HANDBOOK OF Magnetism AND ADVANCED MAGNETIC MATERIALS

1

Fundamentals and Theory

Micromagnetism

Novel Techniques for Characterizing and Preparing Samples

Novel Materials

Spintronics and Magnetoelectronics

Editors

HELMUT KRONMÜLLER

STUART PARKIN

WILEY

Density-functional Theory of Magnetism

Gustav Bihlmayer
Institut für Festkörperforschung, Jülich, Germany

1 INTRODUCTION

The description of many physical properties of condensed matter involves the theoretical treatment of an inhomogeneous electron gas in the potential of atomic nuclei. The ground-state structure, the vibrational and optical properties, and the magnetic properties of a solid are determined by the electrons and their interactions, quantum mechanically described by the (many-body) Schrödinger equation. Wave function–based approximations, like the Hartree–Fock method, have a long tradition of dealing with this complicated many-body problem. In the last 40 years, density-functional theory (DFT) has developed into a successful alternative to these methods and it seems to be currently one of the most widespread methods in computational solid-state theory (Argaman and Makov, 2000). It has applications in diverse fields like studying the properties of defects in solids, heterogeneous catalysis, organic and biomolecular reactions, and also magnetism.

Handbook of Magnetism and Advanced Magnetic Materials. Edited by Helmut Kronmüller and Stuart Parkin. Volume 1: *Fundamentals and Theory*. ISBN: 978-0-470-02217-7.

Magnetism in the solid state comprises a large variety of phenomena that can be characterized by quantities like the magnetic moment, the magnetic order, the ordering temperature, the magnetization direction, and so on. The physical concepts, used to describe these quantities on a theoretical basis, are again diverse and include relativistic quantum mechanics, statistical theories, and classical electrodynamics. The magnetic moment of a solid can be obtained, for example, by quantum-mechanical theories, while ordering temperatures can be accessed by statistical theories which use input parameters of quantum-mechanical calculations. Exchange interactions have to be described on a quantum-mechanical basis, but it is usually sufficient to describe dipole–dipole interactions classically.

Although there is no single theoretical approach to all magnetic phenomena, it can be stated that magnetism is a uniquely quantum-mechanical phenomenon and, in the solid state, DFT is the most widespread theoretical method used to determine the magnetic properties of matter. Vector-spin DFT allows – at least in principle – the access to the spin magnetic moment and the magnetic order of the ground state and it can serve to extract other quantities, like exchange interactions, that can serve as input for other theoretical approaches. Although DFT is designed as a ground-state method, that is, all results refer to a temperature of zero Kelvin, it can, nevertheless, be used to infer some finite-temperature properties of materials. This contribution starts with an outline of DFT and describes the successes and current limitations of the theory. Some methods to overcome these limitations, like self-interaction correction (SIC) or orbital polarization (OP), are discussed. Concepts to formulate spin dynamics based on DFT are presented and strategies to determine the magnetic ground state of a system are discussed. This involves also the mapping of DFT results on model Hamiltonians, which can be used to describe

other properties – like ordering temperatures – in a certain approximation. Orbital magnetism, which is particularly important in low-dimensional systems, is briefly discussed here and – in more detail – in later chapters.

Most examples given in this contribution are metallic systems, typically transition metals and their alloys and compounds. DFT has proved to be particularly valuable in the description of these materials, while other classes of magnetic systems – like magnetic insulators – have been traditionally approached with other methods. Modern magnetoelectronic and spintronic applications involving orbitally ordered systems, low-dimensional structures, and so on, may require theoretical approaches beyond those presented here. But for the majority of magnetic systems DFT presents a good starting point for a theoretical description.

2 DENSITY-FUNCTIONAL THEORY

In any realistic calculation, the straightforward quantum-mechanical treatment of a system of identical particles is limited to a very small number of particles. This is mainly due to the appearance of the many-body wave function, which contains a tremendous amount of information – but typically we are interested only in a limited number of physical observables. DFT starts directly from the density of the particles in question (in our case electrons) and, bypassing the troublesome many-body wave function, allows thereby the treatment of a large number of particles. In this section, only a short and certainly incomplete review of DFT can be given. For a more detailed account of this theory, the reader is referred to the review of Jones and Gunnarsson (1989) or to the books of Parr and Yang (1989) and Eschrig (2003).

2.1 The non-spin-polarized version of DFT

Hohenberg and Kohn (1964) worked out two central theorems that form the basis of DFT: For a system of N particles (e.g., electrons) moving in an external potential $v(\mathbf{r})$ (caused by, e.g., nuclei) in a nondegenerate ground state, (i) the many-body wave function Ψ and $v(\mathbf{r})$ are uniquely determined by the particle density distribution $n(\mathbf{r})$ and (ii) there exists an energy functional of this density, $E[n(\mathbf{r})]$, which is stationary with respect to variations of the ground-state density. These two theorems allow – at least in principle – the determination of the ground-state density and energy of an N-particle system. Extracting the classical Coulomb interaction energy, such a Hohenberg–Kohn energy functional takes the form

$$E[n(\mathbf{r})] = \int v(\mathbf{r})n(\mathbf{r})\mathrm{d}\mathbf{r} + \frac{1}{2}\int\int \frac{n(\mathbf{r})n(\mathbf{r}')}{|\mathbf{r}-\mathbf{r}'|}\mathrm{d}\mathbf{r}\mathrm{d}\mathbf{r}' + G[n(\mathbf{r})] \quad (1)$$

where the functional $G[n(\mathbf{r})]$ contains all other contributions.

If we succeed in finding the functional $G[n(\mathbf{r})]$ or a good approximation to it, the immediate advantage of DFT is that, instead of dealing with the full many-body wave function, $\Psi(\mathbf{r}_1, \mathbf{r}_2, \ldots, \mathbf{r}_N)$, we can work with the much more tractable density, $n(\mathbf{r})$. Although more information is directly accessible from the wave function than from the density,

$$n(\mathbf{r}) = \int \mathrm{d}\mathbf{r}_2 \ldots \int \mathrm{d}\mathbf{r}_N \Psi^*(\mathbf{r}, \mathbf{r}_2, \ldots, \mathbf{r}_N) \times \Psi(\mathbf{r}, \mathbf{r}_2, \ldots, \mathbf{r}_N) \quad (2)$$

in DFT many physical quantities, like the structural properties or bond strength, can be obtained for large systems, where a many-body wave function would be impossible to access. For example, calculations of the ground-state energies for different external potentials, as they result from a variation of the lattice parameters in a periodic solid, allow the determination of the equilibrium lattice constant, which is nowadays possible to within a few percents. Early attempts to use the density as a key parameter for calculations of periodic solids were made by Lenz (1932) based on the statistical method of Thomas (1927) and Fermi (1928). In this approach, $G[n(\mathbf{r})]$ was considered to contain the kinetic energy density (taken to be proportional to $[n(\mathbf{r})]^{(5/3)}$). In the Thomas–Fermi–Dirac method $G[n(\mathbf{r})]$ even contains an exchange energy density term proposed by Dirac (1930) (proportional to $[n(\mathbf{r})]^{(1/3)}$). Although the Thomas–Fermi theory still has its applications today, it never became useful as a theoretical method for the prediction of material properties (Slater and Krutter, 1934).

The key idea, that made DFT a success, was to extract from $G[n(\mathbf{r})]$ the kinetic energy T_0 of a noninteracting electron gas in its ground state which has the same density distribution, $n(\mathbf{r})$, as the interacting system. In this Kohn–Sham theory (Kohn and Sham, 1965), a new functional

$$E_{\mathrm{xc}}[n(\mathbf{r})] = G[n(\mathbf{r})] - T_0[n(\mathbf{r})] \quad (3)$$

appears, that remains to be determined. E_{xc} is a much smaller term than G and is called *exchange-correlation energy functional*, since – as we will see in the following text – without E_{xc} our energy functional E would yield just the energy in the Hartree approximation. If we take into account that particle conservation, that is, $N = \int n(\mathbf{r})\mathrm{d}\mathbf{r}$, has to be ensured,

we can formulate the stationarity of E in equation (1) with respect to variations of the ground-state density, n, as

$$\frac{\delta T_0}{\delta n(\mathbf{r})} + v(\mathbf{r}) + \int \frac{n(\mathbf{r}')}{|\mathbf{r}-\mathbf{r}'|}\mathrm{d}\mathbf{r}' + \frac{\delta E_{\mathrm{xc}}}{\delta n(\mathbf{r})} - \lambda = 0 \qquad (4)$$

where the Lagrange parameter λ ensures the particle conservation. Expressing the kinetic energy of the noninteracting particles via their wave functions, ϕ_i, we can recast equation (4) in the form of an effective single-particle Schrödinger equation, the Kohn–Sham equation:

$$\left[-\frac{\hbar^2}{2m}\nabla^2 + v(\mathbf{r}) + \int \frac{n(\mathbf{r}')}{|\mathbf{r}-\mathbf{r}'|}\mathrm{d}\mathbf{r}' + \frac{\delta E_{\mathrm{xc}}}{\delta n(\mathbf{r})}\right]\phi_i(\mathbf{r}) = \epsilon_i\phi_i(\mathbf{r}) \qquad (5)$$

which has to be solved self-consistently since $n(\mathbf{r}) = \sum_{i=1}^{N}|\phi_i(\mathbf{r})|^2$. We can see now that without E_{xc} equation (5) reduces to the Hartree equation. Therefore, this last term of the Hamiltonian is called the *exchange-correlation potential*.

Although λ was introduced as a Lagrange multiplier and the ϵ_i's also should be strictly interpreted in this way, it is usual to derive from the ϵ_i's band structures of a crystal and use the wave functions $\phi_i(\mathbf{r})$ as approximations to true quasiparticle wave functions. Some justification will be given below and comparison with experimental data often confirms this point of view, but there are also well-known examples, where this interpretation leads to significant 'errors', like in the comparison of the band gaps of semiconductors and insulators with band structures derived from these ϵ_i's.

2.2 The density and potential matrix

DFT allows us – at least in principle – to determine the correct ground-state charge density. For a magnetic system we are interested not only in $n(\mathbf{r})$ but also in accessing the magnetization density, $\mathbf{m}(\mathbf{r})$, directly. If $\psi_\alpha(\mathbf{r})$ is the field operator for a particle of spin α, the particle and the magnetization density can be formulated as

$$n(\mathbf{r}) = \sum_\alpha \langle\Psi|\psi_\alpha^+(\mathbf{r})\psi_\alpha(\mathbf{r})|\Psi\rangle;$$
$$\mathbf{m}(\mathbf{r}) = -\mu_{\mathrm{B}}\sum_{\alpha,\beta}\langle\Psi|\psi_\beta^+\boldsymbol{\sigma}_{\alpha\beta}\psi_\alpha(\mathbf{r})|\Psi\rangle \qquad (6)$$

where we introduced the Bohr magneton, $\mu_{\mathrm{B}} = (e\hbar/2mc)$, and the Pauli matrices (underlined symbols denote 2×2 matrices):

$$\underline{\sigma_x} = \begin{pmatrix} 0 & 1 \\ 1 & 0 \end{pmatrix}, \underline{\sigma_y} = \begin{pmatrix} 0 & -i \\ i & 0 \end{pmatrix}, \underline{\sigma_z} = \begin{pmatrix} 1 & 0 \\ 0 & -1 \end{pmatrix} \qquad (7)$$

Instead of $n(\mathbf{r})$ and $\mathbf{m}(\mathbf{r})$, we can now introduce a hermitian 2×2 spin-density matrix, $\underline{n}(\mathbf{r})$, with components defined as

$$n_{\alpha\beta}(\mathbf{r}) = \langle\Psi|\psi_\beta^+(\mathbf{r})\psi_\alpha(\mathbf{r})|\Psi\rangle \qquad (8)$$

The density matrix can then be decomposed into a scalar and a vectorial part, corresponding to the particle and spin density:

$$\underline{n}(\mathbf{r}) = \frac{1}{2}\left(n(\mathbf{r})\underline{\mathrm{I}} + \underline{\boldsymbol{\sigma}}\cdot\mathbf{s}(\mathbf{r})\right) = \frac{1}{2}\begin{pmatrix} n(\mathbf{r})+s_z(\mathbf{r}) & s_x(\mathbf{r})-is_y(\mathbf{r}) \\ s_x(\mathbf{r})+is_y(\mathbf{r}) & n(\mathbf{r})-s_z(\mathbf{r}) \end{pmatrix} \qquad (9)$$

where $\underline{\mathrm{I}}$ is a 2×2 unit matrix and $\mathbf{s}(\mathbf{r})$ is the spin density that differs from the magnetization density by a factor of $-\mu_{\mathrm{B}}$. Likewise, a potential matrix corresponding to this spin-density matrix is denoted as $\underline{v}(\mathbf{r})$ and can be written in terms of a scalar potential and magnetic field, $\mathbf{B}(\mathbf{r})$:

$$\underline{v}(\mathbf{r}) = v(\mathbf{r})\underline{\mathrm{I}} + \mu_{\mathrm{B}}\underline{\boldsymbol{\sigma}}\cdot\mathbf{B}(\mathbf{r}) \qquad (10)$$

In 1972, von Barth and Hedin used these matrices to extend the DFT concept to spin-polarized systems (von Barth and Hedin, 1972), replacing the scalar quantities by their 2×2 matrix counterparts. In this way, they were able to derive a spin-polarized version of the Kohn–Sham equations:

$$\left[\left(-\frac{\hbar^2}{2m}\nabla^2 + \sum_\alpha\int\frac{n_{\alpha\alpha}(\mathbf{r}')}{|\mathbf{r}-\mathbf{r}'|}\mathrm{d}\mathbf{r}'\right)\underline{\mathrm{I}} + \underline{v}(\mathbf{r}) + \frac{\delta E_{\mathrm{xc}}}{\delta\underline{n}(\mathbf{r})}\right] \times \begin{pmatrix} \phi_i^{(+)}(\mathbf{r}) \\ \phi_i^{(-)}(\mathbf{r}) \end{pmatrix} = \epsilon_i\begin{pmatrix} \phi_i^{(+)}(\mathbf{r}) \\ \phi_i^{(-)}(\mathbf{r}) \end{pmatrix} \qquad (11)$$

In contrast to the original, non-spin-polarized, version of DFT, here the uniqueness of the potential is not guaranteed (Capelle and Vignale, 2001), but for most practical purposes this poses no problems. We can now write the exchange-correlation potential also as a 2×2 matrix:

$$\frac{\delta E_{\mathrm{xc}}}{\delta\underline{n}(\mathbf{r})} = \underline{v}_{\mathrm{xc}}(\mathbf{r}) = v_{\mathrm{xc}}(\mathbf{r})\underline{\mathrm{I}} + \mu_{\mathrm{B}}\underline{\boldsymbol{\sigma}}\cdot\mathbf{B}_{\mathrm{xc}}(\mathbf{r}) \qquad (12)$$

for which suitable approximations have to be found. A solution of equation (11) yields again Kohn–Sham wave functions, from which the density matrix can be determined:

$$n_{\alpha\beta}(\mathbf{r}) = \sum_{i=1}^{N}\phi_i^{*\alpha}(\mathbf{r})\phi_i^{\beta}(\mathbf{r}) \quad \text{where} \quad \alpha,\beta = (+),(-) \qquad (13)$$

As in the non-spin-polarized theory, a solution for equations (11) and (13) has to be obtained self-consistently.

If the density matrix turns out to be diagonal, at any point in space the magnetic moments are aligned along the same direction (z) and the magnetization is called *collinear*. Otherwise, we speak of noncollinear magnetic structures. Examples of collinear magnetization densities are displayed in Figure 1 for bcc and fcc Fe. Experimentally, fcc Fe can be stabilized as precipitate in Cu and was found to have a noncollinear magnetic structure (Tsunoda, 1989).

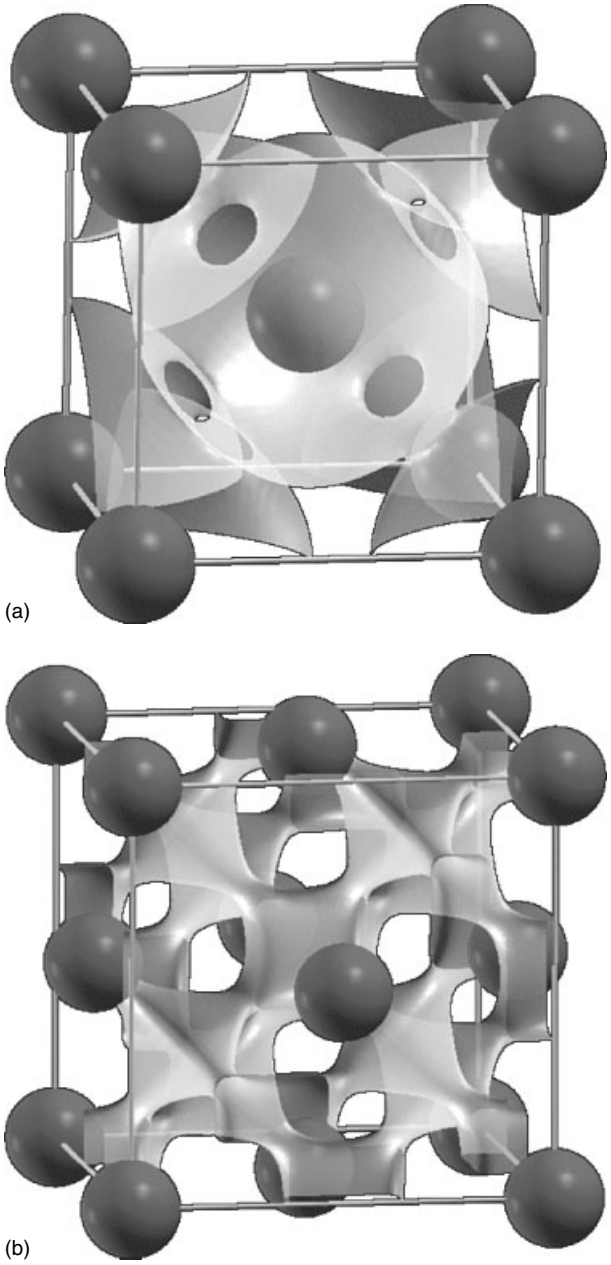

Figure 1. Isosurfaces of the magnetization density of ferromagnetic bcc Fe (a) and a (hypothetical) ferromagnetic fcc Fe with the lattice constant of bulk Cu (b). The isosurface in bcc Fe shows the boundary between regions of positive and negative magnetization density; in fcc Fe a small but negative magnetization density, m_z, is plotted. Plots were generated with a program of Kokalj (2003).

Numerically, equation (11) can be solved by expanding $\phi_i(\mathbf{r})$ in a linear combination of suitable basis functions $\chi_j(\mathbf{r})$. Then equation (11) transforms into a problem of linear algebra, that is, to find the eigenvalues and eigenvectors of a matrix. The eigenvectors, that have to be determined, give the linear combination coefficients, c_{ij}, of the expansion $\phi_i(\mathbf{r}) = \sum_j c_{ij}\chi_j(\mathbf{r})$. In such an eigenvalue problem, the computational effort scales in the most general case with the third power of the number of basis functions. Compared to the nonmagnetic problem, equation (5), this number is doubled in equation (11). Therefore, the computational effort for a general, noncollinear calculation is increased by a factor 8 as compared to the nonmagnetic calculation.

2.3 Collinear magnetic structures within DFT

Supposing that the potential matrices in equations (10) and (12) are diagonal (i.e., the magnetic and exchange fields point in z direction), equation (11) decouples into two equations of the type of equation (5):

$$\begin{aligned}
&\left(-\frac{\hbar^2}{2m}\nabla^2 + v_{\mathrm{Coul}}(\mathbf{r}) + v(\mathbf{r}) + B_z(\mathbf{r}) + v_{\mathrm{xc}}^{(+)}(\mathbf{r})\right)\\
&\quad\times \phi_i^{(+)}(\mathbf{r}) = \epsilon_i^{(+)}\phi_i^{(+)}(\mathbf{r})\\
&\left(-\frac{\hbar^2}{2m}\nabla^2 + v_{\mathrm{Coul}}(\mathbf{r}) + v(\mathbf{r}) - B_z(\mathbf{r}) + v_{\mathrm{xc}}^{(-)}(\mathbf{r})\right)\\
&\quad\times \phi_i^{(-)}(\mathbf{r}) = \epsilon_i^{(-)}\phi_i^{(-)}(\mathbf{r}) \qquad (14)
\end{aligned}$$

where v_{Coul} now denotes the classical Coulomb potential and $v_{\mathrm{xc}}^{(\pm)}$ the exchange-correlation potential that arises from the functional derivative of the exchange-correlation energy with respect to the spin-up (+) or spin-down (−) part of the diagonal density matrix.

The spin-up and spin-down part of the density can be calculated from the wave functions as

$$\begin{aligned}
n^{(+)}(\mathbf{r}) &= \sum_i w_i^{(+)}|\phi_i^{(+)}(\mathbf{r})|^2 \quad \text{and}\\
n^{(-)}(\mathbf{r}) &= \sum_i w_i^{(-)}|\phi_i^{(-)}(\mathbf{r})|^2 \qquad (15)
\end{aligned}$$

where the weight factors, w_i, are determined such that the density of states (DOS), $N(E)$, integrated up to the same

Fermi level, E_F, yields the correct number of particles:

$$N = \int^{E_F} [N^{(+)}(E) + N^{(-)}(E)]\mathrm{d}E \quad \text{where}$$
$$N^{(\pm)}(E) = \sum_i \delta(E - \epsilon_i^{(\pm)}) \tag{16}$$

In this way, the two equations (14) are coupled in the self-consistency cycle. Furthermore, a coupling occurs via the Coulomb potential and the exchange-correlation potential,

$$v_{xc}^{(\pm)} = v + B^{(\pm)} = \frac{\delta E_{xc}[n_{(+)}, n_{(-)}]}{\delta n_{(\pm)}(\vec{r})} \tag{17}$$

depending on the functional form of E_{xc}. A particularly simple form can be derived from the local approximation to Hartree–Fock theory and includes only the exchange part:

$$E_{xc} = E_x = -\frac{3}{2}\left(\frac{3}{4\pi}\right)^{\frac{1}{3}} \int \mathrm{d}\mathbf{r}\left[(n^{(+)}(\mathbf{r}))^{\frac{4}{3}} + (n^{(-)}(\mathbf{r}))^{\frac{4}{3}}\right] \tag{18}$$

Empirical modifications by a multiplicative factor have been used to compensate for the missing correlation energy, but modern functionals include reliable estimates for the correlation, so that no adjustable parameters are needed.

Systems that can be described by equation (14) are all kinds of magnetic materials that assume a collinear magnetic order, for example, ferromagnetic, antiferromagnetic, or ferrimagnetic states. Since the two equations (14) can be solved independently, the computational effort for a collinear calculation seems to be just twice the effort for a nonmagnetic calculation. However, most magnetic calculations are computationally considerably more demanding since the quantities in question (magnetic moments, energy differences between various magnetic configurations) require much higher accuracy than what is needed for nonmagnetic systems. To explore different magnetic orders in a system, unit cells much larger than the chemical unit cell are required, for example, antiferromagnetic body-centered cubic (bcc) chromium requires a calculation with at least two atoms in the unit cell (as compared to one, in a nonmagnetic calculation).

The ground-state density is a property that can – at least in principle – be obtained exactly in DFT. In the same way, the magnetization density is a property that can be obtained directly from spin-polarized DFT:

$$\mathbf{m}(\mathbf{r}) = -\mu_B \sum_{\alpha,\beta} \phi_\alpha^*(\mathbf{r})\boldsymbol{\sigma}_{\alpha\beta}\phi_\beta(\mathbf{r}) \tag{19}$$

The integral magnetic (spin) moment, M, for a collinear system is then (in units of μ_B) simply

$$M = |\int \mathbf{m}(\mathbf{r})\mathrm{d}\mathbf{r}| = \int (n^{(+)}(\mathbf{r}) - n^{(-)}(\mathbf{r}))\mathrm{d}\mathbf{r} \tag{20}$$

But what is essentially responsible for the formation of a magnetic moment in the DFT framework, that is, which term has to be included in the exchange-correlation potential to describe magnetic systems? For a qualitative understanding of this problem, it is instructive to develop a simple model for magnetism in the next subsection.

2.4 A Stoner-like model for magnetism

Consider a simple elemental magnet with a magnetic moment, M, per atom (again in units of μ_B). The exchange-correlation **B**-field, $v_{xc}^{(+)} - v_{xc}^{(-)}$, can be expanded in orders of M:

$$v_{xc}^{(+)} - v_{xc}^{(-)} = M v_{xc}^{(1)} + \mathcal{O}(M^2) \quad \text{where}$$
$$M = \int^{E_F} [N^{(+)}(E) - N^{(-)}(E)]\mathrm{d}E \tag{21}$$

This potential difference acts as a magnetic field that splits the eigenvalues, ϵ_i, according to

$$\Delta\epsilon_i = \epsilon_i^{(+)} - \epsilon_i^{(-)} \approx M\langle\phi_i|v_{xc}^{(1)}|\phi_i\rangle \tag{22}$$

that is, it introduces a shift of the eigenvalues of $\pm\frac{1}{2}MI(\epsilon_i)$. In the Stoner model (Stoner, 1939), it is assumed that all states are shifted by $\pm\frac{1}{2}MI$, where I is an energy-independent exchange integral, the Stoner parameter. Within DFT, a generalized Stoner parameter $I(\epsilon)$ can be introduced and calculated (Gunnarsson, 1976).

In the Stoner model, the magnetization that results from the splitting of the eigenvalues by $\pm\frac{1}{2}MI$ is given by

$$F(M) = \int^{E_F} \left[N\left(E + \frac{1}{2}IM\right) - N\left(E - \frac{1}{2}IM\right)\right]\mathrm{d}E \tag{23}$$

and this magnetization, $F(M)$, has to correspond to the magnetic moment M that induces the splitting. Since the DOS is always positive, $F(M)$ can only grow monotonously with M. Furthermore, we see from equation (23) that $F(M) = -F(-M)$ and in the limit $M \to \pm\infty$ it levels off to $\pm N$ (full spin polarization). From these conditions, we can derive that the equation $F(M) = M$ has the trivial solution $M = 0$ and two nontrivial solutions if $(\mathrm{d}F(M)/\mathrm{d}M)|_0 > 1$. This leads to the famous Stoner criterion

$$\frac{\mathrm{d}F(M)}{\mathrm{d}M}|_0 = IN(E_F) > 1 \tag{24}$$

Within DFT the Stoner parameter can be calculated from a given exchange-correlation potential and the wave functions. Typically, values around $0.4 - 0.5$ eV are obtained for transition metals and I turns out to be only weakly material dependent. Therefore, it is mainly the variation in the DOS at the Fermi level, $N(E_F)$, that determines whether a material is magnetic or not. DFT calculations of the (paramagnetic) DOS of a material already offer a first indication of whether (ferro)magnetism has to be expected or not. Assuming a parabolic DOS of the d-states, this explains why the magnetic moment is large in the middle of the 3d transition metals (Mn) and gets smaller for elements with almost filled or almost empty d-band. This behavior is similar to Hund's first rule, and can be observed well for thin magnetic films (See also **Magnetism of Low-dimensional Systems: Theory, Volume 1**).

Of course, the self-consistent calculation with spin-polarized DFT will give a much more accurate estimate of the magnetic moments than this model. But a comparison between the predictions of the Stoner-like model and the actual DFT calculation of the magnetic system (Figure 2) for bcc Fe shows that our simple Stoner-like model is not so far from a self-consistent, spin-polarized DFT solution.

An exchange-correlation potential that gives a reasonable estimate for the (generalized) Stoner parameter, I, can be expected to also give reasonable magnetizations. Therefore, even relatively simple exchange correlation energy functionals, like given in equation (18), describe magnetic trends in DFT qualitatively correct, provided the nonmagnetic DOS is also described correctly. Properties that are required for a (non)spin-polarized exchange correlation potential will be discussed in the next subsection.

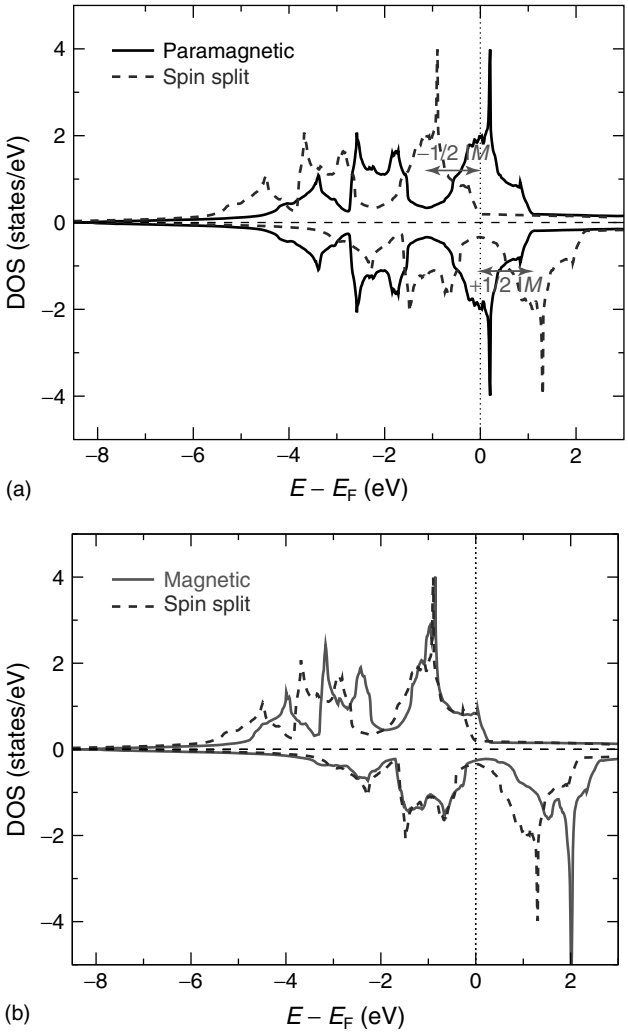

Figure 2. (a) Paramagnetic DOS of bcc Fe (black, full line) shifted by $\pm\frac{1}{2}IM$. The resulting DOS (dashed line) is compared (b) to the result of a spin-polarized DFT calculation (gray, full line). The spin-down DOS are plotted with negative values.

2.5 Exchange-correlation energy functionals

One of the first interpretations of the term, which emerged as the exchange-correlation potential in DFT, was given by Slater and Krutter (1934) in the context of the Thomas–Fermi method and later in connection with the Hartree–Fock method (Slater, 1951). Essentially, it describes the interaction of a particle with the 'hole' that is created by its own presence in the gas of the other particles. This means that the probability of finding an electron at a position $\mathbf{r}$ reduces the probability of finding another electron at a position $\mathbf{r}'$ nearby, depending of course also on the spin of the two particles (therefore, in the Hartree–Fock method this hole has been given the name 'exchange hole').

To derive some properties of the exchange-correlation energy functional, it is useful to write this 'hole' (exchange-correlation hole in DFT), n_{xc}, in terms of a two-particle correlation function, $g(\mathbf{r}, \mathbf{r}')$ (Kohn and Vashista, 1983):

$$n_{xc}(\mathbf{r}, \mathbf{r}') = n(\mathbf{r}') \int_0^1 d\lambda [g_n(\mathbf{r}, \mathbf{r}', \lambda) - 1]$$
$$\equiv n(\mathbf{r}') h(\mathbf{r}, \mathbf{r}') \qquad (25)$$

Here, $g_n(\mathbf{r}, \mathbf{r}', \lambda)$ is the correlation function of a system of charged particles where the Coulomb interaction is scaled by a factor λ and a λ-dependent potential has been added, so that the density, $n(\mathbf{r})$, is independent of λ. Additionally, the so-called hole function, $h(\mathbf{r}, \mathbf{r}')$, was introduced. The exchange-correlation energy can then be written as

$$E_{xc}[n(\mathbf{r})] = \frac{1}{2} \int d\mathbf{r} n(\mathbf{r}) \int d\mathbf{r}' \frac{1}{|\mathbf{r} - \mathbf{r}'|} n_{xc}(\mathbf{r}, \mathbf{r}') \qquad (26)$$

Although the exchange-correlation hole can be very complicated in shape, it was soon realized that only its radial dependence enters in the exchange-correlation energy (Gunnarsson, Jonson and Lundqvist, 1979). This means that, in practice, $E_{\rm xc}$ is rather insensitive to details of shape of $n_{\rm xc}$. Some properties of the exchange-correlation hole can be derived from the definition via the correlation function g, for example, there is a sum rule which states that $n_{\rm xc}$ corresponds exactly to one electron, that is, that

$$\int {\rm d}\mathbf{r}' n_{\rm xc}(\mathbf{r}, \mathbf{r}') = -1 \tag{27}$$

has to be fulfilled. Such relations can guide the construction of exchange-correlation functionals or help in judging the validity of existing approximations to $E_{\rm xc}$.

One of the big surprises in the early days of DFT was certainly the fact that even a simple exchange-correlation functional like the LDA leads to relatively convincing results. The LDA starts from the limit of the homogeneous electron gas, assuming $E_{\rm xc}$ rather as a function than as a functional of $n(\mathbf{r})$. Its success can now be explained by the fact that the exchange-correlation hole in the LDA is of the form

$$n_{\rm xc}^{\rm LDA}(\mathbf{r}, \mathbf{r}') = n(\mathbf{r}') h_0(|\mathbf{r} - \mathbf{r}'|; n(\mathbf{r}')) \tag{28}$$

where $h_0(|\mathbf{r} - \mathbf{r}'|; n)$ is the hole function of a uniform interacting electron gas of density n. For a uniform density, this exchange-correlation hole satisfies equation (27). For a nonuniform density, the sum rule should be at least approximately fulfilled and Gunnarsson and Lundqvist (1976) showed that in LDA this is, on average, the case. This, together with the fact that $E_{\rm xc}$ depends only on the spherical average of $n_{\rm xc}$, is mainly responsible for the success of the LDA.

Also modern, spin-dependent exchange-correlation functionals including gradient corrections are constructed in such a form that they fulfill certain conditions that are known exactly in different limits (like high or low density, constant or slowly varying density, etc.). In this way, exchange-correlation potentials are improved on a parameter-free basis. Alternatively, the functionals (or parts of the functionals, e.g. the correlation energy) can be fitted to numerical results from many-body calculations. Another strategy – often used in the chemical literature – is to adjust the functional to yield best results (like bond length, dissociation energies, etc.) for a given set of systems.

Although the exchange-correlation potential of spin-dependent DFT was first formulated in terms of 2×2 spin matrices, almost all practically used exchange-correlation functionals are restricted to the form

$$E_{\rm xc}[n^{(+)}(\mathbf{r}), n^{(-)}(\mathbf{r})] = \int {\rm d}\mathbf{r} n(\mathbf{r}) \varepsilon_{\rm xc}(n^{(+)}(\mathbf{r}), n^{(-)}(\mathbf{r})) \tag{29}$$

(local spin-density approximation, LSDA) and possibly also containing the gradients of $n^{(\pm)}(\mathbf{r})$ (GGA). There are also formulations including the kinetic energy density, $\tau^{(\pm)}(\mathbf{r})$, (meta-GGA) and other hybrid schemes (Tao, Perdew, Staroverov and Scuseria, 2003), which will not be discussed here since extensive tests on magnetic systems are not yet available. But all these schemes work basically with 'spin-up' and 'spin-down' quantities, and a study that went beyond this approximation (proposing a spin angular gradient approximation to DFT) indicated rather small effects on the calculated properties as compared to the collinear version of $E_{\rm xc}$ (Katsnelson and Antropov, 2003).

Early calculations of elemental ferromagnets demonstrated that LSDA is rather successful in the prediction of the (spin) magnetic moments. The increase of the magnetic moment with decreasing coordination (e.g., at surfaces or in thin films) is well described by DFT and chemical trends similar to Hund's first rule can be observed in lower dimensions. Some examples are presented in **Magnetism of Low-dimensional Systems: Theory, Volume 1**; some results for bulk systems are given in Table 1. It can be seen that spin polarization leads to a significant expansion of the lattice constant not only for Fe and Co but also for Mn and several magnetic alloys. This magnetovolume effect can be explained by the exchange splitting of the d-band, as observed in Figure 2 for Fe: It leads to an enhanced population of antibonding majority-spin states (at the top of the band) and a reduced population of bonding and nonbonding states (bottom and middle of the band) in the minority spin channel. The weaker bonding leads to an expansion of the lattice and also reduces the bulk modulus of these metals (Janak and Williams, 1976). While spin polarization improves the lattice constant as compared to non-spin-polarized LDA, for 3d metals LSDA still gives smaller values than observed experimentally. The use of gradient corrections and a correct treatment of the nonspherical charge distribution in the solid finally leads to reliable lattice constants for these transition metals (Asato *et al.*, 1999).

Here, one has to note that the LSDA results for the magnetic moments in Table 1 were obtained from calculations assuming the experimental lattice constants of the elements. Attempts to theoretically describe both the magnetic and structural properties of iron showed that LSDA predicts an fcc ground state with an almost vanishing magnetic moment (Wang, Klein and Krakauer, 1985). For this system, it turned out that only inclusion of gradient corrections can save the situation and GGA calculations finally correctly predicted a

Table 1. Magnetic moments (in μ_B per atom) and lattice constants (in Å) of ferromagnetic elements in the bulk. The experimentally determined total magnetization, M_{tot}, consists of spin and orbital moment contributions. The LDA (non-spin-polarized) and LSDA (spin-polarized) results for Fe, Co, and Ni are taken from Moruzzi, Janak and Williams (1978); the GGA values of the magnetic moments, from Shallcross, Kissavos, Meded and Ruban (2005) where experimental values are also quoted. The calculated Gd data is from Kurz, Bihlmayer and Blügel (2002) and the experimental one is from White *et al*. (1975). The GGA values of the lattice constants of Fe and Ni are from Asato *et al*. (1999) and the Co lattice constant is from Battocletti, Ebert and Akai (1996).

Property	Source	Fe (bcc)	Co (fcc)	Ni (fcc)	Gd (hcp)
M_{spin}	LSDA	2.15	1.56	0.59	7.63
M_{spin}	GGA	2.22	1.62	0.62	7.65
M_{spin}	Experiment	2.12	1.57	0.55	
M_{tot}	Experiment	2.22	1.71	0.61	7.63
a_0	LDA	2.73	3.41	3.47	
a_0	LSDA	2.76	3.47	3.47	3.58
a_0	GGA	2.83	3.55	3.55	3.69
a_0	Experiment	2.86	3.53	3.53	3.63

bcc ground state structure with a magnetic moment that is slightly larger than the experimental one (Asada and Terakura, 1992).

As noted above, for 3d transition metals GGA improves the lattice constants and, thereby, in most cases also the magnetic moments. This success of the GGA is contrasted here with the case of Cr, where up to now no satisfactory agreement with experimental results was obtained: while LSDA calculations of antiferromagnetic Cr at the experimental lattice constant give a magnetic moment in good agreement with experimental data ($0.5 - 0.6\,\mu_B$), and also a slight stabilization of the experimentally observed incommensurate sinusoidal modulation of the antiferromagnetic structure was predicted (Hirai, 1998), calculations at the lattice constant determined with LSDA (which is 3% too small) yield a nonmagnetic ground state. GGA calculations, on the other hand, give a reasonable lattice constant but the magnetic moment is more than 60% too large (Singh and Ashkenazi, 1992). Furthermore, the unmodulated antiferromagnetic structure of Cr seems to be stabilized by GGA, whereas a modulated structure is observed experimentally (Hafner, Spišák, Lorenz and Hafner, 2002).

Despite these critical remarks on the success of DFT in describing Fe and Cr (and much more could be said on Mn (Hobbs and Hafner, 2003)), it should be emphasized that DFT is an excellent theory for the prediction of magnetic properties of materials – despite some limitations. As the vast amount of literature in this field shows, the area of applicability of this method is constantly expanding. Recent examples from the field of magnetism in low dimensions can be found in **Magnetism of Low-dimensional Systems: Theory, Volume 1**.

Up to now, we focused on the spin density and the resulting, in most cases collinear, magnetization. We should notice that the direction of this magnetization with respect to the lattice did not enter in the formalism and we relied on the assumption that the total energy is invariant with respect to a uniform rotation of the magnetization direction. This was implicitly assumed when we arbitrarily (or, better, for convenience) selected in equation (14) the z direction as global magnetization axis. Indeed, in the absence of an external **B**-field (or in its presence, as long as it is oriented in the z direction) this implies no loss in generality, if the interactions included in v_{xc} are isotropic in space. If we start from a Schrödinger–Pauli-like theory, there is indeed no term that could couple the spin space to the lattice. The dipole–dipole interaction, which can introduce a magnetic anisotropy, results from a relativistic two-particle term and is not contained in LSDA or GGA (but it can be added as a classical magnetostatic term 'by hand', if the magnetic moment is known). However, the presence of an orbital moment can introduce a coupling between spin and lattice by the spin-orbit coupling term, which follows from the single-particle Dirac equation. The formation of orbital moments in DFT will be discussed in the next subsection.

2.6 Orbital magnetism

The magnetization density and the magnetization, equation (19), are clearly a consequence of the imbalance of electrons with spin-up or spin-down and, therefore, the quantity defined in equation (20) is called *spin moment*. From atomic physics we know that the total magnetic moment is a sum of spin and orbital contributions, $M_{tot} = M_{spin} + M_{orb}$. The orbital moment results, in a classical picture, from the orbital motion of the electron

around the nucleus. Compared to the situation in a free atom, where M_{orb} can be even larger than M_{spin}, in a solid this motion is restricted by the crystal field that quenches the orbital moment. In bulk samples, small moments (typically 0.1–0.2 μ_{B}) can be found (compare Table 1).

DFT in the known LSDA or GGA formulations provides no term that could lead to the formation of an orbital moment in the presence of a crystal field. In an atomic LSDA calculation of scandium ($3d^1$ configuration), all d-levels of a given spin ($m_l = -2, -1, \ldots, 2$) are energetically degenerate if no external magnetic field is present. A small crystal field would immediately lead to the formation of linear combinations of these levels (e.g., d_{xy} or $d_{x^2-y^2}$) which carry no orbital moment. Current- and spin-density functional theory (Vignale and Rasolt, 1988) would provide a natural starting point for the description of orbital magnetism, but so far the success is limited.

As noted above, the Dirac equation provides a term that couples the spin to the orbital moment and, thereby, counteracts the influence of the crystal field and leads to the formation of an orbital moment. For a deep and fundamental discussion of relativistic effects in DFT, we refer the reader to a paper by Jansen (1988) and the review of Staunton (1994). Here, we take a simpler approach: interpreting the Kohn–Sham equation or its spin-polarized form, equation (11), like a single-particle Schrödinger equation, we can compare this equation with a two-component approximation to the Dirac equation from relativistic quantum mechanics (Bethe and Salpeter, 1977). This Pauli equation has the same form as the Schrödinger equation, but additionally several terms, like the Darwin or mass-velocity term, appear as a consequence of the relativistic treatment. If these terms are now included in the Kohn–Sham equation, we can hope to improve the description of heavier elements, without having to modify the exchange-correlation potential; for example, the scalar-relativistic approximation takes over from the Pauli equation these terms that are diagonal in spin and prove to be essential for the description of 5d elements.

Another term of the Pauli equation, the spin-orbit coupling term, couples up- and down-spin and also provides a mechanism that leads to orbital polarization, that is, the formation of an orbital moment. The electron, traveling on a classical trajectory around the nucleus, experiences the electric field (from the screened nucleus) as a magnetic field. This field couples to the magnetic (spin) moment of the electron and, thus, leads to a preferential orientation of the spin to the orbital motion. Using the orbital moment operator $\mathbf{L} = \mathbf{r} \times \mathbf{v}$, we can write the spin-orbit coupling term in the vicinity of a nucleus with a radial potential $v(r)$ as

$$H_{\mathrm{so}} = \frac{1}{r}\frac{\mathrm{d}v(r)}{\mathrm{d}r}(\boldsymbol{\sigma} \cdot \mathbf{L}) \tag{30}$$

Adding this term to equation (11) will destroy the decoupling of spin-up and -down equations like in equation (14). It also invalidates the aforementioned assumption that the total energy is not affected by a uniform rotation of the spin directions: the crystal field in a solid acts on the orbital motion of the electron so that there is a preferential plane for this orbital motion. Therefore, a total energy difference arises when the solid is magnetized in two different directions (Stöhr, 1999). This difference, the magnetocrystalline anisotropy energy (MCA) energy, is small for bulk systems with high symmetry, for example, cubic crystals like Fe or Ni. It is larger for crystals with a unique crystallographic axis, like hexagonal Co. But for lower-dimensional systems, thin films, or atomic wires, the MCA will essentially determine the magnetic properties, especially at finite temperatures (Bihlmayer, 2005). Examples of calculations of the MCA within DFT can be found in Wu and Freeman (1999). The MCA energy is also discussed in **Theory of Magnetocrystalline Anisotropy and Magnetoelasticity in Transition-metal Systems, Volume 1**.

The orbital magnetization can be defined in analogy to the spin magnetization, equation (19), now expressed in single-particle wave functions ϕ_i:

$$\mathbf{m}^{\mathrm{orb}}(\mathbf{r}) = -\mu_{\mathrm{B}} \sum_i \langle \phi_i | \mathbf{r} \times \mathbf{v} | \phi_i \rangle \tag{31}$$

At a certain atom ν, the orbital moment $\mathbf{M}_\nu^{\mathrm{orb}}$ can then be obtained by an integration (denoted $\langle\rangle_\nu$) in a sphere centered around this atom:

$$\mathbf{M}_\nu^{\mathrm{orb}} = -\mu_{\mathrm{B}} \sum_i \langle \phi_i | \mathbf{L} | \phi_i \rangle_\nu \tag{32}$$

Although this definition of the orbital moment poses no difficulties in periodic solids, we note here that the evaluation of the total orbital moment of a periodic crystal is more involved (Thonhauser, Ceresoli, Vanderbilt and Resta, 2005). As will be shown in later chapters, relativistic DFT calculations successfully predict the chemical trends (similar to Hund's second and third rules), the changes of the orbital moment with the coordination of the atom or the dimensionality of the system, and the variation of the orbital moment with the magnetization direction. It should be noted that in most cases the atomic orbital moments and also the MCA energies, obtained in DFT calculations, are too small compared to experiment; for example, the calculated orbital moments of Fe, Co, and Ni in LSDA are 0.05, 0.08, and 0.05 μ_{B}, respectively (Beiden *et al.*, 1998). Compared to the experimental values (Table 1, difference between total and spin moment) the values of Fe and Co are about 50% too small, for Ni the value is surprisingly

good. Orbital polarization can be incorporated in DFT to compensate for this deficiency at least partially (Solovyev, 2005). Similar approaches to correct the magnetic anisotropy energy have also been discussed in the literature (Yang, Savrasov and Kotliar, 2001). Some account of these methods will be presented in the next section. Finally, we should notice that the orbital moment, as expressed in equation (32), is not a quantity that can be directly accessed in DFT. In this equation, single-particle wave functions have been used that describe a noninteracting electronic system in an effective potential, and they yield the correct ground-state density but do not necessarily lead to the correct orbital moments.

The computational effort for calculations that include the spin-orbit coupling term, equation (30), in a straightforward way is comparable to a noncollinear calculation, even if collinear systems are considered. This effort can be reduced if this term is considered as a small perturbation to the nonrelativistic Schrödinger-Pauli Hamiltonian. Furthermore, the so-called magnetic force theorem (Weinert, Watson and Davenport, 1985) can be used to evaluate quantities like the MCA. But even these calculations require considerable computational resources, since the energy differences to be determined are very small and – compared to normal calculations – drastically increased numerical cutoffs can be necessary. Systems in which spin-orbit coupling is strong require a self-consistent treatment including equation (30) in the Hamiltonian. In these systems, of course, the relativistic effects are stronger so that moderate numerical cutoffs can be used, but the computational complexity brought by the spin-orbit coupling term and the loss of symmetry leads to an increased computational effort.

3 EXTENSIONS TO 'STANDARD DFT' APPROACHES

While the 'standard DFT' approaches, like LSDA or GGA, are quite successful for many metals, semiconductors, and most insulators, it was realized that there are certain classes of materials that require an extension to the usual exchange-correlation terms (van der Marel and Sawatzky, 1988); for example, many transition metal oxides, like FeO or CoO, turn out to be metallic in LSDA, while they are actually wide band gap insulating. Problems also occur with 4f metals, where the treatment of the localized f-electrons with LDA or GGA is often insufficient. Some strategies to overcome these problems are presented in this section. A more detailed account of some of these methods will follow in later chapters of this book.

3.1 Self-interaction correction

Let us consider DFT in the LDA for a single particle in a potential $v(\mathbf{r})$. Our equation,

$$E^{\mathrm{SP}}[n(\mathbf{r})] = T_0 + \int v(\mathbf{r})n(\mathbf{r})\mathrm{d}\mathbf{r} + \frac{1}{2}\int\int \frac{n(\mathbf{r})n(\mathbf{r}')}{|\mathbf{r}-\mathbf{r}'|}\mathrm{d}\mathbf{r}\mathrm{d}\mathbf{r}' + \int n(\mathbf{r})\varepsilon_{\mathrm{xc}}(n(\mathbf{r}))\mathrm{d}\mathbf{r} \tag{33}$$

would be correct, that is, its functional derivative with respect to the density would lead to the ordinary Schrödinger equation, if in the last term $\varepsilon_{\mathrm{xc}}$ would compensate for the spurious Coulomb interaction of the single electron interacting with itself,

$$U^{\mathrm{SP}}[n(\mathbf{r})] = +\frac{1}{2}\int\int \frac{n(\mathbf{r})n(\mathbf{r}')}{|\mathbf{r}-\mathbf{r}'|}\mathrm{d}\mathbf{r}\mathrm{d}\mathbf{r}' \tag{34}$$

This means that the exact 'exchange-correlation energy density for a single particle' (which certainly does not deserve this name) would have the form

$$\varepsilon_{\mathrm{xc}}^{\mathrm{SP}}(n(\mathbf{r})) = -\frac{1}{2}\int \frac{n(\mathbf{r}')}{|\mathbf{r}-\mathbf{r}'|}\mathrm{d}\mathbf{r}' \tag{35}$$

More properly, this last term should be named a *self-interaction correction* (*SIC*). While the situation is simple for one particle, in DFT normally many particles are described. To eliminate the self-interaction for a many-particle system is naturally more complicated than the case studied above.

Since the exact DFT energy functional has to be self-interaction-free, E_{xc} has to account in some way for a correction. Although in the limit of very low densities SIC can be seen to give only a small contribution, for very localized electrons this correction can be important. One of the first attempts to include SIC in DFT was made by Perdew and Zunger (1981). Their idea was to introduce an orbital-wise removal of the self-interaction on top of a given approximation to the exchange-correlation potential. If the density of single, fully occupied orbital of spin α is $n_{i,\alpha} = |\phi_{i,\alpha}|^2$, then the self-interaction-corrected version of an exchange-correlation energy (e.g., in LSDA) would be

$$E_{\mathrm{xc}}^{\mathrm{SIC}} = E_{\mathrm{xc}}^{\mathrm{LSDA}}[n^{(+)}(\mathbf{r}), n^{(-)}(\mathbf{r})] - \sum_{i,\alpha}\left(U[n_{i,\alpha}(\mathbf{r})] - E_{\mathrm{xc}}^{\mathrm{LSDA}}[n_{i,\alpha}(\mathbf{r}), 0]\right) \tag{36}$$

If we use for an estimate of this correction the inequality (Gadre, Bartolotti and Handy, 1980)

$$U[n(\mathbf{r})] \leq 1.092N^{\frac{2}{3}}\int [n(\mathbf{r})]^{\frac{4}{3}}\mathrm{d}\mathbf{r} \quad \text{where} \quad N = \int n(\mathbf{r})\mathrm{d}\mathbf{r} \tag{37}$$

and compare this to equation (18), we see that for an orbital i, α the correction $\delta_{i,\alpha}$ is bounded by

$$\delta_{i,\alpha} \leq 0.16 \int [n_{i,\alpha}(\mathbf{r})]^{\frac{4}{3}} \mathrm{d}\mathbf{r} \quad \text{and} \quad E_{\mathrm{xc}}^{\mathrm{SIC}} = E_{\mathrm{xc}}^{\mathrm{LSDA}} - \sum_{i,\alpha} \delta_{i,\alpha} \tag{38}$$

Here, the correction amounts to about 17% of the $E_{\mathrm{x}}^{\mathrm{HF}}$ evaluated for a single orbital. In any case, the SIC introduces a significant complication of the Kohn–Sham equations, since the exchange-correlation potential that follows from (36) is now orbital dependent. This leads to the SIC equations (Svane, 1996):

$$(H^{\mathrm{LSDA}} + V_{i,\alpha}^{\mathrm{SIC}})\phi_{i,\alpha} = \epsilon_{i,\alpha}\phi_{i,\alpha} + \sum_{\{i,\alpha\}'}^{occ'} \lambda_{\{i,\alpha\},\{i,\alpha\}'}\phi_{\{i,\alpha\}'} \tag{39}$$

where the Lagrange multipliers $\lambda_{\{i,\alpha\},\{i,\alpha\}'}$ ensure orthogonality of the wave functions. The SIC potential, $V_{i,\alpha}^{\mathrm{SIC}}$ is the functional derivative of $E_{\mathrm{xc}}^{\mathrm{SIC}}$ as defined in equation (36) with respect to the density of the state $\{i, \alpha\}$. Methods exist to solve these equations at different levels of approximations; for a review see Temmerman *et al*. (2000).

As a typical system where SIC helps improve the DFT results we consider NiO here. In LDA a small gap of 0.2–0.5 eV is found, while experimentally it is more than 4.0 eV. Of course we should be careful when comparing Kohn–Sham band structures with real spectra, but in this case the error is exceptionally large. Also, the band ordering turns out to be wrong and – most disturbingly – the magnetic moment is only $1.0\,\mu_{\mathrm{B}}$ as compared to the experimental value of $1.7\,\mu_{\mathrm{B}}$ (Anisimov, Zaanen and Andersen, 1991). If the strongly localized d-electrons of Ni in NiO are the sources of the error here, we can suspect that SIC can help improve the situation. Indeed, an inclusion of SICs not only increases the magnetic moment to $1.6\,\mu_{\mathrm{B}}$ but also opens up the band gap to more than 3.0 eV and considerably improves the calculated spectra (Dudarev *et al*., 1998). Other examples, like the 4f metal Ce, can be found in Temmerman *et al*. (2000).

3.2 The LDA+U method

Dealing with f and some d transition metals and their compounds, it was realized that, while the s, p and some d electrons can successfully be described in standard DFT methods, for the strongly localized electrons an atomic-like description is appropriate (van der Marel and Sawatzky, 1988). Taking into account the different atomic potentials and the stronger screening in the metal, an atomic theory (Slater, 1929) for these localized states can describe the situation quite satisfactorily. Following this approach, Anisimov, Zaanen and Andersen (1991) merged this atomic picture with band theory (i.e. standard DFT), to get a 'band approach' to Hubbard-type models: for the localized d and f states, the Coulomb interaction of the electrons is formulated in the spirit of the Anderson model:

$$E_{\mathrm{ee}} = \frac{1}{2} U \sum_{i \neq j} n_i n_j \tag{40}$$

where the n's are the d-orbital occupation numbers here and U is the famous Hubbard parameter, describing the on-site Coulomb interaction. In the LDA to this model, the energy of the d–d interaction is (Anisimov, Aryasetiawan and Lichtenstein, 1997)

$$E_{\mathrm{ee}}^{\mathrm{LDA}} = \frac{1}{2} U N(N-1) \quad \text{where} \quad N = \sum_i n_i \tag{41}$$

If we add E_{ee} from equation (40) to the LDA energy functional, $E_{\mathrm{ee}}^{\mathrm{LDA}}$ should be subtracted, so that

$$E^{\mathrm{LDA}+U} = E^{\mathrm{LDA}} + \frac{1}{2} U \sum_{i \neq j} n_i n_j - \frac{1}{2} U N(N-1) \tag{42}$$

This is a simple version of the LDA+U method. Such a modification of the LDA results in a shift of the LDA eigenvalues:

$$\epsilon_i = \frac{\mathrm{d}E}{\mathrm{d}n_i} = \epsilon_i^{\mathrm{LDA}} + U\left(\frac{1}{2} - n_i\right) \tag{43}$$

that is, more-than-half-filled bands are shifted down in energy, while less-than-half-filled bands are shifted up. Despite the formal similarity with the Stoner model of section 2.4, it should be noted that the physical background of this model is quite different (Anisimov, Zaanen and Andersen, 1991). A simple example is given in Figure 3, where the LDA+U method was used to correct the positions of the $4f$ states in ferromagnetic bcc Eu. It is easy to see that the correction has almost no effect on the s and p states, but shifts down the occupied $4f$ states (an enhanced localization of these states can be seen by the narrowing of the band) and pushes the unoccupied 4f levels to higher energies. How large this shift is depends of course on the chosen U. Before we turn to the question of how to obtain a reasonable estimate for U, we have to refine the model to see how we can apply the LDA+U method on a certain set of states (e.g., 4f) at a given atom.

To separate the localized orbitals from the itinerant states, for which the LDA already provides a good description, one chooses a site-centered, $\{l, m\}$-dependent orbital basis,

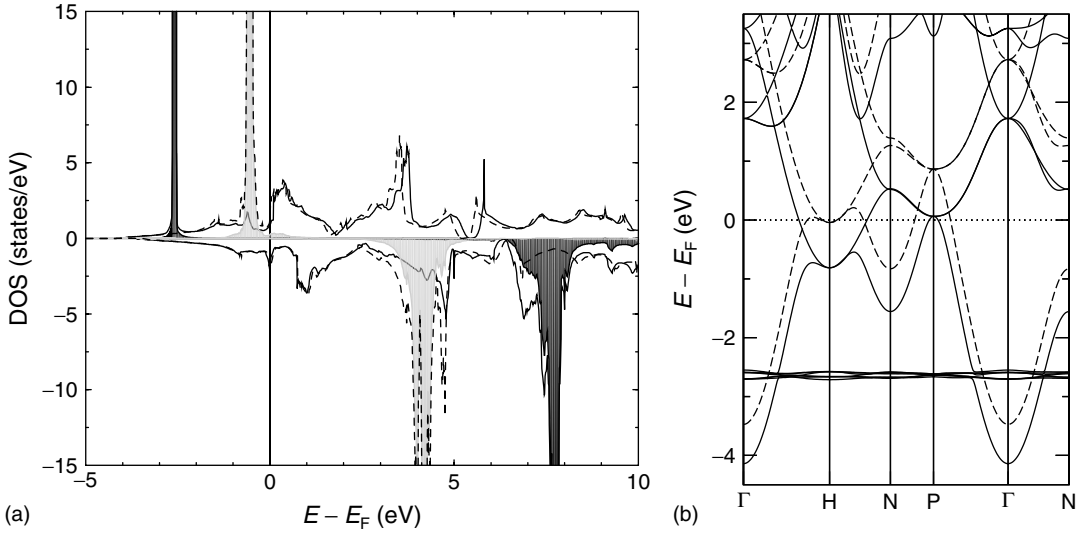

Figure 3. (a) Density of states of bcc Eu calculated with standard LDA (dashed line) and the LDA+U (full line) method. A Hubbard U of about 6 eV was used to correct the positions of the $4f$ states. The local partial 4f DOS as obtained in LDA is shown as gray shaded area, the LDA+U result in black. (b) Eu band structure obtained in the LDA+U method: majority-spin states (full lines) and minority-spin states (broken lines).

$|\nu, l, m\rangle$, where ν is the site index of the selected atom and l and m are the angular and azimuthal quantum numbers, respectively. If the density is given by Kohn–Sham orbitals like in equation (15), we can define a density matrix for spin α in m, m'-space:

$$n^{\alpha\nu}_{mm'} = \sum_i w_i^\alpha \langle \nu, l, m|\phi_i^\alpha\rangle\langle\phi_i^\alpha|\nu, l, m'\rangle \tag{44}$$

If we want to apply the LDA+U method on $4f$ states, we need for each spin a 7×7 density matrix, where the diagonal elements give the occupancy of the $l = 3, m = -3, -2, \ldots, 3$ orbitals of the selected atom. Using this density matrix, the electron–electron interaction energy can be formulated as (Liechtenstein, Anisimov and Zaanen, 1995)

$$E_{ee} = \frac{1}{2}\sum_\nu \sum_{mm'pq}^{\alpha,\beta} n^{\alpha\nu}_{mm'}\Big[\langle m, p|V_{ee}|m', q\rangle - \langle m, p|V_{ee}|q, m'\rangle\delta_{\alpha\beta}\Big]n^{\beta\nu}_{pq} \tag{45}$$

and used instead of the simpler version, equation (40). Here, the electron–electron interaction can be expressed in terms of an angular part, contained in a_k, and the radial part that is given by the effective Slater integrals (Slater, 1929), F_k:

$$\langle m, p|V_{ee}|m', q\rangle = \sum_k a_k(m, p, m', q)F_k; \quad 0 \le k \le 2l \tag{46}$$

In terms of the screened Coulomb and exchange parameters, U and J, the Slater integrals can be approximated, for example, for $l = 2$, as

$$U = F_0; \quad J = \frac{F_2 + F_4}{14} \quad \text{and} \quad \frac{F_4}{F_2} = \frac{5}{8} \tag{47}$$

and the a_k are sums of integrals of the angular part of the wave function with spherical harmonics. Then, we can define an orbital selective potential,

$$V^{\alpha\nu}_{mm'} = \sum_{pq\beta}\big[\langle m, p|V_{ee}|m', q\rangle - \langle m, p|V_{ee}|q, m'\rangle\delta_{\alpha\beta}\big]n^{\beta\nu}_{pq} - \left[U\left(n^\nu - \frac{1}{2}\right) - J\left(n^{\alpha\nu} - \frac{1}{2}\right)\right]\delta_{mm'} \tag{48}$$

where $n^{\alpha\nu} = \sum_m n^{\alpha\nu}_{mm}$ and $n^\nu = \sum_\alpha n^{\alpha\nu}$. This spin-, site- and l, m-dependent potential now enters the Kohn–Sham equation via

$$\big[-\nabla^2 + V^\alpha_{LDA}(\vec{r})\big]\phi_i^\alpha + \sum_\nu\sum_{mm'} V^{\alpha\nu}_{mm'}\frac{\delta n^{\alpha\nu}_{mm'}}{\delta\phi_i^\alpha} = \epsilon_i^\alpha\phi_i^\alpha \tag{49}$$

Thus, we have introduced a Hartree–Fock-like potential term that acts on a certain subset of the orbitals, leaving the others (in a first approximation) unchanged. Equation (49) has to be solved self-consistently, until both the density and the density matrix are converged. If the Kohn–Sham equations are solved by expanding the wave function into some basis set, for different types of basis sets also a different

orbital basis, $|\nu, l, m\rangle$, will be convenient. It is clear that the result of the LDA+U calculation will also depend, to some extent, on the choice of the orbital basis, but in practice for the same parameters U and J also qualitatively the same answers are reached.

When applied to 4f metals like Eu or Gd, one can use the LDA+U method to shift the position of the 4f as a function of U. A comparison to the position where they are spectroscopically measured can be used to determine a value for U, although other methods are described below. One of the problems of LSDA, the prediction of an antiferromagnetic ground state for hcp Gd, is resolved when the LDA+U method is applied in this way (Kurz, Bihlmayer and Blügel, 2002). Another success of the LDA+U approach can be seen in the case of Eu, where LDA would predict a much too small lattice constant, while LDA+U removes this overbinding caused by the $4f$ states (Turek *et al.*, 2003). Also the problems in NiO, mentioned in the last section in connection with the SIC, can be resolved in this way (Dudarev *et al.*, 1998).

Although the LDA+U method is rather simple and quite successful, it faces the problem that it introduces an external parameter and thus destroys the *ab initio* character of the conventional LDA approach. Therefore, concepts to calculate U within constrained DFT (Solovyev, Dederichs and Anisimov, 1994) (see also subsection 4.2) and with the GW method (Solovyev and Imada, 2005) (cf. subsection 3.4) have been developed. Fortunately, in many cases the results do not depend too sensitively on the exact values of U and J. But there are also systems, like $YMnO_3$, where depending on the value of U different magnetic ground states can be stabilized (Picozzi, Yamauchi, Bihlmayer and Blügel, 2006). A collection of applications of the LDA+U method can be found in Anisimov, Aryasetiawan and Lichtenstein (1997).

3.3 Orbital polarization

As we noted in subsection 2.6, one of the deficiencies of standard DFT approaches is to underestimate the orbital moments in solids, especially in lower dimensions (thin films, chains, adatoms). To get a better description of the total moments of bulk actinides, Brooks (1985) proposed a correction term inspired by Hartree–Fock theory, which induces a splitting of the eigenvalues of states with positive and negative azimuthal quantum number m, proportional to the difference in population of states with positive and negative m:

$$\epsilon(m^{(+)}) - \epsilon(m^{(-)}) = -I^{\mathrm{OP}}\left(N(m^{(+)}) - N(m^{(-)})\right) \qquad (50)$$

where I^{OP} can be estimated from a Slater-type atomic theory. The structure of this correction looks similar to the simple LDA+U approach of equation (43). Later Eriksson, Brooks and Johansson (1990) refined this idea, again based on the atomic theory of the orbital moments. They followed an analogy of the mean-field-like approach (MFA) to the interaction between spin moments **s**:

$$-\sum_{\nu\nu'} \mathbf{s}_\nu \mathbf{s}_{\nu'} \xrightarrow{\mathrm{MFA}} -\left(\sum_\nu s_\nu^z\right)\left(\sum_{\nu'} s_{\nu'}^z\right) = -S_z^2 \qquad (51)$$

which leads to a spin-polarization energy of $-I S_z^2$ where I is the Stoner parameter (subsection 2.4). The same approach for the orbital moment **l**,

$$-\sum_{\nu\nu'} \mathbf{l}_\nu \mathbf{l}_{\nu'} \xrightarrow{\mathrm{MFA}} -\left(\sum_\nu l_\nu^z\right)\left(\sum_{\nu'} l_{\nu'}^z\right) = -L_z^2 \quad \text{leads to}$$

$$E^{\mathrm{OP}} = -\frac{1}{2} I^{\mathrm{OP}} L_z^2 \qquad (52)$$

so that an orbital-dependent potential for a state with the quantum number m_l was proposed:

$$\Delta V_{m_l} = -\frac{1}{2} I^{\mathrm{OP}} L_z \hat{m}_l \quad \text{where} \quad L_z = \sum_i w_i \langle \phi_i | \hat{m}_l | \phi_i \rangle \qquad (53)$$

and $\hat{m}_l$ is the z-component of the angular momentum operator (again the magnetization is assumed to be oriented along z). For d electrons I^{OP} is the Racah parameter, B, and can be obtained from the Slater integrals similar to U and J. For f-electrons this term is denoted as $E^{(3)}$. This OP was used successfully for bulk metals (Rodriguez *et al.*, 2001) and systems of different dimensionality (Ederer, Komelj and Fähnle, 2003), although sometimes a rescaling of the Racah parameter obtained from the Slater integrals of the local atomic wave functions is necessary (Gambardella *et al.*, 2003). Like in the LDA+U approach, this then introduces an external parameter in the DFT and destroys the *ab initio* character of the method.

Although the proposed OP provides an intuitive and often successful approach to include OP in DFT, its physical interpretation remains somewhat unclear. Solovyev, Liechtenstein and Terakura (1998) derived an OP term in the framework of open-shell Hartree–Fock theory as a limiting case, which is generally more complicated than the OP suggested in equation (53). This simple form can be recovered when $U \approx 1.5J$ (for d electrons). For this choice of U and J, the LDA+U method is close to the OP scheme derived above. It is clear that the LDA+U method can also be used to include OP in DFT and successes in this direction have been reported by Shick and Mryasov (2003). A comparison can be found in Table 2.

Table 2. Orbital moments of Fe and Co with the magnetization oriented along the direction $\hat{M}$. The LDA and OP (1) results are from Rodriguez *et al*. (2001), OP (2) is from Trygg, Johansson, Eriksson and Wills (1995), while the LDA+U calculations were performed by Shick and Mryasov (2003). The experimental values are quoted in these references.

	$\hat{M}$	$M^{\mathrm{orb}}(\mu_{\mathrm{B}})$				
		LDA	OP (1)	OP (2)	LDA+U	Experimental
Fe (bcc)	[001]	0.048	0.086	0.078	0.085	0.08
Co (hcp)	[0001]	0.079	0.13	0.123	0.153	0.14

3.4 Methods using DFT output: *GW* and LDA+DMFT

In many cases, it is also desirable to go beyond DFT because one is interested in properties that cannot be accessed directly in conventional DFT, for example, band gaps or finite-temperature properties. To describe spectral properties or lifetimes of quasiparticle states, it is therefore more natural to start from many-body theory, where the quasiparticle equation (Hedin, 1965) can be studied. It has a similar structure as the Kohn–Sham equation, but the nonlocal, energy-dependent, self-energy $\Sigma(\mathbf{r}, \mathbf{r}', \epsilon)$ takes the role of the exchange-correlation potential here. The wave functions describe now quasiparticles and the eigenvalues are energies that are required to remove or add an electron. In principle, the solution of such an equation gives just the quantities lacking in conventional DFT schemes, but in practice these equations are too complicated to solve except for some special cases. Therefore, they are often used to provide a 'correction' to the Kohn–Sham eigenvalues. One of these schemes is the many-body perturbation theory in the GW approximation (Aryasetiawan and Gunnarsson, 1998), where the self-energy is approximated by the product of a Green function G and the screened Coulomb interaction W, both obtained from the output quantities of a DFT calculation. Of course there are DFT-based methods, like time-dependent density-functional theory (TDDFT), which provide a way to calculate spectra and there are also temperature-dependent nonlocal exchange-correlation potentials. It is too early to say whether these methods will become more popular than other well-established methods like the GW method, but some, like TDDFT, are active research fields today (Onida, Reining and Rubio, 2002).

In the last three subsections we discussed different extensions of the conventional DFT schemes that are designed to circumvent some of the problems of the common LSDA or GGA functionals. In general they consist of an orbital-dependent potential, that is added to the Kohn–Sham equation, which is solved self-consistently. In this way, 'many-body effects' are incorporated in an approximate form, for example, static correlations that are underestimated by LDA are included by the LDA+U method. But these are mean-field-type approximations that cannot describe dynamical correlation effects that go beyond Hartree–Fock-like methods. If dynamical correlations are important for the description of a certain property of a specific material, then it is necessary to go beyond these approaches. To study such many-body effects, one has to start from an explicit many-body problem which normally can only be solved for model Hamiltonians under special conditions. To account for the realistic material properties, DFT results are then incorporated in these many-body theories, hoping that this synthesis provides a realistic description both of the many-body effects and of the material properties.

As an example for a method that is used to study magnetism in the solid state, we mention here the dynamical mean field theory (DMFT) which, in conjunction with LDA or GGA band structures, is a popular approach to describe dynamical correlations in realistic materials. Correlations can determine order parameters in transition-metal oxides (Tokura and Nagaosa, 2000) or phase transitions in low-dimensional systems (Sachedev, 2000) which are outside a mean-field description. Since lattice Hamiltonians, like the Hubbard Hamiltonian, give at least the right qualitative behavior of many quantities of interest, one starts from a multiband Hubbard model:

$$H = -\sum_{\nu\nu'}\sum_{mm'}^{\alpha} t_{mm'}^{\alpha\nu\nu'}(c_m^{\alpha\nu})^{\dagger}c_{m'}^{\alpha\nu'} + \frac{1}{2}\sum_{\nu} \times \left(\sum_{mm'}^{\alpha\neq\beta} U_{mm'}^{\nu} n_m^{\alpha\nu} n_{m'}^{\beta\nu} + \sum_{m\neq m'}^{\alpha} (U_{mm'}^{\nu} - J_{mm'}^{\nu}) n_m^{\alpha\nu} n_{m'}^{\alpha\nu}\right) \quad (54)$$

This can be interpreted as hopping terms between an orbital m on site ν and an orbital m' on site ν' plus an electron–electron interaction term as encountered in the LDA+U method, equation (40), but keeping only the diagonal of the density matrix. If the hopping parameters t are taken from a DFT calculation, a Hartree–Fock-like solution of this model is similar to the first iteration in the LDA+U method. The DMFT goes beyond Hartree–Fock, but at the expense of other simplifications, like the use of a local

self-energy instead of a nonlocal or momentum-dependent one (Liechtenstein and Katsnelson, 2001). A description of this method and its extensions is given in **Dynamical Mean-field Theory of Itinerant Electron Magnetism, Volume 1**. Here, it should be sufficient to say that this LDA+DMFT approach was successfully applied to the description of many transition-metal oxides, orbitally ordered systems, and actinides. For a review, see Held *et al*. (2002).

4 THE MAGNETIC GROUND STATE AND BEYOND

In the first section, we dealt with the problem of finding the magnetic ground state in DFT without worrying about possible metastable solutions or local minima on the total energy surface. Indeed, non-spin-polarized DFT calculations for a given external potential (i.e., a selected arrangement of the atomic nuclei) normally lead to a single solution. In spin-polarized calculations it is possible to start the calculations from different initial magnetizations and to stabilize different magnetic solutions, say a ferromagnetic and an antiferromagnetic one, and obtain total energies for both magnetic states. In this section, we will discuss methods to find the magnetic state of lowest energy, the ground state.

To determine the magnetic ground state it is possible to follow several directions: similar to molecular-dynamics calculations, spin dynamics allows the study of the magnetic degrees of freedom by exploring the ground state configuration. Another possibility is to determine the magnetic interactions between the atoms by DFT calculations which are then mapped onto a model (in the simplest case a classical Heisenberg model). This model is then solved, either analytically or numerically. In both cases we introduce a discretization of the (vector) magnetization density: In spin dynamics, the evolution of discrete spins, that is, vectors attached to certain (atomic) positions can be monitored. Also mapping the *ab initio* results to a model Hamiltonian which contains interactions between spins requires that it is possible to assign a definite spin to an atom, so that it should be possible to write in the vicinity of an atom ν, for example, within some sphere centered at the nucleus, the magnetization density, $\mathbf{m}(\mathbf{r})$, as

$$\mathbf{m}(\mathbf{r}) = |\langle \mathbf{m}(\mathbf{r}) \rangle_\nu | \hat{\mathbf{e}}_\nu = M_\nu \hat{\mathbf{e}}_\nu \tag{55}$$

where M_ν is the magnetization and $\hat{\mathbf{e}}_\nu$ is the magnetization direction. Vector-spin DFT calculations allow the estimation of whether equation (55) is a good approximation or not (cf. Figure 4).

If the magnetization density in the vicinity of some atom ν is expressible by equation (55), then the total energy of a magnetic system as a function of its magnetic structure can be described as a functional $E[\{\hat{\mathbf{e}}_\nu\}]$ of the directions of the magnetic moments at the atoms ν in the magnetic unit cell. In this context, collinear states ($\hat{\mathbf{e}}_\nu$ is parallel for all atoms) are special solutions where $E[\{\hat{\mathbf{e}}_\nu\}]$ has a local or global extremum. Therefore, they constitute an important class of magnetic configurations that are often realized in magnetic materials in the ground state. But to describe magnetic materials at elevated temperatures even in this case more general, noncollinear, magnetic configurations have to be calculated. Some techniques will be presented in this

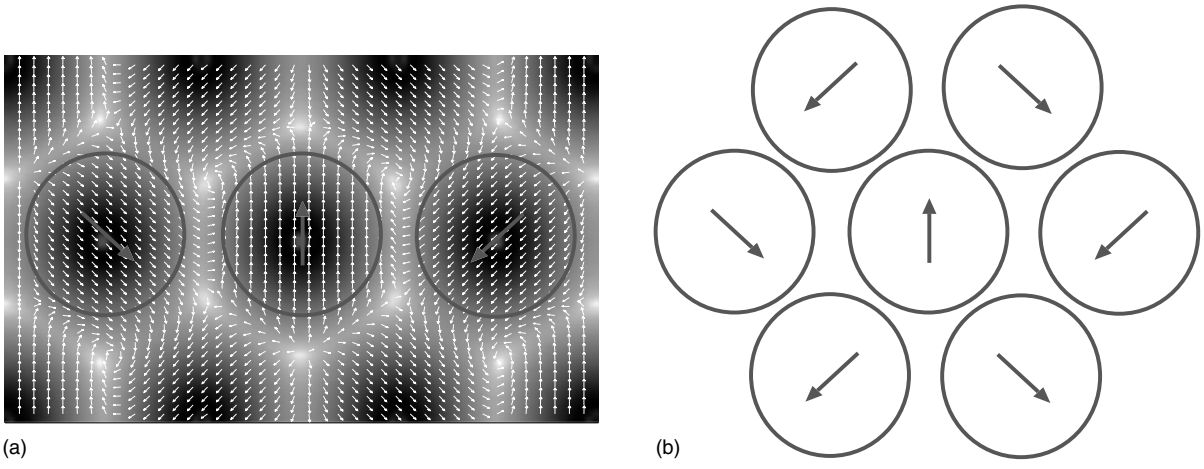

Figure 4. (a) Ground-state magnetization density of a hexagonal Cr monolayer with the Cu(111) in-plane lattice constant; the absolute value of the magnetization is shown in grayscale and the local directions are marked by small arrows. The average magnetization direction around an atom is indicated as gray arrow. (b) Schematic picture of the magnetic structure (Néel state) of the hexagonal Cr monolayer. (Reprinted figures from Kurz, P., Bihlmayer, G., Hirai, K. and Blügel, S. Three-Dimensional Spin Structure on a Two-Dimensional Lattice: Mn/Cu(111), *Phys. Rev. Lett* **86**, 1106–1109. Copyright 2004 by the American Physical Society.)

section. A more detailed presentation can be found in the book of Kübler (2000).

4.1 Spin dynamics, magnetic torque

If one is interested in the magnetic ground state of a system of given chemical composition and atomic positions, the final goal is to minimize the functional $E[\{\hat{\mathbf{e}}_\nu\}]$. The dimensionality of this problem will, of course, depend on the size of the chosen unit cell (some multiple of the chemical unit cell) and this minimization will involve the tricky task of determining the absolute minimum on a high-dimensional total energy surface. In analogy to molecular dynamics, that is, the problem of minimizing the energy as a function of the atomic positions, we introduce here a spin dynamics, where the magnetic orientations, $\hat{\mathbf{e}}_\nu$, take the role of the variables.

Any vector-spin DFT calculation has to start with a reasonably chosen spin configuration in a prescribed unit cell. On a simple level, one can 'relax' the directions of the magnetization at the atoms by allowing the directions $\hat{\mathbf{e}}_\nu$ to change during the self-consistency cycle. The magnetization directions will then change to minimize the total energy (cf. Figure 5), but the final magnetic state that will be reached will, in general, depend on the starting point of the calculation. Therefore, a more elaborate technique will be needed to avoid being trapped in some local minimum of $E[\{\hat{\mathbf{e}}_\nu\}]$.

To this end, we have to develop an equation of motion for the magnetization of an atom. To keep things simple, we will focus on the case where the magnetization stays collinear within the vicinity of the atom. Let us start from the Hamiltonian of equation (11) and assume that the external potential matrix, $\underline{v}(\mathbf{r})$, has been chosen to be diagonal and the exchange-correlation potential is separated into diagonal and off-diagonal parts. Following Antropov, Katsnelson, van Schilfgaarde and Harmon (1995) and Antropov *et al*. (1996) we set up a time-dependent analogon of equation (11):

$$i\frac{\mathrm{d}\Phi}{\mathrm{d}t} = \left[H_\mathrm{d} - \underline{\boldsymbol{\sigma}}\cdot\mathbf{B}(\mathbf{r},t)\right]\Phi \text{ where } \Phi = \begin{pmatrix}\phi^{(+)}\\ \phi^{(-)}\end{pmatrix} \quad (56)$$

and H_d is the Hamiltonian that now contains only diagonal parts.

In the spirit of the Born–Oppenheimer approximation, we can separate the evolution of the magnetization into fast (value of the magnetization) and slow (direction of the magnetization) degrees of freedom. The former part will be described quantum mechanically, while the latter is treated on a semiclassical level. At a given time, t, the time-independent version of equation (56) can be solved for a given magnetization characterized by $\{\hat{\mathbf{e}}_\nu\}$. Now we have to determine an equation of motion for the magnetization $\mathbf{m}(\mathbf{r},t)$.

This equation of motion can be obtained by multiplying equation (56) from the left with $\Phi^*\underline{\boldsymbol{\sigma}}$ and adding the complex conjugate equation. Comparing with the time derivative of equation (19) and using the relation $\underline{\boldsymbol{\sigma}}(\underline{\boldsymbol{\sigma}}\cdot\mathbf{B}) = \mathbf{B} - i\underline{\boldsymbol{\sigma}}\times\mathbf{B}$,

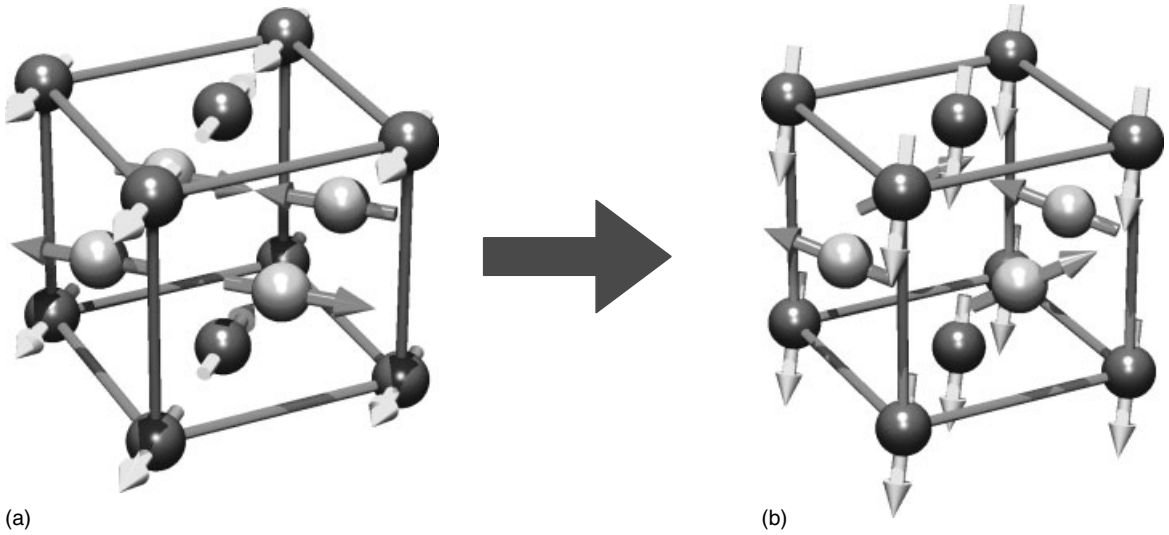

Figure 5. Determination of the magnetic ground state of ordered FeMn. Experimentally, FeMn is a disordered alloy and the 2**q**-state is the magnetic ground state. This is the initial magnetic configuration for a simulated ordered alloy (a). A more complex magnetic arrangement is obtained (b) when the local spin directions are allowed to change in the simulation. The Fe moments are shown by lighter arrows, the Mn moments by darker arrows.

we get in units of μ_B

$$\frac{d\mathbf{m}(\mathbf{r},t)}{dt} = 2\mathbf{m}\times\mathbf{B} + \frac{i}{2}\nabla(\Phi^*\underline{\boldsymbol{\sigma}}\cdot\nabla\Phi - c.c.) \qquad (57)$$

The second term on the right side is complicated and describes longitudinal changes of the magnetization, which we will not consider at this level. Omitting this term, equation (57) describes the precession of the magnetization direction at an atom under the influence of the magnetic field generated by the atom itself and other atoms of the crystal.

Returning once more to equation (55), we can simplify equation (57) and write for the evolution of the magnetization direction in atom ν

$$\frac{d\hat{\mathbf{e}}_\nu}{dt} = -\frac{2}{\mu_B}\hat{\mathbf{e}}_\nu\times\mathbf{I}_\nu \qquad (58)$$

where $\mathbf{I}_\nu = \mu_B\mathbf{B}$. If we explicitly also want to take into account the effect of other fields acting onto a magnetization direction, for example, stemming from the spin-orbit interaction (magnetic anisotropy) or dipole–dipole interaction, these fields can be added to equation (58) into $\mathbf{I} = \mathbf{I}_\nu + \mathbf{I}_{SO} + \mathbf{I}_{d\text{–}d}$. More general expressions of equation (58), suitable for spin dynamics with finite temperatures included, can be found in the paper of Antropov *et al*. (1996).

The next question, that has to be answered, is how to determine the fields $\mathbf{I}_\nu$, that is, given a certain set of magnetization directions $\{\hat{\mathbf{e}}_\nu\}$ what is the torque on a selected magnetic moment (Stocks *et al*., 1998)? This problem can be solved in constrained vector-spin DFT, as introduced in the next section.

4.2 Constrained DFT

In general, an arbitrary magnetic configuration given by a set of local (atomic) magnetization directions $\{\hat{\mathbf{e}}_\nu\}$ is not an extremum or a stationary solution of the total energy functional $E\left[\underline{n}(\mathbf{r})\right]$. Exceptions are high-symmetry states, like collinear magnetic states, a certain class of spin-spiral states (see Section 4.3) and particular linear superpositions of several spin-spiral states. The constrained DFT developed by Dederichs, Blügel, Zeller and Akai (1984) provides the necessary generalization to deal with arbitrary magnetic configurations, that is, configurations where the orientations of the local moments are constrained to nonequilibrium directions. We define a generalized energy functional $\tilde{E}\left[\underline{n}(\mathbf{r})|\{\hat{\mathbf{e}}_\nu\}\right]$, where we ensure that the average magnetization in an atom, $\langle\mathbf{m}\rangle_\nu$, points in the direction $\hat{\mathbf{e}}_\nu$. This condition, $\hat{\mathbf{e}}_\nu\times\langle\mathbf{m}\rangle_\nu = 0$, is introduced by a Lagrange multiplier, $\boldsymbol{\lambda}$, so that (Kurz *et al*., 2004)

$$\begin{aligned}\tilde{E}\left[\underline{n}(\mathbf{r})|\{\hat{\mathbf{e}}_\nu\}\right] &= E\left[\underline{n}(\mathbf{r})\right] + \sum_\nu \boldsymbol{\lambda}^\nu\cdot(\hat{\mathbf{e}}_\nu\times\langle\mathbf{m}\rangle_\nu)\\ &= E\left[\underline{n}(\mathbf{r})\right] + \mu_B\sum_\nu \mathbf{B}_c^\nu\cdot\langle\mathbf{m}\rangle_\nu \qquad (59)\end{aligned}$$

Here, we recast the Lagrange multiplier in the form of a magnetic field, $\mathbf{B}_c^\nu$, which is the constraining field in atom ν that keeps the local (integrated) magnetic moment, that is, the magnetization density averaged over the sphere where equation (55) holds,

$$\langle\mathbf{m}(r)\rangle_\nu = \mathbf{M}^\nu = \int_{MT^\nu}\mathbf{m}(\mathbf{r})\,d^3r \qquad (60)$$

parallel to the prescribed direction $\hat{\mathbf{e}}_\nu$.

In an actual constrained local moment (CLM) calculation, $\underline{n}(\mathbf{r})$ and $\mathbf{B}_c^\nu$ have to be determined self-consistently. The density matrix is calculated in the usual self-consistency cycle. At the same time, the local constraint fields $\mathbf{B}_c^\nu$ have to be adjusted, until the constraint conditions, $\hat{\mathbf{e}}_\nu\times\langle\mathbf{m}\rangle_\nu = 0$, are fulfilled (cf. Figure 6). At the end of such a calculation, we obtain the self-consistent densities and a set of local constraint $\mathbf{B}$ fields. The total energy of the system is given by the constrained energy functional, equation (59).

According to the Hellmann–Feynman theorem we find that the change of the energy due to a change in magnetization direction, $d\hat{\mathbf{e}}_\nu$, is given by $dE = -\mu_B\mathbf{M}^\nu\cdot(\mathbf{B}_c^\nu\times d\hat{\mathbf{e}}_\nu)$. Therefore, the constraint field can be interpreted as a torque acting on the magnetic moment, in the spirit of the spin dynamics, formulated in the previous section. Combined with techniques known from molecular dynamics, like simulated annealing, this provides a formalism that allows the finding – at least in principle – of the magnetic ground state of a system (Újfalussy *et al*., 1999). The chapter **Dissipative Magnetization Dynamics Close to the Adiabatic Regime, Volume 1** gives a more complete account of adiabatic spin dynamics and its applications.

CLM calculations can also be used in a different way. In the next section, we describe how they can be used to determine the exchange interactions in a system and utilize these results in models, such as the classical Heisenberg model, to obtain information about the ground state, but also about excited states of a magnetic system. Of course, constrained DFT can also be used to fix the value of the magnetic moment (Dederichs, Blügel, Zeller and Akai, 1984) (in this case, the constraining field is a longitudinal magnetic field, in contrast to the transverse field discussed above) or to vary the occupation numbers of a certain band (e.g., the *d* band) for an estimate of the Hubbard parameter U (Solovyev, Dederichs and Anisimov, 1994).

4.3 Mapping on model Hamiltonians

From the classical Heisenberg model, we can derive a Hamiltonian that describes the interaction between two spins **S** at sites ν and ν' in the form

$$H = -\sum_{\nu\nu'} J_{\nu\nu'} \mathbf{S}_\nu \cdot \mathbf{S}_{\nu'} \tag{61}$$

where $J_{\nu\nu'}$ is the exchange coupling constant between the two spins. The sign of $J_{\nu\nu'}$ determines whether a parallel (ferromagnetic) or antiparallel (antiferromagnetic) alignment of $\mathbf{S}_\nu$ and $\mathbf{S}_{\nu'}$ is preferred. This can be used as a phenomenological starting point in the investigation of the magnetic interaction in a crystal. Although the Heisenberg model was originally introduced for magnetic insulators with localized moments (Anderson, 1963), we can also apply equation (61) to metallic systems, as shown in Figure 7. In these hexagonal unsupported monolayers the behavior of the total energy as a function of the relative angle between the atoms can be described as cosinelike function, the exchange coupling constant being negative for Cr and Mn (preferring antiferromagnetic coupling) and positive for Fe (leading to a ferromagnetic ground state). The total energy has been calculated by a constrained DFT calculation as described above. We further see that the magnetic moment does not change significantly as the spins are rotated, an important requirement for the application of the classical Heisenberg model. For spin systems which do not fulfill this requirement, a spin-cluster expansion has been developed to map energetics obtained by DFT calculations on a more general model that has been inspired by alloy theory (Drautz and Fähnle, 2004).

From the right part of Figure 7 we can see that rotating the local magnetic moment direction of one atom in the two-atom unit cell of the hexagonal lattice will change the relative orientation of that atom to four nearest neighbors, but does not affect two of the nearest-neighbor (NN) atoms. Likewise, only four of the six second-NN atoms will change the relative orientation to the original atom. This leads to an expression for the total energy in the classical Heisenberg model up to second-NN:

$$E = -S^2(J_1 + J_2)(2 + 4\cos\theta) \tag{62}$$

if **S** is now the total spin moment treated as a classical vector. This means, from a CLM calculation we can at least estimate the size of $(J_1 + J_2)$. It is not difficult to find other unit cells and rotations that allow the determination of other linear combinations of J_1 and J_2, thereby separating the individual

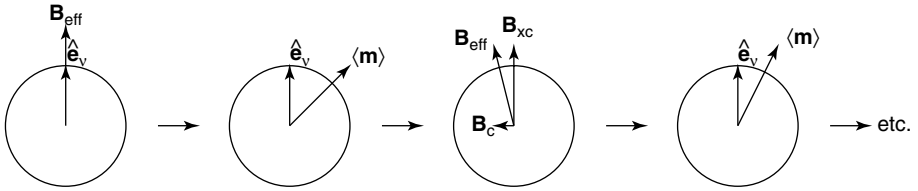

Figure 6. Determination of the constraint field: Initially, the effective **B** field is parallel to the prescribed direction $\hat{\mathbf{e}}^\nu$ (left). The resulting magnetization, $\langle \mathbf{m} \rangle$, is generally not parallel to this direction. Therefore, a constraint field $\mathbf{B}_c$ is introduced that points in a direction opposite to the component of the magnetization that is perpendicular to $\hat{\mathbf{e}}^\nu$. Using this $\mathbf{B}_{\text{eff}}$, the direction of the magnetization is then adjusted toward $\hat{\mathbf{e}}^\nu$ (right).

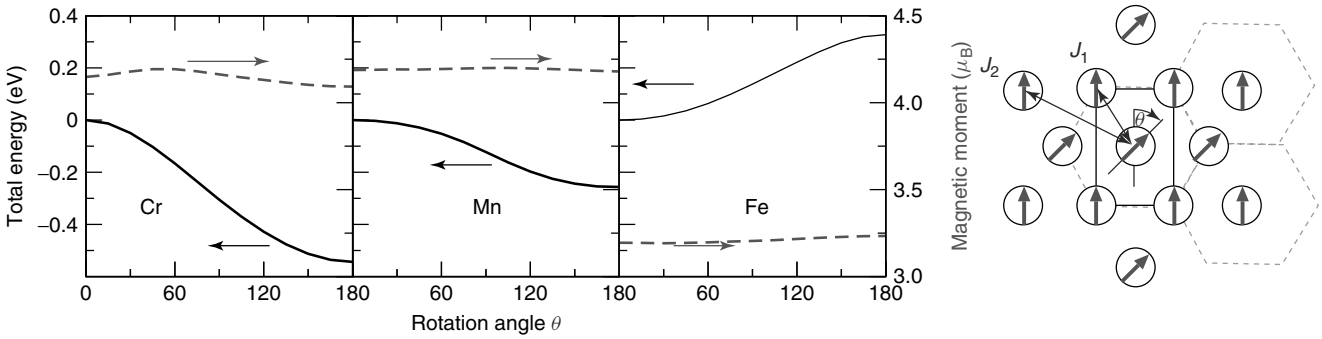

Figure 7. Total energy (full black line) and magnetic moment (dashed gray line) of hexagonal monolayers of Cr, Mn, and Fe as a function of the angle of the magnetization in a two-atom unit cell (right). $\theta = 0^\circ$ corresponds to a ferromagnetic state, $\theta = 180^\circ$ is a row-wise antiferromagnetic state. As lattice constant we chose the parameters of the Ag(111) surface. In the schematic picture of the hexagonal monolayer (right), the coupling to nearest neighbors (J_1) and next-nearest neighbors (J_2) is indicated.

exchange coupling constants (Kurz, Bihlmayer, Hirai and Blügel, 2001).

Of course, the energies obtained from the CLM calculation contain contributions of all J_ν and also from interactions that are not described by the Heisenberg model. Examples such as the biquadratic interaction or the four-spin interaction result from processes that have to be described by an Hamiltonian which includes a product of four spin operators. Taking spin-orbit interaction into account gives rise to a third-order process, the so-called Dzyaloshinsky–Moriya interaction (Yosida, 1996). All these different interaction terms can be extracted from a set of suitable *ab initio* calculations (possibly including spin-orbit interaction) and can be used to determine the magnetic ground state within the chosen model.

4.4 Low temperatures: magnons and spin waves

In a periodic crystal, it is convenient to replace the quantities in equation (61) by their Fourier-transformed equivalents:

$$\mathbf{S}(\mathbf{q}) = \frac{1}{N}\sum_\nu \mathbf{S}_\nu \mathrm{e}^{-i\mathbf{q}R_\nu} \quad \text{and} \quad J(\mathbf{q}) = \sum_\nu J_{0\nu}\mathrm{e}^{-i\mathbf{q}R_\nu} \tag{63}$$

Exploiting the translational invariance of the lattice, we can then rewrite equation (61) as

$$H = -N\sum_{\mathbf{q}} J(\mathbf{q})\mathbf{S}(\mathbf{q})\cdot\mathbf{S}(-\mathbf{q}) \tag{64}$$

where we have to ensure that the length of all spins $\mathbf{S}_\nu^2 = S^2$ is conserved on all sites ν. This condition is fulfilled by solutions of the type (Yosida, 1996)

$$\mathbf{S}_\nu = S\left(\hat{\mathbf{e}}_x\cos(\mathbf{q}\cdot\mathbf{R}_\nu) + \hat{\mathbf{e}}_y\sin(\mathbf{q}\cdot\mathbf{R}_\nu)\right) \tag{65}$$

where the unit vectors $\hat{\mathbf{e}}_x$ and $\hat{\mathbf{e}}_y$ just have to be perpendicular to each other, otherwise their directions are arbitrary. Equation (65) describes an spiral spin density wave (SSDW)

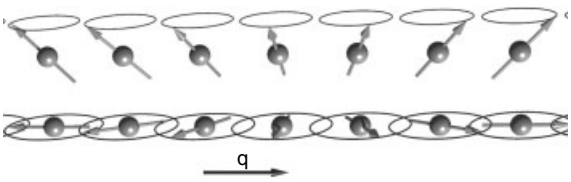

Figure 8. Spiral spin-density wave (SSDW) or spin spiral propagating along the with a wave vector $\mathbf{q}$. The opening angle is 45° in the upper and 90° in the lower example. (Reprinted figures from Kurz, P., Bihlmayer, G., Hirai, K. and Blügel, S. Three-Dimensional Spin Structure on a Two-Dimensional Lattice: Mn/Cu(111), *Phys. Rev. Lett* **86**, 1106–1109. Copyright 2004 by the American Physical Society.)

as shown in the lower half of Figure 8. A more general form of SSDWs can be obtained, when the magnetization precesses on a cone with an opening angle ϑ:

$$\mathbf{S}_\nu = S\left(\hat{\mathbf{e}}_x\cos(\mathbf{q}\cdot\mathbf{R}_\nu)\sin\vartheta + \hat{\mathbf{e}}_y\sin(\mathbf{q}\cdot\mathbf{R}_\nu)\sin\vartheta + \hat{\mathbf{e}}_z\cos\vartheta\right) \tag{66}$$

as shown in the upper half of Figure 8.

All solutions of the classical Heisenberg model can be described as SSDWs or, if there are several degenerate solutions, as linear combination of SSDWs. From equation (64), we can conclude that the SSDW with the lowest total energy will be the one with the propagation vector $\mathbf{Q}$ which maximizes $J(\mathbf{q})$. If $\mathbf{Q} = 0$ maximizes $J(\mathbf{q})$, the solution corresponds to the ferromagnetic state; if $\mathbf{Q} = \hat{\mathbf{e}}_z\frac{\pi}{a_z}$ and a_z is the lattice constant in z-direction, then the structure is layered antiferromagnetic in z-direction. Three examples for bcc crystals are illustrated in Figure 9: Cr is a typical antiferromagnet, where no stable ferromagnetic solution can be found and magnetic moments form only for large $\mathbf{q}$-vectors. In Mn both a ferro- and an antiferromagnetic phase can be formed, the former with a smaller and the latter with a larger magnetic moment. From the energy $E(\mathbf{q})$ it can be seen that bcc Mn is antiferromagnetic, while bcc Fe is ferromagnetic. In Fe, the magnetic moment changes continuously from the ferromagnetic solution ($2.2\,\mu_\mathrm{B}$) to the antiferromagnetic one ($1.5\,\mu_\mathrm{B}$).

SSDWs are sometimes also called *frozen magnons*, since a spin-spiral looks like a 'snapshot' of a single magnon at a fixed time. Spin-spiral calculations can therefore be used to simulate the effect of temperature on a magnetic system in the adiabatic approximation, in particular at very low temperatures, when magnons with long wavelengths dominate. But also at $T = 0$ many compounds and even elements show SSDW ground states. Some examples are shown in Figure 10.

At low, but finite temperatures, collective spin-wave excitations or magnons are excited in the ferromagnetic crystal. These magnons can again be characterized by their wave vector $\mathbf{q}$. In the long wavelength limit, that is, around $\mathbf{q} = 0$, the spin-wave dispersion behaves almost quadratically and can be described as $E(\mathbf{q}) = Dq^2$. The spin stiffness, D, characterizes the magnetic properties of a ferromagnet at low temperatures and can be calculated from the exchange coupling constants in real space (Pajda *et al*., 2001). Since

$$E(\mathbf{q}) = E(\mathbf{0}) + 2S\sum_{\nu\neq 0} J_{0\nu}\left(1 - \mathrm{e}^{i\mathbf{q}R_\nu}\right) \tag{67}$$

by differentiation D is obtained as

$$D = \frac{M}{6\mu_\mathrm{B}}\sum_\nu J_{0\nu}R_\nu^2 \tag{68}$$

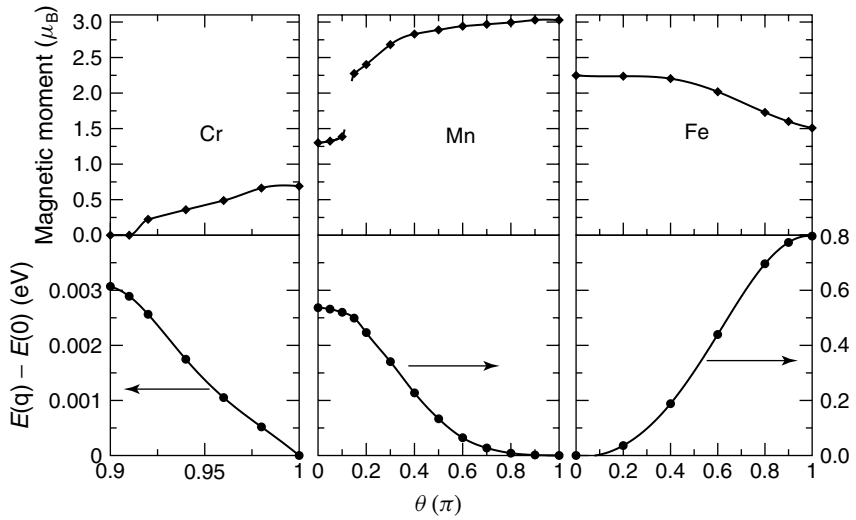

Figure 9. Change of the energy, $E(\mathbf{q})$, and the local magnetic moments, M, in bcc Cr, Mn, and Fe in a spin-spiral state as a function of the turning angle θ between the magnetization axes of two consecutive (001) planes. Magnetic moments are aligned ferromagnetically within each (001) plane. Results are calculated for the experimental lattice constants. ($\theta = \pi$) $\theta = 0$ corresponds to the (anti)ferromagnetic state. Note the different energy and θ scale for bcc Cr.

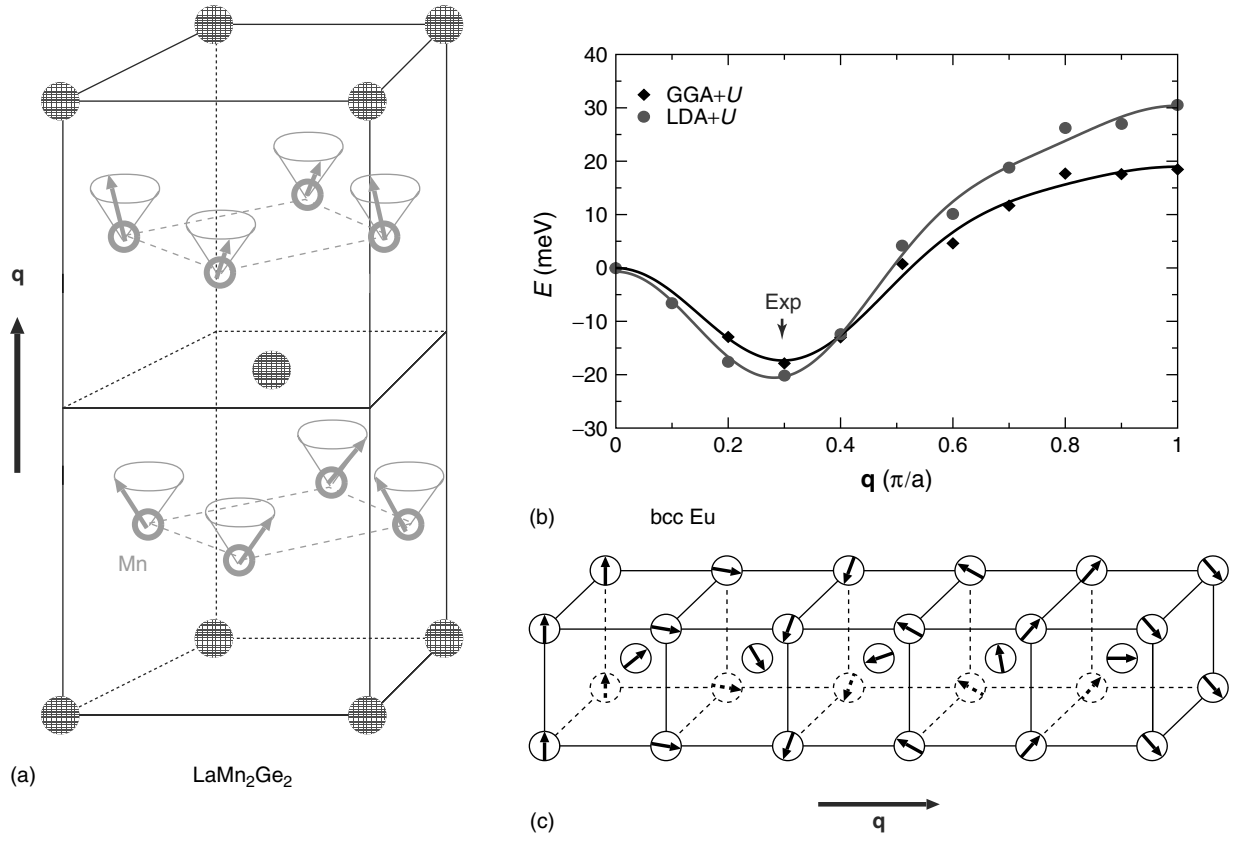

Figure 10. Examples of noncollinear ground states: (a) in $LaMn_2Ge_2$ the spins on the Mn sublattice can be described by a conical spin spiral, that is, the magnetization precesses on a cone with a semi-cone angle of 58° from layer to layer in z direction. The turning angle per layer is 128°. The magnetic structure is in good agreement with first-principles calculations (di Napoli *et al.*, 2004). Bulk bcc europium has a flat spiral in [001] direction as ground state (c), the length of the **q**-vector, describing this precession, is correctly reproduced in DFT calculations (Turek *et al.*, 2003) (b).

Here, $M = 2\,\mu_B S$ is the magnetic moment of the ferromagnetic state. Some results of *ab initio* calculations are given in Table 3. For Fe and Co, agreement with experimental data is reasonable, but for Ni most methods fail to reproduce the experimental spin stiffness. More about spin waves can be found in **Spin Waves: History and a Summary of Recent Developments, Volume 1** and in the review of Staunton (1994).

Owing to the long-range nature of the exchange interactions in itinerant magnets, the so-called Rudermann–Kittel–Kasuya–Yoshida (RKKY) interaction, the evaluation of equation (68) is problematic (Pajda *et al.*, 2001). Therefore, it is more natural to evaluate $E(\mathbf{q})$ directly in reciprocal space. This can be efficiently done, using the generalized Bloch theorem introduced in the next subsection.

4.5 Spin spirals and the generalized Bloch theorem

A very elegant treatment of spin spirals by first-principles calculations is possible when the generalized Bloch theorem (Herring, 1966; Sandratskii, 1986) is applied. However, this theorem can only be proved when spin-orbit coupling is neglected. For this reason, the spin-rotation axis will always be considered parallel to the z axis of the spin coordinate frame. Thus, only the m_x and m_y components are rotated, while m_z does not change. Following Sandratskii (1986) we can define a generalized translation, $\mathcal{T}_\nu$, that combines a lattice translation, $\mathbf{R}_\nu$, and a spin rotation $\mathbf{U}$ that commutes with the Hamiltonian H. Applying such a generalized translation to $H\Phi$ yields

$$\begin{aligned}\mathcal{T}_\nu H(\mathbf{r})\Phi(\mathbf{r}) &= \mathbf{U}(-\mathbf{q}\mathbf{R}_\nu)H(\mathbf{r}+\mathbf{R}_\nu)\mathbf{U}^\dagger(-\mathbf{q}\mathbf{R}_\nu)\mathbf{U}(-\mathbf{q}\mathbf{R}_\nu)\\ &\times \Phi(\mathbf{r}+\mathbf{R}_\nu) = H(\mathbf{r})\mathbf{U}(-\mathbf{q}\mathbf{R}_\nu)\Phi(\mathbf{r}+\mathbf{R}_\nu) \qquad (69)\end{aligned}$$

where $\mathbf{U}(\mathbf{q}\mathbf{R}_\nu)$ is the spin 1/2 rotation matrix

$$\mathbf{U}(\mathbf{q}\mathbf{R}_\nu) = \begin{pmatrix} \mathrm{e}^{-i\varphi/2} & 0 \\ 0 & \mathrm{e}^{i\varphi/2} \end{pmatrix}, \quad \varphi = \mathbf{q}\cdot\mathbf{R}_\nu \qquad (70)$$

In analogy with the proof of Bloch's theorem (Ashcroft and Mermin, 1976), it follows that the eigenstates can be chosen such that

$$\mathcal{T}_\nu\Phi(\mathbf{k},\mathbf{r}) = \mathbf{U}(-\mathbf{q}\mathbf{R}_\nu)\Phi(\mathbf{k},\mathbf{r}+\mathbf{R}_\nu) = \mathrm{e}^{i\mathbf{k}\cdot\mathbf{R}_\nu}\Phi(\mathbf{k},\mathbf{r}) \quad (71)$$

Since these eigenstates are labeled with the same Bloch vector $\mathbf{k}$ as the eigenstates of the translation operator without the spin rotation, the lattice periodic part of these states follows the chemical lattice, $\mathbf{R}_\nu$, that is, we can calculate the spin-spiral state in the chemical unit cell. In a reciprocal-space method, that is, when all quantities like potential or wave functions are expressed as Fourier transforms, the computational effort scales with the volume of the unit cell. Without the application of the generalized Bloch theorem the investigation of spin-spiral states requires very large unit cells, and a description of SSDWs that are incommensurate with the lattice would be not possible. Within this formalism, incommensurate magnetic structures can also be described in the framework on DFT. Two recent examples, $LaMn_2Ge_2$ and bcc Eu (Turek *et al.*, 2003), are shown in Figure 10.

Since the spin spiral is the exact solution of the classical Heisenberg model at $T = 0$, it is believed that it covers a large and important part of the phase space of possible spin states. Thus, among all possible magnetic states, spin spirals are the next relevant class of spin states besides the high-symmetry magnetic states, that is, the ferromagnetic, antiferromagnetic, or ferrimagnetic configurations.

A further computational simplification can be reached when the SSDW is considered just as a small perturbation to the parent (most often ferromagnetic) structure. This may be justified in the limit of small $\mathbf{q}$-vectors or small opening angles ϑ (cf. equation (66)). The limit of $\vartheta \to 0$ is particularly important in the study of finite temperature effects, since it describes elementary perturbations of the collinear ground state. In this limit, the magnetic force theorem (Weinert, Watson and Davenport, 1985) can be applied again, thus reducing the computational efforts significantly (Ležaić, 2005).

In real-space methods the calculation of $J(\mathbf{q})$ is most conveniently done via the right of equation (63), that is, the evaluation of $J_{0\nu}$. In this case the direction of the magnetization at a reference atom, 0, is perturbed and the response on the other atoms, ν, calculated. Also in this case, a kind of magnetic force theorem can be used (Turek *et al.*, 2003).

4.6 High temperatures: T_C and T_N

Let us now see how higher temperatures influence the magnetic order in a ferromagnetic solid. Staying within the Heisenberg model, we will assume that the magnitude of the magnetic moments at the atoms will – in first approximation – not be changed, and discuss just their mutual orientation. At $T = 0$, the spin at a selected atom will be fixed in parallel direction to the spins at all other atoms by an effective field that will be proportional to $S\sum_{\nu\neq 0} J_{0\nu} = SJ_0$. At a finite temperature T, this field, that acts on the spin at site 0, is reduced owing to the thermal fluctuation on the sites ν. The thermal average of the projection of the spin at site ν on the spin at site 0 is denoted as $\langle S(\mathbf{R}_\nu)\rangle$. In the 'mean-field approximation' (MFA), it is assumed

Table 3. Calculated and experimental spin-wave stiffness (D) for Fe, Co, and Ni. The theoretical data was obtained in different approximations as described by Rosengaard and Johansson (1997) (theoretical (1)), Kübler (2000) (theoretical (2)), Shallcross, Kissavos, Meded and Ruban (2005) (theoretical (3)), and Pajda *et al*. (2001) (theoretical (4)); the experimental data was taken as cited in these references.

	D (meV Å^2)				
	Theoretical (1)	Theoretical (2)	Theoretical (3)	Theoretical (4)	Experimental
Fe (bcc)	247	355	322, 313	250	280, 314, 330
Co (fcc)	502	510	480, 520	663	510, 580
Ni (fcc)	739	790	541, 1796	756	422, 550, 555

that the effective field at finite temperatures that acts on spin 0 is

$$B_{\text{eff}} = \sum_{\nu} J_{0\nu} \langle S(\mathbf{R}_\nu) \rangle \tag{72}$$

In this model it is possible to calculate the temperature dependence of the average magnetization of the solid and, specifically, the temperature where the average magnetization vanishes, the critical temperature. For a ferromagnet this temperature is called *Curie temperature* and in the MFA it is given by

$$T_{\text{C}} = \frac{2S(S+1)}{3k_{\text{B}}} J_0 \tag{73}$$

It has to be mentioned that in most cases the MFA severely overestimates T_{C} (in bulk crystals by about 20 to 50%, depending on the lattice; in lower dimensions MFA is even qualitatively wrong). Nevertheless, it gives a simple estimate of the ordering temperature in bulk systems, where the approximations of the Heisenberg model are reasonable. On the other hand, some properties, like the – material independent – critical exponents, are in any case not usefully reproduced by the MFA.

On a more sophisticated level, the 'random phase approximation' (RPA) can give quite reliable results. In contrast to the MFA, where the thermal averaging was done over the sites ν that determine B_{eff}, here the Hamiltonian is first transformed into reciprocal space (equation (64)), and then the averaging is done over one of the Fourier components:

$$H = -N \sum_{\mathbf{q}} J(\mathbf{q}) \mathbf{S}(\mathbf{q}) \cdot \langle \mathbf{S}(-\mathbf{q}) \rangle \tag{74}$$

If the term $S(S+1)$ (in a classical model S^2) is included in the exchange coupling constants (as it is usually done, when the J's are determined from first-principles calculations), then the Curie temperature in the MFA and RPA can be expressed as

$$k_{\text{B}} T_{\text{C}}^{\text{MFA}} = \frac{2}{3} J_0 = \frac{2}{3} \sum_{\nu} J_{0\nu} = \frac{M}{6\mu_{\text{B}}} \frac{1}{N} \sum_{\mathbf{q}} E(\mathbf{q}) \tag{75}$$

$$k_{\text{B}} T_{\text{C}}^{\text{RPA}} = \frac{2}{3} N \left(\sum_{\mathbf{q}} \frac{1}{J(\mathbf{0}) - J(\mathbf{q})} \right)^{-1} = \frac{M}{6\mu_{\text{B}}} N \left(\sum_{\mathbf{q}} \frac{1}{E(\mathbf{q})} \right)^{-1} \tag{76}$$

where N is the number of $\mathbf{q}$-vectors included in the sum. If the exchange coupling constants are calculated in reciprocal space ($J(\mathbf{q})$) by using the generalized Bloch theorem, the calculation of T_{C} requires a dense $\mathbf{q}$-point sampling in both approximations. From equations (75) and (76) it can be seen that MFA gives more weight to the interaction with near neighbors, while in RPA the exchange interaction with distant neighbors is emphasized. Therefore, the Curie temperature in RPA is smaller than in MFA and usually also in better agreement with experimental values.

Also for antiferromagnets (or generally spin-spiral states characterized by a vector $\mathbf{Q}$) expressions for the ordering temperature, the Néel temperature T_{N}, can be derived. In the MFA with $S(S+1)$ again included in J, this is given simply by

$$k_{\text{B}} T_{\text{N}}^{\text{MFA}} = \frac{2}{3} J(\mathbf{Q}) \tag{77}$$

while a slightly more involved expression can be derived in the random phase approximation (Turek *et al*., 2003). Comparison of these results with experimental values gave reasonable results, for example, for bcc europium, Néel temperatures of 147 K and 110 K were obtained in MFA and RPA, respectively (Turek *et al*., 2003). These values have to be compared with the experimental T_{N} of 90.5 ± 0.5 K.

Although there exist several additional methods to calculate critical temperatures from DFT results, we outline just one further possibility here, which seems to be rather flexible and appropriate for many systems with different

Table 4. Calculated and experimental Curie temperature T_C for some ferromagnetic materials. MFA and RPA data for Fe, Co, and Ni taken from Pajda *et al*. (2001), MFA2 results and experimental values as quoted by Shallcross, Kissavos, Meded and Ruban (2005), while the MC results were obtained by Rosengaard and Johansson (1997). Spin dynamics (SD) calculations have been performed by Antropov (2005). Data for Gd can be found in the papers of Kurz, Bihlmayer and Blügel (2002) and Turek, Kudrnovský, Bihlmayer and Blügel (2003).

	T_C (K)					
	MFA	MFA2	RPA	MC	SD	Experimental
Fe (bcc)	1414	550, 1190	950	1060	1070	1044–1045
Co (fcc)	1645	1120, 1350	1311	1080		1388–1390
Ni (fcc)	397	320, 820	350	510	470	624–631
Gd (hcp)	334					293

magnetic ground states: the Monte Carlo technique (MC) allows the study of finite-temperature magnetic properties by implementation of a Heisenberg Hamiltonian (equation (61), possible with extensions like biquadratic terms or a uniaxial anisotropy (see following text)), into a Metropolis algorithm (Metropolis *et al*., 1953). Unit cells of different size are then studied so that finite-size effects can be eliminated. In these unit cells, the evolution of the magnetic property in question (in our case the average magnetization) as a function of temperature can then be monitored.

Results of *ab initio* calculations of the Curie temperature of Fe, Co, and Ni are presented in Table 4. From this table one can easily see that, compared to RPA, the MFA typically overestimates T_C by 25–50%. For Fe and Co, RPA gives quite good estimates of the Curie temperature, while for Ni, T_C is underestimated in both approximations. MC simulations work better for Ni and Fe, but give too low a T_C for Co. Finally, the results of spin dynamics calculations, performed along the line sketched in subsection 4.1, give results comparable to MC calculations for Fe and Ni, but have the advantage that they do not rely on a model Hamiltonian (Antropov, 2005). More information on finite-temperature effects and their calculation can be found in **Electron Theory of Finite Temperature Magnetism, Volume 1**.

While we quoted here results for 'simple' metals, it is nowadays possible to investigate in the same manner the temperature-dependent properties of complex multicomponent systems, for example, half-metallic Heusler alloys (Şaşıoğlu, Sandratskii and Bruno, 2005) or dilute magnetic semiconductors (Sato, Dederichs and Katayama-Yoshida, 2005). In this way, materials for modern spintronic applications can be studied at physically relevant temperatures and their detailed magnetic properties can be predicted on the basis of quantum mechanics. The combination of advanced numerical techniques and massively parallel supercomputers makes computational material science based on DFT one of the most rapidly growing fields of physics with relevance for basic and applied science. It covers many aspects of magnetism and some of them have been outlined in this chapter. A more complete and more detailed presentation will be given in the following chapters.

ACKNOWLEDGMENTS

The author gratefully acknowledges valuable discussions with S. Blügel, M. Heide, M. Ležaić, and D. Wortmann.

REFERENCES

Anderson, P.W. (1963). Theory of magnetic exchange interactions: exchange in insulators and semiconductors. *Solid State Physics*, **14**, 99–214.

Anisimov, V.I., Aryasetiawan, F. and Lichtenstein, A.I. (1997). First-principles calculations of the electronic structure and spectra of strongly correlated systems: the LSDA+U method. *Journal of Physics: Condensed Matter*, **9**, 767–808.

Anisimov, V.I., Zaanen, J. and Andersen, O.K. (1991). Band theory and Mott insulators: Hubbard U instead of Stoner I. *Physical Review B*, **44**, 943–954.

Antropov, V. (2005). Magnetic short-range order above the Curie temperature of Fe and Ni. *Physical Review B*, **72**, 140406(R)/1–140406(R)/4.

Antropov, V.P., Katsnelson, M.I., Harmon, B.N., *et al*. (1996). Spin dynamics in magnets: equation of motion and finite temperature effects. *Physical Review B*, **54**, 1019–1035.

Antropov, V.P., Katsnelson, M.I., van Schilfgaarde, M. and Harmon, B.N. (1995). Ab initio spin dynamics in magnets. *Physical Review Letters*, **75**, 729–732.

Argaman, N. and Makov, G. (2000). Density functional theory: an introduction. *American Journal of Physics*, **68**, 69–79.

Aryasetiawan, F. and Gunnarsson, O. (1998). The GW method. *Reports on Progress in Physics*, **61**, 237–312.

Asada, T. and Terakura, K. (1992). Cohesive properties of iron obtained by use of the generalized gradient approximation. *Physical Review B*, **46**, 13599–13602.

Asato, M., Settels, A., Hoshino, T., *et al*. (1999). Full-potential KKR calculations for metals and semiconductors. *Physical Review B*, **60**, 5202–5210.

Ashcroft, N.W. and Mermin, N.D. (1976). *Solid State Physics*, Saunders College: Philadelphia.

von Barth, U. and Hedin, L. (1972). A local exchange-correlation potential for the spin polarized case: I. *Journal of Physics C: Solid State Physics*, **5**, 1629–1642.

Battocletti, M., Ebert, H. and Akai, H. (1996). Influence of gradient corrections to the local-density-approximation on the calculation of hyperfine fields in ferromagnetic Fe, Co, and Ni. *Physical Review B*, **53**, 9776–9783.

Beiden, S.V., Temmerman, W.M., Szotek, Z., *et al*. (1998). Real-space approach to the calculation of magnetocrystalline anisotropy in metals. *Physical Review B*, **57**, 14247–14253.

Bethe, H.A. and Salpeter, E.E. (1977). *Quantum Mechanics of One- and Two-electron Systems*, Plenum Publishing: New York.

Bihlmayer, G. (2005). Reduced dimensions: magnetic anisotropy. *Magnetism Goes Nano*, *Matter and Materials Volume 26*, Schriften des FZ-Jülich Forschungszentrum Jülich GmbH: Jülich, pp. C21–C24.

Brooks, M.S.S. (1985). Ground state properties of light actinide metals and their compounds. *Physica B*, **130**, 6–12.

Capelle, K. and Vignale, G. (2001). Nonuniqueness of the potentials of spin-density-functional theory. *Physical Review Letters*, **86**, 5546–5549.

Dederichs, P.H., Blügel, S., Zeller, R. and Akai, H. (1984). Ground states of constrained systems: application to cerium impurities. *Physical Review Letters*, **53**, 2512–2515.

Dirac, P.A.M. (1930). Note on exchange phenomena in the Thomas–Fermi atom. *Proceedings of the Cambridge Philosophical Society*, **26**, 376–385.

Drautz, R. and Fähnle, M. (2004). Spin-cluster expansion: parametrization of the general adiabatic magnetic energy surface with ab initio accuracy. *Physical Review B*, **69**, 104404/1–104404/6.

Dudarev, S.L., Botton, G.A., Savrasov, S.Y., *et al*. (1998). Electronic structure and elastic properties of strongly correlated metal oxides from first principles: LSDA+U, SIC-LSDA and EELS study of UO_2 and NiO. *Physical Status Solidi A*, **166**, 429–443.

Ederer, C., Komelj, M. and Fähnle, M. (2003). Magnetism in systems with various dimensionalities: a comparison between Fe and Co. *Physical Review B*, **68**, 052402/1–052402/4.

Eriksson, O., Brooks, M.S.S. and Johansson, B. (1990). Orbital polarization in narrow-band systems: application to volume collapses in light lanthanides. *Physical Review B*, **41**, 7311–7314.

Eschrig, H. (2003). *The Fundamentals of Density Functional Theory*, Edition am Gutenbergplatz: Leipzig.

Fermi, E. (1928). Eine statistische Methode zur Bestimmung einiger Eigenschaften des Atoms und ihre Anwendung auf die Theorie des periodischen Systems der Elemente. *Zeitschrift für Physik*, **48**, 73–79.

Gadre, S.R., Bartolotti, L.J. and Handy, N.C. (1980). Bounds for Coulomb energies. *Journal of Chemical Physics*, **72**, 1034–1038.

Gambardella, P., Rusponi, S., Veronese, M., *et al*. (2003). Giant magnetic anisotropy of single cobalt atoms and nanoparticles. *Science*, **300**, 1130–1133.

Gunnarsson, O. (1976). Band model for magnetism of transition metals in the spin-density-functional formalism. *Journal of Physics F: Metal Physics*, **6**, 587–606.

Gunnarsson, O., Jonson, M. and Lundqvist, B.I. (1979). Descriptions of exchange and correlation effects in inhomogeneous electron systems. *Physical Review B*, **20**, 3136–3164.

Gunnarsson, O. and Lundqvist, B.I. (1976). Exchange and correlation in atoms, molecules, and solids by the spin-density-functional formalism. *Physical Review B*, **13**, 4274–4298.

Hafner, R., Spišák, D., Lorenz, R. and Hafner, J. (2002). Magnetic ground state of Cr in density-functional theory. *Physical Review B*, **65**, 184432/1–184432/9.

Hedin, L. (1965). New method for calculating the one-particle Green's function with application to the electron-gas problem. *Physical Review*, **139**, A796–A823.

Held, K., Anisimov, V.I., Nekrasov, I.A., *et al*. (2002). The LDA+DMFT approach to materials with strong electronic correlations. In *Quantum Simulations of Complex Many-body Systems: From Theory to Algorithms*, *Volume 10 of NIC Series*, Grotendorst, J., Marx, D. and Muramatsu, A. (Eds.), Research Center Jülich: Jülich, pp. 175–209.

Herring, C. (1966), Exchange interactions among itinerant electrons. In *Magnetism IV*, Rado, G.T. and Suhl, H. (Eds.), Academic Press: New York, London.

Hirai, K. (1998). Total energy calculations for spin-density-wave chromium. *Journal of the Physical Society of Japan*, **67**, 1776–1783.

Hobbs, D. and Hafner, J. (2003). Understanding the complex metallic element Mn. I. crystalline and noncollinear magnetic structure of α-Mn. *Physical Review B*, **68**, 14407/1–14407/18.

Hohenberg, P. and Kohn, W. (1964). Inhomogeneous electron gas. *Physical Review*, **136**, B864–B871.

Janak, J.F. and Williams, A.R. (1976). Giant internal magnetic pressure and compressibility anomalies. *Physical Review B*, **14**, 4199–4204.

Jansen, H.J.F. (1988). Magnetic anisotropy in density-functional theory. *Physical Review B*, **38**, 8022–8029.

Jones, R.O. and Gunnarsson, O. (1989). The density functional formalism, its applications and prospects. *Reviews of Modern Physics*, **61**, 689–746.

Katsnelson, M.I. and Antropov, V.P. (2003). Spin angular gradient approximation in the density functional theory. *Physical Review B*, **67**, 140406(R)/1–140406(R)/4.

Kohn, W. and Sham, L.J. (1965). Self-consistent equations including exchange and correlation effects. *Physical Review*, **140**, A1133–A1138.

Kohn, W. and Vashista, P. (1983). General density functional theory. In *Theory of the Inhomogeneous Electron Gas*, Lundqvist, S. and March, N.H. (Eds.), Plenum Publishing: New York, pp. 79–147.

Kokalj, A. (2003). Computer graphics and graphical user interfaces as tools in simulations of matter at the atomic scale. *Computational Materials Science*, **28**, 155–168.

Kübler, J. (2000). *Theory of Itinerant Electron Magnetism*, *Volume 106 of International Series of Monographs in Physics*, Clarendon Press: Oxford.

Kurz, P., Bihlmayer, G. and Blügel, S. (2002). Magnetism and electronic structure of hcp Gd and the Gd(0001) surface. *Journal of Physics: Condensed Matter*, **14**, 6353–6371.

Kurz, P., Bihlmayer, G., Hirai, K. and Blügel, S. (2001). Three-dimensional spin structure on a two-dimensional lattice: Mn/Cu(111). *Physical Review Letters*, **86**, 1106–1109.

Kurz, P., Förster, F., Nordström, L., *et al*. (2004). *Ab initio* treatment of noncollinear magnets with the full-potential linearized augmented plane wave method. *Physical Review B*, **69**, 024415/1–024415/15.

Lenz, W. (1932). Über die Anwendbarkeit der statistischen Methode auf ionengitter. *Zeitschrift für Physik*, **77**, 713–721.

Ležaić, M. (2005). *Spin-Gap Materials from First Principles: Properties and Applications of Half-Metallic Ferromagnets*, Ph.D. Thesis, RWTH, Aachen.

Liechtenstein, A.I., Anisimov, V.I. and Zaanen, J. (1995). Density-functional theory and strong interactions: orbital ordering in Mott-Hubbard insulators. *Physical Review B*, **52**, R5467–R5470.

Liechtenstein, A.I. and Katsnelson, M.I. (2001). Magnetism of correlated systems: beyond LDA. In *Band-ferromagnetism: Ground-state and Finite Temperature Phenomena*, *Volume 580 of Lecture Notes in Physics*, Baberschke, K., Donath, M. and Nolting, W. (Eds.), Springer: Berlin, Heidelberg, pp. 75–93.

van der Marel, D. and Sawatzky, G.A. (1988). Electron-electron interaction and localization in *d* and *f* transition metals. *Physical Review B*, **37**, 10674–10684.

Metropolis, N., Rosenbluth, A.W., Rosenbluth, M.N., *et al*. (1953). Equation of state calculations by fast computing machines. *Journal of Chemical Physics*, **21**, 1087–1092.

Moruzzi, V.L., Janak, J.F. and Williams, A.R. (1978). *Calculated Electronic Properties of Metals*, Pergamon Press: New York.

di Napoli, S., Llois, A.M., Bihlmayer, G., *et al*. (2004). Magnetic structure and transport properties of noncollinear $LaMn_2X_2$ (X = Ge,Si) systems. *Physical Review B*, **70**, 174418/1–174418/10.

Onida, G., Reining, L. and Rubio, A. (2002). Electronic excitations: density-functional versus many-body Green's-function approaches. *Reviews of Modern Physics*, **74**, 601–659.

Pajda, M., Kudrnovský, J., Turek, I., *et al*. (2001). *Ab initio* calculations of exchange interactions, spin-wave stiffness constants, and Curie temperatures of Fe, Co, and Ni. *Physical Review B*, **64**, 174402/1–174402/9.

Parr, R.G. and Yang, W. (1989). *Density Functional Theory of Atoms and Molecules*, Oxford University Press: New York.

Perdew, J.P. and Zunger, A. (1981). Self-interaction correction to density-functional approximations for many-electron systems. *Physical Review B*, **23**, 5048–5079.

Picozzi, S., Yamauchi, K., Bihlmayer, G. and Blügel, S. (2006). First-principles stabilization of an unconventional collinear magnetic ordering in distorted manganites. *Physical Review B*, **74**, 094402.

Rodriguez, C.O., Ganduglia-Pirovano, M.V., Peltzer y Blancá, E.L, *et al*. (2001). Orbital and dipolar contributions to the hyperfine fields in bulk bcc Fe, hcp Co, and at the Fe/Ag(100) interface: the inclusion of orbital polarization. *Physical Review B*, **63**, 184413–184419.

Rosengaard, N.M. and Johansson, B. (1997). Finite-temperature study of itinerant ferromagnetism in Fe, Co, and Ni. *Physical Review B*, **55**, 14975–14986.

Sachedev, S. (2000). Quantum criticality: competing ground states in low dimensions. *Science*, **288**, 475–480.

Sandratskii, L.M. (1986). Energy band structure calculations for crystals with spiral magnetic structure. *Physical Status Solidi B*, **136**, 167–180.

Şaşıoğlu, E., Sandratskii, L.M. and Bruno, P. (2005). Above-room-temperature ferromagnetism in half-metallic Heusler compounds NiCrP, NiCrSe, NiCrTe, and NiVAs: a first-principles study. *Journal of Applied Physics*, **98**, 063523/1–063523/6.

Sato, K., Dederichs, P.H. and Katayama-Yoshida, H. (2005). Is high T_c possible in (Ga,Mn)N?: Monte Carlo simulation vs. mean field approximation. *Journal of Superconductivity*, **18**, 33–36.

Shallcross, S., Kissavos, A.E., Meded, V. and Ruban, A.V. (2005). An *ab initio* effective Hamiltonian for magnetism including longitudinal spin fluctuations. *Physical Review B*, **72**, 104437/1–104437/8.

Shick, A.B. and Mryasov, O.N. (2003). Coulomb correlations and magnetic anisotropy in ordered $L1_0$ CoPt and FePt alloys. *Physical Review B*, **67**, 172407/1–172407/4.

Singh, D.J. and Ashkenazi, J. (1992). Magnetism with generalized-gradient-approximation density functionals. *Physical Review B*, **46**, 11570–11577.

Slater, J.C. (1929). The theory of complex spectra. *Physical Review*, **34**, 1293–1322.

Slater, J.C. (1951). A simplification of the Hartree-Fock method. *Physical Review*, **81**, 385–390.

Slater, J.C. and Krutter, H.M. (1934). The Thomas-Fermi method for metals. *Physical Review*, **47**, 559–568.

Solovyev, I.V. (2005). Orbital polarization in itinerant magnets. *Physical Review Letters*, **95**, 267205/1–267205/4.

Solovyev, I.V., Dederichs, P.H. and Anisimov, V.I. (1994). Corrected atomic limit in the local-density approximation and the electronic structure of *d* impurities in Rb. *Physical Review B*, **50**, 16861–16871.

Solovyev, I.V. and Imada, M. (2005). Screening of Coulomb interactions in transition metals. *Physical Review B*, **71**, 045103/1–045103/11.

Solovyev, I.V., Liechtenstein, A.I. and Terakura, K. (1998). Is Hund's second rule responsible for the orbital magnetism in solids? *Physical Review Letters*, **80**, 5758–5761.

Staunton, J.B. (1994). Electronic structure of magnetic transition metallic materials. *Reports on Progress in Physics*, **57**, 1289–1344.

Stocks, G.M., Újfalussy, B., Wang, X-D., *et al*. (1998). Towards a constrained local moment model for first principles spin dynamics. *Philosophical Magazine B*, **78**, 665–673.

Stöhr, J. (1999). Exploring the microscopic origin of magnetic anisotropies with X-ray magnetic circular dichroism (XMCD) spectroscopy. *Journal of Magnetism and Magnetic Materials*, **200**, 470–497.

Stoner, E.C. (1939). Collective electron ferromagnetism II. Energy and specific heat. *Proceedings of the Royal Society of London Series A*, **169**, 339.

Svane, A. (1996). Electronic structure of cerium in the self-interaction-corrected local-spin-density approximation. *Physical Review B*, **53**, 4275–4286.

Tao, J., Perdew, J.P., Staroverov, V.N. and Scuseria, G.E. (2003). Climbing the density functional ladder: nonempirical meta-generalized gradient approximation designed for molecules and solids. *Physical Review Letters*, **91**, 146401/1–146401/4.

Temmerman, W.M., Svane, A., Szotek, Z., *et al*. (2000). On the implementation of the self-interaction corrected local spin density approximation for d- and f-electron systems. In *Electronic Structure and Physical Properties of Solids: The Uses of the LMTO Method*, *Volume 535 of Lecture Notes in Physics*, Dreyssé, H. (Ed.), Springer: Berlin, Heidelberg, pp. 286–312.

Thomas, L.H. (1927). The calculation of atomic fields. *Proceedings of the Cambridge Philosophical Society*, **23**, 542–548.

Thonhauser, T., Ceresoli, D., Vanderbilt, D. and Resta, R. (2005). Orbital magnetization in periodic insulators. *Physical Review Letters*, **95**, 137205/1–137205/4.

Tokura, Y. and Nagaosa, N. (2000). Orbital physics in transition-metal oxides. *Science*, **288**, 462–468.

Trygg, J., Johansson, B., Eriksson, O. and Wills, J.M. (1995). Total energy calculation of the magnetocrystalline anisotropy energy in the ferromagnetic 3*d* metals. *Physical Review Letters*, **75**, 2871–2874.

Tsunoda, Y. (1989). Spin-density wave in cubic γ-Fe and γ-$Fe_{100-x}Co_x$ precipitates in Cu. *Journal of Physics: Condensed Matter*, **1**, 10427–10438.

Turek, I., Kudrnovský, J., Bihlmayer, G. and Blügel, S. (2003). *Ab initio* theory of exchange interactions and the Curie temperature of bulk Gd. *Journal of Physics: Condensed Matter*, **15**, 2771–2782.

Turek, I., Kudrnovský, J., Diviš, M., *et al*. (2003). A first-principle study of electronic structure and exchange interactions in bcc europium. *Physical Review B*, **68**, 224431/1–224431/7.

Újfalussy, B., Wang, X-D., Nicholson, D.M.C., *et al*. (1999). Constrained density functional theory for first principles spin dynamics. *Journal of Applied Physics*, **85**, 4824–4826.

Vignale, G. and Rasolt, M. (1988). Current and spin-density-functional theory for inhomogeneous electronic systems in strong magnetic fields. *Physical Review B*, **37**, 10685–10696.

Wang, C.S., Klein, B.M. and Krakauer, H. (1985). Theory of magnetic and structural ordering in iron. *Physical Review Letters*, **54**, 1852–1855.

Weinert, M., Watson, R.E. and Davenport, J.W. (1985). Total-energy differences and eigenvalue sums. *Physical Review B*, **32**, 2115–2119.

White, H.W., Beaudry, B.J., Burgardt, P., *et al*. (1975). Magnetic moments of ferromagnetic gadolinium alloys. *AIP Conference Proceedings*, **29**, 329.

Wu, R. and Freeman, A.J. (1999). Spin-orbit induced magnetic phenomena in bulk metals and their surfaces and interfaces. *Journal of Magnetism and Magnetic Materials*, **200**, 498–514.

Yang, I., Savrasov, S.Y. and Kotliar, G. (2001). Importance of correlation effects on magnetic anisotropy in Fe and Ni. *Physical Review Letters*, **87**, 216405/1–216405/4.

Yosida, K. (1996). *Theory of Magnetism*, Springer: Berlin, Heidelberg.

Multiband Hubbard Models and the Transition Metals

Gernot Stollhoff
Max-Planck-Institut für Festkörperforschung, Stuttgart, Germany

1 INTRODUCTION

A breakthrough in the understanding of the itinerant ferromagnetism of the 3d transition metals occurred when density-functional (DF) calculations, performed in the local density approximation (LDA) (Hohenberg and Kohn, 1964; Kohn and Sham, 1965) or rather its spin generalized variant, local spin-density approximation (LSDA) (Gunnarsson and Lundqvist, 1976), obtained seemingly perfect values for the magnetic moments of the metals. Good results were also obtained for other ground-state properties: binding energies, equilibrium volumes, bulk moduli, and Fermi surfaces, to name a few (Poulson, Kollar and Anderson, 1976; Janak and Williams, 1976; Callaway, 1981).

A crucial aspect in this context is the behavior of the 3d electrons. The 3d atomic orbitals are largely localized in space around the nuclei, and form rather narrow tight-binding bands with a width of roughly 5 eV. This localization is considerably stronger for the 3d than for the heavier 4d or 5d transition metals. In the following work, the consequences of this localization are investigated for the 3d transition metals.

While there have been many speculations about a full localization of the 3d electrons and about a representation of their degrees of freedom by spin Hamiltonians, the delocalization is a feature that is strongly supported by experiment. Already before the success of LSDA, the experimental binding energies were unambiguously connected to delocalized 3d electrons (Friedel, 1969). In LSDA, the explicit part of the kinetic energy is obtained from a maximally delocalized single-determinant reference state while correlation corrections are contained in a functional. Consequently the former part represents the limit of maximal delocalization of the 3d electrons. On the other hand, there is evidence that the LSDA results overemphasize binding by up to 20% (Moruzzi, Janak and Williams, 1978), possibly owing to a mishandling of correlation corrections. This deviation in turn sets an upper limit to possible correlation corrections. In particular, strong correlations or electronic degrees of freedom that can be described in terms of atomic moments are ruled out.

With the 3d electrons basically delocalized in tight-binding bands, magnetism must result from the electronic interactions. As already mentioned, these cannot be so strong that localized atomic moments arise. Even more, it needs to

Handbook of Magnetism and Advanced Magnetic Materials. Edited by Helmut Kronmüller and Stuart Parkin. Volume 1: *Fundamentals and Theory*. ISBN: 978-0-470-02217-7.

be understood why the LSDA is apparently able to handle these interactions that are definitely connected to the spatially strongly localized atomic orbital representation of the 3d electrons. It is hard to imagine how a homogeneous electron-gas exchange-correlation potential can adequately deal with such inhomogeneous atomic features. In fact it cannot.

Bare local Coulomb-interaction matrix elements between electrons in these atomic orbitals are of the order of 20 eV, far larger than the kinetic energy gained from delocalization into bands. Therefore, a second problem is to understand how these bare interactions are reduced into the required smaller interactions.

The optimal way to deal with these questions would be a full *ab initio* correlation calculation. The only method available for such a treatment is the local ansatz (LA) (Stollhoff and Fulde, 1980; Stollhoff, 1996). It starts from Hartree–Fock (HF) *ab initio* calculations for solids and adds correlations in a variational way like quantum chemistry (QC) methods do. However, it differs from these methods by using specifically constructed subsets of correlation operators with a well-defined local meaning instead of trying to cover the whole correlation space in an orthogonal representation. This results in a loss of typically one to a few percent of the correlation energy in a given basis, but it leads to a large gain in efficiency, and it enables the LA to treat metals. First *ab initio* calculations for metals (Heilingbrunner and Stollhoff, 1993) and for a metallic transition metal compound (Stollhoff, 1998) have already been performed, and calculations for nonmagnetic transition metals are under way (Stollhoff, unpublished), but a complete coverage of the magnetic problem has not yet been obtained. Therefore, the problems mentioned above could so far only be addressed using correlation calculations for models.

The minimal level of complexity for such models is well defined: a tight-binding Hamiltonian for the 3d electrons, that is, a five-band (per spin) Hamiltonian. The hope is that the 4s and 4p orbitals of the transition metals do not need to be explicitly included for the basic understanding of magnetism, since they contribute little to the electronic density of states in the relevant energy range around the Fermi energy. This omission certainly causes defects, for example, of the Fermi surface. For the interactions, a first choice is the inclusion of only local (atomic) interactions of the 3d electrons. It is known that these can be condensed into three Slater parameters. We will, in the following, rearrange those terms and call the resulting interactions Hubbard (U) interaction, Hund's rule exchange terms (J), and anisotropy terms (ΔJ) (Kleinmann and Mednick, 1981). The underlying assumption is that longer-range contributions of the Coulomb interaction are almost perfectly screened for these metals.

Such models have for long been the basis of attempts to understand the itinerant ferromagnetism. However, these attempts were mostly restricted to simplified single-band models and/or to the approximate treatment of the interaction in HF approximation, or when the treatment was extended to finite temperatures within a functional integral formulation, in an equivalent static approximation. For an early overview, refer to Moriya (1981).

Here, the LA led to a sizable improvement. Since it can be applied to models as well as to *ab initio* calculations, we were able to perform satisfactory correlation calculations for the model described above, and we have computed the nonmagnetic (Stollhoff and Thalmeier, 1981) as well as the magnetic (Oleś and Stollhoff, 1984) cases. The tool to understand the magnetic phase transition for the case of delocalized electrons is the Stoner–Wohlfarth theory (Stoner, 1938; Wohlfarth, 1949). Such an analysis had been earlier performed in the case of LSDA computations (Gunnarsson, 1976). We also analyzed our results in the same way (Oleś and Stollhoff, 1988; Stollhoff, Oleś and Heine, 1990), and managed to work out why the LSDA calculations had been so successful for the transition metals but had failed for a set of transition-metal compounds (Stollhoff, Oleś and Heine, 1990, 1996). We abstained from any attempts to generalize the treatment of the order parameter beyond a mean-field (or Stoner–Wohlfarth) approximation. It should be noted that for the simplified handling of the interaction in HF or static approximation, a generalized spin fluctuation theory is available (Moriya, 1985).

It turned out from our analysis that the fivefold degeneracy of the model bands is very relevant. Single-band or two-band models are not able to catch the essence of the 3d magnetism at all. Many of the degeneracy features also are lost when restricting to a HF or static approximation. As will be shown in the subsequent text, a reduction of the degeneracy would require also larger and larger interactions and would incorrectly push the treatment into a strong-correlation direction which is inadequate for the 3d transition metals.

Five-band models have been rarely treated by other methods beyond HF approximation. A first attempt was made in the context of an insufficient second-order perturbation computation (Kajzar and Friedel, 1978; Treglia, Ducastelle and Spanjaard, 1980). Quasiparticle calculations followed using the Kanamori t-matrix approach (Kanamori, 1963) for almost filled degenerate band systems such as Ni (Liebsch, 1979, 1981; Penn, 1979; Davis and Feldkamp, 1980). Recently, calculations have been performed for nine-band models starting from an $R = 0$ approximation that had also been used by the LA but employing a full configuration interaction (CI) calculation instead of the weak-correlation expansion or of a two-particle excitation CI calculation both within the LA (Bünemann, Weber and Gebhard, 1998; Bünemann *et al*., 2003). Finally, the dynamical mean-field theory (DMFT) has been used for such a model (Lichtenstein, Katsnelson and

Kotliar, 2001). The latter is the appropriate generalization of the functional integral schemes just mentioned, and goes beyond the static approximation.

We will in the following introduce the five-band model plus its interactions, and describe in detail the LA treatment and the different approximations made. We will also establish connections to the other computational schemes.

In a next step, results of the calculations for the nonmagnetic case will be presented, and the different approximations will be tested. A further step is to compute and analyze the magnetic results for Fe, Co, and Ni. Based on them, conclusions on the comparability to experiment and on specific deficiencies of the LSDA and its results will be made.

Finally, connections between the model and first *ab initio* correlation results will be made, and the limits of the Hubbard-model scenario will be revealed.

2 MODEL HAMILTONIAN AND SINGLE-PARTICLE GROUND STATE

The aim of the qualitative treatment is to understand the delocalization and interaction of the 3d electrons which is the expected key for the understanding of magnetism in the 3d-elemental solids. There are five 3d electrons per spin and site (atom). A compact description of their delocalization is in the form of canonical d bands (Andersen and Jepsen, 1977). This is essentially a tight-binding description and has the additional advantage of containing only a single open parameter, namely, the 3d bandwidth W. The single-particle part of the model Hamiltonian (H_0) is given in terms of these orbitals in eigenvalue representation. In the computations, these bands are constructed for the two relevant lattices, bcc and fcc.

For these electrons we further assume that they only interact when they are on the same atom l. These interactions can be given in terms of three Slater interactions; here we choose a slightly different but equivalent notation. The full Hamiltonian H reads as

$$H = H_0 + H_1 \tag{1}$$

$$H_0 = \sum_{\nu\sigma\mathbf{k}} e_\nu(\mathbf{k}) n_{\nu\sigma}(\mathbf{k}) \tag{2}$$

$$H_1 = \sum_{\mathbf{l}} H_1(\mathbf{l}) \tag{3}$$

$$\begin{aligned} H_1(\mathbf{l}) = {} & \frac{1}{2}\sum_{ij\sigma\sigma} U_{ij} a^\dagger_{i\sigma}(l) a^\dagger_{j\sigma'}(l) a_{j\sigma'}(l) a_{i\sigma}(l) \\ & + \frac{1}{2}\sum_{ij\sigma\sigma} J_{ij} \Big[a^\dagger_{i\sigma}(l) a^\dagger_{j\sigma'}(l) a_{i\sigma'}(l) a_{j\sigma}(l) \\ & + a^\dagger_{i\sigma}(l) a^\dagger_{i\sigma'}(l) a_{j\sigma'}(l) a_{j\sigma}(l) \Big] \end{aligned} \tag{4}$$

The $e_\nu(\mathbf{k})$ represent the five ($\nu = 1.5$) canonical bands, and the $n_{\nu\sigma}(\mathbf{k})$ the corresponding number operators of the Bloch eigenstates, whose creation and annihilation operators are $c^\dagger_{\nu\sigma}(\mathbf{k}), c_{\nu\sigma}(\mathbf{k})$. The U_{ij} and J_{ij} are the local (atomic) interaction matrices and are related by

$$U_{ij} = U + 2J - 2J_{ij} \tag{5}$$

where U and J are the average Coulomb and exchange interaction constants. The matrix J_{ij} contains the third interaction parameter ΔJ that is a measure of the difference between the e_g and t_{2g} interactions. For details of this matrix, we refer to Kleinmann and Mednick (1981) and Oleś and Stollhoff (1984). For $\Delta J = 0$, it holds that $J_{ij} = J$. The interactions are expressed in terms of the five local 3d orbitals i on atomic positions l whose creation and annihilation operators are given as $a^\dagger_{i\sigma}(l), a_{i\sigma}(l)$.

The size of these parameters will be fixed later. Typically, it holds that the bandwidth W that scales the single-particle part H_0 is roughly 5 eV. The interactions are reduced to a single free parameter by setting $J \simeq 0.2U$ and $\Delta J \simeq 0.2J$. For U it holds that typically $U \simeq 0.5W$.

Starting point of the following correlation treatment is the solution to the single-particle Hamiltonian H_0, called Ψ_0. This is written as

$$|\Psi_0(n_d, 0)\rangle = \prod_{\substack{\mathbf{k}\nu\sigma \\ e_{\mathbf{k}\nu} \le e_\mathrm{F}(n_d)}} c^\dagger_{\nu\sigma}(\mathbf{k})|0\rangle \tag{6}$$

This solution differs slightly from the self-consistent field (SCF) solution of the full model Hamiltonian H. The latter generates additional self-consistently obtained crystal-field terms that may lead to charge redistributions between the e_g and t_{2g} orbitals. However, since the interactions are not too large, and the original site occupations are almost degenerate, these redistributions can be almost neglected. An exception that will be discussed later is the case of ferromagnetic Ni where the second requirement does not hold. Such a solution is found for all fillings n_d per atom of the five-band system, with n_d ranging from 0 to 10. $e_\mathrm{F}(n_d)$ is the occupation-dependent Fermi energy.

In addition to this nonmagnetic solution, magnetic solutions with a moment m are constructed by generating states

$$|\Psi_0(n_d, m)\rangle = \prod_{\substack{\mathbf{k}\nu \\ e_{\mathbf{k}\nu} \le e_\mathrm{F}(n_d+m)}} \prod_{\substack{\mathbf{k}'\nu \\ e_{\mathbf{k}'\nu} \le e_\mathrm{F}(n_d-m)}} c^\dagger_{\nu\uparrow}(\mathbf{k}) c^\dagger_{\nu\downarrow}(\mathbf{k}')|0\rangle \tag{7}$$

Here, the majority band with spin up is occupied with $(n_d + m)/2$ electrons, and the minority band with spin down with $(n_d - m)/2$. This ansatz is a rigid band approach. Again, a self-consistent solution might lead to small charge

redistributions in the minority and majority bands if these are not empty or filled, respectively.

The Fermi energy for the individual cases like Fe, Co, Ni is chosen so that the maximal magnetic moment agrees with the same one of the LSDA calculations. This implies an occupation of 7.4, 8.4, 9.4 for Fe, Co, and Ni, respectively. It is known from more careful charge analyzes that the true atomic 3d occupations are somewhat smaller. For Fe for example they amount to 6.5. Consequently, the d orbitals of this model Hamiltonian are not maximally localized 3d tight-binding orbitals but their tails have small 4s, 4p contributions.

3 CORRELATED GROUND STATE

3.1 Deficiencies of the single-particle ground state

The single-particle ground state Ψ_0 is an eigenstate for the single-particle part of the Hamiltonian but results in a poor coverage of the interaction part. Being represented by eigenfunctions in momentum space, this state has maximal local charge fluctuations that are uncorrelated for the different bands. A measure of these charge fluctuations is the atomic quantity Δn^2 for a given wave function. It is given as

$$\Delta n^2 = \langle\Psi|n^2(l)|\Psi\rangle - \langle\Psi|n(l)|\Psi\rangle^2 \tag{8}$$

$$n(l) = \sum_{i\sigma} n_{i\sigma}(l) \tag{9}$$

where $n_{i\sigma}(l)$ is the density operator for an electron with spin σ in orbital i on site l.

For the single-particle ground state, it holds that

$$\Delta n^2(\Psi_0(n_d, 0)) = \sum_{i\sigma} n_{i\sigma}(1 - n_{i\sigma}) \tag{10}$$

$$n_{i\sigma} = \langle\Psi_0|n_{i\sigma}(l)|\Psi_0\rangle \tag{11}$$

These fluctuations increase linearly with the number of bands. For the half-filled five-band case with degenerate occupation we find that $\Delta n^2 = 2.5$. Correspondingly, the interaction energy costs per atom of this state in comparison to the disordered atomic limit amount to $1.25\left(U - \frac{2}{9}J\right)$. This needs to be compared to a kinetic energy gain, which for a roughly constant density of states equals $-1.25W$. This indicates that half the delocalization energy is lost in this approximation for a ratio $U \simeq 0.5W$. However, the electrons on the individual atoms order by Hund's rule and can gain an energy of $-\frac{70}{9}J$ at half-filling. Consequently even for this relatively modest screened interaction, the solid is no longer bound in single-particle approximation, and a better treatment is required, that is, the correlated ground state needs to be computed. Without including correlations explicitly, any broken symmetry, even disordered local moments would be favorable.

3.2 The local ansatz

For a three-dimensional model with five degenerate bands, the correlation treatment cannot be done exactly but only approximately. Since the parameter choice let us expect that the electrons are not too strongly correlated, the natural approach is to start from the single-particle ground state and add correlations as corrections.

This is how the LA is set up. Here, the following variational ansatz is made for the correlated ground state:

$$|\Psi_{\text{corr}}\rangle = e^{-S}|\Psi_0\rangle \tag{12}$$

$$S = \sum_{\nu} \eta_\nu O_\nu \tag{13}$$

$$O_\nu = \begin{cases} n_{i\uparrow}(l)n_{i\downarrow}(l) \\ n_i(l)n_j(l') \\ \vec{s}_i(l)\cdot\vec{s}_j(l') \end{cases} \tag{14}$$

The $n_{i\sigma}(l)$ and $\vec{s}_i(l)$ are density and spin operators for an electron in the local orbital i on site l. The operators have a transparent meaning. For example, the first operator $n_{i\uparrow}(l)n_{i\downarrow}(l)$, when applied to $|\Psi_0\rangle$, picks out all configurations with two electrons in orbital i. When applied with a variational parameter η_ν, as in equation (12), it partially suppresses those configurations. For a single-band Hubbard model such an ansatz was first made by Gutzwiller (1965). Similarly, the operators $n_i(l)n_j(l')$ introduce density correlations between electrons in local orbitals i, j either on the same site or on different sites l, l'. The wave function generated by these two sets of operators, when applied to the homogeneous electron gas problem, is the Jastrow function (Jastrow, 1955). The operators $\vec{s}_i \cdot \vec{s}_j$ generate spin correlations. On the same site, they introduce Hund's rule correlations, while when applied for different sites they result in magnetic correlations.

For the same sites, all these operators are directly connected to H_1. They allow to correct exactly those features that are addressed by the interaction terms.

In the following, we will no longer use the full operators but only their two-particle excitation contributions. The standard approximation to derive the energy and to obtain the variational parameters is an expansion in powers of η, up to second order,

$$E_{\text{G}} = E_{\text{SCF}} + E_{\text{corr}} \tag{15}$$

$$E_{\text{corr}} = -2\sum_{\nu} \eta_\nu \langle O_\nu^\dagger H\rangle + \sum_{\mu\nu} \eta_\nu\eta_\mu \langle O_\nu^\dagger H O_\mu\rangle_{\text{c}} \tag{16}$$

When optimizing this energy, the following equations arise that determine the energy and the variational parameters.

$$E_{\mathrm{corr}} = -\sum_{\nu} \eta_\nu \langle O_\nu^\dagger H \rangle \tag{17}$$

$$0 = -\langle O_\nu^\dagger H \rangle + \sum_{\mu} \eta_\mu \langle O_\nu^\dagger H O_\mu \rangle_{\mathrm{c}} \tag{18}$$

Here, $\langle A \rangle$ is the expectation value of the operator A within $|\Psi_0\rangle$, and $\langle\rangle_{\mathrm{c}}$ indicates that only connected contributions are included. It holds that $E_{\mathrm{SCF}} = \langle H \rangle$ These equations can also be identified as a linearized coupled-cluster expansion with singles and doubles (LCCSD), restricted to particular two-particle (double) and one-particle (single) excitations. The concept of coupled-cluster (CC) equations was introduced into many-body physics and into QC a long time ago (Coester, 1958; Coester and Kümmel, 1960; Cizek, 1966, 1969). In the presented calculations on models, single-particle excitations were, in contrast to the *ab initio* calculations, not included in the correlation treatment itself, but were covered by direct modifications in the trial single-particle wave functions.

The full treatment of these equations poses no problems, in particular, when the operators are restricted to on-site terms. Then, without consideration of intrinsic symmetries, one has 5 Gutzwiller-like operators and 10 density and spin operators each. The most expensive step is the solution of a set of linear equations with dimension 25.

3.3 The $R = 0$ approximation and alternatives to the local ansatz

The correlation calculations can be performed in a further approximation in which one may go beyond the LCCSD equations. This approximation applies only when restricting to on-site operators. In this case, one can approximately set all those terms in the matrices $\langle OH \rangle$ and $\langle OHO \rangle$ equal to zero where the operators in the O or in H_1 are not on the same site. In this approximation, the full correlation treatment separates into independent contributions covering a single site each in a noncorrelated and noninteracting environment. This approximation is called *single-site* or $R = 0$ *approximation*. It was introduced for the first time in a second-order perturbation treatment of a five-band Hamiltonian that is very similar to the one used here. There, however, no restriction to a particular choice of correlation operators was made but the full two-particle operator space was covered (Treglia, Ducastelle and Spanjaard, 1980). In the single-site approximation of the LA, all required terms are simply obtained from two sets of single-particle elements, the individual occupations $n_{i\sigma}$ and the average energies on these sites, $e_{i\sigma}$, are given as

$$e_{i\sigma} = \int_{-\infty}^{e_{\mathrm{F}}} e n_{i\sigma}(e)\, \mathrm{d}e \tag{19}$$

where $n_{i\sigma}(e)$ is the local partial density of states for orbital i with spin σ. More details can be found in Stollhoff and Thalmeier (1981) and Oleś and Stollhoff (1984). All terms that are left out in the single-site approximation contain nondiagonal density matrix elements of the form $P_{ij}(l, l') = \langle a_i^\dagger(l) a_j(l') \rangle$ with $R = l - l' \neq 0$, explaining the name. With rising number of nearest neighbors, these contributions shrink in weight and disappear for the limit of infinitely many neighbors (or equivalently dimensions d). The approximation was therefore more recently called $d = \infty$ approximation (Vollhardt *et al.*, 1999).

In a way, this approximation represents the correlation generalization of an approximate coherent potential approximation (CPA) where a single-site mean-field calculation with broken symmetry is performed which leads to disordered local moments. With on-site correlations properly included, a broken symmetry result no longer arises, at least not prior to a Mott–Hubbard transition. Or, in other words, disordered local moments are a poor man's approach to correlations.

This single-site approximation allows a more general treatment than the LCCSD approximation. One possibility is to perform a CI calculation for this single site. The exact energy of the variational state with two-particle excitations included is obtained. It represents a lower limit to the exact result, while the LCCSD approximation usually overshoots the latter. The correlated wave function for the single site l is defined as

$$|\Psi_{\mathrm{corr}}(l)\rangle = \left(1 - \sum_{\nu \in l} O_\nu\right) |\Psi_0\rangle \tag{20}$$

Its exact energy is

$$E_{\mathrm{G}}(l) = E_{\mathrm{SCF}} + E_{\mathrm{corr}}(l) \tag{21}$$

$$E_{\mathrm{corr}}(l) = \frac{-2 \sum_{\nu}{}' \eta_\nu \langle O_\nu^\dagger H' \rangle + \sum_{\mu\nu}{}' \eta_\nu \eta_\mu \langle O_\nu^\dagger H' O_\mu \rangle_{\mathrm{c}}}{1 + \sum_{\mu\nu}{}' \eta_\nu \eta_\mu \langle O_\nu^\dagger O_\mu \rangle_{\mathrm{c}}} \tag{22}$$

Here the $\sum'$ indicates a restriction of the summation to operators on site l, and $H' = H_0 + H_1(l)$. When optimizing this energy, the resulting equations that determine the energy and the variational parameters can be written in close

similarity to the LCCSD equations (17) and (18).

$$E_{\mathrm{corr}}(l) = -\sum_{\nu}{}' \eta_\nu \langle O_\nu^\dagger H' \rangle \tag{23}$$

$$0 = -\langle O_\nu^\dagger H' \rangle + \sum_{\mu}{}' \eta_\mu \langle O_\nu^\dagger H' O_\mu \rangle_{\mathrm{c}} + \sum_{\mu}{}' \eta_\mu \langle O_\nu^\dagger O_\mu \rangle_{\mathrm{c}} \sum_{\mu'}{}' \eta_{\mu'} \langle H' O_{\mu'} \rangle_{\mathrm{c}} \tag{24}$$

The newly added terms in equation (24) are responsible for the difference. One may generalize in this approximation and perform a full CI calculation not restricted to two-particle operators. The system of equations (20), (22)–(24) stays the same but the operators O_ν are not restricted to two-particle excitations. The available operator space explodes exponentially with degeneracy, and the numerical demands rise sharply, but recently even nine-band models could be addressed this way (i.e., the 3d plus the 4s and 4p orbitals were included) (Bünemann, Weber and Gebhard, 1998; Bünemann *et al*., 2003).

An even more extended approach is to perform an exact calculation for the single-site problem, based on dynamically fluctuating disordered local moments, called DMFT (for an introduction of its origins, see Vollhardt *et al*., 1999). This computation is based on a Green's function formalism, and is by far the most expensive method. Formally, the operator space is extended beyond strictly local operators. Not all electrons are covered equally but their treatment is influenced by their individual energies. Applications for a nine-band model were done for Fe and Ni (Lichtenstein, Katsnelson and Kotliar, 2001) by this method. A further advantage of this scheme is that quasiparticle results can be obtained and a transition to thermodynamic quantities is possible since the computations are performed on a Green's function level.

Let's return to the most simple scheme, the LA. In contrast to the other methods, it cannot be applied to the Mott–Hubbard transition. However, it is the only scheme that can be extended beyond $R = 0$ and can treat finite dimension corrections. Furthermore, it can deal with long-range interactions, and even manage *ab initio* calculations with the full interaction.

There is actually a rather simple extension of the LA that makes it more tolerant of stronger correlations. This is the application of the full coupled-cluster expansion with singles and doubles (CCSD) equations. They arise from a full equation of motion of the original ansatz for the wave function, and not from a weak coupling approximation. The resulting equations read as follows:

$$E_{\mathrm{corr}} = -\sum_{\nu} \eta_\nu \langle O_\nu^\dagger H \rangle \tag{25}$$

$$0 = -\langle O_\nu^\dagger H \rangle + \sum_{\mu} \eta_\mu \langle O_\nu^\dagger H O_\mu \rangle_{\mathrm{c}} - \frac{1}{2} \sum_{\mu\mu'} \eta_\mu \eta_{\mu'} \langle O_\nu^\dagger H O_\mu O_{\mu'} \rangle_{\mathrm{c}} \tag{26}$$

This generalization would improve the results for larger ratios of U/W. When applied to a single-band Hamiltonian in $R = 0$ approximation, the result should, with single-particle operators properly added, reproduce the Gutzwiller approximation (Stollhoff and Heilingbrunner, 1991).

3.4 Error estimates of the different approximations in the local ansatz

In the present treatment of the LA, three approximations are made that need to be controlled.

The first is the weak-correlation approximation. It may be tested by a comparison of the LCCSD and the CI result in the $R = 0$ approximation.

The second is the $R = 0$ approximation itself. It can be tested only in the weak-correlation approximation.

The last is the restriction in correlation operator space. Again, this will be tested in the weak-correlation expansion.

The last restriction is best tested for the one-dimensional single-band Hubbard model. Here, the exact energy is known, and also its weak-correlation limit. The corresponding Gutzwiller ansatz, which contains only single-site operators yields 92% of the exact correlation energy in this limit for the half-filled case. A large fraction of the missing energy can be obtained by longer-range density and spin correlations.

The situation is worse for almost empty bands. Here, additional correlation operators of the form $[H_0, O_\nu]$ are required for a satisfactory result. Such operators do not open new correlation channels but allow us to take into account the band energies of the electrons involved in the correlation process. Such operators are included in the *ab initio* scheme and have turned out to be important in a different context (Stollhoff, 1996). We had found for the nonmagnetic five-band calculations (Stollhoff and Thalmeier, 1981; Stollhoff, 1986) that these operators do not lead to noticeable changes. Although being of nonlocal nature, such operators contribute in $R = 0$ approximation, and bridge the difference between a correlation calculation restricted to local correlation operators and a DMFT calculation.

For the five-band model, we had also included nearest-neighbor operators in the nonmagnetic calculations (Stollhoff and Thalmeier, 1981). The energy gain due to these terms was only a few percent; thus we can trust the results of calculations restricted to on-site correlations for the five-band Hamiltonian.

The $R = 0$ approximation depends on the number of neighbors. For a two-site problem with a single orbital each, the $R = 0$ result is only half the correct result. For the one-dimensional Hubbard model, the $R = 0$ result needs to be enhanced by 33% to obtain the final LA result with on-site operators for half-filling, but already nearest neighbor or $R = 1$ corrections reduce the deficiency to 1%. For the five-band problems treated here, the $R = 1$ corrections turned out to be 2–3% for fcc or bcc, respectively (Stollhoff and Thalmeier, 1981). Most of our calculations and all calculations for the magnetic state were therefore restricted to the $R = 0$ approximation. On the other hand, these results indicate that an $R = 0$ or d_∞ approximation should not be applied to systems with less than six neighbors.

Let's finally turn to the validity of the weak-correlation approximation. It will definitely fail around half-filling for ratios $(U/W) > 1$. In Figure 1, correlation energies in the $R = 0$ approximation are given for a ratio of $U = 0.5W$. The dashed curve gives the HF-energy costs $\Delta E_{\mathrm{SCF}} = E_{\mathrm{SCF}} - \langle H_0 \rangle$. The topmost curve gives the result of a correlation calculation performed in second-order perturbation (MP2) expansion (the LCCSD equation can be reduced to MP2 by replacing $\langle OHO \rangle$ by $\langle OH_0O \rangle$). This result overshoots the HF term and is definitely wrong. The second solid curve gives the final result in LCCSD, and the dotted curve below it gives the CI result. The maximal relative difference around half-filling amounts to 25%. When considering that the CI result is a true lower limit, the LCCSD result should not overshoot the correct result by more than 5%. The lowest curves display the energies that are lost when spin correlations are omitted. Here, the relative differences between CI and LCCSD are considerably larger but again the true result is expected to be close to the LCCSD result.

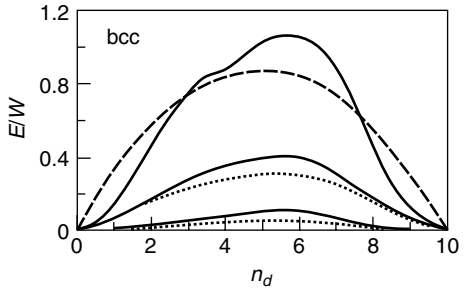

Figure 1. Several energies in units of W as a function of band filling n_d. The interaction energy costs in SCF approximation are given by the dashed line. The top full line gives the MP2 correlation result, the second full line the LCCSD result, and the dotted line just below it the CI result. The lowest full line and the dotted line below give the amount of correlation energy that is lost when the spin correlation operators are omitted from the LCCSD or CI calculations, respectively. All correlation calculations were performed for the bcc case and in the $R = 0$ approximation. (Reproduced from G. Stollhoff and P. Thalmeier: 'Variational Treatment of Electronic Correlations in d-Band Metals', *Z. Physik B* **43**, 13 (1981) with permission from Springer Science and Business Media.)

These particular features are closely connected to the degeneracy. As mentioned before, fluctuation costs arise in five channels i in the HF approximation. The correlation ansatz however makes 15 density correlation channels i, j available. Thus, treating these channels independently as is done in perturbation theory very soon overscreens the fluctuations. The term H_1 in $\langle OHO \rangle$ by which the LCCSD equations differ from MP2 guarantees that the different channels take note of each other and act coherently. This distribution of correlation corrections among many different states also makes it plausible why the CI and LCCSD results are so close to each other although five degenerate orbitals need to be treated.

For the spin correlations, the situation is different. Here each pair i, j can gain an interaction energy J independent of each other. This is reproduced in the LCCSD equations, while it is a particular feature of the CI calculations restricted to two-particle excitations that at each moment one has either the one or the other electron pair corrected. Thus, the different contributions, also the spin and density contributions actually impede each other, and a considerably smaller energy is obtained. This explains why the largest part of the difference between the two schemes in the full calculation arises from the addition of the spin correlations. On a CI level, this deficiency might only be corrected by including in the variational ansatz for the CI wave function not only 2-particle excitations but also their products, and finally up to 10-particle excitations.

The failure of MP2 found here is related to the failure of this approximation when the screening of the long-range Coulomb interactions in metals is concerned. There fluctuations are also diagonal, that is, connected to the local sites l. The correlation space, however, offers l, l' density correlations that are independent in MP2 and cause the well-known divergence of the correlation energy. The LCCSD scheme used here does not result in a divergence but it is not perfect either for the homogeneous electron gas. It generates only half of the screening of the long-range charge fluctuations (Stollhoff and Heilingbrunner, 1991).

The weak-correlation expansion used here, looks very simple, but this is not at all the case when evaluated in a diagrammatic representation. In the linear equations (17) and (18) the interaction is included in both sets of terms. In a

diagram representation, this means that infinite orders of diagrams are summed up. The LCCSD approximation includes the Tamm–Dancoff approximation plus all related exchange diagram corrections, and also contains the Kanamori limit. It does not yet contain the random phase approximation (RPA) limit (plus all exchange corrections). The RPA limit is covered by the full CCSD equations in (25) and (26).

These findings also explain why reliable Green's function results for the transition metals are rare. The only area well accessible was the almost empty or filled band case, the Kanamori limit (Liebsch, 1979, 1981; Penn, 1979; Davis and Feldkamp, 1980). For the case of Fe, one was restricted to MP2 calculations that are more or less empirically renormalized (Unger, Igarashi and Fulde, 1994; Katsnelson and Lichtenstein, 1999). Only the DMFT has made a significant progress by the use of large scale Monte Carlo computations (Lichtenstein, Katsnelson and Kotliar, 2001).

4 RESULTS FOR THE NONMAGNETIC GROUND STATE

4.1 Ground-state energies

In the last section, some specific total energy contributions have been analyzed. Here, we discuss them in more detail. The results discussed represent the bcc case, and the ratio $(U/W) = (1/2)$ is used. Also ΔJ is disregarded in the qualitative discussion for simplicity.

All total energies are related to an average interaction energy of electrons with the same occupation with localized electrons and without Hund's rule ordering:

$$E_0(n_d) = \left(U - \frac{2}{9}J\right) n_d(n_d - 1) \tag{27}$$

The Hund's rule energy gain for the ordered atoms is then

$$E_{\text{atom}}(n_d) = -\frac{7}{18} J \tilde{n}_d(\tilde{n}_d - 1) \quad \text{where} \tag{28}$$

$$\tilde{n}_d = \begin{cases} n_d \text{ for } n_d \leq 5 \\ (10 - n_d) \text{ for } n_d \geq 5 \end{cases} \tag{29}$$

The occupation dependence of this energy is shown in Figure 2 (upper full line). It is strongly peaked at $n_d = 5$. It is compared to the ground-state energy for H_0 that is contained in the figure as the lowest solid line. This figure indicates the binding due to the 3d electron delocalization. Disregarding slight shifts, the difference between these two extremal curves is a good representation of the LDA binding energy contributions of the 3d electrons. This can be seen when comparing Figure 2 with the LDA binding energy Figure 1.1 in Moruzzi, Janak and Williams (1978). Two corrections should be made. The first one is that the real atoms have occupations differing from the solids (Fe atom, $n_d = 6$ vs $n_d = 7.4$ in the model), and the second one is that the bands are narrower for the heavier elements. By setting $W = 5\,\text{eV}$, a typical binding of 2.5 eV arises.

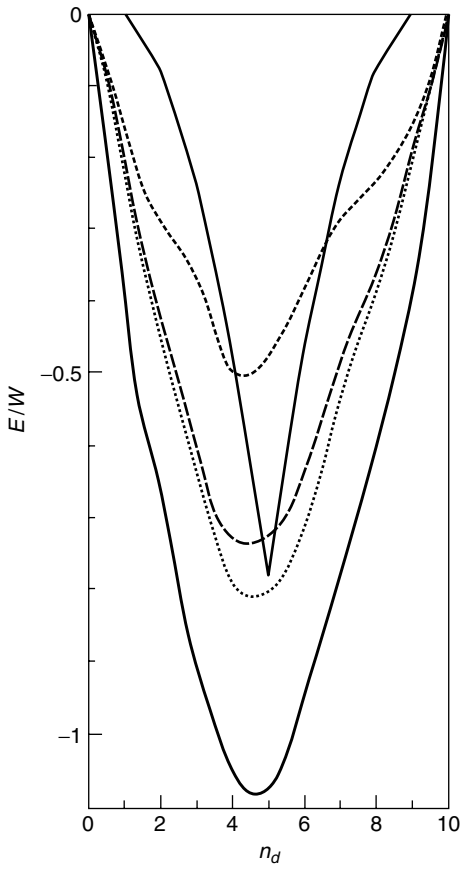

Figure 2. Energies for various approximations of the ground state in powers of W as a function of band filling n_d for the bcc case. The upper solid line represents the atomic energy, the lowest solid line the kinetic energy. The upper broken line represents the HF energy, the lower broken line, the result with density correlations included, and the dotted line, the final LA result.

The upper broken curve in Figure 2 represents the HF energy. As already mentioned, half of the band energy gain is lost. Even worse, the uncorrelated ground state is no longer binding in the occupation range from 4 to 7. The situation is corrected when the full correlation treatment is performed (dotted curve). The correlated ground state is always bound, although marginally at half-filling. This is in rough agreement with experiment, where the d-orbital contributions to the binding in Mn are not larger than 1 eV. Actually, the difference between the noninteracting and the fully correlated result matches roughly the difference between the LSDA and experimental binding energies for these cases (see again

Figure 1.1 in Moruzzi, Janak and Williams, 1978), and might well explain it as will be discussed later. The figure also contains the energy when spin correlations are omitted (lower broken curve). As can be seen, the contributions of the spin correlations to the total energy are not large but important.

4.2 Correlation functions

From our calculations, local correlation functions for the transition metals were obtained for the first time. The effects of the correlations are large, and should be basically experimentally accessible wasn't it for the yet lacking spatial resolution of X-rays, and for the too small energies of the neutrons. But it is still valuable to discuss a few theoretical results. The first correlation function is the atomic charge fluctuation Δn^2. The reduction of this quantity due to correlations is shown in Figure 3. As can be seen, it is sizable, although the electrons are not strongly correlated. This is due to the many available correlation channels. When turning to the spin correlation function S^2, one has to be aware that the autocorrelation of the electrons leads to a finite value even in the uncorrelated state. This is given as the lower broken line in Figure 3(b). Of importance is also the fully localized limit whose values of S^2 are given as the dotted line in this figure. The correlation result is given as the full line. As can be seen, spin correlations are strong, but significantly smaller than in the localized limit. They are almost halfway in between, the relative change being 0.45, almost independent of band filling. This also indicates that the proximity of the energy to the atomic limit at half-filling (see Figure 2) does not yet cause a resonance-like correlation enhancement.

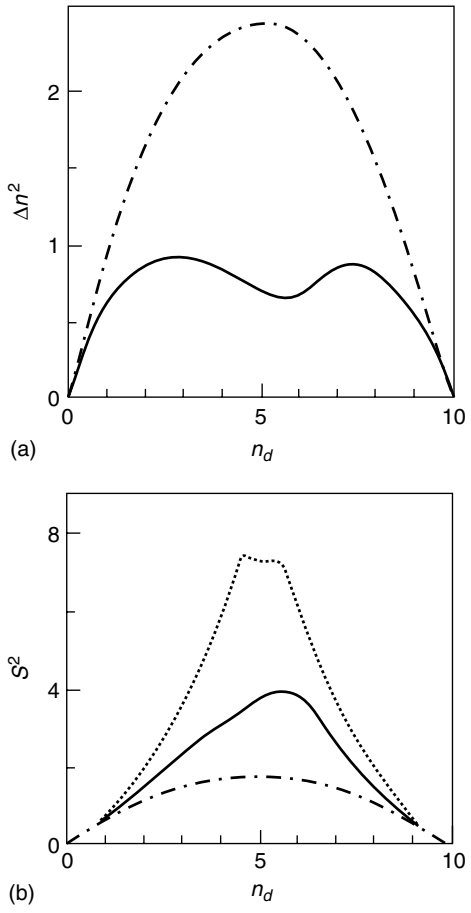

Figure 3. (a) Charge fluctuations as function of d-band filling n_d (bcc). Upper curve without correlations, lower curve with correlations included. (b) Local spin correlations S^2 as function of d-band filling n_d (bcc). Upper curve: Atomic limit, lower curve: SCF result. Full line: LA result. (Reproduced from G. Stollhoff and P. Thalmeier: 'Variational Treatment of Electronic Correlations in d-Band Metals', *Z. Physik B* **43**, 13 (1981) with permission from Springer Science and Business Media.)

This presence of relatively strong spin correlations poses the question whether these can be treated in a good approximation as quasilocal moments, whether they for example, already require a different timescale, or whether these correlations decay as fast as the electrons move, and only form a polarization cloud around the moving electrons.

The answer cannot be directly obtained from ground-state calculations. There is, however, an indirect way to address this question, where one includes short-range magnetic correlations into the LA calculation. There is no direct neighbor interaction in the Hamiltonian. Thus a strong magnetic neighbor correlation would indicate the formation of local moments, at least in cases when the nonmagnetic ground state is only metastable, and a ferromagnetic ground state exists. The calculation can be easily done by adding neighbor spin operators to the correlation treatment. This rules out an $R=0$ approximation. In the required computation, all matrix elements $P_{ij}(0,l)$ with l nearest neighbors are included, and all nearest-neighbor correlations are added up (Stollhoff, 1986).

The discussion of the obtained quantities requires some care because the nonmagnetic ground state is a singlet. This implies that the positive magnetic correlation function on the same site must be compensated by short-range antiferromagnetic correlations in order to obtain $S^2_{\rm tot}|\Psi_i\rangle = 0$, no matter whether the single particle ($i=0$) or correlated ($i=$ corr) ground state is concerned. Neighbor antiferromagnetic correlations have therefore no relevance as such, but only their eventual changes due to added degrees of freedom are of importance. Consequently, we compare for every filling every change in correlation with the maximal possible change, namely, the local moment formation. We discuss therefore the quantity

$$\Delta S^2_\delta = \frac{C(\delta) - C_0(\delta)}{S^2_{\rm loc} - S^2_0} \tag{30}$$

Here, it holds that

$$C(\delta) = \langle \Psi_{\text{corr}} | S(l) S(l+\delta) | \Psi_{\text{corr}} \rangle \tag{31}$$

$$C_0(\delta) = \langle \Psi_0 | S(l) S(l+\delta) | \Psi_0 \rangle \tag{32}$$

Figure 4 displays these relative changes. In the upper part, the relative change of the on-site spin correlation is given, in the lower part the one of the neighbor functions. The solid line displays the result without neighbor correlations that had just been discussed. The upper curve indicates on an average 45% of the maximal correlation, and the lower curve indicates the required antiferromagnetic reordering due to the on-site correlations in the neighbor function. This calculation was performed for the bcc case. As can be seen, the ratio is a slightly lesser than 1/4. Therefore additional longer-range compensation effects are expected. The most interesting result is the changes due to added neighbor correlations. The resulting curves are given in Figure 4 as dotted lines. These changes are very small. However, it is interesting that they recover the expected trends correctly. They indicate a tendency toward antiferromagnetism only around half-filling (from occupations of $3.5 < n_d < 6.5$). Apparently, the magnetic susceptibilities are slightly enhanced for the proper magnetic ordering. However, the moments themselves do not change at all, except around half-filling. Here, the stability of the nonmagnetic state is smallest, as discussed above. It should be noted that for this choice of parameters, the stable ground state is ferromagnetic for band fillings of $n_d > 7.0$.

To conclude, on-site correlations on neighbor atoms do not support each other. Barely, noticeable neighbor correlations form. These results strongly contradict a local moment assumption. The energy gain due to the added operators

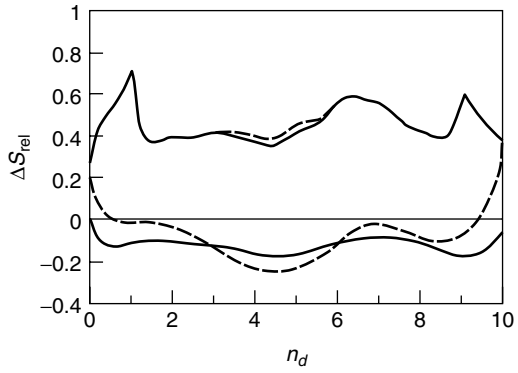

Figure 4. Relative change of the spin correlation function as function of band filling. Upper curves: change of on-site correlations, lower curves: change of neighbor correlations. Full lines without neighbor correlations, broken curves with neighbor correlations added. (Reproduced from G. Stollhoff: 'Magnetic correlations in the paramagnetic state of 3d-transition metals', *J. Magn. Magn. Mat.* 1043 (1986), copyright © 1986, with permission from Elsevier.)

is small – it amounts to less than 100 K per atom for Fe. Consequently, the strong on-site correlations cannot be interpreted as quasi static local moments. Magnetic ordering restricted to nearest neighbors does not exist in these compounds. If magnetic order exists – and it must exist – then it is only for domains considerably larger than a single atom and its neighbors. This demonstrates again that the electrons in the transition metals are delocalized, and that spin fluctuations can only exist for small moments q, as experiments demonstrate (the stiffness constant of Fe, for example, allows magnetic excitations with energies smaller than T_c only for moments q smaller than one fifth of the Brillouin zone). If there is really a need to address the strong magnetic scattering above T_c for Ni, (Brown, Deportes, Givord and Ziebeck, 1982), by methods extending beyond a critical Stoner enhancement that was computed in Steiner, Albers and Sham (1992), then this can only be done by long-range spin or order parameter fluctuation theories (Korenman, Murray and Prange, 1977; Capellmann, 1974, 1979).

4.3 Compton scattering

While experiments have not yet been able to provide information about correlation functions, they have succeeded for another quantity that displays correlation effects: the density distribution in momentum space, $n(\mathbf{k})$. The scattering intensity $I(\mathbf{q})$ measured in Compton scattering is given by the integral over all densities $n(\mathbf{k})$ with $\mathbf{kq} = \mathbf{q}^2$. The variation in $I(\mathbf{q})$ with direction $\mathbf{q}$ provides a direct measure of the anisotropy of the Fermi surface (Bauer and Schneider, 1985). These experimental results are in good qualitative agreement with Fermi surfaces obtained in LSDA for Cu (Bauer and Schneider, 1985), Va (Rollason, Cooper and Holt, 1983; Wakoh and Matsumoto, 1990), Cr (Wakoh and Matsumoto, 1990), and Ni (Anastassopoulos *et al.*, 1991) with exception of a constant scaling factor. For Fe (Rollason, Holt and Cooper, 1983; Sundararajan, Kanhere and Singru, 1991), the agreement is less good.

This constant scaling factor provides a measure of the correlation correction. In the single-particle approximation, all states with energies smaller than the Fermi energy are filled and the others are empty. This implies a maximal step at $n(\mathbf{k_F})$. This result is changed by correlations. The changes are qualitatively depicted in Figure 5(a). For simplicity let us assume that correlations cause a constant shift α in occupations for the occupied and unoccupied parts of the partially filled bands. Then this correction α can be directly extracted from the scaling factor by which experiments (correlations included) and single-particle calculations (no correlations included) differ.

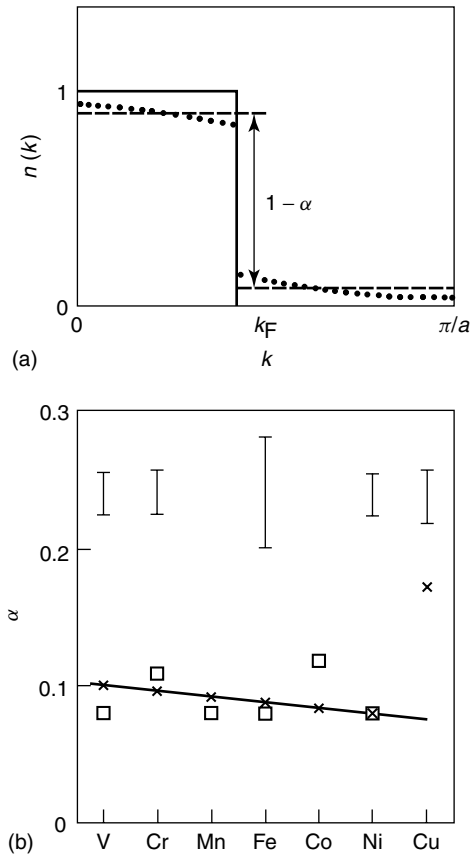

Figure 5. (a) Qualitative picture of changes in occupation around the Fermi energy owing to correlations. Dots represent the real behavior, and the dotted line the average change. (b) Values of the quantity α in the left figure for different transition metals. The bars represent the values deduced from experiment in comparison to LSDA results. Crosses give a homogeneous electron gas estimate α_{hom}, and squares give the contributions α_{LA} due to the atomic correlations of the screened d electrons alone to this value. (From Stollhoff, 1995a.)

Figure 5(b) contains the values for α for the mentioned transition metals and for Cu as deduced from experiment. As can be seen, this reduction amounts to 20–25% in all cases.

This reduction α can be compared to its counterpart α_{hom} obtained for a homogeneous system with the same average density. For its derivation, we refer to Bauer and Schneider (1985) and Stollhoff (1995a). When taking for Cu a single valence electron only (i.e., considering the d electrons as part of the core), the experimental value is regained. This indicates that as far as this property is concerned, the 4s (and 4p) electrons correlate as a homogeneous system of the same average density. For the transition metals, on the other hand, the d electrons need to be incorporated into the estimate. The resulting r_s value is much smaller than in the case of Cu which implies – within the theory of the homogeneous electron gas – a smaller reduction of the occupation. The latter amounts to less than half of the correlation effects determined experimentally.

Within our scheme, the reduction α_{LA} is obtained from the change of the expectation value of H_0, the so-called kinetic or band energy, with correlations. For the uncorrelated ground state, it holds that

$$E(\text{band})_0 = \langle \Psi_o | H_0 | \Psi_0 \rangle = \sum_{\nu\sigma} \int_{e_\nu(\mathbf{k}) \le e_F(\sigma)} d^3\mathbf{k} e_\nu(\mathbf{k}) \quad (33)$$

while the band energy of the correlated ground state is

$$E(\text{band}) = \langle \Psi_{\text{corr}} | H_0 | \Psi_{\text{corr}} \rangle = (1 - \alpha_{\text{LA}}) E(\text{band})_0 \quad (34)$$

because the model Hamiltonian is constructed such that $\text{Tr}(H_0) = 0$. Thus, the quantity α_{LA} also represents the relative change of the band or kinetic energy of the model by correlations. For the magnetic cases, the values for the magnetic ground state are selected. The interaction parameters are chosen so that they correspond to the actual transition metals. The values found indicate again that the electrons are weakly correlated. Only 10% of the kinetic energy is lost due to atomic correlations.

The restriction to this model implies that only a part of the correlation corrections α can be obtained, namely, the one that arises from the atomic correlations due to the strongly screened atomic d-electron interactions. The contributions of the screening itself to the momentum density, for example, are not included in this estimate. As can be seen from Figure 5, the particular atomic correlation contributions α_{LA} alone as derived from the model computations are as large as the total homogeneous electron gas values α_{hom}. Therefore, they must to a large extent be neglected in a homogeneous electron gas approximation as was explained before. They amount to almost half the experimental value α and can therefore explain the largest part of the deficit of a homogeneous electron gas treatment.

Correlations are included in a homogeneous electron gas approximation when LSDA calculations are performed. Such calculations must therefore lack a satisfactory description of these atomic correlations for the case of the transition metals.

5 RESULTS FOR THE MAGNETIC GROUND STATE

5.1 Parameterization of the Hubbard Hamiltonian

Of main interest in the case of the magnetic transition metals is the magnetic moment itself. So far, for Hubbard models the interaction parameters were always chosen such

Table 1. Parameters for our model (energies in electron volts). (From Oleś and Stollhoff, 1984.)

	Fe	Co	Ni
n	7.4	8.4	9.4
m	2.1	1.6	0.6
W	5.4	4.8	4.3
U	2.4	3.1	3.3

that the experimental magnetic moment was obtained. It is an indication for the accuracy of the different discussed correlation treatments that these parameters are now closely related. Global differences for the most typical value $U + 2J$ are not larger than 10% and are connected with band structure differences between five-band and nine-band models. This holds true as long as the interaction is restricted. When interactions on and between the 4s, 4p orbitals are also included, the 3d interaction also needs to be enhanced and the screening of the latter interaction by the 4s, 4p electrons is explicitly covered.

The values for W and U for our model are given in Table 1 together with the moment used. In all cases, the ratio $J = 0.2 * U$ was kept. Only for the case of Fe was U unambiguously determined from the magnetic moment. In the other cases, we had only lower limits which were 2.6 and 3.1 eV for Co and Ni, respectively. We will, in the subsequent text, make comparison between the values of U, obtained here, and the ones obtained from other sources.

5.2 Dependence of magnetism on degeneracy

The degeneracy of the energy bands of the transition metals is of vital importance for magnetism itself, and also imposes strict boundary conditions on the possible treatments. To explain this, the magnetic energy gain and its magnetic moment dependence are analyzed as a function of the represented method i for the actual moment m_0.

$$\Delta E_i(m_0) = E_i(m_0) - E_i(0) \tag{35}$$

This energy gain as a function of magnetization is rewritten in the following form:

$$\Delta E_i(m_0) = \frac{1}{4}\int_0^{m_0^2} D(m)\mathrm{d}m^2 - \frac{1}{4}\int_0^{m_0^2} I_i(m)\mathrm{d}m^2 \tag{36}$$

Here, the first term describes the loss in (noninteracting) band or kinetic energy. It holds that

$$D(0) = \frac{1}{n(E_\mathrm{F})} \tag{37}$$

is the inverse total density of states per spin at the Fermi energy. Its generalization for finite m is simple and can be found in Stollhoff, Oleś and Heine (1990). The second part describes the interaction energy gain and is defined by this function. It is a generalized Stoner parameter. The optimal magnetic moment in approximation i is defined by the condition

$$D(m_0) = I_i(m_0) \tag{38}$$

For $m_0 = 0$, this is the standard Stoner criterion, and the Stoner parameter I_i is the limiting $I_i(O)$. For a system with orbital degeneracy N and a Hubbard interaction in the form of equation (4), it holds in HF approximation

$$I_\mathrm{SCF}(m_0) = \frac{1}{N}(U + J(N+1)) \tag{39}$$

If we assume a structureless density of states with a bandwidth W, then $D(0) = W/N$, and for the single-band model the Stoner criterion in SCF approximation reads $U + 2J = W$. In a single-band Hamiltonian, the interaction terms are usually condensed into a single U, but for the degeneracy treatment we will stay in our notation. Ferromagnetism in a single-band system can therefore only be expected for a strong interaction with $U \geq W$ where correlations are important. Correlations however, strongly diminish I from I_SCF, and shift the onset of magnetism to an even larger interaction. Thus, if spurious magnetism due to peaks in the density of states is disregarded, itinerant magnetism with large moments and weak correlations can arise only for highly degenerate systems. This is why we could obtain magnetism for five-band systems with rather weak interactions of $U/W \geq 0.5$. The atomic exchange interaction J is the relevant quantity in this respect, and it requires an adequate treatment. Note that for the case with the smallest interaction, Fe, magnetism is strongly supported by a peak in the density of states, and that Fe does not become fully magnetic.

We had already mentioned that the treatment of degenerate band systems puts strong additional demands on the many-body methods used. This also is the case for magnetic properties. Figure 6 contains for the bcc Fe case the correlated Stoner parameter $I(0)$ as a function of interaction U, renormalized by the SCF Stoner parameter (roughly $(U + 6J)$) to $\overline{I}$. For $U = 0$, $\overline{I}(0)$ is therefore equal to 1, and it decreases due to correlation corrections. As can be seen, there is first a fast decrease, but then, at $U/W = 0.1$ a rigorous slowing down of the screening occurs. From the logarithmic derivative, it can be seen that the exponent changes from 2 to 1/2. This is the point where a second-order perturbation treatment is no longer sufficient, and a better approach is necessary.

Owing to these experiences we decided to include in this review neither contributions that used false degeneracies nor

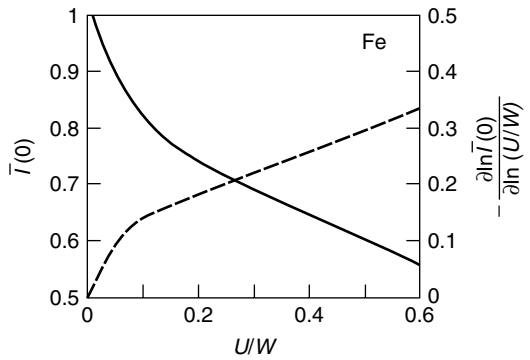

Figure 6. $I(0)$ as depending on the ratio (U/W) for Fe. In addition, the logarithmic deviation is given. (Reproduced with permission from fig. 5 in G. Stollhoff, A. M. Oles, and V. Heine: 'Stoner exchange interaction in transition metals', *Phys. Rev. B* **41**, 7028 (1990), copyright © 1990 by the American Physical Society.)

contributions that are unable to treat degenerate systems well. Therefore, we did not cover work that is based on MP2 or lowest-order diagram techniques. Besides the LA only the full CI method given in Bünemann, Weber and Gebhard (1998) and Bünemann *et al*. (2003); Kanamori t-matrix applications, and the first full application of the DMFT to the transition metals (Lichtenstein, Katsnelson and Kotliar, 2001) remained.

5.3 Magnetic energy gains, Stoner parameter, and T_c

Besides the moment that was taken from experiment, the most basic ground-state quantity connected with the broken symmetry is the magnetization energy gain ΔE.

The values of the energy gain are given in Table 2 for our calculations in the single-particle approximation, for the full treatment of correlations, and for LSDA calculations (Gunnarsson, 1976). A comparison of ΔE_{HF} and ΔE_{corr} shows how correlations reduce the magnetization energy gains. Be aware that the interactions employed are already strongly reduced screened interactions. When comparing the model and LSDA magnetic energy gains, the LSDA quantities come out twice as large for Fe and Ni. Without caring for any specific dependences on details of the density of states, this would imply a corresponding reduction in the Stoner T_c. An exception is the case of Co but here we had possibly chosen a model interaction that was too large for reasons explained in the subsequent text.

Table 2. Magnetic energy gain in HF approximation and for the correlated ground state (Oleś and Stollhoff, 1984) and from LSDA calculations (Gunnarsson, 1976). Stoner-transition temperatures from LSDA calculations (Gunnarsson, 1976), DMFT (Lichtenstein, Katsnelson and Kotliar, 2001), and experiment.

	Fe	Co	Ni
ΔE_{HF} (eV)	0.56	0.43	0.12
ΔE_{corr}	0.15	0.13	0.03
ΔE_{LSDA}	0.28	0.10	0.08
T_c(LSDA)(K)	4400	3300	2900
T_c(DMFT)	2000		700
T_c(exp)	1040	1400	631

The differences between the LA and the LSDA results can be understood by a discussion of the Stoner parameter $I(m)$. In the SCF-approximation, it holds for the degenerate band case

$$I_{\mathrm{SCF}}(m) = \frac{1}{5}(U + 6J) \tag{40}$$

(the terms ΔJ are disregarded). I_{SCF} is independent of magnetization. The function ΔE_{LSDA} contains the same expression for the kinetic energy as the quantities defined in the preceding text because in this approximation the uncorrelated kinetic energy of the reference wave function is used, and also I_{LSDA} turns out to be independent of magnetic moment. Even more important, I_{LSDA} is also essentially independent of the kind of transition-metal atom and its environment. It holds (within 10% variation) $I_{\mathrm{LSDA}} = 0.9\,\mathrm{eV}$ (Gunnarsson, 1976).

While in LSDA, the uncorrelated kinetic energy is used, and the losses in band energy due to magnetism are large, correlations reduce these losses for Fe by 30% (Stollhoff, Oleś and Heine, 1990). These corrections are included in $I(m)$. In particular, if $D(m)$ changes with m, then a partial, compensating change must occur in this function. This holds true for Fe, where it is well known that $D(m)$ strongly rises with m and cuts off the magnetic moment before the maximum. It holds that $D(m_0) = 1.6 \times D(0)$ (Stollhoff, Oleś and Heine, 1990). Correspondingly, $I_{\mathrm{corr}}(m)$ must contain a correcting change. Since $I_{\mathrm{corr}}(m_0) = D(m_0)$, it holds that $I_{\mathrm{corr}}(m_0) = 1.2 I_{\mathrm{corr}}(0)$ due to this effect alone.

There is a further interesting correction that can be seen immediately for Co where the density of states is constant and causes no m dependences in $I(m)$. Figure 7 displays the function $I_{\mathrm{corr}}(m)$, (called $I(m)$ in the figure) in comparison to $D(m)$. As can be seen, it increases sizably with m. The origin is due to spin correlations. When these are turned off in the correlation calculation, the resulting quantity $I_2(m)$ no longer displays m dependencies. Spin correlations are most relevant in the nonmagnetic state and die out in the full magnetic limit. Also contained in the figure is the quantity $I_3(m)$ which is obtained when all interaction contributions originating from J are treated in the HF approximation.

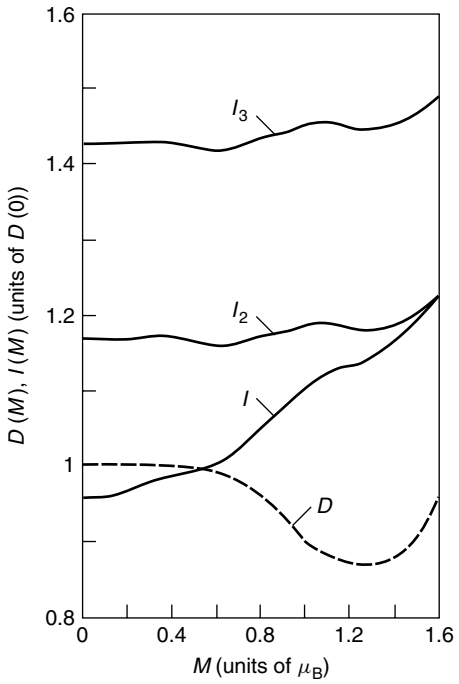

Figure 7. Kinetic energy loss function $D(M)$ in comparison to the Stoner parameter $I(M)$, obtained correctly (I), without inclusions of spin correlations I_2, and without any correlation corrections for the J contributions, I_3. (Reproduced with permission from fig. 3 in G. Stollhoff, A. M. Oles, and V. Heine: 'Stoner exchange interaction in transition metals', *Phys. Rev. B* **41**, 7028 (1990), copyright © 1990 by the American Physical Society.)

This proper treatment of Hund's rule effects which corrects the Stoner parameter, strongly contrasts to fictitious disordered local moments that result from a locally symmetry broken HF treatment of the exchange interaction. If such local moments existed in reality, then they would from the beginning prefer to order and to enhance the kinetic energy of the electrons.

The effect seen here is a quasi 'antidisordered' local moment effect. It definitely squeezes Co into a first-order magnetic phase transition. The nonmagnetic ground state for Co is even metastable at $T = 0$. It requires a polarization beyond a critical size to destabilize it toward the ground state. Consequently, we would expect that the LSDA value for the transition temperature is not only overestimated due to a missing correlation correction of the kinetic energy loss, but that the true first-order transition is considerably below that corrected quantity. We have not performed thermodynamic estimates but it looks as if the experimental T_c for Co might be reached this way. Our original choice of U for Co (Oleś and Stollhoff, 1984) had been motivated by the wish to bring Co close to a second-order phase transition.

Where Ni is concerned, our results indicate a strong reduction of the magnetic energy in comparison to LSDA. For this case, a proper thermodynamic treatment has been made in DMFT (Lichtenstein, Katsnelson and Kotliar, 2001). The Hamiltonian was very close to the one that we used, and here also a local mean field or Stoner theory was applied. The outcome was a T_c slightly above the experimental value. Also the critical spin fluctuations due to Stoner enhancement just above T_c were in good qualitative agreement with experiment. Corrections by spin-wave fluctuations that were disregarded in the DMFT calculations are definitely of relevance but have apparently little effect. One should remember, though, that the values of the interaction U are not unambiguously fixed for the Ni-model calculations. The agreement of the DMFT calculations and experiment might originate in part from a value for U that is slightly too small. On the other hand, there is again the trend that $I(m_0)$ is 20% larger than $I(m)$ (Stollhoff, Oleś and Heine, 1990), in part due to the spin correlations, and in part due to a small reduction of the change in $D(m)$. Since these two corrections are missing in LSDA calculations, one would expect that the true Stoner T_c is considerably smaller than the LSDA T_c.

For Fe, relative changes in the partial n_{e_g} and $n_{t_{2g}}$ occupations with magnetization arise as artifacts of the five-band model. These cause an enhancement of $I_{SCF}(m)$ for small m. Being only partly screened by correlations, this partially compensates the above mentioned corrections for small m. Nevertheless, a reduction of the magnetic energy by half was still found (Stollhoff, Oleś and Heine, 1990). However, this should, due to the pathology of the Fe density of states, only lead to a reduction of T_c by less than half (Gunnarsson, 1976). The DMFT calculation for a nine-band Hamiltonian for Fe produced a T_c of 2000 K (Lichtenstein, Katsnelson and Kotliar, 2001), which is unsatisfactory. Here, the interactions were unambiguously fixed, and the deficiencies of the five-band model should not occur.

Thus Fe is the only case that still poses a major problem. There are two possible scenarios for its solution: either the phase transition in Fe is not at all correctly described by a Stoner-like picture but rather by spin-wave fluctuation theories (for the earliest ones, see Korenman, Murray and Prange, 1977; Capellmann, 1974, 1979), or alternatively the starting point, the rigid band system derived from LSDA together with local Hubbard interactions is insufficient. Very recently, we obtained evidence (Stollhoff, unpublished) that the latter case holds true. Its discussion is necessary for an understanding of the limits of a Hubbard-model treatment but goes beyond the original scope of this contribution. It will therefore be shortly addressed at the end.

5.4 Anisotropic exchange splitting for Ni

For ferromagnetic Ni, an interesting anisotropy occurs. The majority bands are completely filled. The charge in

the minority bands is not equally distributed among the different 3d orbitals, but charge is missing almost exclusively from the t_{2g} orbitals which form the most antibonding band states. This anisotropic charge distribution is to a smaller amount already present for the nonmagnetic state without interaction (occupations of 0.98 or 0.92 for the e_g and t_{2g} orbitals, respectively). In the SCF approximation, already for the nonmagnetic state, an anisotropic crystal field exists. Even more interesting, for the ferromagnetic state, an anisotropic exchange splitting builds up. With exchange splitting, we refer to the difference between majority and minority crystal-field terms. In the SCF approximation, it holds for the splitting $\Delta_{\mathrm{SCF}}(i)$ (with terms in the Hamiltonian ΔJ disregarded)

$$\Delta_{\mathrm{SCF}}(i) = (U + J)(n_{i\uparrow} - n_{i\downarrow}) + Js_z \tag{41}$$

where

$$s_z = \sum_i (n_{i\uparrow} - n_{i\downarrow}) \tag{42}$$

While the second term is isotropic and amounts to 0.4 eV for Ni, the first one contributes a splitting of 0.7 eV only for the t_{2g} orbitals.

With correlations, the interaction effects are partially screened. Also, a single-particle potential is no longer unambiguously defined. We obtained approximate values from our ground-state calculations by keeping the correlation operators restricted to two-particle excitations, and by energy optimizing correlated states starting from different single-determinant trial states that were each generated with particular exchange splittings. The optimal trial state determined the ground-state exchange splitting. We obtained for Ni exchange splittings of $\Delta_{\mathrm{corr}}(e_g) = 0.15\,\mathrm{eV}$ and $\Delta_{\mathrm{corr}}(t_{2g}) = 0.57\,\mathrm{eV}$ (Oleś and Stollhoff, 1984). Actually, here interaction terms ΔJ contributed. Without them, the splittings would be 0.27 and 0.50 eV, respectively. These changes indicate a screening of the J contributions by almost half, and of the U contributions by more than half. Exchange splittings from LSDA come out isotropic and amount to 0.6 eV.

These anisotropies were measured in angle-resolved photoemission experiments (Eastman, Himpsel and Knapp, 1978; Eberhardt and Plummer, 1980) and came out as 0.1 or 0.4 eV, respectively. The agreement with our values is good particularly, if one takes into account that we computed our splitting for non-renormalized bands while in photoemission experiments the 15–20% mass renormalization due to many-body effects is included (Eastman, Himpsel and Knapp, 1980; Cooke, Lynn and Davis, 1980).

Many-body calculations for quasiparticle properties had actually been done before for a five-band Hamiltonian with very similar interactions (lacking the ΔJ contributions). This calculation was based on the Kanamori t-matrix approximation and had obtained splittings of 0.21 and 0.37 eV, with which our results agreed well. That computation had not only obtained the anisotropic splitting but also reasonable band renormalizations of 15% and even the experimentally seen shake-up peak (Liebsch, 1979, 1981). Very recently, ground-state calculations for a Hamiltonian similar to ours were performed, this time again within the $R = 0$ approximation but for a nine-band model Hamiltonian, and by a full CI calculation. The agreement for the exchange splitting was again very good (0.16 and 0.38 eV), but this time also relativistic contributions were included, and the experimental Fermi surface was reproduced with high quality (Bünemann *et al.*, 2003). Here, the anisotropic exchange splitting plays a big role, and the Fermi surface of the LSDA is false.

In the computations, such anisotropies in the exchange splitting did not show up for Co, but we found them for Fe. In Fe, the e_g orbitals carry a larger moment because the majority states are completely filled, but the minority bands are less populated than the t_{2g} analogs. We had found splittings of $\Delta(e_g) = 1.74\,\mathrm{eV}$ and $\Delta(t_{2g}) = 1.30\,\mathrm{eV}$. LSDA calculations obtain an isotropic splitting of 1.55 eV, and experiments obtain 1.45 eV (Eastman, Himpsel and Knapp, 1980) but cannot resolve an anisotropy.

6 INTERACTION PARAMETERS U

It is of interest to compare the interaction parameters U obtained for Fe to Ni to parameters obtained by other means, and to try to gain a more global understanding. Figure 8 contains these parameters as functions of the band filling.

Spectroscopy experiments for transition-metal impurities in noble metals were interpreted with the help of atomic interactions (van der Marel and Sawatzky, 1988). The values of the resulting quantity, U (or F_0, as it is called in van der Marel and Sawatzky, 1988), are given in Figure 8, too. They are in very good agreement with the values of U obtained by the LA, in particular, if one considers the different environments. This indicates that the screening patterns must be similar, and must also originate from the 4s, 4p orbitals on the one hand, or from the 5s, 5p orbitals on the other. In the impurity case, results exist for a whole range of transition metal impurities. The maximal reduction is obtained for the half-filled case (Cr) with $U = 0.9\,\mathrm{eV}$ taken from spectroscopy results, while for less then half-filling, the interaction increases again (van der Marel and Sawatzky, 1988).

The occupation dependence of U can be understood with the help of a residual neighbor electron interaction V.

It has been worked out before for a single-band model (Stollhoff, 1995b), how a Hamiltonian with on-site and

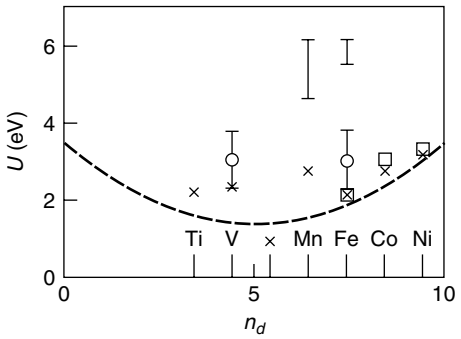

Figure 8. Values of the interaction U, obtained for different transition metals as a function of band filling. The values obtained by the LA are given as squares, the ones obtained from core spectroscopy (van der Marel and Sawatzky, 1988) are given by crosses. The full curve indicates the occupation dependence when a residual neighbor interaction V is included. Bars with circles indicate estimates of U, obtained from *ab initio* LA calculations (Stollhoff, unpublished), bars without circles estimates from frozen charge approximation computations (Anisimov and Gunnarsson, 1991; Drchal, Gunnarsson and Jepsen, 1991).

neighbor interactions,

$$H_{\text{int}} = U_0 \sum_i n_\uparrow(i) n_\downarrow(i) + \frac{V}{2} \sum_{(i,j)} a^\dagger_\sigma(i) a^\dagger_{\sigma'}(j) a_{\sigma'}(j) a_\sigma(i) \tag{43}$$

can be mapped into the Hubbard interaction $H_{\text{int}} = U \sum_i n_\uparrow(i) n_\downarrow(i)$. The sum over (i, j) runs over the z nearest neighbors j for each atom i. Here, it is implicitly assumed that all longer-range interactions are equal to zero. For the Hamiltonian with only on-site interactions, the only meaningful response to the interaction can be condensed into the expectation value $\langle n_\uparrow(i) n_\downarrow(i) H_{\text{int}} \rangle$. It is therefore plausible to choose U so that it yields the same response as the pair U_0, V. Assuming for Ψ_0 the following relations for the single-particle density matrix, $P(0) = \langle |n_\sigma(0)| \rangle = n$, $P(0, l) = \langle |a^\dagger_\sigma(0) a_\sigma(l)| \rangle \simeq p$ for (l) nearest neighbors, and zero elsewhere, one obtains

$$\langle |\overline{n_{i\uparrow} n_{i\downarrow}} H_{\text{int}}| \rangle = U_0((n(1-n))^2 + zp^4) - 2Vzn(1-n)p^2 \tag{44}$$

and

$$U = U_0 - \frac{2Vzn(1-n)p^2}{(n(1-n))^2 + zp^4} = U_0 - \alpha V \tag{45}$$

The parameter U depends therefore on band filling as well as on the number of nearest neighbors. For almost empty bands, it holds that $p \simeq n$ since $k_{\text{F}} \ll 1/(|\vec{R}_i - \vec{R}_j|)$ and consequently $U \simeq U_0$. At half-filling, it holds from $P^2 = P$, that $n \simeq n^2 + zp^2$ and therefore $\alpha = 2z/(z+1)$. For almost completely filled bands it holds that $\alpha \sim \delta n$, where δn represents the number of holes. The curve drawn into Figure 8 is based on an $U_0 = 3.5\,\text{eV}$ and a $V = 1.2\,\text{eV}$. It is deliberately put 0.5–1.0 eV below the data points. Apparently, a pair of interactions $U = 4.2\,\text{eV}$, $V = 1.2\,\text{eV}$ can replace the so far independent terms for the specific elements.

Accepting such a residual interaction V for the transition metals resolves a further problem. The LDA bandwidth for transition metals is known to roughly agree with experiment for Fe but to be too large for Co and Ni (Cooke, Lynn and Davis, 1980; Eastman, Himpsel and Knapp, 1980). The latter deficiency has been understood to arise from correlations caused by the on-site interactions (Liebsch, 1979). From model calculations with the LA (Oleś and Stollhoff, 1984; Stollhoff, Oleś and Heine, 1990), it can be deduced that the reduction of the bandwidth δW due to U is similar in all three (!) cases. The apparent discrepancy for the case of Fe can be resolved when a neighbor interaction $V = 1.2\,\text{eV}$ is included. The exchange broadening δW due to V increases the bandwidth of Fe by 10% which partly compensates the correlation correction due to U. The exchange corrections for Co and Ni are smaller since it holds again that $\delta W \sim V \delta n$.

Effective local interactions U were computed from LDA frozen charge calculations for the transition metal Fe and for Mn impurities in Ag (Anisimov and Gunnarsson, 1991; Drchal, Gunnarsson and Jepsen, 1991). They are plotted in Figure 8 as well. Apparently, these results do not depend on band filling. They are of the same size as for the case of Cu with a completely filled 3d band (Anisimov and Gunnarsson, 1991). There, they match experiment. These frozen charge calculations actually computed the interaction costs to bring two electrons together from infinite distance but not the change in interaction from a neighbor site to the same site which is the relevant quantity in a half-filled band system. It is thus not astonishing that frozen charge LDA calculations are unable to treat band filling effects on effective local interactions.

The convolution of a longer-range interaction into an on-site term alone is not sufficient to determine a model U. A model always lacks degrees of freedom that are present in the *ab initio* calculation. If degrees of freedom were removed, then there is an alternative procedure to obtain a residual local interaction U. It is to require that particular correlation properties of the model are identical to the same *ab initio* quantities. Owing to the restriction of the model interaction to atomic terms, the relevant properties are atomic correlations. For the cases discussed here, the proper representative is the change of the atomic charge fluctuations Δn^2. For the model, this quantity was discussed in Section 4.2. Exactly the same quantity can be calculated from *ab initio* calculations. There, atomic orbitals are unambiguously defined, the same operators are included into the correlation calculations, and the same correlation function is available. U is then chosen

so that the model correlation function matches the *ab initio* result. First applications have been presented in Stollhoff, 1995b. From first *ab initio* calculations, correlation functions for V and Fe are available (Stollhoff, unpublished). They lead to values of U that are also included in Figure 8. The big error bars originate from a mismatch of the five-band Hamiltonian to the correct atomic orbitals. We did not want to enter poorly described 3d orbitals with 4s and 4p tails into the *ab initio* calculations. On the other hand, lacking a general tight-binding program, we could not improve the model. Also, in our *ab initio* calculation, we did not treat the very short-range part of the correlation hole well. Thus, our *ab initio* results rather represent an upper limit to the U.

Even for these error bars, the results show that an unambiguous convolution and condensation of the full Coulomb interaction into meaningful model interactions is possible. So far, model interactions were always chosen to fit a model to experiment. We had done so for the transition metals, and had obtained good agreement, but we had encountered other cases where a particular physical effect was incorrectly connected solely to an on-site interaction, and the resulting fit led to a wrong U. The case we have in mind is polyacetylene whose bond alternations also depends on interactions but not solely on a local term U (König and Stollhoff, 1990; Stollhoff, 1995b).

Of interest is also the case of the high-T_c superconducting compounds where we had performed such an analysis (Stollhoff, 1998, 2002).

7 RELATION OF THE HUBBARD-MODEL RESULTS TO THE LSDA

In the previous sections, we had shown how difficult an adequate treatment even of model interactions is. This makes it even more astonishing that LSDA calculations managed to get sizable parts of magnetism correct, in particular, the magnetic moments of the transition metals. To a certain degree this results from the fact that the 3d electrons are not too strongly correlated, and that for the delocalized electrons extended-Hückel features prevail, which the LSDA describes well. This may explain the cases of Co and Ni, where the magnetic moment is maximal, provided the 3d-band occupation is correct.

But as our evaluations have made clear, the correct magnitude of the magnetic moment of Fe required an accuracy that the LSDA cannot possess. Consequently, the correct result can only arise due to a chance compensation of a set of errors. As was shown, the magnetic moment is determined by the Stoner parameter I, which depends equally on the local interactions U and J for fivefold degenerate systems.

Let us first sum up all contributions where U alone is relevant, and connect these to LSDA deficiencies. U dominates the strength of correlations. Owing to it, electrons lose considerably more kinetic or band energy than would be expected for a homogeneous electron gas approximation. This can be seen in the Compton scattering. From the latter, one gets the impression that a treatment based on homogeneous electron gas ideas must miss most of U.

The next topics are binding energies, equilibrium distances, and magnetovolume effect. All transition metals have LSDA binding energies that are too large – actually almost exactly by the amount which is removed by the residual U. Also the equilibrium distances are too short. The LSDA magnetovolume effect is always too large – in part, it can be corrected by effects of the residual U (Stollhoff, Oleś and Heine, 1990; Kaiser, Oleś and Stollhoff, 1988).

Finally, the interaction U causes sensitivities to charge anisotropies. This is relevant for the anisotropic exchange splitting of Ni. Owing to its effect on the Fermi surface, it is basically a ground-state property. LSDA lacks this splitting.

Consequently one may safely conclude that LSDA misses all U contributions, or more cautiously expressed, it reduces U to J (this would avoid attractive interactions). This finding, however, raises a problem. U is very important for the Stoner parameter and for the magnetic moment. Roughly half of the weight in the latter comes from U. Consequently, a second error in connection with J must occur.

J leaves a direct imprint only on a single feature, namely, the m dependence of $I(m)$. Owing to the inclusion of spin correlations, $I(0)$ is typically reduced by 10–20% in comparison to $I(m)$. Sadly, other contributions (in particular, correlation effects due to U cause a magnetic moment dependence too. There is a single exception, Co. LSDA shows no feature like this, but on the other hand, there is not yet experimental evidence for this effect.

It is worthwhile to investigate in more detail how I_{LSDA} is obtained from LSDA calculations. As mentioned before, whenever an LSDA calculation is made, even for atoms, I_{LSDA} has the same value. In the atomic case, LSDA is assumed to describe the Hund's rule ground state, and LDA is usually assumed to describe an average over all possible atomic states. Consequently, I_{LSDA} must describe just the atomic exchange J, and it must do so in a mean-field approximation – no moment without broken symmetry. In this respect, it must behave exactly like a HF theory, or like the incorrect SCF approximation of our model Hamiltonian.

Only if LSDA behaves this way can one understand why it obtains the correct moment for Fe (Stollhoff, Oleś and Heine, 1990, 1996). I depends roughly to equal parts on U and J. Correlations reduce the effects of these terms by 40% from the SCF limit. As a consequence, the error involved in skipping U (or in reducing it to J) is almost

exactly compensated by the error in not correlating J. For magnetism in general, this compensation works only for fivefold degeneracy. The error on the U side is considerably larger than the error on the J side for a single-band system. Consequently the LDA must and usually does underestimate magnetism in general.

This latter deficiency is actually known, as the popularity of more recent 'LDA plus U' approximations demonstrates. Here, a local interaction is added and treated in mean-field approximation to boost magnetism. However, all attempts to generate a kind of compensation within the DF framework to upkeep the correct magnetic moment of Fe have failed. They had to fail because the second error, the one for J is of a different origin and thus independent. Even worse, these two are not the only LDA errors in the transition-metal context as will be demonstrated in the next section.

These findings also call a particular field of LSDA applications into question, namely, all so-called *ab initio* disordered local moment calculations with which one has attempted to correct the false LSDA Stoner theory results. As just derived, these LSDA disordered local moments are nothing but the false and inadequate model disordered local moment approximations for the Hubbard model. The local degrees of freedom generated by either method are artifacts of the approximation and have no connection to reality.

The only meaningful extensions of LDA schemes are like the ones we had made for the first time a quarter century ago (Stollhoff and Thalmeier, 1981; Oleś and Stollhoff, 1984) and like those that are now made in connection with DMFT applications (Lichtenstein, Katsnelson and Kotliar, 2001): to condense the LDA results into a tight-binding Hamiltonian, to connect it to a local model interaction and to perform a careful correlation treatment of the latter.

A problem arises with the charge distributions in the ground state of these models. It is often but not always a good choice to freeze the charge distribution of this state to the one of the LDA input. Counterexamples are the changes in the Fermi surface of Ni that would not show up this way, or the inverse magnetovolume effect of Ni that arises from anisotropic exchange contributions that cause a charge transfer from the 4s, 4p to the 3d orbitals. There are also systems like the high-T_c superconductors where the LDA-charge distribution is wrong (Stollhoff, 1998, 2002). As shown next, the case of Fe is another example where it does not pay off to stay close to LSDA results even for the charge distribution.

8 *AB INITIO* CORRELATION CALCULATIONS FOR Fe

As mentioned before, the model calculations using the LA are only a special application of the original *ab initio* scheme. Here, first results of an *ab initio* calculation for nonmagnetic Fe will be presented in order to contribute to the resolution of the open problem of T_c. We address nonmagnetic Fe because we assume that the ferromagnetic state is rather well reproduced in LSDA. The moment is correct, and also the Fermi surface seems to be in agreement with experiment. The deficiencies in the description of the magnetic phase transition might instead be connected to the nonmagnetic ground state.

Like the nonmagnetic HF ground state and the LDA ground state, the correlated nonmagnetic ground state is theoretically well defined. The only possible problem in the latter case might be that the added correlations allow long-range ferromagnetic patterns, and that in the approximation used the calculations turn instable. We proceeded only up to second nearest-neighbor corrections for the case of Fe, and found no instability up to this range.

The details of the calculation will be given elsewhere (Stollhoff, unpublished). It should just be mentioned that for the HF calculation and the parallel LDA calculation the program Crystal was used (Saunders *et al*., 1998). The basis set quality was of double-ζ quality, and better for the 3d electrons, and the computation was performed at the experimental lattice constant. A first correlation calculation starting from the LDA ground state single determinant worked fine. Although the calculation was performed with the full and unscreened interaction, the electrons in the nine valence orbitals screened each other perfectly. Correlations were as weak as for the model calculation with screened interaction. Note that this time for the 9 fluctuating channels, 45 correlation channels were available.

From the 3d-correlation patterns we could also obtain an estimate on the effective local interactions, as mentioned before. This turned out to be 3 ± 1 eV and was in reasonable agreement with the interaction needed for the Hubbard-model treatment.

The LDA-charge distribution was analyzed using the LA. Within this scheme, precise atomic orbitals are required for correlation purposes. A method had been developed to unambiguously obtain these from the single-particle density matrix $P_{ij}(l, l')$ (Pardon, Gräfenstein and Stollhoff, 1995). For a similar application, see Stollhoff (1998, 2002). The two right columns of Table 3 contain our charge analysis in comparison to a standard tight-binding fit (Papaconstantopoulos, 1968). There is good agreement, except a small charge transfer from the 4p orbitals into the 3d orbitals in the case of the fit. We assume that this occurs because for the fit, the completely empty 4p bands needed to be included which probably hybridize with the 4d bands. This apparently has an effect on the resulting charge distribution. In our numerical determination, only the occupied part of the bands was of relevance. The occupation anisotropy $\Delta = n_{t_{2g}} - n_{e_g}$ which is most relevant comes out the same.

Table 3. Charge distributions for bcc nonmagnetic Fe. Given are values for the HF, LA, and LDA calculations. Also values of a LDA tight-binding fit (Papaconstantopoulos, 1968) are included.

Orbital	HF	LA	LDA	LDA(tbf)
4s	0.272	0.273	0.288	0.29
4p	0.203	0.173	0.163	0.06
3d(t_{2g})	0.966	0.715	0.678	0.73
3d(e_g)	0.100	0.542	0.611	0.66
Δ	0.866	0.173	0.067	0.07

While performing the HF calculation, a very different charge distribution was obtained. The 4s- and 4p-orbital occupations did not change but a complete charge rearrangement occurred for the 3d orbitals. The t_{2g} orbitals were almost completely filled, and the e_g orbitals almost empty. This charge distribution is definitely incorrect. It would never deliver the required sizable binding energy contributions of the 3d bands. The values for the true ground state are also given. In particular Δ is considerably closer to the LDA value.

This charge transfer represented by Δ is originally not connected to on-site interactions. Neither did our correlation calculation based on the LDA ground state show instabilities toward a charge transfer, nor had the earlier model calculations given any hint for such a behavior.

Rather, this charge transfer is due to a quantity that has been almost completely disregarded in the past: the nonlocal exchange. The long-range exchange contributions per site are formally of the form

$$\Delta E_{\text{exch}} = -\sum_{ijl} V(i,0;\,j,l)\,P_{ij}(0,l)^2 \tag{46}$$

Here, V is the Coulomb-interaction term between orbital i on site 0 and orbital j on site l, and $P_{ij}(0,l)$ the corresponding density matrix that was introduced above. For the density matrix of a single-determinant state, the following sum rule applies

$$\sum_{jl} P_{ij}(0,l)^2 = n_i \tag{47}$$

As a consequence, delocalization pushes weight from neighbor terms into longer-range terms and costs considerable exchange energy. The amount is related to the size of long-range fluctuations and depends strongly on the density of states $n(E_{\text{F}})$. The latter, and even more the peak structure around it, is very large for nonmagnetic Fe and is extremely costly in exchange energy. The peak structure is formed by antibinding e_g and t_{2g} orbitals. For the only nonlocal contribution to the LDA calculation, the kinetic energy, this peak is apparently irrelevant, but adding only a small part of the nonlocal exchange immediately starts to separate the different contributions. The e_g orbitals are pushed up, and the t_{2g} orbitals are pushed down. When computed using the LDA, then the big charge transfer toward the LA ground state costs less than 0.1 eV per atom in energy. This is negligibly small in comparison to the binding energy and still smaller than the magnetization energy. However, 1.5 eV are gained from the full exchange, and 0.3 eV remain when the latter is screened. The ground-state charge distribution is then further influenced by the strong spin correlations between the e_g electrons forming when these reach half-filling.

The most relevant quantity in our context is the resulting density of states. The LDA total density of states (summed over spins) and the one of the LA ground state are given in Figure 9. As can be seen, the LDA peak close to the Fermi energy splits and is shifted to both sides of it. $n(e_{\text{F}})$ is reduced from 3.2 to 1.1 eV^{-1}. It becomes so small that the Stoner criterion is no longer fulfilled. Consequently, there is a true metastable nonmagnetic bcc ground state for Fe, and the magnetic phase transition is of first order. Thus it is no wonder that there has been no chance to obtain a reasonable transition temperature starting from the unphysical nonmagnetic ground state of the LDA. The instability of the LDA state is such that already an admixture of only 5% of nonlocal exchange is sufficient to reduce the density of state at the Fermi energy by half.

These nonlocal exchange effects create a general trend toward weak localization. In Fe, they can act without symmetry breaking, but for single-band systems they would enter mostly via a symmetry lowering charge-density wave instability.

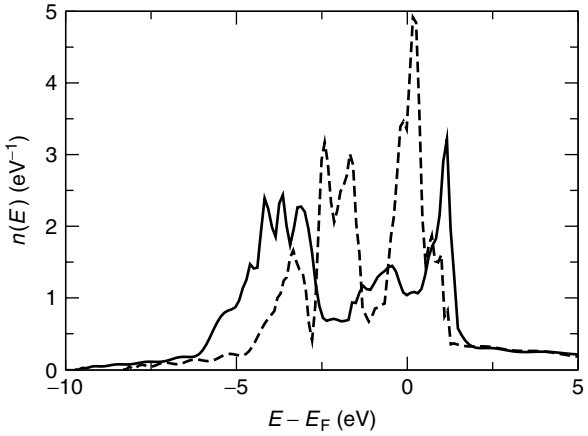

Figure 9. Total density of states $n(E)$ for bcc nonmagnetic Fe, obtained in LDA (dotted line) and by the LA (full line). E_{F} is set to zero for both cases.

The LA density of states indicates a widening of the 3d bands by 1.0 eV. It has been obtained from a single-particle calculation with such a fraction of the nonlocal exchange added that the correct charge distribution was reproduced. Neither this density of states nor the original LDA density of states contain any mass enhancements due to further many-body contributions. The latter should amount to 15–20% and shrink the bandwidths accordingly.

Sadly, no experimental information about the density of states above the magnetic transition temperature is available. They might immediately verify our results since these differ strongly from LDA, and also from the ferromagnetic results obtained either experimentally or in LSDA. There is no strong peak just below the Fermi energy either, as it originates from the majority states in the ferromagnetic case.

There is an experiment, though, that can be explained by these new results: the measurements of the unoccupied Fe energy bands (Kirschner, Gloebl, Dose and Scheidt, 1984).

For this purpose, the energy bands of the LDA and of the LA ground state are presented in Figure 10.

The full lines represent the LA case, and the dotted lines the LDA case. This time, the LA bands have been renormalized so that the occupied width matches the LDA case, in order to facilitate comparison. The renormalization factor is 0.8, and may be deduced from Figure 9. As can be seen, nonlocal exchange has pushed the bands with e_g-character around E_F roughly 1 eV above E_F, while bands with t_{2g} character are a little lowered (around the H and N points). This explains the changes in the density of states.

It is of interest to compare the energy bands of the true nonmagnetic state with the ones of the ferromagnetic ground state. The latter can be derived from the LDA bands by either an upward shift by 1 eV for the minority bands or a downward shift by the same amount for the majority bands. As a consequence, the unoccupied minority bands are almost exactly where the corresponding nonmagnetic bands are. An exception is the H point where minority and majority bands enclose the nonmagnetic band asymmetrically.

With temperature increasing toward T_c, the unoccupied minority bands are therefore expected to stay in place while the bands around the H points are shifted. This is exactly what has been measured. The unoccupied minority and majority bands around the H point are shifted towards a center position, the former slightly more. The minority bands measured in the vicinity of the P point and in between N and P points did not shift at all, however (Kirschner, Gloebl, Dose and Scheidt, 1984). These experiments fully confirm our results for the nonmagnetic ground state.

So far, the experimental results have been interpreted differently. It has been speculated that parts of the magnetic order do not break down when T_c is reached, and that certain directions in momentum space might keep a magnetic memory for some unknown reasons. It would be worthwhile to reanalyze the experimental data and also to extract how the majority bands become unfilled and jump towards the true nonmagnetic bands.

The proper computation of the first order phase transition remains a topic to be adressed in the future. On the model level, this would imply the inclusion of at least neighbor interactions,

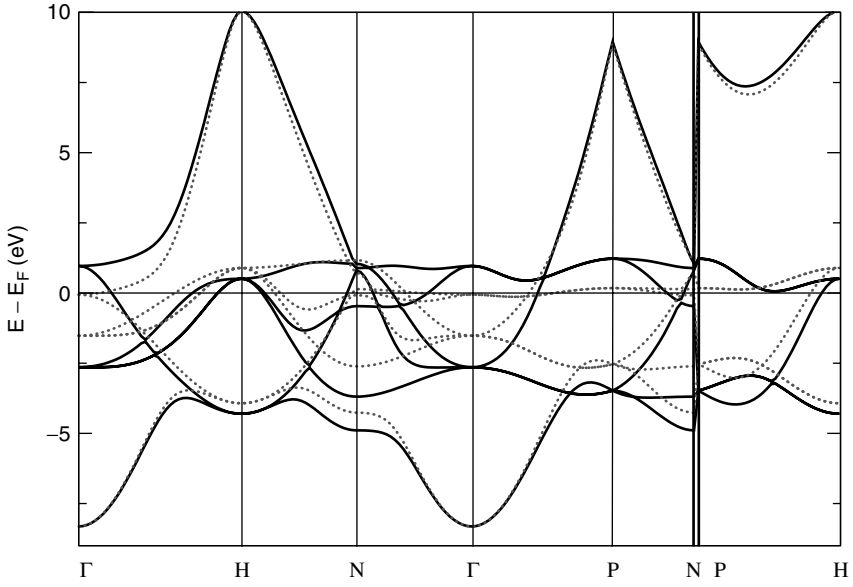

Figure 10. Energy bands of nonmagnetic bcc Fe from the LDA calculation (dots) and from the LA calculation (full lines). The occupied bandwidth of the latter bands is renormalized to the one of the LDA bands.

and is definitely out of the range for the present DMFT. Further speculations on giant spin fluctuation theories should be put on hold, however, because it is very probable that they will never be needed for Fe, either.

We do not expect that nonlocal exchange contributions play a role for the ferromagnetic ground state of Fe, except for a certain band widening as discussed above (this is also why we have rescaled the LA bands to the LDA bands in Figure 10). $n(E_F)$ is already rather low for the ferromagnetic case. The role of nonlocal exchange contributions shrinks further when dealing with more strongly occupied bands as for Co and Ni. Also, there is no peak in the density of states at the Fermi energy in these systems that might be removed.

On the other hand, we expect that these nonlocal exchange contributions play a significant role for the Fe compounds. It is known that the LSDA usually does not treat these correctly, but it does so without an apparent systematic trend. The Fe–O compounds come out more magnetic in reality than using the LSDA while for the Fe–Al compounds the inverse holds true. In all these cases, there is a sizable crystal field that Fe itself lacks. This would make these compounds even more susceptible to a charge redistribution and accompanying weak localization than Fe itself.

There is not only a competition between nonmagnetic and magnetic states for the transition metals, but also one between more or less weakly localized states. While the interactions behind the former competition are U and J, the ones behind the latter are V.

9 CONCLUSION

The aim of this work has been to present theoretical achievements in the computation of multiband Hubbard models for transition metals. Luckily, this application turned out to be sufficiently remote from any kind of Mott–Hubbard transition so that currently well-controlled weak-correlation expansions could be used. As a consequence, we can be certain that a model and not a deficiency in the treatment is responsible if we do not match experiment. We could exclude a strong correlation scenario for a set of experimental findings, but the strongest argument against this scenario is the not fully magnetized ground state of Fe.

This weak-correlation scenario also made it possible to connect with LSDA calculations, and to analyze and explain a set of errors, even failures of the latter method.

Our findings indicate the seeming success of LSDA for the magnetism of the transition metals is basically due to a chance compensation of two big errors, an overscreening of U on the one hand, and a mishandling of the atomic exchange interaction J in a mean-field approximation on the other.

We have shown that these model interactions are of very similar size when obtained from fits to different experiments, and that it is even possible to understand the trend among these values for different transition metals. This indicates that these model interactions are more meaningful quantities than just fitting parameters. We have also given an indication of how these parameters will, in the future, be directly computed from *ab initio* correlation calculations using the LA.

On the model level, a set of different properties could be understood. Also with the help of more extensive CI calculations (Bünemann *et al*., 2003), and in particular, thanks to quasiparticle calculations using the DMFT (Lichtenstein, Katsnelson and Kotliar, 2001), a basic understanding has finally been reached of the problems that had been raised half a century ago (Stoner, 1938; van Vleck, 1945; Wohlfarth, 1949; Gutzwiller, 1965; Herring, 1966), and that had been mostly put aside in the last 40 years as far as the DF approach was concerned.

We now know that the magnetic phase transition of the transition metals can basically be described following the ideas of Stoner and Wohlfarth, and that the electrons stay almost completely delocalized. We also know that orbital degeneracy plays the most important role in this context, and that the atomic exchange interaction is of great importance.

A very surprising twist is that for the magnetism of Fe, also residual nonlocal interactions seem to be relevant. There has been earlier evidence that they are present in Fe, originating from trends in the dependence of U on the individual atoms, and from matches and mismatches of theoretical and experimental photoemission results. These nonlocal interaction contributions lead to big changes of the LDA results for the nonmagnetic ground state, although those latter results were and still are the basis of a satisfying description of the ferromagnetic ground state.

All these findings demonstrate how important it is to understand and to treat the interactions of the electrons directly. It is an advantage of the LA that the correlation treatment does not disappear within the black box of a numerical program but that all different correlation details can be obtained directly and understood. One aim of this contribution was to present, with the help of the LA, a lucid and understandable decomposition of the complex many-body world.

REFERENCES

Anastassopoulos, D.L., Priftis, G.D., Papanicolaou, N.I., *et al*. (1991). Calculation of the electron moment density and Compton scattering measurements for Ni. *Journal of Physics: Condensed Matter*, **3**, 1099.

Andersen, O.K. and Jepsen, O. (1977). Advances in the theory of one-electron energy states. *Physica*, **B 91**, 317.

Anisimov, V.I. and Gunnarsson, O. (1991). Density-functional calculation of effective Coulomb interactions in metals. *Physical Review B*, **43**, 7570.

Bauer, G.E. and Schneider, J.R. (1985). Electron correlation effect in the momentum density of copper metal. *Physical Review*, **B 31**, 681.

Brown, P.J., Deportes, D., Givord, D. and Ziebeck, K.R.A. (1982). Paramagnetic scattering studies of the short-range order above T_c in 3*d* transition metals compounds and pure Fe. *Journal of Applied Physics*, **53**, 1973.

Bünemann, J., Gebhard, F., Ohm, T., *et al*. (2003). Atomic correlations in itinerant ferromagnets: quasi-particle bands of Ni. *Europhysics Letters*, **61**, 667.

Bünemann, J., Weber, W. and Gebhard, F. (1998). Multiband Gutzwiller wave functions for general on-site interactions. *Physical Review B*, **57**, 6896.

Callaway, J. (1981). *Physics of Transition Metals*, Institute of Physics: Bristol.

Capellmann, H. (1974). Ferromagnetism and strong correlations in metals. *Journal of Physics*, **F 4**, 1466.

Capellmann, H. (1979). Theory of itinerant ferromagnetism in the 3*d*-transition metals. *Zeitschrift fur Physik*, **B 34**, 29.

Cizek, J. (1966). On the correlation problem in atomic and molecular physics. *Journal of Chemical Physics*, **45**, 4256.

Cizek, J. (1969). Use of the cluster expansion and the technique of diagrams in calculations of correlation effects in atoms and molecules. *Advances in Chemical Physics*, **14**, 35.

Coester, F. (1958). Bound states of a many-particle system. *Nuclear Physics*, **7**, 421.

Coester, F. and Kümmel, H. (1960). Short-range correlations in nuclear wave functions. *Nuclear Physics*, **17**, 477.

Cooke, J.F., Lynn, J.W. and Davis, H.L. (1980). Calculations of the dynamic susceptibility of Ni and Fe. *Physical Review*, **B 21**, 4118.

Davis, L.C. and Feldkamp, L.A. (1980). Quasi-particle energies and two-hole xps satellite in Ni. *Solid State Communications*, **34**, 141.

Drchal, V., Gunnarsson, O. and Jepsen, O. (1991). Effective Coulomb interaction in metallic 3*d*-systems: comparison of theory and experiment for Mn in Ag. *Physical Review B*, **44**, 3518.

Eastman, D.E., Himpsel, F.J. and Knapp, J.A. (1978). Experimental band structure and temperature-dependent magnetic exchange splitting of Ni using angle-resolved photoemission. *Physical Review Letters*, **40**, 1514.

Eastman, D.E., Himpsel, F.J. and Knapp, J.A. (1980). Experimental exchange-split energy-band dispersions for Fe, Co, Ni. *Physical Review Letters*, **44**, 95.

Eberhardt, W. and Plummer, E.W. (1980). Angle-resolved photoemission determination of the band structure and multielectron excitations in Ni. *Physical Review*, **B 21**, 3245.

Friedel, J. (1969). *The Physics of Metals*, Cambridge University Press: Cambridge.

Gunnarsson, O. (1976). Band model for magnetism of transition metals in the spin-density-functional formalism. *Journal of Physics F*, **6**, 587.

Gunnarsson, O. and Lundqvist, B.I. (1976). Exchange and correlation in atoms, molecules, and solids by the spin-density-functional formalism. *Physical Review*, **B13**, 4274.

Gutzwiller, M.C. (1965). Correlation of electrons in a narrow *s* band. *Physical Review*, **137**, 1726.

Heilingbrunner, A. and Stollhoff, G. (1993). Ab-initio correlation calculation for metallic lithium. *Journal of Chemical Physics*, **99**, 6799.

Herring, C. (1966). In *Magnetism*, Rado, G. and Suhl, H. (Eds.), Academic Press.

Hohenberg, P. and Kohn, W. (1964). Inhomogeneous electron gas. *Physical Review*, **136**, 864.

Janak, J.F. and Williams, A.R. (1976). Giant internal magnetic pressure and compressibility anomalies. *Physical Review*, **B14**, 4199.

Jastrow, R. (1955). Many-body problem with strong forces. *Physical Review*, **98**, 1479.

König, G. and Stollhoff, G. (1990). Why polyacetylene dimerizes: results of ab initio computations. *Physical Review Letters*, **65**, 1239.

Kaiser, A.B., Oleś, A.M. and Stollhoff, G. (1988). Volume dependence of the Stoner parameter in transition metals. *Physica Scripta*, **37**, 935.

Kajzar, F. and Friedel, J. (1978). Role of the intraatomic Coulomb correlation on the energy of cohesion in narrow band metals. *Journal de Physique*, **39**, 397.

Kanamori, J. (1963). Electron correlation and ferromagnetism in transition metals. *Progress of Theoretical Physics*, **30**, 275.

Katsnelson, M.I. and Lichtenstein, A.I. (1999). LDA++approach to the electronic structure of magnets: correlation effects in Fe. *Journal of Physics: Condensed Matter*, **11**, 1037.

Kirschner, J., Gloebl, M., Dose, V. and Scheidt, H. (1984). Wave-vector-dependent temperature behaviour of empty bands in ferromagnetic iron. *Physical Review Letters*, **53**, 612.

Kleinmann, L. and Mednick, K. (1981). Self-energy contributions to the electronic structure of Ni. *Physical Review*, **B24**, 6880.

Kohn, W. and Sham, L.J. (1965). Self consistent equations including exchange and correlation effects. *Physical Review*, **140**, 1133.

Korenman, V., Murray, J.L. and Prange, R.E. (1977). Local band theory of itinerant ferromagnetism. I Fermi-liquid theory. *Physical Review*, **B16**, 4032.

Lichtenstein, A., Katsnelson, M.I. and Kotliar, G. (2001). Finite-temperature magnetism of transition metals: an ab initio dynamical mean-field theory. *Physical Review Letters*, **87**, 067205.

Liebsch, A. (1979). Effect of self-energy on the valence-band photoemission spectra of Ni. *Physical Review Letters*, **43**, 1431.

Liebsch, A. (1981). Ni *d*-band self-energy beyond the low-density limit. *Physical Review*, **B23**, 5203.

van der Marel, D. and Sawatzky, G.A. (1988). Electron-electron interaction and localization in *d* and *f* transition metals. *Physical Review B*, **37**, 10674.

Moriya, T. (Ed.) (1981). *Electron Correlation and Magnetism in Narrow Band Systems*, *Springer Series in Solid-State Science, Vol 29*, Springer: Berlin.

Moriya,T. (1985). *Spin Fluctuations in Itinerant Electron Magnetism*, *Springer Series in Solid-State Science, Vol 56*, Springer: Berlin.

Moruzzi, V.L., Janak, J.F. and Williams, A.R. (1978). *Calculated Electronic Properties of Metals*, Pergamon Press: New York.

Oleś, A.M. and Stollhoff, G. (1984). Correlation effects in ferromagnetism transition metals. *Physical Review B*, **29**, 314.

Oleś, A.M. and Stollhoff, G. (1988). Correlation corrections for the Stoner parameter of ferromagnetic transition metals. *Europhysics Letters*, **5**, 175.

Papaconstantopoulos, D.A. (1968). *The Band Structure of Elemental Solids*, Plenum Publishing: New York.

Pardon, R., Gräfenstein, J. and Stollhoff, G. (1995). Ab initio ground-state correlation calculations for semiconductors with the local ansatz. *Physical Review B*, **51**, 10556.

Penn, D. (1979). Effect of bound hole pairs on the *d*-band photoemission spectrum of Ni. *Physical Review Letters*, **42**, 921.

Poulson, U.K., Kollar, J. and Anderson, O.K. (1976). Magnetic and cohesive properties from canonical bands. *Journal of Physics*, **F6**, L 241.

Rollason, A.J., Cooper, M. and Holt, R.S. (1983). Directional Compton profiles and the electron density distribution in V. *Philosophical Magazine*, **B 47**, 51.

Rollason, A.J., Holt, R.S. and Cooper, M.J. (1983). Directional Compton profiles and the electron density distribution in Fe. *Journal of Physics*, **F 13**, 1807.

Saunders, V.R., Dovesi, R., Roetti, C., *et al*. (1998). *Crystal98 User's Manual*, University of Torino.

Steiner, M.M., Albers, R.C. and Sham, L.J. (1992). Quasiparticle properties of Fe, Co, and Ni. *Physical Review*, **B 45**, 13272.

Stollhoff, G., unpublished.

Stollhoff, G. (1986). Magnetic correlations in the paramagnetic state of 3*d*-transition metals. *Journal of Magnetism and Magnetic Materials*, **54–57**, 1043.

Stollhoff, G. (1995a). Compton scattering and electron correlations in the transition metals. *Europhysics Letters*, **29**, 463.

Stollhoff, G. (1995b). From ab-initio calculations to the Hubbard model and beyond. *Europhysics Letters*, **30**, 99.

Stollhoff, G. (1996). The local ansatz extended. *Journal of Chemical Physics*, **105**, 227.

Stollhoff, G. (1998). Electrons in high-T_c compounds: ab-initio correlation results. *Physical Review B*, **58**, 9826.

Stollhoff, G. (2002). Electron correlations in the high-T_c compounds, *Proceedings of CIMTEC 2002 Forum on New Materials*, Florence, 3, p. 229.

Stollhoff, G. and Fulde, P. (1980). On the computation of electronic correlation energies within the local approach. *Journal of Chemical Physics*, **73**(9), 4548.

Stollhoff, G. and Heilingbrunner, A. (1991). Coupled-cluster equations for the local ansatz. *Zeitschrift fur Physik*, **B83**, 85.

Stollhoff, G., Oleś, A.M. and Heine, V. (1990). Stoner exchange interaction in transition metals. *Physical Review B*, **41**, 7028.

Stollhoff, G., Oleś, A.M. and Heine, V. (1996). Comment on relationship between the Coulomb integral U and the Stoner parameter I. *Physical Review Letters*, **76**, 855.

Stollhoff, G. and Thalmeier, P. (1981). Variational treatment of electronic correlations in *d*-band metals. *Zeitschrift fur Physik B*, **43**, 13.

Stoner, E.C. (1938). Collective electron ferromagnetism. *Proceedings of the Royal Society of London, Series A*, **165**, 372.

Sundararajan, V., Kanhere, D.G. and Singru, R.M. (1991). Calculation of spin-dependent momentum distributions in Fe: Compton scattering and positron annihilation. *Journal of Physics: Condensed Matter*, **3**, 1113.

Treglia, G., Ducastelle, F. and Spanjaard, D. (1980). Perturbation treatment of correlations in transition metals. *Journal de Physique*, **41**, 281.

Unger, P., Igarashi, J. and Fulde, P. (1994). Electronic excitations in 3*d* transition metals. *Physical Review B*, **50**, 10485.

van Vleck, J.H. (1945). *Reviews of Modern Physics*, **17**, 27.

Vollhardt, D., Blümer, N., Held, K., *et al*. (1999). Metallic ferromagnetism: progress in our understanding of an old strong-coupling problem. *Advances in Solid State Physics*, **38**, 383.

Wakoh, S. and Matsumoto, M. (1990). Correlation correction on Compton profiles of V and Cr. *Journal of Physics Condensed Matter*, **2**, 797.

Wohlfarth, E.P. (1949). Collective electron ferromagnetism III nickel and nickel-copper alloys. *Proceedings of the Royal Society of London, Series A*, **195**, 434.

Dynamical Mean-field Theory of Itinerant Electron Magnetism

Alexander I. Lichtenstein[1] and Mikhail I. Katsnelson[2]

[1] *Universität Hamburg, Hamburg, Germany*
[2] *Radboud University Nijmegen, Nijmegen, The Netherlands*

1 INTRODUCTION

The theory of electronic structure and magnetism of solids has historically been split into two distinct parts, namely, the model investigations of many-body effects and the calculations of the energy spectra and properties of specific compounds in the framework of density functional theory (DFT) (Hohenberg and Kohn, 1964; Kohn and Sham, 1965; Jones and Gunnarsson, 1989). Recently, within the dynamical mean-field theory (DMFT, for a review see Georges, Kotliar, Krauth and Rozenberg, 1996) correlation effects have been incorporated into realistic electronic structure calculations (Anisimov *et al*., 1997; Lichtenstein and Katsnelson, 1997, 1998; Katsnelson and Lichtenstein, 1999, 2000; Chitra and Kotliar, 2000; Held *et al*., 2001b; Lichtenstein and Katsnelson, 2001; Lichtenstein, Katsnelson and Kotliar, 2002; Savrasov and Kotliar, 2004; Kotliar and Vollhardt, 2004). This method has been successfully applied to a number of classical problems of solid state physics such as the finite-temperature magnetism of iron group metals (Lichtenstein, Katsnelson and Kotliar, 2001), $\alpha - \delta$ transition in plutonium (Savrasov, Kotliar and Abrahams, 2001), and electronic structure of doped Mott insulators (Held *et al*., 2001a). In contrast with the standard DFT scheme, in this new approach known as *local density approximation* (LDA)+DMFT (Anisimov *et al*., 1997; Lichtenstein and Katsnelson, 1997, 1998), the total energy of the system (or, more accurately, thermodynamic potential Ω) is considered as a functional of the local Green function instead of the density matrix (Katsnelson and Lichtenstein, 2000; Chitra and Kotliar, 2000; Lichtenstein and Katsnelson, 2001; Lichtenstein, Katsnelson and Kotliar, 2002; Savrasov and Kotliar, 2004). To stress this new feature more explicitly, we will use the term *spectral density functional* (SDF). The analytical properties of the Green function guarantee that the knowledge of the spectral density is equivalent to the knowledge of the time-dependent Green function whereas, the density matrix is just the static value of the latter (Abrikosov, Gorkov and Dzyaloshinski, 1975). Here we will describe the basic ideas of the SDF method, both in the framework of standard DMFT and from a more general point of view, and consider the applications of SDF to the correlation effects and

Handbook of Magnetism and Advanced Magnetic Materials. Edited by Helmut Kronmüller and Stuart Parkin. Volume 1: *Fundamentals and Theory*. ISBN: 978-0-470-02217-7.

magnetism in transition metals and other itinerant-electron magnets.

2 REALISTIC DESCRIPTION OF MAGNETIC CRYSTALS USING DYNAMICAL MEAN-FIELD THEORY

2.1 LDA+DMFT: general considerations

In order to calculate the electronic structure of strongly correlated systems, we have to solve a complicated many-body problem for a crystal corresponding to the inhomogeneous gas of interacting electrons in an external periodic potential. To this aim, the original problem is split into effective *one-particle* problem for the crystal (in DFT approach this is the Kohn–Sham equation, Hohenberg and Kohn, 1964; Kohn and Sham, 1965; Jones and Gunnarsson, 1989) and a many-body problem for some appropriate auxiliary system (for LDA to DFT this is a homogeneous electron gas). Since intra-atomic electron correlations are the strongest and the most important for local-moment formations in metals, we will use DMFT approach as a best local approximation. The DMFT scheme (Georges, Kotliar, Krauth and Rozenberg, 1996) maps the interaction lattice models into *quantum impurity* models (see Figure 1) subject to a self-consistency condition. This quantum impurity is an atom in a self-consistent effective medium. In this sense, the DMFT approach is complementary to the LDA stressing from the beginning atomic-like features in the electronic structure. The resulting many-body multi-orbital impurity problem can be solved by various rigorous approaches (Quantum Monte Carlo (QMC), exact diagonalization, etc.) or by approximate schemes such as iterated perturbation theory (IPT), local fluctuating exchange (FLEX) approximation, or noncrossing approximation (NCA) (Georges, Kotliar, Krauth and Rozenberg, 1996; Lichtenstein and Katsnelson, 1997, 1998; Held *et al*., 2001b; Lichtenstein and Katsnelson, 2001; Lichtenstein, Katsnelson and Kotliar, 2002).

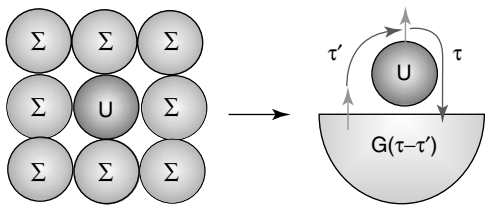

Figure 1. Mapping of the lattice model to the quantum impurity model in the dynamical mean-field theory: the local self-energy one can be obtained from the solution of one correlated site in effective time-dependent fermionic bath $\mathcal{G}(\tau - \tau')$.

In this section, we describe LDA+DMFT approach for the electronic structure calculations. The method was first applied in a simplified one-band approximation to $La_{1-x}Sr_xTiO_3$ (Anisimov *et al*., 1997) which is a classical example of a strongly correlated metal. A general formulation of LDA+DMFT, including the justification of the effective impurity formulation in multiband case has been proposed in Lichtenstein and Katsnelson (1997, 1998) and applied to iron in Katsnelson and Lichtenstein (1999, 2000).

The simplest way to develop the LDA+DMFT scheme is to start with the band-structure approach where an explicit tight-binding Hamiltonian exist, such as a first-principle linear muffin-tin orbital (LMTO) tight-binding method (Andersen, 1975; Andersen and Jepsen, 1984):

$$H_0 = \sum_{ilm,jl'm',\sigma} (\epsilon_{il}\, n_{ilm\sigma}\delta_{ilm,jl'm'} + t_{ilm,jl'm'}\, c^{\dagger}_{ilm\sigma}\, c_{jl'm'\sigma}) \tag{1}$$

where i is site index, lm are orbital indices and σ is spin index, c^+, c are the Fermi creation and annihilation operators ($n = c^+c$); ϵ_{il} are orbital energies and $t_{ilm,jl'm'}$ are hopping matrix elements. Note that the DMFT approach was also implemented in the full-potential LMTO method (Savrasov and Kotliar, 2004) and in multiple-scattering methods such as exact muffin-tin orbital (EMTO) (Chioncel *et al*., 2003b) or Korringa–Kohn–Rostoker (KKR) (Minár *et al*., 2005) schemes.

The LDA one-electron potential (Kohn–Sham potential) is orbital independent and the Coulomb interaction between d-electrons is taken into account in this scheme in an averaged way. In the LDA+DMFT method, as well as in the static limit, which corresponds to LDA+U (Anisimov, Aryasetiawan and Lichtenstein, 1997), this Hamiltonian is generalized for the explicit local Coulomb correlations with the additional interaction term for correlated il shell:

$$H_{int} = \frac{1}{2}\sum_{ilmm'\sigma} U^{il}_{mm'} n_{im\sigma} n_{im'-\sigma} + \frac{1}{2}\sum_{ilm\neq m'\sigma} (U^{il}_{mm'} - J^{il}_{mm'}) n_{im\sigma} n_{im'\sigma} \tag{2}$$

where i is the site index and m is the orbital quantum numbers; $\sigma = \uparrow, \downarrow$ is the spin projection; ϵ and t in equation (1) are effective one-electron energies and hopping parameters obtained from the LDA in the orthogonal LMTO basis set. To avoid double counting of electron–electron interactions one must subtract the averaged Coulomb interaction energy term, which is present in the LDA. In the spirit of LDA+U, we introduce new ϵ^0_d where the d–d Coulomb interaction is excluded. There are few possibilities to subtract the double-counting term coming from average interactions already

taking into account in the LDA: the so-called *fully localized limit* (Anisimov *et al*., 1993; Anisimov, Aryasetiawan and Lichtenstein, 1997) which is suitable for strongly correlated materials and the so-called *around mean field* (Anisimov, Zaanen and Andersen, 1991; Czyzyk and Sawatzky, 1994) which is appropriate for more delocalized systems. We used the first scheme, which corresponds to the following form of subtraction of average atomic Coulomb (U) and exchange (J) interactions

$$\epsilon^0_{d\sigma} = \epsilon_{d\sigma} - U\left(n_d - \frac{1}{2}\right) + \frac{1}{2}J\left(n^\sigma_d - \frac{1}{2}\right) \tag{3}$$

where U and J are the average values of $U_{mm'}$ and $J_{mm'}$ matrices and n_d is the average number of d-electrons.

The screened Coulomb and exchange vertex for the d-electrons are defined as

$$\begin{aligned} U_{mm'} &= <mm'|V_{ee}(\mathbf{r}-\mathbf{r}')|mm'>, \\ J_{mm'} &= <mm'|V_{ee}(\mathbf{r}-\mathbf{r}')|m'm> \end{aligned} \tag{4}$$

Then, the new Hamiltonian will have the following form:

$$\begin{aligned} H &= H_0 + H_{int} \\ H^0 &= \sum_{ilm,jl'm,'\sigma} (\epsilon^0_{il} n_{ilm\sigma}\delta_{ilm,jl'm'} + t_{ilm,jl'm'} c^\dagger_{ilm\sigma} c_{jl'm'\sigma}) \end{aligned} \tag{5}$$

In reciprocal space the matrix elements of the operator H^0 are

$$\begin{aligned} H^0_{qlm,q'l'm'}(\mathbf{k}) = H^{LDA}_{qlm,q'l'm'}(\mathbf{k}) - \delta_{qlm,q'l'm'}\delta_{ql,i_dl_d} \\ \times\left[U\left(n_d - \frac{1}{2}\right) - \frac{1}{2}J\left(n^\sigma_d - \frac{1}{2}\right)\right] \end{aligned} \tag{6}$$

(q is an index of the atom in the elementary unit cell). It is worthwhile to note that the method can also be formulated with a complete rotationally invariant LDA+U Hamiltonian where the interaction is described by complete *four* orbital indices (Lichtenstein and Katsnelson, 1997, 1998; Katsnelson and Lichtenstein, 1999).

One of the main difficulties of standard DFT approach in describing the finite-temperature magnetism is related with the problem of unknown temperature dependence of exchange-correlation potential. In practice, it is not difficult to take into account the Stoner-like temperature effects into the electronic structure calculations via the Fermi distribution function. However, it is well known, that the Bose degrees of freedom such as spin fluctuations are the dominant temperature dependent effects. At the same time both Fermi and Bose excitations can be easily treated in the framework of the SDF using standard many-body Green function approach. For describing the correlations effects in magnets we will use the finite-temperature Matsubara formalism (Abrikosov, Gorkov and Dzyaloshinski, 1975). In the local, frequency dependent, dynamical mean-field theory, the effect of Coulomb correlation is described by the self-energy matrix $\Sigma(i\omega_n)$ in the basis of correlated atomic orbitals. Our main goal within the finite-temperature formalism is to obtain the one-electron Green functions $G_{m,m'}(\tau - \tau') = -\langle T_\tau c^\dagger_m c_{m'}\rangle$ which describe all single particle dynamics of many-body systems (Abrikosov, Gorkov and Dzyaloshinski, 1975). The inverse Green function matrix is defined as

$$\begin{aligned} G^{-1}_{qlm,q'l'm'}(\mathbf{k}, i\omega_n) = (i\omega_n + \mu)\delta_{qlm,q'l'm'} - H^0_{qlm,q'l'm'}(\mathbf{k}) \\ -\delta_{ql,q'l'}\delta_{ql,i_dl_d}\Sigma_{m,m'}(i\omega_n) \end{aligned} \tag{7}$$

where μ is chemical potential, $\omega_n = (2n+1)\pi T$ are the Matsubara frequencies for temperature $T \equiv \beta^{-1}$ ($n = 0, \pm 1, \ldots$) and the local Green function obtained via integration over a Brillouin zone:

$$G_{qlm,q'l'm'}(i\omega_n) = \frac{1}{V_B}\int \mathrm{d}\mathbf{k} G_{qlm,q'l'm'}(\mathbf{k}, i\omega_n) \tag{8}$$

(V_B is the volume of the Brillouin zone).

A so-called *bath Green function* which defines a hybridization with the surrounding crystal in the effective Anderson model and preserves the double-counting of the local self-energy is obtained by a solution of the effective impurity problem (Georges, Kotliar, Krauth and Rozenberg, 1996):

$$\mathcal{G}^{-1}_{m,m'}(i\omega_n) = G^{-1}_{m,m'}(i\omega_n) + \Sigma_{m,m'}(i\omega_n) \tag{9}$$

In the simplest case of massive downfolding to the d-orbital problem, we could incorporate the double counted correction in the chemical potential μ obtained self-consistently from the total number of d-electrons

$$\frac{1}{\beta}\sum_{i\omega_n} e^{i\omega_n 0^+} G(i\omega_n) = N_d \tag{10}$$

Further, one has to find the self-energy $\Sigma_{m,m'}(i\omega_n)$ in terms of the bath Green function $\mathcal{G}_{m,m'}(i\omega_n)$ and use it in the self-consistent LDA+DMFT loop (equations 8 and 9) schematically presented in Figure 2.

2.2 The quantum Monte Carlo solution of the impurity problem

Here we describe the most rigorous way to solve an effective impurity problem using the multiband QMC method

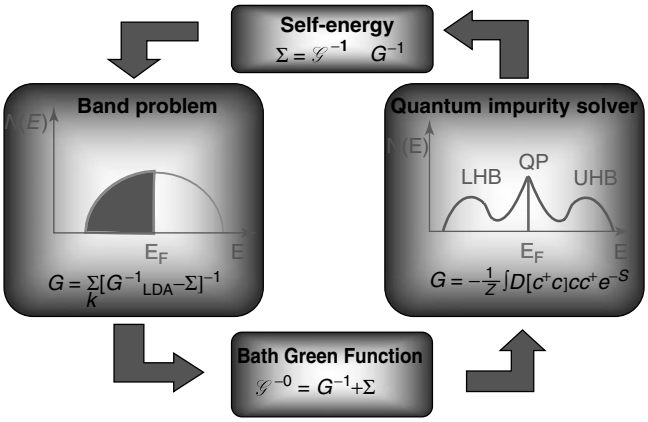

Figure 2. The schematic view of the LDA+DMFT cycle: one can start from a guess for the self-energy, find the local Green function in the electronic structure program, then obtain the effective bath Green function and solve quantum-impurity problem, and then obtain the new self-energy till a self-consistent solution is reached.

(Takegahara, 1993; Rozenberg, 1997). In the framework of the LDA+DMFT, this approach was used first in Katsnelson and Lichtenstein (2000) for the case of ferromagnetic iron. We use the path integral formalism and describe the discrete Hubbard–Stratonovich transformations for calculations of partition functions:

$$Z = \int D[c^{+}(\tau), c(\tau)]e^{-S} \tag{11}$$

and corresponding Green function. In this method, the local Green function is calculated for the imaginary time interval $[0, \beta]$ with the mesh $\tau_l = l\Delta\tau$, $l = 0, \ldots, L-1$, where $\Delta\tau = \beta/L$ ($\beta = \frac{1}{T}$ is the inverse temperature) using the path integral formalism (Georges, Kotliar, Krauth and Rozenberg, 1996). The multi-orbital DMFT problem can be reduced to the general impurity action (see Figure 1):

$$\begin{aligned} S = &- \int_0^\beta \mathrm{d}\tau \int_0^\beta \mathrm{d}\tau' \sum_{i,j} c_i^{+}(\tau)\mathcal{G}_{ij}^{-1}(\tau - \tau')c_j(\tau') \\ &+ \frac{1}{2}\int_0^\beta \mathrm{d}\tau \sum_{i,j} n_i(\tau)U_{ij}n_j(\tau) \end{aligned} \tag{12}$$

where $i = \{m, \sigma\}$ labels both orbital and spin indices (we should remind the reader that we have no site indices since we are now solving the one-site effective impurity problem). Without spin-orbital coupling we have $\mathcal{G}_{ij} = \mathcal{G}^{\sigma}_{m,m'}\delta_{\sigma\sigma'}$.

In the auxiliary fields Green function QMC scheme, one used the discrete Hubbard–Stratonovich transformation introduced by Hirsch and Fye (1986)

$$\begin{aligned} &\exp\left[-\Delta\tau U_{ij}\left(n_i n_j - \frac{1}{2}(n_i + n_j)\right)\right] \\ &= \frac{1}{2}\sum_{s_{ij}=\pm 1} \exp\left[\lambda_{ij}s_{ij}(n_i - n_j)\right] \end{aligned} \tag{13}$$

where $s_{ij}(\tau)$ are the auxiliary Ising fields for each pair of spins, orbitals, and time slices with the strength:

$$\lambda_{ij} = \operatorname{arccosh}\left[\exp\left(\frac{\Delta\tau}{2}U_{ij}\right)\right] \tag{14}$$

Using Hirsch's transformation we can transform the nonlinear action to a normal Gaussian one and exactly integrated out fermionic fields in the path integral (equation 11). Then the resulting partition function and Green function matrix have the following form (Georges, Kotliar, Krauth and Rozenberg, 1996)

$$\begin{aligned} Z &= \frac{1}{2^{N_f L}}\sum_{s_{ij}(\tau)} \det[\widehat{G}^{-1}(s_{ij})] \\ \widehat{G} &= \frac{1}{Z}\frac{1}{2^{N_f L}}\sum_{s_{ij}(\tau)} \widehat{G}(s_{ij}) \det[\widehat{G}^{-1}(s_{ij})] \end{aligned} \tag{15}$$

where N_f is the number of Ising fields, L is the number of time slices, and $\widehat{G}(s_{ij})$ is the Green function of *noninteracting* fermions for a given configuration of the external Ising fields:

$$\begin{aligned} G_{ij}^{-1}(s) &= \mathcal{G}_{ij}^{-1} + \Delta_i\delta_{ij}\delta_{\tau\tau'} \\ \Delta_i &= (e^{V_i} - 1) \\ V_i(\tau) &= \sum_{j(\neq i)} \lambda_{ij}s_{ij}(\tau)\sigma_{ij} \end{aligned} \tag{16}$$

here, we introduce the generalized Pauli matrix:

$$\sigma_{ij} = \begin{cases} +1, i < j \\ -1, i > j \end{cases}$$

For efficient calculation of the Green function $G_{ij}(s)$ for arbitrary configuration of Ising fields one can use the following Dyson equation (Hirsch and Fye, 1986):

$$G' = [1 + (1 - G)(e^{V'-V} - 1)]^{-1}G \tag{17}$$

where V and G are potential and Green function before the Ising spin flip and V' and G' are those after the flip. The QMC important sampling scheme allowed us to integrate over the Ising fields with the modulus of $(\det[\widehat{G}^{-1}(s_{ij})])$

as a stochastic weight (Hirsch and Fye, 1986; Georges, Kotliar, Krauth and Rozenberg, 1996). Using the output local Green function from QMC and input bath Green functions, the new self-energy is obtained via equation (9) and the self-consistent loop can be closed through equation (8) (see Figure 2). The main problem of the multiband QMC formalism is the large number of the auxiliary fields $S^l_{mm'}$. For each time slice l, it is equal to $M(2M-1)$ where M is the total number of the orbitals which gives 45 Ising fields for the d-states case and 91 fields for the f-states. Analytical continuations of the QMC Green functions from the imaginary time to the real energy axis can be done within the maximum entropy method (Jarrell and Gubernatis, 1996).

It is important to emphasize that for the diagonal Green function $G_{ij} = G_i\delta_{ij}$, the determinant ratio is always positive. This means that the sign problem, which is the main obstacle for the application of the QMC method to fermionic problems (von der Linden, 1992), does not arise for this case. Real computational experience shows that even for generic multiband case, the sign problem for the effective impurity calculations is not serious. This means that the QMC solution in the context of DMFT can be considered as a practically exact scheme.

3 SPECTRAL DENSITY VERSUS DENSITY FUNCTIONALS

In the standard DFT approach, the thermodynamic potential Ω^c for noncorrelated conduction – 'c' electrons is represented as a functional of the electron density $\rho(\mathbf{r})$ which is, generally speaking, a matrix in spin indices. Formally it can be represented as a thermodynamic potential of the Kohn–Sham quasiparticles (QPs) (Hohenberg and Kohn, 1964; Kohn and Sham, 1965), Ω_{sp}, minus the contribution of the so-called *double counted* terms, Ω_{dc}:

$$\begin{aligned}
\Omega^c &= \Omega^c_{sp} - \Omega^c_{dc} \\
\Omega^c_{sp} &= -Tr\log[i\omega + \nabla^2/2 - V_{KS}] \\
\Omega^c_{dc} &= \int V_{KS}(\mathbf{r})\rho(\mathbf{r})\,\mathrm{d}\mathbf{r} - \int V_{ext}(\mathbf{r})\rho(\mathbf{r})\,\mathrm{d}\mathbf{r} \\
&\quad -\frac{1}{2}\int \frac{\rho(\mathbf{r})\rho(\mathbf{r}')}{|\mathbf{r}-\mathbf{r}'|}\mathrm{d}\mathbf{r}\mathrm{d}\mathbf{r}' - E_{xc}[\rho]
\end{aligned} \tag{18}$$

where $Tr = Tr_{\omega qL\sigma}$, Tr_ω is the sum over Matsubara frequencies $Tr_\omega \ldots = T\sum_\omega e^{i\omega 0^+}\ldots$, $\omega = \pi T\,(2n+1)$, $n = 0, \pm 1, \ldots$, T is the temperature, and $qL\sigma$ are site numbers (q), orbital quantum numbers ($L = l, m$), and spin projections σ, correspondingly, $V_{ext}(\mathbf{r})$ is the external potential, $E_{xc}[\rho]$ is the exchange-correlation energy, and the Kohn–Sham effective potential is defined as

$$V_{KS}(\mathbf{r}) = V_{ext}(\mathbf{r}) + \int \frac{\rho(\mathbf{r}')}{|\mathbf{r}-\mathbf{r}'|}\mathrm{d}\mathbf{r}' + \frac{\delta E_{xc}[\rho]}{\delta\rho(\mathbf{r})} \tag{19}$$

In contrast to the standard DFT, the SDF approach deals with the real dynamical QPs for correlated 'd-electrons' defined via the local Green functions rather than with Kohn–Sham 'QPs' which are, strictly speaking, only auxiliary states used to calculate the total energy. Therefore, instead of working with the thermodynamic potential Ω as a *density* functional we start from its general expression in terms of an exact Green function (Luttinger and Ward, 1960; Carneiro and Pethick, 1975; Chitra and Kotliar, 2001; Georges, 2004)

$$\begin{aligned}
\Omega^d &= \Omega^d_{sp} - \Omega^d_{dc} \\
\Omega^d_{sp} &= -Tr\left\{\ln\left[\Sigma - G_0^{-1}\right]\right\} \\
\Omega^d_{dc} &= Tr\,\Sigma G - \Phi
\end{aligned} \tag{20}$$

where G, G_0, and Σ are the exact Green function, its bare value, and self-energy, respectively. Φ is the Luttinger-Ward generating functional (sum of the all connected skeleton diagrams without free lines), correspondingly. A complete SDF thermodynamic potential is equal to $\Omega = \Omega^c + \Omega^d$. We have to also keep in mind the Dyson equation

$$G^{-1} = G_0^{-1} - \Sigma \tag{21}$$

and the variational identity

$$\Sigma = \frac{\delta\Phi}{\delta G} \tag{22}$$

When neglecting the QP damping, Ω_{sp} will be nothing but the thermodynamic potential of 'free' fermions but with exact QP energies. Formal analogy between equations (18) and (20), (19) and (22) are obvious: the self-energy plays the role of the Kohn–Sham potential (without the external potential) and the Green function plays the role of the density matrix. As an example of this correspondence one can prove (Katsnelson and Lichtenstein, 2000), in the framework of the SDF, a useful identity known as the *local force theorem* basically in the same way as it has been done in DFT scheme (Mackintosh and Andersen, 1980; Liechtenstein, Katsnelson, Antropov and Gubanov, 1987). We will use this property in the next section to derive the expressions for exchange parameters in LDA+DMFT (Katsnelson and Lichtenstein, 2000).

4 EFFECTIVE EXCHANGE INTERACTIONS

Let us discuss the problem of calculation of effective exchange interactions (J_{ij}) in correlated systems. In principle, the J_{ij} parameters are not well-defined for arbitrary magnetic systems, and the traditional way to study spin excitations is related to the calculation of nonlocal frequency dependent spin susceptibility (Georges, Kotliar, Krauth and Rozenberg, 1996; Aryasetiawan and Karlsson, 1999; Katsnelson and Lichtenstein, 2004). In this case, the auxiliary space–time dependent magnetic field is added to the Hamiltonian: $\boldsymbol{\sigma}\mathbf{h}(\mathbf{r}, \tau)$ and the second derivative of free-energy with respect to magnetic field gives the interacting spin susceptibility: $\chi^{-1} = \chi_0^{-1} - \Gamma$, where χ_0 is an empty-loop susceptibility and Γ is the vertex corrections (Georges, Kotliar, Krauth and Rozenberg, 1996; Aryasetiawan and Karlsson, 1999). Here we consider a simple approximation of 'rigid spin rotation' of spectral density for a small angle:

$$\delta\mathbf{e}_i = \delta\boldsymbol{\varphi}_i \times \mathbf{e}_i, \tag{23}$$

where $\mathbf{e}_i$ is a unit vector determining general direction of constrained effective spin-dependent potential on site i and $\delta\boldsymbol{\varphi}_i$ is an infinithesimal rotation vector. In this case it is useful to write explicitly the spinor structure of the self-energy and Green functions:

$$\begin{aligned} \Sigma_i &= \Sigma_i^c + \boldsymbol{\Sigma}_i^s\boldsymbol{\sigma} \\ G_{ij} &= G_{ij}^c + \mathbf{G}_{ij}^s\boldsymbol{\sigma} \end{aligned} \tag{24}$$

where $\Sigma_i^{(c,s)} = \frac{1}{2}\left(\Sigma_i^{\uparrow} \pm \Sigma_i^{\downarrow}\right)$, $\boldsymbol{\Sigma}_i^s = \Sigma_i^s\mathbf{e}_i$, $\boldsymbol{\sigma} = (\sigma_x, \sigma_y, \sigma_z)$ are Pauli matrices, $G_{ij}^c = \frac{1}{2}Tr_\sigma(G_{ij})$ and $\mathbf{G}_{ij}^s = \frac{1}{2}Tr_\sigma(G_{ij}\boldsymbol{\sigma})$.

We suppose that the bare Green function G^0 does not depend on spin directions and all the spin-dependent terms including the Hartree–Fock terms are incorporated in the self energy. In the rigid spin approximation we assume that the unit vector $\mathbf{e}_i$ does not depend on the energy, orbital indices and represents the direction of the average local magnetic moment on the site i. Note, that the thermodynamic potential Ω should be considered as a constrained SDF which depends on $\mathbf{e}_i$ as external parameter (cf. Stocks *et al.*, 1998). Then the variation of the thermodynamic potential with respect to small-spin rotation can be written as

$$\delta\Omega = \delta^*\Omega_{sp} + \delta_1\Omega_{sp} - \delta\Omega_{dc} \tag{25}$$

where δ^* is the variation without taking into account the change of the 'self-consistent potential' (i.e., self-energy) and δ_1 is the variation due to this change of Σ. Taking into account equation (22) it can be easily shown (cf. Luttinger and Ward, 1960; Carneiro and Pethick, 1975) that

$$\delta_1\Omega_{sp} = \delta\Omega_{dc} = TrG\delta\Sigma \tag{26}$$

and hence

$$\delta\Omega = \delta^*\Omega_{sp} = -\delta^*\ Tr\ln\left[\Sigma - G_0^{-1}\right] \tag{27}$$

which is an analog of the magnetic 'local force theorem' in the DFT (Liechtenstein, Katsnelson, Antropov and Gubanov, 1987).

In the case of rigid spin rotation the corresponding variation of the thermodynamic potential can be written as

$$\delta\Omega = \mathbf{V}_i\delta\boldsymbol{\varphi}_i \tag{28}$$

where the torque $\mathbf{V}_i$ is equal to

$$\mathbf{V}_i = 2Tr_{\omega L}\left[\boldsymbol{\Sigma}_i^s \times \mathbf{G}_{ii}^s\right] \tag{29}$$

On the basis of the expansion of this expression (29) in a sum of pairwise contributions one can obtain a useful formula for the effective magnetic interactions (Katsnelson and Lichtenstein, 2000):

$$J_{ij} = -Tr_{\omega L}\left(\Sigma_i^s G_{ij}^{\uparrow}\Sigma_j^s G_{ji}^{\downarrow}\right) \tag{30}$$

and, correspondingly, for the stiffness tensor of a ferromagnet:

$$D_{\alpha\beta} = -\frac{2}{M}Tr_{\omega L}\sum_{\mathbf{k}}\left(\Sigma^s\frac{\partial G^{\uparrow}(\mathbf{k})}{\partial k_\alpha}\Sigma^s\frac{\partial G^{\downarrow}(\mathbf{k})}{\partial k_\beta}\right) \tag{31}$$

where M is the magnetic moment per unit cell. These results generalize the LDA expressions of Liechtenstein, Katsnelson, Antropov and Gubanov (1987) to the case of correlated systems. Note that the crucial step from equation (29) to equation (30) is not rigorous, since the exchange parameters are connected with the second variations of the Ω-potential and use of the local force theorem cannot be justified. Relations between the local force theorem and more accurate approach based on the magnetic susceptibility is discussed in Katsnelson and Lichtenstein (2004); Bruno (2003) and Antropov (2003). An alternative approach to the exchange parameters in the context of the LDA+DMFT based on the diagrammatic perturbation theory in the rotation angle (Katsnelson and Lichtenstein, 2002) proves that equation (30) corresponds to the 'empty-loop' approximation neglecting the vertex corrections. At the same time, for the stiffness constant the latter are absent and equation (31) appears to be exact provided that the self-energy and three-point vertex are local (as in the DMFT) (Lichtenstein and Katsnelson, 2001).

5 ELECTRON CORRELATIONS AND FINITE-TEMPERATURE MAGNETISM IN IRON AND NICKEL

We now describe the applications of the SDF approach to the classical problem of finite-temperature magnetism of the iron group transition metals (Lichtenstein, Katsnelson and Kotliar, 2001). Despite a lot of attempts starting from the seminal works by Heisenberg and Frenkel (for review of early theories see e.g., Herring, 1966; Vonsovsky, 1974; Moriya, 1985), we have no complete quantitative theory describing their magnetic and spectral properties. In order to describe the magnetic properties of Fe, Co, and Ni, one has to solve the problem of moderately strong electronic correlations for systems where approaches developed both for weakly correlated systems such as normal group metals and to highly correlated systems such as Mott insulators are not reliable. There were a lot of attempts to introduce correlation effects in the real electronic structure of these metals (Liebsch, 1981; Treglia, Ducastelle and Spanjaard, 1982; Manghi, Bellini and Arcangelli, 1997; Manghi *et al*., 1997; Nolting, Rex and Mathi Jaya, 1987; Steiner, Albers and Sham, 1992). But the question of applicability of specific approximations, such as the lowest order perturbation theory (Treglia, Ducastelle and Spanjaard, 1982; Steiner, Albers and Sham, 1992), moment method (Nolting, Rex and Mathi Jaya, 1987), or three-body Faddeev equations (Manghi, Bellini and Arcangelli, 1997; Manghi *et al*., 1997) is still not clear. On other hand, it has been demonstrated in Lichtenstein, Katsnelson and Kotliar (2001) that the *ab initio* dynamical mean-field theory does give a very successful description of both correlation effects in the electron energy spectra and the finite-temperature magnetic properties of Fe and especially, Ni. Here we present the corresponding results.

We start with the LDA Hamiltonian in the tight-binding orthogonal LMTO representation $H^{LDA}_{mm'}(\mathbf{k})$ (1), where m describes the orbital basis set containing $3d$-, $4s$-, and $4p$-states. The interactions are parameterized by the matrix of the screened local Coulomb interactions and a matrix of exchange constants $J_{mm'}$ (2), which are expressed in terms of two screened Hubbard parameters U and J describing the average Coulomb repulsion and the interatomic ferromagnetic exchange respectively. We use the values $U =$ 2.3 (3.0) eV for Fe (Ni) and the same value of the interatomic exchange, $J = 0.9$ eV for both Fe and Ni, a result of constrained LDA calculations (Bandyopadhyay and Sarma, 1989) and the static limit of GW calculations (Aryasetiawan *et al*., 2004). These parameters, which are consistent with those of many other studies result in a very good description of the physical properties of Fe and Ni.

We used the impurity QMC scheme described in the preceding text for the solution of the multiband DMFT equations. In order to sample efficiently all the spin configurations in the multiband QMC scheme, it is important to use 'global' spin-flips: $[s^{\sigma\sigma'}_{mm'}] \rightarrow [-s^{-\sigma-\sigma'}_{mm'}]$, in addition to the local moves of the auxiliary fields (Lichtenstein, Katsnelson and Kotliar, 2001). The number of QMC sweeps was of the order of 10^5. A parallel version of the DMFT program was used to sample the 45 Ising fields for $3d$-orbitals. We used 256 **k**-points in the irreducible part of the Brillouin zone for the **k** integration. Ten to 20 DMFT iterations were sufficient to achieve convergence far from the Curie point. Owing to the cubic symmetry of the bcc (Fe) and fcc (Ni) lattices, the local Green function is diagonal in the basis of real spherical harmonics. The spectral functions for real frequencies were obtained from the QMC data by applying the maximum entropy method.

Our results for the local spectral function for iron and nickel are shown in Figures 3 and 4, respectively. The SDF approach describes well all the qualitative features of the density of states (DOS), which are especially nontrivial for nickel. Our QMC results reproduce well the three main correlation effects of the one-particle spectra below T_C (Iwan, Himpsel and Eastman, 1979; Eberhardt and Plummer, 1980; Altmann *et al*., 2000): the presence of the famous 6 eV satellite; the 30% narrowing of the occupied part of d-band; and the 50% decrease of exchange splitting compared to the LDA results. Note that the satellite in Ni has substantially more spin-up contributions in agreement with photoemission spectra (Altmann *et al*., 2000). The exchange splitting of the d-band depends very weakly on temperature from $T = 0.6T_C$

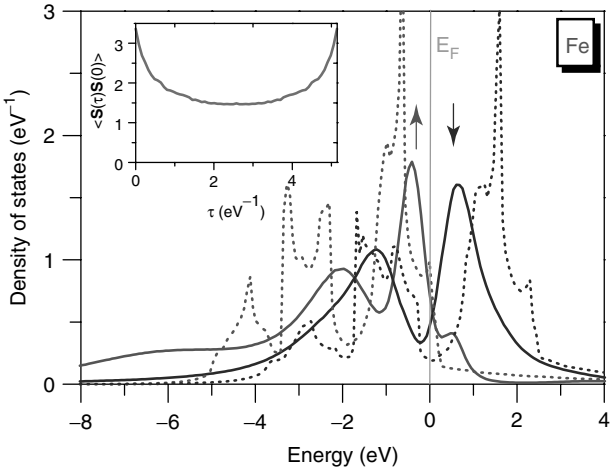

Figure 3. LDA+DMFT results for ferromagnetic iron ($T = 0.8T_C$). The partial densities of d-states (full lines) is compared with the corresponding LSDA results at zero temperature (dashed lines) for the spin-up (arrow up) and spin-down (arrow down) states. The insert shows the spin–spin autocorrelation function for $T = 1.2T_C$.

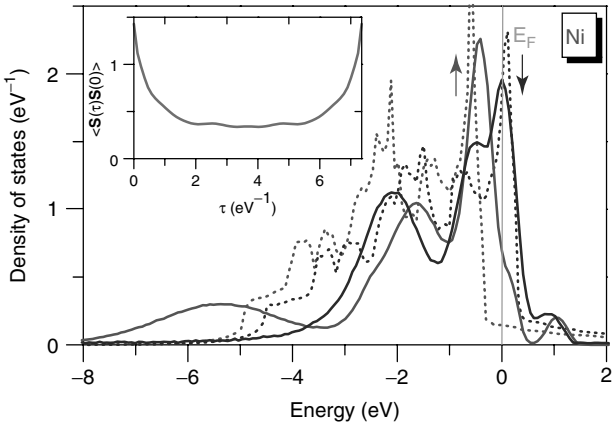

Figure 4. Same quantities as in Figure 3 for ferromagnetic nickel ($T = 0.9T_C$). The insert shows the spin–spin autocorrelation function for $T = 1.8T_C$.

to $T = 0.9T_C$. Correlation effects in Fe are less pronounced than in Ni, due to its large spin splitting and the characteristic bcc structural dip in the DOS for spin-down states near Fermi level, which reduces the DOS for particle hole excitations.

Now we discuss the applications of the SDF approach to the description of finite-temperature magnetic properties of iron and nickel. Although DFT can, in principle, provide a rigorous description of the thermodynamic properties, at present there is no accurate practical implementation available. As a result the finite-temperature properties of magnetic materials are estimated following a simple suggestion (Liechtenstein, Katsnelson, Antropov and Gubanov, 1987), whereby constrained DFT at $T = 0$ is used to extract exchange constants for a *classical* Heisenberg model, which in turn is solved using approximation methods (e.g., random phase approximation (RPA), mean field) from classical statistical mechanics of spin systems (Liechtenstein, Katsnelson, Antropov and Gubanov, 1987; Rosengaard and Johansson, 1997; Halilov, Eschrig, Perlov and Oppeneer, 1998; Antropov *et al*., 1996). The most recent implementation of this approach gives good values for the transition temperature of iron but not of nickel (Pajda *et al*., 2001). Although these localized spin models give, by construction, at high temperatures a Curie–Weiss-like magnetic susceptibility, as observed experimentally in Fe and Ni, they encountered difficulties in predicting the correct values of the Curie constants (Staunton and Gyorffy, 1992).

The uniform spin susceptibility in the paramagnetic state: $\chi_{q=0} = \mathrm{d}M/\mathrm{d}H$ was extracted from the QMC simulations by measuring the induced magnetic moment in a small external magnetic field. It includes the polarization of the impurity Weiss field by the external field (Georges, Kotliar, Krauth and Rozenberg, 1996). The dynamical mean field results account for the Curie–Weiss law which is observed experimentally in Fe and Ni. As the temperature increases above T_C, the atomic character of the system is partially restored resulting in an atomic-like susceptibility with an effective moment:

$$\chi_{q=0} = \frac{\mu_{eff}^2}{3(T - T_C)} \tag{32}$$

The temperature dependence of the ordered magnetic moment below the Curie temperature and the inverse of the uniform susceptibility above the Curie point are plotted in Figure 5 together with the corresponding experimental data for iron and nickel (Wolfarth, 1986). The LDA+DMFT calculations describe the magnetization curve and the slope of the high-temperature Curie–Weiss susceptibility remarkably well. The calculated values of high-temperature magnetic moments extracted from the uniform spin susceptibility are $\mu_{eff} = 3.09\,(1.50)\,\mu_B$ for Fe (Ni), in good agreement with the experimental data $\mu_{eff} = 3.13\,(1.62)\,\mu_B$ for Fe (Ni) (Wolfarth, 1986).

We have estimated the values of the Curie temperatures of Fe and Ni from the disappearance of spin polarization in the self-consistent solution of DMFT problem and from the Curie–Weiss law in equation (32). Our estimates $T_C = 1900\,(700)\,K$ are in reasonable agreement with experimental values of 1043 (631) K for Fe (Ni) respectively (Wolfarth, 1986), considering the single-site nature of the DMFT approach, which is not able to capture the reduction of T_C due to long wavelength spin waves. These effects are governed by the spin-wave stiffness. Since the ratio of the spin-wave stiffness (D) to T_C, $T_C a^2/D$ is nearly a factor of 3 larger for Fe than for Ni (Wolfarth, 1986) (a is the lattice distance), we expect the DMFT T_C to be much higher than the observed Curie temperature in Fe than in Ni. Note that this is a consequence of the long-range oscillating character

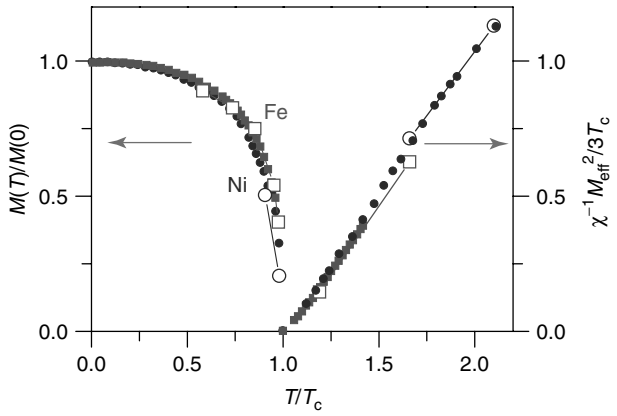

Figure 5. Temperature dependence of ordered moment and the inverse ferromagnetic susceptibility for Fe (open square) and Ni (open circle) compared with experimental results for Fe (square) and Ni (circle).

of exchange interactions in iron compared to short-range ferromagnetic exchange interactions in nickel (Pajda *et al*., 2001). The deeper reason for this difference is the almost half-metallic character of the electron energy spectrum for nickel (with almost complete majority-spin d-band), whereas for well-pronounced Friedel oscillations of the exchange parameters the spectrum should be metallic for both spin projections.

Within DMFT one can also compute the local spin susceptibility defined by

$$\chi_{loc} = \frac{g_s^2}{3} \int_0^\beta \mathrm{d}\tau \, \langle \mathbf{S}(\tau) \, \mathbf{S}(0) \rangle \tag{33}$$

where $g_s = 2$ is the gyromagnetic ratio and $\mathbf{S} = \frac{1}{2} \sum_{m,\sigma,\sigma'} c^\dagger_{m\sigma} \boldsymbol{\sigma}_{\sigma\sigma'} c_{m\sigma'}$ is single-site spin operator. It differs from the $q = 0$ susceptibility, by the absence of spin polarization in the Weiss field of the impurity model. Equation (33) cannot be probed directly in experiments but it is easily computed in DMFT-QMC. Its behavior as a function of temperature, gives a very intuitive picture of the degree of correlations in the system. In a weakly correlated system we expect expression (33) to be nearly temperature independent, whereas in a strongly correlated system we expect a leading Curie–Weiss behavior at high temperatures $\chi_{local} = \mu^2_{loc}/(3T + const)$ where μ_{loc} is an effective local magnetic moment. In the Heisenberg model with spin S, $\mu^2_{loc} = S(S+1)g_s^2$ and well-defined local magnetic moments (e.g., for rare earth magnets), this quantity should be temperature independent. For the itinerant-electron magnets μ_{loc} is temperature dependent due to a variety of competing many-body effects such as Kondo screening, the induction of local magnetic moment by temperature (Moriya, 1985), and thermal fluctuations which disorders the moments (Irkhin and Katsnelson, 1994). All these effects are included in the DMFT calculations. The τ-dependence of the correlation function $\langle \mathbf{S}(\tau) \, \mathbf{S}(0) \rangle$ results in the temperature dependence of μ_{loc} and is displayed in the inserts in the Figures 3 and 4. Iron can be considered as a magnet with very well-defined local moments above T_C (the τ-dependence of the correlation function is relatively weak), whereas nickel is a more itinerant-electron magnet (stronger τ-dependence of the local spin–spin autocorrelation function).

The comparison of the values of the local and the $q = 0$ susceptibility gives a crude measure of the degree of short-range order which is present above T_C. As expected, the moments extracted from the local susceptibility equation (33) are a bit smaller ($2.8\,\mu_B$ for iron and $1.3\,\mu_B$ for nickel) than those extracted from the uniform magnetic susceptibility. This reflects the small degree of the short-range correlations which remain well above T_C (Mook and Lynn, 1985). The high-temperature LDA+DMFT clearly show the presence of a local moment above T_C. This moment is correlated with the presence of high-energy features (of the order of the Coulomb energies) in the photoemission. This is also true below T_C, where the spin dependence of the spectra is more pronounced for the satellite region in nickel than that of the QP bands near the Fermi level (see Figure 4). This can explain the apparent discrepancies between different experimental determinations of the high-temperature magnetic splittings (Kisker, Schröder, Campagna and Gudat, 1984; Sinkovic *et al*., 1997; Kreutz, Greber, Aebi and Osterwalder, 1998) as being the result of probing different energy regions. The resonant photoemission experiments (Sinkovic *et al*., 1997) reflects the presence of local-moment polarization in the high-energy spectrum above Curie temperature in nickel, whereas the low-energy angle-resolved photoemission (ARPES) investigations (Kreutz, Greber, Aebi and Osterwalder, 1998) result in nonmagnetic bands near the Fermi level. This is exactly the DMFT view on the electronic structure of transition metals above T_C. Fluctuating moments and atomic-like configurations are large at short times, which result in correlation effects in the high-energy spectra such as spin-multiplet splitting. The moment is reduced at longer timescales, corresponding to a more band-like, less correlated electronic structure near the Fermi level.

Angle-resolved photoemission spectra of iron, as well as spin-polarized thermoemission data for cesiated iron were discussed in the context of LDA+DMFT in Katsnelson and Lichtenstein (1999), a perturbative FLEX-based solver of the effective impurity problem being used instead of QMC. For both types of spectra, an agreement between theory and experiment is drastically improved in comparison with standard LDA calculations. The QP damping in iron can be as large as 30% of the binding energy for the states in the region of majority-spin DOS peak.

Using the self-consistent values for $\Sigma(i\omega)$ computed by QMC technique, we calculate the exchange interactions (equation 30) and spin-wave spectrum for Fe (Katsnelson and Lichtenstein, 2000) and Ni (Katsnelson and Lichtenstein, 2002). The spin-wave spectrum for ferromagnetic iron is presented in Figure 6 in comparison with the results of LSDA-exchange calculations (Liechtenstein, Katsnelson, Antropov and Gubanov, 1987) and with different experimental data (Lynn, 1975; Mook and Nicklow, 1973; Perring *et al*., 1991). This room-temperature neutron scattering experiments has a sample dependence (Fe-12%Si in Lynn (1975); Perring *et al*. (1991) and Fe-4%Si in Mook and Nicklow (1973)) due to problems with the bcc-Fe crystal growth. Note that for high-energy spin waves the experimental data (Perring *et al*., 1991) has large error-bars due to Stoner damping (we show one experimental point with the uncertainties in the **q** space). On the other hand, the expression of magnon frequency in terms of exchange parameters itself becomes problematic in

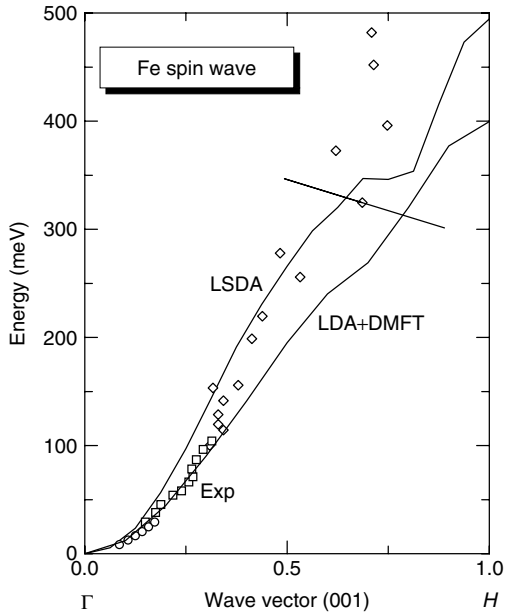

Figure 6. The spin-wave spectrum for ferromagnetic iron in the LSDA and LDA+DMFT approximations compared with different experiments (circles Lynn, 1975, squares Mook and Nicklow, 1973, and diamonds Perring, Boothroyd, Paul, *et al*., 1991).

that region due to the breakdown of adiabatic approximation, as discussed in the preceding text.

Therefore, we think that comparison of theoretical results with experimental spin-wave spectrum for the large energy needs additional investigation of Stoner excitation and requires calculations of dynamical susceptibility in the LDA+DMFT approach (Georges, Kotliar, Krauth and Rozenberg, 1996). Our LSDA spin-wave spectrum agrees well with the results of frozen magnon calculations (Sandratskii and Kübler, 1992; Halilov, Eschrig, Perlov and Oppeneer, 1998). At the lower energy, where the present adiabatic theory is reliable, the LDA+DMFT spin-wave spectrum agrees better with the experiments than the result of the LSDA calculations. Experimental value of the spin-wave stiffness $D = 280\,\text{meV}\,\text{Å}^{-2}$ (Mook and Nicklow, 1973) agrees well with the theoretical LDA+DMFT estimations of $260\,\text{meV}\,\text{Å}^{-2}$ (Katsnelson and Lichtenstein, 2000). We have shown that correlation effects in magnon spectra are less important than in the electron spectra but, in general, an agreement between theory and experiment is also better for the LDA+DMFT approach.

6 CORRELATION EFFECTS IN ARPES: THE CASE OF fcc-Mn

Electronic spectra of transition metals have been probed intensively by angle-resolved photoemission, a technique that allows for the determination of the dispersion law that describes the dependence of the QP energy on quasimomentum. Copper was the first metal to be investigated thoroughly by this technique and the results were in excellent agreement with band structure calculations (Thirty *et al*., 1979; Knapp and Himpsel, 1979). The same technique, however, showed substantial deviations when applied to Ni and provided evidence for many-body behavior, such as the famous 6 eV satellite discussed in the previous section. Correlation effects are indeed important for metals with partially filled 3d bands and should be taken into account for an adequate description of ARPES spectra. Nevertheless, the main part of the spectral density in Fe is related to usual QPs, and the spectral weight of the satellite in Ni amounts to only 20% (Altmann *et al*., 2000). Surprisingly strong correlation effects have been found both experimentally and theoretically for the case of fcc-(γ) phase of manganese (Biermann *et al*., 2004).

Normally the geometrical frustrations in crystals (such as in the fcc lattice) further enhance electronic correlations (Georges, Kotliar, Krauth and Rozenberg, 1996) so that one of the best candidates among the transition metals for the search of strong correlation effects is the fcc-(γ) phase of manganese. It is an example of a very strongly frustrated magnetic system; according to band-structure calculations, (Moruzzi, Marcus and Kübler, 1989) the antiferromagnetic ground state of γ-Mn lies extremely close to the boundary of the nonmagnetic phase. Moreover, an anomalously low value of the bulk modulus (Guillermet and Grimvall, 1989) might be considered as a first experimental hint of strong electronic correlations (Zein, 1995).

The physical properties of bulk γ-Mn are hardly accessible in the experiment, since the γ-phase is only stable at temperatures between 1368 K and 1406 K, where it shows paramagnetic behavior. In Biermann *et al*. (2004) thin films of γ-Mn grown on $Cu_3Au(100)$ substrate have been experimentally investigated by ARPES. The spectra were characterized by two striking features. These are a weakly dispersive QP band near the Fermi level E_F and a broad and almost **k**-independent maximum at approximately 2.7 eV below E_F. This data cannot be understood in the framework of a standard QP picture, since calculations of the first principles of the band structure for different magnetic phases of γ-Mn show an energy dispersion of more than 1.5 eV (Crockford, Bird and Long, 1991). Instead, the overall shape of the experimental spectra is very close to that of the Hubbard model on the metallic side of the Mott transition with a QP band near the Fermi level and a broad Hubbard band (HB) below E_F (Georges, Kotliar, Krauth and Rozenberg, 1996).

To test this hypothesis, LDA+DMFT calculations have been done with the QMC solution of the effective impurity problem within the same approximations as described in the preceding text for Fe and Ni. Carrying out between 10 and 15 DMFT iterations with about 10^5 Quantum Monte

Carlo sweeps allowed us to obtain not only the local Green function $G(\tau)$ but also highly accurate self-energies which can then be used for the computation of the **k**-resolved local Green function. Inversion of the spectral representations of the local Green's function and the dd-block of the **k**-resolved one by means of a Maximum Entropy scheme (Jarrell and Gubernatis, 1996) yields the DOS $\rho(\omega)$ and the spectral function $A(\mathbf{k}, \omega)$.

The results for the **k**-resolved spectral functions $A(\mathbf{k}, i\omega)$ are shown in Figure 7, for **k** points in the Γ-L directions (Biermann, Lichtenstein and Katsnelson, 2001). In the negative energy part (i.e., for the occupied states) of all spectra two main peaks carry – for a given **k**−point – the main part of the spectral weight: a narrow QP feature near the Fermi level and a very broad HB (at about −2.4 eV). These features are shared between the experimental and theoretical curves. Given the facts that (i) the experiments are done at a somewhat lower temperature than the calculations, (ii) we did not take into account matrix elements for interpreting the photoemission data and (iii) using the Maximum Entropy scheme for determining the spectral function introduces a further approximation, the theoretical spectra agree reasonably well with the experimental data. The absence of LDA bands in the energy region near E_F carrying most of the spectral weight around the Γ-point is striking and underlines the necessity of a proper many-body treatment as done in LDA+DMFT. Note that assuming antiferromagnetic order (of the type detailed in the subsequent text) would slightly shift the LDA bands. However, the antiferromagnetic LDA band structure displays a dispersion of more than 2 eV and thus, could not explain the nondispersive photoemission feature.

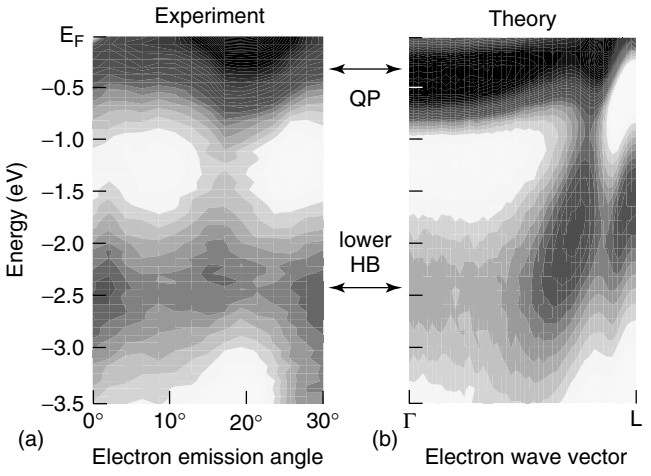

Figure 7. Spectral function for fcc-Mn from ARPES data and calculated within the LDA+DMFT approach, with $U = 3$ eV and $J = 0.9$ eV.

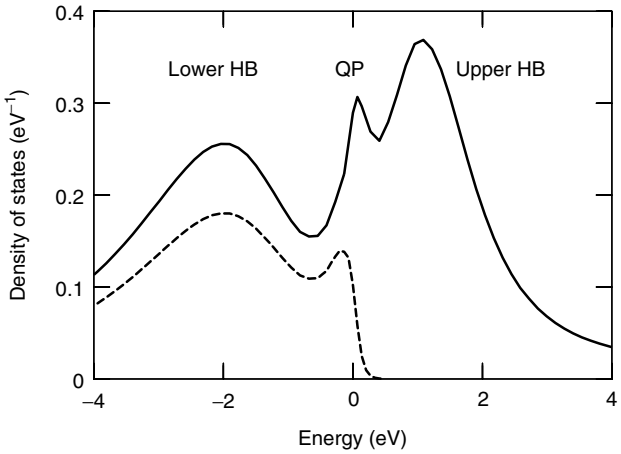

Figure 8. Local DOS for fcc-Mn from LDA+DMFT calculations. The 'three-peak structure' with the two broad HBs and a narrow QP resonance at the Fermi level is typical of strongly correlated systems. The dashed line is the calculated photoemission spectrum.

The calculated (**k**-integrated and **k**-resolved) DOS curves (see Figure 8) demonstrate a characteristic 'three-peak structure', with two broad HBS and a narrow QP Kondo resonance at the Fermi level which is typical of strongly correlated electron systems (Georges, Kotliar, Krauth and Rozenberg, 1996).

The energy scale associated with the correlation effects that lead to the formation of the HBs ($\sim U$) is much larger than that of the magnetic interactions. Therefore, the effects under discussion are not very sensitive to long-range magnetic order. We have carried out the electronic structure calculations for both the paramagnetic and the antiferromagnetic structure with wave vector $\mathrm{Q} = (\pi, 0, 0)$, which is typical of γ-Mn-based alloys (Fishman and Liu, 1999). The magnetic ordering changes the electron spectrum less in comparison with the nonmagnetic case. However, in comparison with the results of standard band theory (Moruzzi, Marcus and Kübler, 1989), the correlation effects stabilize the antiferromagnetic structure leading to a magnetic moment of about $2.9\,\mu_{\mathrm{B}}$.

According to these results, γ-Mn can be considered a unique case of a strongly correlated transition metal. An even larger correlation would transform the system to a Mott insulator where every atomic multiplet forms its own narrow but dispersive HB (Mott, 1974). On the other hand, in most metals correlations are small enough for the QPs to be well-defined in the whole energy region, and usual band theory gives a reasonable description of the energy dispersion. Note that the correlation strength and bandwidth have almost the same magnitude for all 3*d* metals. γ-Mn is probably an exceptional case among the transition elements due to the half-filled d-band and geometric frustrations in the fcc structure.

The ARPES data for the γ-phase of manganese and their theoretical analysis by means of LDA+DMFT, an approach that accounts not only for band-structure effects on the LDA level but also allows for a full description of local effects of strong Coulomb correlations, provide evidence for the formation of HBs in metallic manganese. This is a qualitatively new aspect in the physics of magnetic transition metals.

7 CORRELATION EFFECTS IN HALF-METALLIC FERROMAGNETS

Half-metallic ferromagnets (HMFs) (de Groot, Mueller, van Engen and Buschow, 1983; Irkhin and Katsnelson, 1994; Pickett and Moodera, 2001) recently attracted a great scientific and industrial attention due to their importance for spin-dependent electronics or 'spintronics' Prinz, 1998. The HMFs have metallic electronic structure for one-spin projection (majority- or minority-spin states), but for the opposite spin direction the Fermi level lies in the energy gap (de Groot, Mueller, van Engen and Buschow, 1983). Therefore, the spin-up and spin-down contributions to electronic transport properties have different orders of magnitude, which can result in a huge magnetoresistance for heterostructures containing the HMFs (Irkhin and Katsnelson, 1994).

At the same time, the HMFs are very interesting conceptually as a class of materials which may be suitable for investigation of the essentially many-body physics 'beyond standard band theory'. In most cases, many-body effects lead only to renormalization of the QP parameters in the sense of Landau's Fermi-liquid theory, the electronic *liquid* being *qualitatively* similar to the electron *gas* (see, e.g., Nozieres, 1964; Pines and Nozieres, 1966; Vonsovsky and Katsnelson, 1989a, 1989b). On the other hand, due to specific band structure of the HMF, an important role belongs to incoherent (nonquasiparticle (NQP)) states which occur near the Fermi level because of correlation effects (Irkhin and Katsnelson, 1994). The appearance of NQP states in the energy gap near the Fermi level is one of the most interesting correlation effects typical for the HMFs. The origin of these states is connected with 'spin-polaron' processes: the spin-down low-energy electron excitations, which are forbidden for the HMFs in standard one-particle scheme, turn out to be possible as superpositions of spin-up electron excitations and virtual magnons. The density of these NQP states vanishes at the Fermi level, but increases drastically at the energy scale of the order of a characteristic magnon frequency $\overline{\omega}$. The NQP states were first considered theoretically by (Edwards and Hertz, 1973) in the framework of a broadband Hubbard model for itinerant-electron ferromagnets. Later it was demonstrated (Irkhin and Katsnelson, 1983, 1985) that for a *narrow-band* (infinite-U) Hubbard model, the *whole* spectral weight for one-spin projection belongs to the NQP states which is of crucial importance for the problem of stability of Nagaoka's ferromagnetism (Nagaoka, 1966) and for adequate description of the corresponding excitation spectrum. The NQP states in the $s-d$ exchange model of magnetic semiconductors have been considered in Auslender and Irkhin (1985). It was shown that depending on the sign of the $s-d$ exchange integral, the NQP states can form either only below the Fermi energy E_F or above it. Later it was realized that the HMFs are natural substances for theoretical and experimental investigating of the NQP effects (Irkhin and Katsnelson, 1990). A variety of these effects in the electronic and magnetic properties has been considered (for review of the earlier works see Irkhin and Katsnelson (1994)). As an example of highly unusual properties of the NQP states, we note that they can contribute to the T-linear term in the electron heat capacity (Irkhin and Katsnelson, 1990; Irkhin, Katsnelson and Trefilov, 1989, 1994), despite their density at E_F vanishing at temperature $T = 0$. Existence of the NQP states at the HMFs surface has been predicted in Katsnelson and Edwards (1992) and may be important for their detection by surface-sensitive methods such as the ARPES or by spin-polarized scanning tunneling microscopy. NQP states are also essential for the transport properties of tunneling junctions between HMFs (Irkhin and Katsnelson, 2002; McCann and Fal'ko, 2003), and for the temperature dependence of nuclear magnetic relaxation rate in HMFs (Irkhin and Katsnelson, 2001); they also contribute to their core-level spectra (Irkhin and Katsnelson, 2005). Recently, the density of NQP states has been calculated from first principles for a prototype HMF, NiMnSb (Chioncel, Katsnelson, de Groot and Lichtenstein, 2003a).

Before considering the real HMF case, it is worthwhile to check the applicability of DMFT scheme for quantitative description of the NQP states. Let us start from the DMFT calculations for the one-band Hubbard Hamiltonian

$$H = -\sum_{i,j,\sigma} t_{ij}(c^{\dagger}_{i\sigma}c_{j\sigma} + c^{\dagger}_{j\sigma}c_{i\sigma}) + U\sum_{i} n_{i\uparrow}n_{i\downarrow} \qquad (34)$$

on the Bethe lattice with coordination $z \to \infty$ and nearest-neighbor hoping $t_{ij} = t/\sqrt{z}$ (in this limit the DMFT is formally exact (Georges, Kotliar, Krauth and Rozenberg, 1996). In this case, the DOS have a semicircular form:

$$N(\epsilon) = \frac{1}{2\pi t^2}\sqrt{4t^2 - \epsilon^2} \qquad (35)$$

In order to stabilize the HMF state in our toy model, we have added an external magnetic spin splitting Δ, which mimics the local Hund polarization from other electrons in

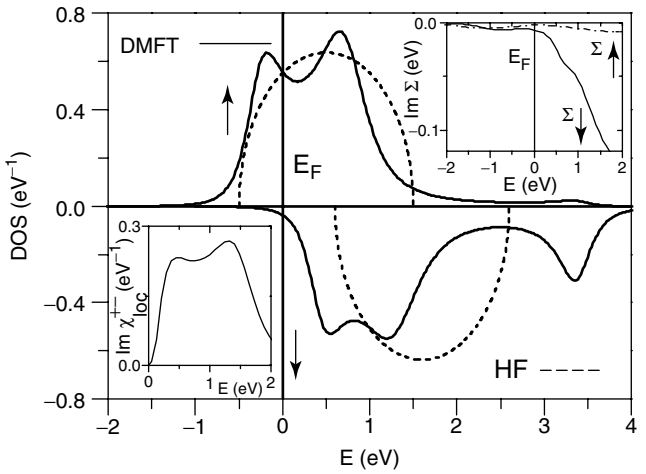

Figure 9. Density of states for HMFs in the Hartree–Fock (HF) approximation (dashed line) and the QMC solution of DMFT problem for semicircular model (solid line) with the bandwidth $W = 2\,\text{eV}$, Coulomb interaction $U = 2\,\text{eV}$, spin splitting $\Delta = 0.5\,\text{eV}$, chemical potential $\mu = -1.5\,\text{eV}$, and temperature $T = 0.25\,\text{eV}$. Insets: imaginary part of the local spin-flip susceptibility (left) and the spin-resolved self-energy (right).

the real NiMnSb compound. This HMF state corresponds to a mean-filed (Hartree–Fock) solution with a LSDA-like DOS (see Figure 9).

We can study an average magnon spectrum in this model through the two-particle correlation function. The local spin-flip susceptibility represents the response function required and can be calculated using the numerically exact enumeration QMC scheme (Georges, Kotliar, Krauth and Rozenberg, 1996). The model DMFT results are presented in Figure 9. In comparison with a simple Hartree–Fock solution (dashed line), one can see an additional well-pronounced states appearing in the spin-down gap region, just above the Fermi level. This new many-body feature corresponds to the NQP states. In addition to these states visible in both spin channels of the DOS around 0.5 eV, a many-body satellite appears at the energy of 3.5 eV.

The left inset in Figure 9 represents the imaginary part of local spin-flip susceptibility. One can see a well pronounced shoulder (around 0.5 eV), which is connected with an average magnon DOS. In addition there is a broad maximum (at 1 eV) corresponding to the Stoner excitation energy. The right inset in Figure 9 represents the imaginary part of self-energy calculated from our 'toy model'. The spin-up channel can be described by a Fermi-liquid type behavior with a parabolic energy dependence $-\text{Im}\Sigma^{\uparrow} \propto (E - E_F)^2$, whereas in the spin-down channel the imaginary part $-\text{Im}\Sigma^{\downarrow}$ shows the 0.5 eV NQP shoulder. Owing to the relatively high temperature of our QMC calculation (an exact enumeration technique with the number of time slices equal to $L = 24$), the NQP tail goes a bit below the Fermi level; at temperature $T = 0$ the NQP tail should end exactly at the Fermi level.

Let us consider now the calculations for real HMF material–NiMnSb. The details of the computational scheme have been described in Chioncel, Katsnelson, de Groot and Lichtenstein (2003a), and only the key points will be mentioned here. In order to integrate the DMFT approach into the band structure calculation, the so-called exact muffin-tin orbital method (EMTO) was used; the implementation of the DMFT scheme in the EMTO method is described in detail in the Chioncel *et al*. (2003b). One should note that in addition to the usual self-consistency of the many-body problem (self-consistency of the self-energy), a charge self-consistency has been achieved.

For the interaction Hamiltonian, a most general rotationally invariant form of the generalized Hubbard Hamiltonian with four-index interaction matrix has been used (Lichtenstein and Katsnelson, 1997, 1998; Katsnelson and Lichtenstein, 1999). The effective many-body impurity problem was solved using the spin polarized T-matrix plus fluctuation-exchange approximation (SPTF) scheme proposed in the Katsnelson and Lichtenstein (2002). It is important that this perturbative scheme includes off-diagonal in spin indices (spin-flip) effective interaction which is responsible for spin-platonic effects.

The results for DOS using LSDA and LDA+DMFT (with $U = 3\,\text{eV}$ and $J = 0.9\,\text{eV}$) approaches are presented in the Figure 10. For the spin-up states we have a normal Fermi-liquid behavior $-\text{Im}\Sigma_d^{\uparrow}(E) \propto (E - E_F)^2$ with a typical

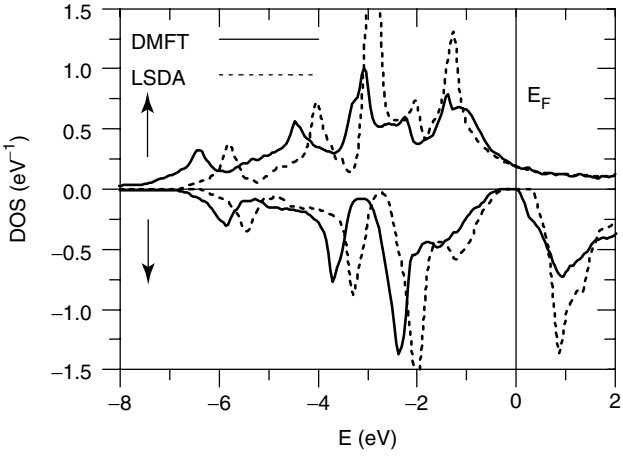

Figure 10. Density of states for HMF NiMnSb in LSDA scheme (dashed line) and in LDA+DMFT scheme (solid line) with effective Coulomb interaction $U = 3\,\text{eV}$, exchange parameter $J = 0.9\,\text{eV}$ and temperature $T = 300\,\text{K}$. The NQP state is evidenced just above the Fermi level for spin-down band.

energy scale of the order of several eV. The spin-down self-energy behaves in a similar way below the Fermi energy, with a slightly smaller energy scale (which is still larger than 1 eV). At the same time, a significant increase in $\mathrm{Im}\Sigma_d^{\downarrow}(E)$ with a much smaller energy scale (few tenths of eV) occurs just above the Fermi level, which is more pronounced for t_{2g} states. The similar behavior of the imaginary part of electronic self-energy and the DOS just above Fermi level is a signature of the NQP states and is also noticed in the model calculation (see Figure 9).

8 CONCLUSIONS

SDF approach in the LDA+DMFT approximation allows the study of correlation effects in solids based on the realistic electronic structure calculations. Among all possible applications we have chosen the magnetism of transition metals and other itinerant-electron magnets. From these examples, one can see all the main advantages of the new approach in comparison with the standard density functional theory. First, we can describe the spectral density transfer phenomena (e.g., the formation of 6 eV satellite in Ni), the QP damping and other effects connected with the frequency dependence of the self-energy, including the formation of NQP states of spin-polaronic origin; all these phenomena are absent completely not only in the DFT approach but also in the Hartree–Fock, LDA+U, or self-interaction corrections approximation. Second, we can adequately describe the contribution of the Bose degrees of freedom (e.g., spin fluctuations) to the electronic structure and thermodynamic properties. In the DFT-based calculations the temperature is taken into account only via the thermal expansion and the Fermi distribution function (Jarlborg, 1997). It was the main reason for which the standard band theory failed to describe the finite-temperature effects in magnetic metals. We show that the LDA+DMFT approach gives satisfactory solution of this complicated problem of itinerant-electron magnetism.

ACKNOWLEDGMENTS

We are grateful to G. Kotliar, A. Georges, L. Chioncel, and S. Biermann for helpful discussions.

REFERENCES

Abrikosov, A.A., Gorkov, L.P. and Dzyaloshinski, I.E. (1975). *Methods of Quantum Field Theory in Statistical Physics*, Dover Publications: New York.

Altmann, K.N., Petrovykh, D.Y., Mankey, G.J., *et al*. (2000). Enhanced spin polarization of conduction electrons in Ni explained by comparison with Cu. *Physical Review B*, **61**, 15661.

Andersen, O.K. (1975). Linear methods in band theory. *Physical Review B*, **12**, 3060.

Andersen, O.K. and Jepsen, O. (1984). Explicit, first-principles tight-binding-theory. *Physical Review Letters*, **53**, 2571.

Anisimov, V.I., Aryasetiawan, F. and Lichtenstein, A.I. (1997). First-principle calculations of the electronic structure and and spectra of strongly correlated systems: the LDA+U method. *Journal of Physics: Condensed Matter*, **9**, 767.

Anisimov, V.I., Poteryaev, A.I., Korotin, M.A., *et al*. (1997). First-principles calculations of the electronic structure and spectra of strongly correlated systems: dynamical mean-field theory. *Journal of Physics: Condensed Matter*, **9**, 7359.

Anisimov, V.I., Solovyev, I.V., Korotin, M.A., *et al*. (1993). Density-functional theory and NiO photoemission spectra. *Physical Review B*, **48**, 16929.

Anisimov, V.I., Zaanen, J. and Andersen, O.K. (1991). Band theory and mott insulators – Hubbard-U instead of Stoner-I. *Physical Review B*, **44**, 943.

Antropov, V.P. (2003). The exchange coupling and spin waves in metallic magnets: removal of the long-wave approximation. *Journal of Magnetism and Magnetic Materials*, **262**, L192.

Antropov, V.P., Katsnelson, M.I., Harmon, B.N., *et al*. (1996). Spin dynamics in magnets: Equation of motion and finite temperature effects. *Physical Review B*, **54**, 1019.

Aryasetiawan, F., Imada, M., Georges, A., *et al*. (2004). Frequency-dependent local interactions and low-energy effective models from electronic structure calculations. *Physical Review B*, **70**, 195104.

Aryasetiawan, F. and Karlsson, K. (1999). Green's function formalism for calculating spin-wave spectra. *Physical Review B*, **60**, 7419.

Auslender, M.I. and Irkhin, V.Yu. (1985). Electron-states in the s-f exchange model of a ferromagnetic semiconductor in the spin-wave region. 2. Degenerate semiconductors. *Journal of Physics C*, **18**, 3533.

Bandyopadhyay, T. and Sarma, D.D. (1989). Calculation of Coulomb interaction strengths for 3d transition-metals and actinides. *Physical Review B*, **39**, 3517.

Biermann, S., Dallmeyer, A., Carbone, C., *et al*. (2004). Observation of Hubbard Bands in γ-Manganese. *JETP Letters*, **80**, 612.

Biermann, S., Lichtenstein, A.I. and Katsnelson, M.I. (2001). unpublished.

Bruno, P. (2003). Exchange interaction parameters and adiabatic spin-wave spectra of ferromagnets: A "renormalized magnetic force theorem". *Physical Review Letters*, **90**, 087205.

Carneiro, G.M. and Pethick, C.J. (1975). Specific-heat of a normal fermi-liquid. 2. Microscopic approach. *Physical Review B*, **11**, 1106.

Chioncel, L., Katsnelson, M.I., de Groot, R.A. and Lichtenstein, A.I. (2003a). Nonquasiparticle states in the half-metallic ferromagnet NiMnSb. *Physical Review B*, **68**, 144425.

Chioncel, L., Vitos, L., Abrikosov, I.A., *et al*. (2003b). Ab initio electronic structure calculations of correlated systems: An EMTO-DMFT approach. *Physical Review B*, **67**, 235106.

Chitra, R. and Kotliar, G. (2000). Dynamical mean-field theory and electronic structure calculations. *Physical Review B*, **62**, 12715.

Chitra, R. and Kotliar, G. (2001). Effective-action approach to strongly correlated fermion systems. *Physical Review B*, **63**, 115110.

Crockford, D.J., Bird, D.M. and Long, M.W. (1991). Band structures of noncollinear magnets in γ-Mn and γ-Fe. *Journal of Physics: Condensed Matter*, **3**, 8665.

Czyzyk, M.T. and Sawatzky, G.A. (1994). Local-density functional and on-site correlations – the electronic-structure of La_2CuO_4 and $LaCuO_3$. *Physical Review B*, **49**, 14211.

Eberhardt, W. and Plummer, E.W. (1980). Angle-resolved photoemission determination of the band-structure and multielectron excitations in Ni. *Physical Review B*, **21**, 3245.

Edwards, D.M. and Hertz, J.A. (1973). Electron-magnon interactions in itinerant ferromagnetism. 2. Strong ferromagnetism. *Journal of Physics F*, **3**, 2191.

Fishman, R.S. and Liu, S.H. (1999). Magnetoelastic effects and spin excitations in γ-Mn alloys. *Physical Review B*, **59**, 8681.

Georges, A. (2004). In *Lectures on the Physics of Highly Correlated Electron Systems VIII*, Avella, A. and Nancini, F. (Eds.), American Institute of Physics: cond-mat/0403123.

Georges, A., Kotliar, G., Krauth, W. and Rozenberg, M. (1996). Dynamical mean-field theory of strongly correlated fermion systems and the limit of infinite dimensions. *Review of Modern Physics*, **68**, 13.

de Groot, R.A., Mueller, F.M., van Engen, P.G. and Buschow, K.H.J. (1983). New class of materials - half-metallic ferromagnets. *Physical Review Letters*, **50**, 2024.

Guillermet, A.F. and Grimvall, G. (1989). Homology of interatomic forces and debye temperatures in transition-metals. *Physical Review B*, **40**, 1521.

Halilov, S.V., Eschrig, H., Perlov, A.Y. and Oppeneer, P.M. (1998). Adiabatic spin dynamics from spin-density-functional theory: Application to Fe, Co, and Ni. *Physical Review B*, **58**, 293.

Held, K., Keller, G., Eyert, V., *et al*. (2001a). Mott-Hubbard metal-insulator transition in paramagnetic V2O3: An LDA+DMFT(QMC) study. *Physical Review Letters*, **86**, 5345.

Held, K., Nekrasov, L.A., Blumer, N., *et al*. (2001b). Realistic modeling of strongly correlated electron systems: An introduction to the LDA plus DMFT approach. *International Journal of Modern Physics. B*, **15**, 2611.

Herring, C. (1966). Exchange interactions among itinerant electrons. In *Magnetism*, Rado G.T. and Suhl H. (Eds.), Academic Press: New York, Vol. 4.

Hirsch, J.E. and Fye, R.M. (1986). Monte-carlo method for magnetic-impurities in metals. *Physical Review Letters*, **25**, 2521.

Hohenberg, P. and Kohn, W. (1964). Inhomogeneous electron gas. *Physical Review*, **136**, B864.

Irkhin, V.Yu. and Katsnelson, M.I. (1983). Charge-carriers in the narrow-band hubbard ferromagnet in the spin-wave temperature-range. *Fizika Tverdogo Tela*, **25**, 3383. [*English Translation in : Soviet Physics-Solid State* **2**5, 1947 (1983)].

Irkhin, V.Yu. and Katsnelson, M.I. (1985). Spin-waves in narrow-band ferromagnets. *Journal of Physics C*, **18**, 4173.

Irkhin, V.Yu. and Katsnelson, M.I. (1990). Ground-state and electron magnon interaction in an itinerant ferromagnet - half-metallic ferromagnets. *Journal of Physics: Condensed Matter*, **2**, 7151.

Irkhin, V.Yu. and Katsnelson, M.I. (1994). Half-metallic ferromagnets. *Uspekhi Fizicheskikh Nauk*, **164**, 705 [*Physics Uspekhi*, **3**7, 659 (1994)].

Irkhin, V.Yu. and Katsnelson, M.I. (2001). Spin-wave contributions to nuclear magnetic relaxation in magnetic metals. *The European Physical Journal*, **B19**, 401.

Irkhin, V.Yu. and Katsnelson, M.I. (2002). Temperature dependences of resistivity and magnetoresistivity for half-metallic ferromagnets. *The European Physical Journal*, **B30**, 481.

Irkhin, V.Yu. and Katsnelson, M.I. (2005). Non-quasiparticle states in the core level spectra of ferromagnetic semiconductors and half-metallic ferromagnets. *The European Physical Journal*, **B43**, 479.

Irkhin, V.Yu., Katsnelson, M.I. and Trefilov, A.V. (1989). On the reconstruction of the conduction electron spectrum in metal-oxide superconductors owing to the interaction with coherent atomic displacements. *Physica C*, **160**, 397.

Irkhin, V.Yu., Katsnelson, M.I. and Trefilov, A.V. (1994). Characteristics of electron and lattice properties of high-temperature superconductors caused by 2-hole potential for apical oxygen. *Zhurnal Eksperimentalnoi I Teoreticheskoi Fiziki*, **105**, 1733 [*Soviet Physics JETP*, **7**8, 936 (1994)].

Iwan, M., Himpsel, F.J. and Eastman, D.E. (1979). Two-electron resonance at the 3p threshold of Cu and Ni. *Physical Review Letters*, **43**, 1829.

Jarlborg, T. (1997). Temperature-dependent electronic structure: from heavy fermion behaviour to phase stability. *Reports on Progress in Physics*, **60**, 1305.

Jarrell, M. and Gubernatis, J.E. (1996). Bayesian inference and the analytic continuation of imaginary-time quantum Monte Carlo data. *Physics Reports*, **269**, 133.

Jones, R.O. and Gunnarsson, O. (1989). The density functional formalism, its applications and prospects. *Reviews of Modern Physics*, **61**, 689.

Kakizaki, A., Fujii, J., Shimada, K., *et al*. (1994). Fluctuating local magnetic moments in ferromagnetic Ni observed by the spin-resolved resonant photoemission. *Physical Review Letters*, **72**, 2781.

Katsnelson, M.I. and Edwards, D.M. (1992). Correlation-effects at the surface of an itinerant electron ferromagnet. *Journal of Physics: Condensed Matter*, **4**, 3289.

Katsnelson, M.I. and Lichtenstein, A.I. (1999). LDA++ approach to the electronic structure of magnets: Correlation effects in iron. *Journal of Physics: Condensed Matter*, **11**, 1037.

Katsnelson, M.I. and Lichtenstein, A.I. (2000). First-principles calculations of magnetic interactions in correlated systems. *Physical Review B*, **61**, 8906.

Katsnelson, M.I. and Lichtenstein, A.I. (2002). Temperature dependences of resistivity and agnetoresistivity for half-metallic ferromagnets. *The European Physical Journal*, **B30**, 9.

Katsnelson, M.I. and Lichtenstein, A.I. (2004). Magnetic susceptibility, exchange interactions and spin-wave spectra in the local spin density approximation. *Journal of Physics: Condensed Matter*, **16**, 7439.

Kisker, E., Schröder, K., Campagna, M. and Gudat, W. (1984). Temperature Dependence of the Exchange Splitting of Fe by Spin-Resolved Photoemission Spectroscopy with Synchrotron Radiation. *Physical Review Letters*, **52**, 2285.

Knapp, J.A. and Himpsel, F.J. (1979). Experimental energy band dispersions and lifetimes for valence and conduction bands of copper using angle-resolved photoemission. *Physical Review B*, **19**, 4952.

Kohn, W. and Sham, L.J. (1965). Self-Consistent Equations Including Exchange and Correlation Effects. *Physical Review*, **140**, A1133.

Kotliar, G. and Vollhardt, D. (2004). Strongly correlated materials: Insights from dynamical mean-field theory. *Physics Today*, **57**(3), 53.

Kreutz, T.J., Greber, T., Aebi, P. and Osterwalder, J. (1998). Temperature-dependent electronic structure of nickel metal. *Physical Review B*, **58**, 1300.

Lichtenstein, A.I. and Katsnelson, M.I. (1997). Dynamical mean field band structure: LDA++ approach. *The Bulletin of American Physical Society*, **42**, 573.

Lichtenstein, A.I. and Katsnelson, M.I. (1998). Ab initio calculations of quasiparticle band structure in correlated systems: LDA++ approach. *Physical Review B*, **57**, 6884.

Lichtenstein, A.I. and Katsnelson, M.I. (2001). Magnetism of correlated systems: beyond LDA. In *Band Ferromagnetism. Ground State and Finite-Temperature Phenomena*, *Lecture Notes in Physics*, Baberschke, K., Donath, M. and Nolting W. (Eds.), Springer: Berlin, p. 75.

Lichtenstein, A.I., Katsnelson, M.I. and Kotliar, G. (2001). Finite-Temperature Magnetism of Transition Metals: An ab initio Dynamical Mean-Field Theory. *Physical Review Letters*, **87**, 067205.

Lichtenstein, A.I., Katsnelson, M.I. and Kotliar, G. (2002). Spectral density functional approach to electronic correlations and magnetism in crystals. In *Electron Correlations and Material Properties 2*, Gonis, A., Kioussis, N. and Ciftan, M. (Eds.), Kluwer Academic Publishers/Plenum: New York, p. 428.

Liebsch, A. (1981). Ni d-band self-energy beyond the low-density limit. *Physical Review B*, **23**, 5203.

Liechtenstein, A.I., Katsnelson, M.I., Antropov, V.P. and Gubanov, V.A. (1987). Local spin-density functional-approach to the theory of exchange interactions in ferromagnetic metals and alloys. *Journal of Magnetism and Magnetic Materials*, **67**, 65.

von der Linden, W. (1992). A quantum monte-carlo approach to many-body physics. *Physics Reports*, **220**, 53.

Luttinger, J.M. and Ward, J.C. (1960). Ground-state energy of a many-fermion system. *Physical Review*, **118**, 1417.

Lynn, J.W. (1975). Temperature dependence of the magnetic excitations in iron. *Physical Review B*, **11**, 2624.

Mackintosh, A.R. and Andersen, O.K. (1980). The Electronic Structure of Transition Metals. In *Electron at the Fermi Surface*, Springford, M. (Eds.), University Press: Cambridge 149.

Manghi, F., Bellini, V. and Arcangelli, C. (1997). On-site correlation in valence and core states of ferromagnetic nickel. *Physical Review B*, **56**, 7149.

Manghi, F., Bellini, V., Osterwalder, J., *et al*. (1999). Correlation effects in the low-energy region of nickel photoemission spectra. *Physical Review B*, **59**, R10409.

McCann, E. and Fal'ko, V.I. (2003). Magnon-assisted transport and thermopower in ferromagnet›normal-metal tunnel junctions. *Physical Review B*, **68**, 172404.

Minár, J., Chioncel, L., Perlov, A., *et al*. (2005). Multiple-scattering formalism for correlated systems: A KKR-DMFT approach. *Physical Review B*, **72**, 045125.

Mook, H.A. and Lynn, J.W. (1985). Measurements of the magnetic excitations above tc in iron and nickel. *Journal of Applied Physics*, **57**, 3006.

Mook, H.A. and Nicklow, R.M. (1973). Neutron-scattering investigation of magnetic excitations in iron. *Physical Review B*, **7**, 336.

Moriya, T. (1985). *Spin Fluctuations in Itinerant Electron Magnetism*, Springer: Berlin.

Moruzzi, V.L., Marcus, P.M. and Kübler, J. (1989). Magneto-volume instabilities and ferromagnetism versus antiferromagnetism in bulk fcc iron and manganese. *Physical Review B*, **39**, 6957.

Mott, N.F. (1974). *Metal-Insulator Transitions*, Taylor and Francis: London.

Nagaoka, Y. (1966). Ferromagnetism in a Narrow, Almost Half-Filled s Band. *Physical Review*, **147**, 392.

Nolting, W., Rex, S. and Mathi Jaya, S. (1987). Valence instability in antiferromagnetically ordered 4f-systems. *Journal of Physics: Condensed Matter*, **9**, 1301.

Nozieres, P. (1964). *Theory of Interacting Fermi Systems*, Benjamin: New York.

Pajda, M., Kudrnovsky, J., Turek, I., *et al*. (2001). Ab initio calculations of exchange interactions, spin-wave stiffness constants, and Curie temperatures of Fe, Co, and Ni. *Physical Review B*, **64**, 174402.

Perring, T.G., Boothroyd, A.T., Paul, D.M., *et al*. (1991). High-energy spin-waves in bcc iron. *Journal of Applied Physics*, **69**, 6219.

Pickett, W.E. and Moodera, J. (2001). Half metallic magnets. *Physics Today*, **54**(6), 39.

Pines, D. and Nozieres, P. (1966). *The Theory of Quantum Liquids*, Benjamin: New York.

Prinz, G.A. (1998). Device physics – Magnetoelectronics. *Science*, **282**, 1660.

Rosengaard, N.M. and Johansson, B. (1997). Finite-temperature study of itinerant ferromagnetism in Fe, Co, and Ni. *Physical Review B*, **55**, 14975.

Rozenberg, M.J. (1997). Integer-filling metal-insulator transitions in the degenerate Hubbard model. *Physical Review B*, **55**, R4855.

Sandratskii, L.M. and Kübler, J. (1992). Static nonuniform magnetic-susceptibility of selected transition-metals. *Journal of Physics: Condensed Matter*, **4**, 6927.

Savrasov, S.Y. and Kotliar, G. (2004). Spectral density functionals for electronic structure calculations. *Physical Review B*, **69**, 245101.

Savrasov, S.Y., Kotliar, G. and Abrahams, E. (2001). Correlated electrons in delta-plutonium within a dynamical mean-field picture. *Nature*, **410**, 793.

Sinkovic, B., Tjeng, L.H., Brookes, N.B., *et al*. (1997). Local electronic and magnetic structure of Ni below and above Tc: a spin-resolved circularly polarized resonant photoemission study. *Physical Review Letters*, **79**, 3510.

Staunton, J.B. and Gyorffy, B.L. (1992). Onsager cavity fields in itinerant-electron paramagnets. *Physical Review Letters*, **69**, 371.

Steiner, M.M., Albers, R.C. and Sham, L.J. (1992). Quasiparticle properties of Fe, Co, and Ni. *Physical Review B*, **45**, 13272.

Stocks, G.M., Ujfalussy, B., Wang, X., *et al*. (1998). Towards a constrained local moment model for first principles spin dynamics. *Philosophical Magazine B*, **78**, 665.

Takegahara, K. (1993). Quantum monte-carlo study of the degenerate anderson model with cubic-crystal field. *Journal of the Physical Society of Japan*, **62**, 1736.

Thiry, P., Chandesris, D., Lecante, J., *et al*. (1979). E vs k $\rightarrow$ and Inverse Lifetime of Cu(110). *Physical Review Letters*, **43**, 82.

Treglia, G., Ducastelle, F. and Spanjaard, D. (1982). Effect of coulomb correlations on energy-bands in ferromagnetic transition-metals – Ni, Co and Fe. *Journal of Physics (Paris)*, **43**, 341.

Vonsovsky, S.V. (1974). *Magnetism*, John Wiley & Sons: New York.

Vonsovsky, S.V. and Katsnelson, M.I. (1989a). *Quantum Solid State Physics*, Springer: Berlin.

Vonsovsky, S.V. and Katsnelson, M.I. (1989b). Evolution of the concepts about the role of many-particle effects in transition-metals, their alloys and compounds. *Physica B*, **159**, 61.

Wolfarth, E.P. (Eds.) (1986). *Ferromagnetic Materials*, North-Holland: Amsterdam, Vol. 1.

Zein, N.E. (1995). Correlation energy functionals for ab initio calculations: Application to transition metals. *Physical Review B*, **52**, 11813.

Quantum Monte Carlo Methods

Fakher F. Assaad[1] and Matthias Troyer[2]

[1] *Universität Würzburg, Würzburg, Germany*
[2] *ETH Zürich, Zürich, Switzerland*

1 INTRODUCTION

The comparison of experimental measurements on quantum magnets to microscopic models requires the ability to accurately calculate magnetic and other thermodynamic properties of these models. Like for most many-body problems, exact solutions are not available except for certain models, such as the two-dimensional classical Ising model or some one-dimensional quantum spin models. While mean-field theories can give reliable results in high-dimensional systems deep inside ordered phases, they are unreliable when fluctuations are strong. These can be either classical thermal fluctuations close to finite-temperature phase transitions or strong quantum fluctuations in low-dimensional systems.

Handbook of Magnetism and Advanced Magnetic Materials. Edited by Helmut Kronmüller and Stuart Parkin. Volume 1: *Fundamentals and Theory*. ISBN: 978-0-470-02217-7.

Unbiased numerical methods are required to obtain reliable results for classical and quantum lattice models of magnetic systems, especially in the vicinity of phase transitions, in frustrated models, and in systems where quantum effects are important. For classical magnets, the Monte Carlo method is the method of choice since it can treat large systems. Using modern sampling algorithms, such as cluster updates, extended ensemble methods, or parallel tempering strategies, most classical magnets can be efficiently simulated with the computational effort scaling, with a low power of the system size, and are usually linear in system size. The notable exceptions are spin glasses, known to be nondeterministic-polynomially (NP) hard (Barahona, 1982) and where, most likely, no polynomial-time algorithm can exist (Cook, 1971).

For quantum magnets, quantum Monte Carlo (QMC) methods are also the methods of choice whenever they are applicable. Over the last decade, the efficient algorithms for classical Monte Carlo simulations have been generalized to quantum systems, and systems with millions of quantum spins have been simulated (Kim and Troyer, 1998).

Unfortunately, in contrast to classical magnets, QMC methods are efficient only for nonfrustrated magnets. Frustration in quantum systems usually leads to the 'negative sign problem', when the weights of some configurations become negative (Troyer and Wiese, 2005). These negative weights cannot be directly interpreted as probabilities in the Monte Carlo process and lead to cancellation effects in the sampling. As a consequence, the statistical errors grow exponentially with inverse temperature and system size, and the QMC methods are restricted to small systems and not too low temperatures. For quasi-one-dimensional quantum systems such as spin chains and spin ladders, the density matrix renormalization group (DMRG) method can be an alternative (White, 1992,1993; Schollwöck, 2005). The problem of simulating

strongly frustrated quantum magnets in more than one dimension and at low temperatures is, however, still an unsolved problem.

In this article, we will review the QMC method for nonfrustrated or weakly frustrated quantum magnets where efficient algorithms are available. We will start in section 2 with an introduction to the general theory of Markov chain Monte Carlo sampling, followed in section 3 by an overview of classical Monte Carlo methods, and how the problem of critical slowing down at phase transition can be solved by using cluster update algorithms or generalized ensembles. Section 4 will provide a review of world-line QMC algorithms for purely magnetic models such as the quantum Heisenberg model and variants thereof. The final section 5 will introduce determinental QMC algorithms for the more microscopic fermionic models of quantum magnets, such as the Hubbard model.

2 THE MONTE CARLO METHOD

In this chapter, we outline the Monte Carlo method for calculating general integrals of the form

$$\langle O \rangle = \int_{\Omega} \mathrm{d}x\, P(x) O(x) \tag{1}$$

Here Ω denotes a discrete or continuous configuration space with elements x and $P(x)$ is a probability distribution on this space, where

$$\int_{\Omega} \mathrm{d}x\, P(x) = 1 \quad \text{and} \quad P(x) \geq 0 \; \forall \; x \in \Omega. \tag{2}$$

O is an observable (or random variable) on the configuration space Ω. In later chapters, we will show how this general method can be applied to quantum magnets.

Stochastic processes are based on the idea that it suffices to sample configurations x according to their importance, $P(x)$. For a given chain of configurations, $x_1, \cdots, x_N$, sampled according to their importance, we can then approximate our observable $\langle O \rangle$ with

$$\langle O \rangle_N \simeq \frac{1}{N} \sum_{i=1}^{N} O(x_i) \tag{3}$$

Clearly the value of $\langle O \rangle_N$ depends on the specific realization of the chain of configurations. However, under the assumptions that $O(x_i)$ are statistically independent and that N is large enough, the central limit theorem tells us that, $\langle O \rangle_N$ follows a Gaussian distribution of width

$$\sigma = \sqrt{\frac{1}{N-1}\left(\frac{1}{N}\sum_{i=1}^{N} O(x_i)^2 - \left(\frac{1}{N}\sum_{i=1}^{N} O(x_i)\right)^2\right)} \tag{4}$$

σ corresponds to the error. Hence, the accuracy of the Monte Carlo approach scales as the inverse square root of the computational time, N, irrespective of the dimensionality of the configuration space. It is this feature which makes the Monte Carlo approach attractive in the limit of large dimensions.

Our task is now to generate a chain of configurations $x_1, \cdots, x_N$, sampled according to $P(x)$. For simplicity let us consider a discrete configurations space Ω. We introduce a Monte Carlo time t and a time-dependent probability distribution $P_t(x)$ which evolves according to a Markov process, that is, the future $(t+1)$ depends only on the present (t). To define the Markov process, we introduce a matrix $T_{y,x}$ which corresponds to the transition probability from state x to state y. The time evolution of $P_t(x)$ is given by:

$$P_{t+1}(y) = \sum_{x} T_{y,x} P_t(x) \tag{5}$$

T has to satisfy the following properties.

$$\sum_{y} T_{y,x} = 1, \quad T_{y,x} \geq 0 \tag{6}$$

Hence, if $P_t(x)$ is a probability distribution then $P_{t+1}(x)$ is equally a probability distribution.
T has to be ergodic:

$$\forall x, \; y \in \Omega \; \exists \, s | \left(T^s\right)_{y,x} > 0 \tag{7}$$

Thus, we are assured of sampling the whole phase space provided the above equation is satisfied. Finally, the requirement of stationarity:

$$\sum_{x} T_{y,x} P(x) = P(y) \tag{8}$$

Once we have reached the desired distribution, $P(x)$, we wish to stay there. Stationarity is automatically satisfied if

$$T_{y,x} P(x) = T_{x,y} P(y) \tag{9}$$

as may be seen by summing on both sides over x. This relation is referred to as detailed balance or microreversibility. However, one has to keep in mind that stationarity and not detailed balance is essential.

As given in the preceding text, in the Monte Carlo simulation we will generate the Markov Chain,

$$x_1, x_2, \cdots, x_N \tag{10}$$

where the conditional probability of sampling the state x_{t+1} given the state x_t reads:

$$P(x_{t+1}|x_t) = T_{x_{t+1},x_t} \tag{11}$$

One can show that as $n \to \infty$ the fraction of the time one can expect the Markov process to be in state x reads $P(x)$ independently of the initial state x_1. More precisely, since the probability of being in state x at time t in the Markov process reads $\left[T^t\right]_{x,x_1}$, one can show that

$$\lim_{n\to\infty} \frac{1}{n} \sum_{t=1}^{n} \left[T^t\right]_{x,x_1} = P(x) \tag{12}$$

irrespective of the starting point x_1. For a demonstration of the above, the reader is referred to (Kemeny and Snell, 1960).

Having defined T, we now have to construct it explicitly. Let $T^0_{y,x}$ be the probability of proposing a transition from x to y and $a_{y,x}$ be the probability of accepting it. $1 - a_{y,x}$ corresponds to the probability of rejecting the move. T^0 is required to satisfy equation (6). Since, in general, we want to propose moves which change the initial configuration, $T^0_{x,x} = 0$. With $a_{y,x}$ and $T^0_{y,x}$ we build $T_{y,x}$ with:

$$T_{y,x} = \begin{cases} T^0_{y,x} a_{y,x} & \text{if} \quad y \neq x \\ \sum_{\substack{z \\ z\neq x}} T^0_{z,x} \left(1 - a_{z,x}\right) & \text{if} \quad y = x \end{cases} \tag{13}$$

Clearly $T_{y,x}$ satisfies equation (6). To satisfy the stationarity, we impose the detailed balance condition to obtain the equality:

$$T^0_{y,x} a_{y,x} P_x = T^0_{x,y} a_{x,y} P_y \tag{14}$$

Let us set:

$$a_{y,x} = \mathcal{F}\left(\frac{T^0_{x,y} P_y}{T^0_{y,x} P_x}\right) \tag{15}$$

with $\mathcal{F}:]0:\infty[\to [0,1]$. Since

$$a_{x,y} = \mathcal{F}\left(\frac{T^0_{y,x} P_x}{T^0_{x,y} P_y}\right) = \mathcal{F}\left(\frac{1}{\frac{T^0_{x,y} P_y}{T^0_{y,x} P_x}}\right) \tag{16}$$

the detailed balance condition reduces to:

$$\frac{\mathcal{F}(Z)}{\mathcal{F}(1/Z)} = Z \quad \text{where} \quad Z = \frac{T^0_{x,y} P_y}{T^0_{y,x} P_x} \tag{17}$$

There are many possible choices. The Metropolis algorithm (Metropolis *et al.*, 1953) is based on the choice:

$$\mathcal{F}(Z) = \min(Z, 1) \tag{18}$$

Thus, one proposes a transition from x to y and accepts it with probability $Z = \frac{T^0_{x,y} P_y}{T^0_{y,x} P_x}$. In the practical implementation, one picks a random number r in the interval $[0, 1]$. If $r < Z (r > Z)$ one accepts (rejects) the move. Alternative choices of $\mathcal{F}(Z)$ are for example:

$$\mathcal{F}(Z) = \frac{Z}{1+Z} \tag{19}$$

which is referred to as the heat bath method.

Whether the so constructed T matrix is ergodic depends upon the choice of T^0. In many cases, one will wish to combine different types of moves to achieve ergodicity. For a specific move i, we construct $T^{(i)}$ as shown above so that $T^{(i)}$ satisfies conditions (6) and (9). The moves may be combined in two ways:

$$T = \sum_i \lambda_i T^{(i)}, \quad \sum_i \lambda_i = 1 \tag{20}$$

which is referred to as random updating since one picks with probability λ_i the move $T^{(i)}$. Clearly, T equally satisfies (6), (9) and if the moves have to be chosen appropriately to satisfy the ergodicity condition. Another choice is sequential updating. A deterministic ordering of the moves is chosen to obtain:

$$T = \prod_i T^{(i)} \tag{21}$$

This choice does not satisfy detailed balance condition, but does satisfy stationarity (8) as well as (6). Again ergodicity has to be *checked* on a case-to-case basis.

The observable O may now be estimated with:

$$\langle O \rangle_P \approx \frac{1}{N} \sum_{t=1}^{N} O(x_t) \tag{22}$$

The required value of N depends on the autocorrelation time of the observable O:

$$C_O(t) = \frac{\frac{1}{N}\sum_{s=1}^{N} O(x_s) O(x_{s+t}) - \left(\frac{1}{N}\sum_{s=1}^{N} O(x_s)\right)^2}{\frac{1}{N}\sum_{s=1}^{N} O(x_s)^2 - \left(\frac{1}{N}\sum_{s=1}^{N} O(x_s)\right)^2} \tag{23}$$

One expects $C_O(t) \sim e^{-t/\tau_O}$ where τ_O corresponds to the autocorrelation time. The autocorrelation time corresponds to

the time scale on which memory of the initial value of the observable is lost. To obtain meaningful results as well as a reliable estimate of the error, $N \gg \tau_O$ is needed.

3 CLASSICAL MONTE CARLO METHODS AND CRITICAL SLOWING DOWN

3.1 The local update algorithm for the Ising model

Before discussing quantum magnets in the following chapters, we first apply the Monte Carlo method to classical lattice models to illustrate the important issues, algorithms, and sampling strategies on simple classical models. We will start with the Ising ferromagnet with Hamilton function

$$H = -J \sum_{\langle i,j \rangle} \sigma_i \sigma_j - g\mu_B h \sum_{i=1}^{N} \sigma_i \tag{24}$$

where J is the exchange constant, h the magnetic field, g the Landee g-factor, μ_B the Bohr magneton, and N the total number of spins. The sum runs over all pairs of nearest neighbors i and j and $\sigma_i = \pm 1$ is the value of the Ising spin at site i.

To calculate the value of an observable, such as the mean magnetization at an inverse temperature $\beta = 1/k_B T$ with T being the temperature and k_B the Boltzmann constant, we need to evaluate

$$\langle m \rangle = \sum_c m(c) \exp(-\beta E(c))/Z \tag{25}$$

where,

$$m(c) = \frac{1}{N} \sum_{i=1}^{N} \sigma_i \tag{26}$$

is the magnetization of the configuration c, $E(c)$ the energy of the configuration and

$$Z = \sum_c \exp(-\beta E(c)) \tag{27}$$

the partition function. Comparing to equation (1) in the previous chapter we identify the space Ω with the space of configurations $\{c\}$, the observable $O(x)$ with the magnetization $m(c)$ and the weight $P(x)$ with the Boltzmann weight $\exp(-\beta E(c))/Z$.

As discussed above, Monte Carlo sampling can be performed using the Metropolis or heat bath methods, which, in their simplest form, are local updates of single spins:

1. Pick a random site i.
2. Calculate the energy cost ΔE for flipping the spin at site i: $\sigma_i \to -\sigma_i$.
3. Flip the spin either with the Metropolis probability $\min[1, \exp(-\beta \Delta E)]$ or the heat bath probability $\exp(-\beta \Delta E)/(1 + \exp(-\beta \Delta E))$. If rejected, keep the original spin value.
4. Perform a measurement independent of whether the spin-flip was accepted or rejected.

The same local update algorithm can be applied to systems with longer-range interactions and with coupling constants that vary from bond to bond. For more complex classical models, such as Heisenberg models, local updates will no longer consist of simple spin flips, but of arbitrary rotations of the local spin vectors.

3.2 Critical slowing down and cluster update algorithms

Local update algorithms are easy to implement and work well away from phase transitions. Problems arise in the vicinity of continuous (second order) phase transitions, when these algorithms suffer from 'critical slowing down' (Swendsen and Wang, 1987). As the correlation length ξ diverges upon approaching the phase transition, the autocorrelation times τ_O also diverge as

$$\tau_O \propto \min(L, \xi)^z \tag{28}$$

with a dynamical critical exponent of $z \approx 2$. L is the linear extent of the system. The origin of critical slowing down is the fact that close to the critical temperature large ordered domains of linear extent ξ are formed and the single-spin updates are not effective in changing these large domains. The value $z \approx 2$ can be understood considering that the time for a domain wall to move a distance ξ by a random walk scales as ξ^2.

The solutions to critical slowing down are cluster updates, flipping carefully selected clusters of spins instead of single spins. Cluster update algorithms were originally invented by Swendsen and Wang for the Ising model (Swendsen and Wang, 1987) and soon generalized to $O(N)$ models, such as the Heisenberg model (Wolff, 1989). These cluster update algorithms are discussed in textbooks on classical Monte Carlo simulations and in computational physics textbooks. While most cluster algorithms require spin-inversion invariance and thus do not allow for external magnetic fields, extensions to spin models in magnetic fields have been proposed (Redner, Machta and Chayes, 1998; Evertz, Erkinger and von der Linden, 2002).

An open-source implementation of local and cluster updates for Ising, Potts, *XY* and Heisenberg models is available through the ALPS (Applications and Libraries for Physics Simulations) project (Alet *et al*., 2005) at the web page http://alps.comp-phys.org/.

3.3 First order phase transitions and the multicanonical ensemble

While cluster updates can solve critical slowing down at second order phase transitions, they are usually inefficient at first order phase transitions and in frustrated systems. Let us consider a first order phase transition, such as in a two-dimensional q-state Potts model with Hamilton function

$$H = -J \sum_{\langle i,j \rangle} \delta_{\sigma_i \sigma_j} \tag{29}$$

where the spins σ_i can now take the integer values $1, \ldots, q$. For $q > 4$ this model exhibits a first order phase transition, accompanied by exponential slowing down of local single-spin updates. The exponential slowdown is caused by the free energy barrier between the two coexisting metastable states at the first order phase transition.

This barrier can be quantified by considering the energy histogram

$$H_{\text{canonical}}[E] = g(E) P_{\text{Boltzmann}}(E) \propto g(E) \exp(-\beta E) \tag{30}$$

which is the probability of encountering a configuration with energy E during the Monte Carlo simulation. Here

$$g(E) = \sum_c \delta_{E,E(c)} \tag{31}$$

is the density of states. Away from first order phase transitions, $H_{\text{canonical}}[E]$ has approximately Gaussian shape, centered around the mean energy. At first order phase transitions where the energy jumps discontinuously, the histogram $H_{\text{canonical}}[E]$ develops a double-peak structure. The minimum of $H_{\text{canonical}}[E]$ between these two peaks, which the simulation has to cross in order to go from one phase to the other, becomes exponentially small upon increasing the system size. This leads to exponentially large autocorrelation times.

A solution to this tunneling problem are extended ensembles, such as the multicanonical ensemble (Berg and Neuhaus, 1991, 1992), where the weight of a configuration c is given by $P_{\text{multicanonical}}(c) \propto 1/g(E(c))$ instead of the Boltzmann weight $\exp(-\beta E(c))$. The multicanonical ensemble leads to a flat histogram in energy space

$$\begin{aligned} H_{\text{multicanonical}}[E] &= g(E) P_{\text{multicanonical}}(E) \propto g(E) \frac{1}{g(E)} \\ &= \text{constant} \end{aligned} \tag{32}$$

removing the exponentially small minimum. After performing a simulation, measurements in the multicanonical ensemble are reweighted by a factor $P_{\text{Boltzmann}}(E)/P_{\text{multicanonical}}(E)$ to obtain averages in the canonical ensemble.

Since the density of states $g(E)$ and thus the multicanonical weights $P_{\text{multicanonical}}$ are not known initially, a scalable algorithm to estimate these quantities is needed. The Wang-Landau algorithm (Wang and Landau, 2001a, b) is a simple iterative method to obtain the density of states $g(E)$ and the multicanonical weights $P_{\text{multicanonical}}(E) \propto 1/g(E)$.

Recent investigations have shown that a flat histogram, as obtained by the multicanonical ensemble, is not optimal but still shows signs of critical slowing down (Dayal *et al*., 2004). Optimized ensembles, assigning larger weights to configurations in the critical region, can be found and lead to further improvements in the efficiency of algorithms by several orders of magnitude (Trebst, Huse and Troyer, 2004).

3.4 Frustrated systems and parallel tempering

The simulation of frustrated systems suffers from a similar tunneling problem as the simulation of first order phase transitions: local minima in energy space are separated by barriers that grow with system size. While the multicanonical or optimized ensembles do not help with the NP-hard problems faced by spin glasses, they are efficient in speeding up simulations of frustrated magnets without disorder.

An alternative to these extended ensembles for the simulation of frustrated magnets is the 'parallel tempering' or 'exchange' Monte Carlo method (Hukushima and Nemoto, 1996). Instead of performing a single simulation at a fixed temperature, simulations are performed for M replicas at a set of inverse temperatures $\beta_1, \ldots, \beta_M$. In addition to standard Monte Carlo updates at a fixed temperature, exchange moves are proposed to swap two replicas between adjacent temperatures. These swaps are accepted with a probability $\min[1, \exp(-\Delta\beta \Delta E)]$, where $\Delta\beta$ is the difference in inverse temperatures and ΔE the difference in energy between the two replicas.

The effect of these exchange moves is that a replica can drift from a local free energy minimum at low temperatures to higher temperatures, where it is easier to cross energy barriers. Upon cooling (by another sequence of exchanges), it can end up in a different local minimum in time that is

much shorter than for a single simulation at a fixed low temperature.

4 QUANTUM MONTE CARLO WORLD-LINE ALGORITHMS

4.1 The $S = 1/2$ quantum XXZ model

In this chapter, we will generalize the Monte Carlo methods described in chapter 3 for classical spin systems to quantum spin systems. As examples we will use the spin-1/2 quantum Heisenberg or XXZ models with Hamiltonian

$$\begin{aligned} H &= \sum_{\langle i,j\rangle}\left[J_z S_i^z S_j^z + J_{xy}\left(S_i^x S_j^x + S_i^y S_j^y\right)\right] - g\mu_B h\sum_{i=1}^{N} S_i^z \\ &= \sum_{\langle i,j\rangle}\left[J_z S_i^z S_j^z + \frac{J_{xy}}{2}\left(S_i^+ S_j^- + S_i^- S_j^+\right)\right] - g\mu_B h\sum_{i=1}^{N} S_i^z \end{aligned} \tag{33}$$

where S_i^α are spin $S = 1/2$ operators fulfilling the standard commutation relations and in the second line, we have replaced S_i^x and S_i^y by the spin raising and lowering operators S_i^+ and S_i^-.

The case $J_{xy} = 0$ corresponds to the classical Ising model (24) up to a change in sign: while in classical Monte Carlo simulations (where there is no difference in the thermodynamics of the ferromagnet and the antiferromagnet) a positive exchange constant J denotes the ferromagnet, the convention for quantum systems is usually opposite with a positive exchange constant denoting the antiferromagnet. The other limit $J_z = 0$ corresponds to the quantum XY-model, while $J_z = J_{xy}$ is the Heisenberg model.

4.2 Representations

The basic problem for Monte Carlo simulations of quantum systems is that the partition function is no longer a simple sum over classical configurations as in equation (27) but an operator expression

$$Z = \mathrm{Tr}\exp(-\beta H) \tag{34}$$

where H is the Hamilton operator and the trace Tr goes over all states in the Hilbert space. Similarly the expression for an observable, like the magnetization, is an operator expression:

$$\langle m\rangle = \frac{1}{Z}\mathrm{Tr}\left[m\exp(-\beta H)\right] \tag{35}$$

and the Monte Carlo method cannot directly be applied except in the classical case where the Hamilton operator H is diagonal and the trace reduces to a sum over all basis states. The first step of any QMC algorithm is thus the mapping of the quantum system to an equivalent classical system

$$\langle m\rangle = \frac{1}{Z}\mathrm{Tr}\left[m\exp(-\beta H)\right] = \sum_c m(c)P(c) \tag{36}$$

where the sum goes over configurations c in an artificial classical system (e.g., a system of world lines), $m(c)$ will be the value of the magnetization or another observable as measured in this classical system and $P(c)$ the weight of the classical configuration. We will now present two different but related methods for this mapping: the path-integral representation and the SSE representation.

4.2.1 The path-integral representation

The path-integral formulation of a quantum system goes back to (Feynman, 1953), and forms the basis of most QMC algorithms. Instead of following the historical route and discussing the Trotter-Suzuki (checkerboard) decomposition (Trotter, 1959; Suzuki, 1976) for path integrals with discrete time steps $\Delta\tau$ we will directly describe the continuous-time formulation used in modern codes.

The starting point is a time-dependent perturbation expansion in imaginary time to evaluate the density matrix operator $\exp(-\beta H)$. Using a basis in which the S^z operators are diagonal, we follow (Prokofev, Svistunov and Tupitsyn, 1998) and split the Hamiltonian $H = H_0 + V$ into a diagonal term H_0, containing the S^z term and an off-diagonal perturbation V, containing the exchange terms $(J_{xy}/2)(S_i^+ S_j^- + S_i^- S_j^+)$. In the interaction representation, the time-dependent perturbation is $V(\tau) = \exp(\tau H_0)V\exp(-\tau H_0)$ and the partition function can be represented as:

$$\begin{aligned} Z &= \mathrm{Tr}\exp(-\beta H) = \mathrm{Tr}\left[\exp(-\beta H_0)\mathcal{T}\exp\int_0^\beta d\tau V(\tau)\right] \\ &= \mathrm{Tr}\left[\exp(-\beta H_0)\left(1 - \int_0^\beta d\tau_1 V(\tau_1) + \frac{1}{2}\int_0^\beta d\tau_1\right.\right. \\ &\quad \left.\left.\times\int_{\tau_1}^\beta d\tau_2 V(\tau_1)V(\tau_2) + \ldots\right)\right] \\ &= \sum_i \langle i|\left[\exp(-\beta H_0)\left(1 - \int_0^\beta d\tau_1 V(\tau_1) + \frac{1}{2}\int_0^\beta d\tau_1\right.\right. \\ &\quad \left.\left.\times\int_{\tau_1}^\beta d\tau_2 V(\tau_1)V(\tau_2) + \ldots\right)\right]|i\rangle \end{aligned} \tag{37}$$

where the symbol $\mathcal{T}$ denotes time-ordering of the exponential and in the last line, we have replaced the trace by a sum over

a complete set of basis states $|i\rangle$, that are eigenstates of the local S^z operators. Note that, in contrast to a real-time path integral, the imaginary-time path integral always converges on finite systems of N spins at finite temperatures β, and the expansion can be truncated at orders $n \gg \beta J_{xy} N$.

Equation (37) is now just a classical sum of integrals and can be evaluated by Monte Carlo sampling in the initial states $|i\rangle$, the order of the perturbation n and the times $\tau_i (i = 1, \ldots, n)$. This is best done by considering a graphical world-line representation of the partition function (37) shown in Figure 1. The zeroth order terms in the sum $\sum_i \langle i| \exp(-\beta H_0)|i\rangle$ are given by straight world lines shown in Figure 1(a). First order terms do not appear since the matrix elements $\langle i|V|i\rangle$ are zero for the *XXZ* model. The first nontrivial terms are appear in second order with two exchanges, as shown in Figure 1(b). A general configuration of higher order is depicted in Figure 2(a).

Since the *XXZ* Hamiltonian commutes with the z-component of total spin $\sum_i S_i^z$, the total magnetization is conserved and all valid configurations are represented by closed world lines as shown in Figures 1 and 2. Models that break this conservation of magnetization, such as general *XYZ* models with different couplings in all directions, models with transverse fields coupling to S_i^x or higher spin models with single ion anisotropies $(S_i^x)^2$ or $(S_i^y)^2$ will in addition contain configurations with broken world-line segments.

4.2.2 The stochastic series expansion representation

An alternative representation is the stochastic series expansion (SSE) (Sandvik and Kurkijärvi, 1991), a generalization of Handscomb's algorithm (Handscomb, 1962) for the Heisenberg model. It starts from a Taylor expansion of the

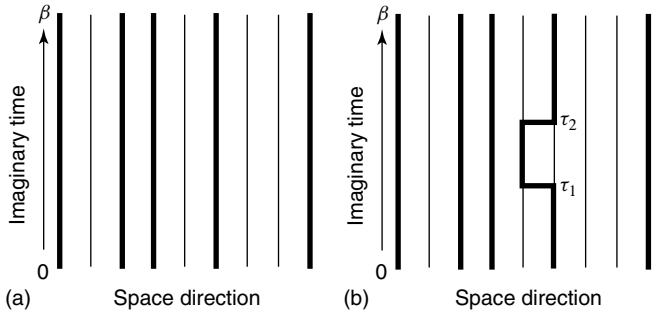

Figure 1. Examples of simple world-line configurations in imaginary time for a quantum spin model. Up-spins are shown by bold lines and down spins by thin lines. (a) a configuration in zeroth order perturbation theory where the spins evolve according to the diagonal term $\exp(-\beta H_0)$ and the weight is given by the classical Boltzmann weight of H_0. (b) a configuration in second order perturbation theory with two exchanges at times τ_1 and τ_2. Its weight is given by the matrix elements of the exchange processes and the classical Boltzmann weight of H_0 of the spins.

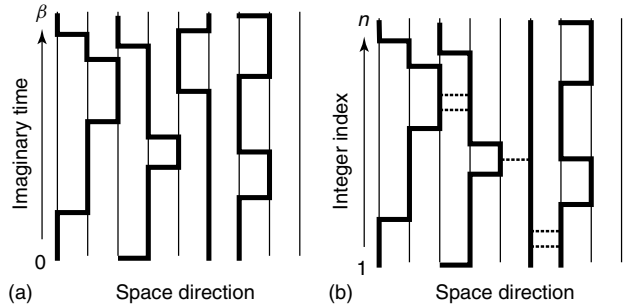

Figure 2. Examples of world-line configurations in (a) a path-integral representation where the time direction is continuous and (b) the stochastic series expansion (SSE) representation where the 'time' direction is discrete. Since the SSE representation perturbs not only in off-diagonal terms but also in diagonal terms, additional diagonal terms are present in the representation, indicated by dashed lines.

partition function in orders of β:

$$\begin{aligned} Z = \mathrm{Tr}\exp(-\beta H) &= \sum_{n=0}^{\infty} \frac{\beta^n}{n!} \mathrm{Tr}(-H)^n \\ &= \sum_{n=0}^{\infty} \frac{\beta^n}{n!} \sum_{\{i_1,\ldots,i_n\}} \sum_{\{b_1,\ldots,b_n\}} \langle i_1| - H_{b_1}|i_2\rangle \\ &\quad \times \langle i_2| - H_{b_2}|i_3\rangle \cdots \langle i_n| - H_{b_n}|i_1\rangle \end{aligned} \tag{38}$$

where, in the second line, we decomposed the Hamiltonian H into a sum of single-bond terms $H = \sum_b H_b$, and again inserted complete sets of basis states. We end up with a similar representation as equation (37) and a related world-line picture shown in Figure 2(b).

The key difference is that the SSE representation is a perturbation expansion in all terms of the Hamiltonian, while the path-integral representation perturbs only in the off-diagonal terms. Although the SSE method thus needs higher expansion orders for a given system, this disadvantage is compensated by a simplification in the algorithms: only integer indices of the operators need to be stored instead of continuous-time variables τ_i. Except in strong magnetic fields or for dissipative quantum spin systems (Sachdev, Werner and Troyer, 2004; Werner, Völker, Troyer and Chakravarty, 2005) the SSE representation is thus the preferred representation for the simulation of quantum magnets.

4.2.3 The negative sign problem

While the mapping from the quantum average to a classical average in equation (36) can be performed for any quantum system, it can happen in frustrated quantum magnets, that some of the weights $P(c)$ in the quantum system are negative, as is shown in Figure 3.

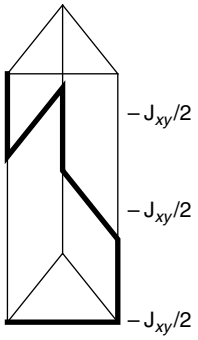

Figure 3. Example of a frustrated world-line configuration in a Heisenberg quantum antiferromagnet on a triangle. The closed world-line configuration contains three exchange processes, each contributing a weight proportional to $-J_{xy}/2$. The overall is proportional to $(-J_{xy}/2)^3$ and is negative, causing a negative sign problem for the antiferromagnet with $J_{xy} > 0$.

Since Monte Carlo sampling requires positive weights $P(c) > 0$, the standard way of dealing with the negative weights of the frustrated quantum magnets is to sample with respect to the unfrustrated system by using the absolute values of the weights $|P(c)|$ and to assign the sign, $s(c) \equiv \text{sign}\, P(c)$ to the quantity being sampled:

$$\langle m \rangle = \frac{\sum_c m(c) P(c)}{\sum_c P(c)} = \frac{\sum_c m(c) s(c) |P(c)| \Big/ \sum_c |P(c)|}{\sum_c s(c) |P(c)| \Big/ \sum_c |P(c)|} \equiv \frac{\langle ms \rangle'}{\langle s \rangle'} \tag{39}$$

While this allows Monte Carlo simulations to be performed, the errors increase exponentially with the particle number N and the inverse temperature β. To see this, consider the mean value of the sign $\langle s \rangle = Z/Z'$, which is just the ratio of the partition functions of the frustrated system $Z = \sum_c p(c)$ with weights $p(c)$ and the unfrustrated system used for sampling with $Z' = \sum_c |p(c)|$. As the partition functions are exponentials of the corresponding free energies, this ratio is an exponential of the differences Δf in the free energy densities:$\langle s \rangle = Z/Z' = \exp(-\beta N \Delta f)$. As a consequence, the relative error $\Delta s / \langle s \rangle$ increases exponentially with increasing particle number and inverse temperature:

$$\frac{\Delta s}{\langle s \rangle} = \frac{\sqrt{\left(\langle s^2 \rangle - \langle s \rangle^2\right)/M}}{\langle s \rangle} = \frac{\sqrt{1 - \langle s \rangle^2}}{\sqrt{M}\langle s \rangle} \sim \frac{\exp(\beta N \Delta f)}{\sqrt{M}} \tag{40}$$

Here M is the number of uncorrelated Monte Carlo samples. Similarly the error for the numerator increases exponentially and the time needed to achieve a given relative error scales exponentially in N and β.

It was recently shown that the negative sign problem is NP-hard, implying that almost certainly no solution for this exponential scaling problem exists (Troyer and Wiese, 2005). Given this exponential scaling of QMC simulations for frustrated quantum magnets, the QMC method is best suited for nonfrustrated magnets and we will restrict ourselves to these sign problem free cases in the following.

4.2.4 Measurements

Physical observables that can be measured in both the path-integral representation and the SSE representation include, next to the energy and the specific heat, any expectation value or correlation function that is diagonal in the basis set $\{|i\rangle\}$. This includes the uniform or staggered magnetization in the z direction, the equal time correlation functions and structure factor of the z-spin components and the z-component uniform and momentum-dependent susceptibilities.

Off-diagonal operators, such as the magnetization in the x- or y-direction, or the corresponding correlation functions, structure factors, and susceptibilities require an extension of the sampling to include configurations with broken world-line segments. These are hard to measure in local update schemes (described in section 4.3) unless open world-line segments are already present when the Hamiltonian does not conserve magnetization, but are easily measured when nonlocal updates are used (see section 4.4 and 4.5).

The spin stiffness ρ_s can be obtained from fluctuations of the winding numbers of the world lines (Pollock and Ceperley, 1987), a measurement which obviously requires nonlocal moves that can change these winding numbers.

Dynamical quantities are harder to obtain, since the QMC representations only give access to imaginary-time correlation function. With the exception of measurements of spin gaps, which can be obtained from an exponential decay of the spin-spin correlation function in imaginary time, the measurement of real-time or real-frequency correlation functions requires an ill-posed analytical continuation of noisy Monte Carlo data, for example using the Maximum Entropy Method (Jarrell and Gubernatis, 1996; von der Linden, 1995; Beach, 2004).

Thermodynamic quantities that cannot be expressed as the expectation value of an operator, such as the free energy or entropy cannot be directly measured but require an extended ensemble simulation, discussed in section 4.6.

4.3 Local updates

To perform a QMC simulation on the world-line representation, update moves that are ergodic and fulfill detailed balance are required. The simplest types of moves are again

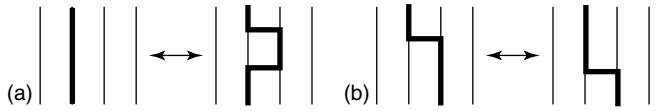

Figure 4. Examples of local updates of world lines. (a) a pair of exchange processes can be inserted or removed; (b) an exchange process is moved in imaginary time.

local updates. Since magnetization conservation prohibits the breaking of world lines, the local updates need to move world lines instead of just changing local states as in a classical model.

A set of local moves for a one-dimensional spin-1/2 model is shown in Figure 4 (Suzuki, Miyashita and Kuroda, 1977; Prokofev, Svistunov and Tupitsyn, 1996). The two required moves are the insertion and removal of a pair of exchange processes (Figure 4a) and the shift in time of an exchange process (Figure 4b). Slightly more complicated local moves are needed for higher-dimensional models, for example, to allow world lines to wind around elementary squares in a square lattice (Makivić and Ding, 1991). Since these local updates cannot change global properties, such as the number of world lines (the magnetization) or their spatial winding, they need to be complemented with global updates (Makivić and Ding, 1991).

While the local update world-line and SSE algorithms enable the simulation of quantum systems they suffer from critical slowing down at second order phase transitions. Even worse, changing the spatial and temporal winding numbers usually has an exponentially small acceptance rate. While the restriction to zero spatial winding can be viewed as a boundary effect, changing the temporal winding number and thus the magnetization is essential for simulations at fixed magnetic fields.

4.4 Cluster updates and the loop algorithm

The ergodicity problems of purely local updates and the critical slowing down observed also in quantum systems require the use of cluster updates. The loop algorithm (Evertz, Lana and Marcu, 1993) and its continuous-time version (Beard and Wiese, 1996), are generalizations of the classical cluster algorithms (Swendsen and Wang, 1987; Wolff, 1989) to quantum systems. They not only solve the problem of critical slowing down, but can also change the magnetization and winding numbers efficiently, avoiding the ergodicity problem of local updates. While the loop algorithm was initially developed for the path-integral representation, it can also be applied to simulations in the SSE representation.

Since there exist extensive recent reviews of the loop algorithm (Evertz, 2003; Kawashima and Harada, 2004), we will only outline the loop algorithm here. It constructs clusters of spins, similar to the Swendsen and Wang (1987) clusters of the classical Ising model (section 3.2). Upon applying the cluster algorithms to world lines in QMC we have to take into account that – in systems with conserved magnetization – the world lines may not be broken. This implies that a single spin cannot be flipped by itself, but, as shown in Figure 5, connected world-line segments of spins must be flipped together. These world-line segments form a closed loop, hence the name 'loop algorithm'.

While the loop algorithm was originally developed only for spin-1/2 models it has been generalized to higher spin models (Kawashima and Gubernatis (1994, 1995); Harada, Troyer and Kawashima, 1998; Todo and Kato, 2001) and anisotropic spin models (Kawashima, 1996). Since an efficient open-source implementation of the loop algorithm is available (see section 4.7) we will not discuss further algorithmic details but refer interested readers to the reviews (Evertz, 2003; Kawashima and Harada, 2004).

4.5 Worm and directed-loop updates

4.5.1 The loop algorithm in a magnetic field

As successful as the loop algorithm is, it is restricted – as most classical cluster algorithms – to models with spin-inversion symmetry. Terms in the Hamiltonian, which break this spin-inversion symmetry, such as a magnetic field, are not taken into account during loop construction. Instead, they enter through the acceptance rate of the loop flip, which can be exponentially small at low temperatures.

As an example consider two $S = 1/2$ quantum spins in a magnetic field:

$$H = J\mathbf{S}_1\mathbf{S}_2 - g\mu_B h(S_1^z + S_2^z) \tag{41}$$

In a field $g\mu_B h = J$, the singlet state $1/\sqrt{2}(|\uparrow\downarrow\rangle - |\downarrow\uparrow\rangle)$ with energy $-3/4J$ is degenerate with the triplet state $|\uparrow\uparrow\rangle$ with energy $1/4J - h = -3/4J$. As illustrated in Figure 6(a), we start from the triplet state $|\uparrow\uparrow\rangle$ and propose

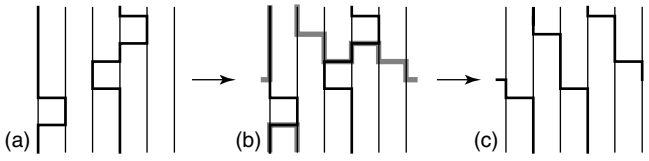

Figure 5. A loop cluster update. (a) world-line configuration before the update, where the world line of an up-spin is drawn as a thick line and that of a down-spin as a thin line; (b) world-line configuration and a loop cluster (grey line); (c) the world-line configurations after all spins along the loop have been flipped.

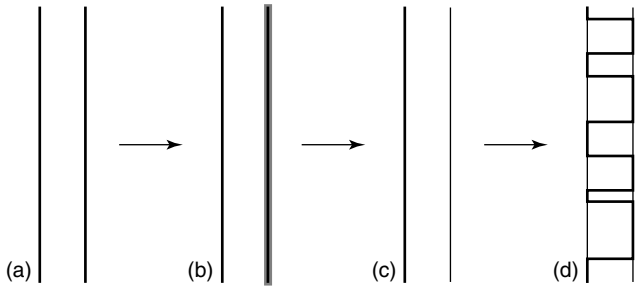

Figure 6. A loop update for two antiferromagnetically coupled spins in a magnetic field with $J = g\mu_B h$. (a) Starting from the triplet configuration $|\uparrow\uparrow\rangle$, (b) a loop is constructed, proposing to go to (c), the intermediate configuration $|\uparrow\downarrow\rangle$, which has an exponentially small acceptance rate, and finally into configurations like (d) which represent the singlet state $1/\sqrt{2}(|\uparrow\downarrow\rangle - |\downarrow\uparrow\rangle)$. As in the previous figure, a thick line denotes an up-spin and a thin line a down-spin.

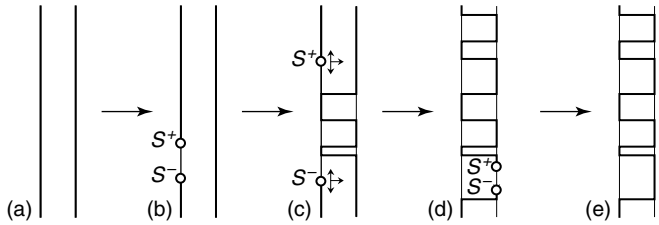

Figure 7. A worm update for two antiferromagnetically coupled spins in a magnetic field with $J = g\mu_B h$. (a) starting from the triplet configuration $|\uparrow\uparrow\rangle$ a worm is constructed in (b) by inserting a pair of S^+ and S^- operators. (c) these 'worm end' operators are then moved by local updates until (d) they meet again, when a move to remove them is proposed, which leads to the closed world-line configuration (e). As in the two previous figures a thick line denotes an up-spin and a thin line a down-spin.

a loop shown in Figure 6(b). The loop construction rules, which ignore the magnetic field, propose to flip one of the spins and go to the intermediate configuration $|\uparrow\downarrow\rangle$ with energy $-1/4J$ shown in Figure 6(c). This move costs potential energy $J/2$ and thus has an *exponentially small acceptance rate* $\exp(-\beta J/2)$. Once we accept this move, immediately many small loops are built, exchanging the spins on the two sites, and gaining exchange energy $J/2$ by going to the spin singlet state. A typical world-line configuration for the singlet is shown in Figure 6d). The reverse move has the same exponentially small probability, since the probability to reach a world-line configuration without any exchange term (Figure 6c) from a spin singlet configuration (Figure 6d) is exponentially small.

This example clearly illustrates the reason for the exponential slowdown: in the first step, we *lose all potential energy*, before *gaining it back in exchange energy*. A faster algorithm could thus be built if, instead of doing the trade in one big step, we could trade potential with exchange energy in small pieces, which is exactly what the worm algorithm does.

4.5.2 The worm algorithm

The worm algorithm (Prokofev, Svistunov and Tupitsyn, 1998) works in an extended configuration space, where in addition to closed world-line configurations one open world-line fragment (the 'worm') is allowed. Formally, this is done by adding a source term to the Hamiltonian, which for a spin model is

$$H_{\text{worm}} = H - \eta \sum_i (S_i^+ + S_i^-) \tag{42}$$

This source term allows world lines to be broken with a matrix element proportional to η. The worm algorithm now proceeds as follows: a worm (i.e., a world-line fragment) is created by inserting a pair (S_i^+, S_i^-) of operators at nearby times, as shown in Figure 7(a) and (b). The ends of this worm are then moved randomly in space and time (Figure 7c), using local Metropolis or heat bath updates until the two ends of the worm meet again as in Figure 7(d). Then an update which removes the worm is proposed, and if accepted we are back in a configuration with closed world lines only, as shown in Figure 7(e).

This algorithm is straightforward, consisting just of local updates of the worm ends in the extended configuration space but it can perform nonlocal changes. A worm end can wind around the lattice in the temporal or spatial direction and in this way change the magnetization and winding number.

In contrast to the loop algorithm in a magnetic field, where the trade between potential and exchange energy is done by first losing all of the potential energy, before gaining back the exchange energy, the worm algorithm performs this trade in small pieces, never suffering from an exponentially small acceptance probability.

While it is not as efficient as the loop algorithm in zero magnetic field (the worm movement follows a random walk while the loop algorithm can be interpreted as a self-avoiding random walk), the big advantage of the worm algorithm is that it remains efficient in the presence of a magnetic field.

4.5.3 The directed-loop algorithm

Algorithms with a similar basic idea as the worm algorithm in the path-integral representations are the operator-loop update (Sandvik, 1999; Dorneich and Troyer, 2001) and the directed-loop algorithms (Syljuasen and Sandvik, 2002) which can be formulated in both an SSE and a world-line representation. Like the worm algorithm, these algorithms create two world-line discontinuities, and move them around by local updates. The main difference compared to the worm algorithm is that

here these movements do not follow an unbiased random walk but have a preferred direction – always trying to move away from the last change, which further speeds up the simulations.

4.6 Extended ensemble methods and parallel tempering

Extended ensemble methods, such as the multicanonical ensemble, Wang-Landau sampling or parallel tempering can also be generalized to quantum systems (Troyer, Wessel and Alet, 2003, 2004). Similar to classical systems, they accelerate the tunneling through free energy barriers and thus speed up simulations at first order phase transitions. Note, however, that frustrated quantum spin systems generally suffer from the negative sign problem. Since the negative sign problem is a property of the representation and not the ensemble or the updates, the scaling will remain exponential even when using improved sampling algorithms, in contrast to classical simulations where extended ensemble algorithms and parallel tempering could speed up the simulations.

The main advantage of generalized ensemble simulations in quantum systems is thus, next to speeding up simulations of first order phase transitions, the ability to directly calculate the density of states and from this to calculate thermodynamic properties such as the entropy or the free energy that are not directly accessible in canonical ensemble simulations.

4.7 Open-source implementations: the ALPS project

The loop, worm, and directed-loop algorithms can be used for the simulation of a wide class of quantum magnets. They are of interest not only to theoretical physicists, but also to experimentalists who want to fit experimental measurements to theoretical models. The wide applicability of these methods has led to the publication of open-source versions of these algorithms as part of the ALPS project (Algorithms and Libraries for Physics Simulations) (Alet *et al*., 2005) on the web page http://alps.comp-phys.org/.

5 DETERMINENTAL ALGORITHMS

In this chapter, we review the basic concepts involved in the formulation of various forms of auxiliary field – or determinental – QMC algorithms. Auxiliary field methods are based on a Hubbard-Stratonovich (HS) decomposition of the two-body interaction term thereby yielding a functional integral expression for the partition function.

$$\mathrm{Tr}\left[e^{-\beta(H-\mu N)}\right] \propto \int \mathrm{d}\Phi(i,\tau) e^{-S[\phi(i,\tau)]} \tag{43}$$

Here, i runs over all lattice sites and τ from 0 to β. For a fixed HS field, $\Phi(i,\tau)$, one has to compute the action, $S[\Phi(i,\tau)]$, corresponding to a problem of noninteracting electrons in an external space and imaginary time-dependent field. The required computational effort depends on the formulation of the algorithm. In the Blankenbecler Scalapino Sugar (BSS) (Blankenbecler, Scalapino and Sugar, 1981) approach, appropriate for lattice models such as the Hubbard Hamiltonian, it scales as βN^3. In the Hirsch-Fye approach (Hirsch and Fye, 1986), appropriate for impurity problems, it scales as $\beta^3 N_{imp}^3$ where N_{imp} corresponds to the number of impurity or correlated sites. Having solved for a fixed HS field, we have to sum over all possible fields. This is done stochastically with the Monte Carlo method.

In comparison to loop algorithms, auxiliary field methods are slow. However, the attractive point of the approach lies in the fact that the sign problem is absent in many nontrivial cases where the loop algorithm fails. Here, we review different formulations appropriate for lattice and impurity problems.

5.1 Lattice methods

To describe the algorithm, we concentrate on the Hubbard model

$$\begin{aligned} H &= H_t + H_U \quad \text{with} \\ H_t &= -t \sum_{\langle \vec{i},\vec{j}\rangle,\sigma} c^\dagger_{\vec{i},\sigma} c_{\vec{j},\sigma} \quad \text{and} \\ H_U &= U \sum_{\vec{i}} \left(n_{\vec{i},\uparrow} - 1/2\right)\left(n_{\vec{i},\downarrow} - 1/2\right) \end{aligned} \tag{44}$$

and show how to compute

$$\langle O\rangle = \frac{\mathrm{Tr}\left[e^{-\beta(H-\mu N)} O\right]}{\mathrm{Tr}\left[e^{-\beta(H-\mu N)}\right]} \tag{45}$$

for an arbitrary observable O.

5.1.1 Formulation of the partition function

We first use the Trotter decomposition to separate the single body Hamiltonian H_t from the two-body interaction term in

the imaginary-time propagation.

$$Z = \mathrm{Tr}\left[e^{-\beta(H-\mu N)}\right] = \mathrm{Tr}\left[\left(e^{-\Delta\tau H_U} e^{-\Delta\tau H_t}\right)^m\right] + \mathcal{O}\left(\Delta\tau^2\right) \tag{46}$$

Here, we have included the chemical potential in a redefinition of H_t, and $m\Delta\tau = \beta$. The systematic error of order $\Delta\tau^2$ will be omitted in the following. There are many possible ways of decoupling the Hubbard interaction and the efficiency as well as the severity of the sign problem will depend upon this choice. The standard procedure is to use a discrete HS transformation introduced by Hirsch in which the field takes two values (Ising spin) and couples to the z-component of the magnetization.

$$e^{-\Delta\tau U\sum_{\vec{i}}\left(n_{\vec{i},\uparrow}-1/2\right)\left(n_{\vec{i},\downarrow}-1/2\right)} = C\sum_{s_1,\ldots,s_N=\pm 1} e^{\alpha\sum_{\vec{i}} s_{\vec{i}}\left(n_{\vec{i},\uparrow}-n_{\vec{i},\downarrow}\right)} \tag{47}$$

where $\cosh(\alpha) = \exp(\Delta\tau U/2)$ and on an N-site lattice, the constant $C = \exp(\Delta\tau U N/4)/2^N$. This equation is readily verified for a single site where the Hilbert space is spanned by the four states: $|\uparrow\rangle$, $|\downarrow\rangle$, $|\uparrow\downarrow\rangle$, and $|0\rangle$.

To simplify the notation we introduce the index $x = (\vec{i}, \sigma)$ to define:

$$H_t = \sum_{x,y} c_x^\dagger T_{x,y} c_y \equiv \vec{c}^\dagger T \vec{c} \quad \text{and}$$

$$\alpha\sum_{\vec{i}} s_{\vec{i}}\left(n_{\vec{i},\uparrow}-n_{\vec{i},\downarrow}\right) = \sum_{x,y} c_x^\dagger V(\vec{s})_{x,y} c_y \equiv \vec{c}^\dagger V(\vec{s})\vec{c} \tag{48}$$

We furthermore define the imaginary-time propagators:

$$U_{\vec{s}}(\tau_2,\tau_1) = \prod_{n=n_1+1}^{n_2} e^{\vec{c}^\dagger V(\vec{s}_n)\vec{c}} e^{-\Delta\tau\vec{c}^\dagger T\vec{c}} \quad \text{and}$$

$$B_{\vec{s}}(\tau_2,\tau_1) = \prod_{n=n_1+1}^{n_2} e^{V(\vec{s}_n)} e^{-\Delta\tau T} \tag{49}$$

where, $n_1\Delta\tau = \tau_1$ and $n_2\Delta\tau = \tau_2$

For a given HS configuration of Ising spins we can now integrate out the fermionic degrees of freedom to obtain:

$$\begin{aligned} Z &= C^m \sum_{\vec{s}_1,\cdots,\vec{s}_m} \mathrm{Tr}\left[U_{\vec{s}}(\beta,0)\right] \\ &= C^m \sum_{\vec{s}_1,\cdots,\vec{s}_m} \det\left[1 + B_{\vec{s}}(\beta,0)\right] \end{aligned} \tag{50}$$

5.1.2 The single particle Green function

One of the big advantages of the auxiliary field approach is its ability of measuring arbitrary observables. This is based on the fact that for a given HS field we have to solve a problem of noninteracting fermions in the external field. Hence Wick's theorem holds for a single HS configuration. Here, we concentrate on equal time observables, show how to compute Green functions, and finally demonstrate the validity of Wick's theorem within the present formulation.

In general, we have to evaluate:

$$\frac{\mathrm{Tr}\left[e^{-\beta H} O\right]}{\mathrm{Tr}\left[e^{-\beta H}\right]} = \sum_{\vec{s}} \mathrm{P}_{\vec{s}} \langle O\rangle_{\vec{s}} \tag{51}$$

where

$$\begin{aligned} \mathrm{P}_{\vec{s}} &= \frac{\det\left(1 + B_{\vec{s}}(\beta,0)\right)}{\sum_{\vec{s}}\det\left(1 + B_{\vec{s}}(\beta,0)\right)}, \\ \langle O\rangle_{\vec{s}} &= \frac{\mathrm{Tr}\left[U_{\vec{s}}(\beta,\tau) O U_{\vec{s}}(\tau,0)\right]}{\mathrm{Tr}\left[U_{\vec{s}}(\beta,0)\right]} \end{aligned}$$

Here, we measure the observable at time τ. Single body observables, $O = \vec{c}^\dagger A \vec{c}$ are given by:

$$\begin{aligned} \langle O\rangle_{\vec{s}} &= \left.\frac{\partial \ln \mathrm{Tr}\left[U_{\vec{s}}(\beta,\tau) e^{\eta O} U_{\vec{s}}(\tau,0)\right]}{\partial\eta}\right|_{\eta=0} \\ &= \left.\frac{\partial \ln \det\left[1 + B_{\vec{s}}(\beta,\tau) e^{\eta A} B_{\vec{s}}(\tau,0)\right]}{\partial\eta}\right|_{\eta=0} \\ &= \left.\frac{\partial \mathrm{Tr} \ln\left[1 + B_{\vec{s}}(\beta,\tau) e^{\eta A} B_{\vec{s}}(\tau,0)\right]}{\partial\eta}\right|_{\eta=0} \\ &= \mathrm{Tr}\left[B_{\vec{s}}(\tau,0)(1 + B_{\vec{s}}(\beta,0))^{-1} B_{\vec{s}}(\beta,\tau) A\right] \\ &= \mathrm{Tr}\left[\left(1 - (1 + B_{\vec{s}}(\tau,0) B_{\vec{s}}(\beta,\tau))^{-1}\right) A\right] \end{aligned} \tag{52}$$

In particular the Green function reads:

$$G_{x,y}(\tau,\tau) = \langle c_x c_y^\dagger\rangle_{\vec{s}} = (1 + B_{\vec{s}}(\tau,0) B_{\vec{s}}(\beta,\tau))^{-1}_{x,y} \tag{53}$$

5.1.3 Wick's theorem

We now show that any multipoint correlation function decouples into a sum of products of the above defined Green functions. First, we define the cumulants:

$$\begin{aligned} &\langle\langle O_n \cdots O_1\rangle\rangle_{\vec{s}} \\ &\quad = \left.\frac{\partial^n \ln \mathrm{Tr}\left[U_{\vec{s}}(\beta,\tau) e^{\eta_n O_n} \cdots e^{\eta_1 O_1} U_{\vec{s}}(\tau,0)\right]}{\partial\eta_n \cdots \partial\eta_1}\right|_{\eta_1\cdots\eta_n=0} \\ &\quad \text{with} \quad O_i = \vec{c}^\dagger A^{(i)} \vec{c} \end{aligned} \tag{54}$$

The following rule, which may be proven by induction (Tsvelik, 1995), emerges:

$$\begin{aligned}\langle O_n \cdots O_1 \rangle_{\vec{s}} = &\langle\langle O_n \cdots O_1 \rangle\rangle_{\vec{s}} \\ &+ \sum_{j=1}^{n} \langle\langle O_n \cdots \widehat{O_j} \cdots O_1 \rangle\rangle_{\vec{s}} \langle\langle O_j \rangle\rangle_{\vec{s}} \\ &+ \sum_{j>i} \langle\langle O_n \cdots \widehat{O_j} \cdots \widehat{O_i} \cdots O_1 \rangle\rangle_{\vec{s}} \langle\langle O_j O_i \rangle\rangle_{\vec{s}} \\ &+ \cdots + \langle\langle O_n \rangle\rangle_{\vec{s}} \cdots \langle\langle O_1 \rangle\rangle_{\vec{s}} \end{aligned} \tag{55}$$

where $\widehat{O_j}$ means that the operator O_j has been omitted from the product.

We can compute the cumulants order by order to see that they depend only on the single particle Green function. For instance, it is easy to show that

$$\begin{aligned}\langle\langle O_2 O_1 \rangle\rangle_{\vec{s}} &= \mathrm{Tr}\left(\overline{G_{\vec{s}}(\tau,\tau)} A^{(2)} G_{\vec{s}}(\tau,\tau) A^{(1)} \right) \\ \text{with} \quad \overline{G} &= 1 - G \end{aligned} \tag{56}$$

or that

$$\begin{aligned}&\langle\langle O_3 O_2 O_1 \rangle\rangle_{\vec{s}} \\ &\quad = \mathrm{Tr}\left(\overline{G_{\vec{s}}(\tau,\tau)} A^{(3)} G_{\vec{s}}(\tau,\tau) A^{(2)} G_{\vec{s}}(\tau,\tau) A^{(1)} \right) \\ &\quad\quad - \mathrm{Tr}\left(\overline{G_{\vec{s}}(\tau,\tau)} A^{(3)} G_{\vec{s}}(\tau,\tau) A^{(1)} \overline{G_{\vec{s}}(\tau,\tau)} A^{(2)} \right) \end{aligned} \tag{57}$$

Hence, with equation (55) we have shown that any n-point correlation function may be calculated from the knowledge of the Green function.

5.1.4 Imaginary-time-displaced Green functions.

Imaginary-time-displaced correlation yield important information. On one hand they may be used to obtain spin and charge gaps (Assaad and Imada, 1996b; Assaad, 1999), as well quasiparticle weights (Brunner, Assaad and Muramatsu, 2000). On the other hand, with the use of the Maximum Entropy method (Jarrell and Gubernatis, 1996; von der Linden, 1995) dynamical properties such as spin and charge dynamical structure factors, optical conductivity, and single particle spectral functions may be computed. Those quantities offer the possibility of direct comparison with experiments, such as photoemission, neutron scattering, and optical measurements.

Since there is again a Wick's theorem for time displaced correlation functions, it suffices to compute the single particle Green function for a given HS configuration. For a given HS field, we evaluate:

$$\begin{aligned} G_{\vec{s}}(\tau_1,\tau_2)_{x,y} &= \langle T c_x(\tau_1) c_y^\dagger(\tau_2) \rangle_{\vec{s}} \\ &= \begin{cases} \langle c_x(\tau_1) c_y^\dagger(\tau_2) \rangle_{\vec{s}} & \text{if} \quad \tau_1 \geq \tau_2 \\ -\langle c_y^\dagger(\tau_2) c_x(\tau_1) \rangle_{\vec{s}} & \text{if} \quad \tau_1 < \tau_2 \end{cases} \end{aligned} \tag{58}$$

where T corresponds to the time ordering. Thus for $\tau_1 > \tau_2 G_{\vec{s}}(\tau_1,\tau_2)_{x,y}$ reduces to

$$\begin{aligned}&\langle c_x(\tau_1) c_y^\dagger(\tau_2) \rangle_{\vec{s}} \\ &\quad = \frac{\mathrm{Tr}\left[U_{\vec{s}}(\beta,\tau_1) c_x U_{\vec{s}}(\tau_1,\tau_2) c_y^\dagger U_{\vec{s}}(\tau_2,0) \right]}{\mathrm{Tr}\left[U_{\vec{s}}(\beta,0) \right]} \\ &\quad = \frac{\mathrm{Tr}\left[U_{\vec{s}}(\beta,\tau_2) U_{\vec{s}}^{-1}(\tau_1,\tau_2) c_x U_{\vec{s}}(\tau_1,\tau_2) c_y^\dagger U_{\vec{s}}(\tau_2,0) \right]}{\mathrm{Tr}\left[U_{\vec{s}}(\beta,0) \right]} \end{aligned} \tag{59}$$

Evaluating $U^{-1}(\tau_1,\tau_2) c_x U_{\vec{s}}(\tau_1,\tau_2)$ boils down to the calculation of

$$c_x(\tau) = e^{\tau \vec{c}^\dagger A \vec{c}} c_x e^{-\tau \vec{c}^\dagger A \vec{c}} \equiv \left(e^{-A} \vec{c} \right)_x$$

We can use the above equation successively to obtain:

$$U_{\vec{s}}^{-1}(\tau_1,\tau_2) c_x U_{\vec{s}}(\tau_1,\tau_2) = (B_{\vec{s}}(\tau_1,\tau_2)\vec{c})_x \tag{60}$$

We can pull out B from the trace in equation (59) to obtain:

$$\begin{aligned} G_{\vec{s}}(\tau_1,\tau_2)_{x,y} &= \langle c_x(\tau_1) c_y^\dagger(\tau_2) \rangle_{\vec{s}} \\ &= [B_{\vec{s}}(\tau_1,\tau_2) G_{\vec{s}}(\tau_2,\tau_2)]_{x,y} \quad \tau_1 > \tau_2 \end{aligned} \tag{61}$$

where $G_{\vec{s}}(\tau_2,\tau_2)$ is the equal time Green function computed previously. A similar calculation will yield for $\tau_2 > \tau_1$

$$\begin{aligned} G_{\vec{s}}(\tau_1,\tau_2)_{x,y} &= -\langle c_y^\dagger(\tau_2) c_x(\tau_1) \rangle_{\vec{s}} \\ &= -\left[(1 - G_{\vec{s}}(\tau_1,\tau_1))\, B_{\vec{s}}^{-1}(\tau_2,\tau_1) \right]_{x,y} \end{aligned} \tag{62}$$

5.1.5 Local updates

Since an exact enumeration of all HS field configuration is out of reach on large lattice sizes, we sample the most relevant ones with the Monte Carlo method. The problem at hand is very similar in nature to the Ising model, presented in section 3. The important difference, however, is that the action is nonlocal. Under a single spin-flip we will have to compute the ratio

$$R = \frac{\mathrm{P}_{\vec{s}'}}{\mathrm{P}_{\vec{s}}} = \frac{\det\left[1 + B_{\vec{s}'}(\beta,0)\right]}{\det\left[1 + B_{\vec{s}}(\beta,0)\right]} \tag{63}$$

to decide if we accept the proposed update or not. Here $\vec{s}$ and $\vec{s}'$ differ only at one point in space and imaginary time, $\vec{i}, n$.

$$s'_{\vec{i}',n'} = \begin{cases} s_{\vec{i}',n'} & \text{if} \quad \vec{i}' \neq \vec{i} \quad \text{and} \quad n' \neq n \\ -s_{\vec{i},n} & \text{if} \quad \vec{i}' = \vec{i} \quad \text{and} \quad n' = n \end{cases} \tag{64}$$

The calculation of R boils down to computing the ratio of two determinants. For the Hubbard interaction with HS transformation of equation (47) only the matrix $V(\vec{s}_n)$ will be affected by the move. Hence, with

$$e^{V(\vec{s}'_n)} = \left[1 + \underbrace{\left(e^{V(\vec{s}'_n)} e^{-V(\vec{s}_n)} - 1 \right)}_{\Delta} \right] e^{V(\vec{s}_n)} \tag{65}$$

we have:

$$B_{\vec{s}'}(\beta, 0) = B_{\vec{s}}(\beta, \tau)\,(1 + \Delta)\,B_{\vec{s}}(\tau, 0) \tag{66}$$

The ratio is then given by:

$$\begin{aligned} R &= \frac{\det\left[1 + B_{\vec{s}}(\beta,\tau)(1+\Delta)B_{\vec{s}}(\tau,0)\right]}{\det\left[1 + B_{\vec{s}}(\beta,0)\right]} \\ &= \det\left[1 + \Delta B_{\vec{s}}(\tau,0)\,(1 + B_{\vec{s}}(\beta,0))^{-1}\,B_{\vec{s}}(\beta,\tau)\right] \\ &= \det\left[1 + \Delta\left(1 - (1 + B_{\vec{s}}(\tau,0)B_{\vec{s}}(\beta,\tau))^{-1}\right)\right] \\ &= \det\left[1 + \Delta\overline{G}_{\vec{s}}(\tau,\tau)\right] \end{aligned} \tag{67}$$

Here we have used the fact that $\det[1 + AB] = \det[1 + BA]$ for arbitrary rectangular matrices. Hence, the Green function determines the Monte Carlo dynamics.

Having calculated the ratio R for a single spin-flip one may now decide stochastically within, for example, a Metropolis scheme if the move is accepted or not. In case of acceptance, we have to update the Green function since this quantity is required at the next step.

Since in general the matrix Δ has only a few non-zero entries, it is convenient to use the Sherman-Morrison formulas (Press, Teukolsky, Vetterling and Flannery, 1992) to update the Green function. This formula states that:

$$(A + \vec{u} \otimes \vec{v})^{-1} = A^{-1} - \frac{\left(A^{-1}\vec{u}\right) \otimes \left(\vec{v}A^{-1}\right)}{1 + \vec{v} \bullet A^{-1}\vec{u}} \tag{68}$$

where A is a $N \times N$ matrix, $\vec{u}$, $\vec{v}$ N-dimensional vectors with tensor product defined as $(\vec{u} \otimes \vec{v})_{x,y} = \vec{u}_x \vec{v}_y$.

To show how to use the above formula for the updating of the Green function, let us first assume that matrix Δ has only one nonvanishing entry: $\Delta_{x,y} = \delta_{x,z}\delta_{y,z'}\eta^{(z,z')}$.

$$\begin{aligned} &G_{\vec{s}'}(\tau) \\ &\quad = [1 + (1 + \Delta)B_{\vec{s}}(\tau,0)B_{\vec{s}}(\beta,\tau)]^{-1} \\ &\quad = B_{\vec{s}}^{-1}(\beta,\tau)\,[1 + B_{\vec{s}}(\beta,\tau)(1+\Delta)B_{\vec{s}}(\tau,0)]^{-1}\,B_{\vec{s}}(\beta,\tau) \\ &\quad = B_{\vec{s}}^{-1}(\beta,\tau)\left[1 + B_{\vec{s}}(\beta,\tau)B_{\vec{s}}(\tau,0) + \vec{u} \otimes \vec{v}\right]^{-1} B_{\vec{s}}(\beta,\tau) \end{aligned} \tag{69}$$

where

$$\vec{u}_x = [B_{\vec{s}}(\beta,\tau)]_{x,z}\,\eta^{(z,z')} \quad \text{and} \quad \vec{v}_x = [B_{\vec{s}}(\tau,0)]_{z',x} \tag{70}$$

Using the Sherman-Morrison formula for inverting $1 + B_{\vec{s}}(\beta,\tau)B_{\vec{s}}(\tau,0) + \vec{u} \otimes \vec{v}$ yields

$$\begin{aligned} &[G_{\vec{s}'}(\tau,\tau)]_{x,y} \\ &\quad = [G_{\vec{s}}(\tau,\tau)]_{x,y} \\ &\qquad - \frac{[G_{\vec{s}}(\tau,\tau)]_{x,z}\,\eta^{(z,z')}\,[1 - G_{\vec{s}}(\tau,\tau)]_{z',y}}{1 + \eta^{(z,z')}\,[1 - G_{\vec{s}}(\tau,\tau)]_{z',z}} \end{aligned} \tag{71}$$

In the above, we have assumed that the matrix Δ has only a single non-zero entry. In general, it is convenient to work on a basis where Δ is diagonal with n nonvanishing eigenvalues. One will then iterate the above procedure n-times to update the Green function.

In principle, we now have all the elements required to carry out a QMC simulation. The space we have to sample is that of Nm Ising spins. Here N is the number of lattice sites and m is the number of imaginary-time slices. It is convenient to adopt a sequential updating scheme so as to sweep from time slice $\tau = 0$ to $\tau = \beta$. After initially computing the Green function on time at $\tau = 0$, we iteratively repeat the following steps:

1. Given the Green function on time slice τ, we sequentially go through all the spins on this time slice. For each Ising spin we compute R and flip the spin with probability $\min[1, R]$ or the heat bath probability $R/(1 + R)$. If accepted we update the Green function, and if rejected we keep the old Green function and old Ising spin configuration.
2. Perform measurements.
3. Propagate the Green function from time slice τ to times slice $\tau + 1$ using the equation

$$G_{\vec{s}}(\tau + 1, \tau + 1) = B_{\vec{s}}(\tau + 1, \tau)G_{\vec{s}}(\tau,\tau)B_{\vec{s}}^{-1}(\tau + 1, \tau) \tag{72}$$

4. Iterate the procedure.

It is to be noted that the implementation of the above algorithm suffers from numerical instabilities at low temperatures. One can, however, stabilize the code by avoiding the

mixing of different scales. An account of those numerical stabilization techniques can be found in (Assaad, 2002b; Loh and Gubernatis, 1992).

5.2 The sign problem

One of the big advantages of the auxiliary field method is that, one can use symmetries to show explicitly that the sign problem does not occur. In the case of the half-filled Hubbard model on a bipartite lattice, particle-hole symmetry ensures that the statistical weight is always positive. The usual proof is based on the factorization of the determinant. Consider the HS transformation of equation (47), then:

$$\det\left(1+B(\beta,0)\right)=\det\left(1+B^{\uparrow}(\beta,0)\right)\det\left(1+B^{\downarrow}(\beta,0)\right) \tag{73}$$

With the particle-hole transformation for a two-dimensional lattice

$$\mathcal{P}^{-1}c_{\vec{i}}^{\dagger}\mathcal{P}=(-1)^{i_x+i_y}c_{\vec{i}} \tag{74}$$

for spinless fermions and $h_t=\sum_{\vec{i},\vec{j}}c_{\vec{i}}^{\dagger}T_{\vec{i},\vec{j}}c_{\vec{j}}$ we have:

$$\begin{aligned}\det\left(1+B^{\uparrow}(\beta,0)\right)&=\mathrm{Tr}\left[\prod_n e^{\alpha\sum_{\vec{i}}s_{\vec{i},n}n_{\vec{i}}}e^{-\Delta\tau h_t}\right]\\&=\mathrm{Tr}\left[\prod_n e^{\alpha\sum_{\vec{i}}s_{\vec{i},n}\mathcal{P}n_{\vec{i}}\mathcal{P}}e^{-\Delta\tau\mathcal{P}^{-1}h_t\mathcal{P}}\right] \qquad (75)\\&=\mathrm{Tr}\left[\prod_n e^{\alpha\sum_{\vec{i}}s_{\vec{i},n}(1-n_{\vec{i}})}e^{-\Delta\tau h_t}\right]\\&=e^{\alpha\sum_{\vec{i},n}s_{\vec{i},n}}\det\left(1+B^{\downarrow}(\beta,0)\right) \qquad (76)\end{aligned}$$

Here, we assumed that $\mathcal{P}^{-1}h_t\mathcal{P}=h_t$ which restricts us to half-filling. Thus the symmetry locks together the sign of both determinants so that no sign problem occurs.

There are more general ways of showing the absence of the sign problem (Wu and Zhang, 2005) which are independent on the factorization of the determinant. If there exists an antiunitary transformation $\mathcal{T}$ such that:

$$\begin{aligned}&\mathcal{T}^{-1}H_t\mathcal{T}=H_t\ \mathcal{T}^{-1}\vec{c}^{\dagger}V(\vec{s}_n)\vec{c}\mathcal{T}=\vec{c}^{\dagger}V(\vec{s}_n)\vec{c}\quad\text{and}\\&\mathcal{T}^2=-1\end{aligned} \tag{77}$$

the eigenvalues of the matrix $1+B(\beta,0)$ always occur in complex conjugate pairs such that:

$$\det\left(1+B(\beta,0)\right)=\prod_i|\lambda_i|^2 \tag{78}$$

Hence, no sign problem occurs.

5.3 The Hirsch-Fye impurity algorithm

This algorithm is used to solve impurity problems such as the Kondo and Anderson models. The strong point of the algorithm is that the CPU time is independent of the volume of the system thus allowing one to carry out simulations directly in the *thermodynamic* limit. The price, however, is a β^3 scaling of the CPU time where β is the inverse temperature. The Hirsch-Fye algorithm is extensively used in the framework of dynamical mean-field theories (DMFT) which become exact in the limit of infinite dimensions. In this limit, the Hubbard model maps onto the single impurity Anderson model (SIAM) supplemented with a self-consistency loop. At each iteration step, an Anderson model has to be solved and this is carried out with the Hirsch-Fye algorithm (Jarrell, 1992; Georges, Kotliar, Krauth and Rozenberg, 1996). In this chapter, we will concentrate on the Anderson model defined as:

$$\begin{aligned}H-\mu N&=H_0+H_U\quad\text{with}\\H_0&=\sum_{\vec{k},\sigma}\left(\epsilon(\vec{k})-\mu\right)c_{\vec{k},\sigma}^{\dagger}c_{\vec{k},\sigma}\\&\quad+\frac{V}{\sqrt{N}}\sum_{\vec{k},\sigma}c_{\vec{k},\sigma}^{\dagger}f_{\sigma}+f_{\sigma}^{\dagger}c_{\vec{k},\sigma}+\epsilon_f\sum_{\sigma}f_{\sigma}^{\dagger}f_{\sigma},\\H_U&=U\left(f_{\uparrow}^{\dagger}f_{\uparrow}-1/2\right)\left(f_{\downarrow}^{\dagger}f_{\downarrow}-1/2\right)\end{aligned} \tag{79}$$

We have shown (see equation (50)) that the grand canonical partition function may be written as:

$$\begin{aligned}Z&\equiv\mathrm{Tr}\left[e^{-\beta(H-\mu N)}\right]\\&=\sum_{\vec{s}}\left[\prod_{\sigma}\det\left[1+B_m^{\sigma}B_{m-1}^{\sigma}\cdots B_1^{\sigma}\right]\right]\end{aligned} \tag{80}$$

with $m\Delta\tau=\beta$.

To define the matrices B_n^{σ}, we will label all the orbitals (conduction and impurity) with the index $\vec{i}$ and use the convention that $\vec{i}=0$ denotes the f-orbital and $\vec{i}=1\cdots N$ the conduction orbitals. We will furthermore define the fermionic operators:

$$a_{\vec{i},\sigma}^{\dagger}=\begin{cases}f_{\sigma}^{\dagger} & \text{if}\quad\vec{i}=0\\ c_{\vec{i},\sigma}^{\dagger} & \text{otherwise}\end{cases} \tag{81}$$

such that the noninteracting term of the Anderson model takes the form:

$$H_0=\sum_{\sigma}H_0^{\sigma},\quad H_0^{\sigma}=\sum_{\vec{i},\vec{j}}a_{\vec{i},\sigma}^{\dagger}(h_0)_{\vec{i},\vec{j}}a_{\vec{j},\sigma} \tag{82}$$

Using the HS transformation of equation (47), the B matrices read:

$$B_n^\sigma = e^{V_n^\sigma} e^{-\Delta\tau h_0}$$
$$(V_n^\sigma)_{\vec{i},\vec{j}} = \delta_{\vec{i},\vec{j}}\delta_{\vec{i},0}\alpha\sigma s_n, \quad \cosh(\alpha) = e^{\Delta\tau U/2} \tag{83}$$

The determinant in a given spin sector may be written as

$$\det\left[1 + B_m^\sigma B_{m-1}^\sigma \cdots B_1^\sigma\right] = \det O^\sigma \quad \text{with} \tag{84}$$

$$O^\sigma = \begin{pmatrix} 1 & 0 & . & . & 0 & B_1^\sigma \\ -B_2^\sigma & 1 & 0 & . & . & 0 \\ 0 & -B_3^\sigma & 1 & . & . & 0 \\ . & 0 & -B_4^\sigma & . & . & . \\ . & . & 0 & . & . & . \\ . & . & . & . & . & . \\ 0 & . & . & 0 & -B_m^\sigma & 1 \end{pmatrix} \tag{85}$$

One can verify that:

$$(O^\sigma)^{-1} \equiv g^\sigma = \begin{pmatrix} G^\sigma(1,1) & G^\sigma(1,2) & . & . & G^\sigma(1,m) \\ G^\sigma(2,1) & G^\sigma(2,2) & . & . & G^\sigma(2,m) \\ . & . & . & . & . \\ G^\sigma(m,1) & G^\sigma(m,2) & . & . & G^\sigma(m,m) \end{pmatrix} \tag{86}$$

where $G^\sigma(n_1, n_2)$ are the time displaced Green functions: defined in Equation (61) and (62). Given a HS configuration $\vec{s}$ and $\vec{s}'$ and associated matrices

$$V^\sigma = \begin{pmatrix} V_1^\sigma & 0 & . & . & . & 0 \\ 0 & V_2^\sigma & 0 & . & . & 0 \\ 0 & 0 & V_3^\sigma & 0 & . & 0 \\ . & . & . & . & . & . \\ 0 & . & . & . & 0 & V_m^\sigma \end{pmatrix} \tag{87}$$

and V'^σ the Green functions g^σ and g'^σ satisfy the following Dyson equation:

$$g^\sigma = g'^\sigma + g'^\sigma\Delta(1 - g^\sigma) \quad \text{with} \quad \Delta^\sigma = (e^{V'^\sigma} e^{-V^\sigma} - 1) \tag{88}$$

To demonstrate the above, we consider

$$\tilde{O}^\sigma = e^{-V^\sigma} O^\sigma = \begin{pmatrix} e^{-V_1^\sigma} & 0 & . & . & 0 & e^{-\Delta\tau h_0} \\ -e^{-\Delta\tau h_0} & e^{-V_2^\sigma} & 0 & . & . & 0 \\ 0 & -e^{-\Delta\tau h_0} & e^{-V_3^\sigma} & . & . & 0 \\ . & 0 & -e^{-\Delta\tau h_0} & . & . & . \\ . & . & 0 & . & . & . \\ . & . & . & . & . & . \\ 0 & . & . & 0 & -e^{-\Delta\tau h_0} & e^{-V_m^\sigma} \end{pmatrix} \tag{89}$$

so that (omitting the spin index σ)

$$\tilde{g} \equiv \tilde{O}^{-1} = [\tilde{O}' + \underbrace{\tilde{O} - \tilde{O}'}_{\equiv e^{-V} - e^{-V'}}]^{-1} = \tilde{g}' - \tilde{g}'\left(e^{-V} - e^{-V'}\right)\tilde{g} \tag{90}$$

The above equation follows from the identity: $\frac{1}{A+B} = \frac{1}{A} - \frac{1}{A}B\frac{1}{A+B}$. Substitution, $\tilde{g} = ge^V$, leads to the Dyson equation (88).

The above Dyson equation is the central identity in the Hirsch-Fye algorithm: all quantities required for the algorithm may be derived directly from this equality. An implementation of the algorithm involves two steps.

5.3.1 Calculation of the impurity Green function for a given HS configuration

The starting point of the algorithm is to compute the green function for a random HS configuration of Ising spins $\vec{s}'$. We will only need the Green function for the impurity f-site. Let $x = (\tau_x, \vec{i}_x)$ with Trotter index τ_x and orbital $\vec{i}_x$. Since

$$(e^{V'}e^{-V} - 1)_{x,y} = (e^{V'}e^{-V} - 1)_{x,x}\delta_{x,y}\delta_{\vec{i}_x,0} \tag{91}$$

we can use the Dyson equation only for the impurity Green function:

$$\left(g^\sigma_{f,f'} = g'^\sigma_{f,f'} + \sum_{f''} g'^\sigma_{f,f''}\Delta^\sigma_{f'',f''}(1 - g^\sigma)_{f'',f'}\right) \tag{92}$$

with indices $f \equiv (\tau, 0)$ running from $1 \cdots m$. Hence, the $m \times m$ impurity Green function matrix,

$$g^{I,\sigma}_{f,f'} = g^\sigma_{f,f'} \tag{93}$$

satisfies the Dyson equation:

$$g^{I,\sigma} = g'^{I,\sigma} + g'^{I,\sigma}\Delta^{I,\sigma}(1 - g^{I,\sigma}) \quad \text{with}$$
$$\Delta^{I,\sigma}_{f,f'} = \Delta^\sigma_{f,f'} \tag{94}$$

For $V = 0$, g^I is nothing but the impurity Green function of the noninteracting Anderson model which may readily be computed. Thus using the Dyson equation, we can compute the Green function g'^I for an arbitrary HS configuration $\vec{s}'$ at the cost of a $m \times m$ matrix inversion. This involves a CPU cost scaling as m^3 or equivalently β^3.

5.3.2 Updating

At this point we have computed the impurity Green function for a given HS configuration $\vec{s}$. Adopting a single-spin flip algorithm we will propose the configuration $\vec{s}'$ which stems from configuration $\vec{s}$ with one flipped spin at time f_1.

We accept this change with probability

$$R = \prod_{\sigma} R^{\sigma} \quad \text{with} \quad R^{\sigma} = \frac{\det\left[1 + B'^{\sigma}_{m} B'^{\sigma}_{m-1} \cdots B'^{\sigma}_{1}\right]}{\det\left[1 + B^{\sigma}_{m} B^{\sigma} m - 1 \cdots B^{\sigma}_{1}\right]}$$
$$= \det\left[g^{\sigma}(g'^{\sigma})^{-1}\right] = \det\left[1 + \Delta^{\sigma}\left(1 - g^{\sigma}\right)\right] \tag{95}$$

The last identity follows from the Dyson equation to express g^{σ} as $g^{\sigma} = g'^{\sigma}\left[1 + \Delta^{\sigma}\left(1 - g^{\sigma}\right)\right]$. Since $\vec{s}$ and $\vec{s}'$ differ only by one entry the matrix Δ^{σ} has one nonzero matrix element: $\Delta^{\sigma}_{f_1,f_1}$. Hence, $R^{\sigma} = 1 + \Delta^{\sigma}_{f_1,f_1}\left(1 - g^{\sigma}_{f_1,f_1}\right)$. Since the impurity Green function $g^{I,\sigma}$ is at hand, we can readily compute R.

If the move (spin-flip) is accepted, we will have to recalculate (update) the impurity Green function. From the Dyson equation (94), we have:

$$g'^{I,\sigma} = g^{I,\sigma}\left[1 + \Delta^{I,\sigma}\left(1 - g^{I,\sigma}\right)\right]^{-1} \tag{96}$$

To compute $\left[1 + \Delta^{I,\sigma}\left(1 - g^{I,\sigma}\right)\right]^{-1}$ we can use the Sherman-Morrison formulas (68) to obtain:

$$g'^{I,\sigma}_{f,f'} = g^{I,\sigma}_{f,f'} + \frac{g^{I,\sigma}_{f,f_1}\Delta^{\sigma}_{f_1,f_1}(g^{I,\sigma} - 1)_{f_1,f'}}{1 + (1 - g^{I,\sigma})_{f_1,f_1}\Delta^{\sigma}_{f_1,f_1}} \tag{97}$$

Thus, the updating of the Green function under a single spin-flip is an operation which scales as m^2. Since for a single sweep we have to visit all spins, the computational cost of a single sweep scales as m^3.

By construction, the Hirsch-Fye algorithm is free from numerical stabilization problems. Furthermore, the absence of the sign problem has recently been proven for the single impurity Anderson model (Yoo *et al.*, 2004). Clearly the attractive feature of the Hirsch-Fye impurity algorithm is that the algorithm may be formulated directly in the thermodynamic limit. This is not possible within the lattice formulation of the auxiliary field QMC method. Within this approach the dimension of the matrices scale as the total number of orbitals, N, and the CPU time for a single sweep as $N^3\beta$. The Hirsch-Fye algorithm is not limited to impurity models. However, when applied to lattice models, such as the Hubbard model, it is not efficient since the CPU time will scale as $(\beta N)^3$.

5.4 Projective methods

Each of the above finite-temperature methods has a projective counterpart to access ground state properties. We can start from a trial wave function $|\Psi_T\rangle$ in which we can embed prior knowledge of the ground state, $|\Psi_0\rangle$ such as symmetries or overlaps. Assuming that the trial wave is nonorthogonal to the ground state,

$$\frac{\langle\Psi_0|O|\Psi_0\rangle}{\langle\Psi_0|\Psi_0\rangle} = \lim_{\beta\to\infty}\frac{\langle\Psi_T|e^{-\beta H}Oe^{-\beta H}|\Psi_T\rangle}{\langle\Psi_T|e^{-2\beta H}|\Psi_T\rangle} \tag{98}$$

The extrapolation to infinite values of the projection parameter, β, is done numerically. A comparison of both algorithms for a SIAM is shown in Figure 8. We note that recently more efficient continuous time algorithms have been developed (Rubtsov, Savkin and Lichtenstein, 2005; Werner *et al.*, 2006; Werner and Millis, 2006) and refer the interested reader to these publications for details.

6 APPLICATIONS

We will finally present typical applications of the above algorithms by reviewing a small and necessarily biased selection.

6.1 Applications of the loop algorithm

The loop algorithm has been applied to a wide range of problems, ranging from purely theoretical questions to experimental data fitting. In the subsequent text, we list a small selection of applications that provide an overview of the possibilities

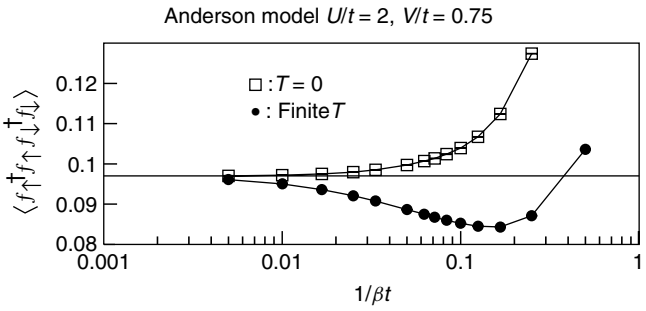

Figure 8. Comparison between the zero temperature (open squares) and finite-temperature Hirsch-Fye (bullets) algorithms for the symmetric Anderson model, with a one-dimensional half-filled density of states. For those parameters, the Kondo temperature is of the order of $0.02t$. In the limit $\beta t \to \infty$ both algorithms yield the same result for the double occupancy. Ground state results are, however, more efficiently obtained within the projective method. Furthermore, the projective approach is extremely efficient when used as an impurity solver in the framework of DMFT of the Hubbard model (Feldbacher, Assaad and Held, 2004).

of the loop algorithm. The first simulation using the loop algorithm was an accurate determination of the ground state properties (staggered magnetization, spin stiffness, and spin wave velocity) of the square-lattice spin-1/2 quantum Heisenberg antiferromagnet (Wiese and Ying, 1992). In a similar spirit the uniform susceptibility, correlation length, and spin gap of spin ladder models (Frischmuth, Ammon and Troyer, 1996; Greven, Birgeneau and Wiese, 1996) and integer spin chains (Todo and Kato, 2001) was calculated, confirming the presence of a spin gapped ground state in even-leg spin ladders and integer spin chains.

As the loop algorithm is efficient also at critical points, it has been used in the first high accuracy simulations of the critical properties of quantum phase transitions by studying the Néel to quantum paramagnet transition in two-dimensional quantum spin systems (Troyer, Imada and Ueda, 1997), for a determination of the low-temperature asymptotic scaling of two-dimensional quantum Heisenberg antiferromagnets (Kim and Troyer, 1998; Beard, Birgeneau, Greven and Wiese, 1998; Harada, Troyer and Kawashima, 1998), and for accurate calculations of the Néel temperature of anisotropic quasi-one- and quasi-two-dimensional antiferromagnets (Yasuda *et al*., 2005).

The loop algorithm is not only restricted to toy models, but can be applied to realistic models of quantum magnets. Comparisons to experimental measurements are done by fitting simulation data to experimental measurements, as for alternating chain compounds (Johnston *et al*., 2000b), spin ladder materials (Johnston, *et al*., 2000a) or frustrated square-lattice antiferromagnets (Melzi *et al*., 1999). In the latter material, the sign problem due to frustration limits the accuracy. As an example, we show in Figure 9 the good quality of a fit of QMC data to experimental measurements on the spin ladder compound $SrCu_2O_3$.

Another interesting application is to simulate realistic models for quantum magnets, using exchange constants calculated by *ab initio* methods. Comparing these *ab initio* QMC data to experimental measurements, as done for a series of vanadates (Korotin *et al*., 1998) and for ladder compounds (Johnston, *et al*., 2000a) allows to quantitatively check the *ab initio* calculations.

6.2 Applications of the worm and directed-loop algorithms

The worm and directed-loop algorithms are applied when magnetic fields are present. Typical examples include the calculation of magnetization curves of quantum magnets (Woodward *et al*., 2002), the determination of the first order nature of the spin flop transition in two dimensions (Schmid, Todo, Troyer and Dorneich, 2002) and the calculation of phase diagrams of dimerized quantum magnets in a magnetic field (Nohadani, Wessel, Normand and Haas, 2004).

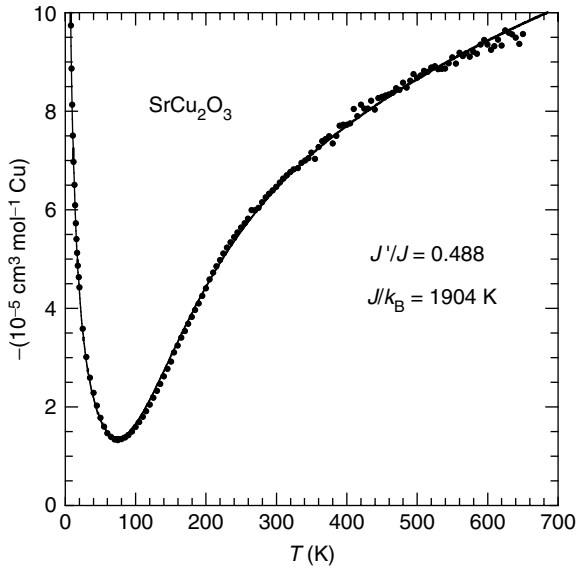

Figure 9. Fits of experimental measurements of the uniform susceptibility of $SrCu_2O_3$. (Azuma *et al*., 1994) to the results of QMC simulations, determining a coupling $J \approx 1904\ K$ along the chains of the ladder and a ratio $J'/J \approx 0.488$ for the rung to chain coupling.

6.3 Applications of the determinental algorithms

The applications of the auxiliary field algorithms to correlated electron systems are numerous. Here, we will only mention a few, starting with the attractive Hubbard model. This model essentially describes the electron–phonon problem in terms of the Holstein model which in the antiadiabatic limit maps onto the attractive Hubbard model (Hirsch and Fradkin, 1983). Both models are free of a sign problem in arbitrary dimensions and on arbitrary lattice topologies. The salient features of those models have been investigated in detail. For instance, the crossover from long coherence length (BCS) to short coherence length superconductors. In the short coherence length limit, a liquid of preformed pairs with non-Fermi liquid character is apparent above the transition temperature (Randeria, Trivedi, Moreo and Scalettar, 1992; Trivedi and Randeria, 1995). Furthermore, the disorder driven superfluid to insulator transition has been studied in the framework of the attractive Hubbard model (Randeria, Trivedi, Moreo and Scalettar, 1996).

Recently, a new class of models of correlated electron models showing no sign problem has been investigated (Assaad *et al*., 2003; Wu, Hu and Zhang, 2003; Capponi, Wu and Zhang, 2004; Wu and Zhang, 2005). Those models

have exotic ground states including phases with circulating currents (Capponi, Wu and Zhang, 2004; Assaad, 2005) striped phases (Assaad *et al*., 2003), as well as possible realizations of gapless spin liquid phases (Assaad, 2005).

A lot of work using the BSS algorithm is centered around the repulsive Hubbard model in two dimensions, as well as the three-band Hubbard model of the CuO_2 planes in the cuprates. On the basis of Monte Carlo simulations, it is now accepted that at half-band filling those models are Mott (charge transfer for the three-band model) insulators with long-range antiferromagnetic order (Hirsch and Tang, 1989; White *et al*., 1989; Dopf, Muramatsu and Hanke, 1992a). In the case of the three-band Hubbard model, a minimal set of parameters were found so as to reproduce experimental findings (Dopf, Muramatsu and Hanke, 1992b). The issue of superconductivity at low doping away from half-filling is still open. General concepts – independent of the symmetry of the pair wave function and including possible retardation effects – such as flux quantization and superfluid density have been used to attempt to answer the above question (Assaad, Hanke and Scalapino, 1994; Scalapino, White and Zhang, 1993). Within the algorithmic limitations, no convincing sign of superconductivity has been found to date.

The nature of the doping induced metal–insulator transition in the two-dimensional Hubbard model has attracted considerable interest (Furukawa and Imada, 1993; Assaad and Imada, 1995, 1996a). In particular, it has been argued the the transition is driven by the divergence of the effective mass rather than by the vanishing of the number of charge carriers. The origin of such a metal–insulator transition is to be found in a very flat dispersion relation around the $(\pi, 0)$ and $(0, \pi)$ points in the Brillouin zone (Dopf *et al*., 1992c; Gröber, Eder and Hanke, 2000). An extensive review of this topic as well as a consistent interpretation of the numerical data in terms of hyperscaling Ansatz may be found in (Imada, Fujimori and Tokura, 1998).

Aspects of the physics of heavy fermion systems have been investigated in the framework of the two-dimensional periodic Anderson model (PAM) (Vekic *et al*., 1995) and of the Kondo lattice model (KLM) (Capponi and Assaad, 2001). It is only recently that a sign free formulation of the KLM for particle-hole symmetric conduction bands has been put forward (Assaad, 1999). Extensive calculations both at $T = 0$ and at finite T allow to investigate the magnetic order–disorder transition triggered by the competition between the RKKY interaction and the Kondo effect (Capponi and Assaad, 2001). Across this quantum phase transition, single hole dynamics as well as spin excitations were investigated in detail. One can show numerically that the quasiparticle residue in the vicinity of $\vec{k} = (\pi, \pi)$ tracks the the Kondo scale of the corresponding single impurity problem. This statement is valid both in the magnetically ordered and disordered phases (Assaad, 2004). This suggests that the coherence temperature tracks the Kondo scale. Furthermore, the effect of a magnetic field on the Kondo insulating state was investigated. For the particle-hole symmetric conduction band, results show a transition from the Kondo insulator to a canted antiferromagnet (Milat, Assaad and Sigrist, 2004; Beach, Lee and Monthoux, 2004). Finally, models with regular depletion of localized spins can be investigated (Assaad, 2002a). Within the framework of those models, the typical form of the resistivity versus temperature can be reproduced.

The most common application of the Hirsch-Fye algorithm is in the framework of dynamical mean-field theories (Georges, Kotliar, Krauth and Rozenberg, 1996) which map the Hubbard model onto an Anderson impurity problem supplemented by a self-consistency loop. At each iteration, the Hirsch-Fye algorithm is used to solve the impurity problem at finite temperature (Jarrell, 1992) or at $T = 0$ (Feldbacher, Assaad and Held, 2004). For this particular problem, many competing methods such as DMRG (Nishimoto, Gebhard and Jeckelmann, 2004) and NRG (Bulla, 1999) are available. In the dynamical mean-field approximation, spatial fluctuations are frozen out. To reintroduce them, one has to generalize to cluster methods such as the dynamical cluster approximation (DCA) (Hettler, Jarrell and Krishnamurthy, 2000) or cellular-DMFT (CDMFT) (Kotliar, Savrasov, Pálsson and Biroli1, 2001). Within these approaches, the complexity of the problem to solve at each iteration is that of an N-impurity Anderson model (N corresponds to the cluster size). Generalizations of DMRG and NRG to solve this problem are difficult. On the other hand, as a function of cluster size the sign problem in the Hirsch-Fye approach becomes more and more severe but is, in many instances, still tractable. It, however, proves to be one of the limiting factors in achieving large cluster sizes.

7 CONCLUSION

To conclude, we discuss which algorithm is preferred for which models. For fermionic models, such as the Hubbard, the determinental quantum Monte Carlo (QMC) algorithm should be employed in more than one dimension because of the reduced sign problem in this formulation. For pure spin models the world-line algorithms are better because of their almost linear scaling with system size, in contrast to the cubic scaling of the determinental algorithms.

Among the world-line algorithms, the loop algorithm is the method of choice for problems with spin-inversion symmetry, that is, in the absence of magnetic fields, whereas

the worm or directed-loop algorithms should be used when magnetic fields are present. Implementations of these world-line QMC algorithms are available through the open-source ALPS project.

A negative sign problem occurs even for pure spin models, in the presence of frustration in the x- and y-components of the exchange couplings. This sign problem restricts simulations to temperatures not lower than the magnitude of the frustrating coupling. As a solution to this sign problem is unlikely (Troyer and Wiese, 2005), alternative methods, such as the density matrix renormalization group method (White, 1992, 1993; Schollwöck, 2005) should be considered for low-dimensional strongly frustrated quantum magnets at low temperatures.

REFERENCES

Alet, F., Dayal, P., Grzesik, A., *et al*. (2005). The ALPS project: open source software for strongly correlated systems. *Journal of the Physical Society of Japan Supplement*, **74**, 30–35.

Assaad, F.F. (1999). Quantum Monte Carlo simulations of the half-filled two-dimensional Kondo lattice model. *Physical Review Letters*, **83**, 796–799.

Assaad, F.F. (2002a). Depleted Kondo lattices: mean-field and quantum Monte Carlo calculations. *Physical Review B*, **65**, 115104.

Assaad, F.F. (2002b). Quantum monte carlo methods on lattices: the determinantal method. In *Lecture Notes of the Winter School on Quantum Simulations of Complex Many-Body Systems: From Theory to Algorithms*. *NIC Series*, Volume 10, Grotendorst, J., Grotendorst, D. and Muramatsu, A. (Eds.), Publication Series of the John von Neumann Institute for Computing: pp. 99–155.

Assaad, F.F. (2004). Coherence scale of the two-dimensional Kondo lattice model. *Physical Review B*, **70**, 020402.

Assaad, F.F. (2005). Phase diagram of the half-filled two-dimensional SU(N) Hubbard-Heisenberg model: a quantum Monte Carlo study. *Physical Review B*, **71**, 075103.

Assaad, F.F., Hanke, W. and Scalapino, D.J. (1994). Flux quantization and temperature derivative of the superfluid density as criteria for superconductivity in two-dimensional Hubbard models. *Physical Review B*, **50**, 12835–12850.

Assaad, F.F. and Imada, M. (1995). Hall coefficient for the two-dimensional Hubbard model. *Physical Review Letters*, **74**, 3868–3871.

Assaad, F.F. and Imada, M. (1996a). Insulator-metal transition in the one- and two-dimensional Hubbard models. *Physical Review Letters*, **76**, 3176–3179.

Assaad, F.F. and Imada, M. (1996b). Stable quantum Monte Carlo algorithm for $T = 0$ calculation of imaginary time Green functions. *Journal of the Physical Society of Japan*, **65**, 189–194.

Assaad, F.F., Rousseau, V., Hébert, F., *et al*. (2003). Spin and charge dynamics of stripes in doped Mott insulators. *Europhysics Letters*, **63**, 569–575.

Azuma, M., Hiroi, Z., Takano, M., *et al*. (1994). Observation of a spin gap in $SrCu_2O_3$ comprising spin-1/2 quasi-1D two-leg ladders. *Physical Review Letters*, **73**, 3463–3466.

Barahona, F. (1982). On the computational complexity of Ising spin glass models. *Journal of Physics A*, **15**, 3241–3253.

Beach, K.S.D. (2004). Identifying the maximum entropy method as a special limit of stochastic analytic continuation. *cond-mat/0403055*.

Beach, K.S.D., Lee, P.A. and Monthoux, P. (2004). Field-induced antiferromagnetism in the Kondo insulator. *Physical Review Letters*, **92**, 026401.

Beard, B.B., Birgeneau, R.J., Greven, M. and Wiese, U.-J. (1998). Square-lattice Heisenberg antiferromagnet at very large correlation lengths. *Physical Review Letters*, **80**, 1742–1745.

Beard, B. and Wiese, U. (1996). Simulations of discrete quantum systems in continuous Euclidean time. *Physical Review Letters*, **77**, 5130–5133.

Berg, B.A. and Neuhaus, T. (1991). Multicanonical algorithms for first order phase transitions. *Physics Letters. [Part B]*, **267**, 249–253.

Berg, B.A. and Neuhaus, T. (1992). Multicanonical ensemble: a new approach to simulate first-order phase transitions. *Physical Review Letters*, **68**, 9–12.

Blankenbecler, R., Scalapino, D.J. and Sugar, R.L. (1981). Monte Carlo calculations of coupled boson-fermion systems. I. *Physical Review D*, **24**, 2278–2286.

Brunner, M., Assaad, F.F. and Muramatsu, A. (2000). Single hole dynamics in the t-J model on a square lattice. *Physical Review B*, **62**, 12395–12407.

Bulla, R. (1999). Zero temperature metal-insulator transition in the infinite-dimensional Hubbard model. *Physical Review Letters*, **83**, 136–139.

Capponi, S. and Assaad, F.F. (2001). Spin and charge dynamics of the ferromagnetic and antiferromagnetic two-dimensional half-filled Kondo lattice model. *Physical Review B*, **63**, 155114.

Capponi, S., Wu, C. and Zhang, S.-C. (2004). Current carrying ground state in a bilayer model of strongly correlated systems. *Physical Review B*, **70**, 220505.

Cook, S. (1971). The complexity of theorem-proving procedures. In *Conference Record of Third Annual ACM Symposium on Theory of Computing*, Shaker Heights, 151–158.

Dayal, P., Trebst, S., Wessel, S., *et al*. (2004). Performance limitations of flat-histogram methods. *Physical Review Letters*, **92**, 097201.

Dopf, G., Muramatsu, A. and Hanke, W. (1992a). Antiferromagnetism and incommensurate order in the three-band Hubbard model. *Europhysics Letters*, **17**, 559.

Dopf, G., Muramatsu, A. and Hanke, W. (1992b). Large-order dimensional perturbation theory for H+2. *Physical Review Letters*, **68**, 1992–1995.

Dopf, G., Wagner, J., Dieterich, P., *et al*. (1992c). Direct comparison of angle-resolved photoemission and numerical simulations for high-T_c superconductors. *Physical Review Letters*, **68**, 2082–2085.

Dorneich, A. and Troyer, M. (2001). Accessing the dynamics of large many-particle systems using the stochastic series expansion. *Physical Review E*, **64**, 066701.

Evertz, H.G. (2003). The loop algorithm. *Advances in Physics*, **52**, 1–66.

Evertz, H., Erkinger, H. and von der Linden, W. (2002). New cluster method for the ising model. In *Computer Simulations in Condensed Matter Physics*, Landau, D., Lewis, S.P. and Schüttler, H.-B. (Eds.), Springer: Berlin, pp. 123, Vol. 14.

Evertz, H.G., Lana, G. and Marcu, M. (1993). Cluster algorithm for vertex models. *Physical Review Letters*, **70**, 875–879.

Feldbacher, M., Assaad, F.F. and Held, K. (2004). Projective auantum Monte Carlo method for the Anderson impurity model and its application to dynamical mean field theory. *Physical Review Letters*, **93**, 136405.

Feynman, R. (1953). Atomic theory of liquid helium near absolute zero. *Physical Review*, **91**, 1301–1308.

Frischmuth, B., Ammon, B. and Troyer, M. (1996). Susceptibility and low-temperature thermodynamics of spin-1/2 Heisenberg ladders. *Physical Review B*, **54**, R3714–R3717.

Furukawa, N. and Imada, M. (1993). Charge mass singularity in two-dimensional Hubbard model. *Journal of the Physical Society of Japan*, **62**, 2557–2560.

Georges, A., Kotliar, G., Krauth, W. and Rozenberg, M.J. (1996). Dynamical mean-field theory of strongly correlated fermion systems and the limit of infinite dimensions. *Reviews of Modern Physics*, **68**, 13–125.

Greven, M., Birgeneau, R.J. and Wiese, U.J. (1996). Monte Carlo study of correlations in quantum spin ladders. *Physical Review Letters*, **77**, 1865–1868.

Gröber, C., Eder, R. and Hanke, W. (2000). Anomalous low-doping phase of the Hubbard model. *Physical Review B*, **62**, 4336–4352.

Handscomb, D. (1962). The Monte Carlo method in quantum statistical mechanic. *Proceedings of the Cambridge Philosophical Society*, **58**, 594–598.

Harada, K., Troyer, M. and Kawashima, N. (1998). The two-dimensional spin-1 quantum Heisenberg antiferromagnet at finite temperatures. *Journal of the Physical Society of Japan*, **67**, 1130–1133.

Hettler, M.M., Jarrell, M. and Krishnamurthy, H.R. (2000). Dynamical cluster approximation: nonlocal dynamics of correlated electron systems. *Physical Review B*, **61**, 12739–12756.

Hirsch, J.E. and Fradkin E.(1983). Phase diagram of one-dimensional electron-phonon systems. II. The molecular-crystal model. *Physical Review B*, **27**, 4302–4316.

Hirsch, J.E. and Fye, R.M. (1986). Monte Carlo method for magnetic impurities in metals. *Physical Review Letters*, **56**, 2521–2524.

Hirsch, J.E. and Tang, S. (1989). Antiferromagnetism in the two-dimensional Hubbard model. *Physical Review Letters*, **62**, 591–594.

Hukushima, K. and Nemoto, Y. (1996). Exchange Monte Carlo method and application to spin glass simulations. *Journal of the Physical Society of Japan*, **65**, 1604–1608.

Imada, M., Fujimori, A. and Tokura, Y. (1998). Metal-insulator transitions. *Reviews of Modern Physics*, **70**, 1039–1263.

Jarrell, M. (1992). Hubbard model in infinite dimensions: a quantum Monte Carlo study. *Physical Review Letters*, **69**, 168–171.

Jarrell, M. and Gubernatis, J. (1996). Bayesian inference and the analytic continuation of imaginary time Monte Carlo data. *Physics Reports*, **269**, 133–195.

Johnston, D.C., Kremer, R.K., Troyer, M., *et al*. (2000a). Thermodynamics of spin S=1/2 antiferromagnetic uniform and alternating-exchange Heisenberg chains. *Physical Review B*, **61**, 9558–9606.

Johnston, D.C., Troyer, M., Miyahara, S., *et al*. (2000b). Magnetic susceptibilities of spin-1/2 antiferromagnetic Heisenberg ladders and applications to ladder oxide compounds. *cond-mat/0001147*.

Kawashima, N. (1996). Cluster algorithms for anisotropic quantum spin models. *Journal of Statistical Physics*, **82**, 131–151.

Kawashima, N. and Gubernatis, J. (1994). Loop algorithms for Monte Carlo simulations of quantum spin systems. *Physical Review Letters*, **73**, 1295–1298.

Kawashima, N. and Gubernatis, J. (1995). Generalization of the Fortuin-Kasteleyn transformation and its application to quantum spin simulations. *Journal of Statistical Physics*, **80**, 169–210.

Kawashima, N. and Harada, K. (2004). Recent developments of world-line Monte Carlo methods. *Journal of the Physical Society of Japan*, **73**, 1379–1414.

Kemeny, G.J. and Snell, J. (1960). *Finite Markov Chains*. *The University Series in Undergraduate Mathematics*, Van Nostrand: New York.

Kim, J. and Troyer, M. (1998). Low temperature behavior and crossovers of the square lattice quantum Heisenberg antiferromagnet. *Physical Review Letters*, **80**, 2705–2708.

Korotin, M.A., Elfimov, I.S., Anisimov, V.I., *et al*. (1998). Exchange interactions and magnetic properties of the layered vanadates CaV_2O_5, MgV_2O_5, CaV_3O_7, and CaV_4O_9. *Physical Review Letters*, **83**, 1387–1390.

Kotliar, G., Savrasov, S.Y., Pálsson, G. and Biroli1, G. (2001). Cellular dynamical mean field approach to strongly correlated systems. *Physical Review Letters*, **87**, 186401.

von der Linden, W. (1995). Maximum-entropy data analysis. *Applied Physics A*, **60**, 155.

Loh, E. and Gubernatis, J. (1992). Stable numerical simulations of models of interacting electrons in condensed-matter physics. In *Modern Problems of Condensed Matter Physics*, Hanke, W. and Kopaev, Y.V. (Eds.), North Holland: Amsterdam, pp. 177, Vol. 32.

Makivić, M.S. and Ding, H.Q. (1991). Two-dimensional spin-1/2 Heisenberg antiferromagnet: a quantum Monte Carlo study. *Physical Review B*, **43**, 3562–3574.

Melzi, R., Carretta, P., Lascialfari, A., *et al*. (1999). $Li_2VO(Si,Ge)O_4$, a prototype of a two-dimensional frustrated quantum Heisenberg antiferromagnet. *Physical Review Letters*, **85**, 1318–1321.

Metropolis, N., Rosenbluth, A.R., Rosenbluth, M.N., *et al*. (1953). Equation of state calculations on fast computing machines. *Journal of Chemical Physics*, **21**, 1087.

Milat, I., Assaad, F. and Sigrist, M. (2004). Field induced magnetic ordering transition in Kondo insulators. *European Physical Journal B*, **38**, 571–580.

Nishimoto, S., Gebhard, F. and Jeckelmann, E. (2004). Dynamical density-matrix renormalization group for the Mott–Hubbard insulator in high dimensions. *Journal of Physics. Condensed Matter*, **16**, 7063–7081.

Nohadani, O., Wessel, S., Normand, B. and Haas, S. (2004). Universal scaling at field-induced magnetic phase transitions. *Physical Review B*, **69**, 220402.

Pollock, E.L. and Ceperley, D.M. (1987). Path-integral computation of superfluid densities. *Physical Review B*, **36**, 8343–8352.

Press, W.H., Teukolsky, S.A., Vetterling, W.T. and Flannery, B.P. (1992). *Numerical Recipes in C*, Cambridge University Press: Cambridge.

Prokofev, N.V., Svistunov, B.V. and Tupitsyn, I.S. (1996). Exact quantum Monte Carlo process for the statistics of discrete systems. *JETP Letters*, **64**, 911.

Prokofev, N.V., Svistunov, B.V. and Tupitsyn, I.S. (1998). Exact, complete, and universal continuous-time worldline Monte Carlo approach to the statistics of discrete quantum systems. *JETP*, **87**, 310–321.

Randeria, M., Trivedi, N., Moreo, A. and Scalettar, R.T. (1992). Pairing and spin gap in the normal state of short coherence length superconductors. *Physical Review Letters*, **69**, 2001–2004.

Randeria, M., Trivedi, N., Moreo, A. and Scalettar, R.T. (1996). Superconductor-insulator transition in a disordered electronic system. *Physical Review B*, **54**, R3756–R3759.

Redner, O., Machta, J. and Chayes, L.F. (1998). Graphical representations and cluster algorithms for critical points with fields. *Physical Review E*, **58**, 2749–2752.

Rubtsov, A.N., Savkin, V.V., Lichtenstein, A.I. (2005). Continuous Time Quantum Monte Carlo method for fermions. *Physical Review B*, **72**, 035122.

Sachdev, S., Werner, P. and Troyer, M. (2004). Universal conductance of quantum wires near the superconductor-metal quantum transition. *Physical Review Letters*, **92**, 237003.

Sandvik, A. (1999). Stochastic series expansion method with operator-loop update. *Physical Review B*, **59**, R14157–R14160.

Sandvik, A. and Kurkijärvi, J. (1991). Quantum Monte Carlo simulation method for spin systems. *Physical Review B*, **43**, 5950–5961.

Scalapino, D.J., White, S. and Zhang, S. (1993). Insulator, metal, or superconductor: the criteria. *Physical Review B*, **47**, 7995–8007.

Schmid, G., Todo, S., Troyer, M. and Dorneich, A. (2002). Finite-temperature phase diagram of hard-core bosons in two dimensions. *Physical Review Letters*, **88**, 167208.

Schollwöck, U. (2005). The density matrix renormalization group method. *Reviews of Modern Physics*, **77**, 259.

Suzuki, M. (1976). Relationship between d-dimensional quantal spin systems and $(d+1)$-dimensional Ising systems – equivalence, critical exponents and systematic approximants of the partition function and spin correlations. *Progress of Theoretical Physics*, **56**, 1454–1469.

Suzuki, M., Miyashita, S. and Kuroda, A. (1977). Monte Carlo simulation of quantum spin systems. I. *Progress of Theoretical Physics*, **58**, 1377–1387.

Swendsen, R. and Wang, J.-S. (1987). Nonuniversal critical dynamics in Monte Carlo simulations. *Physical Review Letters*, **58**, 86–89.

Syljuasen, O. and Sandvik, A.W. (2002). Quantum Monte Carlo with directed loops. *Physical Review E*, **66**, 046701.

Todo, S. and Kato, K. (2001). Cluster algorithms for general-S quantum spin systems. *Physical Review Letters*, **87**, 047203.

Trebst, S., Huse, D. and Troyer, M. (2004). Optimizing the ensemble for equilibration in broad-histogram Monte Carlo simulations. *Physical Review E*, **70**, 046701.

Trivedi, N. and Randeria, M. (1995). Deviations from Fermi-Liquid behavior above T_c in 2D short coherence length superconductors. *Physical Review Letters*, **75**, 312–315.

Trotter, H. (1959). On the product of semi-groups of ooperators. *Proceedings of the American Mathematical Society*, **10**, 545–551.

Troyer, M., Alet, F. and Wessel, S. (2004). Histogram methods for quantum systems: from reweighting to wang-landau sampling. *Brazilian Journal of Physics*, **34**, 377–383.

Troyer, M., Imada, M. and Ueda, K. (1997). Critical exponents of the quantum phase transition in a planar antiferromagnet. *Journal of the Physical Society of Japan*, **66**, 2957–2960.

Troyer, M., Wessel, S. and Alet, F. (2003). Flat histogram methods for quantum systems: algorithms to overcome tunneling problems and calculate the free energy. *Physical Review Letters*, **90**, 120201.

Troyer, M. and Wiese, U.-J. (2005). Computational complexity and fundamental limitations to fermionic quantum Monte Carlo simulations. *Physical Review Letters*, **94**, 170201. *cond-mat/0408370*.

Tsvelik, A.M. (1995). *Quantum Field Theory in Condensed Matter Physics*, Cambridge University Press.

Vekic, M., Cannon, J.W., Scalapino, D.J., *et al*. (1995). Competition between antiferromagnetic order and spin-liquid behavior in the two-dimensional periodic Anderson model at half filling. *Physical Review Letters*, **74**, 2367–2370.

Wang, F. and Landau, D. (2001a). Determining the density of states for classical statistical models: A random walk algorithm to produce a flat histogram. *Physical Review E*, **64**, 056101.

Wang, F. and Landau, D. (2001b). Efficient, multiple-range random walk algorithm to calculate the density of states. *Physical Review Letters*, **86**, 2050–2053.

Werner, P., Völker, K., Troyer, M. and Chakravarty, S. (2005). Phase diagram and critical exponents of a dissipative Ising spin chain in a transverse magnetic field. *Physical Review Letters*, **94**, 047201.

Werner, P., Comanac, A., De Medici, *et al*. (2006). A continuous-time solver for quantum impurity models. *Physical Review Letters*, **97**, 076405.

Werner, P. and Millis, A.J. (2006). Hybridization expansion impurity solver: General formulation and application to Kondo lattice and two-orbital models. *Physical Review B*, **74**, 155107.

White, S. (1992). Density matrix formulation for quantum renormalization groups. *Physical Review Letters*, **69**, 2863–2866.

White, S. (1993). Density-matrix algorithms for quantum renormalization groups. *Physical Review B*, **48**, 10345.

White, S.R., Scalapino, D.J., Sugar, R.L., *et al*. (1989). Numerical study of the two-dimensional Hubbard model. *Physical Review B*, **40**, 506–516.

Wiese, U.-J. and Ying, H.-P. (1992). Blockspin cluster algorithms for quantum spin systems. *Physics Letters A*, **168**, 143–150.

Wolff, U. (1989). Collective Monte Carlo updating for spin systems. *Physical Review Letters*, **62**, 361–364.

Woodward, F., Albrecht, A., Wynn, C., *et al*. (2002). Two-dimensional $S = 1/2$ Heisenberg antiferromagnets: Synthesis, structure, and magnetic properties. *Physical Review B*, **65**, 144412.

Wu, C., Hu, J.P. and Zhang, S.C. (2003). Exact SO(5) symmetry in the spin-3/2 fermionic system. *Physical Review Letters*, **91**, 186402.

Wu, C. and Zhang, S. (2005). A fermionic quantum Monte-Carlo algorithm without the sign problem. *Physical Review B*, **71**, 155115. *cond-mat/0407272*.

Yasuda, C., Todo, S., Hukushima, K., *et al*. (2005). Néel Temperature of quasi-low-dimensional Heisenberg antiferromagnets. *Physical Review Letters*, **94**, 217201. *cond-mat/0312392*.

Yoo, J., Chandrasekharan, S., Kaul, R.K., *et al*. (2004). No sign problem in the Hirsch-Fye algorithm for an Anderson impurity. *cond-mat/0412771*.

Heavy Fermions: Electrons at the Edge of Magnetism

Piers Coleman
Rutgers University, Piscataway, NJ, USA

1 INTRODUCTION: 'ASYMPTOTIC FREEDOM' IN A CRYOSTAT

The term *heavy fermion* was coined by Steglich *et al*. (1976) in the late 1970s to describe the electronic excitations in a new class of intermetallic compound with an electronic density of states as much as 1000 times larger than copper. Since the original discovery of heavy-fermion behavior in $CeAl_3$ by Andres, Graebner and Ott (1975), a diversity of heavy-fermion compounds, including superconductors, antiferromagnets (AFMs), and insulators have been discovered. In the last 10 years, these materials have become the focus of intense interest with the discovery that intermetallic AFMs can be tuned through a quantum phase transition into a heavy-fermion state by pressure, magnetic fields, or chemical doping (von Löhneysen *et al*., 1994; von Löhneysen, 1996; Mathur *et al*., 1998). The 'quantum critical point' (QCP) that separates the heavy-electron ground state from the AFM represents a kind of singularity in the material phase diagram that profoundly modifies the metallic properties, giving them a a predisposition toward superconductivity and other novel states of matter.

One of the goals of modern condensed matter research is to couple magnetic and electronic properties to develop new classes of material behavior, such as high-temperature superconductivity or colossal magnetoresistance materials, spintronics, and the newly discovered multiferroic materials. Heavy-electron materials lie at the very brink of magnetic instability, in a regime where quantum fluctuations of the magnetic and electronic degrees are strongly coupled. As such, they are an important test bed for the development of our understanding about the interaction between magnetic and electronic quantum fluctuations.

Heavy-fermion materials contain rare-earth or actinide ions, forming a matrix of localized magnetic moments. The active physics of these materials results from the immersion of these magnetic moments in a quantum sea of mobile conduction electrons. In most rare-earth metals and insulators, local moments tend to order antiferromagnetically, but, in heavy-electron metals, the quantum-mechanical jiggling of the local moments induced by delocalized electrons is fierce enough to melt the magnetic order.

The mechanism by which this takes place involves a remarkable piece of quantum physics called the *Kondo effect* (Kondo, 1962, 1964; Jones, 2007). The Kondo effect describes the process by which a free magnetic ion, with a Curie magnetic susceptibility at high temperatures, becomes screened by the spins of the conduction sea, to ultimately form a spinless scatering center at low temperatures and low magnetic fields (Figure 1a). In the Kondo effect, this screening process is continuous, and takes place once the

Handbook of Magnetism and Advanced Magnetic Materials. Edited by Helmut Kronmüller and Stuart Parkin. Volume 1: *Fundamentals and Theory*. ISBN: 978-0-470-02217-7.

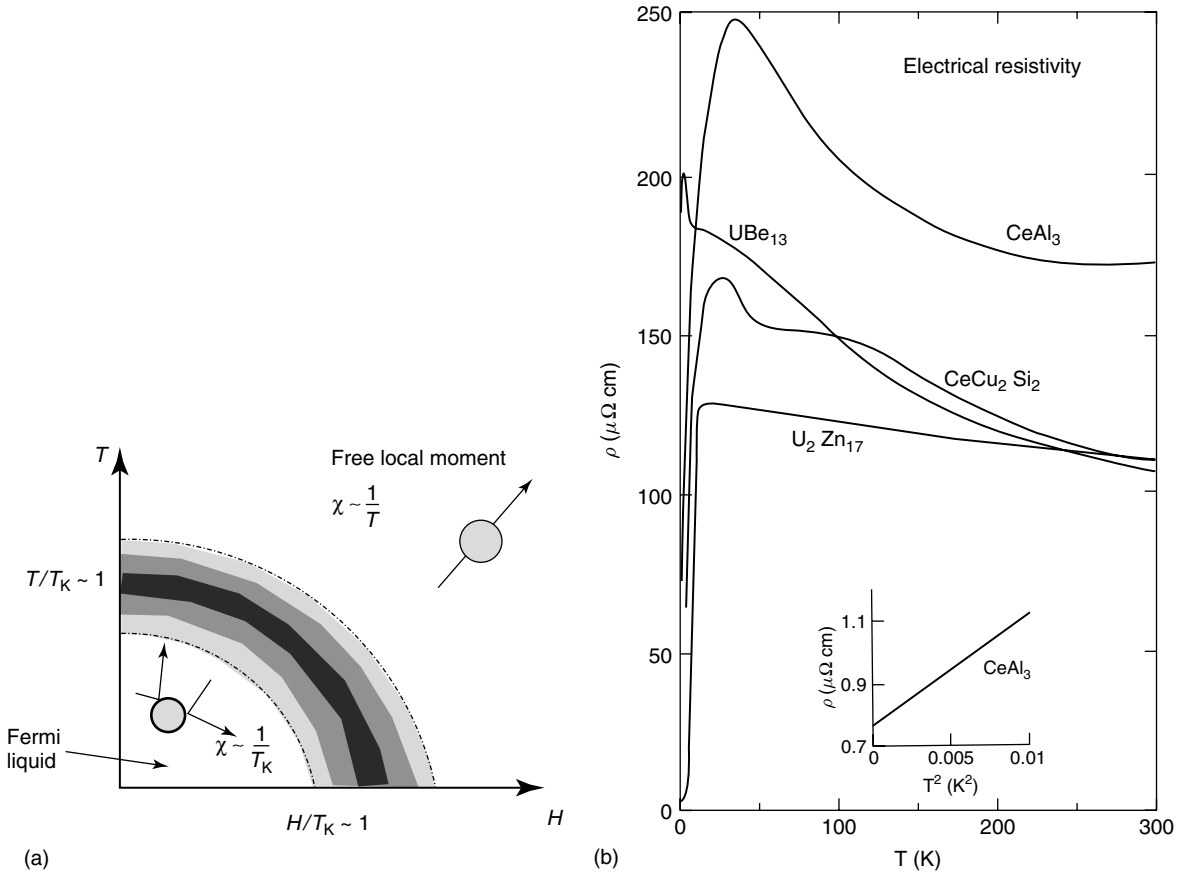

Figure 1. (a) In the Kondo effect, local moments are free at high temperatures and high fields, but become 'screened' at temperatures and magnetic fields that are small compared with the 'Kondo temperature' T_K, forming resonant scattering centers for the electron fluid. The magnetic susceptibility χ changes from a Curie-law $\chi \sim \frac{1}{T}$ at high temperature, but saturates at a constant paramagnetic value $\chi \sim \frac{1}{T_K}$ at low temperatures and fields. (b) The resistivity drops dramatically at low temperatures in heavy fermion materials, indicating the development of phase coherence between the scatering of the lattice of screened magnetic ions. (Reproduced from J.L. Smith and P.S. Riseborough, *J. Mag. Mat.* 47–48, 1985, copyright © 1985, with permission from Elsevier.)

magnetic field, or the temperature drops below a characteristic energy scale called the *Kondo temperature* T_K. Such 'quenched' magnetic moments act as strong elastic scattering potentials for electrons, which gives rise to an increase in resistivity produced by isolated magnetic ions. When the same process takes place inside a heavy-electron material, it leads to a spin quenching at every site in the lattice, but now, the strong scattering at each site develops coherence, leading to a sudden drop in the resistivity at low temperatures (Figure 1b).

Heavy-electron materials involve the dense lattice analog of the single-ion Kondo effect and are often called *Kondo lattice* compounds (Doniach, 1977). In the lattice, the Kondo effect may be alternatively visualized as the dissolution of localized and neutral magnetic f spins into the quantum conduction sea, where they become mobile excitations. Once mobile, these free spins acquire charge and form electrons with a radically enhanced effective mass (Figure 2). The net effect of this process is an increase in the volume of the electronic Fermi surface, accompanied by a profound transformation in the electronic masses and interactions.

A classic example of such behavior is provided by the intermetallic crystal $CeCu_6$. Superficially, this material is copper, alloyed with 14% Cerium. The Cerium Ce^{3+} ions in this material are Ce^{3+} ions in a $4f^1$ configuration with a localized magnetic moment with $J = 5/2$. Yet, at low temperatures, they lose their spin, behaving as if they were Ce^{4+} ions with delocalized f electrons. The heavy electrons that develop in this material are a thousand times 'heavier' than those in metallic copper, and move with a group velocity that is slower than sound. Unlike copper, which has Fermi temperature of the order 10 000 K, that of $CeCu_6$ is of the order 10 K, and above this temperature, the heavy electrons disintegrate to reveal the underlying magnetic moments of the Cerium ions, which manifest themselves as a Curie-law susceptibility $\chi \sim \frac{1}{T}$. There are many hundreds of different

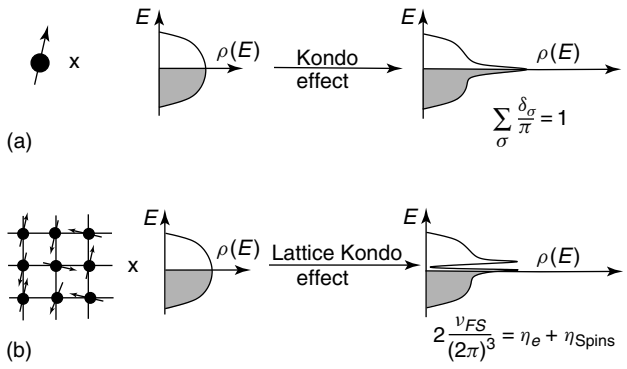

Figure 2. (a) Single-impurity Kondo effect builds a single fermionic level into the conduction sea, which gives rise to a resonance in the conduction electron density of states. (b) Lattice Kondo effect builds a fermionic resonance into the conduction sea in each unit cell. The elastic scattering of this lattice of resonances leads to the formation of a heavy-electron band, of width T_K.

varieties of heavy-electron material, many developing new and exotic phases at low temperatures.

This chapter is intended as a perspective on the the current theoretical and experimental understanding of heavy-electron materials. There are important links between the material in this chapter and the proceeding chapter on the Kondo effect by Jones (2007), the chapter on quantum criticality by Sachdev (2007), and the perspective on spin fluctuation theories of high-temperature superconductivity by Norman (2007). For completeness, I have included references to an extensive list of review articles spanning 30 years of discovery, including books on the Kondo effect and heavy fermions (Hewson, 1993; Cox and Zawadowski, 1999), general reviews on heavy-fermion physics (Stewart, 1984; Lee *et al*., 1986; Ott, 1987; Fulde, Keller and Zwicknagl, 1988; Grewe and Steglich, 1991), early views of Kondo and mixed valence physics (Gruner and Zawadowski, 1974; Varma, 1976), the solution of the Kondo impurity model by renormalization group and the strong coupling expansion (Wilson, 1976; Nozières and Blandin, 1980), the Bethe Ansatz method (Andrei, Furuya and Lowenstein, 1983; Tsvelik and Wiegman, 1983), heavy-fermion superconductivity (Sigrist and Ueda, 1991a; Cox and Maple, 1995), Kondo insulators (Aeppli and Fisk, 1992; Tsunetsugu, Sigrist and Ueda, 1997; Riseborough, 2000), X-ray spectroscopy (Allen *et al*., 1986), optical response in heavy fermions (Degiorgi, 1999), and the latest reviews on non-Fermi liquid behavior and quantum criticality (Stewart, 2001; Coleman, Pépin, Si and Ramazashvili, 2001; Varma, Nussinov and van Saarlos, 2002; von Löhneysen, Rosch, Vojta and Wolfe, 2007; Miranda and Dobrosavljevic, 2005; Flouquet, 2005). There are inevitable apologies, for this chapter is highly selective and, partly owing to lack of space, it neither covers dynamical mean-field theory (DMFT) approaches to heavy-fermion physics (Georges, Kotliar, Krauth and Rozenberg, 1996; Cox and Grewe, 1988; Jarrell, 1995; Vidhyadhiraja, Smith, Logan and Krishnamurthy, 2003) nor the extensive literature on the order-parameter phenomenology of heavy-fermion superconductors (HFSCs) reviewed in Sigrist and Ueda (1991a).

1.1 Brief history

Heavy-electron materials represent a frontier in a journey of discovery in electronic and magnetic materials that spans more than 70 years. During this time, the concepts and understanding have undergone frequent and often dramatic revision.

In the early 1930s, de Haas, de Boer and van der Berg (1933) in Leiden, discovered a 'resistance minimum' that develops in the resistivity of copper, gold, silver, and many other metals at low temperatures (Figure 3). It took a further 30 years before the purity of metals and alloys improved to a point where the resistance minimum could be linked to the presence of magnetic impurities (Clogston *et al*., 1962; Sarachik, Corenzwit and Longinotti, 1964). Clogston, Mathias, and collaborators at Bell Labs (Clogston *et al*., 1962) found they could tune the conditions under which iron impurities in Niobium were magnetic, by alloying with molybdenum. Beyond a certain concentration of molybdenum, the iron impurities become magnetic and a resistance minimum was observed to develop.

In 1961, Anderson formulated the first microscopic model for the formation of magnetic moments in metals. Earlier work by Blandin and Friedel (1958) had observed that localized d states form resonances in the electron sea. Anderson extended this idea and added a new ingredient: the Coulomb interaction between the d-electrons, which he modeled by term

$$H_I = U n_\uparrow n_\downarrow \tag{1}$$

Anderson showed that local moments formed once the Coulomb interaction U became large. One of the unexpected consequences of this theory is that local moments develop an antiferromagnetic coupling with the spin density of the surrounding electron fluid, described by the interaction (Anderson, 1961; Kondo, 1962, 1964; Schrieffer and Wolff, 1966; Coqblin and Schrieffer, 1969)

$$H_I = J\vec{\sigma}(0)\cdot\vec{S} \tag{2}$$

where $\vec{S}$ is the spin of the local moment and $\vec{\sigma}(0)$ is the spin density of the electron fluid. In Japan, Kondo (1962) set out to examine the consequences of this result. He found that when he calculated the scattering rate $\frac{1}{\tau}$ of

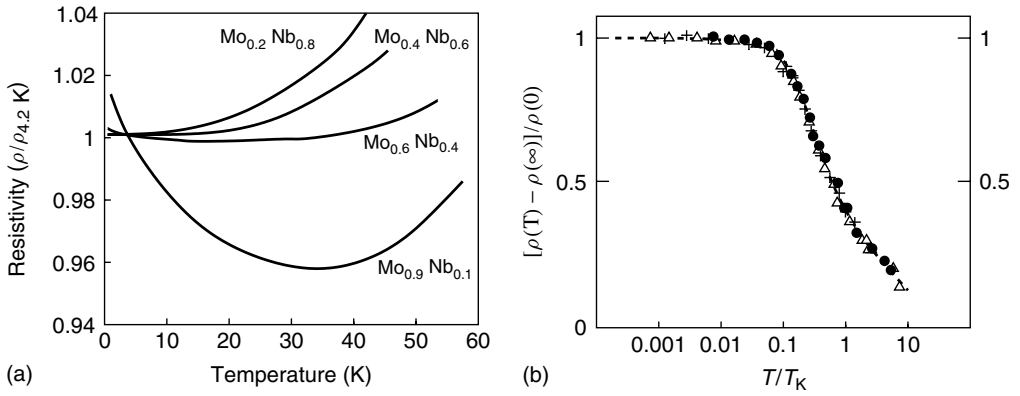

Figure 3. (a) Resistance minimum in Mo_xNb_{1-x}. (Reproduced from M. Sarachik, E. Corenzwit, and L.D. Longinotti, *Phys. Rev.* **135**, 1964, A1041, copyright © by the American Physical Society, with permission of the APS.) (b) Temperature dependence of excess resistivity produced by scattering off a magnetic ion, showing, universal dependence on a single scale, the Kondo temperature. Original data from White and Geballe (1979).

electrons of a magnetic moment to one order higher than Born approximation,

$$\frac{1}{\tau} \propto \left[J\rho + 2(J\rho)^2 \ln \frac{D}{T} \right]^2 \tag{3}$$

where ρ is the density of state of electrons in the conduction sea and D is the width of the electron band. As the temperature is lowered, the logarithmic term grows, and the scattering rate and resistivity ultimately rises, connecting the resistance minimum with the antiferromagnetic interaction between spins and their surroundings.

A deeper understanding of the logarithmic term in this scattering rate required the renormalization group concept (Anderson and Yuval, 1969, 1970, 1971; Fowler and Zawadowskii, 1971; Wilson, 1976; Nozières, 1976; Nozières and Blandin, 1980). The key idea here is that the physics of a spin inside a metal depends on the energy scale at which it is probed. The 'Kondo' effect is a manifestation of the phenomenon of 'asymptotic freedom' that also governs quark physics. Like the quark, at high energies, the local moments inside metals are asymptotically free, but at temperatures and energies below a characteristic scale the Kondo temperature,

$$T_K \sim D e^{-1/(2J\rho)} \tag{4}$$

where ρ is the density of electronic states; they interact so strongly with the surrounding electrons that they become screened into a singlet state, or 'confined' at low energies, ultimately forming a Landau–Fermi liquid (Nozières, 1976; Nozières and Blandin, 1980).

Throughout the 1960s and 1970s, conventional wisdom had it that magnetism and superconductivity are mutually exclusive. Tiny concentrations of magnetic impurities produce a lethal suppression of superconductivity in conventional metals. Early work on the interplay of the Kondo effect and superconductivity by Maple *et al*. (1972) did suggest that the Kondo screening suppresses the pair-breaking effects of magnetic moments, but the implication of these results was only slowly digested. Unfortunately, the belief in the mutual exclusion of local moments and superconductivity was so deeply ingrained that the first observation of superconductivity in the 'local moment' metal UBe_{13} (Bucher *et al*., 1975) was dismissed by its discoverers as an artifact produced by stray filaments of uranium. Heavy-electron metals were discovered by Andres, Graebner and Ott (1975), who observed that the intermetallic $CeAl_3$ forms a metal in which the Pauli susceptibility and linear specific heat capacity are about 1000 times larger than in conventional metals. Few believed their speculation that this might be a lattice version of the Kondo effect, giving rise to a narrow band of 'heavy' f electrons in the lattice. The discovery of superconductivity in $CeCu_2Si_2$ in a similar f-electron fluid, a year later by Steglich *et al*. (1976), was met with widespread disbelief. All the measurements of the crystal structure of this material pointed to the fact that the Ce ions were in a Ce^{3+} or $4f^1$ configuration. Yet, this meant one local moment per unit cell – which required an explanation of how these local moments do not destroy superconductivity, but, rather, are part of its formation.

Doniach (1977), made the visionary proposal that a heavy-electron metal is a dense Kondo lattice (Kasuya, 1956), in which every single local moment in the lattice undergoes the Kondo effect (Figure 2). In this theory, each spin is magnetically screened by the conduction sea. One of the great concerns of the time, raised by Nozières (1985), was whether there could ever be sufficient conduction electrons in a dense Kondo lattice to screen each local moment.

Theoretical work on this problem was initially stalled for want of any controlled way to compute properties of the Kondo lattice. In the early 1980s, Anderson (1981) proposed a way out of this log-jam. Taking a cue from the success of the $1/S$ expansion in spin-wave theory, and the $1/N$ expansion in statistical mechanics and particle physics, he noted that the large magnetic spin degeneracy $N = 2j + 1$ of f moments could be used to generate an expansion in the small parameter $1/N$ about the limit where $N \to \infty$. Anderson's idea prompted a renaissance of theoretical development (Ramakrishnan, 1981; Gunnarsson and Schönhammer, 1983; Read and Newns, 1983a,b; Coleman, 1983, 1987a; Auerbach and Levin, 1986), making it possible to compute the X-ray absorption spectra of these materials and, for the first time, examine how heavy f bands form within the Kondo lattice. By the mid-1980s, the first de Haas van Alphen experiments (Reinders *et al*., 1986; Taillefer and Lonzarich, 1988) had detected cyclotron orbits of heavy electrons in $CeCu_6$ and UPt_3. With these developments, the heavy-fermion concept was cemented.

On a separate experimental front, in Ott, Rudigier, Fisk and Smith (1983), and Ott *et al*. (1984) returned to the material UBe_{13}, and, by measuring a large discontinuity in the bulk specific heat at the resistive superconducting transition, confirmed it as a bulk heavy-electron superconductor. This provided a vital independent confirmation of Steglich's discovery of heavy electron superconductivity, assuaging the old doubts and igniting a huge new interest in heavy-electron physics. The number of heavy-electron metals and superconductors grew rapidly in the mid-1980s (Sigrist and Ueda, 1991b). It became clear from specific heat, NMR, and ultrasound experiments on HFSCs that the gap is anisotropic, with lines of nodes strongly suggesting an electronic, rather than a phonon mechanism of pairing. These discoveries prompted theorists to return to earlier spin-fluctuation-mediated models of anisotropic pairing. In the early summer of 1986, three new theoretical papers were received by *Physical Review*, the first by Monod, Bourbonnais and Emery (1986) working in Orsay, France, followed closely (6 weeks later) by papers from Scalapino, Loh and Hirsch (1986) at UC Santa Barbara, California, and Miyake, Rink and Varma (1986) at Bell Labs, New Jersey. These papers contrasted heavy-electron superconductivity with superfluid He-3. Whereas He-3 is dominated by ferromagnetic interactions, which generate triplet pairing, these works showed that, in heavy-electron systems, soft antiferromagnetic spin fluctuations resulting from the vicinity to an antiferromagnetic instability would drive anisotropic d-wave pairing (Figure 4). The almost coincident discovery of high-temperature superconductivity the very same year, 1986, meant that these early works on heavy-electron superconductivity were destined to exert huge influence on the evolution of ideas about high-temperature

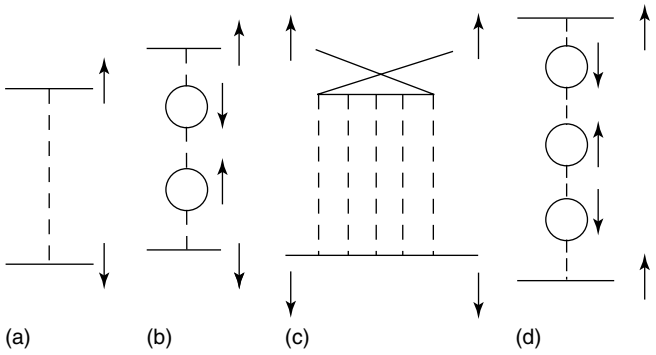

Figure 4. Figure from Monod, Bourbonnais and Emery (1986), one of three path-breaking papers in 1986 to link d-wave pairing to antiferromagnetism. (a) The bare interaction, (b), (c), and (d), the paramagnon-mediated interaction between antiparallel or parallel spins. (Reproduced from M.T.B. Monod, C. Bourbonnais, and V. Emery, *Phys. Rev. B.* **34**, 1986, 7716, copyright © 1986 by the American Physical Society, with permission of the APS.)

superconductivity. Both the resonating valence bond (RVB) and the spin-fluctuation theory of d-wave pairing in the cuprates are, in my opinion, close cousins, if not direct descendents of these early 1986 papers on heavy-electron superconductivity.

After a brief hiatus, interest in heavy-electron physics reignited in the mid-1990s with the discovery of QCPs in these materials. High-temperature superconductivity introduced many important new ideas into our conception of electron fluids, including

- Non-Fermi liquid behavior: the emergence of metallic states that cannot be described as fluids of renormalized quasiparticles.
- Quantum phase transitions and the notion that zero temperature QCPs might profoundly modify finite temperature properties of metal.

Both of these effects are seen in a wide variety of heavy-electron materials, providing an vital alternative venue for research on these still unsolved aspects of interlinked, magnetic, and electronic behavior.

In 1994 Hilbert von Löhneysen and collaborators discovered that by alloying small amounts of gold into $CeCu_6$, one can tune $CeCu_{6-x}Au_x$ through an antiferromagnetic QCP, and then reverse the process by the application of pressure (von Löhneysen, 1996; von Löhneysen *et al*., 1994). These experiments showed that a heavy-electron metal develops 'non-Fermi liquid' properties at a QCP, including a linear temperature dependence of the resistivity and a logarithmic dependence of the specific heat coefficient on temperature. Shortly thereafter, Mathur *et al*. (1998), at Cambridge showed that when pressure is used to drive the AFM $CeIn_3$

through a quantum phase transition, heavy-electron superconductivity develops in the vicinity of the quantum phase transition. Many new examples of heavy-electron system have come to light in the last few years which follow the same pattern. In one fascinating development, (Monthoux and Lonzarich, 1999) suggested that if quasi-two-dimensional versions of the existing materials could be developed, then the superconducting pairing would be less frustrated, leading to a higher transition temperature. This led experimental groups to explore the effect of introducing layers into the material $CeIn_3$, leading to the discovery of the so-called $1-1-5$ compounds, in which an XIn_2 layer has been introduced into the original cubic compound. (Petrovic *et al*., 2001; Sidorov *et al*., 2002). Two notable members of this group are $CeCoIn_5$ and, most recently, $PuCoGa_5$ (Sarrao *et al*., 2002). The transition temperature rose from 0.5 to 2.5 K in moving from $CeIn_3$ to $CeCoIn_5$. Most remarkably, the transition temperature rises to above 18 K in the $PuCoGa_5$ material. This amazing rise in T_c, and its close connection with quantum criticality, are very active areas of research, and may hold important clues (Curro *et al*., 2005) to the ongoing quest to discover room-temperature superconductivity.

1.2 Key elements of heavy-fermion metals

Before examining the theory of heavy-electron materials, we make a brief tour of their key properties. Table 1 shows a selective list of heavy fermion compounds

1.2.1 Spin entropy: a driving force for new physics

The properties of heavy-fermion compounds derive from the partially filled f orbitals of rare-earth or actinide ions (Stewart, 1984; Lee *et al*., 1986; Ott, 1987; Fulde, Keller and Zwicknagl, 1988; Grewe and Steglich, 1991). The large nuclear charge in these ions causes their f orbitals to collapse inside the inert gas core of the ion, turning them into localized magnetic moments.

Moreover, the large spin-orbit coupling in f orbitals combines the spin and angular momentum of the f states into a

Table 1. Selected heavy-fermion compounds.

Type	Material	T^* (K)	$T_c,\ x_c,\ B_c$	Properties	ρ	m J mol^{-1}K^{-2} γ_n	References
Metal	$CeCu_6$	10	–	Simple HF metal	T^2	1600	Stewart, Fisk and Wire (1984a) and Onuki and Komatsubara (1987)
Superconductors	$CeCu_2Si_2$	20	$T_c = 0.17$ K	First HFSC	T^2	800–1250	Steglich *et al*. (1976) and Geibel *et al*. (1991a,b)
	UBe_{13}	2.5	$T_c = 0.86$ K	Incoherent metal→HFSC	$\rho_c \sim 150\,\mu\Omega$ cm	800	Ott, Rudigier, Fisk and Smith (1983, 1984)
	$CeCoIn_5$	38	$T_c = 2.3$	Quasi 2D HFSC	T	750	Petrovic *et al*. (2001) and Sidorov *et al*. (2002)
Kondo insulators	$Ce_3Pt_4Bi_3$	$T_\chi \sim 80$	–	Fully gapped KI	$\sim e^{\Delta/T}$	–	Hundley *et al*. (1990) and Bucher, Schlessinger, Canfield and Fisk (1994)
	CeNiSn	$T_\chi \sim 20$	–	Nodal KI	Poor metal	–	Takabatake *et al*. (1990, 1992) and Izawa *et al*. (1999)
Quantum critical	$CeCu_{6-x}Au_x$	$T_0 \sim 10$	$x_c = 0.1$	Chemically tuned QCP	T	$\sim\frac{1}{T_0}\ln\left(\frac{T_0}{T}\right)$	von Löhneysen *et al*. (1994) and von Löhneysen (1996)
	$YbRh_2Si_2$	$T_0 \sim 24$	$B_\perp = 0.06$ T $B_\parallel = 0.66$ T	Field-tuned QCP	T	$\sim\frac{1}{T_0}\ln\left(\frac{T_0}{T}\right)$	Trovarelli *et al*. (2000), Paschen *et al*. (2004), Custers *et al*. (2003) and Gegenwart *et al*. (2005)
SC + other order	UPd_2Al_3	110	$T_{AF} = 14$ K, $T_{sc} = 2$ K	AFM + HFSC	T^2	210	Geibel *et al*. (1991a), Sato *et al*. (2001) and Tou *et al*. (1995)
	URu_2Si_2	75	$T_1 = 17.5$ K, $T_{sc} = 1.3$ K	Hidden order and HFSC	T^2	120/65	Palstra *et al*. (1985) and Kim *et al*. (2003)

Unless otherwise stated, T^* denotes the temperature of the maximum in resistivity. T_c, x_c, and B_c denote critical temperature, doping, and field. ρ denotes the temperature dependence in the normal state. $\gamma_n = C_V/T$ is the specific heat coefficient in the normal state.

state of definite J, and it is these large quantum spin degrees of freedom that lie at the heart of heavy-fermion physics.

Heavy-fermion materials display properties which change qualitatively, depending on the temperature, so much so, that the room-temperature and low-temperature behavior almost resembles two different materials. At room temperature, high magnetic fields, and high frequencies, they behave as local moment systems, with a Curie-law susceptibility

$$\chi = \frac{M^2}{3T} \qquad M^2 = (g_J \mu_B)^2 J(J+1) \tag{5}$$

where M is the magnetic moment of an f state with total angular momentum J and the gyromagnetic ratio g_J. However, at temperatures beneath a characteristic scale, we call T^* (to distinguish it from the single-ion Kondo temperature T_K), the localized spin degrees of freedom melt into the conduction sea, releasing their spins as mobile, conducting f electrons.

A Curie susceptibility is the hallmark of the decoupled, rotational dynamics of the f moments, associated with an unquenched entropy of $\mathcal{S} = k_B \ln N$ per spin, where $N = 2J + 1$ is the spin degeneracy of an isolated magnetic moment of angular momentum J. For example, in a Cerium-heavy electron material, the $4f^1$ ($L = 3$) configuration of the Ce^{3+} ion is spin-orbit coupled into a state of definite $J = L - S = 5/2$ with $N = 6$. Inside the crystal, the full rotational symmetry of each magnetic f ion is often reduced by crystal fields to a quartet ($N = 4$) or a Kramer's doublet $N = 2$. At the characteristic temperature T^*, as the Kondo effect develops, the spin entropy is rapidly lost from the material, and large quantities of heat are lost from the material. Since the area under the specific heat curve determines the entropy,

$$S(T) = \int_0^T \frac{C_V}{T'} \mathrm{d}T' \tag{6}$$

a rapid loss of spin entropy at low temperatures forces a sudden rise in the specific heat capacity. Figure 5 illustrates this phenomenon with the specific heat capacity of UBe_{13}. Notice how the specific heat coefficient C_V/T rises to a value of order 1 J mol^{-1}K^2, and starts to saturate at about 1 K, indicating the formation of a Fermi liquid with a linear specific heat coefficient. Remarkably, just as the linear specific heat starts to develop, UBe_{13} becomes superconducting, as indicated by the large specific heat anomaly.

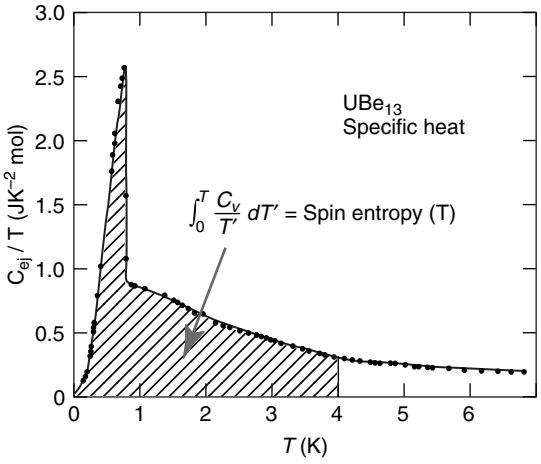

Figure 5. Showing the specific heat coefficient of UBe_{13} after (Ott, Rudigier, Fisk and Smith, 1985). The area under the C_V/T curve up to a temperature T provides a measure of the amount of unquenched spin entropy at that temperature. The condensation entropy of HFSCs is derived from the spin-rotational degrees of freedom of the local moments, and the large scale of the condensation entropy indicates that spins partake in the formation of the order parameter. (Reproduced from H.R. Ott, H. Rudigier, Z. Fisk, and J.L. Smith, in W.J.L. Buyers (ed.): *Proceedings of the NATO Advanced Study Institute on Moment Formation in Solids, Vancouver Island*, August 1983, Valence Fluctuations in Solids (Plenum, 1985), p. 309. with permission of Springer Science and Business Media.)

1.2.2 'Local' Fermi liquids with a single scale

The standard theoretical framework for describing metals is Landau–Fermi liquid theory (Landau, 1957), according to which the excitation spectrum of a metal can be adiabatically connected to those of a noninteracting electron fluid. Heavy-fermion metals are extreme examples of Landau–Fermi liquids which push the idea of adiabaticity into an regime where the bare electron interactions, on the scale of electron volts, are hundreds, even thousands of times larger than the millivolt Fermi energy scale of the heavy-electron quasiparticles. The Landau–Fermi liquid that develops in these materials shares much in common with the Fermi liquid that develops around an isolated magnetic impurity (Nozières, 1976; Nozières and Blandin, 1980), once it is quenched by the conduction sea as part of the Kondo effect. There are three key features of this Fermi liquid:

- *Single scale:* T^* The quasiparticle density of states $\rho^* \sim 1/T^*$ and scattering amplitudes $A_{\mathbf{k}\sigma,\mathbf{k}'\sigma'} \sim T^*$ scale approximately with a single scale T^*.
- *Almost incompressible:* Heavy-electron fluids are 'almost incompressible', in the sense that the charge susceptibility $\chi_c = \mathrm{d}N_e/\mathrm{d}\mu \ll \rho^*$ is unrenormalized and typically more than an order of magnitude smaller than the quasiparticle density of states ρ^*. This is because the lattice of spins severely modifies the quasiparticle density of states, but leaves the charge density of the fluid $n_e(\mu)$, and its dependence on the chemical potential μ unchanged.

- *Local:* Quasiparticles scatter when in the vicinity of a local moment, giving rise to a small momentum dependence to the Landau scattering amplitudes (Yamada, 1975; Yoshida and Yamada, 1975; Engelbrecht and Bedell, 1995).

Landau–Fermi liquid theory relates the properties of a Fermi liquid to the density of states of the quasiparticles and a small number of interaction parameters (Baym and Pethick, 1992). If $E_{\mathbf{k}\sigma}$ is the energy of an isolated quasiparticle, then the quasiparticle density of states $\rho^* = \sum_{\mathbf{k}\sigma} \delta(E_{\mathbf{k}\sigma} - \mu)$ determines the linear specific heat coefficient

$$\gamma = \mathrm{Lim}_{T\to 0}\left(\frac{C_V}{T}\right) = \frac{\pi^2 k_\mathrm{B}^2}{3}\rho^* \tag{7}$$

In conventional metals, the linear specific heat coefficient is of the order 1–10 mJ mol^{-1} K^{-2}. In a system with quadratic dispersion, $E_\mathbf{k} = \frac{\hbar^2 k^2}{2m^*}$, the quasiparticle density of states and effective mass m^* are directly proportional

$$\rho^* = \left(\frac{k_F}{\pi^2\hbar^2}\right) m^* \tag{8}$$

where k_F is the Fermi momentum. In heavy-fermion compounds, the scale of ρ^* varies widely, and specific heat coefficients in the range 100–1600 mJ mol^{-1} K^{-2} have been observed. From this simplified perspective, the quasiparticle effective masses in heavy-electron materials are two or three orders of magnitude 'heavier' than in conventional metals.

In Landau–Fermi liquid theory, a change $\delta n_{\mathbf{k}'\sigma'}$ in the quasiparticle occupancies causes a shift in the quasiparticle energies given by

$$\delta E_{\mathbf{k}\sigma} = \sum_{\mathbf{k}'\sigma'} \mathrm{f}_{\mathbf{k}\sigma,\mathbf{k}\sigma'}\delta n_{\mathbf{k}'\sigma'} \tag{9}$$

In a simplified model with a spherical Fermi surface, the Landau interaction parameters only depend on the relative angle $\theta_{\mathbf{k},\mathbf{k}'}$ between the quasiparticle momenta, and are expanded in terms of Legendre Polynomials as

$$\mathrm{f}_{\mathbf{k}\sigma,\mathbf{k}\sigma'} = \frac{1}{\rho^*}\sum_l (2l+1)P_l(\theta_{\mathbf{k},\mathbf{k}'})[F_l^s + \sigma\sigma' F_l^a] \tag{10}$$

The dimensionless 'Landau parameters' $F_l^{s,a}$ parameterize the detailed quasiparticle interactions. The s-wave ($l = 0$) Landau parameters that determine the magnetic and charge susceptibility of a Landau–Fermi liquid are given by Landau (1957), and Baym and Pethick (1992)

$$\chi_s = \mu_\mathrm{B}^2 \frac{\rho^*}{1+F_0^a} = \mu_\mathrm{B}^2\rho^*\left[1 - A_0^a\right]$$

$$\chi_c = \mathrm{e}^2\frac{\rho^*}{1+F_0^s} = \mathrm{e}^2\rho^*\left[1 - A_0^s\right] \tag{11}$$

where the quantities

$$A_0^{s,a} = \frac{F_0^{s,a}}{1+F_0^{s,a}} \tag{12}$$

are the s-wave Landau scattering amplitudes in the charge (s) and spin (a) channels, respectively (Baym and Pethick, 1992).

The assumption of local scattering and incompressibility in heavy electron fluids simplifies the situation, for, in this case, only the $l = 0$ components of the interaction remain and the quasiparticle scattering amplitudes become

$$A_{\mathbf{k}\sigma,\mathbf{k}'\sigma'} = \frac{1}{\rho^*}\left(A_0^s + \sigma\sigma' A_0^a\right) \tag{13}$$

Moreover, in local scattering, the Pauli principle dictates that quasiparticles scattering at the same point can only scatter when in opposite spin states, so that

$$A_{\uparrow\uparrow}^{(0)} = A_0^s + A_0^a = 0 \tag{14}$$

and hence $A_0^s = -A_0^a$. The additional assumption of incompressibility forces $\chi_c/(e^2\rho^*) \ll 1$, so that now $A_0^s = -A_0^a \approx 1$ and all that remains is a single parameter ρ^*.

This line of reasoning, first developed for the single impurity Kondo model by Nozières and Blandin (1980) and, Nozières (1976) and later extended to a bulk Fermi liquid by Engelbrecht and Bedell (1995), enables us to understand two important scaling trends amongst heavy-electron systems. The first consequence, deduced from equation (11), is that the dimensionless Sommerfeld ratio, or 'Wilson ratio' $W = \left(\frac{\pi^2 k_\mathrm{B}^2}{\mu_\mathrm{B}^2}\right)\frac{\chi_s}{\gamma} \approx 2$. Wilson (1976) found that this ratio is almost exactly equal to 2 in the numerical renormalization group treatment of the impurity Kondo model. The connection between this ratio and the local Fermi liquid theory was first identified by Nozières (1976), and Nozières and Blandin (1980). In real heavy-electron systems, the effect of spin-orbit coupling slightly modifies the precise numerical form for this ratio, nevertheless, the observation that $W \sim 1$ over a wide range of materials in which the density of states vary by more than a factor of 100 is an indication of the incompressible and local character of heavy Fermi liquids (Figure 6).

A second consequence of locality appears in the transport properties. In a Landau–Fermi liquid, inelastic electron–electron scattering produces a quadratic temperature dependence in the resistivity

$$\rho(T) = \rho_0 + AT^2 \tag{15}$$

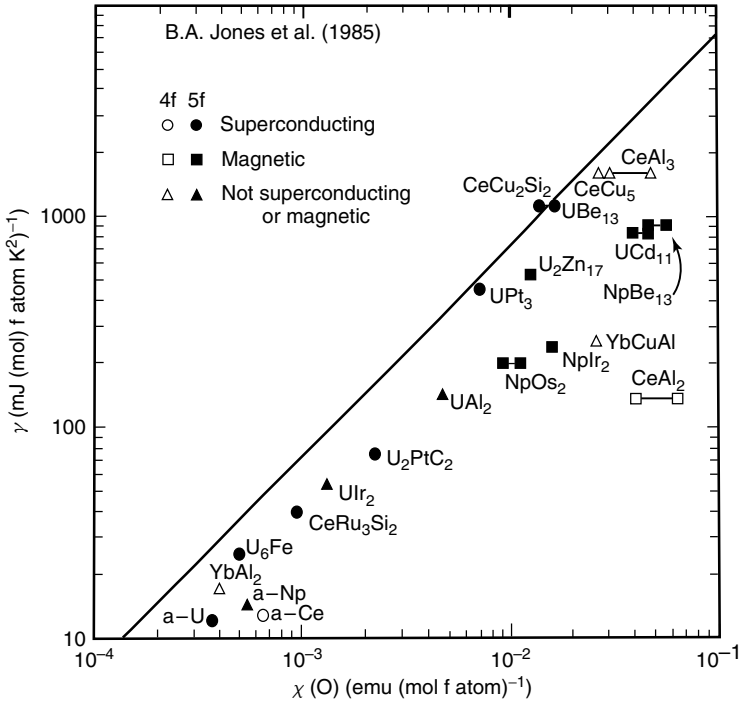

Figure 6. Plot of linear specific heat coefficient versus Pauli susceptibility to show approximate constancy of the Wilson ratio. (Reproduced from P.A. Lee, T.M. Rice, J.W. Serene, L.J. Sham, and J.W. Wilkins, *Comments Condens. Matt. Phys.* 9212, (1986) 99, with permission from Taylaor & Francis Ltd, www.informaworld.com.)

In conventional metals, resistivity is dominated by electron–phonon scattering, and the 'A' coefficient is generally too small for the electron–electron contribution to the resistivity to be observed. In strongly interacting metals, the A coefficient becomes large, and, in a beautiful piece of phenomenology, Kadowaki and Woods (1986), observed that the ratio of A to the square of the specific heat coefficient γ^2

$$\alpha_{\rm KW} = \frac{A}{\gamma^2} \approx (1 \times 10^{-5})\mu\Omega{\rm cm(mol\ K^2 mJ^{-1})} \qquad (16)$$

is approximately constant, over a range of A spanning four orders of magnitude. This can also be simply understood from the local Fermi-liquid theory, where the local scattering amplitudes give rise to an electron mean-free path given by

$$\frac{1}{k_{\rm F} l^*} \sim {\rm constant} + \frac{T^2}{(T^*)^2} \qquad (17)$$

The 'A' coefficient in the electron resistivity that results from the second term satisfies $A \propto \frac{1}{(T^*)^2} \propto \tilde{\gamma}^2$. A more detailed calculation is able to account for the magnitude of the Kadowaki–Woods constant, and its weak residual dependence on the spin degeneracy $N = 2J + 1$ of the magnetic ions (see Figure 7).

The approximate validity of the scaling relations

$$\frac{\chi}{\gamma} \approx {\rm cons}, \qquad \frac{A}{\gamma^2} \approx {\rm cons} \qquad (18)$$

for a wide range of heavy-electron compounds constitutes excellent support for the Fermi-liquid picture of heavy electrons.

A classic signature of heavy-fermion behavior is the dramatic change in transport properties that accompanies the development of a coherent heavy-fermion band structure (Figure 6). At high temperatures, heavy-fermion compounds exhibit a large saturated resistivity, induced by incoherent spin-flip scattering of the conduction electrons of the local f moments. This scattering *grows* as the temperature is lowered, but, at the same time, it becomes increasingly elastic at low temperatures. This leads to the development of phase coherence. the f-electron spins. In the case of heavy-fermion metals, the development of coherence is marked by a rapid reduction in the resistivity, but in a remarkable class of heavy fermion or 'Kondo insulators', the development of coherence leads to a filled band with a tiny insulating gap of the order $T_{\rm K}$. In this case, coherence is marked by a sudden exponential rise in the resistivity and Hall constant.

The classic example of coherence is provided by metallic $CeCu_6$, which develops 'coherence' and a maximum in

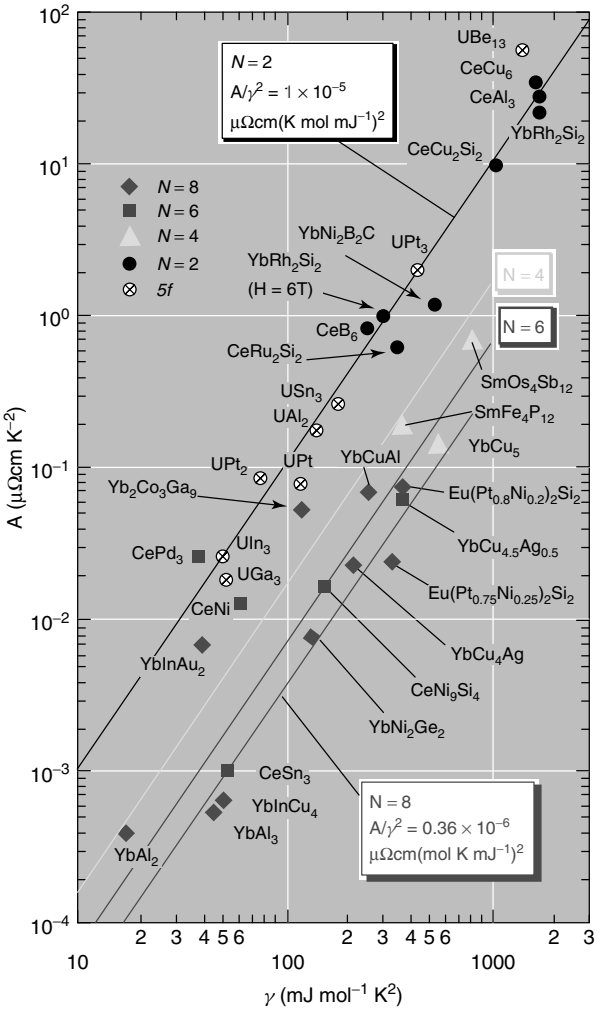

Figure 7. Approximate constancy of the Kadowaki–Woods ratio, for a wide range of heavy electrons. (After Tsujji, Kontani and Yoshimora, 2005.) When spin-orbit effects are taken into account, the Kadowaki–Woods ratio depends on the effective degeneracy $N = 2J + 1$ of the magnetic ion, which when taken into account leads to a far more precise collapse of the data onto a single curve. (Reproduced from H. Tsujji, H. Kontani, and K. Yoshimora, *Phys. Rev. Lett* 94, 2005, copyright © 2005 by the American Physical Sdociety, with permisison of the APS.057201.)

its resistivity around $T = 10\,\mathrm{K}$. Coherent heavy-electron propagation is readily destroyed by substitutional impurities. In $CeCu_6$, Ce^{3+} ions can be continuously substituted with nonmagnetic La^{3+} ions, producing a continuous crossover from coherent Kondo lattice to single impurity behavior (Figure 8).

One of the important principles of the Landau–Fermi liquid is the Fermi surface counting rule, or Luttinger's theorem (Luttinger, 1960). In noninteracting electron band theory, the volume of the Fermi surface counts the number of conduction electrons. For interacting systems, this rule survives (Martin, 1982; Oshikawa, 2000), with the unexpected corollary that

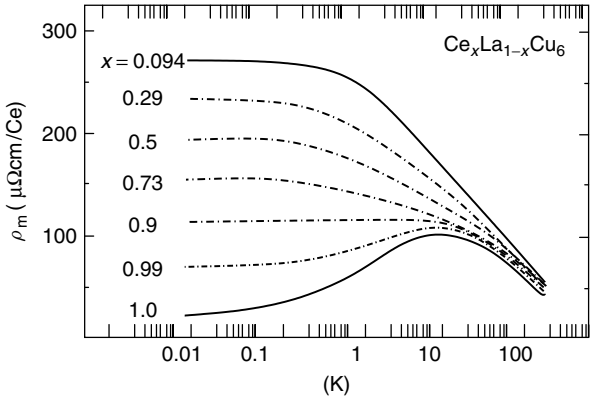

Figure 8. Development of coherence in $Ce_{1-x}La_xCu_6$. (Reproduced from Y. Onuki and T. Komatsubara, *J. Mag. Mat.* 63–64, 1987, 281, copyright © 1987, with permission of Elsevier.)

the spins of the screened local moments are also included in the sum

$$\frac{2V_{\mathrm{FS}}}{(2\pi)^3} = [n_e + n_{\mathrm{spins}}] \tag{19}$$

Remarkably, even though f electrons are localized as magnetic moments at high temperatures, in the heavy Fermi liquid, they contribute to the Fermi surface volume.

The most direct evidence for the large heavy f-Fermi surfaces derives from de Haas van Alphen and Shubnikov de Haas experiments that measure the oscillatory diamagnetism or and resistivity produced by coherent quasiparticle orbits (Figure 9). These experiments provide a direct measure of the heavy-electron mass, the Fermi surface geometry, and volume. Since the pioneering measurements on $CeCu_6$ and UPt_3 by Reinders and Springford, Taillefer, and Lonzarich in the mid-1980s (Reinders *et al*., 1986; Taillefer and Lonzarich, 1988; Taillefer *et al*., 1987), an extensive number of such measurements have been carried out (Onuki and Komatsubara, 1987; Julian, Teunissen and Wiegers, 1992; Kimura *et al*., 1998; McCollam *et al*., 2005). Two key features are observed:

- A Fermi surface volume which counts the f electrons as itinerant quasiparticles.
- Effective masses often in excess of 100 free electron masses. Higher mass quasiparticle orbits, though inferred from thermodynamics, cannot be observed with current measurement techniques.
- Often, but not always, the Fermi surface geometry is in accord with band theory, despite the huge renormalizations of the electron mass.

Additional confirmation of the itinerant nature of the f quasiparticles comes from the observation of a Drude peak in

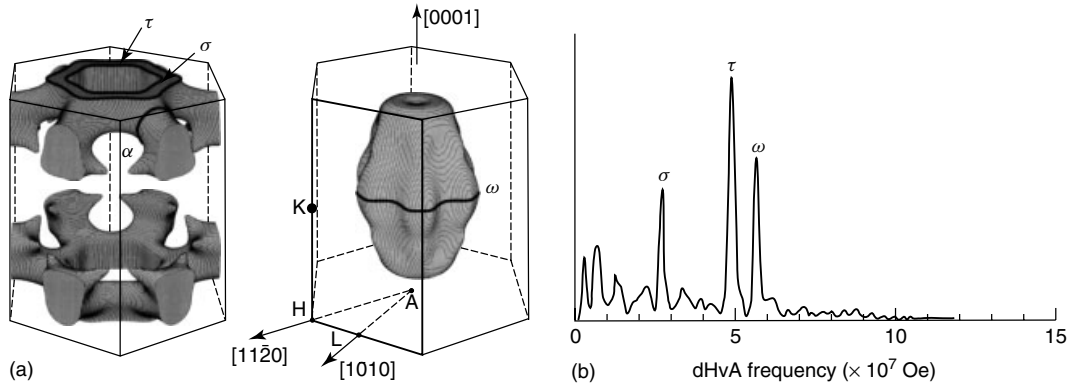

Figure 9. (a) Fermi surface of UPt_3 calculated from band theory assuming itinerant 5f electrons (Oguchi and Freeman, 1985; Wang *et al*., 1987; Norman, Oguchi and Freeman, 1988), showing three orbits (σ, ω and τ) that are identified by dHvA measurements. (After Kimura *et al*., 1998.) (b) Fourier transform of dHvA oscillations identifying σ, ω, and τ orbits shown in (a). (Kimura *et al*., 1998.)

the optical conductivity. At low temperatures, in the coherent regime, an extremely narrow Drude peak can be observed in the optical conductivity of heavy-fermion metals. The weight under the Drude peak is a measure of the plasma frequency: the diamagnetic response of the heavy-fermion metal. This is found to be extremely small, depressed by the large mass enhancement of the quasiparticles (Millis and Lee, 1987a; Degiorgi, 1999).

$$\int_{|\omega| \leq T_K} \frac{d\omega}{\pi} \sigma_{qp}(\omega) = \frac{ne^2}{m^*} \tag{20}$$

Both the optical and dHvA experiments indicate that the presence of f spins depresses both the spin and diamagnetic response of the electron gas down to low temperatures.

2 LOCAL MOMENTS AND THE KONDO LATTICE

2.1 Local moment formation

2.1.1 The Anderson model

We begin with a discussion of how magnetic moments form at high temperatures, and how they are screened again at low temperatures to form a Fermi liquid. The basic model for local moment formation is the Anderson model (Anderson, 1961)

$$H = \overbrace{\sum_{k,\sigma} \epsilon_k n_{k\sigma} + \sum_{k,\sigma} V(k)\left[c^\dagger_{k\sigma} f_\sigma + f^\dagger_\sigma c_{k\sigma}\right]}^{H_{\text{resonance}}} + \underbrace{E_f n_f + U n_{f\uparrow} n_{f\downarrow}}_{H_{\text{atomic}}} \tag{21}$$

where H_{atomic} describes the atomic limit of an isolated magnetic ion and $H_{\text{resonance}}$ describes the hybridization of the localized f electrons in the ion with the Bloch waves of the conduction sea. For pedagogical reasons, our discussion initially focuses on the case where the f state is a Kramer's doublet.

There are two key elements to the Anderson model:

- *Atomic limit:* The atomic physics of an isolated ion with a single f state, described by the model

$$H_{\text{atomic}} = E_f n_f + U n_{f\uparrow} n_{f\downarrow} \tag{22}$$

Here E_f is the energy of the f state and U is the Coulomb energy associated with two electrons in the same orbital. The atomic physics contains the basic mechanism for local moment formation, valid for f electrons, but also seen in a variety of other contexts, such as transition-metal atoms and quantum dots.
The four quantum states of the atomic model are

$$\left.\begin{array}{ll} |f^2\rangle & E(f^2) = 2E_f + U \\ |f^0\rangle & E(f^0) = 0 \end{array}\right\}\text{nonmagnetic}$$
$$|f^1\uparrow\rangle\ |f^1\downarrow\rangle\ \ E(f^1) = E_f \qquad \text{magnetic} \tag{23}$$

In a magnetic ground state, the cost of inducing a 'valence fluctuation' by removing or adding an electron to the f^1 state is positive, that is,

$$\text{removing:} \quad E(f^0) - E(f^1) = -E_f > 0 \Rightarrow \frac{U}{2} > E_f + \frac{U}{2} \tag{24}$$

$$\text{adding:} \quad E(f^2) - E(f^1) = E_f + U > 0 \Rightarrow E_f + \frac{U}{2} > -\frac{U}{2} \tag{25}$$

or (Figure 10).

$$\frac{U}{2} > E_f + \frac{U}{2} > -\frac{U}{2} \tag{26}$$

Under these conditions, a local moment is well defined, provided the temperature is lower than the valence fluctuation scale $T_{\rm VF} = \max(E_{\rm f} + U, -E_{\rm f})$. At lower temperatures, the atom behaves exclusively as a quantum top.

- *Virtual bound-state formation.* When the magnetic ion is immersed in a sea of electrons, the f electrons within the core of the atom hybridize with the Bloch states of surrounding electron sea (Blandin and Friedel, 1958) to form a resonance described by

$$H_{\rm resonance} = \sum_{k,\sigma} \epsilon_k n_{k\sigma} + \sum_{k,\sigma} \left[V(\mathbf{k}) c^\dagger_{k\sigma} f_\sigma + V(\mathbf{k})^* f^\dagger_\sigma c_{k\sigma} \right] \tag{27}$$

where the hybridization matrix element $V(\mathbf{k}) = \langle \mathbf{k} | V_{\rm atomic} | f \rangle$ is the overlap of the atomic potential between a localized f state and a Bloch wave. In the absence of any interactions, the hybridization broadens the localized f state, producing a resonance of width

$$\Delta = \pi \sum_{\mathbf{k}} |V(\mathbf{k})|^2 \delta(\epsilon_{\mathbf{k}} - \mu) = \pi V^2 \rho \tag{28}$$

where V^2 is the average of the hybridization around the Fermi surface.

There are two complementary ways to approach the physics of the Anderson model:

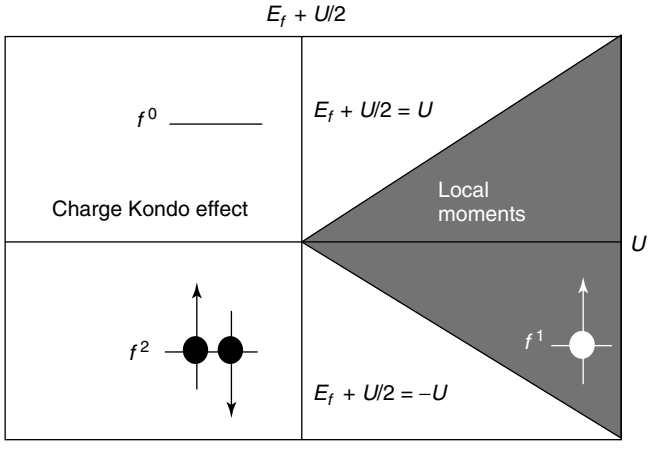

Figure 10. Phase diagram for Anderson impurity model in the atomic limit.

- The 'atomic picture', which starts with the interacting, but isolated atom ($V(k) = 0$), and considers the effect of immersing it in an electron sea by slowly dialing up the hybridization.
- The 'adiabatic picture', which starts with the noninteracting resonant ground state ($U = 0$), and then considers the effect of dialing up the interaction term U.

These approaches paint a contrasting and, at first sight, contradictory picture of a local moment in a Fermi sea. From the adiabatic perspective, the ground state is always a Fermi liquid (see 1.2.2), but from atomic perspective, provided the hybridization is smaller than U, one expects a local magnetic moment, whose low-lying degrees of freedom are purely rotational. How do we resolve this paradox?

Anderson's original work provided a mean-field treatment of the interaction. He found that at interactions larger than $U_c \sim \pi\Delta$ local moments develop with a finite magnetization $M = \langle n_\uparrow \rangle - \langle n_\downarrow \rangle$. The mean-field theory provides an approximate guide to the conditions required for moment formation, but it does not account for the restoration of the singlet symmetry of the ground state at low temperatures. The resolution of the adiabatic and the atomic picture derives from quantum spin fluctuations, which cause the local moment to 'tunnel' on a slow timescale τ_{sf} between the two degenerate 'up' and 'down' configurations.

$$e^-_\downarrow + f^1_\uparrow \rightleftharpoons e^-_\uparrow + f^1_\downarrow \tag{29}$$

These fluctuations are the origin of the Kondo effect. From the energy uncertainty principle, below a temperature $T_{\rm K}$, at which the thermal excitation energy $k_{\rm B}T$ is of the order of the characteristic tunneling rate $\frac{\hbar}{\tau_{sf}}$, a paramagnetic state with a Fermi-liquid resonance forms. The characteristic width of the resonance is then determined by the Kondo energy $k_{\rm B}T_{\rm K} \sim \frac{\hbar}{\tau_{sf}}$. The existence of this resonance was first deduced by Abrikosov (1965), and Suhl (1965), but it is more frequently called the *Kondo resonance*. From perturbative renormalization group reasoning (Haldane, 1978) and the Bethe Ansatz solution of the Anderson model (Wiegmann, 1980; Okiji and Kawakami, 1983), we know that, for large $U \gg \Delta$, the Kondo scale depends exponentially on U. In the symmetric Anderson model, where $E_f = -U/2$,

$$T_K = \sqrt{\frac{2U\Delta}{\pi^2}} \exp\left(-\frac{\pi U}{8\Delta}\right) \tag{30}$$

The temperature $T_{\rm K}$ marks the crossover from a a high-temperature Curie-law $\chi \sim \frac{1}{T}$ susceptibility to a low-temperature paramagnetic susceptibility $\chi \sim 1/T_{\rm K}$.

2.1.2 Adiabaticity and the Kondo resonance

A central quantity in the physics of f-electron systems is the f-spectral function,

$$A_f(\omega) = \frac{1}{\pi}\mathrm{Im}G_f(\omega - i\delta) \tag{31}$$

where $G_f(\omega) = -i\int_{-\infty}^{\infty} \mathrm{d}t\,\langle \mathrm{T} f_\sigma(t) f_\sigma^\dagger(0)\rangle \mathrm{e}^{i\omega t}$ is the Fourier transform of the time-ordered f-Green's function. When an f electron is added, or removed from the f state, the final state has a distribution of energies described by the f-spectral function. From a spectral decomposition of the f-Green's function, the positive energy part of the f-spectral function determines the energy distribution for electron addition, while the negative energy part measures the energy distribution of electron removal:

$$A_f(\omega) = \begin{cases} \overbrace{\sum_\lambda \left|\langle\lambda|f_\sigma^\dagger|\phi_0\rangle\right|^2 \delta(\omega - [E_\lambda - E_0])}^{\text{Energy distribution of state formed by adding one f electron}}, & (\omega > 0) \\ \underbrace{\sum_\lambda \left|\langle\lambda|f_\sigma|\phi_0\rangle\right|^2 \delta(\omega - [E_0 - E_\lambda])}_{\text{Energy distribution of state formed by removing an f electron}}, & (\omega < 0) \end{cases} \tag{32}$$

where E_0 is the energy of the ground state, and E_λ is the energy of an excited state λ, formed by adding or removing an f electron. For negative energies, this spectrum can be measured by measuring the energy distribution of photoelectrons produced by X-ray photoemission, while for positive energies, the spectral function can be measured from inverse X-ray photoemission (Allen *et al.*, 1986; Allen, Oh, Maple and Torikachvili, 1983). The weight beneath the Fermi energy peak determines the f charge of the ion

$$\langle n_f\rangle = 2\int_{-\infty}^{0} \mathrm{d}\omega A_f(\omega) \tag{33}$$

In a magnetic ion, such as a Cerium atom in a $4f^1$ state, this quantity is just a little below unity.

Figure 11 illustrates the effect of the interaction on the f-spectral function. In the noninteracting limit ($U = 0$), the f-spectral function is a Lorentzian of width Δ. If we turn on the interaction U, being careful to shifting the f-level position beneath the Fermi energy to maintain a constant occupancy, the resonance splits into three peaks, two at energies $\omega = E_f$ and $\omega = E_f + U$ corresponding to the energies for a valence fluctuation, plus an additional central 'Kondo resonance' associated with the spin fluctuations of the local moment.

At first sight, once the interaction is much larger than the hybridization width Δ, one might expect there to be no spectral weight left at low energies. But this violates the idea of adiabaticity. In fact, there are always certain adiabatic

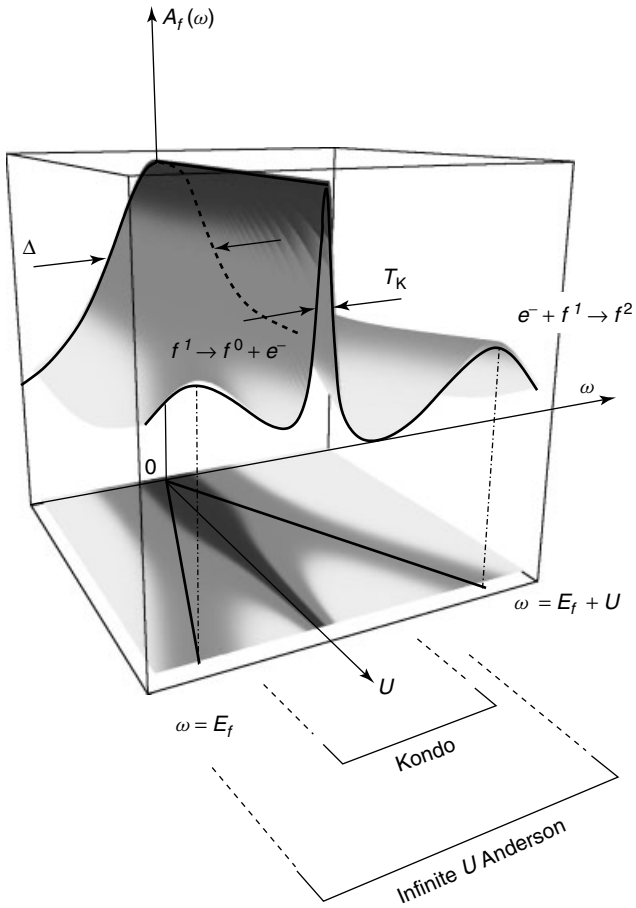

Figure 11. Schematic illustration of the evaluation of the f-spectral function $A_f(\omega)$ as interaction strength U is turned on continuously, maintaining a constant f occupancy by shifting the bare f-level position beneath the Fermi energy. The lower part of diagram is the density plot of f-spectral function, showing how the noninteracting resonance at $U = 0$ splits into an upper and lower atomic peak at $\omega = E_f$ and $\omega = E_f + U$.

invariants that do not change, despite the interaction. One such quantity is the phase shift δ_f associated with the scattering of conduction electrons of the ion; another is the height of the f-spectral function at zero energy, and it turns out that these two quantities are related. A rigorous result owing to (Langreth, 1966) tells us that the spectral function at $\omega = 0$ is directly determined by the f-phase shift, so that its noninteracting value

$$A_f(\omega = 0) = \frac{\sin^2\delta_f}{\pi\Delta} \tag{34}$$

is preserved by adiabaticity. Langreth's result can be heuristically derived by noting that δ_f is the phase of the f-Green's function at the Fermi energy, so that $G_f(0 - i\epsilon)^{-1} = |G_f^{-1}(0)|e^{-i\delta_f}$. Now, in a Fermi liquid, the scattering at the Fermi energy is purely elastic, and this implies

that $ImG_f^{-1}(0 - i\epsilon) = \Delta$, the bare hybridization width. From this, it follows that $ImG_f^{-1}(0) = |G_f^{-1}(0)| \sin\delta_f = \Delta$, so that $G_f(0) = e^{i\delta_f}/(\Delta \sin\delta_f)$, and the preceding result follows.

The phase shift δ_f is set via the Friedel sum rule, according to which the sum of the up-and-down scattering phase shifts, gives the total number of f-bound electrons, or

$$\sum_\sigma \frac{\delta_{f\sigma}}{\pi} = 2\frac{\delta_f}{\pi} = n_f \tag{35}$$

for a twofold degenerate f state. At large distances, the wave function of scattered electrons $\psi_f(r) \sim \sin(k_F r + \delta_f)/r$ is 'shifted inwards' by a distance $\delta_l/k_F = (\lambda_F/2) \times (\delta_l/\pi)$. This sum rule is sometimes called a *node counting* rule because, if you think about a large sphere enclosing the impurity, then each time the phase shift passes through π, a node crosses the spherical boundary and one more electron per channel is bound beneath the Fermi sea. Friedel's sum rule holds for interacting electrons, provided the ground state is adiabatically accessible from the noninteracting system (Langer and Ambegaokar, 1961; Langreth, 1966). Since $n_f = 1$ in an f^1 state, the Friedel sum rule tells us that the phase shift is $\pi/2$ for a twofold degenerate f state. In other words, adiabaticity tell us that the electron is *resonantly scattered* by the quenched local moment.

Photoemission studies do reveal the three-peaked structure characteristic of the Anderson model in many Ce systems, such as $CeIr_2$ and $CeRu_2$ (Allen, Oh, Maple and Torikachvili, 1983) (see Figure 12). Materials in which the Kondo resonance is wide enough to be resolved are more 'mixed valent' materials in which the f valence departs significantly from unity. Three-peaked structures have also been observed in certain U 5f materials such as UPt_3 and UAl_2 (Allen *et al*., 1985) materials, but it has not yet been resolved in UBe_{13}. A three-peaked structure has recently been observed in 4f Yb materials, such as $YbPd_3$, where the $4f^{13}$ configuration contains a single f hole, so that the positions of the three peaks are reversed relative to Ce (Liu *et al*., 1992).

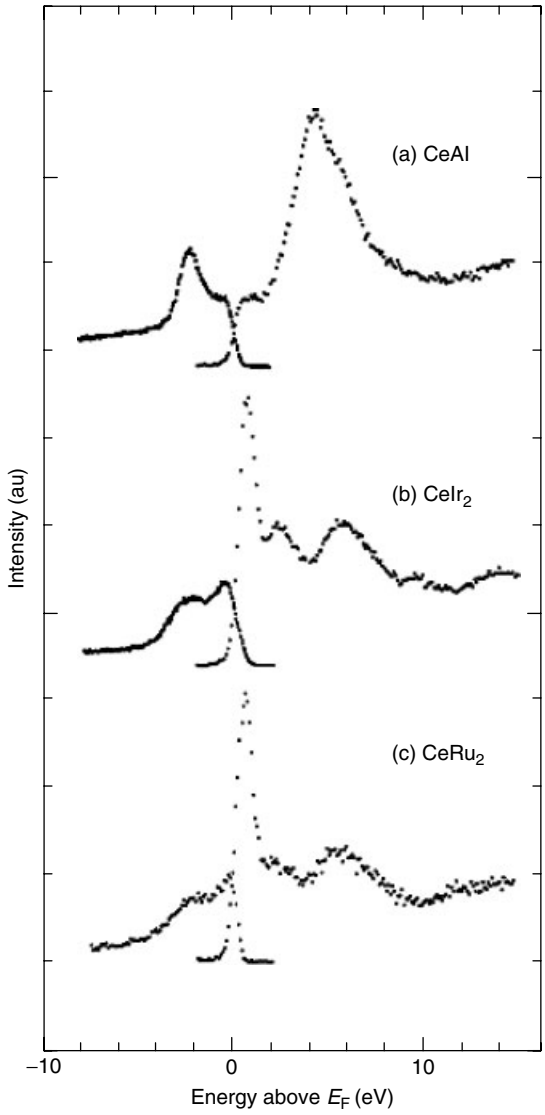

Figure 12. Showing spectral functions for three different Cerium f-electron materials, measured using X-ray photoemission (below the Fermi energy) and inverse X-ray photoemission (above the Fermi energy). CeAl is an AFM and does not display a Kondo resonance. (Reproduced from J.W. Allen, S.J. Oh, M.B. Maple and M.S. Torikachvili: *Phys. Rev.* **28**, 1983, 5347, copyright © 1983 by the American Physical Society, with permission of the APS.)

2.2 Hierarchies of energy scales

2.2.1 Renormalization concept

To understand how a Fermi liquid emerges when a local moment is immersed in a quantum sea of electrons, theorists had to connect physics on several widely spaced energy scales. Photoemission shows that the characteristic energy to produce a valence fluctuation is of the order of volts, or tens of thousands of Kelvin, yet the characteristic physics we are interested in occurs at scales hundreds or thousands of times smaller. How can we distill the essential effects of the atomic physics at electron volt scales on the low-energy physics at millivolt scales?

The essential tool for this task is the 'renormalization group' (Anderson and Yuval, 1969, 1970, 1971; Anderson, 1970, 1973; Wilson, 1976; Nozières and Blandin, 1980; Nozières, 1976), based on the idea that the physics at low-energy scales only depends on a small subset of 'relevant' variables from the original microscopic Hamiltonian. The extraction of these relevant variables is accomplished by

'renormalizing' the Hamiltonian by systematically eliminating the high-energy virtual excitations and adjusting the low-energy Hamiltonian to take care of the interactions that these virtual excitations induce in the low energy Hilbert space. This leads to a family of Hamiltonian's $H(\Lambda)$, each with a different high-energy cutoff Λ, which share the same low-energy physics.

The systematic passage from a Hamiltonian $H(\Lambda)$ to a renormalized Hamiltonian $H(\Lambda')$ with a smaller cutoff $\Lambda' = \Lambda/b$ is accomplished by dividing the eigenstates of H into a a low-energy subspace {L} and a high-energy subspace {H}, with energies $|\epsilon| < \Lambda' = \Lambda/b$ and a $|\epsilon| \in [\Lambda', \Lambda]$ respectively. The Hamiltonian is then broken up into terms that are block-diagonal in these subspaces,

$$H = \left[\begin{array}{c|c} H_{\rm L} & V^\dagger \\ \hline V & H_{\rm H} \end{array}\right] \tag{36}$$

where V and $V^\dagger$ provide the matrix elements between {L} and {H}. The effects of the V are then taken into account by carrying out a unitary (canonical) transformation that block-diagonalizes the Hamiltonian,

$$H(\Lambda) \to UH(\Lambda)U^\dagger = \left[\begin{array}{c|c} \tilde{H}_{\rm L} & 0 \\ \hline 0 & \tilde{H}_{\rm H} \end{array}\right] \tag{37}$$

The renormalized Hamiltonian is then given by $H(\Lambda') = \tilde{H}_{\rm L} = H_{\rm L} + \delta H$. The flow of key parameters in the Hamiltonian resulting from this process is called a *renormalization group flow*.

At certain important crossover energy scales, large tracts of the Hilbert space associated with the Hamiltonian are projected out by the renormalization process, and the character of the Hamiltonian changes qualitatively. In the Anderson model, there are three such important energy scales, (Figure 13)

- $\Lambda_I = E_f + U$, where valence fluctuations $e^- + f^1 \rightleftharpoons f^2$ into the doubly occupied f^2 state are eliminated. For $\Lambda \ll \Lambda_I$, the physics is described by the infinite U Anderson model

$$H = \sum_{k,\sigma} \epsilon_k n_{k\sigma} + \sum_{k,\sigma} V(k)\left[c^\dagger_{k\sigma} X_{0\sigma} + X_{\sigma 0} c_{k\sigma}\right] + E_f \sum_\sigma X_{\sigma\sigma}, \tag{38}$$

  where $X_{\sigma\sigma} = |f^1:\sigma\rangle\langle f^1:\sigma|$, $X_{0\sigma} = |f^0\rangle\langle f^1\sigma|$ and $X_{\sigma 0} = |f^1:\sigma\rangle\langle f^0|$ are 'Hubbard operators' that connect the states in the projected Hilbert space with no double occupancy.
- $\Lambda_{II} \sim |E_f| = -E_f$, where valence fluctuations into the empty state $f^1 \rightleftharpoons f^0 + e^-$ are eliminated to form a local moment. Physics below this scale is described by the Kondo model.
- $\Lambda = T_{\rm K}$, the Kondo temperature below which the local moment is screened to form a resonantly scattering local Fermi liquid.

In the symmetric Anderson model, $\Lambda_I = \Lambda_{II}$, and the transition to local moment behavior occurs in a one-step crossover process.

2.2.2 *Schrieffer–Wolff transformation*

The unitary or canonical transformation that eliminates the charge fluctuations at scales Λ_I and Λ_{II} was first

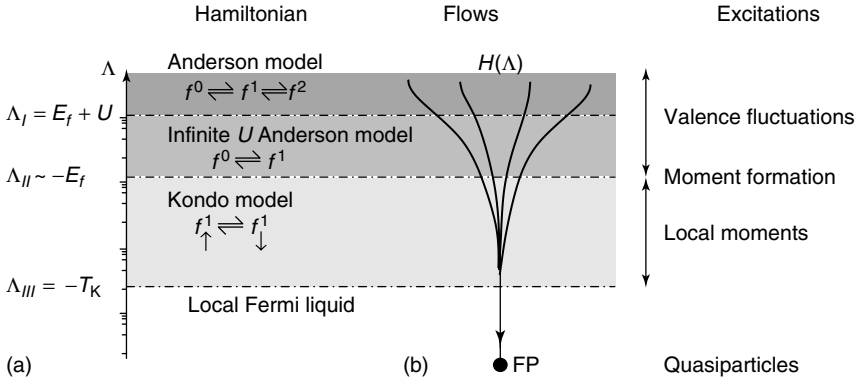

Figure 13. (a) Crossover energy scales for the Anderson model. At scales below Λ_I, valence fluctuations into the doubly occupied state are suppressed. All lower energy physics is described by the infinite U Anderson model. Below Λ_{II}, all valence fluctuations are suppressed, and the physics involves purely the spin degrees of freedom of the ion, coupled to the conduction sea via the Kondo interaction. The Kondo scale renormalizes to strong coupling below Λ_{III}, and the local moment becomes screened to form a local Fermi liquid. (b) Illustrating the idea of renormalization group flows toward a Fermi liquid fixed point.

carried out by Schrieffer and Wolff (1966), and Coqblin and Schrieffer (1969), who showed how this model gives rise to a residual antiferromagnetic interaction between the local moment and conduction electrons. The emergence of this antiferromagnetic interaction is associated with a process called *superexchange*: the virtual process in which an electron or hole briefly migrates off the ion, to be immediately replaced by another with a different spin. When these processes are removed by the canonical transformation, they induce an antiferromagnetic interaction between the local moment and the conduction electrons. This can be seen by considering the two possible spin-exchange processes

$$\begin{aligned} e^-_\uparrow + f^1_\downarrow &\leftrightarrow f^2 \leftrightarrow e^-_\downarrow + f^1_\uparrow \qquad \Delta E_I \sim U + E_f \\ h^+_\uparrow + f^1_\downarrow &\leftrightarrow f^0 \leftrightarrow h^+_\downarrow + f^1_\uparrow \qquad \Delta E_{II} \sim -E_f \end{aligned} \tag{39}$$

Both processes require that the f electron and incoming particle are in a spin-singlet. From second-order perturbation theory, the energy of the singlet is lowered by an amount $-2J$, where

$$J = V^2 \left[\frac{1}{\Delta E_1} + \frac{1}{\Delta E_2} \right] \tag{40}$$

and the factor of two derives from the two ways a singlet can emit an electron or hole into the continuum [1] and $V \sim V(k_{\rm F})$ is the hybridization matrix element near the Fermi surface. For the symmetric Anderson model, where $\Delta E_1 = \Delta E_{II} = U/2$, $J = 4V^2/U$.

If we introduce the electron spin-density operator $\vec{\sigma}(0) = \frac{1}{\mathcal{N}} \sum_{k,k'} c^\dagger_{k\alpha} \vec{\sigma}_{\alpha\beta} c_{k'\beta}$, where $\mathcal{N}$ is the number of sites in the lattice, then the effective interaction has the form

$$H_{\rm K} = -2J P_{S=0} \tag{41}$$

where $P_{S=0} = \left[\frac{1}{4} - \frac{1}{2} \vec{\sigma}(0) \cdot \vec{S}_f \right]$ is the singlet projection operator. If we drop the constant term, then the effective interaction induced by the virtual charge fluctuations must have the form

$$H_{\rm K} = J \vec{\sigma}(0) \cdot \vec{S}_f \tag{42}$$

where $\vec{S}_f$ is the spin of the localized moment. The complete 'Kondo Model', $H = H_c + H_{\rm K}$ describing the conduction electrons and their interaction with the local moment is

$$H = \sum_{\mathbf{k}\sigma} \epsilon_{\mathbf{k}} c^\dagger_{\vec{k}\sigma} c_{\vec{k}\sigma} + J \vec{\sigma}(0) \cdot \vec{S}_f \tag{43}$$

2.2.3 The Kondo effect

The antiferromagnetic sign of the superexchange interaction J in the Kondo Hamiltonian is the origin of the spin-screening physics of the Kondo effect. The bare interaction is weak, but the spin fluctuations it induces have the effect of *antiscreening* the interaction at low energies, renormalizing it to larger and larger values. To see this, we follow an Anderson's 'Poor Man's' scaling procedure (Anderson, 1973, 1970), which takes advantage of the observation that at small J the renormalization in the Hamiltonian associated with the block-diagonalization process $\delta H = \tilde{H}_{\rm L} - H_{\rm L}$ is given by second-order perturbation theory:

$$\delta H_{ab} = \langle a | \delta H | b \rangle = \frac{1}{2} \left[T_{ab}(E_a) + T_{ab}(E_b) \right] \tag{44}$$

where

$$T_{ab}(\omega) = \sum_{|\Lambda\rangle \in \{H\}} \left[\frac{V^\dagger_{a\Lambda} V_{\Lambda b}}{\omega - E_\Lambda} \right] \tag{45}$$

is the many-body 't-matrix' associated with virtual transitions into the high-energy subspace $\{H\}$. For the Kondo model,

$$V = \mathcal{P}_{\rm H} J \vec{S}(0) \cdot \vec{S}_d \mathcal{P}_{\rm L} \tag{46}$$

where $\mathcal{P}_{\rm H}$ projects the intermediate state into the high-energy subspace, while $\mathcal{P}_{\rm L}$ projects the initial state into the low-energy subspace. There are two virtual scattering processes that contribute to the antiscreening effect, involving a high-energy electron (I) or a high-energy hole (II).

Process I is denoted by the diagram

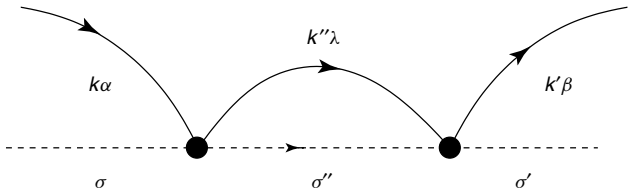

and starts in state $|b\rangle = |k\alpha, \sigma\rangle$, passes through a virtual state $|\Lambda\rangle = |c^\dagger_{k''} \alpha \sigma''\rangle$ where $\epsilon_{k''}$ lies at high energies in the range $\epsilon_{k''} \in [\Lambda/b, \Lambda]$ and ends in state $|a\rangle = |k'\beta, \sigma'\rangle$. The resulting renormalization

$$\begin{aligned} &\langle k'\beta, \sigma' | T^I(E) | k\alpha, \sigma \rangle \\ &\quad = \sum_{\epsilon_{k''} \in [\Lambda - \delta\Lambda, \Lambda]} \left[\frac{1}{E - \epsilon_{k''}} \right] J^2 \times (\sigma^a_{\beta\lambda} \sigma^b_{\lambda\alpha})(S^a_{\sigma'\sigma''} S^b_{\sigma''\sigma}) \\ &\quad \approx J^2 \rho \delta\Lambda \left[\frac{1}{E - \Lambda} \right] (\sigma^a \sigma^b)_{\beta\alpha} (S^a S^b)_{\sigma'\sigma} \end{aligned} \tag{47}$$

In *Process II*, denoted by

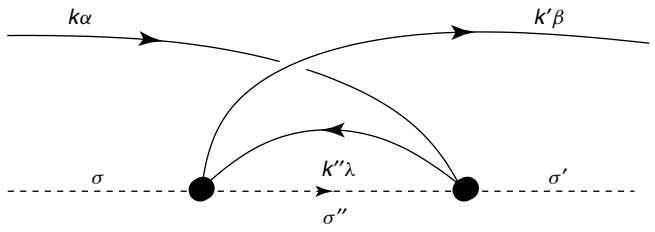

the formation of a virtual hole excitation $|\Lambda\rangle = c_{k''\lambda}|\sigma''\rangle$ introduces an electron line that crosses itself, introducing a negative sign into the scattering amplitude. The spin operators of the conduction sea and AFM reverse their relative order in process II, which introduces a relative minus sign into the T-matrix for scattering into a high-energy hole-state,

$$\begin{aligned}
&\langle k'\beta\sigma'|T^{(II)}(E)|k\alpha\sigma\rangle \\
&\quad = -\sum_{\epsilon_{k''}\in[-\Lambda,-\Lambda+\delta\Lambda]}\left[\frac{1}{E-(\epsilon_k+\epsilon_{k'}-\epsilon_{k''})}\right] \\
&\qquad \times J^2(\sigma^b\sigma^a)_{\beta\alpha}(S^aS^b)_{\sigma'\sigma} \\
&\quad = -J^2\rho\delta\Lambda\left[\frac{1}{E-\Lambda}\right](\sigma^a\sigma^b)_{\beta\alpha}(S^aS^b)_{\sigma'\sigma} \qquad (48)
\end{aligned}$$

where we have assumed that the energies ϵ_k and $\epsilon_{k'}$ are negligible compared with Λ.

Adding equations (47 and 48) gives

$$\begin{aligned}
\delta H^{int}_{k'\beta\sigma';k\alpha\sigma} &= \hat{T}^I + T^{II} = -\frac{J^2\rho\delta\Lambda}{\Lambda}[\sigma^a,\sigma^b]_{\beta\alpha}S^aS^b \\
&= 2\frac{J^2\rho\delta\Lambda}{\Lambda}\vec{\sigma}_{\beta\alpha}\cdot\vec{S}_{\sigma'\sigma} \qquad (49)
\end{aligned}$$

so the high-energy virtual spin fluctuations enhance or 'antiscreen' the Kondo coupling constant

$$J(\Lambda') = J(\Lambda) + 2J^2\rho\frac{\delta\Lambda}{\Lambda} \qquad (50)$$

If we introduce the coupling constant $g = \rho J$, recognizing that $d\ln\Lambda = -\frac{\delta\Lambda}{\Lambda}$, we see that it satisfies

$$\frac{\partial g}{\partial\ln\Lambda} = \beta(g) = -2g^2 + O(g^3) \qquad (51)$$

This is an example of a **negative** β function: a signature of an interaction that grows with the renormalization process. At high energies, the weakly coupled local moment is said to be **asymptotically free**. The solution to the scaling equation is

$$g(\Lambda') = \frac{g_o}{1-2g_o\ln(\Lambda/\Lambda')} \qquad (52)$$

and if we introduce the 'Kondo temperature'

$$T_K = D\exp\left[-\frac{1}{2g_o}\right] \qquad (53)$$

we see that this can be written

$$2g(\Lambda') = \frac{1}{\ln(\Lambda/T_K)} \qquad (54)$$

so that once $\Lambda' \sim T_K$, the coupling constant becomes of the order one – at lower energies, one reaches 'strong coupling' where the Kondo coupling can no longer be treated as a weak perturbation. One of the fascinating things about this flow to strong coupling is that, in the limit $T_K \ll D$, all explicit dependence on the bandwidth D disappears and the Kondo temperature T_K is the only intrinsic energy scale in the physics. Any physical quantity must depend in a universal way on ratios of energy to T_K, thus the universal part of the free energy must have the form

$$F(T) = T_K\Phi\frac{T}{T_K} \qquad (55)$$

where $\Phi(x)$ is universal. We can also understand the resistance created by spin-flip scattering of a magnetic impurity in the same way. The resistivity is given by $\rho_i = \frac{ne^2}{m}\tau(T,H)$, where the scattering rate must also have a scaling form

$$\tau(T,H) = \frac{n_i}{\rho}\Phi_2\left(\frac{T}{T_K},\frac{H}{T_K}\right) \qquad (56)$$

where ρ is the density of states (per spin) of electrons and n_i is the concentration of magnetic impurities and the function $\Phi_2(t,h)$ is universal. To leading order in the Born approximation, the scattering rate is given by $\tau = 2\pi\rho J^2S(S+1) = \frac{2\pi S(S+1)}{\rho}(g_0)^2$ where $g_0 = g(\Lambda_0)$ is the bare coupling at the energy scale that moments form. We can obtain the behavior at a finite temperature by replacing $g_0 \to g(\Lambda = 2\pi T)$, where upon

$$\tau(T) = \frac{2\pi S(S+1)}{\rho}\frac{1}{4\ln^2(2\pi T/T_K)} \qquad (57)$$

gives the leading high-temperature growth of the resistance associated with the Kondo effect.

The kind of perturbative analysis we have gone through here takes us down to the Kondo temperature. The physics at lower energies corresponds to the strong coupling limit of the Kondo model. Qualitatively, once $J\rho \gg 1$, the local moment is bound into a spin-singlet with a conduction electron. The number of bound electrons is $n_f = 1$, so that by the Friedel sum rule (equation (35)) in a paramagnet the phase shift $\delta_\uparrow = \delta_\downarrow = \pi/2$, the unitary limit of scattering. For more

details about the local Fermi liquid that forms, we refer the reader to the accompanying chapter on the Kondo effect by Jones (2007).

2.2.4 *Doniach's Kondo lattice concept*

The discovery of heavy-electron metals prompted Doniach (1977) to make the radical proposal that heavy-electron materials derive from a dense lattice version of the Kondo effect, described by the **Kondo Lattice model** (Kasuya, 1956)

$$H = \sum_{\mathbf{k}\sigma} \epsilon_{\mathbf{k}} c^{\dagger}_{\mathbf{k}\sigma} c_{\mathbf{k}\sigma} + J \sum_j \vec{S}_j \cdot c^{\dagger}_{\mathbf{k}\alpha} \vec{\sigma}_{\alpha\beta} c_{\mathbf{k}'\beta} \mathrm{e}^{i(\mathbf{k}'-\mathbf{k})\cdot\mathbf{R}_j} \tag{58}$$

In effect, Doniach was implicitly proposing that the key physics of heavy-electron materials resides in the interaction of neutral local moments with a charged conduction electron sea.

Most local moment systems develop an antiferromagnetic order at low temperatures. A magnetic moment at location $\mathbf{x}_0$ induces a wave of 'Friedel' oscillations in the electron spin density (Figure 14)

$$\langle \vec{\sigma}(\mathbf{x}) \rangle = -J\chi(\mathbf{x}-\mathbf{x}_0)\langle \vec{S}(\mathbf{x}_0) \rangle \tag{59}$$

where

$$\chi(\mathbf{x}) = 2\sum_{\mathbf{k},\mathbf{k}'} \left(\frac{f(\epsilon_{\mathbf{k}}) - f(\epsilon_{\mathbf{k}'})}{\epsilon_{\mathbf{k}'} - \epsilon_{\mathbf{k}}} \right) e^{i(\mathbf{k}-\mathbf{k}')\cdot\mathbf{x}} \tag{60}$$

is the nonlocal susceptibility of the metal. The sharp discontinuity in the occupancies $f(\epsilon_k)$ at the Fermi surface is responsible for Friedel oscillations in induced spin density that decay with a power law

$$\langle \vec{\sigma}(r) \rangle \sim -J\rho \frac{\cos 2k_{\mathrm{F}} r}{|k_{\mathrm{F}} r|^3} \tag{61}$$

where ρ is the conduction electron density of states and r is the distance from the impurity. If a second local moment is introduced at location $\mathbf{x}$, it couples to this Friedel oscillation with energy $J\langle \vec{S}(\mathbf{x}) \cdot \vec{\sigma}(x) \rangle$, giving rise to the 'RKKY' (Ruderman and Kittel, 1954; Kasuya, 1956; Yosida, 1957) magnetic interaction,

$$H_{\mathrm{RKKY}} = \overbrace{-J^2\chi(\mathbf{x}-\mathbf{x}')}^{J_{\mathrm{RKKY}}(\mathbf{x}-\mathbf{x}')} \vec{S}(\mathbf{x}) \cdot \vec{S}(\mathbf{x}') \tag{62}$$

where

$$J_{\mathrm{RKKY}}(r) \sim -J^2\rho \frac{\cos 2k_{\mathrm{F}} r}{k_{\mathrm{F}} r} \tag{63}$$

In alloys containing a dilute concentration of magnetic transition-metal ions, the oscillatory RKKY interaction gives rise to a frustrated, glassy magnetic state known as a *spin glass*. In dense systems, the RKKY interaction typically gives rise to an ordered antiferromagnetic state with a Néel temperature T_{N} of the order $J^2\rho$. Heavy-electron metals narrowly escape this fate.

Doniach argued that there are two scales in the Kondo lattice, the single-ion Kondo temperature T_{K} and T_{RKKY}, given by

$$\begin{aligned} T_{\mathrm{K}} &= D\mathrm{e}^{-1/(2J\rho)} \\ T_{\mathrm{RKKY}} &= J^2\rho \end{aligned} \tag{64}$$

When $J\rho$ is small, then T_{RKKY} is the largest scale and an antiferromagnetic state is formed, but, when the $J\rho$ is large, the Kondo temperature is the largest scale so a dense Kondo lattice ground state becomes stable. In this paramagnetic state, each site resonantly scatters electrons with a phase shift $\sim\pi/2$. Bloch's theorem then insures that the resonant elastic scattering at each site acts coherently, forming a renormalized band of width $\sim T_{\mathrm{K}}$ (Figure 15).

As in the impurity model, one can identify the Kondo lattice ground state with the large U limit of the Anderson lattice model. By appealing to adiabaticity, one can then link the excitations to the small U Anderson lattice model. According to this line of argument, the quasiparticle Fermi surface volume must count the number of conduction and f electrons (Martin, 1982), even in the large U limit, where it corresponds to the number of electrons *plus* the number of spins

$$2\frac{\mathcal{V}_{\mathrm{FS}}}{(2\pi)^3} = n_e + n_{\mathrm{spins}} \tag{65}$$

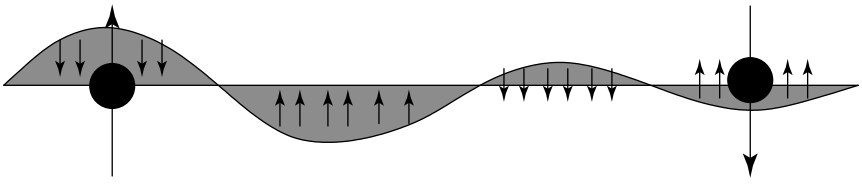

Figure 14. Spin polarization around magnetic impurity contains Friedel oscillations and induces an RKKY interaction between the spins.

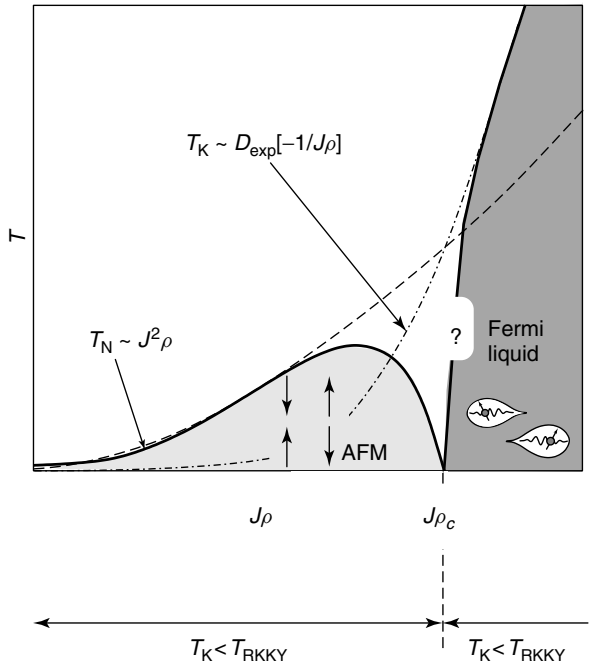

Figure 15. Doniach diagram, illustrating the antiferromagnetic regime, where $T_K < T_{RKKY}$ and the heavy-fermion regime, where $T_K > T_{RKKY}$. Experiment has told us in recent times that the transition between these two regimes is a quantum critical point. The effective Fermi temperature of the heavy Fermi liquid is indicated as a solid line. Circumstantial experimental evidence suggests that this scale drops to zero at the antiferromagnetic quantum critical point, but this is still a matter of controversy.

Using topology, and certain basic assumptions about the response of a Fermi liquid to a flux, Oshikawa (2000) was able to short circuit this tortuous path of reasoning, proving that the Luttinger relationship holds for the Kondo lattice model without reference to its finite U origins.

There are, however, aspects to the Doniach argument that leave cause for concern:

- It is purely a comparison of energy scales and does not provide a detailed mechanism connecting the heavy-fermion phase to the local moment AFM.
- Simple estimates of the value of $J\rho$ required for heavy-electron behavior give an artificially large value of the coupling constant $J\rho \sim 1$. This issue was later resolved by the observation that large spin degeneracy $2j+1$ of the spin-orbit coupled moments, which can be as large as $N = 8$ in Yb materials, enhances the rate of scaling to strong coupling, leading to a Kondo temperature (Coleman, 1983)

$$T_K = D(NJ\rho)^{\frac{1}{N}} \exp\left[-\frac{1}{NJ\rho}\right] \qquad (66)$$

Since the scaling enhancement effect stretches out across decades of energy, it is largely robust against crystal fields (Mekata *et al.*, 1986).

- Nozières' exhaustion paradox (Nozières, 1985). If one considers each local moment to be magnetically screened by a cloud of low-energy electrons within an energy T_K of the Fermi energy, one arrives at an 'exhaustion paradox'. In this interpretation, the number of electrons available to screen each local moment is of the order $T_K/D \ll 1$ per unit cell. Once the concentration of magnetic impurities exceeds $\frac{T_K}{D} \sim 0.1\%$ for ($T_K = 10\,\mathrm{K}$, $D = 10^4\,\mathrm{K}$), the supply of screening electrons would be exhausted, logically excluding any sort of dense Kondo effect. Experimentally, features of single-ion Kondo behavior persist to much higher densities. The resolution to the exhaustion paradox lies in the more modern perception that spin screening of local moments extends *up* in energy, from the Kondo scale T_K out to the bandwidth. In this respect, Kondo screening is reminiscent of Cooper pair formation, which involves electron states that extend upward from the gap energy to the Debye cutoff. From this perspective, the Kondo length scale $\xi \sim v_F/T_K$ is analogous to the coherence length of a superconductor (Burdin, Georges and Grempel, 2000), defining the length scale over which the conduction spin and local moment magnetization are coherent without setting any limit on the degree to which the correlation clouds can overlap (Figure 16).

2.3 The large N Kondo lattice

2.3.1 Gauge theories, large N, and strong correlation

The 'standard model' for metals is built upon the expansion to high orders in the strength of the interaction. This approach, pioneered by Landau, and later formulated in the language of finite temperature perturbation theory by Landau (1957), Pitaevskii (1960), Luttinger and Ward (1960), and Nozières and Luttinger (1962), provides the foundation for our understanding of metallic behavior in most conventional metals.

The development of a parallel formalism and approach for strongly correlated electron systems is still in its infancy, and there is no universally accepted approach. At the heart of the problem are the large interactions, which effectively remove large tracts of Hilbert space and impose strong constraints on the low-energy electronic dynamics. One way to describe these highly constrained Hilbert spaces is through the use of gauge theories. When written as a field theory, local constraints manifest themselves as locally conserved quantities. General principles link these conserved quantities

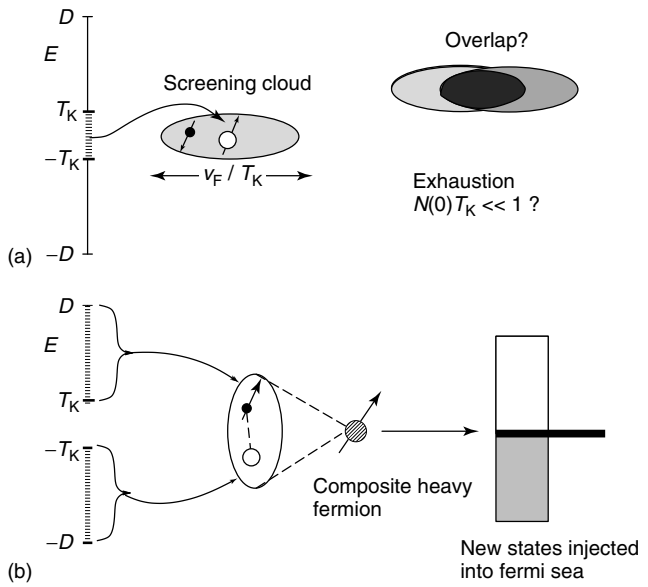

Figure 16. Contrasting (a) the 'screening cloud' picture of the Kondo effect with (b) the composite fermion picture. In (a), low-energy electrons form the Kondo singlet, leading to the exhaustion problem. In (b), the composite heavy electron is a highly localized bound-state between local moments and high-energy electrons, which injects new electronic states into the conduction sea at the chemical potential. Hybridization of these states with conduction electrons produces a singlet ground state, forming a Kondo resonance in the single impurity, and a coherent heavy electron band in the Kondo lattice.

with a set of gauge symmetries. For example, in the Kondo lattice, if a spin $S = 1/2$ operator is represented by fermions,

$$\vec{S}_j = f^\dagger_{j\alpha} \left(\frac{\vec{\sigma}}{2}\right)_{\alpha\beta} f_{j\beta} \tag{67}$$

then the representation must be supplemented by the constraint $n_f(j) = 1$ on the conserved f number at each site. This constraint means one can change the phase of each f fermion at each site arbitrarily

$$f_j \to \mathrm{e}^{i\phi_j} f_j \tag{68}$$

without changing the spin operator $\vec{S}_j$ or the Hamiltonian. This is the local gauge symmetry.

Similar issues also arise in the infinite U Anderson or Hubbard models where the 'no double occupancy' constraint can be established by using a slave boson representation (Barnes, 1976; Coleman, 1984) of Hubbard operators:

$$X_{\sigma 0}(j) = f^\dagger_{j\sigma} b_j, \qquad X_{0\sigma}(j) = b^\dagger_j f_{j\sigma} \tag{69}$$

where $f^\dagger_{j\sigma}$ creates a singly occupied f state, $f^\dagger_{j\sigma}|0\rangle \equiv |f^1, j\sigma\rangle$, while $b^\dagger$ creates an empty f^0 state, $b^\dagger_j|0\rangle = |f^0, j\rangle$. In the slave boson, the gauge charges

$$Q_j = \sum_\sigma f^\dagger_{j\sigma} f_{j\sigma} + b^\dagger_j b_j \tag{70}$$

are conserved and the physical Hilbert space corresponds to $Q_j = 1$ at each site. The gauge symmetry is now $f_{j\sigma} \to e^{i\theta_j} f_{j\sigma}$, $b_j \to e^{i\theta_j} b_j$. These two examples illustrate the link between strong correlation and gauge theories.

$$\begin{aligned} \text{Strong correlation} &\leftrightarrow \text{Constrained Hilbert space} \\ &\leftrightarrow \text{Gauge theories} \end{aligned} \tag{71}$$

A key feature of these gauge theories is the appearance of 'fractionalized fields', which carry either spin or charge, but not both. How, then, can a Landau–Fermi liquid emerge within a Gauge theory with fractional excitations?

Some have suggested that Fermi liquids cannot reconstitute themselves in such strongly constrained gauge theories. Others have advocated against gauge theories, arguing that the only reliable way forward is to return to 'real-world' models with a full fermionic Hilbert space and a finite interaction strength. A third possibility is that the gauge theory approach is valid, but that heavy quasiparticles emerge as bound-states of gauge particles. Quite independently of one's position on the importance of gauge theory approaches, the Kondo lattice poses a severe computational challenge, in no small part, because of the absence of any small parameter for resumed perturbation theory. Perturbation theory in the Kondo coupling constant J always fails below the Kondo temperature. How, then, can one develop a controlled computational tool to explore the transition from local moment magnetism to the heavy Fermi liquid?

One route forward is to seek a family of models that interpolates between the models of physical interest, and a limit where the physics can be solved exactly. One approach, as we shall discuss later, is to consider Kondo lattices in variable dimensions d, and expand in powers of $1/d$ about the limit of infinite dimensionality (Georges, Kotliar, Krauth and Rozenberg, 1996; Jarrell, 1995). In this limit, electron self-energies become momentum independent, the basis of the DMFT. Another approach, with the advantage that it can be married with gauge theory, is the use of large N expansions. The idea here is to generalize the problem to a family of models in which the f-spin degeneracy $N = 2j + 1$ is artificially driven to infinity. In this extreme limit, the key physics is captured as a mean-field theory, and finite N properties are obtained through an expansion in the small parameter $1/N$. Such large N expansions have played an important role in the context of the spherical model of statistical mechanics (Berlin and Kac, 1952) and in field theory (Witten, 1978). The next section discusses how the

gauge theory of the Kondo lattice model can be treated in a large N expansion.

2.3.2 *Mean-field theory of the Kondo lattice*

Quantum large N expansions are a kind of semiclassical limit, where $1/N \sim \hbar$ plays the role of a synthetic Planck's constant. In a Feynman path integral

$$\langle x_f(t)|x_i, 0\rangle = \int \mathcal{D}[x] \exp\left[\frac{i}{\hbar} S[x, \dot{x}]\right] \tag{72}$$

where S is the classical action and the quantum action $A = \frac{1}{\hbar}S$ is 'extensive' in the variable $\frac{1}{\hbar}$. When $\frac{1}{\hbar} \to \infty$, fluctuations around the classical trajectory vanish and the transition amplitude is entirely determined by the classical action to go from i to f. A large N expansion for the partition function Z of a quantum system involves a path integral in imaginary time over the fields ϕ

$$Z = \int \mathcal{D}[\phi] \mathrm{e}^{-NS[\phi,\dot{\phi}]} \tag{73}$$

where NS is the action (or free energy) associated with the field configuration in space and time. By comparison, we see that the large N limit of quantum systems corresponds to an alternative classical mechanics, where $1/N \sim \hbar$ emulates Planck's constant and new types of collective behavior not pertinent to strongly interacting electron systems start to appear.

Our model for a Kondo lattice of spins localized at sites j is

$$H = \sum_{\mathbf{k}\sigma} \epsilon_{\mathbf{k}} c^\dagger_{\mathbf{k}\sigma} c_{\mathbf{k}\sigma} + \sum_j H_I(j) \tag{74}$$

where

$$H_I(j) = \frac{J}{N} S_{\alpha\beta}(j) c^\dagger_{j\beta} c_{j\alpha} \tag{75}$$

is the Coqblin Schrieffer form of the Kondo interaction Hamiltonian (Coqblin and Schrieffer, 1969) between an f spin with $N = 2j + 1$ spin components and the conduction sea. The spin of the local moment at site j is represented as a bilinear of Abrikosov pseudofermions

$$S_{\alpha\beta}(j) = f^\dagger_{j\alpha} f_{j\beta} - \frac{n_f}{N}\delta_{\alpha\beta} \tag{76}$$

and

$$c^\dagger_{j\sigma} = \frac{1}{\sqrt{\mathcal{N}}} \sum_{\mathbf{k}} c^\dagger_{\mathbf{k}\sigma} \mathrm{e}^{-i\mathbf{k}\cdot\vec{R}_j} \tag{77}$$

creates an electron localized at site j, where $\mathcal{N}$ is the number of sites.

Although this is a theorists' idealization – a 'spherical cow approximation', it nevertheless captures key aspects of the physics. This model ascribes a spin degeneracy of $N = 2j + 1$ to both the f electrons *and* the conduction electrons. While this is justified for a single impurity, a more realistic lattice model requires the introduction of Clebsch–Gordon coefficients to link the spin-1/2 conduction electrons with the spin-j conduction electrons.

To obtain a mean-field theory, each term in the Hamiltonian must scale as N. Since the interaction contains two sums over the spin variables, this criterion is met by rescaling the coupling constant replacing $J \to \frac{\tilde{J}}{N}$. Another important aspect to this model is the constraint on charge fluctuations, which in the Kondo limit imposes the constraint $n_f = 1$. Such a constraint can be imposed in a path integral with a Lagrange multiplier term $\lambda(n_f - 1)$. However, with $n_f = 1$, this is not extensive in N, and cannot be treated using a mean-field value for λ. The resolution is to generalize the constraint to $n_f = Q$, where Q is an integer chosen so that as N grows, $q = Q/N$ remains fixed. Thus, for instance, if we are interested in $N = 2$, this corresponds to $q = n_f/N = \frac{1}{2}$. In the large N limit, it is then sufficient to apply the constraint on the average $\langle n_f\rangle = Q$ through a static Lagrange multiplier coupled to the difference $(n_f - Q)$.

The next step is to carry out a 'Hubbard–Stratonovich' transformation on the interaction

$$H_I(j) = -\frac{J}{N}\left(c^\dagger_{j\beta} f_{j\beta}\right)\left(f^\dagger_{j\alpha} c_{j\alpha}\right) \tag{78}$$

Here, we have absorbed the term $-\frac{J}{N} n_f c^\dagger_{j\alpha} c_{j\alpha}$ derived from the spin-diagonal part of (equation (76)) by a shift $\mu \to \mu - \frac{Jn_f}{N^2}$ in the chemical potential. This interaction has the form $-gA^\dagger A$, with $g = \frac{J}{N}$ and $A = f^\dagger_{j\alpha} c_{j\alpha}$, which we factorize using a Hubbard–Stratonovich transformation,

$$-gA^\dagger A \to A^\dagger V + \overline{V} A + \frac{\overline{V} V}{g} \tag{79}$$

so that (Lacroix and Cyrot, 1979; Read and Newns, 1983a)

$$H_I(j) \to H_I[V, j] = \overline{V}_j \left(c^\dagger_{j\sigma} f_{j\sigma}\right) + \left(f^\dagger_{j\sigma} c_{j\sigma}\right) V_j + N\frac{\overline{V}_j V_j}{J} \tag{80}$$

This is an exact transformation, provided the $V_j(\tau)$ are treated as fluctuating variables inside a path integral. The V_j can be regarded as a spinless exchange boson for the Kondo effect. In the parallel treatment of the infinite Anderson model (Coleman, 1987a), $V_j = Vb_j$ is the 'slave boson' field associated with valence fluctuations.

In diagrams:

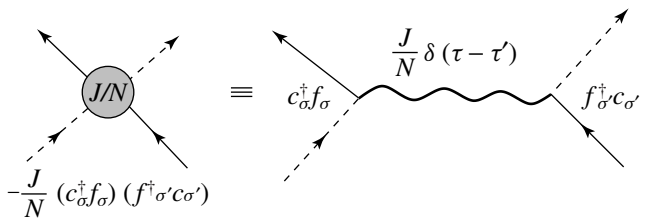

(81)

The path integral for the Kondo lattice is then

$$Z = \int \mathcal{D}[V,\lambda] \overbrace{\int \mathcal{D}[c,f] \exp\left[-\int_0^\beta \left(\sum_{k\sigma} c^\dagger_{\mathbf{k}\sigma}\partial_\tau c_{\mathbf{k}\sigma} + \sum_{j\sigma} f^\dagger_{j\sigma}\partial_\tau f_{j\sigma} + H[V,\lambda]\right)\right]}^{=\mathrm{Tr}\left[T exp\left(-\int_0^\beta H[V,\lambda]d\tau\right)\right]} \tag{82}$$

where

$$H[V,\lambda] = \sum_{\mathbf{k}\sigma} \epsilon_{\mathbf{k}} c^\dagger_{\mathbf{k}\sigma} c_{\mathbf{k}\sigma} + \sum_j \left(H_I[V_j, j] + \lambda_j[n_f(j) - Q]\right) \tag{83}$$

This is the 'Read–Newns' path integral formulation (Read and Newns, 1983a; Auerbach and Levin, 1986) of the Kondo lattice model. The path integral contains an outer integral $\int \mathcal{D}[V,\lambda]$ over the gauge fields V_j and $\lambda_j(\tau)$, and an inner integral $\int \mathcal{D}[c,f]$ over the fermion fields moving in the environment of the gauge fields. The inner path integral is equal to a trace over the time-ordered exponential of $H[V,\lambda]$.

Since the action in this path integral grows extensively with N, the large N limit is saturated by the saddle point configurations of V and λ, eliminating the the outer integral in equation (83). We seek a translationally invariant, static, saddle point, where $\lambda_j(\tau) = \lambda$ and $V_j(\tau) = V$. Since the Hamiltonian is static, the interior path integral can be written as the trace over the Hamiltonian evaluated at the saddle point,

$$Z = \mathrm{Tr} e^{-\beta H_{\mathrm{MFT}}} \qquad (N \to \infty) \tag{84}$$

where

$$H_{\mathrm{MFT}} = H[V,\lambda] = \sum_{\mathbf{k}\sigma} \epsilon_{\mathbf{k}} c^\dagger_{\mathbf{k}\sigma} c_{\mathbf{k}\sigma} + \sum_{j,\sigma}\left(\overline{V} c^\dagger_{j\sigma} f_{j\sigma} + V f^\dagger_{j\sigma} c_{j\sigma} + \lambda f^\dagger_{j\sigma} f_{j\sigma}\right) + Nn\left(\frac{\overline{V}V}{J} - \lambda_o q\right) \tag{85}$$

The saddle point is determined by the condition that the Free energy $F = -T\ln Z$ is stationary with respect to variations in V and λ. To impose this condition, we need to diagonalize H_{MFT} and compute the Free energy. First we rewrite the mean-field Hamiltonian in momentum space,

$$H_{\mathrm{MFT}} = \sum_{\mathbf{k}\sigma} \left(c^\dagger_{\mathbf{k}\sigma}, f^\dagger_{\mathbf{k}\sigma}\right) \begin{bmatrix} \epsilon_{\mathbf{k}} & \overline{V} \\ V & \lambda \end{bmatrix} \begin{pmatrix} c_{\mathbf{k}\sigma} \\ f_{\mathbf{k}\sigma} \end{pmatrix} + Nn\left(\frac{\overline{V}V}{J} - \lambda q\right) \tag{86}$$

where

$$f^\dagger_{\vec{k}\sigma} = \frac{1}{\sqrt{\mathcal{N}}} \sum_j f^\dagger_{j\sigma} e^{i\vec{k}\cdot\vec{R}_j} \tag{87}$$

is the Fourier transform of the f-electron field. This Hamiltonian can then be diagonalized in the form

$$H_{\mathrm{MFT}} = \sum_{\mathbf{k}\sigma} \left(a^\dagger_{\mathbf{k}\sigma}, b^\dagger_{\mathbf{k}\sigma}\right) \begin{bmatrix} E_{\mathbf{k}+} & 0 \\ 0 & E_{\mathbf{k}-} \end{bmatrix} \begin{pmatrix} a_{\mathbf{k}\sigma} \\ b_{\mathbf{k}\sigma} \end{pmatrix} + N\mathcal{N}_s\left(\frac{|V|^2}{J} - \lambda q\right) \tag{88}$$

where $a^\dagger_{\mathbf{k}\sigma}$ and $b^\dagger_{\mathbf{k}\sigma}$ are linear combinations of $c^\dagger_{\mathbf{k}\sigma}$ and $f^\dagger_{\vec{k}\sigma}$, which describe the quasiparticles of the theory. The momentum state eigenvalues $E = E_{\vec{k}\pm}$ are the roots of the equation

$$\mathrm{Det}\left[E\underline{1} - \begin{pmatrix} \epsilon_{\mathbf{k}} & \overline{V} \\ V & \lambda \end{pmatrix}\right] = (E-\epsilon_{\mathbf{k}})(E-\lambda) - |V|^2 = 0 \tag{89}$$

so

$$E_{\mathbf{k}\pm} = \frac{\epsilon_{\mathbf{k}} + \lambda}{2} \pm \left[\left(\frac{\epsilon_{\mathbf{k}} - \lambda}{2}\right)^2 + |V|^2\right]^{\frac{1}{2}} \tag{90}$$

are the energies of the upper and lower bands. The dispersion described by these energies is shown in Figure 17. Notice that:

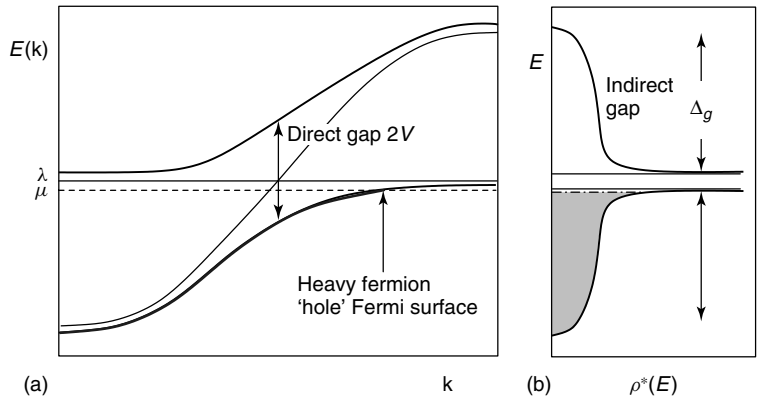

Figure 17. (a) Dispersion produced by the injection of a composite fermion into the conduction sea. (b) Renormalized density of states, showing 'hybridization gap' (Δ_g).

- hybridization between the f-electron states and the conduction electrons builds an upper and lower Fermi band, separated by an indirect 'hybridization gap' of width $\Delta_g = E_g(+) - E_g(-) \sim T_{\rm K}$, where

$$E_g(\pm) = \lambda \pm \frac{V^2}{D_\mp} \tag{91}$$

  and $\pm D_\pm$ are the top and bottom of the conduction band. The 'direct' gap between the upper and lower bands is $2|V|$.
- From (89), the relationship between the energy of the heavy electrons (E) and the energy of the conduction electrons (ϵ) is given by $\epsilon = E - |V|^2/(E-\lambda)$, so that the density of heavy-electron states $\rho^*(E) = \sum_{\mathbf{k},\pm}\delta(E - E^{(\pm)}_{\mathbf{k}})$ is related to the conduction electron density of states $\rho(\epsilon)$ by

$$\rho^*(E) = \rho\frac{{\rm d}\epsilon}{{\rm d}E} = \rho(\epsilon)\left(1 + \frac{|V|^2}{(E-\lambda)^2}\right) \sim \begin{cases} \rho\left(1+\frac{|V|^2}{(E-\lambda)^2}\right) & \text{outside hybridization gap,} \\ 0 & \text{inside hybridization gap,} \end{cases} \tag{92}$$

  so the 'hybridization gap' is flanked by two sharp peaks of approximate width $T_{\rm K}$.
- The Fermi surface volume **expands** in response to the injection of heavy electrons into the conduction sea,

$$Na^D\frac{V_{\rm FS}}{(2\pi)^3} = \left\langle \frac{1}{\mathcal{N}_s}\sum_{\mathbf{k}\sigma} n_{\mathbf{k}\sigma}\right\rangle = Q + n_c \tag{93}$$

  where a^D is the unit cell volume, $n_{\mathbf{k}\sigma} = a^\dagger_{\mathbf{k}\sigma}a_{\mathbf{k}\sigma} + b^\dagger_{\mathbf{k}\sigma}b_{\mathbf{k}\sigma}$ is the quasiparticle number operator and n_c is the number of conduction electrons per unit cell. More instructively, if $n_e = n_c/a^D$ is the electron density,

$$\overbrace{n_e}^{e^-\text{ density}} = \overbrace{N\frac{V_{\rm FS}}{(2\pi)^3}}^{\text{quasi particle density}} - \underbrace{\frac{Q}{a^D}}_{\text{positive background}} \tag{94}$$

  so the electron density n_c divides into a contribution carried by the enlarged Fermi sea, whose enlargement is compensated by the development of a positively charged background. Loosely speaking, each neutral spin in the Kondo lattice has 'ionized' to produce Q negatively charged heavy fermions, leaving behind a Kondo singlet of charge $+Qe$ (Figure 18).

To obtain V and λ, we must compute the free energy

$$\frac{F}{N} = -T\sum_{\mathbf{k},\pm}\ln\left[1 + {\rm e}^{-\beta E_{\mathbf{k}\pm}}\right] + \mathcal{N}_s\left(\frac{|V|^2}{J} - \lambda q\right) \tag{95}$$

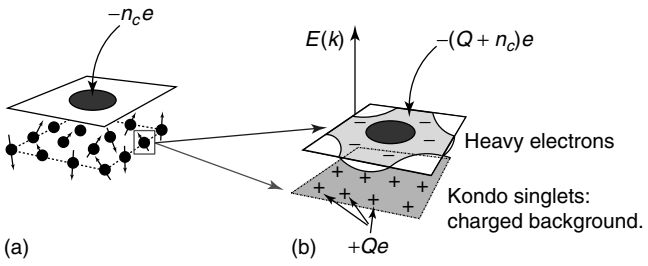

Figure 18. Schematic diagram from Coleman, Paul and Rech (2005a). (a) High-temperature state: small Fermi surface with a background of spins; (b) Low-temperature state, where large Fermi surface develops against a background of positive charge. Each spin 'ionizes' into Q heavy electrons, leaving behind a a Kondo singlet with charge $+Qe$. (Reproduced from P. Coleman, I. Paul, and J. Rech, *Phys. Rev. B* **72**, 2005, 094430, copyright © 2005 by the American Physical Society, with permission of the APS.)

At $T = 0$, the free energy converges the ground-state energy E_0, given by

$$\frac{E_0}{N\mathcal{N}_s} = \int_{-\infty}^{0} \rho^*(E)E + \left(\frac{|V|^2}{J} - \lambda q\right) \tag{96}$$

Using equation (92), the total energy is

$$\begin{aligned}\frac{E_o}{N\mathcal{N}_s} &= \int_{-D}^{0} \mathrm{d}\epsilon \rho E \mathrm{d}E + \int_{-D}^{0} \mathrm{d}E \rho |V|^2 \frac{E}{(E-\lambda)^2} \\ &\quad + \left(\frac{|V|^2}{J} - \lambda q\right) \\ &= \overbrace{-\frac{D^2\rho}{2}}^{E_c/(N\mathcal{N}_s)} + \overbrace{\frac{\Delta}{\pi}\ln\left(\frac{\lambda e}{T_{\mathrm{K}}}\right) - \lambda q}^{E_{\mathrm{K}}/(N\mathcal{N}_s)}\end{aligned} \tag{97}$$

where we have assumed that the upper band is empty and the lower band is partially filled. $T_{\mathrm{K}} = De^{-\frac{1}{J\rho}}$ as before. The first term in (97) is the conduction electron contribution to the energy E_c/Nn_s, while the second term is the lattice 'Kondo' energy $E_{\mathrm{K}}/N_{\mathcal{N}_s}$. If now we impose the constraint $\frac{\partial E_o}{\partial \lambda} = \langle n_f \rangle - Q = 0$ then $\lambda = \frac{\Delta}{\pi q}$ so that the ground-state energy can be written

$$\frac{E_{\mathrm{K}}}{N\mathcal{N}_s} = \frac{\Delta}{\pi}\ln\left(\frac{\Delta e}{\pi q T_{\mathrm{K}}}\right) \tag{98}$$

This energy functional has a 'Mexican Hat' form, with a minimum at

$$\Delta = \frac{\pi q}{e^2} T_{\mathrm{K}} \tag{99}$$

confirming that $\Delta \sim T_{\mathrm{K}}$. If we now return to the quasiparticle density of states ρ^*, we find it has the value

$$\rho^*(0) = \rho + \frac{q}{T_{\mathrm{K}}} \tag{100}$$

at the Fermi energy so the mass enhancement of the heavy electrons is then

$$\frac{m^*}{m} = 1 + \frac{q}{\rho T_{\mathrm{K}}} \sim \frac{qD}{T_{\mathrm{K}}} \tag{101}$$

2.3.3 The charge of the f electron

How does the f electron acquire its charge? We have emphasized from the beginning that the charge degrees of freedom of the original f electrons are irrelevant, indeed, absent from the physics of the Kondo lattice. So how are charged f electrons constructed out of the states of the Kondo lattice, and how do they end up coupling to the electromagnetic field?

The large N theory provides an intriguing answer. The passage from the original Hamiltonian equation (75) to the mean-field Hamiltonian equation (85) is equivalent to the substitution

$$\frac{J}{N} S_{\alpha\beta}(j) c^\dagger_{j\beta} c_{j\alpha} \longrightarrow \overline{V} f^\dagger_{j\alpha} c_{j\alpha} + V c^\dagger_{j\alpha} \mathrm{f}_{j\alpha} \tag{102}$$

In other words, the composite combination of spin and conduction electron are contracted into a single Fermi field

$$\frac{J}{N} \overbrace{S_{\alpha\beta}(j) c_{j\beta}}^{\dagger} = \left(\frac{J}{N} f^\dagger_{j\alpha} \overbrace{f_{j\beta} c_{j\beta}}^{\dagger}\right) \to V f^\dagger_{j\alpha} \tag{103}$$

The amplitude $V = \frac{J}{N} \overbrace{f_{j\beta} c_{j\beta}}^{\dagger} = -\frac{J}{N}\langle c^\dagger_{j\beta} f_{j\beta}\rangle$ involves electron states that extend over decades of energy out to the band edges. In this way, the f electron emerges as a composite bound-state of a spin and an electron. More precisely, in the long-time correlation functions,

$$\begin{aligned}&\langle \left[S_{\gamma\alpha}(i) c_{i\gamma}\right](t) \ \ \left[S_{\alpha\beta}(j) c^\dagger_{j\beta}\right](t')\rangle \\ &\xrightarrow{|t-t'| \gg \hbar/T_K} \frac{N|V^2|}{J^2} \langle f_{i\alpha}(t) f^\dagger_{j\alpha}(t')\rangle\end{aligned} \tag{104}$$

Such 'clustering' of composite operators into a single entity is well-known statistical mechanics as part of the operator product expansion (Cardy, 1996). In many-body physics, we are used to the clustering of fermions pairs into a composite boson, as in the BCS model of superconductivity, $-g\overbrace{\psi_\uparrow(x)\psi_\downarrow(x')} \to \Delta(x - x')$. The unfamiliar aspect of the Kondo effect is the appearance of a composite fermion.

The formation of these composite objects profoundly modifies the conductivity and plasma oscillations of the electron fluid. The Read–Newns path integral has two $U(1)$ gauge invariances – an external electromagnetic gauge invariance associated with the conservation of charge and an internal gauge invariance associated with the local constraints. The f electron couples to the internal gauge fields rather than the external electromagnetic fields, so why is it charged?

The answer lies in the broken symmetry associated with the development of the amplitude V. The phase of V transforms under both internal and external gauge groups. When V develops an amplitude, its phase does not actually order, but it does develop a stiffness which is sufficient to lock the internal and external gauge fields together so that, at low frequencies, they become synonymous. Written in a schematic long-wavelength form, the gauge-sensitive part of

the Kondo lattice Lagrangian is

$$\mathcal{L} = \sum_{\sigma} \int \mathrm{d}^D x \Big[c^{\dagger}_{\sigma}(x)(-i\partial_t + e\Phi(x) + \epsilon_{\mathbf{p}-e\vec{A}})c_{\sigma}(x) + f^{\dagger}_{\sigma}(x)(-i\partial_t + \lambda(x))f_{\sigma}(x) + \Big(\overline{V}(x)c^{\dagger}_{\sigma}(x)f_{\sigma}(x) + \text{ H.c}\Big)\Big] \tag{105}$$

where $\mathbf{p} = -i\vec{\nabla}$. Suppose $V(x) = |V(x)|e^{i\phi(x)}$. There are two independent gauge transformations that increase the phase ϕ of the hybridization. In the external, electromagnetic gauge transformation, the change in phase is absorbed onto the conduction electron and electromagnetic field, so if $V \to Ve^{i\alpha}$,

$$\begin{aligned} &\phi \to \phi + \alpha, \qquad c(x) \to c(x)e^{-i\alpha(x)}, \\ &e\Phi(x) \to e\Phi(x) + \dot{\alpha}(x), \quad e\vec{A} \to e\vec{A} - \vec{\nabla}\alpha(x) \end{aligned} \tag{106}$$

where $(\Phi, \vec{A})$ denotes the electromagnetic scalar and vector potential at site j and $\dot{\alpha} = \partial_t \alpha \equiv -i\partial_\tau \alpha$ denotes the derivative with respect to real time t. By contrast, in the internal gauge transformation, the phase change of V is absorbed onto the f fermion and the internal gauge field (Read and Newns, 1983a), so if $V \to Ve^{i\beta}$,

$$\begin{aligned} &\phi \to \phi + \beta, \qquad f(x) \to f(x)e^{i\beta(x)}, \\ &\lambda(x) \to \lambda(x) - \dot{\beta}(x) \end{aligned} \tag{107}$$

If we expand the mean-field free energy to quadratic order in small, slowly varying changes in $\lambda(x)$, then the change in the action is given by

$$\delta S = -\frac{\chi_Q}{2} \int \mathrm{d}^D x \mathrm{d}\tau \delta\lambda(x)^2 \tag{108}$$

where $\chi_Q = -\delta^2 F/\delta\lambda^2$ is the f-electron susceptibility evaluated in the mean-field theory. However, $\delta\lambda(x)$ is not gauge invariant, so there must be additional terms. To guarantee gauge invariance under both the internal and external transformation, we must replace $\delta\lambda$ by the covariant combination $\delta\lambda + \dot{\phi} - e\Phi$. The first two terms are required for invariance under the internal gauge group, while the last two terms are required for gauge invariance under the external gauge group. The expansion of the action to quadratic order in the gauge fields must therefore have the form

$$S \sim -\frac{\chi_Q}{2} \int \mathrm{d}\tau \sum_j (\dot{\phi} + \delta\lambda(x) - e\Phi(x))^2 \tag{109}$$

so the phase ϕ acquires a rigidity in time that generates a 'mass' or energy cost associated with *difference* of the external and internal potentials. The minimum energy static configuration is when

$$\delta\lambda(\mathbf{x}) + \dot{\phi}(\mathbf{x}) = e\Phi(\mathbf{x}) \tag{110}$$

so when the external potential changes slowly, the internal potential tracks it. It is this effect that keeps the Kondo resonance pinned at the Fermi surface. We can always choose the gauge where the phase velocity $\dot{\phi}$ is absorbed into the local gauge field λ. Recent work by Coleman, Marston and Schofield (2005b) has extended this kind of reasoning to the case where RKKY couplings generate a dispersion $j_{\mathbf{p}-\mathcal{A}}$ for the spinons, where $\mathcal{A}$ is an internal vector potential, which suppresses currents of the gauge charge n_f. In this case, the long-wavelength action has the form

$$S = \frac{1}{2} \int \mathrm{d}^3 x \mathrm{d}\tau \Big[\rho_s \left(e\vec{A} + \vec{\nabla}\phi - \vec{\mathcal{A}}\right)^2 - \chi_Q (e\Phi - \dot{\phi} - \delta\lambda)^2 \Big] \tag{111}$$

In this general form, heavy-electron physics can be seen to involve a kind of 'Meissner effect' that excludes the difference field $e\vec{A} - \vec{\mathcal{A}}$ from within the metal, locking the internal field to the external electromagnetic field, so that the f electrons, which couple to it, now become charged (Figure 19).

2.3.4 *Optical conductivity of the heavy-electron fluid*

One of the interesting consequences of the heavy-electron charge is a complete renormalization of the electronic plasma frequency (Millis, Lavagna and Lee, 1987b). The electronic

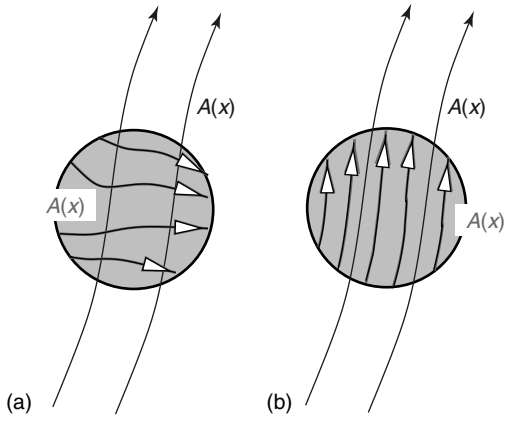

Figure 19. (a) Spin liquid, or local moment phase, internal field $\mathcal{A}$ decoupled from electromagnetic field. (b) Heavy-electron phase, internal gauge field 'locked' together with electromagnetic field. Heavy electrons are now charged and difference field $[e\vec{A}(x) - \mathcal{A}(x)]$ is excluded from the material.

plasma frequency is related via a f-sum rule to the integrated optical conductivity

$$\int_0^\infty \frac{\mathrm{d}\omega}{\pi}\sigma(\omega) = f_1 = \frac{\pi}{2}\left(\frac{n_c e^2}{m}\right) \tag{112}$$

where n_e is the density of electrons [2]. In the absence of local moments, this is the total spectral weight inside the Drude peak of the optical conductivity.

When the heavy-electron fluid forms, we need to consider the plasma oscillations of the enlarged Fermi surface. If the original conduction sea was less than half filled, then the renormalized heavy-electron band is more than half filled, forming a partially filled hole band. The density of electrons in a filled band is N/a^D, so the effective density of hole carriers is then

$$n_{\mathrm{HF}} = (N - Q - \mathcal{N}_c)/a^D = (N - Q)/a^D - n_c \tag{113}$$

The mass of the excitations is also renormalized, $m \to m^*$. The two effects produce a low-frequency 'quasiparticle' Drude peak in the conductivity, with a small total weight

$$\int_0^{\sim V} \mathrm{d}\omega\sigma(\omega) = f_2 = \frac{\pi}{2}\frac{n_{\mathrm{HF}}e^2}{m^*} \sim f_1 \times \frac{m}{m^*}\left(\frac{n_{\mathrm{HF}}}{n_c}\right) \ll f_1 \tag{114}$$

Optical conductivity probes the plasma excitations of the electron fluid at low momenta. The direct gap between the upper and lower bands of the Kondo lattice are separated by a direct hybridization gap of the order $2V \sim \sqrt{DT_{\mathrm{K}}}$. This scale is substantially larger than the Kondo temperature, and it defines the separation between the thin Drude peak of the heavy electrons and the high-frequency contribution from the conduction sea.

In other words, the total spectral weight is divided up into a small 'heavy fermion' Drude peak, of total weight f_2, where

$$\sigma(\omega) = \frac{n_{\mathrm{HF}}e^2}{m^*}\frac{1}{(\tau^*)^{-1} - i\omega} \tag{115}$$

separated off by an energy of the order $V \sim \sqrt{T_{\mathrm{K}}D}$ from an 'interband' component associated with excitations between the lower and upper Kondo bands (Millis and Lee, 1987a; Degiorgi, Anders, Gruner and Society, 2001). This second term carries the bulk $\sim f_1$ of the spectral weight (Figure 20).

Simple calculations, based on the Kubo formula, confirm this basic expectation, (Millis and Lee, 1987a; Degiorgi, Anders, Gruner and Society, 2001) showing that the relationship between the original relaxation rate of the conduction sea and the heavy-electron relaxation rate τ^* is

$$(\tau^*)^{-1} = \frac{m}{m^*}(\tau)^{-1} \tag{116}$$

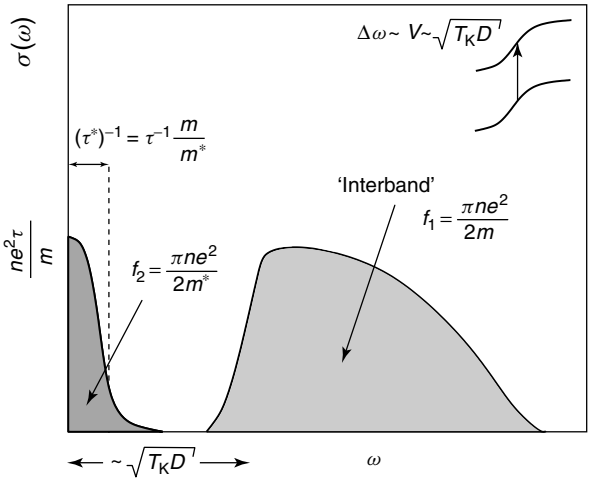

Figure 20. Separation of the optical sum rule in a heavy-fermion system into a high-energy 'interband' component of weight $f_2 \sim ne^2/m$ and a low-energy Drude peak of weight $f_1 \sim ne^2/m^*$.

Notice that this means that the residual resistivity

$$\rho_o = \frac{m^*}{ne^2\tau^*} = \frac{m}{ne^2\tau} \tag{117}$$

is unaffected by the effects of mass renormalization. This can be understood by observing that the heavy-electron Fermi velocity is also renormalized by the effective mass, $v_{\mathrm{F}}^* = \frac{m}{m^*}$, so that the mean-free path of the heavy-electron quasiparticles is unaffected by the Kondo effect.

$$l^* = v_{\mathrm{F}}^*\tau^* = v_{\mathrm{F}}\tau \tag{118}$$

The formation of a narrow Drude peak, and the presence of a direct hybridization gap, have been seen in optical measurements on heavy-electron systems (Schlessinger, Fisk, Zhang and Maple, 1997; Beyerman, Gruner, Dlicheouch and Maple, 1988; Dordevic *et al*., 2001). One of the interesting features about the hybridization gap of size $2V$ is that the mean-field theory predicts that the ratio of the direct to the indirect hybridization gap is given by $\frac{2V}{T_{\mathrm{K}}} \sim \frac{1}{\sqrt{\rho T_{\mathrm{K}}}} \sim \sqrt{\frac{m^*}{m_e}}$, so that the effective mass of the heavy electrons should scale as square of the ratio between the hybridization gap and the characteristic scale T^* of the heavy Fermi liquid

$$\frac{m^*}{m_e} \propto \left(\frac{2V}{T_{\mathrm{K}}}\right)^2 \tag{119}$$

In practical experiments, T_{K} is replaced by the 'coherence temperature' T^*, where the resistivity reaches a maximum. This scaling law is broadly followed (see Figure 21) in measured optical data (Dordevic *et al*., 2001), and provides further confirmation of the correctness of the Kondo lattice picture.

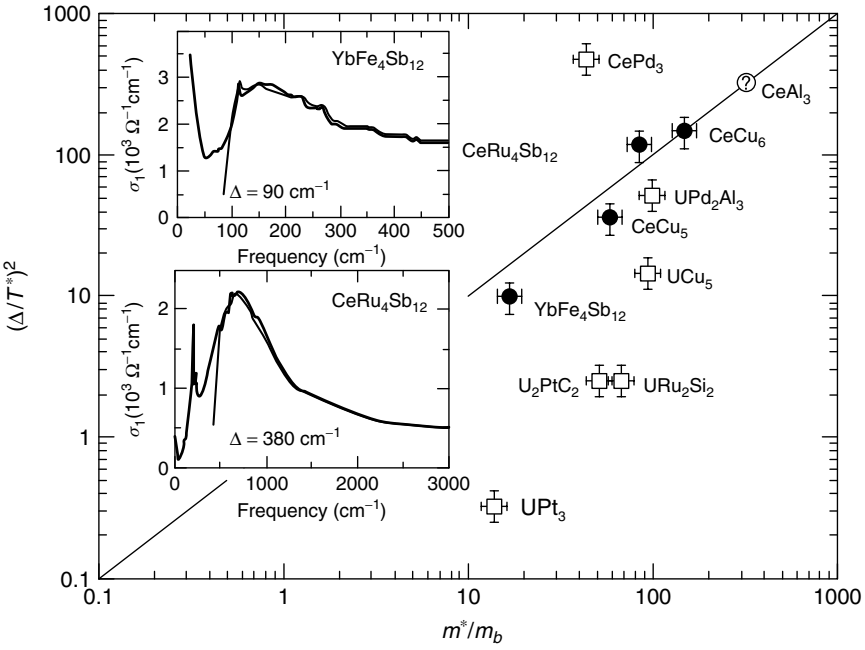

Figure 21. Scaling of the effective mass of heavy electrons with the square of the optical hybridization gap. (Reproduced from S.V. Dordevic, D.N. Basov, N.R. Dilley, E.D. Bauer, and M.B. Maple, *Phys. Rev. Lett.* **86**, 2001, 684, copyright © by the American Physical Society, with permission from the APS.)

2.4 Dynamical mean-field theory

The fermionic large N approach to the Kondo lattice provides an invaluable description of heavy-fermion physics, one that can be improved upon beyond the mean-field level. For example, the fluctuations around the mean-field theory can be used to compute the interactions, the dynamical correlation functions, and the optical conductivity (Coleman, 1987b; Millis and Lee, 1987a). However, the method does face a number of serious outstanding drawbacks:

- False phase transition: In the large N limit, the crossover between the heavy Fermi liquid and the local moment physics sharpens into a phase transition where the $1/N$ expansion becomes singular. There is no known way of eliminating this feature in the $1/N$ expansion.
- Absence of magnetism and superconductivity: The large N approach, based on the $SU(N)$ group, cannot form a two-particle singlet for $N > 2$. The $SU(N)$ group is fine for particle physics, where baryons are bound-states of N quarks, but, for condensed matter physics, we sacrifice the possibility of forming two-particle or two-spin singlets, such as Cooper pairs and spin-singlets. Antiferromagnetism and superconductivity are consequently absent from the mean-field theory.

Amongst the various alternative approaches currently under consideration, one of particular note is the DMFT. The idea of DMFT is to reduce the lattice problem to the physics of a single magnetic ion embedded within a self-consistently determined effective medium (Georges, Kotliar, Krauth and Rozenberg, 1996; Kotliar *et al*., 2006). The effective medium is determined self-consistently from the self-energies of the electrons that scatter off the single impurity. In its more advanced form, the single impurity is replaced by a cluster of magnetic ions.

Early versions of the DMFT were considered by Kuramoto and Watanabe (1987), and Cox and Grewe (1988), and others, who used diagrammatic means to extract the physics of a single impurity. The modern conceptual framework for DMFT was developed by Metzner and Vollhardt (1989), and Georges and Kotliar (1992). The basic idea behind DMFT is linked to early work of Luttinger and Ward (1960), and Kotliar *et al*. (2006), who found a way of writing the free energy as a variational functional of the full electronic Green's function

$$\mathcal{G}_{ij} = -\langle T\psi_i(\tau)\psi_j^\dagger(0)\rangle \tag{120}$$

Luttinger and Ward showed that the free energy is a variational functional of $F[\mathcal{G}]$ from which Dyson's equation relating the $\mathcal{G}$ to the bare Green's function $\mathcal{G}_0$

$$[\mathcal{G}_0^{-1} - \mathcal{G}^{-1}]_{ij} = \Sigma_{ij}[\mathcal{G}] \tag{121}$$

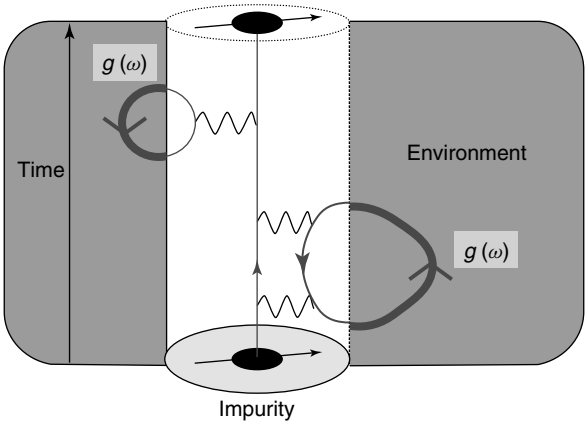

Figure 22. In the dynamical mean-field theory, the many-body physics of the lattice is approximated by a single impurity in a self-consistently determined environment. Each time the electron makes a sortie from the impurity, its propagation through the environment is described by a self-consistently determined local propagator $\mathcal{G}(\omega)$, represented by the thick gray line.

The quantity $\Sigma[\mathcal{G}]$ is a functional, a machine which takes the full propagator of the electron and outputs the self-energy of the electron. Formally, this functional is the sum of the one-particle irreducible Feynman diagrams for the self-energy: while its output depends on the input Greens function, the actual the machinery of the functional is determined solely by the interactions. The only problem is that we do not know how to calculate it.

DMFT solves this problem by approximating this functional by that of a single impurity or a cluster of magnetic impurities (Figure 22). This is an ideal approximation for a local Fermi liquid, where the physics is highly retarded in time, but local in space. The local approximation is also asymptotically exact in the limit of infinite dimensions (Metzner and Vollhardt, 1989). If one approximates the input Green function to Σ by its on-site component $\mathcal{G}_{ij} \approx \mathcal{G}\delta_{ij}$, then the functional becomes the local self-energy functional of a single magnetic impurity,

$$\Sigma_{ij}[\mathcal{G}_{ls}] \approx \Sigma_{ij}[\mathcal{G}\delta_{ls}] \equiv \Sigma_{\text{impurity}}[\mathcal{G}]\delta_{ij} \tag{122}$$

DMFT extracts the local self-energy by solving an Anderson impurity model embedded in an arbitrary electronic environment. The physics of such a model is described by a path integral with the action

$$S = -\int_0^\beta \mathrm{d}\tau \mathrm{d}\tau' f_\sigma^\dagger(\tau)\mathcal{G}_0^{-1}(\tau-\tau')f_\sigma(\tau') + U\int_0^\beta \mathrm{d}\tau n_\uparrow(\tau)n_\downarrow(\tau) \tag{123}$$

where $G_0(\tau)$ describes the bare Green's function of the f electron, hybridized with its dynamic environment. This quantity is self-consistently updated by the DMFT. There are, by now, a large number of superb numerical methods to solve an Anderson model for an arbitrary environment, including the use of exact diagonalization, diagrammatic techniques, and the use of Wilson's renormalization group (Bulla, 2006). Each of these methods is able to take an input 'environment' Green's function providing as output the impurity self-energy $\Sigma[\mathcal{G}_0] = \Sigma(i\omega_n)$.

Briefly, this is how the DMFT computational cycle works. One starts with an estimate for the environment Green's function $\mathcal{G}_0$ and uses this as input to the 'impurity solver' to compute the first estimate $\Sigma(i\omega_n)$ of the local self-energy. The interaction strength is set within the impurity solver. This local self-energy is used to compute the Green's functions of the electrons in the environment. In an Anderson lattice, the Green's function becomes

$$G(\mathbf{k},\omega) = \left[\omega - E_f - \frac{V^2}{\omega-\epsilon_{\mathbf{k}}} - \Sigma(\omega)\right]^{-1} \tag{124}$$

where V is the hybridization and $\epsilon_{\mathbf{k}}$ the dispersion of the conduction electrons. It is through this relationship that the physics of the lattice is fed into the problem. From $G(\mathbf{k},\omega)$, the local propagator is computed

$$\mathcal{G}(\omega) = \sum_{\mathbf{k}}\left[\omega - E_f - \frac{V^2}{\omega-\epsilon_{\mathbf{k}}} - \Sigma(\omega)\right]^{-1} \tag{125}$$

Finally, the new estimate for the bare environment Green's function $\mathcal{G}_0$ is then obtained by inverting the equation $\mathcal{G}^{-1} = \mathcal{G}_0^{-1} - \Sigma$, so that

$$\mathcal{G}_0(\omega) = \left[G^{-1}(\omega) + \Sigma(\omega)\right] \tag{126}$$

This quantity is then reused as the input to an 'impurity solver' to compute the next estimate of $\Sigma(\omega)$. The whole procedure is then reiterated to self-consistency. For the Anderson lattice, Cyzcholl (Schweitzer and Czycholl, 1991) has shown that remarkably good results are obtained using a perturbative expansion for Σ to the order of U^2 (Figure 23). Although this approach is not sufficient to capture the limiting Kondo behavior much, the qualitative physics of the Kondo lattice, including the development of coherence at low temperatures, is already captured by this approach. However, to go to the strongly correlated regime, where the ratio of the interaction to the impurity hybridization width $U/(\pi\Delta)$ is much larger than unity, one requires a more sophisticated solver.

There are many ongoing developments under way using this powerful new computational tool, including the incorporation of realistic descriptions of complex atoms, and the extension to 'cluster DMFT' involving clusters of magnetic moments embedded in a self-consistent environment. Let me

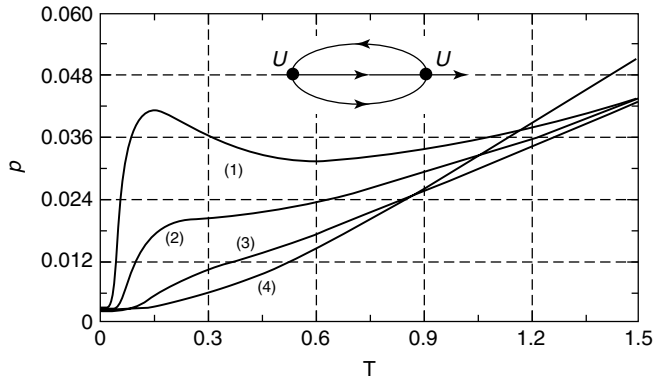

Figure 23. Resistivity for the Anderson lattice, calculated using the DMFT, computing the self-energy to order U^2. (1), (2), (3), and (4) correspond to a sequence of decreasing electron density corresponding to $n_{\mathrm{TOT}} = (0.8, 0.6, 0.4, 0.2)$ respectively. (Reproduced from H. Schweitzer and G. Czycholl, *Phys. Rev. Lett.* **67**, 1991, 3724 copyright © by the American Physical Society, with permission of the APS.)

end this brief summary with a list of a few unsolved issues with this technique

- There is, at present, no way to relate the thermodynamics of the bulk to the impurity thermodynamics.
- At present, there is no natural extension of these methods to the infinite U Anderson or Kondo models that incorporates the Green's functions of the *localized* f-electron degrees of freedom as an integral part of the DMFT.
- The method is largely a numerical black box, making it difficult to compute microscopic quantities beyond the electron-spectral functions. At the human level, it is difficult for students and researchers to separate themselves from the ardors of coding the impurity solvers, and make time to develop new conceptual and qualitative understanding of the physics.

3 KONDO INSULATORS

3.1 Renormalized silicon

The ability of a dense lattice of local moments to transform a metal into an insulator, a 'Kondo insulator' is one of the remarkable and striking consequences of the dense Kondo effect (Aeppli and Fisk, 1992; Tsunetsugu, Sigrist and Ueda, 1997; Riseborough, 2000). Kondo insulators are heavy-electron systems in which the the liberation of mobile charge through the Kondo effect gives rise to a filled heavy-electron band in which the chemical potential lies in the middle of the hybridization gap. From a quasiparticle perspective,

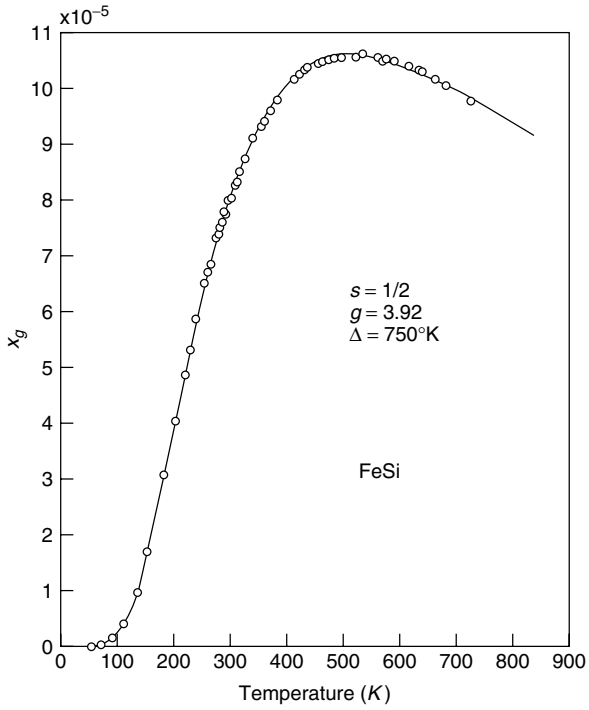

Figure 24. Schematic band picture of Kondo insulator, illustrating how a magnetic field drives a metal-insulator transition. Modified from Aeppli and Fisk (1992). (Reproduced from V. Jaccarino, G.K. Wertheim, J.H. Wernick, C.R. Walker and S. Arajs, *Phys. Rev.* **160**, 1967, 476 copyright © 1967 by the American Physical Society, with permission of the APS.)

Kondo insulators are highly renormalized 'band insulators' (Figure 24). The d-electron Kondo insulator FeSi has been referred to as *renormalized silicon*. However, like Mott–Hubbard insulators, the gap in their spectrum is driven by interaction effects, and they display optical and magnetic properties that cannot be understood with band theory.

There are about a dozen known Kondo insulators, including the rare-earth systems SmB_6 (Menth, Buehler and Geballe, 1969), YB_{12} (Iga, Kasaya and Kasuya, 1988), $CeFe_4P_{12}$ (Meisner *et al.*, 1985), $Ce_3Bi_4Pt_3$ (Hundley *et al.*, 1990), CeNiSn (Takabatake *et al.*, 1992, 1990; Izawa *et al.*, 1999) and CeRhSb (Takabatake *et al.*, 1994), and the d-electron Kondo insulator FeSi. At high temperatures, Kondo insulators are local moment metals, with classic Curie susceptibilities, but, at low temperatures, as the Kondo effect develops coherence, the conductivity and the magnetic susceptibility drop toward zero. Perfect insulating behavior is, however, rarely observed due to difficulty in eliminating impurity band formation in ultranarrow gap systems. One of the cleanest examples of Kondo-insulating behavior occurs in the d-electron system FeSi (Jaccarino *et al.*, 1967; DiTusa *et al.*, 1997). This 'flyweight' heavy-electron system provides a rather clean realization of the phenomena seen in other

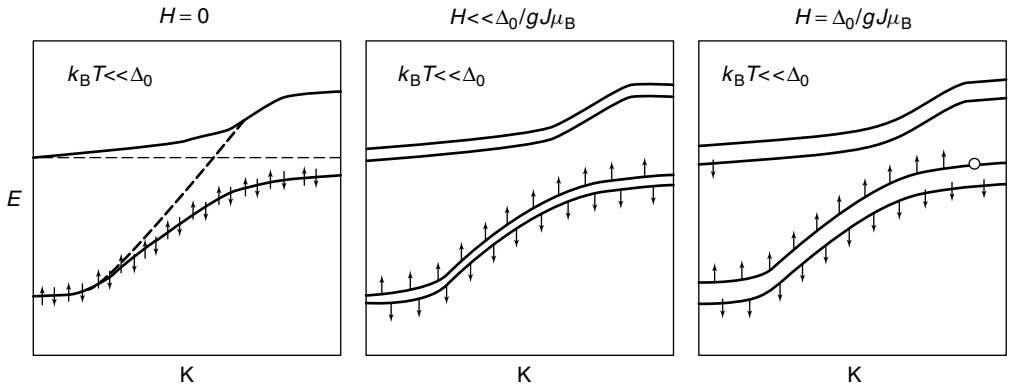

Figure 25. Temperature-dependent susceptibility in FeSi (after Jaccarino *et al*., 1967), fitted to the activated Curie form $\chi(T) = (C/T)e^{-\Delta/(k_B T)}$, with $C = (g\mu_B)^2 j(j+1)$, and $g = 3.92$, $\Delta = 750\,\mathrm{K}$. The Curie tail has been subtracted. (Reproduced from G. Aeppli and Z. Fisk, *Comm. Condens. Matter Phys.* **16** (1992) 155, with permission from Taylor & Franics Ltd, www/.nformaworld.com.)

Kondo insulators, with a spin and charge gap of about 750 K (Schlessinger, Fisk, Zhang and Maple, 1997). Unlike its rare-earth counterparts, the small spin-orbit coupling in this materials eliminates the Van Vleck contribution to the susceptibility at $T = 0$, giving rise to a susceptibility which almost completely vanishes at low temperatures (Jaccarino *et al*., 1967) (Figure 25).

Kondo insulators can be understood as 'half-filled' Kondo lattices in which each quenched moment liberates a negatively charged heavy electron, endowing each magnetic ion an extra unit of positive charge. There are three good pieces of support for this theoretical picture:

- Each Kondo insulator has its fully itinerant semiconducting analog. For example, CeNiSn is isostructural and isoelectronic with the semiconductor TiNiSi containing Ti^{4+} ions, even though the former contains Ce^{3+} ions with localized f moments. Similarly, $Ce_3Bi_4Pt_3$, with a tiny gap of the order 10 meV is isolectronic with semiconducting $Th_3Sb_4Ni_3$, with a 70 meV gap, in which the 5f-electrons of the Th^{4+} ion are entirely delocalized.
- Replacing the magnetic site with isoelectronic nonmagnetic ions is equivalent to doping, thus in $Ce_{1-x}La_xBi_4Pt_3$, each La^{3+} ion behaves as an electron donor in a lattice of effective Ce^{4+} ions. $Ce_{3-x}La_xPt_4Bi_3$ is, in fact, very similar to $CePd_3$, which contains a pseudogap in its optical conductivity, with a tiny Drude peak (Bucher *et al*., 1995).
- The magnetoresistance of Kondo insulators is large and negative, and the 'insulating gap' can be closed by the action of physically accessible fields. Thus, in $Ce_3Bi_4Pt_3$, a 30 T field is sufficient to close the indirect hybridization gap.

These equivalences support the picture of the Kondo effect liberating a composite fermion.

Figure 26(a) shows the sharp rise in the resistivity of $Ce_3Bi_4Pt_3$ as the Kondo-insulating gap forms. In Kondo insulators, the complete elimination of carriers at low temperatures is also manifested in the optical conductivity. Figure 26(b) shows the temperature dependence of the optical conductivity in $Ce_3Bi_4Pt_3$, showing the emergence of a gap in the low-frequency optical response and the loss of carriers at low energies.

The optical conductivity of the Kondo insulators is of particular interest. Like the heavy-electron metals, the development of coherence is marked by the formation of a direct hybridization gap in the optical conductivity. As this forms, a pseudogap develops in the optical conductivity. In a noninteracting band gap, the lost f-sum weight inside the pseudogap would be deposited above the gap. In heavy-fermion metals, a small fraction of this weight is deposited in the Drude peak – however, most of the weight is sent off to energies comparable with the bandwidth of the conduction band. This is one of the most direct pieces of evidence that the formation of Kondo singlets involves electron energies that spread out to the bandwidth. Another fascinating feature of the heavy-electron 'pseudogap' is that it forms at a temperature that is significantly lower than the pseudogap. This is because the pseudogap has a larger width given by the geometric mean of the coherence temperature and the bandwidth $2V \sim \sqrt{T_K D}$. The extreme upward transfer of spectral weight in Kondo insulators has not yet been duplicated in detailed theoretical models. For example, while calculations of the optical conductivity within the DMFT do show spectral weight transfer, it is not yet possible to reduce the indirect band gap to the point where it is radically smaller than the interaction scale U (Rozenberg, Kotliar and Kajueter, 1996). It may be that these discrepancies will disappear in future calculations based on the more extreme physics of the Kondo model, but these calculations have yet to be carried out.

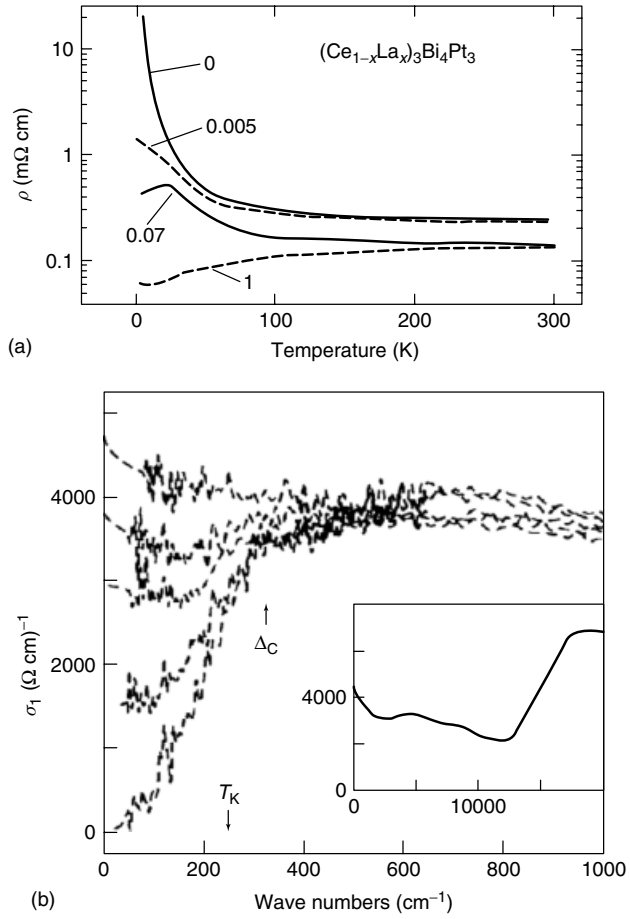

Figure 26. (a) Temperature-dependent resistivity of $Ce_3Pt_4Bi_3$ showing the sharp rise in resistivity at low temperatures. (Reproduced from M.F. Hundley, P.C. Canfield, J.D. Thompson, Z. Fisk, and J.M. Lawrence, *Phys. Rev. B.* **42**, 1990, 6842, copyright © 1990 by the American Physical Society, with permission of the APS.) Replacement of local moments with spinless *La* ions acts like a dopant. (b) Real part of optical conductivity $\sigma_1(\omega)$ for Kondo insulator $Ce_3Pt_4Bi_3$. (Reproduced from B. Bucher, Z. Schlessinger, P.C. Canfield, and Z. Fisk 03/04/2007 *Phys. Rev. Lett* **72**, 1994, 522, copyright © 1994 by the American Physical Society, with permission of the APS.) The formation of the pseudogap associated with the direct hybridization gap leads to the transfer of f-sum spectral weight to high energies of order the bandwidth. The pseudogap forms at temperatures that are much smaller than its width (see text). Insert shows $\sigma_1(\omega)$ in the optical range.

There are, however, a number of aspects of Kondo insulators that are poorly understood from the the simple hybridization picture, in particular,

- The apparent disappearance of RKKY magnetic interactions at low temperatures.
- The nodal character of the hybridization gap that develops in the narrowest gap Kondo insulators CeNiSn and CeRhSb.
- The nature of the metal-insulator transition induced by doping.

3.2 Vanishing of RKKY interactions

There are a number of experimental indications that the low-energy magnetic interactions vanish at low frequencies in a Kondo lattice. The low-temperature product of the susceptibility and temperature χT reported (Aeppli and Fisk, 1992) to scale with the inverse Hall constant $1/R_H$, representing the exponentially suppressed density of carriers, so that

$$\chi \sim \frac{1}{R_{\mathrm{H}} T} \sim \frac{\mathrm{e}^{-\Delta/T}}{T} \tag{127}$$

The important point here is that the activated part of the susceptibility has a vanishing Curie–Weiss temperature. A similar conclusion is reached from inelastic neutron scattering measurements of the magnetic susceptibility $\chi'(q,\omega) \sim$ in CeNiSn and FeSi, which appears to lose all of its momentum dependence at low temperatures and frequencies. There is, to date, no theory that can account for these vanishing interactions.

3.3 Nodal Kondo insulators

The narrowest gap Kondo insulators, CeNiSn and CeRhSb, are effectively semimetals, for although they do display tiny pseudogaps in their spin and charge spectra, the purest samples of these materials develop metallic behavior (Izawa *et al.*, 1999). What is particularly peculiar (Figure 27) about these two materials is that the NMR relaxation rate $1/(T_1)$ shows a T^3 temperature dependence from about 10 to 1 K, followed by a linear Korringa behavior at lower temperatures. The usual rule of thumb is that the NMR relaxation rate is proportional to a product of the temperature and the thermal average of the electronic density of states $N^*(\omega)$

$$\frac{1}{T_1} \sim T\overline{N(\omega)^2} \sim T[N(\omega \sim T)]^2 \tag{128}$$

where $\overline{N(\omega)^2} = \int \mathrm{d}\epsilon \left(-\frac{\partial f(\omega)}{\partial \omega}\right) N(\omega)^2$ is the thermally smeared average of the squared density of states. This suggests that the electronic density of states in these materials has a 'V' shaped form, with a finite value at $\omega = 0$. Ikeda and Miyake (1996) have proposed that the Kondo-insulating state in these materials develops in a crystal-field state with an axially symmetric hybridization vanishing along a single crystal axis. In such a picture, the finite density of states does not derive from a Fermi surface, but from the angular average of the coherence peaks in the density of states. The

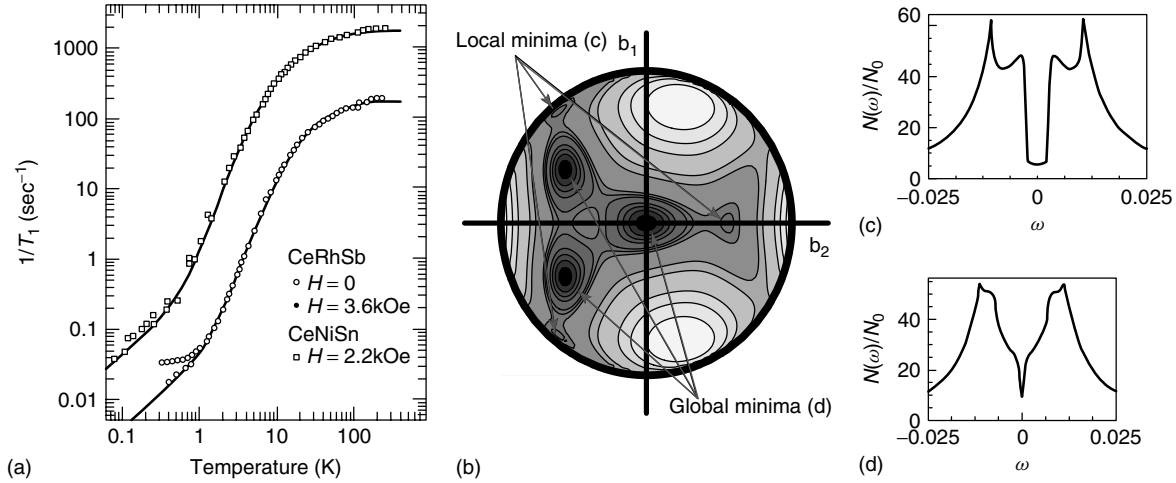

Figure 27. (a) NMR relaxation rate $1/T_1$ in CeRhSb and CeNiSn, showing a T^3 relaxation rate sandwiched between a low- and a high-temperature T-linear Korringa relaxation rate, suggesting a V-shaped density of states. (Reproduced from K. Nakamura, Y. Kitaoka, K. Asayama, T. Takabatake, H. Tanaka, and H. Fujii, *J. Phys. Soc Japan* **63**, 1994, 33, with permission of the Physical Society of Japan.) (b) Contour plot of the ground-state energy in mean-field theory for the narrow gap Kondo insulators, as a function of the two first components of the unit vector $\hat{b}$ (the third one is taken as positive). The darkest regions correspond to lowest values of the free energy. Arrows point to the three global and three local minima that correspond to nodal Kondo insulators. (Reproduced from J. Moreno and P. Coleman, *Phys. Rev. Lett.* **84**, 2000, 342, copyright © 2000 by the American Physical Society, with permission of the APS.) (c) Density of states of Ikeda and Miyake (1996) state that appears as the global minimum of the Kinetic energy. (Reproduced from H. Ikeda, and K. Miyake *J. Phys. Soc. Jpn.* **65**, 1996, 1769, with permission of the Physical Society of Japan.) (d) Density of states of the MC state (Moreno and Coleman, 2000) that appears as a local minimum of the Kinetic energy, with more pronounced 'V'-shaped density of states.

odd thing about this proposal is that CeNiSn and CeRhSb are monoclinic structures, and the low-lying Kramers doublet of the f state can be any combination of the $|\pm\frac{1}{2}\rangle$, $|\pm\frac{3}{2}\rangle$, or $|\pm\frac{5}{2}\rangle$ states:

$$|\pm = b_1|\pm 1/2\rangle + b_2|\pm 5/2\rangle + b_3|\mp 3/2\rangle \qquad (129)$$

where $\hat{b} = (b_1, b_2, b_3)$ could, in principle, point anywhere on the unit sphere, depending on details of the monoclinic crystal field. The Ikeda Miyake model corresponds to three symmetry-related points in the space of crystal-field ground states,

$$\hat{b} = \begin{cases} (\mp\frac{\sqrt{2}}{4}, -\frac{\sqrt{5}}{4}, \frac{3}{4}) \\ (0, 0, 1) \end{cases} \qquad (130)$$

where a node develops along the x, y, or z axis, respectively. But the nodal crystal-field states are isolated 'points' amidst a continuum of fully gapped crystal-field states. Equally strangely, neutron scattering results show no crystal-field satellites in the dynamical spin susceptibility of CeNiSn, suggesting that the crystal electric fields are quenched (Alekseev *et al*., 1994), and that the nodal physics is a many-body effect (Kagan, Kikoin and Prokof'ev, 1993; Moreno and Coleman, 2000). One idea is that Hund's interactions provide the driving force for this selection mechanism. Zwicknagl, Yaresko and Fulde (2002) have suggested that Hund's couplings select the orbitals in multi f electron heavy-electron metals such as UPt_3. Moreno and Coleman (2000) propose a similar idea in which virtual valence fluctuations into the f^2 state generate a many-body or a Weiss effective field that couples to the orbital degrees of freedom, producing an effective *crystal* field that adjusts itself in order to minimize the kinetic energy of the f electrons. This hypothesis is consistent with the observation that the Ikeda Miyake state corresponds to the Kondo-insulating state with the lowest kinetic energy, providing a rational for the selection of the nodal configurations. Moreno and Coleman also found another nodal state with a more marked V-shaped density of states that may fit the observed properties more precisely. This state is also a local minimum of the electron Kinetic energy. These ideas are still in their infancy, and more work needs to be done to examine the controversial idea of a Weiss crystal field, both in the insulators and in the metals.

4 HEAVY-FERMION SUPERCONDUCTIVITY

4.1 A quick tour

Since the discovery (Steglich *et al*., 1976) of superconductivity in $CeCu_2Si_2$, the list of known HFSCs has grown to

include more than a dozen (Sigrist and Ueda, 1991b) materials with a great diversity of properties (Sigrist and Ueda, 1991a; Cox and Maple, 1995). In each of these materials, the jump in the specific heat capacity at the superconducting phase transition is comparable with the normal state specific heat

$$\frac{(C_v^s - C_v^n)}{C_V} \sim 1 - 2 \tag{131}$$

and the integrated entropy beneath the C_v/T curve of the superconductor matches well with the corresponding area for the normal phase obtained when superconductivity is suppressed by disorder or fields

$$\int_0^{T_c} \mathrm{d}T \frac{(C_v^s - C_v^n)}{T} = 0 \tag{132}$$

Since the normal state entropy is derived from the f moments, it follows that these same degrees of freedom are involved in the development of the superconucting state. With the exception of a few anomalous cases, (UBe_{13}, $PuCoGa_5$, and $CeCoIn_5$), heavy-fermion superconductivity develops out of the coherent, paramagnetic heavy Fermi liquid, so heavy fermion superconductivity can be said to involve the pairing of heavy f electrons.

Independent confirmation of the 'heavy' nature of the pairing electrons comes from observed size of the London penetration depth λ_{L} and superconducting coherence length ξ in these systems, both of which reflect the enhanced effective mass. The large mass renormalization enhances the penetration depth, whilst severely contracting the coherence length, making these extreme type-II superconductors. The London penetration depth of HFSCs agree well with the value expected on the assumption that only spectral weight in the quasiparticle Drude peak condenses to form a superconductor by

$$\frac{1}{\mu_o \lambda_{\mathrm{L}}^2} = \frac{ne^2}{m^*} = \int_{\omega \in \mathrm{D.}P} \frac{\mathrm{d}\omega}{\pi} \sigma(\omega) \ll \frac{ne^2}{m} \tag{133}$$

London penetration depths in these compounds are a factor of 20–30 times *longer* (Broholm *et al*., 1990) than in superconductors, reflecting the large enhancement in effective mass. By contrast, the coherence lengths $\xi \sim v_{\mathrm{F}}/\Delta \sim hk_{\mathrm{F}}/(m^*\Delta)$ are severely contracted in a HFSC. The orbitally limited upper critical field is determined by the condition that an area ξ^2 contains a flux quantum $\xi^2 B_c \sim \frac{h}{2e}$. In UBe_{13}, a superconductor with 0.9 K transition temperature, the upper critical field is about 11 T, a value about 20 times larger than a conventional superconductor of the same transition temperature.

Table 2 shows a selected list of HFSCs. 'Canonical' HFSCs, such as $CeCu_2Si_2$ and UPt_3, develop superconductivity out of a paramagnetic Landau–Fermi liquid. 'Preordered' superconductors, such as UPt_2Al_3 (Geibel *et al*., 1991a,b), $CePt_3Si$, and URu_2Si_2, develop another kind of order before going superconducting at a lower temperature. In the case of URu_2Si_2, the nature of the upper ordering transition is still unidentified, but, in the other examples, the upper transition involves the development of antiferromagnetism. 'Quantum critical' superconductors, including $CeIn_3$ and $CeCu_2(Si_{1-x}Ge_x)_2$, develop superconductivity when pressure is tuned close to a QCP. $CeIn_3$ develops superconductivity at the pressure-tuned antiferromagnetic quantum critical point at 2.5 GPa (25 kbar). $CeCu_2$ $(Si,Ge)_2$ has two islands, one associated with antiferromagnetism at low pressure and a second at still higher pressure, thought to be associated with critical valence fluctuations (Yuan *et al*., 2006).

'Strange' superconductors, which include UBe_{13}, the 115 material $CeCoIn_5$, and $PuCoGa_5$, condense into the superconducting state out of an incoherent or strange metallic state. UBe_{13} has a resistance of the order 150 μΩcm at its transition temperature. $CeCoIn_5$ bears superficial resemblance to a high-temperature superconductor, with a linear temperature resistance in its normal state, while its cousin, $PuCoGa_5$ transitions directly from a Curie paramagnet of unquenched f spins into an anisotropically paired, singlet superconductor. These particular materials severely challenge our theoretical understanding, for the heavy-electron quasiparticles appear to form as part of the condensation process, and we are forced to address how the f-spin degrees of freedom incorporate into the superconducting parameter.

4.2 Phenomenology

The main body of theoretical work on heavy-electron systems is driven by experiment, and focuses directly on the phenomenology of the superconducting state. For these purposes, it is generally sufficient to assume a Fermi liquid of preformed mobile heavy electrons, an electronic analog of superfluid Helium-3, in which the quasiparticles interact through a phenomenological BCS model. For most purposes, the Landau–Ginzburg theory is sufficient. I regret that, in this short review, I do not have time to properly represent and discuss the great wealth of fascinating phenomenology, the wealth of multiple phases, and the detailed models that have been developed to describe them. I refer the interested reader to reviews on this subject. (Sigrist and Ueda, 1991a).

On theoretical grounds, the strong Coulomb interactions of the f electrons that lead to moment formation in heavy-fermion compounds are expected to heavily suppress the formation of conventional s-wave pairs in these systems. A large body of evidence favors the idea that the gap function and the anomalous Green function between paired heavy electrons $F_{\alpha\beta}(x) = \langle c_\alpha^\dagger(x) c_\beta^\dagger(0) \rangle$ is spatially

Table 2. Selected HFSCs.

Type	Material	T_c (K)	Knight shift (singlet)	Remarks	Gap symmetry	References
Canonical	$CeCu_2Si_2$	0.7	Singlet	First HFSC	Line nodes	Steglich *et al*. (1976)
	UPt_3	0.48	?	Double transition to T-violating state	Line and point nodes	Stewart, Fisk, Willis and Smith (1984b)
Preordered	UPd_2Al_3	2	Singlet	Néel AFM $T_N = 14\,K$	Line nodes $\Delta \sim \cos 2\chi$	Geibel *et al*. (1991a), Sato *et al*. (2001) and Tou *et al*. (1995)
	URu_2Si_2	1.3	Singlet	Hidden order at $T_0 = 17.5\,K$	Line nodes	Palstra *et al*. (1985) and Kim *et al*. (2003)
	$CePt_3Si$	0.8	Singlet and Triplet	Parity-violating crystal. $T_N = 3.7\,K$	Line nodes	Bauer *et al*. (2004)
Quantum critical	$CeIn_3$	0.2 (2.5 GPa)	Singlet	First quantum critical HFSC	Line nodes	Mathur *et al*. (1998)
	$CeCu_2\ (Si_{1-x}Ge_x)_2$	0.4 (P = 0) 0.95 (5.4 GPa)	Singlet	Two islands of SC as function of pressure	Line nodes	Yuan *et al*. (2006)
Quadrupolar	$PrOs_4Sb_{12}$	1.85	Singlet	Quadrupolar fluctuations	Point nodes	Isawa *et al*. (2003)
Strange	$CeCoIn_5$	2.3	Singlet	Quasi-2D $\rho_n \sim T$	Line nodes $d_{x^2-y^2}$	Petrovic *et al*. (2001)
	UBe_{13}	0.86	?	Incoherent metal at T_c	Line nodes	Andres, Graebner and Ott (1975)
	$PuCoGa_5$	18.5	Singlet	Direct transition Curie metal → HFSC	Line nodes	Sarrao *et al*. (2002)

anisotropic, forming either p-wave triplet or d-wave singlet pairs.

In BCS theory, the superconducting quasiparticle excitations are determined by a one-particle Hamiltonian of the form

$$H = \sum_{\mathbf{k},\sigma} \epsilon_{\mathbf{k}} f^{\dagger}_{\mathbf{k}\alpha} f_{\mathbf{k}\alpha} + \sum_{\mathbf{k}} [f^{\dagger}_{\mathbf{k}\alpha} \Delta_{\alpha\beta}(\mathbf{k}) f^{\dagger}_{-\mathbf{k}\beta} + f_{-\mathbf{k}\beta} \overline{\Delta}_{\beta\alpha}(\mathbf{k}) f_{\mathbf{k}\alpha}] \tag{134}$$

where

$$\Delta_{\alpha\beta}(\mathbf{k}) = \begin{cases} \Delta(\mathbf{k})(i\sigma_2)_{\alpha\beta} & \text{(singlet)} \\ \vec{d}(\mathbf{k}) \cdot (i\sigma_2 \vec{\sigma})_{\alpha\beta} & \text{(triplet)} \end{cases} \tag{135}$$

For singlet pairing, $\Delta(\mathbf{k})$ is an even parity function of $\mathbf{k}$, while for triplet pairing, $\vec{d}(\mathbf{k})$ is a an odd-parity function of $\mathbf{k}$ with three components.

The excitation spectrum of an anisotropically paired singlet superconductor is given by

$$E_{\mathbf{k}} = \sqrt{\epsilon^2_{\mathbf{k}} + |\Delta_{\mathbf{k}}|^2} \tag{136}$$

This expression can also be used for a triplet superconductor that does not break the time-reversal symmetry by making the replacement $|\Delta_{\mathbf{k}}|^2 \equiv \vec{d}^{\dagger}(\mathbf{k}) \cdot \vec{d}(\mathbf{k})$.

Heavy-electron superconductors are anisotropic superconductors, in which the gap function vanishes at points, or, more typically, along lines on the Fermi surface. Unlike s-wave superconductors, magnetic and nonmagnetic impurities are equally effective at pair breaking and suppressing T_c in these materials. A node in the gap is the result of sign changes in the underlying gap function. If the gap function vanishes along surfaces in momentum space, the intersection of these surfaces with the Fermi surface produces 'line nodes' of gapless quasiparticle excitations. As an example, consider UPt_3, where, according to one set of models (Blount, Varma and Aeppli, 1990; Joynt, 1988; Puttika and Joynt, 1988; Hess, Tokuyasu and Sauls, 1990; Machida and Ozaki, 1989), pairing involves a complex d-wave gap

$$\Delta_{\mathbf{k}} \propto k_z(\hat{k}_x \pm i k_y), \qquad |\Delta_{\mathbf{k}}|^2 \propto k_z^2(k_x^2 + k_y^2) \tag{137}$$

Here $\Delta_{\mathbf{k}}$ vanishes along the basal plane $k_z = 0$, producing a line of nodes around the equator of the Fermi surface, and along the z axis, producing a point node at the poles of the Fermi surface.

One of the defining properties of line nodes on the Fermi surface is a quasiparticle density of states that vanishes linearly with energy

$$N^*(E) = 2\sum_{\mathbf{k}} \delta(E - E_{\mathbf{k}}) \propto E \tag{138}$$

The quasiparticles surrounding the line node have a 'relativistic' energy spectrum. In a plane perpendicular to the node, $E_{\mathbf{k}} \sim \sqrt{(v_F k_1)^2 + (\alpha k_2)^2}$, where $\alpha = \mathrm{d}\Delta/\mathrm{d}k_2$ is the gradient of the gap function and k_1 and k_2 the momentum measured in the plane perpendicular to the line node. For a two-dimensional relativistic particle with dispersion $E = ck$, the density of states is given by $N(E) = \frac{|E|}{4\pi c^2}$. For the anisotropic case, we need to replace c by the geometric mean of v_F and α, so $c^2 \to v_F\alpha$. This result must then be doubled to take account of the spin degeneracy and averaged over each line node:

$$N(E) = 2\sum_{\text{nodes}} \int \frac{\mathrm{d}k_\parallel}{2\pi} \frac{|E|}{4\pi v_F \alpha} = |E| \times \sum_{\text{nodes}} \left(\int \frac{\mathrm{d}k_\parallel}{4\pi^2 v_F \alpha} \right) \tag{139}$$

In the presence of pair-breaking impurities and in a vortex state, the quasiparticle nodes are smeared, adding a small constant component to the density of states at low energies.

This linear density of states is manifested in a variety of power laws in the temperature dependence of experimental properties, most notably

- Quadratic temperature dependence of specific heat $C_V \propto T^2$, since the specific heat coefficient is proportional to the thermal average of the density of states

$$\frac{C_V}{T} \propto \overbrace{\overline{N(E)}}^{\propto T} \sim T \tag{140}$$

  where $\overline{N(E)}$ denotes the thermal average of $N(E)$.
- A ubiquitous T^3 temperature dependence in the nuclear magnetic relaxation (NMR) and nuclear quadrupole relaxation (NQR) rates $1/T_1$. The nuclear relaxation rate is proportional to the thermal average of the squared density of states, so, for a superconductor with line nodes,

$$\frac{1}{T_1} \propto T \overbrace{\overline{N(E)^2}}^{\propto T^2} \sim T^3 \tag{141}$$

  Figure 28 shows the T^3 NMR relaxation rate of the Aluminum nucleus in UPd_2Al_3.

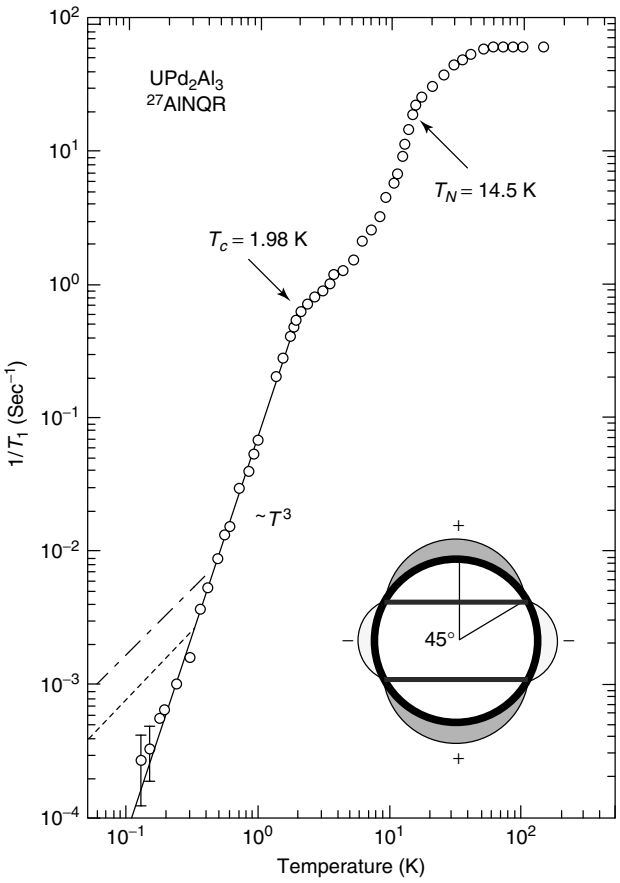

Figure 28. Temperature dependence of the ^{27}Al NQR relaxation rate $1/T_1$ for UPd_2Al_3 (after Tou *et al*., 1995) showing T^3 dependence associated with lines of nodes. Inset showing nodal structure $\Delta \propto \cos(2\theta)$ proposed from analysis of anisotropy of thermal conductivity in Won *et al*. (2004). (Reproduced from H. Tou, Y. Kitaoka, K. Asayama, C. Geibel, C. Schank, and F. Steglich, 1995, *J. Phys. Soc. Japan* **64**, 1995 725, with permission of the Physical Society of Japan.)

Although power laws can distinguish line and point nodes, they do not provide any detailed information about the triplet or singlet character of the order parameter or the location of the nodes. The observation of upper critical fields that are 'Pauli limited' (set by the spin coupling, rather than the diamagnetism), and the observation of a Knight shift in most HFSCs, indicates that they are anisotropically singlet paired. Three notable exceptions to this rule are UPt_3, UBe_{13}, and UNi_2Al_3, which do not display either a Knight shift or a Pauli-limited upper critical field, and are the best candidates for odd-parity triplet pairing. In the special case of $CePt_3Sn$, the crystal structure lacks a center of symmetry and the resulting parity violation must give a mixture of triplet and singlet pairs.

Until comparatively recently, very little was known about the positions of the line nodes in heavy-electron

superconductors. In one exception, experiments carried out almost 20 years ago on UPt_3 observed marked anisotropies in the ultrasound attenuation length and the penetration depth (Bishop *et al*., 1984; Broholm *et al*., 1990) that appear to support a line of nodes in the basal plane. The ultrasonic attenuation $\alpha_s(T)/\alpha_n$ in single crystals of UPt_3 has a T linear dependence when the polarization lies in the basal plane of the gap nodes, but a T^3 dependence when the polarization is along the c axis.

An interesting advance in the experimental analysis of nodal gap structure has recently occurred, owing to new insights into the behavior of the nodal excitation spectrum in the flux phase of HFSCs. In the 1990s, Volovik (1993) observed that the energy of heavy-electron quasiparticles in a flux lattice is 'Doppler shifted' by the superflow around the vortices, giving rise to a finite density of quasiparticle states around the gap nodes. The Doppler shift in the quasiparticle energy resulting from superflow is given by

$$E_{\mathbf{k}} \rightarrow E_{\mathbf{k}} + \vec{p} \cdot \vec{v}_s = E_{\mathbf{k}} + \vec{v}_F \cdot \frac{\hbar}{2}\vec{\nabla}\phi \tag{142}$$

where $\vec{v}_s$ is the superfluid velocity and ϕ the superfluid phase. This has the effect of shifting quasiparticle states by an energy of the order $\Delta E \sim \hbar\frac{v_F}{2R}$, where R is the average distance between vortices in the flux lattice. Writing $\pi H R^2 \sim \Phi_0$, and $\pi H_{c2}\xi^2 \sim \Phi_0$ where $\Phi_0 = \frac{h}{2e}$ is the flux quantum, H_{c2} is the upper critical field, and ξ is the coherence length, it follows that $\frac{1}{R} \sim \frac{1}{\xi}\sqrt{\frac{H}{H_{c2}}}$. Putting $\xi \sim v_F/\Delta$, where Δ is the typical size of the gap, the typical shift in the energy of nodal quasiparticles is of the order $E_H \sim \Delta\sqrt{\frac{H}{H_{c2}}}$. Now since the density of states is of the order $N(E) = \frac{|E|}{\Delta}N(0)$, where $N(0)$ is the density of states in the normal phase, it follows that the smearing of the nodal quasiparticle energies will produce a density of states of the order

$$N^*(H) \sim N(0)\sqrt{\frac{H}{H_{c2}}} \tag{143}$$

This effect, the 'Volovik effect', produces a linear component to the specific heat $C_V/T \propto \sqrt{\frac{H}{H_{c2}}}$. This enhancement of the density of states is largest when the group velocity $\vec{V}_F$ at the node is perpendicular to the applied field $\vec{H}$, and when the field is parallel to $\vec{v}_F$ at a particular node, the node is unaffected by the vortex lattice (Figure 29). This

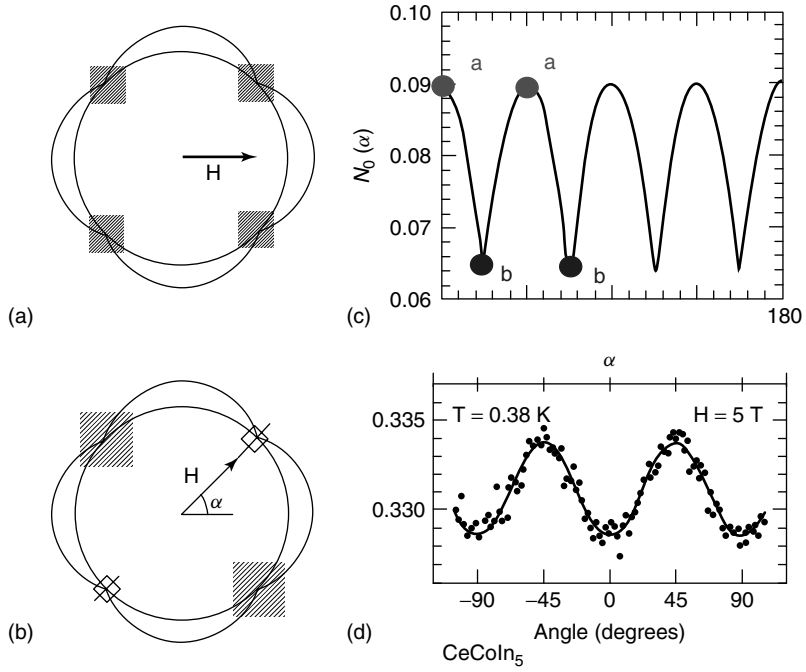

Figure 29. Schematic showing how the nodal quasiparticle density of states depends on field orientation (after Vekhter, Hirschfield, Carbotte and Nicol, 1999). (a) Four nodes are activated when the field points toward an antinode, creating a maximum in density of states. (b) Two nodes activated when the field points toward a node, creating a minimum in the density of states. (c) Theoretical dependence of density of states on angle. (After Vekhter, Hirschfield, Carbotte and Nicol, 1999.) (d) Measured angular dependence of C_v/T (after Aoki *et al*., 2004) is 45° out of phase with prediction. This discrepancy is believed to be due to vortex scattering, and is expected to vanish at lower fields. (Reproduced from I. Vekhter, P. Hirschfield, J.P. Carbotte, and E.J. Nicol, *Phys. Rev. B* **59**, 1998, R9023, copyright © 1998 by the American Physical Society, with permission of the APS.)

gives rise to an angular dependence in the specific heat coefficient and thermodynamics that can be used to measure the gap anisotropy. In practice, the situation is complicated at higher fields where the Andreev scattering of quasiparticles by vortices becomes important. The case of $CeCoIn_5$ is of particular current interest. Analyses of the field-anisotropy of the thermal conductivity in this material was interpreted early on in terms of a gap structure with $d_{x^2-y^2}$, while the anisotropy in the specific heat appears to suggest a d_{xy} symmetry. Recent theoretical work by Vorontsov and Vekhter (2006) suggests that the discrepancy between the two interpretations can be resolved by taking into account the effects of the vortex quasiparticle scattering that were ignored in the specific heat interpretation. They predict that, at lower fields, where vortex scattering effects are weaker, the sign of the anisotropic term in the specific heat reverses, accounting for the discrepancy

It is clear that, despite the teething problems in the interpretation of field-anisotropies in transport and thermodynamics, this is an important emerging tool for the analysis of gap anisotropy, and, to date, it has been used to give tentative assignments to the gap anisotropy of UPd_2Al_3, $CeCoIn_5$, and $PrOs_4Sb_{12}$.

4.3 Microscopic models

4.3.1 Antiferromagnetic fluctuations as a pairing force

The classic theoretical models for heavy-fermion superconductivity treat the heavy-electron fluids as a Fermi liquid with antiferromagnetic interactions amongst their quasiparticles (Monod, Bourbonnais and Emery, 1986; Scalapino, Loh and Hirsch, 1986; Monthoux and Lonzarich, 1999). UPt_3 provided the experimental inspiration for early theories of heavy-fermion superconductivity, for its superconducting state forms from within a well-developed Fermi liquid. Neutron scattering on this material shows signs of antiferromagnetic spin fluctuations (Aeppli *et al*., 1987), making it natural to presuppose that these might be the driving force for heavy-electron pairing.

Since the early 1970s, theoretical models had predicted that strong ferromagnetic spin fluctuations, often called *paramagnons*, could induce p-wave pairing, and this mechanism was widely held to be the driving force for pairing in superfluid He–3. An early proposal that antiferromagnetic interactions could provide the driving force for anisotropic singlet pairing was made by Hirsch (1985). Shortly thereafter, three seminal papers, by Monod, Bourbonnais and Emery (1986) (BBE), Scalapino, Loh and Hirsch (1986) (SLH) and by Miyake, Miyake, Rink and Varma (1986) (MSV), solidified this idea with a concrete demonstration that antiferromagnetic interactions drive an attractive BCS interaction in the d-wave pairing channel. It is a fascinating thought that at the same time that this set of authors was forging the foundations of our current thoughts on the link between antiferromagnetism and d-wave superconductivity, Bednorz and Mueller were in the process of discovering high-temperature superconductivity.

The BBE and SLH papers develop a paramagnon theory for d-wave pairing in a Hubbard model with a contact interaction I, having in mind a system, which in the modern context, would be said to be close to an antiferromagnetic QCP. The MSV paper starts with a model with a preexisting antiferromagnetic interaction, which, in the modern context, would be associated with the 't–J' model. It is this approach that I sketch here. The MSV model is written

$$H = \sum \epsilon_{\mathbf{k}} a^{\dagger}_{\mathbf{k}\sigma} a_{\mathbf{k}\sigma} + H_{\rm int} \tag{144}$$

where

$$H_{\rm int} = \frac{1}{2} \sum_{\mathbf{k},\mathbf{k}'} \sum_{\mathbf{q}} J(\mathbf{k}-\mathbf{k}') \vec{\sigma}_{\alpha\beta} \cdot \vec{\sigma}_{\gamma\delta} \times \left(a^{\dagger}_{\mathbf{k}+\mathbf{q}/2\alpha} a^{\dagger}_{-\mathbf{k}+\mathbf{q}/2\gamma} \right) \left(a_{-\mathbf{k}'+\mathbf{q}/2\delta} a_{\mathbf{k}'+\mathbf{q}/2\beta} \right) \tag{145}$$

describes the antiferromagnetic interactions. There are a number of interesting points to be made here:

- The authors have in mind a strong coupled model, such as the Hubbard model at large U, where the interaction cannot be simply derived from paramagnon theory. In a weak-coupled Hubbard model, a contact interaction I and bare susceptibility $\chi_0(q)$, the induced magnetic interaction can be calculated in a random phase approximation (RPA) (Miyake, Rink and Varma, 1986) as

$$J(q) = -\frac{I}{2[1 + I\chi_0(q)]} \tag{146}$$

  MSV make the point that the detailed mechanism that links the low-energy antiferromagnetic interactions to the microscopic interactions is poorly described by a weak-coupling theory, and is quite likely to involve other processes, such as the RKKY interaction, and the Kondo effect that lie outside this treatment.
- Unlike phonons, magnetic interactions in heavy-fermion systems cannot generally be regarded as retarded interactions, for they extend up to an energy scale ω_0 that is comparable with the heavy-electron bandwidth T^*. In a classic BCS treatment, the electron energy is restricted to lie within a Debye energy of the Fermi energy. But

here, $\omega_0 \sim T^*$, so all momenta are involved in magnetic interactions, and the interaction can transformed to real space as

$$H = \sum \epsilon_{\mathbf{k}} a^\dagger_{\mathbf{k}\sigma} a_{\mathbf{k}\sigma} + \frac{1}{2}\sum_{i,j} J(\mathbf{R}_i - \mathbf{R}_j)\vec{\sigma}_i \cdot \vec{\sigma}_j \quad (147)$$

where $J(\mathbf{R}) = \sum_{\mathbf{q}} e^{i\mathbf{q}\cdot\mathbf{R}} J(\mathbf{q})$ is the Fourier transform of the interaction and $\vec{\sigma}_i = a^\dagger_{i\alpha}\vec{\sigma}_{\alpha\beta}a_{i\beta}$ is the spin density at site i. Written in real space, the MSV model is seen to be an early predecessor of the t–J model used extensively in the context of high-temperature superconductivity.

To see that antiferromagnetic interactions favor d-wave pairing, one can use the 'let us decouple the interaction' in real space in terms of triplet and singlet pairs. Inserting the identity [3]

$$\vec{\sigma}_{\alpha\beta} \cdot \vec{\sigma}_{\gamma\delta} = -\frac{3}{2}(\sigma_2)_{\alpha\gamma}(\sigma_2)_{\beta\delta} + \frac{1}{2}(\vec{\sigma}\sigma_2)_{\alpha\gamma} \cdot (\sigma_2\vec{\sigma})_{\beta\delta} \quad (148)$$

into equation (147) gives

$$H_{\rm int} = -\frac{1}{4}\sum_{i,j} J_{ij}\left[3\Psi^\dagger_{ij}\Psi_{ij} - \vec{\Psi}^\dagger_{ij}\cdot\vec{\Psi}_{ij}\right] \quad (149)$$

where

$$\begin{aligned}\Psi^\dagger_{ij} &= \left(a^\dagger_{i\alpha}(-i\sigma)_{\alpha\gamma}\ a^\dagger_{j\gamma}\right)\\ \vec{\Psi}^\dagger_{ij} &= \left(a^\dagger_{i\alpha}(-i\vec{\sigma}\sigma_2)_{\alpha\gamma}\ a^\dagger_{j\gamma}\right)\end{aligned} \quad (150)$$

create singlet and triplet pairs with electrons located at sites i and j respectively. In real space, it is thus quite clear that an antiferromagnetic interaction $J_{ij} > 0$ induces attraction in the singlet channel, and repulsion in the triplet channel. Returning to momentum space, substitution of equation (148) into (145) gives

$$H_{\rm int} = -\sum_{\mathbf{k},\mathbf{k}',\mathbf{q}} J(\mathbf{k}-\mathbf{k}')\left[3\Psi^\dagger_{\mathbf{k},\ \mathbf{q}}\Psi_{\mathbf{k}',\ \mathbf{q}} - \vec{\Psi}^\dagger_{\mathbf{k},\ \mathbf{q}}\cdot\vec{\Psi}_{\mathbf{k}',\ \mathbf{q}}\right] \quad (151)$$

where $\Psi^\dagger_{\mathbf{k},\mathbf{q}} = \frac{1}{2}\left(a^\dagger_{\mathbf{k}+\mathbf{q}/2\ \alpha}(-i\sigma_2)_{\alpha\gamma}\ a^\dagger_{-\mathbf{k}-\mathbf{q}/2\ \gamma}\right)$ and $\vec{\Psi}^\dagger_{\mathbf{k},\mathbf{q}} = \frac{1}{2}\left(a^\dagger_{\mathbf{k}+\mathbf{q}/2\ \alpha}(-i\vec{\sigma}\sigma_2)_{\alpha\gamma}\ a^\dagger_{-\mathbf{k}-\mathbf{q}/2\ \gamma}\right)$ create singlet and triplet pairs at momentum $\mathbf{q}$ respectively. Pair condensation is described by the zero momentum component of this interaction, which gives

$$H_{\rm int} = \sum_{\mathbf{k},\mathbf{k}'}\left[V^{(s)}_{\mathbf{k},\mathbf{k}'}\Psi^\dagger_{\mathbf{k}}\Psi_{\mathbf{k}'} + V^{(t)}_{\mathbf{k},\mathbf{k}'}\vec{\Psi}^\dagger_{\mathbf{k}}\cdot\vec{\Psi}_{\mathbf{k}'}\right] \quad (152)$$

where $\Psi^\dagger_{\mathbf{k}} = \frac{1}{2}\left(a^\dagger_{\mathbf{k}\alpha}(-i\sigma_2)_{\alpha\beta}\ a^\dagger_{-\mathbf{k}\beta}\right)$ and $\vec{\Psi}^\dagger_{\mathbf{k},\mathbf{q}} = \frac{1}{2}\left(a^\dagger_{\mathbf{k}\alpha}(-i\vec{\sigma}\sigma_2)_{\alpha\beta}\ a^\dagger_{-\mathbf{k}\beta}\right)$ create Cooper pairs and

$$\begin{aligned}V^{(s)}_{\mathbf{k},\mathbf{k}'} &= -3[J(\mathbf{k}-\mathbf{k}') + J(\mathbf{k}+\mathbf{k}')]/2\\ V^{(t)}_{\mathbf{k},\mathbf{k}'} &= \ [J(\mathbf{k}-\mathbf{k}') - J(\mathbf{k}+\mathbf{k}')]/2\end{aligned} \quad (153)$$

are the BCS pairing potentials in the singlet and triplet channel, respectively. (Notice how the even/odd-parity symmetry of the triplet pairs pulls out the corresponding symmetrization of $J(\mathbf{k}-\mathbf{k}')$.)

For a given choice of $J(\mathbf{q})$, it now becomes possible to decouple the interaction in singlet and triplet channels. For example, on a cubic lattice of side length, if the magnetic interaction has the form

$$J(\mathbf{q}) = 2J(\cos(q_x a) + \cos(q_y a) + \cos(q_z a)) \quad (154)$$

which generates soft antiferromagnetic fluctuations at the staggered $\mathbf{Q}$ vector $\mathbf{Q} = (\pi/a, \pi/a, \pi/a)$, then the pairing interaction can be decoupled into singlet and triplet components,

$$\begin{aligned}V^s_{\mathbf{k},\mathbf{k}'} &= -\frac{3J}{2}\big[s(\mathbf{k})s(\mathbf{k}') + \mathrm{d}_{x^2-y^2}(\mathbf{k})\mathrm{d}_{x^2-y^2}(\mathbf{k}')\\ &\qquad + \mathrm{d}_{2z^2-r^2}(\mathbf{k})\mathrm{d}_{2z^2-r^2}(\mathbf{k}')\big]\\ V^t_{\mathbf{k},\mathbf{k}'} &= \frac{J}{2}\sum_{i=x,y,z} p_i(\mathbf{k})\,p_i(\mathbf{k}')\end{aligned} \quad (155)$$

where

$$\begin{aligned}s(\mathbf{k}) &= \sqrt{\tfrac{2}{3}}(\cos(k_x a)\\ &\quad + \cos(k_y a) + \cos(k_z a)) \qquad \text{(extended s-wave)}\\ \left.\begin{aligned}\mathrm{d}_{x^2-y^2}(\mathbf{k}) &= (\cos(k_x a) - \cos(k_y a)\\ \mathrm{d}_{2z^2-r^2}(\mathbf{k}) &= \tfrac{1}{\sqrt{3}}(\cos(k_x a)\\ &\quad + \cos(k_y a) - 2\cos(k_z a))\end{aligned}\right\} &\text{(d-wave)}\end{aligned} \quad (156)$$

are the gap functions for singlet pairing and

$$p_i(\mathbf{q}) = \sqrt{2}\sin(q_i a), \quad (i = x, y, z), \quad \text{(p-wave)} \quad (157)$$

describe three triplet gap functions. For $J > 0$, this particular BCS model then gives rise to extended s- and d-wave superconductivity with approximately the same transition temperatures, given by the gap equation

$$\sum_{\mathbf{k}} \tanh\left(\frac{\epsilon_{\mathbf{k}}}{2T_c}\right)\frac{1}{\epsilon_{\mathbf{k}}}\begin{Bmatrix} s(\mathbf{k})^2 \\ \mathrm{d}_{x^2-y^2}(\mathbf{k})^2 \end{Bmatrix} = \frac{2}{3J} \quad (158)$$

4.3.2 Toward a unified theory of HFSC

Although the spin-fluctuation approach described provides a good starting point for the phenomenology of heavy-fermion superconductivity (HFSC), it leaves open a wide range of questions that suggest this problem is only partially solved:

- How can we reconcile heavy-fermion superconductivity with the local moment origins of the heavy-electron quasiparticles?
- How can the incompressibility of the heavy-electron fluid be incorporated into the theory? In particular, extended s-wave solutions are expected to produce a large singlet f-pairing amplitude, giving rise to a large Coulomb energy. Interactions are expected to significantly depress, if not totally eliminate such extended s-wave solutions.
- Is there a controlled limit where a model of heavy-electron superconductivity can be solved?
- What about the 'strange' HFSCs UBe_{13}, $CeCoIn_5$, and $PuCoGa_5$, where T_c is comparable with the Kondo temperature? In this case, the superconducting order parameter must involve the f spin as a kind of 'composite' order parameter. What is the nature of this order parameter, and what physics drives T_c so high that the Fermi liquid forms at much the same time as the superconductivity develops?

One idea that may help understand the heavy-fermion pairing mechanism is Anderson's RVB theory (Anderson, 1987) of high-temperature superconductivity. Anderson proposed (Anderson, 1987; Baskaran, Zou and Anderson, 1987; Kotliar, 1988) that the parent state of the high-temperature superconductors is a two-dimensional spin liquid of RVBs between spins, which becomes superconducting upon doping with holes. In the early 1990s, Coleman and Andrei (1989) adapted this theory to a Kondo lattice. Although an RVB spin liquid is unstable with respect to the antiferromagnetic order in three dimensions, in situations close to a magnetic instability, where the energy of the antiferromagnetic state is comparable with the Kondo temperature, $E_{\rm AFM} \sim T_{\rm K}$, conduction electrons partially spin-compensate the spin liquid, stabilizing it against magnetism (Figure 30a). In the Kondo-stabilized spin liquid, the Kondo effect induces some RVBs in the f-spin liquid to escape into the conduction fluid where they pair charged electrons to form a heavy-electron superconductor.

A key observation of the RVB theory is that, when charge fluctuations are removed to form a spin fluid, there is no distinction between particle and hole (Affleck, Zou, Hsu and Anderson, 1988). The mathematical consequence of this is that the the spin-1/2 operator

$$\vec{S}_f = f^\dagger_{i\alpha}\left(\frac{\vec{\sigma}}{2}\right)_{\alpha\beta} f^\dagger_\alpha, \qquad n_f = 1 \tag{159}$$

is not only invariant under a change of phase $f_\sigma \to e^{i\phi} f_\sigma$, but it also possesses a continuous particle-hole symmetry

$$f^\dagger_\sigma \to \cos\theta\, f^\dagger_\sigma + \mathrm{sgn}\sigma \sin\theta\, f_{-\sigma} \tag{160}$$

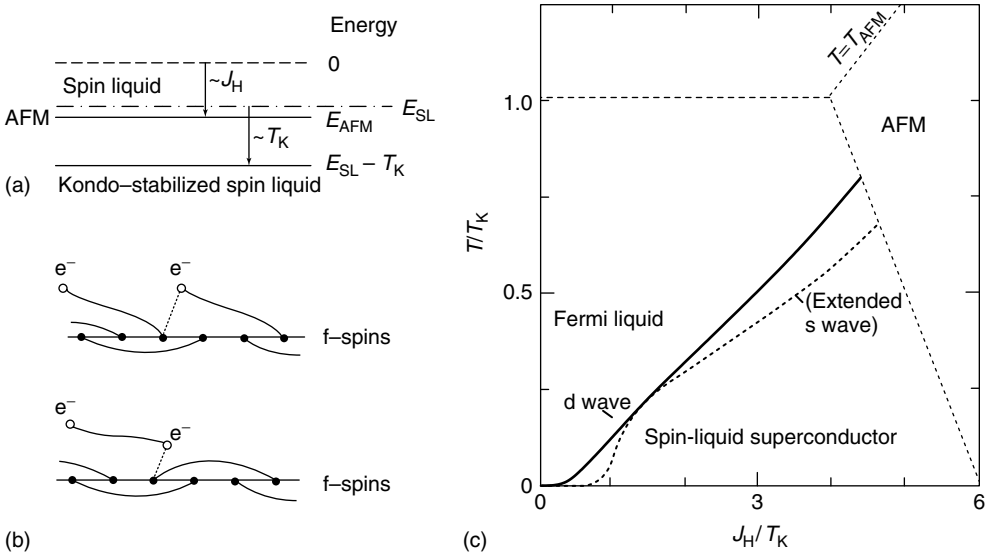

Figure 30. Kondo-stabilized spin liquid, diagram from Coleman and Andrei (1989). (a) Spin liquid stabilized by Kondo effect, (b) Kondo effect causes singlet bonds to form between spin liquid and conduction sea. Escape of these bonds into the conduction sea induces superconductivity. (c) Phase diagram computed using $SU(2)$ mean-field theory of Kondo Heisenberg model. (Reproduced from P. Coleman and N. Andrei, 1989, *J. Phys. Cond. Matt. C* **1** (1989) 4057, with permission of IOP Publishing Ltd.)

These two symmetries combine to create a *local* $SU(2)$ *gauge symmetry*. One of the implications is that the constraint $n_f = 1$ associated with the spin operator is actually part of a triplet of Gutzwiller constraints

$$f^\dagger_{i\uparrow} f_{i\uparrow} - f_{i\downarrow} f^\dagger_{i\downarrow} = 0, \quad f^\dagger_{i\uparrow} f^\dagger_{i\downarrow} = 0, \quad f_{i\downarrow} f_{i\uparrow} = 0 \tag{161}$$

If we introduce the Nambu spinors

$$\tilde{f}_i \equiv \begin{pmatrix} f_{i\uparrow} \\ f^\dagger_{i\downarrow} \end{pmatrix}, \qquad \tilde{f}^\dagger_i = (f^\dagger_{i\uparrow}, f_{i\downarrow}) \tag{162}$$

then this means that all three components of the 'isospin' of the f electrons vanish,

$$\tilde{f}^\dagger_i \vec{\tau} \tilde{f}_i = (f^\dagger_{i\uparrow}, f_{i\downarrow}) \left[\begin{pmatrix} 0 & 1 \\ 1 & 0 \end{pmatrix}, \begin{pmatrix} 0 & -i \\ i & 0 \end{pmatrix}, \begin{pmatrix} 1 & 0 \\ 0 & -1 \end{pmatrix} \right] \times \begin{pmatrix} f_{i\uparrow} \\ f^\dagger_{i\downarrow} \end{pmatrix} = 0 \tag{163}$$

where $\vec{\tau}$ is a triplet of Pauli spin operators that act on the f-Nambu spinors. In other words, in the incompressible f fluid, there can be no *s-wave* singlet pairing.

This symmetry is preserved in spin-1/2 Kondo models. When applied to the Heisenberg Kondo model

$$H = \sum_{\mathbf{k}\sigma} \epsilon_{\mathbf{k}} c^\dagger_{\mathbf{k}\sigma} c_{\mathbf{k}\sigma} + J_H \sum_{(i,j)} \mathbf{S}_i \cdot \mathbf{S}_j + J_K \sum_j c^\dagger_{j\sigma} \vec{\sigma}_{\sigma\sigma'} c_{j\sigma'} \cdot \mathbf{S}_j \tag{164}$$

where $\mathbf{S}_i = f^\dagger_{i\alpha} \left(\frac{\vec{\sigma}}{2}\right)_{\alpha\beta} f_{i\beta}$ represents an f spin at site i, it leads to an $SU(2)$ gauge theory for the Kondo lattice with Hamiltonian

$$H = \sum_{\mathbf{k}} \epsilon_{\mathbf{k}} \tilde{c}^\dagger_{\mathbf{k}} \tau_3 \tilde{c}_{\mathbf{k}} + \sum \vec{\lambda}_j \tilde{f}^\dagger_j \vec{\tau} \tilde{f}_j + \sum_{(i,j)} [\tilde{f}^\dagger_i U_{ij} \tilde{f}_j + \text{H.c}] + \frac{1}{J_\text{H}} \text{Tr}[U^\dagger_{ij} U_{ij}] + \sum_i [\tilde{f}^\dagger_i V_i \tilde{c}_i + \text{H.c}] + \frac{1}{J_\text{K}} \text{Tr}[V^\dagger_i V_i] \tag{165}$$

where λ_j is the Lagrange multiplier that imposes the Gutzwiller constraint $\vec{\tau} = 0$ at each site, $\tilde{c}_k = \begin{pmatrix} c_{k\uparrow} \\ c^\dagger_{-k\downarrow} \end{pmatrix}$ and $\tilde{c}_j = \begin{pmatrix} c_{j\uparrow} \\ c^\dagger_{j\downarrow} \end{pmatrix}$ are Nambu conduction electron spinors in the momentum and position basis, respectively, while

$$U_{ij} = \begin{pmatrix} h_{ij} & \Delta_{ij} \\ \overline{\Delta}_{ij} & -\overline{h}_{ij} \end{pmatrix} \qquad V_i = \begin{pmatrix} V_i & \overline{\alpha}_i \\ \alpha_i & -\overline{V}_i \end{pmatrix} \tag{166}$$

are matrix order parameters associated with the Heisenberg and Kondo decoupling, respectively. This model has the local gauge invariance $\tilde{f}_j \to g_j \tilde{f}_j$, $V_j \to g_j V_j$ $U_{ij} \to g_i U_{ij} g^\dagger_j$, where g_j is an $SU(2)$ matrix. In this kind of model, one can 'gauge fix' the model so that the Kondo effect occurs in the particle-hole channel ($\alpha_i = 0$). When one does so, however, the spin-liquid instability takes place preferentially in an anisotropically paired Cooper channel. Moreover, the constraint on the f electrons not only suppresses singlet s-wave pairing, it also suppresses extended s-wave pairing (Figure 30).

One of the initial difficulties with both the RVB and the Kondo-stabilized spin liquid approaches is that, in its original formulation, it could not be integrated into a large N approach. Recent work indicates that both the fermionic RVB and the Kondo-stabilized spin-liquid picture can be formulated as a controlled $SU(2)$ gauge theory by carrying out a large N expansion using the group $SP(N)$ (Read and Sachdev, 1991), originally introduced by Read and Sachdev for problems in frustrated magnetism, in place of the group $SU(N)$. The local particle-hole symmetry associated with the spin operators in $SU(2)$ is intimately related to the symplectic property of Pauli spin operators

$$\sigma_2 \vec{\sigma}^T \sigma_2 = -\vec{\sigma} \tag{167}$$

where $\vec{\sigma}^T$ is the transpose of the spin operator. This relation, which represents the sign reversal of spin operators under time-reversal, is only satisfied by a subset of the $SU(N)$ spins for $N > 2$. This subset defines the generators of the symplectic subgroup of $SU(N)$, called $SP(N)$.

Concluding this section, I want to briefly mention the challenge posed by the highest T_c superconductor, $PuCoGa_5$ (Sarrao *et al.*, 2002; Curro *et al.*, 2005). This material, discovered some 4 years ago at Los Alamos, undergoes a direct transition from a Curie paramagnet into a heavy-electron superconductor at around $T_c = 19\,\text{K}$ (Figure 31). The Curie paramagnetism is also seen in the Knight shift, which scales with the bulk susceptibility (Curro *et al.*, 2005). The remarkable feature of this material is that the specific heat anomaly has the large size ($110\,\text{mJ}\,\text{mol}^{-1}\,\text{K}^2$ (Sarrao *et al.*, 2002)) characteristic of heavy-fermion superconductivity, yet there are no signs of saturation in the susceptibility as a precursor to superconductivity, suggesting that the heavy quasiparticles do not develop from local moments until the transition. This aspect of the physics cannot be explained by the spin-fluctuation theory (Bang, Balatsky, Wastin and Thompson, 2004), and suggests that the Kondo effect takes place simultaneously with the pairing mechanism. One interesting possibility here is that the development of coherence between the Kondo effect in two different channels created by the different symmetries of the valence fluctuations into the f^6 and f^4 states might be the driver of this intriguing new superconductor (Jarrell, Pang and Cox, 1997; Coleman, Tsvelik, Andrei and Kee, 1999).

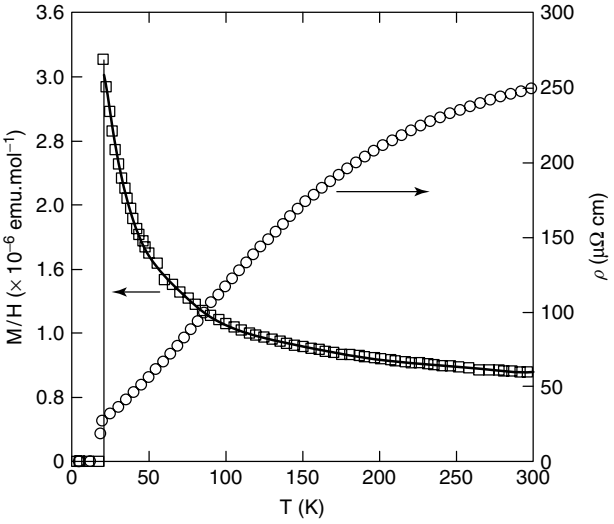

Figure 31. Temperature dependence of the magnetic susceptibility of $PuCoGa_5$. (After Sarrao *et al.*, 2002.) The susceptibility shows a direct transition from Curie–Weiss paramagnet into HFSC, without any intermediate spin quenching. (Reproduced from Sarrao, J.L., L.A. Morales, J.D. Thompson, B.L. Scott, G.R. Stewart, F. Wastlin, J. Rebizant, P. Boulet, E. Colineau, and G.H. Lander, 2002, with permission from Nature Publishing. © 2002.)

5 QUANTUM CRITICALITY

5.1 Singularity in the phase diagram

Many heavy electron systems can be tuned, with pressure, chemical doping, or applied magnetic field, to a point where their antiferromagnetic ordering temperature is driven continuously to zero to produce a 'QCP' (Stewart, 2001, 2006; Coleman, Pépin, Si and Ramazashvili, 2001; Varma, Nussinov and van Saarlos, 2002; von Löhneysen, Rosch, Vojta and Wolfe, 2007; Miranda and Dobrosavljevic, 2005). The remarkable transformation in metallic properties, often referred to as 'non-Fermi liquid behavior', which is induced over a wide range of temperatures above the QCP, together with the marked tendency to develop superconductivity in the vicinity of such 'quantum critical points' has given rise to a resurgence of interest in heavy-fermion materials.

The experimental realization of quantum criticality returns us to central questions left unanswered since the first discovery of heavy-fermion compounds. In particular:

- What is the fate of the Landau quasiparticle when interactions become so large that the ground state is no longer adiabatically connected to a noninteracting system?
- What is the mechanism by which the AFM transforms into the heavy-electron state? Is there a breakdown of the Kondo effect, revealing local moments at the quantum phase transition, or is the transition better regarded as a spin-density wave transition?

Figure 32 illustrates quantum criticality in $YbRh_2Si_2$ (Custers *et al.*, 2003), a material with a 90 mK magnetic transition that can be tuned continuously to zero by a modest magnetic

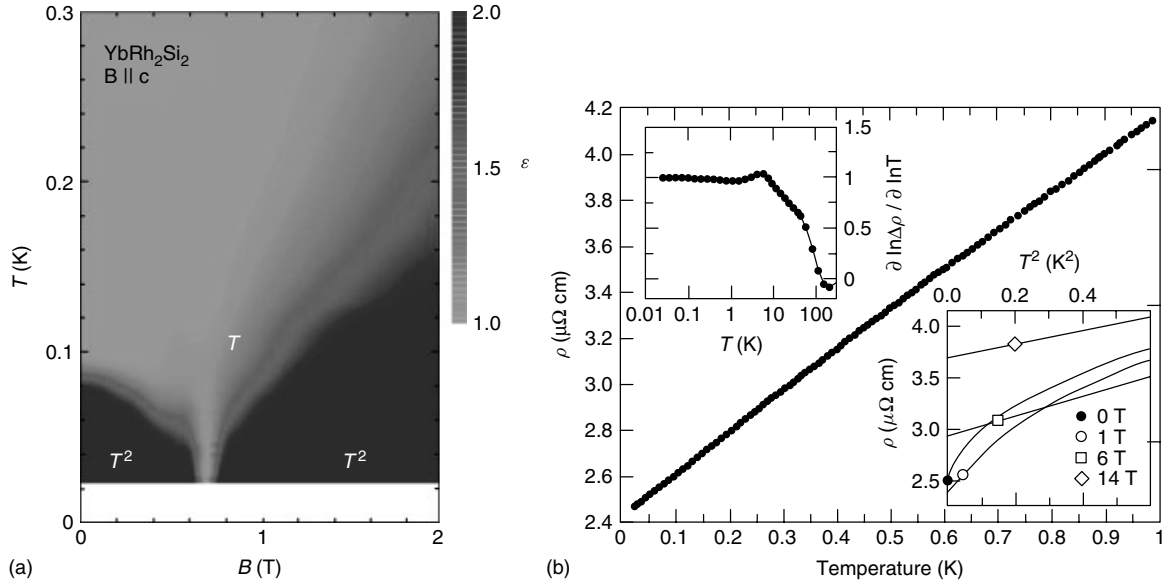

Figure 32. (a) Grayscale plot of the logarithmic derivative of resistivity $d\ln\rho/d\ln T$. (Reproduced from Custers *et al.*, 2003, with permission from Nature Publishing. © 2003.) (b) Resistivity of $YbRh_2Si_2$ in zero magnetic field. Inset shows logarithmic derivative of resistivity. (Reproduced from O. Trovarelli, C. Geibel, S. Mederle, C. Langhammer, F. Grosche, P. Gegenwart, M. Lang, G. Sparn, and F. Steglich, *Phys. Rev. Lett.* **85**, 2000, 626, copyright © 2000 by the American Physical Society, with permission of the APS.)

field. In wedge-shaped regions, either side of the transition, the resistivity displays the T^2 dependence $\rho(T) = \rho_0 + AT^2$ (black) that is the hallmark of Fermi-liquid behavior. Yet, in a tornado shaped region that stretches far above the QCP to about 20 K, the resistivity follows a *linear* dependence over more than three decades. The QCP thus represents a kind of 'singularity' in the material phase diagram.

Experimentally, quantum critical heavy-electron materials fall between two extreme limits that I shall call 'hard' and 'soft' quantum criticality. 'Soft' quantum critical systems are moderately well described in terms quasiparticles interacting with the soft quantum spin fluctuations created by a spin-density wave instability. Theory predicts (Moriya and Kawabata, 1973) that, in a three-dimensional metal, the quantum spin-density wave fluctuations give rise to a weak $\sqrt{T}$ singularity in the low-temperature behavior of the specific heat coefficient

$$\frac{C_V}{T} = \gamma_0 - \gamma_1\sqrt{T} \tag{168}$$

Examples of such behavior include $CeNi_2Ge_2$ (Grosche *et al*., 2000; Küchler *et al*., 2003) chemically doped $Ce_{2-x}La_xRu_2Si_2$ and 'A'-type antiferromagnetic phases of $CeCu_2Si_2$ at a pressure-tuned QCP.

At the other extreme, in 'hard' quantum critical heavy materials, many aspects of the physics appear consistent with a breakdown of the Kondo effect associated with a relocalization of the f electrons into ordered, ordered local moments beyond the QCP. Some of the most heavily studied examples of this behavior occur in the chemically tuned QCP in $CeCu_{6-x}Au_x$ (von Löhneysen *et al*., 1994; von Löhneysen, 1996; Schroeder *et al*., 1998, 2000). and $YbRh_2Si_{2-x}Ge_x$ (Custers *et al*., 2003; Gegenwart *et al*., 2005) and the field-tuned QCP of $YbRh_2Si_2$ (Trovarelli *et al*., 2000) and YbAgGe (Bud'ko, Morosan and Canfield, 2004, 2005; Fak *et al*., 2005; Niklowitz *et al*., 2006). Hallmarks of hard quantum criticality include a logarithmically diverging specific heat coefficient at the QCP,

$$\frac{C_v}{T} \sim \frac{1}{T_0}\ln\left(\frac{T_0}{T}\right) \tag{169}$$

and a quasilinear resistivity

$$\rho(T) \sim T^{1+\eta} \tag{170}$$

where η is in the range 0–0.2. The most impressive results to date have been observed at field-tuned QCPs in $YbRh_2Si_2$ and $CeCoIn_5$, where linear resistivity has been seen to extend over more than two decades of temperature at the field-tuned QCP (Steglich *et al*., 1976; Paglione *et al*., 2003, 2006; Ronning *et al*., 2006). Over the range where linear, where the ratio between the change in the size of the resistivity $\Delta\rho$ to the zero temperature (impurity driven) resistivity ρ_0

$$\Delta\rho/\rho_0 \gg 1 \tag{171}$$

$CeCoIn_5$ is particularly interesting, for, in this case, this resistance ratio exceeds 10^2 for current flow along the c axis (Tanatar, Paglione, Petrovic and Taillefer, 2007). This observation excludes any explanation which attributes the unusual resistivity to an interplay between spin-fluctuation scattering and impurity scattering (Rosch, 1999). Mysteriously, $CeCoIn_5$ also exhibits a $T^{3/2}$ resistivity for resistivity for current flow in the basal plane below about 2 K (Tanatar, Paglione, Petrovic and Taillefer, 2007). Nakasuji, Pines and Fisk (2004) have proposed that this kind of behavior may derive from a *two fluid* character to the underlying conduction fluid.

In quantum critical $YbRh_2Si_{2-x}Ge_x$, the specific heat coefficient develops a $1/T^{1/3}$ divergence at the very lowest temperature. In the approach to a QCP, Fermi liquid behavior is confined to an ever-narrowing range of temperature. Moreover, both the linear coefficient of the specific heat and the the quadratic coefficient A of the resistivity appear to diverge (Estrela *et al*., 2002; Trovarelli *et al*., 2000). Taken together, these results suggests that the Fermi temperature renormalizes to zero and the quasiparticle effective masses diverge

$$T_F^* \to 0 \qquad \frac{m^*}{m} \to \infty \tag{172}$$

at the QCP of these three-dimensional materials. A central property of the Landau quasiparticle is the existence of a finite overlap 'Z', or 'wave function renormalization' between a single quasiparticle state, denoted by $|\mathrm{qp}^-\rangle$ and a bare electron state denoted by $|e^-\rangle = c^\dagger_{\mathbf{k}\sigma}|0\rangle$,

$$Z = |\langle e^-|\mathrm{qp}^-\rangle|^2 \sim \frac{m}{m^*} \tag{173}$$

If the quasiparticle mass diverges, the overlap between the quasiparticle and the electron state from which it is derived is driven to zero, signaling a complete breakdown in the quasiparticle concept at a 'hard' QCP (Varma, Nussinov and van Saarlos, 2002).

Table 3 shows a tabulation of selected quantum critical materials. One interesting variable that exhibits singular behavior at both hard and soft QCPs is the Grüneisen ratio. This quantity, defined as the ratio

$$\Gamma = \frac{\alpha}{C} = -\frac{1}{V}\left.\frac{\partial \ln T}{\partial P}\right|_S \propto \frac{1}{T^\epsilon} \tag{174}$$

Table 3. Selected heavy-fermion compounds with quantum critical points.

	Compound	x_c/H_c	$\frac{C_v}{T}$	$\rho \sim T^a$	$\Gamma(T) = \frac{\alpha}{C_P}$	Other	References
	$CeCu_{6-x}Au_x$	$x_c = 0.1$	$\frac{1}{T_0}\ln\left(\frac{T_0}{T}\right)$	$T + c$	–	$\chi''_{\mathbf{Q}_0}(\omega, T) = \frac{1}{T^{0.7}}F\left[\frac{\omega}{T}\right]$	von Löhneysen *et al*. (1994), von Löhneysen (1996) and Schroeder *et al*. (1998, 2000)
Hard	$YbRh_2Si_2$	$B_{c\|\|} = 0.66\,\mathrm{T}$	–	T	–	Jump in Hall constant	Trovarelli *et al*. (2000) and Paschen *et al*. (2004)
	$YbRh_2Si_{2-x}Ge_x$	$x_c = 0.1$	$\frac{1}{T^{1/3}} \leftrightarrow \frac{1}{T_0}\ln\left(\frac{T_0}{T}\right)$	T	$T^{-0.7}$	–	Custers *et al*. (2003) and Gegenwart *et al*. (2005)
	YbAgGe	$B_{c\|} = 9T$ $B_{c\perp} = 5T$	$\frac{1}{T_0}\ln\left(\frac{T_0}{T}\right)$	T	–	NFL over range of fields	Bud'ko, Morosan and Canfield (2004), Fak *et al*. (2005) and Niklowitz *et al*. (2006)
Soft	$CeCoIn_5$	$B_c = 5\,\mathrm{T}$	$\frac{1}{T_0}\ln\left(\frac{T_0}{T}\right)$	$T/T^{1.5}$	–	$\rho_c \propto T$, $\rho_{ab} \propto T^{1.5}$	Paglione *et al*. (2003, 2006), Ronning *et al*. (2006) and Tanatar, Paglione, Petrovic and Taillefer (2007)
	$CeNi_2Ge_2$	$P_c = 0$	$\gamma_0 - \gamma_1\sqrt{T}$	$T^{1.2-1.5}$	T^{-1}	–	Grosche *et al*. (2000) and Küchler *et al*. (2003)

of the thermal expansion coefficient $\alpha = \frac{1}{V}\frac{\mathrm{d}V}{\mathrm{d}T}$ to the specific heat C, diverges at a QCP. The Grüneisen ratio is a sensitive measure of the rapid acquisition of entropy on warming away from QCP. Theory predicts that $\epsilon = 1$ at a 3D spin density wave critical point, as seen in $CeNi_2Ge_2$. In the 'hard' quantum critical material $YbRh_2Si_{2-x}Ge_x$, $\epsilon = 0.7$ indicates a serious departure from a 3D spin-density wave instability (Küchler *et al*., 2003).

5.2 Quantum versus classical criticality

Figure 33 illustrates some key distinctions between classical and quantum criticality (Sachdev, 2007). Passage through a classical second-order phase transition is achieved by tuning the temperature. Near the transition, the imminent arrival of order is signaled by the growth of droplets of nascent order whose typical size ξ diverges at the critical point. Inside each droplet, fluctuations of the order parameter exhibit a universal power-law dependence on distance

$$\langle \psi(x)\psi(0)\rangle \sim \frac{1}{x^{d-2+\eta}}, \qquad (x \ll \xi) \tag{175}$$

Critical matter 'forgets' about its microscopic origins: Its thermodynamics, scaling laws, and correlation exponents associated with critical matter are so robust and universal that they recur in such diverse contexts as the Curie point of iron or the critical point of water. At a conventional

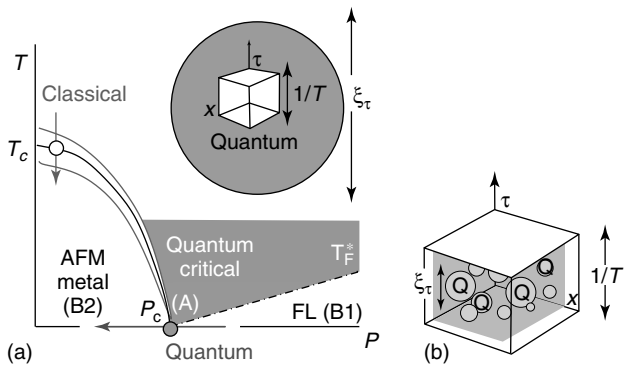

Figure 33. Contrasting classical and quantum criticality in heavy-electron systems. At a QCP, an external parameter P, such as pressure or magnetic field, replaces temperature as the 'tuning parameter'. Temperature assumes the new role of a finite size cutoff $l_\tau \propto 1/T$ on the temporal extent of quantum fluctuations. (a) Quantum critical regime, where $l_\tau < \xi_{\mathrm{tau}}$ probes the interior of the quantum critical matter. (b) Fermi-liquid regime, where $l_\tau > \xi_\tau$, where like soda, bubbles of quantum critical matter fleetingly form within a Fermi liquid that is paramagnetic (B1), or antiferromagnetically ordered (B2).

critical point, order-parameter fluctuations are 'classical', for the characteristic energy of the critical modes $\hbar\omega(q_0)$, evaluated at a wave vector $q_0 \sim \xi^{-1}$, inevitably drops below the thermal energy $\hbar\omega(q_0) \ll k_B T_c$ as $\xi \to \infty$.

In the 1970s, various authors, notably Young (1975) and Hertz (1976), recognized that, if the transition temperature of a continuous phase transition can be depressed to zero, the

critical modes become quantum-mechanical in nature. The partition function for a quantum phase transition is described by a Feynman integral over order-parameter configurations $\{\psi(x,\tau)\}$ in both space *and* imaginary time (Sachdev, 2007; Hertz, 1976)

$$Z_{\text{quantum}} = \sum_{\text{space–time configurations}} \mathrm{e}^{-S[\psi]} \tag{176}$$

where the action

$$S[\psi] = \int_0^{\frac{\hbar}{k_B T}} \mathrm{d}\tau \int_{-\infty}^{\infty} \mathrm{d}^d x L[\psi(x,\tau)] \tag{177}$$

contains an integral of the Lagrangian L over an infinite range in space, but a *finite* time interval

$$l_\tau \equiv \frac{\hbar}{k_{\mathrm{B}} T} \tag{178}$$

Near a QCP, bubbles of quantum critical matter form within a metal, with finite size ξ_x and duration ξ_τ (Figure 33). These two quantities diverge as the quantum critical point is approached, but the rates of divergence are related by a dynamical critical exponent (Hertz, 1976),

$$\xi_\tau \sim (\xi_x)^z \tag{179}$$

One of the consequences of this scaling behavior is that time counts as z spatial dimensions, $[\tau] = [L^z]$ in general.

At a classical critical point, temperature is a tuning parameter that takes one through the transition. The role of temperature is fundamentally different at a quantum critical point: it sets the scale $l_\tau \sim 1/T$ in the time direction, introducing a *finite size correction* to the QCP. When the temperature is raised, l_τ reduces and the quantum fluctuations are probed on shorter and shorter timescales. There are then two regimes to the phase diagram,

$$\text{(a)} \qquad \text{Quantum critical:} \qquad l_\tau \ll \xi_\tau \tag{180}$$

where the physics probes the 'interior' of the quantum critical bubbles, and

$$\text{(b)} \qquad \text{Fermi liquid/AFM} \qquad l_\tau \gg \xi_\tau \tag{181}$$

where the physics probes the quantum fluid 'outside' the quantum critical bubbles. The quantum fluid that forms in this region is a sort of 'quantum soda', containing short-lived bubbles of quantum critical matter surrounded by a paramagnetic (B1) or antiferromagnetically ordered (B2) Landau–Fermi liquid. Unlike a classical phase transition, in which the critical fluctuations are confined to a narrow region either side of the transition, in a quantum critical region (a), fluctuations persist up to temperatures where l_τ becomes comparable the with the microscopic short-time cutoff in the problem (Kopp and Chakravarty, 2005) (which for heavy-electron systems is most likely, the single-ion Kondo temperature $l_\tau \sim \hbar/T_{\mathrm{K}}$).

5.3 Signs of a new universality

The discovery of quantum criticality in heavy-electron systems raises an alluring possibility of *quantum critical matter*, a universal state of matter that, like its classical counterpart, forgets its microscopic, chemical, and electronic origins. There are three pieces of evidence that are particularly fascinating in this respect:

1. Scale invariance, as characterized by E/T scaling in the quantum-critical inelastic spin fluctuations observed in $CeCu_{1-x}Au_x$ (Schroeder *et al.*, 1998, 2000). ($x = x_c = 0.016$),

$$\chi''_{\mathbf{Q}_0}(E,T) = \frac{1}{T^a} F(E/T) \tag{182}$$

   where $a \approx 0.75$ and $F[x] \propto (1 - ix)^{-a}$. Similar behavior has also been seen in powder samples of $UCu_{5-x}Pd_x$ (Aronson *et al.*, 1995).
2. A jump in the Hall constant of $YbRh_2Si_2$ when field tuned through its QCP (Paschen *et al.*, 2004). (see Figure 34a).
3. A sudden change in the area of the extremal Fermi surface orbits observed by de Haas van Alphen at a pressure-tuned QCP in $CeRhin_5$ (Shishido, Settai, Harima and Onuki, 2005). (see Figure 34b).

Features 2 and 3 suggest that the Fermi surface jumps from a 'small' to 'large' Fermi surface as the magnetic order is lost, as if the phase shift associated with the Kondo effect collapses to zero at the critical point, as if the f component of the electron fluid Mott-localizes at the transition. To reconcile a sudden change in the Fermi surface with a second-order phase transition, we are actually forced to infer that the quasiparticle weights vanish at the QCP.

These features are quite incompatible with a spin-density wave QCP. In a spin-density wave scenario, the Fermi surface and Hall constant are expected to evolve continuously through a QCP. Moreover, in an SDW description, the dynamical critical exponent is $z = 2$ so time counts as $z = 2$ dimensions in the scaling theory, and the effective dimensionality $D_{\text{eff}} = d + 2 > 4$ lies above the upper critical dimension, where mean-field theory is applicable and scale-invariant behavior is no longer expected.

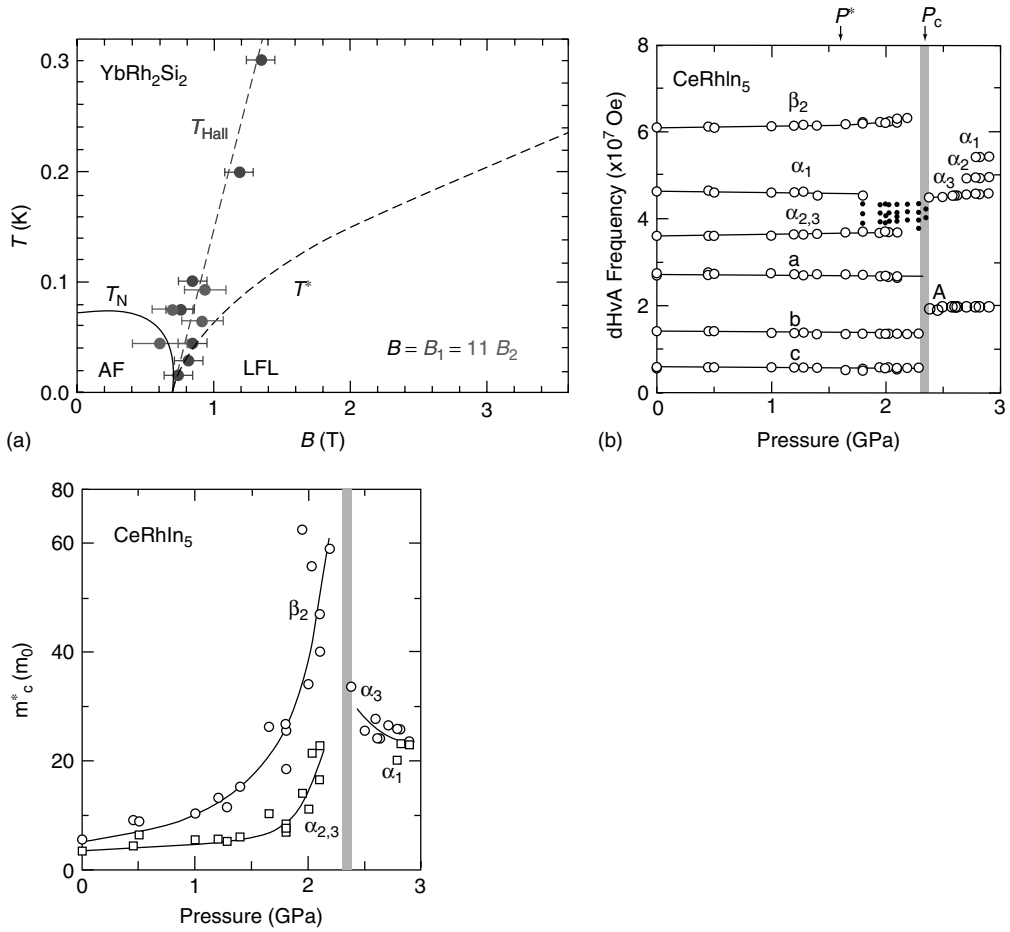

Figure 34. (a) Hall crossover line for sudden evolution of Hall constant in $YbRh_2Si_2$. (Reproduced from Paschen, S., T. Lühmann, S. Wirth, P. Gegenwart, O. Trovarelli, C. Geibel, F. Steglich, P. Coleman, and Q. Si, 2004, *Nature* **432**, 881.) (b) Sudden change in dHvA frequencies and divergence of quasiparticle effective masses at pressure-tuned, finite field QCP in $CeRhIn_5$. (Reproduced from H. Shishido, R. Settai, H. Harima, and Y. Onuki, *Journal of the Physical Society of Japan* **74**, 2005, 1103 weith permission of the Physical Society of Japan.)

These observations have ignited a ferment of theoretical interest in the nature of heavy-fermion criticality. We conclude with a brief discussion of some of the competing ideas currently under consideration.

5.3.1 Local quantum criticality

One of the intriguing observations (Schroeder *et al*., 1998) in $CeCu_{6-x}Au_x$ is that the uniform magnetic susceptibility, $\chi^{-1} \sim T^a + C$, $a = 0.75$ displays the same power-law dependence on temperature observed in the inelastic neutron scattering at the critical wave vector $\mathbf{Q}_0$. A more detailed set of measurements by Schroeder *et al*. (2000) revealed that the scale-invariant component of the dynamical spin susceptibility appears to be momentum independent,

$$\chi^{-1}(\mathbf{q}, E) = T^a[\Phi(E/T)] + \chi_0^{-1}(\mathbf{q}) \tag{183}$$

This behavior suggests that the critical behavior associated with the heavy-fermion QCP contains some kind of *local* critical excitation (Schroeder *et al*., 1998; Coleman, 1999).

One possibility is that this local critical excitation is the spin itself, so that (Coleman, 1999; Sachdev and Ye, 1993; Sengupta, 2000)

$$\langle S(\tau)S(\tau')\rangle = \frac{1}{(\tau - \tau')^{2-\epsilon}} \tag{184}$$

is a power law, but where $\epsilon \neq 0$ signals non-Fermi liquid behavior. This is the basis of the 'local quantum criticality' theory developed by Smith and Si (2000) and Si, Rabello, Ingersent and Smith (2001, 2003). This theory requires that the local spin susceptibility $\chi_{\rm loc} = \sum_{\mathbf{q}} \chi(\mathbf{q}, \omega)_{\omega=0}$ diverges at a heavy-fermion QCP. Using an extension of the methods of DMFT (Georges, Kotliar, Krauth and Rozenberg, 1996; Kotliar *et al*., 2006) Si *et al*. find that it is possible to account

for the local scaling form of the dynamical susceptibility, obtaining exponents that are consistent with the observed properties of $CeCu_{6-x}Au_x$ (Grempel and Si, 2003).

However, there are some significant difficulties with this theory. First, as a local theory, the quantum critical fixed point of this model is expected to possess a finite zero-point entropy per spin, a feature that is, to date, inconsistent with thermodynamic measurements (Custers *et al*., 2003). Second, the requirement of a divergence in the local spin susceptibility imposes the requirement that the surrounding spin fluid behaves as layers of decoupled two-dimensional spin fluids. By expanding $\chi_0^{-1}(\mathbf{q})$ (183) about the critical wave vector $\mathbf{Q}$, one finds that the singular temperature dependence in the local susceptibility is given by

$$\chi_{\rm loc}(T) \sim \int \mathrm{d}^d q \frac{1}{(\mathbf{q}-\mathbf{Q})^2 + T^\alpha} \sim T^{(d-2)\alpha/2} \qquad (185)$$

requiring that $d \leq 2$.

In my judgement, the validity of the original scaling by Schroeder *et al* still stands and that these difficulties stem from a misidentification of the critical local modes driving the scaling seen by neutrons. One possibility, for example, is that the right soft variables are not spin *per se*, but the fluctuations of the phase shift associated with the Kondo effect. This might open up the way to an alternative formulation of local criticality.

5.3.2 *Quasiparticle fractionalization and deconfined criticality*

One of the competing sets of ideas under consideration at present is the idea that, in the process of localizing into an ordered magnetic moment, the composite heavy electron breaks up into constituent spin and charge components. In general,

$$e_\sigma^- \rightleftharpoons s_\sigma + h^- \qquad (186)$$

where s_σ represents a neutral spin-1/2 excitation or 'spinon'. This has led to proposals (Coleman, Pépin, Si and Ramazashvili, 2001; Senthil, Vojta, Sachdev and Vojta, 2003; Pépin, 2005) that gapless spinons develop at the QCP. This idea is faced with a conundrum, for, even if free neutral spin-1/2 excitations can exist at the QCP, they must surely be confined as one tunes away from this point, back into the Fermi liquid. According to the model of 'deconfined criticality' proposed by Senthil *et al*. (2004), the spinon confinement scale ξ_2 introduces a second diverging length scale to the phase transition, where ξ_2 diverges more rapidly to infinity than ξ_1. One possible realization of this proposal is the quantum melting of two-dimensional $S = 1/2$ Heisenberg AFM, where the smaller correlation length ξ_1 is associated with the transition from AFM to spin liquid, and the second correlation length ξ_2 is associated with the confinement of spinons to form a valence bond solid (Figure 35).

It is not yet clear how this scenario will play out for heavy electron systems. Senthil, Sachdev and Vojta (2005) have proposed that, in a heavy-electron system, the intermediate spin liquid state may involve a Fermi surface of neutral (fermionic) spinons coexisting with a small Fermi surface of conduction electrons, which they call an FL* state. In this scenario, the QCP involves an instability of the heavy-electron fluid to the FL* state, which is subsequently unstable to antiferromagnetism. Recent work suggests that the Hall constant can indeed jump at such a transition (Coleman, Marston and Schofield, 2005b).

5.3.3 *Schwinger bosons*

A final approach to quantum criticality, currently under development, attempts to forge a kind of 'spherical model' for the antiferromagnetic QCP through the use of a large N expansion in which the spin is described by Schwinger bosons, rather than fermions (Arovas and Auerbach, 1988; Parcollet and Georges, 1997),

$$S_{ab} = b_a^\dagger b_b - \delta_{ab}\frac{n_b}{N} \qquad (187)$$

where the spin S of the moment is determined by the constraint $n_b = 2S$ on the total number of bosons per site. Schwinger bosons are well suited to describe low-dimensional magnetism (Arovas and Auerbach, 1988). However, unlike fermions, only one boson can enter a Kondo

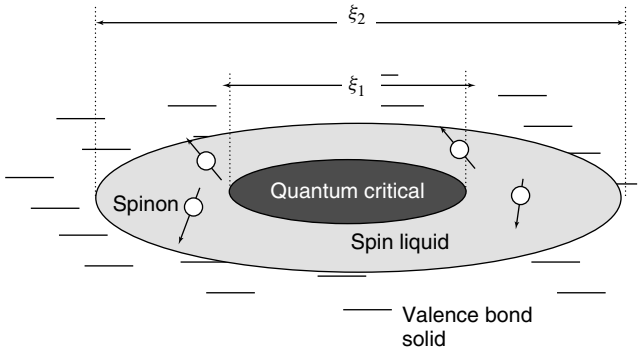

Figure 35. 'Deconfined criticality' (Senthil *et al*., 2004). The quantum critical droplet is defined by two divergent length scales - ξ_1 governing the spin correlation length, ξ_2 on which the spinons confine, in the case of the Heisenberg model, to form a valence bond solid. (Adapted using data from T. Senthil, A. Vishwanath, L. Balents, S. Sachdev and M.P.A. Fisher, *Science* **303** (2004) 1490.)

singlet. To obtain an energy that grows with N, Parcollet and Georges proposed a new class of large N expansion based around the multichannel Kondo model with K channels (Cox and Ruckenstein, 1993; Parcollet and Georges, 1997), where $k = K/N$ is kept fixed. The Kondo interaction takes the form

$$H_{\rm int} = \frac{J_K}{N} \sum_{\nu=1,K,\alpha,\beta} S_{\alpha\beta} c^\dagger_{\nu\beta\mu} c_{\nu\alpha} \qquad (188)$$

where the channel index ν runs from one to K. When written in terms of Schwinger bosons, this interaction can be factorized in terms of a charged, but spinless exchange fermion χ_ν ('holon') as follows:

$$H_{\rm int} \to \sum_{\nu\alpha} \frac{1}{\sqrt{N}} \left[(c^\dagger_{\nu\alpha} b_\alpha) \chi^\dagger_\nu + {\rm H.c} \right] + \sum_\nu \frac{\chi^\dagger_\nu \chi_\nu}{J_K} \qquad (189)$$

Parcollet and Georges originally used this method to study the overscreened Kondo model (Parcollet and Georges, 1997), where $K > 2S$.

Recently, it has proved possible to find the Fermi liquid large N solutions to the fully screened Kondo impurity model, where the number of channels is commensurate with the number of bosons ($K = 2S$) (Rech, Coleman, Parcollet and Zarand, 2006; Lebanon and Coleman, 2007). One of the intriguing features of these solutions is the presence of a gap for spinon excitations, roughly comparable with the Kondo temperature. Once antiferromagnetic interactions are introduced, the spinons pair-condense, forming a state with a *large* Fermi surface, but one that coexists with gapped spinon (and holon) excitations (Coleman, Paul and Rech, 2005a).

The gauge symmetry associated with these particles guarantees that, if the gap for the spinon goes to zero continuously, then the gap for the holon must also go to zero. This raises the possibility that gapless charge degrees of freedom may develop at the very same time as magnetism (Figure 36). In the two impurity model, Rech *et al.* have recently shown that the large N solution contains a 'Jones–Varma' QCP where a static valence bond forms

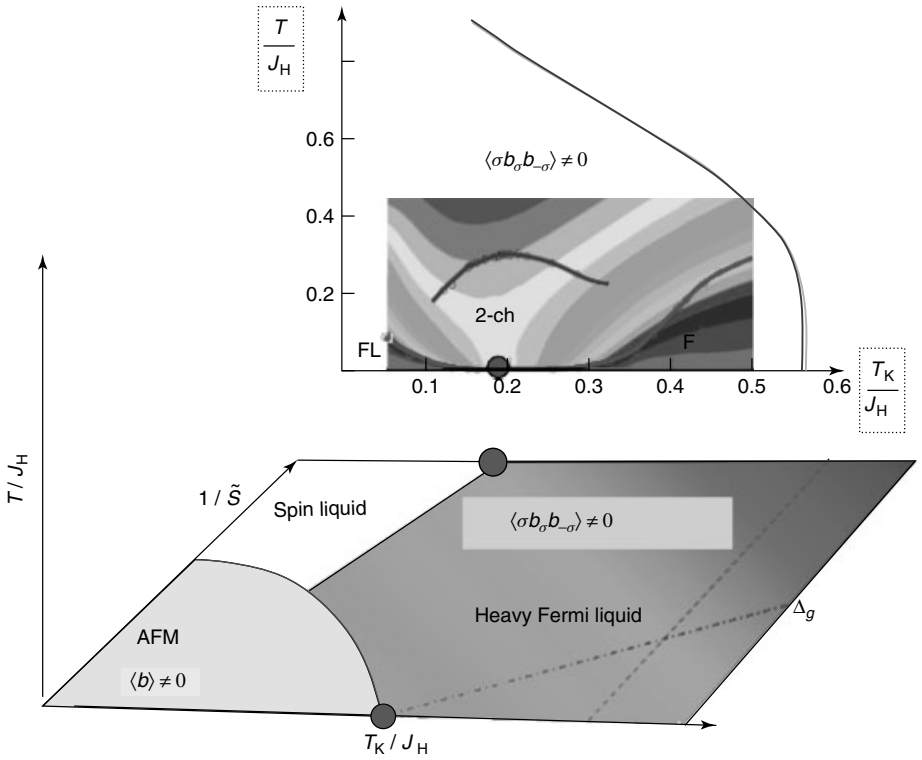

Figure 36. Proposed phase diagram for the large N limit of the two impurity and Kondo lattice models. Background – the two impurity model, showing contours of constant entropy as a function of temperature and the ratio of the Kondo temperature to Heisenberg coupling constant. (Reproduced from Rech, J., P. Coleman, O. Parcollet, and G. Zarand, 2006, *Phys. Rev. Lett* **96**, 016601.) Foreground – proposed phase diagram of the fully screened, multichannel Kondo lattice, where $\tilde{S}$ is the spin of the impurity. At small $\tilde{S}$, there is a phase transition between a spin liquid and heavy-electron phase. At large $\tilde{S}$, a phase transition between the AFM and heavy-electron phase. If this phase transition is continuous in the large N limit, then both the spinon and holon gap are likely to close at the QCP. (Reproduced from Lebanon, E., and P. Coleman, 2007, Fermi liquid identities for the Infinite U Anderson Model, *Phys. Rev. B* (submitted), URL http://arxiv.org/abs/cond-mat/0610027.)

between the Kondo impurities. At this point, the holon and spinon excitations become gapless. On the basis of this result, Lebanon, Rech, Coleman and Parcollet (2006) have recently proposed that the holon spectrum may become gapless at the magnetic QCP (Figure 36) in three dimensions.

6 CONCLUSIONS AND OPEN QUESTIONS

I shall end this chapter with a brief list of open questions in the theory of heavy fermions.

1. To what extent does the mass enhancement in heavy-electron materials owe its size to the vicinity to a nearby quantum phase transitions?
2. What is the microscopic origin of heavy-fermion superconductivity and in theextreme cases UBe_{13} and $PuCoGa_5$ how does the pairing relate to both spin quenching and the Kondo effect?
3. What is the origin of the linear resistivity and the logarithmic divergence of the specific heat at a 'hard' heavy-electron QCP?
4. What happens to magnetic interactions in a Kondo insulator, and why do they appear to vanish?
5. In what new ways can the physics of heavy-electron systems be interfaced with the tremendous current developments in mesoscopics? The Kondo effect is by now a well-established feature of Coulomb blockaded quantum dots (Kouwenhoven and Glazman, 2001), but there may be many other ways in which we can learn about local moment physics from mesoscopic experiments. Is it possible, for example, to observe voltage-driven quantum phase transitions in a mesoscopic heavy-electron wire? This is an area grown with potential.

It should be evident that I believe there is tremendous prospect for concrete progress on many of these issues in the near future. I hope that, in some ways, I have whet your appetite enough to encourage you also to try your hand at their future solution.

NOTES

[1] To calculate the matrix elements associated with valence fluctuations, take

$$|f^1c^1\rangle = \frac{1}{\sqrt{2}}(f^\dagger_\uparrow c^\dagger_\downarrow - c^\dagger_\uparrow f^\dagger_\downarrow)|0\rangle,$$
$$|f^2\rangle = f^\dagger_\uparrow f^\dagger_\downarrow|0\rangle \qquad \text{and} \qquad |c^2\rangle = c^\dagger_\uparrow c^\dagger_\downarrow|0\rangle$$

then $\langle c^2|\sum_\sigma V c^\dagger_\sigma f_\sigma|f^1c^1\rangle = \sqrt{2}V$ and $\langle f^2|\sum_\sigma V f^\dagger_\sigma c_\sigma |f^1c^1\rangle = \sqrt{2}V$

[2] The f-sum rule is a statement about the instantaneous, or short-time diamagnetic response of the metal. At short times $\mathrm{d}j/\mathrm{d}t = (n_c e^2/m)E$, so the high-frequency limit of the conductivity is $\sigma(\omega) = \frac{ne^2}{m}\frac{1}{\delta - i\omega}$. But using the Kramer's Krönig relation

$$\sigma(\omega) = \int \frac{\mathrm{d}x}{i\pi}\frac{\sigma(x)}{x - \omega - i\delta}$$

at large frequencies,

$$\omega(\omega) = \frac{1}{\delta - i\omega}\int \frac{\mathrm{d}x}{\pi}\sigma(x)$$

so that the short-time diamagnetic response implies the f-sum rule.

[3] To prove this identity, first note that any two-dimensional matrix, M, can be expanded as $M = m_0\sigma_2 + \vec{m}\cdot\sigma_2\vec{\sigma}$, $(b = (1, 3))$ where $m_0 = \frac{1}{2}\mathrm{Tr}[M\sigma_2]$ and $\vec{m} = \frac{1}{2}\mathrm{Tr}[M\vec{\sigma}\sigma_2]$, so that in index notation

$$M_{\alpha\gamma} = \frac{1}{2}\mathrm{Tr}[M\sigma_2](\sigma_2)_{\alpha\gamma} + \frac{1}{2}\mathrm{Tr}[M\vec{\sigma}\sigma_2]\cdot(\sigma_2\vec{\sigma})_{\alpha\gamma}$$

Now, if we apply this relationship to the $\alpha\gamma$ components of $\vec{\sigma}_{\alpha\beta}\cdot\vec{\sigma}_{\gamma\delta}$, we obtain

$$\vec{\sigma}_{\alpha\beta}\cdot\vec{\sigma}_{\gamma\delta} = \frac{1}{2}\left(\vec{\sigma}^T\sigma_2\vec{\sigma}\right)_{\delta\beta}(\sigma_2)_{\alpha\gamma} + \frac{1}{2}\sum_{b=1,3}\left(\vec{\sigma}^T\sigma_2\sigma_b\,\vec{\sigma}\right)_{\delta\beta}(\sigma_2\sigma_b)_{\alpha\gamma}$$

If we now use the relation $\vec{\sigma}^T\sigma_2 = -\sigma_2\vec{\sigma}$, together with $\vec{\sigma}\cdot\vec{\sigma} = 3$ and $\vec{\sigma}\sigma_b\vec{\sigma} = -\sigma_b$, we obtain

$$\vec{\sigma}_{\alpha\beta}\cdot\vec{\sigma}_{\gamma\delta} = -\frac{3}{2}(\sigma_2)_{\alpha\gamma}(\sigma_2)_{\delta\beta} + \frac{1}{2}(\vec{\sigma}\sigma_2)_{\alpha\gamma}\cdot(\sigma_2\vec{\sigma})_{\delta\beta}$$

ACKNOWLEDGMENTS

This research was supported by the National Science Foundation grant DMR-0312495. I would like to thank E. Lebanon and T. Senthil for discussions related to this work. I would also like to thank the Aspen Center for Physics, where part of the work for this chapter was carried out.

REFERENCES

Abrikosov, A.A. (1965). Electron scattering on magnetic impurities in metals and anomalous resistivity effects. *Physics*, **2**, 5.

Aeppli, G. and Fisk, Z. (1992). Kondo insulators. *Comments on Condensed Matter Physics*, **16**, 155.

Aeppli, G., Goldman, A., Shirane, G., *et al*. (1987). Development of antiferromagnetic correlations in the heavy-fermion system UPt_3. *Physical Review Letters*, **58**, 808.

Affleck, I., Zou, Z., Hsu, T. and Anderson, P.W. (1988). SU(2) gauge symmetry of the large-U limit of the Hubbard model. *Physical Review B*, **8**, 745.

Alekseev, P.A., Klement'ev, E.S., Lazukov, V., *et al*. (1994). 4f electrons and the formation of the ground state in the Kondo insulator CeNiSn. *JETP*, **79**, 665.

Allen, J.W., Oh, S.J., Maple, M.B. and Torikachvili, M.S. (1983). Large Fermi-level resonance in the electron-addition spectrum of $CeRu_2$ and $CeIr_2$. *Physical Review*, **28**, 5347.

Allen, J.W., Oh, S.J., Cox, L.E., *et al*. (1985). Spectroscopic evidence for the 5f coulomb interaction in UAl_2 and UPt_3. *Physical Review Letters*, **2635**, 54.

Allen, J., Oh, S., Gunnarsson, O., *et al*. (1986). Electronic structure of cerium and light rare-earth intermetallics. *Advances in Physics*, **35**, 275.

Anderson, P.W. (1961). Localized magnetic states in metals. *Physical Review*, **124**, 41.

Anderson, P.W. (1970). Poor Man's derivaton of scaling laws for the Kondo problem. *Journal of Physics C*, **3**, 2346.

Anderson, P.W. (1973). Kondo Effect IV: out of the wilderness. *Comments on Solid State Physics*, **5**, 73.

Anderson, P.W. (1981). Conference summary. In *Valence Fluctuations in Solids*, Falicov, L.M., Hanke, W. and Maple, M.P. (Eds.), North Holland: Amsterdam, p. 451.

Anderson, P.W. (1987). The resonating valence bond state in La_2CuO_4 and superconductivity. *Science*, **235**, 1196.

Anderson, P.W. and Yuval, G. (1969). Exact results in the Kondo problem: equivalence to a classical one-dimensional coulomb gas. *Physical Review Letters*, **45**, 370.

Anderson, P.W. and Yuval, G. (1970). Exact results for the Kondo problem: one-body theory and extension to finite temperature. *Physical Review B*, **1**, 1522.

Anderson, P.W. and Yuval, G. (1971). Some numerical results on the Kondo problem and the inverse square one-dimensional Ising model. *Journal of Physics C*, **4**, 607.

Andrei, N., Furuya, K. and Lowenstein, J. (1983). Solution of the Kondo problem. *Reviews of Modern Physics*, **55**, 331–402.

Andres, K., Graebner, J. and Ott, H.R. (1975). 4f-virtual-bound-state formation in $CeAl_3$ at low temperatures. *Physical Review Letters*, **35**, 1779.

Aoki, H., Sakahibara, T., Shishido, H., *et al*. (2004). Field-angle dependence of the zero-energy density of states in the unconventional heavy-fermion superconductor $CeCoIn_5$. *Journal of Physics: Condensed Matter*, **16**, L13–L19.

Aronson, M., Osborn, R., Robinson, R., *et al*. (1995). Non-Fermi-liquid scaling of the magnetic response in $UCu_{5-x}Pd_x$ ($x = 1, 1.5$). *Physical Review Letters*, **75**, 725.

Arovas, D. and Auerbach, A. (1988). Functional integral theories of low-dimensional quantum Heisenberg models. *Physical Review B*, **38**, 316.

Auerbach, A. and Levin, K. (1986). Kondo bosons and the Kondo lattice: microscopic basis for the heavy Fermi liquid. *Physical Review Letters*, **57**, 877.

Bang, Y., Balatsky, A.V., Wastin, F. and Thompson, J.D. (2004). Possible pairing mechanisms of $PuCoGa_5$ superconductor. *Physical Review*, **70**, 104512.

Barnes, S.E. (1976). New method for the Anderson model. *Journal of Physics*, **F 6**, 1375.

Baskaran, G., Zou, Z. and Anderson, P.W. (1987). The resonating valence bond state and high-T_c superconductivity- a mean field theory. *Solid State Communications*, **63**, 973.

Bauer, E., Michor, G.H.H., Paul, C., *et al*. (2004). Heavy fermion superconductivity and magnetic order in noncentrosymmetric $CePt_3Si$. *Physical Review Letters*, **92**, 027003.

Baym, G. and Pethick, C. (1992). *Landau Fermi-Liquid Theory*, Wiley: New York.

Berlin, T.H. and Kac, M. (1952). The spherical model of a ferromagnet. *Physical Review*, **86**, 821.

Beyerman, W.P., Gruner, G., Dlicheouch, Y. and Maple, M.B. (1988). Frequency-dependent transport properties of UPt_3. *Physical Review B*, **37**, 10353.

Bishop, D.J., Varma, C.M., Batlogg, B., *et al*. (1984). Ultrasonic Attenuation in UPt_3. *Physical Review Letters*, **53**(10), 1009.

Blandin, A. and Friedel, J. (1958). *Journal de Physique et le Radium*, **20**, 160 (1959).

Blount, E.I., Varma, C.M. and Aeppli, G. (1990). Phase diagram of the heavy-fermion superconductor UPt_3. *Physical Review Letters*, **64**, 3074.

Broholm, C., Aeppli, G., Kleiman, R.N., *et al*. (1990). Kondo insulators. *Physical Review Letters*, **65**, 2062.

Bucher, B., Schlessinger, Z., Canfield, P.C. and Fisk, Z. (1994). Charge dynamics in the Kondo insulator Ce_3Bi_4Pt. *Physical Review Letters*, **72**, 522.

Bucher, B., Schlessinger, Z., Mandrus, D., *et al*. (1995). Charge dynamics of Ce-based compounds: connection between the mixed valent and Kondo-insulator states. *Physical Review B*, **53**, R2948.

Bucher, E., Maita, J.P., Hull, G.W., *et al*. (1975). Electronic properties of beryllides of the rare earth and some actinides. *Physical Review B*, **11**, 440.

Bud'ko, S.L., Morosan, E. and Canfield, P.C. (2004). Magnetic field induced non-Fermi-liquid behavior in YbAgGe single crystals. *Physical Review B*, **69**, 014415.

Bud'ko, S.L., Zapf, V., Morosan, E. and Canfield, P.C. (2005). Field-dependent Hall effect in single-crystal heavy-fermion YbAgGe below 1 K. *Physical Review B*, **72**, 172413.

Bulla, R. (2006). Dynamical mean-field theory: from quantum impurity physics to lattice problems. *Philosophical Magazine*, **86**, 1877.

Burdin, S., Georges, A. and Grempel, D.R. (2000). Coherence scale of the Kondo lattice. *Physical Review Letters*, **85**, 1048.

Cardy, J. (1996). *Renormalization in Statistical Physics*, Cambridge University Press: Cambridge.

Clogston, A.M., Mathias, B.T., Peter, M., *et al*. (1962). Local magnetic moment associated with an iron atom dissolved in various transition metal alloys. *Physical Review*, **125**, 541.

Coleman, P. (1983). 1/N expansion for the Kondo lattice. *Physical Review*, **28**, 5255.

Coleman, P. (1984). New approach to the mixed-valence problem. *Physical Review*, **29**, 3035.

Coleman, P. (1987a). Constrained quasiparticles and conduction in heavy-fermion systems. *Physical Review B*, **35**, 5072.

Coleman, P. (1987b). Mixed valence as an almost broken symmetry. *Physical Review Letters*, **59**, 1026.

Coleman, P. (1999). Theories of non-Fermi liquid behavior in heavy fermions. *Physica B*, **259–261**, 353.

Coleman, P. and Andrei, N. (1989). Kondo-stabilized spin liquids and heavy fermion superconductivity. *Journal of Physics: Condensed Matter*, **C 1**, 4057.

Coleman, P., Tsvelik, A.M., Andrei, N. and Kee, H.Y. (1999). Cooperative Kondo effect in the two-channel Kondo lattice. *Physical Review*, **B60**, 3608.

Coleman, P., Pépin, C., Si, Q. and Ramazashvili, R. (2001). How do Fermi liquids get heavy and die?. *Journal of Physics: Condensed Matter*, **13**, 273.

Coleman, P., Paul, I. and Rech, J. (2005a). Sum rules and Ward identities in the Kondo lattice. *Physical Review B*, **72**, 094430.

Coleman, P., Marston, J.B. and Schofield, A.J. (2005b). Transport anomalies in a simplified model for a heavy-electron quantum critical point. *Physical Review*, **72**, 245111.

Coqblin, B. and Schrieffer, J.R. (1969). Exchange interaction in alloys with cerium impurities. *Physical Review*, **185**, 847.

Cox, D. and Grewe, N. (1988). Transport properties of the Anderson lattice. *Zeitschrift fur Physik B*, **71**, 273.

Cox, D. and Maple, M. (1995). Electronic pairing in exotic superconductors. *Physics Today*, **482**, 32.

Cox, D. and Zawadowski, A. (1999). *Exotic Kondo Effects in Metals*, CRC Press: Boca Raton.

Cox, D.L. and Ruckenstein, A.E. (1993). Spin-flavor separation and non-Fermi-liquid behavior in the multichannel Kondo problem: a large-N approach. *Physical Review Letters*, **71**((Sept.)), 1613–1616.

Curro, N.J., Caldwell, T., Bauer, E.D., *et al*. (2005). Unconventional superconductivity in $PuCoGa_5$. *Nature*, **434**, 622.

Custers, J., Gegenwart, P., Wilhelm, H., *et al*. (2003). The break-up of heavy electrons at a quantom critical point. *Nature*, **424**, 524.

de Haas, W.J., de Boer, J. and van der Berg, D. (1933). *Physica*, **1**, 1115.

Degiorgi, L. (1999). The electrodynamic response of heavy-electron compounds. *Reviews of Modern Physics*, **71**, 687.

Degiorgi, L., Anders, F., Gruner, G. and Society, E.P. (2001). Charge excitations in heavy electron metals. *Journal B*, **19**, 167.

DiTusa, J.F., Friemelt, K., Bucher, E., *et al*. (1997). Metal-insulator transitions in the Kondo insulator FeSi and classic semiconductors are similar. *Physical Review Letters*, **831**, 78.

Doniach, S. (1977). Kondo lattice and weak antiferromagnetism. *Physica B*, **91**, 231.

Dordevic, S.V., Basov, D.N., Dilley, N.R., *et al*. (2001). Hybridization gap in 16 heavy fermion compounds. *Physical Review Letters*, **86**, 684.

Engelbrecht, J. and Bedell, K. (1995). Robustness of a local Fermi liquid against ferromagnetism and phase separation. *Physical Review Letters*, **74**, 4265.

Estrela, P., de Visser, A., Naka, T., *et al*. (2002). Resistivity of non-Fermi liquid UPtIn under pressure. *Physica B*, **312–313**, 482.

Fak, B., McMorrow, D.F., Niklowitz, P.G., *et al*. (2005). An inelastic neutron scattering study of single-crystal heavy-fermion YbAgGe. *Journal of Physics: Condensed Matter*, **17**, 301.

Flouquet, J. (2005). *On the Heavy Fermion Road*, http://www.citebase.org/abstract?id=oai:arXiv.org:cond-mat/05 01602.

Fowler, M. and Zawadowskii, A. (1971). Scaling and the renormalization group in the Kondo effect. *Solid State Communications*, **9**, 471.

Fulde, P., Keller, J. and Zwicknagl, G. (1988). Theory of heavy fermion systems. *Solid State Physics*, **41**, 1.

Gegenwart, P., Custers, J., Tokiwa, Y., *et al*. (2005). Ferromagnetic quantum critical fluctuations in $YbRh_2(Si_{0.95}Ge_{0.05})_2$. *Physical Review Letters*, **94**, 076402.

Geibel, C., Schank, C., Thies, S., *et al*. (1991a). Heavy-fermion superconductivity at $T_c = 2K$ in the antiferromagnet UPd_2Al_3. *Zeitschrift fur Physik B*, **84**, 1.

Geibel, C., Thies, S., Kacrowski, D., *et al*. (1991b). A new heavy-fermion superconductor: UNi_2Al_3. *Zeitschrift fur Physik B*, **83**, 305.

Georges, A. and Kotliar, G. (1992). Hubbard model in infinite dimensions. *Physical Review B*, **45**, 6479.

Georges, A., Kotliar, G., Krauth, W. and Rozenberg, M. (1996). Dynamical mean-field theory of strongly correlated fermion systems and the limit of infinite dimensions. *Reviews of Modern Physics*, **68**, 13–125.

Grempel, D.R. and Si, Q. (2003). Locally critical point in an anisotropic Kondo lattice. *Physical Review Letters*, **91**, 026401.

Grewe, N. and Steglich, F. (1991). Heavy Fermions. In *Handbook on the Physics and Chemistry of Rare Earths*, Gschneider, K.A. and Eyring, L. (Eds.), Elsevier: Amsterdam, p. 343, Vol. 14.

Grosche, F.M., Agarwal, P., Julian, S.R., *et al*. (2000). Anomalous low temperature states in $CeNi_2Ge_2$ and $CePd_2Si_2$. *Journal of Physics: Condensed Matter*, **12**, L533.

Gruner, G. and Zawadowski, A. (1974). Magnetic impurities in non-magnetic metals. *Reports on Progress in Physics*, **37**, 1497.

Gunnarsson, O. and Schönhammer, K. (1983). Electron spectroscopies for Ce compounds in the impurity model. *Physical Review B*, **28**, 4315.

Haldane, F.D.M. (1978). Scaling theory of the asymmetric anderson model. *Physical Review Letters*, **40**, 416.

Hertz, J.A. (1976). Quantum critical phenomena. *Physical Review B*, **14**, 1165.

Hess, D.W., Tokuyasu, T.A and Sauls, J.A. (1990). Vortex states in an unconventional superconductor and the mixed phases of UPt_3. *Physical Review B*, **41**, 8891.

Hewson, A.C. (1993). *The Kondo Problem to Heavy Fermions*, Cambridge University Press: Cambridge.

Hirsch, J.E. (1985). Attractive interaction and pairing in fermion systems with strong on-site repulsion. *Physical Review Letters*, **54**, 1317.

Hundley, M.F., Canfield, P.C., Thompson, J.D., *et al*. (1990). Hybridization gap in $Ce_3Bi_4Pt_3$. *Physical Review B*, **42**, 6842.

Iga, F., Kasaya, M. and Kasuya, T. (1988). Specific heat measurements of YbB_{12} and $Yb_xLu_{1-x}B_{12}$. *Journal of Magnetism and Magnetic Materials*, **76–77**, 156.

Ikeda, H. and Miyake, K. (1996). A theory of anisotropic semiconductor of heavy fermions. *Journal of the Physical Society of Japan*, **65**, 1769.

Izawa, K., Suzuki, T., Fujita, T., *et al*. (1999). Metallic ground state of CeNiSn. *Physical Review*, **59**, 2599.

Isawa, K., Goryo, Y.N.J., Matsuda, Y., *et al*. (2003). Multiple Superconducting Phases in New Heavy Fermion Superconductor $PrOs_4Sb)_{12}$. *Physical Review Letters*, **90**, 117001.

Jaccarino, V., Wertheim, G.K., Wernick, J.H., *et al*. (1967). Paramagnetic excited state of FeSi. *Physical Review*, **160**, 476.

Jarrell, M. (1995). Symmetric periodic Anderson model in infinite dimensions. *Physical Review B*, **51**, 7429.

Jarrell, M., Pang, H. and Cox, D.L. (1997). Phase diagram of the two-channel Kondo lattice. *Physical Review Letters*, **78**, 1996.

Jones, B.A. (2007). Kondo effect. In *Handbook of Magnetism and Advanced Magnetic Materials*, Kronmüller, H. and Parkin, S. (Eds.), John Wiley & Sons: Chichester, Vol. 1.

Joynt, R. (1988). Phase diagram of d-wave superconductors in a magnetic field. *Speculations in Science and Technology*, **1**, 210.

Julian, S.R., Teunissen, P.A.A. and Wiegers, S.A.J. (1992). Fermi surface of UPt_3 from 3 to 30 T: field-induced quasiparticle band polarization and the metamagnetic transition. *Physical Review B*, **46**, 9821.

Kadowaki, K. and Woods, S. (1986). Universal relationship of the resistivity and specific heat in heavy-fermion compounds. *Solid State Communications*, **58**, 507.

Kagan, Y., Kikoin, K. and Prokof'ev, N. (1993). Nature of the pseudogap in the energy spectrum of CeNiSn. *JETP Letters*, **57**, 600.

Kasuya, T. (1956). Indirect exchange coupling of nuclear magnetic moments by conduction electrons. *Progress of Theoretical Physics*, **16**, 45.

Kim, K.H., Harrison, N., Jaime, M., *et al*. (2003). Magnetic-field-induced quantum critical point and competing order parameters in URu_2Si_2. *Physical Review Letters*, **91**, 256401.

Kimura, N., Komatsubara, T., Aoki, D., *et al*. (1998). Metamagnetic transition in UPt_3 studied by high-field magnetization and de Haas van Alphen experiments. *Journal of the Physical Society of Japan*, **67**, 2185.

Kondo, J. (1962). g-shift and anomalous Hall effect in gadolinium metals. *Progress of Theoretical Physics*, **28**, 772.

Kondo, J. (1964). Resistance minimum in dilute magnetic alloys. *Progress of Theoretical Physics*, **32**, 37.

Kopp, A. and Chakravarty, S. (2005). Criticality in correlated quantum matter. *Nature Physics*, **1**, 53.

Kotliar, G. (1988). Resonating valence bonds and d-wave superconductivity. *Physical Review B*, **37**, 3664.

Kotliar, G., Savrasov, S.Y., Haule, K., *et al*. (2006). Electronic structure calculations with dynamical mean-field theory. *Reviews of Modern Physics*, **78**, 865.

Kouwenhoven, L. and Glazman, L. (2001). Revival of the Kondo effect. *Physics World*, **14**, 33.

Küchler, R., Oeschler, N., Gegenwart, P., *et al*. (2003). Divergence of the Grüneisen ratio at quantum critical points in heavy fermion metals. *Physical Review Letters*, **91**, 066405.

Kuramoto, Y. and Watanabe, T. (1987). Theory of momentum-dependent magnetic response in heavy-fermion systems. *Physica B*, **148**, 80.

Lacroix, C. and Cyrot, M. (1979). Phase diagram of the kondo lattice. *Physical Review B*, **20**, 1969.

Landau, L. (1957). The theory of a Fermi liquid. *Soviet Physics JETP*, **3**, 920–925.

Langer, J.S. and Ambegaokar, V. (1961). Friedel sum rule for a system of interacting electrons. *Physical Review*, **121**, 1090.

Langreth, D. (1966). Friedel sum rule for Anderson's model of localized impurity states. *Physical Review*, **150**, 516.

Lebanon, E. and Coleman, P. (2007). Fermi liquid identities for the Infinite U Anderson Model, *Physical Review B*, in press, http://arxiv.org/abs/cond-mat/0610027.

Lebanon, E., Rech, J., Coleman, P. and Parcollet, O. (2006). Conserving many body approach to the infinite-U Anderson model. *Physical Review Letters*, **97**, 106604.

Lee, P.A., Rice, T.M., Serene, J.W., *et al*. (1986). Theories of heavy-electron systems. comments condens. *Comments on Condensed Matter Physics*, **12**, 99.

Liu, L.Z., Allen, J.W., Seaman, C.L., *et al*. (1992). Kondo resonance in $Y_{1-x}U_xPd_3$. *Physical Review Letters*, **68**, 1034.

Luttinger, J.M. (1960). Fermi surface and some simple equilibrium properties of a system of interacting fermions. *Physical Review*, **119**, 1153.

Luttinger, J.M. and Ward, J.C. (1960). Ground-state energy of a many-Fermion system. *Physical Review*, **118**, 1417.

Machida, K. and Ozaki, M. (1989). Unconventional superconducting class in a heavy Fermion system UPt_3. *Journal of the Physical Society of Japan*, **58**, 2244.

Maple, B., Fertig, W., Mota, A., *et al*. (1972). The re-entrant superconducting-normal phase boundary of the Kondo system $(La,Ce)Al_2$. *Solid State Communications*, **11**, 829.

Martin, R.M. (1982). Fermi-surface sum rule and its consequences for periodic Kondo and mixed-valence systems. *Physical Review Letters*, **48**, 362.

Mathur, N., Grosche, F.M., Julian, S.R., *et al*. (1998). Magnetically mediated superconductivity in heavy fermion compounds. *Nature*, **394**, 39.

McCollam, A., Julian, S.R., Rourke, P.M.C., *et al*. (2005). Anomalous de Haas van 19 Alphen oscillations in $CeCoIn_5$. *Physical Review Letters*, **94**, 186401.

Meisner, G.P., Torikachvili, M.S., Yang, K.N., *et al*. (1985). UFe_4P_{12} and $CeFe_4P_{12}$: nonmetallic isotypes of superconducting $LaFe_4P_{12}$. *Journal of Applied Physics*, **57**, 3073.

Mekata, M., Ito, S., Sato, N., *et al*. (1986). Spin fluctuations in dense Kondo alloys. *Journal of Magnetism and Magnetic Materials*, **54**, 433.

Menth, A., Buehler, E. and Geballe, T.H. (1969). Magnetic and semiconducting properties of SmB_6. *Physical Review Letters*, **22**, 295.

Metzner, W. and Vollhardt, D. (1989). Correlated lattice fermions in $d = \infty$ dimensions. *Physical Review Letters*, **62**, 324.

Millis, A.J. and Lee, P.A. (1987a). Large-orbital-degeneracy expansion for the lattice Anderson model. *Physical Review B*, **35**(7), 3394–3414.

Millis, A.J., Lavagna, M. and Lee, P.A. (1987b). Plasma oscillations in heavy-fermion materials. *Physical Review*, **36**, 864–867.

Miranda, E. and Dobrosavljevic, V. (2005). Disorder-driven non-Fermi liquid behaviour of correlated electrons. *Reports on Progress in Physics*, **68**, 2337.

Miyake, K., Rink, S.S. and Varma, C.M. (1986). pin-fluctuation-mediated even-parity pairing in heavy fermion superconductors. *Physical Review B*, **34**, 6554.

Monod, M.T.B., Bourbonnais, C. and Emery, V. (1986). Possible superconductivity in nearly antiferromagnetic itinerant fermion systems. *Physical Review B*, **34**, 7716.

Monthoux, P. and Lonzarich, G. (1999). p-wave and d-wave superconductivity in quasi-two-dimensional metals. *Physical Review B*, **59**, 14598.

Moreno, J. and Coleman, P. (2000). Gap-anisotropic model for the narrow-gap Kondo insulators. *Physical Review Letters*, **84**, 342.

Moriya, T. and Kawabata, J. (1973). Effect of spin fluctuations on itinerant electron ferromagnetism. *Journal of the Physical Society of Japan*, **34**, 639.

Nakamura, K., Kitaoka, Y., Asayama, K., *et al*. (1994). NMR investigation of energy gap formation in the valence fluctuating compound CeNiSn. *Journal of the Physical Society of Japan*, **63**, 433.

Nakasuji, S., Pines, D. and Fisk, Z. (2004). Two fluid description of the kondo lattice, *Physical Review Letters*, **92**, 16401–16404.

Niklowitz, P.G., Knebel, G., Flouquet, J., *et al*. (2006). Field-induced non-fermiliquid resistivity of stoichiometric YbAgGe single crystals. *Physical Review B*, **73**, 12501.

Norman, M.R. (2007). High-temperature superconductivity – magnetic mechanisms. In *Handbook of Magnetism and Advanced Magnetic Materials*, Kronmüller, H. and Parkin, S. (Eds.), John Wiley & Sons: Chichester, Vol. 5.

Norman, M.R., Oguchi, T. and Freeman, A.J. (1988). Magnetism in the heavy-electron superconductors UPt_3 and URu_2Si_2. *Physical Review*, **38**, 11193.

Nozières, P. (1976). A "Fermi Liquid" description of the Kondo problem at low tempertures. *Journal de Physique C*, **37**, 1.

Nozières, P. (1985). Magnetic impurities and Kondo effects. *Annales de Physique (Paris)*, **10**, 19–35.

Nozières, P. and Blandin, A. (1980). Kondo effect in real metals. *Journal de Physique*, **41**, 193.

Nozières, P. and Luttinger, J.M. (1962). Derivation of the landau theory of Fermi liquids. *Physical Review*, **127**, 1423.

Oguchi, T. and Freeman, A.J. (1985). Local density band approach to f-electron systems-heavy fermion superconductor UPt_3. *Journal of Magnetism and Magnetic Materials*, **52**, 174.

Okiji, A. and Kawakami, N. (1983). Thermodynamic properties of the Anderson model. *Physical Review Letters*, **50**, 1157.

Onuki, Y. and Komatsubara, T. (1987). Heavy fermion state $CeCu_6$. *Journal of Magnetism and Magnetic Materials*, **63–64**, 281.

Oshikawa, M. (2000). Topological approach to Luttinger's theorem and the Fermi surface of a Kondo lattice. *Physical Review Letters*, **84**, 3370.

Ott, H.R. (1987). Heavy Electron Materials. *Progress in Low Temp Physics*, Brewer, D.F. (ed.), North Holland: Amsterdam, p. 215 Vol. 11.

Ott, H.R., Rudigier, H., Fisk, Z. and Smith, J.L. (1983). UBe_{13}: an unconventional actinide superconductor. *Physical Review Letters*, **50**, 1595.

Ott, H.R., Rudigier, H., Rice, T.M., *et al*. (1984). p-wave superconductivity in UBe_{13}. *Physical Review Letters*, **52**, 1915.

Ott, H.R., Rudigier, H., Fisk, Z. and Smith, J.L. (1985). Superconducting Ground State of a Strongly Interacting Electron System: UBe_{13}. In *Valence Fluctuations in Solids*, Buyers, W.J.L. (Ed.), Plenum, p. 309; *Proceedings of the NATO Advanced Study Institute on Moment Formation in Solids*, Vancouver Island, August 1983.

Paglione, J., Tanatar, M.A., Hawthorn, D.G., *et al*. Field-induced quantum critical point in $CeCoIn_5$. (2003). *Physical Review Letters*, **91**, 246405.

Paglione, J., Tanatar, M.A., Hawthorn, D.G., *et al*. (2006). Nonvanishing energy scales at the quantum critical point of $CeCoIn_5$. *Physical Review Letters*, **97**, 106606.

Palstra, T.T.M., Menovsky, A.A., van den Berg, J., *et al*. (1985). Superconducting and magnetic transitions in the heavy-fermion system URu_2Si_2. *Physical Review Letters*, **55**, 2727.

Parcollet, O. and Georges, A. (1997). Transition from overscreening to underscreening in the multichannel Kondo model: exact solution at large N. *Physical Review Letters*, **79**, 4665.

Paschen, S., Lühmann, T., Wirth, S., *et al*. (2004). Hall-effect evolution across a heavy-fermion quantum critical point. *Nature*, **432**, 881.

Pépin, C. (2005). Fractionalization and Fermi-surface volume in heavy-fermion compounds: the case of $YbRh_2Si_2$. *Physical Review Letters*, **94**, 066402.

Petrovic, C., Pagliuso, P.G., Hundley, M.F., *et al*. (2001). Heavy-fermion superconductivity in $CeCoIn_5$ at 2.3 K. *Journal of Physics: Condensed Matter*, **13**, L337.

Pitaevskii, L.P. (1960). On the superfluidity of liquid He^3. *Zhurnal Eksperimentalnoi i Teoreticheskoi Fiziki*, **37**, 1794.

Puttika, W. and Joynt, R. (1988). Stability of anisotropic superconducting phases in UPt_3. *Physical Review B*, **37**, 2377.

Ramakrishnan, T.V. (1981). In *Valence Fluctuations in Solids*, Falicov, L.M., Hanke, W. and Maple, M.P. (Eds.), North Holland: Amsterdam, p. 13.

Read, N. and Newns, D.M. (1983a). A new functional integral formalism for the degenerate Anderson model. *Journal of Physics C*, **29**, L1055.

Read, N. and Newns, D.M. (1983b). On the solution of the Coqblin-Schreiffer Hamiltonian by the large-N expansion technique. *Journal of Physics C*, **16**, 3274.

Read, N. and Sachdev, S. (1991). Large-N expansion for frustrated quantum antiferromagnets. *Physical Review Letters*, **66**, 1773.

Rech, J., Coleman, P., Parcollet, O. and Zarand, G. (2006). Schwinger Boson approach to the fully screened Kondo model. *Physical Review Letters*, **96**, 016601.

Reinders, P.H.P., Springford, M., Coleridge, P.T., *et al*. (1986). de Haas-van Alphen effect in the heavy-electron compound $CeCu_6$. *Physical Review Letters*, **57**, 1631.

Riseborough, P. (2000). Heavy fermion semiconductors. *Advances in Physics*, **49**, 257.

Ronning, F., Capan, C., Bauer, E.D., *et al*. (2006). Pressure study of quantum criticality in $CeCoIn_5$. *Physical Review*, **73**, 064519.

Rosch, A. (1999). Interplay of disorder and spin fluctuations in the resistivity near a quantum critical point. *Physical Review Letters*, **82**, 4280.

Rozenberg, M.J., Kotliar, G. and Kajueter, H. (1996). Transfer of spectral weight in spectroscopies of correlated electron systems. *Physical Review B*, **54**, 8452.

Ruderman, M.A. and Kittel, C. (1954). Indirect exchange coupling of nuclear magnetic moments by conduction electrons. *Physical Review*, **96**, 99–102.

Sachdev, S. (2007). Quantum phase transitions. In *Handbook of Magnetism and Advanced Magnetic Materials*, Kronmüller, H. and Parkin, S. (Eds.), John Wiley & Sons: Chichester, Vol. 1.

Sachdev, S. and Ye, J. (1993). Gapless spin-fluid ground state in a random quantum Heisenberg magnet. *Physical Review Letters*, **70**, 3339.

Sarachik, M., Corenzwit, E. and Longinotti, L.D. (1964). Resistivity of Mo-Nb and Mo-Re Alloys Containing 1% Fe. *Physical Review*, **135**, A1041.

Sarrao, J.L., Morales, L.A., Thompson, J.D., *et al*. (2002). Plutonium-based superconductivity with a transition temperature above 18 K. *Nature*, **420**, 297.

Sato, N., Aso, N., Miyake, K., *et al*. (2001). Strong coupling between local moments and superconducting 'heavy' electrons in UPd_2Al_3. *Nature*, **410**, 340.

Scalapino, D.J., Loh, E. and Hirsch, J.E. (1986). d-wave pairing near a spin-density-wave instability. *Physical Review B*, **34**, 8190.

Schlessinger, Z., Fisk, Z., Zhang, H.T. and Maple, M.B. (1997). s FeSi a Kondo insulator? *Physica B*, **237–238**, 460–462.

Schrieffer, J.R. and Wolff, P. (1966). Relation between the Anderson and Kondo Hamiltonians. *Physical Review*, **149**, 491.

Schroeder, A., Aeppli, G., Bucher, E., *et al*. (1998). Scaling of magnetic fluctuations near a quantum phase transition. *Physical Review Letters*, **80**, 5623.

Schroeder, A., Coldea, G.A.R., Adams, M., *et al*. (2000). Onset of antiferromagnetism in heavy-fermion metals. *Nature*, **407**, 351.

Schweitzer, H. and Czycholl, G. (1991). Resistivity and thermopower of heavy-fermion systems. *Physical Review Letters*, **67**, 3724.

Sengupta, A.M. (2000). Spin in a fluctuating field: the Bose (+ Fermi) Kondo models. *Physical Review*, **61**, 4041.

Senthil, T., Vojta, M., Sachdev, S. and Vojta, M. (2003). Fractionalized Fermi liquids. *Physical Review Letters*, **90**, 216403.

Senthil, T., Vishwanath, A., Balents, L., *et al*. (2004). Deconfined quantum critical points. *Science*, **303**, 1490.

Senthil, T., Sachdev, S. and Vojta, M. (2005). Deconfined quantum critical points. *Physica B*, **9**, 359–361.

Shishido, H., Settai, R., Harima, H. and Onuki, Y. (2005). A drastic change of the Fermi surface at a critical pressure in $CeRhIn_5$: dHvA study under pressure. *Journal of the Physical Society of Japan*, **74**, 1103.

Si, Q., Rabello, S., Ingersent, K. and Smith, J.L. (2001). Ocally critical quantum phase transitions in strongly correlated metals. *Nature*, **413**, 804.

Si, Q., Rabello, S., Ingersent, K. and Smith, J.L. (2003). Local fluctuations in quantum critical metals. *Physical Review*, **68**, 115103.

Sidorov, V.A., Nicklas, M., Pagliuso, P.G., *et al*. (2002). Superconductivity and quantum criticality in $CeCoIn_5$. *Physical Review Letters*, **89**, 157004.

Sigrist, M. and Ueda, K. (1991a). Unconventional superconductivity. *Reviews of Modern Physics*, **63**, 239.

Sigrist, M. and Ueda, K. (1991b). Phenomenological theory of unconventional superconductivity. *Reviews of Modern Physics*, **63**, 239.

Smith, J.L. and Riseborough, P.S. (1985). Actinides, the narrowest bands. *Journal of Magnetism and Magnetic Materials*, **47–48**, 545.

Smith, J.L. and Si, Q. (2000). Spatial correlations in dynamical mean-field theory. *Physical Review*, **61**, 5184.

Steglich, F., Aarts, J., Bredl, C.D., *et al*. (1976). Superconductivity in the presence of strong pauli paramagnetism: $CeCu_2Si_2$. *Physical Review Letters*, **43**, 1892.

Stewart, G. (1984). Heavy-fermion systems. *Reviews of Modern Physics*, **56**, 755.

Stewart, G. (2001). Heavy-fermion systems. *Reviews of Modern Physics*, **73**, 797.

Stewart, G. (2006). Addendum: non-Fermi-liquid behavior in d-and f-electron metals. *Reviews of Modern Physics*, **78**, 743.

Stewart, G.R., Fisk, Z. and Wire, M.S. (1984a). New Ce heavy-fermion system: $CeCu_6$. *Physical Review*, **30**, 482.

Stewart, G.R., Fisk, Z., Willis, J.O. and Smith, J.L. (1984b). Possibility of coexistence of bulk superconductivity and spin fluctuations in UPt_3. *Physical Review Letters*, **52**, 697.

Suhl, H. (1965). Formation of Local Magnetic Moments in Metals. *Physical Review*, **38A**, 515.

Taillefer, L. and Lonzarich, G.G. (1988). Heavy-fermion quasiparticles in UPt_3. *Physical Review Letters*, **60**, 1570.

Taillefer, L., Newbury, R., Lonzarich, G.G., *et al*. (1987). Direct observation of heavy quasiparticles in UPt_3 via the dHvA effect. *Journal of Magnetism and Magnetic Materials*, **63–64**, 372.

Takabatake, T., Teshima, F., Fujii, H., *et al*. (1990). Formation of an anisotropic energy gap in the valence-fluctuating system of CeNiSn. *Physical Review B*, **41**, 9607.

Takabatake, T., Nagasawa, M., Fujii, H., *et al*. (1992). Anisotropic suppression of the energy gap in CeNiSn by high magnetic fields. *Physical Review*, **45**, 5740.

Takabatake, T., Tanaka, H., Bando, Y., *et al*. (1994). Neling evidence for the quasiparticle Gap in Kondo semiconductors CeNiSn and CeRhSb. *Physical Review B*, **50**, 623.

Tanatar, M.A., Paglione, J., Petrovic, C. and Taillefer, L. (2007). Anisotropic violation of the Wiedemann-Franz law at a quantum critical point. *Science* (in press).

Tou, H., Kitaoka, Y., Asayama, K., *et al*. (1995). d-wave superconductivity in antiferromagnetic heavy-fermion compound UPd_2Al_3-evidence from ^{27}Al NMR/NQR studies. *Journal of the Physical Society of Japan*, **64**, 725.

Trovarelli, O., Geibel, C. Mederle, S., *et al*. (2000). $YbRh_2Si_2$: pronounced non-Fermi-liquid effects above a low-lying magnetic phase transition. *Physical Review Letters*, **85**, 626.

Tsujji, H., Kontani, H. and Yoshimora, K. (2005). Universality in heavy fermion systems with general degeneracy. *Physical Review Letters*, **94**, 057201.

Tsunetsugu, H., Sigrist, M. and Ueda, K. (1997). The ground-state phase diagram of the one-dimensional Kondo lattice model. *Reviews of Modern Physics*, **69**, 809.

Tsvelik, A. and Wiegman, P. (1983). The exact results for magnetic alloys. *Advances in Physics*, **32**, 453.

Varma, C.M. (1976). Mixed-valence compounds. *Reviews of Modern Physics*, **48**, 219.

Varma, C., Nussinov, Z. and van Saarlos, W. (2002). Singular Fermi liquids. *Physics Reports*, **361**, 267.

Vekhter, I., Hirschfield, P., Carbotte, J.P. and Nicol, E.J. (1998). Anisotropic thermodynamics of d-wave superconductors in the vortex state. *Physical Review B*, **59**, R9023.

Vidhyadhiraja, N.S., Smith, V.E., Logan, D.E. and Krishnamurthy, H.R. (2003). Dynamics and transport properties of Kondo insulators. *Journal of Physics: Condensed Matter*, **15**, 4045.

Volovik, G.E. (1993). Superconductivity with lines of GAP nodes: density of states in the vortex. *Soviet Physics JETP Letters*, **58**, 469.

von Löhneysen, H. (1996). Non-Fermi-liquid behaviour in the heavy-fermion system $CeCu_{6-x}Au_x$. *Journal of Physics: Condensed Matter*, **8**, 9689.

von Löhneysen, H., Pietrus, T., Portisch, G., *et al*. (1994). Non-Fermi-liquid behavior in a heavy-fermion alloy at a magnetic instability. *Physical Review Letters*, **72**, 3262.

von Löhneysen, H., Rosch, A., Vojta, M. and Wolfe, P. (2007). Fermi-liquid instabilities at magnetic quantum phase transitions. *Reviews of Modern Physics* (submitted) http://arxiv.org/abs/cond-mat/0606317.

Vorontsov, A. and Vekhter, I. (2006). Nodal structure of quasi-two-dimensional superconductors probed by a magnetic field. *Physical Review Letters*, **96**, 237001.

Wang, C.S., Norman, M.R., Albers, R., *et al*. (1987). Fermi surface of UPt_3 within the local-density approximation. *Physical Review*, **35**, 7260.

White, R.H. and Geballe, T.H. (1979). Long Range Order in Solids. Chap. VII. In *Solid State Physics*, Ehrenreich, H., Seitz, F. and Turnbull, D. (Eds.), Academic Press: New York, p. 283, Vol. 15.

Wiegmann, P.B. (1980a). Towards an exact solution of the Anderson model. *Physics Letters*, **80A**, 163.

Wilson, K.G. (1976). The renormalization group: Critical phenomena and the Kondo problem. *Reviews of Modern Physics*, **47**, 773.

Witten, E. (1978). Chiral symmetry, the 1/N expansion and the SU(N) Thirring model. *Nuclear Physics B*, **145**, 110.

Won, H., Parker, D., Maki, K., *et al*. (2004). Gap symmetry of superconductivity in UPd_2Al_3. *Physical Review B*, **70**, 140509.

Yamada, K. (1975). Perturbation expansion for the Anderson Hamiltonian. II. *Progress of Theoretical Physics*, **53**, 970.

Yoshida, K. and Yamada, K. (1975). Perturbation expansion for the Anderson Hamiltonian. III. *Progress of Theoretical Physics*, **53**, 1286.

Yosida, K. (1957). Magnetic properties of Cu-Mn alloys. *Physical Review*, **106**, 896.

Young, A.P. (1975). Quantum effects in the renormalization group approach to phase transitions. *Journal of Physics C: Solid State Physics*, **8**, L309.

Yuan, H.Q., Grosche, F.M., Deppe, M., *et al*. (2006). Non-Fermi liquid states in the pressurized $CeCu_2(Si_{1-x}Gex)_2$ system: two critical points. *Physical Review Letters*, **96**, 047008.

Zwicknagl, G., Yaresko, A.N. and Fulde, P. (2002). Microscopic description of origin of heavy quasiparticles in UPt_3. *Physical Review*, **65**, 081103.

FURTHER READING

Kawakami, N. and Okiji, A. (1981). Exact expression of the ground-state energy for the symmetric Anderson model. *Physical Review Letters*, **86A**, 483.

The Kondo Effect

Barbara A. Jones
IBM Almaden Research Center, San José, CA, USA

1 INTRODUCTION

The Kondo effect is interesting on a number of fronts, not the least that it is a fully many-body quantum-mechanical effect which can be seen at temperatures as high as room temperature or above, although typical Kondo temperatures are more in the tens, rather than hundreds, of kelvin. Moreover, it is a large effect, causing significant changes to transport and thermodynamics. Originally believed to reside mainly in systems of dilute magnetic impurities in a three-dimensional, metallic, host, Kondo effects are now seen on surfaces, in dense periodic structures such as heavy fermions (see also **Heavy Fermions: Electrons at the Edge of Magnetism, Volume 1**), and even in Kondo insulators (Aeppli and Fisk, 1992), in quantum dots (see also **The Kondo Effect in Mesoscopic Quantum Dots, Volume 5**), and in atomic-scale structures created on surfaces by scanning tunneling microscopes (STM).

The Kondo effect was suspected for some time before it was identified as such. In 1930 Meissner and Voight noted a rise in the resistivity of 'pure gold' below 10 K, in contrast to ordinary metals whose resistivity tends toward zero at low temperatures (owing to a decrease in vibrations). In reality the gold had traces of Fe impurities from the manufacturing process, and these were acting as the Kondo impurities. The effect was first definitively identified by Jun Kondo (1964) as arising from interactions in a system of dilute magnetic impurities in a metal. Later experimentalists would see characteristic peaks in the linear coefficient of specific heat, as well as a flattening in the magnetic susceptibility (see Figure 1). Further experimental signatures also appear in the magnetoresistance, thermopower, and excess entropy extracted from the specific heat.

The essence of the Kondo effect is the exchange interaction between a local magnetic moment and the spin of conduction electrons at the impurity site. As the temperature is lowered, a resonance develops in the interaction, and below a critical, Kondo, temperature, the spin of the local moment is screened. Pauli exclusion effects lead to a resulting increase of scattering at the impurity site. This scattering manifests itself as a resonance in the density of states at the Fermi level with width T_K, where $T_K \sim (\rho J)^{1/2} \exp(-1/\rho J)$; ρ is the density of states. There is evidence that such a resonance can be seen in X-ray photoemission spectroscopy (XPS) and/or bremsstrahlung-isochromat spectroscopy (BIS) experiments (Lee *et al*., 1986). A general review of the Kondo problem for single impurities leading up to heavy fermions is found in Hewson (1993).

The remainder of this review will proceed as follows. In Section 2, we review the now well-understood spin-1/2 single-impurity Kondo model, giving some historical development of the solution, and focusing on the numerical renormalization group (NRG) technique and solution. We next describe the Coqblin–Schrieffer model and the Nozières

Handbook of Magnetism and Advanced Magnetic Materials. Edited by Helmut Kronmüller and Stuart Parkin. Volume 1: *Fundamentals and Theory*. ISBN: 978-0-470-02217-7.

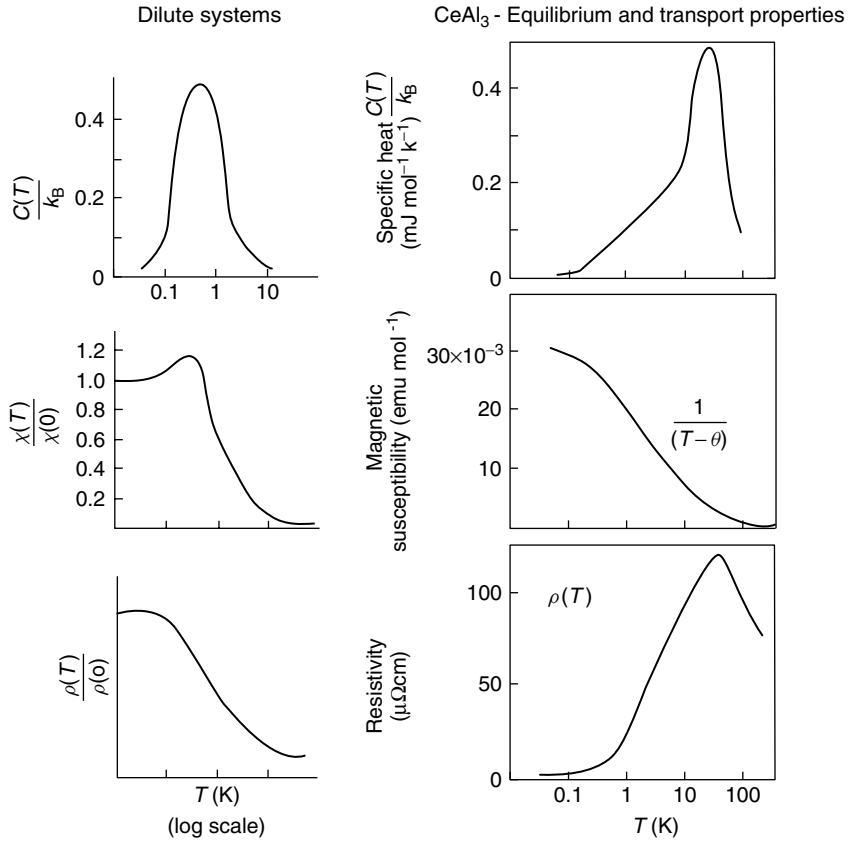

Figure 1. Universal functional forms for the spin-1/2 Kondo systems: specific heat, showing peak with extra ln2 entropy; magnetic susceptibility (note rollover to Pauli paramagnetism at low temperatures); and resistivity, clearly showing rise of scattering at low temperatures. Also for comparison are the same properties for a typical Kondo lattice system. Schematic drawings composed by the author for this article from typical experimental results.

and Blandin phenomenology of Kondo models with multiple channels and spins. An important example of a multichannel model is the two-channel Kondo model, which is described in some detail. We will focus primarily in this review on exact results, but refer to a few key perturbative calculations. In Section 3, we describe the challenges of two-impurity Kondo problems, and the unusual non-Fermi liquid (NFL) fixed point, which can occur for high symmetry. We also describe the effects on the NFL fixed point of the two-channel problem, when a second impurity is added. Section 4 covers the Anderson model, describing how the physics is different from the Kondo model, but related as a more general version of it. This section also covers in more detail the $1/N$ expansion method, reviewing key prior results and discussing its application to the two-impurity infinite-U Anderson model, which maps onto the two-impurity Kondo problem. We also provide a brief review of Kondo lattice physics, but refer the reader to **Heavy Fermions: Electrons at the Edge of Magnetism, Volume 1** for more detail, since the overlap with that subject is considerable. Finally in Section 5 we cover modern experimental developments with few-impurity Kondo systems. The work on quantum dots we refer to **The Kondo Effect in Mesoscopic Quantum Dots, Volume 5**, but cover in detail the experiments with STM in imaging Kondo effects, including interesting physics found outside that predicted by the Hamiltonian calculations of the previous sections. We end with a look at future opportunities in the area of physics of the Kondo effect.

2 SINGLE-IMPURITY KONDO PROBLEMS

The single-impurity Kondo problem is at this point considered completely understood – one of the few many-body quantum models of which this can be said.

The Kondo Hamiltonian for a single impurity is expressed, in second-quantized notation as,

$$H = \sum_{\mathbf{k}\mu} \varepsilon_k c^+_{\mathbf{k}\mu} c_{\mathbf{k}\mu} + J \sum_{\mathbf{k}\mathbf{k}'} \sum_{\mu\mu'} c^+_{\mathbf{k}\mu} \tfrac{1}{2}\boldsymbol{\sigma}_{\mu\mu'} c_{\mathbf{k}'\mu} \cdot \mathbf{S}_0 \quad (1)$$

Here the first term represents the kinetic energy of the sea of conduction electrons and the second term is the exchange interaction between the spin of the conduction electrons at the origin, taken to be the impurity site, and the local moment.

The exchange coupling J can in the abstract be of either sign. However, when derived from a Hamiltonian expressing the hybridization between local and itinerant wave functions (the Anderson model, see subsequently) it is antiferromagnetic, as it is when observed experimentally in many systems.

How such a deceptively simple Hamiltonian can give the dramatic thermodynamic and transport properties is a story that incorporates many of the advanced theoretical developments of the last half-century.

The simplest approach could be to take J to be a small parameter and do a perturbation expansion. However, as was found by Kondo (1964), logarithmic divergences appear at higher order and further expansion becomes invalid. This increase of the expansion parameter does give an indication that growth of the effective J (and of the scattering amplitude at low temperature) is an important part of the physics of the problem.

2.1 'Poor man's' scaling

An early approach was Anderson's poor man's scaling. (Anderson and Yuval, 1969; Anderson, Yuval and Hamann, 1970). Using perturbation theory, scattering processes are successively eliminated at lower and lower energies. Details can be found in the publications and in Anderson's book *Basic Notions of Condensed Matter Physics* (Anderson, 1984). This scaling results in an equation for the coupling $J\tau$ as a function of cutoff energy. (Here τ is the cutoff time, the time for an electron to pass the local spin.) As the cutoff energy is lowered, $J\tau$ increases if the exchange was antiferromagnetic and decreases for ferromagnetic. Thus the ferromagnetic Kondo problem is essentially trivial: the exchange scales to zero as temperature is lowered; the local moment remains essentially free, with no buildup of scattering or increase in resistivity.

For the more usual antiferromagnetic coupling, the exchange scales ever larger, with a cutoff imposed in realistic systems by other scales. If a Kondo temperature is defined by $J\tau = 1$, then an expression for T_K is obtained, $T_K \approx E_C(J\tau)^{1/2}e^{-1/(J\tau)}$, which is remarkably similar to the expression produced by the essentially exact NRG methods obtained by Wilson in the mid-1970s, with the 'cutoff time' replaced by the density of states at the Fermi energy. The physical picture produced by poor man's scaling, of logarithmic contributions to scattering and to the increase of J as temperature is lowered, has been established as correct. What remained as needed was an exact solution which carried all the way from small J, past T_K, down to $T = 0$, and which showed how the low- and high-temperature regimes are connected. For this came Wilson's method of NRG.

2.1.1 Numerical renormalization group

Wilson's method of NRG (Wilson, 1975) comprises several theoretical developments in all. First, it is a unique and insightful way of dividing real and energy space, to focus on behavior at the Fermi energy, and at lower and lower temperatures, and in recasting the Hamiltonian in this form. This aspect is analytical in nature. Second, it is an iterative, computational method for solving a many-body Hamiltonian. And thirdly, it incorporates the concepts of Fermi-liquid theory to extract the exact zero temperature thermodynamic properties, using the numerical results as input to set parameters in analytical expressions.

Wilson's own paper on the solution of the Kondo problem using the NRG is lengthy, and readers are referred to it, and to the exceptionally clear papers by Krishnamurthy, Wilkins, and Wilson (1980a,b) for details of NRG implementation. We will give a summary here.

The first steps are to discretize energy and real space. To prepare, the Hamiltonian is recast from sums over **k** states to integrals over energy. The Fermi surface is assumed to be a single, isotropic conduction band extending from $-D$ to D. New second-quantized operators are defined, which are a set of spherical waves about the impurity site. For a single impurity, only the s-wave states couple. Higher-angular-momentum states come in only in the kinetic energy and do not couple to the impurity; hence they are discarded.

The resulting simplified Hamiltonian is

$$H = \int_{-D}^{D} \mathrm{d}\varepsilon\, \varepsilon a^{+}_{\varepsilon\mu} a_{\varepsilon\mu} + J \iint_{-D}^{D} \mathrm{d}\varepsilon \mathrm{d}\varepsilon' \rho(\varepsilon) a^{+}_{\varepsilon\mu} \tfrac{1}{2}\boldsymbol{\sigma}_{\mu\mu'} a_{\varepsilon'\mu'} \cdot \mathbf{S}_0 \tag{2}$$

Taking $\rho(\varepsilon)$ to be a constant evaluated at the Fermi energy gives the dimensionless parameter ρJ.

Next is the logarithmic discretization of energy and space. A parameter Λ is defined, typically taken to be 2.5 or 3, and energy intervals defined by $\Lambda^{-(n+1)} < \pm\varepsilon < \Lambda^{-n}$. A set of complete orthonormal functions spanning energy space is defined by a Fourier series in each interval, and operators are expanded in this basis. Integrals over energy are now replaced by sums over intervals n. Finally, define new operators so that the first one, f_o, is localized nearest the impurity. Wilson has derived a set of orthonormal operators f_n that couple at most n to $n \pm 1$ in the kinetic energy. The result is an effective Hamiltonian for each energy scale, indexed by N. The zeroth level connects just with the impurity. A recursion relation connects Hamiltonians at level N to those at $N + 1$.

The next step is computational. The iterative procedure is carried out, diagonalizing Ho first, and then using the eigenstates, combined with the next $N = 1$ degree of freedom, to make basis states for the $N = 1$ iteration. At each stage, the Hamiltonian is diagonalized and the lowest energy levels, labeled by spin, are observed. During the first iterations, the energy levels typically change quite rapidly with iteration number. However, after a number of iterations, the eigenstates start to level out, and eventually the levels become exponentially less sensitive to iteration (with an added even-odd iteration differentiation). At this point the iterations are at an eigenstate of the Hamiltonian, and the relative values of the energy levels become meaningful.

Two technical points of the computational part of NRG: First, the rate at which the levels converge is determined by the parameter Λ. The larger Λ, the faster the convergence. The less-fine discretization of energy space results from larger Λ, however, and so the choice of Λ is a tradeoff between these two considerations. A typical range used is 2–3. (Oliveira *et al*. have pioneered the use of a much larger Λ to extract spectral functions and other detail not obtainable with smaller Λ (Campo and Oliveira, 2005; Silva *et al*., 1996), and references therein).) The second point is the imposition at each iteration of an energy cutoff, beyond which states are thrown away. Since every iteration $N \rightarrow N + 1$ introduces a new set of operators, the basis set would quickly grow to unmanageable size if this were not done. However, care must be taken so that the discarded states do not contribute to key energy levels, otherwise this step can be a source of error.

With the eigenstates identified, the final analytic stage of calculating properties can begin. In Fermi-liquid theory, especially as discussed by Nozières (1974), an effective Hamiltonian is formulated for each fixed point, with a certain number of parameters which reflect the low-energy degrees of freedom. In NRG, there is a systematic way to derive these terms, and then the coefficients are derived from the numerical eigenstates. Various thermodynamic properties can then be calculated analytically, using the approach of the energy levels to their fixed point values (i.e., small deviations in energy as a function of iteration number).

For the single-impurity Kondo problem there are two fixed points. The first is the $\rho J = 0$ point, which is free electrons with a free local moment, the so-called weak-coupling fixed point. The second fixed point is $\rho J \rightarrow \infty$. This effectively has the local moment removed from the low-temperature properties, to be replaced by scattering at the unitarity limit, that is, in both up and down spin channels the phase shift is $\pi/2$. By Friedel's sum rule (White, 1983) this means that effectively one electron has been removed from the problem, acting to screen the local moment. (A reminder here that the Kondo effect is not an actual bound state of a conduction electron with the local moment, but rather a resonance–the energy is at the Fermi energy, above the top of the potential 'well', which is the impurity level.) This is known as the *strong coupling fixed point*.

With the only relevant operator ρJ effectively removed from the problem, what remains at low temperatures are the leading irrelevant operators. For the single-impurity problem there are two: a hopping integral, and a local repulsive Coulomb-type interaction $U(n_1 - 1)^2$, involving the nearest-neighbor orbitals. This effective Hamiltonian around the $T = 0$ point enables the calculation of specific heat and susceptibility in the $T = 0$ limit. Wilson formulated a ratio (the Summerfeld–Wilson ratio) of susceptibility to linear coefficient of specific heat γ:

$$R \equiv (4\pi^2/3)(k_B{}^2/g\mu_B)^2 \chi/\gamma \tag{3}$$

This ratio takes the independent, universal value of 2 in the Kondo problem. For free electrons, the value is 1, indicating the enhanced role of spin interactions in the Kondo case.

A notable aspect of Kondo physics is the universal nature of the results. That is, there is only a single parameter, T_K, which governs the energy scale. While the value of the Kondo temperature varies with impurity and host, once the Kondo temperature is determined for a specific system, each physical property has a specific universal shape such that when the experiments are scaled by T_K, the curves all fall on top of one another. For example, as the temperature is lowered, the susceptibility changes near T_K from a Curie law to that of Pauli paramagnetism, indication that the moment has been quenched. The resistivity rises logarithmically and reaches a maximum at zero temperature. Figure 1 illustrates these universal curves.

2.1.2 *Summary of single-impurity spin-1/2 Kondo physics*

At this point we provide a summary of single-impurity Kondo physics. There are, for antiferromagnetic exchange coupling, two fixed points. The $\rho J = 0$ weak-coupling fixed point is unstable, and ρJ effectively scales to infinity as temperature is lowered to zero. The $\rho J = \infty$ fixed point at $T = 0$ is the true Kondo ground state, and it is characterized by scattering at the unitarity limit, $\delta_{\uparrow,\downarrow} = \pi/2$. The spin of the local moment has been screened and disappears from the problem. From an NRG point of view, one conduction electron has been removed from the system to do this screening. The Kondo ground state has universal scaling with the Kondo temperature T_K, and the Wilson ratio takes the universal value 2. In a magnetic field of order T_K, the Kondo effect's many-body spin-symmetric screening is broken, and no Kondo effect is obtained. Finally, the ferromagnetic

Kondo problem has ρJ scaling to 0, and the local moment stays free.

There are other methods which have notably been used for the Kondo problem. One of these is the exact solution by Bethe Ansatz (Andrei, 1980; Andrei and Lowenstein, 1981; Rajan, Lowenstein and Andrei, 1982; Wiegmann, 1980, 1981), obtained in the early 1980s. This solution is very complex, and although it enables the calculation of properties, the primary physical insight is in the nature of the symmetries at the ground state. Another solution method which is not exact, but with far more utility in fitting to a range of experiments, is the $1/N$ expansion (Read and Newns, 1983a,b; Coleman, 1984; Gunnarsson and Schonhammer, 1983; Bickers, Cox and Wilkins, 1987a). This method is remarkably precise in matching a wide range of experimental properties for an extensive range of materials which display single-impurity Kondo behavior. (It should be noted in contrast that for two Kondo impurities, although ferromagnetic interimpurity coupling is reproduced well, the antiferromagnetic regime is less well. More details in the subsequent text.) The $1/N$ expansion is actually implemented on a broader version of the Kondo Hamiltonian, the Anderson model, and will be described in that section.

2.1.3 Coqblin–Schrieffer model

Before moving on to the Anderson model, there are several important variants of the Kondo model. The first variant is to allow the spin to have more than s-wave behavior, and in fact to be larger than spin-1/2. Such a model, with orbital degrees of freedom is the Coqblin–Schrieffer model (Coqblin and Schrieffer, 1969),

$$H = \sum_{\mathbf{k},\alpha} \varepsilon_k \mathrm{c}^{+}_{\mathbf{k}\alpha}\mathrm{c}_{\mathbf{k}\alpha} + J \sum_{\mathbf{k}\mathbf{k}'} \sum_{\alpha\alpha'} \mathrm{c}^{+}_{\mathbf{k}\alpha}\mathrm{c}_{\mathbf{k}'\alpha'}\mathrm{f}^{+}_{\alpha'}\mathrm{f}_{\alpha} \qquad (4)$$

where $\mathrm{c}^{+}_{\mathbf{k}\alpha}$ are creation operators of the conduction electrons' partial harmonics with angular momentum $m = j + 1 - \alpha$, and $\alpha = 1, 2, \ldots 2j + 1$. Here j is the size of the spin. The f^{+}_{α} describe the impurity spin, with degrees of freedom α. Bethe Ansatz methods have been successfully used on this model (Bazhanov, Lukyanov and Tsvelik, 2003). Magnetic fields have a large effect on the Kondo temperature; if small fields, the Kondo temperature is the full value, which may be quite large, hundreds if not thousands of degrees for rare-earth impurities. If larger than T_{K}, magnetic fields can break the full spin symmetry and drive the system to lower-symmetry states with Kondo temperatures of just a few degrees. In general the behavior of this model is more complex than the spin-1/2 model, but tractable by modern methods (i.e., $1/N$, Bethe ansatz, NRG, some forms of scaling).

2.1.4 'M-N-ology'

In general one can consider a Kondo problem of N impurities (spins) and M channels. Multiple scattering channels in a Kondo problem can be obtained, for example, in crystal-electric fields (Cox, 1987) in which orthogonal sets of electrons, interacting with the impurity, can be considered as different 'flavors' of electrons. Using an analysis of channels, spins, and impurities, Nozières and Blandin (1980) have presented a picture which stands the test of time well. It is as follows. For systems in which the number of spin-1/2 impurities equals the number of scattering channels of conduction electrons, a Kondo effect will occur and the ground state will be a Fermi-liquid singlet. If the number of channels is less than the number of spin-1/2 impurities, then a partial Kondo effect will occur, the ground state will be a Fermi liquid, but with a net spin (underscreened case). But if the number of channels is greater than the number of spin-1/2 impurities (overscreened case), then the ground state is predicted to be an NFL unusual state.

We see from sample models how well this holds. For a single-impurity Kondo model, with one impurity and one channel, the ground state is indeed a Fermi liquid. A spin-1 single-impurity, single-channel system has a spin-1/2 Fermi-liquid ground state (Cragg and Lloyd, 1979; Jones and Varma, 1987). We will see below that two spin-1/2 impurities separated by a finite distance have two channels: spin and parity. The ground state is indeed a Fermi-liquid singlet at all parts of its phase space but one. And not all versions of the Fermi-liquid singlet in this case have a full Kondo effect. For the case of a single spin-1/2 with two channels, the so-called multichannel Kondo problem, unusual behavior is predicted – and indeed occurs.

2.1.5 The multichannel Kondo model

The multichannel Kondo Hamiltonian (Nozières and Blandin, 1980) has the form:

$$H = \sum_{\mathbf{k}\mu,\mathrm{n=a,b}} \varepsilon_k \mathrm{c}^{+}_{\mathbf{k}\mu\mathrm{n}}\mathrm{c}_{\mathbf{k}\mu\mathrm{n}} + \sum_{kk'} \sum_{\mu\mu',\mathrm{n=a,b}} J_{\mathrm{n}}\mathrm{c}^{+}_{\mathbf{k}\mu\mathrm{n}}\tfrac{1}{2}\boldsymbol{\sigma}_{\mu\mu'}\mathrm{c}_{\mathbf{k}'\mu'\mathrm{n}} \cdot \mathbf{S}_0 \quad (5)$$

The sources for the two channels can be multiple: crystal-electric field effects in certain heavy fermions (Cox, 1987, 1988; Cox and Jarrell, 1996; Cox and Zawadowski, 1999); electron-assisted tunneling in metallic glasses; and quantum dot systems with multiple explicit channels of conduction electron contacts (see also **The Kondo Effect in Mesoscopic Quantum Dots, Volume 5**).

When $J_{\mathrm{a}} \neq J_{\mathrm{b}}$, the system flows to scaling and a Kondo effect in whichever coupling constant is larger. However, when $J_{\mathrm{a}} = J_{\mathrm{b}}$, the system flows to a stable nontrivial critical point at $T = 0$ which displays NFL behavior such

as logarithmically diverging specific heat coefficient C/T and susceptibility. The residual entropy is $\frac{1}{2}\ln 2$ (that is, $2^{1/2}$ degrees of freedom in the ground state, compared to ln2 as the entropy removed by the regular Kondo effect). This Hamiltonian has been treated by Bethe ansatz (Andrei and Destri, 1984), NRG (Pang and Cox, 1991), and $1/N$ expansion (several authors, e.g., Cox and Ruckenstein, 1993). Of continued interest theoretically is the exact nature of the NFL point, and the relationship of the various solutions to one another. A naïve picture would have the local moment alternatively screened by the spin-up of both a and b channels, then by spin-down of both channels, in concentric rings around the impurity, in each case never obtaining a singlet ground state, extending all the way to infinity. This would have a net spin of 1/2. Some versions of the Bethe ansatz solution are spin symmetric. What then, are the $2^{1/2}$ degrees of freedom? Such can be the nonintuitive aspects of NFL states. Potential multichannel Kondo systems have long been observed in bulk materials, especially those with NFL properties (see also **Heavy Fermions: Electrons at the Edge of Magnetism, Volume 1**), but recently experimental evidence has been given for observing the effect in quantum dots, which should provide a cleaner system for study.

An important theoretical technique adapted from high-energy theory to study condensed matter systems is conformal field theory (CFT), pioneered in Kondo systems by Affleck and Ludwig (Affleck, Ludwig, Pang and Cox, 1992; Affleck and Ludwig, 1993). This is an exact solution, which emphasizes the role of symmetries and extracts the conformal operators for the various fixed points. Although it can identify fixed points independently, it is optimally used in conjunction with the NRG to utilize the energy levels to fix the values of the parameters. CFT was used on the multichannel problem, revealing anomalous critical properties of the NFL state, and was also used to obtain insight into the two-impurity Kondo problem (see subsequent text).

3 TWO-IMPURITY PROBLEMS

The next level of complexity is to introduce a second impurity. This is the simplest level of Hamiltonian to include interimpurity interactions, leading toward models for a lattice. The two-impurity Kondo problem has the form:

$$H = \sum_{\mathbf{k}\mu} \varepsilon_k \mathrm{c}^{+}_{\mathbf{k}\mu}\mathrm{c}_{\mathbf{k}\mu} + J[\mathbf{s_c}(\mathbf{r}_1)\cdot\mathbf{S}_1 + \mathbf{s_c}(\mathbf{r}_2)\cdot\mathbf{S}_2] \qquad (6)$$

where

$$\mathbf{s_c}(\mathrm{r}_i) = \sum_{\mathbf{k}\mathbf{k}'}\sum_{\mu\mu'} \mathrm{e}^{\mathrm{i}(\mathbf{k}'-\mathbf{k})\cdot\mathrm{r}_i}\mathrm{c}^{+}_{\mathbf{k}\mu}\tfrac{1}{2}\boldsymbol{\sigma}_{\mu\mu'}\mathrm{c}_{\mathbf{k}'\mu} \qquad (7)$$

Now the impurities can interact with each other as well as with the conduction electrons. The form of the interimpurity exchange is the Ruderman–Kittel–Kasuya–Yosida (RKKY) interaction (Ruderman and Kittel, 1954). In this interaction, the local moments spin polarize the conduction electron sea around them. There are not enough k vectors to make a delta function of spin at each impurity site, since filling the conduction electron states stops at the Fermi level (and a delta function would need Fourier components all the way to infinity). This sharp cutoff in energy occupation gives an oscillation to the spin polarization. One can calculate this by treating the interaction terms of the Hamiltonian as a perturbation on the kinetic energy, which gives a change in energy of the form $|\rho J|^2 F(R)\mathbf{S}_1\cdot\mathbf{S}_2$, where $F(R)$ is an oscillating function of impurity separation which decays as $\cos(k_\mathrm{F}R)/(k_\mathrm{F}R)^3$ for $R \to \infty$.

For ferromagnetic interactions the moments will just create a larger attraction for the Kondo effect. But for separations for which the interaction is antiferromagnetic, do the moments create their own spin singlet, which will preclude having a Kondo effect? Likewise, if a Kondo effect occurs will this preclude an RKKY interaction, since the moments are screened? How do ferromagnetic and antiferromagnetic sides of the phase diagram connect?

Prior to the exact solution, the thinking was that as soon as there was any antiferromagnetic interaction, the moments would quench each other. Thermodynamic scaling analysis (Jayaprakash, Krishnamurthy and Wilkins, 1981), for example, found an effective Hamiltonian with two parameters, the Kondo and RKKY couplings. For ferromagnetic RKKY, they found a two-stage Kondo effect. This is much in agreement with later NRG calculations. For antiferromagnetic interactions, however, the analysis indicated an either/or scenario: RKKY precluded Kondo and vice versa. Analysis by Doniach of his more complex Kondo necklace model (Doniach, 1977) indicated a similar dichotomy between states. Quantum Monte Carlo (Hirsch and Fye, 1986; Fye, Hirsch and Scalapino, 1987) was also tried on this model, with results which likewise have some comparison with the exact solutions.

The exact solution was obtained by NRG in the late 1980s (Jones and Varma, 1987; Jones, Varma and Wilkins, 1988). Whereas the single-impurity Kondo problem(s) proved eventually amenable to a variety of techniques (poor man's scaling, $1/N$ expansion, Bethe ansatz, NRG, conformal field theories, etc.), all of which gave consistent and correct results in the regimes in which they operated, the two-impurity problem, only one impurity more, and still far to go toward a lattice, produced subtle and unexpected results only completely seen by NRG and CFT (a Bethe ansatz solution for the two-impurity problem remains still problematic at this writing).

What was found by NRG was the following. Because of mirror symmetry about the center of the two impurities, parity is a conserved quantity. All states can be classified as being of either even or odd parity, in addition to having quantum numbers of spin and charge (actually axial charge, a symmetry of Kondo Hamiltonians discovered by the author (Jones, Varma and Wilkins, 1988; Jones, 1990), and later found in other strongly correlated Hamiltonians such as the Hubbard model). Interaction in the Hamiltonian can involve interactions between even parity alone, or odd parity, or a mix of even and odd (and spin-0 and spin-1 states of the impurities). The Hamiltonian in the particle–hole symmetric limit is as follows:

$$H/D = \int \mathrm{d}\varepsilon\, \varepsilon \left[a^{+}_{\varepsilon \mathrm{e}\mu} a_{\varepsilon \mathrm{e}\mu} + a^{+}_{\varepsilon \mathrm{o}\mu} a_{\varepsilon \mathrm{o}\mu}\right] + \rho J_{\mathrm{e}} \mathbf{s}_{\mathrm{e}} \cdot (\mathbf{S}_1 + \mathbf{S}_2) + \rho J_{\mathrm{o}} \mathbf{s}_{\mathrm{o}} \cdot (\mathbf{S}_1 + \mathbf{S}_2) + \rho J_{\mathrm{m}} (\mathbf{s}_{\mathrm{eo}} + \mathbf{s}_{\mathrm{oe}}) \cdot (\mathbf{S}_1 - \mathbf{S}_2),$$

$$\text{where } \mathbf{s}_{\mathrm{pp}'} = \iint \mathrm{d}\varepsilon \mathrm{d}\varepsilon' a^{+}_{\varepsilon \mathrm{p}\mu} \tfrac{1}{2} \boldsymbol{\sigma}_{\mu\mu'} a_{\varepsilon' \mathrm{p}'\mu'} \tag{8}$$

Here the integrals extend from -1 to 1 since the bandwidth has been scaled out. States are labeled by parity as e or o. Only one parity subscript on a spin term represents a repeated value of that parity. (In the most general, particle–hole asymmetric form, there are energy- and distance-dependent form factors within each integral, making it very challenging to implement the Wilson procedure of projection onto Fourier states in each logarithmic energy interval. The approximation represented here thus explores only a portion of phase space.)

Because there are in addition two spin scattering channels, the two-impurity Kondo problem has four channels of conduction electrons. The NRG analysis revealed three low-temperature fixed points, or ground states of the system.

1. For the case of particle–hole symmetry, there is a Kondo effect for all values of RKKY from moderately antiferromagnetic (RKKY/T_{K} near -2.2), through zero RKKY (two independent moments) to all values of ferromagnetic RKKY. For the larger values of ferromagnetic RKKY/T_{K}, there is a two-stage Kondo effect as previously predicted, with the Kondo effect happening separately in the even and the odd channels, with the larger coupling constant having the higher of the two Kondo temperatures. The ground state is a singlet with a $\pi/2$ phase shift in every scattering channel.
2. For larger antiferromagnetic RKKY, with RKKY/T_{K} more negative than -2.2, the moments form a singlet, and no Kondo effect occurs.
3. At a value of RKKY/T_{K} near -2.2, there is an unexpected unstable NFL fixed point. At this point there is a second-order quantum critical point as a function of the parameter RKKY/T_{K}, at $T = 0$. At this point the linear coefficient of specific heat and the magnetic susceptibility diverge. The staggered susceptibility (related to S1−S2) remains finite, with a possible finite discontinuity. These thermodynamics are shown in Figure 2.

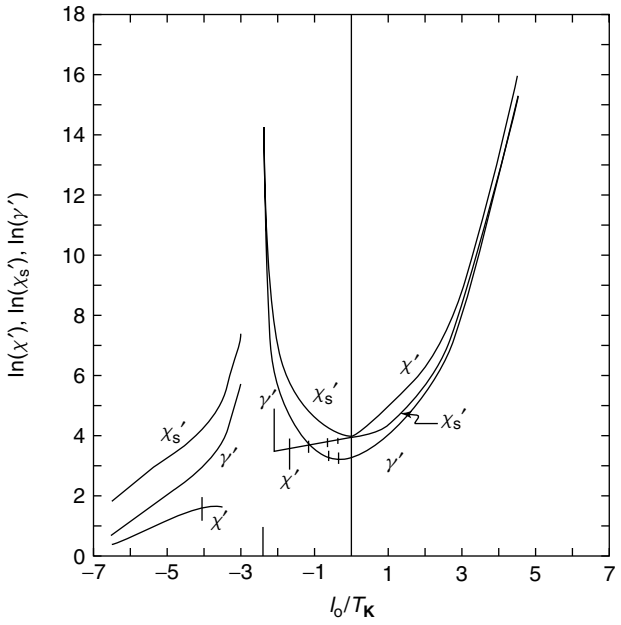

Figure 2. Thermodynamic properties for the two-impurity Kondo Hamiltonian (symmetric case), obtained by NRG. The magnetic susceptibility, the staggered susceptibility (susceptibility under an opposite magnetic field on the two sites), and the linear coefficient of specific heat, all at zero temperature, are plotted as a function of the ratio of the RKKY coupling to the Kondo temperature. Antiferromagnetic RKKY is on the left side of the figure. Note the divergence of staggered susceptibility and linear coefficient of specific heat at the non-Fermi-liquid fixed point, near an antiferromagnetic RKKY/T_{K} ratio of near 2.2. The uniform susceptibility remains finite, if with a possible discontinuity. The system is in a Kondo singlet to the right of the critical point, and in an antiferromagnetic singlet to the left with no Kondo effect. (Reproduced from Jones *et al*., 1988, with permission from the American Physical Society. © 1988.)

Further understanding of the phases of this system is obtained with the calculation of the bare spin−spin correlation function, shown in Figure 3. Notice that the spin−spin correlation function is smooth and continuous throughout the range of parameters, and only becomes ferromagnetic or antiferromagnetic at the extreme range of RKKY. How is this consistent with three separate ground states, one of which is an antiferromagnetic state for a finite range of RKKY? The answer is that the ground state phases are many-body states, involving not only the local moments, but a large percentage of the conduction electrons. The local moments take on intermediate values as the RKKY varies, but the conduction

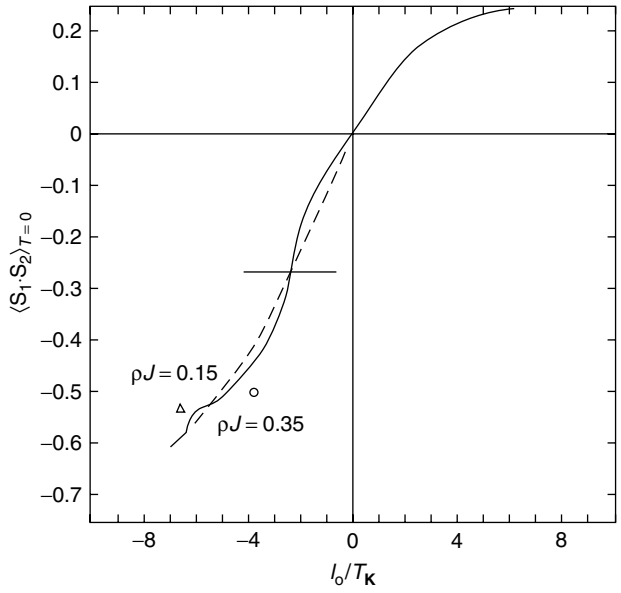

Figure 3. Spin–spin correlation function for the two-impurity Kondo Hamiltonian (symmetric case), obtained by NRG. (Same horizontal axis as Figure 2.) This is the correlation function between the bare local moments; the fixed point represents the moments as dressed by the electrons. Note that exchange coupling exists between the two impurities, even when they are in a Kondo state, and that a pure singlet state only exists at the limit of very large RKKY. Kondo does not preclude RKKY, nor vice versa. The spin–spin correlation function at the critical point takes the value $-1/4$. (Reprinted from Jones B.A. Ph.D. thesis, Cornell University, copyright 1988 by Barbara A. Jones.)

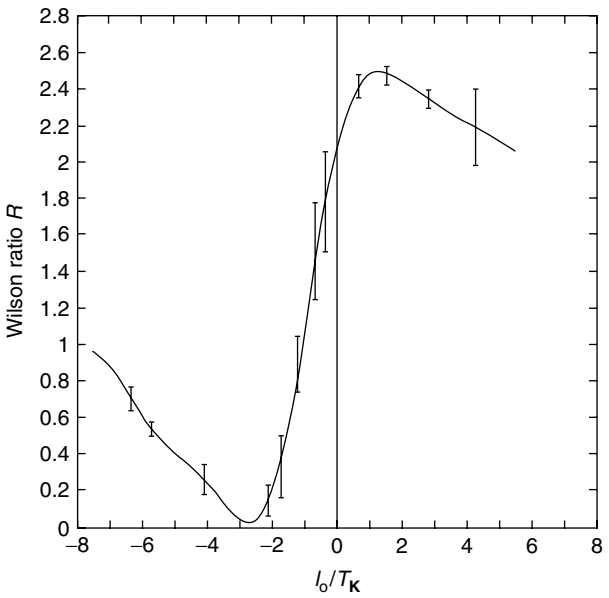

Figure 4. Wilson ratio, proportional to the ratio of the magnetic susceptibility to the linear coefficient of specific heat. The non-constant value shows the nonuniversal nature of the two-impurity system (no single-parameter scaling). Free electrons have value 1, a Kondo effect gives a value 2, and the critical point has a value near if not at 0, showing a suppression of magnetic interactions (or an enhancement of electronic ones). (Reproduced from Jones *et al*., 1988, with permission from the American Physical Society. © 1988.)

electrons have a noncontinuous reaction to this state, deciding that there is enough of a moment to make a Kondo effect for RKKY ratio greater than 2.2, and conversely helping the local moments to form a spin singlet without Kondo effect for larger antiferromagnetic RKKY.

What, then, are the conduction electrons aiding when the local moment spin–spin correlation function is $-1/4$, exactly half way between antiferromagnetic $-3/4$ and ferromagnetic 1/4? This is the location of the unstable NFL point. It seems that the unstable point is the point at which, coming down from more ferromagnetic RKKY, the moment is just barely too small to generate a Kondo effect. The electrons try to form a many-body resonance, but the cloud extends to infinity, and there is no finite-size screening cloud for electrons coming from infinite to scatter off of, and thus define a Fermi liquid (Jones, 1991).

The Wilson ratio has also been calculated and is shown in Figure 4. One can see the Wilson ratio going to the Kondo value of 2 and above for the ferromagnetic side. For the antiferromagnetic side, the Wilson ratio is always less than 2, and in fact goes to 0 at the value of the unstable fixed point. For large antiferromagnetic coupling, the Wilson ratio goes to the free-electron value of 1. One of the central findings of the two-impurity Kondo Hamiltonian is that the results are strongly nonuniversal. There is no one scaling parameter, as there is for the single-impurity case. The variation of R on the ferromagnetic side is less, with perhaps rough scaling possible there, but on the antiferromagnetic side it is clearly ruled out.

It should be noted that for much of the phase diagram, there is simultaneous Kondo effect and RKKY interactions, both ferromagnetic and antiferromagnetic. The RKKY is not stopped by the Kondo effect, nor do antiferromagnetic RKKY interactions necessarily preclude a Kondo effect. In fact, it is proposed that simultaneous antiferromagnetic RKKY and Kondo effect may be what is occurring in the Kondo lattice compounds, where there is a famous conundrum posed by P.W. Anderson, of where the electrons are coming from to form a Kondo singlet with every moment in the dense lattice, if only electrons within T_K of the Fermi energy can participate. In a lattice, there are not nearly enough electrons in that energy range to form a 'sea' for every moment. However, if the moments partially compensate each other, then far fewer compensating electrons are needed.

3.1 Removal of particle–hole symmetry

When the requirement of particle–hole symmetry is lifted (with for example the addition of potential scattering terms to the Hamiltonian above), for most values, the divergences in susceptibility and specific heat coefficient are rounded to peaks, and the quantum phase transition goes away (Jones, 1991). There is no unstable NFL point. All ground states are a Fermi liquid. The phase shifts in this case vary continuously from $\pi/2$ on the ferromagnetic side down to eventually 0 for very large antiferromagnetic RKKY. Thus the ground states for every value of antiferromagnetic RKKY are 'partial Kondo effect', with the moments doing part of the compensating and the electrons doing the rest. The Wilson ratio still varies, however, and the solution is still nonuniversal. Lest one conclude that the critical parameter is purely particle–hole symmetry, however, it should be noted that when potential scattering is added which has parity-symmetric form, although particle–hole symmetry is broken, these Hamiltonians still give a line of NFL fixed points. The symmetry breaking is somewhat subtle, and only has an effect when there is not a reflection symmetry between odd and even.

The exact nature of the critical operators was obtained later by conformal field theoretical analysis (Affleck and Ludwig, 1992; Affleck, Ludwig and Jones, 1995) and an SO(7) complex symmetry identified at the critical point. They calculated the staggered susceptibility at the critical point to depend logarithmically on temperature and frequency.

As a final conclusion, the single-particle result, the Kondo effect, is strongly modified by two-spin results, and hence pair interaction terms must be included in any theories for the lattice. RKKY and Kondo effects are not mutually exclusive, either for ferromagnetic or for antiferromagnetic coupling.

3.1.1 Two-impurity, two-channel Kondo

When adding a second impurity to the two-channel problem, the question naturally arises whether the NFL state for $J_a = J_b$ still remains. This problem has been looked at by NRG, and the solution is as follows (Ingersent, Jones and Wilkins, 1992). The phase diagram is shown in Figure 5. This is the calculation for $J_a = J_b$, and particle–hole symmetry. The previous, single-impurity NFL point is shown in the center of the figure at RKKY $I/T_K = 0$. This fixed point proves to be unstable to any RKKY interactions, ferromagnetic or antiferromagnetic. For antiferromagnetic RKKY, the previous fixed point flows to a line of fixed points, at a critical value of RKKY/T_K. Thus the physics of a bulk two-channel Kondo system should be governed more by the properties of the marginal line of NFL

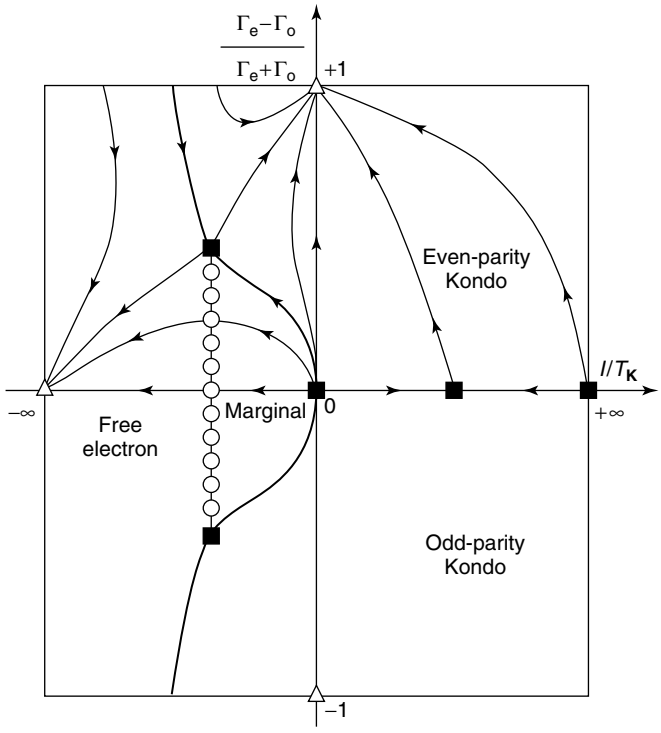

Figure 5. Phase diagram for the two-impurity, two-channel Kondo Hamiltonian in the symmetric case, obtained by NRG. The horizontal axis is the ratio of RKKY to Kondo temperature, as in figures 2–4. The non-Fermi-liquid fixed point for the one impurity case is at the center of the figure at the origin. Note that it is unstable in all directions, either to flow to a Fermi liquid, or to a line of non-Fermi-liquid fixed points at intermediate coupling. Even if the non-Fermi-liquid fixed points were to be changed to crossovers in the presence of particle–hole symmetry breaking, the point at the origin would still be unstable to the Fermi liquid around it. (Reproduced from Ingersent *et al*., 1992, with permission from the American Physical Society. © 1992.)

points, not by the single-impurity point! Similarly to the two-impurity, single-channel problem, for large enough antiferromagnetic RKKY, the moments form their own singlet and no Kondo effect occurs. This is a Fermi-liquid ground state.

For ferromagnetic RKKY, the single-impurity NFL point is again unstable. If there is any even-odd parity asymmetry, the RG flows are to a Kondo effect in either parity channel, with Fermi-liquid ground state. Only in the case of equal even- and odd–parity coupling (isolated points in the phase space of RKKY coupling) does the single-impurity NFL point flow to a new stable ferromagnetic NFL point at intermediate coupling.

In summary, the phase diagram for adding a second impurity to the two-channel problem is surprisingly complex. Unexpectedly, the single-impurity NFL result is unstable to any amount of RKKY coupling. If ferromagnetic, the most

likely result is a Fermi-liquid Kondo ground state with no NFL behavior. If antiferromagnetic coupling, the flow is to a line of new marginal NFL fixed points, with properties different from that of a noninteracting impurity. Two main questions are raised, the first being whether additional impurities add yet more complexity and yet different fixed points, so that it becomes difficult to predict the main interactions for a multichannel lattice. The second challenge is to treat a more general band structure, to see whether particle–hole symmetry has created some nonuniversal effects.

These questions have been looked at with the addition of potential scattering, and it appears that for general values of even- and odd-parity scattering, all the intermediate-RKKY NFL fixed points may be destabilized. A reminder that even though it remains, the NFL point at RKKY = 0, for two independent impurities, is unstable to any RKKY, and will flow to strong coupling fixed points. It appears that a Fermi liquid is the preferred general ground state. For the multichannel Kondo problem, except in special cases, the addition of a second impurity reduces complexity and flows are to stable Fermi-liquid fixed points. Since this Hamiltonian was the hope of modeling NFL in many systems, it raises the final question of where the microscopic Hamiltonian basis of NFL behavior may come from in a lattice model. Certainly at finite temperatures, even low ones, the system could flow near interesting phases in these models, since what is important are the crossover exponents.

4 THE ANDERSON MODEL

So far we have been discussing the Kondo model, in which the local moment occupation is kept fixed, a result of large, tending to infinite Coulomb repulsion. For many systems, however, there is a finite Coulomb repulsion on the impurity site, and fluctuations to double or no occupancy can occur. The more general model for these systems is the Anderson model (Anderson, 1961) with a Hamiltonian as follows:

$$H = \sum_{\mathbf{k}\mu} \varepsilon_k c^+_{\mathbf{k}\mu} c_{\mathbf{k}\mu} + \varepsilon_d c^+_{d\mu} c_{d\mu} + \sum_{\mathbf{k}\mu} (V_{k,d} c^+_{\mathbf{k}\mu} c_{d\mu} + V^*_{k,d} c^+_{d\mu} c_{\mathbf{k}\mu}) + U(c^+_{d\uparrow} c_{\mathbf{k}\uparrow})(c^+_{d\downarrow} c_{\mathbf{k}\downarrow}) \tag{9}$$

Here the first term is the kinetic energy of the conduction electrons; ε_d is the energy of the local level (be it d or f electrons), with operators $c^+_{\mathbf{d}\mu}$; $V_{k,d}$ is the hybridization between the local level and the conduction electrons; and U is the Coulomb repulsion at the local level site.

The Anderson model has some very interesting physics of its own, but first we wish to show how the Anderson and Kondo models are related. This is done by means of a Schrieffer–Wolff transformation (Schrieffer and Wolff, 1966). Assume that U is much larger than V. Then by choosing a generator matrix S, such that

$\tilde{H} = \exp(S)\ H\ \exp(-S)$ and $(I - P)\tilde{H}P = 0$, with P the projector onto the singly-occupied ground state, eliminate V to first order. The resulting Hamiltonian $\tilde{H}$ has a term of the Kondo form, with a coefficient, the effective J, depending on k and k'. Evaluating J at the Fermi energy gives a relation to the parameters of the Anderson model: $J = 2|V_{kf}|^2 U/(\varepsilon_d(\varepsilon_d + U))$. Often the symmetric case is considered, in which $\varepsilon_d = -U/2$, giving $J = -8|V_{kf}|^2/U$. One can see that for large U, J is usually fairly small. However, as we have seen from the single-impurity Kondo results, even small values of J scale to large as temperature is lowered. The Anderson model contains thus a larger subset of physics than the Kondo model, since the Kondo interactions are contained as a limiting case.

We now look at the Anderson model itself. The primary new behavior introduced by such a model is so-called mixed valent physics. That is, it allows the local moment to have an occupancy, which is a mix between two definite values. Such physics is seen in some rare-earth compounds (e.g., α-Ce), and the subject of mixed valent physics has been a very active one both experimentally and theoretically in the past. Unfortunately we do not have room here to review this literature, and will focus on the physics emerging from solutions of the Anderson Hamiltonian above.

The definitive NRG study of this Hamiltonian was done by Krishnamurthy, Wilkins and Wilson (1980a), who studied both the symmetric and asymmetric cases. The results are reviewed here. NRG finds that the local moment behavior described above as the Kondo effect occurs as a fairly large part of phase space. As long as U is roughly greater than the hybridization V, for fairly low temperatures, the system maps onto the spin-1/2 Kondo model with coupling given as per the Schrieffer–Wolff transformation, even up to very large values of ρJ. For U not particularly large, the impurity orbital remains essentially free at high temperatures, and then develops a moment when T drops below U. Finally, for small Coulomb repulsion U, the free impurity orbital flows straight to strong coupling at low temperature. (see Figure 6).

For the asymmetric case, the valence-fluctuating regime is the primary characteristic. This is reached for $-\varepsilon_d \ll T \ll U$. Here the $n_d = 0$ and $n_d = 1$ configurations are equally populated, and the effective impurity level energy becomes temperature dependent, and a function of the hybridization and U as well. Although properties are universal for the symmetric model, the asymmetric model shows evidence of nonuniversal behavior. Several varieties of Bethe ansatz solutions for the Anderson model have also been obtained, such as Schlottmann (1983).

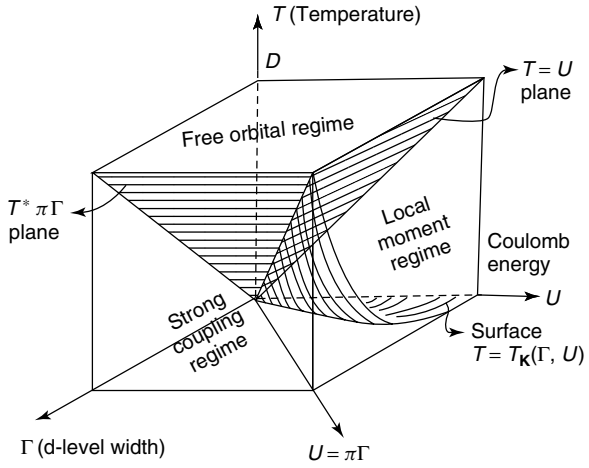

Figure 6. Phase diagram of the symmetric single-impurity Anderson model, with axes as labeled. At low temperature, the system scales to strong coupling for all values of hybridization and Coulomb energy U, even for very small values of U, unless U is identically zero. (Reproduced from Krishnamurthy *et al*., 1980, with permission from the American Physical Society. © 1980.)

4.1 $1/N$ calculations

Besides the NRG, another very successful technique for the single-impurity Anderson model has been the large-N expansion. Here N corresponds to the size of the impurity spin. While in archetypal Kondo systems the spin is 1/2, corresponding to $N = 2$, hardly a large number, in many alloy systems the magnetic moments have a reasonably large angular momentum. The $1/N$ method is in two parts, a mean field approximation, plus corrections, based on Gaussian approximation, to get the fluctuations from the mean field. The fluctuations enable the calculation of thermodynamics. The key benefits of the $1/N$ expansion have been its ability to obtain a unified approach to both the static and dynamic properties of magnetic alloys, and in particular the excitation spectrum. Dynamics are difficult for many techniques, and a good calculation provides insight into many key experiments. Also, unlike many perturbation methods, $1/N$ obtains a singlet ground state for Anderson and Kondo problems, which may be a clue to its success even for $N = 2$, spin-1/2 systems.

Pioneering work was done by Read and Newns, who developed the functional integral approach to $1/N$ calculations for the symmetric Anderson model (Read and Newns, 1983a; Newns and Read, 1987) (using formalism, in particular the slave-boson technique, laid by (Coleman, 1983, 1984, 1987). Over the following years, they and others calculated much of the transport coefficients, finding universal behavior especially in the Kondo regime. For a good review of the groundwork of $1/N$ techniques, see Bickers, (1987b). A major body of work for spectral functions for valence-fluctuating compounds was done using a $1/N$ technique by Gunnarsson and Schonhammer (1983). High-energy spectroscopy data and static susceptibility were calculated and fit to a wide range of materials using a single set of model parameters.

4.2 The two-impurity infinite-U Anderson model

Another advantage of the $1/N$ technique is that it can be straightforwardly extended to multiple impurities and even the lattice. For two impurities, it is the antiferromagnetic side, which poses the greatest challenges, and interest, to many alternative theoretical techniques. An example is the $1/N$ expansion done for the two-impurity problem, explicitly adding an RKKY term in order to span the full range of inter-impurity interactions (Jones, Kotliar and Millis, 1989; Millis, Kotliar and Jones, 1990).

In order to calculate for the Coulomb $U \to \infty$ limit, an auxiliary boson is added in the standard technique, giving a Hamiltonian:

$$\begin{aligned} H = & \sum_{\mathbf{k}\mathrm{m}} \varepsilon_{\mathrm{k}} \mathrm{c}^{+}_{\mathbf{k}\mathrm{m}} \mathrm{c}_{\mathbf{k}\mathrm{m}} + \sum_{\mathrm{m},\alpha=1,2} E_0 f^{+}_{\alpha\mathrm{m}} f_{\alpha\mathrm{m}} \\ & + V N^{1/2} \sum_{\mathbf{k}\mathrm{m},\alpha=1,2} (b^{+}_{\alpha} \mathrm{e}^{i\mathbf{k}\cdot\mathbf{r}\alpha} \mathrm{c}^{+}_{\mathbf{k}\mathrm{m}} f_{\alpha\mathrm{m}} + \mathrm{H.c.}) \\ & + \mathrm{I}/N \sum_{\mathrm{m}'\mathrm{m}} f^{+}_{1\mathrm{m}} f_{2\mathrm{m}} f^{+}_{2\mathrm{m}'} f_{1\mathrm{m}'} \end{aligned} \tag{10}$$

Here α labels spin sites 1 and 2, and the constraint is enforced $n_{\mathrm{f}\alpha} + n_{\mathrm{b}\alpha} = N/2$. In this constraint, $n_{\mathrm{f}\alpha}$ and $n_{\mathrm{b}\alpha}$ are the numbers of f electrons and auxiliary bosons at site α. N is the size of the spin, with the model valid in an $N \to \infty$ limit. I is the RKKY interaction, taken to be antiferromagnetic. Details of the subsequent analysis appear in Jones, Kotliar and Millis (1989).

The $1/N$ approach does find a phase transition for the case of particle-hole symmetry, and at about the right ratio of $T_{\mathrm{K}}/I \approx 0.5$, but (to leading order in $1/N$) it is primarily of first order rather than second. Since the order of the phase transition determines behavior of the thermodynamic properties in the entire region of the critical point, it is the thermodynamics of $1/N$, which differ the most, never diverging or strongly peaking at the critical point, as in the NRG solution. Nevertheless, the $1/N$ calculation does identify a critical parameter associated with particle–hole symmetry breaking, and indicates that breaking particle–hole symmetry can give rise to a gradual crossover rather than a transition, details which were confirmed by NRG calculations.

4.2.1 Multiple impurities and the Kondo lattice

Finally we touch on calculations for the lattice. It is here we overlap most with the chapter on heavy fermions, so this will be kept brief. Interestingly, many $1/N$ calculations for the Kondo lattice model show that Kondo effect occurs, but there is little interaction between local moments in the Kondo state. The ground state is a Fermi liquid. Other effects toward heavy-fermion behavior were shown by the early $1/N$ calculation for the lattice by Coleman (1983). There has been a large body of theoretical work on the Kondo lattice, using a variety of theoretical methods. Fairly recently a two-fluid model for the lattice was put forward (Nakatsuji, Pines and Fisk, 2004) composed of Kondo impurities and heavy electron Fermi liquids. Modern techniques for strongly correlated lattices developed within the last decade and a half include dynamical mean-field theory (Georges *et al*., 1996), a nonperturbative technique which effectively solves the problem at infinite number of dimensions. Also promising is density matrix renormalization group (DMRG) (White, 1992), a real-space renormalization, is an improvement on NRG, which optimizes the set of functions kept for basis states, to enable correct interactions with other sites, as well as on-site terms.

It is interesting to speculate, with all the exotic NFL states, which populate the few-impurity Kondo impurity systems, how much of this is likely to carry to the lattice. With the addition of degrees of freedom, will there be ever more unusual fixed points? A clue to this may be found from the two-impurity work in the most general cases, without particle–hole symmetry. In these, many of the NFL ground states are not reached, and the ground state is a Fermi liquid. It is likely that the most exotic fixed points are a result of a strong amount of local symmetry. In the lattice, there is a new symmetry, the periodicity of the material, which might lead to new types of interesting states, besides the heavy-fermion correlations, which have already been found. At this point a full solution of the Kondo or Anderson lattice is still pending. New experimental approaches such as construction of magnetic nanostructures using STM techniques also open possibilities for future interesting Kondo and Anderson model physics.

5 EXPERIMENTAL IMAGING USING STM TECHNIQUES

Experimentally, among the most promising for realizations of Kondo Hamiltonian systems have been two systems: quantum dots, for which the reader is referred to that chapter of this volume, and systems created by atomic manipulation and imaged by STM. We briefly review here the work on imaging Kondo systems at the atomic scale by STM. The single-impurity Kondo effect was first observed in 1998 for Co atoms on a Au(111) surface and for Ce atoms on a Ag(111) surface (Madhavan *et al*., 1998; Li, Schneider, Berndt and Delley, 1998). They observed a sharp Fano resonance (Újsághy, Kroha, Szunyogh and Zawadowski, 2000; Plihal and Gadzuk, 2001), characteristic of tunneling both into the impurity and also into the conduction states of the surface. The Crommie group subsequently measured the temperature-dependent electronic structure and observed the characteristic broadening of the Kondo resonance as temperature was increased (Nagaoka, Jamneala, Grobis and Crommie, 2002). A Kondo effect of the orbital moments can also occur (Kolesnychenko *et al*., 2002). In 2000 a remarkable feature was observed: the so-called quantum mirage effect (Manoharan, Lutz and Eigler, 2000). An ellipse was built of Co atoms, and one Co atom placed at just one focus of the ellipse. When the STM was placed over the Co atom, a Kondo resonance was observed. However, when imaging over the empty focus site, surprisingly the STM picked up a Kondo resonance as well, although with reduced amplitude: the mirage effect. If the foci were close together, this effect would be expected to include many-body correlations between the two sites. However, experimentally the foci were tens of angstroms apart, and the STM images were fit well by single-particle scattering calculations from a model Kondo phase shift (Fiete *et al*., 2001).

Kondo effects have also been observed in clusters of magnetic atoms. Clusters of Co on metallic single-walled carbon nanotubes give an effectively one-dimensional host for the observed Kondo effect (Odom, Huang, Cheung and Lieber, 2000). An antiferromagnetic trimer of Cr atoms also gives a Kondo effect (Jamneala, Madhavan and Crommie, 2001). Theoretical models indicate that for ferromagnetic clusters, the Kondo coupling is inversely proportional to the total spin of the cluster, and thus the Kondo temperature drops rapidly as the cluster size increases (Fiete, Zarand, Halperin and Oreg, 2002). Clusters can also have mesoscopic fluctuations of charge and magnetization, leading to asymmetric voltage dependence of the spectroscopic features.

The addition of surface layers of adsorbates between the magnetic impurity and the rest of the surface can change the Kondo features (Hirjibehedin, Lutz and Heinrich, 2006; Schneider *et al*., 2005a), leading to questions of whether the surface Kondo effect primarily concerns just the electrons of the surface states, and to what extent the bulk electrons are involved. Experiments show that the surface/bulk contribution ratio varies to some degree based on the combination of magnetic impurity and surface adsorbate layer, but that primarily the Kondo effect is a bulk effect (Knorr, Schneider and Diekhöner, 2002; Schneider *et al*., 2005b). This has been shown theoretically as well,

using properties of the electronic states of both surface and bulk (Lin, Castro Neto and Jones, 2005).

It seems clear that as theorists explore Kondo Hamiltonians of various symmetries, number of impurities, and channels, interesting NFL fixed points, and intriguing phase diagrams in general, will continue to be found. Likewise atomic manipulation on the STM, structures made with quantum dots, and spins in other low-dimensional systems provide a promising experimental ground for exploring Kondo physics, and even tuning the systems to achieve these special critical points predicted by theory which often need high symmetry. Finally, progress on understanding the phase diagram of the Kondo lattice will proceed on (at least) three fronts: with new theoretical techniques and insightful models, with new materials discoveries with bulk Kondo lattice materials, and with increased sophistication and imaging techniques, both real space and spectroscopy, from the STM, which will someday be able to build and measure a purpose built Kondo lattice.

REFERENCES

Aeppli, G. and Fisk, Z. (1992). Kondo insulators. *Comments on Condensed Matter Physics*, **16**, 155–165.

Affleck, I. and Ludwig, A. (1992). Exact critical theory of the two-impurity Kondo model. *Physical Review Letters*, **68**, 1046–1049.

Affleck, I. and Ludwig, A.W.W. (1993). Exact conformal-field-theory results on the multichannel Kondo effect: single-fermion Green's function, self-energy, and resistivity. *Physical Review B*, **48**, 7297–7321.

Affleck, I., Ludwig, A.W.W. and Jones, B.A. (1995). Conformal-field-theory approach to the two-impurity Kondo problem: comparison with numerical renormalization-group results. *Physical Review B*, **52**, 9528–9546.

Affleck, I., Ludwig, A., Pang, H.B. and Cox, D.L. (1992). Relevance of anisotropy in the multichannel Kondo effect: comparison of conformal field theory and numerical renormalization-group results. *Physical Review B*, **45**, 7918–7935.

Anderson, P.W. (1961). Localized magnetic states in metals. *Physical Review*, **124**, 41–53.

Anderson, P.W. (1984). *Basic Notions of Condensed Matter Physics*, The Benjamin/Cummings Publishing Company: Menlo Park.

Anderson, P.W. and Yuval, G. (1969). Exact results in the Kondo problem: equivalence to a classical one-dimensional Coulomb gas. *Physical Review Letters*, **23**, 89–92.

Anderson, P.W., Yuval, G. and Hamann, D.R. (1970). Exact results in the Kondo problem. II. Scaling theory, qualitatively correct solution, and some new results on one-dimensional classical statistical models. *Physical Review B*, **1**, 4464–4473.

Andrei, N. (1980). Diagonalization of the Kondo hamiltonian. *Physical Review Letters*, **45**, 379–382.

Andrei, N. and Destri, C. (1984). Solution of the multichannel Kondo problem. *Physical Review Letters*, **52**, 364–367.

Andrei, N. and Lowenstein, J. (1981). Scales and scaling in the Kondo model. *Physical Review Letters*, **46**, 356–360.

Bazhanov, V.V., Lukyanov, S.L. and Tsvelik, A.M. (2003). Analytical results for the Coqblin-Schrieffer model with generalized magnetic fields. *Physical Review B*, **68**, 94427–94431.

Bickers, N.E., Cox, D.L. and Wilkins, J.W. (1987a). Self-consistent large-N expansion for normal-state properties of dilute magnetic alloys. *Physical Review B*, **36**, 2036–2079.

Bickers, N.E. (1987b). Review of techniques in the large-N expansion for dilute magnetic alloys. *Reviews of Modern Physics*, **59**, 845–939.

Campo, V.L., Jr. and Oliveira, L.N. (2005). Alternative discretization in the numerical renormalization-group method. *Physical Review B*, **72**, 104432–104441.

Coleman, P. (1983). 1/N expansion for the Kondo lattice. *Physical Review B*, **28**, 5255–5262.

Coleman, P. (1984). New approach to the mixed-valence problem. *Physical Review B*, **29**, 3035–3044.

Coleman, P. (1987). Mixed valence as an almost broken symmetry. *Physical Review B*, **35**, 5072–5116.

Coqblin, B. and Schrieffer, J.R. (1969). Exchange interaction in alloys with cerium impurities. *Physical Review*, **185**, 847–853.

Cox, D.L. (1987). Quadrupolar Kondo effect in uranium heavy electron materials? *Physical Review Letters*, **59**, 1240–1243.

Cox, D.L. (1988). The quadrupolar Kondo effect: a new mechanism for heavy electrons. *Journal of Magnetism and Magnetic Materials*, **76**(77), 53–58.

Cox, D.L. and Jarrell, M. (1996). The two-channel Kondo route to non-Fermi liquid physics. *Journal of Physics C*, **8**, 9825–9853.

Cox, D.L. and Ruckenstein, A. (1993). Spin-flavor separation and non-Fermi-liquid behavior in the multichannel Kondo problem: a large-N approach. *Physical Review Letters*, **71**, 1613–1616.

Cox, D.L. and Zawadowski, A. (1999). *Exotic Kondo Effects in Metals*, Taylor & Francis: Philadelphia.

Cragg, D.M. and Lloyd, P. (1979). Kondo hamiltonians with a non-zero ground-state spin. *Journal of Physics C*, **12**, L215–L218.

Doniach, S. (1977). The Kondo lattice and weak antiferromagnetism. *Physica B & C*, **91**, 231–234.

Fiete, G.A., Hersch, J.S., Heller, E.J., *et al*. (2001). Scattering theory of Kondo mirages and observation of single Kondo atom phase shift. *Physical Review Letters*, **86**, 2392–2395.

Fiete, G.A., Zarand, G., Halperin, B.I. and Oreg, Y. (2002). Kondo effect and STM spectra through ferromagnetic nanoclusters. *Physical Review B*, **66**, 24431–24447.

Fye, R.M., Hirsch, J.E. and Scalapino, D.J. (1987). Kondo effect versus indirect exchange in the two-impurity Anderson model: A Monte Carlo study. *Physical Review B*, **35**, 4901–4908.

Georges, A., Kotliar, G., Krauth, W. and Rozenberg, M. (1996). Dynamical mean-field theory of strongly correlated fermion systems and the limit of infinite dimensions. *Reviews of Modern Physics*, **68**, 13–125.

Gunnarsson, O. and Schonhammer, K. (1983). Electron spectroscopies for Ce compounds in the impurity model. *Physical Review B*, **28**, 4315–4341.

Hewson, A.C. (1993). *The Kondo Problem to Heavy Fermions*, Cambridge University Press: Cambridge.

Hirjibehedin, C.F., Lutz, C.P. and Heinrich, A.J. (2006). Spin coupling in engineered atomic structures. *Science*, **312**, 1021–1024.

Hirsch, J.E. and Fye, R.M. (1986). Monte carlo method for magnetic impurities in metals. *Physical Review Letters*, **56**, 2521–2524.

Ingersent, K., Jones, B.A. and Wilkins, J.W. (1992). Study of the two-impurity, two-channel Kondo hamiltonian. *Physical Review Letters*, **69**, 2594–2597.

Jamneala, T., Madhavan, V. and Crommie, M.F. (2001). Kondo response of a single antiferromagnetic chromium trimer. *Physical Review Letters*, **87**, 256804–256807.

Jayaprakash, C., Krishna-murthy, H.R. and Wilkins, J.W. (1981). Two-impurity Kondo problem. *Physical Review Letters*, **47**, 737–740.

Jones, B.A. (1990). Antiferromagnetic phase instability in the two-impurity Kondo problem. In *Field Theories in Condensed Matter Physics*, Tesanovic, Z. (Ed.), Addison-Wesley: Redwood, pp. 87–103.

Jones, B.A. (1991). Pair correlation effects in heavy fermions. *Physica B*, **171**, 53–60.

Jones, B.A., Kotliar, B.G. and Millis, A.J. (1989). Mean-field analysis of two antiferromagnetically coupled Anderson impurities. *Physical Review B*, **39**, 3415–3418.

Jones, B.A. and Varma, C.M. (1987). Study of two magnetic impurities in a Fermi gas. *Physical Review Letters*, **58**, 843–846.

Jones, B.A., Varma, C.M. and Wilkins, J.W. (1988). Low-temperature properties of the two-impurity Kondo hamiltonian. *Physical Review Letters*, **61**, 125–128.

Knorr, N., Schneider, M.A., Diekhöner, L., *et al*. (2002). Kondo effect of single Co adatoms on Cu surfaces. *Physical Review Letters*, **88**, 96804–96807.

Kolesnychenko, O.Yu., De Kort, R., Katsnelson, M.I., *et al*. (2002). Real-space imaging of an orbital Kondo resonance on the Cr(001) surface. *Nature*, **415**, 507–509.

Kondo, J. (1964). Resistance minimum in dilute magnetic alloys. *Progress of Theoretical Physics*, **32**, 37–49.

Krishnamurthy, H.R., Wilkins, J.W. and Wilson, K.G. (1980a). Renormalization-group approach to the Anderson model of dilute magnetic alloys. I. Static properties for the symmetric case. *Physical Review B*, **21**, 1003–1043.

Krishnamurthy, H.R., Wilkins, J.W. and Wilson, K.G. (1980b). Renormalization-group approach to the Anderson model of dilute magnetic alloys. II. Static properties for the asymmetric case. *Physical Review B*, **21**, 1044–1083.

Lee, P.A., Rice, T.M., Serene, J.W., *et al*. (1986). Theories of heavy-electron systems. *Comments on Condensed Matter Physics*, **12**, 99–161.

Li, J., Schneider, W.D., Berndt, R. and Delley, B. (1998). Kondo scattering observed at a single magnetic impurity. *Physical Review Letters*, **80**, 2893–2896.

Lin, C-Y., Castro Neto, A.H. and Jones, B.A. (2005). Microscopic theory of the single impurity surface Kondo resonance. *Physical Review B*, **71**, 35417–35427.

Madhavan, V., Chen, W., Jamneala, T., *et al*. (1998). Tunneling into a single magnetic atom: spectroscopic evidence of the Kondo resonance. *Science*, **280**, 567–569.

Manoharan, H., Lutz, C. and Eigler, D. (2000). Quantum mirages formed by coherent projection of electronic structure. *Nature*, **403**, 512–515.

Millis, A.J., Kotliar, B.G. and Jones, B.A. (1990). Antiferromagnetic phase instability in the two-impurity Kondo problem. In *Field Theories in Condensed Matter Physics*, Tesanovic, Z. (Ed.), Addison-Wesley: Redwood, pp. 159–166.

Nagaoka, K., Jamneala, T., Grobis, M. and Crommie, M.F. (2002). Temperature dependence of a single Kondo impurity. *Physical Review Letters*, **88**, 77205–77208.

Nakatsuji, S., Pines, D. and Fisk, Z. (2004). Two fluid description of the Kondo lattice. *Physical Review Letters*, **92**, 16401–16404.

Newns, D.M. and Read, N. (1987). Mean-field theory of intermediate valence/heavy fermion systems. *Advances in Physics*, **36**, 799–849.

Nozières, P. (1974). A "Fermi-liquid" description of the Kondo problem at low temperatures. *Journal of Low Temperature Physics*, **17**, 31–42.

Nozières, P. and Blandin, A. (1980). Kondo effect in real metals. *Journal de Physique*, **41**, 193–211.

Odom, T.W., Huang, J.L., Cheung, C.L. and Lieber, C.M. (2000). Magnetic clusters on single-walled carbon nanotubes: the Kondo effect in a one-dimensional host. *Science*, **290**, 1549–1552.

Pang, H.B. and Cox, D.L. (1991). On the stability of the fixed-point of the two-channel Kondo hamiltonian. *Physical Review B*, **44**, 9454–9457.

Plihal, M. and Gadzuk, J.W. (2001). Nonequilibrium theory of scanning tunneling spectroscopy via adsorbate resonances: nonmagnetic and Kondo impurities. *Physical Review B*, **63**, 85404–85426.

Rajan, V.T., Lowenstein, J.H. and Andrei, N. (1982). Thermodynamics of the Kondo model. *Physical Review Letters*, **49**, 497–500.

Read, N. and Newns, D. (1983a). A new functional integral formalism for the degenerate Anderson model. *Journal of Physics C-Solid State Physics*, **16**, L1055–L1060.

Read, N. and Newns, D. (1983b). On the solution of the Coqblin-Schreiffer Hamiltonian by the large-N expansion technique. *Journal of Physics C-Solid State Physics*, **16**, 3273–3295.

Ruderman, M.A. and Kittel, C. (1954). Indirect exchange coupling of nuclear magnetic moments by conduction electrons. *Physical Review*, **96**, 99–102.

Schlottmann, P. (1983). Bethe-ansatz solution of the Anderson model of a magnetic impurity with orbital degeneracy. *Physical Review Letters*, **50**, 1697–1700.

Schneider, M.A., Vitali, L., Wahl, P., *et al*. (2005a). Kondo state of Co impurities at noble metal surfaces. *Applied Physics A*, **80**, 937–941.

Schneider, M.A., Wahl, P., Diekhöner, L., *et al*. (2005b). Kondo effect of Co Adatoms on Ag monolayers on noble metal surfaces. *Japanese Journal of Applied Physics*, **44**, 5328–5331.

Schrieffer, J.R. and Wolff, P.A. (1966). Relation between the Anderson and Kondo hamiltonians. *Physical Review*, **149**, 491–492.

Silva, J.B., Lima, W.L.C., Oliveira, W.C., *et al*. (1996). Particle-hole asymmetry in the two-impurity Kondo model. *Physical Review Letters*, **76**, 275–278.

Újsághy, O., Kroha, J., Szunyogh, L. and Zawadowski, A. (2000). Theory of the Fano resonance in the STM tunneling density of states due to a single Kondo impurity. *Physical Review Letters*, **85**, 2557–2560.

White, R.M. (1983). *Quantum Theory of Magnetism*, Springer-Verlag: New York. This reference has a very useful section on the Kondo effect and Anderson model in Chapter 7.

White, S. (1992). Density matrix formulation for quantum renormalization groups. *Physical Review Letters*, **69**, 2863–2866.

Wiegmann, P.B. (1980). Exact solution of s-d exchange model at T=0. *Pis'ma v Zhurnal Eksperimental'noi i Theoreticheskoi Fiziki (Letters to Journal of Experimental and Theoretical Physics)*, **31**, 392–398.

Wiegmann, P.B. (1981). Exact solution of s-d exchange model at T=0. *JETP Letters*, **31**, 364–370.

Wilson, K.G. (1975). The renormalization group: critical phenomena and the Kondo problem. *Reviews of Modern Physics*, **47**, 773–840.

Orbital Physics in Transition-metal Oxides: Magnetism and Optics

Peter Horsch
Max-Planck-Institut für Festkörperforschung, Stuttgart, Germany

1 INTRODUCTION

Strong correlations in transition-metal oxides (TMO) generate spins and orbitals as low-energy degrees of freedom. Their interplay with both real-charge motion and virtual-charge excitations lead to a fascinating richness of spin–charge–orbital-ordered phases, to striking phenomena like the colossal magnetoresistance (CMR), the switching of charge-ordered phases into metallic phases by applied magnetic fields, and many other fascinating effects (Tokura and Nagaosa, 2000; Tokura, 2003; Imada, Fujimori and Tokura, 1998). The focus of this article is on recent developments while discussions of known concepts are kept short. As compensation the article has a large bibliography.

Handbook of Magnetism and Advanced Magnetic Materials. Edited by Helmut Kronmüller and Stuart Parkin. Volume 1: *Fundamentals and Theory*. ISBN: 978-0-470-02217-7.

In undoped compounds, magnetism is determined via Heisenberg–Anderson superexchange (SE) interactions between spins (Anderson, 1959), which result from virtual-charge excitations. In orbital-degenerate systems, magnetism is controlled by spin-orbital models. These models contain apart from the Heisenberg-like spin dynamics also the quantum dynamics of the orbitals themselves as well as coupled spin-orbital interactions; that is, in addition to the relativistic spin-orbit interaction. In simple terms: Orbitals determine the interactions among spins, while spins determine the interaction between orbitals. In certain cases, the exchange interaction between spins may even fluctuate between ferromagnetic (FM) and antiferromagnetic (AF) if orbitals are dominated by quantum fluctuations. However, this subtle interplay may be controlled or quenched via an interaction with the lattice, like the Jahn–Teller (JT) interaction in $LaMnO_3$ which favors alternating orbitals and thereby selects ferromagnetism in the (a, b) plane and antiferromagnetism along c direction. In fact this is the typical case, that is, magnetism controlled by the Goodenough–Kanamori (GK) rules, where fixed, occupied orbitals determine the magnetic structure. Yet there are other systems which show evidence of the more complex interplay of spin and orbital quantum fluctuations. Candidates discussed here are t_{2g} systems like the cubic titanates and vanadates, and the orbital-Peierls effect in YVO_3.

The study of one-dimensional spin-orbital models has been an active field, stimulated by specific analytic and numerical tools. This has given some important deeper insights into the features of spin-orbital models. Some

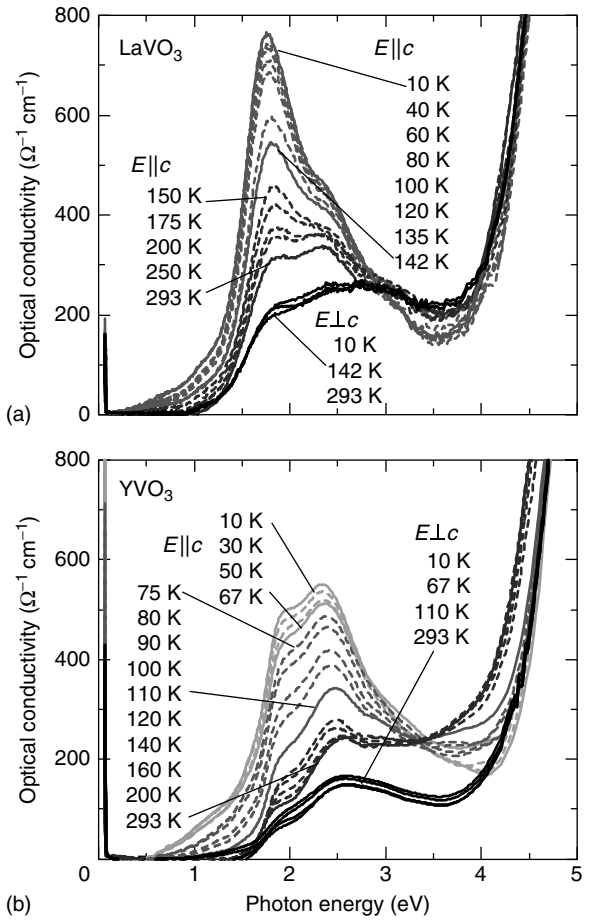

Figure 1. Temperature dependence and anisotropy of optical conductivity of cubic vanadate compounds $LaVO_3$ and YVO_3 reflects the interrelation of spectral weight transfers and magnetic structure (Data reproduced from Miyasaka, Okimoto and Tokura, 2002.) The strong increase of spectral weight for c polarization in the range of the high-spin multiplet transition ($1.5 < \omega < 2.5$ eV) with decreasing temperature reflects the evolution of ferromagnetism along c direction. The strong anisotropy of the basically cubic crystal structure is due to the magnetic anisotropy, that is, the so-called C-type magnetic order with antiferromagnetic correlations in the (ab) plane and ferromagnetism along c.

instructive aspects are described, such as the interplay of orbital and spin correlations in SU(4) and other spin-orbital models, spin-orbital entanglement, and the role of composite spin-orbital fluctuations.

Virtual-charge excitations which determine SE interactions, and thereby magnetism, correspond, on the other hand, to real optical transitions (see Figure 1). This fact provides an important link between the SE energy and the partial sum rules for the different optical multiplet transitions. Thus, the temperature dependence of the optical spectral weights and spectral weight transfers, particularly at phase transitions, are determined by the low-energy spin-orbital model. This leads to the unification of optics and magnetism, that is, in the sense that it allows to combine the interpretation of data obtained by optical spectroscopy and magnetic neutron scattering. Thus it yields important guidance for the further exploration of the electronic structure of TMO.

Finally, key features of the interplay of spin-, charge-, and orbital degrees of freedom in doped TMO are addressed. As examples, some of the complex-ordered phases and the CMR of manganites are discussed. Starting from a generalized orbital-degenerate Kondo-lattice model (KLM) we discuss the double-exchange (DE) interaction and the evidence for the orbital degree of freedom in the intrinsic CMR. Besides, the orbital liquid phase and the complexity of spin-/orbital-ordered phases is touched with a brief discussion of the charge-ordered phases in half-doped manganites.

There is another aspect of general importance and of conceptual novelty. In doped Mott insulators with degenerate or nearly degenerate orbitals charge carriers will move as composite polarons, where the doped holes are not only accompanied (or dressed) by lattice distortions but also by orbital excitations and spin clouds. A particular remarkable example is the orbital polaron in manganites which in combination with spin disorder in the paramagnetic phase offers an explanation for an intrinsic mechanism of CMR.

This field has already a history of about half a century. Its origin is usually connected with the seminal experimental work by Jonker and van Santen (1950) on the magnetotransport of manganites. Subsequently Zener (1951) proposed the DE mechanism and was thereby able to explain the appearance of ferromagnetism and metallicity at moderate doping. The upcoming thermal neutron scattering technique provided deep insight into the magnetic structure. The data obtained in the pioneering neutron work by Wollan and Koehler (1955) was subsequently interpreted by Goodenough, Kanamori, and others (Goodenough, 1955, 1963; Kanamori, 1959). The important insights achieved in those early years, revealed the interplay of magnetic structure and orbital occupation (Pauli principle and Hunds' rule). The insights up to the year 1963 has been summed up by Anderson in an article in 'Magnetism' by Rado and Suhl (Anderson, 1963).

Formally this physics is described by spin-orbital models, which may be interpreted as generalized Heisenberg models, where the magnetic exchange integrals are themselves operators which are controlled by the orbital degrees of freedom. SE models for transition-metal perovskites with partly filled degenerate orbitals have a more complex structure than for nondegenerate orbitals and have been discussed in a seminal review by Kugel and Khomskii (1982a). Such models allow for both AF and FM SE (Kugel and Khomskii, 1982a; Cyrot and Lyon-Caen, 1975; Inagaki, 1975; Castellani, Natoli and Ranninger, 1978). The different contributions to SE results

from the multiplet structure of excited transition metal ions which depends on the Hund's exchange J_H and generates a competition between high-spin and low-spin excitations. The exchange interactions are then intrinsically frustrated *even on a cubic lattice*, which enhances quantum effects both for e_g, (Khaliullin and Oudovenko, 1997; Feiner, Oleś and Zaanen, 1998; Khaliullin and Kilian, 1999; Oleś, Feiner and Zaanen, 2000) and for t_{2g} systems. (Khaliullin and Maekawa, 2000; Khaliullin, 2001; Khaliullin, Horsch and Oleś, 2001). This frustration is partly removed in anisotropic AF phases, which break the cubic symmetry and may lead to dimensionality changes, such as in A-type AF phase realized in $LaMnO_3$, or in C-type AF phase in $LaVO_3$.

The renaissance of orbital physics in the 90th was triggered by the discovery of CMR in the manganites (von Helmolt *et al*., 1993; Jin *et al*., 1994). The experimental and theoretical work on metal–insulator transitions in TMO has been subsequently reviewed by (Imada, Fujimori and Tokura, 1998). CMR has been reviewed by Kaplan and Mahanti (1998) and Tokura (2006) and orbital specific aspects have been addressed by Oleś, Cuoco and Perkins (2000), and Rückamp *et al*. (2005) and Khaliullin (2005). Moreover a number of valuable textbooks have already appeared (Dagotto, 2003; Maekawa *et al*., 2004; Fazekas, 1999).

This chapter describes CMR as an intrinsic phenomenon where the orbital degree of freedom plays a key role. The orbital liquid phase and various spin-, charge-, and orbital-ordered phases are discussed in the framework of theoretical models, such as the orbital degenerated KLM and the orbital $t-J$ model. Although advanced many-body treatment of the quantum physics characteristic for spin-orbital models is required in general, we want to present here simple principles which help to understand the heart of the problem and give some guidelines for interpreting experiments.

This text focuses on the generalization of spin models into spin-orbital models in the case of orbital degeneracy, thereby likewise important developments in the field are not touched. Most importantly the large progress in the field of *ab initio* band-structure methods is not covered. This field has made a significant leap forward through a merger with dynamical mean-field theory (DMFT) (Metzner and Vollhardt, 1989; Georges, Kotliar, Krauth and Rozenberg, 1996; Kotliar and Vollhardt, 2004), which allows to describe the Mott transition, that was out of reach of the traditional density-functional approaches. Still these approaches are not fully *ab initio*, as intermediate multiband Hubbard models need to be defined and then analyzed by help DMFT (Held). Often the more pragmatic LDA + U approach (Anisimov, Zaanen and Andersen, 1991) or the Hartree–Fock method (Solovyev, 2006) are used to compensate for the deficiency of LDA to describe Mott gaps.

2 ORBITAL-DEGENERATE MOTT INSULATORS AND SPIN-ORBITAL MODELS

2.1 Multiband Hubbard model and strong correlations

TMO with integer valence electron number are frequently insulators, that is Mott insulators because of the strong intra-atomic Coulomb interaction, and not because of a gap in the single-particle band structure. Typically this happens when the bandwidth W is smaller than the intraorbital Coulomb matrixelement U. At small hopping t the Mott-insulating state is formed by one single ionic configuration, for example, Mn^{3+} in $LaMnO_3$. All other ionization states are separated by large gaps. Such a state is very distinct from an uncorrelated or Hartree–Fock state where the local charge fluctuates strongly and involves all possible ionization states. In a Mott insulator the neighboring valency, for example, Mn^{2+} in $LaMnO_3$, is suppressed in the wave function by the factor t/U, and Mn^{1+} by $(t/U)^2$. It is this suppression of charge fluctuations and the emergence of the ionic structure which forms the basis of SE, that is, of spin models like the Heisenberg model or in the case of degenerate orbitals the spin-orbital models.

The effective spin-orbital models of TMO with partly filled degenerate orbitals depend in a characteristic way upon those aspects of the electronic structure which decide whether a given strongly correlated system can be classified as a Mott insulator or as a charge transfer (CT) insulator. As suggested in the original classification of Zaanen, Sawatzky and Allen (1985), the energy of the d–p CT excitation Δ has to be compared with the Coulomb interaction U – if $U < \Delta$, the first excitation is at a transition-metal ion and the system is a Mott insulator, otherwise it is a CT insulator. Yet both are strongly correlated insulators, in one limit the dominant virtual excitations are of d–d type, whereas in the other limit they are of p–d type. One may consider this issue more precisely by analyzing the full multiplet structure, and comparing the lowest excitation energy (to a high-spin configuration) *at a transition-metal ion*, $\varepsilon_{HS} = U - 3J_H$, with that of the lowest CT excitation (of energy Δ) *between a transition-metal ion and a ligand ion*. (We note, however, that frequently the average energy of a CT type excitation $\overline{\Delta}$ is considered instead and compared with U.) One can regard a given perovskite as a *charge transfer insulator* if $\varepsilon_{HS} > \Delta$, and as a *Mott–Hubbard insulator* if $\varepsilon_{HS} < \Delta$. By analyzing these parameters it follows that the late TMO may be classified as CT insulators (Imada, Fujimori and Tokura, 1998). In this case, important new contributions to the SE arise (Goodenough, 1963; Zaanen and Oleś, 1988; Eskes

and Jefferson, 1993; Mostovoy and Khomskii, 2004) called *charge transfer terms*. We shall avoid this discussion here, and refer to Oleś, Khaliullin, Horsch and Feiner (2005) for a detailed discussion of CT excitations in $KCuF_3$ and the $LaMnO_3$.

The spin-orbital SE model is an effective low-energy Hamiltonian which allows to discuss excitations on the energy scale $J \sim t^2/U$, such as spin waves and orbital excitations but also polaron formation and transport properties in the doped case. A convenient starting point for the derivation of SE is the multiband Hubbard model for the d-electron bands. First we consider the effective single-particle Hamiltonian operator H_0 for the transition-metal ion states, where the ligand states are integrated out. Hence only the magnetic ions appear explicitly in this formulation:

$$H_0 = \sum_{i\alpha\sigma} \varepsilon_{i\alpha} n_{i\alpha\sigma} + \sum_{ij,\alpha,\beta,\sigma} t_{i,j}^{\alpha,\beta} a_{i\alpha\sigma}^{\dagger} a_{j\beta\sigma} \qquad (1)$$

Here $\varepsilon_{i\alpha}$ is the single-particle energy of an electron in orbital α at site i, $n_{i\alpha\sigma}$ is the number operator that determines the number of electrons with spin σ in orbital α at site i. The second term describes the kinetic energy, that is, the hopping of electrons from site j to site i in terms of annihilation and creation operators $a_{j\beta\sigma}$ and $a_{i\alpha\sigma}^{\dagger}$, respectively. $t_{i,j}^{\alpha,\beta}$ are effective hopping elements via ligand orbitals – they depend on the type of considered orbitals, t_{2g} or e_g (Figure 2), as discussed in Andersen, Klose and Nohl (1978) and Zaanen and Oleś (1993), and are proportional to t_{pd}^2/Δ. The energy scale for the hopping is set by the largest hopping element t: the (ddσ) element in case of e_g systems, and the (ddπ) element when only π bonds are considered in systems with degenerate and partly filled t_{2g} orbitals. Whereas the hopping between t_{2g} orbitals is diagonal along the cubic axis, the e_g electrons do have off-diagonal matrix elements. The orientation of the e_g basis orbitals $\{|x\rangle, |z\rangle\} = \{x^2 - y^2, 3z^2 - r^2\}$ is reflected in the transfer matrices that describe the hopping in the (a, b) plane and along the c axis, respectively.

$$t_{ij||a(b)}^{\alpha,\beta} = \frac{t}{4}\begin{pmatrix} 3 & \mp\sqrt{3} \\ \mp\sqrt{3} & 1 \end{pmatrix}, t_{ij||c}^{\alpha,\beta} = t\begin{pmatrix} 0 & 0 \\ 0 & 1 \end{pmatrix} \qquad (2)$$

Here $\mp$ distinguish hopping along the a and b cubic axis. The flexibility to choose the occupied orbital as some linear combination of the two basis orbitals is the underlying reason for the large flexibility of e_g systems to form complex orbital and spin-ordered patterns. The orbital state at site i:

$$|\theta\rangle = \cos\left(\frac{\theta}{2}\right)|z\rangle + \sin\left(\frac{\theta}{2}\right)|x\rangle \qquad (3)$$

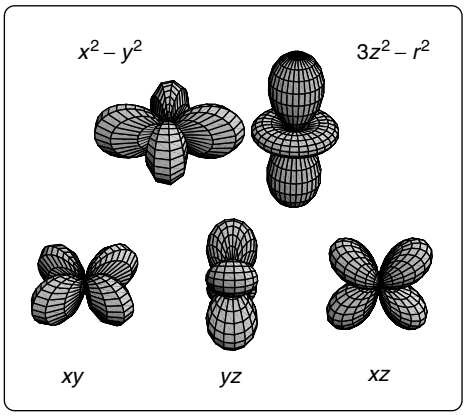

(a)

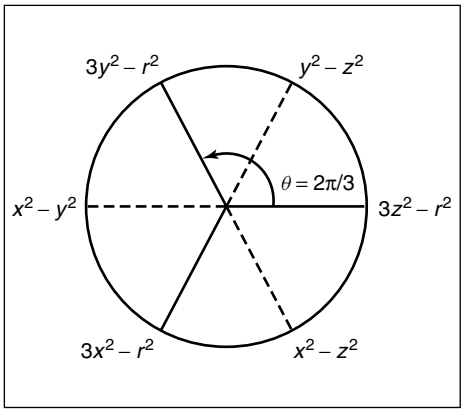

(b)

Figure 2. (a) In a cubic crystal field the degeneracy of d orbitals is lifted. The energy of the e_g orbitals ($x^2 - y^2$ and $3z^2 - r^2$) is higher than the t_{2g} subgroup (xy, yx, zy) because the lobes of e_g orbitals at the transition metal A point toward the negative O ions in the AO_6 octahedra, whereas the t_{2g} orbitals point in between. (b) Schematic representation of states that can be obtained from the two e_g basis states by linear combination (rotation by angle θ, see equation (3)).

is here parameterized by an angle θ which defines the amplitudes of the orbital states

$$|z\rangle \equiv (3z^2 - r^2)/\sqrt{6}, \quad |x\rangle \equiv (x^2 - y^2)/\sqrt{2} \qquad (4)$$

being a local e_g orbital basis at each site. This remarkable flexibility offers the possibility to lower the dimensionality and to optimize thereby the SE energy, or in doped systems the kinetic energy.

For noninteracting electrons the Hamiltonian H_0 would lead to tight-binding bands, but in a Mott insulator the large Coulomb interaction U suppresses charge excitations in the regime of $U \gg t$. Thus for integer electron number per transition-metal ion the hopping elements can

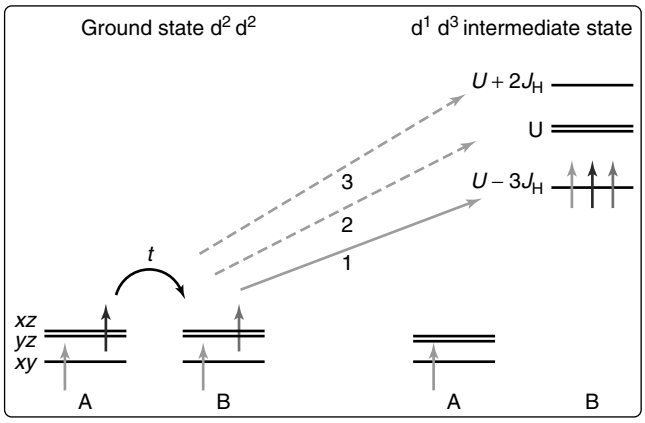

Figure 3. Sketch of superexchange (charge) excitations $\mathrm{d}_i^2\mathrm{d}_j^2 \rightarrow \mathrm{d}_i^3\mathrm{d}_j^1$ between two $S = 1$ V^{2+} ions. Because of Hund's rule the high-spin multiplet state (of the d^3 ion) is the lowest intermediate state ($U - 3J_\mathrm{H}$). Along c direction only xz and yz orbital have finite hopping matrix elements. With one electron in xy due to crystal-field splitting, the remaining electron of ion A is either in xz or yz and can form an orbital singlet with its neighbor B, while spins align ferromagnetically, and thereby profit from the virtual transition into the high-spin state at $U - 3J_\mathrm{H}$.

only contribute via virtual excitations, leading to the SE (Figure 3).

The SE in the 3d *cubic* systems with orbital degeneracy is described by spin-orbital models, which arise from virtual-charge excitations between two neighboring transition-metal ions, $\mathrm{d}_i^m\mathrm{d}_j^m \rightleftharpoons \mathrm{d}_i^{m+1}\mathrm{d}_j^{m-1}$, which involve an increase of energy owing to the Coulomb interactions. Such transitions are mediated by the ligand orbitals between the two ions and have the same roots as the SE in a Mott insulator with nondegenerate orbitals (Anderson, 1959). Their multiplet structure depends on the involved ionic configurations and the strength of the Hund coupling J_H. The relevant multiplet energies have to be determined by analyzing the eigenstates of the local Coulomb interactions H_int, where $H = H_0 + H_\mathrm{int}$ is the multiband Hubbard Hamiltonian:

$$\begin{aligned} H_\mathrm{int} = {} & U\sum_{i\alpha} n_{i\alpha\uparrow}n_{i\alpha\downarrow} \\ & + \sum_{i,\alpha<\beta}\Big(U_{\alpha\beta} - \frac{1}{2}J_{\alpha\beta}\Big)n_{i\alpha}n_{i\beta} - 2\sum_{i,\alpha<\beta} J_{\alpha\beta}\mathbf{S}_{i\alpha}\cdot\mathbf{S}_{i\beta} \\ & + \sum_{i,\alpha<\beta} J_{\alpha\beta}\Big(\mathrm{d}^\dagger_{i\alpha\uparrow}\mathrm{d}^\dagger_{i\alpha\downarrow}\mathrm{d}_{i\beta\downarrow}\mathrm{d}_{i\beta\uparrow} + \mathrm{d}^\dagger_{i\beta\uparrow}\mathrm{d}^\dagger_{i\beta\downarrow}\mathrm{d}_{i\alpha\downarrow}\mathrm{d}_{i\alpha\uparrow}\Big) \end{aligned} \quad (5)$$

with $\overline{\sigma} = -\sigma$. The multiplet structure depends in the general case on three Racah parameters A, B, and C (Griffith, 1971). In solids these parameters are screened and therefore smaller than the tabulated atomic values (Griffith, 1971). Whereas the intraorbital Coulomb element

$$U = A + 4B + 3C \quad (6)$$

is identical for all 3d orbitals, the interorbital Coulomb and exchange elements, $U_{\alpha\beta}$ and $J_{\alpha\beta}$, are anisotropic and depend on the involved pair of orbitals; the values of $J_{\alpha\beta}$ are given in Table 1. The Coulomb and exchange elements are related to the intraorbital element U by a relation which guarantees the invariance of interactions under rotation in the orbital space,

$$U = U_{\alpha\beta} + 2J_{\alpha\beta} \quad (7)$$

In cases where only the orbitals of one type ($\mathrm{e_g}$ or $\mathrm{t_{2g}}$) are partly filled, as, for example, in the titanates, vanadates, or copper fluorides, all relevant exchange elements $J_{\alpha\beta}$ are the same (see Table 1) and one may use a simplified form of on-site interactions (Oleś, 1983)

$$\begin{aligned} H_\mathrm{int}^{(0)} = {} & U\sum_{i\alpha} n_{i\alpha\uparrow}n_{i\alpha\downarrow} + \Big(U - \frac{5}{2}J_\mathrm{H}\Big)\sum_{i,\alpha<\beta} n_{i\alpha}n_{i\beta} \\ & + J_\mathrm{H}\sum_{i,\alpha<\beta}\Big(\mathrm{d}^\dagger_{i\alpha\uparrow}\mathrm{d}^\dagger_{i\alpha\downarrow}\mathrm{d}_{i\beta\downarrow}\mathrm{d}_{i\beta\uparrow} + \mathrm{d}^\dagger_{i\beta\uparrow}\mathrm{d}^\dagger_{i\beta\downarrow}\mathrm{d}_{i\alpha\downarrow}\mathrm{d}_{i\alpha\uparrow}\Big) \\ & - 2J_\mathrm{H}\sum_{i,\alpha<\beta}\mathbf{S}_{i\alpha}\cdot\mathbf{S}_{i\beta} \end{aligned} \quad (8)$$

with only two parameters: the intraorbital Coulomb (or Hubbard) interaction parameter U (6) and the Hund's coupling J_H, being $4B + C$ for $\mathrm{e_g}$ and $3B + C$ for $\mathrm{t_{2g}}$ systems, respectively. However, when both types of orbitals are partly filled (as in the manganites) and therefore both participate in charge excitations, the Hamiltonian (8) is only approximate, and the full excitation spectra of the transition-metal ions (Griffith, 1971) which follow from equation (5) have to be used instead. A few examples of spectra for $\mathrm{d}_i^m\mathrm{d}_j^m \rightleftharpoons \mathrm{d}_i^{m+1}\mathrm{d}_j^{m-1}$ charge excitations at transition-metal ions are shown in Figure 4. As a universal feature, the high-spin excitation is found at energy $U - 3J_H$ in all cases, provided that

Table 1. On-site interorbital exchange elements $J_{\alpha\beta}$ for 3d orbitals as functions of the Racah parameters B and C (for more details see Griffith, 1971).

Orbital	xy	yz	zx	x^2-y^2	$3z^2-r^2$
xy	0	$3B+C$	$3B+C$	C	$4B+C$
yz	$3B+C$	0	$3B+C$	$3B+C$	$B+C$
zx	$3B+C$	$3B+C$	0	$3B+C$	$B+C$
x^2-y^2	C	$3B+C$	$3B+C$	0	$4B+C$
$3z^2-r^2$	$4B+C$	$B+C$	$B+C$	$4B+C$	0

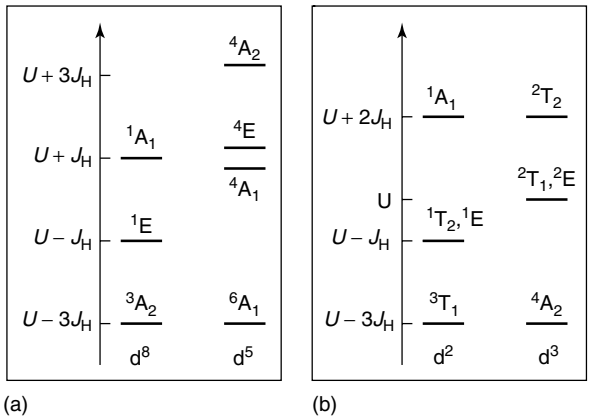

Figure 4. Energies of $d_i^m d_j^m \rightarrow d_i^{m+1} d_j^{m-1}$ charge excitations in selected cubic transition-metal oxides, as obtained from equation (8) for: (a) e_g excitations of Cu^{3+} (d^8) and Mn^{2+} (d^5) ions (in the d^5 case the spectrum was obtained from equation (5)); (b) t_{2g} excitations of Ti^{2+} (d^2) and V^{2+} (d^3) ions. The splittings between different states are due to Hund's exchange element J_H which refers to a pair of e_g electrons in (a), and to a pair of t_{2g} electrons in (b), respectively. (Reproduced from Oles *et al*., 2005, with permission from the American Physical Society. © 2005.)

J_H is understood as Hund's exchange for that partly filled manifold (e_g or t_{2g}) of degenerate d orbitals which participate in charge excitations. The structure of the excited states depends on the partly occupied orbitals (Fractional contributions due to exchange terms $\propto J_H$ shown in the spectrum for the d^5 case (see Figure 4a) follow from the differences between the exchange elements $J_{\alpha\beta}$ in Hamiltonian $H_{\rm int}$ (5) (see Table 1), and were obtained using the relation $C \simeq 4B$ satisfied approximately by the experimental values for Mn^{2+} ions (Zaanen and Sawatzky, 1990) and on the actual valence m – the distance between the high-spin and low-spin excitations increases with the number of electrons for $m \leq 5$ (holes for $m > 5$).

2.2 Superexchange at orbital degeneracy

At orbital degeneracy the SE which connects ions at sites i and j along the bond $\langle ij \rangle$ involves orbital operators which depend on the bond direction. Therefore, it is useful to introduce the index $\gamma = a, b, c$ to label the three *a priori* equivalent directions in a cubic crystal. In order to analyze the consequences of each individual charge excitation n that contributes to the SE in a given transition-metal compound with degenerate d orbitals, we shall use below a general way of writing the effective low-energy Hamiltonian as a superposition of such individual terms on each bond $\langle ij \rangle$,

$$\mathcal{H}_U = \sum_n \sum_{\langle ij \rangle \| \gamma} H_n^{(\gamma)}(ij) \tag{9}$$

with the energy unit (absorbed in individual $H_n^{(\gamma)}(ij)$ terms) given by the SE constant,

$$J = \frac{4t^2}{U} \tag{10}$$

It follows from d−d charge excitations with an effective hopping element t between transition-metal ions, and is the same as that obtained in a Mott insulator with nondegenerate orbitals in the regime of $U \gg t$ (Anderson, 1959).

In the SE Hamiltonian equation (9) the contributions which originate from all possible virtual excitations $d_i^m d_j^m \rightleftharpoons d_i^{m+1} d_j^{m-1}$ just add up to the total SE interaction, in which the individual terms cannot be distinguished. Yet each of these excitations involves a different state in the multiplet structure of at least one of the transition-metal ions, that is, either in the d^{m+1} or in the d^{m-1} configuration or in both, depending on the actual process and on the value of m. The same multiplet transitions also appear in the optical spectra. As pointed out in Khaliullin, Horsch and Oleś (2004), this fact can be used to calculate from the low-energy spin-orbital model the spectral weights of the individual transitions that occur at energies of several electron volts.

The generic structure of each individual SE contribution is for a bond $\langle ij \rangle$ given by

$$\begin{aligned} H_n^{(\gamma)}(ij) &= (a_n + b_n \mathbf{S}_i \cdot \mathbf{S}_j) Q_n^{(\gamma)}(\boldsymbol{\tau}_i, \boldsymbol{\tau}_j) \\ &= a_n Q_n^{(\gamma)}(\boldsymbol{\tau}_i, \boldsymbol{\tau}_j) + b_n Q_n^{(\gamma)}(\boldsymbol{\tau}_i, \boldsymbol{\tau}_j) \mathbf{S}_i \cdot \mathbf{S}_j \end{aligned} \tag{11}$$

where the orbital dependence of the SE is described by means of orbital projection operators $Q_n^{(\gamma)}$ which in the cases discussed here can be expressed in terms of components of orbital pseudospin $T = 1/2$ operators $\boldsymbol{\tau}_i, \boldsymbol{\tau}_j$ at sites i and j. The coefficients a_n and b_n, which measure the strength of the pure orbital part and of the spin and orbital part of the SE, respectively, follow from second-order perturbation theory involving the charge excitation n. In the case of perovskites, where the bond between two transition-metal ions through the ligand ion (F or O) connecting them is close to linear (180°), the coefficients a_n and b_n are of similar magnitude (in contrast to the situation in layered compounds like $LiNiO_2$ with 90° bonds where the pure orbital interaction is stronger by an order of magnitude than the spin and orbital interaction (Mostovoy and Khomskii, 2002; Reitsma, Feiner and Oleś, 2005).

Spin-orbital models have been derived for a number of TMOs, and we refer for the details of such derivations and further reference to the original literature: $KCuF_3$, La_2CuO_4 (Oleś, Feiner and Zaanen, 2000; Oleś, 2003, 2005), $LaTiO_3$ (Khaliullin and Maekawa, 2000; Khaliullin, 2001; Aharony *et al*., 2005), $LaVO_3$ (Khaliullin, Horsch and Oleś, 2001), $LiVO_2$ (Pen, van den Brink, Khomskii and Sawatzky,

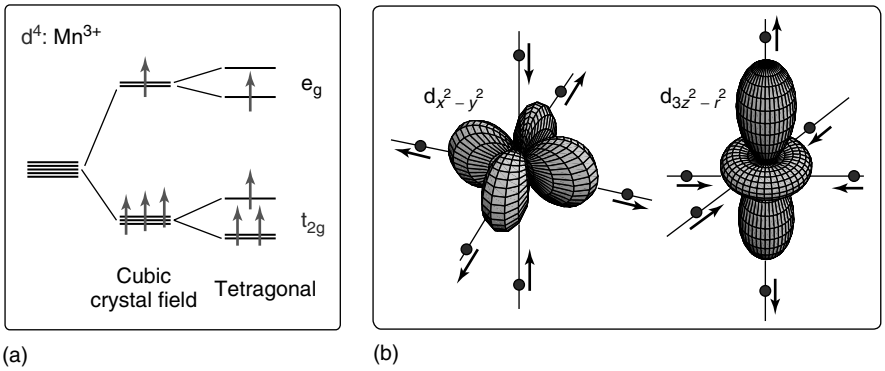

Figure 5. (a) Splitting of d-orbitals in a cubic crystal field ($\Delta E = 10Dq$) and the further splitting of e_g and t_{2g} orbitals in a tetragonal field. The parallel alignment of spins in the $d^4(S = 2)$ configuration of Mn^{3+} is dictated by the strong Hund coupling J_H. (b) Tetragonal symmetry where the oxygen octahedron is elongated (squeezed) along c direction favors the $d_{3z^2-r^2}$ ($d_{x^2-y^2}$) orbital, respectively.

1997), NaV_2O_5 (Mostovoy and Khomskii, 2000; Cuoco, Horsch and Mack, 1999), V_2O_3 (Shiina, Mila, Zhang and Rice, 2001; Di Matteo, Jackeli, Lacroix and Perkins, 2004; Di Matteo, Jackeli and Perkins, 2005), $LaMnO_3$ (Ishihara, Inoue and Maekawa, 1997; Shiina, Nishitani and Shiba, 1997; Feiner and Oleś, 1999), $LiNiO_2$ (Mostovoy and Khomskii, 2002; Reitsma, Feiner and Oleś, 2005; Vernay, Penc, Fazekas and Mila, 2004), the isoelectronic ruthenate alloy $Ca_{2-x}Sr_xRuO_4$ (Sigrist and Troyer, 2004), and the layered cobalt oxides Na_xCoO_2 (Khaliullin, Koshibae and Maekawa, 2004; Khaliullin, 2005).

2.3 Effective spin model and spin waves

Here, we consider systems having cubic symmetry at high temperature. Yet often already at rather high temperature this symmetry is spontaneously broken – usually driven by the joint effect of (i) the orbital part of the SE interaction, and (ii) the JT coupling of the same degenerate (and therefore JT active) 3d orbitals to lattice modes. The result is a simultaneous onset of a macroscopic lattice distortion and of orbital order (OO), that is, a cooperative JT effect. At temperatures well below the transition temperature T_s of this combined structural and orbital ordering phase transition the OO is effectively frozen, and the SE interactions between the spins may then be obtained by replacing the orbital projection operators in equation (9) by their expectation values,

$$Q_n^{(\gamma)}(\boldsymbol{\tau}_i, \boldsymbol{\tau}_j) \longrightarrow \langle Q_n^{(\gamma)}(\boldsymbol{\tau}_i, \boldsymbol{\tau}_j)\rangle = Q_n^{(\gamma)}(\langle\boldsymbol{\tau}_i\rangle, \langle\boldsymbol{\tau}_j\rangle) \quad (12)$$

Obviously, this leads to anisotropic magnetic interactions,

$$H_s = J \sum_n \sum_{\langle ij\rangle\|\gamma} b_n \langle Q_n^{(\gamma)}\rangle \, \mathbf{S}_i \cdot \mathbf{S}_j \quad (13)$$

which will in general induce a further magnetic phase transition at lower temperature. It is noteworthy that in this situation the spin degrees of freedom get decoupled from the orbital degrees of freedom, although the pure orbital (a_n) and spin and orbital (b_n) SE terms are of similar strength. Responsible for this behavior is the JT contribution to the structural phase transition, which enhances T_s above the value it would have if the transition were driven by orbital SE alone. A typical case is $LaMnO_3$ which shows OO below a structural transition at $T_s \sim 780$ K (Murakami *et al.*, 1998).

Thus starting from the microscopic spin-orbital SE model we arrive at low temperature, that is, in the orbital-ordered state, at an effective Heisenberg spin model. Rewritten from equation (13), its generic form is:

$$H_s = J_c \sum_{\langle ij\rangle_c} \mathbf{S}_i \cdot \mathbf{S}_j + J_{ab} \sum_{\langle ij\rangle_{ab}} \mathbf{S}_i \cdot \mathbf{S}_j \quad (14)$$

with two different effective magnetic exchange interactions: J_c along the c axis, and J_{ab} within the ab planes. The latter J_{ab} interactions could in principle still take two different values in case of inequivalent lattice distortions (caused, e.g., by octahedra tilting or pressure effects) making the a and b axes inequivalent. Here, we shall limit the discussion to idealized structures with these two axes being equivalent. The resulting spin–spin correlations along the c axis and within the ab planes,

$$s_c = \langle \mathbf{S}_i \cdot \mathbf{S}_j\rangle_c, \quad s_{ab} = \langle \mathbf{S}_i \cdot \mathbf{S}_j\rangle_{ab} \quad (15)$$

play, as we shall see below, an important role for the interpretation of the optical conductivity data, its anisotropy and its temperature dependence.

2.4 Spin-orbital models: two examples

2.4.1 t_{2g} systems $LaVO_3$ and YVO_3

The orientation of ferromagnetically aligned magnetic moments can be reversed in a sufficiently large magnetic field pointing in the opposite direction. This property is the basis of magnetic recording and storage devices. The cubic vanadate YVO_3 compound shows a very peculiar temperature induced magnetization reversal as reported by Ren *et al.* (1998). Actually there are two reversals in this compound, one at 77 K connected with a first-order structural phase transition. Upon heating the value of the magnetization decreases linearly and leads to another sign change at about ∼95 K. In these compounds, the net magnetic moment results from a tilting of the antiferromagnetically aligned moments of the $(S = 1)$ V^{3+} ions.

The SE in cubic vanadates originates from virtual-charge excitations, $d_i^2 d_j^2 \to d_i^3 d_j^1$, by the hopping t which couples pairs of identical orbitals. As shown in Figure 4 there are three multiplet levels $n = 1, 2, 3$ arising from the transitions to: (i) a high-spin state $^4A_2$ at energy $U - 3J_H$, (ii). two degenerate low-spin states $^2T_1$ and ^2E at U, and (iii) $^2T_2$ low-spin state at $U + 2J_H$. When all processes are analyzed and collected on individual bonds $\langle ij \rangle \parallel \gamma$ along each cubic axis $\gamma = a, b, c$, one finds the spin-orbital Hamiltonian for $S = 1$ spins $(J = 4t^2/U)$ (Khaliullin, Horsch and Oleś, 2001),

$$\mathcal{H} = J \sum_{\gamma} \sum_{\langle ij \rangle \parallel \gamma} \left[\frac{1}{2} (\mathbf{S}_i \cdot \mathbf{S}_j + 1) \hat{J}_{ij}^{(\gamma)} + \hat{K}_{ij}^{(\gamma)} \right] + H' \quad (16)$$

where the orbital operators $\hat{J}_{ij}^{(\gamma)}$ and $\hat{K}_{ij}^{(\gamma)}$ depend on the pseudospin $\tau = 1/2$ operators $\boldsymbol{\tau}_i = \{\tau_i^x, \tau_i^y, \tau_i^z\}$, given by two orbital flavors active along a given direction γ. For instance, yz and zx orbitals are active along c axis, and we label them as a and b, as they lie in the planes orthogonal to these axes. The c (xy) orbitals, on the other hand, have no finite hopping matrixelements $t_{i,j}^{\alpha,\beta}$ along c direction and are therefore inactive on such bonds. H' stands for other relevant (non-SE) interactions, to be discussed later. The general form of the SE (11) was discussed before, and has cubic symmetry in the orbital sector.

There is structural evidence that c (xy) orbitals are shifted to lower energies at the structural transition T_s (Mahajan, Johnston, Torgeson and Borsa, 1992; Noguchi *et al.*, 2000; Ren *et al.*, 2000; Blake *et al.*, 2001, 2002). In YVO_3 the latter occurs at ∼200 K; the subsequent magnetic transitions into the magnetic C (G phase) are at 114(77) K, respectively (Figure 6). $LaVO_3$ has only a C phase with $T_N = 140$ K. Hence, the cubic symmetry is broken and it is assumed that the xy orbitals are occupied $(n_{ic} = 1)$. Actually, this is also concluded from electronic structure calculations (Sawada, Hamada, Terakura and Asada, 1996). The electron densities in a and b orbitals satisfy the local constraint $n_{ia} + n_{ib} = 1$ and therefore can fluctuate along the c direction. Whereas along $a(b)$ direction orbital fluctuations are inhibited because of the occupied xy orbitals. This leads to a dramatic anisotropy of magnetic properties, which are always AF along $a(b)$ directions but can be strongly FM along c, due to orbital-singlet fluctuations.

The exchange constants are now operators depending on the orbital degrees of freedom (which are expressed in the present case by spin-1/2 pseudospin operators controlling the two active orbitals along each Cartesian direction). The interactions along the c axis are expressed as:

$$\hat{J}_{ij}^{(c)} = (1 + 2R)\left(\boldsymbol{\tau}_i \cdot \boldsymbol{\tau}_j + \frac{1}{4}\right) - r\left(\boldsymbol{\tau}_i \otimes \boldsymbol{\tau}_j + \frac{1}{4}\right) - R \quad (17)$$

$$\hat{K}_{ij}^{(c)} = R\left(\boldsymbol{\tau}_i \cdot \boldsymbol{\tau}_j + \frac{1}{4}\right) + r\left(\boldsymbol{\tau}_i \otimes \boldsymbol{\tau}_j + \frac{1}{4}\right) \quad (18)$$

they involve the fluctuations of a and b orbitals $\propto \boldsymbol{\tau}_i \cdot \boldsymbol{\tau}_j$, and $\boldsymbol{\tau}_i \otimes \boldsymbol{\tau}_j = \tau_i^x \tau_j^x - \tau_i^y \tau_j^y + \tau_i^z \tau_j^z$. The interactions along the $\gamma = a(b)$ axis depend on the static correlations $\propto n_{ib} n_{jb}$ $(n_{ia} n_{ja})$ only; for instance:

$$\hat{J}_{ij}^{(a)} = \frac{1}{2}\Big[(1 - r)(1 + n_{ib} n_{jb}) - R(n_{ib} - n_{jb})^2\Big] \quad (19)$$

$$\hat{K}_{ij}^{(a)} = \frac{1}{2}(R + r)(1 + n_{ib} n_{jb}). \quad (20)$$

The Hund's exchange $\eta = J_H/U$ determines the multiplet structure of d^3 excited states which enters via the coefficients: $R = \eta/(1 - 3\eta)$ and $r = \eta/(1 + 2\eta)$. The pseudospin operators in equations (17–18) may be represented by Schwinger bosons: $\tau_i^x = \frac{1}{2}(a_i^\dagger b_i + b_i^\dagger a_i)$, $\tau_i^y = \frac{1}{2} i (a_i^\dagger b_i - b_i^\dagger a_i)$, $\tau_i^z = \frac{1}{2}(n_{ia} - n_{ib})$.

To develop some deeper insight, we consider the limit of vanishing Hund coupling $J_H \to 0$. In this case, the d^3-multiplet splitting shrinks to zero and the SE expression becomes SU(2) symmetric also in the orbital sector:

$$\mathcal{H}_0 = \frac{1}{2} J \sum_{\langle ij \rangle \parallel c} (\mathbf{S}_i \cdot \mathbf{S}_j + 1) \left(\boldsymbol{\tau}_i \cdot \boldsymbol{\tau}_j + \frac{1}{4} n_i n_j\right)^{(c)} \quad (21)$$

where a constant energy of $-2J$ per V^{3+} ion is neglected, and also the coupling in the (a, b) plane is dropped for the moment.

To understand why orbital fluctuations along c direction support FM order it is instructive to consider $\mathcal{H}_0$ with all spins ferromagnetically aligned. The remaining orbital model is a spin-1/2 Heisenberg chain with the known Bethe

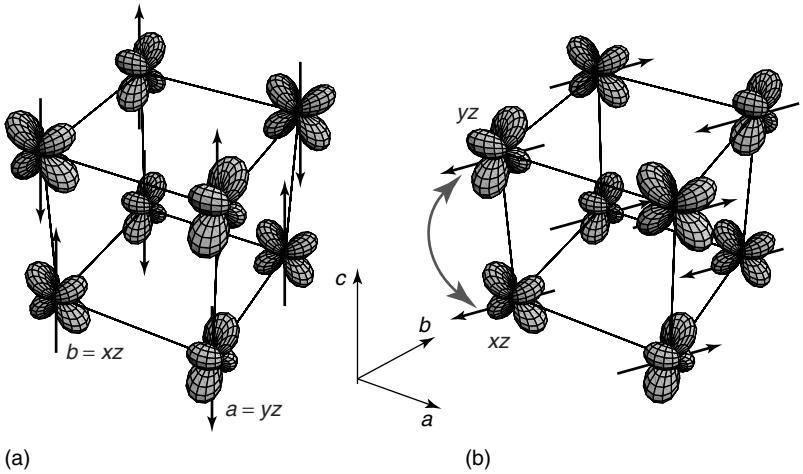

Figure 6. Orientation of occupied t_{2g} orbitals in: (a) the magnetic G type and orbital C type low-temperature structure of YVO_3 and (b) the magnetic C (orbital G) type low-temperature structure of $LaVO_3$. ($S = 1$ spins are indicated by black arrows.) For the C phase a double-side arrow indicates the fluctuating orbital occupation between $a = yz$ and $b = xz$ orbitals along the c direction. A second vanadium t_{2g} electron occupies the xy orbital ($n_c = 1$) at each vanadium ion and is not shown. The occupied xy orbital suppresses orbital fluctuations in the (a, b) plane.

ansatz result $\langle \boldsymbol{\tau_i} \cdot \boldsymbol{\tau_{i+1}} \rangle = -0.443$, that is, for the nearest-neighbor correlation function in the singlet ground state. Owing to the orbital quantum fluctuations this yields a very low energy per bond $E = -0.193J$. It should be noted that for a classical alternating orbital state $\langle \boldsymbol{\tau_i} \cdot \boldsymbol{\tau_{i+1}} \rangle = -1/4$, thus $J_{i,j}^{(c)} = 0$! That is, quantum fluctuations are essential for the ferromagnetism.

Yet surprisingly, the ground state of $\mathcal{H}_0$ is an orbital dimer state or orbital valence bond (OVB) state with energy $E_0 = -0.25J$ per bond. In the OVB state orbital singlets appear together with spin pairs coupled into a $S = 2$ state, the AF arrangement leads to basically decoupled pairs (see Figure 7). Therefore, the system can profit from the orbital dimer energy $\langle \boldsymbol{\tau_i} \cdot \boldsymbol{\tau_{i+1}} \rangle = -3/4$ on each second bond. That is, in the $\eta = 0$ case, the local dimers win over the global singlet. It requires finite Hund coupling J_H to stabilize the C phase (Horsch, Khaliullin and Oleś, 2003) (see Figure 7).

Next we consider the reasons for the stability of the G phase in YVO_3. Unlike $LaVO_3$ with almost equal V–V bonds, this compound crystallizes in the distorted structure (Goodenough, 1955; Kawano, Yoshizawa and Ueda, 1994), indicating that the JT effect plays a significant role. It was suggested that energy may be gained due to C-type orbital ordering, with a and b orbitals staggered in (a, b) planes and repeated along c axis, while $n_{ic} = 1$ (Ren *et al.*, 2000; Mizokawa, Khomskii and Sawatzky, 1999; Sawada and Terakura, 1998). Such ordering can be promoted by Khaliullin, Horsch and Oleś (2001)

$$H_{\rm JT} = -2V \sum_{\langle ij \rangle \| c} \tau_i^z \tau_j^z + V \sum_{\langle ij \rangle \| (a,b)} \tau_i^z \tau_j^z \qquad (22)$$

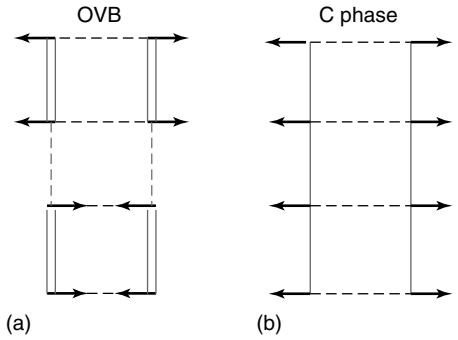

Figure 7. (a) Orbital valence bond (OVB) ground state of $\mathcal{H}_0$, equation (21), consists of orbital singlets (double line). The resulting FM coupling leads to a coupling of pairs of spin 1 into $S = 2$ spin pairs. These are only marginally coupled because of weak AF correlations between dimers. (b) FM aligned $S = 1$ spins lead to a global orbital-singlet state (solid line). Weak AF coupling between different chains along c is indicated by dashed lines.

and competes with the orbital disorder. This behavior is remarkably different from the e_g systems, where the JT effect and SE support each other, inducing orbital ordering (Kugel and Khomskii, 1982a,b; Tokura and Nagaosa, 2000; Oleś, Feiner and Zaanen, 2000). Although $V > 0$ causes orbital splitting by $4V$ and thus lowers the energy of the G phase (E_G), it has little effect on the energy of the C phase.

2.4.2 *e_g system $LaMnO_3$*

Although e_g and t_{2g} electrons behave quite differently in $LaMnO_3$ and are frequently treated as two subsystems, (Dagotto, Hotta and Moreo, 2001; Dagotto, 2003, 2005)

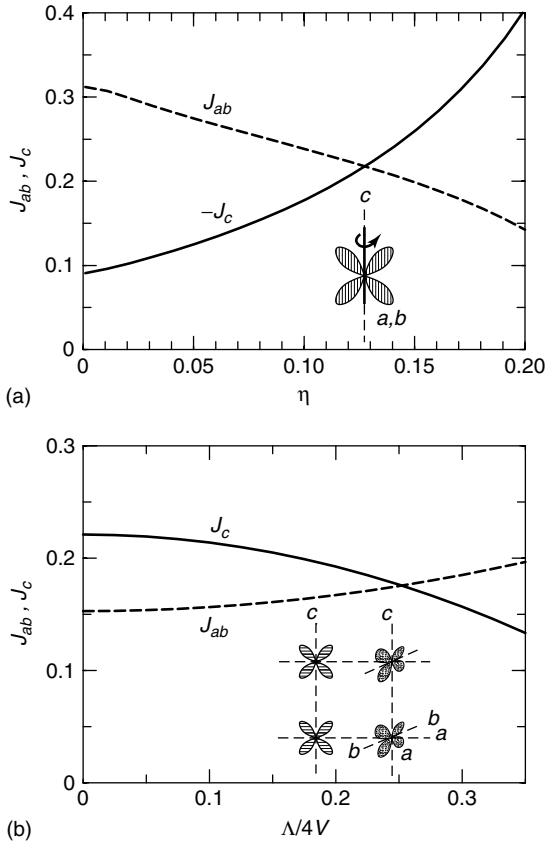

Figure 8. Magnetic exchange couplings J_c and J_{ab} (in units of J): (a) as function of Hund-coupling strength η in the C phase of $LaVO_3$ and YVO_3 with large ferromagnetic J_c due to strong orbital fluctuations along c direction. The inset indicates the fluctuation of $a(b)$ orbital occupancy. (b) Exchange constants in the G-antiferromagnetic low-temperature phase of YVO_3 versus relativistic spin-orbit coupling Λ/V. Inset shows the corresponding C-orbital structure. (Reproduced from Klhallili *et al*., 2001, with permission from the American Physical Society. © 2001.)

the neutron experiments (Hirota, Kaneko, Nishizawa and Endoh, 1996; Moussa, Hennion and Rodríguez-Carvajal, 1996; Biotteau *et al*., 2001) which measure the spin waves in the A−AF phase below T_N leave no doubt that an adequate description of the magnetic properties requires a magnetic Hamiltonian of the form given by equation (14), describing SE between total $S = 2$ spins of the Mn^{3+} ions. The high-spin ^5E ground state at each Mn^{3+} ion is stabilized by the large Hund's exchange J_H. The situation is more complex than in the vanadate system discussed before. The SE terms between Mn^{3+} ions originate from various $d_i^4 d_j^4 \rightleftharpoons d_i^5 d_j^3$ charge excitations, which can originate from transitions of both e_g or t_{2g} electrons. This leads to different excited states in the intermediate d^5 configuration on a $Mn^{2+}(d_i^5)$ ion. Such processes determine the U term $\mathcal{H}_U(d^4)$ defined by equation (9), and were analyzed in detail in (Feiner and Oleś, 1999), and lead to the structure of $\mathcal{H}_U(d^4)$ given below. However, the CT processes, $\mathcal{H}_\Delta(d^4)$, contribute as well and the complete model for $LaMnO_3$ reads

$$\mathcal{H}(d^4) = \mathcal{H}_U(d^4) + \mathcal{H}_\Delta(d^4) \tag{23}$$

The SE constant J is here defined again by equation (10), using an average hopping element along an effective $(dd\sigma)$ bond, $t = t_{pd}^2/\overline{\Delta}$, where $\overline{\Delta}$ is an average CT excitation energy.

We consider here only the more important U terms, $\mathcal{H}_U(d^4)$, due to excitations of e_g electrons (see Figure 4), and refer to Oleś, Khaliullin, Horsch and Feiner (2005) for a discussion of the CT contributions for $LaMnO_3$. The energies of the five possible excited states: Griffith (1971) (i) the high-spin $^6A_1$ state ($S = 5/2$), and (ii–v) the low-spin ($S = 3/2$) states: $^4A_1$, ^4E ($^4E_\epsilon$, $^4E_\theta$), and $^4A_2$, will be parameterized again by the intraorbital Coulomb element U (6), and by Hund's exchange J_H between a pair of e_g electrons. The energies of the excited states are given in terms of the Racah parameters in Griffith (1971); in order to parameterize this spectrum by J_H we apply an approximate relation $4B \simeq C$ which holds for the spectroscopic values of the Racah parameters for a Mn^{2+} (d^5) ion: (Zaanen and Sawatzky, 1990; Bocquet *et al*., 1992) $B = 0.107\,\text{eV}$ and $C = 0.477\,\text{eV}$. One finds then the excitation spectrum: $U - 3J_H$, $U + 3J_H/4$, $U + 5J_H/4$, $U + 5J_H/4$, and $U + 13J_H/4$ (Figure 4a). Unlike J_H, the value of U is known with less accuracy – hence one may use it as a parameter which can be deduced *a posteriori* from the SE J which is able to explain the experimental values for two exchange constants responsible for the A−AF phase observed in $LaMnO_3$ well below the structural transition (here again $T_N \ll T_s$).

Using the spin algebra (Clebsch–Gordon coefficients), and making a rotation of the terms derived for a bond $\langle ij \rangle \parallel c$ to the other two cubic axes a and b, one finds five contributions to $\mathcal{H}_U(d^4)$ due to different $(t_{2g}^3 e_g^1)_i (t_{2g}^3 e_g^1)_j \rightleftharpoons (t_{2g}^3 e_g^2)_i (t_{2g}^3)_j$ excitations by e_g electrons (Feiner and Oleś, 1999). In the following we shall drop the index U and denote the individual multiplet contributions $H_n^{(\gamma)}$:

$$H_1^{(\gamma)} = -\frac{J}{20} r_1 \left(\mathbf{S}_i \cdot \mathbf{S}_j + 6\right)\left(\frac{1}{4} - \tau_i^{(\gamma)} \tau_j^{(\gamma)}\right) \tag{24}$$

$$H_2^{(\gamma)} = \frac{3J}{160} r_2 \left(\mathbf{S}_i \cdot \mathbf{S}_j - 4\right)\left(\frac{1}{4} - \tau_i^{(\gamma)} \tau_j^{(\gamma)}\right) \tag{25}$$

$$H_3^{(\gamma)} = \frac{J}{32} r_3 \left(\mathbf{S}_i \cdot \mathbf{S}_j - 4\right)\left(\frac{1}{4} - \tau_i^{(\gamma)} \tau_j^{(\gamma)}\right) \tag{26}$$

$$H_4^{(\gamma)} = \frac{J}{32} r_4 \left(\mathbf{S}_i \cdot \mathbf{S}_j - 4\right)\left(\frac{1}{2} - \tau_i^{(\gamma)}\right)\left(\frac{1}{2} - \tau_j^{(\gamma)}\right) \tag{27}$$

$$H_5^{(\gamma)} = \frac{J}{32} r_5 \left(\mathbf{S}_i \cdot \mathbf{S}_j - 4\right)\left(\frac{1}{2} - \tau_i^{(\gamma)}\right)\left(\frac{1}{2} - \tau_j^{(\gamma)}\right) \tag{28}$$

The orbital operators $\tau_i^{(\gamma)}$ depend on the direction of a considered bond $\langle ij \rangle$, and are given by

$$\tau_i^{(ab)} = -\frac{1}{4}\left(\sigma_i^z \mp \sqrt{3}\sigma_i^x\right), \tau_i^{(c)} = \frac{1}{2}\sigma_i^z \qquad (29)$$

where σ_i^z and σ_i^x are Pauli matrices acting on the orbital pseudospins and the signs $\pm$ in $\tau_i^{(ab)}$ correspond to a and b axis, respectively. The coefficients

$$r_1 = \frac{1}{1-3\eta}, \quad r_2 = \frac{1}{1+3\eta/4},$$
$$r_3 = r_4 = \frac{1}{1+5\eta/4}, \quad r_5 = \frac{1}{1+13\eta/4} \qquad (30)$$

follow from the above multiplet structure of Mn^{2+} (d^5) ions, and $\eta = J_H/U$ is the Hund-coupling parameter. The meaning of the various terms is straightforward: the first term $H_1^{(\gamma)}$ describes the high-spin excitations to the $^6A_1$ state while the remaining ones, $H_n^{(\gamma)}$ with $n = 2, \ldots, 5$, arise due to the low-spin excited states $^4A_1$, $^4E_\theta$, $^4E_\epsilon$, and $^4A_2$, respectively.

The SE leads in the (a, b) plane to $(|x\rangle \pm |z\rangle)/\sqrt{2}$ OO in combination with ferromagnetism; this is driven by the r_1 term. Similarly OO in $LaMnO_3$ is favored by collective JT distortions (Kanamori, 1959; Goodenough, 1963), which may lead to a further rotation of alternating orbitals toward $d_{3x^2-r^2}$ and $d_{3x^2-r^2}$, respectively. This OO implies as consequence of SE FM spin order in the (a,b) plane, but AF order between planes, and is called *A-type order*. A powerful technique to determine the OO is the resonant X-ray scattering (RXS) technique (for a theoretical discussion, see Ishihara's account in Maekawa *et al*., 2004). The OO of $LaMnO_3$ has been determined by (Murakami *et al*., 1998) using RXS. They have shown that the OO in this compound sets in at $T_O = 780\,K$, while the AF ordering occurs at much lower Neél temperature $T_N = 140\,K$.

2.5 Goodenough–Kanamori rules and spin-orbital order

The magnetism of Mott-insulating TMO is traditionally interpreted by means of the GK rules (Goodenough, 1963; Kanamori, 1959). These rules state that the pattern of occupied orbitals determines the spin structure. In the case of 180° bonds, as shown in Figure 9 for a Mn^{3+}–O–Mn^{3+} bond, there are two key rules (Anderson, 1963):

1. If there is large overlap between partly occupied orbitals at two magnetic ions, the SE interaction between them is strongly AF, because the fluctuating electron meets another electron in the same orbital, thus Pauli principle requires antiparallel spins.
2. Large overlap between partly occupied and unoccupied orbitals on neighboring sites yields weak FM interaction due to Hund's exchange.

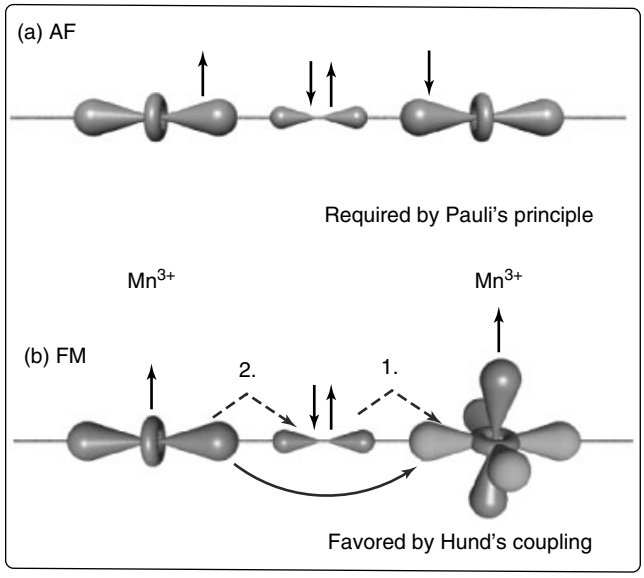

Figure 9. Sketch of Goodenough–Kanamori rules in case of Mn^{3+} with one e_g orbital occupied. (a) Large overlap of occupied orbitals favors antiferromagnetism because of Pauli's principle; In case (b) there is a large overlap between an occupied orbital at the left ion with an unoccupied orbital on the right ion, while in this case AF and FM orientation is possible, Hund's rule on the right ion will favor ferromagnetic alignment. For completeness the intermediate oxygen p orbitals which are active in the superexchange process are shown as well.

Whereas the AF–SE interaction (i) is proportional to t^2/U, the FM interaction (ii) is a weaker interaction $\sim t^2 J_H/U^2$, as it arises from a total balance of AF and FM SE processes, where the FM process wins by a factor J_H/U (see e.g., Figure 3). In the archetypical case of 180° bonds through a single ligand ion, this translates into a complementary interdependence between spin order and OO (Imada, Fujimori and Tokura, 1998): ferro-orbital (FO) order supports strong AF spin order, while alternating orbital (AO) order supports weak FM spin order. The canonical examples for this behavior are $LaMnO_3$ and $KCuF_3$. In $LaMnO_3$ the alternating OO in the (a, b) plane favors ferromagnetism. In $KCuF_3$ weak FM (positive) spin correlations in the ab planes and strong AF (negative) correlations along the c axis are accompanied by alternating OO in the ab planes and FO order along the c axis.

As the bond angle controls the hopping matrix elements it is obvious that the GK rules depend sensitively on the bond angle. Angles close to 90° deserve particular care.

In this case, AF–SE interaction may become small and the total interaction on a bond may become ferromagnetic as other SE channels become relevant (Mizuno *et al*., 1998; Tornow, Entin-Wohlman and Aharony, 1999). Also some compounds have more complex SE channels (Feldkemper and Weber, 1998; Daré, Hayn and Richard, 2003).

2.5.1 Crystal fields and Jahn–Teller distortions

The GK rules have been successful in explaining the magnetic structure in a wide range of materials. This may seem surprising because they presuppose that the orbital occupation is static, whereas it has become clear that if partly filled orbitals are degenerate, both spin and orbital degrees of freedom should be considered as dynamic quantum variables and be described by spin-orbital models as, for example, in equation (16):

$$\mathcal{H} = J \sum_{\gamma} \sum_{\langle ij \rangle \| \gamma} \left[\left(\mathbf{S}_i \cdot \mathbf{S}_j + S^2 \right) \hat{J}_{ij}^{(\gamma)} + \hat{K}_{ij}^{(\gamma)} \right] + \mathcal{H}_{\rm orb} \quad (31)$$

In fact, there are other interactions $\mathcal{H}_{\rm orb}$ between orbitals and the lattice, which can be stronger than the SE interactions and quench the orbital fluctuations. The GK rules work that well because in many compounds a structural phase transition, driven by the JT coupling of degenerate orbitals to the lattice, lifts the degeneracy and fixes the orbital occupation well above the magnetic transition. This happens typically for electrons in e_g orbitals where large cooperative JT distortions favor OO (Millis, 1996; Ahn and Millis, 2000). A good example is $LaMnO_3$ where the alternating OO, Figure 10, and the JT distortion occur simultaneously at $T_{\rm OO} \sim 780\,{\rm K}$ (Imada, Fujimori and Tokura, 1998). For t_{2g} orbitals, however, the JT coupling is rather weak. More significant in cubic vanadates RVO_3 and titanates $RTiO_3$ is the $GdFeO_3$ distortion which controls the t_{2g} level splitting (Mochizuki and Imada, 2003, 2004; Cwik *et al*., 2003; Solovyev, 2004; Pavarini, Yamasaki, Nuss and Andersen, 2005; Pavarini *et al*., 2004). Here, the dominant contribution to the crystal-field stems from the R ions and not from the O neighbors (Pavarini, Yamasaki, Nuss and Andersen, 2005), which reflects the fact that the O octahedra are rotated but only weakly distorted. This leads to a significant variation of orbital ordering transition temperatures in the cubic vanadate systems RVO_3 as function of the cation size which controls the $GdFeO_3$ distortion (Miyasaka, Okimoto, Iwama and Tokura, 2003), Figure 12. In layered ruthenates, the $GdFeO_3$ distortion even induces a metal–insulator transition (see following subsection). Recent experiments in pseudocubic perovskite titanates (Keimer *et al*., 2000) and vanadates (Ulrich *et al*., 2003), however, indicate that the relevant t_{2g} orbital occupations fluctuate and the conditions for applying the GK rules may not be not satisfied.

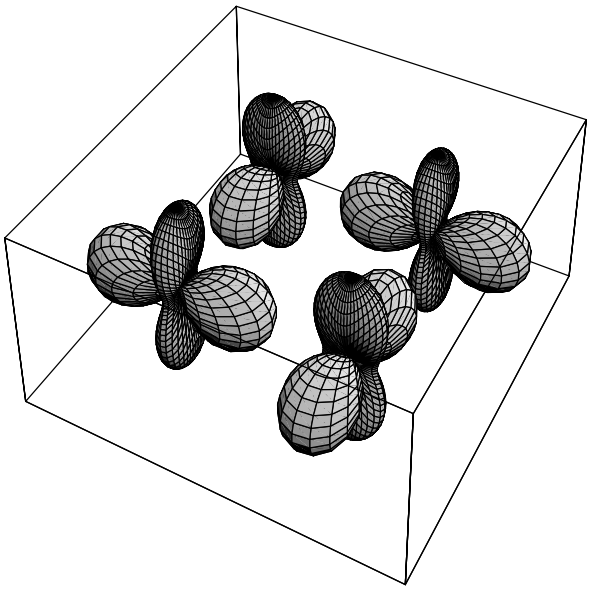

Figure 10. Alternating $(|x\rangle \pm |z\rangle)/\sqrt{2}$ in the ferromagnetic *ab* plane of $LaMnO_3$ as obtained from superexchange. The alternating orbital order is further stabilized by a cooperative Jahn–Teller distortion of the involved MnO_6 octahedra.

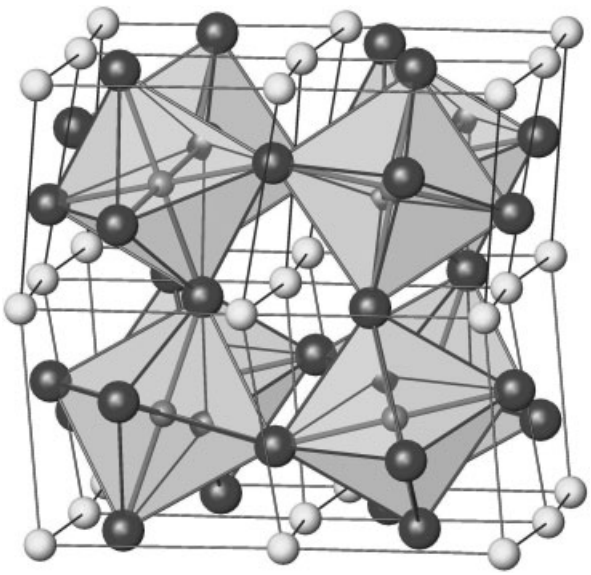

Figure 11. Crystal structure of the $GdFeO_3$ distorted perovskite vanadates RVO_3 and titanates $RTiO_3$ for small R ions. The corner-sharing octahedra are tilted around the *b* axis in alternating directions and subsequently rotated around the *c* axis. (Reproduced from E. Pavarini, Y. Yamasaki, J. Nuss, and O.K. Andersen, *New J. Phys.* **7**, 2005, 188, with permisison from Elsevier.)

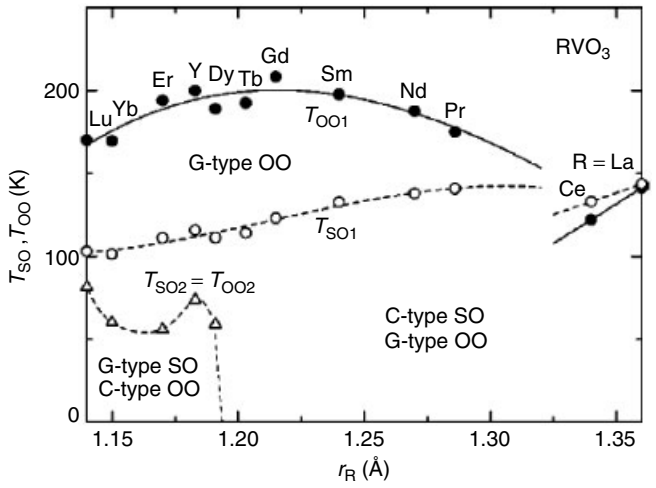

Figure 12. Spin-orbital phase diagram of RVO_3 (R = Lu–La) as function of the cation size r_R. Closed and open circles indicate G-type orbital ordering temperature T_{OO1} and C-type spin ordering T_{SO1}, respectively. Triangles indicate G-type spin (C-type orbital) ordering temperature $T_{SO2} = T_{OO2}$. (Reproduced from Miyasaki *et al*., 2003, with permission from the American Physical Society. © 2003.)

2.5.2 *Orbital-selective Mott transition in layered ruthenates*

The discovery of unconventional superconductivity in Sr_2RuO_4 (Maeno *et al*., 1994) has attracted considerable interest in the electronic properties of layered perovskite ruthenates. With a highest $T_c \sim 1.5\,K$ they are the only superconductors isostructural with the high-temperature superconducting cuprates. In contrast to singlet pairing in high-T_c superconductors, here triplet pairing with p-wave symmetry of the superconducting order parameter is the most probabe scenario. Spin-triplet pairing is favored by strong FM fluctuations that are believed to dominate the pair-formation in Sr_2RuO_4. These aspects have been reviewed in depth by Mackenzie and Maeno (2003).

Surprising insights were obtained when replacing the Sr ion in this compound. For example, the substitution of the smaller Ca^{2+} ions for Sr^{2+} ions does not lead to a more metallic state, as one might naively expect, but to an AF Mott insulator with a staggered moment of $S = 1$ as expected for a localized Ru^{4+} ion which has four electrons in the t_{2g} subshell.

The insulating behavior of Ca_2RuO_4 is triggered by the typical $GdFeO_3$ distortions that appear when small cations are inserted into the perovskite structure (Fang and Terakura, 2001; Anisimov *et al*., 2002; Friedt *et al*., 2001): (i) With the replacement of Sr^{2+} ions by Ca^{2+} ions the RuO_6 octahedra change from *c*-axis elongation to compression. This implies that the xy orbital is shifted below the degenerate xz and yz orbitals, that is, the systems

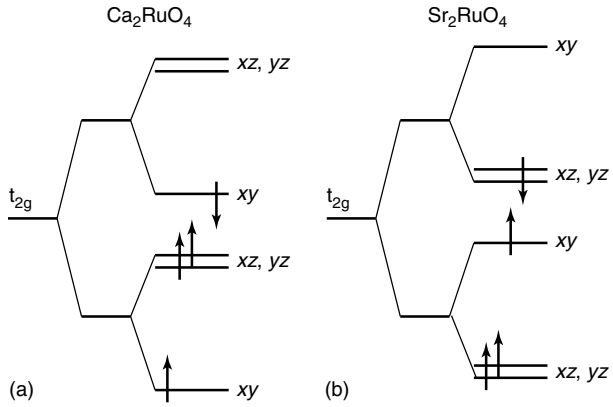

Figure 13. Local electronic structure of the end compounds of the isoelectronic alloy $Ca_{2-x}Sr_xRuO_4$ triggered by the GdFeO lattice distortion connected with the cation size. In Ca_2RuO_4 the down-spin electron occupies the xy-orbital in Ca_2RuO_4 (a), whereas in Sr_2RuO_4 (b) this electron occupies a level with xz/yz orbital degeneracy. (Reproduced from V.I. Anisimov, I.A. Nekrasov, D.E. Kondakov, T.M. Rice, and M. Sigrist, *Eur. Phys. J B* **25**, 2002, 191, with permisison of EDP Sciences.)

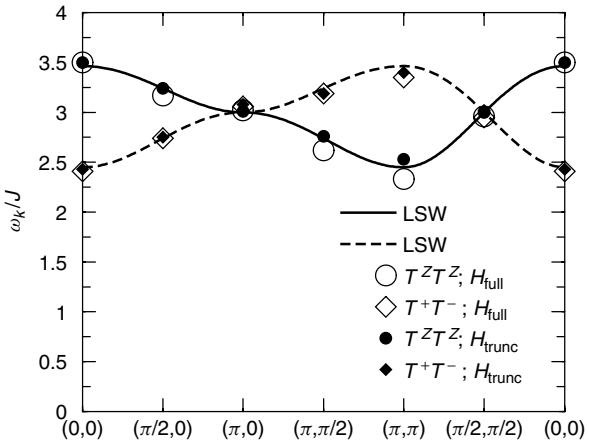

Figure 14. Orbital waves calculated for the alternating orbital order $((|x\rangle \pm |z\rangle)/\sqrt{2})$ of the 2D orbital model that represents the ferromagnetic *ab* plane of $LaMnO_3$. The solid (dashed) lines represent results for the two orbiton modes obtained by the linear spin-wave theory. The symbols indicate the orbital excitation energies obtained by exact diagonalization. (Reproduced from Van den Brink *et al*., 1999, with permission from the American Physical Society. © 1999.)

changes from an orbital-degenerate state into an insulating nondegenerate state in the case of Ca_2RuO_4. (ii) Moreover, the tilt of octahedra associated with the $GdFeO_3$ distortion reduces the resonance integrals. That is, the resulting smaller bandwidth implies stronger correlations. Thus, in combination with the Hund coupling this explains the Mott-insulating behavior of Ca_2RuO_4, as three of the four Ru^{4+} electrons fill the up-spin t_{2g} orbitals while the remaining electron fills the nondegenerate down-spin state with xy

symmetry. It should be seen that these arguments imply that the system is in the strong correlation regime, and the bandwidth is small compared to the relevant level splittings. This also suggests that Sr_2RuO_4 is a correlated metal. Recent high-precision angular resolved photoemission spectroscopy (ARPES) experiments measurements have indeed confirmed that Sr_2RuO_4 represents a Fermi liquid with a relatively strong renormalization of the Fermi velocity due to electron–electron interactions (Ingle *et al*., 2005).

The metal–insulator transition in the isoelectronic alloy $Ca_{2-x}Sr_xRuO_4$ has been dubbed *orbital-selective Mott transition* (Anisimov *et al*., 2002). In this context, degenerate two-band Hubbard models (with diagonal hopping) but with different bandwidth have been explored with different techniques. It was found that for different Coulomb interactions there are separate Mott transitions, that is, allowing for the coexistence of itinerant and localized electrons in the intermediate regime (Koga, Kawakami, Rice and Sigrist, 2004, 2005; Sigrist and Troyer, 2004; Knecht, Blümer and van Dongen, 2005; Liebsch, 2005). The detailed phase diagram of $Ca_{2-x}Sr_xRuO_4$ is discussed in Nakatsuji and Maeno (2000a,b), Friedt *et al*. (2001), and Anisimov *et al*. (2002). Resonant X-ray diffraction experiments indicate the appearance of OO in Ca_2RuO_4 at about 260 K, that is, well above the AF phase transition at $T_N = 110$ K (Zegkinoglou *et al*., 2005).

2.6 Orbital excitations and collective orbital waves

In the presence of OO we expect collective orbital excitations, that is, like phonons in a crystalline lattice. Such orbiton excitations may be visualized as a local orbital excitation that propagates through the orbital-ordered lattice. While a local crystal-field excitation also qualifies as orbiton, we have here in mind moving excitations with pronounced momentum dependence. We begin by considering a simple case, namely, a two-dimensional model for the alternating OO which is relevant for the A phase of $LaMnO_3$ (Figure 10). As the planes are basically saturated ferromagnets at zero temperature, it suffices to consider the orbital degree freedom. Introducing orbital operators $T_i^\alpha = \frac{1}{2}\sigma_i^\alpha$ we obtain from equation (24) the orbital Hamiltonian for the plane (van der Brink, Horsch, Mack and Oleś, 1999; Ishihara, Inoue and Maekawa, 1997; Shiina, Nishitani and Shiba, 1997)

$$H_J = \frac{1}{2}J \sum_{\langle ij\rangle||} \times \left[T_i^z T_j^z + 3T_i^x T_j^x \mp \sqrt{3}(T_i^x T_j^z + T_i^z T_j^x)\right] \qquad (32)$$

where $J = t^2/(U - 3J_H)$ as the high-spin transition is relevant. We will show here that in many cases linear spin-wave (or orbital-wave) theory is the convenient tool to study orbital excitations. One starts by introducing Holstein–Primakoff bosons

$$T_i^+ = \overline{a}_i^\dagger (1 - \overline{a}_i^\dagger \overline{a}_i)^{1/2},$$
$$T_i^- = (1 - \overline{a}_i^\dagger \overline{a}_i)^{1/2} \overline{a}_i,\ T_i^z = \overline{a}_i^\dagger \overline{a}_i - \frac{1}{2} \qquad (33)$$

The linearized Hamiltonian simplifies after Fourier transformation

$$H_{\mathrm{LSW}} = J \sum_k \left[A_k a_k^\dagger a_k + \frac{1}{2} B_k (a_k^\dagger a_{-k}^\dagger + a_k a_{-k})\right] \qquad (34)$$

leading finally to the dispersion

$$\omega_k^\pm = 3J\sqrt{1 \pm \frac{1}{3}\gamma_\parallel(k)},$$
$$\gamma_\parallel(k) = \frac{1}{2}(\cos k_x + \cos k_y) \qquad (35)$$

which consists of two branches, that is, analogous to the case of spin waves in an antiferromagnet.

Different from SU(2) symmetric spin models, the orbital correlation functions sensitively depend on the basis with respect to which the orbital correlation functions are defined. In Figure 15 the two correlation functions $\langle T_q^z T_{-q}^z\rangle$ and $\langle T_q^+ T_{-q}^-\rangle$ are defined with respect to the initial global $|z\rangle$, $|x\rangle$ basis equation (4). In this case the two orbiton branches in Figure 15 are displayed separately. The results obtained by linear spin (orbital) wave theory using the truncated Hamiltonian, where $T^z T^x$ terms have been dropped, coincide with the exact diagonalization results for that model. The numerical spectra for the full Hamiltonian equation (32) are more complex, but still the first moment is well captured by orbital-wave theory.

The alternating orbital order melts for the model defined by equation (32) at $T_O \sim J$ (Horsch, Jaklic and Mack, 1999; Mack and Horsch, 1999). Figure 16 shows the evolution of orbital excitations with temperature. At low temperature, in the (alternating) orbital-orderered phase, the spectra are characterized by a Bragg peak at $q = (\pi, \pi)$ and a well-defined orbital-wave branch. When the OO melts the orbitons disappear and pronounced quasielasic scattering is seen over the whole Brillouin zone and still there is a continuum of spectral weight up to the orbiton energy. That is, there are liquid like excitations up to the bare interaction scale $\sim 3J$.

A calculation of orbitons in $LaMnO_3$ with degenerate e_g orbitals was performed in (Ishihara, Inoue and Maekawa, 1997; Shiina, Nishitani and Shiba, 1997; van der Brink,

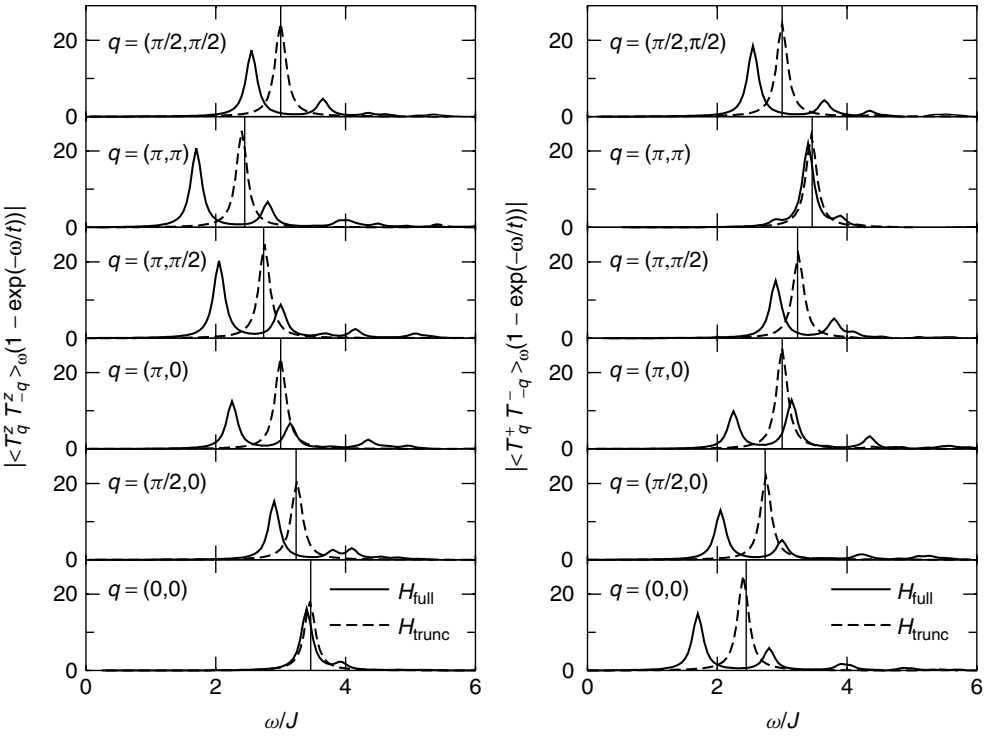

Figure 15. Orbital excitations and spectral functions of the 2D orbital model describing the alternating orbital order $(|x\rangle \pm |z\rangle)/\sqrt{2}$ of the ferromagnetic *ab* plane of $LaMnO_3$: Comparison of spectra $\langle T_q^z T_{-q}^z\rangle$ and $\langle T_q^+ T_{-q}^-\rangle$ obtained by exact diagonalization for (i) the full Hamiltonian (solid lines) and (ii) the truncated Hamiltonian (dashed lines), and the result (iii) from linear spin-wave theory obtained for case (ii) (vertical lines). (Reproduced from Van den Brink *et al*., 1999, with permission from the American Physical Society. © 1999.)

Horsch, Mack and Oleś, 1999). The effect of strong crystal-field splitting which is relevant to the $LaMnO_3$ case because of the strong compression of octahedra has also been considered (van der Brink, Horsch, Mack and Oleś, 1999). More recently Ishihara (Ishihara, 2004; Ishihara *et al*., 2005) has studied orbital waves in the orbital-ordered vanadate compounds $LaVO_3$ and YVO_3 as well as for the titanate $YTiO_3$. The direct observation of orbital waves has proven to be rather difficult, however. Insights concerning the status of experiment may be found in Rückamp *et al*. (2005) and Ishihara *et al*. (2005). Although $LaMnO_3$ appears at first glance an ideal candidate for the observation of orbitons, the evidence of orbitons in Raman scattering (Saitoh *et al*., 2001) has been discussed controversially (Grüninger *et al*., 2002; Saitoh *et al*., 2002). In real materials, the coupling of orbital excitations to lattice distortions (e.g., JT and breathing phonons) may modify the orbital excitation spectra considerably. Theoretical work in this direction has been undertaken in Perebeinos and Allen (2000), van den Brink (2001), Weisse and Fehske (2004), and Schmidt, Grüninger and Uhrig.

Strongly frustrated systems like the titanates may remain in an orbital liquid state or develop only weak OO in a strongly fluctuating orbital system as proposed by Khaliullin and Maekawa (2000) and Khaliullin and Okamoto (2002, 2003). In that case, the orbital excitation spectrum would resemble a (possibly gapped) continuum rather than collective modes. The orbital liquid picture relies on the expectation that crystal fields are sufficiently weak in compounds like $LaTiO_3$ so that the intrinsic frustration of the spin-orbital model leads to strong fluctuations. Recent Raman experiments of $LaTiO_3$ and $YTiO_3$ (Ulrich *et al*., 2006) and NMR data (Kiyama *et al*., 2005) have been indeed interpreted in terms of strongly fluctuating orbitals. However, there are experiments which are interpreted as evidence for strong crystal fields as well (Cwik *et al*., 2003).

While the origin of orbital liquid behavior in undoped systems is the inherent frustration of the spin-orbital SE interaction, that is, not all bonds can be optimized simultaneously, the lowering of symmetry does not help either. In that respect, the $S = 1/2$ cubic titanates are strikingly different from the $S = 1$ vanadate compounds. We shall encounter later in doped manganites another orbital liquid state, namely, the FM metallic phase where orbital liquid behavior is due the hole motion.

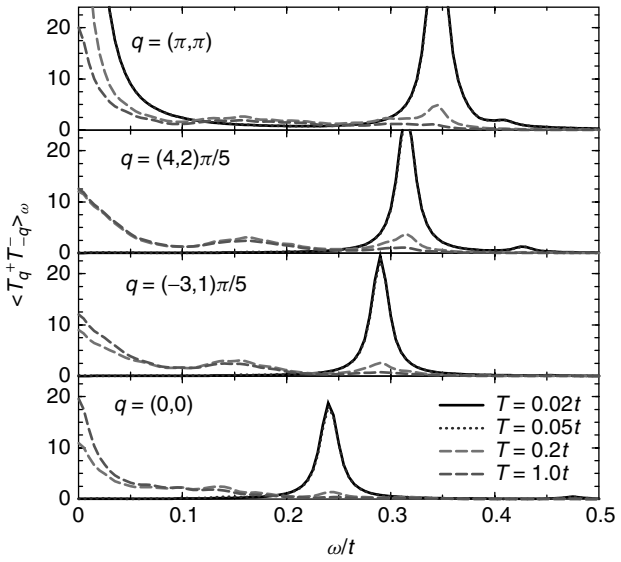

Figure 16. Temperature dependence of orbital excitations calculated for the orbital model (32). Results are obtained by the finite temperature Lanczos method for a 10 site cluster and $J/t = 0.1$. The alternating orbital order melts at about $T_O \sim J$. As the OO melts the orbitons disappear, and the excitation spectrum changes into that of an orbital liquid. (Horsch and Mack, unpublished.)

2.7 Composite spin-orbital phenomena

2.7.1 Spin-orbit coupling

The intrinsic quartic terms of the form $S_i S_j T_i T_j$ in the generic spin-orbital model can lead to entanglement of spin and orbital degrees of freedom. While such terms are not difficult to handle in some cases, as we shall discuss later, they lead in other cases to strong spin-orbital fluctuations and a complete breakdown of any mean-field (MF) theory. We postpone this discussion to Section 3.

Here, we shall address instead the additional coupling between orbital and spin resulting from the relativistic spin-orbit coupling H_λ.

$$H_\lambda = \Lambda \sum_i \mathbf{L}_i \cdot \mathbf{S}_j \tag{36}$$

where we introduce $\lambda = \Lambda/J$ as parameter. This interaction is quenched in the case of real OO, whereas when orbitals fluctuate like in $LaVO_3$ and YVO_3 this interaction can induce orbital moments (OMs) and decide over the alignment of spins (Ulrich *et al.*, 2002; Horsch, Khaliullin and Oleś, 2003). Hence in the t_{2g} systems where orbital fluctuations are strong it is important to include spin-orbit interaction as well. Here we add H_λ simply to the spin-orbital model $\mathcal{H}$, equation (16), for vanadates. An alternative approach would start from the multiband Hubbard model and a derivation of SE with H_λ included from the outset, as in Schmitz *et al.* (2005) for the titanates.

Owing to the $GdFeO_3$ distortion the individual VO_6 octahedra are tilted by the angle $\phi_i = \pm\phi$, which alternate along the c axis (Blake *et al.*, 2001, 2002). As the xy orbital is inactive, two components of the OM $\mathbf{L}_i$ are quenched, while the third one, $L_i^z = 2\tau_i^y$ parallel to the local axis of a VO_6 octahedron, couples to the spin projection. Because of AF correlations of τ_i^y moments, spin-orbit coupling induces a staggered spin component. As the spin interactions are FM, weak spin-orbit coupling would give no energy gain, if the spins were oriented along the c axis. Thus, finite Λ breaks the SU(2) symmetry and favors easy magnetization axis within the (a, b) plane. As quantization axis for $\mathbf{L}_i$ ($\mathbf{S}_i$) we use the octahedral axis. Thus the spin-orbit term is (Horsch, Khaliullin and Oleś, 2003):

$$H_\lambda = 2\Lambda \sum_i \left(S_i^x \cos\phi_i + S_i^z \sin\phi_i\right) \tau_i^y. \tag{37}$$

In Schwinger boson representation $\tau_i^y = \frac{1}{2} i (a_i^+ b_i - b_i^+ a_i)$, that is, this operator leads to local fluctuations of a and b orbital occupancy, whereas SE leads to similar fluctuations by exchanging a and b electrons between neighbor sites along the c axis.

Spin-orbit coupling H_λ competes with Hund's exchange (η terms), which favors real OO, and triggers a novel phase (see Figure 17), where the ordering of the t_{2g} orbital moments is stabilized by the tilting of the VO_6 octahedra. This explains qualitatively spin canting and the reduction of magnetization observed in YVO_3 (Ulrich *et al.*, 2002; Horsch, Khaliullin and Oleś, 2003). Moreover H_λ implies a substantial reduction of spin-wave energies.

2.7.2 Orbital-Peierls distortion in YVO_3

In a neutron scattering study, (Ulrich *et al.*, 2002) found evidence for a dimerization of the finite temperature C phase in YVO_3 (Figure 12) by the observation of a splitting finite temperature magnetic C phase. This was subsequently interpreted as evidence for orbital-Peierls distortion, as no significant lattice dimerization was observed. That is, the proposed mechanism is a modulation of spin exchange constants $J_{c,1}$ and $J_{c,2}$, that is, controlled by orbital dimer formation (Ulrich *et al.*, 2002; Horsch, Khaliullin and Oleś, 2003; Sirker and Khaliullin, 2003).

Thus the underlying idea is, that the system can profit from orbital dimer formation as in the OVB state. However, one also recognizes that the C−AF phase cannot dimerize at $T = 0$ because the FM (along c) state is inert, and does not allow for any modulation in the orbital sector. Orbital singlets need the decoupling via the magnetic sector. That is,

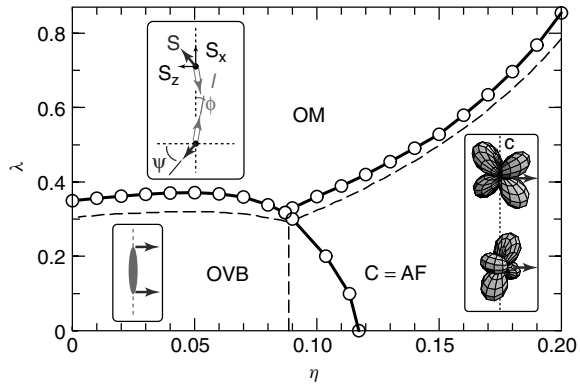

Figure 17. Phase diagram at zero temperature obtained from the spin-orbital model for cubic vanadates. The phase diagram shows the competition of different phases as function of the Hund-coupling constant $\eta = J_{\rm H}/U$ and the relativistic spin-orbit coupling λ. Near the origin the orbital valence bond (OVB) state is the stable solution, large λ favors orbital moment (OM) formation, while large η yields the C-type antiferromagnetic (C-AF) state, with ferromagnetic spin alignment and alternating orbital order along c direction. Solid lines and circles denote results from exact diagonalization, while dashed lines indicate results obtained by mean-field theory. Typical parameters for the vanadates are $\lambda \sim 0.3 - 0.4$ and $\eta \simeq 0.12$. (Reproduced from Horsch *et al*., 2003, with permission from the American Physical Society. © 2003.)

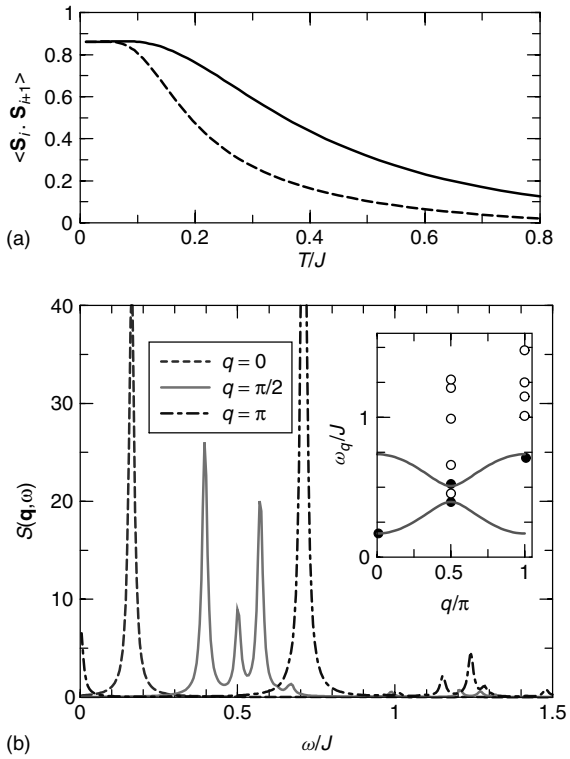

Figure 18. Calculated dimerization and spin-excitation spectra in the C-AF phase at $T > 0$: (a) temperature dependence of spin−spin correlations $\langle \mathbf{S}_i \cdot \mathbf{S}_{i+1} \rangle$ on strong and weak FM bonds (solid and dashed line); (b) spin response $S(\mathbf{q}, \omega)$ in the dimerized C-AF phase for $\mathbf{q} = (0, 0, q)$ with $q = 0, \frac{\pi}{2}, \pi$. Inset: filled (open) circles indicate strong (weak) features in $S(\mathbf{q}, \omega)$; lines show the fitted spin-wave dispersion for: $\eta = 0.12$, $\lambda = 0.4$. (Reproduced from Horsch *et al*., 2003, with permission from the American Physical Society. © 2003.)

the spin correlations $\langle \mathbf{S_i} \cdot \mathbf{S_j} \rangle$ on the adjacent bonds must be weakened by spin deviations, which may occur via thermal fluctuations at higher temperature.

Results obtained by finite temperature diagonalization (Horsch, Khaliullin and Oleś, 2003) show that the chain dimerizes at finite temperatures due to the intrinsic instability toward alternating orbital singlets (Sirker and Khaliullin, 2003). Except at low temperature, the spin correlations $\langle \mathbf{S}_i \cdot \mathbf{S}_{i+1} \rangle$ (Figure 18a), alternate between strong and weak FM bonds due to the orbital-Peierls dimerization, $2\delta_\tau = |\langle \boldsymbol{\tau}_i \cdot \boldsymbol{\tau}_{i+1} \rangle - \langle \boldsymbol{\tau}_i \cdot \boldsymbol{\tau}_{i-1} \rangle|$, which has a distinct maximum at $T \simeq 0.24J$ for $\eta = 0.12$. Consistent with the discussion in the preceding text, the modulation of $\langle \mathbf{S}_i \cdot \mathbf{S}_{i+1} \rangle$ vanishes in the C phase at low T.

Figure 18(b) shows the dynamical spin structure factor $S(\mathbf{q}, \omega)$ obtained by exact diagonalization of a cluster with periodic boundary conditions at $T = 0$, assuming the same orbital dimerization, $\langle \boldsymbol{\tau}_i \cdot \boldsymbol{\tau}_{i+1} \rangle$, as found in the preceding text for $T/J = 0.25$. At $\mathbf{q} = (0, 0, \frac{\pi}{2})$ one finds a splitting of the spin wave similar to experiment. The finite energy of the $\mathbf{q} = (0, 0, 0)$ mode results from the Λ-term in equation (37) and the MF coupling to neighbor chains. Additional features seen in $S(\mathbf{q}, \omega)$, for example, for $q = (0, 0, \pi)$ at $\omega \sim 1.25J$, can be attributed to the coupling to orbital excitations. The spin-wave energies can be fitted by a simple Heisenberg model with two FM coupling constants: $J_{c1} = 5.7$, $J_{c2} = 3.3$ meV, and a small anisotropy term, as shown in the inset (solid lines). A measure for the dimerization strength is the ratio $J_{c1}/J_{c2} \sim 1.73$ consistent with an experimental value 1.82 (Ulrich *et al*., 2002).

Subsequently, the quasi one-dimensional ($S = 1/2$) titanium pyroxene compound $NaTiSi_2O_6$ was proposed to reveal orbital dimerization, and is considered as second system showing the high-temperature orbital-Peierls phase (Konstantinović *et al*., 2004).

3 ONE-DIMENSIONAL SPIN-ORBITAL MODELS

The study of one-dimensional spin-orbital models has been an active field, stimulated by specific analytic and numerical tools. Particularly widely studied are models where it is assumed that also the orbital sector has the full rotational SU(2) symmetry. This has given some important deeper insights into the features of spin-orbital models and the

variety of phases of such models. Some instructive cases are described, such as the interplay of orbital and spin correlations in SU(4) and other spin-orbital models, spin-orbital entanglement and the role of composite spin-orbital fluctuations. One-dimensional spin-orbital models may also represent spin models on two-leg ladders with quartic interactions (Nerseyan and Tsvelik, 1997; Koleshuk and Mikeska, 1998; Mikeska and Koleshuk, 2004).

3.1 Spin-1/2 models

As the most prominent example, among others, the one-dimensional spin-orbital model with SU(4) symmetry, which describes a spin-1/2 system with twofold orbital degeneracy, has been widely investigated (Affleck, 1986; Sutherland, 1975; Itakura and Kawakami, 1995; Yamashita, Shibata and Ueda, 1998; Frischmuth, Mila and Troyer, 1999). A slightly extended 1D spin-orbital model with SU(2)⊗SU(2) symmetry and free constants A and B (Pati, Singh and Khomskii, 1998; Azaria, Gogolin, Lecheminant and Nersesyan, 1999; Azaria, Boulat and Lecheminant, 2000; Yamashita, Shibata and Ueda, 2000; Tsukamoto, Kawakami, Yamashita and Ueda, 2000; Itoi, Qin and Affleck, 2000)

$$\mathcal{H} = J \sum_i \left(\mathbf{S}_i \cdot \mathbf{S}_{i+1} + \frac{A}{4} \right) \left(\mathbf{T}_i \cdot \mathbf{T}_{i+1} + \frac{B}{4} \right) \qquad (38)$$

has been studied in detail. Here $\mathbf{S}_i$ is an $S = 1/2$ spin operator at the ith site and $\mathbf{T}_i$ is a $T = 1/2$ pseudospin operator acting on the doubly degenerate orbital degrees of freedom. In particular, the ground-state phase diagram has been established (Figure 19), which consists of a variety of phases including gapful/gapless spin and orbital phases (Pati, Singh and Khomskii, 1998; Azaria, Gogolin, Lecheminant and Nersesyan, 1999; Azaria, Boulat and Lecheminant, 2000; Yamashita, Shibata and Ueda, 2000; Tsukamoto, Kawakami, Yamashita and Ueda, 2000; Itoi, Qin and Affleck, 2000). At $(A, B) = (1, 1)$ on the I−V phase boundary the model has SU(4) symmetry and is Bethe ansatz integrable (Affleck, 1986; Sutherland, 1975; Itakura and Kawakami, 1995; Yamashita, Shibata and Ueda, 1998; Frischmuth, Mila and Troyer, 1999). The SU(4) symmetry results from the fact that the Hamiltonian in this case consists simply of permutation operators $\left(2\mathbf{S}_i \cdot \mathbf{S}_{i+1} + \frac{1}{2}\right)$, which interchange states on neighbor sites, and also includes the interchange of orbital and spin sector. The low-energy theory is a $SU(4)_1$ Wess–Zumino–Witten model with central charge $c = 3$. One can imagine the ground state formed by spin-singlet (orbital-triplet) pairs fluctuating into orbital-singlet (spin-triplet) pairs and back. A particularly striking result in the SU(4) case is the equality of the spin-, orbital-, and composite correlation

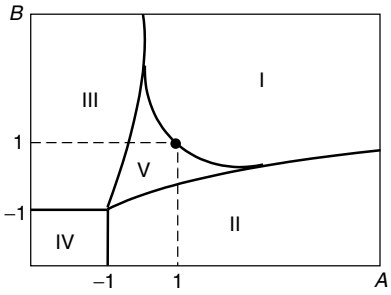

Figure 19. Phase diagram of the $S = 1/2$ spin-orbital model. Phase I is a gapful phase with doubly degenerate ground states which form alternating spin and orbital singlets. In the phase II, the spin degrees of freedom are in the fully polarized ferromagnetic state while the orbitals are in the antiferromagnetic ground state and vice versa in the phase III. Both spin and orbital degrees of freedom are in the fully polarized ferromagnetic states in the phase IV. The phase V is a gapless phase including an integrable SU(4) point ($A = B = 1$). (Reproduced from S. Miyashita and N. Kawakami, *J. Phys. Soc. Jpn.* **74**, 758 (2005), with permission from the Physical Society of Japan.)

functions (Li, Ma, Shi and Zhang, 1998; Frischmuth, Mila and Troyer, 1999):

$$\langle S_i^\alpha S_j^\alpha \rangle = \langle T_i^\alpha T_j^\alpha \rangle = 4 \langle S_i^\alpha S_j^\alpha T_i^\beta T_j^\beta \rangle = w_{i-j} \qquad (39)$$

independent of the indices $\alpha, \beta = x, y, z$. Remarkably the nearest-neighbor correlation functions (CFs) are all negative! For the infinite chain $w_1 = -0.07168(1)$ (Frischmuth, Mila and Troyer, 1999). That is, our usual imagination of MF factorization, that is, $\langle S_i^\alpha S_j^\alpha \rangle \langle T_i^\alpha T_j^\alpha \rangle$, which suggests that, if the individual CFs are negative, the composite CF should be positive, fails here dramatically.

3.2 Spin-1 models

Next we consider the $S = 1$ extension of the 1D spin-orbital model with uniaxial single-ion anisotropy D, which is characterized by two coupling constants A and B related to the spin and orbital degrees of freedom (Miyashita, Kawaguchi, Kawakami and Khaliullin, 2004; Miyashita and Kawakami, 2005). The Hamiltonian reads

$$\mathcal{H} = J \sum_i \left[(\mathbf{S}_i \cdot \mathbf{S}_{i+1} + A) \left(\mathbf{T}_i \cdot \mathbf{T}_{i+1} + \frac{B}{4} \right) \right] + D \sum_i \left(S_i^z \right)^2 \qquad (40)$$

where $\mathbf{S}_i$ is an $S = 1$ spin operator at the ith site and $\mathbf{T}_i$ is a $T = 1/2$ pseudospin operator acting on the doubly degenerate orbital degrees of freedom. J controls the magnitude of the exchange couplings, which will be taken as the energy

unit in the following discussions. The D term represents uniaxial single-ion anisotropy, which has been discussed in detail so far in the Haldane spin chain systems.

The model (40) is regarded as a natural extension of the 1D $S = 1/2$ spin-orbital model with SU(2)⊗SU(2) symmetry, for which the D term is absent, and $A \to A/4$ for the spin ($S = 1/2$) part. As spin $S = 1$ is more classical than $S = 1/2$ the comparison of these two models may allow to clarify the role of spin fluctuations.

At the special point ($A = B = 1$ and $D = 0$), the symmetry is enhanced to SU(2)⊗SU(2). It is known that the ground state in this case is the orbital liquid with a small spin gap, which is called the *orbital valence bond* (OVB) phase (Shen, Xie and Zhang, 2002; Horsch, Khaliullin and Oleś, 2003; Sirker and Khaliullin, 2003; Miyashita, Kawaguchi, Kawakami and Khaliullin, 2004). The spin-orbital model studied by Khaliullin *et al* for the cubic vanadates $LaVO_3$ and YVO_3 (Khaliullin, Horsch and Oleś, 2001; Sirker and Khaliullin, 2003; Horsch, Khaliullin and Oleś, 2003) includes the above special case in the limit of vanishing Hund coupling.

The asymmetry between the spin and orbital sector in the $S = 1$ model is particularly manifest in the OVB state I in Figure 20. Orbital singlets appear together with spin pairs coupled into a $S = 2$ state, the AF arrangement leads to basically decoupled pairs. Instead in phase II all spins are aligned ferromagnetically, while the pseudospins describing the orbitals form a $T = 1/2$ Heisenberg chain. It is quite surprising, that the total energy of phase I which stems from each second bond only can be lower than that of phase II which has a large contribution of the 1D Heisenberg chain on each bond. The OVB state has a small spin gap and a large orbital gap. The phase diagram of the $S = 1$ and the $S = 1/2$ model are quite similar, except that the phase V is missing. Negative uniaxial single-ion anisotropy D leads to further phases (Miyashita and Kawakami, 2005).

3.3 Spin-orbital entanglement and violation of GK rules

Composite spin-orbital excitations and the breakdown of mean-field (MF) theory has been studied by Oleś, Horsch, Feiner and Khaliullin (2006) for several 1D spin-orbital models. Spins and orbitals get entangled due to composite spin-orbital quantum fluctuations and the familiar static GK rules are violated to the extent that even the signs of the magnetic interactions may fluctuate in time. To demonstrate this general feature in the most transparent way, three different spin-orbital models are considered: Correlated insulators with 180° perovskite bonds between d^1, d^2, and d^9 ionic configurations, respectively, where the GK rules (Section 2.5) definitely predict complementary signs of spin and orbital intersite correlations. The first two models are derived for t_{2g} electrons as in $LaTiO_3$ (d^1) and $LaVO_3$ (d^2), and it is demonstrated that the GK rules are violated at small Hund coupling. The third model is for e_g holes as in $KCuF_3$ (d^9), in which the GK rules are perfectly obeyed. The qualitative difference results from the quantum nature of t_{2g} orbitals which may form singlets, while e_g orbitals behave more Ising-like and orbital singlets cannot form. The SE

$$\mathcal{H} = J \sum_{\langle ij \rangle \| c} \left[\left(\mathbf{S}_i \cdot \mathbf{S}_j + S^2 \right) \hat{J}_{ij}^{(c)} + \hat{K}_{ij}^{(c)} \right] + \mathcal{H}_{\rm orb} \qquad (41)$$

contains interactions like $(S_i^+ T_i^-)(S_j^- T_j^+) + (S_i^- T_i^+)(S_j^+ T_j^-)$, which generate *simultaneous* fluctuations of spins and orbitals described by the composite operators $Q_i^+ \equiv S_i^+ T_i^-$, and so on. At finite Hund coupling $\eta = H_{\rm H}/U$ both $\hat{J}_{ij}^{(c)}(d^1)$ and $\hat{J}_{ij}^{(c)}(d^2)$ (see Section 2.4.1) also contain

$$\mathbf{T}_i \otimes \mathbf{T}_j = \tfrac{1}{2}\left(T_i^+ T_j^+ + T_i^- T_j^- \right) + T_i^z T_j^z \qquad (42)$$

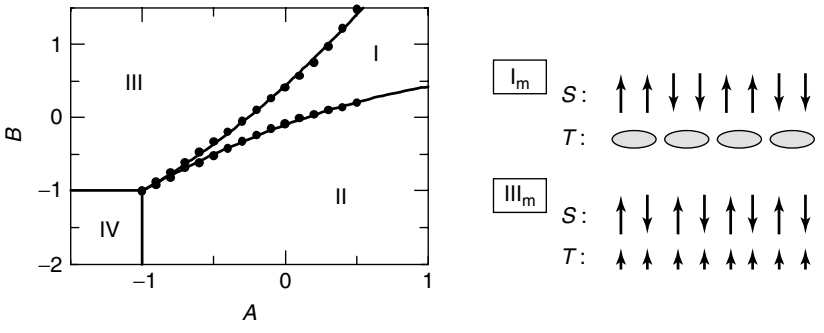

Figure 20. Phase diagram of the 1D $S = 1$ spin-orbital model in the $A - B$ plane without uniaxial single-ion anisotropy. The phase I is the OVB phase (see text). In the phase II, the spin part is in the fully polarized state while the orbital part forms the gapless antiferromagnetic $T = 1/2$ Heisenberg chain. On the other hand, in the phase III, the orbital sector is in the ferromagnetic phase while the spin sector is in the $S = 1$ Haldane phase. Spins and pseudospins are in the fully polarized ferromagnetic states in the phase IV. All the transitions are of first order. (Reproduced from S. Miyashita and N. Kawakami, *J. Phys. Soc. Jpn.* **74**, 758 (2005), with permission from the Physical Society.)

This operator appears because double occupancy of either active (yz or zx) orbital is not an eigenstate of the on-site Coulomb interaction. Consequently, the total T and T^z quantum numbers are not conserved and orbital fluctuations are amplified. Finally, $GdFeO_3$-type distortions induce nearest-neighbor orbital interactions $\mathcal{H}_{\rm orb} = -V \sum_{\langle ij \rangle} T_i^z T_j^z$ favoring FO order along the c axis (Mizokawa, Khomskii and Sawatzky, 1999).

It has been shown that a clear measure of entanglement is provided by the comparison of the intersite spin-, orbital-, and composite spin-orbital correlations. These have been calculated for the above spin-orbital models. To make the results comparable in all cases, the following definitions were chosen:

$$S_{ij} = \langle \mathbf{S}_i \cdot \mathbf{S}_j \rangle / (2S)^2 \tag{43}$$

for the spin correlations. The orbital and spin-orbital correlations are defined for the t_{2g} (d^1 and d^2) models as

$$T_{ij}^{(t)} = \langle \mathbf{T}_i \cdot \mathbf{T}_j \rangle, \tag{44}$$

$$C_{ij}^{(t)} = \left[\langle (\mathbf{S}_i \cdot \mathbf{S}_j)(\mathbf{T}_i \cdot \mathbf{T}_j) \rangle - \langle \mathbf{S}_i \cdot \mathbf{S}_j \rangle \langle \mathbf{T}_i \cdot \mathbf{T}_j \rangle \right] / (2S)^2 \tag{45}$$

If the composite correlation function $C_{ij}^{(t)} = 0$, orbitals and spins are disentangled and the two sectors can be factorized. Alternative measures of spin-orbital entanglement are possible, for example, (Chen, Wang, Li and Zhang, 2006) have used a reduced von Neumann entropy to explore the phase diagram of a spin-orbital chain with $SU(2) \otimes SU(2)$ symmetry. For the e_g (d^9) model the conventions are analogous, for details see Oleś, Horsch, Feiner and Khaliullin (2006). In Figure 21(a) relevant for the d^1 titanates one finds at $\eta = 0$ the SO (4) point where all correlation functions are negative. This exotic phase stops at $\eta S = 0.1$ where the spin correlation get FM and the correlation function C_{ij} that measures the entanglement becomes exactly zero. The anomalous behavior of CF's exists also in Figure 21(b) relevant for the $S = 1$ vanadates. If FM OO is enforced by the $GdFeO_3$-type distortion as in Figure 21(d) the entangled regime is reduced to intermediate values for ηS.

Particularly remarkable is a comparison of spin correlations in Figure 21 and the magnetic exchange constants $J_{ij} = \langle \hat{J}_{ij}^{(c)} \rangle$ (Figure 22) determined via a MF factorization of orbital and spin sector. In Figure 22 the shaded regions in case of t_{2g} models show negative (FM) exchange constant, whereas the actual spin correlations are AF!

Summarizing, in correlated insulators with partly filled t_{2g} shells, orbitals, and spins are entangled, and average spin and orbital correlations are typically in conflict with the (static) GK rules. The key difference between e_g and t_{2g} electrons is that the latter can form orbital singlets. Thus the dynamical spin and orbital correlations are complementary to each other, and fluctuate between orbital-singlet/spin-triplet and orbital-triplet/spin-singlet configurations. This implies the fluctuation of the sign of the spin exchange constants J_{ij}, as can be seen from equation (17).

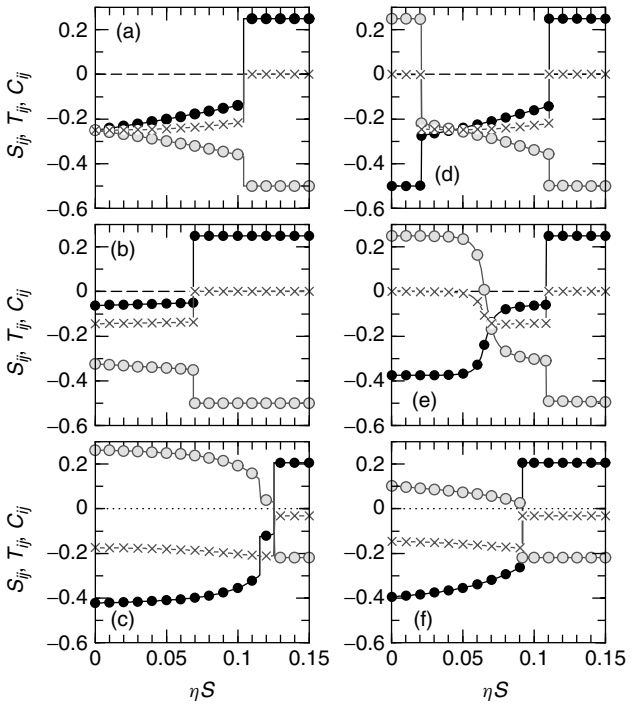

Figure 21. Intersite spin S_{ij} (filled circles), orbital $T_{ij}^{(t,e)}$ (empty circles), and composite spin-orbital $C_{ij}^{(t,e)}$ (crosses) correlations as functions of Hund's exchange ηS, for $V = 0$ (left) and for $V = J$ (right) for: (a,d) d^1 (titanate) model, (b,e) d^2 (vanadate) model, and (c,f) d^9 (cuprate) model. (Reproduced from Oles *et al.*, 2006, with permission from the American Physical Society. © 2006.)

4 SUPEREXCHANGE, MAGNETISM, AND OPTICS

Although this field is already quite mature, it has been realized only recently that the *magnetic* and the *optical* properties of correlated insulators with partly filled d orbitals are intimately related to each other, being just different experimental manifestations of the same underlying spin-orbital physics (Oleś, Khaliullin, Horsch and Feiner, 2005; Khaliullin, Horsch and Oleś, 2004; Lee, Kim and Noh, 2005). On the other hand, it has been well known that the often dramatic temperature dependence of optical spectra is connected to magnetic structure (Miyasaka, Okimoto and Tokura, 2002) and that the variation of spectral weights is controlled by

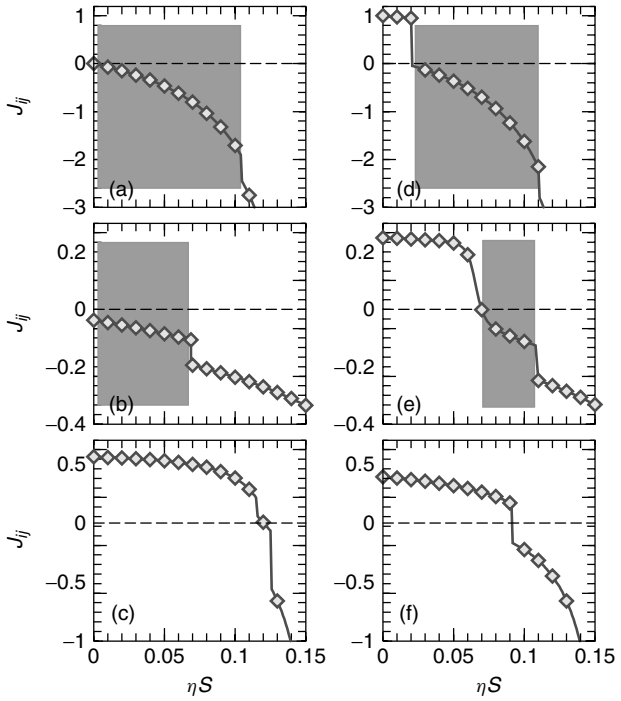

Figure 22. Spin exchange constants $J_{ij} = \langle \hat{J}_{ij}^{(c)} \rangle$ at $V = 0$ (left) and at $V = J$ (right) as functions of Hund's exchange ηS for (a), (d) d^1 model; (b), (e) d^2 model; (c), (f) d^9 model. In the shaded regions in (a), (b), (d), (e), J_{ij} is negative (FM) and yet the spin correlations are AF, $S_{ij} < 0$ (see Figure 21). (Reproduced from Oles *et al*., 2006, with permission from the American Physical Society. © 2006.)

the temperature dependence of the nearest-neighbor spin-correlation functions $\langle \mathbf{S}_i \cdot \mathbf{S}_j \rangle$, that is, by SE energy (Aichhorn, Horsch, von der Linden and Cuoco, 2002). Although it is clear that the *low-energy* effective SE Hamiltonian decides about the magnetic interactions, it is not immediately obvious that the *high-energy* optical excitations and their partial sum rules have the same roots and may be described by the SE as well.

The new concept of partial spectral weights makes it necessary to reanalyze the spin-orbital SE models to obtain the partial optical sum rules. In a further subsection, the three-dimensional spin-orbital model for the cubic vanadate compound $LaVO_3$ is solved approximately to illustrate the interdependence of spin and orbital correlations as well as the emergence of highly anisotropic optical spectral weights.

4.1 Partial optical sum rules and magnetism

The d-d charge excitations that are seen in optics reflect the rich multiplet structure of transition-metal ions determined by Hund's exchange coupling $J_{\rm H}$. The same multiplet transitions that reflect the spin and orbital degrees of freedom determine the SE interactions (Kugel and Khomskii, 1982a; Kugel and Khomskii, 1982b). When spin and orbital correlations change, for example, as function of temperature or magnetic field, the individual components of the optical multiplet reflect characteristic *spectral weight transfer*. Moreover, the cubic symmetry may be broken by orbital and spin order, and thus one expects *anisotropic optical absorption*. Indeed, pronounced anisotropy was reported for $LaMnO_3$ (Tobe, Kimura, Ohimoto and Tokura, 2001), both for the A-type AF phase (A-type (C-type) AF phase consists of ferromagnetic planes (chains) with AF order between them) as well as for the orbital-ordered phase above the Néel temperature $T_{\rm N}$. Recently, the anisotropy in optical absorption and its strong temperature dependence near the magnetic transitions were found for cubic vanadates (Miyasaka, Okimoto and Tokura, 2002; Tsvetkov *et al*., 2004; Motome, Seo, Fang and Nagaosa, 2003). This latter example is even more puzzling as the magnetic properties are anomalous (Mahajan, Johnston, Torgeson and Borsa, 1992; Noguchi *et al*., 2000). Neutron scattering (Ulrich *et al*., 2003) and Raman experiments (Miyasaka *et al*.,) have revealed nontrivial quasi one-dimensional (1D) correlations of spin and orbital degrees of freedom that are surprising for crystals with nearly cubic crystal structure. Indeed, a theory of spin and orbital states in cubic vanadates predicted that quasi-1D orbital fluctuations lead to a spontaneous breaking of the cubic symmetry in the SE model (Khaliullin, Horsch and Oleś, 2001).

The SE interaction in a cubic Mott insulator with orbital degrees of freedom has the generic form,

$$\mathcal{H}_J = H_s + H_\tau + H_{s\tau} = \sum_n \sum_{\langle ij \rangle \| \gamma} H_n^{(\gamma)}(ij) \qquad (46)$$

and consists of separate spin (H_s) and orbital (H_τ) interactions, and of a dynamical coupling between them ($H_{s\tau}$). This complex form of $\mathcal{H}_{\rm J}$, given by equation (46), follows from the terms $H_n^{(\gamma)}(ij)$ for each bond $\langle ij \rangle$ along a given cubic axis $\gamma = a, b, c$, that arise from the transitions to various upper Hubbard bands labeled by n. The *partial optical sum rules* for the different multiplet transitions n and photon polarization γ are determined by the respective terms of the SE energy (Khaliullin, Horsch and Oleś, 2004):

$$\frac{a_0 \hbar^2}{e^2} \int_0^\infty \sigma_n^{(\gamma)}(\omega) {\rm d}\omega = -\frac{\pi}{2} K_n^{(\gamma)} = -\pi \left\langle H_n^{(\gamma)}(ij) \right\rangle \qquad (47)$$

Here the tight-binding model is implied and a_0 is the distance between magnetic ions. $\left\langle H_n^{(\gamma)}(ij) \right\rangle$ is the SE energy for a bond $\langle ij \rangle$ along axis γ and multiplet transition n. The first equality in equation (47) follows from the optical sum rule for a given transition n, and relates the kinetic energy $K_n^{(\gamma)}$ to the optical conductivity $\sigma_n^{(\gamma)}(\omega)$ for this band, while the

second equality relates the associated kinetic energy to the SE energy via the *Hellman–Feynman theorem* (Baeriswyl, Carmelo and Luther, 1986).

Experimental data is often presented in terms of an effective carrier number (see, e.g., equation (2) of (Miyasaka, Okimoto and Tokura, 2002)), $N_{\mathrm{eff},n}^{(\gamma)} = (2m_0 v_0/\pi e^2)\int_0^\infty \sigma_n^{(\gamma)}(\omega)\mathrm{d}\omega$, where m_0 is the free electron mass, and $v_0 = a_0^3$ is the volume per magnetic ion. This gives the *partial optical sum rules* in the following form (Khaliullin, Horsch and Oleś, 2004):

$$N_{\mathrm{eff},n}^{(\gamma)} = -\frac{m_0 a_0^2}{\hbar^2}\, K_n^{(\gamma)} = -\frac{m_0 a_0^2}{\hbar^2}\left\langle 2H_n^{(\gamma)}(ij)\right\rangle \tag{48}$$

Each level n of the multiplet represents an upper Hubbard band with its own spin and orbital quantum numbers. The key point is that while the full kinetic energy and the corresponding total intensity may show only moderate T dependence and weak anisotropy, the behavior of the individual transitions is much richer. In particular, spectral weight transfers between different multiplet transitions directly reflect the change of spin and orbital correlations.

To conclude this section, we note that strong spin-orbital fluctuations imply large virtual kinetic energy, which is measured by the partial spectral weights. Hence by careful quantitative study of optical spectra, their anisotropy and temperature dependence it should be possible to decide whether orbitals fluctuate strongly or whether they are quenched by crystal fields or JT distortions.

4.2 Optical anisotropy and partial sum rules in cubic vanadates

In Mott insulators with orbital degeneracy the orbital occupation and correlation functions determine the interaction between spins, while the resulting spin correlations influence the interaction between orbitals. We have seen that in some cases quantum fluctuations decide about the resulting order, the lowering of dimensionality, and so forth. In the following, this interrelation and the implications for the partial optical spectral weights will be described for one case in more detail. In Section 2.4, we have already discussed the spin-orbital Hamiltonain, equation (16), for $LaVO_3$. Our main task here is to separate this expression into the individual contributions arising from the different multiplet transitions. These individual terms contain precisely the required information for the partial spectral weights of the different optical excitations (see Figure 3). In case of vanadates, one has three optical bands $n = 1, 2, 3$ arising from the transitions to: (i) a high-spin state $^4\mathrm{A}_2$ at energy $U - 3J_\mathrm{H}$, (ii) two degenerate low-spin states $^2\mathrm{T}_1$ and $^2\mathrm{E}$ at U, and (iii) $^2\mathrm{T}_2$ low-spin state at $U + 2J_\mathrm{H}$ (Khaliullin, Horsch and Oleś, 2001). Using $\eta = J_\mathrm{H}/U$, the multiplet structure is parameterized by: $R = 1/(1-3\eta)$ and $r = 1/(1+2\eta)$. In $LaVO_3$ xy orbitals are singly occupied (Mahajan, Johnston, Torgeson and Borsa, 1992; Noguchi *et al.*, 2000). Hence the cubic symmetry is broken and one obtains a high-spin contribution for bonds $\langle ij\rangle$ along c axis:

$$H_1^{(c)} = -\frac{1}{3}JR\sum_{\langle ij\rangle}\Big(\mathbf{S}_i\cdot\mathbf{S}_j + 2\Big)\Big(\frac{1}{4} - \boldsymbol{\tau}_i\cdot\boldsymbol{\tau}_j\Big) \tag{49}$$

while $H_1^{(ab)} = -\frac{1}{6}JR\sum_{\langle ij\rangle}(\mathbf{S}_i\cdot\mathbf{S}_j+2)(\frac{1}{4} - \tau_i^z\tau_j^z)$ for (a,b) planes. In equation (49) pseudospin operators $\boldsymbol{\tau}_i$ describe low-energy dynamics of (initially degenerate) xz and yz orbital doublet at site i; this dynamics is quenched in $H_1^{(ab)}$. The operator $\frac{1}{3}(\mathbf{S}_i\cdot\mathbf{S}_j+2)$ is the projection operator on the *high-spin* state for $S = 1$ spins.

The terms $H_n^{(c)}(ij)$ for *low-spin* excitations ($n = 2, 3$) contain instead the spin operator $(1 - \mathbf{S}_i\cdot\mathbf{S}_j)$ (which guarantees that these terms vanish for fully polarized spins on a considered bond, $\langle \mathbf{S}_i\cdot\mathbf{S}_j\rangle = 1$):

$$\begin{aligned} H_2^{(c)} &= -\frac{1}{12}J\Big(1 - \mathbf{S}_i\cdot\mathbf{S}_j\Big)\Big(\frac{7}{4} - \tau_i^z\tau_j^z - \tau_i^x\tau_j^x + 5\tau_i^y\tau_j^y\Big) \\ H_3^{(c)} &= -\frac{1}{4}Jr\Big(1 - \mathbf{S}_i\cdot\mathbf{S}_j\Big) \\ &\quad\times\Big(\frac{1}{4} + \tau_i^z\tau_j^z + \tau_i^x\tau_j^x - \tau_i^y\tau_j^y\Big) \end{aligned} \tag{50}$$

For the application of the partial sum rules, equation (48), we need to know the temperature dependence of the different spin and orbital correlation functions. One approach is a Bethe–Peierls MF approximation for the spin and orbital bond correlations which are determined self-consistently after decoupling them from each other in $\mathcal{H}_\mathrm{J}$ (46). Within such a MF treatment composite spin-orbital (quartic) interaction terms can be included perturbatively (Khaliullin, Horsch and Oleś, 2004). Spin correlations follow by solution of the effective spin Hamiltonian:

$$H_s = J_{ab}^s\sum_{\langle ij\rangle_{ab}}\mathbf{S}_i\cdot\mathbf{S}_j - J_c^s\sum_{\langle ij\rangle_c}\mathbf{S}_i\cdot\mathbf{S}_j \tag{51}$$

where the exchange integrals along c and $a(b)$ directions:

$$\begin{aligned} J_c^s &= \frac{1}{2}J\Big[\eta R - (R - \eta R - \eta r)\Big(\frac{1}{4} + \langle\boldsymbol{\tau}_i\cdot\boldsymbol{\tau}_j\rangle\Big) \\ &\quad - 2\eta r\langle\tau_i^y\tau_j^y\rangle\Big] \\ J_{ab}^s &= \frac{1}{4}J\Big[1 - \eta R - \eta r + (R - \eta R - \eta r) \\ &\quad\times\Big(\frac{1}{4} + \langle\tau_i^z\tau_j^z\rangle\Big)\Big] \end{aligned} \tag{52}$$

are determined by the corresponding nearest-neighbor orbital correlation functions! Note that J_c^s turns out FM because of singlet fluctuations in the orbital sector (a minus sign in front of J_c^s has been included in equation (51)).

The orbital correlation functions are determined by the orbital Hamiltonian which is given as:

$$H_\tau = \sum_{\langle ij\rangle_c} \left[J_c^\tau \boldsymbol{\tau}_i \cdot \boldsymbol{\tau}_j - J(1-s_c)\eta r \tau_i^y \tau_j^y \right] + J_{ab}^\tau \sum_{\langle ij\rangle_{ab}} \tau_i^z \tau_j^z \qquad (53)$$

with exchange integrals:

$$J_c^\tau = \frac{1}{2} J \Big[(1+s_c)R + (1-s_c)\eta(R+r) \Big]$$
$$J_{ab}^\tau = \frac{1}{4} J \Big[(1-s_{ab})R + (1+s_{ab})\eta(R+r) \Big] \qquad (54)$$

depending on spin correlations: $s_c = \langle \mathbf{S}_i \cdot \mathbf{S}_j \rangle_c$ and $s_{ab} = -\langle \mathbf{S}_i \cdot \mathbf{S}_j \rangle_{ab}$.

In addition to spin-orbital SE $\mathcal{H}_J$ (46), orbitally degenerate systems are sensitive to lattice distortions which may lift orbital degeneracy, like, for example, in the case of the JT effect. In the present vanadate case, the effect of such couplings on the degenerate a and b orbitals can be expressed by the following term (Khaliullin, Horsch and Oleś, 2001):

$$\mathcal{H}_V = V_{ab} \sum_{\langle ij\rangle_{ab}} \tau_i^z \tau_j^z - V_c \sum_{\langle ij\rangle_c} \tau_i^z \tau_j^z \qquad (55)$$

where the interactions $V_{ab} > 0$ originate from the coupling of nearest-neighbor t_{2g} orbitals in (a, b) planes to the bond stretching oxygen vibrations in corner-shared perovskite structure. They generate antidistortive oxygen displacements and staggered OO (supporting SE), whereas the $V_c > 0$ term due to the $GdFeO_3$-type distortion (Mizokawa, Khomskii and Sawatzky, 1999) favors *FO* alignment along c axis, and thus *competes* with SE. The complete model $\mathcal{H} = \mathcal{H}_J + \mathcal{H}_V$ represents a nontrivial many-body problem. Interactions are highly frustrated, leading to strong competition between different spin and orbital states.

It is evident that the calculations need to be done self-consistently. Figure 23 shows the high anisotropy in the orbital sector in the magnetic C phase of $LaVO_3$, that is, below $T_N/J = 0.4$. The quasi-1D behavior documented by the large exchange constant J_c^τ implies strong orbital-singlet fluctuations along the c direction supported by the FM correlations along c in the spin sector. Note that the magnetic structure is 3D, yet highly anisotropic. In particular, the FM J_c^s and the AF J_{ab}^s are of comparable size. The large value of the FM exchange coupling is due to the orbital-singlet

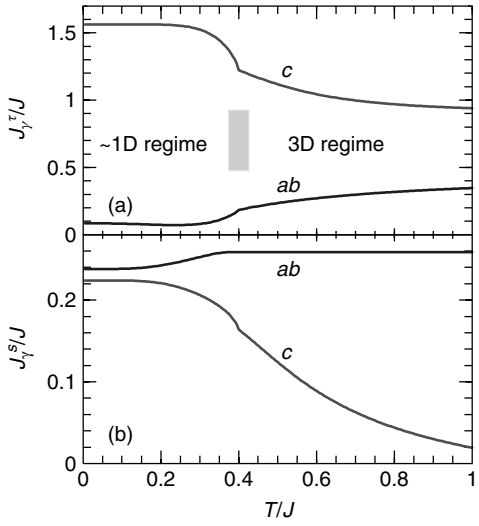

Figure 23. Exchange constants as functions of T along c (a/b) axis: (a) orbital J_γ^τ (54), and (b) spin J_γ^s (52). Parameters: $\eta = 0.12$, $V_c = 0.9J$, $V_{ab} = 0.2J$, $T_N = 0.4J$. (Reproduced from Khaliullin *et al.*, 2004, with permission from the American Physical Society. © 2004.)

fluctuations along c direction. Although the GK rules would also predict FM interaction along c in this case, the large value of the FM coupling J_c^s is unexpected.

Figure 24 shows the temperature dependence of the partial sum rules for the individual multiplet transitions. Because of the FM spin correlations along c in the C phase of $LaVO_3$ basically all weight is in the high-spin transition $n = 1$ below the Neél temperature T_N, whereas above T_N weight is transferred to the low-spin transitions $n = 2, 3$ reflecting the onset of paramagnetic behavior, consistent with experimental data. Because of antiferromagnetism in the ab plane the trends for $a(b)$ polarizations are reversed. At low temperature the main weight is in the low-spin channels, while there is almost no weight in the high-spin channel. This leads to the extreme anisotropy seen in the experimental data (see Figure 1).

Thus the basic experimental findings in the optical spectra of $LaVO_3$, (Miyasaka, Okimoto and Tokura, 2002) such as: (i) pronounced temperature dependence of c axis intensity (changing by a factor of 2 below 300 K), (ii) large anisotropy between the optical spectral weights along c and a/b axis (both below and above T_N), are qualitatively reproduced by this theory (see Figure 24). This strongly supports the picture of quantum orbital chains in the C-AF phase of vanadates.

The basic requirement for the study of partial spectral weights is the subdivision of the spin-orbital SE Hamiltonian into its multiplet contributions. Apart from the cubic vanadates (Khaliullin, Horsch and Oleś, 2004), this has been done in Oleś, Khaliullin, Horsch and Feiner (2005) for $KCuF_3$, $LaMnO_3$, and the cubic titanates. Ellipsometry data

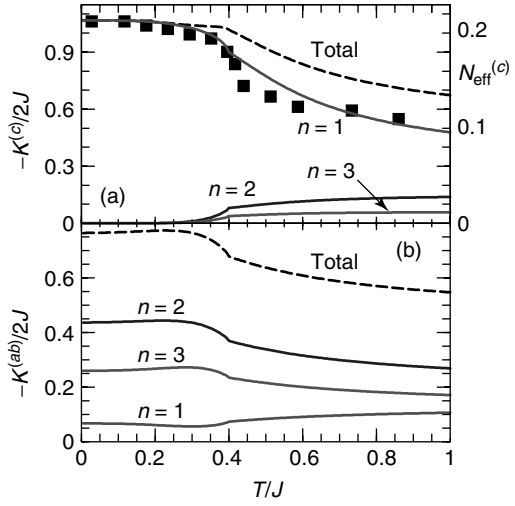

Figure 24. Partial kinetic energies $K_n^{(\gamma)}/2J$ (solid lines) and total kinetic energy (dashed lines) calculated for $LaVO_3$: (a) c axis and (b) ab-plane polarization. Parameters as in Figure 23. Experimental data (squares) for high-spin transition taken from Miyasaka, Okimoto and Tokura (2002). (Reproduced from Khaliullin *et al*., 2004, with permission from the American Physical Society. © 2004.)

of $LaMnO_3$ was analyzed by (Kovaleva *et al*., 2004) using partial sum rules.

5 DOPED MANGANITES: INTERPLAY OF ORBITAL, SPIN, AND CHARGE

5.1 Phase diagram of manganites and double-exchange mechanism

The early history of transport properties of doped manganites starts with the pioneering work of Jonker and van Santen (1950). They observed that the manganite compounds $La_{1-x}A_xMnO_3$ (A = Sr, Ca, Ba) become around $x = 0.3$ FM and good metallic conductors, while they are antiferromagnets and insulators at low doping. The origin of the appearance of ferromagnetism upon doping holes was the central question in the early 1950s. It was answered by Zener (1951) who proposed the so-called double-exchange mechanism. Because of a large Hund coupling J_H the e_g electron spin of Mn^{3+} prefers the high-spin state, that is, to be aligned with the $S = 3/2$ spin of the t_{2g} core electrons (see Figure 25). In the case of doping the e_g electron of a Mn^{3+} ion can move on a Mn^{4+} site. However, to reach again the low-energy (high-spin) state, the t_{2g} spin on the neighbor site should be parallel, whereas for antiparallel alignment hopping is suppressed. Zener did not consider the e_g orbital degeneracy at the Mn^{3+} ion. The name DE stems from the fact that the hopping t between Mn^{3+} to Mn^{4+} involves two

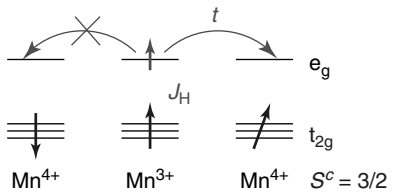

Figure 25. The large Hund coupling J_H forces the e_g electron spin parallel to the core spin $S^c = 3/2$ formed by the three t_{2g} electrons. The kinetic energy of itinerant e_g electrons favors parallel alignment of spins. This so-called double-exchange mechanism is the source of the ferromagnetic metallic phase in manganites at intermediate doping and low temperature.

scattering processes, namely, the creation of a hole in the occupied p orbital of the intermediate oxygen ligand ion and its subsequent annihilation. Thereby the Mn^{3+} and Mn^{4+} ions are interchanged.

The quantum treatment of DE usually starts from the FM KLM (Kubo and Ohata, 1972):

$$H = -t \sum_{\langle i,j\rangle\sigma} \mathrm{d}^\dagger_{i\sigma}\mathrm{d}_{j\sigma} - J_H \sum_{i\sigma\sigma'} \mathbf{S}_i^c \cdot \mathrm{d}^\dagger_{i\sigma}\boldsymbol{\sigma}_{\sigma\sigma'}\mathrm{d}_{i\sigma'} + J_{AF} \sum_{\langle i,j\rangle} \mathbf{S}_i^c \mathbf{S}_j^c \tag{56}$$

The model consists of the kinetic energy and the FM Hund coupling. To reflect the tendency toward antiferromagnetism in the undoped case here an AF interaction between core spins is included. The interplay of global AF interactions (on all bonds) and local FM alignment induced by the motion of an e_g electron via the DE mechanism is a subtle problem. In the high-temperature phase magnetism is controlled by FM polarons which move in the paramagnetic background (Varma, 1996; Horsch, Jaklic and Mack, 1999; Koller, Prüll, Evertz and von der Linden, 2003). The magnetic moment and size of the FM polarons increases with decreasing temperature until the system undergoes the phase transition into the FM phase.

In the paramagnetic phase charge carriers polarize the t_{2g} spins in their neighborhood to optimize their kinetic energy. The total spin of the polaron and its temperature dependence can be estimated using a *FM* spin-polaron picture (Varma, 1996; Horsch, Jaklic and Mack, 1999). The spin polaron is determined by the number P of ferromagnetically aligned spins around the hole which allows the particle to improve its kinetic energy in the paramagnetic system. The gain of kinetic energy is counterbalanced by the loss of spin entropy due to the coupling of P spins S_2, which can no longer rotate independently. An estimate for the change of free energy is $\delta F(P) = at/P^\eta + Pk_BT \ln(2S_2 + 1)$. The kinetic energy exponent $\eta = 2/3, 1, 2$ in

three, two, and one dimensions, respectively, and $S_2 = 2$ for Mn^{3+}. Minimization with respect to P gives the size of the spin polaron and its temperature dependence (Horsch, Jaklic and Mack, 1999):

$$P(T) = \left(\frac{\eta a t}{B k_B T}\right)^{1/(1+\eta)} \tag{57}$$

with $B = \ln(2S_2 + 1)$. The number $P(T)$ of aligned S_2 spins that form the FM polaron depends in a nonlinear fashion on the inverse temperature. This can be used further to calculate the temperature dependence of the susceptibility in the paramagnetic phase – in good agreement with numerical simulations (Horsch, Jaklic and Mack, 1999; Yi, Hur and Yu, 2000).

Thus at sufficiently low temperature the motion of charge carriers overcomes the spin entropy and leads to a full alignment of spins, that is to a paramagnetic to FM transition, where the Curie temperature T_C is expected to scale with doping. This scaling of T_C can be seen in the phase diagrams for $La_{1-x}A_xMnO_3$ (A = Sr, Ca) and $Nd_{1-x}Sr_xMnO_3$ shown in Figure 26. One unsatisfactory aspect of the (orbital nondegenerate) KLM is the high symmetry of the phase diagram with respect to doping, that is, $T_C \sim x(1-x)$ for $J_{AF} = 0$ (Horsch, Jaklic and Mack, 1999).

Often the t_{2g} spins are treated as classical spins, then the effective hopping of e_g electrons can be expressed in terms of the angles Θ_i of the core spins and a phase Φ_i (Müller-Hartmann and Dagotto, 1996):

$$t_{ij}/t = \cos\left(\frac{\Theta_i}{2}\right)\cos\left(\frac{\Theta_j}{2}\right) + \sin\left(\frac{\Theta_i}{2}\right)\sin\left(\frac{\Theta_j}{2}\right)\exp\left[i(\Phi_i - \Phi_j)\right] \tag{58}$$

The phase variable is of quantum-mechanical origin and may have important consequences. Nevertheless, frequently the absolute value $t_{ij} = t\cos(\Theta_{ij}/2)$ of the above expression is used. This model is usually called the *double-exchange model* and depends only on the relative angle Θ_{ij} between the t_{2g} spins (Anderson and Hasegawa, 1955). Recently it has been shown that Zener's model of ferromagnetism is also at work in dilute FM semiconductors like $Ga_{1-x}Mn_xAs$ and $Zn_{1-x}Mn_xTe$, and even allows to estimate relatively reliable values for the Curie temperature T_C (Dietl *et al.*, 2000). Ferromagnetism in dilute magnetic semiconductors depends on the existence of delocalized carriers or shallow impurity states that couple to the spins at the transition-metal site. Systems derived from wide-gap compounds like ZnO are considered particularly promising as candidates for spin-optoelectronic devices (Xu *et al.*, 2006).

5.2 Colossal magnetoresistance and optics

The observation of large magnetoresistance (von Helmolt *et al.*, 1993; Jin *et al.*, 1994) $\Delta R/R = (R_h - R_0)/R_h$ (R_h is the resistance in a magnetic field) in a number of manganite compounds stimulated research in orbital degenerate systems greatly. The name colossal magnetoresistance was proposed by Jin *et al.* (1994) who investigated thin films of $La_{1-x}Ca_xMnO_3$. The data by Tomioka, Asamitsu and Tokura (2000) displayed in Figure 27 shows the dramatic drop of the resistivity $\rho(T)$ in $La_{0.7}Ca_{0.3}MnO_3$ by 2 orders of magnitude. The gradual onset of magnetization at higher temperatures in finite magnetic fields leads to pronounced changes of $\rho(T)$.

An important characteristic feature of CMR is the activated behavior of $\rho(T)$ above the Curie temperature T_C, that is, in the paramagnetic phase. In the phase diagram, Figure 26, this regime is denoted as paramagnetic insulating (PI) phase in contrast to the paramagnetic metallic (PM) phase. CMR is intrinsically connected with the appearance of the PI phase.

The activated behavior of $\rho(T)$ in the PI phase has proven as central theoretical challenge. A short list of possible theoretical explanations includes: (i) Localization due to spin disorder in paramagnetic phase (Varma, 1996), (ii) small lattice polaron formation due to strong JT coupling (but neglect of correlations) (Millis, Littlewood and Shraiman, 1995), (iii) polaron-bipolaron mechanism (Alexandrov and Bratkovsky, 1999), (iv) localization due to charge disorder (Allub and Alascio, 1997), (v) nanoscale phase separation in metallic and insulating domains (Mayr *et al.*, 2001; Burgy, Dagotto and Mayr, 2003), (vi) spin disorder and orbital-polaron formation (Kilian and Khaliullin, 1999).

The localization due to spin disorder alone can be ruled out as mechanism for the strong activated behavior of $\rho(T)$. Calculations of the LKM using quantum spins do not give evidence of significant activated behavior. Nevertheless, spin disorder is crucial as it reduces the kinetic energy in the paramagnetic phase and thereby supports polaron formation and the tendency toward localization in combination with other mechanisms as in (ii), (iii), and (vi). Important further experimental constraints follow from the behavior of the optical conductivity as we shall see next.

The variation of the optical conductivity $\sigma(\omega)$ in manganites as function of doping and temperature is rather complex and is only partially understood. Here, we confine the discussion on the remarkable behavior of $\sigma(\omega)$ in the FM metallic phase and the PI phase, that is the doping range relevant for CMR. Naively one would expect that the FM polarized phase shows simple Drude behavior as spin disorder and fluctuations are frozen out, and only scattering from defects and phonons remain in a homogeneous system. Yet, the optical experiments show a completely different behavior, which was first reported by Okimoto *et al.* (1995, 1997)

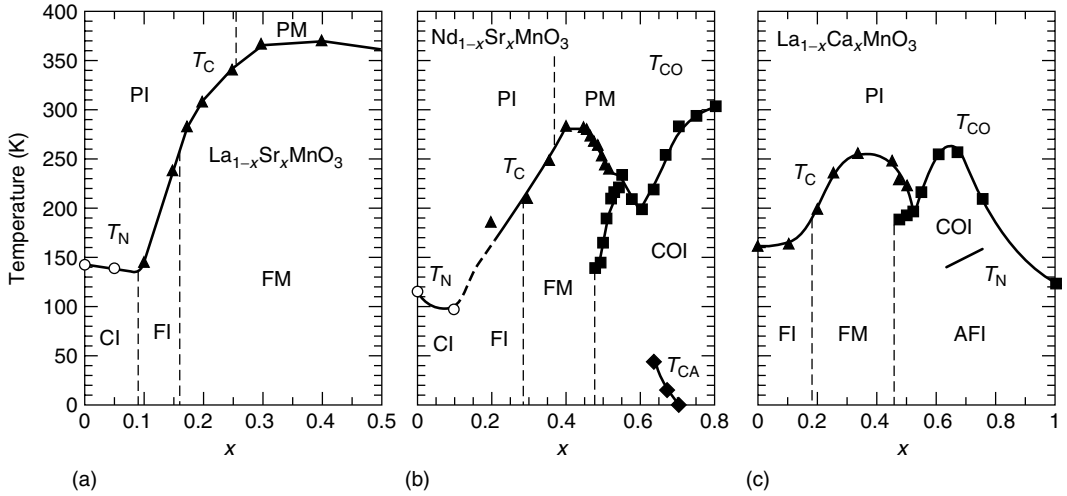

Figure 26. Electronic phase diagrams as function of doping concentration x and temperature T for the perovskite compounds: (a) $La_{1-x}Sr_xMnO_3$, (b) $Nd_{1-x}Sr_xMnO_3$, and (c) $La_{1-x}Ca_xMnO_3$. States are denoted as: PI: paramagnetic insulating; PM: paramagnetic metallic; CI: spin-canted insulating; COI: charge-ordered insulating; AFI: antiferromagnetic insulating, while T_N, T_C, T_{co} denote the Neèl, Curie, and charge-ordering temperature, respectively. (Reproduced from Imada *et al.*, 1998, with permission from the American Physical Society. © 1998.)

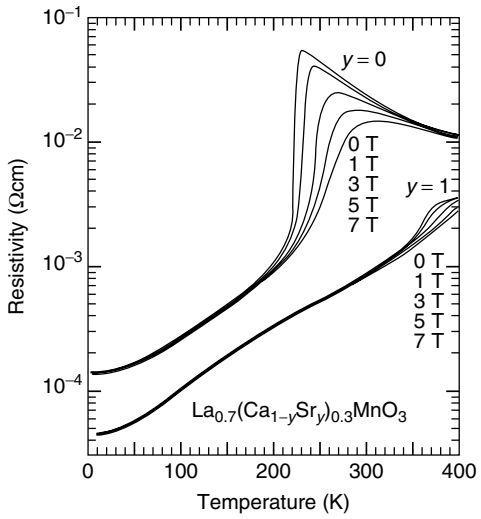

Figure 27. Temperature dependence of resistivity in various magnetic fields for $y = 0$ ($La_{0.7}Ca_{0.3}MnO_3$) and $y = 1$ ($La_{0.7}Sr_{0.3}MnO_3$) as an example of a bandwidth-controlled system. The $y = 0$ compound shows the typical CMR behavior, that is, low resistivity in the ferromagnetic phase and high resistivity together with activated behavior in the paramagnetic insulating (PI) phase. The anomalously large MR or CMR at $y = 0$ changes into a weaker MR behavior at $y = 1$. (Reproduced from Tonioko *et al.*, 2000, with permission from the American Physical Society. © 2000.)

and Saitoh, Asamitsu, Okimoto and Tokura (2000) for the $La_{1-x}Sr_xMnO_3$ compound.

Figure 28 shows the typical temperature dependence of the optical conductivity $\sigma(\omega)$ in the CMR doping regime. We note here four key features: (i) The gradual increase of absorption $\sigma(\omega)$ in the range $\omega < 0.5 - 1.0\,\text{eV}$ with decreasing temperature! That is, in the FM polarized phase this anomalous absorption is particularly large; (ii) this continuum appears to be gapless; (iii) evolution of a narrow Drude peak at low temperatures with strongly suppressed spectral weight (width $\sim 20 - 30\,\text{meV}$, see inset of Figure 28b); (iv) At high temperature, that is, in the PI phase, the optical conductivity develops a pseudogap $\sigma(\omega) \sim \omega$ up to about 1 eV.

This behavior clearly demonstrates, that the change of transport properties is connected with changes of the excitation spectra on the 1-eV scale, for example, distinct from quasielastic impurity scattering. In particular, the activated behavior of $\rho(T)$ in the PI phase is connected with pseudogap formation (iv).

5.3 Orbital $t-J$ model and orbital liquid

The peculiar behavior of the optical conductivity in the uniform FM phase at low temperature, namely, the simultaneous observation of a very narrow Drude absorption and a broad incoherent background of $\sim$1 eV width, finds a natural explanation in the orbital degree of freedom.

Orbital fluctuations in the FM state and their effect on the optical conductivity were studied first by Ishihara, Yamanaka and Nagaosa (1997) who arrived at the conclusion that the quasi-2D nature of orbital fluctuations leads to an orbital liquid in 3D cubic systems. Orbital disorder was treated in a static approximation. Because of this assumption there is no Drude component in the theoretical description of Ishihara, Yamanaka and Nagaosa (1997). Subsequently within a zero

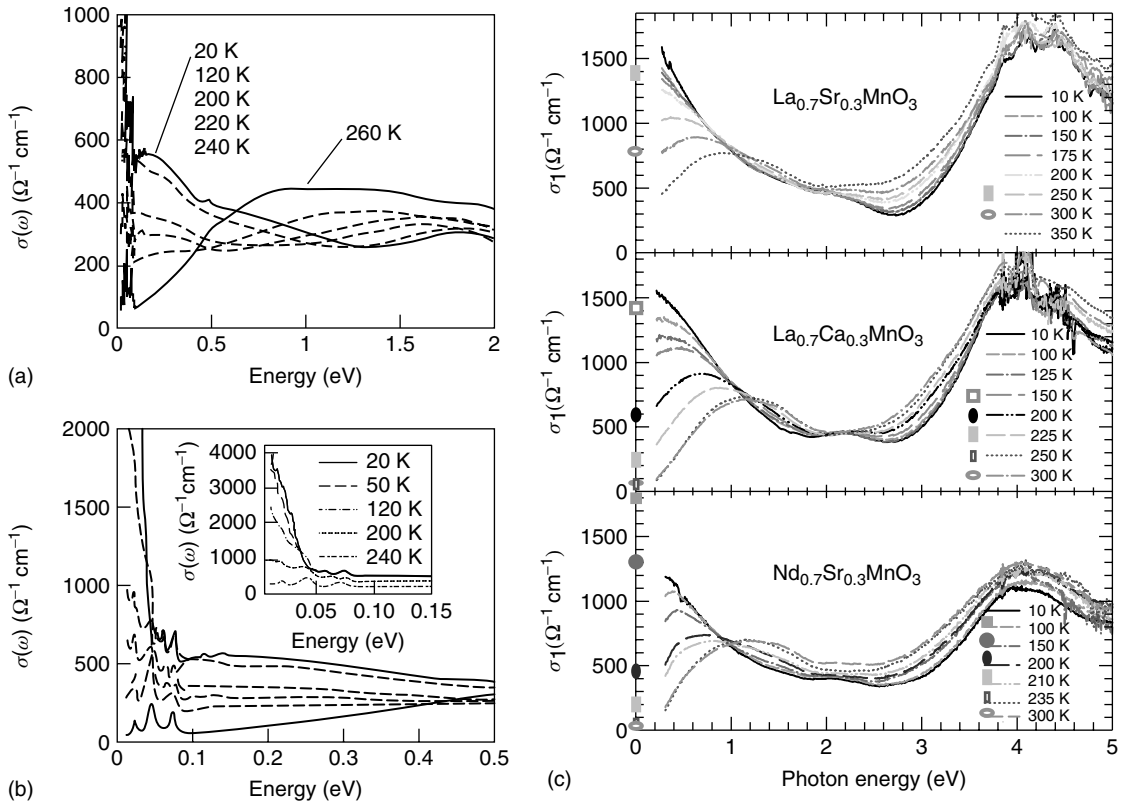

Figure 28. Temperature dependence of optical conductivity $\sigma(\omega)$ in the CMR regime of various compounds: Data of (Kim, Jung and Noh, 1998) for $La_{0.7}Ca_{0.3}MnO_3$ shows the typical behavior of $\sigma(\omega)$ in the CMR regime. (a) There is a strong spectral weight transfer on the 1-eV scale from high energy to low energy as function of decreasing temperature. This implies a continuous increase of the absorption $\sigma(\omega)$ (below 0.5 eV) as temperature decreases and indicates that this scattering has different origin than spin! Inset of (b): Surprisingly, despite of the anomalous low-energy scattering, there is a very narrow Drude peak (width ∼20–30 meV) that develops at low temperature. (c) Data of Quijada *et al*. (1998) for $La_{0.7}Sr_{0.3}MnO_3$, $La_{0.7}Ca_{0.3}MnO_3$ and $Nd_{0.7}Sr_{0.3}MnO_3$ amplifies that this behavior is universal. Notice that here the DC data implies the existence of a narrow Drude peak. Moreover all compounds show a characteristic pseudogap behavior in $\sigma(\omega) \sim \omega$ right above the Curie temperature over a wide energy range (0.5–1 eV)!

temperature slave boson approach Kilian and Khaliullin (1998) could show that there are both features (i) the highly incoherent spectrum due to the scattering of charge carriers from orbital fluctuations and (ii) a Drude peak with strongly reduced spectral weight.

The relevant (and most simple) model for the fully spin-polarized state is the orbital $t-J$ model, which consists of the SE interaction between orbitals and the kinetic energy of holes $H_{\rm kin}$. Actually it turns out that for typical values for the exchange interaction at moderate doping ($xt >> J$) the kinetic energy and the constraint dominate the behavior. The orbital $t-J$ model is defined as:

$$H_{otJ} = -\sum_{\langle ij\rangle_\gamma} \left(t_{ij}^{\alpha\beta} \tilde{d}_{i\alpha}^{\dagger} \tilde{d}_{j\beta} + \text{H.c.} \right) + J \sum_{\langle ij\rangle_\gamma} \left(\tau_i^\gamma \tau_j^\gamma - \frac{1}{4} n_i n_j \right) \tag{59}$$

with the constraint that each site can only be occupied by at most one (e_g) electron, that is, $\tilde{\rm d}_{i\alpha}^{\dagger} = {\rm d}_{i\alpha}^{\dagger}(1 - n_{i\overline{\alpha}})$, $\overline{\alpha}$ denotes the orthogonal e_g orbital with respect to α, and $\gamma = x, y, z$. The orbital SE is defined by pseudospin operators $\tau_i^{x/y} = -\frac{1}{4}(\sigma^z \pm \sqrt{3}\sigma^x)$, $\tau_i^z = \frac{1}{2}\sigma^z$, with Pauli matrices $\sigma_i^{x/z}$ acting on the orbital subspace. The orientation of the basis orbitals $\{|x\rangle, |z\rangle\} = \{x^2 - y^2, 3z^2 - r^2\}$ is reflected in the transfer matrices that describe the hopping in the (*a, b*) plane and along the *c* axis, respectively.

$$t_{ij\|a(b)}^{\alpha\beta} = \frac{t}{4} \begin{pmatrix} 3 & \mp\sqrt{3} \\ \mp\sqrt{3} & 1 \end{pmatrix} \quad t_{ij\|c}^{\alpha\beta} = t \begin{pmatrix} 0 & 0 \\ 0 & 1 \end{pmatrix} \tag{60}$$

Here $\mp$ distinguish hopping along *a* and *b* directions.

This model resembles the $t-J$ model which gives the description of hole motion in quantum antiferromagnets, that is one of the standard models for the high-T_C cuprates. Here the orbital index replaces the spin index in the $t-J$ model, and importantly the hopping has off-diagonal elements.

The $o-t-J$ and the $t-J$ model have in common the large incoherent absorption (with energy scale given by the free bandwidth) and the coherent motion of dressed charge carriers leading to a Drude absorption. A crucial difference of the two models is observed in 2D where the doped $t-J$ model is in a spin-liquid state, whereas due to the off-diagonal hopping elements the o–t–J model selects a long-range ordered state with x^2-y^2 OO that maximizes the kinetic energy in the 2D xy plane. The difference lies in the cubic and SU(2) symmetry of orbitals and spins, respectively. In the 3D cubic orbital t–J model, however, orbitals prefer a liquid state as x^2-y^2, x^2-z^2, and y^2-z^2 orbital correlations are equally possible, and the system is highly frustrated. Yet also the broken symmetry state with x^2-y^2 order appears in the manganite phase diagram as poor metallic highly doped A phase (Mack and Horsch, 1999).

The temperature dependence of the optical conductivity in the orbital $t-J$ model has been studied using finite temperature Lanczos method (Horsch, Jaklic and Mack, 1999). The frequency dependent conductivity $\sigma_0(\omega)$ consists of two parts:

$$\sigma_0(\omega) = 2\pi e^2 D_c \delta(\omega) + \sigma(\omega) \tag{61}$$

namely, the regular finite frequency absorption $\sigma(\omega)$ and a δ-function contribution which is proportional to the charge stiffness D_c (Kohn, 1964; Shastry and Sutherland, 1990). The latter vanishes in insulators. This contribution is broadened into a usual Drude peak in the presence of other scattering processes like impurities which are not contained in the present model. The finite frequency absorption (or regular part) $\sigma(\omega)$ is determined by the current–current correlation function using the Kubo formula

$$\sigma(\omega) = \frac{1-\mathrm{e}^{-\omega/T}}{N\omega}\mathrm{Re}\int_0^\infty \mathrm{d}t\mathrm{e}^{i\omega t}\langle j_x(t)\, j_x\rangle \tag{62}$$

where the x component of the current operator is proportional to the electron charge e and the x component of the hopping vector $\mathbf{u}$

$$j_x = -ie\sum_{j,\mathbf{u},ab} t^{ab}_{j+\mathbf{u}j} u_x \tilde{\mathrm{d}}^\dagger_{j+\mathbf{u}a}\tilde{\mathrm{d}}_{jb} \tag{63}$$

The increase of the anomalous absorption with decreasing temperature is quite natural as it reflects the increase kinetic energy of the orbital t–J model with decreasing T (Horsch, Jaklic and Mack, 1999), and is dictated by the optical sum rule (Baeriswyl, Carmelo and Luther, 1986). (This form of the sum rule applies for nn-hopping, for a more general case (see Aichhorn, Horsch, von der Linden and Cuoco, 2002):

$$\int_{-\infty}^{\infty}\sigma_0(\omega)\mathrm{d}\omega = -\frac{\pi e^2}{N}\langle H^{xx}_{kin}\rangle \tag{64}$$

here xx indicates that only hopping processes along x contribute. It is important to notice that the dominant coupling between charge and orbital degrees of freedom is the kinetic energy H_{kin}, therefore the half-width $\omega_{1/2}\sim 3t$ is related to the bandwidth (Figure 29). For a cubic lattice $\rho_0 = \hbar a/e^2$. If we consider $La_{1-x}Sr_xMnO_3$ with lattice constant $a = 5.5\,\text{Å}$ and $\hbar/e^2 = 4.11\,\mathrm{K\Omega}$ we obtain $\rho_0 = 0.23\cdot 10^{-3}\,\Omega$cm. Interestingly in combination with the sum rule the kinetic energy determines the maximal size of the incoherent absorption (given the energy scale of the continuum) and is consistent with typical experimental data (Horsch, Jaklic and Mack, 1999). The only unknown quantity is the broadening Γ of the δ function. In the inset of Figure 29 a value $\Gamma\sim 20\,\mathrm{meV}$ taken from experiment (Okimoto *et al.*, 1995) was used, and in combination with the calculated charge stiffness D_c this leads to consistent values for the DC conductivity. The scattering processes that determine Γ (and the DC conductivity) are extrinsic with respect to the electronic model (59). That is, Γ is due to impurities, grain boundaries, and at high temperatures also due to scattering with phonons.

Thus, the very peculiar features of the optical conductivity in the uniform FM regime can be naturally explained by orbital degeneracy. On the other hand, typical lattice polaron models require large electron phonon coupling g and large polaron binding energy to generate incoherent absorption up to $\sim$1 eV (Hartinger *et al.*, 2004; Puchkov *et al.*, 1995). However, in such a strong coupling regime no narrow Drude absorption does exist simultaneously (Reik and Heese, 1967).

5.4 Orbital-degenerate Kondo lattice model

For the study of the interplay of charge, orbital, and spin degree freedom in doped manganites a natural starting point is the orbital-degenerate KLM (Horsch, Jaklic and Mack, 1999; Mack and Horsch, 1999). As in the nondegenerate KLM, equation (56), the Mn e_g electrons are coupled ferromagnetically to the t_{2g} core spins via the Hund coupling J_{H}:

$$H_{\mathrm{KLM}} = -\sum_{\langle ij\rangle\alpha\beta,\sigma}\left(t^{\alpha\beta}_{ij}\tilde{\mathrm{d}}^\dagger_{i\alpha\sigma}\tilde{\mathrm{d}}_{j\beta\sigma} + \mathrm{H.c.}\right) - J_{\mathrm{H}}\sum_{\langle ij\rangle\alpha\sigma\sigma'}\mathbf{S}_i\cdot\tilde{\mathrm{d}}^\dagger_{\mathbf{i}\alpha\sigma}\boldsymbol{\sigma}_{\sigma\sigma'}\tilde{\mathrm{d}}_{i\alpha\sigma'} \tag{65}$$

where the kinetic energy matrix is defined as in equation (60) and the creation operators respect the constraint that

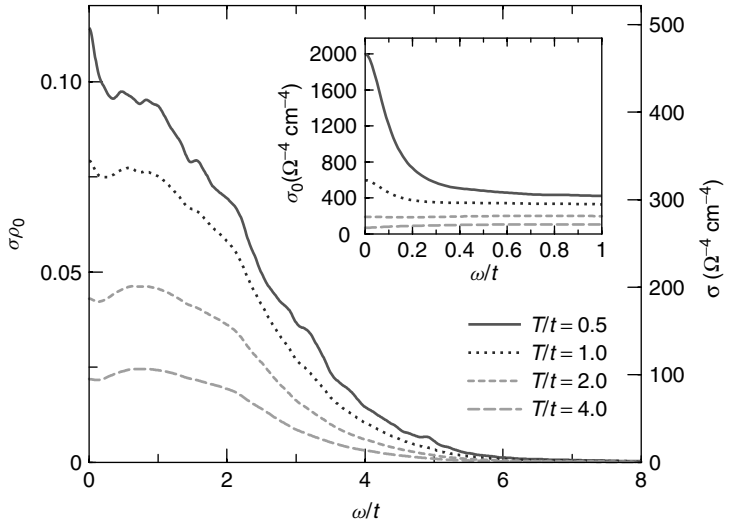

Figure 29. Temperature dependence of optical absorption $\sigma(\omega)$ in the orbital liquid phase. The results obtained for the orbital $t-J$ model at 20% doping show the characteristic increase of absorption with decreasing temperature and the gapless nature of the spectrum. Inset shows the appearance of a narrow Drude peak in $\sigma_0(\omega)$ at low temperature. Typical value for energy scale $t \sim 0.3\,\mathrm{eV}$. (Reproduced from Horsch *et al*., 1999, with permission from the American Physical Society. © 1999.)

allows only Mn^{4+} and Mn^{3+} configurations, that is, $\tilde{d}^{\dagger}_{i\alpha\sigma} = d^{\dagger}_{i\alpha\sigma}(1-n_{i\alpha\bar{\sigma}})\prod_{\sigma'}(1-n_{i\bar{\alpha}\sigma'})$, and all other alternative e_g states are projected out. The total Hamiltonian

$$H = H_{\mathrm{KLM}} + H' \tag{66}$$

usually contains additional relevant interactions that are summarized in H' and whose importance on the electronic properties may depend on the doping regime. Examples are the AF interaction between core spins, Coulomb interaction supporting charge ordering near quarter filling, or effective orbital interactions that simulate cooperative JT interactions.

For example, the tendency toward alternating charge order as in (a,b) plane of undoped or weakly doped $LaMnO_3$ may be expressed by a nearest-neighbor orbital interaction H_{OO}. There are two different mechanisms contributing to the OO interaction: (i) the cooperative JT effect (Feiner and Oleś, 1999) and (ii) SE interactions (Horsch, Jaklic and Mack, 1999; van der Brink, Horsch, Mack and Oleś, 1999). Neglecting more complex spin-orbital terms (Ishihara, Inoue and Maekawa, 1997; Shiina, Nishitani and Shiba, 1997; Feiner and Oleś, 1999) both effects can be described by van der Brink, Horsch, Mack and Oleś (1999)

$$H_{\mathrm{OO}} = 2\kappa \sum_{\langle ij\rangle} T_{ij} \tag{67}$$

where the two-site orbital operator, T_{ij}, between nearest-neighbor Mn sites in the $\{|x\rangle, |z\rangle\}$ basis has the form,

$$T_{ij} = T_i^z T_j^z + 3T_i^x T_j^x \mp \sqrt{3}(T_i^x T_j^z + T_i^z T_j^x) \tag{68}$$

T_i^z and T_i^x are described in terms of pseudospin operators: $T_i^+ = \sum_\sigma \tilde{d}^{\dagger}_{ix\sigma}\tilde{d}_{iz\sigma}$, and $T_i^- = \sum_\sigma \tilde{d}^{\dagger}_{iz\sigma}\tilde{d}_{ix\sigma}$. The sign of the mixed term $\propto \sqrt{3}$ depends on orbital phases and is negative in the a direction and positive in the b direction.

As in the orbital nondegenerate case further simplification can be achieved by introducing classical t_{2g} spins. This allows for the combination of (finite temperature) Monte Carlo simulation of the classical t_{2g} spins with exact diagonalization of the orbital many-body problem (Dagotto, 2003; Daghofer, Oleś, Neuber and von der Linden, 2006).

5.5 Orbital polarons and colossal magnetoresistance

A very important mechanism, that actually can trigger the CMR behavior as well as the appearance of the ferromagnetic insulating (FI) phase, is the orbital polarization around the charge carrier (hole) as proposed by Kilian and Khaliullin (1999),

$$H_{\Delta}^{\mathrm{3D}} = -\frac{1}{2}\Delta \sum_{\gamma} \sum_{\langle ij\rangle \| \gamma} (1-n_i)\tau_j^{\gamma} \tag{69}$$

where $\gamma = a,\ b,\ c$ refers to different lattice directions and the pseudospin operators in the $\{|x\rangle, |z\rangle\}$ orbital basis are defined as:

$$\tau_j^{a(b)} = -\frac{1}{2}\left(T_j^z \mp \sqrt{3}T_j^x\right), \quad \tau_j^c = T_j^z \tag{70}$$

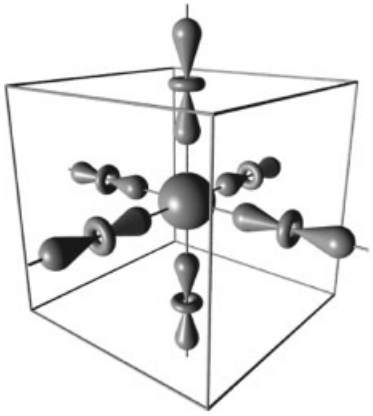

Figure 30. Orbital polaron in the strong coupling limit, where six e_g orbitals point toward the doped hole. This mechanism leads to heavy quasiparticles and eventually to localization. (Reproduced from Kilian & Khaliullin, 1999, with permission from the American Physical Society. © 1999.)

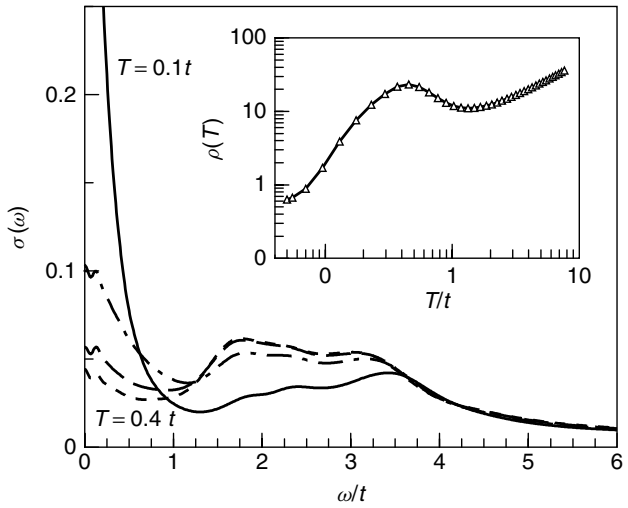

Figure 31. Optical conductivity $\sigma(\omega)$ calculated for a two-dimensional orbital-degenerate Kondo-lattice model at doping $x = 0.25$ for different temperatures $T = 0.1, 0.2, 0.3,$ and $0.4t$. The kinetic energy scale is $t \sim 0.2\,\mathrm{eV}$, the orbital-polaron coupling $\Delta = 2t$ and $\kappa = \Delta/5$. Inset: Resistivity $\rho(T)$ shows activated behavior in the paramagnetic range which is typical for CMR. Note the logarithmic scales. Both ρ and σ are given in dimensionless form. Comparison with experiment can be achieved by identifying the units with $\rho_0 = e^2/\hbar d \sim 0.2 \times 10^{-3}$ (Ωcm) and ρ_0^{-1}, respectively.

The interaction (69) splits locally the e_g states giving preference for the directional orbitals pointing toward an empty neighboring site as shown in Figure 30. Two main mechanisms for this level splitting were proposed: (i) the displacements of oxygen ions around an empty site; (ii) the Coulomb attraction between a hole and electrons on neighboring sites.

Various aspects of orbital polarons have been already investigated (Kilian and Khaliullin, 1999), here we briefly address the effects on optical conductivity and resistivity.The characteristic activated behavior of resisitivity $\rho(T)$ in the paramagnetic phase, and its dramatic decrease in the FM phase, follows in a natural way as a combined effect of orbital-polaron formation and spin disorder. Figure 31 shows results for $\sigma(\omega)$ and the resistivity obtained by the finite temperature Lanzcos method. The activated behavior of $\rho(T)$ is reflected by the evolution of a pseudogap in $\sigma(\omega)$.

We note, that the orbital polaron also describes the transition from the FM metallic into FI phase at low doping (see Figure 26). This is not immediately obvious as insulating implies that carriers do not move, whereas ferromagnetism via DE requires carrier motion! The resolution of this puzzle is straightforward (Kilian and Khaliullin, 1999), the coherent mass of the orbital polaron increases with reduced doping, such that the polaron can get bound by impurities or even form an orbital polaron lattice (at 1/8 filling) (Mizokawa, Khomskii and Sawatzky, 2000). Yet the internal motion of the hole inside the orbital polaron persists, that is the DE mechanism is still active and supports ferromagnetism.

Orbital polarization and its coupling to the lattice exists in the FM and the paramagnetic phase, but its effect is increased due to spin disorder in the paramagnetic regime. Thus leading to the activated behavior in the PI phase.The interplay of orbital-polaron dynamics and phonons is seen, for example, in the neutron scattering data of (Argyriou *et al.*, 2002) for the double layer compound $La_{2-2x}Sr_{1+2x}Mn_2O_7$, ($x = 0.38$), which shows a strongly coupled transverse optical phonon below the Curie temperature T_C but not above.

The properties of composite polarons are subtle as different mechanisms and energy scales are involved in renormalization of the charge carriers which may support or compete with each other. Other examples are the spin-lattice polarons (Ramšak, Horsch and Fulde, 1992; Mishenko and Nagaosa, 2004; Rösch *et al.*, 2005; Prelovšek, Zeyher and Horsch, 2006) in high-T_C compounds and spin-orbital polarons in layered cobaltates (Daghofer, Horsch and Khaliullin, 2006).

5.6 Spin waves in the double-exchange regime

In the uniform FM phase the spin-wave stiffness is determined by the kinetic energy, that is, in contrast to magnons in undoped compounds that are controlled by SE. One of the successes of DE theory was the derivation of the FM magnon dispersion ω_q from the (single orbital) KLM (Kubo and Ohata, 1972; Furukawa, 1996). The resulting dispersion corresponds to an isotropic, nearest-neighbor Heisenberg model. This prediction is well satisfied for manganites with large Curie temperature T_C like, for example, $La_{0.7}Pb_{0.3}MnO_3$

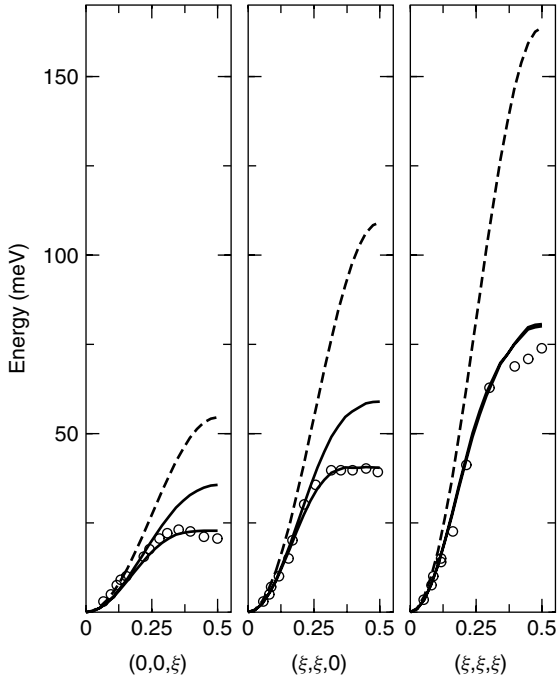

Figure 32. (a) Magnon dispersion of $Pr_{0.63}Sr_{0.37}MnO_3$ along three principal directions (circles) (Hwang *et al.*, 1998); $\xi = 0.5$ corresponds to the cubic Brillouin zone boundary; (b) mean-field dispersion corresponding to nearest-neighbor Heisenberg form (dashed lines); (c) Solid lines, theoretical results including charge, orbital, and lattices effects. (Reproduced from Khalliliun & Kilian, 2000, with permission from the American Physical Society. © 2000.)

(Furukawa, 1996). Yet in compounds with small T_C strong deviations from n.n. Heisenberg behavior were observed at large momentum transfer (see Figure 32).

We focus next on the role of the orbital fluctuations by considering the kinetic energy of the orbital-degenerate model (Khaliullin and Kilian, 2000; Oleś and Feiner, 2002). At small magnon numbers, that is, at low temperatures $T \ll T_C$, the kinetic energy operator in equation (65) can be mapped onto the following expression (Khaliullin and Kilian, 2000):

$$H_t = -\sum_{\langle ij\rangle_\gamma}\sum_{\alpha\beta} t_\gamma^{\alpha\beta}\hat{c}_{i\alpha}^\dagger \hat{c}_{j\beta} \times \left[\frac{3}{4} + \frac{1}{4S^2}\left(S_i^z S_j^z + S_i^- S_j^+\right)\right] + \text{H.c.} \qquad (71)$$

Equation (71) highlights an important point: The strength of DE bonds is a fluctuating complex quantity. Only when treating the orbital and charge sectors on average, that is, when replacing the bond operators $\hat{c}_{i\alpha}^\dagger \hat{c}_{i\beta}$ by their MF value $\langle \hat{c}_{i\alpha}^\dagger \hat{c}_{i\beta}\rangle$, an effective Heisenberg model as in a conventional MF treatment of DE is obtained: $H = J_{\text{DE}} \sum_{\langle ij\rangle} \mathbf{S}_i \mathbf{S}_j$ with the exchange constant dependent on the orbital and charge degrees of freedom:

$$J_{\text{DE}} = \frac{1}{2S^2}\sum_{\alpha\beta} t_\gamma^{\alpha\beta}\langle \hat{c}_{i\alpha}^\dagger \hat{c}_{j\beta}\rangle \qquad (72)$$

This determines the magnon energies $\omega_q = 2zSJ_{\text{DE}}\nu_q$, with $\nu_q = (2 - \cos q_x - \cos q_y)/4$ in 2D, or $\nu_q = (3 - \cos q_x - \cos q_y - \cos q_z)/6$ in 3D. Note that the isotropy of the spin Hamiltonian results from the orbital liquid state, where no direction is preferred.

Next we discuss the modification of the MF picture due to the fluctuations in the bond amplitude. The exchange J_{DE} is actually not a 'constant' but is varying with time. The FM interaction is connected with the hopping process of an e_g electron along a bond. In the case of orbital degeneracy such hopping processes are controlled by the orbital dynamics, that is, by the actual orientation of orbitals that fluctuate in time. As long as the energy scale of orbital fluctuations is large compared to the magnon scale J_{DE}, the magnon spectrum is basically unchanged, and given by time averages which restore the cubic symmetry. On the other hand, if orbitals fluctuate slower than spins or on the same timescale, the anisotropy and the damping of spin waves emerges. Figure 32 shows data from calculations of (Khaliullin and Kilian, 2000). In these calculations, in addition to charge and orbital fluctuations also the presence of JT phonons is considered.

5.7 Ordered and insulating phases prevail

The electronic properties of manganites $R_{1-x}A_xMn\ O_3$ are gradually changing from the wide band materials like (R = La, A = Sr) to the narrow band systems (La, Ca) and (Pr, Ca) as documented in Figure 33. The bandwidth is controlled by the ionic size of the cations R and A, respectively. Small cations lead to large $GdFeO_3$ type distortion (tilt of MnO_6 octahedra) with a large deviation of the Mn–O–Mn angle from 180°, which reduces the effective hopping between the Mn ions (Imada, Fujimori and Tokura, 1998). In the narrow band case the metallic (uniform FM) regime is confined to a narrow doping range, and new insulating phases emerge like the CE phase at and near $x = 0.5$ doping. The name of this phase is due to Goodenough (1955). It is remarkable that in the Orbital-degenerate manganites basically all phases are insulating, with the exception of the uniform FM phase. The A phase near $x = 0.5$ is a poor 2D metallic conductor. This is in striking contrast to the high-T_C cuprates where e_g orbital degeneracy is lifted by ∼1 eV and basically only at low doping insulating behavior is found.

The large variation of physical properties of manganites as function of doping or temperature originates from a complex interplay of spin, orbital, and charge degrees of freedom, as

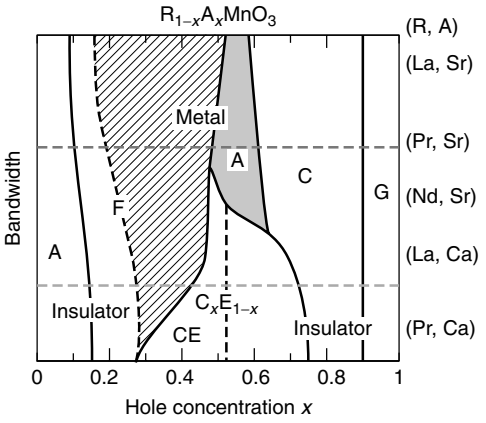

Figure 33. Schematic ground-state phase diagram of $R_{1-x}A_xMnO_3$ perovskites displaying the strong dependence on the bandwidth, that is, bandwidth increases from bottom to top. Here F denotes the FM state, while A, CE, C, and G denote antiferromagnetic states of A type, CE type, and G type, respectively. C_xE_{1-x} represents an incommensurate charge-/orbital-ordered state. (Reproduced from Kajimoto *et al*., 2002, with permission from the American Physical Society. © 2002.)

well as the interaction with the lattice (Tokura and Nagaosa, 2000; Tokura, 2003). An important example for the control of magnetic order due to the orbital degree of freedom is the checkerboard charge-ordered CE phase at quarter filling which we address here briefly. In the CE-phase FM zigzag chains are staggered antiferromagnetically and the occupied e_g orbitals at the Mn^{3+} sites are oriented along the FM bonds in the (a, b) planes (Goodenough, 1955) (Figure 34a,b). The CE structure reflects the cooperative action of AF SE and FM DE. Because of the AF correlations between FM chains, the carrier motion is basically confined to the FM chains. This consideration has stimulated the study of one-dimensional models for the CE phase (van den Brink, Khaliullin and Khomskii, 1999).

Yet it has been argued that these interactions alone do not guarantee the stability of the CE phase (Khomskii and Kugel, 2003; Calderon, Millis and Ahn, 2003; Bała, Horsch and Mack, 2004) and longer distant elastic strain and/or JT interactions are essential for the stability of the CE-OO. This claim is actually supported by the fact that CE-type orbital correlations have also been observed in the absence of antiferromagnetism, namely, in the FM metallic phase of $Nd_{1/2}Sr_{1/2}MnO_3$ (Geck *et al*., 2002). The JT distortion of the O ions and the resulting shift of the position of the Mn^{4+} ions shown in Figure 34(c) leads to a further neighbor JT coupling which supports CE-OO (Bała, Horsch and Mack, 2004; Bala and Horsch, 2005). The AF-CE phase was observed in cubic $(Nd,Pr)_{1/2}(Sr,Ca)_{1/2}MnO_3$ (Tokura and Nagaosa, 2000) and in layered $La_{1/2}Sr_{3/2}MnO_4$ (Sternlieb *et al*., 1996; Murakami *et al*., 1998), $LaSr_2Mn_2O_7$ (Kubota *et al*., 1999) manganites. An alternative proposal for the

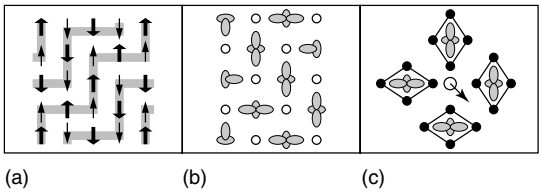

Figure 34. Spin-, orbital-, and charge structure of CE phase. (a) Shows the spin and charge order, where small (large) arrows indicate spin $S = 3/2(2)$ of Mn^{4+} (Mn^{3+}), respectively. (b) Orbital order consistent with the ferromagnetic zigzag chains. (c) Jahn–Teller distortion of the Mn^{3+} octahedra. (Reproduced from Bala & Horsch, 2005, with permission from the American Physical Society. © 2005.)

$x = 0.5$ structure, the Zener polaron picture, where the e_g electrons are centered on bonds (Daoud-Aladine *et al*., 1955; Efremov, van den Brink and Khomskii, 2004) rather than cite centered as in the CE structure, was not confirmed by experiment (Senff *et al*., 2006). An important feature of the CE phase is a large optical gap and a broad absorption maximum at 1–2 eV shifting toward lower frequencies with increasing temperature (Ishikawa, Ookera and Tokura, 1999; Jung *et al*., 2000; Kim *et al*., 2002). Remarkably a similar spectral shift is observed in photoexcitation experiments, which reveal ultrafast response times of such Mott-insulating structures (Tokura, 2003; Ogasawara *et al*., 2002).

It is evident that a real understanding of this or other phases is only achieved if not only the calculated magnetic and orbital structure is right but also the calculated excitation spectra are consistent with experiment. This statement is particularly important when several degrees of freedom act together like in the manganites and complex phase diagrams appear. For example insulating systems with CE structures like $Pr_{1/2}Ca_{1/2}MnO_3$ or $Nd_{1/2}Ca_{1/2}MnO_3$ show an insulator to metal transition connected with the collapse of the electronic gap of $\sim$1 eV in high magnetic fields (Tokura and Nagaosa, 2000). Similar transitions occur in the related Sr compounds at smaller magnetic fields of about 5 T. This suggests that by varying the spin structure the orbital and charge order collapses.

Figure 35 shows the calculated optical conductivity for the CE phase as function of temperature. The calculation was performed by finite temperature diagonalization starting from the KLM $H_{\rm KLM}$ with degenerate orbitals and residual interactions H' which include (i) the AF interaction between core spins, (ii) a nearest-neighbor Coulomb repulsion V which favors checkerboard charge order at quarter filling, and (iii) a second neighbor JT interaction κ' (Bala and Horsch, 2005).

There are still many open questions, for example, concerning the charge modulation of phases beyond $x = 0.5$. Even concerning the strength of charge modulations, that is, weak or strong, there is frequently disagreement among different theoretical approaches and also between different

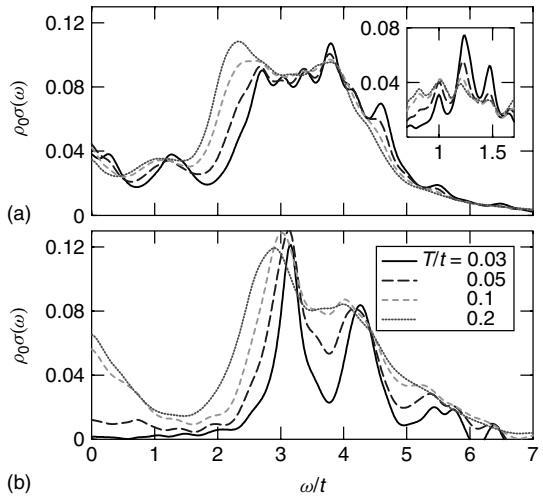

Figure 35. Temperature dependence of the optical conductivity $\sigma(\omega)$ obtained for two cases: (a) AF-CE order in the ground state, and (b) a FM-CE ground state for $J_{\mathrm{AF}} = 0.04t$. Partial melting of electron charge order leads to a reduction of the optical gap. Other parameters: (a) $V = 0.2t$, $\kappa' = 0.15t$; (b) $V = t$, $\kappa' = 0.05t$. The spectra are generated using a Lorentzian broadening $\Gamma = 0.2t$. Inset: Midgap absorption. (Reproduced from Bala & Horsch, 2005, with permission from the American Physical Society. © 2005.)

experimental techniques. Although the definition of the effective charge on an atom or ion is not that well defined, it is worrying that such seemingly simple questions cannot be better resolved. Electron diffraction studies of $La_{1-x}Ca_xMn O_3$ at doping concentrations $x = 0.52, 0.58, 0.67$ are compatible with a weak charge density wave modulation rather than strong charge order with discommensurations (Loudon *et al*., 2005). Thus these investigations suggest weak charge lattice coupling. Weak implies here, that modulations are not to be understood as stripes, that is, soliton-like discommensurations.

6 SUMMARY AND OUTLOOK

Through orbital, spin, and charge degrees of freedom strongly correlated electrons acquire an immense flexibility toward pattern formation. This is reflected in the complex phase diagrams of TMO families. Spin-orbital models that are derived from SE interactions describe the subtle interplay between spin and orbitals in TMO have been presented as useful theoretical approach. Spin-orbital models have only few parameters, the exchange constant J, the Hund-coupling parameter $\eta = J_{\mathrm{H}}/U$, the spin-orbit coupling λ and the JT coupling, for example. In any case a small number compared to multiband Hubbard models. Spin-orbital models allow to calculate orbital and spin ordering, spin excitations – that can be compared with data obtained by neutron scattering or other experiments. Surprisingly, these models also allow to calculate the absolute value of optical spectral weights of multiplet transitions in the electron volt regime. The temperature dependence of the optical weights closely reflects the variation of orbital and magnetic structure. Thus this provides a useful link between magnetic and optical experiments.

The complex electronic properties of TMO can be tuned by various means, for example, by magnetic field, by pressure, by internal pressure, that is chemically via the cation sizes. Charge-ordered states with large energy gap can by switched into conducting states by applying moderate magnetic fields. A new playing ground is opened by nanoscale multilayer interfaces of correlated materials (Okamoto and Millis, 2004). Careful control of orbital structure at interfaces between two materials can generate novel physical phenomena and functionalities, that are not a property of the constituent materials themselves. Examples are bilayers of Mott and band-insulating materials yielding a metallic interface (Ohmoto and Hwang, 2004). Other possibilities are combination of CMR manganite and high- T_{C} superconducting materials (Soltan, Albrecht and Habermeier, 2004; Chakhalian *et al*., 2006).

There are a number of developments that could not be covered here either because of limited space or because they have been discussed recently elsewhere in detail. This list includes, for example, magnetic field and photo-induced phase transitions in charge- and orbital-ordered systems (Tokura and Nagaosa, 2000), colossal electroresistance in perovskite oxides (Beck *et al*., 2000; Liu, Wu and Ignatiev, 2000), multiferroic behavior (Kimura *et al*., 2003; Efremov, van den Brink and Khomskii, 2004; Khomskii, 2006), the magnetoelectric effect (Fiebig, 2005; Katsura, Nagaosa and Balatsky, 2005; Arima *et al*., 2006).

The steady experimental progress in this field will continue to represent a strong stimulation to theory. The full theoretical problem, namely, the description of the interplay of spin, orbital, charge, and lattice degrees of freedom remains a challenge for improved and new simulation techniques. Analytical techniques dealing with these strongly correlated systems need to be developed further in the future and tested against numerical simulation. Last but not least, even the spin-orbital models describing the undoped systems represent a great challenge for theorists. One example is the orbital-Peierls dimerization. Spin-orbital models show more subtle behavior than the Heisenberg and Ising models that have been invented about 80 years ago, and have been explored ever since.

ACKNOWLEDGMENTS

I am grateful to G. Khaliullin and A.M. Oleś for many years of stimulating collaborations on this subject.

REFERENCES

Aharony, A., Entin-Wohlman, O., Korenblit, I.Ya., *et al*. (2005). The cubic Kugel-Khomskii model for triply degenerate t_{2g} electrons, and T. Yildirim. *New Journal of Physics*, **7**, 49.

Affleck, I. (1986). Exact critical exponents for quantum spin chains. *Nuclear Physics B*, **265**, 409.

Ahn, K.H. and Millis, A.J. (2000). Effects of magnetic ordering on the anisotropy and temperature dependence of the optical conductivity in $LaMnO_3$: A tight-binding approach. *Physical Review B*, **61**, 13545.

Aichhorn, M., Horsch, P., von der Linden, W. and Cuoco, M. (2002). Temperature dependence of optical spectral weights in quarter-filled ladder systems. *Physical Review B*, **65**, 201101(R).

Alexandrov, A.S. and Bratkovsky, A.M. (1999). Carrier density collapse and colossal magnetoresistance in doped manganites. *Physical Review Letters*, **82**, 141.

Allub, R. and Alascio, B. (1997). Magnetization and conductivity for $La_{1-x}Sr_xMnO_3$-type crystals. *Physical Review B*, **55**, 14113.

Anderson, P.W. (1959). New approach to the theory of superexchange interactions. *Physical Review*, **115**, 2.

Anderson, P.W. (1963). *Magnetism*, Rado G. and Suhl, H. (Eds.), Academic Press: New York, Vol. I.

Anderson, P.W. and Hasegawa, H. (1955). Considerations on double exchange. *Physical Review*, **100**, 675.

Anisimov, V.I., Nekrasov, I.A., Kondakov, D.E., *et al*. (2002). Orbital-selective Mott-insulator transition in $Ca_{2-x}Sr_xRuO_4$. *European Physical Journal B*, **25**, 191.

Anisimov, V.I., Zaanen, J. and Andersen, O.K. (1991). Band theory and Mott insulators: Hubbard U instead of Stoner I. *Physical Review B*, **44**, 943.

Andersen, O.K., Klose, N. and Nohl, H. (1978). Electronic structure of Chevrel-phase high-critical-field superconductors. *Physical Review B*, **17**, 1209.

Argyriou, D.N., Lynn, J.W., Osborn, R., *et al*. (2002). Glass transition in the polaron dynamics of colossal magnetoresistive manganites. *Physical Review Letters*, **89**, 036401.

Arima, T., Tokunaga, A., Goto, T., *et al*. (2006). Collinear to spiral spin transformation without changing the modulation wavelength upon ferroelectric transition in $Tb_{1-x}Dy_xMnO_3$. *Physical Review Letters*, **96**, 097202.

Azaria, P., Boulat, E. and Lecheminant, P. (2000). Effect of symmetry-breaking perturbations in the one-dimensional SU(4) spin-orbital model. *Physical Review B*, **61**, 12112.

Azaria, P., Gogolin, A.O., Lecheminant, P. and Nersesyan, A.A. (1999). One-Dimensional SU(4) spin-orbital model: a low-energy effective theory. *Physical Review Letters*, **83**, 624.

Baeriswyl, D., Carmelo, J. and Luther, A. (1986). Correlation effects on the oscillator strength of optical absorption: sum rule for the one-dimensional Hubbard model. *Physical Review B*, **33**, 7247.

Bala, J. and Horsch, P. (2005). Spin-orbital physics in the optical conductivity of quarter-filled manganites. *Physical Review B*, **72**, 012404.

Bała, J., Horsch, P. and Mack, F. (2004). Manganites at quarter filling: role of Jahn-Teller interactions. *Physical Review B*, **69**, 094415.

Beck, A., Bednorz, J.G., Gerber, Ch., *et al*. (2000). Reproducible switching effect in thin oxide films for memory applications. *Applied Physics Letters*, **77**, 139.

Biotteau, G., Hennion, M., Moussa, F., *et al*. (2001). Approach to the metal-insulator transition in $La_{1-x}Ca_xMnO_3$ ($0 < x < 0.2$): magnetic inhomogeneity and spin-wave anomaly. *Physical Review B*, **64**, 104421.

Bocquet, A.E., Mizokawa, T., Saitoh, T., *et al*. (1992). Electronic structure of 3d-transition-metal compounds by analysis of the 2p core-level photoemission spectra. *Physical Review B*, **46**, 3771.

Blake, G.R., Palstra, T.T.M., Ren, Y., *et al*. (2001). Transition between orbital orderings in YVO_3. *Physical Review Letters*, **87**, 245501.

Blake, G.R., Palstra, T.T.M., Ren, Y., *et al*. (2002). Transition between orbital orderings in YVO_3. *Physical Review B*, **65**, 174112.

van den Brink, J. (2001). Orbital excitations in $LaMnO_3$. *Physical Review Letters*, **87**, 217202.

van der Brink, J., Horsch, P., Mack, F. and Oleś, A.M. (1999). Orbital dynamics in ferromagnetic transition-metal oxides. *Physical Review B*, **59**, 6795.

van den Brink, J., Khaliullin, G. and Khomskii, D. (1999). Charge and orbital order in half-doped manganites. *Physical Review Letters*, **83**, 5118.

Burgy, J., Dagotto, E. and Mayr, M. (2003). Percolative transitions with first-order characteristics in the context of colossal magnetoresistance manganites. *Physical Review B*, **67**, 014410.

Calderon, M.J., Millis, A.J. and Ahn, K.H. (2003). Strain selection of charge and orbital ordering patterns in half-doped manganites. *Physical Review B*, **68**, R100401.

Castellani, C., Natoli, C.R. and Ranninger, J. (1978). Magnetic structure of V2O3 in the insulating phase. *Physical Review B*, **18**, 4945, 4967 and 5001.

Chakhalian, J., Freeland, J.W., Srajer, G., *et al*. (2006). Magnetism at the interface between ferromagnetic and superconducting oxides. *Nature Physics*, **2**, 244.

Chen, Y., Wang, Z.D., Li, Y.Q. and Zhang, F.C. (2006). Spin-Orbital Entanglement and Phase Diagram of Spin-orbital Chain with SU(2) $\times$ SU(2) Symmetry. cond-mat/0606194.

Cuoco, M., Horsch, P. and Mack, F. (1999). Theoretical study of the optical conductivity of NaV_2O_5. *Physical Review B*, **60**, R8438.

Cyrot, M. and Lyon-Caen, C. (1975). Orbital superlattice in degenerate Hubbard model. *Journal Of Physical (Paris)*, **36**, 253.

Cwik, M., Lorenz, T., Baier, J., *et al*. (2003). Crystal and magnetic structure of $LaTiO_3$: evidence for nondegenerate t2g orbitals. *Physical Review B*, **68**, 060401.

Daghofer, M., Horsch, P. and Khaliullin, G. (2006). Magnetic properties of spin-orbital polarons in lightly doped cobaltates. *Physical Review Letters*, **96**, 216404.

Daghofer, M., Oleś, A.M., Neuber, D.R. and von der Linden, W. (2006). Doping dependence of spin and orbital correlations in layered manganites. *Physical Review B*, **73**, 104451.

Dagotto, E. (2005). Open questions in CMR manganites, relevance of clustered states and analogies with other compounds including the cuprates. *New Journal of Physics*, **7**, 67.

Dagotto, E., Hotta, T. and Moreo, A. (2001). Colossal magnetoresistant materials: the key role of phase separation. *Physics Reports*, **344**, 1.

Dagotto, E. (2003). *Nanoscale Phase Separation and Colossal Magnetoresistance*, *Springer Series in Solid State Sciences*, Springer-Verlag: Heidelberg, Vol. 136.

Daoud-Aladine, A., RodrÃ›guez-Carvajal, J., Pinsard-Gaudart, L. *et al*. (1955). Zener polaron ordering in half-doped manganites. *Physical Review Letters*, **89**, 097205.

Daré, A-M., Hayn, R. and Richard, J-L. (2003). Orbital and spin exchange in $LiNiO_2$. *Europhysics Letters*, **61**, 803.

Dietl, T., Ohno, H., Matsukura, F., *et al*. (2000). Zener model description of ferromagnetism in zinc-blende magnetic semiconductors. *Science*, **287**, 1019.

Efremov, D.V., van den Brink, J. and Khomskii, D.I. (2004). Bond- versus site-centred ordering and possible ferroelectricity in manganites. *Nature Materials*, **3**, 853.

Eskes, H. and Jefferson, J.H. (1993). Superexchange in the cuprates. *Physical Review B*, **48**, 9788.

Fang, Z. and Terakura, K. (2001). Magnetic phase diagram of $Ca_{2-x}Sr_xRuO_4$ governed by structural distortions. *Physical Review B*, **64**, 020509.

Fazekas, P. (1999). *Lecture Notes on Electron Correlation and Magnetism*, World Scientific: Singapore.

Feiner, L.F. and Oleś, A.M. (1999). Electronic origin of magnetic and orbital ordering in insulating $LaMnO_3$. *Physical Review B*, **59**, 3295.

Feiner, L.F., Oleś, A.M. and Zaanen, J. (1998).Quantum disorder versus order-out-of-disorder in the Kugel–Khomskii model. *Journal of Physics: Condensed Matter*, **10**, L555.

Feldkemper, S. and Weber, W. (1998). Generalized calculation of magnetic coupling constants for Mott-Hubbard insulators: application to ferromagnetic Cr compounds. *Physical Review B*, **57**, 7755.

Fiebig, M. (2005). Revival of the magnetoelectric effect. *Journal of Physics D: Applied Physics*, **38**, R123.

Friedt, O., Braden, M., André, G., *et al*. (2001). Structural and magnetic aspects of the metal-insulator transition in Ca2-xSrxRuO4. *Physical Review B*, **63**, 174432.

Frischmuth, B., Mila, F. and Troyer, M. (1999). Thermodynamics of the one-dimensional SU(4) symmetric spin-orbital model. *Physical Review Letters*, **82**, 835.

Furukawa, N. (1996). Spin excitation spectrum of $La_{1-x}A_xMnO_3$. *Journal of the Physical Society of Japan*, **65**, 1174.

Geck, J., Bruns, D., Hess, C., *et al*. (2002). Anisotropic CE-type orbital correlations in the ferromagnetic metallic phase of $Nd_{1/2}Sr_{1/2}MnO_3$. *Physical Review B*, **66**, 184407.

Georges, A., Kotliar, G., Krauth, W. and Rozenberg, M. (1996). Dynamical mean-field theory of strongly correlated fermion systems and the limit of infinite dimensions. *Reviews of Modern Physics*, **68**, 13.

Goodenough, J.B. (1955). Theory of the role of covalence in the Perovskite-type manganites. *Physical Review*, **100**, 564.

Goodenough, J.B. (1963). *Magnetism and the Chemical Bond*, Interscience: New York.

Griffith, J.S. (1971). *The Theory of Transition Metal Ions*, Cambridge University Press: Cambridge.

Grüninger, M., Rückamp, R., Windt, M., *et al*. (2002). Experimental quest for orbital waves. *Nature (London)*, **418**, 39.

Hartinger, Ch., Mayr, F., Deisenhofer, J., *et al*. (2004). Large and small polaron excitations in $La_{2/3}(Sr/Ca)_{1/3}MnO_3$ films. *Physical Review B*, **69**, 100403.

Held, K. *Electronic structure calculations using Dynamical Mean Field Theory*, cond-mat/0511293.

von Helmolt, R., Wecker, J., Holzapfel, B., *et al*. (1993). Giant negative magnetoresistance in perovskitelike $La_{2/3}Ba_{1/3}MnO_x$ ferromagnetic films. *Physical Review Letters*, **71**, 2331.

Horsch, P., Jaklic, J. and Mack, F. (1999). Double-exchange magnets: spin dynamics in the paramagnetic phase. *Physical Review B*, **59**, R14149.

Hirota,K., Kaneko, N., Nishizawa, A. and Endoh, Y. (1996). Two-dimensional planar ferromagnetic coupling in $LaMnO_3$. *Journal of the Physical Society of Japan*, **65**, 3736.

Horsch, P., Khaliullin, G. and Oleś, A.M. (2003). Dimerization versus orbital-moment ordering in a Mott insulator YVO_3. *Physical Review Letters*, **91**, 257203.

Horsch, P., Jaklic, J. and Mack, F. (1999). Optical conductivity of colossal-magnetoresistance compounds: role of orbital degeneracy in the ferromagnetic phase. *Physical Review B*, **59**, 6217.

Hwang, H.Y., Dai, P., Cheong, S-W., *et al*. (1998). Softening and broadening of the zone boundary magnons in $Pr_{0.63}Sr_{0.37}MnO_3$. *Physical Review Letters*, **80**, 1316.

Inagaki, S. (1975). Effect of Orbital Degeneracy and Intra-Atomic Exchange on the Occurrence of Ferromagnetism. *Journal of the Physical Society of Japan*, **39**, 596.

Ingle, N.J.C., *et al*. (2005). Quantitative analysis of Sr_2RuO_4 angle-resolved photoemission spectra: many-body interactions in a model Fermi liquid. *Physical Review B*, **72**, 205114.

Imada, M., Fujimori, A. and Tokura, Y. (1998). Metal-insulator transitions. *Reviews of Modern Physics*, **70**, 1039.

Ishihara, S., Inoue, J. and Maekawa, S. (1997). Effective Hamiltonian in manganites: study of the orbital and spin structures. *Physical Review B* **55**, 8280.

Ishihara, S. (2004). Orbital wave and its observation in orbital-ordered titanates and vanadates. *Physical Review B*, **69**, 075118.

Ishihara, S., Murakami, Y., Inami, T., *et al*. (2005). Theory and experiment of orbital excitations in correlated oxides. *New Journal of Physics*, **7**, 119.

Ishihara, S., Yamanaka, M. and Nagaosa, N. (1997). Orbital liquid in perovskite transition-metal oxides. *Physical Review B*, **56**, 686.

Ishikawa, T., Ookera, K. and Tokura, Y. (1999). Optical response to orbital and charge ordering in a layered manganite: $La_{1/2}Sr_{3/2}MnO_4$. *Physical Review B*, **59**, 8367.

Itakura, T. and Kawakami, N. (1995). Heisenberg model and supersymmetric t-J model with two-band structure in one dimension. *Journal of the Physical Society of Japan*, **64**, 2321.

Itoi, C., Qin, S. and Affleck, I. (2000). Phase diagram of a one-dimensional spin-orbital model. *Physical Review B*, **61**, 6747.

Jin, S., Tiefel, T.H., MacCormack, M., *et al*. (1994). Thousandfold change in resistivity in magnetoresistive La-Ca-Mn-O films. *Science*, **264**, 413.

Jonker, G.H. and van Santen, J.H. (1950). Ferromagnetic compounds of manganese with perovskite structure. *Physica*, **16**, 337.

Jung, J.H., Ahn, J.S., Jaejun, Yu, *et al*. (2000). Optical investigations of the charge gap in orbital-ordered $La_{1/2}Sr_{3/2}MnO_4$. *Physical Review B*, **61**, 6902.

Kajimoto, R., Yoshizawa, H., Tomioka, Y. and Tokura, Y. (2002). Stripe-type charge ordering in the metallic A-type antiferromagnet Pr0.5Sr0.5MnO3. *Physical Review B*, **66**, 180402(R).

Kanamori, J. (1959). Superexchange interaction and symmetry properties of electron orbitals. *Journal of Physics and Chemistry of Solids*, **10**, 87.

Kaplan T.A. and Mahanti S.D. (Eds.) (1998). *Physics of Manganites*, Kluwer Academic/Plenum Publishers, New York.

Katsura, H., Nagaosa, N. and Balatsky, A.V. (2005). Spin current and magnetoelectric effect in noncollinear magnets. *Physical Review Letters*, **95**, 057205.

Kawano, H., Yoshizawa, H. and Ueda, Y. (1994). Magnetic behavior of a Mott-insulator YVO_3. *Journal of the Physical Society of Japan*, **63**, 2857.

Keimer, B., Casa, D., Ivanov, A., *et al*. (2000). Spin dynamics and orbital state in $LaTiO_3$. *Physical Review Letters*, **85**, 3946.

Khaliullin, G. (2001). Order from disorder: quantum spin gap in magnon spectra of $LaTiO_3$. *Physical Review B*, **64**, 212405.

Khaliullin, G. (2005). Orbital order and fluctuations in Mott insulators. *Progress of Theoretical Physics Supplement*, **160**, 155.

Khaliullin, G., Horsch, P. and Oleś, A.M. (2001). Spin order due to orbital fluctuations: cubic vanadates. *Physical Review Letters*, **86**, 3879.

Khaliullin, G., Horsch, P. and Oleś, A.M. (2004). Theory of optical spectral weights in Mott insulators with orbital degrees of freedom. *Physical Review B*, **70**, 195103.

Khaliullin, G. and Kilian,R. (1999). Orbital order out of spin disorder: how to measure the orbital gap. *Journal of Physics: Condensed Matter*, **11**, 9757.

Khaliullin, G. and Kilian, R. (2000). Theory of anomalous magnon softening in ferromagnetic manganites. *Physical Review B*, **61**, 3494.

Khaliullin, G., Koshibae, W. and Maekawa, S. (2004). Low energy electronic states and triplet pairing in layered cobaltate. *Physical Review Letters*, **93**, 176401.

Khaliullin, G. and Okamoto,S. (2002). Quantum behavior of orbitals in ferromagnetic titanates: novel orderings and excitations. *Physical Review Letters*, **89**, 167201.

Khaliullin, G. and Okamoto, S. (2003). Theory of orbital state and spin interactions in ferromagnetic titanates. *Physical Review B*, **68**, 205109.

Khaliullin, G. and Maekawa, S. (2000). Orbital liquid in three-dimensional Mott insulator: $LaTiO_3$. *Physical Review Letters*, **85**, 3950.

Khaliullin, G. and Oudovenko, V. (1997). Spin and orbital excitation spectrum in the Kugel–Khomskii model. *Physical Review B*, **56**, 14243(R).

Khomskii, D.I. (2006). Multiferroics: different ways to combine magnetism and ferroelectricity. *Journal of Magnetism and Magnetic Materials*, **306**, 1.

Khomskii, D.I. and Kugel, K.I. (2003). Elastic interactions and superstructures in manganites and other Jahn-Teller systems. *Physical Review B*, **67**, 134401.

Kilian, R. and Khaliullin, G. (1998). Orbital dynamics: the origin of the anomalous optical spectra in ferromagnetic manganites. *Physical Review B*, **58**, R11841.

Kilian, R. and Khaliullin, G. (1999). Orbital polarons in the metal-insulator transition of manganites. *Physical Review B*, **60**, 13458.

Kim, K.H., Jung, J.H. and Noh, T.W. (1998). Polaron absorption in a Perovskite manganite $La_{0.7}Ca_{0.3}MnO_3$. *Physical Review Letters*, **81**, 1517.

Kim, K.H., Lee, S., Noh, T.W., *et al*. (2002). Charge ordering fluctuation and optical pseudogap in $La_{1-x}Ca_xMnO_3$. *Physical Review Letters*, **88**, 167204.

Kimura, T., Goto, T., Shintani, H., *et al*. (2003). Magnetic control of ferroelectric polarization. *Nature*, **426**, 55.

Kiyama, T., Saitoh, H., Itoh, M., *et al*. (2005). Orbital fluctuations in ground state of $YTiO_3$: ^{47,49}Ti NMR study. *Journal of the Physical Society of Japan*, **74**, 1123.

Knecht, C., Blümer, N. and van Dongen, P.G.J. (2005). Orbital-selective Mott transitions in the anisotropic two-band Hubbard model at finite temperatures. *Physical Review B*, **72**, 081103(R).

Koga, A., Kawakami, N., Rice, T.M. and Sigrist, M. (2004). Orbital-selective Mott transitions in the degenerate Hubbard model. *Physical Review Letters*, **92**, 216402.

Koga, A., Kawakami, N., Rice, T.M. and Sigrist, M. (2005). Spin, charge, and orbital fluctuations in a multiorbital Mott insulator. *Physical Review B*, **72**, 045128.

Kohn, W. (1964). Theory of the insulating state. *Physical Review*, **133**, A171.

Koleshuk, A.K. and Mikeska, H-J. (1998). Non-haldane spin-liquid models with exact ground states. *Physical Review Letters*, **80**, 2709.

Koller, W., Prüll, A., Evertz, H.G. and von der Linden, W. (2003). Magnetic polarons in the one-dimensional ferromagnetic Kondo model. *Physical Review B*, **67**, 174418.

Konstantinović, M.J., van den Brink, J., Popović, Z.V., *et al*. (2004). Orbital dimerization in $NaTiSi_2O_6$: An orbital analogue of the spin-peierls phase transition. *Physical Review B*, **69**, 020409(R).

Kotliar, G. and Vollhardt, D. (2004). Strongly correlated materials: insights from dynamic mean-field theory. *Physics Today*, **57**, 53.

Kovaleva, N.N., Boris, A.V., Bernhard, C., *et al*. (2004). Spin-controlled Mott-Hubbard bands in $LaMnO_3$ probed by optical ellipsometry. *Physical Review Letters*, **93**, 147204.

Kubo, K. and Ohata, N. (1972). A quantum theory of double exchange. *Journal of the Physical Society of Japan*, **33**, 21.

Kubota, M., Yoshizawa, H., Moritomo, Y., *et al*. (1999). Interplay of the CE-Type charge ordering and the A-Type spin ordering in half-doped bilayer manganite $LaSr_2Mn_2O_7$. *Journal of the Physical Society of Japan*, **68**, 2202.

Kugel, K.I. and Khomskii, D.I. (1982a). Jahn-Teller effect and magnetism – transition-metal compounds. *Uspekhi Fizicheskikh Nauk*, **136**, 621.

Kugel, K.I. and Khomskii, D.I. (1982b). Jahn-Teller effect and magnetism – transition-metal compounds. *Soviet Physics Uspekhi*, **25**, 231.

Lee, J.S., Kim, M.W. and Noh, T.W. (2005). Optical excitations of transition-metal oxides under the orbital multiplicity effects. *New Journal of Physics*, **7**, 147.

Liebsch, A. (2005). Novel Mott transitions in a nonisotropic two-band Hubbard model. *Physical Review Letters*, **95**, 116402.

Li, Y.Q., Ma, M., Shi, D.N. and Zhang, F.C. (1998). SU(4) theory for spin systems with orbital degeneracy. *Physical Review Letters*, **81**, 3527.

Liu, S.Q., Wu, N.J. and Ignatiev, A. (2000). Electric-pulse-induced reversible resistance change effect in magnetoresistive films. *Applied Physics Letters*, **76**, 2749.

Loudon, J.C., Cox, S., Williams, A.J., *et al*. (2005). Weak charge-lattice coupling requires reinterpretation of stripes of charge order in $La_{1-x}Ca_xMnO_3$. *Physical Review Letters*, **94**, 097202.

Mack, F. and Horsch, P. (1999). Optical conductivity in doped manganites with planar $x^2 - y^2$ orbital order. *Physical Review Letters*, **82**, 3160.

Maekawa, S., Tohyama, T. Barnes, S.E. *et al*. (2004). *Physics of Transition Metal Oxides*, *Springer Series in Solid State Sciences*, Springer-Verlag: Heidelberg, Vol. 144.

Mahajan, A.V., Johnston, D.C., Torgeson, D.R. and Borsa, F. (1992). Magnetic properties of $LaVO_3$. *Physical Review B*, **46**, 10966.

Di Matteo, S., Jackeli, G., Lacroix, C. and Perkins, N.B. (2004). Valence-bond crystal in a pyrochlore antiferromagnet with orbital degeneracy. *Physical Review Letters*, **93**, 077208.

Di Matteo, S., Jackeli, G. and Perkins, N.B. (2005). Valence-bond crystal and lattice distortions in a pyrochlore antiferromagnet with orbital degeneracy. *Physical Review B*, **72**, 024431.

Mackenzie, A.P. and Maeno, Y. (2003). The superconductivity of Sr_2RuO_4 and the physics of spin-triplet pairing. *Reviews of Modern Physics*, **75**, 657.

Maeno, Y., Hashimoto, H., Yoshida, K., *et al*. (1994). Superconductivity in a layered perovskite without copper. *Nature*, **372**, 532.

Mayr, M., Moreo, A., Vergés, J.A, *et al*. (2001). Resistivity of mixed-phase manganites. *Physical Review Letters*, **86**, 135.

Mostovoy, M.V. and Khomskii, D.I. (2000). Charge ordering and opening of spin gap in NaV_2O_5. *Solid State Communications*, **113**, 159.

Metzner, W. and Vollhardt, D. (1989). Correlated lattice fermions in $d = \infty$ dimensions. *Physical Review Letters*, **62**, 324.

Mikeska, H-J.and Koleshuk, A.K.. (2004). In *Quantum Magnetism*, Schollwök,U., Richter, *Lecture Notes in Physics*, J., Farnell, D. and Bishop, R.F. (Eds.), Springer: Berlin.

Millis, A. (1996). Cooperative Jahn-Teller effect and electron-phonon coupling in $La_{1-x}A_xMnO_3$. *Physical Review B*, **53**, 8434.

Millis, A.J., Littlewood, P.B. and Shraiman, B.I. (1995). Double exchange alone does not explain the resistivity of $La_{1-x}Sr_xMnO_3$. *Physical Review Letters*, **74**, 5144.

Mishenko, A.S. and Nagaosa, N. (2004). Electron-phonon coupling and a polaron in the t-J model: from the weak to the strong coupling regime. *Physical Review Letters*, **93**, 036402.

Miyashita, S., Kawaguchi, A., Kawakami, N. and Khaliullin, G. (2004). Quantum phase transitions in the one-dimensional S = 1 spin-orbital model: implications for cubic vanadates. *Physical Review B*, **69**, 104425.

Miyashita, S. and Kawakami, N. (2005). One-dimensional S = 1 spin-orbital model with uniaxial single-ion anisotropy. *Journal of the Physical Society of Japan*, **74**, 758.

Miyasaka, S., Okimoto, Y., Iwama, M. and Tokura, Y. (2003). Spin-orbital phase diagram of perovskite-type RVO_3. *Physical Review B*, **68**, 100406(R).

Miyasaka, S., Okimoto, Y. and Tokura, Y. (2002). Anisotropy of Mott-Hubbard gap transitions due to spin and orbital ordering in $LaVO_3$ and YVO_3. *Journal of the Physical Society of Japan*, **71**, 2086.

Miyasaka, S., Onoda, S., Okimoto, Y., *et al*. (2005). One-dimensional orbital exciations in vanadium oxides. *Physical Review Letters*, **94**, 076405.

Mizokawa, T., Khomskii, D.I. and Sawatzky, G.A. (1999). Interplay between orbital ordering and lattice distortions in $LaMnO_3$, YVO_3, and $YTiO_3$. *Physical Review B*, **60**, 7309.

Mizokawa, T., Khomskii, D.I. and Sawatzky, G.A. (2000). Orbital polarons and ferromagnetic insulators in manganites. *Physical Review B*, **63**, 024403.

Mizuno, Y., Tohyama, T., Maekawa, S., *et al*. (1998). Electronic states and magnetic properties of edge-sharing Cu-O chains. *Physical Review B*, **57**, 5326.

Mochizuki, M. and Imada, M. (2003). Orbital-Spin Structure and lattice coupling in $RTiO_3$ where R = La, Pr, Nd, and Sm. *Physical Review Letters*, **91**, 167203.

Mochizuki, M. and Imada, M. (2004). Orbital physics in the perovskite Ti oxides. *New Journal of Physics*, **6**, 154.

Murakami, Y., Hill, J.P., Gibbs, D., *et al*. (1998). Resonant X-ray scattering from orbital ordering in $LaMnO_3$. *Physical Review Letters*, **81**, 582.

Mostovoy, M.V. and Khomskii, D.I. (2002). Orbital ordering in frustrated Jahn-Teller systems with 90 degree exchange. *Physical Review Letters*, **89**, 227203.

Mostovoy, M.V. and Khomskii, D.I. (2004). Orbital ordering in charge transfer insulators. *Physical Review Letters*, **92**, 167201.

Motome, Y., Seo, H., Fang, Z. and Nagaosa, N. (2003). One-dimensional confinement and enhanced Jahn-Teller instability in $LaVO_3$. *Physical Review Letters*, **90**, 146602.

Moussa, F., Hennion, M., Rodríguez-Carvajal, J. (1996). Spin waves in the antiferromagnet perovskite $LaMnO_3$: a neutron-scattering study. *Physical Review B*, **54**, 15149.

Müller-Hartmann, E. and Dagotto, E. (1996). Electronic Hamiltonian for transition-metal oxide compounds. *Physical Review B*, **54**, R6819.

Nakatsuji, S. and Maeno, Y. (2000a). Quasi-two-dimensional Mott transition system $Ca_{2-x}Sr_xRuO_4$. *Physical Review Letters*, **84**, 2666.

Nakatsuji, S. and Maeno, Y. (2000b). Switching of magnetic coupling by a structural symmetry change near the Mott transition in $Ca_{2-x}Sr_xRuO_4$. *Physical Review B*, **62**, 6458.

Nerseyan, A.A. and Tsvelik, A.M. (1997). One-dimensional spin-liquid without magnon excitations. *Physical Review Letters*, **78**, 3939.

Noguchi, M., Nakazawa, A., Oka, S., *et al*. (2000). Synchrotron X-ray-diffraction study of orbital ordering in YVO_3. *Physical Review B*, **62**, 9271(R).

Ogasawara, T., Tobe, K., Kimura, T., *et al*. (2002). Photo-induced dynamics of charge/orbital order in perovskite manganite $Nd_{0.5}Ca_{0.5}MnO_3$. *Journal of the Physical Society of Japan*, **71**, 2380.

Ohmoto, A. and Hwang, H.Y. (2004). A high-mobility electron gas at the LaAlO3/SrTiO3 heterointerface. *Nature*, **427**, 423.

Okamoto, S. and Millis, A.J. (2004). Electronic reconstruction at an interface between a Mott insulator and a band insulator. *Nature*, **428**, 630.

Okimoto, Y., Katsufuji, T., Ishikawa, T., *et al*. (1995). Anomalous variation of optical spectra with spin polarization in double-exchange ferromagnet: $La_{1-x}Sr_xMnO_3$. *Physical Review Letters*, **75**, 109.

Okimoto, Y., Katsufuji, T., Ishikawa, T., *et al*. (1997). Variation of electronic structure in $La_{1-x}Sr_xMnO_3$ as investigated by optical conductivity spectra. *Physical Review B*, **55**, 4206.

Oleś, A.M. (1983). Antiferromagnetism and correlation of electrons in transition metals. *Physical Review B*, **28**, 327.

Oleś, A.M. (2003). Orbital ordering and orbital fluctuations in transition metal oxides. *Physica Status Solidi B*, **236**, 281.

Oleś, A.M.(2005). Orbital ordering and orbital fluctuations in transition metal oxides. *Physica Status Solidi B*, **242**, 963(E).

Oleś, A.M., Cuoco, M. and Perkins, N.B. (2000). *Lectures on the Physics of Highly Correlated Electron Systems*, Mancini, F. (Ed.), AIP Conference Proceedings 527: New York.

Oleś, A.M. and Feiner, L.F. (2002). Why spin excitations in metallic ferromagnetic manganites are isotropic. *Physical Review B*, **65**, 052414.

Oleś, A.M., Feiner, L.F. and Zaanen, J. (2000). Quantum melting of magnetic long-range order near orbital degeneracy: classical phases and Gaussian fluctuations. *Physical Review B*, **61**, 6257.

Oleś, A.M., Horsch, P., Feiner, L.F. and Khaliullin, G. (2006). Spin-orbital entanglement and violation of the Goodenough-Kanamori rules. *Physical Review Letters*, **96**, 147205.

Oleś, A.M., Khaliullin, G., Horsch, P. and Feiner, L-F. (2005). Fingerprints of spin-orbital physics in cubic Mott insulators: magnetic exchange interactions and optical spectral weights. *Physical Review*, **72**, 214431.

Pati, S.K., Singh, R.R.P. and Khomskii, D.I. (1998). Alternating spin and orbital dimerization and spin-gap formation in coupled spin-orbital systems. *Physical Review Letters*, **81**, 5406.

Pavarini, E., Yamasaki, Y., Nuss, J. and Andersen, O.K. (2005). How chemistry controls electron localization in $3d^1$ perovskites: a Wannier-function study. *New Journal of Physics*, **7**, 188.

Pavarini, E., Biermann, S., Poteryaev, A., *et al*. (2004). Mott transition and suppression of orbital fluctuations in orthorhombic $3d^1$ perovskites. *Physical Review Letters*, **92**, 76403.

Pen, H.F., van den Brink, J., Khomskii, D.I. and Sawatzky, G.A. (1997). Orbital ordering in a two-dimensional triangular lattice. *Physical Review Letters*, **78**, 1323.

Perebeinos, V. and Allen, P.B. (2000). Franck-condon broadened angle-resolved photoemission spectra predicted in $LaMnO_3$. *Physical Review Letters*, **85**, 5178.

Prelovšek, P., Zeyher, R. and Horsch, P. (2006). Self-localization of composite spin-lattice polarons. *Physical Review Letters*, **96**, 086402.

Puchkov, A.V., Timusk, T., Karlov, M.A., *et al*. (1995). Optical conductivity of nonmetallic $Ba_{0.69}K_{0.31}BiO_3$ single crystals: evidence for bipolaron formation. *Physical Review B*, **52**, R9855.

Quijada, M., Cerne, J., Simpson, J.R., *et al*. (1998). Optical conductivity of manganites: crossover from Jahn-Teller small polaron to coherent transport in the ferromagnetic state. *Physical Review B*, **58**, 16093.

Ramšak, A., Horsch, P. and Fulde, P. (1992). Effective mass of quasiparticles in a t-J model with electron-phonon interactions. *Physical Review B*, **46**, R14305.

Reik, H.G. and Heese, D. (1967). Frequency dependence of the electrical conductivity of small polarons for high and low temperatures. *Journal of Physics and Chemistry of Solids*, **28**, 581.

Reitsma, A.J.W., Feiner, L.F. and Oleś, A.M. (2005). Orbital and spin physics in $LiNiO_2$ and NaNiO. *New Journal of Physics*, **7**, 121.

Ren, Y., Palstra, T.T.M., Khomskii, D.I., *et al*. (1998). Temperature-induced magnetization reversal in a YVO_3 single crystal. *Nature*, **396**, 441.

Ren, Y., Palstra, T.T., Khomskii, D.I., *et al*. (2000). Magnetic properties of YVO_3 single crystals. *Physical Review B*, **62**, 6577.

Rösch, O., Gunnarsson, O., Shen, X.J., *et al*. (2005). Polaronic behavior of undoped high-tc cuprate superconductors from angle-resolved photoemission spectra. *Physical Review Letters*, **95**, 227002.

Rückamp, R., Benckiser, E., Haverkort, M.W., *et al*. (2005). Optical study of orbital excitations in transition-metal oxides. *New Journal of Physics*, **7**, 144.

Saitoh, E., Okamoto, S., Takahashi, K.T., *et al*. (2001). Observation of orbital waves as elementary excitations in a solid. *Nature (London)*, **410**, 180.

Saitoh, E., *et al*. (2002). *Nature (London)*, **418**, 40.

Saitoh, E., Asamitsu, A., Okimoto, Y. and Tokura, Y. (2000). Optical study of metal-insulator transition in the ferromagnetic ground state of $La_{1-x}Sr_xMnO_3$. *Journal of the Physical Society of Japan*, **69**, 3614.

Sawada, H., Hamada, N., Terakura, K. and Asada, T. (1996). Orbital and spin orderings in YVO_3 and $LaVO_3$ in the generalized gradient approximation. *Physical Review B*, **53**, 12742.

Sawada, H. and Terakura, K. (1998). Orbital and magnetic orderings in localized t2g systems, $YTiO_3$ and YVO_3. *Physical Review B*, **58**, 6831.

Senff, D., Krüger, F., Scheidl, S., *et al*. (2006). Spin-wave dispersion in orbitally ordered $La_{1/2}Sr_{3/2}MnO_4$. *Physical Review Letters*, **96**, 257201.

Schmidt, K.P., Grüninger, M. and Uhrig, G.S. The fate of orbitons coupled to phonons, cond-mat/0603766.

Schmitz, R., Entin-Wohlman, O., Aharoni, A., *et al*. (2005). Magnetic structure of the Jahn-Teller system $LaTiO_3$. *Physical Review B*, **1**, 144412.

Shastry, B.S. and Sutherland, B. (1990). Twisted boundary conditions and effective mass in Heisenberg-Ising and Hubbard rings. *Physical Review Letters*, **65**, 243.

Shen, S-Q., Xie, X.C. and Zhang, F.C. (2002). High spin systems with orbital degeneracy. *Physical Review Letters*, **88**, 027201.

Shiina, R., Mila, F., Zhang, F-C. and Rice T.M. (2001). Atomic spin, molecular orbitals, and anomalous antiferromagnetism n insulating V_2O_3. *Physical Review B*, **63**, 144422.

Shiina, R., Nishitani, T. and Shiba, H. (1997). Magnetic ordering, orbital state and lattice distortion in Perovskite manganites. *Journal of the Physical Society of Japan*, **66**, 3159.

Sigrist, M. and Troyer, M. (2004). Orbital and spin correlations in $Ca_{2-x}Sr_xRuO_4$: A mean field study. *European Physical Journal B*, **39**, 207.

Sirker, J. and Khaliullin, G. (2003). Entropy driven dimerization in a one-dimensional spin-orbital model. *Physical Review B*, **67**, 100408.

Soltan, S., Albrecht, J. and Habermeier, H-U. (2004). Ferromagnetic/superconducting bilayer structure: a model system for spin diffusion length estimation. *Physical Review B*, **70**, 144517.

Solovyev, I.V. (2004). Lattice distortion and magnetic ground state of YTiO3 and LaTiO3. *Physical Review B*, **69**, 134403.

Solovyev, I.V. (2006). Lattice distortion and magnetism of $3d - t_{2g}$ perovskite oxides. *Physical Review B*, **74**, 054412.

Sternlieb, B.J., Hill, J.P., Wildgruber, U.C., *et al*. (1996). Charge and magnetic order in $La_{0.5}Sr_{1.5}MnO_4$. *Physical Review Letters*, **76**, 2169.

Sutherland, B. (1975). Model for a multicomponent quantum system. *Physical Review B*, **12**, 3795.

Tobe, K., Kimura, T., Ohimoto, Y. and Tokura, Y. (2001). Anisotropic optical spectra in a detwinned $LaMnO_3$ crystal. *Physical Review B*, **64**, 184421.

Tokura, Y. (2003). Correlated electron physics in transition metal oxides. *Physics Today*, **56**, 50.

Tokura, Y. (2006). Critical features of colossal magnetoresistive manganites. *Reports on Progress in Physics*, **69**, 797.

Tokura, Y. and Nagaosa, N. (2000). Orbital physics in transition-metal oxides. *Science*, **288**, 462.

Tomioka, Y., Asamitsu, A. and Tokura, Y. (2000). Magneto-transport properties and magnetostructural phenomenon in single crystals of $La_{0.7}(Ca_{1-y}Sr_y)_{0.3}MnO_3$. *Physical Review B*, **63**, 024421.

Tornow, S., Entin-Wohlman, O. and Aharony, A. (1999). Anisotropic superexchange for nearest and next-nearest coppers in chain, ladder, and lamellar cuprates. *Physical Review B*, **60**, 10206.

Tsukamoto, Y., Kawakami, N., Yamashita, Y. and Ueda, K. (2000). Gap formation for the one-dimensional SU(4) spin-orbital model. *Physica B*, **281–282**, 540.

Tsvetkov, A.A., Mena, F.P., van Loosdrecht, P.H.M., *et al*. (2004). Structural, electronic, and magneto-optical properties of YVO_3. *Physical Review B*, **69**, 075110.

Ulrich, C., Gössling, A., Grüninger, M., *et al*. (2006). Raman Scattering in the Mott insulators $LaTiO_3$ and $YTiO_3$: evidence for orbital excitations. *Physical Review Letters*, **97**, 157401.

Ulrich, C., Khaliullin, G., Okamoto, S., *et al*. (2002). Magnetic order and dynamics in an orbitally degenerate ferromagnetic insulator. *Physical Review Letters*, **89**, 167202.

Ulrich, C., Khaliullin, G., Sirker, J., *et al*. (2003). Magnetic neutron scattering study of YVO_3: evidence for an orbital peierls state. *Physical Review Letters*, **91**, 257202.

Varma, C.M. (1996). Electronic and magnetic states in the giant magnetoresistive compounds. *Physical Review B*, **54**, 7328.

Vernay, F., Penc, K., Fazekas, P. and Mila, F. (2004). Orbital degeneracy as a source of frustration in $LiNiO_2$. *Physical Review B*, **70**, 014428.

Weisse, A. and Fehske, H. (2004). Microscopic modelling of doped manganites. *New Journal of Physics*, **6**, 158.

Wollan, E.O. and Koehler, W.C. (1955). Neutron diffraction study of the magnetic properties of the series of perovskite-type compounds $La_{1-x}Ca_xMnO_3$. *Physical Review*, **100**, 545.

Xu, X.H., Blythe, H.J., Ziese, M., *et al*. (2006). Carrier-induced ferromagnetism in n-type ZnMnAlO and ZnCoAlO thin films at room temperature. *New Jounal of Physics*, **8**, 135.

Yamashita, Y., Shibata, N. and Ueda, K. (1998). SU(4) spin-orbit critical state in one dimension. *Physical Review B*, **58**, 9114.

Yamashita, Y., Shibata, N. and Ueda, K. (2000). Numerical study of the one-dimensional spin-orbit coupled system with SU(2)⊗ SU(2) symmetry. *Journal of the Physical Society of Japan*, **69**, 242.

Yi, Hongsuk., Hur, N.H. and Yu, J. (2000). Anomalous spin susceptibility and magnetic polaron formation in the double-exchange systems. *Physical Review B*, **61**, 9501.

Zaanen, J. and Oleś, A.M. (1988). Canonical perturbation theory and the two-band model for high-Tc superconductors. *Physical Review B*, **37**, 9423.

Zaanen, J. and Oleś, A.M. (1993). Carriers binding to excitons: crystal-field excitations in doped Mott-Hubbard insulators. *Physical Review B*, **48**, 7197.

Zaanen, J., Sawatzky, G.A. and Allen, J.W. (1985). Band gaps and electronic structure of transition-metal compounds. *Physical Review Letters*, **55**, 418.

Zaanen, J. and Sawatzky, G.A. (1990). Systematics in band gaps and optical spectra of 3D transition metal compounds. *Journal of Solid State Chemistry*, **88**, 8.

Zegkinoglou, I., Strempfer, J., Nelson, C.S. *et al*. (2005).Orbital ordering transition in Ca_2RuO_4 observed with resonant X-ray diffraction. *Physical Review Letters*, **95**, 136401.

Zener, C. (1951). Interaction between the d-shells in the transition metals. II. ferromagnetic compounds of manganese with perovskite structure. *Physical Review*, **82**, 403.

FURTHER READING

Mori, S., Chen, C.H. and Cheong, S-W. (1998). Pairing of charge-ordered stripes in (La,Ca)MnO_3. *Nature*, **392**, 473.

Magnetic Spectroscopy

H. Ebert
Universität München, München, Germany

1 INTRODUCTION

In the middle of the 19th century, it was found that linearly polarized light gets elliptically polarized when it is transmitted through a magnetized sample (Faraday, 1846). This was obviously the first clear demonstration that the spectroscopic properties of a solid depend on its magnetic properties. Later on, several other magneto-optical effects have been discovered, such as the Kerr, Zeeman, Voigt, or Cotton–Moutton effect (Reim and Schoenes, 1990), that can be exploited to monitor the magnetic state of a sample. This applies in particular to the magneto-optical Kerr effect (MOKE), which is extensively used for the recording of magnetic hysteresis loops, imaging of magnetic domains (Hubert and Schäfer, 1998), or in sensor and storage technology (Mansuripur, 1995). The various magneto-optical effects were originally observed in the energy regime of conventional optics. However, the availability of tunable synchrotron radiation of high intensity and well-defined polarization allowed the exploration of magneto-optical effects in the X-ray regime also (Beaurepaire, Scheurer, Krill and Kappler, 2001). Apart from the mentioned effects (Mertins *et al*., 2000), the most prominent phenomena are the magnetic linear dichroism in X-ray absorption (XMLD) (van der Laan *et al*., 1986) and magnetic circular dichroism in X-ray absorption (XMCD) (Schütz *et al*., 1987; Wende, 2004), the magnetic dichroism in X-ray fluorescence (Strange, Durham and Györffy, 1991), and the nonresonant and resonant magnetic scattering (Namikawa, Ando, Nakajima and Kawata, 1985; Gibbs *et al*., 1988; Lovesey, 1993). In addition, one has to mention the various dichroic effects in core-level (Baumgarten *et al*., 1990; Roth, Hillebrecht, Rose and Kisker, 1993) and valence-band (Kuch and Schneider, 2001) photoemission. Similar to the MOKE, dichroic effects in the X-ray regime can also be used to probe the magnetization of a sample. Because X-ray absorption and core-level photoemission imply the excitation of tightly bound core electrons, these spectroscopies supply the basis for element-specific hysteresis loop recording (Chen *et al*., 1993) and magneto-microscopy (Schneider *et al*., 1993; Eimüller *et al*., 2001).

Magneto-optical and dichroic effects in spectroscopy not only allow one to image the magnetization of a sample or to follow its variation with time (Ghiringhelli *et al*., 2001) but also supply a very important probe for their electronic structure. For the MOKE, it was shown around 1930 that it is caused by an interplay of magnetization and spin-orbit coupling (Hulme, 1932). This would later on be confirmed by detailed calculations based on an *ab initio* description of the electronic structure (Wang and Callaway, 1974; Oppeneer, Maurer, Sticht and Kübler, 1992). The mechanism leading to the MOKE was expected to give rise also to the XMCD (Erskine and Stern, 1975). Again, this would be confirmed by calculations that accounted for magnetism and spin-orbit coupling at the same time (Ebert, Strange and Györffy, 1988). In addition, it would be shown that XMCD spectra

Handbook of Magnetism and Advanced Magnetic Materials. Edited by Helmut Kronmüller and Stuart Parkin. Volume 1: *Fundamentals and Theory*. ISBN: 978-0-470-02217-7.

essentially reflect the spin and orbital polarization (OP) of the electronic states above the Fermi level. This finding led to the sum rules that supply a formal basis for deducing from XMCD spectra an estimate for the spin and orbital magnetic moment of the absorbing atoms (Thole, Carra, Sette and van der Laan, 1992; Carra, Thole, Altarelli and Wang, 1993). Accordingly, recording the anisotropy of the XMCD signal gives information on the anisotropy of the orbital magnetic moment. Because of the interrelation of the latter and the magnetic anisotropy energy, ΔE_{aniso} (Bruno, 1989), one gets a spectroscopic access to ΔE_{aniso} (Stöhr, 1999). Owing to these outstanding features, the XMCD became a valuable tool to study the properties of a great variety of magnetic solids.

Angle-resolved valence-band photoemission spectroscopy allows one to probe the electronic structure of a solid in a most detailed way (Kevan, 1992). Spin-resolved experiments on magnetic solids, in addition, give access to the dispersion relation $E(\vec{k})$ of the two spin subsystems separately, that can be studied for example, as a function of temperature (Kisker, Schröder, Campagna and Gudat, 1984). The observation of various forms of dichroism, however, showed that such a decomposition is not strictly possible. Corresponding experimental and theoretical investigations demonstrated that spin- and angle-resolved valence-band photoemission spectroscopies – in contrast to all other spectroscopies – allow probing of the hybridization of states with different spin character in a rather direct and detailed way (Feder and Henk, 1996).

Among the various spectroscopies mentioned in the preceding text, the MOKE, the magnetic dichroism in X-ray absorption, and valence-band photoemission will be dealt with in this contribution as important and representative examples. For all three cases, the theoretical basis for a calculation and discussion of the corresponding spectra will be presented together with some examples. In the next section, it will be demonstrated by some simple arguments that the various magneto-optical and dichroic phenomena to be discussed are caused by an interplay of exchange splitting and spin-orbit coupling. For this reason, a brief overview on the techniques used to perform corresponding electronic structure calculations to supply an adequate basis for a quantitative study of the various phenomena is given in addition.

2 THEORETICAL FRAMEWORK

2.1 The importance of spin-orbit coupling for spectroscopy

Many spectroscopic properties of solids can be discussed on the basis of their optical conductivity tensor $\boldsymbol{\sigma}(\omega)$, whose shape reflects the symmetry of its crystal structure (Kleiner, 1966). In the case of a magnetic solid, the magnetic ordering reduces its symmetry compared to the nonmagnetic state, because any symmetry operation not only has to be conform with the crystal structure but also has to leave the magnetization $\vec{M}$ unchanged. For cubic systems for example, the effective symmetry is tetragonal, trigonal, or orthorhombic, respectively, depending on whether the magnetization is aligned along the [001], the [111], or the [110] axis (Cracknell, 1969). As a consequence, there are less restrictions for the shape of $\boldsymbol{\sigma}(\omega)$ leading for example, for the first and last cases to:

$$\boldsymbol{\sigma}^{[001]} = \begin{pmatrix} \sigma_{xx} & \sigma_{xy} & 0 \\ -\sigma_{xy} & \sigma_{xx} & 0 \\ 0 & 0 & \sigma_{zz} \end{pmatrix} \quad \text{and}$$

$$\boldsymbol{\sigma}^{[110]} = \begin{pmatrix} \sigma_{xx} & \sigma_{xy} & \sigma_{xz} \\ \sigma_{xy} & \sigma_{xx} & -\sigma_{xz} \\ -\sigma_{xz} & \sigma_{xz} & \sigma_{zz} \end{pmatrix} \qquad (1)$$

instead of the diagonal degenerate form in the case of a nonmagnetic cubic solid.

It is important to note that the reduction in symmetry due to the magnetization that is reflected by the preceding equations occurs only if spin-orbit coupling is present. If one could switch off spin-orbit coupling for a spin-polarized system, its properties would not depend on the orientation of the magnetization anymore, and, for this reason, its symmetry would be that of the corresponding nonmagnetic state. Thus, it is the magnetization together with spin-orbit coupling that leads to a symmetry reduction as compared to the nonmagnetic case. Accordingly, many important magneto-optical phenomena occur only because of the simultaneous presence of magnetic ordering and spin-orbit coupling. For a shape of the optical conductivity tensor $\boldsymbol{\sigma}(\omega)$ according to the upper part of of equation (1) for example, one can trace back the magneto-optical Faraday and Kerr effect in the optical regime to the occurrence of the off-diagonal element σ_{xy}. Expressing the X-ray absorption coefficient in terms of the absorptive parts of the elements of $\boldsymbol{\sigma}(\omega)$, one finds that magnetic circular dichroism, that is, the difference in absorption for left- and right-circularly polarized light, is again due to σ_{xy}. Magnetic linear dichroism (MLD), on the other hand, is caused by the difference in σ_{xx} and σ_{zz}. Similar symmetry considerations have to be made when dealing with photoemission experiments also. To achieve a full understanding of all observed phenomena, not only the spin-orbit coupling but also the influence of the surface on the symmetry of the system has to be accounted for (Feder and Henk, 1996).

The importance of spin-orbit coupling for the spectroscopy of magnetic solids can also be demonstrated in an alternative way by the excitation scheme shown in Figure 1. Here initial

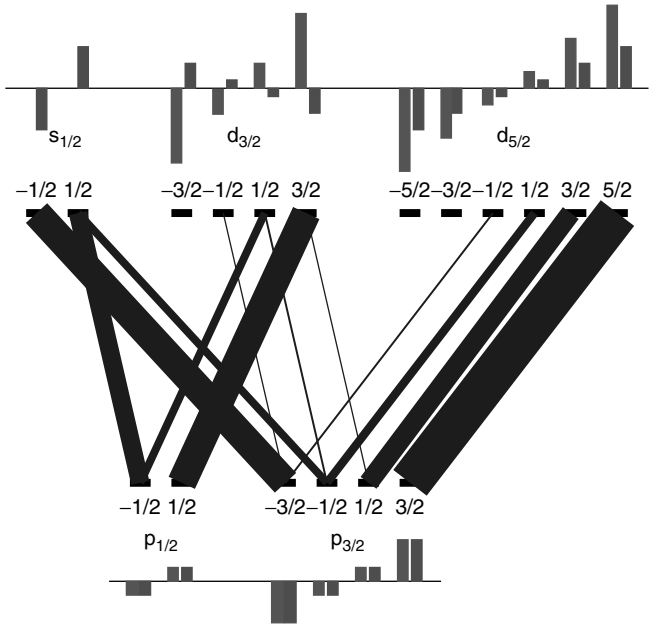

Figure 1. Absorption cross section for left-circularly polarized light represented by the line thickness, for transitions within a system with initial p and final s and d states. The various magnetic sublevels are indexed by the corresponding magnetic quantum number μ. The light and dark bars above and below the excitation scheme represent the expectation values $\langle \chi_\Lambda | \sigma_z | \chi_{\Lambda'} \rangle$ and $\langle \chi_\Lambda | l_z | \chi_{\Lambda'} \rangle$, that is, they are a measure for the spin and orbital magnetic moments, μ_{spin} and μ_{orb}, respectively, of these sublevels.

p and final s and d states that are split owing to the spin-orbit coupling into $j = l \pm 1/2$ levels and resolved according to the magnetic quantum number μ with $\mu = -j, \ldots, +j$ are considered. Using the angular matrix elements for the absorption of left-circularly polarized light (see following text), one arrives at an absorption cross section that strongly depends on the involved initial and final states. In the case of GaAs, one can identify the initial p states with the top of the valence band, while the final s states correspond to the bottom of the conduction band. Because of spin-orbit coupling of the p states, one has only $p_{3/2} \rightarrow s_{1/2}$ transitions at the absorption threshold. Owing to the μ dependence of the absorption cross section, the s states with $\mu = -1/2$ are dominantly populated leading to a spin polarization of the photoelectron current with $P = -50\%$. As long as the energy of the various levels does not depend on the sign of μ, the polarization is just reversed when the helicity of the light is reversed. This observation of spin-polarized photoelectrons from a nonmagnetic sample owing to the use of circularly polarized light is called *Fano effect* (Fano, 1969).

Interchanging the role of initial and final states in Figure 1 and identifying the s states with the 1s core shell and the final states with unoccupied p-like band states of a solid correspond to K-edge X-ray absorption. In this case, one finds that a finite orbital angular momentum is obtained for the final states occupied by absorption of circularly polarized light. Again the sign of the orbital angular momentum is reversed if the helicity is reversed. Shifting the various spin-orbit split levels in Figure 1, one has the excitation scheme for $L_{2,3}$-edge X-ray absorption spectra. Here one finds that the final states carry a spin and an orbital angular momentum that also change their sign upon reversing the helicity of the light. However, if the magnetic ordering destroys the remaining degeneracy with respect to μ, this symmetry disappears. In particular, one finds a magnetic circular dichroism (MCD) that reflects – depending on the involved transitions – the spin and OP of the final states.

These qualitative considerations show that spin-orbit coupling not only influences the spectroscopic properties of solids by its impact on the energy levels but also gives rise to new phenomena. Particularly for magnetic solids, this is the basis for many spectroscopies that allow one to monitor and probe their magnetic properties.

2.2 Electronic structure calculations

From the preceding considerations it is obvious that a full understanding of the spectroscopic properties of magnetic solids on a microscopic level can be achieved only by a description of the underlying electronic structure that accounts for magnetic ordering and spin-orbit coupling at the same time. For this purpose, either a localized or an itinerant point of view is taken depending on which is more appropriate for the system considered.

In the latter case one may assume, in addition, that spin magnetism dominates, implying that spin density functional theory (SDFT) or, in practice, the local spin density approximation (LSDA) supplies a satisfying framework for corresponding electronic structure calculations. To account for relativistic effects, it is quite common to incorporate, as a first step, only the appropriate scalar-relativistic corrections into the radial Kohn–Sham equations (Koelling and Harmon, 1977). These modifications, which represent the Darwin and mass–velocity terms, obviously do not involve the electronic spin. For that reason, they do not affect the symmetry of the system, allowing each subspin system to be treated separately. The spin-orbit coupling term (Rose, 1961):

$$\mathcal{H}_{\text{SOC}} = \frac{\hbar}{4m^2c^2} \frac{1}{r} \frac{\mathrm{d}V}{\mathrm{d}r} \frac{1}{2} \vec{\sigma} \cdot \vec{l} \qquad (2)$$

on the other hand, mixes the two subsystems leading to pronounced changes in the electronic structure.

As a direct consequence, one finds that spin is no more a good quantum number; that is, the expectation value $\langle \psi_{j\vec{k}} | \sigma_z | \psi_{j\vec{k}} \rangle$ for σ_z, with $|\psi_{j\vec{k}}\rangle$ being a Bloch state, is

not restricted to ± 1 but may take any value in between. In particular, the spin character may change continuously from majority to minority or vice versa when going along an electron band $E_{j\vec{k}}$. (An example for this can be found in Figure 8.) Another consequence of spin-orbit coupling is that the orbital angular momentum is no more quenched; that is, the finite expectation value $\langle \psi_{j\vec{k}} | l_z | \psi_{j\vec{k}} \rangle$ leads to a spin-orbit-induced orbital magnetic moment. Finally, it should be noted that the electronic band structure $E_{j\vec{k}}$ depends on the orientation of the magnetization $\vec{M}$ reflecting the magneto-crystalline anisotropy.

Using a conventional band structure scheme that is based on the variational principle, the corresponding basis functions are, in general, calculated on a scalar-relativistic level. Spin-orbit coupling is then accounted for within the variational step; that is, the spin-orbit coupling matrix evaluated using equation (2) and the basis functions are added to the LSDA-based Hamiltonian (Callaway and Wang, 1973). Alternatively, one first solves the LSDA-based band structure problem and then includes the effect of spin-orbit coupling in a second variational step for those states one is interested in (Singh, 1994). Using the Korringa-Kohn-Rostoker (KKR) or multiple-scattering approach instead of a variational method, spin-orbit coupling has to be included when calculating the basis functions (Koelling and Harmon, 1977; MacLaren and Victora, 1994).

All approaches mentioned so far have the common feature that they account for relativistic effects by appropriate corrections to an electronic system dealt on the basis of nonrelativistic SDFT. Accordingly, the underlying two-component basis functions and, with this, all derived electronic properties are classified by the conventional quantum numbers l, m_l and m_s. On the other hand, a scheme that treats spin magnetism and all relativistic effects on the same footing is achieved by starting from the Dirac equation set up within the framework of relativistic SDFT (Rajagopal and Callaway, 1973; MacDonald and Vosko, 1979):

$$\left[\frac{c}{i}\vec{\alpha}\cdot\vec{\nabla} + \frac{c^2}{2}(\beta - I) + V_{\mathrm{H}}(\vec{r}) + \overline{V}_{\mathrm{xc}}(\vec{r}) + \beta\vec{\sigma}\cdot\vec{B}(\vec{r})\right]\phi_i(\vec{r}, E) = E\,\phi_i(\vec{r}, E) \qquad (3)$$

with α_i and β being the standard Dirac matrices and $V_{\mathrm{H}}(\vec{r})$, the Hartree potential. The exchange correlation potential consists of a spin-averaged ($\overline{V}_{\mathrm{xc}}$) and a spin-dependent ($\vec{B}$) part.

Because of the spin-dependent part $\vec{B}$ of the potential, the four-component solutions to equation (3) for an isolated potential well have no unique spin-angular character, but have to be constructed as a superposition (Feder, Rosicky and Ackermann, 1983; Strange, Staunton and Györffy, 1984):

$$\phi_i(\vec{r}, E) = \sum_{\Lambda} \begin{pmatrix} g_{\Lambda i}(r, E)\,\chi_{\Lambda}(\hat{r}) \\ i f_{\Lambda i}(r, E)\,\chi_{-\Lambda}(\hat{r}) \end{pmatrix} \qquad (4)$$

Here $g_\Lambda(r, E)$ and $f_\Lambda(r, E)$ are the major as below and minor radial wave functions, respectively, and $\chi_\Lambda(\hat{r})$ are the spin-angular functions of the relativistic spin-orbit and magnetic quantum numbers κ and μ, respectively, ($\Lambda = (\kappa, \mu)$; $-\Lambda = (-\kappa, \mu)$) (Rose, 1961). Equation (4) implies that the degeneracy of the radial wave functions with respect to the quantum number μ is removed. In addition, for each linearly independent solution i to equation (3) not only a set of radial equations for $g_\Lambda(r, E)$ and $f_\Lambda(r, E)$ has to be solved but instead one also has to deal with an extended set of coupled radial equations depending on the quantum numbers and the geometrical shape of the potential (Huhne *et al.*, 1998). The technical problems caused by basis functions with the form given by equation (4) can be avoided by calculating in a first step the basis functions from equation (3) without the spin-dependent potential $V_{\mathrm{spin}}(\vec{r})$. Using a conventional band structure method this term can then be included in the variational step (Ebert, 1988). As an alternative to this, replacing equations (3–4) by an approximate interpolation scheme, a simpler form of the basis functions could be retained (Ankudinov and Rehr, 1997). In spite of the mentioned technical problems, several band structure schemes have been extended on the basis of equations (3–4) that indeed treat spin magnetism and all relativistic effects on the same level. This applies to several linear methods based on the variational principle (Ebert, 1988; Solovyev *et al.*, 1989; Krutzen and Springelkamp, 1989). For example for the linear muffin-tin orbital (LMTO) method, the Bloch wave functions $\psi_{j\vec{k}}$ can still be written in the standard way:

$$\psi_{j\vec{k}}(\vec{r}, E_{j\vec{k}}) = \sum_i A_i^{j\vec{k}}\phi_{i\nu}(\vec{r}) + B_i^{j\vec{k}}\dot{\phi}_{i\nu}(\vec{r}) \qquad (5)$$

with $\phi_{i\nu}$ and $\dot{\phi}_{i\nu}$ basis functions having the form given by equation (4). The expansion coefficients $A_i^{j\vec{k}}$ and $B_i^{j\vec{k}}$ are determined by the appropriate potential parameters, relativistic LMTO structure constants, and the eigenvectors. In addition, a corresponding extension to the KKR or multiple-scattering approach has been worked out. Again, the electronic Green's function $G(\vec{r}_n, \vec{r}_m, E)$ can be written in the usual way (Ebert, 2000):

$$G(\vec{r}_n, \vec{r}_m, E) = \sum_{\Lambda\Lambda'} Z_\Lambda(\vec{r}_n, E)\tau^{nm}_{\Lambda\Lambda'}(E)Z^{\times}_{\Lambda'}(\vec{r}_m, E) - \sum_{\Lambda} Z_\Lambda(\vec{r}_<, E)J^{\times}_{\Lambda}(\vec{r}_>, E)\delta_{nm} \qquad (6)$$

with $Z_\Lambda(\vec{r}_n, E)$ and $J_\Lambda(\vec{r}_n, E)$ being the solutions to the single-site Dirac equation (3) for site n with their form given by equation (4). The scattering path operator $\tau^{nm}_{\Lambda\Lambda'}(E)$ describes all multiple-scattering events in the system in a self-consistent way.

Compared with variational schemes, the KKR method has a number of appealing features. The calculation of the scattering path operator, that is, solving the band structure problem, can be done in principle for any geometry as, for example, finite, two-dimensional layered or three-dimensional bulk systems. The use of the Dyson equation allows one to deal with complex geometries starting from a simpler reference system as, for example, in the case of clusters deposited on a substrate. Representing the electronic structure in terms of the Green's function also enables the treatment of disordered systems by combining the KKR with the coherent potential approximation (CPA) alloy theory. Finally, the availability of the Green's function makes the KKR method a suitable platform, when dealing with spectroscopic properties.

For many core-level spectroscopies an adequate description of the involved core states that treat exchange splitting and spin-orbit coupling on the same level is indispensable (Mertins *et al*., 2001). This can also be achieved on the basis of the Dirac equation (3) (Ebert, 1989).

Using one of the schemes described in the preceding text to calculate properties that are connected to spin-orbit-induced orbital magnetism, the results are in general too low when compared to experimental data. In addition, one finds that correlation effects are often insufficiently described on the basis of plain LSDA. These problems can in most cases be reduced or removed by applying appropriate corrections to the Hamilton matrix or directly to the Dirac equation (3). This can be done for example, using Brooks' OP scheme (Brooks, 1985) or the LSDA + U method (Anisimov, Aryasetiawan and Lichtenstein, 1997). While the latter approach represents only static correlations, a more accurate treatment of correlation effects is achieved by a combination of LSDA and the dynamical mean field theory (DMFT) (Georges, Kotliar, Krauth and Rozenberg, 1996).

For strongly correlated systems, the various extensions to the LSDA seem to be insufficient and an approach putting strong emphasis on many-body effects is more appropriate. To describe, for example, the pronounced multiplet structure reflected by corresponding core-level spectra of rare earth systems, it is sometimes sufficient to deal with an isolated atom on a Hartree–Fock level (Vogel *et al*., 1991). A simple way to account for the influence of the surrounding on the electronic structure is to include a crystal field having a corresponding symmetry. As an alternative to this configuration interaction (CI), cluster model calculations are done that account for hybridization as well as for electron correlation effects.

2.3 Matrix elements

The various spectroscopies dealt with in the following text have in common that they hinge upon the interaction of electrons and photons. Treating the photon field in a classical way the electron–photon interaction operator is given by

$$X_{\vec{q}\lambda}(\vec{r}) = -\frac{1}{c}\vec{j}_{el} \cdot \hat{a}_\lambda A e^{i\vec{q}\vec{r}} \tag{7}$$

Here the vector potential $\vec{A}_{\vec{q}\lambda}(\vec{r}) = \hat{a}_\lambda A e^{i\vec{q}\vec{r}}$ represents radiation with amplitude A, wave vector $\vec{q}$, and polarization λ, with $\hat{a}_\lambda$ representing the corresponding polarization vector. Adopting a relativistic formulation, the electronic current density operator $\vec{j}_{el} = -ec\vec{\alpha}$ is expressed in terms of the Dirac α matrices.

Investigating electronic transitions on the basis of the description of the electronic structure described in the preceding text, one is led to transition matrix elements of the form

$$M^{\vec{q}\lambda}_{\mathrm{fi}} = \langle \Phi_\mathrm{f} | X_{\vec{q}\lambda} | \Phi_\mathrm{i} \rangle \tag{8}$$

where the initial and final wave functions $\Phi_{\mathrm{i(f)}}$ may stand for itinerant band states or tightly bound core states. Adopting the dipole approximation, the matrix elements connecting states ϕ_Λ with spin-angular character Λ are given by:

$$\begin{aligned} M^{\vec{q}\lambda}_{\Lambda\Lambda'} &= \langle \phi_\Lambda | \vec{\alpha} \cdot \hat{a}_\lambda | \phi_{\Lambda'} \rangle \\ &= i \left[R^1_{\Lambda\Lambda'} A^\lambda_{\Lambda-\Lambda'} - R^2_{\Lambda\Lambda'} A^\lambda_{-\Lambda\Lambda'} \right] \end{aligned} \tag{9}$$

in terms of the radial and angular matrix elements $R^{1(2)}_{\Lambda\Lambda'}$ and $A^\lambda_{\Lambda\Lambda'}$, respectively, with:

$$R^1_{\Lambda\Lambda'} = \int r^2 \, \mathrm{d}r g_\Lambda(r, E) f_{\Lambda'}(r, E') \tag{10}$$

$$R^2_{\Lambda\Lambda'} = \int r^2 \, \mathrm{d}r f_\Lambda(r, E) g_{\Lambda'}(r, E') \tag{11}$$

$$A^\lambda_{\Lambda\Lambda'} = \langle \chi_\Lambda | \vec{\alpha} \cdot \hat{a}_\lambda | \chi_{\Lambda'} \rangle \tag{12}$$

The angular matrix element $A^\lambda_{\Lambda\Lambda'}$ gives rise to the selection rules according to the polarization of the radiation (see Figure 1). The radial matrix elements $R^{1(2)}_{\Lambda\Lambda'}$, on the other hand, depend on the energy owing to the energy dependence of the radial wave functions. In general, the elements $R^{1(2)}_{\Lambda\Lambda'}$ strongly favor transitions with $l \to l' = l + 1$ as compared to those with $l \to l' = l - 1$ (Ebert *et al*., 1996). This, however, does not hold if a Cooper minimum occurs at a certain energy for one of these transitions (Durham, 1984).

Applications using the KKR Green's function method properly account for the energy dependence of the radial matrix elements, as the underlying wave functions $\phi_{\Lambda'}(\vec{r}, E)$ (corresponding to $Z_{\Lambda}(\vec{r}, E)$ and $J_{\Lambda}(\vec{r}, E)$ in equation (6)) are calculated for each energy E. Instead, using a linear band structure method as, for example, the LMTO, the energy dependence is accounted for in an approximate way by using $\phi_{i\nu}(\vec{r})$ and its energy derivative $\dot{\phi}_{i\nu}(\vec{r})$ evaluated at a fixed energy E_ν (see equation (5)). As E_ν can be chosen freely, this is not a severe numerical restriction in practice. However, using the TB formalism, the energy dependence of the radial matrix elements is completely ignored.

3 MAGNETO-OPTICAL PROPERTIES IN THE OPTICAL REGIME

3.1 The optical conductivity tensor and the magneto-optical effects

For many situations, it is adequate to neglect surface effects and to assume that magneto-optical properties reflect the electronic structure of a bulk material. The bridge between both sides is supplied by the dielectric tensor $\boldsymbol{\epsilon}(\omega)$ or, equivalently, the optical conductivity tensor $\boldsymbol{\sigma}(\omega)$, which are linked by the relation $\boldsymbol{\epsilon}(\omega) = 1 + \frac{4\pi i}{\omega}\boldsymbol{\sigma}(\omega)$. An expression for the optical conductivity tensor $\boldsymbol{\sigma}(\omega)$ was derived within the framework of Kubo's linear response formalism (Callaway, 1974):

$$\sigma_{\lambda\lambda'}(\omega) = \frac{ie^2}{m^2\hbar V} \sum_{\substack{j\vec{k}\,\text{occ.} \\ j\vec{k}\,\text{unocc.}}} \frac{1}{\omega_{jj'}} \left[\frac{\Pi^{\lambda}_{j'j}\Pi^{\lambda'}_{jj'}}{\omega - \omega_{jj'} + i/\tau} + \frac{(\Pi^{\lambda}_{j'j}\Pi^{\lambda'}_{jj'})^*}{\omega + \omega_{jj'} + i/\tau} \right] \tag{13}$$

with $\omega_{jj'} = (E_{j\vec{k}} - E_{j'\vec{k}})/\hbar$ and the matrix elements $\Pi^{\lambda}_{jj'} = \langle \Psi_{j\vec{k}} | p_\lambda | \Psi_{j'\vec{k}} \rangle$ of the electronic momentum operator. Here the argument $\vec{k}$ of $\omega_{jj'}$ and $\Pi^{\lambda}_{jj'}$ has been suppressed and $\lambda = \text{x, y, or z}$ denotes one of the Cartesian components. The quantity τ is the relaxation time parameter.

Although equation (13) can be used directly in connection with a nonrelativistic as well as a fully relativistic band structure calculation (Oppeneer and Antonov, 1996), it is advantageous to calculate in a first step only the absorptive parts of the tensor element (Wang and Callaway, 1974). The dispersive parts can then be obtained in a second step by making use of Kramers–Kronig relations (Ebert, 1996b).

The matrix elements $\Pi^{\lambda}_{jj'}$ in equation (13) imply a spatial integration over the whole crystallographic unit cell. Because the square of $\Pi^{\lambda}_{jj'}$ enters the expression for the optical conductivity tensor $\boldsymbol{\sigma}(\omega)$, however, it is not possible to decompose $\boldsymbol{\sigma}(\omega)$ unambiguously into site or component contributions in the case of compounds or multilayer systems. A corresponding decomposition gives rise to cross-term contributions that might be negative or even surpass the site-diagonal contributions (Koenig and Knab, 1990). For multilayer systems, such a decomposition turned out to be very helpful to analyze the rather complex spectra. For this purpose, a so-called layer-resolved optical conductivity tensor $\boldsymbol{\sigma}^{IJ}(\omega)$ was introduced (Perlov and Ebert, 2000) on the basis of equation (13), with I and J numbering the atomic layers within a multilayer. For the absorptive part of the corresponding diagonal tensor element $\sigma^{1\,IJ}_{\lambda\lambda}(\omega)$ one gets, for example, the expression

$$\sigma^{1\,IJ}_{\lambda\lambda}(\omega) = \frac{\pi e^2}{\hbar\omega m^2 V_I} \sum_{\substack{j\vec{k}\,\text{occ.} \\ j\vec{k}\,\text{unocc.}}} \Pi^{I\,\lambda}_{jj'}\,\Pi^{J\,\lambda}_{j'j}\,\delta(\omega - \omega_{jj'}) \tag{14}$$

with the evaluation of the matrix elements $\Pi^{I\,\lambda}_{jj'}$ restricted to layer I with volume V_I. Ignoring the variation of the electric field from layer to layer, a simplification that is in general inherently made when dealing with the optical properties of solids, allows one to introduce the layer-projected optical conductivity:

$$\sigma^{1,I}(\omega) = \sum_{J} \sigma^{1,IJ}(\omega) \tag{15}$$

which can be calculated by making use of Bloch's theorem. This leads to:

$$\sigma^{1\,I}_{\lambda\lambda}(\omega) = \frac{\pi e^2}{\hbar\omega m^2 V_I} \sum_{\substack{j\vec{k}\,\text{occ.} \\ j\vec{k}\,\text{unocc.}}} \Pi^{I\,\lambda}_{jj'}\,\Pi^{\lambda}_{j'j}\,\delta(\omega - \omega_{jj'}) \tag{16}$$

with the conventional matrix elements $\Pi^{\lambda}_{jj'} = \sum_{J\in\text{uc}} \Pi^{J\,\lambda}_{jj'}$ connected with the full unit cell; that is, the summation runs over all sites J within the unit cell. For the special case of a multilayer system, the unit cell is a column of atomic cells representing the stacking sequence of atomic layers. For that reason, the site specific matrix elements $\Pi^{J\,\lambda}_{jj'}$ are representative for the various types of atomic layers.

If the influence of the sample surface has to be accounted for, as for example, in the case of surface layer systems, the preceding expressions for the optical conductivity tensor are of limited use. However, reformulating equation (13) by representing the electronic structure in terms of the Green's function $G(E)$, a very general expression for the spatially resolved optical conductivity $\boldsymbol{\sigma}(\vec{r}, \vec{r}\,', \omega)$ is obtained. For a two-dimensional periodic layered system, the corresponding layer-resolved optical conductivity $\boldsymbol{\sigma}^{IJ}(\omega)$ is given by

(Huhne and Ebert, 1999b):

$$\begin{aligned}
&\sigma^{IJ}_{\lambda\lambda'}(\omega) \\
&\quad = \frac{i\hbar}{\pi^2 A_{WS}\,\mathrm{d}^I}\int_{-\infty}^{E_F}\mathrm{d}E\int_{E_F}^{\infty}\mathrm{d}E'\int_{A^I_{WS}}\mathrm{d}^2r\int_{\text{layer }I}\mathrm{d}r \\
&\qquad \times\int_{\text{layer }J}\mathrm{d}^3r'\frac{\mathrm{Trace}\left\{j_\lambda(\vec{r})\,\Im\,G^+(E')\,j_{\lambda'}(\vec{r}\,')\,\Im\,G^+(E)\right\}}{(E'-E-i\frac{\hbar}{\tau})(\hbar\omega+E-E'+i\frac{\hbar}{\tau})} \\
&\qquad +\frac{\mathrm{Trace}\left\{j_{\lambda'}(\vec{r}\,')\,\Im\,G^+(E')\,j_\lambda(\vec{r})\,\Im\,G^+(E)\right\}}{(E'-E+i\frac{\hbar}{\tau})(\hbar\omega+E'-E+i\frac{\hbar}{\tau})}
\end{aligned} \tag{17}$$

with d^I the thickness of layer I, A^I_{WS} the cross-section area of the corresponding unit cell and $j_{\lambda'}(\vec{r})$ the electronic current density operator.

When discussing magneto-optical phenomena, in general, two special geometric situations are of primary interest. For the Voigt or Cotton–Mouton configuration, the magnetization is aligned perpendicular to the wave vector $\vec{q}$ of the light, while for the Faraday or polar configuration it is parallel or antiparallel to the wave vector. In the case of the later configuration, a linearly polarized light beam that impinges on a magnetized sample will get elliptically polarized upon transmission or reflection. No matter whether the magnetization is present spontaneously or induced by an external magnetic field, these phenomena are called *Faraday* and *Kerr* effect, respectively. In both cases, the polarization ellipsis of the transmitted or reflected, respectively, light is characterized by its ellipticity ϵ and its rotation by the angle θ with respect to the original polarization vector (Reim and Schoenes, 1990). In the case of the Faraday effect, the rotation is a magnetic circular birefringence while the accompanying ellipticity is caused by magnetic circular dichroism. Making use of the connection of the dielectric tensor $\boldsymbol{\epsilon}(\omega)$ and the complex index of refraction $n_{\vec{q}\lambda}(\omega)$, one can express the ellipticity ϵ and rotation angle θ for the Faraday and Kerr effect in terms of the elements of the optical conductivity tensor $\boldsymbol{\sigma}(\omega)$ (Reim and Schoenes, 1990). For the complex Faraday rotation angle $\phi_\mathrm{F} = \theta_\mathrm{F} + i\epsilon_\mathrm{F}$, which combines both quantities, one finds:

$$\phi_\mathrm{F} \simeq \frac{2\pi i d}{c}\,\frac{\sigma_{\mathrm{xy}}}{\sqrt{1-\frac{4\pi i}{\omega}\sigma_{\mathrm{xx}}}} \tag{18}$$

with d the thickness of the sample. Accordingly, one has for the complex Kerr rotation angle $\phi_\mathrm{K} = \theta_\mathrm{K} + i\epsilon_\mathrm{K}$:

$$\phi_\mathrm{K} \simeq \frac{\sigma_{\mathrm{xy}}}{\sigma_{\mathrm{xx}}\sqrt{1-\frac{4\pi i}{\omega}\sigma_{\mathrm{xx}}}} \tag{19}$$

The expressions given in the preceding text for the Faraday and Kerr rotations ϕ_F and ϕ_K, respectively, are sufficiently accurate for angles up to several degrees. For the large rotation angles encountered sometimes in actinide compounds or the giant rotation angles up to 90 °C found for some Ce compounds (Yaresko *et al.*, 1996), one has to use the corresponding exact expressions. Another restriction for the use of equations (18 and 19) is connected with the symmetry of the investigated system. In deriving these equations, a shape of the optical conductivity tensor $\boldsymbol{\sigma}(\omega)$ has been assumed that corresponds to a system with its magnetization aligned to, at least, a threefold rotation axis that in turn is parallel to the light beam. This holds, for example, for cubic systems with the magnetization along one of the cubic axes or the [111] direction, as well as for a tetragonal or hexagonal system with the magnetization along the c axis. For systems with lower symmetry, the expressions for the Faraday and Kerr rotation can still be derived straightforwardly by solving the corresponding Fresnel equation for an anisotropic material. In this case, one will have a superposition of magneto-optical effects and natural birefringence.

Equations (18) and (19) have been derived for a homogeneous magneto-optical medium. An extension to inhomogeneous, that is, for example layered, media is straightforward if the layer thicknesses are relatively large. For thin magnetic surface films, however, the spatial variation of the optical conductivity has to be accounted for. The layer-resolved optical conductivity mentioned in the preceding text allows one to set up and solve the corresponding Maxwell equations for an inhomogeneous system (Huhne and Ebert, 2002). Various techniques to solve these equations have been developed and described in the literature (Huhne and Ebert, 2002; Vernes, Szunyogh and Weinberger, 2002).

Finally, it should be pointed out that equations (18) and (19) reflect the fact that (for the geometries considered in the preceding text) the Kerr effect occurs only for a nonvanishing off-diagonal element $\sigma_{xy}(\omega)$ of the conductivity tensor $\boldsymbol{\sigma}(\omega)$. Expressing $\boldsymbol{\sigma}(\omega)$ with respect to left (+) and right (−) circular and z-linear polarization of the light, one has the relationship $\sigma_\pm(\omega) = \sigma_{xx}(\omega) \mp i\sigma_{xy}(\omega)$. As demonstrated by several authors, $\sigma_+(\omega)$ and $\sigma_-(\omega)$ differ only if spin-orbit coupling and exchange splitting are simultaneously present (Erskine and Stern, 1973; Reim and Schoenes, 1990). This situation is therefore the source for the Kerr effect normally observed in the regime of conventional optics and also for the circular magnetic dichroism in X-ray absorption considered in the following text.

3.2 Magneto-optical properties of bulk materials

The formalism sketched in the preceding text was applied successfully for the first time at the beginning of the 1990s for a calculation of magneto-optical spectra (Oppeneer, Sticht

and Herman, 1991; Oppeneer, Maurer, Sticht and Kübler, 1992). By performing model calculations, with the strength of the spin-orbit coupling ξ and the exchange splitting ΔE_{xc} manipulated, one could demonstrate that the Kerr rotation is nearly proportional to ξ and varies monotonously with ΔE_{xc} (Oppeneer, Maurer, Sticht and Kübler, 1992; Ebert, Freyer, Vernes and Guo, 1996). In particular, for compounds like $CoPt_3$ it could be shown that a normally nonmagnetic component can have a large impact on the Kerr rotation if it possess a large spin-orbit coupling (Weller *et al.*, 1992).

In spite of the connection of the Kerr effect with the spin-orbit coupling and the exchange splitting demonstrated by these model calculations as well as analytical considerations (Erskine and Stern, 1973; Reim and Schoenes, 1990), there is no simple relationship between the Kerr rotation and ellipticity or, equivalently, the $\sigma_{xy}(\omega)$ spectra and the spin and orbital magnetic moments of the investigated solid. However, in analogy to the *f*-sum rule (Wallis and Balkanski, 1986), which relates the total number of electrons in the volume to the integral of the absorptive part of the diagonal optical conductivity $\sigma_{xx}(\omega)$ with respect to the frequency ω, a corresponding sum rule for the off-diagonal element $\sigma_{xy}(\omega)$ could be derived (Kunes and Oppeneer, 2000). Integrating the imaginary part of $\sigma_{xy}(\omega)$ with respect to the frequency ω leads to the total orbital magnetic moment in the volume and an additional term. In contrast to this, the sum rules dealing with the magnetic circular dichroism in X-ray absorption (see following text) imply the restriction to a specific absorption edge and, for that reason, give access to the spin and orbital magnetic moments in an angular momentum- and element-resolved way.

The aforementioned study on pure 3d ferromagnets was followed by a large number of theoretical investigations on a wide range of compounds (Ebert, 1996b; Antonov, Yaresko, Perlov and Nemoshkalenko, 1999). A comparison of theoretical spectra based on different approaches shows that inclusion of the spin-orbit coupling as a perturbation within a scalar-relativistic calculation is well justified in most cases.

When compared to the experimental spectra, a satisfying agreement is found in general for transition metal systems. Figure 2 shows as an example the Kerr rotation and ellipticity spectra for the Heusler alloys NiMnSb, PdMnSb, and PtMnSb, which have the C_{1b} structure. Previous band structure calculations revealed their half-metallic behavior, which was made responsible for the extraordinary Kerr rotation of PtMnSb (de Groot, Mueller, van Engen and Buschow, 1983). Other authors ascribed the high Kerr angle to a low plasma frequency (Feil and Haas, 1987) or to scalar-relativistic effects (Wijngaard, Haas and de Groot, 1989). However, the calculation of the spectra shown in Figure 2 demonstrated that a combination of various favorable properties of the band structure of PtMnSb – in particular the mentioned

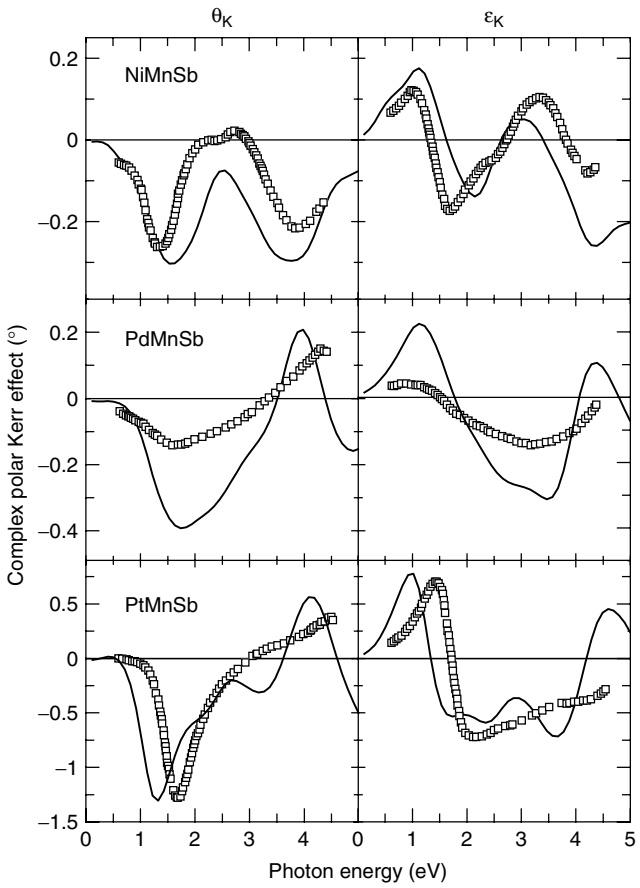

Figure 2. Experimental Kerr rotation and ellipticity spectra of NiMnSb, PdMnSb, and PtMnSb (van Engen, 1983) together with the corresponding theoretical spectra obtained using the relativistic LMTO method (Oppeneer and Antonov, 1996). (Reproduced from Oppeneer, P., *et al.*, 1996, with permission from Springer-Verlag GmbH. © 1996.)

half-metallic behavior and the low plasma frequency – is responsible for its large Kerr rotation.

The examples shown in Figure 2 demonstrate that calculated Kerr spectra may deviate in some cases in a significant way from corresponding experimental data. This is often caused by problems with the sample preparation, as could be convincingly demonstrated, for example for the compounds FeCo and FePt (Weller, 1996). On the other hand, one might ascribe deviations to the neglect of so-called local-field effects when using equation (13) directly. These effects stem from the fact that the actual electric field that acts on an electron differs from the external electric field associated with the light owing to induced charge fluctuations that, in principle, can be accounted for by a self-consistent field scheme (Wallis and Balkanski, 1986). For transition metals, these effects are generally assumed to be negligible. Correlation effects, that are not accounted for within plain SDFT seem to be more important. In fact, the use of Brooks' OP formalism or of

the local density approximation (LDA) + U led in the case of actinide systems to a much better agreement with experiment (Antonov *et al*., 1999). This also applies to calculations for transition metal systems based on the LSDA + DMFT scheme (Perlov, Chadov and Ebert, 2003).

3.3 Magneto-optical properties of layered systems

Most of the experimental as well as theoretical studies on the magneto-optical properties of transition metal systems were motivated by their application in sensor and storage technology (Kryder, 1985). This applies in particular for the investigations on multilayers. These systems allow to some extent the optimization of Kerr rotation spectra with regard to the position and height of prominent peaks by a suitable combination of atomic layers and choice of their thickness. This is demonstrated in Figure 3, which shows Kerr rotation and ellipticity spectra for the multilayer system 6Co/*m*Cu with the thickness *m* of the Co layers varied between 3 and 9 atomic layers (Uba *et al*., 1997). As mentioned in the preceding text, one notes that the peak positions in the theoretical spectra are somewhat shifted as compared to the experimental ones because the local-field and correlation effects are neglected. The various features of the Kerr rotation and ellipticity spectra and their variation with the thickness of the Cu layers, however, are well described by the calculations. This implies, in particular, that imperfections at the Co/Cu interface have only a minor influence on the experimental spectra.

Extensive studies have also been made on the multilayer systems *n*Co/*m*Pd and *n*Co/*m*Pt (Uba *et al*., 1995; Zeper, 1991; Bertero and Sinclair, 1995; Daalderop, 1991) because here the ferromagnetic component Co is combined with an element having a stronger spin-orbit coupling. In addition, Pd and Pt show a pronounced polarizability leading to an induced spin magnetic moment in the order of 0.2 μ_B at the interface (Schütz *et al*., 1993). Furthermore, the high spin-orbit coupling of Pd and Pt is one of the main reasons for the pronounced out-of-plane magnetic anisotropy of these Co-based multilayer systems.

Figure 3 suggests that the calculation of the magneto-optical spectra of multilayer systems should lead, in general, to rather reliable results. On the other hand, it is obviously quite hard or impossible to explain the various spectral features and their variation with the multilayer composition on the basis of such calculations. This severe problem could be reduced to some extent by the introduction of the layer-resolved optical conductivity (Huhne and Ebert, 1999a). The first application of this concept to bcc Fe demonstrated that the contribution of the neighboring atomic layers J to the optical response of an atomic layer I drops off very rapidly with the distance $|I - J|$ between the layers. In particular, it was found that the diagonal tensor element $\sigma_{xx}^{IJ}(\omega)$ is by far dominated by the layer-diagonal term ($I = J$), while for the off-diagonal tensor element $\sigma_{xy}^{IJ}(\omega)$ the contribution from neighboring layers ($|I - J| = 1$) is of the same order of magnitude as the layer-diagonal term ($I = J$). As a consequence, it turned out that it is, in general, sufficient to consider contributions from neighboring layers with $|I - J| = 3$–4 when constructing

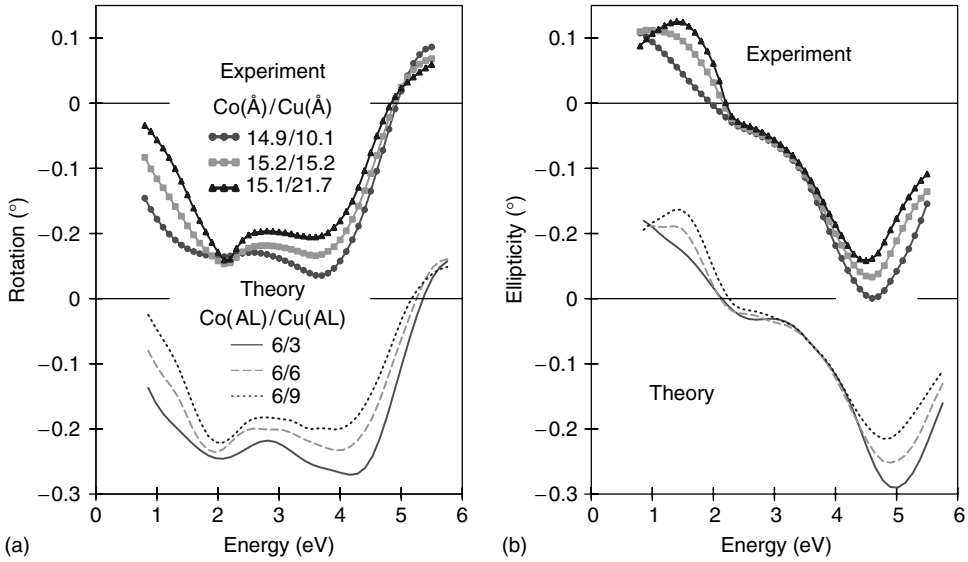

Figure 3. Experimental polar Kerr rotation (a) and ellipticity (b) spectra of Co/Cu multilayer systems. Co and Cu sublayer thicknesses are given in the key in units of Å and atomic layers (AL), respectively. (Reproduced from S. Uba *et al*., 1997, with permission from IOP Publishing Ltd. © 1997.)

the layer-projected optical conductivities $\sigma^I_{xx}(\omega)$ and $\sigma^I_{xy}(\omega)$ for layer I. Corresponding results for the absorptive part of the off-diagonal tensor element $\sigma^I_{xy}(\omega)$ of the multilayer system Co_9/Pd_9 are shown in Figure 4 for the inequivalent layers $I = 1$–10. For the innermost ($I = 1$) of the nine Co layers, one finds that $\sigma^{2,I}_{xy}(\omega)$ is nearly identical to that of pure fcc Co. This reflects the rapid decay of $\sigma^{IJ}_{xy}(\omega)$ with the layer distance $|I - J|$ and implies that the inner Co layers behave essentially like bulk Co concerning their magneto-optical response. Apparently, approaching the Co/Pd interface, $\sigma^{2,I}_{xy}(\omega)$ is more and more modified leading to an appreciable distortion for the spectrum of the Co interface layer ($I = 5$). As mentioned in the preceding text, there is an appreciable moment induced for the Pd layers next to the interface (see the numbers following the layer indices in Figure 4) that rapidly drops with the distance from the interface. The induced moments are reflected by an appreciable nonzero layer-projected off-diagonal tensor element $\sigma^{2,I}_{xy}$ that is most pronounced for the Pd layers close to the interface ($I = 6, 7$) and then decreases very rapidly. For the innermost Pd layer ($I = 10$) $\sigma^{2,I}_{xy}(\omega)$ is close to zero; that is, again one has nearly the magneto-optical behavior of nonmagnetic bulk Pd.

The results shown in Figure 4 imply that for most multilayer systems with relatively large thicknesses of the subsystems one may expect a pronounced variation of the local magneto-optical response only within 3–4 layers next to the interfaces, while the inner regimes should show a bulklike behavior. This property has been exploited with success to construct the magneto-optical response of multilayer systems with large subsystem thicknesses from the layer-projected optical conductivity tensor $\boldsymbol{\sigma}^I(\omega)$ calculated for a multilayer system with the same composition but smaller subsystem thicknesses (Baukasten or modular principle) (Perlov and Ebert, 2000).

The results in Figure 4 also imply that for increasing subsystem thicknesses the influence of the interface regime on the magneto-optical response of the whole layer system will diminish rapidly. As a consequence, representing the subsystems by the optical conductivity of the corresponding bulk material together with a treatment of the whole system by means of classical optics is well justified (Heavens, 1991). This approach has also been used when dealing with magnetic surface layers with a thickness of 20 Å or more on top of a nonmagnetic substrate. For this peculiar situation, one may write for the complex Kerr rotation

$$\phi_K = i\frac{4\pi d}{\lambda}\frac{\sigma_{xy}}{\sigma^{sub}_{xx}} \tag{20}$$

where λ is the wavelength of the radiation and σ^{sub}_{xx} is the diagonal optical conductivity of the substrate (Katayama *et al*., 1988; Reim and Weller, 1989). Equation (20) implies that one can get a resonance-like enhancement of ϕ_K if a suitable substrate is chosen. This holds, for example for Fe films deposited on top of a Cu, Ag, or Au substrate (Katayama *et al*., 1988; Suzuki *et al*., 1992; Suzuki *et al*., 1993) for which σ^{sub}_{xx} is rather small in the vicinity of the plasma edge of the noble metal. In fact, a very satisfying description of available experimental data has been achieved on the basis of equation (20). For thin magnetic films, however, this equation is no more applicable due to the occurrence of quantum confinement effects (Suzuki *et al*., 1992; Bennett, Schwarzacher and Egelhoff, 1990; Carl and Weller, 1995). In particular, it does not describe the oscillations of the Kerr rotation found as a function of the thickness of the magnetic film (Geerts *et al*., 1994) or of a capping nonmagnetic film (Suzuki *et al*., 1998). An explanation for the oscillations observed for the system Au(001)/*n*Fe/*m*Au could be given by a treatment of quantum confinement effects in

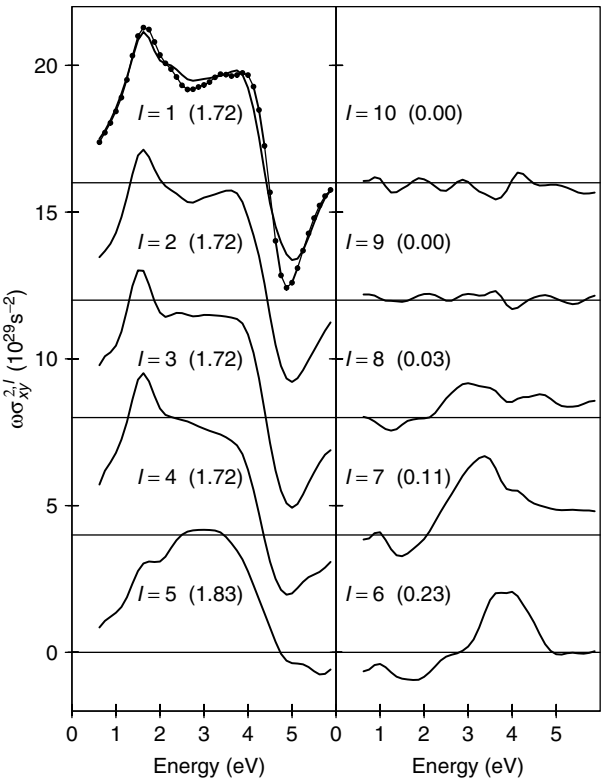

Figure 4. Absorptive part of the off-diagonal layer-projected optical conductivity tensor elements $\sigma^{2,I}_{xy}(\omega)$ for the 10 nonequivalent atomic layers in the multilayer system 9Co/9Pd. The layer index $I = 1$ denotes the innermost Co layer, while $I = 5$ labels the Co layer at the Co/Pd interface. Accordingly $I = 6$ and 10 are the interface and central Pd layers. The numbers accompanying the layer index give the corresponding spin magnetic moments per atom in Bohr magnetons μ_B. The results of bulk calculations for fcc Co are shown by a marked line (Perlov and Ebert, 2000). (Reproduced from Perlov *et al*., 2000, with permission from EDP Sciences. © 2000.)

analogy to the approach used when dealing with the interlayer exchange coupling. This way, the wavelengths of the oscillations were traced back to the bulk electronic structure of the magnetic (Fe) and capping (Au) film material. Calculations of the layer-resolved optical conductivity $\sigma^{IJ}(\omega)$ of Au(001)/nFe/mAu supplied the basis to set up and solve the corresponding inhomogeneous Maxwell equations (Huhne and Ebert, 2002). This approach allowed not only the calculation of the Kerr rotation spectra as a function of the layer thickness n and m, but also the investigation of the distribution of the current density induced by the electromagnetic radiation in the region near the surface. Similar investigations have also been made for the system Pt(111)/nCo (Vernes, Szunyogh and Weinberger, 2002).

4 X-RAY ABSORPTION SPECTROSCOPY

4.1 Absorption coefficient, magnetic dichroism, and sum rules

The absorption coefficient $\mu^{\vec{q}\lambda}(\omega)$ of a sample for radiation of energy $\hbar\omega$, wave vector $\vec{q}$, and polarization λ is determined by its complex index of refraction $n_{\vec{q}\lambda}$. Expressing $n_{\vec{q}\lambda}$ by means of the dielectric function $\epsilon_{\vec{q}\lambda}$ and making use of the relation $\boldsymbol{\epsilon}(\omega) = 1 + \frac{4\pi i}{\omega}\boldsymbol{\sigma}(\omega)$, one can express $\mu^{\vec{q}\lambda}(\omega)$ for the X-ray regime in terms of the absorptive part of the corresponding scalar optical conductivity $\sigma_{\vec{q}\lambda}(\omega)$:

$$\mu^{\vec{q}\lambda}(\omega) = \frac{4\pi}{c}\sigma^{1}_{\vec{q}\lambda}(\omega) \tag{21}$$

Accordingly, using either equation (13) or Fermi's golden rule, $\mu^{\vec{q}\lambda}(\omega)$ can be obtained from:

$$\mu^{\vec{q}\lambda}(\omega) = \frac{\pi c^2}{\hbar\omega m V A^2} \sum_{i\ \mathrm{occ.}} \sum_{f\ \mathrm{unocc.}} |\langle\Psi_f|X_{\vec{q}\lambda}|\Phi_i\rangle|^2 \times\delta(\hbar\omega - E_f + E_i) \tag{22}$$

where A specifies the amplitude of the radiation field according to equation (7).

When studying a specific absorption edge, the summation over the initial states $|\Phi_i\rangle$ can be restricted to the corresponding core shell. On the other hand, the final states $|\Psi_f\rangle$ can be represented by Bloch wave functions $\Psi_{j\vec{k}}$ when dealing with an ordered solid. A more general expression is obtained by representing the final states in terms of the Green's function $G(E)$ to get the form (Shaich, 1984):

$$\mu^{\vec{q}\lambda}(\omega) \propto \sum_{i\ \mathrm{occ.}} \langle\Phi_i|X^{\times}_{\vec{q}\lambda}\,\Im G(E_i + \hbar\omega)\,X_{\vec{q}\lambda}|\Phi_i\rangle \times\theta(E_i + \hbar\omega - E_{\mathrm{F}}) \tag{23}$$

This expression can be evaluated by making use of multiple-scattering theory to determine $G(E)$ (see equation (6)). Accordingly, equation (23) can be applied to arbitrary systems and is the basis for dealing not only with near-edge spectra but also with conventional (Rehr and Albers, 2000) as well as magnetic (Ebert, Popescu and Ahlers, 1999) extended X-ray absorption fine structure (EXAFS). In addition, it supplies an appropriate basis for including many-body effects (Schwitalla and Ebert, 1998).

In the case of rare earth systems, the preceding approach is often inadequate because of the formation of a ground-state electronic configuration according to Hund's rule. Restricting to a free-atom description one gets the corresponding absorption coefficient by considering all transitions from a single ground-state level $|J\,M_J^k\rangle$ to all final states $|J'\,M_J^k + q\rangle$ by absorption of light with polarization λ (Goedkoop *et al.*, 1988):

$$\mu_J^{\lambda k}(\omega) = \sum_{J'} \mu_{JJ'}^{\lambda k}(\omega) = \sum_k \left| \begin{pmatrix} J' & 1 & J \\ -(M_J^k + \lambda) & \lambda & M_J^k \end{pmatrix} \right|^2 \mu_k(\omega) \tag{24}$$

Here $(\ldots)$ is a Wigner 3j symbol and the μ_k are the partial absorption coefficients for the three possible values of $k = \Delta J = -1, 0, +1$.

For a nonmagnetic system, it can be shown that the absorption coefficient $\mu^{\vec{q}\lambda}$ evaluated on the basis of equation (22) or (23) can be written as a sum over partial angular momentum–resolved density of states (DOS) functions $n_\kappa(E)$ weighted by the corresponding absorption cross section $W_{n'\kappa'\to n\kappa}(E)$ (Mattheiss and Dietz, 1980). If an exchange splitting is present in addition to spin-orbit coupling, the degeneracy of the magnetic sublevels is removed (see Figure 1) and magnetic dichroism occurs. Alternatively, this can be demonstrated by considering an exchange-split system with spin-orbit coupling treated as a perturbation. Ignoring the energy and spin dependence of the cross section, the absorption coefficient for the K edge for left- (or right-) circularly polarized light is given by $W_{1s\to np}\sum_{m_s} n_{l=1,m_l,m_s}(E)$ with $m_l = +1(-1)$, where $n_{lm_lm_s}$ is the (l, m_l, m_s)-resolved DOS for p states. The corresponding magnetic dichroic signal $\Delta\mu_{\mathrm{K}} = \mu_{\mathrm{K}}^{+} - \mu_{\mathrm{K}}^{-}$ is therefore given by $W_{1s\to np}\sum_{m_s}(n_{1,+1,m_s}(E) - n_{1,-1,m_s}(E))$. From this expression, it is obvious that $\Delta\mu_{\mathrm{K}}$ vanishes if there is no exchange splitting or if there is no spin-orbit coupling. In addition, one can identify $\Delta\mu_{\mathrm{K}}$ – apart from the cross section – with the orbital polarization $\sum_{m_l}\sum_{m_s} m_l n_{lm_lm_s}(E)$ of the p states. Integrating the dichroic signal over the unoccupied regime of the np shell, one therefore gets a measure for the orbital magnetic moment connected with the p holes, or – by reversing the sign – of

the p electrons. This simple interpretation of the dichroic signal for initial states with s character (e.g., K or L_1 edges) can be expressed by the sum rule (Igarashi and Hirai, 1994):

$$\frac{\int \Delta\mu_{\mathrm{K}} / E \, \mathrm{d}E}{\int \overline{\mu}_{\mathrm{K}} / E \, \mathrm{d}E} = \frac{3}{N_{\mathrm{hp}}} \langle l_{\mathrm{z\,p}} \rangle \tag{25}$$

Here N_{hp} is the number of p holes and $\langle l_z \rangle_{\mathrm{p}}$ is the orbital angular momentum for the p electrons. The integration of the polarization-averaged absorption and dichroic spectra $\overline{\mu}_{\mathrm{K}}(E)$ and $\Delta\mu_{\mathrm{K}}(E)$, respectively, has to be extended from the absorption edge over all unoccupied states of the np shell.

Considerations similar to those presented in the preceding text for the K edge were first made for the $M_{2,3}$ edge of Ni (Erskine and Stern, 1975). Accounting for spin-orbit coupling only for the initial 3p core states and for exchange splitting only for the final 3d states, a relative intensity of the white line peaks at the M_2 and M_3 edges (branching ratio) of 1:2 is expected. For the corresponding circular dichroic signal $\Delta\mu_{\mathrm{M}_{2,3}}$ a ratio of $+1{:}-1$ should occur, with $\Delta\mu_{\mathrm{M}_{2,3}}$ reflecting the spin polarization of the 3d states. Extending the model by accounting, additionally, for the spin-orbit coupling for the final d-like states (Smith, Chen, Sette and Mattheis, 1991; Stöhr, 1999), these ratios deviate from the ideal values. In particular, $\Delta\mu_{\mathrm{M}_{2,3}}$ is now determined by the spin and orbital polarization and by an additional term connected with the magnetic dipole operator $T_{\mathrm{z}} = \frac{1}{2}\big(\vec{\sigma} - 3\hat{\vec{r}}(\hat{\vec{r}} \cdot \vec{\sigma})\big)_{\mathrm{z}}$. The corresponding sum rules for initial states with p character (e.g., $L_{2,3}$ or $M_{2,3}$ edges) are given by (Thole, Carra, Sette and van der Laan, 1992; Carra, Thole, Altarelli and Wang, 1993):

$$\int \left(\Delta\mu_{\mathrm{L}_3} - 2\Delta\mu_{\mathrm{L}_2}\right) \mathrm{d}E = \frac{N}{3N_{\mathrm{hd}}} \left(\langle\sigma_{\mathrm{z}}\rangle + 7\langle T_{\mathrm{z}}\rangle\right) \tag{26}$$

$$\int \left(\Delta\mu_{\mathrm{L}_3} + \Delta\mu_{\mathrm{L}_2}\right) \mathrm{d}E = \frac{N}{2N_{\mathrm{hd}}} \langle l_{\mathrm{z}}\rangle \tag{27}$$

where

$$N = \int \sum_{\lambda=\pm\mathrm{z}} (\mu^{\lambda}_{\mathrm{L}_2} + \mu^{\lambda}_{\mathrm{L}_3}) \, \mathrm{d}E \tag{28}$$

is the polarization-averaged absorption spectrum and N_{hd} is the number of d holes.

The various sum rules obviously supply a formal basis to deduce the spin and orbital magnetic moments from experimental spectra in an element specific way. For transition metal systems for example, the $L_{2,3}$-edge spectra give direct information on the d electrons, which are of central importance for their magnetic properties. Unfortunately, there are a number of problems when applying the sum rules to experimental data. The most obvious are that the number of holes N_{hd} is in general not known, the absorption spectra $\mu^{+(-)}$ have to be separated from the background, and the upper limit for the energy integration has to be fixed.

Originally, the sum rules have been derived on the basis of a localized description for the electronic structure. However, it could be shown that it is also possible to derive them adopting an itinerant description (Ankudinov and Rehr, 1995; Benoist, Carra and Andersen, 2000). Nevertheless, one has to keep in mind that a number of assumptions were made for their derivation. Corresponding test calculations demonstrated that these assumptions are reasonably well justified for many situations (Wu, Wang and Freeman, 1993; Ebert, 1996b). These calculations, in particular, showed that the sum rules also hold in their differential or energy-resolved form that is obtained by dropping the energy integration for the dichroic spectrum $\Delta\mu$ and replacing the expectation values by the corresponding polarization function, that is, replacing, for example, the spin moment $\langle\sigma_z\rangle$ by the spin polarization $\frac{\mathrm{d}}{\mathrm{d}E}\langle\sigma_z\rangle$ that corresponds to the difference of the DOS curves for spin up and down. Finally, it has to be noted that the applicability of the sum rules does not depend on whether the magnetic moment of the absorbing atom is spontaneously formed or whether it is induced via hybridization by neighboring magnetic atoms. This also applies for a magnetic moment that is induced by an external magnetic field. In this case, the sum rules give access to the component-projected spin and orbital magnetic susceptibilities (Ebert and Mankovsky, 2003).

While the sum rules allow one to determine the orbital magnetic moment separately, this is obviously not true for the spin magnetic moment that is connected with the term $\langle T_z\rangle$. The latter term, which has a counterpart in the hyperfine field and the magnetic form factor used when dealing with neutron scattering, can be seen as a measure for the angular variation of the spin magnetization. It is nonzero only for systems having a symmetry that is lower than cubic. For systems with a cubic lattice, $\langle T_z\rangle$ is therefore only nonzero due to the presence of spin-orbit coupling. Accordingly, it should be quite small in that case unless one is dealing with elements with a large atomic number. However, for low-dimensional magnetic systems such as multilayers (Guo, Ebert, Temmerman and Durham, 1994), films, wires (Komelj, Ederer, Davenport and Fähnle, 2002), or clusters (Gambardella *et al.*, 2003) $\langle T_z\rangle$ may be quite large and nonnegligible as compared to $\langle\sigma_z\rangle$.

4.2 Magnetic circular dichroism in X-ray absorption

Owing to technical reasons, the first successful experimental investigations on the XMCD have been made in the hard

X-ray regime. The measurements at the K edge of bcc Fe (Schütz *et al*., 1987) were soon followed by experiments at the $L_{2,3}$ edges of 5d transition metals dissolved substitutionally in bcc Fe (Wienke, Schütz and Ebert, 1991). Owing to the dipole selection rules and the l dependence of the X-ray absorption cross section, the corresponding spectra are dominated by p–d transitions. The strong spin-orbit splitting of the involved initial states, together with the appreciable exchange splitting of the final states – induced by the ferromagnetic host – leads to a relative XMCD signal of up to 20%. These spectra could be reproduced in a very satisfying way by corresponding calculations done on the basis of relativistic multiple-scattering theory (Ebert, 1996b). Use of the sum rules (26) to (27) allowed one to deduce from the experimental XMCD spectra $\Delta\mu_{L_{2,3}}$ the spin and orbital magnetic moments that are induced on the impurity atoms. As the XMCD probes the expectation value of the magnetic moment of the absorbing atom, $\langle\mu\rangle$, not only the magnitude of the induced magnetic moments but also their relative orientation with respect to that of the Fe host could be determined. Obviously, the results given in Figure 5 are in reasonable agreement with corresponding theoretical work (Kornherr, 1997), which allows a more detailed discussion of the data. In particular, theory allows one to ascribe the variation of the spin magnetic moment with the atomic number Z of the impurity atom to the relative position of its d level with respect to the exchange-split d levels of the host. The variation of the orbital magnetic moment, on the other hand, can be explained by treating spin-orbit coupling as a perturbation leading to a direct interrelation with the partial spin-resolved DOS of the impurity atom at the Fermi level (Popescu, Ebert, Nonas and Dederichs, 2001). The magnetic moments deduced from the XMCD spectra are obviously also in reasonable accordance with results of neutron-scattering experiments that, however, do not allow a simple decomposition of the moment into spin and orbital parts. Such a decomposition was possible in the past only by simulations of magnetic neutron-scattering form factors or indirectly on the basis of NMR data (Kawakami, Enokiya and Okamoto, 1985).

Figure 5 demonstrates that the XMCD supplies element-specific information because of the local nature of the involved initial core states. This outstanding feature that has been exploited in many subsequent investigations allowed the probing of the induced magnetic moment of an otherwise nonmagnetic impurity atom. Similar work has also been done on compounds, disordered alloys, and multilayer systems.

Measurements at the $L_{2,3}$ edges of 3d transition metals (Chen, Sette, Ma and Modesti, 1990) opened the way to study the magnetic properties of these important elements in a rather direct and detailed way. The large XMCD signal found normally in experiment can in general be described fairly well on the basis of an itinerant description of the underlying electronic structure. Nevertheless, there are often features in the experimental spectra that cannot be accounted for on the basis of plain LSDA and therefore require extensions to this.

Use of time dependent local density approximation (TDLDA) for example, allowed one to account for dynamical screening effects leading to an improved agreement of theory and experiment concerning the so-called $L_{2,3}$-edge branching ratio in the case of 3d transition metals (Schwitalla and Ebert, 1998; Ankudinov, Nesvizhskii and

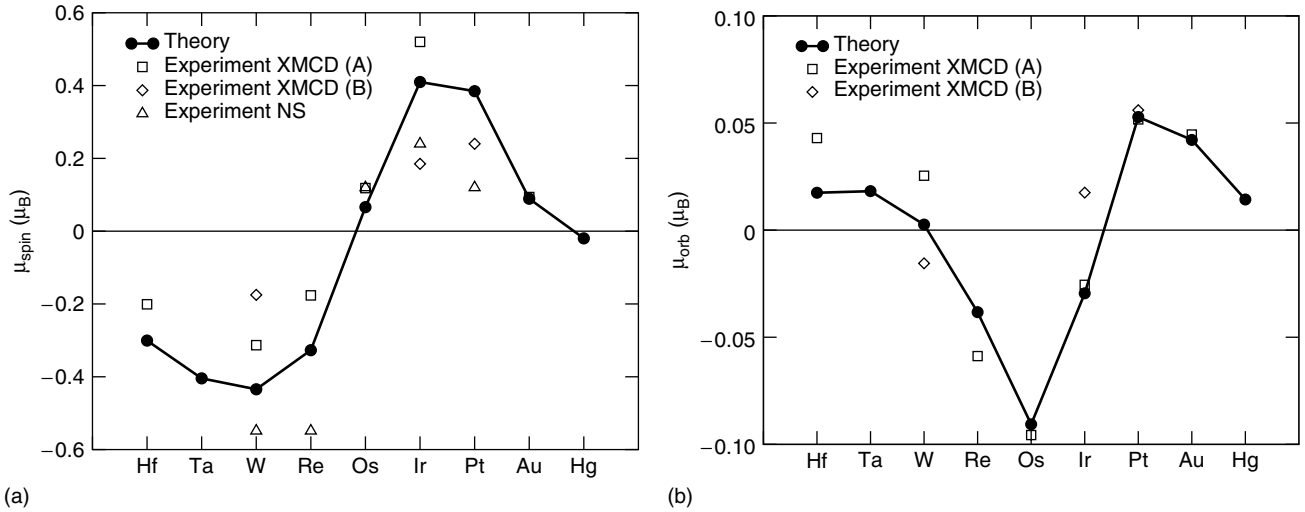

Figure 5. Induced spin (a) and orbital (b) magnetic moment, μ_{spin} and μ_{orb}, respectively, of 5d-transition metal impurities in Fe as deduced from experimental XMCD spectra at the $L_{2,3}$ edges (A: (Wienke, Schütz and Ebert, 1991; Schütz, Knülle and Ebert, 1993), B: (Wilhelm *et al*., 2001)) and neutron-scattering measurements (NS) (Campbell, 1966) and obtained from SPR-KKR band structure calculations (Kornherr, 1997).

Rehr, 2003). This approach led to corresponding changes for the XMCD spectra (Schwitalla, 1997) also. Using plain LSDA to calculate spin-orbit-induced ground-state properties as for example, orbital magnetic moments often gives results that are too small when compared with experiment. An improved description of correlation effects based on Brooks' OP scheme reduces or removes this problem in many cases. Using this approach while calculating XMCD spectra leads to changes with respect to plain-LSDA results that are in full accordance with the corresponding change in the orbital magnetic moment and the sum rules (Ebert, 1996a; Guo, 1997).

Application of the LSDA + U scheme also led in many cases to appreciable improvements compared to work based on plain LSDA. An interesting example for this is a study of the XMCD spectra of Fe in Fe_3O_4 (Antonov, Harmon and Yaresko, 2003) that is ferrimagnetically ordered below ≈850 K. The tetrahedral lattice sites (A) in the inverse spinel structure are occupied by Fe^{3+} ions, whereas the octahedral lattice sites (B) are occupied alternately by equal numbers of Fe^{2+} and Fe^{3+} ions. In contrast to this experimental finding, LSDA-based calculations lead to a half-metallic ferrimagnet, with the Fermi level crossed only by the majority spin bands and equivalent Fe ions on all B sites. The corresponding XMCD spectra for the $L_{2,3}$ edges of the inequivalent A and B sites are shown in Figure 6(a). Obviously, the ferrimagnetic order of the system is reflected by the different sign of the XMCD spectra for the two sites. The resulting total XMCD

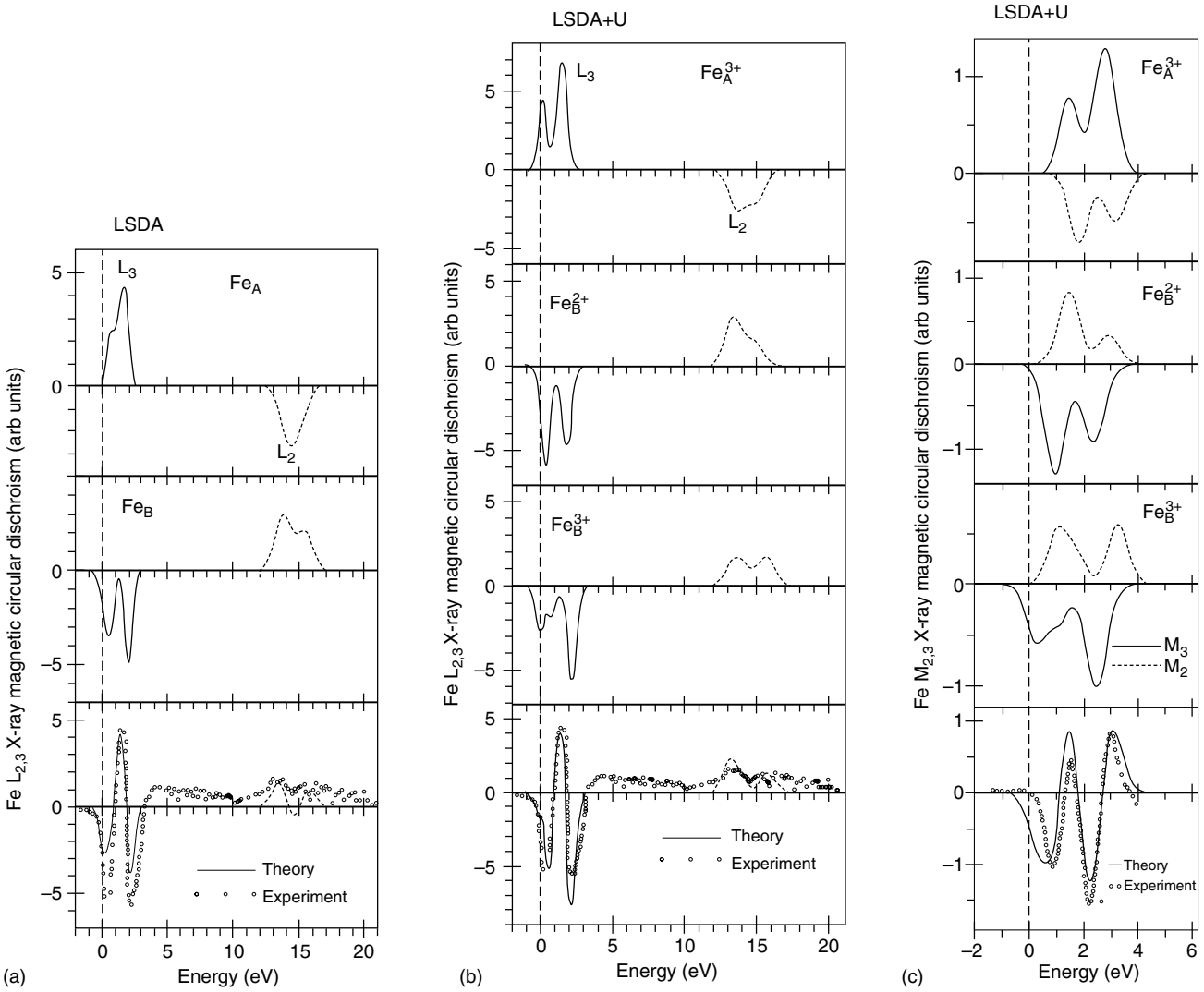

Figure 6. (a) and (b) show results for the total and site-resolved XMCD spectra at the $L_{2,3}$ edges of Fe in Fe_3O_4 obtained on the basis of the LSDA and LSDA + U, respectively, (Antonov, Harmon and Yaresko, 2003) in comparison with experiment (Kuiper *et al*., 1997). (c) shows the corresponding spectra for the $M_{2,3}$ edges of Fe in Fe_3O_4 in comparison with experiment. (Reproduced from Koide *et al*., 1996, with permission from Elsevier. © 1996.)

spectrum is in qualitative agreement with experiment that does not allow one to distinguish the various lattice site contributions. In contrast to LSDA, the use of the LSDA + U leads, in line with experiment, to a charge-ordered insulator with two inequivalent B sites. This qualitative change in the electronic structure is reflected by the various site-resolved XMCD spectra shown in Figure 6(b). As one notes, the resulting total XMCD spectrum is now in much better agreement with experiment. This also holds for $M_{2,3}$ edges for which the LSDA + U-based results are shown in Figure 6(c). Here obviously a strong overlap of the M_2 and M_3 spectra occurs because the spin-orbit splitting of the initial 3p core states is much smaller than that of the 2p core states involved in the $L_{2,3}$ spectra. As a result of this overlap, the total $M_{2,3}$-XMCD spectrum is strongly reduced in amplitude compared to the $L_{2,3}$ spectrum.

While the LSDA + U-based calculations reproduce the experimental $L_{2,3}$ and $M_{2,3}$ spectra very well, they are, nevertheless, not able to describe the small positive shoulder seen at the high-energy side of the main peaks of the L_3 spectrum. Similar problems occurred for other systems also. For example, a satellite at 6 eV above the L_3 absorption edge is found in the experimental XMCD spectrum of Ni, which obviously cannot be described by band structure calculations. On the other hand, adopting a CI viewpoint on the basis of the Anderson impurity model for the Ni d states, this satellite has been ascribed to a superposition of d^8, d^9, and d^{10} configurations for the ground state (Jo and Sawatzky, 1991).

4.3 Magnetic linear dichroism in x-ray absorption

The first successful experimental demonstration of the magnetic dichroism in X-ray absorption was done for the linear dichroism (XMLD) observed at the $M_{4,5}$ edge of Tb in Tb-Fe-garnet (van der Laan *et al*., 1986). These investigations were accompanied by simulations based on atomic Hartree–Fock calculations (Cowan, 1981) for transitions from the $4f^n(J)$ Hund's rule ground state to the manifold of $3d^9 4f^{n+1}(J')$ final states, which allowed the interpretation of the recorded spectra in detail. Results of similar investigations on the M_5 edge of Tb in amorphous Tb_xFe_{1-x} films (Vogel *et al*., 1991) are shown in Figure 7. Here the angular and temperature dependence of the absorption has been analyzed assuming a magnetic interaction that splits the $^7F_6$ ground state of Tb into 13 Zeeman levels. This allowed the estimation of the magnetic parameters in this alloy system as a function of the concentration, leading for example, for the saturation moment normal to the film surface to $5.5\,\mu_B$ and to an effective exchange field of about 14 T.

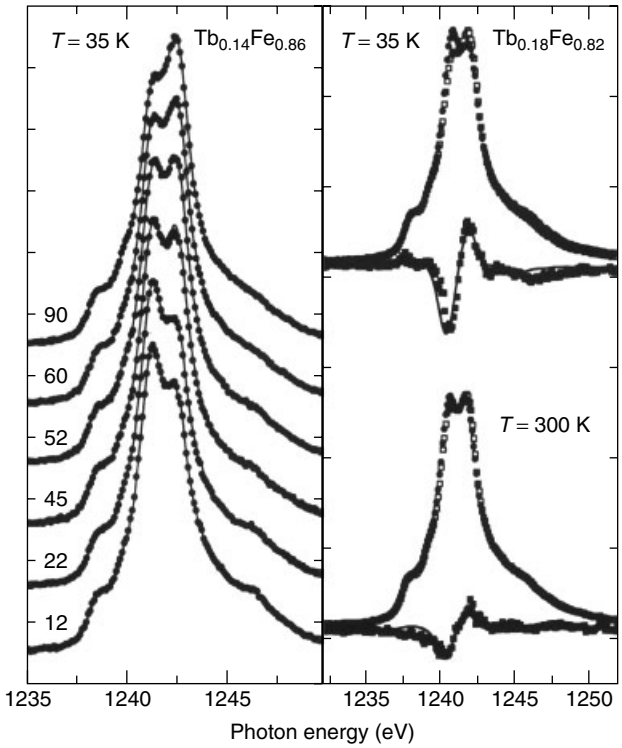

Figure 7. XMLD at the M_5 edge of Tb in amorphous Tb_xFe_{1-x} films as a function of angle (left) and temperature (right). Experimental data are represented by symbols. Theoretical results are given by lines. (Reproduced from Vogel *et al*., 1991, with permission from Elsevier. © 1991.)

Similar to the situation for the magneto-optical effects in the low-energy regime, where most experimental investigations were done for the polar geometry, the XMCD is in general much more pronounced than the XMLD. Nevertheless, the XMLD (Schwickert *et al*., 1998) and related phenomena (Mertins *et al*., 2001) observed in transition metal systems can be described fairly well on the basis of the formalism sketched in the preceding text. In addition, the anisotropy of the XMLD was investigated and found to be quite appreciable (Kunes and Oppeneer, 2003). As was pointed out already in the first XMLD studies on the XMLD (van der Laan *et al*., 1986), the effect measures the expectation value of the square of the magnetic moment of the absorbing atom, $\langle \mu^2 \rangle$. Accordingly, in contrast to the XMCD, the XMLD can also be observed in antiferromagnetic systems. This feature has been exploited, for example, to study the surface magnetism of a NiO(100) film grown on MgO(100) as a function of the temperature (Stöhr *et al*., 1999). Furthermore, the XMLD has been suggested to be used as a probe for the magnetocrystalline anisotropy (van der Laan, 1999). This approach in particular, avoids the determination of the orbital magnetic moment and its anisotropy on the basis of Bruno's model making use of the XMCD (van der Laan, 2001).

5 VALENCE-BAND PHOTOEMISSION

5.1 One-step model of photoemission

The traditional way to discuss valence-band photoemission spectroscopy (VB-PES) of solids is to use the so-called three-step model (Berglund and Spicer, 1964) that divides the photoemission process into excitation, transport to the surface, and escape to the vacuum. This scheme gives some justification for the reconstruction of the bulk dispersion relation $E(\vec{k})$ from experimental angle-resolved ultraviolet photoemission spectroscopy (ARUPS) data. For this procedure, however, a free electron–like dispersion has to be assumed in addition for the final state. More detailed information on the electronic structure of the investigated system is obtained by performing an ARUPS experiment using linearly and/or circularly polarized light together with a spin analysis of the photocurrent. On the basis of the underlying selection rules, information on the spin character and hybridization is gained for the probed electronic states that in principle allows one to map the spin and orbital magnetic moments along the electronic bands in a $\vec{k}$-resolved way (Braun, 1996). As for a magnetic solid, these properties depend strongly on the complex interplay of spin-orbit coupling and exchange splitting, corresponding experimental investigations have to be supported by appropriate accompanying theoretical work.

The most general basis to discuss photoemission experiments is supplied by the one-step model (Feibelman and Eastman, 1974) that describes all steps in a coherent way. Adopting the one-electron approximation and starting from Fermi's golden rule, the photoemission current emitted from a single crystal surface in an angle-resolved experiment is given by:

$$I^{\vec{q}\lambda} = -\frac{1}{\pi}\mathrm{Im}\int \mathrm{d}^3r \int \mathrm{d}^3r' \psi_{\mathrm{f}}^{*}(\vec{r},\vec{k},E_{\mathrm{f}}) X_{\vec{q}\lambda}(\vec{r}) G(\vec{r},\vec{r}\,',E_{\mathrm{i}}) \times X_{\vec{q}\lambda}^{\dagger}(\vec{r}\,')\psi_{\mathrm{f}}(\vec{r}\,',\vec{k},E_{\mathrm{f}}) \tag{29}$$

Here, excitation by light with wave vector $\vec{q}$, frequency ω, and polarization λ is considered with $X_{\vec{q}\lambda}(\vec{r})$ the corresponding electron–photon interaction operator. The manifold possible initial states at energy E_{i} are represented by the Green's function $G(\vec{r},\vec{r}\,',E_{\mathrm{i}})$, while the final states $\psi_{\mathrm{f}}(\vec{r},\vec{k},E_{\mathrm{f}})$ with wave vector $\vec{k}$, and energy $E_{\mathrm{f}} = E_{\mathrm{i}} + \hbar\omega$ are given by a time-reversed low energy electron diffraction (LEED) state (Feibelman and Eastman, 1974). If equation (29) is applied within a nonrelativistic calculation separately to the spin-up ($\uparrow$) and spin-down ($\downarrow$) states of a ferromagnet, one obtains corresponding spin-resolved partial intensities $I^{\uparrow(\downarrow)}$. Reversing the magnetization $\vec{M}$ while keeping all other parameters fixed, just interchanges $I^{\uparrow}$ and $I^{\downarrow}$. As a consequence, the spin polarization $\vec{P} = (I^{\uparrow} - I^{\downarrow})/(I^{\uparrow} + I^{\downarrow})\ \vec{M}/|\vec{M}|$, that is parallel to $\vec{M}$ reverses sign, while the total intensity $I = I^{\uparrow} + I^{\downarrow}$ remains unchanged. This situation, however, changes if the spin-orbit coupling is accounted for in addition to the exchange splitting. Symmetry and analytical considerations allow in this case to predict in detail under which conditions an asymmetry in the spin-averaged photocurrent upon reversal of magnetization, that is, a magnetic dichroism, can be observed (Feder and Henk, 1996; Henk, Scheunemann, Halilov and Feder, 1996).

For this purpose, it is most convenient to introduce the 2×2 spin density matrix (Ginatempo, Durham, Györffy and Temmerman, 1985; Feder and Henk, 1996):

$$\rho_{\sigma\sigma'}^{\vec{q}\lambda} = \frac{1}{2i}\left(I_{\sigma\sigma'}^{\vec{q}\lambda} - I_{\sigma\sigma'}^{\vec{q}\lambda *}\right) \tag{30}$$

with the partial intensity functions

$$I_{\sigma\sigma'}^{\vec{q}\lambda} = -\frac{1}{\pi}\mathrm{Im}\int \mathrm{d}^3r \int \mathrm{d}^3r' \psi_{\mathrm{f}\sigma}^{*}(\vec{r},\vec{k},E_{\mathrm{f}}) X_{\vec{q}\lambda}(\vec{r}) G(\vec{r},\vec{r}\,',E_{\mathrm{i}}) \times X_{\vec{q}\lambda}^{\dagger}(\vec{r}\,')\psi_{\mathrm{f}\sigma'}(\vec{r}\,',\vec{k},E_{\mathrm{f}}) \tag{31}$$

where the final state $\psi_{\mathrm{f}\sigma}(\vec{r},\vec{k},E_{\mathrm{f}})$ is restricted to have the spin character σ with respect to some chosen direction. This way, one has for the total intensity and spin polarization

$$I = \mathrm{Trace}\ \rho \quad \text{and} \quad \vec{P} = \mathrm{Trace}\ \vec{\sigma}\rho/I \tag{32}$$

with $\vec{\sigma}$ the vector of Pauli matrices.

The central condition for the occurrence of magnetic dichroism is that spin-orbit coupling gives rise to a component of the spin polarization $\vec{P}$ along the magnetization $\vec{M}$ if a corresponding nonmagnetic system is considered.

Assuming a sample is magnetized either perpendicular or in-plane with respect to the surface and normal emission induced by light impinging along the surface normal, this condition is met only for certain combinations of the symmetry of the system and polarization of the light. As Table 1 shows, MCD is observed for any system if the magnetization is oriented perpendicular but not if it is oriented in-plane. MLD, on the other hand, may occur for both orientations of the magnetization, depending on the symmetry and the relative orientation of the magnetization and the polarization vector of the light.

Symmetry and analytical considerations allow one to examine in detail the interplay of spin-orbit coupling and exchange splitting, which gives rise to magnetic dichroism in photoemission. A corresponding quantitative description is achieved by evaluating equations (30)–(32) within the framework of the relativistic multiple-scattering or KKR formalism of magnetic solids, which treats spin-orbit coupling and exchange splitting on the same footing. For the partial

Table 1. Magnetic dichroic effects and photoelectron spin-polarization components P_i for perpendicular ($\vec{M}||\hat{\vec{e}}_z$) and in-plane ($\vec{M}||\hat{\vec{e}}_y$) magnetization $\vec{M}$ of surfaces with twofold, threefold, or fourfold rotational axes. *s*, *p*, and *c* stand for s-, p-, and normally incident circularly polarized light. The signs indicate whether the respective component P_i occurs (+ sign) or not (− sign) and whether only spin-orbit coupling (first sign), only exchange splitting (second sign), or both (third sign) are present. MLD (L) and MCD (C) occur if a spin-polarization component parallel to $\vec{M}$ is produced by spin-orbit coupling in the nonmagnetic case, that is, if there is a combination (+, +, +) (Feder and Henk, 1996). (Reproduced from Feder, R. *et al*., 1996, with permission from Springer- Verlag GmbH. © 1996.)

Polarisation	Symmetry	$\vec{M}$ perpendicular				$\vec{M}$ in-plane			
		P_x	P_y	P_z	I	P_x	P_y	P_z	I
s	2mm	−, −, −	−, −, −	+, +, +	L	−, −, +	−, +, +	+, −, +	
	4mm	−, −, −	−, −, −	−, +, +		−, −, +	−, +, +	−, −, +	
	3m	+, −, +	+, −, +	−, +, +		+, −, +	+, +, +	−, −, +	L
p	2mm	+, −, +	+, −, +	+, +, +	L	+, −, +	+, +, +	+, −, +	L
	4mm	+, −, +	+, −, +	−, +, +		+, −, +	+, +, +	−, −, +	L
	3m	+, −, +	+, −, +	−, +, +		+, −, +	+, +, +	−, −, +	L
c	2mm	−, −, −	−, −, −	+, +, +	C	−, −, +	−, +, +	+, −, +	
	4mm	−, −, −	−, −, −	+, +, +	C	−, −, +	−, +, +	+, −, +	
	3m	−, −, −	−, −, −	+, +, +	C	−, −, +	−, +, +	+, −, +	

intensity functions, one is led to the following expression:

$$
\begin{aligned}
&I_{m_s m_s'}(E, \vec{k}; \omega, \vec{q}, \lambda) \\
&\quad = \mathrm{C} \sum_{\Lambda\,\Lambda''} i^{l-l''} C_{\Lambda}^{-m_s} C_{\Lambda''}^{-m_s'} Y_l^{\mu+m_s *}(-\hat{k}) \\
&\qquad \times Y_{l''}^{\mu''+m_s'}(-\hat{k}) \sum_{m\,m'} e^{i\vec{k}(\vec{R}_m - \vec{R}_{m'})} \\
&\qquad \times \sum_{n\,n'} e^{i\vec{q}(\vec{R}_n - \vec{R}_{n'})} \sum_{\Lambda'\,\Lambda'''} \tau_{\Lambda'\Lambda}^{nm}(E') \tau_{\Lambda'''\Lambda''}^{n'm'*}(E') \qquad (33) \\
&\qquad \left[\sum_{\Lambda_1\,\Lambda_2} M_{\Lambda'\Lambda_1}^{\vec{q}\lambda} \tau_{\Lambda_1\Lambda_2}^{nn'}(E) \overline{M}_{\Lambda_2\Lambda'''}^{\vec{q}\lambda} - \delta_{n\,n'} \sum_{\Lambda_1} I_{\Lambda'\Lambda_1\Lambda'''}^{\vec{q}\lambda} \right]
\end{aligned}
$$

Here $M_{\Lambda\Lambda'}^{\vec{q}\lambda}$ and $\overline{M}_{\Lambda\Lambda'}^{\vec{q}\lambda}$ are matrix elements that are usually evaluated making use of the dipole approximation. The additional single-site term $I_{\Lambda\Lambda'\Lambda''}^{\vec{q}\lambda}$ stems from the irregular solution of the Dirac equation and contributes only if one uses a complex energy or self-energy Σ to account for finite lifetime or many-particle effects. Equation (33) involves several summations over lattice sites (n, n', m, m'). This can be evaluated in direct space when a restriction to a finite cluster is made (Woods, Ernst, Strange and Temmerman, 2001). In general, however, a half-infinite crystal is assumed that shows a two-dimensional periodicity for the atomic plane parallel to the surface. In this case the scattering within the planes can be treated by a two-dimensional Fourier transformation. The scattering between the planes is dealt with in a subsequent step either by introducing transmission and reflectivity matrices (Hopkinson, Pendry and Titterington, 1980) or by summing directly in real space (Lüders *et al*., 2001).

For high photon energies, multiple scattering can safely be neglected for the final states (single-scatterer approximation). This assumption seems to be well justified not only for the XPS regime but also down to several tens of eV (Lüders *et al*., 2001; Ostanin and Ebert, 1998). Using this single-scatterer approximation and taking the average with respect to the wave vector $\vec{k}$ of the emitted electrons, one ends up with a simple expression for the angle-integrated photoemission spectrum (PES). In the case of a paramagnetic system, one finds that angle-integrated PES for unpolarized light maps the sum over angular momentum–projected DOS curves that are weighted by a corresponding photoemission cross section (Marksteiner *et al*., 1986). Using circularly polarized light for the excitation, a spin polarization in the photoelectron current is induced; that is, the Fano effect can be observed (Minár *et al*., 2001). Reversing the helicity of the light just reverses the polarization of the photoelectron current. This symmetry is broken for a ferromagnet in the case of a polar geometry, giving rise also to magnetic circular dichroism for an angular-integrated spectrum (Ebert and Schwitalla, 1997).

5.2 Angle-resolved photoemission of transition metals

The formalism sketched in the preceding text allows one to investigate in a very detailed and quantitative way the various

dichroic phenomena observed in core-level (Venus, 1993) as well as valence-band (Kuch and Schneider, 2001) photoemission spectroscopy. As an example for the latter case, Figure 8 summarizes the results of an investigation on the spin- and angle-resolved normal photoemission from Ni(001) (Feder and Henk, 1996). Figure 8(a) of this figure shows the dispersion relation $E(\vec{k})$ for the magnetization $\vec{M}$ perpendicular to the surface. Owing to the inclusion of the spin-orbit coupling, the electronic states have no pure spin character but show only either dominantly spin-up or dominantly spin-down character, indicated by full and dotted lines, respectively. The dash-dotted line represents the relevant allowed final states that have negligible exchange splitting and can be reached with a photon energy of 21.22 eV. As they have been shifted downwards by that energy, the band intersections labeled $a-f$ indicate possible vertical transitions. Because of the symmetry of the system, the spin polarization $\vec{P}$ of the resulting photocurrent has to be aligned along the surface normal; that is, parallel or antiparallel to the magnetization. The corresponding partial and spin-projected intensities $I^{\uparrow}$ and $I^{\downarrow}$, respectively, obtained in a spin-resolved experiment with un- or s-polarized light are shown in panel (d). Obviously, these curves primarily reflect the exchange splitting of the material. As Table 1 suggests, use of circularly polarized radiation will lead to MCD. This is confirmed by the data shown in panel (c), where, instead of spectra for the two opposite orientations of $\vec{M}$, spectra for fixed $\vec{M}$ but opposite circular helicity of the light are presented. The origin of the observed asymmetry in intensity $I(\vec{M},\sigma_+) - I(\vec{M},\sigma_-)$ can be traced back in detail by studying the partial projected intensities $I^{\uparrow(\downarrow)}_{+(-)}$ shown in panel (b) of Figure 8. For the peak labeled b, an admixture of the spin-up character is found owing to spin-orbit coupling. Because of the symmetry-determined selection rules, only the final state with spin-up character can be reached, provided the excitation is done with light that has polarization σ_+. The right-hand side of Figure 8

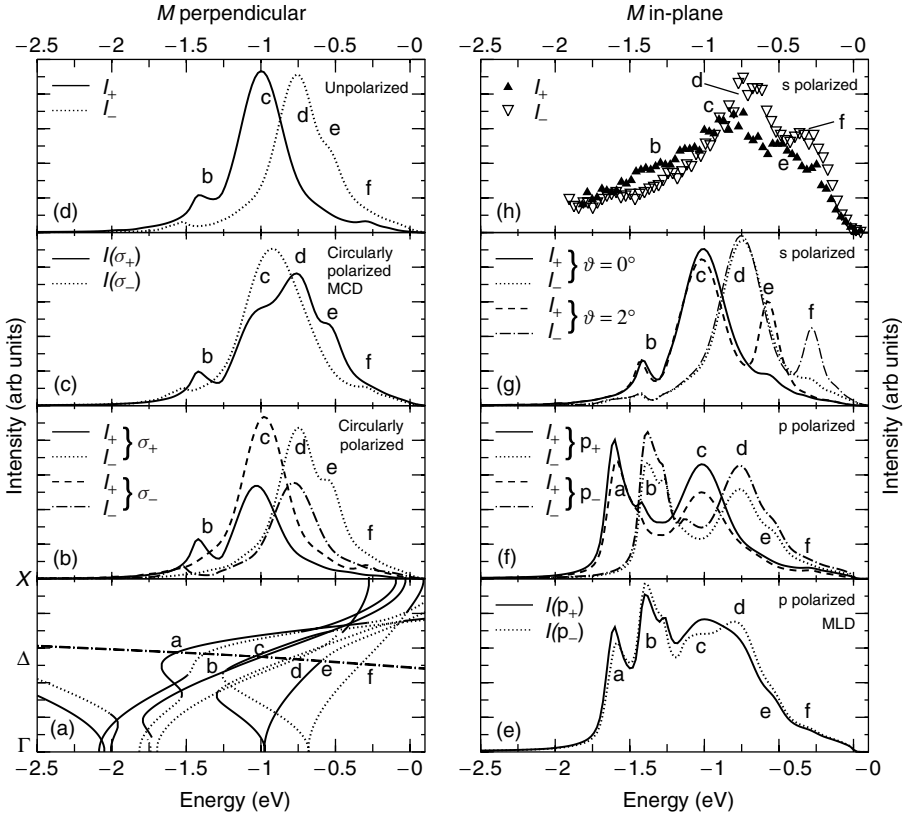

Figure 8. Normal photoemission from Ni(001) for normally incident light with 21.22 eV energy. Left: $\vec{M} \parallel [001]$ perpendicular to the surface: (a) $E(\vec{k})$ along $\Gamma-\Delta-X$. Solid (dashed) lines: states with positive (negative) spin expectation. The final-state bands (dash dotted) are shifted downwards by 21.2 eV. (b) Spin-resolved intensities $I_{\pm}$ for right-(σ_+) and left-(σ_-) circularly polarized light. (c) Spin-averaged spectra obtained from those of (b). (d) Spin-resolved intensities for unpolarized light. Right: $\vec{M} \parallel [110]$ in the surface plane: (e) Spin-averaged intensities for p-polarized light incident off-normally at $\varphi = \pi$ (solid) and $\varphi = 0$ (dotted). (f) Spin-resolved intensities corresponding to those in (a). (g) Spin-resolved intensities for s-polarized light together with off-normal emission spectra ($\vartheta = 2^{\circ}$C). (h) Experimental spin-resolved spectra (Clauberg, Hopster and Raue, 1984) corresponding to (c) (Feder and Henk, 1996). (Reproduced from Feder *et al*., 1996, with permission from Springer-Verlag GmbH. © 1996.)

shows results for the magnetization in-plane along [110]. The two upper panels showing theoretical (g) and experimental (h) spectra for s-polarized light demonstrate that a rather satisfactory agreement between both can be achieved, allowing for an unambiguous interpretation of the experimental spectra. Again, as suggested by Table 1 a linear magnetic dichroism can be expected for p-polarized light. This is confirmed by the results shown in panel (e), which have been obtained for the light incident at polar angle $\theta = 45\,^{\circ}$C in the plane normal to $\vec{M}$ with an azimuthal angle of $0\,^{\circ}$C (p_+) and $180\,^{\circ}$C (p_-). As for the MCD, a detailed analysis is achieved on the basis of the corresponding spin-projected spectra shown in panel (f).

Another example for the occurrence of the MLD in angle-resolved valence-band photoemission is given in Figure 9, which shows the corresponding spectra for normal emission from a seven monolayer Co film with hcp(0001) structure grown on a (110)-oriented W substrate. Within the experiment, the magnetization was aligned along the easy axis that coincides with the $[1\bar{1}0]$ direction of the W substrate. For an orientation of the plane of incidence of the p-polarized light perpendicular to the magnetization, the reversal of the magnetization changes the intensity of the photocurrent in line with the expectations based on Table 1.

When comparing experimental photoemission spectra with corresponding theoretical results based on plain LSDA, a qualitative agreement is found in general. Similar to the case of optical properties, however, the prominent spectral features are usually shifted against one another owing to the influence of many-body effects (Liebsch, 1979). For that reason, a shift of 2 eV in the photon energy has been applied for the theoretical spectra shown in Figure 9. The rather good agreement with experiment obtained this way justifies a detailed analysis of the experimental data on the basis of the theoretical results. As found very often in photoemission experiments on thin films (Henk and Johansson, 1999), the thickness of the Co film already gives rise to a dispersion relation corresponding to that of bulk hcp Co. Accordingly, the main peak seen in the photoemission spectra at around 0.7 eV binding energy, whose position depends only slightly on the photon energy, reflects a rather flat band of the Co band structure. The onset of the peak close to the Fermi level that is observed for the photon energy around 24 eV, on the other hand, is ascribed to a state at the Γ point.

The calculations of the photoemission spectra shown in Figure 9 have been done in a fully relativistic way. For that reason, they are able to reproduce the magnitude and the energy dependence of the observed MLD. From the calculations, it was suggested that the MLD is caused by a strong mixing of the initial-state spin subsystems owing to spin-orbit coupling together with a nonvanishing exchange splitting for the final states. In particular, it could be shown that the observed MLD is nearly exclusively connected with d–f transitions.

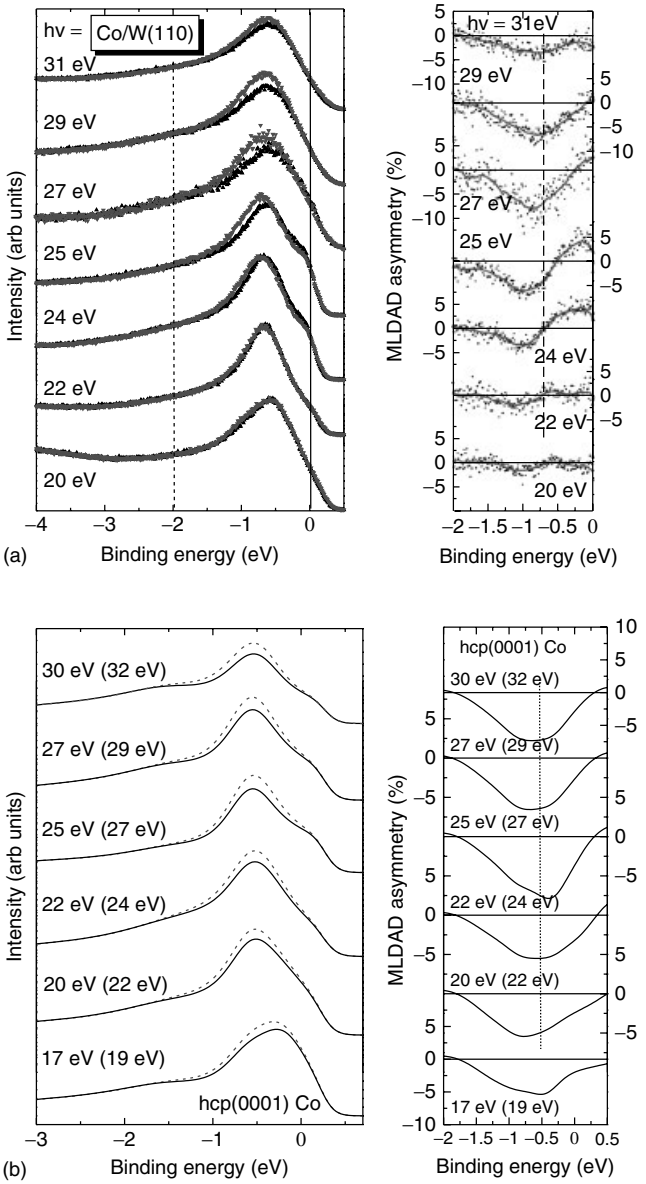

Figure 9. Left: Valence-band photoemission spectra from a seven ML thick hcp(0001) Co film on W substrate, taken with linearly polarized radiation for opposite magnetization directions. Right: Corresponding asymmetry values for binding energies between -2 eV and E_F. (a) Experiment; (b) theory. (Reprinted from Bansmann *et al*., 2000 with permission from Elsevier, © 2000.)

REFERENCES

Anisimov, V., Aryasetiawan, F. and Lichtenstein, A. (1997). First-principles calculations of the electronic structure and spectra

of strongly correlated systems: the LDA+U method. *Journal of Physics. Condensed Matter*, **9**, 767.

Ankudinov, A., Nesvizhskii, A.I. and Rehr, J.J. (2003). Dynamic screening effects in x-ray absorption spectra. *Physical Review B*, **67**, 115120.

Ankudinov, A. and Rehr, J.J. (1995). Sum rules for polarization-dependent x-ray absorption. *Physical Review B*, **51**, 1282.

Ankudinov, A.L. and Rehr, J.J. (1997). Relativistic calculations of spin-dependent x-ray-absorption spectra. *Physical Review B*, **56**, R1712.

Antonov, V.N., Antropov, V.P., Harmon, B.N., *et al*. (1999). Fully relativistic spin-polarized LMTO calculations of the magneto-optical Kerr effect of d and f ferromagnetic materials. III. Uranium chalcogenides and pnictides. *Physical Review B*, **59**, 14571.

Antonov, V.N., Harmon, B.N. and Yaresko, A.N. (2003). Electronic structure and x-ray magnetic circular dichroism in Fe_3O_4 and Mn-, Co-, or Ni-substituted Fe_3O_4. *Physical Review B*, **67**, 24417.

Antonov, V.N., Yaresko, A.N., Perlov, A.Y. and Nemoshkalenko, V.V. (1999). Magneto-optical spectroscopy of d- and f-ferromagnetic materials: recent theoretical progress (review article). *Journal of Low Temperature Physics*, **25**, 387.

Bansmann, J., Lu, L., Getzlaff, M., *et al*. (2000). Epitaxial cobalt films on W(110) -an experimental and theoretical photoemission study with polarized synchrotron radiation. *Surface Science*, **454–456**, 686–691.

Baumgarten, L., Schneider, C.M., Petersen, H., *et al*. (1990). Magnetic x-ray dichroism in core-level photoemission from ferromagnets. *Physical Review Letters*, **65**, 492.

Beaurepaire, E., Scheurer, F., Krill, G. and Kappler, J.P. (Eds.) (2001). *Magnetism and Synchrotron Radiation*, Springer-Verlag: Berlin.

Bennett, W.R., Schwarzacher, W. and Egelhoff, W.F. (1990). Concurrent enhancement of Kerr rotation and antiferromagnetic coupling in epitaxial Fe/Cu/Fe structures. *Physical Review Letters*, **65**, 3169.

Benoist, R., Carra, P. and Andersen, O.K. (2000). Band structure and atomic sum rules for x-ray dichroism. *European Journal of Physics B*, **18**(2), 193.

Berglund, C.N. and Spicer, W.E. (1964). Photoemission studies of copper and silver: theory. *Physical Review*, **136**, A1030.

Bertero, G.A. and Sinclair, R. (1995). Kerr rotations and anisotropy in (Pt/Co/Pt)/X multilayers. *IEEE Transactions on Magnetics*, **31**, 3337.

Braun, J. (1996). The theory of angle-resolved ultraviolet photoemission and its applications to ordered materials. *Reports on Progress in Physics*, **59**, 1267.

Brooks, M.S.S. (1985). Calculated ground state properties of light actinide metals and their compounds. *Physica B*, **130**, 6.

Bruno, P. (1989). Tight-binding approach to the orbital magnetic moment and magnetocrystalline anisotropy of transition-metal monolayers. *Physical Review B*, **39**, 865.

Callaway, J. (1974). *Quantum Theory of the Solid State Part B*, Academic Press: New York.

Callaway, J. and Wang, C.S. (1973). Self-consistent calculation of energy bands in ferromagnetic nickel. *Physical Review B*, **7**, 1096.

Campbell, I.A. (1966). The magnetic moment distributions for transition metal impurities in iron. *Proceedings of the Royal Society of London*, **89**, 71.

Carl, A. and Weller, D. (1995). Oscillatory paramagnetic magneto-optical Kerr effect in Ru wedges on Co. *Physical Review Letters*, **74**, 190.

Carra, P., Thole, B.T., Altarelli, M. and Wang, X. (1993). X-ray circular dichroism and local magnetic fields. *Physical Review Letters*, **70**, 694.

Chen, C.T., Idzerda, Y.U., Lin, H.J., *et al*. (1993). Element-specific magnetic hysteresis as a means for studying heteromagnetic multilayers. *Physical Review B*, **48**, 642.

Chen, C.T., Sette, F., Ma, Y. and Modesti, S. (1990). Soft-x-ray magnetic circular dichroism at the $L_{2,3}$ edges of nickel. *Physical Review B*, **42**, 7262.

Clauberg, R., Hopster, H. and Raue, R. (1984). Reinterpretation of a controversial structure in the photoemission spectrum of Ni(001) by spin analysis. *Physical Review B*, **29**, 4395.

Cowan, R.D. (1981). *The Theory of Atomic Structure and Spectra*, University of California Press: Berkeley.

Cracknell, A.P. (1969). Time-reversal degeneracy in the electronic band structure of a magnetic metal. *Journal of Physics C: Solid State Physics*, **2**, 1425.

Daalderop, G.H.O. (1991). *Magneto-optical Recording Media Based on Co/Pt-multilayers*, Ph.D. Thesis, Technical University Delft.

Durham, P.J. (1984). *The Electronic Structure of Complex Systems*, Plenum Press: New York, p. 709.

Ebert, H. (1988). Two ways to perform spin-polarized relativistic linear muffin-tin-orbital calculations. *Physical Review B*, **38**, 9390.

Ebert, H. (1989). Fully relativistic treatment of core states for spin-dependent potential. *Journal of Physics. Condensed Matter*, **1**, 9111.

Ebert, H. (1996a). Influence of the orbital polarization on the magnetic x-ray dichroism of transition metals. *Solid State Communications*, **100**, 677.

Ebert, H. (1996b). Magneto-optical effects in transition metal systems. *Reports on Progress in Physics*, **59**, 1665.

Ebert, H. (2000). Fully relativistic band structure calculations for magnetic solids – formalism and application. In *Electronic Structure and Physical Properties of Solids*, *Vol. 535 of Lecture Notes in Physics*, Dreyssé, H. (Ed.), Springer: Berlin, p. 191.

Ebert, H., Freyer, H., Vernes, A. and Guo, G.-Y. (1996). Manipulation of the spin-orbit coupling using the Dirac equation for spin-dependent potentials. *Physical Review B*, **53**, 7721.

Ebert, H. and Mankovsky, S. (2003). Field-induced magnetic circular x-ray dichroism in paramagnetic solids: a new magneto-optical effect. *Physical Review Letters*, **90**, 077404.

Ebert, H., Popescu, V. and Ahlers, D. (1999). A fully relativistic theory for magnetic EXAFS – formalism and applications. *Physical Review B*, **60**, 7156.

Ebert, H. and Schwitalla, J. (1997). Magnetic dichroism in valence band x-ray photoemission spectroscopy. *Physical Review B*, **55**, 3100.

Ebert, H., Stöhr, J., Parkin, S.S.P., *et al*. (1996). L-edge x-ray absorption in fcc and bcc Cu metal: comparison of experimental

and first-principle theoretical results. *Physical Review B*, **53**, 16067.

Ebert, H., Strange, P. and Györffy, B.L. (1988). Theory of circularly polarized x-ray absorption by ferromagnetic Fe. *Journal of Applied Physics*, **63**, 3055.

Eimüller, T., Fischer, P., Köhler, M., *et al*. (2001). Transmission x-ray microscopy using x-ray magnetic circular dichroism. *Applied Physics A*, **73**, 697.

van Engen, P.G. (1983). *An Experimental Study of the Magneto-optical Properties of Ferromagnetic Alloys*, Ph.D. Thesis, Technical University of Delft.

Erskine, J.L. and Stern, E.A. (1973). Magneto-optic Kerr effect in Ni, Co and Fe. *Physical Review Letters*, **30**, 1329.

Erskine, J.L. and Stern, E.A. (1975). Calculation of the $M_{2,3}$ magneto-optical absorption spectrum of ferromagnetic nickel. *Physical Review B*, **12**, 5016.

Fano, U. (1969). Spin orientation of photoelectrons ejected by circularly polarized light. *Physical Review*, **178**, 131.

Faraday, M. (1846). Experimental researches in electricity. *Philosophical Transactions of the Royal Society of London*, **136**, 41–62.

Feder, R. and Henk, J. (1996). *Spin-orbit Influenced Spectroscopies of Magnetic Solids*, *Vol. 466 of Lecture Notes in Physics*, Springer: Berlin, p. 85.

Feder, R., Rosicky, F. and Ackermann, B. (1983). Relativistic multiple scattering theory of electrons by ferromagnets. *Zeitschrift fur Physik B*, **52**, 31.

Feibelman, P.J. and Eastman, D.E. (1974). Photoemission spectroscopy-correspondence between quantum theory and experimental phenomenology. *Physical Review B*, **10**, 4932.

Feil, H. and Haas, C. (1987). Magneto-optical Kerr effect, enhanced by the plasma resonance of charge carriers. *Physical Review Letters*, **58**, 65.

Gambardella, P., Rusponi, S., Veronese, M., *et al*. (2003). Giant magnetic anisotropy of single cobalt atoms and nanoparticles. *Science*, **300**, 1130.

Geerts, W., Suzuki, Y., Katayama, T., *et al*. (1994). Thickness-dependent oscillation of the magneto-optical properties of Au-sandwiched (001) Fe films. *Physical Review B*, **50**, 12581.

Georges, A., Kotliar, G., Krauth, W. and Rozenberg, M.J. (1996). Dynamical mean-field theory of strongly correlated fermion systems and the limit of infinite dimensions. *Reviews of Modern Physics*, **68**, 13.

Ghiringhelli, G., Bonfim, M., Brookes, N.B., *et al*. (2001). *X-ray Magnetic Circular Dichroism in the Investigation of Magnetic Dynamics in the Nanosecond Time Scale*, Springer-Verlag: Berlin, p. 347.

Gibbs, D., Harshman, D.R., Isaacs, E.D., *et al*. (1988). Polarization and resonance properties of magnetic x-ray scattering in holmium. *Physical Review Letters*, **61**, 1241.

Ginatempo, B., Durham, P.J., Györffy, B.L. and Temmerman, W.M. (1985). Theory of spin-polarized photoemission from nonmagnetic metals: platinum. *Physical Review Letters*, **54**, 1581.

Goedkoop, J.B., Thole, B.T., van der Laan, G., *et al*. (1988). Calculations of magnetic x-ray dichroism in the 3d absorption spectra of rare-earth compounds. *Physical Review B*, **37**, 2086.

de Groot, R.A., Mueller, F.M., van Engen, P.G. and Buschow, K.H.J. (1983). New class of materials: half-metallic ferromagnets. *Physical Review Letters*, **50**, 2024.

Guo, G.Y. (1997). Spin-ans orbital-polarized multiple scattering effects in fe, co and ni. *Physical Review B*, **55**(17), 11619.

Guo, G.Y., Ebert, H., Temmerman, W.M. and Durham, P.J. (1994). First principles calculation of magnetic x-ray dichroism in Fe and Co multilayers. *Physical Review B*, **50**(6), 3861.

Heavens, O.S. (1991). *Optical Properties of Thin Solid Films*, Dover publications: New York.

Henk, J. and Johansson, B. (1999). Quantum-size effects in photoemission from ultra-thin films: theory and application to Cu-films on fcc-Co(001). *Journal of Electron Spectroscopy and Related Phenomena*, **105**, 187.

Henk, J., Scheunemann, T., Halilov, S.V. and Feder, R. (1996). Magnetic dichroism and electron spin polarization in photoemission: analytical results. *Journal of Physics. Condensed Matter*, **8**, 47.

Hopkinson, J.F.L., Pendry, J.B. and Titterington, D.J. (1980). Calculation of photoemission spectra for surfaces of solids. *Computer Physics Communications*, **19**(1), 69–92.

Hubert, A. and Schäfer, R. (1998). *Magnetic Domains*, Springer: Berlin, New York.

Huhne, T. and Ebert, H. (1999a). Calculation of x-ray absorption coefficients using the full-potential spin-polarized relativistic version of multiple scattering theory. *Solid State Communications*, **109**, 577.

Huhne, T. and Ebert, H. (1999b). A fully relativistic description of the magneto-optical properties of arbitrary layered systems. *Physical Review B*, **60**, 12982.

Huhne, T. and Ebert, H. (2002). Symmetry properties of the scattering path operator for arbitrary translationally invariant systems. *Physical Review B*, **65**, 205125/1.

Huhne, T., Zecha, C., Ebert, H., *et al*. (1998). The full-potential spin-polarized relativistic Korringa-Kohn-Rostoker method – implementation and application to bcc-Fe, fcc-Co and fcc-Ni. *Physical Review B*, **58**, 10236.

Hulme, H.R. (1932). The Faraday effect in ferromagnetics. *Proceedings of the Royal Society of London. Series A*, **135**(826), 237–257.

Igarashi, J. and Hirai, K.M. (1994). Magnetic dichroism at the K-edge of nickel and iron. *Physical Review B*, **50**, 17820.

Jo, T. and Sawatzky, G.A. (1991). Ground state of ferromagnetic nickel and magnetic circular dichroism in Ni 2p core x-ray-absorption spectroscopy. *Physical Review B*, **43**, 8771.

Katayama, T., Suzuki, Y., Awano, H., *et al*. (1988). Enhancement of the magneto-optical Kerr rotation in Fe/Cu bilayered films. *Physical Review Letters*, **60**, 1426.

Kawakami, M., Enokiya, H. and Okamoto, T. (1985). ^{197}Au NMR study of Au impurities in Fe and fcc Co. *Journal of Physics F: Metal Physics*, **15**, 1613.

Kevan, S.V. (1992). *Angle-resolved Photoemission: Theory and Current Applications*, Elsevier: Amsterdam.

Kisker, E., Schröder, K., Campagna, M. and Gudat, W. (1984). Temperature dependence of the exchange splitting of Fe by spin-resolved photoemission spectroscopy with synchrotron radiation. *Physical Review Letters*, **52**(25), 2285.

Kleiner, W.H. (1966). Space-time symmetry of transport coefficients. *Physical Review*, **142**, 318.

Koelling, D.D. and Harmon, B.N. (1977). A technique for relativistic spin-polarised calculations. *Journal of Physics C: Solid State Physics*, **10**, 3107.

Koenig, C. and Knab, D. (1990). LMTO analysis of the optical conductivity of XPd3 compounds (X=Sc, Y, La and Ce). *Solid State Communications*, **74**, 11.

Koide, T., Shidara, T., Yamaguchi, K., *et al*. (1996). Core-level magnetic circular dichroism in Fe_3O_4 and $CoFe_2O_4$. *Journal of Electron Spectroscopy and Related Phenomena*, **78**, 275.

Komelj, M., Ederer, C., Davenport, J.W. and Fähnle, M. (2002). From the bulk to monatomic wires: an ab initio study of magnetism in Co systems with various dimensionality. *Physical Review B*, **66**, 140407.

Kornherr, C. (1997). *Relativistische KKR-Rechnungen für Fremdatome in Magnetischen Wirtsmetallen*, Master's thesis, University of Munich.

Krutzen, B.C.H. and Springelkamp, F. (1989). Spin-polarised relativistic electronic structure calculations. *Journal of Physics. Condensed Matter*, **1**, 8369.

Kryder, M.H. (1985). Magneto-optic recording technology. *Journal of Applied Physics*, **57**, 3913.

Kuch, W. and Schneider, C.-M. (2001). Magnetic dichroism in valence band photoemission. *Reports on Progress in Physics*, **64**, 147.

Kuiper, P., Searle, B.G., Duda, L.C., *et al*. (1997). Fe $L_{2,3}$ linear and circular magnetic dichroism of Fe_3O_4. *Journal of Electron Spectroscopy and Related Phenomena*, **86**, 107.

Kunes, J. and Oppeneer, P.M. (2000). Exact many-body sum rule for the magneto-optical spectrum of solids. *Physical Review B*, **61**, 15774.

Kunes, J. and Oppeneer, P.M. (2003). Anisotropic x-ray magnetic linear dichroism at the $L_{2,3}$ edges of cubic Fe, Co, and Ni: ab initio calculations and model theory. *Physical Review B*, **67**, 24431.

van der Laan, G. (1999). Magnetic linear x-ray dichroism as a probe of the magnetocrystalline anisotropy. *Physical Review Letters*, **82**, 640.

van der Laan, G. (2001). Determination of the element-specific magnetic anisotropy in thin films and surfaces. *Journal of Physics. Condensed Matter*, **13**, 11149.

van der Laan, G., Thole, B.T., Sawatzky, G.A., *et al*. (1986). Experimental proof of magnetic x-ray dichroism. *Physical Review B*, **34**, 6529.

Liebsch, A. (1979). Effect of self-energy corrections on the valence-band photoemission spectra of Ni. *Physical Review Letters*, **43**, 1431.

Lovesey, S.W. (1993). Photon scattering by magnetic solids. *Reports on Progress in Physics*, **56**, 257.

Lüders, M., Ernst, A., Temmerman, W., *et al*. (2001). Ab initio angle-resolved photoemission in multiple-scattering formulation. *Journal of Physics. Condensed Matter*, **13**, 8587.

MacDonald, A.H. and Vosko, S.H. (1979). A relativistic density functional formalism. *Journal of Physics C: Solid State Physics*, **12**, 2977.

MacLaren, J.M. and Victora, R.H. (1994). Theoretical predictions of interface anisotropy in the presence of interdiffusion. *Journal of Applied Physics*, **76**, 6069.

Mansuripur, M. (1995). *The Principles of Magneto-optical Recording*, Cambridge University Press: Cambridge.

Marksteiner, P., Weinberger, P., Albers, R.C., *et al*. (1986). Theoretical x-ray-photoemission-spectroscopy intensities of the actinide compounds UIr_3, UPt_3, and UAu_3. *Physical Review B*, **34**, 6730.

Mattheiss, L.F. and Dietz, R.E. (1980). Relativistic tight-binding calculation of core-valence transitions in pt and au. *Physical Review B*, **22**, 1663.

Mertins, H.C., Oppeneer, P.M., Kunes, J., *et al*. (2001). Observation of the x-ray magneto-optical Voigt effect. *Physical Review Letters*, **87**, 047401.

Mertins, H.C., Schäfers, F., Cann, X.L., *et al*. (2000). Faraday rotation at the 2p edges of Fe, Co, and Ni. *Physical Review B*, **61**, R874.

Minár, J., Ebert, H., Ghiringhelli, G., *et al*. (2001). Theoretical description of the Fano-effect in the angle integrated valence band photoemission of paramagnetic solids. *Physical Review B*, **63**, 144421.

Namikawa, K., Ando, M., Nakajima, T. and Kawata, H. (1985). X-ray resonance magnetic scattering. *Journal of the Physical Society of Japan*, **54**, 4099.

Oppeneer, P.M. and Antonov, V.N. (1996). *Spin-orbit Influenced Spectroscopies of Magnetic Solids*, *Vol. 466 of Lecture Notes in Physics*, Springer: Berlin, p. 29.

Oppeneer, P.M., Maurer, T., Sticht, J. and Kübler, J. (1992). Ab initio calculated magneto-optical Kerr effect of ferromagnetic metals: Fe and Ni. *Physical Review B*, **45**, 10924.

Oppeneer, P.M., Sticht, J. and Herman, F. (1991). Theory of the magneto-optical properties of transition metals and rara-earth compounds. *Journal of the Magnetic Society Japan*, **15**(S1), 73–78.

Ostanin, S. and Ebert, H. (1998). Magnetic dichroism in valence-band photoemission spectroscopy of disordered bcc Fe_xCo_{1-x} alloys. *Physical Review B*, **58**, 11577.

Perlov, A., Chadov, S. and Ebert, H. (2003). Green function approach for the ab initio calculation of the optical and magneto-optical properties of solids: accounting for dynamical many-body effects. *Physical Review B*, **68**, 24511.

Perlov, A. and Ebert, H. (2000). Layer resolved optical conductivity of magnetic multi layers and the *Baukasten principle*. *Europhysics Letters*, **52**, 108.

Popescu, V., Ebert, H., Nonas, B. and Dederichs, P.H. (2001). Spin and orbital magnetic moments of 3d-and 4d-impurities in and on the (001)-surface of bcc-Fe. *Physical Review B*, **64**, 184407.

Rajagopal, A.K. and Callaway, J. (1973). Inhomogeneous electron gas. *Physical Review B*, **7**, 1912.

Rehr, J.J. and Albers, R.C. (2000). Theoretical approaches to x-ray absorption fine structure. *Reviews of Modern Physics*, **72**(3), 621.

Reim, W. and Schoenes, J. (1990). *Ferromagnetic Materials*, North Holland: Amsterdam, Vol. 5.

Reim, W. and Weller, D. (1989). Magneto-optical properties of metallic bilayer thin films. *IEEE Transactions on Magnetics*, **25**, 3752.

Rose, M.E. (1961). *Relativistic Electron Theory*, Wiley: New York.

Roth, C., Hillebrecht, F.U., Rose, H.B. and Kisker, E. (1993). Linear magnetic dichroism in angular resolved Fe 3p core level photoemission. *Physical Review Letters*, **70**, 3479.

Schneider, C.M., Holldack, K., Kinzler, K., *et al*. (1993). Magnetic spectromicroscopy from Fe(100). *Applied Physics Letters*, **63**, 2432.

Schütz, G., Knülle, M. and Ebert, H. (1993). Magnetic circular x-ray dichroism and its relation to local moments. *Physica Scripta*, **T49**, 302.

Schütz, G., Stähler, S., Knülle, M., *et al*. (1993). Distribution of magnetic moments in Co/Pt and Co/Pt/Ir/Pt multilayers detected by magnetic x-ray absorption. *Journal of Applied Physics*, **73**, 6430.

Schütz, G., Wagner, W., Wilhelm, W., *et al*. (1987). Absorption of circularly polarized X-rays in iron. *Physical Review Letters*, **58**, 737.

Schwickert, M.M., Guo, G.Y., Tomaz, M.A., *et al*. (1998). X-ray magnetic linear dichroism in absorption at the L edge of metallic Co, Fe, Cr, and V. *Physical Review B*, **58**(8), R4289.

Schwitalla, J. (1997). *Einfluß der Elektron-Loch-Wechselwirkung auf die Röntgenabsorption in 3d-Metallen*, Ph.D. Thesis, University of München.

Schwitalla, J. and Ebert, H. (1998). Electron core-hole interaction in the x-ray absorption spectroscopy of 3d-transition metals. *Physical Review Letters*, **80**, 4586.

Shaich, W.L. (1984). Derivation of single-scattering formulas for x-ray absorption and high-energy electron-loss spectroscopies. *Physical Review B*, **42**, 6513.

Singh, D. (1994). *Plane Waves, Pseudopotentials and the LAPW Method*, Kluwer Academic Publisher: Amsterdam.

Smith, N.V., Chen, C.T., Sette, F. and Mattheis, L.F. (1991). Relativistic tight-binding calculations of x-ray absorption and magnetic circular dichroism at the L_2 and L_3 edges of nickel and iron. *Physical Review B*, **46**, 1023.

Solovyev, I.V., Shik, A.B., Antropov, V.P., *et al*. (1989). New method for calculating the electronic structure of magnetic crystals containing heavy d and f elements. *Soviet Physics-Solid State*, **31**, 1285.

Stöhr, J. (1999). Exploring the microscopic origin of magnetic anisotropies with X-ray magnetic circular dichroism (XMCD) spectroscopy. *Journal of Magnetism and Magnetic Materials*, **200**, 470.

Stöhr, J., Scholl, A., Regan, T.J., *et al*. (1999). Images of the antiferromagnetic structure of a NiO(100) surface by means of x-ray magnetic linear dichroism spectromicroscopy. *Physical Review Letters*, **83**, 1862.

Strange, P., Durham, P.J. and Györffy, B.L. (1991). Dichroic x-ray fluorescence. *Physical Review Letters*, **67**, 3590.

Strange, P., Staunton, J.B. and Györffy, B.L. (1984). Relativistic spin-polarized scattering theory – solution of the single-site problem. *Journal of Physics C: Solid State Physics*, **17**, 3355.

Suzuki, Y., Katayama, T., Bruno, P., *et al*. (1998). Oscillatory magneto-optical effect in a Au(001) film deposited on Fe: experimental confirmation of a spin-polarized quantum-size effect. *Physical Review Letters*, **80**, 5200.

Suzuki, Y., Katayama, T., Thiaville, A., *et al*. (1993). Magneto-optical properties of Au/Fe/Ag and Ag/Fe/Au(001) sandwich films. *Journal of Magnetism and Magnetic Materials*, **121**, 539.

Suzuki, Y., Katayama, T., Yoshida, S., *et al*. (1992). New magneto-optical transition in ultrathin Fe(100) films. *Physical Review Letters*, **68**, 3355.

Thole, B.T., Carra, P., Sette, F. and van der Laan, G. (1992). X-ray circular dichroism as a probe of orbital magnetization. *Physical Review Letters*, **68**, 1943.

Uba, S., Uba, L., Gontarz, R., *et al*. (1995). Experimental and theoretical study of the magneto-optical properties of Co/Pt multilayers. *Journal of Magnetism and Magnetic Materials*, **144**, 575.

Uba, S., Uba, L., Perlov, A.Y., *et al*. (1997). Experimental and ab initio theoretical study of optical and magneto-optical properties of Co/Cu multilayers. *Journal of Physics. Condensed Matter*, **9**, 447.

Venus, D. (1993). Magnetic circular-dichroism in angular-distributions of core-level photoelectrons. *Physical Review B*, **48**, 6144.

Vernes, A., Szunyogh, L. and Weinberger, P. (2002). Limitations of the two-media approach in calculating magneto-optical properties of layered systems. *Physical Review B*, **66**, 214404.

Vogel, J., Sacchi, M., Kappert, R.J.H., *et al*. (1991). Magnetic properties of Fe and Tb in Tb_xFe_{1-x} amorphous films studied with soft x-ray circular and linear dichroism. *Journal of Magnetism and Magnetic Materials*, **150**, 293.

Wallis, R.F. and Balkanski, M. (1986). *Many Body Aspects of Solid State Spectroscopy*. North Holland: Amsterdam.

Wang, C.S. and Callaway, J. (1974). Band structure of nickel: spin-orbit coupling, the Fermi surface, and the optical conductivity. *Physical Review B*, **9**, 4897.

Weller, D. (1996). *Spin-orbit Influenced Spectroscopies of Magnetic Solids*, *Vol. 466 of Lecture Notes in Physics*, Springer: Berlin, p. 1.

Weller, D., Sticht, J., Harp, G.R., *et al*. (1992). Enhanced orbital magnetic moment on Co atoms in Co/Pd multilayers: a magnetic circular x-ray dichroism study. *Physical Review Letters*, **69**, 2307.

Wende, H. (2004). Recent advances in x-ray absorption spectroscopy. *Reports on Progress in Physics*, **67**, 2105.

Wienke, R., Schütz, G. and Ebert, H. (1991). Determination of local magnetic moments of 5*d*-impurities in iron detected via spin-dependent absorption. *Journal of Applied Physics*, **69**, 6147.

Wijngaard, J.H., Haas, C. and de Groot, R.A. (1989). Origin of the difference in the magneto-optical Kerr effect between PtMnSb and NiMnSb. *Physical Review B*, **40**, 9318.

Wilhelm, F., Poulopoulos, P., Wende, H., *et al*. (2001). Systematics of the induced magnetic moments in 5d layers and the violation of the third Hund's rule. *Physical Review Letters*, **87**(20), 207202–1.

Woods, M., Ernst, A., Strange, P. and Temmerman, W. (2001). Ab initio relativistic spin-polarized theory of angle-resolved photoemission. *Journal of Physics. Condensed Matter*, **13**, 8607.

Wu, R., Wang, D. and Freeman, A.J. (1993). First principles investigation of the validity and range of applicability of the x-ray magnetic circular dichroism sum rule. *Physical Review Letters*, **71**, 3581.

Yaresko, A., Oppeneer, P., Perlov, A., *et al*. (1996). On the nature of the absolute maximal magneto-optical Kerr rotation realized in CeSb. *Europhysics Letters*, **36**, 551.

Zeper, W.B. (1991). *Magneto-optical Recording Media Based on Co/Pt-multilayers*, Ph.D. Thesis, Technical University Delft.

X-ray and Neutron Scattering by Magnetic Materials

S.W. Lovesey[1,2] and Y. Tanaka[2]

[1] *Rutherford Appleton Laboratory, Oxfordshire, UK*
[2] *RIKEN Harima Institute, Hyogo, Japan*

1 INTRODUCTION

The importance of observations made by interpreting the scattering of radiation cannot be overstated. Indeed, many of the most important developments in science during the past century have come from scattering experiments. These developments include Rutherford's discovery of the atomic nucleus, atomic and nuclear structure, nuclear fission, antiferromagnetism, and additions to a classification within the elementary-particle zoo. Today, scattering experiments continually provide vital information in biology, physics, chemistry, and materials science that cannot be obtained by any other experimental technique.

The information derived about a material by shooting radiation at it depends on the nature of the radiation and its interaction with the constituents of the material, namely, electrons and nuclei. Beams of photons, leptons (electrons and muons), and baryons have proved to be the most useful for studies of condensed matter. Here, we discuss the scattering of neutrons and X rays by magnetic materials.

Handbook of Magnetism and Advanced Magnetic Materials. Edited by Helmut Kronmüller and Stuart Parkin. Volume 1: *Fundamentals and Theory*. ISBN: 978-0-470-02217-7.

Neutrons interact strongly with nuclei and, also, the magnetization from unpaired electrons, while the absence of a charge makes them a delicate probe of matter. X rays interact strongly with electrons, and the observations about their magnetization made by interpreting the scattering of X rays nicely complements that derived by interpreting the scattering of neutrons. While the latter is a well-established technique, some of the potential from X-ray scattering to the study of electron magnetism has been realized relatively recently with growth in the availability of bright, energy-tuneable, and polarized beams of X rays from synchrotron sources.

Scattering by a regular array of ions, in a crystal or fabricated structure, contains Bragg reflections that arise only when strict geometric conditions are satisfied. The experimental techniques of neutron and X-ray Bragg diffraction are cornerstones of crystallography. Atomic resonances can significantly influence X-ray scattering, and resonant X-ray Bragg diffraction has received much attention because it yields unique and valuable information in favorable cases. A fundamental limitation on resonant X-ray Bragg diffraction is that the contribution to scattering by the electrons of interest is not precisely factored. X-ray scattering off resonance and most applications of neutron scattering possess a precise factoring of the probe radiation from the electrons.

Bragg diffraction is a purely elastic scattering event, because in the kinematics of the event, the relevant mass is the mass of the sample. It is also purely coherent scattering because any form of disorder (static or dynamic) violates the strict geometric conditions to be satisfied in Bragg reflections. The amplitude for Bragg diffraction is always the mean value of the scattering amplitude, as this amplitude describes a perfect crystal. The Bragg amplitude is to be derived by

averaging the scattering amplitude over all forms of static and dynamic disorders, which may arise from both classical and quantum processes.

Inelastic neutron scattering is an immensely valuable technique, and it provides direct and extensive information on lattice vibrations and their magnetic counterparts called *spin waves* or *magnons*. Inelastic X-ray scattering provides a more limited coverage of lattice vibrations, but the information might be singularly valuable because it is inaccessible with neutron scattering by virtue of kinetic and intensity restrictions in the neutron scattering event. The relative balance in the strengths and weaknesses of neutron versus X-ray scattering techniques changes as the quality of instruments and radiation sources evolve. Certainly, some X-ray experiments recently performed were simply impossible to perform without the development of instruments supplied by synchrotron sources in the preceding decade.

The extreme inelastic X-ray scattering called *Compton scattering* is also incoherent scattering. The information it provides about electron magnetization is confined to spin magnetization. A separation of spin and orbital magnetization can be achieved with X-ray diffraction, whereas neutron diffraction is made by the total magnetization in the sample.

In the following sections, we survey salient features of the theory of neutron and X-ray scattering by magnetic materials. Observations are interpreted with a scattering amplitude (more correctly referred to as a *scattering length* because of its dimension) for each type of radiation. The distribution in space and energy of the radiation deflected by a material is related to a cross section that has the dimension of area divided by energy. The cross section in question is proportional to the square of the modulus of the scattering length and weighted by a δ-function that expresses the conservation of energy. Note that absorption of radiation by a material is related to the imaginary part of the scattering length evaluated for zero deflection. Thus, scattering and absorption of a radiation by a sample are two sides of one coin.

By and large, in this survey of magnetic scattering theory, we adopt the notation and conventions used by Lovesey (1987), Lovesey and Collins (1996) and Lovesey *et al.* (2005). The reader is referred to these articles for much of the background material, such as formal aspects of scattering theory, the description of states of partial polarization, and the Stokes parameters for a beam of X rays. Our survey is skewed toward magnetic X-ray scattering because it is less well established than magnetic neutron scattering which has been thoroughly reviewed in several places. We do not describe sources of radiation, diffraction instruments, or data analysis.

2 X-RAY SCATTERING

A beam of X rays illuminating a sample is principally deflected by the charge, spin, and orbital degree of freedom of the electrons in the sample. The nuclei in the sample also contribute, of course, but, in most cases, their contribution to scattering can be safely neglected because the ratio of the nuclear and electron scattering lengths is of the order of the inverse of the ratio of their masses which is $\approx 1/1836$.

2.1 Thomson scattering by a material with translational order

A translationally ordered material is represented by the regular repetition of a unit cell. The lattice that generates the regular repetition possesses a conjugate lattice defined by reciprocal lattice vectors, which we denote by $\boldsymbol{\tau}$. Bragg reflection can occur when the change in the wave vector of the radiation (X rays), upon scattering, matches a reciprocal lattice vector. Strong Bragg reflections in a diffraction pattern arise from equivalent electron charge densities in the unit cells that are related by translational symmetry. In an atomic model, the densities are attached to sites occupied by ions in the unit cell.

A relatively few electrons in the valence states of a material that possess angular anisotropy and, possibly, a magnetic moment, can cause weak reflections in a diffraction pattern. The importance of observations made by analyzing the weak reflections can hardly be exaggerated, for the valence electrons in question participate in many of the material's properties, including both structural and transport properties.

It is customary to develop the X-ray scattering length in powers of $E/m_e c^2$ where E is the primary energy and the rest mass energy of an electron $m_e c^2 = 0.511$ MeV. The first term in the development is proportional to the spatial Fourier transform of the electron charge density and it is responsible for the Thomson scattering of X rays. (The development referred to is summarized in equation (8.17) in Lovesey and Collins (1996).)

Let $\mathbf{k}$ denote the difference between the primary $\mathbf{q}$ and secondary $\mathbf{q}'$ wave vectors with $\mathbf{k} = \mathbf{q} - \mathbf{q}'$. The corresponding polarization vectors are $\boldsymbol{\varepsilon}$ and $\boldsymbol{\varepsilon}'$ and they satisfy $\mathbf{q}\cdot\boldsymbol{\varepsilon} = \mathbf{q}'\cdot\boldsymbol{\varepsilon}' = 0$. Writing $r_e = \alpha^2 a_0 = 0.282 \times 10^{-12}$ cm for the classical radius of the electron, the Thomson contribution to the X-ray scattering length per unit cell is $-r_e(\boldsymbol{\varepsilon}'\cdot\boldsymbol{\varepsilon})F_c(\mathbf{k})$ where $F_c(\mathbf{k})$ is the appropriate unit cell structure factor. Here, we attach a subscript c to denote the charge density.

In an atomic model of the electron density in the sample, $F_c(\mathbf{k})$ is a sum over every ion in the unit cell that contributes

to scattering. A site in the unit cell is labeled by its position $\mathbf{d}$. We then have

$$F_{\rm c}(\mathbf{k}) = \sum_{\mathbf{d}} {\rm e}^{i\mathbf{k}\cdot\mathbf{d}} \left\langle \sum_j {\rm e}^{i\mathbf{k}\cdot\mathbf{R}_j} \right\rangle_{\mathbf{d}} \tag{1}$$

where angular brackets denote the expectation value, or time-average, of the enclosed quantity and the j sum is over the positions $\mathbf{R}_j$ of the electrons associated with the site $\mathbf{d}$. The quantity $\left\langle \sum_j {\rm e}^{i\mathbf{k}\cdot\mathbf{R}_j} \right\rangle$ is often called an *atomic form factor* and it is equal to the number of electrons when $\mathbf{k} = 0$. If there is translational symmetry between the sites in the cell, $F_{\rm c}(\mathbf{k})$ is simply proportional to the sum of the spatial phase factors ${\rm e}^{i\mathbf{k}\cdot\mathbf{d}}$, and the sum is different from zero for $\mathbf{k} = \boldsymbol{\tau}(hkl)$, where the Miller indices hkl label a space group allowed reflection.

To describe the contribution made by valence electrons to $F_{\rm c}(\mathbf{k})$, we introduce an atomic tensor $\left\langle T_Q^K \right\rangle_{\rm c}$ for each ion. Here the positive integer K is the rank of the spherical tensor and the projection Q can take $(2K+1)$ integer values that satisfy $-K \le Q \le K$. An atomic tensor is also called a *multipole moment* and they are named by the Greek word for the number 2^K. For completeness, Table 1 contains the names of multipoles for $K = 1$ to $K = 6$.

An actual definition of $\left\langle T_Q^K \right\rangle_{\rm c}$ follows by separating the angular dependence of $\mathbf{k}$ and $\mathbf{R}_j$ in ${\rm e}^{i\mathbf{k}\cdot\mathbf{R}_j}$ which is accomplished with the identity,

$${\rm e}^{i\mathbf{k}\cdot\mathbf{R}_j} = 4\pi \sum_{KQ} i^K j_K\left(kR_j\right) \left\{ Y_Q^K(\hat{\mathbf{k}}) \right\}^* Y_Q^K(\hat{\mathbf{R}}_j) \tag{2}$$

Here, $\hat{\mathbf{k}} = \mathbf{k}/k$ and $\hat{\mathbf{R}}_j = \mathbf{R}_j/R_j$ are unit vectors, $j_K(kR_j)$ is a spherical Bessel function, and $Y_Q^K(\hat{\mathbf{k}}) = (-1)^Q \left\{ Y_{-Q}^K(\hat{\mathbf{k}}) \right\}^*$ is a spherical harmonic. Using (2), we write the expectation value of ${\rm e}^{i\mathbf{k}\cdot\mathbf{R}_j}$, which is required in the structure factor as

Table 1. Parity-even multipoles. Even-rank multipoles are time-even. Odd-rank multipoles are time-odd and they vanish in the absence of magnetic order.

Rank K	Name $= 2^K$
$K = 1$	Dipole
$K = 2$	Quadrupole
$K = 3$	Octupole
$K = 4$	Hexadecapole
$K = 5$	Triakontadipole
$K = 6$	Hexacontatetrapole

$$\left\langle \sum_j {\rm e}^{i\mathbf{k}\cdot\mathbf{R}_j} \right\rangle = (4\pi)^{\frac{1}{2}} \sum_{KQ} i^K \left\langle j_K \right\rangle (-1)^Q Y_{-Q}^K(\hat{\mathbf{k}}) \left\langle T_Q^K \right\rangle_{\rm c} \tag{3}$$

with

$$\left\langle T_Q^K \right\rangle_{\rm c} = (4\pi)^{\frac{1}{2}} \sum_j \left\langle Y_Q^K(\hat{\mathbf{R}}_j) \right\rangle \tag{4}$$

We note three properties of the Thomson atomic tensor. First, its Hermitian conjugate $\left(T_Q^K\right)^\dagger = (-1)^Q T_{-Q}^K$ and, secondly, Hermitian conjugation is identical to the reversal of time. Thirdly, under inversion of the electron coordinates $T_Q^K \to (-1)^K T_Q^K$. In equation (3), $\langle j_K(k) \rangle$ is the integral of a spherical Bessel function of order K weighted by the radial density of the valence wave function and $\langle j_k(0) \rangle = 0$ for $K > 0$. The atomic tensor $\left\langle T_Q^K \right\rangle_{\rm c}$ evaluated for $K = Q = 0$ is equal to the number of valence electrons. Weak Bragg reflections arise from tensors with rank $K > 0$.

We have written the right-hand side of (3) as a scalar product of two tensors of equal rank; if $\mathbf{A}$ and $\mathbf{B}$ are vector quantities (tensors of rank 1), their scalar product $\mathbf{A}\cdot\mathbf{B} = A_x B_x + A_y B_y + A_z B_z$ written in terms of spherical components, $A_{+1} = -(A_x + iA_y)/\sqrt{2}$, $A_0 = A_z$, and $A_{-1} = (A_x - iA_y)/\sqrt{2}$ and similar expressions for B_Q, is $\mathbf{A}\cdot\mathbf{B} = \sum_Q (-1)^Q A_{-Q} B_Q$.

After inserting (3) in (1), the Thomson structure factor may be written as

$$F_{\rm c}(\mathbf{k}) = (4\pi)^{\frac{1}{2}} \sum_{KQ} i^K \left\langle j_K \right\rangle (-1)^Q Y_{-Q}^K(\hat{\mathbf{k}}) \Psi_Q^K \tag{5}$$

where

$$\Psi_Q^K = \sum_{\mathbf{d}} {\rm e}^{i\mathbf{k}\cdot\mathbf{d}} \left\langle T_Q^K \right\rangle_{c,\mathbf{d}} \tag{6}$$

We assume that $\langle j_K \rangle$ is the same for each ion that contributes to the weak Bragg reflection in question, for which $\Psi_0^0 = 0$. Note that $F_{\rm c}(\mathbf{k})$ is a scalar product of a tensor $Y_Q^K(\hat{\mathbf{k}})$ associated with the X rays and a tensor Ψ_Q^K associated with the electrons. This feature of the structure factor will appear again and again in scattering processes, including resonant X-ray diffraction.

2.2 Thomson scattering by DyB_2C_2

By way of an example, let us consider diffraction by a crystal of dysprosium borocarbide (DyB_2C_2). On lowering the temperature to $T = 24.7$ K, the material undergoes a continuous structural phase transition in which there is a buckling of B and C rings of ions normal to the crystal c axis.

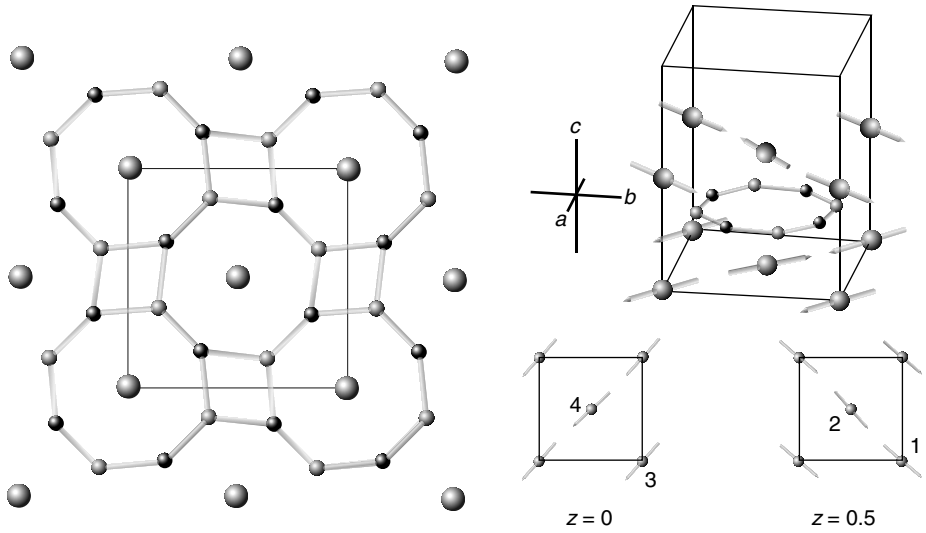

Figure 1. Low-temperature structure of DyB_2C_2 (Tanaka *et al*., 1999). In the left-hand panel, the c axis is normal to the plane of the diagram which contains the Dy ions represented by large shaded circles. The right-hand panel illustrates the configuration of Dy magnetic moments. (Reproduced from Y Tanaka *et al*: *J Phys: Condens. Matter* **11**, 1999, with permission from IOP Publishing Ltd.)

The transition reduces the crystal symmetry to $P4_2/mnm$, down from the crystal symmetry $P4/mbm$ (Tanaka *et al*., 1999). The change in symmetry is accompanied by doubling the unit cell along the c axis, and a reduction in symmetry of the sites occupied by Dy ions to $2/m$ (C_{2h}) from $4/m$ (C_{4h}). Various aspects of the crystal structure are illustrated in Figure 1.

When it comes to calculating Ψ_Q^K, we apply to $\left\langle T_Q^K \right\rangle_{c,\mathbf{d}}$ the symmetry operators that relate the four Dy sites in the unit cell of $P4_2/mnm$. One finds (Lovesey and Knight, 2001)

$$\Psi_Q^K = \left\langle T_Q^K \right\rangle_{c,1} \left\{1 + \nu_Q \mathrm{e}^{i\mathbf{k}\cdot\mathbf{d}_3}\right\} + (-1)^K \nu_Q \left\langle T_{-Q}^K \right\rangle_{c,1} \times \left\{\mathrm{e}^{i\mathbf{k}\cdot\mathbf{d}_2} + \nu_Q \mathrm{e}^{i\mathbf{k}\cdot\mathbf{d}_4}\right\} \tag{7}$$

where $\nu_Q = \mathrm{e}^{iQ\pi/2}$. We consider two classes of space-group forbidden reflections hkl which we label (a) and (b). The corresponding spatial phase factors are as follows:

(a) $h + k$ odd and $l = (2n + 1)/2$,

$$\mathrm{e}^{i\mathbf{k}\cdot\mathbf{d}_2} = \mathrm{e}^{i\mathbf{k}\cdot\mathbf{d}_3} = -1, \ \mathrm{e}^{i\mathbf{k}\cdot\mathbf{d}_4} = +1$$

(b) $h + k$ even and $l = (2n + 1)/2$,

$$\mathrm{e}^{i\mathbf{k}\cdot\mathbf{d}_2} = +1, \ \mathrm{e}^{i\mathbf{k}\cdot\mathbf{d}_3} = \mathrm{e}^{i\mathbf{k}\cdot\mathbf{d}_4} = -1$$

We find

$$\Psi_Q^K(\mathrm{a}) = (1 - \nu_Q) \left\{\left\langle T_Q^K \right\rangle_{c,1} - (-1)^K \nu_Q \left\langle T_{-Q}^K \right\rangle_{c,1}\right\} \tag{8}$$

and

$$\Psi_Q^K(\mathrm{b}) = (1 - \nu_Q) \left\{\left\langle T_Q^K \right\rangle_{c,1} + (-1)^K \nu_Q \left\langle T_{-Q}^K \right\rangle_{c,1}\right\} \tag{9}$$

and the common prefactor guarantees $\Psi_0^K(\mathrm{a}) = \Psi_0^K(\mathrm{b}) = 0$, a result that is a signature of space-group forbidden reflections.

There are more selection rules on K and Q that are derived from Ψ_Q^K. First, for Thomson scattering, K is an even integer, as we mentioned, and the maximum $K = 2l$ when l is the angular momentum of the valence shell occupied by the equivalent electrons. In our example, the valence shell is expected to be formed by the Dy 4f state and $l = 3$. Thus, the possible Ψ_Q^K are Ψ_Q^2, Ψ_Q^4, Ψ_Q^6 which, respectively, are linear combinations of quadrupoles, hexadecapoles, and hexacontatetrapoles of the Dy 4f valence state. The contributions they make to $F_\mathrm{c}(\mathbf{k})$ are weighted by $\langle j_2\rangle$, $\langle j_4\rangle$, and $\langle j_6\rangle$, which vanish as $k = |\mathbf{k}|$ goes to zero, and the magnitude of $\langle j_2\rangle$ is typically much larger than the magnitudes of both $\langle j_4\rangle$ and $\langle j_6\rangle$. Secondly, the diad parallel to the c axis requires that $\left\langle T_Q^K \right\rangle_{c,1}$ be unchanged by a rotation by π about the c axis, that is, $\left\langle T_Q^K \right\rangle_{c,1} = \mathrm{e}^{iQ\pi} \left\langle T_Q^K \right\rangle_{c,1}$. The nontrivial condition is that Q be an even integer $Q = \pm 2, \pm 4, \ldots$. However, a necessary condition for scattering is $\nu_Q = \mathrm{e}^{iQ\pi/2} = -1$, and hence the allowed $Q = \pm 2, \pm 6, \ldots$. Notice that, in the room-temperature structure $P4/mbm$, there is no Thomson scattering because dysprosium ions occupy sites with a tetrad parallel to the c axis, and this rotation symmetry restricts Q to values $0, \pm 4, \pm 8, \ldots$ for which $\Psi_Q^K = 0$.

Below the structural phase transition, at $T = 24.7\,\mathrm{K}$, the structure factor for Thomson scattering is derived from

$$\Psi_Q^K(a) = 2\left\{\langle T_Q^K\rangle_{c,1} + \langle T_{-Q}^K\rangle_{c,1}\right\} = \Psi_{-Q}^K(a) = 4\mathrm{Re}\,\langle T_Q^K\rangle_{c,1} \tag{10}$$

and

$$\begin{aligned}\Psi_Q^K(b) &= 2\left\{\langle T_Q^K\rangle_{c,1} - \langle T_{-Q}^K\rangle_{c,1}\right\} = -\Psi_{-Q}^K(b)\\ &= 4i\,\mathrm{Im}\,\langle T_Q^K\rangle_{c,1}\end{aligned} \tag{11}$$

To express Ψ_Q^K in terms of the real or imaginary parts of $\left\langle T_Q^K\right\rangle_{c,1}$, we have used a result for $\left\langle T_{-Q}^K\right\rangle$ that is valid in the general case, namely, $\left\langle T_{-Q}^K\right\rangle = (-1)^Q\left\langle T_Q^K\right\rangle^*$, together with the fact that Q is an even integer.

The Thomson structure factors are (Tanaka *et al*., 2004)

$$\begin{aligned}F_\mathrm{c}(\mathbf{k}) &= (4\pi)^{\frac{1}{2}}\sum_{K=2,4,6} i^K \sum_{Q=2,6}\left[Y_{-Q}^K(\hat{\mathbf{k}}) + Y_Q^K(\hat{\mathbf{k}})\right]\\ &\quad\times\langle j_K\rangle\,\Psi_Q^K(a)\\ &= -4\sqrt{\frac{15}{2}}\,\langle j_2\rangle\left(\hat{k}_a^2 - \hat{k}_b^2\right)\mathrm{Re}\,\langle T_2^2\rangle_{c,1} + \cdots\end{aligned} \tag{12}$$

and

$$\begin{aligned}F_\mathrm{c}(\mathbf{k}) &= (4\pi)^{\frac{1}{2}}\sum_{K=2,4,6} i^K \sum_{Q=2,6}\left[Y_{-Q}^K(\hat{\mathbf{k}}) - Y_Q^K(\hat{\mathbf{k}})\right]\\ &\quad\times\langle j_K\rangle\,\Psi_Q^K(b)\\ &= -4\sqrt{30}\,\langle j_2\rangle\,\hat{k}_a\,\hat{k}_b\,\mathrm{Im}\,\langle T_2^2\rangle_{c,1} + \cdots\end{aligned} \tag{13}$$

Dots in these expressions denote terms with tensors of rank 4 and rank 6, and $\hat{k}_a$ and $\hat{k}_b$ are proportional to the Miller indices h and k, respectively. Our findings, (12) and (13), are in complete agreement with experimental data reported by Adachi *et al*. (2002), which we display in Figure 2.

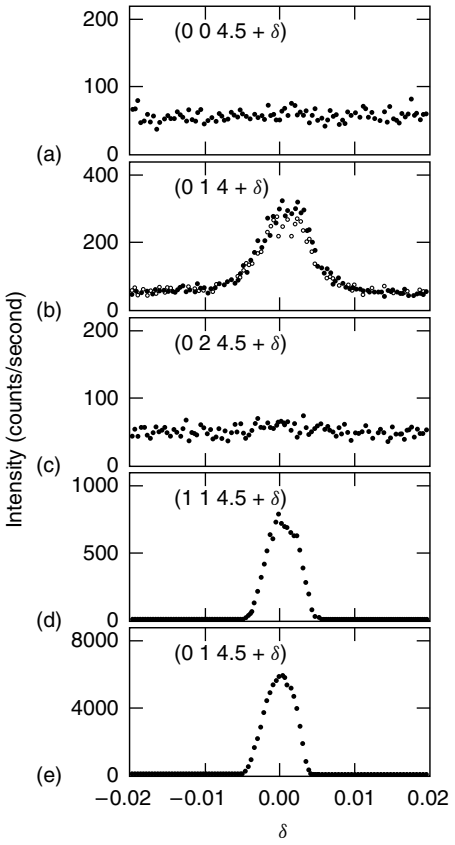

Figure 2. Thomson scattering by DyB_2C_2. Raw data of the l-scan measurements are displayed for various types of reflections. The crystal was held at a temperature of 18 K except for data gathered in scans about (014). Intensities reported in panel (b) were taken at 18 K (solid circles) and 30 K (open circles) and they are attributed to multiple scattering. (Reproduced from Adachi *et al*., 2002, with permission from the American Physical Society. © 2002.)

2.3 Magnetic X-ray scattering

The first correction, in an expansion of E/m_ec^2, to the Thomson contribution of the X-ray scattering length includes magnetic terms. These magnetic terms also appear in the amplitudes for the magnetic scattering of neutrons. In the neutron case, the spin (**S**) and orbital (**L**) magnetic moments of the unpaired electrons in the crystal are linked together and the amplitude is proportional to the total magnetic moment $\mathbf{L} + 2\mathbf{S}$, to a good approximation. By contrast, the magnetic X-ray amplitude is such that the spin and orbital moments can be separately measured (de Bergevin and Brunel, 1981; Brunel and de Bergevin, 1981).

Let us introduce a vector structure factor for spin moments and a vector structure factor for orbital moments, in analogy with the Thomson structure factor $F_\mathrm{c}(\mathbf{k})$. To a first approximation, that is often perfectly adequate for the analysis of observations, our new structure factors are

$$\mathbf{F}_\mathrm{S} \simeq \sum_{\mathbf{d}} f_\mathrm{S}(\mathbf{k};\mathbf{d})\langle\mathbf{S}\rangle_{\mathbf{d}}\mathrm{e}^{i\mathbf{k}\cdot\mathbf{d}} \tag{14}$$

and

$$\mathbf{F}_\mathrm{L} \simeq \frac{1}{2}\sum_{\mathbf{d}} f_\mathrm{L}(\mathbf{k};\mathbf{d})\langle\mathbf{L}\rangle_{\mathbf{d}}\mathrm{e}^{i\mathbf{k}\cdot\mathbf{d}} \tag{15}$$

Here, $f_\mathrm{S}(\mathbf{k};\mathbf{d})$ and $f_\mathrm{L}(\mathbf{k};\mathbf{d})$ are atomic form factors for the spin and orbital moment distributions, respectively, and $f_\mathrm{S}(0;\mathbf{d}) = f_\mathrm{L}(0;\mathbf{d}) = 1$. The general expressions for the

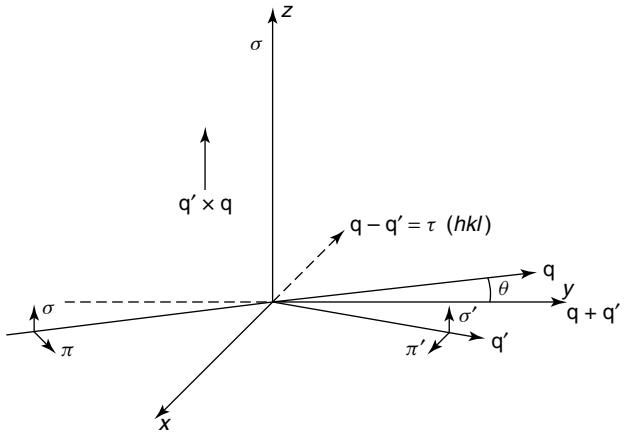

Figure 3. The diagram illustrates the Cartesian coordinate system (xyz) adopted for Bragg diffraction and the relation to the states of polarization, σ and π, in the primary and secondary beams of X rays.

magnetic structure factors can include octupole and higher-order multipole moments.

The magnetic X-ray scattering length has a nontrivial dependence on the polarization in the primary and secondary beams. It is normal practice to label by σ, polarization perpendicular to the plane of scattering, which is defined by $\mathbf{q}$ and $\mathbf{q}'$. Polarization in the plane is labeled by π. Our choice of Cartesian axes (xyz) for the geometry of the experiment is illustrated in Figure 3, where σ and z axis are parallel and $\mathbf{k} = \boldsymbol{\tau}(hkl)$ is directed along $-x$. The X-ray scattering length is expressed as $-r_e\mathrm{G}$, where G is a 2×2 matrix with components $G_{\sigma'\sigma}$, $G_{\pi'\pi}$, $G_{\sigma'\pi}$, and $G_{\pi'\sigma}$. The Thomson structure factor appears in channels where the polarization in the primary beam is not rotated on deflection by the crystal, namely, $G_{\sigma'\sigma}$ and $G_{\pi'\pi}$. These two channels may also contain magnetic components, $F_S^z(\mathbf{k})$ and $F_L^z(\mathbf{k})$, normal to the plane of scattering. The rotated channels, with amplitudes $G_{\sigma'\pi}$ and $G_{\pi'\sigma}$ are purely magnetic, and components of $\mathbf{F}_S(\mathbf{k})$ and $\mathbf{F}_L(\mathbf{k})$ lie in the plane.

It is convenient to express the components of $\mathbf{G}$ in terms of four other quantities specified in the following text:

$$\beta = -\frac{1}{2}(1+\cos 2\theta)\,F_c(\mathbf{k}) - i\delta\sin(2\theta)\left\{F_S^z(\mathbf{k}) + (1-\cos 2\theta)\,F_L^z(\mathbf{k})\right\} \tag{16}$$

$$\alpha_3 = -\frac{1}{2}(1-\cos 2\theta)\,F_c(\mathbf{k}) + i\delta(1-\cos 2\theta) \times \sin(2\theta)F_L^z(\mathbf{k}) \tag{17}$$

$$\alpha_2 = \delta\cos\theta\,(1-\cos 2\theta)\left\{2F_L^y(\mathbf{k}) + F_S^y(\mathbf{k})\right\} \tag{18}$$

$$\alpha_1 = -i\delta\sin\theta\,(1-\cos 2\theta)\,F_S^x(\mathbf{k}) \tag{19}$$

In these expressions, $\delta = E/m_ec^2 = \hbar q/m_ec$, and θ is the Bragg angle illustrated in Figure 3. The virtue in using (16–19), instead of $\mathbf{G}$, lies in the ease of handling polarization. If $\mathbf{P} = (P_1, P_2, P_3)$ is the Stokes vector, the X-ray cross section is simply

$$\frac{d\sigma}{d\Omega} = r_e^2\left\{\boldsymbol{\alpha}^*\cdot\boldsymbol{\alpha} + |\beta|^2 + \beta^*(\mathbf{P}\cdot\boldsymbol{\alpha}) + \left(\mathbf{P}\cdot\boldsymbol{\alpha}^*\right)\beta + i\mathbf{P}\cdot\left(\boldsymbol{\alpha}^*\times\boldsymbol{\alpha}\right)\right\} \tag{20}$$

By way of illustration of (20), let us consider pure charge scattering, that is, set $\mathbf{F}_S(\mathbf{k}) = \mathbf{F}_L(\mathbf{k}) = 0$ in (17–19). The equation (20) then reduces to

$$\frac{d\sigma}{d\Omega} = \frac{1}{2}r_e^2\,|F_c(\mathbf{k})|^2\left\{1+\cos^2(2\theta) + P_3\sin^2(2\theta)\right\} \tag{21}$$

The cross section for X rays polarized perpendicular to the plane $P_3 = +1$ (σ polarization) is larger than the cross section for X rays polarized in the plane $P_3 = -1$ (π polarization).

When the polarization is nearly perfect, the components of $\mathbf{G}$ provide the corresponding cross sections. For example, with pure σ polarization, the unrotated cross section is $r_e|G_{\sigma'\sigma}|^2$. The four components of $\mathbf{G}$ are,

$$\begin{aligned} G_{\sigma'\sigma} &= \beta + \alpha_3 = -F_c(\mathbf{k}) - i\delta\sin(2\theta)F_S^z(\mathbf{k}) \\ G_{\pi'\pi} &= \beta - \alpha_3 \\ G_{\sigma'\pi} &= \alpha_1 - i\alpha_2 \\ G_{\pi'\sigma} &= \alpha_1 + i\alpha_2 \end{aligned} \tag{22}$$

The component $G_{\sigma'\sigma}$ is written out in full to emphasize that it depends on the spin and not on the orbital magnetization.

The spin moment is the dominant magnetic contribution in the limit of small Bragg angles achieved with very hard X rays, and the appropriate cross section has a very simple form. For Bragg diffraction from planes of reflection separated by a distance d and X rays with a wavelength $\lambda \ll d$, the Bragg angle is of the order of (λ/d) and the cross section is

$$\frac{d\sigma}{d\Omega} = r_e^2\left|F_c(\mathbf{k}) + i\left(\frac{\lambda_0}{d}\right)F_S^z(\mathbf{k})\right|^2 \tag{23}$$

Here, $\lambda_0 = (2\pi\alpha a_0) = (2\pi r_e/\alpha) \simeq 0.0243$ Å is the Compton wavelength.

Let us now consider the calculation of $\mathbf{F}_S(\mathbf{k})$ and $\mathbf{F}_L(\mathbf{k})$. Results (14) and (15) are not adequate if the wave vector is large enough for $\langle j_2(k)\rangle$ to be larger than $\langle j_0(k)\rangle$, where $\langle j_K(k)\rangle$ is the Bessel function transform of order K of the radial component of the valence wave function introduced in

Section 2.1. In fact, (14) and (15) become exact in the limit $k \to 0$ at which the atomic form factors are unity.

The definition of $\mathbf{F}_{\mathrm{S}}(\mathbf{k})$ is similar to the definition of the Thomson (charge) structure factor (1), except that $\mathbf{F}_{\mathrm{S}}(\mathbf{k})$ is related to the spatial Fourier transform of the spin density and it is a vector quantity. We have

$$\mathbf{F}_{\mathrm{S}}(\mathbf{k}) = \sum_{\mathbf{d}} \mathrm{e}^{i\mathbf{k}\cdot\mathbf{d}} \left\langle \sum_{j} \mathrm{e}^{i\mathbf{k}\cdot\mathbf{R}_j} \mathbf{s}_j \right\rangle_{\mathbf{d}} \tag{24}$$

where $\mathbf{R}_j$ and $\mathbf{s}_j$ are the position and spin operators of the jth electron associated with the site $\mathbf{d}$ in the unit cell. The orbital structure factor $\mathbf{F}_{\mathrm{L}}(\mathbf{K})$ is constructed from an operator built from $\mathrm{e}^{i\mathbf{k}\cdot\mathbf{R}_j}$ and the linear momentum $\mathbf{p}_j$. One finds

$$\mathbf{F}_{\mathrm{L}}(\mathbf{k}) = \sum_{\mathbf{d}} \mathrm{e}^{i\mathbf{k}\cdot\mathbf{d}} \left\langle \left(\frac{1}{ik^2}\right) \sum_{j} \mathrm{e}^{i\mathbf{k}\cdot\mathbf{R}_j} \left(\mathbf{k} \times \mathbf{p}_j\right) \right\rangle_{\mathbf{d}} \tag{25}$$

In evaluating matrix elements of the operator in (25), one can usefully take advantage of the fact that $\mathbf{F}_{\mathrm{L}}(\mathbf{k})$ appears in $\mathbf{G}$ in a scalar product with vectors that are perpendicular to $\mathbf{k}$, namely, $\mathbf{q} + \mathbf{q}'$ and $\mathbf{q} \times \mathbf{q}'$

Spherical components of structure factors for the magnetic scattering of X rays by spin and orbital moments are

$$\left(\mathbf{F}_{\mathrm{S}}(\mathbf{k})\right)_p = \sum_{KQ} \sum_{K'Q'} (4\pi)^{\frac{1}{2}}\, Y_Q^K(\hat{\mathbf{k}}) \Psi_{Q'}^{K'}(S) \left(KQK'Q'|1p\right) \tag{26}$$

and

$$\left(\mathbf{F}_{\mathrm{L}}(\mathbf{k})\right)_p = \sum_{Q} \sum_{K'Q'} (4\pi)^{\frac{1}{2}}\, Y_Q^{K'-1}(\hat{\mathbf{k}}) \Psi_{Q'}^{K'}(L) \times \left(K'-1QK'Q'|1p\right) \tag{27}$$

In these expressions, $(KQK'Q'|jm)$ is a Clebsch–Gordan coefficient and,

$$\Psi_{Q'}^{K'}(S) = \sum_{\mathbf{d}} \mathrm{e}^{i\mathbf{k}\cdot\mathbf{d}} \left\langle T_{Q'}^{K'} \right\rangle_{S,\mathbf{d}} \tag{28}$$

$$\Psi_{Q'}^{K'}(L) = \sum_{\mathbf{d}} \mathrm{e}^{i\mathbf{k}\cdot\mathbf{d}} \left\langle T_{Q'}^{K'} \right\rangle_{L,\mathbf{d}} \tag{29}$$

Notice that $\mathbf{F}_{\mathrm{S}}$ is essentially a product of two spherical tensors, Y_Q^K and $\Psi_Q^{K'}$, that form a spherical tensor of rank 1 (a vector). The same is true of $\mathbf{F}_{\mathrm{L}}$ and we have in this case added the two contributions $K = K' \pm 1$.

The spherical tensors for spin and orbital magnetization in (28) and (29) are constructed for equivalent electrons in a valence shell with angular momentum quantum number l. For example, in the case of the ion Dy^{+3}, there are nine electrons in the 4f shell ($l = 3$). The spherical tensors are called *Hermitian tensors* for they satisfy (results (30–32) apply to the spin and orbital tensors, and we omit subscripts S and L)

$$\left(T_{Q'}^{K'}\right)^{\dagger} = (-1)^{Q'} T_{-Q'}^{K'} \tag{30}$$

Behavior with respect to time reversal is of paramount importance, and under this transformation

$$T_{Q'}^{K'} \longrightarrow (-1)^{K'+Q'} T_{-Q'}^{K'} \tag{31}$$

The results (30) and (31) tell us how the expectation value $\left\langle T_{Q'}^{K'} \right\rangle$ behaves with respect to reversal of the polarity of a magnetic field acting on the spin. The field, $\mathbf{H}$, can be an applied field or the direction of the spontaneous moment developed by the ion. The requested result is

$$\left\langle T_{Q'}^{K'} \right\rangle_{\mathbf{H}} = (-1)^{K'} \left\langle T_{Q'}^{K'} \right\rangle_{-\mathbf{H}} \tag{32}$$

from which we conclude that multipoles with odd K' are absent in a material with no long-range magnetic order. Tensors with odd (even) K' are said to be time-odd (time-even) on the basis of their behavior with respect to the polarity of $\mathbf{H}$. Under an inversion of the coordinates of the electrons ($\mathbf{R}_j \to -\mathbf{R}_j$ and $\mathbf{s}_j \to \mathbf{s}_j$), the spherical tensors do not change. Tensors with this property are called *parity-even tensors* and they are either true (or polar) tensors that have even K', or pseudotensors (or axial tensors) that have odd K'.

The integer K in (26) is even with $K = 0, 2, 4, \ldots, 2l$. The corresponding integer $K' = K$ and $K' = K \pm 1$. Thus, the spin structure factor can contain both even-rank (polar) tensors and odd-rank (axial) tensors even though the electrons are equivalent and occupy one atomic shell. However, even-rank tensors are often forbidden by a selection rule. One possibility is that $\Psi_{Q'}^{K'}(S)$ vanishes for even K' as a direct result of the motif of magnetic moments. A second possibility is that the reduced matrix element of $T_{Q'}^{K'}$ vanishes for even K'. This is the case when all electrons occupy a single manifold, labeled by quantum numbers S, L, and J. Turning to (27), for the orbital structure factor, the integer K is also even. However, K' is an odd integer and $K' = 1, 3, \ldots, (2l-1)$. In (27), we have exploited a result which relates the two contributions with $K = K' \pm 1$ and a given K'.

Expectation values of the spin and orbital spherical tensors can be calculated, given an appropriate wave function for the valence shell. An individual matrix element in the

expectation value is of the form

$$\left\langle SLJM \left| T^{K'}_{Q'} \right| S'L'J'M' \right\rangle = (-1)^{J-M} \begin{pmatrix} J & K' & J' \\ -M & Q' & M' \end{pmatrix} \times \left(SLJ||T^{K'}||S'L'J' \right) \quad (33)$$

and now we set out expressions for the reduced matrix elements $\left(SLJ||T^{K'}||S'L'J' \right)$. We choose to express the spin and orbital reduced matrix elements in terms of quantities $C(K, K')$ and $A(K, K')$, which are extensively tabulated for 3d and 4f valence shells (Balcar and Lovesey (1989, 2002)). Reduced matrix elements required in (26) and (27) can be derived from the tables in conjunction with the defining relations (Lovesey, 1987)

$$\left(SLJ|| \left(T^{K'} \right)_S ||S'L'J' \right) = i^K (-1)^{J'-J+K'} \times \left\{ \frac{1}{3}(2J+1)(2K'+1) \right\}^{\frac{1}{2}} C(K, K') \quad (34)$$

and

$$\left(SLJ|| \left(T^{K'} \right)_L ||S'L'J' \right) = (-1)^{J'-J+K'} (2J+1)^{\frac{1}{2}} \times \frac{2K'+1}{K'+1} A(K'-1, K') \quad (35)$$

The somewhat awkward form of these relations is a quirk of the historical development of magnetic neutron diffraction in which $C(K, K')$ and $A(K, K')$ were first used. Note that $C(K, K')$ and $A(K, K')$ depend on the full range of quantum numbers required to specify the valence shell of an ion.

We recall that the Thomson atomic tensors introduced in Section 2.1 satisfy (30), while under the time-reversal transform $T^K_Q \to (-1)^Q T^K_{-Q}$ in place of (31). These two properties give $\left\langle T^K_Q \right\rangle_{\mathrm{c},\mathbf{H}} = \left\langle T^K_Q \right\rangle_{\mathrm{c},-\mathbf{H}}$ in place of (32), which confirms that the Thomson atomic tensor is a time-even tensor. It is also a polar tensor.

2.4 Resonant X-ray Bragg diffraction

Figure 4 shows data collected in X-ray Bragg diffraction by V_2O_3 with the sample held at a temperature below its Néel temperature, at which it becomes a fully compensating antiferromagnet Paolasini *et al*. (1999, 2001). The crystal structure is a body-centered cell and all the data in Figure 4 are collected at space-group forbidden reflections, for which the sum of the Miller indices is an odd integer. The panels on the left-hand side of Figure 4 show the intensity as a function of X-ray energy collected near the vanadium K edge, and in the unrotated ($\sigma'\sigma$) and rotated ($\pi'\sigma$) channels of scattering. There is a strong resonance enhancement of the Bragg intensities, and the same phenomenon has been observed with many different resonant ions and many crystal structures. In the case of V_2O_3, the diffraction is due to magnetic multipoles that disorder above the Néel temperature and the Bragg intensities disappear. The strong feature in panel (a) of Figure 4 that sits around 5.475 keV is due to an El event from the vanadium K edge, at which an electron in the 1s core is photoejected in a process that changes orbital angular momentum by one unit. In panel (a), there is a second, weaker feature at an energy of 5.465 eV that is due to an E2 event at the vanadium K edge. With this process, the photoejected electron visits a 3d valence state, which is the state occupied by the unpaired electrons that form the vanadium magnetic moment. Looking at panel (c) in Figure 4, the El event is absent. This observation is one consequence of a selection rule that, for odd h and even $k+l$, forbids resonance events caused by vectorlike interactions, that is, tensors with rank $K = 1$.

Panels (b) and (d) in Figure 4 show Bragg intensities as a function of rotation of the V_2O_3 domain about the Bragg wave vector. If the scattering was from electronic states with no angular anisotropy, the intensity in such scans would be constant. As it is, Bragg intensities depend strongly on the angle of rotation and, also, states of polarization in the diffracted beam.

The data in Figure 4, collected on V_2O_3, nicely illustrates the wealth of information in X-ray resonance-enhanced Bragg diffraction. In this section, we outline a framework for the interpretation of the observations. Applied to V_2O_3, it shows that the observations reported in Figure 4 are in complete accord with the established chemical and magnetic structures. Parity-odd contributions to scattering, which are allowed because the resonant vanadium ions occupy sites that are not centers of inversion symmetry, are not visible in available diffraction data. In particular, data collected in reflections with odd h and even $k+l$ are a direct observation of the vanadium octupole moment created by orbital magnetization in the vanadium 3d valence shell.

Resonance-enhanced Bragg diffraction has most to offer when the intermediate state, visited by the photoejected core electron, is the valence state of the resonant ion occupied by unpaired electrons, namely, 3d, 4f, and 5f states of 3d transition, lanthanide, and actinide ions. In these experiments, the observations are directly related to states that participate in magnetic, magneto-electronic, and charge-ordering effects. Observations on other states of a resonant ion, for example, an El event at the K edge of a 3d transition-metal ion, can provide insight into the valence state of interest but it is less credible because there are more assumptions in the interpretation.

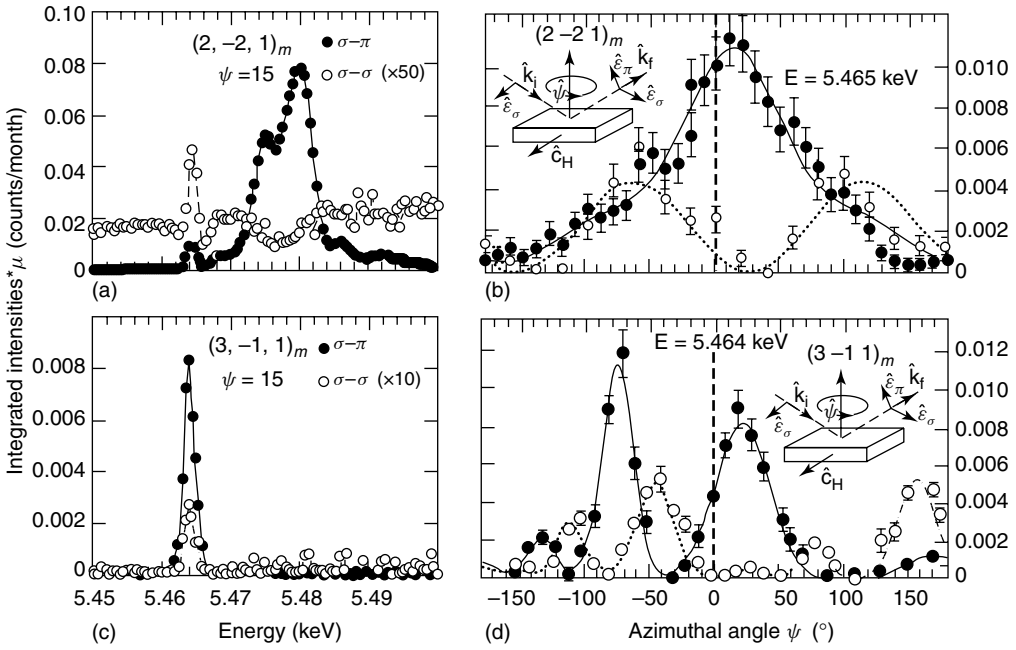

Figure 4. Energy profiles (panels a and c) and azimuthal-angle scans (panels b and d) for resonant Bragg diffraction by a domain within antiferromagnetic V_2O_3. The observations are at space-group forbidden reflections and in channels with unrotated and rotated polarization. (Information taken from Paolasini *et al*., 2001, with permission from Elsevier, and Paolasini *et al*., 1999, with permission from the American Physical Society. © 1999.)

The X-ray scattering length expanded to the first order in E/m_ec^2 has two contributions with denominators that depend explicitly on the X-ray energy. These terms arise in the scattering length from inclusion at the second level of application of the radiation–matter interaction that is linear in the vector potential. To be more specific, the two energy-dependent terms are second order in the current operator, $\mathbf{J}(\mathbf{q}) = \sum(\mathbf{p}_j + i\mathbf{s}_j \times \mathbf{q})e^{i\mathbf{q}\cdot\mathbf{R}_j}$, where $\mathbf{p}_j$, $\mathbf{R}_j$, and $\mathbf{s}_j$ are, respectively, the electron linear momentum, position, and spin operators. We have already encountered these two terms in the limit of large E where they are the source of the contribution to scattering by orbital angular momentum $\mathbf{l} = \mathbf{R} \times \mathbf{p}$. Taken together with the Thomson contribution to the scattering length and the limit of small E, the terms in question produce the Rayleigh limit of the cross section, while the one term that admits an energy resonance gives, in this condition, the Kramers–Heisenberg dispersion formula. Here, we are interested in the energy resonance and its influence on Bragg diffraction, which is a strictly elastic scattering process.

Let us label the virtual intermediate states by the quantum number η. Unlike the initial and final states of the crystal, intermediate states are not from the equilibrium configuration of the crystal and they decay on a timescale $\sim\hbar/\Gamma$, where Γ is the total width of the resonance. The resonant contribution to the scattering length for Bragg diffraction is

$$f = -\left(\frac{r_e}{m_e}\right)\sum_{\eta(\Delta)}\frac{\langle\{\boldsymbol{\varepsilon}'\cdot\mathbf{J}(-\mathbf{q}')|\eta\rangle\langle\eta|\boldsymbol{\varepsilon}\cdot\mathbf{J}(\mathbf{q})\}\rangle}{E-\Delta+i\Gamma/2} \tag{36}$$

where the sum of intermediate states is limited to those that contribute at the resonance energy Δ. Of course, Δ and Γ have a dependence on the intermediate states but this dependence is weak in some cases and the energy profile is observed to be that expected for a single oscillator like (36). Notice that one requires the expectation value of the operators in the numerator of f to describe Bragg diffraction.

Let us examine matrix elements of $\mathbf{J}(\mathbf{q})$. After expanding $\mathbf{J}(\mathbf{q})$ to the first order in $\mathbf{q}$,

$$\langle\eta|\boldsymbol{\varepsilon}\cdot\mathbf{J}(\mathbf{q})|\mu\rangle = (im_e\Delta)\sum_j\left\langle\eta|\boldsymbol{\varepsilon}\cdot\mathbf{R}_j\left(1+\frac{i}{2}\mathbf{q}\cdot\mathbf{R}_j\right)|\mu\right\rangle + \left(\frac{i}{2}\right)\langle\eta|\,(\mathbf{q}\times\boldsymbol{\varepsilon})\cdot(\mathbf{L}+2\mathbf{S})\,|\mu\rangle \tag{37}$$

where $\Delta = E_\eta - E_\mu$ is the energy of the resonance. The first contribution on the right-hand side is the sum of the El and E2 processes, and the second contribution is magnetic and includes a matrix element of the magnetic moment $\mathbf{L} + 2\mathbf{S}$. The relative magnitudes of the magnetic and El contributions is of the order (magnetic dipole/electric dipole) $\sim\mu_B/ea_0$, where μ_B and a_0 are the Bohr magneton and the Bohr radius, and the ratio $\mu_B/ea_0 = \alpha/2$ which leads us to expect that

the El process is the dominant one. On the other hand, the magnitudes of E2 and magnetic processes can be similar at very low energies although evidence in the X-ray region is that the E2 process is the most significant. Similarly, in the X-ray region, E1–E2 interference is more significant than the E1-magnetic interference process. Our calculation of resonant X-ray Bragg diffraction will therefore be based on the El and E2 processes in (37), parity-even events that are pure El or pure E2. Resonant Bragg diffraction in the E1–E2 interference channel, and associated dichroic signals, is discussed by Lovesey *et al*. (2005).

An additional assumption is to neglect in the numerator of (36), its dependence on the projection $\overline{M}$ of the angular momentum of the core state, $\overline{J}$. The assumption is valid in the absence of an interaction between the core state and the photoejected electron, and the absence of a significant exchange coupling of the core and valence states. An energy profile that is very different from a single Lorentzian shape, which is expected for a single oscillator, would suggest that the assumed degeneracy with respect to $\overline{M}$ is not good. The assumption that we make is equivalent to the fast-collision approximation used by Hannon *et al*. (1988, 1989) and Luo *et al*. (1993); See also Carra and Thole (1994).

For an E1 event, we write the resonant X-ray scattering length as

$$f = -\left(\frac{2\pi e}{\lambda}\right)^2 \frac{Z(\mathrm{E1})}{E - \Delta_1 + i\Gamma_1/2} \tag{38}$$

with

$$Z(\mathrm{E1}) = \sum_{\mathbf{d}} \mathrm{e}^{i\mathrm{k}\cdot\mathrm{d}} \sum_{\eta(\Delta)} \left\langle \sum_{j(\mathbf{d})} \{\boldsymbol{\varepsilon}'\cdot\mathbf{R}_j|\eta\rangle\langle\eta|\boldsymbol{\varepsilon}\cdot\mathbf{R}_j\} \right\rangle \tag{39}$$

The prefactor in (38) is obtained by equating Δ with the X-ray energy $E = \hbar cq = 2\pi\hbar c/\lambda$. Since $Z(\mathrm{E1})$ is a scalar quantity, the right-hand side of (39) can be written as a scalar product of a spherical tensor

$$X^K_Q = \sum_{qq'} \varepsilon'_q \varepsilon_{q'} \left(1q\,1q'|K\,Q\right) \tag{40}$$

and an atomic tensor $\left\langle T^K_Q \right\rangle_{\mathrm{E1}}$. The structure factor is

$$F(\mathrm{E1}) = \sum_{K\,Q} (-1)^Q X^K_{-Q} \Psi^K_Q \tag{41}$$

where, as in previous cases,

$$\Psi^K_Q = \sum_{\mathbf{d}} \mathrm{e}^{i\mathbf{k}\cdot\mathbf{d}} \left\langle T^K_Q \right\rangle_{\mathrm{E1},\mathbf{d}} \tag{42}$$

and the sum on **d** is over all resonant ions in the unit cell. Because X^K_Q is constructed from two vector quantities, the triangular condition gives $K = 0$, 1, and 2.

A pure E2 event might be visible in the energy profile at an energy Δ_2 that is usually less than Δ_1. At this juncture, the reader can usefully visit Figure 4. With the assumption that we make, the contribution to the scattering length has the form shown in (38) with a resonance energy and total width Δ_2 and Γ_2, respectively. The numerator $Z(\mathrm{E2})$ is proportional to a structure factor which is a scalar product of H^K_Q that describes the polarization and directions of the primary and secondary X-ray beams, and Ψ^K_Q modeled on (42) but with an atomic tensor $\left\langle T^K_Q \right\rangle_{\mathrm{E2}}$. We find,

$$F(\mathrm{E2}) = \sum_{K\,Q} (-1)^{K+Q} H^K_{-Q} \Psi^K_Q \tag{43}$$

$$\Psi^K_Q = \sum_{\mathbf{d}} \mathrm{e}^{i\mathbf{k}\cdot\mathbf{d}} \left\langle T^K_Q \right\rangle_{\mathrm{E2},\mathbf{d}} \tag{44}$$

The definition of H^K_Q is found in Lovesey *et al*. (2005).

The atomic tensors in (42) and (44) satisfy (30–32). A time-odd contribution to an E1 event can appear in the rotated channel of scattering. This selection rule does not apply to an E2 event.

We see in Figure 4 that the Bragg intensity can vary as the crystal is rotated about the Bragg wave vector $\boldsymbol{\tau}(hkl)$ in an azimuthal-angle scan. The variation is directly related to the angular anisotropy in the valence shell that accommodates the photoejected electron, provided the X-ray beam illuminates a single domain within the crystal. Observations, like the ones reported in Figure 4, thus provide valuable insight into the ordering of the charge and orbital degrees of freedom in the valence shell. In the next section, we examine the observations made on DyB_2C_2.

2.5 Resonant Bragg diffraction by DyB_2C_2

Figure 5 shows the energy spectra of the (0 0 3/2), (0 0 5/2), (1 0 1/2), and (0 0 2) reflections observed for DyB_2C_2 at a temperature below the quadrupole order temperature $T_{\mathrm{Q}} = 24.7\,\mathrm{K}$. The azimuthal angle ψ is defined by the angle between the a axis and the scattering plane. The resonant enhancement at Dy L_{III} absorption edge is successfully interpreted in terms of the coherent sum of two oscillators for E1 and E2 transitions. Here, the E1 transition is from the 2p state to the 5d vacant state, and the E2 is from the 2p state to the 4f vacant state, respectively. Each oscillator is defined by a resonance energy Δ and a width Γ, and the

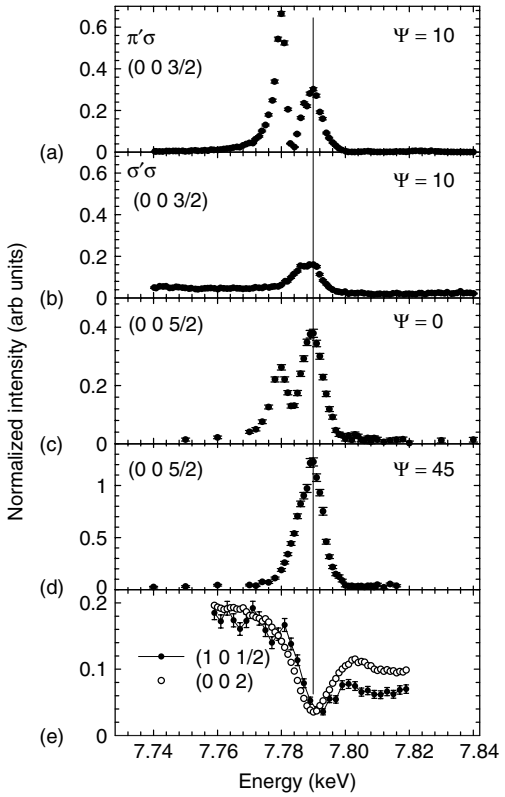

Figure 5. Energy dependence of the intensity of the (0 0 3/2) reflection at $\psi = 10^\circ$ (a) for the $\pi' - \sigma$ channel, (b) that for the $\sigma' - \sigma$ channel; the integrated intensity in ω scans of the (0 0 5/2) (c) at $\psi = 0$ and (d) that at $\psi = 45^\circ$; and (e) intensity of the (1 0 1/2) together with that of the (0 0 2) Bragg reflection. (Reproduced from Tanaka *et al*., 2004, with permission from the American Physical Society. © 2004.)

corresponding scattering length is

$$f_{\mu\nu} = \frac{F_{\mu\nu}^{(E1)}(hkl)}{E - \Delta_1 + \frac{i}{2}\Gamma_1} + r\frac{F_{\mu\nu}^{(E2)}(hkl)}{E - \Delta_2 + \frac{i}{2}\Gamma_2} \tag{45}$$

In this expression μ and ν label the secondary and primary polarizations, respectively, r is an unknown mixing parameter that could depend on μ, ν, and $F_{\mu\nu}^{(E1)}(hkl)$ and $F_{\mu\nu}^{(E2)}(hkl)$ are structure factors for E1 and E2 enhanced diffraction, expressed in terms of mean values of atomic tensors denoted by $\left\langle T_q^{(K)} \right\rangle$.

Scattering enhanced by an E1 event at $(0\,0\,l)$ reflections contain only $\left\langle T_q^{(2)} \right\rangle$. One finds

$$F_{\sigma'\sigma}^{(E1)}(0\,0\,l) = 4\sin(2\psi)\ \mathrm{Im}\left\langle T_{+2}^{(2)} \right\rangle_d \tag{46}$$

$$F_{\pi'\sigma}^{(E1)}(0\,0\,l) = -4\sin\theta\cos(2\psi)\ \mathrm{Im}\left\langle T_{+2}^{(2)} \right\rangle_d \tag{47}$$

In these expressions, we have added a subscript d to atomic tensors to indicate that absorption at the 2p edge and an E1 event lead to a sensitivity to d-like, presumably strongly 5d, valence states. The dependences of E1 structure factors on the azimuthal angle ψ and the Bragg angle θ are consistent with results reported by Tanaka *et al*. (2004).

Structure factors for an E2 event are

$$F_{\sigma'\sigma}^{(E2)}(0\,0\,l) = \sin^2\theta\sin(2\psi)\ \mathrm{Im}\left[3\sqrt{2}\left\langle T_{+2}^{(2)} \right\rangle - \sqrt{11}\left\langle T_{+2}^{(4)} \right\rangle\right] \tag{48}$$

$$F_{\pi'\sigma}^{(E2)}(0\,0\,l) = -\sin\theta\cos(2\psi)\ \mathrm{Im}\left[3\sqrt{2}\left\langle T_{+2}^{(2)} \right\rangle \times(3 - 4\sin^2\theta) + \frac{1}{2}\sqrt{11}\left\langle T_{+2}^{(4)} \right\rangle(1 + \sin^2\theta)\right] \tag{49}$$

The structure factors are linear combinations of the imaginary parts of $\left\langle T_{+2}^{(2)} \right\rangle$ and $\left\langle T_{+2}^{(4)} \right\rangle$, and these atomic tensors describe properties of the Dy 4f valence shell. We note that

$$\left\langle T_{+2}^{(2)} \right\rangle = \frac{1}{\sqrt{6}}\left\langle T_{xx}^{(2)} - T_{yy}^{(2)} + 2iT_{xy}^{(2)} \right\rangle \propto \langle Q_{aa} - Q_{bb} + 2iQ_{ab} \rangle \tag{50}$$

where the Cartesian tensors $\left\langle T_{\alpha\beta}^{(2)} \right\rangle$ are purely real. $F_{\mu\nu}^{(2)}(0\,0\,l)$ contains a component of the quadrupole moment $\left\langle T_{xy}^{(2)} \right\rangle \propto \langle Q_{xy} \rangle$ and that of the hexadecapole $\mathrm{Im}\left\langle T_{+2}^{(4)} \right\rangle$, and all contributions transform according to the representation A_g of $2/m$.

The data shown in panels from (a) to (d) in Figure 5 are interpreted by the coherent sum of two oscillators E1 and E2 transitions as shown in equation 45. The E1 and E2 transitions are located at 7.790 and 7.780 keV, respectively. Note that the E1 event width is so wide that the interference of two oscillators cannot be neglected at $E = \Delta_2$.

Figure 6 shows the azimuthal-angle scans for (0 0 1/2), (0 0 3/2), and (0 0 5/2) reflections, measured at $E = \Delta_1$ and $E = \Delta_2$. The fourfold periodicity and the antiphase signals for the $\sigma' - \sigma$ channel and $\pi' - \sigma$ channel are interpreted by equations from (46) to (49). The mixing parameter, r, in (45) is found to be independent of the states of polarization and independent of the Bragg angle, to a very good approximation. These findings provide confidence in the use of (45) to model the energy profiles.

2.6 Compton scattering

Magnetic Compton scattering is reviewed by Lovesey and Collins (1996) and Cooper *et al*. (2004), where it is argued

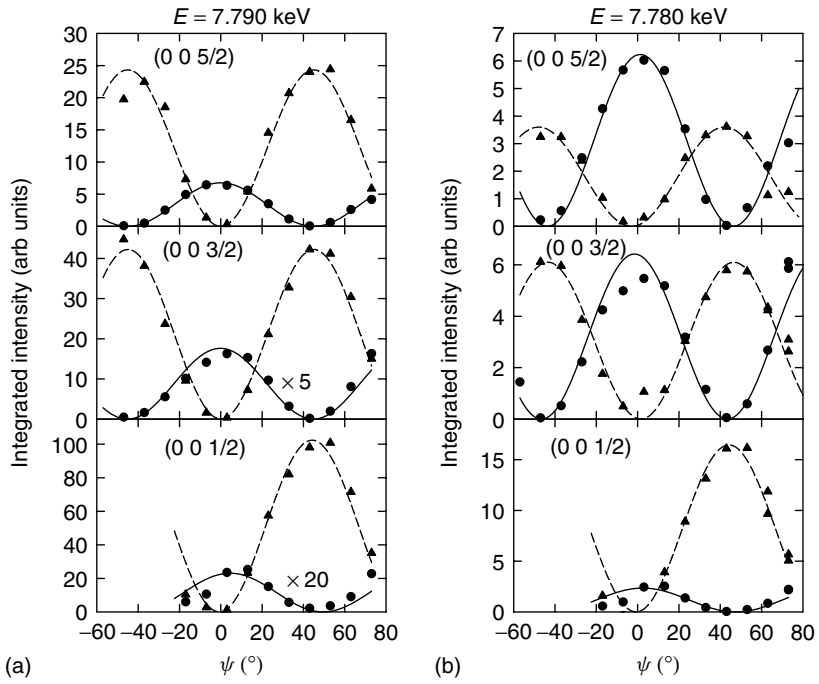

Figure 6. Change of the integrated intensities with the rotation of sample around the reflection vectors, (0 0 1/2), (0 0 3/2), and (0 0 5/2) at (a) 7.790 keV and at (b) 7.780 keV. Azimuthal angle ψ is defined by the angle between the a axis and the scattering plane. Circles (triangles) represent the signal through the $\pi' - \sigma$ ($\sigma' - \sigma$) channel. The full curves and broken curves are squared sinusoidal functions which are fit to each of the data. (Reproduced from Tanaka *et al*., 2004, with permission from the American Physical Society. © 2004.)

that it is a probe of the spin magnetization. Figure 7 shows the Compton profiles observed in extensive experiments on an iron crystal, together with the reconstructed spin density and the corresponding quantity calculated by a band-structure method. Dimunition in density at zero momentum transfer is believed to be a result of negative spin polarization of the s,p-like band electrons, while the surrounding ridge of density is due to d-like electrons in wave functions localized on sites occupied by Fe atoms.

The Compton limit of scattering is achieved with hard X rays. In the energy region $E \sim 40$–60 keV, the parameter $\delta = E/m_e c^2$ is small enough to be a good expansion parameter in which to develop the scattering length, as we indicated in Section 2.3. Experiments performed at much higher energies require, for their interpretation, a theory not based on a simple expansion in powers of δ (Bell, Felsteiner and Pitaevskii, 1996).

Using the scattering length already employed in Section 2.3, and developing the cross section for scattering at the first level of approximation in δ, we find a cross section that is the sum of the standard Compton limit plus an interference between charge and spin amplitudes induced by circular polarization in the primary X-ray beam. The origin of the interference term can be seen in (20). Taking $\mathbf{P} = (0, P_2, 0)$ the polarization dependent terms are of the form $\beta + \alpha_2$ and $\alpha_3 + \alpha_1$. Inspection of (16–19) shows that both $\beta + \alpha_2$ and $\alpha_3 + \alpha_1$ contain contributions of order δ. Only the charge–spin interference contribution to scattering survives in the Compton limit of these two terms.

Let us denote by $\rho(\mathbf{Q})$, the momentum distribution function of the bound electrons in the ground state of the material, namely,

$$\rho(\mathbf{Q}) = \langle \delta(\mathbf{Q} - \mathbf{p}) \rangle \tag{51}$$

where $\mathbf{p}$ in the argument of the δ-function is the operator for the linear momentum of an electron $\hbar = 1$. In the Compton limit of scattering, the conservation of energy is the same as that for scattering by a single, free electron with a wave vector $\mathbf{Q}$, and this is

$$\omega = E_R + \mathbf{k}\cdot\mathbf{Q}/m_e \tag{52}$$

where the recoil energy $E_R = k^2/2m_e$ and ω is the change in energy of the X rays. By setting $Q_0 = m_e(\omega - E_R)/k$ and choosing $\mathbf{k}$ parallel to the z axis, we find

$$\omega - E_R - \mathbf{k}\cdot\mathbf{Q}/m_e = (k/m_e)(Q_0 - Q_z) \tag{53}$$

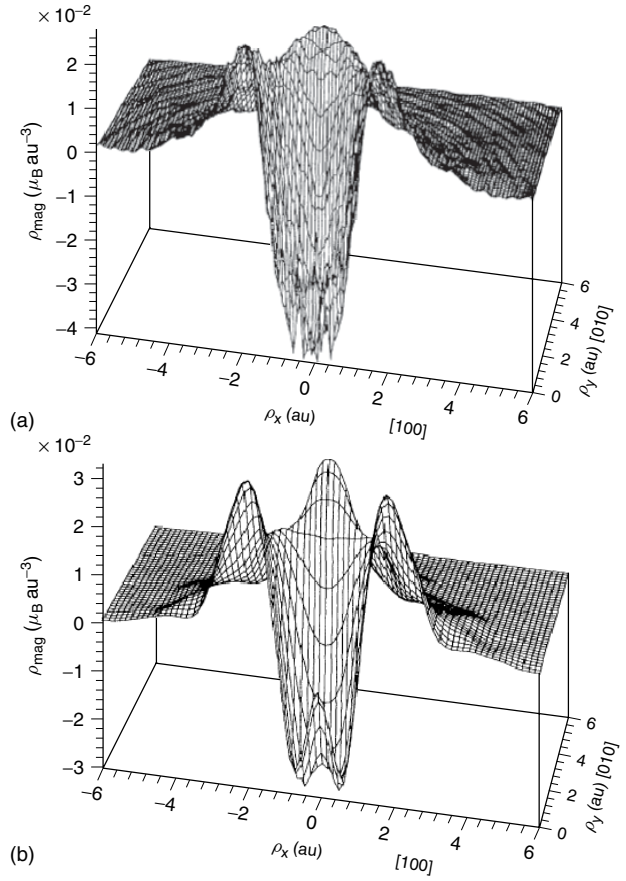

Figure 7. (a) A cross section of the experimental ρ_{mag} in the (001) plane including the Γ point. (b) A cross section of the theoretical ρ_{mag} in the (001) plane including the Γ point. The density is convoluted with the experimental resolution expressed by a Gaussian of full width at half-maximum (FWHM) 0.76 a.u. (Reproduced from Tanaka *et al*., 1993, with permission from the American Physical Society. © 1993.)

With these definitions, the standard Compton limit of scattering is described by a cross section

$$\frac{\mathrm{d}^2\sigma}{\mathrm{d}\Omega \mathrm{d}E'} = \frac{1}{2}(q'/q)r_{\mathrm{e}}^2\left(1+\cos^2 2\theta\right) \times \int \mathrm{d}\mathbf{Q}\rho(\mathbf{Q})\delta(\omega - E_{\mathrm{R}} - \mathbf{k}\cdot\mathbf{Q}/m_{\mathrm{e}}) \quad (54)$$

Here, $E' = E - \omega$ is the final X-ray energy, $\mathrm{d}\Omega$ is the element of solid angle subtended by the X-ray detector, and the X-ray beam is deflected through an angle 2θ. The so-called Compton profile $J(Q)$ is defined by

$$(m_{\mathrm{e}}/k)J(Q_0) = \int \mathrm{d}\mathbf{Q}\rho(\mathbf{Q})\delta(\omega - E_{\mathrm{R}} - \mathbf{k}\cdot\mathbf{Q}/m_{\mathrm{e}}) = (m_{\mathrm{e}}/k)\int \mathrm{d}Q_x \int \mathrm{d}Q_y \rho(Q_x, Q_y, Q_0) \quad (55)$$

We define a spin-weighted Compton profile, $J_S^{\alpha}(Q)$, where α is a Cartesian component, by an expression similar to (55). Let

$$(Nm_{\mathrm{e}}/k)J_S^{\alpha}(Q_0) = \int \mathrm{d}\mathbf{Q}\sum_j \left\langle \delta(\mathbf{Q} - \mathbf{p}_j)s_j^{\alpha}\right\rangle \times \delta(\omega - E_{\mathrm{R}} - \mathbf{k}\cdot\mathbf{Q}/m_{\mathrm{e}}) \quad (56)$$

The integral of $J(Q_0)$ over all Q_0 is unity, whereas the same integral of $\mathbf{J}_S(Q_0)$ is proportional to the spin magnetization.

Adding to (54) the charge–spin interference scattering, we arrive at a cross section

$$\frac{\mathrm{d}^2\sigma}{\mathrm{d}\Omega\,\mathrm{d}E'} = (Nr_{\mathrm{e}}^2 m_{\mathrm{e}}/k)\left\{\frac{1}{2}\left(1+\cos^2 2\theta\right)J(Q_0) - \delta P_2(1-\cos 2\theta)(\hat{\mathbf{q}}\cos 2\theta + \hat{\mathbf{q}}')\times \mathbf{J}_S(Q_0)\right\} \quad (57)$$

In this expression, P_2 is the helicity of the primary beam of X rays, and $\hat{\mathbf{q}}$ and $\hat{\mathbf{q}}'$ are unit vectors with $\hat{\mathbf{q}}\cdot\hat{\mathbf{q}}' = \cos 2\theta$. The charge–spin interference contribution to (57) can be separated from the standard Compton contribution, which is essentially Thomson scattering, by reversing either the magnetizing field applied to the sample or the handedness of primary helicity, P_2. The cross section (57) is the basis of the interpretation of data gathered on iron and displayed in Figure 7.

3 MAGNETIC NEUTRON SCATTERING

Neutrons are scattered by the magnetization in a material that is created by the spin and orbital moments of unpaired electrons (Lovesey, 1987). The orbital interaction is identical to the one encountered in the magnetic scattering of X rays, and the actual operator is displayed in (25). The spin interaction for neutron scattering is also very similar to the spin interaction in X-ray scattering. The one difference between the two cases is that in neutron scattering the spin of an electron is linked to the deflection of the beam in a double vector product $\mathbf{k}\times(\mathbf{s}_j\times\mathbf{k})/k^2$. We denote by $\mathbf{Q}_{\perp}$ the sum of the spin and orbital interactions

$$\mathbf{Q}_{\perp} = \sum_j \mathrm{e}^{i\mathbf{k}\cdot\mathbf{R}_j}\left(\frac{1}{k^2}\right)\left\{\mathbf{k}\times(\mathbf{s}_j\times\mathbf{k}) - i(\mathbf{k}\times\mathbf{p}_j)\right\} \quad (58)$$

A neutron with spin $\mathbf{s}_n$ has a scattering length $\gamma r_{\mathrm{e}}\mathbf{s}_n\cdot\mathbf{Q}_{\perp}$, where $\gamma = -1.9130$ is the gyromagnetic ratio.

The total neutron scattering length is the sum of the nuclear scattering and the magnetic scattering lengths. On borrowing the language adopted in Section 2.3, nuclear

scattering contributes to both β and $\boldsymbol{\alpha}$ while magnetic scattering contributes only to $\boldsymbol{\alpha}$. The cross section for neutron scattering can be derived from (20) where $\mathbf{P}$ is the mean value of $2\mathbf{s}_n$. Purely magnetic contributions to the cross section follow by the identifications $\boldsymbol{\alpha} = \gamma r_e \mathbf{Q}_\perp$ and $\beta = 0$.

3.1 Bragg diffraction

It is often convenient to employ an interaction operator $\mathbf{Q}$ which is related to $\mathbf{Q}_\perp$ through

$$\mathbf{Q}_\perp = \left\{\mathbf{k} \times (\mathbf{Q} \times \mathbf{k})/k^2\right\} \tag{59}$$

In neutron diffraction, we can use $\mathbf{F}_L(\mathbf{k}) + \mathbf{F}_S(\mathbf{k})$ for the expectation value $\langle \mathbf{Q} \rangle$, where the two structure factors are defined by (24) and (25).

For small scattering wave vectors, $\langle \mathbf{Q} \rangle$ is related to magnetic moments. With $\mu = \langle \mathbf{L} + 2\mathbf{S} \rangle$, one has $\mu = g\langle \mathbf{J} \rangle$ for a lanthanide ion, where g is the Landé splitting factor. For a 3d transition-metal ion, $\mu = g\langle \mathbf{S} \rangle$, and the gyromagnetic factor g is close to the value 2 that is correct when the orbital magnetic moment $\langle \mathbf{L} \rangle = (g-2)\langle \mathbf{S} \rangle$ is fully quenched. The small-k limit of $\langle \mathbf{Q} \rangle$ is,

$$\begin{aligned} \langle \mathbf{Q} \rangle &= \mathbf{F}_S(\mathbf{k}) + \mathbf{F}_L(k) \\ &\approx \frac{1}{2} \sum_{\mathbf{d}} e^{i\mathbf{k}\cdot\mathbf{d}} \boldsymbol{\mu}_d \end{aligned} \tag{60}$$

In the more general case, when the scattering wave vector is not particularly small, one needs to use (26) and (27) for the spin and orbital structure factors appearing in (60).

3.2 Inelastic scattering

When both the wave vector and the energy of the radiation change in a scattering event, the cross section is best described in terms of a correlation function. The correlation function in purely magnetic neutron scattering is $\left\langle \mathbf{Q}_\perp^\dagger \cdot \mathbf{Q}_\perp(t) \right\rangle$, where $\mathbf{Q}_\perp(t)$ is the Heisenberg operator created from (58), and $\mathbf{Q}_\perp = \mathbf{Q}_\perp(0)$. The conventional form of the cross section is

$$\frac{d^2\sigma}{d\Omega\, dE'} = (\gamma r_e)^2 (q'/q) S(\mathbf{k}, \omega) \tag{61}$$

where $\mathbf{k} = \mathbf{q} - \mathbf{q}'$ and $\omega = E - E'$ are the changes in the wave vector and the energy ($\hbar = 1$), respectively. $S(\mathbf{k}, \omega)$ in (61) is the Van Hove response function,

$$\begin{aligned} S(\mathbf{k}, \omega) &= \frac{1}{2\pi} \int_{-\infty}^{\infty} dt e^{-i\omega t} \left\langle \mathbf{Q}_\perp^\dagger \cdot \mathbf{Q}_\perp(t) \right\rangle \\ &= \sum_{\alpha\beta} \left(\delta_{\alpha\beta} - \hat{k}_\alpha \hat{k}_\beta\right) \frac{1}{2\pi} \int_{-\infty}^{\infty} dt e^{-i\omega t} \left\langle Q_\alpha Q_\beta(t) \right\rangle \end{aligned} \tag{62}$$

Purely elastic scattering, such as Bragg diffraction, is described by the cross section obtained from (62) with $\left\langle \mathbf{Q}_\perp^\dagger \cdot \mathbf{Q}_\perp(t = \infty) \right\rangle = |\langle \mathbf{Q}_\perp \rangle|^2$.

The most general form of the cross section is derived from (20) treating $\boldsymbol{\alpha}$ and β as operators. Usually, the largest contributions to β and $\boldsymbol{\alpha}$ are the nuclear and magnetic interactions. In the general use of (20), it creates a partial differential cross section, like (61), and each of the five terms on the right-hand side is a response function similar to (62). For example, the third term $\beta^*(\mathbf{P}\cdot\boldsymbol{\alpha})$ in (20) is interpreted as the response function

$$\frac{1}{2\pi} \int_{-\infty}^{\infty} dt e^{-i\omega t} \left\langle \beta^\dagger \mathbf{P}\cdot\boldsymbol{\alpha}(t) \right\rangle \tag{63}$$

Analytic properties of the cross section are discussed by Lovesey and Watson (1998). The cross sections discussed in this section are the basis for the interpretation of data that provides the dispersion of spin waves and critical magnetic fluctuations in magnetic salts and metallic magnets.

REFERENCES

Adachi, H., Kawata, H., Mizumaki, M., *et al*. (2002). Ordered charge asphericity around dysprosium and structural deformation in DyB_2C_2. *Physical Review Letters*, **89**, 206401.

Balcar, E. and Lovesey, S.W. (1989). *Theory of Magnetic Neutron and Photon Scattering*, Clarendon Press: Oxford.

Balcar, E. and Lovesey, S.W. (2002). Neutron diffraction by magnetic crystals: V_2O_3. *Journal of Physics-Condensed Matter*, **14**, 10281–10293.

Bell, F., Felsteiner, J. and Pitaevskii, L.P. (1996). Cross section for Compton scattering by polarized bound electrons. *Physical Review A*, **53**, R1213–R1215.

de Bergevin, F. and Brunel, M. (1981). Diffraction of x-rays by magnetic materials. I. General formulae and measurements on ferro- and ferrimagnetic compounds. *Acta Crystallographica*, **A37**, 314–324.

Brunel, M. and de Bergevin, F. (1981). Diffraction of x-rays by magnetic materials. II. Measurements on antiferromagnetic Fe_2O_3. *Acta Crystallographica*, **A37**, 324–331.

Carra, P. and Thole, B.T. (1994). Anisotropic x-ray anomalous diffraction and forbidden reflections. *Reviews of Modern Physics*, **66**, 1509–1515.

Cooper, M.J., Mijnarends, P.E., Shiotani, N., *et al*. (2004). *X-ray Compton Scattering*, Oxford University Press: Oxford.

Hannon, J.P., Trammell, G.T., Blume, M., *et al*. (1988). X-ray resonance exchange scattering. *Physical Review Letters*, **61**, 1245–1248.

Hannon, J.P., Trammell, G.T., Blume, M., *et al*. (1989). X-ray resonance exchange scattering. *Physical Review Letters*, **62**, 2644.

Lovesey, S.W. (1987). *Theory of Neutron Scattering from Condensed Matter*, Clarendon Press: Oxford, Vol. 1 & 2.

Lovesey, S.W., Balcar, E., Knight, K.S., *et al*. (2005). Electronic properties of crystalline materials observed in x-ray diffraction. *Physics Reports*, **411**, 233–289.

Lovesey, S.W. and Collins, S.P. (1996). *X-ray Scattering and Absorption by Magnetic Materials*, Clarendon Press: Oxford.

Lovesey, S.W. and Knight, K.S. (2001). Calculated x-ray dichroic signals and resonant bragg diffraction structure factors for DyB_2C_2. *Physical Review B*, **64**, 094401.

Lovesey, S.W. and Watson, G.I. (1998). Magnetically scattered polarized neutrons: static and dynamic features of the sample. *Journal of Physics-Condensed Matter*, **10**, 6761–6769.

Luo, J., Trammell, G.T., Hannon, J.P., *et al*. (1993). Scattering operator for elastic and inelastic resonant x-ray scattering. *Physical Review Letters*, **71**, 287–290.

Paolasini, L., Vettier, C., de Bergevin, F., *et al*. (1999). Orbital occupancy order in V_2O_3: resonant x-ray scattering results. *Physical Review Letters*, **82**, 4719–4722.

Paolasini, L., Di Matteo, S., Vettier, C., *et al*. (2001). Interplay between orbital and magnetic long range order by resonant x-ray scattering in $(V_{1-x}Cr_x)_2O_3$. *Journal of Electron Spectroscopy and Related Phenomena*, **120**, 1–10.

Tanaka, Y., Inami, T., Nakamura, T., *et al*. (1999). Evidence of antiferroquadrupolar ordering of DyB_2C_2. *Journal of Physics-Condensed Matter*, **11**, L505–L511.

Tanaka, Y., Inami, T., Lovesey, S.W., *et al*. (2004). Quadrupole and hexadecapole ordering in DyB_2C_2: direct observation with resonant x-ray diffraction. *Physical Review B*, **69**, 024417.

Tanaka, Y., Sakai, N., Kubo, Y., *et al*. (1993). Three-dimensional momentum density of magnetic electrons in ferromagnetic iron. *Physical Review Letters*, **70**, 1537–1540.

Spin Waves: History and a Summary of Recent Developments

D.L. Mills
University of California, Irvine, CA, USA

1 INTRODUCTION

In diverse forms of condensed matter, both the thermodynamic properties and the linear response of materials to external probes are controlled by the nature of the collective excitations in the system of interest. In the case of macroscopic crystals, we have the well-known phonon modes, which are wave like excitations of atomic motions, which propagate through the crystal. Each phonon mode is described by a wave vector $\vec{k}$ which resides in the appropriate Brillouin zone. When $|\vec{k}|a_0 \ll 1$, with a_0 the lattice constant, the dispersion relation of these modes may be described by a continuum theory, the classical theory of elasticity. We must turn to fully microscopic theories when the wavelength and the lattice constant are comparable.

In ordered magnets of all forms (ferromagnets, antiferromagnets, ferrimagnets, . . .) we encounter the spin analog of the phonon modes just described. These are wave like excitations that propagate through the lattice of ordered spins; if we focus on the given spin in the lattice when such a mode is excited, the spin is tipped slightly away from its equilibrium direction and engages in circular or elliptical precession. As one progresses down the lattice of spins in a direction parallel to the wave vector, the phase angle $\varphi(\vec{l})$ associated with the motion of the spin on lattice site $\vec{l}$ varies as $\vec{k} \cdot \vec{l}$, once again with $\vec{k}$ a wave vector in the appropriate Brillouin zone. Introductory descriptions of these excitations may be found in textbooks. For example, see the discussion by Kittel (1976). As in the case of phonons, the energy of spin waves is quantized in units of $\hbar\omega(\vec{k})$, with $\omega(\vec{k})$ the frequency of the spin wave mode with wave vector $\vec{k}$. The relationship between frequency and wave vector is referred to as the *spin-wave dispersion relation*. When one wishes to emphasize the quantum-mechanical character of these collective excitations, one refers to them as *magnons*. For the purposes of this chapter, the term *spin wave* and *magnon* are regarded as interchangeable.

Spin-wave quanta or magnons are thermally excited, and at temperatures well below the magnetic ordering temperature (Curie temperature, Neel temperature) one may develop descriptions of the contribution of the magnetic degrees of freedom to the thermodynamic properties of magnets by combining the dispersion relation with the fact that spin waves are bosons (Kittel, 1963a). We have as an example the celebrated Bloch $T^{3/2}$ law which describes the initial falloff with increasing temperature of the magnetization in ferromagnets (Kittel, 1963a). It is the case as well that spin waves couple to external probes, thus allowing their study by experimental methods such as inelastic neutron scattering (Kittel, 1963b). In addition, they control the response of

Handbook of Magnetism and Advanced Magnetic Materials. Edited by Helmut Kronmüller and Stuart Parkin. Volume 1: *Fundamentals and Theory*. ISBN: 978-0-470-02217-7.

magnetic materials to external probes, so long as one is in the linear response regime. If one wishes to describe a ferromagnetic resonance (FMR) experiment, for example, the physical origin of the resonant absorption is excitation of a long wavelength spin wave by the microwave field which illuminates the sample.

At the time of this writing, the theory of spin waves, along with their interaction with each other and with external probes is a mature, well-developed field. It is the case as well that experimental studies of spin waves and their influence on materials is also very well developed. Owing to this, it is impossible to review the field in any meaningful sense in a brief chapter such as this. We refer the reader to the classic Rado–Suhl volumes (Rado and Suhl, 1963a, 1963b, 1965, 1966), within which the reader will find an excellent collection of articles that describe basic aspects of spin waves and their interactions. These volumes, though published many years ago, still stand as excellent reference material on fundamental aspects of this topic. We shall focus here on recent developments. Our discussion will be focused on the theory and experimental study of the spin wave excitations in the ultrathin ferromagnets, which play such a central role in contemporary nanoscale magnetic devices. We shall also discuss the nature of spin waves in the bulk 3d ferromagnets and the means of studying them experimentally, since this will acquaint us with physics we need to understand spin dynamics in ultrathin metallic magnets. It should be remarked that in our discussion, we not only focus on very recent developments but also cover a considerable amount of material which has appeared after the Rado–Suhl volumes were published but nonetheless some years ago. This is required, in the mind of the author, to set down the conceptual basis for the work of more recent years.

Before we turn to this topic, some additional general remarks are in order. The ultrathin films of current interest are fabricated largely from the 3d ferromagnetic elements or their alloys. Certainly magnetism in bulk forms of the 3d ferromagnets along with that in thick (micron range) films has been studied in great detail for many decades. However, surprisingly our knowledge of the spin waves in these materials is not so complete. FMR studies and Brillouin light scattering (BLS) have provided us with detailed information on spin-wave modes in the regime where the wavelengths are long compared to the lattice constant. FMR probes modes in these metals whose wavelength is comparable to the microwave skin depth, the order of a micron. BLS, a spectroscopy confined to the near surface because of the optical skin depth ($\sim$150–200 Å), allows one to probe modes which propagate parallel to the surface with wavelengths of the order of that of visible light, approximately one-half micron. As we shall see, spin-wave modes of such long wavelengths may be described by a phenomenology similar in spirit to the theory of elasticity when it is applied to the description of phonons.

To obtain truly microscopic information on the physics of the response of the spin system, one needs to study modes whose wavelength is comparable to the underlying lattice constant. The method used standardly in the study of short wavelength collective excitations in condensed matter physics, the inelastic scattering of thermal neutrons, in these materials can probe only the near vicinity of the center of the Brillouin zone, perhaps wave vectors smaller than $10^7\,\mathrm{cm}^{-1}$. The reason for this is that the spin system is very 'stiff' in the 3d ferromagnets, with the consequence that the excitation energy of short wavelength spin waves ($|\vec{k}| \sim 10^8\,\mathrm{cm}^{-1}$) is in the range of 250–300 meV. Such large excitation energies are beyond the reach of thermal neutrons. Spallation sources must then be used, and it is also the case that the neutron excitation cross section is very small at large wave vectors. Experimental studies of short wavelength neutrons in the 3d ferromagnets are thus a challenge, with the consequence that only few studies are found in the literature.

Theoretical description of spin waves in these materials is also a challenge. The materials are itinerant ferromagnets, wherein the magnetic moment carrying electrons reside in the broad 3d energy bands, whose width is the order of 4 eV. (For an introduction to the fundamental physics of itinerant magnets, see the lengthy discussion by Herring, 1966.) Thus, one must begin with a full electronic structure calculation of the ferromagnetic ground state, and then generate a description of the spin waves through use of a methodology such as time dependent density-functional theory. Such an undertaking has been possible for a number of years now for bulk materials, but since data on the short wavelength spin waves is sparse, theoretical efforts which explore the entire Brillouin zone (as opposed to the spin-wave exchange stiffness which controls the long wavelength form of the dispersion relation) are not so large in number. It is curious and surprising that at the time of this writing, our knowledge of short wavelength spin waves in these most common of ferromagnets is less complete than those in very complex materials.

We shall see that a recently developed experimental method, spin polarized electron energy loss spectroscopy (SPEELS), now allows us to examine short wavelength spin waves in ultrathin films out to the boundary of the surface Brillouin zone. The method overcomes the difficulty associated with neutron probes through use of beam electrons with kinetic energy of several electron volts. It is the case as well that one realizes an appreciable cross section for exciting modes of short wavelength with this method.

The outline of this chapter is as follows. In Section 2, we discuss experimental methods of exciting and probing spin waves in the 3d transition-metal ferromagnets, with emphasis

on recent studies of ultrathin films. In Section 3, we discuss theoretical methods for describing these excitations. We remark that in this chapter our aim is to acquaint the reader with basic concepts, and we direct the reader to representative papers in the literature. This is not an exhaustive review, in which all papers in the subarea covered are cited and discussed. Relevant references are found in the papers we cite.

2 EXPERIMENTAL PROBES OF SPIN WAVES IN THE 3D FERROMAGNETS

In this section, we shall survey the principal experimental methods for exciting spin waves in bulk ferromagnetic metals, and also in the ferromagnetic ultrathin films. Two of the methods, FMR and BLS, probe modes whose wavelength is very long compared to the lattice constant. The second two we discuss, inelastic neutron scattering and SPEELS, endow us with the ability to look at modes whose wavelength is comparable to the underlying lattice constant, though neutron scattering has the limitations noted in the preceding text. We begin with some introductory remarks.

If our interest is in spin-wave modes with wavelength long compared to the lattice constant, then a description of the modes may be obtained from a phenomenology based on the Landau–Lifschitz–Gilbert (LLG) equation. This describes the motion of the magnetization per unit volume $\vec{M}(\vec{r}, t)$; the notion is that we may consider a volume whose linear dimensions are small compared to the wavelength of the mode of interest, and within this volume we have a large number of spins coupled together tightly by the strong exchange interactions responsible for the ferromagnetism. The magnetization per unit volume is then a vector of fixed length, which precesses in response to various effective magnetic fields, which exert a torque on it. For our purposes here, we write the LLG equation in the form

$$\frac{\mathrm{d}\vec{M}(\vec{r}, t)}{\mathrm{d}t} = -\gamma[\vec{H}_{\mathrm{eff}}(\vec{r}, t) \times \vec{M}(\vec{r}, t)] - \frac{G}{\gamma M_{\mathrm{S}}^2}\left[\vec{M}(\vec{r}, t) \times \frac{\mathrm{d}\vec{M}(\vec{r}, t)}{\mathrm{d}t}\right] \quad (1)$$

Here γ is the magnitude of the gyromagnetic ratio, and $\vec{H}_{\mathrm{eff}}(\vec{r}, t)$ is the effective magnetic field which drives the spin precession. The second term is a phenomenological damping term. We will have much to say about the appropriateness of this term in our discussion of FMR linewidths in ultrathin films.

The effective magnetic field has several contributions. First, there will be an externally applied Zeeman field, which gives rise to an internal field that one may assume to be constant in magnitude and direction for many simple sample geometries. Anisotropy contributes to the effective field along with macroscopic dipolar fields generated by virtue of motions of the spins. Also exchange interactions between the spins provide a restoring torque, which resists spatial gradients. This leads to a contribution to the effective field of the form $(D/M_{\mathrm{S}})\nabla^2\vec{M}(\vec{r}, t)$, where M_{S} is the saturation magnetization, and D is a parameter called the exchange stiffness, a magnetic analog to the elastic constants of elasticity theory. We shall present a more detailed discussion of this long wavelength phenomenology in Section 3.

The LLG equation is a nonlinear differential equation when written out in full, and allows a discussion of large amplitude motions of the spin system within the framework of its phenomenological basis. Spin waves are the magnetic normal modes, which describe small amplitude deviations of the spins from the ferromagnetic equilibrium orientation. Thus, in the infinitely extended crystal, one obtains a description of spin waves by linearizing the LLG equation and then seeking plane wave solutions where the small deviations have the dependence on space and time given by $\exp[i(\vec{k} \cdot \vec{r} - \omega(\vec{k})t)]$. From this procedure one can generate a dispersion relation for the spin waves. We shall quote the result for a simple case. We consider an infinitely extended ferromagnet with magnetization directed along an easy axis, and external Zeeman field applied parallel to the easy axis. The dispersion relation is then given by (Kittel, 1963a)

$$\omega(\vec{k}) = \gamma[(H + Dk^2)(H + 4\pi M_{\mathrm{S}} \sin^2\theta_{\vec{k}} + Dk^2)]^{1/2} \quad (2)$$

In this expression, $H = H_0 + H_{\mathrm{a}}$ is the sum of the external Zeeman field H_0 and the effective anisotropy field H_{a}, which acts parallel to the easy axis. The angle $\theta_{\vec{k}}$ is the angle between the wave vector $\vec{k}$ and the easy axis.

With the dispersion relation in equation (2) in hand, we can now discuss aspects of FMR and BLS in the metallic ferromagnets. We begin first with bulk materials or thick (several micron) films, and then we turn our attention to ultrathin ferromagnets.

2.1 Ferromagnetic resonance studies of the 3d ferromagnets

2.1.1 Bulk materials

In a FMR study, microwaves illuminate the sample, and one realizes resonant absorption of the microwaves when their frequency matches that of the long wavelength spin waves. In the usual geometry, the magnetization is parallel to the sample surface. The wave vector of the microwaves is normal

to the surface, and hence the wave vectors of the spin waves excited in the experiment are normal to the magnetization and also to the surface. Thus, in this geometry the dispersion relation of the spin waves is given by equation (2), for the case where the angle $\theta_{\vec{k}}$ is 90°.

The wavelength of the microwaves is so long that one might suppose one could also set the wave vector $\vec{k}$ to zero in equation (2). However, in the metallic 3d ferromagnets, the microwave field does not penetrate into the sample in a uniform manner, but is limited to the skin depth δ_0. As one approaches the ferromagnetic resonance frequency of the system, excitation of the spins in the ferromagnet causes the spin depth to contract. The skin depth is given by $\delta(\omega) = \delta_0/\sqrt{\mu_{\text{eff}}(\omega)}$, where $\mu_{\text{eff}}(\omega)$ is an effective susceptibility that peaks strongly on resonance. (For a recent discussion of the influence of the frequency variation of the skin depth on microwave devices, we refer the reader to a paper by Camley and Mills, 1997.) On resonance, the effective skin depth can contract to only a few hundred angstroms. Suppose, under these circumstances, one makes a spatial Fourier decomposition of the microwave field inside the sample. The resulting spectrum will contain a range of wave vectors from zero up to values as large as $10^6\,\text{cm}^{-1}$. Under these circumstances, the microwave field may excite finite wave vector spin waves, with wave vectors extending over this entire range. Thus, the frequency shifts contained in the exchange term Dk^2 must be incorporated into any analysis of data. We may use the value of the exchange stiffness of Fe to set the scale of such effects. In Fe, $D \sim 2.5 \times 10^{-9}\,\text{G-cm}^2$. Thus, in magnetic field units, a spin wave with wave vector of $10^6\,\text{cm}^{-1}$ is shifted away from the nominal FMR frequency $[H(H + 4\pi M_S)]^{1/2}$ by some 250 G.

Under the conditions just described, even in the absence of damping of the spin motions, the FMR spectrum will consist of a rather broad line, with line shape controlled by the spatial Fourier spectrum of the microwave field, which penetrates into the sample. In such experiments, one scans applied field and measures microwave absorption at fixed frequency; one realizes absorption of energy by spin waves over a rather wide range of fields.

It then follows that in such studies, one cannot determine the damping constant G which appears in the LLG equation simply from the observed width of the feature seen in the FMR spectrum. One must fit the spectrum carefully by a description of the absorption provided by an analysis based on application of the Maxwell equations in combination with the LLG equation. The theory of FMR absorption in the ferromagnetic metals was developed many years ago (Amendt and Rado, 1955). We refer the reader to a classic experimental study of ferromagnetic resonance in these materials, where detailed comparisons between theory and experiment were presented (Bhagat and Lubitz, 1974). These authors conclude that the damping term, which appears in the LLG equation accounts very well for their data, and they extract values for the (temperature dependent) damping constant G over a wide range of temperatures. Data is presented for Fe, Ni, and hcp-Co.

2.1.2 *Ultrathin films*

FMR has been used actively in the study of ultrathin ferromagnnets for well over a decade, at the time of this writing. It has proved a powerful means of exploring aspects of magnetism unique to these materials, along with damping or relaxation mechanisms not operative in the bulk ferromagnetic metals. Before we begin our discussion, we remark that the term ultrathin ferromagnet refers to a film consisting of a small number of atomic layers, from two or three layers to perhaps twenty or so. The thickness of these films thus ranges from a few angstroms to perhaps 50 Å.

First, we comment on the spin-wave spectrum of such materials. As noted above in a FMR measurement, one excites spin-wave modes whose wave vector parallel to the surface is very close to zero. In the case of FMR studies of thick, bulk crystals of the 3d ferromagnetic metals, we saw that in such measurements, a continuum of modes are excited; the wave vector perpendicular to the surface can take on any desired value, so long as it lies within the appropriate two-dimensional Brillouin zone. The range of wave vectors excited depends on the spatial profile of the microwave field inside the sample. In films of finite thickness, the perpendicular component of the wave vector is quantized, and assumes values of $\approx n\pi/d$ where d is the film thickness, and n an integer. The lowest mode with $n = 0$ is the uniform mode, wherein all spins in the film precess in phase. Consider the first standing wave mode, with $n = 1$. When we examine the structure of equation (2) in the preceding text, we see that the term $D(\pi/d)^2$ upshifts the mode in frequency in very much the same manner as a larger applied magnetic field. Suppose we consider the magnitude of this shift in a film whose thickness is in the range of 30 Å. We recall from our example in the preceding text that in Fe, we have $D \sim 2.5 \times 10^{-9}\,\text{G-cm}^2$. The exchange induced frequency shift of the first standing wave spin-wave mode for a 30-Å Fe film is thus equivalent to that provided by an effective field in the range of 2.5×10^5 G! The frequency of such a mode is in the 100 GHz range, well outside the regime accessible to conventional FMR spectrometers. Hence, in the ultrathin films under discussion here, the microwaves excite a single mode of the film, the uniform mode wherein all spins precess coherently.

The frequency of the uniform mode provides one with access to key properties of the ultrathin film, such as the anisotropy and also the value of the magnetization M_S.

Of central interest in the study of these materials is the nature of the anisotropy, which can be dramatically different than that found in bulk materials. It is beyond the scope of the present chapter to provide the reader with an understanding of the origin of anisotropy in ferromagnets, but we can provide a brief sketch. There are two forms of anisotropy, each with a very different origin. One, referred to as *shape anisotropy*, has its origin in the fact that ferromagnetic alignment of atomic moments creates a macroscopic dipolar field. If a thin film is magnetized in the z direction normal to its surfaces, one sees easily that magnetic poles on the film surface lead to an internal field of strength $-4\pi M_S \hat{z}$ perpendicular to the film surfaces, and antiparallel to the magnetization. Conversely, if the film is magnetized parallel to its surface, there is no such internal field. A consequence is that shape anisotropy forces the magnetization in ferromagnetic films to lie in plane, under circumstances where it is dominant. The second form of anisotropy has its origin in spin-orbit coupling, and the interaction of the moment bearing ions in the material with crystalline fields from the neighboring ions. This provides the magnetic moments with the means of sensing the local site symmetry. For a magnetic ion which sits in a site of cubic symmetry, the spin orbit induced anisotropy is quite weak, whereas in sites with uniaxial symmetry it can be up to 2 orders of magnitude stronger than for cubic sites. Elsewhere, in an article directed toward ultrathin ferromagnets, the present author has set forth a simple physical picture which allows one to appreciate why this is so (Mills, 1994).

In an ultrathin film, a very large fraction of the magnetic ions sit in either surface or interface sites, whose symmetry is necessarily very low. In a five-layer film, for instance, 40% of the ions sit in such sites. As a consequence, in an ultrathin film of Fe or Ni, the spin-orbit anisotropy can be enormously larger than realized in the bulk. It can overwhelm the shape anisotropy in magnitude and for many film/substrate combinations one can realize films where the easy axis is in fact normal to the surface. An additional source of spin orbit induced anisotropy arises from the mismatch between the lattice constants of the material in the film and the substrate. This results in films whose interior sites have tetragonal rather than cubic symmetry, and once again the easy axis associated with this source can be either normal to or in the plane perpendicular to the film surfaces. Clearly, one can control both the strength and character of the very strong anisotropy realized in ultrathin ferromagnets by varying the growth conditions, the substrate, and also the composition of any capping layer that may be present. This allows one to create materials with desired hysteresis loops or microwave response by design. One may refer to spin engineering in these materials, a magnetic analogue of the band gap engineering so important in semiconductor device design.

FMR proves to be a most powerful means of deducing the nature of the anisotropy present in any sample of interest. The key measurement is the variation of the FMR resonance field with angle relative to the various symmetry axes of the system. Such data can be interpreted in impressive quantitative detail, to provide one with a remarkably detailed picture of all aspects of anisotropy. We refer the reader to excellent articles where such experiments are reviewed, and the analysis required to interpret the data is discussed (Prinz, 1994; Heinrich, 1994).

An issue discussed very actively in the recent literature is the nature of the damping of the spin motions in ultrathin ferromagnets. Is the physics which underlies the damping in these systems the same as in the bulk 3d ferromagnets, or does one have new mechanisms unique to the ultrathin film environment, not present in the bulk? Indeed, one may also inquire if the damping term in the simple LLG equation is applicable to the thin-film environment; perhaps a more complex form is appropriate. These questions are very important from the point of view of contemporary device technology. Devices which contain ultrathin ferromagnets depend on either small amplitude motions of the magnetization, or perhaps its complete reversal as the basis for their operation. The speed of the device is clearly then controlled by damping rates realized on the nanoscale. By now it is very clear that in ultrathin films, new damping mechanisms not present in bulk materials are operative, and these can often be the dominant source damping. It is now well established that in commonly encountered structures, the damping term provided by the LLG phenomenology is qualitatively incorrect. We conclude this section with comments on this issue.

Two mechanisms unique to ultrathin ferromagnets have been invoked in discussions in the literature. One is intrinsic, and operative for ultrathin films on metallic substrates and the second is extrinsic and relies on growth defects to be activated.

The intrinsic mechanism is referred to in the literature as the spin pumping contribution to the damping rate. In physical terms, it is best visualized within the picture where we have local moments of spin $\vec{S}$ localized on each lattice sites. Each such local moment is coupled to conduction electrons by an exchange interaction $-J\vec{S}\cdot\vec{\sigma}$ with $\vec{\sigma}$ the conduction electron spin. While this is surely an oversimplified description of the 3d ferromagnets, which are fully itinerant in character, nonetheless this model has been used frequently in the literature, particularly in the early papers on spin pumping. When the FMR spin wave is excited, the local moments on the lattice engage in coherent precession. Through the exchange interaction just described, they transfer angular momentum to the conduction electrons. This results in a spin current normal to the interface between the film

and the substrate (assumed metallic), and there is thus a loss of spin angular momentum within the system of precessing local moments. This is then a damping mechanism, which relaxes the excited spins by returning them to their equilibrium orientation. This mechanism was first proposed as a relaxation mechanism by Berger (1996) and Slonczewski (1999). FMR studies in which this mechanism was found to play a key role were reported by Urban, Woltersdorf and Heinrich (2001). It should be remarked that this mechanism is fully compatible with the phenomenological damping term in the LLG equation. For instance, it provides a contribution to the FMR linewidth, which scales linearly with frequency, very much as provided by the phenomenology. In the recent literature, theoretical treatments have appeared which recognize the fully itinerant character of the magnetism in the 3d transition-metal films studied in these experiments. We shall discuss these in more detail in Section 3. Thus, we have a new mechanism operative for ultrathin films, and it may be incorporated into LLG phenomenology.

As noted above, a second mechanism found to contribute to the FMR linewidth and to spin damping in ultrathin ferromagnets is extrinsic in origin. This is referred to in the literature as two-magnon damping, a term introduced decades ago in the literature on FMR linewidths in macroscopic garnet samples. Thus, some brief historical remarks will prove useful.

Early experimental studies of FMR linewidths in the garnets encountered lines very much wider than expected from theory applied to the ideal Heisenberg ferromagnet, with localized spins coupled by exchange and dipolar interactions. In a key experimental paper, it was found that the FMR linewidth depended sensitively on the size of grit used to polish the sample surfaces (LeCraw, Spencer and Porter, 1958). In a seminal theoretical paper, Kittel and coworkers developed a theory based on what they called *two-magnon scattering* which provided an excellent account of the observations (Sparks, Loudon and Kittel, 1961). These authors noted that the frequency ω_{FMR} of the FMR modes in the garnet spheres used in the experiments is degenerate in frequency with finite wave vector spin waves, whose dispersion relation is given in equation (2) above for the limit where the wavelength of the spin wave is small compared to the radius of the sphere. Now for an absolutely perfect spherical sample, all of the spin wave modes are independent normal modes of the system, so energy cannot be transferred directly from the uniform precession FMR mode to the degenerate short wavelength spin waves. However, if defects are present in the sample, energy may be scattered from the FMR mode to the degenerate short wavelength spin waves through a matrix element provided by the defect. In the case of the garnet spheres, surface pits produced in the polishing process proved to be the source of the scattering. In the language of resonance physics, the two-magnon contribution to the linewidth is a dephasing mechanism. A process that scatters a spin wave quantum of the FMR mode to a short wavelength spin wave scrambles the phases of the spins all of which initially precess in phase.

It is the case that in ultrathin ferromagnetic films magnetized in plane, there are also finite wave vector spin waves degenerate with the uniform FMR mode. This occurs because of a peculiar aspect of the magnetic dipolar interaction between spins in the two-dimensional environment. If one has a film of thickness d, and considers the influence of dipolar interactions on spin waves whose wave vector satisfies $kd \ll 1$, then the dipolar interaction contributes a term to the dispersion relation *linear* in wave vector. For an in plane magnetized film and for range of propagation angles, the coefficient of this term is negative, so the spin-wave frequency decreases with increasing wave vector. The presence of exchange stiffness provides the contribution Dk^2, very much as in equation (2), so there is a minimum in the dispersion relation at a wave vector k_m which is in the range of $10^5\,\mathrm{cm}^{-1}$ for typical films. (A detailed theory of the contribution of two-magnon scattering in ultrathin films has been presented by Arias and Mills, 1999). Experimental confirmation of key predictions of the theory is found in the studies of Azevedo, Olivera, de Aguiar and Rezende (2000) and in earlier work of the NIST group, who suggested the importance of this mechanism in ultrathin ferromagnets grown on exchange biasing substrates (McMichael, Stiles, Chen and Egelhoff, 1998). It is now clear that this mechanism contributes to the FMR linewidth importantly in diverse ultrathin ferromagnets; it is the case that for films on exchange biased substrates, it is strong and usually dominant. For films on exchange biased substrates, we refer the reader to the theory and fascinating data presented by the Recife group (Rezende, Azevedo, Lucena and Augiar, 2001). We also refer the reader to a review article which discusses early experiments, and the theory (Mills and Rezende, 2003).

A key prediction of the LLG equation is that the FMR linewidth should scale linearly with ω_{FMR}, the frequency of the FMR mode. The theoretical prediction in the paper of Arias and Mills is that when the two-magnon mechanism is dominant, the linewidth should increase much more slowly with frequency than linearly. These authors argued that the observation of apparent linear frequency dependence in early studies (Celinski and Henrich, 1991) is a consequence of sampling a narrow range of FMR frequencies (10, 24, and 36 GHz). It was argued as well that the zero field linewidth inferred indirectly from such data could be an artifact (Arias and Mills, 1999). This discussion stimulated a remarkable series of new measurements of FMR linewidths in ultrathin Fe films, with data from 1 to 80 GHz (Lindner *et al.*, 2003). The data is fitted well by the sublinear dependence predicted

for the two-magnon mechanism, supplemented with a linear term such as that provided by the LLG phenomenology. A possible 'zero field linewidth' was included in the fitting process, but this parameter came out to be vanishingly small. There is also a very large in-plane anisotropy of the linewidth, compatible with the theory if the defects have a symmetry character proposed by Arias and Mills (1999). In the earlier work by the Recife group, it was also established experimentally that one realizes a very strong wave vector dependence in the measured linewidths; an extension of the original theory shows that a fully quantitative account of these observations follows from the two-magnon mechanism (Rezende, Azevedo, Lucena and Augiar, 2001). The LLG phenomenology is a theory of local damping, and there is thus no intrinsic wave vector dependence contained in this picture, in clear disagreement with the data.

Despite the fact the experiments cited in the preceding paragraph shows that the LLG phenomenology commonly provides a qualitatively incorrect description of both the wave vector and the frequency dependence of the linewidths observed in ultrathin ferromagnets, authors still often utilize the predictions of this well-known equation. If one measures the FMR linewidth at rather low frequencies, in the 10 GHz range, and wishes to asses the response characteristics at much higher frequencies, an extrapolation based on an assumed linear frequency dependence can be in serious error. Similarly, as magnetic devices are made smaller and smaller, one will have large spatial gradients in the dynamic magnetization, with the consequence that the strong wave vector dependence absent from LLG phenomenology will be of importance. The reader should keep in mind that for a permalloy film grown on an exchange biased substrate, the linewidth measure in BLS, where the spin-wave vector is in the range of $10^5\ \mathrm{cm}^{-1}$ is over five times larger than that found in FMR on the same sample (Rezende, Azevedo, Lucena and Augiar, 2001). The wave vector dependence can be dramatic, a clear contradiction with the prediction provided by the LLG equation.

Hence unless the origin of the damping mechanism in any given ultrathin film structure is understood, extrapolation of linewidths measured in FMR to higher or lower frequencies must be treated with caution. It is also the case that similar extrapolations to the damping of spin motions with an appreciable spatial gradient can lead to misleading conclusions regarding the damping rate of spin motions.

2.2 Brillouin light scattering studies of spin waves in 3d ferromagnets

We begin with introductory comments. In the BLS experiment, a laser photon is incident on the sample; the photons typically have frequencies in the visible range. The photon may interact with thermal fluctuations in the magnetization within the optical skin depth, typically 100–200 Å for the 3d ferromagnetic metals. Thus, for bulk samples or for films whose thickness is large compared to the optical skin depth, one learns about the nature of spin fluctuations near the surface, whereas in ultrathin films the incident laser fields are uniform throughout the film, to excellent approximation.

In the BLS scattering event, the laser photon can either emit ('Stokes scattering') or absorb ('anti-Stokes scattering') a thermal spin-wave quantum. The frequency ω_S of the scattered photon then follows from energy conservation, $\hbar\omega_S = \hbar\omega_I \pm \hbar\omega_{SW}$, where ω_I is the frequency of the incident photon, and ω_{SW} that of the spin wave involved in the scattering event. If the surfaces are smooth and flat, then the presence of translational symmetry in the plane parallel to the surfaces of the sample (we consider here only bulk, semi-infinite crystals, along with films or multilayers on substrates) requires that wave vector components of the interacting quanta parallel to the surfaces be conserved. Thus, the direction of the outgoing scattered photon is controlled by the conservation condition $\vec{k}_{S\parallel} = \vec{k}_{I\parallel} \pm \vec{k}_{SW\parallel}$. The direction of the outgoing photon is controlled by the wave vector $\vec{k}_{SW\parallel}$, since spin-wave frequencies are orders of magnitude smaller than the photon frequencies. In these statements, $\vec{k}_{\parallel}$ is the projection of $\vec{k}$ onto a plane parallel to the surface. Thus, for a particular scattering geometry, one obtains information regarding the frequencies of the spin waves in the sample whose wave vector projection onto the plane parallel to the surface is $\vec{k}_{SW\parallel}$. In the discussion below, we shall provide examples of BLS spectra taken on thick crystals, in films whose thickness is large compared to the optical skin and also for ultrathin films. Note that the wave vector of the spins probed in such measurements is in the range of that of optical frequency photons, so $|\vec{k}_{SW\parallel}| \sim 10^5\ \mathrm{cm}^{-1}$. Thus, the method reaches out into the Brillouin zone, in contrast to FMR which, as we have seen, samples spin waves for which $\vec{k}_{SW\parallel} \approx 0$. It remains the case, however, that BLS samples spin waves whose wavelength is very long compared to a lattice constant. They are thus well described by the macroscopic phenomenology employed to derive the bulk spin-wave dispersion relation displayed in equation (2), so no truly microscopic information is contained in the data. For this, we require a probe whose wavelength is comparable to a lattice constant. The BLS technique is complementary to FMR. A virtue of BLS is that when the sample is in a fixed external magnetic field, one may scan the frequency response of system in a continuous manner. In contrast, FMR experiment employs a resonant microwave cavity with a single resonance frequency. In FMR, one drives the frequency the spin wave of through the cavity resonance by varying the external magnetic field. In essence, one samples the response

of the system at one single frequency. To scan a broad range of frequencies, one must use several cavities, each with its own resonance frequency. However, the resolution of FMR is far greater than BLS, so FMR allows study linewidths. The BLS method can resolve linewidths only if the modes studies are rather broad.

2.2.1 Spin waves in the BLS spectra of bulk crystals

In this section, we review the information on spin waves one obtains from BLS spectra, which have been taken on thick crystals of the 3d ferromagnets. We should mention that the first BLS study of spin waves in magnetically ordered materials was reported by Grunberg and Metawe, who studied the semiconducting ferromagnet material EuO (Grunberg and Metawe, 1977). A theoretical account of these spectra was given shortly afterward by Camley and the present author (Camley and Mills, 1978a). Very soon after these very beautiful experiments, Sandercock and Wettling reported BLS spectra for thick samples of Fe and Ni. (Sandercock and Wettling, 1978, 1979). Camley and the present author developed the detailed theory of the nature of spin fluctuations near ferromagnetic surfaces, with BLS spectra of the metallic ferromagnets in mind, along with a quantitative theory of the final spectra (Camley and Mills, 1978b). With the emphasis of this chapter in mind, we shall focus our attention on the BLS spectra of the ferromagnetic metals. Before we turn to the nature of the actual spectra we need to comment on the nature of spin wave excitations on the surface of ferromagnetic materials, in the regime where the wavelength is long compared to the underlying lattice constant.

The spin-wave modes of a ferromagnetic film in the usual configuration, magnetized parallel to its surface, were studied in a classic paper by Damon and Eshbach (1960). They employed the magnetostatic approximation, in which the exchange stiffness parameter D is set to zero. By taking the limit as the film thickness becomes infinite and focusing on the near vicinity of the surface, one obtains the spin-wave frequencies and eigenvectors appropriate to the semi-infinite ferromagnet. One has bulk spin waves, whose dispersion relation is described by equation (2) with exchange stiffness set to zero, which can propagate up to and reflect the surface. These have frequencies, which range from γH_0 for propagation parallel to both the surface and the magnetization, to $\gamma[H_0(H_0 + 4\pi M_S)]^{1/2}$ for propagation in plane perpendicular to it. A most striking surface spin wave appears in this theory. Its frequency, $\gamma[H_0 + 2\pi M_S]$ lies *above* the frequency band appropriate to the bulk spin waves. It has the most peculiar feature that it is a 'unidirectional' wave: it will propagate from left to right across the magnetization, but not from right to left. Surface waves with asymmetric left/right propagation characteristics are referred to as having nonreciprocal propagation characteristics. We have here the most dramatic form of nonreciprocal propagation, where one realizes 'one way' propagation only. In a very thick film, with thickness large compared to the penetration depth of the Damon–Eshbach surface wave, on the lower surface of the film, one has a wave which propagates from left to right. The penetration depth of the mode is in fact just $|\vec{k}_{SW\|}|^{-1}$. If the film thickness d is decreased, the eigenvector extends over the entire film when $|\vec{k}_{SW\|}|d \sim 1$, with larger amplitude on the upper surface for right to left propagation, and larger amplitude on the lower surface for left to right propagation. In the thin film limit $|\vec{k}_{SW\|}|d \ll 1$, the eigenvector is uniform across the film and the frequency of the mode drops to the FMR frequency $\gamma[H_0(H_0 + 4\pi M_S)]^{1/2}$. As we shall see shortly, the Damon–Eshbach surface spin wave is a prominent feature in the BLS spectra of thick ferromagnetic crystals. We remark that this mode exists only when the magnetization is parallel to the surface, and there is no analogue of it when the magnetization is normal to the surface. For a discussion of the effects on Damon–Eshbach surface spin waves of tipping the magnetization out of plane, see the discussion presented by Rahman and the present author (Rahman and Mills, 1982).

The discussion in the previous paragraph describes magnetostatic spin waves, that is, modes whose wavelength is sufficiently long that exchange may be ignored in their description. As we see again from equation (2), as wave vector increases, exchange as manifested in the Dk^2 term in this equation, upshifts the frequency of short wavelength bulk spin waves above the upper bound $\gamma[H_0(H_0 + 4\pi M_S)]^{1/2}$ appropriate to the long wavelength magnetostatic waves. Thus, we have short wavelength bulk spin waves, upshifted by exchange, degenerate with the Damon–Eshbach wave. Camley and the present author have carried out detailed theoretical studies which show that even for a perfectly flat surface in the semi-infinite crystal, finite wave vector, Damon–Eshbach surface waves acquire a finite lifetime by decaying onto degenerate bulk spin waves. The lifetime associated with this process decreases with increasing wave vector, and vanishes at zero wave vector (Camley and Mills, 1978b).

The points discussed above are illustrated in Figure 1, where we reproduce a comparison between theory and experiment, for a BLS spectrum taken on bulk crystalline Fe magnetized parallel to its surface. The scattering geometry is arranged so the wave vector transfer is perpendicular to the magnetization. On the Stokes side, we see the strong, sharp peak associated with Brilluoin scattering from the Damon–Eshbach surface spin wave. The absence of such a feature on the anti-Stokes side of the spectrum is an elegant demonstration of the 'one way' character of these modes, as discussed above. If the magnetization is reversed,

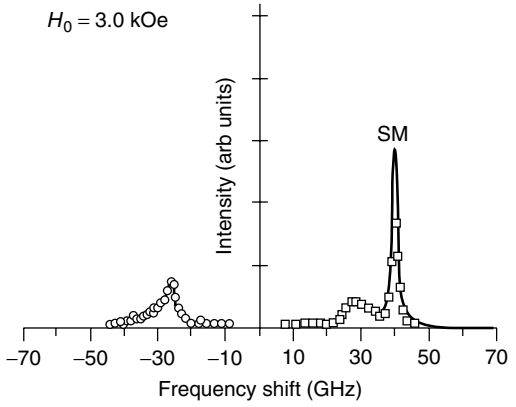

Figure 1. A comparison between theory (solid line) and experiment (open dots), for a Brilluoin light scattering spectrum taken on a single crystal of ferromagnetic Fe. The feature labeled SM is a Stokes feature associated with scattering from the Damon–Eshbach surface spin wave, and the broad bands are scatterings from bulk spin waves. (The data is that of Sandercock and Wettling, 1979, and the figure is taken from the paper by Camley, Rahman and Mills, 1981.)

this feature will appear on the anti-Stokes side, if the scattering geometry is held fixed. The broad asymmetric bands are features produced by scattering from bulk spin waves, which propagate up to and reflect off the surface. These have wavelengths sufficiently short that they are influenced importantly by exchange, so we see that the bulk spin-wave feature extends to frequencies well above that of the Damon–Eshbach wave. This figure shows clearly that the Damon–Eshbach wave sits on top of a manifold of bulk spin waves, and its linewidth in the BLS spectrum shown is influenced substantially by the decay process summarized in the preceeding paragraph. It should be remarked that no adjustable parameters are involved in the theoretically calculated spectrum. All parameters which control the shape of the spectrum are well known.

Very interesting BLS studies of spin waves in Ni/Mo superlattices have been reported by Keuny and collaborators (Kueny, Khan, Schuller and Grimsditch, 1984). There is an interesting issue in regard to such structures. When one considers their dynamic response, does one think of an array of uncoupled ferromagnetic films, or is it that the superlattice structure has its own spectrum of collective excitations, and thus its own unique response characteristics? In essence, have we created a new material?

The question just posed was explored within the theory of magnetostatic spin waves by Camley, Rahman, and Mills (1983). It is the case that magnetic superlattices have a unique collective excitation spectrum, even when the nonmagnetic spacer layer is sufficiently thick that exchange coupling between adjacent ferromagnetic films is negligible. A Damon–Eshbach surface spin wave on a given film generates a dynamic dipole field outside the film, which provides a means of interfilm coupling. One thus realizes collective excitations of the superlattice, where the new collective modes are appropriate linear combinations of single film eigenstates. There is a striking prediction of the theory. Suppose the ferromagnetic constituents have thickness d_1 while the nonmagnetic spacer layers have thickness d_2. If $d_1 > d_2$, the semi-infinite superlattice supports collective Damon–Eshbach wave with frequency identical to that of a semi-infinite whose magnetization is the same as that in the films. As one decreases d_1 for fixed nonmagnetic spacer layer thickness, when d_1 approaches d_2 the high-frequency side of the collective bulk spin-wave modes rises, until the Damon–Eshbach wave is merged into the bulk spin waves. The very extensive BLS studies of NiMo superlattices reported by Kueny *et al*. are in excellent accord with the predictions of Camley, Rahman, and Mills, except for superlattices with nonmagnetic spacer layers so thin that interfilm exchange influences the response characteristics of the sample. These experimental studies are remarkable, it should be said, since the magnetic properties of a very large number of samples were studied. In this work, superlattices whose constituents had thicknesses from 50 to 5000 Å were explored, with the ratio for d_1/d_2 assuming the values 1/3, 1, and 3.

2.2.2 BLS studies of ferromagnetic films

As one moves from very thick crystalline samples to thin ferromagnetic films, the Damon–Eshbach spin wave remains a prominent feature in the spectrum. With exchange neglected, in a film magnetized in plane with finite thickness, its frequency is given by Damon and Eshbach (1960)

$$\omega_{\mathrm{DE}}(k) = \gamma[(H_0 + 2\pi M_{\mathrm{S}})^2 - 4\pi^2 M_{\mathrm{S}}^2 \exp(-2kd)]^{1/2} \quad (3)$$

for the standardly studied case where the mode propagates perpendicular to the magnetization. At fixed wave vector, as the film thickness is decreased, the frequency of the mode decreases from the value appropriate to the semi-infinite crystal, $\gamma[H_0 + 2\pi M_{\mathrm{S}}]$ down to $\gamma[H_0(H_0 + 4\pi M_{\mathrm{S}})]^{1/2}$, which is the FMR frequency of the film, as we have commented earlier.

The bulk spin waves have wave vector component normal to the surface quantized, so the normal component of wave vector becomes $k_\perp = k_\perp^{(n)} \approx n\pi/d$. Thus, the bulk spin-wave continuum evident in the data on very thick crystals as illustrated by Figure 1 breaks up into a series of lines, each associated with a particular standing wave resonance of the film, as we have noted above.

We illustrate this in Figure 2(a) for a film of the amorphous ferromagnetic $Fe_{80}B_{20}$. The data is that of Grimsditch and his collaborators (1979). The thickness of the film used in this

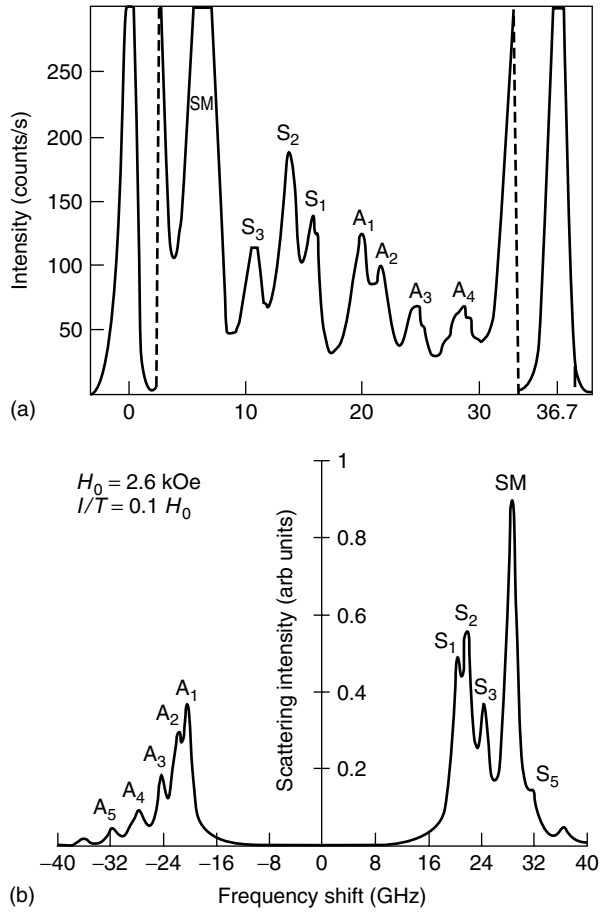

Figure 2. In (a), we show an experimental BLS spectrum taken from an $Fe_{80}B_{20}$ ferromagnetic film whose thickness is 106 nm. The frequency scale is in GHz, and a magnetic field of strength 2.6 kOe is applied in plane. (The data are from the paper by Grimsditch and collaborators, 1979.) In (b) we show theoretical spectra as calculated by Camley and coworkers (1981).)

experiment is 106 nm, and it is magnetized in plane with an external magnetic field of strength 2.6 kOe applied in plane. In order to understand this spectrum, some comments on the nature of the BLS measurement are useful. In these studies, the spectral composition of the scattered light is analyzed through use of a Fabry–Perot interferometer. Let light with only the laser frequency be introduced into this device. One then sees a sequence of interference features associated with the standing wave resonances of the interferometer. In Figure 2(a) two of these structures are evident, at the far left and the far right of the figure. In this particular detector, they are separated by 36.7 GHz, which is referred to as the spectral range of the device. The detector, it should be noted, is placed at an angle removed from that associated with specularly reflected light. Roughness on the surface leads to a bit of elastically scattered light off the specular direction and hence one sees 'markers' at the laser frequency as the spectrum is scanned. The spin-wave signal then consists of peaks, which fall between two such laser structures. The peaks labeled A_i in Figure 2(a) are anti-Stokes scatterings from bulk spin waves associated with the leftmost laser feature, and the peaks labeled S_i are bulk spin wave losses associated with the rightmost laser feature. The strong line labeled SM is the Damon–Eshbach surface magnon, which appears in the Stokes spectrum for this scattering configuration. We clearly see that the bulk spin-wave continuum evident in Figure 1 now consists of individual standing spin-wave modes. From the separation of these modes in frequency, one may infer the value of the exchange stiffness parameter which enters equation (2) in the preceding text.

In Figure 2(b), we reproduce a theoretical spectrum from the paper by Camley and collaborators (1981). One sees that the theory provides a remarkably quantitative account of the data. There is one parameter in the theory. At the film surfaces, the magnetic moments can encounter strong anisotropy fields with origin in the low symmetry of the surface environment, as we have discussed in the section on the FMR spectrum of films. Such anisotropy fields, if sufficiently strong, can 'pin' or suppress the spin motion at the surface. As illustrated in the paper just cited, the presence of surface anisotropy affects the relative intensity of the modes in the bulk spin-wave spectrum. For the particular sample explored in Figure 2(a), the data is accounted for very well assuming that surface anisotropy is absent.

As noted in the preceding text, the data in Figure 2(a) was taken on a rather thick film, with thickness of 106 nm. As the film is made thinner, the standing wave bulk modes shift upward in frequency, through action of the Dk^2 term in equation (2). We have seen one estimating this effect by replacing the k by its quantized value $k_\perp^{(n)} \approx n\pi/d$. In the ultrathin limit, the standing wave modes are shifted well above the spectral range accessible to the BLS technique, very much as in FMR. One is left with the signature of only the Damon–Eshbach mode, whose frequency is now very close to the FMR mode, as one sees from equation (3) with $kd \ll 1$. The eigenvector of this mode is now rather uniform across the film.

In the discussion we have given above, we have remarked that in thick samples, the Damon–Eshbach surface spin wave appears on only one side of the laser line in BLS studies, either the Stokes or the anti-Stokes side, depending on the details of the scattering geometry. In the very thin-film limit where $kd \ll 1$, one finds that the eigenvector of both the mode localized on the upper layer of the film and that localized on its lower surface become uniform across the film. Furthermore, in the ultrathin film limit, the optical skin depth is comparable to or perhaps even larger than the film thickness. In this limit, one should expect to see

the Damon–Eshbach mode on both the Stokes and the anti-Stokes side of the laser line with very close to equal intensity, since the incident light 'sees' both modes in a roughly equal manner. However, early experimental studies of films with thickness in the 10 nm range, where one should be well into the limit just described, a large Stokes/anti-Stokes asymmetry persists (Camley, Grunberg and Mayr, 1982). These authors set forth an elegant theoretical explanation of the data, based on an interesting interference effect in the matrix element for excitation of the Stokes and the anti-Stokes Damon–Eshbach mode.

The discussion in the preceding text sets forth the principal concepts, which control our understanding of BLS in ferromagnetic films. We now turn our attention to the information one may obtain by applying this method to ultrathin ferromagnets and bilayers or superlattices formed from ultrathin ferromagnetic films. There is by now a very extensive literature on this topic. Thus, a complete review of this literature is beyond the scope of the present chapter. In the discussion below, we shall select examples of what may be learned from this technique, which is complementary to FMR. We direct the reader to the excellent article by Cochran, which discusses key concepts and presents a complete list of the earlier seminal papers in this area (Cochran, 1994). Our focus will also be on earlier selected studies, since these set out the principal concepts illustrated by data on important systems.

A first question is whether the BLS technique has the sensitivity to study true ultrathin ferromagnets. In all the examples discussed in the preceding text, recall that the optical skin depth is in the range of 10–20 nm. Thus, the spectra are produced through coupling of the laser light to perhaps 50 or 100 atomic layers of spins. To illustrate spectra that can be measured from truly ultrathin films, in Figure 3, we reproduce data taken on a three monolayer film of Fe grown on the Cu(100) substrate (Dutcher *et al*., 1988). The signal-to-noise ratio in this data is most impressive indeed. Thus, it is clear that the BLS method may be used to probe spin waves down to the single monolayer level, if desired.

As remarked above, the BLS method has been employed to obtain quantitative information on the magnetic properties and response characteristics on diverse ultrathin films and magnetic multilayers. In an interesting early study, Grunberg and his collaborators explored the BLS spectra of ultrathin Fe, Ni, and Permalloy films (Grunberg, Mayr, Vach and Grimsditch, 1982). From the spectra, they extracted all the key magnetic properties of these films. All these materials had been studied earlier by FMR, and they compared the results obtained by BLS and FMR. The agreement is very good.

As we have mentioned in the preceding text in our discussion of FMR, in ultrathin films the strength of the effective anisotropy can be very much larger than in bulk materials with the same atomic constituents, because a large fraction

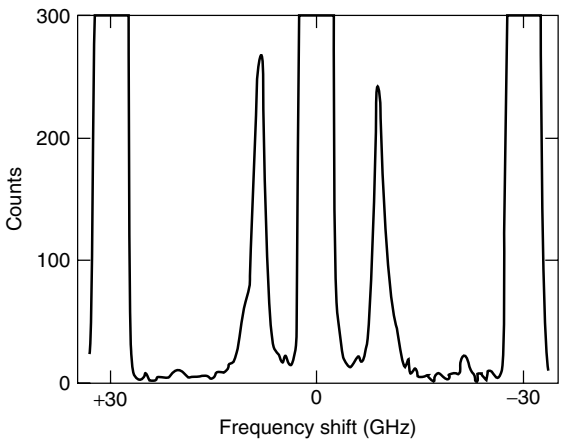

Figure 3. A Brillouin light scattering spectrum of three monolayers of Fe, grown on a Cu(100) substrate. (Reproduced from Dutcher, J.R. ,Heinrich, B., Cochran, J.F., Steigerwald, D.A., and Egelhoff Jr., W.F., (1988), "Magnetic Properties of Sandwiches and Superlattices of FCC Fe(100) Grown on Cu(100) Substrates", *J. Appl. Phys.* **63**, copyright © 1988 American Institute of Physics, with permission from the AIP.)

of atoms reside at surface or interface sites of low symmetry. In a very thin film, the spins are locked together tightly by the very strong exchange interactions as they engage in precession after a long wavelength spin wave is excited. Thus, one measures an effective anisotropy energy averaged over all layers, in both FMR and BLS studies of ultrathin films. Strong surface or interface anisotropy then contributes a term to the average anisotropy, which scales inversely with the film thickness. In BLS data, Hillebrands and coworkers observe very strong surface anisotropy, in BLS studies of ultrathin films of Fe grown on W(110) (Hillebrands, Baumgart and Guntherodt, 1987). The Fe films ranged in thickness from 15 nm down to a few monolayers; below 6 nm in thickness, the spin-wave frequency is found to increase strongly with decreasing thickness until it is larger than that appropriate to the thick films by a factor of 3. This is an illustration of the dramatic effect that the surface anisotropy can have on the dynamic response characteristics of ultrathin ferromagnets.

In the studies cited in the preceding text and many others, BLS is used to determine the fundamental parameters, which control the frequency spectrum of the dynamic response of ultrathin films. Examples are the nature of the anisotropy, the magnetization itself, and the exchange stiffness parameter. Another crucial feature of the response of such systems is the magnitude and nature of the damping of the spin motions. In general, FMR has far higher frequency resolution than BLS, and thus is more frequently used to explore the nature of damping. We presented a discussion of this topic above, in the section on FMR of ultrathin films. However, there are circumstances where BLS can also measure the intrinsic linewidth of spin-wave excitations

under circumstances where the damping is appreciable. It is the case that when films are grown on exchange biasing substrates, the two-magnon mechanism discussed in the preceding text can be very strong. Under such circumstances, the linewidths of the spin-wave modes can be substantial, and accessible to the BLS technique. Earlier we noted the paper by of Rezende *et al*. where large linewidths could be measured directly by the BLS method. These authors measured the linewidth in FMR and also in BLS, for the same samples of exchange biased Permalloy films. The BLS linewidth is five times larger than that found in FMR on the same film. The FMR linewidth is also large, and these authors applied the theory of two-magnon damping (Arias and Mills, 1999) to extract the magnitude of the matrix element which controls this process from the FMR linewidth, under the assumption that two-magnon scattering is dominant. They argue that this source of damping is wave vector dependent, and extended the theory of Arias and Mills to take this feature into account. They show that this is so by comparing theory with the BLS data; through use of exactly the same matrix element extracted from the FMR spectra, they were able to obtain a fully quantitative account of the larger linewidths found in BLS. As noted in our section on FMR in ultrathin films, their conclusion that the linewidth of long wavelength spin waves in ultrathin films is strongly wave vector dependent, combined with the dramatic deviations from the linear law in the dependence of the FMR linewidth in ultrathin films (Lindner *et al*., 2003) show that in materials where the two-magnon mechanism is operative the widely used LLG equation breaks down qualitatively.

In magnetic multilayer or superlattice structures, there will be interactions between adjacent films in the structure, with the consequence that the spin-wave modes are collective excitations of the structure as a whole. We have already encountered an example of such collective modes in our discussion above of the BLS studies of NiMo superlattices (for data see Kueny *et al*., 1984, and for theory related to these experiments, see Camley, Rahman and Mills, 1983). In these samples, the Ni and Mo films were quite thick, and the interfilm coupling responsible for the collective character of the modes studied had their origin in long-ranged dipolar interactions between the ferromagnetic constituents. As the spins in a given ferromagnetic film precess upon excitation of a spin wave within the film, a dynamic, time dependent dipolar field is generated outside the film by the spin motions. This field has strength and range given roughly by $4\pi M_S kd \exp(-kz)$ with d the film thickness, k the wave vector of the spin wave, and z the distance from the film, measured along the normal. Such dynamic fields couple the various films together, to produce collective modes of the structure as a whole as we have discussed.

If we consider a multilayer or superlattice wherein the ferromagnetic films are separated by nonmagnetic metallic spacers as in the example of the NiMo structure, when the spacer layers become very thin there is a direct exchange coupling between adjacent ferromagnetic films with origin in the spin polarization of the conduction electrons in the nonmagnetic spacer layer. The effective exchange coupling necessarily oscillates with the thickness of the spacer layer, as proved theoretically over four decades ago (Bardasis *et al*., 1965). Thus, the interfilm coupling may be antiferromagnetic or ferromagnetic in character, depending on the thickness of the spacer layer. (A recent review of this topic is provided by Stiles 2006.)

Exchange coupled ferromagnetic bilayers, wherein the magnetization of one of the two ferromagnets is pinned by strong anisotropy field provided by the exchange bias mechanism (Berkowitz and Kodama, 2006) are referred to as *spin valves*. These structures play a vital role in current computer technology, as we see from the new generation of read heads, which incorporate spin valves as essential elements. Very high sensitivity in the read head results from the phenomenon of giant magnetoresistance. (Fert, Barthelemy and Petroff, 2006). Thus, there is great interest in the study of the influence of interfilm exchange coupling on the dynamic response of magnetic nanostructures such as spin valves.

The BLS technique offers a means of directly measuring the strength of the exchange between adjacent ferromagnetic films separated by a nonmagnetic spacer. Consider two such films in the form of a ferromagnetic film grown on a substrate, a nonmagnetic spacer is then deposited on this film, and then a second film is deposited on top of the spacer. The system will exhibit collective spin-wave modes, with an in-phase acoustic mode and an out-of-phase 'optical' mode split in frequency by the exchange coupling and/or dipolar interactions between the films. Experimental studies of such modes along with the related theory have been reported by Grunberg and his collaborators, for Fe/Au/Fe and Fe/Cr/Fe structures (Grunberg *et al*., 1986). Subsequent measurements have provided direct access to the oscillatory exchange coupling in the important Co/Ru system. In these measurements, the value of the coupling between neighboring Co films as a function of Ru thicknesswas measured and the period of the oscillation was found to be 1.15 nm (Fassbender *et al*., 1992).

It is possible to grow bilayers or multilayers from ultrathin films in which both constituents are ferromagnets. An example is the Fe/Ni system, whose spin-wave modes have been studied by Heinrich and his colleagues (1988). Here one realizes strong interfilm exchange coupling across the interface between the two constituents. These authors also provided a theoretical analysis of the spin waves in ferromagnetic bilayers, including both the role of the exchange stiffness D discussed above, and also the influence

of dynamic dipole fields generated by the spin motions in the ferromagnets. There is an important comment one must make regarding this analysis and others found in the literature on similar systems. A boundary condition linking the dynamic magnetizations and their derivatives across the interface between the two ferromagnetic films is required, before one can solve the differential equations, which form the basis of the theory. Quite commonly a boundary condition is employed in such calculations (Hoffman, 1970). However, it is the case that the boundary condition found in Hoffman's paper leads to unphysical conclusions, as discussed by the present author (Mills, 1993). An energy conservation law is violated, since the energy transported across the interface is not conserved when the Hoffman boundary connects spin motions on both sides of the interface. Also, in the mathematical limit that the two ferromagnets become identical, the reflectivity can be nonzero. Thus, the Hoffman boundary condition is in fact unphysical. In the paper just cited by the present author, a boundary condition compatible with both of these constraints has been formulated and stated. Clearly for valid quantitative conclusions to be deduced from the data, one must use a boundary condition free of the difficulties found in the Hoffman boundary condition.

In this section on BLS studies of spin waves in ferromagnets, our attention has been directed toward bulk materials, films, ultrathin films, and magnetic multilayers composed of ultrathin films. In the recent literature, the method has been employed to explore patterned media of diverse sorts. This constitutes a most powerful extension of the method. For instance, BLS has been used to study spin dynamics in the vortex state of a circular magnetic dot (Novosad *et al*., 2002). A theoretical study of such spin excitations has been given by Giovanni and his colleagues (2004). An extension of theory and experiment to the study of dots of elliptical shape is given by Gubbiotti *et al*. (2005). A series of BLS studies of the spin-wave excitations of arrays of ferromagnetic ribbons has been carried out by Demokritov and his colleagues. A recent article discusses this work, and also covers the use of spatially resolved BLS to explore nonlinear spin-wave phenomena in systems driven beyond the linear response regime (Demokritov, Hillebrands and Slavin, 2001). We note that Arias and the present author have presented an exact theory of magnetostatic spin waves in ferromagnetic ribbons of arbitrary cross section, and compared the results of theory to the high aspect ratio ribbons studied by Demokritov and his colleagues (Arias and Mills, 2005).

2.3 Some general comments

The last two sections have reviewed both FMR and BLS studies of spin waves in the metallic ferromagnets, again in bulk crystalline form, in films, in ultrathin films, and in magnetic multilayers. We see that both of these important methods provide us with information on the basic magnetic parameters of materials in these diverse forms. Also, they are complementary in that each of these methods can probe different aspects of the response, as we have seen. However, they have one common feature. This is that both probe modes whose wavelength is very long compared to the lattice constant of the underlying material. Thus theoretical descriptions of the modes can be obtained from macroscopic theory constructed through use of phenomenological parameters. We shall review the structure of such theories in Section 3. The parameters generated by such analyses may, of course, be compared with the results of *ab initio* theories, wherein one begins with a density functional description of the ferromagnetic state, and then calculates from this point the relevant parameters deduced from the application of macroscopic theory. The current state of the art is such that we now may obtain reliable and quantitative accounts of these parameters from *ab initio* density functional based theory.

If we set damping parameters aside, by the means just discussed one may extract information from the data on anisotropies, magnetization of various constituents, the exchange stiffness, and in the case of ultrathin multilayer structures the spacer mediated exchange between ferromagnetic constituents, as we have noted in the preceding text. Although one requires a truly dynamical theory to describe the damping of spin motions, these parameters are all ground state parameters, which may be calculated by adiabatic methods from the description of the ground state. One might think that the exchange stiffness D is a dynamical parameter, but in fact in the phenomenology it describes the change in ground state energy with respect to long wavelength static distortions of the spin system. Thus this may be generated from information on the ground state. A recent discussion of this point has been given by Muniz and the present author, for ultrathin ferromagnetic films (Muniz and Mills, 2002).

To obtain truly microscopic information on the nature of spin excitations in any magnetically ordered material, one must study short wavelength spin excitations, with wave vectors of a considerable fraction of the distance from the center of the appropriate Brillouin zone to the zone boundary. The remainder of the present section will be devoted to experiments, which can probe this regime. At least for classical, well-studied materials like the bulk 3d ferromagnets Fe, Co, and Ni and their various alloys, one would think this to be well trodden ground. However, this is not the case. As we shall see, there is still much to learn about these basic and fundamental materials, whose ferromagnetism has been known for centuries.

2.4 Neutron scattering studies of the ferromagnetic transition metals

For many decades now, the technique of inelastic neutron scattering has been one of the most important means of studying diverse elementary excitations in materials. The experiment is conceptually similar to the BLS studies, which have just occupied our attention, except the probe beam now consists of monoenergetic neutrons rather than photons. The loss spectrum is measured as a function of scattering angle, and from the data one may then construct the dispersion curves of phonons, spin waves, and other elementary excitations as well. As we shall see, in contrast to BLS, neutron spectroscopy can reach throughout the entire Brilluoin zone. The kinematics of the excitation process may be described in exactly the same language we have just employed. Let $\vec{k}_{\mathrm{I}}$ be the wave vector of a neutron incident on a crystal, and suppose it creates or absorbs a quantum of an elementary excitation whose wave vector is $\vec{k}$. Then the wave vector of the scattered neutron will be $\vec{k}_{\mathrm{S}} = \vec{k}_{\mathrm{I}} \pm \vec{k}$, with the plus sign chosen for the case where the quantum is absorbed, and the minus sign if it is emitted. Energy conservation then reads $E(\vec{k}_{\mathrm{S}}) = E(\vec{k}_{\mathrm{I}}) \pm \hbar\omega(\vec{k})$. Here, $E(\vec{k}) = \hbar^2 k^2 / 2m_{\mathrm{N}}$ is the energy of a neutron of wave vector $\vec{k}$. Thus, a measurement of the loss spectrum of the neutron as a scattering angle allows one to construct the dispersion curves of elementary excitations of interest. There is by now a very large literature on neutron scattering from spin waves in diverse magnetic crystals, along with other 'magnetically active' excitations. We refer the reader to the excellent text by Lovesey for a detailed exposition of the theory of neutron scattering from spin excitations in magnetic materials (Lovesey, 1984).

Thermal neutrons are commonly used in such experiments, since very high neutron fluxes are generated by nuclear reactors designed for neutron spectroscopy. Thus, the neutrons in the beam have kinetic energies on the order of $k_{\mathrm{B}}T$, where the temperature is roughly room temperature. Thus, typical beam kinetic energies are in the range of 50 meV or somewhat less. The wave vector of such a neutron is approximately $5 \times 10^8\,\mathrm{cm}^{-1}$, so we can appreciate that in contrast to light scattering spectroscopy, we have here a means of reaching out to the boundary of the Brillouin zone. In regard to spin waves, for materials which may be described by a Heisenberg–Hamiltonian, a rule of thumb is that modes at the zone boundary have excitation energies in the range of $k_{\mathrm{B}}T_0$, with T_0 the ordering temperature (the Curie temperature for ferromagnets, or the Neel temperature for antiferromagnets). Almost all insulating magnetic materials have ordering temperatures in the vicinity of room temperature or below, so inelastic neutron scattering is a most powerful probe for the experimental study of spin waves in a very wide class of magnetic materials.

The ferromagnetic transition metals, which are the primary focus of this review have spin waves of a character qualitatively different than discussed in the previous paragraph. First, of course, almost all of these materials have Curie temperatures well above room temperature, in the vicinity of 1000 K. Second, the spin waves in these materials are very 'stiff', and the frequency of short wavelength spins waves can be much higher than $k_{\mathrm{B}}T_{\mathrm{C}}$. Consider, for instance, ferromagnetic Fe. The frequency of a spin wave of wave vector $\vec{k}$ may be approximated by Dk^2, for excitation energies sufficiently large that Zeeman, dipolar, and anisotropy energies may be set aside. For Fe, the low temperature value of the exchange stiffness D is approximately 300 meV Å^2. If we just extrapolate this quadratic form out to the Brillouin zone boundary, we see that spin-wave excitations energies will be in the range of 300 meV, or in temperature units we have 3000 K, far above the range accessible to thermal neutrons. The breakdown of the relationship between spin-wave energy at the zone boundary and $k_{\mathrm{B}}T_{\mathrm{C}}$ has its origin in the fact that these materials are itinerant electron ferromagnets, and a Heisenberg model with short ranged exchange interactions fails very badly for this important class of ferromagnets.

The remarks in the previous paragraph lead to the conclusion that thermal neutrons can explore only spin waves of rather small wave vector, in the 3d ferromagnets. To reach the zone boundary, one requires high-energy neutron beams, from a spallation source. It is the case that the neutron cross section is small at large wave vectors, so such experiments are a major challenge. A consequence is that there is little data in hand, even at this mature state of the field, on the nature of short wave length spin waves in the ferromagnetic transition metals. This situation is remarkable in the view of the present writer. The ferromagnetism of these metals has been known well since antiquity, and historically they have played a central role in electromagnetic technology since the nineteenth century. Indeed, they occupy center stage today, as we see from their role in the remarkable giant magnetoresistance (GMR) read heads, and in magnetic random access memories (MRAMs). Despite the very long history of study of these materials, and their central role in past and current technology, we have less information regarding the nature of their spin excitations than we do of very exotic materials.

2.4.1 Neutron scattering studies of spin waves in the bulk 3d ferromagnets

Early studies of spin waves in Fe, Co, and Ni were carried out by the Brookhaven group. We refer the reader to a review of this data (Shirane, Minkiewicz and Nathans, 1968). The data explored spin waves with excitation energy below

50 meV, and wave vector transfers in the range 0.5 A^{-1} and below. In this regime, the dominant contribution to the spin wave excitation energy is the classical Dk^2 term discussed in the preceding text. The data was fitted with the form $Dk^2(1 - \beta k^2)$, and values of the exchange stiffness D and the parameter β are found in this paper. For hcp-Co, the data explores spin waves, which propagate along the c direction. For the case of fcc-Co, Sinclair and Brockhouse have measured the exchange stiffness, through measurement of the spin-wave dispersion near the center of the Brillouin zone (Sinclair and Brockhouse, 1960). It should be remarked that in some of the measurements just cited, it was not possible to obtain pure single crystals large enough for detectable neutron signals. In the case of Fe and also fcc-Co, it was necessary to add several percent of Si for the purpose of stabilizing large crystals. Thus, the measured spin-wave dispersion in such studies may differ somewhat from that appropriate to the pure single crystal.

Mook and collaborators have extended the measurements to higher spin-wave excitation energies, to approximately 120 meV, and to wave vectors as large as 0.8 A^{-1}. In the case of Ni, they found a dramatic falloff in intensity, for spin waves above 100 meV in energy (Mook, Nicklow, Thompson and Wilkinson, 1969). They attributed this to damping by coupling of the spin wave to Stoner excitations, a process unique to itinerant ferromagnets. We shall discuss this damping process in detail in Section 3, when we turn our attention to theoretical descriptions of spin waves in these materials. Briefly stated, the damping process arises from the following. Imagine one sets up a spin wave in the material at time zero. The precession of the spins take place in a metallic environment, where all electrons reside in spin-polarized energy bands. The electronic system has a continuous energy spectrum of spin triplet particle hole pairs, formed by taking an electron from an occupied state in a majority spin band, thus creating a hole, and placing it in an unfilled state in the minority spin band. The continuum of such particle hole pairs is referred to as the Stoner excitation spectrum. The spin wave may then decay by creating such particle hole pairs. If the spin wave is destroyed by this process, as we know from elementary discussions of the properties of spin waves (Kittel, 1963a), destruction of a spin wave increases the spin angular momentum of the substrate by $\hbar$. Angular momentum conservation requires that the excitation to which its energy is transferred must have angular momentum $-\hbar$. Hence there must be a spin flip in the gas of conduction electrons in the process, which transfers the energy of the spin wave to the band electrons. We shall see that the decay process just described is of central importance when we discuss spin waves in ultrathin metallic ferromagnets. In the case of the neutron scattering studies of Ni, the sudden falloff in intensity found by Mook and coworkers was interpreted in terms of crossing a wave vector threshold for creating Stoner excitations. Mook and Nicklow shortly thereafter reported neutron scattering studies of spin waves in Fe, where similar behavior was found (Mook and Nicklow, 1973).

We shall discuss the theory of itinerant spin waves in the 3d ferromagnetic metals in Section 3. In the present section, we wish to make a comment on a theoretical prediction that has stimulated much discussion. Cooke and his collaborators presented the first theoretical description of spin waves in Ni and Fe, within the framework of the itinerant electron picture of ferromagnetism, combined with use of a realistic electronic band structure (Cooke, Lynn and Davis, 1980). One striking and unexpected feature found in this study was a curious hybridization gap in the spin-wave dispersion relation for Ni and Fe, along the [100] direction. One has an upper branch above this gap which is called an *optical spin wave* by Cooke and his collaborators. These materials are, of course, monatomic crystals with one atom per unit cell, so the appearance of such structures are both surprising, and of course very interesting. We shall discuss this topic in detail in Section 3. It is the view of present writer and his colleagues, based on our studies of spin waves in ultrathin films, that such features are in fact artifacts of poor convergence in the sums over wave vector in the Brillouin zone in constructing the kernal of the integral equation which must be solved to extract information on the spin wave excitations. In our own calculations of the spin-wave spectrum of Fe (Tang, Plihal and Mills, 1998) and Ni (Hong and Mills, 2000) we have not encountered such features. We did find hybridization gaps qualitatively similar to those in the paper of Cooke and his collaborators in our study of spin waves in the Fe monolayer on W(110) (Muniz and Mills, 2002). As we discussed in this paper, upon improving the convergence in our k space sums this feature disappeared.

Evidence for an apparent gap in the spin-wave dispersion relation in Ni along the [100] direction has been provided by Mook and Paul (1985). In the theory to which the data is compared, the hybridization feature is considerably more than that found in the data as one sees from the solid line in Figure 3 of the by Mook and Paul. There are no actual loss spectra displayed, in the wave regime where the hybridization gap is found. Evidently an optical spin-wave feature was not seen directly, but rather structure in the acoustical spin-wave loss peak was assumed to be evidence for the optical mode (Mook, private communication). Studies of high-frequency spin excitations in Fe also suggest that an optical spin-wave feature may have been observed (Perring *et al.*, 1991). Our calculations, however, suggest that this may be structure in the low-lying sector of the Stoner excitations. We refer the reader to Figure 5 of the paper by Tang, Plihal, and the present author, and the associated discussion (Tang, Plihal and Mills, 1998). We thus regard the question of the existence

of hybridization gaps in the spin-wave spectrum of the simple 3d transition-metal ferromagnets to be an open question, from both the experimental and the theoretical point of view.

2.4.2 Neutron scattering from ultrathin films and magnetic multilayers

Quite clearly it is not possible to detect inelastic neutron scattering from a single ultrathin film, simply because the signals will be orders of magnitude smaller than can be detected. The studies of spin waves in bulk materials described in the previous section were carried out on large single crystal samples. As we mentioned, to obtain such large, perfect crystals it was often necessary to allow Fe or Co with Si. Thus, even for the study of bulk spin waves, considerable effort must be expended in sample preparation and sometimes this requires a compromise. As we see, many of the experiments just discussed are carried out on alloys rather than perfect, elemental single crystals.

It is possible to detect magnetic neutron scattering from magnetic multilayers, which incorporate ultrathin films as elements. At the time of this writing, there is a considerable experimental literature devoted to studies of static spin arrangements in magnetic multilayers. A beautiful study of the evolution of the surface spin flop state in finite Fe/Cr superlattices provides one with an illustration of the power and sophistication of such experiments (Te Velthuis, Jiang, Bader and Felcher, 2002). We also refer the reader to a discussion of the application of neutrons to such studies; this paper also contains very impressive data, including preliminary data on inelastic neutron scattering from spin waves in Dy/Y superlattices (Schreyer *et al*., 2000). We are unaware of further studies of spin waves in magnetic multilayers by inelastic neutron scattering at the time of this writing.

2.5 Studies of spin waves by spin polarized electron energy loss spectroscopy (SPEELS)

Because of the limitations of neutron scattering when applied to the study of spin waves in the 3d ferromagnets, most particularly when they are in the form of ultrathin films, until very recently we have had in hand no experimental information on the nature of large wave vector, or short wavelength spin waves in such films. Indeed, as we have just seen, the number of experiments which explore the entire Brillouin zone, is remarkably limited for the bulk materials, even at this very mature point in the field. There is compelling reason to learn about the nature of large wave vector spin waves in ultrathin structures. In the current era, devices based on ultrathin film magnetic structures have had a massive impact on information technology, as we see from the remarkable GMR based read heads. MRAM is just coming on line in early form at the time of this writing. As such devices are made smaller and smaller, we require quantitative information on the nature of spin motions with large spatial gradients, in the materials that are the focus of the present chapter. Much in this area can be learned through the study of large wave vector spin waves in ultrathin films.

For a considerable number of years, there have been discussions in the electron energy loss spectroscopy (EELS) community regarding the possibility of utilizing electrons, spin polarized if possible, as a means of studying spin waves in ultrathin films or on magnetic surfaces. Indeed, the present author proposed this possibility many years ago (Mills, 1967), and explored issues in the area through model calculations of the spin wave contribution to the loss cross section of electrons scattered from the surface of a Heisenberg ferromagnet. An attempt to detect spin waves on a Ni(100) surface in 1983 was unsuccessful (Ibach, private communication), for reasons we now understand (Hong and Mills, 2000). We shall discuss this point in the following text, in the present section.

The use of electrons rather than neutrons to study large wave vector spin waves in ultrathin films overcomes two principal difficulties with neutron scattering. First, typical electron energies utilized in loss studies range from a few electron volts, to a few tens of electron volts. Thus, the incident particle has more than enough kinetic energy to excite spin waves in the 3d ferromagnets, in contrast to thermal neutrons. Furthermore, the mean free path of electrons in the 3d ferromagnets is very short, even for electrons with kinetic energy very close to the vacuum level (Abraham and Hopster, 1987). Thus, beam electrons backscattered from these surfaces sample magnetic moments in the outer surface layer primarily. The short penetration depth thus makes electrons ideal for the study of ultrathin film magnetism. All the electrons, which are detected, carry information primarily about the outer layer of atoms.

It should be remarked that for many years now, EELS has been utilized for the study of phonons on crystal surfaces. With this technique, one may measure dispersion curves of surface phonons out to the Brillouin zone boundary, and probe the influence of bulk phonons on surface vibrations as well. For a discussion of such a study, and a comparison between theory and experiment, we refer the reader to the discussion by Hall and Mills and the references cited therein (Hall and Mills, 1986). As one envisions using this method for the study of spin waves, it is highly desirable to be able to discriminate between losses produced by phonons or other ‘magnetically inactive’ excitations, and spin waves. The use of a highly spin-polarized electron beam allows one to identify spin-wave features in a unique manner.

In elementary text book discussions of spin waves, one sees that when a spin wave is excited in a ferromagnet, the spin angular momentum of the substrate decreases by exactly $\hbar$ (Kittel, 1963a). Suppose such a spin wave is excited by an electron whose spin is antiparallel to the ferromagnetically aligned spins in the sample. Then angular momentum will be conserved in the scattering process if beam electron flips its spin from antiparallel to parallel to the aligned spins in the substrate. If, however, the beam electron has its spin aligned parallel to those in the sample, it cannot excite the spin wave and conserve angular momentum in the scattering event. Hence, if the experiment were to be carried out with an ideal beam that is 100% polarized, one would see spin-wave losses when the spin polarization is antiparallel to the substrate spins, and the spin-wave feature would disappear when the beam polarization (or sample magnetization) is reversed.

Some years ago, there were SPEELS study of the magnetic excitations in both Fe (Venus and Kirschner, 1988) and Ni (Abraham and Hopster, 1989). In both of these experiments, termed *complete experiments*, the incident beam was spin polarized and the spin of the scattered electron was detected as well, a most challenging experimental undertaking. This allowed separation of losses into the two nonspin flip loss channels (both beam and scattered electron parallel or antiparallel to substrate majority spins), and the spin flip processes. The spin flip scattering events provide us with information on the nature of the continuum of Stoner excitations, and as we have seen earlier with sufficient resolution one should also be able to see spin waves. In both of these experiments, only the Stoner regime was studied. In Fe, the peak of this broad continuum is in the 2 eV range, well above the spin-wave loss regime. It is the case that the spectrometer utilized had insufficient energy resolution to explore the low-energy regime where one may expect to find spin waves. Much more interesting, from the perspective of our present discussion, is the data on Ni. In Ni, the exchange splitting in the d bands is roughly 300 meV, and thus the Stoner spectrum lies very close to the spin-wave regime. The data reported by Abraham and Hopster goes down to 100 meV, and the resolution of the instrument, 17 meV, was remarkably high. It is puzzling that under these conditions, no evidence of a spin-wave signal was found. This reminds one of Ibach's early failed attempt to detect spin waves in EELS, also on Ni(100).

The present author and his colleagues have been engaged in the studies of large wave vector spin waves in ultrathin films, and also of the theory of spin-polarized electrons loss spectra. We wish to comment on conclusions reached in these studies, before we introduce the reader to recent SPEELS data in which large wave vector spin waves were studied in very beautiful recent experiments.

A central question that was addressed in our studies was the following. As we have just seen, the spectrum of Stoner excitations had been detected in SPEELS studies of both Fe and Ni quite some time ago. So an important question is the relative intensity of the spin-wave loss feature to that of the Stoner spectrum. Is there enough integrated strength in the spin-wave loss structure at large wave vectors for it to stand out as a clear structure on the background of Stoner excitations? Through use of a microscopic description of the Coulomb exchange matrix element appropriate to SPEELS and a quantitative description of the spin-wave/Stoner excitation spectrum of Fe, it was predicted that in Fe, the spin-wave loss structure should be a prominent feature in the SPEELS spectrum (Plihal and Mills, 1998). The first spin-wave signature SPEELS was reported shortly thereafter, in a study of an ultrathin Fe film on W(110) (Plihal, Mills and Kirschner, 1999). Further study showed that the feature observed failed to disperse with wave vector transfer. Evidently, the Fe film had a substantial concentration of dislocations, with origin of the lattice mismatch between the Fe film and the underlying W(110) substrate. This could cause a breakdown of wave vector conservation in the spin-wave excitation process, thus producing a broad loss feature reminiscent of spectra associated with diffuse neutron scattering from phonons in disordered crystals. In such circumstances, the breakdown of $\vec{k}$ conservation produces a broad structure, which does not disperse with wave vector. It is clear, however, that the feature reported by Plihal *et al*. was a spin-wave structure.

At this point, one must inquire why spin waves were not detected in scattering from Ni(100); two experiments evidently failed to see such structures. We should remark that Ibach's 1983 attempt to observe spin waves was known widely in the electron loss community, and this discouraged attempts to see spin-wave features in the electron loss spectrum. We also know, of course, as discussed in the preceding text that large wave vector spin waves in bulk Ni have been studied by inelastic neutron scattering (Mook and Paul, 1985). Thus, the absence of these features in SPEELS is puzzling.

We have set forth an explanation for the above annoying situation (Hong and Mills, 2000). One must appreciate that the neutron and electron beams create spin waves through different mechanisms. Neutrons interact with electron spins in magnetic materials through the magnetic dipole interaction, which is a long-ranged interaction. Thus, the neutron senses the total magnetic moment in each unit cell, but is not sensitive to its shape or the details of its electronic structure. The theory of inelastic neutron scattering from magnetic materials show that the loss spectrum is controlled by a response function referred to by theorists as the wave vector and frequency dependent susceptibility, written as $\chi_{+,-}(\vec{k}, \omega)$. Here $\vec{k}$ is the wave vector transfer in the

scattering process, and $\hbar\omega$ is the energy loss of the neutron. This response is precisely the same response function which, in linear response theory, provides the magnitude of the transverse magnetic moment induced by a time and spatially dependent applied magnetic field, where the space and time dependence is given by $\cos(\vec{k}\cdot\vec{r}-\omega t)$. We shall have more to say on this topic in Section 3.

In contrast, the excitation of spin waves by electrons involves a Coulomb exchange scattering process, as mentioned earlier. In physical terms, one may picture this as follows. The d electrons inside an Fe or Ni atom reside in 3d orbitals of either e_g or t_g character, if we allow ourselves to think in terms of a localized atom picture for a moment. The incoming electron penetrates into the atom and in the process of creating a spin excitation may transfer a particular electron from one orbital to a distinctly different orbital. The shape of the moment cloud in real space has thus been altered in the excitation process. When the theoretical analysis is completed (Plihal and Mills, 1998), one finds that the SPEELS spectrum is described not by $\chi_{+,-}(\vec{k},\omega)$ but rather by a distinctly different response function we may refer to as $\chi_{\mathrm{SPEELS}}(\vec{k},\omega)$. When we calculate each of these two response functions, we find that the loss spectra described by them are dramatically different. In both bulk crystals and in ultrathin films, our extensive series of calculations show that the Stoner spectrum is virtually absent in $\chi_{+,-}(\vec{k},\omega)$. One sees only spin-wave loss features in this response function, and in our numerical calculations even at large wave vectors, the Stoner region is very weak. We first found this behavior in our studies of spin waves in bulk Fe, and in ultrathin Fe(100) films (Tang, Plihal and Mills, 1998). On the other hand, in both Fe and Ni, in $\chi_{\mathrm{SPEELS}}(\vec{k},\omega)$ the Stoner spectrum is a strong feature, very much as found in the early SPEELS studies of these materials. In Fe, as noted above, we also found a visible, clear spin wave in the low-energy wing of the Stoner loss spectrum, which as mentioned earlier peaks near 2 eV. However, in Ni, the SPEELS response function shows no sign of loss structures from spin waves, save very close to the center of the Brillouin zone. The Stoner spectrum lies very low in energy, in the vicinity of 300 meV as mentioned earlier, and this is all one sees in $\chi_{\mathrm{SPEELS}}(\vec{k},\omega)$. However, when we calculate $\chi_{+,-}(\vec{k},\omega)$ through use of precisely the same description of the electronic structure, we see clear spin-wave loss structures for Ni very much as in the neutron studies (Hong and Mills, 2000).

The remarks in the previous paragraph show that one can then understand the differences between the SPEELS spectra in Fe and Ni; in Fe, one sees clear spin-wave loss features, as predicted by theory Plihal and Mills (1998), while in Ni, so far as we know at present, one sees only the low-lying broad Stoner excitations. Quite in contrast to this, inelastic neutron scattering sees spin waves in both materials, and in the case of Ni the low-lying Stoner excitations are absent. This striking difference between loss spectra taken by the two methods, which seem so similar from the superficial point of view, have their origin in the fact that the neutrons and electrons interact with the magnetic moments in the material in a qualitatively different manner, with the consequence that the loss spectra are described by different response functions. This suggests that to observe spin waves in an itinerant ferromagnet with the SPEELS technique, one may be limited to materials with exchange splittings in the d bands that are large compared to spin-wave excitation energies.

After the observation of the spin-wave loss feature in Fe, a new spectrometer was designed and constructed in Julich, and then rendered operational in the Max Planck Institute in Halle. We now have very beautiful experimental studies in hand of spin wave dispersion and damping in an ultrathin film of Co on Cu(100) (Vollmer *et al*., 2003). As we shall see shortly, the data are in qualitative and quantitative agreement with the picture that has emerged from our theoretical studies. Subsequent studies of other ultrathin films have been completed by the Halle group. We shall not review these experiments in detail here, since an excellent and careful review of this body of data and the related theoretical literature is found elsewhere in this series (Etzkorn, Anil Kumar, and Kirschner, 2007). However, we wish to comment on some general features, and also on the new aspects of short wavelength spin excitations in ultrathin films predicted by theory, and illustrated by the data.

Earlier, we pointed out that by virtue of angular momentum conservation in the excitation process, spin-wave excitation is forbidden if the beam polarization is parallel to the majority spins in the substrate, and allowed only if the beam polarization is antiparallel to the majority spins. This is illustrated well in Figure 4, taken from the paper by Vollmer and collaborators (2003). The curve labeled $I_\downarrow$ is the loss spectrum taken for the case where the beam polarization is antiparallel to the spins of the majority electrons in the sample. We see a very clear loss feature. The curve labeled $I_\uparrow$ is for the case where the beam polarization is parallel to the substrate majority spins. The loss feature is absent, except for a small feature with origin in the fact that the beam is not perfectly polarized. This data serves as a lovely experimental verification of a fundamental conservation law, which follows from the fact that the excitation matrix element has its origin in the spin independent Coulomb interaction. We see clearly from this example that through use of polarized electron beams, one may unambiguously identify loss features as spin waves.

Figure 5, again reproduced from the paper of Vollmer *et al*., shows a series of loss spectra taken for a sequence of wave vector transfer directed along the [11] direction

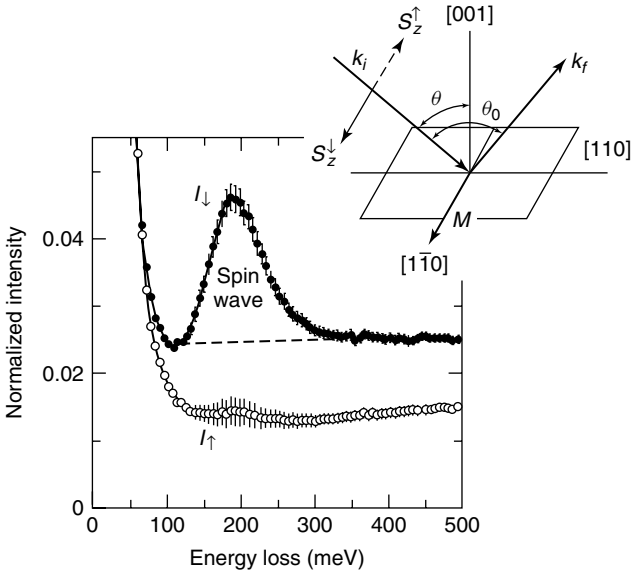

Figure 4. An example of the spin-wave loss feature in the SPEELS spectrum of an ultrathin Co film on Cu(001). The scattering geometry is illustrated in the inset. The curve labeled $I_\downarrow$ is a loss spectrum taken with beam polarization antiparallel to that of the majority spins in the substrate, whereas the curve labeled $I_\uparrow$ is taken with beam polarization parallel to the majority spins in the substrate. (Reproduced from Vollmer *et al*., 2003, with permission from the American Physical Society. © 2003.)

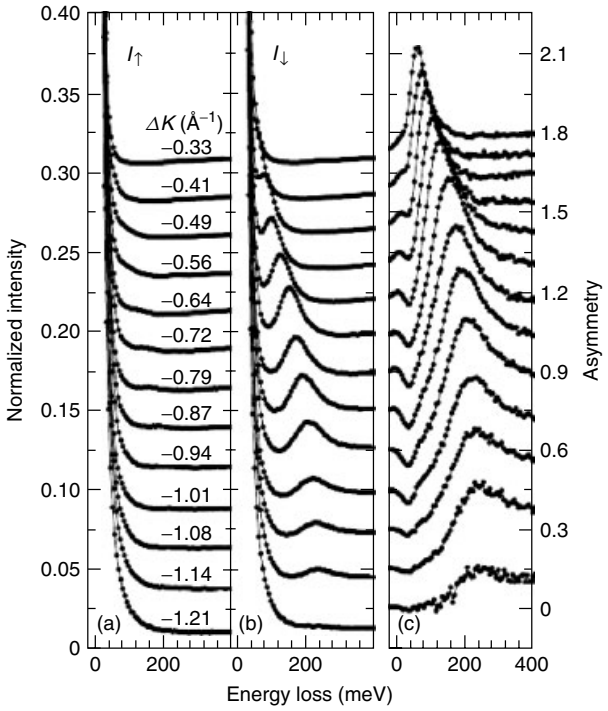

Figure 5. A series of loss spectra illustrating the spin-wave loss feature, taken for various wave vector transfers along the [11] direction of the surface Brillouin zone, for an ultrathin Co film on Cu(001). In (a), the loss spectra are for the case where the beam polarization is parallel to the majority spins in the sample, in (b) the beam polarization is antiparallel to the majority spins in the substrate, and (c) is the asymmetry A, defined as $(I_\downarrow - I_\uparrow)/(I_\downarrow + I_\uparrow)$. (Reproduced from Vollmer *et al*., 2003, with permission from the American Physical Society. © 2003.)

of the two-dimensional Brillouin zone. In (a), we have loss spectra taken with beam polarization parallel to the substrate majority spins, in (b) we have spectra taken for the antiparallel configuration, and in (c) we have the asymmetry A defined as $A = (I_\downarrow - I_\uparrow)/(I_\downarrow + I_\uparrow)$. One sees two key features in these data (i) there is a *single* loss feature, which shows dispersion with wave vector similar to that expected for a spin wave, and (ii) the linewidth increases with wave vector, to become very large at the largest wave vectors explored in the experiment. The spectrometer has resolution to resolve the linewidth in all the loss spectra shown. Thus, as we move out in the Brillouin zone, we have a very heavily damped excitation with a short lifetime.

The spectra just described are striking. To see this, we discuss what is expected on the basis of the commonly used model of spin excitations in ferromagnets, the Heisenberg model. Here one envisions localized magnetic moments on the lattice sites, described by the Hamiltonian $H = -\sum_{i,j} J_{i,j} \vec{S}_i \cdot \vec{S}_j$. If one applies this Hamiltonian to a ferromagnetic film with N layers, the following picture of the spin excitations emerges (Mills, 1970, 1984). First of all, by virtue of translational symmetry in the two directions of the surface all spin-wave modes are characterized by a two-dimensional wave vector $\vec{k}$, which resides in the appropriate two-dimensional Brillouin zone. Then for an N layer film, for each choice of $\vec{k}$, there are precisely N distinct spin-wave frequencies. Each mode, of course shows dispersion as the wave vector is varied. Very importantly, in the Heisenberg model, each of these N modes is an exact excited state of the Hamiltonian and has infinite lifetime. Of course at finite temperatures, there will be a finite linewidth for each mode, but well below the Curie temperature the linewidth calculated from the Heisenberg model is small.

So the spectra reported by Vollmer and coworkers differ qualitatively from the description in the previous paragraph. They are in full agreement with the predictions of our earlier calculations, carried out within the framework of an itinerant description of the metallic ferromagnetic film/substrate combination (Muniz and Mills, 2002; Costa, Muniz and Mills, 2003a,b). While these studies were carried out for Fe films on the W(110) surface rather than Co on Cu(100), as later work shows the qualitative nature of the theoretical spectra seems robust and very similar for these two different systems. The theory shows that near center of the Brillouin zone, one has an acoustical spin-wave mode where the spins

in the various layers precess in phase. This mode is rather weakly damped for small wave vectors. Near the center of the Brillouin zone, one finds higher energy standing spin-wave modes, with wave vector perpendicular to the film given to good approximation by $q_\perp \sim n\pi/d$, with d the film thickness. The Heisenberg model leads one to expect standing wave modes with n ranging from 1 to $N-1$ which, when combined with the acoustic mode provides us with N modes. The theory for these itinerant systems shows that even the mode with $n = 1$ is very heavily damped, and when the spin fluctuation spectrum of the film is calculated this mode has a linewidth larger than that of the acoustic mode by roughly 2 orders of magnitude. The higher order standing wave modes with $n > 1$ are so heavily damped that they are barely perceptible as structures in the spectrum of spin fluctuations. As one proceeds into the Brillouin zone toward the zone boundary, one sees two or three low-lying modes, which become progressively more heavily damped until they merge into a single broad feature. This single broad feature shows dispersion characteristic of a spin very much as we see in the spectra illustrated in Figure 5. The damping mechanism is unique to the metallic state of these ultrathin ferromagnets.

The physical picture of the origin of the damping is as follows. If one imagines setting up a coherent spin wave in the array of atomic moments at time $t = 0$, then the moments are precessing in a gas of conducting electrons. The spin motions are damped through what one might call a kind of friction created by stirring up the conduction electrons. To be more precise, the spin-wave frequency in these systems is embedded within the continuum of Stoner excitations, and thus the spin wave can decay to this manifold of excited states. This mechanism also enters in the metallic ferromagnets as we have seen and as discussed many years ago (Cooke, Lynn and Davis, 1980). However, the calculations for the ultrathin films show this damping to be much more severe than in the bulk materials. It is clear that the metallic nature of the substrate plays a role for the thinnest films. The damping is much less severe for free-standing films, in the theory, than for films adsorbed on metallic substrates. Also, in the bulk materials spin waves are characterized by a three-dimensional wave vector, and there is conservation of wave vector in the damping process. The combined wave vector of the particle and the hole in the final state Stoner excitation is constrained to sum up to that of the spin wave. In the film, the absence of translational symmetry in the system in the direction normal to the surface relaxes of perpendicular wave vector, thus opening up new decay channels.

In Figure 6, we show a comparison between theory and experiment, for data on the eight layer Co film on Cu(001) reported by Vollmer and his collaborators (Vollmer *et al*., 2003) In (a), the data and theory are compared

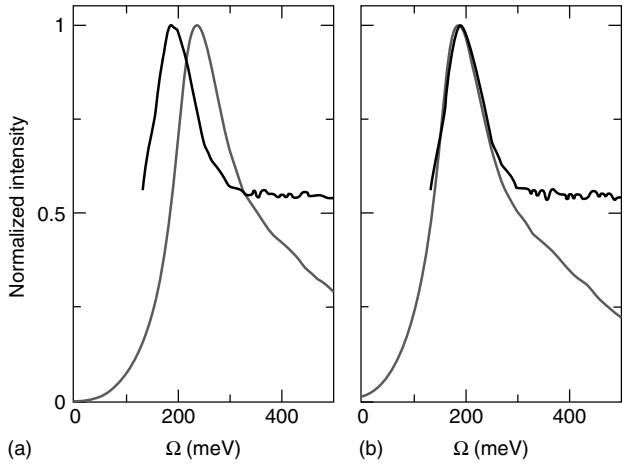

Figure 6. A comparison between theory and experiment, for the case of a spin-wave loss feature for the eight layer Co film on Cu(001). In (a) we have a direct comparison, and in the theory the spin wave is a bit higher in frequency than found in the experiment. In (b) the theoretical curve has been shifted down a bit so the width of the theoretical and experimental feature may be compared directly. (Reproduced from Costa *et al*., 2004, with permission from the American Physical Society. © 2004.)

directly. In the theory, which contains no free parameters, the calculated spin-wave frequency is a bit higher than found in the experiment. In (b), the theoretical curve has been shifted so the calculated linewidth and lineshapes may be compared with experiment. The agreement between theory and experiment is excellent. We note that, as discussed by Costa *et al*., the calculated spin-wave frequencies are found to be quite sensitive to the strength of the intra-atomic Coulomb repulsion between electrons within the 3d shell of the Co atoms (Costa, Muniz and Mills, 2004). A small shift in this parameter, taken from an empirical analysis of exchange splittings within d shells measured by photoemission, can bring the calculated frequencies in line with the data. In the data, we see the spin wave loss structure followed by an upturn in the loss spectrum. The upturn is the low frequency wing of the Stoner spectrum. This is from the theory, since the calculations explore not χ_{SPEELS} but rather $\chi_{+,-}$. The latter can be computed much more easily than the former, particularly for ultrathin films on substrates. A full calculation of χ_{SPEELS} for a multilayer ferromagnetic film on a substrate remains a computational challenge, so we must do with $\chi_{+,-}$ at present.

Thus, we see that the spin-wave features in the SPEELS loss spectra differ qualitatively from the expectations of the Heisenberg model. However, the general features of the observed spectrum are in accord with predictions, and in fact subsequent theory provides an excellent account of the observations. The metallic character of both the ultrathin ferromagnet and the substrate are responsible for the behavior

found. We shall have much more to say about this issue in the following section on theoretical descriptions of spin excitations in the 3d ferromagnets.

At the time of this writing, the experimental study of spin waves by the SPEELS technique is in its early stages. As new and improved spectrometers come on line, we may expect this method to emerge as a powerful tool for the study of spin excitations in diverse magnetic materials.

3 THEORETICAL DESCRIPTIONS OF SPIN WAVES IN THE 3D FERROMAGNETIC METALS

In Section 2, in our discussion of experimental studies of spin waves in the 3d ferromagnetic metals, we cited and discussed numerous theoretical papers which provide a conceptual base for understanding the measurements, and for interpretation of the data. However, we said very little about the theoretical techniques employed in these studies. In this section, we will describe how one goes about generating theoretical descriptions of the spin waves probed in the experiments described in the preceding text. We shall divide the discussion into three parts. First, we have seen that both FMR and BLS studies explore spin waves whose wavelength is long compared to the lattice constant of the material. As we have seen, such long wavelength modes may be described by phenomenology for which ferromagnetism is the analog to the theory of elasticity for the treatment of long wavelength acoustical phonons. We then discuss microscopic theories of spin waves in the bulk 3d ferromagnets, and finally we turn to theoretical descriptions of the ultrathin film systems

3.1 Phenomenological theory of long wavelength spin waves in bulk ferromagnets and in magnetic nanostructures

In remarks above, we outlined very briefly the principal concepts that enter the phenomenology of long wave spin waves in ferromagnets. Here, we discuss the topic in more detail.

The description proceeds by introducing the magnetization per unit volume $\vec{M}(\vec{r}, t)$. We consider a microscopic volume ΔV sufficiently large that many spins are contained within it. The spins within ΔV are tightly coupled by very strong exchange interactions so they always remain parallel and fully ferromagnetically aligned. As we move through the material and sample, the magnetization over length scales very large compared to the linear dimensions of ΔV, this quantity may vary slowly in space and time. As the magnetization precesses in response to an external probe, or engages in thermal fluctuations, this vector remains fixed in length everywhere. Thus, the phenomenology is confined to disturbances in the magnetization whose length scale is sufficiently long that a volume ΔV such as that just defined can be introduced.

To proceed with the discussion of the dynamics of the magnetization, we must construct an underlying Hamiltonian and then we must develop the means of generating an equation of motion from this Hamiltonian. For the purposes of this section, we limit our attention to the case for which the magnetization in its quiescent state is spatially uniform. We then write the magnetization as $\hat{z}M_S$, where M_S is referred to as the *saturation magnetization*. The assumption that the magnetization is uniform in space is adequate for many of the sample configurations encountered in practice. If we consider samples of selected shapes, application of a modest external magnetic field will suffice to remove domains, and produce a state wherein the magnetization is uniform over the sample. This is the case for films, which may be viewed as infinite in extent, for cylinders, for spheres, and more generally for samples of elliptical shape. Films, cylinders, and spheres are all special limits of an ellipsoid of revolution. In samples of more complex shape, such as a rectangular prism, in sufficiently high applied field the magnetization may be regarded as spatially uniform to good approximation, though one must proceed with caution in such situations, since the static internal demagnetizing fields generated by surface magnetic charges can be quite nonuniform in space. A measure of the strength of such fields can generally be taken to be $4\pi M_S$ as a rough guide, and the magnetization will be spatially uniform to good approximation only if the applied external field is large compared to this quantity.

We may construct a phenomenological Hamiltonian as follows. First, we have the Zeeman interaction of the magnetization with the externally applied field. This may be written

$$H_Z = -H_{\text{int}} \int_V M_z(\vec{r})\, \mathrm{d}^3 r \tag{4}$$

We prefer to discuss the phenomenology in the language of the quantum theory, since there are physical situations where we need to describe the quantum nature of the spin-wave excitations. An example is BLS, where single quanta are created or adsorbed in the scattering process. Thus, in equation (4), $M_z(\vec{r})$ is the operator, in the Schrodinger representation of quantum mechanics, corresponding to the z component of magnetization density. We shall have more to say about the structure of this operator shortly. In equation (4), H_{int} is the internal magnetic field, which is parallel to magnetization density for samples of the special

shapes outlined above. Thus, for a sphere, we have $H_{\rm int} = H_0 - 4\pi M_{\rm S}/3$, for a film magnetized parallel to its surface, $H_{\rm int} = H_0$ and for a film magnetized perpendicular to its surface, $H_{\rm int} = H_0 - 4\pi M_{\rm S}$. In the latter case, in the absence of surface anisotropy the perpendicular state is stable only if $H_0 > 4\pi M_{\rm S}$. Here H_0 is the externally applied field.

When the magnetization is set in motion, it generates a dipolar field we may call $\vec{h}_{\rm d}(\vec{r})$. We thus have a second term, the interaction of the magnetization with this dipolar field. This has the form

$$H_{\rm d} = -\frac{1}{2}\int_V \vec{h}^{(\rm d)}(\vec{r}) \cdot \vec{M}(\vec{r})\, {\rm d}^3 r \tag{5}$$

The factor of 1/2 enters equation (5) because, as we see next, the dipolar field is linearly proportional to the spatially varying magnetization itself, so we have here a self energy term in the Hamiltonian.

To excellent approximation, the dipolar field may be calculated from magnetostatics. Thus we may write $\vec{h}^{(\rm d)}(\vec{r}) = -\vec{\nabla}\Phi_{\rm M}(\vec{r})$, where the magnetic potential is found from the condition $\vec{\nabla} \cdot \vec{b} = 0$, with $\vec{b} = \vec{h}^{(\rm d)} + 4\pi\vec{M}$. Thus, we find the magnetic potential from Poisson's equation

$$\nabla^2 \Phi_{\rm M}(\vec{r}) = 4\pi \nabla \cdot \vec{M}(\vec{r}) \tag{6}$$

It is an elementary matter to write down the formal solution to equation (6). When this is used to calculate the dipolar field $\vec{h}^{(\rm d)}(\vec{r})$ and the result inserted into equation (5), one can express $H_{\rm d}$ as a quadratic form in the magnetization density $\vec{M}(\vec{r})$.

Spatial variations in the magnetization are resisted by the strong exchange interactions between the spins, which are responsible for the ferromagnetism in the material. This gives rise to a contribution to the energy density of the material, which is quadratic in the spatial derivatives $\partial M_\alpha/\partial x_\beta$. The coefficients are the analogue of the elastic constants of the theory of elasticity. For this exposition, we confine our attention to the case where the material is cubic in form. Then symmetry reduces the structure to one in which we have a single parameter D, the spin-wave exchange stiffness. We refer to this term as the exchange contribution to the Hamiltonian, and write it as (for the cubic case)

$$H_{\rm ex} = \frac{D}{2M_{\rm S}} \sum_\alpha \int_V \left|\vec{\nabla} M_\alpha(\vec{r})\right|^2 \tag{7}$$

When this formalism is applied to ultrathin films, care must be taken to structure an exchange term compatible with the symmetry of the system considered. For example, films grown on the W(110) surface have a rectangular unit cell. Explicit calculations of the exchange stiffness for an Fe monolayer on W(110) show that there is a very large in-plane exchange anisotropy for this case (Muniz and Mills, 2002). If a film is grown on a substrate where the two-dimensional unit cell is a square, such as the Cu(100) surface, then the lattice mismatch may lead to a unit cell in the film tetragonal in character. Thus, once again we have symmetry much lower than assumed in the commonly used form in equation (7). The in-plane exchange stiffness is necessarily the same in the two principal directions, but may differ substantially from that perpendicular to the plane in the example just cited. An example of a system where such a tetragonal distortion is large and exerts an influence on various magnetic properties has been discussed by Baberschke and his coworkers Schultz and Baberschke (1994). We shall remain here with the simple form in equation (7).

A partial integration on equation (7) yields a more useful form for the exchange energy:

$$\begin{aligned} H_{\rm ex} = &-\frac{D}{2M_{\rm S}} \sum_\alpha \int_V M_\alpha(\vec{r}) \nabla^2 M_\alpha(\vec{r})\, {\rm d}^3 r \\ &+\frac{D}{2M_{\rm S}} \sum_\alpha \int_S M_\alpha(\vec{r}) \hat{n} \cdot \vec{\nabla} M_\alpha(\vec{r})\, {\rm d}S \end{aligned} \tag{8}$$

The second term is an integral over the surface of the sample, with $\hat{n}$ an outward pointing unit normal to the surface.

In our earlier discussion of anisotropy, it was mentioned that there were two sources of anisotropy, the shape anisotropy and a local anisotropy of spin-orbit origin whose form is controlled by the local site symmetries in the material. Shape anisotropy, whose origin is in the long-ranged dipolar fields generated by the magnetization, is included fully by the above structure through $H_{\rm int}$. Anisotropy of spin-orbit origin must be introduced through additional terms in the Hamiltonian. These take the form

$$\begin{aligned} H_{\rm a} = &\sum_{\alpha\beta} \frac{K^{(2)}_{\alpha\beta}}{M_{\rm S}^2} \int_V {\rm d}^3 r\, M_\alpha(\vec{r}) M_\beta(\vec{r})\, {\rm d}^3 r \\ &+ \sum_{\alpha,\ldots\delta} \frac{K^{(4)}_{\alpha\beta\gamma\delta}}{M_{\rm S}^4} \int_V {\rm d}^3 r\, M_\alpha(\vec{r}) M_\beta(\vec{r}) M_\gamma(\vec{r}) M_\delta(\vec{r}) \end{aligned} \tag{9}$$

Time reversal symmetry allows only even powers of the magnetization to appear on the right hand side of equation (9). Symmetry controls which coefficients in equation (9) are nonzero. For the commonly encountered but special case of cubic symmetry, one has $K_{\alpha\beta} = K\delta_{\alpha\beta}$, so the first term is then proportional to $M_x^2 + M_y^2 + M_z^2 = M_{\rm S}^2$. Thus the first term is silent for such materials, and their anisotropy is controlled by the quartic term. We could include higher powers of the magnetization in equation (9), but they will be small

in magnitude because equation (9) can be understood to be a perturbation expansion in powers of the strength of the spin-orbit coupling, which is weak for the 3d ferromagnets. If λ measures the strength of the spin-orbit coupling, and W is the bandwidth of the itinerant 3d electrons which carry the magnetism in the materials of interest, then equation (9), formally, is an expansion in powers of (λ/W) (Mills, 1994).

We have one more term to discuss. This is the surface or interface anisotropy, which we have seen in the preceding text plays a critical role in ultrathin films and more generally in nanoscale magnetic structures. The site symmetry on surfaces and interfaces is uniaxial, and usually the leading term in an expansion such as that in equation (9) is dominant. We may then write the surface anisotropy in the form

$$H_{\mathrm{a}}^{(\mathrm{S})} = \int_{\mathrm{S}} \frac{K_{\mathrm{S}}(\hat{n})}{M_{\mathrm{S}}^2}[\hat{n}\cdot\vec{M}(\vec{r},t)]^2\,\mathrm{d}S \tag{10}$$

When $K_{\mathrm{S}}(\hat{n})$ is positive, the local region on the surface is a hard axis, and when it is negative, we have an easy axis. Here $\hat{n}$ is an outward directed unit vector normal to the surface.

The next step is to generate an equation of motion for the magnetization components. Within our quantum theoretic formulation, we may write down equations of motion for the operators $M_\alpha(\vec{r},t)$ in the Heisenberg representation. These have the well-known form

$$i\hbar\frac{\partial M_\alpha(\vec{r},t)}{\partial t} = [M_\alpha(\vec{r},t), H] \tag{11}$$

To proceed with the construction of the right hand side of equation (11), we require commutation relations between the various components of the magnetization. These have been derived by Kittel (1963a) and take the form

$$[M_x(\vec{r},t), M_y(\vec{r}',t)] = i\mu_0 M_z(\vec{r},t)\delta(\vec{r}-\vec{r}') \tag{12}$$

plus forms generated by permuting x, y, and z. We also have $[M_\alpha(\vec{r},t), M_\alpha(\vec{r}',t)] = 0$. In these expressions, μ_0 is the magnetic moment in each unit cell of the material.

The discussion just given allows one to derive equations of motion that describe not only the small amplitude spin motions of interest to spin-wave theory but also the full nonlinear equations which can be applied to large amplitude spin motions as well. One may show that the right hand side of equation (11) can be written in the form of the first torque term in equation (1), where the effective field $\vec{H}_{\mathrm{eff}}(\vec{r},t)$is given by $\hat{z}H_{\mathrm{int}} + \vec{h}_{\mathrm{d}}(\vec{r},t)$ plus terms from the exchange and anisotropy contributions to the Hamiltonian. We shall not quote the general form of this structure; the interested reader can derive its form for any particular model of interest. The relaxation term at the right hand side of equation (1) does not emerge from the formalism set up so far. This must either be added as a phenomenological structure such as that shown in equation (1) or derived from a suitable microscopic theory, though this cannot be done in general. As we have seen from our discussion of the two-magnon damping mechanism in the section on FMR in ultrathin films, in real materials the simple phenomenological form in equation (1) can prove inadequate.

If our desire is to discuss small amplitude motions of the magnetization appropriate to the description of spin waves, then one proceeds as follows. One writes

$$\vec{M}(\vec{r},t) = M_z(\vec{r},t)\hat{z} + m_x(\vec{r},t)\hat{x} + m_y(\vec{r},t)\hat{y} \tag{13}$$

where $m_{x,y}(\vec{r},t)$ are regarded as small. Then in the limit of small amplitude motions, from the constraint $m_x^2 + m_y^2 + M_z^2 = M_{\mathrm{S}}^2$, we have

$$M_z \cong M_{\mathrm{S}} - \frac{1}{2M_{\mathrm{S}}}(m_x(\vec{r},t)^2 + m_y(\vec{r},t)^2) \tag{14}$$

Through use of equations (13) and (14), the Hamiltonian may be reduced to a quadratic form in the small amplitudes $m_x(\vec{r},t)$ and $m_y(\vec{r},t)$. The relevant commutation relation for use in generating equations of motion for $m_x(\vec{r},t)$ and $m_y(\vec{r},t)$ becomes

$$[m_x(\vec{r},t), m_y(\vec{r},t)] = i\mu_0 M_{\mathrm{S}}\delta(\vec{r}-\vec{r}') \tag{15}$$

Suppose we apply the above formalism to a simple but commonly encountered geometry. This is a film of thickness d magnetized parallel to its surfaces, with surface anisotropy present. We take the z axis parallel to the magnetization, and the y axis normal to the film surfaces, which are then parallel to the xz plane. We have the ultrathin film limit in mind, and we suppose that surface anisotropy is dominant. The Hamiltonian can then be written

$$H = H_{\mathrm{V}} + H_{\mathrm{S}}^{>} + H_{\mathrm{S}}^{<} \tag{16}$$

where

$$\begin{aligned} H_{\mathrm{V}} = {} & \frac{H_0}{2M_{\mathrm{S}}}\int_V \left[m_x(\vec{r})^2 + m_y(\vec{r})^2\right]\mathrm{d}^3r \\ & -\frac{1}{2}\int_V \left[h_x^{(\mathrm{d})}(\vec{r})m_x(\vec{r}) + h_y^{(\mathrm{d})}m_y(\vec{r})\right]\mathrm{d}^3r \\ & -\frac{D}{2M_{\mathrm{S}}}\int_V \left[m_x(\vec{r})\nabla^2 m_x(\vec{r}) + m_y(\vec{r})\nabla^2 m_y(\vec{r})\right]\mathrm{d}^3r \end{aligned} \tag{17}$$

$$H_{\rm S}^{>} = +\frac{D}{2M_{\rm S}} \int\limits_{y=+d/2} \left[m_x(\vec{r}) \frac{\partial m_x(\vec{r})}{\partial y} + m_y \frac{\partial m_y(\vec{r})}{\partial y} \right] {\rm d}x{\rm d}z + \frac{K_{>}^{\rm S}}{M_{\rm S}^2} \int\limits_{y=+d/2} m_y(\vec{r})^2 {\rm d}x{\rm d}z \tag{18}$$

and

$$H_{\rm S}^{<} = -\frac{D}{2M_{\rm S}} \int\limits_{y=-d/2} \left[m_x(\vec{r}) \frac{\partial m_x(\vec{r})}{\partial y} + m_y(\vec{r}) \frac{\partial m_y(\vec{r})}{\partial y} \right] {\rm d}x{\rm d}z + \frac{K_{<}^{\rm S}}{M_{\rm S}^2} \int\limits_{y=-d/2} m_y(\vec{r})^2 \, {\rm d}x{\rm d}z \tag{19}$$

This Hamiltonian structure leads to equations of motion in the bulk of the film, in the regime $-(d/2) < y < +(d/2)$, of the form

$$\frac{\partial m_x}{\partial t} = -\gamma(H_0 - D\nabla^2)m_y + \gamma h_y^{(\rm d)} \tag{20a}$$

$$\frac{\partial m_y}{\partial t} = \gamma(H_0 - D\nabla^2)m_x - \gamma h_x^{(\rm d)} \tag{20b}$$

where once again we have $\vec{h}^{(\rm d)} = -\nabla\Phi_{\rm M}$ and for the film

$$\nabla^2\Phi_{\rm M} = 4\pi \left[\frac{\partial m_x}{\partial x} + \frac{\partial m_y}{\partial y} \right] \tag{20c}$$

We have boundary conditions at each surface of the film, which must be imposed, in order to obtain a solution to these equations. The first two may be called the *electrodynamic boundary conditions*. We must conserve the two tangential components of the dipolar field $\vec{h}^{(\rm d)}$across both surfaces; as we know from textbook discussions of magnetostatics, this is insured if the magnetic potential $\Phi_{\rm M}$ is conserved. Then we must also conserve the normal (y) component of $\vec{b} = \vec{h}^{(\rm d)} + 4\pi\vec{m}$. One must recognize that in general, the spin motion creates time dependent fields of dipolar origin outside the body of the film. One may describe these by introducing a magnetic potential $\Phi_{\rm M}^{(\rm ext)}$ the region outside the film, which satisfies LaPlace's equation.

There are then boundary conditions imposed by the surface terms contained in equations (18) and (19). Formally these introduce terms into the equations of motion for the variables m_x and m_y which are proportional to $\delta(y \pm d/2)$. The boundary conditions follow by requiring equation (19) to be satisfied everywhere in the film including $y = \pm d/2$, and then one must set the coefficients of the two delta functions to zero if this is to be the case. At the upper surface $y = +d/2$ one then has the two conditions,

$$D\frac{\partial m_y}{\partial y} + \frac{2K_{\rm S}^{>}}{M_{\rm S}} m_y \bigg|_{y=+d/2} = D\frac{\partial m_x}{\partial y}\bigg|_{y=+d/2} = 0 \tag{21a}$$

whereas on the lower surface $y = -d/2$ we have

$$D\frac{\partial m_y}{\partial y} - \frac{2K_{\rm S}^{<}}{M_{\rm S}} m_y \bigg|_{y=-d/2} = D\frac{\partial m_x}{\partial y}\bigg|_{y=-d/2} = 0 \tag{21b}$$

We have traced through this particular example to illustrate how the presence surface anisotropy enters the description of spin dynamics in ultrathin films. For this case, and for diverse magnetic nanostructures for which the continuum theory described above is appropriate, the surface anisotropy manifests itself in the boundary conditions applied to the dynamic magnetization at the surface of the sample.

In the exposition in the preceding text, we have phrased the discussion in terms of the quantum theory of magnetization motions, since there are circumstances one encounters where truly quantum phenomena are encountered in ultrathin films and also in other nanostructures. Thus, it is useful to have the full quantum-mechanical formalism in hand. We direct the reader to an excellent discussion by Heinrich and Cochran (Heinrich and Cochran, 1993). These authors frame the discussion entirely in the language of the classical physics. The equations of motion generated by the quantum theory are in fact identical to those generated by the classical approach. The fact that this is so is insured by the correspondence principle of quantum theory, and the fact that the magnetization density as defined here is a macroscopic variable. However, even though this is so, there are circumstances where a quantum theoretic formulation of the problem is essential. This is the case any time we wish to discuss phenomena in which a single spin-wave quantum is created or destroyed; as remarked above, BLS is an example of such a physical process.

Both the classical theory and the quantum theory necessarily produce identical eigenvectors for the spin-wave modes of a sample, since each emerges from the same equation of motion. However, in the discussion of quantum-dominated phenomena, including the calculation of the temperature dependent magnetization at low temperatures, one must phrase the discussion in terms of spin-wave annihilation and creation operators, which destroy or create spin waves described by properly normalized eigenstates. There is no way one can arrive at a normalization criterion through use of the classical approach. To do this properly, a quantum theory is required. Interestingly, for finite samples of general shape, the question of how to properly normalize the eigenfunction has been discussed only very recently, by the present author (Mills, 2006). It should also be remarked that the present author finds it much more straightforward to derive equations of motion in the quantum rather than the classical method, though this clearly is a matter of taste.

We conclude this section by referring once again to the review paper by Heinrich and Cochran cited in the preceding

text (Heinrich and Cochran, 1993). Here one finds application of the theory to the analysis of data on ultrathin films for diverse systems.

3.2 Microscopic theories of spin waves in the bulk 3d ferromagnets

In the previous section, we have seen that long wavelength spin waves in bulk crystals, films, and more generally magnetic nanostructures may be described by a simple phenomenology which involves a small number of parameters which may be fitted to data.

If our interest is in short wavelength spin waves whose wave vector is well out into the Brillouin zone, then we must resort to a microscopic model. For ferromagnets and other forms of magnetically ordered crystals, the standard approach is based on the use of the Heisenberg model, which utilizes a scheme based on the notion that in each unit cell of the material we have a spatially localized magnetic moment. One then envisions that these moments are coupled together by exchange interactions of the classical Heisenberg form; so two neighboring spins interact via the classical exchange interaction, which may be written as $-J_{12}\vec{S}_1\cdot\vec{S}_2$. Such interactions in many materials may extend to next nearest neighbors and beyond.

Although it is not uncommon to see such a picture applied to the 3d ferromagnets, in fact it is clear that the physics of spin excitations in these materials is very different than what follows from the Heisenberg model. We have discussed some of these issues above, and we will address them in more detail here.

The Heisenberg model is appropriate to insulating materials where the 'magnetically active' electrons are very tightly bound within the ions, which sit on the various lattice sites. Overlap between wave functions of the spin-aligned electons on neighboring lattice sites is very small, and the partially filled magnetic shell has wave functions which differ only slightly from those in the free atom. In the language of band theory, these electrons reside in bands of zero width. Such a picture applies very well to transition-metal ions in insulating crystals, and to the rare-earth magnets where the 4f electrons are very tightly bound indeed. A signature of the fact that the magnetic electrons are highly localized is that the magnetic moment associated with the various ions in the crystal lattice is very close to that expected for an isolated atom, influenced by crystal fields. One then finds the magnetic moment per ion to be very close to an integral number of Bohr magnetons. The first clue that this picture fails badly in the 3d ferromagnets is the fact that the moment per ion is a nonintegral number of Bohr magnetons. For example, in Fe, the moment per ion is $2.2\,\mu_B$, in Co $1.7\,\mu_B$, and in Ni one has $0.6\,\mu_B$, with μ_B the Bohr magneton.

At this point, the electronic band structure of the 3d ferromagnets is very well understood. The electrons of interest reside in a series of nine energy bands (per spin direction) formed from the 4p, 4s, and 3d states of the free atom. The Fermi energy intersects this band structure where the 3d admixture into the Bloch functions is very large; the width of this region is roughly 4 eV for the 3d metals, whereas the width of the 4sp complex is in the range of 10 eV. The Bloch functions of general wave vector are admixtures of s, p, and d character as a consequence of hybridization between these states.

Ferromagnetism occurs when the Coulomb interaction between electrons becomes sufficiently strong. A rather simple argument allows one to appreciate why this is so. Suppose we consider electrons in energy bands with a paramagnetic ground state, so for each wave vector $\vec{k}$ below the Fermi energy we have one electron with spin up, and one with spin down. We then have $E_\uparrow(\vec{k}) = E_\downarrow(\vec{k})$, where the subscript refers to spin direction, and also we have $N_\uparrow = N_\downarrow$ in this state.

Now suppose that we create a spin-polarized state by taking all down spin electrons within the energy ΔE of the Fermi level, increase the energy of each electron by ΔE, flip its spin and place in an empty state in the up spin band, just above the Fermi energy E_F. We suppose that $\Delta E \ll E_F$. The change in kinetic energy of the electrons is $\Delta T = \Delta E \Delta N = (\Delta N)^2/N(E_F)$, where ΔN is the number of electrons transferred. Thus, this operation has increased the kinetic energy of the electrons in the energy bands. It costs kinetic energy to create a spin-polarized state.

Now consider the influence of the Coulomb interaction between electrons. If we consider the 'magnetically active' 3d electrons in the transition metals, there is a strong Coulomb interaction between electrons which reside in the 3d shell on a given lattice site. The dominant Coulomb interaction is between antiparallel spins on each site; the Pauli principle does not allow two parallel spins to occupy the same point in space (the many-body wave function vanishes in this circumstance) and by continuity the probability that two parallel spin electrons come close together is small. There is no such restriction on electrons of opposite spin, so to first approximation we may write the Coulomb interaction as $UN_\uparrow N_\downarrow$. After we create the spin-polarized state, we have $N_\uparrow = N + \Delta N$ and $N_\downarrow = N - \Delta N$. Hence the change in Coulomb energy is $\Delta V_C = -U(\Delta N)^2$.

The above argument shows that by creating a net spin polarization in an initially paramagnetic metal, if the Coulomb interaction between antiparallel spins is sufficiently strong that the product $UN(E_F) > 1$, the paramagnetic state is unstable with respect to formation of ferromagnetism.

This is known as the *Stoner criterion*. The criterion, derived above from a crude argument, survives within the framework of contemporary density-functional theory, and in fact the theory provides one with an *ab initio* value for the parameter U (Marcus and Moruzzi, 1988).

We pause to remark that the Stoner criterion allows one to understand the occurrence of ferromagnetism in the 3d metals. As one moves from left to right in a given row of the transition-metal series, the nuclear charge increases and causes the d wave functions to contract. Hence U increases as we move from left to right, since it scales inversely with the radius of the d orbital. This also causes the d bands to narrow, since overlap between neighboring d orbitals decreases. This increases $N(E_F)$, so the Stoner product $UN(E_F)$ increases. The ferromagnetic metals Fe, Co, and Ni lie on the right side of the 3d row. As one moves vertically downward in a given column, the 4d orbitals are spatially more extended than the 3ds, and the 5d orbitals more so than the 4d wave functions. Hence as we go down a column from the 3d row to the 5d row, the Stoner product decreases. The consequence is that ferromagnetism is found only on the right end of the 3d series.

The first step in generating a microscopic description of spin waves in the itinerant 3d ferromagnets is then to complete an electronic structure calculation, wherein the ferromagnetism is driven by the presence of Coulomb interactions between the electrons. It is a nontrivial step to proceed from the electronic band structure calculation to a description of spin waves in the itinerant magnets.

The analysis proceeds by calculating the quantity referred to as the wave vector and frequency dependent susceptibility, denoted usually by $\chi_{+,-}(\vec{k}, \omega)$, and exploring its structure as a function of frequency for fixed wave vector. The physical meaning of this function is as follows. Suppose we take our ferromagnet with magnetization parallel to the z axis, and apply a circularly polarized magnetic field in the xy plane, which oscillates with frequency ω and has a spatial dependence characterized by the wave vector $\vec{k}$. The field is thus $\vec{h}(\vec{r}, t) = h_{\vec{k},\omega}[\hat{x}\cos(\vec{k}\cdot\vec{r} - \omega t) + \hat{y}\sin(\vec{k}\cdot\vec{r} - \omega t)]$. This applied field will excite the spins, and introduce a spatially varying disturbance, which may be written as $\langle S_+(\vec{r}, t)\rangle = \langle S_+\rangle_{\vec{k},\omega}[\hat{x}\cos(\vec{k}\cdot\vec{r} - \omega t) + \hat{y}\sin(\vec{k}\cdot\vec{r} - \omega t)]$. Linear response theory then provides one with a link between the amplitude of the exciting field and the response of the system. One writes

$$\langle S_+\rangle_{\vec{k},\omega} = \chi_{+,-}(\vec{k}, \omega) h_{\vec{k},\omega} \tag{22}$$

Thus, the wave vector and frequency dependent transverse susceptibility is the proportionality constant between the applied transverse field and the amplitude of the transverse spin density induced by the field.

One proceeds to study spin waves by devising a means of calculating the transverse susceptibility just described. For fixed wave vector, if frequency is scanned, there will be a pole of this function at the frequency $\omega(\vec{k})$ of the spin wave with wave vector $\vec{k}$. If the spin wave is damped by some intrinsic process, instead of a pole one will find a resonant peak with finite width; the lifetime of the spin wave is the inverse of this width. In results to be presented below, we shall show calculations of the quantity $\mathrm{Im}[\chi_{+,-}(\vec{k}, \omega)]$. The spin wave appears as a resonant peak in this quantity, centered around the spin-wave frequency $\omega(\vec{k})$.

The calculation of the transverse susceptibility takes one into the realm of many-body theory. One is led to an integral equation, which must be solved numerically for all but the most schematic descriptions of the electron band structure. An introduction to such analyses for the very simple one band Hubbard model, where the analysis is elementary and can be carried out analytically is given by White (1970).

Two methods have been used in the study of spin-wave excitations in the bulk 3d metals. The first, introduced by Cooke and collaborators (1980) utilizes an empirical tight binding description of the electron energy bands. One begins with *ab initio* energy bands for the paramagnetic state of the material of interest, and generates a tight binding description of the 3d/4sp complex by choosing intersite hopping integrals and 3d/4sp hybridization parameters to reproduce the band structure. Ferromagnetism is driven by empirically described Coulomb interactions between electrons, which reside within the 3d shell of an ion on a specific lattice site. Depending on the scheme used, there can be from one to three parameters for this purpose. The Coulomb parameters are adjusted empirically to fit certain ground state properties such as the total magnetic moment, the fraction of the moment of 3d character, which has e_g symmetry, and the fraction which has t_g symmetry. We may refer to such schemes as multiband generalizations of the well-known Hubbard model of magnetism in itinerant systems. One may find descriptions of such analyses in various papers (Cooke, Lynn and Davis, 1980; Tang, Plihal and Mills, 1998). We note that it is essential for the empirical term which describes the Coulomb interaction to be form invariant under spin rotations. The initial studies of Cooke and coworkers used a form that did not have this property (Cooke, Lynn and Davis, 1980), though in subsequent work we see this matter corrected (Blackman *et al.*, 1985).

The scheme just described is based on a realistic underlying electronic band structure, though this is described by the empirical method just discussed. The transverse susceptibility $\chi_{+,-}(\vec{k}, \omega)$ is calculated through use of a many-body scheme known as the *random phase approximation* (RPA). The method leads to a certain integral equation one must solve numerically. The virtue of the empirical tight binding

method is that once the kernal of the integral equation is generated by numerical methods, the actual solution of the integral equation is achieved through simple inversion of a small matrix. For this reason, at present the empirical tight method is the only means of addressing spin-wave excitations in adsorbed ultrathin films, which we discuss in the next section. A full *ab initio* treatment such as that discussed in the next paragraph is still beyond the computational power available at present.

A much more satisfactory means of generating theoretical descriptions of spin waves is through *ab initio* theory, where the spin-polarized version of density-functional theory is used to generate the ground state, without resort to the simple empirical description of the Coulomb interaction employed in the empirical tight binding scheme. The transverse susceptibility is then generated through application of time dependent density-functional theory. In this fully *ab initio* scheme there are no adjustable parameters, of course. Full density-functional calculations of spin waves in bulk Ni and Fe have been reported by Savrasov, and also by Karlsson and Aryasetiawan (Savrasov, 1998; Karlsson and Aryasetiawan, 2000a,b).

While as just stated, full *ab initio* calculations of spin-wave spectra are surely more satisfactory than those based on the empirical tight binding approach, from the perspective of the physics incorporated in the two methods, there are similarities. For instance, both methods utilize a simple self-consistent mean-field description of the ground state. In density-functional theory, the influence of electron correlation beyond that in, say, Hartree–Fock theory is embedded within the exchange correlation potential, which contains no adjustable parameters. In the empirical tight binding methods, correlation effects are surely incorporated into the effective Coulomb matrix elements, but as discussed in the preceding text these are adjusted to fit data on the ground state. If one describes the content of time dependent density-functional theory by Feynman diagrams, the diagrams summed are in fact the same as those, which enter the RPA. Both methods have the feature that once the ground state is described, no further parameters are introduced to generate the description of spin waves.

As one can see from the discussions above, there are important differences in the nature of the spin waves in the itinerant ferromagnets, and those insulating solids for which application of the Heisenberg model is appropriate. In the Heisenberg model, the spin waves are *exact* eigenstates of the Hamiltonian, as excitations from the ground state. This is not the case in the itinerant materials. Here one has, for each wave vector $\vec{k}$, a continuum of spin triplet particle hole excitations formed by taking an electron from a majority spin band, and then placing it in a state in the minority spin band complex after flipping its spin and translating its wave vector by the amount $\vec{k}$. These bands of particle hole excitations are called the *Stoner continuum* as noted in our discussion of neutron scattering from spin waves. As discussed there, spin waves in the itinerant ferromagnets thus have a finite lifetime by virtue of the fact that they can decay into the Stoner continuum. These features appear in the calculations cited in the preceding text, and the onset of strong damping with increasing wave vector is evident in the neutron data we have discussed in Section 2. We shall see in our discussion of spin waves in ultrathin films adsorbed on metal substrates that in such systems, the damping is very severe indeed, to the point where the spin wave 'lives' for only two or three periods, when its wave vector is large.

We wish to conclude this section with comments on an issue that has been discussed since the early work of Cooke and his colleagues (Cooke, Lynn and Davis, 1980). We also mentioned this matter earlier, and here we wish to explore it in more detail. These authors found apparent gaps in the spin-wave dispersion relation in both Fe and Ni, along high symmetry directions and roughly in the middle of the Brillouin zone. The physical reason why such gaps should occur is puzzling, at least to the present author. The piece of dispersion curve on the high-frequency side of the gap was called an *optical spin wave* by Cooke *et al*., though clearly these materials are monatomic in nature. As remarked earlier, in our studies of spin-wave dispersion in both Fe and Ni through use of the empirical tight binding method, we have failed to find such features. We find smooth dispersion curves throughout the Brillouin zone (Tang, Plihal and Mills, 1998; Hong and Mills, 2000).

However, other authors have also found apparent gaps in spin-wave dispersion relations for Fe and Ni. We note that a survey of the literature shows that there is no consensus regarding the direction in the Brilluoin zone or the point at which the apparent gaps occur. For instance, Cooke and coworkers report a doublet in the spectral density of Fe along [100] (Cooke, Lynn and Davis, 1980) while Savrasov finds a smooth featureless dispersion curve in Fe along this same direction, in clear conflict with the earlier paper (Savrasov, 1998). Karlsson and Aryasetiawan find a gap in the spin-wave dispersion along the [111] direction in Ni (Karlsson and Aryasetiawan, 2000a), but Cooke and collaborators find their structures along the [100] direction in Ni. Furthermore the nature of their structures differs qualitatively from the gap reported by Savrasov along Ni [100] (Savrasov, 1998; Cooke, Blackman and Morgan, 1985).

Thus, while various authors have found gaps and unusual structures in the effective spin-wave dispersion relations of both Fe and Ni, no two theoretical papers agree on their nature, or even which symmetry direction in the zone the features are found. With this in mind, we wish to discuss our

own experience in which we encountered such a structure. In our study of the spin waves in an Fe monolayer adsorbed on the W(110) surface, we initially found a dispersion relation with a clear gap when the wave vector was directed along the ΓX direction in the two-dimensional Brillouin zone. The gap in our case was an artifact caused by poor convergence in the k space sums required to construct the kernal of the integral equation one must solve in the RPA description of the transverse susceptibility. The convergence issue involved is quite curious, and we illustrate this in Figure 7, reproduced from our paper on the Fe monolayer on W(110) (Muniz and Mills, 2002). The three panels show

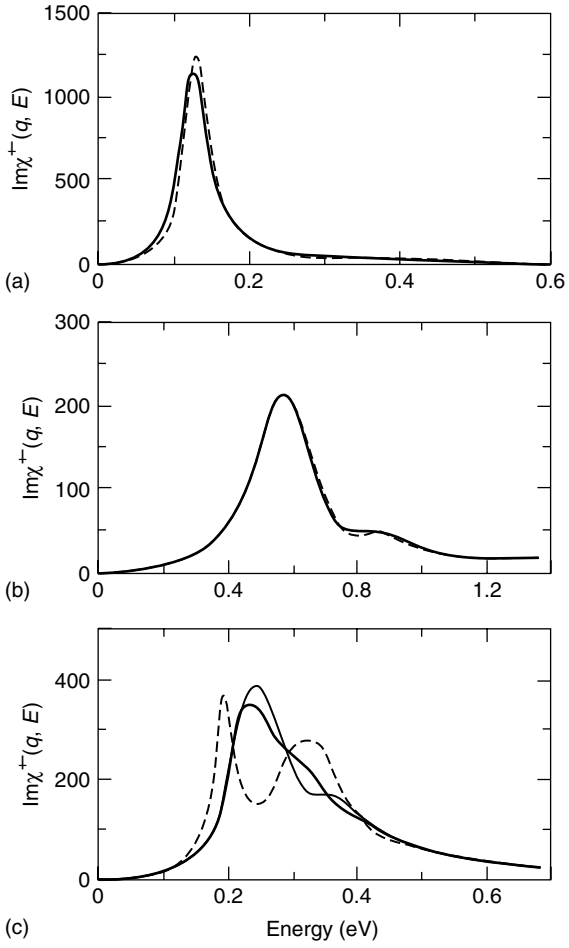

Figure 7. We illustrate convergence issues encountered in our calculation of the spin-wave dispersion relation for the Fe monolayer on W(110). We plot the imaginary part of the transverse susceptibility $\chi_{+,-}$ for selected wave vectors in the two-dimensional Brillouin zone, along the ΓX direction. In (a) the reduced wave vector is 0.25, in (b) it is 0.50, and in (c) it is 0.35. The dashed curve is a calculation based on 262 special points in the irreducible Brillouin zone for the kernal which appears in the RPA integral equation, the light solid curve is for 1036 special points, and the heavy solid curve is for 4120 points. (Reproduced from Muniz & Mills 2002, with permission from the American Physical Society. © 2002.)

the spin-wave resonance in $\mathrm{Im}(\chi_{+,-})$ for three selected reduced wave vectors along the ΓX direction. In (a), we show the calculation for a reduced wave vector of 0.25, in (b) we show the result for 0.50, and in (c) we show the result for 0.35. Let us first look at the results in (a) and in (b). In these figures, the dashed line results from a calculation where the computation of the kernal in the RPA integral equation utilized 262 special points in the irreducible Briilouin zone, and the thin solid line is a calculation, which employed 1036 such points. The dashed curve and the thin solid line nearly lie on top of each other, so it is reasonable to assume that for all wave vectors, adequate convergence can be achieved with use of 262 points. If we proceed to do this, then for a reduced wave vector of 0.35 we generate the double peaked structure evident in part (c) of the figure. If we were to stop here, and plot an effective dispersion for spin waves along the ΓX direction, we would find a gap near the reduced wave vector of 0.35. The dispersion curve and its gap have an appearance qualitatively similar to those found by Savrasov along Ni(100), and that found by Karlsson and Aryasetiawan along the (111) direction in Ni.

However, in our case the apparent gap and the doublet in Figure 7(c) are an artifact produced by poor convergence around the particular wave vector in the figure. When we use 1036 points, the doublet has disappeared (thin solid line), and we are left with a single peak. The calculation has now settled down, since use of 4120 points yields virtually the same structure.

This example, along with the contradictions found in the theoretical literature on spin waves in Fe and Ni suggests that further study of the apparent gaps and optical spin wave features should be undertaken before their existence is viewed as firmly established.

3.3 Theoretical studies of spin waves in ferromagnetic ultrathin films

It was remarked in the previous section that a full density-functional analysis of the spin-wave spectra of ultrathin ferromagnets adsorbed on substrates is beyond our capability at present. It is the case that through use of density-functional methods, one may calculate effective Heisenberg exchange interactions between nearby spins in a ferromagnetic lattice (Frota Pessoa, Muniz and Kudrnovsky, 2000; Grother, Ederer and Fahnle, 2001; Bruno, 2003). Such methods can be applied to ultrathin films to generate spin-wave spectra calculated within the adiabatic approximation (Padja *et al*., 2000; Udvardi, Szunyodh, Palotos and Weinberger, 2003). Such exchange couplings may be inserted into a Heisenberg–Hamiltonian and one may then generate a spin-wave

spectrum for the ultrathin film. In our discussion of the SPEELS data on spin waves in ultrathin films in Section 2, we have seen that a procedure such as this produces a misleading picture of the nature of short wavelength spin waves in ultrathin films. The author and his colleagues have formulated a means by which spin excitations in ultrathin structures on substrates of infinite extent may be described within a fully dynamical theory similar to the RPA descriptions discussed in the previous section of spin waves in the bulk 3d ferromagnets (Tang, Plihal and Mills, 1998; Muniz and Mills, 2002; Costa Muniz and Mills, 2003a). In the discussion presented in the subsequent text, we shall make explicit comparisons between results of full dynamical calculations and those generated from a Heisenberg–Hamiltonian applied to the ultrathin film. The dramatic failure of the latter approach will be evident. We first comment on aspects of the calculation.

A detailed discussion of our method is given in our first paper on adsorbed films (Muniz and Mills, 2002). We employ the empirical tight binding method to the adsorbed film/substrate combination. Thus, the one-electron states extend throughout the system, in general. To generate a description of the ground state of the structure, we require the one-electron Green's function. This can be built up for the film/substrate combination by an iteration method, applied numerically. As in the bulk ferromagnets, we use a mean-field description of the ferromagnetic ground state, but the magnetic moments in the ferromagnetic film are allowed to vary in a layer-by-layer fashion. There are some technical issues that must be addressed here. For instance, the multiband Hubbard model with on-site Coulomb interactions within the 3d shell does not properly incorporate the long-ranged feature of the full Coulomb interaction employed in *ab initio*, density functional based theories. Thus, one finds that the surface layer of the ultrathin film is highly charged, if one works within the multiband Hubbard model. The ground state so generated is thus rather unphysical. One must then adjust the energies of the one-electron orbitals in the surface so the orbital occupancies are brought in line with those generated from *ab initio* studies of the film. A detailed discussion of this issue, and comparisons between the empirical tight binding description of ultrathin films is presented in the paper by Tang and coworkers (1998).

Once a description of the ground state is found, one must set up an appropriate wave vector and frequency dependent susceptibility for the film by extending the concept described in the above for the bulk. This new object is defined as follows. We suppose we subject the film/substrate combination to a circularly polarized transverse magnetic field of frequency ω once again. This field has a wave vector $\vec{k}_\parallel$ in the plane parallel to the film surface, but may vary in the direction normal to the surface in an arbitrary manner. If we use l to label the atomic planes in the structure, then the externally applied field has the form

$$\vec{h}(\vec{r}_\parallel, l; t) = h_{\vec{k}_\parallel,\omega_\parallel}(l)[\hat{x}\cos(\vec{k}_\parallel \cdot \vec{r}_\parallel - \omega t) + \hat{y}\ \sin(\vec{k}_\parallel \cdot r_\parallel - \omega t)] \tag{23}$$

Such an external field induces a transverse moment $\langle S_+(\vec{r}_\parallel, l; t)\rangle$ of the form

$$\langle S_+(\vec{r}_\parallel, l; t)\rangle = \langle S_+(l)\rangle_{\vec{k}_\parallel,\omega_\parallel}(l)[\hat{x}\cos(\vec{k}_\parallel\cdot\vec{r}_\parallel - \omega t) + \hat{y}\sin(\vec{k}_\parallel\cdot r_\parallel - \omega t)] \tag{24}$$

From linear response theory, one finds that one can write

$$\langle S_+(l))\rangle_{\vec{k}_\parallel\omega} = \sum_{l'} \chi_{+,-}(l, l'; \vec{k}_\parallel, \omega)h(l')_{\vec{k}_\parallel,\omega} \tag{25}$$

One may formulate a means of calculating the response function introduced in equation (25) through use of the RPA. There is a kernal, referred to in the literature as the irreducible particle hole propagator, that must be generated from a convolution of two single particle Green's functions, which one knows once the description of the ground state of the system is completed. This object is a matrix structure with elements labeled by plane and orbital indices. A very considerable amount of computational effort is involved in generating the large number of elements to sufficient accuracy to insure converged results. Once this is done, however, for each wave vector and frequency the response function can be generated by means of a straightforward matrix inversion. This step is rendered simple by the fact that the Coulomb interaction between electrons is local in space, confined to the electrons within the 3d shell of a single ion. The computational labor required to carry through a full time dependent density-functional analysis of the large structures we have explored would be some orders of magnitude larger than that expended in our calculations.

A feeling for the physical content of the response function defined in equation (25) may be obtained by displaying its form if we do describe the spin-wave excitations in the film through use of the Heisenberg model. As we have seen, for a film with N layers, for each choice of the wave vector $\vec{k}_\parallel$ we have N spin-wave frequencies we may refer to as $\omega_\alpha(\vec{k}_\parallel)$, where α ranges from 1 to N. Associated with each mode is an eigenvector $e_\alpha(\vec{k}_\parallel; l)$, with l the layer index. The eigenvector tells us the amplitude of mode α on layer l. Then for suitably normalized eigenvectors, one finds

$$\chi_{+,-}(l, l'; \vec{k}_\parallel, \omega) = \sum_{\alpha=1}^{N} \frac{e_\alpha(\vec{k}_\parallel, l)e_\alpha(\vec{k}_\parallel l')}{\omega_\alpha(\vec{k}_\parallel) - \omega - i\eta} \tag{26}$$

Where η is infinitesimal. To illustrate the results generated from our full dynamical calculations we shall display the quantity $S(l;\vec{k}_\parallel,\omega) = (1/\pi)\mathrm{Im}\{\chi_{+,-}(l,l;\vec{k}_\parallel,\omega)\}$. We refer to this quantity as the spectral density of spin fluctuations on layer l of the film. For the Heisenberg model, one has

$$S(l;\vec{k}_\parallel,\omega) = \sum_{\alpha=1}^{N} e_\alpha(\vec{k}_\parallel,l)^2\delta(\omega-\omega_\alpha(\vec{k}_\parallel)) \qquad (27)$$

The spectral density function associated with layer l thus consists of, in the Heisenberg model, a series of delta functions at the spin-wave frequencies associated with the wave vector selected, and the integrated strength of each of the delta functions is the square of the amplitude of the eigenvector of each mode on layer l. When we calculate this function for the itinerant ferromagnetic film adsorbed on the substrate, the damping of each mode provided by its decay to the continuum of Stoner excitations will produce resonances of finite width. The lifetime of the damped spin wave is given by the inverse of this width. The integrated strength of the broadened feature can be taken to be an indication of the square of the amplitude of each of the modes, which appear in the spectrum.

We now turn to a discussion of our results for the layer dependent spectral densities for a five-layer film of bcc-Fe on W(110). These results illustrate the behavior of the spin-wave spectra we have calculated for several ultrathin film/substrate combinations.

In Figure 8(a), we show the layer dependent spectral densities for a reduced wave vector of 0.05 along the [10] direction of the two-dimensional Brillouin zone. The dashed lines are for a free-standing film, whereas the solid lines are for the film adsorbed on the substrate. For the adsorbed film, the low frequency feature is the acoustical spin-wave mode. This mode, extrapolated back to zero wave vector, is the mode one would observe in FMR. The linewidth is very narrow. We shall comment further on intrinsic linewidths in FMR later. Then the second mode is the first standing

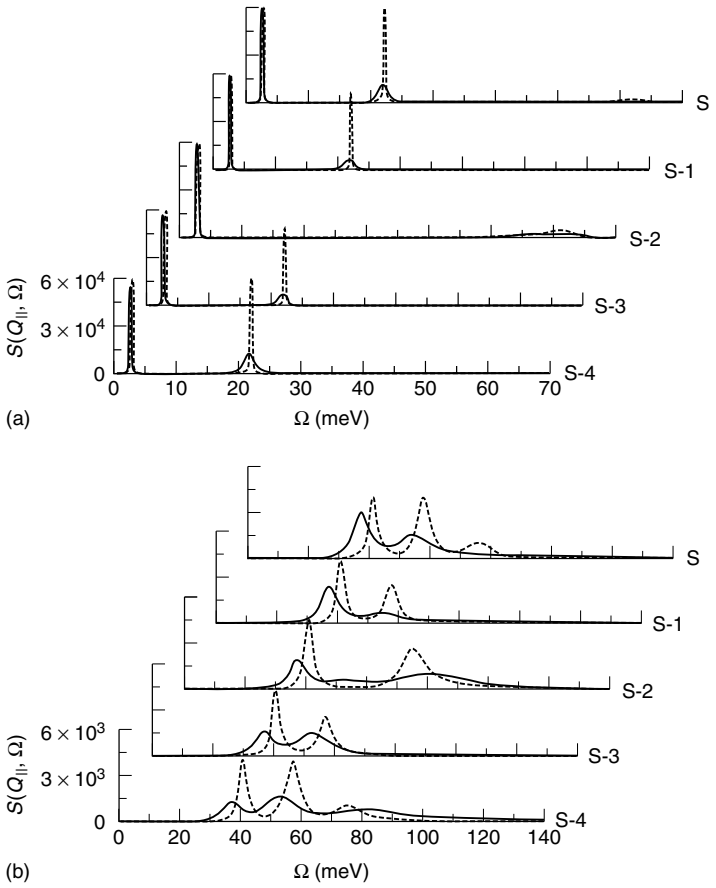

Figure 8. We show spectral densities calculated for a five-layer Fe film on W(110), for selected wave vectors along the [10] direction in the two-dimensional Brillouin zone. These are the layer dependent spectral densities defined in the text. The layer labeled S is the outer layer of the film, and layer 1 is at the interface between the film and substrate. In (a), we have results for the case where the reduced wave vector is 0.05, and in (b) the reduced wave vector is 0.2. (Reproduced from Costa *et al*., 2003, with permission from the American Physical Society. © 2003.)

spin-wave mode, whose eigenvector clearly has the cosine squared form expected through use of equation (27) as a means of representing the layer dependent spectral densities. It is, however, broadened enormously in comparison to the acoustic spin wave. Comparison of this mode with that for the free-standing film (dashed curves in Figure 8(a)) shows that the substrate plays a strong role in providing damping. This mode decays to the continuum of Stoner excitations, which carry off the spin angular momentum stored in the spin wave into the substrate by virtue of hybridization of the Fe film electron wave functions with those of the substrate. The third standing spin-wave mode is broadened so much that it is barely perceptible as a feature in the spectral density. There is a very small, broad feature evident in the middle layer of the film for this mode. Recall that if we apply the Heisenberg model to the film we would expect from equation (27) to see five modes, each with infinite lifetime. Clearly, such a picture is qualitatively wrong for systems such as these.

In Figure 8(b), we show the same information, but now for a reduced wave vector of 0.2. We see three modes, all heavily damped and they are beginning to merge into a single broad structure. Notice the difference in vertical scale between Figure 8(a) and (b). As we see from Figure 9, which shows the spectra for the reduced wave vector of 0.6, in the outer layer of the film probed by the electrons in SPEELS, we see a single broad feature. If one follows the position of this peak as a function of wave vector, one will obtain a spin wave like dispersion curve, as one sees from the example in Figure 2 of Costa Muniz and Mills (2004).

Finally in Figure 10, we show a comparison between spectral densities calculated within the full dynamical theory, and for a Heisenberg model with exchange interactions generated

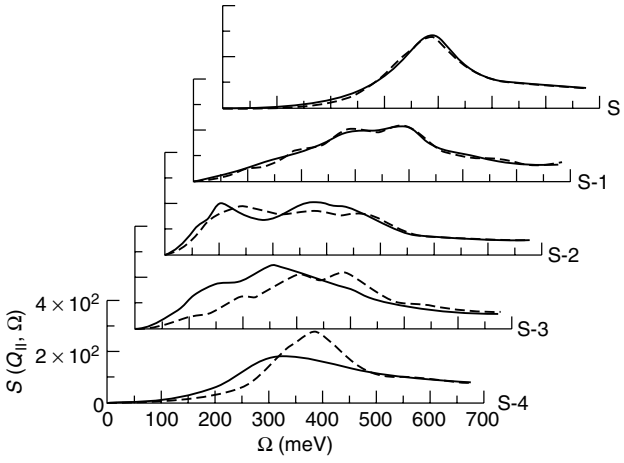

Figure 9. Same as Figure 8, except the reduced wave vector is 0.6. (Reproduced from Costa *et al*., 2003, with permission from the American Physical Society. © 2003.)

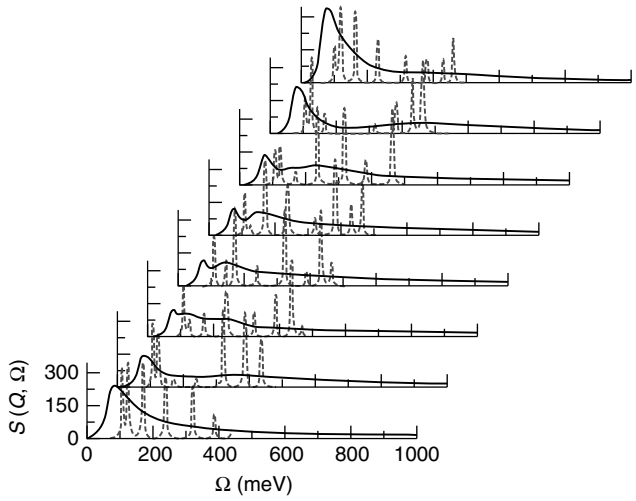

Figure 10. For an eight layer Co film on Cu(100), we show a comparison of the layer-by-layer spectral densities calculated within the full dynamical theory with those for a Heisenberg model of the film whose exchange integrals have been generated from adiabatic theory applied to the same electronic structure utilized in the full dynamical theory. The reduced wave vector is 0.3 along the [11] direction in the surface Brillouin zone. (Reproduced from Costa *et al*., 2004, with permission from the American Physical Society. © 2004.)

by adiabatic theory for the same electronic structure used in the full dynamical calculations. The calculations are for an eight layer fcc-Co film adsorbed on Cu(100), and for a reduced wave vector of 0.3 directed along the [11] direction of the surface Brillouin zone. We remind the reader that this is the system explored in the SPEELS experiments of Vollmer and collaborators (Vollmer *et al*., 2003).

We should comment on the reason for the breakdown of the Heisenberg model, when applied to the itinerant ultrathin ferromagnets. The basis for the Heisenberg model is the assumption that the adiabatic approximation is valid for a description of the spin excitations of the system. If one accepts this assumption, then one proceeds by calculating the exchange interactions between a selected pair of moments from the energy change associated with a static reorientation of the moments. If one tips a selected moment from the direction of the magnetization, torques are felt by neighboring moments, and one may deduce the value of the exchange interactions from the magnitude of the calculated torques. The infinitely long lived spin waves of the Heisenberg model follow by supposing the spin motions are sufficiently slow that adiabatic theory describes their dynamics. The calculations we have shown in Figures 8–10 show that for spin waves in the ultrathin, itinerant ferromagnets, we have a qualitative breakdown of adiabatic theory. The RPA is indeed a approximate many-body technique, but it is a fully dynamical scheme that does not invoke the adiabatic approximation.

We see from Figure 6, discussed above, that the results which emerge from this scheme applied to the empirical tight binding model appear to agree very well with the data.

In calculations of phonon spectra of metals, including that of adsorbate overlayers, the adiabatic approximation is standardly employed and the method works splendidly (Heid and Bohnen, 2003). One is tempted to argue that since the frequency of spin waves in the itinerant magnets is perhaps an order of magnitude larger than that of phonons in these same systems, this offers a basis for the breakdown of adiabatic theory for spin waves. This does not seem correct, however, because the damping rate of both phonons and spin waves scales linearly with frequency to good approximation. The damping of both phonons and spin waves in metals has its origin in decay to particle hole pairs, and if the frequency of both is low to the Fermi energy or any other characteristic energy of the electron band structure, then the damping term in the relevant dynamical response function must vary linearly with frequency. Thus, if there were no other difference, one would expect the 'Q factor' (the number of oscillations in one lifetime) of both spin waves and phonons to be roughly the same.

The breakdown of the adiabatic approximation for spin waves cannot thus be related to the much higher frequency of spin waves. Instead the breakdown has its origin in the fact that the coupling constant of the spin waves to the Stoner continuum is very much larger than the dimensionless electron–phonon coupling constant. In essence, for itinerant ferromagnets the dimensionless coupling constant is the Stoner factor, $UN(E_F)$ encountered in our simple discussion of the instability of the paramagnetic state of electrons with respect to the ferromagnetic state. This is of order unity for the 3d transition-metal ferromagnets, whereas the dimensionless electron–phonon coupling constant is small compared to unity.

We conclude this section with a discussion of one final topic, the intrinsic FMR linewidth in the ultrathin films. As discussed in the section on FMR, in the bulk form of 3d ferromagnets, the linewidth is a spin orbit based mechanism, whereas in the ultrathin films a new intrinsic mechanism is present and can be substantial in magnitude. This is the 'spin pumping' contribution to the linewidth, present when an ultrathin metallic ferromagnet is deposited on a metallic substrate. The picture set forth in the early theoretical papers which predicted the phenomenon (Berger 1996; Slonczewski, 1998) was discussed above. When the spins in the ultrathin ferromagnet are set in motion, angular momentum is transferred to the conduction electrons in these metallic films, and in the process a spin current normal to the interface is created. Thus, spin angular momentum is transported into the substrate where it is ultimately dissipated. These early calculations were based on a rather primitive model of localized spins exchange coupled to conduction electrons, viewed as free electrons. A theory of spin pumping based on one-electron theory has been set forth by Tserkovnyak, Brataas and Bauer (2002a,b) and subsequent calculations based on this formalism applied to a realistic electronic structure account well for data on spin pumping (Zwierzycki *et al*., 2005).

The spin pumping mechanism just described is clearly very much the same mechanism responsible for damping the large wave vector spin waves observed in SPEELS. To explore that this is so, we have applied our response function analyses to the issue of the linewidth in FMR. We may do this by calculating the spectral density functions at the center of the two-dimensional Brillouin zone, and then comparing the calculated linewidths to data. In our method, unfortunately, it is not possible to carry out calculations of the linewidth of the very low frequency modes actually studied in FMR. We must then apply an artificially large Zeeman and exploit the fact that the linewidth varies linearly with frequency. The method provides an excellent account of the data, as we see from Figure 11, where a comparison is made with the original observations of Urban, Woltersdorf and Heinrich (2001). We have applied our methodology also to trilayers (ferromagnetic film/nonmagnetic spacer/ferromagnetic film) adsorbed on metallic substrates, to find very excellent descriptions of the variation of linewidth of the acoustical and optical spin-wave mode of the trilayer with spacer thickness (Costa, Muniz and Mills, 2006).

It thus appears that we now have in hand theoretical descriptions of spin waves and their damping in the ultrathin ferromagnets from the zone center out to large wave vectors,

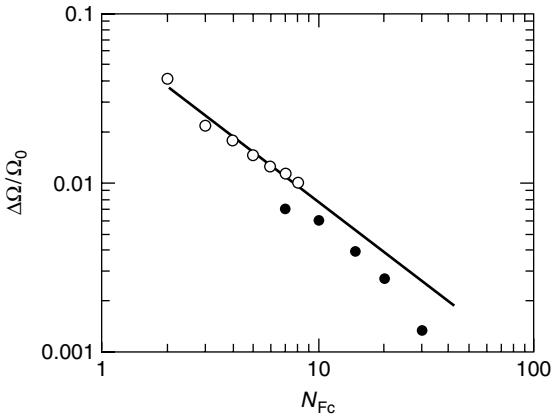

Figure 11. We show a comparison between theory (open circles) and experiment (solid dots) for the spin pumping linewidth, for Fe films on Au(100). For both theory and experiment, we show the linewidth divided by the FMR frequency, as a function of Fe film thickness. (Reproduced from Costa *et al*., 2006, with permission from the American Physical Society. © 2006. The data in the plot has been reported by Urban and coworkers, 2001.)

and the theory provides an excellent account of the data. A most important step remains. This is be the appearance of theoretical studies not based on the empirical tight binding method supplemented by the RPA but on the analyses, which employ full time dependent density-functional theory. It would be of very great interest to see such studies even for relatively small systems such as few layer free-standing films, so the results of full *ab initio* theory can be compared alongside those generated by the empirical approach. It is the view of this writer that we may see studies of small systems in the near future, but we are unfortunately far from the time where full *ab initio* calculations may be applied to the very large systems that have been studied by the empirical tight binding method. In density functional based theories of only the ground state, it is still necessary to approximate a semi-infinite substrate by a small number of layers. It is unlikely that use of such a scheme will provide adequate accounts on the damping of the spin-wave modes in ultrathin films adsorbed on metallic substrates though surely the ground state is well described with only a few substrate layers present.

REFERENCES

Abraham, D. and Hopster, H. (1987). Magnetic probing depth in spin polarized secondary electron spectroscopy. *Physical Review Letters*, **58**, 1352.

Abraham, D. and Hopster, H. (1989). Spin polarized electron energy loss spectroscopy on Ni. *Physical Review Letters*, **62**, 1157.

Amendt, W.S. and Rado, G. (1955). Electromagnetic effects of spin wave resonance in ferromagnetic metals. *Physical Review*, **97**, 1558.

Arias, R. and Mills, D.L. (1999). Extrinsic contributions to the ferromagnetic resonance response of ultrathin films. *Physical Review B*, **60**, 7395.

Arias, R. and Mills, D.L. (2005). Magnetostatic modes in ferromagnetic nanowires II. *Physical Review B*, **72**, 54426.

Azevedo, A., Olivera, A.B., de Aguiar, F.M. and Rezende, S.M. (2000). Extrinsic contribution to spin wave damping and renormalization in thin $Ni_{50}Fe_{50}$ films. *Physical Review B*, **62**, 5331.

Bardasis, A., Falk, D.S., Ferrell, R.A., *et al*. (1965). Possibility of long range spin polarization in a degenerate electron gas. *Physical Review Letters*, **14**, 298.

Berger, L. (1996). Emission of spin waves by a magnetic multilayer traversed by a current. *Physical Review B*, **54**, 9353.

Berkowitz, A. and Kodama, R.H. (2006). Exchange anisotropy. In *Nanomagnetism: Ultrathin Films, Multilayers and Nanostructures*, Mills, D.L. and Bland, J.A.C. (Eds.), Elsevier: pp. 115–152.

Bhagat, S.M. and Lubitz, P. (1974). Temperature variation of ferromagnetic relaxation in the 3d transition metals. *Physical Review B*, **10**, 179.

Blackman, J.A., Morgan, T. and Cooke, J.F. (1985). Prediction of high energy spin wave in iron. *Physical Review Letters*, **55**, 2814.

Bruno, P. (2003). Exchange interaction parameters and adiabatic spin wave spectra of ferromagnets: a "renormalized force theorem". *Physical Review Letters*, **90**, 087205.

Camley, R.E., Grunberg, P. and Mayr, C.M. (1982). Stokes-anti stokes asymmetry in brillouin scattering from magnons in thin ferromagnetic films. *Physical Review B*, **26**, 2609.

Camley, R.E. and Mills, D.L. (1997). Theory of microwave propagation in dielectric/magnetic multilayer structures. *Journal of Applied Physics*, **82**, 3058.

Camley, R.E. and Mills, D.L. (1978a). Light scattering from bulk and surface spin waves in opaque ferromagnets; the influence of quadratic coupling terms. *Solid State Communications*, **28**, 321.

Camley, R.E. and Mills, D.L. (1978b). Surface response of exchange and dipolar coupled ferromagnets; application to light scattering from magnetic surfaces. *Physical Review B*, **18**, 4821.

Camley, R.E., Rahman, T.S. and Mills, D.L. (1981). Theory of light scattering from spin wave excitations of thin ferromagnetic films. *Physical Review B*, **23**, 1226.

Camley, R.E., Rahman, T.S. and Mills, D.L. (1983). Magnetic excitations in layered media; spin waves and the light scattering spectrum. *Physical Review B*, **27**, 261.

Celinski, Z. and Henrich, B. (1991). Linewidth of Fe ultrathin films grown on Cu BCC substrates. *Journal of Applied Physics*, **70**, 5935.

Cochran, J.F. (1994). Light scattering from ultrathin magnetic layers and bilayers. In *Ultrathin Magnetic Structures II*, Bland, J.A.C. and Heinrich, B. (Eds.), Springer-Verlag: Heidelberg, pp. 222–257.

Cooke, J.F., Blackman, J.A. and Morgan, T. (1985). New interpretation of spin wave behavior in Ni. *Physical Review Letters*, **54**, 718.

Cooke, J.F., Lynn, J.W. and Davis, H.L. (1980). Calculations of the dynamical susceptibility of nickel and iron. *Physical Review B*, **21**, 4118.

Costa, A.T., Muniz, R.B. and Mills, D.L. (2003a). Microscopic theory of spin waves in ultrathin ferromagnetic films; Fe on W(110) as an example. *Journal of Physics: Condensed Matter*, **15**, S495.

Costa, A.T., Muniz, R.B. and Mills, D.L. (2003b). Theory of spin excitations in Fe(110) multilayers. *Physical Review B*, **68**, 224435.

Costa, A.T., Muniz, R.B. and Mills, D.L. (2004). Theory of large wave vector spin waves in ultrathin ferromagnetic films; sensitivity to electronic structure. *Physical Review B*, **70**, 054406.

Costa, A.T., Muniz, R.B. and Mills, D.L. (2006). Ferromagnetic resonance linewidths in ultrathin structures: a theoretical study of spin pumping. *Physical Review B*, **73**, 054426.

Damon, R.W. and Eshbach, J.R. (1960). Magnetostatic modes of a ferromagnetic slab. *Journal of Physics and Chemistry of Solids*, **19**, 308.

Demokritov, S., Hillebrands, B. and Slavin, A.N. (2001). Brillouin light scattering studies of confined spin waves. *Physics Reports*, **348**, 441.

Dutcher, J.R., Heinrich, B., Cochran, J.F., *et al*. (1988). Magnetic properties of sandwiches and superlattices of FCC Fe(100) grown on Cu(100) substrates. *Journal of Applied Physics*, **64**, 673.

Etzkorn, M., Anil Kumar, P.S. and Kirschner, J. (2007). High-energy surface spin waves studied by spin-polarized electron energy loss spectroscopy. In *The Handbook of Magnetism and Advanced Magnetic Materials*, Kronmüller, H. and Parkin, S. (Eds.), John Wiley & Sons: Chichester, Vol. 3.

Fassbender, J., Nortemann, F., Stamps, R.L., *et al*. (1992). Oscillatory interlayer exchange coupling of Co/Ru multilayers investigated by brillouin light scattering. *Physical Review*, **46**, 5810.

Fert, A., Barthelemy, A. and Petroff, F. (2006). Spin transport in magnetic multilayers and tunnel junctions. In *Nanomagnetism: Ultrathin Films, Multilayers and Nanostructures*, Mills, D.L. and Bland, J.A.C. (Eds.), Elsevier, pp. 153–226.

Frota Pessoa, S., Muniz, R.B. and Kudrnovsky, J. (2000). Exchange coupling in transition metal ferromagnets. *Physical Review B*, **62**, 5293.

Giovanni, V., Monotoncello, F., Nizzoli, F., *et al*. (2004). Spin excitations of nanometric cylindrical dots in vortex and saturated magnetic states. *Physical Review B*, **70**, 172404.

Grimsditch, M., Malozemoff, A. and Brunsch, A. (1979). Standing spin waves observed by brillouin scattering in amorphous metallic $Fe_{80}B_{20}$ films. *Physical Review Letters*, **43**, 711.

Grother, O., Ederer, C. and Fahnle, M. (2001). Fast Ab Initio method for calculation of adiabatic spin wave spectra in complex systems. *Physical Review B*, **63**, 10041.

Grunberg, P., Mayr, C.M., Vach, W. and Grimsditch, M. (1982). Determination of magnetic parameters by means of brillouin scattering; examples Fe, Ni and $Ni_{0.8}Fe_{0.2}$. *Journal of Magnetism and Magnetic Materials*, **28**, 319.

Grunberg, P. and Metawe, F. (1977). Light scattering from bulk and surface spin waves in EuO. *Physical Review Letters*, **39**, 156.

Grunberg, P., Schreiber, R., Pang, Y., *et al*. (1986). Layered magnetic structures: evidence for antiferromagnetic coupling of Fe layers across Cr interlayers. *Physical Review Letters*, **57**, 2442.

Gubbiotti, G., Carlotti, G., Okuno, T., *et al*. (2005). Spin dynamics in thin nanometric elliptical permalloy dots; a brillouin light scattering investigation as a function of dot eccentricity. *Physical Review B*, **72**, 184419.

Hall, B.M. and Mills, D.L. (1986). Electron energy loss studies of surface vibrations on Ni(100); surface and bulk phonon contributions. *Physical Review B*, **34**, 8318.

Heid, R. and Bohnen, K.P. (2003). Ab Initio lattice dynamics of metal surfaces. *Physics Reports*, **387**, 151.

Heinrich, B. (1994). Ferromagnetic resonance in ultrathin film structures. In *Ultrathin Magnetic Structures II*, Bland, J.A.C. and Heinrich, B. (Eds.), Springer-Verlag: Heidelberg, pp. 195–222.

Heinrich, B. and Cochran, J. (1993). Ultrathin metallic magnetic films; magnetic anisotropies and exchange interactions. *Advances in Physics*, **42**, 523.

Heinrich, B., Purcell, S.T., Dutcher, J.R., *et al*. (1988). Structural and magnetic properties of ultrathin Ni/Fe bilayers grown epitaxially on Ag (100). *Physical Review B*, **38**, 12879.

Herring, C. (1966). *Magnetism*, Rado, G. and Suhl, H. (Eds.), Academic Press: New York, Vol. 4.

Hillebrands, B., Baumgart, P. and Guntherodt, G. (1987). In situ brillouin scattering from surface anisotropy dominated damon eshbach modes in ultrathin epitaxial Fe(110) layers. *Physical Review B*, **36**, 2450.

Hoffman, F. (1970). Dynamic pinning induced by nickel layers on permalloy films. *Physica Status Solidi*, **41**, 807.

Hong, J. and Mills, D.L. (2000). Spin excitations in ferromagnetic Ni; electrons and neutrons as a probe. *Physical Review B*, **58**, R858.

Karlsson, K. and Aryasetiawan, F. (2000a). Spin wave spectra of nickel and iron. *Physical Review B*, **62**, 3006.

Karlsson, K. and Aryasetiawan, F. (2000b). A many approach to spin wave excitations in itinerant magnetic systems. *Journal of Physics:Condensed Matter*, **12**, 7617.

Kittel, C. (1963a). *Quantum Theory of Solids*, John Wiley & Sons: New York, Chapter 4.

Kittel, C. (1963b). *Quantum Theory of Solids*, John Wiley & Sons: New York, Chapter 19.

Kittel, C. (1976). *Introduction to Solid State Physics*, *Fifth Edition*, John Wiley & Sons: New York, pp. 468–476.

Kueny, A., Khan, M.R., Mahbut, R., *et al*. (1984). Magnons in superlattices; A light scattering study. *Physical Review B*, **29**, 2879.

LeCraw, R.C., Spencer, E.G. and Porter, C.S. (1958). Ferromagnetic resonance line widths in yttrium iron garnets. *Physical Review*, **110**, 1311.

Lindner, J., Lenz, K., Kosubek, E., *et al*. (2003). Non gilbert type damping in ultrathin ferromagnets; importance of magnon magnon scattering. *Physical Review B*, **68**, 60102.

Lovesey, S.W. (1984). *Theory of Neutron Scattering from Condensed Matter; Vol 2, Polarization Effects and Magnetic Scattering*, Oxford University Press: Oxford.

Marcus, P.M. and Moruzzi, V.L. (1988). Stoner model of ferromagnetism and total energy band theory. *Physical Review B*, **38**, 6949.

McMichael, R.D., Stiles, M.D., Chen, P.J. and Egelhoff, W.D. Jr. (1998). Ferromagnetic resonance linewidth in thin films coupled to NiO. *Journal of Applied Physics*, **83**, 7037.

Mills, D.L. (2006). Quantum theory of spin waves in finite samples. *Journal of Magnetism and Magnetic Materials*, **306**, 16.

Mills, D.L. (1967). On the magnetic scattering of low energy electrons from the surface of a ferromagnetic crystal. *Journal of Physics and Chemistry of Solids*, **28**, 1855.

Mills, D.L. (1970). Surface corrections to the specific heat of ferromagnetic films. *Physical Review B*, **1**, 264.

Mills, D.L. (1984). Surface spin waves on magnetic crystals. In *Surface Excitations*, Agranovich, V.M. and Loudon, R. (Eds.), North Holland: Amsterdam, Chapter 3.

Mills, D.L. (1993). Spin waves in ultrathin exchange coupled ferromagnetic multilayers:the boundary condition at the interface. *Physical Review B*, **45**, 13100.

Mills, D.L. (1994). Thermodynamic properties of ultrathin ferromagnetic films. In *Ultrathin Magnetic Structures I*, Bland, J.A.C. and Heinrich, B. (Eds.), Springer-Verlag: Heidelberg, Section 3.2.

Mills, D.L. and Rezende, S.M. (2003). *Spin Damping in Ultrathin Magnetic Films*, Hillebrands, B. and Ounadjela, K. (Eds.), Springer-Verlag: Heidelberg.

Mook, H.A. and Nicklow, R.M. (1973). Neutron scattering investigation of the magnetic excitations in Fe. *Physical Review B*, **7**, 336.

Mook, H.A., Nicklow, R.M., Thompson, E.D. and Wilkinson, M.K. (1969). Spin wave spectrum of nickel metal. *Journal of Applied Physics*, **40**, 1450.

Mook, H.A. and Paul, D.McK. (1985). Neutron scattering measurement of the spin wave spectra for Ni. *Physical Review Letters*, **54**, 227.

Muniz, R.B. and Mills, D.L. (2002). Theory of spin excitations in Fe(110) monolayers. *Physical Review B*, **66**, 174417.

Novosad, V., Grimsditch, M., Guslienko, K.Yu., *et al*. (2002). Spin excitations of magnetic vortics in ferromagnetic nanodots. *Physical Review B*, **66**, 052407.

Padja, M., Kudrnovdsky, J., Turek, I., *et al*. (2000). Oscillatory curie temperatures of two dimensional ferromagnets. *Physical Review Letters*, **85**, 5424.

Perring, T.G., Boothroyd, A.T., Paul, D.McK., *et al*. (1991). High energy spin waves in BCC iron. *Journal of Applied Physics*, **69**, 6219.

Plihal, M. and Mills, D.L. (1998). Spin flip exchange scattering of low energy electrons in Fe. *Physical Review B*, **58**, 14407.

Plihal, M., Mills, D.L. and Kirschner, J. (1999). The spin wave signature in the spin polarized electron loss spectrum of ultrathin Fe films; Theory and experiment. *Physical Review Letters*, **82**, 2579.

Prinz, G. (1994). Magnetic metal films on semiconductor structures. In *Ultrathin Magnetic Structures II*, Bland, J.A.C. and Heinrich, B. (Eds.), Springer-Verlag: Heidelberg.

Rado, G. and Suhl, H. (1963a). *Magnetism*, Rado, G. and Suhl, H. (Eds.), Academic Press: New York, Vol. I.

Rado, G. and Suhl, H. (1963b). *Magnetism*, Rado, G. and Suhl, H. (Eds.), Academic Press: New York, Vol. III.

Rado, G. and Suhl, H. (1965). *Magnetism*, Rado, G. and Suhl, H. (Eds.), Academic Press: New York, Vol. IIa.

Rado, G. and Suhl, H. (1966). *Magnetism*, Rado, G. and Suhl, H. (Eds.), Academic Press: New York, Vol. IIb.

Rahman, T.S. and Mills, D.L. (1982). Dipolar surface spin waves in ferromagnetic films. *Journal of Applied Physics*, **53**, 2084.

Rezende, S.M., Azevedo, A., Lucena, M.A. and Augiar, F.M. (2001). Anomalous spin wave damping in exchange biased films. *Physical Review B*, **63**, 214418.

Sandercock, J. and Wettling, W. (1978). Light scattering from thermal magnons in iron and nickel. *IEEE Transactions on Magnetics*, **14**, 442.

Sandercock, J.R. and Wettling, W. (1979). Light scattering from surface and bulk thermal magnons in iron and nickel. *Journal of Applied Physics*, **50**, 7784.

Savrasov, S.Y. (1998). Linear response calculations of spin fluctuations. *Physical Review Letters*, **81**, 2570.

Schreyer, A., Schmitte, T., Siebrecht, R., *et al*. (2000). Neutron scattering on magnetic thin films; Pushing the limits. *Journal of Applied Physics*, **87**, 5443.

Schultz, B. and Baberschke, K. (1994). Crossover from in plane to perpendicular magnetization in ultrathin Ni/Cu(100) films. *Physical Review B*, **50**, 13467.

Shirane, G., Minkiewicz, V. and Nathans, R. (1968). Spin waves in 3d metals. *Journal of Applied Physics*, **39**, 383.

Sinclair, R.N. and Brockhouse, B.N. (1960). Dispersion relation of spin waves in a FCC cobalt alloy. *Physical Review*, **120**, 1638.

Slonczewski, J. (1999). Excitation of spin waves by an electric current. *Journal of Magnetism and Magnetic Materials*, **195**, 261.

Sparks, M., Loudon, R. and Kittel, C. (1961). Ferromagnetic relaxation I:theory of the relaxation of the uniform precession and the degenerate spectrum in insulators at low temperatures. *Physical Review*, **122**, 791.

Stiles, M.D. (2006). Exchange coupling in magnetic multilayers. In *Nanomagnetism: Ultrathin Films, Multilayers and Nanostructures*, Mills, D.L. and Bland, J.A.C. (Eds.), Elsevier, pp. 51–76.

Tang, H., Plihal, M. and Mills, D.L. (1998). Theory of spin dynamics of bulk Fe and ultrathin Fe(100) films. *Journal of Magnetism and Magnetic Materials*, **187**, 23.

Te Velthuis, S.G.E., Jiang, J.S., Bader, S.D. and Felcher, G.P. (2002). Spin flop transition in a finite antiferromagnetic superlattice; evolution of the magnetic structure. *Physical Review Letters*, **89**, 127203.

Tserkovnyak, Y., Brataas, A. and Bauer, G.E.W. (2002a). Enhanced gilbert damping in thin ferromagnetic films. *Physical Review Letters*, **88**, 117601.

Tserkovnyak, Y., Brataas, A. and Bauer, G.E.W. (2002b). Spin pumping and magnetization dynamics in metallic multilayers. *Physical Review B*, **66**, 224403.

Udvardi, L., Szunyodh, L., Palotos, K. and Weinberger, P. (2003). First principles relativistic study of spin waves in thin magnetic films. *Physical Review B*, **68**, 104436.

Urban, R., Woltersdorf, G. and Heinrich, B. (2001). Gilbert damping in single and multilayer ultrathin films; Role of interfaces in nonlocal spin dynamics. *Physical Review Letters*, **87**, 217204.

Venus, D. and Kirschner, J. (1988). Momentum dependence of the stoner excitation spectrum of iron using spin polarized electron energy loss spectroscopy. *Physical Review B*, **37**, 2199.

Vollmer, R., Etzkorn, M., Anil Kumar, P.S., *et al*. (2003). Spin polarized electron energy loss spectroscopy of high energy, large wave vector spin waves in ultrathin BCC Co films on Cu(001). *Physical Review Letters*, **91**, 147201.

White, R.M. (1970). *Quantum Theory of Magnetism*, McGraw Hill: New York, pp. 173–177.

Zwierzycki, M., Tserkovnyak, Y., Kelly, P.J., *et al*. (2005). First principles study of magnetization relaxation enhancement and spin transfer in thin magnetic films. *Physical Review B*, **71**, 064420.

Dissipative Magnetization Dynamics Close to the Adiabatic Regime

Manfred Fähnle and Daniel Steiauf
Max-Planck-Institut für Metallforschung, Stuttgart, Germany

1 INTRODUCTION

In the last few years, there has been extensive research activity to achieve a basic understanding of ultrafast magnetization processes in magnetically ordered materials. From the viewpoint of fundamental research, this issue is very interesting because the coupling of the electronic system to the lattice has to be taken into account for dissipative spin dynamics, and this is often achieved by a combination of methods of electron theory with methods of irreversible thermodynamics. From the viewpoint of magnet technology, a strong impetus came from the promising and possible applications of magnetization dynamics in micro- and nanosized magnets for advanced information storage and data processing devices in which the binary information is stored in two magnetization states, either *up* and *down*, or *up* and *zero* (i.e., demagnetized). Thereby, three different modes are currently discussed for changing the magnetic state (*switching*) – the application of an antiparallel or perpendicular (*precessional switching*) field pulse (Back and Pescia, 2004; Hillebrands and Fassbender, 2002); switching by use of a spin-polarized current (Stiles and Miltat, 2006); or switching by heating up a spot of the sample with an intensive laser pulse followed by demagnetization of the spin systems via thermalization of the highly excited electrons and excitation of phonons (Koopmans, 2003). The ultimate objective is to achieve switching times as short as possible.

The timescale of the magnetization processes is most essential for the physics and for the type of theories that are used to describe them. For near-adiabatic processes, the timescales are longer than typically several picoseconds, and then the electronic system is always close to its ground state with respect to the momentary magnetization configuration (see Section 4). Examples include the dynamics of domain walls (Thiaville, Nakatani, Miltat and Suzuki, 2005), the field- or current-induced magnetization dynamics in nanostructures (Back and Pescia, 2004; Hillebrands and Fassbender, 2002; Stiles and Miltat, 2006), and the propagation of spin waves of long wavelengths (Grotheer, Ederer and Fähnle, 2001). To describe spin waves with shorter wavelength (Costa, Muniz and Mills, 2003) or the relaxation processes on the sub-picosecond timescale after intense laser

Handbook of Magnetism and Advanced Magnetic Materials. Edited by Helmut Kronmüller and Stuart Parkin. Volume 1: *Fundamentals and Theory*. ISBN: 978-0-470-02217-7.

pulses (Koopmans, 2003), strong electronic excitations from these ground states have to be taken into account (see also the contribution of D.L. Mills in volume I). In the present review, we confine ourselves mainly to processes close to the adiabatic limit. The main objective is to figure out the appropriate equation of motion (EOM) for magnetization dynamics, thereby including dissipative processes due to the coupling of magnetic degrees of freedom to the lattice degrees of freedom, which leads to damping. On a phenomenological level ((Kronmüller and Fähnle, 2003), see also the corresponding articles of volume II), magnetization dynamics is often described by the Gilbert equation (Gilbert, 1956) for magnetization $\mathbf{M}(\mathbf{r}, t)$,

$$\frac{\mathrm{d}\mathbf{M}}{\mathrm{d}t} = -\gamma(\mathbf{M} \times \mathbf{H}_{\mathrm{eff}}) + \frac{1}{M}\,\mathbf{M} \times \alpha \frac{\mathrm{d}\mathbf{M}}{\mathrm{d}t} \tag{1}$$

Here, γ is the gyromagnetic ratio; $\mathbf{H}_{\mathrm{eff}}$ is the effective field composed of the external field as well as the exchange, anisotropy, and dipolar fields; and α is a phenomenological damping parameter. We will see that this equation is strictly valid only under very restricted circumstances, and we will discuss appropriate modifications.

In earlier times, the dissipative magnetization dynamics driven by external fields has been discussed. In 1996, two pioneering papers (Slonczewski, 1996; Berger, 1996) initiated an overwhelming activity on magnetization dynamics induced by transport currents mainly in magnetic multilayers with very small layer thickness. In the present review, we concentrate mainly on processes driven by external fields and transport currents in single-phase systems (whereas (Stiles and Miltat (2006) and Heinrich (2005) give excellent overviews on the multilayer systems), and we just make comments on how the physical processes in non-multilayer and multilayer systems are interrelated. Furthermore, we concentrate on the spin dynamics in metals and do not consider insulators or magnetic semiconductors. We also neglect the effect of thermal fluctuations on EOM (for corresponding papers, see, e.g., Safonov and Bertram (2005) and Rebei and Parker (2003)).

A discussion of all the relevant papers on dissipative magnetization dynamics would go far beyond the scope of the present review. Instead, we illustrate the basic physical mechanisms by two intuitive and, in some respect, complementary models – the s–d model and the breathing Fermi surface model. The outline of our review is as follows. In Section 2, we define the dynamical magnetic variables used for various experimental situations, and damping is introduced in Section 3. In Section 4 we discuss two situations without (direct) damping, the case of vanishing and that of infinite scattering time of electrons. The scattering processes leading to direct damping mechanisms are discussed qualitatively in Section 5. In Section 6, we treat using two examples (s–d model and breathing Fermi surface model), how theory can describe damping by including the coupling of magnetization to other degrees of freedom in a phenomenological manner via relaxation times. In Section 7, the present status of spin dynamics simulations by the *ab initio* electron theory is described, and in Section 8, concluding remarks are given.

2 DYNAMICAL MAGNETIC VARIABLES

The starting point of any theory of magnetic dynamics is the definition of appropriate dynamical variables. The choice of these variables depends on the experimental setup that will be used to study magnetization dynamics. Because magnetization arises from spin and orbital degrees of freedom, the most general dynamical variable is the density of spin and orbital magnetic moment, $\mathbf{m}(\mathbf{r}, t) = \mathbf{m}_{\mathrm{s}}(\mathbf{r}, t) + \mathbf{m}_{\mathrm{l}}(\mathbf{r}, t)$, where $\mathbf{m}_{\mathrm{s}}$ and $\mathbf{m}_{\mathrm{l}}$ denote the spin and orbital contributions, respectively, which are defined as the quantum-mechanical expectation values of the corresponding Schrödinger operators,

$$\hat{\mathbf{m}}_{\mathrm{s}}(\mathbf{r}) = -\frac{g\mu_{\mathrm{B}}}{2} \sum_{s,s'} \hat{\psi}_s^{\dagger}(\mathbf{r})\ \hat{\boldsymbol{\sigma}}_{s,s'}\ \hat{\psi}_{s'}(\mathbf{r}) \tag{2}$$

$$\hat{\mathbf{m}}_{\mathrm{l}}(\mathbf{r}) = -\mu_{\mathrm{B}} \sum_{s} \hat{\psi}_s^{\dagger}(\mathbf{r})\ \hat{\mathbf{L}}\ \hat{\psi}_s(\mathbf{r}) \tag{3}$$

In these equations, μ_{B} is Bohr's magneton, $-g\mu_{\mathrm{B}}/2$ is the magnetic moment of the free electron, $\hat{\psi}_s$ is the s component of the spinor field operator, $\hat{\boldsymbol{\sigma}}$ is the vector of Pauli matrices, and $\hat{\mathbf{L}}$ is the angular momentum operator. The time dependencies of $\mathbf{m}(\mathbf{r}, t) = \langle \hat{\mathbf{m}}(\mathbf{r}) \rangle$ and the like arise because the expectation values have to be formed with the many-body Schrödinger wave function $|\psi(t)\rangle$ which is a solution of the time-dependent wave equation,

$$\hat{H}\,|\psi\rangle = \mathrm{i}\hbar\,|\dot{\psi}\rangle \tag{4}$$

where the Hamiltonian in general acts on the positional and spin degrees of freedom of all electrons and nuclei. (In the following, we neglect all effects resulting from dipolar interactions between magnetic moments; to take them into account would require the inclusion of a coupling term between current and vector potential in $\hat{H}$.)

Presently, there is no experimental technique to monitor $\mathbf{m}(\mathbf{r}, t)$ on all scales in space – including the subatomic scale – and on all timescales down to the shortest possible timescale (corresponding to the fast degrees of freedom) which is the electronic intersite hopping time $h/W \approx 10^{-15}$ s (h is Planck's quantum and W is the width of the electronic

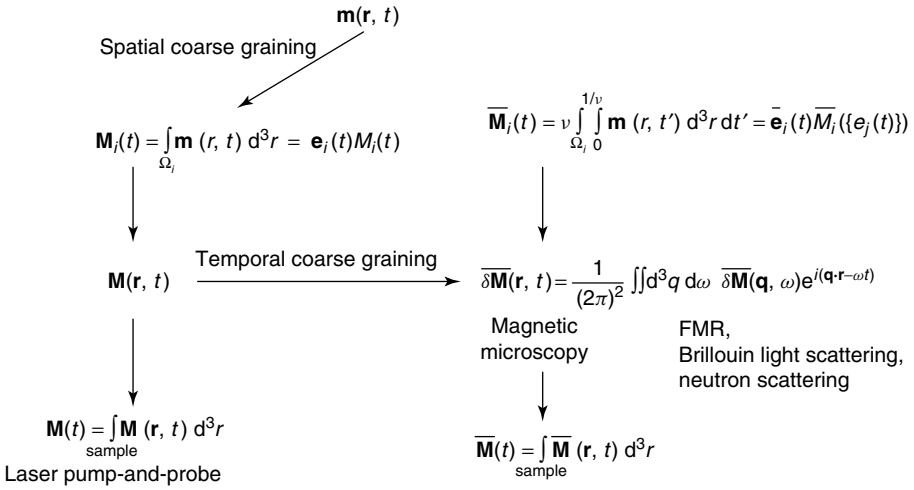

Figure 1. Schematic representation (see text) of the spatial and temporal coarse graining of $\mathbf{m}(\mathbf{r}, t)$ to define the appropriate dynamical variables for various experiments.

energy band in the solid). Therefore $\mathbf{m}(\mathbf{r}, t)$ is not an appropriate dynamical variable, it has to be coarse-grained step by step both in space and in time (see Figure 1). Concerning the coarse graining in space, we first eliminate the information at the subatomic level. To do this, we subdivide the system into disjunct space-filling parts around the atoms at sites i with volumes Ω_i, and we define atomic magnetic moments

$$\mathbf{M}_i(t) = \mathbf{e}_i(t)\, M_i(t) = \langle \hat{\mathbf{M}}_i \rangle \tag{5}$$

as expectation values for the site-moment operators

$$\hat{\mathbf{M}}_i = \int_{\Omega_i} \hat{\mathbf{m}}(\mathbf{r})\, \mathrm{d}^3 r \tag{6}$$

The atomic moments $\mathbf{M}_i(t)$ in equation (5) are characterized by their momentary directions $\mathbf{e}_i(t)$ that represent the transversal degrees of freedom and the magnitudes $M_i(t)$ that represent the longitudinal degrees of freedom. The operators $\hat{\mathbf{M}}_i$ fulfill certain commutation relations, for example, the spin part $\hat{\mathbf{M}}_{\mathrm{s},i}$ obeys

$$[\hat{M}_{\mathrm{s},i\alpha}, \hat{M}_{\mathrm{s},j\beta}] = -\mathrm{i}g\mu_{\mathrm{B}}\ \delta_{ij}\ \varepsilon_{\alpha\beta\gamma}\ \hat{M}_{\mathrm{s},i\gamma} \tag{7}$$

where α, β, and γ refer to the Cartesian indices, and where $\varepsilon_{\alpha\beta\gamma}$ are the components of the antisymmetric tensor of the fundamental three form. In the second step of spatial coarse graining, we get rid of the atomic scale information and keep only the information on the mesoscopic scale via a continuation of the atomic magnetization $\mathbf{M}_i/\Omega_i$, yielding the magnetization field $\mathbf{M}(\mathbf{r}, t)$,

$$\mathbf{M}(\mathbf{r}, t) = \sum_{i \in \Omega(\mathbf{r})} \frac{\mathbf{M}_i(t)}{\Omega_i} \tag{8}$$

where $\Omega(\mathbf{r})$ is the volume of a mesoscopic part of the sample around $\mathbf{r}$. Finally, we can define the magnetic moment $\mathbf{M}(t)$ of the whole sample via

$$\mathbf{M}(t) = \sum_i \mathbf{M}_i(t) = \int_{\mathrm{sample}} \mathbf{M}(\mathbf{r}, t)\, \mathrm{d}^3 r \tag{9}$$

In a typical laser pump-and-probe experiment (Koopmans, 2003), it is often the moment averaged over a more or less macroscopic regime which is monitored on the femtosecond timescale, so that $\mathbf{M}(t)$ as given by equation (9) is the appropriate dynamical variable. Many other experiments, however, explore only the slow magnetic degrees of freedom defined in the following way. Due to the mutual Coulomb and exchange interactions, the electronic intersite hopping is not random but the electrons arrive at an atom and leave the atom in a highly correlated way. As a result, a finite value remains for the time-averaged quantity

$$\overline{\mathbf{M}}_i(t) = \nu \int_0^{t+1/\nu} \mathbf{M}_i(t')\, \mathrm{d}t' \tag{10}$$

where $\nu \approx 10^{13}\,\mathrm{s}^{-1}$ is the frequency of a typical long-wavelength spin wave. On timescales larger than $1/\nu$, the orientations $\bar{\mathbf{e}}_i(t)$ of $\overline{\mathbf{M}}_i$ change in time and represent the independent transversal fluctuations. In contrast, the magnitudes $\overline{M}_i(t)$ are totally determined (see Section 4) by

the orientations $\overline{\mathbf{e}}_j(t)$ at all sites j, that is, the longitudinal fluctuation modes are 'slaved' by the independent transversal modes, and thus we can write

$$\overline{\mathbf{M}}_i(t) = \overline{\mathbf{e}}_i(t)\ \overline{M}_i(\{\overline{\mathbf{e}}_j(t)\}) \tag{11}$$

In analogy to equations (8 and 9), the quantities $\overline{\mathbf{M}}_i(t)$ may be further coarse grained in space, yielding $\overline{\mathbf{M}}(\mathbf{r}, t)$ and $\overline{\mathbf{M}}(t)$. In the following sections, only such situations are discussed, and therefore we omit the 'bar' denoting time average for simplicity, that is, with $\mathbf{M}_i(t)$ or $\mathbf{M}(\mathbf{r}, t)$ we address those slow degrees of freedom. As an example, for the magnetic microscopy on the nanosecond and subnanosecond timescale (e.g., by using (Stoll *et al*., 2004) the X-ray magnetic circular dichroism (XMCD)), the so-defined magnetization field $\mathbf{M}(\mathbf{r}, t)$ is the appropriate dynamical variable. Furthermore, we define the deviation, $\delta\mathbf{M} = \mathbf{M}(\mathbf{r}, t) - \mathbf{M}_{\mathrm{ref}}(\mathbf{r})$, from an appropriately chosen reference state with

$$\delta\mathbf{M}(\mathbf{r}, t) = \frac{1}{(2\pi)^2} \iint \mathrm{d}^3q\ \mathrm{d}\omega\ \ \delta\mathbf{M}(\mathbf{q}, \omega)\ \mathrm{e}^{\mathrm{i}(\mathbf{q}\cdot\mathbf{r} - \omega t)} \tag{12}$$

The limited spatial resolution thereby defines the upper limit for the $\mathbf{q}$ integration in equation (12), that is, the dynamical variable $\mathbf{M}(\mathbf{r}, t)$ also depends on the experimental details. Finally, there are other experiments on the slow timescale that investigate only single Fourier components of the deviation $\delta\mathbf{M}$ from a saturated ferromagnetic reference state. Examples are the ferromagnetic resonance (FMR) experiments (Lindner *et al*., 2003) for the uniform mode $\mathbf{q} = 0$, the Brillouin scattering experiments (Demokritov and Hillebrands, 2002) for spin waves with small $\mathbf{q}$, and the neutron scattering experiments (Mook and Paul, 1985) for spin waves with arbitrary $\mathbf{q}$. In these cases, the considered spin-wave mode $\delta\mathbf{M}(\mathbf{q}, \omega)$ is the appropriate dynamical variable.

Finally, we comment on the spin and orbital contributions to magnetization. When a sample is investigated by a magnetometer (mainly used for static situations), then the experimental signal is directly related to the total magnetic moment including both contributions. However, in most experiments with temporal and spatial resolution, things are more complicated. For instance, the signals from the XMCD microscopy (Stoll *et al*., 2004) at fixed X-ray energy are not proportional to the sum of spin and orbital contributions, but to a more complicated combination of these two contributions plus additional contributions (Ankudinov and Rehr, 1995). The resolution of spin and orbital contributions would require magneto-spectromicroscopy. Fortunately, in many metallic bulk magnets, the contribution of orbital magnetism is small for slow dynamics, and therefore in many papers (including the following sections of the present review), the term *magnetization* is used synonymously with the term *spin magnetization*. For the pump-and-probe experiments on the femtosecond timescale, however, it is important to investigate the transfer of magnetic moment between spin and orbital degrees of freedom. Such an analysis is rendered even more difficult because there is no simple relation (Koopmans, 2003) between the Kerr effect probe signal after the laser pulse and the magnetic moments.

3 DISSIPATION

When we include in the wave equation (4) the couplings between all positional and spin degrees of freedom of all electrons and nuclei, and solve it for $|\psi(t)\rangle$ for a given initial state $|\psi(t = 0)\rangle$, we obtain a quantum-mechanically coherent dynamics for $\mathbf{m}(\mathbf{r}, t)$ which contains far too much information than is required for an interpretation of most experiments. (The coherent part of the dynamics is of relevance only for the femtosecond dynamics after an intense laser pulse (Hübner and Zhang, 1998)). Furthermore, all equations would be local in time and the notion of damping would not appear in such a theory.

However, it is not the objective to investigate the dynamics of $\mathbf{m}(\mathbf{r}, t)$ obtained in this way, but to study the behavior of the dynamical variables that are appropriate for the experiment under consideration, and to write down an EOM that explicitly contains only these variables, for example, by integrating out all the other degrees of freedom. The outcome of this process is that in general the EOM contains terms which depend on the entire history (Suhl, 1998; Capelle and Gyorffy, 2003), and this is the signature for damping processes which describe the transfer of energy and angular momentum (and concomitant magnetic moment) from the considered dynamical variable to the eliminated degrees of freedom. As an example, the damping term in the Gilbert equation (1) may be conceived as the first term of the evaluation of a general damping term that is nonlocal in time, and the dissipated power R due to this term is given by Brown (1963)

$$R = \int \frac{1}{2}\frac{\alpha}{\gamma M}\left(\frac{\mathrm{d}\mathbf{M}}{\mathrm{d}t}\right)^2 \mathrm{d}t \tag{13}$$

When all the eliminated degrees of freedom are nonmagnetic, then damping is denoted as *direct damping*, whereas relaxation processes describing the transfer from the considered dynamical variable to other magnetic degrees of freedom are called *indirect damping* (Suhl, 1998). Direct damping may be subdivided further (Heinrich, 2005) into intrinsic damping (related to 'unavoidable' phonons) and extrinsic damping (related to defects or complex geometrical features of the

sample). An example for indirect damping is the transfer from adiabatic magnetic variables to fast magnetic degrees of freedom (Costa, Muniz and Mills, 2003; Capelle and Gyorffy, 2003). Another example is the transfer from a special $\delta\mathbf{M}(\mathbf{q}, \omega)$ to other modes of the spectrum, for example, from the uniform ferromagnetic mode of an FMR experiment to spin-wave modes of finite wavelengths.

In spite of this well-defined definition of damping in theory, it is in general a delicate problem to analyze damping quantitatively, and to separate direct and indirect damping experimentally. A relatively simple situation arises if a special mode is investigated by external excitations, for example, the uniform mode in an FMR experiment or spin-wave modes in neutron or Brillouin light scattering experiments, because the excitation linewidth is a measure for damping. Furthermore, in FMR experiments on ultrathin ferromagnetic layers, the direct and indirect contributions can be separated by measuring the frequency dependence of the linewidth (Lindner *et al*., 2003). In more general situations, however, a simple procedure would exist only if there were experimentally accessible observables that are constants of motion for the case without damping. The magnetic energy E_{magn} is a constant of motion if there is no direct damping, but it is not a directly accessible observable. Another possible constant of motion is the total angular momentum of the system,

$$\mathbf{J} = \mathbf{L}_{\text{e}} + \mathbf{S}_{\text{e}} + \mathbf{L}_{\text{phonon}} \tag{14}$$

where $\mathbf{L}_{\text{e}}$ and $\mathbf{S}_{\text{e}}$ are the total orbital and total spin moment of the electrons, and $\mathbf{L}_{\text{phonon}}$ is the total lattice (phonon) contribution. (For simplicity, we have omitted the momentum of the electromagnetic field due to radiation at the moment.) If there is no direct damping, the electronic angular momentum $\mathbf{L}_{\text{e}} + \mathbf{S}_{\text{e}}$ is a constant of motion for isotropic systems. This, however, does not mean that the total magnetic moment, derived from equation (9) using equations (2 and 3),

$$\mathbf{M} = -\mu_{\text{B}}(\mathbf{L}_{\text{e}} + g\mathbf{S}_{\text{e}}) \tag{15}$$

is also a constant of motion. Only in bulk metallic systems where the orbital moment $-\mu_{\text{B}}\mathbf{L}_{\text{e}}$ is much smaller than the spin moment $-\mu_{\text{B}}g\mathbf{S}_{\text{e}}$ can we assume that the magnetic moment is approximately a constant of motion for macroscopically isotropic systems. Because the systems are not isotropic in most experiments, the investigation of $\mathbf{M}(t)$ often does not help the analysis of damping. Therefore, for a general situation the procedure to analyze damping is rather complicated. First, we have to determine $\mathbf{M}(\mathbf{r}, t)$ by some kind of magnetic microscopy (Back and Pescia, 2004; Hillebrands and Fassbender, 2002; Stoll *et al*., 2004), with the given resolution, in space and time, of the instrument. Then we compare the measured $\mathbf{M}(\mathbf{r}, t)$ with data from simulations based on an EOM including damping, for example, the Gilbert equation (1) hoping that this EOM describes the situation adequately. The comparison yields the damping constant α that can be compared with theoretical predictions in order to figure out which physical damping mechanism is operative. To check for consistency, we can calculate the magnetic energy E_{magn} from an energy functional $E_{\text{magn}}[\mathbf{M}(\mathbf{r}, t)]$ that is consistent with the nondamped part of the EOM, for example, the micromagnetic energy functional (Kronmüller and Fähnle, 2003) for the slow magnetic degrees of freedom, and E_{magn} should decrease in time if there is direct damping.

From the above discussion, it becomes obvious that damping is intimately related to the choice of the dynamical variable. Therefore it is not guaranteed that the parameters which describe damping for one choice are of much relevance for damping with respect to another choice. For instance, for the dynamics of the adiabatic variables, only electrons close to the Fermi surface are relevant (see Section 6.2), whereas for experiments on the femtosecond timescale after an intense laser pulse, 'hot' electrons are involved. Another example comes from the near-adiabatic regime. Due to the limited spatial resolution of a magnetic microscope, the adiabatic modes with wavelengths shorter than the scale of resolution are already 'integrated out' by the instrument. Therefore, instruments with different spatial resolutions in general yield at least slightly different damping parameters (Miltat, Albuquerque and Thiaville, 2002), and erroneous conclusions arise if this difference is tentatively related to different direct relaxation mechanisms.

The reader might have become disappointed after having heard about all these problems that render an accurate analysis of the data, in terms of damping mechanisms, difficult. Indeed, as is always the case for a complicated physical situation, many different experiments on many different materials will be required to arrive at a description that is at least to some extent consistent. Fortunately, a very detailed analysis is not always required to solve the big question on the ultimate timescales that can be achieved for the switching of the magnetic information in data processing devices. To do this, often the existing order of magnitude estimates are sufficient, and the large variety of experimental and theoretical investigations should be able to clarify this point.

For the rest of the paper, we consider as dynamical variables, mainly, the slow degrees of freedom; then, damping arises from any transfer of energy and angular momentum to other magnetic and nonmagnetic degrees of freedom. Examples of the involvement of the fast magnetic degrees of freedom are considered by Costa, Muniz and Mills (2003) and Capelle and Gyorffy (2003). In the following we discuss only the direct damping mechanisms related to the nonmagnetic degrees of freedom.

4 SITUATIONS WITHOUT DIRECT DAMPING – ZERO AND INFINITE ELECTRONIC SCATTERING TIMES

In the following we describe the system by an effective single-electron representation (e.g., the density-functional electron theory), and we discuss the effect of phonons or lattice defects by a scattering approach via a scattering time τ. Interestingly enough, there are two situations without damping, corresponding to $\tau \to \infty$ and $\tau \to 0$. The first case is intuitively clear because it describes the situation for which there is no coupling of the electronic system to the lattice, and hence no damping. Damping will be related to noninfinite scattering times, and for finite but still large τ we expect an increase of damping with decreasing τ. The second case corresponds to the strictly adiabatic limit ($\tau \to 0$), which will be discussed in the following. We will see that zero scattering time also rules out damping.

For the dynamics of the atomic magnetic moments $\mathbf{M}_i(t)$, we distinguish between transversal degrees of freedom, given by the orientations $\mathbf{e}_i$ of $\mathbf{M}_i = \mathbf{e}_i(t)M_i(t)$, and longitudinal degrees of freedom, given by $M_i(t)$. In the model of a strictly adiabatic situation (Gyorffy *et al.*, 1985), it is assumed that for the timescale of the slow magnetization fluctuations (see Section 2), the primary fluctuation modes of $\mathbf{M}_i(t)$ are the directional fluctuations $\mathbf{e}_i(t)$, whereas the longitudinal fluctuations are 'slaved' by the transversal fluctuations, that is, they are completely determined by the momentary orientational configurations $\{\mathbf{e}_j\}$ of the orientations $\mathbf{e}_j$ at all sites j, $M_i(t) = M_i[\{\mathbf{e}_j(t)\}]$. This means that the electronic system is assumed to be at any instant in its ground state with respect to the momentary configuration $\{\mathbf{e}_j(t)\}$. The operators $\hat{\mathbf{M}}_i$ given by equation (6) may then be represented in the form $\hat{\mathbf{M}}_i = M_i\hat{\mathbf{e}}_i$ where $\hat{\mathbf{e}}_i$ are the operators related to the dynamical variables $\mathbf{e}_i$ and M_i are just numbers at any instant. The idea is similar to the one of the Born–Oppenheimer approximation (Born and Oppenheimer, 1927), which separates the timescales for the dynamics of electrons and nuclei. Nevertheless, the magnetic situation is more complicated because it separates slow and fast degrees of freedom for the same 'species', that is, for the inhomogeneous spin-polarized electron liquid. Therefore, the derivation of an EOM for the slow degrees of freedom, that is, for $\mathbf{e}_i(t)$, is less straightforward. As a result, there are various approaches in the literature (Antropov, Katsnelson, van Schilfgaarde and Harmon, 1995; Antropov *et al.*, 1996; Halilov, Eschrig, Perlov and Oppeneer, 1998; Niu and Kleinman, 1998; Gebauer and Baroni, 2000; Grotheer, 2002) which are formally different but are all based on the same central idea. We present a derivation similar to the one given by Grotheer (2002) which is a variant of the approach of Niu and Kleinman (1998) and Gebauer and Baroni (2000).

We introduce an adiabatic state $|\psi(\{\mathbf{e}_j(t)\})\rangle$ that depends on the whole momentary configuration $\{\mathbf{e}_j(t)\}$ given by the momentary orientations $\mathbf{e}_j(t)$ at all sites j, with the following properties:

1.
$$\langle\psi(\{\mathbf{e}_j(t)\})|\,\hat{\mathbf{e}}_i\,|\psi(\{\mathbf{e}_j(t)\})\rangle = \mathbf{e}_i(t) \tag{16}$$

2. Among all the states compatible with equation (16), we select the one that corresponds to a minimal energy,
$$E(\{\mathbf{e}_j\}) = \langle\psi(\{\mathbf{e}_j(t)\})|\,\hat{H}\,|\psi(\{\mathbf{e}_j(t)\})\rangle = \min \tag{17}$$

From 1 and 2, it follows that $|\psi(\{\mathbf{e}_j(t)\})\rangle$ may be constructed as the ground state of a modified Hamiltonian,

$$\hat{H}' = \hat{H} - \sum_k \boldsymbol{\lambda}_k\hat{\mathbf{e}}_k \tag{18}$$

according to the lowest-energy solution of

$$\hat{H}'|\psi(\{\mathbf{e}_j(t)\})\rangle = E'(\{\mathbf{e}_j\})|\psi(\{\mathbf{e}_j(t)\})\rangle \tag{19}$$

with

$$E'(\{\mathbf{e}_j\}) = E(\{\mathbf{e}_j\}) - \sum_k \boldsymbol{\lambda}_k\mathbf{e}_k \tag{20}$$

Thereby the Lagrangian parameters $\boldsymbol{\lambda}_k = \boldsymbol{\lambda}_k(\{\mathbf{e}_j\})$ were introduced to guarantee that equation (16) is fulfilled. Please note that the state depends parametrically (via the $\mathbf{e}_j(t)$) on the time, but at any instant the state $|\psi(\{\mathbf{e}_j(t)\})\rangle$ is the ground state of the time-independent equation (19).

In the adiabatic approximation, we demand that the development in time of the state $|\psi(t)\rangle$ in Hilbert space is forced to be the one of the adiabatic states $|\psi(\{\mathbf{e}_j(t)\})\rangle$. In reality, however, when we solve the time-dependent wave equation with the initial state $|\psi(t=0)\rangle = |\psi(\{\mathbf{e}_j(t=0)\})\rangle$, the state $|\psi(t)\rangle$ deviates from the adiabatic state $|\psi(\{\mathbf{e}_j(t)\})\rangle$ very quickly if we neglect electronic scattering processes. The only way to realize a strictly adiabatic situation is to assume that the scattering processes instantaneously lead $|\psi(t)\rangle$ back to $|\psi(\{\mathbf{e}_j(t)\})\rangle$, that is, the adiabatic approximation corresponds to $\tau \to 0$. Using Ehrenfest's theorem, we then obtain the following EOM for $\mathbf{e}_k$,

$$\dot{\mathbf{e}}_k = \frac{1}{\mathrm{i}\hbar}\langle\psi(\{\mathbf{e}_j(t)\})|\,[\hat{\mathbf{e}}_k, \hat{H}]\,|\psi(\{\mathbf{e}_j(t)\})\rangle \tag{21}$$

Using equations (18–20) to reexpress $\hat{H}|\psi\rangle$, inserting equations (5–7), and making use of the relation

$$\boldsymbol{\lambda}_k = \frac{\delta E}{\delta \mathbf{e}_k} \tag{22}$$

which may be obtained from equation (19), we finally find the EOM in adiabatic approximation,

$$\dot{\mathbf{e}}_k = -\frac{2\mu_\mathrm{B}}{\hbar} \frac{\partial E}{\partial \mathbf{e}_k} \times \mathbf{e}_k \tag{23}$$

For instance, if the $\mathbf{e}_k$ deviate only slightly from a preferred direction, we can evaluate $E(\{\mathbf{e}_j\})$ into a Taylor series truncated after the second-order term and linearize equation (23) to obtain the well-known adiabatic EOM for spin waves (Grotheer, Ederer and Fähnle, 2001; Halilov, Eschrig, Perlov and Oppeneer, 1998). Of course, equation (23) already has the form of the Gilbert equation (1) without damping, that is, by the assumption $\tau \to 0$ underlying the strictly adiabatic limit, the damping of magnetization dynamics is eliminated. This will become clearer in Sections 6.1 (s–d model) and 6.2 (breathing Fermi surface model). The dissipated power density for magnetization dynamics described by the Gilbert equation (1) is $\frac{1}{2}\frac{\alpha}{\gamma M}(\dot{\mathbf{M}})^2$. Obviously, in the strict adiabatic limit, that is, for $\tau \to 0$ for which there is only a precession term but no damping term in the EOM, there is no energy dissipation. The situation is similar for the Drude model of electrical conductivity for which the dissipated power density is σE^2 with the electric field E and conductivity σ that is proportional to τ, that is, it vanishes for zero scattering time.

According to the above discussed limits of zero damping for $\tau \to 0$ and $\tau \to \infty$, we expect with increasing τ an increase of damping for small τ and a decrease of damping for large τ; see also Sections 5 and 6.

5 QUALITATIVE DISCUSSION OF VARIOUS DIRECT DAMPING MECHANISMS

In the following, the change of magnetic energy via electromagnetic radiation of the time-dependent magnetization field as well as relaxations due to dipolar interactions are neglected. Then a direct damping of spin magnetism is possible only in a system with spin-orbit coupling; otherwise, the Hamiltonian commutes with the operator of the total spin momentum, and the total magnetic spin moment is a constant of motion.

The various theories of direct damping of the slow magnetic degrees of freedom may be subdivided as follows:

1. Theories for the transfer of angular momentum directly from the slow magnetic degrees of freedom to the lattice;
2. Theories that treat this transfer at the electron level.

In class 1 theories, the spin-orbit coupling is taken into account implicitly on a phenomenological level via the magnetoelastic coupling between the magnetization field $\mathbf{M}(\mathbf{r}, t)$ and the lattice strain field $\underline{\underline{\varepsilon}}(\mathbf{r}, t)$ arising from a lattice defect or from a phonon distortion. Most theories determine the time for the scattering of one or more magnons at one or more phonons (Haas and Callen, 1963) or at lattice defects (e.g., Kloss and Kronmüller, 1971). In contrast, in Suhl (1998) the dynamics of a general magnetization field $\mathbf{M}(\mathbf{r}, t)$ is considered by solving the coupled system of EOMs for $\mathbf{M}(\mathbf{r}, t)$ and $\underline{\underline{\varepsilon}}(\mathbf{r}, t)$ which are derived from a general magnetoelastic energy functional. When including a shear viscosity term in the elastic part of this functional, the resulting EOM for $\mathbf{M}(\mathbf{r}, t)$ contains various other damping terms in addition to the Gilbert damping term of equation (1). Physically, damping arises because the magnetoelastic rearrangement of the atoms induced by a change of $\mathbf{M}(\mathbf{r}, t)$ requires a repopulation of phonon modes via phonon scattering ('phonon dragging') and hence requires time.

The theories of class 2 may be subdivided according to the physical mechanisms which transfer energy and magnetic moment from the atomic magnetic moments (describing the slow degree of freedom) to the single electrons, that is, Coulomb interactions or spin-current interactions. An example for the latter case is the eddy-current damping (Kittel, 1958), where the motion of the atomic moments $\mathbf{M}_i(t)$ induces electrical fields that couple to the conduction electrons in a metallic system. This leads to eddy currents which then experience Ohmic damping.

For the final transfer of energy and angular momentum from the electrons of type 2 theories to the lattice, a scattering at impurities or lattice vibrations is required. The eigenstates $\psi_k(\mathbf{r})$ of the band electrons with wave vector $\mathbf{k}$ may be written as

$$\psi_\mathbf{k}(\mathbf{r}) = a_\mathbf{k}(\mathbf{r})|\uparrow\rangle + b_\mathbf{k}(\mathbf{r})|\downarrow\rangle \tag{24}$$

where $|\uparrow\rangle$ and $|\downarrow\rangle$ are the spinor states with spin $\hbar/2$ and $-\hbar/2$, respectively. The two spinor states are in any case mixed by spin-orbit coupling (an additional source for this mixing is a noncollinearity of the magnetic configuration). For the small mixing via spin-orbit coupling the variety of states $\psi_\mathbf{k}$ can be subdivided into those that have predominantly spin-up character ($a_\mathbf{k}(\mathbf{r}) \gg b_\mathbf{k}(\mathbf{r})$, denoted by $\psi_\mathbf{k}^\uparrow(\mathbf{r})$) and those that have predominantly spin-down character ($b_\mathbf{k}(\mathbf{r}) \gg a_\mathbf{k}(\mathbf{r})$, denoted by $\psi_\mathbf{k}^\downarrow(\mathbf{r})$). Deviations from the translationary invariance of the system due to phonons

or lattice defects provide scattering potentials (Yafet, 1965) which mediate transitions between the various $\psi^{\sigma}_{\mathbf{k}}(\mathbf{r})$ which contribute to damping. We can therefore consider ordinary scattering processes (Yafet, 1965; Kamberský, 1970) among $\psi^{\uparrow}_{\mathbf{k}}$ and $\psi^{\uparrow}_{\mathbf{k}'}$ states or among $\psi^{\downarrow}_{\mathbf{k}}$ and $\psi^{\downarrow}_{\mathbf{k}'}$ states. Because states with various $\mathbf{k}$ correspond to different mixtures of $|\uparrow\rangle$ and $|\downarrow\rangle$, such processes will change the probability of finding the considered electron in one of the two spin states, that is, angular momentum will be transferred to the lattice. On the other hand, there are spin-flip processes (Yafet, 1965; Kamberský, 1970) that involve $\psi^{\uparrow}_{\mathbf{k}}$ and $\psi^{\downarrow}_{\mathbf{k}'}$ states, respectively. Finally, there are intraband scattering processes of electrons within the same energy band of the solid (for which the wave functions for different $\mathbf{k}$ often exhibit approximately the same orbital character) as well as interband scattering (for which the orbital character is often different). In Heinrich (2005) and Kamberský (1976, 1984) it is assumed that damping is proportional to the scattering time τ if the energy differences between the scattering states are small compared to $\hbar/\tau$, which is likely for intraband scattering and small τ, whereas it is proportional to τ^{-1} if the energy differences are larger than $\hbar/\tau$, which is likely for interband scattering and large τ. Because for near-adiabatic processes any deviations of the wave functions from the adiabatic wave functions are eliminated almost instantly by scattering, these scattering processes involve only slight changes in electronic single-particle energies, that is, they correspond to intraband scattering.

It is certainly a highly nontrivial problem to figure out which relaxation mechanisms are relevant for damping in a considered magnet. To get information on that, it is important to start with measurements on high-purity bulk crystals to separate the effect of intrinsic damping; then damping can be modified by doping with impurities and by bringing the material to a complex geometrical shape to study extrinsic damping. Systematic studies in this way are still lacking. For high-purity single-crystalline Ni, it was found (Heinrich, Meredith and Cochran, 1979) that the temperature dependence of damping below room temperature is well described by two terms which are equal in strength and proportional to the conductivity σ (ascribed to intraband scattering) and the resistivity ρ (ascribed to interband scattering). The effect of doping of Permalloy with Tb impurities was studied in Russek, McMichael, Donahue and Kaka (2003). A modest concentration of 2% of Tb resulted in a 10-fold increase of damping as measured by FMR (for an interpretation see also (Heinrich, 2005)). Extrinsic damping due to the geometry of an ultrathin film is discussed in Mills and Rezende (2003), and effects of interfaces between magnetic and nonmagnetic metallic layers are studied in Tserkovnyak, Brataas and Bauer (2002) and Berger (2001).

6 TWO QUANTITATIVE MODELS FOR DISSIPATIVE SPIN DYNAMICS

In the present section, we discuss two quantitative models for dissipative spin dynamics, the s–d model (Section 6.1) that covers both the cases of small and large scattering times, and the breathing Fermi surface model (Section 6.2) for small scattering times (Kamberský, 1970). In the s–d model, the electrons are subdivided into two types, itinerant electrons of which those that are close to the Fermi level E_{F} are responsible for spin-dependent transport and are denoted as *s electrons* (although conduction electrons with p character may of course also contribute); and localized electrons far below the Fermi level which form the magnetic moments (inducing in turn a spin polarization of the itinerant electrons) and which are denoted as *d electrons*. While the s–d model may be applied to metallic systems with 4f impurities (the 'd electrons' then represent the 4f electrons) or to sp metal hosts with 3d impurities, its application to 3d impurities in transition-metal hosts (Beuerle, Hummler, Elsässer and Fähnle, 1994) or to concentrated magnetic transition metals and alloys should be considered with much caution. The reason is that in these systems there is considerable weight of the d density of electronic states at the Fermi level so that a subdivision into itinerant and localized magnetic electrons is no longer possible. Because of its conceptual simplicity, the s–d model is used, nevertheless, also for magnetic transition metals. The breathing Fermi surface model does not require the subdivision into itinerant and localized electrons and may be applied to any magnetic system, but it is conceptually more difficult.

6.1 The s–d model

In the literature, there are several variants of the s–d model; our discussion will be based on the paper of Zhang and Li (2004).

In the following, we consider only the magnetization $\mathbf{M}(\mathbf{r}, t)$ related to electronic spin and neglect the orbital contribution. As outlined in the preceding text, in the s–d model, $\mathbf{M}(\mathbf{r}, t)$ is composed of a d contribution $\mathbf{M}_{\mathrm{d}}(\mathbf{r}, t)$ with fixed length M_{d}, and a contribution of the conduction electrons, $\mathbf{m}(\mathbf{r}, t)$

$$\mathbf{M}(\mathbf{r}, t) = \mathbf{M}_{\mathrm{d}}(\mathbf{r}, t) + \mathbf{m}(\mathbf{r}, t) \tag{25}$$

The basic physics of the s–d model is most easily discussed by looking at the homogeneous ferromagnetic precession mode. If there was no spin-flip scattering for the conduction electrons ($\tau_{\mathrm{sf}} \to \infty$), then the d magnetization and the conduction electron magnetization that are coupled

via the s–d exchange interaction would be in parallel alignment and would precess in phase. A finite scattering time τ_{sf} generates a part $\delta\mathbf{m}(\mathbf{r}, t)$ transversal to $\mathbf{M}_d$, as well as a torque acting on $\delta\mathbf{m}$, with a component which leads to a precession of $\delta\mathbf{m}$ around $\mathbf{M}_d$, and a component which turns $\delta\mathbf{m}$ toward $\mathbf{M}_d$. For large τ_{sf}, the latter component, which contributes to damping will increase with increasing scattering rate, that is, decreasing τ_{sf}. For small τ_{sf}, however, the magnitude of $\delta\mathbf{m}$ is reduced because the angular momentum related to $\delta\mathbf{m}$ is very quickly transferred to the lattice, that is, damping will decrease with increasing scattering rate, and finally we end up with the strictly adiabatic situation where the conduction electron magnetization exhibits at any instant its equilibrium value with respect to the momentary configuration $\mathbf{M}_d$. As outlined in Section 4, noninfinite scattering times are required for damping, but zero scattering times rule out damping.

For a quantitative formulation, Zhang and Li (2004) assumed that the dynamics of d magnetization is described by a Gilbert type EOM (see equation (1)) with an additional term $\mathbf{T}(\mathbf{r}, t)$,

$$\frac{\partial \mathbf{M}_d(\mathbf{r}, t)}{\partial t} = -\gamma(\mathbf{M}_d \times \mathbf{H}_{eff,d}) + \frac{1}{M_d}\,\mathbf{M}_d \times \alpha \frac{\partial \mathbf{M}_d}{\partial t} + \mathbf{T}(\mathbf{r}, t) \tag{26}$$

In equation (26), $\mathbf{H}_{eff,d}$ and α are the effective field experienced by the d magnetization and the damping constant that would describe damping of the d magnetization when switching off the conduction electron magnetization, that is, which is due to direct relaxation processes of the d electrons, respectively. The additional term $\mathbf{T}(\mathbf{r}, t)$ describes the torque density exerted on $\mathbf{M}_d(\mathbf{r}, t)$ by $\mathbf{m}(\mathbf{r}, t)$ when these two magnetization fields are not collinear. The two remaining problems are to calculate $\mathbf{T}(\mathbf{r}, t)$ from the two magnetization fields and to determine $\mathbf{m}(\mathbf{r}, t)$.

The first problem is solved by assuming a classical Heisenberg interaction,

$$E_{sd} = -J_{ex}\ \mathbf{s}(\mathbf{r}, t)\cdot\mathbf{S}(\mathbf{r}, t) \tag{27}$$

with the exchange coupling constant J_{ex}, yielding

$$\mathbf{T} = -\frac{1}{\tau_{ex} M_d}\,\mathbf{M}_d \times \mathbf{m} \tag{28}$$

with

$$\tau_{ex} = \frac{\hbar}{S J_{ex}} \tag{29}$$

For the solution of the second problem, the generalized continuity equation for the conduction electron spin density $\mathbf{m}(\mathbf{r}, t)$ is used, which may be written in the form

$$\frac{\partial \mathbf{m}(\mathbf{r}, t)}{\partial t} = \mathbf{T}_m \tag{30}$$

where

$$\mathbf{T}_m = -\nabla\cdot\mathcal{J} - \mathbf{T} - \Gamma_{re} \tag{31}$$

is the total torque density acting on the conducting electron spin density. Thereby $\mathcal{J}$ is the expectation value of the spin-current density tensor operator $\hat{\mathcal{J}}$,

$$\hat{\mathcal{J}} = \mathrm{Re}\sum_{s,s'} \hat{\psi}_s^{\dagger}(\mathbf{r})\ \hat{\boldsymbol{\sigma}}_{ss'} \otimes \hat{\mathbf{v}}\ \hat{\psi}_{s'}(\mathbf{r}) \tag{32}$$

which involves the outer product between $\hat{\boldsymbol{\sigma}}$ and the velocity operator $\hat{\mathbf{v}}$, and Γ_{re} represents the spin relaxation (Section 5) due to spin-flip scattering of the conduction electrons. Equations (30 and 31) tell that the torque on the conduction electron spin density in a volume element of volume $\mathrm{d}V$ arises from the net flux of spin current through the surface $\mathrm{d}\mathbf{S}$ bounding $\mathrm{d}V$, from the torque exerted by the d magnetization which would like to induce a precession of $\mathbf{m}$ around $\mathbf{M}_d$ with frequency τ_{ex}^{-1}, and from the spin-flip relaxation.

To solve equation (30), phenomenological ansatzes are made for the quantities $\mathbf{m}(\mathbf{r}, t)$, $\mathcal{J}(\mathbf{r}, t)$, and Γ_{re}. The conduction electron spin density is separated into two parts,

$$\mathbf{m}(\mathbf{r}, t) = \mathbf{m}_0(\mathbf{r}, t) + \delta\mathbf{m}(\mathbf{r}, t) \tag{33}$$

where $\mathbf{m}_0$ represents the *adiabatic* spin density that would arise if the conduction electron magnetization followed the d magnetization $\mathbf{M}_d(\mathbf{r}, t)$ instantaneously, and $\delta\mathbf{m}(\mathbf{r}, t)$ is the nonadiabatic contribution. In the paper of Zhang and Li (2004) it is assumed that $\mathbf{m}_0(\mathbf{r}, t)$ is parallel to $\mathbf{M}_d(\mathbf{r}, t)$,

$$\mathbf{m}_0(\mathbf{r}, t) = m_0\ \frac{\mathbf{M}_d(\mathbf{r}, t)}{M_d} \tag{34}$$

While equation (34) certainly holds for a spatially homogeneous d magnetization, the situation in general is much more complicated for an inhomogeneous $\mathbf{M}_d(\mathbf{r}, t)$ where the directions of the s and p contributions to the magnetic moments may deviate strongly from the directions of the d contributions (Fähnle, Singer, Steiauf and Antropov, 2006). For strong cantings of the magnetic moments on an atomic scale, for example, in the center of a vortex or in an extremely narrow domain wall, this complication may change the results both qualitatively and quantitatively. For the sake of simplicity we adopt equation (34), and this should be justified for systems with slow spatial variations of $\mathbf{M}_d(\mathbf{r}, t)$.

The spin-current density $\mathcal{J}(\mathbf{r}, t)$ is nonzero even in a situation where there is no transport current. Then $\nabla\cdot\mathcal{J}$

describes the dependence of the kinetic energy on the relative orientations of the magnetic moments, and it has been emphasized repeatedly (see, e.g., Antropov, Harmon and Smirnov, 1999; Grotheer, Ederer and Fähnle, 2001; Stiles and Miltat, 2006) that this kinetic exchange term is very essential. In the paper of Zhang and Li (2004), the kinetic exchange for conduction electrons is neglected (which again may be justified approximately for systems with slow spatial variations of $\mathbf{M}_\mathrm{d}(\mathbf{r}, t)$) and only the contribution of a possible transport spin current is taken into account. In analogy to equation (33), the spin-current density is then subdivided into an adiabatic part $\mathcal{J}_0(\mathbf{r}, t)$ and a nonadiabatic part $\delta\mathcal{J}(\mathbf{r}, t)$,

$$\mathcal{J}(\mathbf{r}, t) = \mathcal{J}_0(\mathbf{r}, t) + \delta\mathcal{J}(\mathbf{r}, t) \tag{35}$$

The adiabatic part $\mathcal{J}_0(\mathbf{r}, t)$ is written in a form that holds for one-dimensional problems (Stiles and Miltat, 2006), that is, as an outer product of the charge current density $\mathbf{j}_\mathrm{e}$ and the spin direction $\mathbf{e}$ of the transport electrons,

$$\mathcal{J}_0(\mathbf{r}, t) = -\frac{\mu_\mathrm{B} P}{e_0}\, \mathbf{j}_\mathrm{e} \otimes \mathbf{e} \tag{36}$$

Here e_0 is the elementary charge, and the quantity P is the modulus of the spin-current polarization in the ferromagnet which is the up spin current minus the down spin current, all divided by the total current. In the paper of Zhang and Li (2004), it is assumed that P is a constant throughout the material, that is, the transport current has a spin polarization of constant magnitude but varying direction, which is certainly an approximation. Furthermore, it is assumed that for the adiabatic part of $\mathcal{J}$, the spin direction $\mathbf{e}$ of the transport electrons is parallel to $\mathbf{M}_\mathrm{d}(\mathbf{r}, t)$ everywhere, that is,

$$\mathbf{e}(\mathbf{r}, t) = \frac{\mathbf{M}_\mathrm{d}(\mathbf{r}, t)}{M_\mathrm{d}} \tag{37}$$

Let us pause to elucidate the physics behind equation (37). The assumption underlying this equation is equivalent to Slonczewski's assumption (Slonczewski, 1996) of complete spin filtering of an ideal, homogeneously magnetized ferromagnetic layer, which is assumed to completely remove that component of the spin polarization of an incident spin-polarized current perpendicular to the layer magnetization. To explain the spin filter effect see, e.g., Stiles and Miltat, 2006, the spinor field of an incident electron with given spin direction is written as a coherent superposition of spinor states with spin up and spin down relative to the direction of the layer magnetization. Because the conduction electrons in the ferromagnet experience an exchange interaction which produces a spin-dependent effective potential, the transmission probability will be larger for spin up than for spin down, that is, the perpendicular component of the spin of an electron entering the ferromagnet is reduced (*spin filtering*) but it is not yet zero. Furthermore, in the ferromagnet the two components of the spinor field with different spin belong to different wave vectors $\mathbf{k}_1$ and $\mathbf{k}_2$ because of the different effective potentials. Therefore the phase between the spin-up and the spin-down part of the spinor field in the ferromagnet, $\exp[\mathrm{i}(k\uparrow - k\downarrow)x]$, changes as the electron penetrates into the magnet, describing the precession of the electron with nonzero perpendicular spin around magnetization. Because electrons on different parts of the Fermi surface precess at different rates, there is a dephasing of different electrons. As a result of this dephasing, the remaining transverse spin current entering the ferromagnet decays with a characteristic decay length which is smaller, the more dissimilar the Fermi surfaces for spin-up and spin-down electrons. When scattering is included, that is, when the assumption of ballistic transport underlying the above reasoning is abandoned and a diffusive transport is considered, then the transverse component of spin polarization (called *spin accumulation*) decays exponentially on a short length scale and then its elimination takes place very close to the interface. (The influence of the small residual transverse spin accumulation which creates an effective field for the precession of the ferromagnetic magnetization is discussed, in Heide, Zilberman and Elliott, 2001; Heide, 2001, 2002). Equation (37) represents a generalization of all these considerations to the case of a continuously varying magnetization configuration. In general, this equation will be valid only if the length that characterizes the magnetization inhomogeneity is much larger than the characteristic decay length for the transverse component of the spin polarization, and this often will require strong scattering. However, in the special case of a domain wall, the conduction electron spin polarization will stay close to the magnetization of the domain wall even in the ballistic limit, because of the special properties of the precession of the conduction electrons in a domain wall (Waintal and Viret, 2004).

In the paper of Zhang and Li (2004) the quantities P and $\mathbf{j}_\mathrm{e}$ appearing in equation (36) are fixed, that is, it is assumed that the transport current $\mathbf{j}_\mathrm{e}$ is constant and has a spin polarization of constant magnitude but varying direction (always parallel to $\mathbf{M}_\mathrm{d}$), which is certainly an approximation. In contrast, for a theoretical description of a multilayer with abrupt changes of magnetization, these quantities are not prescribed but determined by classical or semiclassical transport theories for which the results of the calculations for spin filtering at the interfaces enter as boundary conditions (for a review, see Stiles and Miltat, 2006).

The nonadiabatic contribution $\delta\mathcal{J}$ is related to the nonadiabatic $\delta\mathbf{m}$ via a diffusion equation with diffusion constant D_0,

$$\delta\mathcal{J} = -D_0\ \nabla \otimes \delta\mathbf{m} \tag{38}$$

in very much the same way as the current density is related to the concentration gradient in a nonequilibrium situation. In the following we consider situations where magnetization varies on a length scale much larger than the spin diffusion transport length; then the term $\nabla \otimes \delta\mathbf{m}$ is neglected (Zhang and Li, 2004) in equations (30 and 31) (of course this approximation does not apply for the layer systems with abrupt changes of magnetization).

Finally, for the relaxation term a simple relaxation time approximation is used,

$$\Gamma_{\mathrm{rel}} = \frac{\delta\mathbf{m}(\mathbf{r}, t)}{\tau_{\mathrm{sf}}} \tag{39}$$

with a relaxation time τ_{sf} for the spin-flip scattering of the conduction electrons.

As outlined in Section 5, it is customary to subdivide the scattering processes into ordinary scattering between states with the same spin index ($\uparrow$ or $\downarrow$) and spin-flip scattering between states with different spin index. However, it should be recalled that due to spin-orbit coupling, the up and down states are not pure spin states but states with small spin mixing, so that even ordinary scattering processes change the probability to find the considered electron in one of the spin states $|\uparrow\rangle$ or $|\downarrow\rangle$. The quantity τ_{sf} then encompasses both spin-flip scattering and ordinary scattering.

Solving equations (30, 31, 33–37, and 39) with $\delta\mathcal{J} = 0$, thereby neglecting the higher-order term $\partial\delta\mathbf{m}/\partial t$, yields four contributions to the torque $\mathbf{T}$ on the d magnetization according to equation (28),

$$\mathbf{T} = \sum_{i=1}^{4} \mathbf{T}_i \tag{40}$$

$$\mathbf{T}_1 = \frac{\xi m_0}{(1+\xi^2)M_{\mathrm{d}}^2}\ \mathbf{M}_{\mathrm{d}} \times \frac{\partial \mathbf{M}_{\mathrm{d}}}{\partial t} \tag{41}$$

$$\mathbf{T}_2 = -\frac{m_0}{(1+\xi^2)M_{\mathrm{d}}} \frac{\partial \mathbf{M}_{\mathrm{d}}}{\partial t} \tag{42}$$

$$\mathbf{T}_3 = -\frac{\mu_{\mathrm{B}} P}{(1+\xi^2)e_0 M_{\mathrm{d}}^3}\ \mathbf{M}_{\mathrm{d}} \times [\mathbf{M}_{\mathrm{d}} \times (\mathbf{j}_{\mathrm{e}} \cdot \nabla)\mathbf{M}_{\mathrm{d}}] \tag{43}$$

$$\mathbf{T}_4 = -\frac{\mu_{\mathrm{B}} P \xi}{(1+\xi^2)e_0 M_{\mathrm{d}}^2}\ \mathbf{M}_{\mathrm{d}} \times (\mathbf{j}_{\mathrm{e}} \cdot \nabla)\mathbf{M}_{\mathrm{d}} \tag{44}$$

$$\xi = \frac{\tau_{\mathrm{ex}}}{\tau_{\mathrm{sf}}} \tag{45}$$

While $\mathbf{T}_3$ and $\mathbf{T}_4$ are related to the transport current $\mathbf{j}_{\mathrm{e}}$, the terms $\mathbf{T}_1$ and $\mathbf{T}_2$ do not depend on $\mathbf{j}_{\mathrm{e}}$ but arise as a consequence of the dynamical evolution of the d magnetization, that is, they exist for $\partial\mathbf{M}_{\mathrm{d}}/\partial t \neq 0$. For very strong spin-flip scattering, that is, $\tau_{\mathrm{sf}} \to 0$ and $\xi \to \infty$, the nonadiabatic contribution $\delta\mathbf{m}$ vanishes; that is, $\mathbf{m}$ follows $\mathbf{M}_{\mathrm{d}}$ adiabatically and all contributions $\mathbf{T}_i$ to $\mathbf{T}$ are zero.

First we consider the case without transport current $\mathbf{j}_{\mathrm{e}}$, that is, $\mathbf{T}_3 = \mathbf{T}_4 = 0$. For small τ_{sf} (i.e., large ξ), the torque $\mathbf{T}_1$ results primarily from the relaxation term Γ_{rel} of equations (30 and 31), whereas for large τ_{sf} (small ξ), $\mathbf{T}_2$ is primarily related to the s–d exchange torque $\mathbf{T}$ in these equations that leads to a precession of $\mathbf{m}$ around $\mathbf{M}_{\mathrm{d}}$. The equations (26 and 40–42) yield an EOM of Gilbert form, equation (1), with γ and α replaced by

$$\gamma' = \frac{\gamma}{1+\eta} \tag{46}$$

$$\alpha' = \frac{\alpha + \xi\eta}{1+\eta} \tag{47}$$

$$\eta = \frac{m_0}{(1+\xi^2)M_{\mathrm{d}}} \tag{48}$$

The torque $\mathbf{T}_1$ thereby gives a new contribution,

$$\Delta\alpha = \xi\eta \tag{49}$$

for the damping constant, while $\mathbf{T}_2$ renormalizes γ and $(\alpha + \Delta\alpha)$ by the factor $1/(1+\eta)$.

We note that $\Delta\alpha$ is proportional to τ_{sf}^{-1} for the case of low spin-flip rate, $\tau_{\mathrm{ex}} \ll \tau_{\mathrm{sf}}$, $\xi \ll 1$. As outlined in the introduction of Section 6.1, deviations $\delta\mathbf{m}$ are produced by spin-flip scattering processes and hence damping increases for decreasing τ_{sf} at large values of τ_{sf}. In Tserkovnyak, Fiete and Halperin (2004) it is pointed out that the physics of this low-spin-flip-rate regime is similar to the *spin-pumping* damping (Tserkovnyak, Brataas and Bauer, 2002; Zwierzycki *et al.*, 2005) of a thin ferromagnetic film on a nonmagnetic conductor. The moving magnetization in the film 'pumps' spins into the conduction electron system. For a low spin-flip scattering rate, the spin polarization of these conduction electrons is conserved for a long time and relaxes only far inside the nonmagnetic conductor, leading to a nonlocal damping of magnetization dynamics in the film. The only difference is that in the present section the spins are pumped into the own delocalized states of the magnet rather than in the delocalized states outside the magnet. For the case of high spin-flip rate, $\tau_{\mathrm{ex}} \gg \tau_{\mathrm{sf}}$, $\xi \gg 1$, $\Delta\alpha$ is proportional to τ_{sf}. This corresponds to the situation outlined in the introduction of Section 6.1 that for a high spin-flip rate the magnitude of $\delta\mathbf{m}$ is strongly reduced because the related angular momentum is transferred very quickly to the lattice.

Insofar, the s–d model yields two contributions to damping, the first proportional to τ_{sf}^{-1} and the second one proportional to τ_{sf}. It is tempting to relate these two contributions to the two contributions found experimentally for pure Ni (Heinrich, Meredith and Cochran, 1979) that are proportional to the conductivity $\sigma \sim \tau$ at low temperatures and to the resistivity $\rho \sim \tau^{-1}$ at higher temperatures. However, there are two important differences. First, we have to distinguish between the relaxation time τ_{sf} for spin-flip scattering and the Drude relaxation time τ appearing in the theory of electrical conduction which involves both spin channels. Second, in the experiments the term proportional to τ dominates at large τ (resp. low temperature), whereas in the s–d model the term proportional to τ_{sf} dominates for small τ. See also the next paragraph for the relevance of the s–d damping $\Delta\alpha$.

Estimates for J_{ex} and τ_{sf} are given in Zhang and Li (2004) ($J_{ex} \approx 1.6 \times 10^{-12}$ erg, $\tau_{sf} \approx 10^{-12}$ s) and in Waintal and Viret (2004) ($J_{ex} \approx 10^{-13}$ erg, $\tau_{sf} \approx 5 \times 10^{-14}$ s), yielding the values $\xi \approx 4 \times 10^{-4}$ and $\xi = 10^{-1}$ for $S = 2$. A typical value of $\eta \approx m_0/M_d$ is 1/20. This yields $\Delta\alpha = 2 \times 10^{-5}$ and 0.5×10^{-2}; typical experimental values for the damping constant are in the range of multiples of 10^{-2} to multiples of 10^{-1}. In Zhang and Li (2004), it was therefore concluded that the damping of magnetization dynamics in metals is not dominated by spin-flip scattering of s and p electrons. Probably the factor $\eta \approx m_0/M_d$ which describes the smallness of the conduction electron magnetization as compared to the d magnetization is responsible for this (see also the footnote 5 of Kamberský, 1970). Obviously, a theory of damping in metallic magnets has to include the scattering of the d electrons (as will be the case in the d band models of Kamberský (1976, 1984) and in the breathing Fermi surface model (Kamberský, 1970), see Section 6.2).

We now discuss the influence of a transport current $\mathbf{j}_e$. Equations (43 and 44) show that $\mathbf{j}_e$ is effective only for an inhomogeneous situation, that is, when the direction of $\mathbf{M}_d(\mathbf{r}, t)$ varies in space. The current $\mathbf{j}_e$ enters the EOM (30) for $\mathbf{m}(\mathbf{r}, t)$ via the term $\nabla\cdot\mathcal{J}_0$ (see equation (31)). Because the spin polarization of the conduction electrons is parallel to $\mathbf{M}_d(\mathbf{r}, t)$ everywhere for $\mathcal{J}_0$, the angular momentum of the spin current has to change in space: When the spin-polarized conduction electrons flow into the volume element d^3r around $\mathbf{r}$, that part of the spin polarization which is originally transverse to $\mathbf{M}_d(\mathbf{r}, t)$ will be totally transferred to the surroundings in d^3r. The result is the torque $-\nabla\cdot\mathcal{J}_0$ exerted on the magnetization $\mathbf{m}(\mathbf{r}, t)$, generating a component $\delta\mathbf{m}(\mathbf{r}, t)$ that is not parallel to $\mathbf{M}_d(\mathbf{r}, t)$, that will experience a precession around $\mathbf{M}_d$ via the s–d exchange torque $\mathbf{T}$ in equation (30), and a relaxation via the term Γ_{rel}. It becomes obvious from equation (43) that the term $\mathbf{T}_3$ (denoted (Zhang and Li, 2004) as *adiabatic spin torque*) results primarily (apart from the factor $(1 + \xi^2)$ in the denominator) from the s–d exchange term $\mathbf{T}$ in combination with $\nabla\cdot\mathcal{J}_0$, whereas $\mathbf{T}_4$ (denoted (Zhang and Li, 2004) as *nonadiabatic spin torque*) is primarily related to the relaxation term Γ_{rel} in combination with $\nabla\cdot\mathcal{J}_0$. The term $\mathbf{T}_3$ may be considered (Li and Zhang, 2004) as a generalization to the case of a continuously nonuniform magnetization of the spin-transfer torque due to complete spin filtering introduced by Slonczewski (1996) for multilayers where magnetization changes abruptly at the interface. Formally, the mathematical structure of the term $\mathbf{T}_4$ looks like a corresponding generalization of an additional multilayer torque arising from an effective field generated by the residual transverse spin accumulation (Zhang, Levy and Fert, 2002; Shpiro, Levy and Zhang, 2003). Thiaville, Nakatani, Miltat and Suzuki (2005) have introduced in a phenomenological manner a term of the form $\mathbf{T}_4$ in addition to the torque $\mathbf{T}_3$ to describe the current-driven domain-wall motion.

Zhang and Li (2004) have applied their theory to investigate the effects a spin-polarized transport current on the form and the dynamics of a Néel wall in a nanowire. The adiabatic $\mathbf{T}_3$ term causes a domain-wall distortion and is responsible for the initial velocity of the wall, whereas the terminal velocity of the wall is controlled by the nonadiabatic $\mathbf{T}_4$ term (although it is much smaller in size than $\mathbf{T}_3$). It should be noted that, while in the above discussed paper of Zhang and Li (2004) the diffusive conduction electron flow is considered, Waintal and Viret (2004) determine the torque exerted on the domain wall by the ballistic motion of conduction electrons, yielding other torques that are explicitly related to the precession of the electron spins around the magnetization in the domain wall.

Finally, we note that Xiao, Zangwill and Stiles (2006) argue that the phenomenological form of Γ_{rel} as given by equation (39) should not be used for systems with an inhomogeneous situation, and therefore doubt the existence of the nonadiabatic spin torque. Furthermore, they commented critically on the torque reported by Waintal and Viret (2004).

6.2 Breathing Fermi surface model

As outlined in Section 6.1, a theory of damping in ferromagnetic metals has to take into account the scattering of d electrons, like the breathing Fermi surface model originally introduced by Kamberský (1970) and further developed in Kuneš and Kamberský (2002, 2003) and Steiauf and Fähnle (2005). In the following, we discuss extensively the basic physical assumptions of this phenomenological model and the results of a calculation that determines the quantities entering this model by the *ab initio* density-functional electron theory.

For a complete quantum-mechanical description of the angular momentum and energy transfer from the electrons to the lattice, one had to start from the time-dependent wave equation for electrons and nuclei, involving spin-orbit coupling. Instead, we want to describe the situation approximately by an effective single-particle theory that involves only electrons and that describes the transfer empirically via relaxation times. In such a theory, the expectation values of the observables are determined by the matrix elements of the respective operators formed with the single-particle spinor wave functions $\psi_{j\mathbf{k}}(\mathbf{r}, t)$ – where j and $\mathbf{k}$ denote the band index and the wave vector – and by the occupation numbers $n_{j\mathbf{k}}(t)$ describing the occupation of these states at time t. For instance, the spin magnetization density is given by

$$\mathbf{m}_{\mathrm{s}}(\mathbf{r}, t) = -\frac{g\mu_{\mathrm{B}}}{2} \sum_{\substack{j,\mathbf{k} \\ s,s'}} n_{j\mathbf{k}}(t)\ \psi^{*}_{j\mathbf{k}s}(\mathbf{r}, t)\, \hat{\boldsymbol{\sigma}}_{ss'}\, \psi_{j\mathbf{k}s'}(\mathbf{r}, t) \tag{50}$$

where $\psi_{j\mathbf{k}s}$ is the s component of the spinor $\psi_{j\mathbf{k}}$, and the band-structure energy is

$$\begin{aligned} E_{\mathrm{band}}(t) &= \sum_{j\mathbf{k}} n_{j\mathbf{k}}(t)\ \left\langle \psi_{j\mathbf{k}}(t) \middle| \hat{H} \middle| \psi_{j\mathbf{k}}(t) \right\rangle \\ &= \sum_{j\mathbf{k}} n_{j\mathbf{k}}(t)\ \epsilon_{j\mathbf{k}}(t) \end{aligned} \tag{51}$$

where $\hat{H}$ is the effective single-particle Hamiltonian of the density-functional electron theory.

In principle, the $\psi_{j\mathbf{k}}(\mathbf{r}, t)$ should be determined from the time-dependent single-electron wave equation. In a strictly adiabatic situation, however, the $\psi_{j\mathbf{k}}(\mathbf{r}, t)$ are given by solutions of the time-independent wave equation for the effective potential related to the momentary directions $\{\mathbf{e}_i(t)\}$ of the atomic moments, $\psi_{j\mathbf{k}}(\mathbf{r}, t) = \psi_{j\mathbf{k}}(\mathbf{r}, \{\mathbf{e}_i(t)\})$. Correspondingly, we have $\epsilon_{j\mathbf{k}}(t) = \epsilon_{j\mathbf{k}}[\{\mathbf{e}_i(t)\}]$ and $n_{j\mathbf{k}}(t) = f(\epsilon_{j\mathbf{k}}[\{\mathbf{e}_i(t)\}]) = f_{j\mathbf{k}}$, where the $f_{j\mathbf{k}}$ are the Fermi–Dirac equilibrium occupation numbers, with a Fermi energy $\varepsilon_{\mathrm{F}}[\{\mathbf{e}_i(t)\}]$ and a corresponding Fermi surface. For a noncollinear magnetization configuration, the $\psi_{j\mathbf{k}}$ and $\epsilon_{j\mathbf{k}}$ depend on the orientations $\{\mathbf{e}_i(t)\}$ mainly because the orientations determine the kinetic exchange part of $\hat{H}$. For a homogeneous magnetization, the dependence of the $\epsilon_{j\mathbf{k}}$ on the $\{\mathbf{e}_i\}$ arises from the spin-orbit coupling. When changing $\{\mathbf{e}_i\}$ in time, the adiabatic $\psi_{j\mathbf{k}}$, $\epsilon_{j\mathbf{k}}$, and ε_{F} also change in time and the Fermi surface will continuously attain a slightly different form (*breathing Fermi surface*).

There are two basic assumptions of the breathing Fermi surface model. The first one is that even in a slightly nonadiabatic situation we can insert into equations (50 and 51) the adiabatic wave functions and the adiabatic single-electron energies corresponding to the momentary directions $\{\mathbf{e}_i(t)\}$. The deviation from the adiabatic situation is taken into account only by nonadiabatic occupation numbers $n_{j\mathbf{k}}(t)$ which lag behind the adiabatic occupation numbers $f(\epsilon_{j\mathbf{k}}[\{\mathbf{e}_i(t)\}])$. The reason is that the redistribution of the occupation numbers, which is necessary to adjust to the steadily changing Fermi surface requires scattering processes between various electronic states $j\mathbf{k}$ around the Fermi surface, and hence requires time. For quasistatic changes, the characteristic timescale $\tau_{\mathbf{e}}$ for the changes of the momentary directions $\mathbf{e}_i$ is much larger than the characteristic timescale τ_{s} for the scattering process, $\tau_{\mathbf{e}} \gg \tau_{\mathrm{s}}$, and then $n_{j\mathbf{k}}(t) = f_{j\mathbf{k}}(t)$ at any instant. In the general case, however, $n_{j\mathbf{k}}$ never catches up with $f_{j\mathbf{k}}$, and the deviation between $n_{j\mathbf{k}}$ and the fictitious $f_{j\mathbf{k}}$ generates the dynamical evolution of $n_{j\mathbf{k}}$. In Kamberský's theory, this process is described by a relaxation ansatz (Kamberský, 1970)

$$\frac{\mathrm{d}n_{j\mathbf{k}}(t)}{\mathrm{d}t} = -\frac{1}{\tau_{j\mathbf{k}}} \left[n_{j\mathbf{k}}(t) - f_{j\mathbf{k}}(t) \right] \tag{52}$$

with the relaxation times $\tau_{j\mathbf{k}}$, which in general will depend on the respective electronic state $j\mathbf{k}$. It becomes obvious that the breathing Fermi surface model describes a situation close to the adiabatic limit, that is, for very small relaxation times $\tau_{j\mathbf{k}}$.

The exact solution of equation (52) is

$$n_{j\mathbf{k}}(t) = \int_{t_0}^{t} \frac{1}{\tau_{j\mathbf{k}}} f_{j\mathbf{k}}(t')\ \mathrm{e}^{-(t-t')/\tau_{j\mathbf{k}}}\ \mathrm{d}t' + n_{j\mathbf{k}}(t_0)\ \mathrm{e}^{-(t-t_0)/\tau_{j\mathbf{k}}} \tag{53}$$

Neglecting the second term in equation (53) for $t_0 \to -\infty$ and evaluating $f_{j\mathbf{k}}(t')$ around $t' = t$ into a Taylor series, we find for $n_{j\mathbf{k}}(t)$ a power series in $\tau_{j\mathbf{k}}$,

$$n_{j\mathbf{k}}(t) = f_{j\mathbf{k}}(t) - \tau_{j\mathbf{k}}\, \frac{\mathrm{d}f_{j\mathbf{k}}(t)}{\mathrm{d}t} + \ldots \tag{54}$$

which converges for $\tau_{j\mathbf{k}} \ll \tau_{\mathbf{e}}$. In the case of a large timescale $\tau_{\mathbf{e}}$ for changes of the moment directions the deformation of the Fermi surface is very gradual and requires only scattering processes between electronic states that are close in energy, that is, those belonging to the same energy band j and – in the case of small spin mixing due to spin-orbit coupling – to the subband with the same spin index. Therefore the use of equation (54) implies that we make a theory of damping due to ordinary intraband scattering with small relaxation times.

In the following, we consider a homogeneous situation where $\mathbf{M}_i = \mathbf{M} = M\mathbf{e}$ for all sites i and where the absolute value M depends only slightly on $\mathbf{e}$ so that we take it as a constant. For the strictly adiabatic situation the EOM (23)

then reads

$$\dot{\mathbf{M}}_i = -\gamma(\mathbf{M}_i \times \mathbf{H}_{\mathrm{eff},i}) \tag{55}$$

with the adiabatic effective field

$$\mathbf{H}_{\mathrm{eff},i} = -\frac{1}{M}\frac{\delta E}{\delta \mathbf{e}_i} \tag{56}$$

The second basic assumption of the breathing Fermi surface model is that for the slightly nonadiabatic situation the form of the EOM (55) is retained, with $\mathbf{H}_{\mathrm{eff},i}$ replaced by a nonadiabatic effective field,

$$\tilde{\mathbf{H}}_{\mathrm{eff},i} = -\frac{1}{M}\frac{\delta F_{\mathrm{diss}}}{\delta \mathbf{e}_i} \tag{57}$$

Here the effect of damping is included in a dissipative free-energy functional F_{diss} of the magnetization configuration. For instance, a simple phenomenological F_{diss} has been written down by Brown (1963) by including a Rayleigh dissipation function in the free energy (see equation (13)).

For $T = 0\,\mathrm{K}$, we construct the dissipative free-energy functional for the breathing Fermi surface model from a phenomenological extension of the total energy expression of the density-functional theory,

$$E[n, \{\mathbf{e}_i(t)\}] = \sum_{j\mathbf{k}} n_{j\mathbf{k}}\epsilon_{j\mathbf{k}} + E_{\mathrm{dc}}[n] \tag{58}$$

where $n = [\rho(\mathbf{r}, \{\mathbf{e}_i(t)\}); \mathbf{m}(\mathbf{r}, \{\mathbf{e}_i(t)\})]$ with the electron density ρ. The first (second) term is the band-structure energy (double-counting term), and the phenomenological extension consists of inserting the nonadiabatic occupation numbers $n_{j\mathbf{k}}(t)$, equation (54), rather than the $f_{j\mathbf{k}}(t)$. Using the variational property of $E[n]$, and assuming that changes of the $n_{j\mathbf{k}}$ due to a change of $\{\mathbf{e}_i(t)\}$ occur exclusively for states close to ε_{F} with relaxation times $\tau_{j\mathbf{k}}$ that do not depend on the state $j\mathbf{k}$, that is, $\tau_{j\mathbf{k}} = \tau$, we find

$$\tilde{\mathbf{H}}_{\mathrm{eff}} = -\frac{1}{M}\sum_{j\mathbf{k}} n_{j\mathbf{k}}(\mathbf{e}(t))\,\frac{\partial \epsilon_{j\mathbf{k}}(\mathbf{e}(t))}{\partial \mathbf{e}} \tag{59}$$

Inserting (54) into (59) yields

$$\tilde{\mathbf{H}}_{\mathrm{eff}} = \mathbf{H}_{\mathrm{aniso}} + \mathbf{H}_{\mathrm{damp}} \tag{60}$$

with the anisotropy field

$$\mathbf{H}_{\mathrm{aniso}} = -\frac{1}{M}\sum_{j\mathbf{k}} f_{j\mathbf{k}}\,\frac{\partial \epsilon_{j\mathbf{k}}(\mathbf{e})}{\partial \mathbf{e}} \tag{61}$$

and the damping field

$$\mathbf{H}_{\mathrm{damp}} = -\frac{1}{\gamma M}\,\underline{\underline{\alpha}} \cdot \frac{\mathrm{d}\mathbf{M}}{\mathrm{d}t} \tag{62}$$

with the damping matrix

$$\frac{\alpha_{lm}}{\tau} = -\frac{\gamma}{M}\sum_{j\mathbf{k}} \frac{\partial f_{j\mathbf{k}}}{\partial \epsilon_{j\mathbf{k}}}\,\frac{\partial \epsilon_{j\mathbf{k}}}{\partial e_l}\bigg|_{\mathbf{M}}\,\frac{\partial \epsilon_{j\mathbf{k}}}{\partial e_m}\bigg|_{\mathbf{M}} \tag{63}$$

We note the similarity of equation (63) with the Drude equation for the conductivity tensor $\underline{\underline{\sigma}}$ in semiclassical approximation,

$$\frac{\sigma_{lm}}{\tau} = -e_0^2\sum_{j\mathbf{k}} \frac{\partial f_{j\mathbf{k}}}{\partial \epsilon_{j\mathbf{k}}}\,\frac{\partial \epsilon_{j\mathbf{k}}}{\partial k_l}\,\frac{\partial \epsilon_{j\mathbf{k}}}{\partial k_m} \tag{64}$$

Please note that in equations (63 and 64), the quantity τ describes the Drude relaxation time and not the spin-flip scattering time τ_{sf} that appeared in the s–d model.

Inserting equations (60–62) into equation (55) yields the EOM

$$\dot{\mathbf{M}} = -\gamma\mathbf{M} \times \mathbf{H}_{\mathrm{aniso}} + \frac{1}{M}\mathbf{M} \times \left(\underline{\underline{\alpha}} \cdot \frac{\mathrm{d}\mathbf{M}}{\mathrm{d}t}\right) \tag{65}$$

which looks very much like the original Gilbert equation (1), with the only but very important difference that the damping scalar of equation (1) is replaced by a damping matrix $\underline{\underline{\alpha}}$ of the form (Steiauf and Fähnle, 2005)

$$\begin{bmatrix} a^2 & ab & 0 \\ ab & b^2 & 0 \\ 0 & 0 & 0 \end{bmatrix} \tag{66}$$

so that in general $\mathbf{H}_{\mathrm{damp}}$ is not parallel to $\mathrm{d}\mathbf{M}/\mathrm{d}t$. A Gilbert equation is obtained only for the special case that $\mathrm{d}\mathbf{M}/\mathrm{d}t$ corresponds to one of the two eigenvectors of $\underline{\underline{\alpha}}(\mathbf{M})$, which are orthogonal to the momentary $\mathbf{M}$ and orthogonal to each other (and then the respective momentary damping constant is given by one of the eigenvalues $\tilde{\alpha}_p$, $p = 1, 2$), or if $\mathbf{M}$ is momentarily aligned to a threefold of fourfold symmetry axis of the system. For a general $\mathrm{d}\mathbf{M}/\mathrm{d}t$, it is always possible to write down (Steiauf and Fähnle, 2005) a 'momentary' Gilbert equation with a 'momentary' gyromagnetic ratio $\tilde{\gamma}(\dot{\mathbf{M}}, \mathbf{M})$ and a 'momentary' damping scalar $\tilde{\alpha}(\dot{\mathbf{M}}, \mathbf{M})$ that is between $\tilde{\alpha}_1$ and $\tilde{\alpha}_2$.

Altogether, the breathing Fermi surface model yields an EOM which, to lowest order, in the Taylor expansion (54), that is, for situations very close to the adiabatic limit, is an extension of the Gilbert EOM to the case of a damping matrix. Higher-order terms in equation (54) would contribute

further terms to the EOM. The theory predicts a damping matrix which is proportional to the relaxation time τ as the conductivity σ. It does not yield the contribution proportional to the resistivity $\rho \sim 1/\tau$ found experimentally for high-purity Ni (Heinrich, Meredith and Cochran, 1979; see Section 5). The reason is (see the preceding text) that the theory implies $\tau \ll \tau_{\mathbf{e}}$, and hence it corresponds to the regime with high relaxation rates for which α vanishes for $\tau \to 0$ like σ. Experimentally, the contribution proportional to σ has been found for pure single crystals of Ni (Heinrich, Meredith and Cochran, 1979) and Co (Bhagat and Lubitz, 1974), but not for Fe (Bhagat, Anderson and Hirst, 1966; Bhagat, Anderson and Ning, 1967).

The quantity $\underline{\underline{\alpha}}/\tau$ according to equation (64) has been calculated by the *ab initio* density-functional electron theory for bulk materials (Kuneš and Kamberský, 2002, 2003; Steiauf and Fähnle, 2005), as well as for hexagonal monolayers and for monatomic wires (Steiauf and Fähnle, 2005) of Fe, Co, and Ni, yielding the following results:

(1) For reasonable assumptions about τ, the calculated value of α for bulk Ni is in reasonable agreement with the experimental data at low temperatures (Kuneš and Kamberský, 2002).

(2) The dependence of the two eigenvalues $\tilde{\alpha}_p$ on the orientation of magnetization is already substantial in bulk materials (e.g., variations up to a factor of 4 in hexagonal Co, see Figure 2), and it is very strong for systems with reduced dimensionality like monatomic layers and monatomic wires. In these systems there are orientations of **M** for which damping is identically zero for any $\mathrm{d}\mathbf{M}/\mathrm{d}t$. For the layer, these orientations are perpendicular, in-plane orientations parallel to the most densely packed rows of the layer, and in-plane orientations perpendicular to these rows. For the wire, these are the orientations perpendicular to the wire or in its direction, see Figure 3. Altogether, the dependence of damping on the orientation of **M** represents an additional option to optimize a magnetization reversal process in a nanostructured system by choosing a magnetization trajectory that is most appropriate from the viewpoint of damping. So far the magnetization dynamics in nanostructures has been optimized in micromagnetic simulations only with respect to the shape of the sample, the form of the switching field and the magnitude of the damping scalar are assumed to be independent of the orientation of **M**.

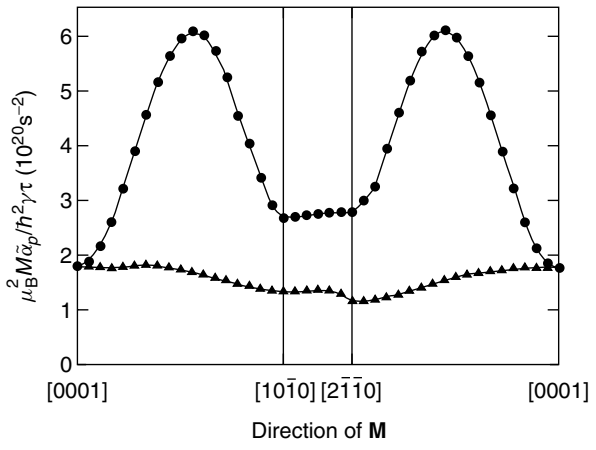

Figure 2. The two eigenvalues $\tilde{\alpha}_p$ (symbols ● and ▲) of $\underline{\underline{\alpha}}$ for different orientations of **M** in bulk hcp Co. (Reprinted figure from Steiauf, D. and Fähnle, M. (2005), *Physical Review B*, **72**, 064450-1–13. With permisson from APS. © 2005.)

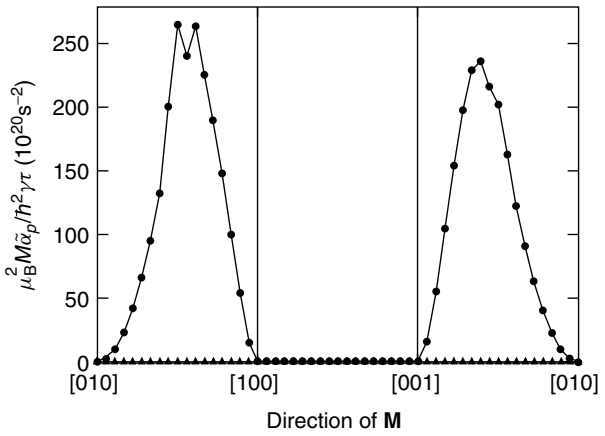

Figure 3. The two eigenvalues $\tilde{\alpha}_p$ of $\underline{\underline{\alpha}}$ for different orientations of **M** in a monatomic wire of Ni. The wire is along [010]. Note that both eigenvalues are zero for **M** perpendicular to the wire or in wire direction, that is, there is no damping for any arbitrary $\mathrm{d}\mathbf{M}/\mathrm{d}t$ out of this direction. In addition, for an arbitrary orientation, the eigenvalue corresponding to a rotation of the magnetization around the wire axis (symbol ▲) is also zero (because this rotation is equivalent to a reverse rotation of the coordinate system which does not change anything), whereas the second eigenvalue (symbol ●) is large. (Reprinted figure from Steiauf, D. and Fähnle, M. (2005), *Physical Review B*, **72**, 064450-1–13. With permisson from APS. © 2005.)

(3) It is often assumed that the larger the damping, the larger the magnetic anisotropy. From the inspection of equations (61 and 64), it becomes clear that this is not at all guaranteed: The anisotropy field contains the derivatives $\partial\epsilon_{j\mathbf{k}}/\partial\mathbf{e}$ linearly. These derivatives may exhibit positive and negative values, which may compensate to a large extent when performing the summation in equation (61). In contrast, the derivatives enter quadratically when calculating α_{ll} from equation (64). In fact, Table 1 shows that there is no simple relation between damping and magnetic anisotropy. For instance, for bulk Co the magnetic anisotropy is 2 orders of magnitude

Table 1. The maximum eigenvalues $\mu_B^2 M\tilde{\alpha}_p/\hbar^2\gamma\tau$ and the maximum anisotropy energies ΔE_{magn} for Co and Ni bulk, monolayer, and wire. The magnetic anisotropies of bulk Co and Ni have not been calculated. The experimental room-temperature anisotropy constants for bulk Fe, Co, and Ni are $K_1 = 4.6 \times 10^5$, 4.1×10^6, -5×10^4 erg cm^{-3} and $K_2 = 1.5 \times 10^5$, 1×10^6, -3×10^4 erg cm^{-3}.

	Bulk	Monolayer	Wire
Co			
$\mu_B^2 M\tilde{\alpha}_p/\hbar^2\gamma\tau$ (10^{20} s^{-2})	6	230	6500
ΔE_{magn}/atom (mRy)	–	6	8
Ni			
$\mu_B^2 M\tilde{\alpha}_p/\hbar^2\gamma\tau$ (10^{20} s^{-2})	15.5	95	250
ΔE_{magn}/atom (mRy)	–	0.1	9

larger than for bulk Ni, but damping of Ni is a factor of 2 larger than the one of Co (when we insert the same τ). For the monolayer, the magnetic anisotropy is a factor of 60 larger in Co than in Ni, but damping is only a factor of about 2.5 larger. Finally, for the wire the magnetic anisotropy is about the same for Co and Ni but damping is a factor of about 30 larger for Co.

In future the theory has to be extended to account for noncollinear magnetization configurations (Fähnle, Singer, Steiauf and Antropov, 2006). For strong noncollinearities on an atomic scale, like in the center of a vortex or in narrow domain walls in nanowires, the electronic eigenvalues $\epsilon_{j\mathbf{k}}$ change strongly when changing the magnetic configuration, and this might result in very strong damping because the Fermi surface shows large deformations in time, which have to be realized by strong redistributions of the occupation numbers via scattering processes. It will be interesting to see whether damping for a strongly noncollinear situation indeed differs from the one of a homogeneous situation.

7 *AB INITIO* SPIN DYNAMICS

The theoretical investigations of magnetization dynamics in the literature may be subdivided essentially in those based on micromagnetic simulations (e.g., see Stiles and Miltat, 2006; Kronmüller and Fähnle, 2003; Thiaville, Nakatani, Miltat and Suzuki, 2005; Thiaville *et al.*, 2003; Leineweber and Kronmüller, 1999; Hertel, 2002; Berkov, 2002; Van Wayenberge, 2006) and those based on the classical nearest-neighbor Heisenberg model (see, e.g., Nowak and Hinzke, 2001). The micromagnetic simulations are designed to resolve magnetization inhomogeneities on a mesoscopic scale, and use mainly the Gilbert equation (1) with the phenomenological micromagnetic effective field $\mathbf{H}_{\text{eff}}(\mathbf{r}, t)$ (Kronmüller and Fähnle, 2003). Forming the scalar product of equation (1) with $\mathbf{M}$ yields

$$\mathbf{M} \cdot \frac{\mathrm{d}\mathbf{M}}{\mathrm{d}t} = \frac{1}{2}\frac{\mathrm{d}}{\mathrm{d}t}\mathbf{M}^2 = \mathbf{M} \cdot \left(-\gamma \mathbf{M} \times \mathbf{H}_{\text{eff}} + \frac{1}{M}\,\mathbf{M} \times \alpha \frac{\mathrm{d}\mathbf{M}}{\mathrm{d}t}\right) = 0 \tag{67}$$

because the vector in the bracket of equation (67) is perpendicular to $\mathbf{M}$. This means that the magnitude $\mathbf{M}(\mathbf{r}, t)$ is conserved at any position $\mathbf{r}$. In the Heisenberg model the magnitudes $\mathbf{M}_i(t)$ of the atomic moments at sites $\mathbf{r}$ are also taken as constants. Therefore both approaches are unable to describe configurations with strong cantings of the magnetic moments on an atomic scale for which the $\mathbf{M}_i(t)$ depend strongly on the orientations of the surrounding magnetic moments (Heine, Lichtenstein and Mryasov, 1990; Turzhevskii, Likhtenshtein and Katsnel'son, 1990; Singer, Fähnle and Bihlmayer, 2005). As an example, Figure 4 shows the magnitude M_0 of a Ni moment $\mathbf{M}_0$ at site $i = 0$, which is surrounded by ferromagnetic Ni bulk and for which the orientation of $\mathbf{M}_0$ is fixed via constraining fields (Singer, Fähnle and Bihlmayer, 2005) with an angle θ_0 between $\mathbf{M}_0$ and the surrounding moments. The magnitude M_0 strongly decreases with increasing θ_0 and collapses to zero for $\theta_0 = 90^\circ$. A similar strong dependence is found for Co albeit the magnitude M_0 never vanishes totally, whereas for Fe the moments are much more stable (Singer, Fähnle and Bihlmayer, 2005). It is thus clear that configurations with atomic scale cantings can be described neither by micromagnetic simulations nor by the Heisenberg model. Finally, the conventional Heisenberg model neglects the influence of multispin interactions (Müller-Hartmann,

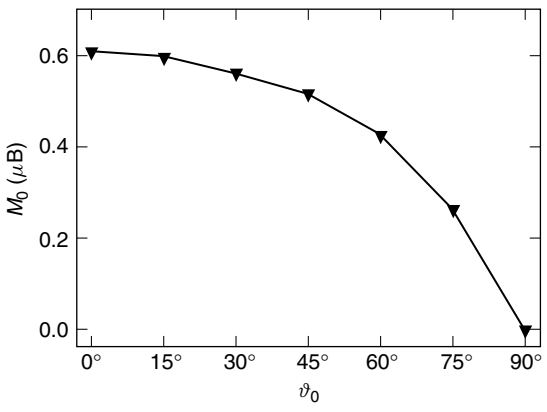

Figure 4. The magnitude M_0 of the magnetic moment $\mathbf{M}_0$ of a Ni atom at site 0 which is rotated by an angle ϑ_0 out of the ferromagnetic alignment of the surrounding fcc Ni bulk. (Reprinted figure from Singer, R., Fähnle, M. and Bihlmayer, G. (2005), *Physical Review B*, **71**, 214435-1–6. With permission from APS. © 2005)

Köbler and Smardz, 1997; Drautz and Fähnle, 2004, 2005), which may also become important for strongly canted configurations. Such configurations often appear in nanoscale materials that may have high-technological relevance in the future, examples are domain walls on the atomic scale in quasi-one-dimensional Fe nanostripes (Pratzer *et al*., 2001), vortex structures in platelets (Miltat and Thiaville, 2002) with a radius of the vortex core of 4–5 nm, and Bloch-point-mediated processes for vortices (Thiaville *et al*., 2003). All the above problems are avoided in microscopic simulations based on the *ab initio* spin density-functional electron theory.

Starting point of the existing *ab initio* spin dynamics simulations is the EOM, equation (23), for the orientations $\mathbf{e}_k$ of the atomic moments at sites k in the strictly adiabatic situation,

$$\dot{\mathbf{e}}_k = -\frac{2\mu_\mathrm{B}}{\hbar}\frac{\partial E(\{\mathbf{e}_i\})}{\partial \mathbf{e}_k} \times \mathbf{e}_k \tag{68}$$

Suggestions on how to take into account the damping of spin systems as well as stochastic fluctuation fields that model finite temperature effects are given in Antropov *et al*. (1996) and Fähnle *et al*. (2005), and a method for simultaneous molecular and spin dynamics is discussed in Antropov *et al*. (1996). In this latter reference, it is also shown that equation (68) holds not only for orientations of the total magnetic moments $\mathbf{M}_k$ composed of different orbital states ν (ν = s, p, d, . . .) but, approximately, also for the separate orbital contributions $\mathbf{M}_{\nu,k}$ with corresponding effective fields $\partial E/\partial \mathbf{e}_{\nu,k}$ for the various orbitals ν.

In principle, simulations based on equation (68) proceed in the following line. First, the initial orientation configuration $\{\mathbf{e}_i(t = t_0)\}$ at the initial time t_0 is generated, in the most strict way by use of constraining fields (Stocks *et al*., 1998; Singer, Fähnle and Bihlmayer, 2005), and the 'slaved' magnitudes $M_k(\{\mathbf{e}_i(t = t_0)\})$ are calculated by the *ab initio* density-functional electron theory, yielding the initial magnetic configuration $\{\mathbf{M}_i(t_0) = M_i(t_0)\,\mathbf{e}(t_0)\}$. Furthermore, the 'effective fields' $\partial E(\{\mathbf{e}_i\})/\partial \mathbf{e}_k$ are calculated by appropriate methods of the *ab initio* electron theory (Stocks *et al*., 1998; Singer, Fähnle and Bihlmayer, 2005). Then the orientational configuration for the time $t_0 + \mathrm{d}t$ is calculated from equation (68), the new magnitudes $M_k(\{\mathbf{e}_i(t_0 + \mathrm{d}t)\})$ and the new effective fields $\partial E/\partial \mathbf{e}_k$ are determined *ab initio*, and so on. By far, the most time-consuming step in this procedure is the *ab initio* calculation of the quantities M_k and $\partial E(\{\mathbf{e}_i\})/\partial \mathbf{e}_k$, which makes the present *ab initio* spin dynamics simulations extremely costly. Therefore, there are so far only extremely few *ab initio* studies of the magnetization dynamics. In Section 7.1 an alternative method is described that circumvents the use of the *ab initio* electron theory for each time step of the solution of equation (68), while still providing near-*ab initio* accuracy. A code based on this new method will probably be very much faster than the existing *ab initio* spin dynamics simulation codes.

7.1 The spin-cluster expansion

The basic idea to facilitate the use of equation (68) for *ab initio* spin dynamics simulations is to construct analytical parameterizations for the functionals $M_k(\{\mathbf{e}_i\})$ and $E(\{\mathbf{e}_i\})$ from which the required quantities M_k and $\partial E/\partial \mathbf{e}_k$ can be calculated analytically so that their *ab initio* determination in each time step can be avoided. In order to obtain near-*ab initio* accuracy, the parameterizations have to be obtained by the use of the *ab initio* electron theory, which will be the most costly part of the method. However, this parameterization has to be done just once before starting the simulation, and the simulation itself will then be very easy.

To obtain the desired parameterization, the recently developed (Drautz and Fähnle, 2004) spin-cluster expansion (SCE) technique, which is an extension of the conventional cluster expansion method in alloy theory (Sanchez, Ducastelle and Gratias, 1984), can be used. In the SCE, it is shown that every quantity $O(\{\mathbf{e}_i\})$ may be written as a sum of contributions of all conceivable spin clusters, α (pairs, triplets, quartets, etc.), in the system,

$$O(\{\mathbf{e}_i\}) = O_0 + \sum_\alpha \sum_\nu O_{\alpha\nu}\Phi_{\alpha\nu}(\{\mathbf{e}_i\}) \tag{69}$$

$$\Phi_{\alpha\nu}(\{\mathbf{e}_i\}) = Y_{\nu_1}(\mathbf{e}_{i_1})Y_{\nu_2}(\mathbf{e}_{i_2})\ldots Y_{\nu_k}(\mathbf{e}_{i_k}) \tag{70}$$

Here $\alpha = (i_1, i_2, \ldots, i_k)$ labels the sites included in the cluster α; $\nu = (\nu_1, \nu_2, \ldots, \nu_k)$ gives the quantum numbers (l, m) characterizing the spherical harmonics Y_{lm}; and $O_{\alpha\nu}$ are expansion coefficients. In a practical calculation, the SCE has to be terminated at a maximum cluster α_max and by a maximum quantum number l_max. The expansion coefficients can then be obtained by fitting the terminated SCE to the observables calculated for a relatively small number of appropriately chosen reference spin configurations $\{\mathbf{e}_i\}_\mathrm{ref}$ by the *ab initio* electron theory for noncollinear spin systems (see, e.g., Grotheer, Ederer and Fähnle, 2001; Antropov *et al*., 1996; Halilov, Eschrig, Perlov and Oppeneer, 1998; Stocks *et al*., 1998; Grotheer, 2002; Singer, Fähnle and Bihlmayer, 2005), prescribing the directions $\mathbf{e}_i$ by local transverse constraining fields (Stocks *et al*., 1998; Singer, Fähnle and Bihlmayer, 2005). When we thereby take into account the spin-orbit coupling, $E(\{\mathbf{e}_i\})$ encompasses the magnetic anisotropy in addition to the exchange energy, and in Drautz and Fähnle (2004), it is shown how the dipolar energy and the Zeeman energy can be incorporated in the SCE. On the basis of the experience gained for conventional

cluster expansions in the alloy theory, we expect that SCEs for $E(\{\mathbf{e}_i\})$ and $M_k(\{\mathbf{e}_i\})$ which exhibit *ab initio* or near *ab initio* accuracy, can be obtained by including relatively few clusters. Finally, it should be noted that $O(\{\mathbf{e}_i\})$ has to fulfill symmetry demands, for example, it must be invariant with respect to the operations of the symmetry group of the magnetic systems. In Singer and Fähnle (2006), it is shown how this can be achieved for the case of magnetically isotropic systems by constructing from the basis functions $\Phi_{\alpha\nu}$ of equation (70), appropriate rotationally invariant basis functions.

8 CONCLUDING REMARKS

From the discussion of the preceding sections, it can be concluded that the basic physics that determines magnetization dynamics in metallic magnets close to the adiabatic limit is known. First, it should be recalled that direct damping is a consequence of the spin-orbit coupling in the system. Second, because of the itineracy of magnetism in 3d transition metals, any theory for these systems should start from the delocalized electronic states. Thereby, the s–d model has shown that damping in metallic bulk magnets results mainly from the scattering of d electrons, and that s and p electrons play only a minor role in situations without transport currents. The breathing Fermi surface model is an intuitive physical model to deal with the scattering of s, p, and d electrons on equal footing in the limit of high scattering rates (i.e., impure crystals and/or high temperatures), and it is able to incorporate in a reliable manner the specific electronic properties of a given material when it is combined with the state-of-the-art *ab initio* density-functional electron theory. It has been shown in Section 6.2 that this is highly important for systems with reduced dimensionality, which are promising candidates for future technological applications. So far this model has been worked out quantitatively only for homogeneous magnetization. For this simple situation, the theory yields an EOM of Gilbert form with the only but very important difference that the damping scalar of the Gilbert equation is replaced by a damping matrix $\underline{\underline{\alpha}}(\mathbf{M})$ which depends on the momentary orientation of $\mathbf{M}$. This dependence can be very large for systems with reduced dimensionality, offering a further option to optimize magnetization dynamics especially in nanostructured materials. The damping matrix is proportional to the electronic relaxation time τ as the conductivity σ, and this results from the fact that the model is designed to describe a near-adiabatic situation with high scattering rates. Damping that is proportional to $1/\tau$ as the resistivity (found in experiments on pure samples) probably arises mainly for small scattering rates, and it is not included in the breathing Fermi surface model. Inserting reasonable values for τ obtained from conductivity measurements yields damping comparable in magnitude to experimentally observed damping. It remains to generalize the model to the case of strongly noncollinear magnetization configurations for which strong damping is expected.

Altogether the breathing Fermi surface model is a powerful model to describe dissipative spin dynamics in metallic magnets in the limit of high scattering rates, for example, in highly doped materials. It is a big challenge to explore the limitations of the near-adiabatic approach. Because the model is designed for a near-adiabatic situation, it probably does not make sense to try to extend it to the regime of small scattering rates. There are other theories including this regime (Kamberský, 1976, 1984; Korenman and Prange, 1972) which, however, are rather formal and do not exhibit the physical intuition of the breathing Fermi surface model.

In our opinion, it is rather difficult to figure out which physical mechanisms (electronic scattering at phonons or various types of lattice defects) determine the damping of a specific material under consideration. In order to investigate the intrinsic damping due to phonons, high-purity crystals have to be used. Research on high-purity crystalline Ni samples has shown convincingly (Heinrich, 2005) that intrinsic damping in Ni is indeed caused by the delocalized nature of the electrons in combination with spin-orbit scattering. Damping may be considerably increased by introducing defects, for example, rare-earth impurities, giving the chance to engineer the desired damping properties for technological applications. Finally, it should be noted that it is possibly questionable whether much information on the damping mechanism can be extracted from the comparison of experiments for the near-adiabatic timescale and for the subpicosecond timescale of laser pump-and-probe experiments because electronic states at different energies are involved in these two situations.

The s–d model – albeit unable to describe damping in metallic bulk magnets – is a good starting point to describe the effect of a transport current on magnetization dynamics, both in bulk materials with continuous inhomogeneous magnetization configurations like domain walls as well as in layered systems with discontinuous changes of magnetization. (In Section 6.1 the interrelations between the torque arising for these two situations are discussed.) Quantitatively there are certainly many open questions for bulk materials already. (For problems in the treatment of layered structures, see Stiles and Miltat, 2006). For instance, the role of noncollinearity between the s, p, and d contributions for situations with strong cantings of magnetic moments has to be figured out. Furthermore, it is an open question as to how the ballistic (Waintal and Viret, 2004) and the diffusive (Zhang and Li, 2004) approach to describe the influence of transport currents on domain walls should be reconciled.

In the last few years, it became possible to treat the adiabatic spin dynamics by means of the *ab initio* density-functional electron theory, albeit the respective computer codes are very time consuming. This latter problem may by overcome by use of the SCE method, as described in Section 7. The remaining challenge is to incorporate into the *ab initio* spin dynamics the effect of damping. One way would be to construct a SCE with expansion coefficients that depend parametrically on the positions of the atoms, thereby including the spin-orbit coupling in the calculation of the magnetic energy of the respective reference configurations. A simultaneous treatment of spin dynamics and atomic dynamics (with *ab initio* determined force constants) would then represent an *ab initio* theory for the spin dynamics including intrinsic damping via phonons.

ACKNOWLEDGMENTS

We acknowledge helpful discussions with V. Antropov, J. Kuneš, R. Singer, A. Thiaville, X. Waintal, and S. Zhang. Part of the work on the breathing Fermi surface was supported by the DFG Schwerpunktprogramm 1133.

REFERENCES

Ankudinov, A. and Rehr, J.J. (1995). Sum rules for polarization-dependent x-ray absorption. *Physical Review B*, **51**, 1282–1285.

Antropov, V.P., Harmon, B.N. and Smirnov, A.N. (1999). Aspects of spin dynamics and magnetic interactions. *Journal of Magnetism and Magnetic Materials*, **200**, 148–166.

Antropov, V.P., Katsnelson, M.I., Harmon, B.N., *et al*. (1996). Spin dynamics in magnets: equation of motion and finite temperature effects. *Physical Review B*, **54**, 1019–1035.

Antropov, V.P., Katsnelson, M.I., van Schilfgaarde, M. and Harmon, B.N. (1995). Ab initio spin dynamics in magnets. *Physical Review Letters*, **75**, 729–732.

Back, C.H. and Pescia, D. (2004). Speed limit ahead. *Nature*, **428**, 808–809.

Berger, L. (1996). Emission of spin waves by a magnetic multilayer traversed by a current. *Physical Review B*, **54**, 9353–9358.

Berger, L. (2001). Effect of interfaces on Gilbert damping and ferromagnetic resonance linewidth in magnetic multilayers. *Journal of Applied Physics*, **90**, 4632–4638.

Berkov, D.V. (2002). Fast switching of magnetic nanoparticles: simulation of thermal noise effects using the Langevin dynamics. *IEEE Transactions on Magnetics*, **38**, 2489–2495.

Beuerle, T., Hummler, K., Elsässer, C. and Fähnle, M. (1994). Formation of magnetic moments on iron impurities in transition-metal hosts. *Physical Review B*, **49**, 8802–8810.

Bhagat, S.M., Anderson, J.R. and Hirst, L.L. (1966). Ferromagnetic resonance in pure iron at low temperatures. *Physical Review Letters*, **16**, 1099–1100.

Bhagat, S.M., Anderson, J.R. and Ning, Wu. (1967). Influence of the anomalous skin effect on the ferromagnetic-resonance linewidth in iron. *Physical Review*, **155**, 510–513.

Bhagat, S.M. and Lubitz, P. (1974). Temperature variation of ferromagnetic relaxation in the 3d transition metals. *Physical Review B*, **10**, 179–185.

Born, M. and Oppenheimer, J.R. (1927). Quantum theory of molecules. *Annalen der Physik*, **84**, 457–484.

Brown, W.F. (1963). *Micromagnetics*, Wiley: New York.

Capelle, K. and Gyorffy, B.L. (2003). Exploring dynamical magnetism with time-dependent density-functional theory: from spin fluctuations to Gilbert damping. *Europhysics Letters*, **61**, 354–360.

Costa, A.T., Muniz, R.B. and Mills, D.L. (2003). Theory of spin excitations in Fe(110) multilayers. *Physical Review B*, **68**, 224435-1–224435–14.

Demokritov, S.O. and Hillebrands, B. (2002). Spinwaves in laterally confined magnetic structures. In *Spin Dynamics in Confined Magnetic Structures I*, Hillebrands, B. and Ounadjela, K. (Eds.), Springer: Berlin, pp. 65–92.

Drautz, R. and Fähnle, M. (2004). Spin-cluster expansion: parametrization of the general adiabatic magnetic energy surface with ab initio accuracy. *Physical Review B*, **69**, 104404-1–104404-6.

Drautz, R. and Fähnle, M. (2005). Parametrization of the magnetic energy at the atomic level. *Physical Review B*, **72**, 212405-1–212405-4.

Fähnle, M., Drautz, R., Singer, R., *et al*. (2005). A fast ab initio approach to the simulation of spin dynamics. *Computational Materials Science*, **32**, 118–122.

Fähnle, M., Singer, R., Steiauf, D. and Antropov, V.P. (2006). Role of nonequilibrium conduction electrons on the magnetization dynamics of ferromagnets in the s-d model. *Physical Review B*, **73**, 172408-1–172408-3.

Gebauer, R. and Baroni, S. (2000). Magnons in real materials from density-functional theory. *Physical Review B*, **61**, R6459–R6462.

Gilbert, T.L. (1956). *Formulation, Foundations and Applications of the Phenomenological Theory of Ferromagnetism*, Ph.D. Thesis, Illinois Institute of Technology, Chicago.

Grotheer, O. (2002). *Ab-initio-Berechnung der Spinwellenspektren von Eisen, Kobalt und Nickel*. Ph.D. Thesis, University of Stuttgart. Cuvillier Verlag, Göttingen.

Grotheer, O., Ederer, C. and Fähnle, M. (2001). Fast *ab initio* methods for the calculation of adiabatic spin wave spectra in complex systems. *Physical Review B*, **63**, 100401.

Gyorffy, B.L., Pindor, A.J., Staunton, J., *et al*. (1985). A first-principles theory of ferromagnetic phase transitions in metals. *Journal of Physics F: Metal Physics*, **15**, 1337–1386.

Haas, C.W. and Callen, H.B. (1963). Ferromagnetic relaxation and resonance line widths. In *Magnetism I*, Rado, G.T. and Suhl, H. (Eds.), Academic Press: New York, London, pp. 449–549.

Halilov, S.V., Eschrig, H., Perlov, A.Y. and Oppeneer, P.M. (1998). Adiabatic spin dynamics from spin-density-functional theory: application to Fe, Co, and Ni. *Physical Review B*, **58**, 293–302.

Heide, C. (2001). Spin currents in magnetic films. *Physical Review Letters*, **87**, 197201-1–197201-4.

Heide, C. (2002). Effects of spin accumulation in magnetic multilayers. *Physical Review B*, **65**, 054401-1–054401-17.

Heide, C., Zilberman, P.E. and Elliott, R.J. (2001). Current-driven switching of magnetic layers. *Physical Review B*, **63**, 064424-1–064424-7.

Heine, V., Lichtenstein, A.I. and Mryasov, O.N. (1990). On the Origin of Short-range order above Tc in Fe, Co, Ni. *Europhysics Letters*, **12**, 545–550.

Heinrich, B. (2005). Spin relaxation in magnetic metallic layers and multilayers. In *Ultrathin Magnetic Structures III*, Bland, J.A.C. and Heinrich, B. (Eds.), Springer: Berlin, Heidelberg, New York, pp. 143–232.

Heinrich, B., Fraitová, D. and Kamberský, V. (1967). Influence of s–d exchange on relaxation of magnons in metals. *Physica Status Solidi B*, **23**, 501–507.

Heinrich, B., Meredith, D.J. and Cochran, J.F. (1979). Wave number and temperature dependent Landau-Lifshitz damping in nickel. *Journal of Applied Physics*, **50**, 7726–7728.

Hertel, R. (2002). Computational micromagnetism of magnetization processes in nickel nanowires. *Journal of Magnetism and Magnetic Materials*, **249**, 251–256.

Hillebrands, B. and Fassbender, J. (2002). Ultrafast magnetic switching. *Nature*, **418**, 493–494.

Hübner, W. and Zhang, G.P. (1998). Ultrafast spin dynamics in nickel. *Physical Review B*, **58**, R5920–R5923.

Kamberský, V. (1970). On the Landau-Lifshitz relaxation in ferromagnetic metals. *Canadian Journal of Physics*, **48**, 2906–2911.

Kamberský, V. (1976). Ferromagnetic resonance damping in metals. *Czechoslovak Journal of Physics Section B*, **26**, 1366–1383.

Kamberský, V. (1984). FMR linewidth and disorder in metals. *Czechoslovak Journal of Physics Section B*, **34**, 1111–1124.

Kittel, C. (1958). Interaction of spin waves and ultrasonic waves in ferromagnetic crystals. *Physical Review*, **110**, 836–841.

Kloss, R. and Kronmüller, H. (1971). Ferromagnetic linewidth broadening by dislocations. *Zeitschrift fur Angewandte Physik*, **32**, 17–22.

Koopmans, B. (2003). Laser-induced magnetization dynamics. In *Spin Dynamics in Confined Magnetic Structures II*, Hillebrands, B. and Ounadjela, K. (Eds.), Springer: Berlin, pp. 253–320.

Korenman, V. and Prange, R.E. (1972). Anomalous damping of spin waves in magnetic metals. *Physical Review B*, **6**, 2769–2777.

Kronmüller, H. and Fähnle, M. (2003). *Micromagnetism and the Microstructure of Ferromagnetic Solids*, Cambridge University Press: Cambridge.

Kuneš, J. and Kamberský, V. (2002). First-principles investigation of the damping of fast magnetization precession in ferromagnetic 3d metals. *Physical Review B*, **65**, 212411-1–212411-3; Erratum (2003). *Physical Review B*, **68**, 019901(E).

Leineweber, T. and Kronmüller, H. (1999). Dynamics of magnetisation states. *Journal of Magnetism and Magnetic Materials*, **192**, 575–590.

Li, Z. and Zhang, S. (2004). Domain-wall dynamics and spin-wave excitations with spin-transfer torques. *Physical Review Letters*, **92**, 207203-1–207203-4.

Lindner, J., Lenz, K., Kosubek, E., *et al*. (2003). Non-Gilbert-type damping of the magnetic relaxation in ultrathin ferromagnets: importance of magnon-magnon scattering. *Physical Review B*, **68**, 060102(R).

Mills, D.L. and Rezende, S.M. (2003). Spin damping in ultrathin magnetic films. In *Spin Dynamics in Confined Magnetic Structures II*, Hillebrands, B. and Ounadjela, K. (Eds.), Springer: Berlin, pp. 27–59.

Miltat, J., Albuquerque, G. and Thiaville, A. (2002). An introduction to micromagnetics in the dynamic regime. In *Spin Dynamics in Confined Magnetic Structures I*, Hillebrands, B. and Ounadjela, K. (Eds.), Springer: Berlin, pp. 1–33.

Miltat, J. and Thiaville, A. (2002). Vortex cores – smaller than small. *Science*, **298**, 555.

Mook, H.A. and Paul, D.McK. (1985). Neutron-scattering measurement of the spin-wave spectra for nickel. *Physical Review Letters*, **54**, 227–229.

Müller-Hartmann, E., Köbler, U. and Smardz, L. (1997). Competing non-Heisenberg interactions in $Eu_xSr_{1-x}S$. *Journal of Magnetism and Magnetic Materials*, **173**, 133–140.

Niu, Q. and Kleinman, L. (1998). Spin-wave dynamics in real crystals. *Physical Review Letters*, **80**, 2205–2208.

Nowak, U. and Hinzke, D. (2001). Magnetic nanoparticles: the simulation of thermodynamic properties. In *Advances in Solid State Physics 41*, Cramer, B. (Ed.), Springer: Berlin, pp. 613–622.

Pratzer, M., Elmers, H.J., Bode, M., *et al*. (2001). Atomic-scale magnetic domain walls in quasi-one-dimensional Fe nanostripes. *Physical Review Letters*, **87**, 127201-1–127201-4.

Rebei, A. and Parker, G.J. (2003). Fluctuations and dissipation of coherent magnetization. *Physical Review B*, **67**, 104434-1–104434-14.

Russek, S.E., McMichael, R.D., Donahue, M.J. and Kaka, S. (2003). High speed switching and rotational dynamics in small magnetic thin film devices. In *Spin Dynamics in Confined Magnetic Structures II*, Hillebrands, B. and Ounadjela, K. (Eds.), Springer: Berlin, pp. 93–156.

Safonov, V.L. and Bertram, H.N. (2005). Fluctuation-dissipation considerations of damping models for ferromagnetic materials. *Physical Review B*, **71**, 224402-1–224402-5.

Sanchez, J.M., Ducastelle, F. and Gratias, D. (1984). Generalized cluster description of multicomponent systems. *Physica A*, **128**, 334–350.

Shpiro, A., Levy, P.M. and Zhang, S. (2003). Self-consistent treatment of nonequilibrium spin torques in magnetic multilayers. *Physical Review B*, **67**, 104430-1–104430-17.

Singer, R. and Fähnle, M. (2006). Construction of basis functions for the spin-cluster expansion of the magnetic energy on the atomic scale in rotationally invariant systems. *Journal of Mathematical Physics*, **47**, 113503-1–113503-10.

Singer, R., Fähnle, M. and Bihlmayer, G. (2005). Constrained spin-density functional theory for excited magnetic configurations in an adiabatic approximation. *Physical Review B*, **71**, 214435-1–214435-6.

Slonczewski, J.C. (1996). Current-driven excitation of magnetic multilayers. *Journal of Magnetism and Magnetic Materials*, **159**, L1–L7.

Steiauf, D. and Fähnle, M. (2005). Damping of spin dynamics in nanostructures: an ab initio study. *Physical Review B*, **72**, 064450-1–064450-13.

Stiles, M.D. and Miltat, J. (2006). Spin transfer torques and dynamics. In *Spin Dynamics in Confined Magnetic Structures III*, Hillebrands, B. and Thiaville, A. (Eds.), Springer: Berlin, pp. 225–308.

Stocks, G.M., Ujfalussy, B., Wang, X., *et al*. (1998). Towards a constrained local moment model for first principles spin dynamics. *Philosophical Magazine B*, **78**, 665–673.

Stoll, H., Puzic, A., van Waeyenberge, B., *et al*. (2004). High-resolution imaging of fast magnetization dynamics in magnetic nanostructures. *Applied Physics Letters*, **84**, 3328–3330.

Suhl, H. (1998). Theory of the magnetic damping constant. *IEEE Transactions on Magnetics*, **34**, 1834–1838.

Thiaville, A., Garcia, J.M., Dittrich, R., *et al*. (2003). Micromagnetic study of Bloch-point-mediated vortex core reversal. *Physical Review B*, **67**, 094410-1–094410-12.

Thiaville, A., Nakatani, Y., Miltat, J. and Suzuki, Y. (2005). Micromagnetic understanding of current-driven domain wall motion in patterned nanowires. *Europhysics Letters*, **69**, 990–996.

Tserkovnyak, Y., Brataas, A. and Bauer, G.E.W. (2002). Enhanced Gilbert damping in thin ferromagnetic films. *Physical Review Letters*, **88**, 117601-1–117601-4.

Tserkovnyak, Y., Fiete, G.A. and Halperin, B.I. (2004). Mean-field magnetization relaxation in conducting ferromagnets. *Applied Physics Letters*, **84**, 5234–5236.

Turzhevskii, S.A., Likhtenshtein, A.I. and Katsnel'son, M.I. (1990). Degree of localization of magnetic moments and the non-Heisenberg nature of exchange interactions in metals and alloys. *Soviet Physics-Solid State*, **32**, 1138–1142.

Van Wayenberge, B., Puzic, A., Stoll, H., *et al*. (2006). Magnetic vortex core reversal by excitation with short bursts of an alternating field. *Nature*, **444**, 461–464.

Waintal, X. and Viret, M. (2004). Current-induced distortion of a magnetic domain wall. *Europhysics Letters*, **65**, 427–433.

Xiao, J., Zangwill, A. and Stiles, M.D. (2006). Spin-transfer torque for continuously variable magnetization. *Physical Review B*, **73**, 054428-1–054428-10.

Yafet, Y. (1965). g-factors and spin-lattice relaxation of conduction electrons. In *Solid State Physics 13*, Seitz, F. and Turnbull, D. (Eds.), Academic Press: New York, London, pp. 1–98.

Zhang, S., Levy, P.M. and Fert, A. (2002). Mechanisms of spin-polarized current-driven magnetization switching. *Physical Review Letters*, **88**, 236601-1–236601-4.

Zhang, S. and Li, Z. (2004). Roles of nonequilibrium conduction electrons on the magnetization dynamics of ferromagnets. *Physical Review Letters*, **93**, 127204-1–127204-4.

Zwierzycki, M., Tserkovnyak, Y., Kelly, P.J., *et al*. (2005). First-principles study of magnetization relaxation enhancement and spin transfer in thin magnetic films. *Physical Review B*, **71**, 064420.

Phase Transitions and Finite Temperature Magnetism: Experiment and Analysis

Sharika Nandan Kaul
University of Hyderabad, Hyderabad, India

1 INTRODUCTION

In magnetic insulator compounds (e.g., transition metal oxides) and the majority of rare earth metals, atomic magnetic moments are localized at lattice sites and have integral magnitudes (amplitudes) that are temperature independent. While superexchange interactions (usually antiferromagnetic in nature) couple magnetic moments in the former type of materials, indirect exchange interaction mediated by conduction electrons performs this function in rare earth metals. Within the framework of the Heisenberg model, the magnetic ground state of the system is determined by the sign of the interatomic exchange interaction constant, J, and the range of exchange interactions. For instance, in the ground state, spins on all the lattice sites are ferromagnetically (antiferromagnetically or ferrimagnetically) coupled in a three-dimensional Heisenberg system with short-range exchange interactions when $J > 0$ ($J < 0$). The Heisenberg (localized-spin) model and the generalizations thereof that make allowance for magnetic anisotropies (of either dipolar or spin-orbit plus crystal-field origin) adequately describe the ground state as well as finite temperature properties of the localized moment systems. In this model, the only form of collective excitations is the thermally excited propagating transverse spin fluctuations (spin waves) which have a small energy dispersion and fill the entire Brillouin zone.

By contrast, the electrons responsible for magnetism in transition metals, alloys, and intermetallic compounds are itinerant and have delocalized wave functions that are phase coherent over large distances at very low temperatures. At every atomic site, the magnetic moment originates from a spin splitting of the d-electron bands owing to the intra-atomic exchange interaction. The typical time, t_q, for a 3d electron to hop from one lattice site to the other is of the order of $t_q \approx h/W \approx 10^{-15}$s, where W is the bandwidth. As a result of the electron hopping, even in the ground state the magnetic moment has very fast quantum fluctuations and hence does not have a constant magnitude. An experiment with a 'time window' larger than t_q will average over the quantum fluctuations and measure the average magnetic moment per atom (or equivalently, 'atomic moment') which is necessarily nonintegral in magnitude. At low temperatures, the spin-flip excitation spectrum consists of single-particle excitations and collective excitations. Spin-up holes and spin-down electrons, created by intra-atomic spin-flip transitions of electrons from a spin-up band to a spin-down band (as sketched in Figure 1(a) and (b) for weak and strong itinerant-electron ferromagnets) and moving independent of one another in a common mean (exchange) field, constitute the single-particle excitations.

Handbook of Magnetism and Advanced Magnetic Materials. Edited by Helmut Kronmüller and Stuart Parkin. Volume 1: *Fundamentals and Theory*. ISBN: 978-0-470-02217-7.

Such excitations form the Stoner continuum, which, at finite momentum transfer q, extends from $E_q = 0$ in Figure 1(a) ($E_q = \Delta' = E_F$(Fermi energy) $- E_\uparrow^{top}$ in Figure 1b) to high energies, as schematically depicted in Figure 2(a) and (b) for weak (strong) itinerant-electron ferromagnets. Single-particle excitations with zero momentum transfer ($q = 0$) cost an energy equal to the exchange splitting Δ (Figure 2). The transfer of an electron–hole pair excitation, which results from a spin flip on an atom, from atom to atom gives rise to spin-wave excitations (Figure 3). The typical spin-wave energy is nearly 2 orders of magnitude smaller than the bandwidth and hence the timescale associated with this energy is $t_{sw} \approx 10^{-13}$s. In itinerant-electron ferromagnets, spin waves exist as well-defined collective excitations only in the small q and small $E_q = \hbar\omega_q$ region in the Brillouin zone (Figure 2), where the Stoner single-particle excitations require high energies of the order of intra-atomic exchange splitting $\Delta = I(n_\uparrow - n_\downarrow)$; I is the intra-atomic exchange interaction and $n_\uparrow(n_\downarrow)$ is the population of the spin-up (spin-down) band (Figures 1 and 3). As the momentum transfer q increases from zero, the energy gap between the Stoner continuum and spin-wave spectrum reduces rapidly such that beyond a certain threshold value of $q = q_{SB}$, the spin-wave dispersion curve enters the Stoner continuum. For $q > q_{SB}$, the spin

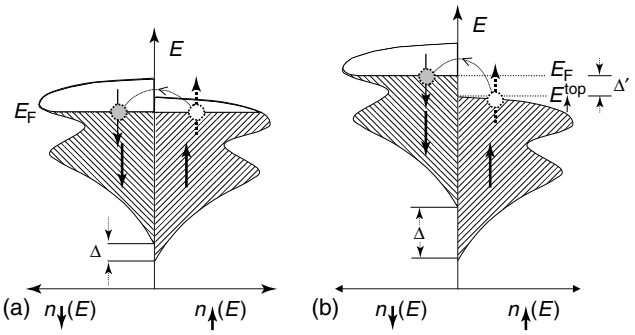

Figure 1. Schematic representation of a spin-flip Stoner single-particle excitation in a (a) weak itinerant-electron ferromagnet and (b) strong itinerant-electron ferromagnet.

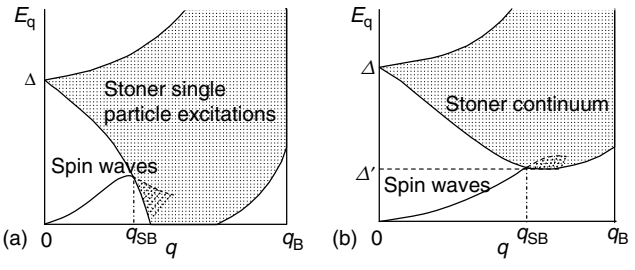

Figure 2. Schematic representation of magnetic dispersion and magnetic excitations in a (a) weak itinerant-electron ferromagnet and (b) strong itinerant-electron ferromagnet.

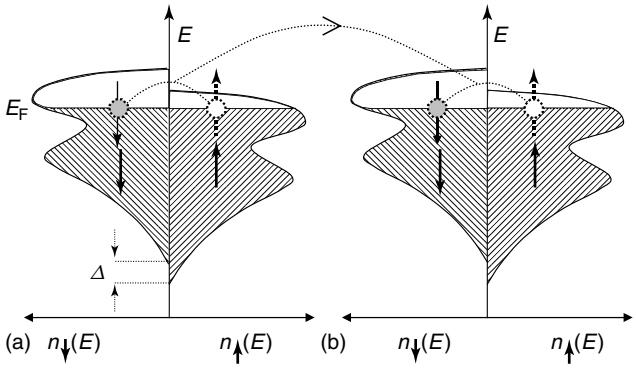

Figure 3. Schematic representation of a spin-wave excitation in a weak itinerant-electron ferromagnet.

waves get damped with the result that the collective magnetic excitations in the Stoner continuum are the overdamped (nonpropagating) modes of exchange-enhanced longitudinal and transverse spin-density fluctuations (Figure 2). For spin fluctuations of given q, in the longitudinal mode, the magnetic moments point in the same direction but their amplitude fluctuates from one lattice site to the other, whereas in the transverse mode, amplitude of the magnetic moments remains nearly constant while their direction varies from site to site. Since spin-wave modes of larger and larger q are excited as the temperature is raised from $T = 0$, the transition at $q = q_{SB}$ from well-defined spin waves to nonpropagating exchange-enhanced transverse spin fluctuations should be observed at a certain finite value of temperature. By contrast, the thermally excited nonpropagating exchange-enhanced longitudinal spin-density fluctuations persist down to $q = 0$ and coexist with, but are swamped by, spin waves for $q \leq q_{SB}$. A detailed description of the nature of magnetic excitations in different systems and their experimental determination is furnished in Section 2.

A phase transition from a magnetically ordered state to a magnetically disordered (paramagnetic) state occurs at a well-defined temperature when critical fluctuations of the order parameter (spontaneous magnetization) get correlated over distances of the order of the system size. At the critical point, spin waves in localized-spin systems and nonpropagating longitudinal as well as transverse spin-density fluctuations in weak itinerant-electron systems destroy long-range magnetic order. The rudiments of thermally driven phase transitions and critical phenomena as well as the intricacies in the data analyses are dealt with at length in Section 3.

For a detailed theoretical background to the nature of magnetic excitations and phase transitions in Heisenberg (localized-spin) and band (itinerant-electron) magnets, the reader is referred to Gautier (1982), Moriya (1985), Capellmann (1987), Barbara, Gignoux and Vettier (1988), Callaway (1991), Yosida (1996), and Mohn (2003), see also

Spin Waves: History and a Summary of Recent Developments, Volume 1 and **Theory of Magnetic Phase Transitions, Volume 1**.

2 MAGNETIC EXCITATIONS

As the temperature of the spin system is raised from very low temperatures, different types of magnetic excitations become important, in the following sequence, in different temperature regimes till the critical point is reached at which the long-range magnetic order is completely destroyed and a phase transition to the magnetically disordered (paramagnetic) state occurs.

2.1 Propagating transverse spin fluctuations (spin waves)

In a wide variety of spin systems regardless of whether they are crystalline or amorphous, insulating (localized-electron) or metallic (itinerant-electron), ferromagnetic or antiferromagnetic, or even ferrimagnetic, spin waves exist as well-defined low-lying (in energy) collective magnetic excitations from the ground state. Spin-wave excitations, involving energy transfers typically of the order of 100 meV, are amenable to direct detection in the inelastic neutron-scattering (INS) experiments on bulk samples.

If z axis is chosen as the spin quantization direction, the partial differential cross-section for the inelastic (*inel*) scattering of unpolarized thermal neutrons due to the magnetic interaction between neutron spin and the spins of unpaired electrons, localized at the lattice sites of a system of N atoms, is given by Squires (1978), Lovesey (1987), and Stirling and McEwen (1987)

$$\left(\frac{\mathrm{d}^2\sigma}{\mathrm{d}\Omega \mathrm{d}E}\right)_{\text{inel}} = \left(\frac{\gamma e^2}{m_e c^2}\right)^2 \frac{k'}{k}\left\{\frac{1}{2}\, g\, F(\mathbf{Q})\right\}^2 \times e^{-2W(\mathbf{Q})}\, \frac{N}{\pi (g\mu_B)^2}\, [1 + n(\omega)] \times \Big[(1 - \hat{\mathbf{Q}}_z^2)\, \mathrm{Im}\chi_{||}(\mathbf{Q}, \omega) + (1 + \hat{\mathbf{Q}}_z^2)\, \mathrm{Im}\chi_{\perp}(\mathbf{Q}, \omega)\Big] \quad (1)$$

In this equation, $\mathbf{k}$ and $\mathbf{k}'$ are the wave vectors of the incident and scattered neutrons, $\mathbf{Q} = \mathbf{k} - \mathbf{k}'$, $\hat{\mathbf{Q}}_z$ is the z component of the unit vector $\hat{\mathbf{Q}} = \mathbf{Q}/|\mathbf{Q}|$, $F(\mathbf{Q})$ and $e^{-2W(\mathbf{Q})}$ are the form factor and the Debye–Waller factor, respectively, for the magnetic lattice, $E = \hbar\omega = (\hbar^2/2m_n)(k^2 - k'^2)$ is the energy transfer, $n(\omega) = [\exp(\hbar\omega/k_B T) - 1]^{-1}$ is the Bose function, $\mathrm{Im}\chi_{||}(\mathbf{Q}, \omega)$ and $\mathrm{Im}\chi_{\perp}(\mathbf{Q}, \omega)$ are the imaginary parts of the longitudinal (i.e., along the direction of magnetization (z axis)) and transverse (i.e., perpendicular to z axis) wave-vector- and frequency-dependent magnetic susceptibilities and the remaining symbols have their usual meaning. In equation (1), the inelastic scattering cross-section is the sum of longitudinal and transverse contributions. At low temperatures, where the linear spin-wave approximation holds and the spin-wave linewidths are negligible, the longitudinal part of the cross section leads (Squires, 1978; Lovesey, 1987) only to elastic scattering, whereas the transverse part takes the form (Squires, 1978; Lovesey, 1987; Stirling and McEwen, 1987):

$$\left(\frac{\mathrm{d}^2\sigma}{\mathrm{d}\Omega \mathrm{d}E}\right)^{\perp}_{\text{inel}} = \left(\frac{\gamma e^2}{m_e c^2}\right)^2 \frac{k'}{k}\left\{\frac{1}{2}\, g\, F(\mathbf{Q})\right\}^2 \times e^{-2W(\mathbf{Q})}\, (1 + \hat{\mathbf{Q}}_z^2)\, \frac{S}{2}\, \frac{(2\pi)^3}{v_0} \times \sum_{\mathbf{q},\boldsymbol{\tau}} \Big\{(n_{\mathbf{q}} + 1)\, \delta(E_{\mathbf{q}} - E)\, \delta(\mathbf{Q} - \mathbf{q} - \boldsymbol{\tau}) + n_{\mathbf{q}}\, \delta(E_{\mathbf{q}} + E)\, \delta(\mathbf{Q} + \mathbf{q} - \boldsymbol{\tau})\Big\} \quad (2)$$

where $n_{\mathbf{q}} = [\exp(\hbar\omega_{\mathbf{q}}/k_B T) - 1]^{-1}$ is the (Boson) occupation factor for the magnons (spin waves) of wave vector $\mathbf{q}$ and energy $E_{\mathbf{q}} = \hbar\omega_{\mathbf{q}}$, $(2\pi)^3/v_0$ is the volume of a unit cell in the reciprocal lattice and $\boldsymbol{\tau}$ is the reciprocal-lattice vector. The first (second) term in the inelastic scattering cross-section corresponds to the creation (annihilation) of an infinite-lifetime magnon and the consequent neutron energy loss (gain). Note that the expression for the transverse inelastic cross section for the scattering of neutrons by spin waves in an itinerant-electron ferromagnet bears a striking similarity (Lovesey, 1987) with equation (2), which is valid for a Heisenberg ferromagnet. Since both momentum- and energy-conservation conditions govern the creation or annihilation of a magnon, the INS experiments provide a direct means of determining the whole spin-wave spectrum (dispersion). Obviously, creation of magnons is favored over annihilation at low temperatures ($k_B T \ll \hbar\omega$). At higher temperatures, dynamic magnon–magnon interactions become important and broaden the spin-wave peaks. In order to fit the constant-q INS scans, the spectral weight function $F_{\perp}(\mathbf{Q}, \omega)$ in the expression $\mathrm{Im}\chi_{\perp}(\mathbf{Q}, \omega) = \pi\omega\, \chi_{\perp}(\mathbf{Q})\, F_{\perp}(\mathbf{Q}, \omega)$ (where $\chi_{\perp}(\mathbf{Q})$ is the static wave vector–dependent susceptibility), and hence in equation (2) via equation (1), is often approximated by either a double Lorentzian (DL)

$$F_{\perp}^{\mathrm{DL}}(\mathbf{q}, E) = \frac{1}{2\pi}\left[\frac{\Gamma_{\mathbf{q}}}{(E - E_{\mathbf{q}})^2 + \Gamma_{\mathbf{q}}^2} + \frac{\Gamma_{\mathbf{q}}}{(E + E_{\mathbf{q}})^2 + \Gamma_{\mathbf{q}}^2}\right] \quad (3)$$

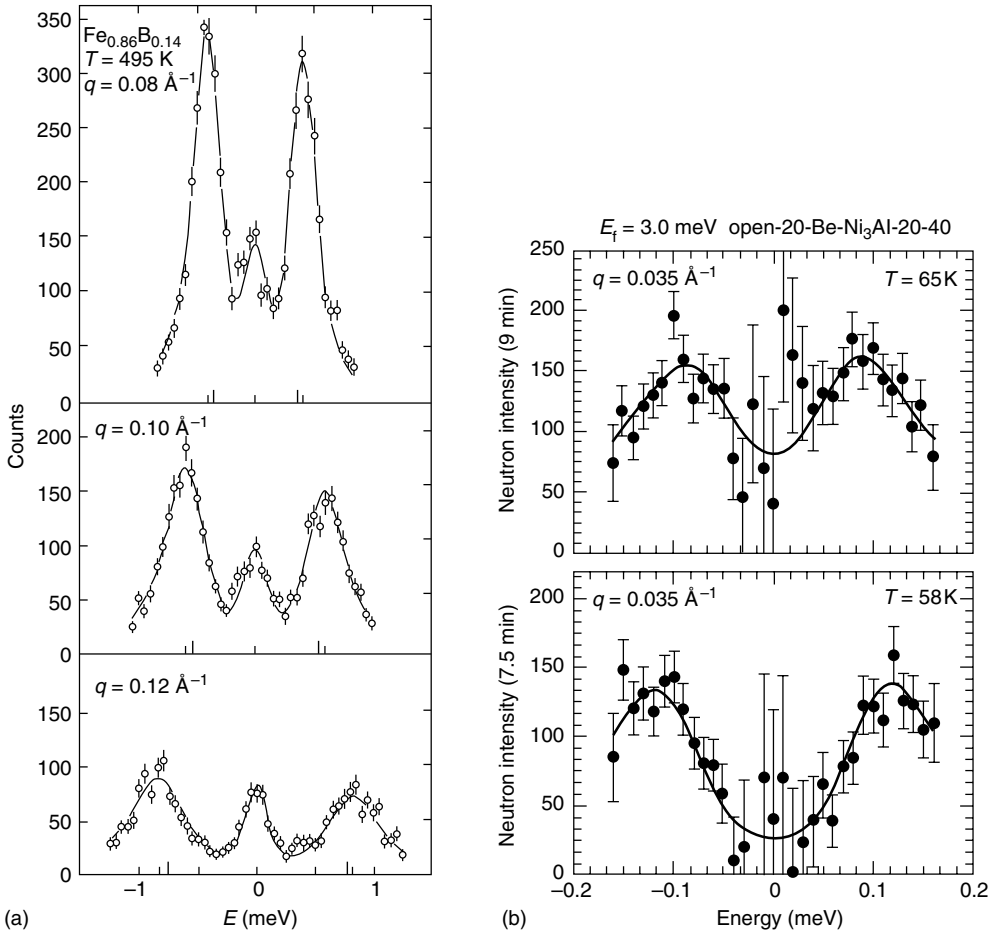

Figure 4. Constant-q scans for (a) amorphous $Fe_{86}B_{14}$ at $q = 0.08$, 0.10, and $0.12\,\text{Å}^{-1}$ and $T = 495\,\text{K}$ and (b) the weak itinerant-electron ferromagnet Ni_3Al at $q = 0.035\,\text{Å}^{-1}$ and $T = 58\,\text{K}$ ($0.8T_C$), 65 K ($0.9T_C$). The solid curves denote the least-squares fits based on equation (3).

or a damped-harmonic-oscillator (DHO) form

$$F_{\perp}^{\text{DHO}}(\mathbf{q}, E) = \frac{1}{\pi} \frac{\Gamma_{\mathbf{q}}(E_{\mathbf{q}}^2 + \Gamma_{\mathbf{q}}^2)}{[(E - E_{\mathbf{q}})^2 + \Gamma_{\mathbf{q}}^2][(E + E_{\mathbf{q}})^2 + \Gamma_{\mathbf{q}}^2]} \quad (4)$$

where $\Gamma_{\mathbf{q}}$ is the $\mathbf{q}$-dependent half-width at half-maximum (HWHM) of the spin-wave peak. Figure 4(a) (taken from Fernandez-Baca, Lynn, Rhyne and Fish, 1987) and 4(b) (taken from Semadeni *et al*., 2000), pertaining, respectively, to the amorphous Invar alloy $Fe_{86}B_{14}$ (which behaves as a Heisenberg ferromagnet but the canonical examples of such a ferromagnet are EuO and EuS) and the well-known weak itinerant-electron ferromagnet Ni_3Al, serve to illustrate as to how the magnon dispersion for a ferromagnet is measured in an INS experiment. In Figure 4, (i) the spin-wave excitations manifest themselves as inelastic peaks centered at $\pm E_{\mathbf{q}}$ (on either side of the elastic peak centered at $E = 0$) in the neutron-scattering intensity versus the energy transfer E isotherm taken at a fixed value of q, (ii) the continuous curves in Figure 4 are the theoretical fits obtained by assuming that the spectral weight function in the transverse (longitudinal) part of the cross section in equation (1) can be approximated by equation (3) (a δ function centered at $E = 0$ in Figure 4a) and treating $E_{\mathbf{q}}$ and $\Gamma_{\mathbf{q}}$ as free parameters, (iii) $E_{\mathbf{q}}$ and $\Gamma_{\mathbf{q}}$ corresponding to different values of q are thus directly obtained from the constant-q scans taken at a given temperature while their temperature variations, $E_{\mathbf{q}}(T)$ and $\Gamma_{\mathbf{q}}(T)$, are determined from the constant-q scans taken at different temperatures. Details about the INS determination of the spin-wave spectrum in a wide variety of magnetic systems are given in Stirling and McEwen (1987), Tomiyoshi *et al*. (1987), Mook (1988), Lynn and Rhyne (1988), Shapiro (1988), and Fernandez-Baca *et al*. (1990); see also **X-ray and Neutron Scattering by Magnetic Materials, Volume 1** and **Spin Structures and Spin Wave Excitations, Volume 3**.

Regardless of the nature (localized or itinerant) of magnetic electrons, the spin-wave dispersion relation has the form

$$E_{\mathbf{q}}(T) = \hbar\omega_{\mathbf{q}}(T) = \Delta_{\mathrm{SW}} + D(T)q^2(1 - \beta q^2) \qquad (5)$$

where Δ_{SW} is an effective energy gap in the spin-wave spectrum originating from dipole–dipole interactions, magnetic anisotropy, and external magnetic field (if present) and the spin-wave stiffness, D, renormalizes with temperature according to the relation

$$D(T) = D(0)(1 - D_2\,T^2 - D_{5/2}\,T^{5/2}) \qquad (6)$$

for both localized-electron (Izuyama and Kubo, 1964; Keffer, 1966) and itinerant-electron (Izuyama and Kubo, 1964; Mathon and Wohlfarth, 1968) models. Within the framework of the Heisenberg model, the T^2 term is appreciable only when the localized spins interact with one another via the spin of conduction electrons and this term is normally several orders of magnitude smaller than the $T^{5/2}$ term, which arises from the magnon–magnon interactions. By contrast, the T^2 term in the band model results from the interaction between spin waves and single-particle excitations and dominates over the $T^{5/2}$ term, which originates from the magnon–magnon interactions, as in the localized-electron case. Thus, the expressions $D(T) = D(0)(1 - D_2\,T^2)$ and $D(T) = D(0)(1 - D_{5/2}\,T^{5/2})$ essentially denote the variation of the spin-wave stiffness with temperature for the itinerant- and localized-electron models, respectively. These models also make specific predictions about the functional dependence of $\Gamma_{\mathbf{q}}$ on q. In the long-wavelength ($q \to 0$) limit, equation (5) reduces to $E_{\mathbf{q}}(T) = D(T)\,q^2$ for an isotropic ferromagnet in the absence of external magnetic field. In the limit as $q \to 0$, $E_{\mathbf{q}}(T) \propto q^2$ ($E_{\mathbf{q}}(T) \propto q$) for a ferrimagnet (antiferromagnet).

By virtue of the fact that the INS experiments directly determine $E_{\mathbf{q}}(q, T)$ (and hence $D(T)$) and $\Gamma_{\mathbf{q}}(q, T)$, the INS technique is the most powerful experimental tool for clearly distinguishing between the localized and band models (and thereby reveal the exact nature of magnetic electrons) by unambiguously verifying their predictions concerning the thermal renormalization of spin-wave stiffness, $D(T)$, and the variations of spin-wave linewidth with q and temperature, $\Gamma_{\mathbf{q}}(q, T)$. This is particularly true when spin waves fill the entire Brillouin zone and the spin-wave dispersion falls within the energy transfer range covered in the INS experiments (as is the case for Heisenberg ferromagnets). However, the INS technique suffers from a number of drawbacks. First, owing to very weak interaction of neutrons with matter, this method has the required sensitivity only for bulk samples or large multilayer systems. Second, it fails to detect other excitations accompanying spin waves. For instance, in those amorphous ferromagnets or Invar systems that have a noncollinear ground-state arrangement of local magnetic moments (caused by a strong competition between the ferromagnetic and antiferromagnetic interactions), the diffusive modes ('diffusons') associated with the longitudinal spin fluctuations contribute to the $T^{3/2}$ decrease of magnetization as significantly as the propagating transverse spin fluctuations (spin waves) do (Continentino and Rivier, 1979; Valiev and Menshikov, 1995; Kaul, 1999). Unlike spin waves, the diffusons show up as the central (elastic) peak (which already contains contributions from small-angle and incoherent scattering from the sample and its environment) in the constant-q INS scans. It is, therefore, not possible to resolve this component from the nuclear scattering. Further complication arises when the coupling between the longitudinal spin fluctuations and the spin-wave modes gives rise to inelastic peaks that are centered at the spin-wave energies (Vaks, Larkin and Pikin, 1968), besides a much smaller central peak corresponding to spin diffusion. Third, the limited range of energy transfer accessible to the INS experiments does not permit a simultaneous detection of spin waves and (high energy) Stoner single-particle excitations, which are present in itinerant-electron ferromagnets. The first and third limitations of the INS method have been overcome in a relatively new experimental technique called the *spin-polarized electron-energy-loss spectroscopy* (SPEELS). In this experiment, the spin-polarized incident electron beam of fixed energy gets scattered from the surface of an itinerant-electron ferromagnet and spin polarization of the scattered beam is measured as a function of the energy loss suffered by the electrons during the scattering process. Recognizing that the energy loss is mainly due to the exchange scattering from electron–hole pair excitations, this technique directly probes the Stoner single-particle (spin-flip or non-spin-flip) excitations (Venus and Kirschner, 1988; Penn and Apell, 1988; Abraham and Hopster, 1989). SPEELS, with considerably improved energy resolution, has recently enabled observation of large wave vector ($\cong 1\,\text{Å}^{-1}$) and large energy ($\cong 250\,\text{meV}$) spin waves in ultrathin Fe or Co films (Plihal, Mills and Kirschner, 1999; Vollmer *et al*., 2003, 2004; see also **High-energy Surface Spin Waves Studied by Spin-polarized Electron Energy Loss Spectroscopy, Volume 3**). Like SPEELS, the ferromagnetic resonance and Brillouin light scattering techniques are extremely powerful surface-sensitive experimental tools but they can detect spin waves of small wave vector ($\leq 0.01\,\text{Å}^{-1}$) only. As far as the second limitation is concerned, a comparison of the value of spin-wave stiffness at 0 K, directly determined from the INS experiments, $D_n(0)$, with that, $D_m(0)$, deduced from the magnetization measurements, reveals the existence or absence of the concomitant excitations and gives important clues about the nature of such excitations (Kaul, 1984a). This calls for high-resolution magnetization measurements and an elaborate data analysis, as elucidated in the following text.

The decline in magnetization, $M(T, H)$, due to the thermally excited long-wavelength spin-wave excitations at temperature, T, and external magnetic field, H, for Heisenberg (Keffer, 1966) as well as band (Kaul, 1999, 2005) ferromagnets is given by

$$M(T, H) = M(0, H) - g\mu_B \int_0^\infty \frac{n_{SW}(\omega)\, d\omega}{e^{(\hbar\omega + g\mu_B H_{eff})/k_B T} - 1} \tag{7}$$

In equation (7), the magnon density of states, $n_{SW}(\omega)$, and the effective field, H_{eff}, have the forms

$$n_{SW}(\omega) = \frac{1}{4\pi^2}\left(\frac{\hbar}{D(T)}\right)^{3/2} \omega^{1/2} \tag{8}$$

and $H_{eff} = H - H_D + H_L + H_A$ with H_D, H_L, and H_A representing the demagnetizing, Lorentz, and anisotropy fields, respectively, while the magnon (Bose) occupation factor makes use of the spin-wave dispersion relation, equation (5), but with $\beta = 0$ (i.e., $\hbar\omega(T) = D(T)\, q^2$) and $\Delta_{SW} = g\mu_B H_{eff}$. In a more general case, where the Bose factor in equation (7) is replaced by $[\exp\{\hbar\omega_{\mathbf{q}}(T)/k_B T\} - 1]^{-1}$ (with $\hbar\omega_{\mathbf{q}}(T)$ given by equation (5)) and $n_{SW}(\omega)$ by $n_{SW}(\omega_{\mathbf{q}})$, and both spin-wave (SW) and Stoner single-particle (SP) excitations contribute to the fractional decrease in magnetization, defined as $\Delta m(T, H) \equiv [M(0, H) - M(T, H)]/M(0, H)$, $\Delta m(T, H)$ has the functional form (Thompson, Wohlfarth and Bryan, 1964; Keffer, 1966)

$$\Delta m(T, H) = \Delta m_{SW}(T, H) + \Delta m_{SP}(T, H) \tag{9}$$

$$\Delta m_{SW}(T, H) = \frac{g\mu_B}{M(0, H)}\left[Z(3/2, t_H)\left(\frac{k_B T}{4\pi D(T)}\right)^{3/2} + 15\pi\beta\, Z(5/2, t_H)\left(\frac{k_B T}{4\pi D(T)}\right)^{5/2}\right] \tag{10}$$

$$\Delta m_{SP}(T, H) = A'(H) T^{3/2} \exp(-\Delta_{SP}/k_B T)$$

for a strong itinerant-electron ferromagnet

$$= A(H) T^2$$

for a weak itinerant-electron ferromagnet

(11)

In equation (10), the Bose–Einstein integral functions $Z(s, t_H) = \sum_{n=1}^{\infty} n^{-s} \exp(-nt_H)$ and $t_H = g\mu_B H_{eff}/k_B T$ allow for the extra energy gap $g\mu_B H_{eff} (= \Delta_{SW} = k_B T_g)$ in the spin-wave spectrum arising from the effective field that the spins experience within the sample, and the $T^{3/2}$ ($T^{5/2}$) term has its origin in the q^2 (q^4) term in the spin-wave dispersion relation, equation (5). Taking cognizance of the theoretical prediction that $D(T)$ in equation (10) varies as T^2 or $T^{5/2}$ for band or Heisenberg ferromagnets, it is obvious from the expressions (10) and (11) that magnetization is expected to be a smoothly varying function of temperature that may include $T^{3/2}$, T^2, $T^{5/2}$, $T^{7/2}$, and exponential terms. An unambiguous determination of the spin-wave and single-particle contributions is, therefore, not possible unless the magnetization is measured with extremely high precision and an elaborate data analysis is carried out. This strategy has been successfully implemented, and has yielded several interesting results, in a number of systems that include Fe and Ni (Ododo and Anyakoha, 1983), crystalline (Nakai, 1983, 1990; Nakai, Ono and Yamada, 1983; Nakai and Maruyama, 1992), and amorphous (Kaul, 1983; Yamada *et al.*, 1986; Nakai *et al.*, 1987; Kaul and Babu, 1994a, 1998; Semwal and Kaul, 1999, 2004) Invar alloys. For instance, from a reanalysis of the already published magnetization data on Fe and Ni, Ododo and Anyakoha (1983) concluded that (i) at low temperatures ($T \leq 0.4T_C$), besides the dominant spin-wave contribution, Stoner non-spin-flip single-particle excitations rather than their spin-flip counterpart significantly contribute to thermal demagnetization in both Fe and Ni, and (ii) a gap between the 'acoustic' and 'optical' branches in the spin-wave dispersion spectrum of Ni occurs at the wave vector $q_{co} = 0.47 \pm 0.01$ Å^{-1} and energy $E_{co} = 120 \pm 6$ meV, and predicted a similar gap between the 'acoustic' and 'optical' magnon branches at $q_{co} = 0.74 \pm 0.02$ Å^{-1} and $E_{co} = 166 \pm 10$ meV in Fe. While the SPEELS (Venus and Kirschner, 1988; Penn and Apell, 1988; Abraham and Hopster, 1989) experiments on Fe and Ni, and INS experiments (Mook and Paul, 1985) on Ni, later confirmed the findings (i) and (ii), the prediction of a gap in the spin-wave spectrum of Fe has found firm support in the recent many-body calculations (Karlsson and Aryasetiawan, 2000). Similarly, in conformity with the results of the magnetoresistance (Kaul and Rosenberg, 1983), spin-polarized photoemission (Hopster *et al.*, 1985), Compton scattering (Anderjczuk *et al.*, 1992), and spin-polarized INS (Lynn, Rosov and Fish, 1993) measurements, an extensive analysis of high-resolution magnetization data (Kaul and Babu, 1994a) reveals that all the compositions in the amorphous $(Fe_pNi_{1-p})_{80}$ $(B,Si)_{20}$ alloy series behave as weak itinerant-electron ferromagnets, while a transition from weak to strong itinerant ferromagnetism occurs at $p \cong 0.75$ in the amorphous $(Fe_pNi_{1-p})_{80}P_{14}B_6$ alloys and that propagating longitudinal spin fluctuations make as significant a contribution to the $T^{3/2}$ decrease of magnetization as their transverse counterpart (spin waves) does for the compositions $p > 0.75$ in both the alloy series. An example (Semwal and Kaul, 1999, 2004), shown in Figure 5, serves to illustrate (see the deviation plots in the lower panel) that at temperatures $T \leq 0.24T_C$ (where T_C is the Curie temperature) spin waves (manifesting themselves as $M(T) \sim T^{3/2}$) swamp the contributions to magnetization arising from both Stoner single-particle ($M(T) \sim T^2$) and nonpropagating collective electron–hole pair ($M^2(T) \sim T^2$; for details,

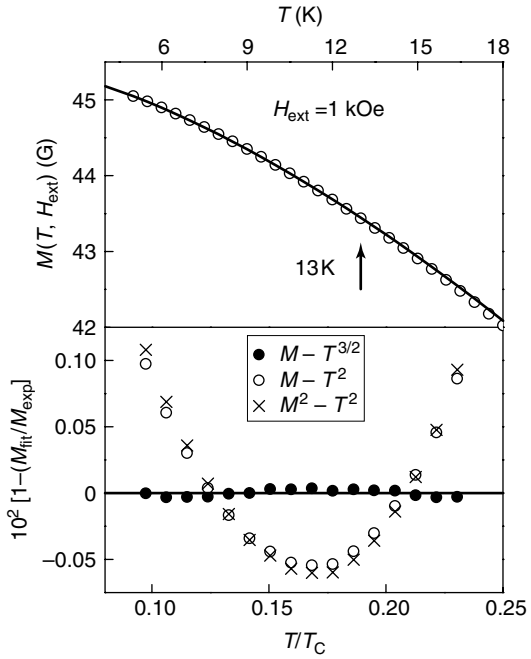

Figure 5. The upper panel depicts the temperature variation of magnetization measured at an external magnetic field of $H_{ext} = 1$ kOe for the weak itinerant-electron ferromagnet Ni_3Al at low temperatures and the continuous curve is the least-squares fit based on equation (10). The lower panel displays the percentage deviation of the data from the least-squares fits based on equations (10) and (11). Notice that the functional form given by equation (10) yields minimum deviations.

see Section 2.3) excitations in the weak itinerant-electron ferromagnet Ni_3Al. Furthermore, the observation (Semwal and Kaul, 1999) that $D_n(0) = D_m(0)$, within the uncertainty limits, permits the conclusion that no diffusons are present in this material.

2.2 Magnon-fracton crossover

Understanding the nature of quantized excitations in fractal networks, the crossover between extended (phonon, magnon) and strongly localized (fracton) excitations, and the effect of this crossover on thermodynamic and transport properties of random physical systems, continues to be a fascinating subject (Nakayama, Yakubo and Orbach, 1994). Alexander and Orbach (1982) determined the density of states and the dispersion relation for vibrational excitations of D_f-dimensional fractal network. They termed such excitations as fractons and conjectured that the *fracton dimensionality* $\tilde{d}_f = 4/3$ for percolation networks with Euclidean dimension $d \geq 2$. One of the well-known realizations of a self-similar (fractal) network is a quenched random site–diluted Heisenberg magnet with the concentration of magnetic atoms (p) near the percolation threshold (p_c). At $p = p_c$, an infinite magnetic cluster first appears (i.e., for $p < p_c$, only finite magnetic clusters are present and no long-range magnetic order exists even for temperatures as low as $T \approx 0$ K), and the percolation correlation length at $T = 0$ K, $\xi_0(p)$, diverges in accordance with the relation (Stauffer and Aharony, 1992)

$$\xi_0(p) = \xi_p (p - p_c)^{-\nu_p} \tag{12}$$

The divergence in $\xi_0(p) \equiv \xi(T = 0, p)$ induces a crossover in the dynamics of Heisenberg spins from hydrodynamic (magnon) behavior for $q\xi < 1$ to critical (fracton) behavior for $q\xi > 1$, where q is the inverse wavelength of spin waves in the hydrodynamic regime and the inverse characteristic length of the localized fracton modes in the critical regime. Change from Euclidean dimension, d, to *fractal dimension*, D_f, causes a crossover in the dispersion relation and the density of states from their long-wavelength (low-frequency, $\omega \ll \omega_{co}$) magnon forms to short length scale (high-frequency, $\omega \gg \omega_{co}$) magnetic fracton forms at a characteristic frequency ω_{co}. Such a crossover has a profound effect on those static thermal properties that are directly related to the excitation of spin waves such as magnetization and specific heat. The dilution-induced hydrodynamic-to-critical crossover in the dynamics of Heisenberg spins on a percolation network and the consequent crossover in the thermal behavior of magnetization for concentrations just above the percolation threshold, has been theoretically studied by Stinchcombe and Pimentel (1988). This crossover is, however, distinctly different from the usual thermal-to-percolation crossover (Stauffer and Aharony, 1992) which occurs when the thermal fluctuations of the order parameter become critical at a concentration-dependent temperature $T_C(p)$, as the percolation critical point $Q(p = p_c, T = 0)$ is approached by reducing the temperature to zero at fixed values of p with $p \to p_c$ in the $T - p$ diagram (Figure 6). For a given concentration, p, of the magnetic atoms, $T_C(p)$ is the temperature at which a transition from a magnetically disordered (paramagnetic) state to a magnetically ordered (ferromagnetic, antiferromagnetic, or ferrimagnetic) state occurs when the temperature is lowered from high temperatures.

In its most general scaling form, the density of vibrational states of a percolating network for $p > p_c$ is given by (Aharony, Alexander, Entin-Wohlman and Orbach, 1985; Aharony, Entin-Wohlman, Alexander and Orbach, 1987)

$$N(\omega) = A\,\omega^{x-1} f(\omega/\omega_{co}) \tag{13}$$

where x is the *fracton* dimensionality whose explicit expression depends on the particular fractal model chosen, ω_{co} is the frequency at which a crossover from hydrodynamic (phonon or magnon) regime to the critical (fracton) regime occurs,

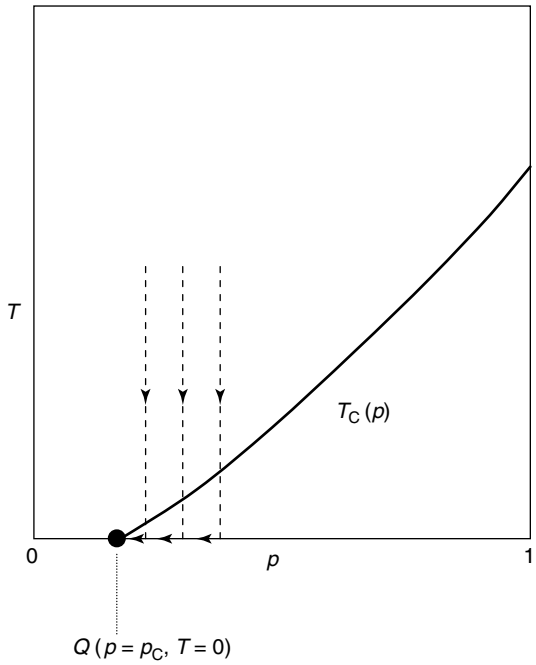

Figure 6. Schematic $T - p$ phase diagram in which the arrows depict the path through which the percolation critical point $Q(p = p_C, T = 0)$ is approached by reducing temperature to zero at fixed values of the concentration, p, of the magnetic atoms for p just above the percolation threshold, p_C. This diagram also roughly sketches a typical thermal-to-percolation crossover line, $T_C(p)$.

and A is a constant independent of ω_{co}. The scaling function in equation (13) has the asymptotic limits $f(z) \to 1$ as $z \to \infty$ and $f(z) \to z^{d'-x}$ as $z \to 0$ so that (Aharony, Alexander, Entin-Wohlman and Orbach, 1985; Aharony, Entin-Wohlman, Alexander and Orbach, 1987)

$$N_{hy}(\omega) = A\,\omega_{co}^{x-d'}\,\omega^{d'-1} \tag{14}$$

in the hydrodynamic ($\omega \ll \omega_{co}$) limit and

$$N_{cr}(\omega) = A\,\omega^{x-1} \tag{15}$$

in the critical ($\omega \gg \omega_{co}$) limit. In the case of magnon–fracton crossover, the fracton dimensionality x and the dimension d' are $x = \tilde{d}_f/2$ and $d' = d/2$. Salamon and Yeshurun (1987) suggested an expression for the effective density of states, $n_{eff}(\omega)$, in $d = 3$ percolating ferromagnetic networks that is supposed to be valid not only in the magnon and fracton regimes but also in the entire crossover region. Early attempts (Salamon and Yeshurun, 1987; Yeshurun and Salamon, 1987; Zadro, 1996) to experimentally determine the fracton contribution to $M(T)$ in site-diluted amorphous ferromagnets with $p \geq p_c$, based on this form of $n_{eff}(\omega)$, however, yielded widely different values for $\tilde{d}_f$. Subsequently, this discrepancy in the values of $\tilde{d}_f$ was traced to a number of major flaws (Kaul and Srinath, 2001) in both the form of the effective density of states and the data analysis used by Salamon and Yeshurun (1987) and Zadro (1996). The extensive investigations of ferromagnetic fractons in quenched random site–diluted ferromagnets (Kaul and Srinath, 2001; Kaul and Semwal, 2004) have completely got rid of these flaws by carrying out a thorough data analysis and by using the density of states of the form

$$n_{eff}(\omega) = \left(\frac{1}{4\pi^2}\right)\left[\frac{\hbar}{D(p)}\right]^{d/2}(p - p_c)^{\nu_p(D_f - d)} \times \omega^{(d/2)-1}\left(1 + \frac{\omega}{\omega_{co}}\right)^{(\tilde{d}_f - d)/2} \tag{16}$$

proposed by Kaul and Srinath (2001). Unlike the earlier (Salamon and Yeshurun, 1987) form of the density of states, equation (16) (i) yields the correct asymptotic forms (Aharony, Alexander, Entin-Wohlman and Orbach, 1985; Aharony, Entin-Wohlman, Alexander and Orbach, 1987; Stauffer and Aharony, 1992)

$$n_{SW}(\omega) = A'\,\omega_{co}^{(\tilde{d}_f - d)/2}\,\omega^{(d/2)-1} \tag{17}$$

and

$$n_{fr}(\omega) = A'\,\omega^{(\tilde{d}_f/2)-1} \tag{18}$$

with $A' = (1/4\pi^2)\{\hbar\omega_p^{[1-(\tilde{d}_f/d)]}/d_p\}^{d/2}$, in the magnon ($\omega \ll \omega_{co}$) (cf. equations (14) and (17)) and fracton ($\omega \gg \omega_{co}$) (cf. equations (15) and (18)) regimes, (ii) ensures a smooth crossover between the two regimes at $\omega = \omega_{co}$, and (iii) consistent with the theoretical predictions (Aharony, Alexander, Entin-Wohlman and Orbach, 1985; Aharony, Entin-Wohlman, Alexander and Orbach, 1987; Stauffer and Aharony, 1992) yields the ratio $n_{fr}(\omega_{co})/n_{SW}(\omega_{co})$, which is a constant independent of ω_{co} (i.e., the ratio is noncritical). In arriving at the equations (17) and (18), use has been made of the following relations (Nakayama, Yakubo and Orbach, 1994)

$$D(p) = d_p\,(p - p_c)^{2\nu_p[(D_f/\tilde{d}_f)-1]} \tag{19}$$

and

$$\omega_{co}(p) = \omega_p\,(p - p_c)^{2\nu_p D_f/\tilde{d}_f} \tag{20}$$

Note that for $d = 3$ equation (17) has the same form as equation (8). For computing magnetization at finite fields and temperatures with greater ease, an alternative form of

equation (16), given below, is preferred (Kaul and Srinath, 2001)

$$n_{\rm eff}(\omega) = \left(\frac{1}{4\pi^2}\right)\left[\frac{\hbar}{D(p)}\right]^{d/2}\left(\frac{m_p^*}{M_0(p)}\right) \times \omega^{(d/2)-1}\left(1+\frac{\omega}{\omega_{\rm co}}\right)^{(\tilde{d}_{\rm f}-d)/2} \quad (21)$$

This expression is obtained from equation (16) by using the relations (Stauffer and Aharony, 1992; Nakayama, Yakubo and Orbach, 1994)

$$D_{\rm f} = d - (\beta_{\rm p}/\nu_{\rm p}) \quad (22)$$

and

$$M_0(p) = m_{\rm p}^*\,(p-p_{\rm c})^{\beta_{\rm p}} = m_{\rm p}\,(p-p_{\rm c})^{\beta_{\rm p}} \times [1 + a\,(p-p_{\rm c})^{\Delta}] \quad (23)$$

The main steps involved in the data analysis are as follows. At first, employing the usual extrapolation (to $H = 0$) method, spontaneous magnetization at 0 K for each composition, $M_0(p) \equiv M(T = 0, p)$, is determined from the $M - H$ isotherm taken at the lowest possible temperature ($T_0 \cong 1$ K). The percolation critical exponent (amplitude), $\beta_{\rm p}\,(m_{\rm p})$, the 'correction-to-scaling' amplitude, a, and the percolation threshold, $p_{\rm c}$, (and hence the quantity $m_{\rm p}^*$) are determined from the best theoretical fit to the $M_0(p)$ data, based on equation (23), in which the 'correction-to-scaling' exponent Δ is fixed at its theoretically predicted value $\Delta = 1$ (Stauffer and Aharony, 1992) while $m_{\rm p}$, $p_{\rm c}$, $\beta_{\rm p}$, and a, are treated as free fitting parameters. Next, the magnetization $M(T, H)$ is calculated from equation (7) by replacing the magnon density of states, $n_{\rm SW}(\omega)$, with the effective density of states, $n_{\rm eff}(\omega)$, given by equation (21), and performing the integration over ω numerically. At any given field strength, the agreement between the observed and calculated values of M at different temperatures $T \le T_{\rm C}$ is optimized, at first, by keeping $\tilde{d}_{\rm f}$ fixed at values differing by 0.01 in the range $1.0 \le \tilde{d}_{\rm f} \le 2.0$ (which embraces the theoretically expected (Alexander and Orbach, 1982) value of $\tilde{d}_{\rm f} = 4/3$ for percolation networks with Euclidean dimension $d \ge 2$) and varying $M(0, H)$, D, and $\omega_{\rm co}$. A cross-check for a correct estimation of these parameters is provided by the stringent conditions that the above optimization process should yield the result $M(0, H) = M(T_0, H)$ (the value of magnetization corresponding to a given field measured at $T = T_0$) and $\tilde{d}_{\rm f}$ independent of both H and p. The values of $M(0, H)$ and $\tilde{d}_{\rm f}$, so obtained, are kept constant in the subsequent fits that involve only two parameters, D and $\omega_{\rm co}$. This procedure not only unravels the true functional form of the thermal renormalization of spin-wave stiffness, $D(T)$, and of the magnetic field dependence of magnon-to-fracton crossover frequency, $\omega_{\rm co}(H)$, but also yields accurate values for $D_0(p) \equiv D(T = 0, p)$, $\omega_{\rm co}(p) \equiv \omega_{\rm co}(p, 0) \equiv \omega_{\rm co}(p, H = 0)$, (and their corresponding percolation critical exponents) and $\tilde{d}_{\rm f}$ for $d = 3$ percolating ferromagnetic networks with the concentration of magnetic atoms, p, just above the percolation threshold, $p_{\rm c}$ (Kaul and Babu, 1994b; Kaul and Srinath, 2001; Kaul and Semwal, 2004).

$\omega_{\rm co}(p)$ permits determination of the temperature $T_{\rm co}^*(p) = \hbar\omega_{\rm co}(p)/k_{\rm B}$ at which the crossover from hydrodynamic regime to critical regime occurs. The locus of $T_{\rm co}^*$ values for different compositions in a given quenched random site-diluted ferromagnetic alloy series is the crossover line that divides the ferromagnetic (FM) phase into two regions (1) and (2) in the magnetic phase diagrams, as illustrated by the dashed curve shown in Figure 7 for the amorphous $(Fe_pNi_{1-p})_{80}B_{16}Si_4$ and $(Co_{p'}Ni_{1-p'})_{80}B_{16}Si_4$ alloys (Kaul and Srinath, 2001). In region (2), thermal demagnetization is solely due to hydrodynamic spin waves, whereas in region (1) both hydrodynamic and critical magnons (i.e.,

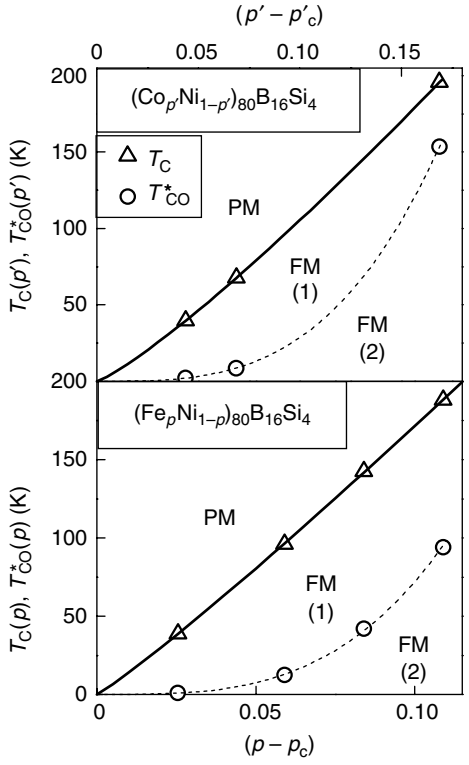

Figure 7. Magnetic phase diagrams for the amorphous alloy series $(Fe_pNi_{1-p})_{80}B_{16}Si_4$ and $(Co_{p'}Ni_{1-p'})_{80}B_{16}Si_4$ that display the two crossover lines: the thermal-to-percolation crossover line, $T_{\rm C}(p)$, (solid curves) and the magnon-to-fracton crossover line, $T_{\rm co}^*(p)$, (dashed curves) within the ferromagnetic (FM) phase.

ferromagnetic fractons) are responsible for the decline of spontaneous magnetization with increasing temperature. The magnon-to-fracton crossover line appears at lower temperatures in addition to the thermal-to-percolation crossover line (continuous curve), that is, the phase boundary between the magnetically *disordered* (paramagnetic, PM) phase and *ordered* (ferromagnetic, FM) phase. The magnetic phase diagram predicted by the theory (Stinchcombe and Pimentel, 1988) for a quenched random site–diluted Heisenberg ferromagnet conforms well to the phase diagrams shown in Figure 7. Note that in the amorphous $(Fe_pNi_{1-p})_{80}M_{20}$ and $(Co_{p'}Ni_{1-p'})_{80}M_{20}$ (M = P,B,Si) alloys Ni atoms (substituting for Fe and Co atoms at random) carry very small magnetic moments (Kaul, 1981; Liebs and Fähnle, 1996) and hence these systems are the experimental realizations of quenched random site–diluted Heisenberg ferromagnets.

Extensive investigations on amorphous (Kaul and Babu, 1994b; Kaul and Srinath, 2001) and crystalline (Kaul and Semwal, 2004) systems (i) enable an accurate determination of the hydrodynamic-to-critical spin-wave crossover line in the magnetic phase diagram, the percolation-to-thermal crossover exponent, the fractal and fracton dimensionalities, the percolation critical exponents for magnetization, and the spin-wave stiffness, (ii) vindicate the Alexander–Orbach conjecture (Alexander and Orbach, 1982) by demonstrating that $\tilde{d}_f \cong 4/3$ for $d = 3$ percolating network, and (iii) conclusively prove that quenched randomness does not alter the critical behavior of percolation on a regular $d = 3$ lattice. A direct experimental evidence for antiferromagnetic fracton excitations in a $d = 3$ site-diluted Heisenberg antiferromagnet with the concentration of the magnetic atoms near the percolation threshold, $RbMn_{0.39}Mg_{0.61}F_3$, has recently been provided by INS experiments (Ikeda *et al*., 1994).

2.3 Nonpropagating exchange-enhanced spin-density fluctuations

Weak itinerant-electron ferromagnets, as opposed to their strong counterparts, facilitate the study of the interaction of collective spin-wave modes with the Stoner single-particle excitations since the relatively small spin splitting of the d band ensures that spin-wave dispersion curve intersects the boundary of Stoner continuum (henceforth referred to as the *Stoner boundary*, SB) tangentially at much lower values of energy, $E_{\mathbf{q}}$, and momentum, $\mathbf{q}$ (Moriya, 1985). Within the $(E_{\mathbf{q}}, \mathbf{q})$ space covered by the Stoner continuum, spin waves are degenerate in energy with single-particle excitations and hence have a short lifetime. The lifetime depends on the density of states of Stoner excitations; the higher the density of states, the shorter the spin-wave lifetime and broader the spin-wave peaks in the INS cross-section. Thus, the spin-wave linewidth increases abruptly at the SB, whereas the integrated intensity (of the spin-wave peaks) starts decreasing before the spin-wave dispersion curve enters the Stoner continuum at a threshold value $q = q_{SB}$ (Figure 2) and falls to very low values above q_{SB}, indicating thereby that the spin waves are severely damped upon crossing the SB. An abrupt increase in the linewidth and a steep drop in the intensity of spin-wave peaks in the inelastic scattering cross-section of unpolarized (spin-polarized) neutrons at the SB has been observed by Ishikawa, Shirane, Tarvin and Kohgi (1977) and Semadeni *et al*. (1999) in the weak itinerant-electron ferromagnet MnSi at the energy transfer $E_{SB} \cong 2.5\,\text{meV}$ ($E_{SB} \cong 3.0\,\text{meV}$) and momentum transfer $q_{SB} \cong 0.25\,\text{Å}^{-1}$ ($q_{SB} \cong 0.36\,\text{Å}^{-1}$), and by Mook, Nicklow, Thompson, and Wilkinson (1969) and Mook and Nicklow (1973) in the early INS experiments on itinerant-electron ferromagnets Fe and Ni at the energies $E_{SB} \cong 80\,\text{meV}$ and $E_{SB} \cong 110\,\text{meV}$, respectively. A drop in the magnon intensity as the SB is approached in an itinerant-electron ferromagnet sharply contrasts with the q-independent spin-wave intensity in the case of localized-spin ferromagnets. An experimental determination of the dependence of magnon intensity on q by INS thus provides a decisive means (Ishikawa, 1978) of ascertaining whether the spins in a given system are localized or itinerant. For $q > q_{SB}$, the collective magnetic excitations in an itinerant-electron ferromagnet are the overdamped (nonpropagating) modes of exchange-enhanced longitudinal and transverse spin-density fluctuations (henceforth simply termed as *spin fluctuations*) that give rise to the elastic peak centered at zero energy transfer, $E = 0$, in the partial differential INS cross-section, $d^2\sigma/d\Omega dE$, versus E plot at a fixed value of q (i.e., in the constant-q scan). At very low temperatures ($T \ll T_C$), spin-wave modes and nonpropagating longitudinal spin fluctuations of q in the range $0 \leq q \leq q^{up}$ (say) are thermally excited. Note that propagating transverse and nonpropagating longitudinal spin fluctuation modes of larger and larger q get thermally excited as the temperature is raised from $T = 0\,\text{K}$ and hence q^{up} increases with temperature. As the temperature is progressively raised, a temperature $T = T_{SB}$ is reached when $q^{up} = q_{SB}$. Consequently, at temperatures $T \leq T_{SB}$, spin waves and longitudinal spin fluctuations of wave vectors $0 \leq q \leq q_{SB}$ coexist, whereas for $T_{SB} < T \leq T_C$, spin-wave modes of $0 \leq q \leq q_{SB}$ accompany longitudinal spin fluctuations of $0 \leq q \leq q^{up}$ as well as transverse spin fluctuations of $q_{SB} < q \leq q^{up}$. Thus, in the constant-q scans taken at temperatures $T \leq T_C$, the inelastic spin-wave peaks centered at $E = \pm E_{\mathbf{q}}$ occur in association with the elastic peak centered at $E = 0$ arising from longitudinal spin fluctuations (both longitudinal and transverse spin fluctuations) for $T \leq T_{SB}$ ($T_{SB} < T \leq T_C$). Occurrence of inelastic peaks alongside an elastic peak, however, limits the energy transfer resolution of the elastic spin-fluctuation

peak. Since spin waves cease to exist at temperatures above the Curie point, spin fluctuations are amenable to an accurate experimental scrutiny only in the paramagnetic state where the spin system is completely isotropic with the result that $\mathrm{Im}\chi(\mathbf{Q},\omega) \equiv \mathrm{Im}\chi_{||}(\mathbf{Q},\omega) \cong \mathrm{Im}\chi_{\perp}(\mathbf{Q},\omega)$ in the partial differential neutron-scattering cross section, given by equation (1). The energy- and momentum-resolved neutron-scattering experiments, employing the time-of-flight technique, on canonical weak itinerant-electron ferromagnets such as Ni_3Al (Bernhoeft, Lonzarich, Paul, and Mitchell, 1986), $ZrZn_2$ (Bernhoeft, Lonzarich, Paul, and Mitchell, 1986; Bernhoeft, Law, Lonzarich and Paul, 1988), and MnSi (Ishikawa *et al*., 1985; Ishikawa, 1986) at temperatures $T > T_C$ as well as on the exchange-enhanced paramagnet Ni_3Ga (Bernhoeft *et al*., 1989) have revealed that the scattering of neutrons from thermally excited nonpropagating spin fluctuations in these materials is characterized by a simple Lorentzian frequency spectrum, that is, by the imaginary part of the dynamic wave vector–dependent susceptibility, $\mathrm{Im}\chi(\mathbf{Q},\omega)$, of the form

$$\mathrm{Im}\chi(\mathbf{Q},\omega) = \omega\,\chi(\mathbf{q})\,\frac{\Gamma(\mathbf{q})}{\omega^2+\Gamma^2(\mathbf{q})} \tag{24}$$

in equation (1), where the momentum transfer $\mathbf{q}$ is measured from a reciprocal-lattice point. In accordance with the predictions of the random phase approximation (RPA) for an electron gas in the low q limit (Moriya, 1985; Lonzarich and Taillefer, 1985), the wave vector-dependent susceptibility, $\chi(\mathbf{q})$, and the relaxation frequency, $\Gamma(\mathbf{q})$, of spin fluctuations, in the above expression, are given by

$$\chi(\mathbf{q}) = \chi(\mathbf{q},\omega=0) = \chi(0)\,\frac{\kappa^2}{\kappa^2+q^2} \tag{25}$$

$$\Gamma(\mathbf{q}) = \gamma q \chi^{-1}(\mathbf{q}) = \gamma\, q\, c\,(\kappa^2+q^2) \tag{26}$$

In equations (25) and (26), $\chi(0) = \chi(\mathbf{q}=0) = (c\kappa^2)^{-1}$ is the bulk static susceptibility, κ is the inverse spin fluctuation–spin fluctuation correlation length, c is a constant which can be identified with the coefficient of the gradient squared term in the Ginzburg–Landau free energy expansion, and γ characterizes the relaxation transport of spin carriers (Lonzarich and Taillefer, 1985); the quantities c and γ depend on the details of the band structure near the Fermi level (Lonzarich and Taillefer, 1985). The neutron-scattering intensity, $I(\mathbf{Q},\omega)$, is calculated from the partial differential scattering cross-section by evaluating the integral

$$I(\mathbf{Q},\omega) = \int \frac{\mathrm{d}^2\sigma}{\mathrm{d}\Omega\mathrm{d}(\hbar\omega)}(\mathbf{Q}',\omega')\,R(\mathbf{Q}-\mathbf{Q}',\omega-\omega')\,\mathrm{d}\omega'\,\mathrm{d}\mathbf{Q}' \tag{27}$$

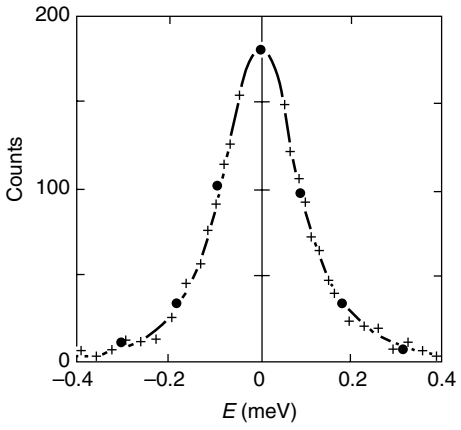

Figure 8. Energy dependence of the neutron-scattering intensity (+) in Ni_3Al at 45 K ($T > T_C$) relative to the 5 K background, measured by the time-of-flight technique for an elastic scattering wave vector $q = 0.063\,\text{Å}^{-1}$ and incident neutron wavelength $\lambda \cong 8\,\text{Å}$. The solid circles represent the scattering intensity calculated from equations (1) and (24–27) using $c = 1.5 \times 10^5\,\text{Å}^2$ and $\hbar\gamma = 3.3\,\mu\text{eV Å}$.

where $R(\mathbf{Q}-\mathbf{Q}',\omega-\omega')$ is the resolution function of the spectrometer. As an illustrative example, Figure 8 (taken from Bernhoeft, Lonzarich, Paul, and Mitchell, 1986) compares the energy transfer dependence of the neutron-scattering intensity observed in Ni_3Al at a temperature $T > T_C$ (plus symbols) with that calculated (solid circles) from the equations (1) and (24–27) by treating the quantities c and γ as free fitting parameters while optimizing agreement between theory and experiment. Note that the band parameter c can also be independently determined from the relation (Moriya, 1985; Lonzarich and Taillefer, 1985) $D(T) = g\,\mu_B\,M(T)\,c$ between the spin-wave stiffness, D, and spontaneous magnetization, M, and once c is known, κ can be calculated from the observed bulk susceptibility, $\chi(0)$, using the relation $\kappa = (c\chi(0))^{-1/2}$. The band parameters c and γ, in turn, permit a quantitative analysis of the thermodynamic properties of weakly or nearly ferromagnetic or antiferromagnetic metals.

Besides complementing the information about the underlying band structure deduced from the neutron-scattering experiments, the bulk magnetization measurements enable a thorough investigation of spin fluctuations at intermediate temperatures and for temperatures close to T_C (the temperature range normally inaccessible to the neutron-scattering experiments so far as an accurate determination of the band parameters c and γ is concerned) because in this temperature range, the contribution due to spin fluctuations to the thermal demagnetization dominates over the spin-wave contribution. For a better understanding of what can be learnt about spin fluctuations from bulk magnetization studies, a brief account of the theoretical developments in this field, given in the

following text, is required. One of the earliest theories that self-consistently renormalizes the mutually coupled modes of exchange-enhanced spin fluctuations (*localized* in the reciprocal (q) space), the so-called self-consistent renormalization theory (Moriya and Kawabata, 1973), yielded the temperature dependence of spontaneous magnetization for weakly ferromagnetic metals as $M^2(0,0) - M^2(T,0) = aT^2$ at low temperatures and $M^2(T,0) = a'(T_C^{4/3} - T^{4/3})$ over a wide temperature range below T_C by taking into account only the transverse modes of thermally excited spin fluctuations. Takeuchi and Masuda (1979) extended this theory to include the effect of external magnetic field on magnetization by using the electron gas model to calculate the magnetic field – and temperature-dependent static susceptibility that is consistent with the magnetic equation of state (MES). A good quantitative agreement between the theoretically predicted and experimentally observed variations of magnetization with temperature and magnetic field in the weak itinerant-electron ferromagnet Sc_3In was achieved (Takeuchi and Masuda, 1979) by using a number of adjustable parameters. Recognizing the importance of longitudinal spin fluctuations and the fact that the electron gas model forms an oversimplified description of the band structure of real weak itinerant-electron magnetic systems, Lonzarich and Taillefer (1985) calculated the MES of nearly or weakly ferromagnetic metals, which includes corrections to the conventional Stoner theory arising from both longitudinal and transverse spin fluctuations, by making use of the band parameters obtained from neutron-scattering experiments rather than the unrealistic electron gas model. The effect of including longitudinal spin fluctuations (in addition to the transverse spin fluctuations) is to (Lonzarich and Taillefer, 1985) widen the temperature range (which now includes intermediate temperatures as well) over which the squared spontaneous magnetization varies with temperature as $M^2(T,0) \sim T^2$ and narrow down the temperature range (so as to restrict it to temperatures not too far from T_C) where $M^2(T,0) \sim T^{4/3}$. The above-mentioned spin-fluctuation models considered only the thermally-excited spin fluctuations but completely ignored the contribution to magnetization due to zero-point (quantum) spin fluctuations whose significance was realized only later (Takahashi, 1986, 2001; Solontsov and Wagner, 1994, 1995; Kaul, 1999; Kaul and Semwal, 1999). Among the theoretical approaches that take into account both thermally excited and zero-point spin fluctuations (Takahashi, 1986, 2001; Kaul, 1999; Kaul and Semwal, 1999), the treatment proposed by Kaul (1999) clearly brings out the roles of zero-point and thermally excited spin fluctuations in the thermal demagnetization of weak itinerant-electron ferromagnets and the extent to which these excitations get suppressed by the external magnetic field. The results of the bulk magnetization studies on amorphous (Kaul and Babu, 1998) and crystalline (Kaul and Semwal, 1999; Semwal and Kaul, 1999, 2004) weakly ferromagnetic metallic alloys validate this theoretical approach (Kaul, 1999), as illustrated in the following text.

The thermal variances of the local magnetization parallel (||), $\langle m_{||}^2 \rangle$, and perpendicular ($\perp$), $\langle m_{\perp}^2 \rangle$, to the average magnetization, **M**, are related to the imaginary part of the dynamical wave-vector-dependent susceptibility, $\mathrm{Im}\chi_\nu(\mathbf{q},\omega)$, where $\nu(= ||, \perp)$ is the polarization index, through the well-known fluctuation-dissipation relation (Moriya, 1985; Lonzarich and Taillefer, 1985; Takahashi, 1986)

$$\langle m_\nu^2 \rangle = 4\hbar \int \frac{\mathrm{d}^3\mathbf{q}}{(2\pi)^3} \int \frac{\mathrm{d}\omega}{2\pi} \left(n(\omega) + \frac{1}{2} \right) \mathrm{Im}\chi_\nu(\mathbf{q},\omega) \quad (28)$$

where the thermally-excited spin fluctuations and zero-point spin fluctuations are represented by the Bose function, $n(\omega)$, and the factor $1/2$, respectively. Calculating the longitudinal, $\langle m_{||}^2 \rangle$, and transverse, $\langle m_{\perp}^2 \rangle$, spin-fluctuation contributions to magnetization (in the ferromagnetic state) from equation (28) by combining the equations (24–26) and (28), and substituting the result in the MES (Lonzarich and Taillefer, 1985; Kaul, 1999)

$$\left[\frac{M(T,H)}{M(0,0)} \right]^2 = 1 - \frac{3\langle m_{||}^2 \rangle + 2\langle m_{\perp}^2 \rangle}{M^2(0,0)} + 2\chi(0,0)\frac{H}{M(T,H)} \quad (29)$$

finally yields the expressions for magnetization (Kaul, 1999)

$$M(T,H) = M(0,H)[1 - (T/T_0)^2 - (T/T_1)^{4/3}]^{1/2} \quad (30)$$

and

$$M(T,H) = M(0,H)[1 - A(H)\,T^{4/3}]^{1/2} \quad (31)$$

at intermediate temperatures and for temperatures close to T_C but outside the critical region, respectively. The expressions (30) and (31) are valid for both zero and finite magnetic fields. The T^2 term in equation (30) originates from thermally-excited spin fluctuations alone and its coefficient T_0^{-2} depends on H through the field dependence of the static susceptibility, $\chi_\nu(0)$. By contrast, the $T^{4/3}$ term in equation (30) is a net outcome of the competing claims made by the thermally-excited and zero-point components of spin fluctuations (the contribution due to thermally-excited spin fluctuations decreases with T as $T^{4/3}$ and is dominated by the one arising from zero-point spin fluctuations, which increases with T as $T^{4/3}$) and its coefficient $T_1^{-4/3}$ is essentially independent of field. Owing to this competition, the $T^{4/3}$ term in equation (30) is very small compared to the T^2 term. In equation (31), the $T^{4/3}$ term for

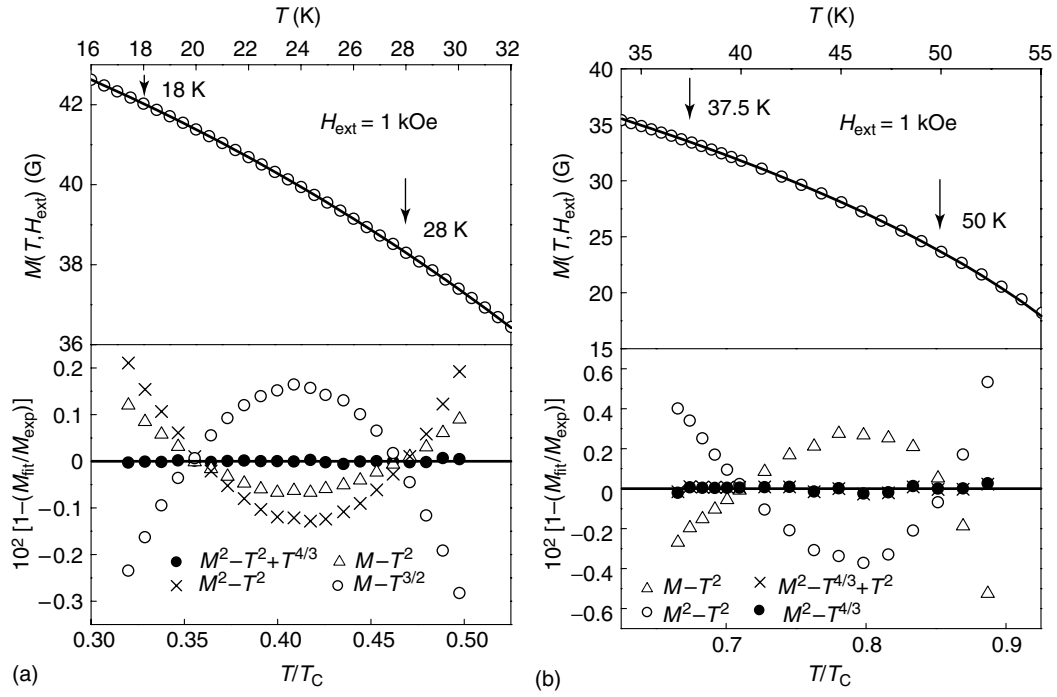

Figure 9. The upper panels depict the temperature variation of magnetization measured at an external magnetic field of $H_{\rm ext} = 1$ kOe for the weak itinerant-electron ferromagnet Ni_3Al at (a) intermediate temperatures and (b) temperatures close to the Curie temperature, and the continuous curves are the least-squares fits based on (a) equation (30) and (b) equation (31). The lower panel displays the percentage deviation of the data from the least-squares fits based on equations (10), (11), (30), and (31). Notice that the functional forms given by equations (30) and (31) yield minimum deviations in the cases (a) and (b), respectively.

$H = 0$ has its origin in both zero-point and thermally excited spin fluctuations (SF) in that their contributions to the coefficient, $A(H = 0) = (T_C^{\rm SF})^{-4/3}$, of this term are additive; however, for $H \neq 0$, the thermally excited spin fluctuations alone are responsible for the coefficient $A(H) = A(H = 0)[1 - \eta\sqrt{H}]$, of the $T^{4/3}$ term. The results of extensive magnetization measurements performed on amorphous weakly ferromagnetic metallic alloys (Kaul and Babu, 1998) and crystalline weak itinerant-electron ferromagnet Ni_3Al with (Semwal and Kaul, 2004) and without site disorder (Kaul and Semwal, 1999; Semwal and Kaul, 1999) corroborate the above theoretical predictions (Kaul, 1999) concerning the relative magnitudes of the zero-point and thermally excited spin-fluctuation contributions to thermal demagnetization and the functional forms of their dependence on temperature and magnetic field in different temperature ranges. Treating the well-known weak itinerant-electron ferromagnet Ni_3Al as an example, Figure 9 (taken from Semwal and Kaul, 1999) and Figure 10 (taken from Semwal and Kaul, 2004), respectively, serve to demonstrate the validity of the theoretical expressions (30), (31), and $A(H) = A(H = 0)[1 - \eta\sqrt{H}]$ (i.e., magnetic field suppresses thermally excited spin fluctuations according to the theoretically predicted $\sqrt{H}$ power law). Nuclear spin-lattice relaxation

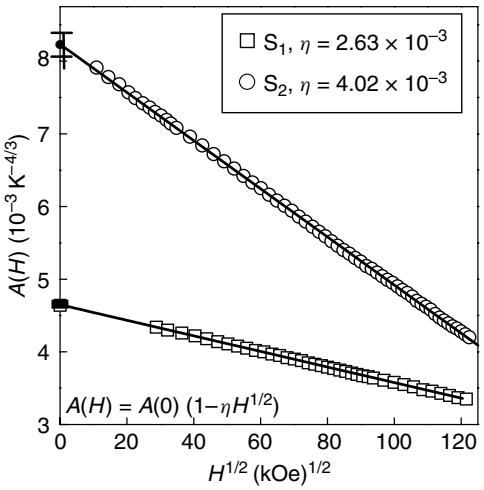

Figure 10. $\sqrt{H}$ variation of the coefficient A of the $T^{4/3}$ term in equation (31) for the annealed (S_1) and quenched (S_2) samples of the weak itinerant-electron ferromagnet Ni_3Al.

provides yet another powerful experimental technique to study spin fluctuations. The relevant details about the theoretical and experimental aspects of this technique are given by Moriya (1985).

3 THERMALLY-DRIVEN MAGNETIC PHASE TRANSITIONS

In the critical region (whose extent depends on the type of material and is typically of the order of $|\varepsilon| = |(T - T_C)/T_C| \leq 0.01$, where T_C is the critical temperature) as the critical temperature is approached, the thermally-excited critical fluctuations of the local spin-density (order parameter) rapidly pick up in amplitude and get correlated in space over larger and larger distances with the result that they destroy the long-range magnetic order at T_C, where the spin-density-fluctuation–spin-density-fluctuation correlation length, $\xi(T = T_C)$, (henceforth referred to as *spin–spin correlation length*, for brevity) diverges and the magnetic order–disorder phase transition occurs. Note that the thermally-driven 'classical' phase transitions are distinctly different from the quantum phase transitions which occur only at the temperature of absolute zero where the quantum (zero-point) fluctuations, demanded by the Heisenberg uncertainty principle, destroy cooperative ordering in the system (the reader is referred to **Quantum Phase Transitions, Volume 1** for a detailed discussion of quantum phase transitions). Experimental investigations in the critical region near a thermally-driven phase transition provide a unique and direct means of probing the type of interactions present and the interplay between them, which finally decides the nature of magnetic order prevailing in the systems under study for temperatures below the transition temperature. This is so because the critical behavior of a system is solely governed by the nature of the underlying interactions. For instance, an interplay between interactions, such as crystal-field (leading to uniaxial anisotropy), isotropic short-range (ISR) Heisenberg, and long-range dipole–dipole interactions, in a localized-spin system gives rise to a series of crossovers from uniaxial dipolar (UD) critical regime (where both uniaxial anisotropy and dipolar interactions dominate) to isotropic dipolar critical regime (where anisotropy is negligibly small and isotropic dipolar interactions take over) to isotropic Heisenberg critical regime (where short-range isotropic Heisenberg interactions become prominent), and so on, as the temperature is raised above T_C in the critical region. To facilitate understanding of the magnetic phase transitions, the prerequisites such as the definition of the asymptotic critical exponents and amplitudes, which quantify the static critical behavior near a magnetic order–disorder phase transition, and the physical concepts relating to the critical phenomena such as the scaling hypothesis, universality, renormalization group (RG) approach, and crossover between different critical regimes, are covered in the following subsections.

3.1 Static critical exponents and amplitudes

In the asymptotic critical region, the behavior of a magnetic system is characterized by a set of critical exponents and amplitudes (Stanley, 1971; Kaul, 1985). Critical exponents are the exponents in the power laws that define the deviations of various thermodynamic quantities from their values at the critical point T_C and the corresponding amplitudes are the forefactors in these power laws. The asymptotic critical exponents and amplitudes for the second-order ferromagnetic (FM) to paramagnetic (PM) phase transition are defined as follows.

3.1.1 Spontaneous magnetization

In the asymptotic critical region, spontaneous magnetization, M_S, the order parameter for the FM–PM phase transition, varies with the reduced temperature $\varepsilon = (T - T_C)/T_C$ as

$$M_S(T) = \lim_{H \to 0} M(T, H) = B\,(-\varepsilon)^{\beta} \qquad \varepsilon < 0 \tag{32}$$

3.1.2 Initial susceptibility

Initial susceptibility, defined as $\chi_0 = \lim_{H \to 0}[\partial M/\partial H]_T$, diverges at T_C as

$$\chi_0(T) = \Gamma^{-}\,(-\varepsilon)^{-\gamma^{-}} \qquad \varepsilon < 0 \tag{33}$$

$$\chi_0(T) = \Gamma^{+}\,\varepsilon^{-\gamma^{+}} \qquad \varepsilon > 0 \tag{34}$$

3.1.3 Critical isotherm

At $T = T_C$, magnetization M varies with field H as

$$M(T_C, H) = A_0\,H^{1/\delta} \qquad \text{or}$$

$$H = D\,M^{\delta} \qquad \varepsilon = 0 \tag{35}$$

3.1.4 Specific heat

Zero-field ($H = 0$) specific heat diverges at T_C as

$$C_{H=0}(T) = \frac{A^{-}}{\alpha^{-}}[(-\varepsilon)^{-\alpha^{-}} - 1] + B^{-} \qquad \varepsilon < 0 \tag{36}$$

$$C_{H=0}(T) = \frac{A^{+}}{\alpha^{+}}[\varepsilon^{-\alpha^{+}} - 1] + B^{+} \qquad \varepsilon > 0 \tag{37}$$

Specific heat exhibits a cusp at T_C when $\alpha < 0$, whereas for $\alpha = 0$ the singularity is logarithmic. B^{-} and B^{+} represent the nonsingular background for $\varepsilon < 0$ and $\varepsilon > 0$, respectively, in the asymptotic critical region.

3.1.5 Spin–spin correlation function

At T_C, the correlation function for the spin fluctuations at the points **0** and **r** in space, $G(\mathbf{r}) \equiv \langle[\mathbf{S}(\mathbf{r}) - \langle\mathbf{S}\rangle][\mathbf{S}(\mathbf{0}) - \langle\mathbf{S}\rangle]\rangle$, decays with distance, r, as

$$G(|\mathbf{r}|) = N\,|\mathbf{r}|^{-(d-2+\eta)} \qquad [\text{large}|\mathbf{r}|, \varepsilon = H = 0] \tag{38}$$

where d is the dimensionality of the lattice and η is a measure of the deviation from the mean-field behavior.

3.1.6 Spin–spin correlation length

Correlation length, ξ, is the distance over which the order parameter fluctuations are correlated and is defined through the relation $G(|\mathbf{r}|) = e^{-|\mathbf{r}|/\xi(T)}/|\mathbf{r}|$, where $|\mathbf{r}| \to \infty$. In the critical region, ξ depends on temperature as

$$\xi(T) = \xi_0^-\,(-\varepsilon)^{-\nu^-} \qquad \varepsilon < 0, H = 0 \tag{39}$$

$$\xi(T) = \xi_0^+\,\varepsilon^{-\nu^+} \qquad \varepsilon > 0, H = 0 \tag{40}$$

In equations (32–40), $\beta, \gamma^-, \gamma^+, \delta, \alpha^-, \alpha^+, \eta, \nu^-$, and ν^+ are the asymptotic critical exponents and $B, \Gamma^-, \Gamma^+, A_0$, or D, A^-, A^+, N, ξ_0^-, and ξ_0^+ are the corresponding asymptotic critical amplitudes. There are nine critical exponents in total but only two of them are independent (Stanley, 1971). This is a consequence of the scaling relations between them, for example, $\alpha^+ = \alpha^-$, $\gamma^+ = \gamma^-$, $\nu^+ = \nu^-$, $\beta\delta = \beta + \gamma$ (Widom equality), $\alpha + 2\beta + \gamma = 2$ (Rushbrooke equality), $\alpha + \beta(\delta + 1) = 2$ (Griffiths equality), $(2 - \eta)\nu = \gamma$ (Fisher equality), and $d\nu = 2 - \alpha$ (Josephson equality), to name a few.

The single power laws are strictly valid only at $T = T_C$. In practice, however, the power laws are fitted to the experimental data over a finite temperature range. Consequently, such an approach yields only average exponent values since, in general, the amplitudes as well as the exponents are temperature-dependent and they assume temperature-independent values only in the asymptotic critical region (Kaul, 1985). In order to tackle this problem effectively, the concept of effective critical exponent was introduced by Riedel and Wegner (1974). The effective critical exponents provide a local measure for the degree of singularity of physical quantities in the critical region. The effective critical exponent, $\lambda_{\text{eff}}(\mu)$, of a function $f(\mu)$ is defined by the logarithmic derivative $\lambda_{\text{eff}}(\mu) = \mathrm{d}\ln f(\mu)/\mathrm{d}\ln\mu$. In the limit $\mu \to 0$, $\lambda_{\text{eff}}(\mu)$ coincides with the asymptotic critical exponent λ.

3.2 Scaling and universality

Historically, the observation that a huge body of experimental data on a variety of systems could be represented in the form of a scaled equation of state led to the scaling hypothesis, which asserts that in the asymptotic critical region the singular part of the Gibbs free energy, $G_s(\varepsilon, H)$, is a generalized homogeneous function (Stanley, 1971) of its arguments ε and H. Scaling hypothesis or, equivalently, the homogeneity postulate makes two specific predictions: (i) it relates various critical exponents through the scaling equalities, and (ii) makes specific predictions concerning the form of the equation of state. For magnetic systems, the scaling hypothesis predicts that all the magnetization, $M(\varepsilon, H)$, curves (either magnetization isotherms at different temperatures or $M(\varepsilon)$ at different fields) taken in the critical region collapse onto two universal curves, one for $\varepsilon < 0$ and the other for $\varepsilon > 0$, if scaled magnetization, $M/|\varepsilon|^\beta$, is plotted against scaled field, $H/|\varepsilon|^\Delta$, where $\Delta = \beta\delta$ is the gap exponent. Both the above-mentioned scaling predictions have been vindicated by experiments on widely different magnetic systems (Stanley, 1971; Kaul, 1985; Kellner, Fähnle, Kronmüller and Kaul, 1987; Fähnle, Kellner and Kronmüller, 1987; Kaul and Sambasiva Rao, 1991, 1994; Sambasiva Rao and Kaul, 1995; Seeger, Kaul, Kronmüller and Reisser, 1995; Babu and Kaul, 1997; Fischer, Kaul and Kronmüller, 2002). The RG approach (Section 3.3) makes use of the homogeneity postulate to relate critical exponents to the eigenvalues of the RG operator and thereby permits quantitative determination of the critical exponents.

A related concept is the universality, which basically amounts to cataloging, under a single category (class), all types of systems that possess the same values for critical exponents and critical amplitude ratios and for which the equation of state and the correlation functions become identical near criticality, provided the order parameter, the ordering field, and the correlation length (time) are scaled properly by material-dependent factors. Thus, the critical exponents and the ratios between critical amplitudes (but not the amplitudes themselves) are universal (Kaul, 1985; Privman, Hohenberg and Aharony, 1991; Kaul and Sambasiva Rao, 1994; Seeger, Kaul, Kronmüller and Reisser, 1995; Babu and Kaul; 1997; Fischer, Kaul and Kronmüller, 2002) in the sense that they possess exactly the same numerical values for a number of widely different systems belonging to the same universality class. The universality class, in turn, is decided by (i) the space dimensionality 'd', (ii) the number of order parameter components, or equivalently, the order parameter dimensionality 'n', (iii) the symmetry of the Hamiltonian, and (iv) the range of interactions. For $d = 3, n = 1$ corresponds to a three-dimensional Ising system in which the spins on a three-dimensional lattice are constrained to point either in the $+z$ (up) or $-z$ (down) directions. In this example, the range of interactions is too short compared to the spin–spin correlation length and the symmetry of the Hamiltonian is reflected through the extremely large uniaxial anisotropy which constrains the spins to point up or down.

3.3 Renormalization group and crossover phenomena

Wilson's RG treatment has provided a powerful theoretical method to accurately calculate not only the asymptotic critical exponents and asymptotic critical amplitude ratios but also the 'correction-to-scaling' critical exponents and critical amplitudes. The RG approach has, therefore, become the subject of many books and reviews, the recent ones being Goldenfeld (1994), Cardy (1996), Domb (1996), and Fisher (1998). The main essence of one of the variants of RG (Ma, 1976) and its practical implications are given in the following text. Starting with an effective cell-Hamiltonian (Ma, 1976) (i.e., the Hamiltonian of a unit cell of spins), the RG transformation proceeds in two steps. First, the cell size in each direction is increased by a factor b and the bigger cell-Hamiltonian is constructed out of the smaller cell-Hamiltonian using the well-known Kadanoff transformation. Second, a scale transformation, in which the length scale changes by a factor $b = \mathrm{e}^{l}$ in all linear dimensions, is performed such that the bigger-cell volume shrinks back to the original smaller-cell volume, that is, $V(l) = \mathrm{e}^{-dl} V(0)$. As a consequence, free energy is left unaltered but the free energy density transforms according to $g_{l=0} = \mathrm{e}^{-dl} g_l$, while the Hamiltonian $\mathcal{H}_0 = \mathcal{H}\{\mu_i\}$ transforms into $\mathcal{H}_l = \mathcal{H}\{\mu_i \mathrm{e}^{y_i l}\}$, where μ_i are the scaling fields and y_i are the scaling exponents. RG transformation thus requires that (Wegner, 1972; Fisher, 1974; Kaul, 1994)

$$g\{\mu_i\} = g(\mu_0) - \mathrm{e}^{-dl}\, g_{\sin g}\{\mu_i\, \mathrm{e}^{y_i l}\} \tag{41}$$

The scaling fields μ_i can be identified with the relevant fields $\mu_\varepsilon = |\varepsilon|$ and $\mu_h = H = h$. Since the parameter l is arbitrary, it can be chosen such that $|\varepsilon|\, \mathrm{e}^{y_\varepsilon l} = 1$ or $\mathrm{e}^{-y_\varepsilon l} = |\varepsilon|$. Thus,

$$\mathrm{e}^{-dl} = (\mathrm{e}^{-y_\varepsilon l})^{d/y_\varepsilon} = |\varepsilon|^{d/y_\varepsilon} = |\varepsilon|^{2-\alpha} \tag{42}$$

and

$$\mathrm{e}^{y_h l} = (\mathrm{e}^{-y_\varepsilon l})^{-y_h/y_\varepsilon} = |\varepsilon|^{-\Delta} \tag{43}$$

where $2 - \alpha = d/y_\varepsilon$ and $\Delta = y_h/y_\varepsilon$. Combining equations (41–43) yields (Kaul, 1994)

$$g(T, H) = g_0(T) - |\varepsilon|^{2-\alpha}\, Y_{\pm}(\pm 1, h/|\varepsilon|^{\Delta}) \tag{44}$$

For the sake of convenience, the microscopic volume of the system is set equal to unity ($V = 1$). Thus, the first- and second-order derivatives of g with respect to H yield magnetization $M(T, H)$ and 'in-field' susceptibility $\chi(T, H)$, respectively, whereas the second-order derivative of g with respect to temperature yields the specific heat, $C(T, H)$. Therefore (Aharony and Fisher, 1983; Kaul, 1994),

$$\begin{aligned} M(T, H) &= -\left(\frac{\partial g(T, H)}{\partial H}\right)_T \\ &= |\varepsilon|^{2-\alpha-\Delta}\left(\frac{\partial Y_{\pm}(\pm 1, h/|\varepsilon|^{\Delta})}{\partial h}\right)_T \quad \text{or} \\ M(\varepsilon, h) &= |\varepsilon|^{\beta} f_{\pm}(h/|\varepsilon|^{\Delta}) \end{aligned} \tag{45}$$

$$\begin{aligned} \chi(T, H) &= \left(\frac{\partial M(T, H)}{\partial H}\right)_T \\ &= |\varepsilon|^{2-\alpha-2\Delta}\left(\frac{\partial f_{\pm}(h/|\varepsilon|^{\Delta})}{\partial h}\right)_T \quad \text{or} \\ \chi(\varepsilon, h) &= |\varepsilon|^{-\gamma}\left(\frac{\partial f_{\pm}(h/|\varepsilon|^{\Delta})}{\partial h}\right)_T \end{aligned} \tag{46}$$

$$\begin{aligned} C(T, 0) &= -T\left(\frac{\partial^2 g}{\partial T^2}\right)_{H=0} = C(\varepsilon, 0) \\ &= (1-\alpha)(2-\alpha) T_{\mathrm{C}}^{-1} Y_{\pm}(0)\, |\varepsilon|^{-\alpha}(1+\varepsilon) \end{aligned} \tag{47}$$

In equations (44–47), $Y_{\pm}(\pm 1, h/|\varepsilon|^{\Delta})$, $f_{\pm}(h/|\varepsilon|^{\Delta})$, $(\partial f_{\pm}(h/|\varepsilon|^{\Delta})/\partial h)_T$ and $Y_{\pm}(0)$ are the scaling functions, which, in the asymptotic limit, assume constant values and $+$ and $-$ signs denote $\varepsilon > 0$ and $\varepsilon < 0$, respectively. A comparison of (45–47) with the definitions (32–34), (36), and (37) reveals that these constant limiting values are nothing but the asymptotic critical amplitudes and that $\beta = 2 - \alpha - \Delta$ and $\gamma = -2 + \alpha + 2\Delta$. From these relations, it immediately follows that $\beta + \gamma = \Delta$ and $\alpha + 2\beta + \gamma = 2$ (which is the Rushbrooke scaling equality). Furthermore, equation (45) is the MES or just the scaling equation of state (SES). As $\varepsilon \to 0$, $|\varepsilon|^{\Delta}/h \to 0$ and the MES can be cast into an alternate form (Aharony and Fisher, 1983; Kaul, 1994)

$$M(\varepsilon, h) = |h|^{\beta/\Delta} f_0\left(\frac{|\varepsilon|}{|h|^{1/\Delta}}\right) \tag{48}$$

In the limit $|\varepsilon|/|h|^{1/\Delta} \ll 1$, the function $f_0(z)$ can be expanded in a Taylor series around $z = 0$ with the result $M(\varepsilon, h) = |h|^{\beta/\Delta}[f_0(0) + (|\varepsilon|/|h|^{1/\Delta}) f_0'(0) + \ldots]$. At $|\varepsilon| = 0$, $M(0, h) = f_0(0)\, |h|^{\beta/\Delta}$ or equivalently,

$$M(0, H) = f_0(0)\, H^{1/\delta} \tag{49}$$

Comparing (49) with (35) gives $\beta/\Delta = 1/\delta$ or $\beta\delta = \Delta$. Now that $\beta + \gamma = \Delta$ (as shown in the preceding text), $\beta + \gamma = \beta\delta$, which is the Widom scaling equality. The foregoing calculations serve to illustrate how the RG approach relates asymptotic critical amplitudes with the scaling functions and provides a theoretical basis for the scaling equalities between asymptotic critical exponents.

Having defined renormalization group, the RG transformation is iterated through the repeated application of the RG operator, $\mathbf{R}$, that is, $\mathcal{H}' = \mathbf{R}[\mathcal{H}], \mathcal{H}'' = \mathbf{R}[\mathcal{H}'], \ldots$, till the fixed point of RG transformation, that is, the critical point, is reached where the Hamiltonian maps onto itself under the RG transformation and such a Hamiltonian is called a *fixed point Hamiltonian*, $\mathcal{H}^*$. The fixed point Hamiltonian is defined by its invariance under RG transformation, that is, $\mathbf{R}[\mathcal{H}^*] = \mathcal{H}^*$. A visualization of the approach to criticality is facilitated when the RG operator is linearized about $\mathcal{H}^*$, for example, (Fisher, 1974)

$$\mathcal{H}' = \mathbf{R}[\mathcal{H}] = \mathbf{R}[\mathcal{H}^* + \mu\mathbf{Q}] = \mathcal{H}^* + \mu\mathbf{L}\mathbf{Q} + \vartheta(\mu^2) \quad (50)$$

where $\mathbf{L}$ is a linear operator defined by the eigenvalue equation

$$\mathbf{L}\,\mathbf{Q}_i = \mathrm{e}^{y_i l}\,\mathbf{Q}_i \quad (51)$$

This equation also defines eigenoperators (or eigenperturbations) $\mathbf{Q}_i$, eigenvalues $\mathrm{e}^{y_i l}$, and scaling exponents y_i. Assuming that the eigenoperators form a complete set of operators, any Hamiltonian $\mathcal{H}_0$ can be expanded in terms of this complete set, that is, $\mathcal{H}_0 = \mathcal{H}^* + \sum_i \mu_i \mathbf{Q}_i$. In this expression, the Hamiltonian is parameterized by the scaling fields μ_i. Thus,

$$\mathcal{H}_l = \mathbf{R}[\mathcal{H}_0] = \mathcal{H}^* + \sum_i \mu_i\,\mathrm{e}^{y_i l}\,\mathbf{Q}_i \quad (52)$$

For instance, we saw earlier that when $\mathcal{H}_0 = \mathcal{H}^* + \mu_\varepsilon\mathbf{Q}_\varepsilon + \mu_h\mathbf{Q}_h$ with $\mu_\varepsilon = |\varepsilon|$ and $\mu_h = h$, the singular part of the free energy density is given by $g_{\sin g}(\varepsilon, h) = |\varepsilon|^{2-\alpha}\,Y_\pm(\pm 1, h/|\varepsilon|^\Delta)$. If one starts with the Hamiltonian $\mathcal{H}_0 = \mathcal{H}^* + \mu_\varepsilon\mathbf{Q}_\varepsilon + \mu_h\mathbf{Q}_h + \mu_i\mathbf{Q}_i$, generalization of this procedure yields, within the linear approximation, the Hamiltonian

$$\mathcal{H}_l = \mathcal{H}^* + \mu_\varepsilon\,\mathrm{e}^{y_\varepsilon l}\,\mathbf{Q}_\varepsilon + \mu_h\,\mathrm{e}^{y_h l}\,\mathbf{Q}_h + \mu_i\,\mathrm{e}^{y_i l}\,\mathbf{Q}_i \quad (53)$$

and the singular part of the free energy density (Wegner, 1972)

$$g_{\sin g}(\varepsilon, h, \mu_i) = |\varepsilon|^{2-\alpha}\,Y_\pm\left(\pm 1, \frac{h}{|\varepsilon|^\Delta}, \frac{\mu_i}{|\varepsilon|^{\phi_i}}\right) \quad (54)$$

Depending upon the sign of the exponent ϕ_i, three different cases arise.

1. $\phi_i < 0$. As the critical point is approached, ($|\varepsilon| \to 0$), the reduced fields $\overline{\mu_i} = \mu_i/|\varepsilon|^{\phi_i}$ tend to zero. The leading singularity in the asymptotic behavior is the same as if all the scaling fields μ_i were zero. Hence the operators $\mathbf{Q}_i$ are irrelevant and μ_i are called *irrelevant scaling fields*. However, a Taylor expansion of the scaling function $Y_\pm(x)$ about $x = 0$ corrects the dominant singular terms by additive terms (called the *correction-to-scaling* terms) proportional to $|\varepsilon|^{2-\alpha+|\phi_i|}$.
2. $\phi_i > 0$. As $|\varepsilon| \to 0$, three distinct temperature regions can be identified, $|\varepsilon|^{\phi_i} \gg \mu_i$, $|\varepsilon|^{\phi_i} \approx \mu_i$, and $|\varepsilon|^{\phi_i} \ll \mu_i$. In the first region, far from the critical point, $\overline{\mu_i}$ are extremely small and the behavior is as if μ_i are zero. In the second region, centered at the crossover temperature $|\varepsilon^*| \approx \mu_i^{1/\phi_i}$, the perturbation begins to make its presence felt. Finally in the third region, closest to the critical point, the reduced fields $\overline{\mu_i}$ become very large and grow rapidly as $|\varepsilon| \to 0$ with the result that the perturbative treatment breaks down. Either there is no critical behavior at all, as, for instance, in the presence of a magnetic field, which suppresses the transition ($\Delta = \beta\delta$ is always positive and hence can be thought of as a crossover exponent ϕ_i), or else the actual critical behavior is quite different from that corresponding to $\mu_i = 0$ and depends on the nature of the operators $\mathbf{Q}_i$ (i.e., the perturbation). Such crossover phenomena from one kind of critical behavior to another reflect competition between two critical regimes; the $\mu_i = 0$ critical behavior yields progressively to the $\mu_i \neq 0$ critical behavior as the critical point is approached such that the latter critical behavior takes over at $\varepsilon = 0$. This also implies that the presence of the relevant operator $\mathbf{Q}_i$ and relevant scaling fields μ_i leads to a crossover from one critical regime to the other and causes a shift in the critical temperature from $T_C(\mu_i = 0)$ to $T_C(\mu_i \neq 0)$. In sharp contrast with a crossover between different critical regimes brought about by the linear relevant scaling fields, the nonlinear relevant (irrelevant) scaling fields give rise to analytic (nonanalytic) 'correction-to-scaling' terms (Aharony and Fisher, 1983; Kaul, 1994) that become important for temperatures far away from the critical point (in the asymptotic critical region).
3. $\phi_i = 0$. In this case, the operators $\mathbf{Q}_i$ and scaling fields μ_i are marginal and they can have various consequences, such as multiplicative logarithmic corrections (MLCs) to the power laws, or critical exponents varying continuously with the strength of the scaling fields μ_i. The subsequent subsections deal with the experimental realizations of the cases (1–3).

3.4 Static critical phenomena

From the foregoing text, it is clear that the critical behavior of a spin system near the magnetic order–disorder phase

transition depends on the nature of the perturbing interactions, that is, whether they are irrelevant, relevant, or marginal in the RG sense, and the physical phenomena in the critical region (i.e., the critical-point phenomena or simply the critical phenomena) are characterized by the asymptotic critical exponents and asymptotic critical amplitude ratios. A vast body of literature exists on the determination of critical exponents for a very large number of magnetic systems using a variety of experimental techniques. Among static critical exponents, the exponents α, β, γ, and δ for 'zero-field' specific heat, spontaneous magnetization, initial magnetic susceptibility, and the magnetization versus magnetic field isotherm at $T = T_C$ have been more frequently determined. In most cases, either the asymptotic analysis (AA) or the SES analysis (for details, see Kaul, 1985) is used to deduce above critical exponents from specific heat or electrical resistivity, magnetization and ac susceptibility data. It is customary to fit the data to single power laws (i.e., equations (32–37)) in AA or to the different forms of the SES in the SES analysis over temperature ranges that lie either completely or partly outside the asymptotic critical region. Now that the single power laws, or equivalently, the scaling, are strictly valid only in the asymptotic critical region, this exercise invariably yields the effective critical exponents (e.g., α_{eff}, β_{eff}, and γ_{eff}) that depend on the temperature range chosen for a given analysis. The effective critical exponents, so obtained, can be quite different (Kellner, Fähnle, Kronmüller and Kaul, 1987; Fähnle, Kellner and Kronmüller, 1987; Kaul, 1988; Kaul and Sambasiva Rao, 1991, 1994; Sambasiva Rao and Kaul, 1995; Babu and Kaul, 1997) from the asymptotic critical exponents. Thus, a quantitative comparison between the values of effective critical exponents and those of the asymptotic critical exponents, yielded by the theory, is rendered meaningless in that no definite conclusions about the nature and origin of the leading singularity at T_C can be drawn. This situation is remedied by the following approach which permits an accurate determination of asymptotic critical exponents and amplitudes.

3.4.1 *Irrelevant scaling fields: additive 'correction-to-scaling' terms*

The RG calculations (Lubensky, 1975; Grinstein and Luther, 1976), based on the random-exchange model (which combines within itself both quenched random site- and bond-diluted spin models), reveal that the asymptotic critical behavior of a quenched random spin system is the same as that of an ordered counterpart if the specific heat critical exponent, α_p, of the ordered system is negative (better known as *Harris criterion*) since in this case the quenched randomness acts as an irrelevant scaling field in the RG sense. Thus, according to these RG calculations, spontaneous magnetization, $M_S(\varepsilon)$, initial susceptibility, $\chi_0(\varepsilon)$, and specific heat or equivalently (Kaul, 1985), the temperature derivative of electrical resistivity normalized to the resistivity value at T_C, $r(\varepsilon) \equiv (\mathrm{d}\rho(T)/\mathrm{d}T)/\rho(T_C)$, of a quenched random Heisenberg system with space dimensionality $d = 3$ and spin dimensionality $n = 3$ are not described by the simple power laws (32–34), (36), and (37) in the asymptotic critical region but by the expressions

$$M_S(\varepsilon) = m_0(-\varepsilon)^{\beta}[1 + a_{M_1}^{-}(-\varepsilon)^{\Delta_1} + a_{M_2}^{-}(-\varepsilon)^{\Delta_2}] \qquad \varepsilon < 0 \tag{55}$$

$$\chi_0(\varepsilon) = \Gamma\varepsilon^{-\gamma}[1 + a_{\chi_1}^{+}\,\varepsilon^{\Delta_1} + a_{\chi_2}^{+}\,\varepsilon^{\Delta_2}] \qquad \varepsilon > 0 \tag{56}$$

$$r(\varepsilon) = (A^{\pm}/\alpha^{\pm})\,(\pm\varepsilon)^{-\alpha^{\pm}}\left[1 + a_{c_1}^{\pm}\,\alpha^{\pm}\,(\pm\varepsilon)^{\Delta_1} + a_{c_2}^{\pm}\,\alpha^{\pm}\,(\pm\varepsilon)^{\Delta_2}\right] - (A^{\pm}/\alpha^{\pm}) + B^{\pm} \tag{57}$$

In equations (55–57), plus and minus signs denote temperatures above and below T_C; m_0, $\Gamma \equiv (m_0/h_0)$, $A^{\pm}(a_{M_1}^{-}, a_{M_2}^{-}; a_{\chi_1}^{+}, a_{\chi_2}^{+}; a_{c_1}^{\pm}, a_{c_2}^{\pm})$ and β, γ, $\alpha^{\pm}$ (Δ_1, Δ_2) are the asymptotic (leading 'correction-to-scaling') critical amplitudes and critical exponents, respectively. It immediately follows that equations (55–57) reduce to the simple power laws (32–34), (36), and (37) only in the limit $\varepsilon \to 0$. Note that, like asymptotic critical exponents and amplitude ratios, the 'correction-to-scaling' critical exponents and amplitude ratios are universal (i.e., they possess unique values for systems falling within a given universality class). However, in practice, simple power laws are fitted to the data taken in a finite temperature range around T_C with the result that both the amplitudes and exponents in these power laws now depend on temperature. In other words, in such a temperature range, the simple power laws assume the modified forms

$$M_S(\varepsilon) = m_0^{\text{eff}}(\varepsilon)\,(-\varepsilon)^{\beta_{\text{eff}}(\varepsilon)} \qquad \varepsilon < 0 \tag{58}$$

$$\chi_0(\varepsilon) = \Gamma_{\text{eff}}(\varepsilon)\,\varepsilon^{-\gamma_{\text{eff}}(\varepsilon)} \qquad \varepsilon > 0 \tag{59}$$

$$r(\varepsilon) = [A_{\text{eff}}^{\pm}(\varepsilon)/\alpha_{\text{eff}}^{\pm}(\varepsilon)]\,[(\pm\varepsilon)^{-\alpha_{\text{eff}}^{\pm}(\varepsilon)} - 1] + B_{\text{eff}}^{\pm}(\varepsilon) \tag{60}$$

The most direct way of determining the asymptotic critical exponents and amplitudes is to fit the expressions (55–57) to the experimental data in the asymptotic critical region and optimize agreement between theory and experiment by treating T_C, asymptotic and 'correction-to-scaling' critical amplitudes and critical exponents as free parameters (Kaul, 1988; Kaul and Sambasiva Rao, 1991, 1994; Sambasiva Rao and Kaul, 1995; Babu and Kaul, 1997). An alternative method of determining these quantities makes use of the relations between the effective and asymptotic critical exponents and amplitudes, as explained in the following text for $M_S(\varepsilon)$ and $\chi_0(\varepsilon)$. Having calculated $M_S(T)$ $[\chi_0^{-1}(T)]$ from the intercepts on the ordinate

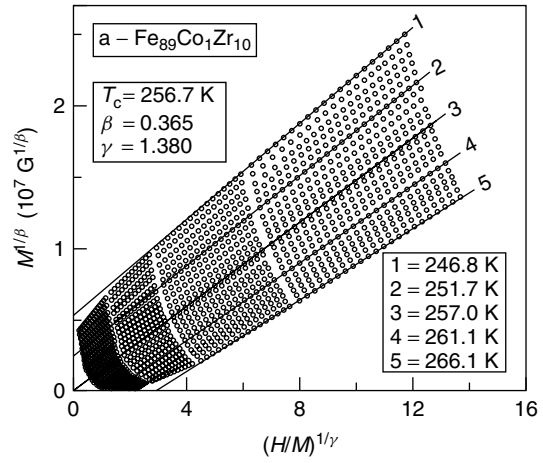

Figure 11. A typical modified Arrott ($M^{1/\beta}$ vs $(H/M)^{1/\gamma}$) plot in the critical region.

(abscissa) at $T < T_C\,[T > T_C]$ obtained by linearly extrapolating the modified Arrott plot (i.e., $[M(T, H)]^{1/\beta}$ versus $[H/M(T, H)]^{1/\gamma}$ plot) isotherms taken in the asymptotic critical region to $H = 0$ (as shown in Figure 11, taken from Babu and Kaul, 1997), the quantities $Y(T)$ and $X(T)$, defined as

$$Y(T) \equiv M_S(T)[dM_S(T)/dT]^{-1} = (T - T_C)/\beta_{eff}(\varepsilon) = [T_C/\beta_{eff}(\varepsilon)]\varepsilon \quad (61)$$

$$X(T) \equiv \chi_0^{-1}(T)[d\chi_0^{-1}(T)/dT]^{-1} = (T - T_C)/\gamma_{eff}(\varepsilon) = [T_C/\gamma_{eff}(\varepsilon)]\varepsilon \quad (62)$$

are computed from the $M_S(T)$ and $\chi_0^{-1}(T)$ data. The right-hand sides of equations (61) and (62) follow from equations (58) and (59). Since β_{eff} and γ_{eff} approach their asymptotic values β and γ only in the limit $T \to T_C$, $Y(T)$ and $X(T)$ plots tend to be linear in the immediate vicinity of T_C so that the $Y(T)$ and $X(T)$ straight lines yield the inverse slopes as β_{eff} and γ_{eff} (which are very close to β and γ) and intercepts on the T axis as T_C^- and T_C^+, respectively. Closer the T_C is approached in a given experiment, closer are the values of β_{eff} and γ_{eff} to β and γ, and more rigorously is the equality $T_C^- = T_C^+$ satisfied. This procedure fixes the value of T_C very accurately. With T_C fixed at the value so obtained, the effective critical exponents β_{eff} and γ_{eff} as functions of temperature are deduced from the $Y(T)$ and $X(T)$ data using equations (61) and (62), that is, the relations $\beta_{eff}(\varepsilon) = T_C\,\varepsilon/Y(T)$ and $\gamma_{eff}(\varepsilon) = T_C\,\varepsilon/X(T)$. In the asymptotic critical region, the effective critical exponents β_{eff} and γ_{eff} are related to the asymptotic critical exponents β and γ through the relations (Kaul, 1988; Kaul and Sambasiva Rao, 1994; Sambasiva Rao and Kaul, 1995; Babu and Kaul, 1997).

$$\beta_{eff}(\varepsilon) = \frac{d[\ln M_S(\varepsilon)]}{d\ln\varepsilon} = \beta + a_{M_1}^-\Delta_1(-\varepsilon)^{\Delta_1} + a_{M_2}^-\Delta_2(-\varepsilon)^{\Delta_2} \quad (63)$$

$$\gamma_{eff}(\varepsilon) = \frac{d[\ln \chi_0^{-1}(\varepsilon)]}{d\ln\varepsilon} = \gamma - a_{\chi_1}^+\Delta_1\varepsilon^{\Delta_1} - a_{\chi_2}^+\Delta_2\varepsilon^{\Delta_2} \quad (64)$$

The corresponding relations between the effective and asymptotic critical amplitudes are (Kaul, 1988; Kaul and Sambasiva Rao, 1994)

$$m_0^{eff}(\varepsilon) = m_0\left[1 + a_{M_1}^-(-\varepsilon)^{\Delta_1} + a_{M_2}^-(-\varepsilon)^{\Delta_2}\right](-\varepsilon)^{-[a_{m_1}^-\Delta_1(-\varepsilon)^{\Delta_1} + a_{M_2}^-\Delta_2(-\varepsilon)^{\Delta_2}]} \quad (65)$$

$$\Gamma_{eff}(\varepsilon) = \Gamma(1 + a_{\chi_1}^+\varepsilon^{\Delta_1} + a_{\chi_2}^+\varepsilon^{\Delta_2})\varepsilon^{-(a_{\chi_1}^+\Delta_1\varepsilon^{\Delta_1} + a_{\chi_2}^+\Delta_2\varepsilon^{\Delta_2})} \quad (66)$$

It is evident from equations (63) and (64) that over a finite temperature range around T_C, where the 'correction-to-scaling' confluent singularity terms are significant, the effective critical exponents can appreciably differ from the asymptotic ones and that $\beta_{eff}(\varepsilon)$ and $\gamma_{eff}(\varepsilon)$ coincide with β and γ only in the limit $|\varepsilon| \to 0$. The $\beta_{eff}(\varepsilon)$ and $\gamma_{eff}(\varepsilon)$ data, typical of amorphous ferromagnets, presented in Figure 12 (taken from Babu and Kaul, 1997) not only testify to the validity of this statement but also depict the optimum theoretical fits (continuous curves), based on equations (63) and (64), obtained by treating β, $a_{M_1}^-$, and $a_{M_2}^-$, and γ, $a_{\chi_1}^+$, and $a_{\chi_2}^+$ as free fitting parameters and fixing Δ_1 and Δ_2 at their theoretically predicted values. The values of β, $a_{M_1}^-$, and $a_{M_2}^-$, and γ, $a_{\chi_1}^+$, and $a_{\chi_2}^+$, so determined, are then used in equations (65) and (66) to compute the values of the asymptotic critical amplitudes m_0 and Γ. This method thus enables an accurate determination of the universal critical exponents $\alpha^{\pm}$, β, γ, critical amplitude ratios A^+/A^-, Dm_0^{δ}/h_0, 'correction-to-scaling' critical exponents Δ_1, Δ_2 (in some cases, Kaul, 1988; Kaul and Sambasiva Rao, 1994) and amplitude ratios $a_{M_1}^-/a_{\chi_1}^+$, $a_{M_2}^-/a_{\chi_2}^+$, $a_{c_1}^+/a_{c_1}^-$, $a_{c_2}^+/a_{c_2}^-$, $a_{c_1}^+/a_{\chi_1}^+$, $a_{c_2}^+/a_{\chi_2}^+$, and thereby allows a complete characterization of the leading singularity at T_C. True asymptotic critical behavior of a large number of ferromagnets with quenched random-exchange disorder (Kaul, 1988; Kaul and Sambasiva Rao, 1991, 1994; Sambasiva Rao and Kaul, 1995; Babu and Kaul, 1997; Peruma *et al*., 2001; Perumal, Srinivas, Rao and Dunlap, 2003) and site-disordered magnetic spinel semiconductors (Tsurkan *et al*., 1999) has been determined by following the above method of analysis. Other important points to note are as follows: (i) ac susceptibility data, taken at a driving ac field of very small root-mean-square amplitude (typically

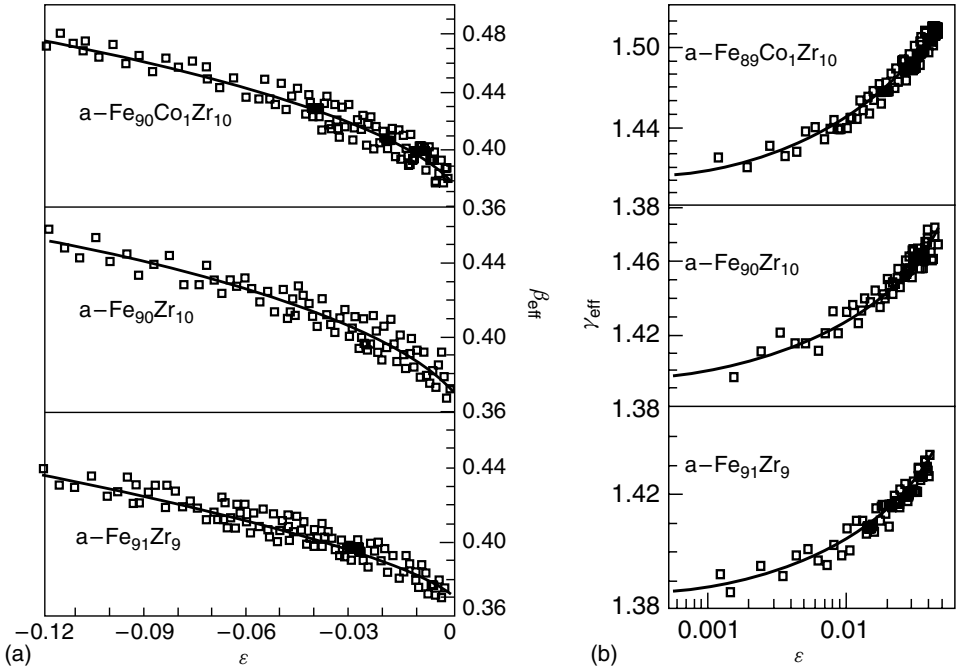

Figure 12. The effective critical exponents (a) for spontaneous magnetization, β_{eff}, and (b) susceptibility, γ_{eff}, as functions of the reduced temperature $\varepsilon = (T - T_{\text{C}})/T_{\text{C}}$ in the asymptotic critical region. The solid curves represent the least-squares fits based on (a) equation (63) and (b) equation (64).

1×10^{-7} or 10^{-6} T) after compensating for the earth's magnetic field, get rid of the errors, if any, introduced by the extrapolation of the modified Arrott plots. The results of the above-mentioned analysis of the ac susceptibility data thus serve as a cross-check (Kaul, 1988; Kaul and Sambasiva Rao, 1994) for those extracted from the extrapolated susceptibility data. (ii) Loss of accuracy suffered in constructing the temperature derivative of resistivity, $\mathrm{d}\rho(T)/\mathrm{d}T$, from $\rho(T)$ data can be avoided by directly measuring $\mathrm{d}\rho(T)/\mathrm{d}T$ employing the heat-pulse method. Recently, the direct relations between the magnetic contributions to sound velocity and 'zero-field' specific heat, and between the magnetic contribution to Young's modulus and inverse magnetic susceptibility have been exploited to accurately determine (Balakrishnan and Kaul, 2002) the specific heat and susceptibility asymptotic and 'correction-to-scaling' critical exponents and amplitudes for amorphous weak itinerant-electron ferromagnets.

3.4.2 Relevant scaling fields: isotropic Heisenberg to isotropic dipolar crossover

In insulating magnetic systems, localized magnetic moments interact with one another not only through Heisenberg exchange interactions but also via relatively weak dipole–dipole interactions. Compared to ISR (Heisenberg) exchange interactions, magnetic dipole–dipole interactions have both a long range and a reduced symmetry. The RG calculations (Aharony and Fisher, 1973; Wilson and Kogut, 1974; Bruce and Aharony, 1974; Bruce, Kosterlitz and Nelson, 1976; Bruce, 1977; Frey and Schwabl, 1991) on ferromagnets with both short-range Heisenberg exchange and long-range dipolar interactions revealed the following. (i) Dipolar perturbations, being relevant scaling fields, make the ISR (nearest-neighbor) Heisenberg fixed point of RG unstable and give rise to a new stable 'dipolar' fixed point, whose nature depends on the type (cubic, XY, Ising) of anisotropy present. (ii) In an isotropic $d = 3, n = 3$ spin system, isotropic dipolar fixed point is characterized by critical exponents whose values differ only slightly from those associated with $d = 3$ pure isotropic Heisenberg ferromagnet. (iii) Even though the asymptotic critical behavior of an isotropic dipolar ferromagnet is practically indistinguishable from that of a $d = 3$ ferromagnet with ISR Heisenberg exchange interactions only, such ferromagnets exhibit a deep minimum (a dip) in the effective critical exponent for susceptibility, γ_{eff}, versus reduced temperature, $\varepsilon = (T - T_{\text{C}})/T_{\text{C}}$, ($T_{\text{C}}$ is the Curie temperature of isotropic dipolar ferromagnet), curve in the crossover region for $\varepsilon > 0$. Such a dip in $\gamma_{\text{eff}}(\varepsilon)$ turns out to be a universal feature of $d = 3$ ferromagnets with weak isotropic dipolar interactions.

The scaling approach (Bruce, Kosterlitz and Nelson, 1976; Bruce, 1977), when applied to the crossover phenomena in a $d = 3$ ISR Heisenberg ferromagnet with weak isotropic dipolar interactions of normalized strength $g_{\rm D}$, yields 'zero-field' susceptibility for temperatures close to criticality as

$$\chi(\varepsilon_H, g_{\rm D}) = \Gamma\, \varepsilon_H^{-\gamma_H}\, X(y) \tag{67}$$

where $\varepsilon_H = [T - T_{\rm C}(0)]/T_{\rm C}(0)$ and Γ is a nonuniversal constant; $T_{\rm C}(0) \equiv T_{\rm C}(g_{\rm D} = 0)$ and γ_H, respectively, are the transition temperature and susceptibility critical exponent of pure ($g_{\rm D} = 0$) ISR Heisenberg ($d = 3, n = 3$) spin system, $y = x/x_g, x \equiv g_{\rm D}/\varepsilon_H^{\phi}, x_g \equiv g_{\rm D}/\varepsilon_g^{\phi}, \varepsilon_g = [T_{\rm C}(g_{\rm D}) - T_{\rm C}(0)]/T_{\rm C}(0)$ is the shift in the transition temperature caused by long-range dipolar interactions, ϕ is the crossover exponent which equals γ_H, and $X(y)$ is the crossover scaling function. As the true transition temperature $T_{\rm C} \equiv T_{\rm C}(g_{\rm D})$, is approached, dipolar interactions dominate and give rise to a singularity in $X(y)$ at $y = 1$ (or equivalently, at $\varepsilon = [(T - T_{\rm C})/T_{\rm C}] = 0$) with the result

$$X(y \approx 1) \sim (1 - y)^{-\gamma_{\rm D}} \tag{68}$$

where $T_{\rm C}$ and $\gamma_{\rm D}$ are the transition temperature and the susceptibility critical exponent of the isotropic dipolar ferromagnet. According to equations (67) and (68), dipolar interactions make their presence felt when a crossover temperature $\varepsilon_{\rm co} \equiv g_{\rm D}^{1/\phi}$ is reached by lowering the temperature from high temperatures ($T \gg T_{\rm C}$) such that for $\varepsilon \gg \varepsilon_{\rm co}$ the spin system behaves as a pure $d = 3, n = 3$ system with only ISR exchange interactions, whereas for $\varepsilon \ll \varepsilon_{\rm co}$ the asymptotic critical behavior is that of a $d = 3$ isotropic dipolar ferromagnet. A detailed RG calculation (Bruce, Kosterlitz and Nelson, 1976; Bruce, 1977) of the crossover scaling function yields the explicit forms of the susceptibility and its effective critical exponent (defined as $\gamma_{\rm eff}(\varepsilon) = {\rm d}[\ln \chi^{-1}(\varepsilon)]/{\rm d}(\ln \varepsilon)$) as

$$\chi(y) = \tilde{\Gamma}\, y^{\gamma_H/\phi}\, (1 - y)^{-\gamma_{\rm D}}\, p(y) \tag{69}$$

and

$$\gamma_{\rm eff}(y) = (1 - y^{1/\phi}) \left[\gamma_H + \phi\, \gamma_{\rm D} \left(\frac{y}{1 - y} \right) + \phi \left(\frac{y\, p'(y)}{p(y)} \right) \right] \tag{70}$$

in terms of the 'correction-to-scaling' function, $p(y)$. The reduced temperature, ε, is related to y as $y^{-1/\phi} - 1 = \hat{\varepsilon} = [(1 + \varepsilon_g)/\varepsilon_g]\, \varepsilon$. The expression (70), like (69), is valid across the entire crossover region and yields the limiting values $\gamma_{\rm D} = \gamma_{\rm eff}(y \to 1)$ and $\gamma_H = \gamma_{\rm eff}(y \ll 1)$ that characterize the critical behavior of susceptibility in the isotropic long-range dipolar (ILD) and ISR Heisenberg regimes, respectively. According to equation (70), $\gamma_{\rm eff}$ as a function of y goes through a minimum at a certain value of $\hat{\varepsilon}$ in the crossover region. Moreover, in the asymptotic critical regime ($0 < \varepsilon \ll \varepsilon_{\rm co}$) $y \cong 1$, the function $p(y)$ in equations (69) and (70) can be expanded to obtain (Kogon and Bruce, 1982) the expressions

$$\chi(\varepsilon) = A_\chi\, \varepsilon^{-\gamma_{\rm D}}\, (1 + a_\chi\, \varepsilon^{\Delta_{\rm D}}) \tag{71}$$

$$\gamma_{\rm eff}(\varepsilon) = \gamma_{\rm D} - a_\chi\, \Delta_{\rm D}\, \varepsilon^{\Delta_{\rm D}} \tag{72}$$

$$a_\chi \cong 0.099\, \varepsilon_g^{-\Delta_{\rm D}} \tag{73}$$

$$\varepsilon_g \cong 0.349\, \dot{\varepsilon} \tag{74}$$

where a_χ and $\Delta_{\rm D}$ are the leading 'correction-to-scaling' amplitude and exponent, respectively, and $\dot{\varepsilon}$ is the reduced temperature ε at which the inverse initial (intrinsic) susceptibility $\chi^{-1} = 4\pi$.

Despite intense efforts (Menyuk, Dwight and Reed, 1971; Høg and Johansson, 1973; Huang, Pindak and Ho, 1974; Berkner, 1975; Kornblit and Ahlers, 1975; Als-Nielsen, Dietrich and Passell, 1976; Kornblit, Ahlers and Buehler, 1978) to unravel the exact nature of the leading singularity in the asymptotic critical region of well-known $d = 3$ dipolar ferromagnets EuO and EuS in the past, the above theoretical predictions had to wait for experimental confirmation till recently when their validity was demonstrated by the results of extensive ac ('zero-field') susceptibility measurements (Srinath, Kaul and Sostarich, 2000; Srinath and Kaul, 2000) on amorphous $(Fe_pNi_{1-p})_{80}B_{16}Si_4$ and $(Co_{p'}Ni_{1-p'})_{80}B_{16}Si_4$ alloys with p and p' just above the respective critical concentrations for the onset of long-range ferromagnetic order, that is, $p_{\rm C} = 0.0285(5)$ and $p'_{\rm C} = 0.0688(5)$. The effective critical exponent for susceptibility as a function of reduced temperature, $\gamma_{\rm eff}(\varepsilon)$, is obtained from the measured ac susceptibility after correcting it for demagnetization by following the procedure described in detail in the previous subsection. $\gamma_{\rm eff}(\varepsilon)$ exhibits a pronounced dip at $\varepsilon_{\rm min}$ and attains the ILD and ISR Heisenberg values $\gamma_{\rm D}$ and γ_H in the limits $\varepsilon \to 0$ and $\varepsilon \to \varepsilon^{**}$ for the alloys with the Fe or Co concentration p or p' just above $p_{\rm C}$ or $p'_{\rm C}$ in which dipolar interactions are comparable in strength to ISR Heisenberg exchange interactions. A detailed quantitative comparison between theory (equations (67–74)) and experiment is depicted in Figure 13 (taken from Srinath, Kaul and Sostarich, 2000). Another important physical implication of the above experimental study (Srinath, Kaul and Sostarich, 2000; Srinath and Kaul, 2000) on amorphous ferromagnets, which either do or do not exhibit reentrant behavior at low temperatures, is that it clearly brings out the importance of isotropic dipolar interactions in establishing long-range ferromagnetic order in reentrant amorphous ferromagnets. For different types of crossover phenomena, the reader is referred to Kaul (2002).

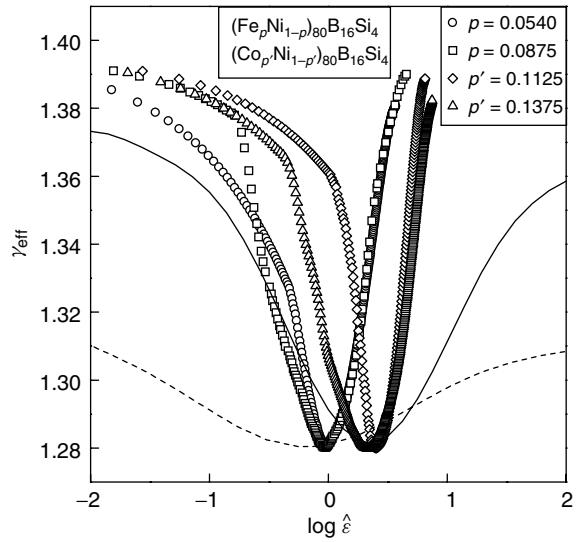

Figure 13. Comparison between the theoretically predicted and experimentally observed temperature variation of the susceptibility effective critical exponent, γ_{eff}, for the amorphous $(Fe_pNi_{1-p})_{80}B_{16}Si_4$ and $(Co_{p'}Ni_{1-p'})_{80}B_{16}Si_4$ alloys with the concentration of magnetic Fe or Co atoms just above the percolation threshold for long-range ferromagnetic order. This figure serves to highlight the dip in $\gamma_{\text{eff}}(\varepsilon)$ that is characteristic of the isotropic long-range dipolar to isotropic short-range Heisenberg crossover.

3.4.3 Marginal scaling fields: multiplicative logarithmic corrections to the power laws

The crossover scenario as well as the asymptotic critical behavior gets more complicated when, in addition to the dipolar interaction, magnetic anisotropy is present in an otherwise ISR $(d = 3, n = 3)$ Heisenberg spin system. In the presence of magneto-crystalline anisotropy, dipolar interactions act as marginal scaling fields and hence modify the critical behavior of the $d = 3, n = 1$ system (i.e., three-dimensional spin system with infinite uniaxial anisotropy) so much so that, instead of behaving as a three-dimensional Ising ferromagnet in the asymptotic critical region, it exhibits mean-field behavior with logarithmic multiplicative corrections (Wegner and Riedel, 1973; Brézin and Zinn-Justin, 1976; Frey and Schwabl, 1990; Ried, Millev, Fähnle and Kronmüller, 1995) in this regime. Elaborate RG study (Frey and Schwabl, 1990; Ried, Millev, Fähnle and Kronmüller, 1995) of the second-order phase transition in a Heisenberg ferromagnet in which, in addition to the dominant short-range exchange interactions, dipole–dipole interactions and uniaxial anisotropy are present, reveals that, due to a competition between the three types of interactions that differ in symmetry and range, the critical region embraces a series of crossovers between four nontrivial fixed points: Gaussian → ISR Heisenberg → isotropic dipolar → uniaxial dipolar, as the critical point is approached from high temperatures. In this case, 'zero-field' susceptibility takes the scaling form

$$\chi(\varepsilon_H, g_{\text{D}}, g_{\text{A}}) \propto \varepsilon_H^{-\gamma_H} X\left(\frac{g_{\text{D}}}{\varepsilon_H^{\phi_{\text{D}}}}, \frac{g_{\text{A}}}{\varepsilon_H^{\phi_A}}\right) \tag{75}$$

where $\varepsilon_H = [T - T_{\text{C}}(0)]/T_{\text{C}}(0), T_{\text{C}}(0) = T_{\text{C}}(g_{\text{D}} = g_{\text{A}} = 0)$ and γ_H, respectively, are the reduced temperature, transition temperature, and susceptibility critical exponent of pure $(g_{\text{D}} = g_{\text{A}} = 0)$ ISR Heisenberg $(d = 3, n = 3)$ spin system. The crossover exponents ϕ_{D} and ϕ_{A} are positive while $g_{\text{D}}\,(g_{\text{A}})$ is the dimensionless ratio of dipolar energy (anisotropy energy) and ISR exchange energy. Alternatively, g_{D} and g_{A} are a direct measure of the dipolar and anisotropy (relevant) perturbations. For sufficiently high temperatures, that is, $\varepsilon_H \gg g_{\text{D}}^{1/\phi_{\text{D}}}, g_{\text{A}}^{1/\phi_{\text{A}}}$, the critical behavior is that of an isotropic Heisenberg ferromagnet. As the temperature is lowered toward the critical point, a series of crossovers occur depending on the initial values of g_{A} and g_{D} and their relative strengths. In the temperature ranges $g_{\text{D}}^{1/\phi_{\text{D}}} \ll \varepsilon_H \ll g_{\text{A}}^{1/\phi_{\text{A}}}$ and $g_{\text{A}}^{1/\phi_{\text{A}}} \ll \varepsilon_H \ll g_{\text{D}}^{1/\phi_{\text{D}}}$, the spin system exhibits anisotropic short-range (e.g., $d = 3, n = 1$) and isotropic dipolar critical behavior, respectively. The behavior of the system in the asymptotic critical region, that is, at temperatures $\varepsilon_H \ll g_{\text{D}}^{1/\phi_{\text{D}}}, g_{\text{A}}^{1/\phi_{\text{A}}}$ or equivalently, in the limit $\varepsilon \to 0$, is determined by both anisotropy and dipolar interactions; the reduced temperature ε measures the temperature deviation from the critical temperature $T_{\text{C}}(g_{\text{D}} \neq 0, g_{\text{A}} \neq 0)$ of the anisotropic dipolar fixed point. The RG calculations (Frey and Schwabl, 1990; Ried, Millev, Fähnle and Kronmüller, 1995) have addressed three distinctly different cases. On the basis of the calculated temperature dependence of the effective critical exponent for susceptibility, $\gamma_{\text{eff}}(\varepsilon) = \mathrm{d}\ln\chi^{-1}(\varepsilon)\mathrm{d}\ln\varepsilon$, at temperatures spanning the asymptotic critical region and crossover regimes, these RG theories predict the following sequences of crossovers as the temperature is lowered from high temperatures to the critical point, T_{C}. Case I: when both g_{D} and uniaxial anisotropy (g_{U}) are extremely large (Frey and Schwabl, 1990), Gaussian regime → short-range Ising (I) → uniaxial dipolar (UD) fixed point (characterized by mean-field power laws with MLCs (Wegner and Riedel, 1973; Brézin and Zinn-Justin, 1976; Frey and Schwabl, 1990; Ried, Millev, Fähnle and Kronmüller, 1995)). Case II: when $g_{\text{U}} \gg g_{\text{D}}$ (Ried, Millev, Fähnle and Kronmüller, 1995), Gaussian → isotropic short-range Heisenberg (IH) → I → UD. Case III: when $g_{\text{U}} \ll g_{\text{D}}$ (Ried, Millev, Fähnle and Kronmüller, 1995), Gaussian → IH → isotropic long-range dipolar (ID) → UD.

The existence of MLCs to the mean-field power laws, characteristic of the UD fixed point, in uniaxial ferromagnets $GdCl_3$, $LiTbF_4$, and $LiHoF_4$ (Kötzler and Scheithe, 1973; Frowein and Kötzler, 1982; Griffin, Huster and Folweiler, 1980; Frowein, Kötzler, Schaub and Schuster, 1982) as well

as a crossover from Ising to asymptotic UD critical behavior in $LiTbF_4$ (Frey and Schwabl, 1990) was confirmed experimentally by Frowein, Kötzler, Schaub and Schuster (1982). Even though early electrical resistivity (Geldart, De'Bell, Cook and Laubitz, 1987) and specific heat (Bednarz, Geldart and White, 1993) data strongly indicated that the asymptotic critical behavior of Gd could be that of a UD ferromagnet, it was only recently that an elaborate analysis of extensive high-resolution ac susceptibility (Srinath, Kaul and Kronmüller, 1999) and bulk magnetization (Srinath and Kaul, 1999) data taken along the c axis (easy direction of magnetization) of a high-purity Gd single crystal over four decades in the reduced temperature $\varepsilon = (T - T_C)/T_C$ provided a conclusive experimental evidence for (i) a UD asymptotic critical behavior, (ii) a sequence of crossovers: UD $\rightarrow$ isotropic dipolar (ID) $\rightarrow$ Gaussian (the latter crossover proceeds without the intervening ID $\rightarrow$ isotropic short-range Heisenberg (IH) crossover, predicted theoretically by Frey and Schwabl (1990) and by Ried, Millev, Fähnle and Kronmüller (1995) for temperatures above T_C (critical temperature corresponding to the UD fixed point) as $T \rightarrow T_C^+$, and (iii) the UD $\rightarrow$ IH crossover as the temperature is lowered below T_C^-. The UD $\rightarrow$ IH crossover is accompanied by a transition from linear (uniaxial dipolar/Ising) domain wall to Bloch (Heisenberg) domain wall and no theoretical predictions exist for this crossover (details given in Srinath and Kaul, 1999). The effective critical exponents $\beta_{\rm eff}(\varepsilon)$ and $\gamma_{\rm eff}(\varepsilon)$ for spontaneous magnetization and 'zero-field' susceptibility (obtained by employing the method of data analysis already described in Section 3.4.1) displayed in Figure 14 (taken from Srinath and Kaul, 1999) highlights the crossovers UD $\rightarrow$ IH for $T < T_C^-$ and UD $\rightarrow$ ID for $T > T_C^+$. A detailed analysis (Srinath and Kaul, 1999) of the spontaneous magnetization, $M(\varepsilon, 0)$, (inverse 'zero-field' susceptibility, $\chi^{-1}(\varepsilon)$) data in the asymptotic critical region, that is, $|\varepsilon| \leq |\varepsilon_{\rm co}^{\rm UD\rightarrow IH}|$ [$|\varepsilon| \leq |\varepsilon_{\rm co}^{\rm UD\rightarrow ID}|$], and the critical $M - H$ isotherm reveals that, in conformity with the RG predictions (Wegner and Riedel, 1973; Brézin and Zinn-Justin, 1976; Frey and Schwabl, 1990; Ried, Millev, Fähnle and Kronmüller, 1995) for a $d = 3$ UD ferromagnet, the asymptotic critical behavior of these quantities is accurately described by the expressions

$$M(\varepsilon, 0) = \hat{B}\,(-\varepsilon)^{\beta}\,|\ln|\varepsilon||^{x^-} \qquad \varepsilon < 0 \qquad (76)$$

$$\chi^{-1}(\varepsilon) = \hat{\Gamma}^{-1}\varepsilon^{\gamma}\,|\ln\varepsilon|^{-x^+} \qquad \varepsilon > 0 \qquad (77)$$

$$H = \hat{D}\,M^{\delta}\,|\ln|M||^{-3x^-} \qquad \varepsilon = 0 \qquad (78)$$

with the asymptotic critical exponents $\beta = 0.5002(6)$, $\gamma = 1.0003(3)$, $\delta = 3.005(5)$, and logarithmic correction exponents $x^- = 0.330(2)$, $x^+ = 0.329(1)$. These experimental values match quite well with the theoretical values $\beta = 0.5$, $\gamma = 1$, $\delta = 3$, and $x^- = 3/(n+8)$, $x^+ = (n+2)/(n+8)$ with $n = 1$. Such a close agreement is also true for the universal amplitude ratio $R_\chi = \hat{D}\hat{B}^{\delta-1}\hat{\Gamma}$ and hence these results unambiguously establish that the asymptotic critical behavior of Gd is that of a $d = 3$ UD ferromagnet.

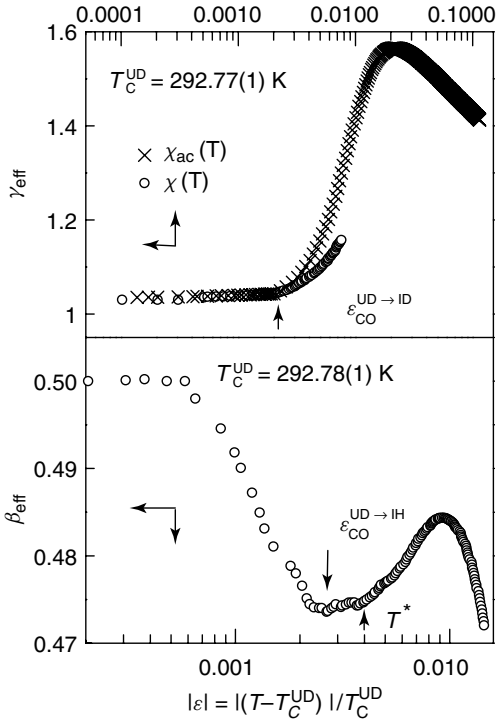

Figure 14. Temperature variations of the effective critical exponents $\beta_{\rm eff}$ (bottom panel) and $\gamma_{\rm eff}$ (top panel) for gadolinium metal. The onset temperatures of the uniaxial dipolar (UD)-to-isotropic Heisenberg (IH) and uniaxial dipolar (UD)-to-isotropic dipolar (ID) crossovers as well as the peak in $\beta_{\rm eff}(\varepsilon)$, where a transition from the linear domain wall to Bloch domain wall occurs, are marked by the arrows.

Another example of marginal scaling fields is provided by the long-range exchange interactions of the specific form $J(r) \sim r^{-(d+\sigma)}$ with $\sigma = d/2$ (Fisher, Ma and Nickel, 1972) that couple spins in an isotropic d-dimensional spin system with n-component order parameter. Such interactions thus give rise to logarithmic corrections (Fisher, Ma and Nickel, 1972) to the mean-field critical behavior. MLCs to the mean-field power laws in the asymptotic critical region (henceforth referred to as the MLC fixed point) of the type given by equations (76–78) and a gradual crossover to the Gaussian fixed point at temperatures outside the critical regime have been unambiguously detected in recent bulk magnetization and ac susceptibility experiments on various polycrystalline samples of $d = 3, n = 3$ weak itinerant-electron ferromagnet $Ni_{75}Al_{25}$ 'prepared' in different states of site disorder (Semwal and Kaul, 2001, 2002). In these samples, crossover to the Gaussian fixed point is followed at

higher temperatures ($T > T_C$) by a crossover from Gaussian (G) to mean-field (MF) regime. Site disorder (or equivalently, quenched random-exchange disorder) turns out to be irrelevant (Semwal and Kaul, 2002) in the RG sense in $Ni_{75}Al_{25}$. The MLC fixed point is distinctly different from the UD fixed point in that the universal amplitude ratio $R_\chi = \hat{D}\hat{B}^{\delta-1}\hat{\Gamma}$ and the logarithmic correction exponents have widely different values (Semwal and Kaul, 2002) in the two cases.

4 CONCLUDING REMARKS

In this brief review of the vast field of finite temperature magnetism and magnetic phase transitions (from the experimental point of view), more emphasis has been deliberately laid on itinerant-electron (band or metallic) magnetism than on localized-spin (Heisenberg) magnetism, for the following reasons. First, itinerant systems form the bulk of real magnetic materials. Second, magnetic excitations and magnetic phase transitions are more varied in nature in metallic systems than in localized systems. Inability of the early INS experiments (due to the limited range of energy transfer accessible to them) to simultaneously detect spin waves and Stoner single-particle excitations, together with nonpropagating longitudinal and transverse spin fluctuations, in strong or weak itinerant-electron systems not only gave birth to SPEELS (a relatively new experimental technique) but also led to significant improvements in the traditional neutron-scattering techniques; one such improvised technique is the spin-polarized neutron scattering with spin-polarized detection. Third, weak itinerant magnets act as model systems for understanding strongly correlated systems, which have gained considerable attention in the scientific community recently because of the discovery of high-temperature superconductivity and magnetically mediated superconductivity, on the one hand, and renewed interest in the metal-insulator transition particularly in the colossal magnetoresistance materials (doped $LaMnO_3$ compounds), on the other.

Phase transitions in spin systems with quenched random-exchange disorder attracted considerable attention in the late 1970s and early 1980s because certain features of the critical behavior, inherent to these systems, were distinctly different from those witnessed earlier in crystalline systems. One such feature is the nonmonotonic temperature dependence of the effective exponent, γ_{eff}, for susceptibility in amorphous ferromagnets (Kaul, 1984b, 1985) over an extremely wide temperature range above the Curie point, T_C (i.e., with temperature increasing above T_C, γ_{eff} increases from a value close to that ($\gamma = 1.386$) for a $d = 3$ Heisenberg ferromagnet in the asymptotic critical region to a broad maximum before decreasing at a very slow rate toward the mean-field value of $\gamma = 1.0$ at $T \gg T_C$). This nonmonotonic behavior of $\gamma_{\text{eff}}(\varepsilon)$ arises from the interplay between the thermal spin–spin correlation length, $\xi(T)$, (of the spins in the ferromagnetic 'backbone'/network) and the length scale characteristic of random structural disorder (temperature-dependent length scale determined by the caliper dimension of the finite spin clusters at $T > T_C$) in the correlated molecular-field theory proposed by Fähnle and Herzer (1984) (in the infinite-ferromagnetic-network plus finite-spin-clusters model due to Kaul (1984b, 1985)). The Monte Carlo simulations of the phase transitions in bond- and site-disordered ferromagnets (Fähnle, 1984, 1985, 1987) revealed that the nonmonotonic temperature dependence of γ_{eff} was mainly due to site disorder.

The experimental techniques and the methods of data analysis used in the literature to study static critical phenomena in magnetic systems were extensively reviewed by Kaul (1985) with particular emphasis on ferromagnets with quenched random-exchange disorder. By contrast, Section 3 of the present article deals exclusively with refinements in the data analyses and recent advances in the experimental detection of the asymptotic (static) critical behavior and crossover between different critical regimes in ISR exchange ferromagnets with or without long-range interactions (e.g., dipole–dipole interactions) and magnetic anisotropy. However, due to space restrictions, this description of the static critical phenomena has in a sense preempted the dynamical aspects of such phenomena, which are equally interesting and sometimes yield more decisive information about the nature of underlying interactions in a given system. One of the most glaring examples where this is indeed the case is the following. The static critical behavior of $d = 3$ ISR Heisenberg ferromagnet is practically indistinguishable from that of $d = 3$ ILD ferromagnet since the values of the static critical exponents for such ferromagnets differ only slightly (by less than 0.5%). By contrast, the dynamical critical exponent z (which characterizes the dynamics of the critical spin fluctuations) has widely different values $z \cong 2$ and $z \cong 2.5$ for the ILD and ISR Heisenberg fixed points and hence permits a clear-cut distinction between them. A 'feel' for the dynamical critical phenomena is essentially conveyed by the observation of a cooperative growth of the short-range magnetic order (or equivalently, spin patches or clusters), characterized by a correlation length, ξ, and a correlation time, τ, both of which diverge at T_C, as the critical point is approached from temperatures above T_C. This is the well-known 'critical slowing down' phenomenon. To account for this dynamical aspect of critical phenomena, the (equal time) correlation function, given earlier by equation (38), should be generalized to include time, that is, $G(\mathbf{r}, \tau) = [\langle \mathbf{S_0}(0) \cdot \mathbf{S_r}(\tau)\rangle - \langle \mathbf{S_0}\rangle\langle \mathbf{S_r}\rangle]$. As a consequence of this generalization, the lifetime of the

spin fluctuations of wave vector q is governed by a temperature dependence $|\varepsilon|^{-z\nu}$ (where z and ν are the dynamical and correlation length critical exponents, respectively), with a characteristic divergence as $T \rightarrow T_C$. Excellent reviews of the subject of dynamical critical phenomena are available in the literature both from theoretical (Hohenberg and Halperin, 1977; Frey and Schwabl, 1994; Henneberger *et al*., 1999) and experimental (Hohenemser, Rosov and Kleinhammes, 1989; Collins, 1989) standpoints.

ACKNOWLEDGMENTS

The author has greatly benefited from discussions or correspondence with A. Aharony, A. S. Arrott, M. Fähnle, D. J. W. Geldart, C. Hohenemser, J. Kötzler, H. Kronmüller and W. Nolting. Thanks are also due to the members of the research groups at the University of Hyderabad, India, and at the Max Planck Institute for Metal Research, Stuttgart, whose contributions have been extensively used in this article. These researchers include P. D. Babu, S. F. Fischer, W.-U. Kellner, Ch. V. Mohan, R. Reisser, M. Sambasiva Rao, M. Seeger, Anita Semwal, V. Siruguri and S. Srinath. The author thanks Sanjeev Kumar for his assistance in preparing the diagrams for this article.

REFERENCES

Abraham, D.L. and Hopster, H. (1989). Spin-polarized electron-energy-loss spectroscopy on Ni. *Physical Review Letters*, **62**, 1157–1160.

Aharony, A., Alexander, S., Entin-Wohlman, O. and Orbach, R. (1985). Nonlinear scaling fields and corrections to scaling near criticality. *Physical Review B*, **31**, 2565–2567.

Aharony, A., Entin-Wohlman, O., Alexander, S. and Orbach, R. (1987). Crossover from phonons to fractons. *Philosophical Magazine B*, **56**, 949–955.

Aharony, A. and Fisher, M.E. (1973). Critical behavior of magnets with dipolar interactions. I. Renormalization group near four dimensions, *Physical Review B*, **8**, 3323–3341.

Aharony, A. and Fisher, M.E. (1983). Nonlinear scaling fields and corrections to scaling near criticality. *Physical Review B*, **27**, 4394–4400.

Alexander, S. and Orbach, R. (1982). Density of states on fractals: fractons. *Journal de Physique Letters, Paris*, **43**, L625–L631.

Als-Nielsen, J., Dietrich, O.W. and Passell, L. (1976). Neutron scattering from the Heisenberg ferromagnets EuO ans EuS. II. Static critical properties. *Physical Review B*, **14**, 4908–4922.

Anderjczuk, A., Dobrzynski, L., Zukowski, E., *et al*. (1992). Compton scattering studies of charge transfer in Fe-Ni-B amorphous alloys. *Journal of Physics: Condensed Matter*, **4**, 2735–2745.

Babu, P.D. and Kaul, S.N. (1997). Scaling behaviour of magnetization for temperatures in the vicinity of, and far from, the ferromagnetic-paramagnetic phase transition in amorphous $Fe_{90-x}Co_xZr_{10}$ and $Fe_{90+y}Zr_{10-y}$ alloys. *Journal of Physics: Condensed Matter*, **9**, 7189–7222.

Balakrishnan, K. and Kaul, S.N. (2002). Determination of susceptibility and specific heat critical exponents for weak itinerant-electron ferromagnets from vibrating reed experiments. *Physical Review B*, **65**, 134412-1–134412-7.

Barbara, B., Gignoux, D. and Vettier, C. (1988). *Lectures on Modern Magnetism*, Springer-Verlag: Berlin.

Bednarz, G., Geldart, D.J.W. and White, M.A. (1993). Heat capacity of gadolinium near the Curie temperature. *Physical Review B*, **47**, 14247–14259.

Berkner, D.D. (1975). Magneto-optic study of the critical region of EuS. *Physics Letters A*, **54**, 396–398.

Bernhoeft, N.R., Hayden, S.M., Lonzarich, G.G., *et al*. (1989). Dispersive magnetic density fluctuations in Ni_3Ga. *Physical Review Letters*, **62**, 657–660.

Bernhoeft, N.R., Law, S.A., Lonzarich, G.G. and Paul, D.Mc.K. (1988). Magnetic excitations in $ZrZn_2$ at low energies and long wavelengths. *Physica Scripta*, **38**, 191–193.

Bernhoeft, N.R., Lonzarich, G.G., Paul, D.Mc.K. and Mitchell, P.W. (1986). Magnetic fluctuation spectra of very weak itinerant ferromagnets. *Physica B*, **136**, 443–446.

Brézin, E. and Zinn-Justin, J. (1976). Critical behavior of uniaxial systems with strong dipolar interactions. *Physical Review B*, **13**, 251–254.

Bruce, A.D. (1977). Susceptibility crossover in dipolar ferromagnets. *Journal of Physics C: Solid State Physics*, **10**, 419–432.

Bruce, A.D. and Aharony, A. (1974). Critical exponents of ferromagnets with dipolar interactions: second-order ε-expansion. *Physical Review B*, **10**, 2078–2087.

Bruce, A.D., Kosterlitz, J.M. and Nelson, D.R. (1976). Crossover phenomena in isotropic dipolar ferromagnets. *Journal of Physics C: Solid State Physics*, **9**, 825–840.

Callaway, J. (1991). *Quantum Theory of the Solid State*, *Second Edition*, Academic Press: New York.

Capellmann, H. (1987). In *Metallic Magnetism*, Capellmann, H. (Ed.), Springer-Verlag: Berlin, pp. 1–13.

Cardy, J.L. (1996). *Scaling and Renormalization in Statistical Physics*, Cambridge University Press: London.

Collins, M.F. (1989). *Magnetic Critical Scattering*, Oxford University Press: Oxford, New York.

Continentino, M.A. and Rivier, N. (1979). On the apparent spin wave stiffness of amorphous ferromagnets. *Journal of Physics F: Metal Physics*, **9**, L145–L150.

Domb, C. (1996). *The Critical Point: A Historical Introduction to the Modern Theory of Critical Phenomena*, Taylor & Francis: London.

Fähnle, M. (1984). Monte Carlo study of phase transitions in bond- and site-disordered Ising and classical Heisenberg ferromagnets. *Journal of Magnetism and Magnetic Materials*, **45**, 279–287.

Fähnle, M. (1985). Behaviour of the effective susceptibility exponent in site-disordered ferromagnets. *Journal of Physics C: Solid State Physics*, **18**, 181–190.

Fähnle, M. (1987). Non-monotonic temperature dependence of the effective susceptibility exponent–a characteristic feature of many

disordered spin systems. *Journal of Magnetism and Magnetic Materials*, **65**, 1–6.

Fähnle, M. and Herzer, G. (1984). On the correlated molecular field theory of amorphous ferromagnets. *Journal of Magnetism and Magnetic Materials*, **44**, 274–278.

Fähnle, M., Kellner, W.U. and Kronmüller, H. (1987). Use of scaling plots in phase-transition studies. *Physical Review B*, **35**, 3640–3642.

Fernandez-Baca, J.A., Lynn, J.W., Rhyne, J.J. and Fish, G.E. (1987). Long-wavelength spin-wave energies and linewidths of the amorphous Invar alloy $Fe_{100-x}B_x$. *Physical Review B*, **36**, 8497–8511.

Fernandez-Baca, J.A., Rhyne, J.J., Fish, G.E., *et al*. (1990). Spin dynamics of amorphous $Fe_{90-x}Ni_xZr_{10}$. *Journal of Applied Physics*, **67**, 5223–5228.

Fischer, S.F., Kaul, S.N. and Kronmüller, H. (2002). Critical magnetic properties of disordered polycrystalline $Cr_{75}Fe_{25}$ and $Cr_{70}Fe_{30}$ alloys. *Physical Review B*, **65**, 064443-1–064443-12.

Fisher, M.E. (1974). The renormalization group in the theory of critical behavior. *Reviews of Modern Physics*, **46**, 597–616.

Fisher, M.E. (1998). Renormalization group theory: its basis and formulation in statistical physics. *Reviews of Modern Physics*, **70**, 653–681.

Fisher, M.E., Ma, S.K. and Nickel, B.G. (1972). Critical exponents for long-range interactions. *Physical Review Letters*, **29**, 917–920.

Frey, E. and Schwabl, F. (1990). Renormalized field theory for the static crossover in uniaxial dipolar ferromagnets. *Physical Review B*, **42**, 8261–8273.

Frey, E. and Schwabl, F. (1991). Renormalized field theory for the static crossover in isotropic dipolar ferromagnets. *Physical Review B*, **43**, 833–841.

Frey, E. and Schwabl, F. (1994). Critical dynamics of magnets. *Advances in Physics*, **43**, 577–683.

Frowein, R. and Kötzler, J. (1982). Direct observation of the logarithmic corrections to Landau's equation of state at marginal dimension. *Physical Review B*, **25**, 3292–3297.

Frowein, R., Kötzler, J., Schaub, B. and Schuster, H.G. (1982). Crossover to mean-field behavior at marginal dimensionality. *Physical Review B*, **25**, 4905–4907.

Gautier, F. (1982). In *Magnetism of Metals and Alloys*, Cyrot, M. (Ed.), North-Holland Publishing: Amsterdam, pp. 1–244.

Geldart, D.J.W., De'Bell, K., Cook, J. and Laubitz, M.J. (1987). Dipole-dipole interactions and the critical resistivity of gadolinium. *Physical Review B*, **35**, 8876–8879.

Goldenfeld, N. (1994). *Renormalization Group in Critical Phenomena*, Addison-Wesley: New York.

Griffin, J.A., Huster, M. and Folweiler, R.J. (1980). Critical behavior of the spontaneous magnetization at marginal dimensionality in $LiHoF_4$. *Physical Review B*, **22**, 4370–4378.

Grinstein, G. and Luther, A. (1976). Application of the renormalization group to phase transitions in disordered systems. *Physical Review B*, **13**, 1329–1343.

Henneberger, S., Frey, E., Maier, P.G., *et al*. (1999). Critical dynamics of a uniaxial and dipolar ferromagnet. *Physical Review B*, **60**, 9630–9649.

Hohenberg, P.C. and Halperin, B.I. (1977). Theory of dynamic critical phenomena. *Reviews of Modern Physics*, **49**, 435–479.

Hohenemser, C., Rosov, N. and Kleinhammes, A. (1989). Critical phenomena studied via nuclear techniques. *Hyperfine Interactions*, **49**, 267–324.

Høg, J. and Johansson, J. (1973). Critical magnetic behaviour of Europium oxide. *International Journal of Magnetism*, **4**, 11–16.

Hopster, H., Kurzawa, R., Raue, R., *et al*. (1985). Spin-polarized photoemission study of Fe-Ni ferromagnetic metallic glasses. *Journal of Physics F: Metal Physics*, **15**, L11–L15.

Huang, C.C., Pindak, R.S. and Ho, J.T. (1974). Critical exponent γ of Europium oxide. *Solid State Communications*, **14**, 559–562.

Ikeda, H., Fernandez-Baca, J.A., Nicklow, R.M., *et al*. (1994). Fracton excitations in a diluted Heisenberg antiferromagnet near the percolation threshold: $RbMn_{0.39}Mg_{0.61}F_3$. *Journal of Physics: Condensed Matter*, **6**, 10543–10549.

Ishikawa, Y. (1978). Neutron scattering studies of itinerant electron magnetism. *Journal of Applied Physics*, **49**, 2125–2130.

Ishikawa, Y. (1986). Paramagnetic spin fluctuations in 3d metals and compounds. *Journal of Magnetism and Magnetic Materials*, **54–57**, 1121–1126.

Ishikawa, Y., Noda, Y., Uemura, Y.J., *et al*. (1985). Paramagnetic spin fluctuations in weak itinerant-electron ferromagnet $MnSi$. *Physical Review B*, **31**, 5884–5893.

Ishikawa, Y., Shirane, G., Tarvin, J.A. and Kohgi, M. (1977). Magnetic excitations in the weak itinerant ferromagnet $MnSi$. *Physical Review B*, **16**, 4956–4970.

Izuyama, T. and Kubo, R. (1964). Some considerations on the magnetic carriers in ferromagnetic transition metals. *Journal of Applied Physics*, **35**, 1074–1081.

Karlsson, K. and Aryasetiawan, F. (2000). A many-body approach to spin-wave excitations in itinerant magnetic systems. *Journal of Physics: Condensed Matter*, **12**, 7617–7631.

Kaul, S.N. (1981). Magnetic properties of amorphous $(Fe, Ni)_{80}B_{20}$, $(Fe, Ni)_{80}B_{19}Si_1$, and $(Fe, Ni)_{80}P_{14}B_6$ alloys. *IEEE Transactions on Magnetics*, **MAG-17**, 1208–1215.

Kaul, S.N. (1983). Low-temperature magnetization and spin-wave excitations in amorphous Ni-rich transition-metal-metalloid alloys. *Physical Review B*, **27**, 5761–5774.

Kaul, S.N. (1984a). Reappraisal of the published neutron scattering data on amorphous ferromagnetic alloys. *Solid State Communications*, **52**, 1015–1019.

Kaul, S.N. (1984b). Critical behavior of amorphous ferromagnetic alloys. *IEEE Transactions on Magnetics*, **MAG-20**, 1290–1295.

Kaul, S.N. (1985). Static critical phenomena in ferromagnets with quenched disorder. *Journal of Magnetism and Magnetic Materials*, **53**, 5–53.

Kaul, S.N. (1988). Asymptotic and leading "correction-to-scaling" susceptibility critical exponents and amplitudes for ferromagnets with quenched disorder. *Physical Review B*, **38**, 9178–9186.

Kaul, S.N. (1994). Nonlinear scaling and its application to ferromagnetic systems. *Phase Transitions*, **47**, 23–57.

Kaul, S.N. (1999). Spin-fluctuation theory for weak itinerant-electron ferromagnets: revisited. *Journal of Physics: Condensed Matter*, **11**, 7597–7614.

Kaul, S.N. (2002). Thermal critical phenomena and crossover between critical regimes in ferromagnets with long-range interactions. *Zeitschrift fur Metallkunde*, **93**, 1024–1029.

Kaul, S.N. (2005). Spin-wave and spin-fluctuation contributions to the magnetoresistance of weak itinerant-electron ferromagnets. *Journal of Physics: Condensed Matter*, **17**, 5595–5612.

Kaul, S.N. and Babu, P.D. (1994a). Detailed magnetization study of quenched random ferromagnets. I. Low-lying magnetic excitations. *Physical Review B*, **50**, 9308–9322.

Kaul, S.N. and Babu, P.D. (1994b). Detailed magnetization study of quenched random ferromagnets. II. Site dilution and percolation exponents. *Physical Review B*, **50**, 9323–9330.

Kaul, S.N. and Babu, P.D. (1998). Low-lying magnetic excitations in amorphous $Fe_{90-x}Co_xZr_{10}$ and $Fe_{90+y}Zr_{10-y}$ alloys. *Journal of Physics: Condensed Matter*, **10**, 1563–1597.

Kaul, S.N. and Rosenberg, M. (1983). Evidence for a transition from weak to strong ferromagnetism from spontaneous resistivity anisotropy and high-field magnetic susceptibility data in amorphous $(Fe-Ni)_{80}(P-B)_{20}$ alloys. *Physical Review B*, **27**, 5698–5705.

Kaul, S.N. and Sambasiva Rao, M. (1991). Asymptotic and leading correction-to-scaling specific-heat critical exponents and amplitudes for quench-disordered ferromagnets from resistivity measurements. *Physical Review B*, **43**, 11240–11248.

Kaul, S.N. and Sambasiva Rao, M. (1994). Asymptotic critical behaviour of quenched random-exchange Heisenberg ferromagnets. *Journal of Physics: Condensed Matter*, **6**, 7403–7435.

Kaul, S.N. and Semwal, A. (1999). Dependence of spin fluctuations on magnetic field in weak itinerant-electron ferromagnets. *Physics Letters A*, **254**, 101–106.

Kaul, S.N. and Semwal, A. (2004). Magnetic properties of the weak itinerant-electron ferromagnet $Ni_{75}Al_{25}$: II. The effect of compositional disorder. *Journal of Physics: Condensed Matter*, **16**, 8695–8712.

Kaul, S.N. and Srinath, S. (2001). Magnon-fracton crossover in quenched random site-diluted ferromagnets. *Physical Review B*, **63**, 094410-1–094410-7.

Keffer, F. (1966). Spin waves. In *Encyclopedia of Physics*, Wijn, H.P.J. (Ed.), Springer-Verlag: Berlin, Ferromagnetism, pp. 1–268, Volume XVIII/2.

Kellner, W.U., Fähnle, M., Kronmüller, H. and Kaul, S.N. (1987). The magnetic phase transition in amorphous and disordered crystalline ferromagnets. *Physical Status Solidi B*, **144**, 397–409.

Kogon, H.S. and Bruce, A.D. (1982). Transition temperature shifts and correction-to-scaling amplitudes in systems exhibiting crossover behaviour. *Journal of Physics C: Solid State Physics*, **15**, 5729–5739.

Kornblit, A. and Ahlers, G. (1975). Heat capacity of EuO near the Curie temperature. *Physical Review B*, **11**, 2678–2688.

Kornblit, A., Ahlers, G. and Buehler, E. (1978). Heat capacity of EuS near the ferromagnetic transition. *Physical Review B*, **17**, 282–292.

Kötzler, J. and Scheithe, W. (1973). Critical exponents of $GdCl_3$: a ferromagnet with long-range interactions. *Solid State Communications*, **12**, 643–647.

Liebs, M. and Fähnle, M. (1996). Are amorphous FeNiB systems non-collinear magnets? *Journal of Physics: Condensed Matter*, **8**, 3207–3213.

Lonzarich, G.G. and Taillefer, L. (1985). Effect of spin fluctuations on the magnetic equation of state of ferromagnetic or nearly ferromagnetic metals. *Journal of Physics C: Solid State Physics*, **18**, 4339–4371.

Lovesey, S.W. (1987). *Theory of Neutron Scattering from Condensed Matter*, *Reprinted Edition*, Oxford University Press: New York.

Lubensky, T.C. (1975). Critical properties of random-spin models from the ε- expansion. *Physical Review B*, **11**, 3573–3580.

Lynn, J.W. and Rhyne, J.J. (1988). Spin dynamics of amorphous magnets. In *Spin Waves and Magnetic Excitations*, Borovik-Romanov, A.S. and Sinha, S.K. (Eds.), North-Holland Publishing: Amsterdam, pp. 177–218.

Lynn, J.W., Rosov, N. and Fish, G.E. (1993). Polarization analysis of the magnetic excitations in Invar and non-Invar amorphous alloys. *Journal of Applied Physics*, **73**, 5369–5371.

Ma, S.K. (1976). *Modern Theory of Critical Phenomena*, W. A. Benjamin, Inc.: Massachusetts.

Mathon, J. and Wohlfarth, E.P. (1968). The temperature dependence of the spin wave energy in the itinerant electron model of ferromagnetism. *Proceedings of the Royal Society of London. Series A*, **302**, 409–418.

Menyuk, N., Dwight, K. and Reed, T.B. (1971). Critical magnetic properties and exchange interactions in EuO. *Physical Review B*, **3**, 1689–1698.

Mohn, P. (2003). *Magnetism in the Solid State: An Introduction*, Springer-Verlag: Berlin.

Mook, H.A. (1988). Neutron scattering studies of magnetic excitations in itinerant magnets. In *Spin Waves and Magnetic Excitations*, Borovik-Romanov, A.S. and Sinha, S.K. (Eds.), North-Holland Publishing: Amsterdam, pp. 425–478.

Mook, H.A. and Nicklow, R.M. (1973). Neutron scattering investigation of the magnetic excitations in iron. *Physical Review B*, **7**, 336–342.

Mook, H.A., Nicklow, R.M., Thompson, E.D. and Wilkinson, M.K. (1969). Spin wave spectrum of nickel metal. *Journal of Applied Physics*, **40**, 1450–1451.

Mook, H.A. and Paul, D.Mc.K. (1985). Neutron scattering measurements of the spin-wave spectra for nickel. *Physical Review Letters*, **54**, 227–229.

Moriya, T. (1985). *Spin Fluctuations in Itinerant Electron Magnetism*, Springer-Verlag: Berlin.

Moriya, T. and Kawabata, A. (1973). Effect of spin fluctuations on itinerant electron ferromagnetism. II. *Journal of the Physical Society of Japan*, **35**, 669–676.

Nakai, I. (1983). Magnetic excitations in fcc Fe-Ni alloys revealed from detailed magnetization measurements. *Journal of the Physical Society of Japan*, **52**, 1781–1790.

Nakai, I. (1990). Field dependence of the Stoner-type contribution to the magnetization of fcc Fe-Ni alloys. *Journal of the Physical Society of Japan*, **59**, 2211–2215.

Nakai, I. and Maruyama, H. (1992). Field dependence of the magnetisation of Fe-Ni Invars. *Journal of Magnetism and Magnetic Materials*, **104–107**, 2053–2054.

Nakai, I., Ono, F. and Yamada, O. (1983). Role of T^2 term in temperature dependence of the magnetization for Fe-Ni Invar alloys. *Journal of the Physical Society of Japan*, **52**, 1791–1798.

Nakai, I., Yamada, O., Mimura, M., *et al*. (1987). Detailed investigation of the magnetization of an amorphous ferromagnet $Fe_{83}B_{17}$. *Journal of the Physical Society of Japan*, **56**, 4056–4063.

Nakayama, T., Yakubo, K. and Orbach, R.L. (1994). Dynamical properties of fractal networks: scaling, numerical simulations and physical realizations. *Reviews of Modern Physics*, **66**, 381–443.

Ododo, J.C. and Anyakoha, M.W. (1983). Magnetic excitations in nickel and iron. *Journal of Physics F: Metal Physics*, **13**, 2335–2349.

Penn, D.R. and Apell, P. (1988). Free-electron-like Stoner excitations in Fe. *Physical Review B*, **38**, 5051–5054.

Perumal, A., Srinivas, V., Kim, K.S., *et al*. (2001). Correction to scaling critical exponents and amplitudes for amorphous Fe-Mn-Zr alloys. *Journal of Magnetism and Magnetic Materials*, **233**, 280–289.

Perumal, A., Srinivas, V., Rao, V.V. and Dunlap, R.A. (2003). Quenched disorder and the critical behavior of a partially frustrated system. *Physical Review Letters*, **91**, 137202-1–137202-4.

Plihal, M., Mills, D.L. and Kirschner, J. (1999). Spin wave signature in the spin polarized electron energy loss spectrum of ultrathin Fe films: theory and experiment. *Physical Review Letters*, **82**, 2579–2582.

Privman, V., Hohenberg, P.C. and Aharony, A. (1991). In *Phase Transitions and Critical Phenomena*, Domb, C. and Lebowitz, J.L. (Eds.), Academic Press: London, New York, pp. 1–134, Vol. 14.

Ried, K., Millev, Y., Fähnle, M. and Kronmüller, H. (1995). Phase transitions in ferromagnets with dipolar interactions and uniaxial anisotropy. *Physical Review B*, **51**, 15229–15249.

Riedel, E.K. and Wegner, F.J. (1974). Effective critical and tricritical exponents. *Physical Review B*, **9**, 294–315.

Salamon, M.B. and Yeshurun, Y. (1987). Spin-fracton effects in dilute amorphous alloys. *Physical Review B*, **36**, 5643–5646.

Sambasiva Rao, M. and Kaul, S.N. (1995). Determination of asymptotic critical exponents and amplitudes for amorphous 3D ferromagnets from bulk magnetization measurements. *Journal of Magnetism and Magnetic Materials*, **147**, 149–159.

Seeger, M., Kaul, S.N., Kronmüller, H. and Reisser, R. (1995). Asymptotic critical behavior of Ni. *Physical Review B*, **51**, 12585–12594.

Semadeni, F., Böni, P., Endoh, Y., *et al*. (1999). Direct observation of spin-flip excitations in $MnSi$. *Physica B*, **267–268**, 248–251.

Semadeni, F., Roessli, B., Böni, P., *et al*. (2000). Critical fluctuations in the weak itinerant ferromagnet Ni_3Al: a comparison between self-consistent renormalization and mode-mode coupling theory. *Physical Review B*, **62**, 1083–1088.

Semwal, A. and Kaul, S.N. (1999). Low-lying magnetic excitations in Ni_3Al and their suppression by a magnetic field. *Physical Review B*, **60**, 12799–12809.

Semwal, A. and Kaul, S.N. (2001). Evidence for logarithmic corrections to the mean-field critical behavior in the weak itinerant ferromagnet Ni_3Al. *Physical Review B*, **64**, 014417-1–014417-8.

Semwal, A. and Kaul, S.N. (2002). Effect of site disorder on the asymptotic critical behaviour of $Ni_{75}Al_{25}$. *Journal of Physics: Condensed Matter*, **14**, 5829–5847.

Semwal, A. and Kaul, S.N. (2004). Magnetic properties of the weak itinerant-electron ferromagnet $Ni_{75}Al_{25}$: I. The effect of site disorder. *Journal of Physics: Condensed Matter*, **16**, 8675–8694.

Shapiro, S.M. (1988). Magnetic excitations in spin glasses. In *Spin Waves and Magnetic Excitations*, Borovik-Romanov, A.S. and Sinha, S.K. (Eds.), North-Holland Publishing: Amsterdam, pp. 219–258.

Solontsov, A.Z. and Wagner, D. (1994). Spin anharmonicity and zero-point fluctuations in weak itinerant electron magnets. *Journal of Physics: Condensed Matter*, **6**, 7395–7402.

Solontsov, A.Z. and Wagner, D. (1995). Zero-point spin fluctuations and magnetovolume effect in itinerant-electron magnetism. *Physical Review B*, **51**, 12410–12417.

Srinath, S. and Kaul, S.N. (1999). Static universality class for gadolinium. *Physical Review B*, **60**, 12166–12176.

Srinath, S. and Kaul, S.N. (2000). Evidence for dipolar-effects in re-entrant amorphous ferromagnets. *Europhysics Letters*, **51**, 441–446.

Srinath, S., Kaul, S.N. and Kronmüller, H. (1999). Observation of isotropic dipolar to uniaxial dipolar crossover in gadolinium. *Physical Review B*, **59**, 1145–1151.

Srinath, S., Kaul, S.N. and Sostarich, M.K. (2000). Isotropic-Heisenberg to isotropic-dipolar crossover in amorphous ferromagnets with composition near the percolation threshold. *Physical Review B*, **62**, 11649–11660.

Stanley, H.E. (1971). *Introduction to Phase Transitions and Critical Phenomena*, Oxford University Press: New York.

Stauffer, D. and Aharony, A. (1992). *Introduction to Percolation Theory*, *Second Edition*, Taylor & Francis: London.

Stinchcombe, R.B. and Pimentel, I.R. (1988). Thermal crossover effects resulting from dilution-induced magnon critical dynamics. *Journal of Physics A: Mathematical and General*, **21**, L807–L811.

Stirling, W.G. and McEwen, K.A. (1987). In *Methods of Experimental Physics*, Sköld, K. and Price, D.L. (Eds.), Academic Press: New York, pp. 159–240, Vol. 23, Part C.

Squires, G.L. (1978). *Introduction to the Theory of Thermal Neutron Scattering*, Cambridge University Press: London, New York.

Takahashi, Y. (1986). On the origin of the Curie-Weiss law of the magnetic susceptibility in itinerant electron ferromagnetism. *Journal of the Physical Society of Japan*, **55**, 3553–3573.

Takahashi, Y. (2001). Quantum spin fluctuation theory of the magnetic equation of state of weak itinerant-electron ferromagnets. *Journal of Physics: Condensed Matter*, **13**, 6323–6358.

Takeuchi, J. and Masuda, T. (1979). Low temperature specific heat of itinerant electron ferromagnet Sc_3In. *Journal of the Physical Society of Japan*, **46**, 468–474.

Thompson, E.D., Wohlfarth, E.P. and Bryan, A.C. (1964). The low temperature variation of the saturation magnetization of

ferromagnetic metals and alloys. *Proceedings of the Physical Society of London*, **83**, 59–70.

Tomiyoshi, S., Yamaguchi, Y., Ohashi, M., *et al*. (1987). Magnetic excitations in the itinerant antiferromagnets Mn_3Si and Fe-doped Mn_3Si. *Physical Review B*, **36**, 2181–2189.

Tsurkan, V., Baran, M., Szewczyk, A., *et al*. (1999). Magnetic phase transition in $MnCr_{2-2x}In_{2x}S_4$ crystals. *Journal of Physics: Condensed Matter*, **11**, 7907–7920.

Vaks, V.G., Larkin, A.I. and Pikin, S.A. (1968). Spin waves and correlation functions in a ferromagnet. *Soviet Physics JETP*, **26**, 647–655.

Valiev, E.Z. and Menshikov, A.Z. (1995). Longitudinal spin fluctuations (hidden magnetic excitations) in Invar alloys. *Journal of Magnetism and Magnetic Materials*, **147**, 189–191.

Venus, D. and Kirschner, J. (1988). Momentum dependence of the Stoner excitation spectrum of iron using spin-polarized electron-energy-loss spectroscopy. *Physical Review B*, **37**, 2199–2211.

Vollmer, R., Etzkorn, M., Anil Kumar, P.S., *et al*. (2003). Spin-polarized electron energy loss spectroscopy of high energy, large wave vector spin waves in ultrathin fcc Co films on Cu(001). *Physical Review Letters*, **91**, 147201-1–147201-4.

Vollmer, R., Etzkorn, M., Anil Kumar, P.S., *et al*. (2004). Spin-polarized electron energy loss spectroscopy: a method to measure magnon energies. *Journal of Magnetism and Magnetic Materials*, **272–276**, 2126–2130.

Wegner, F.J. (1972). Corrections to scaling laws. *Physical Review B*, **5**, 4529–4536.

Wegner, F.J. and Riedel, E.K. (1973). Logarithmic corrections to the molecular-field behavior of critical and tricritical systems. *Physical Review B*, **7**, 248–256.

Wilson, K.G. and Kogut, J. (1974). The renormalization group and the ε-expansion. *Physics Reports*, **12**, 75–200.

Yamada, O., Mimura, M., Maruyama, H., *et al*. (1986). Temperature dependence of the magnetization of amorphous Fe-B Invar alloys. *Journal of Magnetism and Magnetic Materials*, **54–57**, 250–252.

Yeshurun, Y. and Salamon, M.B. (1987). Fractal excitations in dilute magnets. *Philosophical Magazine*, **56**, 957–961.

Yosida, K. (1996). *Theory of Magnetism*, Springer-Verlag: Berlin.

Zadro, K. (1996). Magnetic excitations in $Fe_3Ni_{77}B_{18}Si_2$ amorphous alloy. *Journal of Magnetism and Magnetic Materials*, **163**, L5–L7.

Electron Theory of Finite Temperature Magnetism

Jürgen Kübler
Technische Universität Darmstadt, Darmstadt, Germany

1 INTRODUCTION

Wohlfarth, in an important review (1980), stated that the three ferromagnetic transition metals are of importance to the whole subject of metallic magnetism and their properties should be thoroughly understood before attempting to understand those of the transition-metal alloys. In fact, we repeat only one of Wohlfarth's tables in Table 1 and can now state, clearly, how far our understanding goes and where the challenge lies.

The saturation magnetization appearing in the first two lines of Table 1 can be calculated to very good precision *ab initio* using the density-functional theory in the local spin-density functional approximation (LSDA), an approximation that is well documented and is widely used for calculating ground-state properties. In the next section, some of the salient facts of the LSDA are collected. So, depending somewhat on one's point of view, one can say that these data are well understood.

The Curie temperatures listed in the third line of Table 1 and the fourth line are not so well understood, but progress has been made in the recent past as we have documented here.

Historically, the important question was whether the magnetic carriers were localized or itinerant and each of these two viewpoints had eminent proponents. Although, of course, colloquially, the terms *localized* or *itinerant* seem clear, a physical definition is more helpful. A simple one was given more than 40 years ago by Rhodes and Wohlfarth (1963). This is how they might have argued.

The susceptibility in the paramagnetic state of a local moment ferromagnet is given by the Curie–Weiss law:

$$\chi = \frac{C}{T - T_c} \tag{1}$$

The Curie constant, C can be written as

$$C = \frac{1}{3} q_c (q_c + 2) \mu_B^2 / k_B \tag{2}$$

where q_c is called the *number of magnetic carriers*, which is obtained from the experimental Curie–Weiss susceptibility. In Table 1, the values of q_c are collected and the ratio q_c/q_s is also listed, where q_s is the moment at zero temperature. A local moment system is characterized by the ratio $q_c/q_s = 1$. We see from Table 1 how the elemental ferromagnets Fe, Co, and Ni progressively deviate from locality.

Rhodes and Wohlfarth obtained the ratios of q_c/q_s for a large number of ferromagnetic metallic compounds and alloys from experimental data and plotted them as a function of the measured Curie temperatures. The result is now called the Rhodes-Wohlfarth plot, as shown in Figure 1.

Handbook of Magnetism and Advanced Magnetic Materials. Edited by Helmut Kronmüller and Stuart Parkin. Volume 1: *Fundamentals and Theory*. ISBN: 978-0-470-02217-7.

Table 1. Fundamental magnetic properties of bcc Fe, Co, and fcc Ni (Co is hcp at low and fcc at high temperatures). (Reproduced from E.P. Wohlfarth, 1980, with permission of Elsevier.)

	Fe	Co	Ni
Saturation magnetization [emu g^{-1}]	221.71 ± 0.08	162.55	58.57 ± 0.03
Saturation magnetization (q_s) [μ_B per atom]	2.216	1.715	0.616
Curie temperature (T_c) (K)	1044 ± 2	1388 ± 2	627.4 ± 0.3
kT_c [meV]	90.0	119.6	54.1
Number of magnetic carriers from Curie–Weiss law (q_c)	2.29	2.29	0.90
q_c/q_s	1.03	1.34	1.46

This phenomenological curve gives intuitive insight into the different kinds of magnetism. For, considering a system with localized moments, we do not expect the magnitude of the moment to change much when it is measured below and above T_c, giving ratios q_c/q_s of order unity. Thus, we find systems with localized moments on the line $q_c/q_s = 1$. We attribute the rather systematic deviation of q_c/q_s from unity to magnetic moments due to itinerant, that is, essentially delocalized, magnetic moments. Of course, the saturation moments become small in general for decreasing T_c, but the increase in q_c/q_s is mainly due to increasing effective magnetic carriers at high temperatures. The challenge is that we do not deal with two disjunct cases, localized or itinerant, but with a distribution, which requires a unified treatment that interpolates between the two limits.

The theory of itinerant-electron magnetism has traditionally been pursued along two different directions, until recently by two separate communities. One uses model Hamiltonians, most prominently the Hubbard (1979) model, in conjunction with many-body techniques, the other density-functional theory and its LSDA. In contrast to the former, the latter is an *ab initio* approach that does not require empirical parameters as input. It appears, however, that the two main streams are about to merge into one; of the many examples, only the work of Lichtenstein, Katsnelson and Kotliar (2001) should be mentioned here because of its relevance for the finite-temperature properties of Fe and Ni. Since, otherwise, the model Hamiltonian approach will receive much attention in this volume (see for instance **Density-functional Theory of Magnetism, Volume 1** and **Dynamical Mean-field Theory of Itinerant Electron Magnetism, Volume 1**), we can pass over this important topic here and turn to the density-functional approach, which will carry us a long way.

A readable and clear introduction to the history of magnetism and various ways to the treatment of localized and itinerant-electron magnets can be found in the book by Mohn (2003). In the book by Kübler (2000), much of the methodology is described, which makes the spin-density-functional theory amenable to numerical solutions.

Returning now to the need of a unified treatment of itinerant-electron magnetism, we emphasize the work of Moriya and his students (Moriya and Takahashi, 1978a,b; Moriya, 1985,1987), which supplies such a unified concept and spells out the key approximations, as for instance the *adiabatic approximation* to be dealt with later on. Although

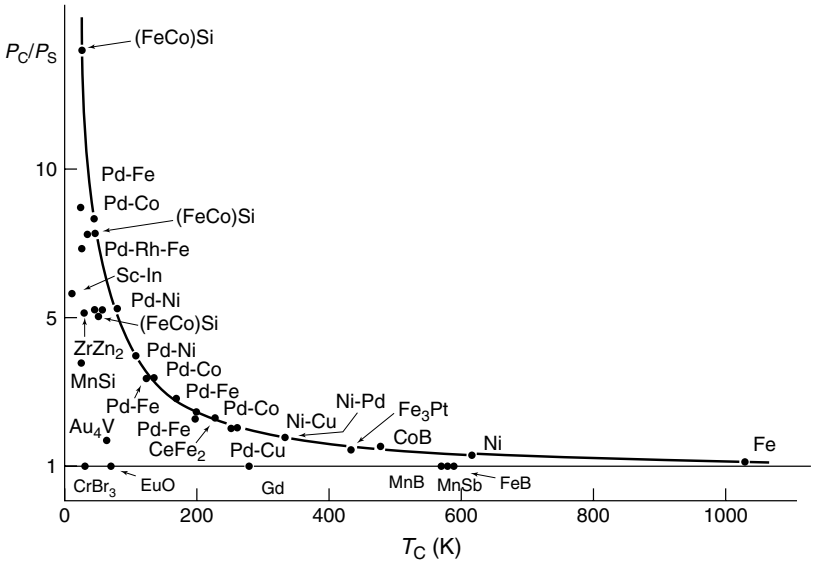

Figure 1. Rhodes–Wohlfarth plot: ratio P_c/P_s, where P_c is obtained from the experimental Curie constant, and P_s is the saturation magnetization versus the Curie temperature. Note that the notation is changed in this historical plot, the letter P replacing q used in the text. (Reproduced from P. Rhodes and E.P. Wohlfarth: *Proceedings of the Royal Society* **A273**, 1963, p 247, with permission from The Royal Society.)

the theory in its entirety is not easily amenable to *ab initio* calculations, which are at the heart of this chapter, we will make an attempt to follow the physical insight it supplies as far as possible without too many formal derivations. It emerges that starting from the elemental metals is not advantageous. It is the limit of the weak ferromagnets with very large values of q_c/q_s that provides initially more insight into the physics of the itinerant-electron magnets.

2 SPIN-DENSITY-FUNCTIONAL THEORY

We begin with a brief excursion into density-functional theory. It is of some didactic advantage to do this using the version by Mermin (1965), which is formulated for finite temperatures. We give an outline of this theory even though we presently do not know a physically meaningful approximation to the finite-temperature exchange-correlation potential. The discussion given in this section, therefore, serves on the one hand to restate, in the modern form, the Stoner–Wohlfarth theory (and why it fails) and, on the other hand, to define our limits of understanding. It should be noted that the formulation that follows – differing from Mermin's – is based on two-component spinor functions this way accounting for the spin of the electron in a sufficiently detailed, yet simple way.

We consider a many-electron system in an external potential giving first the connection of the external potential with the density matrix:

$$V[\tilde{\rho}] = \sum_{\alpha\beta} \int v^{\text{ext}}_{\alpha\beta}(\mathbf{r})\tilde{\rho}_{\beta\alpha}(\mathbf{r})\mathrm{d}\mathbf{r} \tag{3}$$

where $\alpha, \beta = 1, 2$ are spin indices and $\tilde{\rho}_{\beta\alpha}(\mathbf{r})$ are the elements of the density matrix, $\tilde{\rho}$, which define the particle density through the trace

$$\rho(\mathbf{r}) = \text{Tr } \tilde{\rho}(\mathbf{r}) \tag{4}$$

and the vector of the magnetization by

$$\mathbf{m}(\mathbf{r}) = \text{Tr } \boldsymbol{\sigma}\tilde{\rho}(\mathbf{r}) \tag{5}$$

where $\boldsymbol{\sigma}$ is given by the Pauli spin matrices.

Mermin (1965) laid the formal foundations for the proof that in the grand canonical ensemble at a given temperature T and chemical potential μ the equilibrium density matrix $\tilde{\rho}(\mathbf{r})$, that is, the equilibrium particle density $\rho(\mathbf{r})$ and the equilibrium magnetization $\mathbf{m}(\mathbf{r})$ are determined by the external potential and magnetic field that make up $v^{\text{ext}}_{\alpha\beta}(\mathbf{r})$. It must be added, however, that Mermin did not discuss magnetic systems and based his theory on the density, not the density matrix. Allowing for this generalization without any formal proofs, we state that the correct $\rho(\mathbf{r})$ and $\mathbf{m}(\mathbf{r})$ minimize the Gibbs grand potential Ω:

$$\Omega[\tilde{\rho}] = \sum_{\alpha\beta} \int v^{\text{ext}}_{\alpha\beta}(\mathbf{r})\tilde{\rho}_{\beta\alpha}(\mathbf{r})\mathrm{d}\mathbf{r} + \iint \mathrm{d}\mathbf{r}\,\mathrm{d}\mathbf{r}' \frac{\rho(\mathbf{r})\rho(\mathbf{r}')}{|\mathbf{r}-\mathbf{r}'|} - \mu \int \mathrm{d}\mathbf{r}\rho(\mathbf{r}) + G[\tilde{\rho}] \tag{6}$$

where G is a unique functional of charge and magnetization at a given temperature T and chemical potential μ. The reader interested in more details is referred to Mermin's original paper or to reviews like that by Ramana and Rajagopal (1983), Kohn and Vashishta (1983), and Eschrig (1996). The quantity $G[\tilde{\rho}]$ in equation (6) is written as the sum of three terms, that is,

$$G[\tilde{\rho}] = T_0[\tilde{\rho}] - TS_0[\tilde{\rho}] + \Omega_{xc}[\tilde{\rho}] \tag{7}$$

with T_0, S_0 being, respectively, the kinetic energy and entropy of a system of noninteracting electrons with density matrix $\tilde{\rho}$ at a temperature T. The quantity Ω_{xc} is the exchange and correlation contribution to the Gibbs grand potential.

We now construct the minimum of the grand potential using a system of noninteracting electrons moving in an effective potential. We thus assume we can determine single-particle functions $\{\psi_{i\alpha}(\mathbf{r})\}$ that permit us to write the elements of the density matrix as

$$\tilde{\rho}_{\beta\alpha}(\mathbf{r}) = \sum_{i=1}^{\infty} \psi_{i\beta}(\mathbf{r})\psi^*_{i\alpha}(\mathbf{r}) f(\varepsilon_i) \tag{8}$$

where α and β, due to the electron spin, take on the values 1 and 2 and $f(\varepsilon) = \left[1 + \exp\beta(\varepsilon - \mu)\right]^{-1}$ is the Fermi–Dirac distribution function ($\beta = 1/k_B T$). We obtain the single-particle spinor functions by solving the Schrödinger equation

$$\sum_{\beta} [-\delta_{\alpha\beta}\nabla^2 + v'_{\alpha\beta}(\mathbf{r}) - \varepsilon_i\delta_{\alpha\beta}]\psi_{i\beta}(\mathbf{r}) = 0 \tag{9}$$

and attempt to determine the potential, v', by minimizing the grand potential, thus obtaining the effective potential as

$$v'_{\alpha\beta}(\mathbf{r}) \equiv v^{\text{eff}}_{\alpha\beta}(\mathbf{r}) = v^{\text{ext}}_{\alpha\beta}(\mathbf{r}) + 2\delta_{\alpha\beta}\int \frac{\rho(\mathbf{r}')}{|\mathbf{r}-\mathbf{r}'|}\mathrm{d}\mathbf{r}' + v^{xc}_{\alpha\beta}(\mathbf{r}) \tag{10}$$

where

$$v^{xc}_{\alpha\beta}(\mathbf{r}) = \frac{\delta}{\delta\tilde{\rho}_{\beta\alpha}(\mathbf{r})}\Omega_{xc}[\tilde{\rho}] \tag{11}$$

With the result for the effective potential, we may finally rewrite the grand potential as

$$\Omega[\tilde{\rho}] = -\beta^{-1}\sum_{i=1}^{\infty}\ln[1+\exp\beta(\mu-\varepsilon_i)] - \iint \mathrm{d}\mathbf{r}\mathrm{d}\mathbf{r}'\frac{\rho(\mathbf{r})\rho(\mathbf{r}')}{|\mathbf{r}-\mathbf{r}'|} - \sum_{\alpha\beta}\int \mathrm{d}\mathbf{r} v^{xc}_{\alpha\beta}(\mathbf{r})\tilde{\rho}_{\beta\alpha}(\mathbf{r}) + \Omega_{xc}[\tilde{\rho}] \qquad (12)$$

Formally, the problem now appears to be solved: the potential in the Schrödinger equation, equation (9), is given by the equations (10) and (11) in which the density matrix is given by equation (8). For a ferromagnet at zero temperature, we know that the basic Schrödinger equation, in the local-density-functional approximation, is diagonal in spin space and hence easily solved. But, at finite temperatures, the formal expression for the exchange-correlation potential, $v^{xc}_{\alpha\beta}(\mathbf{r})$, equation (11), gives no clue regarding its general properties. If we assume it remains diagonal in spin space and use the zero-temperature exchange-correlation potential, we may again solve the Schrödinger equation, temperature in this case entering only through the Fermi–Dirac distribution in equation (8). This is not a hard calculation and one obtains for the temperature where the magnetization vanishes, values that, compared with the experimental Curie temperatures, are unacceptably large.

This disagreement is part of what is normally called the *failure of Stoner–Wohlfarth theory*. Another well-known defect is the magnetic susceptibility for which one calculates for the temperature range of interest Pauli-like (i.e., temperature independent) behavior. This is in stark contradiction to the well-known, experimentally observed Curie–Weiss law, which receives a lot of attention in Section 3.

We have chosen here to discuss the problem using a version of Mermin's finite-temperature density-functional theory and see that our basic assumption of a diagonal effective potential is most likely the weak part of this treatment. Restricting the effective potential to diagonal form implies that the magnetization decreases as the temperature increases because of excitations that are of the order of the exchange splitting, that is, of rather high energies, since the exchange splitting is large on the scale of the Curie temperatures. We are thus led to look for low-energy excitations to explain the magnetic phase transition.

Awareness of low-energy excitations arose in the 1970s predominantly through the pioneering work of Korenman Murray and Prange (1977), Hubbard (1979), Hasegawa (1979), Edwards (1982), Heine and Samson (1983), Moriya (1985), and Gyorffy *et al*. (1985), and others, the review of Staunton (1994) constituting a clear summary. The broad consensus reached was that *orientational fluctuations of the local magnetization* represent the essential ingredients of a thermodynamic theory. This cannot be incorporated in a straightforward way into the Stoner–Mermin theory.

To proceed with the density-functional theory, one ignores the difficulties connected with the exchange-correlation grand potential and assumes in its place the exchange-correlation total energy at zero temperature making, at the same time, the LSDA. One may use here any of the established schemes like those of von Barth and Hedin (1972) or Perdew and Wang (1992). The next step then is a formulation of the LSDA that allows for general, that is, *noncollinear configurations* of the magnetic moments in a magnetic crystal. To accomplish this, one may proceed as follows.

In its most simple version, one partitions the space in the crystal into atomic spheres over which one integrates the density matrix defined in equation (8), that is, one determines the quantity

$$\rho_{\alpha\beta} = \int_S \tilde{\rho}_{\alpha\beta}(\mathbf{r})\mathrm{d}\mathbf{r} \qquad (13)$$

for the atomic sphere S. Having chosen a quantization axis, usually the z axis, the integrated (or *atomic*) density matrix $\rho_{\alpha\beta}$ will naturally be diagonal for a ferromagnet in the ground state. For other kinds of magnetic systems, it may not be so; in this case, one can diagonalize the magnetic moment by means of the spin-1/2 rotation matrix, $U(\theta,\varphi)$, by performing the operation $U\rho U^{\dagger}$. The spherical polar coordinates, θ and φ then define the orientation of the magnetic moment of the atom in sphere S with respect to the z axis (Kübler, Höck, Sticht and Williams, 1988; Sticht, Höck and Kübler, 1989). We note that the integration in equation (13) to obtain the atomic density matrix is not a necessary step as one can deal directly with the full space dependence of $\tilde{\rho}_{\alpha\beta}(\mathbf{r})$ and calculate polar angles for each point in space as was done by Knöpfle, Sandratskii and Kübler (2000) for the noncollinear ground state of γ-Fe; this topic, however, is not pursued here any further. A relation connecting the diagonal with the nondiagonal atomic density matrix can easily be obtained as

$$\frac{\delta\rho_i}{\delta\rho_{\alpha\beta}} = U_{i\alpha}U^{\dagger}_{\beta i} \qquad (14)$$

Hence, the exchange-correlation potential in equation (11) can be written as

$$v^{xc}_{\alpha\beta}(\mathbf{r}) = \sum_{i=1}^{2} U^{\dagger}_{\alpha i}\left(\frac{\delta\Omega_{xc}}{\delta\rho_i}\right)U_{i\beta} \qquad (15)$$

This allows the determination of the nondiagonal elements of the exchange-correlation potential from the usual functional derivative of the Gibbs potential (total energy).

The next step now is to model the effects of nonzero temperatures by 'freezing in' deviations from the ground-state spin orientation by a meaningful choice of noncollinear moment arrangement. The most appealing approach is that by Herring (1966), which was later independently rediscovered by Sandratskii (1986a,b); they showed that spiral magnetic structures have ideal mathematical properties for this purpose. These are described in reciprocal space. Another approach exists, which, starting with real space, has great virtues when translational symmetry is broken or partially broken. We will deal with this after the reciprocal-space approach.

2.1 Magnetic interactions from a reciprocal-space approach

A spiral magnetic structure is defined by giving the Cartesian coordinates of the magnetization vector, $\mathbf{M}_n$, as

$$\mathbf{M}_n = M\left[\cos(\mathbf{q}\cdot\mathbf{R}_n)\sin\theta, \sin(\mathbf{q}\cdot\mathbf{R}_n)\sin\theta, \cos\theta\right] \quad (16)$$

Here, M is the magnitude of the magnetic moment at site $\mathbf{R}_n$, and $(\mathbf{q}\cdot\mathbf{R}_n)$ as well as θ are polar angles. On first sight, it appears that the periodicity is lost with respect to lattice translations nonorthogonal to $\mathbf{q}$. One should notice, however, that all atoms of the spiral structure separated by a translation $\mathbf{R}_n$ are equivalent, possessing magnetic moments of equal magnitude. This equivalence leads to the useful property for the single-particle spinor functions, which is embodied in a generalized Bloch theorem:

$$\{\mathbf{q}\cdot\mathbf{R}_n|\epsilon|\mathbf{R}_n\}\psi_{\mathbf{k}}(\mathbf{r}) = \mathrm{e}^{i\mathbf{k}\cdot\mathbf{R}_n}\psi_{\mathbf{k}}(\mathbf{r}) \quad (17)$$

where the $\psi_{\mathbf{k}}(\mathbf{r})$ are eigenspinors. The operator $\{\mathbf{q}\cdot\mathbf{R}_n|\epsilon|\mathbf{R}_n\}$ combines a lattice translation $\mathbf{R}_n$ and the identity space rotation, denoted by the identity symbol ϵ, with a spin rotation about the z axis by an angle $\mathbf{q}\cdot\mathbf{R}_n$. The vectors $\mathbf{k}$ lie in the first Brillouin zone, which is defined in the usual way. The spin spiral defined in equation (16) does not break the translational symmetry of the lattice, although, in general, the point-group symmetry is reduced. This statement is independent of the choice of $\mathbf{q}$, which, therefore, need not be commensurate with the lattice. A practical consequence is that no supercell is needed to solve the Schrödinger equation in the presence of spin spirals. From a representation of the generalized translation operator, which is easily obtained from the spin-1/2 rotation matrix as

$$\{\mathbf{q}\cdot\mathbf{R}_n|\epsilon|\mathbf{R}_n\}\psi(\mathbf{r}) = \begin{pmatrix}\exp(\mathrm{i}\mathbf{q}\cdot\mathbf{R}_n/2) & 0\\ 0 & \exp(-\mathrm{i}\mathbf{q}\cdot\mathbf{R}_n/2)\end{pmatrix}\psi(\mathbf{r}-\mathbf{R}_n) \quad (18)$$

one can see that for elemental metals the spiral wave vector $\mathbf{q}$ is chosen from inside the first Brillouin zone; $\mathbf{q}$ vectors outside give nothing new. The details of the underlying analysis can be found in the original literature or the review paper by Sandratskii (1998).

Finally, if the Schrödinger equation (9) is written in the usual form as $\mathcal{H}_{\mathbf{q}}\psi = \varepsilon\psi$, then by means of equation (15), the Hamiltonian, $\mathcal{H}_{\mathbf{q}}$, can be specified in the following form

$$\mathcal{H}_{\mathbf{q}} = -\mathbf{1}\nabla^2 + \sum_n \Theta(|\mathbf{r}_n|)U^{+}(\theta,\varphi,\mathbf{q}) \times \begin{pmatrix} v_{+}^{\mathrm{eff}}(|\mathbf{r}_n|) & 0\\ 0 & v_{-}^{\mathrm{eff}}(|\mathbf{r}_n|)\end{pmatrix} U(\theta,\varphi,\mathbf{q}) \quad (19)$$

where $|\mathbf{r}_n| = |\mathbf{r}-\mathbf{R}_n|$, $\Theta(|\mathbf{r}_n|)$ is the unit step function that vanishes outside the atomic sphere centered at $|\mathbf{R}_n|$ and the indices $+$ and $-$ label the spin-up and spin-down effective potential in the local diagonal frame of reference.

An important observation is that the Hamiltonian in the preceding text, $\mathcal{H}_{\mathbf{q}}$, depends on a parameter $\mathbf{q}$, the wave vector characterizing the spin spiral. Niu and Kleinman (1998) realized that, just like the adiabatic approximation for decoupling the electronic from the ionic motion in solids, this parameter leads to a Berry phase (Berry, 1984). In fact, they, and later Niu *et al*. (1999), showed that the Berry curvatures involved in the equation of motion describe how the total spin component along the symmetry axis changes due to spin deviations from the ground-state configuration. So, if the total energy is calculated by constraining the magnetic moment to the ground-state value M for a small value of θ, then the spin wave energy for an itinerant-electron ferromagnet is (in atomic units) given by

$$\omega(\mathbf{q}) = \lim_{\theta\to 0}\frac{4}{M}\frac{E(\mathbf{q},\theta)}{\sin^2\theta} \quad (20)$$

where the total energy $E(\mathbf{q},\theta)$ is counted from the ground-state value. Since the total energy is very nearly proportional to $\sin^2\theta$, the choice of θ is not very critical. This formula not only establishes the spiral energy as a physical quantity but has also been shown to lead to very good agreement with measured magnon energies for Fe, Co, and Ni (Halilov, Eschrig, Perlov and Oppeneer, 1998; Brown, Nicholson, Wang and Schulthess, 1999; Gebauer and Baroni, 2000).

To summarize, it is the total energy and its changes with some parameters that are at the center of interest. To manage

these calculations, one solves the single-particle equations, equation (9), self-consistently. This means, in particular, a solution of the Schrödinger equation $\mathcal{H}_{\mathbf{q}}\psi = \varepsilon\psi$, where $\mathcal{H}_{\mathbf{q}}$ is given by equation (19); the Bloch function ψ and the energy eigenvalues ε depend on the parameter $\mathbf{q}$, and on the angles θ and φ. To proceed, one commonly expands the Bloch function in terms of suitable basis sets and then uses the variational principle. The result is the total energy, $E(\mathbf{q}, \theta, \varphi)$.

In practical applications, one must bear in mind that, for a general value of θ, that is, $\theta \neq 0$ and $\theta \neq 90^{\circ}$, the magnetic moment experiences a torque; the resulting precession leads to convergence problems and inaccurate values of the total energy change. This problem can be solved by means of constraints that are formulated with appropriate Lagrange multipliers in the Schrödinger equation. An elegant method has been proposed and successfully applied by Grotheer, Ederer and Fähnle (2001).

An alternative way is to employ Green's functions to solve the single-particle Schrödinger equation. The great virtue is their applicability when translational symmetry is broken. Clearly, surfaces and nanostructures call for such a method. But, even if one considers twisting slightly the magnetic moment of one atom in an otherwise ferromagnet environment, one encounters a problem of broken symmetry. Therefore, before we embark on the main topic of this chapter, we now digress and describe the Green's function or real-space approach.

2.2 Magnetic interactions from a real-space approach

The Green's function approach can be expressed as the solution of the multiple scattering problem. Thus, if G describes free particle propagation from any individual scattering event to the next, for which the single-site scattering matrix is denoted by t, we may describe multiple scattering by means of the sum

$$\tau = t + tGt + tGtGt + \cdots = t + tG(t + tGt + tGtGt + \cdots) = t + tG\tau \tag{21}$$

or

$$\tau = (1 - tG)^{-1}t = (t^{-1} - G)^{-1} \tag{22}$$

where τ is called the *scattering path operator* or the *scattering path matrix*.

Next, the total energy change to be effected is written in a simple way by using the so-called *force theorem*. This concept, originally due to Heine (1980) as well as Mackintosh and Andersen (1980) – later extended to magnetic systems by Oswald, Zeller, Braspenning and Dederichs (1985) – allows the total energy change in first order to be written as the change in the sum on the single-particle energies, provided the potential is kept as its unperturbed value. It is brought about by a subtle cancellation of terms. So, looking in particular at equation (12) – for simplicity evaluated at $T = 0$ – a first-order change of the grand potential is the sum of changes in the first term on the right-hand side and the other three terms, the so-called *double-counting terms*; the latter cancel the change in the former. For mathematical details and limitations, see Methfessel and Kübler (1982).

The force theorem was applied by Liechtenstein, Katsnelson and Gubanov (1984) Liechtenstein, Katsnelson, Antropov and Gubanov (1987) to obtain the magnetic interactions as follows.

A total energy change, brought about by a change of the magnetic structure, which changes the density of states (DOS) by $\delta n(\varepsilon)$, is given by

$$\delta E = \int^{E_{\mathrm{F}}} \varepsilon \delta n(\varepsilon)\, \mathrm{d}\varepsilon \tag{23}$$

After integration by parts, one obtains

$$\delta E = -\int^{E_{\mathrm{F}}} \delta N(\varepsilon)\, \mathrm{d}\varepsilon \tag{24}$$

where $N(\varepsilon)$ is the integrated DOS, or $n(\varepsilon) = \mathrm{d}N/\mathrm{d}\varepsilon$. Now, let the magnetic structure be described by the Heisenberg Hamiltonian

$$\mathcal{H} = -\sum_{ij}{}' J_{ij}\mathbf{e}_i \cdot \mathbf{e}_j \tag{25}$$

where J_{ij} are the exchange parameters (including the magnetic moment squared) and $\mathbf{e}_i$ is the unit vector in the direction of the magnetization. Then, the twisting of one magnetic moment at site 0 by the angle θ causes the energy to change by

$$\delta E = 2\sum_j J_{0j}(1 - \cos\theta) \simeq J_0\theta^2 \tag{26}$$

where we defined $J_0 = \sum_j J_{0j}$. Next, one uses the fact that the integrated DOS is connected with the scattering path operator by means of Lloyd's formula (Lloyd and Smith, 1972), that is,

$$N(\varepsilon) = N_0 + \frac{1}{\pi}\mathrm{Im\ tr} \ln \tau(\varepsilon) \tag{27}$$

Thus, equating (26) with equation (24) and using equation (27), one obtains

$$J_0\theta^2 = \frac{1}{\pi}\int^{E_F} \text{Im tr ln}[1 + \delta t^{-1}\tau(\varepsilon)]\,\mathrm{d}\varepsilon \tag{28}$$

Liechtenstein, Katsnelson, Antropov and Gubanov (1987) next specify the form of the t-matrix change at site i as

$$t_i = \frac{1}{2}(t_{i\uparrow} + t_{i\downarrow}) + \frac{1}{2}(t_{i\uparrow} - t_{i\downarrow}) \times (\mathbf{e}_i \cdot \boldsymbol{\sigma}) \tag{29}$$

where the components of the vector $\boldsymbol{\sigma}$ are the Pauli matrices. This implies

$$\delta t_i^{-1} = \frac{1}{2}(t_{i\uparrow}^{-1} - t_{i\downarrow}^{-1}) \times (\delta\mathbf{e}_i \cdot \boldsymbol{\sigma}) \tag{30}$$

which gives with the chosen spin rotation, $\delta\mathbf{e}_0 = (\sin\theta, 0, \cos\theta - 1)$

$$\delta t_i^{-1} = \frac{1}{2}\delta_{i,0}(t_{i\uparrow}^{-1} - t_{i\downarrow}^{-1}) \times \begin{pmatrix} \cos\theta - 1 & \sin\theta \\ \sin\theta & 1 - \cos\theta \end{pmatrix} \tag{31}$$

The trace of the logarithm in spinor-space is now evaluated using the relation tr ln T = ln det T. One obtains from equation (28)

$$J_0 = -\frac{1}{4\pi}\int^{E_F} \text{Im tr}_L[\Delta_0(\tau_\uparrow^{00} - \tau_\downarrow^{00}) + \Delta_0\tau_\uparrow^{00}\Delta_0\tau_\downarrow^{00}] \tag{32}$$

where $\Delta_0 = (t_{i\uparrow}^{-1} - t_{i\downarrow}^{-1})$.

The pair interaction parameter J_{ij} is obtained by rotating two spin moments at the sites i and j by opposite angles $\pm\theta/2$. Taking care of double counting, one obtains the desired parameter from

$$\delta E_{ij} - \delta E_i - \delta E_j \simeq \frac{1}{2}J_{ij}\theta^2 \tag{33}$$

and, after some manipulations, for which the reader can find the details in the paper by Liechtenstein, Katsnelson, Antropov and Gubanov (1987), one finally derives the result

$$J_{ij} = \frac{1}{4\pi}\int^{E_F} \text{Im tr}_L[\Delta_i\tau_\uparrow^{ij}\Delta_j\tau_\downarrow^{ji}] \tag{34}$$

A collection of formulas of the preceding type valid for more general perturbations can be found in the paper by Antropov, Harmon and Smirnov (1999). A brief review of the theory appeared in the book by Gubanov, Liechtenstein and Postnikov (1992), and early numerical applications of the formalism are quite encouraging.

When the formalism is applied to the determination of spin-wave spectra, the parameter θ is no longer small, but is of the order of $\mathbf{q}\cdot\mathbf{R}$, $\mathbf{q}$ being the magnon wave vector. This limits the applicability of the theory to the limit of small $|\mathbf{q}|$. To overcome this limit, Bruno (2003) developed a theory for renormalized magnetic interactions, or a *renormalized magnetic force theorem*.

It is also of interest to point out that the multiple scattering theory sketched in the preceding text is the key to a formulation of the disordered local moment (DLM) picture in the coherent-potential approximation (Gyorffy *et al*., 1985). We will briefly return to this theory in Sections 3.3.3 and 4.3, but continuing here in detail would carry us too far afield.

Finally, a method to calculate the effective exchange interaction parameters for correlated magnetic crystals, for which the LSDA is no longer applicable, has been formulated by Katsnelson and Lichtenstein (2000) very much along the lines of the approach in the preceding text.

3 THERMODYNAMICS

3.1 Weakly ferromagnetic metals: formulation

We begin the thermodynamics with the weakly ferromagnetic metals and later take up the other cases. In Chapter 4 of his book, Moriya (1985) obtained the energies of various spin configurations in metals by using the Hartree–Fock approximation (HFA) and random phase approximation (RPA), whereas here the energies are based on those of spin spirals. It is thus assumed that the frozen-magnon energies represent the relevant excited states sufficiently well. One can put this differently by saying that the adiabatic approximation is invoked, which is loosely justified by observing that the motion of the electrons is much faster than that of the magnetic moments, since the latter possess energies of the order of milli-electron volts, whereas the former move in bands of widths of the order of electron volts. However, it is not *a priori* clear how well this approximation is justified in general.

The space-varying spin density $\mathbf{M}(\mathbf{R})$ is now regarded as a classical field and the free energy F is formally obtained by the following functional integral:

$$F = -k_B T\ \ln\int \delta\mathbf{M}(\mathbf{R})\ \exp\{-\Psi[\mathbf{M}(\mathbf{R})]/k_B T\} \tag{35}$$

where $\Psi[\mathbf{M}(\mathbf{R})]$ is the energy functional of the spin configuration. The latter is written as

$$\mathbf{M}(\mathbf{R}) = M\mathbf{e}_z + \mathbf{m}(\mathbf{R}) = M\mathbf{e}_z + \sum_{j,\mathbf{q}} m_{j\mathbf{q}}\exp(\mathrm{i}\mathbf{q}\cdot\mathbf{R})\mathbf{e}_j \tag{36}$$

Here, M is the magnetization along some direction, say the z-direction, and $\mathbf{m}(\mathbf{R})$ is a local deviation of the magnetization, which is expanded in a Fourier series. Since it is real, the Fourier coefficients obey $m_{j-\mathbf{q}} = m^*_{j\mathbf{q}}$. The quantities $\mathbf{e}_j (j = 1, 2, 3)$ are Cartesian unit vectors.

For weakly ferromagnetic metals, the local amplitude of spin fluctuations, $m_{j\mathbf{q}}$, is expected to be relatively small. Therefore, the energy functional can be expanded in powers of the magnetization. In this step, one follows the work of Murata and Doniach (1972), who, however, took a scalar field for the spin density, whereas here a vector field is employed. The work of Lonzarich and Taillefer (1985) constitutes one of the key papers in the field of weak itinerant ferromagnets, and a lucid introduction to the physics of spin fluctuations can be found in the book by Mohn (2003).

The mode–mode coupling functional proposed is written in two parts

$$\Psi = \Psi_1 + \Psi_2 \tag{37}$$

where

$$\Psi_1 = \frac{1}{2}\alpha \frac{1}{N} \sum_n \mathbf{M}(\mathbf{R}_n)^2 + \frac{1}{4}\beta \frac{1}{N} \sum_n \mathbf{M}(\mathbf{R}_n)^4 \tag{38}$$

and

$$\Psi_2 = \frac{1}{N} \sum_{n,m} J\,(\mathbf{R}_n - \mathbf{R}_m)\, \mathbf{M}(\mathbf{R}_n) \cdot \mathbf{M}(\mathbf{R}_m) \tag{39}$$

where N denotes the number of particles in the system and the coefficients α and β can be viewed as Landau coefficients controlling changes of the size of the magnetization. They here are assumed to be independent of the temperature. The quantity $J(\mathbf{R})$ describes the exchange interaction between sites separated by $\mathbf{R}$. In the weakly ferromagnetic limit, only the fourth-order term in equation (38) is needed, which simplifies the analysis considerably, but carrying the expansion to a higher order poses no real difficulties.

To obtain the free energy, a variational principle is used by employing a Gaussian functional in this subsection

$$\Phi = \sum_{j,\mathbf{q}} a_{j\mathbf{q}} |m_{j\mathbf{q}}|^2 \tag{40}$$

$a_{j\mathbf{q}}$ being variational parameters. Using the convexity properties of exponentials (also called the *Bogoliubov–Peierls* inequality), one writes

$$F < -k_\mathrm{B}T \ \ln \int \delta\mathbf{M} \ \exp\left(\frac{-\Phi}{k_\mathrm{B}T}\right) + \langle \Psi - \Phi \rangle_0 \doteq \tilde{F} \tag{41}$$

The average $< \ldots >_0$ is defined through the Gaussian distribution, equation (40). By substituting equation (36) and Fourier transforming, one obtains after some algebra

$$\begin{aligned} \tilde{F} = &-\frac{1}{2} k_\mathrm{B} T \sum_{j,\mathbf{q}} \ln\left(\pi \left\langle |m_{j\mathbf{q}}|^2 \right\rangle_0\right) + \frac{1}{2}\alpha \left(M^2 + 2m_\perp^2 + m_\parallel^2\right) \\ &+ \frac{1}{4}\beta \Big[M^4 + 2M^2 \left(2m_\perp^2 + 3m_\parallel^2\right) + 8m_\perp^4 + 4m_\perp^2 m_\parallel^2 \\ &+ 3m_\parallel^4 \Big] + 2 \sum_{\mathbf{q}} j(\mathbf{q}) \left\langle |m_{\perp\mathbf{q}}|^2 \right\rangle_0 + \sum_{\mathbf{q}} j(\mathbf{q}) \left\langle |m_{\parallel\mathbf{q}}|^2 \right\rangle_0 \end{aligned} \tag{42}$$

where $j = \perp$ and $j = \parallel$ distinguish the fluctuations perpendicular and parallel to the macroscopic magnetization. Furthermore,

$$m_j^2 = \sum_{\mathbf{q}} \left\langle |m_{j\mathbf{q}}|^2 \right\rangle_0 \tag{43}$$

for $j = \perp$ and $j = \parallel$. The quantity $j(\mathbf{q})$ is defined by the Fourier transform

$$j(\mathbf{q}) = \sum_n J(\mathbf{R}_n) \exp(i\mathbf{q} \cdot \mathbf{R}_n) \tag{44}$$

and describes the exchange interaction in reciprocal space.

The minimization of $\tilde{F}$ with respect to the variational parameter $a_{j\mathbf{q}}$ is equivalent to minimization with respect to the fluctuations because equation (40) implies $\left\langle |m_{j\mathbf{q}}|^2 \right\rangle_0 = k_B T/(2a_{j\mathbf{q}})$. The result of the minimization is most compactly written as

$$m_j^2 = \frac{k_\mathrm{B} T}{N} \sum_{\mathbf{q}} \chi_j(\mathbf{q}) \tag{45}$$

where, one finds for the longitudinal case, $j = \parallel$,

$$\chi_\parallel^{-1}(\mathbf{q}) = \alpha + \beta(3M^2 + 2m_\perp^2 + 3m_\parallel^2) + 2j(\mathbf{q}) \tag{46}$$

and for the perpendicular case, $j = \perp$,

$$\chi_\perp^{-1}(\mathbf{q}) = \alpha + \beta(M^2 + 4m_\perp^2 + m_\parallel^2) + 2j(\mathbf{q}) \tag{47}$$

Equation (45) is the static (or high-temperature) limit of an exact relation, which states that in linear response theory the average fluctuations squared are connected with the frequency-dependent, nonuniform susceptibility $\chi_{nj}(\mathbf{q}, \omega)$ in the form

$$\left\langle |m_{j\mathbf{q}}|^2 \right\rangle = \frac{2}{\pi N} \int_0^\infty \mathrm{d}\omega \ \mathrm{Im}\left\{\chi_j(\mathbf{q}, \omega)\right\} N(\omega) \tag{48}$$

where, $N(\omega)$, omitting zero-point fluctuations, denotes the Planck distribution function. This is the famous *fluctuation-dissipation theorem* (Callen and Welton, 1951; Becker and Sauter, 1968; Jones and March, 1973; White, 1983).

The connection between equation (48) and the equations (43) and (45) is made in the limit of high temperatures and by using the Kramers–Kronig relations.

The partial derivative of the free energy with respect to the magnetization gives the magnetic field. Requiring this to be zero, one obtains

$$\frac{M^2}{M_0^2} = 1 - \frac{(2m_\perp^2 + 3m_\parallel^2)}{M_0^2} \tag{49}$$

known also as the *Moriya relation*. Here, the relation $\alpha = -\beta M_0^2$ was used, which is the minimum condition for the free energy in the absence of all fluctuations, that is, at zero temperature, $T = 0$, at which the magnetization is M_0.

For a vanishing magnetization, that is, above the ordering temperature, the longitudinal and perpendicular fluctuations and susceptibilities become equal. Thus, writing $m_\perp^2 = m_\parallel^2 = m_\mathrm{p}^2$, one determines the paramagnetic fluctuations using

$$m_\mathrm{p}^2 = \sum_{\mathbf{q}} \left\langle |m_{\mathbf{pq}}|^2 \right\rangle_0 = \frac{k_\mathrm{B}T}{N} \sum_{\mathbf{q}} \left[\alpha + 5\beta m_\mathrm{p}^2 + 2j(\mathbf{q}) \right]^{-1} \tag{50}$$

The inverse susceptibility is then given by

$$\chi^{-1} = \alpha(1 - 5m_\mathrm{p}^2/M_0^2) \tag{51}$$

It was initially thought (Uhl and Kübler, 1996; Kübler, 2000, Ch.5) that self-consistent solutions of the basic equations (45)–(47) together with equations (49) and (51) describe the phase transition below and above the Curie temperature for the elemental ferromagnets. We will see that this, unfortunately, is not true. In fact, numerical values for the two Landau coefficients, α and β were obtained by constraining the magnetic moment, M, such that the total energy counted from the nonmagnetic state $E(M)$ is expressed as a function of M. This is achieved by a Langrange multiplier in the total energy calculations (Dederichs, Blügel, Zeller and Akai, 1984). The function $E(M)$ thus obtained can then be identified with equation (38) in the absence of all fluctuations, which is written in this case as $\Psi_1(0)$, a simple fit subsequently giving

$$\Psi_1(0) = \frac{1}{2}\alpha M^2 + \frac{1}{4}\beta M^4 \tag{52}$$

This is very similar to the approach taken by Luchini, Heine and McMullan (1991) to describe the magnetic fluctuations of iron. The other parameter appearing in the basic equations is the exchange function $j(\mathbf{q})$, which was calculated by assuming the noncollinear moment arrangement of the form given in equation (16). The total energy change ensuing, $\Delta E(\mathbf{q})$, gives $j(\mathbf{q})$ through

$$\Delta E(\mathbf{q}) = M_0^2 j(\mathbf{q}) \sin^2\theta \tag{53}$$

choosing $\theta = 90^\circ$ and constraining the magnetic moment to its ground-state value, M_0. This choice of θ leads to a small error, which can be removed by better constraints, as was shown by Grotheer, Ederer and Fähnle (2001) and Singer, Fähnle and Bihlmayer (2005). But, for the sake of simplicity, we stick to this simple choice. No cutoff parameter is needed for the summations (integrations) in reciprocal space since, because of equation (44), the function $j(\mathbf{q})$ is periodic. Finally, if the phase transition calculated is of second order, one obtains from the basic equations the following formula for the Curie temperature:

$$k_\mathrm{B}T_\mathrm{c}^{SF} = \frac{2M_0^2}{5} \left[\frac{1}{N} \sum_{\mathbf{q}} \frac{1}{j(\mathbf{q})} \right]^{-1} \tag{54}$$

which carries the label SF, for spin fluctuation, in order to distinguish it from other expressions that are given in the subsequent text.

Before the partial success and the shortcomings of this approach are discussed, it is worthwhile to improve the approximations by going beyond the static approximation. The essential step here is the replacement of equation (45) by equation (48); the resulting theory is commonly called the *dynamic approximation*. The importance of this step has been stressed repeatedly by Moriya (1985).

One may conveniently start by writing the free energy in the form

$$F(M,T) = \frac{1}{2}\alpha M^2 + \frac{1}{4}\beta M^4 + F_1(M,T) \tag{55}$$

and employ a formula for the free energy part $F_1(M,T)$ that is due to Dzyaloshinski and Kondratenko (1976). This is

$$F_1(M,T) = F_0(T) + \frac{1}{2N} \sum_{j,\mathbf{q}} \int_{-\infty}^{\infty} \frac{\mathrm{d}\omega}{2\pi} \times \mathrm{Im} \left\{ \ln \chi_j^{-1}(\mathbf{q},\omega) \right\} \coth\left(\frac{\omega}{2k_\mathrm{B}T} \right) \tag{56}$$

Here, $F_0(T)$ does not depend on the magnetization and is, therefore, at this point, of no concern. The inverse dynamic susceptibilities are approximated by

$$\chi_j^{-1}(\mathbf{q},\omega) = \chi_j^{-1}(\mathbf{q}) - \frac{i\omega}{\Gamma q} \tag{57}$$

where the real part, $\chi_j^{-1}(\mathbf{q})$, is assumed to be given by the results of the static approximation, equation (46) for $j = \parallel$ and equation (47) for $j = \perp$.

The complex part of the inverse, dynamic susceptibility is a widely used approximation for the weakly ferromagnetic metals, where long wavelength fluctuations of small frequencies predominate. It rests on a broad experimental and theoretical basis (Moriya, 1985; Lonzarich and Taillefer, 1985). The latter has most concisely been summarized by Lonzarich and Taillefer, who give the small ω and small q expansion of the dynamic Lindhard susceptibility as equation (57), valid for a single tight-binding band and omitting matrix elements. In this approximation, one can express the dissipation constant Γ in terms of band-structure quantities as

$$\Gamma = (4/\pi V)\mu_B^2 N_F E_F / k_F \tag{58}$$

where V is the volume of the primitive unit cell, N_F is the DOS at the effective Fermi energy E_F, k_F is the Fermi wave vector, and the magnetization is assumed to be small.

By taking next the second derivative of the free energy, equations (55) and (56) with respect to M (but neglecting derivatives of the fluctuations), one verifies that the uniform, static, longitudinal susceptibility is given by $\chi_\parallel(\mathbf{q} = 0)$, equation (46), provided the fluctuations are connected with the susceptibility through the fluctuation-dissipation theorem, equation (48). The transverse susceptibility, however, is slightly different from $\chi_\perp(\mathbf{q} = 0)$, equation (47). It is believed, though, that this is still a good approximation since numerically the two susceptibilities come out very nearly the same.

The remaining calculation is the evaluation of the fluctuation equation (48). With the preceding approximation for the dynamic susceptibility, the frequency integration can be carried out analytically, as was done by Lonzarich and Taillefer (1985), who refer to a paper by Ramakrishnan (1974), obtaining $\langle |m_{j\mathbf{q}}|^2 \rangle = k_B T \chi_j(\mathbf{q}) g(z)/N$ where $g(z) = 2z\,(\ln z - 1/2z - \psi(z))$, $\psi(z)$ is Euler's psi function and $z = \Gamma|\mathbf{q}|\chi_j^{-1}(\mathbf{q})/2\pi k_B T$. To a very good approximation, one can write $g(z) \simeq 1/(1 + 5.63602z)$, which finally gives

$$\sum_{\mathbf{q}} \langle |m_{j\mathbf{q}}|^2 \rangle = \frac{k_B T}{N} \sum_{\mathbf{q}} \chi_j(\mathbf{q}) - \frac{\xi\Gamma}{N} \sum_{\mathbf{q}} |\mathbf{q}| \times \left[1 + \frac{\xi\Gamma|\mathbf{q}|}{k_B T} \chi_j^{-1}(\mathbf{q}) \right]^{-1} \tag{59}$$

The constant appearing is $\xi = 0.897$. Note that, for $\Gamma = 0$, the results of the static approximation are obtained.

One could now argue that all important quantities are determined by the total energy and the band structure. However, the assumptions underlying equation (58) are heavily idealized, and so this relation can only be expected to give an order of magnitude estimate of the dissipation constant Γ, as we will see. In principle, the dynamic susceptibility can be easily formulated, but, in the appropriate integral equation, a kernel remains unknown (Antropov, Harmon and Smirnov, 1999). A desirable approach would be that of Savrasov (1998), who calculated the dynamical susceptibility *ab initio* but did not direct his attention to the problems addressed here. Similarly, the *ab initio* theory of Staunton *et al*. (2000) should be applied to ferromagnets.

Furthermore, even more serious, as it turns out, is a conceptual error made in the determination of the Landau coefficients α and β from the total energy. This point is exposed in detail in the following examples.

The determination of the exchange function $j(\mathbf{q})$, however, is seen to be quite reliable, thus turning out to be one of the strong points of the theory.

3.2 Weakly ferromagnetic metals: examples

3.2.1 An exploratory calculation for nickel

Although Ni is not understood to be a weakly ferromagnetic metal, we start with this case since the calculations are quickly performed, allowing the formalism to be exposed together with its strengths and weaknesses.

In Table 2, we collect some of the relevant data for nickel. The lattice constant used for the calculations is seen to be somewhat smaller than the experimental value, which is due to the well-known overbinding property of the LSDA. The calculated value of the magnetic moment, M_0, is also listed. Its being smaller than the experimental value is due to the missing orbital and spin-orbit coupling (SOC) contributions. By means of total energy calculations, the input coefficients α, $\beta = -\alpha/M_0^2$, and $j(\mathbf{q})$ are easily obtained and the basic equations (45)–(47) together with equation (49) as well as equations (50) and (51) are solved numerically, first in the static approximation. The Curie temperature given in equation (54) is evaluated and given in Table 2. With the knowledge of the exchange function $j(\mathbf{q})$, other approximations for the Curie temperature can be

Table 2. Calculated and experimental values for Ni: lattice constant, a, calculated spin fluctuation, T_c^{SF}, spherical model, T_c^{SP}, and mean field, T_c^{MF} Curie temperatures, and magnetic moment, M_0.

	a (Å)	T_c^{SF} (K)	T_c^{SP} (K)	T_c^{MF} (K)	M_0 (μ_B)
Calculated	3.468	322	537	643	0.598
Experimental	3.525		627		0.616

obtained. These are

$$k_B T_c^{SP} = \frac{2M_0^2}{3}\left[\frac{1}{N}\sum_{\mathbf{q}}\frac{1}{j(\mathbf{q})}\right]^{-1} \tag{60}$$

which are derived in Section 3.3.1 in the *spherical approximation*. This equation is also known as the *RPA expression*. The well-known *mean-field approximation* gives for the Curie temperature

$$k_B T_c^{MF} = \frac{2M_0^2}{3N}\sum_{\mathbf{q}} j(\mathbf{q}) \tag{61}$$

This is a convenient formula to express the average value of the exchange function $j(\mathbf{q})$. Results obtained in the spherical and mean-field approximations are also listed in Table 2 and are seen to approximate the measured Curie temperature much better than the spin-fluctuation value.

When, however, the basic equations are solved with the value of α obtained from the total energy, the phase transition to the paramagnetic state is found to be weakly of first order, giving a Curie temperature of about 370 K. Although the inverse susceptibility above the Curie point is calculated to be a Curie–Weiss law, its slope is much too large, giving a value for the number of carriers, q_c smaller than q_s, the saturation value at zero temperature.

In an attempt to analyze the situation, one first finds a condition for the transition to be of second order. This is $\alpha M_0^2/J_0 < 1$, where J_0 is the average of $j(\mathbf{q})$ defined by the sum in equation (61). This condition is not satisfied for the value of α used in the preceding text. Next one expresses the coefficient α by the total energy gained in the ferromagnetic state, which in Figure 2(a) is denoted by E_B; this is trivially from equation (52) $\alpha = -4E_B/M_0^2$. To continue, it is convenient to turn to the *dynamic approximation*, choosing a dissipation constant Γ such that the experimental Curie temperature is obtained, assuring, however, that the transition is of second order by using smaller values of α than required by the total energy value E_B. Thus, Figure 2(b) illustrates that the inverse susceptibility shows, indeed, Curie–Weiss behavior; however, its value agrees with the experimental data (also given in the figure) only for a vastly reduced E_B (or α). Can one justify this reduction?

The simple relation $\alpha = -4E_B/M_0^2$ shows that the coefficient α is defined with respect to the nonmagnetic ground state, since this is the offset for E_B. For Ni – or any other ferromagnet – the nonmagnetic ground state, however, is a computational *fiction*. Another reference state should be used, one that is magnetic with no long-range order. In Chapter 7 of his book, Moriya (1985) identified the reference state qualitatively by means of the Anderson condition,

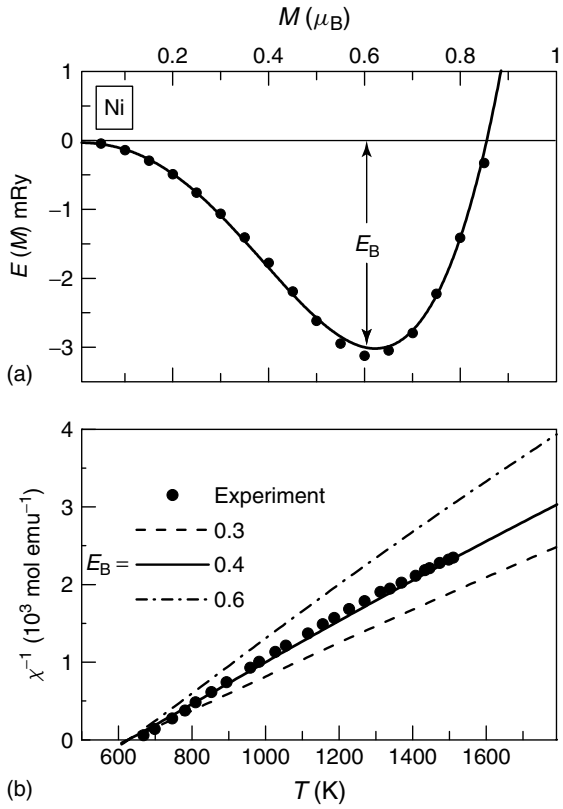

Figure 2. (a) Total energy of Ni as a function of the magnetic moment, M, obtained by a constrained-moment calculation (dots), counted from the nonmagnetic state. Solid line is the fit, equation (52). Label E_B is used as parameter in part (b) of this figure. Inverse susceptibility for Ni above the Curie point. Experimental data (circles) from Shimizu (1981); data calculated in the dynamic approximation are shown for different values of the parameter E_B in mRy.

which marks the appearance of randomly oriented local moments in metals. We will come back to this problem in Section 3.3.

It is clear now that the Landau coefficients must be renormalized. One is tempted therefore to abandon the LSDA in favor of a many-body treatment since there is no formal answer within the theory presented. It is still worthwhile to continue anyway by observing that the appearance (or disappearance) of local moments can clearly be seen in the enhancement of the *nonuniform* susceptibility, $\chi(\mathbf{q})$. The susceptibility enhancement was discussed, for instance, by Sandratskii and Kübler (1992) (see also Kübler, 2000, Ch.4), who obtained $\chi(\mathbf{q})$ by using spiral-moment arrangements in LSDA calculations and demonstrated that it peaks strongly at values of $\mathbf{q}$, where the magnetic moment becomes small. The calculations have been repeated here for Ni with high precision and the results are shown in Figure 3 for $\mathbf{q}$ along the (1,0,0)-direction. Since, locally, in reciprocal space, the

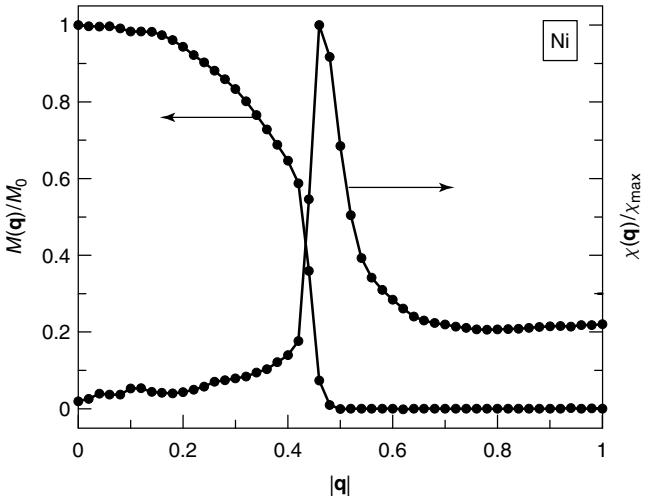

Figure 3. Relative magnetic moment of Ni, $M(\mathbf{q})/M_0$ and relative nonuniform susceptibility $\chi(\mathbf{q})/\chi_{\max}$, both as a function of the wave vector $\mathbf{q} = (q, 0, 0)$ in units of $2\pi/a$. A value of $\chi_{\max} = 149\mu_B^2/Ry = 0.35 \cdot 10^{-3}$emu mol^{-1} is obtained along this direction in the Brillouin zone.

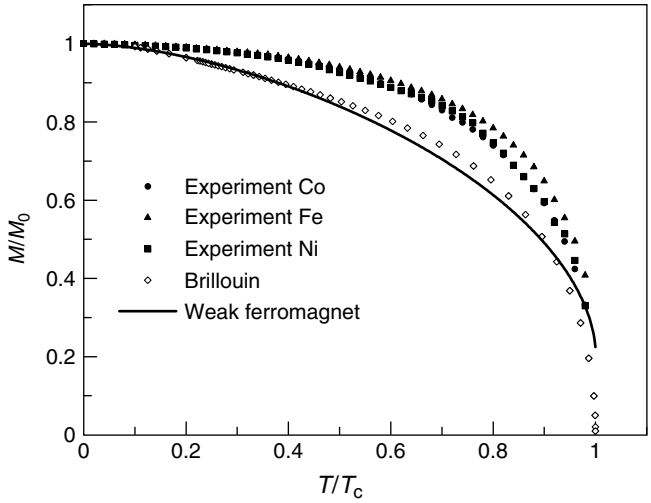

Figure 4. Temperature dependence of the magnetization of Ni in reduced units from theory of weak ferromagnetism.

total energy can be expanded as

$$E(\mathbf{q}, M) = E(\mathbf{q}, M_0(\mathbf{q})) + \frac{(M - M_0(\mathbf{q}))^2}{2\chi(\mathbf{q})} \qquad (62)$$

one sees that the total energy is very flat as a function of M in those regions of the Brillouin zone where the susceptibility becomes large. Proceeding empirically, we assume that it is this value of the total energy that determines the coefficient α and consequently E_B. We are thus led to using $\alpha = -(2\chi_{\max})^{-1}$, which gives $E_B = 0.4$ mRy. Figure 2(b) shows that this leads to very good agreement with the experimental Curie–Weiss susceptibility. We take this agreement as an indication for a useful procedure to apply to all weakly ferromagnetic materials, which are described in the sequel of the chapter.

In Figure 4, we show the magnetization as a function of the temperature for Ni in reduced units. For comparison, the experimental data for Fe, Co, and Ni are also shown together with the well-known Brillouin function valid in the mean-field approximation. One can see that especially at low temperatures the calculated curve does not agree with the experimental values. This is due to an improper treatment of the magnon excitations. As will be explained later, for the case of iron, the low-temperature phase transition is better described by a local moment approximation.

We complete this subsection by giving the value of the dissipation constant that leads to the experimental Curie temperature shown in Figure 2(b); this is $\Gamma = 0.641\,\mu\text{eV}\text{Å}^2$. Although, differing from equation (57), the experimental wave-vector dependence proportional to q^2 was used in the calculations, we cannot expect agreement with the measured value of Γ, which is 3 orders of magnitude larger (Steinsvoll, Majkrzak, Shirane and Wicksted, 1984). This should not be surprising in view of the simplifications made in the modeling of the imaginary part of the susceptibility.

3.2.2 The weakly ferromagnetic compound $ZrZn_2$

$ZrZn_2$, like the compounds Ni_3Al, MnSi, and Sc_3In, belongs to the class of weakly ferromagnetic materials with small magnetic moments (of the order of a tenth of a μ_B) and small Curie temperatures (of the order of 5–40 K). Because of its large effective moment in the paramagnetic phase, it is found on the far left in Figure 1. It was discovered by Matthias and Bozort (1958) to be ferromagnetic. The unit cell of the cubic C15 Laves phase of $ZrZn_2$ contains six atoms, the two Zr atoms occupying a diamond lattice and the four Zn atoms forming tetrahedra in the interstices. A number of generalizations need be done to apply the theory given in Section 3.1 to a crystal structure possessing a basis, as $ZrZn_2$ does. Thus, equation (36) is changed to

$$\mathbf{M}_\tau(\mathbf{R}) = M_\tau \mathbf{e}_z + \sum_{n,j,\mathbf{q}} m_{nj\mathbf{q}} C_{n\tau} \exp(i\mathbf{q}\cdot\mathbf{R})\mathbf{e}_j \qquad (63)$$

where τ labels the basis and the coefficient $C_{n\tau}$ allows one to treat normal modes, which are numbered by n. All other symbols are defined as in equation (36).

Beginning with the *static approximation*, the Curie temperature, the magnetic order parameter, and the high-temperature susceptibility are calculated by evaluating the basic equations (45)–(47) together with equation (49) as

well as equations (50) and (51) as a function of the pressure (volume) (Kübler, 2004). The two equivalent magnetic Zr atoms lead to two normal modes and two exchange functions $j_{11}(\mathbf{q})$ and $j_{12}(\mathbf{q})$, which require a number of simple modifications in the basic equations. Thus, the total energy change, equation (53), is replaced by

$$\Delta E = 2M_0^2 j_{11}(\mathbf{q}) + 2M_0^2 j_{12}(\mathbf{q}) \cos(\mathbf{q} \cdot \boldsymbol{\tau}) \qquad (64)$$

where $\boldsymbol{\tau} = (\frac{1}{4}, \frac{1}{4}, \frac{1}{4})$ in units of the lattice constant is the basis vector for the second magnetic atom in $ZrZn_2$, assuming the first at the origin. The quantity M_0 is the Zr moment in the ground state. Since, by virtue of equation (44), the exchange functions are periodic with the periodicity of the reciprocal lattice, but $\cos(\mathbf{k} \cdot \tau)$ is not, we may determine $j_{11}(\mathbf{q})$ and $j_{12}(\mathbf{q})$ from equation (64) with a choice of a reciprocal lattice vector, $\mathbf{K} = (0, 0, 2)\ 2\pi/a$, where a is the lattice constant. Thus, replacing $\mathbf{q}$ by $\mathbf{q} + \mathbf{K}$, we get an equation to solve for $j_{11}(\mathbf{q})$, finally eliminating the cosine by choosing all phases to be zero to obtain $j_{12}(\mathbf{q})$.

The variation described in Section 3.1 now leads via a standard normal-mode analysis to two inverse static susceptibilities, $\chi^{-1}_{\parallel,\pm}(\mathbf{q})$ and $\chi^{-1}_{\perp,\pm}(\mathbf{q})$, which replace the equations (46)–(47) by changing the single exchange functions there to $j_{11}(\mathbf{q}) \pm j_{12}(\mathbf{q})$. The Curie temperature is then

$$k_B T_c = \frac{4}{5} M_0^2 \cdot \left(\frac{1}{N} \sum_{\mathbf{q}} \frac{1}{j_{11}(\mathbf{q}) + j_{12}(\mathbf{q})} + \frac{1}{N} \sum_{\mathbf{q}} \frac{1}{j_{11}(\mathbf{q}) - j_{12}(\mathbf{q})} \right)^{-1} \qquad (65)$$

instead of equation (60), provided the phase transition is of second order.

The total energy calculations to obtain the exchange functions should be done by constraining the magnetic moments to the ground-state values. Much more efficient, however, is to use the force theorem, that is, by calculating the total energy differences from the band energies, as described and justified in Section 2.2. This was done here, even though an error is to be expected, as pointed out by Bruno (2003). By a somewhat lengthy numerical computation, the error was estimated and found to amount to roughly a factor of 1.7.

Some pertinent experimental and theoretical data for $ZrZn_2$ are collected in Table 3. As in the case of Ni, the coefficient α is to be obtained from the maximum value of the enhanced, nonuniform susceptibility, $\alpha = -\chi^{-1}_{\mathrm{Max}}/2$. We stress that this renormalization is not derived theoretically, but is motivated empirically through the appearance of the magnetic moment in the metal (see also Section 3.2.1). Figure 5 shows that the appearance (or disappearance) of the moment is accompanied by a large enhancement of the susceptibility, which is shown for two different volumes. With this choice of α, the phase transition is calculated to be of second order. The results for the Curie temperature are graphed in Figure 6, where the full pressure range used for the calculations is shown. The measured value of T_c at ambient pressure is 28.1 K where in the calculations – due to the well-known LSDA-overbinding – the pressure is found to be negative. Here, the calculated value of T_c is $T_c = 30$ K. Although it agrees well with the experimental value, we discard it in favor of the calculation at the theoretical equilibrium at $P = 0$: $T_c = 8$ K obtained using the force theorem; this value is underestimated and could be as large as 14 K in a constrained total energy calculation of the type suggested by Grotheer, Ederer and Fähnle (2001) and Singer, Fähnle and Bihlmayer (2005). In the spherical approximation, the Curie temperature

Table 3. Calculated and experimental values for $ZrZn_2$: lattice constant, a, calculated spin fluctuation, T_c^{SF}, spherical model, T_c^{SP} Curie temperatures, magnetic moment, M_0, and Curie–Weiss law ratio q_c/q_s. Values in parentheses are estimates derived from constrained-moment total energy calculations.

	a (Å)	T_c^{SF} (K)	T_c^{SP} (K)	M_0 (μ_B)	q_c/q_s
Calculated	7.284	8.0 (14)	13.3 (23)	0.20	2.8
Experimental	7.393	28.1		0.17	4.1

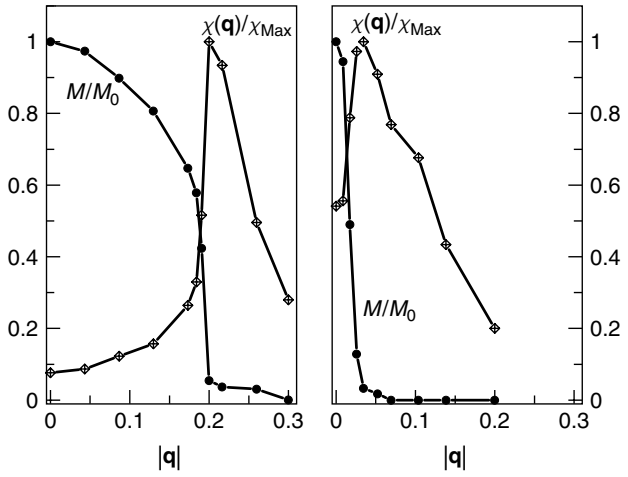

Figure 5. Reduced magnetic moment, M/M_0, and reduced susceptibility, $\chi(\mathbf{q})/\chi_{\mathrm{Max}}$, as a function of the wave vector, $\mathbf{q}$, along the (1,1,1)-direction. Left panel calculated at the experimental lattice constant, $a = 7.393$ Å, right panel calculated for $a = 7.217$ Å, corresponding to the last nonvanishing magnetization before the transition. The values of M_0 and χ_{Max} are $M_0 = 0.36\ \mu_B$ per formula unit and $\chi_{\mathrm{Max}} = 3.111 \cdot 10^{-3}$ emu mol^{-1} on the left; on the right they are $M_0 = 0.079\ \mu_B$ per formula unit and $\chi_{\mathrm{Max}} = 1.652 \cdot 10^{-3}$ emu mol^{-1}.

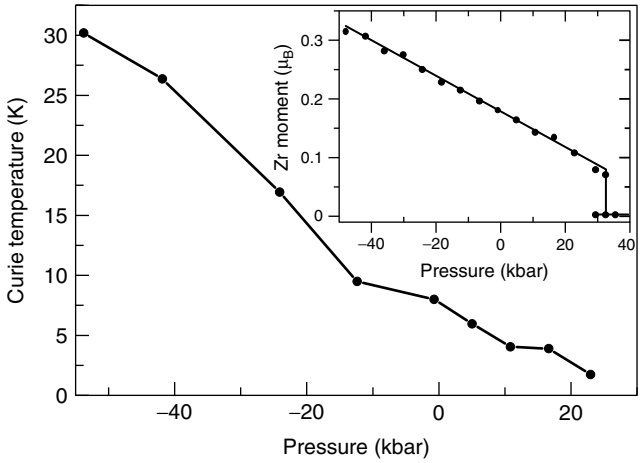

Figure 6. Curie temperature of $ZrZn_2$ as function of the pressure calculated with equation (65) using the force theorem to calculate the exchange functions $j_{11}(\mathbf{q})$ and $j_{12}(\mathbf{q})$. Inset: Magnetic moment of Zr as function of the pressure.

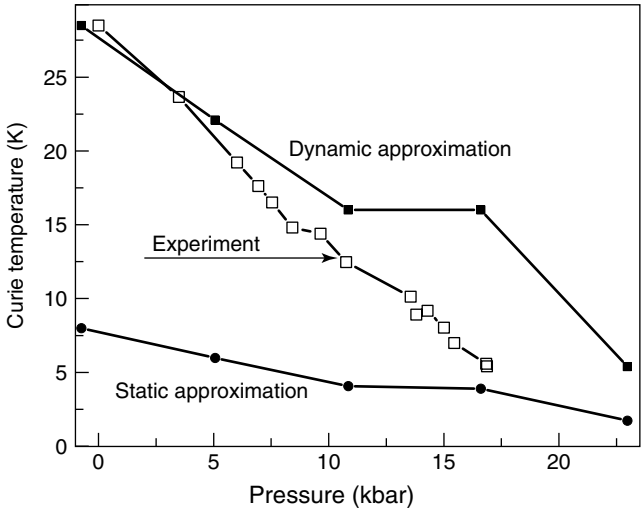

Figure 7. Curie temperature of $ZrZn_2$ as function of the pressure calculated with equation (65) (static approximation with the force theorem) and using finite dissipation constant (see text on dynamic approximation). The experimental data shown are from Pfleiderer *et al*. (2001).

is calculated to be of the order of 13.3–23 K. The estimated values are given in parentheses in Table 3.

Turning now to the *dynamic approximation*, we start the calculation with an experimental value for the dissipation constant, Γ, which was obtained by Bernhoeft, Law, Lonzarich and Paul (1988) by neutron-scattering studies. Above the Curie temperature, this value is given as $\Gamma = 1.8\,\mu\text{eV\AA}$. Inserting this value into our equations, however, we overestimate the Curie temperature by a factor of 2. In fact, the experimental value of the Curie temperature at ambient pressure is obtained by using a value of $\Gamma = 0.44\,\mu\text{eV\AA}$.

We may relate these values to the simple approximation given in equation (58). Taking the calculated value for the density of states at the Fermi energy to be about 40 states per Ry and k_F of the order of $2\pi/a$ (Kübler, 2004), the experimental value of Γ suggests a value of the Fermi energy of about 1.6 eV, whereas the theoretical value would require 0.4 eV, both values being within range of the band structure of $ZrZn_2$. But, a rigorous value of Γ cannot be extracted from equation (58).

In an attempt to use the value of $\Gamma = 0.44\,\mu\text{eV\AA}$ for higher pressures revealed that it must be reduced further for very low temperatures, thus obtaining the pressure dependence shown in Figure 7 (labelled dynamic approximation). The results of the static approximation and the experimental results of Pfleiderer *et al*. (2001) are also shown.

In Figure 8(a), the calculated relative magnetization as a function of the temperature is shown, which is compared with experimental data from Uhlarz, Pfleiderer and Hayden (2004). The agreement is very good. It depends sensitively on the value of the dissipation constant Γ, concerning not only the Curie temperature but also the curvature of the magnetization; smaller values of Γ, in particular the static approximation ($\Gamma = 0$), lead to a much flatter $M(T)$. It should be noticed that the disagreement seen in the calculated magnetization for Ni at low temperatures is not present in this case.

The calculated susceptibility in the paramagnetic temperature range is shown in Figure 8(b). Being very nearly linear, this shows a nice Curie–Weiss law. Its slope depends only very weakly on the dissipation constant, but is largely determined by the value of the coefficient α. The empirical renormalization leads to the value of q_c/q_s given in Table 3, where it is also compared with an experimental estimate of Uhlarz, Pfleiderer and Hayden (2004).

In this context, it is of interest to point out the work of Takahashi (1986), who formulated a theory for the Rhodes–Wohlfarth plot. His theory, however, relies on the zero-point spin fluctuations, which we ignored, and the assumption of a conserved local spin-fluctuation amplitude. Although zero-point spin fluctuations may play a certain role, we cannot make definite *ab initio* estimates because a cutoff frequency is needed.

3.2.3 The weakly ferromagnetic compound Ni_3Al

Another, thoroughly studied itinerant-electron weak ferromagnet is Ni_3Al. Early experimental work is that by De Boer, Schinkel, Biesterbos and Proost (1969), followed by Kortekaas and Franse (1976), Buis, Franse and Brommer (1981), and others. Bernhoeft, Lonzarich, Mitchell and

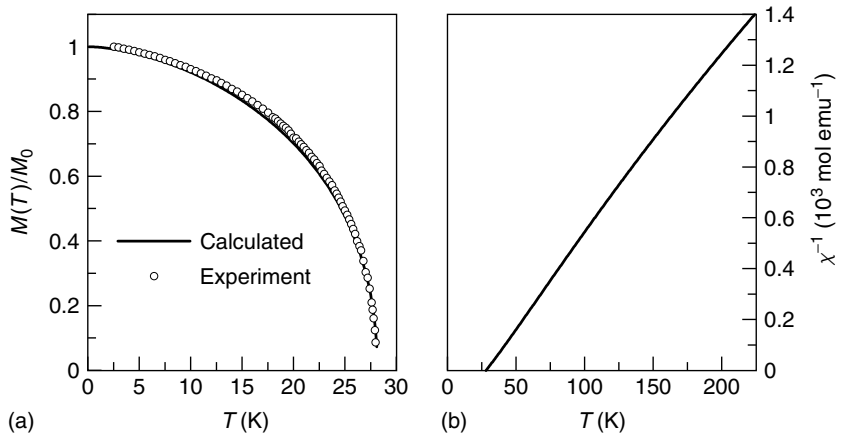

Figure 8. (a) Reduced magnetic moment, M/M_0, as a function of T for $ZrZn_2$. The experimental data (circles) were kindly supplied by Ch. Pfleiderer (Uhlarz, Pfleiderer and Hayden, 2004) (b) Calculated Curie–Weiss law.

Paul (1983) did neutron-scattering studies. In the theoretical work of Lonzarich and Taillefer (1985) and Lonzarich (1986), Ni_3Al was used as the prime example.

Ni_3Al is simple-cubic and has the Cu_3Au structure, which possesses a basis of three atoms. Thus, three normal modes are taken into account in equation (63), of which two are found to be degenerate. One obtains the three inverse static susceptibilities from $\chi^{-1}_{\parallel,\pm}(\mathbf{q})$ and $\chi^{-1}_{\perp,\pm}(\mathbf{q})$ by using that labelled with the minus sign twice. This is defined by changing the single exchange functions in the equations (46)–(47) by the combination $j_{11}(\mathbf{q}) - j_{12}(\mathbf{q})$, whereas the susceptibility labeled with the plus sign is defined by the combination $j_{11}(\mathbf{q}) + 2j_{12}(\mathbf{q})$. The Curie temperature is then given by

$$k_B T_c = \frac{6}{5} M_0^2 \cdot \left(\frac{1}{N} \sum_{\mathbf{q}} \frac{2}{j_{11}(\mathbf{q}) - j_{12}(\mathbf{q})} + \frac{1}{N} \sum_{\mathbf{q}} \frac{1}{j_{11}(\mathbf{q}) + 2j_{12}(\mathbf{q})} \right)^{-1} \tag{66}$$

provided the transition is of second order.

The exchange functions are obtained from the total energy of a spin spiral given in the case of Ni_3Al by

$$\Delta E = M_0^2 [3j_{11}(\mathbf{q}) + 2j_{12}(\mathbf{q}) \sum_{i=1}^{3} \cos(\mathbf{q} \cdot \boldsymbol{\tau}_i)] \tag{67}$$

The quantity M_0 is the Ni moment in the ground state and $\boldsymbol{\tau}_i$ are the basis vectors. Since the exchange functions are periodic with the periodicity of the reciprocal lattice, they are obtained from equation (67) with a choice of three reciprocal lattice vectors, $\mathbf{K}_1 = (1, 0, 0)$, $\mathbf{K}_2 = (0, 1, 0)$, and $\mathbf{K}_3 = (0, 0, 1)$ in units of $2\pi/a$, where a is the lattice constant. Thus, replacing $\mathbf{q}$ by $\mathbf{q} + \mathbf{K}_j$ $j = 1, 2, 3$, we get equations to solve for $j_{11}(\mathbf{q})$, finally eliminating the cosine by choosing all phases to be zero to determine $j_{12}(\mathbf{q})$.

The static approximation gives a second-order phase transition if the coefficient α is obtained from the maximum of the nonuniform susceptibility as described before. Its $\mathbf{q}$-dependence is very similar to that shown for $ZrZn_2$ in Figure 5; its maximum value of $\chi_{\mathrm{Max}} \simeq 0.88 \cdot 10^{-3}\,\mathrm{emu\,mol^{-1}}$ is smaller, however, and occurs at $\mathbf{q} \simeq (0.1, 0, 0)2\pi/a$.

The total energy differences needed to evaluate the exchange functions are obtained by both the force theorem and constrained-moment calculations. Together with other pertinent experimental and theoretical data, the result of the latter is given in Table 4, where it is denoted by T_c^{SF}. As expected, it is larger than the estimate from the force theorem, which leads to $T_c = 12.7$ K.

To obtain the experimental Curie temperature in the *dynamic approximation*, the dissipation constant is chosen as $\Gamma = 0.15\,\mu\mathrm{eV\AA}$. The calculated temperature dependence of the magnetization is shown in Figure 9(a) and is seen to agree nearly perfectly with the experimental data measured by De Boer, Schinkel, Biesterbos and Proost (1969). The value of Γ is, however, considerably smaller than the neutron-scattering value of $\Gamma = 3.3\,\mu\mathrm{eV\AA}$ measured by Bernhoeft, Lonzarich,

Table 4. Calculated and experimental values for Ni_3Al: lattice constant, a, calculated spin fluctuation, T_c^{SF}, spherical model, T_c^{SP} Curie temperatures, magnetic moment, M_0, and Curie–Weiss law ratio q_c/q_s.

	a (Å)	T_c^{SF} (K)	T_c^{SP} (K)	M_0 (μ_B)	q_c/q_s
Calculated	3.5283	18.4	30.6	0.12	1.8
Experimental	3.568		41.0	0.075	7.5

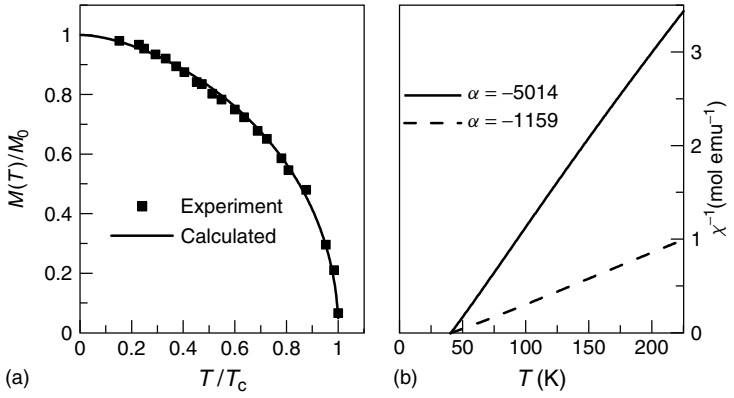

Figure 9. (a) Reduced magnetic moment, $M(T)/M_0$, as a function of the reduced temperature, T/T_c of Ni_3Al. The experimental data (circles) were taken from the paper by Lonzarich (1986) who used data by De Boer, Schinkel, Biesterbos and Proost (1969). (b) Calculated Curie–Weiss law using $\alpha = -5014$ determined with susceptibility maximum, $\chi_{\text{Max}} = 0.88 \cdot 10^{-3}$ emu mol^{-1}, and $\alpha = -1159$. (Reproduced from G.G. Lonzarich and L. Taillefer: 'Effect of spin fluctuations on the magnetic equation of state of ferromagnetic or nearly ferromagnetic metals', *Journal of Physics C: Solid State Physics B* **18** (1985), 4339.)

Mitchell and Paul (1983). Finally, the calculated inverse Curie–Weiss susceptibility shown in Figure 9(b) (solid line with $\alpha = -5014$ in Gaussian units) gives an effective magnetic moment at $T > T_c$ larger than in the ground state, as it should, but the calculated ratio of q_c/q_s given in Table 4 is too small. Possible reasons for this discrepancy may be our empirical renormalization scheme and (or) Stoner excitations, which could decrease the coefficient α considerably. To illustrate the dependence on α, we include in Figure 9(b) (dashed line) the results for a value of $\alpha = -1159$, which was found by Lonzarich and Taillefer (1985) to describe the experimental data. This value gives for the ratio q_c/q_s the value $q_c/q_s = 5$.

3.2.4 The weakly ferromagnetic compound MnSi

As the final example, we discuss the compound MnSi. It is considered to be a weak itinerant-electron ferromagnet (Moriya, 1985; Lonzarich and Taillefer, 1985), although in zero magnetic field it possesses a helical ground state with a very long period (170 Å) (Ishikawa, Tajima, Bloch and Roth, 1976). In recent experimental work (Pfleiderer, McMullan, Julian and Lonzarich, 1997; Pfleiderer *et al.*, 2004), MnSi was studied under hydrostatic pressure, P. At $P = 14.6$ kbar, a phase transition to a state identified as a non-Fermi liquid was found. The neutron diffraction studies of Pfleiderer *et al.* (2004) reveal that long-range magnetic order is suppressed at $P_c = 14.6$ kbar, but sizable quasistatic magnetic moments survive far into the non-Fermi liquid state. It is the helical modulation along a $\mathbf{Q}$ vector in the (111)-direction that is crucial for the experiments, since the corresponding Bragg scattering at $|\mathbf{Q}| = 0.037$ Å^{-1} is easily tracked as a function of the pressure. The findings are a challenge for the theory presented in this chapter.

MnSi is simple-cubic in the B-20 crystal structure possessing four Mn and four Si atoms in the unit cell at the positions (u, u, u), $(\frac{1}{2} + u, \frac{1}{2} - u, -u)$, $(-u, \frac{1}{2} + u, \frac{1}{2} - u)$, and $(\frac{1}{2} - u, -u, \frac{1}{2} + u)$, where for Mn $u = 0.137$ and for Si $u = 0.845$. This structural information is important because the symmetry of the crystal structure and the type of magnetic order are intimately connected (Sandratskii, 1998). The reasoning is as follows.

Beginning an electronic structure calculation with the Hamiltonian given in equation (19) for a spin spiral of a given $\mathbf{q}$, we find for MnSi the total-energy minimum at $\mathbf{q} = 0$. Indeed, from the work of Bak and Jensen (1980), Nakanishi, Yanase, Hasegawa and Kataoka (1980), and Kataoka, Nakanishi, Yanase and Kanamori (1984), it is known that the helical ground state of MnSi has its origin in the SOC, which is neglected in the scalar relativistic Hamiltonian. It is not difficult to add an appropriate SOC Hamiltonian to equation (19) (Sandratskii, 1998) but, since SOC does not commute with the generalized translations introduced in Section 2, a spin spiral or helical structure is unstable. We will immediately come back to this apparent contradiction, but first discuss SOC in MnSi in the *absence* of a helical state. In this case, self-consistent calculations lead to a ferromagnet with slightly canted moments. This type of magnetic order is a consequence of the symmetry of the lattice in combination with the SOC. The latter requires the application of a spin–space group (Sandratskii, 1998), which in this case is D_2. The elements of this group permute the Mn atoms together with their magnetic moments. The canting angles calculated are rather small, being at the theoretical equilibrium lattice constant $\theta_1 \simeq 0.3^\circ$ and $\phi_1 \simeq 120^\circ$ (θ_j and ϕ_j for $j = 1 \ldots 4$ such that a regular rectangle is formed). Under pressure, the canting increases slightly. The calculations reveal, furthermore, a second state with a small

Table 5. Calculated and experimental values for MnSi: lattice constant, a, calculated spin-fluctuation Curie temperature, T_c^{SF}, magnetic moment, M_0, and compressibility, κ.

	a (Å)	T_c^{SF} (K)	M_0 (μ_B)	κ (10^{-4} kbar^{-1})
Calculated	4.483	42	0.55	4.7
Experimental	4.56	30	0.4	6

magnetic moment and slightly higher total energy (fractions of a mRy per unit cell), which possesses canting angles with $\theta_1 \simeq 1.0^\circ$ and $\phi_1 \simeq 143^\circ$.

Some pertinent calculated and experimental data for MnSi are collected in Table 5. The calculated lattice constant is as usual smaller than the experimental one, but is larger than that determined by Yamada and Terao (1999), presumably because they ignored SOC. The calculated magnetic moment is somewhat larger than the experimental one, but is of the same order as that determined by Yamada and Terao at our lattice constant; the compressibility is in moderate agreement with the experiment.

Before we comment on the calculated value of the Curie temperature, we return to the apparent contradiction posed by the observed helical spin structure.

The physics of the observed helical structure is different from that discussed in Section 2. In fact, it was shown (Bak and Jensen, 1980; Nakanishi, Yanase, Hasegawa and Kataoka, 1980; Kataoka, Nakanishi, Yanase and Kanamori, 1984) to come about through the Dzyaloshinski–Moriya exchange interaction (DMI) (Dzyaloshinsky, 1958; Moriya, 1960), which is a consequence of the SOC. It is of the form $\mathbf{D}(\mathbf{S_1} \times \mathbf{S_2})$ and is finite if the crystal lacks an inversion center, as in the case of MnSi. The simultaneous rotation of all magnetic moments about the direction of the 'exchange vector' $\mathbf{D}$ does not change the energy of the system. This property of the DMI allows the symmetry, with respect to the generalized translations, to be maintained, which is a necessary condition for the stability of helical structures (Sandratskii and Lander, 2001). The work of Bak and Jensen (1980), Nakanishi, Yanase, Hasegawa and Kataoka (1980), and Kataoka, Nakanishi, Yanase and Kanamori (1984) reveals that the DMI breaks the symmetry of the wave-vector-dependent susceptibility with respect to the reversal of $\mathbf{q}$, as a consequence of which the total energy $E(\mathbf{q})$ is no longer invariant under a reversal of $\mathbf{q}$, leading to a small shift of the minimum of the total energy to an incommensurate $\mathbf{Q}$. Presently, this cannot be simulated with an *ab initio* total energy calculation.

It should be clear now that, strictly speaking, one cannot use spin spirals to determine the exchange function of MnSi and whence the Curie temperature. However, assuming that SOC has only a small effect on the electronic structure, leaving aside its subtle influence on the magnetic order, we may use the converged potentials to calculate the band structure without SOC and subsequently determine the total energy for spin spirals by employing the force theorem. To do this, one notes that the four magnetic atoms in MnSi require four normal modes in equation (63) and the total energy difference of a spin spiral becomes

$$\Delta E = M_0^2[4j_{11}(\mathbf{q}) + 2j_{12}(\mathbf{q}) \sum_{i=1}^{6} \cos(\mathbf{q} \cdot \boldsymbol{\tau}_i)] \tag{68}$$

where M_0 is the Mn moment in the ground state and $\boldsymbol{\tau}_i$ are the six basis vector differences describing the regular tetrahedron characteristic for the crystal structure of MnSi. To obtain the two exchange functions, one calculates the set of reciprocal lattice vectors, $\{\mathbf{K}_\kappa\}$ for which

$$\sum_{\kappa=1}^{8} \sum_{i=1}^{6} \cos[(\mathbf{q} + \mathbf{K}_\kappa) \cdot \boldsymbol{\tau}_i] = 0 \tag{69}$$

The Curie temperature in the static approximation is then given by

$$k_B T_c = \frac{12}{5} M_0^2 \cdot \left(\frac{1}{N} \sum_{\mathbf{q}} \frac{3}{j_{11}(\mathbf{q}) - j_{12}(\mathbf{q})} + \frac{1}{N} \sum_{\mathbf{q}} \frac{1}{j_{11}(\mathbf{q}) + 3j_{12}(\mathbf{q})} \right)^{-1} \tag{70}$$

where we used the appropriate combinations of the exchange functions that describe the normal modes.

The result of the numerical calculations is given in Table 5 as T_c^{SF}. In contrast to $ZrZn_2$ and Ni_3Al, it is larger than the experimental value and the overestimate increases if the dynamic approximation is applied. Furthermore, it is found that the pressure dependence of the calculated T_c^{SF} is much too weak being near ambient pressure $dT_c/dP \simeq -0.3\,\mathrm{K\,kbar^{-1}}$, which is to be compared with the experimental value of $dT_c/dP \simeq -1.6\,\mathrm{K\,kbar^{-1}}$ (Pfleiderer *et al.*, 2004). Since the calculated compressibility is in fair agreement with the measured value of Pfleiderer *et al.* (2004) (see Table 5), we conclude that the subtle properties of the magnetic structure are ill-described by the naive application of the spin spiral configurations.

3.3 Toward a unified theory

It is desirable to have a theory that covers the whole range of cases, from weak ferromagnets to the local moment limit, ideally all the cases displayed by the Rhodes–Wohlfarth

plot, Figure 1. Such a theory was proposed by Moriya and Takahashi (1978a,b) (Moriya, 1985, Chapters 7–8) who used the Stratonovich–Hubbard functional integral method. One can construct a simple form for the functional that does not contain the original model parameters, thus representing all the spin configurations including intermediate cases in an approximate way. In a notation somewhat different from that of Moriya and Takahashi, the formalism may be described as follows.

A functional $\Psi = \Psi(M, M_{\mathrm{L}}, \mathbf{M_q})$ is constructed that depends on the magnetization, M, the length of the moments, M_{L}, and the fluctuation vector $\mathbf{M_q} = (m_{x\mathbf{q}}, m_{y\mathbf{q}}, m_{z\mathbf{q}})$. The functional integral to be evaluated is then

$$\exp(-F/k_{\mathrm{B}}T) \propto \int \mathrm{d}M_{\mathrm{L}}^2 \int \prod_{\mathbf{q}} \mathrm{d}\mathbf{M_q} \times \exp[-\Psi(M, M_{\mathrm{L}}, \mathbf{M_q})/k_{\mathrm{B}}T] \tag{71}$$

which supplies the free energy, F. An important approximation is now to use Lagrange multipliers, λ_α, to enforce all lengths of the magnetic moments to be near a most probable length, thus writing for the functional

$$\Psi = \sum_{\mathbf{q}} j(M_{\mathrm{L}}^2, \mathbf{q})|\mathbf{M_q}|^2 + E(M, M_{\mathrm{L}}^2) - \sum_{\alpha} \lambda_\alpha \left(M_{\alpha\mathrm{L}}^2 + M^2 - \sum_{\mathbf{q}} |m_{\alpha\mathbf{q}}|^2 \right) \tag{72}$$

Here $j(M_{\mathrm{L}}^2, \mathbf{q})$ is the exchange interaction that may be determined with the methods described in Section 2 and is defined such that $j(M_{\mathrm{L}}^2, \mathbf{q} = 0) = 0$. $E(M, M_{\mathrm{L}}^2)$ is the energy of the configuration having the magnetization M and the local magnetic moment M_{L}. The integral over $\mathbf{M_q}$ can now be carried out easily. But, we single out the $\mathbf{q} = 0$ component $\mathbf{M_{q=0}} = (0, 0, m_{z0}) = (0, 0, M)$, which is identified as the macroscopic magnetization. The result is

$$\exp(-F/k_{\mathrm{B}}T) \propto \int \mathrm{d}M_{\mathrm{L}}^2 \int \mathrm{d}M \times \exp\left\{ -\frac{[E(M, M_{\mathrm{L}}^2) - \sum_\alpha \lambda_\alpha M_{\alpha\mathrm{L}}^2]}{k_{\mathrm{B}}T} - \frac{1}{2} \sum_{\alpha,\mathbf{q}} \ln \frac{\lambda_\alpha + j(M_{\mathrm{L}}^2, \mathbf{q})}{\pi k_{\mathrm{B}}T} \right\} \tag{73}$$

Next, differentiating with respect to λ_α, we get for the length, $M_{\mathrm{L}}^2 = \sum_{\alpha=1}^{3} M_{\alpha\mathrm{L}}^2$,

$$M_{\mathrm{L}}^2 = \frac{k_{\mathrm{B}}T}{N} \sum_{\alpha} \sum_{\mathbf{q}} \chi_\alpha(\mathbf{q}) \tag{74}$$

where

$$\chi_\alpha(\mathbf{q}) = \frac{1}{[2\lambda_\alpha + 2j(M_{\mathrm{L}}^2, \mathbf{q})]} \tag{75}$$

The saddle-point condition for $M_{\alpha\mathrm{L}}^2$ gives another equation by taking the derivative with respect to $M_{\alpha\mathrm{L}}^2$. This gives

$$\lambda_\alpha = \frac{\partial E(M, M_{\mathrm{L}}^2)}{\partial M_{\alpha\mathrm{L}}^2} + \frac{k_{\mathrm{B}}T}{N} \sum_{\mathbf{q}} \chi_\alpha(\mathbf{q}) \frac{\partial j(M_{\mathrm{L}}^2, \mathbf{q})}{\partial M_{\alpha\mathrm{L}}^2} \tag{76}$$

Here the inverse susceptibility is identified with the fluctuation-dissipation theorem in the static approximation. If the magnetization is finite, that is, below the Curie temperature, the integration over M indicated in equation (73) must be carried out. Treating this also with a saddle-point integration, we obtain the condition

$$\frac{\partial E(M, M_{\mathrm{L}}^2)}{\partial M} + \frac{k_{\mathrm{B}}T}{N} \sum_{\alpha} \sum_{\mathbf{q}} \chi_\alpha(\mathbf{q}) \frac{\partial j(M_{\mathrm{L}}^2, \mathbf{q})}{\partial M} = 0 \tag{77}$$

To determine the local magnetic moment, the magnetization and the susceptibility, and thus the Curie temperature, the four equations (74)–(77) must be solved simultaneously.

Unfortunately, this formalism does not provide a new method to determine the energy functional $E(M, M_{\mathrm{L}}^2)$. In the work referred to by Moriya (1985), an approximation to the grand potential defined in equation (12) is employed. Indeed, one can extract the appropriate terms for $E(M, M_{\mathrm{L}}^2)$ from equation (42) and find that the preceding formalism leads exactly to the theory described in Section 3.1 in the *static approximation*, provided the derivatives $\partial j(M_{\mathrm{L}}^2, \mathbf{q})/\partial M_{\alpha\mathrm{L}}^2$ and $\partial j(M_{\mathrm{L}}^2, \mathbf{q})/\partial M$ are neglected in equations (76) and (77). This again implies the need to renormalize the coefficients in equation (42) if one attempts to calculate them in the LSDA. One can construct expansions of order higher than that given in equation (42), which involve the magnetization and the fluctuations, the latter – it must be emphasized – appearing as Gaussian averages. An example of this can be found in the seminal review article by Shimizu (1981), who gives an expansion up to eighth order in M. Actual numerical experiments with expansions of varying order show, however, that only very little is gained in accuracy by high-order expansions compared to the simpler low-order cases. In Chapter 8 of his book, Moriya (1985), correctly points out that the preceding equations are more general than any expansions. They are also useful for explaining physical trends; it must be emphasized, however, that powerful *ab initio* algorithms still have to be developed. For this, a promising approach using a spin-cluster expansion appears to be that recently proposed by Drautz and Fähnle (2004).

The unified approach sketched in the preceding text can still be profitably used for a simple demonstration

of a formula for the Curie temperature in the spherical approximation. Usually, the resulting formula is known as the *RPA formula*, which is derived for localized-moment systems by Green's function methods (see Tahir-Keli and ter Haar, 1962a,b; Tahir-Keli and Jarrett, 1964; Tyablikov, 1969; Wagner, 1972). Furthermore, the unified approach sheds light on bcc Fe above the Curie temperature and provides means to interpolate between the intermediate cases in the Rhodes–Wohlfarth plot. While the interpolation is quite empirical and is not pursued here any further (see Moriya, 1985, Chapter 7), it is worthwhile to use the unified approach for the 'nearly localized' case of bcc Fe at and above the Curie temperature.

3.3.1 The spherical approximation and bcc iron

In the paramagnetic region, that is, above the Curie temperature, $T > T_c$, the equations (74)–(76) simplify because of isotropy and become

$$M_L^2 = \frac{3k_B T}{N} \sum_{\mathbf{q}} \chi(\mathbf{q}) \tag{78}$$

as well as

$$\chi_0^{-1} = 2\frac{\partial E(M_L^2)}{\partial M_L^2} + \frac{6k_B T}{N} \sum_{\mathbf{q}} \chi(\mathbf{q}) \frac{\partial j(M_L^2, \mathbf{q})}{\partial M_L^2} \tag{79}$$

where

$$\chi(\mathbf{q}) = 1/[\chi_0^{-1} + 2j(M_L^2, \mathbf{q})] \tag{80}$$

M_L^2 is the magnetic moment squared at high temperatures, which for a local moment system is equal to the saturation moment squared, $M_L^2 = M_0^2$. Since at the Curie temperature $\chi_0^{-1} = 0$, equations (78) and (80) imply

$$k_B T_c^{SP} = \frac{2}{3} M_0^2 \left[\frac{1}{N} \sum_{\mathbf{q}} \frac{1}{j(M_0^2, \mathbf{q})} \right]^{-1} \tag{81}$$

which gives the Curie temperature in the spherical approximation, or, as was pointed out in the preceding text, in the RPA. Note that equation (79) was ignored in this step. Continuing to ignore this equation, one can discuss a Curie–Weiss law that is obtained by requiring $M_L^2 = M_0^2$ at all temperatures above T_c but calculating χ_0^{-1} by using equation (80) in equation (78). This problem is easily solved numerically and the inverse susceptibility that results is shown as the dashed curve in Figure 10; it can, obviously, not explain the experimental susceptibility. A collection of data pertinent for bcc Fe is given in Table 6.

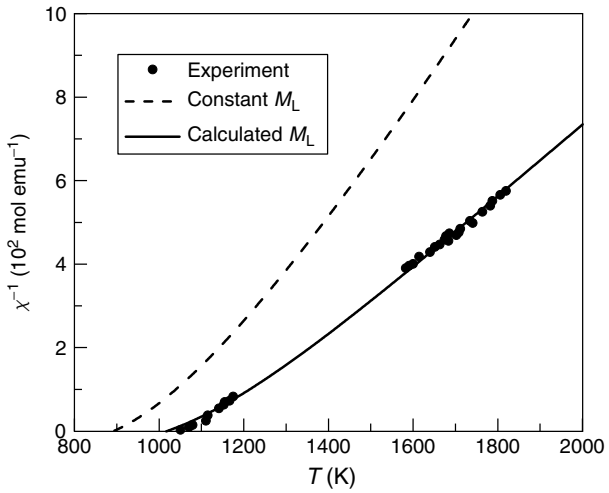

Figure 10. Calculated inverse susceptibility of bcc Fe (for the definition of M_L, see the text). Dashed curve is the spherical approximation inverse susceptibility, solid curve is obtained from solving equations (78)–(80) self-consistently. Experimental data from Shimizu (1981). (Reproduced from J. Kübler, 2006, with permission from IOP Publishing Ltd. © 2006.)

Table 6. Calculated and experimental values for bcc Fe: lattice constant, a, calculated spherical model (RPA), T_c^{SP}, mean field, T_c^{MF} Curie temperatures, magnetic moment, M_0, and Curie temperature.

	a (Å)	T_c^{SP} (K)	T_c^{MF} (K)	$M_0(\mu_B)$	T_c (K)
Calculated[a]	2.8158	893	1343	2.171	1018
Calculated[b]	2.8660	824	1328	2.268	
Calculated[c]	2.8210	790	1150		
Calculated[d]	2.8680	675	1035		
Experiment	2.8660			2.216	1044

[a]This calculation at theoretical lattice constant.
[b]This calculation at experimental lattice constant.
[c]Moran, Ederer and Fähnle (2003).
[d]Moran, Ederer and Fähnle (2003).

The exchange function $j(\mathbf{q})$ was in the cases discussed here obtained by total energy calculations using equation (53) for $\theta = 90^\circ$ constraining the magnetic moment in the atom or local frame of reference to the desired self-consistent ground-state value. Results are given for two lattice constants, the first line in Table 6 applying to the theoretical equilibrium and the second line to the experimental atomic volume. Values for the calculated spherical approximation Curie temperature and the mean-field value from equation (61) for the appropriate atomic volumes are also listed in Table 6. Before discussing these numbers any further, we show that a semiempirical explanation of the Curie–Weiss law is possible by considering equation (79) together with equations (78) and (80).

If one assumes that for the case of a nearly localized ferromagnet an expansion of the energy function $E(M_L^2)$ about the value of $M_L^2/M_0^2 = 1$ is meaningful, then the derivative of the exchange function with respect to M_L^2 in equation (79) might be estimated from $\partial j(M_0^2, \mathbf{q})/\partial M_0^2$, that is, replacing M_L by M_0. The latter derivative can be obtained numerically by finite differences using constrained total energy calculations to values of the magnetic moment, $M_0 \pm \Delta M$.

The derivative calculated for bcc Fe may be characterized by the number

$$\frac{1}{N}\sum_{\mathbf{q}} \frac{\partial \log j(M_0^2, \mathbf{q})}{\partial M_0^2} \simeq -0.129 \tag{82}$$

and an evaluation of the self-consistency equations (78)–(80) gives, using the expansion

$$E(M_L^2) = \frac{1}{4}\chi_{\text{eff}}^{-1}(M_L^2/M_0^2 - 1) \tag{83}$$

the result shown in Figure 10 as solid line. The value used here for the expansion coefficient is $\chi_{\text{eff}} \simeq 0.67 \cdot 10^{-4}$ emu mol^{-1}. The Curie temperature is obtained as $T_c = 1018$ K and is also given in Table 6. The value of the magnetic moment at the calculated Curie temperature is $M_L \simeq 1.07 M_0$. It should be stressed that the only input parameter is χ_{eff}, which together with the *ab initio* exchange function $j(M_0^2, \mathbf{q})$ explains both the slope and the Curie temperature. The expansion coefficient χ_{eff} should be obtained from a renormalized theory, which is beyond the scope of our approach. But it is interesting to observe that it is of the order of magnitude of a Brillouin zone average of the nonuniform susceptibility $\chi(\mathbf{q})$. The agreement with the experimental data is surprising, but perhaps fortuitous.

For completeness, we report results for the magnetization of bcc Fe below the Curie temperature. An application of an expansion of the energy function $E(M, M_L^2)$ in equations (76) and (77) of rather high order cannot explain the magnetization properly. But since the magnon-spectrum can be calculated by means of spiral total energies, using for instance a formula like equation (20), one can resort to established theories for local moment systems. Antropov, Harmon and Smirnov (1999) used an interpolation formula given by Tyablikov (1969) and calculated magnon energies to obtain the magnetization shown in Figure 11, which explains the experimental results to an amazing accuracy. It should be added, however, that the visual agreement is enhanced by using reduced units, which was not done in the original publication by Antropov, Harmon and Smirnov (1999).

We complete the discussion by commenting on the remaining numbers in Table 6. Moran, Ederer and Fähnle (2003)

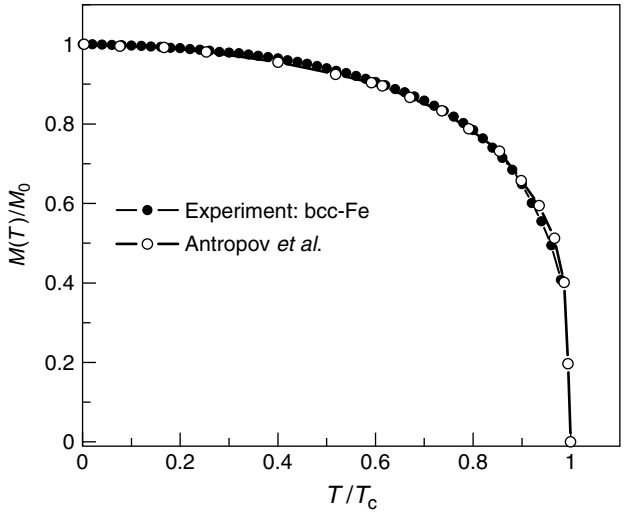

Figure 11. Temperature dependence of the magnetization of bcc Fe in reduced units. The data for the curve labelled Antropov *et al.* were extracted from Figure 13 of the paper of Antropov, Harmon and Smirnov (1999) and are based on the Tyablikov formalism.

calculated the Curie temperature as a function of the volume and found that its value increases as the volume is decreased. Two of their values are included in Table 6 together with two values calculated here. The latter support the calculations of Moran *et al.*, although our rate of change is somewhat smaller, being $\partial T_c^{SP}/\partial P \simeq 0.58$ K kbar^{-1} compared with their value of $\partial T_c^{RPA}/\partial P \simeq 1.8$ K kbar^{-1}. It is not the difference in these numbers that is of importance (our estimate perhaps being less precise because of our simplified constraining scheme, see Grotheer, Ederer and Fähnle, 2001 and Singer, Fähnle and Bihlmayer (2005)), it is the sign that is quite counterintuitive. Indeed, it violates the Bethe–Slater curve, according to which the nearest-neighbor exchange constant for iron should decrease with decreasing interatomic distance (Sommerfeld and Bethe, 1933; see also Kouvel and Wilson, 1961 as well as Jiles, 1998). Moran *et al*. point out that one has to go far beyond the nearest and next-nearest exchange constants to see the origin of the behavior in the rate of change. Since the experimental data give $\partial T_c/\partial P \simeq 0$ (Leger, Loriers-Susse and Vodar, 1972), they conclude that the pressure effect cannot be correctly described by the Heisenberg model. (Note that the quantities T_c^{SP} or T_c^{RPA} or T_c^{MF} depend only on the exchange function $j(\mathbf{q})$). Thus, we have to look at the role of pressure in the energy function $E(M_L^2)$, for which, unfortunately, an *ab initio* expression is lacking.

3.3.2 Other work on elementary magnets

We begin this subsection by referring back to the grand potential given in equation (12) and consider the

paramagnetic state as consisting of local moments that are disordered like atoms in a disordered alloy. To evaluate the grand potential for this situation, one needs a method to solve the single-particle equations in the presence of disorder. A powerful scheme to treat the disorder is the coherent-potential approximation (CPA) (Ehrenreich and Schwartz, 1976), which can be combined with Green's function methods implied in Section 2.2, where the real-space method for obtaining the exchange interactions was sketched. The initial steps of the CPA theory are easily explained.

If we are given a situation where the concentration of A atoms is x, then, in a binary alloy, that of the B atoms is $(1 - x)$ and the average of the scattering path matrix defined in equation (22) is

$$\langle \tau \rangle = x\tau^A + (1 - x)\tau^B \doteq \tau_{\mathrm{C}} \tag{84}$$

where a scattering path operator, τ_{C}, of a coherent medium is defined. Physically, a random crystal potential is replaced by an effective medium that is described with a single scattering path matrix τ_{C}. Starting from here, a single-site t-matrix is defined in correspondence with equation (22). There are a number of different ways to proceed, all are, however, beyond the scope of this chapter. A good discussion can be found in the paper by Gyorffy *et al*. (1985). We stress that the CPA is ideally suited for obtaining the exchange constants from the real-space approach.

The paramagnetic state of a magnet is now modeled as a random distribution of an equal amount of up- and down-spin atoms and the grand potential is determined variationally dropping all double-counting terms. Using this approach, which leads to the so-called *disordered local moment picture* (*DLM*), Staunton, Gyorffy, Stocks and Wadsworth (1986) have derived an expression for the temperature-dependent, paramagnetic spin susceptibility. This approach has been very successful in explaining the magnetic correlations in the paramagnetic state of several magnetic metals and alloys as well as determining the Curie temperatures (Staunton and Gyorffy, 1992).

We begin our comparison of a number of noteworthy, *ab initio* calculations for the Curie temperatures for Fe, Co, and Ni with the results of Staunton and Gyorffy (1992), which appear in the first column of Table 7. This prominent paper also contains a demonstration of the Curie–Weiss law and its relation to experimental data. It should be noted that this theory does not require a mapping onto an effective Heisenberg model.

The remaining entries of Table 7 are calculated with methods more in line with the present review. Thus, the second column summarizes the results of Halilov, Eschrig, Perlov and Oppeneer (1998), who, in an important and very detailed paper, obtained the exchange interaction in the reciprocal-space approach. They also, besides detailed magnon spectra, calculated and showed the magnetization as a function of the temperature for Fe, Co, and Ni, giving the Curie temperatures in the mean-field approximation.

The results obtained by Uhl and Kübler (1996) (Reference[c] in Table 7) were based on the spin-fluctuation theory using, besides the exchange function $j(\mathbf{q})$, the calculated values for the expansion coefficients α and β. This, as was pointed out in the preceding text, unfortunately leads to inaccurate Curie constants.

The results by Rosengaard and Johansson (1997) in the column marked Reference[d] are described in a very inspiring paper, in which the real-space and reciprocal-space approaches for obtaining the exchange interaction are compared. The actual calculations were carried out with exchange constants obtained in the reciprocal space approach using spin spirals. The magnetization as a function of the temperature was determined using the Monte Carlo method, which, in principle, is exact, given exact exchange constants and a sufficiently large sampling volume. Unfortunately, this method cannot be dealt with here, so a reference must suffice (Landau and Binder, 2000). (See also **Quantum Monte**

Table 7. Collection of calculated Curie temperatures and experimental values (from Table 1) in Kelvin of bcc Fe, fcc Co, and fcc Ni.

	Reference[a]	Reference[b]	Reference[c]	Reference[d]	Reference[e]		Reference[f]		Experiment[g]
bcc-Fe	1015	1037	1095	1060	1414	950	1343	893	1044
fcc-Co		1250	1012	1080	1645	1311	1570	1249	1388
fcc-Ni	450	430	412	510	397	350	643	537	627

[a]Staunton and Gyorffy (1992), DLM picture.
[b]Halilov, Eschrig, Perlov and Oppeneer (1998), mean-field approximation.
[c]Uhl and Kübler (1996), spin-fluctuation approximation.
[d]Rosengaard and Johansson (1997), Monte Carlo calculations.
[e]Pajda *et al*. (2001), mean-field and RPA values given.
[f]This work, mean-field and spherical approximation given.
[g]Experimental results, see Table 1.

Carlo Methods, Volume 1). The Curie constants are also obtained and found to be smaller than the experimental values.

Finally, we emphasize that Pajda *et al*. (2001) determine the exchange constants using the real-space approach obtaining the spin-wave stiffness constants, and Curie temperatures of Fe, Co, and Ni in the RPA and mean-field approximation. Their results are shown in Table 7 in the column marked Reference[e]. They are seen to basically agree with ours, given in the column marked Reference[f], although they are not identical.

We close this subsection by briefly remarking on the antiferromagnetic metals fcc Fe and fcc Mn. Their electronic and magnetic structure is unusual, showing for a certain range in the atomic volume noncollinear order, see for instance Chapter 4 in Kübler (2000), and for more recent results Knöpfle, Sandratskii and Kübler (2000) and references therein. The case of fcc Fe is of particular interest because of the possibility of epitaxially growth, which is further discussed in Section 4.3.

Zhou, Wang and Kawazoe (1999) determined for both fcc Fe and fcc Mn 11 pair exchange constants by means of total energy calculations for magnetic supercells of considerable size. By means of the Monte Carlo method, they then computed the Néel temperatures obtaining for fcc Mn a value of $T_N = 383\,\mathrm{K}$, which should be compared with a spin-fluctuation value by Uhl and Kübler (1997) of $T_N = 446\,\mathrm{K}$ and an experimental estimate from Mn alloys of $T_N = 490\,\mathrm{K}$ (Endoh and Ishikawa, 1971). For fcc Fe, their results were $T_N = 156\,\mathrm{K}$. A comparison with an experimental value is not straight forward: neutron diffraction measurements by Onodera *et al*. (1994) on coherent fcc Fe precipitates in Cu yielded a value of $T_N = 67 \pm 2\,\mathrm{K}$, whereas films epitaxially grown on Cu(100) by Qian *et al*. (2001) indicated a Néel temperature of about 275 K.

4 APPLICATIONS FOR MAGNETS DESIGN

In this section, essentially, two formulas are retained, that is, equations (60) and (61), the spherical approximation (or RPA) and the mean-field approximation to predict the Curie temperature of magnetic systems that might be of interest for technological applications. We stress that all these theories require a mapping to an effective Heisenberg model.

Without an attempt at completeness, a number of recent papers concerned with, broadly speaking, spin-electronics (or *spintronics*) are reviewed first, followed by some selected studies on magnet films and multilayers. (See also **Heusler Alloys, Volume 4**).

4.1 Half-metallic ferromagnets

Half-metallic ferromagnets possess the unusual property that in one spin channel the electrons are metallic, in the other they are insulating with a sizable energy gap, provided SOC can be neglected. Thus, at least at the absolute zero, the electrons are 100% spin polarized at the Fermi edge. In the presence of SOC, the degree of polarization is still nearly perfect. An early review is contained in the book by this author (Kübler, 2000, Ch.4). A recent review article containing a large number of original references is that by Shirai (2004); thus, half-metallic ferromagnets may be used as potential materials for spintronic device applications, for example, as an electrode of a magnetic tunnel junction, a source of spin injection into semiconductors, and newly proposed transistors.

4.1.1 Heusler alloys

Examples of half-metallic ferromagnets are the 'classical' $C1_b$-type Heusler alloys NiMnSb, PtMnsb, and so on, magnetite, rutile-type CrO_2, the $L2_1$-type Heusler alloys, perovskite manganites, double perovskites, the diluted magnetic semiconductors, and the recently discovered zinc-blend half-metals, for references see Shirai (2004). For any of these compounds to be of technical use, the Curie point must be above room temperature. Modern simulations thus not only concentrate on the electronic and magnetic properties but also on predictions of the Curie temperature.

To begin with, one needs to know if the techniques described here are sufficiently accurate for meaningful predictions. Calculations by Enkovaara *et al*. (2003) on the $L2_1$-type Heusler alloys Ni_2MnGa and Ni_2MnAl as well as by Sasioglu, Sandratskii and Bruno (2004) on Ni_2MnX (X = Ga,In,Sn,Sb) serve this purpose quite well. Although these compounds are not half-metallic, their finite-temperature properties are quite revealing. Improving considerably earlier work by Kübler, Williams and Sommers (1983), Enkovaara *et al*. and Sasioglu *et al*. used modern calculational method and the LSDA including the generalized gradient approximation (GGA) (Perdew and Wang, 1992) to determine the exchange parameters in the reciprocal-space approach. The Curie temperature is obtained in the mean-field approximation modified by considering more than one magnetic sublattice. The latter improvement is similar to the diagonalization employed for the treatment of the multi-sublattice case in Section 3.2, except for the fact that Sasioglu, Sandratskii and Bruno (2004) use it for the mean-field approximation.

The results of these calculations are extremely satisfying. The experimental Curie temperatures of Ni_2MnX (X = Ga,In,Sn,Sb) are known and found in the range from 315 K to 380 K, the theoretical values deviating in the worst

case by only 9% of the experimental value for the case of Ni_2MnIn, where $T_c^{exp} = 315\,K$ compared with $T_c^{calc} = 343\,K$ (Sasioglu, Sandratskii and Bruno, 2004).

Sasioglu, Sandratskii and Bruno (2005) in another paper considered two further $L2_1$-type Heusler alloys, Mn_2VAl and Mn_2VGe, the former of which was found by Weht and Pickett (1999) to be a half-metallic ferrimagnet with a magnetic moment of 2 μ_B/f.u. The Curie temperature for Mn_2VAl calculated in the same way as in the previous paper (Sasioglu, Sandratskii and Bruno, 2004) comes out to be $T_c^{MF} = 638\,K$, underestimating the experimental value of $T_c = 760\,K$ somewhat. For Mn_2VGe, they predict a Curie point of $T_c^{MF} = 413\,K$. For more recent results see Kübler (2006).

Clearly, it is of interest to calculate the Curie temperatures of the 'classical' $C1_b$-type Heusler alloys first discovered by de Groot, Mueller, van Engen, Buschow and Jongebreur (1983). This was done here using the augmented spherical wave (ASW) method (Williams, Kübler and Gelatt, 1979) in the LSDA, employing the reciprocal-space method and the force theorem to obtain the exchange parameters. The results for Curie temperatures in the spherical and mean-field approximation are collected in Table 8.

For NiMnSb, the lattice constant was optimized; the results are given in footnote a. At the smaller theoretical lattice constant, NiMnSb remains half-metallic but the calculated Curie temperature increases. We draw the attention to the drop in the measured and calculated Curie temperatures for PtMnSn, which is not half-metallic. Furthermore, although overestimates by the mean-filed approximation are not uncommon, it is startling to see the consistent overestimates in the calculated T_cs by the spherical approximation, except for the case of PtMnSn. Unpublished results by this author indicate that the same discrepancy is found in the half-metallic ferromagnet CrO_2. One could argue that estimates of T_c using the static approximation to the spin-fluctuation theory, which are lower by a factor of 0.6 compared with the spherical approximation (compare equation (54) with equation (60)), are more appropriate here. This can be ruled out for the following reasons.

Table 8. Calculated and experimental (van Engen, Buschow and Jongebreur, 1983) values for the 'classical' half-metallic ferromagnets: lattice constant, a, experimental magnetic moments, M_0, calculated magnetic moments, M_0^{calc}, both in μ_B/f.u., experimental Curie temperatures, T_c, calculated Curie temperatures: spherical approximation (RPA) T_c^{SP} and mean-field approximation, T_c^{MF}.

	a (Å)	M_0	M_0^{calc}	T_c (K)	T_c^{SP} (K)	T_c^{MF} (K)
PtMnSb	6.210	3.97	4.02	582	741	991
PdMnSb	6.285	3.95	4.09	500	744	927
NiMnSb[a]	5.920	3.85	4.00	730	1002	1305
PtMnSn[b]	6.264	3.42	3.84	330	188	354

[a]Calculated lattice constant is $a = 5.725$ Å with $T_c^{SP} = 1141\,K$.
[b]Not half-metallic.

Capelle and Vignale (2001) as well as Eschrig and Pickett (2001) in two recent papers drew attention to a nonuniqueness problem in spin-density-functional theory. Eschrig and Pickett start out with the observation that the spin-only magnetic susceptibility is zero for a half-metallic ferromagnet (which it manifestly is), although the conductivity is that of a metal. Zero susceptibility, however, implies that the ground-state spin density does not change when an external magnetic field is changed. They prove that *two magnetic fields whose difference is constant in magnitude, but possibly is nonunidirectional, may give rise to the same ground state.* Both papers arrive at the same conclusions finding that the exchange-correlation energy is not always a differentiable function of the spin density and *the ground state does not contain all information about excited states in the presence of a magnetic field.* As a consequence, applications of the spin-density functional approximation must be critically reexamined.

It is thus not surprising, for instance, that calculations for the ground-state energy, where the magnetic moment is constrained to a given value (the constraint is achieved by a magnetic field (Dederichs, Blügel, Zeller and Akai, 1984)), result in a kink at the ground-state magnetization. The kink implies that a power series expansion of the total energy in terms of the magnetization fails precluding an expansion of the form of equation (38). Since the kink, however, pins the value of the magnetic moment near the ground-state value in the wave-vector-dependent energy changes, the spherical approximation still seems applicable. Furthermore, calculations employing the force theorem are carried out without any constraining magnetic fields, so the information gained in this case seems justified too. The apparent discrepancy remains and could be due to the LSDA. Indications exist that the GGA provides the necessary corrections.

4.1.2 Zinc-blende compounds

In the search for new materials suitable for spintronics applications Akinaga, Manago and Shirai (2000) predicted by LSDA calculations and subsequently grew zinc-blende CrAs (zb-CrAs) on GaAs by molecular-beam epitaxy. It was found to be ferromagnetic at room temperature and the calculations revealed zb-CrAs to be half-metallic.

In fact, a large number of recent electronic structure calculations concentrated on zinc-blende compounds of transition elements, in some cases comparing the electronic properties in the unstable zinc-blende phase with that of the stable NiAs crystal structure (Sanvito and Hill, 2000; Xu, Liu and Pettifor, 2002; Sakuma, 2002). A systematic study of zinc-blende

compounds involving transition-metal elements with N, P, As, Sb, S, Se, and Te is that by Galanakis and Mavropoulos (2003), who also examined the half-metallic behavior of the transition-element-terminated surfaces. Subsequently, there appeared calculations of the Curie temperatures, T_c, of some of the compounds that might be of technological importance. In addition, the calculated trends in T_c were interpreted and related with salient features of the electronic structure (Kübler, 2003; Sanyal, Bergqvist and Eriksson. 2003).

The calculations by this author (Kübler, 2003) were based on spin-fluctuation theory in the LSDA, which is not justified because of the nonuniqueness problem addressed in the preceding text. However, the Landau parameter α plays no prominent role here, therefore the results for the Curie temperatures can easily be scaled up to the spherical approximation (compare equation (54) with equation (60)) and are given in Table 9, which also contains results obtained by Sanyal, Bergqvist and Eriksson (2003), who used the GGA for the determination of the underlying exchange constants.

The calculations were carried out for two lattice constants, namely, those of GaAs (5.65 Å) and InAs (6.06 Å). For both cases, the compounds VAs and CrAs are half-metallic ferromagnets, with magnetic moments of 2 μ_B/f.u. and 3 μ_B/f.u., respectively. The compound MnAs, however, is only half-metallic with a moment of 4 μ_B/f.u. for the larger lattice constant of InAs; for that of GaAs, the Fermi edge, E_F, moves into the conduction band (see for instance Figure 1 of Kübler (2003)) and the magnetic moment drops to 3.65 μ_B/f.u. Connected with this shift of E_F is a large decrease of the calculated Curie temperature, which is seen in the last row of Table 9.

There is only rough agreement between the two sets of numbers appearing in Table 9, the more precise values of Sanyal *et al*. (second and third row) are lower throughout. The differences in the mean-field results indicate different exchange constants, presumably because in one case the GGA was employed. The Monte Carlo results are in principle exact, given exact exchange constants.

Both sets of numbers indicate same orders of magnitude and, in the cases of VAs and CrAs, an increase in the calculated Curie temperatures when the lattice constant is decreased. The same trend is observed in the half-metallic ferromagnet NiMnSb, for which estimates of the Curie temperature are given in Table 8.

This subsection is closed with the remark that experimental observations confirm the theoretical results in that zb-CrAs grown on GaAs possesses a Curie temperature above 400 K (Akinaga, Manago and Shirai, 2000), while that of zb-MnAs is below room temperature (Ono *et al*., 2002).

Table 9. Calculated Curie temperatures for three zinc-blende materials at two different lattice constants, a, which are those of GaAs (5.65 Å) and InAs (6.06 Å). The second and third row are calculations by Sanyal, Bergqvist and Eriksson (2003) using the GGA, the fourth and fifth row are our own results obtained by the LSDA. Mean-field, T_c^{MF}-, Monte Carlo T_c^{MC}-, and spherical approximation T_c^{SP}-results are given in K.

	VAs	VAs	CrAs	CrAs	MnAs	MnAs
a (Å)	5.65	6.06	5.65	6.06	5.65	6.06
T_c^{MF} [a]	990	610	1320	1100		640
T_c^{MC} [a]	830	490	980	790		530
T_c^{MF} [b]		1175		1367	569	1363
T_c^{SP} [b]		882		820	301	953

[a] Calculated by Sanyal, Bergqvist and Eriksson (2003).
[b] Own calculations, obtained from Kübler (2003).

4.2 Diluted magnetic semiconductors

Diluted magnetic semiconductors (DMSs), like the prototypical Mn-doped GaAs, (Ga,Mn)As, and others to be discussed in the subsequent text, are intended to be technologically applied in devices that combine functions of semiconductors and magnetic devices. Here, methods need to be developed to manipulate and propagate the spin polarization in order to control the spin degree of freedom of electrons in semiconductors. These semiconductors are envisioned to be ferromagnetic possessing Curie points above room temperature, in order to realize, for instance, a spin-polarized transistor, integrated spin-logic in a nonvolatile spin memory, and phase-coherence in a quantum computer – just to name some of the presently much talked about key projects.

Because of the great wealth of experimental and theoretical work on DMSs, our treatment here is necessarily incomplete. An earlier review paper on the theoretical side is that by König, Schliemann, Jungwirth and MacDonald (2003) and the experimental situation was covered by Ohno (1999).

Perhaps one of the key materials fabricated is the DMS with the formula $(Ga_{0.947}Mn_{0.053})As$ having a Curie temperature of $T_c = 110$ K (Ku *et al*., 2003). However, fabrication of DMS materials possessing higher Curie temperatures (characterized with unambiguous experimental methods like magnetic circular dichroism) met with difficulties so far, with perhaps one exception discussed in the subsequent text. Numerous theoretical efforts thus concentrated on identifying and understanding those physical mechanisms, which could guide experimental efforts to result in optimized materials. A small selection of these papers are reviewed here.

At present, the DMS materials discussed are (Ga,Mn)As, (In,Mn)As, and (Ga,Mn)N of the III-V type, (Zn,Cr)Te of the II-VI type, and $Ge_{1-x}Mn_x$ of group-IV type. The question to be clarified theoretically concerns mainly the physical mechanism that determines the exchange interactions over

rather large distances. Here, one finds theories that rely on model Hamiltonians, particularly noteworthy being that by Dietl, Ohno and Matsukura (2001). Another approach uses *ab initio* methods, like that by Akai (1998) who extracts concepts for the exchange mechanism from his calculations.

Since we opt for describing results of *ab initio* methods, we should stress that the various exchange mechanisms appear in the calculational results in mixed form. This is in contrast to the model Hamiltonian approach where different perturbational treatments give different exchange interactions, depending on the relative magnitude of the relevant physical properties. Still, it is common to treat the magnetism of a DMS in terms of the competition between the antiferromagnetic superexchange and the ferromagnetic double exchange through charge carriers (Andersen, 1963). In the work, we want to start with (Sandratskii and Bruno, 2002, 2003a,b) the term *double exchange* is replaced by kinetic exchange, since, it is argued that the term *double exchange* occurs in the interpretation of mixed valence systems, which are important in another context. The physics, however, considered in the original definition of double exchange (de Gennes, 1960) is the same as that considered here under the label kinetic exchange (Sandratskii and Bruno, 2003a). This is shown by these authors, who use a simple two-band tight-binding model and varying band occupations.

The supercell calculations have the virtue of great simplicity, but they ignore the role of disorder, thus representing simplifications that could be questioned. Still, the insight gained by the work of Sandratskii and Bruno (2002, 2003a,b) is quite enormous. Furthermore, refined calculations that do consider the role of disorder *ab initio* support the supercell calculations to a large extend, as shown by us in the following text.

Sandratskii and Bruno deal with the DMSs consisting of (Ga,Cr)As, (Ga,Mn)As, (Ga,Fe)As, and (Zn,Cr)Te containing various concentrations of the magnetic ions. For simplicity, we here select results for (Ga,Mn)As and (Zn,Cr)Te and show in Figure 12 the calculated DOS for (Ga,Mn)As for the two Mn concentrations of (i) 25% and (ii) 12.5%. In Figure 12(c), we show the DOS of (Zn,Cr)Te with 25% Cr. They are easily reproduced with the help of a notebook computer using, just as Sandratskii and Bruno, the ASW-method (Williams, Kübler and Gelatt, 1979) in the LSDA. In the original work, to which we refer for all details, one also finds the concentrations 6.25% and 3.125%, obtained in the case of (Ga,Mn)As for the lattice constant of GaAs. We here use a slightly larger lattice constant ($a = 5.87$ Å instead of $a = 5.65$ Å) so that the DMSs are half-metallic for all concentrations. That these DMSs are, indeed, half-metallic, at least in supercell calculations, is one of the first results to be noticed.

In somewhat more detail, the calculations show (Figure 12 and those of Sandratskii and Bruno (2002, 2003a,b)) that the

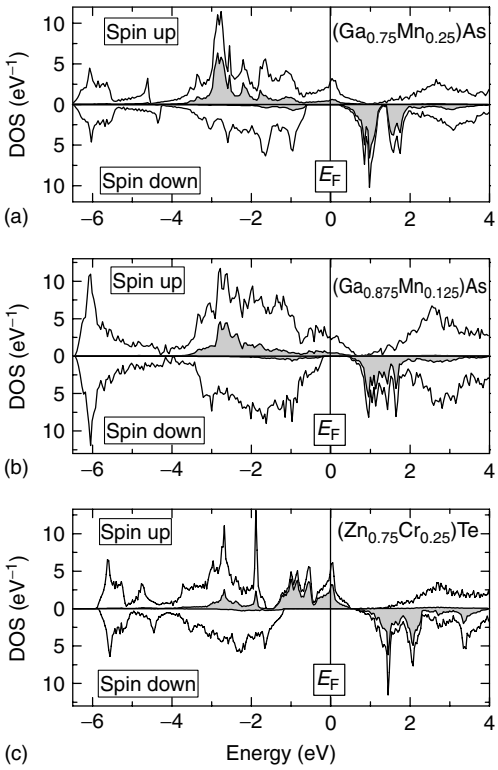

Figure 12. Total and partial density of states (DOS) of (a) $(Ga_{0.75}Mn_{0.25})As$, (b) $(Ga_{0.875}Mn_{0.125})As$, and (c) $(Zn_{0.75}Cr_{0.25})Te$ obtained by supercell calculations. Curves bordering shaded areas depict d-states of Mn or Cr, respectively.

replacement of one Ga atom in the supercell of GaAs by a Mn atom does not change the number of spin-down states in the valence band. In the spin-up states, however, five new hybridized energy bands related to the 3d states of Mn are created. The situation is analogous for the case of ZnTe with Cr. The atomic configurations of Ga being $4s^2 4p^1$ and that of Mn $4s^2 3d^5$ implies that four electrons occupy the five states, leaving one state unoccupied at the top of the valence band, which is interpreted as a hole state. The same hole state appears for ZnTe doped with Cr.

The important issue to be clarified by the calculations is the role of the charge carriers in mediating the exchange interaction. The experimental studies (Ohno, 1999) show that the concentration of holes is lower than the concentration of the Mn atoms. One of the factors leading to the low concentration is the presence of As antisites, that is, a small fraction of As occupies Ga sites. Sandratskii and Bruno now succeed in demonstrating the importance of the hole states by changing their occupation. This is done in a rigid-band approximation for different numbers of electrons, n, changing the charge state of Mn, each time calculating the Curie temperature by both equations (60) and (61), the spherical (or RPA), and the mean-field

approximation, respectively, as a function of n self-consistently. The reciprocal-space approach is used for the determination of the Curie temperatures.

For $n = 0$, that is, the nominal number of carriers, the calculated Curie temperatures are given in Table 10 and compared with experimental values. The DMS (Zn,Cr)Te was grown with a concentration of 20% having an exceptionally large Curie temperature of 300 K (Saito, Zayets, Yamagata and Ando, 2003). It was studied by Sato and Katayama-Yoshida (2001) theoretically and simulated with a supercell containing 25% Cr by Sandratskii and Bruno (2003b), which seems close enough to the experimental value.

For both DMS materials, a decrease in the number of holes ($n > 0$) decreases the exchange interactions and thus both estimates of the Curie temperature. For a small number of holes, when the valence band is nearly filled, the exchange interaction becomes antiferromagnetic, that is, the superexchange mechanism begins to dominate over the kinetic exchange. For an increased number of holes ($n < 0$), the exchange interaction and correspondingly the Curie temperature initially increases. The calculations reported by Sandratskii and Bruno (2002, 2003a,b) cover the range $-2 \leq n \leq 2$ and show oscillatory behavior. The experimental Curie temperatures are found to be in good agreement with the calculations obtained for $n = 0.6$, indicating a hole concentration lower than the concentration of Mn atoms, also agreeing with the experimental observation of Ohno (1999). In the case of $(Zn_{0.75}Cr_{0.25})$Te, the differences between the two calculations cited in Table 10 is somewhat startling and might be due to different precisions in sampling the exchange function $j(\mathbf{q})$.

The next step in theoretical refinements consists in incorporating disorder in the *ab initio* calculations. This is done by employing the CPA, introduced briefly in Section 3.3.3.

In a short paper, Bouzerar, Kudrnovsky, Bergqvist and Bruno (2003) focus their attention on the effects of randomness and the compensating effects by As antisites in the DMSs described by the formula $(Ga_{0.95-y}As_yMn_{0.05})$As. The CPA is used obtaining the exchange constants from the real-space approach. Furthermore, the approximations for the Curie temperature are examined by using the Monte Carlo method (Landau and Binder, 2000) (See also **Quantum Monte Carlo Methods, Volume 1**). As a result, the general picture obtained by the supercell simulations is not changed, although the various approximations for the Curie temperature lead to somewhat higher values, including the Monte Carlo estimate, which is larger by about 30 K compared with the mean-field value given in Table 10. However, a finite concentration of As antisites in both the supercell- and the CPA-approximation leads to decreasing calculated values resulting for $y = 0.01$ in the Monte Carlo approximation in $T_c^{MC} = 117\,\mathrm{K}$.

Table 10. Experimental Curie temperatures for $(Ga_{0.95}Mn_{0.05})$As and $(Zn_{0.8}Cr_{0.2})$Te and results of supercell calculations in the spherical (RPA), T_c^{SP}, and mean-field, T_c^{MF}, approximation.

	$(Ga_{0.95}Mn_{0.05})$As	$(Zn_{0.8}Cr_{0.2})$Te
T_c^{MF} (K)	225[a]	346[c] 429[d]
T_c^{SP} (K)	175[a]	369[d]
T_c^{exp} (K)	110[b]	300[e]

[a]Calculated by Sandratskii and Bruno (2002, 2003a).
[b]Experimental value (Ohno *et al*., 1996).
[c]Calculated by Sandratskii and Bruno (2003b) for $(Zn_{0.75}Cr_{0.25})$Te.
[d]Own calculation for $(Zn_{0.75}Cr_{0.25})$Te.
[e]Experimental value (Saito, Zayets, Yamagata and Ando, 2003).

Sato, Dederichs, Katayama-Yoshida and Kudrnovsky (2004) also employ the CPA to investigate the exchange mechanism and the Curie temperature for the diluted magnetic semiconductors (Ga,Mn)N, (Ga,Mn)P, (Ga,Mn)As, and (Ga,Mn)Sb. A concentration range up to 15% Mn is assumed, for which the Curie temperature is obtained in the mean-field approximation. The exchange constants are determined using the total energy difference between the ferromagnetic state and the 'DLM' state (see Section 3.3.3.), which can be described with the formula $(Ga_{(1-c)}Mn^{\uparrow}_{c/2}Mn^{\downarrow}_{c/2})$X, whereas the ferromagnetic state is denoted by $(Ga_{(1-c)}Mn^{\uparrow}_{c})$X. This means that in the latter state the Mn impurities with concentration c having parallel aligned magnetic moments are randomly distributed at Ga sites, whereas in the former three components, $Mn^{\uparrow}$, $Mn^{\downarrow}$, and Ga are considered on the Ga site.

The calculations by Sato, Dederichs, Katayama-Yoshida and Kudrnovsky (2004) show that the compounds remain half-metallic except for (GaMn)Sb. To compare with the supercell calculations a Curie temperature of $T_c^{MF} \simeq 250\,\mathrm{K}$ for 5% Mn in GaAs can be read from their Figure 1, which is in acceptable agreement with the value given in Table 10. The important thing about this paper is that the exchange mechanism is analyzed in great detail. The concentration dependence of the Curie temperature for small c is found to be $\propto \sqrt{c}$, which is convincingly interpreted to be the signature of kinetic exchange, called *double exchange* by these authors. In contrast to this is the case of (Ga,Mn)Sb, for which the concentration dependence is surprisingly different, being nearly linear in c. Sato *et al*. argue that in this case the magnetic moments are to be considered as localized so that the p-d exchange model seems more suitable here. In fact, this model was employed successfully by Jungwirth, Atkinson, Lee and MacDonald (1999) and by Dietl, Ohno and Matsukura (2001). The p-d-model (in other contexts called the s-f-model) is the basis of the well-known RKKY interaction, but the value of the p-d-exchange integral is a disposable parameter. The transition to localized states seems

to be a possibility here, but more experimental data are needed to establish this firmly.

There are two further notable papers: Kudrnovsky *et al*. (2004a) on (Ga,Mn)As as well as (Ge,Mn) and Kudrnovsky *et al*. (2004b) on the same DMSs and (Zn,Cr)Te. They supply important details and enlarge the scope of the paper by Bouzerar, Kudrnovsky, Bergqvist and Bruno (2003), supporting in all respects the exchange mechanisms exposed in the preceding text and the role of anitsite atoms. They, furthermore, find that due to disorder and the half-metallic character of the systems, the pair exchange interactions are exponentially damped with increasing distance of the Mn atoms. They are also reduced with increasing concentrations of the Mn atoms and the As antisites.

Eriksson *et al*. (2004), finally, are concerned with the stability of the magnetic moment as a function of the As antisite concentration. They argue that agreement between theory and experiment is obtained only when the magnetic atoms are randomly positioned on the Ga or Zn sites. They suggest that the ordering of the DMS materials is heavily influenced by magnetic percolation and that the measured Curie temperatures should be very sensitive to details in the sample preparation, which, indeed, they are.

4.3 Reduced-dimensional magnets

The importance of the magnetism of ultrathin films and multilayers need not really be stressed since their applications in the magnetic storage technology are numerous, as, for instance, the giant magnetoresistance of the multilayer systems employed in present-day read-heads. Equally (or even more) important is the fundamental point of view on epitaxial thin-film materials, which offer opportunities for exploring the relationship between structure and magnetism because new phases of matter can be stabilized on suitable growth templates. It is only natural that the thermal properties of these new phases, in particular, the Curie temperatures of ferromagnets, are of great importance here. Examples are the DMSs in Section 4.2. But the topic of this subsection are other systems, to which we now turn.

A recent experimental study by Vollmer, van Dijken, Schleberger and Kirschner (2000) has shown that the Curie temperature of fcc(001)-Fe ultrathin films on a Cu(001) substrate is modified upon coverage by a Cu-cap layer, varying in a nonmonotonous manner as a function of the Cu-cap layer thickness. Qian *et al*. (2001) noted that the close correlation between magnetism and structure makes this system quite unique. An oscillatory behavior of the Curie temperature as a function of the spacer thickness was also found by Ney *et al*. (1999) in fcc(001)-Co/Cu/Ni trilayers. As Pajda *et al*. (2000) point out, the understanding of these systems in the framework of itinerant-electron magnetism is a very serious challenge. One of the problems is as follows.

In an important paper, Mermin and Wagner (1966) proved rigorously that *the one- and two-dimensional isotropic Heisenberg models with interactions of finite range can be neither ferromagnetic nor antiferromagnetic at nonzero temperature*. This implies that the Heisenberg model, as specified in the preceding text, cannot explain the finite-temperature ferromagnetism observed in ultrathin films. There seem to be (at present) two ways out.

We recall that many of the theories (but not all) require a mapping onto an effective Heisenberg model, which is postulated *ad hoc* in the cases where this applies. Thus, one can either map onto a *modified* effective Heisenberg model or avoid the mapping all together. The first possibility is quite plausible because of SOC, which is a relativistic effect, not included in the Heisenberg model implied by Mermin and Wagner, and known to be more important in thin films than in bulk materials. This line of thought is pursued by Pajda *et al*. (2000), who modify the mapping by using a Heisenberg model with the inclusion of SOC. This manifestly renders the Mermin–Wagner theorem inoperative.

The other possibility is to abandon the Heisenberg model for the description of itinerant-electron magnetism. Thus, one might revisit Moriya's unified approach (Section 3.3), or revert to the DLM picture, which was briefly explained in Section 3.3.3. To the best of the author's knowledge, the unified approach has not yet been used for two-dimensional magnets, but the DLM picture has in papers by Razee, Staunton, Szunyogh and Gyorffy (2002a,b).

We begin with the paper by Pajda *et al*. (2000) on fcc(001)-Fe (or -Co) ultrathin films on Cu(001) covered by a Cu-cap layer of varying thickness. In the first step, they obtain the exchange constants, J_{ij}, for i and j in the Fe- or Co-film by the real-space method, subsequently doing a two-dimensional Fourier transform, which results in the exchange function $j(\mathbf{q}_{||})$, where $\mathbf{q}_{||}$ lies in the fcc(001) surface Brillouin zone.

If one now rewrites equation (60) suitably adopted to the two-dimensional case in terms of the spin-wave spectrum obtainable from $j(\mathbf{q}_{||})$, observing that the latter has a quadratic dispersion, one finds the Curie temperature to be zero, just as required by the Mermin–Wagner theorem. In the presence of SOC, however, the spin-wave spectrum develops a gap at the zone center. Thus, one can write in the RPA or spherical approximation

$$k_{\mathrm{B}}T_{\mathrm{c}}^{RPA} = \frac{2M_0^2}{3}\left[\frac{1}{N_{||}}\sum_{\mathbf{q}_{||}}\frac{1}{[j(\mathbf{q}_{||})+\Delta]}\right]^{-1} \tag{85}$$

where $N_{||}$ is the number of sites per layer, M_0 is the film's magnetic moment, and the sum extends over the fcc(001) surface Brillouin zone. The quantity Δ, except for a constant, is the spin-wave gap, which was estimated roughly.

The calculated Curie temperatures are too large compared with the experimental values, but qualitatively they show the oscillatory behavior seen in the experimental data as a function of the cap thickness, which is interpreted by Pajda *et al*. (2000) as evidence of the oscillatory RKKY character of exchange interactions in itinerant ferromagnets.

In contrast to the work by Pajda *et al*., the theory by Razee, Staunton, Szunyogh and Gyorffy (2002a,b) for the Curie temperature in reduced dimensions does not map onto an effective Heisenberg model. It uses the concept of DLMs above the Curie temperature in the same way as the DLM theory for bulk systems by Gyorffy *et al*. (1985), Staunton, Gyorffy, Stocks and Wadsworth (1986), as well as Staunton and Gyorffy (1992), which was briefly described in Section 3.3.3. Thus, the layer-dependent paramagnetic spin susceptibility of films and multilayers above the Curie temperature is calculated for various geometries and the instability of the paramagnetic state is interpreted as the Curie temperature. Unfortunately, the formal development of the theory is too space consuming to be included here. It is of importance, however, to notice that relativistic effects are not incorporated. Since DLM employ the Bogoliobov–Peierls variational principle and a rather simple trial grand potential, just like the spin-fluctuation theory in Section 3.1 (equations (40) and (41)), this is a mean-field theory, a point which could invite criticism. Yet, even though a rigorous proof for the validity of the DLM theory in lower-dimensional systems is apparently lacking, it does not seem to be justified to treat the DML mean field on the same footing as the Heisenberg mean field, which erroneously gives a nonzero Curie temperature in two (and even in one) dimensions.

Razee, Staunton, Szunyogh and Gyorffy (2002a,b) consider in detail thin films of Fe and Co (1–8 layers) on and embedded in nonmagnetic substrates, specifically bcc Fe/W(100), fcc Fe/Cu(100), and fcc Co/Cu(100). In uncapped Fe/W(100), they find intralayer ferromagnetic correlations in all thicknesses of the iron film except in the layer nearest the W substrate; the interlayer couplings are ferromagnetic and short ranged. There are also ferromagnetic intra- and interlayer couplings throughout the Co films in fcc Co/Cu(100). In the Fe/Cu(100) system, the top two layers are coupled ferromagnetically and the rest antiferromagnetically. Cu capping is found to have a profound effect upon the magnetic coupling in both Fe/Cu(100) and Co/Cu(100) with the Curie temperature showing an oscillatory behavior as a function of the cap layer thickness. As an example, we show in Figure 13 their results for the fcc Fe/Cu(100) system. The oscillations are clearly seen; also seen is that the

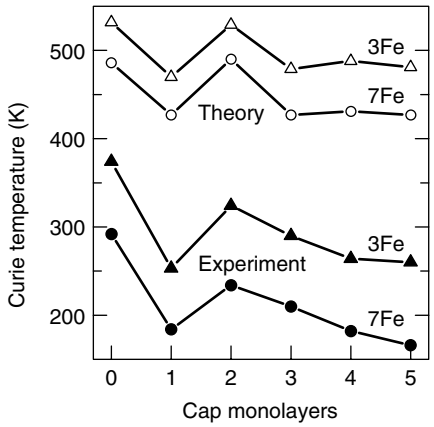

Figure 13. The Curie temperature for 3 and 7 layers of Fe on and embedded in Cu(100) as a function of the number of cap monolayers. The experimental data were extracted by Razee, Staunton, Szunyogh and Gyorffy (2002a) from Kerr data measured by Vollmer, van Dijken, Schleberger and Kirschner (2000). This figure was redrawn using Figure 1 of Razee, Staunton, Szunyogh and Gyorffy (2002a) with permission of the authors.

calculated values overestimate the measured ones, although they are much smaller than mean-field values on the basis of an effective Heisenberg model (Pajda *et al*., 2000).

It is quite certain that much more work will be done on these challenging problems in the future.

5 SUMMARY

The theory of finite-temperature magnetism of metals is formulated within the LSDA, the salient features of which are described briefly. However, calculational details are largely left to the specialized literature. The essential ingredients to the thermodynamic theory are orientational fluctuations of the local magnetization for which an adiabatic principle is postulated. The excitation energies of the fluctuations are determined from frozen magnons or more general frozen configurations, which are modeled by constrained total energy changes or, in justified approximations, from band-energy changes due to noncollinear spin orientations. As a result, exchange constants are defined and determined *ab initio* either in a real- or in a reciprocal-space approach.

The range to be covered to describe the magnetism of itinerant electron metals is a wide one extending from localized or nearly localized systems to the weakly ferromagnetic metallic compounds and alloys. A guide line for this review is Moriya's work that supplies a general framework, even though it does not yet give detailed algorithms for all cases.

The limit of weakly ferromagnetic metals is formulated with special emphasis on dissipation effects, which are incorporated in the nonuniform, dynamical susceptibility, the latter

being treated in a widely used approximation. The resulting static and dynamic approximations to the spin-fluctuation theory are applied to and discussed for the cases of $ZrZn_2$, Ni_3Al, MnSi, and tentatively for nickel. It is pointed out that an *ab initio* theory for the dissipation constant is lacking, although in some cases its order of magnitude can be estimated from the band structure. Furthermore, it becomes apparent that the energy governing the length changes of the magnetic moment, usually formulated in terms of a Landau-type expansion, needs special attention and can only be obtained from the total energy by rescaling (renormalizing) the latter if it is determined from constrained-moment calculation.

Moriya's unified theory is then used to derive the spherical approximation or RPA, which supplies a useful formula also for those cases where a mapping onto an effective Heisenberg model is a necessary approximation. The unified theory is discussed further in view of the static approximation for both the weak ferromagnetism and the opposite limit of the ferromagnetism of iron.

The Curie temperatures of the ferromagnetic metals, Fe, Co, and Ni have been determined by a great number of methods; there is the DLM picture by Staunton and Gyorffy, which is briefly introduced, and there are others that use a mapping onto an effective Heisenberg model obtaining estimates by the mean-field approximation, the RPA, and the Monte Carlo technique. These results for the Curie temperatures, as well as results for Néel temperatures of fcc Fe and fcc Mn, are collected and discussed.

Some selected applications for magnets design, in particular, for the novel field of spintronics, are then introduced. This includes a collection of theoretical and experimental Curie temperatures of half-metallic ferromagnets like Heusler alloys and Zinc-blende compounds, and the diluted magnetic semiconductors. Here, a catalogue of exchange mechanisms and their interpretations play an important role, which are particularly emphasized.

Finally, the finite-temperature properties of epitaxial thin-film materials and multilayers are addressed. The role played by the theorem of Mermin and Wagner is stressed and two different techniques to determine the Curie temperatures of low-dimensional systems are compared. One is a relativistic extension of the mapping onto an effective Heisenberg model and the other is the DLM picture as applied to thin magnetic films on and embedded in Cu substrates.

ACKNOWLEDGMENTS

I am indebted to Peter Mohn for his hospitality and great interest in the topics of this review, for which he supplied much information.

REFERENCES

Akai, H. (1998). Ferromagnetism and its stability in the deluted magnetic semiconductor (In,Mn)As. *Physical Review Letters*, **81**, 3002.

Akinaga, H., Manago, T. and Shirai, M. (2000). Material design of half-metallic zinc-blende CrAs and the synthesis of molecular-beam epitaxy. *Japanese Journal of Applied Physics*, **39**, L1118.

Andersen, P.W. (1963). Exchange in insulators: superexchange, direct exchange, and double exchange. In *Magnetism I*, Rado, G. and Suhl, H. (Eds.), Academic Press: New York, Chap. 2.

Antropov, V.P., Harmon, B.N. and Smirnov, A.N. (1999). Aspects of spin dynamics and magnetic interactions. *Journal of Magnetism and Magnetic Materials*, **200**, 148.

Bak, P. and Jensen, M.H. (1980). Theory of helical magnetic structures and phase transition in MnSi and FeGe. *Journal of Physics C-Solid State Physics*, **13**, L881.

Becker, R. and Sauter, F. (1968). *Theorie der Elektrizität*, B.G. Teubner: Stuttgart, Vol. 3.

Bernhoeft, N.R., Law, S.A., Lonzarich, G.G. and Paul, Mc.K.D. (1988). Magnetic excitations in $ZrZn_2$ at low energies and long wavelengths. *Physica Scripta*, **38**, 191.

Bernhoeft, N.R., Lonzarich, G.G., Mitchell, P.W. and Paul, D.Mc.K. (1983). Magnetic excitations in $ZrZn_2$ at low energies and long wavelengths. *Physical Review B*, **28**, 422.

Berry, M.V. (1984). Quantal phase factors accompanying adiabatic changes. *Proceedings of the Royal Society of London A*, **392**, 45.

de Boer, F.R., Schinkel, C.J., Biesterbos, J. and Proost, S. (1969). Exchange-enhanced paramagnetism and weak ferromagnetism in the Ni_3Al and Ni_3Ga phases; giant moment inducement in Fe-doped Ni_3Ga. *Journal of Applied Physics*, **40**, 1049.

Bouzerar, G., Kudrnovsky, J., Bergqvist, L. and Bruno, P. (2003). Ferromagnetism in diluted magnetic semiconductors: a comparison between *ab initio* mean-field, RPA, and Monte Carlo treatments. *Physical Review B*, **68**, 081203(R).

Brown, R.H., Nicholson, D.M.C., Wang, X. and Schulthess, T.C. (1999). First principles theory of spin waves in Fe, Co, and Ni. *Journal of Applied Physics*, **85**, 4830.

Bruno, P. (2003). Exchange interaction parameters and adiabatic spin-wave spectra of ferromagnets: a "renormalized magnetic force theorem". *Physical Review Letters*, **90**, 087205.

Buis, N., Franse, J.J.M. and Brommer, P.E. (1981). The magnetic properties of Ni_3Al under high pressure. *Physica B*, **106**, 1.

Callen, H.B. and Welton, T.A. (1951). Irreversibility and General Noise. *Physical Review*, **83**, 34.

Capelle, K. and Vignale, G. (2001). Nonuniqueness of the potentials of spin-density-functional theory. *Physical Review Letters*, **86**, 5546.

Dederichs, P.H., Blügel, S., Zeller, R. and Akai, H. (1984). Ground states of constrained systems: application to cerium impurities. *Physical Review Letters*, **53**, 2512.

Dietl, T., Ohno, H. and Matsukura, F. (2001). Hole-mediated ferromagnetism in tetrahedrally coordinated semiconductors. *Physical Review B*, **63**, 195205.

Drautz, R. and Fähnle, M. (2004). Spin-cluster expansion: parametrization of the general adiabatic magnetic energy surface with {ab initio} accuracy. *Physical Review B*, **69**, 104404.

Dzyaloshinski, I.E. and Kondratenko, P.S. (1976). Theory of weak ferromagnetism of a Fermi liquid. *Soviet Physics JETP*, **43**, 1036.

Dzyaloshinsky, I. (1958). A thermodynamic theory of "weak" ferro-. magnetism of antiferromagnetics. *Journal of Physics and Chemistry of Solids*, **4**, 241.

Edwards, D.M. (1982). The paramagnetic state of itinerant electron systems with local magnetic moments: I. Static properties. *Journal of Physics F-Metal Physics*, **12**, 1789.

Ehrenreich, H. and Schwartz, L.M. (1976). In *Solid State Physics*, Ehrenreich, H., Seitz, F. and Turnbull, D. (Eds.), Academic Press: New York, p. 149, Vol. 31.

Endoh, Y. and Ishikawa, Y. (1971). Antiferromagnetism in γ iron manganese alloys. *Journal of the Physical Society of Japan*, **30**, 1614.

van Engen, P.G., Buschow, K.H.J. and Jongebreur, R. (1983). PtMnSb, a material with very high magneto-optical Kerr effect. *Applied Physics Letters*, **42**, 202.

Enkovaara, J., Ayuela, A., Jalkanen, J., *et al*. (2003). First-principles calculations of spin spirals in Ni_2MnGa and Ni_2MnAl. *Physical Review B*, **67**, 054417.

Eriksson, O., Bergqvist, L., Sanyal, B., *et al*. (2004). Electronic structure and magnetism of diluted magnetic semiconductors. *Journal of Physics: Condensed Matter*, **16**, S5481.

Eschrig, H. (1996). *The Fundamentals of Density Functional Theory*, Teubner: Stuttgart.

Eschrig, H. and Pickett, W.E. (2001). Density functional theory of magnetic systems revisited. *Solid State Communications*, **118**, 123.

Galanakis, I. and Mavropoulos, P. (2003). Zinc-blende compounds of transition elements with N, P, As, Sb, S, Se, and Te as half-metallic systems. *Physical Review B*, **67**, 104417.

Gebauer, R. and Baroni, S. (2000). Magnons in real materials from density-functional theory. *Physical Review B*, **61**, R6459.

de Gennes, P-G. (1960). Effects of double exchange in magnetic crystals. *Physical Review*, **118**, 141.

de Groot, R.A., Mueller, F.M., van Engen, P.G. and Buschow, K.H.J. (1983). New class of materials: half-metallic ferromagnets. *Physical Review Letters*, **50**, 2024.

Grotheer, O., Ederer, C. and Fähnle, M. (2001). Fast *ab initio* methods for the calculation of adiabatic spin wave spectra in complex systems. *Physical Review B*, **63**, 100401(R).

Gubanov, V.A., Liechtenstein, A.I. and Postnikov, A.V. (1992). *Magnetism and the Electronic Structure of Crystals*, Springer-Verlag: Berlin, Heidelberg, New York, London.

Gyorffy, B.I., Pindor, A.J., Staunton, J., *et al*. (1985). A first-principles theory of ferromagnetic phase transitions in metals. *Journal of Physics F: Metal Physics*, **15**, 1337.

Halilov, S.V., Eschrig, H., Perlov, A.Y. and Oppeneer, P.M. (1998). Adiabatic spin dynamics from spin-density-functional theory: application to Fe, Co, and Ni. *Physical Review B*, **58**, 293.

Hasegawa, H. (1979). Single-site functional-integral approach to itinerant-electron ferromagnetism. *Journal of the Physical Society of Japan*, **46**, 1504.

Heine, V. (1980). In *Solid State Physics*, Ehrenreich, H., Seitz, F. and Turnbull, P. (Eds.), Academic Press: New York, p. 1, Vol. 35.

Heine, V. and Samson, J.H. (1983). Magnetic, chemical and structural ordering in transition metals. *Journal of Physics F: Metal Physics*, **13**, 2155.

Herring, C. (1966). In *Magnetism IV*, Rado, G. and Suhl, H. (Eds.), Academic Press: New York, Chap. V and XIII.

Hubbard, J. (1979). Magnetism if iron II. *Physical Review B*, **20**, 4584.

Ishikawa, Y., Tajima, K., Bloch, D. and Roth, M. (1976). Helical spin structure in manganese silicide MnSi. *Solid State Communications*, **19**, 525.

Jiles, D. (1998). *Introduction to Magnetism and Magnetic Materials*, Chapman & Hall: London.

Jones, W. and March, N.H. (1973). *Theoretical Solid State Physics*, John Wiley & Sons: London.

Jungwirth, T., Atkinson, W.A., Lee, B.H. and MacDonald, A.H. (1999). Interlayer coupling in ferromagnetic semiconductor superlattices. *Physical Review B*, **59**, 9818.

Kataoka, M., Nakanishi, O., Yanase, A. and Kanamori, J. (1984). Antisymmetric spin interaction in metals. *Journal of the Physical Society of Japan*, **53**, 3642.

Katsnelson, M.I. and Lichtenstein, A.I. (2000). First-principles calculations of magnetic interactions in correlated systems. *Physical Review B*, **61**, 8906.

Knöpfle, K., Sandratskii, L.M. and Kübler, J. (2000). Spin spiral ground state of γ-iron. *Physical Review B*, **62**, 5564.

Kohn, W. and Vashishta, P. (1983). In *Theory of the Inhomogeneous Electron Gas*, Lundqvist, S. and March, N.H. (Eds.), Plenum Press: New York.

König, K., Schliemann, J., Jungwirth, T. and MacDonald, A.H. (2003). In *Electronic Structure and Magnetism in Complex Materials*, Singh, D.J. and Papaconstantopoulus, D.A. (Eds.), Springer-Verlag: Berlin, Heidelberg, New York, London. (Preprint cond-mat/0111314).

Korenman, V., Murray, I.I. and Prange, R.E. (1977). Local-band theory of itinerant ferromagnetism. I. Fermi-liquid theory. *Physical Review B*, **16**, 4032.

Kortekaas, T.F.M. and Franse, J.J.M. (1976). Volume magnetostriction in Ni_3Al and Ni-Pt alloys and its interpretation in the band model of magnetism. *Journal of Physics F: Metal Physics*, **6**, 1161.

Kouvel, J.S. and Wilson, R.H. (1961). Magnetization of iron-nickel alloys under hydrostatic pressure. *Journal of Applied Physics*, **32**, 435.

Ku, K.C., Potashnik, S.J., Wang, R.F., *et al*. (2003). Highly enhanced Curie temperature in low-temperature annealed [Ga,Mn]As epilayers. *Applied Physics Letters*, **82**, 2302.

Kübler, J. (2000). *Theory of Itinerant Electron Magnetism*, Clarendon Press: Oxford.

Kübler, J. (2003). Curie temperatures of zinc-blende half-metallic ferromagents. *Physical Review B*, **67**, 220403(R).

Kübler, J. (2004). Spin fluctuations in ferromagnetic $ZrZn_2$. *Physical Review B*, **70**, 064427.

Kübler, J. (2006). Ab initio estimates of the Curie temperature for magnetic compounds. *Journal of Physics: Condensed Matter*, **18**, 9795.

Kübler, J., Höck, K-H., Sticht, J. and Williams, A.R. (1988). Density functional theory of non-collinear magnetism. *Journal of Physics F: Metal Physics*, **18**, 469.

Kübler, J., Williams, A.R. and Sommers, C.B. (1983). Formation and coupling of magnetic moments in Heusler alloys. *Physical Review B*, **28**, 1745.

Kudrnovsky, J., Turek, I., Drchal, V., *et al*. (2004a). Exchange interaction in III-V and group-IV diluted magnetic semiconductors. *Physical Review B*, **69**, 115208.

Kudrnovsky, J., Drchal, V., Turek, I., *et al*. (2004b). Exchange interaction and critical temperatures in diluted magnetic semiconductors. *Journal of Physics: Condensed Matter*, **16**, S5571.

Landau, D.P. and Binder, K. (2000). *A Guide to Monte Carlo Simulations in Statistical Physics*, Cambridge University Press: Cambridge.

Leger, J.M., Loriers-Susse, C. and Vodar, B. (1972). Pressure effect on the Curie temperature of transition metals and alloys. *Physical Review B*, **6**, 4250.

Liechtenstein, A.I., Katsnelson, M.I., Antropov, V.P. and Gubanov, V.A. (1987). Local spin density functional approach to the theory of exchange interactions in ferromagnetic metals and alloys. *Journal of Magnetism and Magnetic Materials*, **67**, 65.

Liechtenstein, A.I., Katsnelson, M.I. and Gubanov, V.A. (1984). Exchange interactions and spin-wave stiffness in ferromagnetic metals. *Journal of Physics F: Metal Physics*, **14**, L125.

Lichtenstein, A.I., Katsnelson, M.I. and Kotliar, G. (2001). Finite-temperature magnetism of transition metals: an *ab initio* dynamical mean-field theory. *Physical Review Letters*, **87**, 067205.

Lloyd, P. and Smith, P.V. (1972). Multiple scattering theory in condensed matter. *Advances in Physics*, **21**, 69.

Lonzarich, G.G. (1986). The magnetic equation of state and heat capacity in weak itinerant ferromagnets. *Journal of Magnetism and Magnetic Materials*, **54–57**, 612.

Lonzarich, G.G. and Taillefer, L. (1985). Effect of spin fluctuations on the magnetic equation of state of ferromagnetic or nearly ferromagnetic metals. *Journal of Physics C: Solid State Physics*, **18**, 4339.

Luchini, M.U., Heine, V. and McMullan, G.J. (1991). Calculation of longitudinal magnetic fluctuations in iron by a Landau energy and force method. *Journal of Physics: Condensed Matter*, **3**, 8647.

Mackintosh, A.R. and Andersen, O.K. (1980). The structure of transition metals. In *Electrons at the Fermi Surface*, Springford, M. (Ed.), Cambridge University Press: Cambridge, p. 149.

Matthias, B.T. and Bozorth, R.M. (1958). Ferromagnetism of a zirconium-zinc compound. *Physical Review*, **109**, 604.

Mermin, N.D. (1965). Thermal properties of the inhomogeneous electron gas. *Physical Review*, **137**, A1441.

Mermin, N.D. and Wagner, H. (1966). Absence of ferromagnetism or antiferromagnetisn in one- or two-dimensional isotropic Heisenberg models. *Physical Review Letters*, **17**, 1133.

Methfessel, M. and Kübler, J. (1982). Band analysis of heats of formation: application to some group VIII and IB hydrides. *Journal of Physics F: Metal Physics*, **12**, 141.

Mohn, P. (2003). *Magnetism in the Solid State: An Introduction*, Springer-Verlag: Berlin, Heidelberg, New York, London.

Moran, S., Ederer, C. and Fähnle, M. (2003). *Ab initio* electron theory for magnetism in Fe: pressure dependence of spin-wave energies, exchange parameters, and Curie temperature. *Physical Review B*, **67**, 012407.

Moriya, T. (1960). Anisotropic superexchange interaction and weak ferromagnetism. *Physical Review*, **120**, 91.

Moriya, T. (1985). *Spin Fluctuations in Itinerant Electron Magnetism*, Springer-Verlag: Berlin, Heidelberg, New York, London.

Moriya, T. (1987). *A unified picture of magnetism*. In *Metallic Magnetism*, Capellmann, H. (Ed.), Springer-Verlag: Berlin, Heidelberg, New York, London.

Moriya, T. and Takahashi, Y. (1978a). Spin fluctuation theory of itinerant electron ferromagnetism – a unified picture. *Journal of the Physical Society of Japan*, **45**, 397.

Moriya, T. and Takahashi, Y. (1978b). Spin fluctuation theory of itinerant electron ferromagnetism – a unified picture. *Journal de Physique Paris*, **39**, C6–1466.

Murata, K.K. and Doniach, S. (1972). Theory of magnetic fluctuations in itinerant ferromagnets. *Physical Review Letters*, **29**, 285.

Nakanishi, O., Yanase, A., Hasegawa, A. and Kataoka, M. (1980). The origin of the helical spin density in MnSi. *Solid State Communications*, **35**, 995.

Ney, A., Wilhelm, F., Farle, M., *et al*. (1999). Oscillations of the Curie temperature and interlayer exchange coupling in magnetic trilayers. *Physical Review B*, **59**, R3938.

Niu, Q. and Kleinman, L. (1998). Spin-wave dynamics in real crystals. *Physical Review Letters*, **80**, 2205.

Niu, Q., Wang, X., Kleinman, L., *et al*. (1999). Adiabatic dynamics of local spin moments in itinerant magnets. *Physical Review Letters*, **83**, 207.

Ohno, H. (1999). Properties of ferromagnetic III-V semiconductors. *Journal of Magnetism and Magnetic Materials*, **200**, 110.

Ohno, K., Shen, A., Matsukura, F., *et al*., (1996). (Ga,Mn)As: A new diluted magnetic semiconductor based on GaAs. *Applied Physics Letters*, **69**, 363.

Ono, K., Okabayashi, J., Mizuguchi, M., *et al*. (2002). Fabrication, magnetic properties, and electronic structures of nanoscale zinc-blende MnAs dots. *Journal of Applied Physics*, **91**, 8088.

Onodera, A., Tsunoda, Y., Kunitomi, N., *et al*. (1994). Neutron-diffraction studies of γ-Fe at high pressure. *Physical Review B*, **50**, 3532.

Oswald, A., Zeller, R., Braspenning, P.J. and Dederichs, P.H. (1985). Interaction of magnetic impurities in Cu and Ag. *Journal of Physics F: Metal Physics*, **15**, 193.

Pajda, M., Kudrnovsky, J., Turek, I., *et al*. (2000). Oscillatory Curie temperature of two-dimensional ferromagnets. *Physical Review Letters*, **85**, 5424.

Pajda, M., Kudrnovsky, J., Turek, I., *et al*. (2001). *Ab initio* calculations of exchange interactions, spin-wave stiffness constants, and Curie temperatures of Fe, Co, and Ni. *Physical Review B*, **64**, 174402.

Perdew, J.P. and Wang, Y. (1992). Accurate and simple analytic representation of the electron-gas correlation energy. *Physical Review B*, **45**, 13244.

Pfleiderer, C., McMullan, G.J., Julian, S.R. and Lonzarich, G.G. (1997). Magnetic quantum phase transition in MnSi under hydrostatic pressure. *Physical Review B*, **55**, 8330.

Pfleiderer, C., Reznik, D., Pintschovius, L., *et al*. (2004). Partial order in the non-Fermi liquid phase of MnSi. *Nature (London)*, **427**, 227.

Pfleiderer, C., Uhlarz, M., Hayden, S.M., *et al*. (2001). Coexistence of superconductivity and ferromagnetism in the *d*-band metal $ZrZn_2$. *Nature (London)*, **412**, 58.

Qian, D., Jin, X.F., Barthel, J., *et al*. (2001). Spin-density wave in ultrathin Fe films on Cu(100). *Physical Review Letters*, **87**, 227204.

Ramakrishnan, T.V. (1974). Microscopic theory of spin fluctuations in itinerant-electron ferromagnets. I. Paramagnetic phase. *Physical Review B*, **10**, 4014.

Ramana, M.V. and Rajagopal, A.K. (1983). Inhomogeneous relativistic electron systems: a density-functional formalism. *Advances in Chemical Physics*, **54**, 231.

Razee, S.S.A., Staunton, J.B., Szunyogh, L. and Gyorffy, B.L. (2002a). Onset of magnetic order in fcc-Fe films on Cu(100). *Physical Review Letters*, **88**, 147201.

Razee, S.S.A., Staunton, J.B., Szunyogh, L. and Gyorffy, B.L. (2002b). Local moments and magnetic correlations above the Curie temperature in thin films on and embedded in nonmagnetic substrates: Fe/Cu(100), Co/Cu(100), and Fe/W(100). *Physical Review B*, **66**, 094415.

Rhodes, P. and Wohlfarth, E.P. (1963). The effective Curie-Weiss constant in ferromagnetic metals and alloys. *Proceedings of the Royal Society*, **A273**, 247.

Rosengaard, N.M. and Johansson, B. (1997). Finite-temperature study of itinerant ferromagnetism in Fe, Co, and Ni. *Physical Review B*, **55**, 14975.

Saito, H., Zayets, V., Yamagata, S. and Ando, K. (2003). Room-temperature ferromagnetism in a II-VI diluted magnetic semiconductor $Zn_{1-x}Cr_xTe$. *Physical Review Letters*, **90**, 207202.

Sakuma, A. (2002). Stability of half-metallic ferromagnetism of zinc-blende type CrAs and MnM (M=Si, Ge and Sn). *Journal of the Physical Society of Japan*, **71**, 2534.

Sandratskii, L.M. (1986a). *Journal of Physics F: Metal Physics*, **16**, L43.

Sandratskii, L.M. (1986b). *Physical Status Solidi B*, **135**, 167.

Sandratskii, L.M. (1998). Noncollinear magnetism in itinerant-electron systems: theory and applications. *Advances in Physics*, **47**, 91.

Sandratskii, L.M. and Bruno, P. (2002). Exchange interactions and Curie temperature in (Ga,Mn)As. *Physical Review B*, **66**, 134435.

Sandratskii, L.M. and Bruno, P. (2003a). Electronic structure, exchange interactions, and Curie temperature in diluted III-V magnetic semiconductors: (GaCr)As, (GaMn)As, (GaFe)As. *Physical Review B*, **67**, 214402.

Sandratskii, L.M. and Bruno, P. (2003b). Density functional theory of high-T_c ferromagnetism of (ZnCr)Te. *Journal of Physics: Condensed Matter*, **15**, L585.

Sandratskii, L.M., Bruno, P. and Kudrnovsky, J.(2003). On-site Coulomb interaction and the magnetism of (Ga,Mn)N and (GaMn)As. *Physical Review B*, **69**, 195203.

Sandratskii, L.M. and Kübler, J. (1992). Static non-uniform magnetic susceptibility of selected transition metals. *Journal of Physics: Condensed Matter*, **4**, 6927.

Sandratskii, L.M. and Lander, G.H. (2001). Helical magnetic structures in relativistic systems: the case of UPtGe. *Physical Review B*, **63**, 134436.

Sanvito, S. and Hill, N.A. (2000). Ground state of half-metallic zinc-blende MnAs. *Physical Review B*, **62**, 15553.

Sanyal, B., Bergqvist, L. and Eriksson, O. (2003). Ferromagnetic materials in the zinc-blende structure. *Physical Review B*, **68**, 054417.

Sasioglu, E., Sandratskii, L.M. and Bruno, P. (2004). First-principles calculation of the intersublattice exchange interaction and the Curie temperatures of the full Heusler alloys Ni_2MnX (X=Ga, In, Sn, Sb). *Physical Review B*, **70**, 024427.

Sasioglu, E., Sandratskii, L.M. and Bruno, P. (2005). First-principles study of exchange interactions and Curie temperatures of half-metallic ferrimagnetic full Heusler alloys Mn_2VZ (Z=Al,Ge). *Journal of Physics: Condensed Matter*, **17**, 995.

Sato, K., Dederichs, P.H., Katayama-Yoshida, H. and Kudrnovsky, J. (2004). Exchange interactions in diluted magnetic semiconductors. *Journal of Physics: Condensed Matter*, **16**, S5491.

Sato, K. and Katayama-Yoshida, H. (2001). Materials design of transparent and half-metallic ferromagnets in V- or Cr-doped ZnS, ZnSe and ZnTe without p- or n-type doping treatment. *Japanese Journal of Applied Physics*, **40**, L651.

Savrasov, S.Y. (1998). Linear response calculations of spin fluctuations. *Physical Review Letters*, **81**, 2570.

Shimizu, M. (1977). Ferromagnetism in iron, cobalt, nickel and their alloys. *Physica B*, **91**, 14.

Shimizu, M. (1981). Itinerant electron magnetism. *Reports on Progress in Physics*, **44**, 329.

Shirai, M. (2004). The computational design of zinc-blende half-metals and their nanostructures. *Journal of Physics: Condensed Matter*, **16**, S5525.

Singer, R., Fähnle, M. and Bihlmayer, G. (2005). Constrained spin-density functional theory for excited magnetic configurations in an adiabatic approximation. *Physical Review B*, **71**, 214435.

Sommerfeld, A. and Bethe, H. (1933). Elektronentheorie der Metalle. In *Handbuch der Physik*, Geiger, H. and Scheel, K. (Eds.), Springer Verlag: Berlin, p. 595, Vol. 24, Part 2.

Staunton, J.B. (1994). The electronic structure of magnetic transition metal materials. *Reports on Progress in Physics*, **57**, 1289.

Staunton, J.B. and Gyorffy, B.L. (1992). Onsager cavity fields in itinerant-electron paramagnets. *Physical Review Letters*, **69**, 371.

Staunton, J.B., Gyorffy, B.L., Stocks, G.M. and Wadsworth, J. (1986). The static, paramagnetic, spin susceptibility of metals at finite temperatures. *Journal of Physics F: Metal Physics*, **16**, 1761.

Staunton, J.B., Poulter, J., Ginatempo, B., *et al*. (2000). Spin fluctuations in nearly magnetic metals from *ab initio* dynamical spin susceptibility calculations: application to Pd and $Cr_{95}V_5$. *Physical Review B*, **62**, 1075.

Steinsvoll, O., Majkrzak, C.F., Shirane, G. and Wicksted, J. (1984). Paramagnetic scattering from metallic Ni. *Physical Review B*, **30**, 2377.

Sticht, J., Höck, K-H. and Kübler, J. (1989). Non-collinear itinerant magnetism: the case of Mn_3Sn. *Journal of Physics: Condensed Matter*, **1**, 8155.

Tahir-Keli, R.A. and ter Haar, D. (1962a). Use of Green functions in the theory of ferromagnetism. I. General discussion of the spin-S case. *Physical Review*, **127**, 88.

Tahir-Keli, R.A. and ter Haar, D. (1962b).Use of Green functions in the theory of ferromagnetism II. Dyson spin waves. *Physical Review*, **127**, 95.

Tahir-Keli, R.A. and Jarrett, H.S. (1964). Ferromagnetic Curie temperatures in cubic lattices. *Physical Review*, **135**, A1096.

Takahashi, Y. (1986). On the origin of the Curie-Weiss law of the magnetic susceptibility in itinerant electron ferromagnets. *Journal of the Physical Society of Japan*, **55**, 3553.

Tyablikov, S.A. (1969). *Quantum Mechanical Methods in Magnetism*, Consultant Bureau: New York.

Uhl, M. and Kübler, J. (1996). Exchange-coupled spin-fluctuation theory: application to Fe,Co, and Ni. *Physical Review Letters*, **77**, 334.

Uhl, M. and Kübler, J. (1997). Exchange-coupled spin-fluctuation theory: calculation of magneto-elastic properties. *Journal of Physics: Condensed Matter*, **9**, 7885.

Uhlarz, M., Pfleiderer, C. and Hayden, S.M. (2004). Quantum phase transition in the itinerant ferromagnet $ZrZn_2$. *Physical Review Letters*, **93**, 256404.

Udvardi, L., Szunyogh, L., Palotas, K. and Weinberger, P. (2003). First-principles relativistic study of spin waves in thin magnetic films. *Physical Review B*, **68**, 104436.

Vollhardt, D., Blümer, N., Held, K. and Kollar, M. (2001). In *Band-Ferromagnetism*, Baberschke, K., Donat, M. and Nolting, W. (Eds.), Springer Verlag: Berlin, Heidelberg, p. 191.

Vollmer, R., van Dijken, S., Schleberger, M. and Kirschner, J. (2000). Dependence of the Curie temperature on the Cu cover layer in x-Cu/Fe/Cu(001) sandwiches. *Physical Review B*, **61**, 1303.

von Barth, U. and Hedin, L. (1972). A local exchange- correlaion potential for the spin polarized case. *Journal of Physics C: Solid State Physics*, **5**, 1629.

Wagner, D. (1972). *Introduction to the Theory of Magnetism*, Pergamon Press: Oxford, New York, Toronto, Sydney, Braunschweig.

Weht, R. and Pickett, W.E. (1999). Half-metallic ferrimagnetsm in Mn_2VAl. *Physical Review B*, **60**, 13006.

White, R.M. (1983). *Quantum Theory of Magnetism*, Springer-Verlag: Berlin.

Williams, A.R., Kübler, J. and Gelatt, C.D. (1979). Cohesive properties of metallic compounds: augmented-spherical-wave calculations. *Physical Review B*, **19**, 6094.

Wohlfarth, E.P. (1980). *Iron, Cobalt and Nickel*. In *Ferromagnetic Materials*, Wohlfarth, E.P. (Ed.), North-Holland: Amsterdam, Vol. 1.

Xu, Y-Q., Liu, B-G. and Pettifor, D.G. (2002). Half-metallic ferromagnetism of MnBi in the zinc-blende structure. *Physical Review B*, **66**, 184435.

Yamada, H. and Terao, K. (1999). Itinerant-electron metamagnetism of MnSi at high pressure. *Physical Review B*, **59**, 9342.

Zhou, Y., Wang, D. and Kawazoe, Y. (1999). Effective *ab initio* exchange integrals and magnetic phase transition in fcc Fe and Mn antiferromagnets. *Physical Review B*, **59**, 8387.

FURTHER READING

Antropov, V.P., Katsnelson, M.I., Harmon, B.N., *et al*. (1996). Spin dynamics in magnets: equation of motion and finite temperature effects. *Physical Review B*, **54**, 1019.

Kohn, W. and Sham, L.J. (1965). Self-consistent equations including exchange and correlation effects. *Physical Review*, **140**, A1133.

Theory of Magnetic Phase Transitions

David P. Landau
The University of Georgia, Athens, GA, USA

1 INTRODUCTION

The study of phase transitions has played a central role in many subfields of physics and related disciplines, and research in magnetism has been crucial to progress in the understanding of diverse types of phase transitions. This is, in part, because simple magnetic models have time-reversal symmetry that results in symmetries in phase diagrams that are absent in other models in statistical mechanics. In part, it also results from the rich diversity of experimental measurements of magnetic systems that allows comparison between theory and physical reality. Although simple approaches, such as Landau theory (mean-field theory), provide an intuitive picture of magnetic phase transitions, we now know that such approaches are generally inadequate for the provision of a truly quantitative description. More sophisticated methods of investigation have been developed and a mature framework is now in place for the understanding and classification of phase transitions based on a combination of theoretical and numerical approaches.

In general terms, the distinguishing feature of magnetic phase transitions is the appearance of a nonzero value of an 'order parameter' in the ordered phase, below some transition temperature, T_c, which is zero in the disordered phase above T_c. In a ferromagnet, the order parameter is simply the normalized spontaneous magnetization

$$m = \frac{1}{N}\sum_i S_i \tag{1}$$

where S_i is the spin at site i and the sum is over all N sites in the lattice. Of course, in general the spin may have many components; but for simplicity, here we will consider the one-component (scalar) case. In an antiferromagnet, the order parameter is the 'staggered magnetization'

$$m^+ = \frac{1}{N}\sum_i S_i e^{i\vec{k}\cdot\vec{r}} \tag{2}$$

where $\vec{r}$ gives the position of the spin and $\vec{k}$ is the wave vector that characterizes the ordered antiferromagnetic structure for the lattice under consideration.

Other thermodynamic properties will also show discontinuities or singularities at T_c, and these may be measured by a variety of experimental methods. However, even in the disordered state, a system will have microscopic regions in which the local properties of the material are correlated and these can be described quantitatively by a two-point correlation function

$$G(r) = \langle m(0)m(r)\rangle - \langle m\rangle^2 \tag{3}$$

Handbook of Magnetism and Advanced Magnetic Materials. Edited by Helmut Kronmüller and Stuart Parkin. Volume 1: *Fundamentals and Theory*. ISBN: 978-0-470-02217-7.

where r is the spatial distance at which the correlation is being measured and m is the quantity of interest. (The correlations may be both space dependent and time dependent, but for static properties, the equal-time correlations, that is, time-independent correlations, are adequate.) The correlations will decay as a function of distance (although not always monotonically); and the order parameter will be zero at any temperature for which the reduced correlation, that is, the first term in equation (3), decays to zero as the distance goes to infinity.

At a phase transition, the thermodynamic properties may show dramatic changes of different kinds. If the first derivatives of the free energy are discontinuous, the transition is termed first order. The size of the discontinuity is unimportant in terms of the classification of the phase transition, but there are diverse systems with either very large or rather small 'jumps'. In contrast, for second-order phase transitions the first derivatives are continuous, and transitions (critical points) at some temperature T_c (critical temperature) and 'field' H (critical field) are characterized by singularities in the second derivatives of the free energy. Properties of different systems can then be related by considering not the absolute temperature but instead the *reduced distance* from the transition $\varepsilon = |1 - T/T_c|$. (We note that the notation in the literature has varied over time. Initially the symbol ε was used to represent the 'distance' from the critical point, but as expansion methods in renormalization group (RG) theory were developed, the symbol ε took on the meaning of the difference between the spatial dimension of the system and the 'upper critical dimension' at which the transition became mean-field-like. The symbol t was then introduced in the place of ε. Then, however, the increased performance of computers and algorithms made computer simulations more important in the study of magnetic models. In simulations, the symbol t generally represented 'time', so it again became common to use ε to denote the *reduced distance* from the transition. The reader must be careful to determine what convention is being used in a given publication.) At a first-order phase transition, the free-energy curves for ordered and disordered states cross with a finite difference in slope, and both stable and metastable states may exist for some region of temperature beyond the transition. In contrast, at a second-order transition the two free-energy curves meet tangentially and no metastability is seen (in the usual sense). In the following discussion we will consider a portion of the diversity of magnetic phase transitions that may exist and provide estimates for important 'characteristic' quantities. Since first-order phase transitions do not have the same underlying, unifying characteristics that second-order transitions have, very little can be theoretically predicted about them without specific knowledge of the nature and interaction constants for a particular system. Consequently, second-order transitions will prove to be far more interesting and, thus, will consume a greater part of the presentation in the remainder of this article, and the reader is referred elsewhere (Binder, 1987) for a more detailed discussion of first-order transitions.

The wealth of information provided about magnetic phase transitions via numerous careful, high-quality experiments has been important in helping to guide the development of ideas about phase transitions. Nevertheless, substantial difficulties remain for experiments: Sample quality is always a problem, for example, grain boundaries, impurities, and so on, so that the approach to the critical temperature is limited by 'rounding'. Since the asymptotic critical region is often restricted to very small distances from the critical point, experiment may not always explore the asymptotic behavior near T_c. Consequently, computer simulations sometimes provide the best 'experimental' information. On the other hand, a magnetic system may be so complex that appropriate models cannot be solved analytically. In this case, computer simulations provide 'theoretical' information for comparison with experiment. In this article we shall thus include results from a variety of analytical and computational approaches under the general rubric of 'theory', although a more accurate view of approaches to the study of magnetic phase transitions can be depicted schematically by Figure 1.

We wish to emphasize that the theory of magnetic phase transitions is an extremely rich topic (see Fisher, 1967; Landau, 1996 for earlier reviews), and it is impossible to cover all relevant aspects in a limited amount of space. Some (subjective) selection of topics must be made, and the author apologizes at the outset to those researchers whose high-quality work is not mentioned.

In the following section we will review some background and general concepts that are essential for understanding the theory of magnetic phase transitions. In Section 3 we will

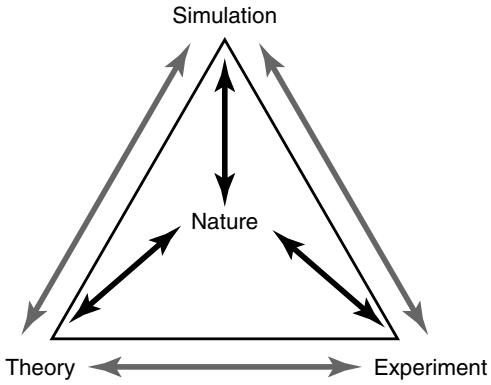

Figure 1. Schematic view of possible approaches that have been applied to the study of magnetic phase transitions.

describe specific theoretical and computational approaches that are applicable to the study of phase transitions. Some detail will be provided about these techniques to help the reader understand the advantages and limitations of each method. In Section 4 we will present some numerical results for several different models and consider the general state of our knowledge. A few final conclusions will be drawn in the final section.

2 BACKGROUND AND GENERAL CONCEPTS

2.1 Static critical behavior and critical exponents

As mentioned in Section 1, the behavior of thermodynamic properties near second-order phase transitions can be described using a formalism in which the fundamental quantity is the reduced distance from the critical temperature. Extensive experimental research has long provided a testing ground for developing theories (Kadanoff *et al*., 1967), and more recently computer simulations have been playing an increasingly important role. Of course, experiments are limited not only by instrumental resolution but also by unavoidable sample imperfections; consequently, the beautiful specific-heat peak for $RbMnF_3$, shown in Figure 2, is quite difficult to characterize for $\varepsilon \leq 10^{-4}$. Data from multiple experiments as well as analytic and numerical results for a number of exactly soluble models show that the thermodynamic properties can be described by a set of simple power laws in the vicinity of the critical point T_c, for example, for a magnetic system, the order parameter m, the specific heat C, the susceptibility χ, and the correlation length ξ vary as (Stanley, 1971; Fisher, 1974)

$$m = m_o \varepsilon^{\beta} \tag{4a}$$

$$\chi = \chi_o \varepsilon^{-\gamma} \tag{4b}$$

$$C = C_o \varepsilon^{-\alpha} \tag{4c}$$

$$\xi = \xi_o \varepsilon^{-v} \tag{4d}$$

where $\varepsilon = |1 - T/T_c|$ and the powers (Greek characters) are termed 'critical exponents'. Note that equations (4a–d) represent asymptotic expressions, which are valid only in the limit as $\varepsilon \to 0$, and more complete forms would include additional 'corrections to scaling' terms, which describe the deviations from the asymptotic behavior. Consequently, the behavior of the susceptibility χ near a critical point is better described by

$$\chi = \chi_o \varepsilon^{-\gamma}(1 + a_\theta \varepsilon^{\theta} + \cdots) \tag{5}$$

where only the first correction term, characterized by the exponent θ, is shown. (Similar corrections are present for other quantities.) The extraction of estimates for this new exponent, however, is notoriously difficult to accomplish.

Although the critical exponents for each thermodynamic quantity are believed to be identical when T_c is approached from above or below (but the singularity in the order parameter occurs only below T_c), the prefactors, or 'critical amplitudes', are usually different, and the estimation of various amplitude ratios has been of extensive interest (Privman, Hohenberg and Aharony, 1991). Lastly, along the critical isotherm, that is, at $T = T_c$, we can define another critical exponent using an expression which for a ferromagnet in a uniform applied field H is

$$m = DH^{1/\delta} \tag{6}$$

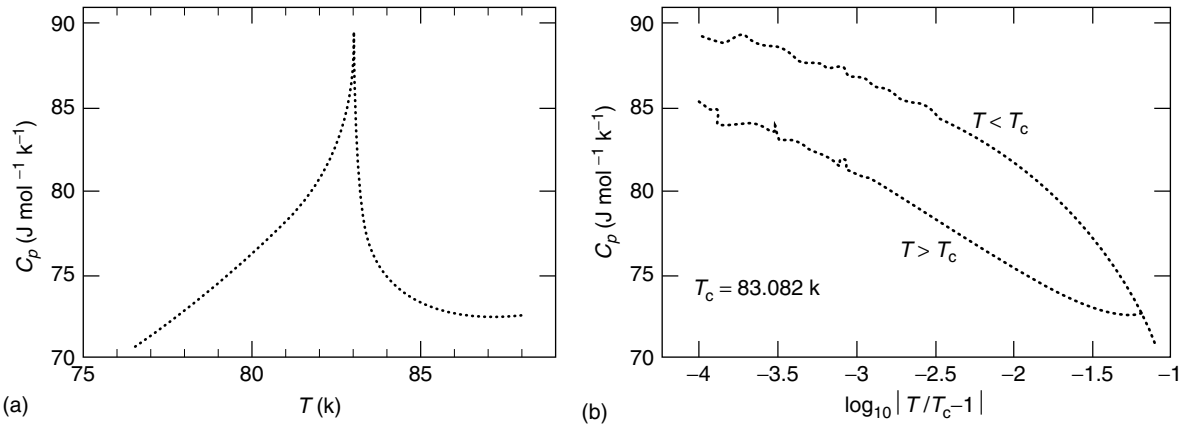

Figure 2. (a) Experimental data and (b) analysis of the critical behavior of the specific heat of the Heisenberg-like antiferromagnet $RbMnF_3$. The critical temperature is T_c. (Reproduced from Kornblit, A. and Ahlers, G. (1973), with permission from the American Physical Society. © 1973.)

(Note that an analogous expression would apply for a liquid–gas system at the critical temperature as a function of the deviation from the critical pressure.) For a system in d dimensions the two-body correlation function defined in equation (3), $G(r)$, should decay with distance well above the critical temperature with the Ornstein–Zernike form

$$G(r) \propto r^{-(d-1)/2} \exp(-r/\xi), \quad r \to \infty \tag{7}$$

Instead, at T_c the decay of the correlation function is given by a power law

$$G(r) = G_o r^{-(d-2+\eta)}, \quad r \to \infty \tag{8}$$

where η is another characteristic critical exponent. Systems that have the same set of critical exponents are said to belong to the same 'universality class'.

2.2 Some systems of special interest

2.2.1 The Ising model

The critical exponents defined in the previous section are known exactly for only a small number of magnetic models, most notably the two-dimensional Ising square lattice (Onsager, 1944), whose exact solution shows a logarithmic divergence of the specific heat. The simple Ising model (Ising, 1925; Brush, 1967), with Hamiltonian

$$\mathcal{H} = -J \sum_{\text{nn}} \sigma_i \sigma_j \tag{9}$$

where $\sigma_i = \pm 1$ has played a special 'fruit fly' role in the development of our understanding of phase transitions. This is, in part, because of its simplicity and, in part, because the model on a square lattice is one of the few cases that can be solved exactly. Onsager's solution yields a critical point at $k_B T_c/J = 2.26159\ldots$ (where k_B is Boltzmann's constant), and the critical exponents for this model are $\alpha = 0$, $\beta = 1/8$, $\gamma = 7/4$, $\nu = 1$, and $\eta = 1/4$. (In three dimensions, however, an exact solution is lacking even after many decades of attempts to find one.) A simple, nearest-neighbor (nn) Ising antiferromagnet on a bipartite lattice in a uniform magnetic field has the same critical exponents for all field values below H_c, the $T = 0$ critical field. This remarkable behavior will become clearer when we consider the problem in the context of RG theory.

2.2.2 The Heisenberg model

Many magnetic systems, however, cannot be described by an Ising model. As an example, we show in Figure 2 that the experimental data for the specific heat of $RbMnF_3$ increases even more slowly than a logarithm as $\varepsilon \to 0$ implying that $\alpha < 0$, that is, the specific heat is nondivergent. In fact, a suitable theoretical model for $RbMnF_3$ is not the Ising model but a 3-dim Heisenberg model with classical spins of unit length and nn interactions

$$\mathcal{H} = -J \sum_{\text{nn}} (S_{ix} S_{jx} + S_{iy} S_{jy} + S_{iz} S_{jz}), \quad |\vec{S}_i| = 1 \tag{10}$$

which has slightly different critical exponents than the Ising model. (The Mn^{2+} ions have spin $S = 5/2$ and can thus be well described by classical spins.) Although no exact solutions are available for Heisenberg models, as we shall see later, quite precise values of the exponents are available from field theoretic RG (Le Guillou and Zinn-Justin, 1980) and extensive Monte Carlo simulations, at least for classical spin version (Chen, Ferrenberg and Landau, 1993). There are even better known magnetic systems, like body centered cubic (bcc) iron, whose behavior also appears to be well described by a classical Heisenberg model. Of course, many real magnetic systems cannot be described by a classical version of the Heisenberg model and, particularly at low temperatures, the quantum effects can become important. Extensive series expansions indicate, however, that near a finite temperature phase transition the critical exponents are independent of spin value, although the critical amplitudes are not. For this reason, we can expect that the essential character of phase transitions in most physical Heisenberg spin systems can be described by classical spin models.

2.2.3 2-dim XY model

The preceding picture is still incomplete because there are special cases that do not fit into that general scheme at all. Most notable are 2-dimensional XY models with Hamiltonian

$$\mathcal{H} = -J \sum_{\text{nn}} (S_{ix} S_{jx} + S_{iy} S_{jy}) \tag{11}$$

where $\vec{S}_i$ is a unit vector that may have either two components (plane-rotator model) or three components (XY model). The Mermin–Wagner theorem has shown that in 2-dim (two spatial dimensions), at any nonzero temperature, classical spin models are unstable against the spontaneous formation of spin waves that destroy the long-range order. Because of this, the 2-dim Heisenberg model shows no phase transition at any $T > 0$. Although the 2-dim XY model also develops no long-range order below any nonzero transition temperature, it does nonetheless possess topological excitations termed vortices and antivortices; and below some transition temperature, T_{KT}, vortex–antivortex pairs become

bound together (Kosterlitz and Thouless, 1973). Both the correlation length and magnetic susceptibility for this model are predicted to diverge exponentially fast as T_{KT} is approached from above, that is,

$$\xi \propto \exp(a\varepsilon^{-\nu}) \tag{12}$$

and every temperature below T_{KT} is a critical point. Furthermore, the value of ν is predicted to be 1/2 for both quantities. At T_{KT} the correlation function should decay with distance, r, as $r^{-\eta}$ with $\eta = 1/4$. For all lower temperatures, the decay should still be a power law, but with a power that becomes smaller with decreasing temperature. Another characteristic of this phase transition is that the helicity modulus Υ drops discontinuously from $\Upsilon = 0.636508\ldots$ to zero at the transition. (The helicity modulus gives the reaction of the system to a twist.) In summary, there are a number of explicit predictions about the character of this unusual transition.

2.2.4 *Blume–Capel model*

As mentioned earlier, not all magnetic phase transitions are of second order. One classic example of a real system is UO_2 which was shown, half a century ago, to possess a first-order transition at about 30 K from a high-temperature paramagnetic state to a low-temperature antiferromagnetic state. Blume (1966) proposed a simple model in which a singlet electronic ground state was separated from a higher-lying triplet at an energy Δ above the ground state. Furthermore, this triplet would be split by near-neighbor exchange couplings, and Blume showed, using mean-field (Landau) theory, that if Δ is sufficiently small, one of the triplet components would lie below the singlet. Hence, an ordered ground state will result. If, however, Δ is sufficiently large, the transition will become first order. Lastly, if Δ exceeds a certain value, the ground state is always a singlet and no magnetic ground state results. A similar scenario was investigated by Capel (1966), who considered a similar Hamiltonian, but with a high-lying doublet instead of a triplet. This latter model has become known as the Blume–Capel model, that is,

$$\mathcal{H} = -J \sum_{\text{nn}} \sigma_i \sigma_j + D \sum_i \sigma_i^2, \quad \sigma_i = 1, 0, -1 \tag{13}$$

The Blume–Capel model has played an important role in the development of our understanding of some multicritical phenomena, which will be outlined in the next section.

2.2.5 *Other interesting models with unusual behavior*

Simple extensions of the 2-dim Ising model, for example, with three-body couplings instead of two-body interactions, known as the Baxter–Wu model (Baxter and Wu, 1973), or with enhanced next-nearest-neighbor (nnn) couplings may have critical behavior that is distinctly different from the simple Ising model. Another 'classic' model is the q-state Potts model (Potts, 1952; Wu, 1982) for which the Hamiltonian is

$$\mathcal{H} = -J \sum_{\text{nn}} \delta_{\sigma_i \sigma_j}, \quad \sigma_i = 1, 2, \ldots q \tag{14}$$

This model may show either first-order or second-order transitions, depending upon the number of states q. There are many other classical spin models with suitable competing interactions or lattice structures that may also show 'unusual' transitions (Landau, 1993), which, in some cases, include different behavior of multiple order parameters at T_c. These models are generally best studied by computer simulation, but to a large extent will not be considered here because of space limitations.

The preceding discussion was limited to static aspects of phase transitions and critical phenomena. The entire question of dynamic behavior will be treated in a later subsection using extensions of the current formulation.

2.3 Scaling and universality

Homogeneity arguments provide a way of simplifying mathematical expressions that contain thermodynamic singularities. As an example, consider a simple Ising ferromagnet in a small uniform magnetic field H at a temperature T that is near T_c. A 'scaling' form can be used to express the singular portion of the free energy $F(T, H)$ as

$$F_s = \varepsilon^{2-\alpha} \Im^{\pm}(H/\varepsilon^{\Delta}) \tag{15}$$

where Δ is termed the 'gap exponent' and is equal to $1/2(2 - \alpha + \gamma)$. $\Im^{\pm}$ is a function of the 'scaled' variable (H/ε^{Δ}) and does not depend upon H and ε independently. This formula has the consequence that the expressions for various thermodynamic quantities, for example, specific heat, susceptibility, and so on, can also be written in scaling forms. Even the correlation function can be expressed in terms of a scaling function but requires an extra variable, that is,

$$G(r, \xi, \varepsilon) = r^{-(d-2+\eta)} \wp(r/\xi, H/\varepsilon^{\Delta}) \tag{16}$$

where $\wp(x, y)$ is now a scaling function of two variables.

With a bit more mathematical development, one can show that not all of the critical exponents defined in the preceding text are independent. Thermodynamic arguments can be used to derive a series of exponent relations called 'scaling laws', which show that only two exponents are generally unrelated.

For example, taking the derivative of the free energy, as expressed in a scaling form, we find that the singular part near a phase transition behaves as

$$-\frac{\partial F_{\sin g}}{\partial H} = M = \varepsilon^{2-\alpha-\Delta}\Im'(H/\varepsilon^{\Delta}) \tag{17}$$

where $\Im'$ is the derivative of the function $\Im$. This equation can be compared directly with the formula for the temperature dependence of the order parameter to show that $\beta = 2 - \alpha - \Delta$. Similarly, by integrating a scaling expression for the magnetic susceptibility

$$\chi = \varepsilon^{-\gamma}\tilde{\chi}(H/\varepsilon^{\Delta}) \tag{18}$$

we find

$$m \propto \varepsilon^{\Delta-\gamma} \tag{19}$$

The combination of these relations yields the 'Rushbrooke equality'

$$\alpha + 2\beta + \gamma = 2 \tag{20}$$

and this relationship should hold regardless of what the individual exponent values are. Another important relationship that exists between critical exponents and the lattice dimensionality d of a system is termed the 'hyperscaling' expression:

$$\mathrm{d}\upsilon = 2 - \alpha \tag{21}$$

The physical justification of the homogeneity assumption given in equation (15) is discussed elsewhere, for example, Yeomans (1992); however, these scaling relations are a prerequisite for the understanding of finite size scaling, which is a basic tool in the analysis of simulational data near phase transitions. Hyperscaling may sometimes be violated, for example, the upper critical (spatial) dimension for the Ising model is $d = 4$ beyond which mean-field (Landau theory) exponents apply and hyperscaling fails. Integration of the spin–spin correlation function over all spatial separation yields the magnetic susceptibility

$$\chi = \varepsilon^{-\upsilon(2-\eta)} \tag{22}$$

and by comparing with the 'definition', cf. equation (4b), of the critical behavior of the susceptibility we easily see that

$$\gamma = \upsilon(2 - \eta) \tag{23}$$

Those systems that have the same set of critical exponents are said to belong to the same 'universality class' (Fisher, 1974), although, some of the critical exponents in different universality classes may be similar. Relevant properties that determine the universality class include spatial dimensionality, spin dimensionality, symmetry of the ordered state, the presence of symmetry-breaking fields, and the range of interaction. Thus, nn Ising ferromagnets on different lattices of the same dimensionality should have identical critical exponents and belong to the same universality class, but square-lattice and sc Ising models would be expected to have different critical behavior.

Some models have simple symmetries that can be easily broken. For example, an isotropic ferromagnet changes from the Heisenberg universality class to the Ising class when exchange anisotropy is introduced:

$$\mathcal{H} = -J\sum_{i,j}[(1-\lambda)(S_{ix}S_{jx} + S_{iy}S_{jy}) + S_{iz}S_{jz}] \tag{24}$$

with $\lambda > 0$. The variation of the critical temperature is then given by

$$T_{\mathrm{c}}(\lambda) - T_{\mathrm{c}}(\lambda = 0) \propto \lambda^{1/\phi} \tag{25}$$

where ϕ is termed the 'crossover exponent' (Riedel and Wegner, 1972). If $\lambda < 0$, however, the model becomes an easy-axis magnet and should have XY-model critical behavior instead.

Before leaving the topic of scaling, we will introduce an important, related approach to the understanding of the behavior of finite system size. At a second-order phase transition, the critical behavior of a system in the thermodynamic limit can be extracted from the size dependence of the singular part of the free energy using finite size scaling theory (Fisher, 1971; Landau, 1976; Privman, 1990; Binder, 1992). If we adopt a scaling ansatz similar to the scaling of the free energy with thermodynamic variables T, H and infinite lattice critical exponents α and υ, we can write the free energy for a system of linear dimension L as

$$F(L, T) = L^{(2-\alpha)/\upsilon}\Im(\varepsilon L^{1/\upsilon}) \tag{26}$$

where $\varepsilon = (T - T_{\mathrm{c}})/T_{\mathrm{c}}$. The choice of the scaling variable $x = \varepsilon L^{1/\nu}$ is motivated by the observation that the correlation length ξ attempts to diverge as $\varepsilon^{-\nu}$ when the transition is approached but is limited by the lattice size L. Thermodynamic properties then also have corresponding scaling forms, for example,

$$m = L^{-\beta/\upsilon}\mathcal{M}^{\mathrm{o}}(\varepsilon L^{1/\upsilon}) \tag{27a}$$

$$\chi = L^{\gamma/\upsilon}\chi^{\mathrm{o}}(\varepsilon L^{1/\upsilon}) \tag{27b}$$

$$C = L^{\alpha/\upsilon}\mathcal{C}^{\mathrm{o}}(\varepsilon L^{1/\upsilon}) \tag{27c}$$

where $\mathcal{M}^{\rm o}$(x), $\chi^{\rm o}$(x), and $\mathcal{C}^{\rm o}$(x) are finite size scaling functions. These expressions are valuable for interpreting data for finite systems obtained by a variety of numerical methods as well as for understanding the relationship between experimental data on small systems and in the corresponding thermodynamic limit. Corrections to scaling and finite size scaling must be taken into account for yet smaller systems and temperatures away from $T_{\rm c}$. Because of the complexity of the origins of these corrections, we direct the reader elsewhere (Liu and Fisher, 1990; Ferrenberg and Landau, 1991) for a detailed discussion of these corrections and techniques for including them in the analysis of MC data.

An alternative form for finite size scaling was proposed (Kim, 1994) in terms of the variable $x = \xi_{\rm L}/L$ where $\xi_{\rm L}$ is the correlation length in a system of linear dimension L. Kim, de Souza and Landau (1996) demonstrated that this approach was surprisingly effective for the Ising model even though the data used in the analysis were taken rather far from the critical temperature.

Finite size scaling has revealed important 'new' information about the nature of critical phenomena. In a classic paper, Binder (1981) examined the distribution functions for the order parameter in finite size systems and in subblocks of such systems. In particular, he showed that in addition to the first two moments of the distribution, that is, the order parameter and the susceptibility, the fourth-order cumulant also provided important information. For a system with time-reversal symmetry, the fourth-order cumulant is defined by

$$U_L = 1 - \frac{\langle m^4 \rangle}{3\langle m^2 \rangle^2} \tag{28}$$

although, in the general case, the full cumulant must be used (included odd moments, which do not then vanish). However, the 'reduced' form (also known as the *Binder parameter*) has become a valuable tool for the determination of the universality class of a model from simulational data.

As mentioned earlier, critical behavior depends upon the dimensionality of the system. An interesting question then arises: how can we understand how the critical behavior changes as the system changes from 2-dim to 3-dim. This too can be predicted using a slight adaptation of finite size scaling. For a system of n layers, the order parameter is given by

$$m = n^{-\beta_3/\nu_3} \mathcal{M}^{\rm o}(\varepsilon n^{1/\nu_3}) \tag{29}$$

where ν_3 describes the divergence of the correlation length in the 3-dim system. For small values of $(z - z_c)$, where $z = (\varepsilon n^{1/\nu_3})$ and z_c is the value obtained using $T_{\rm c}(n)$, the scaling function $\mathcal{M}^{\rm o}(z) \to (z - z_c)^{\beta_2}$. Thus, crossover from 3-dim to 2-dim behavior occurs, and it shows up in the 'critical amplitude' (Binder, 2003). However, as $n \to \infty$, $\mathcal{M}^{\rm o}(x) \to x^{\beta_3}$ so that 3-dim critical behavior is recovered. One consequence is that the shift in critical temperature is expected to be

$$\frac{T_{\rm c}(\infty) - T_{\rm c}(n)}{T(\infty)} \propto n^{-\phi} \tag{30}$$

where ϕ is the 'shift exponent'. Normally, $\phi = 1/\nu_3$, that is, hyperscaling holds.

For first-order transitions, the size dependence is governed by the system volume, that is, L^d, and the underlying theoretical formulations for both temperature-driven phase transitions (Challa, Landau and Binder, 1986) and field-driven phase transitions (Binder and Landau, 1984) have been examined via Monte Carlo simulations.

2.4 Phase diagrams and multicritical behavior

For some magnets, for example, antiferromagnets, phase boundaries will be traced out in a multidimensional thermodynamic parameter when some thermodynamic field, for example, uniform magnetic field, is varied. Perhaps the classic example of a thermodynamic phase diagram is that of water, in which lines of first-order transitions separate ice–water, water–steam, and ice–steam. The three first-order transitions join at a 'triple point', and the water–steam phase line ends at a 'critical point' where a second-order phase transition occurs. A much simpler phase diagram than that for water occurs for the Ising ferromagnet in a magnetic field

$$\mathcal{H} = -J \sum_{\rm nn} \sigma_i \sigma_j - H \sum_i \sigma_i \tag{31}$$

where $\sigma_i = \pm 1$ represents a 'spin' at lattice site i that interacts with nearest neighbors on the lattice with interaction constant $J > 0$. At low temperatures a first-order transition occurs as H is swept through zero, and the phase boundary terminates at the critical temperature $T_{\rm c}$. Time-reversal symmetry requires that the phase boundary must occur at magnetic field $H = 0$ so that the only remaining 'interesting' question is the location of the critical point. For $J < 0$, the antiferromagnetic phase remains stable in nonzero field, although the critical temperature is depressed. The phase boundary for the Ising antiferromagnet has defied analytic solution although there are several rather precise numerical determinations of its shape. As in the case of the ferromagnet, the phase diagram is symmetric about $H = 0$.

Under certain circumstances, the order of a phase transition changes as some thermodynamic parameter is modified. At first glance such behavior appears to violate the principles of universality, but examination of the system in a larger thermodynamic space makes the change easy to understand.

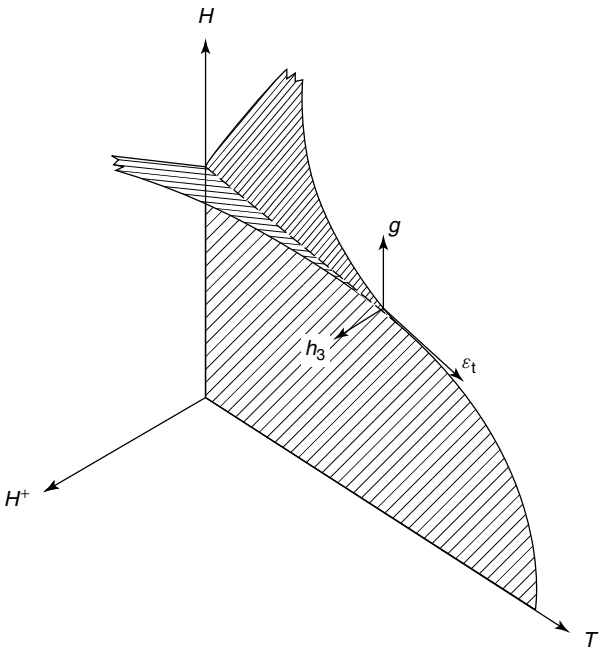

Figure 3. Phase diagram for an Ising antiferromagnet with a tricritical point in the three-dimensional thermodynamic field space, which includes both ordering (H^+) and nonordering (H) fields. Tricritical scaling axes are labeled ε_t, g, and h_3.

The intersection point of multiple curves of second-order phase transitions is known as a multicritical point. Examples include the intersection of three such curves, known as a tricritical point (Griffiths, 1970; Stryjewski and Giordano, 1977; Lawrie and Sarbach, 1984), which occurs in strongly anisotropic ferromagnets. The intersection of two second-order phase boundaries, or a bicritical point (Fisher and Nelson, 1974; Nelson, Kosterlitz and Fisher, 1974), appears on the phase boundary of a moderately anisotropic Heisenberg antiferromagnet in a uniform magnetic field. In this latter system, at low temperature a low-field antiferromagnetic state is separated from a 'spin-flop' state by a line of first-order transitions. This line ends at a bicritical point at which the second-order phase boundaries to the ordered high-field and low-field states meet. The characteristic phase diagram for a tricritical point is shown in Figure 3 in which three first-order surfaces intersect along a line of first-order transitions and the three second-order boundaries to the first-order surfaces of phase transitions meet at the tricritical point. This is one of the simplest cases of a more general set of transitions that are known as multicritical points. One of the well-known models that exhibits such behavior is the Ising antiferromagnet with nn and nnn coupling

$$\mathcal{H} = J_{\mathrm{nn}} \sum_{\mathrm{nn}} \sigma_i \sigma_j - J_{\mathrm{nnn}} \sum_{\mathrm{nnn}} \sigma_i \sigma_j - H \sum_i \sigma_i - H^+ \sum_i \sigma_i \tag{32}$$

where $\sigma_i = \pm 1$, H is the uniform magnetic field, which couples to the uniform magnetization, and H^+ is the staggered magnetic field, which couples to the order parameter (staggered magnetization). The presence of a tricritical point introduces a new 'relevant' field g, which as shown in Figure 3 makes a nonzero angle with the phase boundary, and a second scaling field ε_t, which is tangential to the phase boundary at the tricritical point. Near the tricritical point a 'crossover' scaling expression is valid

$$F(\varepsilon, H^+, g) = |g|^{2-\alpha_\varepsilon} \Im(H^+ |g|^{-\Delta_\varepsilon}, \varepsilon |g|^{-\phi_\varepsilon}) \tag{33}$$

where α_ε is the specific-heat exponent appropriate for a tricritical point, Δ_ε is the corresponding 'gap exponent', and ϕ_ε is a new 'crossover' exponent that describes the separation between the critical region near the second-order line and the tricritical region near the tricritical point. In addition, there are power law relations that describe the vanishing of discontinuities as the tricritical point is approached from below, for example, the jump in the magnetization from M^- to M^+ as the first-order phase boundary is crossed for $T < T_t$ decreases as

$$\Delta M = M^+ - M^- \propto |1 - T/T_{\mathrm{t}}|^{\beta_u} \tag{34}$$

The 'u-subscripted' exponents are related to the 'ε-subscripted' ones by a crossover exponent,

$$\beta_u = (1 - \alpha_\varepsilon)/\phi_\varepsilon \tag{35}$$

as will be discussed subsequently, the mean-field values of the tricritical exponents are $\alpha_\varepsilon = 1/2$, $\Delta_\varepsilon = 5/2$, $\phi_\varepsilon = 1/2$, and hence $\beta_u = 1$. Tricritical points have been explored using both computer simulations of model systems and by experimental investigation of physical systems, and their theoretical aspects have been studied in detail (Lawrie and Sarbach, 1984).

Mean-field theory predicts that for sufficiently strong coupling between spins in the same sublattice, the tricritical point may decompose into a critical endpoint and a double critical point with the topology shown in Figure 4. Qualitatively, the possible occurrence of the phase diagram in Figure 4 rather than of Figure 3 can be understood from mean-field theory, although the quantitative predictions for the conditions for which this should happen turn out to be incorrect.

Another kind of multicritical behavior occurs in an anisotropic Heisenberg antiferromagnet with a uniform magnetic field included. The Hamiltonian is

$$\mathcal{H} = -J \sum_{\mathrm{nn}} [(1 - \lambda) S_{ix} S_{jx} + S_{iy} S_{jy} + S_{iz} S_{jz}] - H \sum_i S_{iz} \tag{36}$$

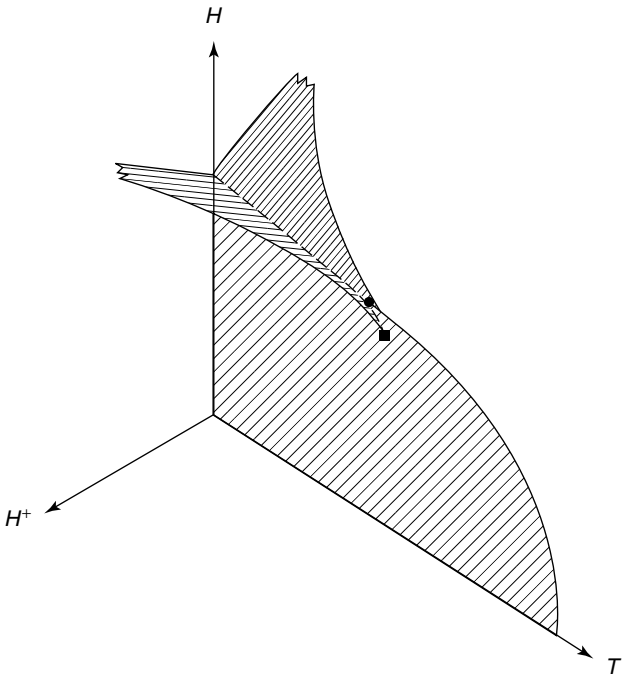

Figure 4. Schematic view of phase diagram for which the tricritical point has decomposed into a critical endpoint (filled circle) and a double critical point (filled square).

For small magnetic fields, there is an ordered antiferromagnetic state at low temperatures and as the temperature is increased an Ising-like transition occurs to the paramagnetic state. If instead, the field is increased, a first-order transition to a 'spin-flop' state takes place. In this state the z components of the spins are aligned along the field but the x and y components are antiferromagnetically aligned. At fields above the spin-flop field, with increasing temperature, there is an XY transition involving the perpendicular spin components. At the confluence of the two phase boundaries, that is, at the end of the spin-flop phase boundary, there is a single bicritical point with Heisenberg behavior. As the phase boundaries approach the bicritical point, they form an umbilicus that is completely missing in mean-field theory. Scaling axes for the bicritical point are predicted to be skew and have the following form

$$g = \Delta(H^2) - p\varepsilon_b \tag{37a}$$

$$\tilde{\varepsilon} = \varepsilon_b + q\Delta(H^2) \tag{37b}$$

where $\Delta(H^2) = H^2 - H_b^2$ and $\varepsilon_b = |1 - T/T_b|$. The shapes of the upper and lower phase boundaries near the bicritical point are predicted to be determined by the crossover scaling form

$$g/\tilde{\varepsilon}^{\phi} = +w_{\perp}, -w_{||} \tag{38}$$

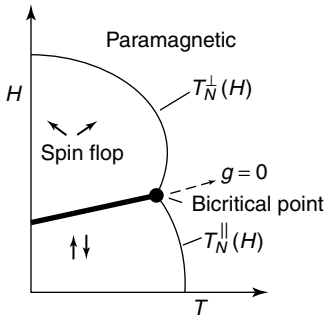

Figure 5. Schematic phase diagram predicted for an anisotropic Heisenberg antiferromagnet. The heavy solid line is a first-order transition and the lighter solid lines are second-order transitions. For fields below the bicritical point, the order parameter is the staggered magnetization component that is parallel to the applied field; above the bicritical point, the perpendicular staggered magnetization is critical.

where $w_{\perp}, w_{||}$ are model dependent and may also differ above and below the bicritical point. This behavior for an anisotropic Heisenberg antiferromagnet is shown schematically in Figure 5. We conclude this section with a comment about analysis of critical exponents when the appropriate scaling fields are not parallel to the 'applied' thermodynamic fields. In such cases, 'field mixing' can complicate the analysis, and we refer the reader elsewhere (Wilding and Bruce, 1992; Wilding, 1995) for a more detailed discussion.

2.5 Surface critical behavior

Although it had long been common to only consider phase transitions in systems of infinite extent, several authors realized that critical behavior that is explicitly associated with surfaces of magnetic systems was itself of interest (for a detailed description of surface transitions, see Binder, 1983). Binder and Hohenberg (1972, 1974) realized that a new set of surface critical exponents could be defined that were not necessarily related to the exponents of the corresponding bulk. For example, if the free energy is separated into a bulk term f_b and a surface term f_s in analogy with the bulk magnetization, defined using a bulk field H,

$$m_{\mathrm{b}} = -\left(\frac{\partial f_{\mathrm{b}}}{\partial H}\right) \tag{39}$$

we can define a surface layer magnetization

$$m_1 = -\left(\frac{\partial f_{\mathrm{s}}}{\partial H_1}\right) \tag{40}$$

where H_1 is a magnetic field that acts only on the surface layer. There are also new thermodynamic response functions,

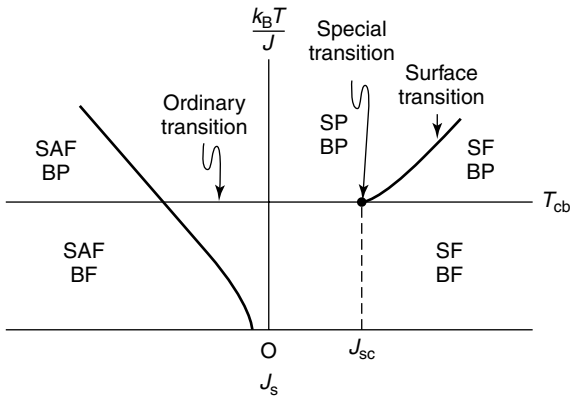

Figure 6. Schematic view of phase transition behavior occurring at the surface of a semi-infinite magnetic system. Each phase is labeled according to whether it is bulk (B) or surface (S) and ferromagnetic (F) or antiferromagnetic (AF). J_{sc} denotes the coupling for the surface–bulk multicritical point. (Reproduced from K. Binder: 'Critical Behavior at Surface' in C. Domb and J.L. Lebowitz (eds): *Phase Transitions and Critical Phenomena*, vol. 8 (Academic Press, 1983), with permission from Elsevier.)

such as the magnetic susceptibility, that appear in addition to the bulk ones, that is,

$$\chi_b = -\left(\frac{\partial^2 f_b}{\partial H^2}\right) \tag{41a}$$

$$\chi_1 = -\left(\frac{\partial^2 f_s}{\partial H \partial H_1}\right) \tag{41b}$$

$$\chi_{1,1} = -\left(\frac{\partial^2 f_s}{\partial H_1^2}\right) \tag{41c}$$

Binder and Hohenberg also worked out a schematic (mean field) phase diagram, shown in Figure 6, that shows the general features for a phase diagram for a simple model with an exchange parameter J in the bulk and a surface interaction constant J_s, as the temperature is varied. The 'special transition' is a multicritical point at which bulk and surface fluctuations become simultaneously critical at temperature $T_{cs} \equiv T_{cb}$. Separate sets of surface critical exponents should describe the different kinds of transitions, for example,

$$m_1 \propto (1 - T/T_{cs})^{\beta_1} \tag{42}$$

The mean-field values of the surface exponents often differ at the ordinary transition, the special transition, and the surface transition and may also differ from the bulk exponents:

$$\beta_b = 1/2; \quad \beta_{ord} = 1; \quad \beta_{sp} = 1/2; \quad \beta_{surf} = 1/2;$$
$$\gamma_b = 1; \quad \gamma_{1,ord} = 1/2; \quad \gamma_{1,sp} = 1; \quad \gamma_{1,surf} = 1;$$
$$\gamma_{11,ord} = -1/2; \quad \gamma_{11,sp} = 1/2; \quad \gamma_{11,surf} = 1$$

There are additional thermodynamic properties that have distinct surface behavior, but we will not discuss this topic further. For more details see Binder (1983).

2.6 Systems with disorder

Systems with extreme disorder that produces frustration develop spin glass order, but this behavior is beyond the scope of this article. In this section we will only be concerned with the introduction of modest amounts of quenched (i.e., nonmobile) site or bond disorder that does not change the nature of the ordered state. When the concentration of impurities exceeds a critical level, the magnetic bonds can no longer percolate, and no long-range order can occur. The seminal paper on the effects of nonmagnetic impurities by Harris (1974) predicted that if random, quenched, nonmagnetic impurities are added to a magnetic system, new critical exponents will be produced only if $\alpha > 0$ in the pure system. Of course, there are other possible types of disorder and these will be discussed briefly later in Section 4.

2.7 Dynamic critical behavior

The framework for understanding the static behavior of magnetic systems near phase transitions has been rather thoroughly developed, in part because of the ability to make high-resolution experiments and in part because of the development of sophisticated numerical techniques. Understanding of the time-dependent behavior of magnetic properties of systems near phase transitions has proved more difficult.

As a critical point T_c is approached, the large spatial correlations that develop have long temporal correlations associated with them as well. At T_c the characteristic time scales diverge in a manner that is determined, in part, by the nature of the conservation laws. This 'critical slowing down' has been observed in multiple physical systems by light-scattering experiments (critical opalescence) as well as by neutron scattering. In a classic work, Hohenberg and Halperin (1977) laid the foundation for understanding dynamic critical behavior by proposing the existence of a number of dynamic universality classes on the basis of the number of degrees of freedom of the order parameter and the lattice and spin dimensionalities as well as any applicable conservation laws. The characteristic feature of the framework of dynamic critical behavior was the introduction of a new, dynamic critical exponent z that was distinct from, and in many cases unrelated to, the static critical exponents. One important conclusion was that multiple classes could exist for models with the same Hamiltonian but different conservation laws.

Two classes were identified as having only stochastic, or 'relaxational', behavior:

Model A – Ising model with neither magnetization nor energy conserved.
Model B – Ising model with conserved magnetization.

The conventional theory of critical slowing down (Van Hove, 1954) predicts that $z = 2 - \eta = 1.75$ for model A Ising critical relaxation, where η is the exponent describing the decay of the static, two-point correlation function at the critical point (equation 8). Model B should describe the growth of magnetic domains in a system with fixed magnetization and, according to Lifshitz–Slyozov theory (Lifshitz and Slyozov, 1961), the characteristic length scale $L(t)$ of the domains should grow as $t^{1/3}$.

Several other classes, however, have true dynamics, that is, deterministic behavior governed by equations of motion, derived from the Hamiltonian:

Model E – Planar spin model, $H_z = 0$
Model F – Planar spin model, $H_z > 0$
Model G – Antiferromagnetic Heisenberg model
Model J – Ferromagnetic Heisenberg model.

One consequence of this classification scheme is that there may be models that are in the same static universality class but in different dynamic classes. For example, an Ising model with 'spin-flip' kinetics and the same Ising model with 'spin-exchange' kinetics may be in different universality classes. Similarly, the Heisenberg model treated by Monte Carlo (stochastic) simulations and the same model solved by integrating coupled equations of motion may also be in different dynamic universality classes.

For relaxational models, such as the stochastic Ising model, the time-dependent behavior is described by a master equation

$$\partial P_n(t)/\partial t = -\sum_{n \neq m} [P_n(t) W_{n \to m} - P_m(t) W_{m \to n}] \qquad (43)$$

where $P_n(t)$ is the probability of the system being in state 'n' at time t, and $W_{n \to m}$ is the transition rate for $n \to m$. The solution to the master equation is a sequence of states developing in time, but the 'time' is a stochastic quantity that is not equivalent to true time. A quantitative measure of time correlations *within* equilibrium is obtained by first defining a relaxation function $\varphi(t)$, for example, for the magnetization M

$$\varphi_{MM}(t) = \frac{\langle M(0)M(t)\rangle - \langle M\rangle^2}{\langle M^2\rangle - \langle M\rangle^2} \qquad (44)$$

and a similar relaxation function can be defined for the internal energy. When normalized as in equation (44), the relaxation function is equal to unity at $t = 0$ and decays to zero as $t \to \infty$. The asymptotic, long-time decay of the relaxation function is exponential, that is,

$$\varphi(t) \to e^{-t/\tau} \qquad (45)$$

and the correlation time τ diverges as T_c is approached. This dynamic (relaxational) critical behavior can be expressed in terms of a power law as well

$$\tau \propto \xi^z \propto \varepsilon^{-\nu z} \qquad (46)$$

where ξ is the (divergent) correlation length, $\varepsilon = |1 - T/T_c|$, and z is the dynamic critical exponent. Estimates for z have been obtained for Ising models by ε-expansion RG theory (Bausch, Dohm, Janssen and Zia, 1981) but numerical estimates (Landau, Tang and Wansleben, 1988; Wansleben and Landau, 1991; Ito, 1993) have been inconsistent and have only recently come to reasonably consistent values.

The approach to equilibrium can be used to define another, nonlinear relaxation function

$$\varphi_M(t) = \frac{\langle M(t) - M(\infty)\rangle}{\langle M(0)\rangle - \langle M(\infty)\rangle} \qquad (47)$$

which also has an exponential decay at long times. According to Fisher and Rácz (1976), however, there is only a single, independent dynamic exponent and

$$z = z_{nl}^M + \beta/\nu \qquad (48)$$

or, in terms of the time dependence for the internal energy, then

$$z = z_{nl}^E + (1 - \alpha)/\nu \qquad (49)$$

At T_c the nonlinear relaxation is expected to decay at long times as a power law

$$m(t) \sim t^{-\beta/z\nu} \qquad (50)$$

and a 'local exponent', λ_m, extracted from Monte Carlo data,

$$\lambda_m = -\frac{\mathrm{d}\log m(t)}{\mathrm{d}\log t} \qquad (51)$$

should extrapolate to $\beta/z\nu$. The critical temperature can be determined by locating the temperature at which the nonlinear (nonequilibrium) relaxation obeys equation (50) and with use of the static critical exponents the dynamic exponent z can be estimated. Somewhat surprisingly, short time dynamics can also be used to extract information about critical dynamics and short time dynamic scaling has been

well established (Janssen, Schaub and Schmittmann, 1989; Zheng, 2006).

There are other systems, such as spin glasses and models with impurities, where the decay of the relaxation function is more complex, for example, a 'stretched exponential'

$$\varphi(t) \propto \exp[-(t/\tau)^n], \quad n < 1 \tag{52}$$

and the correct behavior of τ may not be simple. (In such cases, quite long observation times may be needed to measure the asymptotic behavior of the relaxation function.) Such systems are beyond the scope of this article and will not be considered further.

For continuous-spin systems with true dynamics, the time-dependent properties are determined by the dynamic structure factor

$$S(\vec{q}, \omega) = \frac{1}{2\pi} \sum_{\vec{r},\vec{r}'} e^{i\vec{q}\cdot(\vec{r}-\vec{r}')} \int_{-\infty}^{\infty} e^{i\omega t} C(\vec{r} - \vec{r}', t)\, \mathrm{d}t \tag{53}$$

The dynamic structure factor depends upon the static correlation length ξ and thus shows characteristic behavior as the critical temperature is approached. Near the critical temperature a dynamic scaling hypothesis can be formulated in terms of the behavior of the characteristic frequency ω_m in terms of the wave vector q and the correlation length ξ

$$\omega_m \propto \xi^{-z} \Omega(q\xi) \tag{54}$$

and the dynamic structure factor can also be written in a suitable scaling form

$$S(q, \omega) = \frac{2\pi}{\omega_m} S(q) F\left(\frac{\omega}{\omega_m}, q\xi\right) \tag{55}$$

The functional form for Ω in equation (54) will vary with the details of the model, but the dynamic critical exponent z should be invariant within a given dynamic universality class. The 'conventional theory' of critical dynamics (Van Hove, 1954) predicts that the behavior of the characteristic frequency is

$$\omega \propto \xi^{-z} (q\xi)^2 \tag{56}$$

with $z = 4 - \eta$. Mode-coupling theory and the RG were then used to make predictions about the values of the dynamic critical exponent z, and these generally differed from the predictions of the conventional theory. Within the context of the ε-expansion RG, the prediction for model A is $z = 2 + c\eta$ where $c = [6ln(4/3) - 1]$. The planar magnet is predicted to have exponent $z = d/2 + \alpha'/2\nu$ where $\alpha' = \max(\alpha, 0)$. For the isotropic Heisenberg antiferromagnet, RG theory predicts $z = d/2$, whereas for the isotropic ferromagnet the prediction is $z = (d + 2 - \eta)/2$. For a review of the theory and applicability to real materials see Frey and Schwabl (1994).

3 THEORETICAL APPROACHES

3.1 Landau theory

One of the fundamental approaches used to describe magnetic phase transitions is Landau theory, which begins with the assumption that near the transition the free energy of a system can be expanded in terms of the order parameter. For a d-dimensional system the free energy, in terms of a simple one-component order parameter $m(x)$, is given by

$$F = F_o + \int d^d x \left\{ \frac{1}{2} r m^2(x) + \frac{1}{4} u m^4(x) + \frac{1}{6} v m^6(x) - \frac{H}{k_B T} m(x) + \frac{1}{2d} [R \nabla m(x)]^2 + \ldots \right\} \tag{57}$$

In this equation, a factor of $(k_B T)^{-1}$ has been absorbed so the coefficients r, u, and v are dimensionless. (Time-reversal symmetry has also been used to eliminate all odd order terms for $H = 0$.) For more complex systems, additional terms, for example, cubic products of components of a multicomponent order parameter, might appear; but such considerations are beyond the scope of our present discussion. For a simple, homogeneous system with a spatially uniform order parameter the free energy becomes (V being the volume)

$$F = F_o + V \left(\frac{1}{2} r m^2 + \frac{1}{4} u m^4 + \frac{1}{6} v m^6 - \frac{mH}{k_B T} + \ldots \right) \tag{58}$$

In equilibrium, the free energy must be a minimum, and if $u > 0$ the preceding equation can be truncated and the minimization criterion $\partial F / \partial m = 0$ can be applied to find three possible solutions:

$$m_1 = 0 \tag{59a}$$

$$m_{2,3} = \pm\sqrt{-r/u} \tag{59b}$$

The first solution describes the disordered (i.e., $T > T_c$) state. Expanding r in the vicinity of T_c so that $r = r'(T - T_c)$, we find then for $r < 0$ (i.e., $T < T_c$),

$$m_{2,3} = \pm (r' T_c / u)^{1/2} (1 - T/T_c)^{1/2} \tag{60}$$

Solutions $m_{2,3}$ correspond to behavior below T_c where the order parameter approaches zero with a characteristic

power law (see equation 4a) with critical exponent $\beta = 1/2$. Similarly, an analysis of the susceptibility yields $\gamma = 1$ for the susceptibility and $\delta = 3$ for the order parameter along the critical isotherm. Unfortunately, Landau theory does not correctly describe the behavior of most physical systems that generally have values of $\beta \approx 1/3$ (Kadanoff *et al.*, 1967) instead of the Landau value of $\beta = 1/2$. Lastly, the 'fixed-point' (see the next section) value of the reduced fourth-order cumulant for the Landau (mean field) model with a one-component order parameter is $U^* \sim 0.2705$ (Brézin and Zinn-Justin, 1985).

The appearance of tricritical points can be easily understood within the context of Landau theory by retaining the sixth-order term in equation (58). If the term in m^4 is less than 0, the solutions are as follows:

$$m_1 = 0 \tag{61a}$$

$$m_{2,3} = \pm[\tfrac{1}{2v}(-u + \sqrt{u^2 - 4rv})]^{1/2} \tag{61b}$$

$$m_{4,5} = \pm[\tfrac{1}{2v}(-u - \sqrt{u^2 - 4rv})]^{1/2} \tag{61c}$$

The first solution again describes the disordered state. For positive values of v, there are multiple solutions showing long-range order and the phase transition is first order. A tricritical point appears when $r = u = 0$, and the tricritical exponents that result from this analysis are

$$\alpha_t = 1/2 \tag{62a}$$

$$\beta_t = 1/4 \tag{62b}$$

$$\gamma_t = 1 \tag{62c}$$

$$\delta_t = 5 \tag{62d}$$

Note that most of these tricritical exponents are quite different than those predicted for the critical point. The crossover exponent describing the behavior of the second-order phase boundary in the vicinity of the tricritical point is predicted by Landau theory to be $\phi = 1/2$.

As mentioned earlier, the thermodynamic properties of a system are not constant in time but fluctuate as the system explores different regions of phase space. The relative fluctuations of extensive thermodynamic variables scale inversely with the number of sites N, so that global fluctuations vanish in the thermodynamic limit. Nevertheless, local fluctuations can have dramatic effects and require a separate discussion. As long as fluctuations do not play a significant role, the predictions of Landau theory should be correct. This can be expressed mathematically for the fluctuations in $m(x)$ for a d-dimensional system over the 'correlation volume' ξ^d. If the mean value of the order parameter is m_o, fluctuations can be ignored if

$$\frac{\langle [m(x) - m_o]^2 \rangle}{m_o^2} \ll 1 \tag{63}$$

This inequality, termed the Ginsburg criterion, leads to the expression

$$\xi^d m_o^2 \chi^1 \gg \text{const} \tag{64}$$

Once the appropriate power laws for critical behavior are inserted into equation (64) the inequality becomes

$$\varepsilon^{-\nu d + 2\beta + \gamma} \gg \text{const} \tag{65}$$

This implies that Landau exponents will be valid if

$$\varepsilon^{(d-4)/2} \ll \text{const} \tag{66}$$

that is, the lattice dimensionality must be greater than or equal to an upper critical dimension $d_u = 4$. Below some lower critical dimensionality, d_l, fluctuations completely dominate and no transition will occur. Fluctuations at tricritical points can be examined if the next order term $\sim v m^6$ in the Landau free energy is retained. Mean-field theory (i.e., Landau theory) is also valid for tricritical behavior above some upper critical dimension for the Ising model with competing interactions $d_u = 3$. However, for $d = 3$ there are also logarithmic corrections (Wegner and Riedel, 1973), which complicate the verification of these predictions by numerical means.

Improvements on Landau, that is, mean field, theory are nontrivial to implement, particularly for systems with inhomogeneous interactions, for example, amorphous magnets. However, a correlated mean-field theory (Fähnle, Herzer, Egami and Kronmüller, 1982; Kronmüller and Fähnle, 2003) is able to describe the experimentally observed upward curvature in the inverse susceptibility for random exchange ferromagnets.

3.2 Renormalization group theory

The concepts of scaling and universality can be given a firm foundation through the use of RG theory. The fundamental physical ideas underlying RG theory were introduced by Kadanoff (1971) using a simple coarse-graining approach, and a mathematical basis was provided by Wilson (1971a,b). Instructional overviews of RG theory can be found in Domb and Green (1976) and Fisher (1974). Kadanoff subdivided a system into cells of characteristic size b (in terms of the nn spacing a) and $b < \xi$, where ξ is the correlation length of the system. The starting point is the expression of the singular

part of the free energy in terms of cell variables instead of the original site variables, that is,

$$F_{\text{cell}}(\tilde{\varepsilon}, \tilde{H}) = b^d F_{\text{site}}(\varepsilon, H) \tag{67}$$

where $\varepsilon = |1 - T/T_c|$, $\tilde{\varepsilon}$ and $\tilde{H}$ are cell variables, and d is the spatial dimensionality. Homogeneity of the free energy then implies that

$$F(\lambda^{a_T}\varepsilon, \lambda^{a_H} H) = \lambda F(\varepsilon, H) \tag{68}$$

where a_T and a_H are new exponents that can be related to those already defined. Using formal RG theory, the initial Hamiltonian is transformed, or *renormalized*, to produce a new Hamiltonian. With successive repetitions, the resultant Hamiltonians, enumerated using index n to describe the number of times the transformation has been applied, are related by

$$\mathcal{H}^{(n+1)} = \boldsymbol{R}_b \mathcal{H}^{(n)} \tag{69}$$

Each application of the RG operator $\boldsymbol{R}_b$ reduces the number of degrees of freedom by b^d. New interaction terms that were not present in the original Hamiltonian may appear in the renormalized Hamiltonian, but the partition function Z must not change since it is only being expressed in terms of new variables. Eventually the renormalized Hamiltonian reaches a stable, or 'fixed point', form $\mathcal{H}^*$ and no longer changes with further repetition, that is,

$$\mathcal{H}^* = \boldsymbol{R}_b \mathcal{H}^* \tag{70}$$

Thus, the Hamiltonian of a system at its critical point 'flows' towards the fixed-point Hamiltonian upon successive application of the RG transformation until it no longer changes. For points in Hamiltonian parameter space for which the system is not initially at a critical point, the Hamiltonian instead 'flows' away from the fixed point (Figure 7). For an Ising-type Hamiltonian above T_c there is also a trivial fixed point corresponding to the ideal paramagnet at $T \to \infty$ that is eventually reached. (After a few rescalings, the block size b^n exceeds ξ and the different blocks are then uncorrelated.) For $T < T_c$, the flow is to a different, zero-temperature fixed point. The Hamiltonian is written in the same general framework at each application of the transformation, for example, an Ising-type Hamiltonian

$$\mathcal{H}/k_B T = K_1 \sum_i \sigma_i + K_2 \sum_{\langle i,j \rangle} \sigma_i \sigma_j + K_3 \sum_{\langle i,j,k \rangle} \sigma_i \sigma_j \sigma_k + K_4 \sum_{\langle i,j,k,\ell \rangle} \sigma_i \sigma_j \sigma_k \sigma_{ell} + \cdots \tag{71}$$

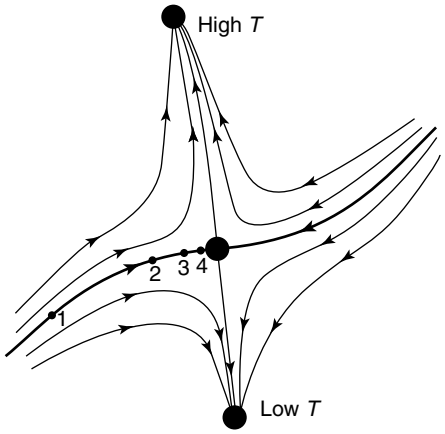

Figure 7. Schematic RG flow diagram in a two-dimensional parameter space. The heavy curve represents the critical hypersurface. Point 1 is the critical value for the initial Hamiltonian and the other points labeled show the flow toward the fixed point (heavy filled circle).

where the set of coupling constants $\{K_1, K_2, \ldots\}$ forms the space in which the flow is considered.

As additional couplings are included in the Hamiltonian, an entire hypersurface of critical points is produced. Whenever the Hamiltonian begins on the critical hypersurface, it should 'flow' towards the fixed point. If, instead, the system is at a multicritical point, the Hamiltonian should flow towards a new 'fixed point' and not towards the critical fixed point. Close to the multicritical point, however, there should be complex 'crossover' behavior: the system may first appear to flow towards a critical fixed point but upon further iteration of the RG transformation begin to flow towards the 'new' fixed point. RG theory provides insight into the principle of universality of critical phenomena because each type of criticality is controlled by a different 'fixed point' of the RG transformation.

Near the fixed point, the problem can be linearized so that the Hamiltonian $\mathcal{H}'$ is related to the fixed point by

$$\mathcal{H}' = \boldsymbol{R}_b[\mathcal{H}^*] + h\boldsymbol{L}\boldsymbol{Q} = \mathcal{H}^* + h\boldsymbol{L}\boldsymbol{Q} + \ldots \tag{72}$$

The linear operator $\boldsymbol{L}$ has the eigenvalue equation

$$\boldsymbol{L}Q_j = \lambda_j Q_j \tag{73}$$

where λ_j is the eigenvalue and Q_j the eigenvector. In terms of the spatial rescaling factor b the eigenvalue is

$$\lambda_j = b^{y_j} \tag{74}$$

where y_j is an 'exponent eigenvalue', which can be related to the usual critical exponents. In terms of these λ_j, the

transformed Hamiltonian can be expressed as

$$\mathcal{H}' = \mathcal{H}^* + \sum h_j \lambda_j Q_j + \ldots \tag{75}$$

and eigenvalues may be extracted from recursion relations ($h_j^{(k+1)} \approx \lambda_j h_j^{(k)}$). The free energy in terms of the original and renormalized variables is again unchanged:

$$f(h_1, h_2, h_3, \ldots) \approx b^{-d} f(b^{\lambda_1} h_1, b^{\lambda_2} h_2, \ldots) \tag{76}$$

where $h_1 = k_1 \varepsilon$, $h_2 = k_2 H$, and so on. Choosing b so that $b^{\lambda_1} \varepsilon = 1$, we can rewrite this equation with k_1, k_2 constants

$$F(\varepsilon, H, h_3) \approx \varepsilon^{d/\lambda_1} f(k_1, k_2 H/\varepsilon^{\lambda_1/\lambda_2}, \ldots) \tag{77}$$

Scaling has then been 'derived' if we identify $d/\lambda_1 = 2 - \alpha$ and $\lambda_2/\lambda_1 = \Delta$.

Alternatively, one may develop a momentum space approach to RG theory in which the coarse-graining and rescaling is defined in k space (momentum space) so that

$$\mathcal{H}(m) = 1/2 \int \mathrm{d}k (k^2 + r_\mathrm{o}) |m(k)|^2 + \ldots \tag{78}$$

A cutoff momentum Λ is introduced, and the k values that lie between Λ and Λ/b are integrated out so the variable of integration is rescaled by $k' = bk$. The order parameter is then renormalized and steps are repeated. A perturbation expansion leads to recursion relations for the effective interaction parameters and their solution gives the 'fixed points'. Perturbation parameters may include the deviation from the upper critical dimension, d_u, or the inverse of the number of components of the order parameter n. For simple magnetic systems with isotropic, short-range couplings, the upper critical dimension is $d_u = 4$ and the leading order estimates (Wilson and Fisher, 1972) for critical exponents from the ε expansion are (note that the parameter ε in the following equation has a special meaning and does *not* refer to the reduced distance from the critical temperature) as follows:

$$\alpha = \frac{4 - n}{2(n + 8)} \varepsilon + \cdots \quad \text{where} \quad \varepsilon = 4 - d \tag{79a}$$

$$\beta = \frac{1}{2} - \frac{3}{2(n + 8)} \varepsilon + \cdots \tag{79b}$$

$$\gamma = 1 + \frac{(n + 2)}{2(n + 8)} \varepsilon + \cdots \tag{79c}$$

Of course, for some simple models higher-order expressions have been derived; and although these expressions do not always vary simply with ε, rather accurate estimates for critical exponents have been extracted, see for example, Brézin, Le Guillou, Zinn-Justin and Nickel (1973) and Le Guillou and Zinn-Justin (1980). A reliable analysis of the expansions generally requires substantial sophistication. RG theory was also applied to tricritical points by Wegner and Riedel (1973), who showed that Landau theory correctly predicted tricritical exponents in 3-dim but that the critical behavior is modified by the presence of logarithmic corrections. Further, an RG analysis of bicritical and related tetracritical points has been carried out by Nelson, Kosterlitz and Fisher (1974). While the momentum space RG has yielded fairly accurate results for the critical exponents of the n-vector model, the accuracy for other problems is far more modest, for example, universal scaling functions describing the equation of state, or describing the crossover from one universality class to another, are typically available only in low-order ε expansion. The momentum space RG, in principle, also yields information about universal properties but not for the critical coupling constants (T_c, etc.) or critical amplitudes. Real space RG, described below, can yield this information. Momentum space RG has been particularly valuable in the examination of systems with dipolar coupling (Fisher and Aharony, 1973), an addition which, of course, has important implications for many real, physical systems. This treatment showed that Ising models with dipolar interactions have mean-field exponents (Larkin and Khmel'nitskii, 1969; Aharony, 1973; Brézin and Zinn-Justin, 1976). Ried, Millev, Fähnle and Kronmüller (1995) extended the momentum space RG to Heisenberg models with uniaxial anisotropy and dipolar coupling. The crossover transitions between four nontrivial fixed points (Heisenberg, Ising, uniaxial dipolar, and isotropic dipolar) were described in terms of an effective exponent. Their results were later confirmed by experiments on Gadolinium (Srinath and Kaul, 1999). Of course, RG theory has been discussed extensively, and the reader is directed elsewhere for a more detailed description (e.g., Domb and Green, 1976).

Several simple RG transformations have been used with generally good success. For these, the space of allowed coupling constants is low-dimensional: This is an uncontrolled approximation but allows rapid calculations that are needed for the actual renormalization transformation. As an example, the 'block-spin' transformation replaces a $b \times b$ block of spins by a 'super spin', whose state is determined by the state of the majority of spins in the block. (When the number of spins in a block is even, one site in each block is chosen as a 'tiebreaker'.) In an nn antiferromagnet, a (2×2) block spin would give zero for all block spins if the system were in the ground state. Instead 'block spins' are best composed of more complex structures where each block resides on a single sublattice. (A $\sqrt{5} \times \sqrt{5}$ transformation rotates the lattice through an angle $\varphi = \pi/4$ so if a second transformation then rotates the lattice through angle $-\varphi$, the original orientation is recovered.) With continued

application of the rescaling transformation, the number of couplings $\{K_i\}$ in the Hamiltonian increases; however, in practice, as the rescaling is iterated, the space of coupling constants has to be truncated. In an analytic approach, other uncontrolled approximations may be necessary to relate the new and old couplings, but with the Monte Carlo renormalization group (MCRG) methods described subsequently such problems can be avoided.

The large-cell MCRG transformation was used to study the 2-dim Ising model with nn coupling (Friedman and Felsteiner, 1977). A system of size $L \times 2L$ was considered and two block spins σ'_1 and σ'_2 were created from application of the majority rule to 'large' cells of size $L \times L$. The block spins interact with Hamiltonian

$$\mathcal{H} = K'\sigma'_1\sigma'_2 \tag{80}$$

where the magnitude of the new effective coupling constant K' is determined from

$$\langle\sigma'_1\sigma'_2\rangle = \tanh(2dK') \tag{81}$$

where d is the spatial dimensionality. Note that this corresponds to a transformation with scale factor $b = L$. The thermal eigenvalue y_T is then determined from the expression

$$\frac{\mathrm{d}K'}{\mathrm{d}K} = L^{y_\mathrm{T}} \tag{82}$$

where the derivative can be calculated via Monte Carlo simulation from averages, that is,

$$\frac{\mathrm{d}K'}{\mathrm{d}K} = \langle\sigma'_1\sigma'_2 S\rangle - \langle\sigma'_1\sigma'_2\rangle\langle S\rangle \tag{83}$$

where $S = \sum \sigma_i\sigma_j$. If L is increased with the system held at the critical coupling the estimates for y_T should converge to the correct value of $1/\nu$.

Methods that require calculation of the renormalized Hamiltonian do not work well. A very different approach that avoids calculation of renormalized couplings is usually more effective. For simplicity, we express the Hamiltonian in the form

$$\mathcal{H} = \sum_\alpha K_\alpha S_\alpha \tag{84}$$

where the various S_α are sums of different products of spin operators and the K_α are the corresponding dimensionless coupling constants. Examples of S_α are as follows:

$$S_1 = \sum \sigma_i \tag{85a}$$

$$S_2 = \sum \sigma_i\sigma_j \tag{85b}$$

$$S_3 = \sum \sigma_i\sigma_j\sigma_k \tag{85c}$$

Near the fixed-point Hamiltonian $\mathcal{H}^*(K^*)$ the linearized transformation takes the form

$$K_\alpha^{(n+1)} - K_\alpha^* = \sum_\beta T^*_{\alpha\beta}(K_\beta^{(n)} - K_\beta^*) \tag{86}$$

where the sum is over all possible couplings. The eigenvalues λ_i of $T^*_{\alpha\beta}$ are related to eigenvalue exponents by

$$\lambda = b^y \tag{87}$$

where the y are related to the usual critical exponents, for example, $y_\mathrm{T} = \nu^{-1}$. The equations are valid for all real space RG methods, and the common challenge becomes the determination of matrix elements $T^*_{\alpha\beta}$ at the fixed point. Perhaps the most successful implementation of real space RG methods has been through the use of MCRG simulations (see Swendsen, 1982). In this approach, the elements of the linearized transformation matrix are written in terms of expectation values of correlation functions at different levels of renormalization. Thus,

$$T_{\alpha\beta} = \frac{\partial K_\alpha^{(n+1)}}{\partial K_\beta^{(n)}} \tag{88}$$

where the elements can be extracted from solution of the chain rule equation

$$\frac{\partial\langle S_\gamma^{(n+1)}\rangle}{\partial K_\beta^{(n)}} = \sum \left\{\frac{\partial K_\alpha^{(n+1)}}{\partial K_\beta^{(n)}}\right\}\left\{\frac{\partial\langle S_\gamma^{(n+1)}\rangle}{\partial K_\alpha^{(n+1)}}\right\} \tag{89}$$

The derivatives can be obtained from correlation functions, which can be evaluated by Monte Carlo simulation, that is,

$$\frac{\partial\langle S_\gamma^{(n+1)}\rangle}{\partial K_\beta^{(n)}} = \langle S_\gamma^{(n+1)} S_\beta{}^{(n)}\rangle - \langle S_\gamma^{(n+1)}\rangle\langle S_\beta^{(n)}\rangle \tag{90}$$

and

$$\frac{\partial\langle S_\gamma^{(n)}\rangle}{\partial K_\alpha^{(n)}} = \langle S_\gamma^{(n)} S_\alpha^{(n)}\rangle - \langle S_\gamma^{(n)}\rangle\langle S_\alpha^{(n)}\rangle \tag{91}$$

In practice, the $T_{\alpha\beta}$ matrix is truncated and the number of renormalizations is also limited. The estimates for eigenvalues need to be examined as a function of the number of

couplings N_c used in the analysis as well as the number of iterations N_r. Exact results are obtained only for $N_r \to \infty$ and $N_c \to \infty$, but convergence is often rapid. Comparisons for different size lattices indicate whether finite lattice effects are biasing the answers.

MCRG may be used to locate critical points by matching correlation functions for transformed and untransformed systems. However, finite size effects can be subtle, so, two different lattices that differ in size by scale factor b are needed. Near a critical point, a linear approximation relates the difference between the original and renormalized correlation functions to the distance to the critical point, that is,

$$\langle S_\alpha^{(n)}\rangle_L - \langle S_\alpha^{(n-1)}\rangle_S = \sum_\beta \left[\frac{\partial \langle S_\alpha^{(n)}\rangle_L}{\partial K_\beta^{(0)}} - \frac{\partial \langle S_\alpha^{(n-1)}\rangle_S}{\partial K_\beta^{(0)}} \right] \delta K_\beta^{(0)} \tag{92}$$

The predicted 'distance' from the critical coupling $\delta K_\beta^{(0)}$ can be extracted by inverting equation (92) for different values of n. Thus, an initial estimate for the critical coupling is chosen, the above process is carried out, and the procedure is iterated.

The methods that have just been described can also be used to investigate multicritical behavior. This usually requires a search in a two-dimensional parameter space; moreover there are usually additional critical eigenvalue exponents due to the presence of additional scaling fields.

Investigations of critical dynamics may also be performed using RG theory and matching, time-dependent correlation functions. A sequence of states that have been blocked at difference levels is generated, and the correlation functions are 'matched' at different blocking levels at different times. The relationship between the blocking level and the time at which they match gives the dynamic exponent z:

$$C(N, m, T_2, t) = C(Nb^d, m+1, T_1, b^z t) \tag{93}$$

where the critical temperature is $T_1 = T_2 = T_c$. Two different size lattices must be used so that there are an identical number of spins in the large lattice after blocking as in the smaller lattice with one less blocking. Of course, the matching can be carried out successfully only for sufficiently large m for which the effect of irrelevant variables is small. This approach was first implemented by Tobochnik, Sarker and Cordery (1981) for simple 1- and 2-dim Ising models. Multiple lattice sizes should be used so that finite size effects can be determined, and the procedure should be repeated for different times to insure that the asymptotic, long-time behavior is being probed.

3.3 Series expansions

The method of series expansions is a well-tested approach that has found great utility in the examination of magnetic phase transitions for over half a decade. The challenges of performing calculations with the series-expansion technique can be subdivided into two types: generation of the series and analysis of the series. Each aspect has its own subtleties and difficulties.

The basic idea of series expansions is rather simple, but the practical implementation of this method demands considerable sophistication. The partition function contains all relevant information about the static properties of a magnetic system:

$$Z = \sum_i e^{-\mathcal{H}/k_B T} \tag{94}$$

where the sum is over all states of the system. At high temperatures, the exponential can be expanded in a power series in T^{-1}or in $\tanh(J/k_B T)$, and at low temperatures an expansion in $\exp\left(-\frac{J}{k_B T}\right)$is possible. The individual terms can generally be computed in terms of the permutations of bonds to form different graphs, and computer algorithms have been devised that allow the precise creation of quite long expansions for simple models. (For more details on how to develop series expansions for magnetic systems, see Domb and Green (1974).)

A series-expansion approach can also be used for critical dynamics. Using the master equation given in equation (43) we can define a time evolution operator

$$\mathcal{L} = \sum_k W_k(S_k)(1 - P_k) \tag{95}$$

where W_k is the spin-flip transition rate and P_k is the spin-flip operator. The long-time behavior is described by

$$\tau \sim \sum_{i,j} \langle s_i \mathcal{L}^{-1} s_j \rangle \tag{96}$$

and τ is estimated by expanding $\mathcal{L}^{-1}$ in a series.

Quite sophisticated methods of analysis have been derived and each approach has its own strengths and weaknesses. (For a more detailed review, see Guttmann (1989) and Adler (1995).) Ratio methods and Padé approximants have long been favorites. The radius of convergence of a series

$$F(z) = \sum_n a_i z^n \tag{97}$$

is determined by a singularity in the complex z plane (not to be confused with the dynamic critical exponent z), and

the strongest singularity on the positive real axis will be identified as the critical point. Of course, there may be other singularities in the complex z plane, so analysis of the series may be nontrivial. In the ratio method, the critical point z_c is estimated by examining ratios of successive prefactors and extrapolating to $n \to \infty$, for example, for the magnetic susceptibility

$$\frac{a_n}{a_{n-1}} = \frac{1}{z_n} = \frac{1}{z_c}\left[1 - \frac{\gamma}{n} + \cdots\right] \tag{98}$$

The ratio method works poorly however, when the coefficients in the series are irregular in sign and/or magnitude. An alternative approach that has great value is that of Padé approximants in which $F(z)$ is approximated by the ratio of two polynomials, that is, the $[L, M]$ approximant is

$$F(z) = \frac{p_0 + p_1 z + \ldots + p_L z^L}{q_0 + q_1 z + \ldots + q_M z^M} \tag{99}$$

The poles and residues of the diagonal approximants are then used to determine the critical points and exponents. If the function $F(z)$ has an algebraic branch cut at $z = z_c$, a new function $G(z)$ can be defined

$$G(z) = F(z)(z_c - z)^{\gamma} z_c^{-\gamma} \tag{100}$$

and the logarithmic derivative

$$D(z) = \frac{\mathrm{d}}{\mathrm{d}z} F(z) = \frac{-\gamma}{z - z_c} + \frac{\mathrm{d}}{\mathrm{d}z} G(z) \tag{101}$$

has a simple pole at $z = z_c$ and the approximant should converge faster for $D(z)$ than for $F(z)$.

Differential approximants have been used to analyze series in terms of singularities with nonanalytic corrections but these have not always been effective. One promising approach has been the Roskies transform in which a change of variables is performed

$$y = 1 - (1 - T/T_c)^{\theta} \tag{102}$$

so that the nonanalytic term in $(T - T_c)$ becomes analytic in $(1 - y)$. The new series only has weaker nonanalytic corrections involving a second irrelevant exponent θ_2.

As the preceding discussion shows, the extraction of critical behavior from series expansions can be subtle, and series that are too short and unreliable analyses have led to controversies in the past literature. Quite long series now exist for a few, simple magnetic models on regular lattices, and we believe that the estimates derived from these series expansions that we shall review later are reliable.

3.4 Monte Carlo simulations

A rich diversity of importance sampling Monte Carlo methods has been used to study magnetic phase transitions (Landau and Binder, 2005). In the classic Metropolis method (Metropolis *et al*., 1953), configurations are generated from a previous state using a transition probability that depends on the energy difference between the initial and final state. The sequence of states produced follow a time-ordered path, but the time in this case is really only a nondeterministic 'Monte Carlo time'. (From a theoretical perspective, the commutator of the Hamiltonian and a spin gives the time dependence of that spin. For the Ising model, this is zero and there is no deterministic behavior.) Instead, for relaxational models, such as the (stochastic) Ising model (Kawasaki, 1972), the time-dependent behavior is described by a master equation (equation (43) for the probability $P_n(t)$ that the system is in state n at time t, and $W_{n\to m}$ is the transition rate for $n \to m$. If the system is in equilibrium, $\partial P_n(t)/\partial t = 0$ and the two terms on the right-hand side of equation (43) must be equal! The resultant expression is known as 'detailed balance':

$$P_n(t) W_{n\to m} = P_m(t) W_{m\to n} \tag{103}$$

The probability of the nth state occurring in a classical system is given by

$$P_n(t) = e^{-E_n/k_B T}/Z \tag{104}$$

where Z is the partition function. This probability is usually not exactly known because of the denominator; however, by generating a Markov chain of states we can avoid the need to determine it. If we generate the nth state from the mth state, the relative probability is the ratio of the individual probabilities and the denominator in equation (104) cancels out. This means that only the difference in energy between the two states is needed, for example,

$$\Delta E = E_n - E_m \tag{105}$$

Any transition rate that satisfies detailed balance is acceptable. The choice of rate initially used in simulations of magnetic systems was the single spin-flip Metropolis form

$$W_{m\to n} = \tau_o^{-1} \exp(-\Delta E/k_B T), \quad \Delta E > 0 \tag{106a}$$

$$= \tau_o^{-1}, \quad \Delta E < 0 \tag{106b}$$

where τ_o is the time required to attempt a spin flip. (Often τ_o is set equal to unity and thus not explicitly shown in the equations.) A spin flip is accepted if a random number r, chosen *uniformly* in the interval [0,1], is less than the flipping probability. (Of course, the random number stream must have

a long period, and successive random numbers should be uncorrelated. Some simulations in the literature have suffered from poor-quality random numbers.) The 'standard' unit of Monte Carlo time is the Monte Carlo step/site (MCS/site), which corresponds to the consideration of every spin in the system once. With this algorithm, states are generated with the correct probability once the initial transients are past. Then, the desired averages $\langle A \rangle = \sum_n P_n A_n$ of a variable A become arithmetic averages over the entire sample of states. Note that if an attempted spin flip is rejected, the old state is counted again in the average.

For early times, the system relaxes towards equilibrium, but the internal energy and magnetization may have different characteristic time scales. At later times, the system is in equilibrium and the properties exhibit thermodynamic fluctuations; and at yet longer times global spin reversal might occur, that is, between states of equal energy and oppositely directed spontaneous magnetization. If sites are selected randomly in a system with N sites, one MCS/site corresponds to the consideration of N randomly chosen sites. Note that, some spins will probably be chosen more than once and some not at all during one MCS/site. The time development of the system will be similar to that for sites being visited in order, but the explicit variation and time scales will differ. Random site selection should be used if dynamic correlation functions of the corresponding stochastic model are to be measured and not just static equilibrium properties.

The Metropolis flipping probability is not a unique solution to the master equation. An alternative method, commonly referred to as 'Glauber dynamics' (Glauber, 1963) uses the single spin-flip transition rate

$$W_{n\to m} = \tau_{\mathrm{o}}^{-1}[1 + \sigma_i \tanh(E_i/k_{\mathrm{B}}T)] \qquad (107)$$

where $\sigma_i E_i$ is the energy of the ith spin in state n. Unlike the Metropolis method, the Glauber rate is antisymmetric about 0.5 for $E_i \to -E_i$. Müller-Krumbhaar and Binder (1973) showed that both Glauber and Metropolis algorithms are just special cases of a more general transition rate form. Note that at very high temperatures, the Metropolis algorithm will flip a spin on *every* attempt because the transition probability approaches 1 for $\Delta E > 0$; the system is then nonergodic and merely oscillates between the two states. With the Glauber algorithm, however, the transition probability approaches 1/2 and the process remains ergodic.

Algorithmic simplifications are possible for the Ising model and these may modify the 'time dependence'. For example, for each spin there are only a small number of different environments that are possible, for example, for a square lattice with nn interactions, there are only five different energy changes associated with a successful spin flip and each flipping probability can be computed and stored in a table. Spins are chosen randomly to be flipped and the time that elapses between flips is determined with another random number. Averages are thus over lifetimes of each state. This 'event-driven' simulation does not give the same sequence of states as the 'time-step-driven' algorithms, for example, the Metropolis method, so the 'dynamic' properties will be different.

The Ising model as originally formulated and discussed in the preceding text may be viewed as a spin-S model with $S = 1/2$, but the definition can be extended to the case of higher spin without difficulty. For example, for $S = 1$ there are three possible states, 1, 0, and -1, at each site. An nn pair can, therefore, have *three* possible states with different energies and the total space of possible lattice configurations is similarly enlarged. A spin-S Ising model can be simulated using the method just described except that the 'new' state to which a given spin attempts to flip must be chosen from among multiple choices using another random number.

Of course, other Monte Carlo algorithms have been developed to overcome the limitations of the Metropolis technique. Cluster algorithms (Swendsen and Wang, 1987; Wolff, 1989), based on the Fortuin–Kasteleyn theorem, have been developed to overcome critical slowing down near phase transitions. Such methods create clusters by randomly adding bonds to a starting site with a characteristic probability, and then entire clusters of spins are flipped. These algorithms greatly reduce the characteristic relaxation times of the sampling. Although the 'dynamic' critical behavior is thus modified, that is, the dynamic exponent z is reduced, the static properties remain unchanged.

A different approach was taken by Berg and Neuhaus (1992) who proposed a new, multicanonical method. They used a sampling probability that differed from the canonical probability in order to increase the sampling of intermediate states between configurations of high probability that were separated by a region of quite low probability. This is the situation at first-order phase transitions and leads to loss of ergodicity. More recently, Wang and Landau (2001a,b) described a quite different approach to Monte Carlo simulations that directly estimated the density of states, that is, rewriting the partition function as

$$Z = \sum_i e^{-E_i/k_{\mathrm{B}}T} \equiv \sum_E g(E) e^{-E/k_{\mathrm{B}}T} \qquad (108)$$

The technique uses a simple 'recipe' to construct $g(E)$ in an iterative fashion. A random walk is performed in energy space using a modified probability that does not depend upon temperature

$$p(E_1 \to E_2) = \min\left(\frac{g(E_1)}{g(E_2)}, 1\right) \qquad (109)$$

Once $g(E)$ has been estimated, the canonical probability, and hence all thermodynamic properties, may be determined for all temperatures, from a single simulation.

The principle of ergodicity requires that all possible configurations of the system should be reachable. Below a phase transition, multiple different-ordered states that are well separated in phase space may appear. If the phase transition from the disordered phase to the ordered phase is associated with 'symmetry breaking', the different-ordered states are related by a symmetry operation (e.g., a reversal of the sign of the order parameter for an Ising ferromagnet). Within the context of dynamical behavior of such systems, symmetry breaking usually means ergodicity breaking, that is, the system stays in one separate region in phase space. For example, in the simulation of an Ising system that may have all spins up or all spins down, we may wish to keep the system from exploring all of phase space so that only positive magnetization values are observed. For a fully ergodic simulation algorithm, both positive and negative values of magnetization will be sampled and the average will be zero.

3.5 Spin dynamics simulations

We have previously mentioned that the Monte Carlo method is fundamentally stochastic in nature, so that there is, in general, no correlation between 'Monte Carlo time' and 'real time', although the static averages are the same. An approach to the investigation of true time-dependent properties is to generate initial states, drawn from a canonical ensemble using Monte Carlo methods and to use these as starting points for the integration of the coupled equations of motion. This approach, referred to as 'spin dynamics', has been quite successful (Landau and Krech, 1999). In the general case, we have a system of N spins, which interact with the general Hamiltonian

$$\mathcal{H} = -J \sum_{\langle i,j \rangle} (S_{ix} S_{jx} + S_{iy} S_{jy} + \lambda S_{iz} S_{jz}) + D \sum_i S_{iz}^2 + H \sum_i S_{iz} \tag{110}$$

where the first sum is over all nn pairs, λ represents exchange anisotropy, D is the single ion anisotropy, and H is the external magnetic field. There are a number of real magnet systems that are well approximated by such Hamiltonians, although one or more of the parameters may vanish in particular cases. For $\lambda = 1$ and $D = 0$, the Hamiltonian describes the isotropic Heisenberg ferromagnet for $J > 0$ or for $J < 0$ the Heisenberg antiferromagnet.

For models with continuous spins, equations of motion can be derived from the quantum mechanical commutator,

$$\frac{\partial \mathbf{S}_i}{\partial t} = -\frac{i}{\hbar}[\mathbf{S}_i, \mathcal{H}] \tag{111}$$

by allowing the spin value to go to infinity and normalizing the length to unity to yield

$$\frac{\mathrm{d}\vec{S}_i}{\mathrm{d}t} = \frac{\partial \mathcal{H}}{\partial \vec{S}_i} \times \vec{S}_i = -\vec{S}_i \times \vec{H}_{\mathrm{eff}} \tag{112}$$

where $\vec{H}_{\mathrm{eff}}$ is an 'effective' interaction field. For the isotropic Heisenberg ferromagnet, $\vec{H}_{\mathrm{eff}} = -J \sum_{\mathrm{nn}} \vec{S}_j$. Through these coupled equations of motion, a spin can be described as precessing about an 'effective interaction field', which itself changes as the other spins move. The time dependence of each spin $S_i(t)$ can be determined by numerical integration of these coupled equations of motion.

The simplest approach is to simply expand about the current spin value using a small-time-step Δ as the expansion variable in a Taylor expansion. The resulting estimate depends upon how many terms are retained in the series. Typical values of Δ that deliver reliable results to a reasonable maximum integration time $t_{\max}$ are $\sim\Delta = 0.005$. A very simple improvement can be made by implementing a 'leapfrog' procedure (Gerling and Landau, 1983)

$$S_i^\alpha(t+\Delta) = S_i^\alpha(t-\Delta) + 2\Delta \dot{S}_i^\alpha(t) + \frac{2}{3!}\Delta^3 \dddot{S}_i^\alpha(t) + \cdots \tag{113}$$

The local error in this integration is $O(\Delta^5)$ and allows larger values of Δ to be used, hence extending the maximum possible integration time, $t_{\max}$. Several standard numerical methods can also be applied, for example, fourth-order predictor–corrector methods have proved quite effective for spin dynamics simulations (local truncation error of $\sim\Delta^5$). Note, however, that the conservation laws discussed below will only be observed within the accuracy set by the truncation error of the method. In practice, this limits the time-step to $\sim\Delta = 0.01/J$ in $d = 3$ (Chen and Landau, 1994) for the isotropic model ($D = 0$), where $t_{\max} \leq 200/J$.

For a typical spin dynamics study, most of the CPU time is consumed by the numerical time integration, so a large time step is most desirable. However, 'standard' methods impose a severe restriction on the size of Δ for which the conservation laws of dynamics are obeyed. Symmetries of the Hamiltonian impose additional conservation laws, so, for the isotropic Heisenberg model, the magnetization $\vec{m}$ is conserved. For an anisotropic Heisenberg model, that is, $\lambda \neq 1$ or $D \neq 0$, only the z component m_z of the magnetization

is conserved. Conservation of spin length and energy is particularly crucial, and it would therefore also be desirable to devise an algorithm that conserves these two quantities exactly. In this spirit, a new, large-time-step integration procedure, which is based on Trotter–Suzuki decompositions of exponential operators and conserves both spin length and energy *exactly* for $D = 0$, has been devised (Krech, Bunker and Landau, 1998). For high order decompositions, time steps as large as $\Delta = 0.2/J$ can be used so that $t_{\max}$ may be greatly extended to $1000/J$ or more. Variants of this method for more general models also allow the use of very large time steps but do not necessarily conserve all quantities exactly.

4 NUMERICAL RESULTS: CURRENT STATUS

4.1 Ising model

The simplest and most-studied magnetic system is surely the Ising model. This model consists of spins $\sigma_i = \pm 1$ placed at lattice sites i, and near neighbors interact. In the simplest case, the coupling is only between nearest neighbors, but the addition of nnn interactions and a magnetic field can lead to a tricritical point. Although the 1-dim model in zero field, solved in Ising's classic paper (Ising, 1925), exhibited no phase transition, Onsager's '*tour de force*' analytic solution of the 2-dim zero-field model showed that there was only a weak divergence of the specific heat with $\alpha = 0$ (a logarithmic divergence); moreover, the spontaneous magnetization goes to zero at T_c with exponent $\beta = 1/8$. These exponent values are quite different from those predicted by Landau theory and are a result of the large fluctuations that exist in two dimensions. Since not all properties of the 2-dim Ising model are known exactly, Monte Carlo simulations are nonetheless of substantial value. For example, Nicolaides and Bruce (1988) have shown that the 'fixed-point' value of the reduced fourth-order cumulant (Binder parameter) for the Ising square lattice is $U^* \sim 0.61562(90)$.

The spin configurations that are generated by Monte Carlo simulations provide substantial insight into the nature of the critical behavior. A 'snapshot' of the 2-dim Ising model at the critical temperature (Figure 8) shows quite clearly that the critical clusters that form are *not* compact but rather quite ramified. At the critical temperature, clusters of all sizes are present, but the slow 'dynamics' result from the slow changes in the largest or 'infinite' cluster.

MCRG simulations have been used to study the proximity of the nn Ising square lattice Hamiltonian to the fixed-point value. The thermal eigenvalue exponent estimates for $L \times L$ square lattices converge quickly to the asymptotic value y_T equals to 1.0 (Swendsen, 1982). As the number of iterations increases, the exponent rapidly approaches the exact value, but this is true only as long as at least one additional coupling is generated. Even for only one iteration and a single nn coupling $y_T = 0.912(2)$, and after three iterations with only two couplings $y_T = 0.998(2)$. Finite size effects also begin to appear slowly and become increasingly important as the iteration number increases. Nonetheless, the conclusion that may be drawn is that the original Hamiltonian is rather close to the fixed point.

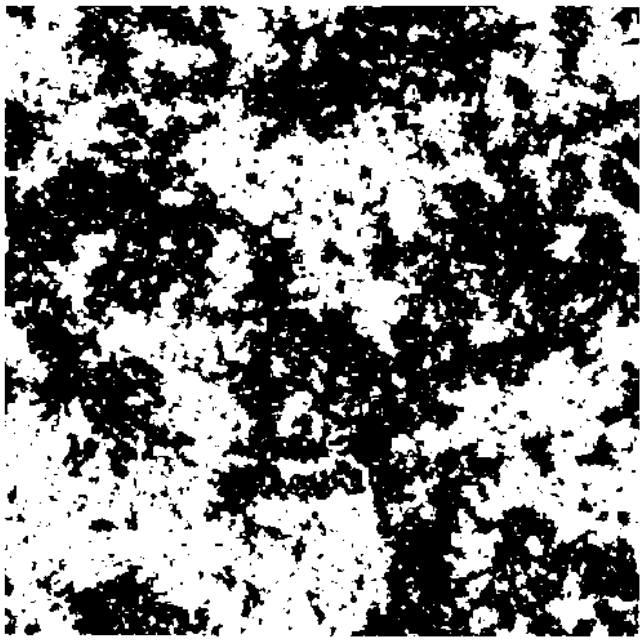

Figure 8. Snapshot generated by a Monte Carlo simulation of a 2-dim Ising model at T_c for a 256×256 lattice with periodic boundary conditions. Dark and light squares represent oppositely directed spins.

Experience with other models, and with the Ising model in higher dimension, has shown that, in general, the convergence of MCRG with iteration is not as rapid as for the 2-dim Ising model, and great care must be used to insure that a sufficient number of couplings and renormalizations have been used. This also means that the lattices must be large enough to avoid finite size effects in the renormalized systems.

Although the 2-dim Ising model has been solved analytically, the 3-dim model has defied exact solution and may not even be solvable. Extensive numerical studies of Ising models on different lattices have given a fairly detailed view of the transition. Several high-quality MCRG studies attempted to deduce the critical behavior for the simple cubic (sc) lattice. In the latest of these studies, Baillie, Gupta, Hawick and Pawley (1992) used lattices as large as 128^3 with 53 even operators and 46 odd operators. They

concluded that $K_c = 0.221652(3)$ and $\nu = 0.624(2)$. Large scale Monte Carlo simulations of the Ising sc model with results analyzed using finite size scaling have given quite precise estimates for both the critical temperature and critical exponents. Using lattices as large as $96 \times 96 \times 96$, Ferrenberg and Landau (1991) estimated $K_c = 0.2216595(26)$ and $\nu = 0.6289(2)$. A reanalysis of the data including corrections to scaling found $\nu = 0.6294(2)$, and by fixing ν, the authors found $K_c = 0.2216574(18)$. Blöte, Luijten and Heringa (1995) made very high statistics runs on many smaller systems, but used more detailed corrections to finite size scaling using correction exponents from RG theory and found $K_c = 0.2216546(10)$. The estimate for the fixed-point value of the fourth-order cumulant was $U^* \sim 0.47$, a value that is far below that of the 2-dim Ising model. Critical behavior has also been estimated from the nonequilibrium time behavior. Ito, Hukushima, Ogawa and Ozeki (2000) used substantial Monte Carlo simulations to study the nonlinear relaxation of the magnetization for large $(405 \times 405 \times 406)$ sc Ising lattices and found $K_c = 0.2216595(15)$ and $\nu = 0.635(5)$. Deng and Blöte (2003) performed extensive Monte Carlo simulations on a number of models that are believed to be in the same universality class. By requiring consistency in the estimates of universal quantities, they concluded that for the sc lattice $K_c = 0.22165455(3)$. This latter value together with the earlier MCRG result and the latest series expansion would seem to exclude the 'exact conjecture' by Rosengren (1986), that is, $\tanh K_c = (\sqrt{5} - 2)\cos(\pi/8)$ or $K_c = 0.22165863$. A good summary of results obtained from different methods for several simple Hamiltonians, including the Ising Hamiltonian, can be found in Pelissetto and Vicari (2002).

The crossover from 2-dim to 3-dim critical behavior in the Ising model was probed by Binder (1974) using Monte Carlo simulations. The observed shift in the critical temperature (due to crossover) is well described by equation (30) with $\phi = 1/\nu_3$ (Figure 9). Of course, the asymptotic behavior is not reached until the number of layers has reached a sufficiently large value. A similar situation in terms of the appropriate variables occurs for other crossover phenomena.

Surface critical behavior in 3-dim Ising models has also been studied using extensive Monte Carlo simulations. Although the qualitative picture presented by mean-field theory seems to be correct, the location of the special transition as well as all of the surface critical exponents are not quantitatively correct. Monte Carlo simulations (Landau and Binder, 1990) first suggested that $J_{sc}/J = 1.52$, but later simulations (Ruge, Dunkelmann, Wagner and Wulf, 1993) suggested that the value was slightly smaller. Instead of the mean-field value $\beta_1 = 1$ at the ordinary transition, Monte Carlo estimates were about 0.78 or 0.80. Field theoretic RG theory predictions (Diehl and Dietrich, 1981; Diehl and Shpot, 1998) were 0.816 and later 0.796. Critical exponents for the special transition have also been estimated by different numerical methods. Instead of the mean-field value $\phi = 1/2$, RG theory first predicted $\phi = 0.68$ and an improved estimate was $\phi = 0.539$. Monte Carlo simulations yielded $\phi = 0.56$, and more recent simulations found smaller values, 0.45 and 0.46 (Deng, Blöte and Nightingale, 2005).

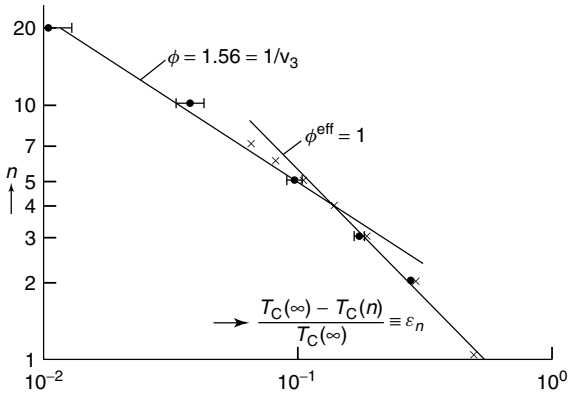

Figure 9. Shift of the critical temperature for Ising films of thickness n. Crosses (x) are series expansions results and the solid points (•) are results from Monte Carlo simulations. (Reproduced from K. Binder: 'Monte Carlo study of thin magnetic Ising films', *Thin Solid Films* **20**, 1974, pp 367–381, copyright © 1974, with permission from Elsevier.)

The determination of 'dynamic' critical exponents for Ising (model A) systems has been an arduous task. For several decades, the estimates for the dynamic exponent in 2-dim varied from study to study and showed little tendency to converge towards 'accepted' values. Finally, a careful series-expansion analysis (Dammann and Reger, 1993, 1995) for the 2-dim Ising model yielded the estimate $z = 2.183(5)$, although a reanalysis of the series by Adler (1996) gave $z = 2.165(15)$. Using extremely large lattices ($L = 496{,}640$), Stauffer (1997) examined the decay of the magnetization at T_c (see equation 50) and concluded that $z = 2.18$. Then, a high precision Monte Carlo study (Wang and Gan, 1998) yielded $z = 2.169(3)$ and a variance-reducing Monte Carlo simulation of the stochastic matrix (Nightingale and Blöte, 1998) gave $z = 2.1665(12)$. It thus appears as though the model A dynamic exponent is now well known for the 2-dim Ising model. For the 3-dim Ising model, rather good estimates were obtained from finite size scaling of the linear correlation time at T_c, $z = 2.04(3)$ (Wansleben and Landau, 1991); and from the 'statistical dependence time', $z = 2.030(4)$ (Kikuchi and Ito, 1993); and from the nonlinear relaxation Ito, Hukushima, Ogawa and Ozeki (2000) estimated $z = 2.055(10)$. Therefore, it appears as though the model A Ising dynamic exponent is smaller in 3-dim than in 2-dim but is still larger than 2.

Rather recently, very high quality series-expansion determinations of critical exponents for general spin Ising models on the sc and bcc lattices have confirmed expectations that the spin value was unimportant in the determination of the static universality class (Butera and Comi, 2002). Using high-temperature series with a large number of terms, through T^{-23} and T^{-25} (for different quantities), they found that $\gamma = 1.2371(1)$, $\nu = 0.6299(2)$, and the leading correction to scaling exponent is $\theta = 0.50$ for spin values between 1/2 and ∞.

4.2 3-dim Heisenberg model

Rather long high-temperature series expansions (Butera and Comi, 1996) have also been used to obtain rather precise values of critical exponents for both the sc and bcc lattices. Including corrections to scaling, they found $K_c = 0.69305(4)$, $\nu = 0.712(10)$, $\gamma = 1.40(1)$ for the sc lattice, and $K_c = 0.486820(4)$, $\nu = 0.714(2)$, $\gamma = 1.402(3)$ for the bcc lattice. These may be compared with results of high-resolution Monte Carlo simulations (Chen, Ferrenberg and Landau, 1993). These produced critical temperature estimates $K_c = 0.693035(37)$, $\nu = 0.7036(23)$, $\gamma = 1.3896(70)$ for the sc lattice and $K_c = 0.486798(12)$, $\nu = 0.7059(37)$, $\gamma = 1.385(10)$ for the bcc lattice. Holm and Janke (1993) obtained similar answers but with larger error bars. Another Monte Carlo study (Ballesteros, Fernandez, Martín-Mayor and Muñoz Sudupe, 1996) compared data from two different size lattices and used finite size scaling to extract the values $K_c = 0.693002(12)$, $\nu = 0.7128(14)$, $\gamma = 1.396(3)$. They also provided the estimate $U^* = 0.6217(8)$. ε-expansion RG calculations have also been performed for the 3-dim Heisenberg model. The estimate (Le Guillou and Zinn-Justin, 1980) $\nu = 0.710(7)$ has been improved by a newer study (Guida and Zinn-Justin, 1998) with smaller errors that predicts $\nu = 0.7096(8)$. Thus, although small differences between different numerical estimates remain, it must be concluded that both critical temperatures and static critical exponents are rather well known.

The 'dynamic' critical behavior of the Heisenberg model is more complex than the static behavior. For the Heisenberg ferromagnet a finite size scaling analysis of spin dynamics simulations data (Chen and Landau, 1994) yielded an estimate for the dynamic exponent $z = 2.478(27)$. This value was in excellent agreement with the dynamic scaling prediction (identical to ε-expansion RG theory) of $z = (d + 2 - \eta)/2 = 2.478(28)$. For the Heisenberg antiferromagnet there was a controversy about the shape of the dynamic structure factor. Although mode-coupling theory predicted that at T_c there would only be a spin wave peak, both inelastic neutron-scattering experiments and spin dynamics simulations found a central peak at T_c, that is, a maximum for $\omega = 0$, in addition to a spin wave peak. In addition, although for the Heisenberg antiferromagnet the theoretical prediction that $z = 1.5$ was not initially confirmed by either experiment or by spin dynamics simulation, a more detailed finite size scaling analysis (Tsai and Landau, 2003) showed that $z = 1.5$ was correct for sufficiently small values of q. If, instead, the time-dependent behavior (critical kinetics) of the Heisenberg model is studied via Monte Carlo simulations, that is, treating the Heisenberg model stochastically as in model A, the dynamic exponent is $z = 1.96(6)$ (Peczak and Landau, 1993). Thus, although there is a single set of static critical exponents for the classical Heisenberg model, there are three different 'dynamic' exponents.

4.3 2-dim *XY* model

Various forms of the 2-dim *XY* model have been extensively studied using Monte Carlo simulations. In most cases, the plane rotator (two-component spins) has been used, but different studies have yielded different, and sometimes contradictory, results. The general feature of the predictions at the transition, that is, the unbinding of vortex pairs has been confirmed by early Monte Carlo simulations (see Figure 10). The vortex-pair density goes up with increasing temperature, and at $T_{KT} \sim 0.9\, J/k_B$ the pairs begin to unbind. Although the systems used in this simulation were relatively small and the numerical values of transition temperature and critical exponents were not terribly precise, this study clearly provided insight into the underlying correctness of the Kosterlitz–Thouless picture. The subsequent estimation of the numerical values for the transition temperature and critical exponents proved quite difficult as various studies yielded different results. The difficulties were, at least in part, due to a slow approach to the asymptotic critical region and corrections to finite size scaling. The most recent and highest-resolution study (Hasenbusch, 2005) has clarified a somewhat murky situation. Hasenbusch simulated plane-rotator models on $L \times L$ square lattices at two different temperatures, $K = 1.1199$ and $K = 1.12091$, which had been estimated as being T_{KT} by two different groups. A single-cluster update algorithm was used with lattices as large as $L = 2048$ and a minimum of 2.5×10^6 MCSs were taken for each temperature and lattice size. An analysis of the second moment correlation length and the helicity modulus confirm $K_c = 1.1199$ as the transition temperature. An analysis of the magnetic susceptibility showed that for sufficiently large L it followed the form

$$\chi \propto L^{2-\eta}(\ln L + C)^{-2r} \tag{114}$$

with the theoretically predicted values of $\eta = 1/2$ and $r = -1/16$.

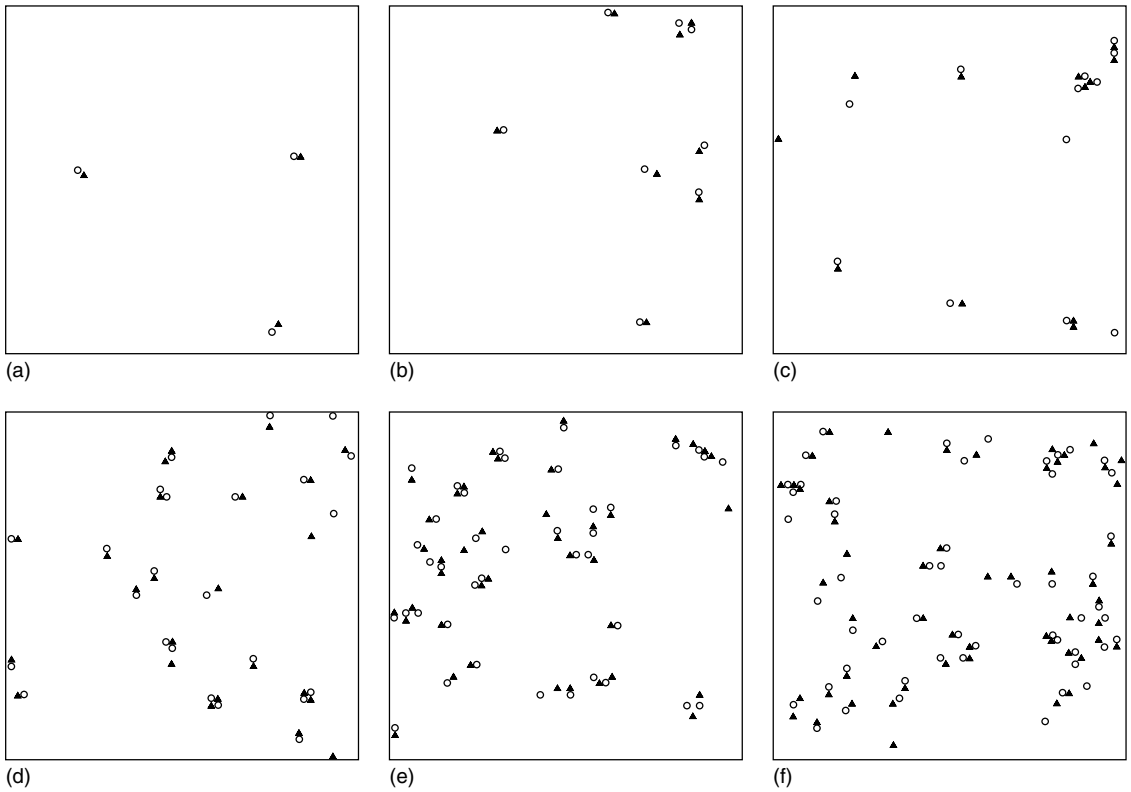

Figure 10. Vortex-pair unbinding in the 2-dim *XY* model. Open circles are vortices and triangles are antivortices: (a) $T = 0.80$; (b) $T = 0.85$; (c) $T = 0.90$; (d) $T = 0.95$; (e) $T = 1.00$; (f) $T = 1.05$, where $J/k_{\mathrm{B}} = 1$. (Reproduced from Tobochnik, J., Sarker, S. and Cordery, R. (1981), with permission from the American Physical Society. © 1981.)

4.4 Blume–Capel model: a window on tricritical behavior

The Blume–Capel model on a face centered cubic (fcc) lattice was studied by Saul, Wortis and Stauffer (1974) using both low-temperature and high-temperature series expansions. They traced out the phase diagram and found a tricritical point at $k_B T_t/J = 3.138(84)$ with a tricritical coupling ratio (see equation 13) of $D_t/J = 5.659(12)$. The tricritical exponents were consistent with the predicted mean-field (Landau) values (or equivalently the Riedel–Wegner Gaussian fixed point). Using Monte Carlo simulations, Jain and Landau (1980) found $k_B T_t/J = 3.072(24)$ with a tricritical coupling ratio of $D_t/J = 5.652(48)$. A finite size scaling analysis also yielded tricritical exponents that were consistent with Gaussian fixed-point predictions, including logarithmic corrections for the order parameter.

The examination of tricritical behavior in 2-dim was perhaps more interesting and more challenging. MCRG methods (Landau and Swendsen, 1986) were used to study the 2-dim Blume–Capel ferromagnet as well as for the 2-dim Ising antiferromagnet with nnn interactions in a magnetic field. The MCRG study showed that for quite a wide range of couplings below the predicted (mean field) critical value, there was only an ordinary tricritical point with no indication of the predicted decomposition into a critical endpoint and double critical point. The numerical estimates obtained for both the dominant and subdominant eigenvalue exponents were also unchanged with modifications in the couplings and agreed well with the predicted values for an ordinary tricritical point. Kimel, Black, Carter and Wang (1987) performed a Monte Carlo study of the antiferromagnetic Blume–Capel model in two dimensions and found similar results, that is, no decomposition of the tricritical point with tricritical exponents that agreed with values extracted for the Blume–Capel ferromagnet. Thus, fluctuations in the 2-dim model completely destroy mean-field behavior and also maintain simple tricritical behavior.

4.5 Bicritical behavior in the anisotropic Heisenberg model

Monte Carlo simulations were carried out for the anisotropic Heisenberg model in 3-dim by Landau and Binder (1978). They found a low-field Ising-like ordered, antiferromagnetic

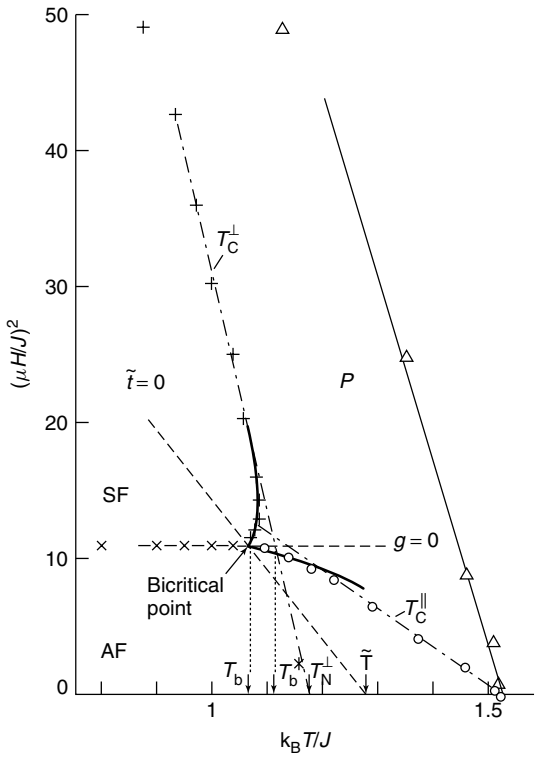

Figure 11. Phase diagram of the anisotropic Heisenberg antiferromagnet in the $H_{||} - T$ plane. The symbols are the results of Monte Carlo simulations, the mean-field lines (·····) and bicritical temperature T_b^* are shown for comparison. The heavy solid curves represent the asymptotic phase boundaries resulting from a fit to equation (38). The dashed lines are theoretical scaling axes. The triangles show the critical field data in the $H_{\perp} - T$ plane. (Reproduced from Landau, D.P. and Binder, K. (1978), with permission from the American Physical Society. © 1978.)

state and as the field was increased, the system underwent a first-order transition to a spin-flop state (Figure 11). The data showed Ising-like critical behavior of the z component of the staggered magnetization for low fields and XY-like critical behavior of the perpendicular component of the staggered magnetization at high fields. They found the predicted bicritical umbilicus and showed that the behavior of the phase boundary in the vicinity of the bicritical point could indeed be described by the predicted nonlinear scaling axes. The indention of the bicritical point was substantially greater than the mean-field prediction. The phase boundary for a perpendicular field, also shown in Figure 11, follows a simple, quadratic dependence upon the field.

4.6 Competing interactions: surprises and unanswered questions

The classical Heisenberg ferromagnet discussed in previous sections has a second-order transition with critical behavior that is now well characterized. The addition of anisotropy can make significant modifications to the phase transition. Mouritsen, Knak Jensen and Bak (1977) used Monte Carlo simulations to examine variation of the Heisenberg model in which fluctuations in the order parameter make a discontinuous transition (first order) energetically favorable. Next-nearest-neighbor couplings as well as fourth-order anisotropy were added to the Hamiltonian. As a consequence, the fourth-order invariants of the six components of the order parameter of this model are the same as for UO_2 or $NdSn_3$ and all three cases should have the same kind of phase transition. Indeed, Monte Carlo calculations by Mouritsen, Knak Jensen and Bak (1977) showed clear hysteresis in both the order parameter and the internal energy (shown in Figure 12) that was indicative of a first-order transition. In contrast, mean-field theory predicts a second-order transition.

The model just described is not the only case in which competition can lead to first-order transitions. The simple Ising model on an fcc lattice with antiferromagnetic nn coupling shows geometric frustration because it is impossible to produce a ground state in which all nn bonds are satisfied. When a magnetic field is added, the system shows 'order out of disorder' in which long-range order is observed. If the fcc lattice is subdivided into four interpenetrating sc sublattices,

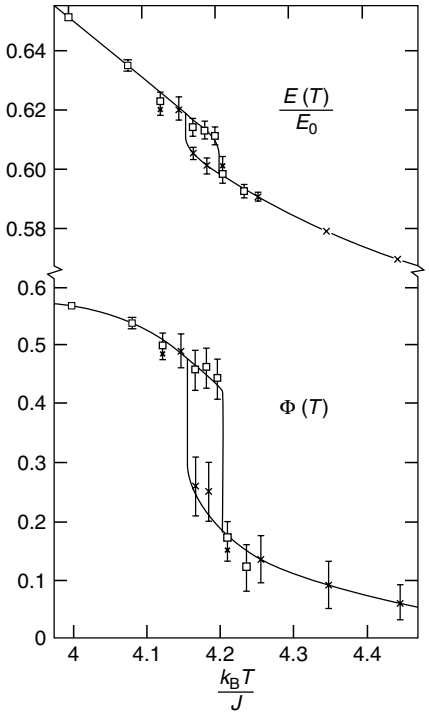

Figure 12. Temperature dependence of the order parameter and internal energy of a competing interaction Heisenberg model with fourth-order anisotropy. (Reproduced from Mouritsen, O.G., Knak Jensen, S.J., and Bak, P. (1977), with permission from the American Physical Society. © 1977.)

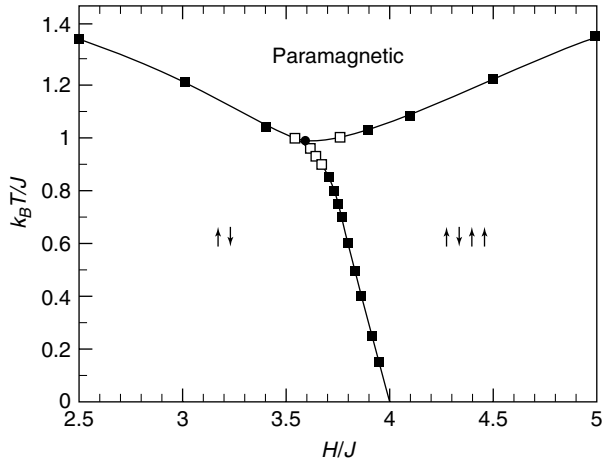

Figure 13. Phase diagram for the fcc lattice with antiferromagnetic nn interactions. The lines connecting the points are guides to the eye and indicate first-order phase boundaries. The intersection of all three boundaries (solid dot) is either a multicritical point or a triple point. (Reproduced from Kämmerer, S., Dünweg, B., K. Binder, and d'Onorio de Meo, M. (1996), with permission from the American Physical Society. © 1996.)

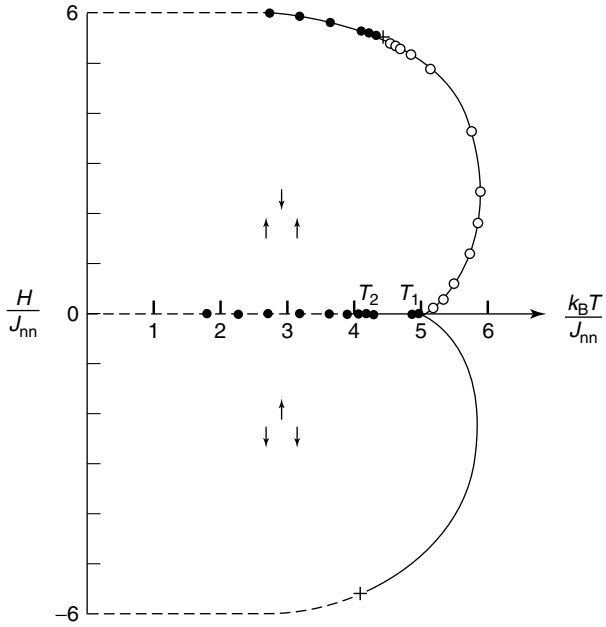

Figure 14. Phase diagram for a triangular Ising antiferromagnet with nnn interactions. The solid curves indicate second-order transitions and the dashed lines indicate first-order transitions. The region between T_1 and T_2 shows Kosterlitz–Thouless behavior. The (+) are tricritical points. (Reproduced from Landau, D.P. (1983), with permission from the American Physical Society. © 1983.)

for low fields a multiply degenerate antiferromagnet is produced in which two of the sublattices are up and two are down, and at higher fields, a ferromagnetic state appears in which three of the four sublattices are up. Although early Monte Carlo simulations were somewhat contradictory, more recent simulations have shown that all phase boundaries are then first order as shown in Figure 13. However, the 'jumps' along the first-order line tend to zero, so it is unclear if the confluence of the three first-order phase boundaries is a triple point or a multicritical point (Kämmerer, Dünweg, Binder and d'Onorio de Meo, 1996).

Another kind of unexpected, and rather complex, behavior occurs in the triangular Ising antiferromagnet with the addition of ferromagnetic nnn interactions (Landau, 1983). With only nn interactions, there is no phase transition in zero magnetic field; however, when a uniform magnetic field is added, a ferrimagnetic phase becomes stable with positive net magnetization for positive field and negative net magnetization for negative field. Each ferrimagnetic state is separated from the paramagnetic state by a three-state Potts-like line of second-order transitions, but the lines only intersect for $T = 0$. When ferromagnetic nnn interactions are included, the unusual phase diagram, depicted in Figure 14 results. At high temperature in zero magnetic field, the system is paramagnetic. Then, as the temperature is lowered to T_1, in zero magnetic field, a Kosterlitz–Thouless-like transition is encountered (even though the model is an Ising model!). At a still lower temperature, T_2, the transition becomes first order. Thus, below T_2, the field-driven transition separating the two ferrimagnetic states is discontinuous. For small magnetic fields, the transition is second order (for both positive and negative fields) and in the three-state Potts universality class, and as the field increases, a three-state Potts-like tricritical point appears on the boundaries. Thus this simple Ising model shows *no* Ising behavior.

4.7 Systems with disorder

The Ising model with site impurities has been studied by Monte Carlo simulations with contradictory results. The relevant issues are reviewed by Selke (1993). Holey and Fähnle (1990) carried out an MCRG study of the sc Ising model with nonmagnetic impurities and concluded that for 20% impurities, the critical behavior was modified with respect to the pure system. (However, for smaller impurity concentrations the asymptotic critical behavior could not be observed.) The estimate $\nu = 0.688(13)$ was only about 8% higher than the pure Ising value, but the error bars clearly excluded the pure Ising estimate. Using Monte Carlo simulations and an analysis that included corrections to scaling, Ballesteros *et al.* (1998) were able to show rather convincingly that the line of phase transitions that results when different amounts of nonmagnetic site impurities are added is controlled by a single impurity fixed point. Their exponent estimates, for example, $\nu = 0.6837(29)$ agreed

with the earlier MCRG values. An important contributory factor to the precision of their analysis was the inclusion of corrections to scaling in their extrapolation to infinite lattice size. Estimates of critical exponents for the dilute Ising model from four-loop field theoretic RG expansions had also indicated a change in exponents but the numerical values were slightly different than those obtained from the high-quality Monte Carlo simulations mentioned in the preceding text.

Matthews-Morgan, Landau and Swendsen (1984) used MCRG to study the isotropic Baxter model (Baxter, 1972) with nonmagnetic site impurities. In the pure system, the critical behavior is nonuniversal and depends upon the ratio of the four-spin and two-spin couplings. In the site dilute case, the MCRG results suggest that the critical exponents can be described by the pure Baxter fixed line for negative four-spin coupling (slightly renormalized in interaction ratio) terminating at an Ising fixed point. These results substantiate the validity of the Harris criterion within the context of a single model with wide-ranging critical exponents.

Another intriguing aspect of critical behavior in systems with 'simple' disorder (Hui and Berker, 1989) was the prediction that any amount of randomness in a system with a first-order transition should lead to a vanishing of the latent heat, that is, the transition should become first order. This was tested for the first-order transition in the eight-state, ferromagnetic Potts model where the magnitude of the ferromagnetic coupling was modified for some of the bonds. Using MCRG simulations, Chen, Ferrenberg and Landau (1992) confirmed the prediction and found exponents that were consistent with Ising values. Cardy and Jesperson (1997) later reexamined this problem for the q-state Potts model using finite size scaling and conformal invariance. They found evidence for exponents that vary with the number of states q, and a value of $\nu \approx 1$ that varies weakly with q. For spatial dimensionality greater than 2, they also predict that a tricritical point should appear.

Clearly, then the effects of disorder can be surprising and rich, and numerical techniques have only just begun to probe these phenomena.

5 SUMMARY AND PERSPECTIVE

The theory of magnetic phase transitions is now a mature endeavor. Although few models can be solved exactly, Landau theory provides some qualitative insight into phase transition behavior, and a variety of computational approaches allow the precise determination of transition temperatures and critical exponents for many models. Quite long series expansions, however, are difficult to produce for all but the simplest models, and RG theory is also difficult to apply for more complex systems. Nevertheless, both methods have led to substantial understanding of many aspects of phase transitions. Computer simulations are quite flexible and can often be applied to more complicated systems. Finite size scaling allows the extrapolation of simulational data to the thermodynamic limit, and simulations are also rapidly approaching the point at which they can predict the behavior for magnetic nanoparticles of sizes that can be studied in the laboratory. Differences remain between various numerical estimates, and it is not unusual to find that as newer studies are performed using improved methods and computers small, systematic differences are found with respect to older work. Nonetheless, the power of numerical methods is now manifest and when used in concert with analytical theory, such techniques can now provide quite precise results for comparison with experiment.

ACKNOWLEDGMENTS

The author is indebted to J. Adler, K. Binder, M. Fähnle, and S.-H. Tsai for helpful comments and suggestions.

REFERENCES

Adler, J. (1995). Modern series analysis techniques and the relation to Monte Carlo results on similar models. In *Computer Simulation Studies in Condensed Matter Physics VIII*, Landau, D.P., Mon, K.K. and Schüttler, H.-B. (Eds.), Springer: Heidelberg, pp. 5–17.

Adler, J. (1996). Series expansions vs simulations. In *Annual Reviews of Computational Physics*, Stauffer, D. (Ed.), World Scientific: Singapore, p. 241, Vol IV.

Aharony, A. (1973). Critical behavior of uniaxial ferromagnets with dipolar interactions. *Physics Letters A*, **44**, 313–314.

Baillie, C.F., Gupta, R., Hawick, K.A. and Pawley, G.S. (1992). Monte Carlo renormalization-group study of the three-dimensional Ising model. *Physical Review B*, **45**, 10438–10453.

Ballesteros, H.G., Fernandez, L.A., Martín-Mayor, V. and Muñoz Sudupe A. (1996). Finite size effects on measures of critical exponents in d = 3 O(N) models. *Physics Letters B*, **387**, 125–131.

Ballesteros, H.G., Fernandez, L.A., Martín-Mayor, V., *et al* (1998). Critical exponents of the three-dimensional diluted Ising model. *Physical Review B*, **58**, 2740–2747.

Bausch, R., Dohm, V., Janssen, H.K. and Zia, R.K.P. (1981). Critical dynamics of an interface in $1 + \varepsilon$ dimensions. *Physical Review Letters*, **47**, 1837–1840.

Baxter, R.J. (1972). Partition function of the eight-vertex lattice model. *Annals of Physics (N.Y.)*, **70**, 193–228.

Baxter, R.J. and Wu, F.Y. (1973). Exact solution of an Ising model with three-spin interactions on a triangular lattice. *Physical Review Letters*, **31**, 1294–1297.

Berg, B. and Neuhaus, T. (1992). Multicanonical ensemble: a new approach to simulate first-order phase transitions. *Physical Review Letters*, **68**, 9–12.

Binder, K. (1974). Monte Carlo study of thin magnetic Ising films. *Thin Solid Films*, **20**, 367–381.

Binder, K. (1981). Finite size scaling analysis of ising model block distribution functions. *Zeitschrift für Physik B: Condensed Matter*, **43**, 119–140.

Binder, K. (1983). Critical behavior at surfaces. In *Phase Transitions and Critical Phenomena*, Domb, C. and Lebowitz, J.L., Academic Press: London, pp. 1–144, Vol. 8.

Binder, K. (1987). Theory of first-order phase transitions. *Reports on Progress in Physics*, **50**, 783–859.

Binder, K. (1992). Finite size effects at phase transitions. In *Computational Methods in Field Theory*, Lang, C.B. and Gausterer, H. (Eds.), Springer: Berlin, pp. 59–125.

Binder, K. (2003). Classical statistical mechanics. In *Computer Simulations of Surfaces and Interfaces*, Dünweg, B., Landau, D.P. and Milchev, A.I. (Eds.), Kluwer: Dordrecht, pp. 3–35.

Binder, K. and Hohenberg, P.C. (1972). Phase transitions and static spin correlations in Ising models with free surfaces. *Physical Review B*, **6**, 3461–3487.

Binder, K. and Hohenberg, P.C. (1974). Surface effects on magnetic phase transitions. *Physical Review B*, **9**, 2194–2214.

Binder, K. and Landau, D.P. (1984). Finite size scaling at first-order phase transitions. *Physical Review B*, **30**, 1477–1485.

Blume, M. (1966). Theory of the first-order magnetic phase change in UO_2. *Physical Review*, **141**, 517–524.

Blöte, H.W.J., Luijten, E. and Heringa, J.R. (1995). Ising universality in three dimensions: a Monte Carlo study. *Journal of Physics A: Mathematical and General*, **28**, 6289–6313.

Brézin, E., Le Guillou, J.C., Zinn-Justin, J. and Nickel, B.G. (1973). Higher order contributions to critical exponents. *Physics Letters A*, **44**, 227–228.

Brézin, E. and Zinn-Justin, J. (1976). Critical behavior of uniaxial systems with strong dipolar interactions. *Physical Review B*, **13**, 251–254.

Brézin, E. and Zinn-Justin, J. (1985). Finite size effects in phase transitions. *Nuclear Physics B*, **257**, 867–893.

Brush, S.G. (1967). History of the Lenz-Ising model. *Reviews of Modern Physics*, **39**, 883–893.

Butera, P. and Comi, M. (1996). N-vector spin models on the simple-cubic and the body-centered-cubic lattices: a study of the critical behavior of the susceptibility and the correlation length by high-temperature series extended to order β^{21}. *Physical Review B*, **56**, 8212–8240.

Butera, P. and Comi, M. (2002). Critical universality and hyperscaling revisited for Ising models of general spin using extended high-temperature series. *Physical Review B*, **65**, 144431–144456.

Capel, H.W. (1966). On the possibility of first-order phase transitions in Ising systems of triplet ions with zero-field splitting. *Physica A*, **32**, 966–988.

Cardy, J. and Jesperson, J.L. (1997). Critical behavior of random-bond Potts models, *Physical Review Letters*, **79**, 4063–4066.

Challa, M.S.S., Landau, D.P. and Binder, K. (1986). Finite-size effects at temperature-driven first-order transitions. *Physical Review B*, **34**, 1841–1852.

Chen, K., Ferrenberg, A.M. and Landau, D.P. (1993). Static critical behavior of three-dimensional classical Heisenberg models: a high-resolution Monte Carlo study. *Physical Review B*, **48**, 3249–3256, and references therein.

Chen, K. and Landau, D.P. (1994). Spin-dynamics study of the dynamic critical behavior of the three-dimensional classical Heisenberg ferromagnet. *Physical Review B*, **49**, 3266–3274.

Chen, S., Ferrenberg, A.M. and Landau, D.P. (1992). Randomness-induced second-order transition in the two-dimensional eight-state Potts model: a Monte Carlo study. *Physical Review Letters*, **69**, 1213–1215.

Dammann, B. and Reger, J. (1993). Dynamical critical exponent of the two-dimensional Ising model. *Europhysics Letters*, **21**, 157–162.

Dammann, B. and Reger, J. (1995). High-temperature series expansion for the relaxation times of the two dimensional Ising model. *Zeitschrift für Physik B: Condensed Matter*, **98**, 97–110.

Deng, Y. and Blöte, H.W.J. (2003). Simultaneous analysis of several models in the three-dimensional Ising universality class. *Physical Review E*, **68**, 036125–036134.

Deng, Y., Blöte, H.W.J. and Nightingale, M.P. (2005). Surface and bulk transitions in three-dimensional O(n) models. *Physical Review E*, **72**, 016128–016139.

Diehl, H.W. and Dietrich, S. (1981). Field-theoretical approach to multicritical behavior near free surfaces. *Physical Review B*, **24**, 2878–2880.

Diehl, H.W. and Shpot, M. (1998). Massive field-theory approach to surface critical behavior in three-dimensional systems. *Nuclear Physics B*, **528**, 595–647.

Domb, C. and Green, M.S. (Eds.) (1974). *Phase Transitions and Critical Phenomena*, Academic Press: New York, London, Vol. 3.

Domb, C. and Green, M.S. (Eds.) (1976). *Phase Transitions and Critical Phenomena*, Academic Press: London, Vol. 6.

Fähnle, M., Herzer, G., Egami, T. and Kronmüller, H. (1982). On the theory of the ferromagnetic phase transition in crystalline and amorphous materials. *Journal of Applied Physics*, **53**, 2326–2328.

Ferrenberg, A.M. and Landau, D.P. (1991). Critical behavior of the three-dimensional Ising model: a high-resolution Monte Carlo study. *Physical Review B*, **44**, 5081–5091.

Fisher, M.E. (1967). The theory of equilibrium critical phenomena. *Reports on Progress in Physics*, **30**, 615–730.

Fisher, M.E. (1971). The theory of critical point singularities. In *Critical Phenomena*, Green, M.S. (Ed.), Academic Press: London, pp. 1–99.

Fisher, M.E. (1974). The renormalization group in the theory of critical behavior. *Reviews of Modern Physics*, **46**, 597–616.

Fisher, M.E. and Aharony, A. (1973). Dipolar interactions at ferromagnetic critical points. *Physical Review Letters*, **30**, 559–562.

Fisher, M.E. and Nelson, D.R. (1974). Spin flop, supersolids and bicritical and tetracritical points. *Physical Review Letters*, **32**, 1350–1353.

Fisher, M.E. and Rácz, Z. (1976). Scaling theory of nonlinear critical relaxation. *Physical Review B*, **13**, 5039–5041.

Frey, E. and Schwabl, F. (1994). Critical dynamics of magnets. *Advances in Physics*, **43**, 577–684.

Friedman, Z. and Felsteiner, J. (1977). Kadanoff block transformation by the Monte Carlo technique. *Physical Review B*, **15**, 5317–5319.

Gerling, R.W. and Landau, D.P. (1983). Static and dynamic properties of the classical *XY* chain. *Physical Review B*, **27**, 1719–1724.

Glauber, R.J. (1963). Time-dependent statistics of the Ising model. *Journal of Mathematical Physics*, **4**, 294–307.

Griffiths, R.B. (1970). Thermodynamics near the two-fluid critical mixing point in He^3-He^4. *Physical Review Letters*, **24**, 715–717.

Guida, R. and Zinn-Justin, J. (1998). Critical exponents of the *N*-vector model. *Journal of Physics A: Mathematical and General*, **31**, 8103–8121.

Guttmann, A.J. (1989). Asymptotic analysis of power-series expansions. In *Phase Transitions and Critical Phenomena*, Domb, C. and Lebowitz, J.L. (Eds.), Academic Press: New York, pp. 1–234, Vol. 13.

Harris, A.B. (1974). Effect of random defects on the critical behaviour of Ising models. *Journal of Physics C*, **7**, 1671–1692.

Hasenbusch, M. (2005). The two-dimensional *XY* model at the transition temperature: a high-precision Monte Carlo study. *Journal of Physics A: Mathematical and General*, **38**, 5869–5883.

Hohenberg, P.C. and Halperin, B.I. (1977). Theory of dynamic critical phenomena. *Reviews of Modern Physics*, **49**, 435–479.

Holey, T. and Fähnle, M. (1990). Monte Carlo renormalization-group study of the site-diluted simple-cubic Ising model. *Physical Review B*, **41**, 11709–11712.

Holm, C. and Janke, W. (1993). Critical exponents of the classical three-dimensional Heisenberg model: a single-cluster Monte Carlo study. *Physical Review B*, **48**, 936–950.

Hui, K. and Berker, A.N. (1989). Random-field mechanism in random-bond multicritical systems. *Physical Review Letters*, **62**, 2507–2510.

Ising, E. (1925). Beitrag zur theorie des ferromagnetismus. *Zeitschrift fur Physik*, **31**, 253–258.

Ito, N. (1993). Non-equilibrium relaxation and interface energy of the Ising model. *Physica A: Statistical and Theoretical Physics*, **196**, 591–614.

Ito, N., Hukushima, K., Ogawa, K. and Ozeki, Y. (2000). Nonequilibrium relaxation of fluctuations of physical quantities. *Journal of the Physical Society of Japan*, **69**, 1931–1934.

Jain, A.K. and Landau, D.P. (1980). Monte Carlo study of the fcc Blume-Capel model. *Physical Review B*, **22**, 445–452.

Janssen, H.K., Schaub, B. and Schmittmann, B. (1989). New universal short-time scaling behaviour of critical relaxation processes. *Zeitschrift fur Physik B*, **73**, 539–549.

Kadanoff, L.P., Goetze, W., Hamblen, D., *et al*. (1967). Static phenomena near critical points theory and experiment. *Reviews of Modern Physics*, **39**, 395–431.

Kadanoff, L.P. (1971). Critical behavior universality and scaling. In *Critical Phenomena*, Green, M.S. (Ed.), Academic Press: London, p. 101.

Kawasaki, K. (1972). Kinetics of ising models. In *Phase Transitions and Critical Phenomena*, Domb, C. and Green, M.S. (Eds.), Academic Press: London, pp. 441–501, Vol. 2.

Kämmerer, S., Dünweg, B., K. Binder and d'Onorio de Meo, M. (1996). Nearest-neighbor Ising antiferromagnet on the fcc lattice: evidence for multicritical behavior. *Physical Review B*, **53**, 2345–2351.

Kikuchi, M. and Ito, N. (1993). Statistical dependence time and its application to dynamical critical exponent. *Journal of the Physical Society of Japan*, **62**, 3052–3061.

Kim, J.-K. (1994). Novel application of finite-size-scaling – a numerical study of the 2-dimensional XY model. *Europhysics Letters*, **28**, 211–216.

Kim, J.-K., de Souza, J.F. and Landau, D.P. (1996). Numerical computation of finite size scaling functions: an alternative approach to finite size scaling. *Physical Review E*, **54**, 2291–2297.

Kimel, J.D., Black, S., Carter, P. and Wang, Y.-L. (1987). Monte Carlo study of the antiferromagnetic two-dimensional Blume-Capel model. *Physical Review B*, **35**, 3347–3353.

Kornblit, A. and Ahlers, G. (1973). Heat capacity of $RbMnF_3$ near the antiferromagnetic transition temperature. *Physical Review B*, **8**, 5163–5174.

Kosterlitz, J.M. and Thouless, D.J. (1973). Ordering, metastability and phase transitions in two-dimensional systems. *Journal of Physics C: Solid State Physics*, **6**, 1181–1203.

Krech, M., Bunker, A. and Landau, D.P. (1998). Fast spin dynamics algorithms for classical spin systems. *Computer Physics Communications*, **111**, 1.

Kronmüller, H. and Fähnle, M. (2003). *Micromagnetism and the Microstructure of Ferromagnetic Solids*, Cambridge University Press: Cambridge.

Landau, D.P. (1976). Finite-size behavior of the Ising square lattice. *Physical Review B*, **13**, 2997–3011.

Landau, D.P. (1983). Critical and multicritical behavior in a triangular-lattice-gas Ising model: repulsive nearest-neighbor and attractive next-nearest-neighbor coupling. *Physical Review B*, **27**, 5604–5617.

Landau, D.P. (1993). Phase transitions in the classical X-Y and some related models. *Journal of Applied Physics*, **73**, 6091–6095.

Landau, D.P. (1996). Theory of phase transitions beyond mean field theory. In *Monte Carlo and Molecular Dynamics of Condensed Matter Systems*, Binder, K. and Ciccotti, G. (Eds.), Societa Italiana di Fisica: Bologna, pp. 181–214.

Landau, D.P. and Binder, K. (1978). Phase diagrams and multicritical behavior of a three-dimensional anisotropic Heisenberg antiferromagnet. *Physical Review B*, **17**, 2328–2342.

Landau, D.P. and Binder, K. (1990). Monte Carlo study of surface phase transitions in the three-dimensional Ising model. *Physical Review B*, **41**, 4633–4645.

Landau, D.P. and Binder, K. (2005). *A Guide to Monte Carlo Simulations in Condensed Matter Physics*, *Second Edition*, Cambridge University Press: Cambridge.

Landau, D.P. and Krech, M. (1999). Spin dynamics simulations of classical ferro- and antiferromagnetic model systems: comparison with theory and experiment. *Journal of Physics: Condensed Matter*, **11**, R179–R213.

Landau, D.P. and Swendsen, R.H. (1986). Monte Carlo renormalization-group study of tricritical behavior in two dimensions. *Physical Review B*, **33**, 7700–7707.

Landau, D.P., Tang, S. and Wansleben, S. (1988). Monte Carlo studies of dynamic critical phenomena. *Journal de Physique*, **49**, C8-1525–C8-1529.

Larkin, A.I. and Khmel'nitskii, D.E. (1969). Phase transition in uniaxial ferroelectrics. *Journal of Experimental and Theoretical Physics Letters*, **29**, 1123–1128.

Lawrie, I.D. and Sarbach, S. (1984). Theory of tricritical points. In *Phase Transitions and Critical Pheomena*, Domb, C. and Lebowitz, L.J. (Eds.), Academic Press: New York, pp. 1–161, Vol. 9.

Le Guillou, J.-C. and Zinn-Justin, J. (1980). Critical exponents from field theory. *Physical Review B*, **21**, 3976–3998.

Lifshitz, I.M. and Slyozov, V.V. (1961). The kinetics of precipitation from supersaturated solid solutions. *Journal of Physics and Chemistry Solids*, **19**, 35–50.

Liu, A.J. and Fisher, M.E. (1990). On the corrections to scaling in three-dimensional Ising models. *Journal of Statistical Physics*, **58**, 431–442.

Matthews-Morgan, D., Landau, D.P. and Swendsen, R.H. (1984). New universal behavior for the impure Baxter model. *Physical Review Letters*, **53**, 679–682.

Metropolis, N., Rosenbluth, A.W., Rosenbluth, M.N., *et al*. (1953). Equation of state calculations by fast computing machines. *Journal of Chemical Physics*, **21**, 1087–1092.

Mouritsen, O.G., Knak Jensen, S.J. and Bak, P. (1977). Fluctuation-induced first-order phase transitions studied by the Monte Carlo technique. *Physical Review Letters*, **39**, 629–632.

Müller-Krumbhaar, H. and Binder, K. (1973). Dynamic properties of the Monte Carlo method in statistical mechanics. *Journal of Statistical Physics*, **8**, 1–24.

Nelson, D.R., Kosterlitz, J.M. and Fisher, M.E. (1974). Renormalization-group analysis of bicritical and tetracritical points. *Physical Review Letters*, **33**, 813–817.

Nicolaides, D. and Bruce, A.D. (1988). Universal configurational structure in two-dimensional scalar models. *Journal of Physics A: Mathematical and General*, **21**, 233–243.

Nightingale, M.P. and Blöte, H.W.J. (1998). Universal dynamics of independent critical relaxation modes. *Physical Review Letters*, **80**, 1007–1010.

Onsager, L. (1944). Crystal statistics. I. A two-dimensional model with an order-disorder transition. *Physical Review*, **65**, 117–149.

Peczak, P. and Landau, D.P. (1993). Dynamical critical behavior of the three-dimensional Heisenberg model. *Physical Review B*, **47**, 14260–14266.

Pelissetto, A. and Vicari, E. (2002). Critical phenomena and renormalization-group theory. *Physics Reports*, **368**, 549–727.

Potts, R.B. (1952). Some generalized order-disorder transformations. *Proceedings of the Cambridge Philosophical Society*, **48**, 106–109.

Privman, V. (Ed.) (1990). *Finite Size Scaling and Numerical Simulation of Statistical Systems*, World Scientific: Singapore.

Privman, V., Hohenberg, P.C. and Aharony, A. (1991). Universal critical point amplitude relations. In *Phase Transitions and Critical Phenomena*, Domb, C. and Lebowitz, J.L. (Eds.), Academic Press: London, pp. 1–134, Vol. 14.

Ried, K., Millev, Y., Fähnle, M. and Kronmüller, H. (1995). Phase transitions in ferromagnets with dipolar interactions and uniaxial anisotropy. *Physical Review B*, **51**, 15229–15249.

Riedel, E.K. and Wegner, F.J. (1972). Tricritical exponents and scaling fields. *Physical Review Letters*, **29**, 349–352.

Rosengren, A. (1986). On the combinatorial solution of the Ising model. *Journal of Physics A: Mathematical and General*, **19**, 1709–1714.

Ruge, C., Dunkelmann, A., Wagner, F. and Wulf, J. (1993). Study of the three-dimensional Ising model on film geometry with the cluster Monte Carlo method. *Journal of Statistical Physics*, **73**, 293–317.

Saul, D.M., Wortis, M. and Stauffer, D. (1974). Tricritical behavior of the Blume-Capel model. *Physical Review B*, **9**, 4964–4980.

Selke, W. (1993). Monte Carlo simulations of dilute ising models. In *Computer Simulation Studies in Condensed Matter Physics IV*, Landau, D.P., Mon, K.K. and Schüttler, H.-B. (Eds.), Springer-Verlag: Heidelberg, pp. 18–27.

Srinath, S. and Kaul, S.N. (1999). Static universality class for gadolinium. *Physical Review B*, **60**, 12166–12176.

Stanley, H.E. (1971). *An Introduction to Phase Transitions and Critical Phenomena*, Oxford University Press: Oxford.

Stauffer, D. (1997). Relaxation of Ising models near and away from criticality. *Physica A*, **244**, 344–357.

Stryjewski, E. and Giordano, N. (1977). Metamagnetism. *Advances in Physics*, **26**, 487–650.

Swendsen, R.H. (1982). Monte Carlo renormalization. In *Real Space Renormalization*, Burkhardt, T.W. and van Leeuwen, J.M.J. (Eds.), Springer-Verlag, Heidelberg, pp. 57–86.

Swendsen, R.H. and Wang, J.-S. (1987). Nonuniversal critical dynamics in Monte Carlo simulations. *Physical Review Letters*, **58**, 86–88.

Tobochnik, J. and Chester, G.V. (1979). Monte Carlo study of the planar spin model. *Physical Review B*, **20**, 3761–3769.

Tobochnik, J., Sarker, S. and Cordery, R. (1981). Dynamic Monte Carlo renormalization group. *Physical Review Letters*, **46**, 1417–1420.

Tsai, S.-H. and Landau, D.P. (2003). Critical dynamics of the simple-cubic Heisenberg antiferromagnet $RbMnF_3$: extrapolation to $q = 0$. *Physical Review B*, **67**, 104411–104417.

Van Hove, L. (1954). Time-dependent correlations between spins and neutron scattering in ferromagnetic crystals. *Physical Review*, **95**, 1374–1384.

Wang, F. and Landau, D.P. (2001a). Efficient, multiple-range random walk algorithm to calculate the density of states. *Physical Review Letters*, **86**, 2050–2053.

Wang, F. and Landau, D.P. (2001b). Determining the density of states for classical statistical models: a random walk algorithm to produce a flat histogram. *Physical Review E*, **64**, 056101–056117.

Wang, J.-S. and Gan, C.K. (1998). Nonequilibrium relaxation of the two-dimensional Ising model: series-expansion and Monte Carlo studies. *Physical Review E*, **57**, 6548–6554.

Wansleben, S. and Landau, D.P. (1991). Monte Carlo investigation of critical dynamics in the three-dimensional Ising model. *Physical Review B*, **43**, 6006–6014.

Wegner, F.J. and Riedel, E.K. (1973). Logarithmic corrections to the molecular-field behavior of critical and tricritical systems. *Physical Review B*, **7**, 248–256.

Wilding, N.B. (1995). Applications of finite-size-scaling techniques. In *Computer Simulation Studies in Condensed Matter Physics VIII*, Landau, D.P., Mon, K.K. and Schüttler, H.-B. (Eds.), Springer, Heidelberg, pp. 18–30.

Wilding, N.B. and Bruce, A.D. (1992). Density fluctuations and field mixing in the critical fluid. *Journal of Physics: Condensed Matter*, **4**, 3087–3108.

Wilson, K.G. (1971a). Renormalization group and critical phenomena I. Renormalization group and the Kadanoff scaling picture. *Physical Review B*, **4**, 3174–3183.

Wilson, K.G. (1971b). Renormalization group and critical phenomena. II. Phase-space cell analysis of critical behavior. *Physical Review B*, **4**, 3184–3205.

Wilson, K.G. and Fisher, M.E. (1972). Critical exponents in 3.99 dimensions. *Physical Review Letters*, **28**, 240–243.

Wolff, U. (1989). Collective Monte Carlo updating for spin systems. *Physical Review Letters*, **62**, 361–364.

Wu, F.Y. (1982). The Potts model. *Reviews of Modern Physics*, **54**, 235–268.

Yeomans, J. (1992). *Statistical Mechanics of Phase Transitions*, Oxford University Press: Oxford.

Zheng, B. (2006). Numerical simulations of critical dynamics far from equilibrium. In *Computer Simulation Studies in Condensed Matter Physics XVII*, Landau, D.P., Lewis, S.P. and Schüttler, H.-B. (Eds.), Springer-Verlag: Heidelberg, pp. 25–40.

FURTHER READING

Aharony, A. (1997). Critical behavior of magnets with dipolar interactions V. Uniaxial magnets in d dimensions. *Physical Review B*, **8**, 3363–3370.

Disordered and Frustrated Spin Systems

Kurt Binder[1] and A. Peter Young[2]

[1] *Johannes Gutenberg Universität, Mainz, Germany*
[2] *University of California, Santa Cruz, CA, USA*

1 INTRODUCTION

Why should we study magnetic systems with disorder? Since perfect crystals are rare in nature we clearly need to understand how disorder changes the behavior of crystals in order to explain experiments on real materials. More importantly, we now realize that disordered systems exhibit *new phenomena* which are not present in perfect crystals, and so are *of interest in their own right*.

The simplest case of disorder is substitutional disorder, in which a ferromagnetic crystal for example, is randomly diluted with nonmagnetic atoms, (see Figure 1 and Stinchcombe, 1973). If the concentration of nonmagnetic atoms is small enough, a percolating 'network' of spins connected by (e.g., nearest neighbor) exchange interactions is still present in the crystal, and so long-range magnetic order is maintained at low enough temperatures. This is the case assumed in Figure 1 since there is a 'cluster' of spins spanning the lattice from the bottom to the top. Figure 1 shows of a simple Ising model, described by the Hamiltonian (Stanley, 1971)

$$\mathcal{H}_{\text{Ising}} = -\sum_{\langle i,j\rangle} J_{ij} S_i S_j - \sum_i H_i S_i, \quad (S_i = \pm 1) \tag{1}$$

where H_i is a magnetic field acting on site i ($H_i = H$ for a uniform field) and J_{ij} are the exchange constants (which depend only on the relative distance between lattice sites i and j in an ideal crystal). Assuming that $J_{ij} = J$ is nonzero only if i, j are nearest neighbors and that the concentration variable x_i is equal to 1 if site i is occupied by a magnetic atom and zero otherwise, we have

$$J_{ij} = \begin{cases} x_i x_j J, & \text{if } i, j \text{are nearest neighbors} \\ 0, & \text{otherwise} \end{cases}$$
$$H_i = x_i H \tag{2}$$

in the case of Figure 1. An alternative to this 'site disorder' is the case of (nearest-neighbor) 'bond disorder' in which exchange constants take values J_1 with probability p and J_2 with probability $1 - p$. In other words, the probability distribution $P(J_{ij})$ has the form

$$P(J_{ij}) = p\delta(J_{ij} - J_1) + (1 - p)\delta(J_{ij} - J_2) \tag{3}$$

Bond dilution (for which $J_1 = J$, $J_2 = 0$) and the $\pm J$ Ising spin glass model (Binder and Young, 1986) (for which $J_1 = J, J_2 = -J$) are special cases of such disorder (which can only be physically realized in the case of indirect exchange between magnetic ions).

Handbook of Magnetism and Advanced Magnetic Materials. Edited by Helmut Kronmüller and Stuart Parkin. Volume 1: *Fundamentals and Theory*. ISBN: 978-0-470-02217-7.

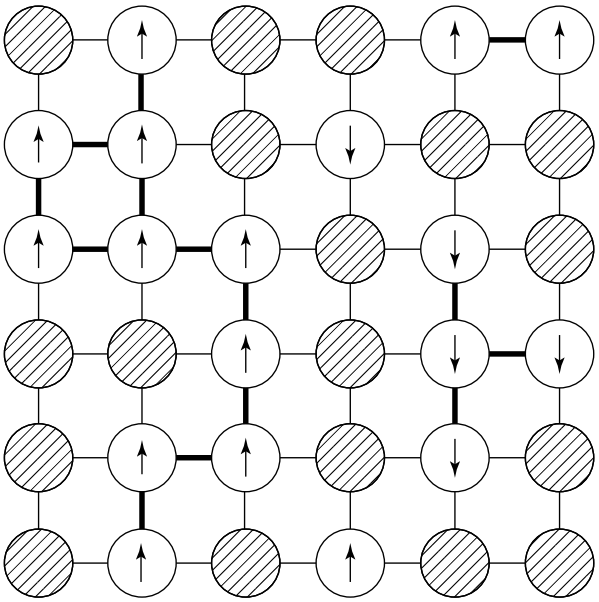

Figure 1. Diluted ferromagnetic Ising model on the square lattice. In the Ising model, spins can point only up or down, as indicated by arrows. Nonmagnetic atoms are shaded. Nearest-neighbor exchange interactions are indicated by thick lines.

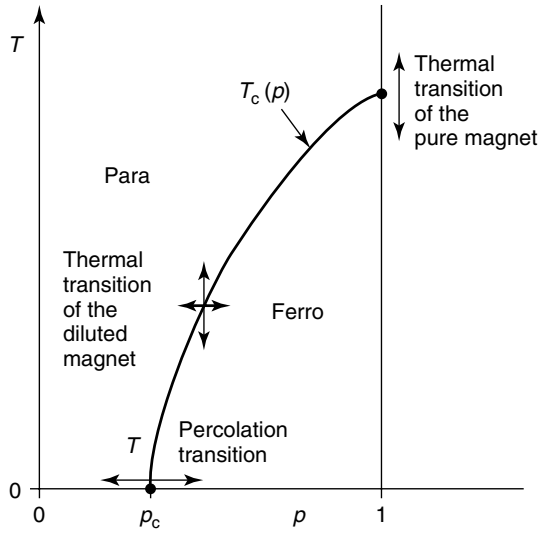

Figure 2. Schematic phase diagram of a bond-diluted nearest-neighbor ferromagnet, using temperature T and the concentration of ferromagnetic bonds as variables. A line of critical points $T_c(p)$ separates the disordered paramagnetic phase (para) from the phase with ferromagnetic long-range order (ferro). This line begins at the critical point of the pure system $\{T_c(p = 1)\}$ and ends at the percolation threshold $\{T_c(p = p_c) = 0\}$. Crossing the line $T_c(p)$ at $T > 0$ one observes a thermal transition, with critical exponents that are believed to be universal along the whole line $T_c(p)$ as long as $p_c < p < 1$ (i.e., excluding the endpoints of this critical line), for three-dimensional Ising systems. With respect to its critical exponents the diluted Ising ferromagnet belongs to a different 'universality class' than the pure model. Still different exponents apply for the percolation transition, which is observed by varying p at $T = 0$. The various phase transitions are indicated by double arrows.

Note that in this article we choose units such that the magnetic moment per spin is incorporated in the magnetic field in equations (1) and (2), so both exchange constants J_{ij} and fields H_i have a dimension of energy. In the limit of a noninteracting Ising paramagnet, the zero-field susceptibility per spin takes the simple form $\chi_0 = (k_B T)^{-1}$, that is, it has the dimension of inverse energy, while the magnetization per spin (M) is dimensionless.

We shall return to the case of spin glasses below; here we focus on the simplest case: the phase diagram of the bond-diluted nearest-neighbor Ising ferromagnet (Figure 2). Disorder has only two effects: (i) a depression of the critical temperature $T_c(p)$ for $p_c < p < 1$ relative to its pure value $T_c(1)$ and (ii) a change of the critical behavior (in the case of Ising ferromagnets in three dimensions). More details on the behavior of diluted ferromagnets will be given in the next section. Particularly interesting is the case $p = p_c$ where $T_c(p) = 0$. This is the concentration below which there is no longer a 'spanning infinite cluster' of spins connected by nearest-neighbor bonds extending throughout the system. At p_c, this infinite cluster (Stauffer and Aharony, 1992) is a 'fractal' (see Section 3 and Meakin, 1998). For $p < p_c$, only finite clusters of spins connected by nearest-neighbor bonds exist, and consequently at low temperature the system behaves as a 'superparamagnet'.

Of course, the assumption that the magnetic interactions extend only to nearest neighbors is inappropriate for many magnetic materials, and the effect of the longer range of the exchange needs to be considered. If the sign of the exchange $J(r)$ is uniformly positive, then, irrespective of the distance r between magnetic atoms, all that happens is that the percolation threshold is shifted to a smaller concentration. However, if ferromagnetic and antiferromagnetic exchange constants (bonds) compete, the magnetic ordering does not energetically satisfy all the bonds. This 'frustration' of some of the bonds combined with the disorder leads to very interesting effects, such as the occurrence of a 'spin glass' phase (Section 4).

Figure 3 qualitatively illustrates the behavior in the case of nearest-neighbor ferromagnetic ($J_{nn} > 0$), and next-nearest-neighbor antiferromagnetic ($J_{nnn} < 0$) exchange interactions in one lattice plane of a simple cubic lattice. In the absence of disorder, if $R \equiv J_{nnn}/J_{nn}$ is greater than some critical value R_m the ground state is still ferromagnetic, while for $R < R_m$ an antiferromagnetic type of order takes over. However, in the case of quenched disorder, there are statistical fluctuations in the concentration of ferromagnetic bonds and as a result, for sufficiently strong dilution and low enough temperature,

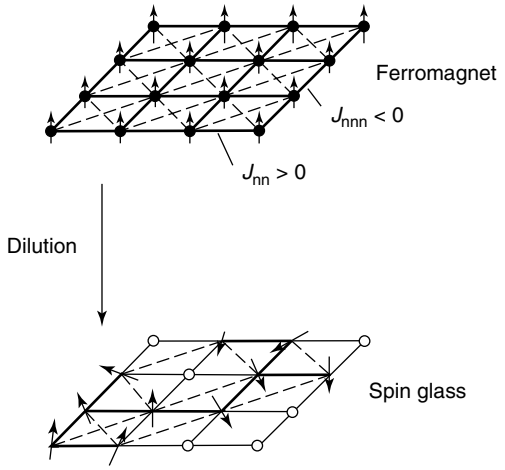

Figure 3. Schematic picture of the spin ordering in one lattice plane of a ferromagnet with nearest-neighbor ferromagnetic exchange J_{nn} (full bonds) and next-nearest-neighbor antiferromagnetic exchange J_{nnn} (broken bonds), upper part. Sufficiently strong dilution (lower part) destroys the conventional magnetic long range of the spins and may lead to a spin glass phase. Nonmagnetic atoms are shown as open circles.

long-range order of either ferromagnetic or antiferromagnetic type is not the equilibrium magnetic structure, but rather the spins 'freeze' into a random-looking state called a *spin glass*. In Figure 3, we have assumed site disorder, since a similar model applies to the face-centered cubic Heisenberg ferromagnet EuS diluted with nonmagnetic Sr (Maletta and Zinn, 1989).

Figure 4 illustrates in a rather speculative way how the phase diagram for a diluted Ising ferromagnet on the simple cubic lattice might look. In particular, there is a 'multicritical point' at $x = x_m$ where paramagnetic, ferromagnetic, and spin glass phases meet. Note that this phase diagram contains several unproven assumptions. Firstly, it is assumed that, for $R_m < R < 0$, the phase boundary of the ferromagnetic phase in the $(T, 1 - x)$ plane is 'reentrant', that is, for $x_c'' < x < x_m$ one observes a transition from paramagnet to ferromagnet *and then to a spin glass*, when the temperature is lowered. This assumption is motivated by experimental observations for some real spin glass systems but has been difficult to reproduce theoretically. Secondly, it is assumed that the zero temperature phase boundary between the spin glass state and the (super)paramagnet does not simply coincide with the next-nearest-neighbor percolation threshold (shown as a broken straight line in Figure 4). This assumption is motivated by some numerical evidence for bond-diluted spin glasses (Aharony and Binder, 1980). The resulting phase at $T = 0$ for $x_p^{nnn} < x < x_c'$ is thought to not exhibit long-range spin correlations of any kind, and this is termed a *cooperative paramagnet* (Binder, Kinzel and Stauffer, 1979) in Figure 4.

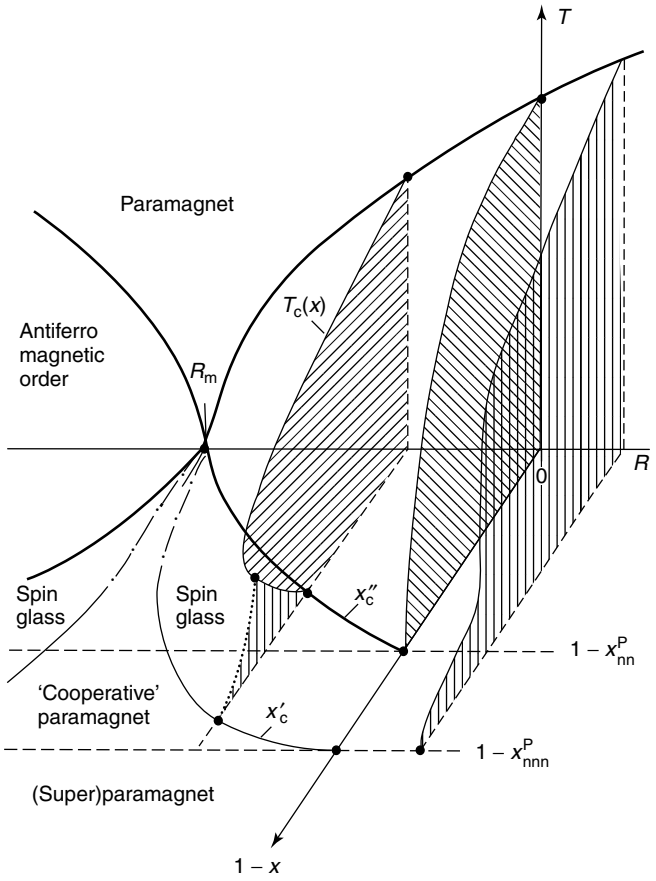

Figure 4. Schematic phase diagram of an Ising model with nearest (J_{nn}) and next-nearest (J_{nnn}) exchange as a function of temperature T, concentration of nonmagnetic ions $1 - x$, and the ratio $R = J_{nnn}/J_{nn}$. Thick curves highlight phase boundaries in the planes $x = 0$ and $T = 0$, respectively. Three phase diagrams are shown (shaded) – for fixed R (for $R_m < R < 0$ a spin glass phase occurs, for $R = 0$ one has the same type of phase diagram as in the case of bond disorder (Figure 2), and for $0 < R - 1 \ll 1$ at low T the stability of the ferromagnetic order extends up to the next-nearest-neighbor site percolation threshold x_{nnn}^p.) For further explanations see text.

Actually, the most commonly studied spin glasses are not diluted magnetic insulators with short-range exchange, modeled as in Figure 3, but rather nonmagnetic noble metals, such as Au, Ag, Cu, or Pt, with a small concentration, of the order of a few percent, of transition-metal magnetic impurities such as Fe or Mn. These magnetic atoms then interact with the indirect exchange mediated by the scattering of conduction ions, the so-called RKKY interaction, $J_{ij}(R) \propto \cos(2k_F R + \varphi_0)/R^3$, in which k_F is the Fermi wave number and φ_0 is a constant. In a dilute system (Figure 5), the distances R between the spins at lattice sites i, j are random, and so some pairs of spins will experience a ferromagnetic and others an antiferromagnetic exchange in a random way. Owing to the long range of this RKKY interaction we expect

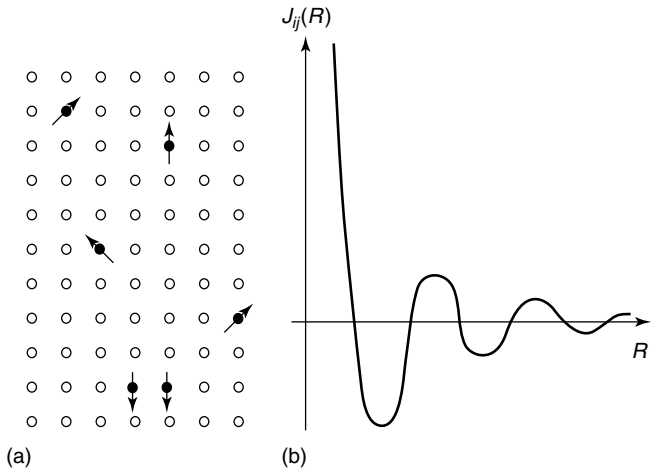

Figure 5. Schematic sketch of magnetic moments (dots with arrows) in a nonmagnetic metallic matrix (open circles, a) and the resulting RKKY exchange plotted as a function of distance R (b).

a random distribution of exchange constants $P(J_{ij})$ strongly peaked at $J_{ij} = 0$.

Disregarding this detailed atomistic structure underlying the problem, Edwards and Anderson (1975) suggested a coarse-grained model, now termed the *Edwards–Anderson model* or *EA model*, which contains what are generally believed to be the two essential ingredients of a spin glass: *disorder* and *frustration*. The Hamiltonian of the EA model is still given by equation (1) but the interactions J_{ij} are chosen to be independent random variables with mean $\overline{J}$ and standard deviation J. Two common choices are the '$\pm J$' model for which

$$P(J_{ij}) = \frac{1}{2}\left[\delta(J_{ij} - J) + \delta(J_{ij} + J)\right] \tag{4}$$

and the Gaussian distribution where

$$P(J_{ij}) = (\sqrt{2\pi}\,J)^{-1} \exp\left[-(J_{ij} - \overline{J})^2/(2J^2)\right] \tag{5}$$

Use of the EA model replaces the original site-disorder problem of Figure 5 by a bond-disorder problem, since the latter is easier to treat by theoretical methods. Many chemically different spin glass systems show qualitatively similar properties, and this supports the view that microscopic details are unimportant and a simple model, such as the EA model, that has disorder and frustration should capture the basic physics of spin glasses. The simplest case, and the one usually taken, is zero mean, $\overline{J} = 0$, since this has no bias toward ferromagnetism or antiferromagnetism.

The EA model, which is described by equation (1) plus the specification of the bond distribution, is generally considered in one of two versions: the short range version where $J_{ij} \neq 0$ only if i, j are nearest-neighbor sites of the lattice, and the long-range version where every spin i in the system interacts with every other spin j with the same (Gaussian) distribution equation (5). However, in the latter case, to ensure a sensible thermodynamic behavior when the number of spins $N \to \infty$, one assumes a scaling $\overline{J} \equiv J_0/N$, $J \equiv \tilde{J}/\sqrt{N}$ with J_0 and $\tilde{J}$ being finite. This Sherrington–Kirkpatrick (SK) model (Sherrington and Kirkpatrick, 1975) has been considered extensively with the motivation that mean-field theory should become exact for infinite-range interactions. However, as briefly discussed further in Section 4, developing a mean-field theory of spin glasses has been a major *tour de force*.

Disorder as shown in Figures 3 and 5 not only prevents the occurrence of conventional magnetic long-range order but it is also rather plausible that the spin arrangement that minimizes the (free) energy of the system is not unique. Consequently, the 'energy landscape' (i.e., the energy of the system as a function of 'phase space coordinates', see Figure 6) contains many (more or less equivalent) 'valleys', separated by large (free) energy barriers. This picture provides a qualitative interpretation of why a very slow relaxation is observed in spin glass systems when one approaches the transition to the spin glass phase from the paramagnetic side. In fact, in the spin glass phase below the transition, the spectrum of relaxation times extends from microscopic times (10^{-12} s or so) up to times considerably longer than that of the experiment. Hence a spin glass at low temperatures is not in equilibrium. Nonequilibrium effects have been conveniently characterized in 'aging' experiments (Nordblad and Svedlindh, 1998), and give rise to surprising and rather poorly understood phenomena such as 'memory' and 'rejuvenation' (Jonason *et al.*, 1998; Bert *et al.*, 2004; Picco, Ricci-Tersenghi and Ritort, 2001).

These slow dynamical aspects of spin glass behavior are qualitatively reminiscent of the behavior of structural glasses,

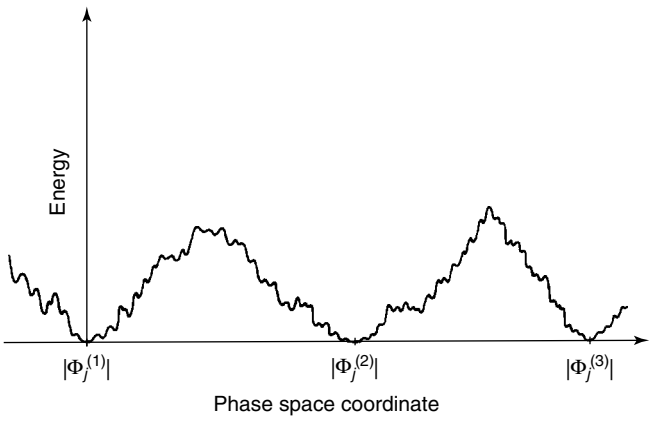

Figure 6. Schematic plot of the coarse-grained free energy of a spin glass plotted versus a phase space coordinate which measures the projection of the considered state to a particular ordered state.

and this is the reason why this kind of disordered magnetic system is called a *spin glass*. However, in the opinion of the authors, there is a significant difference between structural glasses and spin glasses. As we shall see, spin glasses in zero field have an equilibrium transition at finite temperature where there is a divergent correlation length. To our knowledge, no divergent *equilibrium* length scale has been seen in structural glasses.

It should be noted that a complicated energy landscape with many degenerated ground states can be obtained as a result of only frustration without any disorder. The classic example is the nearest-neighbor Ising antiferromagnet on the triangular lattice, which stays disordered at all nonzero temperatures (while on the square lattice the Ising antiferromagnet orders at the same temperature as the Ising ferromagnet). Figure 7 illustrates this concept of frustration for an isolated triangle of spins connected by antiferromagnetic bonds of the same strength, showing that it is not possible to find a spin configuration that is energetically optimal for all three bonds. In the ground state there is always one bond which is 'dissatisfied', that is, 'frustrated'. However, this can be any of the three bonds, and hence there is an enhanced ground-state degeneracy: while a ferromagnetic triangle has a twofold degenerate ground state (all spins up or all spins down) the ground state of the corresponding antiferromagnet is sixfold degenerate, see Figure 7. An infinite triangular lattice with antiferromagnetic bonds between the Ising spins has a nonzero entropy per spin.

Similar frustration effects are also possible on other lattices, for example, the square lattice, when we have both ferro–and antiferromagnetic bonds. Consider, for example, an elementary square with three ferromagnetic and one antiferromagnetic bonds. One finds that this 'plaquette' is frustrated because again no spin configuration can be found that is favorable for all the bonds, and the ground state is now eightfold degenerate. Obviously, any closed loop of bonds on

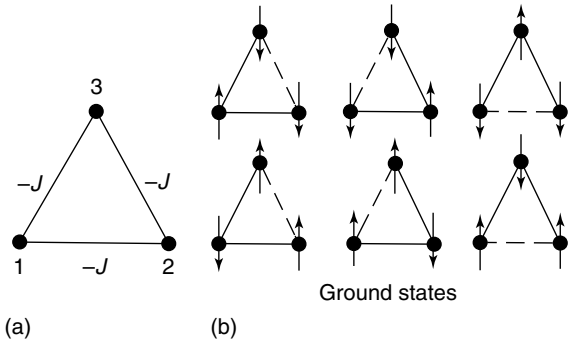

Figure 7. Frustrated triangle of Ising spins (a) and its six ground states (b) where the 'dissatisfied' bonds are shown as broken straight lines.

the lattice is frustrated if the variable $\phi_{\mathrm{p}} \equiv \mathrm{sign}(\prod_{\mathrm{bonds}} J_{ij})$ is equal to -1. One can therefore construct square and simple cubic lattices with a periodic arrangement of frustrated plaquettes, which have very interesting magnetic properties. In particular, for XY spins, that is, a model where magnetic anisotropy constrains the spins to orient isotropically in a particular plane (Stanley, 1971), or for Heisenberg spins (a fully isotropic magnet), noncollinear spin alignments occur. We shall briefly return to such frustrated spin systems without disorder in Section 5.

A still different type of disorder can be obtained when the field H_i in equation (1) is a random variable such that it is zero on average. Again, two common choices are the Gaussian distribution

$$P(H_i) = (2\pi h^2)^{-1/2} \exp\left[-H_i^2/(2h^2)\right] \tag{6}$$

and a two δ function distribution,

$$P(H_i) = \frac{1}{2}\left[\delta(H_i - h) + \delta(H_i + h)\right] \tag{7}$$

In both cases averages over the quenched disorder, indicated by $[\cdots]_{\mathrm{av}}$, have the property

$$[H_i]_{\mathrm{av}} = 0, \quad [H_i^2]_{\mathrm{av}} = h^2 \tag{8}$$

Since such a random field couples linearly to the (local) order parameter (the magnetization of the ferromagnet), even very weak random fields can have drastic effects (Imry and Ma, 1975; Nattermann, 1998). While physical realizations of random fields in ferromagnets are not known, this type of disorder is found in diluted antiferromagnets exposed to a uniform magnetic field (Fishman and Aharony, 1979), since in this way one indirectly creates a random 'staggered field', which couples linearly to the 'staggered magnetization', which is the order parameter of an antiferromagnet. Consequently it has been possible to perform beautiful experiments (Belanger, 1998) testing the theoretical concepts on random fields. We shall briefly return to this problem in Section 6.

2 WEAKLY DILUTED FERRO- AND ANTIFERROMAGNETS

In this section, we discuss the phase transition of ferromagnets (or antiferromagnets in zero magnetic field) which contain quenched disorder due to random dilution with nonmagnetic species (see Figure 2). We restrict attention to short-range exchange forces, disregard long-range correlations in the positions of the impurities, and assume that the

phase transition of the 'pure' system (i.e., an ideal crystal with no impurities) is a second-order transition (Stanley, 1971). In other words, the order parameter ψ, associated susceptibility χ, specific heat C, and correlation length ξ have critical behavior characterized by the following power laws when the temperature is close to the critical temperature $T_c = T_c(p = 1)$:

$$\psi \sim (1 - T/T_c)^{\beta}, \quad \chi \sim |1 - T/T_c|^{-\gamma}$$
$$C \sim |1 - T/T_c\,|^{-\alpha}, \quad \xi \sim |1 - T/T_c|^{-\nu} \tag{9}$$

The many critical exponents $\alpha, \beta, \gamma, \nu$, and so on, are not independent but are related via scaling laws (Stanley, 1971; Fisher, 1974) (see also **Theory of Magnetic Phase Transitions, Volume 1**) such as

$$2\beta + \gamma = 2 - \alpha = d\nu \tag{10}$$

The last of these relations, involving the dimensionality d of the system, is an example of a 'hyperscaling relation'. Critical exponents are 'universal', that is, they do not depend on irrelevant details (such as ratios of exchange constants between nearest and more distant neighbors, lattice symmetry, etc.), but only on the space dimensionality d and the 'spin dimensionality' n, where $n = 1$ is the Ising model, $n = 2$ is the XY model, and $n = 3$ is the Heisenberg model. Thus, critical exponents are the same for all materials in a given 'universality class', and a question of primary interest is how they are affected when quenched disorder occurs.

A rather strong statement on this problem is the 'Harris criterion' (Harris, 1974), which suggests that for $p_c < p < 1$ the critical exponents remain unchanged, that is, they are the same as that of the pure system if the specific-heat exponent of the pure system, α, is negative. This is the case for XY and Heisenberg magnets in $d = 3$, and hence for these systems quenched disorder should be irrelevant. This means that sufficiently close to $T_c(p)$ one should observe the critical exponents of the pure system. Conversely, if $\alpha > 0$, the random system will have new critical exponents $\alpha_r, \beta_r, \gamma_r, \nu_r$. Renormalization group arguments (Stinchcombe, 1973) imply that these new exponents are again universal, and, in particular, should not depend on p (though the temperature range $|T - T_c(p)|$ where they can be observed depends on p and is often very small). Much effort, both experimentally and theoretically, with numerical methods (Monte Carlo simulations, extrapolation of systematic series expansions; see Stinchcombe, 1973) has been devoted to this problem. The asymptotic critical region is so narrow that it is practically inaccessible, and hence in practice one observes 'effective' critical exponents that depend on p. However the data is consistent with the asymptotic behavior being independent of p.

The Harris criterion is inconclusive for the special case $\alpha = 0$, which occurs, for example, for the $d = 2$ Ising model where the specific heat of the pure system has a logarithmic singularity, $C \sim \ln|1 - T/T_c(p)|$. By various theoretical methods, evidence has been accumulated (Selke, 1991) that in this case the critical behavior is altered into an even more subtle logarithmic form, $C \sim \ln|\ln|1 - T/T_c(p)||$.

Finally, we mention that in the diluted system some (exponentially weak) singularities already set in at $T_c(p = 1)$, the critical temperature of the pure system. These 'Griffiths singularities' (Griffiths, 1969) come from statistical fluctuations in the occupancy of the sites in a randomly diluted system. There is always a nonzero probability to find an arbitrarily large region with no dilution sites (though this probability decreases exponentially with the volume of such a region), and these regions already order at T_c. While the effect of these anomalies occurring for $T_c(p) < T < T_c(p = 1)$ on *static* properties is hardly noticeable, they have a bigger effect on *dynamics*, causing a slow stretched exponential relaxation which is not expected in the pure case. Related 'Griffiths–McCoy' singularities have more pronounced effects in quantum spin glasses (Bhatt, 1998), see Section 4.

3 PERCOLATION

Here we continue the discussion of the phase diagram in Figure 2, but now consider the concentration, p_c, where the critical temperature vanishes, $T_c(p = p_c) = 0$. This endpoint of the line $T_c(p)$ is a special multicritical point since a different type of critical behavior is observed when p is varied at $T = 0$ than when the critical line is crossed at finite T. For simplicity we restrict our attention to nearest-neighbor ferromagnetic exchange.

For $p < p_c$, all spins are in finite clusters, where a cluster is defined by the criterion that each spin of the cluster must have at least one bond to another spin in the same cluster. As an example, the 6×6 lattice of Figure 1 contains clusters with $s = 2, 4$, and 10 spins. On a lattice with N sites, it is useful to define a *cluster concentration* $n_s(p) = N_s(p)/N$, where $N_s(p)$ is the number of clusters with s spins. Note that all spins inside a cluster at $T = 0$ are aligned parallel with respect to each other but different clusters can orient independently (Figure 1). Since each spin must belong to some cluster, we have the sum rule

$$\sum_{s=1}^{\infty} s n_s(p) = p, \quad (p < p_c) \tag{11}$$

The restriction $p < p_c$ is because, for $p \geq p_c$, an infinite 'percolating' cluster occurs in an infinite lattice, and this

needs to be considered separately. The probability that a given spin is part of the percolating cluster is called the *percolation probability* $P_\infty(p)$ and is related to the cluster concentrations n_s via

$$P_\infty(p) = 1 - (1/p) \sum_{s=1}^{\infty}{}' s n_s(p), \quad (p > p_c) \tag{12}$$

since spins which do not belong to the infinite cluster must belong to finite clusters. The prime in the sum in equation (12) indicates that the infinite cluster is not included.

The spontaneous magnetization m is obtained by taking the limit of an infinitesimally small field. Finite clusters can point equally in both directions as the field tends to zero and so contribute nothing to m. However, the infinite cluster must point in the direction of the field as long as the field is not strictly zero, and so $P_\infty(p)$ is the spontaneous magnetization per lattice site as $T \to 0$. When $p \to p_c^+$, there occurs a power law analogous to equation (9), $P_\infty(p) \propto (p - p_c)^{\beta_p}$, but the critical exponent β_p differs from β and β_r.

For $p < p_c$ the spontaneous magnetization of the lattice is zero, but we obtain a magnetization applying a magnetic field H

$$M(T, h) = (1/p) \sum_{s=1}^{\infty} n_s s \tanh(s\mu H / k_B T), \quad (T \to 0) \tag{13}$$

μ being the magnetic moment per spin. This is equivalent to the equilibrium magnetization of superparamagnetic particles containing s spins and having a particle size distribution n_s. From equation (13) the zero-field susceptibility is given by

$$\chi_p = (\chi_0/p) \sum_{s=1}^{\infty} n_s s^2 \quad (p < p_c) \tag{14}$$

where χ_0 is the susceptibility of a single spin. An analogous formula holds for $p > p_c$, if the infinite cluster is omitted from the sum. For $p \to p_c$ one finds a power law $\chi_p \propto |p - p_c|^{-\gamma_p}$. The free energy of the superparamagnet in the limit of a vanishingly small field comes from the entropy $(\ln 2)$ of each of the finite clusters. Hence

$$F(T, 0) = -k_B T \ln 2 \sum_{s=1}^{\infty} n_s(p) \tag{15}$$

which has a singular part that can be written as $F_{sing} \propto |p - p_c|^{2-\alpha_p}$ for $p \to p_c$.

Note that the spin–spin correlation function now has the meaning of a 'pair-connectedness function' $G(r)$, see Stauffer and Aharony (1992) for more details, and one can introduce a correlation length ξ_p describing the exponential decay of $G(r)$ with distance r, $G(r) \propto \exp(-r/\xi_p)$. Again a power law holds, $\xi_p \propto |p - p_c|^{-\nu_p}$, and the exponents $\alpha_p, \beta_p, \gamma_p, \nu_p$ satisfy the same type of scaling relations as in equation (9).

Exactly at the percolation concentration p_c, $G(r)$ decays with a power law, $G(r) \propto r^{-(d-2+\eta_p)}$. (There is an analogous relation for the spin correlation function at a thermally driven second-order phase transition.) For the percolation transition, the geometric interpretation of this power law is particularly interesting. Let us consider the number n of sites within a (hyper)sphere of radius R around a site of the (incipient) percolating cluster precisely at $p = p_c$:

$$n = \int \mathrm{d}r [G(r)/P_R] \propto P_R^{-1} \int_0^R G(r) r^{d-1}\, \mathrm{d}r \tag{16}$$

Here $P_R \propto R^{-\beta_p/\nu_p}$ is the probability that an occupied site within the hypersphere belongs to the largest cluster (and not to any of the many smaller clusters that are also present and counted in $G(r)$). Using the power law for $G(r)$ at $p = p_c$ then yields

$$n \propto R^{2-\eta_p+\beta_p/\nu_p} = R^{d_f}, \quad \text{where}$$
$$d_f = 2 - \eta_p + \frac{\beta_p}{\nu_p} = \frac{1}{2}(d + 2 - \eta_p) \tag{17}$$

To get the last relation, we have used another hyperscaling relation. For a compact object of radius R the number of lattice sites in the object, n, is clearly proportional to R^d, so the exponent d_f in equation (17) can be interpreted as a 'fractal dimension' characterizing the geometrical self-similar structure of a noncompact object. It is intuitively clear that $d_f < d$, and this follows because $d - 2 + \eta_p > 0$ since correlations must decrease (rather than increase) with distance at criticality. It turns out that the structure of the spin correlations at the critical point at thermally driven magnetic phase transitions can also be similarly interpreted in terms of the geometric concepts about 'fractals'.

We also mention briefly the nature of long-wavelength magnetic excitations (magnons) in strongly disordered Heisenberg magnets near the percolation threshold. One can show that for wave number $q \to 0$ and near the percolation threshold, the dispersion relation of the characteristic frequency $\omega_c(q)$, has a 'dynamic scaling' structure (Hohenberg and Halperin, 1977)

$$\omega_c(q) \propto q^2 (p - p_c)^{\mu - \beta_p} \tilde{\omega}_p \left(q(p - p_c)^{-\nu_p}\right) \quad (p \geq p_c) \tag{18}$$

where μ is a new exponent and $\tilde{\omega}_p$ a scaling function. The relation $\omega_c \propto q^2$ is just the standard dispersion law

for ferromagnetic spin waves, but the factor $(p - p_c)^{\mu-\beta_p}$ implies that for $p \to p_c$ the spin-wave frequencies vanish, that is, the spin waves become 'soft modes'. Keeping q small but fixed and taking $p \to p_c^+$, the scaling function $\tilde{\omega}_p(\xi)$ must behave as $\tilde{\omega}_p(\xi) \propto \xi^{(\mu-\beta_p)/\nu_p}$ in order to have a well-defined limit for $p \to p_c$, and hence the characteristic frequency $\omega_c(q)$ scales as $\omega_c(q) \propto q^z$, where z, the dynamical exponent is given by $z = 2 + (\mu - \beta_p)/\nu_p$. One sometimes expresses this result in terms of a 'spectral dimension' d_s where $d_s = 2d_f/z$ and d_s is related to the density of energy excitations between w and $\omega + d\omega$ by $g(\omega) \propto \omega^{ds/2-1}$. Unfortunately, the precise estimate of the dynamic exponent z (or equivalently the exponent d_s) is difficult, and also the nature of magnetic excitations in disordered magnets outside the scaling regime near the percolation threshold is a complicated problem (Kovalenko, Krasny and Krey, 2001).

Fractals have many applications outside of magnetic systems also, such as conductivity of disordered materials containing random mixtures of conducting and nonconducting regions, flow of water or oil through porous rocks, diffusion-limited aggregation, and other random growth phenomena (Meakin, 1998). However these are beyond the scope of this article.

4 SPIN GLASSES

Spin glasses are magnetic systems with competing interactions and quenched disorder that is strong enough that no conventional ferro- and antiferromagnetic order can occur, but rather the spins are frozen in random directions. As mentioned in Section 1, there exists a great variety of physical systems that show this behavior. A common feature is a rather sharp cusp in the (frequency-dependent) magnetic susceptibility, but there is no corresponding anomaly in the specific heat. The position of the cusp is weakly dependent on frequency ω but seems to converge toward a static transition temperature T_c, below which hysteresis effects set in. In particular, for $T < T_c$, the zero-field-cooled and field-cooled susceptibilities differ (see Figure 8 and for example, Nagata, Keesom and Harrison, 1979) and aging phenomena are observed (Nordblad and Svedlindh, 1998) as well.

It soon became clear that the observed behavior does not simply come from a gradual slowing down of the dynamics to timescales beyond those of experiments, but is due to an underlying *equilibrium* phase transition. To illustrate how this can lead to a cusp in the susceptibility, consider, for simplicity, a symmetric distribution of bonds, $P(J_{ij}) = P(-J_{ij})$, that is, $\overline{J} = 0$ in equation (5). For this case one can easily show that, on average, magnetic two-spin

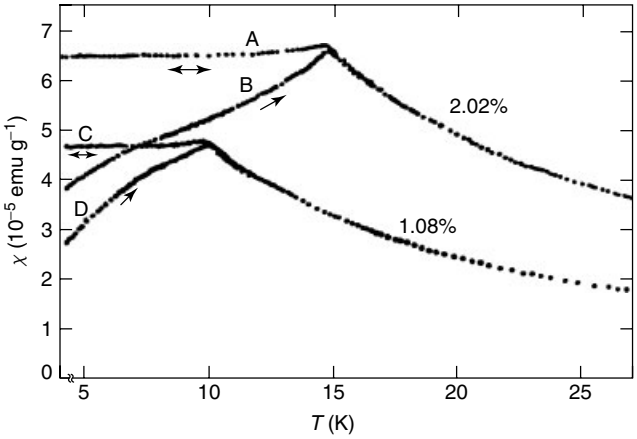

Figure 8. Static susceptibilities of CuMn versus temperature for 1.08 and 2.02 at% Mn. After zero-field cooling ($H < 0.05$ Oe), initial susceptibilities (B) and (D) were taken for increasing temperature in a field of $H = 5.9$ Oe. The susceptibilities (A) and (C) were obtained in the field $H = 5.9$ Oe, which was applied above T_c before cooling the samples. (Reprinted figure with permission from Shoichi Nagata, P.H. Keesom and H.R. Harrison, *Phys. Rev. B.* Vol. 19, 1633–1638 (1979) Copyright 1979 by the American Physical Society.)

correlations are trivial, $[\langle \vec{S}_i \cdot \vec{S}_j \rangle]_{\rm av} = \delta_{ij}$. (Here we have allowed for a vector character of the spins). Using the fluctuation–dissipation relation, which expresses the susceptibility in terms of spin pair correlations, we have, in the limit of vanishingly small field,

$$k_B T \chi = N^{-1} \sum_{i,j} \left[\langle S_i \cdot S_j \rangle_T - \langle S_i \rangle_T \cdot \langle \vec{S}_j \rangle_T \right]_{\rm av}$$
$$= 1 - q \tag{19}$$

where the spin glass order parameter q is defined by $q = [\langle S_i \rangle_T^2]_{\rm av}$. q becomes nonzero for $T < T_c$, $q \propto (1 - T/T_c)^\beta$, which gives a cusp in the zero-field susceptibility.

Actually, as for other critical phenomena, one can identify correlations that become long ranged as one approaches the freezing transition from above, however this correlation is not the standard spin pair correlation but is of a higher order, $g_{\rm SG}(r) = [\langle S_i \cdot S_j \rangle_T^2]_{\rm av}$. The square is needed because the spin–spin correlations can have either sign at random. It is useful to sum $g_{\rm SG}(r)$ over all space to get the spin glass susceptibility, $\chi_{\rm SG} = \sum_r g_{\rm SG}(r)$, since this diverges at the spin glass transition, $\chi_{\rm SG}(T) \propto (T/T_c - 1)^{-\gamma}$. Although $\chi_{\rm SG}$ is not directly measurable it is very closely related to the nonlinear susceptibility, $\chi_{\rm nl}$, defined by

$$M = \chi_0 H - \chi_{\rm nl} H^3 + \cdots \tag{20}$$

where M is the magnetization and H the magnetic field. In fact, for an EA Ising spin glass with a symmetric distribution

of interactions, the relation is

$$(k_{\mathrm{B}}T)^3\chi_{\mathrm{nl}} = \chi_{\mathrm{SG}} - \frac{2}{3} \tag{21}$$

Remember our choice of units, for which the magnetic field has a dimension of energy, magnetization is dimensionless, and hence the (linear) susceptibility has a dimension of inverse energy, the nonlinear susceptibility has a dimension of inverse energy to the minus third power, while the spin glass susceptibility was defined as a dimensionless quantity.

For the case of a nonsymmetric bond distribution, this relation is no longer true but, nonetheless, χ_{nl} and χ_{SG} still diverge in the same way. Experiments, for example, Omari, Préjean and Souletie (1983), suggest that a critical divergence of χ_{nl} does occur ($\gamma \approx 3.25$ in Omari, Préjean and Souletie (1983)). Furthermore, one finds a scaling of the nonlinear part of the magnetization,

$$1 - M/(\chi_0 H) = (1 - T/T_{\mathrm{c}})^{\beta}\widetilde{M}\left\{(H/T)^2(1-T/T_{\mathrm{c}})^{-(\gamma+\beta)}\right\} \tag{22}$$

with $\beta \approx 0.75 - 0.95$ (Omari, Préjean and Souletie, 1983). Note, however, that the critical behavior of the correlation length ξ_{SG} describing the decay of $g_{\mathrm{SG}}(r)$ with distance, $\xi_{\mathrm{SG}} \propto (|T/T_{\mathrm{c}} - 1|^{-\nu})$, cannot be measured directly, and thus can only be inferred indirectly from experimental determinations of β and γ combined with the scaling relation (equation (10)).

Analyzing the dynamic susceptibility near T_{c}, the dramatic increase of the relaxation time τ can be attributed to standard critical slowing down (Hohenberg and Halperin, 1977), $\tau_{\mathrm{SG}} \propto \xi_{\mathrm{SG}}^{z} \propto (T/T_{\mathrm{c}} - 1)^{-\nu z}$, but with an anomalously large dynamic exponent z, giving $z\nu \approx 7.2 \pm 0.5$ (Bontemps, Rajchenbach, Chamberlin and Orbach, 1984). However, when one compares analyses of different groups, one finds a rather large spread in the values of the suggested critical exponents, irrespective of whether these groups analyze the same spin glass systems or different ones (see, e.g., Table 1 of Maletta and Zinn, 1989). Thus, it is fair to say that there is qualitative evidence from experiment that a static phase transition in spin glasses does exist, but the associated critical exponents are not yet accurately known.

Turning to the theoretical work on spin glasses, the first problem to consider is how one can carry out the averaging $[\cdots]_{\mathrm{av}}$ over the random bond distribution. To calculate the average free energy, $[F]_{\mathrm{av}} = -k_{\mathrm{B}}T[\ln Z\{J_{ij}\}]_{\mathrm{av}}$, and its derivatives a common approach is to use the 'replica trick' (Edwards and Anderson, 1975)

$$[\ln Z\{J_{ij}\}]_{\mathrm{av}} = \lim_{n\to 0}\frac{1}{n}\left(\left[Z^n(J_{ij})\right]_{\mathrm{av}} - 1\right) = \lim_{n\to 0}\frac{\partial}{\partial n}\left[Z^n(J_{ij})\right]_{\mathrm{av}} \tag{23}$$

The problem of averaging $\ln Z$ is thus reduced to the problem of averaging Z^n, and, at least for positive integer n, this is a simpler problem since one can interpret Z^n as a product of n identical replicas of the system. At the end of the calculation one takes the limit $n \to 0$.

For nearest-neighbor interactions with the Gaussian distribution in equation (5), it is easy to 'complete the square' and show that $Z_n \equiv [Z^n\{J_{ij}\}]_{\mathrm{av}} = Tr_{\{S_i^\alpha\}}\exp[-\mathcal{H}_n^{\mathrm{eff}}(S_i^\alpha)/k_{\mathrm{B}}T]$, where

$$\mathcal{H}_n^{\mathrm{eff}}\{S_i^\alpha\} = \frac{\overline{J}}{k_{\mathrm{B}}T}\sum_{i\neq j}\sum_{\alpha=1}^{n} S_i^\alpha S_j^\alpha + \frac{1}{2}\left(\frac{J}{k_{\mathrm{B}}T}\right)^2\sum_{i\neq j}\sum_{\alpha,\beta} S_i^\alpha S_j^\alpha S_i^\beta S_j^\beta \tag{24}$$

The initial problem with the Hamiltonian $\mathcal{H}\{J_{i,j}\}$, which lacks translational invariance, has now been replaced by an equivalent problem that *is* translationally invariant (equation (24)). The price of this simplification is that the degrees of freedom S_i^α now carry an additional index α, $1 \leq \alpha \leq n$, the 'replica index', and, owing to disorder, the various replicas of the system get coupled to each other.

In the mean-field approximation, one replaces $S_i^\alpha S_j^\alpha$ by $S_i^\alpha\langle S_j^\alpha\rangle$, and $S_i^\alpha S_i^\beta S_j^\alpha S_j^\beta$ by $S_i^\alpha S_i^\beta\langle S_j^\alpha S_j^\beta\rangle$ and determines self-consistently the 'order parameters' $m_\alpha \equiv \langle S_\alpha^j\rangle$, $q_{\alpha\beta} = \langle S_j^\alpha S_j^\beta\rangle$ ($\alpha \neq \beta$). More precisely, noting from equation (23) that we need to let $n \to 0$ and that no index α should be singled out, one obtains for the magnetization M and the EA order parameter q

$$M = \lim_{n\to 0}\frac{1}{n}\sum_{\alpha=1}^{n}\langle S_i^\alpha\rangle,\quad q = \lim_{n\to 0}\frac{1}{n(n-1)}\sum_{\alpha\neq\beta}\langle S_i^\alpha S_i^\beta\rangle \tag{25}$$

For the infinite-range case, mean-field theory can be obtained rigorously in terms of a saddle point approximation, as worked out by Sherrington and Kirkpatrick (1975) for the 'replica-symmetric' case in which $m_\alpha = M$ and $q_{\alpha\beta} = q$ independent of the replica indices. One finds

$$M = \frac{1}{\sqrt{2\pi}}\int_{-\infty}^{+\infty} \mathrm{d}z\mathrm{e}^{-z^2/2}\tanh\left(\frac{1}{k_{\mathrm{B}}T}\left[\tilde{J}\sqrt{q}z + J_0 M + H\right]\right) \tag{26}$$

and

$$q = \frac{1}{\sqrt{2\pi}}\int_{-\infty}^{+\infty} \mathrm{d}z\mathrm{e}^{-z^2/2}\tanh^2\left(\frac{1}{k_{\mathrm{B}}T}[\tilde{J}\sqrt{q}z + J_0 M + H]\right) \tag{27}$$

which generalizes the well-known result for the Ising ferromagnet, $M = \tanh([J_0 M + H]/k_{\mathrm{B}}T)$. For $H = J_0 = 0$,

equation (27) allows a nonzero solution for q for $T < T_c = \tilde{J}/k_B$, namely, $q = 1 - T/T_c + (1 - T/T_c)^2/3 + \cdots$, so $\beta = 1$ in mean-field theory. The magnetic equation of state for $T > T_c$ becomes

$$M = \frac{H}{k_B T}\left\{1 - \frac{1}{3}\left(\frac{H}{k_B T}\right)^2 \frac{T^2 + 2T_c^2}{T^2 - T_c^2} + \cdots\right\} \qquad (28)$$

which shows that the nonlinear susceptibility does indeed diverge (as stated in Section 1), with the mean-field exponent $\gamma = 1$.

However, a closer look on the SK solution given by equations (26) and (27) shows that it is not acceptable, since at low temperatures the entropy becomes negative, and χ_{SG} for $T \leq T_c$ turns out to be negative as well (de Almeida and Thouless, 1978). The problem lies in the assumption of replica symmetry. However, the means for breaking the symmetry of the matrix $q_{\alpha\beta}$ in the limit $n \to 0$ was not entirely clear. Eventually, in a brilliant piece of work, Parisi (1979) made an ansatz (which appears to be exact for the infinite-range SK model) in which the matrix is reduced to an order parameter function $q(x)$. For $H = J_0 = 0$ and T close to T_c, Parisi finds

$$q(x) = x/2, \ (0 < x \leq x_1),$$
$$q(x) = x_1/2, \ (x_1 \leq x \leq 1) \qquad (29)$$

This order parameter function arises because, for $T < T_c$, the phase space is split into many 'valleys' (compare Figure 6) separated by infinitely high barriers. These valleys or 'ergodic components' are not orthogonal to each other however, but the spin configurations in different valleys have an overlap q. It turns out (Parisi, 1983) that the derivative of the inverse function of $q(x)$, namely, $\mathrm{d}x/\mathrm{d}q$, is the probability, $P(q)$, that there is an overlap q between two states. Note that replica calculations use statistical mechanics, in which there is a nonzero probability of the system being in any of the valleys. By contrast, if one followed the dynamical evolution of the system, the system would be trapped in a single valley, so time averages differ from ensemble averages.

The multivalley structure of an Ising spin glass in the mean-field limit not only exists at zero field, but over a range of fields up to the so-called AT line (de Almeida and Thouless, 1978), which near T_c is given by

$$T_c - T_{AT}(H) \propto H^{2/3} \qquad (30)$$

Of course, experience from standard phase transitions is that mean-field theory is, at best, only qualitatively correct for real systems with short-range forces (Fisher, 1974). Only if the spatial dimensionality d of the system exceeds the 'upper critical dimension', d_u (with $d_u = 4$ for ferromagnets), do the critical exponents of mean-field theory apply to real systems. However, for $d_l < d < d_u$, where d_l is the 'lower critical dimension', the exponents take nontrivial values and depend on d and also on the spin dimensionality. For $d < d_l$, statistical fluctuations (that are neglected by mean-field theory) destroy the phase transition altogether so $T_c = 0$. For ferromagnets, $d_l = 1$ for Ising systems and $d_l = 2$ for isotropic vector models (e.g., XY or Heisenberg).

For spin glasses, however, it turns out that $d_u = 6$, and hence the physical dimensionality $d = 3$ is much less than d_u; so drastic discrepancies between mean-field theory and experiments should be expected. These discrepancies would be even more dramatic if d_l were greater than 3, because then the transition predicted in mean-field theory would not occur at all. However, at least for Ising spin glasses, it is now well established that there *is* a finite-temperature spin glass transition in three dimensions (Ballesteros *et al*., 2002), though not in $d = 2$ (see, for example, Hartmann *et al*., 2002), so d_l lies between 2 and 3.

For XY and Heisenberg ferromagnets, however, the situation has been more controversial. It is known that for the pure case, topological excitations may be important since unbinding of vortex–antivortex pairs controls the phase transition of the XY model (Kosterlitz and Thouless, 1973) in two dimensions. For the pure case, vortices only occur through thermal fluctuations since the ground state is collinear. However, in a model with frustration the ground state is noncollinear, and so one has vortices quenched in even at $T = 0$. It is therefore important to understand the role of vortices (often called chiralities) in XY spin glasses (and the analogous chiralities in Heisenberg spin glasses). While for a long time it was believed that $d_l = 4$, so there would be no order in isotropic spin glass systems in $d = 3$, it was later (Kawamura and Tanumura, 1991) suggested that chiral glass ordering in isotropic vector spin glasses occurs without accompanying spin glass ordering. However, this was not universally accepted, and, in particular, recent, careful Monte Carlo simulations (Lee and Young, 2003) have shown that isotropic spin glasses *d*o have a nonzero *spin glass* transition temperature in $d = 3$, and that chiral and spin glass ordering set in at the same temperature. Thus one can explain the observed finite T_c in spin glasses such as CuMn and $Eu_xSr_{1-x}S$, which are isotropic to a good approximation, without invoking the small anisotropy that these systems must possess.

Even though a spin glass is not in thermal equilibrium below T_c, it is still of theoretical interest to understand the equilibrium state that the system is trying to reach. Two main phenomenological descriptions have been proposed. The first is the 'replica symmetry breaking' (RSB) approach in which

it is supposed that the spin glass state in real systems is similar to the multivalley structure found (Parisi, 1979) in the SK model. This has (i) a nontrivial order parameter function $P(q)$ and (ii) a phase transition (AT line) in a magnetic field. The other approach is the 'droplet picture' developed by Fisher and Huse (1986) (see also Bray and Moore, 1986; McMillan, 1984). In this picture spin glasses have just a single 'pure state' (apart from states related by global symmetry such as spin inversion). Consequently $P(q)$ is trivial (just a delta function at the single order parameter q), and there is no AT line (a field wipes out the transition as it does in a ferromagnet). According to numerics, there does not appear to be an AT line (Katzgraber and Young, 2004), which favors the droplet model, although $P(q)$ appears to be nontrivial (Marinari, Parisi and Ruiz-Lorenzo, 1998; Katzgraber, Palassini and Young, 2001), which favors RSB. Hence an intermediate scenario (Krzakala and Martin, 2000; Palassini and Young, 2000) called *TNT* for *trivial–nontrivial*, fits the data best. However, numerics can only be done on small systems, so it is not clear whether TNT describes the asymptotic behavior on large length scales.

Since a spin glass is not in full equilibrium below T_c, the eventual goal of spin glass theory must be to explain nonequilibrium effects, such as aging (Nordblad and Svedlindh, 1998) and memory and rejuvenation (Jonason *et al.*, 1998; Bert *et al.*, 2004; Picco, Ricci-Tersenghi and Ritort, 2001), referred to in Section 1. There has also been considerable interest in the nature of violations of the fluctuation–dissipation theorem (Bouchaud, Cugliandolo, Kurchan and Mézard, 1998; Crisanti and Ritort, 2003). Unfortunately we do not have space to discuss these fascinating topics here.

In addition, generalizations of the spin glass problem such as the p-spin interaction models and p-state Potts spin glass models have received a lot of attention, because these models are possibly related to the problem of the glass transition of undercooled fluids (Binder, 2004).

Another very interesting extension concerns spin glass models in which quantum fluctuations rather than classical fluctuations play a key role (Bhatt, 1998). An example is the Ising spin glass in a transverse magnetic field at zero temperature, where one can study a quantum phase transition by varying the strength of this field. The diluted dipolar Ising magnet $LiHo_xY_{1-x}F_4$ provides an experimental example (Wu, Bitko, Rosenbaum and Aeppli, 1993). It is interesting to note that quantum spin glasses do have a 'quantum phase transition' (i.e., a transition at $T = 0$) even in $d = 2$ dimensions, and that rare fluctuations of the random distribution can cause a divergence of the nonlinear susceptibility already in the paramagnetic phase of the spin glass (Bhatt, 1998).

5 PERIODIC FRUSTRATED SYSTEMS

Following the pioneering work of Villain (1977), there has been interest in understanding the behavior of models with frustration but without disorder. In addition to theoretical interest, further motivation for studying these models comes from the existence of related experimental systems with which one can compare theoretical predictions (Diep, 1994).

The effect of periodically distributed frustrated 'plaquettes', that is, elementary polygons (triangles on the triangular or face-centered cubic lattices, squares on the square or simple cubic lattices) depends crucially on whether one considers Ising or continuous spins (e.g., XY and Heisenberg models). As already discussed (see Figure 7), the ground state degeneracy in frustrated systems is enhanced relative to that of unfrustrated systems.

Ising models in $d = 2$, such as the triangular antiferromagnet or the 'fully frustrated' square lattice do not order at any temperature. In $d = 3$, the face-centered cubic antiferromagnet in zero field has a first-order transition to the paramagnetic state, that has been carefully studied by Monte Carlo methods. However, the phase diagram of the fcc Ising antiferromagnet in a magnetic field is still not fully understood (Kämmerer, Dünweg, Binder and D'Onorio De Meo, 1996). Ising models on frustrated simple cubic lattices and stacked triangular lattices presumably exhibit second-order phase transitions, which have been studied by Monte Carlo simulations and renormalization group methods (Plumer and Mailhot, 1995).

Ising-like systems on the pyrochlore lattice, such as holmium and dysprosium titanate, have aroused a lot of recent interest (Siddharthan, Shastry and Ramirez, 2001; Melko, den Hertog and Gingras, 2001). This lattice comprises corner-sharing tetrahedra and on each tetrahedron, energetics requires two of the four spins to be 'in' and two 'out', similar to the Bernal–Fowler rules for the hydrogen bonds in ice. In fact, there is a strong similarity between these magnetic systems and ice, even down to the residual entropy at $T = 0$ first calculated for ice by Pauling, so the name *spin ice* has been given to them. The advantage of the magnetic system over ice is that it couples to a continuously variable parameter, the magnetic field, and so complicated phase boundaries can be mapped out. This has been done in detail for a related Heisenberg system (Ramirez *et al.*, 2002).

The behavior of frustrated XY antiferromagnets is also of interest because the spin ordering around a frustrated plaquette is noncollinear, and so chiralities may play a role, as also proposed for XY spin glasses discussed in Section 4. For the frustrated triangular XY antiferromagnet, spins around an elementary triangle are rotated by 120°, and

one has left-handed and right-handed chiral states. Therefore, the symmetry of the order parameter space is $Z_2 \times$ SO(2) instead of the continuous rotational invariance. Similarly, there are chiral as well as spin degrees of freedom in the fully frustrated XY model on the square lattice. The main issue is whether spin and chiralities order at the same temperature, or whether the chiralities order at a higher temperature. There is some evidence (see, e.g., Lee, Lee and Kosterlitz, 1997) for two separate transitions but the difference in transition temperatures is very small so it is difficult to know whether this effect is real or an artifact due to systematic corrections to finite size scaling.

If one stacks triangular lattices to make a three-dimensional lattice, one can have ordering at finite temperature, and Kawamura (1988) pointed out that the transition belongs to a new universality class, assuming it is second order. There has been controversy, which does not seem to be settled, as to whether the transition is really second order, in which case the exponents are close to those expected at a tricritical point ($\beta = 1/4, \gamma = 1, \nu = 1/2$), or whether the transition is weakly first order (see, e.g., Delamotte, Mouhanna and Tissier, 2004). Unfortunately, the wide variety of experimental systems (e.g., $CsMnBr_3$) does not give a clear picture of the critical behavior of these systems (Plumer and Mailhot, 1995).

A variety of complex phase diagrams and multicritical phenomena is expected when one considers frustrated XY and Heisenberg antiferromagnets exposed to magnetic fields. This still is an active area of research (Diep, 1994).

6 RANDOM MAGNETIC FIELDS

In this section we focus on systems where the quenched disorder leads to a local 'field' coupling linearly to the order parameter, and examine how the phase transition, for example, to a ferromagnetic phase, is affected. The simplest model is an n-component ferromagnet with nearest-neighbor exchange J exposed to a random field H_i that acts on every lattice site i and is completely uncorrelated with zero mean and variance h^2:

$$\mathcal{H} = -J \sum_{\langle i,j \rangle} S_i \cdot S_j - \sum_i H_i \cdot S_i,$$
$$[H_i]_{av} = 0, \; [H_i \cdot H_j]_{\text{av}} = h^2 \delta_{ij} \tag{31}$$

A basic question is how to determine the value of the lower critical dimension d_l, below which arbitrarily weak random fields are able to destroy uniform long-range order by breaking the system up into domains (Imry and Ma, 1975). In a domain of linear size L in d dimensions there will be an excess of random fields of either sign of order $L^{d/2}$, due to statistical fluctuations. Thus, overturning the magnetization in this domain causes an energy gain of the order of $hL^{d/2}$. However, for $T < T_c$, creating a domain wall costs an energy of the order of JL^{d-1} in the Ising case and JL^{d-2} in the case of XY and Heisenberg. Balancing these energies, one finds that a uniform magnetization is unstable against domain formation in arbitrarily weak random fields for $d < 2$ in the Ising case and for $d < 4$ in the XY and Heisenberg cases. Thus, a phase transition is still expected to occur for the $d = 3$ Ising model, but not for the $d = 3$ XY and Heisenberg model where arbitrary weak random fields should lead to a rounding of the transition. The transition is also rounded for the $d = 2$ Ising model, for which a more refined analysis shows (Binder, 1983; Moore, Stinchcombe and de Queiroz, 1996) that the domain size scales exponentially with h/J.

Understanding the phase transition of the $d = 3$ random field Ising model has been controversial for a long time, partly because random field systems, like spin glasses, have very slow dynamics around and below T_c. Assuming a second-order transition, one finds that the hyperscaling relation equation (10), needs to be modified as (Nattermann, 1998)

$$2\beta + \gamma = 2 - \alpha = (d - \theta)\nu \tag{32}$$

A heuristic argument to understand equation (32) assumes that the singular part of the free energy of a correlated region of volume ξ^d scales as the energy that is necessary to flip the region. At a thermal transition this is $k_B T$, and hence $k_B T \sim \xi^d \xi^{-(2-\alpha)/\nu}$, which gives equation (10). However, in the present case, thermal fluctuations are irrelevant in comparison with the random fields, and the energy is assumed to be $h\xi^\theta$ rather than $k_B T$, with a new exponent θ, and then equation (32) readily follows. While equation (32) appears to have three independent exponents, there are strong arguments (Nattermann, 1998) that there are actually only two, since there should exist an additional scaling relation $\theta = 2 - \eta$. Evidence from series expansions (Gofman *et al.*, 1996) is compatible with this relation.

Experiments (Belanger, 1998) on random field Ising systems have given beautiful evidence for the destruction of the transition in $d = 2$ and have obtained estimates for critical exponents in $d = 3$. These exponent values are in reasonable agreement with the best numerical study (Middleton and Fisher, 2002), though there is a puzzle concerning the specific heat (Hartmann and Young, 2001). Simulations also find that the order parameter exponent β is very close to $\beta = 0$. A different value is found in experiments (Ye *et al.*, 2002) but the discrepancy is probably because the experiment is done below T_c (the order parameter is only nonzero there),

where the system is not fully in equilibrium (D. P. Belanger, private communication).

Also of interest is the dynamics of domain growth (which is probably logarithmic in time) and the suggestion that the critical dynamics may be of a thermally activated type (Nattermann, 1998).

7 CONCLUSIONS

Disordered and frustrated spin systems are model materials which illuminate the interplay between nonthermal random fluctuations (due to quenched disorder) and thermal fluctuations on ordering phenomena in condensed matter. New types of phase transitions and unconventional types of order, such as the spin glass, are found in these systems, and important concepts of critical phenomena and the statistical mechanics of solids can be exemplified and tested. Many of the new concepts developed first for these magnetic systems have later been carried over to different systems, such as the problem of the glass transition of undercooled fluids, and orientational glass behavior found in diluted dielectric materials and randomly mixed molecular crystals. Random field effects in magnetic systems find counterparts in the behavior of binary fluids in porous media, and in the mesophase formation of binary polymer networks or mixed 'polymer brushes', and even in phase separation phenomena in biological membranes.

Just as magnetic ordering in ideal crystals has played a key role in developing the theory of phase transitions and critical phenomena, disordered magnets are critical for understanding the effects of quenched disorder in condensed matter. Furthermore, theoretical techniques for understanding ground states of spin glasses and random field systems have allowed important spin offs in fields outside of physics, such as neural networks, pattern recognition, optimization problems in computer science, and economics. Despite much effort, there are still many interesting open questions, so we expect that the field will stay an active area of research in the future.

REFERENCES

Aharony, A. and Binder, K. (1980). Low concentration series expansions for dilute spin glasses at zero temperature. *Journal of Physics C*, **13**, 4091–4108.

de Almeida, J.R.L. and Thouless, D.J. (1978). Stability of the Sherrington-Kirkpatrick solution. *Journal of Physics A*, **11**, 983–990.

Ballesteros, H.G., *et al*. (2002) Critical behavior of the three-dimensional Ising spin glass. *Physical Review B*, **62**, 14237.

Belanger, D.P. (1998). Experiments on the random field Ising model. In *Spin Glasses and Random Fields*, Young, A.P. (Ed.), World Scientific: Singapore, pp. 277–298.

Bert, F., Dupuis, V., Vincent, E., *et al*. (2004). Spin anisotropy and slow dynamics in spin glasses. *Physical Review Letters*, **92**, 167203.

Binder, K. (1983). Random-field induced interface widths in Ising systems. *Zeitschrift fur Physik B*, **50**, 343–352.

Binder, K. (2004). Statistical mechanics of undercooled fluids and the glass transition: testing theoretical concepts by computer simulation. In *Proceedings of the International School of Physics "Enrico Fermi" Course CLV*, Mallamace, F. and Stanley, H.E. (Eds.), IOS Press: Amsterdam, pp. 17–82.

Binder, K., Kinzel, W. and Stauffer, D. (1979). Phase diagrams and magnetic properties of diluted Ising and Heisenberg magnets with competing interactions. *Zeitschrift fur Physik B*, **36**, 161–177.

Binder, K. and Young, A.P. (1986). Spin glasses: experimental facts, theoretical concepts, and open questions. *Reviews of Modern Physics*, **58**, 801–976.

Bhatt, R.N. (1998). Quantum spin glasses. In *Spin Glasses and Random Fields*, Young, A.P. (Ed.), World Scientific: Singapore, pp. 225–249.

Bontemps, N., Rajchenbach, J., Chamberlin, R.V. and Orbach, R. (1984). Dynamic scaling in the $Eu_{0.4}$ $Sr_{0.6}S$ spin glass. *Physical Review B*, **30**, 6514–6520.

Bouchaud, J-P., Cugliandolo, L.F., Kurchan, J. and Mézard, M. (1998). *Spin Glasses and Random Fields*, Young, A.P. (Ed.), World Scientific: Singapore.

Bray, A.J. and Moore, M.A. (1986). Scaling theory of the ordered phase of spin glasses. In *Heidelberg Colloquium on Glassy Dynamics and Optimization*, Van Hemmen, L. and Morgenstern, I. (Eds.), Springer, p. 121.

Crisanti, A. and Ritort, F. (2003). Violation of the fluctuation-dissipation theorem in glassy systems: basic notions and the numerical evidence. *Journal of Physics A: Mathematical and General*, **36**, R181–R290.

Delamotte, B., Mouhanna, D. and Tissier, M. (2004). Nonperturbative renormalization group approach to frustrated magnets. *Physical Review B*, **69**, 134413.

Diep, R.T. (Ed.) (1994). *Magnetic Systems with Competing Interactions*, World Scientific: Singapore.

Edwards, S.F. and Anderson, P.W. (1975). Theory of spin glasses. *Journal of Physics F*, **5**, 965–974.

Fisher, M.E. (1974). The renormalization group in the theory of critical behavior. *Reviews of Modern Physics*, **46**, 597–616.

Fisher, D.S. and Huse, D.A. (1986). Ordered phase of short-range Ising spin glasses. *Physical Review Letters*, **56**, 1601–1604.

Fishman, S. and Aharony, A. (1979). Random field effects in disordered anisotropic antiferromagnets. *Journal of Physics C*, **12**, L729–L733.

Gofman, M., Adler, J., Aharony, A., *et al*. (1996). Critical behavior of the random-field Ising model. *Physical Review B*, **53**, 6362.

Griffiths, R.B. (1969). Nonanalytic behavior above the critical point in a random Ising ferromagnet. *Physical Review Letters*, **23**, 17–19.

Harris, A.B. (1974). Effects of random defects on the critical behavior of Ising models. *Journal of Physics C*, **7**, 1671–1692.

Hartmann, A.K., Bray, A.J., Carter, A.C., *et al*. (2002). Stiffness exponent of two-dimensional Ising spin glasses for nonperiodic boundary conditions using aspect-ratio scaling. *Physical Review B*, **66**, 224401-1–224401-4.

Hartmann, A.K. and Young, A.P. (2001). Specific-heat exponent of random-field systems via ground-state calculations. *Physical Review B*, **64**, 214419.

Hohenberg, P.G. and Halperin, B.I. (1977). Theory of dynamic critical phenomena. *Reviews of Modern Physics*, **49**, 435–479.

Imry, Y. and Ma, S.K. (1975). Random-field instability of the ordered state of continuous symmetry. *Physical Review Letters*, **35**, 1399–1402.

Jonason, K., Vincent, E., Hammann, E., *et al*. (1998). Memory and chaos effects in spin glasses. *Physical Review Letters*, **81**, 3243–3246.

Kämmerer, S., Dünweg, B., Binder, K. and D'Onorio De Meo, M. (1996). The nearest neighbor Ising antiferromagnet on the FCC lattice revisited: evidence for a new type of multicritical behavior. *Physical Review B*, **53**, 2345–2351.

Katzgraber, H.G., Palassini, M. and Young, A.P. (2001). Monte Carlo simulations of spin glasses at low temperatures. *Physical Review B*, **63**, 184422.

Katzgraber, H.G. and Young, A.P. (2004). Absence of an Almeida Thouless line in three-dimensional spin glasses (cond-mat/0407 031). *Physical Review Letters*, **93**, 207203.

Kawamura, H. (1988). Renormalization-group analysis of chiral transitions. *Physical Review B*, **38**, 4916.

Kawamura, H. and Tanumura, M.C. (1991). Ordering of XY spin glasses in two and three dimensions – domain-wall renormalization-group studies. *Journal of the Physical Society of Japan*, **60**, 608–613.

Kosterlitz, J.M. and Thouless, D.J. (1973). Ordering, metastability and phase transitions in two-dimensional systems. *Journal of Physics C*, **6**, 1181–1203.

Kovalenko, N.P., Krasny, Y.P. and Krey, U. (2001). *Physics of Amorphous Metals*, Wiley-VCH: Berlin.

Krzakala, F. and Martin, O.C. (2000). Spin and link overlaps in 3-dimensional spin glasses. *Physical Review Letters*, **85**, 3013–3016.

Lee, S., Lee, K-C. and Kosterlitz, J.M. (1997). Phase diagram of the restricted solid-on-solid model coupled to the Ising model. *Physical Review B*, **56**, 340–341.

Lee, L.W. and Young, A.P. (2003). Single spin and chiral glass transition in vector spin glasses in three dimensions. *Physical Review Letters*, **90**, 227203 1–4.

Maletta, H. and Zinn, W. (1989). Spin glasses. In *Handbook on the Physics and Chemistry of Rare Earths*, Gschneidner, K.A. Jr. and Eyring, L. (Eds.), Elsevier Science: Amsterdam, pp. 213–356, Vol. 12.

Marinari, E., Parisi, G. and Ruiz-Lorenzo, J.J. (1998). In *Spin Glasses and Random Fields*, Young, A.P. (Ed.), World Scientific: Singapore, p. 59.

Meakin, P. (1998). *Fractals, Scaling, and Growth Far From Equilibrium*, Cambridge University Press: London.

Melko, R.G., den Hertog, B.C. and Gingras, M.J.P. (2001). Long range order at low temperature in dipolar spin ice. *Physical Review Letters*, **87**, 067203.

McMillan, W. (1984). Scaling theory of Ising spin glasses. *Journal of Physics A*, **17**, 3179.

Middleton, A.A. and Fisher, D.S. (2002). Three-dimensional random-field Ising magnet: interfaces, scaling, and the nature of states. *Physical Review B*, **65**, 134411.

Moore, E.D., Stinchcombe, R.B. and de Queiroz, S.L.A. (1996). Domain scaling and marginality breaking in the random-field Ising model. *Journal of Physics A: Mathematical and General*, **29**, 7409–7438.

Nagata, S., Keesom, P.H. and Harrison, H.R. (1979). Low-dc-field susceptibility of CuMn spin glass. *Physical Review*, **B19**, 1633–1638.

Nattermann, T. (1998). Theory of the random field Ising model. In *Spin Glasses and Random Fields*, Young, A.P. (Ed.), World Scientific: Singapore, pp. 277–298.

Nordblad, P. and Svedlindh, P. (1998). Experiments on spin glasses. In *Spin Glasses and Random Fields*, Young, A.P. (Ed.), World Scientific: Singapore, pp. 1–27.

Omari, R., Préjean, J.J. and Souletie, J. (1983). Critical measurements in the spin glass CuMn. *Journal de Physique*, **44**, 1069–1083.

Palassini, M. and Young, A.P. (2000). Nature of the Spin Glass State. *Physical Review Letters*, **85**, 3017–3020.

Parisi, G. (1979). Infinite number of order parameters for spin glasses. *Physical Review Letters*, **43**, 1754–1757.

Parisi, G. (1983). Order parameter for spin-glasses. *Physical Review Letters*, **50**, 1946–1948.

Picco, M., Ricci-Tersenghi, F. and Ritort, F. (2001). Chaotic, memory, and cooling rate effects in spin glasses: evaluation of the Edwards-Anderson model. *Physical Review B*, **63**, 174412.

Plumer, M.L. and Mailhot, A. (1995). Monte-Carlo simulations of phase transitions in frustrated antiferromagnets. In *Computer Simulation Studies in Condensed Matter Physics VIII. Recent Developments*, Landau, D.P., Mon, K.K. and Schüttler, H-B. (Eds.), Springer: Berlin, pp. 44–56.

Ramirez, A.P., Shastry, B.S., Hayashi, A., *et al*. (2002). Multiple field-induced phase transitions in the geometrically frustrated dipolar magnet: $Gd_2Ti_2O_7$. *Physical Review B*, **63**, 184412.

Selke, W. (1991). Monte Carlo simulations of dilute Ising models. In *Computer Simulations Studies in Condensed Matter Physics IV*, Landau, D.P., Mon, K.K. and Schüttler, H.B. (Eds.), Springer: Berlin, pp. 18–27.

Siddharthan, R., Shastry, B.S. and Ramirez, A.P. (2001). Spin ordering and partial ordering in holmium titanate and related systems. *Physical Review B*, **63**, 184412.

Stanley, H.E. (1971). *An Introduction to Phase Transitions and Critical Phenomena*, Oxford University Press: Oxford.

Stauffer, D. and Aharony, A. (1992). *Introduction to Percolation Theory*, Taylor and Francis: London.

Sherrington, D. and Kirkpatrick, S. (1975). Solvable model of a spin glass. *Physical Review Letters*, **35**, 1972–1975.

Stinchcombe, R.B. (1973). Dilute magnetism. In *Phase Transitions and Critical Phenomena*, Domb, C. and Lebowitz, J.L. (Eds.), Academic Press: London, pp. 150–280, Vol. 7.

Villain, J. (1977). Spin glass with non-random interactions. *Journal of Physics C*, **10**, 1717–1734.

Wu, W., Bitko, D., Rosenbaum, T.F. and Aeppli, G. (1993). Quenching of the nonlinear susceptibility at a $T = 0$ spin glass transition. *Physical Review Letters*, **71**, 1919–1922.

Ye, F., Zhou, L., Larochelle, S., *et al*. (2002). Order parameter criticality of the $d = 3$ random-field Ising antiferromagnet $Fe_{0.85}Zn_{0.15}F_2$. *Physical Review Letters*, **89**, 157202.

Quantum Phase Transitions

Subir Sachdev
Harvard University, Cambridge, MA, USA

1 INTRODUCTION

The study of quantum phase transitions has been a major focus of theoretical and experimental work in systems of correlated electrons and in correlated ultracold atoms in recent years. However, some of the best-characterized and understood examples of quantum phase transitions are found in magnetic materials. These, therefore, serve as a valuable laboratory for testing our understanding of real systems in the vicinity of quantum critical points. We will review some of the simplest model systems in the subsequent text, along with their experimental realizations. This will be followed by a discussion of recent theoretical advances on some novel quantum critical points displayed by quantum magnets that have no direct analog in the theory of classical phase transitions at finite temperature (T). Portions of this article have been adapted from another recent review by the author (Sachdev, 2005).

In all the magnetic systems considered in the subsequent text, there is at least one ground state in which the symmetry of spin rotations is broken. So in this phase we have

$$\langle \hat{S}_j^\alpha \rangle \neq 0 \tag{1}$$

at $T = 0$. Here $\hat{S}$ is the electron spin operator on site j and $\alpha = x, y, z$ are the spin components. In all cases that are considered here, the Hamiltonian has at least a symmetry of spin inversion, and this symmetry is broken by (1). We are quite familiar with such magnetic systems, as all antiferromagnets, ferromagnets, or even spin glasses obey (1) at sufficiently low temperatures.

Let us now try to access a *paramagnetic* phase where

$$\langle \hat{S}_j^\alpha \rangle = 0 \tag{2}$$

Normally, we do this by raising the temperature. The resulting phase transition between phases characterized by (1) and (2) is well understood and described by the well-developed theory of classical phase transitions. This shall *not* be our interest here. Rather, we are interested in moving from a magnetic system obeying (1) to a *quantum paramagnet* obeying (2), by varying a system parameter at $T = 0$. There are many experimental and theoretical examples of such transitions: at the critical point, there is a qualitative change in the nature of the quantum wave function of the ground state.

One crucial feature of quantum phase transitions is that (2) is usually *not* sufficient to characterize the paramagnetic phase. In the Landau–Ginzburg–Wilson (LGW) approach to classical phase transitions, one focuses on the broken symmetry associated with (1) and defines a corresponding order parameter. A field theory of the thermal fluctuations of this order parameter is then sufficient to describe the transition to the paramagnetic phase and also to completely characterize the paramagnet. As we will discuss in

Handbook of Magnetism and Advanced Magnetic Materials. Edited by Helmut Kronmüller and Stuart Parkin. Volume 1: *Fundamentals and Theory*. ISBN: 978-0-470-02217-7.

Section 4, this procedure is not sufficient in some of the most interesting and physically important quantum phase transitions. The paramagnetic phase is not completely characterized by (2) and typically breaks some other symmetry of the Hamiltonian or has a more subtle 'topological' order. Furthermore, this additional 'order' of the paramagnet plays an important role in the theory of the quantum critical point.

We will begin Section 2 by introducing some simple lattice models and their experimental realizations, which exhibit quantum phase transitions. The theory of the critical point in these models is based on a natural extension of the LGW method, and this will be presented in Section 3. This section will also describe the consequences of a zero-temperature critical point on the nonzero-temperature properties. Section 4 will consider more complex models in which quantum interference effects play a more subtle role and which cannot be described in the LGW framework: such quantum critical points are likely to play a central role in the understanding of many of the correlated electron systems of current interest.

2 SIMPLE MODELS

2.1 Ising ferromagnet in a transverse field

This quantum phase transition is realized (Bitko, Rosenbaum and Aeppli, 1996) in the insulator $LiHoF_4$. The Ho ion has an $S = 1/2$ Ising spin that prefers to orient itself either parallel or antiparallel to a particular crystalline axis (say z). These Ising spins interact via the magnetic dipolar coupling and normally form a ferromagnetic ground state that obeys (1) for $\alpha = z$. As described in the subsequent text, upon application of a (transverse) magnetic field in the plane perpendicular to the z axis, quantum fluctuations of the Ising spin are enhanced, and there is eventually a quantum phase transition to a paramagnetic state obeying (2) for $\alpha = z$.

Rather than explore the full complexity of the experimentally relevant model, we will restrict our attention to a simple one-dimensional model with nearest-neighbor couplings that displays much of the same physics. The dynamics of this quantum Ising spin chain is described by the simple Hamiltonian

$$H_I = -J \sum_{j=1}^{N-1} \hat{\sigma}_j^z \hat{\sigma}_{j+1}^z - gJ \sum_{j=1}^{N} \hat{\sigma}_j^x \tag{3}$$

where $\hat{\sigma}_j^\alpha$ are the Pauli matrices, which act on the Ising spin degrees of freedom ($\hat{S}_j^\alpha \propto \hat{\sigma}_j^\alpha$), $J > 0$ is the ferromagnetic coupling between nearest-neighbor spins, and $g \geq 0$ is a dimensionless coupling constant, which determines the strength of the transverse field. In the thermodynamic limit ($N \to \infty$), the ground state of H_I exhibits a second-order quantum phase transition as g is tuned across a critical value $g = g_c$ (for the specific case of H_I it is known that $g_c = 1$), as we will now illustrate.

First, consider the ground state of H_I for $g \ll 1$. At $g = 0$, there are two degenerate *ferromagnetically ordered* ground states

$$|\Uparrow\rangle = \prod_{j=1}^{N} |\uparrow\rangle_j \quad ; \quad |\Downarrow\rangle = \prod_{j=1}^{N} |\downarrow\rangle_j \tag{4}$$

Each of these states breaks a discrete 'Ising' symmetry of the Hamiltonian – rotations of all spins by 180 °C about the x axis. These states are more succinctly characterized by defining the ferromagnetic moment N_0 by

$$N_0 = \langle \Uparrow | \hat{\sigma}_j^z | \Uparrow \rangle = - \langle \Downarrow | \hat{\sigma}_j^z | \Downarrow \rangle \tag{5}$$

At $g = 0$, we clearly have $N_0 = 1$. A key point is that in the thermodynamic limit this simple picture of the ground state survives for a finite range of small g (indeed, for all $g < g_c$), but with $0 < N_0 < 1$. The quantum tunneling between the two ferromagnetic ground states is exponentially small in N (and, so, can be neglected in the thermodynamic limit), and so the ground state remains twofold degenerate, and the discrete Ising symmetry remains broken. The change in the wave functions of these states from equation (4) can be easily determined by perturbation theory in g: these small g quantum fluctuations reduce the value of N_0 from unity but do not cause the ferromagnetism to disappear.

Now consider the ground state of H_I for $g \gg 1$. At $g = \infty$ there is a single *nondegenerate* ground state, which fully preserves all symmetries of H_I:

$$|\Rightarrow\rangle = 2^{-N/2} \prod_{j=1}^{N} \left(|\uparrow\rangle_j + |\downarrow\rangle_j \right) \tag{6}$$

It is easy to verify that this state has no ferromagnetic moment $N_0 = \langle \Rightarrow | \hat{\sigma}_j^z | \Rightarrow \rangle = 0$. Further, perturbation theory in $1/g$ shows that these features of the ground state are preserved for a finite range of large g values (indeed, for all $g > g_c$). One can visualize this ground state as one in which strong quantum fluctuations have destroyed the ferromagnetism, with the local magnetic moments quantum tunneling between 'up' and 'down' on a timescale of the order $\hbar/J$.

Given the very distinct signatures of the small g and large g ground states, it is clear that the ground state cannot evolve smoothly as a function of g. There must be at least one point of nonanalyticity as a function of g: For H_I it is known

that there is only a single nonanalytic point, and this is at the location of a second-order quantum phase transition at $g = g_c = 1$.

The character of the excitations above the ground state also undergoes a qualitative change across the quantum critical point. In both the $g < g_c$ and $g > g_c$ phases, these excitations can be described in the Landau *quasiparticle* scheme, that is, as superpositions of nearly independent particle-like excitations; a single, well-isolated quasiparticle has an infinite lifetime at low excitation energies. However, the physical nature of the quasiparticles is very different in the two phases. In the ferromagnetic phase, with $g < g_c$, the quasiparticles are domain walls between regions of opposite magnetization:

$$|j, j+1\rangle = \prod_{k=1}^{j} |\uparrow\rangle_k \prod_{\ell=j+1}^{N} |\downarrow\rangle_\ell \tag{7}$$

This is the exact wave function of a stationary quasiparticle excitation between sites j and $j+1$ at $g = 0$; for small nonzero g, the quasiparticle acquires a 'cloud' of further spin flips and also becomes mobile. However, its qualitative interpretation as a domain wall between the two degenerate ground states remains valid for all $g < g_c$. In contrast, for $g > g_c$, there is no ferromagnetism, and the nondegenerate paramagnetic state has a distinct quasiparticle excitation:

$$|j\rangle = 2^{-N/2} \left(|\uparrow\rangle_j - |\downarrow\rangle_j\right) \prod_{k \neq j} \left(|\uparrow\rangle_k + |\downarrow\rangle_k\right) \tag{8}$$

This is a stationary 'flipped-spin' quasiparticle at site j, with its wave function exactly at $g = \infty$. Again, this quasiparticle is mobile and applicable for all $g > g_c$, but there is no smooth connection between equations (8) and (7).

2.2 Coupled dimer antiferromagnet

Now we consider a model of $S = 1/2$ spins that interact via an antiferromagnetic exchange, and the Hamiltonian has full SU(2) spin rotation invariance. Physically, the cuprates are by far the most important realization of Hamiltonians in this class. However, rather than facing the daunting complexity of those compounds, it is useful to study simpler insulators in which a quantum phase transition from an antiferromagnet to a paramagnet can be explored. One experimentally and theoretically well-studied system (Tanaka *et al.*, 2001; Oosawa *et al.*, 2003; Rüegg *et al.*, 2003; Matsumoto, Normand, Rice and Sigrist, 2002, 2004) is $TlCuCl_3$. Here the $S = 1/2$ spins reside on the Cu^+ ions, which reside in a rather complicated spatial arrangement. As in Section 2.1, we will not explore the full complexity of the experimental magnet, but be satisfied with a caricature that captures the essential physics. The most important feature of the crystal structure of $TlCuCl_3$ (as will become clear in Section 4) is that it is naturally *dimerized*, that is, there is a pairing between Cu spins that respects all symmetries of the crystal structure. So we will consider the simplest dimer antiferromagnet of $S = 1/2$ spins that exhibits a quantum phase transition essentially equivalent to that found in $TlCuCl_3$.

The Hamiltonian of the dimer antiferromagnet is illustrated in Figure 1 and is given by

$$H_d = J \sum_{\langle jk \rangle \in A} \left(\hat{\sigma}_j^x \hat{\sigma}_k^x + \hat{\sigma}_j^y \hat{\sigma}_k^y + \hat{\sigma}_j^z \hat{\sigma}_k^z\right) + \frac{J}{g} \sum_{\langle jk \rangle \in B} \left(\hat{\sigma}_j^x \hat{\sigma}_k^x + \hat{\sigma}_j^y \hat{\sigma}_k^y + \hat{\sigma}_j^z \hat{\sigma}_k^z\right) \tag{9}$$

where $J > 0$ is the antiferromagnetic exchange constant, $g \geq 1$ is the dimensionless coupling, and the set of nearest-neighbor links $\mathcal{A}$ and $\mathcal{B}$ are defined in Figure 1. An important property of H_d is that it is now invariant under the full SU(2) group of spin rotations under which the $\hat{\sigma}^\alpha$ transform as ordinary vectors (in contrast to the Z_2 symmetry group of H_I). In analogy with H_I, we will find that H_d undergoes a quantum phase transition from a paramagnetic phase that preserves all symmetries of the Hamiltonian at large g to an *antiferromagnetic* phase that breaks the SU(2) symmetry at small g. This transition occurs at a critical value $g = g_c$, and the best current numerical estimate is (Matsumoto, Yasuda, Todo and Takayama, 2002) $1/g_c = 0.52337(3)$.

As in the previous subsection, we can establish the existence of such a quantum phase transition by contrasting the disparate physical properties at large g with those at $g \approx 1$. At $g = \infty$ the exact ground state of H_d is

$$|\text{spin gap}\rangle = \prod_{\langle jk \rangle \in A} \frac{1}{\sqrt{2}} \left(|\uparrow\rangle_j |\downarrow\rangle_k - |\downarrow\rangle_j |\uparrow\rangle_k\right) \tag{10}$$

and is illustrated in Figure 2. This state is nondegenerate and invariant under spin rotations and, so, is a paramagnet: the qubits are paired into spin-singlet valence bonds across

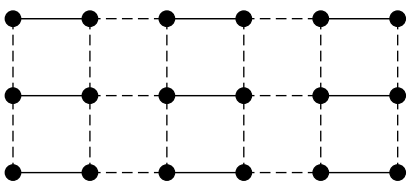

Figure 1. The coupled dimer antiferromagnet. Qubits (i.e., $S = 1/2$ spins) are placed on the sites, the $\mathcal{A}$ links are shown as full lines, and the $\mathcal{B}$ links as dashed lines.

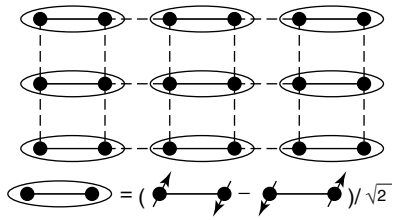

Figure 2. The paramagnetic state of H_d for $g > g_c$. The state illustrated is the exact ground state for $g = \infty$, and it is adiabatically connected to the ground state for all $g > g_c$.

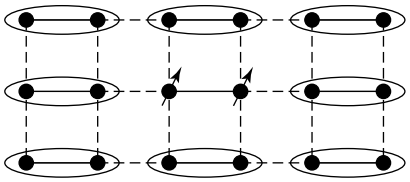

Figure 3. The triplon excitation of the $g > g_c$ paramagnet. The stationary triplon is an eigenstate only for $g = \infty$ but it becomes mobile for finite g.

all the $\mathcal{A}$ links. The excitations above the ground state are created by breaking a valence bond, so that the pair of spins form a spin triplet with total spin $S = 1$ – this is illustrated in Figure 3. It costs a large energy to create this excitation, and at finite g the triplet can hop from link to link, creating a gapped *triplon* quasiparticle excitation. This is similar to the large g paramagnet for H_I, with the important difference that each quasiparticle is now threefold degenerate.

At $g = 1$, the ground state of H_d is not known exactly. However, at this point, H_d becomes equivalent to the nearest-neighbor square-lattice antiferromagnet, and this is known to have antiferromagnetic order in the ground state, as illustrated in Figure 4. This state is similar to the ferromagnetic ground state of H_I, with the difference that the magnetic moment now acquires a staggered pattern on the two sublattices, rather than the uniform moment of the ferromagnet. Thus, in this ground state,

$$\langle \mathrm{AF}| \hat{\sigma}_j^{\alpha} |\mathrm{AF}\rangle = N_0 \eta_j n_{\alpha} \tag{11}$$

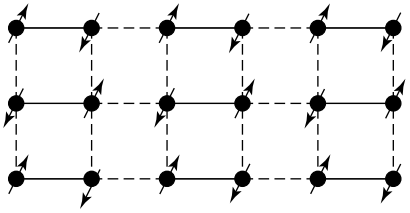

Figure 4. Schematic of the ground state with antiferromagnetic order with $g < g_c$.

where $0 < N_0 < 1$ is the antiferromagnetic (or Néel) moment, $\eta_j = \pm 1$ identifies the two sublattices in Figure 4, and n_{α} is an arbitrary unit vector specifying the orientation of the spontaneous magnetic moment that breaks the O (3) spin rotation invariance of H_d. The excitations of the antiferromagnet are also distinct from those of the paramagnet: they are a *doublet* of spin waves consisting of a spatial variation in the local orientation n_{α} of the antiferromagnetic order; the energy of this excitation vanishes in the limit of long wavelengths, in contrast to the finite energy gap of the triplon excitation of the paramagnet.

As with H_I, we can conclude from the distinct characters of the ground states and excitations for $g \gg 1$ and $g \approx 1$ that there must be a quantum critical point at some intermediate $g = g_c$.

3 QUANTUM CRITICALITY

The simple considerations of Section 2 have given a rather complete description (based on the quasiparticle picture) of the physics for $g \ll g_c$ and $g \gg g_c$. We turn, finally, to the region $g \approx g_c$. For the specific models discussed in Section 2, a useful description is obtained by a method that is a generalization of the LGW method developed earlier for thermal phase transitions. However, some aspects of the critical behavior (e.g., the general forms of equations (14–16)) will apply to the quantum critical point of Section 4 also.

Following the canonical LGW strategy, we need to identify a collective order parameter that distinguishes the two phases. This is clearly given by the ferromagnetic moment in equation (5) for the quantum Ising chain and the antiferromagnetic moment in equation (11) for the coupled dimer antiferromagnet. We coarse-grain these moments over some finite averaging region, and at long wavelengths this yields a real-order parameter field ϕ_{α}, with the index $\alpha = 1 \ldots n$. For the Ising case, we have $n = 1$ and ϕ_{α} is a measure of the local average of N_0 as defined in equation (5). For the antiferromagnet, a extends over the three values x, y, z (so $n = 3$), and the three components of ϕ_{α} specify the magnitude and orientation of the local antiferromagnetic order in equation (11); note that the average orientation of a specific spin at site j is η_j times the local value of ϕ_{α}.

The second step in the LGW approach is to write down a general field theory for the order parameter that is consistent with all symmetries of the underlying model. As we are dealing with a quantum transition, the field theory has to extend over *space–time*, with the temporal fluctuations representing the sum over histories in the Feynman path integral approach. With this reasoning, the proposed partition function for the vicinity of the critical point takes the

following form:

$$\mathcal{Z}_\phi = \int \mathcal{D}\phi_\alpha(x,\tau)\exp\Bigg[-\int \mathrm{d}^d x\,\mathrm{d}\tau\left(\frac{1}{2}\big((\partial_\tau\phi_\alpha)^2 + c^2(\nabla_x\phi_\alpha)^2 + s\phi_\alpha^2\big) + \frac{u}{4!}\left(\phi_\alpha^2\right)^2\right)\Bigg] \tag{12}$$

Here τ is imaginary time, there is an implied summation over the n values of the index a, c is a velocity, and s and $u > 0$ are coupling constants. This is a field theory in $d+1$ space–time dimensions, in which the Ising chain corresponds to $d = 1$ and the dimer antiferromagnet to $d = 2$. The quantum phase transition is accessed by tuning the 'mass' s: There is a quantum critical point at $s = s_c$, and the $s < s_c$ ($s > s_c$) regions correspond to the $g < g_c$ ($g > g_c$) regions of the lattice models. The $s < s_c$ phase has $\langle\phi_\alpha\rangle \neq 0$, and this corresponds to the spontaneous breaking of spin rotation symmetry noted in equations (5) and (11) for the lattice models. The $s > s_c$ phase is the paramagnet with $\langle\phi_\alpha\rangle = 0$. The excitations in this phase can be understood as small harmonic oscillations of ϕ_α about the point (in field space) $\phi_\alpha = 0$. A glance at equation (12) shows that there are n such oscillators for each wave vector. These oscillators clearly constitute the $g > g_c$ quasiparticles found earlier in equation (8) for the Ising chain (with $n = 1$) and the triplon quasiparticle (with $n = 3$, illustrated in Figure 3) for the dimer antiferromagnet.

We have now seen that there is a perfect correspondence between the phases of the quantum field theory $\mathcal{Z}_\phi$ and those of the lattice models H_I and H_d. The power of the representation in equation (12) is that it also allows us to get a simple description of the quantum critical point. In particular, readers may already have noticed that if we interpret the temporal direction τ in equation (12) as another spatial direction, then $\mathcal{Z}_\phi$ is simply the classical partition function for a thermal phase transition in a ferromagnet in $d+1$ dimensions: this is the canonical model for which the LGW theory was originally developed. We can now take over standard results for this classical critical point and obtain some useful predictions for the quantum critical point of $\mathcal{Z}_\phi$. It is useful to express these in terms of the dynamic susceptibility defined by

$$\chi(k,\omega) = \frac{i}{\hbar}\int \mathrm{d}^d x \int_0^\infty \mathrm{d}t\,\left\langle\left[\hat{\phi}(x,t),\hat{\phi}(0,0)\right]\right\rangle_T e^{-ikx+i\omega t} \tag{13}$$

Here $\hat{\phi}$ is the Heisenberg field operator corresponding to the path integral in equation (12), the square brackets represent a commutator, and the angular brackets an average over the partition function at a temperature T. The structure of χ can be deduced from the knowledge that the quantum correlators of $\mathcal{Z}_\phi$ are related by analytic continuation in time to the corresponding correlators of the classical statistical mechanics problem in $d+1$ dimensions. The latter are known to diverge at the critical point as $\sim 1/p^{2-\eta}$ where p is the $(d+1)$-dimensional momentum, η is the anomalous dimension of the order parameter ($\eta = 1/4$ for the quantum Ising chain). Knowing this, we can deduce the form of the quantum correlator in equation (13) at the zero-temperature quantum critical point

$$\chi(k,\omega) \sim \frac{1}{(c^2k^2-\omega^2)^{1-\eta/2}}\ ;\ T = 0,\ g = g_c \tag{14}$$

The most important property of equation (14) is the absence of a quasiparticle pole in the spectral density. Instead, $\mathrm{Im}\,(\chi(k,\omega))$ is nonzero for all $\omega > ck$, reflecting the presence of a continuum of critical excitations. Thus the stable quasiparticles found at low enough energies for all $g \neq g_c$ are absent at the quantum critical point.

We now briefly discuss the nature of the phase diagram for $T > 0$ with g near g_c. In general, the interplay between quantum and thermal fluctuations near a quantum critical point can be quite complicated (Sachdev, 1999), and we cannot discuss it in any detail here. However, the physics of the quantum Ising chain is relatively simple and also captures many key features found in more complex situations and is summarized in Figure 5. For all $g \neq g_c$ there is a range of low temperatures ($T \lesssim |g - g_c|$) where the long-time dynamics can be described using a dilute gas of thermally excited quasiparticles. Further, the dynamics of these quasiparticles is quasiclassical, although we reiterate that the nature of the quasiparticles is entirely distinct on opposite sides of the quantum critical point. Most interesting, however, is the novel *quantum critical* region $T \gtrsim |g - g_c|$ where neither a quasiparticle picture nor a quasiclassical description are appropriate. Instead, we have to understand

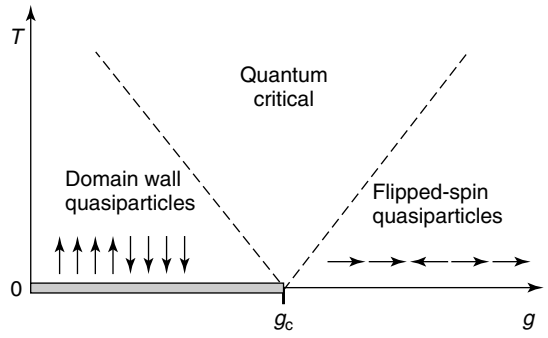

Figure 5. Nonzero-temperature phase diagram of H_I. The ferromagnetic order is present only at $T = 0$ on the shaded line with $g < g_c$. The dashed lines at finite T are crossovers out of the low T quasiparticle regimes where a quasiclassical description applies. The state sketched on the paramagnetic side used the notation $|{\rightarrow}\rangle_j = 2^{-1/2}(|{\uparrow}\rangle_j + |{\downarrow}\rangle_j)$ and $|{\leftarrow}\rangle_j = 2^{-1/2}(|{\uparrow}\rangle_j - |{\downarrow}\rangle_j)$.

the influence of temperature on the critical continuum associated with equation (14). This is aided by scaling arguments, which show that the only important frequency scale that characterizes the spectrum is $k_B T/\hbar$, and the crossovers near this scale are universal, that is, independent of specific microscopic details of the lattice Hamiltonian. Consequently, the zero-momentum dynamic susceptibility in the quantum critical region takes the following form at small frequencies:

$$\chi(k=0,\omega) \sim \frac{1}{T^{2-\eta}} \frac{1}{(1-i\omega/\Gamma_R)} \tag{15}$$

This has the structure of the response of an overdamped oscillator, and the damping frequency Γ_R is given by the universal expression

$$\Gamma_R = \left(2\tan\frac{\pi}{16}\right)\frac{k_B T}{\hbar} \tag{16}$$

The numerical proportionality constant in equation (16) is specific to the quantum Ising chain; other models also obey equation (16), but with a different numerical value for this constant.

4 BEYOND LGW THEORY

The quantum transitions discussed so far have a critical theory identical to that found for classical thermal transitions in $d+1$ dimensions. Over the last decade, it has become clear that there are numerous models of key physical importance for which such a simple classical correspondence does not exist. In these models, quantum *Berry phases* are crucial in establishing the nature of the phases and of the critical boundaries between them. In less technical terms, a signature of this subtlety is an important simplifying feature that was crucial in the analyses of Section 2: both models had a straightforward $g \to \infty$ limit in which we were able to write down a simple, nondegenerate, ground-state wave function of the 'disordered' paramagnet. In many other models, identification of the 'disordered' phase is not as straightforward: specifying absence of a particular magnetic order as in (2) is *not* enough to identify a quantum state, as we still need to write down a suitable wave function. Often, subtle quantum interference effects induce new types of order in the 'disordered' state, and such effects are entirely absent in the LGW theory.

An important example of a system displaying such phenomena is the $S = 1/2$ square-lattice antiferromagnet with additional frustrating interactions. The quantum degrees of freedom are identical to those of the coupled dimer antiferromagnet, but the Hamiltonian preserves the full point-group symmetry of the square lattice:

$$H_s = \sum_{j<k} J_{jk}\left(\hat{\sigma}_j^x\hat{\sigma}_k^x + \hat{\sigma}_j^y\hat{\sigma}_k^y + \hat{\sigma}_j^z\hat{\sigma}_k^z\right) + \ldots \tag{17}$$

Here the $J_{jk} > 0$ are short-range exchange interactions that preserve the square-lattice symmetry and the ellipses represent possible multiple spin terms. Now imagine tuning all the non-nearest-neighbor terms as a function of some generic coupling constant g. For small g, when H_s is nearly the square-lattice antiferromagnet, the ground state has antiferromagnetic order as in Figure 4 and equation (11). What is the 'disordered' ground state for large g now? One natural candidate is the spin-singlet paramagnet in Figure 2. However, because all nearest-neighbor bonds of the square lattice are now equivalent, the state in Figure 2 is degenerate with three other states obtained by successive 90 °C rotations about a lattice site. In other words, the state in Figure 2, when transferred to the square lattice, *breaks* the symmetry of lattice rotations by 90 °C. Consequently it has a new type of order, often called *valence-bond-solid* (VBS) order. It is now believed (Senthil *et al*., 2004a, b) that a large class of models like H_s do indeed exhibit a second-order quantum phase transition between the antiferromagnetic state and a VBS state (Figure 6). The existence of VBS order in the paramagnet and a second-order quantum transition are both features that are not predicted by LGW theory: these can only be understood by a careful study of quantum interference effects associated with Berry phases of spin fluctuations about the antiferromagnetic state.

We will now review the manner in which Berry phases lead to a breakdown of LGW field theory. We begin with the field theory $\mathcal{Z}_\phi$ in equation (12) for the coupled dimer antiferromagnet and modify it to include Berry phases of the spin. For each spin, the partition function acquires a

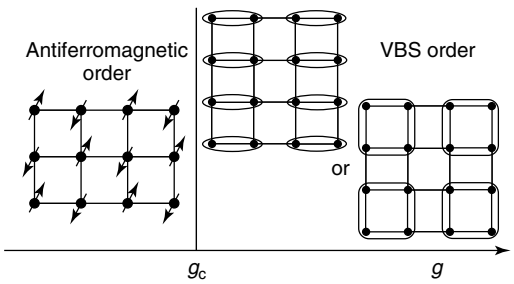

Figure 6. Phase diagram of H_s. Two possible VBS states are shown: one that is the analog Figure 2 and the other in which spins form singlets in a plaquette pattern. Both VBS states have a fourfold degeneracy due to breaking of square-lattice symmetry. So the novel critical point at $g = g_c$ (described by $\mathcal{Z}_z$) has the antiferromagnetic and VBS orders vanishing as it is approached from either side: this coincident vanishing of orders is generically forbidden in LGW theories.

phase factor $e^{iA/2}$, where A is the area enclosed by the world line of the spin on the unit sphere in spin space. To include this contribution, it is necessary to rewrite equation (12) in terms of a 'hard-spin' unit vector field $\mathbf{n}$, rather than the soft-spin field ϕ_α. The direction of $\mathbf{n}$ then represents the local orientation of the antiferromagnetic order parameter. Furthermore, the Berry phase contributions oscillate rapidly from site to site, and, so, we have to write them down on the underlying lattice and cannot directly take the continuum limit. In this manner, we obtain from equation (12)

$$\mathcal{Z}_{\mathbf{n}} = \int \mathcal{D}\mathbf{n}(r,\tau)\delta(\mathbf{n}^2(r,\tau)-1) \times \exp\left[\frac{i}{2}\sum_j \eta_j \int \mathrm{d}\tau \mathcal{A}_\tau(\mathbf{n}(r_j,\tau)) - \frac{1}{2gc}\int \mathrm{d}^2 r \mathrm{d}\tau \left((\partial_\tau \mathbf{n})^2 + c^2(\nabla_r \mathbf{n})^2\right)\right] \quad (18)$$

Excluding the first Berry phase term, this is the action of the so-called O (3) nonlinear sigma model in three space–time dimensions. Here, we are primarily interested in the consequences of the Berry phases: $\mathcal{A}_\tau(\mathbf{n}(\tau))\mathrm{d}\tau$ is defined as the oriented area of the spherical triangle defined by $\mathbf{n}(\tau)$, $\mathbf{n}(\tau+\mathrm{d}\tau)$, and an arbitrary reference point $\mathbf{n}_0$ (which is usually the north pole).

The theory in equation (18) can be considered as the 'minimal model' of quantum antiferromagnets on the square lattice. At small g there is the conventional magnetically ordered 'Néel' phase with $\langle\mathbf{n}\rangle \neq 0$, while at large g there is a 'quantum-disordered' paramagnetic phase, which preserves spin rotation invariance with $\langle\mathbf{n}\rangle = 0$. We are especially interested here in the nature of this paramagnetic state.

The key to an analysis of the large-g regime is a better understanding of the nature of $\mathcal{A}_\tau$. We will see that $\mathcal{A}_\tau$ behaves in many respects like the time component of a compact U(1) gauge field, and, indeed, this accounts for the suggestive notation. All physical results should be independent of the choice of the reference point $\mathbf{n}_0$, and it is easy to see by drawing triangles on the surface of a sphere that changes in $\mathbf{n}_0$ amount to gauge transformations of $\mathcal{A}_\tau$. If we change $\mathbf{n}_0$ to $\mathbf{n}_0'$, then the resulting $\mathcal{A}_\tau'$ is related to $\mathcal{A}_\tau$ by

$$\mathcal{A}_\tau' = \mathcal{A}_\tau - \partial_\tau \phi(\tau) \quad (19)$$

where $\phi(\tau)$ measures the oriented area of the spherical triangle defined by $\mathbf{n}(\tau)$, $\mathbf{n}_0$, and $\mathbf{n}_0'$. Furthermore, as we will discuss more completely in the subsequent text, the area of any spherical triangle is uncertain modulo 4π, and this accounts for the 'compactness' of the U(1) gauge theory.

We proceed with our analysis of $\mathcal{Z}_{\mathbf{n}}$. First, we discretize the gradient terms of the O (3) sigma model. We will limit our considerations here to antiferromagnets on the square lattice, but similar considerations apply to other bipartite lattices. We also discretize the imaginary-time direction, and (by a slight abuse of notation) use the same index j to refer to the sites of a three-dimensional cubic lattice in space–time. On such a lattice we can rewrite (18) as

$$\mathcal{Z}_{\mathbf{n}} = \int \prod_j d\mathbf{n}_j \delta(\mathbf{n}_j^2 - 1) \times \exp\left(\frac{1}{2g}\sum_{j,\mu} \mathbf{n}_j \cdot \mathbf{n}_{j+\hat{\mu}} + \frac{i}{2}\sum_j \eta_j \mathcal{A}_{j\tau}\right) \quad (20)$$

where the sum over μ extends over the three space–time directions, and $\mathcal{A}_{j\mu}$ is defined to equal the oriented area of the spherical triangle formed by $\mathbf{n}_j$, $\mathbf{n}_{j+\mu}$, and the arbitrary (but fixed) reference point $\mathbf{n}_0$. We have also dropped unimportant factors of the lattice spacing and the spin-wave velocity in (20).

The theory equation (20) is still cumbersome to work with because $\mathcal{A}_{j\tau}$ is a complicated function of $\mathbf{n}_j$. However, a purely local formulation can be found by reexpressing $\mathbf{n}_j$ in terms of *spinor* variables. We write

$$n_{j\alpha} = z_{ja}^* \sigma_{ab}^\alpha z_{jb} \quad (21)$$

where σ^α are the Pauli matrices, the z_{ja} are two-component complex spinor fields residing on the sites of the cubic lattice, and a is a *spinor* index that extends over $\uparrow$ and $\downarrow$. It is an interesting classical result in spherical trigonometry that the area of a spherical triangle can be expressed quite simply in terms of the spinor coordinates of its vertices. We will not explicitly review this analysis here, but refer the reader to a separate review (Sachdev, 2004). Using this result, it is not difficult to show that equation (20) is very closely related to the following partition function on the cubic lattice

$$\mathcal{Z}_z = \prod_{j\mu}\int_0^{2\pi} \frac{\mathrm{d}A_{j\mu}}{2\pi} \prod_{ja}\int \mathrm{d}z_{ja} \prod_j \delta\left(|z_{ja}|^2 - 1\right) \times \exp\left(\frac{1}{g}\sum_{j\mu}\left(z_{ja}^* e^{-iA_{j\mu}} z_{j+\mu,a} + \text{c.c.}\right) + i\sum_j \eta_j A_{j\tau}\right) \quad (22)$$

Note that we have introduced a new field $A_{j\mu}$ on each link of the cubic lattice, which is integrated over. This is a compact U(1) gauge field, which has replaced $\mathcal{A}_{j\mu}$ in equation (20): it can be shown (Sachdev, 2004) that the integral over $A_{j\mu}$ in equation (22) is dominated by values $A_{j\mu} \approx \mathcal{A}_{j\mu}/2$, and the resulting action differs

from equation (20) only in unimportant details. The crucial advantage of equation (22) is, of course, that there are no constraints between the z_{ja} and the $A_{j\mu}$, and we now have to deal with a purely local lattice gauge theory.

The theory $\mathcal{Z}_z$ now allows us to address the key questions linked to the breakdown of LGW theory. At small g, we have, as before, a Néel state with $\langle z_a \rangle \neq 0$, and hence from equation (21) $\langle \mathbf{n} \rangle \neq 0$. We will now describe the nature of the large g paramagnetic phase and of the transition between the small- and large-g phases in the subsections in the following text.

4.1 Nature of the paramagnet

For large g, there are strong fluctuations of the z_{ja}, and it therefore pays to integrate out the z_{ja} from $\mathcal{Z}_z$ and obtain an effective theory for the $A_{j\mu}$. This can be done order by order in $1/g$ in a 'high-temperature' expansion. The powers of $1/g$ yield terms dependent upon gauge-invariant U(1) fluxes on loops of all sizes residing on the links of the cubic lattice. For our purposes, it is sufficient to retain only the simplest such term on elementary square plaquettes, yielding the partition function

$$\mathcal{Z}_A = \prod_{j\mu} \int_0^{2\pi} \frac{\mathrm{d}A_{j\mu}}{2\pi} \times \exp\left(\frac{1}{e^2} \sum_{\square} \cos\left(\epsilon_{\mu\nu\lambda} \Delta_\nu A_{j\lambda} \right) + i \sum_j \eta_j A_{j\tau} \right) \tag{23}$$

where $\epsilon_{\mu\nu\lambda}$ is the totally antisymmetric tensor in three space–time dimensions. Here the cosine term represents the conventional Maxwell action for a compact U(1) gauge theory: it is the simplest local term which is consistent with the gauge symmetry and periodic under $A_{j\mu} \to A_{j\mu} + 2\pi$. The sum over $\square$ in (23) extends over all plaquettes of the cubic lattice, Δ_μ is the standard discrete lattice derivative ($\Delta_\mu f_j \equiv f_{j+\mu} - f_j$ for any f_j), and e^2 is a coupling constant. We expect the value of e to increase monotonically with g.

The properties of a pure compact U(1) theory have been described by Polyakov (1987). Here we need to extend his analysis to include the all-important Berry phases in $\mathcal{Z}_A$. The Berry phase has the interpretation of a $\int J_\mu A_\mu$ coupling to a static matter field with 'current' $J_\mu = \delta_{\mu\tau}$, that is, static charges ± 1 on the two sublattices. It is this matter field that will crucially control the nature of the paramagnet.

Polyakov showed that the quantum fluctuations of the pure compact U(1) gauge theory were controlled by *monopole* tunneling events at which the U(1) gauge flux changed by 2π. In particular, at all values of the coupling e, the monopoles eventually proliferate at long enough distances and lead to confinement of 'electric' charges: here these electric charges are the $S = 1/2$ z_a quanta (also known as *spinons*).

For our purposes, we need to understand the influence of the Berry phase terms in $\mathcal{Z}_A$ on the monopoles. This is a subtle computation (Haldane, 1988; Read and Sachdev, 1990) that has been reviewed elsewhere (Sachdev, 2004). The final result is that each monopole can also be associated with a Berry phase factor. If $m_j^\dagger$ is the monopole creation at site j, then this appears in the partition function as

$$m_j^\dagger \zeta_j \tag{24}$$

where ζ_j is a fixed field taking the values 1, i, -1, $-i$ on the four square sublattices as shown in Figure 7.

An important consequence of these Berry phases is that the monopole operator now transforms nontrivially under the operations of the square-lattice space group. Indeed, the partition function of the antiferromagnet must be invariant under all space group operations, and, so, by demanding the invariance of equation (24), we deduce the transformation properties of the monopole operator. A simple analysis of equation (24) then shows that

$$\begin{aligned} T_x &: m \to i m^\dagger \\ T_y &: m \to -i m^\dagger \\ R^{\mathrm{dual}}_{\pi/2} &: m \to m^\dagger \\ I^{\mathrm{dual}}_x &: m \to m \\ \mathcal{T} &: m \to m \end{aligned} \tag{25}$$

Here $T_{x,y}$ are translations by one lattice spacing along the x,y axes, $R^{\mathrm{dual}}_{\pi/2}$ is a rotation by $\pi/2$ about a site of the dual lattice, I^{dual}_x is reflection about the y axis of the dual lattice, and $\mathcal{T}$ is time reversal.

The transformation properties in equation (25) now allow us to relate the monopole operator to physical observables by searching for combinations of spin operators that have

1	i	1	i
$-i$	-1	$-i$	-1
1	i	1	i
$-i$	-1	$-i$	-1

Figure 7. The values of the fixed field ζ_i that specify the Berry phase of the monopole tunneling events. The monopoles are assumed to be centered on the sites of the dual lattice.

the same signature under space group operations. It turns out that the monopole operator is connected to the VBS order parameter (Read and Sachdev, 1990). From Figure 6, we note that VBS order is associated with modulations in the value of the nearest-neighbor spin-singlet correlations. So we can define a complex order parameter, $\psi_{\rm VBS}$, such that

$$\begin{aligned} {\rm Re}\left[\psi_{\rm VBS}\right] &= (-1)^{j_x} \sum_\alpha \hat{\sigma}^\alpha_j \hat{\sigma}^\alpha_{j+x} \\ {\rm Im}\left[\psi_{\rm VBS}\right] &= (-1)^{j_y} \sum_\alpha \hat{\sigma}^\alpha_j \hat{\sigma}^\alpha_{j+y} \end{aligned} \tag{26}$$

It is now easy to work out the space group transformations of $\psi_{\rm VBS}$. These lead to the important correspondence (Read and Sachdev, 1990; Senthil *et al*., 2004a, b)

$$m \sim e^{-i\pi/4}\psi_{\rm VBS} \tag{27}$$

We have now assembled all the ingredients necessary to describe the interplay between the monopole dynamics and the Berry phases in the paramagnetic phase. Using a mapping from the compact U(1) gauge theory to a dual effective action for monopoles, the proliferation of monopoles can be argued (Sachdev, 2004) to be equivalent to their 'condensation' with $\langle m_j \rangle \neq 0$. This argument also applies in the presence of Berry phases although cancellations among the phases now leads to a significantly smaller value of $\langle m_j \rangle$. Nevertheless, it can be shown that $\langle m_j \rangle$ is nonzero in the paramagnetic phase. Because of the nontrivial transformation properties of m_j under the square-lattice space group noted in the preceding text, it is then clear that a nonzero $\langle m_j \rangle$ spontaneously breaks the space group symmetry. Indeed, the connection in equation (27) shows that this broken symmetry is reflected in the appearance of VBS order. The precise configuration of the VBS order depends on the value of Arg$[\langle m \rangle]$. Using equation (27) and the space group transformations in the preceding text, the two VBS configurations shown in Figure 6 appear for Arg$[\langle m \rangle]$ equal to $\pi/4, 3\pi/4, 5\pi/4, 7\pi/4$ or $0, \pi/2, \pi, 3\pi/2$.

We have now established the breakdown of LGW theory induced by the Berry phases in $\mathcal{Z}_{\mathbf{n}}$ in equation (18). A theory of the quantum fluctuations of the LGW antiferromagnetic order parameter $\mathbf{n}$ does not lead to a featureless 'quantum disordered' paramagnetic state. Rather, subtle quantum interference effects induce a new VBS order parameter and an associated broken symmetry.

4.2 Deconfined criticality

We now turn to a brief discussion of the quantum phase transition between the small-g Néel phase with $\langle \mathbf{n} \rangle \neq 0$ and $\langle \psi_{\rm VBS} \rangle = 0$ and the large-g paramagnetic phase with $\langle \mathbf{n} \rangle = 0$ and $\langle \psi_{\rm VBS} \rangle \neq 0$. The two phases are characterized by two apparently independent order parameters, transforming very differently under spin and lattice symmetries. Given these order parameters, LGW theory predicts that there can be no direct second-order phase transition between them, except with fine tuning.

Recent work by Senthil *et al*. (2004a, b) has shown that this expectation is incorrect. Central to their argument is the demonstration that at a possible quantum critical point the monopole Berry phases in equation (24) lead to complete cancellation of monopole effects even at the longest distance scales. Recall that in the $g > g_c$ paramagnetic phase, Berry phases did lead to a partial cancellation of monopole contributions, but a residual effect was present at the longest scales. In contrast, the monopole suppression is complete at the $g = g_c$ quantum critical point.

With the suppression of monopoles, the identification of the continuum critical theory turns out to be quite straightforward. We simply treat $A_{j\mu}$ as a noncompact U(1) gauge field and take the naive continuum limit of the partition function $\mathcal{Z}_z$ in equation (22) while ignoring the monopoles and their Berry phases. This leads to the field theory

$$\begin{aligned} \mathcal{Z}_{zc} = \int \mathcal{D}z_a(x,\tau)\mathcal{D}A_\mu(x,\tau) \\ \times \exp\Bigg(-\int d^2x d\tau \Bigg[|(\partial_\mu - iA_\mu)z_a|^2 + s|z_a|^2 \\ + \frac{u}{2}(|z_a|^2)^2 + \frac{1}{2e^2}(\epsilon_{\mu\nu\lambda}\partial_\nu A_\lambda)^2\Bigg]\Bigg) \end{aligned} \tag{28}$$

In comparing $\mathcal{Z}_{zc}$ to the continuum theory $\mathcal{Z}_\phi$ for the coupling dimer antiferromagnet, note that the vector order parameter ϕ_α has been replaced by a spinor z_a, and these are related by $\phi_\alpha \sim z^*_a \sigma^\alpha_{ab} z_b$, from equation (21). So the order parameter has *fractionalized* into the z_a spinons. A second novel property of $\mathcal{Z}_z$ is the presence of a U(1) gauge field A_μ: this gauge field emerges near the critical point, even though the underlying model in equation (17) has only simple two-spin interactions.

Studies of fractionalized critical theories like $\mathcal{Z}_{zc}$ in other models with spin and/or charge excitations is an exciting avenue for further theoretical research and promises to have significant applications in a variety of correlated electron systems (Senthil, Sachdev and Vojta, 2005; Balents *et al*., 2005).

REFERENCES

Balents, L., Bartosch, L., Burkov, A., *et al*. (2005). Putting competing orders in their place near the Mott transition. *Physical Review B*, **71**, 144508.

Bitko, D., Rosenbaum, T.F. and Aeppli, G. (1996). Quantum critical behavior for a model magnet. *Physical Review Letters*, **77**, 940.

Haldane, F.D.M. (1988). O(3) nonlinear σ model and the topological distinction between integer- and half-integer-spin antiferromagnets in two dimensions. *Physical Review B*, **61**, 1029.

Matsumoto, M., Normand, B., Rice T.M. and Sigrist, M. (2002). Magnon dispersion in the field-induced magnetically ordered phase of $TlCuCl_3$. *Physical Review Letters*, **89**, 077203.

Matsumoto, M., Normand, B., Rice T.M. and Sigrist, M. (2004). Field- and pressure-induced magnetic quantum phase transitions in $TlCuCl_3$. *Physical Review B*, **69**, 054423.

Matsumoto, M., Yasuda, C., Todo, S. and Takayama, H. (2002). Ground-state phase diagram of quantum Heisenberg antiferromagnets on the anisotropic dimerized square lattice. *Physical Review B*, **65**, 014407.

Oosawa, A., Fujisawa, M., Osakabe, T., *et al*. (2003). Neutron diffraction study of the pressure-induced magnetic ordering in the spin gap system $TlCuCl_3$. *Journal of the Physical Society of Japan*, **72**, 1026.

Polyakov, A.M. (1987). *Gauge Fields and Strings*, Harwood Academic: New York.

Read, N. and Sachdev, S. (1990). Spin-Peierls, valence-bond solid, and Néel ground states of low-dimensional quantum antiferromagnets. *Physical Review B*, **42**, 4568.

Rüegg, Ch., Cavadini, N., Furrer, A., *et al*. (2003). Bose-Einstein condensation of the triplet states in the magnetic insulator $TlCuCl_3$. *Nature (London)*, **423**, 62.

Sachdev, S. (1999). *Quantum Phase Transitions*, Cambridge University Press: Cambridge.

Sachdev, S. (2004). In *Quantum Magnetism*, *Lecture Notes in Physics*, Schöllwock, U., Richter, J., Farnell, D.J.J. and Bishop R.A. (Eds.), Springer: Berlin, cond-mat/0401041.

Sachdev, S. (2005). Quantum phase transitions. In *Encyclopedia of Mathematical Physics*, Francoise, J-P., Naber, G. and Tsun, T.S.(Eds.), Elsevier: Amsterdam.

Senthil, T., Sachdev, S. and Vojta, M. (2005). Quantum phase transitions out of the heavy Fermi liquid. *Physica B*, **359–361**, 9.

Senthil, T., Vishwanath, A., Balents, L., *et al*. (2004a). Deconfined quantum critical points. *Science*, **303**, 1490.

Senthil, T., Balents, L., Sachdev, S., *et al*. (2004b). Quantum criticality beyond the Landau-Ginzburg-Wilson paradigm. *Physical Review B*, **70**, 144407.

Tanaka, H., Oosawa, A., Kato, T., *et al*. (2001). Observation of field-induced transverse Néel ordering in the spin gap system $TlCuCl_3$. *Journal of the Physical Society of Japan*, **70**, 939.

Theory of Magnetocrystalline Anisotropy and Magnetoelasticity in Transition-metal Systems

Ruqian Wu
University of California, Irvine, CA, USA

1 INTRODUCTION

The application of innovative experimental tools and the desire to grow nanostructures and novel materials in a controlled manner have produced an urgent need for highly reliable, robust, and predictive theoretical models and tools to achieve a quantitative understanding of their growth dynamics and the size, shape, and process dependencies of their physical properties. It has been recognized in many fields of materials science that state-of-the-art *ab initio* electronic structure calculations based on the density-functional theory (DFT) (Hohenberg and Kohn, 1964; Kohn and Sham, 1965) have been enormously successful, in both explaining existing phenomena and, more importantly, in predicting the properties of new systems. For example, the prediction of enhanced magnetic moments with lowered coordination numbers at clean metal surfaces has stimulated both theoretical and experimental explorations for new magnetic systems and phenomena in man-made nanostructures (Freeman and Wu, 1991; Freeman, 2002). Synergistic applications of theory and experiment, as demonstrated repeatedly in many areas of materials science, become a 'must' to further advance our understanding of magnetism in reduced dimensions.

It is known that the magnetism of ultrasmall entities is not stable due to super paramagnetism (Mermin and Wanger, 1966). Thermal fluctuation is the major obstacle for further size reduction of magnetic devices and has become an urgent issue for fundamental research. Innovative strategies to block thermal fluctuation with high magnetic anisotropy energy (MAE) have attracted enormous attention in recent years. Moreover, it is preferred to have the easy axis aligned along the perpendicular direction, a stipulation for the next generation high-density magnetic recording media (Weller and Moser, 1999; Weller *et al*., 2000; Wood, 2000; Bertram and Williams, 2000; Bertram and Shimizu, 2003). Experimental studies for spin reorientation transition (SRT) in various magnetic thin films have been very fruitful (Allenspach and Bischof, 1992; Li *et al*., 1994; Durr *et al*., 1997; Farle, 1998; Hope, Gu, Choi and Bland, 1998; Bland, Hope, Choi and Bode, 1999; Sander, 2004). Many possible tactics have been found to tailor magnetic anisotropies of nanostructured magnetic materials by manipulating lattice strains, compositions, capping layers, growth procedures, and surface adsorbates (Qiu, Pearson and Bader, 1993; Kawakami, Escorcia-Aparicio and Qiu, 1996; O'Brien, Droubay and Tonner, 1996; Millev and Kirschner, 1996; Oepen, Speckmann,

Handbook of Magnetism and Advanced Magnetic Materials. Edited by Helmut Kronmüller and Stuart Parkin. Volume 1: *Fundamentals and Theory*. ISBN: 978-0-470-02217-7.

Millev and Kirschner, 1997; Farle *et al*., 1997; van Dijken, Vollmer, Poelsema and Kirschner, 2000; Baberschke, Donath and Nolting, 2001; Yin *et al*., 2006), and the underlying electronic mechanism has been extensively explored through density-functional calculations (Johnson, Bloemen, den Broedert and de Vries, 1996; Wu and Freeman, 1999; Weinberger and Szunyogh, 2000; Hong *et al*., 2004). Furthermore, the strain dependence of MAE is the origin of another important magnetic phenomenon: magnetostriction (Gibbs, 2001; Engdahl, 2002). Anisotropic magnetostriction is generally described as the deformation of a body in response to a change in its direction of magnetization through the application of a magnetic field. Strongly magnetostrictive materials are widely utilized in various MEMS, sensor, actuator, and transducer applications. On the other hand, materials with extremely small magnetostrictive coefficients, λ (defined as $\lambda \propto \Delta l/l$, here l denotes the length of a sample), are desired in electric transformers, motor shielding, and magnetic recording. Innovative magnetic materials that have strong magnetostrictive yet ductile mechanical properties attract renewed attention for the miniaturization of operation devices (Clark *et al*., 2000; Clark, Wun-Fogle, Restorff and Lograsso, 2001). Owing to its intrinsic complexity, however, magnetostriction in transition-metal systems has rarely been tackled theoretically until very recently (Wu and Freeman, 1999).

In this chapter, I will review the current status of theoretical determination for magnetic anisotropy and magnetostriction of transition-metal systems. Examples used here, mainly from our own work, will elucidate the main challenges, solutions, and prospects of these vigorous research fields.

2 THEORETICAL BACKGROUND

Magnetic anisotropy depends on two factors: the spin-orbit coupling (SOC, the contribution from this part is called *magnetocrystalline anisotropy*, E_{MCA}) and the magnetostatic dipole–dipole interaction (this part of the anisotropy is called *shape anisotropy*). The shape anisotropy can be evaluated through summing up over discrete lattice

$$E_{\mathrm{shape}} = A \sum_{i \neq j} \left[\frac{(\vec{m}_i \cdot \vec{m}_j)}{|r_{ij}|^3} - \frac{3}{|\vec{r}_{ij}|^5} (\vec{m}_i \cdot \vec{r}_{ij})(\vec{m}_j \cdot \vec{r}_{ij}) \right] \tag{1}$$

Here A is a unit-dependent constant; $\vec{m}$ and $\vec{r}$ are local magnetic moments and position vectors, respectively. The determination of E_{MCA}, on the other hand, was a major challenge for theoretical calculations in the last two decades. The reliable determination of E_{MCA} for a given material requires highly accurate electronic structures and proper treatment of the weak SOC Hamiltonian. The single-particle energy (ε) and wave function (Ψ), the bases for predictions of almost all physical properties of real materials, can be obtained by solving the Kohn–Sham equation

$$\left[-\frac{1}{2}\nabla^2 + V_{\mathrm{ext}} + V_{\mathrm{c}} + V_{\mathrm{xc}} \right] \Psi = \varepsilon \Psi \tag{2}$$

Here, V_{ext} and V_{c} are the external potential and the Coulomb potential among electrons, while V_{xc} is the exchange-correlation potential that takes into account all the complexities of many-body interactions. In practical calculations, the local spin density approximation (LSDA) and the more advanced generalized gradient approximation (GGA) are usually adopted for V_{xc}. By using different basis functions, equation (2) is typically solved as a generalized matrix diagonalization problem of $H - \varepsilon S = 0$, where H and S are the matrices of Hamiltonian and overlap. In the implementation of the all-electron full-potential linearized augmented plane wave (FLAPW) method (Wimmer, Krakaur, Weinert and Freeman, 1981; Weinert, Wimmer and Freeman, 1982), the space is divided into three regions, namely, the near nucleus muffin-tin region, the vacuum region, and the remaining interstitial region. The wave function, potential, and charge density are expended in a 'natural' way without any artificial shape approximations. The spin-orbit coupling term is usually omitted in most of the DFT calculations hitherto. The so-called scalar-relativistic or semirelativistic (Koelling and Harmon, 1977) approaches significantly reduce computational demands but still provide good results for various physical properties such as optimized geometry, spin magnetic moment, and magnetic ordering. For the determination of E_{MCA} and λ, the relativistic SOC is essential. To the order of $(v/c)^2$, the SOC Hamiltonian is expressed as

$$H^{\mathrm{SOC}} = \frac{\hbar^2}{4m^2c^2} \frac{\partial V(r)}{r\,\partial r} \vec{l} \cdot \vec{S} = \xi(\vec{l} \cdot \vec{S}) \tag{3}$$

In practical calculations, the SOC Hamiltonian is expressed in a matrix format in the spin space (the two states are denoted as $\uparrow$ and $\downarrow$, respectively) as,

$$\vec{l} \cdot \vec{S} = \begin{pmatrix} \dfrac{A_+ + A_-}{2} \sin\theta + L_z \cos\theta & \left(A_- \cos^2\dfrac{\theta}{2} - A_+ \sin^2\dfrac{\theta}{2} - L_z \sin\theta \right) \mathrm{e}^{-i\phi} \\ \left(A_+ \cos^2\dfrac{\theta}{2} - A_- \sin^2\dfrac{\theta}{2} - L_z \sin\theta \right) \mathrm{e}^{i\phi} & -\dfrac{A_+ + A_-}{2} \sin\theta - L_z \cos\theta \end{pmatrix} \tag{4}$$

Here θ and ϕ are for polar and azimuthal angles of magnetization and $A^+ = e^{-i\phi}(L_x + iL_y)$ while $A^- = e^{i\phi}(L_x - iL_y)$. For 3d transition metals, it has been shown that involvement of H^{SOC} alters charge density, spin density, and spin moment negligibly (Wu and Freeman, 1999). In contrast, H^{SOC} has to be invoked in the self-consistence loop for the solution of the Kohn–Sham equations when heavy elements are involved, especially in nanoentities in which 4d and 5d elements are also magnetic.

In low dimensions, the leading term in E_{MCA} is the uniaxial anisotropy, $E_{MCA} = K\sin^2\theta + O(\sin^4\theta, \sin^4\phi)$. For the determination of K, the magnetocrystalline anisotropy force theorem (Daalderop, Kelly and Schuurmans, 1990; Wang, Wang, Wu and Freeman, 1996a)

$$E_{MCA} \equiv E(90^\circ) - E(0^\circ) \approx \sum_{occ'} \varepsilon_i(90^\circ) - \sum_{occ''} \varepsilon_i(0^\circ) \quad (5)$$

was adopted in most previous *ab initio* calculations. Because the sets of occupied states, that is, {occ′} and {occ″}, were determined through the Fermi filling scheme, which relies on very limited information from ε_i alone, a huge number of k points (>10 000 in the two dimensional Brillouin zone for thin films) are needed to restrain the numerical fluctuation (Gay and Richter, 1986; Daalderop, Kelly and Schuurmans, 1990). This hurdle was overcome in the last decade by using various broadening techniques (Trygg, Johansson, Eriksson and Wills, 1995; Hjortstam *et al*., 1997) and the state-tracking (Wang, Wu and Freeman, 1993) and the torque (Wang, Wang, Wu and Freeman, 1996b) schemes. Particularly, the torque method circumvents the need to differentiate energies. Instead, E_{MCA} is evaluated through the expectation values of the angular derivative of H^{SOC} with wave function at a magic angle $\Psi'(\theta_m, \phi_m)$. Here the prime indicates that the SOC is taken into account.

$$E_{MCA} = \sum_{i\in occ} \langle \Psi_i'(\theta_m, \phi_m)| \frac{\partial H^{SOC}}{\partial \theta} |\Psi_i'(\theta_m, \phi_m)\rangle \quad (6)$$

The magic angle (θ_m, ϕ_m) can be found from the symmetry, or more explicitly the form of angular dependence of total energy. For a uniaxial system, it can be proved that $\theta_m = 45^\circ$ and $\phi_m = 0^\circ$. Very stable results of uniaxial E_{MCA} have been obtained with a manageable number of k points, as elucidated in examples in the subsequent text.

The determination of magnetostrictive coefficients for real materials is another difficult problem for modern electronic structure theory (Wu and Freeman, 1999; Fahnle, Komelj, Wu and Guo, 2002; Komelj and Fahnle, 2006). In general, the size of the magnetoelastic strain induced by rotation of the magnetization depends on the directions of the measured strain and the spin moment. For a cubic material, the directional dependence of the fractional change in length can be expressed in terms of the direction cosines of the magnetization (α) and of the strain measurement (β) with respect to the crystalline axes

$$\frac{\Delta l}{l_0} = \frac{3}{2}\lambda_{001}\left[\sum_{i=1}^{3}\alpha_i^2\beta_i^2 - \frac{1}{3}\right] + 3\lambda_{111}\sum_{i\neq j}^{3}\alpha_i\alpha_j\beta_i\beta_j \quad (7)$$

If the measurement is carried out along the (001) direction, for example, $\alpha_x = \alpha_y = 0$ and $\alpha_z = 1$, then equation (7) can be simplified as $\Delta l/l_0 = 3/2\lambda_{001}[\alpha_z^2 - 1/3]$ or further, for systems with a single domain,

$$\lambda_{001} = \frac{1}{3}\frac{l_0(\theta = 0^\circ) - l_0(\theta = 90^\circ)}{l_0(\theta = 0^\circ) + l_0(\theta = 90^\circ)} \quad (8)$$

Clearly, λ_{001} represents the change in length along (001) when the magnetization turns from the x, y plane to the z direction. As a normal practice, the equilibrium lengths, $l_0(\theta)$, can be obtained by fitting the calculated total energies in a quadratic form

$$E(\theta = 0^\circ) = al^2 + bl + c; \quad \text{and}$$
$$E(\theta = 90^\circ) = al^2 + bl + c + E_{MCA} \quad (9)$$

From equation (8), one can get

$$\lambda_{001} = -\frac{2}{3}\frac{\frac{dE_{MCA}}{dl}}{b} \quad (10)$$

Since b is negative (a and l_0 are positive), λ and $\frac{dE_{MCA}}{dl}$ should *always* have the same sign. Obviously, the major challenge for first-principles calculations is the determination of $\frac{dE_{MCA}}{dl}$, which is typically very small.

3 MAGNETIC ANISOTROPY OF THIN FILMS

In most of the magnetic thin films, large uniaxial MAEs are induced not only by the surface and interface effects but also by lattice strains due to lattice mismatches and the presence of step edges (Baberschke, 1996; Kawakami, Escorcia-Aparicio and Qiu, 1996). The surface and interface contributions sensitively depend on the atomic relaxations, chemisorptions, and growth morphologies. Well-optimized structures are hence prerequisites for the determination of E_{MCA} through DFT calculations. Fortunately, most of the modern DFT packages can directly calculate atomic forces to expedite the structural optimization procedures. Nevertheless, one should note that while GGA significantly

improves the results of atomic structures for 3d transition metals over LSDA, it overestimates the volume of 4d and 5d elements as well as oxides. Extra care is thus needed to handle systems with mixing building blocks.

To understand complex magnetic films, it is instructive to first analyze the electronic origin of the E_{MCA} for a free-standing magnetic monolayer. The k distributions of E_{MCA} and the band structures of a Co monolayer, for example, are plotted in Figure 1 along the high-symmetry directions in the 2D Brillouin zone. Obvious correlation between the abrupt changes in E_{MCA} and the locations where bands cross the Fermi level discloses simple physics. Clearly, the large negative E_{MCA} for the Co monolayer (-1.34 meV/atom) mainly stems from contributions around the M point. This can be further traced to SOC interaction(s) between the occupied $d_{xz,yz}$ states ($m = \pm 1$, denoted as state 5 in Figure 1) and the unoccupied d_{z^2} state ($m = 0$, denoted as state 1 in Figure 1). Note only the pair across E_{F} with the same (different) magnetic quantum number(s) leads to a positive (negative) contribution to E_{MCA}. By knowing the origin of E_{MCA} of simple systems, one can tailor magnetic anisotropy by engineering the bands of the magnetic layer. For example, owing to the Co–Cu d-band hybridization, the Co-$d_{xz,yz}$ states are lowered in energy in Co/Cu(001) and Cu/Co/Cu(001). As a result, E_{MCA} becomes less negative in Co/Cu(001)and is positive in Cu/Co/Cu(001) (Gavrilenko and Wu, 1999), in good accordance with experimental data (Krams *et al*., 1992). Many calculations have been done in the last decade to study the effects of metal substrates or capping layers on the E_{MCA} of ultrathin magnetic thin films (Wu and Freeman, 1999; Weinberger and Szunyogh, 2000). It is now well established that values of K for magnetic films can be determined through high-quality DFT calculations with satisfactory accuracy; some of the calculations also give atom-resolved contributions from different layers (Uiberacker *et al*., 1999).

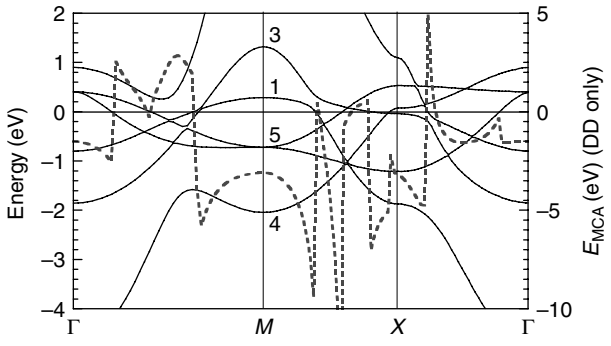

Figure 1. The band structure (thin solid lines, for minority spin only) and the EMCA (bold dashed line) of the Co(001) monolayer ($a = 4.8$ au) through LSDA calculations.

Interestingly, E_{MCA} of Fe, Co, and Ni films can be tuned by surface chemisorptions of O, CO, and H (Baek, Lee, Kim and Vescovo, 2003; Vollmer *et al*., 1999; Vollmer and Kirschner, 2000; van Dijken, Vollmer, Poelsema and Kirschner, 2000; Matsumura *et al*., 2002; Sander *et al*., 2004), and the underlying electronic mechanism has been actively explored through theory and experiment interplays. Figure 2 illustrates theoretical and experimental results of MAEs for O/Ni/Cu(001) from different regions, namely, the y interception of the $K(1/d)$ line is for bulk and its slope is for surface/interface (Hong *et al*., 2004). For O/Ni/Cu(001), the bulk contribution is 27 meV/atom, primarily caused by the tetragonal distortion in the Ni films grown on Cu(001) (Farle *et al*., 1997; Wu, Chen and Freeman, 1997a; Hjortstam *et al*., 1997). Contributions from the Cu/Ni and O/Ni interfaces are -59 and $-17\,\mu$eV/atom, respectively. The dramatic decrease in magnitude at the O/Ni interface leads to a shift of critical thickness for SRT from 10 Ni MLs in vacuum/Ni/Cu(001) to 5 Ni MLs in O/Ni/Cu(001), as given by the interception between the K(1/d) line with the horizontal line of $2\pi M^2$ in Figure 2(a). This brings the optimum record up to date for SRT in Ni/Cu(001), as compared to cases using Cu, hydrogen, or CO. Theoretical calculations reproduced the trend of experimental data very well, indicating the appropriateness of models. Analyses in electronic structures furthermore attributed the O-induced change in E_{MCA} to the new surface state with the d_{xz} feature caused by the O adlayer. O- and H-induced relaxation and buckling in the second layer also play a role. Surprisingly, the presence of O does not purge the magnetization in the surface region (Hong *et al*., 2004). Instead, the Ni surface magnetic moments are significantly enhanced (by more than 5% for Ni alone), especially when the sizable spin polarization of oxygen ($m_{\mathrm{O}} = 0.18\,\mu_{\mathrm{B}}$) is included. However, the magnetic moments of both O and Ni are significantly reduced if the atomic structure is optimized with LDA that produces better agreement with experimental X-ray magnetic circular dichroism data (Sorg *et al*., 2006).

4 MAGNETIC ANISOTROPY OF WIRES AND CHAINS

Ultrasmall monatomic chains, the smallest possible magnetic recording units (for 100–1000 TB in.$^{-2}$), are grown on vicinal substrates (Gambardella *et al*., 2002) or built by Scanning Tunnelling Microscope (STM) tip manipulation (Nilius, Wallis and Ho, 2002). Investigations of MAEs of magnetic clusters including molecule magnets are getting extensive attention for spintronics applications in the future (Sessoli, Gatteschi, Caneschi and Novak, 1993; Respaud,

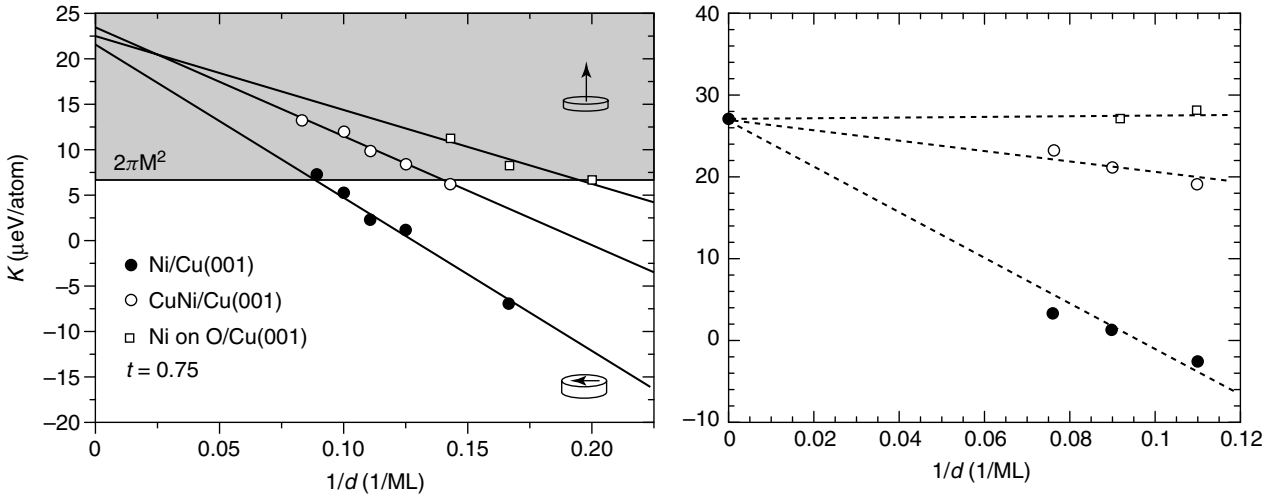

Figure 2. The experimental and theoretical results of magnetic anisotropy energies for Ni/Cu(001), Cu/Ni/Cu(001), and O/Ni/Cu(001).

1998; Caneschi *et al*., 1999; Waldmann *et al*., 2001). The bottleneck for exploitation of nanomagnets is thermal fluctuation, which produces super paramagnetism at finite temperature. A high MAE barrier is vital to maintain ferromagnetic ordering or hold up the magnetic relaxation. Experimentally, Jamet *et al*. studied magnetic anisotropy in a 3-nm cobalt cluster embedded in a niobium matrix and found the dominating role of atoms on the cluster surface (Barra, 1999; Jamet *et al*., 2001, 2004). Gambardella *et al*. reported giant MAEs of Co particles on Pt(111) (Gambardella *et al*., 2003, 2004). They also found that the easy axis of magnetization, the MAE, and the coercive field oscillate as a function of the transverse width of the Co wires on Pt(997). Rusponi *et al*. (2003) attempted to separate contributions of differently coordinated atoms in Co patches deposited on Pt(111) and concluded that the edge atoms play the dominant role in the perpendicular uniaxial anisotropy. Pratzer *et al*. studied Fe stripes on stepped W(110) and found an extremely narrow domain wall, as thin as 6 Å, presumably due to large MAE (Pratzer *et al*., 2001; Pratzer and Elmers, 2003).

Figure 3 displays magnetic phase diagram for a 10-atom monatomic chain, obtained through classical Monte Carlo simulations based on a classical model Hamiltonian. To have high blocking temperature (e.g., 300 K), below which the magnetization of each atom aligns along the easy axis and hence forms a ferromagnetic structure, stringent conditions are required, namely, $J = 320–420$ meV and $K = 30–50$ meV/atom. Such a large E_{MCA} cannot be achieved in nanoentities solely with 3d elements. For the free-standing or supported Co monatomic chains, for example, the amplitude of E_{MCA} is still a few tenths meV/atom (Hong and Wu, 2003). For Co chains on Pt(111), Lazarovits, Szunyogh, and Weinberger (2003). found that the easy axis is perpendicular to the surface, independent of the length of the chains. Fe_n

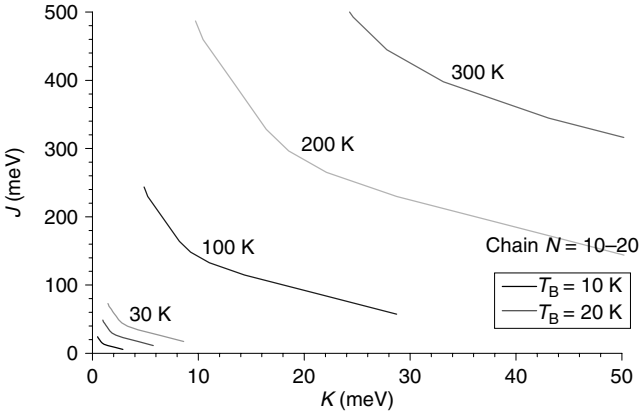

Figure 3. The phase diagram for a free-standing chain of 10 atoms, generated through classical Monte Carlo simulations.

chains grown on Cu(001), Cu(111) as well as embedded in the bulk Cu were also studied (Hong and Wu, 2003). Shick *et al*. found that a quasi-one-dimensional Co chain at the Pt(111) step edge has an easy axis at an odd angle of 20° toward the Pt step (Shick, Gornostyrev and Freeman, 1999; Shick, Maca and Oppeneer, 2004). In addition, the spin and orbital magnetic moments are noncollinear. The proportionality between MAE and the anisotropy of the orbital moment, a conjecture that is adopted for the measurement of E_{MCA} through the X-ray magnetic circular dichroism technique, was also examined for several systems (Ederer, Komelj and Fahnle, 2003; Hong and Wu, 2004).

Intriguingly, giant K up to 30–50 meV/atom was found possible through our recent DFT calculations as illustrated in Table 1. Model calculations for 3d–5d trimers, especially FeOsFe and FeIrFe, revealed large E_{MCA} up to 108 meV, due to both the high spin polarization of Fe and the strong SOC from the 5d atoms. In addition, all 5d atoms possess

Table 1. The calculated K, spin, and orbital magnetic moments distributed in different atoms. The easy axis for positive (negative) E_{MCA} is along (perpendicular to) the chain.

System and magnetic ordering	M_s (μ_B)		M_L (μ_B)		E_{MCA} (meV)
	3d	5d	3d	5d	
FeTaFe (↑↓↑)	2.99	−1.96	−0.16	0.30	−21
FeWFe (↑↓↑)	2.93	−2.85	0.10	0.13	−31
FeReFe (↑↑↑)	3.22	2.94	−0.03	−0.04	−31
FeOsFe (↑↑↑)	3.32	3.21	0.60	0.57	−75
FeIrFe (↑↑↑)	3.36	1.58	0.00	1.53	+108
FePtFe (↑↑↑)	3.34	0.69	0.20	0.34	−27

extraordinarily large spin and in some cases also orbital magnetic moments. In all the trimers, the Fe spin moment is stable and remains 2.99–3.36 μ_B. The spin moments of Ta and W align in an antiparallel manner to that of the adjacent Fe. The maximum induced spin moment occurs for Os, whereas the maximum induced orbital moment occurs for Ir. As indicated by the resonant features in their density of states, strong hybridization is found between Fe and 5d elements. For the FeIr trimer, analyses suggests that the contribution from spin-orbit interaction among the majority spin states, $E_{MCA}(\uparrow\uparrow)$, is negligible compared to $E_{MCA}(\downarrow\downarrow)$. Giant values of 30–60 meV/atom were also reported for stretched Ru or Rh wires by Mokrousov, Bihlmayer, Heinze and Blugel (2006) through FLAPW calculations.

5 MAGNETOSTRICTION OF TRANSITION-METAL BULKS AND ALLOYS

Despite the tremendous advances in modern electronic structure theory for studies in materials science, magnetostriction has been rarely tackled until very recently, due to its intrinsic complexity (Wu and Freeman, 1996; Wu, Chen and Freeman, 1997b, 1998). Benchmark calculations for cubic bulk Fe, Co, and Ni resulted in a good agreement when compared to experiment for λ_{001}. In contrast, the calculated λ_{111} ($+12 \times 10^{-6}$) differs in sign from the experimental data (-23×10^{-6}) (Fahnle, Komelj, Wu and Guo, 2002). This discrepancy was attributed to the incapability of LSDA, but the reliability of experimental data was also questioned with possible involvement of Si impurities. Komelj and Fahnle (2000, 2001, 2002, 2006) investigated the high-order magnetoelastic coefficients of bulk Fe, Co, and Ni. Burkert *et al.* also found that the MAE of FeCo alloy can be exceedingly large when the lattice is tetragonally distorted to a certain c/a ratio (Burkert, Nordstrom, Eriksson and Heinonen, 2004; Burkert *et al.*, 2004; Andersson *et al.*, 2006). One of the most interesting examples is the determination of λ for $Fe_{1-x}Ga_x$ alloys. It was recently found by Clark and collaborators (Clark *et al.*, 2000; Clark, Wun-Fogle, Restorff and Lograsso, 2001; Guruswamy *et al.*, 2000; Cullen *et al.*, 2001; Kellogg *et al.*, 2002) that Ga, when substituted for Fe in the common bcc Fe structure, increases the tetragonal magnetostriction, λ_{001}, over 10-fold above the magnetostriction of the pure bcc bulk Fe ($\lambda_{001} \approx 20 \times 10^{-6}$). As shown in Figure 4, λ_{001} increases with the Ga concentration monotonically when $x < 0.19$; decreases thereafter for $0.19 < x < 0.25$; and increases again if more Ga is added. This promises a possibility of achieving strong magnetostriction in ductile metallic materials, instead of in brittle rare-earth metal compounds (e.g., TERFENOL-D, etc.) (Engdahl, 2002). Strikingly, recent experiments revealed substantial softening in this alloy (Clark *et al.*, 2003). The value of its tetragonal shear elastic constant, $c' = (c_{11} - c_{12})/2$, decreases to 6.8 GPa at $x = 0.27$. Meanwhile, the magnetostrictive coefficients also depend on the quenching history, which indicates that the large magnetostriction is likely to associate with metastable geometries rather than the ground state one (Clark, Wun-Fogle, Restorff and Lograsso, 2001). Nonetheless, the mechanism of such an extraordinary enhancement is unclear.

While the structural phase diagram for $Fe_{1-x}Ga_x$ is rather complex, it is helpful to explore three basic simple structures for $x = 0.25$, namely, DO_3, B_2 like (or L_{60}), and $L1_2$. To determine magnetostrictive coefficients, lattice strain along the z axis (c/c_0) is used as a parameter. Explicitly, the constant-volume mode was adopted in lattice distortion for the $L1_2$ and DO_3 structures, whereas constant-area mode was adopted for the B_2-like structure. The calculated results of

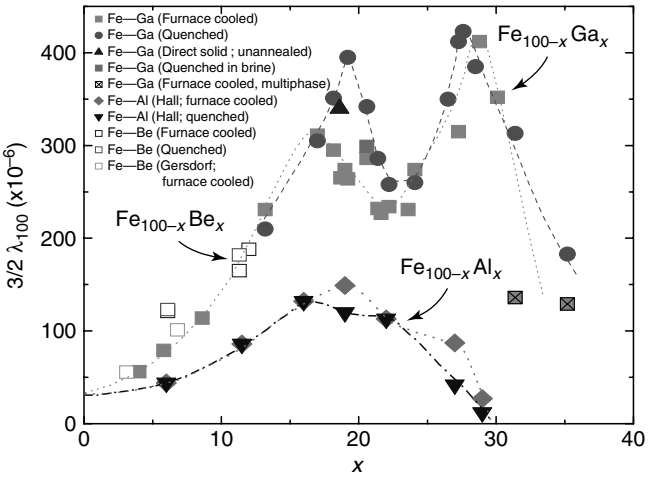

Figure 4. Magnetostrictive coefficients of $Fe_{1-x}Ga_x$ measured by A.E. Clark *et al.*

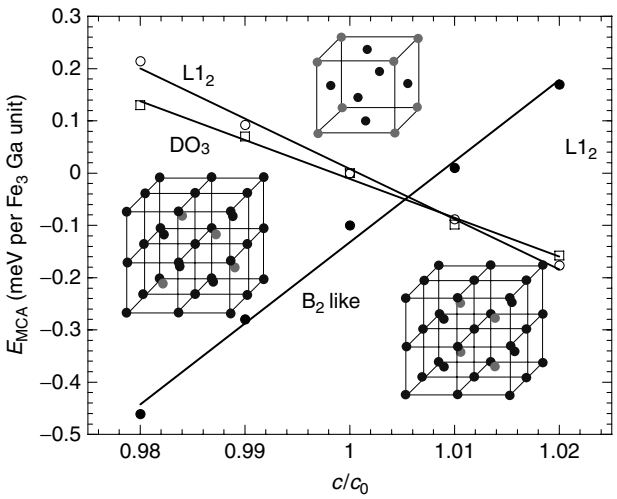

Figure 5. The calculated strain dependence of E_{MCA} of $Fe_{0.75}Ga_{0.25}$ in simple structures.

strain-dependent E_{MCA} are plotted in Figure 5. Interestingly, the calculated slope of E_{MCA} is positive only for the B_2-like structure. Quantitatively, the calculated values of λ_{001} are -107×10^{-6}, -298×10^{-6}, and $+380 \times 10^{-6}$ for the DO_3, $L1_2$, and B_2-like structures, respectively. Overall, the magnitude of λ_{001} for all these three structures is much larger than that for the pure bcc bulk Fe (20×10^{-6}), due to the stronger magnetoelastic coupling as well as the smaller Young's modulus. Experimentally, λ_{001} for $Fe_{1-x}Ga_x$ is $+150 \sim +200 \times 10^{-6}$ when x is 0.25. This indicates that the local B_2-like structure plays a key role in the strong positive magnetostriction of FeGa alloys (Wu, 2002). The change in sign of λ_{001} from the DO_3 structure to the B_2-like structure is very fascinating, since only the second-neighbor arrangement is altered. The calculated magnetic moments in the B_2-like structure ($2.48\,\mu_{\mathrm{B}}$ for Fe(1) in the mixed layer, $2.08\,\mu_{\mathrm{B}}$ for Fe(2) in the pure layer, and $-0.08\,\mu_{\mathrm{B}}$ for Ga) are very close to those in the DO_3 structure ($2.41\,\mu_{\mathrm{B}}$ for Fe(1), $1.96\,\mu_{\mathrm{B}}$ for Fe(2), and $-0.07\,\mu_{\mathrm{B}}$ for Ga). The difference originates from very subtle changes in their band structures. In the DO_3 structure, the negative magnetostriction is associated with strain dependence of the d_{z^2} and $d_{x^2-y^2}$ states in the unoccupied regime. Meanwhile, some of the Fe(2)-$d_{xz,yz}$ and -d_{xy} states become nonbonding states and they lie around the Fermi level in the minority spin channel. This enhances the SOC interaction between occupied t_{2g} states and the unoccupied e_g states and leads to large negative magnetostriction. For the B_2-like structure, the Fe(2)-$d_{xz,yz}$ states in the minority spin band become nondegenerate and some of them are unoccupied because of lower symmetry. Since they have the same magnetic quantum numbers ($m = \pm 1$), the SOC interaction between them leads to a positive magnetostriction.

Unfortunately, the B_2-like structure in the small cell is unstable under tetragonal distortion and one thus needs to consider more complex geometries. Our recent calculations found that the B_2-like structure can be stabilized either by mixing with the DO_3 structure or by removing some Ga atoms from the lattice. For the latter case, large magnetostrictive coefficient, $\lambda_{001} = +188 \times 10^{-6}$, is found for the $Fe_{0.81}Ga_{0.19}$ alloy in the B_2-like structure (by substituting one Ga atom with Fe in a 16-atom unit cell). In contrast, the DO_3-like structure still contributes a negative λ_{001} (-70×10^{-6}). Calculations using a large unit cell for $Fe_{0.75}Ga_{0.25}$ that combines the B_2-like and DO_3 structure result in a positive magnetostriction, $\lambda_{001} = +90 \times 10^{-6}$. Obviously, involvement of the B_2-like geometry is very important for attaining large positive magnetostriction. Total energy calculations also indicate that Ga atoms tend to distribute away from each other. Furthermore, the random alloy is less favorable in energy than those that retain pure Fe layers adjacent to the mixed layers.

6 CONCLUSIONS

As discussed through several examples in the preceding text, high-quality density-functional calculations can provide reliable results for magnetocrystalline anisotropy and magnetostriction in transition-metal systems. The insights revealed through analyses of electronic structures are imperative in guiding experimental procedures for the design of novel nanomagnetic materials. To determine E_{MCA} of nanostructures, a general treatment including noncollinear ordering is necessary, as was done in several recent studies (Nordstrom and Singh, 1996; Nakamura *et al*., 2004). The correlation and orbital polarization effects on E_{MCA} should also be examined, especially when the system has only a few atoms (Yang, Savrasov and Kotliar, 2001; Solovyev, 2005). Furthermore, *ab initio* treatment for spin relaxation, spin waves, and spin transport has been developed recently to explain experimental observations (Vomir *et al*., 2005; Steiauf and Fahnle, 2005) but more efforts are needed to enhance the capability and reliability of theoretical tools. Some of these topics are discussed more extensively in other chapters in this handbook.

ACKNOWLEDGMENTS

The author is indebted to Profs A.J. Freeman, D.S. Wang, D.L. Mills and Drs A.E. Clark, and K.B. Hathaway for helpful discussions. Part of the calculations was done by Prof. J.S. Hong. The work is supported by the DOE-BES (DE-FG02-05ER46237).

REFERENCES

Allenspach, R. and Bischof, A. (1992). Magnetization direction switching in Fe/Cu(100) epitaxial films: temperature and thickness dependence. *Physical Review Letters*, **69**, 3385–3388.

Andersson, G., Burkert, T., Warnicke, P., *et al*. (2006). Perpendicular magnetocrystalline anisotropy in tetragonally distorted Fe-Co alloys. *Physical Review Letters*, **96**, 037205.

Baberschke, K. (1996). The magnetism of nickel monolayers. *Applied Physics A*, **62**, 417–427.

Baberschke, K., Donath, M. and Nolting, W. (Eds.) (2001). *Band-ferromagnetism*, Springer-Verlag: Berlin.

Baek, I.G., Lee, H.G., Kim, H.K. and Vescovo, E. (2003). Spin reorientation transition in Fe(110) thin films: the role of surface anisotropy. *Physical Review B*, **67**, 075401.

Barra, A.L. (1999). Single-molecule magnet behavior of a tetranuclear iron(III) complex. The origin of slow magnetic relaxation in iron(III) clusters. *Journal of the American Chemical Society*, **121**, 5302–5310.

Bertram, H.N. and Williams, M. (2000). SNR and density limit estimates: a comparison of longitudinal and perpendicular recording. *IEEE Transactions on Magnetics*, **36**, 4.

Bertram, H.N. and Shimizu, Y. (2003). Micromagnetic study of the transition parameter and position jitter in perpendicular recording. *IEEE Transactions on Magnetics*, **39**, 1846.

Bland, J.A.C., Hope, S., Choi, B. and Bode, P. (1999). Magnetic anisotropy engineering in in-plane magnetized ultrathin ferromagnetic films. *Journal of Applied Physics*, **85**, 4613–4618.

Burkert, T., Nordstrom, L., Eriksson, O. and Heinonen, O. (2004). Giant magnetic anisotropy in tetragonal FeCo alloys. *Physical Review Letters*, **93**, 027203.

Burkert, T., Eriksson, O., James, P., *et al*. (2004). Calculation of uniaxial magnetic anisotropy energy of tetragonal and trigonal Fe, Co, and Ni. *Physical Review B*, **69**, 104426.

Caneschi, A., Gatteschi, D., Sangregorio, C., *et al*. (1999). Molecular approach to nanoscale magnetism. *Journal of Magnetism and Magnetic Materials*, **200**, 182–201.

Clark, A.E., Wun-Fogle, M., Restorff, J.B. and Lograsso, T.A. (2001). Effect of quenching on the magnetostriction of Fe1-xGax ($0.13 < x < 0.21$). *IEEE Transactions on Magnetics*, **37**, 2678–2680.

Clark, A.E., Hathaway, K.B., Wun-Fogle, M., *et al*. (2003). Extraordinary magnetoelasticity and lattice softening in bcc Fe-Ga alloys. *Journal of Applied Physics*, **93**, 8621–8623.

Clark, A.E., Restorff, J.B., Wun-Fogle, M., *et al*. (2000). Magnetostrictive properties of body-centered cubic Fe-Ga and Fe-Ga-Al alloys. *IEEE Transactions on Magnetics*, **36**, 3238–3240.

Cullen, J.R., Clark, A.E., Wun-Fogle, M., *et al*. (2001). Magnetoelasticity of Fe-Ga and Fe-Al alloys. *Journal of Magnetism and Magnetic Materials*, **226-230**, 948.

Daalderop, G.H.O., Kelly, P.J. and Schuurmans, M.F.H. (1990). 1st-Principles calculation of the magnetocrystalline anisotropy energy of iron, cobalt and nickel. *Physical Review B*, **42**, 11919–11937.

van Dijken, S., Vollmer, R., Poelsema, B. and Kirschner, J. (2000). Influence of CO and H_2 adsorption on the spin reorientation transition in Ni/Cu(001). *Journal of Magnetism and Magnetic Materials*, **210**, 316–328.

Durr, H.A., Guo, G.Y., van der Laan, G., *et al*. (1997). Element-specific magnetic anisotropy determined by transverse magnetic circular x-ray dichroism. *Science*, **277**, 213–215.

Ederer, C., Komelj, M. and Fahnle, M. (2003). Magnetism in systems with various dimensionalities: a comparison between Fe and Co. *Physical Review B*, **68**, 052402.

Engdahl, G. (Ed.) (2002). *Handbook of Giant Magnetostrictive Materials*, Academic Press: San Diego.

Fahnle, M., Komelj, M., Wu, R.Q. and Guo, G.Y. (2002). Magnetoelasticity of Fe: possible failure of ab initio electron theory with the local-spin-density approximation and with the generalized-gradient approximation. *Physical Review B*, **65**, 144436.

Farle, M. (1998). Ferromagnetic resonance of ultrathin metallic layers. *Reports on Progress in Physics*, **61**, 755–826.

Farle, M., Mirwald–Schulz, B., Anisimov, A.N., *et al*. (1997). Higher-order magnetic anisotropies and the nature of the spin-reorientation transition in face-centered tetragonal Ni(001)/Cu(001). *Physical Review B*, **55**, 3708–3715.

Freeman, A.J. (2002). Materials by design and the exciting role of quantum computation/simulation. *Journal of Computational and Applied Mathematics*, **149**, 27–56.

Freeman, A.J. and Wu, R.Q. (1991). Electronic structure theory of surface, interface and thin film magnetism. *Journal of Magnetism and Magnetic Materials*, **100**, 497–514.

Gambardella, P., Dallmeyer, A., Maiti, K., *et al*. (2002). Ferromagnetism in one-dimensional monatomic metal chains. *Nature*, **416**, 301–304.

Gambardella, P., Dallmeyer, A., Maiti, K., *et al*. (2004). Oscillatory magnetic anisotropy in one-dimensional atomic wires. *Physical Review Letters*, **93**, 077203.

Gambardella, P., Rusponi, S., Veronese, M., *et al*. (2003). Giant magnetic anisotropy of single cobalt atoms and nanoparticles. *Science*, **300**, 1130–1133.

Gavrilenko, V.G. and Wu, R.Q. (1999). Effects of Cu coverage on the magnetic anisotropy of Co/Cu(001). *Physical Review B*, **60**, 9539.

Gay, J.G. and Richter, R. (1986). Spin-anisotropy of ferromagnetic films. *Physical Review Letters*, **56**, 2728.

Gibbs, M.R.J. (Ed.) (2001). *Modern Trends in Magnetostriction Study and Application*, Kluwer Academic Publishers: London.

Guruswamy, S., Srisukhumbowornchai, N., Clark, A.E., *et al*. (2000). Strong, ductile, and low-field-magnetostrictive alloys based on Fe-Ga. *Scripta Materialia*, **43**, 239–244.

Hjortstam, O., Baberschke, K., Wills, J.M., *et al*. (1997). Magnetic anisotropy and magnetostriction in tetragonal and cubic Ni. *Physical Review B*, **55**, 15026–15032.

Hohenberg, P. and Kohn, W. (1964). Inhomogeneous electron gas. *Physical Review B*, **136**, 864.

Hong, J.S. and Wu, R.Q. (2003). First principles calculations of magnetic anisotropy energy of Co monatomic wires. *Physical Review B*, **67**, 020406.

Hong, J.S. and Wu, R.Q. (2004). Magnetic properties of Co nanochains. *Physical Review B*, **70**, 060406.

Hong, J.S., Wu, R.Q., Lindner, J., *et al*. (2004). Manipulation of spin reorientation transition by oxygen surfactant growth: a combined theoretical and experimental approach. *Physical Review Letters*, **92**, 147202.

Hope, S., Gu, E., Choi, B. and Bland, J.A.C. (1998). Spin engineering in ultrathin Cu/Co/Cu(110). *Physical Review Letters*, **80**, 1750.

Jamet, M., Wernsdorfer, W., Thirion, C., *et al*. (2001). Magnetic anisotropy of a single cobalt nanocluster. *Physical Review Letters*, **86**, 4676–4679.

Jamet, M., Wernsdorfer, W., Thirion, C., *et al*. (2004), Magnetic anisotropy in single clusters. *Physical Review Letters*, **69**, 024401.

Johnson, M.T., Bloemen, P.J.H., den Broedert, F.J.A. and de Vries, J.J. (1996). Magnetic anisotropy in metallic multilayers. *Reports on Progress in Physics*, **59**, 1409–1458.

Kawakami, R.K., Escorcia-Aparicio, E.J. and Qiu, Z.Q. (1996). Symmetry-induced magnetic anisotropy in Fe films grown on stepped Ag(001). *Physical Review Letters*, **77**, 2570–2573.

Kellogg, R.A., Flatau, A.B., Clark, A.E. *et al*. (2002). Temperature and stress dependencies of the magnetic and magnetostrictive properties of Fe0.81Ga0.19. *Journal of Applied Physics*, **91**, 7821–7823.

Koelling, D.D. and Harmon, B.N. (1977). Technique for relativistic spin polarized calculations. *Journal of Physics C*, **10**, 3107–3114.

Kohn, W. and Sham, L.J. (1965). Self-consistent equations including exchange and correlation effects. *Physical Review A*, **140**, 1133.

Komelj, M. and Fahnle, M. (2000). Nonlinear magnetoelastic coupling coefficients in Fe from an ab initio calculation. *Journal of Magnetism and Magnetic Materials*, **220**, L8–L12.

Komelj, M. and Fahnle, M. (2001). Nonlinear magnetoelastic effects in ultrathin epitaxial FCCCo(001) films: an ab initio study. *Journal of Magnetism and Magnetic Materials*, **224**, L1–L4.

Komelj, M. and Fahnle, M. (2002). Shear-strain-related nonlinear magnetoelastic properties of epitaxial films. *Physical Review B*, **65**, 92403.

Komelj, M. and Fahnle, M. (2006). Nonlinear magnetoelastic behavior of the bcc phases of Co and Ni: importance of third-order contributions for bcc Ni. *Physical Review B*, **73**, 012404.

Krams, P., Lauks, F., Stamps, R.L., *et al*. (1992). Magnetic anisotropies if ultrathin Co(001) films on Cu(001). *Physical Review Letters*, **69**, 3674–3677.

Lazarovits, B., Szunyogh, L. and Weinberger, P. (2003). Magnetic properties of finite Co chains on Pt(111). *Physical Review B*, **67**, 024415.

Li, D.Q., Freitag, M., Pearson, J., *et al*. (1994). Magnetic phases of ultrathin Fe grown on Cu(100) as epitaxial wedges. *Physical Review Letters*, **72**, 3112–3115.

Matsumura, D., Yokoyama, T., Amemiya, K., *et al*. (2002). X-ray magnetic circular dichroism study of spin reorientation transitions of magnetic thin films induced by surface chemisorption. *Physical Review B*, **66**, 024402.

Mermin, N.D. and Wanger, H. (1966). Absence of ferromagnetism or antiferromagnetism in one-or two-dimensional isotropic Heisenberg models. *Physical Review Letters*, **17**, 1133.

Millev, Y. and Kirschner, J. (1996). Reorientation transitions in ultrathin ferromagnetic films by thickness-and temperature-driven anisotropy flows. *Physical Review B*, **54**, 4137–4145.

Mokrousov, Y., Bihlmayer, G., Heinze, S. and Blugel, S. (2006). Giant magnetocrystalline anisotropies of 4*d* transition-metal monowires. *Physical Review Letters*, **96**, 147201.

Nakamura, K., Takeda, Y., Akiyama, T., *et al*. (2004). Atomically sharp magnetic domain wall in thin film Fe(110): a first principles noncollinear magnetism study. *Physical Review Letters*, **93**, 057202.

Nilius, N., Wallis, T.N. and Ho, W. (2002). Development of one-dimensional band structure in artificial gold chains. *Science*, **297**, 1853–1856.

Nordstrom, L. and Singh, D.J. (1996). Noncollinear intra-atomic magnetism. *Physical Review Letters*, **76**, 4420–4423.

O'Brien, W.L., Droubay, T. and Tonner, B.P. (1996). Transitions in the direction of magnetism in Ni/Cu(001) ultrathin films and the effects of capping layers. *Physical Review B*, **54**, 9297–9303.

Oepen, H.P., Speckmann, M., Millev, Y. and Kirschner, J. (1997). Unified approach to thickness-driven magnetic reorientation transitions. *Physical Review B*, **55**, 2752–2755.

Pratzer, M. and Elmers, H.J. (2003). Domain wall energy in quasi-one dimensional Fe/W(110) nanostripes. *Physical Review B*, **67**, 944161–944167.

Pratzer, M., Elmers, H.J., Bode, M., *et al*. (2001). Atomic-scale magnetic domain walls in quasi-one-dimensional Fe nanostripes. *Physical Review Letters*, **87**, 127201.

Qiu, Z.Q., Pearson, J. and Bader, S.D. (1993). Asymmetry of the spin reorientation transition in ultrathin Fe films and wedges grown on Ag(100). *Physical Review Letters*, **70**, 1006–1009.

Respaud, M. (1998). Surface effects on the magnetic properties of ultrafine cobalt particles. *Physical Review B*, **57**, 2925–2935.

Rusponi, S., Cren, T., Weiss, N., *et al*. (2003). The remarkable difference between surface and step atoms in the magnetic anisotropy of two-dimensional nanostructures. *Nature Materials*, **2**, 546–551.

Sander, D. (2004). The magnetic anisotropy and spin reorientation of nanostructures and nanoscale films. *Journal of Physics. Condensed Matter*, **16**, R603–R636.

Sander, D., Pan, W., Ouazi, S., *et al*. (2004). Reversible H-induced switching of the magnetic easy axis in Ni=Cu(001) thin films. *Physical Review Letters*, **93**, 247203.

Sessoli, R., Gatteschi, D., Caneschi, A. and Novak, M.A. (1993). Magnetic bistability in a metal-ion cluster. *Nature*, **365**, 141–143.

Shick, A.B., Gornostyrev, Y.N. and Freeman, A.J. (1999). Magnetoelastic mechanism of spin reorientation transitions at step edges. *Physical Review B*, **60**, 3029–3032.

Shick, A.B., Maca, F. and Oppeneer, P.M. (2004). Anomalous ferromagnetism of a monatomic Co wire at the Pt(111) surface step edge. *Physical Review B*, **69**, 212410.

Solovyev, I.V. (2005). Orbital polarization in itinerant magnets. *Physical Review Letters*, **95**, 267205.

Sorg, C., Ponpandian, N., Bernien, M., *et al*. (2006). Induced magnetism of oxygen in surfactant grown Fe, Co, and Ni monolayers. *Physical Review B*, **73**, 064409.

Steiauf, D. and Fahnle, M. (2005). Damping of spin dynamics in nanostructures: an ab initio study. *Physical Review B*, **72**, 064450.

Trygg, J., Johansson, B., Eriksson, O. and Wills, J.M. (1995). Total-energy calculation of the magnetocrystalline anisotropy energy in the ferromagnetic 3d metals. *Physical Review Letters*, **75**, 2871–2874.

Uiberacker, C., Zabloudil, J., Weinberger, P., *et al*. (1999). Lattice relaxation driven reorientation transition in Ni_n/Cu(100). *Physical Review Letters*, **82**, 1289–1292.

Vollmer, R. and Kirschner, J. (2000). Influence of H_2 adsorption on magnetic properties of Fe films on Cu(0 0 1). *Physical Review B*, **61**, 4146.

Vollmer, R., Gutjahr-Löser, Th. and Kirschner, J., *et al*. (1999). Spin-reorientation transition in Ni films on Cu(001): the influence of H_2 adsorption. *Physical Review B*, **60**, 6277–6280.

Vomir, M., Andrade, L.H.F., Guidoni, L., *et al*. (2005). Real space trajectory of the ultrafast magnetization dynamics in ferromagnetic metals. *Physical Review Letters*, **94**, 237601.

Waldmann, O., Koch, R., Schromm, S., *et al*. (2001). Magnetic anisotropy of a cyclic octanuclear Fe(III) cluster and magneto-structural correlations in molecular ferric wheels. *Inorganic Chemistry*, **40**, 2986–2995.

Wang, X.D., Wang, D.S., Wu, R.Q. and Freeman, A.J. (1996a). Validity of the force theorem for magnetocrystalline anisotropy. *Journal of Magnetism and Magnetic Materials*, **159**, 337–341.

Wang, X.D., Wang, D.S., Wu, R.Q. and Freeman, A.J. (1996b). Torque method for the theoretical determination of magnetocrystalline anisotropy. *Physical Review B*, **54**, 61–64.

Wang, D.S., Wu, R.Q. and Freeman, A.J. (1993). State-tracking 1st principles determination of magnetocrystalline anisotropy. *Physical Review Letters*, **70**, 869–872.

Weinberger, P. and Szunyogh, L. (2000). Perpendicular magnetism in magnetic multilayer systems. *Computation Materials Science*, **17**, 414–437.

Weinert, M., Wimmer, E. and Freeman, A.J. (1982). Total-energy all-electron density functional method for bulk solids and surfaces. *Physical Review B*, **26**, 4571–4578.

Weller, D. and Moser, A. (1999). Thermal effect limits in ultrahigh-density magnetic recording. *IEEE Transactions on Magnetics*, **35**, 4423–4439.

Weller, D., Moser, A., Folks, L., *et al*. (2000). High K-u materials approach to 100 Gbits/in^2. *IEEE Transactions on Magnetics*, **36**, 10–15.

Wimmer, E., Krakaur, H., Weinert, M. and Freeman, A.J. (1981). Full-potential self-consistent linearized-augmented-plane-wave method for calculating the electronic structure of molecules and surfaces: O2 molecule. *Physical Review B*, **24**, 864–875.

Wood, W. (2000). The feasibility of magnetic recording at 1 Terabit per square inch. *IEEE Transactions on Magnetics*, **36**, 36–42.

Wu, R.Q. (2002). Origin of large magnetostriction in FeGa alloys. *Journal of Applied Physics*, **91**, 7358–7360.

Wu, R.Q., Chen, L.J. and Freeman, A.J. (1997a). Strain induced magneto-crystalline anisotropy in fct Ni/Cu(001), *Journal of Applied Physics*, **81**, 4417–4419.

Wu, R.Q., Chen, L.J. and Freeman, A.J. (1997b). First principles determination of magnetostriction in bulk transition metals and thin films. *Journal of Magnetism and Magnetic Materials*, **170**, 103–109.

Wu, R.Q., Chen, L.J. and Freeman, A.J. (1998). First principles determinations of magneto-crystalline anisotropy and magnetostriction in bulk and thin-film transition metals. *Journal of Magnetism and Magnetic Materials*, **177**, 1216–1219.

Wu, R.Q. and Freeman, A.J. (1996). First principles determinations of magnetostriction in transition metals. *Journal of Applied Physics*, **79**, 6209–6212.

Wu, R.Q. and Freeman, A.J. (1999). Spin-orbit induced magnetic phenomena in bulk metals and their surfaces and interfaces. *Journal of Magnetism and Magnetic Materials*, **200**, 498–514.

Yang, I., Savrasov, S.Y. and Kotliar, G. (2001). Importance of correlation effects on magnetic anisotropy in Fe and Ni. *Physical Review Letters*, **87**, 216405.

Yin, L.F., Wei, D.H., Lei, N., *et al*. (2006). Magnetocrystalline anisotropy in permalloy revisited. *Physical Review Letters*, **97**, 067203.

FURTHER READING

Chuang, D.S., Ballentine, C.A. and O'Handley, R.C. (1994). Surface and step magnetic anisotropy. *Physical Review B*, **49**, 15084–15095.

Lazarovits, B., Szunyogh, L., Weinberger, P. and Ujfalussy, B. (2003). Magnetic properties of finite Fe chains at fcc Cu(001) and Cu(111) surfaces. *Physical Review B*, **68**, 024433.

Theory of Magnetocrystalline Anisotropy and Magnetoelasticity in 4f and 5f Metals

Børje Johansson and Michael S.S. Brooks
Uppsala University, Uppsala, Sweden

1 INTRODUCTION

The differences in the nature of the chemical bonding in the d, 4f, and 5f series is illustrated by the atomic volumes shown in Figure 1. The parabolic decrease in volumes across the transition-metal series is mirrored by the early part of the 5f series as each added electron changes the bonding. The lanthanide contraction across the 4f series is relatively small and monotonic except for the anomalous divalent elements, Eu and Yb, and the actinide contraction of the heavy 5f elements is similar to that of the rare-earth series with a large expansion for the divalent element, Es. The difference in volume between the divalent and trivalent metals is approximately due to one extra bonding d electron and it is evident that the f electrons are not bonding. Most elements lose their magnetic moments in the metallic state. The exceptions are a few transition metals, some actinides, and most rare earths. The 3d transition metals Fe, Co, Ni, and Mn order magnetically. Otherwise transition metals are paramagnets with enhanced susceptibilities, the enhancement being mostly due to exchange interactions between the d electrons that are also involved in cohesion and the determination of structure (Friedel, 1969; Pettifor, 1970; Skriver, 1985). Nearly all of the rare-earth metals are magnetically ordered at low temperatures. The 4f shell is chemically inert, the bonding and structure being due to the conduction electrons (Duthie and Pettifor, 1977; Skriver, 1983). The rare-earth metals are therefore 5d transition metals with about two 5d electrons. The origin of the magnetism is the localized 4f shell (Jensen and Mackintosh, 1991). However, there is little in the way of direct magnetic interaction between the 4f shells on different atoms, and if the 4f electrons on their own were responsible for the magnetism, the rare earths would be paramagnets down to the lowest temperatures. Exchange interactions between 4f and conduction electrons provide the mechanism for indirect interaction between 4f shells that is finally responsible for magnetic order. The actinide metals are more complex. The light actinides are 5f transition metals, whereas the heavy actinides are 6d transition metals since their 5f shell is chemically inert (Skriver, 1985). The light actinide metals are Pauli paramagnets but magnetic order is to be found in many of their compounds, as is the case for transition metals.

The absence of magnetic order in light actinide elemental metals has changed the way magnetism has been studied in light actinides. Studies of magnetism in transition metals and rare earths began with the elemental metals, and models for their compounds were built on that basis. Fundamental studies of magnetism in light actinides begin with their compounds. Perhaps the most basic empirical result is that there are critical An–An interatomic distances in actinide compounds above which magnetic order occurs. The systematic absence of

Handbook of Magnetism and Advanced Magnetic Materials. Edited by Helmut Kronmüller and Stuart Parkin. Volume 1: *Fundamentals and Theory*. ISBN: 978-0-470-02217-7.

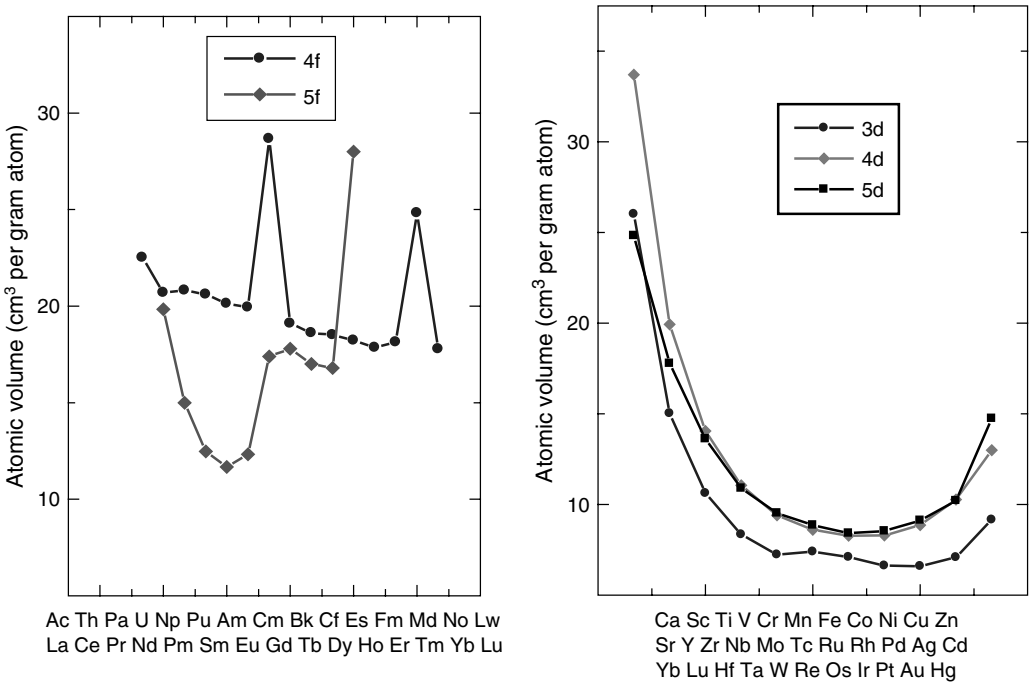

Figure 1. Atomic volumes of the 3d, 4d, 5d, 4f, and 5f elemental metals in the solid state.

magnetism in compounds with small An–An separation (Hill, 1970) suggests that magnetic ordering is due to the competition between kinetic and magnetic energies as in transition metals. However magnetic actinide compounds have, in contrast to transition metals, large orbital magnetic moments – a property that is normally associated with rare earths.

1.1 Free lanthanide and actinide atoms

The single electron wave functions, ψ_{nlm}, are products, $R_{nl}(r)Y_{lm}$, and 4f and 5f atoms have the same angular properties. The radial part of the wave functions differs, Figure 2, because not only are the actinides larger atoms but also the radial 5f wave functions have an extra node and are more extended. The more extended 5f radial densities are responsible for major differences in the magnetic properties of 4f and 5f metals. The densities in Figure 2 are the result of self-consistent field atomic calculations. Exact solutions to the Schrödinger or Dirac equations for large atoms are not achievable but the effect of the Coulomb interactions between electrons can be approximated by a self-consistent field (See also **Density-functional Theory of Magnetism, Volume 1**). The single electron wave equation is solved at a given potential for each of the occupied states and the resulting wave functions used to calculate the electron density. The density is then used to recalculate the potential and the process repeated until the calculated electron density differs from the electron density in the previous iteration by less than a specified amount. The iterative procedure in self-consistent field calculations allows the effect of screening of the Coulomb interactions to be approximated reasonably accurately. For example, the contraction of the f shell across the 4f and 5f series is reproduced, due to incomplete screening of nuclear potential as each f electron is added. For free atoms, the number of electrons is fixed and an issue occurs for 4f and 5f atoms since the f shells are not full. In self-consistent field calculations, the energy is minimized when the energies of the outermost occupied orbitals are equal, and this rarely leads to integral occupation numbers for the different orbitals. In practice, the occupation number of the 4f and 5f states is fixed to its known integer value and the calculation made subject to this constraint. When the f states are truly localized, as in most of the rare earths, the constraint may also be used in the solid state although there are other ways to ensure that the number of f states remains approximately integral (Svane and Gunnarsson, 1990; Anisimov, Aryasetiawan and Lichtenstein, 1997) (See also **Dynamical Mean-field Theory of Itinerant Electron Magnetism, Volume 1**).

The angular properties of the ground state of f shells are obtained from the Russell–Saunders coupling scheme in which direct Coulomb and exchange interactions are the largest parts of the electron Hamiltonian. Since electron–electron interactions are unchanged by simultaneous rotations of all the electrons, the total spin, $\boldsymbol{S}$, and orbital angular

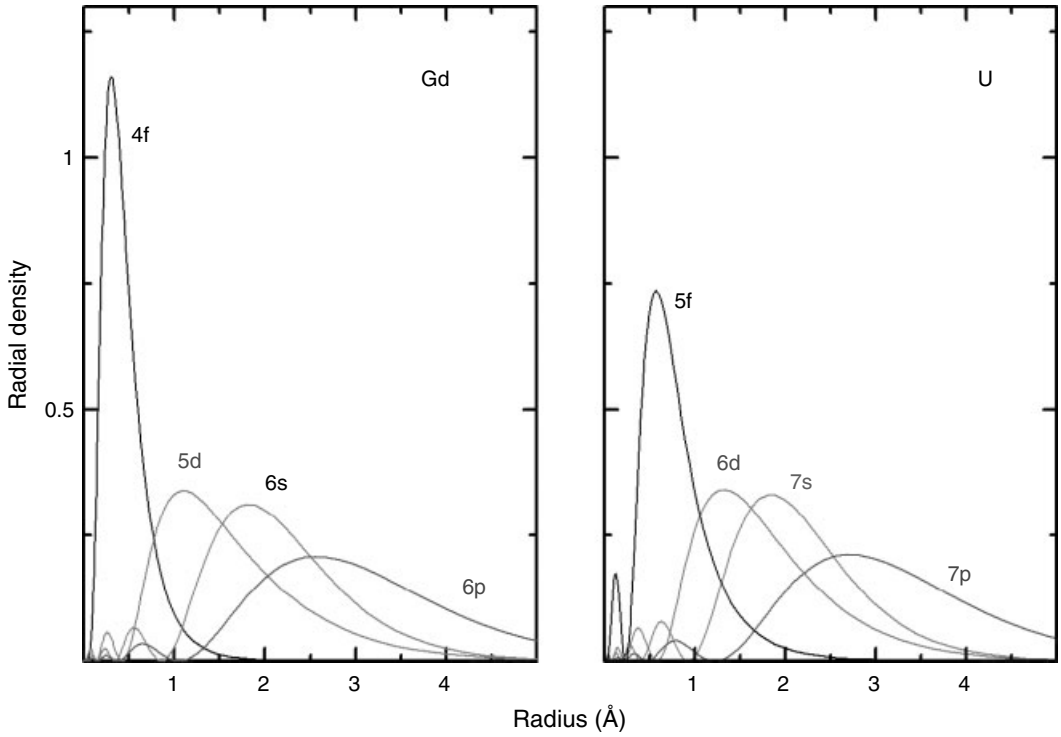

Figure 2. Calculated radial densities ($= 4\pi r^2 R_n^2(r)$) of the valence electrons in Gd and U.

momentum, $\boldsymbol{L}$, are conserved. The smaller spin-orbit interaction is a perturbation that couples $\boldsymbol{L}$ and $\boldsymbol{S}$ to a total angular momentum $\boldsymbol{J}$. It is a consequence of the strong coupling of the electrons to first $\boldsymbol{S}$ and $\boldsymbol{L}$, and then $\boldsymbol{J}$, involving a high degree of electron correlation that the matrix elements of all operators in the ground state are proportional to those of $\boldsymbol{J}$

$$\boldsymbol{O} = \frac{\langle J||\boldsymbol{O}||J\rangle}{\langle J||\boldsymbol{J}|J|\rangle}\boldsymbol{J} \tag{1}$$

where $\langle||\cdots||\rangle$ denotes a reduced matrix element. For example, the saturated ground state f moment, $\boldsymbol{\mu} = \boldsymbol{L} + 2\boldsymbol{S}$, is a product of $\boldsymbol{J}$ with the Landé factor, g_J, that is just the ratio of the reduced matrix elements of $\boldsymbol{\mu}$ and $\boldsymbol{J}$. Equation (1), a consequence of the Wigner–Eckart theorem, becomes particularly useful when the crystal field is added to the electron Hamiltonian.

1.2 Electronic structure of 4f and 5f metals

The standard model for the rare-earth metals (Jensen and Mackintosh, 1991) approximates the rare-earth atoms in the solid by retaining the free atom properties of the open 4f shell and allowing either two or three electrons to enter the conduction (or valence) bands resulting in a solid of divalent or trivalent ions immersed in a sea of conduction electrons. In practice, the orbital degeneracy of the 4f ground state is partially or fully removed in the solid by the crystalline electric field (CEF), which has crystal point group rather than full rotational symmetry. The CEF is therefore an origin of magnetocrystalline anisotropy energy (MAE) for the 4f magnetism. Anisotropic interion interactions (AII) may also play a role. The volume and strain dependence of the CEF and AII produce magnetoelastic effects special to the 4f electrons. Both the CEF and conduction electron–mediated AII depend on the electronic structure of the conduction electrons, primarily 5d electrons. The magnetic properties of 4f metals therefore depend on the electronic structure of both localized and itinerant electrons and the interactions between them.

At temperatures high enough that all crystal-field levels are populated, the Curie–Weiss law for the paramagnetic susceptibility is obeyed with an effective moment of $g_J\sqrt{J(J+1)}$. The Russell–Saunders coupling scheme provides a direct relationship between the number of 4f electrons, the magnitude of the total angular momentum, $\boldsymbol{J}$, and the paramagnetic moment. These relationships are less reliable in actinide compounds where, due to the more extended 5f wave functions, the effects of the CEF are far larger or the 5f electrons are even involved in chemical bonding. A thorough knowledge of the conduction electron wave functions, usually including the 5f wave functions, is required to describe 5f magnetism.

While localized electrons in their ground state always have a maximum spin moment, this is not the case for itinerant electrons. When the energy bands spin polarize, the kinetic energy of the occupied majority spin states increases more rapidly than the kinetic energy of the minority spin states decreases. As a consequence, the total kinetic energy is increased and must be compensated by a gain in exchange energy. The increase in kinetic energy, ΔT_s, is smaller for narrow bands and vanishes in the atomic limit. The balance is quantified by the Stoner criterion, $ID(E_F)/2 > 1$, for the appearance of magnetism, where I is the exchange integral and $D(E_F)$ is the density of states at the Fermi energy. Typically the exchange integral is about 1 and 0.5 eV in 3d transition metals and actinide metals, respectively. The lighter actinide metals and some actinide compounds, for example, UC, with small lattice constants are Pauli paramagnets, and have been found not to satisfy the Stoner criterion (Brooks, 1984; Trygg *et al*., 1995).

The 4f bandwidths in the actinides (typically 3 eV) are less than the 3d bandwidths in transition metals (typically 6 eV), whereas the spin-orbit splitting of 0.7 eV in U is an order of magnitude larger than in Fe where it is about 0.05 eV. The spin-orbit interaction mixes an orbital moment into the ground state. The mixing is from states across the energy bands, and when the bandwidth is large compared to the spin-orbit splitting, the mixing is small; hence the orbital moment is almost entirely quenched in 3d transition metals. The large spin-orbit interaction in light actinide compounds is responsible for large orbital moments in itinerant actinide magnets and concomitantly large MAE (Brooks and Kelly, 1983).

Hohenberg and Kohn (1964) proved that the ground state energy of a system of interacting electrons is a functional of the single electron density and derived a variational principle for the ground state energy. The general theory is known as *density-functional theory* (*DFT*) (See also **Density-functional Theory of Magnetism, Volume 1**). The variational principle was converted to a computationally viable form for self-consistent electron density calculations for atoms and solids by Kohn and Sham (1965). The essence of the Kohn and Sham (1965) procedure is to subdivide the total energy into large contributions that are either well-known functionals, such as the Hartree and kinetic energies and a much smaller remainder, E_{xc}, the exchange and correlation energy. Approximations to E_{xc} *hopefully* produce reasonably small errors. Calculations may then be made without adjustable parameters. A numerically tractable formulation is provided by the Kohn and Sham (1965) equations

$$\left(-\frac{1}{2}\nabla^2 + V_{\text{eff}}\right)\phi_i = \varepsilon_i \phi_i \tag{2}$$

with the effective potential

$$V_{\text{eff}} = V(\boldsymbol{r}) + \int \mathrm{d}\boldsymbol{r}\, \frac{n(\boldsymbol{r}')}{|\boldsymbol{r} - \boldsymbol{r}'|} + \mu_{\text{xc}} \tag{3}$$

consisting of external, Hartree, and exchange-correlation potentials. The latter is given by $\mu_{\text{xc}} = \delta E_{\text{xc}}/\delta n$. The density is reconstructed from solutions to these equations forming a nonlinear system of integrodifferential equations that are solved by iteration. Due to the complexity of the Kohn–Sham equations, more than one stationary solution may exist, for example, metastable magnetic states such as low and high-spin states. The simplest approximation for E_{xc} is the local spin density approximation (LSDA),

$$E_{\text{xc}}^{LSDA}[n_\uparrow, n_\downarrow] = \int \mathrm{d}\boldsymbol{r}\; n(\boldsymbol{r})\epsilon_{\text{xc}}\left(n_\uparrow(\boldsymbol{r}), n_\downarrow(\boldsymbol{r})\right) \tag{4}$$

where ϵ_{xc} is the exchange-correlation energy per electron of the homogeneous electron gas, and $n_\uparrow(\boldsymbol{r})$ and $n_\downarrow(\boldsymbol{r})$ are the spin-up and spin-down electron densities.

2 MAGNETIC INTERACTIONS AND MAGNETOCRYSTALLINE ANISOTROPY ENERGY

2.1 Exchange interactions

The simplest possible exchange interaction between the localized 4f shell and the conduction electrons at rare-earth sites is isotropic

$$\mathcal{H}_{\text{4f-c}} = -\frac{1}{g_j \mu_B^2}\tilde{j}\boldsymbol{\mu}_{\text{4f}}^s \cdot \boldsymbol{\mu}_{\text{c}} = -2\tilde{j}\boldsymbol{S}_{\text{4f}} \cdot \boldsymbol{S}_{\text{c}} \tag{5}$$

where $\boldsymbol{S}_{\text{c}}$, $\boldsymbol{S}_{\text{4f}}$, $\boldsymbol{\mu}_{\text{c}}$, and $\boldsymbol{\mu}_{\text{4f}}^s$ are the conduction electron and 4f spin and spin moments, respectively, and g_j is the 4f g-factor. The local exchange interaction, $\tilde{j}$, depends on the local electron density in LSDA (See also **Density-functional Theory of Magnetism, Volume 1**). More generally, direct and exchange interactions between 4f shell and conduction electrons leads to scattering of conduction electrons accompanied by transitions within the lowest J manifold of the localized 4f electrons. The annihilation and creation operators for the latter transitions may be reexpressed in terms of irreducible tensor operators, $\tilde{O}_K^Q$, so that the Hamiltonian is expanded in multipoles (Teitelbaum and Levy, 1976)

$$\mathcal{H}_{\text{4f-c}} = -\sum_{knLk'n'L'KQ} \tilde{j}_{knLk'n'L'K}^Q \tilde{O}_K^Q(\boldsymbol{J}_j) c_{k'n'L'}^\dagger c_{knL} \tag{6}$$

where the c's are conduction band creation and annihilation operators, n labels the band, and the elements of $\tilde{j}$ are constructed to make $\mathcal{H}_{4f-c}$ symmetry invariant (Hirst, 1978). Another way to view equation (5) is that the conduction electrons interact with an effective inhomogeneous magnetic field $\boldsymbol{H}_i = \tilde{j}_i \boldsymbol{S}_i/\mu_B$ provided by the spin of the 4f shell. The conduction electron moment induced by the field at a site $\boldsymbol{R_j}$ in the crystal is given by

$$\boldsymbol{\mu}_j = \boldsymbol{\chi}_{ji}(\boldsymbol{R})\cdot\boldsymbol{H}_i \tag{7}$$

where $\boldsymbol{\chi}$ is the conduction electron susceptibility tensor and $\boldsymbol{R} = \boldsymbol{R_j} - \boldsymbol{R_i}$. The interaction between the induced moment and the 4f spin at site $\boldsymbol{R_j}$ produces an effective interaction between the f shells at the two sites

$$\mathcal{H}_{ij} = -\frac{\tilde{j}^2}{\mu_B^2}\boldsymbol{S}_i\cdot\boldsymbol{\chi}_{ij}(\boldsymbol{R})\cdot\boldsymbol{S}_j \tag{8}$$

If the conduction electrons were free electrons,

$$\chi(\boldsymbol{R}) = \chi(R) = -4\pi^3\frac{k_F}{R^2}j_1(2k_F R) \tag{9}$$

where j is a spherical Bessel function. The Fourier transform of $\chi(R)$ is the Lindhard function

$$\chi(\boldsymbol{q}) = \sum_{\boldsymbol{k}}\frac{f_{\boldsymbol{k}} - f_{\boldsymbol{k}-\boldsymbol{q}}}{E_{\boldsymbol{k}-\boldsymbol{q}} - E_{\boldsymbol{k}}} \tag{10}$$

where f is the Fermi–Dirac distribution function. The wave-vector-dependent susceptibility may be calculated if the energy band structure is known (Lindgård, Harmon and Freeman, 1975). However it is already clear from the free electron approximation to $\chi(\boldsymbol{q})$ that the main contributions come from pairs of states, one filled and one empty, close to the Fermi energy and separated by wave vector $\boldsymbol{q}$. The peaks in $\chi(\boldsymbol{q})$, or Kohn anomalies, correspond to Friedel oscillations in the real space $\chi(\boldsymbol{R})$. For a real band structure the susceptibility tensor is anisotropic.

More generally, the coupling between the 4f shells on different sites may be expanded in multipole–multipole interactions (Elliott and Thorpe, 1968)

$$\mathcal{H}_{ij} = -\sum_{KLL'}\mathcal{J}^K_{LL'}(\boldsymbol{R})\langle\tilde{O}_K\rangle\tilde{O}_L(\boldsymbol{J}_j)\tilde{O}_{L'}(\boldsymbol{J}_i) \tag{11}$$

where $L = (lm)$ and $K = (kn)$. The $\tilde{O}_L$ are Racah operator equivalents and the effect of the environment has been approximated by a mean field (Jensen, Houmann and Møller, 1975). If all of the $\mathcal{J}_{LL'}$ were zero except for $l = 1$ then $\mathcal{J}_{mm'} = \mathcal{J}_{1,0} = -\mathcal{J}_{1,1} = -\mathcal{J}_{1,-1} = \mathcal{J}$,

$$\mathcal{H}_{ij} = -\mathcal{J}\sum_m(-)^m\tilde{O}_{1,m}(\boldsymbol{J}_j)\tilde{O}_{1,-m}(\boldsymbol{J}_i) = -\mathcal{J}\boldsymbol{J}_j\cdot\boldsymbol{J}_j \tag{12}$$

and isotropic exchange is recovered. The origins of the anisotropic direct and exchange interactions have been studied in detail by Kaplan and Lyons (1963), Specht (1967), Elliott and Thorpe (1968), and Levy (1969). The conduction electron wave functions may be expanded in multipoles about any given site. The monopole is responsible for the $\boldsymbol{s}_c\cdot\boldsymbol{S}_{4f}$ interaction but higher multipoles are responsible for anisotropic exchange (Kaplan and Lyons, 1963; Specht, 1967). Kaplan and Lyons (1963) estimated a pseudodipolar interaction of about 10% of isotropic exchange. An effective spin Hamiltonian such as equation (11) contains the effects of the conduction band MAE and spin-orbit interaction but it *appears* as a part of the anisotropic 4f–4f interaction. Direct electric multipole–multipole interactions between the ions are also present, although probably small in metals due to screening of the Coulomb interactions by conduction electrons. More important are probably the multipole–multipole interactions propagated by lattice strain.

The predominant approximation now used to compute the electronic charge and spin densities in solids from first principles is LSDA (See also **Density-functional Theory of Magnetism, Volume 1**). Gunnarsson (1976) showed how to extract *local* exchange integrals from LSDA, and the variational principle of DFT was used by Brooks and Johansson (1983) to extract local exchange integrals for transition metals, rare earths, and actinide atoms. The 4f–5d and 5d–5d exchange integrals are 94 meV and 0.5 eV, respectively, in gadolinium. The 5f–5f, 5f–4d, and 5d–5d exchange integrals are 0.44, 0.15, and 0.35 eV, respectively, for uranium. Since the ions and ionic magnetic moments in a metal move far more slowly than the conduction electrons, it is a good approximation to assume that the conduction electrons adjust instantaneously to any given ionic moment configuration. The spin-wave dispersion relations in Gd metal, calculated by Lindgård, Harmon and Freeman (1975), were in good agreement with measurements as regards the dispersion, suggesting that the results for the wave-vector-dependent susceptibility were good. However, the exchange interactions were calculated using unscreened Coulomb integrals – a method that predated LSDA – and were too large. The exchange integrals obtained from LSDA, if used in the analysis, would have yielded good agreement with measurements. Indirect exchange interactions may also be extracted from self-consistent energy band calculations where the total energy is calculated for different spiral configurations (Sandratskii, 1998; Kurz *et al*., 2004). It is also possible to extract interionic exchange interactions by using the magnetic force theorem (Liechtenstein, Katsnelson and Gubanov, 1984; Liechtenstein, Katsnelson, Antropov and Gubanov, 1987; Bruno, 2003).

It is evident from the foregoing that if the local exchange interactions between the 4f shell and the conduction electrons

can be obtained reasonably accurately from LSDA, the remaining task is to calculate the conduction band interatomic susceptibility, and various methods for doing this have been devised (Cooke, Lynn and Davis, 1980; Callaway, Chatterjee, Singhal and Ziegler, 1983; Savrasov, 1998; Antropov, Katsnelson, van Schilfgaarde and Harmon, 1995). Application has been to magnetic 3d transition metals, but since the rare earths are 5d transition metals, the same techniques should be even more effective as the 5d bands are very broad and their magnetism is induced, reducing the problems of electron correlation. How this may be done has been illustrated by Perlov, Havilov and Eschrig (2000) who have calculated magnon spectra for the heavy rare-earth metals from a Hamiltonian that contained, apart from the crystal fields, parameters evaluated *ab initio* from LSDA. They also found that the conduction electron spin density is not always necessarily collinear with the 4f spin density at a rare-earth site.

Indirect exchange interactions between the rare and transition-metal sublattices in rare-earth intermetallics were calculated from the difference in total energy between ferromagnetic and ferrimagnetic alignment of the sublattices by Liebs, Hummler and Fähnle (1992). Examples of how the local exchange integrals may be used to determine the indirect exchange coupling between rare earth and transition-metal ions in rare earth–transition metal intermetallics have been given by Brooks, Nordström and Johansson (1991).

2.2 The crystalline electric field

Although known as the *crystalline electric field*, or *CEF*, it is the potential and the potential energy that are the subject of calculations. The potential due to a charge distribution, $\rho(\boldsymbol{r}')$, is

$$V_{\text{cef}}(\boldsymbol{r}) = \int \frac{\rho(\boldsymbol{r}')}{|\boldsymbol{r}-\boldsymbol{r}'|}\,\mathrm{d}\boldsymbol{r}' = \sum_{nm} B_{nm}(r)C_{nm}(\hat{\boldsymbol{r}}) \tag{13}$$

where

$$B_{nm}(r) = \left(\frac{2n+1}{4\pi}\right)^{1/2}\left[r^n a_{nm} + r^{-n-1}a'_{nm}\right] \tag{14}$$

with

$$a_{nm} = \frac{4\pi}{2n+1}\int_r^\infty \mathrm{d}\boldsymbol{r}'\rho(\boldsymbol{r}')\left(\frac{1}{r'}\right)^{n+1} Y_{nm}(\hat{\boldsymbol{r}}')$$
$$a'_{nm} = \frac{4\pi}{2n+1}\int_0^r \mathrm{d}\boldsymbol{r}'\rho(\boldsymbol{r}')(r')^n Y_{nm}(\hat{\boldsymbol{r}}') \tag{15}$$

and

$$C_{nm}(\boldsymbol{r}) = \tilde{Y}_{nm}(\boldsymbol{r}) = \left(\frac{4\pi}{2n+1}\right)^{1/2} Y_{nm}(\boldsymbol{r}) \tag{16}$$

is a tensor operator.

If the charge distribution in the solid is known, the integrals in equation (15) may be calculated. Then the potential is a linear combination of products of spherical harmonics and CEF parameters. The ground state electron density is therefore used to calculate the parameters, a_{nm}, and the radial integrals $\langle r^n\rangle$ and $\langle(1/r)^{n+1}\rangle$.

The matrix elements of the potential for a localized state characterized by L, S, J may be reduced by the Wigner–Eckart theorem and evaluated. Alternatively, since the matrix elements of the CEF are proportional to those of operator equivalents (Stevens, 1952) written in terms of the total angular momentum, $\boldsymbol{J}$, the CEF Hamiltonian may be replaced by a Hamiltonian expressed in terms of the operator equivalents, $\tilde{O}_{nm}(\boldsymbol{J})$.

In the single electron basis, $i^l R_l Y_{lm}\chi = |m\sigma\rangle$ and the N-electron state $|LSJM\rangle$ is (Judd, 1967)

$$|LSJM\rangle = a_N^\dagger \ldots a_1^\dagger|0\rangle \tag{17}$$

where the $a_i^\dagger$ are electron creation operators and $i = (nlm_l m_s)$. A spin-independent single electron operator, $F = \sum_i f_i$, in this basis is

$$F = \sum_i f_i = \sum_{mm'\sigma} a^\dagger_{m'\sigma}\langle m'\sigma|f|m\sigma\rangle a_{m\sigma} \tag{18}$$

where, for $f(\boldsymbol{r}) = B_{nm}(r)C_{nm}(\hat{\boldsymbol{r}})$

$$\langle m'\sigma|f|m\sigma\rangle = \int Y^*_{lm'}(\hat{\boldsymbol{r}})C_{nm}(\hat{\boldsymbol{r}})Y_{lm}(\hat{\boldsymbol{r}})\,\mathrm{d}\hat{\boldsymbol{r}} \times \int r^2 R_l^2(r)B_{nm}(r)\,\mathrm{d}r = \langle B_{nm}\rangle\langle m'|C_{nm}|m\rangle \tag{19}$$

Since the radial wave function, R_l, is the same for all localized electrons of a given l, the $\langle B_{nm}\rangle$ are factorized out and only the matrix elements of the tensor operator

$$A_{nm} = \sum_{mm'\sigma} a^\dagger_{m'\sigma}\langle m'\sigma|C_{nm}|m\sigma\rangle a_{m\sigma} \tag{20}$$

in the basis $|LSJM\rangle$ are required. Then the CEF contribution to the Hamiltonian is

$$V_{\text{cef}} = \sum_{nm}\langle B_{nm}\rangle A_{nm} \tag{21}$$

If the Wigner–Eckart theorem is applied to A_{nm}

$$\langle LSJM'|A_{nm}|LSJM\rangle = (-1)^{J-M'}\begin{pmatrix} J & n & J \\ -M' & m & M\end{pmatrix} \times \langle LSJ||\boldsymbol{A}^{(n)}||LSJ\rangle \tag{22}$$

where $\boldsymbol{A}^{(n)}$ is a reduced operator. Since $\boldsymbol{A}^{(n)}$ operates only on the spatial variables, the reduced matrix element may be further factored

$$\langle LSJ||\boldsymbol{A}^{(k)}||LSJ\rangle = (-1)^{L+S+J+n}(2J+1) \times \langle L||\boldsymbol{A}^{(n)}||L\rangle \begin{Bmatrix} J & J & n \\ L & L & S \end{Bmatrix} \quad (23)$$

The remaining reduced matrix element may be evaluated by observing that in the basis $|LM_LSM_S\rangle$, the state $|LLSS\rangle$ is a single Slater determinant for which the matrix elements of A_{mn} are easy to evaluate. Then

$$\langle L||\boldsymbol{A}^{(n)}||L\rangle = (2l+1)\frac{\begin{pmatrix} l & n & l \\ 0 & 0 & 0 \end{pmatrix}}{\begin{pmatrix} L & n & L \\ -L & 0 & L \end{pmatrix}} \times \sum_{m=l+1-N}^{l} (-1)^m \begin{pmatrix} l & n & l \\ -m & 0 & m \end{pmatrix} \quad (24)$$

The matrix elements of the crystal field are then evaluated from equation (22) by substituting from equations (23) and (24) for the reduced matrix elements (Colarieti-Tosti, 2004).

The matrix elements of the tensor operator equivalent, $\tilde{O}_{nm}(\boldsymbol{J})$, for the manifold $|JM\rangle$ are, from the Wigner–Eckart theorem,

$$\langle JM'|\tilde{O}_{nm}(\boldsymbol{J})|JM\rangle = (-1)^{J-M'} \begin{pmatrix} J & n & J \\ -M' & m & M \end{pmatrix} \times \langle J||\tilde{\boldsymbol{O}}^{(n)}||J\rangle \quad (25)$$

The operator equivalents are functions purely of the operators J_z and $J_\pm$, and may be obtained from the generating function

$$\sum_m \tilde{O}_{nm}(\boldsymbol{J})\frac{2^n n! t^m}{[(n+m)!(n-m)!]^{1/2}} = \left[-J_+ t + 2J_z + J_-/t\right]^n \quad (26)$$

Consequently, it may be shown that the reduced matrix element of $\tilde{O}_{nm}(\boldsymbol{J})$ is given by (Egami and Brooks, 1975)

$$\langle J||\tilde{\boldsymbol{O}}^{(n)}||J\rangle = \frac{1}{2^k}\left[\frac{(2J+n+1)!}{(2J-n)!}\right]^{1/2} \quad (27)$$

The ratios

$$f_N^n = \frac{\langle LSJM'|A_{nm}|LSJM\rangle}{\langle JM'|\tilde{O}_{nm}(\mathbf{J})|JM\rangle} = (-1)^{L+S+J+n}(2J+1)\begin{Bmatrix} J & J & n \\ L & L & S \end{Bmatrix}\frac{\langle L||\boldsymbol{A}^{(n)}||L\rangle}{\langle J||\tilde{\boldsymbol{O}}^{(n)}||J\rangle} \quad (28)$$

are the Stevens factors used to replace the crystal-field matrix elements by operator equivalents. The matrix elements of the crystal field may be written in terms of either set of tensor operators

$$\langle LSJM'|V_{\text{cef}}|LSJM\rangle = \sum_{nm}\langle B_{nm}\rangle\langle LSJM'|C_{nm}|LSJM\rangle = \sum_{nm} f_N^n\langle B_{nm}\rangle\langle LSJM'|\tilde{O}_{nm}|LSJM\rangle \quad (29)$$

CEF excitations may be observed directly by inelastic scattering of neutrons, and their single-ion nature is evident from their lack of energy dispersion (See also **X-ray and Neutron Scattering by Magnetic Materials, Volume 1**).

Since the self-consistent electron density used to evaluate the CEF is obtained from energy band calculations, it is useful to set this treatment in the context of DFT. An expression similar to equation (13) has been derived from LSDA by Fähnle (1995) who considered the change of energy due to rotations of the 4f shell. The aspherical electron density of a 4f crystal-field state may be thought of as a small impurity charge, $t(\mathbf{r})$ (which integrates to zero), added to the electron density obtained from a self-consistent calculation. The conduction electron density in the crystal will relax to screen the impurity. The energy functional may be partitioned into a part depending on the original density and a part depending on both the original density and the test charge. Since the original density, $\overline{n}$, was at a variational minimum with respect to variations in the density due to the self-consistent nature of the original energy band calculation, the changes in energy due to the screening density cancel to $O(\delta n)$. In addition, the change in kinetic energy of the 4f shell is zero due to Russell–Saunders coupling, leaving a residual energy change of

$$\delta E = E[\overline{n}, t] = \int \overline{V}(\mathbf{r})t(\mathbf{r})\,\mathrm{d}\mathbf{r} \quad (30)$$

where

$$\overline{V}(\mathbf{r}) = V_N(\overline{n}) + V_H(\overline{n}) + \mu_{\text{xc}}(\overline{n}) \quad (31)$$

is the total potential due to all of the charge except for the nonspherical 4f density (Fähnle, 1995), and it includes an exchange contribution.

2.3 Magnetocrystalline anisotropy energy

The free energy of a magnetic crystal depends on the direction of the magnetic moment but must be invariant under the symmetry operations of the lattice which imposes

conditions on the MAE coefficients, κ_{nm}, in the expansion

$$F(\theta, \phi) = \sum_{n,m} \kappa_{nm} Y_{nm}(\theta, \phi) = \sum_{n,m} K_n^m \sin^n \theta \cos m\phi \quad (32)$$

where θ and ϕ are the angles that magnetization makes with a crystal axis and Y_{nm} are the spherical harmonics. The set of K_n^m are MAE constants and it is straightforward to evaluate κ_{nm} in terms of K_n^m. In a general sense, the origin of MAE is the spin-orbit interaction since there is no other interaction in the electron Hamiltonian coupling the spin direction to the crystal lattice. In 4f metals the spin-orbit interaction is responsible for coupling $\boldsymbol{L}$ and $\boldsymbol{S}$ in the 4f shells. The orientation of an aspherical 4f shell is then related to the direction of the total magnetic moment. One source of MAE is the interaction between the CEF and the multipole moments of the 4f shell. Another is the classical dipole–dipole interaction between the magnetic moments that is particularly important in Gd where the 4f shell is half filled. Although the dipole–dipole interaction energy is usually far smaller than the CEF energy it has a very long range and is responsible for the demagnetization field. Indirect exchange interactions – mediated by conduction electrons – between the 4f ions are also anisotropic, due to both multipolar interaction with the conduction bands and spin-orbit coupling in the conduction electron bands, and may be expanded in two-ion multipole–multipole interactions, equation (11). The Coulomb interactions between the 4f aspherical charge clouds may also be expanded in multipole–multipole interactions, again leading to MAE. In addition, multipole–multipole interactions between the 4f shells may be mediated by lattice strain. Despite the multiplicity of ways that MAE can be produced, it is believed that the CEF is the largest source in rare-earth metals.

Similar considerations should apply to the heavy actinides although there are no measurements available. The origin of MAE in compounds of light actinides is more complex and depends on whether the 5f electrons are itinerant or localized. There is strong evidence that the light actinide dioxides, which are semiconductors, have a localized 5f shell and crystal-field excitations have been observed (Amoretti *et al*., 1989; Fournier *et al*., 1991a; Kern *et al*., 1990). Sharp crystal-field excitations have been observed in one metallic compound, UPd_3. In these cases multipolar interactions are also important. In many compounds, such as the NaCl compounds US and UN, evidence is that the 4f electrons are itinerant, and in these cases the spin-orbit interaction enters at the single electron level, coupling spin and orbit in the conduction bands (Brooks and Kelly, 1983). The spin-orbit splitting between $j = l \pm 1/2$ states ranges from 0.7 to 0.9 eV from U to Pu compared with 0.4 eV in Ce. The MAE is an order of magnitude larger than in 4f metals and 4 orders of magnitude larger than in 3d transition metals (Lander *et al*., 1990).

2.4 Magnetoelastic interactions

All magnetic crystals have some type of MAE and magnetoelastic interactions. By the latter, we mean that a magnetic field affects the elastic properties and that stress affects the magnetic properties. In particular, anomalies in magnetic and elastic properties are produced by structural and magnetic phase transitions, respectively. The MAE originates in the coupling of magnetic moments to the directional properties of the crystal lattice, and the magnetoelastic interactions arise because the MAE *always* changes with changes in the lattice. A change in magnetic state produces a change in the (static) homogeneous strain known as *magnetostriction*. If the MAE is expanded for small strains, the leading term – linear in strain and magnetic variables – is responsible for magnetostriction. The term *quadratic in strain* is responsible for a magnetic contribution to the elastic constants and thus the sound velocity. The dynamic effects of the interaction between inhomogeneous strain and magnetic variables include magnetoelastic waves and magnon–phonon scattering.

When the magnetic interion interactions are large compared to the ion–lattice interactions, phase transitions are driven by the magnetic interactions and the accompanying lattice distortion is magnetostriction. When the ionic ground state has an unquenched orbital moment and ion–lattice interactions are larger than the magnetic interion interactions, local Jahn–Teller (JT) distortions can interact to drive a cooperative structural phase transition known as the *cooperative Jahn–Teller* (*CJT*) *effect*. The magnetic transition then often occurs at a lower temperature to a phase of lower symmetry. A CJT transition is characterized by the softening of one or more elastic constants, whereas in a magnetic transition the effect of magnetostriction on the elastic properties is relatively small (Lines, 1979). The interaction between JT ions, T, is usually quadrupolar (Sivardière and Blume, 1972). Large magnetic interion interactions, M, lead to a second-order magnetic dipole transition ($M \gg T$) where the quadrupolar interactions produce magnetostriction in the ordered phase. The sound velocity remains finite. As M/T decreases, the still magnetic transition changes to first order with both dipolar and quadrupolar order parameters discontinuous at the transition. For $T \gg M$, there are two transitions with decreasing temperature, the first being either a first- or second-order CJT transition for the latter of which an elastic constant softens; the second being the magnetic transition which occurs at a lower temperature and is first or second order depending on its closeness to the CJT transition.

Magnetoelastic coupling manifests itself in quite different ways in 4f and 5f metals and compounds. In the heavy rare earths, the large molecular fields due to the large 4f spin moments mean that magnetic effects dominate, but MAE and magnetostriction are very important, influencing the spin-wave energies and producing magnon–phonon interactions. In some compounds of light actinides, particularly small moment antiferromagnets, JT-induced quadrupolar coupling is large.

2.5 Anisotropy and magnetic structure

In the absence of MAE, the magnetic structure is determined by the isotropic exchange interaction, since in the paramagnetic phase, $1/\chi(\boldsymbol{q}) = 1/\chi^0(\boldsymbol{q}) - \mathcal{J}(\boldsymbol{q})$, and the magnet will order with a $\boldsymbol{Q}$ vector corresponding to a maximum in $\mathcal{J}(\boldsymbol{q})$ that will not necessarily be commensurable with the crystal lattice. In the heavy rare earths, $\boldsymbol{Q} = \boldsymbol{Q}_\parallel$ is parallel to the c axis of the hcp structure. The MAE determines the direction of the magnetic moment and also favors commensurable magnetic structures since the MAE is lower when the magnetic moments lie along easy directions. The sign of the dominant axial CEF parameter, $\langle B_{20}\rangle$ (equation (14)), produces an MAE that confines the magnetic moments of Tb and Dy to the hexagonal plane of the hcp structure. This leads to incommensurable *helical magnetic structures* with the magnetic moments parallel within the hexagonal planes but changing in direction along the c axis with wave vector $\boldsymbol{Q}$. The Stevens factor (equation (28)), is of opposite sign for Tm – reversing the sign of the MAE and confining the magnetic moments to the c axis. The resulting incommensurable *c-axis modulated structure* is described by

$$J_\parallel(\boldsymbol{R}_i) = J\cos(\boldsymbol{Q}\cdot\boldsymbol{R}_i + \phi) \tag{33}$$

with the wave vector $\boldsymbol{Q}$ parallel to the c axis, whereas the helical structure has two oscillating components in the hexagonal plane. For larger MAE, as in Ho at low temperature, the hexagonal plane MAE is large enough to force the helical magnetic order to become commensurable. Apart from these simple examples, the rich variety of magnetic structures observed for the rare-earth metals is due to this competition between isotropic exchange and single- and two-ion anisotropic interactions as explained in detail by Jensen and Mackintosh (1991).

The magnetic structure described by equation (33) is known as a *single-q structure* since only a single $\boldsymbol{Q}$ vector is involved. If, however, $\boldsymbol{Q} = \boldsymbol{Q}_\perp$ is in the hexagonal plane there are three distinct values of $\boldsymbol{Q}$ that are equivalent by symmetry, therefore a possible multiple-$\boldsymbol{Q}$ ($m > 1$) magnetic structure is

$$\boldsymbol{J}(\boldsymbol{R}_i) = \sum_m \boldsymbol{J}_m \mathrm{e}^{i(\boldsymbol{Q}_m\cdot\boldsymbol{R}_i + \phi_m)} \tag{34}$$

where the set of vectors $\{\boldsymbol{Q}\}$ lie in the star of $\boldsymbol{Q}_1$. In Nd, where the MAE (as a result of both CEF and anisotropic two-ion interactions) is relatively larger than in the heavy rare earths, the magnetic order is multi-$\boldsymbol{Q}$ (Bak and Lebech, 1978; Forgan, 1982; Walker and McEwen, 1983; McEwen and Walker, 1986).

The Landau expansion of free energy for the set $\{\boldsymbol{Q}\}$ in powers of the magnetic moment is (Jensen and Mackintosh, 1991; Rossat-Mignod, 1987)

$$F\{\boldsymbol{Q}\} = F_0 + a_{\boldsymbol{Q}} \sum_m J_{\boldsymbol{Q}_m} J_{-\boldsymbol{Q}_m} + b_{\boldsymbol{Q}} \sum_m J^4_{\boldsymbol{Q}_m} + b'_{\boldsymbol{Q}} \sum_{m\neq m'} J^2_{\boldsymbol{Q}_m} J^2_{\boldsymbol{Q}_{m'}} + \cdots \tag{35}$$

and at least fourth order terms are required to remove the degeneracy between multiple-$\boldsymbol{Q}$ structures. Consequently, higher order crystal-field terms or quadrupolar coupling are important in the stabilization of multiple-$\boldsymbol{Q}$ structures.

3 RARE EARTHS

3.1 Crystalline-electric-field anisotropy

Since the CEF is the simplest and usually the principal origin of MAE in 4f metals, we establish the relationship between the CEF parameters (equations (13) and (29)), and the MAE coefficients (equation (32)), in the expansion of the free energy (Callen and Callen, 1965; Brooks and Egami, 1973; Jensen and Mackintosh, 1991). Some care should be taken with regard to the balance between the torque from the applied field and the torque from the MAE (Kanamori and Minatono, 1962; Brooks and Egami, 1973), especially when the MAE is large, but the argument is briefly as follows. Since $F = -\ln Z/\beta$ where $Z = Tre^{-\beta\mathcal{H}}$, the change of free energy on rotation of the moments is $\delta F = \langle\delta\mathcal{H}\rangle$. The CEF Hamiltonian has been expressed in terms of operator equivalents with the direction of magnetic moment (and therefore $\boldsymbol{J}$) along the c axis. Each operator equivalent becomes a linear combination of operator equivalents with the direction of the angular momentum specified by polar angles (θ, ϕ). When the CEF is small enough, the system has cylindrical symmetry about the magnetic moment axis and the only surviving thermal averages of $\tilde{O}_{lm}(\boldsymbol{J})$ are for $m = 0$. Hence

$$\langle\tilde{O}_{lm}(\boldsymbol{J}')\rangle = \tilde{Y}_{lm}(\theta,\phi)\langle\tilde{O}_{l0}(\boldsymbol{J})\rangle \tag{36}$$

The thermal average of the crystal field, (equations (13) and (29)) becomes

$$\langle V_{\text{cef}}\rangle = \sum_{nm} f_N^n \langle B_{nm}\rangle \langle \tilde{O}_{n0}(\boldsymbol{J})\rangle \tilde{Y}_{lm}(\theta,\phi) \tag{37}$$

and comparison with equation (32) yields

$$\kappa_{nm} = f_N^n \langle B_{nm}\rangle \left(\frac{4\pi}{2n+1}\right)^{1/2} \langle \tilde{O}_{n0}\rangle \tag{38}$$

There have been a number of attempts to calculate CEF parameters from first principles. Schmitt (1979a,b) calculated the crystal-field parameters from the aspherical charge density at a rare-earth site although this work predated self-consistent calculations of the charge density. Subsequently LSDA was used to calculate the crystal-field parameters from the self-consistent aspherical charge density (Steinbeck, Richter, Nitzsche and Eschrig, 1996; Richter, Oppeneer, Eschrig and Johansson, 1996; Hummler and Fähnle, 1996a,b; Uebele, Hummler and Fähnle, 1996; Divis and Kuriplach, 1995). The consistency of the application of equation (30) when a nonspherical 4f density is added to the aspherical density of the valence electrons has been investigated by Hummler and Fähnle (1996b) and Fähnle and Buck (1997).

The effects of valence electron screening were included by Brooks, Eriksson, Wills and Johansson (1997) by total energy calculations of the different crystal-field states in PrSb and TmSb. A constrained 4f density corresponding to a particular CEF state was added to the valence electron density and the valence electron density calculated self-consistently, thus allowing it to screen the 4f density. The energies of the crystal field excitations were then obtained as energy differences, as observed in experiments, without the necessity to evaluate CEF parameters. The conditions under which it is necessary to include screening in a total energy calculation have been discussed by Fähnle and Buck (1993) and Brooks, Eriksson, Wills and Johansson (1993).

3.2 Magnetostriction

When the lattice is strained, the magnetic interactions are modified leading to a magnetoelastic coupling between the strain and magnetic moments that is linear in the strain (See also **Magnetostriction and Magnetoelasticity Theory: A Modern View, Volume 1**). The elastic energy, quadratic in the strain, is most conveniently formed from the strains that transform according to the irreducible representations, Γ_n of the chemical point group of the lattice. The hcp lattice occurs frequently for rare earths, in which case the irreducible representations are $\Gamma_\alpha(2)$, $\Gamma_\gamma(2)$, and $\Gamma_\epsilon(2)$ in the notation of Callen and Callen (1965). The elastic energy, invariant under symmetry operations of the crystal, is then

$$\mathcal{H}^e = \frac{1}{2}\sum_{n,m} c_m^n (\varepsilon_m^n)^2 \tag{39}$$

where the c_m^n are elastic constants and the ε_m^n are the irreducible homogeneous strains and m runs over the components of the irreducible representation n. The single-ion magnetoelastic contributions to the Hamiltonian are obtained by forming invariant products of the irreducible strains with linear combinations of tensor operator equivalents transforming according to the irreducible representation Γ_n for the site i

$$\mathcal{H}_i^{me} = -\sum_{n,m} M_m^n \varepsilon_m^n \overline{O}_{nm} \tag{40}$$

where the bar over O denotes the appropriate linear combination. When the magnetoelastic coupling is due to the strain dependence of the CEF it is a single site coupling. There is a similar strain dependence of the interionic interactions leading to two-ion magnetoelastic coupling. Since $\mathcal{H}_i^{me}$ is linear in the strain, the equilibrium strains are never zero when there is magnetic order. The equilibrium strains are obtained by minimizing the free energy with respect to strain. To first order one may use $\partial F/\partial\varepsilon = \langle \partial\mathcal{H}/\partial\varepsilon\rangle = 0$ and the spin Hamiltonian will therefore contain, in addition to the contribution from the unstrained MAE, additional terms arising from equilibrium strains proportional to $M_m^n\langle\overline{O}_{nm}\rangle/c_m^n$. The magnetoelastic contribution to the spin Hamiltonian can be quite large in 4f metals. In the heavy rare-earth metals, where the molecular field is far larger than the crystal field, magnetic dipole order dominates. The magnetostrictive contribution to the spin Hamiltonian has a significant influence on the spin wave energies, especially if the magnetization axis is in the hexagonal plane of the hcp structure (Jensen, Houmann and Møller, 1975), as it is in the ferromagnets Tb and Dy. When the easy axis lies in the hexagonal plane, the energy of the uniform spin-wave mode (or ferromagnetic resonance frequency) in the absence of magnetostriction would be simply proportional to $(K_1 K_3' \cos 6\phi)^{1/2}$, where K_1 and K_3' are the axial and hexagonal plane MAE constants, and ϕ is the angle in the hexagonal plane between the magnetization direction and an easy axis. This is to be expected on physical grounds since the ferromagnetic resonance frequency is proportional to $(F_{\theta\theta}F_{\phi\phi})^{1/2}$, that is, the uniform spin-wave mode just samples the MAE. A magnetic field applied in the hexagonal plane could be used to cancel the hexagonal plane contribution, reducing the resonance frequency to zero. The uniform (static) magnetostrictive strains in these metals prevent the uniform mode frequency from going soft since they add another term to the hexagonal plane contribution to the resonance frequency which is independent

of the direction of magnetic moment in the plane (Cooper, 1968; Brooks, 1970). The strain does not, however, make the same contribution in a static MAE experiment since the uniform strain then adjusts to the direction of magnetization. The effective hexagonal plane MAE is therefore different in dynamic and static experiments. Initially it was believed that the uniform strains could sometimes follow the spin precession dynamically (Vigren and Liu, 1972) partially because the frequency of the uniform mode in Dy was far less than seemed to be obtained from static measurements of MAE and magnetostriction constants. The anomaly, however, is actually due to a renormalization of the planar MAE constant in Dy as a result of zero point fluctuations induced by elliptical spin precession (Egami, 1972). A complete treatment includes both coupled magnon and phonon excitations and the effects of zero point motion (Chow and Keffer, 1973; Jensen and Mackintosh, 1991).

Ab initio calculation of the giant magnetostriction in Tb and Er has been made by Buck and Fähnle (1998) who found that it is dominated by the single-ion 4f contribution and obtained good agreement with experiment. The same authors (Buck and Fähnle, 1999) calculated a large magnetostrictive MAE in $TbFe_2$ arising from the intrinsic electronic structure. A model, based on a rigid band Stoner model, has been used successfully by Kulakowski and Moral (1994) for Y_2Fe_{17}.

3.3 Multipole interactions in 4f Metals

The magnetoelastic interaction causes lattice distortion but may do so in different ways. Magnetic interactions break time reversal symmetry, and when they are larger than higher multipole–multipole interactions, the material undergoes a magnetic phase transition that is *accompanied but not driven by* a lattice distortion due to magnetostriction. It can happen that higher, nonmagnetic, multipole–multipole interactions –usually quadrupole–quadrupole ones – are larger than the magnetic interactions, even when the lattice is rigid. In this case, multipolar ordering (which does not break time reversal symmetry) occurs and is *accompanied but not driven by* a lattice distortion – named *quadrupolar striction* by Levy, Morin and Schmitt (1979) – due to magnetoelastic coupling. If the magnetoelastic interactions are larger than the magnetic and quadrupolar interactions, they can drive a phase transition that is *accompanied but not driven by* multipolar ordering. In this case the transition is caused by a CJT effect. Rare-earth compounds in which quadrupolar ordering with quadrupolar striction occurs before magnetic ordering are TmCd and TmZn (Levy, Morin and Schmitt, 1979). In DySb, the JT, magnetic, and quadrupolar interactions are of comparable size (Levy, 1973).

3.4 Conduction electron magnetocrystalline anisotropy energy in rare earths

Typical MAE energies of rare-earth metals are of the order of millielectron volts per atom. The MAE in Gd metal is 2 orders of magnitude smaller than in other rare earths but of the same order of magnitude as in Co, the most anisotropic of the 3d metals. The first approximation to the ground state of Gd is a half-filled shell with $\boldsymbol{L} = 0$ and zero MAE. It is possible that residual interactions would mix enough orbital moment into the S state to explain this MAE. Another alternative has been explored by Colarieti-Tosti *et al.* (2003). Dipole–dipole interactions between the large spins make a significant contribution (Brooks and Goodings, 1969; Jensen and Mackintosh, 1991) and they contribute an MAE of the form $K_1^0 sin^2\theta$, where θ is the angle between the magnetic moment and the c axis with $K_1^0 = 10.3\,\mu$eV per atom. However, the total MAE measured from experiment is $35.4\,\mu$eV per atom (Franse and Gersdorf, 1980), requiring an additional contribution of $25.1\,\mu$eV per atom. The easy direction is observed to lie at an angle of about 20° to the c axis at low temperatures (Cable and Wollan, 1968), which would not be possible without $sin^n\theta$ contributions ($n > 2$) to the MAE. Colarieti-Tosti *et al.* (2003) suggested that the MAE in Gd is due to a combination of the dipole–dipole interaction and the MAE of the conduction electrons. The 4f spin polarizes the conduction electrons via exchange interaction, which transfers the MAE of the conduction electrons to the 4f spin. They tested the hypothesis with LSDA total energy calculations as a function of the direction of the Gd moment between the hexagonal plane and c axis, obtaining reasonable agreement with the measurements of Franse and Gersdorf (1980). According to this theory, Gd is a 5d transition metal with a large 4f spin and the MAE calculation is very similar to those for Fe, Ni, or Co. This mechanism for the MAE must be present in all of the elemental rare-earth metals and the heavy actinides, but since it is far smaller than the MAE arising from the interaction between the CEF and the electric multipole moments of the 4f charge cloud, it is only important for S state ions. In rare earth–transition metal compounds, the transition metal may also make a contribution to the MAE and this would be expected to be largest for cobalt (Steinbeck, Richter and Eschrig, 2001).

4 ACTINIDES

The elemental light actinide metals do not order magnetically. The complexity of the magnetic and magnetoelastic properties of compounds of light actinides derives from the fact that the 5f orbitals are more extended than the 4f

orbitals in rare earths (Figure 2), but are not so extended that the orbital magnetic moments are quenched, as in many transition metals. The existence of a finite orbital angular momentum is not only responsible for the MAE but it also leads to coupling between charge degrees of freedom and lattice vibrations. The simplest consequence of the more extended 5f orbitals is that the effects of the CEF in actinide compounds are larger than in the corresponding rare earths. It is customary to say that the CEF is larger in actinides although, of course, the electric field itself is not. However the matrix elements of the CEF between 5f states are larger, leading to larger splitting of energy levels by the CEF. Also, CEF excitations have been difficult to find in metallic actinide compounds (Holland-Moritz and Lander, 1994) but they have been unambiguously observed in UPd_3 (McEwen, Steigenberger and Martinez, 1993; McEwen, Steigenberger, Martinez and Abell, 1990) and in actinide dioxides (Amoretti *et al*., 1989; Fournier *et al*., 1991b; Kern *et al*., 1999; Kern *et al*., 1990).

The closeness of the actinide 5f states to delocalization, apart from larger CEF effects, is responsible for other differences between anisotropic and magnetoelastic interactions in actinides and rare earths. Firstly, interactions between 5f and conduction electrons frequently require multipole expansions, rather than the simpler RKKY interaction, leading to indirect multipole–multipole interactions. Although also present in some rare-earth compounds, such interactions are more prevalent in actinide compounds. The larger magnetoelastic interactions that accompany larger CEF splittings produce stronger phonon-mediated indirect interactions between 5f shells, and these interactions are also multipolar. An immediate and important effect of large CEF and higher multipole–multipole interactions in actinides is that multiple-$\boldsymbol{Q}$ structures are often the ground states. Multiple-$\boldsymbol{Q}$ structures are stable only if terms higher than quadratic in the magnetization are present in the Landau expansion of free energy, equation (35), and such terms are present due to the CEF and multipole–multipole interactions (Monachesi and Weling, 1983; Rossat-Mignod, 1987; Sandratskii, 1998). When the 5f states are itinerant, the MAE is due to spin-orbit interaction in the energy bands, and the MAE can be very large.

4.1 Light actinide compounds with localized 5f electrons

Band structure calculations (Kelly and Brooks, 1980; Dudarev, Nguyen-Manh and Sutton, 1997) for UO_2 indicate that, if the 5f states are treated as itinerant, the calculated volumes are far too small, a result consistent with a wealth of experimental evidence that the 5f electrons are localized. A more systematic treatment for the light actinide dioxide series (Kelly and Brooks, 1987) found that the valence band electronic structure varies little across the series, suggesting that the strength of magnetic interactions would also not vary too much apart from small effects due to actinide contraction. This indicates that the strength of the CEF and exchange interactions may therefore be scaled across the actinide oxide series, a simplification confirmed by experiment (Amoretti *et al*., 1992). Even though the actinide dioxides are CEF compounds, their electronic structure is by no means simple, since the CEF, exchange, quadrupolar, and magnetoelastic interactions are all involved with equal magnitude.

The uranium ions in UO_2 are tetravalent with a $5f^2$ configuration. The Γ_1, Γ_3, and Γ_4 CEF states in UO_2 lie between 150 and 170 meV above the Γ_5 ground state (Amoretti *et al*., 1989). UO_2 undergoes a first-order antiferromagnetic phase transition at 30.8 K (Leask, Roberts, Walter and Wolf, 1963; Frazer, Shirane, Cox and Olsen, 1965; Faber and Lander, 1976; Lander, Faber, Freeman and Desclaux, 1976). The correlation length increases below T_N (Buyers and Holden, 1985) without diverging and the elastic constants are discontinuous at T_N (Brandt and Walker, 1967), although, within 50 Å of the surface, the magnetic scattering intensity decreases continuously as the bulk Néel temperature is approached from below (Watson *et al*., 1996). Allen (1968a,b) suggested that the magnetoelastic interaction would mediate quadrupole–quadrupole interactions, since the CEF ground state Γ_5 triplet may have both magnetic dipole and electric quadrupole moments. Resonant X-ray scattering experiments at the uranium M_4 absorption edge have confirmed antiferroquadrupolar (AFQ) ordering of the electric quadrupoles (Wilkins *et al*., 2006). Allen's model is consistent with a softening of the C_{44} elastic constant, which is related to the quadrupolar susceptibility, and neutron diffraction (Faber and Lander, 1976) confirmed the presence of a lattice distortion, albeit not the $\boldsymbol{q} = 0$ optical phonon postulated by Allen. Further, Allen assumed a single-$\boldsymbol{Q}$ magnetic structure, whereas measurements (Burlet *et al*., 1986) were more consistent with a triple-$\boldsymbol{Q}$ structure. Recently, Blackburn *et al*. (2005) have established beyond doubt from the spin-wave polarization that the magnetic structure of UO_2 is triple-$\boldsymbol{Q}$. Additional efforts to explain the magnetic structure (Siemann and Cooper, 1979; Solt and Erdös, 1980; Giannozzi and Erdös, 1987) actually found the single-$\boldsymbol{Q}$ structure to be more stable. The magnon–phonon interaction is observed to be strong in the ordered phase (Cowley and Dolling, 1968) and the spin-wave spectrum (Caciuffo *et al*., 1999) is roughly consistent with theory (Giannozzi and Erdös, 1987) except that three branches are observed over most of the Brillouin zone, whereas only two are expected. Neutron scattering measurements (Amoretti *et al*., 1989) showed that the excited

crystal-field states are split above T_N when theory suggests that they should be degenerate in the paramagnetic phase. However a dynamic JT effect, with proper vibronic states, might well resolve the inconsistencies.

The Np ions in NpO_2, tetravalent with a $5f^3$ configuration, are Kramers ions with a magnetic doublet or quadruplet ground state. Heat capacity (Osborne and Westrum, 1953) and magnetic susceptibility measurements (Erdös *et al*., 1980) indicate a phase transition in NpO_2 at 25 K but there was evidence neither for magnetic ordering nor for lattice distortions (Caciuffo *et al*., 1987). Any ordering with an order parameter even under time reversal does not suppress a diverging magnetic susceptibility at low temperature. The absence of magnetic order in NpO_2 was therefore something of a mystery. Superlattice reflections in resonant X-ray scattering at the Np $M_{4,5}$ absorption edges were observed (Mannix *et al*., 1999; Wilkins *et al*., 2004) and attributed to longitudinal triple-$\boldsymbol{Q}$ antiferromagnetic ordering. It seemed that the magnetic moments ($<0.1\,\mu_B$) were too small to be detectable in the neutron experiments. Further theory (Santini and Amoretti, 2000a,b) and experiments (Paixào *et al*., 2002) revealed quite a different picture in which the superlattice Bragg peaks were due to long-range triple-$\boldsymbol{Q}$ ordering of electric quadrupoles. The absence of magnetic dipole order is consistent with the ordering of magnetic octupoles of Γ_5 symmetry that removes the degeneracy of the ground quartet, producing a singlet ground state with no magnetic dipole moment, and drives the ordering of the electric quadrupoles.

The Pu ions in PuO_2 are tetravalent with a $5f^4$ configuration, and if the CEF and exchange parameters are scaled from those of UO_2 and NpO_2, a Γ_1 ground state, about 110 meV below a Γ_4 triplet, would be expected (Colarieti-Tosti *et al*., 2002). The lowest exited CEF state detected by inelastic neutron scattering (Kern *et al*., 1990, 1999) is at 120 meV. No phase transition has been observed in PuO_2 and the magnetic susceptibility is temperature independent at low temperature (Raphael and Lallement, 1968). The gap between ground (Γ_1) and first excited (Γ_4) CEF states required to fit the temperature independent susceptibility (Raphael and Lallement, 1968) is inconsistent with that measured in the neutron scattering experiments (Kern *et al*., 1990, 1999) by a factor of about two. The inconsistency may be removed (Colarieti-Tosti *et al*., 2002) by antiferromagnetic exchange enhancement scaled from the antiferromagnetic exchange interactions in UO_2, assuming an identical electronic structure apart from the correlated 5f states.

CEF excitations have also been observed in UPd_3 (Buyers and Holden, 1985; McEwen, Steigenberger and Martinez, 1993; McEwen, Steigenberger, Martinez and Abell, 1990). UPd_3 has a double hexagonal close-packed structure with uranium ions at sites with local hexagonal and quasicubic symmetry. Early experiments (Walker *et al*., 1994; McEwen *et al*., 1988) revealed that there are at least three transitions in UPd_3. Quadrupolar order first develops at 7.8 K followed by an AFQ transition at 6.8 K and magnetic antiferromagnetic ordering at 4.4 K. AFQ ordering between 7.8 and 6.8 K was observed by resonant X-ray scattering (McMorrow *et al*., 2001) although below 6.8 K an unambiguous identification of the ordered structure was not possible. Subsequently, ultrasound experiments (Lingg, Maurer, Müller and McEwen, 1999) confirmed that in addition to the magnetic phase transition at 4.4 K, orbital ordering occurs at 7.6 K accompanied by a symmetry change from hexagonal to orthorhombic. The quadrupolar transition at 6.8 K was found to split into a second-order transition at 6.9 K and a first-order transition at 6.70 K. McEwen, Park, Gipson and Gehring (2003) have produced a CEF model based on all the available evidence. The CEF at the hexagonal sites has a singlet ground state and a first excited doublet at 15 meV as also deduced by Buyers and Holden (1985). The CEF at the cubic sites has a ground doublet and a first excited singlet at 4 meV with a doublet CEF ground state and a first excited singlet at 4 meV and antiferromagnetic exchange. The phase transition at 7.8 K is second order with the primary order parameter $Q_{x^2-y^2}$. At 6.9 K there is a second-order transition to a phase with order parameters $Q_{x^2-y^2}$ and Q_{yz}. Then, at 6.7 K there is a first-order transition to a phase with order parameters $Q_{x^2-y^2}$, Q_{zx} and Q_{yz}. Finally, the phase below 4.4 K is AFQ with four sublattices, order parameters $Q_{x^2-y^2}$ and Q_{zx}, and a small magnetic moment.

4.2 Other light actinide compounds

The magnetism of the actinide pnictides and chalcogenides with rock salt structure has been studied thoroughly. It has been found that the MAE is extremely large for cubic compounds (Vogt, 1980) and that multiple-$\boldsymbol{Q}$ magnetic structures are common (Rossat-Mignod *et al*., 1984). Theories incorporating parameterized anisotropic bilinear exchange and CEF interactions (Monachesi and Weling, 1983; Monachesi, 1986) are able to reproduce the multiple-$\boldsymbol{Q}$ magnetic ordering in the uranium pnictides and a hybridization mediated anisotropic two-ion interaction has been derived by Cooper and his collaborators (Thayamballi and Cooper, 1985).

The MAE in the uranium chalcogenides has been calculated from self-consistent DFT calculations under the assumption that the 5f electrons are delocalized. Early calculations (Brooks, Johansson, Eriksson and Skriver, 1986) found the difference in energy between the (100) and the (111) directions of magnetization, ΔE_a to be 180 meV per atom (for $\Delta E_a > 0$, the easy axis is (111)). The comparable

MAE for $TbFe_2$, the most magnetically anisotropic cubic rare-earth compound, is of the order of 10 meV per atom. Subsequent calculations yielded lower, but still very large MAE. The magnitude of the MAE is related to the size of the orbital magnetic moment (Bruno, 1989). Conventional LSDA treatments of orbital magnetism tend to yield orbital magnetic moments that are too small (Brooks, 1985) and therefore an MAE that is also too small. Such calculations should therefore set a lower limit on the MAE. Kraft (1997) obtained values for ΔE_a of about 9, 10 and 16meV for US, USe, and UTe, respectively, whereas Shishidou and Oguchi (2000) obtained values of 14, 7, and 8 meV for the same compounds. Trygg (1995), using conventional, full potential linear muffin-tin orbital (LMTO) calculations, obtained $\Delta E_a = 15$ meV for US. He made additional calculations with orbital polarization corrections (Eriksson, Brooks and Johansson, 1990a) that produced orbital magnetic moments close to those deduced from the analysis of experiments (Wedgwood, 1972) and obtained $\Delta E_a = 55$ meV for US. Measurements of the MAE energy of US are difficult since the MAE is so large that it is not possible to move the magnetic moment away from the easy axis (Vogt, 1980). However, working at higher temperatures where the MAE is smaller, and estimating the temperature dependence of the MAE constants from theory, Lander *et al*. (1990) estimated ΔE_a to be about 100 meV per atom.

There have been a few attempts to calculate the CEF parameters in actinides. Apart from the work on PuO_2 by Colarieti-Tosti *et al*. (2002) in actinides, Divis, Richter, Eschrig and Steinbeck (1996) calculated the CEF parameters for UGa_2, and from them, the anisotropy of the magnetic susceptibility.

The MAE of the laves phase compound UFe_2 (Popov, Levitin, Zelený and Andreev, 1980) was measured to be only a little larger than that of metallic Fe ($K_1 \approx 10^6$ ergs cm^{-3}). Nevertheless it was clear that something more interesting was happening in this compound since Popov, Levitin, Zelený and Andreev (1980) also observed a large magnetoelastic distortion that contributed to K_1, an amount equal to about minus the measured K_1. K_1^0, for the unstrained lattice, was deduced to be $\approx 10^7$ ergs cm^{-3}. Evidently, the small value of the total MAE is due to a cancellation of far larger unstrained and magnetoelastic contributions neither of which would be expected to be due to the Fe alone. The magnetic moment of uranium in UFe_2 is negligible (Wulff, Lander, Lebech and Delapalme, 1989) but that is due to the almost complete cancellation of small spin and orbital moments at the uranium sites (Eriksson, Brooks and Johansson, 1990b; Brooks, 2004). The origin of the large anisotropic magnetoelastic coupling is probably the spin–orbit interaction in uranium and the small orbital moment of uranium. It is quite possible that only the Fe moment is rotated in a torque experiment and that there is a large MAE associated with the U moment. Owing to the cancellation of orbital and spin moments on uranium, no anisotropy in the magnitude of the magnetic moment would be observed. If this were the case the measured unstrained torque would be mostly due to the coupling between Fe and U moments. However no detailed theory has been produced to date.

Neutron diffraction experiments on $PuFe_2$ (Wulff *et al*., 1988) determined the easy direction of magnetization to be (100). It appeared that the magnetic moment could not be moved away from the easy direction in achievable magnetic fields. Since $PuFe_2$ has a relatively high Curie temperature of 564 K, the indications are that it has a very large MAE for a cubic compound.

REFERENCES

Allen, S.J. (1968a). Spin-lattice interaction in UO_2. I. Ground-state and spin-wave excitations. *Physical Review*, **166**, 530–539.

Allen, S.J. (1968b). Spin-lattice interaction in UO_2. II. Theory of the first-order phase transition. *Physical Review*, **168**, 492–496.

Amoretti, G., Blaise, A., Caciuffo, R., *et al*. (1989). 5f-electron states in uranium dioxide investigated using high-resolution neutron spectroscopy. *Physical Review B*, **40**, 1856–1870.

Amoretti, G., Blaise, A., Caciuffo, R., *et al*. (1992). Neutron-scattering investigation of the electronic ground state of neptunium dioxide. *Journal of Physics: Condensed Matter*, **4**, 3459–3478.

Anisimov, V.I., Aryasetiawan, F. and Lichtenstein, A.I. (1997). First-principles calculations of the electronic structure and spectra of strongly correlated systems: the LDA+U method. *Journal of Physics: Condensed Matter*, **9**, 767–808.

Antropov, V.P., Katsnelson, M.I., van Schilfgaarde, M. and Harmon, B.N. (1995). *Ab initio* spin dynamics in magnets. *Physical Review Letters*, **75**, 729–732.

Bak, P. and Lebech, B. (1978). Triple-$\boldsymbol{q}$" modulated magnetic structure and critical behaviour in neodymium. *Physical Review Letters*, **40**, 800–803.

Blackburn, E., Caciuffo, R., Magnani, N., *et al*. (2005). Spherical neutron spin polarimetry of anisotropic magnetic fluctuations in UO_2. *Physical Review B*, **72**, 184411–184421.

Brandt, O.G. and Walker, C.T. (1967). Temperature dependence of elastic constants and thermal expansion for UO_2. *Physical Review Letters*, **18**, 11–13.

Brooks, M.S.S. (1970). Theory of the temperature dependence of the spin-wave excitation energies in the rare earth metals. *Physical Review B*, **1**, 2257–2264.

Brooks, M.S.S. (1984). Electronic structure of NaCl-type compounds of the light actinides. I. UN, UC, and UO. *Journal of Physics F-Metal Physics*, **14**, 639–652.

Brooks, M.S.S. (1985). Calculated ground state properties of light actinide metals and their compounds. *Physica B*, **130**, 6–12.

Brooks, M.S.S. (2004). Orbital magnetism in UFe_2. *Journal of Magnetism and Magnetic Materials* **272–276**, E331–E332.

Brooks, M.S.S. and Egami, T. (1973). Theory of highly anisotropic ferromagnets I. Magnetic anisotropy and magnetostriction. *Journal of Physics C-Solid State Physics*, **6**, 513–531.

Brooks, M.S.S. and Goodings, D. (1969). Spin-wave theory of the magnetocrystalline anisotropy in gadolinium metal. *Journal of Physics C-Solid State Physics*, **1**, 1279–1287.

Brooks, M.S.S. and Johansson, B. (1983). Exchange integral matrices and cohesive energies of transition metal atoms. *Journal of Physics F-Metal Physics*, **13**, L197–L202.

Brooks, M.S.S. and Kelly, P.J. (1983). Large orbital-moment contribution to 5f band magnetism. *Physical Review Letters*, **51**, 1708.

Brooks, M.S.S., Eriksson, O., Wills, J.M. and Johansson, B. (1993). Comment on density functional theory of crystal field quasi-particle excitations and the *ab initio* calculation of spin Hamiltonian parameters: reply. *Physical Review Letters*, **80**, 4108.

Brooks, M.S.S., Eriksson, O., Wills, J. and Johansson, B. (1997). Density functional theory of crystal field quasiparticle excitations and the ab initio calculation of spin Hamiltonian parameters. *Physical Review Letters*, **79**, 2546–2549.

Brooks, M.S.S., Johansson, B., Eriksson, O. and Skriver, H.L. (1986). Relativistic effects in heavy elements. *Physica B*, **144**, 1–13.

Brooks, M.S.S., Nordström, L. and Johansson, B. (1991). Origin and *ab initio* evaluation of magnetic interactions in rare earth intermetallics. *Journal of Physics: Condensed Matter*, **3**, 3393–3396.

Bruno, P. (1989). Tight-binding approach to the orbital magnetic moment and magnetocrystalline anisotropy of transition-metal monolayers. *Physical Review B*, **39**, 865–868.

Bruno, P. (2003). Exchange interaction parameters and adiabatic spin-wave spectra of ferromagnets: A "renormalized magnetic force theorem". *Physical Review Letters*, **90**, 087205.

Buck, S. and Fähnle, M. (1998). *Ab initio* calculation of the giant magnetostriction in terbium and erbium. *Physical Review B*, **57**, R14044–R14047.

Buck, S. and Fähnle, M. (1999). Magnetostriction in $TbFe_2$: weak influence of the internal structural distortion. *Journal of Magnetism and Magnetic Materials*, **204**, 1–4.

Burlet, P., Rossat-Mignod, J., Vuevel, S., *et al*. (1986). Neutron diffraction on actinides. *Journal of the Less Common Metals*, **121**, 121–139.

Buyers, W.J.L. and Holden, T.M. (1985). Neutron scattering from spins and phonons in actinide systems. In *Handbook on the Physics and Chemistry of the Actinides*, Freeman, A.J. and Lander, G.H. (Eds.), North-Holland: New York, Vol. 2.

Cable, J.W. and Wollan, E.O. (1968). Neutron diffraction study of the magnetic behavior of gadolinium. *Physical Review*, **165**, 733–734.

Caciuffo, R., Amoretti, G., Santini, P., *et al*. (1999). Magnetic excitations and dynamical jahn-teller distortions in UO_2. *Physical Review B*, **59**, 13892–13900.

Caciuffo, R., Lander, G.H., Spirlet, J.C., *et al*. (1987). A search for anharmonic effects in NpO_2 at low temperature by neutron diffraction. *Solid State Communications*, **64**, 149–152.

Callaway, J., Chatterjee, A.K., Singhal, S.P. and Ziegler, A. (1983). Magnetic susceptibility of ferromagnetic metals: application to nickel. *Physical Review B*, **28**, 3818–3830.

Callen, E. and Callen, H.B. (1965). Magnetostriction, forced magnetostriction, and anomalous thermal expansion in ferromagnets. *Physical Review*, **139**, A455–A471.

Chow, H. and Keffer, F. (1973). Phenomenological theory of magnetoelastic modes in hexagonal ferromagnets of easy-plane type. *Physical Review B*, **7**, 2028–2038.

Colarieti-Tosti, M. (2004). *Theory of Crystal Fields and Magnetism of f-Electron Systems*, PhD Thesis, Uppsala University.

Colarieti-Tosti, M., Eriksson, O., Nordström, L., *et al*. (2002). Crystal-field levels and magnetic susceptibility in PuO_2. *Physical Review B*, **65**, 195102–195108.

Colarieti-Tosti, M., Simak, S.I., Ahuja, R., *et al*. (2003). Origin of magnetic anisotropy of Gd metal. *Physical Review Letters*, **91**, 157201–157204.

Cooke, J.F., Lynn, J.W. and Davis, H.L. (1980). Calculations of the dynamic susceptibility of nickel and iron. *Physical Review B*, **21**, 4118–4131.

Cooper, B.R. (1968). Spin waves and magnetic resonance in rare-earth metals: thermal, applied-field, and magnetoelastic effects. *Physical Review*, **169**, 281–294.

Cowley, R.A. and Dolling, G. (1968). Magnetic excitations in uranium dioxide. *Physical Review*, **167**, 464–477.

Divis, M. and Kuriplach, J. (1995). Crystal field in rare earth intermetallics with CsCl structure. *Physica B*, **205**, 353–364.

Divis, M., Richter, M., Eschrig, H. and Steinbeck, L. (1996). *Ab initio* electronic structure, magnetism, and magnetocrystalline anisotropy of UGa_2. *Physical Review B*, **53**, 9658–9665.

Dudarev, S., Nguyen-Manh, D. and Sutton, A. (1997). Effect of Mott-Hubbard correlations on the electronic structure and structural stability of uranium dioxide. *Philosophical Magazine Part B*, **75**, 613–628.

Duthie, J. and Pettifor, D. (1977). Correlation between d-band occupancy and crystal structure in the rare earths. *Physical Review Letters*, **38**, 564–567.

Egami, T. (1972). Effect of zero-point energy on magnetocrystalline anisotropy of the rare earth metals. *Journal of Physics C-Solid State Physics*, **5**, L85–L88.

Egami, T. and Brooks, M.S.S. (1975). Theory of collective magnetic excitations in strong crystal fields. I. Dynamics of the angular momentum tensor operators. *Physical Review B*, **12**, 1021–1028.

Elliott, R.J. and Thorpe, M.F. (1968). Orbital effects on exchange interactions. *Journal of Applied Physics*, **39**, 802–807.

Erdös, P., Solt, G., Zolnierek, Z., *et al*. (1980). Magnetic susceptibility and the phase transition of NpO_2. *Physica B*, **102**, 164–170.

Eriksson, O., Brooks, M.S.S. and Johansson, B. (1990a). Orbital polarization in narrow-band systems: application to volume collapses in light lanthanides. *Physical Review B*, **41**, 7311–7314.

Eriksson, O., Brooks, M.S.S. and Johansson, B. (1990b). Theoretical aspects of the magnetism in the ferromagnetic AFe_2 systems (A=U, Np, Pu, and Am). *Physical Review B*, **41**, 9087–9094.

Faber, J.J. and Lander, G.H. (1976). Neutron diffraction study of UO_2: antiferromagnetic state. *Physical Review B*, **14**, 1151–1164.

Fähnle, M. (1995). Mapping of the density functional theory on the crystal field theory of rare earth systems. *Journal of Magnetism and Magnetic Materials*, **151**, 151.

Fähnle, M. and Buck, S. (1993). Comment on density functional theory of crystal field quasiparticle excitations and the ab initio calculation of spin Hamiltonian parameters. *Physical Review Letters*, **80**, 4107.

Fähnle, M. and Buck, S. (1997). Rare-earth magnetic anisotropy: Is the crystal field theory valid? *Journal of Magnetism and Magnetic Materials*, **166**, 297–302.

Forgan, E.M. (1982). The magnetic structure of neodymium below 20K: a first principles mean field theory for two-dimensionally modulated spin patterns in an antiferromagnet. *Journal of Physics F-Metal Physics*, **12**, 779–793.

Fournier, J., Blaise, A., Amoretti, G., *et al*. (1991a). High-energy-neutron spectroscopy of crystal-field excitations in NpO_2. *Physical Review B*, **43**, 1142–1145.

Fournier, J.M., Blaise, A., Amoretti, G., *et al*. (1991b). High-energy-neutron spectroscopy of crystal-field excitations in NpO_2. *Physical Review B*, **43**, 1142–1145.

Franse, J.J.M. and Gersdorf, R. (1980). Magnetic anisotropy of Gd metal at 4K under pressure. *Physical Review Letters*, **45**, 50–53.

Frazer, B.C., Shirane, G., Cox, D.E. and Olsen, C.E. (1965). Neutron-diffraction study of antiferromagnetism in UO_2. *Physical Review*, **140**, A1448–A1452.

Friedel, J. (1969). Chapter 8. In *The Physics of Metals*, Ziman, J. (Ed.), Cambridge University Press: Cambridge, pp. 341–494.

Giannozzi, P. and Erdös, P. (1987). Theoretical analysis of the 3-k magnetic structure and distortion of uranium dioxide. *Journal of Magnetism and Magnetic Materials*, **67**, 75–87.

Gunnarsson, O. (1976). Band model for magnetism of transition metals in the spin-density-functional formalism. *Journal of Physics F-Metal Physics*, **6**, 587–606.

Hill, H.H. (1970). The early actinides: the periodic systems f electron transition metal series. In *Plutonium 1970*, Miner W.N. (Ed.), Metallurgical Society of AIME: New York, pp. 2–19.

Hirst, L.L. (1978). Theory of the coupling between conduction electrons and moments of 3d and 4f ions in metals. *Advances in Physics*, **27**, 231–285.

Hohenberg, P. and Kohn, W. (1964). Inhomogeneous electron gas. *Physical Review*, **136**, 864–871.

Holland-Moritz, E. and Lander, G.H. (1994). Neutron elastic scattering from actinides and anomalous lanthanides. In *Handbook on the Physics and Chemistry of the Rare Earths*, Gschniedner, G.H.L.K., Eyring, L. and Choppin, G. (Eds.), North-Holland Physics: Amsterdam, pp. 1–121, Vol. 19.

Hummler, K. and Fähnle, M. (1996a). Full-potential linear-muffin-tin-orbital calculations of the magnetic properties of rare-earth transition-metal intermetallics. I. description of the formalism and application to the series RCo_5 (R=rare-earth atom). *Physical Review B*, **53**, 3272–3289.

Hummler, K. and Fähnle, M. (1996b). Full-potential linear-muffin-tin-orbital calculations of the magnetic properties of rare-earth transition-metal intermetallics. II. $Nd_2Fe_{14}B$. *Physical Review B*, **53**, 3290–3295.

Jensen, J., Houmann, J.G. and Møller, H.B. (1975). Spin waves in terbium. I. Two-ion magnetic anisotropy. *Physical Review B*, **12**, 303–319.

Jensen, J. and Mackintosh, A. (1991). *Rare Earth Magnetism, Structures and Excitations*, Oxford Science Publications, Clarendon Press: Oxford.

Judd, B.R. (1967). *Second Quantization and Atomic Spectroscopy*, John Hopkins: Baltimore.

Kanamori, J. and Minatono, H. (1962). The magnetic anisotropy constant in the case of strong anisotropy. *Journal of the Physical Society of Japan*, **17**, 1759–1766.

Kaplan, T.A. and Lyons, D.H. (1963). Theory of indirect exchange interactions in Rare-Earth metals. *Physical Review*, **129**, 2072–2086.

Kelly, P.J. and Brooks, M.S.S. (1980). Cohesive properties of CaF_2 and UO_2 in the atomic sphere approximation. *Journal of Physics C-Solid State Physics*, **13**, L939–L945.

Kelly, P.J. and Brooks, M.S.S. (1987). Electronic structure and ground state properties of the actinide dioxides. *Journal of the Chemical Society-Faraday Transactions*, **83**, 1189–1203.

Kern, S., Loong, C.K., Goodman, G.L., *et al*. (1990). Crystal-field spectroscopy of PuO_2: further complications in actinide dioxides. *Journal of Physics: Condensed Matter*, **2**, 1933–1940.

Kern, S., Robinson, R.A., Nakotte, H., *et al*. (1999). Crystal-field transition in PuO_2. *Physical Review B*, **59**, 104–106.

Kohn, W. and Sham, L.J. (1965). Self-consistent equations including exchange and correlation effects. *Physical Review*, **140**, A1133–A1138.

Kraft, T. (1997). *Magneto-Optischer Kerr-effect und Magneto-optische Spektren von 4f und 5f Systemen*, PhD Thesis, Technische Universitat Dresden.

Kulakowski, K. and Moral, A. (1994). Model calculation of the crystal-field magnetostriction and its temperature dependence in the itinerant uniaxial ferromagnet Y_2Fe_{17}. *Physical Review B*, **50**, 234–241.

Kurz, P., Förster, F., Nordström, L., *et al*. (2004). *Ab initio* treatment of noncollinear magnets with the full-potential linearized augmented plane wave method. *Physical Review B*, **69**, 24415–24429.

Lander, G.H., Brooks, M.S.S., Lebech, B., *et al*. (1990). Measurement of giant magnetic anisotropy in a uranium compound. *Applied Physics Letters*, **57**, 989–991.

Lander, G.H., Faber, J. Jr., Freeman A.J. and Desclaux, J.P. (1976). Neutron-diffraction study of UO_2: paramagnetic state. *Physical Review B*, **13**, 1177–1182.

Leask, M.J.M., Roberts, L.E.J., Walter, A.J. and Wolf, W.P. (1963). Low-temperature magnetic properties of some uranium oxides. *Journal of the Chemical Society*, **75**, 4788–4794.

Levy, P.M. (1969). Anisotropy in two-center exchange interactions. *Physical Review*, **177**, 509–525.

Levy, P.M. (1973). A theoretical study of the elastic properties of dysprosium antimonide. *Journal of Physics C-Solid State Physics*, **6**, 3545–3555.

Levy, P.M., Morin, P. and Schmitt, D. (1979). Large quadrupolar interactions in rare earth compounds. *Physical Review Letters*, **42**, 1417–1420.

Liebs, M., Hummler, K. and Fähnle, M. (1992). Effective intersublattice exchange couplings in rare-earth transition-metal intermetallics from an *ab initio* calculation. *Physical Review B*, **46**, 11201–11203.

Liechtenstein, A.I., Katsnelson, M.I., Antropov, V.P. and Gubanov, V.A. (1987). Local spin density functional approach to the theory of exchange interactions in ferromagnetic metals and alloys. *Journal of Magnetism and Magnetic Materials*, **67**, 65–74.

Liechtenstein, A.I., Katsnelson, M.I. and Gubanov, V.A. (1984). Exchange interactions and spin-wave stiffness in ferromagnetic metals. *Journal of Physics F-Metal Physics*, **14**, L125–L128.

Lindgård, P.A., Harmon, B.N. and Freeman, A.J. (1975). Theoretical magnon dispersion curves for Gd. *Physical Review Letters*, **35**, 383–386.

Lines, M.E. (1979). Elastic properties of magnetic materials. *Physics Reports*, **55**, 133–181.

Lingg, N., Maurer, D., Müller, V. and McEwen, K.A. (1999). Ultrasound investigations of orbital quadrupolar ordering in UPd_3. *Physical Review B*, **60**, R8430–R8433.

Mannix, D., Lander, G.H., Rebizant, J., *et al*. (1999). Unusual magnetism of NpO_2: A study with resonant x-ray scattering. *Physical Review B*, **60**, 15187–15193.

McEwen, K.A., Park, J-G., Gipson, A.J. and Gehring, G.A. (2003). A new model for the crystal field and the quadrupolar phase transitions of UPd_3. *Journal of Physics: Condensed Matter*, **15**, S1923–S1935.

McEwen, K.A., Steigenberger, U., Clausen, K.N., *et al*. (1988). Quadrupolar and magnetic transitions in UPd_3. *Journal of Magnetism and Magnetic Materials*, **177–181**, 37–40.

McEwen, K.A., Steigenberger, U. and Martinez, J.L. (1993). Magnetic excitations and phase transitions in UPd_3. *Physica B*, **186–188**, 670–674.

McEwen, K.A., Steigenberger, U., Martinez, J.L. and Abell, J.S. (1990). Magnetic excitations in single crystal $U(Pd_{1-x}Pt_x)_3$. *Physica B*, **163**, 371–374.

McEwen, K.A. and Walker, M.B. (1986). Free energy analysis of single-$\boldsymbol{q}$ and double-$\boldsymbol{q}$ magnetic structures of neodymium. *Physical Review B*, **34**, 1781–1783.

McMorrow, D.F., McEwen, K.A., Steigenberger, U., *et al*. (2001). X-ray resonant scattering study of the quadrupolar order in UPd_3. *Physical Review Letters*, **87**, 57201–57204.

Monachesi, P. (1986). Multiaxial magnetic structures in cubic compounds: uranium monopnictides and manganese alloys. *Journal of Magnetism and Magnetic Materials*, **54–57**, 555–556.

Monachesi, P. and Weling, F. (1983). Low-temperature magnetic structures of uranium pnictides. *Physical Review B*, **28**, 270–277.

Osborne, D.W. and Westrum, E.F. Jr. (1953). The heat capacity of thorium dioxide from 10 to 305°k. the heat capacity anomalies in uranium dioxide and neptunium dioxide. *Journal of Chemical Physics*, **21**, 1884–1887.

Paixào, J.A., Detlefs, C., Longfield, M.J., *et al*. (2002). Triple-$\boldsymbol{q}$ $\rightarrow$ octupolar ordering in NpO_2. *Physical Review Letters*, **89**, 187202.

Perlov, A.Y., Havilov, S.V. and Eschrig, H. (2000). Rare-earth magnetism and adiabatic magnon spectra. *Physical Review B*, **61**, 4070–4081.

Pettifor, D. (1970). Theory of the crystal structures of transition metals. *Journal of Physics C-Solid State Physics*, **3**, 367–377.

Popov, Y.F., Levitin, R.Z.M., Zelený, A.V.D. and Andreev, A.V. (1980), Giant magnetoelastic distortions of the crystal structure of the weakly anisotropic compound UFe_2. *Soviet Physics JETP*, **51**, 1223–1226.

Raphael, G. and Lallement, R. (1968). Susceptibilite magnetique de PuO_2. *Solid State Communications*, **6**, 383–385.

Richter, M., Oppeneer, P.M., Eschrig, H. and Johansson, B. (1996). Calculated crystal-field parameters of $SmCo_5$. *Physical Review B*, **46**, 13919–13927.

Rossat-Mignod, J. (1987). Magnetic structures. In Sköld, K. and Price, D.L. (Eds.), *Neutron Scattering*, Academic Press: New York, Vol. 23C.

Rossat-Mignod, J., Lander, G.H., Burlet, P., *et al*. (1984). Neutron elastic scattering of the actinides. In *Handbook on the Physics and Chemistry of the Actinides*, North-Holland: New York, Vol. 1.

Sandratskii, L.M. (1998). Noncollinear magnetism in itinerant-electron systems: theory and application. *Advances in Physics*, **47**, 91–160.

Santini, P. and Amoretti, G. (2000a). Erratum: Magnetic-octupole order in neptunium dioxide? *Physical Review Letters*, **88**, 5481–5668.

Santini, P. and Amoretti, G. (2000b). Magnetic-octupole order in neptunium dioxide? *Physical Review Letters*, **85**, 2188–2191.

Savrasov, S.Y. (1998). Linear response calculations of spin fluctuations. *Physical Review Letters*, **81**, 2570–2573.

Schmitt, D. (1979a). Contribution of the conduction electrons to the crystalline electric field. I. Direct Coulombic part. *Journal of Physics F-Metal Physics*, **9**, 1745–1758.

Schmitt, D. (1979b). Contribution of the conduction electrons to the crystalline electric field. II. Exchange Coulombic part. *Journal of Physics F-Metal Physics*, **9**, 1759–1770.

Shishidou, T. and Oguchi, T. (2000). Band-theoretical prediction of magnetic anisotropy in uranium monochalcogenides. *Physical Review B*, **62**, 11747–11750.

Siemann, R. and Cooper, B.R. (1979). Theory of the magnetic ordering and lattice internal rearrangement transition in UO_2. *Physical Review B*, **20**, 2869–2885.

Sivardière, J. and Blume, M. (1972). Dipolar and quadrupolar ordering in $S = 3/2$ Ising systems. *Physical Review B*, **5**, 1126–1134.

Skriver, H. (1983). Electronic structure and cohesion in the rare earth metals. In *Systematics and Properties of the Lanthanides*, Sinha, S. (Ed.), Reidel: Dordrecht, pp. 213–253.

Skriver, H. (1985). Crystal structure from one-electron theory. *Physical Review B*, **31**, 1909–1923.

Solt, G. and Erdös, P. (1980). Lattice distortion and quadrupolar ordering in UO_2. *Physical Review B*, **22**, 4718–4726.

Specht, F. (1967). Indirect exchange interactions in Rare-Earth metals. *Physical Review*, **162**, 389–398.

Steinbeck, L., Richter, M. and Eschrig, H. (2001). Magnetocrystalline anisotropy of RCo_5 intermetallics: itinerant-electron contribution. *Journal of Magnetism and Magnetic Materials*, **226**, 1011–1013.

Steinbeck, L., Richter, M., Nitzsche, U. and Eschrig, H. (1996). *Ab initio* calculation of electronic structure, crystal field, and intrinsic magnetic properties of Sm_2Fe_{17}, $Sm_2Fe_{17}N_3$, $Sm_2Fe_{17}C_3$, and Sm_2Co_{17}. *Physical Review B*, **53**, 7111–7127.

Stevens, K.W.H. (1952). Matrix elements and operator equivalents connected with the properties of rare earth ions. *Proceedings of the Physical Society A*, **65**, 209–215.

Svane, A. and Gunnarsson, O. (1990). Transition-metal oxides in the self-interaction corrected density-functional formalism. *Physical Review Letters*, **65**, 1148–1151.

Teitelbaum, H.H. and Levy, P.M. (1976). Indirect multipole interactions in metallic rare-earth compounds. *Physical Review B*, **14**, 3058–3081.

Thayamballi, P. and Cooper, B.R. (1985). Hybridization-mediated interaction and the equilibrium magnetic behavior in uranium monopnictides. *Physical Review B*, **31**, 6004–6007.

Trygg, J. (1995), *First Principles Studies of Magnetic and Structural Properties of Metallic Systems*, PhD Thesis, Uppsala University.

Trygg, J., Wills, J.M., Brooks, M.S.S., *et al*. (1995). Calculation of elastic constants in UC, US, and UTe. *Physical Review B*, **52**, 2496–2503.

Uebele, P., Hummler, K. and Fähnle, M. (1996). Full-potential linear-muffin-tin-orbital calculations of the magnetic properties of rare-earth transition-metal intermetallics. III. $Gd_2Fe_{17}Z_3$ (Z = C,N,O,F). *Physical Review B*, **53**, 3296–3303.

Vigren, D.T. and Liu, S.H. (1972). Static and dynamic effects of the magnetoelastic interaction in terbium and dysprosium metals. *Physical Review B*, **5**, 2719–2734.

Vogt, O. (1980). Magnetization measurements on single crystals of uranium chalcogenides and pnictides. *Physica B*, **102**, 206–211.

Walker, M.B., Kappler, C., McEwen, K.A., *et al*. (1994). Triple-q quadrupolar order in UPd_3. *Journal of Physics-Condensed Matter*, **6**, 7365–7371.

Walker, M.B. and McEwen, K.A. (1983). Models determining the magnetic structure of neodymium near t_n'. *Journal of Physics F-Metal Physics*, **13**, 139–144.

Watson, G.M., Gibbs, D., Lander, G.H., *et al*. (1996). X-ray scattering study of the magnetic structure near the (001) surface of UO_2. *Physical Review Letters*, **77**, 751–754.

Wedgwood, F.A. (1972). Magnetic moment distribution in uranium monosulphide. *Journal of Physics C-Solid State Physics*, **5**, 2427–2444.

Wilkins, S.B., Caciuffo, R., Detlefs, C., *et al*. (2006). Direct observation of electric-quadrupolar order in UO_2. *Physical Review B*, **73**, 060406–10(R).

Wilkins, S.B., Paixào, J.A., Caciuffo, R., *et al*. (2004). Resonant x-ray scattering study of magnetic-dipole and electric-quadrupole order in $U_{0.75}$ $Np_{0.25}$ O_2. *Physical Review B*, **70**, 214402.

Wulff, M., Lander, G.H., Lebech, B. and Delapalme, A. (1989). Cancellation of orbital and spin magnetism in UFe_2. *Physical Review B*, **39**, 4719–4721.

Wulff, M., Lander, G.H., Rebizant, J., *et al*. (1988). Magnetic moments and Pu form factor in $PuFe_2$. *Physical Review B*, **37**, 5577–5585.

Magnetostriction and Magnetoelasticity Theory: A Modern View

A. del Moral

Universidad de Zaragoza and Instituto de Ciencia de Materiales de Aragón (CSIC), Zaragoza, Spain

Handbook of Magnetism and Advanced Magnetic Materials. Edited by Helmut Kronmüller and Stuart Parkin. Volume 1: *Fundamentals and Theory*.

ISBN: 978-0-470-02217-7.

1 INTRODUCTION: MAGNETOELASTIC (MEL) COUPLING AND MAGNETOSTRICTION (MS); CRYSTAL SYMMETRY-BASED PHENOMENOLOGICAL THEORY; ROTATIONAL STRAINS AND NONLINEAR MEL THEORY

Magnetostriction (MS) is the deformation (denoted by $\lambda = \Delta l/l$ for linear distortion and $\omega = \Delta V/V$ for volume dilatation), of a material body when it is magnetized, either when crossing down the magnetic ordering temperature (spontaneous MS) or a magnetic field, **H**, is applied. However MS is also observed in the paramagnetic (PM) regime (*parastriction*, *PS*), and is useful when we want to remove exchange effects, leaving only the *crystal electric field* (CEF) effect. MS is usually expressed in terms of Cartesian *symmetric* strains $\varepsilon_{ij} = (1/2)(u_{ij} + u_{ji})$, where $\mathbf{u} = \mathbf{x} - \mathbf{X}$ is the point displacement of a point $\mathbf{X}$ for a new position $\mathbf{x}$ and $u_{ij} = \partial u_i/\partial X_j$, the *distortion*. The inverse MS effect (*inverse Wiedemann effect* (*IWE*)) consists in the change of magnetization vector, **M** (by rotation or $|\mathbf{M}|$ variation, mainly in itinerant magnets) when a mechanical stress is applied. In the *direct Wiedemann effect* (DWE) a *rotational strain* (*RS*) *MS*, $\omega_{ij} = (1/2)(u_{ij} - u_{ji})$ is produced under application of a helicoidal **H** to a wire or ribbon (Hernando and Bariandarán, 1980), such that it is antisymmetric ($\omega_{ij} = -\omega_{ji}$). However, introduction of RS is paramount in the propagation of an elastic wave (EW) in a magnetized crystal (*magnetoacoustic* (*MA*)

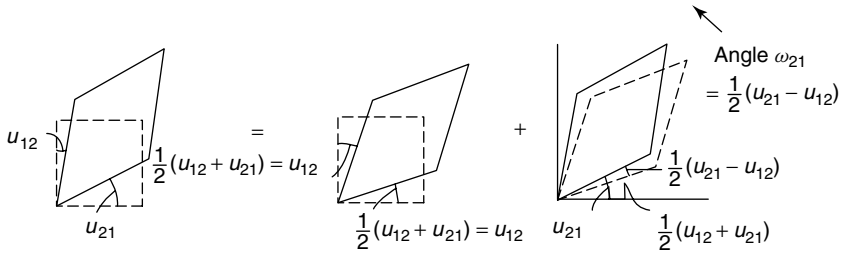

Figure 1. Decomposition of a general deformation in pure strain, ε_{12} and rotation, ω_{12} (Nye, 1976).

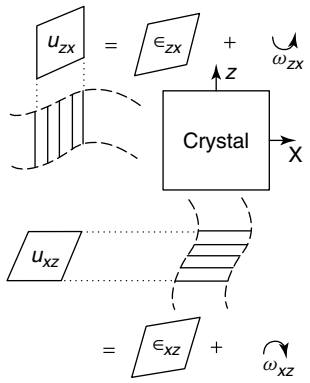

Figure 2. Unequivalence of u_{zx} and u_{xz} shear elastic waves propagating along Z and X axes, due to their antisymmetric rotations, $\omega_{xz} = -\omega_{zx}$, added to otherwise symmetric $\varepsilon_{xz} = \varepsilon_{zx}$ strains (Lüthi, 1976).

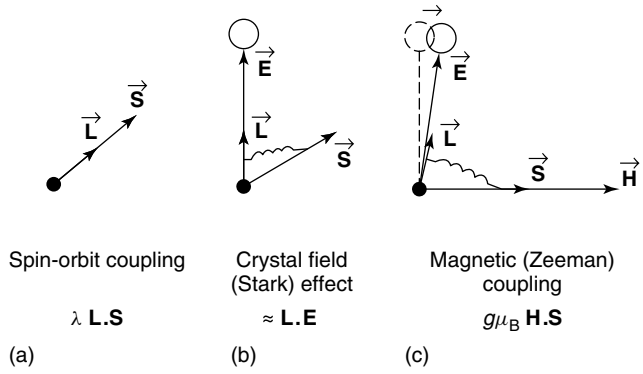

Figure 3. The physical origin of CEF magnetostriction: (a) spin-orbit (SO) coupling; (b) CEF, **E** overrides SO between **L** and **S**; (c) magnetic anisotropy requires stronger **H** to align **S**. Rotation of residual unquenched **L** through SO coupling causes *magnetostrictive* rotation of **E** (Dionne, 1979).

wave), since then, only one distortion is singled out and ω_{ij} is manifested, since $u_{ij} = \varepsilon_{ij} + \omega_{ij}$ (Figures 1 and 2). MS, being an ubiquitous effect in solids, has been observed in every kind of magnetic material (del Moral, 2007). MS is the result of an internal *magnetoelastic* (MEL) *stress*, here denoted as $\overline{\mathrm{M}}_{ij}$ ($\equiv B_{ij}$ in Kittel's notation, see del Moral, 2007) and has its origin in the variation in volume and/or change in shape when the atomic magnetic moment, $\boldsymbol{\mu}$ is modified, either by rotation or by $|\boldsymbol{\mu}|$ variation (this latter called *paraprocess*, manifested in itinerant ferromagnets (FMs)). Effectively, when an atom or ion is magnetized it changes its shape, so modifying the surrounding lattice for accommodating the distortion (*shape or anisotropic magnetostriction* (*AMS*)), or just its volume (*volume or isotropic magnetostriction* (*VMS*)). The mechanism for AMS (but there can also be VMS of this kind) is as sketched in Figure 3.

1. In a free atom the spin-orbit (SO) coupling (Hamiltonian $H_{\mathrm{so}} = \lambda \mathbf{L} \cdot \mathbf{S}$) aligns the orbital, **L** and spin, **S** angular momenta (AM).
2. When the atom is within the solid the highly inhomogeneous CEF, $\mathbf{E}_{\mathrm{CEF}}$, aligns **L** with it (via Stark coupling of energy $\propto \mathbf{L} \cdot \mathbf{E}_{\mathrm{CEF}}$), so overriding the SO coupling. As consequence the expected $\langle\psi|\mathbf{L}|\psi\rangle$ ($|\psi\rangle$ is the magnetic ion wave function within the solid) is usually reduced (*quenching*), that is, some SO coupling survives (except for a singlet where $\langle\psi|\mu|\psi\rangle = 0$).
3. When **H** is applied, this tries to align **S** (via Zeeman coupling, $H_Z = -\boldsymbol{\mu}_S \cdot \mathbf{H}$, with $\boldsymbol{\mu} = \boldsymbol{\mu}_{\mathrm{L}} + \boldsymbol{\mu}_{\mathrm{S}}$, the total magnetic moment), which in turn pulls **L** (atom/ion charge aspherical cloud, $\mathrm{e}\langle\psi|\psi\rangle$) *via* SO coupling, **L** which again pulls $\mathbf{E}_{\mathrm{CEF}}$ and so the ions lattice (which create $\mathbf{E}_{\mathrm{CEF}}$) are displaced. This AMS is called *CEF-MS* (although those mechanisms can also produce VMS). So MS is basically a relativistic (SO) and quantum-mechanical effect.

When a magnetic-order phase transition occurs (or also **H** is applied), usually an isotropic variation of the lattice cell parameter is produced (manifested as an *anomalous thermal expansion* (TH.E.)), so modifying the exchange coupling constant, $J(H_{\mathrm{EX}} = -2J(\mathbf{R}_j - \mathbf{R}_i)\mathbf{S}_i \cdot \mathbf{S}_j$ is the isotropic exchange Hamiltonian between two spins at sites i, j) and we talk of *exchange magnetostriction* (EX-MS) (if exchange is anisotropic, that is $J_x \neq J_y \neq J_z$, an AMS is instead

Table 1. Isomorphisms of spherical harmonics, elastic strain components, one-ion spin operators, two-ion spin operators, and $\alpha_i^{\mu,2}$ polynomials. (From Callen and Callen, 1965.)

Classical polynomials or spherical harmonics[a]	Strain functions	One-ion operators of spherical tensor operators[b]	Two-ion spin operators	Bilinear direction cosines
$1 = (4\pi)^{1/2} Y_0^0$	$\epsilon^{\alpha,1} = \epsilon_{xx} + \epsilon_{yy} + \epsilon_{zz}$	$1 = (2S+1)^{1/2} \Upsilon_0^0$	$\mathrm{S}_f \cdot \mathrm{S}_g$	1
$(\sqrt{3}/2)(z^2 - 1/3) = cY_2^0$	$\epsilon^{\gamma,1} = (\sqrt{3}/2)\lfloor \epsilon_{zz} - \epsilon^{\alpha,1}/3 \rfloor$	$(\sqrt{3}/2)[(S^z)^2 - (1/3)S(S+1)] = (1/\sqrt{2}\mathrm{n}_2)\Upsilon_2^0$	$(\sqrt{3}/2)\lfloor S_f^z S_g^z - \frac{1}{3}\mathbf{S}_f \cdot \mathbf{S}_g \rfloor$	$(\sqrt{3}/2)\lfloor \alpha_z^2 - 1/3 \rfloor$
$(1/2)(x^2 - y^2) = (c/\sqrt{2})\lfloor Y_2^2 + Y_2^{-2} \rfloor$	$\epsilon^{\gamma,2} = (1/2)[\epsilon_{zz} - \epsilon_{yy}]$	$(1/2)[(S^x)^2 - (S^y)^2] = (1/2n_2)[\Upsilon_2^2 + \Upsilon_2^{-2}]$	$1/2\lfloor S_f^x S_g^y - S_f^y S_g^x \rfloor$	$(1/2)\lfloor \alpha_x^2 - \alpha_y^2 \rfloor$
$xy = (-ic/\sqrt{2})\lfloor Y_2^2 - Y_2^{-2} \rfloor$	$\epsilon^{\varepsilon,1} = \epsilon_{xy}$	$(1/2)\lfloor S^x S^y + S^y S^x \rfloor = (-i/2n_2)\lfloor \Upsilon_2^2 - \Upsilon_2^{-2} \rfloor$	$(1/2)\lfloor S_f^x S_g^y + S_f^y S_g^x \rfloor$	$\alpha_x \alpha_y$
$yz = (ic/\sqrt{2})\lfloor Y_2^1 + Y_2^{-1} \rfloor$	$\epsilon^{\varepsilon,2} = \epsilon_{yz}$	$(1/2)\lfloor S^y S^z + S^z S^y \rfloor = (-i/2n_2)\lfloor \Upsilon_2^1 + \Upsilon_2^{-1} \rfloor$	$(1/2)\lfloor S_f^y S_g^z + S_f^z S_g^y \rfloor$	$\alpha_y \alpha_z$
$xz = -(c/\sqrt{2})\lfloor Y_2^1 - Y_2^{-1} \rfloor$	$\epsilon^{\varepsilon,3} = \epsilon_{zx}$	$(1/2)\lfloor S^x S^z + S^z S^x \rfloor = (-i/2n_2)\lfloor \Upsilon_2^1 - \Upsilon_2^{-1} \rfloor$	$(1/2)\lfloor S_f^z S_g^x + S_f^x S_g^z \rfloor$	$\alpha_z \alpha_x$

[a] Here $c = (4\pi/15)^{1/2}$.

[b] In Stevens–Buckmaster's notation these operators are denominated $\widetilde{O}_0^0$, $\widetilde{O}_2^0$, $\overline{O}_2^2$, $\widehat{O}_2^2$, $\overline{O}_2^1$, $\widehat{O}_2^1$ respectively, n_2 is a normalization factor.

produced); *quadrupolar* (*QP*) interaction $\overset{\leftrightarrow}{O}{}^{\eta}_{2,i}$ $\overset{\leftrightarrow}{O}{}^{\eta}_{2,j}$ instead manifests in PS. Therefore MS is a *fundamental* effect in condensed matter physics (either in crystalline or amorphous materials), and the order of magnitude of the associated MEL free energy $F_{\rm mel} = (1/2)c\lambda^2$ (where c is an *elastic constant* (EC)) amounts $\approx 1\,\mu$eV/atom in 3d metals (Fe) and 1–10 meV/ion in a rare-earth (RE) metals (e.g., Dy and Tb metals).

Experimentally it is found that MS depends on the direction of the magnetization, $\boldsymbol{\alpha}$, and that of measurement, $\boldsymbol{\beta}$ with respect to the chosen crystal axes, this means that it is a property related to crystal symmetry. Therefore the natural way to derive the MEL free energy, $F_{\rm mel}$ is making it invariant against the point symmetry group (PSG) operations of the magnetic ion in the crystal. For this we define the *irreducible strains* (*ISs*), ε_i^{μ} which form the bases (i is the basis component index) for the irreducible representations (IRs) of the PSG (Γ^{μ}) and multiply them by polynomials of the direction cosines $\boldsymbol{\alpha}$ (α_i) pertaining to the same representation, in order to obtain products invariant against the symmetry operations of the PSG (i.e., pertaining to the fully symmetric representation Γ^{α}) (Callen and Callen, 1964, 1965). The ISs, ε_i^{μ} are of the same form for all PSG (although with different μ denomination) and for the cubic (CUB) PSGs are given in the second column of Table 1. The forms of these ISs for cubic symmetry are displayed in Figure 4, and those for hexagonal (HEX) ones are shown in Figure 5 (here assuming cylindrical symmetry for the hexagonal unit cell). For some representations, for instance for cubic PSGs, the $\mu = \alpha, \gamma$, and ε correspond to externally manifested strictions, meanwhile for $\mu = \beta', \delta'$ the ISs are internal, and can be only externally manifested if they couple to external

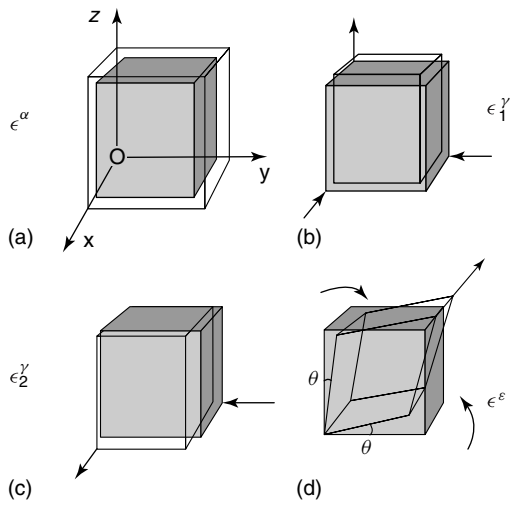

Figure 4. Irreducible strains for cubic symmetry (de Lacheisserie, 1993).

ones, as it happens for example in the cubic Laves-phase intermetallic $DyFe_2$ (Cullen and Clark, 1977); and H_0/Lu superlattices (del Moral, 2007). But before continuing, MS strains can be small (infinitesimal, ε_i^{μ}) or finite, $\mathcal{E}_i^{\mu}$. A kind of *finite* (Brown, 1965) normal ISs are the *Lagrangian strains*, η_{ij} (Eastman, 1966), which include rotations, up to order 2, as well as the local *RSs*, $\mathcal{R}_{ij}$ and which are respectively of the forms (in Cartesian strains),

$$\eta_{ij} = \left(\frac{1}{2}\right)(u_{ij} + u_{ji} + \Sigma_k u_{ki}u_{kj}) = \varepsilon_{ij} + \left(\frac{1}{2}\right) \times \Sigma_k(\varepsilon_{kj} + \omega_{kj})(\varepsilon_{ki} + \omega_{ki}) \cong \varepsilon_{ij} + \left(\frac{1}{2}\right)\Sigma_k \varepsilon_{ki}\varepsilon_{kj} \tag{1}$$

$$\mathcal{R}_{ij} = \omega_{ij} + \left(\frac{1}{2}\right)\Sigma_k(\varepsilon_{jk} + \omega_{jk})(\varepsilon_{ik} - \omega_{ik}) \cong \omega_{ij} - \left(\frac{1}{2}\right)\Sigma_k \omega_{ki}\omega_{kj} \tag{2}$$

(pure RSs ω_{xy}, ω_{zx}, ω_{yz}, bases of $\Gamma^{\delta'}$ are internal). Last expressions for $\eta_{ij}(\mathcal{R}_{ij})$ apply for infinitesimal ω_{ij} (ε_{ij}) strains. We will call all those strains (45 in number) as the ISs π_{ij}^{μ}. These ISs pertain to the same IRs mentioned earlier, where j is the basis-IS number within the basis i for Γ^{μ} IRs (see for a systematic description del Moral, 2007 or Rouchy and de Lacheisserie, 1979). They are of the kinds: purely quadratic in ε_{ij} (21 in number, e.g., $\pi_{11}^{\alpha} = (1/3)(\varepsilon_{xx}^2 + \text{c.p.})$, $\pi_{11}^{\gamma} = (\sqrt{3}/2)(\varepsilon_{zz}^2 - \pi_1^{\alpha})$, $\pi_{11}^{\varepsilon} = \varepsilon_{xx}\varepsilon_{yy}$, etc.); other in ω_{ij} (6 in number, e.g., $\pi_{41}^{\alpha} = \omega_{xy}^2 + \text{c.p.}$, $\pi_{41}^{\gamma} = (\sqrt{3}/2)(\omega_{xy}^2 - \pi_{14}^{\alpha}/3)$, $\pi_{61}^{\varepsilon} = \omega_{zx}\omega_{xy}$, etc.); and remainder are in products $\varepsilon_{ij}\omega_{kl}$ (e.g., $\pi_{14}^{\varepsilon} = (\varepsilon_{yy} - \varepsilon_{zz})\omega_{yz}$, $\pi_{15}^{\gamma} = (\sqrt{3}/2)(\varepsilon_{xy}\omega_{xy} - (1/3)(\varepsilon_{xy}\omega_{xy} + \text{c.p.}))$, etc.). According to the aforesaid we write the MEL free energy for the normal ISs as,

$$F_{\rm mel} = \Sigma_{\mu,l}\overline{\rm M}^{\mu,l}\Sigma_i \alpha_i^{\mu,l}\varepsilon_i^{\mu} \tag{3}$$

where $\overline{\rm M}^{\mu,l}$ are the irreducible *MEL constants* ($\equiv {\rm B}^{\mu,l}$ in popular *Kittel's notation*) and $\alpha_i^{\mu,l}$ are polynomials of $\boldsymbol{\alpha}$ of l-degree bases of Γ^{μ}, isomorphous of ε_i^{μ} and given for $l = 2$ in Table 1 (polynomials of higher order are possible). The MEL free energy then adopts the forms, for cubic and hexagonal symmetries, respectively,

$$F_{\rm mel}^{\rm CUB} = \Sigma_{\ell=0,4,6,\ldots}\overline{\rm M}^{\alpha,\ell}\varepsilon^{\alpha}K^{\alpha,\ell} + \Sigma_{\ell=2,4,6}\overline{\rm M}^{\gamma,\ell} \times \Sigma_{i=1,2}\varepsilon_i^{\gamma}K_i^{\gamma,\ell} + \Sigma_{\ell=2,4,6,6'}\overline{\rm M}^{\varepsilon,\ell}\Sigma_{i=1,2}\varepsilon_i^{\varepsilon}K_i^{\varepsilon,\ell} \tag{4}$$

$$F_{\rm mel}^{\rm HEX} = \Sigma_{\ell=0,2,4,4',\ldots}\Sigma_{i=1,2}\overline{\rm M}_i^{\alpha,\ell}\varepsilon_i^{\alpha}H^{\alpha,\ell} + \Sigma_{\ell}\Sigma_{\mu=\gamma,\varepsilon}\overline{\rm M}^{\mu,\ell}\Sigma_{i=1,2}\varepsilon_i^{\mu}H_i^{\mu,\ell} \tag{5}$$

where $K_i^{\mu,\ell}(\boldsymbol{\alpha})$ and $H_i^{\mu,\ell}(\boldsymbol{\alpha})$ are cubic and hexagonal harmonics, which are tabulated (del Moral, 2007). In order

to obtain the equilibrium strains we have to add the elastic energy, which is of the general diagonal form $F_{\rm el} = (1/2)\Sigma_\mu c^\mu \Sigma_i (\varepsilon_i^\mu)^2$, and minimize the full F (i.e., making $\partial(F_{\rm mel} + F_{\rm el})/\partial\varepsilon_i^\mu = 0$), so obtaining the MSs, which for example, for cubic symmetry have the expressions,

$$\varepsilon^\alpha = -\Sigma_\ell \left(\frac{\overline{\rm M}^{\alpha,\ell}}{c^\alpha}\right) K^{\alpha,\ell},\ \varepsilon^\gamma_{i=1,2} = -\Sigma_\ell \left(\frac{\overline{\rm M}^{\gamma,\ell}}{c^\gamma}\right) K_i^{\gamma,\ell},$$

$$\varepsilon^\varepsilon_{i=1,2,3} = -\Sigma_\ell \left(\frac{\overline{\rm M}^{\varepsilon,\ell}}{c^\gamma}\right) K_i^{\varepsilon,\ell} \qquad (6)$$

and similarly for other classes of symmetry, and where c^μ are the *symmetry ECs*. If we now define the *Clark's MS constants* as $\lambda^{\mu,\ell} = -(\overline{\rm M}^{\mu,\ell}/c^\mu)$ (Clark, DeSavage and Bozorth, 1965; see Figure 5) and notice that for the $\boldsymbol{\beta}$ direction of MS measurement we have to multiply by $\boldsymbol{\beta}$–polynomials, $\beta_i^{\mu,\ell}$, isomorphous to the $\boldsymbol{\alpha}$ ones (of Table 1), we have that,

$$\lambda(\boldsymbol{\alpha}, \boldsymbol{\beta}) = \Sigma_{\mu=\alpha,\gamma,\varepsilon} \Sigma_\ell \lambda^{\mu,\ell} \Sigma_i \beta_i^{\mu,\ell} K_i^{\mu,\ell} \qquad (7)$$

In the same way we can write the MEL free energy in the Lagrangian strains, obtaining $F_{\rm mel}^{\rm 2nd-order} = \Sigma_{i,\mu,\ell,j} \overline{\rm N}^{\mu,\ell} \pi_{ij}^\mu K_i^{\mu,\ell}$, for the cubic PSGs, where $\overline{\rm N}_j^{\mu,\ell}$ are the second-order MEL constants, or *morphic* constants of MS, since they linearly modify the $\overline{\rm M}^{\mu,\ell}$ (*morphic* effect of MEL coupling) ones in the ISs. Now to get the equilibrium finite strains we have to introduce an elastic energy in the third rank (contracted) ECs, C_{ijk} and third-order finite ISs. The importance of higher order than one in u_{ij} MEL coupling is mainly manifested in *EW* propagation in magnetic materials where for a

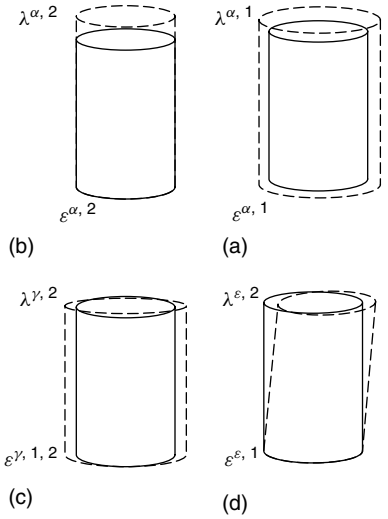

Figure 5. Irreducible strains (down corners) and Clark's MS constants (up corners) for uniaxial symmetry (Clark, DeSavage and Bozorth, 1965).

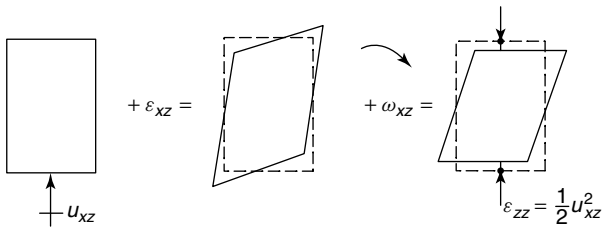

Figure 6. A finite shear gradient u_{xz} is equivalent to a finite strain $\mathcal{E}_{zz}$. (From Bonsall and Melcher, 1976.)

plane wave impressed distortion $u_{xz} = \varepsilon_{xz} + \omega_{xz}$ we end up with a finite Cartesian strain $\mathcal{E}_{zz} = (1/2)u_{xz}^2$ (Figure 6).

To conclude with this phenomenological study of MS sometimes it is better to work with Cartesian strains, and for cubic symmetry we obtain (Lee, 1955),

$$\lambda(\boldsymbol{\alpha}, \boldsymbol{\beta}) = (3/)\lambda_{100}\left(\Sigma_i \alpha_i^2 \beta_i^2 - \frac{1}{3}\right) + 3\lambda_{111}(\alpha_1\alpha_2\beta_1\beta_2 + \text{c.p.}) + \lambda_v\left(\alpha_1^2\alpha_2^2 + \text{c.p.} - \frac{1}{3}\right) \qquad (8)$$

and where the two Kittel's MS constants are $\lambda_{100} \equiv h_1 = -(2/3)\overline{\rm M}_1/(c_{11} - c_{12})$ and $\lambda_{111} \equiv (2/3)h_2 = -(1/3)(\overline{\rm M}_2/c_{44})$, which respectively are the MSs measured along [100] for $\mathbf{M}\|[100]$ and along [111] for $\mathbf{M}\|[111]$ and $\lambda_v \equiv h_3$ the anisotropic volume MS constant, independent of $\boldsymbol{\beta}$ (h_i are the classical *Becker and Döring MS constants*). When the material is polycrystalline or amorphous a number of approaches have been followed to average equation (8) over the 'crystallites' (averages at constant stress, constant strain, fluctuating MS, (Fähnle *et al*., 1990)). A good approximation used for cubic and amorphous materials for AMS being $\lambda_\parallel - \lambda_\perp \equiv \lambda_t = (3/2)(\cos^2\theta - 1/3)$, where θ is the angle

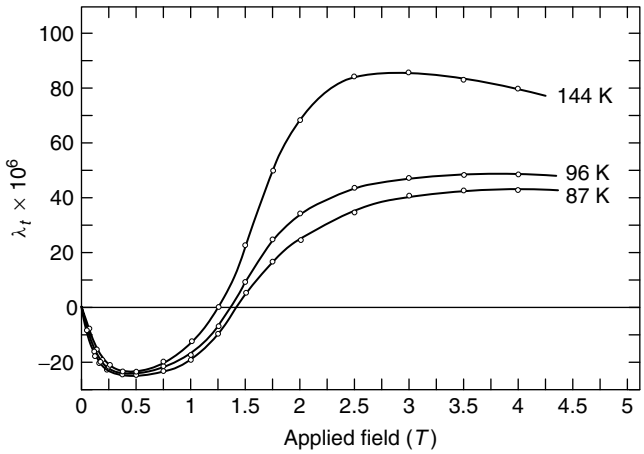

Figure 7. Isotherms of λ_t (H) for polycrystalline MnAs (Choudhury, Lee and Melville, 1974).

($\mathbf{M}$, $\boldsymbol{\beta}$) and λ_s the *saturation MS*. In fact MS adequately maps the different magnetization processes (in fact, MS is superior since it has a sign), that is, domain wall (DW) displacement (MS appears if those are different of 180°), rotation of $\mathbf{M}_s$, and approach to saturation. The $\lambda_t(H)$ isotherms for the hexagonal FM MnAs ($T_c = 393$ K) are portrayed in Figure 7, where the initial decrease is due to DW displacements, the minimum is $\lambda^{\gamma,2}$ (Figure 4c), and the saturation value is $\lambda^{\alpha,2}$ (Figure 4b), the latter two being the MSs due to $\mathbf{M}_s$ rotation.

2 STANDARD THEORY OF MAGNETOELASTIC COUPLING AND MAGNETOSTRICTION (STM): ONE-ION AND TWO-ION MSS; ANTIFERROMAGNETS; SPIN-WAVE APPROACH; PARASTRICTION; MEL PARAMETERS CALCULATION; MS OF RE INTERMETALLICS

The phenomenological theory of MS is firmly based in a microscopic quantum-mechanical one, called *Standard Theory of Magnetostriction* (*STM*), mainly due to Callen and Callen (1964, 1965), which follows the same group theory arguments used before, for obtaining now the *MEL Hamiltonians*. We will distinguish between single-ion CEF and two-ion (bilinear and QP exchanges) MEL couplings.

2.1 Single-ion CEF-MS

MS reduces the point symmetry and therefore, with new terms, adds or modifies the highly inhomogeneous CEF potential, $V(\mathbf{r})$ which can be expanded around the probe ion (i) in the multipolar expansion, either in terms of Cartesian coordinates (x, y, z) polynomials, $f_{n,m}(x, y, z)$ or in terms of spherical harmonics (SH), $Y_n^m(\theta, \phi)$ with coefficients which are proportional to the $V(\mathbf{r})$ *CEF gradients*, A_n^m, that is,

$$V(\mathbf{r}) = \Sigma_{n,m} A_n^m r^n f_{n,m}(x, y, z) = \Sigma_{n,m} A_n^m r^n Y_n^m(\theta, \phi) \quad (9)$$

It is far better to work in terms of so-called *Stevens* AM, $\mathbf{J}$ *operators*, $O_n^m(\mathbf{J})$ by application of the Wigner–Eckart (W–E) theorem to $V(\mathbf{r})$, so obtaining the equivalence $\Sigma_i f_{n,m}(x_i, y_i, z_i) \equiv \theta_n \langle r^n \rangle O_n^m(\mathbf{J})$, where $\mathbf{r}_i$ are the magnetic electron coordinates, $\langle r^n \rangle$ a radial average and θ_n the W–E reduced matrix elements, depending on J (i.e., on the 3d, 4f, 5f ions). Therefore the CEF Hamiltonian can be written as,

$$H_{\mathrm{CEF}} = \Sigma_{n,m} B_n^m O_n^m \quad (10)$$

The Stevens operators (S.Op.) are tabulated (Hutchings, 1964). When the solid is distorted under MS, so it is H_{CEF},

$$H_{\mathrm{CEF}} = \Sigma_{\Gamma,\ell,i,j} \left\{ B^0_{\Gamma,\ell} + \left(\frac{\partial B^{\Gamma,\ell}}{\partial \varepsilon_i^\Gamma} \right)_0 \varepsilon_i^\Gamma + \left(\frac{1}{2} \right) \left(\frac{\partial B^{\Gamma,\ell}}{\partial \pi_{ij}^\Gamma} \right)_0 \pi_{ij}^\Gamma + \cdots \right\} O_i^{\Gamma,\ell} \quad (11)$$

where H_{CEF} is now written in an irreducible form ($\{i, j\}$ span the IR bases) and $M^\Gamma_{n,m} = (\partial B^\Gamma_{n,m}/\partial \varepsilon_i^\Gamma)_{\varepsilon_i^\Gamma = 0}$ are the microscopic *MEL parameters* (first order) whose determination (theoretical or experimentally) is a paramount issue. $N^{\Gamma,\ell} = (1/2)(\partial B^{\Gamma,\ell}/\partial \pi_{ij}^\Gamma)_{\pi_{ij}^\Gamma = 0}$ are the *nonlinear* (*NL*) MEL parameters (second order), which are essential in the magnetoacoustic wave propagation. Now, the single-ion CEF-MEL *coupling* Hamiltonian, $H^{\mathrm{I}}_{\mathrm{mel}}$ is formed as the MEL free energy, just multiplying the strains and AM operators pertaining to the same representation, and therefore the products being invariant against the PSG operations (i.e., pertaining to Γ^α). Although by the deformation the PSG is changed (symmetry lowering by MS) in a first approximation we neglect this effect (it cannot be like that if the strains are finite, thus having the *morphic effect* of MS upon the MEL parameters). Therefore, $H^{\mathrm{I}}_{\mathrm{mel}}$ adopts the *general* form (for any PSG and several ions, f as the lattice point motif; note the negative sign),

$$H^{\mathrm{I}}_{\mathrm{mel}} = -\Sigma_f \Sigma_{\Gamma,\ell} \Sigma_i M^{\Gamma,\ell}(f) \varepsilon_i^\Gamma \mathcal{J}_i^{\Gamma,\ell}(f) \quad (12)$$

where the Racah AM operators $\mathcal{J}_i^{\Gamma,\ell}$ (Kubic Tensor Operator, KTO of cubic PSG, $\mathcal{K}_i^{\Gamma,\ell}$) of order l, are linear combinations of the spherical tensor operators, $\Upsilon_n^{\pm m}$ (isomorphous of the SH), of the form shown in Table 1 for second order (however, we will use the Stevens–Buckmaster's notation (Buckmaster, 1966), shown at the bottom of the table, and where the AM operators are denoted by $\tilde{\mathrm{O}}_n^m$). For finite strains we have to add to the equation (12) the NL-MEL Hamiltonian, of the form $H^{\mathrm{NL}}_{\mathrm{mel}} = -\Sigma_f \Sigma_{\Gamma,\ell} \Sigma_{ij} N^{\Gamma,\ell}(f) \pi_{ij}^\Gamma \mathcal{J}_i^{\Gamma,\ell}(f)$, where $N^{\Gamma,\ell}$ are the NL-MEL parameters. For the most frequent cubic and hexagonal symmetries up to $l = 2$ the MEL Hamiltonians read,

$$H^{\mathrm{CUB}}_{\mathrm{mel}} = -M^{\alpha,0} \mathbf{J}^2 \varepsilon^\alpha - M^{\gamma,2} \left(\varepsilon_1^\gamma \tilde{\mathrm{O}}_2^0 + \left(\frac{1}{\sqrt{2}} \right) \varepsilon_2^\gamma \overline{\mathrm{O}}_2^2 \right) - M^{\gamma,2} \left(\varepsilon_1^\varepsilon i \overline{\mathrm{O}}_2^1 - \varepsilon_2^\varepsilon i \hat{\mathrm{O}}_2^1 + \varepsilon_3^\varepsilon i \hat{\mathrm{O}}_2^2 \right) \quad (13)$$

$$H^{\mathrm{HEX}}_{\mathrm{mel}} = -M_1^{\alpha,2} \varepsilon_1^\alpha \tilde{\mathrm{O}}_2^0 - M_2^{\alpha,2} \varepsilon_1^{\alpha,2} \tilde{\mathrm{O}}_2^0 - M^{\gamma,2} \left(\varepsilon_1^\gamma \overline{\mathrm{O}}_2^2 + i \varepsilon_2^\gamma \hat{\mathrm{O}}_2^2 \right) - M^{\varepsilon,2} \left(\varepsilon_1^\varepsilon i \hat{\mathrm{O}}_2^1 + \varepsilon_2^\varepsilon \overline{\mathrm{O}}_2^1 \right) \quad (14)$$

For lower symmetries the number of independent MEL parameters just increases. To obtain the equilibrium MS

strains, $\overline{\varepsilon}_i^{\Gamma}$ we take the thermal average $\langle H_{\rm mel}\rangle$, add $F_{\rm el}$ and minimize, obtaining for *all* symmetries that

$$\overline{\varepsilon}_i^{\mu} = (1/c^{\mu})\Sigma_{\ell} M^{\mu,\ell}\langle \mathcal{J}_i^{\Gamma,\ell}\rangle \tag{15}$$

where $\langle \mathcal{J}_i^{\Gamma,\ell}\rangle$ has to be substituted by the corresponding Stevens operators of for example, equations (13 and 14).

2.2 Thermal dependence of MS

We are now going to obtain one of the most significant characteristics of MS, which is its *thermal dependence*, which allows one to distinguish between CEF and EX-MSs. For this investigation we consider the cubic symmetry (for remainder ones is the same) and expand $\langle \mathcal{K}_i^{\mu,\ell}\rangle = \sum_m a_{i,m}^{\mu,\ell}\langle \Upsilon_{\ell}^{m}\rangle$. Next we perform the frame rotation (x, y, z)-> (ξ, η, ζ) so that the axis $O\zeta \| \mathbf{M}_{\rm s}$ spontaneous magnetization (Figure 8). Taking into account how the SH are transformed under rotation and the isomorphism between Υ_l^m and Y_l^m, it is easy to show that $\langle \Upsilon_l^m\rangle = \sum_{\mathbf{m}'}\langle Y_{l(\boldsymbol{\zeta})}^{m'}|Y_l^m\rangle\langle \Upsilon_{l(\boldsymbol{\zeta})}^{m'}\rangle$, where $\Upsilon_{l(\zeta)}^{m'}$ refer to the rotated frame. Now under a rotation φ about $\boldsymbol{\zeta}$, $\Upsilon_{l(\zeta)}^{m'}$ transforms as $\mathrm{e}^{im'\varphi}$ and since the spin system (or $\mathbf{M}_{\rm s}$) has cylindrical symmetry around $\boldsymbol{\zeta}$ (keeping only the exchange interaction), $\langle \Upsilon_{l(\zeta)}^{m}\rangle = 0$, except for $m' = 0$. Therefore we have $\langle \mathcal{K}_i^{\mu,l}\rangle = \langle \Upsilon_{l(\zeta)}^{0}\rangle \mathrm{K}_i^{\mu,l}(\zeta)$ and accordingly we end up with $\langle \mathcal{K}_i^{\mu,l}\rangle = \langle \Upsilon_{l(\boldsymbol{\zeta})}^{0}\rangle \Sigma_m a_{i,m}^{\mu,l} = \mathrm{K}_i^{\mu,l}(\zeta)\langle \Upsilon_{l(\boldsymbol{\zeta})}^{0}\rangle$, which provides for the thermal dependence of the MEL constants, being defined as $\overline{\mathrm{M}}^{\Gamma,\ell} \equiv M^{\Gamma,\ell}\langle \Upsilon_{\ell(\boldsymbol{\zeta})}^{0}\rangle_T$. For lowest order $l = 2$, $\Upsilon_{2(\zeta)}^{0} \propto O_{2(\boldsymbol{\zeta})}^{0} = (\sqrt{3}/2)(3J_{\zeta}^2 - J(J+1))$ and if the temperature is low enough only the two first levels of the J manifold will be populated. Expressing $J_{\zeta} = J - \sigma = J - a^{+}a$, with σ, the deviations number operator, we obtain for the eigenvalues $\sigma = 0, 1$ and cutting the expansion that $(1 - \sigma/J)^3 \cong 1 - 3/J$. Therefore, we obtain $\langle \Upsilon_{2(\boldsymbol{\zeta})}^{0}\rangle \approx (2J - 1)J\left[1 - 3\langle\sigma\rangle/J\right] \approx (M/M_0)^3 = m(T)^3$, which for any l adopts the general form

$$\overline{\mathrm{M}}_{j,l}^{\mu}(T)\big/\overline{\mathrm{M}}_{j,l}^{\mu}(0) = \frac{\langle \Upsilon_l^0(\mathbf{J}')\rangle_T}{\langle \Upsilon_l^0(\mathbf{J}')\rangle_0} = \left(\frac{M(T)}{M(0)}\right)^{l(l+1)/2} \tag{16}$$

which is the famous *Akulov–Zener–Callen l(l+1)/2 power law* (AZC) of thermal variation of MS, applicable to FM insulators. This law can be generalized considering that the full J manifold $(-J \le m' \le J)$ is populated (high temperatures). In this case, using the density matrix technique for getting the thermal averages, we have that

$$\langle \Upsilon_l^0(J')\rangle = \sum_{-J}^{J}\langle m'\left|\Upsilon_l^0\right|m'\rangle \frac{\exp[Xm']}{\sum_{-J}^{J}\exp[Xm']} \tag{17}$$

and taking into account that $\int_{-1}^{1} Y_l^0(m')\exp\left[Xm'\right]\mathrm{d}m' = I_{l+1/2}(X)$, where $I_{\ell+1/2}(X)$ is a Bessel function, and defining the reduced Bessel function as $\hat{I}_{\ell+1/2}(X) \equiv I_{\ell+1/2}(X)\big/ I_{1/2}(X)$, we end up with

$$\overline{\mathrm{M}}_{j,l}^{\Gamma}(T) = \overline{\mathrm{M}}_{j,l}^{\Gamma}(0)\hat{I}_{l+1/2}(L^{-1}(m)) \tag{18}$$

where $L^{-1}(m)$ is the inverse Langevin function. However his law is quite general, including all theories based on quasiparticle collective excitations, of which the mean-field approximation (MFA) is a particular case and where the variable $X = ng\mu_{\rm B}\langle m'\rangle/k_{\rm B}T$ (n is the mean-field (MF) constant). Now the reduced magnetization, $m(T)$ along $\boldsymbol{\zeta}$, adopts the form $m(T) = \langle\cos\theta'\rangle = \langle Y_l^0(\mathbf{J}')\rangle_{\rm T}/\langle Y_l^0(\mathbf{J}')\rangle_0 = \hat{I}_{3/2}(X)$. In Figure 9 are shown the reduced $\langle\tilde{\Upsilon}_2^0\rangle(m)$ versus m for several J $(= S)$ values and in Figure 10 the fits of $\lambda^{\gamma,2}\big/2$ and $-\lambda^{\gamma,4}$ thermal variation for Tb metal; also in Figure 11 is shown how the general AZC law is well accomplished for Dy and Er metals (See also **Theory of Magnetocrystalline Anisotropy and Magnetoelasticity in 4f and 5f Metals, Volume 1**). Substituting now equation (15) (for cubic symmetry) into $F_{\rm mel} = \langle H_{\rm mel}\rangle$ we obtain again the same expression for the free energy of equation (3), and if we add $F_{\rm el}$ and the magnetocrystalline anisotropy (MCA) energy, of the form $F_{\rm K} = \Sigma_{\ell}\kappa_{\ell}K^{\alpha,\ell}$, we see that a MEL contribution to the MCA constants, κ_l appears (or *MEL anisotropy* energy), of the form

$$\overline{\kappa}_1^{\rm eff} = \kappa_1 - \left(\frac{1}{2}\right)\Sigma_{\mu}\Sigma_j\left(\frac{1}{c_{\mu}^{\mu}}\right)\Sigma_{l_1,l_2}k_{l_1l_2}^{\mu,l}\overline{\mathrm{M}}_j^{\mu,l_1}\overline{\mathrm{M}}_j^{\mu,l_2} \tag{19}$$

where the k numbers are tabulated (see del Moral, 2007).

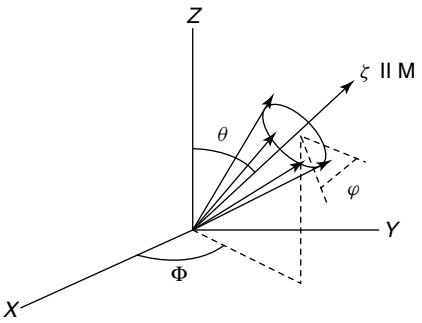

Figure 8. Cylindrical symmetry spin directions distribution around magnetization **M**, at finite temperature (del Moral, 2007.)

2.3 Two-ion (exchange) MS

We will now consider the afore mentioned exchange interaction MS and consider that an exchange interaction exists

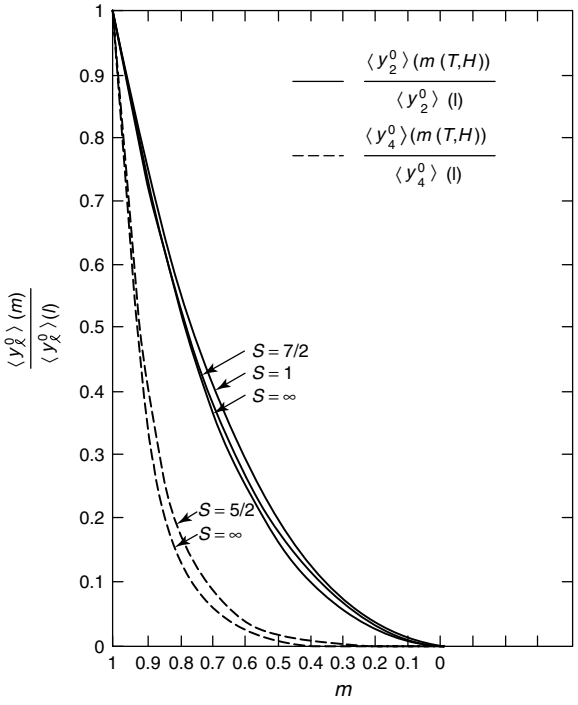

Figure 9. Thermal dependence of longitudinal spin-correlation functions $\ell = 2, 4$, versus reduced $m(T)$ for several spin values, S (Callen and Callen, 1965).

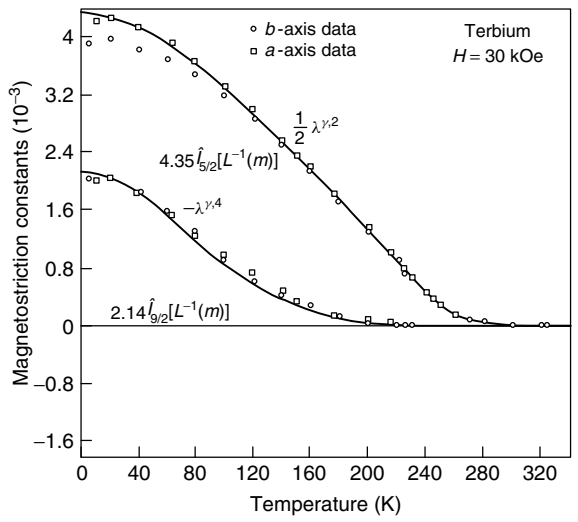

Figure 10. Clark's MS constants, $\lambda^{\gamma,2}$ and $\lambda^{\gamma,4}$ (tetragonal strain) thermal dependence for Tb metal; lines are the STM theoretical fits by reduced Bessel functions $\hat{I}_{\ell+1/2}$ (L^{-1}(m)) with $\ell = 2, 4$ respectively (Rhyne and Legvold, 1965).

between the ion pairs (f, g) of the forms mentioned in Section 1. Now the *two-ion MEL Hamiltonian* takes the form,

$$H_{\rm me}^{\rm II} = -\Sigma_{(f,g)}\Sigma_\Gamma \Sigma_{jj'} D_{jj'}^\Gamma(f,g)\Sigma_i \varepsilon_i^{\Gamma,j}\mathcal{J}_i^{\Gamma,j'}(f,g) \qquad (20)$$

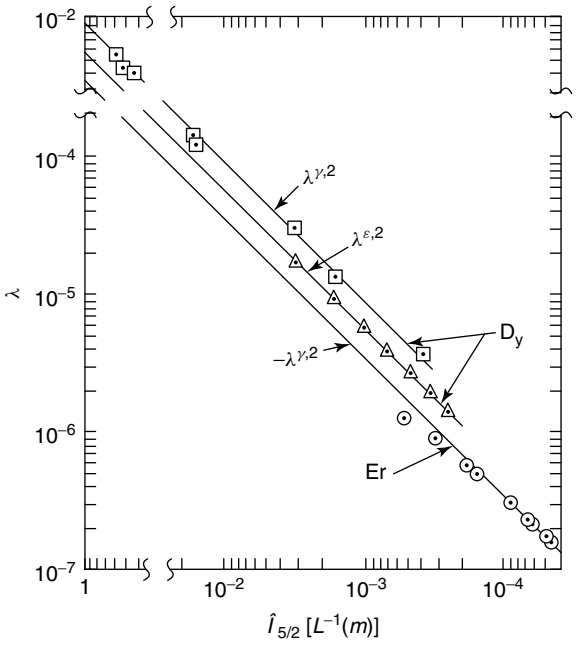

Figure 11. The linear dependence of Clark's MS constants $\lambda^{\gamma,2}$ and $\lambda^{\varepsilon,2}$ with reduced Bessel function $\hat{I}_{5/2}$ (L^{-1} (m)) confirms the STM equation (18) (Tsuya, Clark and Bozorth, 1964).

$D_{JJ'}^\Gamma$ are the EX-MEL parameters and $\mathcal{J}_i^\Gamma(f,g)$, two-ion AM operators, isomorphous of the Stevens operators (see Table 1), and where first correspond to isotropic EX-MS (independent of $\mathbf{M}_s$ orientation) and the remainder to anisotropic EX-MS. In the case of cubic and hexagonal symmetries, $H_{\rm mel}^{\rm II}$ is simply obtained by substituting $J^2 \to J_f \cdot J_g$ and the squared components J_i^2 $(i = x, y, z)$ by $J_f^i J_g^i$ in equations (13 and 14). Now there are four MEL parameters for Γ^α strains, D_{i1} $(i = 1, 2)$ for the isotropic exchange and D_{i2} $(i = 1, 2)$ for the anisotropic one. In this way we obtain three *spin-correlation functions* (SCFs): one-ion longitudinal ($\mathcal{L}_f \sim \langle S_z^2 - (1/3)S(S+1)\rangle$), and two-ion longitudinal ($\mathcal{L}_{fg}(T, H) \sim \langle S_f^z S_g^z - (1/3)S_f S_g\rangle$), and two-ion isotropic ($I_{fg}(T, H) \sim \langle \mathbf{S}_f \cdot \mathbf{S}_g\rangle$), which provide for the thermal dependence of the EX-MSs. In the same way as before the MEL free energy is obtained by taking the thermal average $\langle H_{\rm EX}^{\rm II}\rangle$ and therefore the equilibrium MS becomes $\overline{\varepsilon}_i^\Gamma = (c^\Gamma)^{-1}\Sigma_{(f,g)} D^\Gamma(f,g)\langle \mathcal{J}_i^\Gamma(f,g)\rangle$.

Other theories than the MFA have been developed for explaining the thermal dependence of CEF-MS, such as the one based on a generalization of the Brillouin function theory (Kuz'min, 1992) and including CEF splitting (i.e., unevenly spaced levels), well applicable to RE intermetallics, and the one based on the spin-wave approximation (del Moral and Brooks, 1974). Also a number of techniques have been developed to calculate the two-ion SCFs, such as the cluster one (Bethe–Peierls–Weiss, BPW) and the one based on

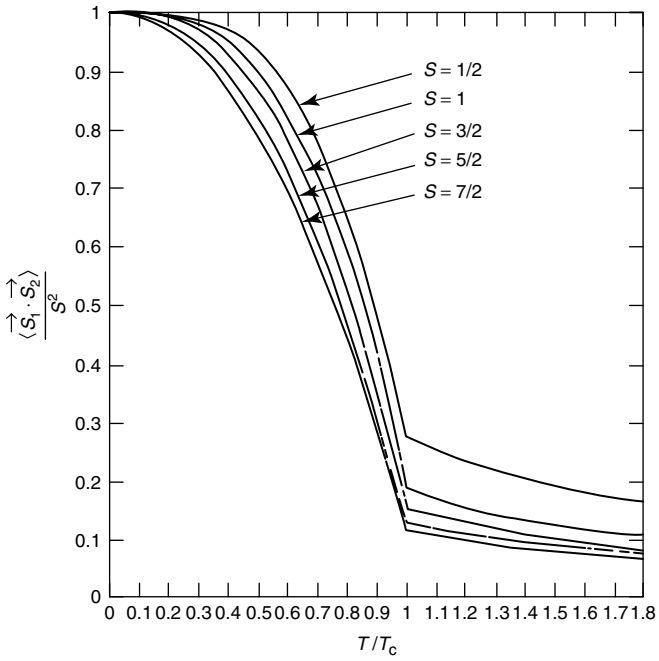

Figure 12. Thermal dependence of isotropic two-ion spin-correlation functions (Callen and Callen, 1964).

the thermodynamic Green function technique. In Figure 12 is shown the thermal variation of $I_{fg}(T)$ for several S values calculated according to the two-atom cluster theory, meanwhile $\mathcal{L}_{fg}(T, H)$ changes as m^2, which distinguishes EX-MS from the CEF-MS, changing as m^3 at low T.

At the Curie temperature, T_c, in FMs, MS manifests *spontaneously*, giving rise to *anomalies* in the volume and anisotropic TH.E.s. For example, for hexagonal symmetry the Γ^α IR anomalous strictions are for volume and tetragonal distortions respectively of the forms,

$$\overline{\epsilon}^{\alpha,1} = \frac{\Delta V}{V} = \lambda_{11}^{\alpha}(T, H) + \lambda_{12}^{\alpha}(T, H)\left(\frac{\sqrt{3}}{2}\right)\left(\alpha_z^2 - \left(\frac{1}{3}\right)\right)$$

$$\overline{\epsilon}^{\alpha,2} = \left(\frac{\sqrt{3}}{2}\right)\left(\overline{\epsilon}_{zz} - \left(\frac{1}{3}\right)\overline{\epsilon}^{\alpha,1}\right) = \lambda_{21}^{\alpha}(T, H) + \lambda_{22}^{\alpha}(T, H)\left(\frac{\sqrt{3}}{2}\right)\left(\alpha_z^2 - \left(\frac{1}{3}\right)\right) \quad (21)$$

where $\lambda_{ij}(T, H) = (1/\Delta_\alpha)\Sigma_{(f,g)}[c_{jj}^{\alpha} D_{ij}^{\alpha}(f, g) - c_{ij}^{\alpha} D_{ji}^{\alpha}(f, g)] I_{f,g}(T, H)$, $i, j = 1, 2$, meanwhile, λ_{12}^{α} and λ_{22}^{α} depend on both $\mathcal{L}_f$ and $\mathcal{L}_{fg}$ (c_{ij}^{α} are symmetry ECs and $\Delta_\alpha \equiv c_{11}^{\alpha} c_{22}^{\alpha} - (c_{12}^{\alpha})^2$). In Figure 13 is shown the *magnetic TH.E.*, $(\Delta V/V)_{\text{isotr}} = \lambda_{11}(T)$, for the cubic Laves-phase polycrystalline $GdNi_2$ compound, with the anomaly

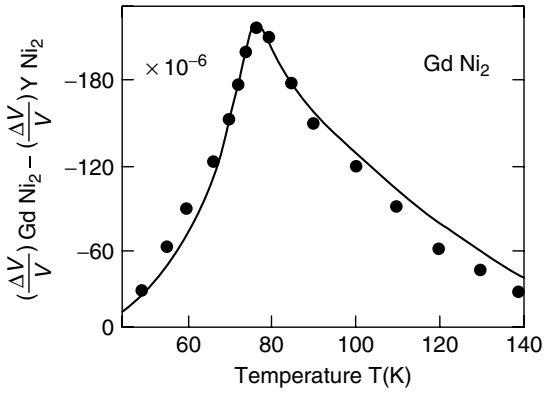

Figure 13. Volume thermal expansion of $GdNi_2$; $\left(\frac{\Delta V}{V}\right)YNi_2$ is the lattice contribution; the line is the theoretical fit (del Moral and Ibarra, 1985).

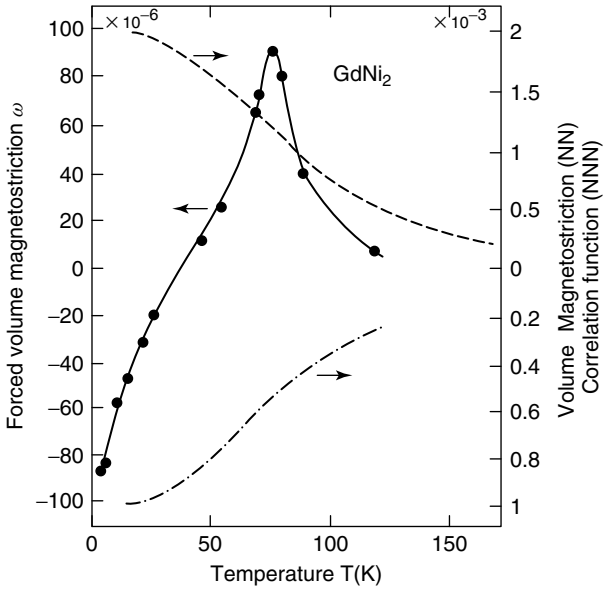

Figure 14. Forced volume MS of $GdNi_2$ and NN and NNN spin-correlation functions (del Moral and Ibarra, 1985).

at $T_c = 75$ K. Also, the volume *forced magnetostriction* (*FMS*), $\partial\omega/\partial H$ is shown to be given by $(\partial\omega/\partial H) = (2/c^{\alpha})\Sigma_{j(f,g)} D_{11}^{\alpha}(f, g)\langle S_j^z \mathrm{S}_f \cdot \mathrm{S}_g\rangle$, with a triple SCF (solved e.g., by decoupling $\langle S_j^z\rangle\langle \mathrm{S}_f \cdot \mathrm{S}_g\rangle$), and in Figure 14 it is shown $\omega(H)$ for $GdNi_2$, together with the *two-spin cluster* BPW theoretical fit. This theory, extended to nearest-neighbours (NN) and next-nearest-neighbour (NNN), explains well the T and H dependencies for archetypal FMs such as EuO, EuS, and the magnetic semiconductor EuSe (del Moral, 2007). Finally note that MS shows critical behavior at T_c with critical exponents $2\beta, 2/\delta$ (FM regime), and -2γ (PM one), as expected (Vázquez, Hernando and Kronmüller, 1986).

2.4 Antiferromagnets

MS in collinear antiferromagnets (AFMs) can be obtained just by applying the STM to each sublattice and adding the contributions. However a phenomenological Landau–Ginzburg (L–G) theory, based on *Dzyaloshinskii's* magnetic symmetry group (MSG) theory arguments (Wolf and Huan, 1988a,b), is more physical and powerful. In those canted AFMs, such as the tetragonal halides MnF_2 and CoF_2 ($T_N = 67.5$, 38 K) and the cubic garnet DyAlG ($T_N = 2.54$ K), instead of $\mathbf{M} = (2M_0)\mathbf{m} = \mathbf{M}_1 + \mathbf{M}_2$ ($= 0$ at 0 K and without canting), the order parameter is $(2M_0)\boldsymbol{\eta} = \boldsymbol{l} = \mathbf{M}_1 - \mathbf{M}_2$, or Néel AFM vector (always non-null, see Figure 15, and where $\mathbf{M}_i$ are the sublattice magnetizations). The MEL free energy must be invariant against the MSG operations and for the simplest case of cubic symmetry (MSG for DyAlG is $Ia3d \times R$, where R is the time inversion operator) the MEL plus elastic free energy is,

$$F_{\text{mel}} + F_{\text{el}} = \overline{D}_1 l^2 \varepsilon + \left(\frac{1}{2}\right)\overline{G}_1 l^2 \varepsilon^2 + \overline{D}_2 m^2 \varepsilon + \overline{D}_3 lm\varepsilon + \cdots + \left(\frac{1}{2}\right) c_0 \varepsilon^2 \qquad (22)$$

where terms odd in $\boldsymbol{\eta}$ are only allowed if $\boldsymbol{\eta}$ is translationally invariant, which only happens if the AFM is commensurate. From the minimization, $\partial(F_{\text{mel}} + F_{\text{el}})/\partial\varepsilon = 0$, we obtain,

$$\overline{\varepsilon} = -\frac{(\overline{D}_1 l^2 + \overline{D}_2 m^2 + \overline{D}_3 ml)}{(c_0 + \overline{G}_1 l^2)} \qquad (23)$$

Without $\mathbf{M}_i$ canting, $\mathbf{m} = 0$ and the MS is determined by $\boldsymbol{l}$ (also $\boldsymbol{l}$ gives rise to an *MEL effect* on the 'bare' EC c_0). In Figure 16a is shown $\overline{\varepsilon}_{xy}$ versus $\mathbf{H}_\perp \| [1\ \overline{1}\ 0]$ for tetragonal CoF_2 (at 4.2 K), noticing a quadratic dependence, and noticing also the dominance of $\boldsymbol{l}$ *rotation* within the [110] plane (term in $\overline{D}_1$). Instead for $\mathbf{H}_\parallel \| [1\ \overline{1}\ 0]$, $\overline{\varepsilon}_{xy}$ changes linearly (Figure 16b), indicating the dominance of the l^2 term, if induced canting is neglected. A similar study has been performed for AFM MnF_2 ($T_N = 67.3$ K) (Shapira, Yacovicht and Nelson, 1975).

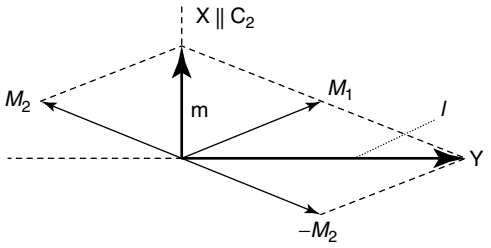

Figure 15. Magnetization, $\mathbf{m}$ and Néel AFM vector, $\boldsymbol{l}$ for AFM; C_2 is a twofold axis (del Moral, 2007).

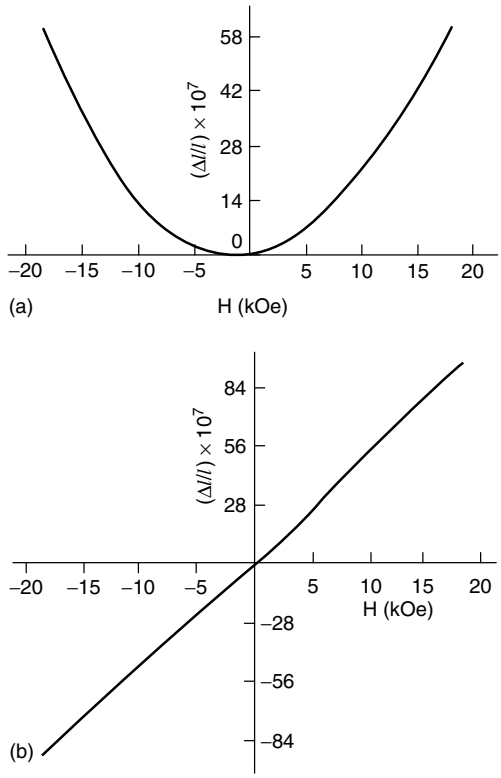

Figure 16. MS $\lambda([1\overline{1}0], [110])$ (a) and $\lambda([001], [110])$ (b) for CoF_2 at 4.2 K (Prokorov and Rudashevskii, 1969).

2.5 Spin-wave approximation for MS

This model is of interest because it provides the MS field dependence in cubic FMs, AFMs, and ferrimagnets (for helical phases in hcp rare-earth metals (REMs) the situation is more complicated). Transformation $S_l^{\pm} \cong \sqrt{2S}a_l^{\pm}$ ($\boldsymbol{l}$ is a lattice site) to boson creation and annihilation operators, immediately yields $\langle \tilde{O}_n^0 \rangle = Q[1 - (n(n+1)/2)(1/M_{\text{so}})g\mu_{\text{B}}\Sigma_l \langle a_l^+ a_l^- \rangle]$, where Q is a constant and $M_{\text{so}} = NgS\mu_{\text{B}}$, or 0 K spontaneous sublattice magnetization. The excited magnon number, at T and applied field H is then $\langle n \rangle_{T,H} = \Sigma_l \langle a_l^+ a_l^- \rangle = (g\mu_{\text{B}})^{-1}[M_{so} - M(T, H)]$. Calling $\Delta m = 1 - m$, we obtain $\langle \tilde{O}_n^0 \rangle = Q[1 - (n(n+1)/2)\Delta m] \approx Q[1 - \Delta m]^{n(n+1)2} = \mathrm{Q}m^{n(n+1)2}$, which again constitutes the AZC power law. Transforming now to magnon operators $a_k^{\pm}$ by Fourier expansion, we obtain $\langle \tilde{O}_n^0 \rangle = Q[1 - (n(n+1)/2NS)\Sigma_k \langle n_k \rangle]$, where $\langle n_k \rangle = \{\exp[\beta E(\mathbf{k}) - 1]\}^{-1}$, or $\mathbf{k}$-magnon number. In a similar way we can calculate the two-ion MS. Assuming a quadratic magnon dispersion $E(\mathbf{k})$ we obtain for the general full MS the expansion,

$$\lambda = \lambda_0 + \lambda_1(T)\sqrt{H} + \lambda_2(T)H + \lambda_3(T)H^{3/2} + \lambda_4(T)H^2 + \lambda_5(T)H^3 + \cdots \qquad (24)$$

The leading term in H applies for α mode (as well as $H^{3/2}$), being of exchange origin. For CEF γ and ε strictions the leading CEF term is in $\sqrt{H}$, that is, nonanalytic (however, exchange α mode has also a $\sqrt{H}$ contribution). Therefore for AMS, $\sqrt{H}$ dependence singles out the CEF-MS origin, as does the H dependence for exchange origin in the volume MS, ω.

Another important aspect manifested by MS is the *spin dimensionality* (Callen, 1982). The AZC law has been derived for spatial $d = 3$ dimension and Heisenberg spins ($D = 3$). We will consider now what happens when the moments are constrained to a plane ($d = 2$, the possible case of ultrathin films, monolayers, and interfaces (IFs) in superlattices (SLs)) and also $D = 2$ (XY magnet), and in general for any D, as we know that MFA is exact for $D = 4$ (for fixed $|\boldsymbol{\mu}|$ the degrees of freedom (DOF) are reduced to $D - 1$). Considering $2D$ spins, the DOF is the angle θ of $\langle \mathbf{S} \rangle$, formed with the MCA *easy direction* (ED), and we will perform a classical calculation of MEL energy. This will be expanded in Legendre polynomials $P_l(\cos\theta)$, where l should be even. In order to obtain $\langle P_l(\cos\theta)\rangle$ we write the partition function as $Z_0 = \int_0^\pi \mathrm{e}^{a\cos\theta} d\theta$, with $a \equiv \langle E\rangle / k_\mathrm{B}T$, where $\langle E\rangle$ is the unperturbed ionic MF energy. Noticing that needed $\langle \cos^n\theta\rangle \sim \partial^n Z_0/\partial a^n$, and that for low-T $\theta = \varepsilon$ is small we perform the expansion, $Z_0 \cong \varepsilon \mathrm{e}^a(1 - a\varepsilon^2/6)$ and therefore we obtain $m = (Z_1/Z_0) \cong 1 - \varepsilon^2/6$, and therefore we obtain $\langle \cos^n\theta\rangle = (Z_n/Z_0) = 1 - n\Delta m$. Then for any l we obtain,

$$\frac{\overline{\mathrm{M}}_i^{\Gamma,l}(T)}{\overline{\mathrm{M}}_i^{\Gamma,l}(0)} = 1 - l^2\Delta m \cong m^{l^2} \tag{25}$$

giving a quite different dependence for $d = D = 2$ than for $D = 3$ spins, that is, an m^4 dependence (or $(l + 0)/1$ power for DOF $n = 2 - 1$). In order to generalize to n DOF, we notice that for $D = 3$ ($n = 3 - 1 = 2$) the power is $l(l + 1)/2$, which by induction gives a general power $l(l + n - 1)/2$. A general proof of the preceding conjecture for all l, all symmetries, and all D does not exist, as the corresponding mathematics does not exist. The exceptions are uniaxial crystals in d dimensions.

2.6 Parastriction

The STM also provides a description of the PS, although a direct calculation of the strictions, through the diagonalization of the full Hamiltonian (including QP exchange interaction), and using perturbation theory has provided a good explanation of PS in cubic-CsCl REM (M = Zn, Ag, Cu, Sb, Cd, P, As) intermetallics, showing FM, AFM, QP, and anti ferro-quadrupolar (AFQP) orderings, in cubic Laves-phase REM_2 (M = Al, Ni, Cu) and hexagonal RENi_5 (del Moral, 2007). We have no space here to develop such a detailed theory (Morin, Schmitt and de Lacheisserie, 1980), and we take recourse to the usual STM, where CEF effects are disregarded (instead in CEF-PS theory we end up, after a perturbation expansion of F, with MSs $\overline{\varepsilon}^\Gamma = (M^{\Gamma,2}/c_0^\Gamma)\chi_Q^\Gamma H^2$, $\Gamma = \gamma(\varepsilon)$, where $\chi_Q^\gamma = \partial Q/\partial(H)^2$ is the QP-field susceptibility, for QP moment $Q = \langle \tilde{O}_2^0\rangle$ ($\langle \overline{O}_2^2\rangle$, etc. for χ_Q^ε). Effectively, in PM regime ($T > T_\mathrm{c}$ or T_N), $X = \beta\mu(H_\mathrm{MF} + H)$ is small and therefore the small $m(T, H) = \hat{I}_{3/2}(X) = (1/3)X + \cdots$ expansion is also allowed, as well as $\hat{I}_{l+1/2}(X) = [1/(2l + 1)!!]X^l + \cdots$, $X \ll 1$. Therefore we obtain $\hat{I}_{l+1/2}(X) \approx 3^l m^l(T, H)/(2l + 1)!!$, $m \gg 1$, and for order $l = 2$ we deduce that

$$\frac{\overline{\mathrm{M}}_{j,2}^\Gamma(T)}{\overline{\mathrm{M}}_{j,2}^\Gamma(0)} = \hat{I}_{5/2}(X) = \left(\frac{9}{15}\right) m^2(T, H) = \left(\frac{9\chi^2(T)}{15M_0^2}\right) H^2, T \gg T_\mathrm{c} \tag{26}$$

where $\chi(T)$ is the first-order PM (Curie) susceptibility and $M_0 = M(0, 0)$. This H^2 dependence is the finger point for a true paramagnet (although higher even powers appear for $T \cong T_\mathrm{c}$). For higher order MEL constants the dependence is as m^ℓ indeed.

Finally we have to mention that in AFM helical systems such as hcp RE metals, MS should be in principle *nonuniform*, the lattice deforming in each crystal plane along the local magnetization. But if we assume such a strain and call by (ξ, η, ζ) the local frame attached to the rotating spin, with turn angle ψ between NN spins along c axis, we obtain the expression for the (l, m, n) site displacement, $u_{lmn} = \int A(\xi, \eta, \zeta) e^{i(\xi l + \eta m + \zeta n)}\, \mathrm{d}\xi\mathrm{d}\eta\mathrm{d}\zeta$ and also the condition $\cos\eta = 2 - \cos 2\psi > 1$, which means that η is imaginary and therefore u is damped as moving away from the crystal surface. This means that for instance, the ε^γ modes are clamped within the lattice, and that the crystal is only strained within a thin surface layer (few lattice constants) (Evenson and Liu, 1969). For a bulk crystal this is insignificant but not for a very thin film (TF).

2.7 Magnetoelastic parameters calculation and MS of RE intermetallics

MEL parameters $M_i^{\Gamma,\ell}$ are the best piece of information about MEL coupling at a microscopic level, and therefore their experimental determination and theoretical calculation are paramount. The simplest way to calculate them is assuming that the ligand ions producing the CEF are point charges, q_i

(*point charge model*, PCM), although PCM is so simplified that it seldom agrees with experiment. A better way is to use the *superposition model*, which assumes axial symmetry along each bond axis, and from A_n^0 build the remaining CEF parameters (Newman and Ng, 1989). The way to proceed is by writing the undistorted CEF gradient (even if it is zero by, e.g., cubic symmetry), and expanding it in the corresponding strain. For instance let us calculate $M^{\gamma,2}$ (for orthorhombic basal plane distortion, $\varepsilon_1^\gamma = (1/2)(\varepsilon_{xx} - \varepsilon_{yy})$) for hexagonal symmetry. We start with the CEF parameter

$$B^{\gamma,2} = +\left(\frac{3}{4}\right) Z|\mathrm{e}|\alpha_J \langle r^2\rangle \Sigma_i q_i \left(\frac{(x_i^2 - y_i^2)}{R_i^5}\right) \tag{27}$$

where (x_i, y_i, z_i) are the point ligand positions (of charge $Z|\mathrm{e}|$) and R_i their distances to the probe ion. $\alpha_J \equiv \theta_2$ is the second-order W–E coefficient. If we now distort the coordinates as $x_i \to x_i(1+\varepsilon_{xx})$, $y_i \to y_i(1+\varepsilon_{yy})$, $z_i \to z_i$ and preserve the volume (i.e., $\varepsilon_{xx} = -\varepsilon_{yy} = \varepsilon_1^\gamma$) we obtain the lattice summation $S = 2\varepsilon_1^\gamma \Sigma_i[(x_i^2 + y_i^2)/R_i^5] - 5\varepsilon_1^\gamma \Sigma_i[(x_i^4 - y_i^4)/R_i^7]$, plus B_2^0. In this form the MEL parameter becomes,

$$M^{\gamma,2} = \left(\frac{3}{4}\right) Z|\mathrm{e}|\alpha_J \langle r^2\rangle \left[\frac{2\Sigma_i\left(x_i^2 + y_i^2\right)}{R_i^5} - 5\Sigma_i \frac{(x_i^4 - y_i^4)}{R_i^7}\right] \tag{28}$$

We can proceed in similar way with other ISs and other symmetries and even with more complex structures (polyatomic motives; the lattice summations are well known, del Moral, 2007). The results of this model can be compared with the measured MEL parameters, obtained from MS measurements, the best way being by studying $\overline{\mathrm{M}}^{\gamma,\ell}$ temperature dependence. This has been performed with the RE metals (hcp structure), many RE intermetallics, such as REM_2 (Laves phases), REM_5 (hexagonal) (M is a metallic atom), and RE impurities in nonmagnetic hosts, a good way to avoid MS exchange contribution. Considering only NN ligands, for the REM_2 the tetragonal distortion, ε_1^γ MEL parameter becomes, $M^{\gamma,2} = \sqrt{6}\mathrm{e}^2\alpha_J\langle r^2\rangle \left\{\frac{4}{3}\left[Z(\mathrm{RE})/R^3(\mathrm{RE})\right] - (156/121)\left[Z(\mathrm{M})/R^3(\mathrm{M})\right]\right\}$, where Z is the ligand charge.

We present an example to show how to proceed for the derivation of the MEL parameter, studying the thermal variation of ISs in the archetypal FM Laves-phase REAl_2, in concrete the *saturation* (spontaneous after DW displacements) tetragonal $\varepsilon_1^\gamma(\varepsilon_{xx} = \varepsilon_{yy} = -\varepsilon_{zz}/2)$ distortion in Pr Al_2 ($T_\mathrm{c} = 33\,\mathrm{K}$; $\langle 100\rangle$ EDs) (Abell, del Moral, Ibarra and Lee, 1983; see del Moral *et al.*, 1986), for $\mathrm{Gd}_{1-x}\mathrm{Tb}_x\mathrm{Al}_2$, where exchange is tailored). The same kind of study has been performed in dilute $\mathrm{Y}_{1-x}\mathrm{RE}_x$ (Pureur, Creuzet and Fert, 1985) and noble metal–rare earth (NMRE) alloys (Creuzet and Campbell, 1981). The thermal variation of the MSs difference giving $\overline{\varepsilon}_1^\gamma$ is shown in Figure 17, together with the theoretical fit by $\overline{\varepsilon}_1^\gamma = (M^{\gamma,2}/c_0^\gamma)\langle\tilde{\mathrm{O}}_2^0\rangle + (M^{\gamma,4}/c^\gamma)\left[\langle\tilde{\mathrm{O}}_4^0\rangle - (14/5)\langle\overline{\mathrm{O}}_4^4\rangle\right]$, where $c_0^\gamma = c_{11}^0 - c_{12}^0 = 4.52 \times 10^5$ K/ion. The thermal averages are calculated by the diagonalization of the unperturbed Hamiltonian $H = H_\mathrm{EX} + H_\mathrm{CEF} + H_\mathrm{Z}$, expressing $H_\mathrm{EX} = g\mu_\mathrm{B}\mathbf{J}\cdot\mathbf{H}_\mathrm{MF}$ within the MFA, obtaining the Pr^{3+} ion energy levels and eigen functions, those mixtures of pure $|\mathrm{J}M_J\rangle$ ones. From the fit we obtain the $M^{\gamma,2}$ value given in Table 2, but a better fit is obtained adding the fourth-order MEL contribution (M_4^γ term in the MEL Hamiltonian). In this table the MEL parameters for other REAl_2 together with PCM calculated parameters are given. As we can see the PCM generally fails, either in magnitude or sign (less). This is because of the neglecting of the *screening* of the CEF by the *distorted* conduction band electrons (CEs) charge density, which is very strong, since the proximity of CE to the probe ion can produce a CEF even *stronger* than the NN ions. However ratios such as $M^{\varepsilon,2}/M^{\gamma,2}$ are dictated *only* by symmetry, being model independent (e.g., $-4/3$ for the RE^{3+} diamond lattice in REM_2).

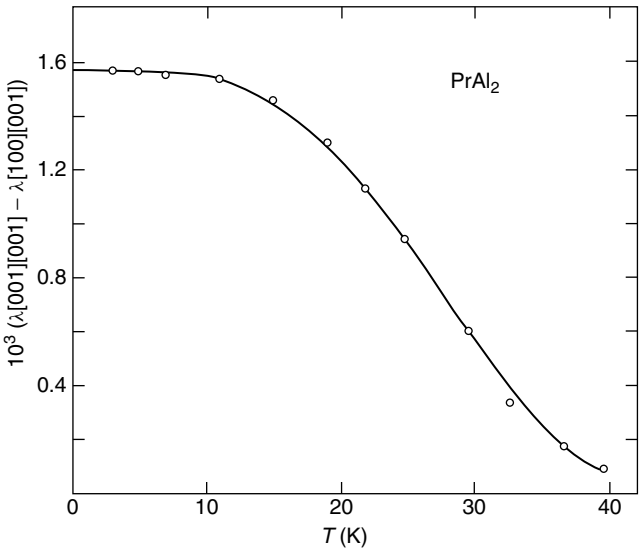

Figure 17. Spontaneous MS ε_1^γ (T) variation for cubic Pr Al_2; line is the theoretical fit (see text) (Abell, del Moral, Ibarra and Lee, 1983).

There are two models to introduce screening in the MEL parameters, both distorting the electronic charge density, $\rho(\mathbf{r} - \mathbf{R}_i)$: one calculates the distortion of the reciprocal space ($\mathbf{q}$) and of the Lindhard's dielectric constant of CE, $\varepsilon(\mathbf{q})$, introducing exchange and correlation between CE, and assumes an spatial charge distribution (Gaussian) for the ligands (del Moral, Echenique and Corrales, 1983); the other just considers the distorted $\rho(\mathbf{r} - \mathbf{R}_i)$, after a previous

Table 2. Magnetoelastic parameters in K/ion for $REAl_2$. (From Abell, del Moral, Ibarra and Lee, 1983.)

Compound	M_2^γ	M_2^ε	M_4^γ	M_4^ε
$PrAl_2$–I	−52	+487	–	–
$PrAl_2$–II	+132	–	−12	–
$PrAl_2$–IV	−97	+130	–	–
$TbAl_2$–I	−3.5	+20	–	–
$TbAl_2$–III	–	40	–	+0.1
$TbAl_2$–IV	−35	+46	–	–
$NdAl_2$–I	−32	+65	–	–
$NdAl_2$–IV	−82	+109	–	–

I–derived from experimental data using second-order terms only.
II–derived from experimental data including fourth-order terms in ε_1^γ.
III–derived from experimental data including fourth-order terms in ε^ε.
IV–calculated from point-charge model–nearest-neighbor RE ions only; zero charge on Al.

undistorted band structure calculation (Morin and Schmitt, 1981). It has been shown that the first approach is superior, the second one failing in the sign and/or order of magnitude. For instance in the case of $NdAl_2$, introduction of CE exchange is essential (positive Fermi holes introduction) and the experimental values are well reproduced (same happens for RE = Pr, Tb).

3 ITINERANT ELECTRON MAGNETOSTRICTION; BAND MODELS; HUBBARD FORCED MAGNETOSTRICTION; STRONGLY CORRELATED SYSTEMS MAGNETOSTRICTION; SPIN-FLUCTUATIONS THEORY; ITINERANT WEAK FERROMAGNETS; *AB INITIO* MS CALCULATION METHODS

Calculation of MS and MEL effects in metals, semiconductors, and alloys is the most difficult task of MS theory. Several theories have been proposed so far (del Moral, 2007): the *Stoner model* of spontaneous magnetovolume (MV), ω_s developed below T_c, and of forced VMS, $\partial\omega/\partial H$ (near saturation); the use of *Hubbard model* (HM); the *band models* (BMs, one of which is the pioneering *Brooks–Fletcher–Katayama* (BFK) one (Fletcher, 1954); see also Tatebayashi, Ohtsuka, Ukai, and Mori (1986)), based on *MS perturbation of tight binding approximation* (*TBA*) *bands* (Mori, 1969a,b; Kondorskii and Straube, 1973; Mori, Fukuda and Ukai, 1974; Otha and Shimizu, 1982), and a simplified BM (band-degeneration and Brillouin zone symmetry (BD-BZS)) of it; and the *ab initio* (AI) calculations (based on first-principles calculations) will be considered. The Stoner model is developed in many text books, and therefore we focus on the BMs (for CEF-MS) and the HM for two-ion MS, as well as in AI methods. In all BMs some conditions to get MS are required: (i) the band must be *orbitally degenerated* to have $\langle \mathbf{L}\rangle \neq 0$ and so non-null SO coupling; (ii) $\mathbf{k}$ points of high symmetry (HS) within the Brillouin zone (BZ) are the main contributors to MS (e.g., Γ point in fcc and bcc-BZs), since only in this case moving out the HS $\mathbf{k}$ point some degeneracy is retained; (iii) only bands near E_F which are partially occupied, yield $\langle \mathbf{L}\rangle \neq 0$ and $\langle \mathbf{S}\rangle \neq 0$; (iv) the SO coupling finally splits the degenerate CEF levels (centers of bands) and mixes the t_{2g} and $e_g\langle \mathbf{L}\rangle = 0$ orbitals (see subsequent text), in this way giving $\langle \mathbf{L}\rangle \neq 0$.

3.1 Band-degeneration (BD) and Brillouin zone symmetry model (BZS)

In the BD-BZS model (Kulakowski and del Moral, 1994) one considers rigid bands within the TBA (with wave functions $\psi_{\mathbf{k},\lambda}(\mathbf{r}) = \Sigma_l a_l \varphi_\lambda(\mathbf{r}-\boldsymbol{l})e^{\mathbf{k}\cdot\boldsymbol{l}}$), centered around the CEF 3d-electron energy levels, E_λ, with density of states (DOS) $D(E-E_\lambda)$. The bands are taken to be of elliptical or Lorentzian shape, obtained by fitting the real DOS band calculations. Also few $\mathbf{k}$ points near the Fermi surface (FS) are considered. Under MS and the MF field, $\mathbf{H}_{MF} = n\mathbf{M}$ (proportional to the Stoner spin-polarized band splitting), there is a rigid band shift $\Delta E_\lambda(\varepsilon_i^\Gamma, \mathbf{H}_{MF})$, and electron number variation, Δn_λ, by transference to other 3d bands ($e_g : \varphi_\lambda = \{3z^2 - r^2, x^2 - y^2\}$; $t_{2g} : \varphi_\lambda = \{xy,yz,zx\}$ for cubic symmetry). Since $\Sigma_\lambda \Delta n_\lambda = 0$, there must be a ΔE_F variation, such that $\Delta n_\lambda = D_\lambda(\mu)\Delta\mu - D_\lambda(\mu)\Delta E_\lambda$, from where ΔE_F is obtained under the preceding constraint. The energy variation is therefore given by $\Delta F(\mathbf{H}_{eff}, \varepsilon_i^\Gamma) = \Sigma_\lambda(\Delta F_\lambda^{(1)} + \Delta F_\lambda^{(2)} + \Delta F_\lambda^{(3)})$, where $\Delta F_\lambda^{(1)} = -n_\lambda \Delta E_\lambda$, or energy gain under rigid sub-band shift; $\Delta F_\lambda^{(2)} = E_F D_\lambda(E_F)\Delta E_\lambda$, or energy cost to keep E_F constant for the exchange polarized bands; $\Delta F_\lambda^{(3)} = -E_F \Delta E_F D_\lambda(E_F)$, or gain under E_F modification ($\mathbf{H} = \mathbf{H}_{app} + \mathbf{H}_{MF}$). Introducing ΔE_F in the total ΔF, we obtain the net variation, $\Delta F_m(\mathbf{H}_{eff}, \varepsilon_i^\Gamma) = -\Sigma_\lambda n_\lambda \Delta E_\lambda$, from where for instance for α strains,

$$\frac{\partial F_m}{\partial \varepsilon_i^\alpha} = -\Sigma_{\lambda=1}^{10}\left(\frac{\partial E_\lambda}{\partial \varepsilon_i^\alpha}\right) \quad (i = 1, 2) \tag{29}$$

which allows the MS calculation, just minimizing, that is, making $\partial(F_m + F_{el})/\partial\varepsilon_i^\Gamma = 0$. The free energy is calculated in itinerant FMs as $F_m = \Sigma_\lambda \int_{-\infty}^{\mu}(E-E_\lambda)^\nu D_\lambda(E-E_\lambda) f_{FD}(\beta(E-E_\lambda))dE$ (with $\nu = 1$) and the band filling, n taking $\nu = 0$.

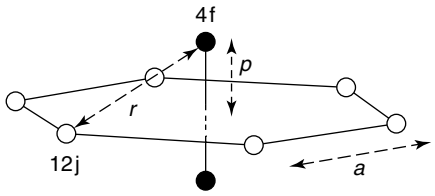

Figure 18. Fe pair atoms (4f sites) in uniaxial Y_2Fe_{17} intermetallic (Kulakowski and del Moral, 1995).

This model has been successfully applied to iron-rich *uniaxial* intermetallics and to Ni and Fe. In the former, for example, for the Y_2Fe_{17} (2–17), with hexagonal structure formed out of pairs of magnetostrictive Fe atoms ('dumbbells') (see Figure 18), **a** ED and with two magnetostrictive doublets ($\{|xz\rangle, |yz\rangle\}$ and $\{|xy\rangle, |x^2 - y^2\rangle\}$), these produced by the CEF splitting. The MEL Hamiltonian is equation (14). From the preceding considerations we immediately obtain for the spontaneous $\overline{\varepsilon}_i^{\alpha}$ MSs ($i = 1, 2$) that

$$\overline{\varepsilon}_i^{\alpha} = \Delta_{\alpha}^{-1}\left[c_{jj}^{\alpha}\left(-\frac{\partial \mathrm{F}_m}{\partial \varepsilon_i^{\alpha}}\right) - c_{12}^{\alpha}\left(-\frac{\partial F_m}{\partial \varepsilon_j^{\alpha}}\right)\right]$$
$$i, j = 1, 2;\ j \neq i \tag{30}$$

By applying field we rotate $\mathbf{M}\|\mathbf{a}$ to $\mathbf{M}\|\mathbf{c}$, and we obtain the rotational or CEF-MSs $\Delta\varepsilon_i^{\alpha} = \varepsilon_i^{\alpha}(\mathbf{c}) - \varepsilon_i^{\alpha}(\mathbf{a})$, where the thermal variation of shape MS $\Delta\varepsilon_2^{\alpha}$ is shown in Figure 19, where we notice a nonmonotonous or non-STM variation, as a consequence of a population of the first doublet, $\langle \mathbf{L} \rangle$ becoming quenched and MS decreasing for $T < 150$ K, as the numerical calculation shows. Same happens with volume MS $\Delta\varepsilon_1^{\alpha}$. The fitted MEL parameters are (in 10^3 K/Fe atom) $M_1^{\alpha,2} = -9.0$ and $M_2^{\alpha,2} = -1.8$, much larger than for RE intermetallics ($\approx 10 - 100$ K/RE^{3+}), due to the much weaker CEF screening in 3d metals. Therefore this model gives a good account of the complicated MS thermal variation (also shown by $Y_2Fe_{14}B$ (2–14), with Tetragonal (TETR) structure and **c** ED) and has been also successful in explaining the maximum shown by $-\lambda^{\gamma,2}$ in iron, below T_c. In iron the use of localized STM gives an AZC exponent $a = 4.9$, which means a breaking of $m^3(T)$ law (Kulakowski and de Lacheisserie, 1989).

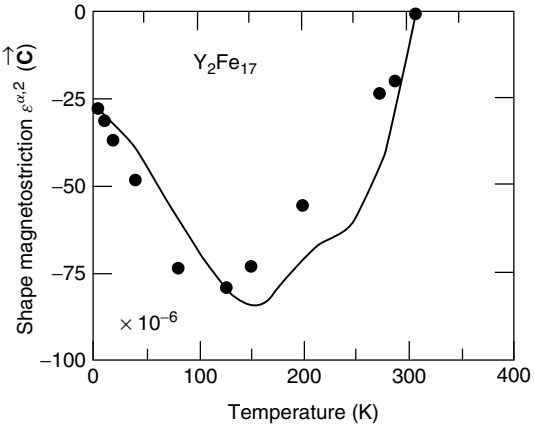

Figure 19. Irreducible ε_2^{α} (**c**) thermal variation in Y_2Fe_{17}; line is the theoretical fit ($\varepsilon_2^{\alpha}(\mathbf{a}) \approx 0$)(Kulakowski and del Moral, 1994).

3.2 Hubbard forced MS

In the preceding Fe intermetallics the magnetostrictive atom pairs are well 'separated' *via* electron hopping from the surroundings, and so the FMS can be calculated in a rather exact way (in fact those systems MS recall the classical *pair-atom* Néel MS model). The important fact is that this simple system shows up that FMS is a consequence of the 3d-electron repulsion, U within the pair. The pair Hamiltonian is the Hubbard one, $H_h = \Sigma_{i=1,2}\Sigma_{\rho,\rho',\sigma} t_{12}(\rho, \rho') c_{i\rho\sigma}^{+} c_{3-i\rho'\sigma} + U_{\mathrm{int}}$, where $|\rho\rangle$ and $|\rho'\rangle$ are t_{2g} states, i the dumbbell sites, $t_{12}(\rho, \rho')$ the hopping matrix elements (Slater–Koster overlapping integrals, depending on the direction cosines of the atoms bond) and U_{int} the intra-atomic electron coulomb repulsion. The preceding Hamiltonian can be transformed to one where the *effective* coulomb interaction depends on the electrons' distance, $U_{\rho\rho'}^{\mathrm{eff}}(r)$, and takes the many-body form $H = U^{\mathrm{eff}}\Sigma_{i=1,2} n_{i,\sigma} n_{i,-\sigma}$ ($n_{i,\sigma}$ is the occupation operator) with a quasi-ground state (QGS) energy level $E_{\mathrm{QGS}} = U^{\mathrm{eff}}$ and

$$U^{\mathrm{eff}} = \left(\frac{U}{2}\right)\left(1 + \frac{r}{2} - \left[1 + (1-r)^2 - 16\left(\frac{t_i}{U}\right)^2\right]^{1/2}\right)$$
$$r \equiv \frac{3J}{4U} \tag{31}$$

strongly reduced from the bare U value ($\cong$1 eV for Y_2Fe_{17}), that is, to 0.1 and 3 meV for 2–17 and 2–14 compounds. But this reduction is only accomplished if t_{12} (= 0.24 and 0.15 eV) is taken as purely *imaginary*, that is, the Bloch pair state QGS is bonding. It can be shown from equation (29) that the FMS, $\chi_{\mathrm{mel}}^{\alpha,i} = \partial\varepsilon_i^{\alpha}/\partial H$ has a contribution such that $\chi_{\mathrm{mel}}^{\alpha,i} = \chi_{\mathrm{mel},0}^{\alpha,i} - (1/c_{ii}^{\alpha})(U_n^{\mathrm{eff}}/4)(\partial/\partial\varepsilon^{\alpha,i}\left[\chi_{hf}(T)m(T)\right])_{\mathrm{T}}$, $i = 1, 2$ (del Moral, Abadia and Garcia-Landa, 2000), which allows to derive U^{eff} from the slopes of the plots of Figure 20 (χ_{hf} is the paraprocess susceptibility, $\partial M_s/\partial H$, and $\chi_{\mathrm{mel},0}^{\alpha,i}$ the combined CEF and Fe–Fe exchange, J, FMS) (del Moral *et al.*, 2007).

3.3 Spin-fluctuations theory of MS

There are RE intermetallics, notably the $REMn_2$ (including Y) and some alloys such as $ZrZn_2$, MnSi and Sc_3In where

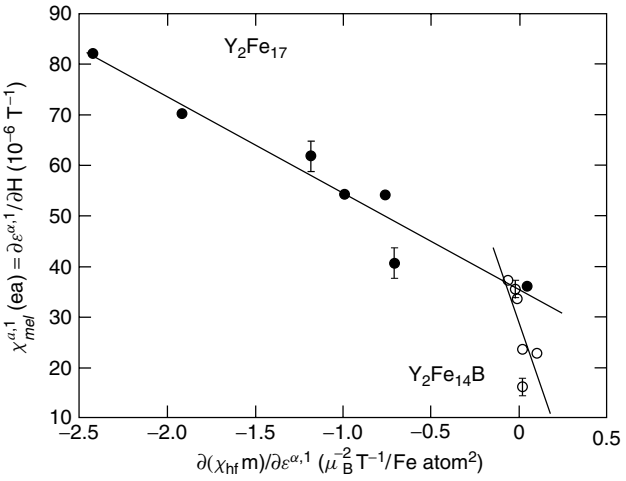

Figure 20. Strain susceptibility for iron intermetallics; see text (del Moral *et al*., 2007).

the Stoner and BM of MS do not work, needing the *spin-fluctuation* (SF) theory of MS for weak ferromagnet (WFM) and weak antiferromagnet (WAFM). In SF theory (Moriya, 1985) we work in the reciprocal $(\mathbf{k}, \omega)$ space as follows. The spin fluctuation is given by $\delta\mathbf{S} = \mathbf{S} - \langle\mathbf{S}\rangle_T$ and there will exist a correlation $S(\mathbf{r}, \mathbf{r}', t - t') = \langle\delta\mathbf{S}(\mathbf{r}, t) \cdot \delta\mathbf{S}(\mathbf{r}', t')\rangle$, which when adequately Fourier transformed gives rise to a dynamical susceptibility $\chi(\mathbf{k}, \omega)$, whose imaginary part can be measured by inelastic neutron scattering. Moreover in spin-localized magnets SFs are spatially localized, and therefore delocalized in *reciprocal* space, around $\mathbf{k} = 0$ or $\mathbf{k} = \mathbf{K}$ in WAFMs ($\mathbf{K}$ is the magnetic structure propagation vector). In SF systems just the opposite occurs, fluctuations are localized around $\mathbf{k} = 0$ (or $\mathbf{K}$) but spatially *extended*. In itinerant magnets those SFs are mainly longitudinal, due to the up and down fluctuation of the spin-polarized subbands. These SFs are therefore the very existing local average spin (local moment), whose mean-squared local amplitude, $S_L^2(T)$ must be T dependent (it is not a true moment $\boldsymbol{\mu} = g\mu_B\mathbf{S}$), that is, self-sustained by thermal fluctuations only. The main result of SF theory for PM regime is that there exists the relationship $S_L^2(T) - S_L^2(T_c) = (3/5)gN^2(1/\chi)$, so that $S_L^2(T)$ increases with T (from 3/5 of its 0 K value; g is a factor function of the DOS slope and curvature at E_F), (see Figure 21). With this background the TH.E. MV can be obtained, just writing $F_{mel} = -\omega\Sigma_{\mathbf{k}}D_{\mathbf{k}}\left[\langle S_{\mathbf{k}}^2\rangle_T - \langle S_{\mathbf{k}}^2\rangle_0\right]$ (Moriya and Usami, 1980). Adding the elastic energy $F_{el} = (1/2)B\omega^2$ (where B is the bulk modulus) and minimizing full F we obtain

$$\omega_s(T) = N^2\left(\frac{D_0}{B}\right)\left[S_L^2(T) - S_L^2(0)\right] \qquad (32)$$

which follows the variation shown in Figure 21, having at T_c^+ (or T_N^+) a discontinuity in the MV of

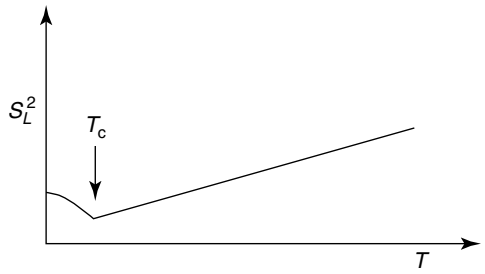

Figure 21. Local spin for spin fluctuation weak FM and AFM (Shiga, 1988).

$\omega_s(T_c) = -(2/5)(D_0/B)[M(0)]^2$, which means that the *atom volume expands* when it acquires a magnetic moment, an interesting result (we assume that the MEL constant is for $\mathbf{k} = 0$, due to the small electron kinetic energy involved). A renormalization of the SFs, long and complicated, transforms equation (32) in an interpolated expression useful for experimental comparison and valid for $T < T_c$, obtaining

$$\omega_s(T) = -\left(\frac{2}{5}\right)\left(\frac{D_0}{B}\right)\left\{[M(0)]^2 - [M(T)]^2\right\},$$

$$\omega_{mel}(T) - \omega_{mel}(T_c) = \left(\frac{3D_0}{5Bg}\right)\frac{1}{\chi(T)} \quad (T > T_c) \qquad (33)$$

and since $1/\chi(T)$ increases with T at PM regime, VMS increases. In Figure 22 is shown the volume TH.E. for the SF Laves-phase series $Y(Mn_{1-x}Ni_x)_2$, where we notice the first-order MV jump, and how small Ni addition suppress the WFM phase, due to the strong SF suppression of μ_{Mn}.

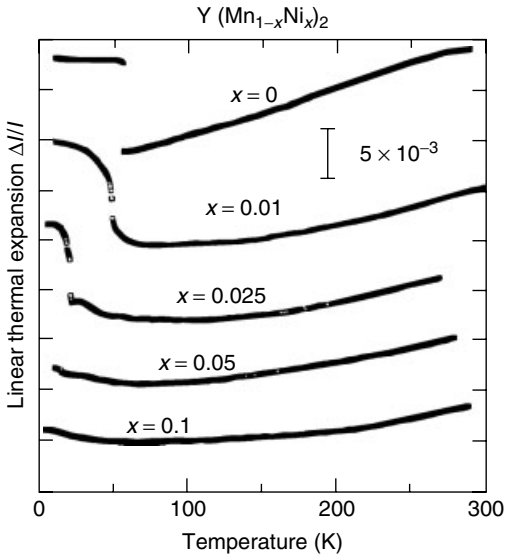

Figure 22. Thermal expansion of cubic $Y(Mn_{1-x}Ni_x)_2$ intermetallics (Ibarra, Garcıa-Olza and del Moral, 1992).

This theory also explains well the MS mentioned in the WFMs, as we will see in the subsequent text.

3.4 Itinerant weak FM magnetostriction

Several theories have been put forward for explaining MS in WFMs such as the archetypal $ZrZn_2$, Sc_3In, MnSi, Ni_3Al, the alloys Fe_xNi_{1-x}, Ni_xAl_{1-x}, and $TiBe_{2-x}Cu_x$, the transition metal (TM)-rich intermetallics, Y_nTM_m(TM = Fe, Ni) and many other alloys. Many of them show the *invar effect*, consisting in the very weak temperature dependence of MV, ω_s below T_c. Others show the *elinvar effect* or constancy also of B bulk modulus below T_c (and other ECs). Of those theories we will consider the Stoner–Wohlfarth–Edwards (SWE) one (Edwards and Wohlfarth, 1968; Mathon and Wohlfarth, 1968) and the SFs one (Moriya, 1985), quite similar to the preceding SF theory; the Shiga's model (Shiga, 1981) based on local spin-polarized bands (of rather clear physical picture) and the field theoretic one (Kakehashi–Liberman–Pettifor, more complex, (Kakehashi, 1981)) may be found elsewhere (del Moral, 2007). In SWE model the free energy, $F(M, \omega)$ adopts a L–G expansion in M, and if the material deforms (either spontaneously or forced by H), the coefficient $A(\omega) = A(\omega_0) - 2\overline{D}^{\alpha}(\omega - \omega_0)$, and therefore,

$$F = F_{00} + \left(\frac{1}{2}\right) AM^2 + \left(\frac{1}{4}\right) BM^4 - HM + \left(\frac{1}{2\kappa}\right) \omega^2 - \overline{D}^{\alpha}\left(M^2 - M_0^2\right)\omega + p\omega \qquad (34)$$

where $F_{00} = F(0, 0)$, $\kappa = 1/B$ is the compressibility, $M = M(T, H)$, $M_0 = M(T, 0)$ (spontaneous magnetization for $T < T_c$), and therefore $\overline{D}^{\alpha}$ is the *MV constant* (p is the applied pressure). Minimizations $\partial F/\partial M = \partial F/\partial \omega = 0$, in particular yield,

$$\omega(H, T) = \kappa \overline{D}^{\alpha}(M^2(H, T) - M_0^2) - \kappa p \qquad (35)$$

where the first term is the *MV* effect. Therefore for $H = 0$, a *spontaneous MV* $\omega_s = \kappa \overline{D}^{\alpha}(M(T, 0)^2 - M(0, 0)^2)$ appears below T_c, and a minimum at T_c (see such a behavior in Figure 23). This appears as an anomalous TH.E. in WFMs, superposed to the lattice one. $\overline{D}^{\alpha}$ is determined from $A(T_c) = 0$ in a second-order transition, that yields $\partial T_c/\partial \omega = -2\overline{D}^{\alpha}\chi_0 T_c$, where $\chi_0 = \left[\partial M(H, 0)/\partial H\right]$ is the 0 K paraprocess (high field) susceptibility at FM regime. It can be also shown that $\overline{D}^{\alpha}_{FM} = -(1/4\chi_0^2)(\partial \chi/\partial \omega) = (1/2)\overline{D}^{\alpha}_{PM}$. Also the forced MS becomes $(\partial \omega/\partial H)_{T\to 0} = 2\kappa \overline{D}^{\alpha} M \chi_0$. The calculation of $\overline{D}^{\alpha}$ is paramount in this theory, and many-body interactions influence it, through the U enhancement of χ_0, yielding at FM regime and 0 K,

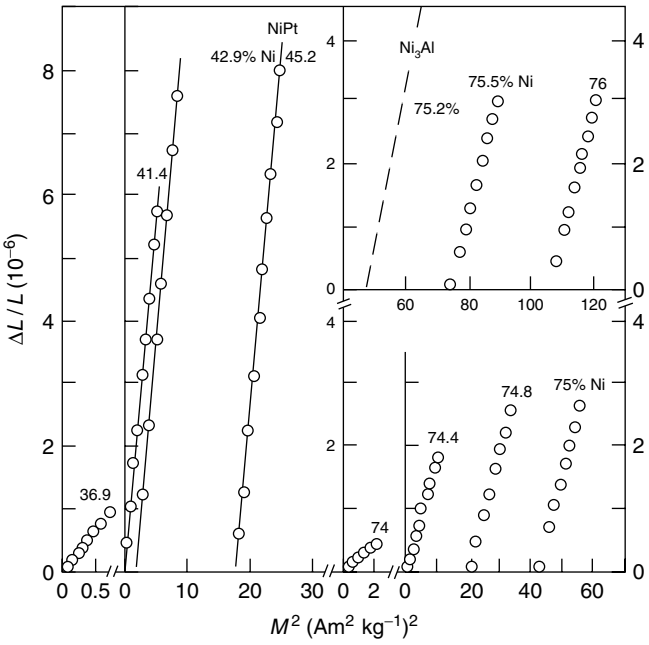

Figure 23. Linear TH.E. Vs M^2 for several weak FMS; see text (Brommer and Franse, 1990).

$$\overline{D}^{\alpha} = \left(\frac{1}{4ND(E_F)\mu_B^2}\right)\left(\frac{\partial \ln D(E_F)}{\partial \ln \omega} + \overline{U}\left(\frac{\partial \ln U}{\partial \omega}\right)\right) \qquad (36)$$

where $\overline{U} = UD(E_F)$ ($\cong 1$ is the Stoner criterion for FM). An important consequence from equation (36) is that $\overline{D}^{\alpha}$ is positive and decreases with increasing T.

In SWE theory we have single-particle excitations, without spin-fluctuations allowance. In fact a strong discrepancy of this theory with experiment is observed, as shown in Table 3. If SFs are taken into account, we obtain in similar way as in the preceding SF theory $\omega_s = \Sigma_{\mathbf{k}}(D_{\mathbf{k}}/B)\left[\langle M_{\mathbf{k}}^2\rangle - \langle M_{\mathbf{k}}^2\rangle_0\right]$, which can be transformed to $\omega_s = (D_0 M_0^2/B)(\eta - 1)$, where $\eta = \langle M_{loc}^2\rangle/M_0^2$, where M_{loc} and M_0 are the local and uniform magnetizations respectively. If we now compare with SWE theory where for $T < T_c$, $\eta_{SW}(T) = (M_T/M_0)^2 = 1 - (T/T_c)^2$ (= 0, for $T > T_c$) and expand $1 - \eta(T) \approx [1 - \eta(T_c)]\,(1 - M(T)/M_0)$, we obtain that $\langle M_{loc}^2\rangle_{T_c} = (3/5)M_0^2$ and therefore the important relation $\omega_s^{SF}/\omega_s^{SWE} = 2/5$, in qualitative agreement with Table 3. Moreover, for $T > T_c$, $\omega_s^{SWE} = 0$, whereas in the SF theory $\omega_s(T) - \omega_s(T_c) = (3D_0/5\gamma)(1/\chi) > 0$ increases with temperature, as observed experimentally. When $\omega_{nm}(T) + \omega_s(T) = 0$, where ω_{nm} is the lattice TH.E., we have the *invar effect* for $T < T_c$ (see Figure 24 for the alloys $Fe_{65}(Ni_{1-x}Mn_x)_{35}$).

Table 3. Experimental values for ω_{exp} thermal expansion relative to ω_{SWE} and other related magnitudes. (From Moriya and Usami, 1980.)

	T_c(K)	M_0 (emu g^{-1})	D_0/B(emu g^{-1})$^{-2}$	$\omega_{exp}/\omega_{SWE}$
Sc_3In	7.5	≈ 3	$1- \approx 1.6 \times 10^{-6}$	$0.3- \approx 0.5$
$ZrZn_2$	18	3	5	≈ 0.6
$Ni_xAl_{1-x}(x = 0.755- \approx 0.76)$	$59- \approx 72$	$8.7- \approx 10$	0.7	≈ 0.3
$Ni_xPt_{1-x}(x = 0.452)$	55	4.2	3.3	≈ 0.2

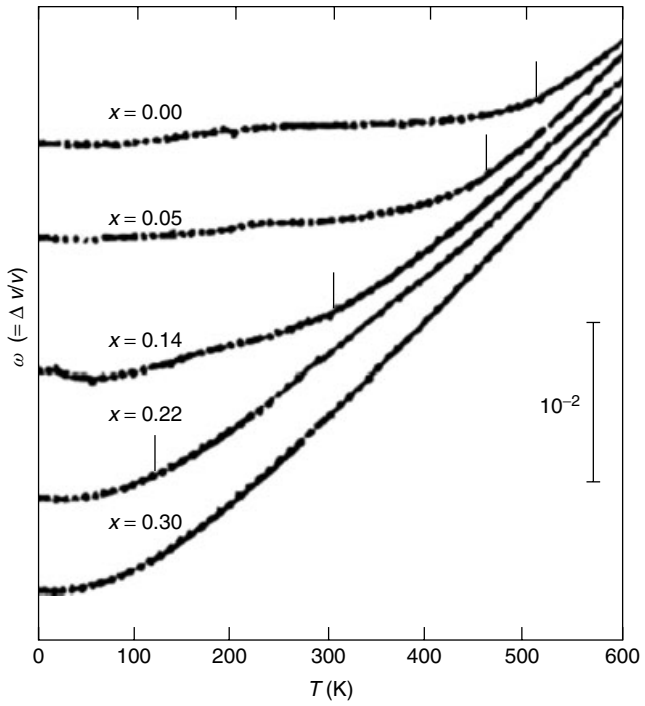

Figure 24. Spontaneous ω_s (T) and invar effect in $Fe_{65}(Ni_{1-x}Mn_x)_{35}$; bar signals T_c (Hayase, Shiga and Nakamura, 1971).

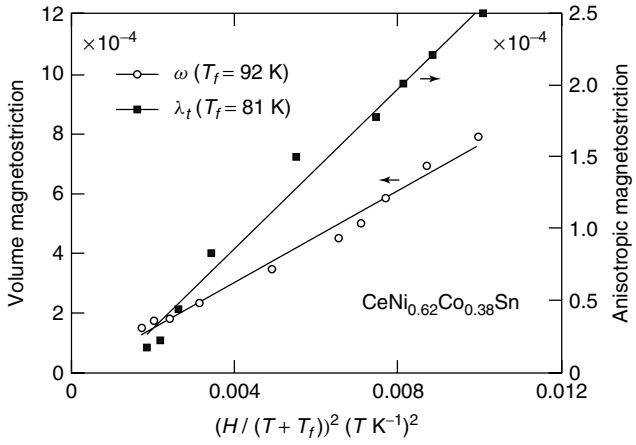

Figure 25. See text for meaning (Adroja *et al.*, 1995).

3.5 Strongly correlated systems (SCS)-MS

Several models have been proposed to explain MS in strongly correlated systems (SCS), where its main characteristic is the instability of the ion f shell, giving rise to Kondo (K), fluctuating valence (FV) and heavy fermion (HF) behaviors (see also **Heavy Fermions: Electrons at the Edge of Magnetism, Volume 1** and **The Kondo Effect, Volume 1**). Of those models we will consider the *interconfigurational* (ICF) one (Zieglowski, Häfner and Wohlleben, 1986), consisting in assuming that $4f^n$-shell valence, ν fluctuates between $4f^n \leftrightarrow 4f^{n\pm1}$ (−:Ce,Eu; +: Yb), so that with macroscopic probes the valence appears as intermediate. One of characteristics of susceptibility and MS in FV materials is that they show a broad maximum around the fluctuation temperature, T_f, and that the H-dependence is quadratic. In the case of ω, we assume the Vegard's ansatz $\Delta V/V = V^{-1}(\partial V/\partial \nu)\Delta\nu(H)$, where $\Delta\nu(H)$ is consequence of the E_F reduction for the higher moment configuration. Assuming the two configurations (separated by energy E_{exc}) with probabilities ε and $(1-\varepsilon)$, and their CEF manifold levels, it is easy to obtain the partition function, $Z_i(H) = \sum_k \exp\left[-E_{ik}(0)/k_B T^*\right]\left[\exp(-\mu_{ik}H/k_B T^*) + \exp(\mu_{ik}H/k_B T^*)\right]$, where $T^* = T + T_f$, E_{ik} are the CEF levels for i-configuration, and μ_{ik} the corresponding moments. From an expansion of $Z_i(H/T^*)$ and preceding considerations the VMS is given by

$$\frac{\Delta V}{V} \equiv \omega = \left[\pm\left(\frac{\nu_0(1-\nu_0)}{2}\right)\left(\frac{(V_{n+1}-V_n)}{V}\right)\left(\frac{\mu_z^2}{k_B^2}\right)\right] \times \frac{H^2}{(T+T_f)^2} \tag{37}$$

This kind of dependence is well manifested in Figure 25 for ω and also λ_t of $Ce(Ni_{1-x}Co_x)Sn$ intermetallics and it is also well followed at high enough field by many SCS (Häfner, 1985).

3.6 *Ab initio* MS calculation methods

First-principles calculations based on the determination of the electronic structure for the MS distorted solid provide a very accurate MEL energy obtention, and have been used

for MS calculation in TMs (Wu and Freeman, 1999; Wu, Gravilenko and Freeman, 2001; Komelj and Fähnle, 2000) and also in REMs and RE intermetallics (Buck and Fähnle 1998, 1999; Wu, 1999). They are based on the powerful nonrelativistic (i.e., without spin consideration) *density-functional approximation* (*DFA*) (Hohenberg and Kohn 1964; Kohn and Sham, 1965) and the relativistic *spin-density* (*functional*) *approximation* (*SDA*) (von Barth and Hedin, 1972), together with some added practical modifications, the *local-density approximation* (*LDA*), *local spin-density approximation* (*LSDA*), the *generalized gradient approximation* (*GGA*), the *full potential linearized augmented plane wave* (*FLAPW*) (Weinert, Wimmer and Freeman, 1982), *force theorem* (*FT*) and *state tracking* (*ST*) methods, and the very practical *torque method* (*TQ*), required to calculate MCA and MEL energies as tiny as respectively $\approx 0.1-1$ and $\approx 0.01\,\mu$eV/atom respectively in TM and alloys. Those theories take resort to **k** space, in order to introduce **k** points of low symmetry, which are also magnetostrictive, and because 'Fermi energy filling' of levels, $\varepsilon(\mathbf{k})$ can introduce some **k** states below E_F in detriment of others contributing more to MEL energy (and MCA). However, it is tried to reduce **k** points to a minimum ($\leq 10^3$), and therefore these methods are more accurate for calculating MS in standing monolayers, overlayers, and very thin multilayers (MLs) (see Section 6). Here, we can only very briefly treat all those approximations (see **Theory of Magnetocrystalline Anisotropy and Magnetoelasticity in Transition-metal Systems, Volume 1** for further details): DFA, and its local (**r** dependent) LDA, consist in writing electrons nonrelativistic Hamiltonian, H in second quantized field operator form and then $H = T + V_{CEF} + E_{EX} + U$ terms as integral *functionals*, $F\,[n(\mathbf{r})]$ of the electron density, $n(\mathbf{r})$, the system becoming an inhomogeneous *quantum liquid* of single-particles (e.g., kinetic energy $T \equiv (1/2)\int \nabla\psi^+(\mathbf{r})\nabla\psi(\mathbf{r})d\mathbf{r}$ in terms of *field* operators, ψ^+, ψ, afterwards transformed to $T[n]$). When H is the relativistic Dirac Hamiltonian, we end up with the FLAPW method, where the functionals are $F\,[n(\mathbf{r}), \mathbf{m}(\mathbf{r})]$, with $\mathbf{m}(\mathbf{r})$ being the local magnetization. In augmented plane wave APW + LSDA + FT *brute force* method, introduction of H_{SO} and H_{CEF} allows calculation of MCA and CEF-MEL energies in terms of the *total* electronic energy ($\approx 1 - 10$ eV) difference when $\mathbf{M}_s$ is rotated from ED (1) to another hard one (2), that is,

$$\Delta E_{MEL} = \sum_{i,\boldsymbol{k}}^{occ} \varepsilon_i^0(\hat{\mathbf{m}}_1, \mathbf{k}) - \sum_{i,\boldsymbol{k}}^{occ} \varepsilon_i^0(\hat{\mathbf{m}}_2, \mathbf{k}) \qquad (38)$$

or *FT* (Daalderop, Kelly and Schuurmans, 1990) (occ. means states occupied up to E_F; i is the band index; superindex 0 means without SO coupling; $\hat{\mathbf{m}}_i$, unitary vector). One must insure that for both directions large direct-Coulomb and intra-atomic-exchange energies are the same, because of the *very weak* MEL energy compared with the band one, therefore requiring the use of a large number of **k** points: $\approx 10^6$ for bulk 3d metals and $\approx 10^4$ for monolayers and overlayers. Results with this method for Ni are only qualitative, $\lambda_{100} = -245$ and $\lambda_{111} = -107$ (in 10^{-6}), about three times the values at 0 K, although results improve for fcc Co.

Calculation of MS much improves with the *tour de force* FLAPW + LSAD + GGA + ST + TQ method, which avoids the use of total energy and FT (Wu and Freeman, 1999). GGA briefly consists in expanding $E_{EX}\,[n]$ as shown in $E_{EX}[n] = \int n(\mathbf{r})\varepsilon_{xc}(n(\mathbf{r}))d\mathbf{r}$, where ε_{xc} is the exchange plus correlation, energy per electron, keeping only $n(\mathbf{r})$ and $\nabla n(\mathbf{r})$, but indeed separating out up and down spins (Perdew *et al*., 1992). But the core of the method is: (i) the mentioned ST, by which the levels filling is done keeping charge and spin densities practically constant, energy difference of equation (38) reflecting certainly the MEL (or MCA) energy; the name is because the initially FLAPW calculated basis state $|\psi_i\rangle$ can be 'tracked' when forming new basis states due to the perturbation introduced by H_{SO} and H_{mel} ('Fermi **k** filling'). The practical consequence is the *large reduction* in the number of **k** states needed ($\approx 0.5 - 1 \times 10^3$) for good energy convergence. (ii) Since MEL energy is the strain dependence of MCA energy, TQ method comes into its calculation, in terms of MCA torque $T(\theta)$. This is calculated using *Feynman–Hellman* theorem, that is, $T(\theta) = \sum_{occ}\langle\psi^{so}_{i,\boldsymbol{k}}\,|\partial H_{so}/\partial\theta|\,\psi^{so}_{i,\boldsymbol{k}}\rangle$, which again avoids calculation of total energy, since SO interaction is introduced from the beginning of the calculation. Those methods have been developed for calculation of MS and MEL constants in 3d metals, RE metals, and RE intermetallics, summarizing the results in Table 4, and comparing with experiment, from where we can realize the degrees of agreement attained, still not quite the experimental values (see **Theory of Magnetocrystalline Anisotropy and Magnetoelasticity in Transition-metal Systems, Volume 1** for further details).

4 MAGNETOELASTICITY DYNAMICS: MAGNETOACOUSTIC (MA) WAVES AND BIREFRINGENCE; ELASTIC CONSTANTS MAGNETOELASTIC CONTRIBUTION; SIMON EFFECT; ROTATIONAL INVARIANCE THEORY; FARADAY EFFECT

Another as powerful a way as MS for studying the MEL coupling and magnetoelasticity is through the ECs or elastic moduli (EM) (polycrystals), because the EWs in magnets are modified by MEL energy (*MA waves*), giving rise to a variety

Table 4. MS (in 10^{-6}, except when quoted otherwise) and MEL constants for 3d metals, RE metals, and RE intermetallics. The main step(s) in the calculation method are indicated (Wu and Freeman, 1999; Wu *et al*., 2001; Komelj and Fähnle, 2000; Buck and Fähnle, 1998, 1999; Wu 1999).

Material	λ_{100} (LDA)	λ_{100} (GGA)	λ_{100} (EXP)	$\overline{M}_1$ (FLAPW + LDA + ST) (meV/au)	λ_{111}(APW + LSDA)/ EXP	$\overline{M}^{\gamma,2}$ (FLAPW+ LSDA/GG)/ EXP (MJ m^{-3})	$\lambda_2^{\alpha,2}$(APW+ LSDA)/EXP (in 10^{-2})	$\lambda^{\gamma,2}$ (ibid.)/ EXP (in 10^{-2})
Bcc Fe	52	29	21					
Fcc Co	92	56	79					
Fcc Ni	−63	−56	−49					
Co/Cu(111)				−0.37				
Co/Pd(001)				+1.87				
Co/Pd(111)				<±0.1				
Bcc-Fe film	4.9([a])	11.8	2.4			(−10.09, /−2.42)/−3.1		
Tb							1.71/1.5	1.00/0.95
Er							−0.41/−0.59	−0.47/−0.5
$GdFe_2$[b]	44/39							
$GdCo_2$[b]	−327/−1200							
$TbFe_2$	-0.14×10^3				$8.3/4.4 \times 10^3$			

[a](LSDA).
[b]FLAPW + LSDA + ST + TQ.

of interesting effects, all of them of the kind of *inverse MEL effects* (see del Moral, 2007). Well known are the ΔE and Δc_{ij} effects related to the DW magnetization process. Let us consider the Δc_{ij}*-effect* in cubic crystals (de Lacheisserie, Morin and Rouchy, 1978), at the end of the DW magnetization process (usually at weak H), before the intradomain $\mathbf{M}_s$ rotation toward applied $\mathbf{H}$. The MCA and MEL energies add to

$$F_m = \kappa_4\left(\alpha_1^4+\alpha_2^4+\alpha_3^4-\frac{3}{5}\right)+\overline{M}^{\gamma,2}\Big[\varepsilon_{xx}\left(\alpha_1^2-\frac{1}{3}\right) + \varepsilon_{yy}\left(\alpha_2^2-\frac{1}{3}\right)+\varepsilon_{zz}\left(\alpha_3^2-\frac{1}{3}\right)\Big] \tag{39}$$

where $\overline{M}^{\gamma,2}$ is the tetragonal MEL constant, and minimizing against $\boldsymbol{\alpha}$, if $K_1 = -2\kappa_4 + c^{\gamma}(\lambda^{\gamma,2})^2 < 0$ ($\langle 111\rangle$ EDs), the $\mathbf{M}_s$ direction under strain becomes $\alpha_i^2 = 1/3 - (\overline{M}^{\gamma,2}/2\kappa_4)(2\varepsilon_{ii}-\varepsilon_{jj}-\varepsilon_{kk})/3$, $i\neq j\neq k$ and bringing them to F_m, we obtain the *MEL contribution* to the effective elastic energy, $\Delta F_{\rm el} = -\big[(\overline{M}^{\gamma,2})^2/6\kappa_4\big]\big\{(\varepsilon_{xx}^2+\varepsilon_{yy}^2+\varepsilon_{zz}^2) - (\varepsilon_{yy}\varepsilon_{zz}+\varepsilon_{zz}\varepsilon_{xx}+\varepsilon_{xx}\varepsilon_{yy})\big\}$. Therefore the EC variations are ($\Delta c_{ij} = c_{ij}^M - c_{ij}^0$, with c_{ij}^0 the without interactions (bare) EC),

$$\Delta c_{11} = -\frac{(\overline{M}^{\gamma,2})^2}{3\kappa_4}, \quad \Delta c_{12} = \frac{(\overline{M}^{\gamma,2})^2}{6\kappa_4} \tag{40}$$

and therefore $c^{\gamma} = c_{11} - c_{12}$ *decreases* (the material softens for $\mathbf{H}\perp\mathbf{u}$, Figure 27) under magnetization, typical of the ΔE effect for low applied fields (DW displacements) in soft magnetic alloys such as Fe_xNi_{1-x} (Carr, 1966).

4.1 Simon effect

The Simon effect (Simon, 1958) is the modification of ECs during the intradomain $\mathbf{M}_s$ rotation process, manifested in the different EW velocity for $\mathbf{H}\|\boldsymbol{\varepsilon}$ and $\mathbf{H}\perp\boldsymbol{\varepsilon}$, where $\boldsymbol{\varepsilon}$ is the shear EW strain (in Voigt's notation), as seen in

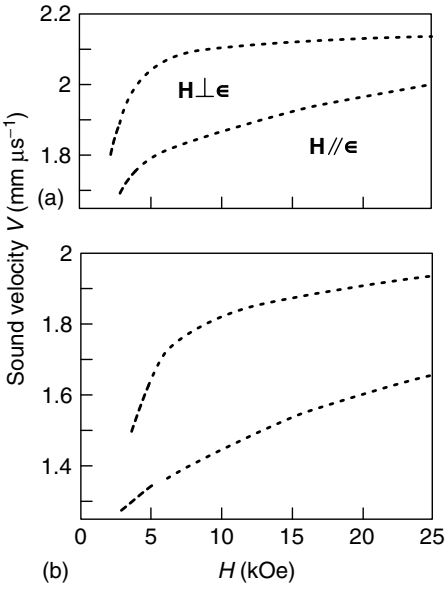

Figure 26. Magnetoacoustic birefringence in $Tb_{0.3}Dy_{0.7}Fe_2$ (a) and $Sm_{0.88}Dy_{0.12}Fe_2$ (b). The saturation sound velocity is unmodified when magnetic field $\mathbf{H}\perp\boldsymbol{\in}$ (polarization), but it is strongly reduced when $\mathbf{H}\|\boldsymbol{\in}$ (Cullen, 1978).

Figure 26 for the 'giant' (≈1%) AMS $Tb_{0.3}Dy_{0.7}Fe_2$ (Terfenol) and $Sm_{0.7}Ho_{0.3}Fe_2$ polycrystalline materials. We will first consider our FM material to be isotropic (polycrystalline or amorphous), where a shear EW ($\boldsymbol{\varepsilon} \perp \mathbf{k}$) is propagating and where $\mathbf{H}$ is set for the preceding two geometries. It is observed that when the angle $\theta = \widehat{\boldsymbol{\varepsilon}, \mathbf{H}}$ is 0 or $\pi/2$ a single wave propagates but for intermediate θ two waves with different velocities, v_T are observed, the faster ($\mathbf{H} \perp \boldsymbol{\varepsilon}$) with small $\mathbf{H}$ dispersion (except at the beginning due to the DW ΔG *effect*; G is the shear modulus), but with strong dependence for the slower ($\mathbf{H} \| \boldsymbol{\varepsilon}$), this effect being known as *MA birefringence* (Figure 26). We write $F_{\text{mel}} = \overline{\text{M}}^{\text{is}} \Sigma_{ij} \varepsilon_{ij} (m_i m_j - (1/3)\delta_{ij})$, where $\overline{\text{M}}^{\text{is}}$ is the isotropic MEL constant and $\mathbf{m} = \mathbf{M}/M_s$. If we set $\mathbf{M} \| \mathbf{H} \| \text{OZ}$, $\mathbf{k} \| \text{OY}$ and the EW displacement $\mathbf{u} \perp \mathbf{k}$, the only nonzero strains are ε_{xz} and ε_{xy}, and since $m_z \cong 1$, the other $\mathbf{m}$ components are of the same order as the strains and therefore only ε_{xz} couples to $\mathbf{M}$, so we have $F_{\text{mel}} = \overline{\text{M}}^{\text{is}} m_z m_x \varepsilon_{xz}$. Now $m_x = \chi_\perp H_x^{\text{mel}}/M_s$, where $\mathbf{H}^{\text{mel}}$ is the *MEL anisotropy field* (defined as $M_s H_x^{\text{mel}} = -\partial F_{\text{mel}}/\partial m_x = -\overline{\text{M}}^{\text{is}} m_z \varepsilon_{xz}$) and therefore we have for the total energy, $F_t = (1/2)G_0(\varepsilon_{xz}^2 + \varepsilon_{xy}^2) - (\overline{\text{M}}^{\text{is}}/M_s)^2 m_z^2 \chi_\perp \varepsilon_{xz}^2$, where G_0 is the zero-field (bare) shear modulus. Therefore the EM for the two strains ε_{xz} and ε_{xy} are different,

$$G = G_0 - (\overline{\text{M}}^{\text{is}})^2 (\chi_\perp M_s^2) m_z^2, \quad G = G_0 \tag{41}$$

respectively, a result that embodies the *Simon effect* of EM, giving rise to the waves with different velocities $v_T = \sqrt{G/\rho}$, the slower being the MA wave. Therefore $\mathbf{H}$ application breaks the isotropy of G in the isotropic medium. This result also applies to cubic crystals within the elastically isotropic {100} planes, since $\overline{\text{M}}^{\text{is}} = 2\overline{\text{M}}_2$.

Extension of the preceding theory to crystals complicates calculations, but not the physics. Then if $\mathbf{M}$ rotates under $\mathbf{H}$ application against MCA field $\mathbf{H}_K$, we have the experimental picture of Figure 27 for a Terfenol crystal, for $c^\gamma = (1/2)(c_{11} - c_{12})(\mathbf{u} \| [1\bar{1}0])$ and $c^\varepsilon = c_{44}(\mathbf{u} \| [001])$, with enormous softening of c_{44} under $\mathbf{H}$ rotation from $\perp \mathbf{u}$ to $\| \mathbf{u}$ within the elastically anisotropic [110] plane. The effect is larger for c^ε than for c^γ because $\overline{\text{M}}_2 >> \overline{\text{M}}_1$ and according to equation (8) $\overline{\text{M}}_2$ couples shear strains ε_{ij} to $\mathbf{M}$ (c_{44} mode), meanwhile $\overline{\text{M}}_1$ does it for linear ε_{ii} strains (c^γ mode). The case of c_{44} mode is the more difficult mathematically (del Moral, 2007) and therefore we will consider a shear ε_{xy}, consisting in a wave with $\mathbf{u} \| [100]$ (OX) and propagation $\mathbf{k} \| [010]$ (OY) and with $\mathbf{H} \| \text{OX}$, so that $\mathbf{M}_s$ is near to OX ($\alpha_x \cong 1$). Now we will consider first the strains as dependent variables and minimize full energy $F = F_K + F_Z + F_{\text{mel}} + F_{\text{el}}$ against ε_{ij}, obtaining the equilibrium strains, $\varepsilon_{ij}^{\text{eq}}$ (or MS) in terms of fixed $\boldsymbol{\alpha}$. In this case the free energy becomes

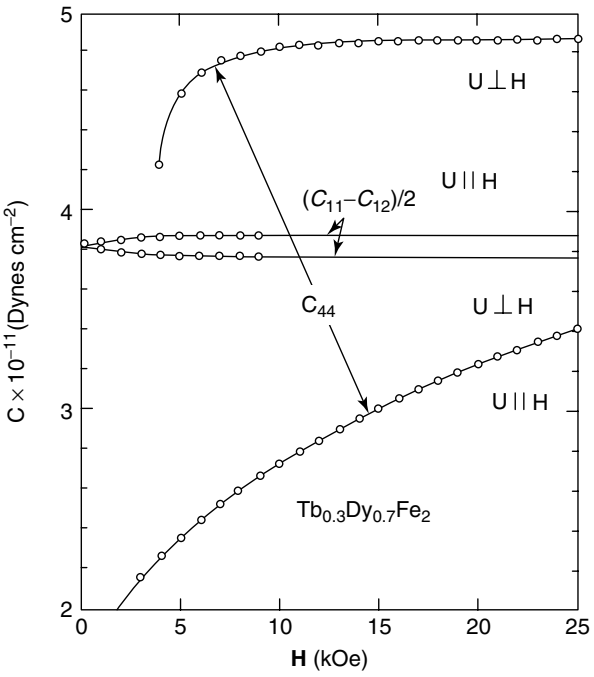

Figure 27. Magnetoacoustic birefringence in Terfenol single crystal for symmetry ECs $(1/2)(c_{11} - c_{12})$ and c_{44}, similarly to Figure 26 ($\mathbf{U} \equiv \boldsymbol{\epsilon}$) (Cullen, Rinaldi and Blessing, 1978).

$$\begin{aligned} F = {} & K_1(\alpha_x^2\alpha_y^2 + \alpha_y^2\alpha_z^2 + \alpha_z^2\alpha_x^2) - HM_s\alpha_x \\ & + \overline{\text{M}}_2\alpha_x\alpha_y \in_{xy} + \left(\frac{1}{2}\right) c_{44}^0 \in_{xy}^2 + \overline{\text{M}}_2(\alpha_y\alpha_z \in_{yz}^{\text{eq}} \\ & + \alpha_z\alpha_x \in_{zx}^{\text{eq}}) + \left(\frac{1}{2}\right) c_{44}^0((\in_{yz}^{\text{eq}})^2 + (\in_{zx}^{\text{eq}})^2) + \cdots \end{aligned} \tag{42}$$

Conversely if we set ε_{ij} as independent (externally *impressed* by a transducer) we find the equilibrium $\boldsymbol{\alpha}$, by making $(\partial F/\partial \alpha_k)_\varepsilon = 0$. From the equivalent zero anisotropy torque $\Gamma_z = M_y \partial F/\partial M_x - M_x \partial F/\partial M_y$ we obtain $\alpha_x^{\text{eq}}\alpha_y^{\text{eq}} = (-\overline{M}_2/(2K_1 + MH) \in_{xy}$, and from $\Gamma_y = 0$, $\alpha_z^{\text{eq}} = 0$. Using the constraint $\alpha_x^2 + \alpha_y^2 \cong 1$, we obtain $\alpha_x^{\text{eq}} \cong 1 - (1/2)(\alpha_y^{\text{eq}})^2 = 1 - (1/2)\left[\overline{\text{M}}_2^2/(2K_1 + MH)^2\right] \in_{xy}^2$, and substituting α^{eq} in equation (42) we obtain the equilibrium energy $F^{\text{eq}} = (1/2)(c_{44}^0 - \overline{\text{M}}_2^2/(2K_1 + MH)) \in_{xy}^2 - M_s H$. Therefore c_{44}^{eff} (the coefficient of $(1/2)\varepsilon_{xy}^2$) becomes (Clark, 1980),

$$c_{44}^{\text{eff}} = c_{44}^0 - \frac{\overline{\text{M}}_2^2}{(2K_1 + M_s H)} = c_{44}^0 - \frac{\overline{\text{M}}_2^2}{M_s(H + H_K)} \tag{43}$$

where $H_K = 2K_1/M_s$ is the [100] *anisotropy field* (in metallic materials and high-frequency ultrasound the skin effect eddy currents (within the surface [100] plane) produces a dipolar demagnetizing field, $H_D = 4\pi M_s$ which adds

to $H + H_K$). Therefore a decrease (*softening*) of c^{ε} is always expected under magnetization rotation when $\mathbf{H}\|\mathbf{u}$ with respect to the unmagnetized crystal, whereas for $\mathbf{H} \perp \mathbf{u}$, $c_{44}^{\text{eff}} \cong c_{44}^{0}$ (if DW process Δc_{44} is excluded). Also, when the effect is larger the stronger is the MS, as for example, in Terfenol where it is gigantic, of $\approx$100%. Moreover under H increase c_{44}^{eff} increases, approaching c_{44}^{0} for $H \gg H_K$, the opposite to the low field Δc_{ij} effect discussed in the preceding text. This is a way of distinguishing between the two magnetization processes, based on magnetoelasticity.

4.2 Magnetoacoustic Faraday effect

This effect consists in the polarization rotation of an ultrasound wave under **H** rotation in FM crystals, more accused in strongly magnetostrictive ones (Rinaldi and Cullen, 1978). For cubic crystals an initially polarized, $\mathbf{u}_T$ shear wave in the elastically anisotropic [110] planes splits in two waves with polarizations **u** along [100] and $[\bar{1}10]$ directions, which are the normal modes, $\mathbf{u}_I$ and $\mathbf{u}_{II}$ (Figure 28). Therefore the MEL coupling can not fully tilt $\mathbf{u}\,\|[001]$ parallel to $\mathbf{M}\|\mathbf{H}$, then the normal mode $\mathbf{u}_I$ forming an angle Φ with [001], which increases with the **H** rotation, the material becoming *magnetoacoustically active*. This angle is weak in weakly magnetostrictive materials, but it is large when MS is gigantic. We will now calculate Φ, and for that we set the EW (*Christoffel's*) (plane, $\mathbf{u} = \mathbf{u}_0 \exp i(\mathbf{k}\cdot\mathbf{r} - \omega t)$) and **M** (*Larmors's*) motion equations in the respective forms (ρ is the density),

$$-\rho\omega^2 \mathrm{u}_i = \Sigma_j \left(\frac{\partial}{\partial x_j}\right)\left(\frac{\partial F}{\partial \varepsilon_{ij}}\right) \tag{44}$$

$$\frac{\partial \mathbf{M}}{\partial t} = \gamma\left(\mathbf{M} \times \left(\frac{\partial F}{\partial \mathbf{M}}\right)\right) \tag{45}$$

which are coupled via the MEL coupling (*MA wave equations*). For $\mathbf{k}\|[110]$ and for sufficiently low frequencies such that $\dot{\mathbf{M}} \cong 0$, the coupled equations are,

$$\rho\omega^2 u_t = k^2 u_t \left(\frac{(c_{11} - c_{12})}{2} - \left(\frac{\overline{\mathrm{M}}_1^2 M_x^2}{M_s^3 H}\right)\right) - k^2 u_z \overline{\mathrm{M}}_1 \overline{\mathrm{M}}_2 \left(\frac{M_x M_z}{M_s^3 H}\right) \tag{46}$$

$$\rho\omega^2 u_z = k^2 u_z \left(c_{44} - \left(\frac{\overline{\mathrm{M}}_2^2 M_z^2}{M_s^3 H}\right)\right) - k^2 u_t \overline{\mathrm{M}}_1 \overline{\mathrm{M}}_2 \left(\frac{M_x M_z}{M_s^3 H}\right) \tag{47}$$

where $u_t \equiv u_x - u_y$ and $H = H_{\text{app}} + H_K + 4\pi M_s$. We notice that the equations coupling is *via* $\overline{M}_1\overline{M}_2$. Setting now $u_t = u_0 \sin\Phi$, $u_z = u_0 \cos\Phi$ and $M_z/M_s = \sin\theta$, we obtain from equations (46 and 47) a linear system of equations in $(\sin\Phi, \cos\Phi)$, whose secular determinant yields $(\omega/k)^2$, and therefore the phase velocities ($v = \omega/k$), $\rho v_{\pm}^2 = \frac{1}{2}(C' + C) \pm \left\{\left[\frac{1}{2}(C' - C)\right]^2 + B^2\right\}^{1/2}$, where C and C' are constants related to the problem parameters, depending on field as $1/H$, B being the coupling constant. We also obtain the polarization angles of rotation for the two normal modes,

$$\tan\Phi_{\pm} = -B\left\{\frac{1}{2}(C - C') \pm \left[\frac{1}{2}(C' - C)^2 + B^2\right]^{1/2}\right\}^{-1} \tag{48}$$

which embodies the *MA Faraday effect*. $B \equiv \overline{\mathrm{M}}_1\overline{\mathrm{M}}_2(\sin 2\theta / 2HM_s)$, where θ is the angle (**M**, [001]), introducing a NL dependence. In Figure 29 is shown the calculated Φ_- versus θ for Terfenol. Another prediction is the interference between the two normal modes, when projected into the reception transducer axis, $\hat{\mathbf{u}}_R$, the maximum occurring for an angle $\theta_R(H)$, which decreases with H, as observed.

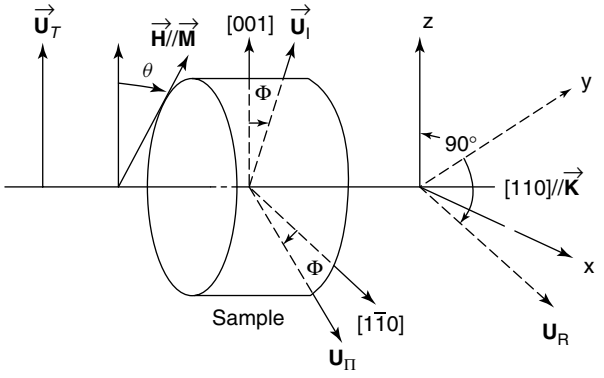

Figure 28. Magnetoacoustic Faraday rotation geometry (Rinaldi and Cullen, 1978).

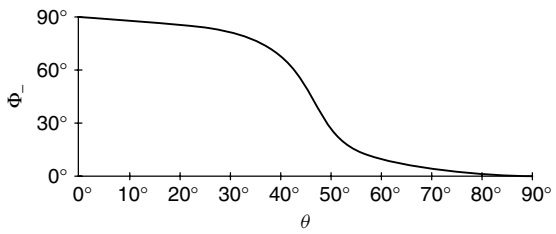

Figure 29. Magnetoacoustic Faraday rotation angle, Φ_- versus **H** rotation angle, θ (Rinaldi and Cullen, 1978).

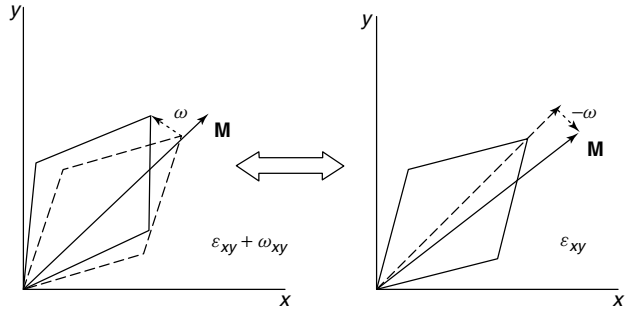

Figure 30. Rotational invariance principle of magnetoelasticity (del Moral, 2007).

4.3 General magnetoelasticity dynamics; rotational invariance

A general theory of magnetoelasticity dynamics has been developed, which includes as a central part the quantum-mechanical *rotational invariance* principle (Brown, 1965; Melcher, 1972; Dohm and Fulde, 1975; Wang and Lüthi, 1977), based on the invariance of angular momentum under spatial rotation. In the most general form the theorem is expressed in terms of *finite* strains (or Lagrangian, η_{ij} if the strains are small) and states that the MEL Hamiltonian for a magnetized crystal under pure strains, $\overleftrightarrow{\mathcal{E}}$ and rotational ones, $\overleftrightarrow{\mathcal{R}}$ is the same if the crystal is only $\overleftrightarrow{\mathcal{E}}$ strained and the AM **J** and applied **H** are rotated back by $\mathcal{R}^{-1}(=\mathcal{R}^t)$ ($\overleftrightarrow{\mathcal{E}}$ is rotationally invariant) (see Figure 30). Therefore we write

$$\hat{H}\left(J_i, H_i, \frac{\partial x_i}{\partial X_j}\right) = H(J_k^*, H_k^*, \mathcal{E}_{kl}) \tag{49}$$

where

$$\begin{aligned} J_k^* &= J_i \mathcal{R}_{ik}, \quad H_k^* = H_i \mathcal{R}_{ik}, \\ \mathcal{E}_{kl} &= \left(\frac{1}{2}\right)\left[\left(\frac{\partial x_i}{\partial X_k}\right)\left(\frac{\partial x_i}{\partial X_l}\right) - \delta_{kl}\right] \end{aligned} \tag{50}$$

where $\partial x_i/\partial X_j$ in $\hat{H}$ mean pure strains. If the RSs, $\boldsymbol{\omega}(\omega_{yz}, \omega_{zx}, \omega_{xy})$ are small this theorem adopts this other more manageable form, which also allows the derivation of the rotational part of Hamiltonian, $H_{\rm rot}$ and where $\hat{H}_{\rm Spin} = \hat{H}_{\rm CEF} + \hat{H}_{\rm strain}$,

$$\begin{aligned} &\exp[-i\hbar^{-1}\boldsymbol{\omega}\cdot\mathbf{J}]\hat{H}_{\rm Spin}(\mathbf{J})\exp[i\hbar^{-1}\boldsymbol{\omega}\cdot\mathbf{J}] \\ &\quad = H_{\rm CEF}(\mathbf{J}) + H_{\rm strain}(\mathbf{J}) + H_{\rm rotation}(\mathbf{J}) \end{aligned} \tag{51}$$

There are some dramatic consequences of this theorem, the most spectacular one is the inequivalence of the EWs shown in Figure 2 when the crystal is magnetized for example,

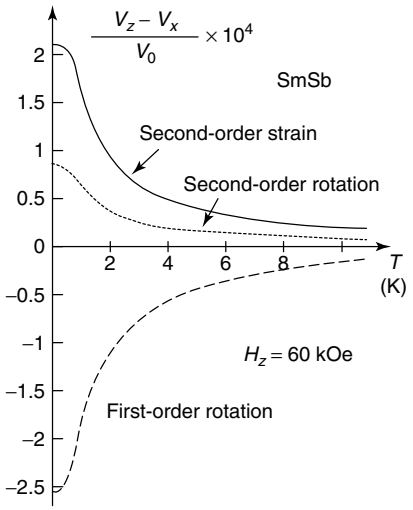

Figure 31. Magnetoacoustic birefringence contributions (Dohm, 1976).

along OZ‖[001] in a cubic crystal, which constitutes in fact the birefringence at *PM regime* (however, it remains at FM regime if $H_{\rm EX}$ is expressed in the MFA). This result has been applied to hcp RE metals, cubic RE intermetallics and to the archetypal RE vanadates ($REVO_4$) (see del Moral, 2007). Let us study in detail the case of cubic (CsCl structure) pnictides RESb, which show a rich variety of magnetic and QP structures, and magnetostructural transitions. From transformation of equation (51) we immediately obtain, after $e^{\pm i\omega_{zx}J_y}$ expansion, $H_{\rm rotation}(c_{44}) = -20B_4\omega_{xz}\Lambda_{xz} + 40B_4\omega_{xz}^2\lambda_{xz} + 2G_3\varepsilon_{xz}\omega_{xz}(J_x^2 - J_z^2)$, where $\Lambda_{zx} = i[H_{\rm CEF}, J_y]$, $\lambda_{zx} = (i/2)[\Lambda_{zx}, J_y]$, plus a 2nd-order term in the strains $H_{\rm str}^{(2)}(c_{44})$ if finite pure strains $\mathcal{E}_{xx}, \mathcal{E}_{zz}$ are considered (see Figure 31). Calculating the full H energy levels, the free energy and using the EC expression variations $\Delta c_{ij}(T, \mathbf{H}) = (\partial^2 F/\partial u_{ij}^2)_T$ we obtain velocity shifts, $\Delta v_{xz}/v_0$ and $\Delta v_{zx}/v_0$, different for the two modes (k_z, u_x) and (k_x, u_z), and respectively

$$\begin{aligned} \Delta v_{\substack{zx \\ xz}}/v_0 = \left(\frac{N}{2\rho v_0^2}\right)\Big\{\left(\frac{1}{4}\right)\chi\{G_3(J_xJ_z + J_zJ_x) \\ \mp 20B_4\Lambda_{xz}\} + 20B_4\langle\lambda_{xz}\rangle + G_3\langle J_x^2 - J_z^2\rangle\Big\} \end{aligned} \tag{52}$$

where $G_3 \equiv -M^{\varepsilon,2}/2$. $\chi\{\ldots\}$ is the *dynamical strain* susceptibility, appearing also in the PS calculation, and calculated using the thermodynamic Green function technique (del Moral, 2007). This susceptibility is defined as $\chi_2^{\varepsilon} = (1/M^{\varepsilon,2})(\partial\langle\tilde{O}_2^0\rangle_{\rm T}/\partial\varepsilon_{xz})$, taking into account the strain dependence of the RE^{3+} QP moment, $\langle\tilde{O}_2^0\rangle$, and for a doublet GS (of splitting Δ), $\chi\{\hat{O}_2^1, \omega\} = -(160/3)p(T)(\Delta/(\Delta^2 - \omega^2))$,

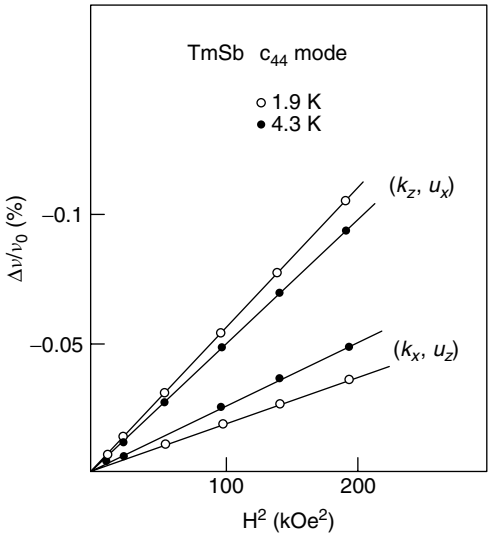

Figure 32. RI breaking of cubic degeneration in TmSb (Wang and Lüthi, 1977).

where $p(T)$ is the high level atom population. In Figure 31 the calculated thermal variations of the different contributions to the velocity birefringence in cubic SmSb (1^{st}-order strain contribution does not appear in birefringence) are shown. In Figure 32 the T and H^2 dependencies of the velocity shifts for TmSb, split by the field, which breaks the cubic axes degeneration are shown. Therefore the birefringence has a quantum-mechanical origin.

5 MAGNETOSTRICTION OF MAGNETICALLY DISORDERED MAGNETS: RANDOM MAGNETIC ANISOTROPY (RMA) AND AMORPHOUS MATERIALS

Disordered magnets, with structural (amorphous) and/or spin disorder (spin glasses and random magnetic anisotropy (RMA) ones) show peculiar characteristics in their MS behaviors and pose difficult problems to MS calculation.

5.1 RMA magnets MS

In the case of RMA (del Moral and Arnaudas, 1989) hard magnets, the local CEF easy axis, $\hat{\mathbf{a}}(\mathbf{r})$ changes randomly through the lattice and the exchange and CEF Hamiltonian has the form $H_{\mathrm{EX+CEF}} = -J_0 \Sigma_{(\mathbf{r},r)} \mathbf{S}(\mathbf{r}) \cdot \mathbf{S}(\mathbf{r}') - D_0 \Sigma_{\mathbf{r}} [\hat{\mathbf{a}}(\mathbf{r}) \cdot \mathbf{S}(\mathbf{r})]^2$. An order parameter, q (of *Edwards–Anderson*) is defined at each site i which takes into account the time autocorrelation instead of the nonexistent spatial one, of the form $q = \lim_{t\to\infty} \langle \langle S_i(0) S_i(t) \rangle_T \rangle_r$, where the average r is over the structural disorder. From the use of statistical mechanics *replica technique* it can be shown that

$$p = \int_{-\infty}^{\infty} \left(\frac{dx}{\sqrt{2\pi}} \right) e^{-x^2/2} \langle S_z^2 \rangle, \; q = p - \left(\frac{1}{\gamma} \right) \times \int_{-\infty}^{\infty} \left(\frac{\mathrm{d}x}{\sqrt{2\pi}} \right) x \mathrm{e}^{-x^2/2} \langle S_z \rangle$$
$$M = \int_{-\infty}^{\infty} \left(\frac{\mathrm{d}x}{\sqrt{2\pi}} \right) \mathrm{e}^{-x^2/2} \langle S_z \rangle \tag{53}$$

where $\gamma = (2/5)^{1/2} \beta \sqrt{q} D_0$, and therefore q, p (QP moment) and M must be solved self-consistently. The effect now of the MEL coupling of probe ion $\mathbf{S}$ to its local CEF is assumed to rearrange the local environment, modifying D_0, but keeping fixed $\hat{\mathbf{a}}(\mathbf{r})$ as in crystalline FMs. If the local strain projected along $\hat{\mathbf{a}}(\mathbf{r})$ is $\varepsilon_{\hat{\mathbf{a}}\hat{\mathbf{a}}}$, the simplest MEL Hamiltonian takes the form, $H_{\mathrm{me}} = -M_2 \Sigma_{\mathrm{r}} [\hat{\mathbf{a}}(\mathbf{r}) \cdot \mathbf{S}(\mathbf{r})]^2 \varepsilon_{\hat{\mathbf{a}}\hat{\mathbf{a}}}(\mathbf{r})$, where the MEL parameter is $M_2 = (\partial D_0 / \partial \varepsilon_{\hat{\mathbf{a}}\hat{\mathbf{a}}})$. Under field application $\mathbf{H} \| \mathrm{OZ}$, where OZ is the macroscopic MS strain, ε_{zz} measurement axis and $\varepsilon_{\hat{\mathbf{a}}\hat{\mathbf{a}}} = \varepsilon_{zz} \cos^2 \theta(\mathbf{r})$, where $\theta(\mathbf{r})$ is the angle formed by $\mathbf{S}(\mathbf{r})$ with OZ. Using the 'replica trick' where the free energy is given by $F = -(k_{\mathrm{B}} T) \lim_{n\to 0} (1/n) (T r_n \mathrm{e}^{-\beta H_{\mathrm{mel}}} - 1)$, where we assume an n-times replicated spin system for taking the trace, it is possible to show from preceding H_{mel} that the effective MEL Hamiltonian takes the form,

$$\tilde{H}_{\mathrm{me}} = -\left(\frac{3M_2}{5} \right) \varepsilon_{zz} \Sigma_{\mathrm{r}} \Sigma_{\alpha} [S_z^{\alpha}(\mathbf{r})]^2 - \left(\frac{2 D_0 M_2}{105} \right) \varepsilon_{zz} \times \Sigma_{\mathbf{r}} \Sigma_{\alpha,\beta} \Sigma_{i,j} S_i^{\alpha}(\mathbf{r}) S_j^{\alpha}(\mathbf{r}) S_i^{\beta}(\mathbf{r}) S_j^{\beta}(\mathbf{r}) \tag{54}$$

The replica trick free energy is too long to be presented here, but from the minimization $\partial (F_{\mathrm{mel}} + \frac{1}{10} N c_{\mathrm{el}} \varepsilon_{zz}^2) / \partial \varepsilon_{zz} = 0$ it is finally obtained that the macroscopic shape MS (Figure 33) becomes,

$$\lambda_t = \left(\frac{M_2}{3 c_{\mathrm{e}}} \right) \left[p - \frac{S(S+1)}{3} \right] = \left(\frac{M_2}{c_{\mathrm{e}}} \right) \int_{-\infty}^{\infty} \left(\frac{\mathrm{d}x}{\sqrt{2\pi}} \right) \mathrm{e}^{-x^2/2} \langle \tilde{\mathrm{O}}_2^{\mathrm{o}} \rangle \tag{55}$$

which takes the usual form for ordered FMs but on top of the thermal average we have to perform the average over the spin disorder (integral). This theory has been applied to a series of RE metallic glasses such as a-$\mathrm{RE}_{40}\mathrm{Y}_{23}\mathrm{Cu}_{37}$, a-$\mathrm{Tb}_2\mathrm{Fe}_{1-x}\mathrm{Ni}_x$ and a-$(\mathrm{Gd}_{1-x}\mathrm{Tb}_x)_2\mathrm{Cu}$ and crystalline $\mathrm{Tb}_x\mathrm{Y}_{1-x}\mathrm{Al}_2$, where in the latter Y substitutions produces the RMA (del Moral, 2007). In Figure 34 the MS thermal variation for RE = Dy (with $T_{\mathrm{SG}} = 23$ K, $D_0 = 1.25$ K, $J_0 = 0.66$ K), together with

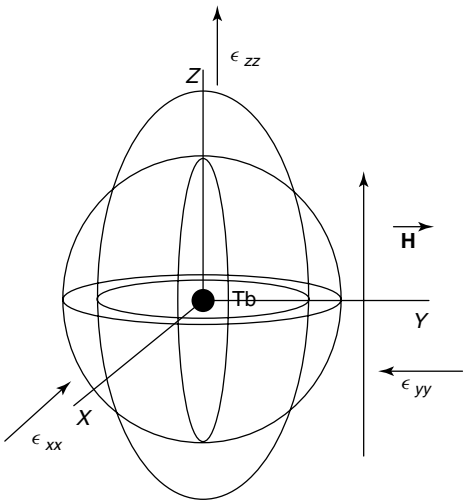

Figure 33. Tetragonal distortion of spherical symmetry in amorphous material (de la Fuente, unpublished).

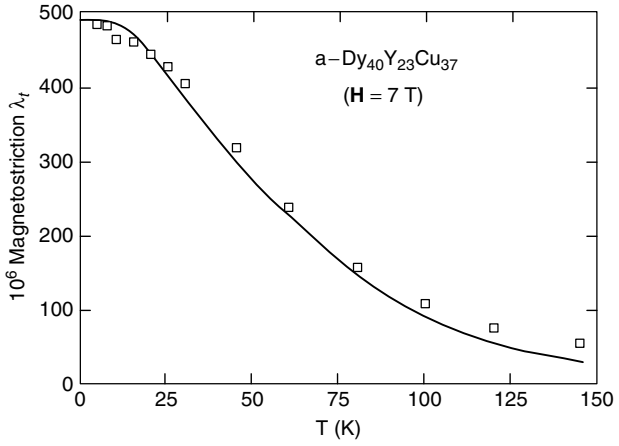

Figure 34. Shape MS thermal variation for a-$Dy_{40}Y_{23}Cu_{37}$; line is the replica model fit (del Moral and Arnaudas, 1989).

the good fit by equation (55), which yields $M_2/c_{\rm el} = 9.2 \times 10^{-6}$, is shown.

5.2 Breaking of AZC law in RMA magnets

We will consider for RMA magnets (del Moral, de la Fuente and Arnaudas, 1996), the ferromagnetic wandering axis regime, where long-range FM order is formed along applied **H**, but the transverse order is limited to a length $R_\perp = (\mathrm{H_{EX}}/\mathrm{H})R_\mathrm{a}$, where R_a is the structural correlation length (SCL) (Chudnovsky, Saslow and Serota, 1986). Therefore we will assume that the system $\mathbf{M}\|\mathbf{H}$ is almost saturated and therefore spin-wave excitations are proper. Instead of only using dynamic magnon operators (α_l, α_l^+ at site $\boldsymbol{l}$), to diagonalize H we will use the transformations (del Moral and Cullen, 1995) $a_l = (1+u_l)\alpha_l + v_l\alpha_l^+ + c_l$ and c.c., c_l, c_l^+ being the disorder spin deviations ('frozen'-in SWs) and u_l, v_l Fourier transforms of the magnon scattering matrices due to RMA disorder. Now we use the same calculation as for FMs, but we have $M(0,H)/gJ\mu_\mathrm{B} = 1 - J^{-1}\{\langle c_l^+ c_l\rangle_r + \langle v_l^+ v_l\rangle_r\}$ and $\langle\langle Y_2^0(\boldsymbol{J})\rangle_\mathrm{T}\rangle_\mathrm{r} = 3J^2 - J(J+1) - 3(2J-1)\langle\langle a_l^+ a_l\rangle_\mathrm{T}\rangle_\mathrm{r} + 3\langle\langle a_l^+ a_l^+ a_l a_l\rangle_\mathrm{T}\rangle_\mathrm{r}$, obtained from the preceding transformations, and from where we have after some easy calculations that order $l = 2$ MS becomes,

$$\frac{\lambda_2(T,H)}{\lambda_2(0,H)} = 1 - 3\xi(1 - m(T,H)) \cong m(T,H)^p \qquad (56)$$

where $p = 3\xi = 3[J(2J-1) - 6J\delta + \delta(1+4\delta)]/[J(2J-1) - 6J\delta + 3\delta(1+2\delta)]$, with $\delta = J\Delta m(0,H)$, and $\Delta m(0,H)$ the *zero-point* magnetization defect, due to the static disorder. Therefore p exponent becomes smaller than 3, which constitutes a *quantum effect*. In Figure 35 we show the double-log plots of $\lambda_2(T)$ versus $M(T)$ at $H = 3\mathrm{T}$ for $\mathrm{Tb}_x\mathrm{Y}_{1-x}\mathrm{Al}_2$ intermetallics, from the straight line slopes obtaining p, which becomes much smaller than 3 (see inset), in agreement with the model. Also p increases toward 3 with H increasing (12 T), as expected.

5.3 Soft metallics glasses MS models

Soft (low MCA) magnetic glasses are rather important materials for technological applications, as seen in other chapters of this Handbook (e.g. in **Magnetostrictive Materials and Magnetic Shape Memory Materials, Volume 4**). For some alloys $\lambda_\mathrm{s}(T)$ shows the same single-ion CEF $\hat{\mathrm{I}}_{l+1/2}(m)$ dependence of crystalline FMs with *localized* moments. The reason is that, although they are RMA materials, the magnetic correlation length (MCL), $L \cong 0.02(l_{ex}^4/l^3)$ (where $l_\mathrm{ex} = \pi\sqrt{A/D_0}$ is the DW width (A is exchange stiffness

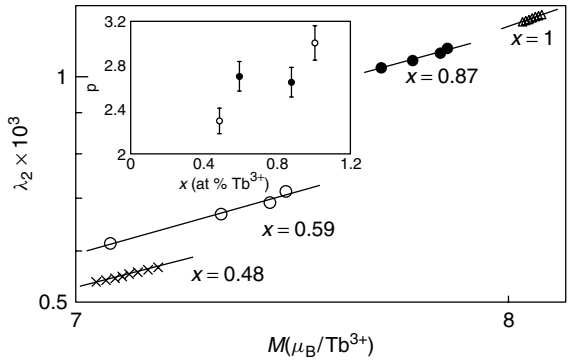

Figure 35. Magnetostriction of $\mathrm{Tb_x\ Y_{1-x}\ Al_2}$ interuetallic vs. magnetization; see text (del Moral, de la Fuente and Arnaudas, 1996).

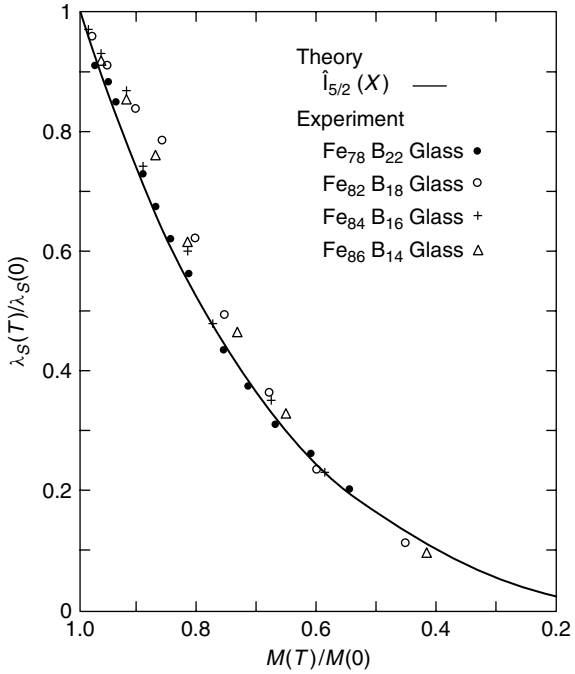

Figure 36. Shape MS thermal variation for a-$Fe_{100-x}B_x$ (O'Handley, Narasimham and Sullivan, 1979).

constant) and l the short range SCL) is so large that the material is quasi-FM. This is the case of the a-$Fe_{1-x}B_x$ alloys shown in Figure 36. However for other more complex alloys $\lambda_s(T)$ shows broad maxima or even changes the sign (see Figure 37). In this case two models can explain such a behavior. In the first one (O'Handley, 1978a) a competition in sign is assumed between the CEF and two-ion MSs, in such a way that

$$\lambda_s(T) = \left(\frac{\overline{M}^s(0)}{c^\gamma}\right)\hat{I}_{5/2}(X) + \left(\frac{\overline{D}^s(0)}{c^\gamma}\right)m^2 \equiv C_1\hat{I}_{5/2}(X) + C_2m^2 \qquad (57)$$

Since the CEF-MS evolves more rapidly ($\propto m^3$) with temperature than the exchange one, this is predominant near T_c, and if $C_1 < 0 < C_2$ and $|C_1| > |C_2|$ a sign variation of λ_s is possible, as it happens for the alloys shown in Figure 37, where the lines are the fits by equation (57). But another explanation is found within the itinerant moment BD-BZS model studied in Section 3, now assuming that we have a RMA, that also explains the broad maxima shown by $\lambda_s(T)$ (see Figure 38 for a pseudobinary alloy, where the continuous line is the theory). In the calculation the random CEF is represented by a random matrix, $R_{\mu\nu}(c)$, where c points to the CEF energy variation with the local atom cluster tetragonal deformation, ε_2^α (e.g., a Bernal polyhedron tetragonally deformed along OZ), and $H_{\text{CEF+mel}} = \Sigma_{i,\mu,\nu,\sigma}R_{\mu\nu}(c)a^+_{i\mu\sigma}a_{i\nu\sigma} + M^{\alpha,2}\varepsilon_2^\alpha[3\delta_{\mu,xy} - 1]$, where i are sites, μ, ν orbitals (t_{2g} with a magnetostrictive doublet $\{xz, yz\}$ near to E_F and the preceding xy singlet or conversely) and $\sigma = \pm 1/2$ is the spin, H_{CEF} giving the d-electron scattering by the disorder. The remainder Hamiltonian is the same as for a crystalline material (del Moral *et al.*, 1998a).

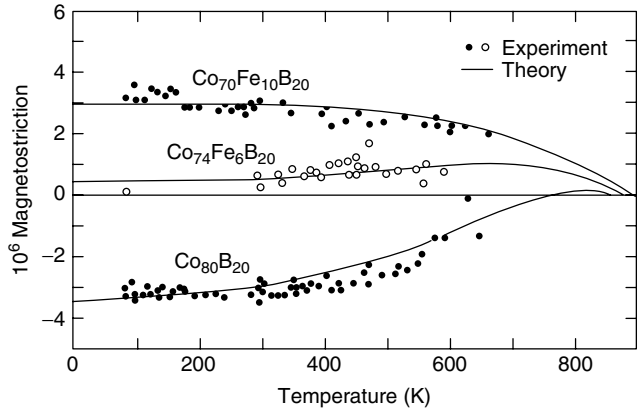

Figure 37. Shape MS thermal variation for a-$(Co_{1-y}Fe_y)_{80}B_{20}$ (O'Handley, 1978a).

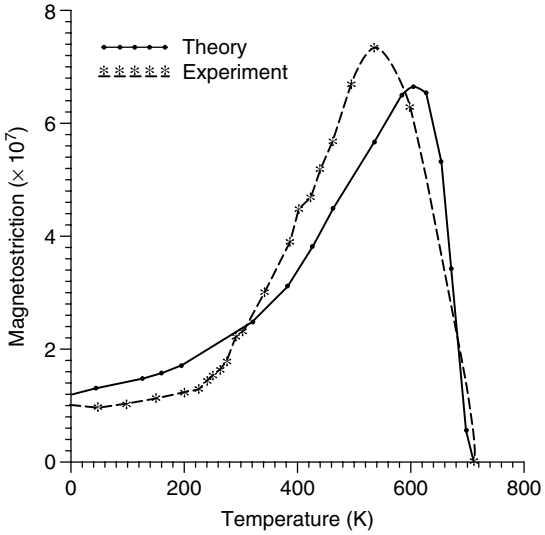

Figure 38. Shape MS thermal variation for a-$Fe_5Co_{71}Si_{12}B_{12}$, experiment and itinerant theory (Kulakowski, Maksymowicz and Magdón, 1993).

5.4 Zero-λ_s alloys; split-band model

Some alloys of technological use, crystalline, and amorphous, show zero λ_s for certain compositions. Generally within the 3d metals and alloys λ_s *oscillates* with band electron filling, n a property well explained using the simplified

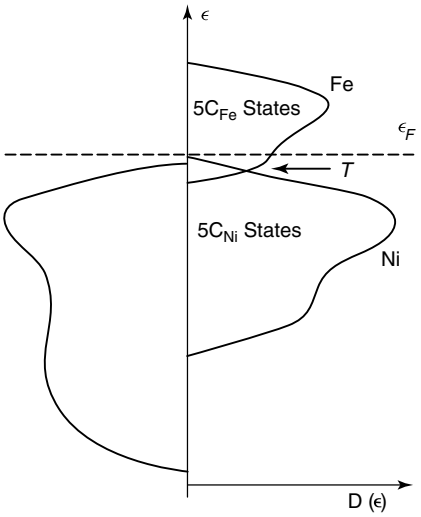

Figure 39. Split bands for binary $Fe_{1-x}Ni_x$ alloys (Berger, 1977).

Berger's *split-band model* (SBM, Berger, 1977) (a Green function theory of itinerant MS does the same, Heine, Kox and Nex, 1984), quite suitable for alloys where a TBA or *AI* MS calculation is difficult. In the SBM one assumes that the bands DOS and their centers, E_p for the alloy partners (e.g., crystalline (c-)Fe_xNi_{1-x} or a $-$ $(Fe_xNi_{1-x})_{80}B_{20}$) do not modify on alloying, the alloy DOS being just the addition of partner DOS (see Figure 39 for c-Fe_xNi_{1-x}, where $E_{Fe} > E_{Ni}$, because the Fe nuclear charge is smaller than Ni one; on the left is the added DOS for down spins ($\downarrow$), on the right the spin up ($\uparrow$) individual bands). Let us assume the existence of a DOSs crossing point T and see at which x E_F traverses T, where $\lambda_s = 0$, as the hole number, n_h in the $\downarrow$ band is zero (strong-FM). In c-Fe_xNi_{1-x}, clearly $n_h = 0.55 + 2C_{Fe}$ in the alloy ($C \equiv x$). Because the Fe state number in the minority band (mB, $\downarrow$) is $5C_{Fe}$, crossing occurs when $n_h = 5C_{Fe}$, that is, when the Ni band holes are filled by the Fe-band electrons, giving $x_0 = 0.18$, or concentration for zero-MS. In this case the total orbital momentum (OM), $\langle L_z\rangle_{alloy} = \Sigma_b \langle b|L_z|b\rangle$ must be zero at E_F (b are band states), since $\lambda_s \propto \langle L_z(E_F)\rangle_{alloy}$. A second-order perturbation calculation upon H_{SO} yields

$$\langle L_z^t\rangle = \sum \langle L_z\rangle = \left(\frac{1}{n_{at}}\right) \Sigma_{i,j,m,n} f_m^i \times \left(\frac{\xi\left(\frac{1}{2}\right) |\langle L_z\rangle_{mn}^{ij}|^2}{(E_m^i - E_n^j)}\right) \tag{58}$$

where $i(j)$ are Fe and Ni bands, $m(n)$ unperturbed $\downarrow$ Bloch states of energy E_m^i, f_m^i the Fermi–Dirac function, $\langle L_z\rangle_{mn}^{ij} = \langle mi|L_z|nj\rangle$ and n_{at} the atom number. Passing equation (58) to continuous DOS, the calculated $\langle L_z\rangle_{alloy}$ is shown in Figure 40, where α_{NiFe} is the $\langle \mathbf{L}\rangle$ quenching parameter and z

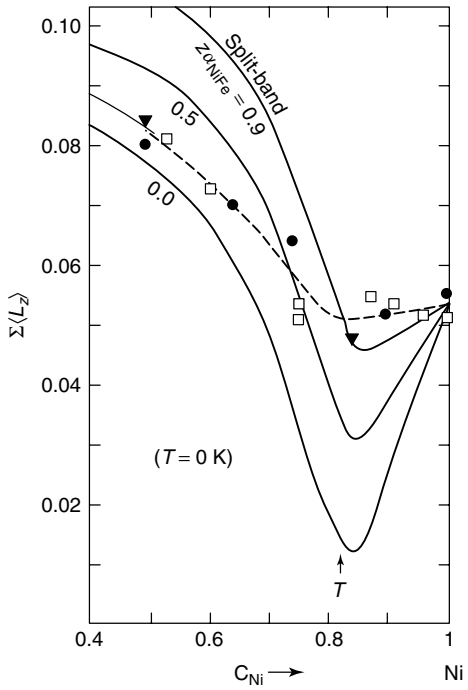

Figure 40. $Fe_{1-x}Ni_x$ alloys, see text for meaning (points are from different probes) (Berger, 1977).

the NN number. We see that $\langle L_z\rangle_{alloy}$ is minimum at T point or for $x_0 = 0.18$, as experimentally observed from different probes. For a $-$ $(Fe_xNi_{1-x})_{80}B_{20}$ alloys, the $\lambda_s = 0$ condition is $5C_{Fe} = 2.55C_{Fe} + 0.55_{Ni} - 1.6C_B$ with $C_{Fe} + C_{Ni} = 0.8$, $C_B = 0.2$, since there is a charge transfer of 1.6 e/B-atom to the TM bands, yielding $x_0 = 0.06$, that is, a strong shifting down. For a-$(Fe_xCo_yNi_{1-x\cdot y})_{80}B_{20}$ pseudoternary alloys the $\lambda_s = 0$ 'point' transform in a $\lambda_s = 0$ 'line' when we trace a triangular MS phase diagram (O'Handley, 1978b) (see **Magnetostrictive Materials and Magnetic Shape Memory Materials, Volume 4**).

6 SURFACE, INTERFACE, AND MAGNETIC THIN FILMS AND SUPERLATTICES MAGNETOSTRICTIONS

Nanostructured materials in the form of TFs, MLs, and SLs encounter increasing technological applications (see **Hard Magnetic Films, Volume 4**, **Ferromagnetic Manganite Films, Volume 5**). However the knowledge of MS in those structures is also important because the reduction to $2d$ (ultrathin films; see **Magnetic Ultrathin Films, Volume 4**) and because the existence of highly perfectioned surfaces (SF) and IFs reveal magnetic properties different

to the bulk. For instance depending on (l, m, n) indices, SF crystal symmetry is reduced (see Figure 41 for bulk fcc lattice) and therefore $H_{\rm CEF}$ becomes modified; in SFs moment is enhanced (to 0.73 and 2.98 $\mu_{\rm B}$ in [100] Ni and Fe SFs respectively); and MCA anisotropy can become perpendicular to SF. In ML or SL the mismatch, $\eta = (a_{\rm m} - a_{\rm nm})/a_{\rm nm}$ between blocks (magnetic and nonmagnetic) lattice parameters gives rise to a *misfit strain*, which for epitaxial growth is $\varepsilon_{\rm mf} \cong \eta(t_{\rm nm}/(t_{\rm m} + t_{\rm nm}))$, although it can be partially released by IF dislocations. Let us first consider the *surface MEL coupling*, where the MCA and MEL free energy is written as $F_{\rm mel}(z) = K^s_{ij}\delta(z)\alpha_i\alpha_j + \overline{\rm M}^{*s}_{ij}\,\delta(z)\alpha_i\alpha_j\varepsilon_{ij}$, where z is the distance from the SF ($z = 0$) and $\overline{\rm M}^*_{ij} = \overline{\rm M}_{ij} + \overline{\rm N}_{ijkl}\varepsilon_{kl}$, introducing NL-MEL coupling due to the large $\varepsilon_{\rm mf}$ (O'Handley and Sun, 1992). Adding the bulk MCA and averaging $F(z)$ over the crystal thickness, t we obtain

$$\langle F\rangle = \left(\frac{1}{t}\right)\int_0^t F(z){\rm d}z = K_{ij}\alpha_i\alpha_j + \left(\frac{K^s_{ij}}{t}\right)\alpha^0_i\alpha^0_j + \overline{\rm M}^*_{ij}\alpha_i\alpha_j\varepsilon_{ij} + \left(\frac{\overline{\rm M}^{*s}_{ij}}{t}\right)\alpha^0_i\alpha^0_j\varepsilon^{s,0}_{ij} \qquad (59)$$

where we see that the SF MCA and MEL constants show a $1/t$ dependence (consequence of converting them to bulk like constants, Néel's assumption). $\boldsymbol{\alpha}^0$ is the unstrained film $\mathbf{M}_{\rm s}$ direction at the SF and $\varepsilon^{s,0}_{ij}$ the SF strains (misfit and MS). Therefore for a crystal block in a ML or SL (two SFs), the MEL constant becomes, $\overline{\rm M}^{\rm eff} = \overline{\rm M}^{v} + 2\overline{\rm M}^{*s}/t$. This Dirac δ(z) approximation is not very realistic as the 'surface' monolayers (ML) extend beyond $z = 0$. For thin blocks and $\varepsilon_{\rm mf} \approx 1\%$ ($\varepsilon_{\rm mf} >> \lambda_{\rm s}$ for 3d metals, but becomes comparable for RE materials), SF-MS can be comparable to bulk (v) one, for example in Ni/Ag MLs, $\lambda^{\rm v}_{\rm s} = -34$ and $\lambda^{\rm sf}_{\rm s} = -35.4/t(\times 10^{-6}$, t in nm) (Zuberek *et al.*, 1998). SF MEL constants can be directly measured using the SESPA technique.

If we now introduce crystal symmetry, the rules for building the MEL Hamiltonian, $H^{\rm sf}_{\rm mel}$ are the same as for the bulk crystal seen in the STM, but reducing the symmetry accordingly with the SF (l, m, n) indices, and the same applies to $F^{\rm sf}_{\rm mel}$. Therefore the MEL constants for a [110] SF (ORTH) of a BCC film have the form $\overline{\rm M}^{\Gamma,l}_{\rm f} = \overline{\rm M}^{\Gamma,l}_{\rm v} + (2/t)\overline{\rm M}^{\Gamma,l}_{\rm s}$, where there are for $l = 2$, three bulk MEL constants ($\Gamma = \alpha, \gamma, \varepsilon$), but four for the SF ($\Gamma = \alpha 1, \alpha 2, \varepsilon, \varsigma$). We will now apply this MEL theory to 3d-metal films and RE SLs.

6.1 Cu/Ni/Cu trilayers

In this structure we have a substrate onto which the magnetic Ni film is deposited, and it is capped with another Cu film to avoid corrosion. The misfit strain in the Ni TF is biaxial, that is, $\varepsilon_{xx} = \varepsilon_{yy} = \varepsilon_{\rm mf}$ in plane and if stress $\sigma_{zz} = 0$, $\varepsilon_{zz} = \nu\varepsilon_{\rm mf}$ with $\nu = -2(c_{11}/c_{12})$, or Poisson ratio (Figure 42). Therefore the misfit MEL energy easily becomes,

$$F^{\rm t}_{\rm me} \cong -(\overline{\rm M}_{11} + \overline{\rm M}_{12} + \overline{\rm M}_{13})\varepsilon_{\rm mf}\cos^2\theta \qquad (60)$$

which adds to the MCA energy $F_{\rm K} = K_1\cos^2\theta$, where θ is the angle of $\mathbf{M}_{\rm s}$ with the film normal OZ. Therefore the effective MA constant takes the form,

$$K^{\rm eff}t = 2(K^{\rm s} + \overline{\rm M}^{\rm s}\varepsilon_{\rm mf} + \overline{\rm N}^{\rm s}\varepsilon^2_{\rm mf}) + \left(\overline{\rm M}^{\rm v}_1\left(\frac{1 + 2c_{11}}{c_{12}}\right) + \overline{\rm N}^{\rm v}\varepsilon_{\rm mf}\right)\varepsilon_{\rm mf}t - 2\pi M^2_{\rm s}t \qquad (61)$$

where NL-MEL energy is included, for volume (v) and SFs (s) (Ni/Cu IFs), as well as the demagnetizing energy (last term) trying to keep $\mathbf{M}_{\rm s}$ in plane. In Figure 43 are shown $K^{\rm eff}t$ for three trilayers prepared under different conditions, where we see that in the range $t \cong 20$–135 Å, the ED is perpendicular to plane (PMA) ('window' effect), a property quite used in magnetic recording to reduce the domain size.

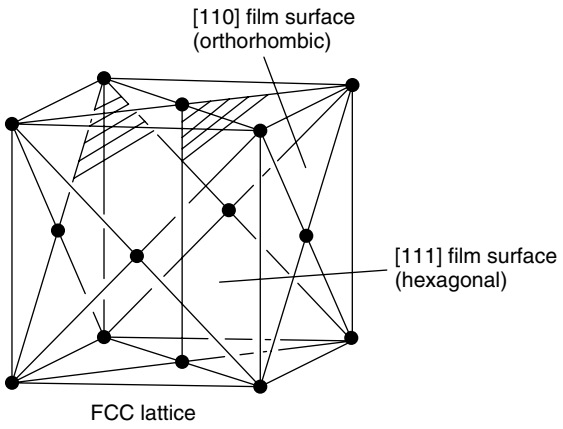

Figure 41. Surface symmetry reductions for fcc lattice (del Moral, 2007).

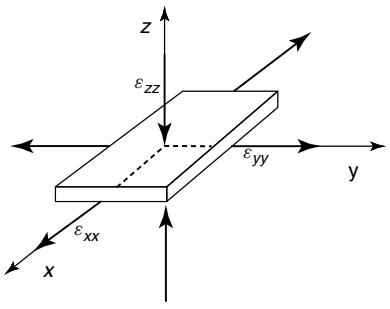

Figure 42. Biaxial strain in a thin film (O'Handley, Sun and Ballentine, 1993).

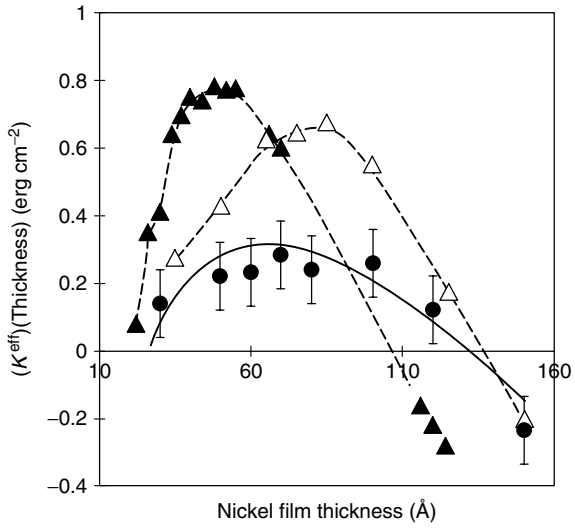

Figure 43. Effective MA in Cu/Ni/Cu trilayers (Ha and O'Handley, 1999).

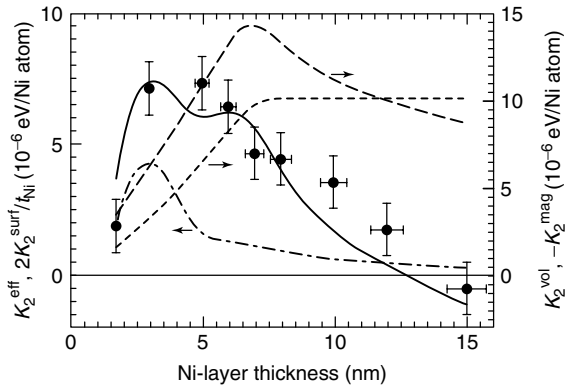

Figure 44. MA constant K_{eff} (•; plain line, theory) ant its contributions, K_2^{vol} (dash), surface (dash-dot), K_2^{mag} (dot) (del Moral *et al.*, unpublished).

The fit by equation (61) (continuous line) is attained with, $K_1 \cong 0$, $K^s = 0.76$, $\overline{M}^s = -1.22$ (erg cm^{-2}), $\overline{N}^v = -1.11 \times 10^{10}$, $2\pi M_s^2 = 1.5 \times 10^6$ (erg cm^{-3}) and $\overline{N}^s = -1.97$ erg cm^{-1}. Since $K^s > 0$ the *spin reorientation* for $t > \approx 20$ Å is due to the bulk NL contribution, which contributes negatively to K^{eff}, whereas the $\overline{M}^s$ contribution is negligible. Assuming that the film is tetragonally distorted, the itinerant BD-BZS model of Section 3 yields the contributions and kind of fit shown in Figure 44 with only $K_2^{eff} = K_2^{vol} + (2K_2^{sf}/t_{Ni}) - 2\pi M_s^2$ contributions (del Moral *et al.*, unpublished). This model also explains the t dependence of $\overline{M}^{\gamma,2}$, due to the SF $2\overline{M}_{sf}^{\gamma,2}/t$ contribution, for $t < 100$ Å, for above the concourse of NL $\overline{N}^{\gamma,2}\varepsilon_{1,mf}^{\gamma}$ being needed, in order to explain the observed 'window'of $\overline{M}^{\gamma,2}$ with t (Ciria *et al.*, 2004).

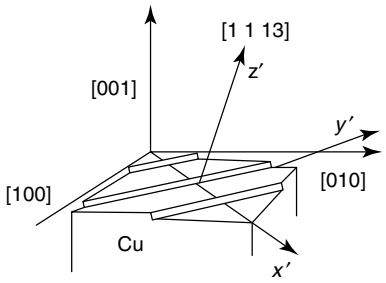

Figure 45. Vicinal surface [1113] terraces (Oepen *et al.*, 1993).

The growth of a SF 'vicinal' to a [001] one, with normal [1113] in fcc Co/Cu ultrathin films (few ML) gives rise to the appearing of steps (Figure 45), which allows study of MEL coupling in one dimension, since a MEL anisotropy is developed along the terrace line. The Néel's *pair-atom MEL model* mentioned explains well the observations, the anisotropy energy density becoming, $E_{film} = E_{bulk} - 2E_{sf}/t - 2E_{step\ edge}/td - 2E_{step\ corner}/td$, where d is the steps distance (an *AI* calculation does exist, Victora and MacLaren, 1993).

6.2 RE superlattices

In RE/Y, RE/Lu, and RE/Sc SLs the oscillatory RKKY exchange interaction is propagated through the NM blocks, the ordering temperatures (T_N, T_c) are strongly modified, a *finite size* effect is manifested for very thin RE blocks in the helical structure and new magnetic phases appear in the (H, T) diagram (Jehan *et al.*, 1993). Since the moments are now truly localized we can write for the orthorhombic MS in basal plane, ε_1^{γ} that thickness and T dependencies respectively are,

$$\overline{M}_{th}^{\gamma} = \overline{M}_{v0}^{\gamma} + \left(\frac{2\overline{M}_s^{\gamma}}{t_{Ho}}\right) + \overline{N}_v^{\gamma}\eta\left(\frac{t_{Lu}}{(\alpha t_{Ho} + t_{Lu})}\right) \qquad (62)$$

$$\overline{M}_{th}^{\gamma}(m) = (\overline{M}_{v0}^{\gamma} + \overline{N}_v^{\gamma}\varepsilon_{mf})\hat{I}_{5/2}(L^{-1}(m)) + \left(\frac{2\overline{M}_s^{\gamma}}{t_{Ho}}\right)m^{\alpha} \qquad (63)$$

In equation (63) the last term is the thermal variation for the IF-MS, which according to STM for $d = D = 2$, gives $\alpha = 4$ at low T ($\alpha = 2$ at high T), our case. In Figure 46 $\overline{M}_{th}^{\gamma,2}$ given by equation (62) is adequately compared with the saturation ($H = 12$ T) and 10 K $\overline{M}_{exp}^{\gamma,2}$ for $[Ho_n/Lu_{15}]_{x50}$ [0001] SLs where the Ho ML number is $n = 8 - 80$ (plus bulk films, o symbol), the Lu block thickness being constant (Ho block in under misfit compression, opposite to Y spacer SLs). From the fit we obtain that $\overline{M}_{v0}^{\gamma,2} = -0.89$, $\overline{M}_{sf}^{\gamma,2}/(c/2) = 7$, $N_v^{\gamma,2} = 185$ (all in GPa), with $\eta = -1.44\%$. In Figure 47 are shown the $\overline{M}^{\gamma,2}(T)$

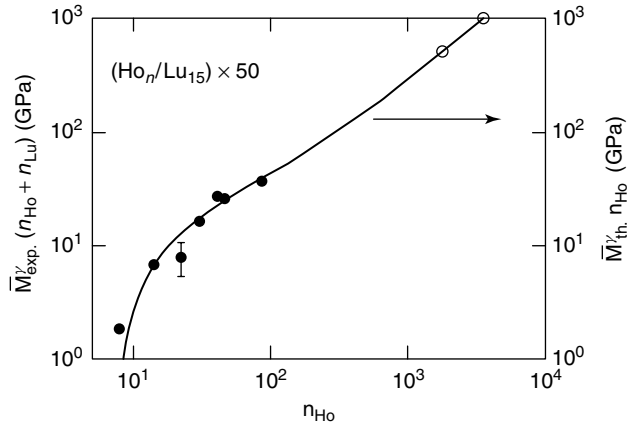

Figure 46. See text for meaning (del Moral *et al*., 1998b).

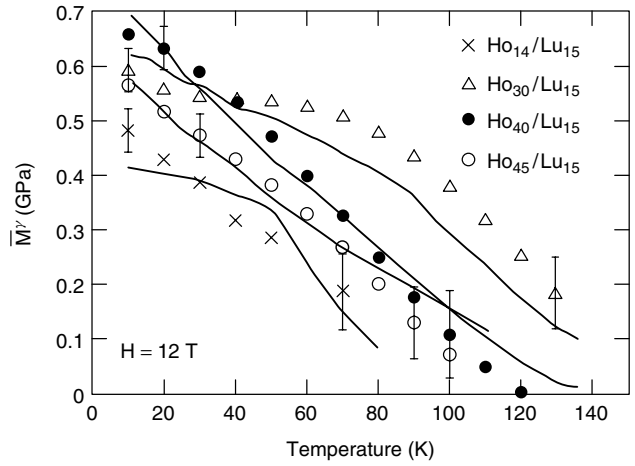

Figure 47. $\overline{M}^{\gamma,2}$ (T) thermal variations for Ho_n/Lu_{15} superlattices; lines are the theory (del Moral *et al*., 1998b).

variations together with the fits by equation (63), using the *same* MEL parameters, the opposite sing IF contribution being needed. Therefore STM is as well behaved in RE SLs as in bulk REMs.

REFERENCES

Abell, S., del Moral, A., Ibarra, M.R. and Lee, E.W. (1983). *Journal of Physics C: Solid State Physics*, **16**, 769.

Adroja, D.T., del Moral, A., De Teresa, J.M., *et al*. (1995). *Journal of Magnetism and Magnetic Materials*, **140–144**, 1219.

von Barth, U. and Hedin, L. (1972). *Journal of Physics C*, **5**, 1629.

Bonsall, L. and Melcher, R.L. (1976). *Physical Review B*, **14**, 1128.

Berger, L. (1977). *Physica B*, **91**, 31.

Brommer, P.E. and Franse, J.J.M. (1990). In *Handbook of Ferromagnetic Materials*, *First Edition*, Wohlfarth, E.P. (Ed.), North Holland: Amsterdam.

Brown, W.F. Jr., (1965). *Journal of Applied Physics*, **36**, 994.

Buck, S. and Fähnle, M. (1998). *Physical Review B*, **57**, R14044.

Buck, S. and Fähnle, M. (1999). *Journal of Magnetism and Magnetic Materials*, **204**, L1.

Buckmaster, H.A. (1966). *Canadian Journal of Physics*, **44**, 2525.

Callen, E.R. (1982). *Journal of Applied Physics*, **53**, 8139.

Callen, H.B. and Callen, E.R. (1964). *Physical Review*, **136**, A1675.

Callen, E.R. and Callen, H.B. (1965). *Physical Review*, **139**, A455.

Carr, W.J. (1966). In *Handbuch der Physik*, Flügge, S. (Ed.), Springer: Berlin, Vol. 18/2.

Choudhury, G.M., Lee, E.W. and Melville, D. (1974). *High Magnetic Fields Conference Proceedings*, CNRS: Grenoble.

Chudnovsky, E.M., Saslow, W.M. and Serota, R.A. (1986). *Physical Review B*, **33**, 251.

Ciria, M., Arnaudas, J.I., del Moral, A. and O'Handley, R.C. (2004). *Physical Review B*, **70**, 5443.

Clark, A.E. (1980). In *Handbook of Ferromagnetic Materials*, *First Edition*, Wohlfarth, E.P. (Ed.), North Holland: Amsterdam.

Clark, A.E., DeSavage, B.F. and Bozorth, R. (1965). *Physical Review*, **138**, A216.

Creuzet, G. and Campbell, I.A. (1981). *Physical Review B*, **23**, 3375.

Cullen, J.R., Rinaldi, S. and Blessing, G.V. (1978). *Journal of Applied Physics*, **49**, 1960.

Cullen, J.R. and Clark, A.E. (1977). *Physical Review B*, **15**, 4510.

Daalderop, G.H.O., Kelly, P.J. and Schuurmans, M.F.H. (1990). *Physical Review B*, **41**, 11919.

de la Fuente, (1995). Ph.D. Thesis, University of Zaragoza, unpublished.

Dionne, G.F. (1979). *Journal of Applied Physics*, **50**, 4263.

Dohm, V. (1976). *Zeitschrift fur Physik*, **23**, 153.

Dohm, V. and Fulde, P. (1975). *Zeitschrift fur Physik*, **21**, 369.

Eastman, D.E. (1966). *Physical Review*, **148**, 530.

Edwards, D.M. and Wohlfarth, E.P. (1968). *Proceedings of the Royal Society of London Series A*, **303**, 127.

Evenson, W.E. and Liu, S.H. (1969). *Physical Review*, **178**, 783.

Fähnle, M., Furthmüller, J., Pawellek, R., *et al*. (1990) In *Physics of Magnetic Materials*, Gorzkowski W., Gutowski, M., Lachowicz, K.H., Szymczak, H., *et al.* (Eds.), World Scientific: Singapore.

Fletcher, G.C. (1954). *Proceedings of the Physical Society*, **A67**, 505.

Ha, K. and O'Handley, R.C. (1999). *Journal of Applied Physics*, **85**, 5282.

Häfner, H.U. (1985). *Journal of Magnetism and Magnetic Materials*, **47–48**, 299.

Hayase, M., Shiga, M. and Nakamura, Y. (1971). *Journal of the Physical Society of Japan*, **30**, 729.

Heine, V., Kox, W.C. and Nex, C.C.M. (1984). *Journal of Magnetism and Magnetic Materials*, **43**, 61.

Hernando, A. and Bariandarán, M. (1980). *Physical Review B*, **22**, 2445.

Hohenberg, P. and Kohn, W. (1964). *Physical Review B*, **136**, 864.

Hutchings, M.T. (1964). *Solid State Physics*, **16**, 277.

Ibarra, M.R., Garcıa-Olza, L. and del Moral, A. (1992). *Solid State Communications*, **84**, 875.

Jehan, D.A., McMorrow, D.F., Cowley, R.C., *et al*, (1993). *Physical Review B*, **48**, 5594.

Kakehashi, Y. (1981). *Journal of the Physical Society of Japan*, **50**, 1925.

Kohn, W. and Sham, L.J. (1965). *Physical Review B*, **140**, A1133.

Komelj, M. and Fähnle, M. (2000). *Journal of Magnetism and Magnetic Materials*, **220**, L8.

Kondorskii, E.I. and Straube, E. (1973). *Soviet Physics JETP*, **36**, 188.

Kulakowski, K. and de Lacheisserie, E.T. (1989). *Journal of Magnetism and Magnetic Materials*, **81**, 349.

Kulakowski, K., Maksymowicz, A.Z. and Magdón, M. (1993). In *Magnetoelastic Effects and Applications*, Lanotte, L. (Ed.), Kluwer: Amsterdam.

Kulakowski, K. and del Moral, A. (1994). *Physical Review B*, **50**, 234.

Kulakowski, K. and del Moral, A. (1995). *Physical Review B*, **52**, 15943.

Kuz'min, M.D. (1992). *Physical Review B*, **46**, 8219.

de Lacheisserie, E.T. (1993). *Magnetostriction*, CRC Press: Boca Raton.

de Lacheisserie, E.T., Morin, P. and Rouchy, J. (1978). *Annales de Physique (Paris)*, **3**, 479.

Lee, E.W. (1955). *Reports on Progress in Physics*, **18**, 184.

Lüthi, B. (1976), Magnetism and Magnetic Materials, *AIP Conference Proceedings no 34 (Joint MMM-INTERMAG 7)*, Pittsburg.

Mathon, J. and Wohlfarth, E.P. (1968). *Physica Status Solidi*, **30**, K131.

Melcher, R.L. (1972). *Physical Review Letters*, **28**, 165.

del Moral, A. (2007). *Handbook of Magnetostriction and Magnetostrictive Materials*, CRC/Taylor & Francis: Boca Raton.

del Moral, A. and Cullen, J. (1995). *Journal of Magnetism and Magnetic Materials*, **139**, 39.

del Moral, A. and Arnaudas, J.I. (1989). *Physical Review B*, **39**, 9453.

del Moral, A., Arnaudas, J.I., Ibarra, M.R., *et al*. (1986). *Journal of Physics C: Solid State Physics*, **19**, 579.

del Moral, A. and Brooks, M.S.S. (1974). *Journal of Physics C: Solid State Physics*, **7**, 2540.

del Moral, A., Ciria, M., Arnaudas, J.I., *et al*. (1998b). *Journal of Physics: Condensed Matter*, **10**, L139.

del Moral, A., Echenique, P.M. and Corrales, J.A. (1983). *Journal of Physics C: Solid State Physics*, **16**, 4637.

del Moral, A., de la Fuente, C. and Arnaudas, J.I. (1996). *Journal of Physics: Condensed Matter*, **8**, 6945.

del Moral, A. and Ibarra, M.R. (1985). *Journal of Physics and Chemistry of Solids*, **46**, 127.

del Moral, A., Kulakowski, K., de la Fuente, C. (1998a). *Physical Review B*, **57**, 5320.

del Moral, A., Abadia, C. and Garcia-Landa, B. (2000). *Physical Review B*, **61**, 6879.

del Moral, A., Kulakowski, K., Fraile, A., *et al*. (2007), to be published.

Mori, N. (1969a). *Journal of the Physical Society of Japan*, **27**, 307.

Mori, N. (1969b). *Journal of the Physical Society of Japan*, **27**, 1374.

Mori, N., Fukuda, Y. and Ukai, T. (1974). *Journal of the Physical Society of Japan*, **37**, 1263.

Morin, P. and Schmitt, D. (1981). *Physical Review B*, **23**, 2278.

Morin, P., Schmitt, D. and de Lacheisserie, E.T. (1980). *Physical Review B*, **21**, 1742.

Moriya, T. (1985). *Spin Fluctuations in Itinerant Electron Magnetism*, Springer: Berlin.

Moriya, T. and Usami, K. (1980). *Solid State Communications*, **34**, 95.

Newman, D.J. and Ng, B. (1989). *Reports on Progress in Physics*, **52**, 699.

Nye, J.F. (1976). *Physical Properties of Crystals*, Oxford University Press: Oxford.

O'Handley, R.C. (1978a). *Physical Review B*, **18**, 930.

O'Handley, R.C. (1978b). *Physical Review B*, **18**, 2577.

O'Handley, R.C., Narasimham, M.C. and Sullivan, M.O. (1979). *Journal of Applied Physics*, **50**, 1633.

O'Handley, R.C. and Sun, S.W. (1992). *Journal of Magnetism and Magnetic Materials*, **104–107**, 1717.

O'Handley, R.C., Sun, S.W. and Ballentine, C.A. (1993). *Journal of Applied Physics*, **74**, 6302.

Oepen, H.P., Schneider, C.M., Chuang, D.S., *et al*. (1993). *Journal of Applied Physics*, **73**, 6186.

Otha, Y. and Shimizu, M. (1982). *Journal of Physics F: Metal Physics*, **12**, 1045.

Perdew, J.P., Chevray, J.A., Vosko, S.H., *et al*. (1992). *Physical Review B*, **46**, 6671.

Prokorov, A.S. and Rudashevskii, E.G. (1969). *Zhurnal Eksperimentalnoi i Teoreticheskoi Fiziki (Soviet Physics JETP)*, **10**, 175.

Pureur, P., Creuzet, G. and Fert, A. (1985). *Journal of Magnetism and Magnetic Materials*, **53**, 121.

Rhyne, J.J. and Legvold, S. (1965). *Physical Review*, **138**, A507.

Rinaldi, S. and Cullen, J. (1978). *Physical Review B*, **18**, 3677.

Rouchy, J. and de Lacheisserie, E.T. (1979). *Zeitschrift fur Physik B*, **36**, 67.

Shapira, Y., Yacovicht, R.D. and Nelson, D.R. (1975). *Solid State Communications*, **17**, 175.

Shiga, M. (1981). *Journal of the Physical Society of Japan*, **50**, 2573.

Shiga, M. (1988). *Physica B*, **149**, 293.

Simon, S. (1958). *Zeitschrift fur Naturforschung*, **A13**, 84.

Tatebayashi, T., Ohtsuka, S., Ukai, T. and Mori, N. (1986). *Journal of Magnetism and Magnetic Materials*, **54–57**, 973.

Tsuya, N., Clark, A.E. and Bozorth, R.M. (1964) *Proceedings of the International Conference on Magnetism*, Institute of Physics: London.

Vázquez, M., Hernando, A. and Kronmüller, H. (1986). *Physica Status Solidi*, **b133**, 167.

Victora, R.H. and MacLaren, J.M. (1993). *Physical Review B*, **47**, 11583.

Weinert, M., Wimmer, E. and Freeman, A.J. (1982). *Physical Review B*, **26**, 4571.

Wolf, W.P. and Huan, C.H.A. (1988a). *Journal of Applied Physics*, **63**, 3904.

Wolf, W.P. and Huan, C.H.A. (1988b). *Physical Review*, **37**, 2033.

Wu, R. (1999). *Journal of Applied Physics*, **85**, 6217.

Wu, R. and Freeman, A.J. (1999). *Journal of Magnetism and Magnetic Materials*, **200**, 498.

Wu, R., Gravilenko, V.I. and Freeman, A.J. (2001), In *Modern Trends in Magnetostriction Study and Applications*, *NATO ASI Series*, Gibbs, M.R.J. (Ed.), Kluwer: Dordrecht, p. 1.

Zieglowski, J., Häfner, H.U. and Wohlleben, D. (1986). *Physical Review Letters*, **56**, 193.

Zuberek, R., Szymczak, H., Krishanan, R. and Tessier, M. (1988). *Journal de Physique*, **49**, c81761.

FURTHER READING

Callen, H.B. and Callen, E.R. (1966). *Journal of Physics and Chemistry of Solids*, **27**, 1271.

del Moral, A. (1993). *Introduction Talk, in Magnetoelastic Effects and Applications*, Lanotte, L. (Ed.), Elsevier, Amsterdam, p. 1.

Wang, P.S. and Lüthi, B. (1977). *Physical Review B*, **15**, 2718.

Exchange Coupling in Magnetic Multilayers

David M. Edwards[1] and Andrey Umerski[2]

[1] *Imperial College London, London, UK*
[2] *Open University, Milton Keynes, UK*

1 INTRODUCTION

The recent intensive investigation of magnetic layered structures followed advances in molecular-beam epitaxy (MBE) techniques for preparing samples with atomically flat interfaces between layers. Antiferromagnetic (AF) exchange coupling between ferromagnetic (FM) films across a nonferromagnetic metallic spacer was first clearly observed in Fe/Cr/Fe(001) structures by Grünberg *et al*. (1986). About the same time, the study of exchange coupling in rare-earth-based multilayers also began (Majkrzak *et al*., 1986; Salamon *et al*., 1986). Work on transition metal (TM)-based multilayers intensified following the discovery of the giant magnetoresistance (GMR) effect in antiferromagnetically coupled Fe/Cr systems (Baibich *et al*., 1988; Binasch, Grünberg, Saurenbach and Zinn, 1989). In this chapter, we confine ourselves to the discussion of interlayer exchange coupling (IEC) in TM-based systems.

An important early development in the study of IEC was the discovery by Parkin, More and Roche (1990) that the nature of the coupling oscillates between AF and FM alignments, as the thickness of the spacer is varied. In samples with AF coupling, the strength of the coupling was measured by the magnetic field required to saturate the total moment of the system. In the case of FM coupling, all the moments are aligned parallel, and only a small field, unrelated to the coupling strength, is required for saturation. The first measurements of oscillatory exchange coupling, made on sputtered Fe/Cr/Fe and Fe/Ru/Fe multilayers, were followed by similar ones with a wide range of 3d, 4d, and 5d TM spacers (Parkin, Bhadra and Roche, 1991). Surprisingly, all samples exhibited only long-wavelength oscillations with the same period of about 10 Å, with the exception of Cr where the observed period was about 18 Å. These results were clearly inconsistent with the emerging Ruderman–Kittel–Kasuya–Yosida (RKKY) (Bruno and Chappert, 1991, 1992) and quantum well (QW) (Edwards and Mathon, 1991; Edwards, Mathon, Muniz and Phan, 1991a,b) theories. As discussed later, in these theories, oscillation periods are related to spanning vectors of the spacer Fermi surface and should therefore vary from metal to metal. The source of this discrepancy must lie in the sputtering method of preparing the multilayers. This technique is quick and relatively inexpensive, as required for production of GMR devices, but the resultant structure is not well known. It has been

Handbook of Magnetism and Advanced Magnetic Materials. Edited by Helmut Kronmüller and Stuart Parkin. Volume 1: *Fundamentals and Theory*. ISBN: 978-0-470-02217-7.

suggested that polycrystallinity with different grain orientations could lead to an averaging effect which might produce Parkin's almost universal 10 Å period. The result still remains mysterious.

The MBE technique has several advantages over sputtering, including generally sharper interfaces, with less interdiffusion, and epitaxial growth with known crystal orientation. The greater speed of deposition by sputtering is offset, in studies of oscillatory exchange coupling, by the ability of MBE to produce samples with a wedged shaped spacer layer. Measurements of the IEC can then be carried out for many different spacer thicknesses on a single sample. The wedge geometry is obtained by moving a shutter in front of the sample during deposition of the spacer material. The gradient of the sloping face of the wedge can be as small as 1 monolayer (ML) per mm with sample sizes of up to 10 mm. Local measurements of the IEC for many different spacer thicknesses are then not affected by the wedge geometry. The wedged-spacer technique was pioneered by Grünberg's group using Fe/Cr/Fe samples grown on GaAs substrates (Demokritov, Wolf and Grüunberg, 1991), where they found only strongly damped long-wavelength oscillations of the IEC with a period of about 12 ML ($\simeq$17 Å).

A major breakthrough in the study of IEC occurred with the discovery of short-wavelength oscillations in Fe/Cr/Fe(001). The NIST group (Unguris, Celotta and Pierce, 1991; Unguris, Pierce, Celotta and Stroscio, 1993; Pierce, Unguris and Celotta, 1994) found oscillations of the exchange coupling with Cr thickness, with a period of about 2 ML. In these samples, a Cr wedge was grown on an atomically flat Fe whisker substrate at a raised temperature ($>$250 °C). Measurements on samples grown at lower substrate temperatures revealed only the long 12 ML period. It was concluded that the IEC is the sum of two components with long and short periods. These results demonstrate the importance of having smooth interfaces for a complete study of IEC. It is, of course, not surprising that local variations in spacer thickness will wash out 2 ML period oscillations. The NIST work made use of a scanning electron microscope with polarization analysis (SEMPA) which detects the sign of the coupling but not its magnitude. In later work on Fe/Au/Fe(001), the same group combined this technique with magneto-optical Kerr effect (MOKE) measurements which additionally determine the magnitude of the coupling (Unguris, Celotta and Pierce, 1997). These measurements are discussed later in Section 7.1, since they represent one of the very few cases where a meaningful comparison can be made between experiment and theoretical calculations based on perfect interfaces.

We present this brief history of IEC as a background to the theoretical work, which is the main concern of this chapter. It is clear that one must beware of too naive a comparison between theory and experiment.

So far, we have only considered coupling between magnetic layers that is either FM or AF, leading to parallel or antiparallel orientations of the two magnetizations. In fact, 90° coupling with magnetizations at right angles is also observed. To describe this possibility, it is conventional to introduce a phenomenological coupling energy, per unit interfacial area, of the form

$$\begin{aligned} E(\theta) &= -J_1 \mathbf{m}_1.\mathbf{m}_2 - J_2(\mathbf{m}_1.\mathbf{m}_2)^2 \\ &= -J_1 \cos\theta - J_2 \cos^2\theta \end{aligned} \tag{1}$$

where $\mathbf{m}_1$ and $\mathbf{m}_2$ are unit vectors in the directions of the two magnetizations and θ is the angle between them. The parameters J_1 and J_2 determine the type and the strength of the coupling. If the term J_1 dominates, the coupling is FM (AF) for positive (negative) J_1, respectively. If the term J_2 dominates and J_2 is negative, the energy is a minimum for $\theta = \pi/2$, so that 90° coupling is stable. The J_2 term is called *biquadratic coupling* and the J_1 term is sometimes called *bilinear coupling*. In much of the theoretical work the quantity calculated is $E(0) - E(\pi) = E_{\mathrm{FM}} - E_{\mathrm{AF}} = -2J_1$.

It is expected that some readers of this chapter will not wish to explore the finer details of the theory. Section 2 is therefore intended to give a broad overview of exchange coupling between magnetic layers and its relation to the existence of QW states and resonances in the spacer region. In Section 3, we describe a simple free-electron model which demonstrates many important features with explicit analytic formulas. These features include the oscillations of the bilinear and intrinsic biquadratic coupling as a function of spacer thickness, the temperature dependence of these couplings, and the nature of the induced moment within the spacer. In Section 4, we sketch the methods used for obtaining quantitative results for the IEC in real systems. Section 5 is concerned with intrinsic and nonintrinsic mechanisms for biquadratic coupling, with particular reference to the role of interface roughness. In Section 6, it is shown how temperature dependence of the IEC arises from both single-particle and spin-wave excitations. Theory and experiment are brought together in Section 7 for systems with spacers classified as noble metal, TM, and AF metal (particularly chromium) or insulator. In the final section, the current status of the IEC is summarized and the outlook for future work is discussed.

2 QUANTUM WELL STATES AND EXCHANGE COUPLING

In this section, we discuss some of the basic theoretical ideas behind the QW theory of the IEC. In Section 2.1,

we apply the free-electron model to a simple QW. We calculate the density of states for this system and observe that this oscillates both as a function of the well width and as a function of the electron energy relative to the bottom of the well. Although this model is simple, it contains many of the essential features of more sophisticated models, and we can compare it qualitatively to results obtained from photoemission experiments. In Section 2.2, we discuss two methods of calculating the exchange coupling between magnetic layers, and show how its oscillations, as a function of spacer thickness, are related to QW states, with periods determined by extremal points of the spacer Fermi surface. Finally in Section 2.3, we describe a quantitative calculation of exchange coupling in a Co/Cu/Co(001) trilayer (Mathon *et al*., 1995, 1997). We interpret the results on the basis of our findings in the earlier two subsections, and compare with experiment.

2.1 QW states in a trilayer

Consider a simple free-electron model of an A/B/A trilayer. The potential energy is depicted in Figure 1(a), where y is the electron coordinate perpendicular to the layers. The thickness of the B layer is l and the depth of the well is V. Electron states Ψ satisfy the Schrödinger equation

$$\frac{-\hbar^2}{2m}\nabla^2\Psi + V(y)\Psi = E\Psi \tag{2}$$

and, owing to in-plane translational symmetry, are classified by a Bloch wave vector $\boldsymbol{k}_\parallel = (k_x, 0, k_z)$. Thus,

$$\Psi = e^{i\boldsymbol{k}_\parallel\cdot\mathbf{r}}u(y) \tag{3}$$

where the electron position $\mathbf{r} = (x, y, z)$. On substituting equation (3) in equation (2) we find that $u(y)$ satisfies the one-dimensional (1D) Schrödinger equation

$$\mathcal{H}u \equiv \frac{-\hbar^2}{2m}\frac{d^2u}{dy^2} + V(y)u = E'u \tag{4}$$

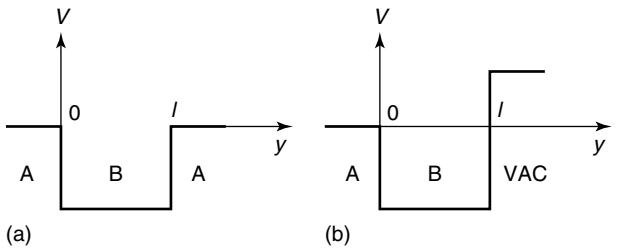

Figure 1. Potential energy $V(y)$ of an electron in (a) an A/B/A trilayer (b) an A/B/VAC system corresponding to a B overlayer on an A substrate.

with $E' = E - \hbar^2\boldsymbol{k}_\parallel{}^2/(2m)$. For a given $\boldsymbol{k}_\parallel$, we take the zero of energy to be such that $E' = 0$ corresponds to the bottom of the well. Thus if E_F is the actual Fermi energy measured from the bottom of the well, electrons fill states in the 1D well up to $E'_\mathrm{F} = E_\mathrm{F} - \hbar^2\boldsymbol{k}_\parallel{}^2/(2m)$. If $E'_\mathrm{F} \le 0$, there are no occupied states with the given $\boldsymbol{k}_\parallel$. Figure 1(b) shows the potential $V(y)$ for the system A/B/VAC, where an overlayer B of thickness l separates the semi-infinite layer A from the vacuum. This is the potential corresponding to angle-resolved photoemission (ARPES) from an overlayer in which electrons are emitted from states of definite $\boldsymbol{k}_\parallel$, for example, $\boldsymbol{k}_\parallel = 0$. The measurement probes the density of states $\rho(E, l)$ of the 1D well. For the present simple discussion, it is sufficient to consider the symmetric well of Figure 1(a).

In general, the eigenstates of the 1D well consist of a number of discrete bound states with $E' < V$ and a continuum of states with $E' > V$. As $\boldsymbol{k}_\parallel$ is varied, we may have a change in the nature of states near the effective Fermi level from continuum for $\boldsymbol{k}_\parallel = 0$ to bound states for some finite $\boldsymbol{k}_\parallel$. The density of states in the region of the well is given by

$$\rho(\mathrm{E}', l) = \int_0^l \mathrm{d}y \sum_i |u_i(y)|^2\,\delta(E' - E_i) \tag{5}$$

$$= -\frac{1}{\pi}\mathrm{Im}\int_0^l \mathrm{d}y\; G(y, y, E'_+) \tag{6}$$

Here $u_i(y)$ and E_i are the eigenfunctions and eigenvalues of the Hamiltonian $\mathcal{H}$ in equation (4) and $G(y, y', E'_+)$ is the one-particle Green function $\langle y\,|(E' - \mathcal{H})^{-1}|\,y'\rangle$. E'_+ signifies that E' has an infinitesimal positive imaginary part. The Green function is straightforward to calculate and we find that, in the continuum region $E' > V$,

$$\pi V\rho(E', l) = \frac{d(2\varepsilon - 1)(\varepsilon - 1)^{1/2}}{\sin^2(d\sqrt{\varepsilon}) + 4\varepsilon(\varepsilon - 1)} \tag{7}$$

where $\varepsilon = E'/V$ and $d = l(2mV/\hbar^2)^{1/2}$ are dimensionless energy and well-width variables. Now

$$d\sqrt{\varepsilon} = l\sqrt{\frac{2E'm}{\hbar^2}} = k_y l \tag{8}$$

where $E = (\hbar^2/2m)(\boldsymbol{k}_\parallel{}^2 + k_y^2)$. Thus $k_y(\boldsymbol{k}_\parallel, E)$ is the k_y coordinate of a point on the constant energy surface of energy E and with a given $\boldsymbol{k}_\parallel$. Clearly, from equation (7), $l^{-1}\rho(\mathrm{E}', l)$ is a periodic function of l with period π/k_y. In the later development, this periodicity property of the density of states turns out to be very useful, and even for nonspherical energy surfaces, the period is found to be determined by the same dimension k_y of the constant energy surface.

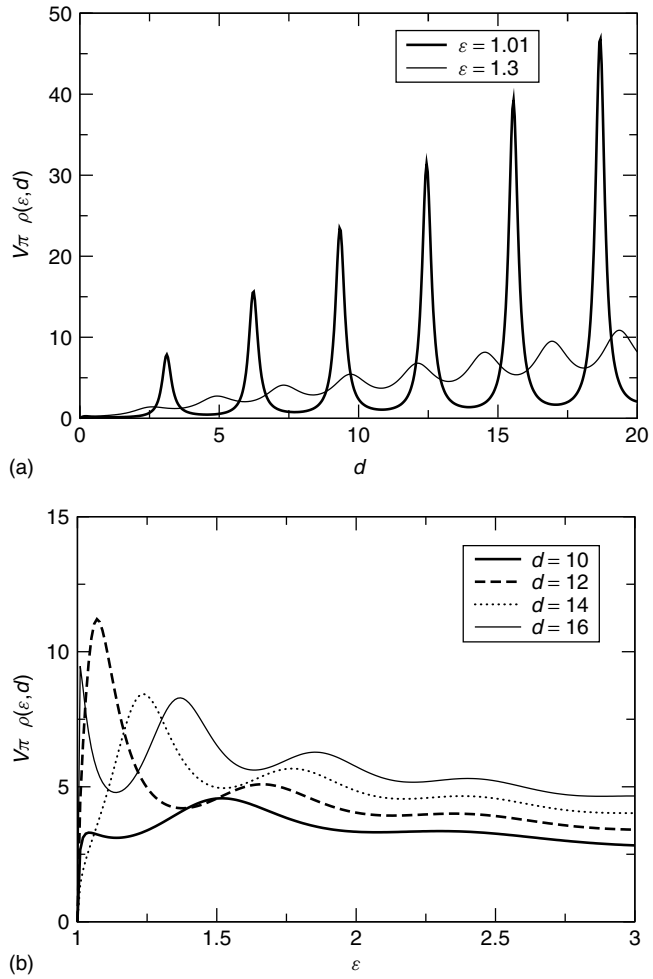

Figure 2. (a) Scaled density of states in the well region (RH side of equation (7)), as a function of dimensionless well width d, for reduced energies $\varepsilon = 1.01$ (thick line) and $\varepsilon = 1.3$ (thin line). (b) Same scaled density of states as in (a), as a function of reduced energy ε for $d = 10, 12, 14, 16$.

In Figure 2(a), the right-hand (RH) side of equation (7) is plotted as a function of d, the dimensionless width of the well, for two energies $\varepsilon = 1.01$ and 1.3. The first case corresponds to an energy E' just above the top of the well and sharp resonances, corresponding to nearly bound states, pass through this energy as d is varied. For $\varepsilon = 1.3$ the resonances are much broader. For E' below the top of the well ($\varepsilon < 1$) the resonances would become δ-functions, corresponding to bound states. In Figure 2(b), the RH side of equation (7) is plotted as a function of ε ($\varepsilon > 1$) for various values of d. This shows how the resonances seen in the density of states shift in energy with changing well width.

Figure 2(a) and (b) may be compared qualitatively with the spectral density observed by Ortega, Himpsel, Mankey and Willis (1993), in ARPES and inverse photoemission with $\boldsymbol{k}_\parallel = 0$, from Cu overlayers on Co(001) or Fe(001). The results of Ortega, Himpsel, Mankey and Willis (1993) shown in Figure 3(a), corresponding to electrons emitted from the Fermi level, are similar to the plots in Figure 2(a). This shows that QW resonances exist in the Cu overlayer and the relation of the oscillation period to the Cu Fermi surface is discussed later. The simple linear increase in amplitude is not observed since not all the photoemitted electrons originate in the overlayer, and in any case, emission is not uniform throughout the overlayer. The spectra shown in Figure 3(b) may be compared with Figure 2(b) with a similar upward shift in resonances as the Cu thickness increases.

Electrons in a ferromagnet such as Co and Fe have a spin-dependent potential energy, the difference in energy between that for minority and majority spin corresponding to an exchange splitting of 1 or 2 eV. Consequently, the QW in a nonmagnetic overlayer has a different depth for the two spin orientations. The effect of this is seen in the spin-resolved photoemission results of Garrison, Chang and Johnson (1993), shown in Figure 3(c), where QW resonances are seen clearly only for minority spins. In general, oscillations in the spectral density of large amplitude are associated with QW states strongly confined in the nonmagnetic layer.

2.2 Relation of QW states to exchange coupling

There are two starting points for a quantitative calculation of exchange coupling. The first proceeds directly from the definition of exchange coupling between two semi-infinite magnetic layers across a nonmagnetic spacer layer of thickness $l = Nd$. Here, d is the interplane spacing and N is the number of atomic planes in the spacer. Thus, we define the exchange coupling as

$$J(l) = \Omega_{\uparrow\uparrow} - \Omega_{\uparrow\downarrow} \tag{9}$$

where $\Omega_{\uparrow\uparrow}$ and $\Omega_{\uparrow\downarrow}$ are thermodynamic potentials of the trilayer per unit cross-sectional area for the parallel and antiparallel configuration of the magnetic moments of the magnetic layers, respectively. The first method of calculating $J(l)$, which we use in this section, is to calculate this energy difference directly.

A second method, which we discuss later, is the torque method in which we consider the nonequilibrium situation where the magnetic moments of the two magnetic layers make an arbitrary angle θ with each other. If the corresponding thermodynamic potential is $\Omega(\theta)$ we define

$$J(l, \theta) = \Omega(0) - \Omega(\theta) = \int_0^\theta -\frac{\mathrm{d}\Omega}{\mathrm{d}\theta}\,\mathrm{d}\theta \tag{10}$$

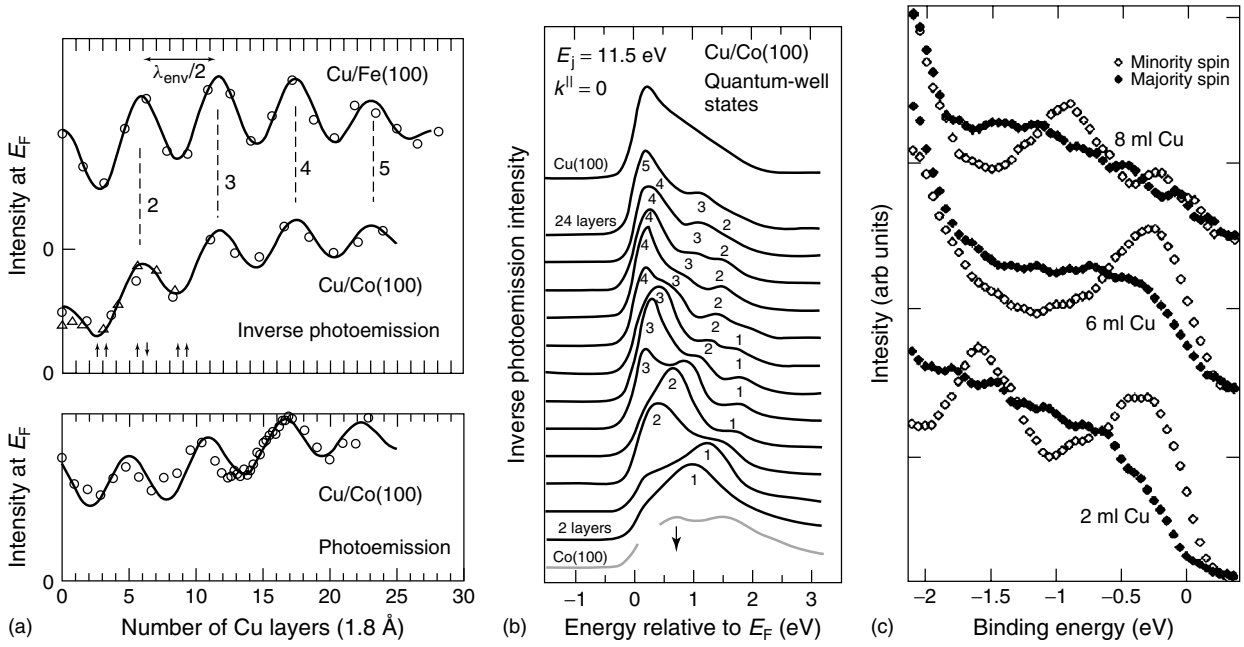

Figure 3. (a) Quantum well resonances in Cu overlayers on Co(001) observed by Ortega, Himpsel, Mankey and Willis (1993) cf. simple theoretical picture of Figure 2(a). (Reprinted figure Ortega, J.E., Himpsel, F.J., Mankey G.J., and Willis, R.F., (1993), *Phys. Rev. B*, **47**, 1540–1552. © 1993 by the American Physical Society.) (b) Inverse photoemission spectra for Cu overlayers of different thickness on Co(001) (Ortega, Himpsel, Mankey and Willis, 1993) cf. simple theoretical picture of Figure 2(b). (Reprinted figure Ortega, J.E., Himpsel, F.J., Mankey G.J., and Willis, R.F., (1993), *Phys. Rev. B*, **47**, 1540–1552. © 1993 by the American Physical Society.) (c) Spin-resolved photoemission spectra (Garrison, Chang and Johnson, 1993) for Cu overlayers on Co(001) showing distinct QW resonances for minority spin only. (Reprinted figure from Garrison, K., Chang Y., and Johnson, P.D., (1993), *Phys. Rev. Lett.*, **71**, 2801–2804. © 1993, by the American Physical Socirty.)

The integrand $-\mathrm{d}\Omega/\mathrm{d}\theta$ is the torque exerted on one magnetic moment by the other and is related to the spin current flowing across the spacer in the nonequilibrium configuration considered. We discuss this in Section 3. Clearly, from equations (9) and (10), $J(l) = J(l, \pi)$ so that $J(l)$ can be calculated by integrating torque instead of taking the energy difference. Both methods have been used and are known to be equivalent (Umerski unpublished; and see Edwards, Robinson and Mathon (1995) for the one-band case). The torque method was first used by Slonczewski (1989) for the case of an insulating spacer.

To evaluate equation (9) we make two approximations. The first is the so-called force theorem (Pettifor and Varma, 1979), which states that a good approximation to a total energy difference between different structures (in this case, magnetic) is obtained by comparing sums of one-electron energies, using atomic potentials which are independent of the magnetic configurations. The second approximation is to neglect the dependence of the local densities of states within the magnetic layers on the magnetic configuration. This approximation can be checked and is found to be a good one, at least for spacer thicknesses that are not too small. Thus, at temperature $T = 0$,

$$J(l) = \sum_{\boldsymbol{k}_\parallel} \int_{-\infty}^{\mu} (E - \mu) \left\{ [\rho_\uparrow + \rho_\downarrow]_{\mathrm{FM}} - [\rho_\uparrow + \rho_\downarrow]_{\mathrm{AF}} \right\} \mathrm{d}E \tag{11}$$

where μ is the chemical potential. Here $\rho_\sigma = \rho_\sigma(\boldsymbol{k}_\parallel, E, l)$ is the density of states within the spacer for a given wave vector $\boldsymbol{k}_\parallel$ and spin $\sigma = \{\uparrow, \downarrow\}$; these densities of states are calculated for the FM and AF configurations as indicated. At finite temperature T, the factor $E - \mu$ is replaced by $-k_\mathrm{B}T \ln(1 + \exp((\mu - E)/k_\mathrm{B}T))$.

Now, as pointed out in Section 2.1, $l^{-1}\rho_\sigma(\boldsymbol{k}_\parallel, E, l)$ is a periodic function of l with period π/k_y where $k_y = k_y(\boldsymbol{k}_\parallel, E)$ defines the bulk spacer constant energy surface with energy E. This periodicity property has been rigorously proved by Umerski (1997). Thus, we may introduce the Fourier series

$$l^{-1}\rho_\sigma(\boldsymbol{k}_\parallel, E, l) = \sum_n c_{n\sigma}(\boldsymbol{k}_\parallel, E) e^{2inlk_y(\boldsymbol{k}_\parallel, E)} \tag{12}$$

and substitute into equation (11). This is very convenient because for large l we may use the stationary phase approximation (SPA) to evaluate the integrals over $\boldsymbol{k}_\parallel$ and E in

equation (11). The dominant contribution arises from $E \sim \mu$ and from points $\boldsymbol{k}_\parallel = \boldsymbol{k}_\parallel{}^0$ where the function $k_y(\boldsymbol{k}_\parallel, \mu)$ is stationary. Thus oscillations in $\rho_\sigma(\boldsymbol{k}_\parallel{}^0, \mu, l)$, which arise from QW states passing through the Fermi level μ as spacer thickness l varies, give rise to corresponding oscillations in the exchange coupling $J(l)$. Oscillations of large amplitude are associated with strongly confined QW states, as pointed out in Section 2.1, so that one of the terms in equation (11), for example, $[\rho_\downarrow]_{\mathrm{FM}}$ in the case of Co/Cu/Co(001), may be the most significant. We discuss the Co/Cu/Co example further in the next section.

2.3 Co/Cu/Co(001) trilayers

Figure 4 shows a sketch of a cross section of part of the Cu Fermi surface. k_y is in the (001) direction and $\boldsymbol{k}_\parallel$ in the (110) direction. The dashed line is the zone boundary $k_y = \pi/d$. The two stationary points of $k_y(\boldsymbol{k}_\parallel, \mu)$ are indicated: $k_y = k_y^B$ occurs at $\boldsymbol{k}_\parallel = \boldsymbol{0}$ and the other $k_y = k_y^N$ at a finite value $\boldsymbol{k}_\parallel{}^0$. The corresponding oscillation periods are influenced by the discrete nature of the lattice, which we have not considered before. Thus $l = Nd$ where N is an integer, and in this case d is the interplanar Cu distance, so that $\exp(2inlk_y) = \exp(2inl(k_y - \pi/d))$. When $\pi/d - k_y < k_y$ the observed period, considering the function of l only at discrete points Nd, is $\pi/(\pi/d - k_y)$ rather than π/k_y (this is known as the *aliasing effect*). The stationary point at $\boldsymbol{k}_\parallel = \boldsymbol{0}$ therefore corresponds to a long period, in fact 5.9 ML, which is the one seen in Figure 3(a). The other stationary point corresponds to a shorter period of 2.6 ML (∼4.7 Å) and contributions with both periods should occur in the exchange coupling. Recently, the shorter period has been observed (Klässges *et al*., 1998) in ARPES from Cu overlayers on Co(001) with $\boldsymbol{k}_\parallel \sim \boldsymbol{k}_\parallel{}^0$.

Mathon *et al*. (1995, 1997) calculated the exchange coupling in Co/Cu/Co(001) trilayers using a fully numerical method, based on the torque (or 'cleavage') formalism, as well as the semi-analytic SPA described above. Both methods use a tight-binding model, with nine orbitals (3d, 4s, 4p) and parameters fitted to first-principles calculations for the bulk metals. Given this model, the fully numerical method relies further only on the force theorem, and the stationary phase method should give the same results for large l. Here, we just discuss the results since more detail is given in Mathon *et al*. (1995, 1997) and in Section 4 of this chapter.

In Figure 5, we show a comparison between the numerical results for exchange coupling J and the SPA. As expected, the latter is very accurate when the number N of Cu planes is large. Clearly the oscillatory exchange coupling is dominated by the short-period contribution. The SPA, which has the advantage of being able to separate the two contributions, shows that the long-period contribution is less than 1% of the total. The reason for this is easy to understand in terms of confinement of QW states.

Figure 6(a) shows the energy bands for bulk Co (majority and minority spin) and for Cu, along a line in **k** space in the k_y direction with $\boldsymbol{k}_\parallel = \boldsymbol{k}_\parallel{}^0$ corresponding to a short-period Fermi-surface extremum (see Figure 4). There is a good match between the sp-like bands for Cu and Co majority spin where they cross the Fermi level $\mu = E_{\mathrm{F}}$. However, for Co minority spin, the Fermi level falls in an almost

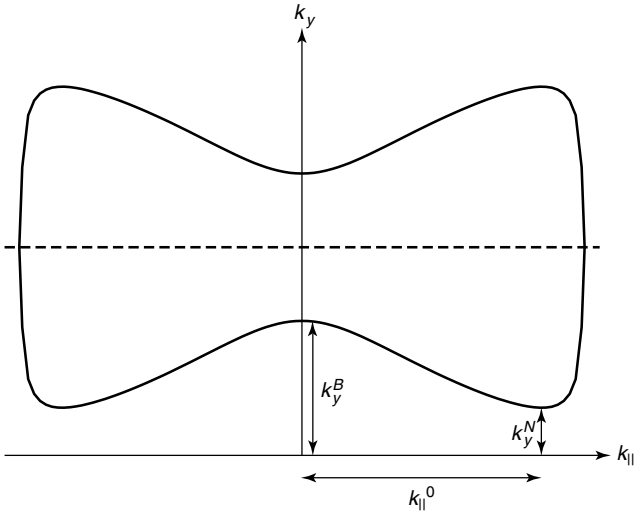

Figure 4. Sketch of a cross section of part of the Cu Fermi surface, showing two extreme values of k_y, namely, k_y^B and k_y^N, which occur at $\boldsymbol{k}_\parallel = 0$ and $\boldsymbol{k}_\parallel = \boldsymbol{k}_\parallel{}^0$ respectively.

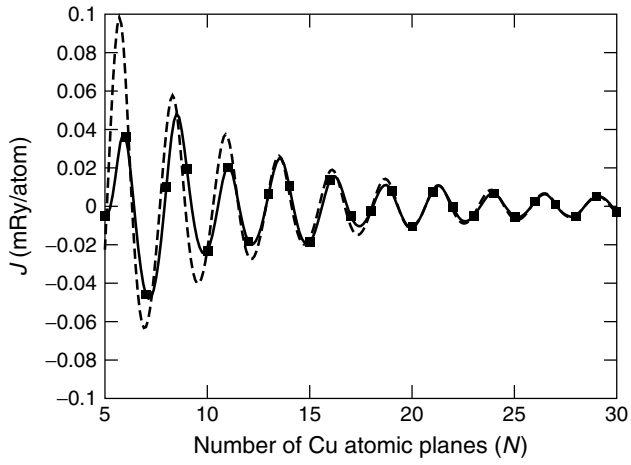

Figure 5. Exchange coupling in a Co/Cu/Co(001) trilayer calculated as a function of Cu thickness, fully numerically (full line) and using SPA (dashed line). (Reprinted figure Mathon, J. *et al*., 1997, *Phys. Rev. B*, **56**, 11797–11809. © 1997 by the American Physical Society.)

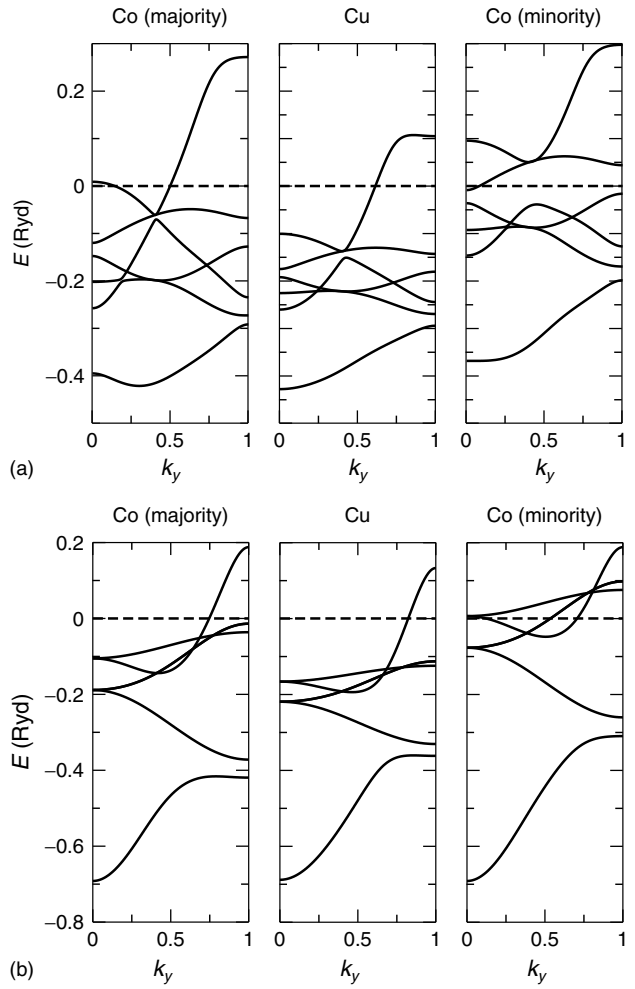

Figure 6. (a) Energy bands for Cu and FM fcc Co along a line in the k_y direction with $\boldsymbol{k}_\parallel = \boldsymbol{k}_\parallel{}^0$ corresponding to a short-period Fermi-surface extremum (see Figure 4). (Reprinted figure Mathon, J. *et al*., 1997, *Phys. Rev. B*, **56**, 11797–11809. © 1997 by the American Physical Society.) (b) Energy bands as in (a) but with $\boldsymbol{k}_\parallel = 0$ corresponding to the long-period Fermi-surface extremum. (Reprinted figure Mathon, J. *et al*., 1997, *Phys. Rev. B*, **56**, 11797–11809. © 1997 by the American Physical Society.)

complete hybridization gap. Thus, in the FM configuration of the Co/Cu/Co trilayer, minority spin electrons at the Fermi level are strongly confined in the Cu layer, which therefore acts like a deep QW in the simple free-electron picture we used in Section 2.1. However, the majority spin electrons are hardly confined at all and will make only a small contribution to QW oscillations in photoemission and exchange coupling. In the AF configuration, electrons of both spin are free to escape into one of the Co layers and therefore contribute weakly to QW oscillations. Thus, the short-period oscillations of Figure 5 arise largely from the minority spin spectral density $[\rho_\downarrow]_{\mathrm{FM}}$ in equation (11). The situation is quite different for $\boldsymbol{k}_\parallel = 0$, corresponding to the long-period Fermi-surface extremum. The sp-like band crosses E_{F} at very similar values in both spin bands of Co and in Cu, as shown in Figure 6(b). Thus, there are no strongly confined QW states of either spin for $\boldsymbol{k}_\parallel = 0$. Consequently, the long-period oscillations in J are much weaker than the short-period ones, as found in the calculations. Nevertheless, the long-period oscillations can be seen in photoemission, at least for minority spin electrons, as described earlier.

The experimental situation is complicated by interfacial roughness. For an oscillation period close to 2 ML, the sign of the exchange coupling is changed by adding a spacer atomic layer. Thus, the presence of steps will tend to reduce the amplitude of this component when averaged over the sample. The short-period oscillation in Cu is clearly much more susceptible to this effect than the long-period one. Johnson *et al*. (1993) and Bloemen *et al*. (1993) found in their experiments that the amplitudes of the short- and long-period oscillations are comparable. Their value of J at the first AF peak ($0.4\,\mathrm{mJ\,m^{-2}}$) is about three times smaller than that found by Mathon *et al*. (1997), which may well be attributed to roughness. Kawakami *et al*. (1999) also concluded that the amplitude ratio is about 1 and discuss their results in terms of QW states observed in ARPES (see also Qiu and Smith, 2002). Weber, Allenspach and Bischof (1995), using a SEMPA, estimate that, in their 'best' samples, the amplitude of the short-period oscillation is at least a factor 7 larger than that of the long-period oscillation. This is more in accord with the predictions of Mathon *et al*. (1997). Unfortunately, SEMPA does not give the absolute values of the exchange coupling.

3 CALCULATION OF THE EXCHANGE COUPLING AND INDUCED MAGNETIZATION IN A PARABOLIC BAND MODEL

In this section, we consider a particularly simple free-electron model (Hathaway and Cullen 1992; Edwards, Ward and Mathon, 1993) of a magnetic trilayer, consisting of two FM metallic layers separated by a nonmagnetic metallic spacer layer. We assume infinite exchange splitting in the ferromagnets, so that minority spin electrons do not penetrate them at all and assume that majority spin electrons experience the same constant potential (taken as zero) as the spin independent potential in the spacer. The advantage of this somewhat idealized model is that it is fully solvable, and contains much of the physical behavior observed in more sophisticated tight-binding or *ab initio* calculations of realistic systems (Edwards, Ward and Mathon, 1993; Mathon *et al*., 2000).

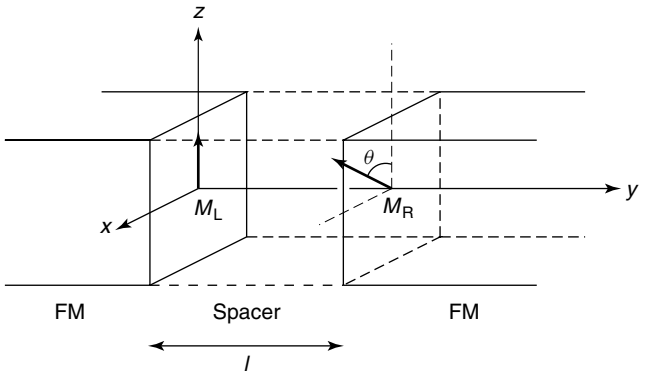

Figure 7. Schematic representation of a trilayer, showing left and right semi-infinite ferromagnets separated by a nonmagnetic spacer layer of width l. The magnetization in the LH ferromagnet is along the z axis while that in the RH ferromagnet makes an angle θ with the z axis. The growth axis is along y.

The geometry of the system is depicted in Figure 7. We select a Cartesian system of coordinates with the x and z axes in the plane of the layers and the y axis along the growth direction. We suppose that the spacer has width l and occupies the region $|y| < l/2$, whereas the ferromagnets occupy the regions $l/2 < |y| < L$. We also assume that the potential is infinite for $|y| > L$, but eventually let $L \to \infty$ so that the ferromagnets become semi-infinite. The magnetizations of the left-hand (LH) and RH ferromagnets are constrained to be in the directions shown in Figure 7, making an angle θ with each other.

The electron eigenstates ψ are classified by a wave vector $\boldsymbol{k}_\parallel$ parallel to the layers and either an energy E or a wave vector k_y in the spacer, such that $E = \hbar^2(k_\parallel^2 + k_y^2)/2m$. The spin current $j(\boldsymbol{k}_\parallel, k_y)$ carried by an electron in this state is given by

$$\mathbf{j}(\boldsymbol{k}_\parallel, k_y) = \frac{i\hbar^2}{4m}\left(\frac{\mathrm{d}\boldsymbol{\psi}^\dagger}{\mathrm{d}y}\boldsymbol{\sigma}\boldsymbol{\psi} - \boldsymbol{\psi}^\dagger\boldsymbol{\sigma}\frac{\mathrm{d}\boldsymbol{\psi}}{\mathrm{d}y}\right) \qquad \text{where}$$
$$\boldsymbol{\psi} = \begin{pmatrix}\psi_\uparrow \\ \psi_\downarrow\end{pmatrix} \tag{13}$$

and $\boldsymbol{\sigma} = (\boldsymbol{\sigma}_x, \boldsymbol{\sigma}_y, \boldsymbol{\sigma}_z)$ are Pauli matrices with spin quantized with respect to the z axis. Note that if $\hbar/2\boldsymbol{\sigma}$ is replaced by the unit matrix, we recover the usual expression for the particle current. The spin current in the spacer is independent of position y, owing to spin conservation, and the only nonzero component of $\mathbf{j}$ is the y component j_y. On summing $j_y(\boldsymbol{k}_\parallel, k_y)$ over all occupied states (such that $E < \mu$ at $T = 0$), one obtains the rate of transfer of the y component of spin angular momentum across the spacer, and hence the torque $-\mathrm{d}\Omega/\mathrm{d}\theta$ which enters equation (10) for the exchange coupling $J(l, \theta)$. The reason for the torque to be in the y direction in the present geometry is that the constrained RH ferromagnet, for example, is trying to precess about an effective field in the z direction arising from the LH magnet.

The integration over θ in equation (10) is done by expanding $j(\boldsymbol{k}_\parallel, k_y)$ in a Fourier series in k_y. Eventually, one obtains an exact result for the exchange coupling at $T = 0$ and for spacer thickness l

$$J(\theta) = \frac{N_{2\mathrm{d}}E_\mathrm{F}^2}{\pi k_\mathrm{F}^2 l^2}\sum_{s=1}^{\infty}\frac{1}{s^3}\left[1 - \cos^{2s}\left(\frac{\theta}{2}\right)\right] \times\left[\left(1 - \frac{3}{(2sk_\mathrm{F}l)^2}\right)\sin(2sk_\mathrm{F}l) + \frac{3}{2sk_\mathrm{F}l}\cos(2sk_\mathrm{F}l)\right] \tag{14}$$

Here, k_F is the Fermi wave vector in the spacer, E_F is the corresponding Fermi energy, and $N_{2\mathrm{d}}$ is the constant density of states per unit area of the electron gas in two dimensions.

The $s = 1$ term in equation (14) gives the fundamental oscillation in $J(\theta)$ as a function of the spacer thickness l with period π/k_F. If J is only observed at discrete thicknesses $l = Nd$, a longer period of $\pi/|k_\mathrm{F} - \pi/d|$ may be observed owing to the 'aliasing effect', as described in Section 2.3. Subsequent terms $s = 2, 3, \ldots$ give higher harmonics with dependencies on angle θ of increasing complexity. The angular factor may be written as $(1 - \cos\theta)/2$ for the $s = 1$ term and as $(3 - 2\cos\theta - \cos^2\theta)/4$ for the $s = 2$ term. So the biquadratic exchange first occurs in the $s = 2$ harmonic, and generally a $\cos^s\theta$ term first occurs in the sth harmonic.

It is straightforward to include Fermi factors in the sum of the spin current over occupied states, in order to investigate the temperature dependence of the exchange coupling. The result in the limit of large spacer thickness l is

$$J(\theta) = \frac{N_{2\mathrm{d}}E_\mathrm{F}}{\beta\pi k_\mathrm{F} l}\sum_{s=1}^{\infty}\frac{1}{s^2}\left[1 - \cos^{2s}\left(\frac{\theta}{2}\right)\right] \times\left[\frac{\sin(2sk_\mathrm{F}l)}{\sinh(s\pi k_\mathrm{F}l/\beta E_\mathrm{F})}\right] \tag{15}$$

where $\beta = (k_\mathrm{B}T)^{-1}$. Clearly, the sth harmonic is damped exponentially for $T > T_s$, where $k_\mathrm{B}T_s = \hbar v_\mathrm{F}/2s\pi l$, v_F being the Fermi velocity. Thus higher harmonics, including the biquadratic exchange, decay more rapidly than the fundamental oscillation with $s = 1$. Impurity scattering in the spacer also damps the oscillations in the IEC exponentially (see e.g., Levy, Maekawa and Bruno, 1998). The analogy between IEC oscillations and de Haas van Alphen oscillations, where similar damping occurs, has been pointed out by Edwards, Mathon, Muniz and Phan (1991a). In order to make the temperature dependence of the exchange coupling explicit, it is

instructive to write equation (15) as

$$J(T,\theta) = \sum_{s=1}^{\infty} J_s(T,\theta) \qquad \text{where}$$

$$J_s(T,\theta) = J_s(0,\theta)\frac{T/T_s}{\sinh(T/T_s)} \tag{16}$$

The temperature dependence exhibited in this simple free-electron model closely resembles the temperature dependence of the exchange coupling for very general spacer band structures which we explore in Section 6.

The nonmagnetic spacer between the two magnetic layers acquires an induced magnetic moment due to the different confinement conditions of up- and down-spin electrons (Mathon *et al.*, 2000). The wave function ψ introduced in the preceding text can be used to calculate this spin density. It is found that the induced magnetization $\boldsymbol{P}(y)$ is coplanar with the magnetizations of the two magnetic layers. Thus $\boldsymbol{P}(y) = P(y)(\sin\phi(y), 0, \cos\phi(y))$, where the 'twist angle' $\phi(y)$ determines how the induced magnetization rotates about the y axis in the spacer. The components of $\boldsymbol{P}(y)$ oscillate with the same period π/k_F as the exchange coupling.

When the magnetizations of the two FM layers are collinear ($\theta = 0$ or π), the twist angle $\phi(y) = 0$, so that the induced moment is also collinear. In the general case when $\theta \neq 0$, Mathon *et al.* (2000) have shown, both for the simple free-electron model considered here and for a multiorbital tight-binding calculation of a Co/Cu/Co(001) trilayer, that the induced moment rotates along a complex three-dimensional spiral and can undergo many complete 360° rotations. Figure 8 displays $\phi(y)$ as a function of y for spacers of thicknesses $l = 8, 10, 14, 16$, with $\theta = \pi/2$. For $l = 8$, the induced moment rotates straightforwardly from 0 to $\pi/2$ with most of the rotation occurring near the middle of the spacer. For $l = 10$, the behavior is already strikingly different. Rather than a rotation from 0 to $\pi/2$, the induced moment reaches $\pi/2$ at $y = l$ by undergoing a slow rotation through an angle of $-3\pi/2$. For $l = 14, 16$, we now reach the typical behavior of induced moment. It rotates through $\pi/2$ several times before finally aligning itself with the magnetization in the right ferromagnet. Not only does this mean that the induced moment rotates by more than 2π but the manner of rotation is itself remarkable. The angle ϕ shows almost constant plateaus, followed by sharp variations.

Several factors probably contribute to this rather bizarre behavior. Firstly, the induced moment is very small and, secondly, electron–electron interactions in the spacer have been neglected. One can imagine a different situation with a spacer such as Pd, which is a paramagnet on the verge of ferromagnetism owing to electron interaction. The induced moments would be larger and would possess an exchange stiffness, which would inhibit rapid rotation. A rather uniform simple twist might be expected as in a domain wall of a ferromagnet. Similar behavior is discussed in Section 7.3 for an AF spacer. The actual behavior of the induced moment in noble metal and TM spacers deserves further consideration.

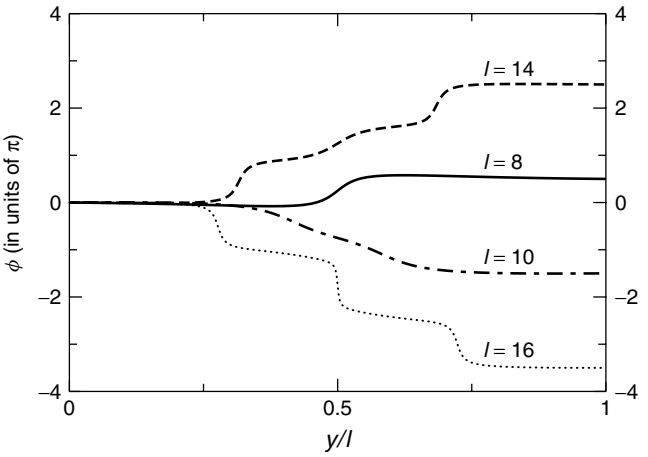

Figure 8. Dependence of the twist angle $\phi(y)$ on the distance from the left ferromagnet/spacer interface for spacer thicknesses $l = 8, 10, 14, 16$ and $\theta = \pi/2$.

4 CALCULATION OF IEC IN MODELS OF REAL SYSTEMS

The standard approach to realistic calculation of the ground state properties of an electronic system makes use of density-functional theory within the local spin-density approximation (LSDA). For a magnetic trilayer or superlattice the total energies of the FM and AF configurations may be calculated and the IEC must then be obtained as the small difference between these two large energies. The one-electron spin-dependent potentials are determined self-consistently in each configuration. This is a computationally slow and difficult task, since typically 10^4 k-points in the in-plane Brillouin zone must be summed over to achieve the required accuracy (Mathon *et al.*, 1997). So the method is usually restricted to relatively thin spacers, where fewer k-points may be used. A much more practical approach is to use the force theorem or frozen potential approximation. Both of these closely related approaches approximate the total energy difference by the difference of sums of one-electron energies over occupied states. In frozen potential approximation, the local one-electron potentials are frequently taken as those corresponding to the bulk magnetic and spacer metals. (For further details and comparison of these methods see Szunyogh, Újfalussy, Weinberger and Sommers, 1996.)

One-electron energies in the given potentials are usually determined by the Korringa–Kohn–Rostocker (KKR) method, the related tight-binding linear muffin tin orbital (TB-LMTO) method or by a straightforward multiorbital tight-binding method. The last method has the advantage of conceptual simplicity and we shall use this approach to sketch the formalism for calculating the IEC in real trilayers. An explicit formula for the IEC is obtained in Section 4.2 which is exact for thick spacers and separates clearly the various oscillatory components.

4.1 The cleavage formula for IEC

The general method is most easily described for a multiorbital tight-binding model with s, p, d orbitals whose one-electron parameters are fitted to first-principles bulk band structure or obtained within an *ab initio* LMTO-tight-binding formulation. Within the one-electron approximation of Section 2.2, we write the Hamiltonian for the magnetic trilayer of Figure 7, in the form

$$H = H_0 + H_P \tag{17}$$

where the one-electron hopping term H_0 is given by

$$H_0 = \sum_{\boldsymbol{k}_\parallel \sigma} \sum_{m\mu,n\nu} t_{m\mu,n\nu}(\boldsymbol{k}_\parallel) c^\dagger_{\boldsymbol{k}_\parallel m\mu\sigma} c_{\boldsymbol{k}_\parallel n\nu\sigma} \tag{18}$$

and H_P contains on-site potentials. These are independent of spin in the spacer, but contain exchange splitting in the ferromagnets. The spin dependence of the exchange potentials in the two ferromagnets is chosen appropriately for their different directions of magnetization. In equation (18), $c^\dagger_{\boldsymbol{k}_\parallel m\mu\sigma}$ creates an electron in a Bloch state, with in-plane wave vector $\boldsymbol{k}_\parallel$ and spin σ, formed from a given atomic orbital μ in plane m. The easiest method of deriving an expression for the IEC within this formulation is to consider a pair of neighboring planes in the spacer (labeled by say n and $n-1$) and to initially 'switch off' the hoppings between them, so that the trilayer is 'cleaved' into two semi-infinite systems. The final expression for the IEC is independent of the position of the 'cleavage plane' within the spacer. Then the Hamiltonian may be written as follows:

$$\begin{aligned} H(\lambda) &= H_{\mathrm{L}} + H_{\mathrm{R}}(\theta) + \lambda H_{\mathrm{LR}} \qquad \text{where} \\ H_{\mathrm{LR}} &= \sum_{\boldsymbol{k}_\parallel \sigma} \sum_{\mu,\nu} t_{n-1\mu,n\nu}(\boldsymbol{k}_\parallel)\; c^\dagger_{\boldsymbol{k}_\parallel n-1\mu\sigma}\; c_{\boldsymbol{k}_\parallel n\nu\sigma} \end{aligned} \tag{19}$$

and H_{L} is the Hamiltonian for the LH semi-infinite system, with the magnetization of the LH ferromagnet in the (0, 0, 1) direction, and H_{R} is the Hamiltonian for the RH semi-infinite system, with the magnetization of the RH ferromagnet in the $(\sin\theta, 0, \cos\theta)$ direction (see Figure 7). The parameter λ represents a coupling constant between the LH and RH systems, so that $H(0)$ corresponds to a cleaved system with no hopping across the cleavage plane, and $H(1) = H$ is the original Hamiltonian.

There are a number of ways in which a formula for the IEC can be derived. One can use a generalization of the energy difference method given in Mathon *et al*. (1997) or the torque method described in Section 3 of this chapter (see also Edwards, 2002) or a method based on Lloyd's formula (Drchal, Kudrnovsky, Turek and Weinberger, 1996). Alternatively, the coupling constant integration method may be used (e.g., Doniach and Sondheimer, 1998). In this case, the change in thermodynamic potential between the cleaved and uncleaved system, obtained by turning on the coupling constant λ, is given by $\delta\Omega = \int_0^1 \langle H_{\mathrm{LR}}\rangle_\lambda \, \mathrm{d}\lambda$, where $\langle H_{\mathrm{LR}}\rangle_\lambda$ denotes the thermal average in the grand canonical ensemble, calculated using the Hamiltonian $H(\lambda)$. The thermodynamic potential of the cleaved system is independent of θ so that the IEC can be written (see equation (10))

$$J(\theta) = \Omega(0) - \Omega(\theta) = \delta\Omega(0) - \delta\Omega(\theta) \tag{20}$$

which after some algebra can be expressed in the form

$$\begin{aligned} J(\theta) = \frac{-1}{\pi} \sum_{\boldsymbol{k}_\parallel} \mathrm{Im} \int dE f(E-\mu) \\ \times \mathrm{Tr} \ln \left(1 - \frac{1-\cos\theta}{2}\mathbf{M}\right) \end{aligned} \tag{21}$$

where

$$\begin{aligned} \mathbf{M} = \mathbf{1} - (\mathbf{1} - \boldsymbol{g}_{\mathrm{R}}^{\uparrow}\boldsymbol{t}^\dagger \boldsymbol{g}_{\mathrm{L}}^{\uparrow}\boldsymbol{t})^{-1}(\mathbf{1} - \boldsymbol{g}_{\mathrm{R}}^{\uparrow}\boldsymbol{t}^\dagger \boldsymbol{g}_{\mathrm{L}}^{\downarrow}\boldsymbol{t})(\mathbf{1} - \boldsymbol{g}_{\mathrm{R}}^{\downarrow}\boldsymbol{t}^\dagger \boldsymbol{g}_{\mathrm{L}}^{\downarrow}\boldsymbol{t})^{-1} \\ \times(\mathbf{1} - \boldsymbol{g}_{\mathrm{R}}^{\downarrow}\boldsymbol{t}^\dagger \boldsymbol{g}_{\mathrm{L}}^{\uparrow}\boldsymbol{t}) \end{aligned} \tag{22}$$

Here, $f(E-\mu)$ is the Fermi function with chemical potential μ, and $\boldsymbol{g}_{\mathrm{L}}^{\sigma}$ and $\boldsymbol{g}_{\mathrm{R}}^{\sigma}$ are surface Green's functions (SGF) for the LH and RH cleaved systems with Hamiltonians H_{L} and H_{R}, respectively. These are matrices with elements $g_{\mu,\nu}$, where μ, ν label the orbitals, and the trace is over these indices. The spin index $\sigma = \uparrow, \downarrow$ refers to the majority and minority spin directions of the corresponding ferromagnet. $\boldsymbol{t}$ is a matrix with μ, ν elements $t_{n-1\mu,n\nu}$ and $\boldsymbol{t}^\dagger$ is its hermitian conjugate.

This form of the IEC was first given by Drchal, Kudrnovsky, Turek and Weinberger (1996), and when $\theta = \pi$ it reduces to the formula of Mathon *et al*. (1997). It is a particularly convenient expression, since the θ dependence is explicit, and does not occur in the calculation of $\mathbf{M}$. The

expansion of this formula in powers of $1-\cos\theta$ to determine the bilinear and biquadratic coupling has been discussed by Drchal, Kudrnovsky, Turek and Weinberger (1996).

Alternative expressions for the IEC have been given by Bruno (1995) and Stiles (1996b, 1999) in terms of reflection and transmission coefficients at interfaces, rather than Green's functions. The form for the IEC, which is usually considered in this approach is one valid in the limit of weak confinement. This approximation amounts to replacing a $\ln(1-X)$ term, similar to that in equation (21), by the leading term X in its power series expansion. The method is not very well adapted to accurate calculation of the IEC in real systems. Quantitative work along these lines for a real trilayer such as Co/Cu/Co(001) is usually restricted to calculation of reflection coefficients (Bruno, 1995), possibly followed by an uncontrolled estimate of the IEC using the weak-confinement approximation (Stiles, 1996b).

4.2 The stationary phase approximation (SPA)

Consider the integrand $F(E,\boldsymbol{k}_\parallel,\theta,l)=Tr\ln(1-\mathbf{M}(1-\cos\theta)/2)$ of equation (21). For each value of $E,\boldsymbol{k}_\parallel,\theta$, it can be shown that (see Umerski, 1997; Mathon and Umerski, 2006; Edwards, 2002) this can be expanded in a Fourier type series:

$$F(E,\boldsymbol{k}_\parallel,\theta,l)=\sum_{\vec{s}} c_{\vec{s}}\,e^{il\phi_{\vec{s}}} \qquad \text{where}$$
$$\phi_{\vec{s}}\equiv 2(s_1k_{y1}+\cdots+s_Pk_{yP}) \qquad (23)$$

where $s_1,\ s_2,\ \ldots,\ s_P$ are integers and $\{\pm k_{y1},\pm k_{y2},\ldots\pm k_{yP}\}$ are the $2P$ solutions of the perpendicular wave vector obtained from the bulk spacer dispersion relation $E(\boldsymbol{k}_\parallel,k_y)=E$. To simplify the present discussion, we restrict ourselves to the case of Fermi surfaces which are symmetric about the $k_y=0$ plane, but see Edwards (2002) for the general case. When the Fermi surface has a single sheet, there are just two solutions $\pm k_y$, and so $\phi_s\equiv 2sk_y$. In this case, $F(E,\boldsymbol{k}_\parallel,\theta,l)$ is a periodic function of the spacer thickness l, with period π/k_y, and the expansion is a standard Fourier series. This case is closely related to the periodicity of the integrand of equation (11), and the expansion corresponds to that of equation (12).

For multisheet Fermi surfaces, the integrand F is said to be a quasiperiodic function of the spacer thickness l, with periods $\pi/k_{y1},\pi/k_{y2},\ldots,\pi/k_{yP}$. Evaluation of the Fourier-like coefficients in this case requires use of the matrix Möbius transformation (Umerski, 1997), and we refer the interested reader to the review articles of Mathon and Umerski (2006) and Edwards (2002). Equation (23) can be substituted into equation (21) for the IEC, and the same argument following that of equation (12) of Section 3 can be applied to obtain a SPA of the IEC. The result is a formula for the exchange coupling, which is asymptotically exact in the limit of large spacer thickness ($l\to\infty$):

$$J(l)=-\frac{(2\pi)^2k_BT}{2lA_{BZ}}\sum_{\vec{s}}\sum_{\mathbf{k}^0_{\parallel\vec{s}}}\mathrm{Re}$$
$$\times\left(\frac{\tau c_{\vec{s}}e^{il\phi_{\vec{s}}}}{|\det(\partial^2\phi_{\vec{s}})|^{1/2}\sinh(\pi k_BT[l\phi'_{\vec{s}}+\psi'_{\vec{s}}])}\right)\Bigg|_{\mu,\mathbf{k}^0_{\parallel\vec{s}}} \qquad (24)$$

Here, $(\partial^2\phi_{\vec{s}})$ is the 2×2 Hessian matrix $(\partial^2\phi_{\vec{s}})_{\alpha,\beta}\equiv\partial^2\phi_{\vec{s}}/\partial k_{\parallel\alpha}\partial k_{\parallel\beta}$, and $\tau=i$ when both eigenvalues of the Hessian matrix are positive, $\tau=-i$ when they are negative, and $\tau=1$ when they have opposite signs. $\phi'_{\vec{s}}\equiv \mathrm{d}\phi_{\vec{s}}/\mathrm{d}E$, $\psi'_{\vec{s}}$ is the derivative of the phase of $c_{\vec{s}}$ with respect to E, and A_{BZ} is the area of the in-plane Brillouin zone. All quantities in equation (24) are evaluated at the chemical potential of the spacer $E=\mu$, and the sum over $\{\mathbf{k}^0_{\parallel\vec{s}}\}$ is over the set of points in the two-dimensional in-plane Brillouin zone at which $\phi_{\vec{s}}(\mathbf{k}_\parallel)$ is stationary.

In the case of a single sheet Fermi surface which is symmetric about the $\boldsymbol{k}_\parallel$ plane, these stationary points coincide with the stationary points of the spacer Fermi surface (i.e., where $k_y(E=\mu,\boldsymbol{k}_\parallel)$) is stationary), and the periods are related to the spanning vectors of the Fermi surface. In the case of Co/Cu/Co(001), these are k_y^B and k_y^N depicted in Figure 4, and equation (24) was used to determine the dashed SPA to Figure 5. For multisheet Fermi surfaces, the stationary points of $\phi_{\vec{s}}$ will include all RKKY periods derived from the extrema of Fermi-surface spanning vectors. However, additional periods arising from more complex linear combinations of Fermi-surface wave vectors are also obtained. In general, these are not merely harmonics of RKKY periods. Such non-RKKY periods even occur in simple models, for example, in a single orbital fcc (110) tight-binding model (Ferreira, d'Albuquerque e Castro, Edwards and Mathon, 1996), as well as in more complex realistic systems such as Fe/Mo/Fe(001) (Edwards, 2002).

It should be noted that a fundamental assumption of the SPA is that the coefficients $c_{\vec{s}}$ of equation (23) are slowly varying functions of the energy, near E_F. Whereas this is found to be true for many realistic systems, Costa, d'Albuquerque e Castro and Muniz (1999) have found that this is not the case for Fe/Au/Fe and Fe/Ag/Fe(001), since electrons at the Fermi energy are very close to deconfinement, and hence their wave functions vary rapidly as a function of energy. As a result, the SPA only becomes an accurate approximation in these systems for extremely thick spacer layers.

5 BIQUADRATIC EXCHANGE COUPLING

5.1 Measurement

Consider two coupled magnetic layers with, for simplicity, the same thickness and magnetization M_0. The magnetocrystalline anisotropy is assumed to have fourfold symmetry and a magnetic field of magnitude H is applied in the plane of the layer (zx plane) along an easy axis (z axis). The magnetic moments of the two layers lie in plane in directions $\mathbf{m}_1 = (\sin\theta_1, 0, \cos\theta_1)$ and $\mathbf{m}_2 = (\sin\theta_2, 0, \cos\theta_2)$. The total energy per unit interfacial area may be written as

$$E_{\text{tot}} = -M_0 D(\cos\theta_1 + \cos\theta_2)H - \frac{KD}{8}(\cos 4\theta_1 + \cos 4\theta_2) - \bar{J}_1\cos(\theta_1 - \theta_2) - \bar{J}_2\cos^2(\theta_1 - \theta_2) \tag{25}$$

where K is the anisotropy constant, $\bar{J}_1$, $\bar{J}_2$ are the bilinear and biquadratic couplings and D is the ferromagnet thickness. In this section, we distinguish between the quantities $\bar{J}_1$, $\bar{J}_2$ which enter E_{tot} for a real, generally imperfect, sample and the couplings J_1, J_2 which pertain to an ideal system with perfect interfaces. For $\bar{J}_2 < 0$ the biquadratic term favors noncollinear alignment of the magnetizations, whereas for $\bar{J}_2 > 0$ it merely reinforces collinear alignment and has essentially no influence on the magnetic properties of the system. Consequently, only negative values of $\bar{J}_2$ are measurable. Following Demokritov (1998), we assume that anisotropy is dominant, this being a common experimental situation. In this case, $\mathbf{m}_1$ and $\mathbf{m}_2$ cannot deviate from the easy axes and only three ground state configurations are possible: FM, AF, and perpendicular (90° coupling). For $H \geq 0$, the corresponding energies E_{tot} are (ignoring the constant term $-KD/4$) $E_{\text{FM}} = -\bar{J}_1 - \bar{J}_2 - 2M_0DH$, $E_{\text{AF}} = \bar{J}_1 - \bar{J}_2$ and $E_{90^\circ} = -M_0DH$, respectively. The most important case is when $\bar{J}_1 < \bar{J}_2 < 0$ so that $\bar{J}_1 - \bar{J}_2 < 0$ and $-\bar{J}_1 - \bar{J}_2 > 0$. The energies E_{FM}, E_{AF}, E_{90° for this case are plotted schematically as functions of H in Figure 9. Here $H_1 = -(\bar{J}_1 + \bar{J}_2)/M_0D$ and $H_2 = -(\bar{J}_1 - \bar{J}_2)/M_0D$. As H increases, transitions occur from the AF configuration to the 90° one at $H = H_2$ and then to the FM configuration at $H = H_1$. The corresponding steps in the normalized magnetization component $M_{||}/M_s$ in the direction of the field, where M_s is the saturation value in the FM state, are shown for a real Fe/Ag/Fe structure in Figure 10 (Schäfer *et al.*, 1995).

The length of the plateau with $M_{||} = M_s/2$ is $H_p = H_1 - H_2 = -2\bar{J}_2/M_0D$ and both $\bar{J}_1$ and $\bar{J}_2$ can be deduced from the observed fields H_1 and H_2.

If $\bar{J}_2 < 0$, $|\bar{J}_1| < -\bar{J}_2$ it is easily seen that the ground state is the 90° one. In this case, only one step occurs, at $H = H_1$, so that only the sum $\bar{J}_1 + \bar{J}_2$ is determined.

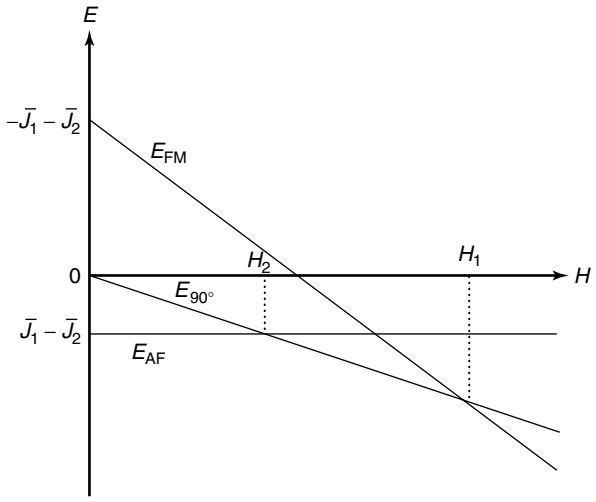

Figure 9. The energies E_{FM}, E_{AF}, E_{90°, defined in the text, schematically plotted as a function of the applied field H, for the case $\bar{J}_1 < \bar{J}_2 < 0$.

5.2 Mechanisms

There is no general theory of biquadratic coupling, which can be applied to all systems. We shall consider four different mechanisms and discuss their limits of applicability.

5.2.1 The intrinsic mechanism

In Section 3, we presented an exact expression (equation (14)) for the exchange energy of a trilayer, as a function of the angle θ between the magnetizations of the magnetic layers, for a simple free-electron model with perfect interfaces. The $s = 1$ term in equation (14) gives the

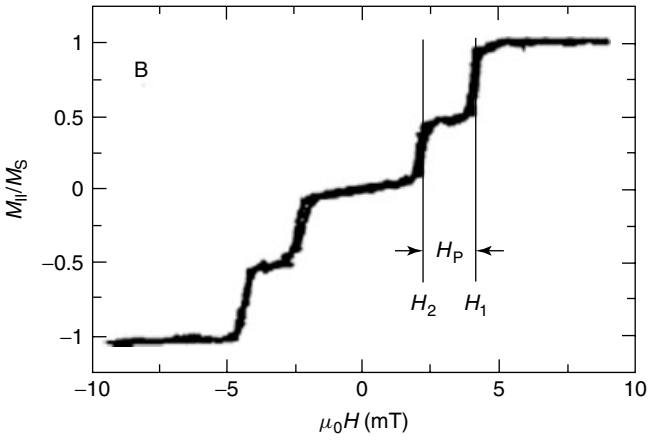

Figure 10. A $M(H)$ loop with hysteresis effects removed (anhysteretic measurement), for an antiferromagnetically coupled Fe/Ag/Fe structure with Ag thickness of 18.5 Å. (Reprinted with permission from Schäfer *et al.*, 1995, © 1995, American Institute of Physics.)

fundamental oscillation of the exchange coupling as a function of the spacer thickness with period π/k_F, where k_F is the Fermi wave vector in the spacer. The biquadratic exchange first occurs in the $s = 2$ harmonic, and, consequently, is much smaller than the bilinear coupling (Edwards, Ward and Mathon, 1993). The same result is obtained in several other model calculations (Erickson, Hathaway and Cullen, 1993; Slonczewski 1993a; d'Albuquerque e Castro, Ferreira and Muniz, 1994). This feature of simple models seems to be a general property and appears in first-principles calculations for real systems (Drchal, Kudrnovsky, Turek and Weinberger, 1996). One may conclude that for ideal multilayers with perfect interfaces, the biquadratic coupling is an order of magnitude smaller than the bilinear coupling. Thus observation of biquadratic coupling $\bar{J}_2$ with magnitude comparable to that of the bilinear coupling $\bar{J}_1$ is indicative of deviations from an ideal structure, for example, interface roughness.

In this section, we shall discuss how interface roughness can result in intrinsic biquadratic coupling becoming much more important owing to the observed bilinear coupling being strongly reduced from its intrinsic value. In the next section, we describe Slonczewski's (1991) 'fluctuation mechanism' of biquadratic coupling, which also relies on interface roughness. The couplings, which arise from intrinsic and fluctuation mechanisms are considered additive. For both mechanisms, it is important that the oscillatory intrinsic bilinear coupling $J_1(N)$, where N is the spacer thickness in MLs, has a dominant short-period component, the period being close to 2 ML. Strong biquadratic coupling is most commonly observed in systems with Cu, Au, Ag, and Cr spacers (Demokritov, 1998) of which all except Ag have such a dominant short-period component. Another exception seems to be Fe/Al/Fe which is discussed in Section 5.2.3.

Drchal, Kudrnovsky, Turek and Weinberger (1996) calculated the intrinsic bilinear and biquadratic coupling, $J_1(N)$ and $J_2(N)$, respectively, for Co/Cu/Co(001) trilayers with Cu thickness N ranging from 1 to 50 ML, and with Co thicknesses of 5 ML and infinity. We shall concentrate on the case of thick Co layers. The bilinear coupling $J_1(N)$ is dominated by a short-period (2.53 ML) oscillation, and the results are in close agreement with those of Mathon *et al*. (1997). The long-period contribution associated with the belly part of the Cu Fermi surface is negligible for thick Co layers. The intrinsic biquadratic coupling $J_2(N)$ is an order of magnitude smaller that $J_1(N)$ and oscillates about zero with a period of about 5 ML. This period is easily understood as follows. $J_2(N)$ oscillates as an $s = 2$ harmonic so its period should be $2.53/2 = 1.27$ ML. However, since N is an integer, an oscillatory term $\sin(2\pi N\lambda^{-1}) = -\sin(2\pi N(1-\lambda^{-1}))$, which corresponds to an actual period of $\lambda/(\lambda-1) = 4.7$ ML for $\lambda = 1.27$. This effect of a discrete lattice on the observed period is known as the *aliasing effect*, and is also described in Section 2.3. To model the effect of interfacial roughness Drchal, Kudrnovsky, Turek and Weinberger (1996), following Kudrnovsky *et al*. (1996), introduced a discrete probability distribution $w(N-P)$ specifying the probability that the spacer layer is P ML thick for a nominal thickness N. Thus, the observed bilinear and biquadratic couplings are related to the intrinsic ones by

$$\bar{J}_{1,2}(N) = \sum_P w(N-P) J_{1,2}(P) \tag{26}$$

Kudrnovsky *et al*. (1996) assumed a distribution of the form $w(0) = (1-2r)^2 + 2r^2$, $w(\pm 1) = 2r(1-2r)$, $w(\pm 2) = r^2$ and $w(m) = 0$ for $|m| > 2$. This corresponds to each Co/Cu interface deviating from its nominal position by ± 1 ML, each with probability r, the steps on the two interfaces being uncorrelated. For the averaging process in equation (26) to be valid, the terrace widths between the steps must not be too small, certainly not less than the spacer thickness. On the other hand, the terrace widths must not be larger than the width of a domain wall in the Co layers ($\sim$100 nm). If this condition is not satisfied the Co magnetizations will adopt the energetically favorable AF or FM configurations locally and the concept of exchange coupling between magnetic layers with essentially uniform magnetization breaks down.

The averaging process of equation (26) essentially washes out the fundamental short-period oscillation of $J_1(P)$, but the $s = 2$ harmonic with period 4.7 ML is largely unaffected. The same applies to $J_2(P)$ so that $\bar{J}_2(N) \approx J_2(N)$. Kudrnovsky *et al*. (1996) calculated $\bar{J}_1(N)$ with a reasonable roughness parameter $r = 0.25$ and it is found to oscillate with a period of about 5 ML, as expected, and with an amplitude about one-fifth of the short-period amplitude in $J_1(N)$ (actually the calculation was performed for Co thickness of 5 ML where the long-period oscillation in $J_1(N)$ is not completely negligible, as it is for thick Co layers. Thus, $\bar{J}_1(N)$ has a contribution from the long-period oscillation period 5.7 ML, in addition to that from the short-period harmonic). Clearly, the effect of interface roughness is to reduce the intrinsic bilinear coupling $J_1(N)$ by a substantial factor to its observable value $\bar{J}_1(N)$; $J_2(N)$ is hardly affected so that $\bar{J}_1(N)$ and $\bar{J}_2(N)$ become comparable in magnitude. Drchal, Kudrnovsky, Turek and Weinberger (1996) investigated the total exchange energy for thick Co layers and found that the 90° coupling is never the ground state configuration for $r \leq 0.1$. However, for $r = 0.2$ and $r = 0.25$, 90° coupling occurs for some Cu thicknesses.

The general belief that intrinsic biquadratic coupling is too small to account for observed values is based on results for simple models with ideal interfaces. The calculations of Drchal, Kudrnovsky, Turek and Weinberger (1996) for Co/Cu/Co(001) with the effect of rough interfaces taken into

account, show that this is not always the case. In fact it is interesting to return to the free-electron model of Section 3, but consider the effect of a lattice with interplanar spacing d. Then $J(\theta)$ is only observed at discrete spacer thicknesses $l = Pd$ taking values $J(P, \theta)$. The fundamental period of the bilinear coupling is π/k_F, where k_F is the Fermi wave vector, and suppose that this is close to $2d$ so that the $s = 1$ term in equation (14) oscillates with a period close to 2 ML. The $s = 2$ term has a long period when observed at discrete spacer thicknesses Nd, due to the aliasing effect. Suppose that roughness subjects $J(P, \theta)$ to an averaging of the type specified in equation (26). The $s = 1$ term in $J(P, \theta)$ is thus largely eliminated and the observed exchange energy $\bar{J}(N, \theta)$ is dominated by the $s = 2$ term with angular dependence $(3 - 2\cos\theta - \cos^2\theta)/4$. Hence $\bar{J}_1(N) = 2\bar{J}_2(N)$ and for spacer thicknesses N with $\bar{J}_1(N) < 0$, corresponding to AF coupling, we have $\bar{J}_1(N) < \bar{J}_2(N) < 0$ which leads to a $M(H)$ curve of the type shown in Figure 10. Further work, both experimental and theoretical, is required on biquadratic coupling as a function of spacer thickness.

5.2.2 *The fluctuation mechanism*

We once again consider a trilayer in which the intrinsic bilinear coupling $J_1(N)$ oscillates with a dominant short period of approximately 2 ML. At a ML step on an interface J_1 therefore changes sign taking values $\pm\Delta J$. Suppose that the terrace width L between steps is considerably less than the width of the domain wall in a magnetic layer. The magnetization in each magnetic layer can therefore only respond to the changing sign of the bilinear coupling by small deviations from its average direction. Slonczewski (1991) showed that the energy of the system is minimized when these average directions are at right angles, that is, 90° coupling is favored.

Figure 11 shows a section of the trilayer where the FM layers have thicknesses D and D'. The corresponding magnetization vectors $\mathbf{M}$ and $\mathbf{M}'$ are oriented in the $x - z$ plane at angles $\theta(y, z)$ and $\theta'(y', z)$ measured from a common axis. For simplicity a periodic structure is assumed with ML steps on one interface of the spacer creating terraces of constant width L. The intrinsic bilinear coupling $J_1(z)$ is therefore a periodic step function of the form

$$J_1(z) = \Delta J \ \ \mathrm{sgn}\left[\sin\left(\frac{\pi z}{L}\right)\right] \approx \frac{4\Delta J}{\pi}\sin\left(\frac{\pi z}{L}\right) \quad (27)$$

The last expression approximates $J_1(z)$ by the first term in its Fourier expansion and only leads to a small error in the final result (Slonczewski, 1991). The sum of the exchange energies per unit area due to interlayer coupling and intralayer FM stiffness may be written as

$$W = \frac{1}{2L}\int_0^{2L} \mathrm{d}z\Big(-J_1(z)\cos(\theta(0,z) - \theta'(0,z)) + A\int_0^D \mathrm{d}y \times(\theta_y^2 + \theta_z^2) + A'\int_0^{D'} \mathrm{d}y'\left(\theta'^2_{y'} + \theta'^2_z\right)\Big) \quad (28)$$

where A, A' are the Bloch wall stiffnesses of the magnetic layers. At the outer surfaces $y = D$ and $y' = D'$ the magnetizations are free so that we have boundary conditions $\theta_y(D, z) = \theta'_{y'}(D', z) = 0$. Minimization of W with respect to variations in $\theta(y, z)$, $\theta'(y', z)$ leads to two-dimensional Laplace equations for θ, θ' with boundary conditions relating $\theta_y(0, z)$, $\theta'_{y'}(0, z)$ to $J_1(z)$. The boundary conditions are

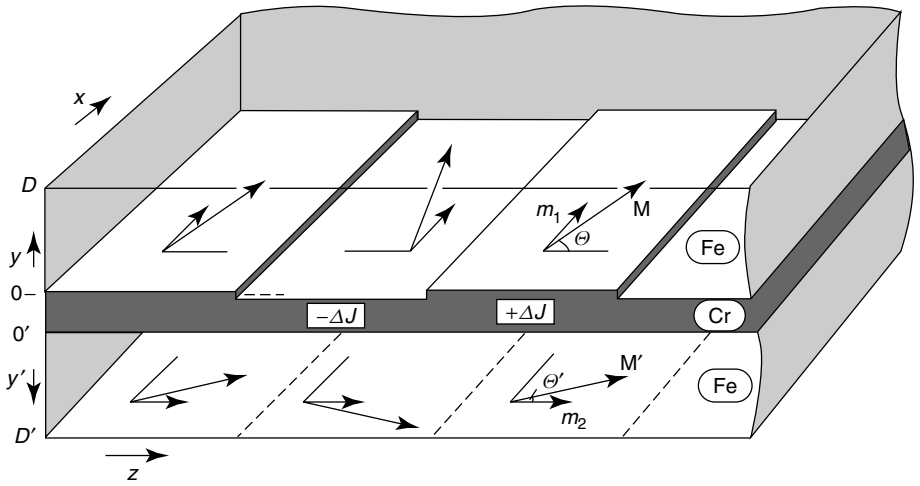

Figure 11. Section of an epitaxial magnetic trilayer, with periodic ML interface terraces. Arrows schematically indicate the fluctuations in magnetizations $\mathbf{M}(y, z)$ and $\mathbf{M}'(y', z)$ in the $x - z$ plane due to fluctuations in the exchange coupling $J(z)$. (Reprinted figure from Slonczewski, J.C., (1991), *Phys. Rev. Lett.*, **67**, 3172–3175. © 1991, by the American Physical Society.)

linearized by assuming that deviations of θ, θ' from their average values $\bar{\theta}$, $\bar{\theta'}$ are small. The result for $\theta(y, z)$ is

$$\theta = \overline{\theta} - \frac{2L\Delta J}{\pi^2 A \sinh\left(\frac{\pi D}{L}\right)} \sin\left(\frac{\pi z}{L}\right) \cosh\left(\frac{\pi}{L}(D-y)\right) \times \sin(\overline{\theta} - \overline{\theta}') \tag{29}$$

with a similar expression for θ'. On introducing these expressions into equation (28) we obtain an energy of the biquadratic form $W = \bar{J}_2[1 - \cos^2(\overline{\theta} - \overline{\theta}')]$ with

$$\bar{J}_2 = -\frac{4(\Delta J)^2 L}{\pi^3 A} \coth\left(\frac{\pi D}{L}\right) \tag{30}$$

We have assumed here equivalent FM layers with $A = A'$, $D = D'$. We note that $\bar{J}_2 < 0$ so that 90° coupling is always favored by the fluctuation mechanism. It is important to stress that ΔJ is the amplitude of the short-period *intrinsic* bilinear coupling J_1 which is not observable in the presence of the roughness responsible for the observed $\bar{J}_2$. Slonczewski (1991) pointed out that measurement of $\bar{J}_2$ in specimens with rough interfaces can therefore give information about the short-period coupling in the ideal system, as long as the terrace width L can be reasonably estimated and the fluctuation mechanism makes the dominant contribution to $\bar{J}_2$. The idea has been cleverly implemented by Heinrich and Cochran (1993) to deduce $J_1(N)$ for bcc Fe/Cu/Fe(001) from the observed $\bar{J}_1(N)$, $\bar{J}_2(N)$. In deriving equation (29) and hence (30), it was required that $\theta - \overline{\theta} \ll \pi/2$ which implies $|\bar{J}_2| \ll \Delta J$. Clearly until this condition breaks down, $|\bar{J}_2|$ is an increasing function of the terrace width L. If $D \ll L$, $|\bar{J}_2| \propto L^2$ and the condition $|\bar{J}_2| \ll \Delta J$ implies $L \ll \pi l$ where $l = \frac{\pi}{2}\sqrt{AD/\Delta J}$ is the domain wall width in the FM layer, interlayer coupling playing the role of anisotropy (Pierce, Unguris, Celotta and Stiles, 1999). Ribas and Dieny (1993) have carried out a numerical study of the fluctuation mechanism, with magnetocrystalline anisotropy included in the magnetic layers. For a model of Fe/Cr/Fe in which one of the Fe layers is thin ($D = 10$ nm) they find a crossover from 90° coupling of the Slonczewski type when $L = 25$ nm, to the appearance in this layer of domains, in which the Fe magnetization adopts the energetically favorable AF or FM configurations locally, for $L = 125$ nm. This is in accordance with a domain wall width of about 50 nm. Moser, Berger, Margulies and Fullerton (2003) have studied this type of crossover experimentally. If the magnetic layers are both thick ($D \gg L$), $|\bar{J}_2| \propto L$ with a condition for validity of equation (30) of the form $L \ll \pi^2 A/(4\Delta J)$. It follows from equation (29) that the magnetization only deviates from a uniform direction within a distance L of the interface with the spacer.

5.2.3 *'Loose spin' model*

Some measurements of $\bar{J}_2$ in Fe/Al/Fe (Gutierrez, Krebs, Filipkowski and Prinz, 1992) and Fe/Au/Fe (Fuss, Wolf and Grünberg, 1992) have shown that it decreases much more rapidly with increasing temperature than can be easily understood within the intrinsic or fluctuation mechanisms. In an attempt to explain this behavior Slonczewski (1993b) proposed that the source of the biquadratic coupling was the polarization of magnetic impurities located in the spacer. A given impurity with spin $\mathbf{S}$ ('loose spin') has an effective Hamiltonian $(\mathbf{U}_1 + \mathbf{U}_2).\mathbf{S}/S$ where $\mathbf{U}_1 = U_1\mathbf{m}_1$, $\mathbf{U}_2 = U_2\mathbf{m}_2$ are the exchange fields due to coupling with the magnetic layers. $\mathbf{m}_1$ and $\mathbf{m}_2$ are unit vectors in the magnetization directions of the magnetic layers. U_1 and U_2 are fields of the RKKY type and therefore fluctuate in sign as the spatial position of the impurity is varied. The energy levels of the impurity are $-mU(\theta)/S$ with $m = -S, -S+1, \ldots, S$, and

$$U(\theta) = |\mathbf{U}_1 + \mathbf{U}_2| = (U_1^2 + U_2^2 + 2U_1U_2\cos\theta)^{1/2} \tag{31}$$

where θ is the angle between $\mathbf{m}_1$ and $\mathbf{m}_2$ as usual. It follows that the free energy of the loose spin at temperature T is

$$f(T,\theta) = -k_B T \ln\left(\frac{\sinh\left([1+(2S)^{-1}]U(\theta)/(k_B T)\right)}{\sinh\left(U(\theta)/(2Sk_B T)\right)}\right) \tag{32}$$

and at $T = 0$, $f(0, \theta) = -U(\theta)$. Slonczewski does not carry out a configurational average over impurity positions, but assumes that each impurity experiences the same exchange fields U_1, U_2. The macroscopic free energy F per unit area is then $F(T, \theta) = \rho f(T, \theta)$, where ρ is the areal density of the impurities. This may be written approximately in the usual form

$$F(T,\theta) = F(T,\pi/2) - \bar{J}_1^{LS}\cos\theta - \bar{J}_2^{LS}\cos^2\theta \tag{33}$$

either by expanding in powers of $\cos\theta$, for small $\cos\theta$, or by choosing $\bar{J}_1^{LS}$, $\bar{J}_2^{LS}$ so as to reproduce $F(T, 0)$ and $F(T, \pi)$ correctly. Either way, at $T = 0$, we find that the sign of $\bar{J}_1^{LS}$ is that of U_1U_2, whereas $\bar{J}_2^{LS}$ is always positive. Hence the failure to take a configurational average is qualitatively not so serious for $\bar{J}_2^{LS}$, the main object of interest. On the other hand, $\bar{J}_1^{LS}$ fluctuates in sign for different impurity positions so will tend to average to zero.

Slonczewski fitted his theory to the observed temperature dependence of $\bar{J}_2$ in Fe/Al/Fe and Fe/Au/Fe in two ways. He first assumed that most of the impurities were positioned far from the interface with $|U_1| \approx |U_2|$. However, exchange fields $|U_{1,2}|/k_B \sim 250 - 400$ K were required, which is unrealistically large. Slonczewski's second type of fit is based on the assumption that the loose spins actually comprise the

last atomic layer of the ferromagnets. Then one exchange field is very large and the other small. The concept of independent loose spins at the surface of an itinerant electron ferromagnet is of doubtful validity.

Slonczewski (1993b) pointed out that a system to which the loose spin model would apply could be constructed by deliberate deposition of magnetic impurities in an atomic layer within the spacer. Following earlier work by Heinrich and Cochran (1993) this has been achieved by Schäfer *et al*. (1995) in Fe/Ag/Fe with a submonolayer of Fe in the center of the Ag spacer. A contribution to biquadratic coupling proportional to the Fe concentration and rapidly decreasing in temperature was observed.

Heinrich and Cochran (1993) proposed an alternative source of strongly temperature dependent biquadratic coupling in Fe/Al/Fe. Interfaces in this structure are known to be rough (Gutierrez, Krebs, Filipkowski and Prinz, 1992), and, with spacer thicknesses of 6–8 ML, magnetic bridges or pinholes are possible. If these exist the exchange coupling would vary between FM through the pinholes and AF elsewhere (the overall bilinear coupling is observed to be AF). If the spacing between pinholes is less than a domain wall width in an Fe layer, the Slonczewski (1991) fluctuation mechanism for 90° coupling could operate. The rapid decay of $\bar{J}_2$ with increasing temperature would be associated with the decay of magnetization in the thin magnetic bridge.

5.2.4 *Magnetic-dipole mechanism*

The magnetic-dipole mechanism is a variant of the fluctuation mechanism where the spatially fluctuating coupling between rough magnetic layers is not due to exchange coupling but due to a magnetic field. A perfect infinite magnetic layer produces a magnetic field outside itself only within a range of the order of the lattice constant (Heinrich *et al*., 1988). However, a rough magnetic layer, with a periodic array of terraces of width L (as in Figure 11), produces a magnetic field which oscillates about zero with lateral periodicity $2L$ and which has a range of the order of $2L$ (Demokritov, Tsymbal, Grünberg and Zinn, 1994). The effect on the magnetization of a smooth magnetic layer, separated from the rough layer by a spacer of thickness t with $t < L$ is therefore similar to that of the fluctuating exchange field in the fluctuation mechanism. Thus a positive contribution to $\bar{J}_2$ is obtained which increases with L until the theory breaks down for L of the order of a domain wall width, just as in the fluctuation mechanism. The two mechanisms may sometimes be difficult to distinguish in practice. Rücker *et al*. (1995) claim to have shown that the magnetic-dipole mechanism is the source of the biquadratic coupling in their rough Fe/Au/Fe trilayers. However, they eliminate the fluctuation mechanism on the grounds that the predicted $\bar{J}_2$ is too small. It is now known (Unguris, Celotta and Pierce, 1997) that the amplitude of the short-period oscillation in J_1 (ΔJ in equation (27)) is at least five times larger than their estimate, which increases their estimate of the contribution of the fluctuation mechanism to $\bar{J}_2$ by a factor of 25. It is thus of the same magnitude as their estimated magnetic-dipole contribution.

6 TEMPERATURE DEPENDENCE OF INTERLAYER EXCHANGE COUPLING

In earlier sections, we noted the temperature dependence of IEC owing to single-particle excitations around the Fermi level. The bulk spacer Fermi surface is given by $E(\boldsymbol{k}_\parallel, k_y) = \mu$, where $E(\boldsymbol{k}_\parallel, k_y)$ defines the bulk band structure with $\boldsymbol{k}_\parallel$ in the plane of the layers and k_y in the perpendicular direction. Consider the simplest case where, for a given $\boldsymbol{k}_\parallel$, there are just two points $k_y = \pm k(\boldsymbol{k}_\parallel)$ on the Fermi surface. In the limit of large l, where l is the spacer thickness, the bilinear exchange coupling is a sum of oscillatory terms with periods determined by extremal values of k_y (see equation (24)). For each period λ there is a series of harmonics $s = 1, 2, \ldots$. The bilinear exchange coupling may be written as

$$J_1(l, T) = \sum_{\lambda, s} J_{1\lambda s}(l, 0)\, f_{\lambda s l}(T) \tag{34}$$

where

$$f_{\lambda s l}(T) = \frac{T/T_{\lambda s l}}{\sinh(T/T_{\lambda s l})} = 1 - \frac{1}{6}\left(\frac{T}{T_{\lambda s l}}\right)^2 + \cdots \tag{35}$$

with

$$k_{\mathrm{B}} T_{\lambda s l} = \pi^{-1}(2 l s k'_{y\lambda} + \psi'_{\lambda s})^{-1} \tag{36}$$

Here $k'_{y\lambda} = \mathrm{d}k_y/\mathrm{d}E = (\hbar v_{\mathrm{F}\lambda})^{-1}$ where $v_{\mathrm{F}\lambda}$ is the Fermi velocity at the relevant extremal point of the Fermi surface. The $\psi'_{\lambda s}$ term, which is the energy derivative of the phase of the relevant coefficient in the Fourier expansion of the spectral density, is zero for the simple parabolic band model with infinite exchange splitting in the ferromagnets, considered in Section 3 (compare equation (36) with equation (16)). In that case there is only one period and $T_{\lambda s l}$ is determined entirely by the spacer Fermi-surface velocity v_{F}. However, d'Albuquerque e Castro, Mathon, Villeret and Umerski (1996) showed that $\psi'_{\lambda s}$ can become large when the condition for confinement of electrons of one spin is just satisfied. They showed that this 'confinement mechanism' for decreasing $T_{\lambda s l}$, which depends on the spacer-ferromagnet interface, operates importantly in Co/Cu/Co(001). They also

showed that for a parabolic band model with perfect matching for one spin-channel, and complete confinement for the other spin-channel, $\psi'_{\lambda s} = s\psi'_{\lambda 1}$, and that this relationship is also satisfied to a good approximation in Co/Cu/Co. (In fact it can be proved rigorously that for nonmagnetic spacers with a single Fermi surface, this condition is exactly satisfied when there is exact matching between one of the spin bands in the ferromagnet and the spacer.) Hence, even in the presence of the confinement mechanism, $T_{\lambda sl} \simeq s^{-1} T_{\lambda 1 l}$. This means that an $s = 2$ harmonic of the oscillatory IEC varies more rapidly with temperature than the corresponding fundamental ($s = 1$). Consequently, the intrinsic biquadratic coupling varies more strongly with temperature than the bilinear coupling.

Combining equations (34) and (35) we find

$$J_1(l, T) = J_1(l, 0) f_e(T) = J_1(l, 0) \left[1 - \frac{1}{6} (T/T_l)^2 \ldots \right] \quad (37)$$

where

$$T_l^{-2} = \frac{\sum_{\lambda s} T_{\lambda s l}^{-2} J_{1\lambda s}(l, 0)}{\sum_{\lambda s} J_{1\lambda s}(l, 0)} \quad (38)$$

If the sign of the term $J_{1\lambda s}(l, 0)$ varies, cancellation can occur in the denominator of equation (38), so that T_l^{-2} can be much larger than any of the $T_{\lambda s l}^{-2}$. Hence T_l can be much smaller than one would expect from any of the Fermi velocities. In addition, it is possible for T_l^{-2}, the coefficient of T^2 in equation (37), to be negative so that the coupling increases with temperature. This occurs in calculations by Costa, d'Albuquerque e Castro and Muniz (1997a) for bcc Fe/Cu/Fe(001) with l corresponding to 13 ML. In this case, terms with three different periods and comparable amplitudes contribute to the coupling. In the usual experimental situation with rough interfaces T_l may differ markedly from its value for ideal interfaces when the ideal couplings $J_{1\lambda s}$ are replaced by averages of the type given by equation (26). The range of temperature over which an expansion like that in equation (35) is valid can be extended by using $x/\sinh x \simeq 1 - 0.15x^{1.82}$, which is an excellent approximation for $0 < x < 1$, in the above analysis. Another discussion of the temperature dependence of the IEC due to single-electron excitation is given by Drchal *et al.* (1999).

Cullen and Hathaway (1993) first pointed out another source of temperature dependence in IEC owing to thermal excitation of spin waves. They considered an effective Heisenberg model in which two FM films are coupled by a weak nearest-neighbor IEC J_I. They also considered a superlattice case of an infinite number of coupled films, but we shall restrict our attention here to the model of the trilayer. Cullen and Hathaway adopted a thermodynamic approach, involving the free energy of the system in different magnetic configurations, and recently Schwieger and Nolting (2004) have followed the same line. Almeida, Mills and Teitelman (1995), using the same model, adopted a dynamic approach involving a Hartree–Fock type of decoupling of the equation of motion for spin waves. Here, we use the method of coupling constant integration (e.g., Doniach and Sondheimer, 1998) to obtain a result which we can relate to those of Cullen and Hathaway (1993) and Almeida, Mills and Teitelman (1995).

The model Hamiltonian is $\mathcal{H}(1)$ where

$$\mathcal{H}(\gamma) = \mathcal{H}_0 - \gamma J_I \sum \mathbf{S}_{\mathrm{L}} \cdot \mathbf{S}_{\mathrm{R}} \quad (39)$$

and the sum is over nearest-neighbor pairs with site L in the interface plane of the LH magnet and site R in the interface plane of the RH magnet. We suppose that the magnetizations of the two magnetic layers are constrained to make an angle θ with each other. The change in free energy when J_I is turned on from zero is given exactly by

$$\delta F(\theta) = F(J_I) - F(J_I = 0) = -J_I \sum \int_0^1 \mathrm{d}\gamma \langle \mathbf{S}_{\mathrm{L}} \cdot \mathbf{S}_{\mathrm{R}} \rangle_\gamma \quad (40)$$

where the thermal average is to be calculated using the Hamiltonian equation (39). In the case of thick magnetic films and $J_I \ll J$, the bulk exchange parameter, the spins $\mathbf{S}_{\mathrm{L}}$ and $\mathbf{S}_{\mathrm{R}}$ are very weakly correlated, except at very low temperature where $k_{\mathrm{B}}T < J_I$. Hence $\langle \mathbf{S}_{\mathrm{L}} \cdot \mathbf{S}_{\mathrm{R}} \rangle_\gamma \simeq \langle \mathbf{S}_{\mathrm{L}} \rangle_{\gamma=0} \cdot \langle \mathbf{S}_{\mathrm{R}} \rangle_{\gamma=0}$ and $\delta F(\theta) = -J_I S^2 \cos\theta \;\; m_{\mathrm{L}}(T) m_{\mathrm{R}}(T)$, where $m_{\mathrm{L}}(T)$, $m_{\mathrm{R}}(T)$ are the reduced magnetizations in the free surface planes of the two ferromagnets, which may be of different materials. If, as assumed by Almeida, Mills and Teitelman (1995), the magnetic films are thick, $m_i(T) = 1 - c_i T^{3/2}$ $(i = L, R)$ and it is well known that $c_i = 2c'_i$, where the bulk magnetization varies as $M_i(T) = M_i(0)(1 - c'_i T^{3/2})$, in the spin-wave regime (Mills and Maradudin, 1967). This simple relation between surface and bulk T dependence breaks down if there is significant variation in the exchange parameters within the ferromagnet near its surface (Mathon, 1988). Thus for thick FM layers, the temperature dependence of IEC due to spin-wave excitations is approximately given by a factor $1 - 2\bar{c}T^{3/2}$, where $\bar{c} = (c_{\mathrm{L}} + c_{\mathrm{R}})/2$. The coefficient of $T^{3/2}$ is twice that found by Almeida, Mills and Teitelman (1995) using the equation of motion method. It appears that the quantity appearing in the equations of motion is different from the thermodynamical IEC, which would be measured by saturation fields (Schwieger and Nolting, 2004). When $k_{\mathrm{B}}T < D\pi^2/t^2$, where D is the spin-wave stiffness and t the thickness of a FM layer, two-dimensional behavior appears and the $T^{3/2}$ law does not apply. Cullen

and Hathaway (1993) consider thin FM layers where J_1, and dipolar coupling within each layer, play an important role in stabilizing two-dimensional ferromagnetism at finite T. Referring to equation (40) they effectively take $\langle \mathbf{S}_L.\mathbf{S}_R\rangle_\gamma = \langle \mathbf{S}_L.\mathbf{S}_R\rangle_{\gamma=1}$. They find that for ferromagnets with a thickness of one or two ML the IEC decreases linearly with T, except at extremely low temperature. If a phenomenological biquadratic coupling $-J_{12}\ (\mathbf{S}_i.\mathbf{S}_j)^2$ is introduced into the Heisenberg model, a similar analysis yields a temperature dependent biquadratic coupling $-J_{12}S^4\cos^2(\theta)\ (1-6\bar{c}T^{3/2})$ due to spin-wave excitations in thick FM layers.

Finally, we comment on how the two contributions to the T dependence of the IEC are to be combined. Since at low temperatures one-electron excitations and spin waves are essentially independent we expect, as proposed by Almeida, Mills and Teitelman (1995), that the total T dependence is determined by a product of an electronic factor $f_e(T)$ and a suitable spin-wave factor.

The attribution of experimentally observed T dependence of IEC to electronic or spin-wave factors is sometimes confused by the fact that $x/\sinh x \simeq 1.025 - 0.175x^{3/2}$ is an excellent approximation for $0.4 < x^{3/2} < 2$. An important distinction is that the spin-wave factor $1-2\bar{c}T^{3/2}$ is independent of spacer thickness, whereas the electronic factor $f_e(T)$ has, in general, a strong dependence on l (equations (36)–(38)). Thus in work on IEC in $Ni_7/Cu_N/Co_2/Cu(001)$ trilayers, Lindner and Baberschke (2003a,b) found a much more rapid temperature dependence for $N = 9$ than for $N = 5$. Nevertheless, on the basis of linear $T^{3/2}$ plots, they ascribe the main source of the T dependence to spin-wave excitation. Actually pure $T^{3/2}$ behavior is not expected for such a thin Co layer. The authors dismiss a reasonable fit of the $(T/T_l)/\sinh(T/T_l)$ type, with $T_l = 120\,\mathrm{K}$ for $N = 9$, on the grounds that T_l is much smaller than expected from Fermi velocities in Cu. A similar problem is reported by Persat and Dinia (1997). However, we have discussed how T_l may be strongly reduced both by the confinement mechanism and by cancellations in the sums of equation (38). Such cancellation may be strongly influenced by roughness which, as in the case of Co/Cu/Co(001), discussed in Section 5.2.1, can suppress a strong contribution with short period λ leaving a weaker $s = 2$ harmonic with an intrinsically smaller characteristic temperature $T_{\lambda 2l}$ (cf. equation (36)).

Clearly much more experimental and theoretical work on the temperature dependence of IEC, particularly its dependence on spacer thickness, is required for a full understanding. A fully satisfactory theory, in which both the single-electron and spin-wave excitations are treated within a tight-binding model with interacting electrons, is not yet available.

7 THEORY AND EXPERIMENT

7.1 Noble metal spacers

In general, agreement between theory and experiment is good with regard to the periods of oscillation of IEC as a function of spacer thickness. This is to be expected since these periods are determined entirely by the nature of the spacer Fermi surface. The situation regarding amplitude and phase of the oscillations is much less satisfactory where wide discrepancies frequently exist not only between theory and experiment but also between different calculations. Observed IEC is invariably smaller than that calculated and this can be understood qualitatively to be due to interface roughness and interfacial diffusion (Kudrnovsky *et al*., 1996; Costa, d'Albuquerque e Castro and Muniz, 1997b; Inoue, 1994). Comparison between theory and experiment is then difficult because the exact nature of roughness and interfacial diffusion in an experiment is largely unknown. Possibly, the only system where direct comparison is possible between experiment and calculations for ideal interfaces is Fe/Au/Fe(001). Unguris, Celotta and Pierce (1997) made SEMPA and MOKE measurements on wedge structures grown on single crystal Fe whiskers, which provide very flat substrates. The angle of the Au wedge is about 0.001° so that the Au thickness increases by 1 ML over steps which are about 10 μm apart. Owing to a dominant short-period contribution to the coupling ($\simeq$2.5 ML), these steps are signaled in SEMPA measurements by a reversal of the magnetization in the top Fe layer. The magnitude of the AF peaks in the coupling was measured by MOKE as shown in Figure 12.

Ninety degree coupling is observed in SEMPA at the transition regions, between regions which are ferromagnetically

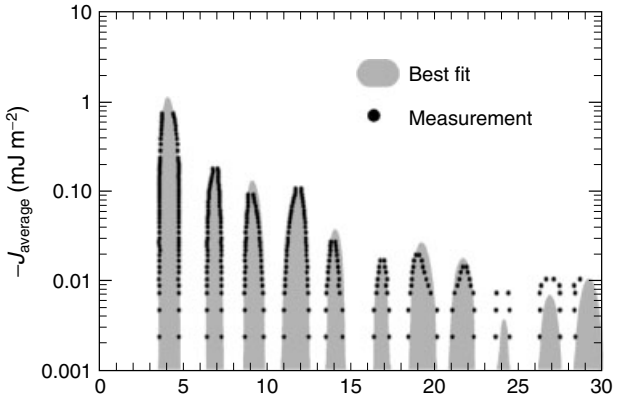

Figure 12. Measured values of coupling strength on Fe/Au/Fe(100) whiskers, as a function Au thickness (in monolayers). (Reprinted figure from Unguris, J., Celotta, R.J., and Pierce, D.T., (1997), *Phys. Rev. Lett.*, **79**, 2734–2737. © 1997 by the American Physical Society.)

and antiferromagnetically coupled. These transition regions are too wide to be merely due to Néel-type domain walls and indicate the existence of weak, but observable biquadratic coupling. Unfortunately, measurements of the magnetization curve $M(H)$ to determine its strength were not carried out. Such measurements would be very valuable because the biquadratic coupling in these samples with very smooth interfaces is presumably intrinsic. One indication that this is indeed the case is an apparent reduction in its strength, reflected in reduced transition region widths, on capping the top Fe layer with a Au layer. In fact, Unguris, Celotta and Pierce (1997) tentatively ascribe this to 'changes in boundary conditions of the spin-dependent quantum well'. The effect of a capping layer on bilinear coupling has been investigated experimentally and theoretically for a Co/Cu/Co structure by de Vries *et al*. (1995). Results of calculations of IEC in Fe/Au/Fe(001) differ widely. Opitz, Zahn, Binder and Mertig (2000), in LSDA calculations within the frozen potential approximation, report couplings an order of magnitude larger than observed by Unguris, Celotta and Pierce (1997). Hafner, Spišák, Lorentz and Hafner (2002), in total energy LSDA calculations, report results four times larger than Opitz, Zahn, Binder and Mertig (2000) and attribute the difference to the use of the frozen potential approximation by the latter authors. Much more reasonable results were obtained by Costa, d'Albuquerque e Castro and Muniz (1997b) using the tight-binding formulation described in Section 4.1. Although $J_1(N)$ does not agree with experiment in detail, as a function of Au thickness N, the order of magnitude is correct. Thus a calculated AF maximum at $N = 8$ ML with $J_1 = -0.5$ mJ m^{-2} may be compared with a measured $J_1 = -0.2$ mJ m^{-2} at the corresponding maximum of $N = 7$ ML. Costa, d'Albuquerque e Castro and Muniz (1997b) show how interplanar distance relaxation at the Fe/Au interface could reduce the calculated J_1 by a factor of 3. These authors also find that the short-period component of the IEC is completely dominant, which agrees with the large ratio of short-period to long-period amplitudes of 7 in experiment (Unguris, Celotta and Pierce, 1997). Stiles (1996b) estimated the size of the two components of J_1 from calculated reflection amplitudes at interfaces; he obtained reasonable magnitudes but an amplitude ratio of 2.

Costa, d'Albuquerque e Castro and Muniz (1997b) also calculated the IEC in Fe/Ag/Fe(001) trilayer and found that $J_1(N)$ exhibited the expected long period of about 5.3 ML. A short period (2.4 ML) of comparable amplitude is also present but produces no sign alternations on the 2 ML scale. The agreement with measurements of Celinski, Heinrich and Cochran (1993) and Unguris, Celotta and Pierce (1993) is excellent apart from theory being four times larger than experiment. The absence of sign alternations in $J_1(N)$ corresponding to a 2 ML period, in calculations for ideal interfaces precludes the Slonczewski fluctuation mechanism for biquadratic coupling. The biquadratic coupling observed by Schäfer *et al*. (1995) and Unguris, Celotta and Pierce (1993) is relatively weak ($J_1/J_2 \simeq 6$ at low T for an Au thickness of 1.8 nm) and is probably intrinsic, contrary to the interpretations of Schäfer *et al*. These authors find that J_1 is strongly temperature dependent, as in the calculations of Costa *et al*., with J_2 even more so. This is as expected for a J_2 of intrinsic origin.

The case of Co/Cu/Co(001) has already been discussed in Sections 2.3 and 5.2.1. We now briefly discuss some systems with TM spacers.

7.2 Transition-metal spacers

TM spacers have not been studied experimentally or theoretically as thoroughly as the noble metal spacers. Theoretical analysis of the IEC is complicated by multisheet Fermi surfaces associated with a partially filled d band. Parkin (1991) measured the IEC of multilayers $(\text{Co}(15\,\text{Å})/\text{TM})_{16}$ for nearly all TM spacers of the 3d, 4d, and 5d series. However, his failure to observe any oscillations with spacer thickness of period less than 10 Å suggests that the sputtered samples suffered from considerable interface roughness and interdiffusion. It is therefore uncertain how much significance should be attributed to Parkin's remarkable observation of an exponentially increasing coupling strength as one moves from left to right along each TM series. Nevertheless Mathon, Villeret and Edwards (1993) presented a plausible explanation of this effect on the basis of QW theory, with variable matching of the Co and spacer d bands as the latter band fills on moving along the series. Stoeffler and Gautier (1990) made more detailed calculations for Co/Ru and Fe/V superlattices. These were based on tight-binding calculations involving d orbitals with on-site electron interactions treated within the unrestricted Hartree–Fock approximation. They could consider only thin spacers and found large coupling strength, for example, about 30 mJ m^{-2} for a bcc $\text{Fe}_3\text{V}_2(001)$ superlattice. One important result is that the effect of electron interaction is to increase the coupling strength by only about 50% above its value for noninteracting electrons.

Realistic calculations for Fe/Mo/Fe(001) have been carried out by Mirbt, Niklasson, Johansson and Skriver (1996), using the LSDA approximation, and by Umerski and Mathon (unpublished, but see Edwards (2002)), using the method of Section 4.1. Umerski and Mathon find a large coupling strength, with $|J_1| \simeq 5$ mJ m^{-2} for a Mo thickness of 10 ML. Mirbt *et al*. find a somewhat larger coupling, which might be expected since electron interaction is included in the LSDA calculations. Both groups find a dominant 2 ML period associated with nesting of the Mo Fermi surface,

similar to that which gives rise to antiferromagnetism in the corresponding 3d metal Cr. Experimentally Qiu, Pearson, Berger and Bader (1992) and Qiu, Pearson and Bader (1993) found a coupling strength nearly 2 orders of magnitude smaller than the theoretical one and with a period of about 3 ML. A large discrepancy between theoretical and experimental coupling strength is also found for the AF spacer Cr, as discussed in the next section.

7.3 Antiferromagnetic Spacers

A huge body of experimental work exists involving trilayers and multilayers with AF Cr as the spacer. Excellent reviews exist on the Fe/Cr system (Pierce, Unguris, Celotta and Stiles, 1999; Fishman, 2001) and here we have space only for a few salient points. Antiferromagnetism in bulk bcc Cr takes the form of a spin-density wave (SDW) which is incommensurate (I) with the lattice, having a wave vector $\mathbf{q} = (2\pi/a)(1 \pm \delta')\hat{\mathbf{y}}$ where a is the lattice constant and $\hat{\mathbf{y}}$ is a unit vector along a cubic axis. The parameter δ' is temperature dependent and $0 \leq \delta' \leq \delta$ where $\pm\delta$ ($\simeq$0.05) corresponds to nesting wave vectors which link planar parts of the paramagnetic Cr Fermi surface. The spin on a site with coordinate y in the I SDW is given by

$$\mathbf{S}_{\mathrm{Cr}}(y) = (-1)^{2y/a}\hat{\mathbf{m}}g(T)\cos((2\pi/a)y\delta' + \theta) \qquad (41)$$

where $\hat{\mathbf{m}}$ is a unit vector perpendicular or parallel to $\hat{\mathbf{y}}$, corresponding to transverse (T) or longitudinal (L) phases, respectively, and θ is an arbitrary phase. Bulk Cr undergoes a Néel transition at $T_{\mathrm{N}}^{\mathrm{bulk}} = 311$ K, into a T SDW phase which changes to a L SDW state below 123 K. At low temperatures, the SDW amplitude $g(T)$ corresponds to a maximum Cr moment of about $0.6\,\mu_{\mathrm{B}}$. Doping with 0.2% Mn or 2.4% Fe drives δ' to zero so that the SDW becomes commensurate (C). Another type of SDW, which does not occur in bulk Cr but may appear in trilayers and multilayers, is a noncollinear helical (H) one with

$$\mathbf{S}_{\mathrm{Cr}}(y) = (-1)^{2y/a}g(T)(\hat{\mathbf{z}}\cos((2\pi/a)y\delta' + \theta) \pm \hat{\mathbf{x}}\sin((2\pi/a)y\delta' + \theta)) \qquad (42)$$

A simple picture of IEC in a Fe/Cr/Fe(001) trilayer combines a strong AF coupling $J_i\mathbf{S}_{\mathrm{Fe}}.\mathbf{S}_{\mathrm{Cr}}$ at the interfaces with a C SDW ($\delta' = 0$) in the Cr layer. For a Cr thickness of N ML this clearly leads to FM coupling between the Fe layers for N odd and to AF coupling for N even. The picture of alternating FM and AF coupling is valid for $9 \leq N < 24$ except that the sign is reversed in SEMPA measurements (Pierce, Unguris, Celotta and Stiles, 1999). Freyss, Stoeffler and Dreyssé (1997) have shown theoretically how this sign reversal may occur because of interface diffusion. Using a tight-binding d-band Hamiltonian, with electron interaction treated in an unrestricted Hartree–Fock approximation, they show that a Cr plane containing more than 20% of Fe acts as if it were part of the FM Fe layer rather than acting as part of the Cr spacer layer. Heinrich, Cochran, Monchevsky and Urban (1999) point out that interfacial mixing occurs at the relevant temperatures when Cr is deposited on Fe but is unimportant for deposition of Fe on Cr. Consequently, interfacial mixing occurs at only one interface, thus effectively reducing N by 1. The work of Freyss, Stoeffler and Dreyssé (1997) also indicates that interfacial alloying is the cause of the delayed onset of the clear 2 ML period in IEC which is only established for $N > 8$ (Pierce, Unguris, Celotta and Stiles, 1999; Heinrich, Cochran, Monchevsky and Urban, 1999).

SEMPA measurements (Pierce, Unguris, Celotta and Stiles, 1999) show that at room temperature the C SDW gives way to a I SDW for $N > 24$. The IEC is FM for both $N = 24$ and 25, so that a phase slip occurs in the alternation between FM and AF coupling. Further phase slips are observed at $N = 44$–45 and 64–65. The phase slips move to larger N as temperature T increases, the first phase slip occurring at $N = 38$–39 at 550 K. It is remarkable that the IEC associated with the Cr SDW persists far above the bulk Néel temperature. A good account of these phenomena is afforded by a phenomenological model based on a free energy expression which is a sum of interfacial couplings $J_i\mathbf{S}_{\mathrm{Fe}}.\mathbf{S}_{\mathrm{Cr}}$ and a free energy corresponding to the bulk SDW of equation (41) (Shi and Fishman, 1997; Fishman and Shi, 1998, 1999). The latter energy is calculated for interacting electrons with nested bands within the random phase approximation and the total free energy is minimized with respect to g, δ', and θ for given N and T. The calculated bilinear coupling $|J_1| \simeq 10$ mJ m^{-2} at $N = 10$ which is about 15 times larger than observed for good samples grown on an Fe whisker (Heinrich, Cochran, Monchevsky and Urban, 1999). Tight-binding d-band calculations which include electron–electron interaction (Stoeffler and Gautier, 1991) give $|J_1| \simeq 25\,\mathrm{mJ\,m^{-2}}$. First-principles calculations based on LSDA (Mirbt, Niklasson, Johansson and Skriver, 1996) also give a large coupling $|J_1| \simeq 30\,\mathrm{mJ\,m^{-2}}$ for $N = 10$. Mirbt *et al.* simulated a Cr spacer without exchange enhancement due to electron interaction and found that the Cr moments were reduced by a factor of 20 from the interacting case while the IEC retained a 2 ML period and was reduced only by a factor of 3 with $|J_1| \simeq 10\,\mathrm{mJ\,m^{-2}}$. This is only slightly larger than the value obtained by standard methods assuming Cr to be paramagnetic with noninteracting electrons (Costa, d'Albuquerque e Castro and Muniz, 1999). Costa *et al.* investigated the

effect of interfacial alloying on the IEC but were unable to account for the very large discrepancy between theory and experiment.

In samples where terrace lengths are short enough for the 2 ML period coupling to be averaged out, a long-period component with a period of about 12 ML is observed (Unguris, Celotta and Pierce, 1991; Demokritov, Wolf and Grüunberg, 1991). The origin of this long period is still controversial. The general consensus is that it is associated with the spanning vector of a small ellipsoidal part of the paramagnetic Cr Fermi surface surrounding the N-point in the Brillouin zone (Stiles, 1996a, 1999; Tsetseris, Lee and Chan, 1997; Bürgler, Grünberg, Demokritov and Johnson, 2001). This part of the Fermi surface should not be much disturbed by the existence of an SDW.

In the work discussed in the preceding text it is assumed that, when the angle θ between the magnetizations of the magnetic layers is equal to 0 or π, the Cr moments are collinear. This is not necessarily the case, as shown schematically for an ideal Fe/Cr_{10}/Fe trilayer in Figure 13.

For $N = 10$ the Fe magnetizations are antiparallel ($\theta = \pi$) in the stable configuration. The figure illustrates the parallel ($\theta = 0$) configuration, which would occur in a saturating magnetic field, and shows three possible SDW states in the Cr layer. The C SDW is the stable one for $\theta = \pi$ and is ruled out for $\theta = 0$ in the presence of strong AF Fe/Cr interfacial coupling. The magnitude of the IEC is determined by the energy difference between the energy of

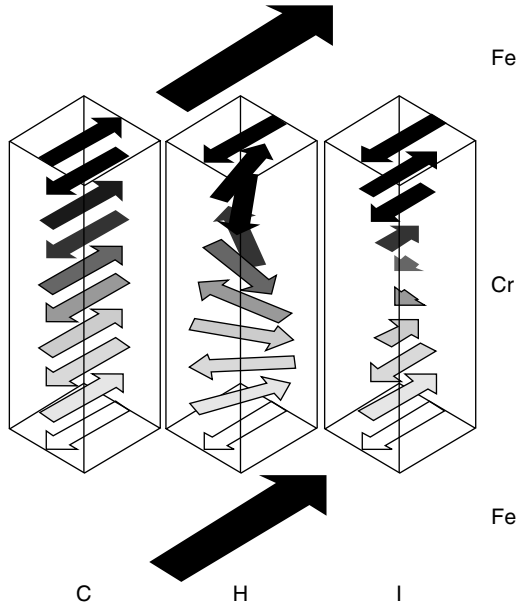

Figure 13. Three possible SDW states in Fe/Cr_{10}/Fe with parallel Fe magnetizations. (Reproduced from Fishman, R.S. (2001), *J. Phys.: Condens. Matter*, **13**, R235–R269, with permission from IOP Publishing Ltd. © 2001.)

the H SDW or I SDW – whichever is lower – and that of the C SDW. Stoeffler and Gautier (1993a,b), using a d-band tight-binding model which apparently favors C over I SDWs in bulk Cr, find that the H SDW has a lower energy than the I SDW for $N \geq 24$. Allowing a nonuniform twist in the helix stabilizes the noncollinear state for $N \geq 20$. The energy of the I SDW, relative to that of the C SDW, tends to a positive constant as $N \to \infty$ owing to the continuing presence of a magnetic defect in the center of the Cr layer where Cr moments are suppressed due to frustrated antiferromagnetism. The energy of the H SDW relative to that of the C SDW tends to zero as $1/N$. Slonczewski (1995) pointed out that, for N not too small, the energy of a H SDW for general θ may be written as $J_+(N)(\pi - \theta)^2$ for even N, as considered above, and as $J_-(N)\theta^2$ for odd N. Here, $0 \leq \theta \leq \pi$ and J_+, J_- are positive stiffness constants such that $J_\pm \propto N^{-1}$. Slonczewski proposed a torsion model for Fe/Cr/Fe in which these energy expressions replace the standard $-J_1 \cos\theta - J_2 \cos^2\theta$ expression. From the work of Stoeffler and Gautier (1993a,b) one would expect this to be valid only for $N \geq 24$ when the H SDW is stable for all θ. But surprisingly Freyss, Stoeffler and Dreyssé (1996) found a stable noncollinear state, with energy $J_+(\pi - \theta)^2$ for $0 \leq \theta \leq \pi$, even for $N = 6$. However, recent, improved tight-binding calculations by Cornea and Stoeffler (2000), which include s, p, and d orbitals, show that for even (odd) N the central Cr moments in a H-type SDW are suppressed as $\theta \to 0(\pi)$. The SDW then becomes incommensurate and collinear and the calculated energies are fitted excellently over the whole range $0 \leq \theta \leq \pi$ by the standard expression, and not by the torsion model, for the cases $N = 4, 5, 10, 11$ considered. For $N = 10$ and 11 it is found that the intrinsic biquadratic coupling $J_2 \simeq |J_1|/3$ in agreement with the measurements of Heinrich, Cochran, Monchevsky and Urban (1999) on trilayers with smooth interfaces. For interfacial terrace lengths less than the domain wall width in Fe the Slonczewski fluctuation mechanism comes into play with a further tendency toward 90° coupling. In Fe/Cr/Fe(001) multilayers with short terraces, Schreyer *et al.* (1995) found a noncollinear orientation of the moments of Fe layers, with a slow approach to saturation in an applied field, which they interpret in terms of the torsion model. This interpretation is challenged by Heinrich, Cochran, Monchevsky and Urban (1999) and by Cornea and Stoeffler (2000).

The torsion model has been used successfully to interpret IEC in systems with Mn spacers (Yan *et al.*, 1999; Filipkowski, Krebs, Prinz and Guttierez, 1995; Krebs, Prinz, Filipkowski and Gutierrez, 1996). Mn is another AF metal, which normally exhibits a C SDW. For rough interfaces, the coupling energy for a given nominal spacer thickness takes the form $c_+(\pi - \theta)^2 + c_-\theta^2$. Here $c_+ = p_+\bar{J}_+$, $c_- = p_-\bar{J}_-$ where p_+, p_- are the fractions of the cross-sectional area

with, respectively, even and odd numbers of planes in the spacer ($p_+ + p_- = 1$) and $\bar{J}_+$, $\bar{J}_-$ are the relevant average stiffness constants. The minimum energy in zero field, with anisotropy neglected, occurs for $\theta = \pi c_+/(c_+ + c_-)$ which gives 90° coupling for $c_+ = c_-$. Yan *et al.* (1999) deduce from $M(H)$ curves that this is the case in Fe/Mn/Fe trilayers with the Mn thickness in the range 1.2–2.45 nm.

7.4 IEC with insulating and semiconducting spacers

Slonczewski (1989) introduced the torque method to calculate the IEC for a free-electron model of two FM metals separated by a potential barrier. Bruno (1995) solved the same problem using the energy difference method. The main result is that the IEC, which may be FM or AF, decays exponentially with increasing barrier width (spacer thickness) at a rate determined by the height of the barrier. This contrasts with the slowly decaying oscillatory coupling for metal spacers. In the latter case, the amplitude of the oscillations decreases with increasing temperature owing to smearing of the Fermi surface (see Section 6). For the insulating barrier case, Bruno (1995) found that the coupling strength increases with temperature owing to the enhanced tunneling of thermally occupied states above the Fermi level. The experimental situation, reviewed by Bürgler, Grünberg, Demokritov and Johnson (2001), is quite confused. Possibly some light is shed on the matter by the very recent theoretical work of Zhuravlev, Tsymbal and Vedyayev (2005). They consider the same free-electron barrier model used by Slonczewski and Bruno, but with the addition of an impurity potential well within the barrier. This creates an impurity level below the top of the potential barrier. A strong resonant AF peak in the IEC appears as the impurity level passes through the Fermi level. The peak reduces slightly with increasing temperature so that the IEC weakens. This temperature dependence contrasts with Bruno's result for the pure barrier and agrees with some experiments. However, the success of the model depends on having a sufficient number of impurity states close to the Fermi level of the ferromagnets.

No quantitative calculations for the IEC on real materials such as epitaxial Fe/MgO/Fe(001) have been made; they are perfectly feasible using the same methods as for existing calculations of tunneling magnetoresistance in this system (Mathon and Umerski, 2001). A large AF coupling ($J_1 \simeq -0.26$ mJ m^{-2}) has been observed in this system with a thin MgO layer of 6 Å (Faure-Vincent *et al.*, 2002). Multiorbital tight-binding calculations for valence-band electrons in all-semiconductor IV-VI magnetic/nonmagnetic superlattices have yielded values for the IEC (Blinowski and Kacman, 2001). J_1 has been calculated for EuS/PbS(001) with PbS thicknesses of $N = 1$–8 ML; it is negative and decreases exponentially with N. Experimental estimates of J_1 exist for $N = 1, 2, 3$ and the calculated values of $-J_1 = 0.77, 0.33, 0.18$ mJ m^{-2}, respectively, follow them closely apart from being larger by an almost constant factor of 10.

8 OUTLOOK

The essential theoretical concepts for understanding IEC were in place soon after its experimental discovery. Ten years ago quantitative calculations of IEC for real systems were already being made. At this time, the emphasis on magnetic multilayer research changed to nonequilibrium phenomena such as tunneling magnetoresistance and, most recently, current-induced switching of magnetization. This has left many issues concerning IEC unresolved. One important issue is the order-of-magnitude discrepancy between theory and experiment for systems with TM spacers (see Section 7.2). Another open topic is the unambiguous observation of intrinsic biquadratic exchange, with evidence for its oscillatory behavior as a function of spacer thickness. This should be possible in systems such as Fe/Au/Fe and Fe/Ag/Fe (see Section 7.1). We expect that work on these and other issues will progress steadily and that maybe there are still some surprises in store.

ACKNOWLEDGMENTS

The authors wish to thank J. Mathon, M. Villeret, J. d'Albuquerque e Castro, and R.B. Muniz for many years of enjoyable collaboration in this subject. We are grateful to the UK Engineering and Physical Sciences Research Council (EPSRC) for continuous support.

REFERENCES

d'Albuquerque e Castro, J., Ferreira, M.S. and Muniz, R.B. (1994). Theory of the exchange coupling in magnetic metallic multilayers. *Physical Review B*, **49**, 16062–16065.

d'Albuquerque e Castro, J., Mathon, J., Villeret, M. and Umerski, A. (1996). Confinement mechanism for strong temperature dependence of the interlayer exchange coupling in Co/Cu(001). *Physical Review B*, **53**, R13306–R13309.

Almeida, N.S., Mills, D.L. and Teitelman, M. (1995). Temperature variation of the interfilm exchange in magnetic multilayers: the influence of spin wave interactions. *Physical Review Letters*, **75**, 733–736.

Baibich, M.N., Broto, J.M., Fert, A., *et al.* (1988). Giant magnetoresistance of (001)Fe/(001)Cr magnetic superlattices. *Physical Review Letters*, **61**, 2472–2475.

Binasch, G., Grünberg, P., Saurenbach, F. and Zinn, W. (1989). Enhanced magnetoresistance in layered magnetic structures with antiferromagnetic interlayer exchange. *Physical Review B*, **39**, 4828–4830.

Blinowski, J. and Kacman, P. (2001). Interlayer exchange coupling mediated by valence-band electrons. *Physical Review B*, **64**, 045302–045308.

Bloemen, P.J.H., van Dalen, R., de Jonge, W.J.M., *et al*. (1993). Short-period oscillation of the interlayer exchange coupling in the ferromagnetic regime in Co/Cu/Co(100). *Journal of Applied Physics*, **73**, 5972–5974.

Bruno, P. (1995). Theory of interlayer magnetic coupling. *Physical Review B*, **52**, 411–439.

Bruno, P. and Chappert, C. (1991). Oscillatory coupling between ferromagnetic layers separated by a nonmagnetic metal spacer. *Physical Review Letters*, **67**, 1602–1605.

Bruno, P. and Chappert, C. (1992). Ruderman-Kittel theory of oscillatory interlayer exchange coupling. *Physical Review B*, **46**, 261–270.

Bürgler, D.E., Grünberg, P., Demokritov, S.O. and Johnson, M.T., (2001). *Handbook of Magnetic Materials*, Buschow, K.H.J. (Ed.), Elsevier Science B.V., Vol. 13, Chapter 1.

Celinski, Z., Heinrich, B. and Cochran, J.F. (1993). Analysis of bilinear and biquadratic exchange coupling in Fe/Ag/Fe(001) trilayers. *Journal of Applied Physics*, **73**, 5966–5968.

Cornea, C. and Stoeffler, D. (2000). Calculated interlayer magnetic couplings in Fe/Cr superlattices. *Europhysics Letters*, **49**, 217–223.

Costa, A.T. Jr., d'Albuquerque e Castro, J. and Muniz, R.B. (1997a). Exchange coupling between iron layers separated by bcc copper. *Physical Review B*, **55**, 3724–3727.

Costa, A.T. Jr., d'Albuquerque e Castro, J. and Muniz, R.B. (1997b). Exchange coupling between iron layers separated by silver and gold. *Physical Review B*, **56**, 13697–13700.

Costa, A.T. Jr., d'Albuquerque e Castro, J. and Muniz, R.B. (1999). Oscillatory exchange coupling between iron layers separated by chromium. *Physical Review B*, **59**, 11424–11431.

Cullen, J.R. and Hathaway, K.B. (1993). Temperature dependence of the exchange energy and critical field for antiferromagnetically coupled thin films and superlattices. *Physical Review B*, **47**, 14998–15006.

Demokritov, S.O. (1998). Biquadratic interlayer coupling in layered magnetic systems. *Journal of Physics D: Applied Physics*, **31**, 925–941.

Demokritov, S., Tsymbal, E., Grünberg, P. and Zinn, W. (1994). Magnetic-dipole mechanism for biquadratic interlayer coupling. *Physical Review B*, **49**, 720–723.

Demokritov, S., Wolf, J.A. and Grüunberg, P. (1991). Evidence for oscillations in the interlayer coupling of Fe films across Cr films from spin-waves and M(H) curves. *Europhysics Letters*, **15**, 881–886.

Doniach, S. and Sondheimer, E.H. (1998). *Green's Functions for Solid State Physicists*, Imperial College Press.

Drchal, V., Kudrnovsky, J., Bruno, P., *et al*. (1999). Temperature dependence of the interlayer exchange coupling in magnetic multilayers: an ab initio approach. *Physical Review B*, **60**, 9588–9595.

Drchal, V., Kudrnovsky, J., Turek, I. and Weinberger, P. (1996). Interlayer magnetic coupling: the torque method. *Physical Review B*, **53**, 15036–15044.

Edwards, D.M., (2002). In *Exotic States in Quantum Nanostructures*, Sarkar, S. (Ed.), Kluwer Academic Press.

Edwards, D.M. and Mathon, J. (1991). Oscillations in exchange coupling across a nonmagnetic metallic layer. *Journal of Magnetism and Magnetic Materials*, **93**, 85–88.

Edwards, D.M., Mathon, J., Muniz, R.B. and Phan, M.S. (1991a). Oscillations of the exchange in magnetic multilayers as an analog of de Haas–van Alphen effect. *Physical Review Letters*, **67**, 493–496.

Edwards, D.M., Mathon, J., Muniz, R.B. and Phan, M.S. (1991b). Oscillations in the exchange coupling of ferromagnetic layers separated by a nonmagnetic metallic layer. *Journal of Physics: Condensed Matter*, **3**, 4941–4958.

Edwards, D.M., Robinson, A.M. and Mathon, J. (1995). The torque method for exchange coupling in magnetic trilayers. *Journal of Magnetism and Magnetic Materials*, **140**, 517–518.

Edwards, D.M., Ward, J.M. and Mathon, J. (1993). Intrinsic and secondary mechanisms for biquadratic exchange coupling in magnetic trilayers. *Journal of Magnetism and Magnetic Materials*, **126**, 380–383.

Erickson, R.P., Hathaway, K.B. and Cullen, J.R. (1993). Mechanism for non-Heisenberg-exchange coupling between ferromagnetic layers. *Physical Review B*, **47**, 2626–2635.

Faure-Vincent, J., Tiusan, C., Bellouard, C., *et al*. (2002). Interlayer magnetic coupling interactions of two ferromagnetic layers by spin polarized tunneling. *Physical Review Letters*, **89**, 107206–107209.

Ferreira, M.S., d'Albuquerque e Castro, J., Edwards, D.M. and Mathon, J. (1996). Fundamental oscillation periods of the interlayer exchange coupling beyond the RKKY approximation. *Journal of Physics: Condensed Matter*, **8**, 11259–11276.

Filipkowski, M.E., Krebs, J.J., Prinz, G.A. and Guttierez, C.J. (1995). Giant near-90 degree coupling in epitaxial CoFe/Mn/CoFe sandwich structures. *Physical Review Letters*, **75**, 1847–1850.

Fishman, R.S. (2001). Spin-density waves in Fe/Cr trilayers and multilayers. *Journal of Physics: Condensed Matter*, **13**, R235–R269.

Fishman, R.S. and Shi, Z-P. (1998). Magnetic phase diagram of Fe/Cr multilayers and wedges. *Journal of Physics: Condensed Matter*, **10**, L277–L282.

Fishman, R.S. and Shi, Z-P. (1999). Collinear spin-density-wave ordering in Fe/Cr multilayers and wedges. *Physical Review B*, **59**, 13849–13860.

Freyss, M., Stoeffler, D. and Dreyssé, H. (1996). Noncollinear order contribution to the exchange coupling in Fe/Cr(001) superlattices. *Physical Review B*, **54**, R12677–R12680.

Freyss, M., Stoeffler, D. and Dreyssé, H. (1997). Interfacial alloying and interfacial coupling in Cr/Fe(001). *Physical Review B*, **56**, 6047–6055.

Fuss, A., Wolf, J.A. and Grünberg, P.A. (1992). Exchange of Fe layers across interlayers with good match. *Physica Scripta*, **T45**, 95–98.

Garrison, K., Chang, Y. and Johnson, P.D. (1993). Spin polarization of quantum well states in copper thin films deposited on a Co(001) substrate. *Physical Review Letters*, **71**, 2801–2804.

Grünberg, P., Schreiber, R., Pang, Y., *et al*. (1986). Layered magnetic structures: evidence for antiferromagnetic coupling of Fe layers across Cr interlayers. *Physical Review Letters*, **57**, 2442–2445.

Gutierrez, C.J., Krebs, J.J., Filipkowski, M.E. and Prinz, G.A. (1992). Strong temperature-dependence of the 90-degrees coupling in Fe/Al/Fe(001) magnetic trilayers. *Journal of Magnetism and Magnetic Materials*, **116**, L305–L310.

Hafner, R., Spišák, D., Lorentz, R. and Hafner, J. (2002). Ab initio local-spin-density study of oscillatory exchange coupling in Fe/Au multilayers. *Journal of Physics: Condensed Matter*, **14**, 4297–4307.

Hathaway, K.B. and Cullen, J.R. (1992). A free-electron model for the exchange coupling of ferromagnets through paramagnetic metals. *Journal of Magnetism and Magnetic Materials*, **104–107**, 1840–1842.

Heinrich, B. and Cochran, J.F. (1993). Ultrathin metallic magnetic-films – magnetic anisotropies and exchange interactions. *Advances in Physics*, **42**, 523–639.

Heinrich, B., Cochran, J.F., Monchevsky, T. and Urban, R. (1999). Exchange coupling through spin-density waves in Cr(001) structures: Fe-whisker/Cr/Fe(001) studies. *Physical Review B*, **59**, 14520–14532.

Heinrich, B., Purcell, S.T., Dutcher, J.R., *et al*. (1988). Structural and magnetic properties of ultrathin Ni/Fe bilayers grown epitaxially on Ag(001). *Physical Review B*, **38**, 12879–12896.

Inoue, J. (1994). Effects of randomness at interfaces on the exchange coupling in magnetic multilayers. *Physical Review B*, **50**, 13541–13546.

Johnson, M.T., Bloemen, P.J.H., Coehoorn, R., *et al*. (1993). In *Magnetic Ultrathin Films, Multilayers, and Surfaces/Interfaces and Characterization*, MRS Symposia Proceedings No.313, Jonker, B.T., Chambers, S.A., Farrow, R.F.C., *et al*. (Eds.), Materials Research Society: Pittsburgh, p. 93.

Kawakami, R.K., Rotenberg, F., Escorcia-Aparacio, E.J., *et al*. (1999). Determination of the magnetic coupling in the Co/Cu/Co (100) system with momentum-resolved quantum well states. *Physical Review Letters*, **82**, 4098–4101.

Kläsges, R., Schmitz, D., Carbone, C., *et al*. (1998). Short-period oscillations in photoemission from Cu films on Co(100). *Physical Review B*, **57**, R696–R699.

Krebs, J.J., Prinz, G.A., Filipkowski, M.E. and Gutierrez, C.J. (1996). Interlayer thickness dependence of the strong 90 degrees coupling in epitaxial CoFe/Mn/CoFe trilayers. *Journal of Applied Physics*, **79**, 4525–4527.

Kudrnovsky, J., Drchal, V., Turek, I., *et al*. (1996). Interlayer magnetic coupling: effect of interface roughness. *Physical Review B*, **53**, 5125–5128.

Levy, P.M., Maekawa, S. and Bruno, P. (1998). Range dependence of interlayer exchange coupling. *Physical Review B*, **58**, 5588–5593.

Lindner, J. and Baberschke, K. (2003a). Ferromagnetic resonance in coupled ultrathin films. *Journal of Physics: Condensed Matter*, **15**, S465–S478.

Lindner, J. and Baberschke, K. (2003b). In situ ferromagnetic resonance: an ultimate tool to investigate the coupling in ultrathin magnetic films. *Journal of Physics: Condensed Matter*, **15**, R193–R232.

Majkrzak, C.F., Cable, J.W., Kwo, J., *et al*. (1986). Observation of a magnetic antiphase domain structure with long-range order in a synthetic Gd-Y superlattice. *Physical Review Letters*, **56**, 2700–2703.

Mathon, J. (1988). Magnetism at transition-metal surfaces. *Reports on Progress in Physics*, **51**, 1–56.

Mathon, J. and Umerski, A. (2001). Theory of tunneling magnetoresistance of an epitaxial Fe/MgO/Fe(001) junction. *Physical Review B*, **63**, 220403(R), (4 pages).

Mathon, J. and Umerski, A. (2006). In *Handbook of Theoretical and Computational Nanotechnology*, Rieth, M. and Schommers, W. (Eds.), American Scientific Publishers.

Mathon, J., Umerski, A., Villeret, M., *et al*. (2000). Induced magnetization spiral in a nonmagnetic metal sandwiched between two ferromagnets. *Journal of Magnetism and Magnetic Materials*, **217**, 188–198.

Mathon, J., Villeret, M. and Edwards, D.M. (1993). Theory of the systematic variation of the exchange coupling strength in magnetic multilayers. *Journal of Magnetism and Magnetic Materials*, **127**, L261–L266.

Mathon, J., Villeret, M., Muniz, R.B., *et al*. (1995). Quantum well theory of the exchange coupling in Co/Cu/Co(001). *Physical Review Letters*, **74**, 3696–3699.

Mathon, J., Villeret, M., Umerski, A., *et al*. (1997). Quantum-well theory of the exchange coupling in magnetic multilayers with application to Co/Cu/Co(001). *Physical Review B*, **56**, 11797–11809.

Mills, D.L. and Maradudin, A.A. (1967). Some thermodynamic properties of a semi-infinite Heisenberg ferromagnet. *Journal of Physics and Chemistry of Solids*, **28**, 1855.

Mirbt, S., Niklasson, A.M.N., Johansson, B. and Skriver, H.L. (1996). Calculated oscillation periods of the interlayer coupling in Fe/Cr/Fe and Fe/Mo/Fe sandwiches. *Physical Review B*, **54**, 6382–6392.

Moser, A., Berger, A., Margulies, D.J. and Fullerton, E.E. (2003). Magnetic tuning of biquadratic exchange coupling in magnetic thin films. *Physical Review Letters*, **91**, 097203.

Opitz, J., Zahn, P., Binder, J. and Mertig, I. (2000). Interlayer exchange coupling in Fe/Au multilayers. *Journal of Applied Physics*, **87**, 6588–6590.

Ortega, J.E., Himpsel, F.J., Mankey, G.J. and Willis, R.F. (1993). Quantum-well states and magnetic coupling between ferromagnets through a noble-metal layer. *Physical Review B*, **47**, 1540–1552.

Parkin, S.S.P. (1991). Systematic variation of the strength and oscillation period of indirect magnetic exchange coupling through the 3D, 4D, and 5D transition-metals. *Physical Review Letters*, **67**, 3598–3601.

Parkin, S.S.P., Bhadra, R. and Roche, K.P. (1991). Oscillatory magnetic exchange coupling through thin copper layers. *Physical Review Letters*, **66**, 2152–2155.

Parkin, S.S.P., More, N. and Roche, K.P. (1990). Oscillations in exchange coupling and magnetoresistance in metallic superlattice structures: Co/Ru, Co/Cr, and Fe/Cr. *Physical Review Letters*, **64**, 2304–2307.

Persat, N. and Dinia, A. (1997). Strong temperature dependence of the interlayer exchange coupling strength in Co/Cu/Co sandwiches. *Physical Review B*, **56**, 2676–2679.

Pettifor, D.G. and Varma, C. (1979). Heat of formation within the density functional formalism. *Journal of Physics C*, **12**, L253–L255.

Pierce, D.T., Unguris, J. and Celotta, R.J. (1994). *Ultrathin Magnetic Structures*, Heinrich, B. and Bland, J.A.C. (Eds.), Springer: Berlin, Vol II.

Pierce, D.T., Unguris, J., Celotta, R.J. and Stiles, M.D. (1999). Effect of roughness, frustration, and antiferromagnetic order on magnetic coupling of Fe/Cr multilayers. *Journal of Magnetism and Magnetic Materials*, **200**, 290–321.

Qiu, Z.Q., Pearson, J. and Bader, S.D. (1993). Magnetic coupling of Fe/Mo/Fe and Co/Cu/Co sandwiches across wedged spacer layers. *Journal of Applied Physics*, **73**, 5765–5770.

Qiu, Z.Q., Pearson, J., Berger, A. and Bader, S.D. (1992). Short-period oscillations in the interlayer magnetic coupling of wedged Fe(100)/Mo(100)/Fe(100) grown on Mo(100) by molecular-beam epitaxy. *Physical Review Letters*, **68**, 1398–1401.

Qiu, Z.Q. and Smith, N.V. (2002). Quantum well states and oscillatory magnetic interlayer coupling. *Journal of Physics: Condensed Matter*, **14**, R169–R193.

Ribas, R. and Dieny, B. (1993). Numerical investigation of 90-degrees coupling in magnetic sandwiches – thermal variation, influence of anisotropy. *Journal of Magnetism and Magnetic Materials*, **121**, 313–317.

Rücker, U., Demokritov, S., Tsymbal, E., *et al*. (1995). Biquadratic coupling in Fe/Au/Fe trilayers – experimental-evidence for the magnetic-dipole mechanism. *Journal of Applied Physics*, **78**, 387–391.

Salamon, M.B., Sinha, S., Rhyne, J.J., *et al*. (1986). Long-range incommensurate magnetic order in a Dy-Y multilayer. *Physical Review Letters*, **56**, 259–262.

Schäfer, M., Demokritov, S., Mtiller-Pfeiffer, S., *et al*. (1995). Investigation of 90-degrees coupling in Fe/Ag/Fe structures – loose spins and fluctuation mechanism. *Journal of Applied Physics*, **77**, 6432–6438.

Schreyer, A., Ankner, J.F., Zeidler, T., *et al*. (1995). Noncollinear and collinear magnetic structures in exchange coupled Fe/Cr(001) superlattices. *Physical Review B*, **52**, 16066–16085.

Schwieger, S. and Nolting, W. (2004). Origin of the temperature dependence of interlayer exchange coupling in metallic trilayers. *Physical Review B*, **69**, 224413, (7 pages).

Shi, Z-P. and Fishman, R.S. (1997). Interplay between spin-density wave and proximity magnetic layers. *Physical Review Letters*, **78**, 1351–1354.

Slonczewski, J.C. (1989). Conductance and exchange coupling of two ferromagnets separated by a tunneling barrier. *Physical Review B*, **39**, 6995–7002.

Slonczewski, J.C. (1991). Fluctuation mechanism for biquadratic exchange coupling in magnetic multilayers. *Physical Review Letters*, **67**, 3172–3175.

Slonczewski, J.C. (1993a). Mechanism of interlayer exchange in magnetic multilayers. *Journal of Magnetism and Magnetic Materials*, **126**, 374–379.

Slonczewski, J.C. (1993b). Origin of biquadratic exchange in magnetic multilayers. *Journal of Applied Physics*, **73**, 5957–5962.

Slonczewski, J. (1995). Overview of interlayer exchange theory. *Journal of Magnetism and Magnetic Materials*, **150**, 13–24.

Stiles, M.D. (1996a). Oscillatory exchange coupling in Fe/Cr multilayers. *Physical Review B*, **54**, 14679–14685.

Stiles, M.D. (1996b). Spin-dependent interface transmission and reflection in magnetic multilayers. *Journal of Applied Physics*, **79**, 5805–5810.

Stiles, M.D. (1999). Interlayer exchange coupling. *Journal of Magnetism and Magnetic Materials*, **200**, 322–337.

Stoeffler, D. and Gautier, F. (1990). Electronic-structure, magnetic order and interlayer magnetic couplings in metallic superlattices. *Progress of Theoretical Physics Supplement*, **101**, 139–157.

Stoeffler, D. and Gautier, F. (1991). Interface roughness, magnetic moments, and couplings in (A)m/(Cr)n (001) superlattices (A = Fe, Co, Ni). *Physical Review B*, **44**, 10389–10392.

Stoeffler, D. and Gautier, F. (1993a). Magnetic couplings in Fe/Mn and Fe/Cr superlattices. *Journal of Magnetism and Magnetic Materials*, **121**, 259–265.

Stoeffler, D. and Gautier, F. (1993b). In *Magnetism and Structure in Systems of Reduced Dimension*, Farrow, R.F.C., Dieny, B. and Donath, M., (Eds.), Plenum Press: New York, p. 411.

Szunyogh, L., Újfalussy, B., Weinberger, P. and Sommers, C. (1996). Fully relativistic spin-polarized description of magnetic interface coupling: Fe multilayers in Au(100). *Physical Review B*, **54**, 6430–6436.

Tsetseris, L., Lee, B. and Chan, Y-C. (1997). Interlayer exchange coupling in Fe/Cr multilayers. *Physical Review B*, **55**, 11586–11592.

Umerski, A. (1997). Closed-form solutions to surface Green's functions. *Physical Review B*, **55**, 5266–5275.

Unguris, J., Celotta, R.J. and Pierce, D.T. (1991). Observation of two different oscillation periods in the exchange coupling of Fe/Cr/Fe(100). *Physical Review Letters*, **67**, 140–143.

Unguris, J., Celotta, R.J. and Pierce, D.J. (1993). Oscillatory magnetic coupling in Fe/Ag/Fe(100) sandwich structures. *Journal of Magnetism and Magnetic Materials*, **127**, 205–213.

Unguris, J., Celotta, R.J. and Pierce, D.T. (1997). Determination of the exchange coupling strengths for Fe/Au/Fe. *Physical Review Letters*, **79**, 2734–2737.

Unguris, J., Pierce, D.T., Celotta, R.J. and Stroscio, J.A., (1993). In *Magnetism and Structure in Systems of Reduced Dimension*, Farrow, R.F.C., *et al*. (Eds.), Plenum Press: New York, p. 101.

de Vries, J.J., Schudelavo, A.A.P., Jungblut, R., *et al*. (1995). Oscillatory interlayer exchange coupling with the Cu cap layer thickness in Co/Cu/Co/Cu(100). *Physical Review Letters*, **75**, 4306–4309.

Weber, W., Allenspach, R. and Bischof, A. (1995). Exchange coupling across Cu(100) – a high-precision study. *Europhysics Letters*, **31**, 491–496.

Yan, S-S., Schreiber, R., Voges, F., *et al*. (1999). Oscillatory interlayer coupling in Fe/Mn/Fe trilayers. *Physical Review B*, **59**, R11641–R11644.

Zhuravlev, M.Ye., Tsymbal, E.Y. and Vedyayev, A.V. (2005). Impurity-assisted interlayer exchange coupling across a tunnel barrier. *Physical Review Letters*., **94**, 026806.

Enhanced Magnetoresistance

Peter Zahn and Ingrid Mertig
Martin Luther University, Halle, Germany

1 INTRODUCTION

Magnetoresistance (MR) effects are known since the discovery of the anisotropic magnetoresistance (AMR) in metals in 1857 by William Thomson where the resistance depends on the direction of the current with respect to the material's magnetization. A revival of the MR effect occurred in the late 1980s with the discovery of giant magnetoresistance (GMR). GMR is related to nanofabrication technology. Artificially layered structures, so-called magnetic multilayers, show a drastic change of resistance as a function of relative orientation of layer magnetization. The high potential of future application was realized in the 1990s and a large effort in basic and applied research was initiated. Thereby, two major application areas are in the focus of commercial interests – magnetoresistive sensors and information technology. Read heads in magnetic hard disk drives and nonvolatile memory are expected to beat conventional systems with respect to performance and costs.

The discovery of the GMR effect is a result of up-to-date solid state physics at the nanometer scale. The microscopic understanding of the effect is based on quantum mechanics starting from the atomic level and combines modern concepts of transport theory with material-specific *ab initio* calculations. The main idea of this chapter is to introduce the basic components of the theoretical description and to elucidate the macroscopic phenomenon by means of qualitative microscopic pictures confirmed by quantitative *ab initio* electronic structure calculations.

Handbook of Magnetism and Advanced Magnetic Materials. Edited by Helmut Kronmüller and Stuart Parkin. Volume 1: *Fundamentals and Theory*. © 2007 John Wiley & Sons, Ltd. ISBN: 978-0-470-02217-7.

1.1 Limiting cases

While measuring the resistance of a sample, two regimes have to be distinguished (see Figure 1). In the diffusive limit the mean free path Λ of the electrons is much shorter than the dimension of the sample. The mean free path is a measure of the distance an electron travels in the sample without being affected by the scattering processes.

In the diffusive regime the resistance R is given by Ohm's law and is proportional to the length L and the cross section A of the sample assuming current and voltage measurement in the same direction

$$R = \rho \frac{L}{A} \tag{1}$$

A material-specific proportionality constant ρ, the resistivity, is defined. In general the resistivity is a tensor $\underline{\underline{\rho}}$, which reflects the anisotropy of the crystal in different spatial directions.

A similar relation holds for the conductance g and the conductivity σ

$$g = \sigma \frac{A}{L} \tag{2}$$

Conductance and resistance are related to each other by $g = R^{-1}$. As a consequence, conductivity and resistivity are also inversely proportional $\sigma = \rho^{-1}$ in the diffusive limit. In general, conductivity is also a tensor $\underline{\underline{\sigma}}$.

In the ballistic limit, the dimensions of the sample are shorter than the mean free path of the electrons and the transport cannot be characterized by a material-specific constant only. The resistance and conductance can change in a nonmonotonic way with the length of the sample. This is the nonohmic limit.

1.2 Magnetoresistance

Owing to the general definition the resistivity, ρ can be expressed as a three-dimensional tensor of rank 2. For systems with time-reversal symmetry this tensor can be diagonalized with components ρ_{xx}, ρ_{yy}, and ρ_{zz}

$$\underline{\underline{\rho}} = \begin{pmatrix} \rho_{xx} & 0 & 0 \\ 0 & \rho_{yy} & 0 \\ 0 & 0 & \rho_{zz} \end{pmatrix} \tag{3}$$

This is valid for vanishing spin-orbit coupling and without magnetic field. In isotropic and cubic systems the material-specific resistivity is a single scalar $\rho = \rho_{xx} = \rho_{yy} = \rho_{zz}$.

If one direction is preferred by a symmetry breaking field, two components $\rho_{\parallel}$ and $\rho_{\perp}$ for the transport parallel and perpendicular to the corresponding axis have to be distinguished. This is, for example, the case in hexagonal systems and causes the so-called resistivity anisotropy.

Another way of breaking the symmetry is by means of an external magnetic field. An external magnetic field of strength B can influence the resistivity by the acting Lorentz force. The increase of the diagonal elements of the resistivity caused by the Lorentz force is called *longitudinal and transversal magnetoresistance* according to the relative orientation of the current and the external magnetic field, respectively.

The relative change in resistance (MR ratio) characterizes the enhanced MR

$$\frac{\Delta R}{R} = \frac{R(B) - R(B=0)}{R(B=0)} \tag{4}$$

In the diffusive limit this is equivalent to the relative change in resistivity

$$\frac{\Delta \rho}{\rho} = \frac{\rho(B) - \rho(B=0)}{\rho(B=0)} \tag{5}$$

In magnetic systems the role of an external magnetic field is replaced by the internal magnetization. Crystal anisotropy causes a preferred orientation of the magnetization along the so-called easy axes. Resistances measured parallel or perpendicular to the magnetization direction are different. The ratio is called *anisotropic magnetoresistance*.

Finally, an external magnetic field can be used to change the magnetic order in the sample which can be accompanied by a drastic change of the resistance.

A well-known example is GMR. The effect occurs in magnetic multilayers. Ferromagnetic layers are separated by non(ferro)magnetic metallic layers. The relative change of the layer magnetizations with respect to each other causes an enormous change of the resistance at considerably small fields. This effect is much stronger than the Lorentz force effect.

If the metallic layers are replaced by insulating layers so-called tunneling magnetoresistance (TMR) is obtained (Julliere, 1975; Moodera, Kinder, Wong and Meservey, 1995; Meservey and Tedrow, 1994), (see also **Theory of Spin-dependent Tunneling, Volume 1**).

In colossal magnetoresistance (CMR) systems (von Helmolt *et al*., 1993) the action of the external field causes a magnetic phase transition which is accompanied by a metal–insulator transition. This changes the resistance by orders of magnitude but the strength of the required fields prevent, until now, application in sensor and information technology.

1.3 Giant magnetoresistance

1.3.1 GMR ratio

The discovery of GMR in magnetic multilayer systems (Baibich *et al*., 1988; Binasch, Grünberg, Saurenbach and Zinn, 1989) initiated a variety of experimental and theoretical investigations to elucidate the microscopic origin of the phenomenon. The effect was first discovered in metallic multilayers made up of magnetic layers separated by non(ferro)magnetic layers. The effect is closely linked to the effect of interlayer exchange coupling (IEC) which was discovered some years earlier by Grünberg *et al*. (1986) (see also **Exchange Coupling in Magnetic Multilayers, Volume 1**). In those samples a magnetic coupling of adjacent magnetic layers occurs which is mediated by the electrons of the nonmagnetic layer. The strength J_{AF} and the sign of the coupling depend on the thickness of the nonmagnetic layer (Parkin, 1991; Bruno and Chappert, 1991).

If the layer magnetizations are antiparallel in the ground state, the relative orientation of the layer magnetizations can be changed by means of an external magnetic field. In systems without an intrinsic coupling of the magnetic layers the switching of the magnetic layers can be triggered by their magnetic anisotropy caused by different layer thicknesses, crystal structures, and alloying. The change of magnetic

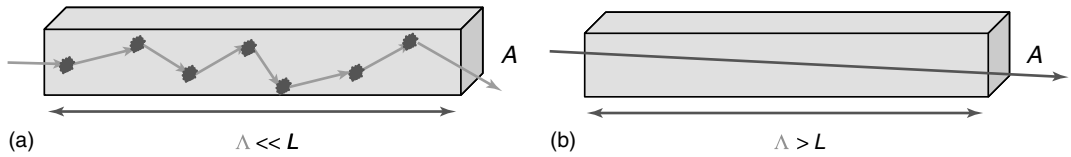

Figure 1. Transport measurements in the diffusive limit (a) and the coherent limit (b). The cross section of the sample is A and the length along the current directions is L, Λ denotes the mean free path.

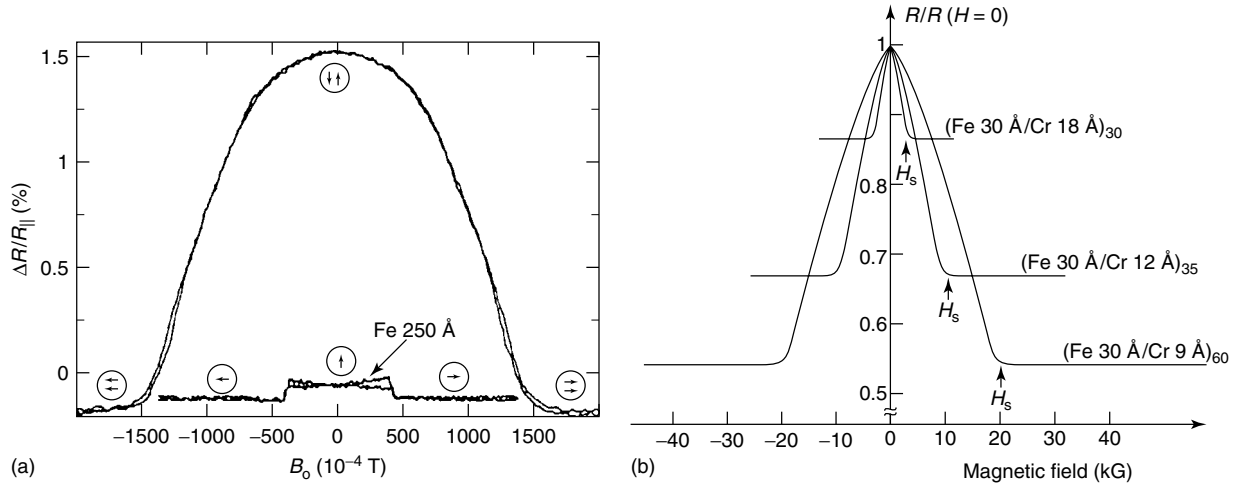

Figure 2. First experimental GMR results obtained in Fe/Cr/Fe systems: trilayer result from Binasch, Grünberg, Saurenbach and Zinn (1989) (a), multilayer result from Baibich *et al*. (1988) (b). (Reproduced from Binasch *et al*., 1989/Baibich *et al*., 1998, with permission from the American Physical Society. © 1989/1998.)

order is accompanied by a drastic change of resistance. The first experiments were carried out at Fe/Cr multilayers and changes up to 50% were achieved, see Figure 2. The close link of the behavior of resistance and magnetization is sketched in Figure 3.

To quantify the GMR effect the following ratio was introduced

$$GMR = \frac{R^{\mathrm{AP}} - R^{\mathrm{P}}}{R^{\mathrm{P}}} = \frac{\rho^{\mathrm{AP}} - \rho^{\mathrm{P}}}{\rho^{\mathrm{P}}} = \frac{\sigma^{\mathrm{P}}}{\sigma^{\mathrm{AP}}} - 1 \qquad (6)$$

This definition is the so-called optimistic one, because it can reach values much larger than 1. It will be used throughout this chapter. Some authors prefer to use the pessimistic definition, which is limited in cases of positive GMR ($\rho^{\mathrm{AP}} > \rho^{\mathrm{P}}$) to values smaller than 100%, and is given by

$$GMR' = \frac{\rho^{\mathrm{AP}} - \rho^{\mathrm{P}}}{\rho^{\mathrm{AP}}} = 1 - \frac{\sigma^{\mathrm{AP}}}{\sigma^{\mathrm{P}}} \qquad (7)$$

It was shown by several authors (Oguchi, 1993; Zahn, Mertig, Richter and Eschrig, 1995; Schep, Kelly and Bauer, 1995; Butler, MacLaren and Zhang, 1993) that GMR in magnetic multilayers is strongly influenced by the electronic structure of the layered system as a function of the magnetic configuration. That is, the differences in Fermi velocities of the multilayers for parallel or antiparallel alignment of magnetic moments in adjacent magnetic layers cause GMR by themselves. Since this effect is a result of Bragg reflection in ideal multilayers, it might be less important in dirty samples that still have remarkable GMR amplitude. Consequently, spin-dependent scattering (Camley and Barnaś, 1989; Levy, Zhang and Fert, 1990; Inoue, Oguri and Maekawa, 1991; Hood and Falicov, 1992; Valet and Fert, 1993; Levy, 1994) is assumed to play a crucial role for GMR. Experiments (Parkin, Modak and Smith, 1993; Enders *et al*., 2001; Santamaria *et al*., 2001) and corresponding calculations (Schep *et al*., 1997; Zahn *et al*., 1998; Zahn, Binder and Mertig, 2003) demonstrated that spin-dependent interface scattering is especially important for the size of the effect.

The idea of the review is to present an overview of the material-specific trends for the standard systems of magnetoelectronics. The general trends are elucidated by a detailed analysis of the spin-dependent scattering cross sections in layered structures.

1.3.2 Geometry

For GMR measurements two geometrical arrangements can be distinguished with respect to the direction of the current relative to layer orientation. The current-in-plane (CIP)

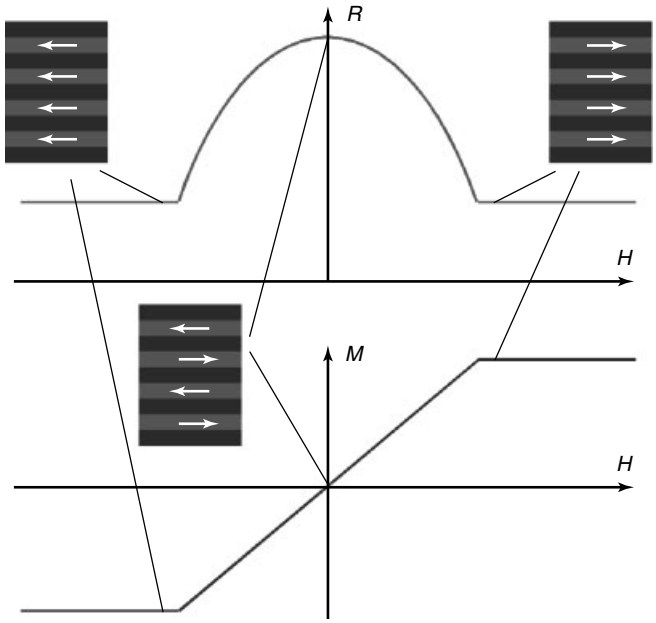

Figure 3. Multilayer structure, resistivity, and magnetization as a function of the external magnetic field.

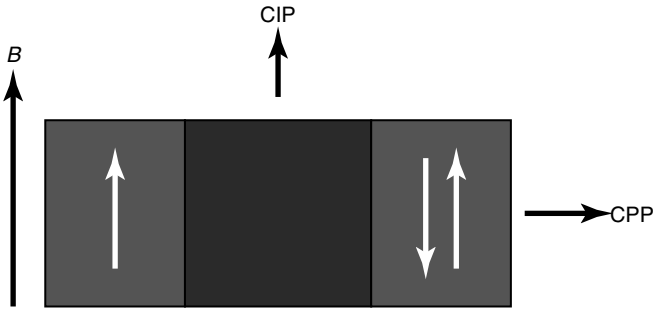

Figure 4. Geometries for GMR transport measurements.

geometry is characterized by a current flowing parallel to the layers. Contrarily, in the current perpendicular to the planes (CPP) geometry the current is driven perpendicular to the planes, as sketched in Figure 4.

In CIP geometry trilayers and multilayers are used. In trilayers one of the magnetic layers, the hard layer, is pinned to a natural or artificial antiferromagnet (Nogues and Schuller, 1999; van den Berg *et al*., 1999). The soft magnetic layer is often made from an alloy to reduce the magnetocrystalline anisotropy. In multilayers the different coercivities of the magnetic layers are obtained by different layer thicknesses or by exploiting the effect of magnetic IEC.

In CPP geometry, several configurations have been used for transport measurements. Planar junctions (Gijs, Lenczowski and Giesbers, 1993), sawtooth samples, which allow measurements in CIP and CPP at one and the same sample (Pratt *et al*., 1991), and multilayer pillars grown in polymer foil holes with a large number of bilayers have been investigated (Piraux, Dubois and Fert, 1996; Piraux *et al*., 1997).

Owing to the symmetry of crystalline layered systems the conductivity tensor $\underline{\underline{\sigma}}$ consists of two different diagonal elements. If the current flows perpendicular to the layers that is, parallel to the crystal z axis

$$\sigma_{\mathrm{CPP}} = \sigma_{zz} = \sigma_{\perp} \tag{8}$$

is obtained and

$$\sigma_{\mathrm{CIP}} = \sigma_{xx} = \sigma_{yy} = \sigma_{\parallel} \tag{9}$$

is observed if the current flows in the layer direction.

2 TRANSPORT THEORY

Starting from density-functional theory (DFT), the one-electron wave functions have to fulfill a Schrödinger equation with an effective one-particle Hamiltonian (Hohenberg and Kohn, 1964; Kohn and Sham, 1965)

$$H(\mathbf{r})\psi_k(\mathbf{r}) = E_k\psi_k(\mathbf{r}) \tag{10}$$

with $H(\mathbf{r}) = -\nabla_r^2 + V_{\mathrm{eff}}(\mathbf{r})$ and the eigenfunctions $\psi_k(\mathbf{r})$. The effective potential $V_{\mathrm{eff}}(\mathbf{r})$ contains by construction all exchange and correlation effects. k is a shorthand notation for Bloch vector $\mathbf{k}$, band index ν and for magnetic systems all properties are spin dependent. Throughout this section the spin quantum number σ will, however, be omitted for reasons of clarity. All equations are given in real-space representation. Atomic units are used by setting $\hbar = 2m = \epsilon^2/2 = 1$.

The starting point is an unperturbed system which might be translational invariant in certain directions and is described by the Hamiltonian $\mathring{H}(\mathbf{r}) = -\nabla_r^2 + \mathring{V}_{\mathrm{eff}}(\mathbf{r})$.

A potential perturbation $\Delta V(\mathbf{r})$ defines a new system $H(\mathbf{r}) = -\nabla_r^2 + V_{\mathrm{eff}}(\mathbf{r}) = \mathring{H}(\mathbf{r}) + \Delta V(\mathbf{r})$.

Both systems can be equivalently described by means of Green's functions defined as

$$(E - H(\mathbf{r}))\, G(\mathbf{r}, \mathbf{r}', E) = \delta(\mathbf{r} - \mathbf{r}') \tag{11}$$

$$\left(E - \mathring{H}(\mathbf{r})\right) \mathring{G}(\mathbf{r}, \mathbf{r}', E) = \delta(\mathbf{r} - \mathbf{r}') \tag{12}$$

instead of Schrödinger equations.

The advantage of Green's functions is that they are related to each other by the Dyson equation

$$G(\mathbf{r}, \mathbf{r}', E) = \mathring{G}(\mathbf{r}, \mathbf{r}', E) + \int \mathrm{d}\mathbf{r}'' \mathring{G}(\mathbf{r}, \mathbf{r}'', E) \times \Delta V(\mathbf{r}'') G(\mathbf{r}'', \mathbf{r}', E) \tag{13}$$

Using cell-centered coordinates for the description of the local potentials and scattering solutions this results in a system of linear equations which can be solved very efficiently (Zeller and Dederichs, 1979; Mertig, Mrosan and Ziesche, 1987).

The local density of states (LDOS) is obtained from the diagonal part of the Green's function

$$n(\mathbf{r}, E) = -\frac{1}{\pi} Im\, G(\mathbf{r}, \mathbf{r}, E) \tag{14}$$

which can be used to calculate the charge density

$$\begin{aligned} n(\mathbf{r}) &= \int_{-\infty}^{E_\mathrm{F}} \mathrm{d}E\, n(\mathbf{r}, E) \\ &= \sum_{E_k \le E_\mathrm{F}} |\psi_k(\mathbf{r})|^2 \end{aligned} \tag{15}$$

and the density of states (DOS)

$$n(E) = \int \mathrm{d}\mathbf{r}\, n(\mathbf{r}, E) \tag{16}$$

with E_F being the Fermi level.

It has been shown that the variational principle of DFT can be reformulated for the case of magnetic systems by introducing the charge and magnetization density, respectively (von Barth and Hedin, 1972)

$$n(\mathbf{r}) = n^{\uparrow}(\mathbf{r}) + n^{\downarrow}(\mathbf{r}) \tag{17}$$

$$m(\mathbf{r}) = n^{\uparrow}(\mathbf{r}) - n^{\downarrow}(\mathbf{r}) \tag{18}$$

$\sigma = \uparrow, \downarrow$ denotes the spin directions 'up' for majority states and 'down' for minority states. The total magnetization of the system is given by

$$M = \int \mathrm{d}\mathbf{r}\, m(\mathbf{r}) \tag{19}$$

In the following $\mathring{V}_\mathrm{eff}(\mathbf{r})$ describes the unperturbed system with periodicity in certain directions and $\Delta V(\mathbf{r})$ describes point defects or, more generally, spatially localized potential perturbations.

2.1 Boltzmann theory

The Boltzmann theory is a quasiclassical theory and combines quantum-mechanical information of the electronic structure with a classical description of the transport. The solution of the Boltzmann equation is a classical distribution function $f_k(\mathbf{r}, t)$ which determines the number of carriers in phase-space volume characterized by k, and the position in real space $\mathbf{r}$. k is related to the wave vector $\mathbf{k}$, the band index ν, and for magnetic systems the spin σ. In the following derivations the spin is neglected for the sake of simplicity and an explicit dependence of the distribution function on time and magnetic field is excluded. The real-space dependence vanishes because of the restriction to homogeneous systems. In the steady state the total rate of change has to vanish, and from the conservation of phase-space volume a master equation for the distribution function is derived

$$\dot{\mathbf{k}} \frac{\partial f_k}{\partial E_k} \frac{\partial E_k}{\partial \mathbf{k}} - \left.\frac{\partial f_k}{\partial t}\right|_\mathrm{scatt} = 0 \tag{20}$$

with the Fermi velocity

$$\mathbf{v}_k = \frac{\partial E_k}{\partial \mathbf{k}} \tag{21}$$

The field term is determined by the external electric field $\mathbf{E}$ with e the electron charge $e = -|e|$ and $\dot{\mathbf{k}} = e\mathbf{E}$. The second term in equation (20) describes the change of carriers in state k due to scattering and is determined by the microscopic transition probability $P_{kk'}$ via equation (22). These scattering processes can be caused, for example, by lattice defects, imperfections, or thermally activated quasiparticles.

The microscopic transition probability $P_{kk'}$ is given by Fermi's golden rule

$$P_{kk'} = 2\pi c N |T_{kk'}|^2 \delta(E_k - E_{k'}) \tag{22}$$

$T_{kk'}$ describes the scattering at one impurity. cN is the total number of impurities in the sample where c is the relative concentration of defects and N is the total number of atoms in the system.

In the framework of a Korringa-Kohn-Rostoker (KKR) Green's function formalism the transition matrix elements $T_{kk'}$ can be calculated without an adjustable parameter using the self-consistently determined impurity potentials in an otherwise perfect matrix (Mertig, Zeller and Dederichs, 1993; Mertig *et al.*, 1995).

Exploiting the microscopic reversibility $P_{kk'} = P_{k'k}$, considering only elastic scattering processes, and introducing a small deviation $g_k = f_k - \mathring{f}_k$ from the equilibrium distribution function $\mathring{f}_k$, the change of the distribution function due to scattering is given by

$$\left.\frac{\partial f_k}{\partial t}\right|_\mathrm{scatt} = \sum_{k'} P_{kk'}(g_{k'} - g_k) \tag{23}$$

In the limit of linear response, the proportionality of g_k and the external field $\mathbf{E}$ is given by the vector mean free path $\mathbf{\Lambda}_k$ using the ansatz

$$g_k = -e \frac{\partial \mathring{f}_k}{\partial E} \mathbf{\Lambda}_k \mathbf{E} \tag{24}$$

The Fermi surface average of the vector mean free path $\mathbf{\Lambda}_k$ is related to the mean free path Λ discussed in Section 1. Using the relaxation time $[\tau_k]^{-1} = \sum_{k'} P_{kk'}$ one obtains with equations (20) and (23) the linearized Boltzmann equation

$$\mathbf{\Lambda}_k = \tau_k \left[\mathbf{v}_k + \sum_{k'} P_{kk'} \mathbf{\Lambda}_{k'} \right] \tag{25}$$

The first term on the rhs describes the mean free path in the relaxation time approximation $\mathbf{\Lambda}_k = \tau_k \mathbf{v}_k$ known from textbooks. The second term on the rhs is the so-called scattering-in term which counts the scattering events from states k' back to the considered state k. It causes the vertex corrections of the mean free path. In the limit of zero temperature, the integration of equation (25) has to be performed for electronic states on the anisotropic Fermi surface of the system under consideration. For magnetic systems the spin degeneracy is lifted and the spin variable σ has to be included explicitly. As a result equation (25) becomes a set of integral equations for majority and minority electrons, separately.

Introducing a diagonal matrix τ containing the Boltzmann relaxation times $\tau = \{\delta_{\mathbf{kk}'} \tau_{\mathbf{k}}\}$ an exact solution for a (super)vector containing the group velocities can be given

$$\mathbf{\Lambda} = [1 - \tau P]^{-1} \tau \mathbf{v} \quad \text{or} \tag{26}$$

$$\mathbf{\Lambda}_k = \sum_{k'} [1 - \tau P]^{-1}_{kk'} \tau_{k'} \mathbf{v}_{k'} \tag{27}$$

The required number of k points to sample the Fermi surface properly prevents a direct evaluation of this equation. Nevertheless this formal solution clearly shows the equivalence of the Boltzmann and Kubo formalisms in the weak scattering limit (see also Butler, 1985). To calculate the residual resistivity, that is the resistivity at zero temperature caused by scattering at defects only, the current density is expressed by the deviation g_k of the distribution function

$$\mathbf{j} = -\frac{e}{V} \sum_k \mathbf{v}_k g_k \tag{28}$$

The contribution of the equilibrium occupation function $\mathring{f}$ vanishes. In the limit of zero temperature and linear response, the nonzero contributions of g_k are restricted to the Fermi surface and the current density can be expressed by a Fermi surface integral, using the ansatz in equation (24)

$$\sigma_{ij} = \frac{e^2}{V} \sum_k \delta(E_k - E_\mathrm{F})\, v_{k,i} \Lambda_{k,j} \tag{29}$$

with i and j as the Cartesian coordinates. For ferromagnetic systems a sum over the spin directions has to be performed which results in a factor 2 for nonmagnetic systems.

Applying the relaxation time approximation for the evaluation of the vector mean free path, the Fermi surface integral for the conductivity contains the tensor of the Fermi velocities scaled by the state-dependent relaxation time

$$\sigma_{ij} = \frac{e^2}{V} \sum_k \delta(E_k - E_\mathrm{F}) v_{k,i} v_{k,j} \tau_k \tag{30}$$

The Fermi surface integral contains information about the band structure of the unperturbed system only and τ_k contains information about the scattering properties. This approximation will be used later on to explain the origin of intrinsic and extrinsic GMR since the band structure and the scattering properties can be nicely separated.

2.2 Landauer theory

For mesoscopic systems where the system size plays a crucial role for transport properties the Landauer–Büttiker theory is an established method (Landauer, 1970; Landauer, 1988; Büttiker, 1988; Datta, 1995). The considered device contains a scattering region, which is connected to electron reservoirs by ideal leads which feed the current in and take it out. The measurement geometry is illustrated in Figure 5 and determines the assumption to be made in the application of the formalism. A two-terminal device is characterized by two reservoirs and current as well as voltage are measured at the same leads. In the case of zero temperature and within linear response, the Landauer conductance becomes

$$g = \frac{e^2}{h} \sum_{\substack{k_\mathrm{L}, k_\mathrm{R} \\ E_{k_\mathrm{L}} = E_{k_\mathrm{R}} = E_\mathrm{F}}} T_{k_\mathrm{L} k_\mathrm{R}} \tag{31}$$

with $T_{k_\mathrm{L} k_\mathrm{R}}$ the quantum-mechanical probability for a state k_L incident from the left reservoir to be transmitted into state k_R of the right-hand side reservoir. k_L and k_R are the quantum numbers of the eigenstates in the left- and right-hand side electrode, respectively, which are normalized to carry a unit current.

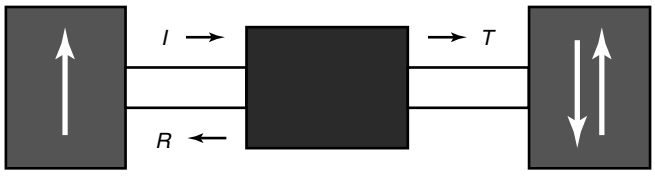

Figure 5. Geometry for the conductance measurement in mesoscopic systems with magnetic electrodes: a scattering region is connected by ideal leads to electron reservoirs (bath), which determine the voltage drop at the junction.

This formula was empirically derived for one-dimensional systems. Fisher and Lee have later shown that equation (31) can be extended to systems of higher dimensions using the transmission matrix t connecting the incident flux in the various channels k_L to the outgoing flux in the channels k_R on the other side (Fisher and Lee, 1981).

For planar tunnel junctions with an in-plane translational invariance and magnetic electrodes, k_L and k_R are shorthand notations for $(\mathbf{k}_\parallel, \nu, \sigma)$, the in-plane wave vector $\mathbf{k}_\parallel$, band index ν, and spin σ in the left or right lead, respectively.

The transmission as introduced by Landauer can be computed by means of the Green's function of the semi-infinite system (Baranger and Stone, 1989). The conductance g for planar junctions with an in-plane translational invariance is obtained by a two-dimensional integration in the surface Brillouin zone (Mavropoulos, Papanikolaou and Dederichs, 2004)

$$g = \frac{e^2}{h} \int \mathrm{d}^2\mathbf{k}_\parallel T_{\mathbf{k}_\parallel}(E_\mathrm{F}) \tag{32}$$

$$T_{\mathbf{k}_\parallel}(E) = \mathrm{tr}\left[J_\mathrm{L}(E) G_\mathrm{LR}(\mathbf{k}_\parallel, E) J_\mathrm{R}(E) G_\mathrm{RL}(\mathbf{k}_\parallel, E)\right] \tag{33}$$

The planes L and R are situated on both sides of the barrier in the unperturbed electrode regions. $J_\mathrm{L}(E)$ and $J_\mathrm{R}(E)$ are the current operator matrices and $G_\mathrm{LR}(\mathbf{k}_\parallel, E)$ are the Green's function elements connecting both sides of the junction. The transmission $T_{\mathbf{k}_\parallel}(E)$ contains as eigenvalues of the matrix the transmission coefficients T_m of the states fed by the reservoirs as introduced by Büttiker, Imry, Landauer and Pinhas (1985).

Transforming equation (31) for a three-dimensional electron gas and perfect transmission to a Fermi surface integral the ballistic or Sharvin conductance (Sharvin, 1965) is obtained

$$g(\mathbf{n}) = \frac{e^2}{h} \frac{A}{4\pi^2} \frac{1}{2} \sum_k \delta(E_k - E_\mathrm{F}) \, |\mathbf{n} \cdot \mathbf{v}_k| \tag{34}$$

$A/4\pi^2$ denotes the density of states of transverse modes and $|\mathbf{n} \cdot \mathbf{v}_k|$ is the Fermi velocity projection on the current direction $\mathbf{n}$. The factor $1/2$ accounts for the electrons moving in the direction of the current. It describes the conductance of a narrow region with cross section A which is connected to two electrodes. It is referred to as ballistic point contact when the diameter of the narrow region is much smaller than the mean free path and much larger than the electron wavelength. In multilayer geometry the vector $\mathbf{n}$ perpendicular to the planes describes the CPP geometry and $\mathbf{n}$ parallel to the planes of the CIP geometry. Although in most experiments this situation is not realized, the formalism was applied to elucidate the microscopic origin of intrinsic GMR (Schep, Kelly and Bauer, 1995; Gijs and Bauer, 1997).

2.3 Kubo formalism

A method of evaluating the response of a quantum mechanical system to an external potential was developed by Kubo in the 1950s, in particular, the current in response to an electric field (Kubo, 1957). In the linear response the two are related by a conductivity which is given in terms of the equilibrium properties of the system, that is, in zero field. Therefore, to calculate the conductivity it is necessary to start from the Hamiltonian that describes the ground state of the conduction electrons. Also we are primarily interested in transport at $T = 0\,\mathrm{K}$, so processes that occur at finite temperature are omitted. Using the Kubo formalism conductivity is evaluated entirely quantum mechanically by the current–current correlation function for the ground state (Kubo, 1957). It is a form of the fluctuation-dissipation theorem (Kubo, 1966), relating a transport coefficient, which characterizes a dissipative process, to the fluctuations at equilibrium. It gives the transport coefficient in the linear response regime and there are no restrictions concerning the strength of the scattering occurring in the system.

First, the expression for the conductivity will be derived starting from the Kubo–Greenwood formula and using the one-particle Green's function. Zero temperature conductivity can be obtained from the current operator by the commonly used expression (Kubo, 1957; Greenwood, 1958; Velický, 1969)

$$\sigma_{ij} = \frac{\pi}{N\Omega} \langle \mathrm{Tr}\, \mathcal{J}_i \delta(E - \mathcal{H}) \mathcal{J}_j \delta(E - \mathcal{H}) \rangle_\mathrm{conf} \Big|_{E=E_\mathrm{F}} \quad \text{with}$$

$$\mathcal{J}_i = -2\imath e \frac{\partial}{\partial x_i} \tag{35}$$

It can be considered in terms of nonlocal conductivities connecting the external field in direction i at one site to the induced current in direction j at another site. N denotes the number of atoms in the sample, Ω is the volume per atom. For systems with a basis it is replaced by the normalization volume $V_\diamond$ of the wave function. In the following the formalism will be given for a bulk system with one atom per unit cell. For systems with a layered structure as considered in Weinberger *et al.* (1996) or bulk systems with an atomic basis a thorough bookkeeping of the layer, unit cell, and atomic indices has to be performed. We consider a sample containing defects μ at random positions $\mathbf{r}_\mu$ with relative concentrations c_μ which give the number of defects per normalization volume. $\mathcal{H}$ is the Hamilton operator of one configuration of the random potential. The large brackets $\langle\rangle_\mathrm{conf}$ denote the configurational average. x_i is a Cartesian coordinate of the real-space vector $\mathbf{r} = (x_1, x_2, x_3)$. For simplicity a compact operator representation is used in this chapter. By means of the Green's function the δ functions

can be replaced by

$$\delta(E-\mathcal{H}) = -\frac{1}{\pi} Im\mathcal{G}(E^+) = -\frac{1}{2\pi\imath}\left[\mathcal{G}(E^+)-\mathcal{G}(E^-)\right], \text{ with } E^\pm = E \pm \imath 0 \tag{36}$$

and the expression from equation (35) splits into four parts

$$\sigma_{ij} = \frac{1}{4}\left(\sigma_{ij}^{++} + \sigma_{ij}^{--} - \sigma_{ij}^{-+} - \sigma_{ij}^{+-}\right), \quad \text{with}$$

$$\sigma_{ij}^{\pm\pm} = -\frac{1}{\pi N\Omega}\,\langle \mathrm{Tr}\ \mathcal{J}_i\ \mathcal{G}(E^\pm)\mathcal{J}_j\ \mathcal{G}(E^\pm)\rangle_{\mathrm{conf}}\big|_{E=E_\mathrm{F}} \tag{37}$$

To evaluate the configurational average over the Green's function $\mathcal{G}(E^\pm)$ the coherent-potential approximation (CPA) first proposed by Velicky and others (Velický, 1969; Gyorffy, 1972; Butler, 1985) might be used. Using the Green's function of the coherent medium and the transition matrices of the single defects, the correspondence of the exact solution of the Boltzmann equation (27) can be demonstrated and the criteria for the applicability of the Boltzmann approach can easily be deduced.

2.4 Magnetic systems

The basic output of a self-consistent electronic structure calculation is the local electron density. In addition, the energy bands E_k and eigenstates Bloch functions ψ_k defined by the Kohn–Sham equation (10) are obtained (Kohn and Sham, 1965). As before, the index k is a shorthand notation for the wave vector $\mathbf{k}$, the band index ν, and the spin index σ. In systems with a net magnetization, the spin degeneracy is lifted and at a given energy eigenstates of rather different character can be found. A prominent example is the relative shift of the spectra in both spin channels, which is obvious for the spin-dependent DOS for Co and Fe in Figure 6.

The properties at the Fermi level are of special interest in the following transport calculations, since they are the main ingredients to calculate the transport coefficients within the chosen approximation. The Fermi velocities are defined by the derivative of the energy bands given in equation (21). The Fermi surface contains all k points with an eigenvalue of the energy E_k^σ equal to the Fermi level E_F. Examples for Fermi surfaces are given in Figure 6 and can be found on the web at http://www.physik.tu-dresden.de/∼fermisur (1998) together with the corresponding Fermi velocity distribution and at http://www.phys.ufl.edu/fermisurface (2005).

For magnetic systems the properties of both spin channels differ quite strongly, which is illustrated by the spin-dependent Fermi surface of Co and the spin-dependent DOS for Co and Fe in Figure 6. For some material combinations the properties of one spin channel coincide to a large extent. This is the case for the majority channels of Co and Cu, which can be seen from the Fermi surfaces and from the DOS in Figure 6. The similarities in the minority channel in Cr, which is actually antiferromagnetic, and Fe can be deduced from the comparison of the LDOS in Figure 6.

In magnetic systems with negligible spin-flip scattering, both spin channels contribute to the current in parallel applying Mott's two-current model, see Figure 7 (Mott, 1964). This applies to systems with collinear magnetic order in the nonrelativistic case. This causes spin-dependent scattering events which change the momentum $\mathbf{k}$ but keep the spin unchanged, so that the scattering probability becomes diagonal in spin space

$$P_{kk'}^{\sigma\sigma'} = \delta_{\sigma\sigma'} P_{kk'} \tag{38}$$

The neglected transition probability amplitudes $P_{kk'}^{\sigma\overline{\sigma}}$ are marked by dashed lines in Figure 8. As a consequence, the conductivity or resistivity are split in majority and minority contributions

$$\sigma = \sigma^\uparrow + \sigma^\downarrow \tag{39}$$

$$\frac{1}{\rho} = \frac{1}{\rho^\uparrow} + \frac{1}{\rho^\downarrow} \tag{40}$$

A similar separation of the spin contributions holds for the conductance or resistance in this case

$$g = g^\uparrow + g^\downarrow \tag{41}$$

$$\frac{1}{R} = \frac{1}{R^\uparrow} + \frac{1}{R^\downarrow} \tag{42}$$

To quantify the contribution of the spin channels, the spin-anisotropy ratio

$$\alpha = \frac{\rho^\uparrow}{\rho^\downarrow} = \frac{\sigma^\downarrow}{\sigma^\uparrow} \tag{43}$$

is defined. In nonmagnetic systems α equals unity and strong deviations from one point to the dominance of one spin channel. For a given host material, the spin anisotropy can vary strongly with the type of defects considered. This is discussed in Mertig (1999) for bulk systems and illustrated in Section 4, Figure 25 for layered structures.

The anisotropy of scattering is characterized by the ratio

$$\beta = \frac{\tau^\uparrow}{\tau^\downarrow} \tag{44}$$

which gives the differences in the averaged electron momentum lifetimes for both spin channels.

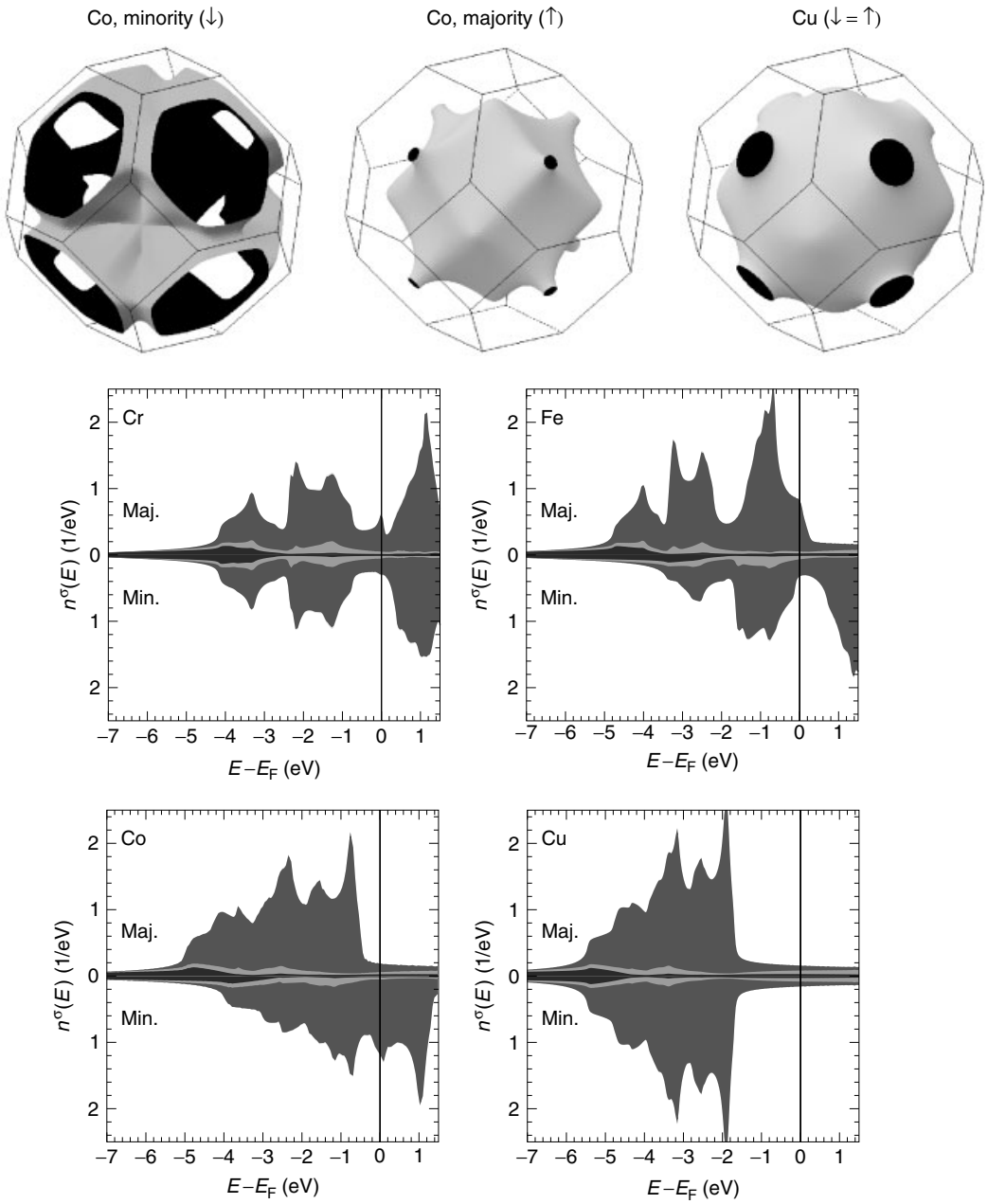

Figure 6. Spin dependence of eigenvalue spectra: Fermi surfaces for Co minority electrons (contribution from the fifth band), Co majority electrons and Cu electrons (top row from left) and spin-dependent density of states for Cr, Fe, Co, and Cu; the colors indicate the amount of s electrons (black), p electrons (light gray), and d electrons (dark gray).

In the above discussion we neglected spin-flip scattering. If one includes spin-flip scattering, the two spin currents are mixed, that is, they are not independent of each other any more. At low temperature, the primary source of spin-flip scattering comes from impurities with spin-orbit coupling or paramagnetic ones for which spin flip is an elastic process. As most of the scattering encountered in magnetic multilayers at low temperature does not flip spin as this costs energy, that is, it is inelastic, the spin diffusion length is usually much longer than the mean free path (Valet and Fert, 1993), so that for CIP where transport is controlled by Λ the presence of spin-flip processes and the subsequent breakdown of the two-current model is not perceived. However for CPP, where Λ does not control GMR, spin-flips limit the distance over which the two spin currents are independent, and concomitantly reduce the GMR in this geometry. This has been nicely demonstrated in a series of experiments in which the amount of spin-flip scatterers, spin-orbit coupled and paramagnetic impurities,

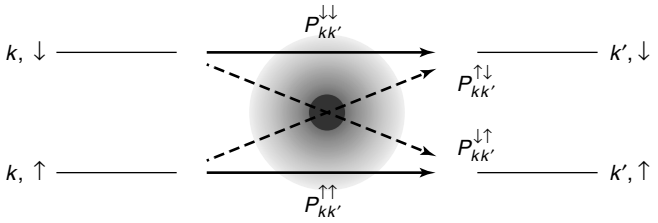

Figure 7. Two-current model: spin-dependent resistors in parallel.

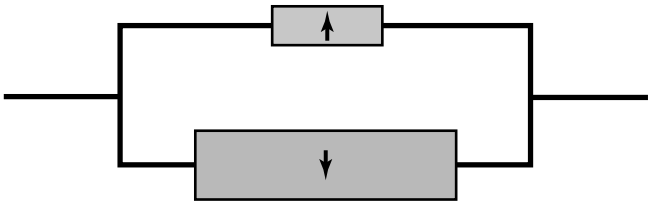

Figure 8. Spin-flip and spin-conserving transition probabilities in magnetic systems.

has been shown to mix the two currents and significantly reduce the GMR (Bass *et al*., 1994; Yang *et al*., 1994). At higher temperatures inelastic spin-flip processes occur. Without introducing impurities, for example, electron–magnon scattering, however, the resistivity assigned to each channel does not increase since momentum is conserved (Fert, 1969; Fert and Campbell, 1976; Campbell and Fert, 1982).

The basis for the simple parameterization of transport in the two-current model is usually assigning one scattering rate τ^{σ} to all the currents with one spin direction. While this may have some validity for homogeneous materials it is not correct for multilayers, except for the local limit which is attained in magnetically layered nanowires (Piraux, Dubois and Fert, 1996; Piraux *et al*., 1997; Piraux, Dubois, Fert and Belliard, 1998). As we show in Section 4 scattering depends on momentum as well as spin; there are as many scattering rates as there are states in a multilayered structure. Parenthetically, as transport is primarily confined to the Fermi surface, by momentum we mean the Fermi momentum. While it is nigh impossible for toy models to account for this, *ab initio* calculations are ideally suited for this task (Binder *et al*., 1998; Blaas *et al*., 1999). Calculations which are completely *ab initio* include the two-current model automatically; however, these calculations have been found to be extremely time consuming. One compromise has been to perform *ab initio* calculations of the band structure and assign different spin-dependent scattering rates to layers and interfaces that are independent of the electron's momentum (Butler *et al*., 1999). This provides a convenient way to include the effects of band structure and a parameterization of the scattering in the different regions with a reasonable number of unknown constants that are determined by fits to experimental data. The concern one might have is that the neglect of the dependence of scattering rates on momentum yields unrealistic scattering rates.

One final source for breakdown of the independence of the up-and-down spin currents is the noncollinearity of the spin structure. For noncollinear structures the eigenstates are not pure spin states, so that when electrons undergo non-spin-flip scattering they nonetheless mix the currents being conducted in eigenstates. This mixing has been identified as a source of resistivity of walls between oppositely oriented magnetic domains (Levy and Zhang, 1997; Brataas, Bauer and Kelly, 2006).

3 MICROSCOPIC SCATTERING THEORY

This section is addressed to the properties of point defects, including the perturbation of the electron density, the perturbed wave functions, and the transition matrix elements. Defects with finite dimensions in all directions, so-called point defects or zero-dimensional defects are considered in the following. The unperturbed system we start from will be a superlattice, a system with three-dimensional periodicity. One single defect will be considered in the following neglecting the interaction of defects and limiting the considerations to the case of dilute alloys. The position of the defect in the unperturbed system is essential for the scattering properties and all derived quantities. For example, in layered systems described by a large unit cell, there are quite different positions for defects, for example, inside the different layers or with respect to the interfaces Figure 9.

The Green's functions of the perturbed system and the unperturbed system are connected by a Dyson equation, see equation (13). The unperturbed system $\mathring{G}$ is now the periodic system without defects and G describes the system with one defect at a specific position μ. The difference of the effective potential $\Delta V^{\mu}(\mathbf{r})$ describes the potential perturbation caused by the defects. Owing to the effective

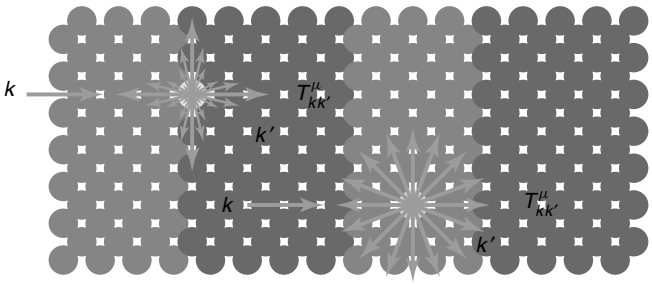

Figure 9. Source of resistance: scattering from a state k into possible states k' at impurities in a multilayer at different positions μ and μ'.

screening of the perturbation in metallic systems, the charge and magnetization relaxation are mainly restricted to the vicinity of several coordination spheres around the defect. The solution of equation (13) can be restricted to a number of neighboring sites next to the defect. Using the Green's function G of the perturbed system the changes in charge and magnetization density can be calculated self-consistently.

The perturbation of the potential $\Delta V^{\mu}(\mathbf{r})$ causes scattering processes of the unperturbed Bloch states which keep the spin and the energy unchanged. The neglect of spin-flip processes is justified by experimental results that in 3d transition metals the scattering cross section for these processes is about 2 orders of magnitude smaller than that for spin-conserving processes (Fert and Campbell, 1976). The scattering at the potential perturbation $\Delta V^{\mu}(\mathbf{r})$ can be expressed by the transition matrix T

$$T^{\mu}_{kk'} = \left(\mathring{\psi}_k(\mathbf{r})|\Delta V^{\mu}(\mathbf{r})|\psi_{k'}(\mathbf{r})\right) = \int \mathrm{d}\mathbf{r}\mathring{\psi}^{*}_k(\mathbf{r})\Delta V^{\mu}(\mathbf{r})\psi_{k'}(\mathbf{r}) \tag{45}$$

which is the quantum-mechanical matrix element.

Providing that the wave functions $\psi^{\mu}_{k'}(\mathbf{r})$ of the perturbed systems can be calculated from the unperturbed ones $\mathring{\psi}_k(\mathbf{r})$ by a Lippman–Schwinger equation

$$\psi^{\mu}_{k'}(\mathbf{r}) = \mathring{\psi}_k(\mathbf{r}) + \int \mathrm{d}\mathbf{r}'\mathring{G}(\mathbf{r},\mathbf{r}',E)\Delta V^{\mu}(\mathbf{r}')\psi^{\mu}_k(\mathbf{r}) \tag{46}$$

the transition matrix can be expressed using only the eigenstates of the unperturbed system and the potential perturbation. By multiple scattering theory, the full perturbation series can be included by inversion, so that the theory is restricted to the dilute limit, which means noninteracting impurities, but is not restricted to weak scattering (Mertig, Mrosan and Ziesche, 1987; Mertig, 1999).

4 MICROSCOPIC THEORY OF GMR

4.1 Intrinsic GMR

The GMR ratio equation (6) calculated within the relaxation time approximation $\mathbf{\Lambda}_k = \tau_k \mathbf{v}_k$ (compare equation (25)) assuming a k-independent relaxation time becomes (Zahn, Mertig, Richter and Eschrig, 1995)

$$GMR = \frac{\sum_k \delta(E^{\uparrow}_k - E_{\mathrm{F}})\, v^{\uparrow}_{k,i}{}^2 + \sum_k \delta(E^{\downarrow}_k - E_{\mathrm{F}})\, v^{\downarrow}_{k,i}{}^2}{2\sum_k \delta(E^{\mathrm{AP}}_k - E_{\mathrm{F}})\, v^{\mathrm{AP}2}_{k,i}} - 1 \tag{47}$$

where $v_{k,i}$ with $i = (\parallel, \perp)$ are the Cartesian components of the velocity parallel and perpendicular to the layers. As we have not considered the spin dependence of the relaxation times, they cancel out, and the GMR ratio is only determined by the intrinsic electronic structure of the system. For concreteness, but without loss of generality, we focus on a Co/Cu multilayered structure. A detailed analysis of the GMR ratio depending on the spacer thickness (equation (47)) for $\mathrm{Co}_n\mathrm{Cu}_m$ multilayers is shown in Figure 10. The CPP-GMR is always larger than the CIP-GMR, and the ratios decrease with increasing Cu-layer thickness (see also Levy, 1994). For a better understanding of these results we can approximate the GMR ratio by using the density of states at the Fermi level $n^{\sigma}(E_{\mathrm{F}}) = \sum_k \delta(E^{\sigma}_k - E_{\mathrm{F}})$, and a Fermi surface average of the square of the velocity components

$$\overline{v^{\sigma}_{k,i}{}^2} = \frac{\sum_k \delta(E^{\sigma}_k - E_{\mathrm{F}})\, v^{\sigma}_{k,i}{}^2}{\sum_k \delta(E^{\sigma}_k - E_{\mathrm{F}})} \tag{48}$$

this leads to

$$GMR \approx \frac{n^{\uparrow}(E_{\mathrm{F}})\,\overline{v^{\uparrow}_{k,i}{}^2} + n^{\downarrow}(E_{\mathrm{F}})\,\overline{v^{\downarrow}_{k,i}{}^2}}{2\, n^{\mathrm{AP}}(E_{\mathrm{F}})\,\overline{v^{\mathrm{AP}2}_{k,i}}} - 1 \tag{49}$$

4.1.1 *Electronic structure of the multilayer*

The electronic structure of the majority bands of Co and Cu are very similar (see also Figure 6). The majority d bands are fully occupied and lie below the Fermi level. However, since Co has two electrons less than Cu, the minority band of Co is less occupied and the electronic structure of the minority band at the Fermi energy is very different for both

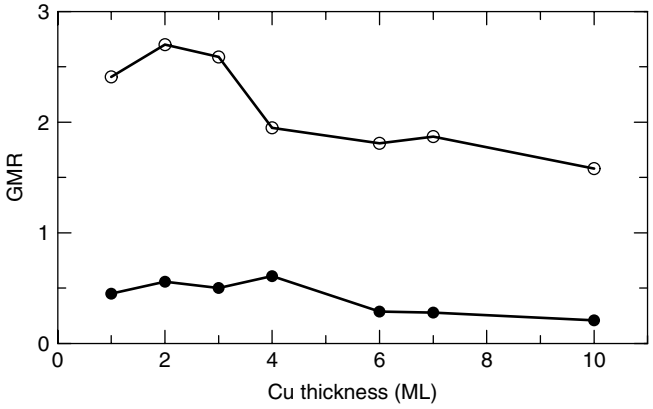

Figure 10. Calculated GMR ratios for Co/Cu(100) multilayers as a function of the Cu layer thickness, CIP-GMR (filled circles) and CPP-GMR (open circles).

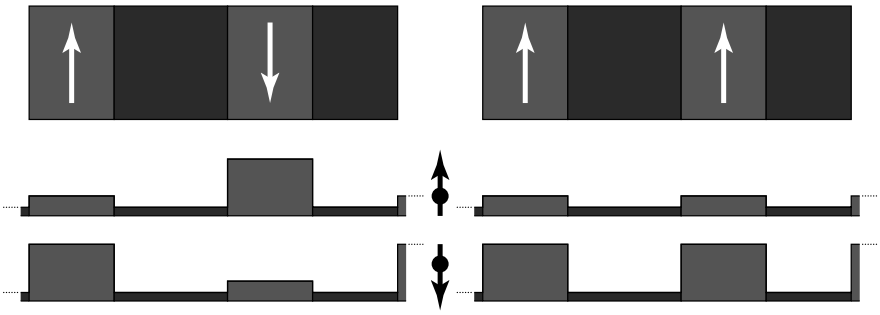

Figure 11. Spin-dependent potentials in a magnetic multilayer for the AP and P configurations for majority and minority electrons.

metals. The majority electrons of a multilayer at E_F with their moments aligned in parallel traverse easily through the system; the reason is that the potential landscape is very flat (see Figure 11) since the bandwidth is nearly the same in each layer. On the contrary, minority electrons at E_F experience high potential steps and are reflected at the Co/Cu interfaces. As a result, the Fermi velocity of the majority electrons is much larger than the Fermi velocity of the minority electrons, $v_F^{\uparrow} \gg v_F^{\downarrow}$ (see also Figure 13). A multilayer with antiparallel moments consists of a potential with a potential well in alternate layers since the spin character of the electrons (majority, minority) changes in every other layer (see Figure 11); also both spin channels are degenerate. The velocity of the electrons is mainly determined by the largest potential step. For this reason the Fermi velocity of the electrons in an AP-ordered multilayer is nearly the same as for the minority electrons, $v_F^{\uparrow} \gg v_F^{AP} \geq v_F^{\downarrow}$ (see also Figure 13).

The densities of states at the Fermi level for P and AP configurations as a function of Cu-layer thickness are shown in Figure 12. When one adds the majority and minority density of states in P configuration they are quite close to the density of states in AP configuration, so that they are neither responsible for the positive GMR ratios nor account for the differences between the CIP- and CPP-GMR; rather these result from differences of the averaged velocities as a function of the magnetic configuration (Figure 13).

If we compare the averaged velocities of the majority and minority electrons in the parallel configuration with those in

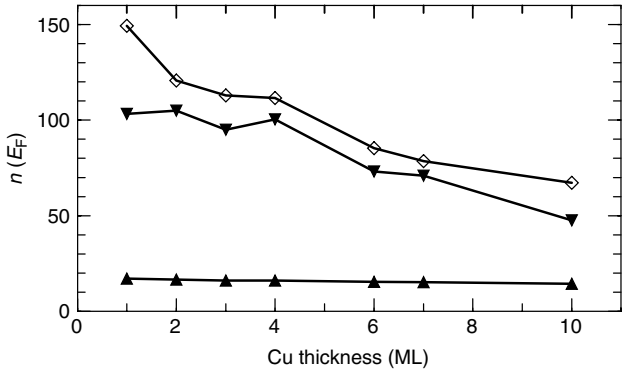

Figure 12. Densities of states at the Fermi energy for Co/Cu(100) multilayers as a function of Cu-layer thickness for majority electrons (triangle upwards) and minority electrons (triangle downwards) in P configuration and in AP configuration (diamonds). (Reproduced from I. Mertig, P. Zahn, M. Richter, H. Eschrig, R. Zeller & P.H. Dederichs: 'Ab initio calculation of residual resisistivity in dilute Fe alloys and giant magnetoresistance in Fe/Cr multilayers', *J. Mag. Mag. Mat.* **151** (1995), copyright © 1995, with permission from Elsevier.)

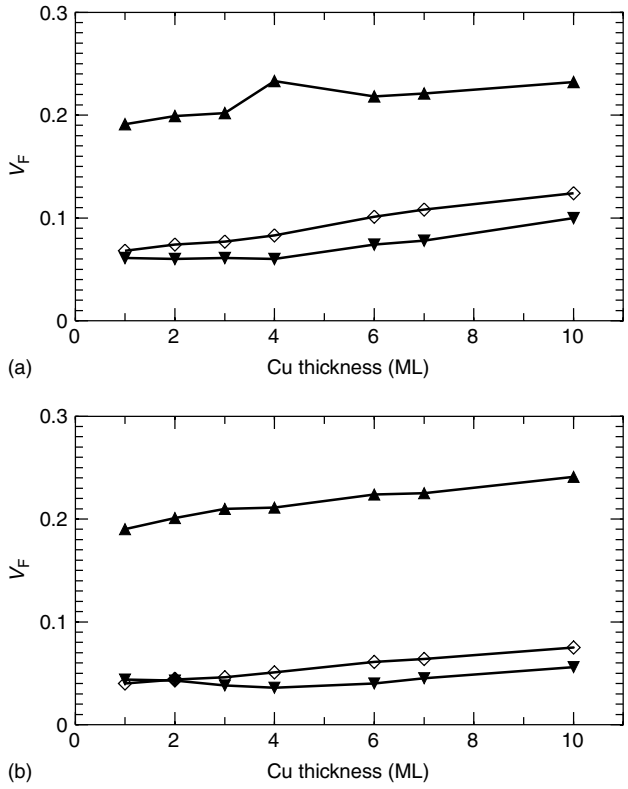

Figure 13. The average of the Fermi velocities in the plane of the layers $\sqrt{\overline{v_{\parallel}^2}}$ (a) and perpendicular to the layers $\sqrt{\overline{v_{\perp}^2}}$ (b) for majority (triangle upwards) and minority (triangle downwards) electrons in P and in AP configuration (diamonds) (Zahn, Mertig, Richter and Eschrig, 1995, 1998; Mertig *et al*., 1995).

the antiparallel configuration we notice that this would lead to a positive GMR ratio. For the components in the plane of the layers $v_{\parallel}$, the CIP-GMR is obtained, whereas $v_{\perp}$ leads to CPP-GMR. When we compare the in-plane components of the velocity with the components perpendicular to the plane (Figure 13) we can even explain the differences of the CIP- and CPP-GMR. Similar conclusions have been drawn by Oguchi (1993) and Butler, MacLaren and Zhang (1993, 1996).

The same result was obtained by calculating the GMR of point contacts in the ballistic limit of transport by using the conductance of equation (34) (Schep, Kelly and Bauer, 1995; Gijs and Bauer, 1997).

4.1.2 Eigenstates of the multilayers

An important ingredient to the microscopic understanding of the conductivity is the layerwise decomposed density of states. The LDOS is calculated from the diagonal part of the spin-dependent one-particle Green's function of the multilayer system (see equation (14)). They can be resolved by means of the spectral representation of the Green's function into a superposition of probability amplitudes of all eigenstates at energy E_{F}.

The LDOS at E_{F} of the P configuration is shown in Figure 14(a) and is nearly the same at all monolayers in the majority channel. The minority electrons are characterized by a very inhomogeneous profile. The LDOS in Co layers is much higher than that in Cu layers. The largest values are obtained for the Co layers at the interface. This is a general behavior independent of Co- or Cu-layer thicknesses. This profile can easily be interpreted by means of probability amplitudes of the eigenstates. Owing to a smooth potential profile most of the eigenstates in the majority bands are extended with a constant probability amplitude for all layers (Figure 14b). In contrast, the minority electrons move in a multiwell potential with a periodicity perpendicular to the layers (z direction). For this reason quantum well states appear which are well localized in z direction but extended in plane. Besides quantum well states with a localization in the center of the Co and Cu layers (Figure 14c,d) pronounced interface states in the Co layers are formed as shown in Figure 14(e). The interface state can be understood in terms of resonant scattering and compares to the virtual bound state (VBS) of a Co impurity in a Cu matrix (Dederichs and Zeller, 1981).

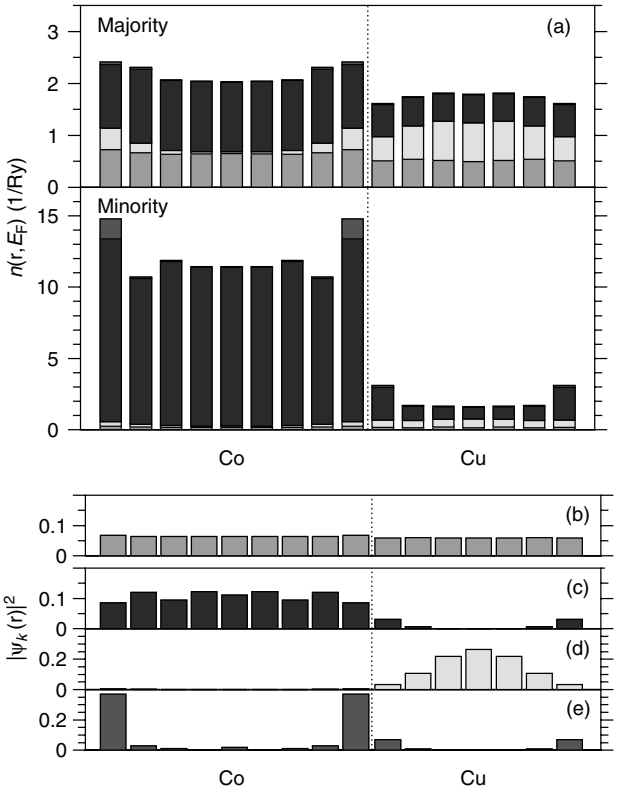

Figure 14. Co_9Cu_7 in P configuration: spin-resolved local density of states at E_{F} in (au) (a), probability amplitude of an extended majority state (b) and of different quantum well and interface states in the minority band (c–e). (Reproduced from Zahn *et al*., 1998, with permission from the American Physical Society. © 1998.)

4.2 Extrinsic GMR

It was shown in the last section that the GMR effect has an intrinsic origin determined by the electronic structure of the magnetic multilayer. Since the intrinsic effect is based on the coherent electronic structure, the samples have to be of high quality. Another rather robust mechanism is spin-dependent scattering in magnetic multilayers. The scattering properties of impurities in magnetic systems exhibit a spin anisotropy (Mertig, 1999). That is, majority and minority electrons undergo a scattering process of different strength. As a measure, the so-called scattering anisotropy of the resistivity (equation (43)) is used. This property, namely, spin-dependent impurity scattering in multilayers causes the GMR effect. The mechanism is illustrated in Figure 15. Let us consider an impurity atom with a scattering anisotropy $\alpha < 1$. The majority electrons are weakly scattered by the impurity in the magnetic layer and cause a small resistance $R^{\uparrow}$ and a large current. The minority electrons, however, are scattered strongly at the same impurities in the magnetic layer which results in a large resistance $R^{\downarrow}$ and a small current. The total resistance R^{P} is small since the fast majority channel determines the transport. In the AP configuration both channels have the same resistance. Strong and weak scattering alternate from layer to layer for the electrons of both spin directions and produce a resistance $R^{\mathrm{AP}} > R^{\mathrm{P}}$ which corresponds to a positive MR effect.

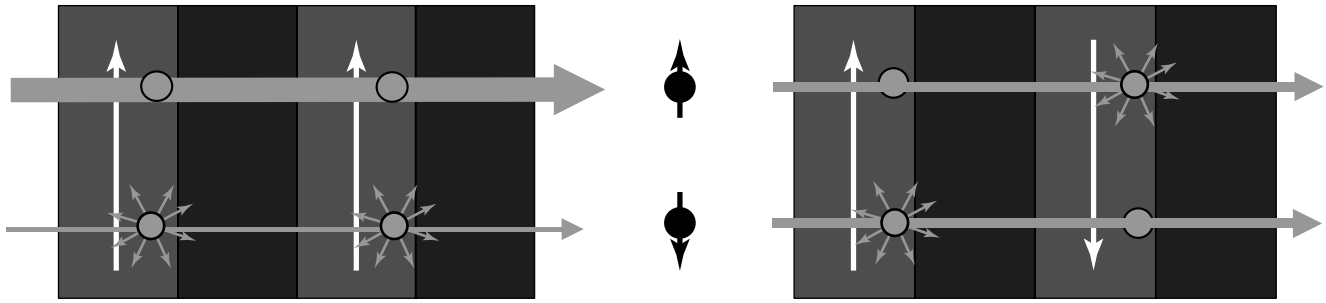

Figure 15. Extrinsic GMR: spin-dependent scattering in magnetic multilayers.

The qualitative picture discussed above will be manifested in a quantitative analysis of the scattering properties of impurities in magnetic multilayers. The results are based on *ab initio* electronic structure calculations. The data demonstrate the diversity of the considered systems, explain obtained experimental trends, and can be understood as instructions to tailor GMR systems of desired properties. Combination of impurities with opposite spin anisotropy can even cause inverse GMR.

4.2.1 Electronic structure of impurities in magnetic multilayers

Impurities are a perturbation of the host material and cause charge and magnetization relaxation. As a result of a self-consistent impurity calculation, the density of states at the impurity site includes all the necessary information. Impurities in a multilayer show a strong dependence on their position with respect to the interfaces. If the impurities are situated in the center of a layer, the LDOS is similar to the corresponding bulk system. At the interfaces the properties are changed.

In this section the LDOS of the 3d transition-metal impurities in Co/Cu multilayers are presented in Figure 16. The data are for impurities in the center and at the interface of the magnetic and of the nonmagnetic layer to demonstrate the differences as a function of the impurity position in the multilayer. Co in Co and Cu in Cu characterize the corresponding host properties, that is, the LDOS in the center and at the interface of the Co and Cu layer. Obviously, the Co and Cu density of states in the center of the Co layer is the same as in bulk (see also Figure 6). Co is magnetic with a moment of $1.64\,\mu_B$. The Co moment at the interface is reduced to $1.55\,\mu_B$. The Cu interface layer is also magnetic with a very small moment parallel to the Co moments of $0.01\,\mu_B$. The central Cu layer is nonmagnetic. The LDOS are shown from left to right corresponding to their position in the unit cell: central Co layer, Co and Cu interface layers, and the central Cu layer. The LDOS in the central layers coincides with the respective properties of bulk defects (for comparison see Stepanyuk, Zeller, Dederichs and Mertig, 1994; Braspenning, Zeller, Lodder and Dederichs, 1984; Mertig, 1999).

In the central Cu layer all defects show a tendency to form VBSs. Their positions shift according to the band filling and for Co, Fe, Mn, Cr, and V a magnetic moment is formed. This tendency is enhanced when the defects are moved closer to the Co layer. In the Cu interface layer in close contact to the Co layer all 3d defects possess a magnetic moment. The orientation of the moment is opposite to the adjacent Co moment for Cr, V, Ti, and Sc in accordance with the less-than-half-filled 3d band. For Cr, V, and Ti an interesting feature is obtained: two VBSs at the upper band edges of the 3d states of the adjacent Co and Cu atoms, which are below and above the Fermi level are formed in the minority channel. The influence on the local magnetic moment and the DOS at the Fermi level is quite small and a smooth transition from the Co central position to the Cu central position is obtained.

The behavior of the 3d impurities in the Co central layer is dominated by the competition of the local electrostatic potential at the defect site which is weaker in the beginning of the row and larger for Ni and Cu. For Ni the reduced moment causes a reduction of the exchange energy which acts in the opposite direction to the Coulomb potential shift in the majority band and in the same direction for the minority electrons. So, the moment at the Ni impurities is suppressed, and the same holds for Cu atoms in the Co layer. The opposite shift, which is connected with a large local moment, is obtained for the minority states of Fe defects. For Mn and the earlier 3d elements the weakening of the electrostatic potential can no longer be counterbalanced by an increasing exchange potential, since the local moment cannot increase sufficiently. So, at Mn a VBS is formed in the majority channel just below the Fermi energy destabilizing the ferromagnetic solution. For Mn, Cr, V, Ti, and Sc an antiferromagnetic alignment of the local magnetic moment relative to the surrounding Co sites is obtained. This tendency is maintained for all sites in the Co layer, as can be recognized from the LDOS of the impurities at the Co interface position.

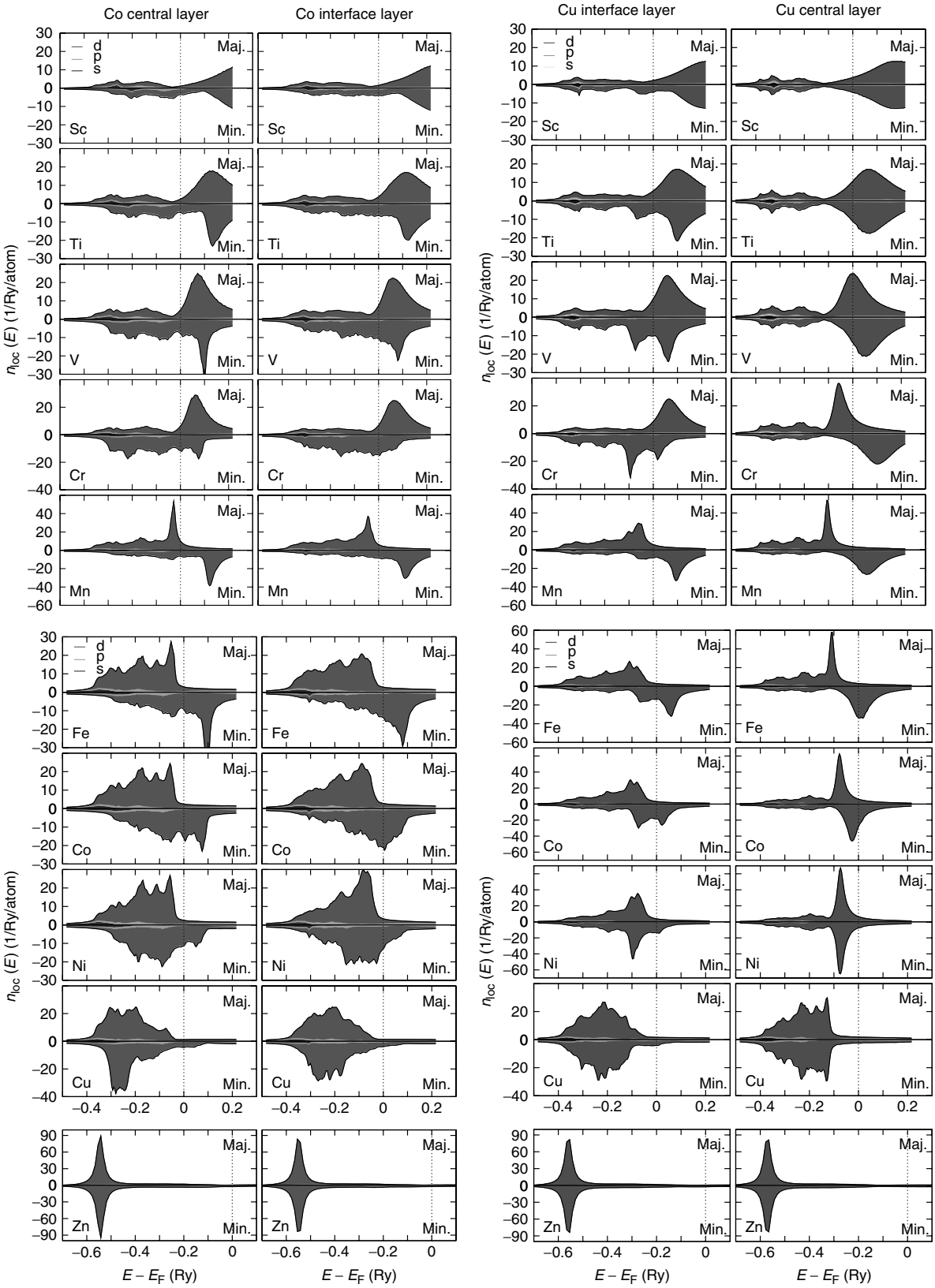

Figure 16. Local partial density of states for 3d transition-metal impurities at the central and interface sites of the Co and Cu layers of a $Co_9Cu_7(001)$ multilayer in P configuration; the color code is the same as in Figure 6.

4.2.2 Scattering anisotropy in bulk materials

The scattering properties of an impurity atom in a bulk system are highly anisotropic, that is, the relaxation times τ_k^σ vary strongly for different states. As an example, the relaxation time anisotropy is shown for a Cu impurity in Co bulk at the Fermi surface (Figure 17). The relaxation times of the minority electrons (Figure 17a) are on average shorter by 1 order of magnitude in comparison to those of the majority electrons (Figure 17b). Shorter relaxation times mean stronger scattering and, in principle, cause larger resistance. The relaxation times per Fermi surface sheet vary by a factor of 2 in bulk systems.

The scattering anisotropy in general is, however, hidden in the microscopic scattering probability $P_{kk'}$, which is an enormous amount of data. An example of a magnetic Co impurity in Cu bulk is given in Figure 18. The spin-conserving scattering probabilities of one initial state $\mathbf{k}$ fixed to (100) into all other states $\mathbf{k}'$ is visualized as a function of the scattering angle (a) or at the Fermi surface (b and c) for majority and minority electrons separately.

Assuming that the system without and with defects is invariant under time-reversal symmetry, one obtains

$$\mathbf{v}_{-k} = -\mathbf{v}_k \quad \text{and} \tag{50}$$

$$\mathbf{\Lambda}_{-k} = -\mathbf{\Lambda}_k \tag{51}$$

where $-k$ should denote the state with a reversed wave vector $-\mathbf{k}$ but the same band index ν. Using the symmetric and antisymmetric part of the transition probability matrix

$$P_{kk'}^{\mathrm{S}} = \frac{P_{kk'} + P_{k-k'}}{2} \quad \text{and} \tag{52}$$

$$P_{kk'}^{\mathrm{A}} = \frac{P_{kk'} - P_{k-k'}}{2} \tag{53}$$

one can rewrite the Boltzmann equation (25) as

$$\mathbf{v}_k = \sum_{k'} \left(P_{kk'}^{\mathrm{S}} \mathbf{\Lambda}_k - P_{kk'}^{\mathrm{A}} \mathbf{\Lambda}_{k'} \right) \tag{54}$$

From this equation it is evident that the Boltzmann relaxation time is determined by the symmetric part of $P_{kk'}$ and the vertex corrections in equation (25) by the antisymmetric contribution

$$\tau_k = \left[\sum_{k'} P_{kk'}^{\mathrm{S}} \right]^{-1} \quad \text{and} \tag{55}$$

$$\sum_{k'} P_{kk'} \mathbf{\Lambda}_{k'} = \sum_{k'} P_{kk'}^{\mathrm{A}} \mathbf{\Lambda}_{k'} \tag{56}$$

To quantify these contributions, the following anisotropies will be defined. The anisotropy α_k^{P} of forward and backward scattering is determined by the ratio of P_{kk} and P_{k-k} and is closely related to the ratio α_k^{A} of the antisymmetric scattering probability to the probability of forward scattering

$$\alpha_k^{\mathrm{P}} = \frac{P_{kk}}{P_{k-k}} \quad \text{and} \tag{57}$$

$$\alpha_k^{\mathrm{A}} = 1 - \frac{1}{\alpha_k^{\mathrm{P}}} = 2\frac{P_{kk}^{\mathrm{A}}}{P_{kk}} \tag{58}$$

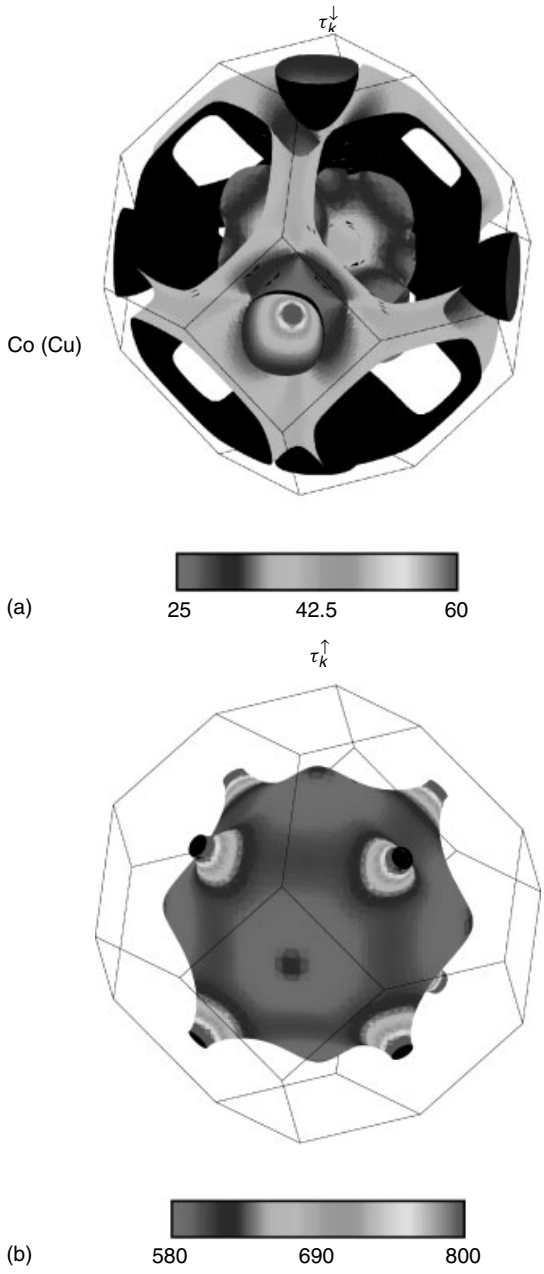

Figure 17. Anisotropic relaxation times τ_k^σ for Cu defects in a magnetic Co host.

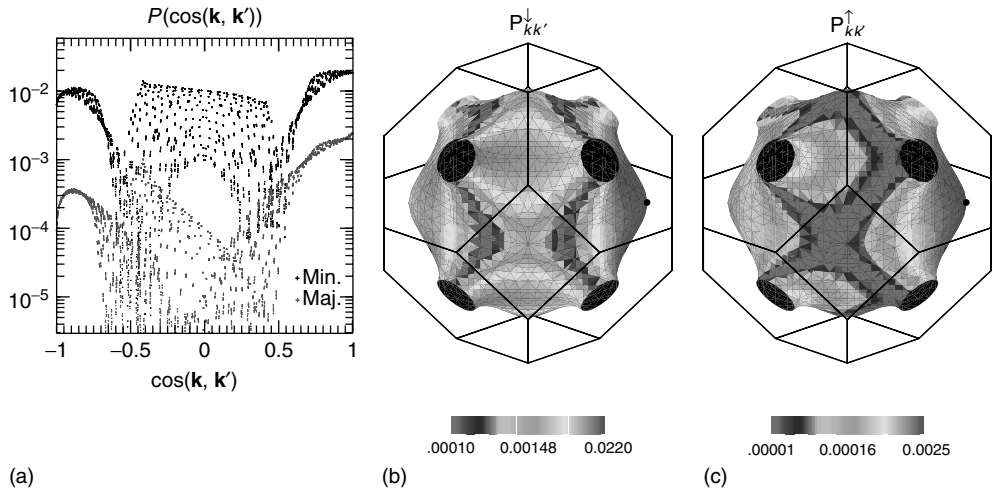

Figure 18. Microscopic transition probability $P_{kk'}$ for magnetic Co defects in a Cu matrix (a); $P_{kk'}$ as a function of the angle between **k** and **k**′ (b and c); $P_{kk'}$ for minority and majority channel, respectively. The initial state **k** is fixed to (100) and is marked by a black dot on the right-hand side.

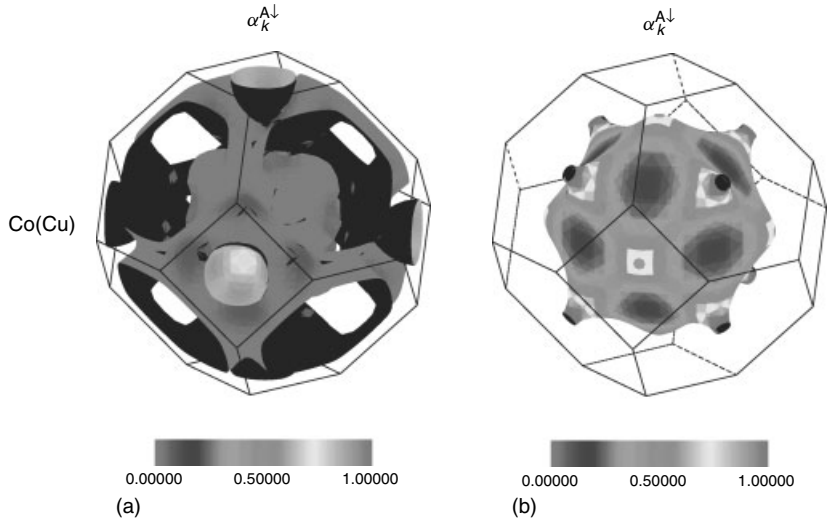

Figure 19. Scattering asymmetry of transition probability α_k^{A} for Cu defects in a magnetic Co matrix (a) minority electrons and (b) majority electrons.

These quantities are state dependent and characterize in short the anisotropy of the scattering and allow for an estimate of the importance of the vertex corrections in equation (25).

The results for a Cu impurity in Co are shown in Figure 19. The scattering asymmetry of the minority electrons is rather low in comparison to the majority electrons which predicts that the vertex corrections will be negligible for the minority electrons but rather important for the majority electrons. Quantitative results are discussed in Section 4.2.4.

4.2.3 Variation of relaxation times

Besides the state and spin dependence of the relaxation times in bulk systems (see discussion above), the relaxation times of impurity states in a multilayer are determined by the relative position of the impurity atom with respect to the interfaces. The interplay of the quantum size effects of the multilayer wave functions (see Section 4.1.2) and the properties of the impurity potential in different positions in the multilayer (see Section 3 and Figure 20) cause variations of the relaxation time.

All Bloch states with a finite probability amplitude at the impurity site are strongly scattered and have a relatively short relaxation time. On the other hand, states with a nearly zero probability amplitude at the impurity site undergo a weak scattering and cause extremely large relaxation times. The state-dependent relaxation times are distributed over several orders of magnitude. This occurs especially for defects inside

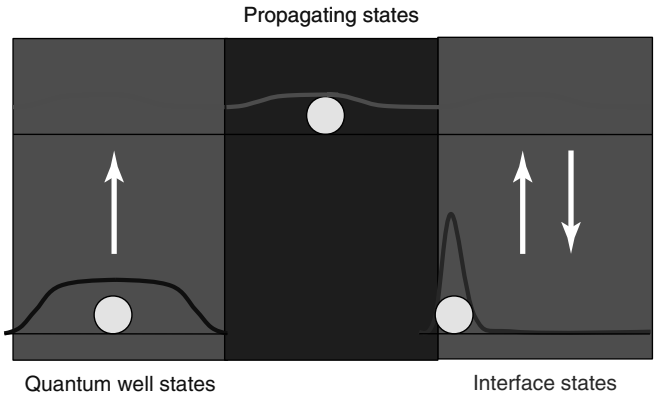

Figure 20. Quantum confinement of eigenstates in a metallic multilayer and characteristic defect positions: the electronic states are described by their probability amplitude.

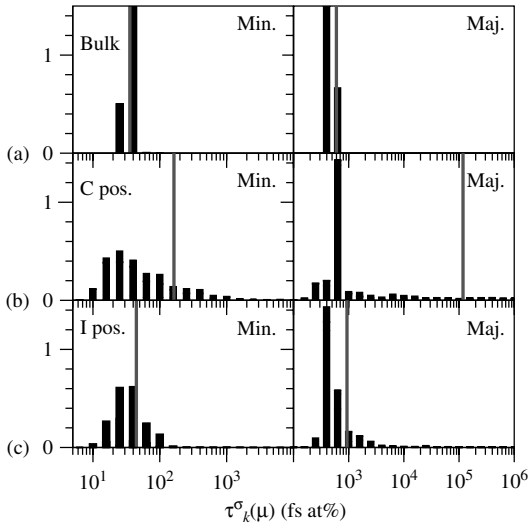

Figure 21. Histogram of spin-dependent, anisotropic relaxation times of Cu impurities in Co_9Cu_7 multilayers for P alignment; bulk impurities (a) are compared with impurities in the center (b) and at the interface (c) of the Co layer (Zahn, Binder and Mertig, 2005). The Fermi surface average of the relaxation times is indicated by a dark gray line. (Reproduced from Zahn *et al*., 2005, with permission from the American Physical Society. © 2005.)

the metallic layers (see Figure 21). This is a new effect that does not happen in bulk systems. Figure 21 shows the relative amount of relaxation times τ_k for the states at the Fermi level for Cu impurities in Co bulk and in the center and at the interface of the Co layer of a Co_9Cu_7 multilayer.

For defects inside the magnetic layer, the maximum of the distribution coincides with that in the bulk material. In addition, a long tail for high values occurs caused by states which have a small probability amplitude at the defect position, for example, quantum well states in the nonmagnetic layer or interface states. This fact is also reflected by the Fermi surface average of the relaxation times indicated by a dark grey line. The averaged relaxation times of bulk impurities and impurities at the interface are nearly the same since all states have a finite probability amplitude at the interface. The averaged relaxation times for impurities in the center of the magnetic layer, however, are quite different. This fact should be borne in mind for the evaluation of theoretical results calculated with constant relaxation times. Comparing the electronic properties of bulk impurities with impurities in a multilayer we can conclude that the electronic structure of impurities in the center of the layer are the same as in bulk; the scattering properties are, however, different. Because of quantum size effects the averaged relaxation times for impurities in the center of the layer are much larger than for bulk impurities in contrast to impurities at the interface, which are comparable.

The states with large relaxation times, although not numerous, are highly conducting and nearly provoke a short circuit. This is the case for Cu impurities in the Co layer of the Co/Cu multilayer, compare Figure 21. This effect is mainly obtained for impurities in the center of the layers and is related to the fact that in-plane transport is mostly driven by quantum well states (Zahn *et al*., 1998). This peculiar behavior is in agreement with the results of Blaas *et al*. (1999) who found higher resistivities for Co/Cu multilayers with interdiffusion restricted to the interface layers than for alloying with Cu atoms in the Co layers.

The multilayer modulation of the relaxation times is quite a robust effect, which was experimentally confirmed for the conductivity and the GMR effect (Marrows and Hickey, 2001).

4.2.4 Vertex corrections in multilayers

The influence of the vertex corrections in the solution of the Boltzmann equation was investigated for the $Co_9Cu_7(100)$ multilayer. The resistances obtained by evaluation of the vector mean free path by equation (25) $\mathring{\rho}_{\parallel}$ and with $\mathbf{\Lambda}_k$ in relaxation time approximation $\rho_{\parallel}$ are compared in Figure 22.

In general the vertex corrections are less important for the minority electrons in comparison to the majority electrons. The scattering anisotropy of the minority electrons is much lower (see also Figure 6) than that for the majority electrons which is related to the character of the electronic states. Scattering of s and p states is highly anisotropic, whereas scattering of the d state is isotropic. The largest deviations occur in the minority channel for a Cr defect and in the majority channel for the defects from Fe to Zn. The latter is caused by the dominating sp scattering since the d states are fully occupied. The large deviation for the Fe defect is comparable to the case of Cu defects in a Co host with large asymmetries of the scattering probability. Compare

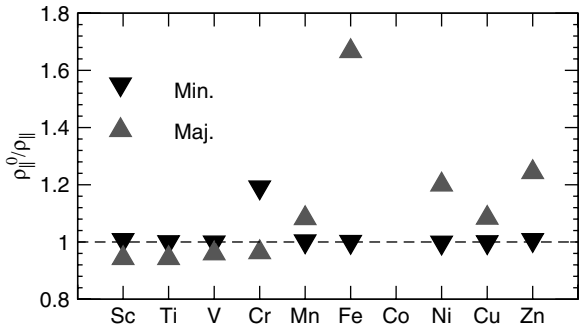

Figure 22. $Co_9Cu_7(100)$: different defects at the Co interface site are treated to consider the ratio $\mathring{\rho}_{\|}/\rho_{\|}$ of CIP conductivities calculated with and without vertex corrections, respectively.

also the bottom panel in Figure 19(b). For pure d scattering or dominating d character of the states (minority channel) the corrections due to the vertex term are small. Zhang and Butler (2000) proposed a simplified scheme to treat the vertex corrections. The main purpose was to increase the scattering probabilities to account for the asymmetry of the scattering, which was determined by the anisotropy of the bulk relaxation times.

4.3 Resistivity and spin anisotropy

4.3.1 Spin anisotropy of resistivity

In the following, the trends of the residual resistivities and the corresponding spin anisotropy of resistivity defined in equation (43) are discussed for $Co_9Cu_7(001)$ multilayers with 3d impurities in the Cu (Figure 23) and the Co layer (Figure 24) in the central and in the interface position in comparison with bulk results. Besides the spin-resolved results for the systems, the total resistivities of the P and AP configurations are presented. The idea of this section is to discuss some general trends that are confirmed by the quantitative results. First, the spin-resolved and total resistivities of the bulk systems are largest in comparison to the multilayer results (P configuration). Second, the general trend of the resistivities for interface impurities in multilayers is very similar to the trend for the bulk systems. Third, the resistivities for impurities in the central position of the Cu or Co layer are very small which is related to the quantum confinement of the wave functions in the multilayer and the large relaxation times of quantum well states. The effect was discussed in Section 4.2.3. The trend of the total resistivity in P configuration is determined by the trend of the spin channel with lower resistivity. The resistivities in the AP configuration are for all systems larger than the resistivities in the P configuration which leads to positive GMR (see Section 4.4.1).

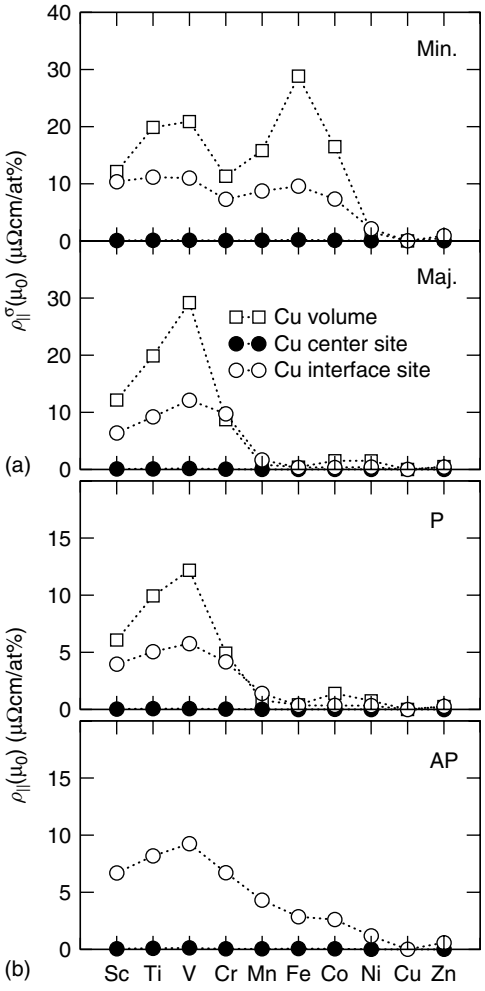

Figure 23. CIP resistivities of $Co_9Cu_7(001)$ multilayers with 3d defects in the Cu layer (central and interface position) in comparison with bulk results, (a) spin-resolved contributions for the P configuration and (b) total resistivities for P and AP configurations.

To understand the physics behind the trend we have to examine the LDOS (Figure 16). The trend is determined by resonance scattering. As soon as the VBS formed by the impurity approaches the Fermi level resonance scattering occurs and causes a large resistivity.

Considering the spin-anisotropy ratio α (equation (43), Figure 25): The trend obtained for bulk impurities coincides with the trend for the corresponding impurities at the interfaces of the layers. A strong shift of the anisotropy to values of $\alpha < 1$ is found for impurities in the central position of the Co layer. The spin-anisotropy ratio is decreased because of the channeling states in the Cu layer $\rho^{\uparrow} << \rho^{\downarrow}$. Strong anisotropy is found for defects with a nuclear charge close to the host material. Since the impurity potential is nearly degenerated with the host potential in one of the spin channels, the corresponding scattering cross section vanishes.

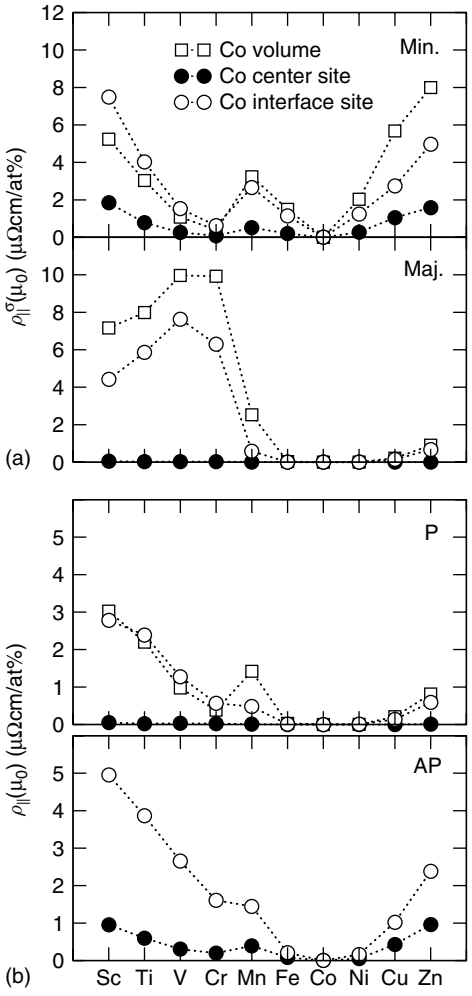

Figure 24. CIP resistivities of $Co_9Cu_7(001)$ multilayers with 3d defects in the Co layer (central and interface position) in comparison with bulk results, (a) spin-resolved contributions for the P configuration and (b) total resistivities for P and AP configurations.

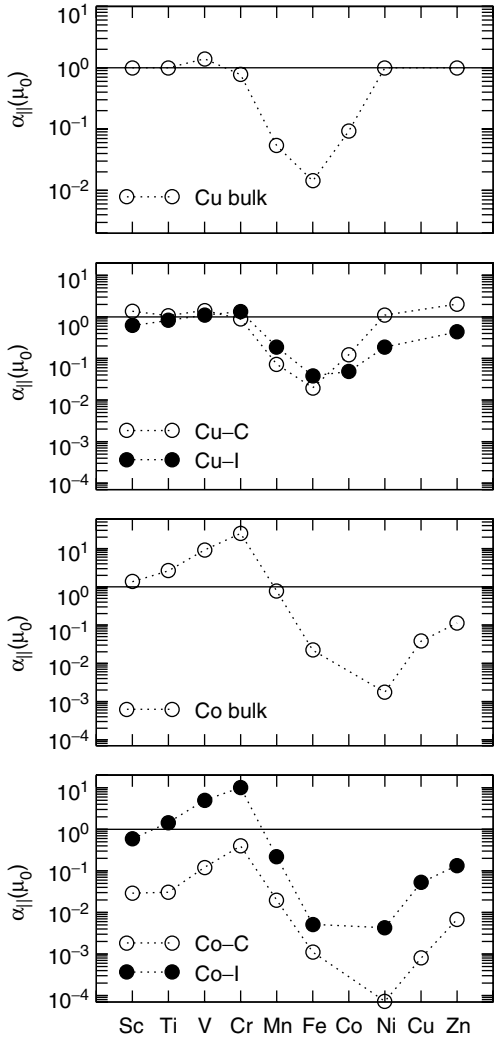

Figure 25. Spin anisotropy α (equation (43)) of the CIP resistivities of $Co_9Cu_7(001)$ multilayers with 3d defects in the Co or Cu layer (central and interface position) in comparison with corresponding bulk results.

4.3.2 Inverse GMR

On the basis of the strong differences in the spin anisotropy it became clear that the amplitude of the GMR effect can be tailored by the chemical composition of the multilayer with appropriate impurity atoms. In particular the GMR ratio could be inverted by combination of impurities with opposite spin-anisotropy ratio (George *et al*., 1994). The mechanism is illustrated in Figure 26. Two types of defects with opposite spin-anisotropy ratio are deposited in adjacent magnetic layers. So that the scattering for electrons with one spin direction changes from strong to weak in the P configuration of the magnetic multilayer. As a result the resistivity of the two spin channels is comparable. In the AP configuration, however, the opposite spin-anisotropy ratio of the impurity atom is counterbalanced by the change of the magnetization direction. As a result a channel with low resistivity is created so that $\rho^{AP} < \rho^{P}$ and the inverse GMR effect is created.

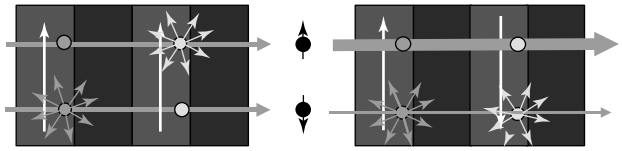

Figure 26. Inverse GMR: spin-dependent scattering.

To simulate a system with inverse GMR, impurities with opposite spin-anisotropy ratio β (see equation (46)) are combined.

To describe a multilayer with two types of noninteracting impurities (A and B), we use the following ansatz for the

microscopic transition probability per spin direction in the parallel alignment

$$P_{kk'}^{\sigma\,\mathrm{P}} = x\,P_{kk'}^{\sigma\,\mathrm{A}} + (1-x)\,P_{kk'}^{\sigma\,\mathrm{B}} \tag{59}$$

and in the antiparallel alignment

$$P_{kk'}^{\sigma\,\mathrm{AP}} = x\,P_{kk'}^{\sigma\,\mathrm{A}} + (1-x)\,P_{kk'}^{-\sigma\,\mathrm{B}} \tag{60}$$

Correspondingly, the electron lifetime becomes

$$\frac{1}{\tau_{\mathrm{P}}^{\sigma}} = x\,\frac{1}{\tau_{\mathrm{A}}^{\sigma}} + (1-x)\frac{1}{\tau_{\mathrm{B}}^{\sigma}} \tag{61}$$

in the parallel configuration and

$$\frac{1}{\tau_{\mathrm{AP}}^{\sigma}} = x\,\frac{1}{\tau_{\mathrm{A}}^{\sigma}} + (1-x)\,\frac{1}{\tau_{\mathrm{B}}^{-\sigma}} \tag{62}$$

in the antiparallel configuration. The parameter x determines the concentration of impurities A relative to B. In the limit $x = 1$ the relaxation time of impurity A with an anisotropy ratio β_{A} and in the limit $x = 0$ the relaxation time of impurity B with an anisotropy ratio β_{B} is reached.

In our calculations A is associated with V impurities in the Fe layers (denoted by Fe(V)) and B is either a Cu impurity in Co layers (Co(Cu)) or a magnetic Co impurity in Cu layers (Cu(Co)). The inverse relaxation times and the anisotropy ratios are shown in Table 1. The spin-anisotropy ratio of Co(Cu) and Cu(Co) is smaller than 1. Both defects cause, in principle, the same scattering behavior of the wave function. The anisotropy ratio of Fe(V) is opposite, that is, in parallel configuration the majority electrons (spin up, ↑) are strongly scattered at the V impurities in the Fe layers and are weakly scattered at the Cu impurities in the Co layers or in the Co-containing Cu layers whereas the minority electrons (spin down, ↓) are weakly scattered at V impurities in Fe layers but strongly scattered at Cu impurities in Co or Co-containing Cu layers. For the antiparallel configuration the scattering channels are mixed. The majority electrons are scattered strongly in each layer and the minority electrons are scattered weakly in each layer. Consequently, a slow and a fast channel occur which results in a low resistivity.

The results of the calculation as a function of impurity concentration and Fe layer thickness are shown in Figure 27. As expected from the simple model, the GMR ratio switches from positive to negative values as a function of the relative impurity concentration x.

Table 1. Anisotropy ratios β (equation (46)) and Fermi surface average of the relaxation times per spin direction τ^{σ} in arbitrary units for the dilute bulk alloys Co(Cu), Cu(Co), and Fe(V).

Impurity	Co(Cu)	Cu(Co)	Fe(V)
β	0.0701	0.1413	21.55
$\tau^{\downarrow}$	2.52	0.42	38.0
$\tau^{\uparrow}$	35.9	2.95	1.76

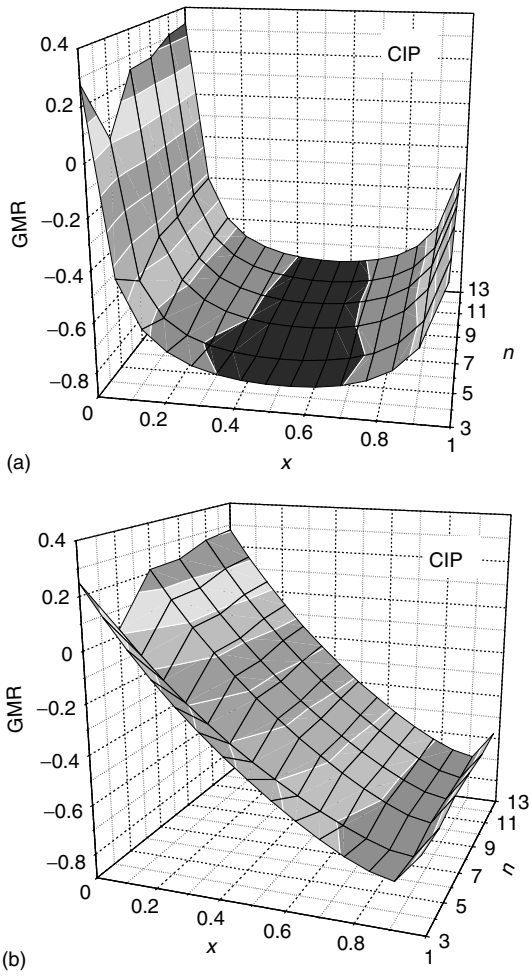

Figure 27. Calculated CIP-GMR of $Fe_n Cu_6 Co_2 Cu_6$ versus Fe layer thickness n and relative defect concentration x; (a) for V impurities in Fe layers combined with Cu impurities in Co layers, (b) for V impurities in Fe layers combined with magnetic Co impurities in Cu layers.

4.4 GMR: defect dependence

4.4.1 Position dependence

The GMR ratios derived from the resistivity calculation of Figures 23 and 24 are shown in Figure 28. The trends

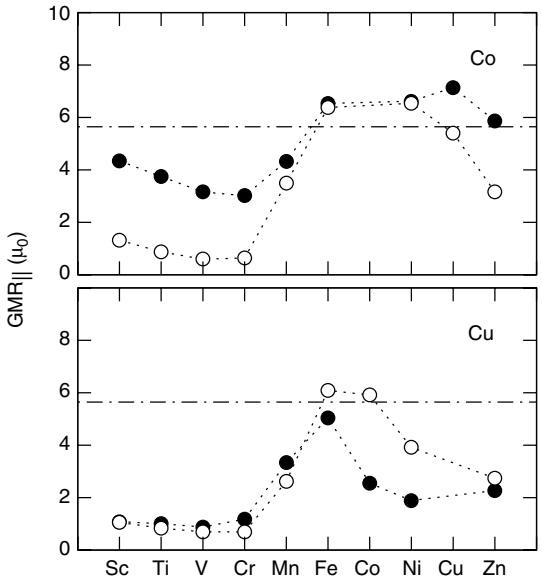

Figure 28. GMR ratio of $Co_9Cu_7(100)$ multilayers for δ layers of 3d transition-metal impurities in the center and at the interface of the Co or Cu layers; the symbols of each subpanel denote the δ layer position; closed symbols: center of the layer and open symbols: interface position; the dashed line indicates the GMR value caused by interface scattering only.

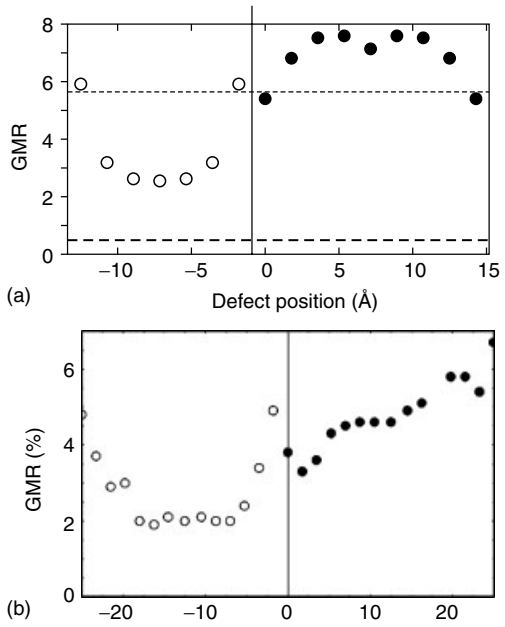

Figure 29. Dependence of the GMR in $Co_9Cu_7(100)$ multilayers on the position of Co impurities in the Cu layer and Cu impurities in the Co layer assuming δ layer scattering and interface scattering with equal weights. The thick dashed line indicates the intrinsic GMR and the thin dashed line the GMR value caused by interface scattering only, from Zahn, Binder and Mertig (2003), (b) shows the experimental results by Marrows and Hickey (2001). (Reproduced from Zahn *et al*., 2003/Marrows & Hickey 2001, with permission from the American Physical Society. © 2001/2003.)

imply that the larger the spin anisotropy α (see Figure 25) the larger the GMR ratio. Although defects in the center of the layers cause a much smaller resistivity than defects at the interfaces (see Figures 23 and 24), they are equally efficient like defects at the interface to induce large GMR. Dependence of the GMR in $Co_9Cu_7(100)$ multilayers on self defects in any of the multilayer position is presented in Figure 29. For the calculation, δ layers of Cu impurities in the Co layer or δ layers of Co impurities in the Cu layer and interface scattering are taken into account with equal weights. The thin dashed line is the GMR value caused by interface scattering only, from Zahn, Binder and Mertig (2003). This value would correspond to the reference value in the experiments of Marrows and Hickey without the δ layer (Marrows and Hickey, 2001). The thick dashed line in Figure 29 gives the GMR value obtained with the assumption of a constant relaxation time without any spin or state dependence (intrinsic GMR). In comparison to this case of isotropic scattering the insertion of an additional δ layer increases GMR, mostly at the interfaces.

Comparing the trend of GMR an excellent agreement with the experiment (Figure 29b) is obtained for the Co/Cu system which is a confirmation of the microscopic picture.

The very good agreement with experimental results is not limited to self defects. Investigations of all the 3d transition-metal impurities deposited as δ layers in the Co/Cu spin valve have been performed, (Marrows and Hickey, 2001) and they substantiate the basic concept of spin-dependent scattering in magnetic multilayers (see Figure 30) (Zahn, Binder and Mertig, 2003).

We still have to mention, that the calculated values are 2 orders of magnitude larger than the experimental ones. The reason is the restriction to substitutional point defects. In addition to these, other scattering processes occur in real samples. Assuming self-averaging, the results could be corrected toward the experimental ones by an additional spin- and state-independent relaxation time τ (thick dashed line in Figure 29) (Zahn *et al*., 1998). In contrast to Zahn *et al*. (1998), the present results were obtained assuming only the impurity distribution described above and are focused on the impurity scattering rates only. Another difference from the experimental setup in Marrows and Hickey (2001) is the geometry. The experimentally investigated samples have been Co/Cu/Co spin valves grown on a buffer layer and protected by a cap layer. As a consequence, the GMR ratios are nearly symmetric as a function of the impurity position in the Cu layer but asymmetric for defects in the Co layer. The calculations are performed in supercell geometry and this is reflected in the symmetry of the results with respect to the defect position in both layers, Cu and Co. A possible

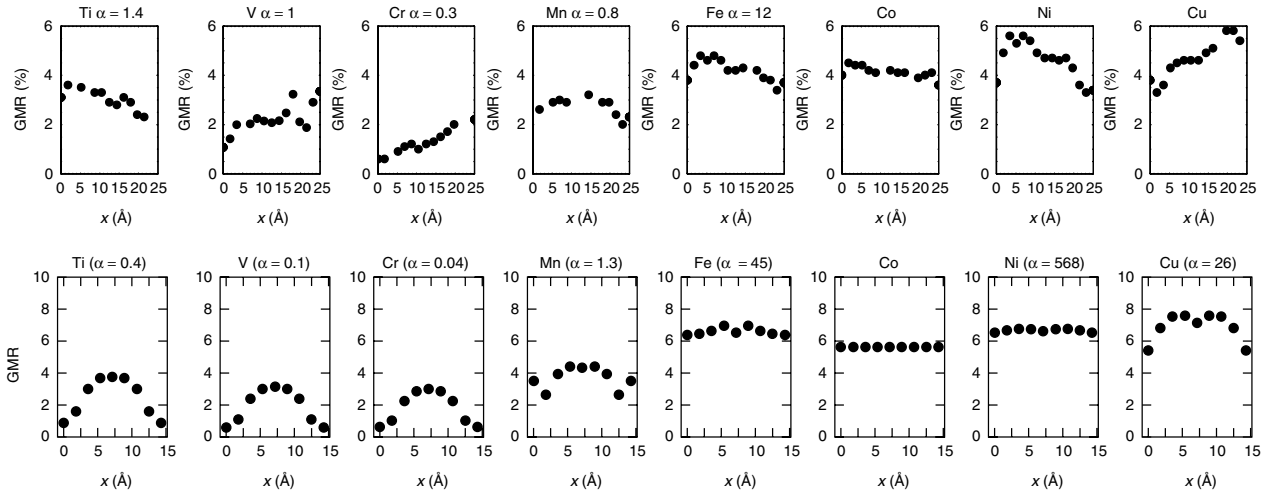

Figure 30. Dependence of the GMR on the position of 3d impurities in the Co layer; upper row: experimental results by Marrows and Hickey (Figure 1 reproduced from Marrows & Hickey 2001, with permission from the American Physical Society. © 2001.); lower row: our calculation (Zahn, Binder and Mertig, 2003). $x = 0$ corresponds to the position of the Cu/Co interface. α values are calculated for the corresponding impurities in bulk Co.

influence of superlattice effects in metallic multilayers was shown to be negligible (Erler, Zahn and Mertig, 2001).

4.5 CPP-GMR

In contrast to the CIP geometry, where the current is flowing parallel to the layers, the CPP geometry is characterized by a current perpendicular to the layers. Owing to the reduced device dimension in current direction microfabrication or even nanofabrication technologies have to be used to enhance the resistivity and resistivity changes. This is necessary to allow for a reliable detection of the effect. The effect was first measured with superconducting contacts (Pratt *et al.*, 1991), which unfortunately implies that the low-temperature regime is accessible only, but allows for a simultaneous measurement of the CIP and CPP effect on the same sample, see Figure 31. Other setups which avoid this restriction are microstructured pillars (Gijs, Lenczowski and Giesbers, 1993), a growth on structured substrates (Ono and Shinjo, 1995; Gijs *et al.*, 1995), and electrodeposition of nanowires into pores of a polymer foil (Blondel, Meier, Doudin and Ansermet, 1994; Piraux *et al.*, 1994). Surveys about the experimental and theoretical achievements are given in (Levy, 1994; Gijs and Bauer, 1997; Barthélémy, Fert and Petroff, 1999; Tsymbal and Pettifor, 2001; Brataas, Bauer and Kelly, 2006).

From a theoretical point of view, the CPP-GMR effect is less complex than the CIP equivalent, because the high symmetry of the former reduces the effort by approximations using model Hamiltonians.

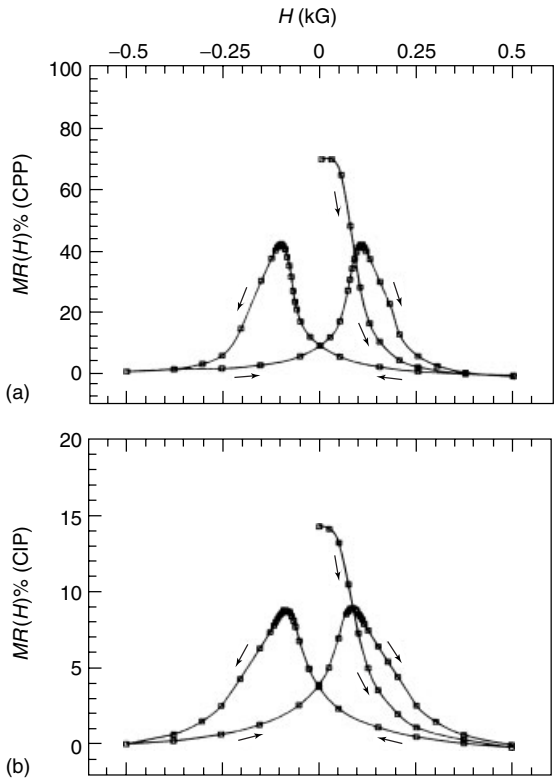

Figure 31. $MR(H) = (R(H) - R_{\mathrm{satt}})/R_{\mathrm{satt}}$ for a Ag (6 nm)/Co (6 nm) multilayer with Nb cross strips simultaneously measured for CPP geometry (a) and CIP geometry (b). (Figure 2 reproduced from Pratt *et al.*, 1991, with permission from the American Physical Society. © 1991.)

The models applied are aimed at the linear response of the system and are based on a quasiclassical approach using the Boltzmann equation and a fully quantum-mechanical

description starting from the Kubo–Greenwood approach, respectively. In the following, considerations are restricted to calculational schemes applied to the CPP geometry. Valet and Fert treated bulk, interface, and spin-flip scattering on the same footing starting from the quasiclassical distribution function (Valet and Fert, 1993). They have shown that the correct treatment of the spin accumulation caused by the spin-dependent bulk and interface resistivities is necessary to describe systems with layer thicknesses of the order of the spin diffusion length. That is the length scale at which the currents in both spin channels are equilibrated by spin-flip scattering processes.

For multilayer systems, the global solution of the Boltzmann equation is obtained by an appropriate coupling of the piecewise solutions inside the layers analogous to the Fuchs–Sondheimer theory (Fuchs, 1938; Sondheimer, 1952), as was shown by Falicov and Hood for the CIP geometry (Falicov and Hood, 1993). Zhang and Levy have demonstrated that the interface resistance and the CPP-GMR are very sensitive to the scattering at the interfaces and that diffusive scattering can assist or suppress the effect depending on the interface reflectivity (Zhang and Levy, 1998). This is illustrated in Figure 32. $(1 - S)$ measures the diffusive scattering and T characterizes the transmission. This quasiclassical approach was later generalized by Butler and coworkers to include the bulk and interface resistivities from *ab initio* calculations (Zhang and Butler, 1995; Butler, Zhang and MacLaren, 2000). Transmission coefficients across a ferromagnet/nonmagnet interface which are essential ingredients for CPP-GMR were first obtained by matching the generalized Bloch states of the two semi-infinite crystals (Stiles, 1996), or from a surface embedding Green's function technique (Schep *et al*., 1997).

A quasiclassical approach including the coherent scattering by the *ab initio* band structure of the multilayer and the diffuse scattering by appropriate spin-dependent relaxation times was developed by the authors. The presented results are, however, limited to the very special case that the mean free path Λ is much larger than the unit cell. Since the CPP geometry is characterized by an alignment of the current and the direction of the quantum confinement effects that occur in this limit because of coherent scattering at the interfaces, the obtained CPP-GMR is much larger than CIP-GMR ratio, both in theory (Zhang and Levy, 1991; Zahn, Mertig, Richter and Eschrig, 1995; Zahn *et al*., 1998) and in experiment (Pratt *et al*., 1991). Compare Figures 33 and 31(a,b), respectively.

To describe the transport in the linear response regime on the basis of quantum mechanics alone the Kubo formula is well suited and it is explained in great detail in text books (Mahan, 1981). The correspondence of the quantum approach starting from the Kubo formula (Kubo, 1957) and the quasiclassical approach for the case of multilayers was shown by Camblong and Levy (1992). Following the description of the CIP-GMR (Levy, Zhang and Fert, 1990), it was applied to the CPP geometry by Zhang and Levy (1991). To include typical features of the electronic structure of the metals forming the multilayer, tight-binding Hamiltonians were included in the consideration to elucidate the role of defects and layer thickness on the MR effect (Tsymbal and Pettifor, 2000; Mathon, 1996). An oscillatory

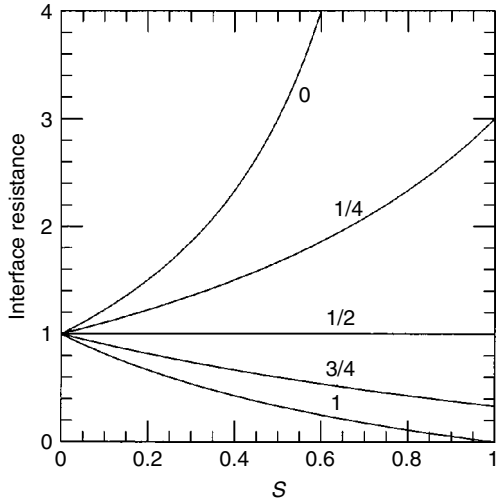

Figure 32. Interface resistance as a function of the diffuse scattering parameter S for a set of transmission coefficients T. $S = 0$ represents total diffuse scattering, while for $S = 1$ there is no diffuse scattering. (Reproduced from Zhang & Levy 1998, with permission from the American Physical Society. © 1998.)

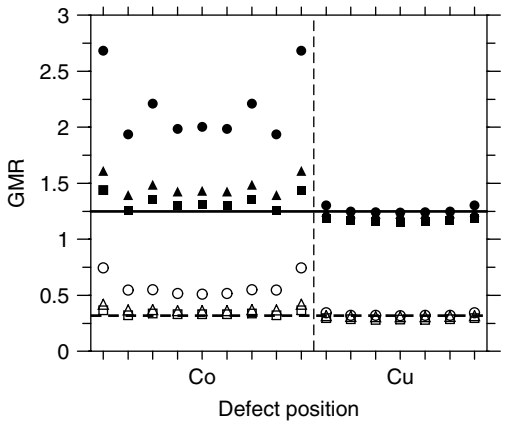

Figure 33. GMR of a Co (1.6 nm)/Cu (1.25 nm) multilayer in dependence on the impurity position in the Co and Cu layers: open symbols for CIP-GMR, closed symbols for CPP-GMR for a set of spin asymmetry of the defect scattering strength $\beta = 0.25$ (squares), $\beta = 1.0$ (triangles), $\beta = 4.0$ (circles). Dashed and full lines are the values with a constant spin-independent relaxation time. (Reproduced from Zahn *et al*., 1998, with permission from the American Physical Society. © 1998.)

behavior similar to the IEC was predicted for the coherent limit of very high quality samples (Mathon *et al*., 1995). The generalization of the Kubo formula to inhomogeneous layered systems was derived (Butler, Zhang, Nicholson and MacLaren, 1994; Weinberger *et al*., 1996), but the highly demanding vertex corrections within the CPA to describe defects and interdiffusion prevented a numerical evaluation of the CPP transport coefficients.

A fully *ab initio* level of description was reached by Kudrnovský *et al*. taking advantage of a supercell approach to model the influence of disorder and interdiffusion (Kudrnovský and Bruno, 2000; Xia *et al*., 2001; Drchal *et al*., 2002). This method allows for the description of specular and diffuse scattering at the interfaces and inside the layers on an equal footing. By this approach, the evaluation of the resistivity of a single interface between two metals was performed, which provides parameters for a simplified resistor model of the structure (Bauer *et al*., 2001).

REFERENCES

Baibich, M.N., Broto, J.M., Fert, A., *et al*. (1988). Giant magnetoresistance of (001)Fe/(001)Cr magnetic superlattices. *Physical Review Letters*, **61**, 2472.

Baranger, H. and Stone, A. (1989). Electrical linear-response theory in an arbitrary magnetic field: a new Fermi-surface formation. *Physical Review B*, **40**, 8169.

von Barth, U. and Hedin, L. (1972). A local exchange-correlation potential for the spin-polarized case. *Journal of Physics C*, **5**, 1629.

Barthélémy, A., Fert, A. and Petroff, F. (1999). GMR in magnetic multilayers. In *Handbook of Magnetic Materials*, Buschow, K.H.J. (Ed.), Elsevier, Vol. 12.

Bass, J., Yang, Q., Lee, S.F., *et al*. (1994). How to isolate effects of spin-flip scattering on giant magnetoresistance in magnetic multilayers. *Journal of Applied Physics*, **75**, 6699.

Bauer, G., Nazarov, Y., Huertas-Hernando, D., *et al*. (2001). Semiclassical concepts in magnetoelectronics. *Materials Science and Engineering B*, **84**, 31.

van den Berg, H.A.M., Altmann, J., Bar, L., *et al*. (1999). Magnetic tunnel sensors with Co-Cu artificial antiferromagnetic (aaf) hard subsystem. *IEEE Transactions on Magnetics*, **35**, 2892–2894.

Binasch, G., Grünberg, P., Saurenbach, F. and Zinn, W. (1989). Enhanced magnetoresistance in layered magnetic structures with antiferromagnetic interlayer exchange. *Physical Review B*, **39**, R4828.

Binder, J., Zahn, P., Mertig, I., *et al*. (1998). Magnetic properties of impurities and impurity pairs in magnetic multilayers. *Philosophical Magazine B*, **78**, 537.

Blaas, C., Weinberger, P., Szunyogh, L., *et al*. (1999). Ab initio calculations of magnetotransport for magnetic multilayers. *Physical Review B*, **60**, 492.

Blondel, A., Meier, J.P., Doudin, B. and Ansermet, J-P. (1994). Giant magnetoresistance of nanowires of multilayers. *Applied Physics Letters*, **65**, 3019.

Braspenning, P., Zeller, R., Lodder, A. and Dederichs, P. (1984). Self-consistent cluster calculations with correct embedding for 3d, 4d and some sp impurities in copper. *Physical Review B*, **29**, 703.

Brataas, A., Bauer, G.E.W. and Kelly, P. (2006). Non-collinear magnetoelectronics. *Physics Reports*, **472**, 157–255.

Bruno, P. and Chappert, C. (1991). Oscillatory coupling between ferromagnetic layers separated by a nonmagnetic metal spacer. *Physical Review Letters*, **67**, 1602, 2592(E).

Butler, W. (1985). Theory of electronic transport in random alloys: Korringa-Kohn-Rostoker coherent-potential approximation. *Physical Review B*, **31**, 3260.

Butler, W., MacLaren, J. and Zhang, X. (1993). Giant magnetoresistance calculated from first principles. *Materials Research Society Symposium Proceedings*, **313**, 59.

Butler, W.H., Zhang, X-G. and MacLaren, J.M. (2000). Solution to the Boltzmann equation for layered systems for current perpendicular to the planes. *Journal of Applied Physics*, **87**, 5173.

Butler, W.H., Zhang, X-G., Nicholson, D.M.C. and MacLaren, J. (1994). Theory of transport in inhomogeneous systems and application to magnetic multilayer systems. *Journal of Applied Physics*, **76**, 6808.

Butler, W.H., Zhang, X-G., Nicholson, D.M.C., *et al*. (1996). Giant magnetoresistance from an electron waveguide effect in cobalt-copper multilayers. *Physical Review Letters*, **76**, 3216.

Butler, W., Zhang, X-G., Schulthess, T., *et al*. (1999). First principles modelling of magnet random access memory devices. *Journal of Applied Physics*, **85**, 5834.

Büttiker, M. (1988). Symmetry of electrical conduction. *IBM Journal of Research and Development*, **32**, 317.

Büttiker, M., Imry, Y., Landauer, R. and Pinhas, S. (1985). Generalized many-channel conductance formula with application to small rings. *Physical Review B*, **31**, 6207.

Camblong, H.E. and Levy, P.M. (1992). Novel results for quasiclassical linear transport in metallic multilayers. *Physical Review Letters*, **69**, 2835.

Camley, R.E. and Barnaś, J. (1989). Theory of giant magnetoresistance effects in magnetic layered structures with antiferromagnetic coupling. *Physical Review Letters*, **63**, 664.

Campbell, I.A. and Fert, A. (1982). Transport properties of ferromagnets. In *Ferromagnetic Materials*, Wohlfahrt, E.P. (Ed.), North Holland: Amsterdam, pp. 769, Vol. 3.

Datta, S. (1995). *Electronic Transport in Mesoscopic Systems*, Cambridge University Press: Cambridge.

Dederichs, P. and Zeller, R. (1981). *Festkörperprobleme (Advances in Solid States Physics)*, Vieweg: Braunschweig, pp. 243–269, Vol. XXI.

Drchal, V., Kudrnovský, J., Bruno, P., *et al*. (2002). Electron transport in magnetic multilayers: effect of disorder. *Physical Review B*, **65**, 214414.

Enders, A., Monchesky, T.L., Myrtle, K., *et al*. (2001). The role of interfaces in the magnetoresistance of Au/Fe/Au/Fe/GaAs(001). *Journal of Applied Physics*, **89**, 7110.

Erler, F., Zahn, P. and Mertig, I. (2001). Finite-size effects in giant magnetoresistance: an ab initio calculation. *Physical Review B*, **64**, 094408.

Falicov, L.M. and Hood, R.Q. (1993). A Boltzmann-equation approach to the magnetoresistance of ferromagnetic normal metallic multilayers. *Journal of Magnetism and Magnetic Materials*, **121**, 362.

Fert, A. (1969). Two-current conduction in ferromagnetic metals and spin wave-electron collisions. *Journal of Physics C*, **2**, 1784.

Fert, A. and Campbell, I. (1976). Electrical resistivity of ferromagnetic nickel and iron based alloys. *Journal of Physics F*, **6**, 849.

Fisher, D. and Lee, P. (1981). Relation between conductivity and transmission matrix. *Physical Review B*, **23**, 6851.

Fuchs, K. (1938). The conductivity of thin metallic films according to the electron theory of metals. *Proceedings of the Royal Society of London Series A*, **34**, 100.

George, J., Pereira, L., Barthélémy, A., *et al*. (1994). Inverse spin-valve-type magnetoresistance in spin engineered multilayered structures. *Physical Review Letters*, **72**, 408.

Gijs, M. and Bauer, G. (1997). Perpendicular giant magnetoresistance of magnetic multilayers. *Advances in Physics*, **46**, 285–445.

Gijs, M., Giesbers, J., Johnson, M., *et al*. (1995). *Perpendicular giant magnetoresistance using microlithography and substrate patterning techniques*, pp. 333–340.

Gijs, M., Lenczowski, S. and Giesbers, J. (1993). Perpendicular GMR of microstructured Fe/Cr magnetic multilayers from 4.2 to 300k. *Physical Review Letters*, **70**, 3343.

Greenwood, D.A. (1958). The Boltzmann equation in the theory of electrical conduction in metals. *Proceedings of the Physical Society*, **71**, 585.

Grünberg, P., Schreiber, R., Pang, Y., *et al*. (1986). Layered magnetic structures: evidence for antiferromagnetic coupling of Fe layers across Cr interlayers. *Physical Review Letters*, **57**, 2442.

Gyorffy, B. (1972). Coherent-potential approximation for a nonoverlapping-muffin-tin-potential model of random substitutional alloys. *Physical Review B*, **5**, 2382.

von Helmolt, R., Wecker, J., Holzapfel, B., *et al*. (1993). Giant negative magnetoresistance in perovskite-like $La_{2/3}Ba_{1/3}MnO_x$ ferromagnetic-films. *Physical Review Letters*, **71**, 2331.

Hohenberg, P. and Kohn, W. (1964). Inhomogeneous electron gas. *Physical Review*, **136**, 864.

Hood, R.Q. and Falicov, L.M. (1992). Boltzmann-equation approach to the negative magnetoresistance of ferromagnetic/normal-metal multilayers. *Physical Review B*, **46**, 8287.

http://www.physik.tu-dresden.de/∼fermisur (1998). Fermi surfaces.

http://www.phys.ufl.edu/fermisurface, (2005). Fermi surface database.

Inoue, J., Oguri, A. and Maekawa, S. (1991). Theory of giant magnetoresistance in metallic superlattices. *Journal of the Physical Society of Japan*, **60**, 376.

Julliere, M. (1975). Tunneling between ferromagnetic-films. *Physics Letters A*, **54A**, 225.

Kohn, W. and Sham, L. (1965). Self-consistent equations including exchange and correlation effects. *Physical Review*, **140**, A1133.

Kubo, R. (1957). Statistical-mechanical theory of irreversible processes I. *Journal of the Physical Society of Japan*, **12**, 570.

Kubo, R. (1966). The fluctuation-dissipation theorem. *Reports on Progress in Physics*, **29**, 255–284.

Kudrnovský, J. and Bruno, P. (2000). Ab initio theory of perpendicular magnetotransport in metallic multilayers. *Physical Review B*, **62**, 15084.

Landauer, R. (1970). Electrical resistance of disordered one-dimensional lattices. *Philosophical Magazine*, **21**, 863.

Landauer, R. (1988). Spatial variation of currents and fields due to localized scatterers in metallic conduction. *IBM Journal of Research and Development*, **32**, 306.

Levy, P.M. (1994). Giant magnetoresistance in magnetic layered and granular materials. *Solid State Physics*, **47**, 367–462.

Levy, P. and Zhang, S. (1997). Resistivity due to domain wall scattering. *Physical Review Letters*, **79**, 5110.

Levy, P., Zhang, S. and Fert, A. (1990). Electrical conductivity of magnetic multilayered structures. *Physical Review Letters*, **65**, 1643.

Mahan, G. (1981). *Many-Particle Physics*, Plenum Press: New York.

Marrows, C.H. and Hickey, B.J. (2001). Impurity scattering from δ-layers in giant magnetoresistance systems. *Physical Review B*, **63**, 220405(R).

Mathon, T. (1996). Large enhancement of the perpendicular GMR in pseudorandom magnetic multilayers. *Physical Review B*, **54**, 55.

Mathon, J., Villeret, M., Muniz, R., *et al*. (1995). Quantum well theory of the exchange coupling in Co/Cu/Co(001). *Physical Review Letters*, **74**, 3696.

Mavropoulos, P., Papanikolaou, N. and Dederichs, P. (2004). A KKR green function formalism for ballistic transport. *Physical Review B*, **69**, 125104.

Mertig, I. (1999). Transport properties of dilute alloys. *Reports on Progress in Physics*, **62**, 237.

Mertig, I., Mrosan, E. and Ziesche, P. (1987). *Multiple Scattering Theory of Point Defects in Metals: Electronic Properties*, Teubner-Verlag: Leipzig.

Mertig, I., Zahn, P., Richter, M., *et al*. (1995). Ab initio calculation of residual resistivity in dilute Fe alloys and giant magnetoresistance in Fe/Cr multilayers. *Journal of Magnetism and Magnetic Materials*, **151**, 363.

Mertig, I., Zeller, R. and Dederichs, P. (1993). Ab initio calculations of residual resistivities for dilute Ni alloys. *Physical Review B*, **47**, 16178.

Meservey, R. and Tedrow, P. (1994). Spin-polarized electron-tunneling. *Physics Reports*, **238**, 173–243.

Moodera, J., Kinder, L., Wong, T. and Meservey, R. (1995). Large magnetoresistance at room temperature in ferromagnetic thin film tunnel junctions. *Physical Review Letters*, **74**, 3273.

Mott, N. (1964). Electrons in transition metals. *Advances in Physics*, **13**, 325.

Nogues, J. and Schuller, I. (1999). Exchange bias. *Journal of Magnetism and Magnetic Materials*, **192**, 203–232.

Oguchi, T. (1993). Fermi-velocity effect on magnetoresistance in Fe/transition-metal multilayers. *Journal of Magnetism and Magnetic Materials*, **126**, 519.

Ono, T. and Shinjo, T. (1995). Magnetoresistance of multilayers prepared on microstructured substrates. *Journal of the Physical Society of Japan*, **64**, 363.

Parkin, S. (1991). Systematic variation of the strength and oscillation period of indirect magnetic exchange coupling through the 3d, 4d, and 5d transition metals. *Physical Review Letters*, **67**, 3598.

Parkin, S., Modak, A. and Smith, D. (1993). Dependence of giant magnetoresistance on Cu-layer thickness in Co/Cu multilayers: a simple dilution effect. *Physical Review B*, **47**, 9136.

Piraux, L., Dubois, S., Duvail, J.L., *et al*. (1997). Arrays of nanowires of magnetic metals and multilayers: perpendicular GMR and magnetic properties. *Journal of Magnetism and Magnetic Materials*, **175**, 127.

Piraux, L., Dubois, S. and Fert, A. (1996). Perpendicular giant magnetoresistance in magnetic multilayered nanowires. *Journal of Magnetism and Magnetic Materials*, **159**, L287.

Piraux, L., Dubois, S., Fert, A. and Belliard, L. (1998). The temperature dependence of the perpendicular giant magnetoresistance in co/cu multilayered nanowires. *European Physical Journal B*, **4**, 413.

Piraux, L., George, J., Despres, J., *et al*. (1994). Giant magnetoresistance in magnetic multilayered nanowires. *Applied Physics Letters*, **65**, 2484.

Pratt W.P. Jr., Lee, S-F., Slaughter, J.M., *et al*. (1991). Perpendicular giant magnetoresistance of ag/co multilayers. *Physical Review Letters*, **66**, 3060.

Santamaria, J., Gomez, M-E., Cyrille, M-C., *et al*. (2001). Interfacially dominated giant magnetoresistance in Fe/Cr superlattices. *Physical Review B*, **65**, 012412.

Schep, K., van Hoof, J., Kelly, P., *et al*. (1997). Interface resistances of magnetic multilayers. *Physical Review B*, **56**, 10805.

Schep, K., Kelly, P. and Bauer, G. (1995). Giant magnetoresistance without defect scattering. *Physical Review Letters*, **74**, 586.

Sharvin, Y. (1965). A possible method for studying Fermi surfaces. *Soviet Physics JETP*, **21**, 655.

Sondheimer, E.H. (1952). The mean free path of electrons in metals. *Advances in Physics*, **1**, 1.

Stepanyuk, V., Zeller, R., Dederichs, P. and Mertig, I. (1994). Electronic structure and magnetic properties of dilute Co alloys with transition metal impurities. *Physical Review B*, **49**, 5157.

Stiles, M. (1996). Spin-dependent interface transmission and reflection in magnetic multilayers. *Journal of Applied Physics*, **79**, 5805.

Tsymbal, E. and Pettifor, D. (2000). Quantum-well resistivity for perpendicular transport in magnetic layered systems. *Physical Review B*, **61**, 506.

Tsymbal, E.Y. and Pettifor, D.G. (2001). Local impurity-assisted conductance in magnetic tunnel junctions. *Physical Review B*, **64**, 212401.

Valet, T. and Fert, A. (1993). Theory of the perpendicular magnetoresistance in magnetic multilayers. *Physical Review B*, **48**, 7099.

Velický, B. (1969). Theory of electronic transport in disordered binary alloys: Coherent-potential approximation. *Physical Review*, **184**, 614.

Weinberger, P., Levy, P., Banhart, J., *et al*. (1996) Band structure and electrical conductivity of disordered layered systems. *Journal of Physics: Condensed Matter*, **8**, 7677.

Xia, K., Kelly, P.J., Bauer, G.E.W., *et al*. (2001). Interface resistance of disordered magnetic multilayers. *Physical Review B*, **63**, 064407.

Yang, Q., Holody, P., Lee, S., *et al*. (1994). Spin flip diffusion length and giant magnetoresistance at low temperatures. *Physical Review Letters*, **72**, 3274.

Zahn, P., Binder, J. and Mertig, I. (2003). Impurity scattering and quantum confinement in giant magnetoresistive systems. *Physical Review B*, **68**, 100403(R).

Zahn, P., Binder, J. and Mertig, I. (2005). Impurity scattering and quantum confinement in giant magnetoresistance systems: a comparative ab initio study. *Physical Review B*, **72**, 174425.

Zahn, P., Binder, J., Mertig, I., *et al*. (1998). Origin of giant magnetoresistance: Bulk or interface scattering. *Physical Review Letters*, **80**, 4309.

Zahn, P., Mertig, I., Richter, M. and Eschrig, H. (1995). Ab initio calculations of the giant magnetoresistance. *Physical Review Letters*, **75**, 2996.

Zeller, R. and Dederichs, P.H. (1979). Electronic-structure of impurities in Cu, calculated self-consistently by Korringa-Kohn-Rostoker Green's-function method. *Physical Review Letters*, **42**, 1713.

Zhang, X-G. and Butler, W.H. (1995). Conductivity of metallic films and multilayers. *Physical Review B*, **51**, 10085–10103.

Zhang, X-G. and Butler, W.H. (2000). A simple treatment of the 'scattering-in' term of the Boltzmann equation for multilayers. *Journal of Applied Physics*, **87**, 5176.

Zhang, S. and Levy, P. (1991). Conductivity perpendicular to plane of multilayered structures. *Journal of Applied Physics*, **69**, 4786.

Zhang, S. and Levy, P.M. (1998). Interplay of the specular and diffuse scattering at interfaces of magnetic multilayers. *Physical Review B*, **57**, 5336.

The Berry Phase in Magnetism and the Anomalous Hall Effect

Patrick Bruno
Max-Planck-Institut für Mikrostrukturphysik, Halle, Germany

1 INTRODUCTION

In 1983, Berry made the surprising discovery that a quantum system adiabatically transported round a closed circuit $\mathcal{C}$ in the space of external parameters acquires, besides the familiar dynamical phase, a nonintegrable phase depending only on the geometry of the circuit $\mathcal{C}$ (Berry, 1984). This Berry phase, which had been overlooked for more than half a century, provides us a very deep insight into the geometric structure of quantum mechanics and gives rise to various observable effects. The concept of the Berry phase has now become a central unifying concept in quantum mechanics, with applications in fields ranging from chemistry to condensed-matter physics (Shapere and Wilczek, 1989; Bohm *et al*., 2003).

The aim of this article is to give an elementary introduction to the Berry phase, and to discuss its various implications in the field of magnetism, where it plays an increasingly important role. The reader is referred to specialized textbooks (Shapere and Wilczek, 1989; Bohm *et al*., 2003) for a more comprehensive presentation of the field of geometrical phases. Particular emphasis will be given to the discussion of the anomalous Hall effect, the theory of which has been considerably renewed recently, on the basis of the concept of Berry phase.

2 PARALLEL TRANSPORT IN GEOMETRY

The importance of the Berry phase stems from the fact that it reveals the intimate geometrical structure underlying quantum mechanics. It is therefore appropriate to start with an introduction to the fundamental concept of *parallel transport* in a purely geometrical context; here, we follow the discussion given by Berry (1990).

This is best illustrated by means of a simple example. Consider a surface Σ (e.g., a plane, a sphere, a cone, etc.) and a vector constrained to lie everywhere in the plane tangent to the surface. Next, we wish to transport the vector on the surface, *without rotating it around the axis normal to the surface*, as illustrated in Figure 1. We are interested, in particular, in the case, in which the arrow is transported round a closed circuit $\mathcal{C} \equiv (1 \rightarrow 2 \rightarrow 3 \rightarrow 1)$. We may encounter two different situations: (i) if the surface is flat,

Handbook of Magnetism and Advanced Magnetic Materials. Edited by Helmut Kronmüller and Stuart Parkin. Volume 1: *Fundamentals and Theory*. ISBN: 978-0-470-02217-7.

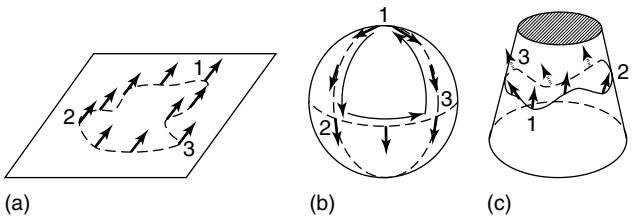

Figure 1. Sketch of parallel transport on (a) a plane, (b) a sphere, and (c) a cone.

as in Figure 1(a), then the arrow always remains parallel to its original orientation, and is, therefore, unchanged after completion of the circuit $\mathcal{C}$; (ii) if, however, the surface Σ is curved as in Figure 1(b) and (c), the arrow, being constrained to lie in the local tangent plane, cannot remain parallel to its original orientation, and after completion of the circuit $\mathcal{C}$, has clearly undergone a rotation by an angle $\theta(\mathcal{C})$, a phenomenon referred to as *anholonomy*.

Let us now formalize this procedure. The arrow is represented by a tangent unit vector $\mathbf{e}^1$, transported along a circuit $\mathcal{C} \equiv \{\mathbf{r}(t)|t = 0 \to T\}$ on the surface. Defining $\mathbf{n}(\mathbf{r})$ as the unit vector normal to the surface at point $\mathbf{r}$, we define a second tangent unit vector $\mathbf{e}^2 \equiv \mathbf{n} \times \mathbf{e}^1$, which is also parallel transported on the surface along $\mathcal{C}$. The three unit vectors $(\mathbf{n}, \mathbf{e}^1, \mathbf{e}^2)$ form an orthonormal reference frame. As $\mathbf{e}^1$ and $\mathbf{e}^2$ are transported, they have to rotate with an angular velocity $\boldsymbol{\omega}$ (to be determined) if the surface is not flat, that is, the equation of motion of $\mathbf{e}^1$ and $\mathbf{e}^2$ is

$$\dot{\mathbf{e}}^r = \boldsymbol{\omega} \times \mathbf{e}^r \quad (r = 1, 2) \tag{1}$$

where the overdot indicates the time derivative. One can easily see that in order to fulfill the requirements that $\mathbf{e}^1$ and $\mathbf{e}^2$ remain tangent unit vectors (i.e., $\mathbf{e}^r \cdot \mathbf{n} = 0$, $(r = 1, 2)$) and never rotate around $\mathbf{n}$ (i.e., $\boldsymbol{\omega} \cdot \mathbf{n} = 0$), the angular velocity has to be given by

$$\boldsymbol{\omega} = \mathbf{n} \times \dot{\mathbf{n}} \tag{2}$$

The law of parallel transport is therefore,

$$\dot{\mathbf{e}}^r = (\mathbf{n} \times \dot{\mathbf{n}}) \times \mathbf{e}^r = -(\mathbf{e}^r \cdot \dot{\mathbf{n}})\mathbf{n} \tag{3}$$

This law can be expressed in a form more suitable for generalization to the case of quantum mechanics, by defining the complex unit vector,

$$\boldsymbol{\phi} \equiv \frac{\mathbf{e}^1 + \mathrm{i}\mathbf{e}^2}{\sqrt{2}} \tag{4}$$

with

$$\boldsymbol{\phi}^\star \cdot \boldsymbol{\phi} = 1 \tag{5}$$

The law of parallel transport now reads,

$$\boldsymbol{\phi}^\star \cdot \dot{\boldsymbol{\phi}} = 0 \tag{6}$$

In order to express the rotation of the unit vectors $(\mathbf{e}^1, \mathbf{e}^2)$ as they move around $\mathcal{C}$, we need to choose a *fixed* local orthonormal frame $(\mathbf{n}(\mathbf{r}), \mathbf{t}^1(\mathbf{r}), \mathbf{t}^2(\mathbf{r}))$ on the surface. The normal unit vector $\mathbf{n}(\mathbf{r})$ is, of course, uniquely determined by the surface, but we have an infinity of possible choices for $\mathbf{t}^1(\mathbf{r})$ (we simply impose that it is a smooth function of $\mathbf{r}$), which corresponds to a gauge freedom; once we have made a choice for $\mathbf{t}^1(\mathbf{r})$, then $\mathbf{t}^2(\mathbf{r})$ is of course uniquely determined. We next define the complex unit vector,

$$\mathbf{u}(\mathbf{r}) \equiv \frac{\mathbf{t}^1(\mathbf{r}) + \mathrm{i}\mathbf{t}^2(\mathbf{r})}{\sqrt{2}} \tag{7}$$

with, of course,

$$\mathbf{u}^\star(\mathbf{r}) \cdot \mathbf{u}(\mathbf{r}) = 1 \tag{8}$$

The relation between the parallel transported frame and the fixed one is expressed as

$$\boldsymbol{\phi}(t) = \exp[-\mathrm{i}\theta(t)]\ \mathbf{u}\,(\mathbf{r}(t)) \tag{9}$$

where $\theta(t)$ is the angle by which $(\mathbf{t}^1, \mathbf{t}^2)$ must be rotated to coincide with $(\mathbf{e}^1, \mathbf{e}^2)$. We obtain the equation satisfied by $\theta(t)$ by inserting the preceding definition in the equation of parallel transport (6), and obtain

$$0 = \boldsymbol{\phi}^\star \cdot \dot{\boldsymbol{\phi}} = -\mathrm{i}\,\dot{\theta}\mathbf{u}^\star \cdot \mathbf{u} + \mathbf{u}^\star \cdot \dot{\mathbf{u}} \tag{10}$$

Since $\mathbf{u}^\star \cdot \mathbf{u} = 1$ and $\mathbf{u}^\star \cdot \dot{\mathbf{u}}$ is imaginary, we get

$$\dot{\theta} = \mathrm{Im}(\mathbf{u}^\star \cdot \dot{\mathbf{u}}) \tag{11}$$

so that

$$\theta(\mathcal{C}) = \mathrm{Im} \oint_{\mathcal{C}} \mathbf{u}^\star \cdot \mathrm{d}\mathbf{u} \tag{12}$$

$$= -\oint_{\mathcal{C}} \mathbf{t}^2 \cdot \mathrm{d}\mathbf{t}^1 \tag{13}$$

If we choose a coordinate system (X_1, X_2) on our surface Σ and define the vector field $\mathbf{A}(\mathbf{r})$ (usually called a *connection*) on Σ as

$$A_i(\mathbf{X}) \equiv \mathrm{Im}\left[u_j^\star(\mathbf{X})\frac{\partial u_j(\mathbf{X})}{\partial X_i}\right] \tag{14}$$

where we have used Einstein's convention of summation over repeated indices, we get

$$\theta(\mathcal{C}) = \oint_{\mathcal{C}} \mathbf{A}(\mathbf{X}) \cdot \mathrm{d}\mathbf{X} \tag{15}$$

which constitutes the *1-form* expression of the anholonomy angle $\theta(\mathcal{C})$. The connection $\mathbf{A}(\mathbf{X})$ depends on our particular gauge choice for $\mathbf{t}^1(\mathbf{X})$: if we make a new choice $\mathbf{t}^{1'}(\mathbf{X})$ which is brought in coincidence with $\mathbf{t}^1(\mathbf{X})$ by a rotation of angle $\mu(\mathbf{X})$, that is, if we make the gauge transformation

$$\mathbf{u}(\mathbf{X}) \rightarrow \mathbf{u}'(\mathbf{X}) \equiv \exp\left(-\mathrm{i}\mu(\mathbf{X})\right) \mathbf{u}(\mathbf{X}) \tag{16}$$

we obtain a new connection

$$A'_i(\mathbf{X}) \equiv \mathrm{Im}\left[u^{\star}_{j'}(\mathbf{X}) \frac{\partial u_{j'}(\mathbf{X})}{\partial X_i}\right] = A_i(\mathbf{X}) - \frac{\partial \mu(\mathbf{X})}{\partial X_i} \tag{17}$$

However, since

$$\oint_{\mathcal{C}} \nabla\mu(\mathbf{r}) \cdot \mathrm{d}\mathbf{r} = \oint_{\mathcal{C}} \mathrm{d}\mu(\mathbf{r}) = 0 \tag{18}$$

we can see that the expression (15) for the anholonomy angle $\theta(\mathcal{C})$ is indeed gauge invariant, as it should be.

A more intuitive understanding of the anholonomy angle may be obtained if we use Stokes' theorem to express it as a surface integral. In doing so, however, we should pay attention to the possible existence of holes in the surface Σ. If this is the case, Σ is said to be nonsimply connected. An example is sketched in Figure 2, where the surface Σ has two holes limited by the contours $\mathcal{C}_1$ and $\mathcal{C}_2$ (hatched areas in Figure 2). Applying Stokes' theorem, we then obtain

$$\theta(\mathcal{C}) = \iint_{\mathcal{S}} B(\mathbf{X}) \mathrm{d}X_1\, \mathrm{d}X_2 \; + \sum_i N_i(\mathcal{C}) \theta(\mathcal{C}_i) \tag{19}$$

where the surface $\mathcal{S}$ is the subset of the surface Σ that is limited by the circuit (dotted area in Figure 2), $\mathcal{C}$, $N_i(\mathcal{C})$ is the winding number of circuit $\mathcal{C}$ around the hole i (i.e., the difference between the number of turns in counterclockwise and clockwise directions),

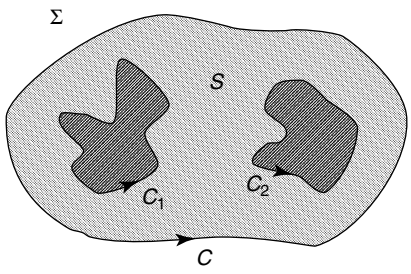

Figure 2. Sketch of a nonsimply connected surface Σ, with two holes (hatched areas), limited by the contours $\mathcal{C}_1$ and $\mathcal{C}_2$.

$$\theta(\mathcal{C}_i) \equiv \oint_{\mathcal{C}_i} \mathbf{A}(\mathbf{X}) \cdot \mathrm{d}\mathbf{X} \tag{20}$$

is the anholonomy angle of circuit $\mathcal{C}_i$ and

$$B(\mathbf{X}) \equiv \left(\frac{\partial A_2}{\partial X_1} - \frac{\partial A_1}{\partial X_2}\right) = \mathrm{Im}\left[\frac{\partial \mathbf{u}^{\star}}{\partial X_1} \cdot \frac{\partial \mathbf{u}}{\partial X_2} - \frac{\partial \mathbf{u}^{\star}}{\partial X_2} \cdot \frac{\partial \mathbf{u}}{\partial X_1}\right] \tag{21}$$

Equation (19) constitutes the *2-form* expression of the anholonomy angle $\theta(\mathcal{C})$. One can see immediately that, unlike the connection $\mathbf{A}(\mathbf{X})$, the quantity $B(\mathbf{X})$ is gauge invariant. The geometrical meaning of $B(\mathbf{X})$ stems from its relation to the *Gaussian curvature* K of Σ at point $\mathbf{X}$, that is,

$$B(\mathbf{X}) \mathrm{d}X_1 \mathrm{d}X_2 = K\, \mathrm{d}S \equiv \frac{\mathrm{d}S}{R_1(\mathbf{X})\, R_2(\mathbf{X})} \tag{22}$$

where $R_1(\mathbf{X})$ and $R_2(\mathbf{X})$ are the principal curvature radii at point $\mathbf{X}$. In the case of the sphere, this is easily checked by explicit calculation, taking the usual spherical angles (θ, φ) as variables (X_1, X_2). Since the Gaussian curvature is related to the solid angle Ω spanned by the normal unit vector $\mathbf{n}$ by

$$B = \frac{\mathrm{d}^2\Omega}{\mathrm{d}X_1\, \mathrm{d}X_2} \tag{23}$$

we finally get

$$\theta(\mathcal{C}) - \sum_i N_i(\mathcal{C}) \theta(\mathcal{C}_i) = \iint_{\mathcal{S}} \frac{\mathrm{d}^2\Omega}{\mathrm{d}X_1\, \mathrm{d}X_2} \mathrm{d}X_1\, \mathrm{d}X_2 = \iint_{\mathcal{S}} \mathrm{d}^2\Omega = \Omega(\mathcal{S}) \tag{24}$$

where $\Omega(\mathcal{S})$ is the solid angle described by the normal vector $\mathbf{n}$ on the surface $\mathcal{S}$. That the above results hold not only for a sphere but also for any surface can be understood easily from the following argument: Equation (3) shows that the trajectory of the parallel transported tangent vectors is entirely determined by the trajectory of the normal unit vector $\mathbf{n}$ along $\mathcal{C}$. We can therefore map the trajectory $\mathcal{C}$ on the surface Σ to a trajectory $\mathcal{C}'$ on the sphere of unit radius S^2, by mapping each point of Σ onto the point of S^2 with the same normal vector $\mathbf{n}$. This implies that we can restrict ourselves to studying the case of parallel transport on S^2 and obtain conclusions valid for parallel transport on any surface Σ.

Let us examine these results for the examples sketched in Figure 1. For the case of the plane, the anholonomy of course trivially vanishes. For the sphere, the anholonomy angle is

given by the solid angle $\Omega(\mathcal{S})$ and is therefore a *geometric* property of the circuit $\mathcal{C}$; this can easily be checked through the following experiment: take your pen in you left hand, and raise your arm above you head, the pen pointing in front of you; then rotate your arm until it is horizontal in front of you, without twisting your hand; then rotate it by 90° to your left; finally rotate your arm back to the vertical (pay attention to never twist your hand in whole process); the pen is now pointing to your left, that is, it has rotated by $4\pi/8 = \pi/2$. For the case of the cone, the Gaussian curvature vanishes everywhere (a cone can be fabricated by rolling a sheet of paper), so that the anholonomy angle is in fact a *topological* property of the circuit $\mathcal{C}$, given by the winding number of the circuit $\mathcal{C}$ around the cone (multiplied by the solid angle of the cone).

3 PARALLEL TRANSPORT IN CLASSICAL MECHANICS: FOUCAULT'S PENDULUM AND THE GYROSCOPE

Let us now consider the famous experiment of Foucault's pendulum that demonstrated the earth's rotation. If the pendulum trajectory is originally planar (swinging oscillation), the vertical component of the angular momentum vanishes. Since forces exerted on the pendulum (gravity and wire tension) produce a vanishing vertical torque, the vertical component of the angular momentum has to be conserved. The absence of any vertical torque imposes that the swing plane has to follow a law of parallel transport as the direction of gravity slowly changes because of the earth's rotation. Therefore, within 1 day it rotates by an angle equal to the solid angle described by the vertical $2\pi(1 - \cos\theta)$, where θ is the colatitude.

The parallel transport may also affect the phase of the periodic motion of the Foucault pendulum or the rotation phase of a gyroscope. Let us consider a gyroscope whose rotation axis is constrained to remain parallel to the axis $\mathbf{n}$; let us now move the rotation axis $\mathbf{n}$ round a closed circuit $\mathcal{C}$. The rotation angle of the gyroscope will be the sum of the *dynamic rotation angle* ωt and the *geometric anholonomy angle* $\theta(\mathcal{C})$ equal to the solid angle described by the rotation axis. Thus if we have two synchronous gyroscopes and perform different circuits with the rotation axes, they will eventually be dephased with respect to each other, an effect that could easily be observed by stroboscopy. This geometric anholonomy angle is known as *Hannay's angle* (Hannay, 1985; Berry, 1985). If the Foucault pendulum is given a conical oscillation instead of a planar swing, then we have exactly the same situation as described in the preceding text for the gyroscope, and the rotation angle will have an anholonomy excess angle given by the solid angle described by the vertical. Thus, two identical Foucault pendula (i.e., of same length) with circular oscillations in opposite directions will have slightly different oscillation frequencies and will progressively get dephased with respect to each other. The swinging motion of the usual Foucault may be viewed as the superposition of circular motions in opposite directions, so that the rotation of the swinging plane may be viewed as resulting from the previously mentioned frequency shift.

4 PARALLEL TRANSPORT IN QUANTUM MECHANICS: THE BERRY PHASE

Let us now consider a quantum mechanical system described by a Hamiltonian controlled by a set of external parameters $(R_1, R_2, \ldots)$, which we describe collectively as a vector $\mathbf{R}$ in some abstract parameter space. Physically, the external parameters may be magnetic or electric fields, and so on. For each value $\mathbf{R}$ of the external parameters, the Hamiltonian $H(\mathbf{R})$ has eigenvalues $E_n(\mathbf{R})$ and eigenvectors $|n(\mathbf{R})\rangle$ satisfying the independent Schrödinger equation, that is,

$$H(\mathbf{R})\,|n(\mathbf{R})\rangle = E_n(\mathbf{R})\,|n(\mathbf{R})\rangle \tag{25}$$

The eigenvectors $|n(\mathbf{R})\rangle$ are defined up to an arbitrary phase, and there is *a priori* no particular phase relation between eigenstates corresponding to different values of the parameter $\mathbf{R}$. We make a particular choice for the phase of the eigenstates, simply requiring that $|n(\mathbf{R})\rangle$ varies smoothly with $\mathbf{R}$ in the region of interest. It may happen that the eigenstates we have chosen are not single-valued functions of $\mathbf{R}$. If this happens, special care must be given to this point.

Let us perform an adiabatic closed circuit $\mathcal{C} \equiv \{\mathbf{R}(t)|t = 0 \to T\}$ in the parameter space. The adiabatic theorem (Messiah, 1991) tells us that if the rate of variation of the external parameters is low enough, a system that is initially in the nth stationary state $|n\rangle$ (assumed nondegenerate) of the Hamiltonian will remain continuously in the state $|n\rangle$. The condition of adiabaticity is that the stationary state under consideration remains nondegenerate, and the rate of variation of the Hamiltonian is low enough to make the probability of transition to another state $|m\rangle$ vanishingly small, that is,

$$\hbar|\langle m|\dot{H}|n\rangle| \ll |E_m - E_n|^2 \quad \forall\, m \neq n \tag{26}$$

Then of course, if one performs a closed adiabatic circuit $\mathcal{C}$, the system has to return to its original state.

Berry (1984) asked the following question: what will be the phase of the state after completion of the circuit $\mathcal{C}$? It may be difficult at first sight to realize that this question may be of any interest. Indeed, the expectation value of any observable quantity A,

$$\langle A\rangle \equiv \langle\psi|A|\psi\rangle \tag{27}$$

does not depend on the phase of $|\psi\rangle$. This lack of interest is certainly the main reason why the Berry phase was (almost) completely overlooked for more than half a century of quantum mechanics. One should mention here that there has been, prior to Berry's seminal paper (Berry, 1984), a number of precursor works on effects related to the Berry phase, including, notably, Pancharatnam's work on optical polarization (Pancharatnam, 1956), Aharonov and Bohm's work on the phase due to the electromagnetic potential vector (Aharonov and Bohm, 1959), and Mead and Truhlar's work on the molecular Aharonov–Bohm effect in the Born–Oppenheimer theory of molecular vibrations (Mead and Truhlar, 1979). However, Berry (1984) was the first to point out the geometric significance and the generality of the adiabatic geometric phase. After the publication of Berry's paper, the generality and the fecundity of this new concept has been widely recognized, soon leading to a considerable amount of developments (Shapere and Wilczek, 1989; Bohm *et al*., 2003).

So, following Berry, taking

$$|\psi(t=0)\rangle \equiv |n(\mathbf{R}(t=0))\rangle \tag{28}$$

we express the state $|\psi(t)\rangle$ at a latter time t as

$$|\psi(t)\rangle \equiv \exp\left[\frac{-\mathrm{i}}{\hbar}\int_0^t \mathrm{d}t'\, E_n(\mathbf{r}(t'))\right]|\phi_n(t)\rangle \tag{29}$$

that is, we introduce an auxiliary wave function $|\phi_n(t)\rangle$ with a zero dynamical phase. Using the time-dependent Schrödinger equation,

$$\mathrm{i}\hbar|\dot{\psi}(t)\rangle = H(t)|\psi(t)\rangle \tag{30}$$

and projecting it on $\langle\psi(t)|$, we get

$$\begin{aligned} 0 &= \langle\psi(t)|\left(H(t) - \mathrm{i}\hbar\frac{\partial}{\partial t}\right)|\psi(t)\rangle \\ &= \langle\phi_n(t)|\dot{\phi}_n(t)\rangle \end{aligned} \tag{31}$$

where we have used the relation

$$\langle\psi(t)|H(t)|\psi(t)\rangle = E_n(t) \tag{32}$$

which follows from the adiabatic theorem. Equation (31) shows that the wave function $|\phi_n(t)\rangle$ obeys a quantum mechanical analog of the law of parallel transport (6).

In complete analogy with the problem of parallel transport on a surface, we now express the parallel transported state $|\phi_n(t)\rangle$ in terms of the fixed eigenstates $|n(\mathbf{R})\rangle$ as

$$|\phi_n(t)\rangle \equiv \exp((\mathrm{i}\gamma_n(t))\,|n(\mathbf{R})\rangle \tag{33}$$

where the phase $\gamma_n(t)$ plays the same role as the angle $-\theta(t)$ for the problem of parallel transport on a surface. We then immediately get the equation of motion of $\gamma_n(t)$, that is,

$$\dot{\gamma}_n(t) = \mathrm{i}\langle n|\dot{n}\rangle = -\mathrm{Im}\langle n(\mathbf{R}(t))|\frac{\mathrm{d}}{\mathrm{d}t}n(\mathbf{R}(t))\rangle \tag{34}$$

which is analogous to equation (11).

Finally, the answer to the question originally asked by Berry is

$$|\psi(T)\rangle = \exp\left[\mathrm{i}(\delta_n + \gamma_n(\mathcal{C}))\right]|\psi(0)\rangle \tag{35}$$

where

$$\delta_n \equiv \frac{-1}{\hbar}\int_0^T E_n(\mathbf{R}(t))\,\mathrm{d}t \tag{36}$$

is the dynamical phase, and

$$\gamma_n(\mathcal{C}) \equiv -\mathrm{Im}\left[\oint_{\mathcal{C}}\langle n(\mathbf{R})|\partial_{\mathbf{R}}|n(\mathbf{R})\rangle\cdot\mathrm{d}\mathbf{R}\right] - \alpha_n(\mathcal{C}) \tag{37}$$

is the Berry phase. The last term in the latter equation arises when the states $|n(\mathbf{R})\rangle$ are not a single-valued function of $\mathbf{R}$ in the region of interest of the parameter space and is given by

$$\alpha_n(\mathcal{C}) = \mathrm{i}\ln\left[\langle n(\mathbf{R}(0))|n(\mathbf{R}(T))\rangle\right] \tag{38}$$

Note that this term was absent in Berry's original paper (Berry, 1984), because the basis states $|n(\mathbf{R})\rangle$ were assumed to be single valued. We shall omit this term in the subsequent text, and consider only the case of single-valued basis states.

We note the very close analogy between the results obtained for quantum and classical systems. The dynamical phase of a quantum system is analogous to the rotation angle ωT in classical mechanics, whereas the Berry phase is analogous to Hannay's angle (they both arise from the anholonomy of parallel transport).

Defining the connection $\mathbf{A}^n(\mathbf{R})$ as

$$\mathbf{A}^n(\mathbf{R}) \equiv -\mathrm{Im}\left[\langle n(\mathbf{R})|\partial_{\mathbf{R}}n(\mathbf{R})\rangle\right] \tag{39}$$

we reexpress the Berry phase as

$$\gamma_n(\mathcal{C}) \equiv \oint_{\mathcal{C}} \mathbf{A}^n(\mathbf{R}) \cdot \mathrm{d}\mathbf{R} \tag{40}$$

which constitutes the 1-form expression of the Berry phase. The latter clearly depends only on the geometry of the circuit $\mathcal{C}$. The connection $\mathbf{A}^n(\mathbf{R})$ is not gauge invariant – if we make a new choice for the phase of the reference state, that is,

$$|n(\mathbf{R})\rangle' = \exp(-i\,\mu(\mathbf{R}))|n(\mathbf{R})\rangle \tag{41}$$

with a single-valued function $\mu(\mathbf{R})$, we obtain a different connection

$$\mathbf{A}^{n\prime}(\mathbf{R}) = \mathbf{A}^n(\mathbf{R}) + \partial_{\mathbf{R}}\mu(\mathbf{R}) \tag{42}$$

However, the Berry phase $\gamma_n(\mathcal{C})$ is gauge invariant, as it should be.

As for the geometric parallel transport on surfaces, we may obtain a gauge-invariant and more transparent expression by transforming the preceding result to a surface integral using Stokes' theorem. Here too, we have to pay attention to the existence of holes in the parameter space – if the parameter space is multiply connected, and if the circuit $\mathcal{C}$ cannot be continuously deformed to a point (i.e., it is not *homotopic* to a point), we must take into account terms associated with the winding of $\mathcal{C}$ around holes of the parameter space.

The formulation of the Berry phase as a surface integral in a form that is independent of a particular choice of coordinates of the parameter space generally requires the use of mathematical formalism of differential forms (Bohm *et al*., 2003), which is beyond the scope of this article. We can nevertheless obtain a useful result without resorting to any advanced mathematics if we make a suitable choice of coordinates of the parameter space. Let us choose a surface $\mathcal{S}$ in the parameter space which is bound by the circuit $\mathcal{C}$, and a parameterization (R_1, R_2) of the surface $\mathcal{S}$. Using Stokes' theorem, we then get

$$\gamma_n(\mathcal{C}) = \iint_{\mathcal{S}} B^n(\mathbf{R})\mathrm{d}R_1\,\mathrm{d}R_2 + \sum_i N_i(\mathcal{C})\gamma_n(\mathcal{C}_i) \tag{43}$$

where $\mathcal{C}_i$ are the circuits bounding the holes of the parameter space and N_i, the corresponding winding numbers of the circuit $\mathcal{C}$ around them, and where

$$\begin{aligned} B^n(\mathbf{R}) &\equiv \left(\partial_{R_1} A_2^n - \partial_{R_2} A_1^n\right) \\ &= -\mathrm{Im}\left[\langle \partial_{R_1} n(\mathbf{R})|\partial_{R_2} n(\mathbf{R})\rangle - \langle \partial_{R_2} n(\mathbf{R})|\partial_{R_1} n(\mathbf{R})\rangle\right] \end{aligned} \tag{44}$$

is the *Berry curvature*. In the case where the parameter space is three-dimensional, we can use the familiar language of vector calculus, as in electrodynamics, and Stokes' theorem yields

$$\gamma_n(\mathcal{C}) = \iint_{\mathcal{S}} \mathbf{B}^b(\mathbf{R}) \cdot \mathbf{n}\,\mathrm{d}S + \sum_i N_i(\mathcal{C})\gamma_n(\mathcal{C}_i) \tag{45}$$

$$\begin{aligned} \mathbf{B}^n(\mathbf{R}) &\equiv \nabla \times \mathbf{A}^n(\mathbf{R}) \\ &= -\mathrm{Im}\left[\langle \nabla n(\mathbf{R})| \times |\nabla n(\mathbf{R})\rangle\right] \qquad (46) \\ &= -\mathrm{Im}\sum_{m\neq n} \langle \nabla n(\mathbf{R})|m(\mathbf{R})\rangle \times \langle m(\mathbf{R})|\nabla n(\mathbf{R})\rangle \qquad (47) \end{aligned}$$

Making use of the relation

$$\langle m|\nabla n\rangle = \frac{\langle m|\nabla H|n\rangle}{E_n - E_m} \tag{48}$$

one eventually gets

$$\begin{aligned} \mathbf{B}^n(\mathbf{R}) = -\mathrm{Im}&\sum_{m\neq n} \\ &\times \frac{\langle n(\mathbf{R})|\nabla H(\mathbf{R})|m(\mathbf{R})\rangle \times \langle m(\mathbf{R})|\nabla H(\mathbf{R})|n(\mathbf{R})\rangle}{(E_m(\mathbf{R}) - E_n(\mathbf{R}))^2} \end{aligned} \tag{49}$$

Obviously, the Berry curvature is gauge invariant. As the notation suggests, the Berry curvature $\mathbf{B}^n$ plays the role of a magnetic field in the space of parameters, whose vector potential is the Berry connection $\mathbf{A}^n$.

The energy denominator in equation (49) shows that if the circuit $\mathcal{C}$ lies in a region of the parameter space that is close to a point $\mathbf{R}^\star$ of twofold degeneracy involving the two states labeled $+$ and $-$, the corresponding Berry connections $\mathbf{B}_+$ and $\mathbf{B}_-$ are dominated by the term involving the denominator $(E_+ - E_-)^2$ and the contribution involving other states can be neglected. So, to first order in $\mathbf{R} - \mathbf{R}^\star$, one has

$$\begin{aligned} \mathbf{B}_+(\mathbf{R}) = -\mathbf{B}_-(\mathbf{R}) = -\mathrm{Im}&\\ &\times \frac{\langle +(\mathbf{R})|\nabla H(\mathbf{R}^\star)| -(\mathbf{R})\rangle \times \langle -(\mathbf{R})|\nabla H(\mathbf{R}^\star)| +(\mathbf{R})\rangle}{(E_+(\mathbf{R}) - E_-(\mathbf{R}))^2} \end{aligned} \tag{50}$$

The general form of the Hamiltonian $H(\mathbf{R})$ of a two-level system is (without loss of generality, we may take $\mathbf{R}^\star = 0$)

$$H(\mathbf{R}) \equiv \frac{1}{2}\begin{pmatrix} Z & X - \mathrm{i}Y \\ X + \mathrm{i}Y & -Z \end{pmatrix} \tag{51}$$

with eigenvalues

$$E_+(\mathbf{R}) = -E_-(\mathbf{R}) = \frac{1}{2}R \tag{52}$$

This illustrates a theorem due to von Neumann and Wigner (1929), stating that it is necessary to adjust three independent parameters in order to obtain a twofold degeneracy from a Hermitian matrix. The gradient of the Hamiltonian is

$$\nabla H = \frac{1}{2}\boldsymbol{\sigma} \tag{53}$$

where $\boldsymbol{\sigma}$ is the vector matrix whose components are the familiar Pauli matrices. Simple algebra then yields

$$\mathbf{B}_+ = -\mathbf{B}_- = -\frac{\mathbf{R}}{R^3} \tag{54}$$

The preceding Berry curvature $\mathbf{B}_\pm$ is the magnetic field in parameter space generated by a Dirac magnetic monopole (Dirac, 1931) of strength $\mp 1/2$. Thus, the Berry phase $\gamma_\pm(\mathcal{C})$ of a circuit $\mathcal{C}$ is given by the flux of the monopole through the surface $\mathcal{S}$ subtended by the circuit $\mathcal{C}$, which, by Gauss' theorem, is nothing but $\mp\Omega(\mathcal{C})$, where $\Omega(\mathcal{C})$ is the solid angle described by $\mathbf{R}$ along the circuit $\mathcal{C}$.

The corresponding vector potential (or Berry connection) $\mathbf{A}_\pm$ (not calculated here) has an essential singularity along a line (Dirac string) ending at the origin and carrying a 'flux' of magnitude $\pm 2\pi$. The position of the Dirac string can be moved (but not removed!) by a gauge transformation, as sketched in Figure 3. If the Dirac string happens to cross the surface $\mathcal{S}$, the Berry phase remains unchanged (modulo 2π), so that the result is indeed gauge invariant.

5 EXAMPLES OF BERRY PHASE

5.1 Spin in a magnetic field

As the first example, we consider the case of a single spin (of magnitude S) in a magnetic field, which is both the most immediate application of the formal theory presented in the preceding text and one of the most frequent cases encountered in experimentally relevant situations. The Hamiltonian considered is

$$H(\mathbf{b}) \equiv -\mathbf{b}\cdot\mathbf{S} \tag{55}$$

with the magnetic field $\mathbf{b}$ being the external parameter. The eigenvalues are

$$E_n(\mathbf{b}) = -nb \tag{56}$$

with $2n$ integer and $-S \le n \le S$. For $\mathbf{b} = 0$, the $2S+1$ eigenstates are degenerate, so the circuit $\mathcal{C}$ has to avoid the origin. The Berry connection can be calculated using equation (49) and well-known properties of the spin operators, and one gets

$$\mathbf{B}^n(\mathbf{b}) = -n\frac{\mathbf{b}}{b^3} \tag{57}$$

which is the 'magnetic field' (in parameter space) of a monopole of strength $-n$, located at the origin. The Berry phase is thus

$$\gamma_n(\mathcal{C}) = -n\Omega(\mathcal{C}) \tag{58}$$

where $\Omega(\mathcal{C})$ is the solid angle described by the field $\mathbf{b}$ along the circuit $\mathcal{C}$. For $S = 1/2$, this of course reduces to the result obtained in the preceding text for the two-level problem. Note that the Berry phase $\gamma_n(\mathcal{C})$ depends only on the quantum number n (projection of $\mathbf{S}$ on $\mathbf{b}$) and not on the magnitude S of the spin. Note also, that while $H(\mathbf{b})$ is the most general Hamiltonian for a spin $S = 1/2$, this is not the case for a spin $S \ge 1$; in the latter case, we restrict ourselves to a subspace of the full parameter space. If a more general Hamiltonian and a wider parameter space is considered, the simple result obtained in the preceding text would not hold any more.

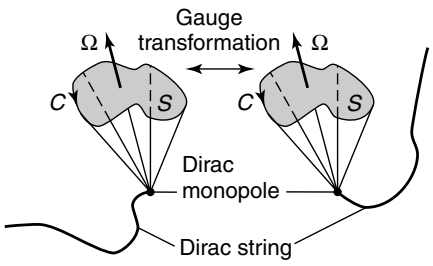

Figure 3. Sketch showing the flux of the Dirac monopole through the circuit $\mathcal{C}$, and the effect of a gauge transformation.

5.2 Aharonov–Bohm effect

Another example that is of great interest, both conceptually and experimentally is the well-known Aharonov–Bohm effect (Aharonov and Bohm, 1959). We follow here the presentation of the Aharonov–Bohm effect given by Berry (1984).

Let us consider the situation depicted in Figure 4, namely, a magnetic field confined in a tube with flux Φ and a box, located at $\mathbf{R}$, in which particles of charge q are confined. The magnetic field vanishes everywhere outside the flux tube and, in particular, inside the box. Let $\mathbf{A}(\mathbf{r})$ be the corresponding vector potential. The latter generally does not vanish in the regions of vanishing field (unless the flux Φ is a multiple of the flux quantum $\Phi_0 \equiv h/e$).

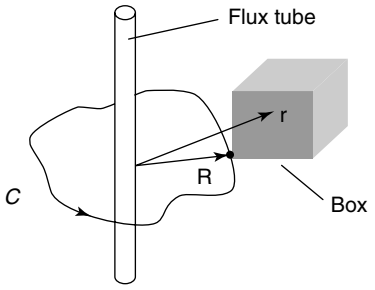

Figure 4. Sketch describing the Aharonov–Bohm effect.

Let the Hamiltonian describing the particles in the box be $H(\mathbf{p}, \mathbf{r}-\mathbf{R})$; the corresponding wave functions, for a vanishing vector potential, are of the form $\psi_n(\mathbf{r}-\mathbf{R})$, with energies E_n independent of $\mathbf{R}$. When the flux is nonzero, we can choose as basis states $|n(\mathbf{R})\rangle$, satisfying

$$H(\mathbf{p}-q\mathbf{A}(\mathbf{r}), \mathbf{r}-\mathbf{R})|n(\mathbf{R})\rangle = E_n|n(\mathbf{R})\rangle \tag{59}$$

whose solutions are given by

$$\langle \mathbf{r}|n(\mathbf{R})\rangle = \exp\left[\frac{\mathrm{i}q}{\hbar}\int_{\mathbf{R}}^{\mathbf{r}} \mathrm{d}\mathbf{r}'\cdot\mathbf{A}(\mathbf{r}')\right]\psi_n(\mathbf{r}-\mathbf{R}) \tag{60}$$

where the integral is performed along a path contained in the box. The energies E_n are independent of the vector potential, because it is always possible to find a gauge transformation that would make it zero in the box (but not everywhere in space!).

The Hamiltonian depends on the position $\mathbf{R}$ of the box via the vector potential. Thus, our parameter space, in this example, is nothing but the real space, with exclusion of the region of the flux tube. If we transport the box around a closed circuit $\mathcal{C}$, the Berry phase will be given by

$$\gamma_n(\mathcal{C}) \equiv \oint_{\mathcal{C}} \mathbf{A}^n(\mathbf{R})\cdot\mathrm{d}\mathbf{R} \tag{61}$$

with the Berry connection

$$\begin{aligned}\mathbf{A}^n(\mathbf{R}) &\equiv -\mathrm{Im}\left[\langle n(\mathbf{R})|\partial_{\mathbf{R}} n(\mathbf{R})\rangle\right] \\ &= -\mathrm{Im}\iiint \mathrm{d}^3\mathbf{r}\psi_n^\star(\mathbf{r}-\mathbf{R}) \\ &\quad\times\left[\frac{-\mathrm{i}q}{\hbar}\mathbf{A}(\mathbf{R})\psi_n(\mathbf{r}-\mathbf{R}) + \partial_{\mathbf{R}}\psi_n(\mathbf{r}-\mathbf{R})\right] \\ &= \frac{q}{\hbar}\mathbf{A}(\mathbf{R})\end{aligned} \tag{62}$$

The Berry curvature $\mathbf{B}^n(\mathbf{R}) = \nabla\times\mathbf{A}^n(\mathbf{R}) = (q/\hbar)\mathbf{B}(\mathbf{R})$ is just given by the magnetic field and vanishes everywhere outside the flux tube. But because the tube region is excluded from the allowed parameter space, the latter is multiply connected, and the Berry phase is purely topological, given by the winding number $N(\mathcal{C})$ of the circuit $\mathcal{C}$ around the flux tube, and by the flux Φ

$$\gamma_n(\mathcal{C}) = 2\pi N(\mathcal{C})\frac{q}{h}\Phi \tag{63}$$

The Aharonov–Bohm effect was confirmed experimentally by electron holography by Tonomura *et al*. (1986) in a configuration where the magnetic field truly vanishes, and plays an outstanding role in the physics of mesoscopic systems; here, it gives rise to conductance oscillations and to persistent currents in mesoscopic metallic rings threaded by a magnetic flux (Olariu and Popescu, 1985; Aronov and Sharvin, 1987; Washburn and Webb, 1992).

5.3 Thomas precession and spin-orbit coupling

In relativistic kinematics, space–time coordinates perceived by observers in different inertial frames are related to each other by Lorentz transformations. The latter may consist of pure Lorentz boosts, pure rotations, or combinations of a boost and a rotation. As is well known, Lorentz boosts with different velocity axes do not commute with each other, and the product of two pure Lorentz boosts with different axes is not a pure Lorentz boost but the product of a Lorentz boost and a rotation. This effect gives rise to the phenomenon of Thomas precession (Thomas, 1926, 1927), which is one of the contributions to the spin-orbit coupling (the other contribution being the result of the Lorentz transformation of the electric field).

Recently, it has been pointed out that the Thomas precession may be understood as an anholonomy associated with the parallel transport on the manifold Lorentz boosts (Jordan, 1988; Aravind, 1997; Rhodes and Semon, 2004). This important result is briefly outlined here.

For simplicity, we restrict to Lorentz boosts in the xy plane and rotations around the z axis. A Lorentz boost of velocity $\mathbf{v}\equiv(v_x, v_y)$ can be characterized by a point (ct, x, y) on the hyperboloid $(ct)^2-(x^2+y^2)=1$ $(t\geq 0)$, such that $(v_x, v_y) = (x/t, y/t)$. Thus a closed trajectory in the space of Lorentz boosts is characterized by a closed loop on the hyperboloid. One can show (Jordan, 1988; Aravind, 1997; Rhodes and Semon, 2004) that upon such a closed loop the system does not return to the initial inertial frame but to an inertial frame that differs from the initial one by a rotation around the z axis, of angle $\theta = -A$, where A is the area enclosed by the loop on the hyperboloid. This rotation is precisely the Thomas precession (Thomas, 1926, 1927), the geometrical nature of which appears clearly from the present formulation. For a quantum spin, a Berry phase

results from the Thomas precession. Another contribution (for charged particles) arises from the Lorentz transformation of the electric field and combines with the Thomas precession to give the familiar spin-orbit coupling of the electron.

For velocities much smaller than the velocity of light, the Berry phase corresponding to a closed loop $\mathcal{C}$ in the (v_x, v_y) plane due to the spin-orbit coupling (including both the Thomas precession contribution and the Lorentz transformation of the electric field) is given by the simple expression

$$\gamma_\sigma(\mathcal{C}) = -\sigma \oint_{\mathcal{C}} \frac{\mathbf{v} \times \mathrm{d}\mathbf{v}}{4c^2} = -\sigma \frac{A(\mathcal{C})}{4c^2} \tag{64}$$

with $\sigma = \pm 1$ for $s_z = \pm 1/2$, respectively, and where $A(\mathcal{C})$ is the area swept in the (v_x, v_y) plane.

The geometric character of the spin-orbit coupling appears clearly from the preceding expression. For an electron in a periodic orbit, the Berry phase accumulates linearly in time, which amounts to an additional term in the dynamical phase, that is, to the spin-orbit coupling term of the Hamiltonian, which is given by the following expression (for velocities much smaller than c):

$$H_{\mathrm{SO}} = \hbar \mathbf{s} \cdot \left(\frac{\mathbf{v} \times \mathbf{a}}{2c^2} \right) \tag{65}$$

where **a** is the acceleration.

The preceding formulation of the spin-orbit coupling allows us to understand qualitatively why electrons with group velocities much smaller than c may nevertheless have a spin-orbit splitting, several orders of magnitude larger than that of free electrons with equivalent velocity. In a quasiclassical picture, the motion of electrons in a solid may be viewed as consisting mostly of periodic orbital motion around nuclei, combined with a hopping interatomic motion. The hopping frequency from atom to atom, which determines the average electron velocity, is typically much smaller than the frequency of the intra-atomic orbital motion around the nuclei. The Berry phase accumulated between two successive hopping events, determined essentially by this intra-atomic orbital motion, is considerably larger than the one accumulated in the interatomic hopping motion, so that the effective spin-orbit coupling of Bloch electrons in a solid may be enhanced by a factor of the order of 10^4 as compared to the spin-orbit coupling of free electrons.

5.4 Experimental observations of the Berry phase for a single spin

Let us now discuss how the Berry phase could be detected experimentally. As already mentioned, this is not immediately clear since the expectation value of any observable would be independent of the phase of the system. As always, when considering phases, some kind of interference has to be observed. There are various ways in which this can be done.

- Berry's original proposal (Berry, 1984) was as follows: A monoenergetic polarized beam of particles in the spin state n along the magnetic field **b** is split into two beams. For one of the beams, the field **b** is kept constant in magnitude and direction, whereas for the second beam, the magnitude of **b** is kept constant and its direction is slowly varied along a circuit $\mathcal{C}$ subtending a solid angle Ω. The two beams are then recombined to interfere, and the intensity is monitored as a function of the solid angle Ω. Since the dynamical phase is the same for both beams, the phase difference between the two beams is given purely by the Berry phase (plus a propagation factor is determined by the phase shift for $\Omega = 0$). Although conceptually possible, it seems unlikely that such an experiment would be feasible in practice. In particular, it would be extremely difficult to ensure that the difference between the dynamical phases of the two beams is smaller than the Berry phase one wants to detect, unless some physical principle enforces it. This kind of experiment may be said to be of type 'one state – two Hamiltonians'. This kind of experiment, being based on interferences, is truly quantum mechanical.
- An alternative approach, more amenable to an experimental test, is to prepare the system into a superposition of two states, that is,

$$|\psi(t=0)\rangle = \alpha |n(\mathbf{R}(t=0))\rangle + \beta |m(\mathbf{R}(t=0))\rangle \tag{66}$$

with $m = n - 1$ and $|\alpha|^2 + |\beta|^2 = 1$, for example, by polarizing it along a direction perpendicular to the field **b**. The orientation of the transverse component of the spin is given by the angle $\theta(t=0) \equiv \arg(\beta) - \arg(\alpha)$. The spin of course precesses at around **b** at the Larmor frequency $\omega_L = b/\hbar$. After completion of the circuit $\mathcal{C}$, the system state has evolved to

$$|\psi(T)\rangle = \alpha \exp[\mathrm{i}(\delta_n + \gamma_n(\mathcal{C}))] |n(\mathbf{R}(t=0))\rangle + \beta \exp[\mathrm{i}(\delta_m + \gamma_m(\mathcal{C}))] |m(\mathbf{R}(t=0))\rangle \tag{67}$$

and the polarization angle has evolved to $\theta(T) = \theta(t=0) + \Delta\theta$ with

$$\Delta\theta = \Delta\theta_{\mathrm{dyn}} + \Delta\theta_{\mathrm{B}} \tag{68}$$

$$\Delta\theta_{\mathrm{dyn}} \equiv \delta_m - \delta_n = \omega_L T \tag{69}$$

$$\Delta\theta_{\mathrm{B}} \equiv \gamma_m(\mathcal{C})) - \gamma_n(\mathcal{C})) \tag{70}$$

Here the angle $\Delta\theta_{\mathrm{dyn}}$ gives the polarization rotation due to the Larmor precession (dynamic phase), while $\Delta\theta_{\mathrm{B}}$ is the polarization rotation due to the Berry phase accumulated along the circuit $\mathcal{C}$. Thus by investigating how the polarization varies as the circuit $\mathcal{C}$ is modified, the Berry phase can be detected. Such an experiment may be said to be of the type 'two states – one Hamiltonian'. Note that this type of experiment can be interpreted in purely classical terms (Cina, 1986) (it bears a clear analogy to the rotation of the swinging plane of the Foucault pendulum); this is related to the fact that only Berry phase differences between two states, and not the absolute Berry phase of a given state, are detected.

- A further possibility consists in repeating the circuit $\mathcal{C}$ in a periodic manner. Thus, the Berry phase is accumulated linearly in time, just as the dynamical phase, and leads to an apparent energy shift for the state n,

$$\Delta E_n = \frac{\hbar}{T}\gamma_n(\mathcal{C}) \tag{71}$$

which gives rise to an observable shift of the transition between two levels n and m. Such an experiment too is of type 'two states – one Hamiltonian'. It can also be interpreted in classical terms and has close analogy to the period shift of a Foucault pendulum with circular oscillation.

The Berry phase has been observed for neutrons ($S = 1/2$) by Bitter and Dubbers (1987), who used the experiment shown in Figure 5. A slow ($v \simeq 500\,\mathrm{ms}^{-1}$), monochromatic beam of neutrons polarized ($P \simeq 0.97$) along an axis perpendicular to the beam axis z is injected in a cylinder with a helical magnetic field with longitudinal component B_z and transverse component B_1 making a right-handed turn of 2π. Depending on the values of B_z and B_1, various values of the solid angle Ω may be achieved.

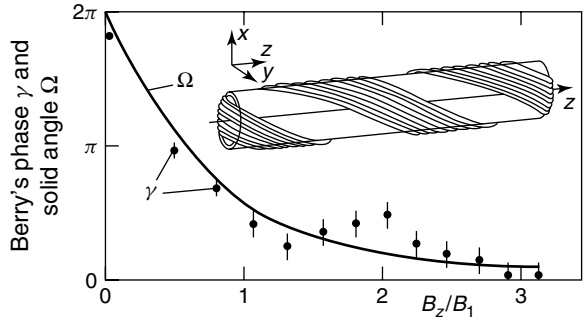

Figure 5. Measurement of Berry phase of neutrons. The inset shows the arrangement of the coil giving a helical field; the neutron beam is along z; length: 40 cm, diameter: 8 cm; an axial coil (not shown) produces a field B_z. The curve shows the Berry phase (more precisely $\gamma_{-1/2} - \gamma_{1/2}$) and solid angle Ω as a function of the ratio B_z/B_1. (Reproduced from Bitter & Dubber 1987, with permission from the American Physical Society. © 1987.)

After having traversed the cylinder, the polarization of the beam is measured, from which the Berry phase can be extracted. The comparison of the measured Berry phase (or more precisely the difference of Berry phase between states $S_z = +1/2$ and $S_z = -1/2$) and of the solid angle is shown in Figure 5. The observation is in good agreement with the theoretical prediction.

The Berry phase has also been confirmed for photons ($S = 1$) by Tomita and Chiao (1986) using an experimental procedure proposed by Chiao and Wu (1986); for protons ($S = 1/2$) by Suter, Chingas, Harris and Pines (1987) following a proposal of Moody, Shapere and Wilczek (1986); and for ^{35}Cl nuclei by Tycko (1987).

6 ANOMALOUS HALL EFFECT

The Berry phase plays an important role in the modern understanding of the anomalous Hall effect. Therefore this problem will be discussed here in a detailed manner.

6.1 Brief historical sketch and survey of the state of the art

The history of the anomalous Hall effect has been quite a turbulent one, rich in misconceptions and controversies, and the reader approaching the corresponding literature without a sufficient overview of the historical developments might easily get lost in details of controversial debates. Therefore, it appears useful to briefly sketch the main stages in the historical development of the field.

Soon after his discovery of the Hall effect of normal metals subject to an external magnetic field (Hall, 1880a), Erwin H. Hall discovered that ferromagnetic metals may exhibit a spontaneous (i.e., in the absence of an external magnetic field) Hall effect (Hall, 1880b, 1881). Toward the end of the nineteenth century and in the first half of the twentieth century, extensive experimental and phenomenological investigations of the anomalous Hall effect of ferromagnetic metals and alloys were carried out (Kundt, 1893; Smith, 1910; Perrier, 1930a,b; Pugh, Rostoker and Schindler, 1950; Smit and Volger, 1953; Pugh and Rostoker, 1953).

From these early studies, the following phenomenological description emerged. In linear response regime, the electric field $\mathbf{E}$ is linearly related to the current density $\mathbf{j}$ by

$$\mathbf{E} = \boldsymbol{\rho}\mathbf{j} \tag{72}$$

with a resistivity tensor $\boldsymbol{\rho}$ (for a magnetic field and/or magnetization parallel to the z-axis) of the form

$$\boldsymbol{\rho} = \begin{pmatrix} \rho_{xx} & \rho_{xy} & 0 \\ -\rho_{xy} & \rho_{xx} & 0 \\ 0 & 0 & \rho_{zz} \end{pmatrix} \tag{73}$$

The Hall effect is given by the antisymmetric part of the resistivity tensor, giving rise to a voltage that is transverse to both the current and the magnetic field (or magnetization). In a ferromagnet, the Hall resistivity $\rho_H = -\rho_{xy}$ is experimentally found to be of the form

$$\rho_H = R_0 H + R_S M \tag{74}$$

where H is the magnetic field, M, the magnetization, R_0, the normal Hall coefficient, and R_S, the anomalous Hall coefficient (the quantity of interest here). Alternatively, the Hall effect may be expressed in terms of the conductivity tensor, $\boldsymbol{\sigma} \equiv \boldsymbol{\rho}^{-1}$. Another important quantity measuring the Hall effect is the Hall angle θ_H (the angle between the electric field and the current) given by

$$\tan\theta_H \equiv \frac{-\sigma_{xy}}{\sigma_{xx}} = \frac{\rho_{xy}}{\rho_{xy}} \tag{75}$$

For values of the magnetic field usually available experimentally, the spontaneous contribution is usually much larger than the normal contribution in ferromagnets. In many cases, it has been found that as the temperature varies, the anomalous Hall resistivity varies as ρ_{xx}^2, which implies that the Hall conductivity σ_{xy} is essentially independent of the relaxation time.

Various mechanisms contribute to the anomalous Hall effect of homogenously magnetized systems:

- the Karplus–Luttinger mechanism (Karplus and Luttinger, 1954)
- the skew-scattering mechanism (Smit, 1955)
- the side-jump mechanism (Berger, 1970).

All three mechanisms rely on the combined effect of exchange and spin-orbit interactions. This can be easily understood from the following considerations. From the Onsager–Casimir symmetry relations (Onsager, 1931; Casimir, 1945), it follows that the antisymmetric part of the resistivity (or conductivity) tensor, that is, the Hall effect, is antisymmetric with respect to time-reversal invariance. In ferromagnets, time-reversal invariance is spontaneously broken by the appearance of the exchange splitting of the band structure. This fact, however, is not sufficient to explain the existence of the Hall effect; indeed, in the absence of spin-orbit interaction, the spin (magnetization) and orbital (electronic motion) degrees of freedom are completely independent of each other. This implies that all properties of the system (including the resistivity tensor) would be invariant under a continuous uniform rotation of the magnetization, resulting in a vanishing Hall effect. This state changes, however, when the electron motion and spin are coupled to each other via the spin-orbit coupling, so that the physical properties are no longer invariant under a global rotation of the magnetization, resulting in the possibility of a nonzero spontaneous Hall effect.

Although sharing a common microscopic origin, the three mechanisms mentioned in the preceding text are quite different in the way they depend on the electronic structure and/or on the impurities present in the ferromagnet.

The Karplus–Luttinger mechanism (Karplus and Luttinger, 1954) results from a velocity correction (the anomalous velocity) due to interband matrix elements of the velocity operator. It yields a Hall conductivity that is essentially a property of the pure Ferromagnet and (for low impurity concentration) is independent of the nature and concentration of impurities, that is, to a Hall resistivity proportional to ρ_{xx}^2, as observed in many cases. The original derivation by Karplus and Luttinger is quite involved and not really physically transparent. This, together with various other theoretical difficulties, led to misunderstanding and controversies that could be definitely lifted only quite recently, through the reinterpretation of the Karplus–Luttinger mechanism in terms of the Berry phase (Chang and Niu, 1996; Sundaram and Niu, 1999; Jungwirth, Niu and MacDonald, 2002). Interestingly, this important progress emerged from concepts developed in the context of the quantum Hall effect (Thouless, Kohmoto, Nightingale and den Nijs, 1982; Avron, Seiler and Simon, 1983; Simon, 1983; Thouless, 1984, 1994; Niu and Thouless, 1984; Niu, Thouless and Wu, 1985; Kohmoto, 1985,1993), which allowed the interpretation of the quantized Hall conductance as a topological invariant, expressed as the integral of a Berry curvature over a closed manifold.

The skew-scattering mechanism (Smit, 1955) arises from the Mott scattering (Mott, 1929) at impurities, that is, from the fact that, owing to spin-orbit interaction, the scattering amplitude depends on the relative orientation of the spin with respect to the scattering plane. An illustrative picture of this mechanism is given in Figure 6(a) (Crépieux and Bruno, 2001). Consider an incident plane wave characterized by a wave vector **k**, which is scattered by a central potential owing to, for example, impurity. In the presence of spin-orbit coupling, the amplitude of the wave packet becomes anisotropic in the sense that it depends on the relative directions of the scattered and incident waves and the spin. After a succession of scattering events, the average trajectory of the electron is deflected by a spin-dependent angle,

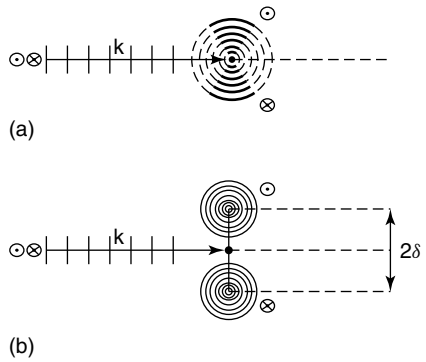

Figure 6. Sketch of the skew-scattering (a) and side-jump (b) mechanisms. (Reproduced from Crepieux & Bruno, 2001, with permission from the American Physical Society. © 2001.)

which is typically of the order of 10^{-2} rad. Because the skew scattering yields an *angular* deflection of scattered electrons, it induces a Hall angle that is *independent* of the impurity density (for sufficiently low impurity density), or in other words, a Hall resistivity that is proportional to the longitudinal resistivity.

The side-jump mechanism (Berger, 1970) arises from the fact that as a plane wave is scattered at an impurity, the outgoing scattered wave is generally not centered exactly at the impurity, but may be slightly shifted away from the impurity, as depicted in Figure 6(b) (Crépieux and Bruno, 2001). This shift can be transverse and/or longitudinal (with respect to the incident wave vector). The longitudinal shift is not directly relevant to the Hall effect and will be ignored here. The transverse shift (side jump) is due to the effect of the spin-orbit coupling and changes sign as the spin component perpendicular to the scattering plane is reversed. The existence of the side jump may be easily understood by examining the reflection of a free electron on a potential barrier under the influence of the spin-orbit coupling (Crépieux and Bruno, 2001). For free electrons, the magnitude of the side jump is of the order of $k\lambda_C{}^2/4 \simeq 10^{-15}$ m, where $\lambda_C \equiv \hbar/(mc)$ is the Compton wavelength. As pointed out by Berger (1970), and discussed in Section 5.3 in the preceding text, band-structure considerably enhance the effective spin-orbit coupling experienced by electrons in solids, and yield an enhancement factor of the order of 10^4 of the magnitude of the side jump. The side jump contributes to the Hall current in two ways: (i) the side jumps experienced at each collision add up to yield a transverse current, and (ii) in the presence of an external electric field, the side jump induces a shift of the electron distribution function away from the Dirac distribution, yielding another contribution to the transverse current (Berger, 1970). The two contributions can be shown to be identical. The most important feature of the side-jump contribution is that it yields a Hall conductivity that is independent of the impurity concentration (and, at least for s-scattering, independent of the sign and magnitude of the scattering potential). Thus, it is essentially an *intrinsic* contribution to the total Hall conductivity just like the Karplus–Luttinger term, and, therefore, yields a contribution to the Hall resistivity that is proportional to ρ_{xx}^2 (Berger, 1970).

Until recently, it was believed that spin-orbit coupling is an essential ingredient to obtain a nonvanishing anomalous Hall effect. This belief is indeed correct in uniformly magnetized ferromagnets for the reasons explained in the preceding text. However, the argument put forward to justify the necessity of the spin-orbit coupling does not hold any more for magnetic systems with noncollinear magnetization. In fact, in general, a time-reversed magnetic configuration (i.e., with all magnetic moments flipped) cannot be obtained by a global rotation of the magnetic moments, unless the magnetization is collinear or coplanar. Therefore, from symmetry considerations, a nonvanishing anomalous Hall effect may be expected, even without spin-orbit coupling, in a magnetic system with a chiral spin texture. Quite recently, it has been proposed that the chiral textured magnetic system may exhibit anomalous Hall effect not (directly) related to the spin-orbit coupling (Ye *et al*., 1999; Ohgushi, Murakami and Nagaosa, 2000; Chun *et al*., 2000; Taguchi and Tokura, 2001; Taguchi *et al*., 2001, 2003, 2004; Lyanda-Geller *et al*., 2001; Shindou and Nagaosa, 2001; Yanagihara and Salamon, 2002; Tatara and Kawamura, 2002; Onoda and Nagaosa, 2002, 2003a,b; Bruno, Dugaev and Taillefumier, 2004; Onoda, Tatara and Nagaosa, 2004; Baily and Salamon, 2005; Kézsmárki *et al*., 2005). The mechanism responsible for the anomalous Hall effect, in this case, relies on the Berry phase accumulated as an electron moves in a textured exchange field. If the exchange splitting is large enough and the electron velocity small enough, the electron spin must adiabatically follow the direction of the local exchange field as it moves through the lattice. In the reference frame where the electron is at rest, it experiences an adiabatically moving exchange field, and the associated geometrical phase in turn generates a fictitious Aharonov–Bohm phase as the electron moves through the lattice. The electron's orbital degree of freedom is coupled to the fictitious field in exactly the same way as to a real magnetic field, and therefore also responds in the same way. In particular, it experiences a Lorentz force that can give rise to a nonvanishing anomalous Hall effect if a net chirality is present.

It is worth pointing out that the theory of the anomalous Hall effect involves the Berry phase in two distinct ways:

1. In the anomalous Hall effect of homogenous ferromagnets, the Karplus–Luttinger contribution can be interpreted as a Berry phase in momentum space.

2. In chiral textured ferromagnets, the anomalous Hall effect arises from the Berry phase due to the exchange field texture in real space.

In the following text, we shall discuss in more detail the interplay of the Berry phase and anomalous Hall effect in these two different contexts.

6.2 Berry phase and the anomalous Hall effect in homogenous ferromagnets

From Kubo's linear response theory, the conductivity tensor for independent electrons is given by Luttinger (1969)

$$\sigma_{ij} = \frac{\mathrm{i}e^2\hbar}{\Omega}\lim_{s\to 0^+} \times \left\langle \sum_{n,m} \frac{f(\varepsilon_n) - f(\varepsilon_m)}{\varepsilon_m - \varepsilon_n} \frac{\langle n|\, v_j\, |m\rangle \langle m|\, v_i\, |n\rangle}{\varepsilon_n - \varepsilon_m + \mathrm{i}s} \right\rangle_c \quad (76)$$

In this equation, n, m label the eigenstates, the thermodynamic limit is implied (volume Ω tending to infinity), and $\langle \ldots \rangle_c$ indicates averaging over impurity configuration. For metals, particular care is needed to perform the limit $s \to 0^+$. Simply setting $s = 0$ yields the Karplus–Luttinger term. The remaining contributions arise from the vicinity of the Fermi level and yield the skew-scattering and side-jump contributions. Here, we are interested in the Karplus–Luttinger term. Disorder is usually considered to be of minor importance for the Karplus–Luttinger term and will be neglected from now on, so that the eigenstates are labeled by the band index n and the wave vector $\mathbf{k}$ in the first Brillouin zone. We thus get

$$\sigma_{ij}^{KL} = -e^2\hbar \int_{1BZ} \frac{\mathrm{d}^D\mathbf{k}}{(2\pi)^D} \sum_{n\neq m} (f(\varepsilon_n(\mathbf{k})) - f(\varepsilon_m(\mathbf{k}))) \times \frac{\mathrm{Im}\left[\langle n\mathbf{k}|\, v_j\, |m\mathbf{k}\rangle \langle m\mathbf{k}|\, v_i\, |n\mathbf{k}\rangle\right]}{(\varepsilon_n(\mathbf{k}) - \varepsilon_m(\mathbf{k}))^2} \quad (77)$$

Using the fact that, for $m \neq n$,

$$\langle n\mathbf{k}|\, H\, |m\mathbf{k}\rangle = 0 \quad (78)$$

one obtains

$$\langle \partial_{\mathbf{k}}(n\mathbf{k})|\, m\mathbf{k}\rangle\, \varepsilon_m(\mathbf{k}) + \langle n\mathbf{k}|\, \partial_{\mathbf{k}}(m\mathbf{k})\rangle\, \varepsilon_n(\mathbf{k}) + \langle m\mathbf{k}|\, \frac{\partial H(\mathbf{k})}{\partial \mathbf{k}}\, |n\mathbf{k}\rangle = 0 \quad (79)$$

Similarly, $\langle n\mathbf{k}|\ m\mathbf{k}\rangle = 0$ implies that

$$\langle \partial_{\mathbf{k}}(n\mathbf{k})|\, m\mathbf{k}\rangle + \langle n\mathbf{k}|\, \partial_{\mathbf{k}}(m\mathbf{k})\rangle = 0 \quad (80)$$

so that

$$\frac{\langle n\mathbf{k}|\, v_j\, |m\mathbf{k}\rangle}{\varepsilon_n(\mathbf{k}) - \varepsilon_m(\mathbf{k})} = \frac{1}{\hbar} \langle \partial_{k_j}(n\mathbf{k})|\ m\mathbf{k}\rangle \quad (81)$$

Finally, we get

$$\sigma_{ij}^{KL} = -\frac{2e^2}{\hbar} \int_{1BZ} \frac{\mathrm{d}^D\mathbf{k}}{(2\pi)^D} \sum_n f(\varepsilon_n(\mathbf{k}))\, \mathrm{Im} \times \left[\langle \partial_{k_j}(n\mathbf{k})|\ \partial_{k_i}(n\mathbf{k})\rangle\right] \quad (82)$$

Defining the Berry curvature in band n as

$$\mathbf{\Omega}^{(n)} \equiv -\mathrm{Im}\left(\langle \partial_{\mathbf{k}}(n\mathbf{k})| \times |\partial_{\mathbf{k}}(n\mathbf{k})\rangle\right) \quad (83)$$

we finally obtain

$$\sigma_{ij}^{KL} = -\frac{e^2}{\hbar} \int_{1BZ} \frac{\mathrm{d}^D\mathbf{k}}{(2\pi)^D} \sum_n f\left({}^{(n)}\varepsilon_n(\mathbf{k})\right) \varepsilon_{ijk}\Omega_k(\mathbf{k}) \quad (84)$$

where ε_{ijk} is the fully antisymmetric tensor. This result is best understood for two-dimensional systems ($D = 2$), where only σ_{xy} and $\Omega_z^{(n)}$ are of interest. There the contribution of the band of index n to the Karplus–Luttinger term is simply determined by the Berry phase associated with parallel transport (with the $\mathbf{k}$-plane playing the role of the parameter space) around the Fermi surface (which is a line in two dimensions).

The case of an insulating system is of particular interest. In this case, there are no Fermi surface contributions (skew scattering and side jump) to the Hall conductivity, and the latter thus reduces to the Karplus–Luttinger term. The contribution of the occupied bands is thus given by an integral over the whole first Brillouin zone (empty bands do not contribute). Because the first Brillouin zone may be viewed as a closed surface (torus), the conductance is topologically quantized in multiples of the quantum of conductance, e^2/h. Since the longitudinal conductance vanishes, we obtain the integer quantum Hall effect without an external magnetic field. This result is completely analogous to the quantum Hall effect obtained in the problem of the Hofstadter butterfly (Hofstadter, 1976; Thouless, Kohmoto, Nightingale and den Nijs, 1982; Avron, Seiler and Simon, 1983).

It is completely similar to the Bonnet theorem in differential geometry (Nakahara, 1990), which relates the integral of the Gaussian curvature (which is a local geometrical property) over a closed surface to its Euler index (which is a global topological invariant).

The simplest example for the Berry phase formulation of the Karplus–Luttinger term is given by the two-dimensional electron gas in the presence of Rashba spin-orbit coupling

and exchange splitting. It is described by the following Hamiltonian:

$$\mathcal{H} = \frac{\hbar^2 \mathbf{k}^2}{2m^*} + \alpha \left(\sigma_x k_y - \sigma_y k_x\right) - M\sigma_z \tag{85}$$

The eigenvalues (shown in Figure 7) are

$$E^{\pm}_{\mathbf{k}} = \frac{\hbar^2 k^2}{2m^*} \mp \lambda(k) \tag{86}$$

with

$$\lambda(k) \equiv \sqrt{M^2 + \alpha^2 k^2} \tag{87}$$

The eigenstates $|\mathbf{k}, \pm\rangle$ are polarized along (resp. against) the unit vector

$$\mathbf{n}(\mathbf{k}) \equiv \left(\frac{\alpha k_y}{\lambda(k)}, \frac{-M}{\lambda(k)}, \frac{\alpha k_y}{\lambda(k)}\right) \tag{88}$$

Thus, as one performs a closed loop around the Fermi line, the spin quantization axis describes a cone, the solid angle of which determines the Berry phase, and, hence, the Karplus–Luttinger contribution to the anomalous Hall effect. We have

$$\sigma^{KL}_{xy} = -\frac{e^2}{h}\frac{1}{4\pi}\int \mathrm{d}^2\mathbf{k}\left[f(E^+_{\mathbf{k}}) - f(E^-_{\mathbf{k}})\right]\varepsilon_{\alpha\beta\gamma} n_\alpha \frac{\partial n_\beta}{\partial k_x}\frac{\partial n_\gamma}{\partial k_y} \tag{89}$$

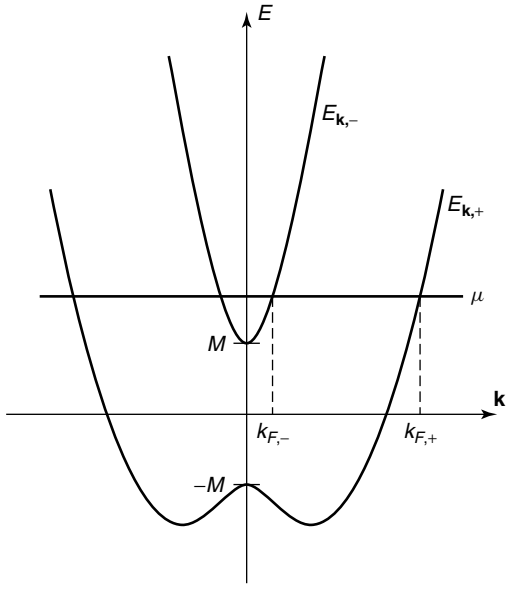

Figure 7. Energy spectrum of electrons in a two-dimensional ferromagnet with Rashba spin-orbit interaction (schematically). (Reproduced from Dugaev *et al*., 2005, with permission from the American Physical Society. © 2005.)

which, for weak spin-orbit coupling ($\alpha k_F \ll M$), finally yields

$$\sigma^{KL}_{xy} \simeq \frac{e^2}{h}\frac{m^*\alpha^2}{M}\left[\theta(M - \varepsilon_F)\frac{\varepsilon_F + M}{2M} + \theta(\varepsilon_F - M)\right] \tag{90}$$

For more extensive discussions, the reader is referred to original publications (Jungwirth, Niu and MacDonald, 2002; Fang *et al*., 2003; Culcer, MacDonald and Niu, 2003; Yao *et al*., 2004; Lee *et al*., 2004; Haldane, 2004; Sinova, Jungwirth and Černe, 2004; Dugaev *et al*., 2005; Sinitsyn, Niu, Sinova and Nomura, 2005).

6.3 Berry phase and the anomalous Hall effect in chiral textured ferromagnets

Let us consider here a system with the Hamiltonian

$$\mathcal{H} \equiv \frac{\mathbf{p}^2}{2m^*} - \mathbf{\Delta}(\mathbf{r})\cdot\boldsymbol{\sigma} \tag{91}$$

where $\mathbf{\Delta}(\mathbf{r}) \equiv \Delta(\mathbf{r})\mathbf{n}(\mathbf{r})$ is a spatially varying exchange potential. Here the quantization axis is chosen to be along z everywhere. This choice is arbitrary, however (it is in fact a gauge choice), and any other choice could be made. In particular, the exchange term becomes simpler if we choose a gauge such that the quantization axis is everywhere along $\mathbf{n}(\mathbf{r})$, that is, if we perform the unitary transformation

$$\mathcal{H} \to \tilde{\mathcal{H}} \equiv \mathcal{T}^\dagger \mathcal{H} \mathcal{T} \tag{92}$$

with

$$\mathcal{T}^\dagger(\mathbf{r})\left[\mathbf{n}(\mathbf{r})\cdot\boldsymbol{\sigma}\right]\mathcal{T}(\mathbf{r}) = \sigma_z \tag{93}$$

However, we should pay attention to the fact that the unitary operator $\mathcal{T}(\mathbf{r})$ does not commute with the momentum operator $\mathbf{p} \equiv -\mathrm{i}\hbar\partial/\partial\mathbf{r}$. Thus, the price to pay for the simplification of the exchange term is a more complicated expression of the kinetic energy term, and the transformed Hamiltonian reads

$$\tilde{\mathcal{H}} = \frac{1}{2m^*}\left(\mathbf{p} + e\mathbf{A}(\mathbf{r})\right)^2 - \Delta(\mathbf{r})\sigma_z \tag{94}$$

where $\mathbf{A}(\mathbf{r})$ is a nonabelian (2×2-spinor) gauge potential given by

$$A_i(\mathbf{r}) \equiv 2\mathrm{i}\pi\phi_0 \mathcal{T}^\dagger(\mathbf{r})\partial_i \mathcal{T}(\mathbf{r}) \tag{95}$$

Note that in the definition of the gauge potential $\mathbf{A}(\mathbf{r})$, we have introduced the flux quantum $\phi_0 \equiv h/e$ for convenience, in order to be able to express the gauge potential in the same

units as a usual vector potential. It is important to realize, however, that this is merely a convention – the electron charge (being absent from the original Hamiltonian) plays no role here, and we would have obtained the same result for a neutral particle, such as the neutron.

It may seem at first sight that we have made no real progress by changing to a new gauge – the exchange has been simplified, but the kinetic energy has taken a more complicated form. However, if the exchange splitting is large enough compared to the rate of variation of $\mathbf{n}(\mathbf{r})$ (as seen in the reference frame in which the electron is at rest), spin flip terms due to the kinetic energy term become negligible, and the spin has to adiabatically follow the local direction of $\mathbf{n}(\mathbf{r})$. More precisely, the condition of adiabaticity (for an electron at the Fermi level) reads:

$$\alpha \equiv \frac{\hbar^2 k_F}{m^* \xi \Delta} \ll 1 \tag{96}$$

where ξ is the typical length on which the direction of $\mathbf{n}(\mathbf{r})$ makes a change of the order of π. If the adiabaticity condition is satisfied, the two-spin channels decouple and one gets:

$$\tilde{\mathcal{H}} = \begin{pmatrix} \tilde{\mathcal{H}}_\uparrow & 0 \\ 0 & \tilde{\mathcal{H}}_\downarrow \end{pmatrix} \tag{97}$$

with

$$\tilde{\mathcal{H}}_\sigma \equiv \frac{1}{2m^*} \left(\mathbf{p} + \sigma e \mathbf{a}(\mathbf{r})\right)^2 - \sigma \Delta(\mathbf{r}) + V(\mathbf{r}) \tag{98}$$

with $\sigma = +1$ (-1) for $\uparrow$ $(\downarrow)$, respectively, and where the effective vector and scalar potentials are respectively given by

$$a_i(\mathbf{r}) = \pi \phi_0 \frac{n_x \partial_i n_y - n_y \partial_i n_x}{1 + n_z} \tag{99}$$

and

$$V(\mathbf{r}) \equiv \frac{\hbar^2}{8m^*} \sum_{i,\mu} \left(\partial_i n_\mu\right)^2 \tag{100}$$

Thus, we have mapped the original problem onto that of spinless particles subject to spin-dependent vector and scalar potentials. The effective magnetic field associated with the effective vector potential is defined as usual by

$$\mathbf{b} = \nabla \times \mathbf{a} \tag{101}$$

and is given in terms of $n(\mathbf{r})$ by

$$b_i = \frac{\phi_0}{8\pi} \varepsilon_{ijk} \varepsilon_{\mu\nu\lambda} n_\mu (\partial_j n_\nu)(\partial_k n_\lambda) \tag{102}$$

where Einstein's convention of summation over repeated dummy indices is implied. One can check that the effective Aharonov–Bohm phase associated with a closed path in space corresponds exactly with the Berry phase for a spin $1/2$ for the corresponding path in $\mathbf{n}$ space, that is, $\pm\Omega/2$, where Ω is the solid angle described by $\mathbf{n}$. This observation establishes the link between the effective magnetic field experienced by the electron because of the exchange field texture and the concept of the Berry phase.

The electron couples to the effective vector potential in exactly the same way as it would couple to a real vector potential, and therefore the same physical consequences are expected, and obtained. These effects can be classified into two categories:

- nonlocal effects due to quantum interferences, such as the Aharonov–Bohm effect and associated persistent currents; intrinsically, these effects are of quantum mechanical nature and require phase coherence.
- local effects such as the Lorentz force and it consequences like the Hall effect; these effects are *not* quantum mechanical in essence, but classical, and do not rely on phase coherence. An insightful paper by Aharonov and Stern (1992) beautifully explains how the effective Lorentz force arises in a classical description.

A good example of the anomalous Hall effect due to a chiral texture is provided by the pyrochlore compound $Nd_2Mo_2O_7$ (Taguchi *et al.*, 2001). The structure and magnetic ordering are displayed in Figure 8. The electronic transport takes place on Mo sites, which adopt a chiral 'umbrella' spin texture owing to the exchange coupling to the Nd moments. The hopping of an electron around any Mo triangle gives rise to a Berry phase related to the solid angle described by the magnetic moments, and hence to a chirality-induced anomalous Hall effect. This is corroborated by the fact that the application of a large magnetic field closes the 'umbrella' texture, thereby suppressing the solid angle and the anomalous Hall effect.

7 OUTLOOK AND CONCLUSIONS

Besides the applications that have been discussed in the preceding text, the concept of Berry phase has been of great importance to a number of topics in solid-state physics. In the theory of the fractional quantum Hall effect, the occurrence of excitations with fractional charges comes naturally out of a Berry phase argument and gives rise to the concept of *anyon* (Wilczek, 1990). In quantum Hall ferromagnets, the Berry phase gives rise to topological excitations, called *skyrmions*

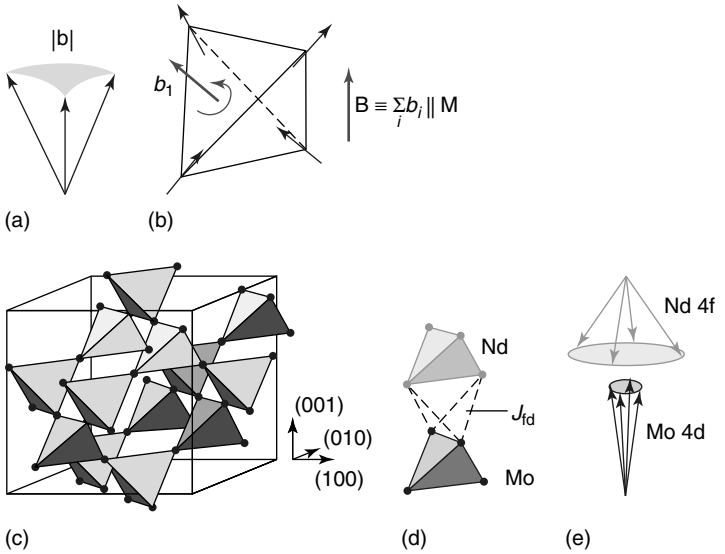

Figure 8. Schematic magnetic and crystal structures of pyrochlore. (a) Spin chirality, that is, the solid angle subtended by the three spins. (b) 'Two-in, two-out' spin structure, in which each spin points along the line that connects the center of the tetrahedron and the vertex. The total fictitious magnetic field is the vector sum of each fictitious magnetic flux that penetrates each plaquette. (c) The B sublattice of pyrochlore structure $A_2B_2O_7$. The A sublattice is structurally identical with this one, but is displaced by half a lattice constant. (d) Relative position of Nd tetrahedron (gray circles) and Mo tetrahedron (black circles) in $Nd_2Mo_2O_7$ pyrochlore. (e) The 'umbrella' structure observed for $Nd_2Mo_2O_7$ (A = Nd, B = Mo) by a neutron diffraction study. A magnetic unit cell contains four inequivalent Nd 4f moments $\mathbf{n}_i$ and four Mo 4d moments $\mathbf{m}_i$. In the umbrella structure, $(\mathbf{m}_i - \mathbf{m}) \perp \mathbf{m}$ and $(\mathbf{n}_i - \mathbf{n}) \perp \mathbf{n}$ for each $\mathbf{m}_i$ and $\mathbf{n}_i$, where $\mathbf{m}$ and $\mathbf{n}$ are the average moments of four $\mathbf{m}_i$ and four $\mathbf{n}_i$, respectively. (Reproduced from Y. Taguchi *et al*: Spin chirality, Berry phase, and anomalous Hall effect in a Frustrated Ferromagnet. *Science* **29**, (2001) 2573–76, with permission from AAAS.)

(Girvin, 1999) with novel properties. In one- and two-dimensional quantum spin systems, the physical properties depend, in a crucial manner, on whether the spin is integer or half-integer (Haldane, 1983, 1988), a phenomenon that is best understood in terms of Berry phase considerations (Loss, 1998). In molecular magnets, the Berry phase can induce destructive interferences of macroscopic tunneling between classically degenerate states, giving rise to the occurrence of *diabolical points* (Loss, DiVincenzo and Grinstein, 1992; von Delft and Henley, 1992; Garg, 1993; Wernsdorfer and Sessoli, 1999; Villain, 2003; Bruno, 2006).

The concept of the Berry phase appears as one of the most profound and insightful concepts in quantum mechanics. This article aimed at giving an introduction to this topic and illustrating its importance and versatility by means of a number of examples in the field of magnetism.

REFERENCES

Aharonov, Y. and Bohm, D. (1959). Significance of electromagnetic potentials in the quantum theory. *Physical Review*, **115**, 485–491.

Aharonov, Y. and Stern, A. (1992). Origin of the geometric forces accompanying Berry's geometric potentials. *Physical Review Letters*, **69**, 3593–3596.

Aravind, P.K. (1997). The Wigner angle as an anholonomy in rapidity space. *American Journal of Physics*, **65**, 634–636.

Aronov, A.G. and Sharvin, Y.V. (1987). Magnetic flux effects in disordered conductors. *Reviews of Modern Physics*, **59**, 755–779.

Avron, J.E., Seiler, R. and Simon, B. (1983). Homotopy and quantization in condensed matter physics. *Physical Review Letters*, **51**, 51–53.

Baily, S.A. and Salamon, M.B. (2005). Berry-phase contribution to the anomalous Hall effect in gadolinium. *Physical Review B*, **71**, 104407-1–104407-6.

Berger, L. (1970). Side-jump mechanism for the Hall effect of ferromagnets. *Physical Review B*, **2**, 4559–4566.

Berry, M.V. (1984). Quantal phases accompanying adiabatic changes. *Proceedings of the Royal Society of London Series A*, **392**, 45–57.

Berry, M.V. (1985). Classical adiabatic angles and quantal adiabatic phase. *Journal of Physics A: Mathematical and General*, **18**, 15–27.

Berry, M.V. (1990). Quantum adiabatic anholonomy. In *Anomalies, Phase, Defects*, Bregola, U.M., Marmo, G. and Morandi, G. (Eds.), Bibliopolis: Naples, pp. 125–181; also available at http://www.phy.bris.ac.uk/research/theory/Berry.

Bitter, T. and Dubbers, D. (1987). Manifestation of Berry's topological phase in neutron spin rotation. *Physical Review Letters*, **59**, 251–254.

Bohm, A., Mostafazadeh, A., Koizumi, H., *et al*. (2003). *The Geometric Phase in Quantum Systems*, Springer-Verlag: Berlin.

Bruno, P. (2006). Berry phase, topology, and degeneracies in quantum nanomagnets. *Physical Review Letters*, **96**, 117208-1–117208-4.

Bruno, P., Dugaev, V.K. and Taillefumier, M. (2004). Topological Hall effect and Berry phase in magnetic nanostructures. *Physical Review Letters*, **93**, 096806-1–096806-4.

Casimir, H.B.G. (1945). On Onsager's principle of microscopic reversibility. *Reviews of Modern Physics*, **17**, 343–350.

Chang, M.C. and Niu, Q. (1996). Berry phase, hyperorbits, and the Hofstadter spectrum: semiclassical dynamics in magnetic Bloch bands. *Physical Review B*, **53**, 7010–7023.

Chiao, R.Y. and Wu, Y.S. (1986). Manifestations of Berry's topological phase for the photon. *Physical Review Letters*, **57**, 933–936.

Chun, S.H., Salamon, M.B., Lyanda-Geller, Y., *et al*. (2000). Magnetotransport in manganites and the role of quantal phases: theory and experiment. *Physical Review Letters*, **84**, 757–760.

Cina, J.A. (1986). Classical adiabatic angle and geometric phase in spin precession. *Chemical Physics Letters*, **132**, 393–395.

Crépieux, A. and Bruno, P. (2001). Theory of the anomalous Hall effect from the Kubo formula and the Dirac equation. *Physical Review B*, **64**, 014416-1–014416-16.

Culcer, D., MacDonald, A.H. and Niu, Q. (2003). Anomalous Hall effect in paramagnetic two-dimensional systems. *Physical Review B*, **68**, 045327-1–045327-9.

von Delft, J. and Henley, C.H. (1992). Destructive quantum interference in spin tunnelling problems. *Physical Review Letters*, **69**, 3236–3239.

Dirac, P.A.M. (1931). Quantised singularities in the electromagnetic field. *Proceedings of the Royal Society of London Series A*, **133**, 60–72.

Dugaev, V.K., Bruno, P., Taillefumier, M., *et al*. (2005). Anomalous Hall effect in a two-dimensional electron gas with spin-orbit interaction. *Physical Review B*, **71**, 224423-1–224423-8.

Fang, Z., Nagaosa, N., Takahashi, K.S., *et al*. (2003). The anomalous Hall effect and magnetic monopoles in momentum space. *Science*, **302**, 92–95.

Garg, A. (1993). Topologically quenched tunnel splitting in spin systems without Kramers' degeneracy. *Europhysics Letters*, **22**, 205–210.

Girvin, S.M. (1999). Quantum Hall effect: novel excitations and broken symmetries. In *Topological Aspects of Low Dimensional Systems*, Comtet, A., Jolicoeur, T., Ouvry, S. and David, F. (Eds.), Springer-Verlag: Berlin.

Haldane, F.M.D. (1983). Nonlinear field theory of large-spin Heisenberg Antiferromagnets: semiclassically quantized solitons of the one-dimensional easy-axis Néel state. *Physical Review Letters*, **50**, 1053–1056.

Haldane, F.M.D. (1988). O(3) nonlinear σ model and the topological distinction between integer-and-half-integer-spin antiferromagnets in two dimensions. *Physical Review Letters*, **61**, 1029–1032.

Haldane, F.M.D. (2004). Berry curvature on the fermi surface: anomalous Hall effect as a topological fermi-liquid property. *Physical Review Letters*, **93**, 206602-1–206602-4.

Hall, E.H. (1880a). On a new action of the magnet on electric currents. *Philosophical Magazine*, **9**, 225–230.

Hall, E.H. (1880b). On the new action of magnetism on a permanent electric current. *Philosophical Magazine*, **10**, 301–328.

Hall, E.H. (1881). On the "rotational coefficient" in nickel and cobalt. *Philosophical Magazine*, **12**, 157–172.

Hannay, J.H. (1985). Angle variable holonomy in adiabatic excursion of an integrable Hamiltonian. *Journal of Physics A: Mathematical and General*, **18**, 221–230.

Hofstadter, D.R. (1976). Energy levels and wave functions of Bloch electrons in rational and irrational magnetic fields. *Physics Review B*, **14**, 2239–2249.

Jordan, T.F. (1988). Berry phases and unitary transformations. *Journal of Mathematical Physics*, **29**, 2042–2052.

Jungwirth, T., Niu, Q. and MacDonald, A.H. (2002). Anomalous Hall effect in ferromagnetic semiconductors. *Physical Review Letters*, **88**, 227208-1–227208-4.

Karplus, R. and Luttinger, J.M. (1954). Theory of the Hall effect in ferromagnetic substances. *Physical Review*, **95**, 1154–1160.

Kézsmárki, I., Onoda, S., Taguchi, Y., *et al*. (2005). Magneto-optical effect induced by spin chirality of the itinerant ferromagnet $Nd_2Mo_2O_7$. *Physical Review B*, **72**, 094427-1–094427-6.

Kohmoto, M. (1985). Topological invariant and the quantization of the hall conductance. *Annals of Physics*, **160**, 343–354.

Kohmoto, M. (1993). Berry's phase of Bloch electrons in electromagnetic fields. *Journal of the Physical Society of Japan*, **62**, 659–663.

Kundt, A. (1893). Das Hall'sche Phänomen in Eisen, Kobalt, und Nickel. *Annalen der Physik (Leipzig)*, **49**, 257–271.

Lee, W.L., Watauchi, S., Miller, V.L., *et al*. (2004). Dissipationless anomalous Hall current in the ferromagnetic spinel $CuCr_2Se_{4?x}Br_x$. *Science*, **303**, 1647–1649.

Loss, D. (1998). Quantum dynamics in mesoscopic magnetism. In *Dynamical Properties of Unconventional Magnetic Systems*, Skjeltorp, A.P. and Sherrington, D. (Eds.), Kluwer Academic Publishers: The Netherlands, pp. 29–75.

Loss, D., DiVincenzo, D.P. and Grinstein, G. (1992). Suppression of tunnelling by interference in half-integer-spin particles. *Physical Review Letters*, **69**, 3232–3236.

Luttinger, J.M. (1969). Transport theory. In *Mathematical Methods in Solid State and Superfluid Theory*, Clark, R.C. and Derrick, G.H. (Eds.), Oliver and Boyd: Edinburgh, pp. 157–193.

Lyanda-Geller, Y., Chun, Y., Salamon, M.B., *et al*. (2001). Charge transport in manganites: hopping conduction, the anomalous Hall effect, and universal scaling. *Physical Review B*, **63**, 184426-1–184426-27.

Mead, C.A. and Truhlar, D.G. (1979). On the determination of the Born-Oppenheimer nuclear motion wave functions including complications due to conical intersections and identical nuclei. *Journal of Chemical Physics*, **70**, 2284–2296.

Messiah, A. (1991). *Quantum Mechanics*, North Holland: Amsterdam, Vol. 2.

Moody, J., Shapere, A. and Wilczek, F. (1986). Realizations of magnetic-monopole gauge fields: diatoms and spin precession. *Physical Review Letters*, **56**, 893–896.

Mott, N.F. (1929). The scattering of fast electrons by atomic nuclei. *Proceedings of the Royal Society of London Series A*, **124**, 425–441.

Nakahara, M. (1990). *Geometry, Topology, and Physics*, Institute of Physics Publishing: Bristol.

von Neumann, J. and Wigner, E.P. (1929). Über das Verhalten von Eigenwerten bei adiabatischen Prozessen. *Physikalische Zeitschrift*, **30**, 467–470.

Niu, Q. and Thouless, D.J. (1984). Quantised adiabatic charge transport in the presence of substrate disorder and many-body interaction. *Journal of Physics A: Mathematical and General*, **17**, 2453–2462.

Niu, Q., Thouless, D.J. and Wu, Y.S. (1985). Quantized Hall conductance as a topological invariant. *Physical Review B*, **31**, 3372–3377.

Ohgushi, K., Murakami, S. and Nagaosa, N. (2000). Spin anisotropy and quantum Hall effect in the kagomé lattice: chiral spin state based on a ferromagnet. *Physical Review B*, **62**, R6065–R6068.

Olariu, S. and Popescu, I.I. (1985). The quantum effects of electromagnetic fluxes. *Reviews of Modern Physics*, **57**, 339–436.

Onoda, M. and Nagaosa, N. (2002). Topological nature of anomalous Hall effect in ferromagnets. *Journal of the Physical Society of Japan*, **71**, 19–22.

Onoda, M. and Nagaosa, N. (2003a). Spin chirality fluctuations and anomalous Hall effect in itinerant ferromagnets. *Physical Review Letters*, **90**, 196602-1–196602-4.

Onoda, M. and Nagaosa, N. (2003b). Quantized anomalous Hall effect in two-dimensional ferromagnets: quantum Hall effect in metals. *Physical Review Letters*, **90**, 206601-1–206601-4.

Onoda, M., Tatara, G. and Nagaosa, N. (2004). Anomalous Hall effect and skyrmion number in real and momentum spaces. *Journal of the Physical Society of Japan*, **73**, 2624–2627.

Onsager, L. (1931). Reciprocal relations in irreversible processes. II. *Physical Review*, **38**, 2265–2279.

Pancharatnam, S. (1956). Generalized theory of interference, and its application. *Proceedings of the Indian Academy of Sciences*, **44**, 247–262. (Also reprinted in Shapere and Wilczek, 1989.)

Perrier, A. (1930a). Grandeurs et formules théoriques nouvelles pour les phénomènes galvanomagnétiques et thermomagnétiques. *Helvetica Physica Acta*, **3**, 317–328.

Perrier, A. (1930b). Interprétation unitaire des particularités de la conduction des milieux ferromagnétiques. *Helvetica Physica Acta*, **3**, 400–427.

Pugh, E.M. and Rostoker, N. (1953). Hall effect in ferromagnetic materials. *Reviews of Modern Physics*, **25**, 151–157.

Pugh, E.M., Rostoker, N. and Schindler, A. (1950). On the Hall effect in ferromagnetics. *Physical Review*, **80**, 688–692.

Rhodes, J.A. and Semon, M.D. (2004). Relativistic velocity space, Wigner rotation and Thomas precession. *American Journal of Physics*, **72**, 943–960.

Shapere, A. and Wilczek, F. (Eds.) (1989). *Geometric Phases in Physics*, World Scientific: Singapore.

Shindou, R. and Nagaosa, N. (2001). Orbital ferromagnetism and anomalous Hall effect in antiferromagnets on the distorted fcc lattice. *Physical Review Letters*, **87**, 116801-1–116801-4.

Simon, B. (1983). Holonomy, the quantum adiabatic theorem and Berry's phase. *Physical Review Letters*, **51**, 2167–2170.

Sinova, J., Jungwirth, T. and Černe, J. (2004). Magneto-transport and magneto-optical properties of ferromagnetic (III,Mn)V semiconductors: a review. *International Journal of Modern Physics. B*, **18**, 1083–1118.

Sinitsyn, N.A., Niu, Q., Sinova, J. and Nomura, K. (2005). Disorder effects in the anomalous Hall effect induced by Berry curvature. *Physical Review B*, **72**, 045346-1–045346-11.

Smit, J. and Volger, J. (1953). Spontaneous Hall effect in ferromagnetics. *Physical Review*, **92**, 1576–1577.

Smit, J. (1955). The spontaneous Hall effect in ferromagnetics I. *Physica*, **21**, 877–887.

Smith, A.W. (1910). The variation of the Hall effect in metals with change of temperature. *Physical Review*, **30**, 1–34.

Sundaram, G. and Niu, Q. (1999). Wave-packet dynamics in slowly perturbed crystals: gradient corrections and Berry-phase effects. *Physical Review B*, **59**, 14915–14925.

Suter, D., Chingas, G.C., Harris, R.A. and Pines, A. (1987). Berry's phase in magnetic resonance. *Molecular Physics*, **61**, 1327–1340.

Taguchi, Y., Oohara, Y., Yoshizawa, H., *et al*. (2001). Spin chirality, Berry phase, and anomalous Hall effect in a frustrated ferromagnet. *Science*, **291**, 2573–2576.

Taguchi, Y., Oohara, Y., Yoshizawa, H., *et al*. (2004). The spin chirality induced anomalous Hall effect in pyrochlore ferromagnets. *Journal of Physics. Condensed Matter*, **16**, S599–S606.

Taguchi, Y., Sasaki, T., Awaji, S., *et al*. (2003). Magnetic field induced sign reversal of the anomalous Hall effect in a pyrochlore ferromagnet $Nd_2Mo_2O_7$: evidence for a spin chirality mechanism. *Physical Review Letters*, **90**, 257202-1–257202-4.

Taguchi, Y. and Tokura, Y. (2001). Enhancement of anomalous Hall effect in a filling-changed pyrochlore-type molybdate. *Europhysics Letters*, **54**, 401–406.

Tatara, G. and Kawamura, H. (2002). Chirality-driven anomalous Hall effect in weak coupling regime. *Journal of the Physical Society of Japan*, **71**, 2613–2616.

Thomas, L.H. (1926). The motion of the spinning electron. *Nature*, **117**, 514.

Thomas, L.H. (1927). The kinematics of an electron with an axis. *Philosophical Magazine*, **3**, 1–22.

Thouless, D.J. (1984). Quantized Hall effect in two-dimensional periodic potentials. *Physics Reports*, **110**, 279–291.

Thouless, D.J. (1994). Topological interpretations of quantum Hall conductance. *Journal of Mathematical Physics*, **35**, 5362–5372.

Thouless, D.J., Kohmoto, M., Nightingale, M.P. and den Nijs, M. (1982). Quantized Hall conductance in a two-dimensional periodic potential. *Physical Review Letters*, **49**, 405–408.

Tomita, A. and Chiao, R.Y. (1986). Observation of Berry's topological phase by using an optical fiber. *Physical Review Letters*, **57**, 937–940.

Tonomura, A., Osakabe, N., Matsuda, T., *et al*. (1986). Evidence for Aharonov-Bohm effect with magnetic field completely shielded from electron wave. *Physical Review Letters*, **56**, 792–795.

Tycko, R. (1987). Adiabatic rotational splittings Berry's phase in nuclear quadrupole resonance. *Physical Review Letters*, **58**, 2281–2284.

Villain, J. (2003). Magnétisme des cristaux de molécules à grand spin. *Annales de Physique*, **28**, 1–96.

Washburn, S. and Webb, R.A. (1992). Quantum transport in small disordered from the diffusive to the ballistic regime. *Reports on Progress in Physics*, **55**, 1311–1383.

Wernsdorfer, W. and Sessoli, R. (1999). Quantum phase interference and parity effects in magnetic molecular clusters. *Science*, **284**, 133–135.

Wilczek, F. (1990). *Fractional Statistics and Anyon Superconductivity*, World Scientific: Singapore.

Yanagihara, H. and Salamon, M.B. (2002). Skyrmion strings and the anomalous Hall effect in CrO_2. *Physical Review Letters*, **89**, 187201-1–187201-4.

Yao, Y., Kleinman, L., MacDonald, A.H., *et al*. (2004). First principles calculation of anomalous Hall conductivity in ferromagnetic bcc Fe. *Physical Review Letters*, **92**, 037204-1–037204-4.

Ye, J., Kim, Y.B., Millis, A.J., *et al*. (1999). Berry phase theory of the anomalous Hall effect: application to colossal magnetoresistance manganites. *Physical Review Letters*, **83**, 3737–3740.

FURTHER READING

Dirac, P.A.M. (1948). The theory of magnetic poles. *Physical Review*, **74**, 817–830.

Hofstadter, D.R. (1983). Energy levels and wave functions of Bloch electrons in rational and irrational magnetic fields. *Physical Review B*, **14**, 2239–2249.

Theory of Spin-dependent Tunneling

Hiroshi Imamura[1,2] and Sadamichi Maekawa[2]

[1] *National Institute of Advanced Industrial Science and Technology (AIST), Tsukuba, Japan*
[2] *Tohoku University, Sendai, Japan*

1 INTRODUCTION

Spin is an intrinsic property of elementary particles and participates in magnetic interactions. An electron is an elementary particle that carries a negative electric charge $-e$ and a spin $1/2$ corresponding to the magnetic moment of $e\hbar/(2mc) = 9.285 \times 10^{-24}$ $(\mathrm{J\,T^{-1}})$. We cannot separate a spin from a charge when we deal with electrons. When the electric current flows in a wire, both charge and spin are carried by electrons. In contrast to the electric charge, the spin of an electron has two directions, up or down. In nonmagnetic conductors such as Cu, Al, and Au, spin-dependent phenomena are not observed, since the same number of spin-up and spin-down electrons are present. However, in magnetic materials such as Fe, Co, and Ni, the number of electrons with spin up is different from that with spin down. Therefore, the transport properties of magnetic materials are spin dependent. We can vary the resistance by applying a magnetic field to change the direction of magnetization. This phenomenon is called *magnetoresistance* (MR) and is applied to magnetoresistive devices such as hard-disk drives.

Electron tunneling is a basic phenomenon in quantum mechanics by which electric current can pass from one electrode through a thin insulating barrier layer into a second electrode. The recent nanofabrication technology enables us to control single-electron tunneling through a small island called a *quantum dot*. Electron tunneling is one of the key concepts in nanotechnologies and has many technological applications: the Schottky diode is a basic element of semiconductor heterostructures, the superconducting quantum interference device (SQUID) is a high-sensitivity magnetic sensor, and the scanning tunneling microscope (STM) is an atomic-resolution microscope in which an electron tunnels through a vacuum instead of an insulating barrier. However, all these devices utilize charge degrees of freedom – rather than spin degrees of freedom – of electrons.

Recently, spin-dependent tunneling in magnetic tunnel junctions has attracted enormous attention because of its potential applications in high-density magnetic recording devices and nonvolatile magnetic random access memory (MRAM). Spin-dependent tunneling is also important from a scientific point of view, since it provides much information about the physical properties of magnetic materials. In fact, the concept of spin-dependent tunneling has a long history in physics. In the early 1970s, Meservey and Tedrow (1994) developed a spin-polarized electron tunneling technique that used special properties of the superconducting states to probe spin-dependent features of the electron density of states

Handbook of Magnetism and Advanced Magnetic Materials. Edited by Helmut Kronmüller and Stuart Parkin. Volume 1: *Fundamentals and Theory*. ISBN: 978-0-470-02217-7.

of ferromagnets (FMs). Applying this technique to various FMs in FM/Al_2O_3/Al tunnel junctions, they showed that the tunneling electrons from FMs are spin polarized, and obtained detailed information about the spin polarization of the conduction electrons near the Fermi level.

The first experiment on spin-dependent tunneling in magnetic tunnel junctions was reported by Julliere (1975). He measured the tunnel conductance of Fe/Ge/Co junctions and showed that it was dependent on the relative orientation of the magnetizations of electrodes. This effect is now called the *tunnel magnetoresistance* (TMR) effect. Subsequently, Maekawa and Gäfvart Maekawa and Gäfvert (1982) demonstrated a strong correlation between the tunnel conductance and magnetization process in Ni/NiO/FM junctions with Ni, Fe, or Co as the counterelectrode. However, these pioneering works on TMR did not attract much attention until the mid-1990s, since the measured TMR values remained very small at room temperature.

In 1995, the first breakthrough for large TMR was brought about by Miyazaki and Tezuka (1995) and Moodera, Kinder, Wong and Meservey (1995), who developed superior fabrication methods for magnetic tunnel junctions with an amorphous Al_2O_3barrier. In the last decade, much effort has been devoted to improving the TMR ratio of magnetic tunnel junctions with an amorphous Al_2O_3barrier. Currently, the record for the largest TMR ratio of the magnetic tunnel junctions with amorphous $Al_2O_3$is 70.4 % at room temperature (Wang *et al*., 2004). The second breakthrough was the discovery of a high TMR in epitaxial magnetic tunnel junctions with MgO barrier (Bowen *et al*., 2001). In 2001, Bowen *et al*. fabricated Fe(001)/MgO(20 Å)/FeCo(001) single-crystal epitaxial junctions and observed a 27% TMR at 300 K, which increased to 60% at 30 K. Although the observed TMR was much smaller than the values predicted by Butler, Zhang, Schulthess and MacLaren (2001) and Mathon and Umerski (2001), it was larger than that obtained on the (001)-oriented Fe/amorphous Al_2O_3/FeCo junction by Yuasa *et al*. (2000). The predicted values of TMR for Fe(100)/Mg(100)/Fe(100) were in excess of 1000% (Butler, Zhang, Schulthess and MacLaren, 2001; Mathon and Umerski, 2001). Owing to the rapid progress in fabrication techniques, the TMR of the epitaxial magnetic tunnel junction has increased rapidly, as shown in Figure 1. The record for the largest TMR ratio of a magnetic tunnel junction with an MgO barrier is 410% at room temperature (Yuasa, 2006).

In the early studies on spin-dependent tunneling, the theoretical interpretation was based on a simple model in which the spin is conserved in the tunneling process and the conductance of each spin direction is proportional to the densities of states of that spin in each electrode. In this model, the tunnel current is larger when the magnetizations of the two electrodes are parallel than when they are antiparallel, which explains the strong dependence of the tunneling current on the relative orientation of the magnetizations of the ferromagnetic electrodes. However, the model does not explain the experimental results that the TMR exhibits rather large bias and temperature dependencies.

Another approach based on the single-electron Schrödinger equation was proposed by Slonczewski (1989). By extending the free-electron model of tunneling in nonmagnetic tunnel junctions (Burstein and Lundqvist, 1969) to magnetic tunnel junctions, Slonczewski found that the polarization of tunneling electrons depends not only on the electronic density of states of FMs but also on the potential height of the tunnel barriers (Slonczewski, 1989). In this approach, the electrodes and the insulating barrier are treated as a single quantum-mechanical system and the wave functions of up and down electrons are constructed by solving the Schrödinger equation in the whole system. While the free-electron model captures some essential features, their predictions for TMR are quantitatively unreliable because the lattice structure of the electrodes and the variation of the band structure near the insulating barrier are overlooked (Zhang and Levy, 1999).

The tight-binding model gives more realistic descriptions for TMR (Zhang and Levy, 1999; Moodera and Mathon, 1999; Asano, Oguri and Maekawa, 1993; Mathon, 1997; Tsymbal and Pettifor, 1998; Mathon and Umerski, 1999; Itoh *et al*., 1999; Itoh, Ohsawa and Inoue, 2000). This approach allows one to distinguish electronic structures at interfaces from that in the bulk and to study the effect of the interface roughness, although it contains some empirical parameters. One can easily see that the single-band tight-binding model reduces to the free-electron model. It is also shown that the conductance of the tight-binding method reduces to the usual expression for the conductance obtained in the classical theory of tunneling when the electron hopping between the electrodes is weak and the coherence across the barrier is completely lost.

A nonempirical description of spin-dependent tunneling of epitaxial magnetic tunnel junctions is provided by the first-principles methods based on density-functional theory within the local spin-density approximation (LSDA) for the electronic structure and the Landauer–Büttiker formula for the conductance (MacLaren *et al*., 1990; MacLaren, Zhang, Butler and Wang, 1999; Butler, Zhang, Schulthess and MacLaren, 2001). Butler, Zhang, Schulthess and MacLaren (2001) studied the spin-dependent tunneling in epitaxial Fe/MgO/Fe magnetic tunnel junctions by using the layer Korringa–Kohn–Rostoker (LKKR) method based on the first-principles method, and predicted a TMR ratio as high as 6000%. They showed that the high TMR ratio in epitaxial magnetic tunnel junctions with an MgO barrier is due to the symmetry of the evanescent wave in the barrier. The symmetry of the current carrying state in the barrier is Δ_1 and

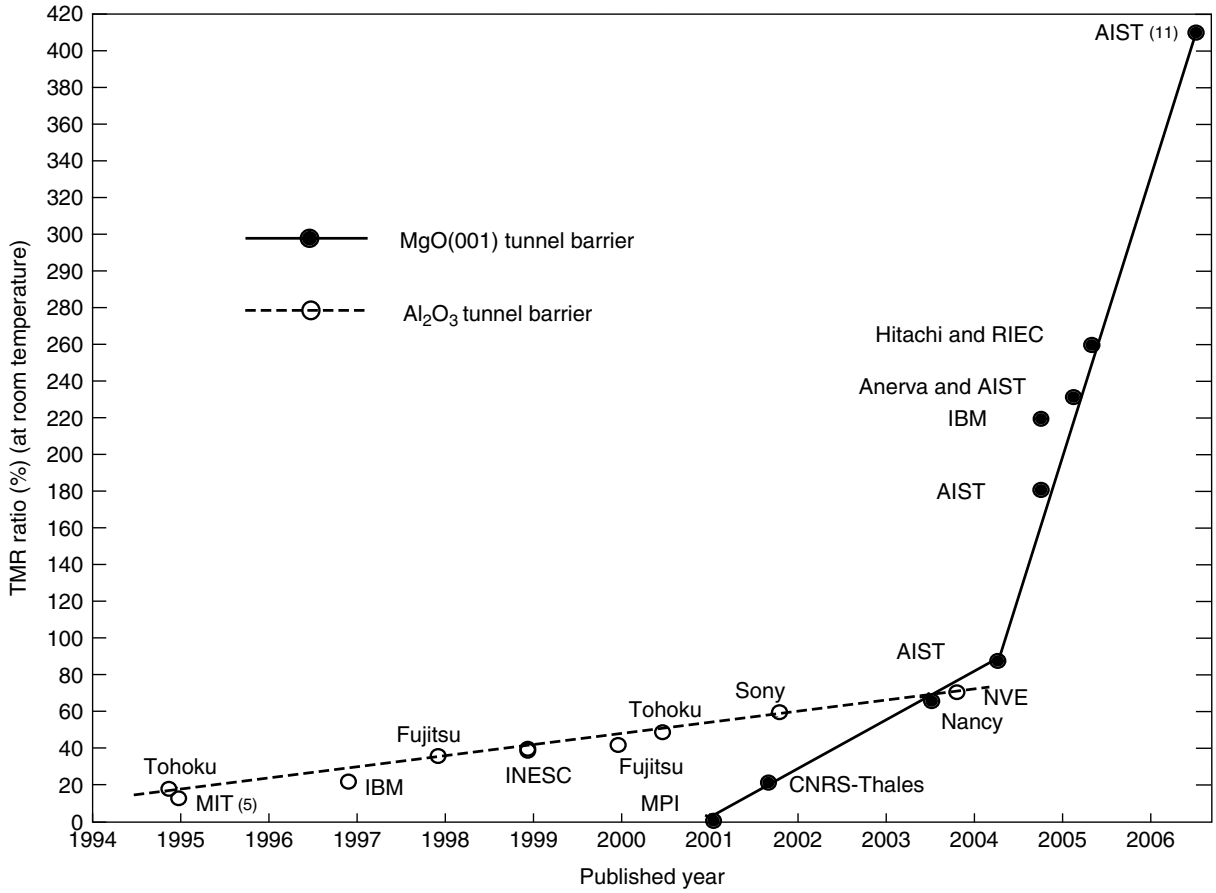

Figure 1. Evolution of the magnetoresistance of magnetic tunnel junctions with Al_2O_3(open circles) and MgO (filled circles) tunnel barriers at room temperature.

the spin polarization of the Δ_1 band in the Fe electrodes is 100%, that is, half-metallic. Mathon and Umerski (2001) arrived at qualitatively identical conclusions independently by using the multiband tight-binding model.

In this chapter, we provide a review of the theories of spin-dependent tunneling in magnetic tunnel junctions. The chapter is organized as follows. The tunneling Hamiltonian model is described in Section 2. We explain the basic ideas for dealing with the electron tunneling and derive the expression of the tunneling current and TMR. We also show some recent advances in the theory of spin-dependent tunneling in a Coulomb blockade regime. In Section 3, we provide a brief review of the free-electron model and show that the TMR is not a monotonic function of the barrier height. In Section 4, we review the theory of spin-dependent tunneling based on the tight-binding model and its application to various magnetic tunnel junctions. The first-principles model and its applications to the epitaxial magnetic tunnel junctions with MgO barriers are described in Section 5.

2 TUNNEL HAMILTONIAN MODEL

Let us consider a tunnel junction where two metallic electrodes are separated by a thin insulating barrier as shown in Figure 2. In the classical mechanics picture, the electrodes cannot exchange electrons through the barrier because the potential of the barrier is higher than the Fermi energy of the electrodes. However, quantum mechanics tells us that there is a nonzero probability of charge transfer by quantum-mechanical tunneling of electrons. The basic idea of the tunnel Hamiltonian model is to write the Hamiltonian of the system as

$$\mathcal{H} = \mathcal{H}_{\mathrm{L}} + \mathcal{H}_{\mathrm{R}} + \mathcal{H}_{\mathrm{T}} \tag{1}$$

where $\mathcal{H}_{\mathrm{L}}$ and $\mathcal{H}_{\mathrm{R}}$ are the Hamiltonians of the left and right electrodes, respectively, and the tunneling process is described by the tunnel Hamiltonian $\mathcal{H}_{\mathrm{T}}$. The tunneling probability decreases exponentially with the thickness of the barrier and is dependent on the characteristics of the

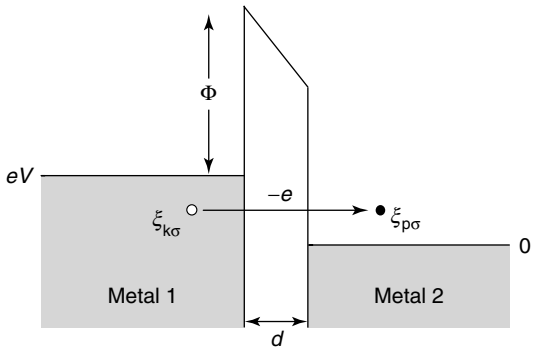

Figure 2. Electron tunneling between two normal metals. The arrow indicates the electron with spin σ transferred through the oxide barrier.

insulating material, but these aspects are absorbed in the phenomenological tunneling matrix elements $\hat{T}^{\sigma}_{\boldsymbol{pk}}$. Thus we write the effective tunnel Hamiltonian in the form

$$\mathcal{H}_{\mathrm{T}} = \sum_{\boldsymbol{kp}\sigma} \hat{T}^{\sigma}_{\boldsymbol{pk}} a^{\dagger}_{\boldsymbol{p}\sigma} a_{\boldsymbol{k}\sigma} + \mathrm{h.c} \tag{2}$$

where $a_{\boldsymbol{k}\sigma}$ is the annihilation operator of an electron with wave vector $\boldsymbol{k}$ and spin σ on the left electrode, $a^{\dagger}_{\boldsymbol{p}\sigma}$ is the creation operator of an electron with wave vector $\boldsymbol{p}$ and spin σ on the right electrode, and no spin flip is assumed in the tunneling process.

When the bias voltage V is applied to the tunnel junction, the tunneling rate $\vec{\Gamma}_{\sigma}(V)$ at which electrons with spin σ are transferred from the left to the right electrodes is calculated by Fermi's golden rule as

$$\vec{\Gamma}_{\sigma}(V) = \frac{2\pi}{\hbar} \sum_{\boldsymbol{k},\boldsymbol{p},\sigma} |\hat{T}^{\sigma}_{\boldsymbol{pk}}|^2 f(\xi_{\boldsymbol{k}\sigma}) \left[1 - f(\xi_{\boldsymbol{p}\sigma})\right] \times \delta(\xi_{\boldsymbol{k}\sigma} - \xi_{\boldsymbol{p}\sigma} + eV) \tag{3}$$

where $\xi_{\boldsymbol{k}}$ and $\xi_{\boldsymbol{p}}$ are one-electron energies measured from the Fermi levels and $f(\xi_{\boldsymbol{k}\sigma}) = \langle a^{\dagger}_{\boldsymbol{k}\sigma} a_{\boldsymbol{k}\sigma} \rangle = 1/[\exp(\xi_{\boldsymbol{k}\sigma}/k_{\mathrm{B}}T) + 1]$ is the Fermi distribution function.

The steady-state current through the junction is determined by the difference between the forward and backward tunneling rates:

$$I_{\sigma}(V) = e\left[\vec{\Gamma}_{\sigma}(V) - \overleftarrow{\Gamma}_{\sigma}(V)\right] \tag{4}$$

where $\overleftarrow{\Gamma}_{\sigma}(V)$ is the tunneling rate at which electrons with spin σ are transferred from the right to the left electrodes and is related to $\vec{\Gamma}_{\sigma}(V)$ by $\overleftarrow{\Gamma}_{\sigma}(V) = \vec{\Gamma}_{\sigma}(-V)$. Substituting equation (3) into equation (4), the tunnel current I_{σ} for the spin channel σ becomes

$$I_{\sigma}(V) = \frac{2\pi e}{\hbar} \langle |\hat{T}^{\sigma}_{\boldsymbol{pk}}|^2 \rangle \int_{-\infty}^{\infty} \mathcal{D}_{1\sigma}(\xi - eV)\mathcal{D}_{2\sigma}(\xi) \times \left[f(\xi - eV) - f(\xi)\right] \mathrm{d}\xi \tag{5}$$

where $\mathcal{D}_{1\sigma}(\xi)$ and $\mathcal{D}_{2\sigma}(\xi)$ are the *tunneling* densities of states with spin σ in the left and right electrodes, respectively, and $\langle |\hat{T}^{\sigma}_{\boldsymbol{pk}}|^2 \rangle$ is the averaged tunneling probability and taken to be a constant proportional to $\exp(-2\kappa d)$, where $\kappa = \sqrt{2m\Phi}/\hbar$ is the decay constant of the evanescent wave in the barrier and Φ is the barrier height. The total current I is given by the sum of the currents in the up- and down-spin channels: $I = I_{\uparrow} + I_{\downarrow}$.

Electron tunneling from ferromagnetic transition metals and alloys into a superconducting Al electrode through an insulating Al_2O_3barrier is one of the most powerful tools for studying the spin-polarized electronic states of FMs. In the early 1970s, Meservey and Tedrow (1994) found that, in a thin film of superconducting Al, the BCS density of states splits into up and down states by application of a magnetic field. This splitting originates from the Zeeman splitting in the quasiparticle dispersion in a magnetic field H:

$$E_{\boldsymbol{k}\sigma} = \left(\xi^2_{\boldsymbol{k}} + \Delta^2\right)^{1/2} - \sigma\mu_{\mathrm{B}}H \tag{6}$$

where Δ is the superconducting energy gap. In the absence of spin-flip scattering, the spin-dependent densities of states of quasiparticles in superconductor (SC) is given by

$$\begin{aligned} \mathcal{D}_{i\uparrow}(E) &= \mathcal{D}_{\mathrm{BCS}}(E - \mu_{\mathrm{B}}H), \\ \mathcal{D}_{i\downarrow}(E) &= \mathcal{D}_{\mathrm{BCS}}(E + \mu_{\mathrm{B}}H) \end{aligned} \tag{7}$$

where i represents the index of electrodes and $\mathcal{D}_{\mathrm{BCS}}(E)$ is the BCS density of states defined as

$$\frac{\mathcal{D}_{\mathrm{BCS}}(E)}{\mathcal{D}_{\mathrm{N}}} = \mathrm{Re}\left[\frac{|E|}{\sqrt{E^2 - \Delta^2}}\right] \tag{8}$$

where $\mathcal{D}_{\mathrm{N}}$ is the density of the state of SC in the normal state. Figure 3(a) illustrates the splitting of the BCS density of states in a magnetic field H.

The Zeeman splitting in the density of states of SC enables one to extract the spin polarization of various FMs using ferromagnet/insulator/superconductor (FM/I/SC) junctions. In magnetic fields, the densities of states of the up- and down-spin bands in FM correspond to those of the majority and minority spin bands, $\mathcal{D}_{1\uparrow} = \mathcal{D}_{\mathrm{M}}$ and $\mathcal{D}_{1\downarrow} = \mathcal{D}_{\mathrm{m}}$, respectively, while those in the SC electrode $\mathcal{D}_{2\sigma}$ are given by equation (7). Then, from equation (5), the conductance

$G = \mathrm{d}I/\mathrm{d}V$ of the junction is given by the sum of the conductance for the two independent spin directions:

$$G(V)/G_{\mathrm{N}} = \left(\frac{1+P}{2}\right)\int_{-\infty}^{\infty}\frac{\mathcal{D}_{\mathrm{BCS}}(E-\mu_{\mathrm{B}}H)/\mathcal{D}_{\mathrm{N}}}{\cosh^2\left[(E-eV)/2k_{\mathrm{B}}T\right]}\frac{\mathrm{d}E}{4k_{\mathrm{B}}T} + \left(\frac{1-P}{2}\right)\int_{-\infty}^{\infty}\frac{\mathcal{D}_{\mathrm{BCS}}(E+\mu_{\mathrm{B}}H)/\mathcal{D}_{\mathrm{N}}}{\cosh^2\left[(E-eV)/2k_{\mathrm{B}}T\right]} \times \frac{\mathrm{d}E}{4k_{\mathrm{B}}T} \tag{9}$$

where $G_{\mathrm{N}} = G_{\mathrm{N}}^{\uparrow} + G_{\mathrm{N}}^{\downarrow}$ ($G_{\mathrm{N}}^{\sigma} = (2\pi e^2/\hbar)\langle|\hat{T}_{\boldsymbol{pk}}^{\sigma}|^2\rangle\mathcal{D}_{\sigma}\mathcal{D}_{\mathrm{N}}$) is the conductance when SC is in the normal state and P is the tunneling spin polarization defined by the relative conductance between the spin-up and spin-down channels:

$$P = \frac{G_{\mathrm{N}}^{\uparrow} - G_{\mathrm{N}}^{\downarrow}}{G_{\mathrm{N}}^{\uparrow} + G_{\mathrm{N}}^{\downarrow}} = \frac{\mathcal{D}_{\mathrm{M}} - \mathcal{D}_{\mathrm{m}}}{\mathcal{D}_{\mathrm{M}} + \mathcal{D}_{\mathrm{m}}} \tag{10}$$

If $\langle|\hat{T}_{\boldsymbol{pk}}^{\sigma}|^2\rangle$ is spin independent, then P is expressed in terms of the densities of states of FM as in the third term of equation (10). In Figure 3(b), the conductance G_{σ} for each spin direction (dashed or dotted) and the total conductance $G = G_{\uparrow} + G_{\downarrow}$ (solid curve) are shown for $P = 0.5$ and $T/T_{\mathrm{c}} = 0.15$. The most striking feature of G is its asymmetry around $V = 0$. The degree of the asymmetry is directly related to the value of P through the weighted factors $\frac{1}{2}(1+P)$ and $\frac{1}{2}(1-P)$ in equation (9).

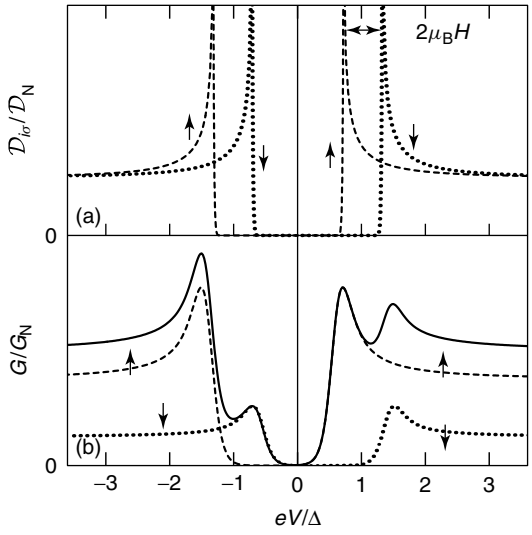

Figure 3. (a) Zeeman splitting of the BCS density of states into spin-up (dashed) and spin-down (dotted) densities of states in a magnetic field H, showing a splitting of $2\mu_{\mathrm{B}}H$. (b) Spin-up conductance (dashed), spin-down conductance (dotted), and total conductance (solid curve).

In the experiments of Tedrow and Meservey, electron tunneling between Al and ferromagnetic metals and alloys in high magnetic fields are used to measure the tunnel conductance. An analysis of the measured conductance based on equation (9) yields the spin polarization P for various FMs. In Table 1, the spin polarization P is listed for various ferromagnetic materials (Moodera and Mathon, 1999; Monsma and Parkin, 2000; Worledge and Geballe, 2000) recently measured by using improved junction preparation conditions, including samples grown by molecular-beam epitaxy (MBE).

As seen in Table 1, the values of the tunneling spin polarization P are positive, that is, $P > 0$, for all of the 3d ferromagnetic metals; the majority spin electrons are predominant in the tunnel current in all cases. From the tunneling experiments, it has been established that the tunnel currents from FM into other metals through the Al_2O_3barrier are dominated by majority spins for Ni, Co, Fe, and their alloys, and the tunneling spin polarization is correlated with the magnetic moment of the electrode. However, the positive sign of P is surprising, especially for metals such as Co and Ni, in which a negative polarization is expected owing to the smaller density of states of the majority spin band at the Fermi level, since the majority d band is below the Fermi level.

Various theoretical explanations have been proposed to explain the positive value of the spin polarization. Stearns (1977) explained this tendency by observing that the ferromagnetic transition metal has a large fraction of d electrons of free-electron-like character at the Fermi surface. Hertz and Aoi argued that the s electrons are responsible for the tunneling and the tunnel currents are proportional to the density of s states at the Fermi level, despite the much higher density of d states in 3d ferromagnetic metals (Hertz and Aoi, 1973). Recent first-principle band calculations support the idea that tunneling is dominated by electrons of s or p character; for Al_2O_3barriers and Co electrodes, the positive spin polarization might be explained by the strong bonding between the d orbitals of Co and the sp orbitals of Al (or the p orbitals of O) at the interface, which results in an almost unoccupied

Table 1. Spin polarization P for various ferromagnetic metals and alloys.

Materials	Ni	Co	Fe	$Ni_{80}Fe_{20}$	$Co_{50}Fe_{50}$	$La_{0.7}Sr_{0.3}MnO_3$
P^{a}(%)	33	45	44	48	51	–
P^{b}(%)	31	42	45	45	50	–
P^{c}(%)	–	–	–	–	–	72

[a]Moodera and Mathon (1999).
[b]Monsma and Parkin (2000).
[c]Worledge and Geballe (2000).

minority sp density of states on Al (or the minority p density of states on O) (Nyugen-Mahn *et al*., 1998; Tsymbal and Pettifor, 2000).

Now we consider the spin-dependent tunneling of magnetic tunnel junctions and derive the TMR ratio. In the low bias regime, where the bias voltage V is much smaller than the bandwidth (of order of eV) and the density of states is nearly constant, the conductance $G_\sigma = \mathrm{d}I_\sigma/\mathrm{d}V$ for each spin channel is given from equation (5) as

$$G_\sigma(V) \approx \frac{2\pi e^2}{\hbar}\langle|\hat{T}^\sigma_{\boldsymbol{pk}}|^2\rangle \mathcal{D}_{1\sigma}\mathcal{D}_{2\sigma} \tag{11}$$

where $\mathcal{D}_{1\sigma}$ and $\mathcal{D}_{2\sigma}$ are the densities of states of the spin σ band at the Fermi levels in the ferromagnetic electrodes.

Assuming that the magnetic moments of the electrodes FM1 and FM2 are aligned to be ferromagnetic (F) in applied magnetic fields, and aligned to be antiferromagnetic (A) in zero magnetic field, the total conductance $G = G_\uparrow + G_\downarrow$ in the F alignment is given by

$$G_\mathrm{F} = G^\uparrow_\mathrm{F} + G^\downarrow_\mathrm{F} \propto \mathcal{D}_{\mathrm{M}1}\mathcal{D}_{\mathrm{M}2} + \mathcal{D}_{\mathrm{m}1}\mathcal{D}_{\mathrm{m}2} \tag{12}$$

and in the A alignment it is given by

$$G_\mathrm{A} = G^\uparrow_\mathrm{A} + G^\downarrow_\mathrm{A} \propto \mathcal{D}_{\mathrm{M}1}\mathcal{D}_{\mathrm{m}2} + \mathcal{D}_{\mathrm{m}1}\mathcal{D}_{\mathrm{M}2} \tag{13}$$

where $\mathcal{D}_{\mathrm{M}i}$ and $\mathcal{D}_{\mathrm{m}i}$ are the densities of states for the majority and minority spin bands in the ith electrode, respectively (see Figure 4a and b). The TMR ratio is defined as

$$\begin{aligned} TMR &= \frac{\Delta R}{R_\mathrm{F}} = \frac{R_\mathrm{A} - R_\mathrm{F}}{R_\mathrm{F}} = \frac{G_\mathrm{F} - G_\mathrm{A}}{G_\mathrm{A}} \\ &= \frac{2P_1P_2}{1 - P_1P_2} \end{aligned} \tag{14}$$

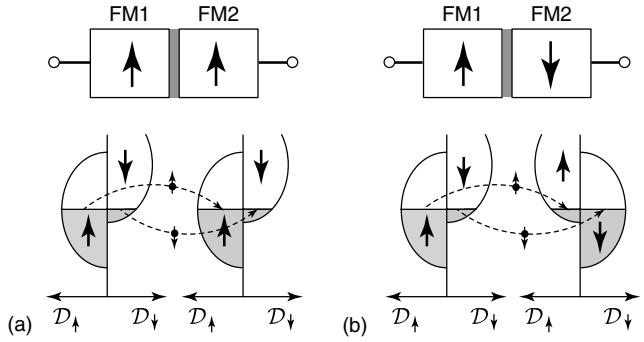

Figure 4. Ferromagnet/insulator/ferromagnet (FM1/I/FM2) tunnel junction and corresponding densities of states of FM1 and FM2 in the ferromagnetic (a) and antiferromagnetic (b) alignments of magnetizations.

where P_i is the spin polarization of the ith electrode defined by

$$P_i = \frac{\mathcal{D}_{\mathrm{M}i} - \mathcal{D}_{\mathrm{m}i}}{\mathcal{D}_{\mathrm{M}i} + \mathcal{D}_{\mathrm{m}i}} \tag{15}$$

Note that another definition, $TMR = \Delta R/R_\mathrm{A} = 2P_1P_2/(1 + P_1P_2)$, is also used in the literature.

One of the advantages of the tunnel Hamiltonian model is that the charging effect, that is, the Coulomb interaction, can be treated easily within this model. The charging energy plays an important role when we consider the charge transport through a very small island. If an electron tunnels into or out of a small island, the electrostatic charging energy changes by $e^2/2C$, where e is the electronic charge and C is the capacitance of the island. The capacitance is proportional to the size of the island and the charging energy $e^2/2C$ can take a high value for a very small island. Therefore, unless the charging energy is overcome by bias potential (eV) or thermal energy ($k_\mathrm{B}T$), an electron is not able to propagate between the electrodes. This is called the *Coulomb blockade* (CB). Since the CB is caused by the charge degrees of freedom of electrons, little attention has been paid to the spin degrees of freedom. However, in the late 1990s, improvements in nanofabrication technology enabled us to fabricate magnetic tunnel junctions in which CB phenomena were observed.

Ono *et al*. have measured the TMR in the Ni/NiO/Co/NiO/Co double junctions and observed Coulomb oscillations in the R_α versus V_g curves (Ono, Shimada and Ootuka, 1997). They found that off resonance the TMR ratio, $\Delta R/R_\mathrm{F} = (R_\mathrm{A} - R_\mathrm{F})/R_\mathrm{F}$, is enhanced to 40%, which is larger than the value of 17.5% expected from $P_\mathrm{Co} = 0.35$ and $P_\mathrm{Ni} = 0.23$ in the absence of the CB effect. The cotunneling theory (Takahashi and Maekawa, 1998) explains this enhancement, since $\Delta R/R_\mathrm{F} = 4P_\mathrm{Co}P_\mathrm{Ni}/(1 - P_\mathrm{Co}P_\mathrm{Ni})^2 = 0.38$, that is, the TMR is 38%. However, they found a TMR of $\sim$4% at resonance, which is considerably smaller than the expected TMR of 17.5%. A reduction in TMR at resonance may occur in the case of a strong tunneling of $R^\alpha_\mathrm{T} < R_\mathrm{K}$, where $R_\mathrm{K} \equiv (h/e^2) \simeq 25.8\,\Omega$ is the quantum resistance.

Recent experiments and theories for the single electron transistor (SET) have shown that the conductance in the strong tunneling case significantly deviates from that in the weak tunneling case $R^\alpha_\mathrm{T} \gg R_\mathrm{K}$. According to the theory of König and Schön (1997), on resonance the bare values of the parameters, E_c and R^s_T, are renormalized so that the conductance becomes logarithmic temperature-dependent, yielding a TMR at low temperatures

$$\left(\frac{\Delta R}{R_\mathrm{F}}\right)_\mathrm{on} = \frac{2P^2}{(1 - P^2)}\left\{1 - \frac{R_\mathrm{K}}{2\pi^2 R^{(\mathrm{F})}_\mathrm{T}}\left[\gamma_\mathrm{E} + \ln\left(\frac{E_\mathrm{c}}{\pi T}\right)\right]\right\} \tag{16}$$

where γ_E is Euler's constant. Therefore, the value of TMR at low temperatures ($k_B T \ll E_c$) is considerably reduced from that at high temperatures. If this is the case for the Ni/NiO/Co/NiO/Co double junctions, we can explain the small value of TMR mentioned above. In contrast, the TMR off resonance remains unaltered (Schoeller and Schön, 1994).

3 FREE-ELECTRON MODEL

In the tunnel Hamiltonian model in the preceding section, we assumed that the tunneling matrix elements and the spin-up and spin-down electrons can be treated as constants. In other words, the wave function in the barrier region is assumed to be independent of the wave vector and spin. However, it is not obvious that the above assumptions are justified. In 1989, Slonczewski proposed another approach for the spin-dependent tunneling based on the free-electron model, where the exact wave function in the barrier region is used (Slonczewski, 1989). He showed that TMR is determined not only by the spin polarization of FM electrodes, P, but also by the potential height of the insulating barrier. Introducing the effective spin polarization of the ferromagnetic electrode, P_{eff}, which ranges from $-P$ to P depending on the potential height of the barrier, the TMR is expressed using the same formula as that derived from the tunnel Hamiltonian model.

Before studying the spin-dependent tunneling in ferromagnetic tunnel junctions, it is convenient to consider the nonmagnetic tunnel junctions and derive an approximate form of the tunnel conductance in weak transmitting limit (Burstein and Lundqvist, 1969). When the bias voltage V is applied, electrons incident from the left electrode tunnel through the insulating barrier, resulting in a tunnel current, as shown in Figure 5(a) and (b). We assume that the system has translational symmetry in the transverse (x and y) direction and therefore the wave vector parallel to the barrier surface $\boldsymbol{k}_\parallel = (k_x, k_y)$ is conserved during the tunneling. We also assume that the temperature is zero. The number of electrons incident from the left electrode per unit time with wave vector $\boldsymbol{k}_\parallel$ is given by

$$N(\boldsymbol{k}_\parallel) = 2 \times \frac{1}{2} \int_0^{eV} \mathrm{d}E\, v_z(E, \boldsymbol{k}_\parallel) \frac{1}{\pi \hbar v_z(E, \boldsymbol{k}_\parallel)} = 2\frac{eV}{h} \tag{17}$$

where $v_z(\boldsymbol{k}_\parallel)$ is the velocity along the z direction and $1/\pi\hbar v_z(\boldsymbol{k}_\parallel)$ is the corresponding 1D density of states for the one spin channel. The factor 2 in equation (17) is due to the spin-degeneracy of the energy bands in the nonmagnetic electrode. Note that the number of incident electrons is independent of the wave vector $\boldsymbol{k}_\parallel$. The tunnel current density

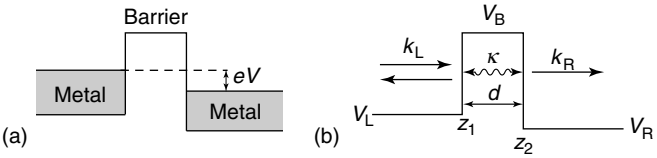

Figure 5. (a) Potential energy diagram for a metal/insulator/metal tunnel junction with the bias voltage V. The shaded area represents the occupied states of electrons at zero temperature. Electrons are transmitted from the occupied states in the left electrode to the unoccupied states in the right electrode. (b) The geometry of one-electron potential for the Hamiltonian given by equation (20). The left and right boundaries of the insulating barrier are indicated by z_1 and z_2, respectively.

is obtained by summing up the number of electrons tunneling through the barrier:

$$I = e \int \frac{\mathrm{d}k_\parallel^2}{(2\pi)^2} N(\boldsymbol{k}_\parallel) T(\boldsymbol{k}_\parallel) = 2\frac{e^2 V}{h} \int \frac{\mathrm{d}k_\parallel^2}{(2\pi)^2} T(\boldsymbol{k}_\parallel) \tag{18}$$

where $T(\boldsymbol{k}_\parallel)$ is the transmission probability defined as the ratio between the probability current densities of incident and transmitting waves. Here we assume the bias voltage V is so small that we can neglect the energy dependence of the transmission probability. The differential conductance per unit area is written in terms of the transmission probability as

$$G \equiv \frac{\mathrm{d}I}{\mathrm{d}V} = 2\frac{e^2}{h} \int \frac{\mathrm{d}k_{\parallel^2}}{(2\pi)^2} T(\boldsymbol{k}_\parallel) \tag{19}$$

The transmission probability $T(\boldsymbol{k}_\parallel)$ is obtained by solving the 1D Schrödinger equation:

$$-\frac{\hbar^2}{2m}\frac{\partial^2}{\partial z^2}\psi(z) = \left(E - V(z) - \frac{\hbar^2}{2m}\boldsymbol{k}_\parallel^2\right)\psi(z) \tag{20}$$

in the geometry shown in Figure 5(b). The general solutions of equation (20) in the left (L) electrode, barrier (B), and right (R) electrode are, respectively, of the forms

$$\begin{aligned} \psi_L(z) &= a_L e^{ik_L z} + b_L e^{-ik_L z}, && \text{for } z \le z_1 \\ \psi_B(z) &= a_B e^{\kappa z} + b_B e^{-\kappa z}, && \text{for } z_1 < z \le z_2 \\ \psi_R(z) &= a_R e^{ik_R z} + b_R e^{-ik_R z}, && \text{for } z > z_2 \end{aligned} \tag{21}$$

where the z components of the wave numbers are defined as

$$\begin{aligned} k_L &= \sqrt{(2m/\hbar^2)(E - V_L) - \boldsymbol{k}_\parallel^2} \\ \kappa &= \sqrt{k_\parallel^2 - (2m/\hbar^2)(E - V_B)} \\ k_R &= \sqrt{(2m/\hbar^2)(E - V_R) - \boldsymbol{k}_\parallel^2} \end{aligned} \tag{22}$$

The scattering wave in the whole system is given by the combination of eigen functions in equation (21). The

coefficients a_L, b_L, a_B, b_B, a_R, and b_R are determined by matching the slope and value of the wave function across the interface (Burstein and Lundqvist, 1969). The matching conditions at $z = z_1$ are conveniently described as a 2×2 matrix R_1 operating on the 2D vectors as

$$\begin{pmatrix} a_L \\ b_L \end{pmatrix} = R_1 \begin{pmatrix} a_B \\ b_B \end{pmatrix} \tag{23}$$

where

$$R_1 = \frac{1}{2k_L} \times \begin{pmatrix} (k_L - i\kappa)e^{(-ik_L+\kappa)z_1} & (k_L + i\kappa)e^{(-ik_L-\kappa)z_1} \\ (k_L + i\kappa)e^{(ik_L+\kappa)z_1} & (k_L - i\kappa)e^{(ik_L-\kappa)z_1} \end{pmatrix} \tag{24}$$

In the same manner, the matching conditions at $z = z_2$ are written as

$$\begin{pmatrix} a_B \\ b_B \end{pmatrix} = R_2 \begin{pmatrix} a_R \\ b_R \end{pmatrix} \tag{25}$$

where

$$R_2 = \frac{i}{2\kappa} \times \begin{pmatrix} (k_R - i\kappa)e^{(ik_R-\kappa)z_2} & -(k_R + i\kappa)e^{-(ik_R+\kappa)z_2} \\ -(k_R + i\kappa)e^{(ik_R+\kappa)z_2} & (k_R - i\kappa)e^{-(ik_R-\kappa)z_2} \end{pmatrix} \tag{26}$$

Since the quantity that we wish to compute is the transmission probability for the electron incident from the left electrode, only a transmitted wave exists in the right electrode and $b_R = 0$. The relation between the coefficients a_L, b_L, and a_R is

$$\begin{pmatrix} a_L \\ b_L \end{pmatrix} = R_1 R_2 \begin{pmatrix} a_R \\ 0 \end{pmatrix} \tag{27}$$

Thus, the transmission probability is

$$T(\boldsymbol{k}_\parallel) = \frac{|a_R|^2 k_R}{|a_L|^2 k_L} = \frac{k_R}{k_L} \frac{1}{|(R_1 R_2)_{11}|^2} \simeq \frac{16 k_L \kappa^2 k_R}{(k_L^2 + \kappa^2)(k_R^2 + \kappa^2)} e^{-2\kappa d} \tag{28}$$

where $d = z_2 - z_1$ is the thickness of the barrier. In the last equality of equation (28), we use the condition $e^{-2\kappa d} \ll 1$ because we are interested in the weak transmitting limit $T(\boldsymbol{k}_\parallel) \ll 1$. Substituting equation (28) into equation (19), the conductance is written as

$$G = 2\frac{e^2}{h} \int \frac{dk_\parallel^2}{(2\pi)^2} \frac{16 k_L \kappa^2 k_R}{(k_L^2 + \kappa^2)(k_R^2 + \kappa^2)} e^{-2\kappa d} \tag{29}$$

We introduce the symbols k_{L0}, k_{R0} and κ_0 to represent the wave numbers with $\boldsymbol{k}_\parallel = 0$. In equation (29), the value of $\boldsymbol{k}_\parallel$ is limited to the range of $0 \le \boldsymbol{k}_\parallel < \min[k_{L0}, k_{R0}]$. For the high barrier, $\kappa_0 \gg \boldsymbol{k}_\parallel$, and the wave number κ can be expressed as

$$\kappa = \kappa_0 \left[1 + \frac{1}{2} \left(\frac{\boldsymbol{k}_\parallel}{\kappa_0} \right)^2 \right] = \kappa_0 + \frac{\boldsymbol{k}_\parallel^2}{2\kappa_0} \tag{30}$$

Since we consider an elliptical energy band, it is often convenient to use

$$\int \frac{d^2 \boldsymbol{k}_\parallel}{(2\pi)^2} = \int \rho_\parallel(E_\parallel)\, dE_\parallel \tag{31}$$

where $E_\parallel = (\hbar^2/2m)\boldsymbol{k}_\parallel^2$ and the 2D density of states $\rho_\parallel(E_\parallel) = (m/2\pi\hbar^2)$. Therefore, the conductance can be written as

$$G = 2\frac{e^2}{h} \rho_\parallel \int_0^{\frac{\hbar^2}{2m}\min(k_{L0}^2, k_{R0}^2)} T(E_\parallel)\, dE_\parallel \tag{32}$$

where

$$T(E_\parallel) = \frac{16 e^{-2\kappa_0 d}}{(V_L - V_B)(V_R - V_B)} \times \sqrt{\frac{\hbar^2}{2m}k_{L0}^2 - E_\parallel} \sqrt{\frac{\hbar^2}{2m}k_{R0}^2 - E_\parallel} \times \left(\frac{\hbar^2}{2m}\kappa_0^2 + E_\parallel \right) \exp\left(-\frac{d}{\kappa_0} \frac{2m}{\hbar^2} E_\parallel \right) \tag{33}$$

For large d, the important region in the integral of equation (32) is $E_\parallel \simeq 0$, and we have

$$G = 2\frac{e^2}{h} \frac{\kappa_0}{4\pi d} T(0) = 2\frac{e^2}{h} \frac{4\kappa_0}{\pi d} \frac{k_{L0} \kappa_0^2 k_{R0}}{(k_{L0}^2 + \kappa_0^2)(k_{R0}^2 + \kappa_0^2)} e^{-2\kappa_0 d} \tag{34}$$

The conductance for spin-up and spin-down electrons is given by half of the total conductance in equation (34) as

$$G_\uparrow = G_\downarrow = \frac{e^2}{h} \frac{4\kappa_0}{\pi d} \frac{k_{L0} \kappa_0^2 k_{R0}}{(k_{L0}^2 + \kappa_0^2)(k_{R0}^2 + \kappa_0^2)} e^{-2\kappa_0 d} \tag{35}$$

Next, let us consider the magnetic tunnel junctions, where the conductance is spin-dependent. In the magnetic electrodes, spin-up and spin-down electrons feel the different exchange potentials h_0 and $-h_0$, respectively. The matching condition depends on the relative angle between the magnetization vectors of left and right electrodes. For simplicity, we

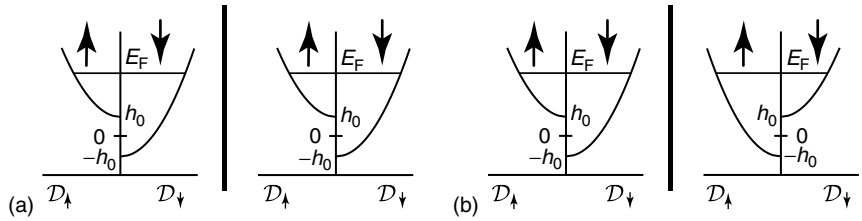

Figure 6. Densities of states for spin-up ($\mathcal{D}_\uparrow$) and spin-down ($\mathcal{D}_\downarrow$) electrons in the F alignment (a) and those in the A alignment (b).

consider two types of alignments of magnetization vectors, ferromagnetic (F) and antiferromagnetic (A) alignments, as shown in Figure 6(a) and (b). The spin quantization axis is taken to be parallel to the magnetization vector in the left electrode. For the F alignment, where the magnetization vectors are parallel, we have two tunneling processes: electrons incident from the left majority (minority) spin band tunnel to the right majority (minority) spin band. Potential diagrams for these two tunneling processes are shown in Figure 7(a) and (b), respectively. The wave numbers of electrons in the majority and minority spin bands are

$$k_{\mathrm{M}} = \sqrt{(2m/\hbar^2)(E - h_0) - \boldsymbol{k}_\parallel^2} \quad \text{(majority)} \tag{36}$$

$$k_{\mathrm{m}} = \sqrt{(2m/\hbar^2)(E + h_0) - k_\parallel^2} \quad \text{(minority)} \tag{37}$$

The conductance for spin-up (spin-down) electrons is obtained from equation (35) by setting $k_{\mathrm{L0}} = k_{\mathrm{R0}} = k_{\mathrm{M0}}(k_{\mathrm{m0}})$, where $k_{\mathrm{M0}}(k_{\mathrm{m0}})$ is the wave number for the electrons in the majority (minority) spin band with $k_\parallel = 0$:

$$G_\uparrow^{\mathrm{F}} = \frac{e^2}{h}\frac{4\kappa_0^3}{\pi d}\frac{k_{\mathrm{m0}}^2}{(k_{\mathrm{m0}}^2 + \kappa_0^2)^2}\mathrm{e}^{-2\kappa_0 d},$$

$$G_\downarrow^{\mathrm{F}} = \frac{e^2}{h}\frac{4\kappa_0^3}{\pi d}\frac{k_{\mathrm{M0}}^2}{(k_{\mathrm{M0}}^2 + \kappa_0^2)^2}\mathrm{e}^{-2\kappa_0 d} \tag{38}$$

The total conductance for the F alignment takes the form

$$G^{\mathrm{F}} = G_\uparrow^{\mathrm{F}} + G_\downarrow^{\mathrm{F}}$$

$$= \frac{e^2}{h}\frac{4\kappa_0^3}{\pi d}\left[\frac{k_{\mathrm{m0}}^2}{(k_{\mathrm{m0}}^2 + \kappa_0^2)^2} + \frac{k_{\mathrm{M0}}^2}{(k_{\mathrm{M0}}^2 + \kappa_0^2)^2}\right]\mathrm{e}^{-2\kappa_0 d} \tag{39}$$

In contrast, for the A alignment where the magnetization vectors are antiparallel, electrons incident from the left majority (minority) spin band tunnel to the right minority (majority) spin band. The potential diagrams for spin-up and spin-down electrons are depicted in Figure 7(c) and 7(d), respectively. The conductance for the A alignment is given by

$$G_\uparrow^{\mathrm{A}} = G_\downarrow^{\mathrm{A}} = \frac{e^2}{h}\frac{4\kappa_0^3}{\pi d}\frac{k_{\mathrm{m0}}k_{\mathrm{M0}}}{(k_{\mathrm{m0}}^2 + \kappa_0^2)(k_{\mathrm{M0}}^2 + \kappa_0^2)}\mathrm{e}^{-2\kappa_0 d}$$

$$G^{\mathrm{A}} = G_\uparrow^{\mathrm{A}} + G_\downarrow^{\mathrm{A}}$$

$$= \frac{e^2}{h}\frac{4\kappa_0^3}{\pi d}\frac{2k_{\mathrm{m0}}k_{\mathrm{M0}}}{(k_{\mathrm{m0}}^2 + \kappa_0^2)(k_{\mathrm{M0}}^2 + \kappa_0^2)}\mathrm{e}^{-2\kappa_0 d} \tag{40}$$

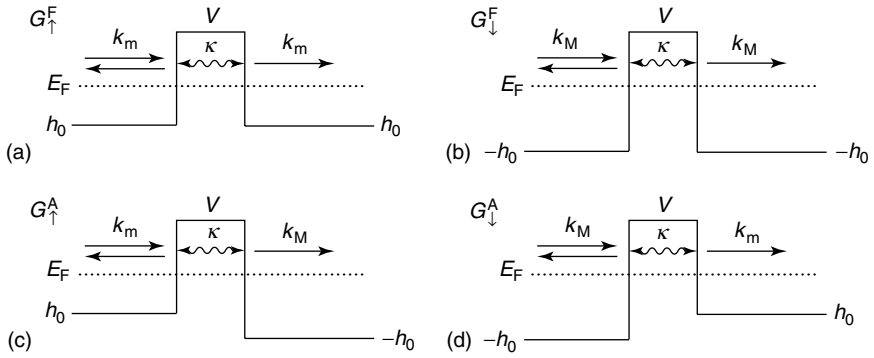

Figure 7. Geometries of the potentials for spin-up and spin-down electrons in the F alignment are shown in panels a) and (b), and those in the A alignment are shown in (c) and (d), respectively.

Using equations (39) and (40), the TMR is expressed as (Slonczewski, 1989)

$$TMR = \frac{G^{\mathrm{F}} - G^{\mathrm{A}}}{G^{\mathrm{A}}} = \frac{(k_{\mathrm{m0}} - k_{\mathrm{M0}})^2(\kappa_0^2 - k_{\mathrm{m0}}k_{\mathrm{M0}})^2}{2k_{\mathrm{m0}}k_{\mathrm{M0}}(k_{\mathrm{m0}}^2 + \kappa_0^2)(k_{\mathrm{M0}}^2 + \kappa_0^2)} = \frac{2P_{\mathrm{eff}}^2}{1 - P_{\mathrm{eff}}^2} \tag{41}$$

where P_{eff} is the effective spin polarization defined as

$$P_{\mathrm{eff}} = \frac{\kappa_0^2 - k_{\mathrm{m0}}k_{\mathrm{M0}}}{\kappa_0^2 + k_{\mathrm{m0}}k_{\mathrm{M0}}} P \tag{42}$$

in which $P = (k_{\mathrm{M0}} - k_{\mathrm{m0}})/(k_{\mathrm{M0}} + k_{\mathrm{m0}})$ is the spin polarization of the ferromagnetic electrode with an elliptical energy band.

Since the wave number in the barrier region κ_0 ranges from 0 (low barrier limit) to ∞ (high barrier limit), we have $-P < P_{\mathrm{eff}} < P$. In the high barrier limit, the TMR is the same as that obtained by the tunneling Hamiltonian method. One interesting result of the free-electron model is that P_{eff} is diminished, and therefore the TMR for values of the barrier height ($\kappa_0 \sim k_{\mathrm{m0}}k_{\mathrm{M0}}$) is diminished. This variation of the TMR has been experimentally observed by Tezuka and Miyazaki (1998) as shown in Figure 8.

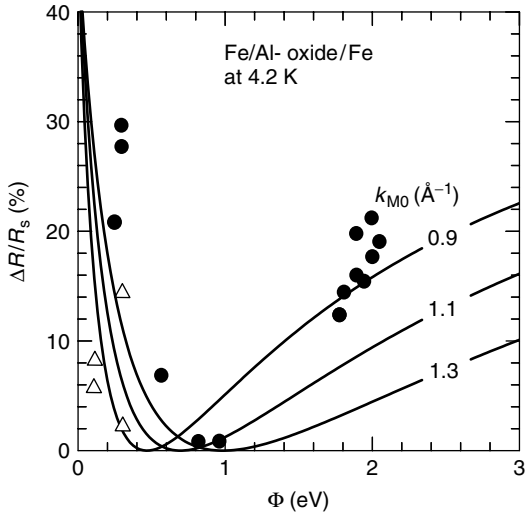

Figure 8. Dependence of TMR on the barrier height Φ at 4.2 K. The horizontal axis is the barrier height obtained by fitting the I–V curves to Simmon's relation (Simmons, 1963). The solid curves are the calculated values using the free-electron model. (Reproduced from N. Tezuka and T. Miyazaki, *J. Magn. Magn. Mater.* **177-181**, 1998, 1283, copyright © 1998, with permission from Elsevier.)

4 TIGHT-BINDING MODEL

Recently, more realistic calculation methods based on the tight-binding Hamiltonian and the Kubo–Landauer formula have been developed by several authors (Zhang and Levy, 1999; Moodera and Mathon, 1999; Asano, Oguri and Maekawa, 1993; Mathon, 1997; Tsymbal and Pettifor, 1998; Mathon and Umerski, 1999; Itoh *et al.*, 1999; Itoh, Ohsawa and Inoue, 2000). The tight-binding model is of great use both in dealing with multiorbital systems having a realistic band structure and in studying the effect of the disorder and roughness of the insulating barrier on the spin-dependent tunneling. In order to understand the basic formalism of the conductance calculation in the tight-binding model, we first consider the 1D chain shown in Figure 9, which is expressed by the following 1D Hamiltonian:

$$\mathcal{H} = -t \sum_{\langle n,n' \rangle} c_n^\dagger c_{n'} + \sum_n \varepsilon_n c_n^\dagger c_n \tag{43}$$

where t is the hopping matrix element and ε_n is the on-site energy at the nth site. The spin indices are dropped for simplicity. In the low bias regime, the conductance G at zero temperature is given by the Kubo formula as

$$G = \frac{\pi\hbar}{N^2} \sum_{\alpha\beta} \left| \sum_{n=1}^{N} \langle \alpha | J(n) | \beta \rangle \right|^2 \times \delta(E_{\mathrm{F}} - E_\alpha)\delta(E_{\mathrm{F}} - E_\beta) \tag{44}$$

where $|\alpha\rangle$ and $|\beta\rangle$ are the eigenstates of the system with energies E_α and E_β, respectively, and the current operator at site n is defined as

$$J(n) = \frac{ie}{\hbar} \left[t c_{n+1}^\dagger c_n - t c_n^\dagger c_{n+1} \right] \tag{45}$$

In the stationary state of the system, the current conservation requires that $J(n)$ is independent of n, and thus the

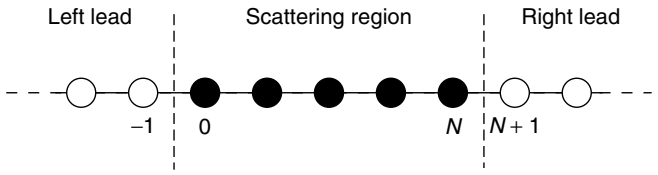

Figure 9. Schematic of the 1D chain including the scattering region, which is indicated by filled circles. The scattering region is connected with the left and right ideal leads.

conductance reduces to

$$\begin{aligned} G = \frac{\pi e^2}{\hbar} t^2 \sum_{\alpha\beta} \Big[& \langle n+1|\alpha\rangle\langle\alpha|n+1\rangle\langle n|\beta\rangle\langle\beta|n\rangle \\ & - \langle n|\alpha\rangle\langle\alpha|n+1\rangle\langle n|\beta\rangle\langle\beta|n+1\rangle \\ & - \langle n+1|\alpha\rangle\langle\alpha|n\rangle\langle n+1|\beta\rangle\langle\beta|n\rangle \\ & + \langle n|\alpha\rangle\langle\alpha|n\rangle\langle n+1|\beta\rangle\langle\beta|n+1\rangle \Big] \\ & \times \delta(E_{\mathrm{F}} - E_\alpha)\delta(E_{\mathrm{F}} - E_\beta) \end{aligned} \tag{46}$$

where $|n\rangle$ is the one-particle state created by the operator $c_n^\dagger$. Let us introduce the Green function:

$$\begin{aligned} \tilde{\mathcal{G}}(n,n') &= \frac{i}{2}\left[\mathcal{G}^+(n,n') - \mathcal{G}^-(n,n')\right] \\ &= \pi \sum_\alpha \langle n|\alpha\rangle\langle\alpha|n'\rangle \delta(E - E_\alpha) \end{aligned} \tag{47}$$

where $\mathcal{G}^+$ and $\mathcal{G}^-$ are the retarded and advanced one-electron Green functions expressed as

$$\mathcal{G}^\pm(n,n') = \left\langle n \left| \frac{1}{E - \mathcal{H} \pm i\delta} \right| n' \right\rangle \tag{48}$$

Here, $\mathcal{H}$ is the total Hamiltonian and δ is a small positive number. Using the Green function defined by equation (47), the conductance can be written as

$$\begin{aligned} G = \frac{4e^2}{h} \Big[& t\tilde{\mathcal{G}}(n,n) t\tilde{\mathcal{G}}(n+1,n+1) \\ & - t\tilde{\mathcal{G}}(n,n+1) t\tilde{\mathcal{G}}(n,n+1) \Big] \end{aligned} \tag{49}$$

The advanced and retarded Green functions are easily obtained by the recursion method (Thouless and Kirkpatrick, 1981; Lee and Fisher, 1981). In the matrix form, the Hamiltonian is given by

$$\mathsf{H} = \begin{pmatrix} \cdots & -t & 0 & 0 & 0 \\ -t & \varepsilon_0 & -t & 0 & 0 \\ 0 & -t & \varepsilon_1 & -t & 0 \\ 0 & 0 & -t & \varepsilon_2 & -t \\ 0 & 0 & 0 & -t & \cdots \end{pmatrix} \tag{50}$$

where the dimension of the matrix is infinite since we consider an open system. Let us define the Green function for the system in which all sites $n > n_0$ are deleted as

$$\mathsf{G}_{n_0}^{\mathrm{L}\pm} = \left[(E \pm i\eta)\mathsf{I} - \mathsf{H}_{n_0}^{\mathrm{L}} \right]^{-1} \tag{51}$$

where the Hamiltonian $\mathsf{H}_{n_0}^{\mathrm{L}}$ consists of sites $n \geq n_0$. The Green function for the system $H_{n_0+1}^{\mathrm{L}}$ satisfies the following equation:

$$\left[(E \pm i\eta)\mathsf{I} - \mathsf{H}_{n_0+1}^{\mathrm{L}} \right] \mathsf{G}_{n_0+1}^{\mathrm{L}\pm} = \mathsf{I} \tag{52}$$

$$\begin{aligned} & \begin{pmatrix} (E \pm i\eta)\mathsf{I} - \mathsf{H}^{\mathrm{L}}(n_0) & -t \\ -t^\dagger & E \pm i\eta - \varepsilon_{n_0+1} \end{pmatrix} \\ & \times \begin{pmatrix} \mathsf{A}_1 & \mathsf{A}_2 \\ \mathsf{A}_3 & \mathcal{G}_{n_0+1}^{\mathrm{L}\pm}(n_0+1, n_0+1) \end{pmatrix} = \mathsf{I} \end{aligned} \tag{53}$$

where $t^\dagger = (0, \cdots, 0, t)$. It follows that the Green function $\mathcal{G}_n^{\mathrm{L}\pm}(n,n)$ satisfies the following recursive relation:

$$\mathcal{G}_{n_0+1}^{\mathrm{L}\pm}(n_0+1, n_0+1) = \left[g^\pm(n_0+1)^{-1} - t\mathcal{G}_{n_0}^{\mathrm{L}\pm}(n_0,n_0)t \right]^{-1} \tag{54}$$

where $g^\pm(n) = (E \pm i\eta - \varepsilon_{n_0+1})^{-1}$ is the Green function for the isolated site $n_0 + 1$. Starting from the left semi-infinite ideal lead, where the exact Green function is analytically given, we can evaluate the Green function $\mathcal{G}_n^{\mathrm{L}\pm}(n,n)$ at arbitrary site $n \geq 1$.

The Green function for the whole system satisfies

$$\begin{aligned} & \begin{pmatrix} (E \pm i\eta)\mathsf{I} - \mathsf{H}_{n-1}^{\mathrm{L}} & -t & 0 \\ -t^\dagger & E \pm i\eta - \varepsilon_n & -t \\ 0 & -t^\dagger & (E \pm i\eta)\mathsf{I} - \mathsf{H}_{n+1}^{\mathrm{R}} \end{pmatrix} \\ & \times \begin{pmatrix} \mathsf{A}_1 & \mathsf{A}_2 & \mathsf{A}_3 \\ \mathsf{A}_4 & \mathcal{G}^\pm(n,n) & \mathsf{A}_5 \\ \mathsf{A}_6 & \mathsf{A}_7 & \mathsf{A}_8 \end{pmatrix} = \mathsf{I} \end{aligned} \tag{55}$$

where $\mathsf{H}_{n_0}^{\mathrm{R}}$ is the Hamiltonian for the semi-infinite system in which all sites $n < n_0$ are deleted. The Green function for the isolated right electrode is calculated by using the following recursive relation:

$$\mathcal{G}_{n_0}^{\mathrm{R}\pm}(n_0,n_0) = \left[g^\pm(n_0)^{-1} - t\mathcal{G}_{n_0+1}^{\mathrm{R}\pm}(n_0+1, n_0+1)t \right]^{-1} \tag{56}$$

The diagonal element of the advanced and retarded Green function for the whole system $\mathcal{G}^\pm(n,n)$ is given by

$$\begin{aligned} \mathcal{G}^\pm(n,n) = \big[& g^\pm(n)^{-1} - t\mathcal{G}_{n-1}^{\mathrm{L}\pm}(n-1,n-1)t - t \\ & \times \mathcal{G}_{n+1}^{\mathrm{R}\pm}(n+1,n+1)t \big]^{-1} \end{aligned} \tag{57}$$

It is also easy to show that the off-diagonal element is given by

$$\mathcal{G}^\pm(n,n+1) = \mathcal{G}^\pm(n,n)t\mathcal{G} \pm {}^{\mathrm{R}}{}_{n+1}(n+1,n+1) \tag{58}$$

Finally, the total conductance for each spin direction is calculated by using equations (49)–(58).

The tight-binding model described above is easily generalized to a 3D junction with a multiorbital system. The Hamiltonian is given by

$$\mathcal{H} = -\sum_{\langle n,n'\rangle,\alpha,\beta,\sigma} t_{n\alpha,n'\beta} c^{\dagger}_{n\alpha\sigma} c_{n'\beta\sigma} + \sum_{n,\alpha,\sigma} \varepsilon_{n\alpha\sigma} c^{\dagger}_{n\alpha\sigma} c_{n\alpha\sigma} \tag{59}$$

where the lattice sites are labeled by indices n and n', and $c^{\dagger}_{n\alpha\sigma}(c_{n\alpha\sigma})$ is the creation (annihilation) operator of an electron with spin σ and orbital α on the lattice site n. The hopping energy is $t_{nn'\alpha\beta}$, and the summation $\langle n, n'\rangle$ runs over nearest-neighbor sites. The spin-dependent on-site potential $\varepsilon_{n\alpha\sigma}$ includes the exchange potential in the FM, and the disorder and roughness of the insulating barrier are described by the variation of the hopping $t_{n\alpha,n'\beta}$ and on-site energy $\varepsilon_{n\alpha\sigma}$ (Itoh *et al*., 1999).

Mathon has studied the continuous transition from the current-perpendicular-to-plane giant magnetoresistance (CPP-GMR) of metallic systems to the TMR of tunnel junctions with a vacuum gap and an insulating barrier (Mathon, 1997). The tunnel junction with a vacuum gap is obtained by gradually turning off the overlap matrix elements between the ferromagnetic electrodes. The insulating barrier is obtained by varying the on-site potentials in the spacer so that the Fermi level in the spacer layer moves into the band gap. It is shown that the tunneling across the vacuum gap and through an insulating barrier leads to the same TMR provided the barrier is at least as high as the conduction bandwidth and the barrier is narrow, not wider than a few atomic planes. It is also shown that the tunneling current across the vacuum gap is carried only by the s−p electrons in the tunneling regime, though a significant proportion of the current in the magnetic metal (Co) is carried by d electrons that are highly spin polarized. The switching from d electrons to s−p electrons can explain the value of the TMR ratio and the change in the sign of spin polarization P of tunneling electrons.

The effect of disorder and roughness of the insulating barrier on TMR has been studied by several authors (Zhang and Levy, 1999; Mathon, 1997; Tsymbal and Pettifor, 1998; Mathon and Umerski, 1999; Itoh *et al*., 1999). Figure 10 shows the TMR ratio R_{MR} of the magnetic tunnel junctions with and without interface roughness calculated by Itoh *et al*. (1999). The interface roughness is treated with the help of the coherent potential approximation (Soven, 1967; Velický, 1969). One can see that R_{MR} for $E_{\mathrm{F}} = -5t$ is enhanced by the interface roughness while that for $E_{\mathrm{F}} = 0$ is suppressed. They found that the diffusive conductance originating from the interface roughness was highly dependent on the shape of the Fermi surface.

The tight-binding model has also been used to study the TMR for half-metallic systems by using the double exchange

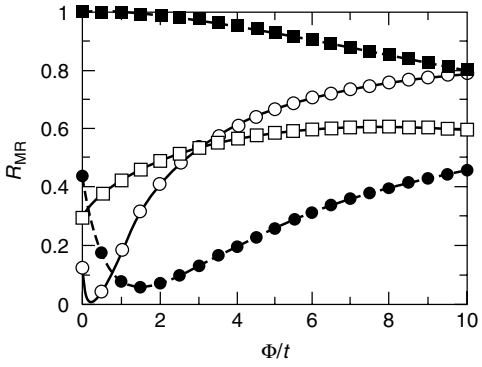

Figure 10. TMR ratio R_{MR} as a function of the barrier height Φ for $E_{\mathrm{F}} = -5t$ (solid and open circles) and $E_{\mathrm{F}} = 0$ (solid and open squares). Solid and open symbols denote the results without (c = 0) and with (c = 0.5) randomness, respectively. The average barrier thickness is taken to be 11 atomic layers. (Reproduced from H. Itoh, A. Shibata, T. Kumazaki, J. Inoue, and S. Maekawa, *J. Phys. Soc. Jpn.* **68**, 1632 (1999), with permission from the Physical Society of Japan.)

model (Itoh, Ohsawa and Inoue, 2000). It is shown that the strong exchange coupling in the double exchange model plays an important role in the temperature dependence of both P and the TMR ratio; their values can be less than the maximum values expected for half-metallic systems at low temperatures, and the TMR ratio decreases more rapidly than P with increasing temperature. The calculated results, however, indicate that the TMR ratio may still be large at high temperatures near the Curie temperature.

The TMR of an epitaxial Fe/MgO/Fe(001) junction was calculated by Mathon and Umerski (2001) and independently by Butler, Zhang, Schulthess and MacLaren (2001). Mathon and Umerski used the tight-binding model with the bands fitted to an *ab initio* band structure of Fe and MgO. The calculated TMR ratio is 1200% for 20 atomic planes of MgO. As mentioned earlier, the larger TMR ratio in epitaxial magnetic tunnel junctions has been observed by several groups (Bowen *et al*., 2001; Faure-Vincent *et al*., 2003); Parkin *et al*., 2004; Yuasa *et al*., 2004; Djayaprawira *et al*., 2005; Hayakawa *et al*., 2005; Yuasa, 2006). The most powerful method to study the spin-dependent tunneling in an epitaxial magnetic tunnel junction is given by the first-principles model, as discussed in the next section.

5 FIRST-PRINCIPLES MODEL

In 1999, MacLaren, Zhang, Butler and Wang (1999) developed a calculation technique for spin-dependent tunneling in magnetic tunnel junctions based on the LKKR method (MacLaren *et al*., 1990). The LKKR method is a self-consistent electronic structure method, based on the LSDA or on some other approximation to density-functional theory,

which may be used to calculate the electronic structure of a three-dimensional solid without requiring the usual constraint of three-dimensional translational symmetry. The LKKR calculation for an interface proceeds as follows: first, a bulk calculation is performed to find the self-consistent potentials for the two leads far from the interface. Then, the whole system with the interface is set up, and the spin-up and spin-down potentials on atomic layers within the sample and within the leads near the interface are allowed to relax through the iterative procedure until electrostatic self-consistency is achieved through the system. Since the plane-wave reflection and transmission coefficients are generated by the LKKR method, the reflection and transmission coefficients for Bloch waves incident on the sample from one of the leads can be obtained easily after a few algebraic steps (MacLaren, Zhang, Butler and Wang, 1999). Then the conductance is obtained by using the Landauer–Büttiker formalism.

MacLaren *et al*. applied the LKKR-based first-principles method to the spin-dependent tunneling in Fe/ZnSe/Fe(100) tunnel junctions and predicted that the TMR ratio reaches as high a value as about 2000%. However, it is difficult to fabricate the epitaxial magnetic tunnel junction with ZnSe showing a larger TMR ratio. Gustavsson, George, Etgens and Eddrief (2001) fabricated an epitaxial Fe/ZnSe/FeCo junction on ZnSe(001)-buffered GaAs(001) substrates by MBE. The transport measurement on microfabricated tunnel junctions yielded up to 16% at 10 K. Butler, Zhang, Schulthess and MacLaren (2001) studied the spin-dependent tunneling in Fe/MgO/Fe junctions by using the LKKR-based first-principles method (MacLaren, Zhang, Butler and Wang, 1999), and predicted a TMR ratio of as high a value as 6000%. As mentioned in the preceding section, Mathon and Umerski (2001) arrived at qualitatively identical conclusions by using the multiband tight-binding description for the electronic structure. Soon after the publication of these two theoretical papers, Bowen *et al*. (2001) reported that a TMR ratio of 27% was observed at 300 K in Fe/MgO/FeCo(001) epitaxial junctions. Encouraged by this work, many groups (Faure-Vincent *et al*., 2003); Parkin *et al*., 2004; Yuasa *et al*., 2004; Djayaprawira *et al*., 2005; Hayakawa *et al*., 2005; Yuasa, 2006) have made substantial efforts for developing epitaxial magnetic tunnel junctions with an MgO barrier having a high TMR ratio, as shown in Figure 1.

The key to understanding the origin of the high TMR ratio observed in the MgO system is the evanescent gap state in the MgO barrier. The decay rate of the evanescent waves in the MgO barrier depends strongly on the symmetry of the wave function. Figure 11 shows the dispersion $k^2(E)$ for MgO in the vicinity of the gap along Δ (100) (Butler, Zhang, Schulthess and MacLaren, 2001). There are three kinds of evanescent waves with different symmetries within the gap, Δ_1, $\Delta_{2'}$, and Δ_5. The horizontal axis is $(k\Delta z)^2$, where k is in the (001) direction and Δz is the interplanar spacing for MgO(001). Negative values of $(k\Delta z)^2$ determine the exponential decay rates for various Bloch states. As shown in Figure 11, the weakest decay is for the state with Δ_1 symmetry, which implies that the evanescent wave with Δ_1 symmetry gives the dominant contribution to the tunneling current. The proportion of the tunneling current carried by the Δ_1 states increases with increasing barrier thickness.

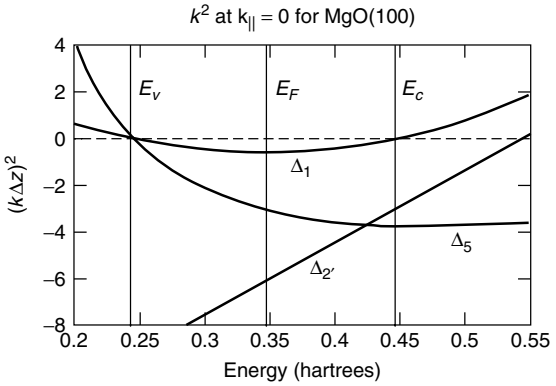

Figure 11. Dispersion $k^2(E)$ for MgO in the vicinity of the gap along Δ (100). k is in the (001) direction and Δz is the interplanar spacing for MgO(001). E_F is the Fermi energy. E_v is the top of the valence band. E_c is the bottom of the conduction band. (Reproduced from Butler *et al*. 2001, with permission from the American Physical Society. © 2001.)

Figure 12 shows the energy band structure of Fe(001) calculated by the LKKR method (Nagahama, Yuasa, Tamura and Suzuki, 2005). The majority and minority spin bans are represented by thin and thick lines, respectively, and the energy bands with Δ_1 symmetry are plotted with solid lines. One can see that the minority spin band with Δ_1 symmetry is absent at the Fermi energy. In contrast, there are majority spin states with Δ_1 symmetry at the Fermi energy. Therefore, the tunneling of electrons with majority spin dominates the current, which yields a high TMR ratio for sufficiently thick barriers. The situation is clearly shown by the tunneling density of states (TDOS) plotted in Figure 12 (b). The TDOS is defined as the density of electronic states subject to the following boundary conditions: on the left-hand side of the interface, there is an incoming Bloch state with unit flux and the corresponding Bloch state with unit flux and the corresponding reflected Bloch states; on the right-hand side are the corresponding transmitted Bloch states (Butler, Zhang, Schulthess and MacLaren, 2001). The states with Δ_2, $\Delta_{2'}$, Δ_5 symmetry decay much faster than that with Δ_1 symmetry. When the magnetizations of Fe electrodes are aligned so as to be antiparallel, only one electrode has the state with Δ_1 symmetry. Therefore, the current is much suppressed than in the case with the parallel alignment, and we have a high TMR ratio.

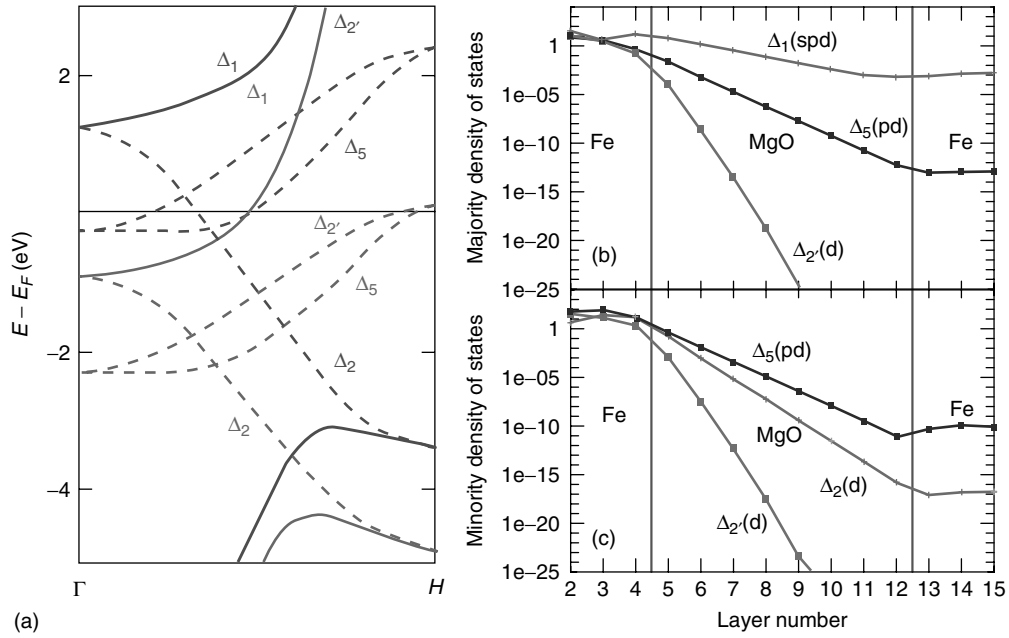

Figure 12. (a) Band structure of Fe(001) calculated by the LKKR method. Solid lines indicate the Δ_1 band, and broken lines indicate other bands. Thick curves represent the band of minority spin, and thin curves the band of majority spin. The majority spin has a Δ_1 band at the Fermi level. (Reproduced from Nagahama *et al*., 2005, with permission from the American Physical Society. © 2005.) (b) Tunneling density of states (TDOS) of the majority spin band for Fe(100)/MgO/Fe(100). (c) TDOS of the minority spin band for Fe(100)/MgO/Fe(100). (Reproduced from Butler *et al*., 2001, with permission from the American Physical Society. © 2001.) Each TDOS curve is labeled by the symmetry of the incident Bloch state in the left Fe electrode, and the magnetizations of Fe(100) electrodes are aligned so as to be parallel.

The transmission electron microscope (TEM) image of a single-crystal magnetic tunnel junction with Fe(001)/MgO (001)(1.8 nm)/Fe(001) fabricated by Yuasa's group (AIST) and the observed TMR ratio are shown in Figure 13(a) and (b), respectively (Yuasa *et al*., 2004). In the TEM image the lattice dislocations are indicated by circles. The lattice of the top Fe electrode is slightly expanded along the [110] axis. The existence of the lattice dislocations is the clear difference between the theoretical model and the real system, and should be considered if we want to construct a more accurate theoretical model of epitaxial tunnel junctions. If we treat the effect of the lattice dislocation on the spin-dependent tunneling in an appropriate way, the quantitative disagreement of the TMR ratio between the theoretical prediction and experimental results will be settled. The predicted TMR ratio is more than 10 times larger than the experimentally observed one. As mentioned before, as the thickness of the MgO barrier increases, the contribution from the states with Δ_1 symmetry increases and therefore the TMR ratio increases, as shown in Figure 13(b). One surprising finding is that the TMR ratio exhibits clear oscillatory behavior as a function of the thickness of the MgO barrier, t_{MgO}. The period of the oscillations (0.30 nm) is independent of temperature and bias voltage, but the amplitude of the oscillation decreases with increasing bias voltage. The origin of the oscillation might be an interference effect, since the period is inconsistent with the thickness of a monoatomic MgO(001) layer (0.22 nm). However, this is still an open question, and further development of the theoretical understanding of this system is required.

6 CONCLUSION

In this chapter, we have described the theoretical models of spin-dependent tunneling in magnetic tunnel junctions, that is, the tunneling Hamiltonian model, free-electron model, tight-binding model, and first principles model. Each model has its own merits and demerits and we should choose the right model for each system. The tunneling Hamiltonian model is a phenomenological model that introduces a crude approximation of constant values for the tunneling matrix elements. However, it gives an intuitive picture of tunneling and a quite useful expression of the TMR ratio. The free-electron model is the simplest of the models that include the quantum coherence. It can explain the anomalous dependence of the TMR ratio on the barrier height, although it cannot handle the multiorbit effect and the scattering due to the disorder. The tight-binding model is a very powerful tool that can treat the complex band structure of materials and

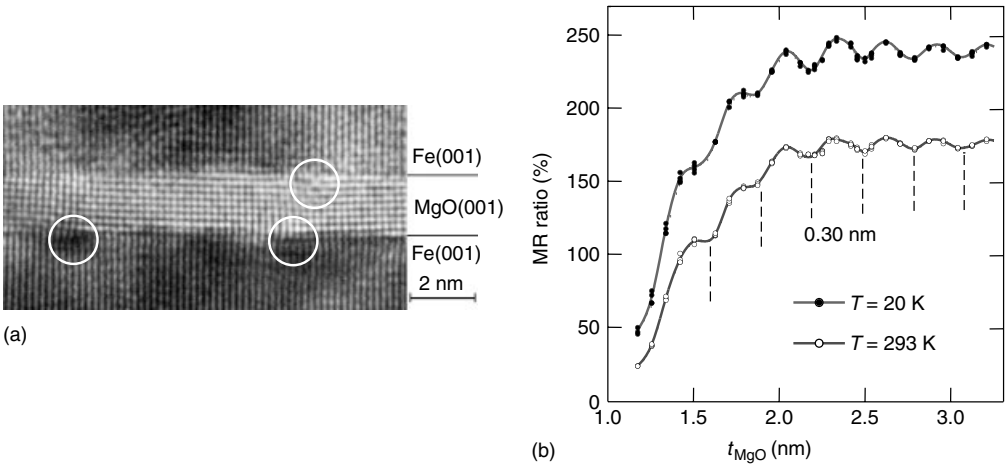

Figure 13. (a) High-resolution TEM image of a single-crystal magnetic tunnel junction with Fe(001)/MgO(001)(1.8 nm)/Fe(001) structure. The vertical and horizontal directions respectively correspond to the MgO[001](Fe[001]) axis and MgO[100](Fe[110]) axis. Lattice dislocations are circled. (b) TMR ratio at T = 293 and 20 K (measured at a bias voltage of 10 mV) versus t_{MgO}. (Reproduced from Yuasa, T. Nagahama, A. Fukushima, Y. Suzuki, and K. Ando, *Nature Materials* **3**, 868 (2004), with permission from Nature Publishing Group.)

disorder at the interface. The model can be applied to both the magnetic tunnel junctions with an amorphous Al_2O_3barrier and those with an epitaxial MgO barrier. However, the model has many parameters that must be determined empirically by fitting the first-principles calculation. The first-principles model has no empirical parameters by definition. However, its computational cost is expensive and it requires two-dimensional translational symmetry.

In order to develop efficient spin-electronic devices, the materials and device designs based on the appropriate theoretical model are required. One successful example is the high TMR ratio realized in the epitaxial magnetic tunnel junctions with MgO barrier, as described in Section 5. The theoretical understanding of the physics of spin-dependent tunneling promises further development of spin electronics and related fields. Further improvements in our theoretical understanding of the physics of spin-dependent tunneling will lead to advances in spin electronics and related fields.

REFERENCES

Asano, Y., Oguri, A. and Maekawa, S. (1993). Parallel anda perpendicular transport in multilayered structures. *Physical Review B*, **48**, 6192.

Bowen, M., Cros, V., Petroff, F., *et al*. (2001). Large magnetoresistance in Fe/MgO/FeCo(001) epitaxial tunnel junctions on GaAs(001). *Applied Physics Letters*, **79**, 1655.

Burstein, E. and Lundqvist, S. (Eds.) (1969). *Tunneling Phenomena in Solids*, Plenum Press: New York.

Butler, W.H., Zhang, X.G., Schulthess, T.C. and MacLaren, J.M. (2001). Spin-dependent tunneling conductance of Fe vertical bar MgO vertical bar Fe sandwiches. *Physical Review B*, **63**, 054416.

Djayaprawira, D.D., Tsunekawa, K., Nagai, M., *et al*. (2005). 230% room-temperature magnetoresistance in CoFeB/MgO/CoFeB magnetic tunnel junctions. *Applied Physics Letters*, **86**, 092502.

Faure-Vincent, J., Tiusan, C., Jouguelet, E., *et al*. (2003). High tunnel magnetoresistance in epitaxial Fe/MgO/Fe tunnel junctions. *Applied Physics Letters*, **82**, 4507.

Gustavsson, F., George, J-M., Etgens, V.H. and Eddrief, M. (2001). Structural and transport properties of epitaxial Fe/ZnSe/FeCo magnetic tunnel junctions. *Physical Review B*, **64**, 184422.

Hayakawa, J., Ikeda, S., Matsukura, F., *et al*. (2005). Dependence of giant tunnel magnetoresistance of sputtered CoFeB/MgO/CoFeB magnetic tunnel junctions on MgO barrier thickness and annealing temperature. *Japanese Journal of Applied Physics*, **44**, L587.

Hertz, J. and Aoi, K. (1973). Spin-Dependent Tunneling from Transition-Metal Ferroagnets. *Physical Review B*, **8**, 3252.

Itoh, H., Ohsawa, T. and Inoue, J. (2000). Magnetoresistance of ferromagnetic tunnel junctions in the double-exchange model. *Physical Review Letters*, **84**, 2501.

Itoh, H., Shibata, A., Kumazaki, T., *et al*. (1999). Effects of randomness on tunnel conductance and magnetoresistance in ferromagnetic tunnel junctions. *Journal of the Physical Society of Japan*, **68**, 1632.

Julliere, M. (1975). Tunneling between ferromagnetic films. *Physics Letters*, **54A**, 225.

König, H.S.J. and Schön, G. (1997). Cotunneling at resonance for the single-electron transistor. *Physical Review Letters*, **78**, 4482.

Lee, P. and Fisher, D. (1981). Anderson Localization in Two Dimensions. *Physical Review Letters*, **47**, 882.

MacLaren, J.M., Crampin, S., Vvedensky, D., *et al*. (1990). Layer Korringa-Kohn-Rostoker electronic-structure code for bulk and interface geometries. *Computer Physics Communications*, **60**, 365.

MacLaren, J.M., Zhang, X.G., Butler, W.H. and Wang, X. (1999). Layer KKR approach to Bloch-wave transmission and reflection:

Application to spin-dependent tunneling. *Physical Review B*, **59**, 5470.

Maekawa, S. and Gäfvert, U. (1982). Electron-tunneling between ferromagnetic-films. *IEEE Transactions on Magnetics*, **18**, 707.

Mathon, J. (1997). Tight-binding theory of tunneling giant magnetoresistance. *Physical Review B*, **56**, 11810.

Mathon, J. and Umerski, A. (1999). Theory of tunneling magnetoresistance in a junction with a nonmagnetic metallic interlayer. *Physical Review B*, **60**, 1117.

Mathon, J. and Umerski, A. (2001). Theory of tunneling magnetoresistance of an epitaxial Fe/MgO/Fe(001) junction. *Physical Review B*, **63**, 220403.

Meservey, R. and Tedrow, P. (1994). Spin-polarized electron-tunneling. *Physics Reports*, **238**, 173.

Miyazaki, T. and Tezuka, N. (1995). Giant magnetic tunneling effect in Fe/Al_2O_3/Fe junction. *Journal of Magnetism and Magnetic Materials*, **139**, L231.

Monsma, D. and Parkin, S. (2000). Spin polarization of tunneling current from ferromagnet/Al_2O_3 interfaces using copper-doped aluminum superconducting films. *Applied Physics Letters*, **77**, 720.

Moodera, J., Kinder, L., Wong, T. and Meservey, R. (1995). Large magnetoresistance at room-temperature in ferromagnetic thin-film tunnel-junctions. *Physical Review Letters*, **74**, 3273.

Moodera, J. and Mathon, G. (1999). Spin polarized tunneling in ferromagnetic junctions. *Journal of Magnetism and Magnetic Materials*, **200**, 248.

Nagahama, T., Yuasa, S., Tamura, T. and Suzuki, Y. (2005). Spin-dependent tunneling in magnetic tunnel junctions with a layered antiferromagnetic Cr(001) spacer: Role of band structure and interface scattering. *Physical Review Letters*, **95**, 086602.

Nyugen-Mahn, D., Tsymbal, E., Pettifor, D., *et al*. (1998). Spin-polarized density of states and electron tunnelling from the Co/Al_2O_3 interface. *Materials Research Society Symposia Proceedings*, **492**, 319.

Ono, K., Shimada, H. and Ootuka, Y. (1997). Enhanced magnetic valve effect and magneto-Coulomb oscillations in ferromagnetic single electron transistor. *Journal of the Physical Society Of Japan*, **66**, 1261.

Parkin, S., Kaiser, C., Panchula, A., *et al*. (2004). Giant tunnelling magnetoresistance at room temperature with MgO (100) tunnel barriers. *Nature Materials*, **3**, 862.

Schoeller, H. and Schön, G. (1994). Mesoscopic quantum transport: Resonant tunneling in the presence of a strong Coulomb interaction. *Physical Review B*, **50**, 18436.

Simmons, J. (1963). Generalized Formula for the Electric Tunnel Effect between Similar Electrodes Separated by a Thin Insulating Film. *Journal of Applied Physics*, **34**, 1793.

Slonczewski, J. (1989). Conductance and exchange coupling of two ferromagnets separated by a tunneling barrier. *Physical Review B*, **39**, 6995.

Soven, P. (1967). Coherent-Potential Model of Substitutional Disordered Alloys. *Physical Review*, **156**, 809.

Stearns, M. (1977). Simple explanation of tunneling spin-polarization of Fe, Co, Ni and its alloys. *Journal of Magnetism and Magnetic Materials*, **5**, 167.

Takahashi, S. and Maekawa, S. (1998). Effect of Coulomb Blockade on Magnetoresistance in Ferromagnetic Tunnel Junctions. *Physical Review Letters*, **80**, 1758.

Tezuka, N. and Miyazaki, T. (1998). Barrier height dependence of MR ratio in Fe/A1-oxide/Fe junctions. *Journal of Magnetism and Magnetic Materials*, **177–181**, 1283.

Thouless, D. and Kirkpatrick, S. (1981). Conductivity of the disordered linear-chain. *Journal of Physics C-Solid State Physics*, **14**, 235.

Tsymbal, E. and Pettifor, D. (1998). Spin-polarized electron tunneling across a disordered insulator. *Physical Review B*, **58**, 432.

Tsymbal, E. and Pettifor, D. (2000). Oxygen-induced positive spin polarization from Fe into the vacuum barrier. *Journal of Applied Physics*, **87**, 5230.

Velický, B. (1969). Theory of Electronic Transport in Disordered Binary Alloys: Coherent-Potential Approximation. *Physical Review*, **184**, 614.

Wang, D., Nordman, C., Daughton, J.M., *et al*. (2004). 70% TMR at room temperature for SDT sandwich junctions with CoFeB as free and reference layers. *IEEE Transactions on Magnetics*, **40**, 2269.

Worledge, D. and Geballe, T. (2000). Spin-polarized tunneling in $La_{0.67}Sr_{0.33}MnO_3$. *Applied Physics Letters*, **76**, 900.

Yuasa S.(2006) Giant tunneling magnetoresistance up to 410% at room temperature in fully epitaxial Co/MgO/Co magnetic tunnel junctions with bcc Co(001) electrodes. *Applied Physics Letters*, **89**, 042505.

Yuasa, S., Nagahama, T., Fukushima, A., *et al*. (2004). Giant room-temperature magnetoresistance in single-crystal Fe/MgO/Fe magnetic tunnel junctions. *Nature Materials*, **3**, 868.

Yuasa, S., Sato, T., Tamura, E., *et al*. (2000). Magnetic tunnel junctions with single-crystal electrodes: A crystal anisotropy of tunnel magneto-resistance. *European Physics Letters*, **52**, 344.

Zhang, S. and Levy, P. (1999). Models for magnetoresistance in tunnel junctions. *European Physical Journal B*, **10**, 599.

Magnetism of Low-dimensional Metallic Structures

Axel Enders[1], Pietro Gambardella[2,3] and Klaus Kern[1,2]

[1] *Max-Planck-Institut für Festkörperforschung, Stuttgart, Germany*
[2] *Ecole Polytechnique Fédérale de Lausanne (EPFL), Lausanne, Switzerland*
[3] *Catalan Institute of Research and Advanced Studies (ICREA), Barcelona, Spain*

1 INTRODUCTION

Many elements in the periodic table show a magnetic moment as free atoms. However, only iron, cobalt, nickel, and a few rare-earths and their alloys exhibit ferromagnetic properties in bulk compounds. The evolution of the atomic magnetic moments, their mutual coupling (which ultimately produces macroscopic magnetism), and the appearance of magnetic anisotropy in molecules, nanosized aggregates, and solids are the subjects of intense investigation. Besides being of fundamental interest, such questions bear on the design of novel magnetic devices with one or more dimensions reduced to the length scale of interatomic cooperative magnetic behavior. Understandably, we have good theoretical models and plenty of experimental data that tell us how magnetism works in free atoms and crystalline solids. However, as we explore the realm in between these two limits, we face a remarkable paucity of experimental information. The relevant length scale of the exchange interaction in most magnetic materials is only a few atomic spacings. This is the reason why the exploration of magnetic nanostructures has traditionally lagged behind the semiconductor field. Whereas in semiconductors the dimensions of the system influence the charge carriers' behavior already for typical lengths of tens of nanometers, magnetic materials must be engineered down to the Angstrom scale. It is only in the last two decades that advances in growth and characterization methods have allowed us to investigate and produce artificial structures with magnetic properties controlled with nanometer precision. Such progress has given rise to a wealth of technological applications, such as magnetic sensors and hard disk read heads making use of giant magnetoresistance effects, spin-based electronics, and new magnetic media.

Here, we are concerned with fundamental issues that govern the magnetic behavior of nanostructured materials as well as that of magnetic alloys down to the ultimate atomic scale. We describe the fabrication and the magnetic properties of zero-dimensional (0D), one-dimensional (1D), and two-dimensional (2D) nanostructures of Co and Fe, outlining the governing principles for self-organized growth of metallic nanostructures on crystalline substrates. By exploiting the hierarchy of diffusion processes on flat and stepped metal surfaces, we are able to construct low-dimensional magnetic systems almost atom-by-atom, which gives us an unprecedented view on the evolution of magnetization, magnetic anisotropy,

Handbook of Magnetism and Advanced Magnetic Materials. Edited by Helmut Kronmüller and Stuart Parkin. Volume 1: *Fundamentals and Theory*. ISBN: 978-0-470-02217-7.

and magnetic order from atoms to solids. Starting from individual impurities, we let ensembles of dimers, trimers, and larger clusters self-assemble by controlling their coverage and substrate temperature. Surfaces with regular arrays of monatomic steps are used to induce the formation of 1D atomic chains. With increasing coverage the chains evolve into stripes in a row-by-row fashion, and finally into 2D atomically thin layers. The investigation of such structures has revealed exciting and unexpected properties. As one important result we demonstrate how the superparamagnetic limit – encountered in samples too small to provide sufficient long-term stability of ferromagnetic order and a well-known limit to the increase of the bit density in magnetic memories – can be elegantly circumvented in nanostructures. The key is in the very large magnetic anisotropy of some of the nanostructures, which results from their reduced atomic coordination on one hand, and the electronic hybridization with substrate atoms on the other hand. The discussed examples demonstrate how nanoscale structures can provide practical solutions to elude classical difficulties in the use of magnetic materials as well as fundamental input to our understanding of magnetic phenomena.

2 SELF-ORGANIZED GROWTH OF METALLIC NANOSTRUCTURES

Common to all bottom-up strategies for the fabrication of metallic nanostructures at surfaces is that they are essentially based on growth phenomena. Atoms are deposited on the substrate in vacuum, and nanoscale structures evolve as the result of a multitude of atomistic processes. This is inherently a nonequilibrium phenomenon. Any growth scenario is governed by the competition between kinetics and thermodynamics. In thermodynamic equilibrium, detailed balance requires that all atomistic processes proceed in opposite directions at equal rate. Hence, at finite temperature, the system fluctuates around equilibrium configurations and no net growth occurs – a situation well described by statistical mechanics. The formation of nanostructures at surfaces requires nonequilibrium. A measure for the degree of nonequilibrium is the supersaturation, defined as the actual adatom/admolecule density normalized to the equilibrium adatom/admolecule density $(\rho - \rho_e)/\rho_e$. The supersaturation describes to which extent the evolving structures will be determined by the growth kinetics or by thermodynamic parameters, such as the surface and interface free energy. The larger the supersaturation, the more decisive the kinetic processes.

In a growth experiment, where atoms are deposited at a surface with a constant rate F, the diffusivity D determines the average distance l an adatom has to travel to meet another one to nucleate a new aggregate or to attach to an already formed island. In the nucleation stage at very low coverage this length decreases rapidly and eventually becomes constant, typically at coverages above a few percent of a monolayer (Brune, Roder, Boragno and Kern, 1994). In this saturation regime any further deposition will exclusively lead to the growth of existing islands. The average diffusion length l, and correspondingly the nucleation density at saturation, only depends on the ratio D:F (Pimpinelli, Villain and Wolf, 1992). The ratio of deposition to diffusion rate is thus the key quantity characterizing the growth kinetics and a measure for the supersaturation. If the deposition is slow with respect to the diffusivity, the supersaturation is low and growth takes place close to equilibrium conditions; that is, adatoms or admolecules have enough time to explore the potential energy surface to reach a minimum energy configuration. If the deposition is fast with respect to the diffusivity, the individual atomistic processes become increasingly important and the growth scenario is essentially determined by kinetics.

2.1 The hierarchy of activated motion

Of particular interest within this chapter are metal nanostructures on metal surfaces. At low substrate temperature, the growth of such a system is a prototype for the kinetically dominated growth regime. The shape and size of the nanostructures are largely determined by the competition of the active diffusion processes and can be controlled by the external parameters temperature and deposition flux and by the appropriate choice of the substrate symmetry (Röder *et al*., 1993). The central atomic processes are surface diffusion processes of single adatoms, comprising diffusion on terraces (characterized by the diffusion barrier E_d), over steps (E_s), along edges (E_e), and across corners (E_c). All these diffusion processes are thermally activated, with the respective rate depending exponentially on the potential energy barrier. To first order, these barriers scale with the local coordination; that is, terrace diffusion has a lower barrier than edge diffusion and corner crossing (Stumpf and Scheffler, 1994). Edge descend is often more costly than terrace diffusion due to an extra barrier at the edge of an island, known as the *Schwoebel–Ehrlich barrier* (Ehrlich and Hudda, 1966). For a given material system we have thus a natural hierarchy of the relevant diffusion barriers. By selective activation/freezing of a certain diffusion process we can shape the growing aggregates.

As already mentioned, the terrace diffusion barrier determines the mean free path of a diffusing adatom on the substrate surface and also on top of islands, which build up during deposition. The barrier for crossing a step fixes the average number of attempts necessary for an adatom

to descend the edge. It is the interplay between these two parameters, which determines whether an aggregate grows 2D or three-dimensionally (3D). If atoms nucleate on top of islands without having visited their edge at all, or after they have visited it too few times to descend, the aggregates grow 3D. Otherwise, the downward flux of adatoms is large enough so that no nucleation occurs on top of an island and the aggregates grow only laterally.

If the Schwoebel–Ehrlich barrier is not too large, one can always find growth conditions where the interlayer diffusion is fast enough to prevent any 3D growth. The aggregates then grow in 2D or 1D shape depending on the interplay of the various intralayer diffusion processes. Even 1D growth of aggregates can be easily initiated by choosing a substrate with an intrinsic diffusion anisotropy (Röder *et al*., 1993; Mo, Kleiner, Webb and Lagally 1991). The fcc(110) surface is such a substrate. Due to the particular structure of this surface with troughs along the [1–10] direction, diffusion is much faster along this direction than in the orthogonal [001] direction. This diffusion anisotropy and the fact that corner crossing is also anisotropic can be exploited for the growth of 1D chains (Li *et al*., 1997) (Figure 1a). Another, particularly intriguing way to promote the formation of 1D atomic chains is the use of substrate steps, as will be discussed later in this section.

On substrates with no terrace diffusion anisotropy, aggregates show 2D with the shape determined by the competition between terrace and edge diffusion. On close-packed surfaces large compact islands can only be grown at sufficiently high temperature, where edge diffusion is active and island corners can be crossed (Röder *et al*., 1993; Michely and Comsa, 1991; Morgenstern, Rosenfeld and Comsa, 1996) (Figure 1b). At low temperature, the mobility of adatoms attached to island edges is limited or frozen and the aggregates grow in ramified island shapes (Hwang, Schroder, Gunther and Behm, 1991; Brune, Romainczyk, Roder and Kern, 1994) (Figure 1c). The metal aggregation on fcc(111) surfaces at low temperature is thus a nice model system for fractal growth in the diffusion limited aggregation scenario (Witten and Sander, 1981). The branches can be randomly ramified or grow into crystallographic well-determined directions. The latter is termed *dendritic growth* and the dominant atomistic process here is the anisotropy in the corner crossing (Brune *et al*., 1996). For square lattices, on the other hand, edge and terrace diffusion are too close in energy leading to compact island shapes even at low temperature (Zhang, Chen and Lagally, 1994).

The size of nanostructures formed in the diffusion limited regime can be controlled directly by temperature, flux, and coverage. Owing to the inherent stochastic nature of the nucleation and growth process, however, the possibility of tuning the size distribution is somewhat limited. Narrowed size distribution can be obtained by either Ostwald ripening, confined nucleation, or self-limiting processes. The nucleation regime is ideally suited to synthesize very small clusters comprising just a few atoms. The size distribution achieved here is characterized by a standard deviation roughly scaling with $<n>^{1/2}$, where n is the number of atoms. Larger particle sizes with substantially narrowed size distribution, $0.3<n>$, can be synthesized by the Ostwald ripening technique (Röder *et al*., 1993). Such size distributions are, however, often sufficiently narrow to explore the size dependence of the physical and chemical properties of metallic nanostructures, such as their magnetism.

2.2 Steering and positioning

Any application of magnetic nanostructures requires the fabrication of ordered nanostructure arrays with individually

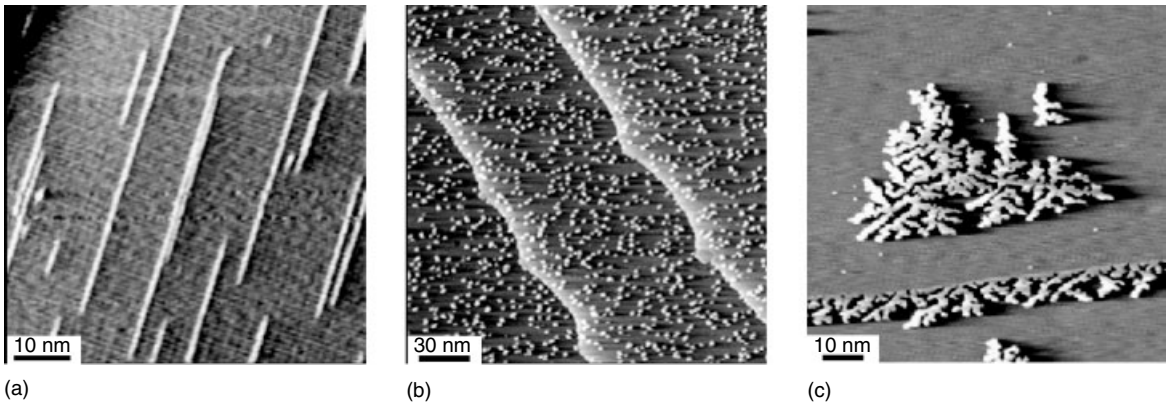

Figure 1. Atomic architecture at surfaces by control of growth kinetics. (a) Formation of monatomic Cu chains on the anisotropic Pd(110) substrate. (b) and (c) Ag nanostructures on Pt(111); size and shape are determined by controlling the kinetic growth parameters deposition flux and temperature.

addressable units. Moreover, uniformity in position and spacing are important considerations because the properties of the nanostructures may not only depend on their size and shape but also on their mutual interactions. Thus, growth strategies need to be developed providing nearly monodisperse nanostructures, which are organized in regular arrangements.

Lateral ordering of the nanostructures can be achieved by (i) self-ordering due to mutual long-range interactions and (ii) directed growth on patterned substrates. The latter approach turned out as particularly successful for guiding nanostructure formation. The patterned surfaces serve as nanotemplates with predefined nucleation sites or energetic sinks (Brune, Giovannini, Bromann and Kern, 1998; Nötzel, 1996; Temmyo, Kuramochi, Kamada and Tamamura, 1998). With this directed self-ordering strategy, the position of each nanostructure is exactly defined by the template, thus yielding nucleation sites predictable with nanometer accuracy. Depending on the required length scale, artificially or naturally structured surfaces can be employed. Natural nanotemplates are surfaces with reconstructions (Barth, Brune, Ertl and Behm, 1990), periodic dislocation networks (Brune, Roder, Boragno and Kern, 1994), or regularly spaced steps (Hahn *et al*., 1994; Kirakosian *et al*., 2001). In these systems periodic spacings ranging from a few angstroms up to a few nanometers are provided. If larger spacings are needed, the usual top-down fabrication techniques can be applied for the fabrication of prestructured substrates (Nötzel, 1996).

Important progress in the fabrication of 2D nanostructure arrays could be made by employing substrates with dislocation networks. These dislocation networks occur naturally on some surfaces (Barth, Brune, Ertl and Behm, 1990) and can also be produced in a controlled way in thin epitaxial films (Brune, Roder, Boragno and Kern, 1994) or by wafer bonding (Leroy, Eymery, Gentile and Fournel, 2002). Typical periodicities range between 2 and 20 nm. The dislocation lines are in general found to be repulsive toward diffusing atoms (Brune, Giovannini, Bromann and Kern, 1998; Fischer *et al*., 1999), while dislocation elbows can act as sinks for mobile atoms (Chambliss, Wilson and Chiang, 1991). For a well-defined set of growth parameters, the adatoms are, therefore, in the first case confined within the dislocation network unit cells, exactly nucleating one island per unit cell. In the second case, islands preferentially nucleate at the attractive defects. These techniques have successfully been applied in the growth of metal or semiconductor nanostructure arrays and even magnetic nanopillars (Fruchart, Klaua, Barthel and Kirschner, 1999). A valuable side effect of the nucleation and growth on such patterned substrates is the typically enhanced size uniformity. In this case, the size distribution becomes binominal and the size uniformity is determined by the statistical fluctuations in the deposition process. As the homogeneity increases with the size of the atom collecting area, the monodispersity becomes better with increasing island distance (Brune, Giovannini, Bromann and Kern, 1998).

As mentioned earlier, regularly stepped surfaces can serve as natural nanotemplates for the self-organized growth of 1D nanoarrays. The step edges act as preferential nucleation sites for the deposited material due to the increased coordination with respect to the terrace sites. A row-by-row decoration of the steps can be achieved if (i) the terrace mobility is high enough that all adatoms can reach the steps and (ii) the mobility of the atoms once attached to the steps is still sufficient to ensure 1D nucleation and growth (Gambardella *et al*., 2000). At appropriate deposition temperatures, the width of the adlayer chains can be changed discretely from monatomic to diatomic, triatomic and so on, simply by controlling the total coverage. Perfect 1D nanotemplates are for example, the (557) surface of Si and the (997) surface of Pt, which had been proven to show highly ordered step structures (Hahn *et al*., 1994; Kirakosian *et al*., 2001). As an example, the Pt(997) surface composed of (111) oriented terraces of 20.2 Å in width, separated by monatomic steps, is shown in Figure 2(a). The regular step ordering is mediated by the repulsive step–step interactions, which suppress step meandering. As examples for nanotemplate supported growth, arrays of 1D Co and Fe chains fabricated on Pt(997) will be discussed within this chapter (see Figure 2b and inset in Figure 8a).

3 MAGNETISM OF ZERO- AND ONE-DIMENSIONAL STRUCTURES

3.1 Magnetic atoms on nonmagnetic substrates

In this chapter, we are concerned with fundamental issues that govern the intrinsic magnetic properties of low-dimensional metal systems fabricated by molecular beam epitaxy on nonmagnetic substrates. We define as *intrinsic* those properties that depend on atomic scale magnetism and crystalline structure, such as the magnetic moment, the magnetocrystalline anisotropy, and magnetic order, as opposed to the *extrinsic* properties that depend on the microstructure and magnetostatic interactions (Kronmüller, 2003; Skomski and Coey, 1999). The main focus will be on 0D and 1D systems, where the influence of size and dimensionality effects on the intrinsic magnetization parameters is largest. For a thorough treatment of 2D systems such as magnetic thin films and multilayers, we refer to the extensive monographs published on the subject (Gradmann, 1993; Schneider and Kirschner, 2000; Bland and Heinrich, 2005) and to other chapters of

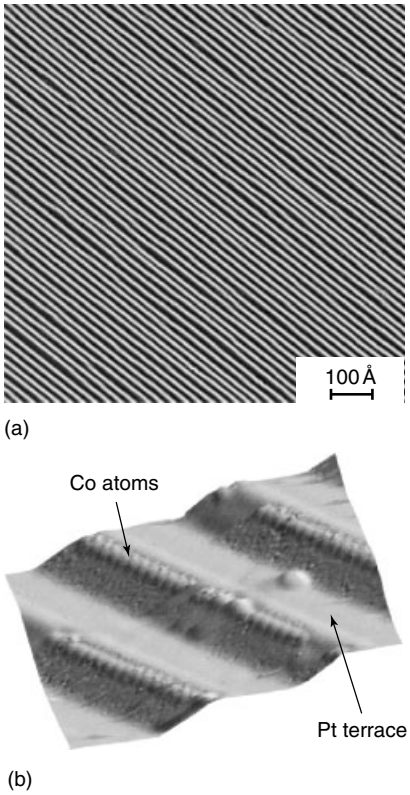

Figure 2. (a) The STM image of a Pt(997) surface shows (111)-oriented terraces of 20 Å width, separated by monatomic steps. The high degree of order makes this substrate an ideal nanotemplate for nanostructure fabrication. (b) Formation of monatomic chains of Co atoms by substrate step decoration.

this handbook (see **Magnetism of Low-dimensional Systems: Theory, Volume 1** and **Magnetic Ultrathin Films, Volume 4**).

The fabrication of magnetic nanostructures and thin films by molecular beam epitaxy (MBE) methods is typically initiated by the deposition of magnetic atoms from the vapor-phase onto a nonmagnetic substrate, as discussed in the preceding text. A first point of fundamental and practical interest, in this context, is the extent to which the local magnetic moment of a transition metal impurity is modified by the interaction with the supporting substrate. The role played by magnetic/nonmagnetic interfaces in determining the magnetization and particularly the anisotropy fields in ultrathin films has been widely investigated in the past (Gradmann, 1993; Sander, 2004). With the aim of controlling the magnetic behavior of structures with ever reducing dimensions, however, our knowledge must progress toward the atomic size level. Identifying and distinguishing local substrate-impurity hybridization effects from coordination and magnetoelastic effects in thin films, for instance, provide useful guidelines to tailor the intrinsic magnetization parameters in finite-sized supported particles, optimize sensitive interface properties that govern electron transport in magnetoelectronic devices (Jansen and Moodera, 1998), and test current theoretical models of low-dimensional magnetic systems (see also **Magnetism of Low-dimensional Systems: Theory, Volume 1**).

Most transition metal atoms in the gas phase possess large spin (m_S) and orbital (m_L) magnetic moments due to the incomplete filling of the d-shell and the atomic correlation effects exemplified by the Hund's rules. In the solid state, electron delocalization and crystal field effects compete with intra-atomic Coulomb interactions causing a substantial or total decrease of m_S and quenching of m_L. Theoretical calculations, however, predict such effects to be strongly reduced at surfaces owing to the decreased coordination of transition metal impurities (see also **Magnetism of Low-dimensional Systems: Theory, Volume 1**; Stepanyuk *et al*., 1996; Nonas *et al*., 2001). As a case experimental system, we consider the magnetic properties of Co. As free atom in the ground state d^7 configuration, Co displays significant spin and orbital magnetism with $m_S = m_L = 3\,\mu_B$, and Brillouin-like isotropic magnetization (Figure 3a). In the bulk hexagonal close-packed structure Co is a strong ferromagnet with $m_S = 1.52$ and $m_L = 0.15\,\mu_B$ and exhibits a fairly large magnetocrystalline anisotropy energy (MCA) compared to bulk Fe and Ni, with a uniaxial anisotropy energy constant $K = 0.05$ meV per atom (Bonnenberg, Hempel and Wijn, 1986).

Once deposited onto a metal surface, we expect the magnetic moment of Co atoms to vary according to the degree of d-orbital hybridization with the conduction electron states of the substrate (Gambardella *et al*., 2002b; Song and Bergmann, 2001). This will depend on the reduced number of neighbors around the impurity as well as on the host band structure, similar to dilute alloys with nonmagnetic metals (Mydosh and Nieuwenhuys, 1980). In dealing with surface impurities, the experimental challenge lies in probing extremely reduced amounts of magnetic atoms (typically the order of 10^{14} atoms cm^{-2} or less, deposited at cryogenic temperature to avoid cluster formation) on a macroscopic metal surface with nonnegligible para- or diamagnetic response. To achieve the required element-specific sensitivity, the method of choice is the absorption of circularly polarized light in the soft X-ray range, described in the chapters **Magnetic Spectroscopy, Volume 1** and **Synchrotron Radiation Techniques Based on X-ray Magnetic Circular Dichroism, Volume 3**. The lineshape of the X-ray absorption spectra (XAS) at the $L_{2,3}$ edges of 3d transition metals ($2p^6 3d^n$ to $2p^5 3d^{n+1}$ excitations) contains information about the electronic configuration of the impurities (van der Laan and Thole, 1991). Simultaneously, as the X-ray absorption cross-section depends on the orientation of the spin and orbital moment of the 3d electrons relative to the X-ray polarization direction, magnetic sensitivity is achieved

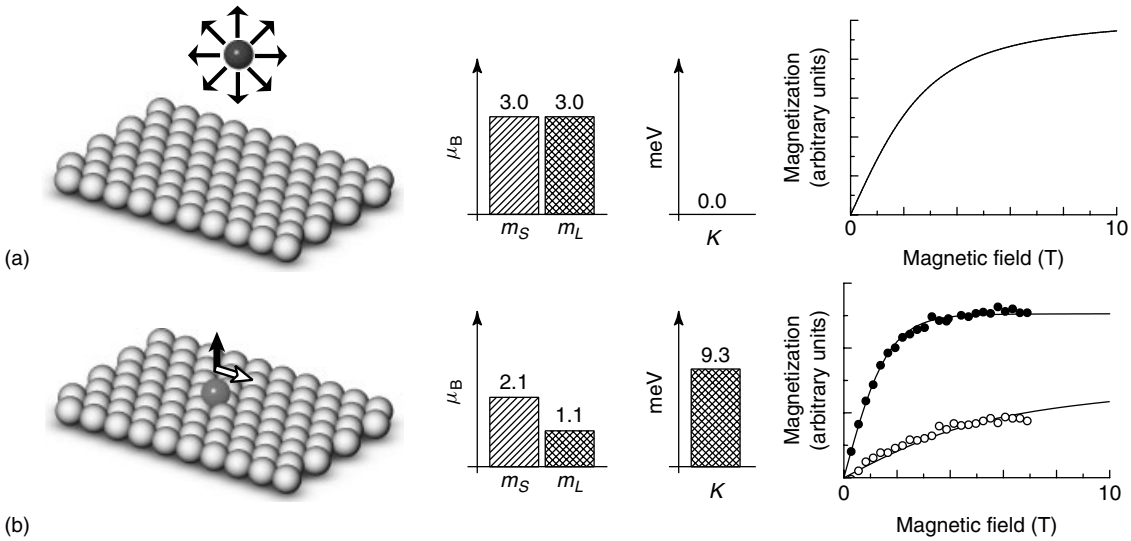

Figure 3. (a) Spin and orbital magnetic moment of a gas phase Co atom as given by the Hund's rules for the d^7 electronic configuration. The magnetic anisotropy energy equals zero due to the spherical symmetry of the system. The isotropic magnetization is represented by a Brillouin function for the d^7 state calculated at $T = 5.5$ K. (b) Spin and orbital magnetic moment and magnetic anisotropy energy of an individual Co atom deposited on the Pt(111) surface. The anisotropic magnetization is measured at $T = 5.5$ K by recording the XMCD intensity at the Co L_3 edge as a function of applied field in the easy (out-of-plane, filled circles) and hard (in-plane, empty circles) direction.

by taking the difference of the XAS spectra for parallel (I_+) and antiparallel (I_-) alignment of the X-ray polarization with respect to the sample magnetization. The X-ray magnetic circular dichroism (XMCD) spectra obtained in this way allow to identify the magnetization direction and strength of a given element (Stöhr, 1999), and to estimate quantitatively m_S and m_L by means of the so-called *XMCD sum rules* (Thole, Carra, Sette and Van der Laan, 1992; Carra, Thole, Altarelli and Wang, 1993; Chen *et al*., 1995).

As an example of a strongly interacting substrate we present data obtained for the Pt(111) surface. The XAS of isolated Co impurities deposited in ultra-high-vacuum on Pt(111) (Figure 4a) reveals broad features typical of Co metal (Figure 4b) that are drastically different from the XAS calculated for the atomic d^7 configuration (Figure 4c) and observed in the vapor-phase (Martins, Godehusen, Richter and Zimmermann, 2003). The spectrum of Co/Pt(111) differs also from that of Co impurities deposited on free-electron metals, such as K, where the narrow XAS multiplet structure indicates that the Co ground state has d^8 atomic-like character (Figure 4c). In the latter case s-d charge transfer takes place, but the Co 3d states remain essentially localized with both m_S and m_L close to the integer Hund's rule limit (Gambardella *et al*., 2002b). On a transition metal surface such as Pt, on the other hand, the electron density is much larger and the impurity 3d-states can hybridize with both the s- and d-states of the substrate. This leads to a strong reduction of m_S and m_L compared to the vapor-phase. Owing to its reduced coordination, the impurity magnetic moment

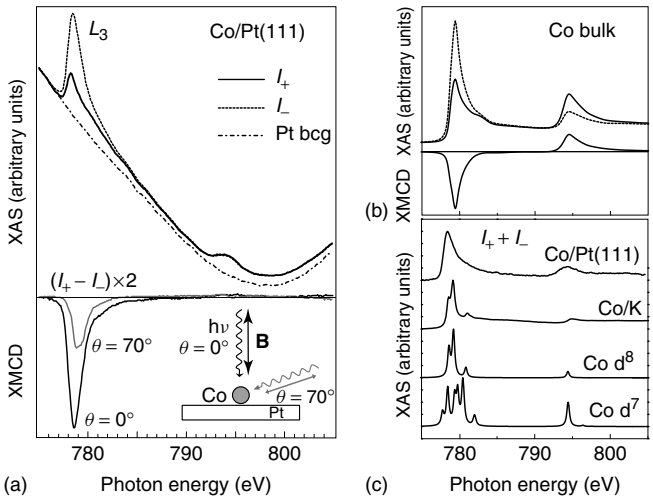

Figure 4. (a) $L_{3,2}$ XAS spectra of Co impurities (0.03 ML) deposited on Pt(111) recorded at $T = 5.5$ K, $\mathbf{B} = 7$ T with parallel (I_+) and antiparallel (I_-) alignment of the photon helicity with respect to $\mathbf{B}$ at an angle $\theta = 0^\circ$ relative to the surface normal. The Co XAS appears superimposed on the background signal of the Pt substrate (dotted line). The XMCD ($I_+ - I_-$) is shown at the bottom for $\theta = 0^\circ$ and 70°. (b) XAS and XMCD spectra of bulk Co. (c) Comparison between the total XAS ($I_+ + I_-$) after background subtraction for Co impurities on Pt(111), Co impurities on a K film, and the calculated XAS for atomic-like d^8 and d^7 configurations.

is nonetheless significantly enhanced with respect to 2D films (Tischer *et al*., 1995; Weller *et al*., 1995), supported nanoparticles (Dürr *et al*., 1999; Koide *et al*., 2001), and 1D

atomic chains (Gambardella *et al.*, 2002a). According to the XMCD sum rules, the vanishing intensity of the XMCD at the L_2 edge in Figure 4(a) compared, for example, to Figure 4(b) indicates that the largest enhancement is that of the orbital component of the magnetic moment, for which we get $m_L = 1.1 \pm 0.1\,\mu_B$.

The presence of strong orbital magnetism allows unusually large MCA through the spin-orbit interaction (Bruno, 1989; Dürr *et al.*, 1997). The MCA energy can be determined by means of XMCD by measuring the magnetization of the Co atoms in an external field applied along different directions with respect to the substrate normal, as shown in Figures 3(b) and 4(a). The solid lines represent fits of the data by means of numerical integration of the equation that describes the impurity magnetization in the presence of the applied field and uniaxial anisotropy energy (Gambardella *et al.*, 2003). For isolated impurities we have $K = 9.3 \pm 1.6$ meV per atom, a remarkable value compared to typical systems with high MCA such as $SmCo_5$ ($K = 1.8$ meV per Co atom Weller and Moser, 1999), Co/Pt and Co/Au multilayers ($K = 0.3$ meV, Nakajima *et al.*, 1998; Weller *et al.*, 1995). Different effects combine in establishing the giant MCA of Co atoms on the Pt surface. The main point is the reduced atomic coordination, which results into narrow 3d-electron bands localized at the impurity sites with augmented spin-orbit interaction due to the increase of the local density of states near the Fermi level (Bruno, 1989; Dürr *et al.*, 1997) and 3d–5d hybridization. Further, the Pt atoms close to Co are magnetically polarized and present an additional MCA due to the strong spin-orbit coupling of the Pt 5d-states. Theoretical calculations indicate the first effect to be dominant (Gambardella *et al.*, 2003) although the two contributions cannot be separated experimentally because of exchange coupling between the Co and Pt magnetic moments.

3.2 Magnetic moment and magnetic anisotropy in finite-sized particles

It is well-known that size effects in metal particles containing a nonnegligible ratio of surface to volume atoms influence the saturation magnetization and MCA properties in cluster beams (Billas, Chatelain and de Heer, 1994; Apsel, Emmert, Deng and Bloomfield, 1996; Knickelbein, 2001) as well as in surface-supported systems (Dürr *et al.*, 1999; Edmonds *et al.*, 1999; Koide *et al.*, 2001; Ohresser *et al.*, 2001; Lau *et al.*, 2002; Rusponi *et al.*, 2004; Bansmann *et al.*, 2005). Such effects become dominant as we reach down to nanometer dimensions. In this critical size regime, key questions are: how the MCA evolves from single atoms to finite-sized particles; how it correlates to atomic magnetic moments; and how both depend on the details of the atomic coordination. By exploiting the energetic hierarchy and temperature dependence of surface diffusion and nucleation processes, the bottom-up approach described in Section 2 allows us to study the development of the magnetization and MCA in magnetic particles constructed on a nonmagnetic substrate starting from isolated magnetic atoms and increasing the particle size almost in an atom-by-atom fashion. Following the previous section, we consider monolayer Co particles grown on Pt(111) as model system. While m_S is expected to vary in a fairly restricted range between 2.1 and 2.2 μ_B for an individual impurity (Gambardella *et al.*, 2003; Lazarovits, Szunyogh, Weinberger and Újfalussy, 2003) to 1.8–1.9 μ_B for a continuous 2D layer (Wu, Li and Freeman, 1991), since the majority spin band is almost filled in all cases, m_L is shown to be much more sensitive to changes in the atomic coordination, reflecting its closer link with the symmetry and

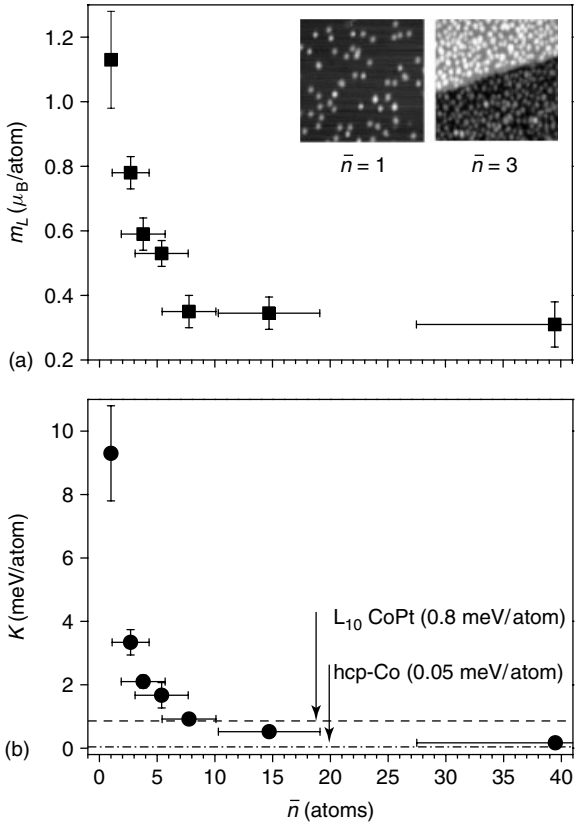

Figure 5. (a) Orbital magnetic moment of monolayer Co nanoparticles deposited on Pt(111) as a function of their average size measured along the easy magnetization direction ($\theta = 0^\circ$). (b) Magnetic anisotropy energy as a function of average particle size. The dashed and dashed-dot lines indicate the magnetic anisotropy energy per Co atom of the CoPt $L1_0$ alloy and *hcp*-Co, respectively. The error bars on the horizontal scale in (a) and (b) represent the standard deviation of the size distribution as determined by STM. The inset shows $180 \times 180\,\text{Å}^2$ STM images of Co impurities and particles with average size $\bar{n} = 1 \pm 0.1$ and 3 ± 1 atoms.

relative filling of different d-orbitals. Figure 5(a) reports the progressive quenching of m_L as a function of average particle size $\overline{n}$. Remarkably, the largest changes of m_L are observed for the smallest particles: for $\overline{n} = 3$ and 4 atoms, m_L has already reduced to 0.78 and 0.59 μ_B, respectively. The MCA energy, due to its spin-orbit origin (Bruno, 1989; Dürr *et al*., 1997), is found to be strongly correlated to the decrease of m_L (Figure 5b). Similar to m_L, drastic changes of K are observed for one-atom variations of the atomic coordination: for $\overline{n} = 3$ atoms, $K = 3.3$ meV amounts to only 30% of the individual impurity value, while already for $\overline{n} > 10$, K drops below the anisotropy energy of the equi-atomic CoPt alloy.

The trend evidenced in Figure 5(b) shows that a huge gain in MCA with respect to bulk or 2D films can be obtained by reducing the size of magnetic particles to a few tens of atoms or less on suitable substrates. Whereas this holds on a per atom basis, it is obvious that the overall stability of the particle magnetization is governed by the sum of the atomic MCA contributions. As more atoms are assembled together to fabricate particles with a large total magnetic moment and total MCA strong enough to stabilize ferromagnetic behavior against thermal fluctuations, this gain is countered by the decrease of K with increasing $\overline{n}$. The problem, however, can be circumvented by noting that the atomic coordination rather than the absolute particle size is the key parameter that governs the magnitude of K, m_L, and m_S. Nanostructures where the shape and composition are tuned so as to control the coordination of the magnetic atoms and maximize useful interface effects, such as in nanowires (Gambardella *et al*., 2002a, 2004) and core-shell particles (Rusponi *et al*., 2004), offer very interesting opportunities to exploit the effects highlighted in this section.

3.3 Magnetic moment and magnetic anisotropy in 1D atomic chains

The dependence of intrinsic magnetization properties on the atomic coordination gives rise to a very diverse magnetic behavior in metal systems that span the 1D–2D limit. As described in Section 2, epitaxial growth on stepped surfaces can be employed to fabricate arrays of nanowires whose thickness and separation are independently adjusted by controlling the coverage and vicinal angle of the substrate. A large number of parallel nanowires are obtained using this method, which allows to use spatially integrating techniques with magnetic sensitivity such as Kerr magnetometry and XMCD. This approach was first explored by Elmers *et al*. (1994) and Pratzer *et al*. (2001) in the study of Fe monolayer stripes grown on stepped W(110). This system presents in-plane anisotropy, scaling of the ordering temperature of each Fe stripe typical of a finite-sized 2D Ising lattice, and a relaxation-free ferromagnetic phase transition due to dipolar coupling across adjacent stripes (Hauschild, Elmers and Gradmann, 1998). Shen *et al*. (1997a,b) found a pronounced temperature- and time-dependent magnetic relaxation for mono- and bilayer Fe stripes on stepped Cu(111) with out-of-plane anisotropy, due to the formation of 1D Ising-coupled spin blocks. Fe stripes on vicinal Pd(110) also present perpendicular anisotropy (Li *et al*., 2001), but the magnetization was found to be time-independent. Recently, Co wires of monatomic thickness have been grown at the step edges of Pt(997) (Figure 2) (Gambardella *et al*., 2000, 2002a) and along the close-packed atomic rows of Pd(110) (Yan *et al*., 2005).

In the limit of atomically thin metal chains, *ab initio* electronic calculations predict large exchange splittings and strongly increased m_S and m_L relative to those of the bulk and 2D monolayers (Weinert and Freeman, 1983; Komelj, Ederer, Davenport and Fähnle, 2002; Ederer, Komelj and Fähnle, 2003; Spisák and Hafner, 2002; Lazarovits, Szunyogh and Weinberger, 2003; Shick, Máca and Oppeneer, 2004) as well as MCA energies exceeding 1 meV per atom (Lazarovits, Szunyogh and Weinberger, 2003; Hong and Wu, 2003, 2004; Újfalussy *et al*., 2004; Shick, Máca and Oppeneer, 2004). Similar to the case of individual impurities, these variations are attributed to the reduced overlap between the d-orbitals in 1D structures. Angle-resolved photoemission experiments on Co monatomic chains grown along the step edges of Pt(997) corroborate the prediction of large exchange splitting of the Co 3d states (2.1 eV Dallmeyer *et al*., 2000) compared to thin films (1.4–1.9 eV) and bulk Co (1.4 eV) (Schneider *et al*., 1990; Clemens *et al*., 1992), suggesting that m_S is of the order of 2 μ_B (Himpsel, Ortega, Mankey and Willis, 1998). XMCD measurements on the same system show that m_L is 0.68 μ_B in the monatomic chain limit, more than twice the value found for a Co monolayer on Pt(997), but drops already to 0.37 μ_B per atom in chains with biatomic thickness (Gambardella *et al*., 2002a). Such values can be rationalized within the trend framed in the previous section, where the average coordination among Co atoms determines large differences of m_L. On the basis of Figure 5(a), for instance, we expect $m_L \approx 0.7\,\mu_B$ per atom for $\overline{n} = 3$, that is, for Co atoms with an average of two Co neighbors, which corresponds to the Co coordination in the monatomic chains.

The sensitivity to the transverse structure of the chains concerns also the orientation of the easy axis and the magnitude of the MCA (Gambardella *et al*., 2004). In Figure 6, we report the magnetization of Co chains with different thickness measured in the plane perpendicular to the chain axis. The magnetization, measured near-remanence at angles θ with respect to the (111) direction, is typical of a uniaxial system and presents a sinusoidal behavior whose maximum indicates the orientation of the easy axis.

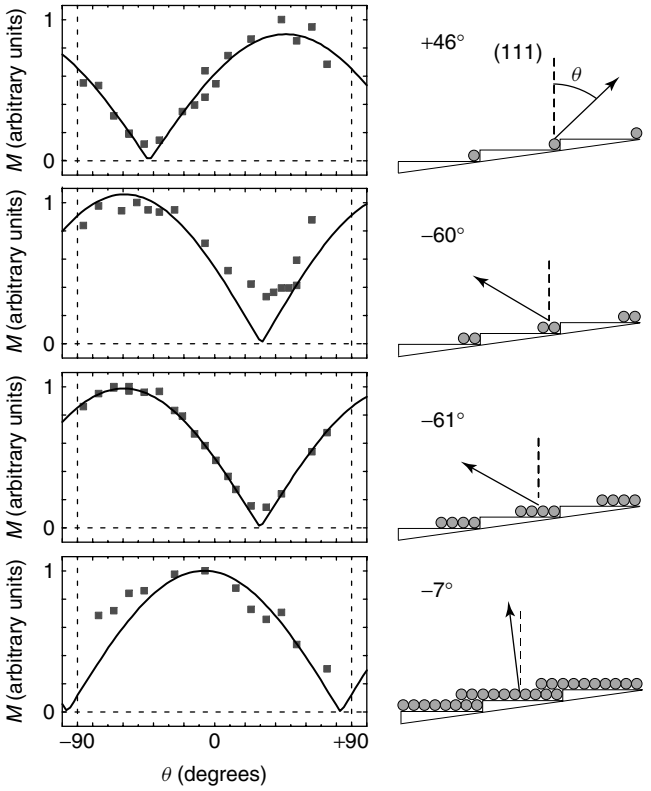

Figure 6. Near-remanence magnetization of Co chains deposited on Pt(997) as a function of the angle θ between the incident photon beam and (111) direction in the plane perpendicular to the chain axis. The data points represent the XMCD signal at the L_3 Co edge. The solid lines fit a $|\cos(\theta - \theta_0)|$ behavior as expected for uniaxial anisotropy. The diagrams indicate the chain thickness and the easy axis direction given by the maximum of the $|\cos|$ function.

In the monatomic chains the easy axis is canted toward the step-up direction due to the reduced symmetry at the Pt step edges, an effect that has been reproduced by first principles relativistic calculations (Újfalussy *et al*., 2004; Shick, Máca and Oppeneer, 2004). With increasing chain thickness unusual oscillations of the easy magnetization direction are observed in the plane perpendicular to the chains (Gambardella *et al*., 2004). The easy axis rotates abruptly from $\theta = +46^\circ$ in the monatomic chains to -60° in the biatomic chains and reverses back toward the surface normal in the monolayer limit as shown in Figure 6. The analysis of the easy and hard magnetization curves reported in Figure 7 reveals further that the magnitude of the MCA has a nonmonotonic behavior with chain thickness. In the monatomic limit $K = 2$ meV per atom at $T = 45$ K, a value enhanced by 1–2 orders of magnitude compared to 2D films (Gradmann, 1993), but in line with expectations based on theoretical calculations (Dorantes-Dávila and Pastor, 1998; Félix-Medina, Dorantes-Dávila and Pastor, 2002; Lazarovits, Szunyogh and Weinberger, 2003; Hong and Wu, 2003, 2004; Újfalussy *et al*., 2004; Shick, Máca and Oppeneer, 2004) and the experiments presented in the previous section. Given that in nanoparticles K is a rapidly decreasing function of the local coordination (Figure 5b), it is not surprising that K reduces to 0.33 meV per atom in the biatomic chains. In triple chains, however, K shows a significant and unexpected increment, upto 0.45 meV per atom, before decreasing again in the monolayer limit. These oscillations as well as the sign inversion of the MCA represented by the rotation of the easy axis appear to be due to thickness-dependent changes in the electronic band structure of the chains rather than to extrinsic (dipolar) effects (Gambardella *et al*., 2004; Vindigni *et al*., 2006), as shown also by tight binding calculations of both free-standing and Pd-supported Co chains one to three atoms thick (Dorantes-Dávila and Pastor, 1998; Félix-Medina, Dorantes-Dávila and Pastor, 2002). Reducing the dimensions of a magnetic layer down to 1D, therefore, reveals a nontrivial magnetic behavior and new opportunities to tune the magnetization properties in metal nanostructures. Examples include the high anisotropy of the 1D-modulated FePt surface alloy presented in Section 4 and the emergence of magnetism in chains of 4d and 5d metals (Bellini, Papanikolaou, Zeller and Dederichs, 2001; Spisák and Hafner, 2003; Rodrigues, Bettini, Silva and Ugarte, 2003).

3.4 Magnetic order in 1D atomic chains

The dimensionality of a magnetic lattice is known to affect not only local properties such as the magnetic moments and MCA but also its thermodynamic properties and in particular order–disorder magnetic phenomena. Ferromagnetism in 2D films is typically more sensitive to temperature-induced fluctuations of the magnetization compared to 3D systems due to the reduced number of atoms contributing to the total exchange interaction (Gradmann, 1993; Schneider and Kirschner, 2000; Poulopoulos and Baberschke, 1999). In the well-known case of the Heisenberg and Ising models, the thermodynamic limit of a 1D spin chain of infinite length is characterized by the absence of long-range magnetic order at any nonzero temperature (Ising, 1925; Mermin and Wagner, 1966; Bruno, 2001). In the past, quasi-1D insulating inorganic crystals have been investigated as Heisenberg model systems to test predictions about magnetism in 1D (De Jongh and Miedema, 1974; Hone and Richards, 1974); typical examples include tetramethylammonium copper and manganese chloride compounds, where Cu^{2+} and Mn^{2+} ions couple ferromagnetically or antiferromagnetically, respectively, along weakly interacting linear chains separated by intervening nonmagnetic complexes (Dingle, Lines and Holt, 1969; Landee and Willett, 1979; Dupas, Renard, Seiden

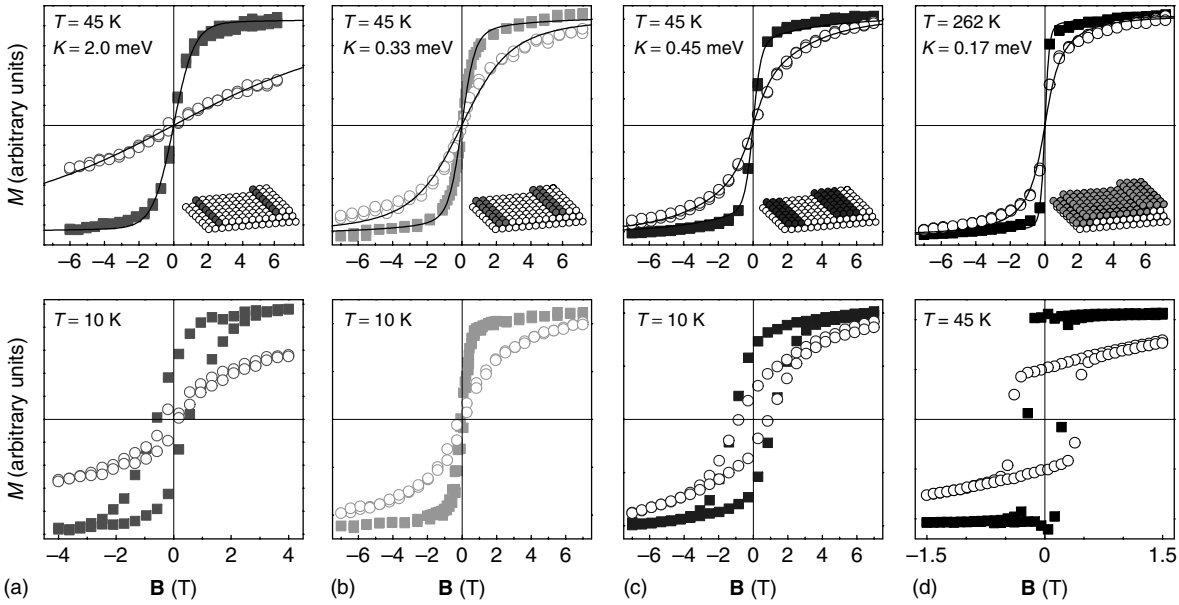

Figure 7. Magnetization of (a) monatomic Co chains, (b) double chains, (c) triple chains, (d) 1.3 monolayers in the easy (filled squares) and hard direction (empty circles). The data points represent the XMCD intensity at the Co L_3 edge as a function of applied field. The solid lines in the top panels are fits of the data in the superparamagnetic regime as described in Gambardella *et al*. (2002a).

and Cheikh-Rouhou, 1982). More recently, the synthesis of molecular ferri- and ferromagnetic chainlike compounds containing magnetically anisotropic ions has allowed to realize 1D Ising model systems where the absence of permanent magnetic order is accompanied by the slow relaxation of the magnetization (Caneschi *et al*., 2001; Bogani *et al*., 2004; Clérac, Miyasaka, Yamashita and Coulon, 2002; Lescouëzec *et al*., 2003) as predicted by Glauber more than 40 years ago (Glauber, 1963). The fabrication of 1D chains of magnetic atoms deposited on a nonmagnetic substrate with the methods described in Section 2 opens up the possibility of extending the investigation of 1D magnetic behavior to metal systems.

The magnetic response of a set of monatomic Co chains at $T = 45$ K (Figure 7a) reveals zero remanent magnetization and the absence of long-range ferromagnetic order. The shape of the magnetization curves, however, indicates the presence of short-range order, that is, of significant interatomic exchange coupling in the chains (Gambardella *et al*., 2002a; Vindigni *et al*., 2006). The observed behavior is that of a 1D superparamagnetic system, that is, a system composed by segments, or spin blocks, each containing N exchange-coupled Co atoms, whose resultant magnetization orientation is unstable due to thermal fluctuations. Fitting the magnetization curves assuming uniaxial MCA and a Boltzmann distribution of the energy states accessible by the system (solid lines) gives the average value $N = 15$ atoms, smaller than the average length of the Co chains, which is estimated to be about 80 atoms from the extension of the atomically straight sections of the Pt steps that act as deposition template. A simple argument of Landau (Landau and Lifshitz, 1959) shows that this result does not contradict the predicted absence of magnetic order in 1D by spin lattice models as long as $N \leq e^{2J/kT}$, where J represents the exchange interaction among adjacent spins ($J \approx 15$ meV Frôta-Pessoa, Muniz and Kudrnovský, 2000; Pratzer *et al*., 2001). However, by lowering the sample temperature below 15 K, we observe a transition to a ferromagnetically ordered state with long-range order and finite remanence at zero field (Figure 7a, bottom panel). This order transition is not dominated by the exchange interaction as in 3D crystals, but rather by the presence of large MCA energy barriers that effectively inhibit the spin fluctuations that lead to the zero remanence thermodynamic limit expected for 1D systems. Below the blocking temperature the magnetization of each spin segment aligns along the common easy axis direction and the system becomes ferromagnetic on a macroscopic scale. Long-range order in 1D metal chains therefore appears as a metastable state, thanks to slow magnetic relaxation. It is interesting to note that as the system evolves toward a 2D film and the number of exchange-coupled Co atoms increases (Figure 5b), we would expect a stronger tendency toward magnetic order. Contrary to expectations, however, in the biatomic chains we observe vanishing long-range magnetic order even at low temperature (Figure 5b). In this case, the tendency toward order is counteracted by the drastic reduction of the MCA energy per Co atom. Paradoxically, therefore, the 1D character of the monatomic chains favors rather than disrupts

ferromagnetic order owing to the minimal coordination of the Co atoms and related enhanced MCA.

4 TOWARD TWO-DIMENSIONAL MAGNETIC STRUCTURES

It is commonly believed that, of all 3d elements, the magnetism of Fe based nanostructures depends the most on the local atomic environment and the interaction with the underlying substrate. This is due to the fact that Fe is a 'borderline ferromagnet' with an exchange interaction sensitively depending in magnitude and sign on the structure at the atomic level (Pajda *et al*., 2000, 2001; Bruno and Sandratskii, 2005). Being a weak ferromagnet, the presence of empty states at the Fermi energy in the minority and majority subband results in a complex dependency of the magnetic properties on the d-band width and occupation, which are controlled by the local atomic coordination. As constructed from Hund's rules, free Fe atoms in the $3d^6 4s^2$ ground state possess spin- and orbital moments of $m_S = m_L = 2\,\mu_B$. In the bulk phase the electron hybridization quenches the orbital moment to $m_L = 0.1\,\mu_B$ (Chen *et al*., 1995). Low-dimensional Fe nanostructures at surfaces are useful to address open questions about the magnetic anisotropy on the atomic level. Of particular interest in the following sections are changes in the magnetism with dimensionality during the crossover from 1D Fe monatomic wires to a 2D Fe or FePt monolayer. As seen in Section 3, the interaction with the substrate has also a decisive influence on the magnetism and can be exploited to tune many of the magnetic properties in low-dimensional structures. The traits of Pt – large Stoner-enhanced susceptibility together with the strong spin-orbit coupling of the 5d states – make it an attractive substrate material for magnetic nanostructures. In contact with 3d magnetic elements Pt acquires a sizable magnetic polarization and gives an important contribution to the magnetocrystalline anisotropy. The role of the substrate will be discussed in the following for all investigated Fe structures, but becomes most apparent for FePt surface alloy layers.

4.1 Fe on Pt – from atomic chains to layered films

Since the early experiments on Fe stripes of finite width prepared on W(110) by Elmers *et al*. (1994) 1D linear Fe nanostructures have been prepared successfully also on vicinal Au (Kawagoe, Sogabe, Kondoh and Narusawa, 1998; Shiraki, Fujisawa, Nantoh and Kawai, 2004, 2005), Cu (Shen *et al*., 1997b; Boeglin *et al*., 2002; Fruchart *et al*., 2004) or Si substrates (Lin *et al*., 2001), on reconstructed Ir surfaces (Klein, Schmidt, Hammer and Heinz, 2004), or by organic patterning (Ma *et al*., 2004). Also on the vicinal Pt(997) surface, Fe shows a strong tendency toward substrate step decoration. Fe atoms arrange themselves to segments of atomic chains at the step edges at growth temperatures between 200 K and 450 K (Lee, Sarbach, Kuhnke and Kern, 2006). Extended monatomic chains of Fe are thus formed at a coverage of $\Theta_{Fe} = 0.13$ monolayer (ML) limited in length only by kinks at step edges or by point defects. The wire formation is, hence, in analogy to the Co chains described in the previous chapter. After complete step decoration, the growth proceeds in the step flow mode until the first Fe monolayer is completed. The layer-wise growth is promoted by the presence of the dense array of substrate steps (Lee, Sarbach, Kuhnke and Kern, 2006).

The evolution of the magnetic anisotropy of Fe stripes with increasing stripe width shows distinctive differences to the Co chains presented in the previous section. The XMCD data in Figure 8 reveal that for a coverage corresponding to 1 atomic row in (a) the preferred magnetization direction is perpendicular to the wire axis, but close to the substrate surface. With increasing coverage the magnetization axis reorients gradually toward the out-of-plane direction. For a coverage corresponding to 3 atomic rows in (b) no distinctive difference between out-of-plane and in-plane magnetization loops is visible, while for 6 rows in (c) the easy magnetization axis points out of the surface plane. For all samples investigated, the in-plane axis along the wire represented the hard magnetization direction. The comparison with Co allows for two important conclusions: (i) In both systems

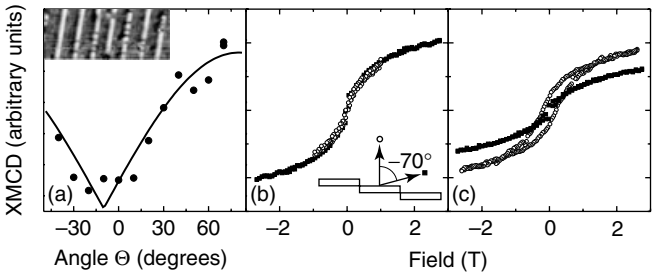

Figure 8. XMCD measurements taken at the Fe L_3 absorption edge as a function of field at 10 K of (a) 0.13 ML Fe (monatomic Fe chain) as a function of polar angle Θ in a constant magnetic field of 1 T. The solid line is a $|\cos(\Theta - \Theta_0)|$ – fit to the data. (b) Hysteresis loops of 0.38 ML Fe (3 atomic stripe), and (c) 0.8 ML (6 atomic stripe). Measurements are taken along the surface normal (o) and under a polar angle of 70° in the direction perpendicular to the step edges (■). A reorientation of the preferred magnetization axis from in-plane perpendicular to the step edges (a) toward perpendicular to the surface (c) occurs with increasing Fe coverage. Inset: STM image of 0.11 ML Fe/Pt(997) showing the wire formation by step decoration.

a preferred magnetization perpendicular to the chain axis is found. Whereas Co chains exhibit an oscillatory reorientation of the magnetization with increasing width, Fe chains rather show a gradual transition from in-plane to out-of-plane magnetization. Complete Fe and Co monolayers have an easy axis close to the sample normal. (ii) The MCA in Fe single atomic chains is 0.56 meV per atom, as determined from fits to angular dependent hysteresis loops. This value is significantly enhanced with respect to the Fe bulk value, but smaller compared to Co chains of equal thickness ($\sim$2 meV per atom, see previous section). Unlike in Co, the MCA of monatomic Fe chains is not sufficient to stabilize remanent magnetization at 10 K, in contrast to Co. In both systems the enhanced MCA goes along with an increase of the orbital moment per atom with respect to bulk, as will be discussed later in this section.

Ab initio electron theory suggests strong similarities in the physics of Co and Fe monatomic chains (Ederer, Komelj and Fähnle, 2003; Shick, Máca and Oppeneer, 2005). The observed ferromagnetic ordering and the enhanced magnetic moments have been predicted theoretically for free and supported atomic chains of Fe (Spisák and Hafner, 2002; Dorantes-Dávila and Pastor, 1998; Lazarovits, Szunyogh, Weinberger and Újfalussy, 2003; Jin, Kim and Lee, 2004). The easy magnetization axis is found perpendicular to the wire axis in all published calculations, as a result of strong Fe–Fe bonds along the chains and the resulting intrachain exchange coupling in this direction. However, the calculated tilt angle of $+30^\circ$ to the surface normal (Shick, Máca and Oppeneer, 2005) is in contrast to our experiment. The calculated tendency of the magnetization to be perpendicular to the Fe–Fe bonding direction may explain the reorientation of the easy axis toward out-of-plane when increasing the Fe coverage above the monochain coverage. Already for chains of 2 atoms in width the intrawire coupling strength perpendicular to the wire axis is of the same order of magnitude as found along the wire (Lazarovits, Szunyogh, Weinberger and Újfalussy, 2003). The intra- and interchain magnetic coupling exceed the dipolar interaction by 2 orders of magnitude and thus dominate the magnetic anisotropy (Spisák and Hafner, 2002). The dipolar interaction would favor ferromagnetically ordered arrays of wires with an in-plane magnetization direction along the wires, which is clearly not observed.

It is important to note that the interaction with the substrate affects the MCA of the wires. This can be seen from a comparison of the experimental data with calculations on free wires which show preferred magnetization *along* the wire axis (Dorantes-Dávila and Pastor, 1998). The role of the substrate is to contribute its spin-orbit coupling to the whole system, thus increasing the total MCA (Dorantes-Dávila and Pastor, 1998), to alter the density of states at the Fermi level (Lazarovits, Szunyogh, Weinberger and Újfalussy, 2003), and possibly to establish interchain coupling by RKKY interaction via intervening substrate sp-electrons (Spisák and Hafner, 2002). The induced magnetic moment in the substrate surface, and thus the substrate contribution to the overlayer magnetism, is one order of magnitude larger for Pt substrates than for Cu substrates (Ederer, Komelj and Fähnle, 2003; Lazarovits, Szunyogh and Weinberger, 2003). Details of the film-substrate interaction will be discussed in the next section.

Further investigation of the magnetism of Fe/Pt(997) in the thickness range between 0.5 and 5 atomic layers shows the evolution of the anisotropy for this system during the transition toward 2D layers (Figure 9). The system has a perpendicular easy magnetization axis up to a film thickness of 3 ML. The reorientation of **M** into the film plane occurs gradually between 2.6 and 3 ML via a canted magnetization state. The spin reorientation is accompanied by a structural transition from fcc(111) to bcc(110) layers with Kurdjumov–Sachs orientation to the substrate. Above 3 ML coverage the easy axis is found within the plane in the direction along the substrate steps. Perpendicular to the steps only hard axis loops with no remanence are found. The strong in-plane anisotropy is attributed to peculiarities of the bcc

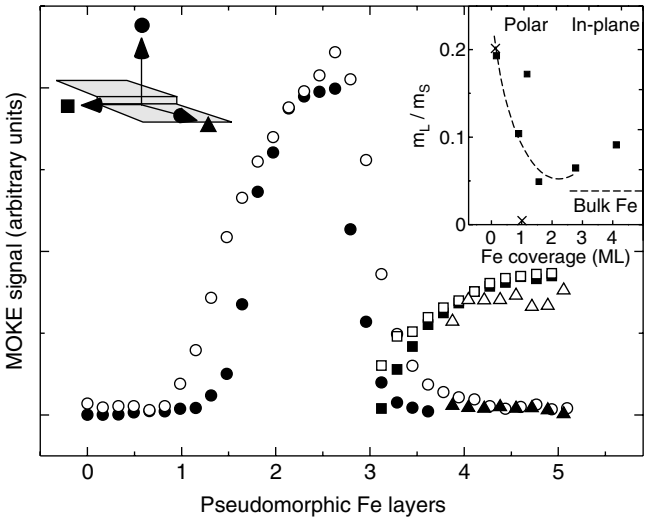

Figure 9. Evolution of the easy magnetization axis for 2D Fe films on Pt substrates with Fe coverage. Open and solid symbols correspond to the saturation and remanent magnetization as obtained from MOKE hysteresis loops at 300 K. A spin reorientation from perpendicular to in-plane direction is observed at the critical thickness of $t_{crit} = 2.8$ atomic layers. Above t_{crit} the films show pronounced in-plane anisotropy with the easy axis along the step edges. Inset: For films thinner than 1 atomic layer the ratio m_L/m_S (from XMCD measurements) increases in favor of larger m_L values, in qualitative agreement with calculations ($\times$, from reference Ederer, Komelj and Fähnle, 2003).

structure of the film in this thickness range (Repetto *et al*., 2006). It is interesting to note that Fe films on Pt(100) substrate, in contrast, do not show perpendicular magnetization at any thickness (He *et al*., 2005). The occurrence of perpendicular magnetization in the monolayer thickness range is commonly ascribed to anisotropy contributions arising at the film's interfaces (see recent overview articles on this field, such as Gradmann, 1993; Shen and Kirschner, 2002; Sander, 2004). More detailed analysis connects the perpendicular magnetic anisotropy of this system with the strong film–substrate interaction. The bonding to the substrate in surface normal direction – which is particularly large for Pt substrates – disturbs orbital motion of the electrons perpendicular to the film plane and significantly increases the bandwidth in this direction, thus promoting perpendicular magnetization (Wang, Wu and Freeman, 1994; Stöhr, 1999). The choice of substrate material and the local atomic arrangement within the nanostructures has decisive influence on the magnetic anisotropy, a fact that will be illustrated more profoundly in the following section.

The measurement of the ratio of orbital to spin magnetic moment reveals an enhancement of the ratio m_L:m_S by a factor of 5 when going from bulk to monatomic chains (see inset in Figure 9). This increase is completely attributed to m_L since below 1 ML Fe coverage m_S is expected to change only slightly (Ederer, Komelj and Fähnle, 2003). In analogy to the discussion of Co clusters in the previous chapter the large m_L is explained by the unquenching of orbital electron motion due to decreased coordination. The latter results in more localized d-bands, and therefore in an increased density of states at E_F and in enhanced moments of the d-electrons. In addition, the exchange splitting between majority and minority electrons is large not only for d-bands but also for sp-bands (Spisák and Hafner, 2002), which may result in sizeable additional contributions to the overall magnetic moment. The minimum in m_L:m_S observed for 1 ML Fe is in qualitative agreement with first principles calculations for Pt-supported fcc(111) Fe monolayers which predict a minimal m_L at this coverage (Ederer, Komelj and Fähnle, 2003).

4.2 High coercivity FePt surface alloy

In Section 3, we elaborated on the importance of high magnetocrystalline anisotropy energy for establishing ferromagnetism in low-dimensional systems. Indeed, nanostructured materials with MCA beyond $10^8\,\mathrm{erg\,cm^{-3}}$ (>1 meV per atom) are being considered for upcoming high-density storage media. Thin films (Yan, Zeng Powers and Sellmyer, 2002; Kanazawa, Lauhoff and Suzuki, 2000; Okamoto *et al*., 2002), multilayers (Johnson, Bloemen, den Broeder and de Vries, 1996), and nanoparticles (Sun *et al*., 2000; Okamoto *et al*., 2002) of intermetallic phases exhibiting the $L1_0$ structure, such as the FePt alloy, fulfill this requirement and are currently in the focus of experimental and theoretical research (2005). The $L1_0$ structure is obtained by alternative stacking of fcc(100) oriented layers of two different materials, such as 3d and 5d elements. Currently, the high anisotropy of FePt alloy is described as the result of 3D coordination of Fe atoms with Pt neighbors. The exchange interaction between Fe atoms across adjacent fcc(100) layers, and hence the 3D nature of the alloy, is considered to be important for large MCA. A key role is played by the induced magnetism in Pt which gives additional MCA contributions due to its large spin-orbit interaction (Ravindran *et al*., 2001). Tetragonal lattice distortion and chemical disorder are found to give access not only to the magnetic anisotropy energy but also to the Curie temperature T_C, exchange interaction J, or saturation magnetization M_S. In this section, we demonstrate on the example of 2D $Fe_{50}Pt_{50}$ surface alloys that the $L1_0$ structure is not required to obtain a large anisotropy. The coordination of Fe with Pt atoms in monolayer thin films increases the MCA so that values close to bulk FePt could be measured (Honolka *et al*., unpublished).

$Fe_{50}Pt_{50}$ surface alloys are obtained by deposition of 0.5 atomic layers of Fe on the Pt(997) substrate at 525 K. The thermally activated diffusion of Fe into the Pt terraces results in the formation of monatomic chain segments of Fe embedded in the Pt surface (Lee, Sarbach, Kuhnke and Kern, 2006), similar to surface alloying of Fe on Pt(111) (Schmid and Varga, 2002). The average spacing between Fe chain segments depends on the amount of deposited Fe and is 5.54 Å (two Pt row spacings) for the idealized $Fe_{50}Pt_{50}$ surface alloy. The element specificity of the XMCD is ideal for probing the magnetism of the Fe and Pt sublattices separately. Typical XAS and XMCD spectra at the Fe $L_{3,2}$ and the Pt $N_{7,6}$ absorption edges are displayed for $Fe_{50}Pt_{50}$ in Figure 10(a). A large dichroic signal was detected at both absorption edges. The presence of a dichroic signal for Pt is the result of an induced magnetic moment due to the hybridization between Fe 3d and Pt 5d states. The existence of a magnetic moment in Pt evidences ferromagnetic coupling between the Fe chains. Antiferromagnetic ordering of the Fe moments would rather result only in negligible Pt moments (Skomski, Kashyap and Sellmyer, 2003; Skomski, Kashyap and Zhou, 2005). The sign relationship of the XMCD signals at the Fe $L_{3,2}$ and the Pt $N_{7,6}$ absorption edges reveals parallel spin alignment of the Fe and Pt sublattices (Shishidou *et al*., 1997). The coupled magnetization of Fe and Pt results in congruent *M-H* magnetization loops which are obtained at each constituent's absorption edge (Figure 10b and c). The preferential magnetization axis is along the surface normal. The large coercive field of $H_C = 0.71$ T is of the same order

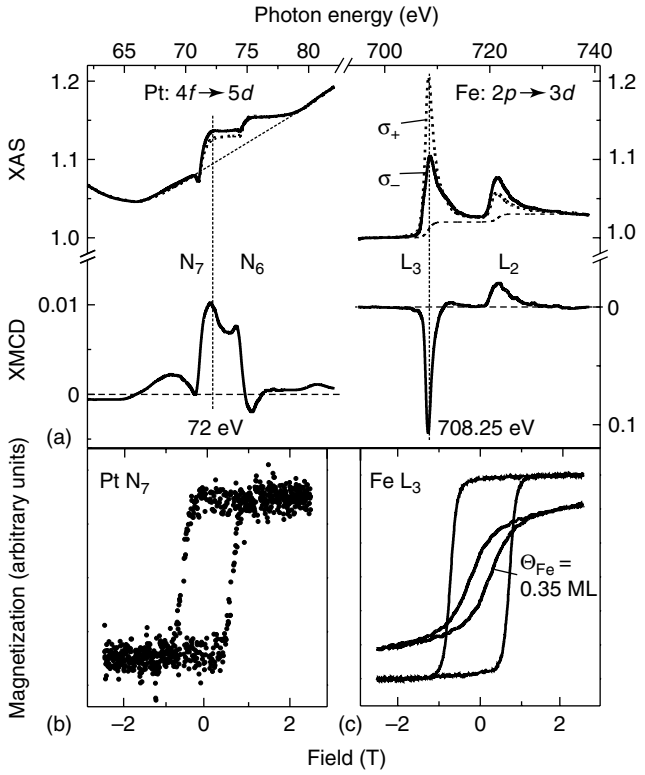

Figure 10. (a) X-ray absorption and XMCD spectra at the Pt $N_{7,6}$ and the Fe $L_{3,2}$ absorption edges of a single, two-dimensional $Fe_{50}Pt_{50}$ surface alloy layer. (b) and (c) The dichroic signal was used to obtain element-specific hysteresis loops of the Fe and Pt sublattice of the same film at 12 ± 1 K. The hysteresis loop of the Fe sublattice is compared to the Fe L_3 loop of a diluted $Fe_{35}Pt_{65}$ monolayer.

of magnitude as the values found for the bulk FePt $L1_0$ phase and demonstrates the presence of a considerable anisotropy energy barrier.

From the XMCD spectrum in Figure 10(a) a total spin moment of $(2.4 \pm 0.2)\mu_B$ per Fe atom is determined. This experimental value is 18% smaller than theoretically predicted Fe moments of $2.93\,\mu_B$ (Staunton *et al.*, 2004a) and $2.92\,\mu_B$ (Kashyap *et al.*, 2004). The determination of the Pt moment from the N-edge dichroism provides a challenge to theorists since the interaction between discrete-like and continuum states during the 4f → 5d dipole transition leads to a Fano-type interference effect and have to be treated accordingly (Shishidou *et al.*, 1997). As a lower limit, a Pt moment of $>0.2\,\mu_B$ per Pt atom is estimated from a comparison of the normalized XMCD signals with $CoPt_3$ bulk samples where the Pt moment is known (Menzinger and Paoletti, 1966). This value is close to calculated Pt spin moments of $0.24\,\mu_B$ per atom in the top layer of Pt(111) covered by one monolayer of Fe (Ederer, Komelj and Fähnle, 2003), and of $0.29\,\mu_B$ (Staunton *et al.*, 2004a) and $0.35\,\mu_B$ (Kashyap *et al.*, 2004) in $L1_0$ ordered FePt. However, at Co/Pt interfaces an induced spin moment as large as $0.53\,\mu_B$ per Pt atom has been determined from XMCD measurements at the Pt $L_{2,3}$ edge (Suzuki *et al.*, 2005).

The MCA of the surface alloy is calculated from angular dependent XMCD measurements to $K = 0.42$ meV per formula unit. Strikingly, this value for the alloyed monolayer is only about a factor of 2–3 smaller than 0.6–1 meV per atom which is typically found for FePt-$L1_0$ bulk samples (Shima, Moriguchi, Mitani and Takanash, 2002; Shima, Takanashi, Takahashi and Hono, 2002; Farrow *et al.*, 1996). As was mentioned already in the preceding text, the MCA is usually related to the orbital moment anisotropy, Δm_L (Bruno, 1989). For the $Fe_{50}Pt_{50}$ surface alloy we determined $\Delta m_L^{alloy} = m_L^{\perp} - m_L^{||} = 0.025 \pm 0.004\,\mu_B$ per hole. This value is close to the measured orbital anisotropy of nonalloyed Fe adlayers on Pt(997) of similar Fe content, $\Delta m_L^{stripe} = 0.035 \pm 0.009\,\mu_B$ per hole. This experimental observation has important implications for the interpretation of the origin of the MCA in alloys, as will be shown in the following text. It is worth to note that both experimental values are by a factor of 2 larger than calculated values, as for instance, in Solovyev, Dederichs and Mertig (1995).

The comparison of the hysteresis loop of $Fe_{50}Pt_{50}$ with those of nonalloyed submonolayer Fe stripes in Figure 8 shows that the alloy has a much stronger tendency toward magnetic ordering, together with a significantly enhanced coercivity. A key role for the conservation of the saturation magnetization in remanence observed for the 2D alloy, and more importantly for the large anisotropy, is obviously played by the magnetism of the Pt atoms. Although the induced exchange splitting in Pt is much weaker than in bulk Fe, its spin-orbit coupling is one order of magnitude larger ($\xi_{Pt} = 0.6$ eV Misemer, 1988 vs $\xi_{Fe} = 0.07$ eV Mackintosh and Andersen, 1980). In result, the Pt orbital moments are expected to be comparable to those of Fe (comparable also to induced Pt orbital moments in the vicinity of Fe chains, $m_L \approx 0.04\,\mu_B$ Ederer *et al.*, 2003). In this simple but quite instructive picture the Fe acts only as the source of magnetization, whereas the Pt sublattice, owing to its large spin-orbit interaction, provides the main contribution to the large MCA. Attempts have been made to express the MCA of binary and multicomponent systems by the sum of the magnetic anisotropy of each constituent (Ravindran *et al.*, 2001; Solovyev, Dederichs and Mertig, 1995). This means that the total MCA is made large by the spin-orbit coupling of the Pt, while the orbital anisotropy of Fe alone remains unchanged – something that our experimental values in the preceding text show. Support of this viewpoint comes from calculations, showing that suppressing the spin-orbit interaction in the 4d/5d constituent reduces the calculated

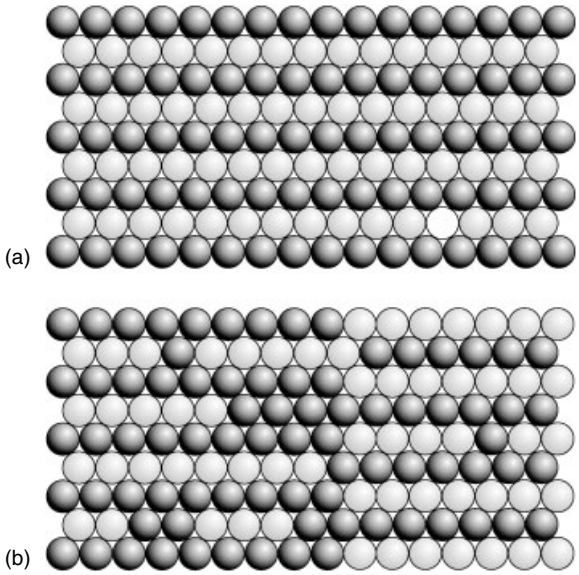

Figure 11. Ordered (a) and disordered (b) structure of a linear, two-dimensional FePt surface alloy. Fe and Pt atoms are represented by dark and bright colors. Deviations from the ideal structure result mostly in ferromagnetic interchain bridges, which promote ferromagnetism in the Fe sublattice and reduce the in-plane anisotropy.

total anisotropy (Burkert *et al*., 2005; Daalderop, Kelly and Schuurmans, 1990).

As has been discussed by several authors, the description of MCA is complicated by chemical disorder (Brown *et al*., 2003; Skomski, Kashyap, Zhou 2005; Okamoto *et al*., 2002; Staunton *et al*., 2004b; Sun *et al*., 2000; Burkert *et al*., 2005), tetragonal distortion (Ravindran *et al*., 2001; Brown *et al*., 2003; Burkert *et al*., 2005), dimensionality, local atomic coordination, and crystal field asymmetry (Ravindran *et al*., 2001). For the surface alloys in this section the chemical disorder, that is, 3d and 5d substitutions as schematically shown in Figure 11(b), plays an important role. Fe atoms in antisite positions bridge the Pt chains and are found to stabilize ferromagnetic ordering of the Fe sublattice, which is predicted to be antiferromagnetic in the ideal structure as in Figure 11(a) (Brown *et al*., 2003). Such disorder can also be assumed to reduce the in-plane magnetic anisotropy of the alloy drastically, as was found experimentally (Honolka *et al*., unpublished).

The experiments point out that the coordination of Fe atoms with Pt, along with strong covalent 3d–5d hybridization, is necessary to achieve large MCA. The importance of Fe-Pt coordination is demonstrated by comparing the hysteresis loop of the $Fe_{50}Pt_{50}$ surface alloy with that of a Fe-poor, diluted $Fe_{35}Pt_{75}$ surface alloy (Figure 10c). Reducing of the Fe concentration by only 30% results in S-shaped loops with the remanence reduced by 78% and the coercivity by 68%. The shape of the loop is similar to the magnetization curve of the nonalloyed Fe stripe in Figure 8(c), for which full spin alignment has only been achieved in external fields of $H > 6$ T. One can say that the increased average spacing between Fe atoms destabilizes the magnetization. It leads on the one hand to narrower Fe d-bands, and in consequence to reduced hybridization and smaller anisotropy. On the other hand, separation of Fe chains by more than one Pt covalent radius significantly decreases the induced net moment in Pt (Ederer, Komelj and Fähnle, 2003) and hence diminishes the Pt's contribution to the magnetism of the surface layer. This is consistent with the observation that Fe-poor FePt bulk alloys exhibit reduced stability of the ferromagnetic order (Brown *et al*., 2003).

5 CONCLUSION

With the ability to control the fabrication of 0D, 1D, and 2D structures of 3d metals by self-organized growth we are capable to study magnetic phenomena in solid-state systems with atomic scale control over their size and crystalline structure. Co and Fe structures of reduced dimensionality reveal a strikingly rich magnetic behavior. Impurity atoms of Co on Pt surfaces have extraordinarily large MCA values and spin and orbital moments halfway between the values of free atoms and bulk Co. The MCA is decreasing with increasing Co coordination when forming small clusters or chains, but still sufficiently large in monatomic Co chains to stabilize a ferromagnetic long-range ordered state at finite temperature. The effect of local atomic coordination on the magnetism of Co and Fe manifests itself in the observed fluctuations of the easy axis with increasing stripe width, as well as in strong orbital magnetism. In all structures investigated a key role is played by the supporting substrate. Pt is found to contribute to the nanostructure's MCA via strong electronic hybridization and even dominates the magnetic anisotropy in the FePt surface alloy. An important consequence of the hybridization is the induced magnetization in Pt.

The basic experiments presented in this chapter contribute to a fundamental understanding of the magnetic properties of finite-sized particles. These results further elucidate the interplay between local coordination, orbital magnetism, and magnetic anisotropy. The link is provided by the electronic structure of the d-states, which sensitively responds to the local atomic arrangement, that is, the number and the electronic nature of the neighboring atoms as well as their interatomic spacing. This knowledge is not only of importance for testing detailed theoretical models used in the prediction and interpretation of magnetic phenomena but also for the conceptual design of nanosized magnetic structures that elude the superparamagnetic limit. In this context, our data show that particles containing only about 400 Co atoms

can behave as ferromagnets at room temperature. Besides the geometry of the atomic arrangement, additional leverage on the magnetic properties is obtained from the choice of the material of the coordinating atoms. When forming a binary alloy the overall magnetism strongly depends also on the nonmagnetic constituent. This is particularly true for nanostructures, such as for the FePt surface alloy, where the low-coordinated Pt atoms acquire a sizeable magnetic moment and contribute with their large spin-orbit coupling to the total magnetic anisotropy.

The work presented in this chapter has only just opened the door toward complex and functional nanostructure networks. Expanded and highly ordered 2D and even 3D networks of nanoscale building blocks can be fabricated by self-organized growth, aided by functionalized molecules, biotemplates or in combination with top-down approaches. It is expected that magnetic nanostructures will play a key role to add functionality to such structures by exploiting their magnetic moments and magnetic ordering associated with magneto-transport or quantum effects. Future experiments may show and exploit ferromagnetism in nanostructures of elements which are nonmagnetic in the bulk, thus opening up additional possibilities. At the frontiers to atomic and nanometer scale structures we will enjoy virtually unlimited avenues for research and promising chances for applications in the near future.

ACKNOWLEDGMENTS

The authors would like to thank Jan Honolka, Klaus Kuhnke, Kai Fauth, Arne Dallmeyer, Carlo Carbone, Stefano Rusponi, Harald Brune, and Sarnjeet S. Dhesi for their valuable contributions to this work.

REFERENCES

Apsel, S.E., Emmert, J.W., Deng, J. and Bloomfield, L.A. (1996). Surface-enhanced magnetism in nickel clusters. *Physical Review Letters*, **76**, 1441.

Bansmann, J., Baker, S., Binns C., *et al*. (2005). Magnetic and structural properties of isolated and assembled clusters. *Surface Science Reports*, **56**, 189.

Barth, J.V., Brune, H., Ertl, G. and Behm, R.J. (1990). Scanning tunneling microscopy observations on the reconstructed Au(111) surface – atomic-structure, long-range superstructure, rotational domains, and surface-defects. *Physical Review B*, **42**, 9307–9318.

Bellini, V., Papanikolaou, N., Zeller, R. and Dederichs, P.H. (2001). Magnetic 4d monoatomic rows on Ag vicinal surfaces. *Physical Review B*, **64**, 094403.

Billas, I.M.L., Chatelain, A. and de Heer, W.A. (1994). Magnetism from the atom to the bulk in iron, cobalt, and nickel clusters. *Science*, **265**, 1682.

Bland, J.A.C. and Heinrich, B. (Eds.) (2005). *Ultrathin Magnetic Structures I*, Springer: Berlin.

Boeglin, C., Stanescu, J.P., Deville, P., *et al*. (2002). In-plane magnetocrystalline anisotropy observed on Fe/Cu(111) nanostructures grown on stepped surfaces. *Physical Review B*, **66**, 014439.

Bogani, L., Caneschi, A., Fedi M., *et al*. (2004). Finite-size effects in single chain magnets: An experimental and theoretical study. *Physical Review Letters*, **92**, 207204.

Bonnenberg, D., Hempel, K.A. and Wijn, H.P.J. (1986). In *Magnetic Properties of 3d, 4d, and 5d Elements, Alloys and Compounds*, *Landolt-Bornstein, New Series*, Hellwege, K.-H. and Madelung, O. (Eds.), Springer-Verlag: Berlin, p. 178, Vol. III/19a.

Brown, G., Kraczek, B., Janotti A., *et al*. (2003). Competition between ferromagnetism and antiferromagnetism in FePt. *Physical Review B*, **68**, 052405.

Brune, H., Giovannini, M., Bromann, K. and Kern, K. (1998). Self-organized growth of nanostructure arrays on strain-relief patterns. *Nature*, **394**, 451–453.

Brune, H., Roder, H., Boragno, C. and Kern, K. (1994). Strain relief at hexagonal-close-packed interfaces. *Physical Review B*, **49**, 2997–3000.

Brune, H., Romainczyk, C., Roder, H. and Kern, K. (1994). Mechanism of the transition from fractal to dendritic growth of surface aggregates. *Nature*, **369**, 469–471.

Brune, H., Roder, H., Bromann, K., *et al*. (1996). Anisotropic corner diffusion as origin for dendritic growth on hexagonal substrates. *Surface Science*, **349**, L115–L122.

Bruno, P. (1989). Tight-binding approach to the orbital magnetic-moment and magnetocrystalline anisotropy of transition-metal monolayers. *Physical Review B*, **39**, 865.

Bruno, P. (2001). Absence of spontaneous magnetic order at nonzero temperature in one- and two-dimensional Heisenberg and XY systems with long-range interactions. *Physical Review Letters*, **87**, 137203.

Bruno, P. and Sandratskii, L.M. (2005). Schizophrenes Eisen. *Physik Journal*, **4**(5), 21.

Burkert, T., Eriksson, O., Simak S.I., *et al*. (2005). Magnetic anisotropy of L1(0) FePt and $Fe_{1-x}Mn_xPt$. *Physical Review B*, **71**, 134441.

Caneschi, A., Gatteschi, D., Lalioti N., *et al*. (2001). Cobalt(II)-nitronyl nitroxide chains as molecular magnetic nanowires. *Angewandte Chemie (International ed. in English)*, **40**, 1760.

Carra, P., Thole, B.T., Altarelli, M. and Wang, X. (1993). X-ray circular-dichroism and local magnetic-fields. *Physical Review Letters*, **70**, 694.

Chambliss, D.D., Wilson, R.J. and Chiang, S. (1991). Nucleation of ordered Ni island arrays on Au(111) by surface-lattice dislocations. *Physical Review Letters*, **66**, 1721–1724.

Chen, C.T., Idzerda, Y.U., Lin H.-J., *et al*. (1995). Experimental confirmation of the x-ray magnetic circular-dichroism sum-rules for iron and cobalt. *Physical Review Letters*, **75**, 152.

Clemens, W., Kachel, T., Rader O., *et al*. (1992). Quantum size effects and the enhancement of the exchange splitting in ultrathin Co overlayers on Cu(100). *Solid State Communications*, **81**, 739.

Clérac, R., Miyasaka, H., Yamashita, M. and Coulon, C. (2002). Evidence for single-chain magnet behavior in a Mn-III-Ni-II chain designed with high spin magnetic units: A route to high temperature metastable magnets. *Journal of the American Chemical Society*, **124**, 12837.

Daalderop, G.H.O., Kelly, P.J. and Schuurmans, M.F.H. (1990). 1st-principles calculation of the magnetic-anisotropy energy of (Co)N/(X)M multilayers. *Physical Review B*, **42**(11), 7270.

Dallmeyer, A., Carbone, C. Eberhardt, W., *et al*. (2000). Electronic states and magnetism of monatomic Co and Cu wires. *Physical Review B*, **61**, R5133.

De Jongh, L.J. and Miedema, A.R. (1974). Experiments on simple magnetic model systems. *Advances in Physics*, **23**, 1.

Dingle, R., Lines, M.E. and Holt, S.L. (1969). Linear-chain antiferromagnetism in $[(CH_3)_4N][MnCl_3]$. *Physical Review*, **187**, 643.

Dorantes-Dávila, J. and Pastor, G.M. (1998). Magnetic anisotropy of one-dimensional nanostructures of transition metals. *Physical Review Letters*, **81**(1), 208.

Dupas, C., Renard, J.P., Seiden, J. and Cheikh-Rouhou, A. (1982). Static magnetic-properties of $(CH_3)_4NMn_xCu_{1-x}Cl_3$, a quantum ferromagnetic chain with classical impurities – experiment and theory. *Physical Review B*, **25**, 3261.

Dürr, H.A., Dhesi, S.S., Dudzik E., *et al*. (1999). Spin and orbital magnetization in self-assembled Co clusters on Au(111). *Physical Review B*, **59**, R701.

Dürr, H.A., Guo, G.Y., van der Laan G., *et al*. (1997). Element-specific magnetic anisotropy determined by transverse magnetic circular x-ray dichroism. *Science*, **277**, 213.

Ederer, C., Komelj, M. and Fähnle, M. (2003). Magnetism in systems with various dimensionalities: A comparison between Fe and Co. *Physical Review B*, **68**, 52402.

Edmonds, K.W., Binns, C., Baker, S.H., *et al*. (1999). Doubling of the orbital magnetic moment in nanoscale Fe clusters. *Physical Review B*, **60**(1), 472.

Ehrlich, G. and Hudda, F.G. (1966). Atomic view of surface self-diffusion – tungsten on tungsten. *Journal of Chemical Physics*, **44**, 1039.

Elmers, H.J., Hauschild, J., Höche, H., *et al*. (1994). Submonolayer magnetism of Fe(110) on W(110) – finite-width scaling of stripes and percolation between islands. *Physical Review Letters*, **73**(6), 898.

Farrow, R.F.C., Weller, D., Marks, R.F., *et al*. (1996). Control of the axis of chemical ordering and magnetic anisotropy in epitaxial FePt films. *Journal of Applied Physics*, **79**(8), 5967.

Félix-Medina, R., Dorantes-Dávila, J. and Pastor, G.M. (2002). Spin moments, orbital moments and magnetic anisotropy of finite-length Co wires deposited on Pd(110). *New Journal of Physics*, **4**, 100.

Fischer, B., Brune, H., Barth, J.V., *et al*. (1999). Nucleation kinetics on inhomogeneous substrates: Al/Au(111). *Physical Review Letters*, **82**, 1732–1735.

Frôta-Pessoa, S., Muniz, R.B. and Kudrnovský, J. (2000). Exchange coupling in transition-metal ferromagnets. *Physical Review B*, **62**, 5293.

Fruchart, O., Eleoui, M., Vogel, J., *et al*. (2004). Nanometers-thick self-organized Fe stripes: bridging the gap between surfaces and magnetic materials. *Applied Physics Letters*, **84**(8), 1335.

Fruchart, O., Klaua, M., Barthel, J. and Kirschner, J. (1999). Self-organized growth of nanosized vertical magnetic Co pillars on Au(111). *Physical Review Letters*, **83**, 2769–2772.

Gambardella, P., Blanc, M., Brune H., *et al*. (2000). One-dimensional metal chains on Pt vicinal surfaces. *Physical Review B*, **61**, 2254.

Gambardella, P., Dallmeyer, A., Maiti K., *et al*. (2002a). Ferromagnetism in one-dimensional monatomic metal chains. *Nature*, **416**, 301.

Gambardella, P., Dhesi S.S., Gardonio S., *et al*. (2002b). Localized magnetic states of Fe, Co, and Ni impurities on alkali metal films,. *Physical Review Letters*, **88**, 047202.

Gambardella, P., Dallmeyer, A., Maiti K., *et al*. (2004). Oscillatory magnetic anisotropy in one-dimensional atomic wires. *Physical Review Letters*, **93**, 077203.

Gambardella, P., Rusponi, S., Veronese M., *et al*. (2003). Giant magnetic anisotropy of single cobalt atoms and nanoparticles. *Science*, **300**, 1130.

Glauber, R.J. (1963). Time-dependent statistics of ising model. *Journal of Mathematical Physics*, **4**, 294.

Gradmann, U. (1993). In *Handbook of Magnetic Materials*, Buschow, K.H.J. (Ed.), Elsevier Science Publishers B. V.: New York, Vol. 7.

Hahn, E., Schief, H., Marsico, V., *et al*. (1994). Orientational instability of vicinal Pt surfaces close to (111). *Physical Review Letters*, **72**, 3378–3381.

Hauschild, J., Elmers, H.J. and Gradmann, U. (1998). Dipolar superferromagnetism in monolayer nanostripes of Fe(110) on vicinal W(110) surfaces. *Physical Review B*, **57**, R677.

He, K., Zhang, L.J., Ma, X.C., *et al*. (2005). Growth and magnetism of ultrathin Fe films on Pt(100). *Physical Review B*, **72**, 155432.

Himpsel, F.J., Ortega, J.E., Mankey, G.J. and Willis, R.F. (1998). Magnetic nanostructures. *Advances in Physics*, **47**, 511.

Hone, D.W. and Richards, P.M. (1974). One- and two-dimensional magnetic systems. *Annual Review of Materials Science*, **4**, 337.

Hong, J. and Wu, R.Q. (2003). First principles calculations of magnetic anisotropy energy of Co monatomic wires. *Physical Review B*, **67**, 020406.

Hong, J. and Wu, R.Q. (2004). Magnetic properties of Co nanochains. *Physical Review B*, **70**, 060406.

Honolka, J., *et al*. unpublished.

Hwang, R.Q., Schroder, J., Gunther, C. and Behm, R.J. (1991). Fractal growth of 2-dimenstional islands – Au on Ru(0001). *Physical Review Letters*, **67**, 3279–3282.

Ising, E. (1925). Report on the theory of ferromagnetism. *Zeitschrift Fur Physik*, **31**, 253.

Jansen, R. and Moodera, J.S. (1998). Influence of barrier impurities on the magnetoresistance in ferromagnetic tunnel junctions. *Journal of Applied Physics*, **83**, 6682.

Jin, Y.J., Kim, I.G. and Lee, J.I. (2004). A first-principles study on the magnetism of an Fe chain along the [110] direction on Cu(001). *Physica Status Solidi B-Basic Research*, **241**(7), 1431.

Johnson, M.T., Bloemen, P.J.H., den Broeder, F.J.A. and de Vries, J.J. (1996). Magnetic anisotropy in metallic multilayers. *Reports on Progress in Physics*, **59**, 1409.

Kanazawa, H., Lauhoff, G. and Suzuki, T. (2000). Magnetic and structural properties of (CoxFe100-x)(50)Pt-50 alloy thin films. *Journal of Applied Physics*, **87**, 6143.

Kashyap, A., Skomski, R., Solanki, A.K., *et al*. (2004). Magnetism of L1(0) compounds with the composition MT (M = Rh, Pd, Pt, Ir and T = Mn, Fe, Co, Ni). *Journal of Applied Physics*, **95**(11), 7480.

Kawagoe, T., Sogabe, K., Kondoh, N., *et al*. (1998). Scanning tunneling microscopy study of Fe submonolayer film on vicinal Au(001). *Japanese Journal of Applied Physics*, **37**, 3796.

Kirakosian, A., Bennewitz, R., Crain J.N., *et al*. (2001). Atomically accurate Si grating with 5.73 nm period. *Applied Physics Letters*, **79**, 1608–1610.

Klein, A., Schmidt, A., Hammer, L. and Heinz, K. (2004). Lateral nanoscale Fe-Ir superlattices on Ir(100). *Europhysics Letters*, **65**(6), 830.

Knickelbein, M.B. (2001). Experimental observation of superparamagnetism in manganese clusters. *Physical Review Letters*, **86**, 5255.

Koide, T., Miyauchi, H., Okamoto, J., *et al*. (2001). Direct determination of interfacial magnetic moments with a magnetic phase transition in Co nanoclusters on Au(111). *Physical Review Letters*, **87**, 257201.

Komelj, M., Ederer, C., Davenport, J.W. and Fähnle, M. (2002). From the bulk to monatomic wires: An ab initio study of magnetism in Co systems with various dimensionality. *Physical Review B*, **66**, 140407.

Kronmüller, H. (2003). *Micromagnetism and The Microstructure of Ferromagnetic Solids*, Cambridge University Press: Cambridge.

van der Laan, G. and Thole, B.T. (1991). Strong magnetic x-ray dichroism in 2p absorption spectra of 3d transition-metal ions. *Physical Review B*, **43**, 13401.

Landau, L.D. and Lifshitz, E.M. (1959). In *Statistical Physics*, Pergamon: London, p. 482, Vol. 5.

Landee, C.P. and Willett, R.D. (1979). Tetramethylammonium copper chloride and TRIS (Trimethylammonium) copper chloride – S = 1/2 Heisenberg one-dimensional ferromagnets. *Physical Review Letters*, **43**, 463.

Lau, J.T., Föhlisch, A., Nietubyc, R., *et al*. (2002). Size-dependent magnetism of deposited small iron clusters studied by x-ray magnetic circular dichroism. *Physical Review Letters*, **89**, 057201.

Lazarovits, B., Szunyogh, L. and Weinberger, P. (2003). Magnetic properties of finite Co chains on Pt(111). *Physical Review B*, **67**, 024415.

Lazarovits, B., Szunyogh, L., Weinberger, P. and Újfalussy, B. (2003). Magnetic properties of finite Fe chains at fcc Cu(001) and Cu(111) surfaces. *Physical Review B*, **68**, 024433.

Lee, T.-Y., Sarbach, S., Kuhnke, K. and Kern, K. (2006). Growth and surface alloying of Fe on Pt(997). *Surface Science 600*, **16**, 3266–3273.

Leroy, F., Eymery, J., Gentile, P. and Fournel, F. (2002). Ordering of Ge quantum dots with buried Si dislocation networks. *Applied Physics Letters*, **80**, 3078–3080.

Lescouëzec, R., Vaissermann, J., Ruiz-Pérez, C., *et al*. (2003). Cyanidebridged iron(III)-cobalt(II) double zigzag ferromagnetic chains: Two new molecular magnetic nanowires. *Angewandte Chemie (International ed. in English)*, **42**, 1483.

Li, D., Cuenya, B.R., Pearson, J., *et al*. (2001). Magnetism of step-decorated Fe on Pd(110). *Physical Review B*, **64**, 144410.

Li, Y.G., Bartelt, M.C., Evans, J.W., *et al*. (1997). Transition from one- to two-dimensional island growth on metal (110) surfaces induced by anisotropic corner rounding. *Physical Review B*, **56**, 12539–12543.

Lin, J.L., Petrovykh, D.Y., Kirakosian, A., *et al*. (2001). Self-assembled Fe nanowires using organometallic chemical vapor deposition and CaF2 masks on stepped Si(111). *Applied Physics Letters*, **78**, 829.

Ma, X., Meyerheim, H.L., Barthel, J., *et al*. (2004). Self-assembled magnetic nanostripes by organic patterning. *Applied Physics Letters*, **84**(20), 4038.

Mackintosh, A.R. and Andersen, O.K. (1980). In *Electrons at the Fermi Surface*, Springford, M. (Eds.), Cambridge University Press: Cambridge, p. 149.

Martins, M., Godehusen, K., Richter, T. and Zimmermann, P. (2003). 2p photoionization of atomic cobalt and nickel. *Aip Conference Proceedings*, **652**, 153.

McHenry, M. and Soffa, W.A. (2005). Preface to viewpoint set on: L10 phases for permanent magnet and recording applications. *Scripta Materialia*, **53**, 381.

Menzinger, F. and Paoletti, A. (1966). Magnetic moments and unpaired-electron densities in $CoPt_3$. *Physical Review*, **143**, 365.

Mermin, N.D. and Wagner, H. (1966). Absence of ferromagnetism or antiferromagnetism in one- or 2-dimenstional isotropic Heisenberg models. *Physical Review Letters*, **17**, 1133.

Michely, T. and Comsa, G. (1991). Temperature-dependence of the sputtering morphology of Pt(111). *Surface Science*, **256**, 217–226.

Misemer, D.K. (1988). The effect of spin orbit interaction and exhange splitting on magneto-optic coefficients. *Journal of Magnetism and Magnetic Materials*, **72**, 267.

Mo, Y.W., Kleiner, J., Webb, M.B. and Lagally, M.G. (1991). Activation-energy for surface-diffusion of Si on Si(001) – a scanning-tunneling-microscopy study. *Physical Review Letters*, **66**, 1998–2001.

Morgenstern, K., Rosenfeld, G. and Comsa, G. (1996). Decay of two-dimensional Ag islands on Ag(111). *Physical Review Letters*, **76**, 2113–2116.

Mydosh, J.A. and Nieuwenhuys, G.J. (1980). In *Ferromagnetic Materials*, Wohlfarth, E.P. (Ed.), North-Holland: Amsterdam, p. 7.

Nakajima, N., Koide, T., Shidara, T., *et al*. (1998). Decay of two-dimensional Ag islands on Ag(111). *Physical Review Letters*, **81**, 5229.

Nonas, B., Cabria, I., Zeller, R., *et al*. (2001). Strongly enhanced orbital moments and anisotropies of adatoms on the Ag(001) surface. *Physical Review Letters*, **86**, 2146.

Nötzel, R. (1996). Self-organized growth of quantum-dot structures. *Semiconductor Science and Technology*, **11**, 1365–1379.

Ohresser, P., Brookes, N.B., Padovani, S., *et al*. (2001). Magnetism of small Fe clusters on Au(111) studied by x-ray magnetic circular dichroism. *Physical Review B*, **64**, 104429.

Okamoto, S., Kikuchi, N., Kitakami, O., *et al*. (2002). Chemical-order-dependent magnetic anisotropy and exchange stiffness constant of FePt (001) epitaxial films. *Physical Review B*, **66**, 024413.

Okamoto, S., Kitakami, O., Kikuchi, N., *et al*. (2002). Preface to viewpoint set on: L10 phases for permanent magnet and recording applications (2005). *Physical Review B*, **66**, 24413.

Pajda, M., Kudrnovský, J., Turek, I., *et al*. (2000). Oscillatory Curie temperature of two-dimensional ferromagnets. *Physical Review Letters*, **85**(25), 5424.

Pajda, M., Kudrnovský, J., Turek, I., *et al*. (2001). Ab initio calculations of exchange interactions, spin-wave stiffness constants, and Curie temperatures of Fe, Co, and Ni. *Physical Review B*, **64**, 174402.

Pimpinelli, A., Villain, J. and Wolf, D.E. (1992). Surface-diffusion and island density. *Physical Review Letters*, **69**, 985–985.

Poulopoulos, P. and Baberschke, K. (1999). Magnetism in thin films. *Journal of Physics-Condensed Matter*, **11**, 9495.

Pratzer, M., Elmers, H.J., Bode, M., *et al*. (2001). Atomic-scale magnetic domain walls in quasi-one-dimensional Fe nanostripes,. *Physical Review Letters*, **87**, 127201.

Ravindran, P., Kjekshus, A., Fjellvåg, H., *et al*. (2001). Large magnetocrystalline anisotropy in bilayer transition metal phases from first-principles full-potential calculations. *Physical Review B*, **63**, 144409.

Repetto, D., Lee, T.Y., Rusponi, S., *et al*. (2006). Structure and magnetism of a atomically thin Fe layers on flat and vicinal Pt surfaces. *Physical Review B*, **74**, 054408.

Röder, H., Hahn, E., Brune, H., *et al*. (1993). Building one-dimensional and 2-dimenstional nanostructures by diffusion-controlled aggregation at surfaces. *Nature*, **366**, 141–143.

Rodrigues, V., Bettini, J., Silva, P.C. and Ugarte, D. (2003). Evidence for spontaneous spin-polarized transport in magnetic nanowires. *Physical Review Letters*, **91**, 096801.

Rusponi, S., Cren, T., Weiss, N., *et al*. (2004). The remarkable difference between surface and step atoms in the magnetic anisotropy of two-dimensional nanostructures. *Nature Materials*, **2**, 546.

Sander, D. (2004). The magnetic anisotropy and spin reorientation of nanostructures and nanoscale films, Journal of Physics-Condensed Matter. *Journal of Physics-Condensed Matter*, **16**, R603–R636.

Schmid, M. and Varga, P. (2002). Segregation and surface chemical ordering – an experimental view on the atomic scale. *The Chemical Physics of Solid Surfaces*. **10**, 118–151.

Schneider, C.M. and Kirschner, J. (2000). In *Handbook of Surface Science*, Horn, K. and Scheffler, M. (Eds.), Elsevier: Amsterdam, p. 511, Vol. 2.

Schneider, C.M., de Miguel, J.J., Bressler, P., *et al*. (1990). Spin-resolved and angle-resolved photoemission from single-crystals and epitaxial-films using circularly polarized synchrotron radiation. *Journal of Electron Spectroscopy and Related Phenomena*, **51**, 263.

Shen, J. and Kirschner, J. (2002). Tailoring magnetism in artificially structured materials: the new frontier. *Surface Science*, **500**, 300.

Shen, J., Klaua, M., Ohresser, P., *et al*. (1997a). Structural and magnetic phase transitions of Fe on stepped Cu(111). *Physical Review B*, **56**, 11134.

Shen, J., Skomski, R., Klaua, M., *et al*. (1997b). Magnetism in one dimension: Fe on Cu(111). *Physical Review B*, **56**, 2340.

Shick, A.B., Máca, F. and Oppeneer, P.M. (2004). Anomalous ferromagnetism of a monatomic Co wire at the Pt(111) surface step edge. *Physical Review B*, **69**, 212410.

Shick, A.B., Máca, F. and Oppeneer, P.M. (2005). Monatomic Fe and Co wires at the Pt surface step edge: theory of the unconventional magnetic anisotropy. *Journal of Magnetism and Magnetic Materials*, **290–291**, 257.

Shima, T., Moriguchi, T., Mitani, S. and Takanashi, K. (2002). Low-temperature fabrication of L1(0) ordered FePt alloy by alternate monatomic layer deposition. *Applied Physics Letters*, **80**(2), 288.

Shima, T., Takanashi, K., Takahashi, Y.K. and Hono, K. (2002). Preparation and magnetic properties of highly coercive FePt films. *Applied Physics Letters*, **81**(6), 1050.

Shiraki, S., Fujisawa, H., Nantoh, M. and Kawai, M. (2004). The growth of Fe, Ni and Co on vicinal Au(111) surfaces. *Applied Surface Science*, **237**, 284.

Shiraki, S., Fujisawa, H., Nantoh, M. and Kawai, M. (2005). One-dimensional Fe nanostructures formed on vicinal Au(111) surfaces. *Journal of the Physical Society of Japan*, **74**(7), 2033.

Shishidou, T., Imada, S., Muro, T., *et al*. (1997). Strong Fano effect in the magnetic circular dichroism of the Pt N-6,N-7 core absorption of ferromagnetic CoPt3. *Physical Review B*, **55**, 3749.

Skomski, R. and Coey, J.M.D. (1999). *Permanent Magnetism*, Institute of Physics Publishing: Bristol.

Skomski, R., Kashyap, A. and Sellmyer, D.J. (2003). Finite-temperature anisotropy of PtCo magnets. *IEEE Transactions on Magnetics*, **39**, 2917.

Skomski, R., Kashyap, A. and Zhou, J. (2005). Atomic and micromagnetic aspects of L1(0) magnetism. *Scripta Materialia*, **53**, 389.

Solovyev, I.V., Dederichs, P.H. and Mertig, I. (1995). Origin of orbital magnetization and magnetocrystalline anisotropy in TX ordered alloys (where T=Fe, Co AND X=Pd, Pt). *Physical Review B*, **52**(18), 13419.

Song, F. and Bergmann, G. (2001). Magnetic Behavior of Na Films with Fe, Co, and Ni Impurities. *Physical Review Letters*, **86**, 2138.

Spisák, D. and Hafner, J. (2002). Fe nanowires on vicinal Cu surfaces: Ab initio study. *Physical Review B*, **65**, 235405.

Spisák, D. and Hafner, J. (2003). Magnetism of ultrathin wires suspended in free space and adsorbed on vicinal surfaces. *Physical Review B*, **67**, 214416.

Staunton, J.B., Ostantin, S., Razee, S.S.A., *et al*. (2004a). Temperature dependent magnetic anisotropy in metallic magnets from an ab initio electronic structure theory: L1(0)-ordered FePt. *Physical Review Letters*, **93**, 257204.

Staunton, J.B., Ostantin, S., Razee, S.S.A., *et al*., (2004b). Long-range chemical order effects upon the magnetic anisotropy of

FePt alloys from an ab initio electronic structure theory. *Journal of Physics-Condensed Matter*, **16**, S5623.

Stepanyuk, V.S., Hergert, W., Wildberger, K., *et al*. (1996). Magnetism of 3d, 4d, and 5d transition-metal impurities on Pd(001) and Pt(001) surfaces. *Physical Review B*, **53**(4), 2121.

Stöhr, J. (1999). Exploring the microscopic origin of magnetic anisotropies with X-ray magnetic circular dichroism (XMCD) spectroscopy. *Journal of Magnetism and Magnetic Materials*, **200**, 470.

Stumpf, R. and Scheffler, M. (1994). Theory of self-diffusion at and growth of Al(111). *Physical Review Letters*, **72**, 254–257.

Sun, S., Murray, C.B., Weller, D., *et al*. (2000). Monodisperse FePt nanoparticles and ferromagnetic FePt nanocrystal superlattices. *Science*, **287**, 1989.

Suzuki, M., Muraoka, H., Inaba, Y., *et al*. (2005). Depth profile of spin and orbital magnetic moments in a subnanometer Pt film on Co. *Physical Review B*, **72**, 054430.

Temmyo, J., Kuramochi, E., Kamada, H. and Tamamura, T. (1998). Resonant self-organization in semiconductor growth. *Journal of Crystal Growth*, **195**, 516–523.

Thole, B.T., Carra, P., Sette, F. and Van der Laan, G. (1992). X-ray circular-dischroism as a probe of orbital magnetization. *Physical Review Letters*, **68**, 1943.

Tischer, M., Hjortstam, O., Arvanitis, D., *et al*. (1995). Enhancement of orbital magnetism at surfaces – Co on Cu(100). *Physical Review Letters*, **75**, 1602.

Újfalussy, B., Lazarovits, B., Szunyogh, L., *et al*. (2004). Ab initio spin dynamics applied to nanoparticles: Canted magnetism of a finite Co chain along a Pt(111) surface step edge. *Physical Review B*, **70**, 100404.

Vindigni, A., Rettori, A., Pini, M.G., *et al*. (2006). Ab initio spin dynamics applied to nanoparticles: Canted magnetism of a finite Co chain along a Pt(111) surface step edge. *Applied Physics A*, **82**, 385–394.

Wang, D.S., Wu, R. and Freeman, A.J. (1994). Magnetocrystalline anisotropy of interfaces – first-principles theory for Co-Cu interface and interpretation by an effective ligand interaction-model. *Journal of Magnetism and Magnetic Materials*, **129**, 237.

Weinert, M. and Freeman, A.J. (1983). Magnetism at surfaces and interfaces. *Journal of Magnetism and Magnetic Materials*, **38**, 23.

Weller, D. and Moser, A. (1999). Thermal effect limits in ultrahigh-density magnetic recording. *IEEE Transactions on Magnetics*, **35**, 4423.

Weller, D., Stöhr, J., Nakajiama, R., *et al*. (1995). Microscopic origin of magnetic-anisotropy in Au/Co/Au probed with x-ray magnetic circular-dischroism. *Physical Review Letters*, **75**(20), 3752.

Witten, T.A. and Sander, L.M. (1981). Diffusion-limited aggregation, a kinetic critical phenomenon. *Physical Review Letters*, **47**, 1400–1403.

Wu, R., Li, C. and Freeman, A.J. (1991). Structural, electronic and magnetic-properties of Co/Pd(111 = and Co/Pt(111). *Journal of Magnetism and Magnetic Materials*, **99**, 71.

Yan, L., Przybylski, M., Lu, Y., *et al*. (2005). Fabrication and uniaxial magnetic anisotropy of Co nanowires on a Pd(110) surface. *Applied Physics Letters*, **86**, 102503.

Yan, M.L., Zeng, H., Powers, N. and Sellmyer, D.J. (2002). L1(0),(001)-oriented FePt: B2O3 composite films for perpendicular recording. *Journal of Applied Physics*, **91**, 8471.

Zhang, Z.Y., Chen, X. and Lagally, M.G. (1994). Bonding-geometry dependence of fractal growth on metal-surfaces. *Physical Review Letters*, **73**, 1829–1832.

FURTHER READING

Aguilera-Granja, F., Montejano-Carrizales, J.M. and Morán-López, J.L. (1998). Magnetic moments of iron clusters: a simple theoretical model. *Physics Letters A*, **242**, 255.

Barth, J.V. (2000). Transport of adsorbates at metal surfaces: From thermal migration to hot precursors. *Surface Science Reports*, **40**, 75–150.

Bromann, K., Felix, C., Brune, H., *et al*. (1996). Controlled deposition of size-selected silver nanoclusters. *Science*, **274**, 956.

Brune, H., Roder, H., Boragno, C. and Kern, K. (1994). Microscopic view of nucleation on surfaces. *Physical Review Letters*, **73**, 1955–1958.

Chikazumi, S. (1997). *Physics of Ferromagnetism*, *Second Edition*, Oxford University Press, p. 546.

Dürr, H.A., van der Laan, G. and Thole, B.T. (1996). Microscopic origin of magnetic anisotropy in Au/Co/Au probed with x-ray magnetic circular dichroism – Comment. *Physical Review Letters*, **76**, 3464.

Garibay-Alonso, R. and López-Sandoval, R. (2005). Ground state spin local magnetic moments of deposited Fe clusters. *Solid State Communications*, **134**, 503.

Guirado-López, R.A., Dorantes-Dávila, J. and Pastor, G.M. (2003). Orbital magnetism in transition-metal clusters: From Hund's rules to bulk quenching. *Physical Review Letters*, **90**(22), 226402.

Haley, C. and Weaver, J. (2002). Buffer-layer-assisted nanostructure growth via two-dimensional cluster-cluster aggregation. *Surface Science*, **518**, 243.

Huang, L., Chey, S.J. and Weaver, J. (1998). Buffer-Layer-Assisted Growth of Nanocrystals: Ag-Xe-Si(111). *Physical Review Letters*, **80**(18), 4095.

Kechrakos, D. and Trohidou, K. (1998). Magnetic properties of dipolar interacting single-domain particles. *Physical Review B*, **58**, 12169.

Knorr, N., Brune, H., Epple, M., Hirstein, M.A., *et al*., (2002). Long-range adsorbate interactions mediated by a two-dimensional electron gas. *Physical Review B*, **65**, 115420.

van der Laan, G. (1998). Microscopic origin of magnetocrystalline anisotropy in transition metal thin films. *Journal of Physics-Condensed Matter*, **30**, 3239.

Lee, H.K., Schulthess, T.C., Landau, D.P., *et al*. (2002). Monte Carlo simulations of interacting magnetic nanoparticles. *Journal of Applied Physics*, **91**(10), 6926.

Novosad, V., Guslienko, K.Y., Shima, H., *et al*. (2002). Effect of interdot magnetostatic interaction on magnetization reversal in circular dot arrays. *Physical Review B*, **65**, 060402.

Ohresser, P., Ghiringhelli, G., Tjernberg, O., *et al*. (2000). Magnetism of nanostructures studied by x-ray magnetic circular dichroism: Fe on Cu(111). *Physical Review B*, **62**, 5803.

Pierce, J., Torija, M., Gai, Z., *et al*. (2004). Ferromagnetic stability in Fe nanodot assemblies on Cu(111) induced by indirect coupling through the substrate. *Physical Review Letters*, **92**(23), 237201.

Repetto, D., Honolka, J., Rusponi, S., *et al*., (2006). Magnetism of Fe clusters and islands on Pt surfaces. *Applied Physics A*, **82**, 109–112.

Shen, J., Pierce, J.P., Plummer, E.W. and Kirschner, J. (2003). The effect of spatial confinement on magnetism: films, stripes and dots of Fe on Cu(111). *Journal of Physics-Condensed Matter*, **15**, R1.

Sipr, O., Košuth, M. and Ebert, H. (2004). Magnetic structure of free iron clusters compared to iron crystal surfaces. *Physical Review B*, **70**, 174423.

Wang, D.S., Wu, R. and Freeman, A.J. (1993). Magnetocrystalline anisotropy of Co-Pd-interfaces. *Physical Review B*, **48**, 15886.

Wang, D.S., Wu, R. and Freeman, A.J. (1994). Local spin-density theory of interface and surface magnetocrystalline anisotropy – Pd/Co/Pd(001) and Cu/Co/Cu(001) sandwiches. *Journal of Applied Physics*, **75**(10), 6409.

Weaver, J. and Antonov, V.N. (2004). Synthesis and patterning of nanostructures of (almost) anything on anything. *Surface Science*, **557**(1–3), 1.

Weaver, J. and Waddill, G. (1991). Cluster assembly of interfaces – nanoscaple engineering. *Science*, **251**, 1444.

Zhao, J., Chen, X., Sun, Q., *et al*. (1995). A simple-band model for the magnetic property of ferromagnetic transition-metal clusters. *Physics Letters A*, **205**, 308.

An STM movie for Cu diffusion on the Cu(111) surface is shown at http://www.mpi-stuttgart.mpg.de/kern/res_act/supmat_1.html, 2006.

Magnetism of Low-dimensional Systems: Theory

Stefan Blügel and Gustav Bihlmayer
Institut für Festkörperforschung, Jülich, Germany

1 INTRODUCTION

We explore the magnetic ground-state properties of low-dimensional systems to investigate which systems are magnetic, what is the magnetic ground-state structure, and what is the orientation of the magnetization with respect to the crystal lattice.

In this article we focus on the dimensional aspect of itinerant magnetism, in particular, of those systems including d electrons, as relevant for the magnetic ground-state properties of metallic interfaces, multilayers, ultrathin films, step edges, wires or chains, or magnetic clusters deposited on surfaces. Considering the vast number of possible systems – a number growing fast with the number of constituent atoms – the surface or interface orientation, the chemical and structural roughness at interfaces, and the electronic nature of the substrate (metal, semiconductor, insulator), an exhaustive review is unattainable. Instead we discuss chemical trends in order to develop an intuition helpful to understand new systems or envisage new effects that have not been investigated yet.

The simplest low-dimensional systems are isolated atoms, whose spin moments as a function of the number of d electrons are well described by Hund's first rule: the spins of all electrons are aligned in parallel up to a maximum value of $S_z = 5/2$. Thus, nearly all of the 30 transition-metal atoms have magnetic spin moments. The largest possible d moments occur at the center of each series, that is, $5\,\mu_B$ for Cr and Mn in the 3d series. On the other hand, it is well known that only 5 of 30 transition metals remain magnetic in their bulk crystalline phase: Co and Ni are ferromagnetic (FM), Cr is antiferromagnetic (AFM), and Mn and Fe are FM or AFM depending on their crystal structure (cf. Figure 1). Low-dimensional transition metals should fall in between these two extremes. A magnetic material that is nonmagnetic as bulk metal but magnetic as nanostructure may be envisaged. Although these arguments do apply, band narrowing, charge transfer, lift of degeneracies, structural, morphological, or thermodynamical changes mire the interpolation and it took about 10 years to settle the 'relatively simple' problem of the surface magnetism of Ni(100) (Donath, 1994). The magnetic coupling between the moments of atoms in systems of reduced dimensions is totally unclear, in particular if the frustration of the magnetic interactions comes into play as for example in exchange-bias systems.

The magnetic ground-state properties may be divided into (i) the formation of local spin and orbital moments of different sizes, (ii) the interaction between the local moments responsible for the formation of the magnetic order, the magnetic coupling at interfaces or across spacer layers, and (iii) the magnetic anisotropy energy (MAE), which couples the direction of the magnetization to the lattice and determines the easy and hard axes of the magnetization. At this point it may be useful to put the magnetic energies involved

Handbook of Magnetism and Advanced Magnetic Materials. Edited by Helmut Kronmüller and Stuart Parkin. Volume 1: *Fundamentals and Theory*. ISBN: 978-0-470-02217-7.

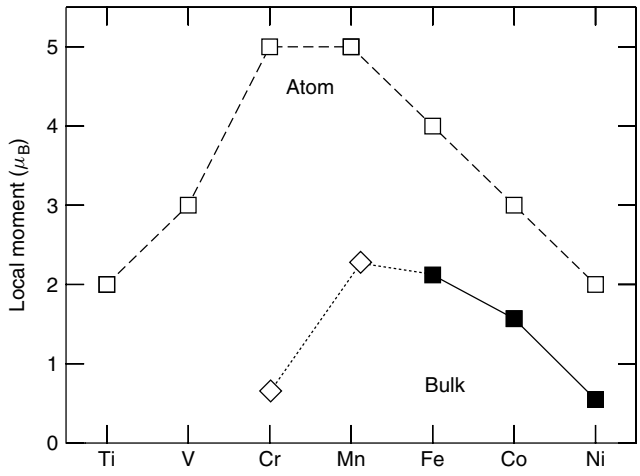

Figure 1. Local spin magnetic moments of isolated 3d atoms (empty squares connected by dashed line), ferromagnetic (solid squares connected by solid line) and antiferromagnetic (diamonds connected by dotted line) 3d bulk metals. The magnetism of the atom includes only the moment due to the d electrons. For the bulk metals, the experimental spin moments are shown.

Table 1. Typical ground-state energies E in eV/atom for 3d metal films.

	E (eV/atom)
Cohesive energy	5.5
Local moment formation	1.0
Alloy formation	0.5
Magnetic order	0.2
Structural relaxation	0.05
Magnetic anisotropy	$0.0001 \div 0.002$

in (i)–(iii) into a general perspective by comparing them in Table 1 with the structural and compositional ground-state energies.

From the relative importance of the different energies it is evident that the local moment formation has a considerable influence on stability, alloy formation, atom arrangement, and atom relaxation at the interface. Since the local moments may change quite substantially at the interface, materials with new and unknown phases (Blügel, 1996), crystal structures, and magnetic structures (Kurz, Bihlmayer, Hirai and Blügel, 2001) are to be expected. Obviously, the anisotropy energy is a rather small quantity, energetically nearly decoupled from the rest and can therefore be treated separately. In magnetism, tiny energies can matter. The anisotropy energy is, technologically speaking, the most important quantity in magnetism as it determines the bimodal state of the magnetization, which can for example be related to bit '0' or '1' and it is an important quantity determining the finite temperature properties of thin films. The anisotropy energy, which depends on all structural and electronic details of a low-dimensional system, is the origin of the magnetostriction, but otherwise does not have much influence on structural aspects. In this sense the problem of the magnetic anisotropy can be tackled after all other aspects of the low-dimensional system have been completely determined.

There are several low-dimensional systems and phenomena that are not covered in this chapter. To these belong the *magnetic nanoparticles* and *magnetic clusters* in the gas phase. The *molecular magnets* and the *Kondo-effect* at surfaces are discussed in detail in **Molecular Magnets: Phenomenology and Theory, Volume 1** and **The Kondo Effect, Volume 1**. When the growth of thin films is repeated to form multilayers, in particular, those of thin magnetic films separated by nonmagnetic spacer layers, an exchange interaction between the films across the spacer layer occurs, which is known as the *interlayer exchange coupling* (see **Exchange Coupling in Magnetic Multilayers, Volume 1**). Here, we do not include the thermodynamic properties of low-dimensional systems, which are partly discussed in **Theory of Magnetic Phase Transitions, Volume 1** and **Electron Theory of Finite Temperature Magnetism, Volume 1**. The works that we present here are basically predictions, analyses, and understanding of the magnetic spin and orbital moment, the magnetic structure and the magnetic orientation on the basis of the electronic structure – results obtained from the density-functional theory are introduced in **Density-functional Theory of Magnetism, Volume 1**. The experimental counterpart can be found in the chapter **Magnetism of Low-dimensional Metallic Structures, Volume 1**

2 THEORY AND MODELS

In this section, the reader is reminded about the theoretical concepts used to predict and analyze the results. The theories have been introduced in other chapters. Further, simple models are discussed to rationalize the results.

2.1 Density-functional theory: noncollinear magnetism

Density-functional theory (Hohenberg and Kohn, 1964) in the local spin-density approximation (LSDA) (von Barth and Hedin, 1972; Kübler, 2000) or the more recent generalized gradient approximation (GGA) (Perdew *et al*., 1992) has been the main underlying basis for the first-principles electronic structure calculations of magnetic systems in reduced dimensions. The theory has been introduced in **Density-functional Theory of Magnetism, Volume 1**. It is based on the Hohenberg–Kohn theorem stating that the ground-state

energy E of a many-body system is a unique functional of the charge density $n(\vec{r})$ and the vector-magnetization density $\vec{m}(\vec{r})$ and is minimal for the true ground-state densities.

In many applications, for example, in FM and AFM solids, there is a common magnetization axis for all atoms. For these collinear cases, a global z axis can be chosen along the direction of the magnetic field. In this case, the energy and all other physical observables become functions of the electron density and the magnetization density $m(\vec{r}) = (\vec{m}(\vec{r}))_z$ rather than $\vec{m}(\vec{r})$, or, equivalently, of the spin-up and spin-down electron densities $n_\uparrow(\vec{r})$ and $n_\downarrow(\vec{r})$. As an example of such computational results we compare in Table 2 the calculated magnetic moments of the elemental bulk ferromagnets with the experimental ones.

This formalism also allows the calculation of complex magnetic structures such as noncollinear magnets, in general, or systems with incommensurate spiral spin-density waves (SSDW) in particular. Such magnetic structures exist in a great variety of systems. They often occur in topologically frustrated antiferromagnets (e.g., antiferromagnets on a triangular lattice or antiferromagnets in contact with ferromagnets with atomically rough interfaces as in exchange-bias systems) or in materials with competing exchange interactions as for example in fcc Fe or Mn.

Non collinear magnets are characterized by a set of magnetization axes $\{\hat{\vec{e}}\}$, which may change from atom to atom in order to minimize the energy functional $E[n(\vec{r}), \vec{m}(\vec{r})|\{\hat{\vec{e}}\}]$ and determine the magnetic structure. The spin spiral is a particular noncollinear magnetic structure with moments that are rotated by a constant angle from atom to atom along a certain direction of the crystal. It can be described by the propagation vector of the spin-spiral $\vec{q}$, the rotation axis (which, in the absence of the spin-orbit or dipole–dipole interaction, is not fixed with respect to the lattice) and the relative (cone-)angle ϑ between the local quantization axis and the rotation axis. The rotation angle of the magnetic moment of an atom at the position $\vec{R}_i$ is then given by $\varphi = \vec{q}\cdot\vec{R}_i$. For a rotation around the z axis the magnetic moment of an atom at the position $\vec{R}_i$ is given by

$$\vec{M}_i = M(\cos(\vec{q}\cdot\vec{R}_i)\sin\vartheta, \sin(\vec{q}\cdot\vec{R}_i)\sin\vartheta, \cos\vartheta) \quad (1)$$

The great value of this type of noncollinear calculations rests in determining from $E[n(\vec{r}),\ \vec{m}(\vec{r})|\{\hat{\vec{e}}\}]$ or $E[n(\vec{r}), \vec{m}(\vec{r})|\{\vec{q}\}, \{\vartheta\}]$ the magnetic ground state as well as the exchange parameters J_{ij}. They enter the Heisenberg model, giving access to magnon spectra, spin-wave stiffness constants, magnetic phase diagrams, finite temperature properties, and magnetic excitations of the low-dimensional system at hand (Sandratskii, 1998; Pajda, *et al*., 2001; Turek, Kudrnovský, Drchal and Bruno, 2006).

Table 2. Magnetic moments M_{LSDA} in μ_{B}/atom for Fe, Co, and Ni calculated using the local spin-density approximation (LSDA) (Moruzzi, Janak and Williams, 1978). Values are compared with experimental data for the pure spin moment M_{spin} and with the total moment M_{tot} including orbital contributions.

Metal	M_{LSDA}	M_{spin}	M_{tot}
Fe	2.15	2.12	2.22
Co	1.56	1.57	1.71
Ni	0.59	0.55	0.61

2.2 Heisenberg model and beyond

Predicting the magnetic ground state of a low-dimensional magnetic system can be a highly nontrivial problem. In cases, for example, where competing exchange interactions between neighboring atoms cannot be satisfied, exchange interactions are frustrated giving rise to a multitude of possible spin structures. In the past, the magnetism of complex spin structures of itinerant magnets was discussed almost exclusively within the framework of model Hamiltonians, for example, the classical Heisenberg Hamiltonian,

$$H_{2\text{-spin}} = -\sum_{i,j} J_{ij}\ \vec{S}_i \cdot \vec{S}_j \quad (2)$$

The spins localized on the lattice sites i, j are considered as classical vectors $\vec{S}$, with the assumption that the spins on all lattice sites have the same magnitude S:

$$\vec{S}_i^2 = S^2, \text{ for all } i \quad (3)$$

The exchange interaction between the spins is isotropic and is described by the pair interaction J_{ij}. In localized spin systems the J_{ij} can be safely approximated by the FM ($J_1 > 0$) or AFM ($J_1 < 0$) nearest-neighbor (nn) interaction, that is, $J_{ij} = 0$ for all i, j, except for $J_{\mathrm{nn}} = J_1$. Also in itinerant magnets J_1 often dominates over the rest of the more distant pairs, however, an attempt to reproduce the Curie temperature T_{C} solely from J_1 produces results of limited quality. In many cases interactions between atoms as distant as 20 sites need to be included to give reliable results.

Exchange interactions beyond the classical Heisenberg model can be motivated from a perturbation expansion of the Hubbard model (Takahashi, 1977). Expanding the Hubbard model into a spin model and replacing the spin operators by classical spin vectors, a second-order perturbation expansion reproduces the classical Heisenberg model. The fourth-order

perturbation treatment (the third order is zero in the absence of spin-orbit interaction) yields two additional terms of a different form. One is the four-spin exchange interaction:

$$H_{4\text{-spin}} = -\sum_{ijkl} K_{ijkl}\big[(\vec{S}_i\vec{S}_j)(\vec{S}_k\vec{S}_l) + (\vec{S}_j\vec{S}_k)(\vec{S}_l\vec{S}_i) - (\vec{S}_i\vec{S}_k)(\vec{S}_j\vec{S}_l)\big] \quad (4)$$

The four-spin interaction arises from the hopping of electrons over four sites, that is, the process $1 \to 2 \to 3 \to 4 \to 1$. The second term, resulting from the hopping $1 \to 2 \to 1 \to 2 \to 1$, is the biquadratic exchange:

$$H_{\text{biquadr}} = -\sum_{ij} B_{ij}(\vec{S}_i \cdot \vec{S}_j)^2 \quad (5)$$

The exchange parameters J_{ij}, K_{ijkl}, and B_{ij} depend on the details of the electronic structure and it is known (Terakura, Hamada, Oguchi and Asada, 1982) that for transition metals the sign and magnitude are rapidly varying functions of the d-band filling. In thin films, the nearest-neighbor exchange constants scaled by the appropriate power of the magnetic moment, S^4K_1 and S^4B_1, are about one order of magnitude smaller than S^2J_1, which is for example for Mn/Cu(111) about 30 meV (Kurz, Bihlmayer, Hirai and Blügel, 2002). The higher-order spin interactions have then the effect, depending on the sign and value, of lifting the degeneracy of magnetic states that are degenerate in the Heisenberg model.

In itinerant magnets, the electrons that are responsible for the formation of the magnetic state do participate in the formation of the Fermi surface and hop across the lattice. Thus, it is by no means clear how far a short-ranged nn interaction or even how far the Heisenberg model, and models beyond that, can go in giving a sufficiently good description of the physics of itinerant magnets at surfaces and films. We believe that the interplay of *ab initio* calculations with model Hamiltonians provides a powerful approach to investigate the magnetic structures of complex magnetic systems such as low-dimensional magnets and to deal with their thermodynamical properties.

For our purpose here, the value of the Heisenberg model lies in two facts: (i) to construct a zero-temperature phase diagram of relevant spin states as a function of the exchange parameters J_{ij} and (ii) that a spin-spiral state, SSDW, with a propagation vector $\vec{q}$ in the first Brillouin zone (BZ) is a fundamental solution of the Heisenberg model for a Bravais lattice. On a Bravais lattice it is convenient to write the spin on lattice sites in terms of their discrete Fourier components $\vec{S}_{\vec{q}}$. The Heisenberg Hamiltonian can then be written in the simple form

$$H_{2\text{-spin}} = -N\sum_{\vec{q}} J(\vec{q})\ \vec{S}_{\vec{q}} \cdot \vec{S}_{-\vec{q}} \quad (6)$$

The summation goes over the reciprocal lattice vectors $\vec{q}$. N denotes the number of lattice sites in the crystal.

$$J(\vec{q}) = \sum_{i,j} J_{i-j}\ \mathrm{e}^{-i\vec{q}(\vec{R}_j-\vec{R}_i)} = \sum_{\vec{0}-\vec{R}_i} J_{\vec{0}-\vec{R}_i}\ \mathrm{e}^{-i\vec{q}(\vec{0}-\vec{R}_i)} = J(-\vec{q}) = J(\vec{q})^* \quad (7)$$

are the Fourier transformed exchange constants and $\vec{R}_i$ is the real-space coordinate of lattice site i. The lowest energy

$$E(\vec{Q}) = -NS^2J(\vec{Q}) \quad (8)$$

is found for the magnetic ground state $\vec{S}_{\vec{Q}}$ of the SSDW with wave vectors $\pm\vec{Q}$ (as well as symmetry-related $\vec{Q}$ vectors) which are obtained by minimizing the energy equation (6) under the condition equation (3). The corresponding spin structures are helical spin spirals (equation (1) for $\vartheta = 90^\circ$) and $\vec{M}_i = -g\mu_B\vec{S}_i$. For particular $\vec{Q}$ vectors, for example, $\vec{Q} = \pm 2\pi/a(0, 0, 1/2)$, one may find the *uudd* state as ground state, a collinear bilayer AFM state of FM double layers (DLs), which couple antiferromagnetically. This state, for example, was found in calculations for regime II of fcc-Fe films on Cu(001) (Asada and Blügel, 1997b).

In two dimensions, $\vec{Q}$ is typically located at high-symmetry points (lines) of the two-dimensional (2D) Brillouin zone, where the energy equation (8) as function of the $\vec{q}$-vector should have an extremum, a maximum, a minimum (or a saddle point), depending on the exchange constants J_{ij} and the symmetry of the high-symmetry point. In principle, one cannot rule out that the minimum of the energy will be located at any arbitrary point along the high-symmetry lines, representing an incommensurate spiral spin-density wave. In practice, we perform first-principles total energy calculations, that is, we study $E\left[n(r), m(r)|\{q\}\right]$ of flat spin spirals along the high-symmetry lines to gain an overview of possible minimum energies $E(\vec{Q})$. The role of higher-order spin interactions is then investigated, carrying out constraint calculations of the total energy $E[n(\vec{r}), \vec{m}(\vec{r})|\{\hat{\vec{e}}\}]$ for particular paths of magnetic configurations. Zero-temperature phase diagrams in the $J_{01} \cdots J_{0i}$ space are very helpful to reduce the relevant phase space of possible spin structures. This method is followed in Sections 3.1.2 and 3.2.2 to explore the magnetic ground state of thin films. The previously described mapping of *ab initio* calculations to spin models relies on the assumption that the magnetic moment does not depend

on the relative difference of the magnetization axis between atoms. For itinerant systems this is not necessarily guaranteed. The change of the moment with respect to the relative quantization axis can be mapped on spin models introducing higher-order spin interactions as well.

2.3 Critical temperature

It is well known that magnetic excitations in itinerant ferromagnets are basically of two different types, namely, the Stoner excitations, associated with longitudinal fluctuations of the magnetizations, and the spin waves or magnons, which correspond to collective transverse fluctuations of the magnetization direction. Near the bottom of the excitation spectrum, the density of states (DOS) of magnons is considerably larger than that of the Stoner excitations, so that the thermodynamics in the low-temperature regime is completely dominated by magnons. Stoner excitations can be safely ignored. Thus, it seems reasonable to extend this approximation up to the critical temperature, T_C, to neglect the Stoner excitation systematically, and to describe the transversal fluctuations by the Heisenberg model expressed in equation (2) with exchange parameters determined from first principles. An overview of the current applications along this line of mapping first-principles results on Heisenberg-type Hamiltonians to study the thermodynamical properties of bulk and low-dimensional magnets can be found in the paper of Turek, Kudrnovský, Drchal and Bruno (2006).

Below the critical temperature, the so-called Curie temperature T_C for ferromagnets, or the Néel temperature, T_N, for magnets with more complex magnetic phases, the spontaneous magnetization remains finite, while it is zero above T_C. The phase transition is of second order, that is the spontaneous magnetization which is the order parameter characterizing the phase transition, vanishes continuously at T_C. A second-order phase transition is governed by the principle of universality, where a system close to the phase transition does not depend on details of the system such as its material parameters or the geometry of the sample, but rather on the symmetry of the underlying model and the dimension of the spin, which is three for the Heisenberg model. In this chapter we are interested in estimating the critical temperatures as these are nonuniversal quantities and are of great practical importance. It is certainly important to know whether cryogenic, room temperature, or elevated temperatures are required to observe particular phenomena.

A first simple estimate of the Néel temperature for a three-dimensional system exhibiting a helical spin-spiral ground state with wave vector $\vec{Q}$ is given by the mean-field approximation (MFA) to the Heisenberg Hamiltonian, which leads to

$$k_B T_N^{MFA} = \frac{2}{3} S^2 J(\vec{Q}) \quad \text{and} \quad k_B T_C^{MFA}(\text{n.n.}) = \frac{2}{3} S^2 N_{nn} J_1 \tag{9}$$

where k_B is the Boltzmann constant. For the FM state, $\vec{Q} = (0, 0, 0)$, the left equation (9) gives the Curie temperature in the MFA, T_C^{MFA}, expressed explicitly in the equation on the right in the nearest-neighbor approximation to the exchange interaction. N_{nn} is the coordination number of nearest neighbor atoms and J_1 is the interaction strength as introduced in Section 2.2. The MFA gives the right proportionality of T_C with respect to the number of neighbors, but also has a few deficiencies. Besides overestimating T_C for three-dimensional systems by typically about 20%, T_C^{MFA} does not depend on the lattice structure or the dimensionality of the system. These shortcomings are remedied by treating the Heisenberg model in the random phase approximation (RPA) (Tyablikov, 1967; Turek *et al*., 2003), which gives for the critical temperatures,

$$\frac{1}{k_B T_N^{RPA}} = \frac{3}{4} \frac{1}{N S^2} \sum_{\vec{q}} \left[\frac{1}{J(\vec{Q}) - J(\vec{q})} + \frac{1}{J(\vec{Q}) - \frac{1}{2} J(\vec{q} + \vec{Q}) - \frac{1}{2} J(\vec{q} - \vec{Q})} \right]$$

$$\text{and } k_B T_C^{RPA}(\text{n.n.}) = \frac{2}{3} S^2 N_{nn} J_1 \cdot \begin{cases} 0.660 & \text{sc} \\ 0.718 & \text{bcc} \\ 0.744 & \text{fcc} \end{cases} \tag{10}$$

The RPA gives weight to the low-energy magnon excitations $E(q) \propto J(\vec{Q}) - J(\vec{q})$ in the summation over all modes. This provides estimates of T_C in close vicinity to the numerical analysis using classical Monte Carlo simulations (Metropolis *et al*., 1953) discussed in detail in the book of Landau and Binder (2000).

Both approximations show that the Curie and Néel temperatures depend on the number of nearest neighbors, and one expects that the critical temperature T_C decreases if the dimensionality of the system is reduced. But both approximations show a qualitatively different behavior for low-dimensional magnets. MFA overestimates the tendency for long-range order and predicts always a phase transition to FM order in the Heisenberg model, regardless of whether we have a one-, two-, or three-dimensional system, whereas $T_C^{RPA} = 0$ already for 2D systems. This is consistent with the theorem of Mermin and Wagner (1966), which states that in two dimensions there is no spontaneous long-range FM order for isotropic Heisenberg models with short-range interaction ($\sum_j J_{ij} r_{ij}^2 < \infty$) at finite temperature. In thin films, the long-range order at finite temperature is stabilized by the magnetic anisotropy, which is practically always present. It

opens a gap Δ in the excitation spectrum of the spin waves, $E(q) \propto \Delta + J(\vec{Q}) - J(\vec{q})$, and suppresses low-energy long-wavelength fluctuations, which occur for low temperatures. According to a renormalization group analysis by Erickson and Mills (1991) and Mills (1994), the transition temperature in two dimensions, $T_C^{(2D)}$, scales with the transition temperature of the three-dimensional Heisenberg model which is renormalized by a logarithmic factor,

$$T_C^{(2D)} = T_C^{(3D)} \frac{2}{\ln\left(\frac{3\pi}{4}\frac{k_B T_C^{(3D)}}{K}\right)} \tag{11}$$

which contains the strength of the uniaxial magnetic anisotropy in terms of a constant K (see Section 2.6). This result is displayed in Figure 2. T_C vanishes in the isotropic limit ($K \to 0$) in accordance with the Mermin–Wagner theorem. Interestingly, for finite K there is a rapid increase of T_C reaching reasonable values, of say 20% of the critical temperature in three dimensional systems, for anisotropy values of less than a percent of the FM coupling constant. Consider for example Fe, with a shape anisotropy of 0.140 meV, which corresponds to 1.63 K on the temperature scale. This is only 0.14% of the Curie temperature of Fe, $T_C^{(3D)}(\text{Fe}) = 1183\,\text{K}$, but already causes a Curie temperature for an Fe film of $T_C^{(2D)}(\text{Fe}) = 0.27 \cdot T_C^{(3D)}(\text{Fe}) = 320\,\text{K}$.

Thus at any finite anisotropy, there is a critical temperature, where the spin degree of freedom is frozen out owing to the presence of the anisotropy, that is the dimension of the spin is reduced from three for the Heisenberg model to one – spin up and down. In terms of universality, the Heisenberg model with any finite anisotropy value is in the universality class of the Ising model, and the Ising model shows a phase transition in two dimensions.

In one dimension even the Ising model does not show long-range order at finite temperatures. Although for quasi-one-dimensional magnetic chains – these are chains of finite size – there is, strictly speaking, no remanent magnetization

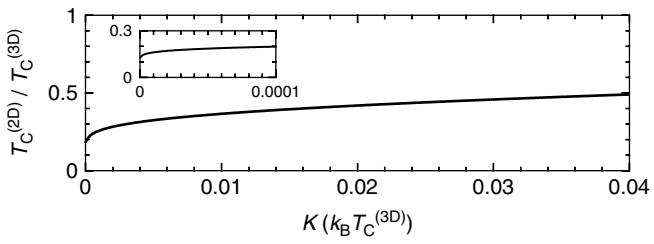

Figure 2. Critical temperature of a two-dimensional magnet as a function of the uniaxial anisotropy following equation (11). The function starts at zero for $K = 0$. Note its rapid growth in the vicinity of the origin as shown in the inset at magnified scale.

or long-range order, but there is a temperature, known as *blocking temperature*, below which a finite chain seems to a have a spontaneous and remanent magnetization, with long-range order in the chain. In reality, this magnetic order is accompanied by a slow relaxation (Glauber, 1963). The relaxation rate depends on the magnetic anisotropy and can be of macroscopic times, such that a quasi-one-dimensional chain appears as a ferromagnet as occurs in the experiments of Gambardella *et al*. (2002).

2.4 Stoner model

The occurrence of ferromagnetism can be studied on the basis of the Stoner criterion introduced in **Density-functional Theory of Magnetism, Volume 1**:

$$I\, n(E_F) > 1 \tag{12}$$

The Stoner criterion is an instability condition that expresses the competition between the exchange interaction in terms of the exchange integral I, which drives the system into ferromagnetism for large I, and the kinetic energy in terms of the nonmagnetic density of states (DOS), $n(E_F)$ at the Fermi energy E_F. The kinetic energy rises if the system becomes magnetic. This effect will be most pronounced for systems with wide bandwidth or low density of states. A big exchange integral and a large nonmagnetic DOS at the Fermi energy favors ferromagnetism. When ferromagnetism occurs, the double degeneracy of the energy bands $\varepsilon_{\vec{k}}$ is lifted, and majority states $\varepsilon_{k\uparrow}$ and minority states $\varepsilon_{k\downarrow}$ are rigidly shifted in energy by the exchange splitting IM, where M is the value of the local magnetic moment,

$$\varepsilon_{k\uparrow} = \varepsilon_{\vec{k}} - \frac{1}{2}IM \quad \text{and} \quad \varepsilon_{k\downarrow} = \varepsilon_{\vec{k}} + \frac{1}{2}IM \tag{13}$$

The rigid band shift is a good model if the shift is small as in the case of bulk ferromagnets. Deviations can be found for thin films, as the magnetic moments and thus the exchange splitting is large.

The Stoner criterion in equation (12) can be generalized, describing the instability against the formation of a frozen spin wave of wave vector $\vec{q}$,

$$I\, \chi_{\vec{q}}(E_F) > 1 \tag{14}$$

Obviously the local DOS was replaced by the $\vec{q}$-dependent susceptibility $\chi_{\vec{q}}$, a quantity that is expressed in the Heisenberg model by $J(\vec{q})$. Within equation (14), antiferromagnetism is just a special case. While the DOS at E_F can be easily assessed by experiment or electronic structure calculations, the static susceptibilities $\chi_{\vec{q}}(E_F)$ are more difficult to

measure. To make use of equation (14), an approximate criterion for antiferromagnetism is derived which makes explicit use of the local DOS. Small magnetic moments with the same magnitude M, but possibly different directions $\widehat{\vec{M}_j}$ at different sites j, induce in linear response theory local moments $\vec{M}_i$ at sites i

$$\vec{M}_i = \sum_j \chi_{ij}(E_\mathrm{F})\, M\, \widehat{\vec{M}_j} \tag{15}$$

The staggered susceptibility describing a particular magnetic state (M) is then expressed as

$$\chi_\mathrm{M} = \sum_i \chi_{0i}\, \widehat{\vec{M}_0}\cdot\widehat{\vec{M}_i} \tag{16}$$

Particular examples of this staggered susceptibility are the FM (χ_FM)

$$\chi_\mathrm{FM} = n = \sum_i \chi_{0i} \tag{17}$$

and the AFM (χ_AFM)

$$\chi_\mathrm{AFM} = \sum_i (-1)^{(i)}\, \chi_{0i} \tag{18}$$

susceptibilities. Assuming that for 3d metals the nearest-neighbor interaction is the most dominating one, χ_{0i} can be neglected for all sites beyond nearest neighbors ($\chi_{0i} = 0$ for $i > 1$), and χ_FM and χ_AFM are given approximately by

$$\begin{aligned} n(E) &\approx \chi_{00}(E) + \chi_{01}(E), \quad \text{and} \\ \chi_\mathrm{AFM}(E) &\approx \chi_{00}(E) - \chi_{01}(E) \end{aligned} \tag{19}$$

where $\chi_{00}(E)$ is the local or atomic susceptibility, respectively, at the energy E. The energy dependence of χ_{00} is fairly simple. It follows from atomic Hund's rule–type arguments: the maximum spin M occurs for half-band filling, hence the atomic (local) susceptibility $\chi = \partial M/\partial H$ will also be largest. From equation (19), we can obtain an approximate form for χ_AFM using only DOS information. This is illustrated in Figure 3. As function of the d-band filling, from V to Ni, the Fermi energy sweeps from the left to the right through the DOS. If the Fermi energy is positioned at the center of the band as for Cr, the DOS is low but the AFM susceptibility is high and antiferromagnetism is expected. If the Fermi energy is closer to the end of the band, the AFM susceptibility is small but the DOS is large and ferromagnetism is expected as for Fe, Co, and Ni. Mn and Fe are at the edge of both magnetic states and, depending on circumstances, different magnetic ground states can be found. Compare also to the calculated DOS, Figure 9 in Section 3.1.1

2.5 Role of coordination number

As discussed in Section 2.4 the Stoner criterion for ferromagnetism, equation (12), depends on (i) the Stoner parameter I and (ii) the DOS $n(E_\mathrm{F})$ at the Fermi energy E_F.

(i) The exchange integral I is an intra-atomic, element-specific quantity, and in the simplest approximation it is independent of the local environment, the structure, and the site of a given atom, for example, surface atom or bulk atom. According to Gunnarsson (1976) and Janak (1977) a global trend

$$I_\mathrm{3d} > I_\mathrm{4d} > I_\mathrm{5d} \tag{20}$$

was found for the exchange integrals of the 3d, 4d, and 5d transition-metal series.

(ii) Focusing on the d electrons as relevant electrons for itinerant magnetism, the DOS depends on both the coordination number N_nn and the hopping matrix elements h_d between the d electrons. This can be understood as follows: The energy integral $\int_W n_\ell(\varepsilon)\,\mathrm{d}\varepsilon = 2\ell + 1$ over the bandwidth, W, of the local DOS of the angular momentum quantum number $\ell(= 2)$ is normalized to $2\ell + 1$ states. Thus, in the simplest approximation possible (e.g., rectangle-shaped

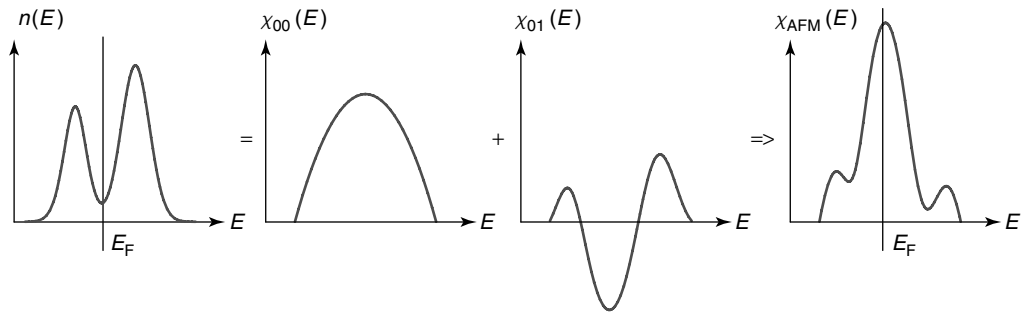

Figure 3. Graphical illustration of equation (19) for a DOS typical for transition-metal monolayers on (001)-oriented noble-metal substrates.

DOS), one can assume that the local DOS scales inversely proportional to the bandwidth, W,

$$n(E_{\mathrm{F}}) \sim \frac{1}{W} \tag{21}$$

At the atomic limit, the bandwidth converges to zero, the Stoner criterion is always fulfilled, and moments in accordance with Hund's first rule will be found. In general the DOS consists of contributions from electrons in s, p, d, and f states. For transition metals, by far the largest contribution comes from the d electrons, and the d–d hybridization determines the shape of the density of states. Therefore, in the following discussion we restrict ourselves to d electrons and write

$$n(E_{\mathrm{F}}) \approx n_{\mathrm{d}}(E_{\mathrm{F}}) \sim \frac{1}{W_{\mathrm{d}}} \tag{22}$$

The average local bandwidth $\overline{W_{\mathrm{d}}}(\vec{R}_i)$ for an atom i at position $\vec{R}_i$ can be estimated in a nearest-neighbor tight-binding model – applicable for the itinerant but tightly bound d electrons of transition-metal atoms – to be

$$W_{\mathrm{d}} \approx \overline{W_{\mathrm{d}}}(\vec{R}_i) = 2\sqrt{N_{\mathrm{nn}}(\vec{R}_i)}h_{\mathrm{d}}(R_{\mathrm{nn}}) \tag{23}$$

According to equation (23) the bandwidth depends on two quantities: (i) the hopping matrix element h_{d} of the d electrons and (ii) the number of nearest-neighbor atoms or coordination number N_{nn}.

(i) The hopping matrix element depends on the overlap of the d wave functions. It decreases with increasing lattice constant or distance R_{nn} to the nearest-neighbor atom, and for a given lattice constant it increases with the extension of the wave function or, equivalently, the number of nodes. In Figure 4 the bandwidths of 3d, 4d, and 5d bulk transition metals are schematically shown, together with the bandwidths of rare earths and actinides. In line with the arguments of increasing number of nodes from 3d to 5d wave functions, a clear 'macro trend' is visible for the transition-metal series, and it is summarized as follows:

$$h_{3\mathrm{d}} < h_{4\mathrm{d}} < h_{5\mathrm{d}} \Rightarrow W_{3\mathrm{d}} < W_{4\mathrm{d}} < W_{5\mathrm{d}} \Rightarrow n_{3\mathrm{d}} > n_{4\mathrm{d}} > n_{5\mathrm{d}} \tag{24}$$

Additionally, within each transition-metal series there exists a 'micro trend' due to the incomplete screening of the Coulomb potential of the nucleus by the d electrons. The d wave functions at the beginning of the transition-metal series are more extensive than at the end of the series, thus the hopping matrix element at the beginning of the series is larger than at the end, with well-known consequences for the bandwidth W and the DOS $n(E_{\mathrm{F}})$.

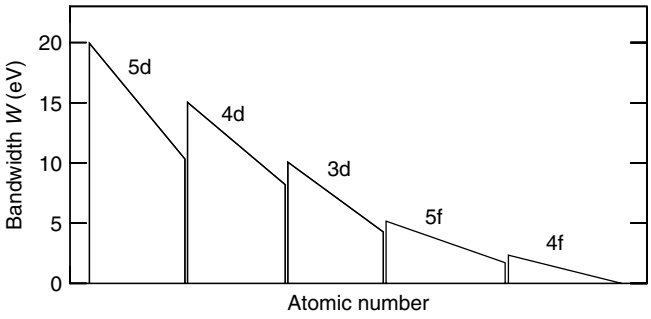

Figure 4. Schematic illustration of the bandwidth W of the transition metals together with rare earths (4f) and actinides (5f), all in the bulk phase. The 5f electrons of the early actinides and the 3d electrons of transition metals from the middle to the end of the 3d series (Cr to Ni) show itinerant magnetism, while the magnetism of the late actinides and the rare earths is best described as localized magnetism, and their magnetic properties can in good approximation be explained in terms of Hund's rule.

(ii) The smaller the coordination number N_{nn} the smaller the d–d hybridization and the smaller the bandwidth. Let us consider for example the coordination number of an atom in the environment of an fcc crystal ($N_{\mathrm{fcc}} = 12$), of an atom in the (001) surface of the fcc crystal ($N_{(001)} = 8$), located in a two-dimensional (001) monolayer (ML) film ($N_{\mathrm{ML}} = 4$) and of an atom in a monatomic chain ($N_{\mathrm{chain}} = 2$), keeping the nearest-neighbor distance ($R_{\mathrm{nn}} = \text{constant}$) and the bonding strength fixed ($h_{\mathrm{d}} = \text{constant}$). Under these circumstances, one obtains for the ratio of the bandwidths

$$W_d{}^{\mathrm{chain}}{:}W_d{}^{\mathrm{ML}}{:}W_d^{(001)}{:}W_d^{\mathrm{fcc}} = 0.41{:}0.58{:}0.82{:}1$$

or that of the local DOS

$$n_d^{\mathrm{chain}}{:}n_d^{\mathrm{ML}}{:}n_d^{(001)}{:}n_d^{\mathrm{fcc}} = 2.45{:}1.73{:}1.22{:}1 \tag{25}$$

Thus, the reduction of the coordination number leads to less d–d hybridization, which consequently leads to band narrowing, and in low-dimensional structures the tendency towards magnetism is considerably boosted. Accordingly, one can expect that transition metals, which are nonmagnetic as bulk metals, may become magnetic at surfaces or as ultrathin films. A nice manifestation of these arguments was recently reported for the size and shape dependence of the local magnetic moments in Fe clusters on the Ni(100) surface (Mavropoulos, Lounis, Zeller and Blügel, 2006) summarized in Section 5.2. The arguments put forward here for the increased ferromagnetism in reduced dimensions can be carried over directly to the increased AFM susceptibility.

The magnetic properties are expected to depend on the surface or film orientation also, because the coordination number N_{nn} (cf. Table 3) as well as the nearest-neighbor

Table 3. Coordination number N_{nn}, interlayer distance d, point symmetry S, and packing density ρ (fraction of the area of the surface unit cell, covered by atoms with an atom radius of touching bulk atoms) for an fcc lattice. Only the three low-index surfaces (001), (011), and (111) are considered. a is the lattice parameter of the simple cubic unit cell.

	N_{nn}	S	d/a	ρ
(111)	9	C_{3v}	0.5774	0.9068
(001)	8	C_{4v}	0.5000	0.7854
(011)	7	C_{2v}	0.3536	0.5554

distance $R_{\parallel}$ between the surface atoms and $R_{\perp}$ between the surface atoms and the atoms in the next layer change along with a change of the surface orientation. For an fcc lattice, the (111) surface is the most densely packed one, and we expect for it the smallest enhancement of the magnetic moments. Among the three low-index surfaces, with the orientation (001), (011), and (111), the (011) surface leads to the most open surface. For the latter we expect the largest magnetic moments. At surfaces or ultrathin films of bcc lattice type the trend should be exactly the opposite. The most densely packed surface is the (011) surface for which we expected the smallest enhancements of the magnetic moments. The (111) surface is the most open one. This surface is already close to a stepped one.

The implication of the coordination number, discussed so far, is an important aspect in interface magnetism but it is not the whole story. Further important aspects, neglected so far, have to be taken into account in order to give a qualitatively correct description of the magnetism at interfaces.

Point symmetry: The disruption of the translational symmetry due to a given interface reduces, in general, the point symmetry. Degeneracies typical for cubic bulk metals may be lifted. One example is the threefold degenerate t_{2g} bulk state, which is split at a (001) surface into a twofold degenerate state and a singly degenerate state. This symmetry break induces a splitting or broadening of the DOS and makes magnetism unfavorable. A famous victim of this scenario is Pd. Bulk Pd has a large DOS at the Fermi energy which contributes to a large exchange enhanced susceptibility. Thus, bulk Pd is nearly FM. The band narrowing experienced at the surface because of the reduction of the coordination number should drive the surface of Pd into the FM state. But this is not the case. Instead, the change of the surface symmetry splits the states at the Fermi energy, broadens the DOS, and counteracts the band narrowing. The surface of Pd(001) remains nonmagnetic.

Shift of the d band relative to the sp band: Compared to a single isolated atom, the d electrons in a solid are in a state of compression. Therefore, in a solid their energy levels are positioned at a much higher energy than in an atom. At the surface, the charge density of the d electrons can relax and their energy levels move downwards. They are situated closer to the bottom of the sp band and the number of d electrons is increased, or the d holes are decreased. This downward shift is often facilitated by a significant hybridization of the d electrons with sp electrons or holes for example, of the substrate. As depicted in Figure 5 this leads to a Lorentzian tail of the DOS. If this tail is positioned close to the Fermi energy, magnetism can be drastically reduced as for example, for a single Ni monolayer on Cu(100), for which the local Ni moment amounts to $0.33\,\mu_B$ as compared to the magnetic Ni moment at the Ni(100) surface ($0.72\,\mu_B$). For a monolayer Pd on Ag(100) magnetism is even absent. In both cases we would expect an increase of the moment due to the reduction of the coordination number by a factor 2 when compared to the respective (100) surface. On the other hand, elements at the beginning of the transition-metal series, such as V, profit from this effect and magnetism is more likely to appear.

sp–d dehybridization: The main carriers of itinerant magnetism are the d electrons. For atoms, we know that the number of d electrons are integer numbers. In metallic systems, this is not the case, the number of d electrons is a noninteger number and depends on the hybridization with the s and p electrons, besides depending on the dominating d–d hybridization. Owing to the hybridization of the d electrons with the sp electrons, d states below the Fermi energy are hybridized into unoccupied sp hybrids and the number of d electrons is reduced when compared to the isolated atom. This so-called sp–d dehybridization changes, as a function of the coordination number or the nearest-neighbor distance, the fractional number of d electrons without any topological change of the DOS. This is illustrated in Figure 6. Surfaces and monolayers with their smaller coordination numbers have, therefore, a higher number of d electrons favorable for magnetism. For an illustration, in a computer experiment we investigated the

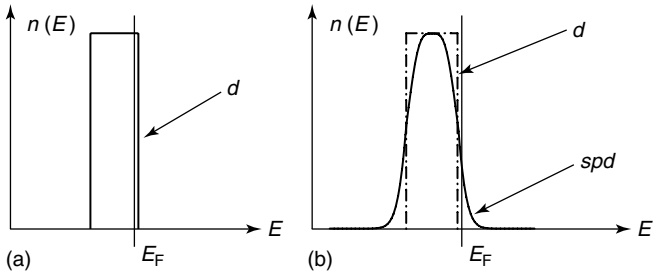

Figure 5. Schematic illustration of the hybridization of the overlayer d electrons with the sp electrons for example, of the substrate, on the density of states, (a) without and (b) with hybridization.

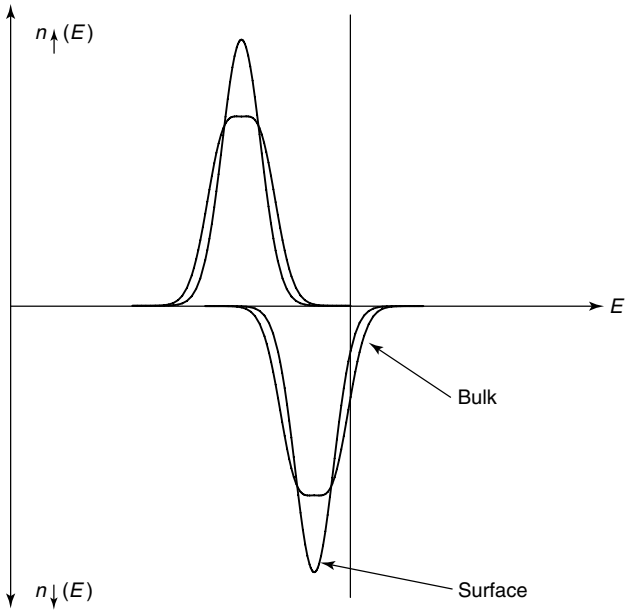

Figure 6. Schematic illustration of the role of the sp–d dehybridization on the density of states of the d electrons $n_d(E)$. The integrated density of d states for the surface is larger than that for the bulk.

Table 4. Calculated magnetic moments in units of μ_B for Ni(001) as an unsupported, freestanding monolayer (coordination number $N_{nn} = 4$), as a function of the lattice constant: $a_{Ag} = 7.79$ au, $a_{Pd} = 7.42$ au, $a_{Cu} = 6.76$ au, and $a_{Ni} = 6.65$ au. $N_{nn} = 8$ indicates the local magnetic moment of the Ni(001) surface and $N_{nn} = 12$ indicates the bulk value. The local magnetic moment of the Ni(011) surface ($N_{nn} = 7$) is also included.

N_{nn}	Lattice parameter			
	Ag	Pd	Cu	Ni
4	1.02	0.96	0.87	0.85
7	–	–	–	0.74
8	–	–	–	0.72
12	–	–	–	0.59

magnetic moment of one layer of Ni for various lattice parameters and coordination numbers. In Table 4 one finds that with decreasing coordination number and increasing atom separation, the magnetic moment increases although the Ni majority band is always completely filled.

Charge neutrality: The local charge neutrality has to be fulfilled in order to avoid the strong Coulomb forces that appear otherwise. It again induces a band alignment. Band narrowing (at interfaces) automatically means that the number of electrons must change. To avoid charged interfaces, a realignment of the center of gravity of the bands occurs. The d band, which moved to lower energy in order to relax the compression, now moves upward again. Owing to an upward shift in the energy, the minority and majority electrons become depopulated differently, and together with the change of the number of majority electrons due to the sp–d dehybridization the magnetic moment increases. All together we find a complex alignment of all the bands, individually, for each symmetry of the electrons.

Strong and weak ferromagnets: Despite the drastic change of the coordination number and the lattice parameter, the Ni moment in Table 4 changes only in the range of $\pm 20\%$. This is typical for strong ferromagnets (magnets with filled majority band). In general, one can say that the magnetism of strong ferromagnets is rather robust against any environmental changes. Weak ferromagnets (magnets with partly occupied majority bands) are sensitive to any environmental changes, and their moments collapse easily.

Using model Hamiltonians, these interwoven effects were frequently neglected. However, they are readily included in self-consistent first-principles results.

2.6 Orbital moment and magnetic anisotropy

A piece of magnetic material is typically magnetically anisotropic. This means that besides the isotropic exchange interaction there are additional interactions, which make the total energy depend on the orientation of the magnetization as measured with respect to the crystal axes and the sample shape. This orientation-dependent energy contribution is called the *magnetic anisotropy energy* (*MAE*), E_{MAE}, given in units of energy/atom throughout this article. Without this effect of the magnetic anisotropy, magnetism would have been hard to discover and possibly useless. In some way or the other, almost all applications of magnetic materials hinge on the fact that it is easier to magnetize a magnetic material in one direction than in another. The magnetic anisotropy is responsible for the occurrence of easy and hard axes, stabilizes magnetic order against thermal fluctuations in dimensions where the exchange interaction alone would not suffice (see Section2.3), and limits the width of a magnetic domain wall. It is, for example, responsible for the bimodal stability of magnetic domains with uniaxial symmetry, which allows the two possible magnetization directions in space to be interpreted in terms of bit '0' or '1'. This makes magnetism very valuable for magnetic storage media. Since the magnetic anisotropy is strongly related to the crystalline symmetry and the shape of the samples, a general expression of E_{MAE} will be a complex function of the orientation of the magnetization relative to the crystal axes. In low-dimensional

systems twofold symmetries are the most relevant ones and the magnetic anisotropy is then expressed as

$$H_{\mathrm{MAE}} = \sum_i \vec{S}_i \cdot \vec{\vec{K}}_i \cdot \vec{S}_i \tag{26}$$

where the tensor of single-site anisotropy constants, $\vec{\vec{K}}$, determines the strength of the anisotropy as well as the direction of minimal and maximal energy, named *easy* and *hard axes*, respectively. In perfect thin films and wires, the presence of a surface is then responsible for a uniaxial anisotropy energy normal to the surface, that is all components of $\vec{\vec{K}}_i$ are zero except $K_i^{zz} = K\delta^{zz}$ for perfect films and $K_i^{xx} = 1/2K\delta^{xx}$ and $K_i^{yy} = 1/2K\delta^{yy}$ for isolated wires. After expressing $\vec{S}_i$ in the form of equation (1), the uniaxial MAE takes the angular dependence

$$E_{\mathrm{MAE}}(\theta) = -K\cos^2\theta \tag{27}$$

θ denotes the angle between the magnetization and the film or wire normal and $K = \Delta E_{\mathrm{MAE}} = E_{\mathrm{MAE}}^{(\parallel)} - E_{\mathrm{MAE}}^{(\perp)}$ is the uniaxial anisotropy constant also given in energy/atom. The total MAE, $E_{\mathrm{MAE}}^{(\mathrm{tot})} = N_{\mathrm{A}} E_{\mathrm{MAE}} = V\mathcal{E}_{\mathrm{MAE}}$, of the system depends then on the number of atoms, N_{A}, in it. Frequently, the MAE is also expressed in terms of an energy density $\mathcal{E}_{\mathrm{MAE}}$. By definition, $K > 0$ ($K < 0$) describes the case of a preferred direction of the magnetization perpendicular, $\perp$, (parallel, $\parallel$) to the film plane or wire axis. Additional higher symmetries in place, for example a fourfold symmetry in a (100)-oriented film plane, corresponds to anisotropy contributions that are smaller in energy than the uniaxial anisotropy and are neglected here. The anisotropy constant depends sensitively on the chemical elements involved, structural details, details of the electronic structure, and the dimensionality of the system.

The microscopic origins of the magnetic anisotropy are the magnetic dipolar interaction and the spin-orbit interaction. The dipolar interaction is of long range and senses the outer boundaries of the sample. This results in shape anisotropy. Discussing long-range contributions, the underlying atomistic lattice describing the crystallinity of the system can be neglected and the shape anisotropy is described in terms of a continuum theory. Any contribution to the MAE, that is due to effects beyond continuum theory and explicitly takes the crystallinity of the system into account, is summarized as magnetocrystalline anisotropy energy (MCA). Both the dipolar and the spin-orbit interaction contribute to the MCA and the total anisotropy constant K,

$$K = K_{\mathrm{shape}} + K_{\mathrm{MCA}}^{(\mathrm{dip})} + K_{\mathrm{MCA}}^{(\mathrm{so})} \tag{28}$$

is just a linear superposition of the different contributions.

The shape anisotropy constant, K_{shape} in atomic Rydberg units/atom of a perfectly flat film of infinite extension or an infinitely long perfectly cylindrical wire is given by the local magnetic moment m and the atomic volume V as

$$K_{\mathrm{shape}}^{\mathrm{film}} = -2\pi\frac{2}{c^2}\frac{m^2}{V} \quad \text{and} \quad K_{\mathrm{shape}}^{\mathrm{wire}} = -\pi\frac{2}{c^2}\frac{m^2}{V} \tag{29}$$

all expressed in atomic units (au), m in μ_{B}/atom, V in au^3, and the speed of light, c, by the inverse of the fine-structure constant α, $c = 2/\alpha$. The negative sign denotes that the shape anisotropy pulls the magnetization into the film plane or along the wire axis. For bcc Fe, for instance, with a bulk magnetic moment of 2.215 μ_{B}/atom and a lattice constant of 5.42 au, $K_{\mathrm{shape}}^{\mathrm{film}}$ is equal to -0.140 meV/atom. The long-range interaction also senses the interface or surface roughness that is always present in real films. According to Bruno (1988) the roughness gives rise to an effective perpendicular contribution to the shape anisotropy the order of magnitude of which depends on the parameters characterizing the roughness. Obviously $K_{\mathrm{shape}}^{\mathrm{film}}$ and $K_{\mathrm{shape}}^{\mathrm{wire}}$ are the same for all atoms irrespective of their position and K is thus homogeneous across the film or wire. The same is true for any finite ellipsoidal structure, for any other finite structure, for example, a nanopattern structure on a surface, K_{shape} becomes inhomogeneous and typically much smaller at the boundary of the structure. For bulk samples, thick films, patterned nanostructures, and wires, the shape anisotropy is frequently the most important of the anisotropies.

For thin films and wires of a few atomic layers, the assumption that the magnetization can be treated as a continuous magnetic medium is no longer valid. Instead, the magnetic dipole-dipole energy has to be evaluated explicitly. In transition metals, the magnetization distribution around the atom is almost spherical and can thus be treated to a good approximation as a collection of discrete magnetic dipoles that are regularly arranged on a crystalline lattice. The dipolar energy E_{dip} per atom experienced by a dipole at site i because of the presence of ferromagnetically aligned dipoles on all other sites j can then be expressed as

$$E_{\mathrm{dip}}^{(i)}(\theta) = K_{\mathrm{dip}}^{(i)}\cos^2\theta = \frac{2}{c^2}\frac{1}{2}\sum_{j(j\neq i)}\frac{m_i m_j}{R_{i,j}^3}\left(1 - 3\cos^2\theta_{ij}\right) \tag{30}$$

θ_{ij} is the angle between the direction of the magnetic moment m of the dipoles at sites i or j given in units of μ_{B} and the vector $\vec{R}_{i,j}$ connecting atoms i and j. $R_{i,j}$ denotes the relative distance between these dipoles or atoms, respectively. The θ dependence explicitly expresses the fact that the dipole–dipole interaction contributes to the magnetic anisotropy. Obviously, in thin films and wires the anisotropy

energy depends on the position of the atom i normal to the surface or wire axis, respectively, and as such explicitly on the film thickness or wire diameter (in contrast to K_{shape} where all atoms have the same value). For crystalline thin wires and films, the sum in equation (30) can be evaluated straightforwardly with fast-converging summation techniques (Topping, 1927; Szunyogh, Újfalussy and Weinberger, 1995). Draaisma and de Jonge (1988) have worked out in detail the layer-dependent dipolar anisotropy $K_{\text{dip}}^{(i)}$. In general, the outer atoms experience values of K_{dip} that are appreciably smaller than those of the inner layers, which finally approach K_{shape}. The inner atoms reach 95% of K_{shape} after about 15 Å below the surface. The exact details depend on the crystal structure and surface orientation, for example, a reduction between 25 and 45% of K_{shape} was reported for a (100)-oriented fcc or bcc monolayer, respectively. The deviation of K_{dip} from K_{shape} gives $K_{\text{MCA}}^{(\text{dip})}$ in equation (28), the dipolar contribution to the MCA which occurs here owing to the presence of a surface or interface and is sometimes also called the *surface contribution* of the dipolar anisotropy. If the MAE is expressed in terms of energy densities $\mathcal{E}$, this $K_{\text{MCA}}^{(\text{dip})}$ is expressed in terms of an areal density. The dipolar energy contributes to the MCA of bulk systems or thick films or wires also, if the underlying lattice structure has a twofold symmetry. For this three-dimensional case more sophisticated summation techniques such as the Ewald summation method (Ewald, 1921) are required to obtain reliable results for equation (30).

The spin-orbit interaction, treated typically by a Pauli-type addition to the Hamiltonian as:

$$H_{\text{so}} = \vec{\sigma}\cdot(\vec{E}(\vec{r}) \times \vec{p}) = \vec{\sigma}\cdot(\nabla V(r) \times \vec{p}) \tag{31}$$

provides the essential contribution to the MCA. This Pauli approximation derives naturally from the Dirac equation and is normally sufficient for treating relativistic effects in transition-metal magnets. For a radially symmetric potential we can rewrite equation (31):

$$H_{\text{so}} = \frac{1}{r}\frac{\mathrm{d}V(r)}{\mathrm{d}r}\vec{\sigma}\cdot(\vec{r} \times \vec{p}) = \frac{1}{r}\frac{\mathrm{d}V(r)}{\mathrm{d}r}(\vec{\sigma}\cdot\vec{L}) = \xi(\vec{r})\vec{\sigma}\cdot\vec{L} \tag{32}$$

where $\vec{L}$ is the angular momentum operator. Since the radial derivative of the potential in a crystal will be largest in the vicinity of a nucleus, we can expect that the major contribution to the spin-orbit interaction will come from this region. Furthermore, since for small r the potential will be Coulomb-like, $(V = -\frac{Z}{r})$, the radial expectation value of $\xi(r)$ leads to a material-dependent spin-orbit coupling constant ξ, which is roughly proportional to the square of the nuclear number Z, $\xi \propto Z^2$. In low-dimensional systems the MCA dominates over the shape anisotropy. The anisotropy depends crucially on the symmetry of the system.

In a solid, where the symmetry of the states is determined by the crystal field, spin-orbit coupling can now introduce orbital moments and magnetocrystalline anisotropies by coupling states that carry no orbital momentum, for example, a d_{xy} and a $\mathrm{d}_{x^2-y^2}$ orbital, such that the combination forms an orbital moment in the z direction. In second-order perturbation theory the expectation value of the orbital moment operator $\mu_{\text{B}}\vec{L}$ can be written as:

$$m_{\text{l}} = \mu_{\text{B}}\langle\vec{L}\rangle = \mu_{\text{B}}\sum_{i,j}\frac{\langle\psi_i|\vec{L}|\psi_j\rangle\langle\psi_j|H_{\text{so}}|\psi_i\rangle}{\varepsilon_i - \varepsilon_j} \times f(\varepsilon_i)\left[1 - f(\varepsilon_j)\right] \tag{33}$$

where f is the Fermi function ensuring that the wave function ψ_i is occupied and ψ_j is unoccupied. In a metal, where several bands are crossing the Fermi level, E_{F}, it is basically the sum of all contributions from bands near E_{F} that determines the orbital moment. van der Laan (1998) has shown, that in the absence of spin-flip terms (i.e., when the majority and minority bands are well separated by the exchange interaction), the spin-orbit coupling changes the total energy of a system in second-order perturbation theory as:

$$\delta E = \sum_{i,j}\frac{\langle\psi_i|H_{\text{so}}|\psi_j\rangle\langle\psi_j|H_{\text{so}}|\psi_i\rangle}{\varepsilon_i - \varepsilon_j}f(\varepsilon_i)\left[1 - f(\varepsilon_j)\right] \approx -\frac{\xi}{4\mu_{\text{B}}}\widehat{m}_{\text{s}}\cdot\left[\vec{m}_{\text{l}}^{\downarrow} - \vec{m}_{\text{l}}^{\uparrow}\right] \tag{34}$$

where $\widehat{m}_{\text{s}}$ is the direction of the spin moment and $\vec{m}_{\text{l}}^{\downarrow}$ and $\vec{m}_{\text{l}}^{\uparrow}$ are the orbital moment vectors of the spin-down and spin-up bands, respectively. If the spin-up band is completely filled, we see that energy change, δE, is proportional to the size of the orbital moment and the MCA, that is, the difference of δE for two different magnetization directions will be proportional to the difference in the orbital moments. This relation between orbital moment anisotropy and MCA was first derived by Bruno (1989).

We have discussed that the reduced coordination number in low-dimensional systems favors the increase of the spin moment. But it also enables the formation of large orbital moments, as can be seen from most atoms. Also in the case of the orbital moment, the hybridization with some neighboring orbitals 'locks' the electrons in place and quenches the orbital moment. Imagine a Sc atom with only one d electron: as an atom, according to Hund's rules, the orbital moment will be maximized and antiparallel to the spin moment. But when Sc atoms are assembled in a square lattice, orbitals with $m = -2$ and $m = +2$ will form linear combinations to build d_{xy} and $\mathrm{d}_{x^2-y^2}$ orbitals of which the latter will be occupied. The more

these two levels are split in energy, the more difficult it will be for the electron to 'circle' around the atom and, therefore, to form an orbital moment.

In Table 5 some representative values of spin and orbital momentum have been collected. These calculations yield very small orbital moments: $0.05\,\mu_B$, $0.08\,\mu_B$, and $0.05\,\mu_B$ for bcc Fe, hcp Co, and fcc Ni, respectively (and about twice the value if the orbital polarization (OP) proposed by Brooks (1985) is included). It is well known that the orbital moments are quenched in the bulk because of the strong hybridization with neighboring atoms. Larger orbital moments are obtained for the (111)-oriented unsupported 3d monolayers. For Fe, Co, and Ni the values are 2–3 times larger than the corresponding bulk values. Thus, in monolayer films the quenching of the orbital moments is less pronounced because of the reduced hybridization. However, it is important to realize that these enhanced orbital moments are still an order of magnitude smaller than the corresponding free-atom values, as given by Hund's second rule (last row in Table 5). Consequently, we expect for atomic-scale magnetic structures such as wires, small clusters, and adatoms strong changes in the orbital moment and, in turn, large values of the MCA. In practice, these films are deposited on substrates. This will once more quench the values, especially for the orbital moments. But the spin polarization of the substrate can lead to additional large contributions to the MCA in particular for substrates with large Z, such as Pt or Ir.

Typically, first-principles calculations based on the LSDA or GGA underestimate the orbital moments. In the literature several methods have been discussed as to how this deficiency can be overcome (Brooks, 1985; Solovyev, Liechtenstein and Terakura, 1988; Solovyev, 2005). For example, the orbital moments of the bulk magnets are about twice the value if Brooks' OP is applied (Eriksson, Brooks and Johansson, 1991b; Hjortstam *et al*., 1996). The effect of OP is much more drastic in low dimensions (Nonas *et al*., 2001). A systematic comparison of LSDA results for Pt-supported and unsupported Fe and Co magnets in various dimensions can be found in the works of Komelj, Ederer, Davenport and Fähnle (2002) and Ederer, Komelj and Fähnle (2003).

In order to interpret *ab initio* results on thin films we discuss the case of an unsupported, (100)-oriented d-metal monolayer, in terms of a simple model following Stöhr (1999). Assume that the d band is substantially exchange split and more than half filled, so that we only have to consider the (partially filled) minority band. The d orbitals at each atom site experience in the monolayer plane a crystal field V, that leads to a splitting of these levels: if the surface normal is assumed to be in z direction, the d_{xy} and $d_{x^2-y^2}$ levels will experience a stronger field than the out-of-plane directed d_{zx}, d_{yz}, and d_{z^2} orbitals. The crystal field leads to a splitting of $2V_\parallel$ for the in-plane oriented orbitals and $2V_\perp$ for the out-of-plane oriented ones. In a band picture, these splittings can be translated into bandwidths W, which will then be twice as large (cf. Figure 7). Normally, $V_\parallel$ will be larger than $V_\perp$, so that $R = V_\perp / V_\parallel < 1$. (If, however, the monolayer is sandwiched between two slabs of nonmagnetic material the situation could be changed.)

Assume that – like in the case of Co – the minority band is half filled; the d_{xy} and $d_{x^2-y^2}$ states will split symmetrically by $\pm V_\parallel$ around the Fermi level, the (d_{zx}, d_{yz}) and d_{z^2} states by $\pm V_\perp$. In a band-picture, these splittings will of course depend on the considered $\vec{k}_\parallel$ point. Now we can use perturbation theory equation (33) to calculate the orbital moments. The result (Stöhr, 1999)

$$m_l^\parallel = \frac{\xi \mu_B}{2V_\parallel}\left(\frac{3}{R} + \frac{2}{R+1}\right) \quad \text{and} \quad m_l^\perp = 4\frac{\xi \mu_B}{2V_\parallel} \tag{35}$$

Table 5. Local spin (m_s) and orbital (m_l) magnetic moments in units of μ_B of Fe, Co, and Ni atoms in bulk materials ($n = 3$), unsupported thin films ($n = 2$), wires ($n = 1$), and as isolated atoms ($n = 0$). For bulk crystals the variation of the orbital moment with direction is small, but for films and wires the orbital moments parallel ($\parallel$) and perpendicular ($\perp$) to the film plane or wire axis are given. The geometry is chosen as if the film or wire would have been grown epitaxially on a Pt(111) substrate. The column $|K_{MCA}|$ indicates the order of magnitude of the MCA for different dimensions. The results were obtained in the GGA to the density-functional theory.

	Fe			Co			Ni			$\lvert K_{MCA}\rvert$
n	m_s	m_l		m_s	m_l		m_s	m_l		(meV/atom)
		$\parallel$	$\perp$		$\parallel$	$\perp$		$\parallel$	$\perp$	
3	2.05	0.05		1.59	0.08		0.62	0.05		0.01
2	3.07	0.07	0.10	2.09	0.20	0.19	0.94	0.18	0.14	1.00
1	3.22	0.72	0.27	2.32	0.98	0.77	1.18	0.84	0.44	10.00
0	4	2		3	3		2	3		-

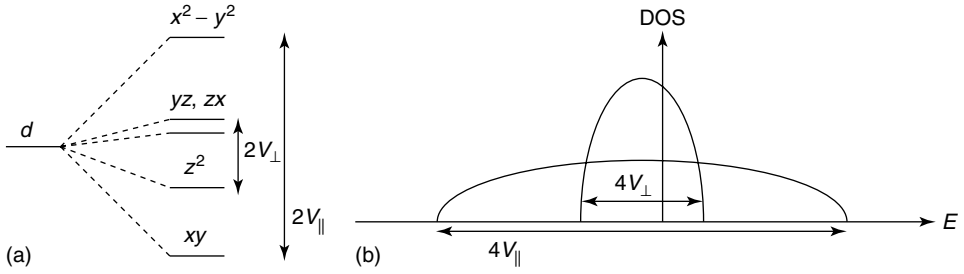

Figure 7. d-level splittings shown in (a) at a given **k** point due to a crystal field in a square monolayer result in a density of states, shown in (b).

shows that only the in-plane orbital moment, $m_l^\parallel$ depends on the splitting of the out-of-plane oriented states, while the out-of-plane orbital moment is only quenched by the in-plane crystal field. This is intuitively clear, since $m_l^\perp$ corresponds to an in-plane motion of the electron, that is, a hopping between the d_{xy} and $d_{x^2-y^2}$ states that are separated by $V_\parallel$. For the calculation of the magnetocrystalline anisotropy energy we can use equation (34), which gives:

$$K_{\mathrm{MCA}} = E_{\mathrm{MCA}}^\parallel - E_{\mathrm{MCA}}^\perp = -\frac{\xi}{4\mu_{\mathrm{B}}}\left(m_l^\parallel - m_l^\perp\right)$$
$$= -\frac{\xi^2}{8V_\parallel}\left(\frac{3}{R} + \frac{2}{R+1} - 4\right) \qquad (36)$$

From this equation we see that, as long as $R < 1$, an in-plane magnetization is obtained, while for $R > 1$ an out-of-plane easy axis is possible. Indeed it is observed that Co monolayers on a weakly interacting substrate (like Cu(001)) have an in-plane easy axis, while a Co layer sandwiched in Pt has a perpendicular magnetization. Taking typical values for 3d-metal monolayers, a spin-orbit coupling strength $\xi \approx 75\,\mathrm{meV}$ and bandwidths $W^\parallel \approx 3\,\mathrm{eV}$ and $W^\perp \approx 2\,\mathrm{eV}$, one arrives at orbital moments of $m_l^\parallel = 0.285\,\mu_{\mathrm{B}}$ and $m_l^\perp = 0.200\,\mu_{\mathrm{B}}$ and the MCA per atom of $K_{\mathrm{MCA}} = 1.6\,\mathrm{meV}$, values in the range of the *ab initio* results given in Table 5.

2.7 Dzyaloshinsky–Moriya interaction

Magnets in low dimensions frequently face a structure inversion asymmetric environment. Consider for example a thin magnetic film on a substrate with the vacuum potential on one side and the potential to the substrate on the other side. This inversion asymmetry leads to a gradient of the potential that can be interpreted in first approximation as an electric field normal to the film surface. In the rest frame of moving electrons, the electric field $\vec{E}$ appears by Lorentz transformation as a magnetic field $\vec{B} \propto \vec{p} \times \vec{E}$, which interacts then with the spin $\vec{\sigma}$ of the electron, giving rise to an additional term in the Hamiltonian, which was already encountered in equation (31) in the context of spin-orbit coupling. Here, instead of an orbital motion, a linear motion of an electron with momentum $\vec{k}$ in an electric field oriented along $\vec{e}_z$ is considered. This can be described by a Hamiltonian $H = \alpha_R \vec{\sigma} \cdot (\vec{k} \times \vec{e}_z)$, known as the *Rashba term* (Bychkov and Rashba, 1984). The strength described by the Rashba parameter, α_R, is determined for example, by the asymmetry of the wave function due to the asymmetry of the potential or the electric field, respectively, and the spin-orbit interaction of the electrons involved.

The magnetic interaction between the spin $\vec{S}_i$ at lattice site i and $\vec{S}_j$ at lattice site j is caused by electrons which hop from site i to site j and back. Electrons in a magnetic film propagate in an exchange field $\pm 1/2IM$ (cf. equation (13)), the bands are exchange split, and the time-inversion symmetry is lost. Owing to the spin-orbit interaction caused by the Rashba term, electrons experience a kinetic energy with an additional weak spin-dependent potential, which depends on the propagation direction $\vec{p}$ of the electrons. Thus, the motion from site i to j and the back motion from j to i is slightly different. The same is true for the time inverse hopping process, the electron hopping first from site j to i and then back. At first sight, both processes look identical and indeed both contribute equally to the isotropic Heisenberg exchange equation (2). But owing to the presence of the spin-orbit interaction, the inversion asymmetric environment, and the lack of time-inversion symmetry, the interference of both processes does not cancel out completely. Instead, it gives rise to an additional antisymmetric exchange interaction between these sites, known as the *Dzyaloshinsky–Moriya* (*DM*) (Dzyaloshinsky, 1958; Moriya, 1960) interaction

$$H_{\mathrm{DM}} = \sum_{i,j} \vec{D}_{ij} \cdot \left(\vec{S}_i \times \vec{S}_j\right) \qquad (37)$$

where $\vec{D}$ is a constant vector, which depends on the symmetry of the system and on the real-space direction given by two sites i and j. For example, for typical (100) and

(110) low-index surfaces of metals, $\vec{D}$ lies in the film plane and points perpendicular to the direction (i, j) connecting two surface atoms, if the two surface atoms are placed along a high-symmetry line. The DM interaction arises as the first-order perturbation in the spin-orbit interaction, and might for this reason be stronger than the magnetocrystalline anisotropy. This chiral interaction tends to orient the spin S_i and S_j orthogonal to each other and to $\vec{D}$, destabilizing a uniform FM or AFM order and can cause, depending on the strength D, a canting of the magnetization at different atoms, a helical or cycloidal spin wave. The sign of $\vec{D}$ defines the chirality of the canting. The DM interaction is practically unknown in metallic bulk magnets, since most metals crystallize in structures with centrosymmetric symmetries. Surprisingly, after 20 years of research on low-dimensional magnetism, the magnitude of $\vec{D}$ has not been established so far and there is currently active research going on to clarify its relevance for the magnetic order in nanomagnets.

3 ULTRATHIN FILMS

The transition-metal monolayers on noble-metal substrates are the classical systems exhibiting two-dimensional magnetism. Because of the reduced coordination number of nearest-neighbor transition-metal atoms in a monolayer film, the d bandwidth in two dimensions is considerably smaller and correspondingly the local density of states (LDOS) at the Fermi energy E_F is considerably larger than in the bulk situation. Thus, magnetism should occur for a much wider variety of transition-metal elements. Following this line of argument it is clear that the strength of the d–d hybridization between monolayer and substrate is an additional parameter which controls the d bandwidth of the monolayer. For instance, a large-band-gap material, for example, MgO(100), used as a substrate allows the formation of two-dimensional monolayer bands within the band gap of the substrate material. In this case the impact on the magnetization of the monolayer due to the substrate is expected to be small. The same is true for noble-metal substrates, which have d bands well below the Fermi energy. The width of the monolayer d band is not significantly broadened by the monolayer–substrate d–d interaction, and magnetism is restricted to the monolayer. Increasing the d–d hybridization by choosing appropriate nonmagnetic transition-metal substrates, for example, Pd(100) or W(110), will lead to a considerable broadening of the monolayer bands and introduce a significant spin polarization of the substrate until we have changed from the two-dimensional limit to the semi-infinite regime. Choosing a magnetic substrate an additional complexity arises owing to the competition of the magnetic coupling in the monolayer and between monolayer and substrate.

3.1 (100)-oriented monolayers on nonmagnetic substrates

3.1.1 Ferromagnetic monolayers

A systematic investigation of the magnetism of all possible 3d, 4d, and 5d transition-metal monolayers on Ag(001) is collected in Figure 8 and in Table 6. One finds that all 3d-metal monolayers (Ti, V, Cr, Mn, Fe, Co, Ni) on Ag(001) substrate show FM solutions. Tc, Ru, and Rh are FM among the 4d metals, and Os and Ir are FM among the 5d metals on Ag(001). The local magnetic moments are partly very large, not only for the 3d monolayers but surprisingly also for the 4d and 5d ones. In the 3d series the overall trend of the local moments follows Hund's first rule. The largest local moment of about $4\,\mu_B$ was found for Mn and from Mn to Ni the magnetic moment decreases in steps of $1\,\mu_B$. The latter is a consequence of the strong ferromagnetism in

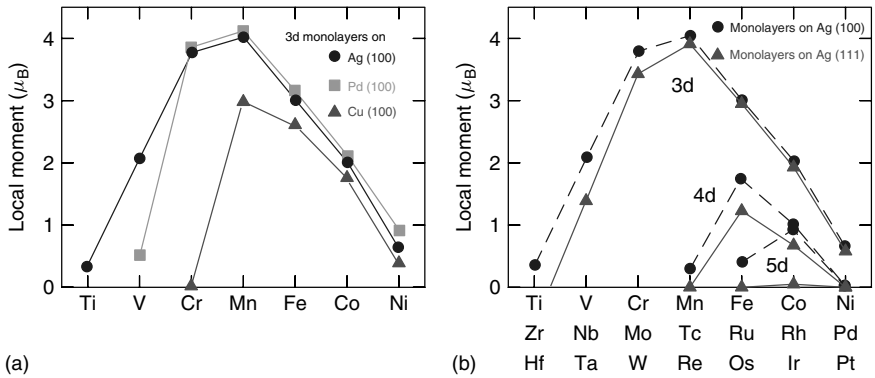

Figure 8. Local magnetic moments as calculated for ferromagnetic (a) 3d-metal monolayers on Ag(100) (Blügel and Dederichs, 1989) (dots), Pd(100) (Blügel, 1988) (squares), and Cu(001) (Blügel, 1996) (triangles), and (b) 3d, 4d (Blügel, 1992a), and 5d (Blügel, 1992b) monolayers on Ag(001) (dots) and Ag(111) (Redinger, Blügel and Podloucky, 1995) (triangles).

Table 6. Local magnetic moments in μ_B/atom for 3d transition-metal atoms as ferromagnetic (F) and antiferromagnetic (AF) 3d monolayers on Ag(001) (Blügel and Dederichs, 1989), Pd(001) (Blügel, 1988), W(001) (Ferriani, Heinze, Bihlmayer and Blügel, 2005), and on Cu(001) (Blügel, 1996; Asada and Blügel, 1997a); compared with results for 3d monolayers as interlayers (IL) in Cu(001) (Blügel, 1996), unsupported (001) monolayers (UL) in the lattice constant of Cu(111), Ag(001) (Blügel, Drittler, Zeller and Dederichs, 1989) and W(001) (Ferriani, Heinze, Bihlmayer and Blügel, 2005), and with results for ferromagnetic 3d monolayers on Cu(111) and Ag(111) (Redinger, Blügel and Podloucky, 1995) as well as on W(110) (Nie, Heinze, Bihlmayer and Blügel, 2007a). '–' indicates that no calculation was performed for this system. '0' indicates that the calculated moment was smaller than the numerical accuracy estimated to be about $0.02\,\mu_B$/atom. '?' indicates a system, for which the calculation was not finished up to self-consistency, but the result is approximately correct.

				Ti	V	Cr	Mn	Fe	Co	Ni
Ag	ML	on Ag(001)	F	0.34	2.09	3.78	4.04	3.01	2.03	0.65
			AF	0	2.08	3.57	4.11	3.06	1.9	0
	UL	– Ag(001)	F	1.72	2.87	4.50	4.32	3.29	2.20	1.02
			AF	0	2.59	4.09	4.32	3.32	2.10	0
	ML	on Ag(111)	F	0	1.39	3.43	3.91	2.95	1.93	0.51
Pd	ML	on Pd(001)	F	0	0.51	3.87	4.11	3.19	2.12	0.89
			AF	0	1.39	3.46	4.05	3.20	1.99	0.59
Cu	ML	on Cu(001)	F	–	0	0	2.97	2.61	1.76	0.33
			AF	–	0	2.52	2.92	2.35	1.3	0
	IL	in Cu(001)	F	–	0	0	2.01	2.39	1.51	0
			AF	–	0	1.84	2.15	–	–	–
	ML	on Cu(111)	F	–	0	0	3.05	2.69	–	–
	UL	– Cu(111)	F	–	0	0	3.06	2.75	–	–
W	ML	on W(110)	F	–	0.00	–	2.97	2.37	1.14	0.00
			AF	–	0.00	2.52	3.32	–	–	0.00
	ML	on W(001)	F	–	1.54	2.55	3.49	2.05	0.69	0.00
			AF	–	0.97	1.80	3.69	2.67	1.46	0.00
	UL	– W(001)	F	–	3.00	4.19	4.33	3.31	2.23	1.03
			AF	–	2.78	4.10	4.37	3.32	2.24	1.02

these monolayers. The magnetic moments of Ti, V, and Cr monolayers show a pronounced dependence on the substrate: Ti is magnetic on Ag, but nonmagnetic on Pd; the magnetic moment of V is reduced by more than $1.5\,\mu_B$ when changing the substrate from Ag to Pd; and for Cr the magnetic moment changes from $3.8\,\mu_B$ as an adlayer on Ag or Pd to zero as an adlayer on Cu. Although not as dramatic, the reduction is also visible for Mn. We attribute the drastic reductions of the monolayer moments to the reduction of the lattice constants in the sequence Ag to Pd to Cu.

When comparing the results of the local moments between 3d, 4d, and 5d monolayers on Ag(001) an interesting trend is observed: the element with the largest magnetic moment among each transition-metal series is shifted from Mn to Ru (isoelectronic to Fe) and at last to Ir (isoelectronic to Co), respectively. Following these trends we do not expect ferromagnetism for any other 4d or 5d metal on noble-metal (001) substrates, and indeed Mo and Re remained nonmagnetic. The overall picture of monolayers on Ag and Au is the same, but the different substrate interactions cause Tc and Os on Au to be nonmagnetic and lead to a slightly larger moment for Rh. Pd and Pt are predicted to be nonmagnetic. With the exception of Ru, for which a rather small magnetic moment of 0.2 μ_B was calculated, no monolayer magnetism was found for 4d metals on Pd(100). Investigations (Újfalussy, Szunyogh and Weinberger, 1995) taking into account the spin-orbit interaction have shown that the spin-orbit interactions significantly reduces the magnetic spin moment of the 5d-metal monolayers, and depending on the interlayer relaxation the spin moment might be suppressed.

3.1.2 Antiferromagnetic monolayers

It is by no means clear whether the FM state is actually the magnetic ground state. Looking at the LDOS of the 3d monolayers in Figure 9 and considering the analysis of the AFM susceptibility equation (19) we expect an AFM phase for Cr and possibly also for V and Mn monolayers. In reality, various AFM states as well as noncollinear spin configurations could be anticipated. Studying an Heisenberg model equation (2) for a square lattice as formed by the (001) monolayers up to the second-nearest-neighbor interaction (J_1, J_2) the situation becomes relatively simple. As

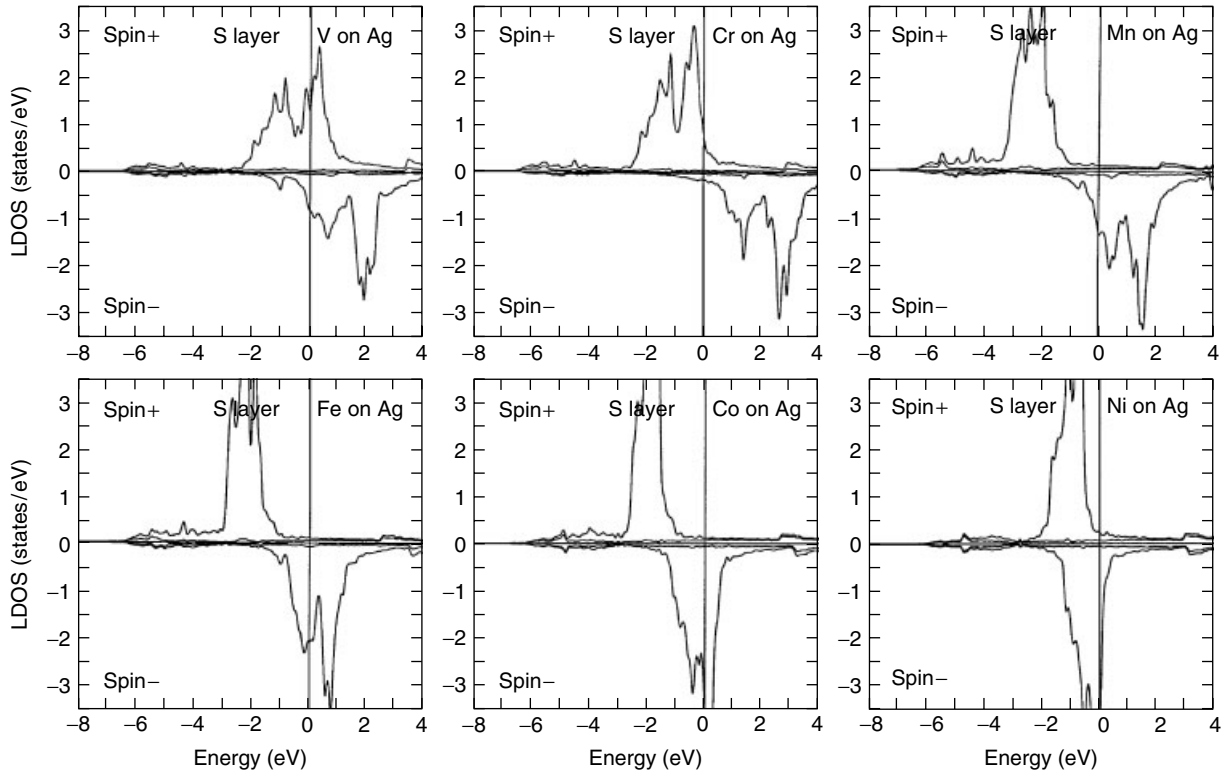

Figure 9. Local density of states (LDOS) of ferromagnetic 3d-metal monolayers on Ag(100). The Fermi energy defines the origin of the energy scale, separating occupied (at negative energies) from unoccupied states (at positive energies). Majority (minority) states are indicated by positive (negative) values of LDOS.

long as the nearest-neighbor interaction is the dominating one, there are only two phases to be considered: the FM p(1 × 1) structure ($J_1 > 0$) discussed in the previous section and the AFM c(2 × 2) superstructure ($J_1 < 0$, a checkerboard arrangement of up and down spins similar to the c(2 × 2) ferrimagnetic (FI) structure in Figure 17, but with moments of identical size on both sublattices). The c(2 × 2) structure corresponds to the $\overline{\mathrm{M}}$ point in the two-dimensional Brillouin zone (2DBZ) of the square lattice. If the next-nearest-neighbor interaction is AFM, $J_2 < 0$, and sufficiently strong, $|J_1| < 2|J_2|$, then the magnetic structure with a 2D $\vec{Q}_{\parallel}$ vector of the $\overline{\mathrm{X}}$ point in the 2DBZ, corresponding to an AFM p(2 × 1) or p(1 × 2) structure (FM rows of atoms along the [100] or [010] direction coupling antiferromagnetically from row to row) becomes the magnetic ground state.

Figure 10 shows the local moments for the FM and c(2 × 2) AFM phase of 3d monolayers on Cu(001). It becomes evident that, for many systems (see also Table 6) both configurations exist with moments of similar values. Depending on the in-plane lattice constant, differences in the local moments for the two magnetic phases develop for earlier transition metals, for example, for Cr on Cu(001), for V on Pd(001), or for Ti on Ag(001). Figure 10 also shows the energy differences $\Delta E = E_{AFM} - E_{FM}$ per atom between the c(2 × 2) AFM and the FM configuration for 3d-metal monolayers on Cu(001) and Ag(001). A clear trend emerges: the Ni, Co, and Fe overlayers ($\Delta E > 0$) prefer the FM configuration and the Mn, Cr, and V ones favor the AFM one. From the strong similarities of the monolayer trends for these two substrates we conclude that this is a general trend: Fe, Co, and Ni favor the p(1 × 1) ferromagnetism on the (001) surfaces of Pd, Pt, and the noble metals Cu, Ag, and Au (Freeman and Fu, 1987); whereas V, Cr, and Mn monolayers prefer the c(2 × 2) AFM configuration. The same trend was recently found for monolayers on W(110) (Nie, Heinze, Bihlmayer and Blügel, 2007a) and is expected for Al substrates although V and Ni might then be nonmagnetic. Since $\Delta E \approx 8S^2 J_1$, ΔE reflects basically the change of J_1 as a function of the band filling (number of d electrons) or how E_{F} moves through the LDOS in Figure 9. For Mn on Ag(001), where ΔE or J_1, respectively, is relatively small, the J's between more distant pairs may determine the picture. We investigated by total-energy calculations the stability of the possible p(2 × 1) structure and found that the c(2 × 2) structure is indeed the magnetic ground state.

The c(2 × 2) AFM phase was first predicted by theory. After the prediction several experiments indicated that the c(2 × 2) state may indeed exist: no FM long-range order was

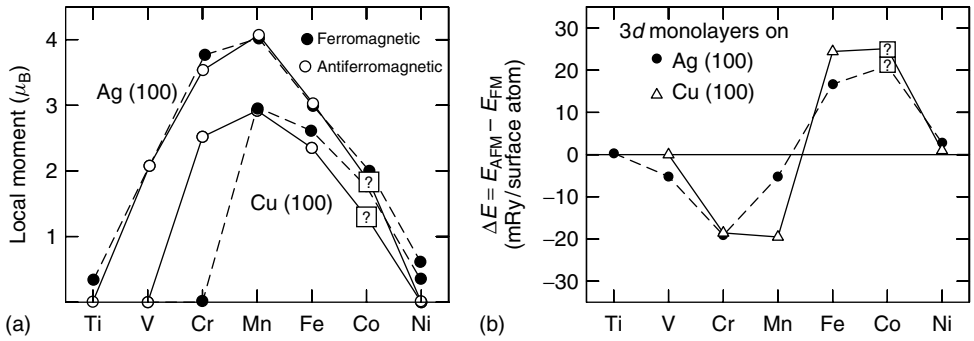

Figure 10. (a) Local magnetic moments of 3d monolayers on Cu(100) (Blügel, 1996) and Ag(100) (Blügel and Dederichs, 1989) calculated for the p(1 × 1) ferromagnetic (solid circles connected by dashed line) and the c(2 × 2) antiferromagnetic configuration (open circles connected by solid line). (b) Total energy difference $\Delta E = E_{AFM} - E_{FM}$ per 3d atom between the c(2 × 2) antiferromagnetic and p(1 × 1) ferromagnetic phase for 3d monolayers on Cu(100) (triangle connected by full line) and Ag(001) (solid circles connected by dashed line). $\Delta E > 0$ (< 0) means the ferromagnetic (antiferromagnetic) configuration is the most stable one. '?' indicates a result that is not fully converged.

found at low temperatures for a V monolayer on Ag(100) (Stampanoni *et al*., 1988), but a local exchange splitting was found for V, Cr, and Mn monolayers on Ag(100) (Ortega and Himpsel, 1993). More than 10 years after the theoretical prediction a direct proof of the c(2 × 2) AFM state became for the first time possible by using the spin-polarized scanning tunneling microscopy in the constant-current mode (Heinze *et al*., 2000; Bode *et al*., 2002). The experiments were carried out for a Mn monolayer on W(110).

3.1.3 Strongly hybridizing substrates

Strong interfacial d-band hybridization between adlayers and transition-metal substrates can modify or even destroy the adlayer magnetization. In the case of strong hybridization, the electronic structure of an interface cannot be deduced from the individual constituents, but rather the interface itself must be considered as a new material that determines the magnetic properties. Strongly hybridizing substrates are for example 4d (Nb, Mo, Ru, Rh, Pd) or 5d (Ta, W, Re, Os, Ir, Pt) metals.

As an example we present here a case study of 3d-metal monolayers on W(001) (Ferriani, Heinze, Bihlmayer and Blügel, 2005). The large surface energy of W leads to experimental conditions that permit an almost perfect preparation of ideal adlayer systems that exhibit pseudomorphic growth at the monolayer range with very little propensity to segregation. The results are summarized in Figure 11. On W(001), we find that the ground state is FM for V, Cr, and Mn, while it is c(2 × 2) AFM for Fe and Co with large energy differences between the two magnetic solutions. The observed trend across the 3d series is rather surprising as it is

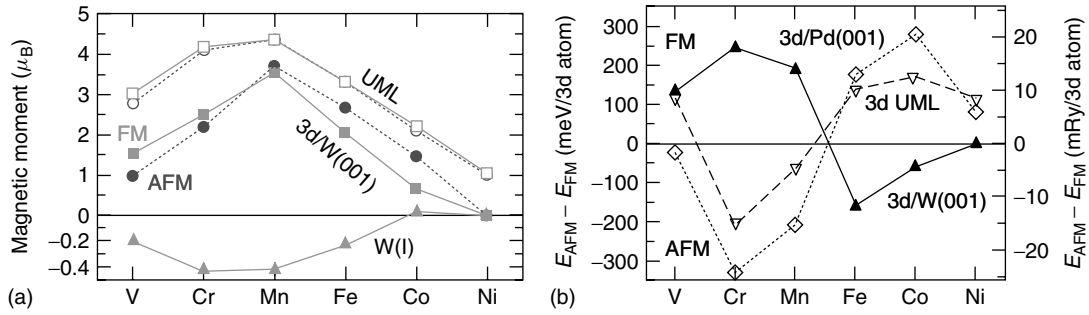

Figure 11. (a) Local magnetic moments of 3d monolayers on W(001) (Ferriani, Heinze, Bihlmayer and Blügel, 2005) and unsupported 3d monolayer (UML) in the lattice constant of W(001) calculated for the p(1 × 1) ferromagnetic (squares connected by full lines) and the c(2 × 2) antiferromagnetic configuration (circles connected by dotted lines). For the FM case, the magnetic moment of interface W atoms is given by triangles. (b) Total energy difference $\Delta E = E_{AFM} - E_{FM}$ per 3d atom between the c(2 × 2) antiferromagnetic and p(1 × 1) ferromagnetic phase for 3d monolayers on W(001), (solid triangles connected by full line), Pd(001) (Blügel, Weinert and Dederichs, 1988) (open squares connected by dotted line), and UML(001) (open triangles connected by dashed line). $\Delta E > 0$ (< 0) means the ferromagnetic (antiferromagnetic) configuration is the most stable one.

exactly opposite to the one expected from the discussion in Section 3.1.2. The theoretical predictions (Ferriani, Heinze, Bihlmayer and Blügel, 2005; Wu and Freeman, 1992b; Qian and Hübner, 2003; Sandratskii, Şaşıoğlu and Bruno, 2006) of an AFM Fe monolayer on W(001) has recently been confirmed experimentally by spin-polarized scanning tunneling microscopy (SPSTM) (Kubetzka *et al*., 2005).

Transition-metal monolayers without substrate, so-called unsupported monolayers (UMLs) and those on Pd(001) have been included for comparison. These monolayers behave as ideal two-dimensional magnets. Their trends in the magnetic phases are indeed inverted with respect to the W(001) substrate, with energy differences of similar magnitude. The results exhibited in Figure 11 are also surprising in comparison to the results of 3d-metal monolayers on W(011), showing exactly the same behavior as on noble metal substrates or Pd. This clearly gives evidence that results on W(001) are an interface effect. In the case of strong overlayer–substrate hybridization, the coordination number, symmetry, and interlayer distance is decisive in the determination of the magnetic properties of the system.

A closer look reveals a significant difference between a bcc substrate such as W and a fcc substrate such as Cu, Pd, Ag, or Au. For a bcc substrate, each transition-metal atom has four nearest W atoms at the interface, while the surrounding transition-metal atoms in the overlayer are only next-nearest-neighbor atoms. Considering that the 5d orbitals of W are more extended than the 3d ones of the overlayer and taking the additional interlayer relaxation into account, we can conclude that here the overlayer–substrate hybridization is more important than the 3d hybridization between the transition metals in the monolayer plane. Thus, the nature of the 3d–5d bond determines the physics. The chemical trend discussed here for the W(001) substrate should also hold for Mo(001), but the magnetic order of 3d metals on other bcc(001) surfaces such V, Nb, Ta is not yet clear.

The strong 3d–5d hybridization also affects the magnetic moments, displayed in Figure 11. As in previous sections the overall trend of the spin moments across the 3d series follows Hund's first rule. This atomic-like behavior indicates that the magnetism is dominated by the local intra-atomic contribution. A comparison with UMLs in the experimental W lattice constant shows that the interaction with the substrate reduces the magnetic moment of the 3d overlayer, a consequence of the 3d–5d hybridization. The magnetism of the overlayer also polarizes the substrate. For the FM configuration, W atoms at the interface are antiferromagnetically coupled to the monolayer (apart from the case of Co) and carry a moment that is roughly proportional to that of the 3d TM. The induced polarization decreases rapidly with distance from the interface into the bulk and is already one order of magnitude lower at the second W layer. The sign of the magnetization oscillates from one W layer to the next, indicating a layered antiferromagnetic (LAF) susceptibility of W(001). For AFM monolayers, the W moments are suppressed owing to symmetry.

3.1.4 Magnetointerlayer relaxation

In order to give the reader an impression (i) how strongly the formation of large monolayer moments may affect the interlayer relaxation and (ii) what is the influence of the magnetic order on the interlayer distance, total-energy calculations as a function of the interlayer distances are presented for two selected systems: Mn/Ag(001) and Mn/Cu(001). Prior to these calculations we determined the in-plane lattice constants, which are taken to be the bulk lattice constants of the substrate; we found a value of $a_0^{Cu} = 6.65\,\text{au}$ for Cu and $a_0^{Ag} = 7.58\,\text{au}$ for Ag. Clearly, the Mn monolayers show the largest magnetic moments on any substrate and the magnetovolume effects should be most substantial.

Figure 12 shows the total energy as a function of the interlayer distance for a Mn monolayer on Cu(001) and Ag(100) for three different magnetic states: nonmagnetic, FM, and c(2×2)AFM. We find, as already discussed in Section 3.1.2 that the nonmagnetic solution is the highest in energy and the AFM one is the lowest-energy magnetic state. Second, we find a substantial change of the minimum-energy interlayer distances with change of the magnetic state. On Cu(100) the most contracted minimum-energy distance was found for the nonmagnetic solution with $\Delta z_N = 1.39\%$. For the FM state a relaxation of $\Delta z_F = 4.02\%$ and for the AFM state a relaxation of $\Delta z_{AF} = 5.41\%$ was determined. We find that the effect of the long-range magnetic ground state on the relaxation is as important as the formation of moments itself: the formation of a magnetic moment expands the interlayer distance by about 2.6% and the change in the magnetic state changes the interlayer distance by 1.4%. This coincides with the energy differences between the FM state and the nonmagnetic state, which is comparable to the energy difference between the AFM state and the FM one.

On Ag(001), the interlayer relaxations for the nonmagnetic, FM, and AFM Mn monolayers are determined to be $\Delta z_N = -13.4\%$, $\Delta z_F = -6.75\%$, and $\Delta z_{AF} = -5.94\%$, respectively. The lattice constant of Ag is 14% larger than the lattice constant of Cu. Consequently the Mn atoms relax inwards on these substrates. Owing to the large Mn moments, around $4\,\mu_B$ on these substrates (recall that the moment of Mn on Cu is slightly below $3\,\mu_B$), the magnetovolume effect is very large. The FM Mn monolayers experience a large expansion of their minimum-energy interlayer distance of about 7%, much larger than for Cu and the magnetic configuration modifies this expansion by an other 1–2%. The

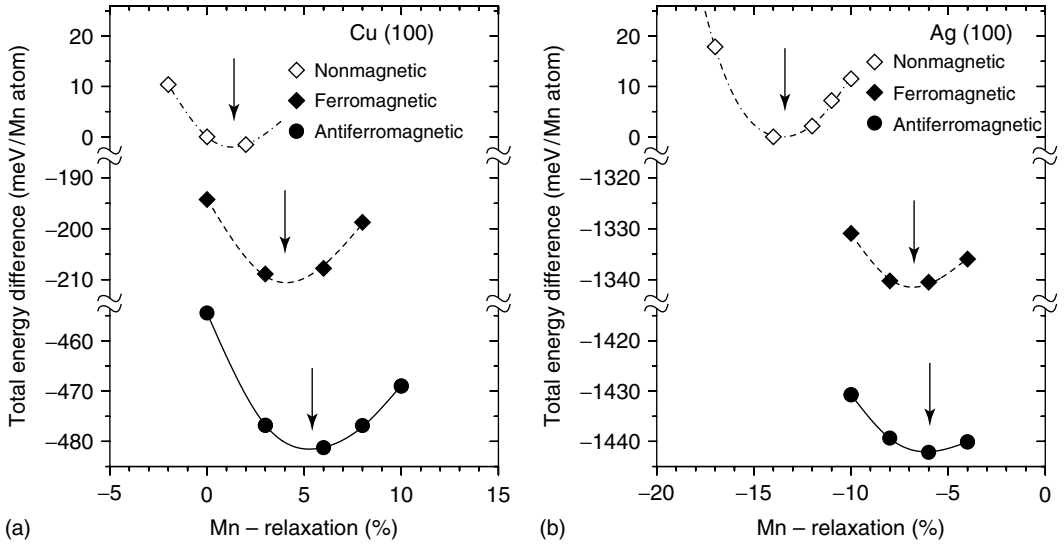

Figure 12. Total energies as a function of the interlayer relaxation for nonmagnetic (open diamonds), ferromagnetic (solid diamonds), and c(2 × 2) antiferromagnetic (solid circles) Mn monolayers on Cu(001) and Ag(001). The energy of the nonmagnetic monolayer at 0% relaxation was chosen as the origin of the total energy scale. The interlayer relaxation is given in relative units with respect to the interlayer distance of the substrate. The vertical arrows indicate the minimum-energy interlayer relaxation.

impact of the magnetic order on the interlayer distance is within about 2%, but the magnetovolume effect due to the formation of large magnetic moments is much larger for Mn on Ag than for Mn on Cu. This is in line with the arguments based on energy differences. The energy difference between the AFM state and the FM state is for all Mn systems in the same range of about 300 meV/Mn atom (cf. Table 1), while the formation energy of local moments is at large difference: about 200 meV for Mn on Cu but 1300 meV for Mn on Ag. This explains the large difference in the magnetovolume effects between Mn on Cu and Mn on Ag. In all cases the relaxations stabilize the FM and AFM phases, respectively.

In conclusion, the atomic volume depends on the magnetism, mostly on the size of the moment and to a smaller extent on the magnetic state. An extreme example of this is the experimentally observed unusually large atomic buckling of the c(2 × 2)MnCu/Cu(001) (Wuttig, Knight, Flores and Gauthier, 1993b) and c(2 × 2)MnNi/Ni(001) (Wuttig, Knight, Flores and Gauthier, 1993b) surface alloys. In these alloys a buckling of the surface atoms of 0.30Å (MnCu) (Wuttig, Knight, Flores and Gauthier, 1993b) and 0.25Å (MnNi) (Wuttig, Knight, Flores and Gauthier, 1993b) was found. Although the atomic radii of Pd and Au are much larger than for Mn, the buckling of the c(2 × 2)CuPd/Cu(001) and c(2 × 2)CuAu/Cu(001) atoms was observed to be just 0.02 Å (Wu *et al.*, 1988) and 0.10 Å (Wang *et al.*, 1987), respectively. It was shown that this buckling was a consequence of the magnetovolume effect due to the large moments of Mn (3.75 μ_B) in Cu (Wuttig, Gauthier and Blügel, 1993a) and Ni (3.55 μ_B) (Rader *et al.*, 1997).

3.2 (111)-oriented monolayers on nonmagnetic substrates

3.2.1 Ferromagnetic monolayers

The (0001) surface of an hcp crystal and the (111) surface of an fcc crystal establish a triangular lattice. Compared to the (100) surface, the coordination number changes from 4 to 6 and the symmetry changes from fourfold to threefold or sixfold, respectively. Moreover, the differences in the magnetic properties between films on a square lattice and on a triangular lattice give an estimate of the importance of the pseudomorphic growth condition for the magnetism of the films.

Figure 8 exhibits the general trend that the magnetic moments of the sixfold coordinated monolayers on Ag(111) are smaller in magnitude than those of the fourfold coordinated ones on Ag(001). On the Ag(111) surface we found magnetism for all 3d metals with the exception of Ti, the magnetism of which was very small anyway. There is nearly no difference between the monolayer moments of Mn, Fe, Co, and Ni on the differently oriented Ag substrates. A comparatively larger reduction of the magnetic moments is found at the beginning of the 3d series where the wave function is more extended than it is at the end of the series. Thus, changing the coordination number from 4 to 6, does not significantly change the local moments. One consequence of this

result is that for monolayers that do not grow pseudomorphically on any substrate but keep an average distance between monolayer atoms similar to the pseudomorphic films, no dramatic difference in the formation of large local moments is expected.

With the exception of Ru ($1.23\,\mu_B$) and Rh ($0.67\,\mu_B$) and a tiny moment for Ir ($0.05\,\mu_B$) among the 5d metals, no ferromagnetism was found for any other 4d and 5d monolayers on Ag(111). For the 4d-metal monolayers Ru and Rh, the moments are reduced to about 70% of the (001) values, and for the 5d metal Ir only a tiny magnetic moment of $0.05\,\mu_B$, about 15% of the (001) value, remains. Obviously, the degree of the reduction of the magnetic moments due to the increase of the hybridization with the increase of the coordination number from 4 to 6 simply follows the increasing degree of delocalization of the d wave function when moving from the 3d to the 4d and 5d transition-metal wave functions.

3.2.2 Monolayers with complex spin structures

AFM interactions on a triangular lattice are the origin of frustrated spin systems. The epitaxial growth of such ultrathin films has been studied intensively by various experimental techniques. In particular, pseudohexagonal c(8×2)Mn films on Cu(100) (Flores, Hansen and Wuttig, 1992), Mn films on the (111) surfaces of fcc Pd (Tian *et al*., 1992b); Ir (Andrieu *et al*., 1996); Cu (Tian, Begley and Jona, 1992a; Grigorov and Walker, 1997; Grigorov *et al*., 1998), and MgO (Grigorov, Fitzsimmons, Siu and Walker, 1999), and on the (0001) surface of Ru (Arrott *et al*., 1987) and Co (Ounadjela *et al*., 1994) have been prepared and analyzed. But also other ultrathin hexagonal films, for example, Cr and V on Pt(111) and Ru(0001) (Zhang, Kuhn and Diebold, 1997; Albrecht *et al*., 1998; Sambi and Granozzi, 1999), or Fe on Ir(111) (von Bergmann *et al*., 2006) have been investigated.

To obtain an overview of all relevant spin structures we develop first a zero-temperature phase diagram in the context of the Heisenberg model. As discussed in Section 2.2 the magnetic ground states are SSDWs, most likely with a commensurate propagation vector $\vec{q}_\parallel$ located at the high-symmetry points in the first 2DBZ of a 2D Bravais lattice. For the 2DBZ of the triangular (hexagonal) lattice, displayed in Figure 13 (a), the high-symmetry points are the corner points $\overline{\Gamma}$, $\overline{\mathrm{K}}$, and $\overline{\mathrm{M}}$ of the irreducible wedge of the 2DBZ (I2DBZ). The $\overline{\Gamma}$ point corresponds to the FM solution. The $\overline{\mathrm{K}}$ point corresponds to a 120° Néel state (Figure 13c), a 2D coplanar spin structure with three atoms in a $(\sqrt{3} \times \sqrt{3})$ R30° unit cell for which the relative angle between the spins at the different sites is always 120°. The $\overline{\mathrm{M}}$ point corresponds to a row-wise antiferromagnetic (RW-AFM) configuration (Figure 13b), which can be described by a rectangular unit cell with two antiferromagnetically aligned atoms. Magnetic ground states with incommensurate $\vec{q}_\parallel$ vectors are also possible preferentially with $\vec{q}_\parallel$ vectors from the connecting high-symmetry lines $\overline{\mathrm{M}}$-$\overline{\Gamma}$-$\overline{\mathrm{K}}$-$\overline{\mathrm{M}}$.

Along the line $\overline{\mathrm{M}}$-$\overline{\Gamma}$-$\overline{\mathrm{K}}$-$\overline{\mathrm{M}}$ we investigated the energetics within the Heisenberg model up to the second-nearest-neighbor interaction, that is, including the exchange constants J_1, J_2. The results are summarized in Figure 14 in terms of a zero-temperature phase diagram.

Depending on the signs and values of J_1 and J_2, four kinds of possible magnetic ground states exist: FM, RW-AFM, 120° Néel, and SSDW. If J_2 is zero or positive (FM) than there are only two possible magnetic ground states, determined by the sign of J_1 – the FM and the Néel state. But small values of J_2 are already sufficient to change the magnetic ground state and an infinite number of

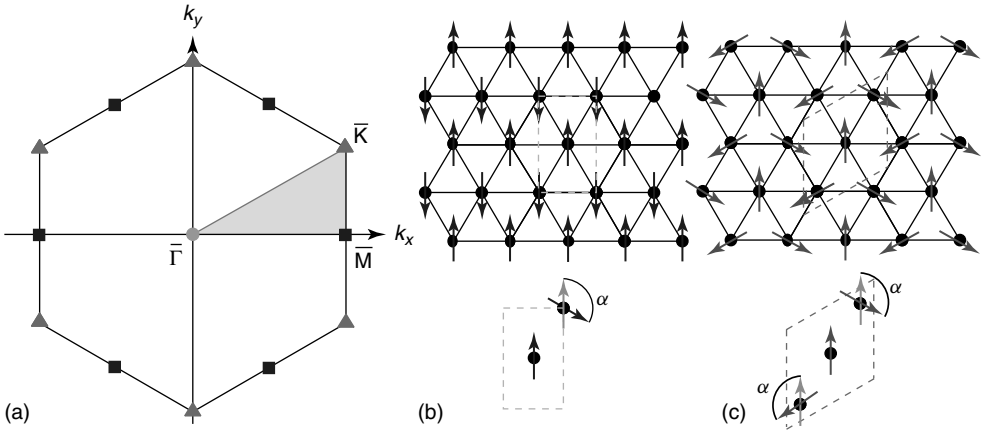

Figure 13. (a) The hexagon shows the first BZ of the 2D hexagonal Bravais lattice. The gray-shaded area indicates the irreducible part. (b) The RW-AFM structure. (c) The coplanar noncollinear Néel (120°) structure. Indicated are the corresponding two- and three-atom unit cells and the continuous paths, which connect the corresponding magnetic structure to the FM state.

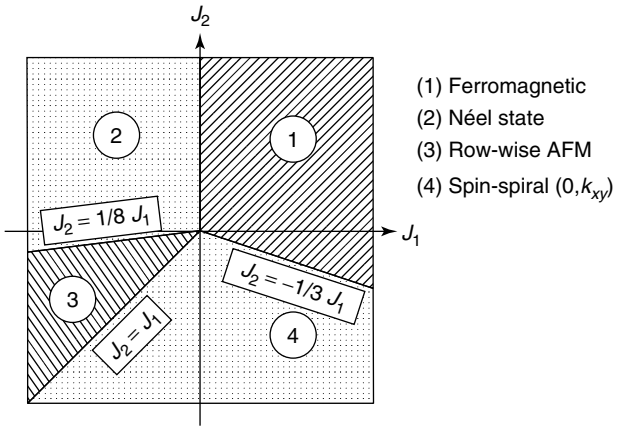

Figure 14. Zero-temperature phase diagram in the (J_1, J_2) space for the triangular lattice indicating the regions of the four possible magnetic states.

magnetic states becomes possible, the RW-AFM state or the incommensurable SSDW at any possible wave vector $\vec{q}_\parallel$ at the high-symmetry line $\overline{\Gamma}$-$\overline{\mathrm{M}}$. Extending the model by also including J_3, a magnetic state with a $\vec{q}_\parallel$ at any high-symmetry line can become a ground state.

Since the J's are rapidly varying functions of the number of d electrons, *ab initio* calculations are carried out to determine the element-specific ground states. Since the calculations are very time consuming, the full overview has been worked out only for unsupported, freestanding monolayers (UMLs). Figure 15 shows for the UMLs with the Cu lattice constant the total energy $E(\vec{q}_\parallel)$ and the magnetic moments $M(\vec{q}_\parallel)$ calculated for a discrete set of the spin spiral $\vec{q}s_\parallel$ vectors along the high-symmetry lines. Among all the SSDWs calculated, the high-symmetry points have the lowest energies: the 120° Néel state ($\overline{\mathrm{K}}$ point) for Cr(111), the RW-AFM state ($\overline{\mathrm{M}}$ point) for Mn(111), and the FM state ($\overline{\Gamma}$ point) for Fe(111). For Fe and Mn, the $M(\vec{q}_\parallel)$ are nearly a constant, but the Cr moments change drastically, as no FM solution could be found for Cr(111). Another interesting observation is the local minimum of $E(\vec{q}_\parallel)$ for Mn on the line $\overline{\Gamma}$-$\overline{\mathrm{K}}$, which is only 21 meV higher in energy than the RW-AFM state. We expect that a small change in the d-band filling, for example, due to alloying with Fe, may change the energetics and an incommensurate SSDW may become the magnetic ground state.

For Mn, the lowest-energy magnetic state found so far is the RW-AFM state, which corresponds to the commensurate SSDW state with one single $\vec{Q}_\parallel$ vector at the $\overline{\mathrm{M}}$ point of the 2DBZ, and the RW-AFM is also called *single-*$\vec{Q}_\parallel$ (1Q) *state*. In the 2DBZ there are three $\overline{\mathrm{M}}$ points corresponding to the three possible directions of the long axis of the RW-AFM unit cell on a triangular lattice. They are equivalent in symmetry but are different from each other with $\vec{Q}_\parallel$ vectors, $\vec{Q}_\parallel^{(k)}$, for

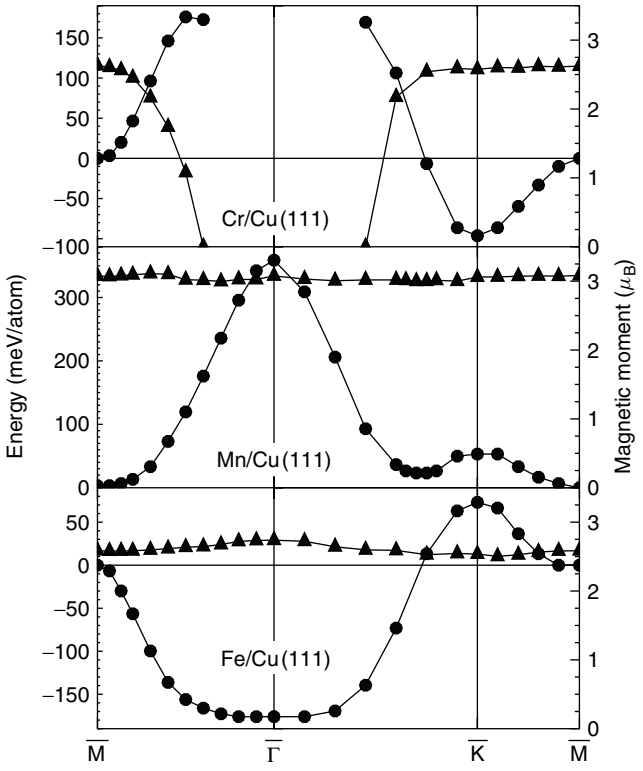

Figure 15. Calculated total energies (circles, left scale) and magnetic moments (triangles, right scale) for spin-spiral states in 3d UMLs with the Cu(111) geometry as function of the 2D wave vector $\vec{q}_\parallel$ along the high-symmetry lines of the 2DBZ. The energy is shown relative to the energy of the RW-AFM state.

$k = 1, 2, 3$. Within the Heisenberg model, the energy of each SSDW denoted by one of the three wave vectors $\vec{Q}_\parallel^{(k)}$ or any SSDW being an orthogonalized linear combination of these vectors is degenerate. Higher-order spin interactions (equations (4) and (5)) may lift this degeneracy and a so-called triple-$\vec{Q}_\parallel$ (3Q)-state, may become lower in energy. The 3Q state is a three-dimensional noncollinear spin structure on a 2D lattice (see Figure 16) with four chemically identical atoms per surface unit cell, where the relative angle between all nearest-neighbor spins is given by the tetrahedron angle of 109.47°. The 3Q state is formed as a linear combination of the three RW-AFM (1Q) structures orthogonal in spin space, each having one of the three $\vec{Q}_\parallel^{(k)}$ vectors of the $\overline{\mathrm{M}}$ points:

$$\vec{m}(\vec{r} + \vec{R}_i) = m(\vec{r}) \times \frac{1}{\sqrt{3}} \sum_{k=1}^{3} e^{i\,\vec{Q}_\parallel^{(k)}\,\vec{R}_i}\,\vec{e}^{(k)} \qquad (38)$$

where the $\vec{e}^{(k)}$ are orthogonal unit vectors in spin space. We see that in the nearest-neighbor approximation to the higher-order exchange contributions, the sign of K_1 and B_1 determine the sign of the energy difference $\Delta E = E_{3Q} - E_{1Q} = 16/3S^4(2K_1 + B_1)$ and thus whether the 3Q or the

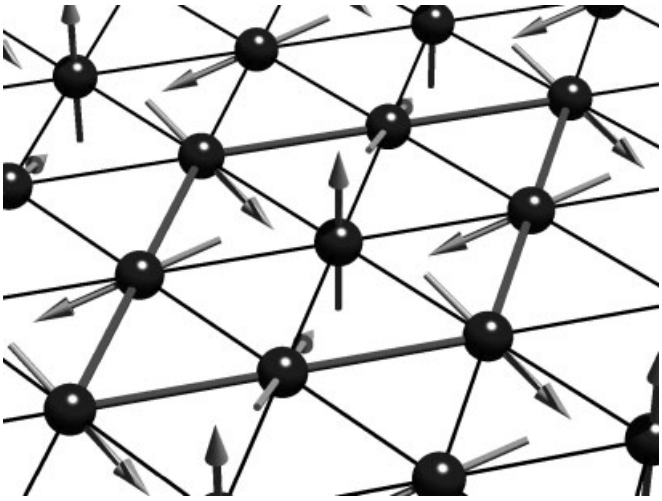

Figure 16. An image of the magnetic 3Q structure, with spins pointing in all three directions of the spin space. Note that, because the spin-orbit interaction is neglected, only the relative orientation of the moments is specified.

1Q state becomes the magnetic ground state. From the *ab initio* calculations for the Mn UML in the geometry of Cu(111) we (Kurz, Bihlmayer, Hirai and Blügel, 2001) found that the 3Q state is 15 meV/atom lower in energy than the 1Q state.

Calculations including the Cu(111) substrate show that the energy differences between different magnetic states change because of the presence of the substrate, but the magnetic ground state remains unaltered: Cr/Cu(111) exhibits the 120° Néel state ($2.35\,\mu_B$), Mn/Cu(111) the 3Q structure ($2.74\,\mu_B$), which is 17 meV lower in energy than the 1Q state ($3.00\,\mu_B$), and Fe/Cu(111) is FM ($2.63\,\mu_B$). On the Ag(111) substrate (Heinze *et al*., 2002) the overall picture is the same, but two differences were noticed: V/Ag(111) is magnetic ($2.19\,\mu_B$) and exhibits as Cr/Ag(111) ($3.65\,\mu_B$) the 120° Néel state and the magnetic ground state of Mn/Ag(111) is the RW-AFM state ($3.91\,\mu_B$) and not the 3Q state ($3.88\,\mu_B$). Fe/Ag(111) is FM ($3.02\,\mu_B$). We believe that the complex spin structures presented here can be resolved using the SPSTM in the constant-current mode (Wortmann *et al*., 2001; Heinze *et al*., 2002). In fact, recent SPSTM results (von Bergmann *et al*., 2006) of an Fe monolayer on the strongly hybridizing Ir(111) substrate yielded a very surprising and unprecedented nanometer-size spin structure exemplifying again that the arguments on the magnetic structure developed for weakly interacting substrates cannot be carried over easily for strongly hybridizing substrates. Since strongly hybridizing substrates have been investigated only recently, great surprises on the magnetic spin structures can be expected in the future.

3.3 Magnetic substrate: magnetic exchange coupling of 3d metals on Fe(001)

3.3.1 Monolayers

3d-metal monolayers on Fe(001) are prototypical systems where the in-plane magnetic interactions, described by the exchange coupling parameter $J_\parallel$, compete with the strong magnetic interactions $J_\perp$ between the monolayer and the substrate. Depending on the signs and values of $J_\parallel$ and $J_\perp$, complex spin structures as ground states can be anticipated. Finally, total-energy calculations are required to determine the minimum-energy magnetic state among the various metastable solutions. We recently carried out calculations (Handschuh and Blügel, 1998; Asada *et al*., 2000) which considered three competing spin structures: the p(1 × 1) FM, the p(1 × 1) LAF and the c(2 × 2) FI spin configurations displayed in Figure 17.

Figure 18 summarizes the results from calculations for structurally unrelaxed monolayers, that is, where the monolayer atoms are located at the ideal, bulk truncated, pseudomorphic Fe atom sites. For most 3d-metal overlayers (Cr, Mn, Fe, Co) on Fe(001) all three configurations exist and are energetically stable. Only the V and Ni monolayers were found to couple exclusively layered antiferromagnetically or ferromagnetically, respectively, to the Fe(001) substrate. Surprisingly, the FM ($M > 0$), the LAF ($M < 0$), and the two different magnetic moments ($M_1 > 0$ and $M_2 < 0$) for the FI phase are all similar in size. The largest magnetic moment of about 3 μ_B was found for Mn, and then the magnetic

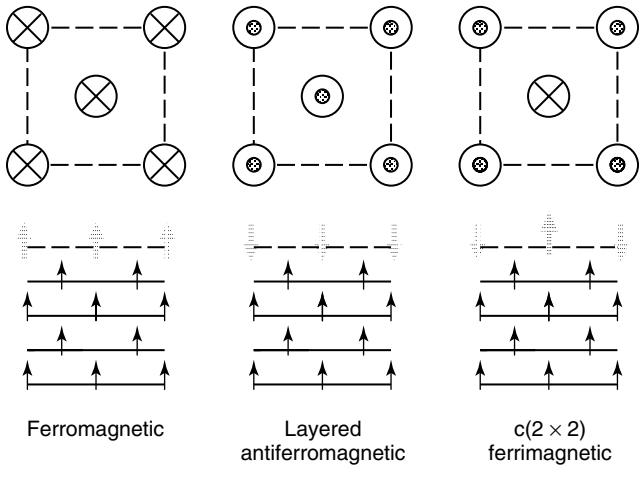

Figure 17. Schematic representation of a ferromagnetic, a layered antiferromagnetic, and a c(2 × 2) (anti)ferrimagnetic superstructure of a monolayer film (broken line) grown as overlayer on a magnetic substrate (full line). Upper panel shows view onto the surface, lower panel shows side view. Arrows indicate the relative spin direction at the positions of the atoms.

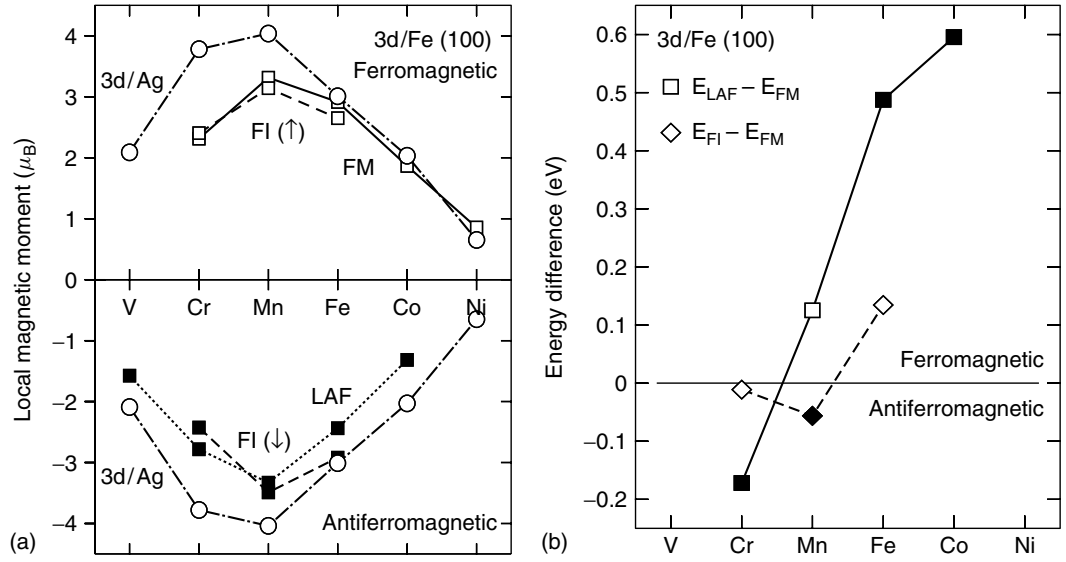

Figure 18. (a) Local magnetic moments of unrelaxed 3*d* transition-metal monolayers on Fe(001). Positive (negative) sign of moments indicates an (anti)ferromagnetic, FM (AF), spin alignment to the Fe substrate, emphasized by open filled) symbols. Shown are results of three different spin configurations: p(1 × 1) FM (solid line), p(1 × 1) LAF (dotted line), and the c(2 × 2) FI (dashed lines) for positive and negative moments. The figure is complemented with results for 3d monolayers on Ag(001) (◯ connected by dash-dotted line). As the Ag substrate is nonmagnetic, ferro-, and antiferromagnetic spin alignment is indistinguishable and moments are identical and are shown twice, once for positive and negative sign. (b) Total energy difference $\Delta E_1 = E_{\mathrm{LAF}} - E_{\mathrm{FM}}$ between the p(1 × 1) layered antiferromagnetic and the ferromagnetic coupling (squares connected by solid lines) and $\Delta E_2 = E_{\mathrm{FI}} - E_{\mathrm{FM}}$ between the c(2 × 2) ferrimagnetic and the p(1 × 1) ferromagnetic coupling (diamonds connect by dashed lines) of 3d transition-metal monolayers with Fe(001). The ferromagnetic (layered antiferromagnetic or ferrimagnetic) coupling has lower energy for $\Delta E > 0$ (<0) and is therefore favored. The layered antiferromagnetic coupling is preferred over the ferrimagnetic one if $\Delta E_1 < \Delta E_2$. Filled squares or diamonds indicate the magnetic ground state. For V and Ni only one magnetic state has been found.

moments drop for elements to the left and right of Mn, reminiscent of the behavior on the noble-metal substrates.

In order to see the effect of the hybridization between the substrate and the overlayer on the size of the local moments, the local magnetic moments of 3d-metal monolayers on Ag(001) (Blügel and Dederichs, 1989) are included for comparison. Fe ($a_{\parallel} = 5.33$ au) and Ag ($a_{\parallel} = 5.51$ au) have very similar in-plane lattice constants and thus very similar in-plane d–d hybridizations may be expected for the monolayer, but the d–d hybridization across the interface is largely different. From Figure 18(a) one infers that the magnetic moments for the Fe, Co, and Ni monolayers are rather independent of the substrate, but increasing deviations are obtained for the monolayer moments in the sequence from Mn to V. The extent of the 3d wave function increases for chemical elements from the end of the 3d series to the beginning of the series. Accordingly, the d–d hybridization within the monolayer and between the monolayer and the Fe substrate increases. As a consequence, the magnetic moments for Mn, Cr, and V overlayers are visibly reduced.

Since the local magnetic moments of the three different magnetic states for Cr, Mn, Fe, and Co monolayers on Fe(001) are very similar in size, total-energy calculations have been performed to determine the minimum-energy magnetic configuration. The energy difference $\Delta E_1 = E_{\mathrm{LAF}} - E_{\mathrm{FM}}$ between the LAF and FM configurations and $\Delta E_2 = E_{\mathrm{FI}} - E_{\mathrm{FM}}$ between the c(2 × 2) FI and the FM configurations, ignoring again any monolayer relaxation, are shown in Figure 18(b). For V and Ni monolayers, which show only one magnetic solution, no data points are included. As reported in the literature (Mirbt, Eriksson, Johansson and Skriver, 1995; Handschuh and Blügel, 1998; Wu and Freeman, 1995) we find with the exception of Cr, that the FM coupling ($\Delta E_1 > 0$) is energetically always more favorable than the LAF one and that for Cr and Mn the FI coupling ($E_2 < 0$) is energetically preferred over the FM one. For Fe, Co, and Ni, the FM solution is the most stable one. When we compare for Cr or Mn the energies among the three different magnetic phases, we find that for Cr the LAF coupling is the magnetic ground state, energetically followed by the FI and the FM coupling, which are metastable phases. The calculated total-energy differences between FM and LAF configurations and between FM and FI show some differences from those of Handschuh *et al.* (Handschuh and Blügel, 1998) mostly due to the different choice of the in-plane lattice constant. Summarizing, (i) the magnetic ground-state structures

are LAF for V and Cr, FI for Mn, FM for Fe, Co, and Ni; (ii) for the Mn monolayer we find a second spin configuration with an energy of about 55 meV/Mn above the ground-state structure.

Therefore, extending the search for the magnetic ground state of Mn to larger surface unit cells may lead to a more complicated ground-state spin structure. Elmouhssine, Moraïtis, Demangeat and Parlebas (1997) and Asada *et al*. (1999) investigated the possibility of additional low-energy Spin structures in the p(2 × 2) surface unit cell containing four Mn surface atoms. Two additional spin structures were included: the p(2 × 2) FM magnetic structure with three Mn atoms out of four coupling ferromagnetically to the Fe substrate and one Mn atom coupling antiferromagnetically, as well as the p(2 × 2) AF structure, which is the LAF version of p(2 × 2) FM, where three Mn atoms couple antiferromagnetically and one atom couples ferromagnetically to Fe. Indeed the calculations reveal that on Fe(001), the Mn c(2 × 2) FI, and the p(2 × 2) FM are nearly degenerate ground states. This is obvious from Figure 19, which displays the energies of the different configurations relative to the c(2 × 2) FI state energy. Tight-binding linear muffin-tin orbital calculations by Elmouhssine *et al*. found that the p(2 × 2) FM superstructure is 15 meV higher in energy than the c(2 × 2) one, while Asada *et al*. found by full-potential linearized augmented planewave (FLAPW) calculations that the total energy of the p(2 × 2) FM superstructure is slightly lower (∼6.4 meV/Mn) than the c(2 × 2) FI structure. The interlayer distances of relevant magnetic configurations had been fully optimized by the use of force calculations; however this is not shown here and these relaxations do not change this picture. The energy differences are comparable to the thermal energy at room temperature. Thus, surface roughness and thermal excitations in true experimental situations could lead to the coexistence of these two magnetic configurations and thus the appearance of magnetic domains within the Mn monolayer. At present one cannot exclude the possibility of magnetic states with even lower energy that have not been investigated yet.

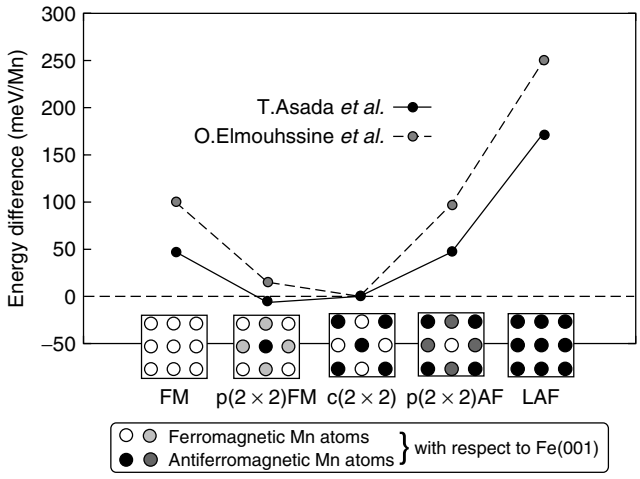

Figure 19. Relative energy $E - E_{c(2\times2)}$ for the five magnetic configurations. The small energy difference between the c(2 × 2) FI state and the p(2 × 2) FM configurations indicates that the two solutions are nearly degenerate ground states.

3.3.2 *Double layers*

In order to demonstrate the complexity of the systems we show here the results of the 3d metal bilayers on Fe(001) as well. For the double layer systems, we have examined all possible magnetic configurations within the c(2 × 2) unit cell. With the exception of Mn all stable magnetic configurations found have the magnetic p(1 × 1) structure. The magnetic ground states are the p(1 × 1) LAF one for V, Cr, and Mn, and the p(1 × 1) FM one for Fe, Co, and Ni bilayers on Fe(001). For Mn we found in addition to the p(1 × 1) LAF ground-state structure also the superstructure ($[\uparrow\downarrow]_S$ $\downarrow_{S-1}$ | ↑ Fe) as a stable solution with a total energy of 43.2 meV/Mn higher than the LAF structure. The magnetic moments for the bilayer systems are collected in Figure 20. Please note for the case of the LAF Mn double layer the almost vanishing magnetic moment of the subsurface atom. Furthermore, for the Mn bilayer, in addition to those two configurations, the ground state ($\uparrow_S$ $\downarrow_{S-1}$ | ↑ Fe) and the

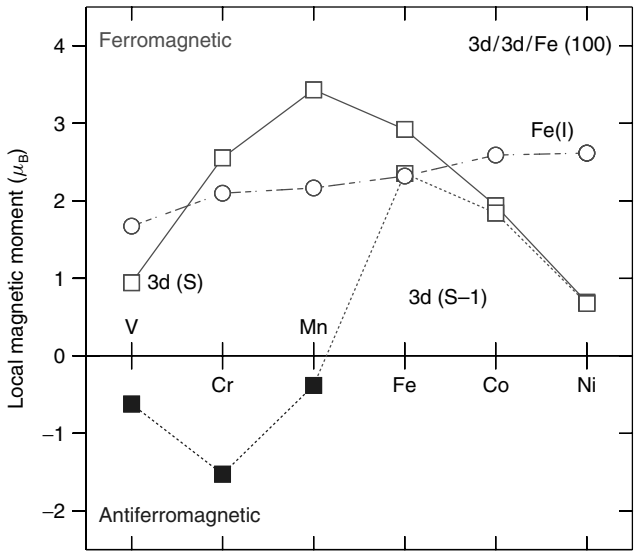

Figure 20. Local magnetic moments (M) for the ground-state spin configurations of unrelaxed 3d transition-metal double layers on Fe(001). The solid line denotes the 3d surface atoms (3d(S)) aligned parallel ($M > 0$) to the Fe substrate, the dotted line denotes the 3d subsurface atoms (3d (S − 1)), whose coupling changes from LAF ($M < 0$) to FM ($M > 0$) from early to late 3d elements. The chained line denotes the interface Fe atoms (Fe(I)).

superstructure stated in the preceding text, we also found a third configuration, ($\downarrow_S \uparrow_{S-1} \mid \uparrow$ Fe), which is about 9 meV/Mn higher in energy than the ground state. Thus, there exist three states within an energy range corresponding to about 400 K. We believe that this gives already a glimpse of the difficulties involved in dealing with thicker Mn overlayers on Fe(001) (Pfandzelter, Igel and Winter, 1997).

For a Cr monolayer the measured magnetic moment was found to be at most 1 μ_B (Hillebrecht *et al*., 1992; Jungblut, Roth, Hillebrecht and Kisker, 1991), which is less than half of the theoretical prediction (Mirbt, Eriksson, Johansson and Skriver, 1995; Handschuh and Blügel, 1998). It was also reported that the layer-by-layer growth leads to a strong intermixing with the substrate Fe layers (Venus and Heinrich, 1996; Pfandzelter, Igel and Winter, 1996; Davies, Stroscio, Pierce and Celotta, 1996). Mn overlayers seem to be even more involved. There is a general experimental consensus that for Mn around 1 ML coverage, the signals related to the magnetization disappear. The microscopic origin for this observation is under strong debate. One explanation supported by theory (Handschuh and Blügel, 1998; Wu and Freeman, 1995) is a possible onset of the in-plane FI coupling. On the other hand, strong interfacial alloying has been observed (Igel, Pfandzelter and Winter, 1998), which may lead to the same results. A third option is the possibility of a double layer growth mode, which may also lead to the disappearance of magnetic signals. The difficulty in controlling and characterizing the morphology of the interface seems to be intimately related to the difficulties in understanding the interfacial magnetism of those systems. A complete picture requires additional theoretical investigations including the possibility of interdiffusion and surface alloying.

3.4 Orbital moment and magnetic anisotropy

3.4.1 Trends in unsupported (100) monolayers

The orbital magnetic moments (m_l) and the MCA are fairly small quantities compared to spin moments and exchange energies. This holds at least for 3d transition metals. These quantities depend on fine details of the electronic structure which changes with lattice constant, film thickness, choice of substrate, and surface orientation. Although it is important to know the actual values of the m_l and the MCA for particular systems, in this subsection we try to provide insight and intuition into the behavior of these quantities by studying the chemical trend of these properties across the transition-metal series. We focus on (100)-oriented unsupported 3d, 4d, and 5d transition-metal monolayers in the lattice constant of Ag(100) ($a_0/\sqrt{2} = 5.459$ au). In order to proceed with a fine scale analysis of these properties as function of the electronic structure or the band filling, respectively, the relativistic density-functional calculations are carried out for films of hypothetical atoms with noninteger nuclear numbers. The rationale behind this *modus operandi* is the idea that owing to the required charge neutrality, the nuclear number and the number of electrons are the same. Thus, a fine change of the nuclear number is followed by a fine change of the number of electrons, caused by the adjustment of the Fermi energy. This facilitates a fine scan of m_l and the MCA as a function of the band filling across the transition-metal series. For example, for the 3d monolayers we have varied the nuclear number Z from the beginning to the end of the transition-metal series, for example, from $Z = 21$ with $N_V = 3$ valence electrons till Cu, $Z = 29$ with $N_V = 11$ valence electrons, in steps of approximately $\Delta Z = 0.10 \sim 0.15$.

The results are summarized in Figure 21. For each Z, two self-consistent relativistic *ab initio* calculations have been carried out, one with the magnetization direction perpendicular to the film plane, $\widehat{m} = \uparrow$, and one with the magnetization parallel to the film plane along the [100] direction, $\widehat{m} = \rightarrow$. The results obtained are the orientation-dependent spin moments, $m_s(\uparrow)$ and $m_s(\rightarrow)$, orbital moments, $m_l(\uparrow)$ and $m_l(\rightarrow)$, and electronic total energies, $E(\uparrow)$ and $E(\rightarrow)$. Here we focus on the FM phase.

The magnetic spin moments exhibited in Figure 21(a), follow the trend discussed in Section 3.1.1: The 3d monolayers behave according to Hund's first rule with a maximum moment of more than 4 μ_B in the center of the series. Also 4d- and 5d-metal monolayers are magnetic for elements between Mo till close to Pd and between W till close to Pt. The magnetic moments decrease from the 3d to the 4d and 5d series and at the same time the element with the maximum magnetic moment in each series shifts to the right in the series. The anisotropy of the spin moments, $\Delta m_s = m_s(\uparrow) - m_s(\rightarrow)$, is very small, for example the calculation of an Ir monolayer yields $m_s(\uparrow) = 1.044\,\mu_B$ and $m_s(\rightarrow) = 1.012\,\mu_B$ and is therefore not further considered. However, for 5d elements, relativistic calculations have an impact on the size of the spin moments. For example, the spin-orbit interaction reduces the magnetic moment of Ir by 0.5 μ_B to about 1 μ_B.

According to equation (30), E_{dip} is proportional to m_s^2 and inversely proportional to third power of the lattice constant, a. Since the lattice constants of all systems are fixed to the one of Ag, Figure 21(a) mirrors the functional behavior of the dipole energy E_{dip} with respect to the band filling. Since the dipolar anisotropy or shape anisotropy in the continuum limit, respectively, $K_{dip} = \Delta E_{dip} = E_{dip}(\rightarrow) - E_{dip}(\uparrow)$, always favors a magnetization in the film plane, the shape anisotropy is strictly negative according to our sign convention for the magnetic anisotropy. The largest value is obtained for a film with elements

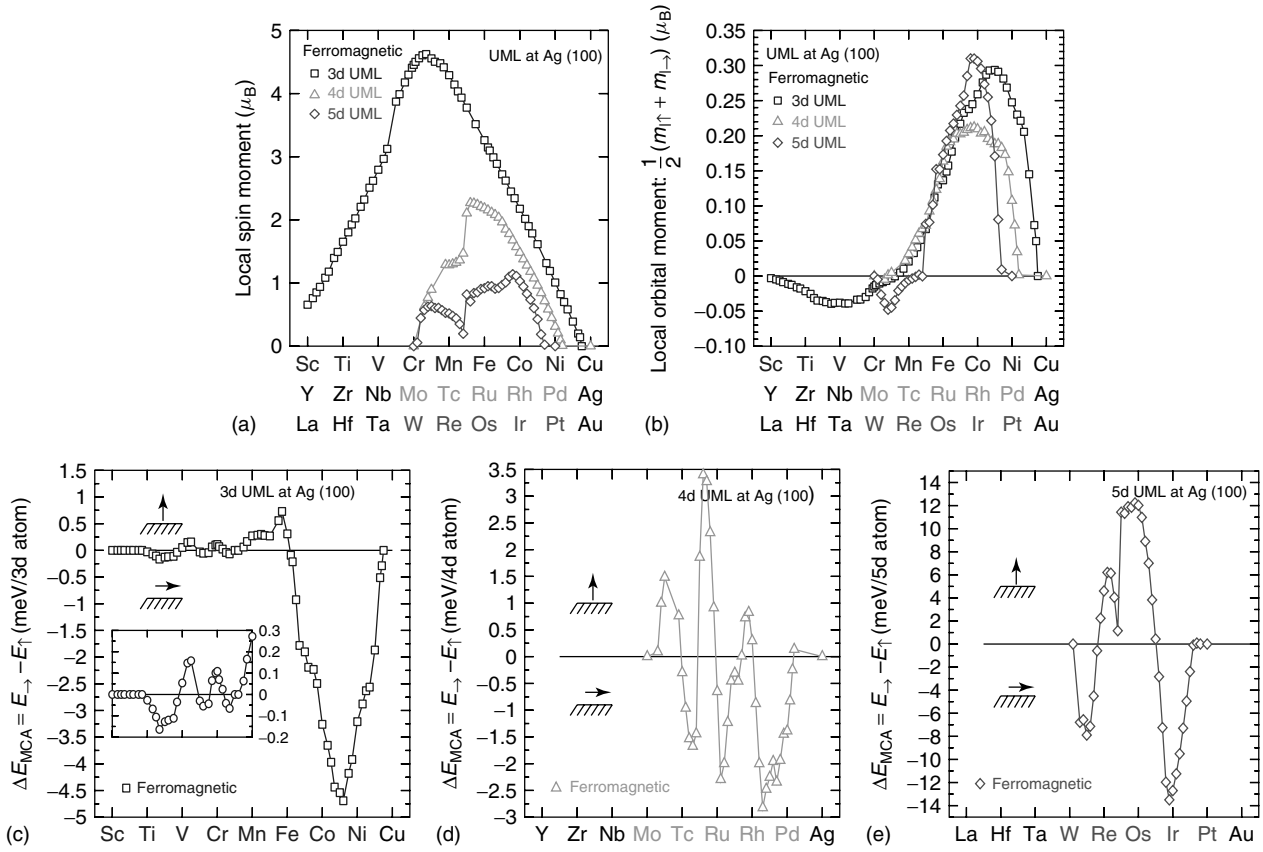

Figure 21. Local magnetic spin moments (a) and orbital moments (b), magnetocrystalline anisotropy constant $K_{MCA} = \Delta E_{MCA}$ calculated as energy difference between two magnetization directions, the magnetization in the film plane ($\rightarrow$) and out of the film plane ($\uparrow$), calculated for ferromagnetic, freestanding, unsupported 3d- (squares) (c), 4d- (triangles) (d), and 5d- (diamonds) (e) metal monolayers (UML) in the (100) surface orientation and in the lateral lattice constant of the Ag(100) substrate (Nie, Bihlmayer and Blügel, 2006). In (b) the average orbital moments between those of the out-of-plane, $m_{l\uparrow}$, and in-plane, $m_{l\rightarrow}$, magnetization directions are shown. The difference of the spin moments on the magnetization direction is difficult to distinguish on the scale of (a) and is not shown. Positive energies in (c)–(e) mean that the out-of-plane magnetization is energetically preferred.

between Cr and Mn and the dipolar anisotropy amounts to $K_{dip} = -0.32$ meV/atom. This is about 30% of the value of K_{shape} as calculated according to equation (29) using continuum theory, in good agreement with the results of Draaisma and de Jonge (1988).

Also the orbital moments, collected in Figure 21(b) exhibit a clear trend: the orbital moments are negative in the first half of the transition-metal series, for example, between Sc and Mn, and positive in the second half of the transition-metal series. The change in sign is reminiscent of Hund's third rule which governs the coupling of the spin and orbital moment. A negative (positive) sign of the orbital moment means that the orbital moment couples opposite (parallel) to the spin moment. The orbital moments of elements in the second half of the transition-metal series are an order of magnitude larger than in the first one. It is surprising that the orbital moments in films made of the 3d, 4d, or 5d elements in the second half of the corresponding transition-metal series show very similar values although the spin moments are substantially different. We recall from equation (35) that for uniaxial symmetry as present in thin films, the orbital moment scales as $m_l \propto \xi \propto Z^2$, which explains the increase of m_l for a given spin moment m_s when switching from the 3d to the 4d and 5d transition-metal series. The anisotropy of the orbital moments, Δm_l, has maximum values of about $\pm 0.07\,\mu_B$ in each series and cannot be neglected. Therefore, in Figure 21(b) the average moments are shown. Δm_l is a rapidly varying function with respect to the band filling and relates according the equation (36) to the corresponding rapid oscillation of the magnetocrystalline anisotropy.

The uniaxial magnetocrystalline anisotropy constants $K_{MCA} = \Delta E_{MCA} = E(\rightarrow) - E(\uparrow)$, calculated as total energy differences for magnetizations in and out of the film plane are exhibited in Figure 21(c–e). Indeed, results show a continuous and very rapidly varying behavior as function of the band filling. We focus first on the 3d-metal monolayers

(Figure 21c). Between Fe and Cu the MCA is negative and the magnetization lies in the film plane. Between Mn and Fe the magnetization normal to the film plane is energetically most favorable. A closer look reveals several changes of sign as a function of the band filling. The large variation of the value of K as function of band filling from 4.75 meV for a band filling between Co and Ni ($N_V = 9.5$) and 0.15 meV for V is surprising. Noninteger band filling is not only of theoretical interest but has a concrete meaning in the spirit of the virtual crystal approximation. For example, we calculated an ordered c(2×2) CoNi UML film, which also has a band filling of $N_V = 9.5$ per atom. K is practically on the spot of the curve Figure 21(c). Adding K_{dip} on top of K_{MCA} one finds that with the exception of a small interval between Mn and Fe, where the positive K_{MCA} exceeds the negative K_{dip}, the magnetization is energetically most favorable to be in the film plane. Thus, among the 3d-metal monolayers (integer nuclear number) only the Fe(100) UML has a magnetization direction out of plane.

Comparing the K_{MCA} values of the 3d, 4d, and 5d monolayers, remarkable results are observed. The most spectacular results are the gigantic K_{MCA} values for the 5d UMLs, which reach values of 12.32 meV for Os and -13.50 meV for Ir. Although the maximum magnetic spin moment within each transition-metal series drops from $4.6\,\mu_{\mathrm{B}}$ in the 3d series to $2.3\,\mu_{\mathrm{B}}$ and $1.1\,\mu_{\mathrm{B}}$ in the 4d and 5d series, respectively, and the orbital moments are roughly the same between the transition-metal series, K_{MCA} varies from -4.69 to 0.73 meV in the 3d series, and from 3.40 to 2.82 meV in the 4d series and to truly gigantic values of -13.50 to 12.32 meV in the 5d series. One further notices that the latter is accompanied by a rapid change of K_{MCA} of about 25 meV when going from Os to its chemical neighbor Ir. One further notices that the functional characteristics of K_{MCA} shows a much more oscillatory behavior in the 4d and 5d series, both exhibiting two maxima and three minima, than in the 3d one with one minimum, one maximum, and then several small rapidly oscillating peaks.

These results can be interpreted on the basis of the corresponding band structures and the second-order perturbation theory of the MCA as presented in Section 2.6. As an example, the Fe monolayer in the Ag(100) lattice constant is analyzed: as can be inferred from Figure 9, the majority d band of Fe on Ag(100) is filled, so that these states will not contribute to equation (34), where only pairs of occupied and unoccupied states near the Fermi level can contribute significantly. Therefore, we can focus on the minority states, and the corresponding band structure is shown in Figure 22. The matrix elements in equation (34) depend on the symmetry of the states, ψ, and the spin-orbit operator (van der Laan, 1998). The spatial part of H_{so} has the symmetry of the orbital moment operator,

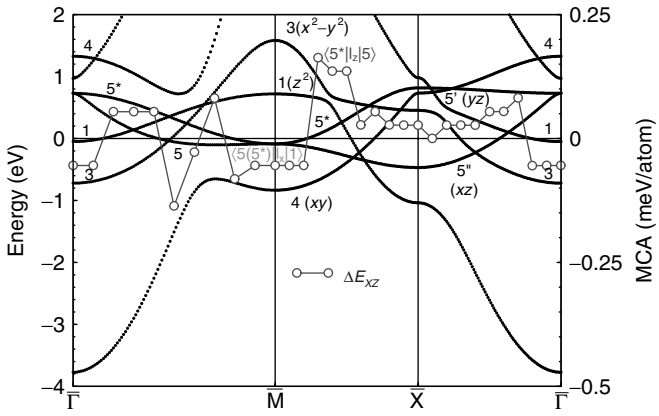

Figure 22. Minority-spin band structure (black) and statewise contribution to K_{MCA} (circles) calculated by perturbation theory for Fe(100) UML in the lattice constant of Ag. The symmetry of the bands is indicated as well as some matrix elements which contribute to K_{MCA} (see text).

for example, l_x or l_z. Therefore it is possible to find out which pairs of states can lead to nonzero matrix elements in equation (34), depending of course on the magnetization direction. For an estimate of the MCA, at each $\vec{k}$ point $K_{\mathrm{MCA}} = \delta E(l_x) - \delta E(l_z) = \Delta E_{xz}$ can be calculated individually, as shown in Figure 22. For example, near the M point, states of d_{xz}, $\mathrm{d}_{yz}(5, 5^*)$ symmetry are just below the Fermi level and states of $d_{z^2}(1)$ symmetry are above it. These states are coupled by the l_x operator, therefore the bands in this region will contribute more to $\delta E(l_x)$ than to $\delta E(l_z)$, favoring an in-plane magnetization. Between $\overline{\mathrm{M}}$ and $\overline{\mathrm{X}}$, a coupling of states with 5 and 5^* symmetry favors an out-of-plane magnetization. After summation over the whole Brillouin zone, the latter contributions dominate and, in accordance with Figure 21(c), Fe/Ag(100) has an out-of-plane magnetization.

If the Fermi level is shifted to higher energies (or the band filling increases), the band with 5^* symmetry gets more occupied and the coupling of the 5 and 5^* states is no longer possible. The contribution of the $\langle 5(5^*)|l_x|1\rangle$ matrix elements near M gets stronger. Finally, K_{MCA} changes sign (see Figure 21c) and the Co UML is in-plane magnetized. As can be inferred from Figure 22, the contributions to the MCA oscillate strongly in $\vec{k}$ space and for an accurate summation a fine resolution in reciprocal space, that is, a fine $\vec{k}$-point mesh, is necessary. It should also be noticed that the decoupling of majority and minority bands used above can only be applied for 3d metals. In 4d or 5d monolayers, the exchange splitting is much smaller and both spin channels give contributions to the MCA. Therefore, a much more complex behavior of the anisotropy as function of the band filling can be seen in Figure 21(d) and (e).

These results give an excellent overview of the trends of the uniaxial anisotropy K of magnetic monolayers. However, the substrate also plays an important role. For weakly magnetically polarizing substrates, for example, Cu and Ag, the same trend is expected although the actual values will change. Substrates with large nuclear numbers and thus large spin-orbit interactions, which have in addition a large Stoner-enhanced susceptibility, for example, W or Pt, and can thus be easily magnetically polarized, may in the end determine the magnetic anisotropy of these systems. For example, in the light of the experimental results of ultrathin Co films in contact with other metal films, as sandwiches or as multilayers, for example, Co/Pd(100) (den Broeder, Kuiper, Donkersloot and Hoving, 1989) or Co/Pt(100) (Lin *et al.*, 1991) the large negative K_{MCA} value of the unsupported Co monolayer, which is in accordance with results of Bruno (1989) based on perturbation theory, is a fairly surprising result. In order to get a better understanding of the influence of the substrate on the magnetocrystalline anisotropy, we compared the uniaxial K_{MCA} for a Co monolayer with and without substrate and found, $K_{\mathrm{MCA}} = -4.75\,\mathrm{meV}$ for a UML(100) in the lattice constant of Ag and $K_{\mathrm{MCA}} = -1.39\,\mathrm{meV}$ on Ag(100), $K_{\mathrm{MCA}} = -1.33\,\mathrm{meV}$ for an UML(100) in the lattice constant of Cu, and $K_{\mathrm{MCA}} = -0.32\,\mathrm{meV}$ on Cu(100). This can be understood in the spirit of the model of Stöhr (1999), introduced in Section 2.6, realizing that the presence of a substrate quenches predominantly the in-plane orbital moment. Therefore, we observe a clear reduction of K_{MCA} due to the presence of the substrate, but the general trend across the transition-metal series will still hold. At arbitrary substrates 4d- and 5d-metal monolayers will be nonmagnetic. But thin films show a significant Stoner-enhanced susceptibility. In contact with 3d transition metals they may develop a magnetic moment, an electronic structure, and a uniaxial K_{MCA} comparable to the isolated monolayers. In turn, strongly spin-polarized substrates with large nuclear number change even the sign of the MCA from in plane to out of plane and will be discussed in Section 3.4.3.

3.4.2 Magnetic reorientation transition: Ni/Cu(100)

If more than one or two layers of magnetic material are deposited as thin film, the layers that are not forming an interface (to the vacuum or the substrate) will show more bulklike properties. It is common to separate the volume-like contributions to the effective anisotropy constants, K^V (energy/unit volume), from the surface term K^S and interface term K^I (energy unit/area). This yields for the effective magnetic anisotropy K of a magnetic layer of thickness t

$$K^{\mathrm{eff}} = K^V + \frac{(K^S + K^I)}{t} \tag{39}$$

All three anisotropy constants K contain contributions of the dipolar and the spin-orbit-derived anisotropy. On phenomenological grounds the dipolar anisotropy is also split into a volume term, K^V_{shape}, namely the shape anisotropy due to the average dipolar energy as obtained by the continuum theory and the contribution due to the reduction of the dipole anisotropy field experienced by the atoms in the surface and interface region, $K^{S\,(\mathrm{dip})}_{\mathrm{MCA}} + K^{I\,(\mathrm{dip})}_{\mathrm{MCA}}$. Thus, we can write for the volume term $K^V = K^V_{\mathrm{shape}} + K^V_{\mathrm{MCA}}$, and for the surface term $K^S = K^{S\,(\mathrm{dip})}_{\mathrm{MCA}} + K^{S\,(\mathrm{so})}_{\mathrm{MCA}}$ and analogously for the interface term. While for smaller thicknesses K^S_{MCA} and K^I_{MCA} can dominate, for thick films the negative shape anisotropy which has a constant value per atom and thus increases with thickness of the film can determine the easy axis.

If these terms have different signs, a reorientation transition of the easy axis can occur. A well investigated example is the system Ni/Cu(001) (Baberschke, 1996): For up to seven layers Ni, an in-plane easy axis of the Ni film is found. Then a reorientation to perpendicular magnetization sets in and only very thick films (more than 50 ML) show again in-plane magnetization. Here K^S is negative, about $-85\,\mu\mathrm{eV/atom}$ at room temperature, while K^V_{MCA} is positive, approximately $30\,\mu\mathrm{eV/atom}$. So we expect a reorientation between 5 and 6 ML, but actually the shape anisotropy contributes another $-10\,\mu\mathrm{eV/atom}$ to K^V (the shape anisotropy in thin films always favors in-plane magnetization). Therefore, the transition sets in after 7 ML thicknesses as illustrated in Figure 23. But we have to realize, that the value of K^V is much larger than the bulk value of fcc Ni. In fact, low energy electron diffraction (LEED) measurements demonstrated that Ni grown on Cu(001) is actually strained, the in-plane lattice constant is 1.6% larger than in fcc Ni. To compensate this strain, the spacing between the Ni layers is smaller than in the bulk. From the arguments put forward in the last paragraph we would now suppose that $V_\perp > V_\parallel$, therefore $R > 1$ and, indeed, K^V favors perpendicular magnetization (although the band filling of Ni does not correspond to the assumptions underlying equation (36)). In very thick films, the structure of Ni relaxes back to fcc and the size of K^V decreases until the influence of the shape anisotropy once more brings the easy axis back in plane.

3.4.3 Monolayers on early transition metals: Fe/W(110)

In the previous sections trends of the magnetic anisotropy of transition-metal layers as a function of band filling and layer thickness were discussed. On weakly interacting, late transition-metal substrates – like Cu or Ag – these results are more or less transferable from one substrate to another. But for early transition-metal substrates, also the influence of the

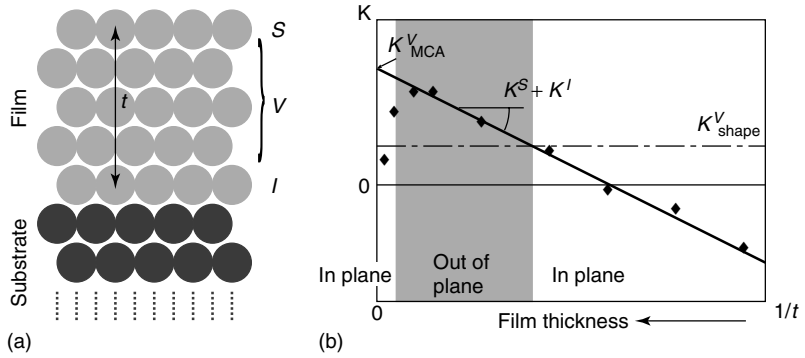

Figure 23. (a) Schematic illustration of a 5 ML Ni film on a Cu substrate; the bulklike, surface and interface regions are marked as V, S, and I, respectively. (b) Schematic plot of the anisotropy (K) versus inverse film thickness (t): the volume-like contribution, K^V, is given by the intersection with the ordinate, the surface- and interface-like term, $K^S + K^I$, can be deduced from the slope of the curve. Together with the (volume) shape anisotropy, K^V_{shape}, these values determine the in-plane/out-of-plane/in-plane transition of the easy axis for Ni films on Cu(001).

substrate has to be taken into account, as demonstrated in this section.

Fe films on W(110) are one the most intensively studied systems (Przybylski and Gradmann, 1987; Hong, Freeman and Fu, 1988; Elmers *et al*., 1994; Weber *et al*., 1997; Sander *et al*., 1997; Qian and Hübner, 1999), as they exhibit unique structural and magnetic properties. It was found that ultrathin Fe films grow pseudomorphically and without intermixing in a layer-by-layer growth mode up to 1.2 ML on the flat W(110) surface and up to 1.8 ML on a vicinal surface. Thus, it developed into a model system of two-dimensional magnetism. The magnetic easy axis switches from in plane for 1 ML Fe coverage to out of plane for a DL Fe coverage, and back to in plane for films grown beyond the pseudomorphic DL (Elmers, Hauschild and Gradmann, 1999). The sequence of the magnetic reorientation transition as function of the film thickness between 1 and 2 ML is rather unique and serves to illustrate the influence of the tungsten substrate on the magnetic anisotropy.

Ab initio calculations (Galanakis, Alouani and Dreyseé, 2000) find in agreement with experiment the reorientation transition between 1 and 2 ML: at 1 ML Fe coverage the easy axis is in the substrate plane and for 2 ML Fe coverage the easy axis switches to the out-of-plane direction. Irrespective of the structural relaxations, the shape anisotropy determines the magnetization direction for thicknesses beyond 2 ML Fe coverages, and the easy axis returns to an in-plane direction.

Interestingly, an unsupported Fe (110) monolayer, with the same lattice constants as in Fe/W(110) shows an out-of-plane magnetization. When put on the W substrate, two things happen: (i) the Fe–W hybridization changes the magnetic properties of Fe (like for Fe/W(100) as discussed in Section 3.1.3) and (ii) Fe induces a considerable spin moment (about $-0.1\ \mu_B$) in the W atoms at the interface and smaller, but finite moments in deeper substrate layers. Since W is a rather heavy element, relativistic effects – like the magnetocrystalline anisotropy – can be large even if the spin- and orbital moments are small. To separate the importance of (i) and (ii) for the MCA of Fe/W(110), a comparison to the system Fe/Mo(110) is helpful: Since in the periodic table Mo is just above W, the Fe–Mo hybridization should be similar to Fe–W. But relativistic effects are much smaller in the light Mo ($Z = 42$) than in the heavy W ($Z = 74$). Both experimentally (Bode, Pietzsch, Kubetzka and Wiesendanger, 2004) and theoretically (Nie, Heide, Bihlmayer and Blügel, 2007b) Fe/Mo(110) was found to have an out-of-plane magnetization. So it is likely that the (induced) magnetic anisotropy of tungsten at the interface is decisive for the in-plane magnetization of Fe/W(110). Layer-resolved *ab initio* calculations (Nie, Heide, Bihlmayer and Blügel, 2007b), which can separate the contribution of each layer to the total MCA, confirm this picture. These calculations also show, that a second Fe layer on W(110) quenches the orbital moment of the interface W from about 0.020 μ_B for the monolayer case to 0.007 μ_B in the double layer one (these values are for out-of-plane magnetization, for other directions of the magnetization they follow a similar trend). Thus, tungsten's influence on the MCA decreases and a double layer Fe on W(110) has out-of-plane magnetization (the same is found for Mo(110) covered with a double layer of iron).

Ab initio calculations show that a similar reorientation transition can be obtained when a capping layer of Au or Ag is put on top of the single Fe monolayer on W(110). Also here, it is the quenching of the interface W orbital moment that is responsible for the change of the easy magnetization axis. Experimentally, Fe islands on W(110) covered with Ag have been reported to have out-of-plane magnetization (Röhlsberger *et al*., 2001). Although stress effects can be important in this system and alter the MAE, it is likely that

the Ag overlayer will also contribute to the observed easy axis by the mechanism explained in this section.

4 WIRES AND CHAINS

Simple in their structure and seemingly easy to understand, metallic monowires not only present a great challenge for experimentalists, but are also an exciting playground for theory. Particularly significant are the consequences of the novel one-dimensional (1D) physics for magnetism in these systems. Electrons, restricted in their dynamics to only one dimension, compensate the lack of hopping between the nearest neighbors by giving *carte blanche* to exchange. This leads to a nonzero magnetization not only in the monowires for most transition metals but also for sp-metals (Zabala, Puska and Nieminen, 1998), for instance Al (Auyela, Raebiger, Puska and Nieminen, 2002). Typically, monowires are created on a substrate by atomic manipulation or self-assembly, allowing the creation of stable artificial structures for further investigations. The hopping and consequently the magnetic properties can change significantly upon structural changes such as dimerization, the formation of zigzag chains, or the stretching of wires. The latter is possible by pulling chains off the surface after a, scanning tunneling microscopy (STM) tip was rammed into the surface and pulled out again. Further, monowires present perhaps the most elementary bridge between the physics of itinerant electrons and molecular physics, and are doubtlessly a fruitful playground for testing the validity and limitations of the models, characteristic in both fields.

Starting from the early pioneering work by Weinert and Freeman (1983) on the magnetic properties of Fe and Ni linear chains, the variety of intriguing properties and aspects of the magnetism in metallic monowires investigated grows every year, spanning over the freestanding (Dorantes-Dávila and Pastor, 1998; Spišák and Hafner, 2003; Delin and Tosatti, 2003; Delin, Tosatti and Weht, 2004; Mokrousov, Bihlmayer, Heinze and Blügel, 2006), as well as substrate-deposited configurations. Among those are predominantly Fe or Co chains on Cu(100) (Spišák and Hafner, 2002), Pd(110) (Robles, Izquierdo and Vega, 2000), Pt(111) (Komelj, Ederer, Davenport and Fähnle, 2002; Ederer, Komelj and Fähnle, 2003; Shick, Maca and Oppeneer, 2004; Újfalussy *et al*., 2004; Baud, Bihlmayer, Blügel and Ramseyer, 2006a,b; Komelj, Steiauf and Fähnle, 2006) and W(110) (Spišák and Hafner, 2004) substrates, Rh (Bazhanov *et al*., 2000) and other 4d metals (Bellini, Papanikolau, Zeller and Dederichs, 2001) on Ag(100) substrate and on insulating substrates such as NaCl (Zabala, Puska and Nieminen, 1998; Auyela, Raebiger, Puska and Nieminen, 2002; Calzolari and Nardelli, 2005), where the hybridization is particularly small.

In this respect, the latest experiments by Hirjibehedin, Lutz and Heinrich (2006), where imaging and manipulation capabilities of the STM were used for studying the spin excitation spectra in linear chains of Mn atoms on CuN insulator, are worth mentioning as they bring the practical realization of spin-based computational schemes and atomic-scale storage devices, stemming from the fascinating abilities of low-dimensional magnetism, one step closer. It is important to notice that the future use of this atomic-scale magnetism in the context of spin-manipulation hinges directly on one quantity: the MCA. In the case of the linear chains, where each atom has only two nearest neighbors, the MCA appears to reach values unattainable in the physics of higher dimensions. The first tight-binding model calculations of the MCA were reported for bare Co and Fe chains (Dorantes-Dávila and Pastor, 1998) and a Co chain deposited on a Pd surface (Robles, Izquierdo and Vega, 2000). In the following subsections, we discuss the *ab initio* values of the MCA and orbital magnetic moments for Co chains deposited on Pt and report on freestanding chains of 4d and 5d transition metals.

4.1 Co on stepped Pt(111)

In the last years, the controlled growth of stripes and wires on step edges (Dallmeyer *et al*., 2000) and semiconductor surfaces (Segovia, Purdie, Hengsberger and Baer, 1999) allowed the investigation of 1D structures. Experimentally, ferromagnetism was reported in Co chains deposited on Pt(997) step-edges: Gambardella *et al*. (2002) found an orbital moment for Co chains on Pt(997) of 0.68 μ_B, the easy axis being tilted by 43° to the surface normal with an MCA of about 2 meV/atom at 45 K. Depositing more than one strand of Co on this surface leads to an oscillation of the easy axis in the plane perpendicular to the wire direction (Gambardella *et al*., 2004) (see also Chapter **Magnetism of Low-dimensional Metallic Structures, Volume 1**

Let us first discuss the magnetic properties of a single, infinite, unsupported FM Co chain following Weinert and Freeman (1983). The local magnetic moment amounts to 2.33 μ_B. The shape anisotropy of a chain has already been discussed in Section 2.6. For an understanding of the orbital magnetism and the spin-orbit coupling in this system we start from a Co dimer. The schematic energy-level diagram is shown in Figure 24. For simplicity we only consider the minority 3d levels and their hybridization: Assuming that the dimer axis is in the z direction, we expect that the d_{z^2} orbitals will form σ bonds, the d_{zx} and d_{yz} orbitals will combine to form π bonds, while the d_{xy} and $d_{x^2-y^2}$ orbitals will be mainly nonbonding (since they are directed perpendicular to the dimer axis). But since these nonbonding states are only singly occupied, now more 'atomic-like' linear combinations

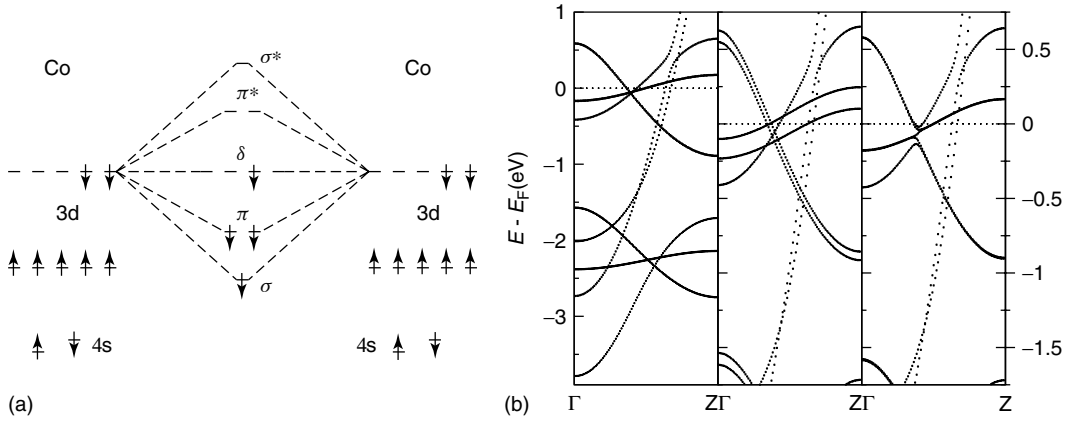

Figure 24. (a) Schematic energy-level diagram of a Co dimer. Only the hybridization between the minority 3d levels is indicated. (b) LSDA band structure of an unsupported Co monowire without (left panel) and with spin-orbit coupling included with the spin-quantization axis parallel (middle panel) or perpendicular (right panel) to the chain direction. Note the different energy scales for the band structure calculation without spin-orbit coupling (left panel), which shows the separation between majority and minority bands, and the middle and right panels, where mainly the spin-orbit splitting of the minority bands can be seen.

can be formed. Remember, that the d_{xy} and $d_{x^2-y^2}$ orbitals are linear combinations of the atomic $m = +2$ and $m = -2$ levels. This means, that a $m = 2$ orbital can be formed, and, if occupied, an orbital moment of 2 can be obtained.

If we look now at the spin-split band structure of such an infinite Co monowire (Figure 24b), we can more or less identify the bands corresponding to the Co dimer levels: Bands with strong positive dispersion correspond to σ bonds, those with negative dispersion to π bonds. But most prominent at the Fermi level is the very flat minority band with small positive dispersion; this is the equivalent of the nonbonding minority δ states. Notice that without spin-orbit coupling (left band structure) this band is doubly degenerate: there are no contributions in the LSDA functional that lead to an OP. But with spin-orbit coupling included, these bands can be seen to split: if the spin-quantization axis is parallel to the wire direction (middle band structure), one of the bands gets preferentially occupied. This is the band that – if fully occupied – leads to an orbital moment of $m_l = +2\,\mu_B$. Actually a smaller orbital moment of $0.9\,\mu_B$ is obtained. When the spin-quantization axis is perpendicular to the chain direction, other bands are mixing and the orbital moment is even smaller. As we know from our previous discussion, the anisotropy in the orbital moment is approximately proportional to the magnetocrystalline anisotropy and, therefore, the easy axis is parallel to the wire direction.

According to experimental findings, a Co chain on Pt(111) has an easy axis perpendicular to the chain direction. This seems to have its origin in the interactions with the Pt substrate. Apart from its two nearest Co neighbors and the reduction of the magnetic moment to about $2.1\,\mu_B$ per Co atom, a Co atom in a chain deposited on a (997) surface actually has five nearest Pt neighbors. Recent calculations (Shick, Maca and Oppeneer, 2004; Újfalussy *et al.*, 2004; Baud, Ramseyer, Bihlmayer and Blügel, 2006b) indeed confirm an easy axis that has a large component perpendicular to the surface. A detailed analysis shows that the Co atoms magnetically polarize the Pt atoms. Consequently, they produce large orbital moments because of their large spin-orbit interaction, which can then dominate the total magnetization direction. The strength of the Pt polarization, and as such the magnetization direction, depends sensitively on the structural relaxation of the Co chain (Baud, Ramseyer, Bihlmayer and Blügel, 2006b). For a Co monowire on a stepped Pt surface a rather large MCA of almost 2.5 meV and an easy axis that is tilted by $\theta = 51^\circ$ were determined with respect to the surface normal in the direction of the upper terrace. Both, the experimentally observed MCA and the orbital moment are smaller than the LSDA results for an unsupported chain, but the orbital moment of a supported wire is severely underestimated in LSDA (and GGA) calculations. In the literature several methods to overcome this deficiency have been discussed (Solovyev, Liechtenstein and Terakura, 1988; Solovyev, 2005). A systematic comparison of LSDA results with and without OP for unsupported and Pt-supported Fe and Co magnets in various dimensions can be found in the papers of Komelj, Ederer, Davenport and Fähnle (2002) and Ederer, Komelj and Fähnle (2003).

The first-principles study (Baud, Bihlmayer, Blügel and Ramseyer, 2006a) of Co chains of different widths, $n = 1, \ldots, 6$ strands, at the stepped Pt surface results, in accordance with experimental observations, in oscillations of the easy axis as a function of chain width around the terrace

normal, and the MCA shows a nonmonotonic behavior. For example, in sharp contrast to the result of the deposited Co monowire the Co double-wire shows a much smaller magnetic anisotropy (0.15 meV) and an easy axis with an angle $\theta = -19^\circ$, that is, pointing away from the upper terrace. This drop of MCA is also accompanied by a decrease of orbital moment anisotropy, that is, the average orbital moment of the double chain is almost constant as a function of the angle θ. The n chains with $n = 3 - 5$ show again larger magnetic anisotropies and the direction of the easy axis varies from -15° for the three-wire to -40° and $+14^\circ$ for the four- and five-wires. As we increase the number of strands beyond three, the MCA decreases again, from 0.99 meV for the three-wire to 0.82 meV and 0.50 meV/Co atom for the four- and five-wires, respectively. We attribute these findings to the individual contributions of the Co chains to the MCA and the total orbital moment. Depending on the position of the Co atom in the chain (at the step edge, in the terrace, in the innermost strand), these contributions can be very different due to the different number of Co and Pt neighbors, even of different sign, and can cancel each other, resulting in this complex behavior of the magnetic properties.

4.2 4d and 5d transition-metal monowires

A large number of metals that are nonmagnetic in the bulk can become magnetic in an 1D arrangement. Since the spin-orbit constant ξ (see equation (32)) increases approximately proportional to the square of the nuclear number, the magnetic anisotropy of unsupported, isolated 4d and 5d transition-metal chains has been investigated in detail. The results (Mokrousov, Bihlmayer, Heinze and Blügel, 2006) are summarized in Figure 25. FM ground states are found for Zr, Ru, Rh, and Pd, and AFM ones for Mo and Tc. Y and Nb wires, being borderline cases, are nonmagnetic. This is in agreement with the results of Spišák and Hafner (2003).

As seen in Figure 24 including the spin-orbit interaction results in a removal of band degeneracies and orbital moments arise (see Figure 25b). For the early 4d metals, left part of the 4d row, the values of m_l are rather small since most occupied bands are involved in chemical bonding. At the same time, Tc, Ru, and Rh monowires exhibit values of 0.2–0.4 μ_B. This is in the range of 0.2–0.3 μ_B obtained for an Fe monowire (Mokrousov, Bihlmayer and Blügel, 2005). For the latter chains we observed a strong dependence of the orbital moment on the magnetization direction. Typically, the axial magnetization leads to values $m_l(\vec{z})$, that are significantly larger than those for the radial magnetization, $m_l(\vec{r})$.

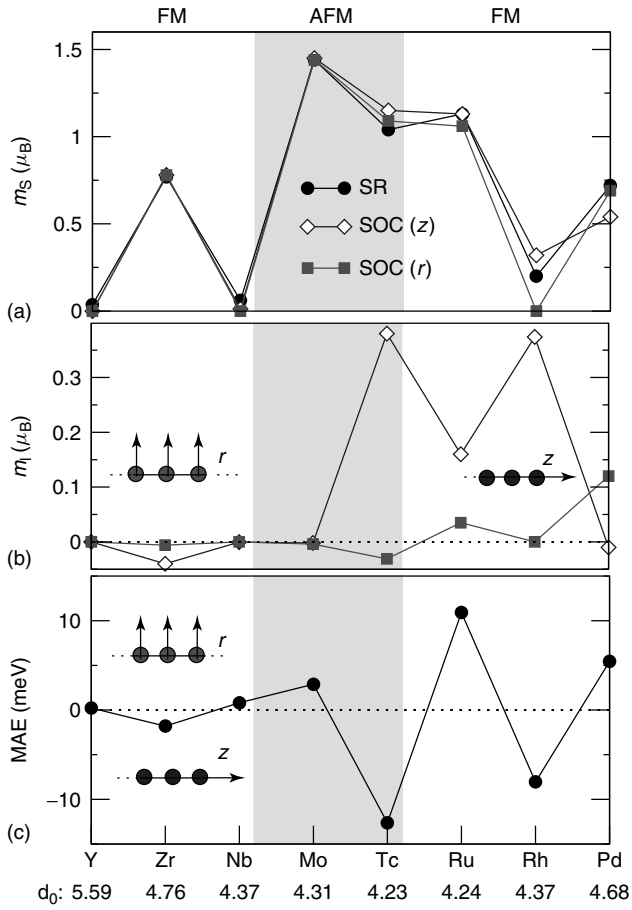

Figure 25. Magnetism in 4d transition-metal monowires at the equilibrium interatomic distance d_0 (Mokrousov, Bihlmayer, Heinze and Blügel, 2006): (a) total (for elements with FM ground state) and muffin-tin (for AFM ground states) magnetic moment without and with spin-orbit interaction (for both magnetization directions), (b) orbital magnetic moments for both magnetization directions, (c) magnetocrystalline anisotropy energy. SR stands for the scalar-relativistic approximation, that is, calculations without spin-orbit interaction. The equilibrium (SR) interatomic distances d_0 are given in atomic units. (Reproduced from Mokrousov *et al*., 2006, with permission from the American Physical Society. © 2006.)

The MCA (Figure 25c) as a function of the nuclear number or of the band filling, respectively, follows roughly the same trend as the orbital moment $m_l(\vec{z})$. The argument that the energy induced by spin-orbit interaction can be assumed to be proportional to the projection of the spin on the orbital momentum $-\vec{S}\cdot\vec{L}$, leading to an easy magnetization axis in the direction of maximum orbital moment, is hardly anymore applicable for heavier 4d transition-metal chains. Here, the spin-orbit interaction becomes stronger and the exchange splitting smaller than in 3d metals. Nevertheless, we observe that in the case when $m_l(\vec{z}) \gg m_l(\vec{r})$ the easy magnetization axis always points along the chain. On the other hand, whenever the difference $|m_l(\vec{z}) - m_l(\vec{r})|$ approaches 0.1 μ_B,

no predictions on the preferred magnetization direction can be made *a priori*. The calculated values of the MCA at the equilibrium interatomic distance d_0 are in the range of 6-12 meV/atom and thus much larger than those for the 3d transition-metal monowires.

Bare infinite monowires do not exist in nature. They are either deposited on a surface or created in a break junction or may be filled in a tubular structure. In either case, monatomic metallic chains would have an interatomic distance, d, different from the calculated equilibrium values for freestanding wires. In the work of Spišák and Hafner (2003) and Mokrousov, Bihlmayer, Heinze and Blügel (2006) it was found that Ru, Rh, and Pd monowires exhibit an FM ground state over a large range of interatomic distances. For Ru and Rh, already for $d > 5$ au, the spin moments saturate at their atomic-like values. The orbital moments gradually rise with d. For $d > 6.3$ au giant values of 1.5 μ_B for $m_l(\vec{z})$ and 0.7 μ_B for $m_l(\vec{r})$ for both monowires are reached. An increase of d leads to a narrowing of the δ-state- and π-state-derived bands in Figure 24, and, eventually, bands with different angular momentum, m_l, become almost fully occupied or fully unoccupied, giving rise to a large value of the orbital moment. In case of Pd, for large distances, the s electron is transferred into the d shell and closes the d shell with 10 electrons, and spin and orbital moments disappear (Delin, Tosatti and Weht, 2004). The combination of high values for spin and orbital moments with the large difference between $m_l(\vec{r})$ and $m_l(\vec{z})$ results in giant values of the MCA (Bruno, 1989). For example, already at $d = 5.5$ au, the MCA of the Rh chain reaches -40 meV/atom and gets as large as -60 meV/atom for $d = 6.3$ au.

As compared to 4d chains, the magnetism of 5d transition-metal monowires is characterized by an even larger spin-orbit strength but generally smaller or even suppressed magnetic moments (Delin and Tosatti, 2003) due to the larger overlap of the 5d wave functions. For example, among the late 5d metals at their respective equilibrium lattice constants we found the largest MCA value for an Os monowire reaching only 2 meV/atom and a spin moment $m_s(\vec{z})$ of 0.36 μ_B. At a strained interatomic distance of 6.3 au, where the values of the spin moments of FM Os, Ir, and Pt chains are already well saturated to 3.53 μ_B, 2.39 μ_B, and 1.13 μ_B, respectively, the respective MCA values of 115, -60, and 44 meV/atom are – at least for Os – colossal in size and can exceed the record value of the Rh chain.

5 ATOMIC-SCALE STRUCTURES

5.1 Adatoms

Single transition-metal adatoms adsorbed on (100) substrates of Cu, Ag, Au (Lang *et al*., 1994; Nonas *et al*., 2001), Pd, and Pt (Stepanyuk *et al*., 1996) have been investigated by first-principles calculations. When the 3d overlayer and adatom moments on Ag(100) are compared as shown in Figure 26, a surprising similarity in the general trend and the magnitude of the magnetic moments is found. Obviously the local moments of monolayers follow Hund's first rule of the adatoms. In other words, if we decompose the DOS according to equation (17) in terms of the local (χ_{00}) and the interatomic nonlocal susceptibilities ($\chi_{0i}, i > 1$), then for the adatoms the nonlocal susceptibilities are basically zero, by definition, but also for the monolayers χ_{00} dominates over χ_{0i}. Fe, Co, and Ni monolayers and adatoms have in each case about the same maximally possible magnetic moments. This will not change for other atomic-scale structures such as chains. For example recent calculations of one-atomic Fe, Co, Ni wires along the ⟨111⟩-type step edge of the Pt(111) surface discussed in Section 4.1 exhibit local moments of 3.18 μ_B, 2.12 μ_B, and

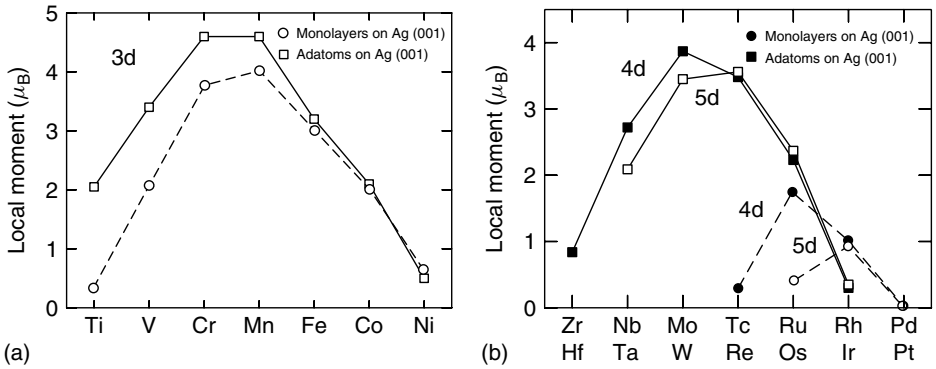

Figure 26. Local magnetic moments calculated for 3d (Nonas *et al*., 2001) (a), 4d (b, solid symbols), and 5d (b, empty symbols) transition-metal adatoms at the hollow-site of Ag(100) (squares connected by full lines) (Lang *et al*., 1994) and monolayers as overlayers on Ag(100) (Blügel, 1992b) (circles connected by dashed lines).

0.83 μ_B, respectively. From Mn to Ti, monolayer and adatom moments deviate systematically because of the increasing extent of 3d wave function and the respective increase of the d–d hybridization in the monolayer.

For the 4d and 5d transition-metal adatoms the comparison to the monolayers on Ag(100) looks radically different. While the adatoms still follow Hund's first rule with maximal moments at the center of each series, the magnetism of monolayers is obviously largely determined by the nonlocal susceptibilities χ_{0i}, which add an essential contribution to χ_{00} necessary to fulfill the Stoner criterion, equation (12). This is a consequence of the large extent of the 4d and 5d wave functions. Since χ_{0i} depends on all details of the local environment, each atomic-scale structure of 4d and 5d metals will have a different collection of magnetic moments. This observation motivated the work on atomic-scale clusters.

5.2 Clusters

Small atomic clusters on surfaces constitute very interesting subjects, as their electronic structure and subsequently their magnetic properties depend, in addition to other factors mentioned in the preceding text, on the individual cluster shape and size. In order to explore the consequences of this statement we explore the spin moment of Fe on a Ni(100) surface (Mavropoulos, Lounis, Zeller and Blügel, 2006). The clusters considered are shown schematically in Figure 27(a), viewed from the top (all atoms lie on the surface). The view is adapted to the surface geometry, meaning that it is rotated by 45° with respect to the in-plane fcc cubic axes of the underlying substrate lattice. The smallest cluster is a single Fe adatom, while the largest consists of nine Fe atoms. On each atom, the calculated spin moment is written, and the average (per atom) moment of each cluster is also given. The Fe moment is always ferromagnetically coupled to the Ni substrate moment. Already, at a first glance it is obvious that the average moment of the clusters depends on the cluster size. The single adatom has manifestly the highest moment (3.24 μ_B), while the nine-atom cluster shows a lower average moment of 2.85 μ_B.

From what has been said in Section 2.5 this behavior is expected on the grounds of hybridization of the atomic d levels with the neighbors. Atoms in larger clusters have, on the average, higher coordination, thus their d wave functions are more hybridized; this leads to lesser localization and lesser tendency to magnetism.

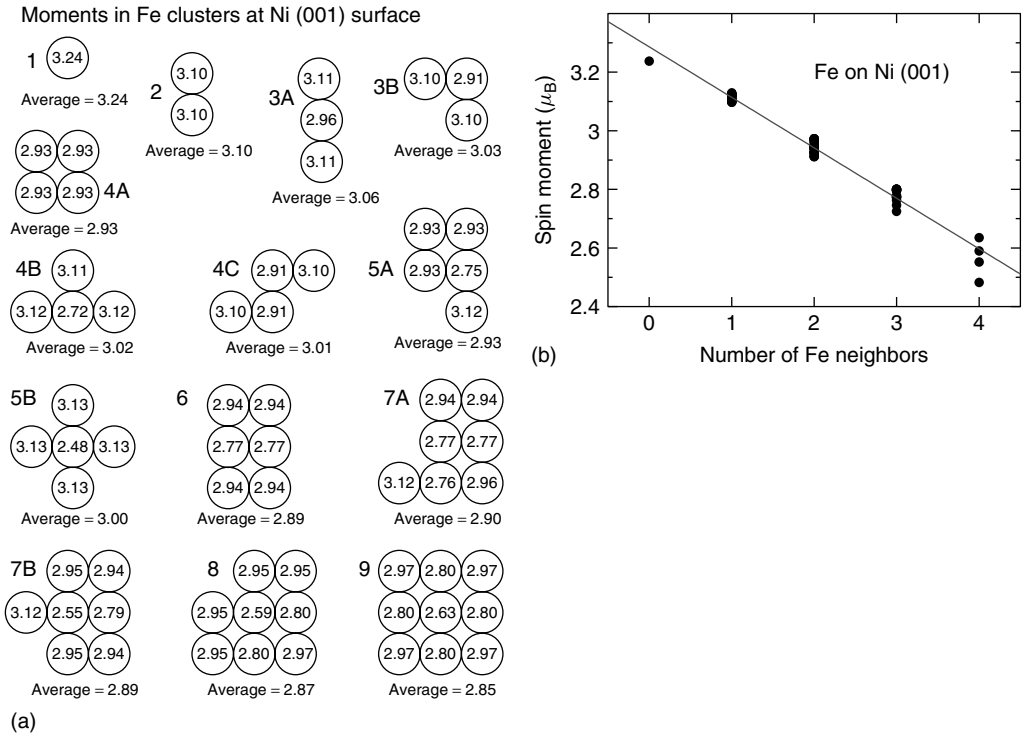

Figure 27. (a) Spin moment (in μ_B) of atoms of Fe clusters at Ni(001) surface, and average (per atom) moment of the clusters (the view is surface adapted, that is, rotated by 45° with respect to the in-plane fcc cubic axes; the clusters are viewed from the top, that is, all atoms lie on the surface). (b) Linear trend for the atomic Fe spin moment as function of the coordination to Fe neighbors. (Reproduced from P. Mavropoulos, S. Lounis, R. Zeller and S. Blugel: Fe clusters on Ni and Cu: size and shape dependence of the spin moment, *Appl. Phys. A* **82**, 2006, 103–107, with permission from Springer Science and Business Media.)

To pursue this idea further, we tried to correlate the local atomic spin moment to the coordination N_c of each atom in the cluster, irrespective of the form or size of the cluster. For instance, let us focus on all Fe atoms which have only one first Fe neighbor, that is, $N_c = 1$ (the coordination to the substrate is the same, $N_s = 4$, for all Fe atoms). Such atoms appear in the clusters with size 2, 3, 4, 5, and 7; there are, in total, 10 such examples (having excluded cases which are trivially equivalent by symmetry). *All* of them have spin moments ranging in the small interval between 3.10 and 3.13 μ_B. Similarly, for the Fe atoms with two Fe neighbors the spin moment ranges from 2.91 to 2.97 μ_B. Collecting all possible cases, from $N_c = 0$ (single adatom) to $N_c = 4$, we present the results in Figure 27(b). One finds an almost linear dependence of the spin moment on the coordination number, $M = -aN_c + b$, with $a = 0.17\,\mu_B$ and $b = 3.29\,\mu_B$. In accordance with the analysis of the 3d transition-metal films, Fe has a strong intra-atomic exchange field, arising from rather localized 3d wave functions resulting in strong intra-atomic susceptibility. Such a linear relation was also found for Fe clusters (Mavropoulos, Lounis, Zeller and Blügel, 2006) on Ni(111), Cu(100), and Cu(111) and for Co clusters on Ni(100). The local magnetic moments of Ni atoms in clusters on Cu surfaces cannot be described by such a simple linear relationship, because the hybridization of the Ni d states with substrate sp electrons enters as an additional important factor (see Figure 5).

In many cases for homo-atomic and mass-selected FM clusters, it is very difficult to address experimentally the magnetic properties of each individual cluster or even each atom in a cluster. Often just the average magnetic moment of clusters of particular sizes or the average local magnetic moment per atom averaged over an ensemble of clusters of the same size but different shapes can be determined. Using this scaling behavior it is possible to estimate the magnetic moments of clusters if the shape is known.

In light of what has been said in Section 5.1 for the 4d and 5d adatoms on surfaces, this rule will not apply to the general case of arbitrary atoms. For example, the magnetism of small 4d and 5d clusters on Ag(100) shows highly nonlocal susceptibilities, resulting even in an increase of the spin moment with coordination. This is connected to the larger extent of the 4d states compared to the 3d of Fe. The magnetic properties of several linear chains (C) and plane islands (I) of 4d (Wildberger *et al*., 1995) and 5d atoms have been calculated in structures as shown in Figure 28. In particular, linear chains of two (dimers, C2), three, and four adatoms (C3 and C4) have been considered, oriented in the [110] direction, in addition to three compact islands with four, five, and nine adatoms (I4, I5, and I9).

Figure 29 shows the calculated moments per adatom for these nanostructures. Since several nonequivalent atoms exist for the clusters C3, C4, I5, and I9, only the average moment is given. For the linear chains quite large moments are obtained, but the behavior with size is nonregular. While the C2 and C4 moments are very similar, the C3 moments of Mo and Tc are much smaller. In this context it is interesting to compare the moments of the inner and outer chain atoms.

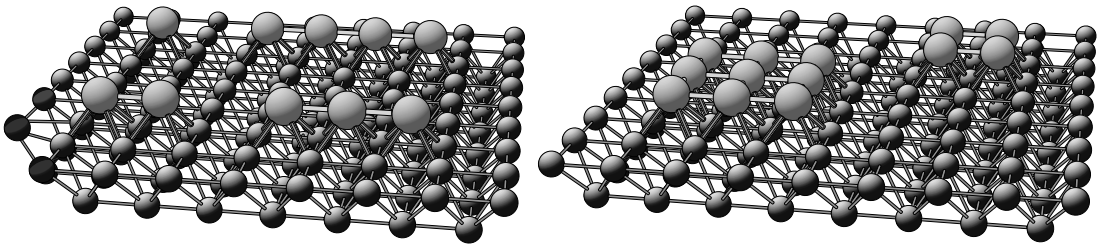

Figure 28. Magnetic clusters of a particular transition metal deposited on an (100)-oriented Ag substrate.

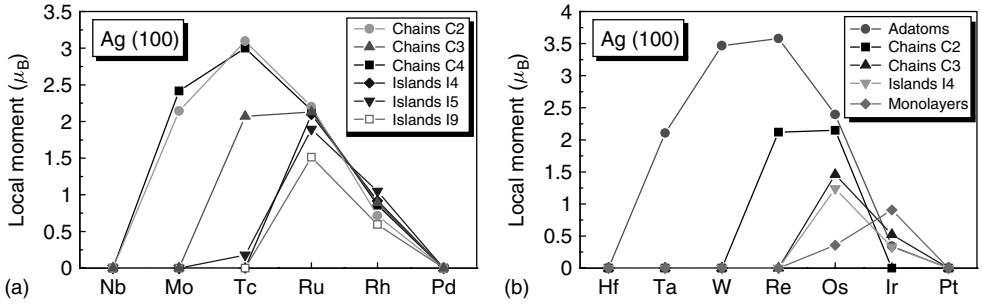

Figure 29. Average magnetic moment per adatom for ferromagnetic 4d (Wildberger *et al*., 1995) (a) and 5d (b) clusters. (Reproduced from Wildberger *et al*., 1995, with permission from the American Physical Society. © 1995)

For Mo and Tc the outer atoms of C3 and C4 have larger moments than the inner ones. In the C4 chain, for instance, the two inner Mo atoms have moments of $1.85\,\mu_B$, while the outer atoms carry moments of $3.00\,\mu_B$. Moving to Ru and Rh the situation changes. In the Ru chains both types of atoms have about the same moments, whereas in the case of Rh the inner atoms carry larger moments. In the Rh C4 chain the inner atoms have moments of $0.96\,\mu_B$ but the outer ones only $0.76\,\mu_B$. This is because the higher coordination of the inner atoms tends to enhance the moments for Rh while Ru is an intermediate case being insensitive to environmental changes. The large moments obtained for all three chain structures indicate that infinite chains of these atoms should also show appreciable moments.

For the considered linear structures also AFM solutions (not shown in Figure 29) have been obtained, which are the most stable configurations for elements in the middle of the transition-metal series. The local moments can be quite large. For instance, for the Mo chains C2, C3, and C4 the local atomic moments are larger than $3\,\mu_B$.

For the compact islands (I4, I5, and I9) the hybridization effects within the cluster are even larger. Similar to the magnetic monolayers (Blügel, 1992a; Eriksson, Albers and Boring, 1991a; Wu and Freeman, 1992a) discussed in Section 3.1.1 appreciable moments are found only for the Ru and Rh nanostructures, whereas zero or very small moments are found for Mo and Tc. This is a consequence of the large spatial extent of 4d wave functions being more important for the compact islands than for the chain structures. Within the Ru structures I5 and I9 we observe that the outer atoms carry a larger moment than the inner ones, the same effect as the one found earlier for the linear structure of Mo and Tc. For Rh the situation is more complicated. For the I5 island the inner moment ($1.00\,\mu_B$) is larger than the outer one ($0.66\,\mu_B$), in agreement with the preceding rule, while the central atom in the I9 cluster has a very small moment of $0.16\,\mu_B$, and the outer atoms have moments of $0.62\,\mu_B$ and $0.64\,\mu_B$. Thus, by comparing the islands with the chain structures, not only is the peak of the moment curve shifted to even larger valences, that is, from Tc to Ru, but the transition from surface enhancement of the moments to surface suppression is also shifted: for the chains this turnover occurs at Ru, but for the more compact islands it occurs at about Rh. The very small moment obtained for the central atom of I9 seems to be in conflict with the results of monolayers for a Rh overlayer on Ag(100) which should have a moment of about $1\,\mu_B$. Calculations for larger Rh islands lead for the inner Rh atoms to considerably larger moments ($0.66\,\mu_B$). Thus, we conclude from these calculations, as well as from the strong difference obtained for the different linear chains C2, C3, and C4, that the moments of the 4d clusters show an unusual and oscillatory dependence on the cluster size.

Preparing clusters with constituent atoms that are subject to an AFM exchange interaction can lead to complex noncollinear magnetism inside the cluster in order to avoid magnetic frustrations due to competing interactions caused by cluster shape and substrate interactions. Obvious examples are Cr and Mn clusters with triangular shapes or those deposited on FM substrates. The actual magnetic structure depends, besides on the cluster shape, on the relative strength of the intracluster exchange interaction of the Cr and Mn atoms versus the cluster–substrate interaction, which can be AFM for Cr and FM for Mn, depending on the substrate. Recent first-principles calculations on Cr and Mn dimers on Ni(100) (Lounis, Mavropoulos, Dederichs and Blügel, 2005) verify the presence of a noncollinear ground state for nearest-neighbor Mn dimers. We see in Figure 30(a) the antiferromagnetically aligned Mn moments are symmetrically tilted under the presence of the FM exchange interaction of the Ni substrate by $\approx \pm 72.6^\circ$ with respect to the direction of the underlying substrate moments. Also the nearest-neighbor Ni moments are tilted by 7.4°. The magnetic ground state of larger Mn compact clusters on Ni(100) remains collinear while Mn chains have a noncollinear ground state similar to the magnetic configuration of the Mn dimer. Cr and Mn clusters on Fe and Co substrates are subject to much larger cluster–substrate interactions and one expects noncollinear magnetism in Cr and Mn clusters of larger size. For example, a Mn trimer on fcc Fe, shown in Figure 30(b) is nearly collinear within the Mn cluster, but is not collinear with respect to the magnetic moments of the underlying Fe substrate. The two outer Mn moments are rotated by 170° and have a value of $3.61\,\mu_B$. The central moment is rotated by 20° and has a value of $3.14\,\mu_B$. This leads to an uncompensated total magnetic moment in the Mn cluster of $-4.16\,\mu_B$ in the direction parallel to the Fe moments, but with opposite sign, and a moment of $0.18\,\mu_B$ normal to the Fe moments. Figure 30(c) shows the ground-state configuration for the Mn tetramer. All neighboring Mn moments are antiferromagnetically aligned and share one plane, which is roughly perpendicular to the substrate magnetization. For clusters on Fe substrates we found that fairly reliable ground-state structures can be obtained from a nearest-neighbor Heisenberg model

Figure 30. Side view of the magnetic ground-state configuration of a Mn dimer on Ni(100) (Lounis, Mavropoulos, Dederichs and Blügel, 2005) (a), of a Mn trimer (b), and tetramer (c) on fcc Fe(100). In (b), moments of two Mn atoms are pointing down (the second one cannot be seen) and one moment is pointing up.

(equation (2)) with exchange parameters obtained from *ab initio* results, where the nearest-neighbor exchange constants for the atoms in the cluster and the interaction between the atoms in the cluster and the substrate enter. This works much less reliably for the Ni substate, as the size of the Ni moment changes dramatically with respect to the relative orientation between the Ni moment and the moments in the cluster.

ACKNOWLEDGMENTS

The authors gratefully acknowledge the valuable discussions and collaborations with Drs P.H. Dederichs, P. Ferriani, M. Heide, S. Heinze, Ph. Kurz, M. Ležaić, S. Lounis, Ph. Mavropoulos, Y. Mokrousov, I. Turek, and X. Nie that made this contribution possible.

REFERENCES

Albrecht, M., Pohl, J., Wider, H., *et al*. (1998). V and Cr on Ru surfaces. *Surface Science*, **397**, 354–360.

Andrieu, S., Fischer, H.M., Piecuch, M., *et al*. (1996). Structure of Mn films grown on (111) and (001) fcc Ir determined by EXAFS and the multiple-scattering approach. *Physical Review B*, **54**, 2822–2829.

Arrott, A.S., Heinrich, B., Purcell, S.T., *et al*. (1987). Engineering magnetic materials on the atomic scale. *Journal of Applied Physics*, **61**, 3721–3728.

Asada, T., Bihlmayer, G., Handschuh, S., *et al*. (1999). First-principles theory of ultrathin magnetic films. *Journal of Physics: Condensed Matter*, **11**, 9347–9363.

Asada, T. and Blügel, S. (1997a). First-principles calculation of Cu(100)c(2×2)Cu3*d* surface alloy formation energy: improvement by generalized gradient approximation. *Physica B*, **237**(238), 359–360.

Asada, T. and Blügel, S. (1997b). Total energy spectra of complete sets of magnetic states for fcc-Fe films on Cu(100). *Physical Review Letters*, **79**, 507–510.

Asada, T., Blügel, S., Bihlmayer, G., *et al*. (2000). First-principles investigation of the stability of 3d monolayer/Fe(001) against bilayer formation. *Journal of Applied Physics*, **87**, 5935–5937.

Auyela, A., Raebiger, H., Puska, M.J. and Nieminen, R.M. (2002). Spontaneous magnetization of aluminum nanowires deposited on the NaCl(100) surface. *Physical Review B*, **66**, 035417-1–035417-8.

Baberschke, K. (1996). The magnetism of nickel monolayers. *Applied Physics A*, **62**, 417–427.

von Barth, U. and Hedin, L. (1972). A local exchange-correlation potential for the spin polarized case. *Journal of Physics C*, **5**, 1629–1642.

Baud, S., Bihlmayer, G., Blügel, S. and Ramseyer, C. (2006a). First-principles investigation of Co wires at Pt(111) step-edges. *Surface Science*, **600**, 4301–4304.

Baud, S., Ramseyer, C., Bihlmayer, G. and Blügel, S. (2006b). Relaxation effects on the magnetism of decorated step edges: Co/Pt(664). *Physical Review B*, **73**, 104427-1–104427-7.

Bazhanov, D.I., Hergert, W., Stepanyuk, V.S., *et al*. (2000). One-dimensional magnetism of Rh chains on the Ag(001) surface. *Physical Review B*, **62**, 6415–6420.

Bellini, V., Papanikolau, N., Zeller, R. and Dederichs, P.H. (2001). Magnetic 4*d* monoatomic rows on Ag vicinal surfaces. *Physical Review B*, **64**, 094403-1–094403-8.

von Bergmann, K., Heinze, S., Bode, M., *et al*. (2006). Observation of a complex nanoscale magnetic structure in a hexagonal Fe monolayer. *Physical Review Letters*, **96**, 167203-1–167203-4.

Blügel, S. (1992a). Ferromagnetism of 4d-metal monolayers on Ag and Au and Pd(001) surfaces. *Europhysics Letters*, **18**, 257–262.

Blügel, S. (1992b). Two-dimensional ferromagnetism of 3d and 4d and 5d transition metal monolayers on noble metal (001) substrates. *Physical Review Letters*, **68**, 851–854.

Blügel, S. (1996). Magnetically stabilized surface alloys. *Applied Physics A*, **63**, 595–504.

Blügel, S. (1988). Strong ferromagnetism of 3d-metal overlayers on Pd(001). *Europhysics Letters*, **7**, 743–748.

Blügel, S. and Dederichs, P.H. (1989). Ferromagnetism and antiferromagnetism of 3d metal overlayers on noble-metal substrates. *Europhysics Letters*, **9**, 597–602.

Blügel, S., Drittler, D., Zeller, R. and Dederichs, P.H. (1989). Magnetic properties of 3d transition metal monolayers on metal substrates. *Applied Physics A*, **49**, 547–562.

Blügel, S., Weinert, M. and Dederichs, P.H. (1988). Ferromagnetism and antiferromagnetism of 3d-metal overlayers on metals. *Physical Review Letters*, **60**, 1077–1080.

Bode, M., Heinze, S., Kubetzka, A., *et al*. (2002). Structural, electronic, and magnetic properties of a Mn monolayer on W(110). *Physical Review B*, **66**, 014425-1–014425-16.

Bode, M., Pietzsch, O., Kubetzka, A. and Wiesendanger, R. (2004). Shape-dependent thermal switching behavior of superparamagnetic nanoislands. *Physical Review Letters*, **92**, 067201-1–067201-4.

den Broeder, F.J.A., Kuiper, D., Donkersloot, H.C. and Hoving, W. (1989). A comparison of the magnetic anisotropy of [001] and [111] oriented Co/Pd multilayers. *Applied Physics A*, **49**, 507–512.

Brooks, M.S.S. (1985). Calculated ground state properties of light actinide metals and their compounds. *Physica B*, **130**, 6–12.

Bruno, P. (1988). Dipolar magnetic surface anisotropy in ferromagnetic thin films with interfacial roughness. *Journal of Applied Physics*, **64**, 3153–3156.

Bruno, P. (1989). Tight-binding approach to the orbital magnetic moment and magnetocrystalline anisotropy of transition-metal monolayers. *Physical Review B*, **39**, 865–868.

Bychkov, Y.A. and Rashba, E.I. (1984). Oscillatory effects and the magnetic susceptibility of carriers in inversion layers. *Journal of Physics C-Solid State Physics*, **17**, 6039–6045.

Calzolari, A. and Nardelli, M.B. (2005). First principles theory of artificial metal chains on NiAl(110) surface. *Physical Review B*, **72**, 045416-1–045416-8.

Dallmeyer, A., Carbone, C., Eberhardt, W., *et al*. (2000). Electronic states and magnetism of monatomic Co and Cu wires. *Physical Review B*, **61**, R5133–R5136.

Davies, A., Stroscio, J.A., Pierce, D.T. and Celotta, R. (1996). Atomic-scale observations of alloying at the Cr-Fe(001) interface. *Physical Review Letters*, **76**, 4175–4178.

Delin, A. and Tosatti, E. (2003). Magnetic phenomena in 5*d* transition metal monowires. *Physical Review B*, **68**, 144434-1–144434-8.

Delin, A., Tosatti, E. and Weht, R. (2004). Magnetism in atomic-size palladium contacts and nanowires. *Physical Review Letters*, **92**, 057201-1–057201-4.

Donath, M. (1994). Spin-dependent electronic structure at magnetic surfaces: the low-Miller-index surfaces of nickel. *Surface Science Reports*, **20**, 251–316.

Dorantes-Dávila, J. and Pastor, G.M. (1998). Magnetic anisotropy of one-dimensional nanostructures of transition metals. *Physical Review Letters*, **81**, 208–211.

Draaisma, H.J.G. and de Jonge, W.J.M. (1988). Surface and volume anisotropy from dipole-dipole interactions in ultrathin ferromagnetic films. *Journal of Applied Physics*, **64**, 3610–3613.

Dzyaloshinsky, I. (1958). A thermodynamic theory of "weak" ferromagnetism of antiferromagnetics. *Journal of Physics and Chemistry of Solids*, **4**, 241–255.

Ederer, C., Komelj, M. and Fähnle, M. (2003). Magnetism in systems with various dimensionalities: a comparison between Fe and Co. *Physical Review B*, **68**, 052402-1–052402-4.

Elmers, H.J., Hauschild, J. and Gradmann, U. (1999). Onset of perpendicular magnetization in nanostripe arrays of Fe on stepped W(110) surfaces. *Physical Review B*, **59**, 3688–3695.

Elmers, H.J., Hauschild, J., Höche, H., *et al*. (1994). Submonolayer magnetism of Fe(110) on W(110): finite width scaling of stripes and percolation between islands. *Physical Review Letters*, **73**, 898–901.

Elmouhssine, O., Moraïtis, G., Demangeat, C. and Parlebas, J. (1997). p(2×2) versus c(2×2) configurations for one Mn monolayer on Fe(001). *Physical Review B*, **55**, R7410–R7413.

Erickson, R.P. and Mills, D.L. (1991). Anisotropy–driven long–range order in ultrathin ferromagnetic films. *Physical Review B*, **43**, 11527–11530.

Eriksson, O., Albers, R.C. and Boring, A.M. (1991a). Prediction of ferromagnetism and metamagnetism in 4d transition-metal overlayers on the (001) surface of Ag (4d = Tc, Ru, Rh, and Pd). *Physical Review Letters*, **66**, 1350–1353.

Eriksson, O., Brooks, M.S.S. and Johansson, B. (1991b). Orbital polarization in narrow-band systems: application to volume collapses in light lanthanides. *Physical Review B*, **41**, 7311–7314.

Ewald, P.P. (1921). Die Berechnung optischer und elektrostatischer Gitterpotentiale. *Annalen der Physik*, **64**, 253–287.

Ferriani, P., Heinze, S., Bihlmayer, G. and Blügel, S. (2005). Unexpected trend of magnetic order of 3*d* transition-metal monolayers on W(001). *Physical Review B*, **72**, 024452-1–024452-4.

Flores, T., Hansen, M. and Wuttig, M. (1992). Structure and growth of Mn on Cu(100). *Surface Science*, **279**, 251–264.

Freeman, A.J. and Fu, C.L. (1987). Strongly enhanced 2D magnetism at surfaces and interfaces. *Journal of Applied Physics*, **61**, 3356–3361.

Galanakis, I., Alouani, M. and Dreyseé, H. (2000). Interface magnetism in ultrathin Fe/W(110) films from first principles. *Physical Review B*, **62**, 3923–3928.

Gambardella, P., Dallmeyer, A., Maiti, K., *et al*. (2002). Ferromagnetism in one-dimensional monatomic metal chains. *Nature*, **416**, 301–304.

Gambardella, P., Dallmeyer, A., Maiti, K., *et al*. (2004). Oscillatory magnetic anisotropy in one-dimensional atomic wires. *Physical Review Letters*, **93**, 077203-1–077203-4.

Glauber, R.J. (1963). Time-dependent statistics of the Ising model. *Journal of Mathematical Physics*, **4**, 294–307.

Grigorov, I.L., Fitzsimmons, M.R., Siu, I-L. and Walker, J.C. (1999). Observation and analysis of multidomain epitaxy of α-Mn on MgO(111). *Physical Review Letters*, **82**, 5309–5312.

Grigorov, I.L. and Walker, J.C. (1997). Structural and magnetic properties of Mn epitaxially grown on Cu(111) (abstract). *Journal of Applied Physics*, **81**, 3907.

Grigorov, I.L., Walker, J.C., Hawley, M.E., *et al*. (1998). Structural and magnetic properties of "expanded" Mn. *Journal of Applied Physics*, **83**, 7010–7012.

Gunnarsson, O. (1976). Band model for magnetism of transition metals in the spin-density-functional formalism. *Journal of Physics F-Metal Physics*, **6**, 587–606.

Handschuh, S. and Blügel, S. (1998). Magnetic exchange coupling of 3d metal monolayers on Fe(001). *Solid State Communications*, **105**, 633–637.

Heinze, S., Bode, M., Kubetzka, A., *et al*. (2000). Real-space imaging of two-dimensional antiferromagnetism on the atomic scale. *Science*, **288**, 1805–1808.

Heinze, S., Kurz, P., Wortmann, D., *et al*. (2002). Complex magnetism in ultra-thin films: atomic-scale spin structures and resolution by the spin-polarized scanning tunneling microscope. *Applied Physics A*, **75**, 25–36.

Hillebrecht, F.U., Roth, C., Jungblut, R., *et al*. (1992). Antiferromagnetic coupling of a Cr overlayer to Fe(100). *Europhysics Letters*, **19**, 711–716.

Hirjibehedin, C.F., Lutz, C.P. and Heinrich, A.J. (2006). Spin coupling in engineering atomic structures. *Science*, **312**, 1021–1024.

Hjortstam, O., Trygg, J., Wills, J.M., *et al*. (1996). Calculated spin and orbital moments in the surfaces of the 3d metals Fe, Co, and Ni and their overlayers on Cu(001). *Physical Review B*, **53**, 9204–9213.

Hohenberg, P. and Kohn, W. (1964). Inhomogeneous electron gas. *Physical Review*, **136**, B864–B871.

Hong, S.C., Freeman, A.J. and Fu, C.L. (1988). Structural, electronic, and magnetic properties of clean and Ag-covered Fe monolayers on W(110). *Physical Review B*, **38**, 12156–12163.

Igel, T., Pfandzelter, R. and Winter, H. (1998). Proton-induced Auger electrons from ultrathin Mn films on Fe(100). *Surface Science*, **405**, 182–191.

Janak, J.F. (1977). Uniform susceptibilities of metallic elements. *Physical Review B*, **16**, 255–262.

Jungblut, R., Roth, C., Hillebrecht, F.U. and Kisker, E. (1991). Magnetic properties of Cr overlayers on Fe. *Journal of Applied Physics*, **70**, 5923–5928.

Komelj, M., Ederer, C., Davenport, J.W. and Fähnle, M. (2002). From the bulk to monatomic wires: an ab initio study of magnetism in Co systems with various dimensionality. *Physical Review B*, **66**, 140407-1–140407-4.

Komelj, M., Steiauf, D. and Fähnle, M. (2006). Influence of the substrate on the magnetic anisotropy of monoatomic wires. *Physical Review B*, **73**, 134428-1–134428-5.

Kubetzka, A., Ferriani, P., Bode, M., *et al*. (2005). Revealing antiferromagnetic order of the Fe monolayer on W(001): spin-polarized scanning tunneling microscopy and first-principles calculations. *Physical Review Letters*, **94**, 087204-1–087204-4.

Kübler, J. (2000). *Theory of Itinerant Electron Magnetism*, *Vol. 106 of International. Series of Monographs on Physics*, Clarendon Press: Oxford, UK, chapter 2: Derivation of the Single-Particle Schrödinger Equation: Density and Spin-Density Functional Theory.

Kurz, P., Bihlmayer, G., Hirai, K. and Blügel, S. (2001). Three-dimensional spin structure on a two-dimensional lattice: Mn/Cu(111). *Physical Review Letters*, **86**, 1106–1109.

Kurz, P., Bihlmayer, G., Hirai, K. and Blügel, S. (2002). Itinerant magnets on a triangular Cu(111) lattice. *Phase Transitions*, **75**, 101–112.

van der Laan, G. (1998). Microscopic origin of magnetocrystalline anisotropy in transition metal thin films. *Journal of Physics. Condensed Matter*, **10**, 3239–3253.

Landau, D.P. and Binder, K. (2000). *A Guide to Monte Carlo Simulations in Statistical Physics*, Cambridge University Press: Cambridge UK.

Lang, P., Stepanyuk, V.S., Wildberger, K., *et al*. (1994). Local moments of 3d, 4d, and 5d atoms at Cu and Ag(001) surfaces. *Solid State Communications*, **92**, 755–759.

Lin, C.J., Gorman, G.L., Lee, C.H., *et al*. (1991). Magnetic and structural properties of Co/Pt multilayers. *Journal of Magnetism and Magnetic Materials*, **93**, 194–206.

Lounis, S., Mavropoulos, P., Dederichs, P.H. and Blügel, S. (2005). Noncollinear Korringa-Kohn-Rostoker Green function method: application to 3d nanostructures on Ni(001). *Physical Review B*, **72**, 224437-1–224437-11.

Mavropoulos, P., Lounis, S., Zeller, R. and Blügel, S. (2006). Fe clusters on Ni and Cu: size and shape dependence of the spin moment. *Applied Physics A*, **82**, 103–107.

Mermin, N.D. and Wagner, H. (1966). Absence of ferromagnetism or antiferromagnetism in one- or two-dimensional isotropic Heisenberg models. *Physical Review Letters*, **17**, 1133–1136.

Metropolis, N., Rosenbluth, A.W., Rosenbluth, M.N., *et al*.(1953). Equation of state calculations by fast computing machines. *Journal of Chemical Physics*, **21**, 1087–1092.

Mills, D.L. (1994). Thermodynamic properties of ultrathin ferromagnetic films. In *Ultrathin Magnetic Structures*, Bland, J.A.C. and Heinrich, B. (Eds.), Springer–Verlag: Berlin/Heidelberg, Vol. I, pp. 91–122.

Mirbt, S., Eriksson, O., Johansson, B. and Skriver, H.L. (1995). Magnetic coupling in 3d transition-metal monolayers and bilayers on bcc (100) iron. *Physical Review B*, **52**, 15070–15073.

Mokrousov, Y., Bihlmayer, G. and Blügel, S. (2005). Full-potential linearized augmented plane-wave method for one-dimensional systems: gold nanowire and iron monowires in a gold tube. *Physical Review B*, **72**, 045402-1–045402-15.

Mokrousov, Y., Bihlmayer, G., Heinze, S. and Blügel, S. (2006). Magnetocrystalline anisotropies of 4*d* transition-metal monowires. *Physical Review Letters*, **96**, 147201-1–147201-4.

Moriya, T. (1960). Anisotropic superexchange interaction and weak ferromagnetism. *Physical Review*, **120**, 91–98.

Moruzzi, V.L., Janak, J.F. and Williams, A.R. (1978). *Calculated Electronic Properties of Metals*, Pergamon Press: New York.

Nie, X., Bihlmayer, G. and Blügel, S. (2006). 'Relativistic total energy magnetic anisotropy calculations for transition metals: free-standing monolayers' (unpublished).

Nie, X., Heinze, S., Bihlmayer, G. and Blügel, S. (2007a).'Ferromagnetism and Antiferromagnetism of 3d Transition Metal Monolayers on W(110)'(unpublished).

Nie, X.L., Heide, M., Bihlmayer, G. and Blügel, S. (2007b). Spin reorientation controlled by interface orbital moment quenching: Fe/W(110) (unpublished).

Nonas, B., Cabria, I., Zeller, R., *et al*.(2001). Strongly enhanced orbital moments and anisotropies of adatoms on the Ag(001) surface. *Physical Review Letters*, **86**, 2146–2149.

Ortega, J.E. and Himpsel, F.J. (1993). Inverse photoemission from V, Cr, Mn, Fe, and Co monolayers on Ag(100). *Physical Review B*, **47**, 16441–16446.

Ounadjela, K., Vennegues, P., Henry, Y., *et al*. (1994). Structural changes in metastable epitaxial Co/Mn superlattices. *Physical Review B*, **49**, 8561–8573.

Pajda, M., Kudrnovský, J., Turek, I., *et al*. (2001). Ab initio calculations of exchange interactions, spin-wave stiffness constants, and Curie temperatures of Fe, Co, and Ni. *Physical Review B*, **64**, 174402-1–174402-9.

Perdew, J.P., Chevary, J.A., Vosko, S.H., *et al*. (1992). Atoms, molecules, solids, and surfaces: applications of the generalized gradient approximation for exchange and correlation. *Physical Review B*, **46**, 6671–6687.

Pfandzelter, R., Igel, T. and Winter, H. (1996). Intermixing during growth of Cr on Fe(100) studied by proton- and electron-induced auger-electron spectroscopy. *Physical Review B*, **54**, 4496–4499.

Pfandzelter, R., Igel, T. and Winter, H. (1997). Growth and structure of ultrathin Mn films on Fe(001). *Surface Science*, **389**, 317–328.

Przybylski, M. and Gradmann, U. (1987). Ferromagnetic order in a Fe(110) monolayer on W(110) by Mössbauer spectroscopy. *Physical Review Letters*, **59**, 1152–1155.

Qian, X. and Hübner, W. (1999). First-principles calculation of structural and magnetic properties for Fe monolayers and bilayers on W(110). *Physical Review B*, **60**, 16192–16197.

Qian, X. and Hübner, W. (2003). Symmetry and substrate effects on magnetic interactions from first principles: a comparison between Fe/W(100) and Fe/W(110). *Physical Review B*, **67**, 184414-1–184414-7.

Rader, O., Gudat, W., Carbone, C., *et al*. (1997). Electronic structure of two-dimensional magnetic alloys: c(2×2) Mn on Cu(100) and Ni(100). *Physical Review B*, **55**, 5404–5415.

Redinger, J., Blügel, S. and Podloucky, R. (1995). Ferromagnetism of 4d and 5d transition-metal monolayers on Ag(111). *Physical Review B*, **51**, 13852–13855.

Robles, R., Izquierdo, J. and Vega, A. (2000). Magnetic behavior of monoatomic Co wires on Pd(110). *Physical Review B*, **61**, 6848–6853.

Röhlsberger, R., Bansmann, J., Senz, V., *et al*. (2001). Perpendicular spin orientation in ultrasmall Fe Islands on W(110). *Physical Review Letters*, **86**, 5597–5600.

Sambi, M. and Granozzi, G. (1999). Ultrathin V films on Pt(111): a structural study by means of X-ray photoelectron spectroscopy and diffraction. *Surface Science*, **426**, 235–250.

Sander, D., Skomski, R., Schmidthals, C., *et al*. (1997). Film stress and domain wall pinning in sesquilayer iron films on W(110). *Physical Review Letters*, **77**, 2566–2569.

Sandratskii, L.M. (1998). Noncollinear magnetism in itinerant-electron systems: theory and application. *Advances in Physics*, **47**, 91–160.

Sandratskii, L., Şaşıoğlu, E. and Bruno, P. (2006). Exchange interactions and Néel temperature of a Fe monolayer on W(001): a first-principles study. *Physical Review B*, **73**, 014430-1–014430-6.

Segovia, P., Purdie, D., Hengsberger, M. and Baer, Y. (1999). Observation of spin and charge collective modes in one-dimensional metallic chains. *Nature*, **402**, 504–507.

Shick, A.B., Maca, F. and Oppeneer, P.M. (2004). Anomalous ferromagnetism of a monatomic Co wire at the Pt(111) surface step edge. *Physical Review B*, **69**, 212410-1–212410-4.

Solovyev, I.V. (2005). Orbital polarization in itinerant magnets. *Physical Review Letters*, **95**, 267205-1–267205-4.

Solovyev, I.V., Liechtenstein, A.I. and Terakura, K. (1988). Is Hund's second rule responsible for the orbital magnetism in solids? *Physical Review Letters*, **80**, 5758–5761.

Spišák, D. and Hafner, J. (2002). Fe nanowires on vicinal Cu surfaces: Ab initio study. *Physical Review B*, **65**, 235405-1–235405-7.

Spišák, D. and Hafner, J. (2003). Magnetism of ultrathin wires suspended in free space and adsorbed on vicinal surfaces. *Physical Review B*, **67**, 214416-1–214416-13.

Spišák, D. and Hafner, J. (2004). Magnetism of Fe-Co nanostructures on flat stepped W(110) surfaces: effects of dimensionality and substrate. *Physical Review B*, **70**, 014430-1–014430-10.

Stampanoni, M., Vaterlaus, A., Pescia, D., *et al*. (1988). Lack of evidence for ferromagnetism in the vanadium monolayer on Ag(001). *Physical Review B*, **37**, 10380–10382.

Stepanyuk, V.S., Hergert, W., Wildberger, K., *et al*. (1996). Magnetism of 3d, 4d, and 5d transition-metal impurities on Pd(001) and Pt(001) surfaces. *Physical Review B*, **53**, 2121–2125.

Stöhr, J. (1999). Exploring the microscopic origin of magnetic anisotropies with X-ray magnetic circular dichroism (XMCD) spectroscopy. *Journal of Magnetism and Magnetic Materials*, **200**, 470–497.

Szunyogh, L., Újfalussy, B. and Weinberger, P. (1995). Magnetic anisotropy of iron multilayers in Au(001): first-principles calculations in terms of the fully relativistic spin-polarized screened KKR method. *Physical Review B*, **51**, 9552–9559.

Takahashi, M. (1977). Half-filled Hubbard model at low temperature. *Journal of Physics C*, **10**, 1289–1301.

Terakura, K., Hamada, N., Oguchi, T. and Asada, T. (1982). Local and non-local spin susceptibilities of transition metals. *Journal of Physics F-Metal Physics*, **12**, 1661–1678.

Tian, D., Begley, A.M. and Jona, F. (1992a). New metastable phase of Mn by epitaxy on Cu(111). *Surface Science Letters*, **273**, L393–L398.

Tian, D., Li, H., Wu, S.C., *et al*. (1992b). Atomic and electronic structure of thin films of Mn on Pd(111). *Physical Review B*, **45**, 3749–3754.

Topping, J. (1927). On the mutual potential energy of a plane network of doublets. *Proceedings of the Royal Society of London. Series B*, **114**, 67–72.

Turek, I., Kudrnovský, J., Diviš, M., *et al*. (2003). First-principles study of the electronic structure and exchange interactions in bcc europium. *Physical Review B*, **68**, 224431-1–224431-7.

Turek, I., Kudrnovský, J., Drchal, V. and Bruno, P. (2006). Exchange interactions, spin waves, and transition temperatures in itinerant magnets. *Philosophical Magazine*, **86**, 1713–1752.

Tyablikov, S.V. (1967). *Methods of Quantum Theory of Magnetism*, Plenum Press, New York.

Újfalussy, B., Lazarovits, B., Szunyogh, L., *et al*. (2004). Ab initio spin dynamics applied to nanoparticles: canted magnetism of a finite Co chain along a Pt(111) surface step edge. *Physical Review B*, **70**, 100404-R-1–100404-R-4.

Újfalussy, B., Szunyogh, L. and Weinberger, P. (1995). Magnetism of 4d and 5d adlayers on Ag(001) and Au(001): comparison between a nonrelativistic and a fully relativistic approach. *Physical Review B*, **51**, 12836–12839.

Venus, D. and Heinrich, B. (1996). Interfacial mixing of ultrathin Cr films grown on an Fe whisker. *Physical Review B*, **53**, R1733–R1736.

Wang, Z.Q., Li, Y.S., Lok, C.K.C., *et al*. (1987). Atomic and electronic structure of a surface alloy - comparison with the bulk alloy. *Solid State Communications*, **62**, 181–185.

Weber, N., Wagner, K., Elmers, H.J., *et al*. (1997). Nanoscale spatial switching of magnetic anisotropy in pseudomorphic Fe(110) on W(110). *Physical Review B*, **55**, 14121–14124.

Weinert, M. and Freeman, A.J. (1983). Magnetism of linear chains. *Journal of Magnetism and Magnetic Materials*, **38**, 23–33.

Wildberger, K., Stepanyuk, V.S., Lang, P., *et al*. (1995). Magnetic nanostructures: 4d clusters on Ag(001). *Physical Review Letters*, **75**, 509–512.

Wortmann, D., Heinze, S., Kurz, P., *et al*. (2001). Resolving complex atomic-scale spin structures by spin-polarized scanning tunneling microscopy. *Physical Review Letters*, **86**, 4132–4135.

Wu, R. and Freeman, A.J. (1992a). Possible 4d ferromagnetism of Rh and Ru overlayers on a Ag(001) substrate. *Physical Review B*, **45**, 7222–7228.

Wu, R-Q. and Freeman, A.J. (1992b). Magnetic properties of Fe overlayers on W(001) and the effects of oxygen adsorption. *Physical Review B*, **45**, 7532–7535.

Wu, R. and Freeman, A.J. (1995). Predicted c(2 × 2) buckling reconstruction of monolayer Mn on Fe(001) and its importance to the interfacial magnetic ordering. *Physical Review B*, **51**, 17131–17134.

Wu, S.C., Lu, S.H., Wang, Z.Q., *et al*. (1988). Cu(001)c(2 × 2)-Pd: an ordered surface alloy. *Physical Review B*, **38**, 5363–5370.

Wuttig, M., Gauthier, Y. and Blügel, S. (1993a). Magnetically driven buckling and stability of ordered surface alloys: Cu(100)c(2 × 2)Mn. *Physical Review Letters*, **70**, 3619–3621.

Wuttig, M., Knight, C.C., Flores, T. and Gauthier, Y. (1993b). LEED structure determination of two ordered surface alloys: Cu(100)–c(2 × 2) Mn and Ni(100)–c(2 × 2) Mn. *Surface Science*, **292**, 189–195.

Zabala, N., Puska, M.J. and Nieminen, R.M. (1998). Spontaneous magnetization of simple metal nanowires. *Physical Review Letters*, **80**, 3336–3339.

Zhang, L., Kuhn, M. and Diebold, U. (1997). Growth and structure of ultrathin Cr films on Pt(111). *Surface Science*, **371**, 223–234.

Molecular Magnets: Phenomenology and Theory

Mark R. Pederson[1] and Tunna Baruah[2]

[1] *Naval Research Laboratory, Washington, DC, USA*
[2] *University of Texas at El Paso, El Paso, TX, USA*

1 INTRODUCTION

The field of molecular magnetism is indeed quite broad and much has been written on many aspects of this field. Discussions, by many of the pioneers and practioners in this field, including Kahn, Barbara, Verdaguer and others may be found in References Kahn, 1993; 2000; Barbara and Gunther, 1999; Ferlay *et al*., 1995; Turnbull, Sugimot and Thompson, 1996; Postnikov, Kortus and Pederson, 2006; Pederson, Park and Baruah, 2006. A single concise definition is difficult and would probably not satisfy all researchers in this field. Further, it is not possible to review all aspects of this interdisciplinary field, especially given the diverse set of scientific skills and expertise needed to look at all aspects. Before focusing the attention on the theoretical study of one class of molecular magnets, it is useful to give a slightly broader overview of all the molecular systems that may be referred to as *molecular magnets* and give some discussion as to how they are related and different. In general, molecular magnetism deals with any molecular system or collection of atoms that is finite, unreactive, and contains at least one but probably two or more unpaired electrons. However, there is another class of related bulk magnetic materials, assembled from transition-metal molecules, that exhibit interesting magnetic and photomagnetic effects such as the Prussian-blue analogs (Ferlay *et al*., 1995) and spin crossover compounds (Gaspar *et al*., 2003). Although unpaired electrons exist in both molecular magnets and radicals, the distinction between these two systems is that on-site exchange effects in a molecular magnet inhibit unpaired electrons from forming bonds with unpaired electrons on neighboring molecules. This unreactive behavior is generally accomplished by intramolecular charge transfer between the moment-carrying sites and the nominally spin-unpolarized part of the molecule. Rather than forming covalent bonds, the resulting sites are more likely to coordinate with an oppositely charged closed-shell entity such as an O^{2-} anion, a dehydrogenated acidic molecule, or the lone pair on a threefold coordinated nitrogen atom. Within this class of systems, one must distinguish between purely organic systems (Palacio and Markova, 2006) and those containing metal ions.

In the former class for which the molecular oxygen may be the simplest example, the moments are generally more delocalized, less likely to be centered on a single ion, and can have distances between neighboring local moments that are small since they are controlled by covalent bonding. These

Handbook of Magnetism and Advanced Magnetic Materials. Edited by Helmut Kronmüller and Stuart Parkin. Volume 1: *Fundamentals and Theory*.

characteristics lead to magnetic or paramagnetic behavior that is governed by different interactions than those that contain metal ions. The combination of the short bond lengths and small spin-orbit splitting leads to multiplet structures exhibiting smaller zero-field splittings. Further, because the spin-orbit splitting is small and the distance (R) between moments is small, the dipolar interaction, which scales as $1/R^3$, leads to an anisotropy energy that depends on both second-order spin-orbit effects and classical dipolar interactions. Excluding the intramolecular dipolar interactions in these systems is expected to lead to errors in the magnetic anisotropy. However, even with the inclusion of these effects, it appears that the role of magnetic anisotropy in organic molecular magnets is small and most of the physics is related to energetics associated with changes in spin ordering between neighboring localized spins rather than global changes in spin projections. While the remainder of this chapter does not directly pertain to this subclass of molecular magnets, some of the physics associated with one class of transition-metal-based molecular magnets coincides with this class of molecules. There are excellent reviews on this subject as well as many recent papers. The interested reader is referred to these (Palacio and Markova, 2006) references.

For the class of molecular magnets that contain transition-metal ions, (see Fig. 1) exclusion of the intramolecular dipolar interactions is at least the best starting point due to the larger distances between neighboring moments. These systems are unreactive because they have a relatively large energy gap between the occupied and unoccupied electronic states. The local filling of the d electrons is determined by relatively strong Jahn–Teller distortions of the sixfold coordinated environment around a given transition-metal atom. Under these conditions, the lowest-energy excitations in these systems are governed by a combination of the interionic exchange interactions, which govern spin ordering, and the spin-orbit interaction. For cases where the spin-orbit interaction is small, the only low-energy excitations are between different spin manifolds each of which would have a degeneracy given by $2S + 1$. The so-called V_{15} molecule exemplifies this type of molecular magnet (Gatteschi *et al*., 1991; Kortus, Hellberg and Pederson, 2001). The spin excitations in these systems can be studied in a straightforward manner from the perspective of Heisenberg Hamiltonians and their extensions. Although straightforward, the computational problem is indeed challenging due to the high dimension of the matrices that need to be diagonalized. For the purpose of discussion, we refer to these molecules as spin systems and put forth the viewpoint that referring to these systems as a 'molecular magnet' is indeed a misnomer despite the fact that the properties of these systems are quite interesting.

For cases where the spin-orbit interaction is large, a simple and very interesting collective behavior emerges if the on-molecule interionic exchange interactions are very large. For discussion in this chapter, we refer to this class of molecular magnets as anisotropic molecular magnets (AMMs) (Friedman *et al*., 1996; Thomas *et al*., 1996; Barra *et al*., 1996; Sangregorio *et al*., 1997; Wernsdorfer and Sessoli, 1999; Wernsdorfer *et al*., 1999). The Mn_{12}-acetate molecule, synthesized by Lis (1980) is the quintessential example of an AMM. Ten years ago, two groups (Friedman *et al*., 1996; Thomas *et al*., 1996) independently observed a phenomenon, now known as *resonant tunneling of magnetization*, in this molecule. It is this class of molecular magnets that most of the discussion will be devoted to. The experiments on these systems will be discussed and the phenomenological Hamiltonian that describes their behavior will be introduced. Then we will discuss how a first-principles theory such as the density-functional theory (Hohenberg and Kohn, 1964; Kohn and Sham, 1965; Perdew *et al*., 1992; Perdew, Burke and Ernzerhof, 1996) may be used to determine the phenomenological Hamiltonian without any adjustable parameters (Pederson and Khanna, 1999).

It should be noted that there is certainly no guarantee that the relative energy scales associated with electronic excitations, spin-ordering changes, and spin-orbit couplings will always lead to a situation that gives rise to a simple collective behavior in an arbitrary molecular material containing transition-metal ions. Because of this, a significant effort will be made to fully discuss the derivations of the computational and theoretical methods that lead to the two simplified extremes. In addition, an attempt is made to identify additional interactions that could lead to a quantitative theory that describes more complicated molecular magnetic materials. It is possible, even likely, that simplified collective behavior appears in these systems as well. However, the theoretical and computational tools that need to be developed to quantify the behavior in this general range are quite significant.

The key experiments, mentioned in the preceding text, have motivated many new experimental and theoretical developments. Because this chapter is being written with some hindsight, an attempt will be made to discuss the problem as to how it may have evolved in the most orderly way, which necessarily means that the chronology of how the field has actually evolved will be primarily apparent from the references. This chapter is not aimed at experts in the field of molecular magnetism. Rather, it is hoped that this chapter will be useful to two audiences. First, it should serve as a good starting point for a researcher who wishes to learn about the fundamental questions in molecular magnets. Second, the derivation for the first-principles determination of the magnetic anisotropy Hamiltonian is aimed at practitioners

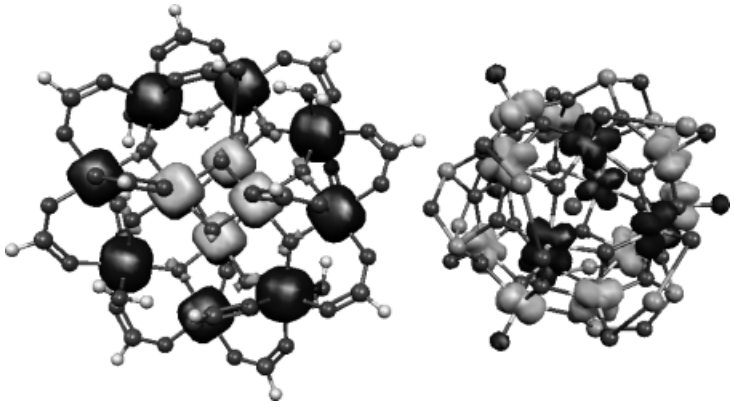

Figure 1. Two types of transition-metal coordinated complexes. On the left is the Mn_{12}-acetate molecular magnet and on the right is the V_{15} spin system. The low-energy excitations in these systems are governed by magnetic anisotropy and spin excitations, respectively.

in electronic structure who are interested in improving the theory or converting a standard electronic structure program into one that can determine magnetic anisotropies. In the first section, the phenomenology of a simple spin system will be discussed. This will include consideration of the Hamiltonians that are most relevant to the spin molecular magnets (SMMs)- and AMMs. With regard to AMMs, we describe the effects of longitudinal resonant tunneling of magnetization, transverse Berry's phase oscillations (Garg, 1993) and the suppression or complication of the latter effect due to higher-order terms in the Hamiltonian (del Barco *et al*., 2004). With regard to the SMMs, we discuss the simplest Heisenberg Hamiltonian that can be used for describing the spin excitations.

After reviewing the fundamental physics that comes out of the spin Hamiltonians, we discuss the first-principles determination of these phenomenological Hamiltonians from a point of view of density-functional theory or other mean-field methods. The derivation of the phenomenological anisotropy Hamiltonian presented here includes additional details and discussion that have not appeared in the original or subsequent work of the NRL group. In doing so, it is hoped that new efforts will be made to improve upon the current computational schemes. There have been two other very complete reviews on applications of the existing formalism published recently. In addition to directing the reader to this work, we briefly discuss more recent theoretical studies of molecular magnets within density-functional theory.

2 PHENOMENOLOGY

2.1 Hamiltonian for a spin molecular magnet

The introduction of spin into electronic wave functions leads to several different effects related to spin polarization. Owing to the nature of fermions, the electronic wave function must be antisymmetric. Because of this, in addition to the repulsive coulomb interaction between electrons, an additional attractive term, between same-spin electrons arises and is referred to as the *electronic exchange interaction*. In an open-shell system, the spin is maximized for cases containing well-localized electronic wave functions that are orthogonal and degenerate, usually, due to orbital symmetry. If two wave functions are orthogonal by symmetry, there is no kinetic energy penalty associated with placing them in parallel spin states and the exchange term will stabilize the high-spin state relative to the lower-spin-state exchange interaction. While this effect is generally referred to as *ferromagnetic behavior*, we emphasize here that it is only one of two necessary conditions to achieve a magnetic state.

Another manifestation of spin polarization arises when we consider two well-separated open-shell atoms or ions (hereafter referred to as a *center*). For this case, the phenomenon referred to as *antiferromagnetic behavior* may be observed. On-site coulomb exchange dictates that each center prefers to have a net moment. However, as the wave function overlap between the two centers increases, the Pauli principle requires orthogonality between all states to be satisfied. The system may accomplish this by choosing antiparallel moments which are orthogonal in spin space. In the antiparallel arrangement, the states associated with a given site tend to delocalize slightly so their positive kinetic energy decreases. This decrease in kinetic energy is partially countered by a decrease in the on-site coulomb exchange energy. The alternative is to choose parallel moments derived from localized wave functions that are orthogonal to those on neighboring atoms. In the parallel arrangement, additional orthogonality constraints cause an increase in the systems' kinetic energy since wiggles in the wave function tails are required to achieve spatial orthogonality. The increase in kinetic energy is partially compensated by an increase in coulomb exchange

energy due to overlap between states on different sites. In a mean-field picture with one fully occupied wave function for each electron, the configuration with the lowest energy depends on the precise characteristics of the occupied wave functions. Often, the lowest-energy configuration leads to a symmetry that is lower than would be expected on the basis of the symmetry of the molecule. The parallel and antiparallel arrangements of neighboring sites are commonly, and again slightly inappropriately, referred to as *ferromagnetic* and *antiferromagnetic spin ordering*. Pictured in Figure 1 are two systems that lead to spin-ordered states.

To systematically determine the classical spin ordering of such systems the energy is parameterized according to:

$$E_{\text{spin}} = \sum_{(\mu,\nu)} J_{\mu\nu} \mathbf{S}_\mu \cdot \mathbf{S}_\nu \tag{1}$$

where S_μ and S_ν are localized spins at site ν and μ respectively and $J_{\mu\nu}$, the exchange coupling constants, are usually only nonnegligible for nearest-neighbor centers. To calculate these parameters, one needs to calculate energies as a function of different spin orderings, know the local moments, and then invert the expression to obtain the exchange couplings. Once the exchange coupling constants are known, the expression may be 'requantized' leading to a spin Hamiltonian of the form:

$$H_{\text{spin}} = \sum_{(\mu,\nu)} J_{\mu\nu} \mathbf{S}_\mu \cdot \mathbf{S}_\nu \tag{2}$$

By constructing all possible product states of the form $\Pi_\nu |S_\nu M_\nu\rangle$, and constructing a very large Hamiltonian matrix, the ground state of the Hamiltonian may be determined. This prescription has been carried out for both the V_{15} spin system (Kortus, Hellberg and Pederson, 2001) and the Mn_{12}-acetate molecular magnet using the density-functional theory described in the subsequent text. In both cases, the lowest-energy spin configuration and low-energy spin excitations were found to be in qualitative accord with experiment. For example, for the case of Mn_{12}-acetate, the wave function consisted of a sum of 10^8 possible configurations. The lowest energy $S = 10$ configuration had 13 states that had reasonably large coefficients (Park, Pederson and Hellberg, 2004). The ferrimagnetic configuration pictured in Figure 1 had an amplitude of 0.6. This configuration agrees qualitatively with the classical ordering determined experimentally (Robinson *et al*., 2000; Mirebeau *et al*., 1999; Petukhov *et al*., 2004).

Assuming that the spin excitations obtained from a Heisenberg Hamiltonian lead to a large gap between the lowest-energy spin multiplet and the first excited spin-multiplet, the system may behave as an AMM. For this case, each spin manifold exhibits zero-field splittings which breaks a $2S + 1$ degenerate multiplet into a set of lower-degeneracy multiplets. Symmetry plays a significant role in determining the size of these zero-field splittings and the number of submanifolds. An $S = 10$ system with uniaxial symmetry would break into S doublets and 1 singlet. The size of these zero-field splittings is also mandated by symmetry. For an O_h system, the barrier would scale as $\frac{1}{16c^8}$ with c the speed of light. For a system without symmetry or with uniaxial symmetry the splittings would scale as $\frac{1}{4c^2}$. Symmetry considerations suggest that magnets with lower symmetry should be stronger. However, there is also a scaling with nuclear charge that could reverse this trend for centers that are heavy enough.

2.2 Hamiltonian for an anisotropic molecular magnet

2.2.1 The second-order Hamiltonian

To the degree that a given system behaves as a single quantum-mechanical spin, the most general second-order anisotropy Hamiltonian for this spin, in the presence of a magnetic field, is given by:

$$H = \sum_i B'_i S'_i + \sum_{ij} \gamma_{ij} S'_i S'_j \tag{3}$$

(with $i, j = x, y, z$). Here, $\mathbf{S}'$, $\mathbf{B}'$ are the standard total spin operators and externally applied magnetic-field components with respect to an arbitrary coordinate system. In the preceding expression, γ_{ij} is referred to as the *second-order anisotropy tensor*. Here, we assume an isotropic g tensor and absorb this term into the definition of the applied magnetic field. Further, it should be noted that general arguments, discussed later, tell us that the phenomenological anisotropy Hamiltonian scales as $\frac{1}{4c^4}$ where c is the speed of light. In atomic units $c = 137$. The preceding Hamiltonian can be immediately simplified by diagonalizing this tensor to find the eigenvalues (λ_i) and eigenvectors which effectively determine the principal axes of magnetization. The Hamiltonian is then most commonly expressed according to:

$$H = \mathbf{B} \cdot \mathbf{S} + \sum_i \lambda_i S_i S_i, \tag{4}$$

$$= AS^2 + DS_z^2 + E(S_x^2 - S_y^2) + \mathbf{B} \cdot \mathbf{S} \tag{5}$$

with $A = \frac{\lambda_x + \lambda_y + \lambda_z}{3}$, $D = \frac{\lambda_z - (\lambda_y + \lambda_x)/2}{3}$, and $E = \frac{\lambda_x - \lambda_y}{2}$. Once the preceding Hamiltonian is adopted, the parameter A is generally taken to be zero since it is isotropic. In the next section, we discuss a means for calculating A, D, and E from

the density-functional theory. The constant, AS^2, is probably very weakly dependent on spin ordering (based on results from Baruah *et al*. 2004). However, some investigation into possible shifts in spin-manifold gaps due to this constant term should be investigated at some point. The parameters D and E are referred to as the *second-order longitudinal and transverse anisotropy parameters*, respectively. Classically, the difference in energy, or energy barrier, for the spin aligned along the z axis rather than the y and x axes would be $(D + E)S^2$ and $(D - E)S^2$, respectively.

Several points should be made. A large barrier for an actual molecular magnet is currently found to be approximately 60–70 K. Before continuing, it is worthwhile dispelling one incorrect notion that can be concluded from the preceding phenomenological Hamiltonian. Examination of this Hamiltonian incorrectly suggests that such barriers could be enhanced by simply engineering larger spin systems and further suggests that an antiferromagnetically ordered molecular magnet, devoid of a net spin, would observe no energy barrier associated with spin reversal. On the contrary, the results of the first-principles derivation, discussed in the subsequent text, show that the barrier scales roughly as $(N_{\text{sites}} \times N_{\text{occ}} \times N_{\text{virt}})$ where N_{sites} are the number of atoms or ions with unpaired localized electrons, and N_{occ} and N_{virt} are characteristic numbers of unpaired states in the occupied and unoccupied manifolds. The derivation shows a hidden inverse square dependence of the γ tensor on the magnitude of the local moments. Thus, an antiferromagnetically ordered set of spins could indeed have an anisotropy and could, for example, be useful for an exchange-biasing application when coupled to a weak paramagnetic molecule with a net spin. The same line of derivation shows that the phenomenological Hamiltonian shown in the preceding text is quantitatively valid only for a given spin manifold. While difficult to prove, it is more likely that the D parameter for two different low-lying spin manifolds would differ by the ratio of $(S_1/S_2)^2$ rather than a factor of unity. However, this Hamiltonian contains all the physics necessary to understand the essence of resonant tunneling of magnetization and oscillations in tunnel splittings. Before considering additional complexities, we consider these two effects.

2.2.2 *Resonant tunneling of magnetization*

To determine the eigenvalues of the above Hamiltonian, it is necessary to construct the $(2S + 1) \times (2S + 1)$ Hamiltonian matrix $\langle SM|H|SM'\rangle$. Setting $A = 0$ and considering the case for $E = 0$ first, it is easy to verify that the eigenvalues of this Hamiltonian, as a function of longitudinal field, are given by

$$E(M) = DM^2 + B_z M \tag{6}$$

At zero field, it is readily apparent that the $(2S + 1)$ levels are split into S doublets (M and $-M$) and one singlet (for an integer spin case). If a longitudinal field is turned on, the S doublets split. However, $S - n$ quasi-doublet degeneracies are restored whenever the magnetic field is chosen such that $B_z = nD$ (with $n = 0, 1, \ldots, S - 1$). With this understanding it is possible to discuss one aspect of the resonant tunneling of magnetization experiments (Friedman *et al*., 1996; Thomas *et al*., 1996).

For the situation where $D < 0$, one may apply a large enough magnetic field so that the spin relaxes to the state $M = S$. If the field were suddenly turned off and then replaced by an infinitesimal field in the opposite direction, the $M = -S$ state would be the new ground state of the system. Classically, the time constant governing relaxation from the $M = S$ to $M = -S$ state would be given by an Ahrrenius behavior:

$$\frac{1}{\tau} = \nu \times e^{(-U/kT)} \tag{7}$$

where ν is referred to as an *attempt frequency* and $U = |D|S^2$ is the activation barrier at zero magnetic field. Given a lattice of noninteracting spins, an experiment which measured magnetization or other observables that depend on the moment projection would allow for the determination of the longitudinal anisotropy constant. For the classical moment, if the antiparallel field is now slowly increased, the energy barrier in the exponential changes continuously according to $U = (|D|S^2 - |BS|)$ and the time constant would also be expected to change continuously with field. However, for a quantum-mechanical spin, the relaxation rate exhibits a much richer dependence on the magnetic field. When the magnetic field is chosen such that the occupied and/or virtual M state aligns perfectly with a state of different M on the other side of the barrier (e.g., $B_z = nD$ for some integer $n < S - 1$), the possibility of tunneling through the barrier, rather than classically jumping over the barrier, exists as well. This leads to a near discontinuity in the tunneling rate and describes the underlying physics observed by Friedman *et al*. and Sessoli *et al*. For the perfect second-order case, multiple state alignments occur simultaneously. Thus, multiple pathways exist for tunneling phenomena and the fastest pathway determines the overall relaxation time. This argument shows the magnetic fields at which tunneling will be allowed based on the consideration of energetics. However, it neither describes the complicated dynamics which lead to resonant tunnelling of magnetization (RTM) nor allows us to directly determine a blocking temperature. However, it is clear from equation (7) that the blocking temperature will be larger if the activation barrier, or magnetic anisotropy, can be increased.

2.2.3 *Tunnel-splitting oscillations*

If the transverse anisotropy (E) is nonzero, an additional quantum-mechanical phenomena can occur for a single quantum-mechanical spin interacting with a magnetic field. This phenomenon was originally predicted by Garg (1993) and subsequently observed by Wernsdorfer and Sessoli (Wernsdorfer and Sessoli, 1999).

Pictured in the upper panel of Figure 2 are the energy levels of an $S = 10$ molecular magnet or quantum spin with anisotropy parameter of $D = -0.25$K and $E = 0.05$ K respectively as a function of a magnetic field applied along the x axis. Following Garg's analytic formula, the units of the magnetic field are given by $B_x^o = [2E(|D| + E)]^{1/2}$. The energy levels as a function of applied field show a series of fascinating crossings or avoided crossing at values of $(N + \frac{1}{2})B_x^o$ and (NB_x^o), respectively. Also pictured in the lower panel of Figure 2 is the logarithm of the energy difference between the two lowest-energy states as a function of magnetic field. There are a total of six different calculations as a function of angle between the in-plane magnetic field and the x axis. This picture shows that the tunnel splittings depend strongly on perfect alignment between the x-axis and the applied magnetic field.

2.2.4 *Effects of higher-order contributions to the anisotropy Hamiltonian*

When higher-order terms are added to the Hamiltonian, for example, terms like $BS_z^4 + C(S_+^4 + S_-^4)$, several effects occur. The S_z^4 term adds a perturbation to the different M states and prevents perfect simultaneous alignments of energy levels in the longitudinal tunneling experiments. The transverse term breaks the perfect periodicity of the tunnel-splitting oscillations in the transverse experiments. Also the relative orientation between the transverse second-order terms and the transverse fourth-order terms changes the orientation of the magnetic fields required for observation of these splittings. This provides a very useful diagnostic tool for the symmetry around a quantum spin and these effects have been observed experimentally and theoretically in relation to the Mn_{12}-acetate molecule. For this case, Cornia identified a weak symmetry-breaking term in the crystal containing these molecules. Weak hydrogen bonds between space-filling acetic acids of crystallization were predicted to lead to three types of spin Hamiltonians with $E = 0, 0.008$, and 0.016 (Cornia *et al.*, 2002; Park, Baruah, Bernstein and Pederson, 2004). Further Pederson, Bernstein and Kortus (Pederson, Bernstein and Kortus, 2002) showed qualitatively from calculations that Raman-active vibrations lead to interactions in the Mn_{12}-acetate which cause an additional transverse term and identify the intrinsic fourth-order axis. The misalignment between the intrinsic transverse axes and those determined from the actual placement of the acetic acids of crystallization provide a system where the tunnel-splitting oscillations can be used as a probe of the local structure around a quantum spin. This has been investigated experimentally and is now quite well understood (del Barco *et al.*, 2004; Hill *et al.*, 2003; Park *et al.*, 2005).

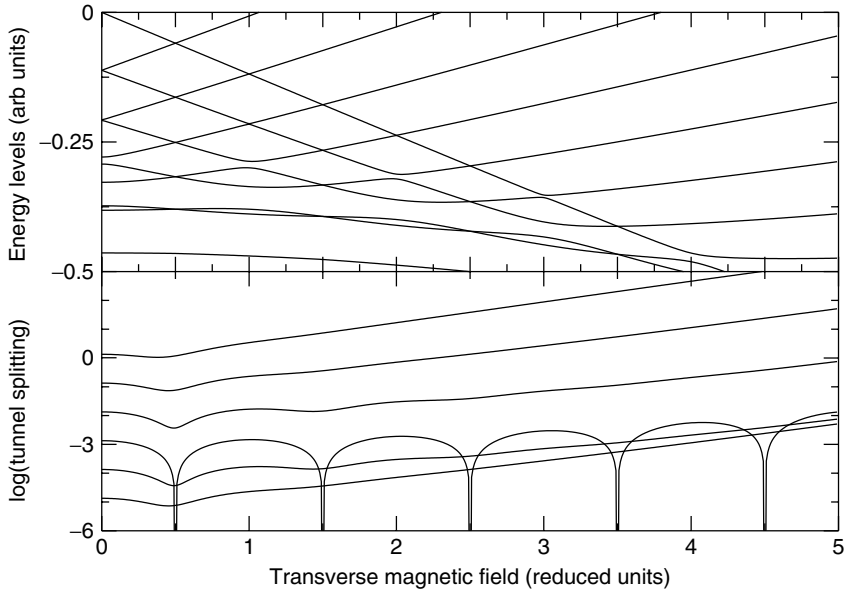

Figure 2. Uppermost energy levels (upper panel) and log (tunnel splittings) of two most stable states for an $S = 10$ quantum spin. The Hamiltonian is field $H = -DS_z^2 - E(S_x^2 + S_y^2) + BS_x$ with $D = -0.25$ and $E = 0.05$. The physical reduced units of the transverse magnetic field are $[2|E|(|D| + |E|]^{1/2}$ as shown by Garg.

2.3 Heisenberg Hamiltonians with anisotropy

As discussed in the subsequent text, the origin of the spin-orbit interaction leads to anisotropy in a molecular system. A general feature of the spin-orbit interaction is that the expectation value of this operator is zero for any wave function that is purely real. This is known as *time-reversal symmetry* but follows immediately if we believe that the expectation value of a physical operator, that is purely imaginary, must be real. Simply appending the phenomenological Hamiltonian to a Heisenberg Hamiltonian leads to splittings in the multiplets; however, there are two main problems with this approximation. First, as already stated, the derivation presented in the subsequent text shows that the anisotropy tensor contains hidden dependencies on the spin of the system. There is not a single phenomenological Hamiltonian that is equally applicable to each state. Second, the operator itself is real and at least quadratic in spin operators. The expectation value of this operator for an arbitrary real wave function is nonzero, which indicates that such a Hamiltonian has some basic physics missing. Alternative approaches have been to include local anisotropy terms (e.g., $\sum_i D_i S_z^i S_z^i$). While these terms describe the energetics of a localized uncoupled spin flip correctly, it has been shown that the energy associated with the simultaneous flipping of a collection of these spins is not equal to the sum of the energies. This is unphysical. Katsnelson, Dobrovitski and Harmon (1999) discuss the use of the Dzyaloshinskii-Moriya (DM) interaction in the Mn_{12}-acetate molecule to build in some of the anisotropic effects.

3 DENSITY-FUNCTIONAL-BASED DERIVATION OF ANISOTROPY HAMILTONIANS

The purpose of this section is to show how to determine the previously discussed phenomenological model from an all-electron mean-field theory. The original derivation of some of the equations here appears in Pederson and Khanna (1999). In that paper, the discussion concentrated on how the change in eigenvalue sum, or trace, was considered when the spin-orbit interaction was included in a quantum-mechanical treatment. The derivation is exact for a collection of electrons moving in an external Hamiltonian. However, if the total energy of the system depends self-consistently on the electronic wave functions, it is really the change in total energy, rather than the change in eigenvalue sum, that one should be interested in addressing. Electric polarizabilities represent a well-known example where a perturbative expression based on the perturbation of a trace gives very different polarizabilities than the correct self-consistent polarizabilities. More generally, in a mean-field theory, the sum of the eigenvalues is not the total energy due to the so-called *double counting* of the coulomb and exchange interactions in the Hamiltonian. Indeed, the electron–electron coulomb contributions to the total energy are exactly half as large in the total energy as they are in the eigenvalue sum. For the spin-orbit interaction, the response of the eigenvalue sum is a very good approximation to the response of the total energy rather than a factor of 2 overestimate. This point is neither immediately obvious nor general to all possible types of perturbations. We discuss the method carefully to show why the method works as well as it does and to aid in identifying the regime of validity.

It should be emphasized that the phenomenological Hamiltonian can in principle be determined numerically using standard self-consistent field (SCF) methods that include the spin-orbit interaction in the energy. However, it has long been recognized that the spin-orbit contribution is the primary interaction leading to magnetic anisotropy. The spin-orbit operator, in atomic units, has a $\frac{1}{2c^2}$ prefactor which leads to lowest-order contributions to the magnetic anisotropy of order $\frac{1}{4c^4}$. These are small numbers which immediately raise questions about the use of an inexact self-consistent numerical treatment. For example, it is well known that the spin-orbit interaction felt by a given electron depends on the electric field observed by that electron. This electric field depends on all charges in the problem including those associated with the other electrons. In the subsequent text, using the proper many-electron wave function and Hamiltonian, we derive the expression for the contributions to the spin-orbit energy due to the electronic coulomb potential. It is not surprising that this exactly reproduces the term one expects from the expression one would derive based on a classical electron moving through an arbitrary coulomb potential. The complication in using this exact expression arises when one invokes the standard variational principle to derive the self-consistent Hamiltonian. Performing this exercise leads to an SCF Hamiltonian that has both the intuitive spin-orbit term and a more complicated term due to the variation of the electric field or coulomb potential of the electronic wave functions. Ignoring this nonlocal term, which has a $\frac{1}{2c^2}$ prefactor in the Hamiltonian, will introduce an error in the total energy that scales as $\frac{1}{2c^4}$ which is the same size as the anisotropy term.

There are two additional problems associated with using a full numerical variational approach. The first is related to the need for a noncollinear treatment of the electronic wave functions because the spin-orbit interaction mixes states of different spin projection. This means that the spin-density matrix is not diagonal and must in principle be rediagonalized at each point in space to construct the energy within a density-functional approach. Noncollinear SCF methods have been used and represent an additional important modification

to a standard SCF procedure that must be performed to obtain energies that are correct to the order of $\frac{1}{4c^4}$. The second problem in relation to the calculation of magnetic anisotropies is that one is not only interested in minimizing the total energy of the system with the spin-orbit interaction turned on. Since the magnetic anisotropy of a molecular magnet or nanoparticle is the target, one is actually interested in minimizing the total energy subject to the constraint that the axis of quantization, which defines the 'z' axis for the spinors, is in an arbitrary but fixed position relative to the molecular axes. Constrained minimizations are also very difficult to do.

Although the numerical determination of magnetic anisotropy is challenging, an entirely analytic approach to a complicated many-electron system is probably futile. Even for the simple triplet state of molecular oxygen, the analytic expressions derived from the magnetic anisotropy are sufficiently complicated that it is difficult to guess whether the molecule is easy axis or easy plane by staring at the formula. Because of these difficulties, we have relied on a partially analytical and partially numerical approach. The approach allows one to derive expressions for the magnetic anisotropy that are variational with respect to a single parameter and alleviates the need for the calculation of some of the more complex terms that would occur in the exact self-consistent Hamiltonian. Further, it leads to a formalism that is easily incorporated into standard codes based upon density-functional theory. We discuss the general idea. First, it is assumed that one has found the occupied and unoccupied electronic wave functions that self-consistently minimize a mean-field energy expression (such as that found in density-functional theory or Hartree-Fock). Second, we append the spin-orbit energy to this expression. Third, we assume that we have a physically motivated means for guessing the form of the wave functions that minimize the energy with the spin-orbit interaction turned on. The starting point for the expression of the new wave functions will correspond to those determined from exact perturbation theory using the full, but not self-consistent, coulomb contributions to the spin-orbit interaction but multiplied by a variational parameter γ. The energy of this expression as a function of γ will then be minimized leading to a variational bound on the energy as a function of a given axis of quantization.

Neglecting spin-orbit effects, in a mean-field theory the part of the total energy of a system of electrons that depends on the electronic wave functions may be written according to:

$$E_{\text{elec}} = \sum_{n\sigma} \langle \psi_{n\sigma} | -\frac{1}{2}\nabla^2 + V_{\text{nuc}} | \psi_{n\sigma} \rangle + \frac{1}{2} \int \mathrm{d}^3 r \times \int \mathrm{d}^3 r' \frac{\rho(\mathbf{r})\rho(\mathbf{r}')}{|\mathbf{r}-\mathbf{r}'|} + \int \mathrm{d}^3 r \, \rho(\mathbf{r}) \epsilon_{xc}(\rho_\sigma, \rho'_\sigma) \quad (8)$$

$$\rho_\sigma(\mathbf{r}) = \sum_n |\psi_{n\sigma}(\mathbf{r})|^2 = \sum_n |\phi_{n\sigma}(\mathbf{r})|^2 \quad (9)$$

$$\rho_\sigma(\mathbf{r}) = \rho_\sigma(\mathbf{r}) + \rho'_\sigma(\mathbf{r}) \quad (10)$$

For the purpose of simplicity, the above equation refers specifically to the local-density approximation. The first three terms represent the electronic kinetic energy, the coulomb interaction of the electrons with the nuclei and the electronic coulomb energy, respectively. The last term represents the local-density approximation to electron correlation and exchange effects. The first three terms are common to most, if not all, mean-field expressions while the last term changes depending on which level of density-functional theory is being used or if one is using exact exchange. The details of the exchange-correlation function do not affect the formalism discussed here. However, the accuracy of the results will of course depend, albeit mildly, on how well the exchange-correlation effects are represented. Requiring that the energy is minimized with respect to the choice of spin orbitals leads to the following Schroedinger-like equation, which must be solved self-consistently.

$$\langle \delta\psi_{n\sigma} | -\frac{1}{2}\nabla^2 + V_{nuc} + \int \mathrm{d}^3 r' \frac{\rho(\mathbf{r}')}{|\mathbf{r}-\mathbf{r}'|} + \mu^\sigma_{xc}(\mathbf{r}) - \epsilon_{n\sigma} | \psi_{n\sigma} \rangle = \langle \delta\psi_{n\sigma} | H_o - \epsilon_{n\sigma} | \psi_{n\sigma} \rangle = 0 \quad (11)$$

where μ^σ_{xc} is the exchange-correlation potential determined from the functional derivative of the exchange-correlation energy. For further details on the self-consistent field method, density-functional theory, and other mean-field approximations, the interested reader is referred to the references. There are many different numerical strategies for solving the preceding equations. One can expand the wave functions in terms of many different types of basis functions including Gaussian-type orbitals, plane waves, augmented plane waves, or linear-muffin-tin orbitals. Discussion of the basis-set dependent numerical details can be found in many places and will not be repeated here. Suppose both the occupied and unoccupied wave functions which satisfy equation (11) have been determined. In preparation for the following perturbative arguments, let us assume that we define a new set of orthonormal wave functions $\{\psi^\gamma_{n\sigma}\}$ which depend continuously upon a variational parameter γ and coincide exactly with the solutions to equation (11) when $\gamma = 0$. An additional constraint on this set of functions will be that $\langle \frac{\mathrm{d}\psi_{n\sigma}}{\mathrm{d}\gamma} | \psi_{m\sigma} \rangle = 0$ for $m = n$. However, without loss of generality it is convenient to make this constraint true for all pairs of occupied wave functions. The energy for this set of orthonormal wave functions $\psi^\gamma_{n\sigma}$ can be expressed in terms

of a Taylor's series in γ. At $\gamma = 0$, the wave functions satisfy equation (10) so there is no first-order change in the energy. Therefore, to second order in γ, the change in energy is given by:

$$\delta E = \frac{\gamma^2}{2}\sum_{n\sigma}\left\{\left\langle\frac{\mathrm{d}^2\psi_{n\sigma}}{\mathrm{d}\gamma^2}|H|\psi_{n\sigma}\right\rangle + \frac{1}{2}\left\langle\frac{\mathrm{d}\psi_{n\sigma}}{\mathrm{d}\gamma}|H|\frac{\mathrm{d}\psi_{n\sigma}}{\mathrm{d}\gamma}\right\rangle + \left\langle\frac{\mathrm{d}\psi_{n\sigma}}{\mathrm{d}\gamma}|\frac{\mathrm{d}H}{\mathrm{d}\gamma}|\psi_{n\sigma}\right\rangle\right\} + c.c \tag{12}$$

The right-most term in the preceding equation is not generally zero but is small for the case of current interest. Neglecting this term, the second-order change in the mean-field energy becomes:

$$\delta E = \frac{\gamma^2}{2}\sum_{n\sigma}\left\{\left\langle\frac{\mathrm{d}^2\psi_{n\sigma}}{\mathrm{d}\gamma^2}|H|\psi_{n\sigma}\right\rangle + c.c\right\} + \left\langle\frac{\mathrm{d}\psi_{n\sigma}}{\mathrm{d}\gamma}|H|\frac{\mathrm{d}\psi_{n\sigma}}{\mathrm{d}\gamma}\right\rangle \tag{13}$$

Now, consider the energy of the γ-dependent choice of wave functions when a very small purely imaginary perturbation ($\mathrm{i}\Delta$) of the form,

$$E(i\Delta) = E'_{\mathrm{elec}} + \sum_{n\sigma}\langle\psi'_{n\sigma}|i\Delta|\psi'_{n\sigma}\rangle \tag{14}$$

is added. For the above energy, the task is to determine very good approximations for the orthonormal wave functions ($\psi'_{n\sigma} = \psi_{n\sigma} + \delta\psi_{n\sigma}$) that minimize the above expression for a given Δ.

As noted in the preceding text, the primed wave functions that minimize equation (14) can be found by the same variational procedure that one uses to perform standard self-consistent field equations. However, for an arbitrary choice of a purely imaginary perturbation operator, $\mathrm{i}\Delta$, it may be that a standard off-the-shelf electronic structure code does not have the necessary numerical techniques to solve the new set of SCF equations. This is especially true when $i\Delta$ becomes the exact spin-orbit interaction. In this case, the electronic coulomb potential appears in the expression for $i\Delta$ and the functional derivative of this term leads to a term in the one-electron Hamiltonian that is cumbersome. For the case that $i\Delta$ is small, such as spin orbit where it has a prefactor of $\frac{1}{2c^2}$, the self-consistent procedure can, to an excellent approximation, be performed *analytically* by adopting the following physically motivated and nearly exact *ansatz* for the perturbation of each occupied wave functions $\psi_\alpha = \phi_m\chi_\sigma$.

$$|\delta\psi_\alpha\rangle = \gamma\sum_\beta|\psi_\beta\rangle\frac{\langle\psi_\beta|i\Delta|\psi_\alpha\rangle}{\epsilon_\alpha - \epsilon_\beta} - \frac{\gamma^2}{2}|\psi_\alpha\rangle\sum_\beta\frac{|\langle\psi_\beta|\Delta|\psi_\alpha\rangle|^2}{(\epsilon_\alpha - \epsilon_\alpha)^2} \tag{15}$$

where the sum over β includes only the unoccupied states. It is easily verified that the preceding wave function remains normalized to second order to the term that is quadratic in γ and that the derivatives satisfy the necessary constraints discussed in the preceding text. Note that Δ or the other factor containing $1/c^2$ is the small parameter in the preceding equation. For a noninteracting collection of electrons it follows immediately that $\gamma = 1$. With respect to the energy for the $\Delta = 0$ limit, (ΔE) for this set of wave functions is to order $(\Delta 2)$ given by:

$$\Delta E = \delta E + \sum_\alpha[(\langle\delta\psi_\alpha|i\Delta|\psi_\alpha\rangle + c.c) + \langle\psi_\alpha|i\Delta|\psi_\alpha\rangle] \tag{16}$$

Now, *if and only if* the perturbing operator $\mathrm{i}\Delta$ yields a vanishing expectation value for each occupied orbital, that is, $\langle\psi_\alpha|i\Delta|\psi_\alpha\rangle = 0$, to second order in γ, the above energy reduces to:

$$\Delta E = -\gamma^2\sum_{\alpha\beta}\frac{|\langle\psi_\alpha|\Delta|\psi_\beta\rangle|^2}{\epsilon_\alpha - \epsilon_\beta} + 2\gamma\sum_{\alpha\beta}\frac{|\langle\psi_\alpha|\Delta|\psi_\beta\rangle|^2}{\epsilon_\alpha - \epsilon_\beta} \tag{17}$$

Since $\epsilon_\beta > \epsilon_\alpha$ for all pairs of occupied and unoccupied states, differentiating the preceding equation with respect to the self-consistency parameter (γ) leads to the conclusion that $\gamma = 1$ for this specific case. Therefore, an upper bound to the second-order energy for a given δ is given by:

$$\Delta E = \sum_{\alpha\beta}\frac{|\langle\psi_\alpha|\Delta|\psi_\beta\rangle|^2}{\epsilon_\alpha - \epsilon_\beta} \tag{18}$$

Now, to connect the preceding formalism to the determination of a phenomenological magnetic anisotropy Hamiltonian, we must start by deriving the spin-orbit energy of a Slater determinant composed of a set of orthonormal single-particle spin orbitals $(\psi_{1\sigma}, \ldots, \psi_{N_\sigma\sigma}, \psi_{1\sigma'}, \ldots, \psi_{N'_\sigma\sigma'})$ where N_σ and N'_σ are the number of electrons for each spin type. Each of these orbitals is a product of a spatial function and a spinor according to:

$$|\psi_{n\sigma}\rangle = \phi_n(\mathbf{r})|\chi_\sigma\rangle \tag{19}$$

$$\langle\phi_{n\sigma}|\phi_{m\sigma}\rangle = \delta_{mn} \tag{20}$$

$$\langle\chi_\sigma|\chi_{\sigma'}\rangle = \delta_{\sigma\sigma'} \tag{21}$$

Note that there is no constraint assumed about the orthonormality of the spatial functions with a different spin index. However, with the exception of the unpaired electrons, the spatial wave functions for antiparallel spin orbitals are nearly identical especially for the core states. Further, we have not yet specified an axis of quantization for the spinors. For now, this choice is assumed to be arbitrary. It is convenient and physically useful to specify the axis of quantization of the spinors with respect to one particular spinor-choice, or alternatively molecular axis, according to:

$$|\chi_1\rangle = \cos\frac{\theta}{2}|\uparrow\rangle + e^{i\phi}\sin\frac{\theta}{2}|\downarrow\rangle$$
$$|\chi_2\rangle = -e^{-i\phi}\sin\frac{\theta}{2}|\uparrow\rangle + \cos\frac{\theta}{2}|\downarrow\rangle \tag{22}$$

The many-electron spin-orbit operator may be written in terms of single-particle operators, corresponding to spin-orbit interactions between the electrons and the coulomb potential of the nuclei and two-particle operators, corresponding to spin-orbit interactions between an electron and the coulomb potential of the other electrons. We discuss the two-particle term in detail and merely give the results of the more-commonly discussed one-electron contributions. The exact two-electron spin-orbit operator may be written in a manifestly symmetric form according to:

$$G_{ls} = \frac{1}{4c^2}\sum_{i,j\neq i}\left[S_i\cdot\nabla_i\frac{1}{r_{ij}}\times p_i + S_j\cdot\nabla_j\frac{1}{r_{ji}}\times p_j\right] \tag{23}$$

$$G_{ls} = \sum_{i,j\neq i} g_{ij} \tag{24}$$

Given an antisymmetrized many-electron Slater determinant composed of the preceding single-particle orbitals, the expectation value of this operator can be evaluated following standard analytic procedures outlined by Slater. The energy is found to be:

$$\langle\Psi|G_{ls}|\Psi\rangle = C_{ls} + E_{ls} \tag{25}$$
$$C_{ls} = \sum_{\alpha\beta}\langle\psi_\alpha(1)\psi_\beta(2)|g_{12}|\psi_\alpha(1)\psi_\beta(2)\rangle \tag{26}$$
$$E_{ls} = -\sum_{\alpha\beta}\langle\psi_\alpha(1)\psi_\beta(2)|g_{12}|\psi_\beta(1)\psi_\alpha(2)\rangle \tag{27}$$

with C_{ls} and E_{ls} the coulomb and exchange contributions to the spin-orbit energy, respectively. Note that the above term is zero if all the above wave functions are real or if there is a set of real wave functions that are related to the above wave functions by a unitary transformation. The constraint of real unperturbed wave functions is important here and in other parts of the derivation. In the preceding equation the summation indices (α, β) include both spatial and spin indices (e.g., $\alpha = n, \sigma$). The exchange contribution manifests itself from the Pauli principle. The coulomb contribution to the spin-orbit term reduces to

$$C_{ls} = \frac{1}{2c^2}\sum_\alpha\langle\psi_\alpha|\mathbf{S}\cdot\boldsymbol{\nabla}\boldsymbol{\Phi}_{\mathrm{e-e}}(\mathbf{r})\times\mathbf{p}|\psi_\alpha\rangle \tag{28}$$

where $\Phi_{\mathrm{e-e}}(\mathbf{r})$ is the electronic coulomb potential. Since we are interested in determining quantities such as $\frac{\mathrm{d}C_{ls}}{\mathrm{d}\gamma}$, we note here that for real zeroth order wave functions it is the explicit dependencies on ψ_α in preceding equation. The coulomb potential changes but since it remains real (i.e., not complex), the change in electronic coulomb potential does not contribute to the first derivative of the coulomb contributions to the spin-orbit energy if the zeroth order wave functions are real.

However, when the single-electron operators associated with the spin-orbit coupling with the nuclei are included, one finds an expression identical to that above, with Φ_{nuc}, the coulomb potential of the nuclei or other applied coulomb field, replacing the electronic coulomb term. Thus, the spin-orbit interaction due to the entire coulomb field Φ is simply

$$C_{ls} = \frac{1}{2c^2}\sum_\alpha\langle\psi_\alpha|\mathbf{S}\cdot\boldsymbol{\nabla}\boldsymbol{\Phi}(\mathbf{r})\times\mathbf{p}|\psi_\alpha\rangle \tag{29}$$

The exchange contributions will be discussed further in the following section. In all of the previous calculations by the NRL group and in most calculations the author is aware of the exchange term has been neglected.

Now that the spin-orbit energy and the perturbative expression for the anisotropy have been developed, it is possible to discuss how these two techniques can be used to derive the phenomenological Hamiltonians that describe molecular magnets. We start by noting that the momentum operator $\mathbf{p} = -i\nabla$ and combine equations (18) and (29) to yield a bound on the second-order spin-orbit energy for a specific set of angles (θ, ϕ). We find:

$$\Delta E = \frac{1}{4c^4}\sum_{\alpha\beta}\frac{\langle\psi_\alpha|\mathbf{S}\cdot\boldsymbol{\nabla}\boldsymbol{\Phi}\times\boldsymbol{\nabla}|\psi_\beta\rangle\langle\psi_\beta|\mathbf{S}\cdot\boldsymbol{\nabla}\boldsymbol{\Phi}\times\boldsymbol{\nabla}|\psi_\alpha\rangle}{\epsilon_\alpha - \epsilon_\beta} \tag{30}$$

$$\Delta E = \frac{1}{4c^4}\sum_{ij}\sum_{\sigma\sigma'}\langle\chi'_\sigma|S_i|\chi_\sigma\rangle\langle\chi_\sigma|S_j|\chi'_\sigma\rangle \times\sum_{nm}\frac{\langle\phi_{n\sigma}|V_i|\phi_{m\sigma}\rangle\langle\phi_{m\sigma}|V_j|\phi_{n\sigma}\rangle}{\epsilon_{n\sigma} - \epsilon_{m\sigma'}} \tag{31}$$

$$V_j = (\mathbf{S}\cdot\boldsymbol{\nabla}\boldsymbol{\Phi}\times\boldsymbol{\nabla})_j \tag{32}$$

To simplify the notation, it is useful to make the following definition for the matrix $M_{ij}^{\sigma\sigma'}$ and note the following

simplification for the matrix elements $\langle\phi_m|V_i|\phi_n\rangle$.

$$M_{ij}^{\sigma\sigma'} = \frac{1}{4c^4}\sum_{nm}\frac{\langle\phi_n|V_i|\phi_m\rangle\langle\phi_m|V_j|\phi_n\rangle}{\epsilon_{n\sigma}-\epsilon_{m\sigma'}} \tag{33}$$

$$S_i^{\sigma\sigma'} = \langle\chi_\sigma|S_i|\chi'_\sigma\rangle \tag{34}$$

$$\langle\phi_{n\sigma}|V_x|\phi_{m\sigma'}\rangle = \left\langle\frac{\mathrm{d}\phi_{n\sigma}}{\mathrm{d}z}|\Phi|\frac{\mathrm{d}\phi_{m\sigma'}}{\mathrm{d}y}\right\rangle - \left\langle\frac{\mathrm{d}\phi_{n\sigma}}{\mathrm{d}y}|\Phi|\frac{\mathrm{d}\phi_{m\sigma'}}{\mathrm{d}z}\right\rangle \tag{35}$$

The matrix elements V_x and V_y are determined from cyclical permutations of the preceding equations. This equation can be derived from the more standard expression of the spin-orbit interaction through an integration by parts (see (Pederson and Khanna, 1999)). With these definitions, the anisotropy energy as a function of spin quantization axis takes the following form

$$\Delta E = \sum_{ij}\sum_{\sigma\sigma'} M_{ij}^{\sigma\sigma'} S_i^{\sigma\sigma'} S_j^{\sigma'\sigma} \tag{36}$$

The final step in understanding magnetization in a molecular magnet is to notice that equation (37) still depends on the angles (θ, ϕ) in the unitary transformation (equation (22)). Therefore, the energy ΔE explicitly depends on these values of angles. Conceptually, one would be interested in mapping out the energy as a function of these two angles. It is worth mentioning that with the specific parameterization of the unitary transformation (equation (22)), the angles correspond to the two rotation angles used in a spherical coordinate system. One approach is to calculate $\Delta E(\theta, \phi)$ and find the vectors/angles which find the critical points of the second-order spin-orbit interaction. For the case of a uniaxial molecule, this was worked out in detail by Pederson and Khanna. However, there is a more elegant way to rewrite the preceding equations in terms of the usually physically meaningful expectation values of $\langle S_i\rangle$. Following (Postnikov, Kortus and Pederson, 2006), we note:

$$\langle S_i\rangle = \sum_{n\sigma}\langle\psi_{n\sigma}|S_i|\psi_{n\sigma}\rangle \tag{37}$$

$$= [N_\sigma - N_{\sigma'}]\langle\chi_\sigma|S_i|\chi_\sigma\rangle = \Delta N\langle\chi_\sigma|S_i|\chi_\sigma\rangle \tag{38}$$

$$= [N_{\sigma'} - N_\sigma]\langle\chi'_\sigma|S_i|\chi'_\sigma\rangle = -\Delta N\langle\chi'_\sigma|S_i|\chi'_\sigma\rangle \tag{39}$$

where ΔN is the total moment of the molecule. In addition, it can be shown, for $\sigma \neq \sigma'$, that:

$$\langle\chi_\sigma|S_i|\chi'_\sigma\rangle\langle\chi'_\sigma|S_j|\chi_\sigma\rangle = \langle\chi_\sigma|S_iS_j|\chi_\sigma\rangle - \langle\chi_\sigma|S_i|\chi_\sigma\rangle\langle\chi_\sigma|S_j|\chi_\sigma\rangle \tag{40}$$

$$= \frac{\delta_{ij}}{4} - \frac{\langle S_i\rangle\langle S_j\rangle}{\Delta N^2} \tag{41}$$

Substituting these expressions for $\langle\chi_\sigma|S_i|\chi'_\sigma\rangle$ in equation 37 gives the second-order spin-orbit energy as a function of $\langle S_i\rangle$. It is:

$$\Delta E = \sum_{ij}\langle S_i\rangle\langle S_j\rangle\frac{1}{\Delta N^2}[M_{ij}^{11} + M_{ij}^{22} - M_{ij}^{12} - M_{ij}^{21}] + \frac{1}{4}\sum_i(M_{ii}^{12} + M_{ii}^{21}) \tag{42}$$

From this, it follows that the effective anisotropy tensor is defined according to:

$$\gamma_{ij} = \frac{1}{\Delta N^2}[M_{ij}^{11} + M_{ij}^{22} - M_{ij}^{12} - M_{ij}^{21}] \tag{43}$$

and we arrive at the final expression for the second-order spin-orbit energy as a function of spin projection. It is:

$$\Delta E = \sum_{ij}\gamma_{ij}\langle S_i\rangle\langle S_j\rangle \tag{44}$$

For any vector of length $|\mathbf{S}| = \frac{\Delta N}{2}$ the spin-orbit energy may be found as a function of orientation. It seems reasonable to requantize this expression and write the phenomenological Hamiltonian as

$$H = \sum_{ij}\gamma_{ij}S_iS_j \tag{45}$$

By diagonalizing the anisotropy tensor, it is possible to recast the preceding equation in the phenomenological form given in equation (1). The division by ΔN^2 in equation (44) is convenient except for the case that an antiferromagnetic system, with zero net spin, is being studied. Under this condition, the expression for the energy as a function of angles in the unitary transformation, or possibly Neel vector, would be a better way of representing the physics.

4 RECENT APPLICATIONS

Two very good reviews on applications of density-functional theory to molecular magnets are about to be published (Postnikov, Kortus and Pederson, 2006; Pederson, Park and Baruah, 2006). However, most of the applications discussed in this work were published prior to 2003. In this section, we primarily give a survey of work that has been completed since then that does not appear in the other reviews.

The method described in the preceding text has been implemented in the NRLMOL code (Pederson and Lin, 1987; Pederson and Jackson, 1990, 1991; Jackson and Pederson, 1990; Quong, Pederson and Feldman, 1993; Pederson, Broughton and Klein, 1988; Porezag and Pederson,

1996, 1999; Briley *et al*., 1998) a few years ago. Since then it has been used to study the anisotropy parameters, local anisotropy axes, and parameters. The first calculations carried out on the Mn_{12}-acetate could correctly predict the anisotropy parameter D within less than 1% error. Since then several different types of molecular magnets have been studied. The density-functional parameters of the spin Hamiltonian, that is, the D and E parameters in equation 5 for various molecular magnets are listed in Table 1 and compared with the available experimental values.

The density-functional theory (DFT) studies on Mn_{12}, Fe_8, Mn_{10}, Co_4, and Mn_4 have been discussed extensively in previous articles (Pederson and Khanna, 1999; Kortus, Pederson, Hellberg and Khanna, 2001; Pederson, Kortus and Khanna, 2002; Baruah *et al*., 2004; Kortus, Hellberg and Pederson, 2001; Kortus, Baruah, Bernstein and Pederson, 2002; Baruah and Pederson, 2002; Baruah and Pederson, 2003; Kortus *et al*., 2003). The energy band gap in the system plays an important role in determining the parameters, which are obtained through a perturbative treatment. However, surprisingly, in Mn_{12}, the DFT calculation gives a very good agreement with experiment for the D parameter. In Mn_{12}, which has S_4 symmetry, the E parameter turns out to be zero by symmetry. However, experiments show tunneling which violates the selection rules applicable to S_4 symmetry. The presence of a small E contribution can possibly arise due to the presence of symmetry-breaking ligands or presence of an extra electron. Incorporation of these effects yields an E parameter 0.016 K (Park, Baruah, Bernstein and Pederson, 2004). The other cases where the DFT calculations give very good agreement with experiment are $[Mn_{10}O_4(2,2'\text{-biphenoxide})_4Br_{12}]^{4-}$, $[Mn_4\ O_3Cl_4(O_2CCH_3CH_2)_3(C_5H_5N)_3]$, and Fe_4 (Kortus, Baruah, Bernstein and Pederson, 2002; Park *et al*., 2003; Kortus *et al*., 2003). The disagreement for the Co_4 molecule is controversial in the sense that there is a lack of reliable experimental data (Yang *et al*., 2002) to compare with. When compared to Co_6 (Murrie, Teat, Stoeckli-Evans and Güdel, 2003) which also has the same cubane structure at the center, the calculated values of the anisotropy barrier agrees well with experimental values. Among all the tabulated systems, the most glaring discrepancy is seen for the $Fe_8O_2OH_{12}(tacn)_6]^{8+}Br_87(H_2O)$ molecule. The Fe_8 molecule is very well studied experimentally and the experimental D parameter is -0.29 K. The Br–Fe_8 molecule has C_1 symmetry but in most calculations which are done at the all-electron level, some symmetry is enforced to make the calculations tractable. This is not unreasonable considering the fact that the calculations are done on the core molecule in the $+2$ charged state without the accompanying symmetry-breaking water molecules and the bromine ions. The calculated gap is small in the Fe_8 and further corrections due to self-interaction may be required. Another example where theory and experiment differ is the Ni_4 analog of Co_4. The Ni_4 molecule has been synthesized with different ligands such as CH_3, CH_2CH_3, or $(CH_2)_2C(CH_3)_3$. The measured electron paramagnetic resonance (EPR) spectra yield values of D between 0.72 and 1.03 K but the calculations found D to be between 0.25 and 0.37 K. Interestingly, DFT finds the $S = 0$ state as the lowest-energy state.

The organic ligands compensate the charges of the transition-metal centers. However, the role of the ligands does not stop there. They also produce the crystal field, and changing the type of ligands can lead to an enhancement of the effective barrier. One example of such barrier enhancement is the $Fe_4(OMe)_6(dpm)_6$ and $Fe_4(thme)_6(dpm)_6$ molecules (Figure 3). The $Fe_4(OMe)_6(dpm)_6$ has C_2 symmetry and four iron atoms lie on a plane such that three of the atoms form an isosceles triangle and the C_2 axis passes through the central iron and one of the apical ones. The

Table 1. Calculated and experimental magnetic anisotropy parameters for different molecular magnets.

Molecular magnet system	Symmetry	Spin S	Gap (eV)	D (K)	E (K)	Experiment D(K), E(K)
$Mn_{12}O_{12}(CH_3COOH)_164(H_2O)$	S4	10	0.45–2.08	−0.55	0.0	−0.56, 0.0
$Fe_8O_2OH_{12}(tacn)_6]^{8+}Br_87(H_2O)$	I,D2	10	0.15–0.54	−0.54 to −0.72	0.05	−0.29, 0.05
Co_4 $(hmp)_4(CH3OH)_4Cl_4$	S4	6	0.55	−0.64	0.0	2.8 −5.6
$[Mn_{10}O_4(2,2'\text{-biphenoxide})_4Br_{12}]^{4-}$	Td	13	–	−0.56	0.06	−0.57, 0.05
$[Mn_4\ O_3Cl_4(O_2CCH_3CH_2)_3(C_5H_5N)_3]$	I	9/2	1.02–2.42	−0.55 to −0.60	−0.72	–
$Fe_4(OMe)_6(dpm)_6$	C2	5	1.04–1.16	−0.071	−0.043	−0.29, 0.01
$Fe_4(thme)_6(dpm)_6$	D3	5	0.81–1.13	−0.64	0.00	−0.64, 0.014
$Fe_4(sae)_4(MeOH)_4$	C1	8	0.48	0.25	0.00	1.14
$Fe_4(sap)_4(MeOH)_4$	S4	8	0.31	−0.10	0.004	−1.09/−0.44
Fe_4	S4	5	–	−0.56	0.06	−0.57, 0.05
$Ni_4(hmp)_4(ROH)_4$	S4	0/4	1.47–2.18	0.25–0.37	0.0	0.72 − 1.03

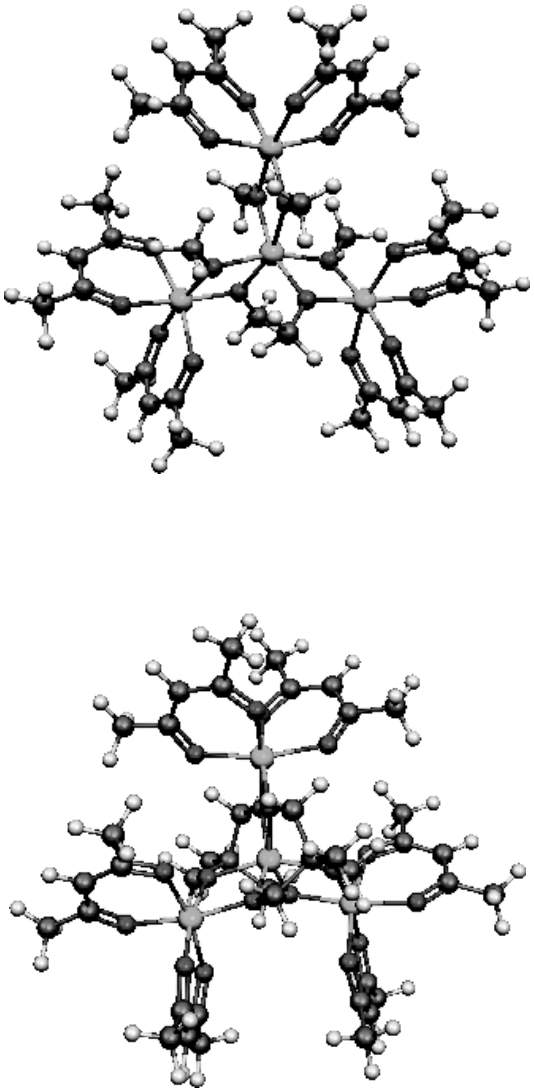

Figure 3. The molecular structures of $Fe_4(OMe)_6(dpm)_6$ and $Fe_4(thme)_6(dpm)_6$.

$Fe_4(thme)_6(dpm)_6$ molecule possesses D_3 symmetry with three iron atoms forming an equilateral triangle with the fourth at the center. Both the molecules have total spin $S = 5$, but the magnetic anisotropy barrier in the $Fe_4(thme)_6(dpm)_6$ is 15.6 K while that of the $Fe_4(OMe)_6(dpm)_6$ is 3.5 K.

The spin interaction between the iron atoms shows similar characteristics in both the molecules – ferromagnetic interaction between the peripheral atoms and antiferromagnetic interaction between the pheral and central atom. Both the molecules are uniaxial with the easy axis coinciding with the C_2 and C_3 axes of symmetry. The main structural difference between the two systems is seen at the position of the central atom. However, elongation of bonds or rotation of the ligands pertaining to the central atom does not fully explain the difference in magnetism between the two molecules. The atom-projected anisotropies show that the orientation of the projected local anisotropy axes are completely different in the two systems. It is the collinear alignment of the local easy axes that leads to a global easy axis system in $Fe_4(thme)_6(dpm)_6$.

The other two Fe_4 compounds are remarkable in that both have a Fe_4O_4 cubane structure but the ligands are slightly different. The $(sap)^{-2}$ has a six-membered ring while the $(sae)^{-2}$ contains a five-membered ring thus leading to different steric strains on the Fe(II) ions. The consequences are that the one with the five-membered ring shows single-molecule magnet behavior while the other does not. This is another example of the ligand changing the magnetic behavior of the molecule.

The calculations on these series of molecules are preliminary, but conclusively show that the π-back donation from the Fe(II) to the ligands allows control of the sign and magnitude of the D parameter. In the $Fe_4(sae)_4(MeOH)_4$ the local easy axes are nearly orthogonal ($\sim 73^\circ$) to the S_4 symmetry axis. In the $Fe_4(sap)_4(MeOH)_4$ cluster, which has nearly S_4 symmetry, the local easy axis has more overlap on the pseudo-S_4 axis leading to a global easy axis system. Further, switching the positions of the imine fragment and a hydroxyl ligand can enhance the barrier by a factor of 6, which is remarkable. This study shows that the steric strains and the orientation of the local axes can enhance or reduce the global SMM behavior.

5 SUMMARY

During the last eight years, the ability to perform calculations on molecular magnets has grown due to new algorithms, faster computers, and an increasing number of researchers interested in this field. This chapter has discussed the basic phenomenological Hamiltonians and a formalism for developing these Hamiltonians from a first-principles methodology such as density-functional theory. There is now a large set of calculated results, which are generally in qualitative accord and often in quantitative accord with experiment. It is hoped that additional work will be performed to further improve computational methodologies for molecular magnets.

Future improvements in the computational methods are likely to concentrate on several different problems. First, pursuit of an improved description of exchange and correlation within a density-functional framework should be one area of concentration. Second, the formalisms discussed here concentrate on two extremes in transition-metal-containing molecules. In one case, the low-energy excitations are determined entirely from exact diagonalization of a many-spin Hamiltonian. In the other case, it is assumed that the leading term from this exact diagonalization will provide a good

anisotropy Hamiltonian. Discussions as to why this is *sometimes* the case have been recently held. However, it is most desirable to develop a formalism that can account directly for multiconfiguration contributions to the magnetic anisotropy. Finally, there is still not much success in quantitatively understanding the higher-order corrections to the magnetic anisotropy Hamiltonian. Future efforts aimed at this problem will be both challenging and useful. It is quite possible that such efforts will require a self-consistent constrained solution to the electronic Hamiltonian. This calls for strong efforts at extending many different electronic structure methods.

ACKNOWLEDGMENTS

This work was supported in part by ONR and NSF. The authors thank Prof. S.N. Khanna, J. Kortus, S. Hellberg, N. Bernstein, K. Park, and J. Ribas for many interesting collaborations on molecular magnetism. It should also be noted that without early developmental efforts by K.A. Jackson, D.V. Porezag, and D. Patton on the nonmagnetic code, it would have been difficult to convert the preceding formalism into an efficient code for understanding molecular magnetism. We thank the editors of this handbook for encouraging us to complete this chapter and for their patience.

REFERENCES

Barbara, B. and Gunther, L. (1999). Magnets, molecules and quantum mechanics. *Physics World*, **12**(3), 35–39.

del Barco, E., Kent, A.D., Chakov, N.E., *et al*. (2004). Distribution of internal transverse magnetic fields in a Mn_{12}-based single molecule magnet. *Physical Review B*, **69**, 020411.

Barra, A-L., Brunner, P., Gatteschi, D., *et al*. (1996). Superparamagnetic-like behavior in an octanuclear iron cluster. *Europhysics Letters* **35**, 133.

Baruah, T. and Pederson, M.R. (2002). Electronic structure and magnetic anisotropy of the $[Co_4(hmp)_4(CH_3OH)_4C_{l4}]$ molecule. *Chemical Physics Letters*, **360**, 144.

Baruah, T. and Pederson, M.R. (2003). Density functional study of the conformers of Co_4-based single-molecule magnet. *International Journal of Quantum Chemistry*, **93**, 324.

Baruah, T., Kortus, J., Pederson, M.R., *et al*. (2004). Understanding the electronic structure, optical, and vibrational properties of the Fe_8Br_8 single-molecule magnet. *Physical Review B*, **70**, 214410.

Briley, A., Pederson, M.R., Jackson, K.A., *et al*. (1998). Vibrational frequencies and intensities of small molecules: all-electron, pseudo-and mixed-potential methodologies. *Physical Review B*, **58**, 1786.

Cornia, A., Sessoli, R., Sorace, L., *et al*. (2002). Origin of second-order transverse magnetic anisotropy in Mn12-acetate. *Physical Review Letters*, **89**, 257201.

Ferlay, S., Mallah, T., Ouahes, R., *et al*. (1995). A room-temperature organometallic magnet based on Prussian blue. *Nature*, **378**, 701–703.

Friedman, J., Sarachik, M.P., Tejeda, J., *et al*. (1996). Macroscopic measurement of resonant magnetization tunneling in high-spin molecules. *Physical Review Letters*, **76**, 3820.

Gaspar, A.B., Munoz, M.C., Moliner, N., *et al*. (2003). Polymorphism and pressure driven thermal spin crossover phenomenon in Fe(abpt)(2)(NCX)(2) (X = S, and Se): synthesis, structure and magnetic properties. *Monatshefte fur Chemie*, **134**, 285–294.

Gatteschi, D., Pardi, L., Barra, A.L., *et al*. (1991). Layered magnetic structure of a metal cluster polyanion. *Nature*, **354**, 463.

Garg, A. (1993). Topologically quenched tunnel splitting in spin systems without Kramers' degeneracy. *Europhysics Letters*, **22**, 205.

Hill, S., Edwards, R.S., Jones, S.I., *et al*. (2003). Definitive spectroscopic determination of the transverse interactions responsible for the magnetic quantum tunneling in Mn_{12}-acetate. *Physical Review Letters*, **90**, 217204.

Hohenberg, P. and Kohn, W. (1964). Inhomogeneous electron gas. *Physical Review*, **136**, B864.

Jackson, K.A. and Pederson, M.R. (1990). Accurate forces in a local-orbital approach to the local-density approximation. *Physical Review B*, **42**, 3276.

Kahn, O. (1993). *Molecular Magnetism*, John Wiley & Sons: Singapore.

Katsnelson, M.I., Dobrovitski, V.V. and Harmon, B.N. (1999). Many-spin interactions and spin excitations in Mn_{12}. *Physical Review B*, **59**, 6919.

Kohn, W. and Sham, L.J. (1965). Self-consistent equations including exchange and correlation effects. *Physical Review*, **140**, A1133.

Kortus, J., Baruah, T., Bernstein, N. and Pederson, M.R. (2002). Magnetic ordering, electronic structure, and magnetic anisotropy energy in the high-spin Mn_{10} single molecule magnet. *Physical Review B*, **66**, 092403.

Kortus, J., Hellberg, C.S. and Pederson, M.R. (2001). Hamiltonian of the V_{15} spin system from first-principles density-functional calculations. *Physical Review Letters*, **86**, 3400.

Kortus, J., Pederson, M.R., Hellberg, C.S. and Khanna, S.N. (2001). DFT studies of the molecular nanomagnet Fe_8 and the V_{15} spin system: electronic structure and magnetic ordering. *European Physical Journal D*, **16**, 177.

Kortus, J., Pederson, M.R., Baruah, T., *et al*. (2003). Density functional studies of single molecule magnets. *Polyhedron*, **22**, 1871.

Lis, T. (1980). Preparation, structure and magnetic properties of a dodecanuclear mixed-valence manganese carboxylate. *Acta Crystallographica, Section B, Structural Science*, **36**, 2042.

Mirebeau, I., Hennion, M., Casalta, H., *et al*. (1999). Low-energy magnetic excitations of the Mn_{12}-acetate spin cluster observed by neutron scattering. *Physical Review Letters*, **83**, 628.

Miller J.S. and Epstein A.J. (Eds.) (2000) Molecule-based magnets. *MRS Bulletin*. **25** No. 11.

Murrie, M., Teat, S.J., Stoeckli-Evans, H. and Güdel, H.U. (2003). Synthesis and characterization of a cobalt(II) single-molecule magnet. *Angewandte Chemie International Edition*, **42**, 4633.

Thomas, L., Lionti, F., Ballou, R., *et al*. (1996). Macroscopic quantum tunnelling of magnetization in a single crystal of nanomagnets. *Nature (London)*, **383**, 145.

Turnbull, M.M., Sugimot, T. and Thompson, L.K. (Eds.) (1996). *Molecule-Based Magnetic Materials, Theory, Techniques and Applications*, Oxford University Press.

Palacio, F. and Markova, T. (Eds.) (2006). *Carbon-based Magnetism: An Overview of the Magnetism of Metal-free Carbon-based Compounds and Materials*, Elsevier.

Park, K., Baruah, T., Bernstein, N. and Pederson, M.R. (2004). Second-order transverse magnetic anisotropy induced by disorders in the single-molecule magnet Mn_{12}. *Physical Review B*, **69**, 144426.

Park, K., Pederson, M.R. and Hellberg, C.S. (2004). Properties of low-lying excited manifolds in the Mn_{12} acetate. *Physical Review B*, **69**, 014416.

Park, K., Pederson, M.R., Richardson, S.L., *et al*. (2003). Density-functional theory calculation of the intermolecular exchange interaction in the magnetic Mn4 dimer. *Physical Review B*, **68**, 020405(R).

Pederson, M.R., Bernstein, N. and Kortus, J. (2002). Fourth-order magnetic anisotropy and tunnel splittings in Mn_{12} from spin-orbit-vibron interactions. *Physical Review Letters*, **89**, 097202.

Pederson, M.R., Broughton, J.Q. and Klein, B.M. (1988). Simulated Annealing with Floating Gaussians: Hellmann-Feynman Forces without Corrections. *Physical Review B*, **38**, 3825.

Pederson, M.R. and Jackson, K.A. (1990). Variational mesh for quantum-mechanical simulations. *Physical Review B*, **41**, 7453.

Pederson, M.R. and Jackson, K.A. (1991). Pseudoenergies for simulations on metallic systems. *Physical Review B*, **43**, 7312.

Pederson, M.R. and Khanna, S.N. (1999). Magnetic anisotropy barrier for spin tunneling in $Mn_{12}O_{12}$ molecules. *Physical Review B*, **60**, 9566.

Pederson, M.R., Kortus, J. and Khanna, S.N. (2002). Electronic-structure-based investigation of magnetism in the Fe_8 molecular magnet. *Journal of Applied Physics*, **91**, 7149.

Pederson, M.R. and Lin, C.C. (1987). All-electron self-consistent variational method for Wannier-type functions: applications to the silicon crystal. *Physical Review B*, **35**, 2273.

Pederson, M.R., Park, K. and Baruah, T. (2006). Density-Functional Based Investigation of Molecular Magnets, *Current Trends in Computational Chemistry*, Vol. 10, Leszczynski, J. (Ed.), World Scientific: pp. 83–120.

Park K., Pederson, M.R., Baruah T., *et al*. (2005). Incommensurate transverse anisotropy induced by disorder and spin-orb it-vibron coupling in Mn-12 acetate. *Journal of Applied Physics*, **97**, 10M505.

Perdew, J.P., Burke, K. and Ernzerhof, M. (1996). Generalized gradient approximation made simple. *Physical Review Letters*, **77**, 3865.

Perdew, J.P., Chevary, J.A., Vosko, S.H., *et al*. (1992). Atoms, molecules, solids, and surfaces: applications of the generalized gradient approximation for exchange and correlation. *Physical Review B*, **45**, 6671.

Petukhov, K., Hill, S., Chakov, N.E., *et al*. (2004). Evidence for the $S = 9$ excited state in Mn_{12}-bromoacetate measured by electron paramagnetic resonance. *Physical Review B*, **70**, 05446, preprint cond-mat/0403435.

Porezag, D.V. and Pederson, M.R. (1996). Infrared intensities and Raman-scattering activities within density-functional theory. *Physical Review B*, **54**, 7830.

Porezag, D. and Pederson, M.R. (1999). Optimization of Gaussian basis sets for density-functional calculations. *Physical Review A*, **60**, 9566.

Postnikov, A.V., Kortus, J. and Pederson, M.R. (2006). Density Functional Studies of Molecular Magnets. *Physica Status Solidi*, **243**, 2533–2572.

Quong, A.A., Pederson, M.R. and Feldman, J.L. (1993). First-Principles Determination of the Interatomic Force-Constant Tensor of the Fullerene Molecule. *Solid State Communications*, **87**, 535.

Robinson, R.A., Brown, P.J., Argyriou, D.N., *et al*. (2000). Internal magnetic structure of Mn_{12} acetate by polarized neutron diffraction. *Journal of Physics. Condensed Matter*, **12**, 2805.

Sangregorio, C., Ohm, T., Paulsen, C., *et al*. (1997). Quantum tunneling of the magnetization in an iron cluster nanomagnet. *Physical Review Letters*, **78**, 4645.

Wernsdorfer, W. and Sessoli, R. (1999). Oscillations and parity effects in the tunneling rate of the magnetization of Fe_8 molecular clusters due to quantum phase interference. *Science*, **284**, 133.

Wernsdorfer, W., Ohm, T., Sangregorio, C., *et al*. (1999). Observation of the distribution of molecular spin states by resonant quantum tunneling of the magnetization. *Physical Review Letters*, **82**, 3903.

Yang, E.C., Hendrickson, D.N., Wernsdorfer, W., *et al*. (2002). Cobalt single-molecule magnet. *Applied Physics Letters*, **91**, 7382.

FURTHER READING

Cornia, A., Fabretti, A.C., Garrisi, P., *et al*. (2004). Energy-barrier enhancement by ligand substitution in tetrairon(III) single-molecule magnets. *Angewandte Chemie International Edition*, **43**, 1136.

Oshio, H., Hoshino, N. and Ito, T. (2000). Superparamagnetic behavior in Alkoxo-bridged iron(II) cube. *Journal of the American Chemical Society*, **122**, 12602.

Oshio, H., Hoshino, N., Ito, T. and Nakano, M. (2004). Single molecule magnets of ferrous cubes: structurally controlled magnetic anisotropy. *Journal of the American Chemical Society*, **126**, 8805.

Ribas-Arino, J., Baruah, T. and Pederson, M.R. (2005). Density-functional study of two Fe_4-based single-molecule magnets. *Journal of Chemical Physics*, **123**, 044303.

Ribas-Arino, J., Baruah, T. and Pederson, M.R. (2005). Density-functional study of two Fe4- based single-molecule magnets. *Journal of Chemical Physics* **123**, 044303.

Interplay of Superconductivity and Magnetism

Saburo Takahashi and Sadamichi Maekawa
Tohoku University, Sendai, Japan

1 INTRODUCTION

The interplay of superconductivity and magnetism is a long-standing and fascinating research subject in condensed-matter physics (Buzdin, 2005; Golubov, Kupriyanov and Il'ichev, 2005; Bergeret, Volkov and Efetov, 2005; Izyumov, Proshin and Khusainov, 2002). It is widely recognized that superconductivity and magnetism are mutually exclusive because of their essentially different ordered states. Superconductivity in conventional superconductors is due to Cooper pairs of two electrons with opposite spin and momentum ($k\uparrow, -k\downarrow$). The attractive interaction between electrons creates Cooper pairs in a singlet state. In contrast, the ferromagnetic exchange interaction forces electron spins to align in parallel and produces ferromagnetism. Therefore, when the Zeeman energy of an electron pair in the exchange field $h_{\rm ex}$ exceeds the condensation energy of the pair, which is measured by the superconducting gap Δ, the superconducting state is destroyed. The corresponding depairing exchange field is $h_{\rm ex} \sim \Delta/\mu_{\rm B}$, where $\mu_{\rm B}$ is the Bohr magneton. It was predicted a long time ago that a spatially inhomogeneous order parameter with Cooper pairs of nonzero-momentum state appears near the depairing field. This state is called the *Fulde–Ferrell–Larkin–Ovchinnikov* (*FFLO*) state (Fulde and Ferrel, 1964; Larkin and Ovchinnikov, 1965). However, there has been no clear observation in bulk materials with the possible exception of the heavy-fermion superconductor $CeCoIn_5$ (Bianchi *et al*., 2003; Kakuyanagi *et al*., 2005).

For the preceding reasons, the coexistence of superconducting order and ferromagnetic order is quite unlikely in bulk materials. However, recent advances in nanofabrication techniques make it possible to study the interplay of superconductivity and ferromagnetism by artificially preparing ferromagnet/superconductor (F/S) systems consisting of ferromagnetic and superconducting layers in the form of bilayers, trilayers, multilayers, and other structures. In these hybrid structures, the superconducting order parameter penetrates into the F layer owing to the proximity effect. Numerous theoretical and experimental studies on F/S structures (Figure 1) revealed a nonmonotonic temperature dependence of the superconducting transition temperature $T_{\rm c}$ on the thickness of the ferromagnetic layer due to the proximity effect (Radovic *et al*., 1991; Jiang, Davidović, Reich and Chein, 1995; Mühge *et al*., 1996; Aarts *et al*., 1997; Tagirov, 1999; Gu *et al*., 2002; Krunavakarn, Sritrakool and Yoksan, 2004; Obi, Ikebe and Fujishiro, 2005; Moraru, Pratt and Birge, 2006).

Of particular interest is a Josephson junction containing a ferromagnet, in which novel phenomena due to the competition between ferromagnetism and superconductivity arise. When Cooper pairs penetrate from a superconductor

Handbook of Magnetism and Advanced Magnetic Materials. Edited by Helmut Kronmüller and Stuart Parkin. Volume 1: *Fundamentals and Theory*. ISBN: 978-0-470-02217-7.

into a ferromagnet across the interface of an F/S junction, the Cooper pairs in a clean F have a finite momentum $q \sim h_{\rm ex}/v_{\rm F}$ ($v_{\rm F}$ is the Fermi velocity), because of the exchange splitting $h_{\rm ex}$ between the up-spin and the down-spin bands (Bulaevskii, Kuzii and Sobyanin, 1977; Buzdin, Bulaevskii and Panyukov, 1982; Demler, Arnold and Beasley, 1997; Kontos, Aprili, Lesueur and Grison, 2001). Consequently, the superconducting pair amplitude oscillates as $\cos(2qz)$ along the direction perpendicular to the interface. Recently, it has been demonstrated that such oscillation can be induced in a weak ferromagnet sandwiched between two superconductors, in which the current-phase relation in the Josephson current is shifted by π compared to the conventional Josephson relation (Ryazanov *et al*., 2001; Kontos *et al*., 2002; Blum, Tsukernik, Karpovski and Palevski, 2002; Sellier, Baraduc, Lefloch and Calemczuk, 2003; Frolov *et al*., 2004; Oboznov *et al*., 2006; Weides *et al*., 2006). The π state offers a new route for studying the interplay of superconductivity and magnetism and is also important to superconducting electronics, for example, quantum computing.

The spin injection technique offers a new type of F/S device (spin switching) based on the interplay of superconductivity and spin accumulation created in S. This technique allows us to electronically control the mutual influence between superconductivity and magnetism in hybrid structures, leading to spin electronics applications (Maekawa, 2006; Maekawa and Shinjo, 2002; Žutić, Fabian and Das Sarma, 2004).

2 PROXIMITY EFFECT IN S/F STRUCTURES

Let us consider the interplay of superconductivity and magnetism in a hybrid structure consisting of a superconductor and a ferromagnet, as shown in Figure 1, in which the proximity effect plays a central role. For simplicity, we concentrate on the proximity effect near the superconducting transition temperature $T_{\rm c}$, and derive a basic equation for the superconducting pair amplitude in F/S structures. The self-consistency equation for the superconducting order parameter $\Delta(\mathbf{r})$ near $T_{\rm c}$ is linearized in the form (de Gennes, 1966; Takahashi and Tachiki, 1986; Ketterson and Song, 1999)

$$\Delta(\mathbf{r}) = V(\mathbf{r}) k_{\rm B} T \sum_{\omega} \int {\rm d}\mathbf{r}' Q_{\omega}(\mathbf{r}, \mathbf{r}') \Delta(\mathbf{r}') \tag{1}$$

where $\omega = (2n+1)\pi k_{\rm B} T$, with n being an integer, $V(\mathbf{r})$ is the position-dependent pairing interaction, and $Q_{\omega}(\mathbf{r}, \mathbf{r}')$ is a

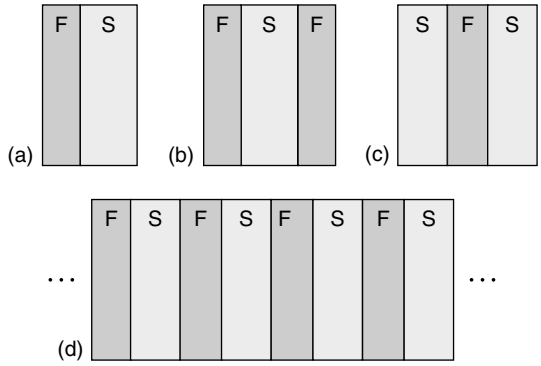

Figure 1. Various types of F/S structures. (a) F/S bilayer, (b) F/S/F trilayer, (c) S/F/S trilayer, and (d) F/S multilayer.

kernel defined by

$$Q_{\omega}(\mathbf{r}, \mathbf{r}') = \frac{1}{2} \sum_{\sigma} \sum_{m,n} \frac{\phi^*_{n\sigma}(\mathbf{r}') \phi_{n\sigma}(\mathbf{r}) \phi^*_{m-\sigma}(\mathbf{r}') \phi_{m-\sigma}(\mathbf{r})}{(i\omega - \xi_{n\sigma})(i\omega + \xi_{m-\sigma})} \tag{2}$$

where $\phi_{n\sigma}(\mathbf{r})$ is the one-electron wave function with energy $\xi_{n\sigma}$ and spin σ in the normal state. The motion of one-electron in a diffusive conductor is described by the one-electron correlation function $g_{\sigma}(\mathbf{r}', \mathbf{r}, t)$ satisfying

$$\left[\hbar \frac{\partial}{\partial t} - \hbar D(\mathbf{r}) \nabla^2 + 2i h_{\rm ex}(\mathbf{r}) \hat{\sigma}_z^{\sigma\sigma} \right] g_{\sigma}(\mathbf{r}', \mathbf{r}, t) = 0 \tag{3}$$

where $D(\mathbf{r})$ is the diffusion constant and $h_{\rm ex}(\mathbf{r})$ is the exchange potential (Zeeman energy) acting on conduction electrons, and $\hat{\sigma}_z$ is the Pauli spin operator. For $t \to 0$, $g_{\sigma}(\mathbf{r}', \mathbf{r}, t)$ reduces to the initial condition $g_{\sigma}(\mathbf{r}', \mathbf{r}, 0) = (1/2)\delta(\mathbf{r} - \mathbf{r}') N_{\sigma}(\mathbf{r})$, where $N_{\sigma}(\mathbf{r})$ is the density of states of the spin-σ band. The kernel $Q_{\omega}(\mathbf{r}, \mathbf{r}')$ and its auxiliary kernel $R_{\omega}(\mathbf{r}, \mathbf{r}')$ are written as (Takahashi and Tachiki, 1986)

$$Q_{\omega}(\mathbf{r}, \mathbf{r}') = 2\pi \int_0^{\infty} {\rm d}t \left[g_{\uparrow}(\mathbf{r}', \mathbf{r}, t) + g_{\downarrow}(\mathbf{r}', \mathbf{r}, t) \right] e^{-2|\omega|t} \tag{4}$$

$$R_{\omega}(\mathbf{r}, \mathbf{r}') = 2\pi \frac{\omega}{|\omega|} \times \int_0^{\infty} {\rm d}t \left[g_{\uparrow}(\mathbf{r}', \mathbf{r}, t) - g_{\downarrow}(\mathbf{r}', \mathbf{r}, t) \right] e^{-2|\omega|t} \tag{5}$$

If we introduce the quantities

$$\mathcal{F}^{(e)}_{\omega}(\mathbf{r}) = \int {\rm d}^3 r' Q_{\omega}(\mathbf{r}, \mathbf{r}') \Delta(\mathbf{r}'),$$
$$\mathcal{F}^{(o)}_{\omega}(\mathbf{r}) = \int {\rm d}^3 r' R_{\omega}(\mathbf{r}, \mathbf{r}') \Delta(\mathbf{r}') \tag{6}$$

we have the coupled equations (Takahashi and Tachiki, 1986; Usadel, 1970):

$$\left[2|\omega| - \hbar D(\mathbf{r})\nabla^2\right] \mathcal{F}_\omega^{(e)}(\mathbf{r}) + 2ih_\omega(\mathbf{r})\mathcal{F}_\omega^{(o)}(\mathbf{r}) = \pi N(\mathbf{r})\Delta(\mathbf{r}) \tag{7}$$

$$\left[2|\omega| - \hbar D(\mathbf{r})\nabla^2\right] \mathcal{F}_\omega^{(o)}(\mathbf{r}) + 2ih_\omega(\mathbf{r})\mathcal{F}_\omega^{(e)}(\mathbf{r}) = 0 \tag{8}$$

where $h_\omega(\mathbf{r}) = (\omega/|\omega|)h_{\rm ex}(\mathbf{r})$ and $N(\mathbf{r}) = N_\uparrow(\mathbf{r}) + N_\downarrow(\mathbf{r})$ is the electronic density of states [1]. Note that $\mathcal{F}_\omega^{(e)}(\mathbf{r}) = \mathcal{F}_{-\omega}^{(e)}(\mathbf{r})$ and $\mathcal{F}_\omega^{(o)}(\mathbf{r}) = -\mathcal{F}_{-\omega}^{(o)}(\mathbf{r})$, so that $\mathcal{F}_\omega^{(e)}(\mathbf{r})$ and $\mathcal{F}_\omega^{(o)}(\mathbf{r})$ correspond to the spin-singlet and spin-triplet components of pair amplitudes with the even- and odd-frequency dependence, respectively (Bergeret, Volkov and Efetov, 2005).

Since the pair function $F(\mathbf{r}) = \Delta(\mathbf{r})/V(\mathbf{r})$ is written as

$$F(\mathbf{r}) = k_{\rm B}T \sum_\omega \mathcal{F}_\omega^{(e)}(\mathbf{r}) \tag{9}$$

equations (7)–(9) yield the self-consistent equations for $F(\mathbf{r})$. In order to solve the self-consistent equation, we introduce the eigenfunction ψ_n and the eigenvalue ϵ_n, which satisfy

$$-\hbar D(\mathbf{r})\nabla^2\psi_n(\mathbf{r}) = \epsilon_n\psi_n(\mathbf{r}) \tag{10}$$

with the boundary conditions that $F(\mathbf{r})/N(\mathbf{r})$ and $D(\mathbf{r})$ $(\hat{\mathbf{n}}\cdot\nabla)F(\mathbf{r})$, $\hat{\mathbf{n}}$ being the unit vector normal to the interface, are continuous at the interfaces. These boundary conditions are applicable to the case that the boundary resistance is negligible [2]. Using the expansion $F(\mathbf{r}) = \sum_n a_n\psi_n(\mathbf{r})$ in the self-consistent equation, we derive the secular equation that determines the superconducting transition temperature $T_{\rm c}$ in a F/S system (Takahashi and Tachiki, 1986)

$$\det\left|\delta_{nn'} - 2\pi k_{\rm B}T\sum_\omega\sum_m \Gamma_{nm}^{-1}\langle m|VN|n'\rangle\right| = 0 \tag{11}$$

where Γ_{nm}^{-1} is the inverse of the matrix Γ with the element

$$\Gamma_{nm} = \left(|\omega| + \frac{1}{2}\epsilon_n\right)\delta_{nm} + \sum_l \frac{\langle n|h_{\rm ex}|l\rangle\langle l|h_{\rm ex}|m\rangle}{|\omega| + \frac{1}{2}\epsilon_l} \tag{12}$$

and $\langle n|VN|n'\rangle$ and $\langle n|h_{\rm ex}|n'\rangle$ are the matrix elements defined by

$$\langle n|\mathcal{O}|n'\rangle = \int {\rm d}^3r\,\psi_n^*(\mathbf{r})\mathcal{O}(\mathbf{r})\psi_n(\mathbf{r}) \tag{13}$$

The superconducting transition temperature $T_{\rm c}$ of F/S structures is determined as the highest temperature among the solutions of equation (11).

2.1 F/S interface

We consider an F/S system where the left side is occupied by S and the right side by F, as shown in Figure 2. In the F region, $\Delta(z) = 0$ $(V(z) = 0)$, so that equations (7) and (8) become

$$\left(\left[2|\omega| - \hbar D_{\rm F}\nabla^2\right]^2 + 4h_\omega^2\right)\mathcal{F}_\omega^{(e)}(z) = 0 \tag{14}$$

which has the solution $\mathcal{F}_\omega^{(e)}(z) \propto \exp(ikz)$ with the wave number k,

$$\left(2|\omega| + \hbar D_{\rm F}k^2\right)^2 + 4h_\omega^2 = 0 \tag{15}$$

yielding $k = \pm\sqrt{(-2|\omega| \mp ih_{\rm ex})/\hbar D_{\rm F}} = \pm\xi_{\rm F1}^{-1} + i\xi_{\rm F2}^{-1}$:

$$\begin{aligned}\xi_{\rm F1} &= \xi_{\rm F}^0\left[\sqrt{1 + \omega^2/h_{\rm ex}^2} - |\omega|/h_{\rm ex}\right]^{1/2}\\ \xi_{\rm F2} &= \xi_{\rm F}^0\left[\sqrt{1 + \omega^2/h_{\rm ex}^2} + |\omega|/h_{\rm ex}\right]^{1/2}\end{aligned} \tag{16}$$

where $\xi_{\rm F}^0 = \sqrt{\hbar D_{\rm F}/h_{\rm ex}}$ and $D_{\rm F}$ is the diffusion constant of F. Therefore, in the F region of the F/S interface, we have

$$\mathcal{F}_\omega^{(e)}(z) \propto \exp\left(\pm iz/\xi_{\rm F1}\right)\exp\left(-z/\xi_{\rm F2}\right) \tag{17}$$

Near $T_{\rm c}$, one can make a lowest-frequency approximation by replacing $|\omega|$ with $\pi k_{\rm B}T$, so that the pair function (9) becomes (Ryazanov *et al.*, 2001)

$$F(z) \propto \cos\left(z/\xi_{\rm F1}\right)\exp\left(-z/\xi_{\rm F2}\right) \tag{18}$$

where $(\xi_{\rm F1}, \xi_{\rm F2}) = \xi_{\rm F}^0[\sqrt{1 + (\pi k_{\rm B}T/h_{\rm ex})^2} \mp (\pi k_{\rm B}T/h_{\rm ex})]^{1/2}$. The main consequence of the complex wave number in the F region is that $F(z)$ oscillates with the period of $\xi_{\rm F1}$ and decays on the scale of $\xi_{\rm F2}$, as depicted in Figure 2. When F is a strong ferromagnet, that is, $h_{\rm ex} \gg k_{\rm B}T$, like a transition-metal ferromagnet (Fe, Co, Ni), both length scales are nearly equal, $\xi_{\rm F1} \approx \xi_{\rm F2} \approx \xi_{\rm F}^0$, and very short. On the other hand, when F is a weak ferromagnet, like a diluted

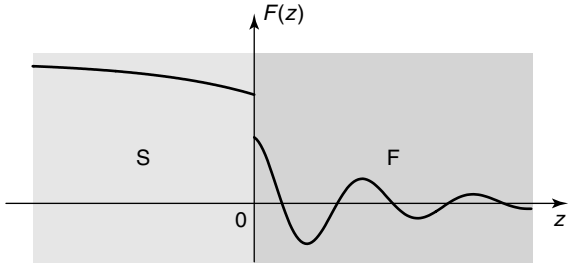

Figure 2. Superconducting pair function $F(z) = \Delta(z)/V(z)$ across the F/S interface.

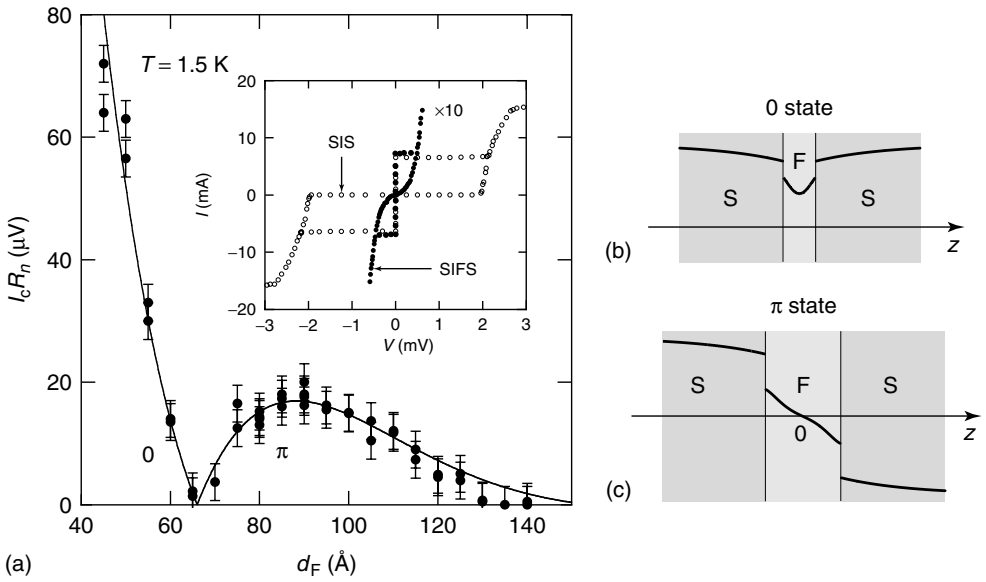

Figure 3. (a) Josephson critical current I_c as a function of thickness d_F of palladium nickel (PdNi) layer (Kontos *et al*., 2002). (Reproduced from Kontos *et al*., 2001, with permission from the American Physical Society. © 2001.) The solid curve is a theoretical fit (Kontos *et al*., 2002). I_c has a zero crossing at $d_F \approx 65$ Å, indicating the transition between the 0 and π states. Inset shows typical I–V characteristics of junctions with (full circles) and without (empty circles) PdNi layer. Spatial variation of the pair amplitude $F(z)$ in the 0 state (b) and in the π state (c).

ferromagnetic alloy (PdNi, CuNi, $\cdots$), in which the exchange field and temperature are the same order of magnitude, $h_{ex} \sim k_B T_c$, both length scales become of the order of tens of nanometers (nm), and, in addition, have a significant temperature dependence.

3 FERROMAGNETIC π JUNCTION

One of the most novel phenomena caused by the interplay of ferromagnetism and superconductivity is the 'π state', which appears in S/F/S junctions and F/S multilayers. It was predicted (Bulaevskii, Kuzii and Sobyanin, 1977; Buzdin, Bulaevskii and Panyukov, 1982) that the Josephson coupling energy takes a minimum at the phase difference equal to π. This state is called the π *state*, and the Josephson junction with the π state is called the π *junction*. In a π junction, the phase in the current-phase relation is shifted by π from that of a conventional Josephson junction (0 junction), so that the Josephson current in the π junction is opposite in sign to that in the 0 junction.

The π state in an S/F/S junction originates from the oscillation of the superconducting pair amplitude $F(z)$ in the presence of the exchange field h_{ex} in F. As shown in Figure 2, at the interface in the S/F junction, the pair amplitude penetrates into F in an oscillatory fashion $F(z) \propto \cos(z/\xi_{F1}) \exp(-z/\xi_{F2})$ in the direction perpendicular to the interface. When the thickness d_F of F in an S/F/S junction is about half the period of the oscillation, that is, $d_F \sim \pi\xi_{F1}$, the pair amplitude of the left and right S's has opposite signs, as shown in Figure 3(c). As a result, the system is stable with the phase difference equal to π, and the current-phase relation is shifted by π from that of the 0 junction in Figure 2(b).

Recent experimental observation of the π state in S/F/S Josephson junctions has opened new research fields. Ryazanov *et al*. have revealed the evidence for the π state by measuring the temperature dependence of the Josephson critical current I_c in Nb/CuNi/Nb junctions (Ryazanov *et al*., 2001), in which the zero crossing of I_c takes place, indicating the transition between the 0 and π states. Kontos *et al*. have measured the dependence of the Josephson current on the thickness of PdNi in a Nb/PdNi/Nb junction as shown in Figure 3(a) (Kontos *et al*., 2002). The transition between the 0 and π states occurs at the zero crossing point ($d_F \approx 65$ Å) of the critical current. In addition, the π state has been observed in a superconducting quantum interference device (SQUID)-type structure with insulating and ferromagnetic Josephson junctions as a π shift in the magnetic field dependence of the critical current (Guichard *et al*., 2003), and in a relatively large superconducting loop with a ferromagnet Josephson junction as a spontaneous current flowing in the loop (Bauer *et al*., 2004. It has been reported recently that, using strong ferromagnets (Co, Ni, and $Ni_{80}Fe_{20}$), multiple 0–π transitions with a short period occur in the thickness dependence of the critical current

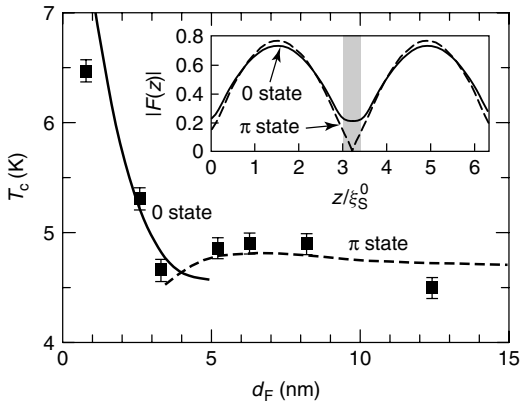

Figure 4. Superconducting transition temperature T_c of the 0 and π states as a function of F-layer thickness d_F for the exchange field $h_{ex} = 10k_B T_{cS}$ and $T_{cS} = 8.8$ K (Kuboya and Takanaka, 1998). The symbols are the experimental data of Nb/CuMu multilayers (Mercaldo *et al*., 1996). The inset shows the spatial variation of the absolute value of the pair amplitude $|F(z)|$. The shaded area is the F layer.

(Robinson *et al*., 2006), and are explained in terms of clean limit results with the oscillation period $\xi_{F1} \sim v_F/2h_{ex}$ and the decay length $\xi_{F2} \sim v_F/2k_B T$, the length scales of which are independent of each other (Born *et al*., 2006), in contrast to the dirty limit results.

The 0–π transition has been observed in F/S multilayers (Jiang, Davidović, Reich and Chein, 1995; Mercaldo *et al*., 1996; Shelukhin *et al*., 2006). In an F/S multilayer system, in addition to the boundary conditions at the interfaces, we impose the Bloch condition $\psi_n(z + L) = \pm\psi_n(z)$, where $L = d_S + d_F$ is the period of the multilayer, and '+' and '−' signs correspond to the 0 state and the π state respectively. Under these boundary conditions, equation (11) is solved numerically (Kuboya and Takanaka, 1998). Figure 4 shows the superconducting transition temperature T_c of the 0 and π states as a function of d_F for $h_{ex} = 10k_B T_{cS}$, $T_{cS} = 8.8$ K, $d_S/\xi_S^0 = 3$, and $\xi_S^0 = 8$ nm, where ξ_S^0 is the coherence length of the bulk S at zero temperature. As d_F is increased, T_c changes from the 0 state to the π state at the thickness $d_F \sim 4$ nm. The symbols are the experimental data of T_c in Nb/CuMn multilayers with fixed Nb layer thickness (∼250 Å) (Mercaldo *et al*., 1996).

4 ANDREEV REFLECTION AT F/S POINT CONTACTS

Andreev reflection (AR) is a fundamental process that occurs at the interface between a normal metal and a superconductor (Andreev, 1964; Blonder, Tinkham and Klapwijk, 1982). In the normal side of the interface, an incident electron with spin σ takes another electron with opposite spin $-\sigma$ to enter the superconductor in the form of a Copper pair, thereby reflecting a positively charged hole. This process allows the current to flow across the N/S interface for bias voltages below the superconducting gap Δ. Recently, a new technique based on AR has been used in F/S point contacts to determine the spin polarization of various ferromagnetic metals (Soulen *et al*., 1998; Upadhyay, Palanisami, Louie and Buhrman, 1998). Figure 5(b) shows experimental results for Andreev reflection for several ferromagnetic materials placed in contact with a superconducting Nb (Soulen *et al*., 1998).

The AR at the interface of a ferromagnetic metal and a superconductor is strongly modified because the incident electrons and the reflected holes occupy the states of the opposite spin bands with different values of the densities of states in the ferromagnet (see Figure 5a). de Jong and Beenakker (de Jong and Beenakker, 1995) have given an intuitive and simple argument for the conductance through a ballistic F/S point contact at zero temperature. A ferromagnet contacts a superconductor through a small area, where the number of up-spin channels $N_\uparrow$ is larger than that

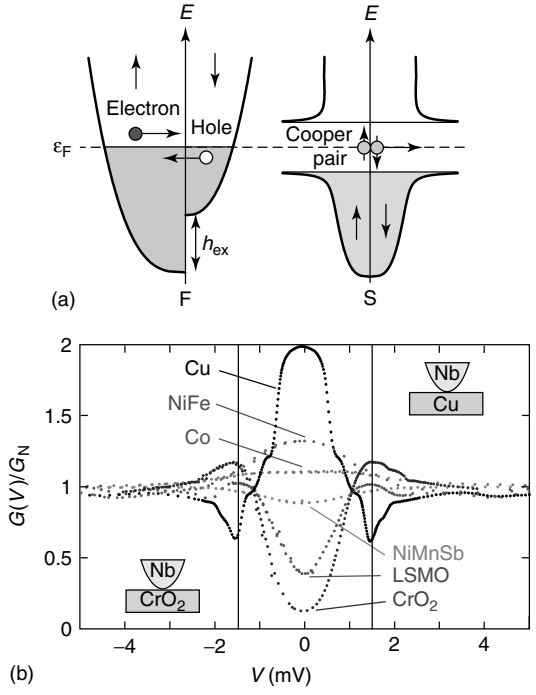

Figure 5. (a) Andreev reflection in a ferromagnet/superconductor (F/S) junction. The up- and down-spin bands are split by the exchange field h_{ex}. (b) Normalized conductance versus bias voltage in normal metal/superconductor (N/S) and ferromagnet/superconductor (F/S) point contacts. (Reproduced from fig 2 in R.J. Soulen Jr., J.M. Byers, M.S. Osofsky, B. Nadgorny, T. Ambrose, S.F. Cheng, P.R. Broussard, C.T. Tanaka, J. Nowak, J.S. Moodera, A. Barry, and J.M.D. Coey, *Science* **282**, (1998) 85, with permission from AAAS.)

of down-spin channels $N_\downarrow$, that is, $N_\uparrow \geq N_\downarrow$. When the superconductor is in the normal state, all scattering channels (transverse modes in the point contact at the Fermi level) are fully transmitted, yielding the conductance

$$G_N = (e^2/\hbar)\left(N_\uparrow + N_\downarrow\right) \tag{19}$$

In the superconducting state, the down-spin electrons in the $N_\downarrow$ channels are all reflected as the Andreev holes, making the conductance double, since $2e$ is transferred at each AR. However, only a fraction $(N_\downarrow/N_\uparrow)$ of up-spin electrons in the $N_\uparrow$ channels is allowed for the AR, because the density of states in the down-spin band is lower than that in the up-spin band in ferromagnets. Therefore, the conductance at zero bias ($V = 0$) is

$$G = (e^2/h)\left[2N_\downarrow + 2(N_\downarrow/N_\uparrow)N_\uparrow\right] = 4(e^2/h)N_\downarrow \tag{20}$$

The ratio of equation (20) to equation (19) gives the normalized conductance

$$G/G_N = 2\,(1 - P_c) \tag{21}$$

where P_c is the point-contact spin polarization

$$P_c = \frac{(N_\uparrow - N_\downarrow)}{(N_\uparrow + N_\downarrow)} \tag{22}$$

The spin polarizations P_c of various ferromagnets can be estimated directly from the conductance values at $V = 0$ by applying equation (21) to experimental results, for example, those of Figure 5. The measured P_c of various ferromagnets are $P_c = 42\%$ for Co (Soulen *et al.*, 1998), $P_c = 42$–46% for Fe (Soulen *et al.*, 1998), $P_c = 43$–46% for Ni (Soulen *et al.*, 1998), $P_c = 49.5\%$ for permalloy ($Ni_{80}Fe_{20}$) (Osofsky *et al.*, 2000), $P_c = 85\%$ for $La_{0.7}Sr_{0.3}MnO_3$ (Braden *et al.*, 2003), and $P_c = 96\%$ for CrO_2 (Ji *et al.*, 2001; Parker, Watts, Ivanov and Xiong, 2002). The role of a point contact and a base electrode can be interchanged between F and S, which brings about no significant difference in the measured $G(V)$ curves or in the estimated value of P_c.

Let us consider a pedagogical mode for the AR in a point contact with S occupying the right half space and an F wire of width w. The wave functions of quasiparticles (QPs) with excitation energy E in the electrodes are calculated from the Bogoliubov–de Gennes equation. For simplicity, the calculation is restricted to the case where only the lowest subband is occupied by electrons or holes in the wires. When an electron with energy E in the majority band (symbol '0' in Figure 6) is incident from the F lead into S, the wave

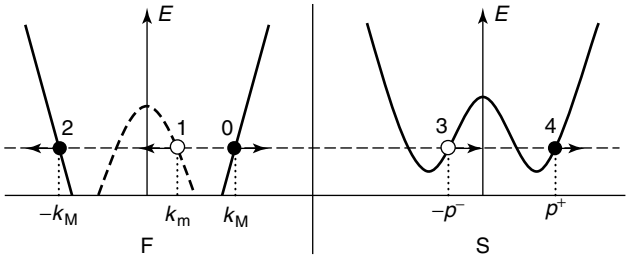

Figure 6. Andreev reflection process at the F/S interface. The open and filled circles represent hole and electron respectively, and the arrows represent the direction of the group velocity. The symbol '0' denotes an incident electron, '1' a reflected Andreev hole, '2' a reflected electron, and '3' and '4' are transmitted holelike and electron-like quasiparticles in S.

function in the lead is given by

$$\Psi_F(x, y) = \left(\begin{bmatrix} 1 \\ 0 \end{bmatrix} e^{ik_M x} + r^{ee}_{MM}\begin{bmatrix} 0 \\ 1 \end{bmatrix} e^{-ik_M x} + r^{eh}_{Mm}\begin{bmatrix} 0 \\ 1 \end{bmatrix} e^{ik_m x}\right)\chi(y) \tag{23}$$

where k_M and k_m are the wave numbers of electron and hole in the majority and minority bands, respectively, $k_\alpha = [2mE + k^2_{F,\alpha} - (\pi/w)^2]^{1/2}$ ($\alpha = M,m$), $k_{F,\alpha}$ is the Fermi momentum of the α band, $\chi(y) = (2/w)^{1/2}\sin\left[(\pi/w)\,(y + w/2)\right]$ is the transverse wave function of the wire, and r^{ee}_{MM} and r^{eh}_{Mm} are the amplitudes of the normal reflection (NR) and the AR, respectively. A similar treatment is made for an incident electron from the minority band. Since $(E, \Delta) \ll \epsilon_{F,\alpha}$, we put $k_\alpha \approx k_{F,\alpha}[1 - (\pi/k_{F,\alpha}w)^2]^{1/2}$ in the following.

Making use of the Andreev approximation (Blonder, Tinkham and Klapwijk, 1982), where $p^\pm$ in Figure 6 is replaced by $(p_F^2 - p_y^2)^{1/2}$, we put the wave function in S as follows:

$$\Psi_S = \int_{-p_F}^{p_F} t_s^{ee}(p_y)\begin{bmatrix} \Delta \\ E - \Omega \end{bmatrix} e^{i\sqrt{p_F^2 - p_y^2}\,x} e^{ip_y y}\mathrm{d}p_y + \int_{-p_F}^{p_F} t_s^{eh}(p_y)\begin{bmatrix} \Delta \\ E + \Omega \end{bmatrix} e^{-i\sqrt{p_F^2 - p_y^2}\,x} e^{ip_y y}\mathrm{d}p_y \tag{24}$$

where $t_s^{ee}(p_y)$ and $t_s^{eh}(p_y)$ are the transmission coefficients and $\Omega = \sqrt{E^2 - \Delta^2}$. The barrier potential at the interface between the wire and S is taken into account by the δ-function-type potential with the amplitude $(\hbar^2 p_F/2m)Z$, Z being a dimensionless barrier-height parameter (Blonder, Tinkham and Klapwijk, 1982). The matching conditions for the wave functions at the interfaces are $\Psi_S(0, y) = \Psi_F(0, y)$ and $[\partial_x\Psi_S(x, y) - \partial_x\Psi_F(x, y)]_{x=0} = p_F Z\Psi_F(0, y)$ appropriate for the $\delta(x)$ barrier potential. The matching technique

to the boundary conditions (Szafer and Stone, 1989) yields the reflection and transmission coefficients.

When the bias voltage V is applied to the wire, the conductance G at zero temperature ($T = 0$) is calculated by putting $E = eV$ as

$$G(V) = \frac{e^2}{h}\left(1 - |r^{ee}_{\mathrm{MM}}|^2 + |r^{eh}_{\mathrm{Mm}}|^2\right) + \frac{e^2}{h}\left(1 - |r^{ee}_{\mathrm{mm}}|^2 + |r^{eh}_{\mathrm{mM}}|^2\right) \tag{25}$$

where h is the Planck's constant and $h/e^2 \approx 25.8\,\mathrm{k\Omega}$ is the quantum resistance.

In the normal state, the transmission probability $\mathcal{T}^{\alpha}_{\mathrm{N}} = 1 - |r^{ee}_{\alpha\alpha}|^2$ ($\alpha = \mathrm{M,m}$) of the majority and minority electrons is

$$\mathcal{T}^{\alpha}_{\mathrm{N}} = 4k_{\alpha}\frac{\Lambda}{[(k_{\alpha} + \Lambda)^2 + Z^2]} \tag{26}$$

where $\Lambda = \int_0^{p_{\mathrm{F}}} (\mathrm{d}q/\pi)\sqrt{p_{\mathrm{F}}^2 - q^2}\,|\langle q|\chi\rangle|^2$ ($0 \le \Lambda \le p_{\mathrm{F}}$) with the overlap integral $\langle q|\chi\rangle$ between e^{ipy} and $\chi(y)$: $\langle q|\chi\rangle = \sqrt{8w/\pi^2}\cos(qw/2)/\left[1 - (qw/\pi)^2\right]$. The spin polarization of the point contact is introduced as

$$P_{\mathrm{c}} = \frac{(\mathcal{T}^{\mathrm{M}}_{\mathrm{N}} - \mathcal{T}^{\mathrm{m}}_{\mathrm{N}})}{(\mathcal{T}^{\mathrm{M}}_{\mathrm{N}} + \mathcal{T}^{\mathrm{m}}_{\mathrm{N}})} \tag{27}$$

For the special case of $\mathcal{T}^{\mathrm{M}}_{\mathrm{N}} = 1$ ($Z = 0$, $k_{\mathrm{M}} = \Lambda$), the conductance for $eV < \Delta$ is calculated as

$$G/G_N = 2(1 - P_{\mathrm{c}}) \tag{28}$$

which is exactly the same as equation (21).

Figure 7 shows the conductance G of F/S point contact as a function of bias voltage V for the barrier heights of $Z = 0$ and $Z = 0.4$ at $T = 0$. The conductance is normalized to the normal-state value $G_N = G(\Delta = 0)$. As can be seen in Figure 7(a), the normalized conductance is flat inside the gap and follows the relation equation (28) for the special case of the perfect transmission of the majority electrons. However, when a small interfacial barrier potential is introduced, as in Figure 7(b), the conductance curves show the peak structure at the gap edge for smaller P_{c}, while they show the dip structure without such peaks for larger P_{c}. These features in the conductance curves have been observed in F/S point-contact experiments.

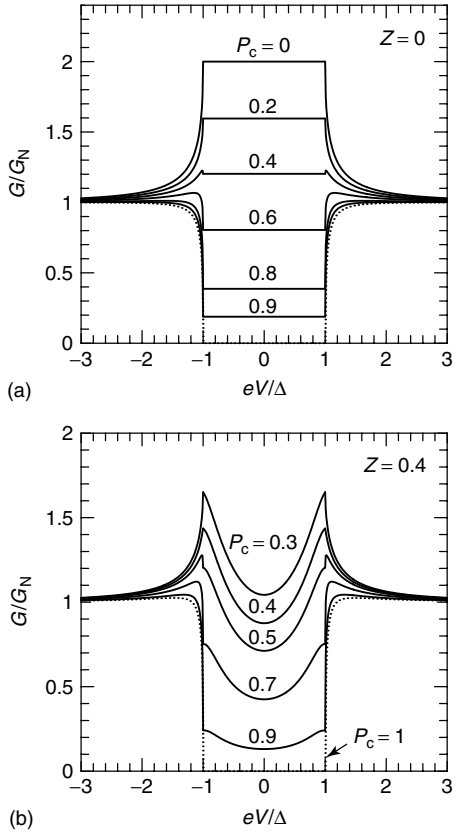

Figure 7. Conductance for the F/S point contacts as a function of bias voltage at $T = 0$. The barrier height is taken to be $Z = 0$ for panel (a) and $Z = 0.4$ for panel (b), for various values of the spin polarization P_{c} at $T = 0$.

5 SUPERCONDUCTING π QUBIT

In quantum computers, information is stored in a basic element called the *qubit*, which is a quantum coherent two-level system. The superposition of the two-level states is utilized in the processing of quantum computing. For physical realization of the qubit, various systems have been proposed, for example, ion traps, nuclear spins, and photons. Among them, solid-state qubits have the advantage of large-scale integration and flexibility of layout. Recently, several qubits based on the Josephson effect have been proposed. One of the proposals is a charge qubit, which uses the charging effect of excess Cooper pairs in a box (Nakamura, Pashkin and Tsai, 1999). Another example is a flux qubit, which uses the superconducting phase. Mooij *et al*. have proposed a flux qubit, which consists of a superconducting loop with three Josephson junctions (Mooij *et al*., 1999). In the flux qubit, degenerate double minima appear in the superconducting phase space under the external magnetic field at which the loop flux corresponds to half the unit magnetic flux. The bonding and antibonding states are formed because of the tunneling between these degenerate states, and are used as the coherent two-level states. Experimentally, the microwave-induced transition between the two-level states, the entanglement of the states,

and the coupling between two qubits have been observed (van der Wal *et al*., 2000; Chiorescu, Nakamura, Harmans and Mooij, 2003; Ciuhu and Lodder, 2001; Majer *et al*., 2005; Izmalkov *et al*., 2004; Chiorescu *et al*., 2004).

Recent advances in nanofabrication techniques have brought a variety of spin-electronic devices. In F/S structures, novel quantum phenomena, such as the π state in ferromagnetic Josephson junctions, arise from the interplay of ferromagnetism and superconductivity. In this respect, recent experimental observations of the π state in those junctions are quite promising for the practical development of superconducting π-shift devices.

Here, we consider a qubit of a superconducting loop consisting of a π junction and a 0 junction (Yamashita, Tanikawa, Takahashi and Maekawa, 2005; Yamashita, Takahashi and Maekawa, 2006). In this system, the potential energy has double minima in the phase space without external magnetic fields because of spontaneous magnetic flux generated by the π junction. The bonding and antibonding states (coherent states), which are formed because of the quantum tunneling between the two degenerate states, are used as a bit in the qubit. A small external magnetic field is enough to manipulate the state of the qubit. These features lead to a smaller size of qubit that is resistant to the decoherence by the external noise.

5.1 Two-junction π qubit

We consider a qubit of a superconducting loop with an S/I/S Josephson junction (0 junction) and an S/F/S Josephson junction (π junction), as shown in Figure 8. In the loop, the 0 junction has the Josephson energy

$$U_0(\theta_0) = -E_{\mathrm{J}}^0 \cos\theta_0 \tag{29}$$

where E_{J}^0 is the Josephson coupling energy and θ_0 is the phase difference in the 0 junction. The current-phase relation is $I = I_0 \sin\theta_0$ with the critical current $I_0 = (2e/\hbar)E_{\mathrm{J}}^0$. On the other hand, the S/F/S junction is a clean and metallic π junction with negligible interface resistance, for which the Josephson energy is well described in the form (Yamashita, Tanikawa, Takahashi and Maekawa, 2005)

$$U_\pi(\theta_\pi) \approx -E_{\mathrm{J}}^\pi \left|\cos\frac{1}{2}(\theta_\pi + \pi)\right| \tag{30}$$

where E_{J}^π is the Josephson coupling energy and θ_π is the phase difference in the π junction. This particular form is realized if appropriate values are chosen for $h_{\mathrm{ex}}/\epsilon_{\mathrm{F}}$ and $k_{\mathrm{F}}d_{\mathrm{F}}$, and leads to the current-phase relation $I \approx -(I_\pi/2)\sin\left[(\theta_\pi + \pi)/2\right]$ for $0 < \theta < 2\pi$ with the critical current $I_\pi = (2e/\hbar)E_{\mathrm{J}}^\pi$.

The total Hamiltonian of the loop is written as $H = K + U_0 + U_\pi + U_L$, where $K = -4E_{\mathrm{c}}^0\left(\partial^2/\partial\theta_0^2\right)$ is the electrostatic energy, $E_{\mathrm{c}}^0 = e^2/(2C_0)$ is the charging energy with the capacitance C_0 of the 0 junction, and U_L is the magnetic energy stored in the loop. The electrostatic energy in the π junction is neglected. The magnetic energy U_L is given by $U_L = (\Phi - \Phi_{\mathrm{ext}})^2/(2L_{\mathrm{s}})$, where Φ is the total flux, L_{s} is the self-inductance of the loop, and Φ_{ext} is the external magnetic flux. The total flux and the phase differences satisfy the relation

$$\theta_\pi + \theta_0 = 2\pi\,(\Phi/\Phi_0) - 2\pi l \tag{31}$$

where $\Phi_0 = hc/2e$ is the unit flux and l is an integer. The total Hamiltonian H is analogous to that describing the motion of a particle with kinetic energy K and in a potential $U = U_0 + U_\pi + U_L$. Minimizing U with respect to θ_0 and

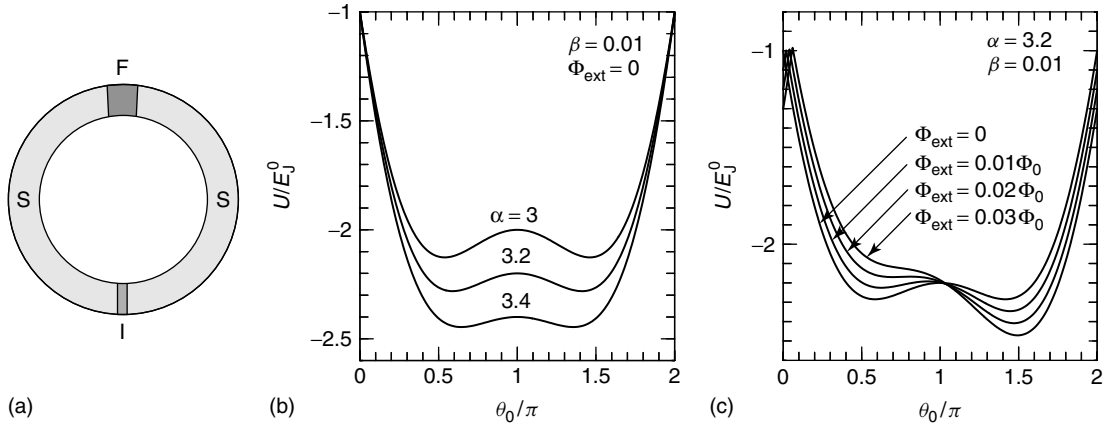

Figure 8. (a) Schematic diagram of a superconducting loop with an insulator and a ferromagnet. The S/I/S junction is a 0 junction (a conventional Josephson junction), and the S/F/S junction is a metallic π junction. (b) Normalized U versus phase θ_0 for $\beta = 1 \times 10^{-2}$ in zero external magnetic field ($\Phi_{\mathrm{ext}} = 0$). (c) Normalized U versus phase θ_0 under the external magnetic fields of $\Phi_{\mathrm{ext}}/\Phi_0 = 0.0$–$0.03$.

θ_π, and eliminating θ_π and Φ from U, we obtain

$$U/E_J^0 = -\cos\theta_0 + \frac{\beta}{2}\sin^2\theta_0 - \alpha\left|\sin\left(\frac{\theta_0}{2} + \frac{\beta}{2}\sin\theta_0 + \pi\frac{\Phi_{\rm ext}}{\Phi_0}\right)\right| \quad (32)$$

where $\alpha = I_\pi/I_0$ and $\beta = (2\pi/\Phi_0)^2 I_0 E_J^0 L_s$, and $\Phi(\theta_0) = \Phi_{\rm ext} + (\Phi_0/2\pi)\beta\sin\theta_0$.

Figure 8(b) shows the θ_0 dependence of U in zero external magnetic field ($\Phi_{\rm ext} = 0$) for several values of α and $\beta = 0.01$. The value $\beta = 0.01$ corresponds to the loop with the inductance $L_s = 2\times10^{-12}$ H with a diameter 2 μm and $I_0 = 500$ nA. As seen in Figure 8(b), the potential has double minima at $\theta_0 \approx \pi/2$ and $3\pi/2$, and the barrier height between the two degenerate states, $|\uparrow\rangle$ ($\theta_0 \approx \pi/2$) and $|\downarrow\rangle$ ($\theta_0 \approx 3\pi/2$), is controlled by α. The value of α can be adjusted by changing the thickness of the insulating barrier or of the ferromagnet. In the $|\uparrow\rangle$ and $|\downarrow\rangle$ states, the supercurrent flows in the clockwise and counterclockwise directions, respectively, inducing flux $\Phi = L_s I \approx \pm 4.8\times10^{-4}\,\Phi_0$.

In the loop, the bonding $|0\rangle \propto |\uparrow\rangle + |\downarrow\rangle$ and the antibonding $|1\rangle \propto |\uparrow\rangle - |\downarrow\rangle$ states are formed via the quantum tunneling between $|\uparrow\rangle$ and $|\downarrow\rangle$, yielding a two-level quantum system. For an alumina barrier with junction area 0.1 μm^2 and thickness 1 nm, $E_c^0 \approx 0.01$ meV and $E_J^0/E_c^0 \approx 96$. In this case, a numerical simulation for $\alpha = 3$ gives the energy gap $\Delta E \approx 0.02$ meV ($\Delta E/h \approx 5$ GHz) between the ground state $|0\rangle$ and the first excited state $|1\rangle$. Microwave absorption is used to measure this two-level quantum state.

Figure 8(c) shows the θ_0 dependence of U in different external magnetic fields and for $\alpha = 3$. The degeneracy of the states $|0\rangle$ and $|1\rangle$ is lifted by applying an external magnetic field. In a small external magnetic field $\Phi_{\rm ext} = \pm0.01\Phi_0$, the double-well potential becomes asymmetric, and one of the components ($|\uparrow\rangle$ or $|\downarrow\rangle$) is lower than the other in the ground state $|0\rangle$, and vice versa in the first excited state $|1\rangle$. In a larger external magnetic field $\Phi_{\rm ext} = \pm0.03\Phi_0$, the double-well potential disappears and the ground state is either $|\uparrow\rangle$ or $|\downarrow\rangle$. Therefore, the currents flow in opposite directions for the $|0\rangle$ and $|1\rangle$ states, when an external magnetic field is applied. As a result, the $|0\rangle$ and $|1\rangle$ states are detected by measuring the current flowing in the loop with a SQUID placed around the loop.

Here, we discuss the dissipation in the metallic π junction. In a small metallic π junction, the discrete Andreev bound states are formed. When the thickness d_F of F is much less than the coherence length, only one Andreev bound state appears in the gap Δ for each spin state σ. The energy, E_σ, of the Andreev bound is gapless ($E_\sigma \approx 0$) at $\theta_\pi = 0$ and 2π, where noise due to thermally excited QPs increases. However, in the π qubit discussed in the preceding text, the quantum tunneling occurs between $\theta_0 \approx \theta_\pi \approx \pi/2$ and $\theta_0 \approx \theta_\pi \approx 3\pi/2$ (Figure 8), for which the Andreev bound state lies near the gap energy. This indicates that the metallic π junction is well gapped in the relevant phase region where the quantum tunneling occurs. Therefore, the QP tunnel dissipation is strongly suppressed at low temperatures and low voltages.

5.2 Three-junction π qubit

Let us next consider a qubit with two 0 junctions and one π junction shown in Figure 9(a) (Yamashita, Takahashi and Maekawa, 2006). The three-junction qubit also does not need an external magnetic field for the formation of the coherent two-level states and is manipulated by a small external field. In addition, this qubit does not require a clean and metallic S/F/S junction, as in the case of the two-junction qubit in the previous section, and works for π junctions with a tunnel barrier between S and F, which are underdamped tunnel π junctions and are robust for decoherence due to thermally excited quasiparticles (Weides *et al*., 2006).

In the three-junction qubit, the first and second 0 junctions have the phase differences θ_1 and θ_2, and the π junction has the phase difference θ_π. The total energy of the system consists of the electrostatic energy and the potential energy of the junctions. The electrostatic energy K is written as

$$K = \frac{4E_c^0}{E_c^\pi + 2E_c^0} \times\left[\left(E_c^\pi + E_c^0\right)\left(\frac{\partial^2}{\partial\theta_1^2} + \frac{\partial^2}{\partial\theta_2^2}\right) - 2E_c^0\frac{\partial^2}{\partial\theta_1\partial\theta_2}\right] \quad (33)$$

where $E_c^0 = e^2/(2C_0)$ and $E_c^\pi = e^2/(2C_\pi)$ are the charging energies of the zero and π junctions, and C_0 and C_π are the capacitances of those junctions. The potential energy U is

$$U = -E_J^0(\cos\theta_1 + \cos\theta_2) - E_J^\pi\cos(\theta_\pi + \pi) + (\Phi - \Phi_0)^2/(2L_s) \quad (34)$$

where E_J^0 and E_J^π are the Josephson coupling energies of the 0 and π junctions, Φ is the total flux in the loop, $\Phi_{\rm ext}$ is the external flux, and L_s is the self-inductance of the loop. A single-valuedness of the wave function along the loop gives the relation

$$\theta_1 + \theta_2 + \theta_\pi = 2\pi(\Phi/\Phi_0) - 2\pi l \quad (35)$$

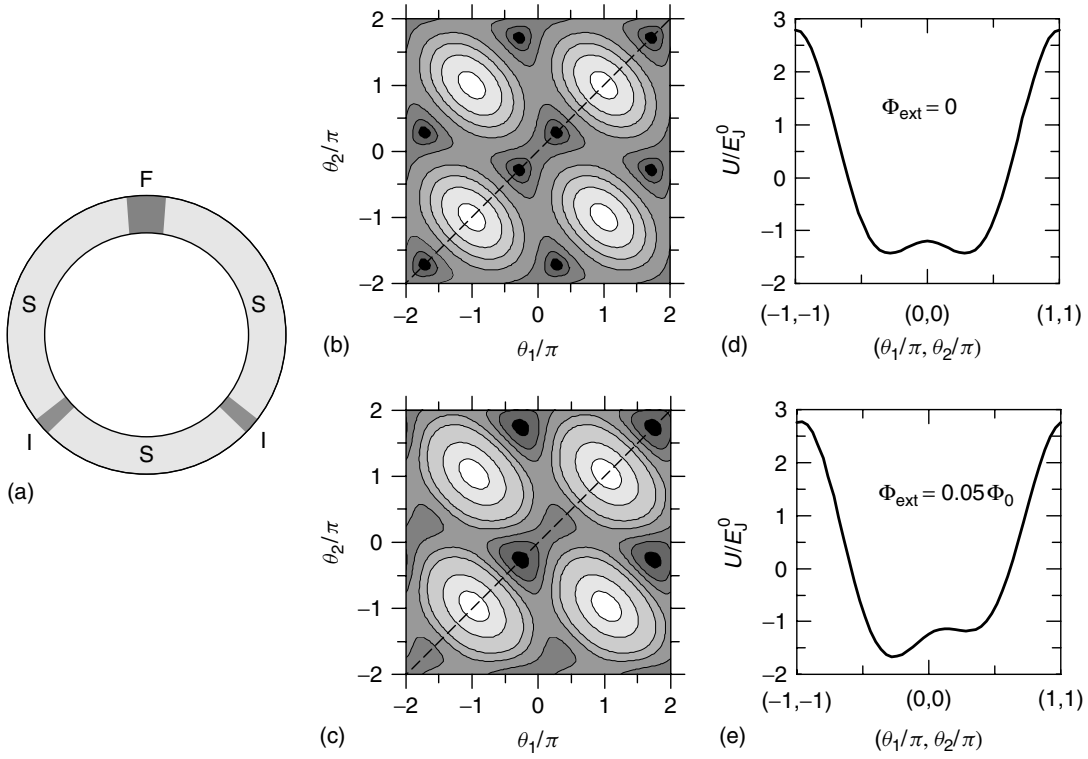

Figure 9. (a) Schematic diagram of a superconducting loop with a π junction and two 0 junctions. Contour plot of the total potential U/E_J^0 in the θ_1–θ_2 plane in zero external magnetic field (b) and in a small external magnetic field of $\Phi_{ext} = 0.05$ (c) for $\alpha = 0.8$ and $\beta = 3.0 \times 10^{-3}$. The phase dependence of U along the dashed lines in (b) and (c) in zero external magnetic flux (d) and in the external magnetic flux $\Phi_{ext} = 0.05\Phi_0$ (e), respectively.

where Φ_0 is the unit flux and l is an integer. Using equation (35) in equation (34), we obtain

$$U = -E_J^0(\cos\theta_1 + \cos\theta_2) - E_J^\pi \cos\left(2\pi\frac{\Phi}{\Phi_0} - \theta_1 - \theta_2\right) + \frac{(\Phi - \Phi_0)^2}{2L_s} \tag{36}$$

Minimizing U with respect to Φ, we obtain the self-consistent equation

$$\alpha\beta \sin\left[2(\Phi/\Phi_0) - \theta_1 - \theta_2\right] = 2\pi(\Phi - \Phi_{ext})/\Phi_0 \tag{37}$$

where $\alpha = E_J^\pi/E_J^0$ and $\beta = 4\pi^2 E_J^0 L_s/\Phi_0^2$. The numerical solution $\Phi = \Phi(\theta_1, \theta_2)$ of equation (37) is used to calculate $U = U(\theta_1, \theta_2)$ as a function of θ_1 and θ_2. In the following, we assume $E_c^0/E_c^\pi = E_J^\pi/E_J^0$, and take $\alpha = 0.8$ and $\beta = 3.0 \times 10^{-3}$. The value of α is controllable by changing the junction area, the barrier height, and the thickness of the ferromagnet. The value of β is suitable for the micrometer-size loop and the Josephson junction with several hundred nanoamperes of the critical current.

Figure 9(b) and (d) shows the potential energy U in the θ_1–θ_2 plane in zero external magnetic flux ($\Phi_{ext} = 0$). As seen in Figure 9, $U(\theta_1, \theta_2)$ has double minima in the phase space. The degenerate $|\uparrow\rangle$ and $|\downarrow\rangle$ states at the minima have the circulating supercurrents of magnitude $\approx 0.8I_0$ in the clockwise and anticlockwise directions, respectively, where I_0 is the critical current in the 0 junctions. Quantum tunneling between the degenerate $|\uparrow\rangle$ and $|\downarrow\rangle$ states creates the bonding $|0\rangle \propto |\uparrow\rangle + |\downarrow\rangle$ and the antibonding $|1\rangle \propto |\uparrow\rangle - |\downarrow\rangle$ states, which are used as a quantum bit. The $|0\rangle$ and $|1\rangle$ states are the states of vanishing circulating current because of the superposition of $|\uparrow\rangle$ and $|\downarrow\rangle$ with equal weight, and have the energy gap ΔE between the $|0\rangle$ and $|1\rangle$ states due to the quantum tunneling. The gap is measured by microwave resonance. From the numerical calculation, the resonance frequency $\Delta E/h \approx 4.4\,\mathrm{GHz}$ for $E_J^0/E_c^0 = 30$.

Figure 9(c) and (e) shows the potential energy U in the θ_1–θ_2 plane in the external magnetic flux $\Phi_{ext} = 0.05\Phi_0$. As seen in the Figure 9(e), the degeneracy of the $|\uparrow\rangle$ and $|\downarrow\rangle$ states is lifted by small external magnetic fields. In the bonding $|0\rangle$ state, the $|\uparrow\rangle$ component increases and the $|\downarrow\rangle$ component decreases, while in the antibonding $|1\rangle$ state the components change in a reversed way. Therefore,

spontaneous circulating currents flow in the clockwise and anticlockwise directions at the $|0\rangle$ and $|1\rangle$ states respectively, producing the spontaneous magnetic flux in the loop. One can detect the states of the qubit through the measurement of the spontaneous flux by a SQUID placed around the loop.

The common features of the two-junction and three-junction π qubits are the formation of the coherent two-level states without external magnetic fields; thus, a small external magnetic field is enough to manipulate and detect the states as compared to the external half unit flux $\Phi_0/2$ required in the proposal of Mooij *et al*. (1999). For example, for a small qubit with the dimensions of several hundred nanometers, a small magnetic field of the order of millitesla is enough for manipulating our qubit. This feature allows us to make qubits of smaller size, which is advantageous in large-scale integration. This type of qubit is also resistant to external noise and has longer decoherence time.

6 SPIN INJECTION INTO SUPERCONDUCTORS

Johnson and Silsbee (1985) first reported that nonequilibrium spins injected from ferromagnets diffuse into Al films over the spin-diffusion length of the order of 1 μm. Johnson (1993) proposed a spin injection technique in an F1/N/F2 structure (F1 is an injector and F2 a detector). Recent experimental studies have demonstrated that the spin-polarized carriers injected from F (NiFe, Co, CoFe,$\cdots$) into N (Cu, Al, Ag,$\cdots$) (Jedema, Filip and van Wees, 2001; Jedema *et al*., 2002; Kimura, Hamrle and Otani, 2004, 2005, 2006; Garzon, Žutić and Webb, 2005; Godfrey and Johnson, 2006; Valenzuela and Tinkham, 2006) and into S (Al,$\cdots$) (Chen *et al*., 2002; Johansson, Urech, Haviland and Korenivski, 2003; Wang and Lu, 2005; Daibou, Oogane, Ando and Miyazaki, unpublished; Urech *et al*., 2006; Miura, Kasai, Kobayashi and Ono, 2006) create a spin accumulation in nonmagnetic metals. Using tunnel devices consisting of a high-T_c cuprate and a ferromagnetic manganite, strong suppression of superconductivity by spin injection has been reported (Vas'ko *et al*., 1997; Dong *et al*., 1997; Yeh *et al*., 1999).

In this section, we discuss nonequilibrium spin accumulation created by a spin-polarized tunnel current and its competition with superconducting condensate in S sandwiched between two ferromagnets (F1/S/F2) (Takahashi, Imamura and Maekawa, 1999, 2000; Takahashi and Maekawa, 2003; Johansson, Korenivski, Haviland and Brataas, 2004). A particular emphasis is placed on the spin-dependent effect, that is, the dependence of the transport properties on the relative orientation of the magnetizations in the F electrodes. In the following, we describe how the spin density is accumulated in S and suppresses the superconductivity, depending on the relative orientation of the magnetizations.

We consider an F1/S/F2 double tunnel junction, as shown in Figure 10(a). The left and right electrodes are made of the same ferromagnets and the central one is a superconductor with thickness d_S. The magnetization of F1 is chosen to point up and that of F2 is either up or down. We assume a symmetric junction, which is characterized by the same tunnel conductance of the tunnel barriers. In the following, we restrict ourselves to the case that the thickness d_S of S is much smaller than the spin-diffusion length $\lambda_S = \sqrt{D\tau_S}$, D being the diffusion constant, so that the spin density accumulated in S is spatially uniform in S.

We calculate the tunnel current using a phenomenological model for tunneling. If S is in the superconducting state, it is convenient to write the electron operators $a_{\mathbf{k}\sigma}$ in S in terms of the QP operators $\gamma_{\mathbf{k}\sigma}$ using the Bogoliubov transformation (Tinkham, 1996)

$$a_{\mathbf{k}\uparrow} = u_{\mathbf{k}}\gamma_{\mathbf{k}\uparrow} + v^*_{\mathbf{k}}\gamma^\dagger_{-\mathbf{k}\downarrow}, \quad a^\dagger_{-\mathbf{k}\downarrow} = -v_{\mathbf{k}}\gamma_{\mathbf{k}\uparrow} + u^*_{\mathbf{k}}\gamma^\dagger_{-\mathbf{k}\downarrow}$$

where $|u_{\mathbf{k}}|^2 = 1 - |v_{\mathbf{k}}|^2 = \frac{1}{2}(1 + \xi_{\mathbf{k}}/E_{\mathbf{k}})$ with the QP dispersion $E_{\mathbf{k}} = \sqrt{\xi^2_{\mathbf{k}} + \Delta^2}$ of S, $\xi_{\mathbf{k}}$ being the one-electron energy relative to the chemical potential and Δ being the gap parameter. Using the golden rule formula, we obtain the spin-dependent currents $I_{i\sigma}$ across junction 1 and 2 (Takahashi,

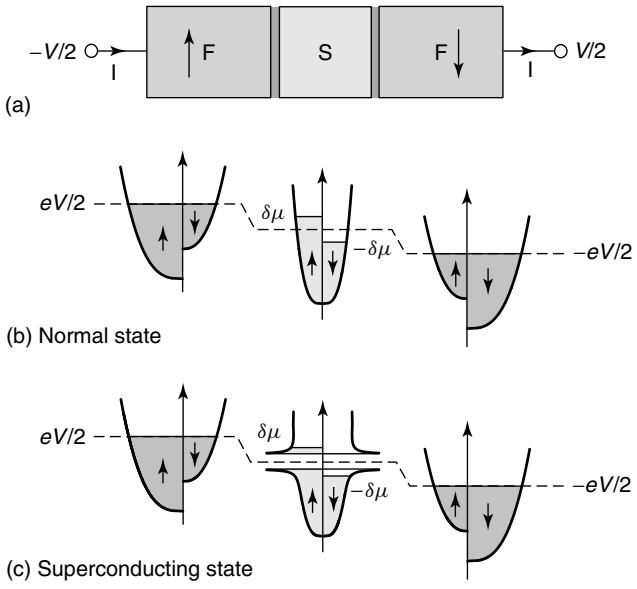

Figure 10. (a) Double-tunnel junction consisting of two ferromagnets (F) and a superconductor (S) separated by insulating barriers. The densities of states of F's (left and right) and S (middle) in the antiparallel magnetizations of F's in the normal state (b) and the superconducting state (c). $\delta\mu$ denotes the chemical-potential shift in S.

Imamura and Maekawa, 1999):

$$I_{1\uparrow} = (G_{1\uparrow}/e)\,(\mathcal{N} - \mathcal{S})\,, \quad I_{1\downarrow} = (G_{1\downarrow}/e)\,(\mathcal{N} + \mathcal{S}) \quad (38)$$

$$I_{2\uparrow} = (G_{2\uparrow}/e)\,(\mathcal{N} + \mathcal{S})\,, \quad I_{2\downarrow} = (G_{2\downarrow}/e)\,(\mathcal{N} - \mathcal{S}) \quad (39)$$

where $G_{i\sigma}$ is the normal-state tunnel conductance of ith junction for electrons with spin σ. Here, the nonequilibrium charge imbalance (Clarke, 1972; Pethick and Smith, 1980) is neglected because it has little effect on the spin-dependent effect in the symmetric junction (Takahashi, Imamura and Maekawa, 2000). The quantity $\mathcal{N}$ is given by (Tinkham, 1972)

$$\mathcal{N}(V) = \frac{1}{2}\int_{-\infty}^{\infty} \mathrm{d}\xi_{\mathbf{k}}\Big[f_0\big(E_{\mathbf{k}} - eV/2\big) - f_0\big(E_{\mathbf{k}} + eV/2\big)\Big] \quad (40)$$

where $f_0(E) = 1/[\exp(E/k_{\mathrm{B}}T) + 1]$ is the Fermi distribution function and $V/2$ is the voltage drop at the barriers. In the normal state, $\mathcal{N}(V) = eV/2$. The quantity $\mathcal{S}$ is the spin density normalized by the normal-state density of states N_{S} in S, and is calculated on the basis of the semiconductor model (Tinkham, 1996):

$$\mathcal{S} = \frac{1}{2}\int_{-\infty}^{\infty} \mathrm{d}\xi_{\mathbf{k}}\Big[f_0\,(E_{\mathbf{k}} - \delta\mu) - f_0\big(E_{\mathbf{k}} + \delta\mu\big)\Big] \quad (41)$$

where the electrochemical potentials of up and down spins are shifted by $\pm\delta\mu$ from equilibrium (see Figure 10).

The injected spin density is determined by balancing the spin injection rate $N_{\mathrm{S}}\,(\mathrm{d}\mathcal{S}/\mathrm{d}t)_{\mathrm{inj}} = [(I_{1\uparrow} - I_{1\downarrow}) - (I_{2\uparrow} - I_{2\downarrow})]/2e$ with the spin relaxation rate $N_{\mathrm{S}}\mathcal{S}/\tau_{\mathrm{S}}$, where τ_{S} is the spin-relaxation time. The result for the parallel (P) and the antiparallel (AP) alignment of magnetizations is

$$\mathcal{S}_{\mathrm{P}} = 0, \quad \mathcal{S}_{\mathrm{AP}} = \frac{P}{1 + \Gamma_{\mathrm{s}}}\mathcal{N}_{\mathrm{AP}} \quad (42)$$

where $P = |G_{i\uparrow} - G_{i\downarrow}|/(G_{i\uparrow} + G_{i\downarrow})$ $(i = 1, 2)$ is the tunnel spin polarization, $\Gamma_{\mathrm{s}} = (\tau_t/\tau_{\mathrm{S}})$ is a spin relaxation parameter, $\tau_t = e^2 N_{\mathrm{S}} R A d_{\mathrm{S}}$ is a characteristic dwell time of an electron in S, A is the junction area, and $R = 1/(G_{i\uparrow} + G_{i\downarrow})$ is the tunnel resistance. The tunnel spin polarization ranges around 30–40% for alumina barriers (Meservey and Tedrow, 1994), and $P \sim 85\%$ for MgO barriers (Parkin *et al.*, 2004). The result (42) indicates that spins accumulate in the AP alignment, while no spins accumulated in the P alignment in the symmetric junction. Therefore, we expect the suppression of superconductivity by spin accumulation in the AP alignment. In the normal state, $\mathcal{S}_{\mathrm{AP}} = P_{\mathrm{eff}} eV/2$ with the effective spin polarization $P_{\mathrm{eff}} = P/(1 + \Gamma_{\mathrm{s}})$.

The superconducting gap Δ in S is determined by $f_{\mathbf{k}\sigma}$ through the BCS gap equation (Tinkham, 1996)

$$\frac{1}{N_{\mathrm{S}} V_{\mathrm{BCS}}} = \int_0^{\omega_{\mathrm{D}}} \frac{\mathrm{d}\xi_{\mathbf{k}}}{2E_{\mathbf{k}}}\left[\tanh\left(\frac{E_{\mathbf{k}} - \delta\mu}{2k_{\mathrm{B}}T}\right) + \tanh\left(\frac{E_{\mathbf{k}} + \delta\mu}{2k_{\mathrm{B}}T}\right)\right] \quad (43)$$

where V_{BCS} is the attractive interaction between electrons and ω_{D} is the Debye frequency in S.

The self-consistent equations, (42) and (43), are solved in terms of Δ and $\delta\mu$ for the P and AP alignments. The results are used to calculate the tunnel current $I = I_\uparrow + I_\downarrow$ as a function of V for the P and AP alignments:

$$I_{\mathrm{P}} = \frac{\mathcal{N}_{\mathrm{P}}(V)}{eR}, \quad I_{\mathrm{AP}} = \left(\frac{1 - P^2 + \Gamma_{\mathrm{s}}}{1 + \Gamma_{\mathrm{s}}}\right)\frac{\mathcal{N}_{\mathrm{AP}}(V)}{eR} \quad (44)$$

In the current bias, $\mathcal{S}_{\mathrm{AP}}$ is directly connected to the injection current I

$$\mathcal{S}_{\mathrm{AP}} = \frac{P}{1 - P^2 + \Gamma_{\mathrm{s}}} eRI \quad (45)$$

It is interesting to note that the spin current $I_{\mathrm{spin}} = I_{i\uparrow} - I_{i\downarrow}$ flows through S with $I_{\mathrm{spin}}^{\mathrm{P}} = PI$ in the P alignment, while $I_{\mathrm{spin}}^{\mathrm{AP}} = 0$ in the AP alignment.

A key parameter for the efficient spin injection into S is the effective spin polarization $P_{\mathrm{eff}} = P/(1 + \Gamma_{\mathrm{s}})$; it depends strongly on the spin relaxation parameter Γ_{s}, which is reexpressed as $\Gamma_{\mathrm{s}} = (1/2)(RA/\rho_N\lambda_{\mathrm{S}})(d_{\mathrm{S}}/\lambda_{\mathrm{S}})$, where RA is the specific (area) tunnel resistance, ρ_N the resistivity, and λ_{S} the spin-diffusion length. For an efficient spin injection into S, it is crucial to make Γ_{s} as small as possible by using a junction with very small RA, a large $\rho_N\lambda_{\mathrm{S}}$, and thin d_{S}. The parameter RA is variable in a wide range by changing the barrier thickness, ranging from $RA \sim 1\,\Omega\mu\mathrm{m}^2$ to $10^4\,\Omega\mu\mathrm{m}^2$. For an Al with thickness $d_{\mathrm{S}} \sim 5\,\mathrm{nm}$, $\rho_N \sim 5\,\mu\Omega\mathrm{cm}$, and $\lambda_{\mathrm{S}} \sim 700\,\mathrm{nm}$ (Jedema *et al.*, 2002; Valenzuela and Tinkham, 2006), we have a condition $RA < 15\,\Omega\mu\mathrm{m}^2$ for realizing that Γ_{s} is comparable to or smaller than unity ($\Gamma_{\mathrm{s}} < 1$). This condition is fulfilled by using a thin MgO barrier with low tunnel resistance and a CoFe-electrode with high P (Parkin *et al.*, 2004), so that a CoFe/MgO/Al/MgO/CoFe structure is most suitable for exploring the effect of spin injection on superconductivity (Yang, H., Yang, S.-H. and Parkin, S.S.P. private communications).

Figure 11(a) shows the superconducting gap Δ_{AP} in the AP alignment as a function of voltage V for $P = 0.4$ (Meservey and Tedrow, 1994) and $\Gamma_{\mathrm{s}} = 0$. The quantity Δ_0 denotes the value of Δ at $V = 0$ and $T = 0$. The gap Δ_{AP} decreases with increasing V and vanishes at

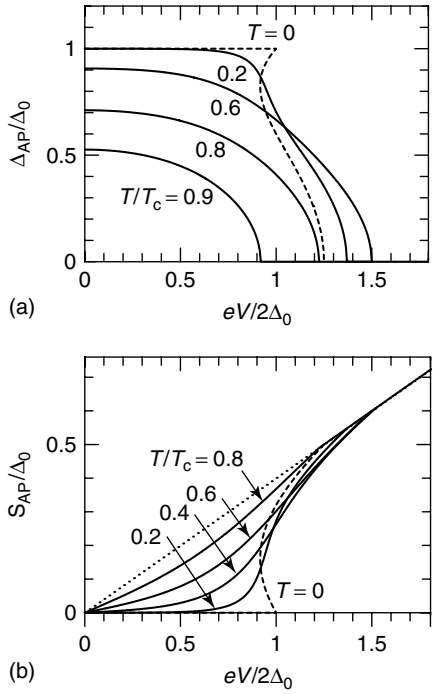

Figure 11. (a) Energy gap Δ_{AP} in S as a function of voltage V for different temperatures in the AP orientation of magnetizations. (b) Spin accumulation $\mathcal{S}_{AP}$ in S as a function of V.

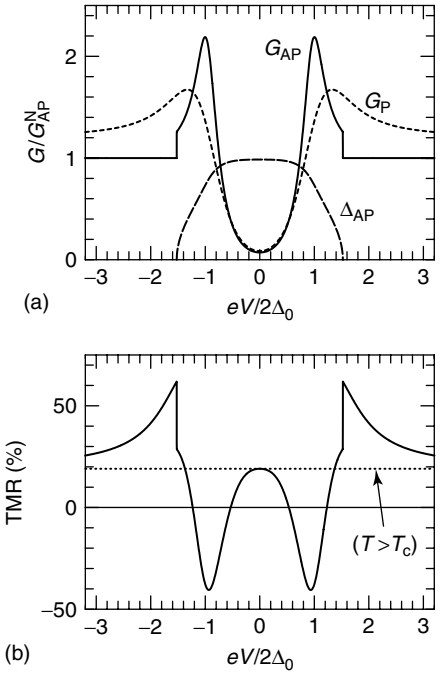

Figure 12. (a) Tunnel conductance as a function of bias voltage. The dashed and solid curves indicate the conductances G_P and G_{AP} for the P and AP alignments respectively, and the long-dashed curve indicates the superconducting gap parameter Δ in the AP alignment. (b) Tunnel magnetoresistance (TMR) as a function of bias voltage. The dotted line indicates TMR $= P^2/(1-P^2)$ in the normal state.

the critical voltage V_c. At very low temperatures, Δ_{AP} becomes multivalued in a certain range of eV; at $T = 0$, it has three solutions: $\Delta_{AP} = \Delta_0$ and $\Delta_{AP} = \Delta_0[1 - 2P^2 \pm 2P\sqrt{(eV/2\Delta_0)^2 + P^2 - 1}]^{1/2}$ for $0.92 < eV/2\Delta_0 < 1$. This suggests that a spatially inhomogeneous FFLO state appears in the narrow range of V at $T \sim 0$. Figure 11(b) shows the voltage dependence of the spin density $\mathcal{S}_{AP}$ in the AP alignment. The dotted line indicates the value of $\mathcal{S}_{AP} = \frac{1}{2}PeV$ in the normal state. As T is lowered below T_c, $\mathcal{S}_{AP}$ is suppressed below V_c by opening of the energy gap. At and near $T = 0$, $\mathcal{S}_{AP}$ shows the S-shaped anomaly around $eV_c \sim 2\Delta_0$, which corresponds to the multiplicity of Δ_{AP} in Figure 11(a). In the P alignment, Δ_P is independent of V and $\mathcal{S}_P = 0$ in the symmetric junction.

Figure 12(a) shows the voltage dependence of the differential conductance G_P and G_{AP} for the P and AP alignments at $T/T_c = 0.4$ and $\Gamma_s = 0$. The G_P shows the ordinary dependence on V expected for the constant gap Δ. In contrast, because of the decrease in Δ_{AP} with increasing voltage, G_{AP} increases with voltage more rapidly than G_P, forming a higher peak than G_P, and then decreases steeply. At the critical voltage V_c, G_{AP} jumps to the conductance G^N_{AP} in the normal state. The TMR is calculated by the formula: TMR $= (G_P/G_{AP}) - 1$. Using the values of Figure 12(a), we obtain the V dependence of TMR shown in Figure 12(b). At $V = 0$, TMR takes the same value as in the normal state. A deep negative dip appears at $eV/2\Delta_0 \sim 1$, where Δ_{AP} steeply decreases, exhibiting an inverse TMR effect ($G_{AP} > G_P$), and is followed by the discontinuous jump at V_c above which TMR is highly enhanced compared to that in the normal state. When the effect of spin relaxation in S is taken into account, the TMR value is reduced roughly by the factor $1/(1 + \Gamma_s)$ because of the reduction of the effective spin polarization $P_{eff} = P/(1 + \Gamma_s)$.

The suppression of the superconducting gap Δ by spin injection is detected by measuring the superconducting critical current I_c. According to the Ginzburg–Landau theory, I_c is proportional to Δ^3 because $I_c \propto \Delta^2 v_c$ with the critical superfluid velocity $v_c \propto \Delta$ (Tinkham, 1996). Figure 13 shows the normalized critical current (I_c/I_{c0}) as a function of injection current I at $T/T_c = 0.9$ for $P_1 = 0.8$, $P_2 = 0$, 0.4, 0.8, and $\Gamma_s = 0$. In the case of symmetric junction, the same spin polarizations (Figure 13a), the critical current I_c in the AP alignment steeply decreases and vanishes at a small value of I, whereas I_c in the P alignment shows no dependence on I. In the case of an asymmetric junction with different spin polarizations (Figure 13b), the critical current decreases with increasing injection current in both alignments but in a different way; I_c decreases more slowly in the P alignment than in the AP alignment.

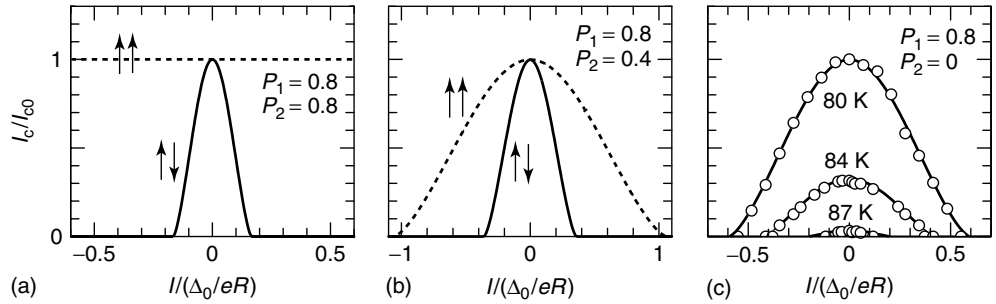

Figure 13. Dependence of the critical current I_c on the injection current I for the spin polarization $P_1 = 0.8$ of F1 and different values of P_2 of F2. The open circles indicate the critical current measured at $T = 80$, 84, and 87 K ($T_c \sim 89$ K) by Dong *et al.* (1997) in a F/S/N junction made of a high-T_c S and ferromagnetic manganite with $P \sim 100\%$.

If one of the ferromagnets, F2, is replaced by a normal metal (N), we have a heterostructure F1/S/N junction with $P_2 = 0$ (Figure 13c). The critical current suppression by spin injection observed in heterostructure junctions consisting of a high-T_c cuprate and a ferromagnetic manganite with a large spin polarization is reproduced well by the calculated result (Vas'ko *et al.*, 1997; Dong *et al.*, 1997; Yeh *et al.*, 1999).

7 SUMMARY AND DISCUSSIONS

In this chapter, we have discussed the novel phenomena arising from the interplay between superconductivity and ferromagnetism in hybrid F/S structures. The most striking consequence due to the proximity effect in the F/S structures is a damped oscillatory behavior of the Cooper-pair wave function in ferromagnets, leading to the formation of the π state in S/F/S Josephson junctions and F/S multilayers. Applications of π junctions to quantum computing devices (qubits) open up a new possibility in the research field of superconducting spin electronics.

AR is a spin-sensitive scattering process at the F/S interface, which provides a powerful tool for probing the spin polarization of various ferromagnets. This spin sensitivity of AR is also capable of probing nonlocality of AR by using the crossed AR between two ferromagnetic leads in contact with a superconductor (Deutscher and Feinberg, 2000; Beckmann, Weber and Löhneysen, 2004).

There is rapidly growing interest in the Josephson current through strong ferromagnets, such as transition-metal ferromagnets or oxide ferromagnets. As shown in Section 2, the Cooper-pair wave function in the spin-singlet state is quickly decayed in strong ferromagnets, and the penetration of singlet pairs into strong ferromagnets is at most only $\sim$1 nm. However, recent observation of the Josephson supercurrent through a half-metallic ferromagnet CrO_2 (Keizer *et al.*, 2006) over several hundreds of nanometers strongly suggested that spin-triplet superconductivity is induced in the half-metallic ferromagnet. The underlying mechanism for occurring spin-triplet superconductivity is a conversion from spin-singlet to spin-triplet pairs due to the spin-mixing or spin-flip scattering at the interface (Bergeret, Volkov and Efetov, 2001; Eschrig, Kopu, Cuevas and Schön, 2003 Asano, Tanaka and Golubov, unpublished).

The dynamics of magnetization and its effect on the proximity effect in S/F structures will offer a new research field. In particular, the effects of spin dynamics (spin-wave emission and absorption, and precession of magnetization) on the proximity effect, the AR (McCann and Fal'ko, 2001), and the Josephson effect (Zhu, Nussinov, Shnirman and Balatsky, 2004; Takahashi *et al.*, unpublished) are important issues to be explored in this fascinating field. The interplay between superconductivity and magnetism provides new electronics devices based on spin and supercurrent.

NOTES

[1] The right-hand side of equation (8) is $\pi[N_\uparrow(\mathbf{r}) - N_\uparrow(\mathbf{r})]\Delta$, which vanishes in F/S structures with the sharp boundaries, because $N_\uparrow(\mathbf{r}) = N_\downarrow(\mathbf{r})$ in N and $\Delta = 0$ in F.

[2] In the presence of boundary resistance, the boundary conditions (Kupriyanov and Lukichev, 1988) are $D(\mathbf{r})\partial F(\mathbf{r})/\partial z\big|_{\mathbf{r}_i^+} = D(\mathbf{r})\partial F(\mathbf{r})/\partial z\big|_{\mathbf{r}_i^-} = (1/e^2R_b)[F(\mathbf{r}_i^+)/N(\mathbf{r}_i^+) - F(\mathbf{r}_i^-)/N(\mathbf{r}_i^-)]$, where R_b is the specific (area) boundary resistance and $\mathbf{r}_i^\pm = \mathbf{r}_i \pm 0$ is the position of the boundaries.

REFERENCES

Aarts, J., Geers, J.M.E., Bruck, E., *et al.* (1997). Interface transparency of superconductor/ferromagnetic multilayers. *Physical Review B*, **56**, 2779.

Andreev, A.F. (1964). The thermal conductivity of the intermediate state in superconductors. *Soviet Physics JETP*, **19**, 1228.

Asano, Y., Tanaka, Y. and Golubov, A.A. (2007) Josephson effect due to odd-frequency pairs in diffusive half metals. *Physical Review Letters*, **98**, 107002.

Bauer, A., Bentner, J., Aprili, M., *et al*. (2004). Spontaneous supercurrent induced by ferromagnetic π junctions. *Physical Review Letters*, **92**, 217001.

Beckmann, D., Weber, H.B. and Löhneysen, H.V. (2004). Evidence for crossed Andreev reflection in superconductor-ferromagnet hybrid structures. *Physical Review Letters*, **93**, 197003.

Bergeret, F.S., Volkov, A.F. and Efetov, K.B. (2001). Long-range proximity effects in superconductor-ferromagnet structures. *Physical Review Letters*, **86**, 4096.

Bergeret, F.S., Volkov, A.F. and Efetov, K.B. (2005). Odd triplet superconductivity and related phenomena in superconductor-ferromagnet structures. *Reviews of Modern Physics*, **77**, 1321.

Bianchi, A., Movshovich, R., Capan, C., *et al*. (2003). Possible Fulde-Ferrell-Larkin-Ovchinnikov superconducting state in $CeCoIn_5$. *Physical Review Letters*, **91**, 187004.

Blonder, G.E., Tinkham, M. and Klapwijk, T.M. (1982). Transition from metallic to tunneling regimes in superconducting micro-constrictions: Excess current, charge imbalance, and supercurrent conversion. *Physical Review B*, **25**, 4515.

Blum, Y., Tsukernik, A., Karpovski, M. and Palevski, A. (2002). Oscillations of the superconducting critical current in Nb-Cu-Ni-Cu-Nb junctions. *Physical Review Letters*, **89**, 187004.

Born, F., Siegel, M., Hollmann, E.K., *et al*. (2006). Multiple 0–π transitions in superconductor/insulator/ferromagnet/superconductor Josephson tunnel junctions. *Physical Review B*, **74**, 140501(R).

Braden, J.G., Parker, J.S., Xiong, P., *et al*. (2003). Direct measurement of the spin polarization of the magnetic semiconductor (Ga,Mn)As. *Physical Review Letters*, **91**, 056602.

Bulaevskii, L.N., Kuzii, V.V. and Sobyanin, A.A. (1977). Superconducting system with weak coupling to the current in the ground state. *JETP Letters*, **25**, 290.

Buzdin, A. (2005). Proximity effects in superconductor-ferromagnet heterostructures. Reviews Modern Physics. *Reviews of Modern Physics*, **77**, 935.

Buzdin, A.I., Bulaevskii, L.N. and Panyukov, S.V. (1982). Critical-current oscillations as a function of the exchange field and thickness of the ferromagnetic metal (F) in an S-F-S Josephson junction. *JETP Letters*, **35**, 178.

Chen, C.D., Kuo, W., Chung, D.S., *et al*. (2002). Evidence for suppression of superconductivity by spin imbalance in Co-Al-Co single-electron transistors. *Physical Review Letters*, **88**, 047004.

Chiorescu, I., Bertet, P., Semba, K., *et al*. (2004). Coherent dynamics of a flux qubit coupled to a harmonic oscillator. *Nature*, **431**, 159.

Chiorescu, I., Nakamura, Y., Harmans, C.J.P.M. and Mooij, J.E. (2003). Coherent quantum dynamics of a superconducting flux qubit. *Science*, **299**, 1869.

Ciuhu, C. and Lodder, A. (2001). Influence of the boundary resistivity on the proximity effect. *Physical Review B*, **64**, 224526.

Clarke, J. (1972). Experimental observation of pair-quasiparticle potential difference in nonequilibrium superconductors. *Physical Review Letters*, **28**, 1363.

Daibou, T., Oogane, M., Ando, Y. and Miyazaki, T. (2005). Study of spin injection into a superconductor in a ferromagnetic double tunnel junction. PhD thesis, Tohoku University.

Demler, E.A., Arnold, G.B. and Beasley, M.R. (1997). Superconducting proximity effects in magnetic metals. *Physical Review B*, **55**, 15174.

Deutscher, G. and Feinberg, D. (2000). Coupling superconducting-ferromagnetic point contacts by Andreev reflections. *Applied Physics Letters*, **76**, 487.

Dong, Z.W., Ramesh, R., Venkatesan, T., *et al*. (1997). Spin-polarized quasiparticle injection devices using $Au/YBa_2Cu_3O_7/LaAlO_3/Nd_{0.7}Sr_{0.3}MnO_3$ heterostructures. *Applied Physics Letters*, **71**, 1718.

Eschrig, M., Kopu, J., Cuevas, J.C. and Schön, G. (2003). Theory of half-metal/superconductor heterostructures. *Physical Review Letters*, **90**, 137003.

Frolov, S.M., Harlingen, D.J.V., Oboznov, V.A., *et al*. (2004). Measurement of the current-phase relation of superconductor/ferromagnet/superconductor π Josephson junctions. *Physical Review B*, **70**, 144505.

Fulde, P. and Ferrell, R.A. (1964). Superconductivity in a strong spin-exchange field. *Physical Review*, **135**, A550.

Garzon, S., Žutić, I. and Webb, R.A. (2005). Temperature-dependent asymmetry of the nonlocal spin-injection resistance: Evidence for spin nonconserving interface scattering. *Physical Review Letters*, **94**, 176601.

de Gennes, P.G. (1966). *Superconductivity of Metals and Alloys*, Benjamin.

Golubov, A.A., Kupriyanov, M.Yu. and Il'ichev, E. (2005). The current-phase relation in Josephson junctions. *Reviews of Modern Physics*, **76**, 411.

Gu, J.Y., You, C.Y., Jiang, J.S., *et al*. (2002). Magnetization-orientation dependence of the superconducting transition temperature in the ferromagnet-superconductor-ferromagnet system: CuNi/Nb/CuNi. *Physical Review Letters*, **89**, 267001.

Guichard, W., Aprili, M., Bourgeois, O., *et al*. (2003). Phase sensitive experiments in ferromagnetic-based josephson junctions. *Physical Review Letters*, **90**, 167001.

Godfrey, R. and Johnson, M. (2006). Spin injection in mesoscopic silver wires: Experimental test of resistance mismatch. *Physical Review Letters*, **96**, 136601.

Izmalkov, A., Grajcar, M., Il'ichev, E., *et al*. (2004). Evidence for entangled states of two coupled flux qubits. *Physical Review Letters*, **93**, 037003.

Izyumov, Y.A., Proshin, Y.N. and Khusainov, M.G. (2002). Competition between superconductivity and magnetism in ferromagnet/superconductor heterostructures. *Physics – Uspekhi*, **45**, 109.

Jedema, F.J., Filip, A.T. and van Wees, B.J. (2001). Electrical spin injection and accumulation at room temperature in an all-metal mesoscopic spin valve. *Nature*, **410**, 345.

Jedema, F.J., Heersche, H.B., Filip, A.T., *et al*. (2002). Electrical detection of spin precession in a metallic mesoscopic spin valve. *Nature*, **416**, 713.

Ji, Y., Strijkers, G.J., Yang, F.Y., *et al*. (2001). Determination of the spin polarization of half-metallic CrO_2 by point contact Andreev reflection. *Physical Review Letters*, **86**, 5585.

Jiang, J.S., Davidović, D., Reich, D.H. and Chein, C.L. (1995). Oscillatory superconducting transition temperature in Nb/Gd multilayers. *Physical Review Letters*, **74**, 314.

Johnson, M. (1993). Spin accumulation in gold films. *Physical Review Letters*, **70**, 2142.

Johansson, J., Korenivski, V., Haviland, D.B. and Brataas, A. (2004). Giant fluctuations of superconducting order parameter in ferromagnet-superconductor single-electron transistors. *Physical Review Letters*, **93**, 216805.

Johansson, J., Urech, M., Haviland, D. and Korenivski, V. (2003). Suppression of superconductivity due to spin imbalance in Co/Al/Co single electron transistor. *Journal of Applied Physics*, **93**, 8650.

Johnson, M. and Silsbee, R.H. (1985). Interfacial charge-spin coupling: Injection and detection of spin magnetization in metals. *Physical Review Letters*, **55**, 1790.

de Jong, M.J.M. and Beenakker, C.W.J. (1995). Andreev reflection in ferromagnet-superconductor junctions. *Physical Review Letters*, **74**, 1657.

Kakuyanagi, K., Saitoh, M., Kumagai, K., *et al*. (2005). Texture in the superconducting order parameter of CeCoIn5 revealed by nuclear magnetic resonance. *Physical Review Letters*, **94**, 047602.

Keizer, R.S., Goennenwein, S.T.B., Klapwijk, T.M., *et al*. (2006). A spin triplet supercurrent through the half-metallic ferromagnet CrO_2. *Nature*, **439**, 825.

Ketterson, J.B. and Song, S.N. (1999). *Superconductivity*, Cambridge University Press.

Kimura, T., Hamrle, J. and Otani, Y. (2004). Suppression of spin accumulation in nonmagnet due to ferromagnetic ohmic contact. *Applied Physics Letters*, **85**, 3795.

Kimura, T., Hamrle, J. and Otani, Y. (2005). Estimation of spin-diffusion length from the magnitude of spin-current absorption: Multiterminal ferromagnetic/nonferromagnetic hybrid structures. *Physical Review B*, **72**, 014461.

Kimura, T., Hamrle, J. and Otani, Y. (2006). Switching magnetization of a nanoscale ferromagnetic particle using nonlocal spin injection. *Physical Review Letters*, **96**, 037201.

Kontos, T., Aprili, M., Lesueur, J., *et al*. (2002). Josephson junction through a thin ferromagnetic layer: negative coupling. *Physical Review Letters*, **89**, 137007.

Kontos, T., Aprili, M., Lesueur, J. and Grison, X. (2001). Inhomogeneous superconductivity induced in a ferromagnet by proximity effect. *Physical Review Letters*, **86**, 304.

Krunavakarn, B., Sritrakool, W. and Yoksan, S. (2004). Nonmonotonic critical temperature in ferromagnet/superconductor/ferromagnet trilayers. *Physica C*, **406**, 46.

Kuboya, K. and Takanaka, K. (1998). Upper critical field and transition temperature of superconducting/ferromagnetic superlattices. *Physical Review B*, **57**, 6022.

Kupriyanov, M.Y. and Lukichev, V.F. (1988). Influence of boundary transparency on the critical current of dirty SSS structures. *Soviet Physics JETP*, **67**, 1163.

Larkin, A.I. and Ovchinnikov, Yu.N. (1965). Inhomogeneous state of superconductors. *Soviet Physics JETP*, **20**, 762.

Maekawa, S. (Eds.) (2006). *Concepts in Spin Electronics*, Oxford University Press.

Maekawa, S. and Shinjo, T. (Eds.) (2002). *Spin Dependent Transport in Magnetic Nanostructures*, Taylor and Francis.

Majer, J.B., Paauw, F.G., ter Haar, A.C.J., *et al*. (2005). Spectroscopy on two coupled superconducting flux qubits. *Physical Review Letters*, **94**, 090501.

McCann, E. and Fal'ko, V.I. (2001). Magnon-assisted Andreev reflection in a ferromagnet-superconductor junction. *Europhysics Letters*, **56**, 583.

Mercaldo, L.V., Attanasio, C., Coccorese, C., *et al*. (1996). Superconducting-critical-temperature oscillations in Nb/CuMn multilayers. *Physical Review B*, **53**, 14040.

Meservey, R. and Tedrow, P.M. (1994). Spin-polarized electron tunnelling. *Physics Reports*, **238**, 173.

Miura, K., Kasai1, S., Kobayashi1, K. and Ono, T. (2006). Non local spin detection in ferromagnet/superconductor/ferromagnet spin-valve device with double-tunnel junctions. *Japanese Journal of Applied Physics*, **45**, 2888.

Mooij, J.E., Orlando, T.P., Levitov, L., *et al*. (1999). Josephson persistent-current qubit. *Science*, **285**, 1036.

Moraru, I.C., Pratt, W.P. Jr. and Birge, N.O. (2006). Magnetization-dependent T_c shift in ferromagnet/superconductor/ferromagnet trilayers with a strong ferromagnet. *Physical Review Letters*, **96**, 037004.

Mühge, T., Garifyanov, N.N., Goryunov, Yu.V., *et al*. (1996). Possible origin for oscillatory superconducting transition temperature in superconductor/ferromagnet multilayers. *Physical Review Letters*, **77**, 1857.

Nakamura, Y., Pashkin, Yu.A. and Tsai, J.S. (1999). Coherent control of macroscopic quantum states in a single-Cooper-pair box. *Nature*, **398**, 786.

Obi, Y., Ikebe, M. and Fujishiro, H. (2005). Evidence for zero- and -phase order parameters of superconducting Nb/Co tri- and pentalayers from the oscillatory behavior of the transition temperature. *Physical Review Letters*, **94**, 057008.

Oboznov, V.A., Bol'ginov, V.V., Feofanov, A.K., *et al*. (2006). Thickness dependence of the Josephson ground states of superconductor-ferromagnet-superconductor junctions. *Physical Review Letters*, **96**, 197003.

Osofsky, M.S., Mazin, I.I., Laprade, G., *et al*. (2000). Transport spin polarization of Ni_xFe_{1-x}: Electronic kinematics and band structure. *Physical Review B*, **61**, R3788.

Parker, J.S., Watts, S.M., Ivanov, P.G. and Xiong, P. (2002). Spin polarization of CrO_2 at and across an artificial barrier. *Physical Review Letters*, **88**, 196601.

Parkin, S.S.P., Kaiser, C., Panchula, A., *et al*. (2004). Giant tunnelling magnetoresistance at room temperature with MgO (100) tunnel barriers. *Nature Materials*, **3**, 862.

Pethick, C. and Smith, H. (1980). Charge imbalance in nonequilibrium superconductors. *Journal of Physics C: Solid State Physics*. **13**, 6313.

Radovic, Z., Ledvij, M., Dobrosavljevic-Grujic, L., *et al*. (1991). Transition temperatures of superconductor-ferromagnet superlattices. *Physical Review*, **B 44**, 759.

Robinson, J.W.A., Piano, S., Burnell, G., *et al*. (2006). Critical current oscillations in strong ferromagnetic π junctions. *Physical Review Letters*, **97**, 177003.

Ryazanov, V.V., Oboznov, V.A., Rusanov, A.Y., *et al*. (2001). Coupling of two superconductors through a ferromagnet: Evidence for a π junction. *Physical Review Letters*, **86**, 2427.

Sellier, H., Baraduc, C., Lefloch, F. and Calemczuk, R. (2003). Temperature-induced crossover between 0 and π states in S/F/S junctions. *Physical Review B*, **68**, 054531.

Shelukhin, V., Tsukernik, A., Karpovski, M., *et al*. (2006). Observation of periodic π-phase shifts in ferromagnet-superconductor multilayers. *Physical Review B*, **73**, 174506.

Soulen, R.J. Jr., Byers, J.M., Osofsky, M.S., *et al*. (1998). Measuring the spin polarization of a metal with a superconducting point contact *Science*, **282**, 85.

Szafer, A. and Stone, A.D. (1989). Theory of quantum conduction through a constriction. *Physical Review Letters*, **62**, 300.

Tagirov, L.R. (1999). Low-field superconducting spin switch based on a superconductor /ferromagnet multilayer. *Physical Review Letters*, **83**, 2058.

Takahashi, S., Hikino, S., Mori, M., *et al*. Supercurrent pumping in Josephson junctions with a half-metallic ferromagnet. (unpublished).

Takahashi, S., Imamura, H. and Maekawa, S. (2000). Spin injection in ferromagnet/superconductor/ferromagnet tunnel junctions. *Physica C*, **341–348**, 1515.

Takahashi, S. and Tachiki, M. (1986). Theory of the upper critical field of superconducting superlattices. *Physical Review B*, **33**, 4620.

Tinkham, M. (1996). *Introduction to Superconductivity*, McGraw-Hill: New York.

Tinkham, M. (1972). Tunneling generation, relaxation, and tunneling detection of hole-electron imbalance in superconductors. *Physical Review B*, **6**, 1747.

Takahashi, S., Imamura, H. and Maekawa, S. (1999). Spin imbalance and magnetoresistance in ferromagnet/superconductor/ferromagnet double tunnel junctions. *Physical Review Letters*, **82**, 3911.

Takahashi, S., Imamura, H. and Maekawa, S. (2000). Spin injection and magnetoresistance in ferromagnet/superconductor/ferromagnet tunnel junctions. *Journal of Applied Physics*, **87**, 5227.

Takahashi, S. and Maekawa, S. (2003). Spin injection and detection in magnetic nanostructures. *Physical Review B*, **67**, 052409.

Upadhyay, S.K., Palanisami, A., Louie, R.N. and Buhrman, R.A. (1998). Probing ferromagnets with Andreev reflection. *Physical Review Letters*, **81**, 3247.

Urech, M., Johansson, J., Poli, N., *et al*. (2006). Enhanced spin accumulation in a superconductor. *Journal of Applied Physics*, **99**, 08M513.

Usadel, K.D. (1970). Generalized diffusion equation for superconducting alloys. *Physical Review Letters*, **25**, 507.

Valenzuela, S.O. and Tinkham, M. (2006). Direct electronic measurement of the spin Hall effect. *Nature*, **442**, 176.

van der Wal, C.H., ter Haar, A.C.J., Wilhelm, F.K., *et al*. (2000). Quantum superposition of macroscopic persistent-current states. *Science*, **290**, 773.

Vas'ko, V.A., Larkin, V.A., Kraus, P.A., *et al*. (1997). Critical current suppression in a superconductor by injection of spin-polarized carriers from a ferromagnet. *Physical Review Letters*, **78**, 1134.

Wang, D. and Lu, J.G. (2005). Spin dependent transport in ferromagnet/superconductor/ferromagnet single electron transistor. *Journal of Applied Physics*, **97**, 10A708.

Weides, M., Kemmler M., Kohlstedt H., *et al*. (2006). 0–π Josephson Tunnel Junctions with Ferromagnetic Barrier. *Physical Review Letters*, **97**, 247001.

Yamashita, T., Takahashi, S. and Maekawa, S. (2006) Superconducting π qubit with three Josephson junctions. *Applied Physics Letters*, **88**, 132501.

Yamashita, T., Tanikawa, K., Takahashi, S. and Maekawa, S. (2005). Superconducting π qubit with a ferromagnetic josephson junction. *Physical Review Letters*, **95**, 097001.

Yeh, N-C., Vasquez, R., Fu, C., *et al*. (1999). Nonequilibrium superconductivity under spin-polarized quasiparticle currents in perovskite ferromagnet-insulator-superconductor heterostructures. *Physical Review B*, **60**, 10522.

Zhu, J-X., Nussinov, Z., Shnirman, A. and Balatsky, A.V. (2004). Novel spin dynamics in a Josephson junction. *Physical Review Letters*, **92**, 107001.

Žutić, I., Fabian, J. and Das Sarma, S. (2004). Spintronics: fundamentals and applications. *Reviews of Modern Physics*, **76**, 323.

Magnetic Superconductors

A. Buzdin[1,2] and J. Flouquet[3]

[1] *Institut Universitaire de France, Paris, France*
[2] *Université Bordeaux I, Talence, France*
[3] *RFMC, SPSMS, CEA-Grenoble, Grenoble, France*

1 INTRODUCTION

Two fundamental properties of the superconducting (SC) state are the zero electrical resistance and the Meissner-Ochsenfeld effect (the expulsion of the magnetic field from the volume of a superconductor). Similarly, superconductivity can be destroyed by applying a magnetic field exceeding some critical value. This demonstrates the antagonistic character of superconductivity and magnetism, and explains the interest to their possible coexistence. Such a problem was first addressed theoretically by Ginzburg (1956) in the framework of the model of the electromagnetic (orbital) interaction between superconductivity and ferromagnetism. After the advent of the microscopic theory of the superconductivity by Bardeen, Cooper and Schrieffer (1957) it became clear that the singlet superconductivity could also be destroyed by an exchange mechanism. The exchange field in the ferromagnetic (FM) state tends to align spins of Cooper pairs in the same direction, thus preventing pairing. This is the so-called Pauli paramagnetic effect which is related with the Zeeman energy of electron spins – the magnetic field favors the orientation of the electron spins along the field direction. The Cooper pair is formed with two electrons with opposite spins (singlet superconductivity), and when the gain of the energy due to the spin reorientation ($\mu_B H$) becomes comparable with the Cooper pair superconducting coupling energy (which is of the order of the superconducting critical temperature T_c), the singlet superconductivity is destroyed. Therefore we obtain the following estimate (see, e.g., Abrikosov, 1988) for the paramagnetic limit of singlet superconductivity existence $H_p \approx 1.24 T_c/\mu_B$ or, in Tesla, $1.8 T_c$ (K). However, in usual superconductors the orbital effect is more important for superconductivity destruction by the magnetic field. In ferromagnetic superconductors the situation is different. The internal magnetic induction does not exceed several kilo-oersted which is smaller than the typical upper critical field in type II superconductors, and then is not harmful for superconductivity. On the other hand, the effective internal field h (which plays the role of Zeeman energy $\mu_B H$) acting on the electron spins due to the exchange interaction is very high. Typically, if expressed in the energy units $h \sim 100$–1000 K, which substantially exceed the superconducting critical temperature T_c, it makes the exchange interaction the main mechanism of superconductivity destruction. This strong exchange interaction is at the origin of very strong suppression of superconductivity by

Handbook of Magnetism and Advanced Magnetic Materials. Edited by Helmut Kronmüller and Stuart Parkin. Volume 1: *Fundamentals and Theory*. © 2007 John Wiley & Sons, Ltd. ISBN: 978-0-470-02217-7.

the magnetic impurities. The early experiments (Matthias, Suhl and Corenzwit, 1958) demonstrated that even a very small concentration (several percents) of magnetic atoms is enough to completely destroy the superconductivity. The influence of magnetic impurities on superconductivity was described by the now classical Abrikosov–Gorkov theory (Abrikosov and Gorkov, 1960).

The small allowed concentration of magnetic atoms in superconducting alloys was not enough to produce the FM ordering. The first regular superconducting single crystals with a regular sublattice of rare earth magnetic atoms have been discovered in 1976, which produced the real breakthrough in studies of magnetism and superconductivity coexistence. They are ternary rare earth (RE) compounds, (RE)Rh_4B_4 and (RE)Mo_6S_8, (RE)Mo_6Se_8; for a review, see, for example, Maple and Fisher (1982) and Fisher (1990) and Kulić (2006). It turned out that in many of these systems superconductivity coexists with antiferromagnetic (AF) order with the Néel temperature $T_N < T_c$. The peaceful coexistence of superconductivity with antiferromagnetism is understandable because, on average, the exchange and orbital fields are zero at distances of the order of superconducting coherence length ξ. Recently, the coexistence of superconductivity and antiferromagnetism was discovered in the series of quaternary intermetallic compounds (RE)Ni_2B_2C. The properties of these compounds are discussed in the reviews (Müller and Narozhnyi, 2001) and (Bud'ko and Canfield, 2006).

The question about FM and SC coexistence appears to be much more fascinating. Such a situation is realized in $ErRh_4B_4$ and $HoMo_6S_8$ compounds. In the superconducting phase below the Curie temperature, instead of the FM ordering, the long period modulated magnetic structure appears. Further cooling provokes the reentrant transition into the normal ferromagnetic phase. The nonuniform magnetic structure in superconductors was predicted a long time ago by Anderson and Suhl (1959), and the theory of the coexistence phase is discussed in detail by Bulaevskii, Buzdin, Kulić and Panjukov (1985).

The example of $ErRh_4B_4$ and $HoMo_6S_8$ shows that ferromagnetism does not coexist with superconductivity in these compounds, instead it is transformed into the modulated magnetic structure in the narrow temperature interval of magnetism and superconductivity coexistence. The first truly ferromagnetic superconductors UGe_2 (Saxena *et al*., 2000) and URhGe (Aoki *et al*., 2001) were discovered only recently, and attracted a lot of interest. Apparently these systems display the triplet superconductivity with parallel spin orientation of electrons in Cooper pair, thus withdrawing the paramagnetic limit. Another interesting problem is the interplay between superconductivity and itinerant-like magnetism in heavy-fermion matter, in the compounds like URu_2Si_2, UPd_2Al_3, UBe_{13}, and so on – for the recent review see Flouquet *et al*. (2006).

The coexistence of superconductivity and ferromagnetism may be easily achieved in artificially fabricated superconductor/ferromagnet heterostructures. Due to the proximity effect, the Cooper pairs penetrate into the F layer and we have the unique possibility to study the properties of superconducting electrons under the influence of the huge exchange field. Moreover, varying in the controllable manner the thicknesses of the ferromagnetic and superconducting layers it is possible to change the relative strength of two competing ordering. The Josephson junctions with ferromagnetic layers reveal many unusual properties quite interesting for applications, in particular, the so-called π-Josephson junction (with the π-phase difference in the ground state) was fabricated (Buzdin, 2005; Bergeret, Volkov and Efetov, 2005).

2 INTERACTION BETWEEN CONDUCTING ELECTRONS AND LOCALIZED MOMENT: ANTIFERROMAGNETIC SUPERCONDUCTORS

2.1 Role of magnetic scattering

The strong pair-breaking effect of magnetic impurities on superconductivity is illustrated in Figure 1 where it is clearly seen that the concentration more than 0.6 at% of Gd

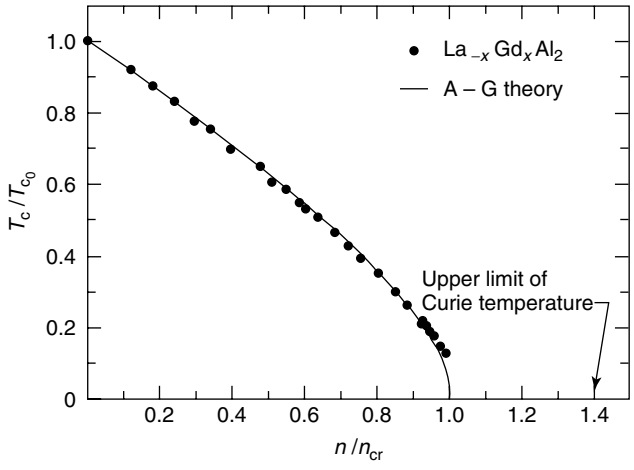

Figure 1. The critical temperature variation versus the concentration n of the Gd atoms in $La_{1-x}Gd_xAl_2$ alloys (Maple, 1968). $T_{c_0} = 3.24$ K and $n_{cr} = 0.590$ at % Gd. (Reprinted from *Physics Letters A*, Vol 26A, 1968, Page 513, Maple, with permission from Elsevier.)

completely destroys the superconductivity in $La_{1-x}Gd_xAl_2$ alloys (Maple, 1968).

The exchange interaction between the spin of the magnetic impurities and spin of electron of the Cooper pairs leads to the spin-flip scattering destroying pair. The theory of this phenomenon was proposed by Abrikosov and Gorkov (1960).

This Abrikosov–Gorkov theory provided an excellent description of the properties of superconductor with magnetic impurities.

The Hamiltonian of the interaction between RE magnetic moments localized in the sites $\vec{r}_i$ and the electron spins is

$$H_{\text{int}} = \int \mathrm{d}^3 r \Psi^+(\vec{r}) \left\{ \sum_i I(\vec{r} - \vec{r}_i)(g_J - 1)\vec{J}_i\vec{\sigma} \right\} \Psi(\vec{r}) \quad (1)$$

where $\Psi(\vec{r})$ is the electron spinor operator, $\vec{\sigma} = \{\sigma_x, \sigma_y, \sigma_z\}$ are the Pauli matrices, $I(\vec{r})$ is the exchange integral, and we take into account that for the RE atoms the total angular momentum $\vec{J}_i$ is quenched and g_J is the Landé g-factor for the Hund's rule ground state of RE. Following the A–G theory (Abrikosov and Gorkov, 1960) the decrease of the critical temperature T_c with the concentration n of magnetic impurities follows the law

$$\frac{\mathrm{d}T_c}{\mathrm{d}n} = -\frac{\pi^2}{2} N(0) \langle I^2(p_F) \rangle (g_J - 1)^2 J(J+1) \quad (2)$$

where $\langle I^2(p_F) \rangle$ is averaged value of the square of the Fourier transform of the exchange interaction over the Fermi surface, $N(0)$ is the electron density of the state at the Fermi energy. The pair-breaking strength of the magnetic scattering occurs to be proportional to the so-called De Gennes factor $\mathrm{d}G = (g_J - 1)^2 J(J+1)$. If all magnetic atoms substitute the nonmagnetic ones, they form a regular lattice and their concentration reaches the same order of magnitude as the concentration of the electrons. The most common mechanism of magnetic ordering in metal RE compounds is the Ruderman-Kittel-Kasuya-Yosida (RKKY) interaction and then the magnetic transition temperature may be estimated as $\Theta_m \approx \mathrm{d}G \frac{I^2}{E_F}$. Following equation (2), the decrease of the T_c being $\frac{\mathrm{d}T_c}{\mathrm{d}x} \approx -\Theta_m x$, where x is the relative concentration of the magnetic atoms. Therefore, the addition of the magnetic atoms of iron (having high Curie temperature) usually destroys superconductivity at a very small concentration (less than 1%). The very informative approach is the comparative studies of the properties of ternary $(RE)Rh_4B_4$ and $(RE)Mo_6S_8$ or quaternary $(RE)Ni_2B_2C$ compounds with different RE atoms and with nonmagnetic RE atoms partially substituted by the magnetic ones. Such substitution practically does not perturb the host matrix responsible for superconductivity but permits to vary the magnetic scattering in a controllable manner. An interesting example of the influence of the magnetic scattering on T_c in the $(Lu_{1-x}Dy_x)Ni_2B_2C$ series (Cho, Canfield and Johnston, 1996) is presented in Figure 2. For low Dy concentration we have the quite expected decrease of T_c, which vanishes at $x \approx 0.7$.

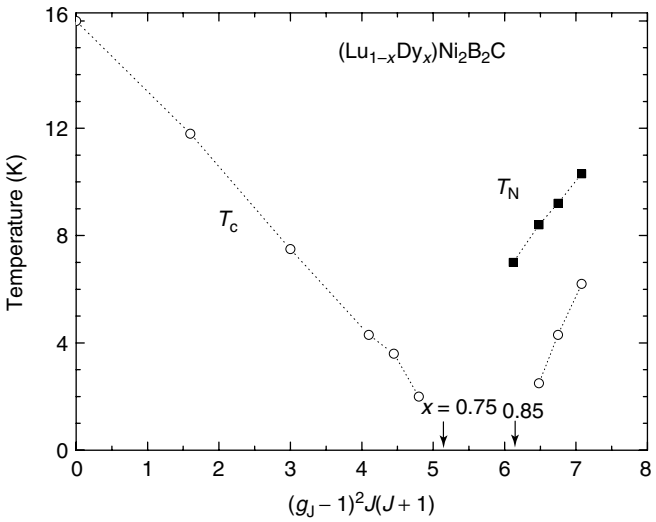

Figure 2. The variation of the critical temperature T_c in the $(Lu_{1-x}Dy_x)Ni_2B_2C$ series. (Reprinted figure with permission from Cho *et al.*, *Phys. Rev. Lett.* Vol 77, 163 (1996) Copyright 1996 by the American Physical Society.)

For $x = 1$ in $DyNi_2B_2C$ the Néel temperature $T_N = 11\,\mathrm{K}$ and superconductivity appears in the antiferromagnetic phase below $T_c = 6.2\,\mathrm{K}$. In the antiferromagnetic state the RE magnetic moments are ordered which decreases the magnetic scattering. They may be considered as magnetic impurities only above the Néel temperature when the RE magnetic moments chaotically change their directions with time. Below T_N they freeze out and the magnetic scattering may occur only via the electrons interaction with the spin waves. On the other hand the average exchange and orbital fields in the antiferromagnetic state are absent and superconductivity appears at lower temperature. The decrease of Dy concentration introduces the disorder in the magnetic sublattice which decreases T_N, and at the same time increases the magnetic scattering and decreases T_c. $DyNi_2B_2C$ only superconducts because the antiferromagnetic ordering reduces the magnetic scattering (Cho, Canfield and Johnston, 1996).

2.2 Antiferromagnetic superconductors

Neutron scattering experiments have shown that usually in ternary $(RE)Rh_4B_4$ (Maple, Hamaker and Woolf, 1982), $(RE)Mo_6S_8$ and $(RE)Mo_6Se_8$ (Thomlinson, Shirane, Lynn and Moncton, 1982), or quaternary $(RE)Ni_2B_2C$ (Müller and

Narozhnyi, 2001) compounds there is the long-range antiferromagnetic order that appears in the superconducting phase. The mutual influence of superconductivity and magnetism in antiferromagnetic superconductors occurs to be rather weak. Indeed, in the case of antiferromagnetism, an average value of magnetic induction and an exchange interaction (exchange field) are practically zero on the scale of Cooper pair size. On the other hand, the Meissner screening of the magnetic field, oscillating on the atomic distance is vanishing. The London penetration depth λ is the characteristic length of the magnetic field screening and typically $\lambda \sim 100–10\,000$ Å, and then it is much larger than the period of antiferromagnetic ordering, which makes its screening impossible. Then we may conclude that the coexistence of superconductivity and antiferromagnetism is quite peaceful – for T_c and T_N of typical antiferromagnetic superconductors see Table 1.

Interestingly, the appearance of magnetic ordering below T_N is at the origin of the anomalous temperature dependence of the upper critical H_{c_2}(T) in antiferromagnetic superconductors. Some typical examples of the H_{c_2}(T) curves measured for the $TmNi_2B_2C$ and $ErNi_2B_2C$ are presented in Figure 3 (Bud'ko and Canfield, 2006). The increase of the H_{c_2} below T_N in $ErNi_2B_2C$ may be related with the decrease of magnetic scattering. It is interesting that the anisotropy of the magnetic subsystem induces the anisotropy of the upper critical field. As it may be seen from Figure 3 near T_c the H_{c_2} along *a* and *c* axis is practically the same. At lower temperature the critical fields are smaller for the orientations corresponding to the easy magnetization directions.

For $TmNi_2B_2C$ it is *c* axis and for $ErNi_2B_2C$ it is the *ab* plane. The decrease of the upper critical field comparing with its value extrapolated from the initial slope near T_c is due to the internal exchange field h created by the polarized magnetic atoms. This field is $\vec{h} = I(g_J - 1)\langle\vec{J}_i\rangle$, where $\langle\vec{J}_i\rangle$ is the moment induced by the applied field which is proportional to the magnetic susceptibility of the RE compound. Then the internal exchange field reflects the anisotropy of magnetic susceptibility and induces the corresponding anisotropy of the H_{c_2} (for more information on the critical fields of the antiferromagnetic superconductors see Buzdin and Bulaevskii (1986)).

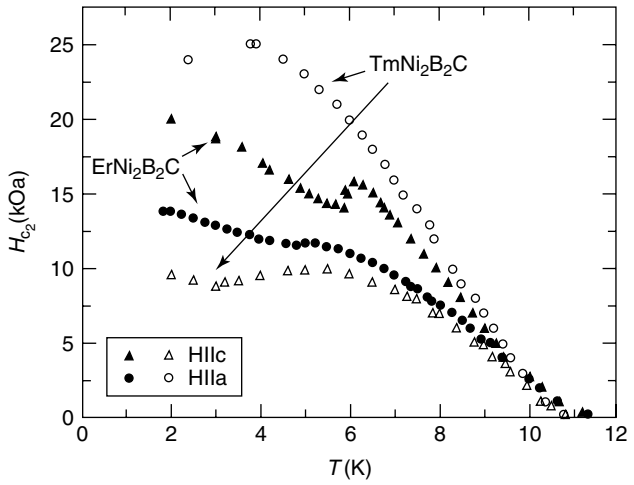

Figure 3. Anisotropic upper critical field $H_{c_2}(T)$ in antiferromagnetic superconductors $TmNi_2B_2C$ and $ErNi_2B_2C$. (Bud'ko and Canfield, 2006. Magnetism and superconductivity in rare earth-nickel-borocarbides. *Comptes Rendus Physique*, **7**, 56–67, with permission from Elsevier.)

Table 1. Antiferromagnetic superconductors.

	T_c (K)	T_N (K)
$NdRh_4B_4$	5.3	1.31
$SmRh_4B_4$	2.7	0.87
$TmRh_4B_4$	9.8	0.4
$GdMo_6S_8$	1.4	0.84
$TbMo_6S_8$	2.05	1.05
$DyMo_6S_8$	2.05	0.4
$ErMo_6S_8$	2.2	0.2
$GdMo_6Se_8$	5.6	0.75
$ErMo_6Se_8$	6.0	1.1
$DyNi_2B_2C$	6.2	11
$ErNi_2B_2C$	10.5	6.8
$TmNi_2B_2C$	11	1.5
$HoNi_2B_2C$	8	5

The data for (RE)Ni_2B_2C compounds are taken from the reviews (Müller and Narozhnyi, 2001) and (Bud'ko and Canfield, 2006) and for (RE)Rh_4B_4 – (Maple, Hamaker and Woolf, 1982) and (RE)Mo_6S_8, (RE)Mo_6Se_8 – (Thomlinson, Shirane, Lynn and Moncton, 1982).

2.3 Field induced superconductivity

A long time ago Jaccarino and Peter (1962) pointed out the possibility of the compensation of Zeeman field by the internal field created by magnetic moment. The total field acting on the electrons spin is $\vec{h}_{tot} = \mu_B\vec{H} + I(g_J - 1)\langle\vec{J}_i\rangle$, and if the sign of the exchange integral I is negative, the compensation Jaccarino–Peter effect occurs. Such behavior was indeed observed in an extremely unusual way in the compound $Eu_{0.75}Sn_{0.25}Mo_6S_{7.2}Se_{0.8}$ (Meul *et al.*, 1984)-Figure 4. The very high orbital critical field in this compound makes it essential to take into account the paramagnetic effect. The presence of localized Eu magnetic moments with negative exchange integral I leads to the possibility of the cancellation of this paramagnetic effect. In a magnetic field, the Eu moments orient along the field, which leads by virtue of the exchange interaction with electrons to the destruction of superconductivity. At low field, the exchange field dominates in $\vec{h}_{tot}$. A further increase of the magnetic field has only a

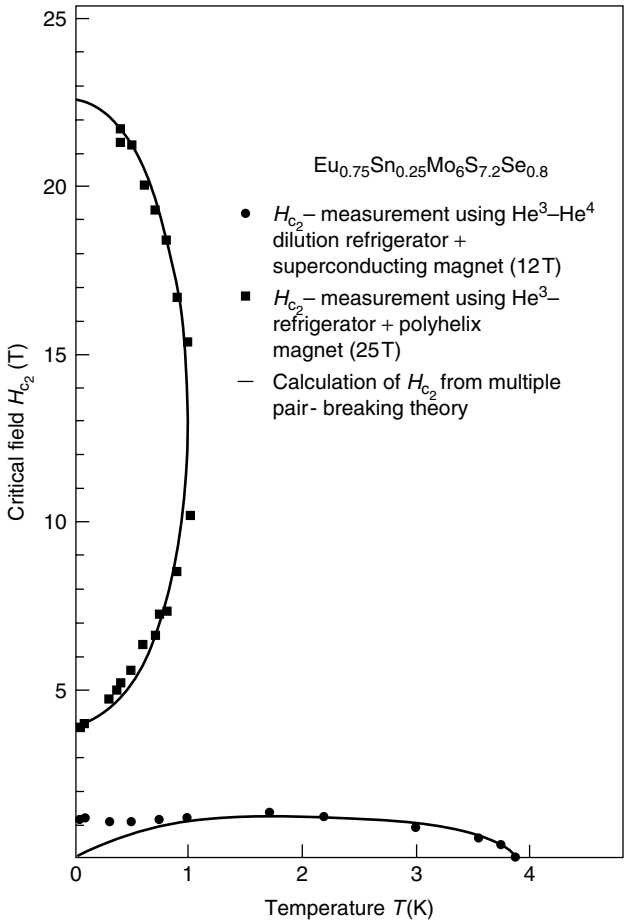

Figure 4. Field induced superconductivity in $Eu_{0.75}Sn_{0.25}Mo_6S_{7.2}Se_{0.8}$ compound (Meul *et al*., 1984). The unusual shape of the (H, T) diagram is a consequence of the Jaccarino–Peter mechanism, that is, the cancellation of the paramagnetic effect by the exchange field produced by polarized Eu atoms. (Reprinted figure from Meul *et al*., *Phys. Rev. Lett.* Vol. 53, 497 (1984). Copyright (1984) by the American Physical Society.)

slight effect on the exchange field of the Eu atoms, since their moment tends toward saturation. On the other hand the Zeeman field linearly increases with H and then finally compensates exchange field. At low temperature the condition of superconductivity existence is $|\vec{h}_{\rm tot}| < 1.24\,T_{\rm c}$ which leads to the restoration of superconductivity when the field is increased. Superconductivity is destroyed again at fields at which the orbital effect becomes important or there is the overcompensation of the exchange field.

Note that recently the magnetic-field-induced superconductivity has been observed in the quasi-two-dimensional organic conductor λ-(bis(ethylenedithio)tetraselenafulvalene, $BETS)_2$ $FeCl_4$ (Uji *et al*., 2001). However at zero magnetic field the superconductivity in this compound is absent due to the antiferromagnetic ordering of Fe^{3+} provoking the metal–insulator transition. A magnetic field above 10 T restores the metal phase. Further increase of the magnetic field induces the superconductivity at $H \approx 17$ T because of the partial compensation of the exchange field of aligned Fe^{3+} spins through the Jaccarino–Peter effect.

2.4 Magnetic high temperature superconductors

The question about the magnetism and superconductivity interplay in high $T_{\rm c}$ superconductor is well beyond the scope of this article. The mechanism of high temperature superconductivity still remains open though many theoretical approaches to handle this problem were proposed (see, e.g., Carlson, Emery, Kivelson and Orgad, 2004; Chubukov, Pines and Schmalian, 2004; Bonn, 2006).

In the $(RE)Ba_2Cu_3O_{6+x}$ and $(La_{2-x}Sr_x)CuO_{4-\delta}$ compounds the oxygen concentration is a very important parameter controlling the Cu ions magnetism. For small x and δ the compounds are insulators and Cu ions order antiferromagnetically with $T_{\rm N} \sim (300–500)$ K (see, e.g., Lynn, 1990). For optimally doped compounds the Cu antiferromagnetic transition is absent, and $T_{\rm c}$ is around 40 and 95 K for $(La_{2-x}Sr_x)CuO_{4-\delta}$ and $(RE)Ba_2Cu_3O_{6+x}$ respectively. The trivalent RE have very little effect on the superconducting properties of $(RE)Ba_2Cu_3O_{6+x}$ compounds. The REorder antiferromagnetically at low temperature $T_{\rm N} \sim (0.5–2)$ K (Lynn, 1990). The RE are very weakly coupled with superconducting Cu–O planes and the exchange interaction between RE and electrons is small (the magnetodipole and RKKY mechanisms give comparable contribution to the antiferromagnetic ordering energy). The condition $T_{\rm N} \ll T_{\rm c}$ ensure quite weak interplay of magnetic and superconducting subsystems in $(RE)Ba_2Cu_3O_{6+x}$.

Nowadays several types of layered compounds, where superconducting and magnetic layers alternate, are known. For example in $Sm_{1.85}Ce_{0.15}CuO_4$ (Sumarlin *et al*., 1992), which reveals superconductivity at $T_{\rm c} = 23.5$ K, the superconducting layers are separated by two ferromagnetic layers with opposite orientations of the magnetic moments and the Néel temperature is $T_{\rm N} = 5.9$ K. Several years ago, a new class of magnetic superconductors based on the layered perovskite ruthenocuprate compound $RuSr_2GdCu_2O_8$ comprising CuO_2 bilayers and RuO_2 monolayers has been synthesized (McLaughlin *et al*., 1999), and as a recent review see Nachtrab *et al*. (2006). In $RuSr_2GdCu_2O_8$, the magnetic transition occurs at $T_{\rm M} \sim 130–140$ K and superconductivity appears at $T_{\rm c} \sim 30–50$ K. Apparently, it is a weak ferromagnetic order, which is realized in this compound. Though the magnetization measurements give evidence of the small ferromagnetic component, the neutron diffraction data on $RuSr_2GdCu_2O_8$ (Lynn *et al*., 2000) revealed the dominant antiferromagnetic ordering in all three directions. Later,

the presence of ferromagnetic in-plane component of about $(0.1-0.3)\mu_B$ has been confirmed by neutron scattering on isostructural $RuSr_2YCu_2O_8$ (Tokunaga *et al.*, 2001).

3 FERROMAGNETIC CONVENTIONAL SUPERCONDUCTORS

As it has been already noted the antiferromagnetism and superconductivity are not in fact incompatible and may easily coexist. The question about ferromagnetism and superconductivity interplay appears to be much more fascinating. Such a situation is realized in $ErRh_4B_4$ and $HoMo_6S_8$ compounds, and leads to the destruction of the superconductivity. For example, in $ErRh_4B_4$ the superconductivity appears below $T_c = 8.7\,K$ and at the Curie temperature $\Theta \approx 0.9\,K$ instead of the ferromagnetic ordering the long period modulated magnetic structure appears. The appearance of this structure has been detected by neutrons scattering experiments (Sinha, Crabtree, Hinks and Mook, 1982), and its period occurs to be around 100 Å. However, a further cooling provokes at the temperature $T_{cr} \approx 0.7\,K$, a first-order phase transition into (or to) a ferromagnetic phase with simultaneous destruction of superconductivity. The transition at $T = T_{cr}$ is called *reentrant transition* because the superconductor goes back into the normal phase. The temperature dependence of the resistivity in the reentrant superconductor $ErRh_4B_4$ is presented in the Figure 5 (Fertig *et al.*, 1977). Similarly in $HoMo_6S_8$ superconductivity appears below $T_c = 1.8\,K$ and in the narrow temperature interval between 0.7 and 0.64 K the nonuniform magnetic structure coexists with superconductivity (Lynn *et al.*, 1981). Further

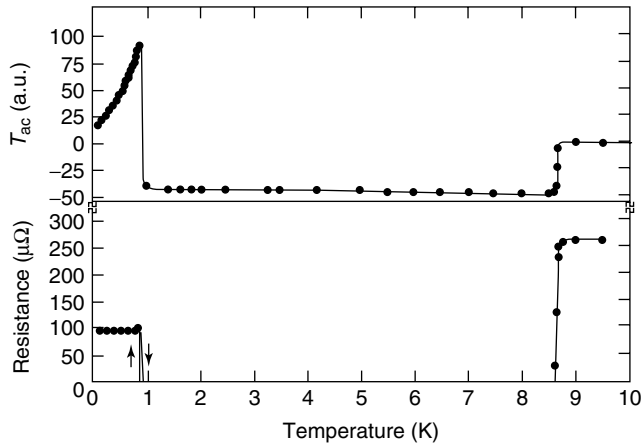

Figure 5. A.C. (alternate current) susceptibility and resistance versus temperature in $ErRh_4B_4$. (Reprinted figure from Fertig *et al.*, *Phys. Rev. Lett.* Vol. 38, 987, 1977. Copyright 1977 by the American Physical Society.)

cooling provokes the destruction of the superconductivity below $T_{cr} \approx 0.64\,K$ and the transition to the ferromagnetic state. Note that the ferromagnetic superconductors give a very rare example of the superconductivity destruction with lowering temperature.

The compound $HoMo_6Se_8$ is quite similar to $HoMo_6S_8$ but has a higher $T_c = 5.5\,K$, and in the superconducting phase also the nonuniform magnetic structure with wave vector $Q \approx 0.09\,Å^{-1}$ appears at $\Theta \approx 0.53\,K$ (Lynn *et al.*, 1984). Unlike $HoMo_6S_8$, however, the superconductivity is not destroyed in $HoMo_6Se_8$, and the nonuniform magnetic structure coexists with it. At low temperature the wave vector decreases down to $Q \approx 0.06\,Å^{-1}$.

What is the origin of such behavior and what is the nature of the coexistence phase in the temperature interval between Θ and T_{cr}? Let us start first with the estimate of the characteristic energy of magnetic interaction. In the case of the RKKY interaction it is the electronic spin susceptibility χ that is responsible for the magnetic ordering and the energy of this interaction may be written as

$$E_m = -\sum_Q \frac{\chi(Q)}{2}|h_Q|^2 \tag{3}$$

where $\chi(Q)$ and h_Q are the Fourier components of the electronic spin susceptibility and exchange field respectively. It is convenient to write $h(\vec{r}) = h_0 S(\vec{r})$, introducing the normalized magnetization $S(\vec{r}) = M(\vec{r})/M_0$, where M_0 and h_0 are the saturated magnetization and the exchange field at $T = 0\,K$. For the ferromagnetic ordering we may easily estimate from (3) the characteristic energy per one magnetic moment (or electron as the electrons' concentration is of the same order of magnitude as the magnetic atoms concentration) as $|E_m| \propto \Theta_{ex} = \frac{N(0)}{2}h_0^2 \propto \Theta$, where $N(0)$ is the electron density of state at the Fermi energy. On the other hand the energy of the superconducting condensation (Abrikosov, 1988) $E_s = -\frac{N(0)}{2}\Delta^2$, and Δ is the superconducting gap. The energy gain per one electron is very small $|E_s| \propto T_c\frac{T_c}{E_F} \ll T_c$. The reason is that the formation of the Cooper pairs modifies the electronic spectrum only in the immediate vicinity near the Fermi surface.

The factor $\frac{T_c}{E_F} \ll 1$ made the superconducting condensation energy very small compared to the magnetic energy. Even in the case $\Theta < T_c$ we have $|E_s| \ll |E_m|$, and so we must conclude that magnetism is a very robust phenomenon compared to superconductivity. Therefore, superconductivity cannot prevent the magnetic ordering and may only modify it. On the contrary, ferromagnetism can easily destroy superconductivity.

Let us address now the question of the type of magnetic transition in superconducting phase. Near the Curie temperature we may describe the magnetic transition in the

framework of Landau functional. For ferromagnetic transition in the normal metal it reads

$$F_{\mathrm{m}} = \tilde{\Theta} \sum_{Q} \lfloor \tau |S_Q|^2 + Q^2 a^2 |S_Q|^2 \rfloor \tag{4}$$

where $\tau = \frac{T-\Theta}{\Theta}$, the energy constant $\tilde{\Theta} \propto \Theta$ and the constant a is the magnetic stiffness being of the order of the interatomic distance. The functional (4) is very general one and its coefficients describe the entropy as well as magnetic energy contributions. The form (4) corresponds to the case of ferromagnetic transition because, namely, $Q = 0$ gives the highest transition temperature Θ. This transition temperature and the wave vector Q are readily determined from (4) as the condition of the vanishing of the coefficient on the $|S_Q|^2$ harmonic.

The question about the type of the magnetic ordering in the superconducting state in the presence of the exchange interaction was first addressed by Anderson and Suhl (1959). In the superconducting state the electronic susceptibility $\chi_{\mathrm{s}}(Q)$ changes comparing with that of normal metal $\chi(Q)$, and to take this into account we need to add to the functional (4) the corresponding term

$$F_{\mathrm{int}}^{\mathrm{ex}} = -\sum_{Q} \frac{\chi_{\mathrm{s}}(Q) - \chi(Q)}{2} |h_Q|^2 \tag{5}$$

The dispersions of the electronic spin susceptibility in normal and superconducting states are schematically presented in Figure 6. The main difference is the vanishing of $\chi_{\mathrm{s}}(Q)$ for $Q = 0$. For large wave vectors $Q\xi_0 \gg 1$ the spin susceptibilities in the superconducting and normal states practically coincide. This explains why superconductivity has no effect

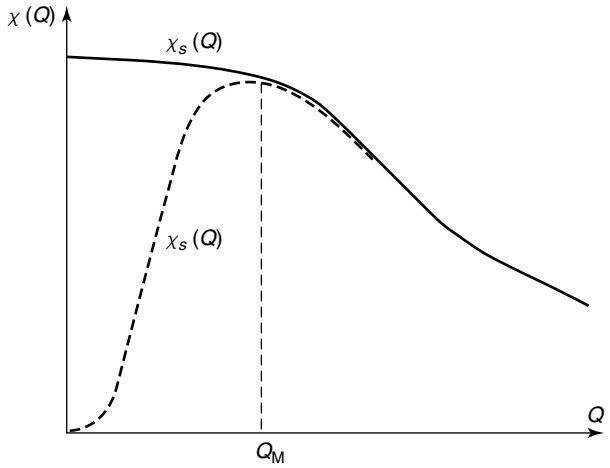

Figure 6. Schematic behavior of the spin susceptibility in normal $\chi(Q)$ and superconducting $\chi_{\mathrm{s}}(Q)$ states.

on the appearance of antiferromagnetic ordering with wave vectors $Q \approx a^{-1}$.

In the superconducting phase the magnetic functional (the energy is calculated per one magnetic atom) becomes

$$\begin{aligned} F_{\mathrm{m}}^{\mathrm{s}} &= F_{\mathrm{m}} + F_{\mathrm{int}}^{\mathrm{ex}} \\ &= \tilde{\Theta} \sum_{Q} \left[\tau + Q^2 a^2 - \frac{\chi_{\mathrm{s}}(Q) - \chi(Q)}{\chi(0)} \frac{\Theta_{\mathrm{ex}}}{\tilde{\Theta}} \right] |S_Q|^2 \end{aligned} \tag{6}$$

At $T = 0$ and $Q\xi_0 \gg 1$ following (Anderson and Suhl, 1959) $\frac{\chi_{\mathrm{s}}(Q)-\chi(Q)}{\chi(0)} = \frac{\pi}{2Q\xi_0}$ and we readily find from (6) the maximum critical temperature corresponds to the nonuniform magnetic structure with $Q_{\mathrm{M}} \approx (a^2\xi_0)^{-1/3}$ (Anderson and Suhl, 1959). The transition temperature Θ_{M} is only slightly smaller than the Curie temperature Θ in the absence of superconductivity: $\frac{\Theta-\Theta_{\mathrm{M}}}{\Theta} \approx (\frac{a}{\xi_0})^{2/3} \ll 1$. Anderson and Suhl called this magnetic structure *cryptoferromagnetic*.

In addition to the exchange mechanism there always exists the electromagnetic mechanism of superconductivity and magnetism interaction which is related with Meissner screening of the magnetic induction created by the magnetization $M(\vec{r}) = M_0 S(\vec{r})$. This mechanism also favors the nonuniform magnetic structure instead of ferromagnetic one (Krey, 1973; Blount and Varma, 1979; Ferrell, Bhattacharjee and Bagchi, 1979; Matsumoto, Umezawa and Tachiki, 1979). The contribution to the free energy from the screening may be readily written as

$$F_{\mathrm{int}}^{\mathrm{em}} = \sum_{Q} \frac{K(Q)}{2} |A_Q|^2 \tag{7}$$

where $K(Q)$ is the electromagnetic kernel in superconductor (see, e.g., Abrikosov, 1988), and A is the vector potential of the magnetic induction in superconductor. Assuming $Q\lambda_L \gg 1$ the vector potential satisfies $i[\vec{Q}\vec{A}_{\vec{Q}}] = 4\pi n M_0 \vec{S}_{\vec{Q}}$, the energy (7) per one magnetic atom reads

$$F_{\mathrm{int}}^{\mathrm{em}} = \Theta_{\mathrm{em}} \sum_{Q} \frac{|S_Q|^2}{Q^2 \lambda_L^2} \tag{8}$$

where $\Theta_{\mathrm{em}} = 2\pi n M_0^2$ and the expression for the kernel $K(Q) = \frac{1}{4\pi\lambda_L^2}$ in the local limit was used. The parameter Θ_{em} describes the strength of the magnetodipole interaction between magnetic atoms, and does not exceed 1 K in the ternary and quaternary magnetic superconductors. Combining (8) and (4) we find the magnetic transition occurs into the nonuniform state with $Q_{\mathrm{M}} \approx \left(\frac{\Theta_{\mathrm{em}}}{\tilde{\Theta}}\right)^{1/4} (a\lambda_L)^{-1/2}$.

The sinusoidally modulated magnetic coexistence phase perfectly resolves an antagonism problem between superconductivity and ferromagnetism. Indeed, from the 'point

of view of superconductivity' such a magnetic structure is like an antiferromagnetic one as $Q_M\lambda_L \gg 1$ and $Q_M\xi_0 \gg 1$. On the other hand, it is like a ferromagnetic one from the 'point of view of magnetism' as $Q_M a \ll 1$. Then it is really a compromise structure. Further lowering of the temperature will favor the structure with the constant modulus of magnetic moment, which is close to its value in the ferromagnet. The full theoretical description of the coexistence phase needs to take into account the magnetic anisotropy and both mechanisms of superconductivity and magnetism interaction (Bulaevskii, Buzdin, Kulić and Panjukov, 1985). The conclusion is that the sinusoidal modulation transforms into the domain phase with the period $d \approx \sqrt{a\xi_0}$ and the main role in the real compounds is played by the exchange interaction. The relative strength of electromagnetic and exchange interaction is controlled by the parameter $r = \frac{F_{\text{int}}^{\text{em}}}{F_{\text{int}}^{\text{ex}}} = \frac{\Theta_{\text{em}}}{\Theta_{\text{ex}}} \frac{1}{Q^2\lambda_{L^2}}$. Due to the large value of $Q\lambda_L \gg 1$ in all ternary ferromagnetic superconductors, the exchange interaction dominates in the formation of the domain coexistence phase. The superconductivity will be destroyed when the additional energy associated with the domain phase will compensate the superconducting condensation energy. This gives the following condition for the transition into the normal ferromagnetic state $S_c(T) \approx \frac{T_c}{h_0}(\xi_0/a)^{1/4}$. If $S_c > 1$ it simply means that the domain phase will be stable till 0 K without the reentrant superconducting transition. This situation is realized in $HoMo_6Se_8$ where the transition into the ferromagnetic state is lacking.

The unambiguous experimental evidence of the existence of the nonuniform magnetic structures were obtained in the neutron diffraction measurements in $ErRh_4B_4$ (Sinha, Crabtree, Hinks and Mook, 1982), $HoMo_6S_8$ (Lynn *et al*., 1981), and $HoMo_6Se_8$ (Lynn *et al*., 1984). For example in Figure 7 it is demonstrated that in $ErRh_4B_4$ (Sinha, Crabtree, Hinks and Mook, 1982) just below the Curie temperature in the superconducting phase the satellite neutron Bragg scattering appears in the narrow temperature interval around (0.1–0.2) K below the magnetic transition. Further lowering of the temperature provokes the transition into the ferromagnetic state with the simultaneous destruction of superconductivity.

Recently the coexistence of superconductivity and nuclear magnetic order has been reported in $AuIn_2$ (Rehmann, Herrmannsdörfer and Pobell, 1997). The superconducting critical temperature of this compound is $T_c = 0.207$ K and the magnetic transition temperature $\Theta \approx 35\,\mu$K though the type of the nuclear magnetic order is not yet known. The hyperfine interaction may play the same role as the exchange interaction and in superconducting $AuIn_2$ nonuniform nuclear magnetic ordering could be expected (Kulić, Bulaevskii and Buzdin, 1997). Coexistence of superconductivity with magnetism gives an interesting opportunity for studying these phenomena when the electronic temperature could be very different from the nuclear one.

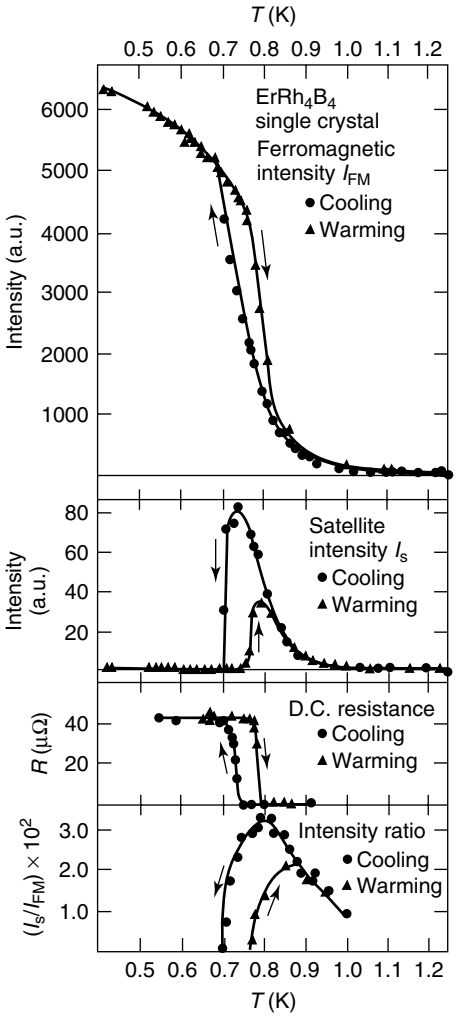

Figure 7. Intensity of the neutron Bragg scattering and resistance as a function of temperature in an $ErRh_4B_4$ (Sinha, Crabtree, Hinks and Mook, 1982). The satellite position corresponds to the wavelength of the modulated magnetic structure around 92 Å. (Reprinted figure from Sinha *et al*., *Phys. Rev. Lett.* Vol. 48, 950, 1982. Copyright 1982 by the American Physical Society.)

4 UNCONVENTIONAL SUPERCONDUCTIVITY: CASE OF HEAVY FERMION COMPOUNDS

In the previous examples, two separated baths exist: one with the localized magnetic centers, another with the Fermi sea. In strongly correlated electronic systems as high T_c oxide, organic conductor, or HFCs this separation is not justified. The spin dynamics and the electronic motion are strongly

coupled; the effective mass m^* of the itinerant electron depends on the proximity to instability points of the magnetism, the valence, or the charge. We will focus here on HFCs, which are intermetallic compounds of 4f or 5f electron (often cerium or uranium atoms). On cooling, the remaining large magnetic entropy ($S = R$ Log 2 for a doublet) is transferred to the Fermi sea for the creation of heavy quasiparticles; m^* is often 2 orders of magnitude larger than the bare electronic mass m_0. The weak delocalization of the 4f or 5f electrons from its site is produced by its hybridization with the other light electrons of the Fermi sea. The corresponding small effective Fermi temperature $T_F \sim 100\,K$ is mainly given by the Kondo temperature T_K of the single 4f or 5f ion. For example, at high temperature ($T > T_K$), the 4f electron of the Ce site behaves as a paramagnetic center with a local Kondo energy. Below T_K, each Ce site is no more independent from the others; heavy quasiparticles are formed in a strongly renormalized band (Flouquet, 2005).

The duality between the localized and itinerant character of the 4f (or 5f) electrons leads to the competition between the long-range magnetic order (AF or FM) and paramagnetism (PM). In Ce HFC, as T_K increases under pressure, the critical magnetic temperature T_N or T_{Curie} collapses at a critical pressure P_C. If the magnetism disappearance occurs continuously through a second-order phase transition (the collapse of T_N is associated with that of the sublattice magnetization M_o), P_C is referred to as the *magnetic quantum critical point*. In the vicinity of P_C, the standard Fermi liquid properties such as temperature dependence of the resistivity in AT^2 can only be observed below a characteristic temperature T_I which collapses right at P_C (Figure 8a).

4.1 Heavy-fermion antiferromagnets and superconductivity

In various cerium HFCs which are AF below P_C, a superconducting dome appears between $P_{+S} - P_{-S}$ tight to P_C (Figure 8b). The quasicoincidence of the pressure of maxima of T_c with P_C suggests a magnetic origin for the pairing. Early theoretical works on superconductivity mediated by AF fluctuations can be found in Emery (1983), Hirsch (1985), and Miyake, Schmitt-Rink and Varma (1986). Recent reviews can be found in Moriya (2003) and Chubukov, Pines and Schmalian (2004). Another source of pairing can originate from valence fluctuations near the pressure P_V where large fluctuations may occur in the occupation number n_f of the 4f shell (Onishi and Miyake, 2000). In Ce HFC, the valence is equal to $v = 4 - n_f$ while T_K is proportional to $1 - n_f$. The evidence of this extramechanism is mainly given by the observation of a maxima of T_c at a pressure far higher than P_C in $CeCu_2Si_2$ and $CeCu_2Ge_2$ (Holmes, Jaccard and Miyake, 2004), and near the pressure P_V where strong valence fluctuations are expected. Quite often P_C and P_V coincide as the collapse of AF corresponds to a strong increase of T_K which drives the system through P_V (Flouquet, 2005).

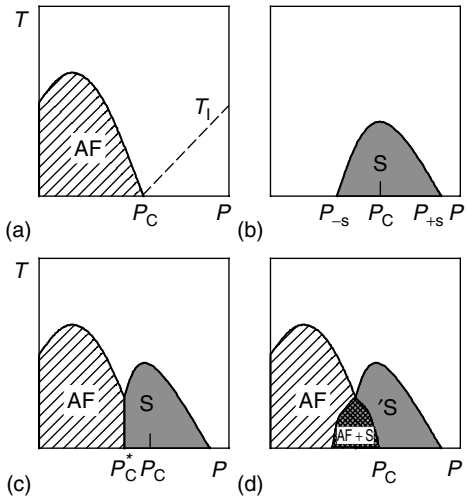

Figure 8. (a) P variation of the Néel temperature (T_N) and the temperature T_I below which Fermi liquid properties are observed without SC. (b) P variation of the superconducting critical temperature T_c neglecting AF order parameter. (c) Possibility of bicritical point if AF and SC expel each other. (d) Coexistence of AF and SC with a tetracritical point.

4.2 Unconventional superconductivity

Due to the strong on-site repulsion among the f electrons, the existence of a previous s-wave superconductivity with finite amplitude of the Cooper pair on a given site is precluded. An anisotropic pairing either a triplet like the p wave of ^3He or a single d wave occurs. In this unconventional superconductor, another symmetry other than the gauge one is broken: point group, odd parity, or time reversal. Often, the order parameter $\Delta(k)$ vanishes on point nodes or line nodes on the Fermi surface (Mineev and Samokhin, 1999). That leads to low energy excitations highly sensitive to any type of impurities and also to the Doppler shift produced by a magnetic field. In these unconventional superconductors, the clean limit is required, that is, the electronic mean free path ℓ must be higher than the superconducting coherence length ξ. Increasing ℓ leads to optimize T_c and $H_{c_2}(0)$.

The consequence of a huge m^* is a large orbital limit, proportional to the product $H_{c_2}^{orb}(0) \sim m^{*2} T_c$. If the zero component of the spin of the Cooper pair exists, the Pauli–Zeeman effect is efficient to break the Cooper pair. In case of equal spin pairing (ESP) between $\uparrow\uparrow$ and $\downarrow\downarrow$ spins, no Pauli

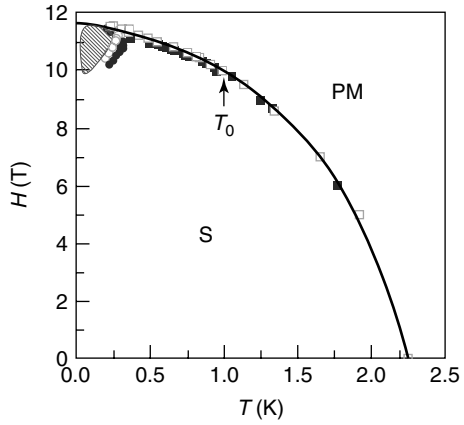

Figure 9. H, T phase diagram of $CeCoIn_5$ with H//110 (filled symbols) and H//100 (open symbols). The hatched domain is the new mixed superconducting phase which may be a FFLO state. (Reprinted figure from Bianchi *et al.*, *Phys. Rev. Lett.* Vol. 91, 187004, 2003. Copyright 2003 by the American Physical Society.)

limit occurs. An interesting possibility, as discussed later, is the appearance of a Fulde–Ferrell–Larkin–Ovchinnikov (FFLO) phase at high magnetic and low temperature (Larkin and Ovchinnikov, 1964; Fulde and Ferrell, 1964). This is possible if the Pauli limit dominates the behavior of H_{c_2} at low temperature. Such a possibility seems realized in $CeCoIn_5$ (Radovan *et al.*, 2003; Bianchi *et al.*, 2003) as an extra phase exists in this limit (Figure 9); however, other mechanisms can occur as reentrant long-range magnetism. A FFLO state was claimed for UPd_2Al_3 (Gloss *et al.*, 1993), and was also suggested for UBe_{13} (Glémot *et al.*, 1999), but with no further confirmation.

4.3 Ce heavy-fermion superconductors

After the unexpected discovery of superconductivity in $CeCu_2Si_2$ (Steglich *et al.*, 1979) at $P = 0$ (almost near the quantum critical pressure P_c), the main steps were:

- the pressure variation of T_C in $CeCu_2Si_2$ and the evidence of similar phenomena in $CeCu_2Ge_2$ (see Holmes, Jaccard and Miyake, 2004),
- the successive discovery of superconductivity in $CeRh_2Si_2$ (Movshovich *et al.*, 1996), $CePd_2Si_2$ and $CeIn_3$ (Mathur *et al.*, 1998) close to P_C,
- the boost on T_c by increasing the two dimensional characters with the insertion of a TIn_2 block ($T =$ Co, Rh, Ir) in the cubic structure of $CeIn_3$; T_c jumps by 1 order of magnitude (Thompson *et al.*, 2001),
- the possibility of SC in the noncentrosymmetric crystal of $CePt_3Si$ (Bauer *et al.*, 2004),
- the direct observation of long-range incommensurate AF order on a $CeCu_2Si_2$ crystal (Stockert *et al.*, 2004), which suggests a spin density wave instability for the origin of its quantum criticality (see Thalmeier *et al.*, 2004).

As an illustrating example let us focus on the interplay between antiferromagnetism and superconductivity in the 1, 1, 5 compound $CeRhIn_5$ with the possibility to tune through the different phases by the two P and H external variables. The increase in the two dimensional character leads to the favorable situation of quite comparable values in the maxima of their transition temperature $T_c = 2.4\,K$ and $T_N = 4\,K$: an ideal example for the study of the interplay between AF and SC (Figure 10).

A key question is the domain of the coexistence of AF and SC. If SC will not appear, the popular view of Ce HFC is that T_N collapses almost linearly with the pressure at P_C as shown in Figure 8(a). Neglecting the AF boundary, SC will appear between P_{-S} and P_{+S} with a temperature maxima T_c near P_C (Figure 8b). For the interference of both AF and SC order parameter, the simple approach is to consider an extra coupled term β in the Landau energy. If $\beta > 0$, superconductivity and magnetism compete. A bicritical point exists with a first-order separation between AF and SC phases at P_C^* (Figure 8c). If $\beta < 0$ a tetracritical point appears and each phase enhances the other (Figure 8d) (Flouquet *et al.*, 2006). Of course in this correlated system, β may depend on P.

At $P = 0$, $CeRhIn_5$ is a AF with $T_N = 3.8\,K$. In this AF state the normal state persists down to 0 K up to 0.8 GPa. Zero resistivity SC anomalies are detected between 0.8 and 1.5 GPa. Only above 1.5 GPa up to $P_C^* \sim 2\,GPa$,

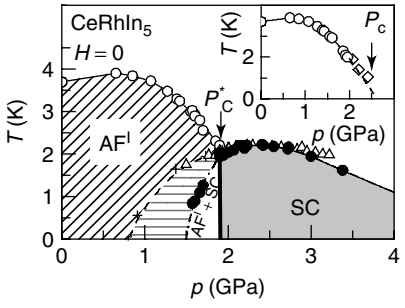

Figure 10. P, T phase diagram of $CeRhIn_5$ from specific heat (○, ●) susceptibility (Δ), and resistivity (X) measurements. Below 1.5 GPa $CeRhIn_5$ is an incommensurate AF in a normal state, the hatched region indicates an inhomogeneous SC state, the white one is the region ($AF^I + SC$) where a SC specific heat anomaly is detected below T_N for $P < P_c^*$. A pure SC without AF is realized for $P > P_c^*$. The inset show the extrapolation of T_N to zero at P_C in absence of SC, the (◇) indicates the temperature where above P_c^*, T_N (H) crosses T_c (H) (Knebel *et al.*, 2006). (Reprinted figure from J. Flouquet *et al.*, *Phys. Rev. B* Vol. 74, 020501 (2006).)

a broadened specific heat appears below T_N linked to SC, however, its temperature maxima T_c(C) is higher than the one detected in susceptibility $T_c(\chi)$ or in resistivity $T_c(\rho)$ (Knebel *et al*., 2004). At least, the SC phase transition is inhomogeneous. Surprisingly, NMR experiments lead to the conclusion of homogeneous gapless superconductivity below $T_c(P)$ (Kawasaki *et al*., 2003). At the opposite end above P_C^*, only a sharp specific heat anomaly characteristic of SC is detected on cooling for $H = 0$. The reason is that, just below P_C^*, where $T_N > T_c$, only few parts of the Fermi surface are involved by AF, and SC is not precluded below T_N. While, above P_C^*, when T_c will be greater than T_N, a large part of the FS is gapped, and thus, AF cannot appear. At first glance, AF and SC are antagonist (Figure 10) but these qualitative arguments do not exclude the possibility of a narrow P domain of a coexistence of SC and AF with a tetracritical point. At least, without SC, AF will collapse at higher pressure P_C than P_C^* defined by $T_c(P_C^*) = T_N\ (P_C^*)$.

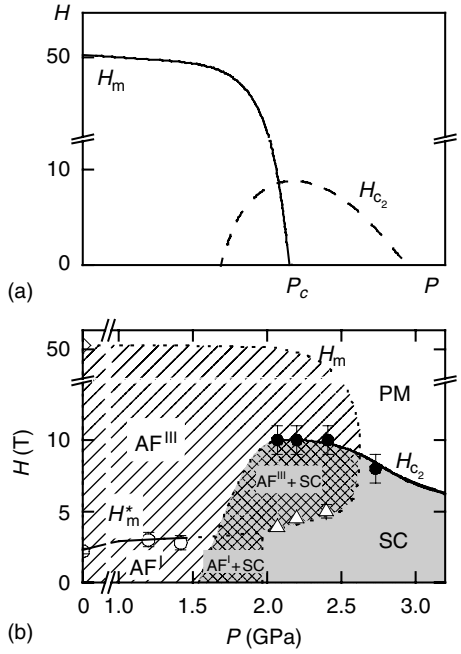

Figure 11. (a) At $T = 0$ K, expected pressure dependence of the magnetic critical field H_m between AF and PM states and the uppercritical field $H_{c_2}(0)$. (b) At $T = 0$ K, the extrapolated phase diagram of $CeRhIn_5$ for H in the basal plane. At zero pressure, the AF is incommensurate (AF^I); above $H_m^* = 2.5$ T, it becomes commensurate (AF^{III}). For $P > P_C^*$ and H H_m^*, SC and AF are suspected to coexist. $AF^I + SC$ and $AF^{III} + SC$ are the coexistence regimes of AF^I and AF^{III} with SC, respectively. SC represents a pure superconducting phase (●) and (○) indicates to $T = 0$ extrapolated values of H_{c_2} and H_m^* from the experiment of Knebel *et al*. (2006), respectively. (Δ) gives the lowest field at which the induced transition at TM is observed (◇) is the value of H_m at $p = 0$ (Takeuchi *et al*., 2001).

The magnetic field can modify the AF–SC boundary. As indicated Figure 11(a), in $CeRhIn_5$, the critical magnetic field H_m between AF and PM domain is high: $H_m \sim 50$ T (Takeuchi *et al*., 2001) for $H//a$ axis while $H_{c_2}(0)$ between P_C and P_C^* is around 8 T. Furthermore, it is expected that H_m will depend weakly on P for $P < P_C^*$. Thus applying a magnetic field can lead to recover the situation where T_N $(P, H) > T_c$ (P, H), and thus, of H reentrance of AF. At first approximation between P_C and P_C^*, T_c (P, H) depends strongly on H but weakly on P, while T_N (P, H) depends weakly on H and strongly on P:

$$T_N(P, H) = T_N(P_C^*)\frac{P_C - P}{P_C - P_c^*} \quad T_c(P, H) \sim T_c(P_C^*)\frac{H_0 - H}{H_0} \tag{9}$$

H reentrance of AF will appear for $H_{1,2}$ equal to

$$H_{1,2} = H_0 - H_0\frac{P_C - P}{P_C - P_C^*} \tag{10}$$

Specific heat experiments have been realized recently in Los Alamos (Park *et al*., 2006) and Grenoble (Knebel *et al*., 2006). Outside differences in the values of P_C^* 1.8 and 1.95 GPa respectively, both measurements show the H emergence of another phase below a pressure around P_C. Figure 12 shows at 2.4 GPa the two phase transitions already for $H > 4$ T: the first one is purely SC, the second one at lower temperature implies presumably an order parameter where SC and AF are coupled. Above P_C, for example,

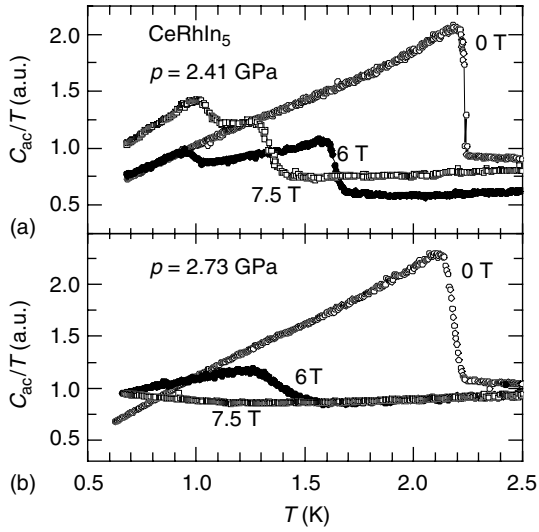

Figure 12. Results of ac microcalorimetry experiments: (a) C/T in arbitrary unit at 2.41 GPa ($P < P_C$) with the appearance of the second phase transition in the SC phase and (b) at 2.73 GPa ($P > P_C$) with the disappearance of the second phase transition (Knebel *et al*., 2006). (Reprinted figure from J. Flouquet *et al*., *Phys. Rev. B* Vol. 74, 020501 (2006).)

at 2.7 GPa, this anomaly disappears and only a unique SC phase transition is observed. As H_c^* is lower than $H_{1,2}$, AF may reappear in a dense vortex matter. One of the peculiarity of the system close to P_C is that, here, superconducting (ξ_0) and magnetic coherent (ξ_m) lengths have a comparable nanometer scale in contrast to previous normal RE intermetallic compounds where ξ_m ($T = 0$ K) corresponds to atomic distances. The Figure 11(b) shows an extrapolation of the H, P phase diagram at $H = 0$ K for H in the basal plane. Above H^*m, the AF structure has switched from incommensurate to commensurate.

At $H = 0$, SC precludes to reach the magnetic quantum critical point, however, the magnetic field can restore its vicinity. That may be the situation for $CeCoIn_5$ with the magnetic field applied along the c axis (Paglione *et al.*, 2003). For the superconductors $CeIn_3$, $CeRh_2Si_2$, $CeCu_2Si_2$, $CePd_2Si_2$, and $CePtSi_3$, AF looks to collapse via a first-order transition. Table 2 lists for different Ce HFC superconductors the value of T_N (max), T_c (max), and the corresponding pressures P_C and $P(T_c$ (max)), as well as the estimated value of the T linear coefficient γ of the specific heat in its normal state at $P = 0$. Table 3 shows the parameter for the uranium HFC which becomes superconductor (see Flouquet, 2005). These observations after the discovery of SC in $CeCu_2Si_2$ have boosted the studies of SC. As excellent crystals can be obtained, for the superconductors already at zero pressure careful experiments have largely contributed to progress on unconventional superconductivity.

Table 2. Parameters of some Ce heavy-fermion superconductors: T_N (max) and T_c (max) in Kelvin, the temperature maxima of their Néel and superconducting temperatures. P_c the critical pressure where T_N is suspected to collapse, $P(T_c$ (max)) the pressure (in GPa) where T_c reaches its maxima in pressure. The linear T term (γ) of the specific heat at $P = 0$ in mJ mol^{-1} K^{-2}. The superconducting coherence length ξ_0 is between 30 and 200 Å.

	T_N (max)	T_c (max)	P_C	$P(T_c$ (max))	$\gamma(P = 0)$
$CeCu_2Si_2$	–	2.5	0	4	1000
$CeCu_2Ge_2$	4	2	10	16	–
$CeIn_3$	10	0.2	2.5	2.4	140
$CeRh_2Si_2$	36	0.5	1.0	1.0	22
$CePd_2Si_2$	8	0.4	2.7	2.6	250
$CeRhIn_5$	3.8	2.4	2.5	2.5	150
$CeIrIn_5$	–	0.7	0	0	720
$CeCoIn_5$	–	2.4	1.5	1.5	1000
$CePt_3Si$	2.2	0.8	0.6	0	400

Table 3. The same parameters for some U heavy-fermion superconductors. For UGe_2 and URhGe, the order is ferromagnetic, T_N is replaced by T_{Curie}.

	T_N (max) or T_{Curie} (max)	T_c (max)	P_C	$P(T_c$ (max))	$\gamma P = 0$
UBe_{13}	–	0.95	–	0	1000
UPt_3	6	0.55	0.6	0.	457
URu_2Si_2	>20	1.2	>12	0	70
UPd_2Al_3	14	2	>40	0	140
UGe_2	54	0.7	1.6	1.2	35
URhGe	>10	0.3	>10	0	160

4.4 Ferromagnetic superconductors: UGe2 and URhGe

The discovery of superconductivity in UGe_2 under pressure (Saxena *et al.*, 2000), deep inside its ferromagnetic phase, was unexpected. At $P = 0$, UGe_2 is a ferromagnet with $T_{Curie} = 54$ K and a sublattice magnetization $M_o = 1.48\,\mu_B$/U atom; its γ term is 35 mJ mol^{-1} K^{-2}. The 5f electrons of the U atom are considered to be itinerant. As reported now for many itinerant ferromagnets, FM disappears at $P_C = 1.6$ GPa through a first-order transition characterized by a jump ΔM_o of M_o equal to $0.8\,\mu_B$/U atom. P studies show two FM phases, FM_1 and FM_2 (Figure 13). The FM_2–FM_1 boundary terminates at P_X ($T = 0$) ~ 1.2 GPa at $T = 0$ K, and the first-order line (P_X, T_X) seems to end up at a critical point around $T_X^c \sim 15$ K and $P_X^c \sim 0.7$ GPa (Huxley *et al.*, 2001). Superconductivity appears above 1.0 GPa when T_{Curie} is still high and M_o large ($\sim 1\,\mu_B$); T_c (max) ~ 700 mK for $P = P_X$. The estimation of the exchange field (100 T) seems to preclude a singlet component. Furthermore triplet ESP is suspected with even the possibility of only majority spin pairing. Flux flow experiments have supported the bulk

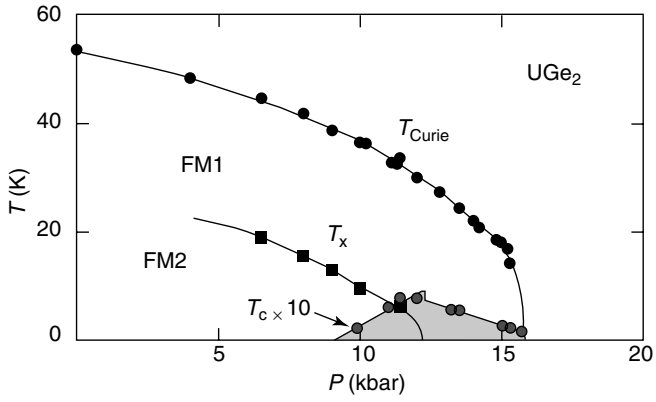

Figure 13. T, P phase diagram of the ferromagnetic superconductors UGe_2. The Curie temperature T_{Curie} (●), the supplementary temperature T_X (■) which leads to first-order transition at $T \to 0$ K and the superconducting temperature T_c (●) are shown. (Reprinted figure from Huxley *et al.*, *Phys. Rev. B* Vol. 63, 144519, 2001. Copyright 2001 by the American Physical Society.)

nature of superconductivity which were confirmed by direct specific heat measurements (Tateiwa *et al*., 2004). The coexistence of superconductivity and ferromagnetism was verified by neutron scattering and recently by NQR measurements on Ge sites (Harada *et al*., 2005). The nuclear relaxation rate T_1^{-1} exhibits a peak at T_{Curie} and a change of slope at T_c from a Korringa law to a T^3 law compatible with unconventional superconductivity with ESP.

Open questions are the mechanism of superconductivity and the variation of the SC order parameter on both side of the first-order line (T_X, P_X). An appealing possibility is that a charge-density wave plays a major role (Watanabe and Miyake, 2002). However, no extra reflections have been detected in neutron diffraction experiments; evidence may have been found in careful calorimetric measurements (Lashley *et al*., 2006).

Applying a magnetic field along the easy axis of the orthorhombic crystal above P_X leads to jump at H_X from FM_1 to FM_2, and even from PM to FM_1 and FM_2 above P_C. The interesting feature is that just above P_X for $P = 1.35$ GPa, the metamagnetic jump from FM_1 to FM_2 at $H_X \sim 1$ T modifies the SC properties, $H_{c_2}(0)$ jumping from 2 to 3 T: *de facto* it corresponds to two different T_c. A recent spectacular example is given later with the H reentrance of SC in URhGe.

A progress in ferromagnetic superconductors seems to be achieved with the observation of SC already at $P = 0$ in the ferromagnet URhGe with $T_c \sim 300$ mK for $T_{\text{Curie}} = 10$ K and $M_o = 0.4\,\mu_B$/U atom (Aoki *et al*., 2001). SC specific heat jump $\frac{\Delta C}{\gamma T_c} \sim 0.45$ was detected on polycrystals. Under pressure, T_{Curie} increases linearly with P reaching 20 K at 12 GPa while $P_{+S} \sim 4.5$ GPa. The growth of small clean crystals allows H_{c_2} measurements along the three a, b, c axis of the orthorhombic crystal; the easy magnetization axis is c (Figure 14) (Hardy and Huxley, 2005). Good fits are obtained with only the orbital limit. Taking into account the relative temperature variation of $H_{c_2}^a$, $H_{c_2}^b$, $H_{c_2}^c$, it was proposed as an ESP between the majority spin paired of the $k_a|\uparrow\uparrow\rangle$ state.

The surprise was the observation of H reentrant SC for $H//b$ associated with a field reorientation of the ordered magnetization M_o from c to b axis at $H_R \sim 12$ T (Figure 15) (Levy *et al*., 2005). In this strongly correlated system, a field reorientation of the magnetic structure is presumably associated with a modification of the spin fluctuation spectrum, which may react on the pairing mechanism. The jump of the b component of M_o is reminiscent of the metamagnetic phenomena extensively studied in the HFC $CeRu_2Si_2$ and URu_2Si_2 with the consequence on the dressing of the quasiparticles (m^*) (see Flouquet, 2005).

Progress in ferromagnetic superconductors requires a new generation of crystals. Up to now, the attempts to discover Ce ferromagnetic SC have failed. The fast claim of

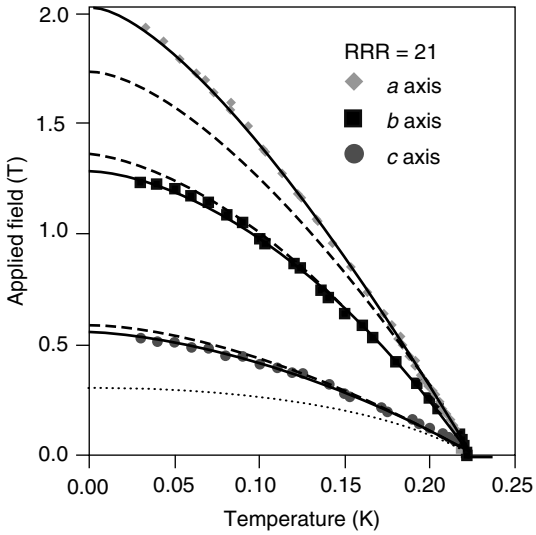

Figure 14. In URhGe, temperature variation of the upper critical field $H_{c_2}(T)$ measured along the a, b, and c axis of a simple crystal with residual resistivity ratio RRR = 21. The solid line show the prediction of the polar state $k_a|\uparrow\uparrow\rangle$. The dotted line is the BCS dependence for the c axis including the paramagnetic limitation and the dashed lines the calculated BCS dependence without paramagnetic limitation (Hardy and Huxley, 2005). (Reprinted figure from Hardy *et al*., *Phys. Rev. Lett.* Vol. 94, 247006, 2005. Copyright 2005 by the American Physical Society.)

superconductivity in the $ZrZn_2$ ferromagnet appears erroneous (Pfleiderer *et al*., 2001; Flouquet, 2005).

On the theoretical side, classification of the SC order parameter was made on general symmetry arguments (Samokhin and Walker, 2002; Mineev, 2002). The stabilization of superconductivity on the FM_1 side ($P < P_C$) was discussed on the basis of a positive feedback between magnetic moments of the Cooper pair and the magnetization density (Walker and Samokhin, 2002; Mineev, 2002). An alternative idea, if the magnetic anisotropy is weak, is the enhancement of T_c due to the coupling of the magnons to the longitudinal magnetic susceptibility (Kirkpatrick, Belitz, Vojta and Narayanan, 2001). As mentioned, an interesting proposal is that CDW are associated with FM. A phenomenological twin peak electronic structure was also developed to explain the maxima of T_c at P_X in UGe_2 (Sandeman, Lonzarich and Schofield, 2003). Possibility of s-wave superconductivity was pointed out by Suhl (2001) and Abrikosov (2002), but ferromagnetism needs to be localized. In UGe_2, the 5f electrons are considered to be itinerant and the reported preliminary experiments favor a triplet pairing.

With a SC order parameter coupled with M_o, one may ask if domain walls are weak links (Machida and Ohmi, 2001; Fomin, 2001), the occurrence of domain wall superconductivity (Buzdin and Mel'nikov, 2003), and finally the evolution of the FM domain structure through SC (Faure and

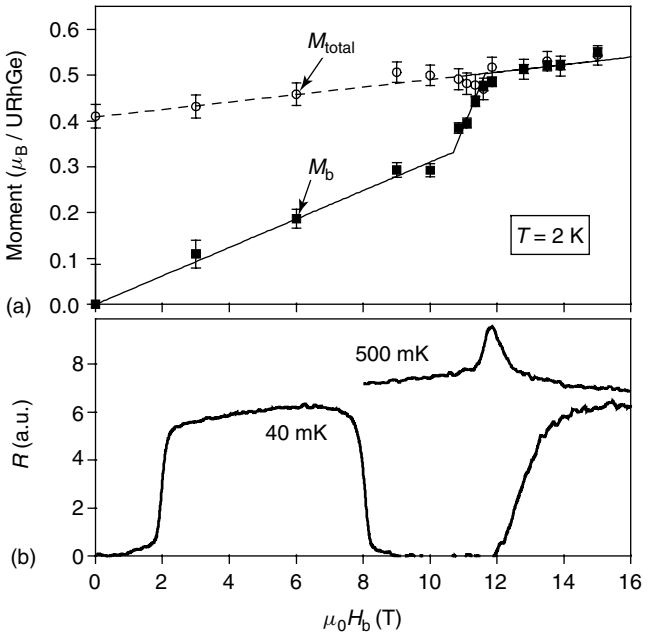

Figure 15. In (a) The total magnetic moment M total and the component Mb measured for H//to the b axis. In (b), variation of the resistance at 40 and 500 mK with the field reentrance of SC between 8 and 12 T (Levy, Sheikin, Grenier and Huxley, 2005). (From Levy *et al*., SCIENCE 309: 1343 (2005). Reprinted with permission from AAAS.)

Buzdin, 2005). A shrinkage of the domain width below T_c is proposed with, furthermore, quite a different T behavior between singlet and triplet pairing.

5 SUPERCONDUCTOR/FERROMAGNET HETEROSTRUCTURES

5.1 Proximity effect in ferromagnets

The coexistence of singlet superconductivity with ferromagnetism was not observed in bulk compounds, but it may be easily achieved in artificially fabricated layered ferromagnet/superconductors (F/S) systems. Due to the proximity effect, the Cooper pairs can penetrate into the F layer and induce superconductivity there. This provides the unique possibility to study the properties of superconducting electrons under the influence of a huge constant exchange field acting on the electron spins. In addition, it is possible to study the interplay between superconductivity and magnetism in a controlled manner, since by varying the layer thicknesses and magnetic content of F layers we change the relative strength of two competing orderings. The behavior of the superconducting condensate under these conditions is quite peculiar (see as reviews Buzdin, 2005; Bergeret, Volkov and Efetov, 2005).

Long time ago Larkin and Ovchinnikov (1964) and Fulde and Ferrell (1964) demonstrated that in a pure superconductor at low temperature the paramagnetic effect leads to the nonuniform superconductivity (it is the so-called FFLO or LOFF state). The appearance of modulation of the superconducting order parameter in FFLO state is related to the Zeeman's splitting of the electron's level under magnetic field acting on electron spins. To demonstrate this, we may consider the simplest case of the 1D superconductor. In the absence of the field, a Cooper pair is formed by two electrons with opposite momenta $+k_F$ and $-k_F$ and opposite spins ($\uparrow$) and ($\downarrow$) respectively. The resulting momentum of the Cooper pair $k_F + (-k_F) = 0$. Under a magnetic field, because of the Zeeman's splitting, the Fermi momentum of the electron with spin ($\uparrow$) will shift from k_F to $k_1 = k_F + \delta k_F$, where $\delta k_F = \mu_B H/v_F$ and v_F is the Fermi velocity. Similarly, the Fermi momentum of an electron with spin ($\downarrow$) will shift from $-k_F$ to $k_2 = -k_F + \delta k_F$ (see Figure 16). Then, the resulting momentum of the Cooper pair will be $k_1 + k_2 = 2\delta k_F \neq 0$, which just implies the space modulation of the superconducting order parameter with a resulting wave vector $2\delta k_F$.

Due to the incompatibility of ferromagnetism and superconductivity, it is not easy to verify this prediction on experiment. Moreover the electron scattering on the impurities destroys the FFLO state very quickly and its observation is possible only in the clean limit (Aslamazov, 1968). It happens that in a ferromagnet in contact with a superconductor the Cooper pair wave function has a damped oscillatory behavior (Buzdin, Bulaevskii and Panjukov, 1982), which may be considered in some sense as an analogy with the decaying nonuniform FFLO superconducting state. Indeed,

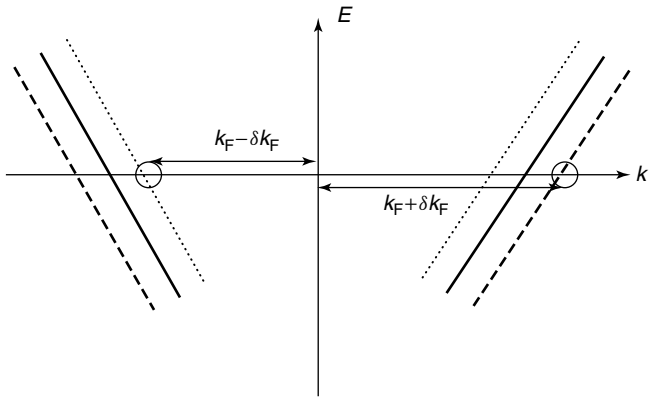

Figure 16. Energy band of the 1D superconductor near the Fermi energy. Due to Zeeman splitting, the energy of the electrons with spin orientation along the magnetic field ($\uparrow$) decreases, dotted line, while the energy of the electrons with the opposite spin orientation ($\downarrow$) increases, dotted line. For more details see text.

when a superconductor is in a contact with a normal metal the Cooper pairs penetrate across the interface at some distance inside the metal. A Cooper pair in a superconductor comprises two electrons with opposite spins and momenta. In a ferromagnet the up spin electron (with the spin orientation along the exchange field) decreases its energy by h, while the down spin electron increases its energy by the same value. To compensate this energy variation, the up spin electron increases its kinetic energy, while the down spin electron decreases it. In the result, the Cooper pair acquires a center of mass momentum $2\delta k_{\mathrm{F}} = 2h/v_{\mathrm{F}}$ which implies the modulation of the order parameter with the period $\pi v_{\mathrm{F}}/h$. The direction of the modulation wave vector must be perpendicular to the interface, because only this orientation is compatible with the uniform order parameter in the superconductor. This phenomenon, however, is quite general and must be present in both the clean and dirty limits (Buzdin and Kuprianov, 1990). It results in many interesting effects: the spatial oscillations of the electron's density of states, the nonmonotonous dependence of the critical temperature of S/F multilayers and bilayers on the ferromagnet layer thickness, the realization of the Josephson 'π' junctions in S/F/S systems. The interplay between the superconductivity and the magnetism in S/F structures occurs at the nanoscopic range of layer thicknesses and the observation of these effects became possible only recently due to the great progress in the preparation of high-quality hybrid F/S systems.

Let us consider the question of the proximity effect for a weak ferromagnet described by the decay of the superconducting correlations in a ferromagnet ($x > 0$) in contact with a superconductor ($x < 0$). If the electron scattering mean free path l is small (which is usually the case in S/F systems), the most natural approach is to use the Usadel equations (Usadel, 1970) for the Green's functions averaged over the Fermi surface. The linearized Usadel equation for the anomalous Green function F_{f} in the ferromagnet reads

$$\left(|\omega| + ih\,\mathrm{sgn}(\omega) + \frac{1}{\tau_{\mathrm{s}}}\right) F_{\mathrm{f}} - \frac{D_{\mathrm{f}}}{2}\frac{\partial^2 F_{\mathrm{f}}}{\partial x^2} = 0 \qquad (11)$$

where $\omega = (2n+1)\pi T$ are the Matsubara frequencies, and $D_{\mathrm{f}} = (1/3)v_{\mathrm{F}}1$ is the diffusion coefficient in the ferromagnet. The parameter $\frac{1}{\tau_{\mathrm{s}}}$ describes the magnetic scattering in the ferromagnetic alloys used as F layers. Note that this form of the Usadel equation in the ferromagnet implies a strong magnetic uniaxial anisotropy, when the magnetic scattering in the plane (xy) perpendicular to the anisotropy axis is negligible (Buzdin, 2005). In the F region, we may neglect the Matsubara frequencies compared to the large exchange field ($h \gg T_{\mathrm{c}}$). Also assuming first that the magnetic scattering is weak, we readily obtain the decaying solution for F_{f}

$$F_{\mathrm{f}}(x, \omega > 0) = A \exp\left(-\frac{1+i}{\xi_{\mathrm{f}}}x\right) \qquad (12)$$

where $\xi_{\mathrm{f}} = \sqrt{D_{\mathrm{f}}/h}$ is the characteristic length of the superconducting correlations decay (with oscillations) in F layer. Due to the condition $h \gg T_{\mathrm{c}}$, this length is much smaller than the superconducting coherence length $\xi_{0\mathrm{s}} = \sqrt{D_{\mathrm{s}}/(2\pi T_{\mathrm{c}})}$ (where D_{s} is the diffusion constant in the superconductor), that is, $\xi_{\mathrm{f}} \ll \xi_{0\mathrm{s}}$. In a ferromagnet, the role of the Cooper pair wave function is played by Ψ that decays as

$$\Psi \propto \sum_{\omega} F_{\mathrm{f}}(x, \omega) \propto \Delta \exp\left(-\frac{x}{\xi_{\mathrm{f}}}\right)\cos\left(\frac{x}{\xi_{\mathrm{f}}}\right) \qquad (13)$$

The presented analysis brings in evidence of the appearance of the oscillations of the order parameter in the presence of an exchange field. The different behavior of the superconducting order parameter in S/F and S/N systems is illustrated schematically in Figure 17.

The damping oscillatory behavior of Ψ is the fundamental difference between the proximity effect in S/F and S/N systems, and it is at the origin of many peculiar characteristics of S/F heterostructures. In the absence of the magnetic scattering the scale for the oscillation and decay of the Cooper pair wave function in a ferromagnet is the same. If we

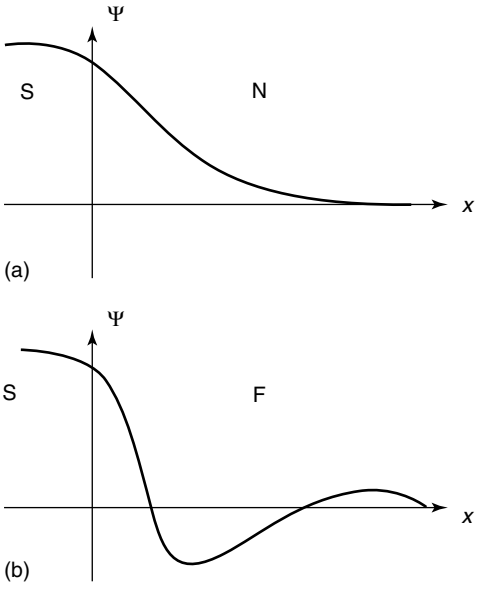

Figure 17. Schematic behavior of the superconducting order parameter near the (a) superconductor–normal metal and (b) superconductor–ferromagnet interfaces. The continuity of the order parameter at the interface implies the absence of the potential barrier. In the general case at the interface the jump of the superconducting order parameter occurs.

take into account the magnetic scattering, then the decaying length ξ_{f1} becomes smaller than the oscillating length ξ_{f2}. Namely $\xi_{f1} = \frac{\xi_f}{\sqrt{\sqrt{1+\alpha^2}+\alpha}}$ and $\xi_{f2} = \frac{\xi_f}{\sqrt{\sqrt{1+\alpha^2}-\alpha}}$, where the parameter $\alpha = \frac{1}{\tau_s h}$ characterizes the relative strength of the magnetic scattering. The damped oscillatory behavior of the order parameter may lead to the electronic density of states oscillations in a ferromagnet in contact with a superconductor (Buzdin, 2000). This prediction has been confirmed by the experiment by Kontos, Aprili, Lesueur and Grison (2001), which up to now remains the only experimental observation of the density of states oscillations in the F layer. The magnetic scattering effect complicates this type of experiment, strongly reducing the amplitude of the oscillations.

5.2 Oscillatory superconducting transition temperature in S/F multilayers and bilayers

The damped oscillatory behavior of the superconducting order parameter in ferromagnets may produce the commensurability effects between the period of the order parameter oscillation (which is of the order of ξ_{f2}) and the thickness of a F layer. This results in the striking nonmonotonous superconducting transition temperature dependence on the F-layer thickness in S/F multilayers and bilayers. Indeed, for a F-layer thickness smaller than ξ_{f2}, the pair wave function in the F layer changes a little and the superconducting order parameter in the adjacent S layers must be the same. The phase difference between the superconducting order parameters in the S layers is absent and we call this state the '0' phase. On the other hand, if the F-layer thickness becomes of the order of ξ_{f2} the pair wave function may go through zero at the center of the F layer providing the state with the opposite sign (or shift of the phase) of the superconducting order parameter in the adjacent S layers, the so-called 'π' phase. The increase of the thickness of the F layers may provoke the subsequent transitions from '0' to 'π' phases, which superpose on the commensurability effect and results in a very special dependence of the critical temperature on the F-layer thickness (Buzdin and Kuprianov, 1990; Radovic *et al*., 1991). The experimental observation (Jiang, Davidović, Reich and Chien, 1995) of this unusual dependence in Nb/Gd was the first strong evidence in favor of the 'π'-phase appearance – see Figure 18.

For the S/F bilayers, the transitions between '0' and 'π' phases are impossible; nevertheless, the commensurability effect between ξ_{f2} and the F-layer thickness also leads to the nonmonotonous dependence of T_c on the F-layer thickness. Processes of the normal quasiparticle reflection at the free F-layer boundary and Andreev reflection at SF interface interfere and this results in T_c minima that is

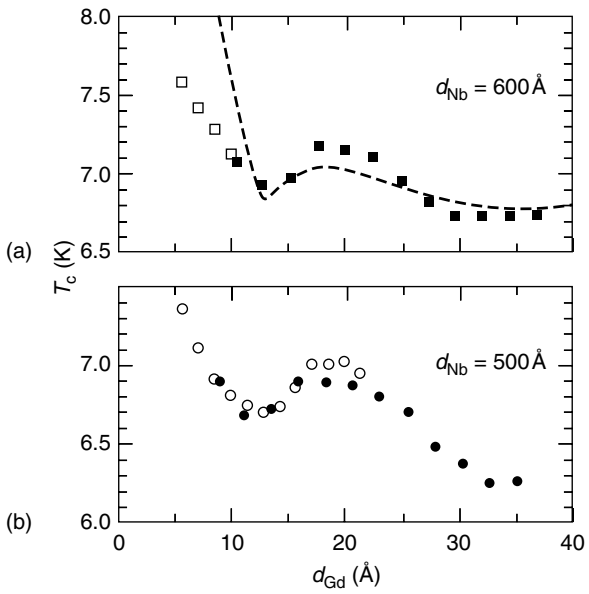

Figure 18. Oscillatory-like dependence of the critical temperature of Nb/Gd multilayers versus thickness of Gd layer (Jiang, Davidović, Reich and Chien, 1995). Dashed line in (a) is a fit using the theory (Radovic *et al*., 1991). (Reprinted figure from Jiang *et al*., *Phys, Rev. Lett.* Vol 74, 314, 1995. Copyright 1995 by the American Physical Society.)

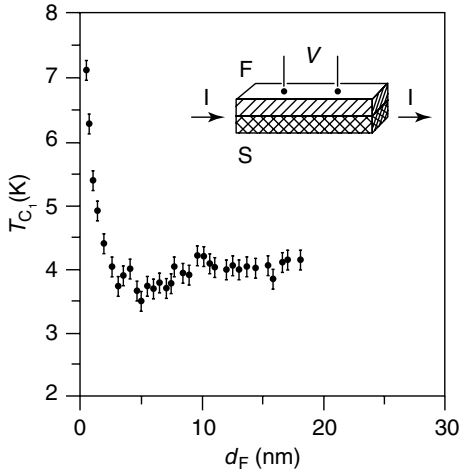

Figure 19. Critical temperature of $Nb/Cu_{0.43}Ni_{0.57}$ bilayer versus the thickness of the ferromagnetic layer (Ryazanov *et al*., 2004). (With kind permission of Springer Science and Business Media: *Journal of Low temp. Physics.*, v 136, 2004, 385, Ryazanov *et al*., figure 3.)

reached when the F-layer thickness is close to a quarter of the spatial oscillation period. The dependence of the T_c of $Nb/Cu_{0.43}Ni_{0.57}$ bilayer on the F-layer thickness (Ryazanov *et al*., 2004) is presented in Figure 19.

5.3 Superconductor-ferromagnet-superconductor 'π' junction

The experiments on the critical temperature of the S/F multilayers and bilayers attracted a lot of interest to the proximity effect in S/F systems but their interpretations were controversial due to the very small value of the characteristic length ξ_{f2} (only several nanometers). The most direct proof of the 'π'-phase observation would be the observation following the theoretical predictions (Buzdin, Bulaevskii and Panjukov, 1982; Buzdin and Kuprianov, 1991) of the vanishing of the critical current at the '0'- to 'π'-phase transition. The first experimental evidence of a '0'–'π' transition in S/F/S (Nb–Cu_xNi_{1-x}–Nb) Josephson junction was obtained in Ryazanov *et al*. (2001) from the measurements of the temperature dependence of the critical current. The '0'–'π' transition was signaled by the vanishing of the critical current with the temperature decrease. Such a behavior is observed for a F-layer thickness d close to some critical value d_c. In fact, it simply means that the critical thickness d_c slightly depends on the temperature. The temperature variation serves as fine tuning and permits one to study this transition in detail. Later, the damped oscillations of the critical current as a function of the F-layer thickness were observed in Nb/Al/Al_2O_3/PdNi/Nb (Kontos *et al*., 2002) and Nb/Cu/Ni/Cu/Nb (Blum, Tsukernik, Karpovski and Palevski, 2002) junctions. Very recent experiments (Oboznov *et al*., 2006) have enabled observation of the two-node thickness dependence of the critical current in Josephson SFS junctions with a ferromagnetic interlayer, that is, both direct transition into π state and reverse one from π into 0 state (Figure 20).

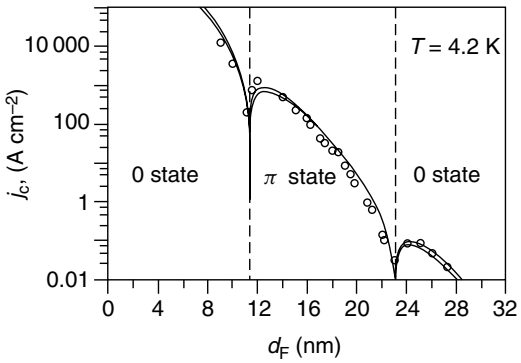

Figure 20. The double-reversal F-layer thickness dependence of the critical current density for Nb/$Cu_{0.47}Ni_{0.53}$/Nb junctions at temperature 4.2 K (Oboznov *et al*., 2006). The open circles present experimental results, the dashed line shows the fit using equation (14). (Reprinted figure from Oboznov, Buzdin *et al*., *Phys. Rev. Lett.* Vol. 96, 197003, 2006. Copyright 2006 by the American Physical Society.)

This revealed that the observed in Ryazanov, Oboznov, Veretennikov and Rusanov (2001) the '0' to 'π' transition with the F-layer thicknesses was the second one. The first transition occurs for F-layer thickness around 10 nm. The temperature dependences of the critical current near the first and the second '0' to 'π' transitions are presented in Figure 21.

The complete quantitative analysis of the S/F/S junctions is rather complicated, because the ferromagnetic layer may strongly modify superconductivity near the S/F interface. In addition, the boundary transparency and electron mean free path, as well as magnetic scattering, are important parameters affecting the critical current. In the case of small conductivity of the F layer or small interface transparency, the 'rigid boundary' conditions (Golubov, Kupriyanov and Il'ichev, 2004) are applied, and the influence of the ferromagnet on the superconducting order parameter in the electrodes may be neglected. This solution of (11) describes the $F(x)$ behavior near the critical temperature and gives the sinusoidal current-phase dependence $I_s(\varphi) = I_c \sin(\varphi)$ where φ is the phase difference on the junction. The critical current I_c passes through zero and changes its sign with the increase of the F-layer thickness.

In the most interesting limit from the practical point of view, when the F-layer thickness is $d_f > \xi_{f1}$ the universal expression for the $I_c(d_f)$ dependence is (Buzdin, 2005)

$$I_c \infty \exp\left(-\frac{d_f}{\xi_{f1}}\right) \sin\left(\frac{d_f}{\xi_{f2}} + \alpha\right) \tag{14}$$

where the angle $\pi/4 < \alpha < \pi/2$ depends on the magnetic scattering amplitude and the boundary transparencies.

Bulaevskii, Kuzii and Sobyanin (1977) pointed out that 'π' junction incorporated into a superconducting ring would generate a spontaneous current, and a corresponding magnetic flux would be half a flux quantum $\Phi_0 = h/2e$. The appearance of the spontaneous current is related to the fact that the ground state of the 'π' junction corresponds to the phase difference π and so, this phase difference will generate a supercurrent in the ring which short circuits the junction. Naturally the spontaneous current is generated if there is any odd number of 'π' junctions in the ring. This circumstance has been exploited in an elegant way (Ryazanov, Oboznov, Veretennikov and Rusanov, 2001) to provide unambiguous proof of the 'π'-phase transition. The observed half-period shift of the external magnetic field dependence of the transport critical current in triangular S/F/S arrays was observed on the '0–π' transition occurred with temperature variation.

The current-phase relation for Josephson junction is sinusoidal $I_s(\phi) = I_1 \sin(\phi)$ only near the critical temperature T_c (Abrikosov, 1988). At low temperature the higher harmonic terms appear. However, in the diffusive limit at $d_f > \xi_{f1}$

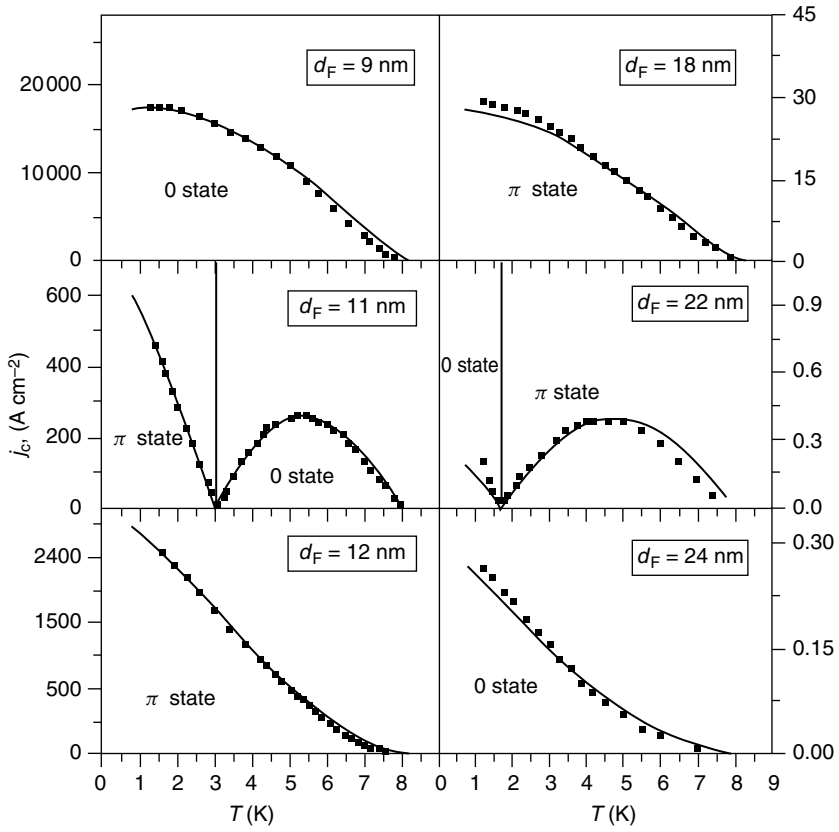

Figure 21. Temperature dependence of the Nb/$Cu_{0.47}Ni_{0.53}$/Nb junctions critical current density at several F-layer thicknesses close to the critical ones (Oboznov *et al*., 2006). The dashed lines show the calculation results based on the solution of the nonlinear Usadel equation. (Reprinted figure from Oboznov, Buzdin *et al*., *Phys. Rev. Lett.* Vol. 96, 197003, 2006. Copyright 2006 by the American Physical Society.)

they are very small and in the usual junctions their presence is hardly to be observed. In S/F/S junctions in general in the dirty limit $I_1 \sim \exp(-d_f/\xi_{f1})$ and the second harmonic contribution happens to be very small and positive $\sim \exp(-2d_f/\xi_{f1})$. The peculiarity of the situation with the '0'–'π' transition is that in the transition region the first harmonic term changes its sign passing through zero and then the role of the second harmonic contribution becomes predominant! To study the scenario of the '0'–'π' transition let us address the general current-phase relation

$$j(\varphi) = I_1 \sin(\varphi) + I_2 \sin(2\varphi) \tag{15}$$

which corresponds to the following phase dependent contribution to energy of the Josephson junction

$$E_J(\varphi) = \frac{\Phi_0}{2\pi c}\left[-I_1 \cos(\varphi) - \frac{I_2}{2}\cos(2\varphi)\right] \tag{16}$$

If we neglect the second harmonic term, then the 0 state occurs for $I_1 > 0$. Near a '0'–'π' transition $I_1 \to 0$ and the second harmonic term becomes important. The critical current at the transition $j_c = |I_2|$ and if $I_2 > 0$, the minimum energy always occurs at $\varphi = 0$ or $\varphi = \pi$.

In the opposite case ($I_2 < 0$) the transition from 0 to π state is continuous, and there is region where the equilibrium phase difference takes any value $0 < \varphi_0 < \pi$. The characteristics of such a 'φ junction' are very peculiar but at the moment there are no experimental evidences of its observation.

5.4 F /S /F spin-valve sandwiches

The strong proximity effect in superconductor-metallic ferromagnet structures could lead to the phenomenon of spin-orientation-dependent superconductivity in F/S/F spin-valve sandwiches. A long time ago De Gennes (1966) considered theoretically the system consisting of a thin superconducting layer in between two ferromagnetic insulators. He argued that the parallel orientation of the magnetic moments is more harmful for superconductivity because of the presence of the nonzero averaged exchange field acting on the surface of the superconductor. This prediction has been confirmed on

experiment by Hauser on In film sandwiched between two Fe_3O_4 films (Hauser, 1969), and on a In film between oxidized FeNi and Ni layers (Deutscher and Meunier, 1969).

A similar effect has been predicted for metallic F/S/F sandwiches (Tagirov, 1999; Buzdin, Vedyayev and Ryzhanova, 1999) and later observed on experiment in CuNi/Nb/CuNi (Gu *et al*., 2002) and Ni/Nb/Ni (Moraru *et al*., 2006) systems.

In the diffusive regime the proximity effect in S/F structures with local inhomogeneity of the magnetization may be rather special (Bergeret, Volkov and Efetov, 2005). The varying in space magnetization generates the triplet component of the anomalous Green's function $\sim \langle \Psi_\uparrow \Psi_\uparrow \rangle$ which may penetrate in the ferromagnet at distances much larger than ξ_f. It is not, however, the triplet superconductivity itself because the corresponding triplet order parameter would be equal to zero, unlike the superfluidity in He^3, for example. In general, the triplet components of the anomalous Green's function always appear at the description of the singlet superconductivity in the presence of rotating in space exchange field. An important finding (Bergeret, Volkov and Efetov, 2005) was the demonstration that in some sense the triplet component is insensitive to pair breaking by the exchange field and can generate the triplet long-range proximity effect. The special long-range triplet proximity effect was predicted to exist in the dirty limit. In the clean limit it disappears, the spin-orbit and magnetic scattering also destroy this effect. Up to know there are no reports on its experimental observation.

The proximity effect is related to the passing of electrons across the superconductor/ferromagnet interface. In addition to this effect if the magnetic field created by the ferromagnet penetrates into a superconductor, it switches on the orbital mechanism of superconductivity and magnetism interaction. The situation when it is the only one mechanism of superconductivity and magnetism interaction is naturally realized in the case, when the ferromagnet is an insulator or the buffer oxide layer separates the superconductor and the ferromagnet. The ferromagnet in such a case plays the role of the additional source of the local magnetic field. In particular the nucleation of superconductivity in the presence of domain structure occurs near the domain walls (Buzdin and Mel'nikov, 2003; Moshchalkov, Ducan, Gobulovic and Mathieu, 2006). The hybrid S/F systems have been intensively studied in connection with the problem of the controlled flux pinning. Enhancement of the critical current has been observed experimentally for superconducting films with arrays of submicron magnetic dots and antidotes (as a review on this subject see Lyuksyutov and Pokrovsky, 2005).

During the last 5 years an enormous progress in the controllable fabrication of the superconductor-ferromagnet heterostructures has been achieved. The peculiar effects predicted earlier were observed in experiments and we have a general understanding of the mechanism of the superconductivity and ferromagnetism interplay in S/F systems. Now this domain of research enters into a period where design of new types of devices becomes feasible and we may expect a lot of interesting findings in the near future.

6 CONCLUSION AND PERSPECTIVES

The RE ternary and quaternary compounds display a rich physics of magnetism and singlet superconductivity coexistence. The reentrant superconductivity and the nonuniform magnetic structure formation in $ErRh_4B_4$ and $HoMo_6S_8$ compounds may be very well described in the framework of the existing theoretical background. It exists a good understanding of the physics of the antiferromagnetic superconductors with localized magnetic moment. On the other hand, a substantial theoretical progress is needed to attend a breakthrough in the problems of the interplay between the itinerant magnetism and superconductivity and heavy-fermion superconductivity.

The studies of HFC have opened the field of unconventional superconductivity. The domain which had been in a shadow during the rush on high T_c superconductors knows again a new boost with the discovery of new materials (the 1,1,5 cerium family, uranium ferromagnetic superconductors, the interplay of superconductivity with multipolar ordering), and also with the necessity to make precise the role of quantum critical points on superconductivity with fine P or H tuning (conditions often easy achieved in HFC). For the general problems under debate on the unconventional superconductivity and its links with normal phase properties, HFCs are excellent systems to observe in great detail SC interplay with the magnetic and valence phase diagrams. Key questions are:

- the evolution of the Fermi surface in the vicinity of P_C^* or P_C,
- the role of impurities on the magnetic and SC boundaries,
- direct observation of first order transition (search for discontinues in volume or sublattice magnetization),
- unambiguous evidence of a valence transition (progress in the resolution of high energy spectroscopy are promising) for the mechanism
- the development of a new generation of measurements for the determination of the order parameter under pressure.

Finally the artificial superconductor-ferromagnet heterostructures provide a possibility to study the interplay between

superconductivity and magnetism in a controlled manner. The oscillatory behavior of the Cooper pair wave function in ferromagnet permits fabrication of the new type of Josephson junction – 'π junction' which opens an interesting perspective for the potential applications of these S/F heterostructures.

REFERENCES

Abrikosov, A.A. (1988). *Fundamentals of the Theory of Metals*, North Holland: Netherlands.

Abrikosov, A.A. (2002). Superconductivity due to ferromagnetically ordered localized spins. *Journal of Physics: Condensed Matter*, **13**, L943–L947.

Abrikosov, A.A. and Gorkov, L.P. (1960). Contribution to the theory of superconducting alloys with paramagnetic impurities. *Zhurnal Eksperimentalnoi i Teoreticheskoi Fiziki*, **39**, 1781–1796 [*Soviet Physics JETP*, **12**, 1243–1253 (1961)].

Anderson, P.W. and Suhl, H. (1959). Spin alignment in the superconducting state. *Physical Review*, **116**, 898–900.

Aoki, D., Huxley, A., Ressouche, E., *et al*. (2001). Coexistence of superconductivity and ferromagnetism in URhGe. *Nature*, **413**, 613–616.

Aslamazov, L.G. (1968). Influence of impurities on the existence of an inhomogeneous state in a ferromagnetic superconductor. *Zhurnal Eksperimentalnoi i Teoreticheskoi Fiziki*, **55**, 1477–1482 [*Soviet Physics JETP*, **28**, 773–775 (1969)].

Bardeen, J., Cooper, L.N. and Schrieffer, J.R. (1957). Theory of superconductivity. *Physical Review*, **108**, 1175–11204.

Bauer, E., Hischler, G., Michor, H., *et al*. (2004). Heavy fermion superconductivity and magnetic order in non centro-symmetric $CePt_3Si$. *Physical Review Letters*, **92**, 066401.

Bergeret, F.S., Volkov, A.F. and Efetov, K.B. (2005). Odd triplet superconductivity and related phenomena in superconductor-ferromagnet structures. *Reviews of Modern Physics*, **77**, 1321–1373.

Bianchi, A., Movshovic, R., Capan, C., *et al*. (2003). Possible Fulde Ferrell Larkin Ovchinnikov superconducting state in $CeCoIn_5$. *Physical Review Letters*, **91**, 187004.

Blount, E.I. and Varma, C.M. (1979). Electromagnetic effects near the superconductor-to-ferromagnet transition. *Physical Review Letters*, **42**, 1079–1082.

Blum, Y., Tsukernik, A., Karpovski, M. and Palevski, A. (2002). Oscillations of the superconducting critical current in Nb-Cu-Ni-Cu-Nb junctions. *Physical Review Letters*, **89**, 187004.

Bonn, D.A. (2006). Are high temperature superconductor exotic? *Nature Physics*, **2**, 159–168.

Bud'ko, S.L. and Canfield, P.C. (2006). Magnetism and superconductivity in rare earth-nickel-borocarbides. *Comptes Rendus Physique*, **7**, 56–67.

Bulaevskii, L.N., Buzdin, A.I., Kulić, M.L. and Panjukov, S.V. (1985). Coexistence of superconductivity and magnetism. Theoretical predictions and experimental results. *Advances in Physics*, **34**, 175–261.

Bulaevskii, L.N., Kuzii, V.V. and Sobyanin, A.A. (1977). Superconducting system with weak coupling with a current in the ground state. *Pis'ma v Zhurnal Eksperimental noi i Teoreticheskoi Fiziki*, **25**, 314–318 [*JETP Letters*, **25**, 290–294 (1977)].

Buzdin, A.I. (2000). Density of states oscillations in a ferromagnetic metal in contact with superconductor. *Physical Review B*, **62**, 11377–11379.

Buzdin, A.I. (2005). Proximity effects in superconductor-ferromagnet heterostructures. *Reviews of Modern Physics*, **77**, 935–976.

Buzdin, A.I. and Bulaevskii, L.N. (1986). Antiferromagnetic superconductors. *Soviet Physics Uspekhi*, **29**, 412–425 [*Uspekhi Fizicheskikh Nauk*, **149**, 45–67 (1986)].

Buzdin, A.I., Bulaevskii, L.N. and Panjukov, S.V. (1982). Critical-current oscillations as a function of the exchange field and thickness of the ferromagnetic metal (F) in a S-F-S Josephson junction. *Pis'ma v Zhurnal Eksperimental noi i Teoreticheskoi Fiziki*, **35**, 147–148 [*JETP Letters*, **35**, 178–180 (1982)].

Buzdin, A.I. and Kuprianov, M.Y. (1990). Transition temperature of a superconductor-ferromagnet superlattice. *Pis'ma v Zhurnal Eksperimental noi i Teoreticheskoi Fiziki*, **52**, 1089–1091 [*JETP Letters*, **52**, 487–491 (1990)].

Buzdin, A.I. and Kuprianov, M.Y. (1991). Josephson junction with a ferromagnetic layer. *Pis'ma v Zhurnal Eksperimental noi i Teoreticheskoi Fiziki*, **53**, 308–312 [*JETP Letters*, **53**, 321–326 (1991)].

Buzdin, A.I. and Mel'nikov, A.S. (2003). Domain wall superconductivity in ferromagnetic superconductors. *Physical Review B*, **67**, R020503.

Buzdin, A.I., Vedyayev, A.V. and Ryzhanova, N.V. (1999). Spin-orientation-dependent superconductivity in S/F/S structures. *Europhys. Lett.* **48**, 686–691.

Carlson, E.W., Emery, V.J., Kivelson, S.A. and Orgad, D. (2004). Concepts in high temperature superconductivity. In *The Physics of Superconductors*, *Vol. II. Superconductivity in Nanostructures, High-T_c and Novel Superconductors, Organic Superconductors*, Benneman, K.H. and Ketterson, J.B. (Eds.), Springer-Verlag: Berlin, Heidelberg, pp. 275–452.

Cho, B.K., Canfield, P.C. and Johnston, D.C. (1996). Breakdown of de Gennes scaling in $(R_{1-x}R_x')Ni_2B_2C$ compounds. *Physical Review Letters*, **77**, 163–166.

Chubukov, A.V., Pines, D. and Schmalian, J. (2004). A spin fluctuation model for D-wave superconductivity. In *The Physics of Superconductors,* Vol. 1, Bennemann, K. H. and Ketterson, J.B. (Eds.), Springer-Verlag: Berlin, Heidelberg, New York, pp. 495–590.

De Gennes, P.G. (1966). Coupling between ferromagnets through a superconducting layer. *Physics Letters*, **23**, 10–11.

Deutscher, G. and Meunier, F. (1969). Coupling between ferromagnetic layers through a superconductor. *Physical Review Letters*, **22**, 395–396.

Emery, V.J. (1983). Some basic questions in organic superconductivity. *Journal de Physique (Paris), Colloque 44*, **C3**, 977.

Faure, M. and Buzdin, A.I. (2005). Domain structure in a superconducting ferromagnet. *Physical Review Letters*, **94**, 187202.

Ferrell, R.A., Bhattacharjee, J.K. and Bagchi, A. (1979). Effect of nonlocality on the spin correlations in ferromagnetic superconductors. *Physical Review Letters*, **43**, 154–157.

Fertig, W.A., Johnston, D.C., DeLong, L.E., *et al*. (1977). Destruction of superconductivity at the onset of long-range magnetic order in the compound $ErRh_4B_4$. *Physical Review Letters*, **38**, 987–990.

Fisher, Ø. (1990). Magnetic superconductors. In *Ferromagnetic Materials*, Buschow, K.H.J. and Wohlfahrth, E.P. (Eds.), Elsevier: New York, pp. 465–510, Vol. 5.

Flouquet, J. (2005). On the heavy fermion road. In *Progress in Low Temperature Physics*, Halperin, W.P. (Ed.), Elsevier, pp. 139–281, Vol. XV.

Flouquet, J., Knebel, G., Braithwaite, D., *et al*. (2006). Magnetism and superconductivity of heavy fermion matter. *Comptes Rendus Physique*, **7**, 22–34.

Fomin, I.A. (2001). Symmetry of the order parameter in the UGe_2 superconductor. *JETP Letters*, **74**, 111–114.

Fulde, P. and Ferrell, R.A. (1964). Superconductivity in a strong spin-exchange field. *Physical Review*, **135**, A550–A563.

Ginzburg, V.L. (1956). Ferromagnetic superconductors. *Zhurnal Eksperimentalnoi i Teoreticheskoi Fiziki*, **31**, 202–214 [*Soviet Physics JETP,* **4**, 153–161 (1957)].

Glémot, L., Brison, J.P., Flouquet, J., *et al*. (1999). Pressure dependence of the upper critical field of the heavy fermion superconductor UBe_{13}. *Physical Review Letters*, **8**, 169–172.

Gloss, K., Modler, R., Schimanski, H., *et al*. (1993). Possible formation of a nonuniform superconducting state in the heavy fermion compound UPd_2Al_3. *Physical Review Letters*, **70**, 501.

Golubov, A.A., Kupriyanov, M.Yu. and Il'ichev, E. (2004). The current-phase relation in Josephson junctions. *Reviews of Modern Physics*, **76**, 411–469.

Gu, J.Y., You, C.-Y., Jiang, J.S., *et al*. (2002). Magnetization-orientation dependence of the superconducting transition temperature in the ferromagnet-superconductor-ferromagnet system: CuNi/Nb/CuNi. *Physical Review Letters*, **89**, 267001.

Harada, A., Kawasaki, S., Kotegawa, H., *et al*. (2005). Cooperative phenomena of ferromagnetism and unconventional superconductivity in UGe_2: A^{73}Ge-NQR study under pressure. *Journal of the Physical Society of Japan*, **74**, 2675–2678.

Hardy, F. and Huxley, A. (2005). P wave superconductivity in the ferromagnetic superconductor URhGe. *Physical Review Letters*, **94**, 247006.

Hauser, J.J. (1969). Coupling between ferromagnetic insulators through a superconducting layer. *Physical Review Letters*, **23**, 374–377.

Hirsch, J.E. (1985). Attractive interaction and pairing in fermion systems with strong on-site repulsion. *Physical Review Letters*, **54**, 1317–1321.

Holmes, A.T., Jaccard, D. and Miyake, K. (2004). Signatures of valence fluctuation in $CeCu_2Si_2$ under high pressure. *Physical Review B*, **69**, 024508.

Huxley, A., Sheikin, I., Ressouche, E., *et al*. (2001). UGe_2 a ferromagnetic spin triplet superconductor. *Physical Review B*, **63**, 144519.

Jaccarino, V. and Peter, M. (1962). Ultra-high-field superconductivity. *Physical Review Letters*, **9**, 290–292.

Jiang, J.S., Davidović, D., Reich, D.H. and Chien, C.L. (1995). Oscillatory superconducting transition temperature in Nb/Gd multilayers. *Physical Review Letters*, **74**, 314–317.

Kawasaki, S., Mito, T., Kawasaki, Y., *et al*. (2003). Gapless magnetic and quasiparticle excitations due to the coexistence of antiferromagnetism and superconductivity in $CeRhIn_5$: a study of ^{115}In NQR under pressure. *Physical Review Letters*, **91**, 137001.

Kirkpatrick, T.R., Belitz, D., Vojta, T. and Narayanan, N.R. (2001). Strong enhancement of superconducting Tc in ferromagnetic phases. *Physical Review Letters*, **87**, 127003.

Knebel, G., Aoki, D., Braithwaite, D., *et al*. (2006). Coexistence of antiferromagnetism and superconductivity in $CeRhIn_5$ under high pressure and magnetic field. *Physical Review B* **74**, 020501.

Knebel, G., Measson, M.A., Salce, B., *et al*. (2004). High pressure phase diagrams of $CeRhIn_5$ and $CeCoIn_5$ under pressure. *Journal of Physics: Condensed Matter*, **16**, 8905–8922.

Kontos, T., Aprili, M., Lesueur, J., *et al*. (2002). Josephson junction through a thin ferromagnetic layer: negative coupling. *Physical Review Letters*, **89**, 137007.

Kontos, T., Aprili, M., Lesueur, J. and Grison, X. (2001). Inhomogeneous superconductivity induced in a ferromagnet by proximity effect. *Physical Review Letters*, **86**, 304307.

Krey, U. (1973). Micromagnetic theory of ferromagnetic superconductors. *International Journal of Magnetism*, **3**, 65–73.

Kulić, M.L., Bulaevskii, L.N. and Buzdin, A.I. (1997). Theory of interplay of nuclear magnetism and superconductivity in $AuIn_2$. *Physical Review B*, **56**, R11415–R11418.

Kulić, M.L. (2006). Conventional magnetic superconductors: coexistence of singlet superconductivity and magnetic order. *Comptes Rendus Physique*, **7**, 4–21.

Larkin, A.I. and Ovchinnikov, Y.N. (1964). Inhomogeneous state of superconductors. *Zhurnal Eksperimentalnoi i Teoreticheskoi Fiziki*, **47**, 1136–1146 [*Soviet Physics JETP,* **20**, 762–769 (1965)].

Lashley, D.C., Fisher, R.A., Flouquet, J., *et al*. (2006). Ambient pressure specific heat of single crystal of UGe_2. *Physica B*, **378–380**, 961–962.

Levy, F., Sheikin, I., Grenier, B. and Huxley, A.D. (2005). Magnetic field induced superconductivity in the ferromagnet URhGe. *Science*, **309**, 1343–1346.

Lynn, J.W. (1990). Magnetic properties. In *High Temperature Superconductivity*, Lynn, J.W. (Ed.), Springer-Verlag: New York, Berlin, Heidelberg, London, Paris, Tokyo, Hong Kong, pp. 268–302.

Lynn, J.W., Gotaas, J.A., Erwin, R.W., *et al*. (1984). Temperature-dependent sinusoidal magnetic order in the superconductor $HoMo_6\,Se_8$. *Physical Review Letters*, **52**, 133–136.

Lynn, J.W., Keimer, B., Ulrich, C., *et al*. (2000). Antiferromagnetic ordering of Ru and Gd in superconducting $RuSr_2GdCu_2O_8$. *Physical Review B*, **61**, R14964–R14967.

Lynn, J.W., Shirane, G., Thomlinson, W., *et al*. (1981). Magnetic properties of the reentrant ferromagnetic superconductor $HoMo_6S_8$. *Physical Review B*, **24**, 3817–3829.

Lyuksyutov, I.F. and Pokrovsky, V.L. (2005). Ferromagnet-superconductor hybrids. *Advances in Physics*, **54**, 67–136.

Machida, K. and Ohmi, T. (2001). Phenomenological theory of ferromagnetic superconductivity. *Physical Review Letters*, **86**, 850–853.

Maple, M.B. (1968). The superconducting transition temperature of $La_{1-x}Gd_xAl_2$. *Physics Letters*, **26A**, 513–514.

Maple, M.B. and Fisher, Ø. (1982). Magnetic superconductors. In *Superconductivity in Ternary Compounds II, Topics in Current Physics*, Maple, M.B. and Fisher, Ø. (Eds.), Springer-Verlag: Berlin, pp. 1–8.

Maple, M.B., Hamaker, H.C. and Woolf, L.D. (1982). Superconductivity, magnetism and their mutual interaction in ternary rare earth rodium borides and some ternary rare earth transition metal stannides. In *Superconductivity in Ternary Compounds II, Topics in Current Physics*, Maple, M.B. and Fisher, Ø. (Eds.), Springer-Verlag: Berlin, pp. 99–141.

Mathur, N.D., Grotsche, F.M., Julian, S., *et al*. (1998). Magnetically mediated superconductivity in heavy fermion compounds. *Nature*, **394**, 39–43.

Matsumoto, H., Umezawa, H. and Tachiki, M. (1979). A new phase in the magnetic superconductors. *Solid State Communications*, **31**, 157–161.

Matthias, B.T., Suhl, H. and Corenzwit, E. (1958). Spin exchange in superconductors. *Physical Review Letters*, **1**, 92–94.

Meul, H.W., Rossel, C., Decroux, M., *et al*. (1984). Observation of magnetic-field-induced superconductivity. *Physical Review Letters*, **53**, 497–500.

Mineev, V. (2002). Superconducting states in ferromagnetic metals. *Physical Review B*, **66**, 134504.

Mineev, V. and Samokhin, K.V. (1999). *Introduction to Unconventional Superconductivity*, Gordon and Breach SV Publishers: New York.

Miyake, K., Schmitt-Rink, S. and Varma, C.M. (1986). Spin fluctuation mediated even parity pairing in heavy fermion superconductors. *Physical Review*, **34**, 6554.

McLaughlin, A.C., Zhou, W., Attfield, J.P., *et al*. (1999). Structure and microstructure of the ferromagnetic superconductor $RuSr_2GdCu_2O_8$. *Physical Review B*, **60**, 7512–7516.

Moraru, I.C., Pratt, W.P. Jr. and Birge, N.O. (2006). Magnetization-dependent T_c shift in ferromagnet/superconductor/ferromagnet trilayers with a strong ferromagnet. *Physical Review Letters*, **96**, 037004.

Moriya, T. (2003). Spin fluctuations and superconductivity around the magnetic instability. *Acta Physica Polonica*, **34**, 287–302.

Moshchalkov, V.V., Ducan, S., Gobulovic, S. and Mathieu, M. (2006). Nucleation of superconductivity and vortex matter in hybrid superconductor ferromagnet nanostructures. *Comptes Rendus Physique*, **7**, 86–98.

Movshovich, R., Graf, T., Mandrus, D., *et al*. (1996). Response of $CeRh_2Si_2$ under pressure. *Physica B*, **223–224**, 126–127.

Müller, K.-H. and Narozhnyi, V.N. (2001). Interaction of superconductivity and magnetism in borocarbide superconductors. *Reports on Progress in Physics*, **64**, 943–1008.

Nachtrab, T., Bernhard, C., Lin, C., *et al*. (2006). The ruthenocuprates: natural superconductor-ferromagnet multilayers. *Comptes Rendus Physique*, **7**, 68–85.

Oboznov, V.A., Bol'ginov, V.V., Feofanov, A.K., *et al*. (2006). Double-reversal thickness dependence of critical current in superconductor-ferromagnet-superconductor Josephson junctions. *Physical Review Letters*, **96**, 197003.

Onishi, Y. and Miyake, K. (2000). Enhanced valence fluctuations: possible origin of pressure induced enhancement of T_C in CeCuGe2 and related compounds. *Journal of the Physical Society of Japan*, **69**, 3955–3964.

Paglione, S., Tanatar, M.A., Hawthorn, D.G., *et al*. (2003). Field induced quantum critical point in $CeCoIn_5$. *Physical Review Letters*, **91**, 246405.

Park, T., Ronning, F., Yuan, H.Q., *et al*. (2006). Hidden magnetism and quantum criticality in the heavy fermion superconductor $CeRhIn_5$. *Nature*, **440**, 65–68.

Pfleiderer, C., Uhlarz, M., Hayden, S.M., *et al*. (2001). Coexistence of superconductivity and ferromagnetism in d band metal ZrZn2. *Nature*, **412**, 58–61.

Radovan, H.A., Fortune, N.A., Murphy, P., *et al*. (2003). Magnetic enhancement of superconductivity from electron spin domains. *Nature*, **425**, 51–55.

Radovic, Z., Ledvij, M., Dobrosaljevic-Grujic, L., *et al*. (1991). Transition temperature of superconductor-ferromagnet superlattices. *Physical Review B*, **44**, 759–764.

Rehmann, S., Herrmannsdörfer, T. and Pobell, F. (1997). Interplay of nuclear magnetism and superconductivity in $AuIn_2$. *Physical Review Letters*, **78**, 1122–1125.

Ryazanov, V.V., Oboznov, V.A., Prokof'ev, A.S., *et al*. (2004). Superconductor-ferromagnet-superconductor junctions. *Journal of Low Temperature Physics*, **136**, 385–400.

Ryazanov, V.V., Oboznov, V.A., Rusanov, A.Yu., *et al*. (2001). Coupling of two superconductors through a ferromagnet: evidence for a π-junction. *Physical Review Letters*, **86**, 2427–2430.

Ryazanov, V.V., Oboznov, V.A., Veretennikov, A.V. and Rusanov, A.Yu. (2001). Intrinsically frustrated superconducting array of superconductor-ferromagnet-superconductor π junctions. *Physical Review B*, **65**, R020501.

Samokhin, K.V. and Walker, M.B. (2002). Symmetry of the order parameter in superconducting $ZrZn_2$.*Physical Review B*, **66**, 024512.

Sandeman, K., Lonzarich, G.G. and Schofield, A.J. (2003). Ferromagnetic superconductivity driven by changing Fermi surface topology. *Physical Review Letters*, **90**, 167005.

Saxena, S.S., Agarwal, P., Ahilan, K., *et al*. (2000). Superconductivity on the border of itinerant-electron ferromagnetism in UGe_2. *Nature*, **406**, 587–592.

Sinha, S.K., Crabtree, G.W., Hinks, D.G. and Mook, H. (1982). Study of coexistence of ferromagnetism and superconductivity in single-crystal $ErRh_4B_4$. *Physical Review Letters*, **48**, 950–953.

Steglich, F., Aarts, J., Bredl, C., *et al*. (1979). Superconductivity in the presence of strong Pauli paramagnetism in $CeCu_2Si_2$. *Physical Review Letters*, **43**, 1892–1895.

Stockert, O., Faulhaber, E., Zwicknagl, G., *et al*. (2004). Nature of the A phase in $CeCu_2Si_2$. *Physical Review Letters*, **92**, 136401.

Suhl, H. (2001). Simultaneous onset of ferromagnetism and superconductivity. *Physical Review Letters*, **87**, 167007.

Sumarlin, I.W., Skanthakumar, S., Lynn, J.W., *et al*. (1992). Magnetic ordering of Sm in Sm_2CuO_4. *Physical Review Letters*, **68**, 2228–2231.

Tagirov, L.R. (1999). Low-field superconducting spin switch based on a superconductor/ferromagnet multilayer. *Physical Review Letters*, **83**, 2058–2061.

Takeuchi, T., Inoue, T., Sugiyama, K., *et al*. (2001). Magnetic and thermal properties of $CeIrIn_5$ and $CeRhIn_5$. *Journal of the Physical Society of Japan*, **70**, 877–883.

Tateiwa, N., Kobayashi, T.C., Amaya, K., *et al*. (2004). Heat capacity anomalies at T_C and T_X in the ferromagnetic superconductors UGe_2. *Physical Review B*, **69**, 180513.

Thalmeier, P., Zwicknagl, G., Stockert, O., *et al*. (2004). Superconductivity in HFC. In *Frontiers in Superconducting Materials*, Narlikar, A.V. (Ed.), Springer-Verlag: Berlin.

Thomlinson, W., Shirane, G., Lynn, J.W. and Moncton, D.E. (1982). Neutron scattering studies of magnetic ordering in ternary superconductors. In *Superconductivity in Ternary Compounds II, Topics in Current Physics*, Maple, M.B. and Fisher, Ø. (Eds.), Springer-Verlag: Berlin, pp. 229–248.

Thompson, J., Movshovich, R., Fisk, Z., *et al*. (2001). Superconductivity and magnetism in a new class of heavy fermion materials. *Journal of Magnetism and Magnetic Materials*, **226–230**, 5.

Tokunaga, Y., Kotegawa, H., Ishida, K., *et al*. (2001). NMR evidence for coexistence of superconductivity and ferromagnetic component in magnetic superconductor $RuSr_2YCu_2O_8$: ^{99,101}Ru and ^{63}Cu NMR. *Physical Review Letters*, **86**, 5767–5770.

Uji, S., Shinagawa, H., Terashima, T., *et al*. (2001). Magnetic-field-induced superconductivity in a two-dimensional organic conductor. *Nature*, **410**, 908–910.

Usadel, L. (1970). Generalized diffusion equation for superconducting alloys. *Physical Review Letters*, **25**, 507–509.

Walker, M.B. and Samokhin, K.V. (2002). Model for ferromagnetic ZrZn2. *Physical Review Letters*, **88**, 207001.

Watanabe, S. and Miyake, K. (2002). Coupled charge and spin fluctuations and mechanisms of superconductivity in UGe_2 under pressures. *Physica B*, **312–313**, 115.

General Micromagnetic Theory

Helmut Kronmüller
Max-Planck-Institut für Metallforschung, Stuttgart, Germany

1 INTRODUCTION

The continuum theory of micromagnetism, which was developed in the 1930s and 1940s, was intended to bridge the gap between the phenomenological Maxwell's theory of electromagnetic fields and quantum theory based on atomic backgrounds. In Maxwell' s theory material properties are described by global permeabilities and susceptibilities valid for macroscopic dimensions. On the other hand quantum theory allows a description of magnetic properties on the atomistic level. Both theories are not suitable to describe cooperative and interactive phenomena such as macroscopic magnetization processes or hysteresis loops of ordered spin structures. The requirement to bridge the gap between Maxwell's theory and quantum theory became very urgent after Barkhausen's experiment known as *Barkhausen's jumps* (Barkhausen, 1919) and Sixtus' and Tonks' experiment on the domain wall velocity (Sixtus and Tonks, 1931).

A further landmark that proved the existence of the so-called Weiss domains (Weiss, 1907) was the Bitter experiment (Bitter, 1931), where by using the dipolar interactions between magnetic ferrofluids and the magnetic stray fields exerting from domain walls the domain patterns were clearly visible.

After the explanation of ferromagnetism by Heisenberg (1928) and Dirac (1928) on the basis of exchange interactions, the door was wide opened toward a mesoscopic theory of magnetism combining Maxwell's and quantum theory. A first attempt to treat inhomogeneous magnetic states is due to Bloch (1932) who showed that as a consequence of exchange interactions the transition regions between the Weiss domains have a finite width. Actually Bloch considered a type of domain wall, today called *Néel wall*; however, Bloch neglects the dipolar stray field energy, thus obtaining the result of the stray field free domain wall, now called the *Bloch wall*. The different type of domain walls have been outlined later by Néel (1955a,b), who gave a first approximate calculation of the so-called Néel wall.

The breakthrough toward a continuum theory of magnetism is due to Landau and Lifshitz (1935), who derived a continuum expression for the exchange energy and gave a first interpretation of domain patterns. In this context, the work by Akulov (1928–1931) should be mentioned, who derived continuum expressions for the magnetocrystalline energy. For a further development of the mesoscopic theory, the book by Becker and Döring (1939) became very important. Here for the first time the interaction between magnetization and the microstructure has been considered by the derivation of the so-called magnetoelastic coupling energy for cubic crystals.

Handbook of Magnetism and Advanced Magnetic Materials. Edited by Helmut Kronmüller and Stuart Parkin. Volume 2: *Micromagnetism*. ISBN: 978-0-470-02217-7.

It was the progress made in the 1930s with respect to microstructures, for example, the definition of dislocations as the sources of internal strains, which inspired W. F. Brown to publish in 1940 and 1941 two basic papers from which the modern theory of micromagnetism emerged (Brown, 1940, 1941). Brown in these papers for the first time considered the effect of local perturbations of the direction of magnetization on the law of approach to ferromagnetic saturation in order to find an explanation for the 1/H term usually found experimentally. There were further papers by Kittel, Stoner–Wohlfarth, Néel, Aharoni, Strikman, Treves and of course also Brown in the 1950s, who established the theory of micromagnetism as an efficient tool to describe magnetization processes and the characteristic properties of the hysteresis loop.

Whereas in the second half of the twentieth century micromagnetism was applied mainly to the classical problems of ferromagnetic materials in the twenty-first century the problems of magnetoelectronics and spintronics became relevant. Here the recent developments in computational micromagnetism play an important role. These techniques allow solutions of the nonlinear micromagnetic equations, determination of spin distribution of magnetic ground states, the determination of single-domain configurations and vortex states as well as the investigation of the dynamics of magnetization processes. These theories represent the content of different articles of Volume II.

2 MAGNETIC GIBBS FREE ENERGY

2.1 General remarks

Within the framework of micromagnetism the magnetic state is fully described if for given temperature, applied field, and elastic stresses the distribution of the spontaneous polarization $\boldsymbol{J}_\mathrm{s}(\boldsymbol{r})$, or of the spontaneous magnetization, $\boldsymbol{M}_\mathrm{s}(\boldsymbol{r})$ are well defined by the modulation and their direction cosines $\gamma_i(\boldsymbol{r})$. The spontaneous polarization

$$\boldsymbol{J}_\mathrm{s}(\boldsymbol{r}) = \mu_0 \boldsymbol{M}_\mathrm{s}(\boldsymbol{r}) = |J_\mathrm{s}(\boldsymbol{r})| \sum_{i=1}^{3} \boldsymbol{i}_i \gamma_i(\boldsymbol{r}) \tag{1}$$

is related to the z-component of S_z, of the spin, $\boldsymbol{S}$, of the magnetic ion at position, $\boldsymbol{r}$, by

$$\boldsymbol{J}_\mathrm{s}(\boldsymbol{r}) = \mu_0 \boldsymbol{M}_\mathrm{s}(\boldsymbol{r}) = g\mu_\mathrm{B} S_z(\boldsymbol{r})/\Omega(\boldsymbol{r}) \tag{2}$$

with g the Landé factor given by $\simeq 2$ in case of metal systems with quenched orbital moments, μ_B the Bohr magneton and $\Omega(\boldsymbol{r})$ the local atomic volume per magnetic ion. The local magnetic moment being given by $g\mu_\mathrm{B} S_z(\boldsymbol{r})$.

Micromagnetism in general deals with the determination of the polarization vector $\boldsymbol{J}_\mathrm{s}(\boldsymbol{r})$. Depending on the type of problem either the direction cosines $\gamma_i(\boldsymbol{r})$ or spatial average $\langle \gamma_i(\boldsymbol{r}) \rangle_\mathrm{r}$ or even the spatial and the thermal averages $\langle \langle \gamma_i(\boldsymbol{r}) \rangle_\mathrm{r} \rangle_\mathrm{T}$ have to be determined. The basis for these calculations is the Gibbs free energy with the free variable temperature T, elastic stress tensor $\boldsymbol{\sigma}$, and applied magnetic field $\boldsymbol{H}_\mathrm{ext}$. In terms of energy densities the total Gibbs free energy density is given by

$$\phi'_\mathrm{t} = U - TS - \boldsymbol{\sigma} \cdot \cdot \boldsymbol{\varepsilon} - \boldsymbol{J}_\mathrm{s} \cdot \boldsymbol{H}_\mathrm{ext} \tag{3}$$

Here U, S, $\boldsymbol{\varepsilon}$, and $\boldsymbol{\sigma}$ denote the internal energy density, the entropy per unit volume, the strain tensor, and the stress tensor, respectively. The free energy $U - TS$ includes the exchange, magnetocrystalline, dipolar and magnetoelastic energies as well as the Ginzburg–Landau ordering energy. The last two terms denote the elastic and magnetostatic interaction energies. In the thermodynamic equilibrium the total Gibbs free energy corresponds to a minimum, that is,

$$\delta\phi_\mathrm{t} = \delta \int_V \phi'_\mathrm{t} \, \mathrm{d}V = 0 \tag{4}$$

where at constant T, $\boldsymbol{\sigma}$ and $\boldsymbol{H}_\mathrm{ext}$ the variation has to be performed with respect to the internal magnetic variables of the system. In case where only the angular distribution of $\boldsymbol{J}_\mathrm{s}$ is of interest, the variation of ϕ_t is taken with respect to the direction cosines γ_i or the components $J_{\mathrm{s},i}$ where $|\boldsymbol{J}_\mathrm{s}|$ or $|\boldsymbol{M}_\mathrm{s}|$ are kept constant. Considering the magnetic phase transition at the Curie temperature, T_C, the variation is taken with respect to the components $J_{\mathrm{s},i}$ or $M_\mathrm{s,i}$ leading to the well-known results of the Landau theory (Landau and Lifshitz, 1971), for example, the critical exponents of the molecular field theory (Kronmüller and Fähnle, 1980; Fähnle and Kronmüller, 1980; Herzer, Fähnle, Egami and Kronmüller, 1980; Fähnle, 1981).

Micromagnetism is based on continuum theoretical expressions for the intrinsic energy terms contained in the internal energy U. These terms are either derived from symmetry considerations or by a continuation of quantum theoretical expressions by replacing, for example, localized spins S_z by $\boldsymbol{J}_\mathrm{s}$ according to equation (2). In the following we summarize all continuum theoretical expressions required for the theory of micromagnetism.

2.2 Exchange energy

In order to derive the continuum expression for the exchange energy, Landau and Lifshitz (1935) calculated the exchange energy for small deviations of the magnetization from a homogeneously magnetized ground state. Because only

inhomogeneous magnetic states increase the exchange energy the first deviations, $\nabla\gamma_i$ of the direction cosines γ_i must occur quadratically in the energy expression. Both considerations are fulfilled by the differential operators $(\mathrm{grad}\boldsymbol{J})^2$, $(\mathrm{div}\boldsymbol{J})^2$ and $(\mathrm{curl}\boldsymbol{J})^2$. Kittel and Herring (1951) discussed that $(\mathrm{grad}\boldsymbol{J}_\mathrm{s})$ is the correct description of the excess exchange energy because $\mathrm{div}\boldsymbol{J}_\mathrm{s}$ and $\mathrm{curl}\boldsymbol{J}_\mathrm{s}$ would lead to zero exchange energies in case of $\mathrm{div}\boldsymbol{J}_\mathrm{s} = 0$ or $\mathrm{curl}\boldsymbol{J}_\mathrm{s} = 0$ in spite of the fact that in both cases an inhomogeneous magnetization exists.

In the case of cubic crystals or amorphous materials accordingly the exchange energy density may be written as

$$\phi'_\mathrm{ex} = A\left\{(\nabla\gamma_1)^2 + (\nabla\gamma_2)^2 + (\nabla\gamma_3)^2\right\} \tag{5}$$

The exchange stiffness constant A is related to the exchange integral $J_{i,j}$, between spin $\boldsymbol{S}_i$ and $\boldsymbol{S}_j$ at position $\boldsymbol{r}_i$ and $\boldsymbol{r}_j$. This relation may be derived by calculating the continuum expression (5) from the Heisenberg exchange Hamiltonian (Heisenberg, 1928)

$$H_\mathrm{ex} = -2\sum_{i\neq j} J_{ij}\left(\boldsymbol{r}_{ij}\right)\boldsymbol{S}_i\left(\boldsymbol{r}_i\right)\cdot\boldsymbol{S}_j\left(\boldsymbol{r}_j\right) \tag{6}$$

where J_{ij} denotes the exchange integral between the ions of spin $\boldsymbol{S}_i$ and $\boldsymbol{S}_j$ with distance $\boldsymbol{r}_{ij} = \boldsymbol{r}_j - \boldsymbol{r}_i$.

2.2.1 Short-range exchange interactions

In the case of localized electrons with small changes of the spin orientations between neighboring ions and only nearest neighbor interactions, J_0, the exchange energy density may be written as (Figure 1)

$$\phi'_\mathrm{ex} = -2S^2 J_0 \frac{1}{\Omega}\sum_{j\neq i}^{\mathrm{nn}} \cos\varphi_{ij} \tag{7}$$

where within the framework of the vector model φ_{ij} denotes the angle between neighboring spins. The expression (5) is

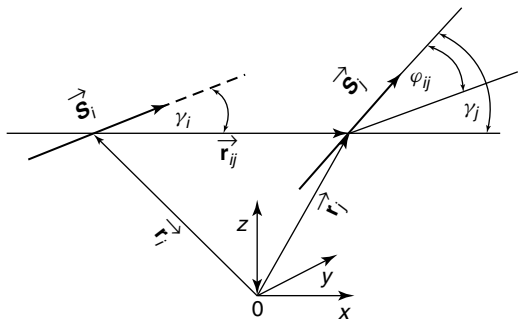

Figure 1. Spacial and angular coordinates of two neighboring spins (Kronmüller and Fähnle (2003)).

obtained from equation (7) by replacing $\cos\varphi_{ij}$ by $\cos\varphi_{ij} = \sum_{n=1}^{3}\gamma_{n,i}(r_i)\gamma_{n,j}(r_j)$ and developing $\gamma_{n,i,j}$ into the Taylor series. In the case of cubic lattices the summation over nearest neighbor ions leads to

$$A = \frac{2J_0S^2}{a}\cdot c \tag{8}$$

where the constant c is given by $c = 1$ for the cubic primitive lattice, $c = 2$ for the bcc lattice and $c = 4$ for the fcc lattice. If in the case of finite temperatures S is replaced by its thermal average $\langle S\rangle$ and necessarily by the spontaneous magnetization $M_\mathrm{s}(T)$ the exchange constant is

$$A = \frac{2J_0M_\mathrm{s}^2}{N^2g^2\mu_\mathrm{B}^2a}\cdot c \tag{9}$$

According to equation (9) the temperature dependence of A follows that of $M_\mathrm{s}^2(T)$. Since the exchange integral J_0 is related to the Curie temperature T_C, within the framework of the molecular field theory (see e.g., Morrish, 1965; Jiles, 1990) the exchange constant is given by

$$A = \frac{3k_\mathrm{B}T_\mathrm{C}S\cdot c'}{2\alpha(S+1)} \tag{10}$$

with $c = 1/6$, 1/4, 1/3 for sc, bcc, and fcc lattices. In the case of uniaxial crystals as tetragonal, trigonal, or hexagonal crystals the exchange energy is

$$\phi'_\mathrm{ex} = A_\perp\sum_{i=1,2}(\nabla\gamma_i)^2 + A_\parallel(\nabla\gamma_3)^2 \tag{11}$$

where $i = 1, 2$ refer to the coordinates perpendicular to the preferred trigonal, quaternary, or hexagonal axis (see Kronmüller and Fähnle, 2003). The exchange stiffness constants determined by equation (10) in general lead to somewhat small values because the molecular field theory neglects the low-energy spin-wave extension. Therefore, values of A either determined from the spin wave dispersion law $E = Dk^2$ as measured by inelastic neutron scattering or from specific domain wall energies are more reliable. In Table 1 experimental results for A are summarized as obtained by the latter two methods.

2.2.2 Long-range exchange interactions

The continuum expression (5) may be clarified from the Heisenberg-type exchange interaction between nearest neighbor atoms. However, in the metallic ferromagnets besides the nearest neighbor interaction exchange interaction also the so-called indirect exchange interaction may be important. This type of indirect exchange interactions originally has been

Table 1. Intrinsic magnetic material constants of transition metals, intermetallic compounds and oxides at room temperature. Values taken from Kronmüller and Fähnle (2003). (Reproduced from H. Kronmüller and M. Fähnle: Micromagnetization and the Microstructure of Ferromagnetic Solids (CUP, 2003), with permission from Cambridge University Press.)

Magnet	J_s (T)	A (pJ m^{-1})	K_1 (J m^{-3})	K_2 (J m^{-3})	$\lambda \times 10^6$	T_C (K)
α-Fe	2.185	$20.7 - 22.8$	4.8×10^4	-1.0×10^4	$\lambda_{100} = 22$, $\lambda_{111} = -21$	1043
Co	1.79	$30.2 - 31.4$	45.3×10^4	14.5×10^4	$\lambda_{11} = -45$, $\lambda_{12} = -45$, $\lambda_{33} = 110$, $\lambda_{44} = -260$	1403
Ni	0.62	$7.2 - 8.5$	-4.5×10^3	-2.5×10^3	$\lambda_{100} = -55$, $\lambda_{111} = -23$	627
Ni_3Fe	1.1	7.1	1.2×10^2	–	$\lambda_{100} = 18$, $\lambda_{111} = 5$	873
$Nd_2Fe_{14}B$	1.61	$7.3 - 8.4$	4.3×10^6	0.65×10^6		588
$Pr_2Fe_{14}B$	1.56	12	5.6×10^6	≈ 0		565
$SmCo_5$	1.05	12	1.7×10^7		$\lambda_{11} = -762$, $\lambda_{12} = -181$, $\lambda_{33} = -47$, $\lambda_{44} = 243$	993
Sm_2Co_{17}	1.29	14	4.2×10^6			1070
$Sm_2Fe_{17}N_2$	1.56	12	8.6×10^6			749
$BaFe_{12}O_{19}$	0.48	63	3.2×10^5	$<0.1 \times 10^6$	$\lambda_{11} = -15$, $\lambda_{12} = 16$, $\lambda_{33} = -11$, $\lambda_{44} = -48$	723
Fe_3O_4	0.60		-11×10^3	-3×10^3	$\lambda_{100} = -20$, $\lambda_{111} = 78$	585
PtFe	1.43	10	6.6×10^6			683

developed by Zener (1951a,b), Ruderman and Kittel (1954), Kasuya (1956), and Yosida (1957) (RKKY-interaction). The indirect exchange interaction is based on the interaction of localized spin of d or f electrons and the sea of delocalized s electrons. Localized spin moments induce an oscillating spin polarization of the s electrons. Other localized spin moments will interact with this polarization cloud. Accordingly, distant spin moments become magnetically exchange coupled via the oscillating polarization of the s electrons. If the s–d- or s–f interaction corresponds to a δ-function the effective exchange integral between the localized spin moments of distance $|\boldsymbol{r}_{ij}| \, | \, |\boldsymbol{r}_j - \boldsymbol{r}_i| = r$ according to Ruderman and Kittel (1954) is given by

$$J(r) = \frac{J_{sf}^2}{(2k_F r)^4}(2k_F r \cos 2k_F r - \sin 2k_F r) \qquad (12)$$

where k_F denotes the modulus of the Fermi wave vector and J_{sf} the exchange integral between s- and f electrons. Due to the long-range exchange interaction the energy density ϕ'_{ex} is given by the following integral:

$$\phi'_{ex}(\boldsymbol{r}) = -\frac{2}{(g\mu_B)^2} \int J\left(|\, \boldsymbol{r} - \boldsymbol{r}' \,|\right) M(\boldsymbol{r}) \cdot M(\boldsymbol{r}') \, \mathrm{d}^3\boldsymbol{r}' \quad (13)$$

where we have replaced $\boldsymbol{S}(\boldsymbol{r})$ by $\boldsymbol{M}(\boldsymbol{r})$ of equation (2). Introducing Fourier transforms

$$\begin{aligned} J(\boldsymbol{k}) &= \int J(\boldsymbol{r}) e^{i\boldsymbol{k}\cdot\boldsymbol{r}} \, \mathrm{d}^3\boldsymbol{r} \\ M(\boldsymbol{k}) &= \int M(\boldsymbol{r}) e^{i\boldsymbol{k}\cdot\boldsymbol{r}} \, \mathrm{d}^3\boldsymbol{r} \end{aligned} \qquad (14)$$

and applying the convolution theorem we obtain

$$\phi'_{ex}(\boldsymbol{r}) = -\frac{2}{(2\pi)^3 (g\mu_B)^2} \frac{1}{\Omega} \int J(\boldsymbol{k}) M(\boldsymbol{k}) \cdot M(-\boldsymbol{k}) \, \mathrm{d}^3\boldsymbol{k} \qquad (15)$$

where according to Ruderman and Kittel (1954) in case of pointlike localized spins $J(\boldsymbol{k})$ is given by

$$J(\boldsymbol{k}) = \frac{3\Omega z J_{sd}^2}{16 E_F} \left\{ 1 + \frac{4k_F - k^2}{4k_F k} \ln \frac{2k_F + k}{2k_F - k} \right\} \qquad (16)$$

(z = number of s electrons per atom, E_F = Fermi energy), J_{sd} = exchange integral between s and d electrons. Within the framework of Ruderman–Kittel's approximation $J(r)$ becomes infinite at $r \to 0$. Since the s–d or s–f interaction actually has a finite range, instead a constant J_{sd} in equation (16) a k-dependent $J_{sd}(k)$, which decreases with increasing k should be introduced. According to Yosida (1957) a suitable Ansatz for $J(k)$ is

$$\begin{aligned} J(\boldsymbol{k}) &= J(0) \qquad \text{for} \quad k \le 2k_F \\ J(\boldsymbol{k}) &= 0 \qquad\quad \text{for} \quad k > 2k_F \end{aligned} \qquad (17)$$

For $k < k_F$ we obtain from equation (16), $J(0) - J(\boldsymbol{k}) \frac{z J_{sd}^2 \Omega}{32 E_F} \frac{k^2}{k_F^2}$. Figure 2 shows the k-dependence for the Ruderman–Kittel and the Yosida model.

2.3 The magnetocrystalline anisotropy energy

The magnetic properties of spin-ordered crystals in general reveal a marked anisotropy. For example, depending on the

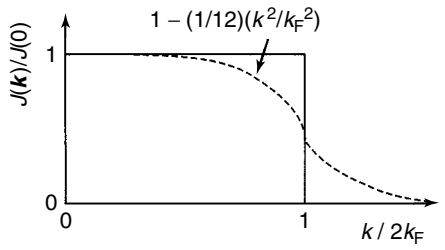

Figure 2. Fourier transform $J(\mathbf{k})$ of the indirect exchange integral for the model according to Yosida (1957) and according to Ruderman and Kittel (1954) (Kronmüller and Fähnle (2003)). (Reproduced from Ruderman & Kittel, 1954, with permisison from Cambridge University Press. © 1954.)

orientation of single crystals the saturation magnetization is approached by small or large magnetic fields. Therefore it is common to speak of hard and easy magnetic directions. The magnetocrystalline energy originates from the coupling between spin and orbital moments (L-S coupling) and the interaction between the ions and the crystal field. In 3d transition metals the orbital moments are nearly completely quenched and consequently the coupling between the orbital moments and the crystal field remains small leading to moderate magnetocrystalline energies. In contrast, in the case of intermetallic compounds, where rare-earth metals are involved, the 4-f electrons are characterized by strong L-S coupling and Hund's rules are valid, the anisotropic charge cloud of 4f electrons interacts strongly with the crystal field resulting in the largest anisotropies measured so far.

The angular dependence of the magnetocrystalline energy was derived for the first time by Akulov (1928–1931) for cubic crystals. Because the magnetocrystalline energy must be invariant with respect to rotations of $\boldsymbol{M}_\mathrm{s}$ by 180° the energy expression must be an even function of the direction cosines γ_i, which have to be taken with respect to the symmetry axes of the point group of the crystal under calculation. A general expression for the magnetocrystalline energy density is (Birss, 1964)

$$\phi'_\mathrm{k}(\boldsymbol{r}) = k_0(\boldsymbol{r}) + \sum_{i\neq j} k_{ij}(\boldsymbol{r})\gamma_i(\boldsymbol{r})\gamma_j(\boldsymbol{r}) + \sum_{i,j,k,l} k_{ijkl}(\boldsymbol{r})\boldsymbol{\gamma}_i(\boldsymbol{r})\gamma_j(\boldsymbol{r})\gamma_h(\boldsymbol{r})\gamma_l(\boldsymbol{r}) + \cdots \quad (18)$$

With diagonalized property tensors $\boldsymbol{k}\phi'_\mathrm{k}$ becomes

$$\phi'_\mathrm{k}(r) = k_0(\boldsymbol{r}) + \sum_i k_i(\boldsymbol{r})\gamma_i^2(r) + \sum_i k_{2i}(\boldsymbol{r})\gamma_i^4(\boldsymbol{r}) + \sum_{i\neq j} k_{3ij}(\boldsymbol{r})\gamma_i^2(\boldsymbol{r})\gamma_j^2(\boldsymbol{r}) + \cdots \quad (19)$$

By specifying the property tensors $\boldsymbol{k}$ to the symmetry requirements of the point groups of a crystal we may derive anisotropy expressions for cubic, hexagonal, tetragonal and orthorhombic crystals.

1. *Cubic symmetry*: (γ_i refer to cubic axes)

$$\phi'_\mathrm{k}(\boldsymbol{r}) = K_0(\boldsymbol{r}) + K_1(\boldsymbol{r})\sum_{i\neq j}\gamma_i^2(\boldsymbol{r})\gamma_j^2(\boldsymbol{r}) + K_2(\boldsymbol{r})\gamma_1^2(\boldsymbol{r})\cdot\gamma_2^2(\boldsymbol{r})\gamma_3^2(\boldsymbol{r}) \quad (20)$$

2. *Hexagonal symmetry*: Here we introduce the angle φ between $\boldsymbol{M}_\mathrm{s}$ and the hexagonal c axis (z axis) and the angle ψ of the projection of $\boldsymbol{M}_\mathrm{s}$ on the hexagonal plane taken with respect to the x axis. Equation (19) now may be rearranged as

$$\phi'_k(\boldsymbol{r}) = K_0(\boldsymbol{r}) + K_1(\boldsymbol{r})\sin^2\varphi(\boldsymbol{r}) + K_2(\boldsymbol{r})\sin^4\varphi(\boldsymbol{r}) + K_3(\boldsymbol{r})\sin^6\varphi(\boldsymbol{r}) + K_4(\boldsymbol{r})\sin^6\varphi(\boldsymbol{r})\cos(6\psi(\boldsymbol{r})) \quad (21)$$

3. *Tetragonal symmetry*: With a similar definition of the angles φ and ψ as in the hexagonal crystal we obtain

$$\phi'_\mathrm{k}(\boldsymbol{r}) = K_0(\boldsymbol{r}) + K_1(\boldsymbol{r})\sin^2\varphi(\boldsymbol{r}) + K_2(\boldsymbol{r})\sin^4\varphi(\boldsymbol{r}) + K_3(\boldsymbol{r})\sin^4\varphi(\boldsymbol{r})\cos(4\psi(\boldsymbol{r}) + \cdots \quad (22)$$

4. *Orthorhombic symmetry*: Equation (19) describes ϕ'_k for orthorhombic symmetry with the direction cosines $\gamma_i(\boldsymbol{r})$ taken with respect to the three two-fold symmetry axes.

   The so-called easy directions are determined by the extrema conditions $\partial\phi'_\mathrm{k}/\partial\gamma_i = 0$ and $\partial^2\phi'_\mathrm{k}/\partial\gamma_i^2 > 0$. Taking into account the anisotropy constants K_1 and K_2 only the easy directions for cubic crystals are the following ones:

   1. $\langle 100\rangle$ directions, $K_1 > 0, K_2 > 0; K_1 > -\frac{1}{9}K_2, K_2 < 0$.
   2. $\langle 111\rangle$ directions, $K_1 < -\frac{1}{9}K_2; K_2 < 0, K_1 < -\frac{4}{9}K_2; K_2 > 0$.
   3. $\langle 110\rangle$ directions, $-\frac{4}{9}K_2\langle K_1 < 0; K_2\rangle 0$.

   For α-Fe at RT Case 1 holds and for Ni Case 2.
   In the case of hexagonal uniaxial crystals also three types of easy directions have to be distinguished:

   1. $\langle 0001\rangle$ - directions ($\pm$c axis): $K_1 > 0; K_1 > -K_2, K_2 < 0, K_{3,4} = 0$
   2. All directions within the basal plane, $K_1 < -K_2, K_2 < 0; K_1 < -2K_2, K_2 > 0; K_{3,4} = 0$
   3. All directions on the surface of a cone with angle $\sin\varphi\sqrt{-K_1/2K_2}$; $-2K_2 < K_1 < 0; K_{3,4} = 0$.

For Co case 1 holds for $T < 520\,\mathrm{K}$, case 2 for $T > 605\,\mathrm{K}$ and case 3 for $520\,\mathrm{K} < T < 605\,\mathrm{K}$. In the case of the hard magnetic compound $Nd_2Fe_{14}B$ the c axis throughout is easy direction in spite of the fact that $K_1 < 0$ holds below 125 K because always $2K_2 > (-)K_1$ holds.

Phase diagrams of the easy directions for cubic and uniaxial crystals as function of K_1 and K_2 are shown in Figure 3.

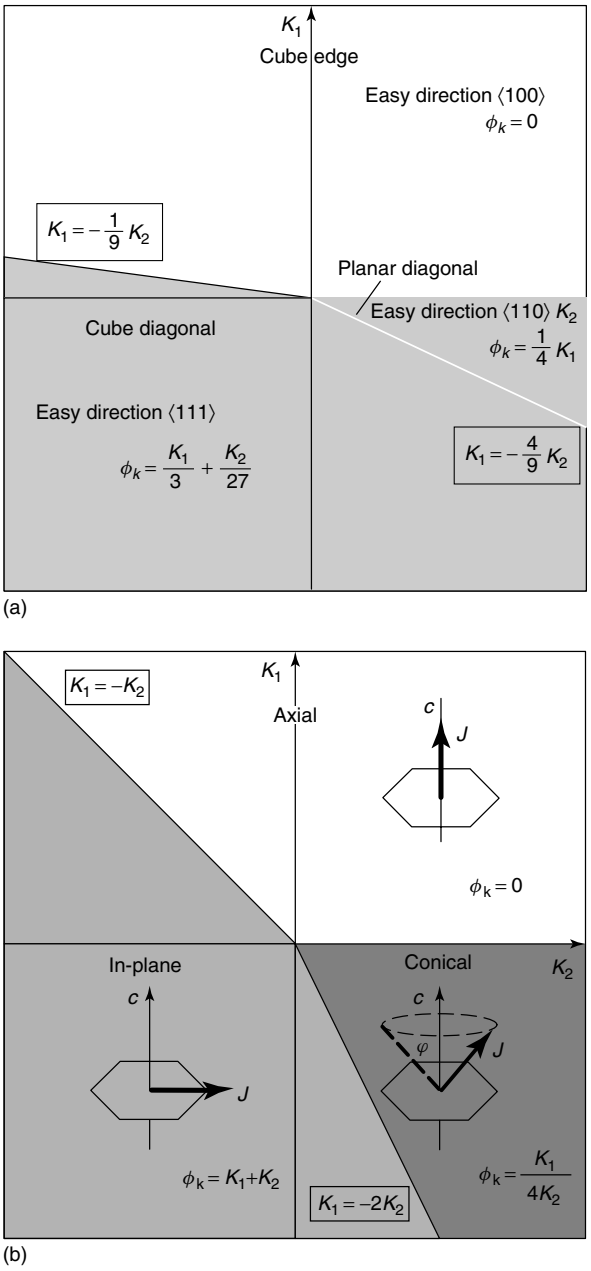

Figure 3. Phase diagrams of easy directions in (a) cubic and (b) uniaxial crystals. (Reproduced with permission from Cambridge University Press.)

2.4 Magnetostatic energies

2.4.1 External field

The magnetostatic energies are related to tow different sources of magnetic fields: The external or applied magnetic field, $\boldsymbol{H}_{\mathrm{ext}}$, and the so-called dipolar fields, $\boldsymbol{H}_{\mathrm{s}}$, resulting from magnetization $\boldsymbol{M}_{\mathrm{s}}$. The magnetostatic energy of the external field, the so-called Zeemann energy may be written as the sum of the interaction energies of local moments $\mu_i g \mu_{\mathrm{B}} \boldsymbol{S}_i(\boldsymbol{r})$ with the external magnetic flux density $\boldsymbol{B}_{\mathrm{ext}}$ giving

$$\phi'_{\mathrm{h}} = -g\mu_{\mathrm{B}} \sum_i \boldsymbol{S}_i(\boldsymbol{r}) \cdot \boldsymbol{B}_{\mathrm{ext}} = g\mu_{\mathrm{B}}\mu_0 \sum_i \boldsymbol{S}_i(\boldsymbol{r}_i) \cdot \boldsymbol{H}_{\mathrm{ext}} \tag{23}$$

By using equation (2) the magnetostatic energy density is,

$$\phi'_{\mathrm{h}} = -\mu_0 \boldsymbol{H}_{\mathrm{ext}}(\boldsymbol{r}) \cdot \boldsymbol{M}_{\mathrm{s}}(\boldsymbol{r}) = -\boldsymbol{H}_{\mathrm{ext}}(\boldsymbol{r}) \cdot \boldsymbol{J}_{\mathrm{s}}(\boldsymbol{r}) \tag{24}$$

2.4.2 Dipolar fields

The role of dipolar fields in magnetism and in particular for the formation of domain patterns has been outlined by Landau and Lifshitz (1935) and Kittel and Galt (1956). Brown (1962) considered the role of dipolar fields, also denoted as stray fields, in the case of micromagnetic problems. In particular, Brown (1962) gave an extensive description of magnetostatic principles. Within the framework of an atomistic description of magnetic moments $\boldsymbol{\mu}_i(\boldsymbol{r})_i = g\mu_{\mathrm{B}} \boldsymbol{S}_i(\boldsymbol{r}_i)$ the macroscopic stray field is determined by a sum over all dipole fields of the magnetic moments $\mu_i(\boldsymbol{r}_i)$.

$$\boldsymbol{H}_{\mathrm{s}}(\boldsymbol{r}) = \frac{1}{4\pi} \sum_i \left(\frac{\boldsymbol{\mu}_i(\boldsymbol{r}_i)}{R^3} - \frac{3\left(\boldsymbol{\mu}_i(\boldsymbol{r}_i) \cdot \boldsymbol{R}\right) \cdot \boldsymbol{R}}{R^5} \right) \tag{25}$$

with $\boldsymbol{R} = \boldsymbol{r} - \boldsymbol{r}_i$. In the continuum theory of micromagnetism the calculation of stray fields starts from the Maxwell equation

$$\mathrm{div}\boldsymbol{B} = 0 \tag{26}$$

where in the case of $\boldsymbol{H}_{\mathrm{ext}} = 0$ the magnetic flux density $\boldsymbol{B}$ is given by

$$\boldsymbol{B}(\boldsymbol{r}) = \mu_0 \boldsymbol{H}_{\mathrm{s}}(\boldsymbol{r}) + \mu_0 \boldsymbol{M}_{\mathrm{s}}(\boldsymbol{r}) = \mu_0 \boldsymbol{H}_{\mathrm{s}}(\boldsymbol{r}) + \boldsymbol{J}_{\mathrm{s}}(\boldsymbol{r}) \tag{27}$$

Since $\boldsymbol{H}_{\mathrm{s}}$ derives from magnetic dipoles the condition curl $\boldsymbol{H}_{\mathrm{s}} = 0$ holds, and $\boldsymbol{H}_{\mathrm{s}}$ derives from a scalar potential $U(\boldsymbol{r})$ according to

$$\boldsymbol{H}_{\mathrm{s}}(\boldsymbol{r}) = -\nabla U(\boldsymbol{r}) \tag{28}$$

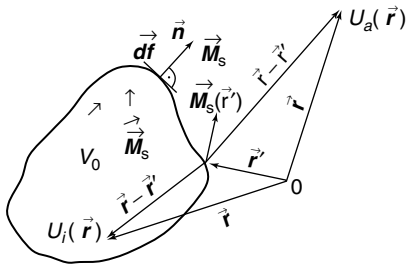

Figure 4. Spacial coordinates and integration variables for the internal potential $U_i(\boldsymbol{r})$ and the external potential $U_a(\boldsymbol{r})$ due to surface charges $\sigma(\boldsymbol{r}') = \boldsymbol{M}_s(\boldsymbol{r}') \cdot \boldsymbol{n}$.

With equation (26) $U(\boldsymbol{r})$ derives from the Poisson equation

$$\Delta U = \text{div } \boldsymbol{M}_s(\boldsymbol{r}) = \frac{1}{\mu_0}\text{div}\boldsymbol{J}_s(\boldsymbol{r}) = -\rho(\boldsymbol{r}) \qquad (29)$$

where we have introduced the magnetic charge density $\rho(\boldsymbol{r}) = -\text{div}\boldsymbol{M}_s(\boldsymbol{r})$. The notation stray field for $\boldsymbol{H}_s$ becomes evident from the Poisson equation, which shows that $\boldsymbol{H}_s$ exists only in cases of a spatially inhomogeneous $\boldsymbol{M}_s$ either in orientation or in the modulus $\mid \boldsymbol{M}_s(\boldsymbol{r}) \mid$. The general solution of Poisson's equation is written as the sum of a volume (V_0) and a surface S integral

$$U(\boldsymbol{r}) = \frac{1}{4\pi}\int_{V_0}\frac{\rho(\boldsymbol{r}')}{\mid \boldsymbol{r}-\boldsymbol{r}' \mid}\text{d}^3\boldsymbol{r}' + \frac{1}{4\pi}\int_S \frac{\boldsymbol{\sigma}(\boldsymbol{r}')\cdot\text{d}f'}{\mid \boldsymbol{r}-\boldsymbol{r}' \mid} \qquad (30)$$

The first term in equation (30) takes care of the volume charges and the second term takes into account the surface charges $\sigma(\boldsymbol{r})\boldsymbol{n} \cdot \boldsymbol{M}_s(r')$ as shown presented in Figure 4.

The magnetostatic strayfield is related with a magnetostatic self-energy density, also denoted as dipolar energy given by

$$\phi'_s(r) = \frac{\mu_0}{2}\cdot\boldsymbol{H}_s^2(\boldsymbol{r}) \qquad (31)$$

In the case of discrete magnetic moment, $\boldsymbol{\mu}_i(\boldsymbol{r}_i)$, its interaction energy with all other magnetic dipoles is given by

$$\phi'^{(i)}_s(r_i) = -\mu_0\boldsymbol{\mu}_i(\boldsymbol{r}_i)\sum_{j\neq i}\boldsymbol{H}_s^{(j)}(r_i) \qquad (32)$$

where the sum extends over all field contributions $\boldsymbol{H}_s^{(j)}$ at $\boldsymbol{r}_i$ of all other dipoles j. The total stray field energy now is given by

$$\phi_s = \frac{1}{2}\sum_i \phi_s^{(i)} = -\frac{1}{2}\mu_0\sum_{j\neq i}\boldsymbol{\mu}_i(\boldsymbol{r}_i)\cdot\boldsymbol{H}_s^{(j)}(\boldsymbol{r}_i) \qquad (33)$$

where the factor 1/2 takes into account that the interaction energy between two dipoles has to be counted only once because $\boldsymbol{\mu}_i(\boldsymbol{r}_i)\boldsymbol{H}_s^{(j)}(\boldsymbol{r}_i) = \boldsymbol{\mu}_j(\boldsymbol{r}_j)\boldsymbol{H}_s^{(j)}(\boldsymbol{r}_j)$ holds. Replacing the magnetic moments by the continuum variables $\boldsymbol{M}_s$ by

$$\boldsymbol{\mu}(\boldsymbol{r}) = \boldsymbol{M}_s(\boldsymbol{r})\,\text{d}V \qquad (34)$$

equation (33) transforms into the integral

$$\phi_s = -\frac{1}{2}\int_{V_0}\boldsymbol{H}_s(\boldsymbol{r})\cdot\boldsymbol{J}_s(\boldsymbol{r})\ \text{d}^3\boldsymbol{r} = \frac{1}{2}\mu_0\int_V \boldsymbol{H}_s^2(\boldsymbol{r})\ \text{d}^3\boldsymbol{r} \qquad (35)$$

It is of interest to note that the first integral extends only over the volume of the magnet and the second one over the total space. By means of Green's theorems equation (35) may be transformed into a surface and a volume integral:

$$\phi_s = \frac{1}{2}\int_S U(\boldsymbol{r})\boldsymbol{J}_s(\boldsymbol{r})\cdot\text{d}\boldsymbol{f} - \frac{1}{2}\int_{V_0}U(\boldsymbol{r})\text{div}\ \boldsymbol{J}_s(\boldsymbol{r})\,\text{d}^3\boldsymbol{r} \qquad (36)$$

$$= \frac{1}{2}\mu_0\int_S \sigma(\boldsymbol{r})\cdot U(\boldsymbol{r})\ \text{d}f + \frac{1}{2}\mu_0\int_{V_0}U(\boldsymbol{r})\rho(\boldsymbol{r})\ \text{d}^3\boldsymbol{r}$$

In the case of a multiconnected homogeneously magnet, that is, $\rho = 0, \phi_s$ is given by a double integral

$$\phi_s = \frac{1}{8\pi}\int_s\int_S\frac{\sigma(\boldsymbol{r})\cdot\sigma(r')}{\mid \boldsymbol{r}-\boldsymbol{r}' \mid}\ \text{d}f'\text{d}f \qquad (37)$$

where the integrals extend over the surfaces f and f'. For $f = f'$ equation (37) describes the self-energy of surface charges.

2.5 Magnetostrictive energy terms

2.5.1 Strain tensors in magnetic materials

Magnetostrictive interactions between elastic stresses and the spontaneous magnetization are one of the main sources of the influence of microstructures on magnetic properties. These interactions are the origin of the pinning of domain walls, the arrangement of domains and deviations from magnetic saturation. First treatments of magnetostrictive interactions are due to Becker (1930; 1932; 1934) and Becker and Döring (1939). These results are one of the basis for the micromagnetic continuum theory as developed by Brown (1940; 1941) who introduced the concept of lattice imperfections into micromagnetism. More recent self-consistent elasticity theories of magnetostrictive interactions have been published by Brown (1966), Rieder (1959), Kronmüller (1967), and Kléman (1980). Elasticity problems in magnetostrictive materials in general are rather complex because not only the intrinsic spontaneous magnetization as described in chapter **Magnetostriction and Magnetoelasticity Theory: A Modern View, Volume 1** play a role

but also rotations of volume elements that result from magnetic torques due to the magnetocrystalline energy in the case of rotational magnetization processes. The role of these rotational processes concerning induced elastic stresses in general can be neglected (Kronmüller and Fähnle, 2003). Therefore, in the following we neglect magnetic torques that contribute to the asymmetric part of the strain tensors. The symmetric part of the strain tensor is composed of four contributions

$$\boldsymbol{\varepsilon}^{\mathrm{T}} = \boldsymbol{\varepsilon}^{\mathrm{ext}} + \boldsymbol{\varepsilon}^{\mathrm{def}} + \boldsymbol{\varepsilon}^{\mathrm{Q}} + \boldsymbol{\varepsilon}^{\mathrm{el}} \tag{38}$$

with the following origins:

1. $\boldsymbol{\varepsilon}^{\mathrm{ext}}$ = external strain tensor of applied stresses.
2. $\boldsymbol{\varepsilon}^{\mathrm{def}}$ = internal strain tensor due to defects.
3. $\boldsymbol{\varepsilon}^{\mathrm{Q}}$ = spontaneous magnetostrictive strain tensor due to spin ordering.
4. $\boldsymbol{\varepsilon}^{\mathrm{el}}$ = elastic strain tensor due to inhomogeneous magnetostrictive strain $\boldsymbol{\varepsilon}^{\mathrm{Q}}$.
5. $\boldsymbol{\varepsilon}^{\mathrm{m}} = \boldsymbol{\varepsilon}^{\mathrm{Q}} + \boldsymbol{\varepsilon}^{\mathrm{el}}$ = total strain tensor due to magnetostriction.

2.5.2 *Determination of stress tensors*

The different contributions of the strain tensors to the elastic stresses have to be determined by different methods because the spontaneous magnetostrictive strains correspond to so-called quasiplastic strains. Within the framework of linear elasticity theory Hoock's law holds:

$$\boldsymbol{\sigma} = \boldsymbol{c} \cdot \cdot \boldsymbol{\varepsilon} \tag{39}$$

where $\boldsymbol{c}$ denotes the fourth rank tensor of elastic constants. The stress tensor, $\boldsymbol{\sigma}$, is determined by the mechanical equilibrium surface conditions ($\boldsymbol{n}$ = surface normal)

$$\left.\begin{array}{ll} \mathrm{Div}\ \boldsymbol{\sigma} + \boldsymbol{f} & = 0 \\ \boldsymbol{n} \cdot \boldsymbol{\sigma}^{\mathrm{ext}}|_{\mathrm{surface}} & \boldsymbol{F}_{\mathrm{surface}} \end{array}\right\} \tag{40}$$

where $\boldsymbol{f}$ corresponds to the volume forces and $\boldsymbol{F}_{\mathrm{surface}}$ to the surface forces. The elastic strain and stress fields $\boldsymbol{\varepsilon}^{\mathrm{def}}$ and $\boldsymbol{\sigma}^{\mathrm{def}}$ of defects are well known. For example, in case of linear dislocations the stress field components vary as $1/r$ and in case of point defects as $1/r^3$. External stresses in general lead to homogeneous stress states if the samples shape is prismatic or cylindrical.

The calculation of the elastic strain fields due to inhomogeneous spontaneous magnetostrictions $\boldsymbol{\varepsilon}^{\mathrm{Q}}$, requires special considerations because just these strains usually are omitted in micromagnetic problems.

The spontaneous magnetostrictive strains $\boldsymbol{\varepsilon}^{\mathrm{Q}}$ have been derived by Becker and Döring (1939) with the components

$$\varepsilon_{ij}^{\mathrm{Q}} = \lambda_{ijkl}\gamma_k\gamma_l \tag{41}$$

where Einstein's sum convention holds (summation from $i = 1$ to 3 if a suffix appears twice). The fourth rank tensor, $\boldsymbol{\lambda}$, possesses the symmetry of the atomic structure, that is, the crystal symmetry or short-range order in otherwise disordered materials. For cubic crystals $\boldsymbol{\varepsilon}^{\mathrm{Q}}$ is given by:

$$\boldsymbol{\varepsilon}^{\mathrm{Q}} = \begin{pmatrix} \frac{3}{2}\lambda_{100}\left(\gamma_i^2 - \frac{1}{3}\right) & \frac{3}{2}\lambda_{111}\gamma_i\gamma_2 & \frac{3}{2}\lambda_{111}\gamma_i\gamma_3 \\ \frac{3}{2}\lambda_{111}\gamma_1\gamma_2 & \frac{3}{2}\lambda_{100}\left(\gamma_2^2 - \frac{1}{3}\right) & \frac{3}{2}\lambda_{111}\gamma_2\gamma_3 \\ \frac{3}{2}\lambda_{111}\gamma_1\gamma_3 & \frac{3}{2}\lambda_{111}\gamma_2\gamma_3 & \frac{3}{2}\lambda_{100}\left(\gamma_3^2 - \frac{1}{3}\right) \end{pmatrix} \tag{42}$$

The magnetostriction constants λ_{100} and λ_{111} have the following meaning: λ_{100} corresponds to the fractional length change upon saturation in ⟨100⟩-direction and λ_{111} has the same meaning for saturation in ⟨111⟩-direction. In the case of hexagonal crystals we deal with four magnetostriction constants and a magnetostriction tensor given by:

$$\boldsymbol{\varepsilon}^{\mathrm{Q}} = \begin{pmatrix} \left(\lambda_{11}\gamma_i^2 + \lambda_{12}\gamma_2^2\right) & \left(\lambda_{11} - \lambda_{12}\right)\gamma_i\gamma_2 & \frac{1}{2}\lambda_{44}\gamma_i\gamma_3 \\ & \left(\lambda_{12}\gamma_1^2 + \lambda_{11}\gamma_2^2\right) & \frac{1}{2}\lambda_{44}\gamma_2\gamma_3 \\ & & \lambda_{33}\gamma_3^2 \end{pmatrix} \tag{43}$$

Isotropic or amorphous materials are characterized by diagonal components

$$\varepsilon_{ii} = \frac{3}{2}\lambda_{\mathrm{s}}\left(\gamma_i^2 - \frac{1}{3}\right), \quad i = 1, 2, 3 \tag{44}$$

and off-diagonal components

$$\varepsilon_{ij}^{\mathrm{Q}} = \frac{3}{2}\lambda_{\mathrm{s}}\gamma_i\gamma_j, \quad i \neq j \tag{45}$$

with λ_{s} the isotropic magnetostrictive constant. The elastic stresses $\boldsymbol{\sigma}^{\mathrm{m}}$ due to the elastic strains $\boldsymbol{\varepsilon}^{\mathrm{el}}$ follow from the condition that the total strain $\boldsymbol{\varepsilon}^{\mathrm{m}}\boldsymbol{\varepsilon}^{\mathrm{Q}} + \boldsymbol{\varepsilon}^{\mathrm{el}}$ can be derived from a displacement field, $\boldsymbol{s}^{\mathrm{m}}$, according to

$$\boldsymbol{\varepsilon}^{\mathrm{m}} = \mathrm{Def}\ \boldsymbol{s}^{\mathrm{m}} \tag{46}$$

where the definition of the operator Def follows from

$$\varepsilon_{ij}^{\mathrm{m}} = \frac{1}{2}\left(\frac{\partial s_i^{\mathrm{m}}}{\partial x_j} + \frac{\partial s_j^{\mathrm{m}}}{\partial x_i}\right) \tag{47}$$

and the elastic stress due to magnetostriction is given by

$$\boldsymbol{\sigma}^{\mathrm{m}} = \boldsymbol{c} \cdot \cdot \boldsymbol{\varepsilon}^{\mathrm{el}} \tag{48}$$

$\boldsymbol{\sigma}^{\mathrm{m}}$ obeys the mechanical equilibrium condition

$$\mathrm{Div}\ \boldsymbol{\sigma}^{\mathrm{m}} = 0 \tag{49}$$

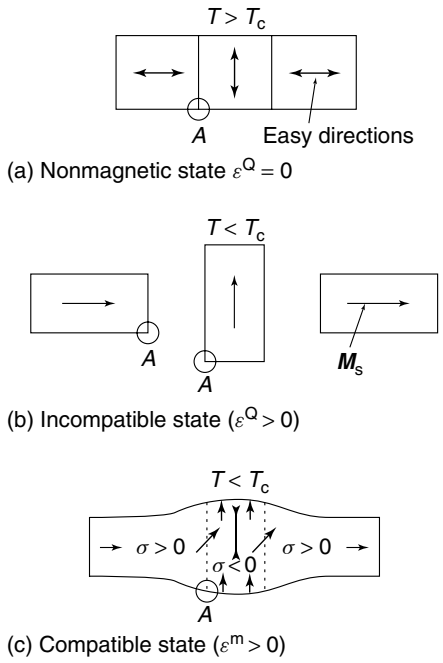

Figure 5. Formation of elastic strains by inhomogeneous spontaneous magnetostrictive strains. The cutting model demonstrates the existence of elastic strains due to the connection of the sites A. (Reproduced with permission from Cambridge University Press.)

and since equation (47) holds

$$\text{Div}\ (\boldsymbol{c}\cdot\cdot\boldsymbol{\varepsilon}^{\text{el}}) = \text{Div}\ \boldsymbol{c}\cdot\cdot\text{Def}\,\boldsymbol{s}^{\text{m}}) - \text{Div}\ (\boldsymbol{c}\cdot\cdot\boldsymbol{\varepsilon}^{\text{Q}}) = 0 \tag{50}$$

The three sets of equations (50) do not allow the determination of the six components $\varepsilon_{ij}^{\text{m}}$. Since $\boldsymbol{\varepsilon}^{\text{m}}$ derives from $\boldsymbol{\varepsilon}^{\text{m}}\text{Def}\boldsymbol{s}^{\text{m}}$, additional relations hold for $\boldsymbol{\varepsilon}^{\text{m}}$, which may be written in the comprehensive form

$$\text{Ink}\ \boldsymbol{\varepsilon}^{\text{m}} = \nabla\times\boldsymbol{\varepsilon}^{\text{m}}\times\nabla = 0 \tag{51}$$

Equation (51) takes into account that the total strain tensor $\boldsymbol{\varepsilon}^{\text{m}}$ describes a compatible continuous deformation without discontinuities. The combination of equations (51) and (50) leads to the so-called Beltrami equations (Kröner, 1958), which for elastic anisotropy is written as (G = shear modulus, ν = Poisson ratio, $\delta_{ij} = 0$ for $i \neq j$, $\delta_{ij} = 1$ for $i = j$, $\sigma_{kk} = \sum_{i=1}^{3}\sigma_{ii}^{\text{m}}$):

$$\Delta\sigma_i + \frac{\nu}{1+\nu}\left(\nabla_i\,\nabla_j\sigma_{kk}^{\text{m}} - \Delta\sigma_{kk}^{\text{m}}\right) = 2G\eta_{ij}^{\text{Q}} \tag{52}$$

where the incompatibility tensor $\boldsymbol{\eta}^{\text{Q}}$ is defined as

$$\boldsymbol{\eta}^{\text{Q}} = (-)\text{Ink}\ \boldsymbol{\varepsilon}^{\text{Q}} = \text{Ink}\boldsymbol{\varepsilon}^{\text{el}} \tag{53}$$

Equation (52) clearly shows that the sources of the elastic magnetostrictive stresses are inhomogeneous spontaneous magnetostrictions. In order to obtain a direct understanding of the formation of elastic magnetostrictive strains the magnetoelastic potential is magnetized homogeneously. Starting from a hypothetical nonmagnetic material with $\boldsymbol{\varepsilon}^{\text{Q}} \equiv 0$ above the Curie temperature, below the Curie temperature spontaneous magnetostrictive strains $\boldsymbol{\varepsilon}^{\text{Q}}$ are formed. In the case of a homogeneously magnetized specimen with $\boldsymbol{\varepsilon}^{\text{Q}} = \text{const}$ no elastic stresses are induced. As shown in Figure 5, in the case of an inhomogeneous magnetization, the different parts of the specimen suffer incompatible spontaneous deformations which develop freely of the specimen is cut into individual parts. According equation (46), however, the displacement field should be continuous without any cracks. According to Figure 5, the individual parts have to be fitted together in order to keep up a continuous displacement field.

This fitting is performed by the application of the elastic strains $\boldsymbol{\varepsilon}^{\text{el}}$, which guarantee the compatible state fulfilling the condition $\text{Ink}\,\boldsymbol{\varepsilon}^{\text{m}} = 0$. This consideration gives a direct insight into the stress-producing role of the incompatibility tensor $\boldsymbol{\eta}^{\text{Q}} = -\text{Ink}\,\boldsymbol{\varepsilon}^{\text{Q}}$.

2.5.3 The magnetoelastic potential – stress tensors in domain walls

In the following the magnetic Gibbs free energy is taken with respect to a hypothetical nonmagnetic state, that is, $\boldsymbol{\varepsilon}^{\text{Q}} = 0$. Below the Curie temperature $\boldsymbol{\varepsilon}^{\text{Q}}$ and its elastic stresses $\boldsymbol{\varepsilon}^{\text{el}}$ appear and the Gibbs free energy according to equation (3) is given by

$$\phi_{\text{t}} = \int\left(\phi_0 + \frac{1}{2}\ \boldsymbol{\varepsilon}^{\text{T}}\cdot\cdot\boldsymbol{c}\cdot\cdot\boldsymbol{\varepsilon}^{\text{T}} - \boldsymbol{\sigma}\cdot\cdot\boldsymbol{\varepsilon}^{\text{T}}\right)\text{d}^3\,\boldsymbol{r} \tag{54}$$

where ϕ_0 contains ϕ_{ex}', ϕ_k' and ϕ_{s}' which are assumed to be independent of strains, minimization of ϕ_{t} with respect to $\boldsymbol{\varepsilon}^{\text{T}}$ leads to Hook's law, $\boldsymbol{\sigma} = \boldsymbol{c}\cdot\cdot\boldsymbol{\varepsilon}^{\text{T}}$, and which allows to rewrite ϕ_{t} as follows:

$$\phi_{\text{t}} = \int\left(\phi_0 - \frac{1}{2}\ \boldsymbol{\varepsilon}^{\text{T}}\cdot\cdot\boldsymbol{c}\cdot\cdot,\boldsymbol{\varepsilon}^{\text{T}}\right)\text{d}^3\,\boldsymbol{r} \tag{55}$$

Inserting for $\boldsymbol{\varepsilon}^{\text{T}}$ equation (39) we may derive the different types of magnetostrictive energy terms. Excluding energy terms, which vanish after integration and taking into account only terms of magnetic origin the magnetic elastic potential is written as

$$\phi_{\text{el}} = -\frac{1}{2}\int\left\{\boldsymbol{\varepsilon}^{\text{Q}}\cdot\cdot\boldsymbol{c}\cdot\cdot\boldsymbol{\varepsilon}^{\text{Q}} - \boldsymbol{\varepsilon}^{\text{el}}\cdot\cdot\boldsymbol{c}\cdot\cdot\boldsymbol{\varepsilon}^{\text{el}}\right\}\text{d}^3\,\boldsymbol{r} - \int\left\{\boldsymbol{\varepsilon}^{\text{def}} + \boldsymbol{\varepsilon}^{\text{ext}}\right\}\cdot\cdot\boldsymbol{c}\cdot\cdot\left(\boldsymbol{\varepsilon}^{\text{Q}} + \boldsymbol{\varepsilon}^{\text{el}}\right)\ \text{d}^3\,\boldsymbol{r} \tag{56}$$

Here the first two terms correspond to self energies of the free spontaneous magnetostrictive strains and of the elastic magnetostrictive strains induced by inhomogeneous spontaneous magnetization. The third term describes interactions between external and defect stresses and the magnetostrictive strains. In order to understand this complex situation we consider three characteristic cases:

1. *Ideal homogeneously magnetized ferromagnet without defects*: In this case no elastic stresses exist, $\boldsymbol{\varepsilon}^{\mathrm{ext}}$, $\boldsymbol{\varepsilon}^{\mathrm{def}}$, $\boldsymbol{\varepsilon}^{\mathrm{el}} = 0$).

$$\phi_{\mathrm{el}} = -\frac{1}{2}\int \boldsymbol{\varepsilon}^{\mathrm{Q}} \cdot\cdot \boldsymbol{c} \cdot\cdot \boldsymbol{\varepsilon}^{\mathrm{Q}}\ \mathrm{d}^3 r \tag{57}$$

   This energy term corresponds to a contribution to the magnetocrystalline energy ϕ_{k}. Inserting $\boldsymbol{\varepsilon}^{\mathrm{Q}}$'s for cubic crystals gives for the elastic energy density

$$\phi'_{\mathrm{el}} = \left\{\frac{9}{4}\ (\mathrm{c}_{11} - \mathrm{c}_{12})\ \lambda_{100}^2 - \frac{9}{4}\ \mathrm{c}_{44}\ \lambda_{111}^2\right\}\ \sum_{i\neq j}\gamma_i^2\,\gamma_j^3 \tag{58}$$

   where c_{ij} corresponds to the cubic elastic constants in Voigt's notation. ϕ_{el} has the symmetry of the magnetocrystalline energy and therefore adds to ϕ_k.
2. *Inhomogeneous magnetization without defects*: Inhomogeneous states of magnetization exist in domain walls, in small particles and in the form of vortices and at the edges and corners of polyhedral small particles. If no defects and external stresses are present, the elastic potential is given by

$$\phi_{\mathrm{el}} = -\frac{1}{2}\int \left\{\boldsymbol{\varepsilon}^{\mathrm{Q}} \cdot\cdot \boldsymbol{c}, \cdot\cdot\ \boldsymbol{\varepsilon}^{\mathrm{Q}} - \boldsymbol{\varepsilon}^{\mathrm{el}} \cdot\cdot \boldsymbol{c} \cdot\cdot \boldsymbol{\varepsilon}^{\mathrm{el}}\right\}\ \mathrm{d}^3\,\boldsymbol{r} \tag{59}$$

   In equation (59) the elastic magnetostrictive self-energy appears, which is of particular interest for domain walls that otherwise would split up into two partial domain walls (e.g., (100)–180°-walls in α-Fe, or the (100)–109°-walls in Ni). For the most important domain walls in α-Fe, Ni, and Co the strain terms $\boldsymbol{\varepsilon}^{\mathrm{el}}$ have been determined. Solution of the elastic equations leads for the (001)–180° wall of the cubic α-Fe to the following stress and stress components using the coordinate system of Figure 6(a):

$$\begin{aligned}
\sigma_{11}^{\mathrm{m}} &= \frac{3}{2}\lambda_{100}(c_{11} - c_{12})\sin^2\varphi,\\
\sigma_{22}^{\mathrm{m}} &= -\frac{3}{2}\lambda_{100}(c_{11} - c_{12}\sin^2\varphi)\\
\sigma_{12}^{\mathrm{m}} &= -\frac{3}{2}\lambda_{111}c_{44}\sin 2\varphi\\
\varepsilon_{11}^{\mathrm{el}} &= \frac{3}{2}\lambda_{100}\sin^2\varphi;\ \varepsilon_{22}^{\mathrm{el}} = -\frac{3}{2}\lambda_{100}\sin^2\varphi,\\
\varepsilon_{12}^{\mathrm{el}} &= -\frac{3}{4}\lambda_{111}\sin 2\varphi
\end{aligned} \tag{60}$$

The magnetostrictive elastic self-energy density for the (100)–180° wall is given by

$$\begin{aligned}
\phi'_{\mathrm{el}} = -\frac{1}{2}\,\sigma_{ij}^{\mathrm{m}}\,\varepsilon_{ij}^{\mathrm{el}} &= \frac{9}{4}\ \lambda_{100}\ (c_{11} - c_{12})\sin^2\varphi\\
&\quad -\frac{9}{4}(\lambda_{100}(c_{11} - c_{12}) - 2\lambda_{111}c_{44})\sin^2\varphi\cos^2\varphi
\end{aligned} \tag{61}$$

In the case of an elastically and magnetically isotropic material ϕ'_{el} is found to be

$$\phi'_{\mathrm{el}} = \frac{9}{2}\,\mathrm{G}\,\lambda_{\mathrm{S}}\ \sin^2\ \varphi \tag{62}$$

These results may be used to determine specific domain wall energies in crystalline and isotropic materials.

Whereas in the case of the (100)–180° dw in α-Fe the elastic strains and stresses vanish within the domains

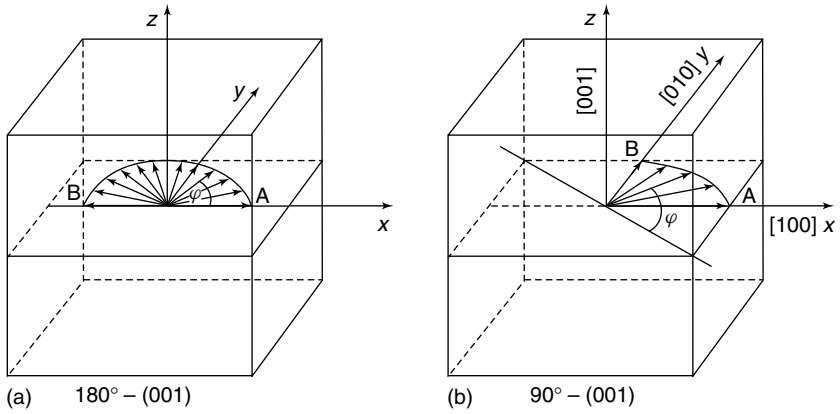

Figure 6. Coordinate systems used for the (001)–180° walls and the (001)–90° walls in cubic α-iron.

for $\varphi = 0$ and $\varphi = \pi$ the situation is different for the (001)–90° wall the geometry of which is shown in Figure 6(b). The rotation of $\boldsymbol{J}_S$ from A to B is described by the direction cosines $\gamma_1 = +\cos(\varphi - \frac{\pi}{4})$, $\gamma_2 \sin(\varphi - \frac{\pi}{4})$, $\gamma_3 = 0$. Strain and stress components are given by

$$\begin{aligned}
\varepsilon_{11}^{\mathrm{el}} &= -\frac{3}{4}\lambda_{100}\,\sin 2\varphi;\ \varepsilon_{22}^{\mathrm{el}} = \frac{3}{4}\lambda_{100}\sin 2\,\varphi;\\
\varepsilon_{12} &= -\frac{3}{4}\lambda_{111}\cos 2\varphi\\
\sigma_{11}^{\mathrm{m}} &= -\frac{3}{4}\lambda_{100}(c_{11}-c_{12})\sin 2\varphi,\\
\sigma_{22}^{\mathrm{m}} &= \frac{3}{4}\lambda_{100}(c_{11}-c_{12})\sin 2\varphi\\
\sigma_{12}^{\mathrm{m}} &= -\frac{3}{2}\lambda_{111}c_{44}\cos 2\varphi
\end{aligned} \tag{63}$$

Within the domains at $\varphi = \frac{\pi}{4}$ and $\varphi = \frac{3\pi}{4}$ the stress components are

$$\begin{aligned}
\sigma_{11}^{\mathrm{m}} &= -\frac{3}{4}\lambda_{100}\,(c_{11}-c_{12}) = -\sigma_{22}^{\mathrm{m}};\quad \sigma_{12}^{\mathrm{m}} = 0\\
\sigma_{11}^{\mathrm{m}} &= \frac{3}{4}\lambda_{100}\,(c_{11}-c_{12}) = -\sigma_{22}^{\mathrm{m}};\quad \sigma_{12}^{\mathrm{m}} = 0
\end{aligned} \tag{64}$$

According to equation (64) the elastic magnetostrictive stresses are finite within the domains. As a consequence this type of dws = domain walls are exposed to strong interactions with stress centers as, for example, dislocations. Therefore 90°-walls in general are less mobile than 180°-walls.

3. *Homogeneous magnetization and external* $\boldsymbol{\sigma}^{\mathrm{ext}}$ *or internal,* $\boldsymbol{\sigma}^{\mathrm{def}}$*, stresses:* In the case of a homogeneously magnetized ferromagnet exposed to external or internal stresses the elastic potential is written as

$$\phi_{\mathrm{el}} = -\frac{1}{2}\int \boldsymbol{\varepsilon}^{\mathrm{Q}}\cdot\cdot\boldsymbol{c}\ \cdot\cdot\boldsymbol{\varepsilon}^{\mathrm{Q}}\ \mathrm{d}^3\boldsymbol{r} - \int \boldsymbol{\sigma}\cdot\cdot\boldsymbol{\varepsilon}^{\mathrm{Q}}\ \mathrm{d}^3\boldsymbol{r} \tag{65}$$

where $\boldsymbol{\sigma}$ means either $\boldsymbol{\sigma}^{\mathrm{ext}}$ or $\boldsymbol{\sigma}^{\mathrm{def}}$ or the sum of both. Here again the first term corresponds to the contribution of the spontaneous magnetization to the magnetocrystalline energy and the second term describes the interaction energy, $\boldsymbol{\varepsilon}^{\mathrm{Q}}$, with external stresses. This latter term was originally developed by Becker and Döring (1939) and is known as the so-called magnetoelastic coupling energy, which for cubic crystals is given by

$$\phi'_{\sigma} = -\frac{3}{2}\,\lambda_{100}\,\sum_{i=1}^{3}\sigma_{ii}\,\gamma_i^2 - \frac{3}{2}\,\lambda_{111}\,\sum_{i\neq j}\sigma_{ij}\gamma_i\gamma_j \tag{66}$$

where $\boldsymbol{\sigma}$ and the γ_i refer to the cubic coordinate system. For isotropic materials as for example, amorphous alloys equation (66) is

$$\phi_{\sigma} = -\frac{3}{2}\lambda_{\mathrm{S}}\left\{\sum_{i=1}^{3}\sigma_{ii}\gamma_i^2 + \sum_{i\neq j}\sigma_{ij}\gamma_i\gamma_j\right\} \tag{67}$$

The stress tensor $\boldsymbol{\sigma}$ in equation (66) and equation (67) either may correspond to external or internal stresses. Equation (67) is the basis for investigating the influence of stresses on the arrangement of domain patterns or the determination of spontaneous magnetization in the neighborhood of stress-active defects. Some examples of this type of interactions will be given in chapter 5.

2.6 Summary

According to the results of Sections 2.1–2.5 the total magnetic Gibbs free energy density is composed of five terms

$$\phi'_{\mathrm{t}} = \phi'_{\mathrm{ex}} + \phi'_{\mathrm{k}} + \phi'_{\mathrm{el}} + \phi'_{\mathrm{s}} + \phi'_{\mathrm{h}} \tag{68}$$

Depending on the problem to be solved in many cases not all of these energy terms have to be taken into account. For example, for the treatment of Blochwall ϕ'_{s} and ϕ'_{H} may be omitted whereas in the case of soft magnetic materials ϕ_{k} plays only a minor role. In the treatment of internal stresses ϕ'_{el} has to be replaced by ϕ'_{σ}. For a crystal of cubic symmetry, the total magnetic Gibbs free energy density in this case is written as

$$\begin{aligned}
\phi'_{\mathrm{t}} = {} & A\sum_i(\nabla\gamma_i)^2 + K_1\sum_{i\neq j}\gamma_i^2\gamma_j^2 + K_2\gamma_1^2\gamma_2^2\gamma_3^2\\
& - \frac{3}{2}\lambda_{100}\sum_{i=1}\sigma_{ii}\gamma_i^2 - \frac{3}{2}\lambda_{111}\sum_{i\neq j}\sigma_{ij}\gamma_i\gamma_j\\
& - \frac{1}{2}\boldsymbol{H}_{\mathrm{s}}\cdot\boldsymbol{J}_{\mathrm{s}} - \boldsymbol{H}_{\mathrm{ext}}\cdot\boldsymbol{J}_{\mathrm{s}}
\end{aligned} \tag{69}$$

where γ_i and $\boldsymbol{\sigma}$ refer to the cubic coordinate system.

Each of these energy terms has a specific influence on the distribution of the directions of the spontaneous magnetization, which will be outlined in the following section.

It is of interest to remember that the continuum expressions (69) for ϕ'_{t} has a quantum theoretical analogon in the

Hamiltonian

$$H = -2\sum_{i\neq j} J_{ij}\, \boldsymbol{S}_i \cdot \boldsymbol{S}_j + \lambda_{\mathrm{SO}} \sum_i \boldsymbol{L}_i \cdot \boldsymbol{S}_i - \frac{\mu_0 (g\mu_{\mathrm{B}})^2}{4\pi} \sum_{i\neq j} \left(\frac{\boldsymbol{S}_i \cdot \boldsymbol{S}_j}{R_{ij}^3} - \frac{3(\boldsymbol{S}_i \cdot \boldsymbol{R}_{ij})(\boldsymbol{S}_j \cdot \boldsymbol{R}_{ij})}{R_{ij}^5} \right) - g\mu_0\mu_{\mathrm{B}} \sum_i \boldsymbol{S}_i \cdot \boldsymbol{H}_{\mathrm{ext}} \tag{70}$$

Here the second term denotes the spin-orbit coupling energy as one of the sources of the magnetoelastic energy is included in equation (70) by the strain dependence of the spin-orbit coupling constant λ_{SO}. The third term corresponds to the dipolar stray field energy and the last term is known as the Zeeman energy.

3 MICROMAGNETIC EQUILIBRIUM EQUATIONS

Micromagnetic equilibrium conditions usually are derived with respect to the orientation of the vector of spontaneous polarization or magnetization. Accordingly, the magnetic Gibbs free energy is mimimalized with respect to the direction cosines γ of $\boldsymbol{J}_{\mathrm{s}}$, where the modulus of $\boldsymbol{J}_{\mathrm{s}}$ is kept constant, that is, the condition

$$\sum_{i=1}^{3} \gamma_i^2 = 1 \quad \text{or} \quad \sum_{i=1}^{3} J_{\mathrm{s},i}^2 = J_{\mathrm{s}}^2 \tag{71}$$

holds. Presenting the results of the following considerations the static equilibrium equations are written as a torque equation

$$\boldsymbol{L} = [\boldsymbol{J}_{\mathrm{s}} \times \boldsymbol{H}_{\mathrm{eff}}] = 0 \tag{72}$$

Here, $\boldsymbol{H}_{\mathrm{eff}}$ denotes the so-called effective field, which is composed of four contributions: external field, dipolar field (stray field), magnetocrystalline field, magnetoelastic field. A trivial solution of equation (72), of course, is $H_{\mathrm{eff}} \equiv 0$. The torque equation for an isotropic medium also may be interpreted as

$$\boldsymbol{J}_{\mathrm{s}} = \mu_0(\mu - 1)\boldsymbol{H}_{\mathrm{eff}},\ \boldsymbol{M}_{\mathrm{s}} = \chi\ \boldsymbol{H}_{\mathrm{eff}}$$

or

$$\mu - 1 = \frac{J_{\mathrm{s}}}{\mu_0 |\boldsymbol{H}_{\mathrm{eff}}|}, \quad \chi = \frac{M_{\mathrm{s}}}{|\ \boldsymbol{H}_{\mathrm{eff}}\ |} \tag{73}$$

In the general case the permeability μ and the susceptibility χ correspond to tensors of second order. In order to derive the micromagnetic equilibrium equations the magnetic Gibbs free energy ϕ_{t} has to be minimized with respect to γ_i taking into account the constraint (71). This leads to the variational equation

$$\delta_{\gamma_i}\phi_{\mathrm{t}} = \delta_{\gamma_i} \int \left\{ \phi'_{\mathrm{ex}} + \phi'_{\mathrm{k}} + \phi'_{\mathrm{el}} + \phi'_{\mathrm{s}} + \phi'_{\mathrm{H}} + \lambda \left(\sum_{i=1}^{3} \gamma_i^2 - 1 \right) \right\} \mathrm{d}^3\boldsymbol{r} = 0 \tag{74}$$

The last term in equation (74) takes care of the constraint (71) by a Lagrange parameter λ. Performing the variational operation of equation (74) gives

$$\delta_{\gamma_i}\phi_{\mathrm{t}} = \int \left\{ 2A \sum_{i=1}^{3} \nabla\gamma_i\ \delta\left(\nabla\gamma_i\right) + \sum_{i=1}^{3} \left(\frac{\partial \phi'_{\mathrm{k}}}{\partial \gamma_i} + \frac{\partial \phi_{\mathrm{el}}}{\partial \gamma_i} - J_{\mathrm{s}} H_{\mathrm{ext},i} - 2\lambda\gamma_i \right) \delta\gamma_i - \frac{1}{2}\left(\boldsymbol{H}_{\mathrm{s}} \cdot \delta \boldsymbol{J}_{\mathrm{s}} + \boldsymbol{J}_{\mathrm{s}} \cdot \delta \boldsymbol{H}_{\mathrm{s}}\right) \right\} \mathrm{d}^3\,\boldsymbol{r} \tag{75}$$

Interchanging the operator $\partial_i = \frac{\partial}{\partial x_i}$ and the variation δ and applying Gauss's theorem the variation of the exchange energy gives

$$\int 2A \sum_{i=1}^{3} \nabla\gamma_i\ \delta\nabla\gamma_i\ \mathrm{d}^3\,\boldsymbol{r} = 2A \int_S \nabla\gamma_i\ \delta\gamma_i\ \mathrm{d}\,\boldsymbol{f} - 2A \int_V \Delta\gamma_i\ \delta\gamma_i\ \mathrm{d}^3\,\boldsymbol{r} \tag{76}$$

where the first term on the right side extends over the surface S of the magnet. Concerning the variation of the dipolar energy according to Brown (1962) because of $\mathrm{div}\boldsymbol{B} = 0$ and rot $\boldsymbol{H}_{\mathrm{s}} = 0$ the relation

$$\int \boldsymbol{H}_{\mathrm{s}} \cdot \delta\, \boldsymbol{J}_{\mathrm{s}}\ \mathrm{d}^3\,\boldsymbol{r} = \int \boldsymbol{J}_{\mathrm{s}} \cdot \delta\, \boldsymbol{H}_{\mathrm{s}}\ \mathrm{d}^3\,\boldsymbol{r} \tag{77}$$

holds. Inserting equations (76 and 77) into equation (75) gives

$$\delta_{\gamma_i}\phi_{\mathrm{t}} = \int_V \left\{ -2A\,\Delta\gamma_i + \left(\frac{\partial \phi'_{\mathrm{k}}}{\partial \gamma_i} + \frac{\partial \phi'_{\mathrm{el}}}{\partial\, \gamma_i} \right) - H_{\mathrm{s},i}\ J_{\mathrm{s}} - H_{\mathrm{ext},i}\ J_{\mathrm{s}} + 2\,\lambda\gamma_i \right\} \delta\gamma_i\ \mathrm{d}^3\,\boldsymbol{r} + 2A \int_S \nabla\gamma_i \delta\gamma_i \cdot \mathrm{d}\,\boldsymbol{f}\,\delta\gamma_i = 0 \tag{78}$$

According to equation (78) the variations $\delta\phi_t$ vanishes if the integrands of the volume and of the surface integrals vanish. The differential equations obtained by this procedure still contain the Lagrange parameter λ. Elimination of λ is performed by multiplying the differential equation for γ_i by γ_j and vice versa and subtracting the corresponding expressions of the type $J_{s,j}H_{eff,i} - J_{s,i}H_{eff,j} = 0$, which correspond to the components of the vector product of $\boldsymbol{J}_s$ and an effective field, $\boldsymbol{H}_{eff}$. Accordingly, the equilibrium condition in the volume is

$$[\boldsymbol{J}_s \times \boldsymbol{H}_{eff}] = 0 \tag{79}$$

and

$$[\boldsymbol{J}_s \times \nabla_n \boldsymbol{M}_s] = 0$$

on the surface. The components of the effective field are given by

$$\begin{aligned} H_{eff,i} = -\frac{1}{J_s}\frac{\partial \phi'_t}{\partial \gamma_i} = \frac{2A}{J_s}\Delta\gamma_i + H_{k,i} \\ + H_{\sigma,i} + H_{s,i} + H_{ext,i} \end{aligned} \tag{80}$$

Here we have introduced the effective fields of the anisotropy and magnetoelastic energy

$$H_{k,i} = -\frac{1}{J_s}\frac{\partial \phi'_k}{\partial \gamma_i}, \quad H_{\sigma,i} = -\frac{1}{J_s}\frac{\partial \phi'_{el}}{\partial \gamma_i} \tag{81}$$

In addition to the above, micromagnetic equilibrium conditions the Maxwell equation $\mathrm{div}\,\boldsymbol{B} = 0$ has to be fulfilled. This leads to the Poisson equation inside the volume

$$\begin{aligned} \Delta U^{(i)} &= \mathrm{div}\ \boldsymbol{M}_s(r) = -\rho(\boldsymbol{r}) \\ \text{with } \boldsymbol{H}_s^{(i)} &= -\nabla\ U^{(i)} \end{aligned} \tag{82}$$

and the Laplace equation

$$\begin{aligned} \Delta U^{(0)} &= 0 \\ \boldsymbol{H}_s^{(0)} &= -\nabla\ U^{(0)} \end{aligned} \tag{83}$$

outside the volume. $U^{(1)}$ and $U^{(0)}$ have to fulfill the following boundary conditions

$$U^{(i)}(\boldsymbol{r}) = U^{(a)}(\boldsymbol{r}) \tag{84}$$

at the surface. Furthermore, the normal component of $\boldsymbol{B}$ at the surface (o) has to be continuous, that is:

$$\left.\begin{aligned} H_{s,0}^{(i)} + M_{s,n} &= H_{s,0}^{(0)} \\ -\nabla_n U_0^{(i)} + M_{s,n} &= -\nabla_n U_0^{(0)} \end{aligned}\right\} \tag{85}$$

In the most general case also the elastic equilibrium conditions has to be taken into account in the volume and at the surface with surface forces $\boldsymbol{F}$, respectively

$$\left.\begin{aligned} \mathrm{Div}(\boldsymbol{c}\cdot\cdot\boldsymbol{\varepsilon}^{el}) &= -\mathrm{Div}(\boldsymbol{c}\cdot\cdot\boldsymbol{\varepsilon}^{Q}) \\ \boldsymbol{n}\cdot\boldsymbol{\sigma} &= \boldsymbol{F} \end{aligned}\right\} \tag{86}$$

In order to formulate equilibrium equations free from the Lagrange parameter and the condition (71) spherical angular coordinates φ and θ are introduced where φ denotes the azimuthal and θ the polar angle. The direction cosines γ_i are replaced by

$$\gamma_1 = \sin\theta\ \cos\varphi,\ \ \gamma_2 = \sin\theta\ \sin\varphi,\ \ \gamma_3 = \cos\theta \tag{87}$$

Now the equilibrium conditions write:

$$\begin{aligned} &2A\Delta\theta - A\ \sin 2\theta(\nabla\varphi)^2 \\ &\quad - \frac{\partial}{\partial\theta}\left(\phi'_k + \phi'_{el} + \phi'_s - \boldsymbol{J}_s\cdot\boldsymbol{H}_{ext}\right) = 0 \\ &2A\left\{\sin^2\theta\Delta\varphi + \sin 2\theta\ (\nabla\varphi)\cdot(\nabla\theta)\right\} \\ &\quad - \frac{\partial}{\partial\varphi}\ \left(\phi'_k + \phi'_{el} + \phi'_s - \boldsymbol{J}_s\cdot\boldsymbol{H}_{ext}\right) = 0 \end{aligned} \tag{88}$$

The micromagnetic equations given by equations (79)–(88) correspond to a system of coupled differential equations for the unknown variables γ_i. Since the stray fields $\boldsymbol{H}_s$ and the elastic tensor $\boldsymbol{\varepsilon}^{el}$ in principle can be represented as integrals (e.g., see equation (30)), it becomes obvious that the micromagnetic equation correspond to a rather complicated system of coupled nonlinear integro-differential equations.

Explicit solutions of the micromagnetic equations have been obtained for a number of fundamental problems as domain walls in bulk materials and thin films (Kronmüller and Fähnle, 2003; Riedel and Seeger, 1971; Lilley, 1950; Rieder, 1959) for nucleation problems (Frei, Shtrikman and Treves, 1957; Aharoni and Shtrikman, 1958; Kronmüller, 1987) the high-field susceptibility in the approach to ferromagnetic saturation (Brown, 1940, 1941; Becker and Döring, 1939; Seeger and Kronmüller, 1960; Kronmüller and Seeger, 1961).

4 SOLUTIONS OF MICROMAGNETIC EQUATIONS

There are only a few cases where explicit solutions of the micromagnetic equations are available. Some of them will be summarized in the following. Many micromagnetic problems have to be solved numerically by the recently developed methods of computational micromagnetism that are summarized in **Numerical Micromagnetics: Finite Difference**

Methods, Volume 2 and **Numerical Methods in Micromagnetics (Finite Element Method), Volume 2**. Explicit solutions have been obtained for a number of fundamental micromagnetic problems as domain walls, nucleation problems, domain patterns, and the law of approach to ferromagnetic saturation. Many problems dealing with the interaction between magnetic and microstructural problems have been solved approximately.

4.1 Domain walls

4.1.1 Bloch walls

The spin distribution in planar Bloch walls in general is described by the spherical angles φ and θ, where θ is kept as a constant and the angle of φ describes the rotation of the spontaneous magnetization along the z-coordinate, which is taken as the domain wall normal $\boldsymbol{n}$ (see Figure 7). Bloch walls are characterized by a vanishing stray field ($\operatorname{div} \boldsymbol{M}_s = 0$), that is, the component of $\boldsymbol{J}_s$ with respect to the wall normal, $\boldsymbol{n}$, is constant

$$\boldsymbol{J}_s \cdot \boldsymbol{n} = J_s \cos\theta = \text{constant} \tag{89}$$

Owing to the vanishing stray field energy, the basic equation for planar Bloch walls according to equation (88) is

$$2A \sin^2\theta \frac{d^2\varphi}{dz^2} - \frac{\partial}{\partial\varphi}\left(\phi'_B\right) = 0 \tag{90}$$

where $\phi'_B = \phi'_k + \phi'_{el}$ includes anisotropy energy and magnetoelastic energies. Integration of equation (90) leads to

$$A \sin^2\theta \left(\frac{d\varphi}{dz}\right)^2 - \left(\phi'_B(\varphi) - \phi'_B(\varphi_i)\right) = 0$$

$$z = \sqrt{A}\sin\theta \int_{\varphi_i}^{\varphi} \frac{d\varphi}{\left(\phi'_B(\varphi) - \phi'_B(\varphi_i)\right)^{1/2}} \tag{91}$$

where $\phi'_B(\varphi_i)$ denotes the value of ϕ'_B in the domain for $z \to -\infty$ where $\varphi = \varphi_i$ holds.

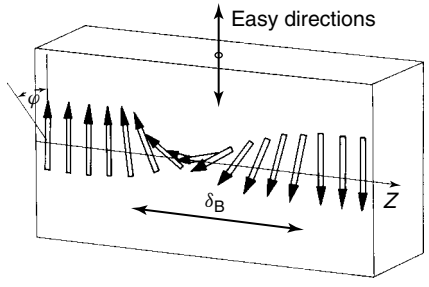

Figure 7. Distribution of magnetization within a 180° wall.

For uniaxial crystals with $\phi'_B = K_1 \sin^2\varphi$ and $\theta = \frac{\pi}{2}$ (180°-wall), the solution is

$$\operatorname{tg}\frac{\varphi}{2} = e^{-z/\delta_0} \text{ or } \sin\varphi = \frac{1}{\operatorname{ch}\left(\frac{z}{\delta_0}\right)}, \quad \cos\varphi = \operatorname{th}\left(\frac{z}{\delta_0}\right) \tag{92}$$

with

$$\delta_0 = \kappa_k^{-1} = \sqrt{\frac{A}{K_1}} \tag{93}$$

which denotes the so-called Bloch wall parameter. In spite of the fact that a domain wall extends from $z = -\infty$ to $z = +\infty$ according to Lilley (1950), Hubert and Schäfer (1998), and Kronmüller and Fähnle (2003) a domain wall width δ_B is defined by the distance between the intersections of the tangent with the largest slope at the $\varphi(z)$ curve with the lines for $\varphi = \varphi_i, \varphi_{ii}$ (see Figure 8):

$$\delta_B = \frac{(\varphi_{ii} - \varphi_i)}{(d\varphi/dz)_{max}} \tag{94}$$

In the case of the 180°-wall in uniaxial materials this gives

$$\delta_B = \pi\delta_0 = \pi\sqrt{\frac{A}{K_1}} \tag{95}$$

and $\delta_B = \sqrt{A/(K_1 + K_2)}$ if the second anisotropy constant is taken into account. For the specific wall energy defined as

$$\gamma_B = 2\sqrt{A}\sin\theta \int_{\varphi_i}^{\varphi_{ii}} \left(\phi'_B(\varphi) - \phi'_B(\varphi_i)\right)^{1/2} d\varphi \tag{96}$$

for the 180° wall with $\varphi_i = 0, \varphi_{ii} = \pi, \theta = \frac{\pi}{2}$

$$\gamma_B = 4\sqrt{A\ K_1} = 4K_1\delta_0 \tag{97}$$

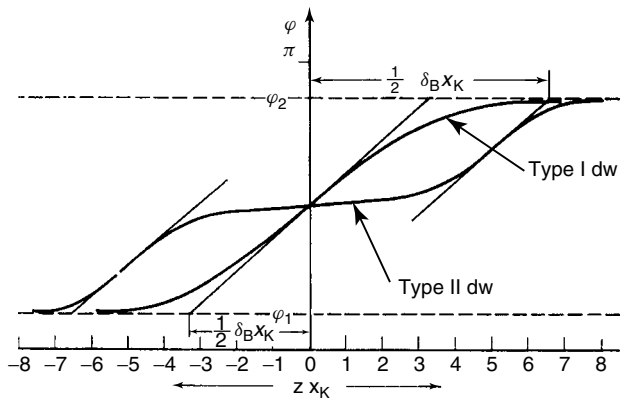

Figure 8. Wall width defined as the intersections of tangents at the steepest slope of φ(z)-curve (Kronmüller and Fähnle (2003)). (Reproduced with permmission from Cambridge University Press.)

is obtained. Whereas in uniaxial crystals the dws are characterized by a single point of inflection of the $\varphi(z)$ curve the situation is more complex in the case of some 180° walls in cubic crystals. For example, the following walls split into two 90° walls if the magnetoelastic energy term ϕ_{el} is neglected: α-Fe: (011)–180°, Ni: (110)–180°, (001)–109,47°. As shown in Figure (8) in this case three points of infliction exist and the $\varphi(z)$-curve is described by

$$\operatorname{ctg}\varphi = -A\cdot \operatorname{sh}\frac{z}{\alpha\delta_0} + \rho \tag{98}$$

Values for A and ρ are given by Lilley (1950) and Kronmüller and Fähnle (2003). In the special case of the (001)–180° wall in α-Fe A, α and ρ are given by

$$A = \frac{3}{2}\lambda_{100}\alpha\sqrt{\frac{c_{11}-c_{12}}{K_1}},$$
$$\alpha = \left(1+\frac{9\lambda_{111}^2 c_{44}}{2K_1}\right)^{-1/2}, \quad \rho = 0 \tag{99}$$

($A = 2.94\cdot 10^{-2}$, $\alpha \approx 1$, $\rho = 0$).

The constricting role of the magnetoelastic energy ϕ_{el} becomes obvious from equation (61) where a term $\propto \sin^2\varphi$ appears, whereas in ϕ_k only terms $\sin^2 2\varphi$ appear that result in a splitting of the 180° wall.

Another important feature of the different types of domain walls in cubic materials is the existence of elastic stresses. In the type I dws there exist long-range stresses within the domains (α-Fe: (100)–90°, (111)–90°. Nickel: (100)–70.53°, (110)–70.53°, (110)–109.47°, (111)–109.47. In the type II dws magnetoelastic stresses exist only within the dws (α-Fe: (001)–180°, (110)–180°, (110)–90°. Nickel: (001)–109.47°, (110)–180°. Kobalt: (001)–180°). As a consequence type I dws have a strong interaction with stress sources, whereas type II dws have a much weaker interaction and therefore are much more mobile than type I dws.

4.1.2 Néel walls

Besides the so-called Bloch walls there exist another type of dws, the so-called Néel walls characterized by the existence of dipolar fields because in this case $\theta = \theta(z)$ and $\varphi =$ const holds. Accordingly there exist volume charges $\rho(z) = -\boldsymbol{M}_s \operatorname{div}\theta(z)$. In bulk materials in general no Néel walls exist. It is the merit of L. Néel (1955a,b), who has shown that in thin films the Bloch walls become instable because of their large dipolar energy due to magnetic surface charges (see Figure 9), which are avoided by the Néel wall type at the expense of volume charges, which, however, lead to a smaller dipolar stray field energy than the surface charges of the Bloch-type wall.

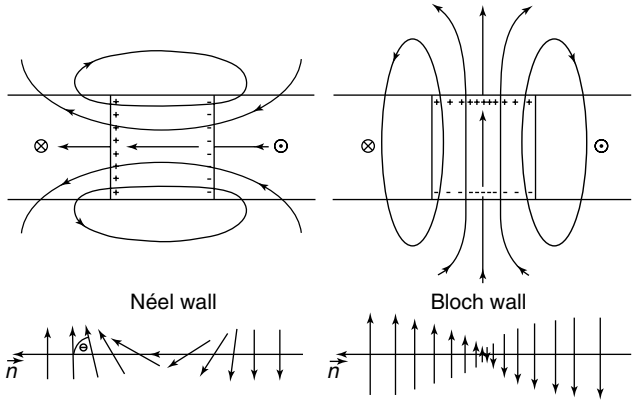

Figure 9. Distribution of magnetization and stray field of Bloch and Néel walls in thin films. (Reproduced with permmission from Cambridge University Press.)

In order to reveal the differences between Bloch and Néel walls in bulk materials we consider a planar 180° Néel wall where the polar angle θ varies from $\theta = \frac{\pi}{2}$ to $\theta = -\frac{\pi}{2}$ (see Figure 9). Solution of the Poisson equation (29) with $\rho = -M_s \operatorname{div}\cos\theta(z)$ gives $H_{z,s} = -M_s\cos\theta(z)$ and $\phi_s = \frac{1}{2}M_s J_s \cos^2\theta(z)$. The differential equation of the Néel wall is obtained from equation (88) for $\varphi = 0$ giving after integration

$$A\left(\frac{\mathrm{d}\theta}{\mathrm{d}z}\right)^2 = \left(\phi_k' + \phi_s'\right) \tag{100}$$

and

$$\operatorname{tg}\left(\frac{\theta}{2}+\frac{\pi}{4}\right) = \exp\left[-z\left(\frac{K_1}{A}+\frac{\mu_0 M_s^2}{2A}\right)^{1/2}\right] \tag{101}$$

For the wall width this gives

$$\delta_{Né} = \frac{\pi}{\left(\frac{K_1}{A}+\frac{\mu_0 M_s^2}{2A}\right)^{1/2}} \tag{102}$$

and the specific wall energy is found to be

$$\gamma_{Né} = 4\ \cdot\sqrt{A\left(K_1+\frac{1}{2}\,\mu_0 M_s^2\right)} \tag{103}$$

From these results it has to be concluded that in bulk materials the Neel wall always has a larger specific wall energy than the Bloch wall, however, its wall width is found to be smaller owing to the constricting role of the dipolar stray field energy.

As mentioned above the situation is different in the case of thin films. Here no rigorous analytical solution of the micromagnetic equation is possible. After the pioneering work by

Néel (1955a,b) numerous approximate and numerical solutions have been published (Dietze and Thomas, 1961; Brown and LaBonte, 1965; Kirchner and Döring, 1968; Holz and Hubert, 1969; Riedel and Seeger, 1971; La Bonte, 1969; Aharoni, 1973, 1975; Aharoni and Jacubovics, 1990). In thin films Néel walls became energetically favored because of their smaller dipolar energy. The distribution of magnetization within a one-dimensional Néel wall depends on the so-called quality parameter $Q = 2K_1/M_s J_s$ and the thickness of the film. The cosine of the rotation angle θ as shown in Figure 10 follows three stages:

1. Kernel region: $\cos\theta(z) \propto \Delta_N^2/(\Delta_N^2 + z^2)$
2. Logarithmic region: $\cos\theta(z) \propto \ln(z)(D)$
3. Dipolar tail: $\cos\theta(z) \propto 1/z^2$.

In stage I the magnetocrystalline energy determines $\cos\theta$ whereas in stage II the local stray field is dominant and in stage III $\cos\theta$ is governed by the long-range dipolar field exerted from stages I and II. According to Aharoni the wall parameter Δ_N and $\gamma_{Né}^{180^\circ}$ approximately are given by

$$\Delta_N = 2\sqrt{\frac{(\sqrt{2}-1)A\ (K_1 - J_s^2 D^2)}{(96\mu_0 K_1)}}$$

$$\gamma_{Né}^{180^\circ} = 2\pi\sqrt{\sqrt{2}-1}\ \sqrt{A\ K_1} + \frac{\pi}{16}\ J_s\ M_s\ D \quad (104)$$

For $D \to 0$ $\gamma_{Né}^{180^\circ}$ approaches the wall energy of the Bloch wall $4 \cdot \sqrt{A\ K_1}$. As analyzed by Hubert (1974) and Hubert and Schäfer (1998) in thin films a large multitude of different types of dws exist, depending on the film thickness, the wall angle and the applied field. The phase diagram shown in Figure 11 shows the ranges where Néel, Bloch, and intermediate wall types are stable in the case of permalloy

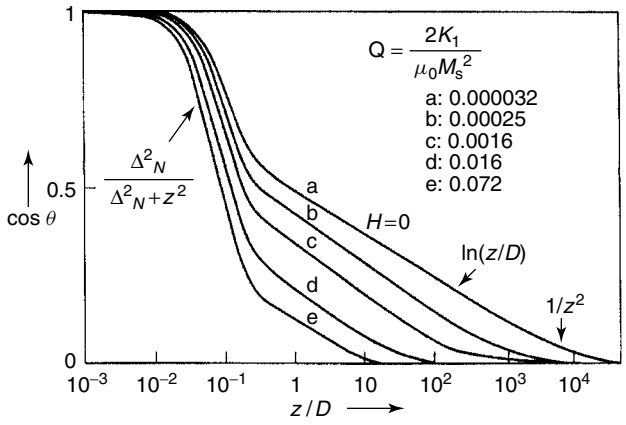

Figure 10. Rotation angle θ of a one-dimensional symmetric Néel wall for different quality parameters $Q = 2K_1/(M_s J_s)$ in reduced length scale $z' = z/D$ (D = film thickness).

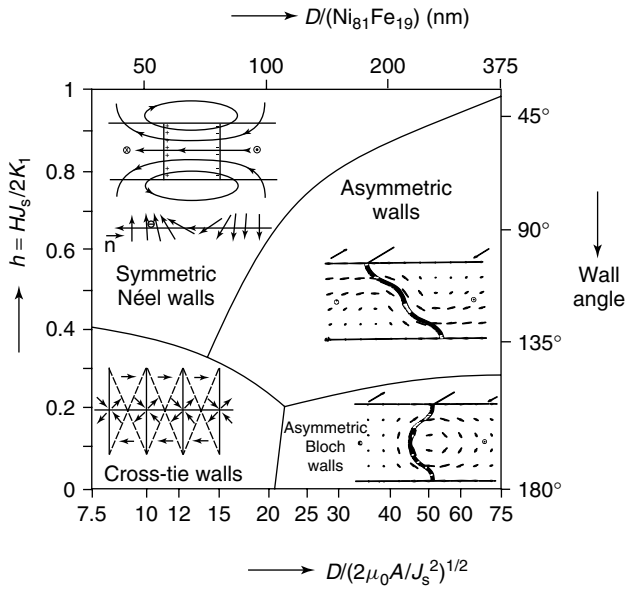

Figure 11. Phase diagram of the main wall types in permalloy with $Q = 0.00025$ according to Hubert and Schäfer (1998).

with $Q = 0.00025$, that is, an extremely soft magnetic material.

4.2 Nucleation fields

Single-domain particles with uniaxial anisotropy in general are characterized by a rectangular hysteresis loop. The critical field under which the spontaneous magnetization reverses spontaneously its direction is called the *nucleation field*, which in case of hard magnetic materials is given by $H_N = 2K_1/(\mu_0 M_s)$. It was W. F. Brown (Brown, 1945, 1963) who pointed out the discrepancy between theory and experiment (Brown's paradox) concerning the nucleation fields, which were found to be a factor of 3 to 4 smaller than predicted. Later on, it has been shown that demagnetization fields and reduced anisotropies at the surface of particles are responsible for these discrepancies (Kronmüller, 1987). Reversal of magnetization in small particles may take place by different types of magnetization modes: homogeneous rotation, curling, buckling, or even more complex nucleation processes at the surfaces. In the following the results for homogeneous rotation and the curling mode are outlined.

4.2.1 Homogeneous rotation in cylindrical particles

The total Gibbs free energy density for homogeneous rotation in the case of a uniaxial anisotropy with the easy axis parallel to the cylinder axis and an applied field under an angle ψ_0

with respect to the negative easy axis is given by

$$\phi'_{\mathrm{t}} = K_1 \sin^2\varphi + K_2 \ \sin^4\varphi + \frac{1}{2}\mu_0 \ M_{\mathrm{s}}^2 \ N_\perp \sin^2\varphi + \frac{1}{2} \ \mu_o \ M_{\mathrm{s}}^2 \ N_\parallel \ \cos^2\varphi + \mu_0 H_{\mathrm{ext}} M_{\mathrm{s}} \cos(\psi_0 + \varphi) \tag{105}$$

where φ denotes the angle between $\boldsymbol{M}_{\mathrm{s}}$ and the positive easy axis. The conditions for a spontaneous rotation of $\boldsymbol{M}_{\mathrm{s}}$ into the opposite direction are a vanishing derivative $\mathrm{d}\phi_{\mathrm{t}}/\mathrm{d}\varphi = 0$ and a second derivative $\mathrm{d}^2\phi_{\mathrm{t}}/\mathrm{d}\varphi^2 \leq 0$. These conditions write

$$\frac{\mathrm{d}\phi'_{\mathrm{t}}}{\mathrm{d}\varphi} = (K_1 + K_{\mathrm{d}}) \sin \ 2\varphi + 2K_2 \sin^2\varphi \sin 2\varphi - \mu_0 \mathrm{M}_{\mathrm{s}} H_{\mathrm{ext}} \ \sin(\psi_0 + \varphi) = 0 \tag{106}$$

and

$$\frac{\mathrm{d}^2\phi'_{\mathrm{t}}}{\mathrm{d}\varphi^2} = 2 \ (K_1 + K_{\mathrm{d}}) \cos \ 2 \ \varphi + 4 \ K_2 \left(3 \sin^2\varphi \cos^2\varphi - \sin^4 \ \varphi\right) - \mu_0 M_{\mathrm{s}} H_{\mathrm{ext}} \cos\left(\varphi + \psi_0\right) \leq 0 \tag{107}$$

Here the magnetostatic dipolar anisotropy constant

$$K_{\mathrm{d}} = \frac{1}{2} \ \mu_0 M_{\mathrm{s}}^2 \ \left(N_\perp - N_\parallel\right) \tag{108}$$

has been introduced, where $N_\perp$ and $N_\parallel$ denote the demagnetization factors of the cylinder perpendicular and parallel to the cylinder axis. The nucleation field for $\psi_0 = 0$ follows from equation (106) by linearization

$$\left[2 \ (K_1 + K_{\mathrm{d}}) - \mu_0 \ M_{\mathrm{s}} H_{\mathrm{ext}}\right] \ \varphi = 0 \tag{109}$$

Taking care of the stability condition (107) the solutions of (107) are $\varphi = 0$ for $H_{\mathrm{ext}} \leq H_{\mathrm{N}}$ and $\varphi \geq 0$ for

$$H_{\mathrm{ext}} = H_{\mathrm{N}} = \frac{2 \ K_1}{\mu_0 \ M_{\mathrm{s}}} + (N_\perp - N_\parallel) \ M_{\mathrm{s}} \tag{110}$$

Taking care of the stability relation (107), it turns out that for $K_1 + K_{\mathrm{d}} \geq 4K_2$ the spontaneous magnetization rotates spontaneously into the opposite direction. However, for $K_1 + K_{\mathrm{d}} \leq 4K_2$ the condition $\mathrm{d}^2\phi_{\mathrm{t}}/\mathrm{d}\varphi^2 \geq 0$ holds and therefore at $H_{\mathrm{ext}} = H_{\mathrm{N}}$, $\boldsymbol{M}_{\mathrm{s}}$ starts to rotate reversibly out of the c axis. The spontaneous reversal of $\boldsymbol{M}_{\mathrm{s}}$ in this case occurs at (Herzer, Fernengel and Adler 1986; Kronmüller, 1985, 1991) a second nucleation field

$$H'_{\mathrm{N}} = \frac{4}{3 \cdot \sqrt{6}} \frac{K_2}{\mu_0 \ M_{\mathrm{s}}} \ \left[1 + \frac{K_1 + K_{\mathrm{d}}}{K_2}\right]^{3/2} \tag{111}$$

According to equation (110) the nucleation field is independent of the particle and the second anisotropy constant K_2 and only depends on the ratio of the ellipsoidal particle axes by $N_\perp$ and $N_\parallel$. From equation (110) we obtain a lower bound of H_{N} for a plate with perpendicular easy axis ($N_\perp = 0$, $N_\parallel = 1$)

$$H_{\mathrm{N}}^{\mathrm{min}} = \frac{2 \ K_1}{\mu_0 \ M_s} - M_{\mathrm{s}} \tag{112}$$

and an upper bound for an in-plane easy axis

$$H_{\mathrm{N}}^{\mathrm{max}} = \frac{2 \ K_1}{\mu_0 M_{\mathrm{s}}} + M_{\mathrm{s}} \tag{113}$$

An intermediate nucleation field is obtained for a sphere ($N_\parallel = N_\perp = 1/3$)

$$H_{\mathrm{N}}^{\mathrm{sph}} = 2K_1/\mu_0 M_{\mathrm{s}} \tag{114}$$

For a cylindrical particle ($N_\perp = \frac{1}{2}$; $N_\parallel = 0$) equation (110) gives

$$H_{\mathrm{N}}^{\mathrm{cyl}} = \frac{2 \ K_1}{\mu_0 \ M_{\mathrm{s}}} \ \pm \frac{1}{2} \ M_{\mathrm{s}} \tag{115}$$

where the (+) and (−) signs hold for an easy axis parallel or perpendicular to the cylinder axis.

4.2.2 The Stoner–Wohlfarth model

For oblique applied magnetic field the basic equation (106) and (107) have been solved by Stoner and Wohlfarth for vanishing higher order anisotropy constants. An extension of their results including the second anisotropy constant has been given by Kronmüller, Durst and Martinek (1987), for K_1, $K_2 \geq 0$ leading to

$$H_{\mathrm{N}}(\psi_0) = \frac{2(K_1 + K_{\mathrm{d}})}{\mu_0 M_{\mathrm{s}}} \frac{1}{\left[(\cos\psi_0)^{2/3} + (\sin\psi_0)^{2/3}\right]^{3/2}} \times \left\{1 + \frac{2 \ K_2}{K_1 + K_{\mathrm{d}}} \frac{(\sin\psi_0)^{2/3}}{\left[(\cos \ \psi_0)^{2/3} + (\sin\psi_0)^{2/3}\right]}\right\} \tag{116}$$

The angle φ_{N} at which a spontaneous nucleation takes place is given by

$$\varphi_{\mathrm{N}} = \mathrm{arctg} \ \sqrt[3]{\mathrm{tg}\psi_0} + \frac{2}{3} \ \frac{K_2}{K_1 + K_{\mathrm{d}}} \tag{117}$$

Figure 12 shows the angular dependence of $H_{\mathrm{N}}(\psi_0)$ for the material constants of $Nd_2Fe_{14}B$ as determined by Hock and Kronmüller (1987). It should be noted that the asymmetry of

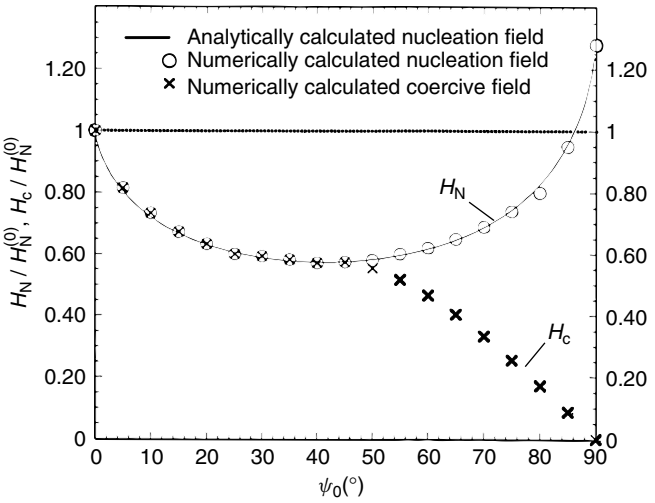

Figure 12. Angular dependence of the nucleation field and the coercive field of $Nd_2Fe_{14}B$ according to equation (116).

the $H_N(\psi_0)$ curve is due to the K_2-term in equation (116). Alternative to Figure 12 the angular dependence of H_N over 2π may be represented in the so-called Stoner–Wohlfarth asteroid where $H_N(\psi_0)$ is plotted as a function of the field components parallel or perpendicular to the c axis. Experimental results of this kind are shown in the article by Kläui and Vaz.

4.2.3 Inhomogeneous rotation by curling

Whereas in the homogeneous rotation mode the reversal of M_s is governed by crystal anisotropy and surface charges the curling mode is governed by exchange energy. Volume charges $\mathrm{div}\boldsymbol{M}_s$ and surface charges $\boldsymbol{n} \cdot \boldsymbol{M}_s$ vanish with the exception of charges at the front sides of a finite cylinder.

In cylindrical polar coordinates the linearized micromagnetic equations give

$$2A \left\{ \frac{\mathrm{d}^2\varphi(r)}{\mathrm{d}r^2} + \frac{1}{r} \frac{\partial\varphi}{\partial r} - \frac{1}{r^2} \varphi(r) \right\} - (2K_1 - \mu_0 M_s H_{ext} - N_\parallel \mu_0 M_s^2)\, \varphi(r) = 0 \quad (118)$$

The solution of equation (118) corresponds to the Bessel function of first order

$$\varphi(r) = \varphi_0 J_1 \left[r \cdot \left(\frac{\mu_0 M_s H_{ext} - N_\parallel \mu_0 M_s^2 - 2K_1}{2A} \right)^{1/2} \right] \quad (119)$$

The nucleation field follows from the boundary condition $\mathrm{d}\varphi/\mathrm{d}r|_{r=R=0}$, which leads to

$$J_1'(R) = 0 \quad (120)$$

The smallest zero of $J_1'(\mathrm{R})$ gives the largest nucleation field (Aharoni and Shtrikman, 1958; Aharoni, 1997)

$$H_N = \frac{2K_1}{\mu_0 M_s} - N_\parallel M_s + \frac{2A}{\mu_0 M_s} \left(\frac{1.84}{R} \right)^2 \quad (121)$$

Here the last term is due to the exchange energy. This term exceeds the nucleation field of the homogeneous rotation at a radius of ($N_\perp = 1/2$)

$$R_{crit}^{nuc} = 3.68 \sqrt{\frac{A}{\mu_0 M_s^2}} = 2.60 l_s \quad (122)$$

($l_s = \sqrt{2A/\mu_0 M_s^2}$, see equation (133)). As a consequence the nucleation fields at small radii are determined by homogeneous rotation and at larger radii by the curling mode. Typical values of R_{crit}^{nuc} are 10–20 nm in the case of soft and hard magnetic materials (like permalloy or $Nd_2Fe_{14}B$). At very large radii, the nucleation field approaches the value of the crystal field $2K_1/(\mu_0 M_s)$.

4.2.4 Critical diameters of small particles

Besides the critical diameter R_{crit}^{nuc} for the transition between nucleation modes there exist two further critical diameters related to superparamagnetism and to multidomain formation.

For the application of small particles as permanent magnets or magnetic recording their thermal stability for time intervals of decades of years is an absolute prerequisite. At a critical diameter D_{crit}^{th} the nucleation fields as given by equations (110) and (121) no longer govern the reversal of magnetization. Reversal of magnetization is initiated by thermal fluctuation. The thermal energy kT is large enough to overcome the effective anisotropy energy $K_{eff} = K_1 + \frac{1}{2}(N_\perp - N_\parallel)\, \mu_0 M_s^2$. The average lifetime of a particle of volume V is given by the Arrhenius law (Néel, 1949a; 1949b, 1950)

$$\tau = \tau_0 \exp\left[-K_{eff}\, V/(kT) \right] \quad (123)$$

where the pre-exponential factor τ_0 is determined approximately by $\tau_0^{-1} = (2\pi)^{-1} \gamma H_{eff}$ (γ gyromagnetic ratio, $H_{eff} = 2K_{eff}/(\mu_0 M_s)$. The lifetime τ depends sensitively on the particle volume as demonstrated by Figure 13 for a material with $K_{eff} = 10^5\,\mathrm{J\,m^{-3}}$, $\tau_0 = 10^{-8}\,\mathrm{s}$, $T = 300\,\mathrm{K}$ and a spherical particle of $V = \frac{\pi}{6} D^3$. For a diameter of 11.5 nm the lifetime is $\tau = 0.1\,\mathrm{s}$, whereas for $D = 14.5\,\mathrm{nm}$ a lifetime of $10^8\,\mathrm{s}$ is obtained. Accordingly there exists a very narrow range of diameters where the transition from a stable configuration to an unstable configuration takes place. For the

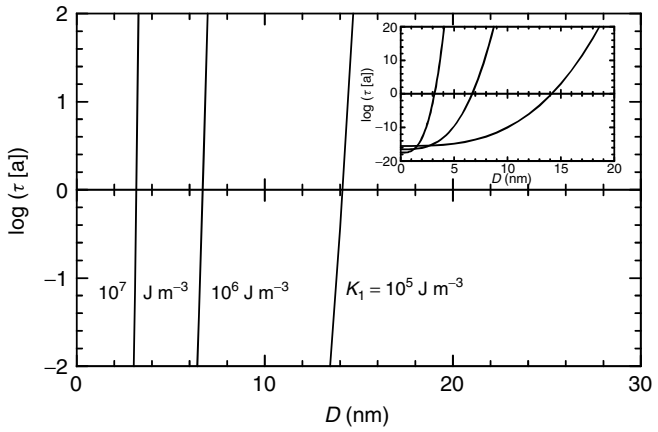

Figure 13. Lifetime of magnetization of a spherical particle of diameter, D, for $K_{\text{eff}} = 10^5$ J/m^{-3}, $\tau_0 = 10^{-8}$s, $T = 300$ K.

material parameters of Co and lifetimes of 0.1 and 10^{10} s the critical diameters are 3.7 and 4.8 nm.

A further critical diameter is determined by the formation of domains due to the increasing magnetostatic stray field energy. For the transition from a single-domain state to a two-domain state the critical diameter for a spherical particle is given by

$$D_{\text{crit}}^{\text{do}} = \frac{9\gamma_{\text{B}}}{(1-\alpha)\mu_0 M_{\text{s}}^2} = \frac{36\sqrt{AK_1}}{(1-\alpha)\mu_0 M_{\text{s}}^2} \qquad (124)$$

where α denotes the factor by which the stray field energy of the homogeneously magnetized single-domain particle is reduced by the formation of a two-domain state. For a sphere, this reduction parameter is found to be $\alpha = 0.4725$ (Goll, Berkowitz and Bertram, 2004), which is very near to the approximate value of $\alpha = 0.5$ as given by Kittel (1949). Table 2 gives a summary of critical diameters $D_{\text{crit}}^{\text{do}}$. Figure 14 shows the dependence of $D_{\text{crit}}^{\text{do}}$ as

Table 2. Critical single-domain diameters of spherical particles according to equation (124). Values for Fe_3O_4, CrO_2 and MnBi were taken from Kronmüller (1991).

Magnet	$\mu_0 M_{\text{s}}^{-2}$ (MJ m^{-3})	γ_{B} (mJ m^{-2})	$D_{\text{crit}}^{\text{do}}$ (nm)
α-Fe	3.82	2.1	9.7
Co	2.54	7.84	55.5
Ni	0.31	0.39	22.6
Fe_3O_4	0.29	2.0	12.4
CrO_2	0.20	2.0	180
MnBi	0.45	12	480
$Nd_2Fe_{14}B$	2.06	24	210
$SmCo_5$	0.88	57	1170
Sm_2O_{17}	1.33	31	420
FePt	1.44	32	340
$BaFe_{12}O_{19}$	0.183	6.3	62

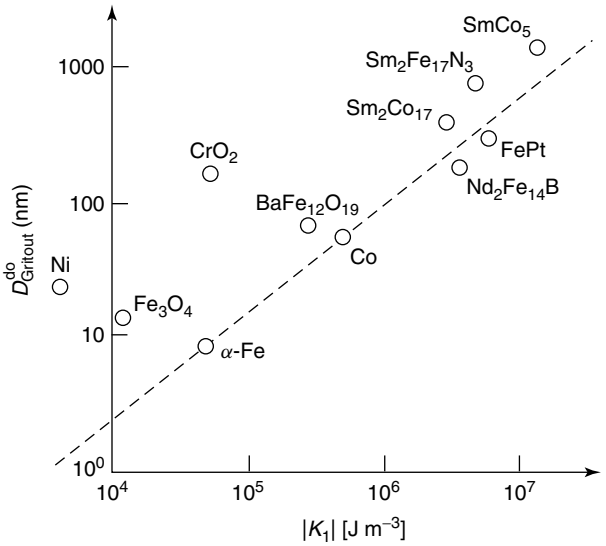

Figure 14. Critical diameters according to equation (124) as a function of K_1.

a function of the anisotropy constant. The low remanence materials do not fit into the empirical law $D_{\text{crit}}^{\text{do}} = (K_1/2.5 \times 10^3\,\text{J m}^{-3})^{0.77}$ (nm). Here it is noteworthy that small critical radii are obtained for α-Fe with $D_{\text{crit}}^{\text{do}} \approx 10$ nm and largest diameter for Co_5Sm with $D_{\text{crit}}^{\text{do}} = 1.17\,\mu$m. Single-domain configurations also have been investigated by the methods of computational micromagnetism. Hertel and Kronmüller (2002) have shown that in cube particles with a quality factor $2K_1/(\mu_0 M_{\text{s}}^2) = 0.1$ (permalloy) the transition from a so-called twisted flower state to a vortex state takes place at an edge length of $8.56\sqrt{2A/(\mu_0 M_{\text{s}}^2)}$ Similarly, Goll, Schütz and Kronmüller (2003) have shown that a square of edge length 1 µm transforms from a four domain Landau structure into a single domain structure at a thickness of 1.5 nm in the case of permalloy and at 2.5 nm and 4 nm in the case of α-Fe and Co, respectively. Hertel (2002) performed similar calculations for rectangular platelets of permalloy of aspect ratio 2:1 and determined the phase diagram of C-state, Landau state, and diamond configurations. It should be noted that these numerical calculations support the analytical calculations of Aharoni (1996) who determined upper and lower bounds for the single domain diameter.

5 LINEARIZED MICROMAGNETIC EQUATIONS

5.1 Brown's equations and the exchange lengths

In cases where the spontaneous magnetization deviates only slightly from a preferred direction the micromagnetic

equations may be linearized in γ_i. This condition exists at large applied fields H_{ext} and large magnetocrystalline energies. Linearization leads to differential equations of second order with constant coefficients. In the following we choose the y axis as the preferred direction either corresponding to the direction of the applied field $H_{\text{ext},2}$ or to an easy direction. Within this coordinate system denoted as Brown's coordinate system the direction cosines follow the conditions

$$\begin{aligned} &\gamma_{1,3} \ll 1; \gamma_2 \sim 1 \\ &\gamma_2 = \sqrt{1-\gamma_1^2-\gamma_2^2} \sim 1 - \frac{1}{2}(\gamma_1^2+\gamma_2^2) \end{aligned} \quad (125)$$

With the condition $\gamma_2 \simeq 1$ the constraint (71) is fulfilled leading to the equilibrium condition

$$\begin{aligned} H_{\text{eff},1} &- \gamma_1 \left(\frac{\partial \phi'_{\text{k}}}{\partial \gamma_2} + \frac{\partial \phi'_{\text{el}}}{\partial \gamma_2} + H_{\text{ext},2} \right) = 0 \\ H_{\text{eff},3} &- \gamma_3 \left(\frac{\partial \phi'_{\text{k}}}{\partial \gamma_2} + \frac{\partial \phi'_{\text{el}}}{\partial \gamma_2} + H_{\text{ext},2} \right) = 0 \end{aligned} \quad (126)$$

To obtain more explicit expressions we develop ϕ'_k and ϕ'_{el} into Taylor series with respect to Brown's coordinates and retain only terms up to the second order in γ_i. With

$$\begin{aligned} \phi'_k(\gamma_i) &= g_0^{\text{k}} + g_i^{\text{k}}\gamma_i + \frac{1}{2} g_{ij}^{\text{k}} \gamma_i \gamma_j \\ &\quad i, j \neq 2 \\ \phi'_{\text{el}}(\gamma_i &= g_0^{\text{el}} + g_i^{\text{el}}\gamma_i + \frac{1}{2}\, g_{ij}^{\text{el}}\, \gamma_i\, \gamma_j \end{aligned} \quad (127)$$

we obtain from equation (127) the linearized micromagnetic equations

$$\begin{aligned} &2A\Delta\gamma_i - J_{\text{s}}(H_{\text{ext}} + H_{\text{s},2})\gamma_i - (g_{ii}^{\text{k}} + g_{ii}^{\text{el}})\gamma_i \\ &-(g_{ij}^{\text{k}} + g_{ij}^{\text{el}})\, \gamma_j + J_{\text{s}} H_{\text{s},i} = g_i^{\text{k}} + g_i^{\text{el}};\ i, j = 1, 3 \end{aligned} \quad (128)$$

and the surface condition

$$\nabla_n \gamma_i = 0, \quad i = 1, 3 \quad (129)$$

Within the framework of linearized equations Poisson' s equation Is written as

$$\Delta U = M_{\text{s}} \left(\frac{\text{d}\gamma_1}{\text{d}x} + \frac{\text{d}\gamma_3}{\text{dz}} \right) \quad (130)$$

A solution of these linearized second-order differential equations is easily obtained by introducing Fourier transforms. With the Fourier transform

$$\left.\begin{aligned} \tilde{\gamma}_i(\boldsymbol{k}) &= \frac{1}{(2\pi)^{3/2}} \int \gamma_i(r) e^{-i\boldsymbol{k}\cdot\boldsymbol{r}}\ \text{d}^3\boldsymbol{r} \\ \gamma_i(\boldsymbol{r}) &= \frac{1}{(2\pi)^{3/2}} \int \tilde{\gamma}_i(k) e^{i\boldsymbol{k}\cdot\boldsymbol{r}}\ \text{d}\boldsymbol{k} \end{aligned}\right\} \quad (131)$$

and the corresponding ones for $U(\boldsymbol{r})$ and $g_i^{\text{k,el}}(\boldsymbol{r})$ the solutions of equations (128) and (130) write (neglecting the terms in g_{ii} and g_{ij}):

$$\left.\begin{aligned} \tilde{\gamma}_i(\boldsymbol{k}) &= -\tfrac{1}{2A}\tfrac{\tilde{g}_i}{k^2+\kappa_{\text{H}}^2} + \tfrac{\kappa_{\text{s}}^2}{2A} \times \tfrac{k_i}{k^2+\kappa_{\text{H}}^2} \times \tfrac{\tilde{g}_x k_x + \tilde{g}_z k_z}{k^4 + (\kappa_{\text{H}}^2+\kappa_{\text{s}}^2)k^2 - \kappa_{\text{s}}^2 k_y^2} \\ \tilde{U}(\boldsymbol{k}) &= -\tfrac{M_{\text{s}}}{k^2}(ik_x\tilde{\gamma}_1 + ik_z\tilde{\gamma}_3) \\ \tilde{H}_{\text{s}}(\boldsymbol{k}) &= -i\boldsymbol{k} \times \tilde{U}(\boldsymbol{k})/(2\pi)^{3/2} \end{aligned}\right\} \quad (132)$$

In the case of long-range RKKY exchange interactions the term Ak^2 has to be replaced by $(J(0) - J(\boldsymbol{k}))M_{\text{s}}^2/(g\mu_{\text{B}})^2$. Equations (132) contain the so-called exchange lengths of the external and of the dipolar fields:

$$l_{\text{H}} = \kappa_{\text{H}}^{-1} = \sqrt{\frac{2A}{J_{\text{s}} H_{\text{ext}}}} \quad l_{\text{s}} = \kappa^{-1} = \sqrt{\frac{2A}{J_{\text{s}} M_{\text{s}}}} \quad (133)$$

If we take into account the magnetocrystalline and the magnetostrictive energy terms in equation (128) two further exchange lengths may be derived. The so-called domain wall parameter and the stress exchange length

$$l_{\text{k}} = \kappa_{\text{k}}^{-1} = \sqrt{\frac{A}{K_1}}, \quad l_\sigma = \kappa_\sigma^{-1} = \sqrt{\frac{2A}{3\lambda_{100}\sigma_{ii}}} \quad (134)$$

The physical meaning of the exchange lengths becomes obvious if we consider δ-function like planar perturbations of the type $g_i \cdot \delta(x)$ and taking into account the torque exerted by only one of the magnetic energies. In the case of a planar perturbation in the (x, z)-plane and a preferred easy axis in y-direction the solution of equation (128) is given by

$$\gamma_i(y) = \gamma_0\, e^{-|y|/l_i}\ (i = 1, 3) \quad (135)$$

where for l_i the dominant exchange length has to be inserted. Values for exchange lengths at room temperature are given in Table 3 together with the wall widths and energies using the characteristic values for A, $J_{\text{s}}, M_{\text{s}}, K_i, \lambda_{ijk}, \delta_{\text{B}}, T_{\text{C}}$ of Table 1. According to equation (135) a local perturbation of the spin orientation leads to an extended deviation of the spin system governed by the exchange lengths as shown in Figure 15. There exist rather large variations of the exchange lengths l_{k} because the K_1-values may vary over 6 orders of magnitude, whereas l_{s} varies only between

Table 3. Exchange lengths, wall widths (in nm) and specific wall energy of transition metals, intermetallic compounds, and oxides at room temperature (l_H determined for $H = 1000\,Oe = 10^6/4\pi$ [A/m], l_σ determined for $\sigma = 10$ MN/m^2).

Magnet	l_k	l_s	l_H	l_σ	δ_B	$\gamma_B\,(10^{-2}\,J\,m^{-2})$
α-Fe	21	3.3	15.6	80	220	0.21(100) − 180°
Co	8.3	4.9	20.4	56	22.3	1.49(0001) − 180°
Ni	42	8.7	16.1	31		0.035 (110); (112)
Ni_3Fe	240	3.7	12.7	51		0.006
$Nd_2Fe_{14}B$	1.4	2.8	11.2		3.82	2.24
$Pr_2Fe_{14}B$	1.4	3.1	14.0		4.4	3.30
$SmCo_5$	0.84	5.3	17.1		2.64	5.71
Sm_2Co_{17}	1.83	4.6	16.6		5.74	3.07
$Sm_2Fe_{17}N_3$	1.18	4.4	14.0		3.36	4.06
$BaFe_{12}O_{19}$	4.45	8.3	18.2		13.94	0.57
PtFe	1.26	3.5	13.3		3.95	3.24

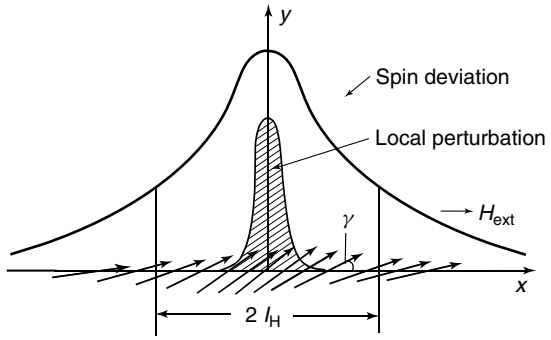

Figure 15. Spin distribution around a local planar perturbation of the orientation of the local magnetization. The extension of the perturbation is determined by the leading exchange length, here l_H.

3 and 10 nm because the interesting magnetic materials have similar polarizations from 0.5 to 2 T and also similar exchange constants between 10 and 30 pJ m^{-1}. In general, that exchange length dominates the spin distribution which leads to the lowest energy state, that is, either the spin system avoids excitation of the high energy modes and if this is not possible owing to boundary conditions the spin inhomogeneities become extended or constricted.

5.2 Applications of Brown's equations

5.2.1 Nucleation processes

The determination of nucleation fields of single-domain configurations has been one of the big successes of the linearized micromagnetic equations. Brown (1945) raised the problem that the coercive fields of real materials in general is much smaller than the nucleation fields as discussed in Section 4.2. There are many experimental efforts to solve this so-called Brown's paradox. Lubersky and Morelock (1964) showed that by the use of Fe-whiskers with diameters larger than 10 nm the nucleation field of the curling mode (see equation (121)) may be approached. Also for Ni-wires the curling modes have been realized by Lederman *et al.* (1995). Measurements of the Stoner–Wohlfarth asteroids have been performed for two-fold anisotropy as Co (Bonet *et al.*, 1999) and for four-fold anisotropy by Thirion *et al.* (2006). Details of these experiments are discussed in **Magnetization Configurations and Reversal in Small Magnetic Elements, Volume 2**.

A further problem treated by Brown's equations is the nucleation in inhomogeneous materials where there exist a local perturbation of the crystal anisotropy constant. The nucleation fields for planar Gaussian perturbations $K_1(z) = K_s + \Delta K(1 - e^{-z^2/r_0^2})$ and hyperbolic perturbations, $K_1(z) = K_1(\infty) - \Delta K/\mathrm{ch}^2(z/r_0)$. ($K_s$ = anisotropy at the center of the planar perturbation, $K_1(\infty) = K_s + \Delta K$, anisotropy constant in the unperturbed matrix) have been determined (Kronmüller, 1987; Kronmüller and Fähnle, 2003) leading to a modified nucleation field

$$H_N = \frac{2K_1}{\mu_0 M_s}\,\alpha_k - N_{eff}\,M_s \tag{136}$$

where the microstructural parameters α_k and N_{eff} depend on the properties of the perturbation, that is, r_0 and ΔK, as well as on the geometry of the perturbation. In the special case where $\Delta K = K_1(\infty)$, the α-parameter for inhomogeneities of average thickness $r_0 > \delta_B$ corresponds to

$$\alpha_k = \frac{\delta_B}{\pi r_0} \tag{137}$$

Experimental values for α_k and N_{eff} are discussed in details by Kronmüller and Fähnle (2003) and in **Micromagnetism–Microstructure Relations and the Hysteresis Loop, Volume 2**. Of course there exist further deteriorating effects as misaligned particles or exchange coupled particles the effects of which are taken into account by microstructural parameters α_ψ and α_{ex} (see Kronmüller and Fähnle, 2003 and **Micromagnetism–Microstructure Relations and the Hysteresis Loop, Volume 2**).

5.2.2 Law of approach to ferromagnetic saturation (LAFS)

Modern theory of micromagnetism has been born by Brown's attempt to explain the so far unexplained $1/H$ term in the law of approach to ferromagnetic saturation (LAFS) (Brown, 1940, 1941). The conventional LAFS $J(H) = J_s - a_1/H - a_2/H^2$ later on has been found to contain also broken

exponents (Kronmüller, 1959; 1967)

$$J(H) = J_s - \frac{a_{1/2}}{H^{1/2}} = \frac{a_1}{H} - \frac{a_{3/2}}{H^{3/2}} - \frac{a_2}{H^2} + \frac{a_3}{H^3} + \alpha T\sqrt{H} + \chi_p \mu_0 H \tag{138}$$

The existence of the field dependent terms in equation (138) makes it difficult to determine the spontaneous polarization J_s for $H = 0$ and any temperature. Furthermore it has to be noted that the coefficients $a_{n/2}$ result from intrinsic and extrinsic properties. In particular, the term $\propto \sqrt{H}$ results from the field dependence of the spectrum of spin-wave excitations (Holstein and Primakoff, 1940; Kronmüller and Fähnle, 2003). The linear term is due to the Pauli paramagnetism, which is described in ferromagnetic materials by an enhanced parasusceptibility χ_p. Whereas these latter two terms have to be determined on the basis of quantum mechanics the $a_{n/2}$ terms are determined by the concepts of micromagnetism. Which one of the $a_{n/2}$ terms dominates depends on the material parameters and the microstructure of the material.

1. *Intrinsic effects*:
   (a) *Uniaxial and cubic crystals*: In uniaxial and cubic crystals the LAFS is described by $1/H^2$ and $1/H^3$ terms if the magnetic field is misaligned with respect to one of the main crystal axes: $\langle 1000\rangle$ in hexagonal crystals and $\langle 100\rangle$, $\langle 110\rangle$ and $\langle 111\rangle$ in cubic crystals. In the case of uniaxial crystals for large fields $H > 2K_1/J_s$, the LAFS is

$$J(H) = J_s\left(1 - \left(\frac{K_1 \sin 2\psi_0}{2K_1 \cos 2\psi_0 + HJ_s}\right)^2\right) \tag{139}$$

where ψ_0 corresponds to the angle between H and the [0001] axis. By averaging over all possible easy directions of the upper half sphere and taking into account the second anisotropy constant the LAFS is (Néel, Pauthenet, Rimet and Giron, 1960)

$$J(H) = J_s\left(1 - \left[\frac{4K_1^2}{15J_s^2} - \frac{64}{105}\frac{K_1K_2}{J_s^2} - \frac{128}{315}\frac{K_2^2}{J_s^2}\right]\frac{1}{H^2}\right) \tag{140}$$

The LAFS of cubic crystals has been treated by Akulov (1928–1931), Gans (1932), and Becker and Döring (1939). The latter authors have determined the full angular dependence of the LAFS. In the case of a polycrystal the averaging over all possible orientations of crystal grains gives

$$J(H) = J_s\left(1 - \frac{8}{105}\frac{K_1}{J_s^2}\frac{1}{H^2} - \frac{192}{5005}\frac{K_1^3}{J_s^3}\frac{1}{H^3}\right) \tag{141}$$

According to equations (140 and 141) from measurements of the high-field polarization the anisotropy constant K_1 can be determined.

   (b) *Amorphous alloys*: In amorphous alloys the intrinsic material parameters are fluctuating quantities as

$$\left.\begin{aligned} J_2(\boldsymbol{r}) &= \langle J_2(\boldsymbol{r})\rangle + \delta J_2(\boldsymbol{r}) \\ g_{ij}^k(r) &= \langle g_{ij}^k(\boldsymbol{r})\rangle + \delta g_{ij}^K(\boldsymbol{r}) \end{aligned}\right\} \tag{142}$$

where $\langle J_2(\boldsymbol{r})\rangle = J_s$, $\langle g_{ij}^k\rangle = 0$, $\langle \delta J_2(\boldsymbol{r})\rangle = 0$.
The effect of these fluctuations has been treated by Kronmüller and Ulner (1977) and by Fähnle and Kronmüller (1978) under the assumption of uncorrelated fluctuations of the material properties. Fluctuations in the polarization result in volume charges, $\mathrm{div}\delta\boldsymbol{J}$ and the exerted dipolar fields produce further inhomogeneities of the orientation of the local magnetization. The micromagnetic equation for the case of magnetostatic fluctuations and a large applied field, H, parallel to the γ-direction, are given by ($i = 1, 3$):

$$\begin{aligned} 2A\ \Delta\gamma_i + \langle J_2(\boldsymbol{r})\rangle\ H_{s,i}(\boldsymbol{r}) - \langle J_2(\boldsymbol{r})\rangle H\ \gamma_i &= 0 \\ \Delta U = \frac{1}{\mu_0}\,\mathrm{div}\ \boldsymbol{J}_2(\boldsymbol{r}) = \frac{1}{\mu_0}\frac{\partial}{\partial y}\ (\delta \boldsymbol{J}_2(\boldsymbol{r})) & \end{aligned} \tag{143}$$

For a spatially random distribution of magnetizations the fluctuations $\delta\boldsymbol{J}_2(\boldsymbol{r})$ obey the following relation

$$\langle \delta \boldsymbol{J}_2(\boldsymbol{r})\ \delta \boldsymbol{J}_2(r')\rangle = \Omega_0 J_s(\boldsymbol{r}) \cdot \delta\left(\boldsymbol{r} - \boldsymbol{r}'\right) \tag{144}$$

where Ω_0 denotes the atomic volume and $\langle \boldsymbol{J}\rangle = \boldsymbol{J}_s$ holds. According to Kronmüller and Ulner (1977) the solutions for γ_i lead to the following LAFS:

$$\begin{aligned} J(H) = J_s 1 - \Omega_0 \frac{(2A/J_s)^{1/2}}{120\pi}\kappa_s^4 \\ \times\left(\frac{1}{H^{1/2}} - \frac{1}{2}\frac{M_s}{H^{3/2}}\right) \\ \text{for } \kappa_H^2 > \kappa_s^2, \text{ and} \\ J(H) = J_s\left(1 - 14 \cdot 10^3\, \Omega_0 \kappa_s^3\right) \end{aligned} \tag{145}$$

for $\kappa_H^2 \geq \kappa_s^2$. The latter equation shows that the dipolar fluctuations in the ground state at $H = 0$

reduce the spontaneous polarization by 10–20%. Taking into account magnetocrystalline fluctuations

$$\langle g_{i2}^{\mathrm{k}}\ (\boldsymbol{r}) \cdot g_{i2}^{\mathrm{k}}\ (\boldsymbol{r}')\rangle = \langle(\delta\ g_{i2}^{\mathrm{k}}(\boldsymbol{r}))^2\rangle\delta(\boldsymbol{r}-\boldsymbol{r}') + \langle g_{i2}(\boldsymbol{r})\rangle^2 \quad (146)$$

the result for the LAFS is

$$J(H) = J_{\mathrm{s}} - \frac{a_{1/2}}{H^{1/2}} - \frac{a_2}{H^2} \quad (147)$$

where the $a_{1/2}$ term results from short-range fluctuations and the $1/H^2$ term takes care of a long-range anisotropy $k_{i2} \neq 0$.

2. *Extrinsic effects*:

(a) *Elastic stress sources in crystalline materials*: Originally Brown (1940, 1941) developed the continuum theory of micromagnetism in order to explain the $1/H$ terms in the LAFS. The basis for this type of calculations was the linearized micromagnetic equation ($i = 1, 3$)

$$2A\Delta\gamma_i - J_{\mathrm{s}}H_{\mathrm{ext}}\gamma_i = g_i^{\mathrm{el}}(\boldsymbol{r}),$$
$$\text{where } g_i^{\mathrm{el}} = \frac{\partial\phi'_{\mathrm{el}}}{\partial\gamma_i}\Big|_{\gamma_{i,1,3}\ll 1}^{\gamma_2=1} \propto \sigma_{\mathrm{kl}} \quad (148)$$

Equation (148) has been applied to all types of stress sources leading to characteristic field dependences of the LAFS:

– Atomic spherical defects and dislocation loops for small radii $\kappa_{\mathrm{H}}r_0 < 1$
These types of defects corresponds to elastic dipoles:

$$\sigma \propto \frac{1}{r^3} \quad J(H) = J_{\mathrm{s}} - \frac{a_{1/2}}{H^{1/2}} \quad \text{for } \kappa_{\mathrm{H}}r_0 < 1$$
$$J(H) = \boldsymbol{J}_{\mathrm{s}} - \frac{a_1}{H} - \frac{a_2}{H^2} \quad \text{for } \kappa_{\mathrm{H}}r_0 \gg 0 \quad (149)$$

– Straight dislocation lines:

$$\sigma \propto \frac{1}{r}; \quad J(H) = J_{\mathrm{s}} - \frac{a_2}{H^2} \quad (150)$$

– Straight dislocation dipoles:

$$\sigma \propto \frac{1}{r^2}: \ J(H) = J_{\mathrm{s}} - \frac{a_1}{H} \quad (151)$$

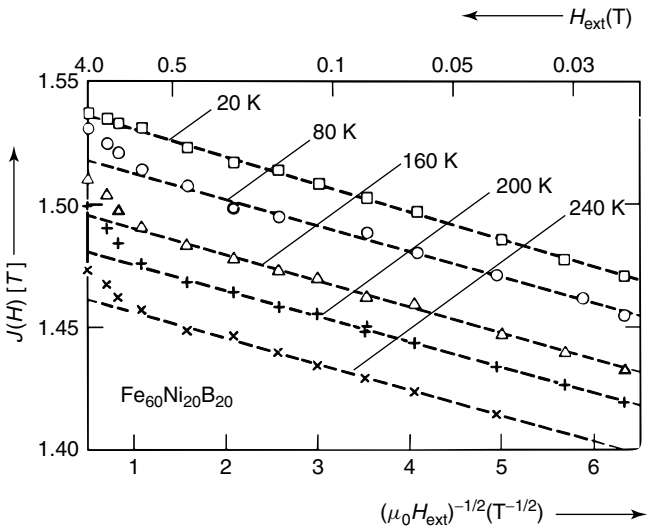

Figure 16. High-field polarization as a function of $1/(\mu_0 H)^{1/2}$ of amorphous thin films of $Fe_{60}Ni_{20}B_{20}$ for different temperatures.

(b) *Spherical nonmagnetic inclusions of radius* r_0:

$$J(H) = J_{\mathrm{s}} - \frac{a_{1/2}}{H^{1/2}} \text{ for } 1 < 8\kappa_{\mathrm{H}}r_0 < 17 + \kappa_{\mathrm{s}}^2 r_0^2$$
$$J(H) = J_{\mathrm{s}} - \frac{a_{3/2}}{H^{3/2}} \text{ for } 8\kappa_{\mathrm{H}}r_0 \gg 17 + \kappa_{\mathrm{s}}^2\ r_0^2 \quad (152)$$

Measurements of the LAFS have revealed the $a_{1/2}, a_1, a_2$ terms in crystalline and amorphous materials. As on example Figure 16 shows the $a_{1/2}$-term for sputtered thin films of amorphous $Fe_{80}B_{20}$ for different temperatures between 20 K and 240 K (Lenge and Kronmüller, 1986). A detailed analysis of these results considering magnetocrystalline fluctuations and the presence of pointlike defects have been performed previously (Kronmüller, Durst and Martinek, 1987; Kronmüller and Fähnle, 2003) showing that both contributions, magnetocrystalline fluctuations as well as pointlike stress centers contribute to $a_{1/2}$. The existence of the $1/H$-term has been detected in as-quenched and plastically deformed amorphous alloys of $Fe_{40}Ni_{40}P_{14}B_6$ (Grimm and Kronmïller, 1980, 1983; Kronmüller *et al.*, 1979). This $1/H$-term results from small linearly extended elastic dipoles due to the agglomeration of vacancy type so-called free volumes (Kronmüller and Fähnle, 2003; Kronmüller, Lenge and Habermaier, 1984). The $1/H^2$-term, which is the result of long-range stresses or magnetocrystalline anisotropies, and also induced anisotropies is the dominant term in crystalline materials, and, in particular, in plastically deformed materials (Kronmüller, 1959; Köster, 1967; Grimm and Kronmüller, 1983; Domann, Grimm and Kronmüller, 1979). Examples of this kind are presented in contributions

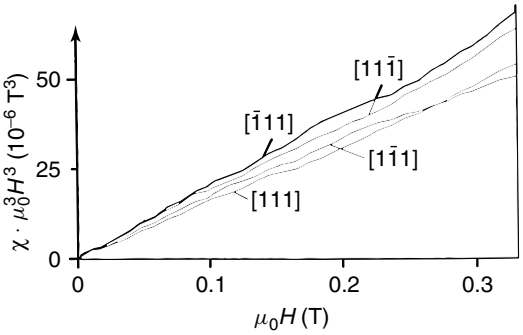

Figure 17. Analysis of the high-field susceptibility of a cyclically deformed Ni single crystal. χH^3 measured parallel to the four ⟨111⟩-directions. Accumulated plastic strain $a_{\mathrm{pl}} = 50$, amplitude per cycle 0.075, flow stress 56.6 MPa (Kronmüller and Fähnle (2003)). (Reproduced with permmission from Cambridge University Press.)

Micromagnetism–Microstructure Relations and the Hysteresis Loop, Volume 2. As a further example Figure 17 shows the analysis of the high-field susceptibility of a cyclically deformed Ni single crystal. In this case the quantity χH^3 follows a linear relation in H thus pointing to the presence of dislocation dipoles. The existence of dense linear clusters of dipole bundles has been proven by transmission electron microscopy (Kronmüller and Fähnle, 2003).

The analysis of the LAFS allows the determination of the temperature dependence of the spontaneous magnetization at $H = 0$. From the $T^{3/2}$-Bloch law the spin-wave stiffness constant and the related exchange energy can be determined if the $1/H^{n/2}$- plots are extrapolated to $H \to 0$. Furthermore from the existence of the $a_{n/2}$ parameters the kind of microstructures can be analyzed (dislocations, dislocation dipoles, point defects, para-, and diamagnetic precipitations).

Extended reviews of this type of analysis have been previously given (Kronmüller and Fähnle, 2003; Kronmüller, 1979, 1981; Umakoshi and Kronmüller, 1981; Grimm and Kronmïller, 1980, 1983; Domann, Grimm and Kronmüller, 1979; Vasquez, Fernengel and Kronmüller, 1989; Kronmüller *et al*., 1979).

6 MICROMAGNETISM OF DOMAIN PATTERNS

6.1 Laminar domain patterns

Analytical determinations of domain patterns by solving the integro-differential equations as derived in Section 3 so far do not exist owing to the complexity of the nonlinear differential equations, which are combined with the differential equations for the long-range dipolar fields. The usual procedure to determine the parameters of domain patterns therefore is based on four steps in order to approximate the true magnetic structure:

1. The existence of dws characterized by their specific wall energy, γ_{B}, is presupposed.
2. Assumptions are made concerning the arrangements of dws.
3. The total Gibbs free energy of dws arrangement is minimized with respect to the geometry of the dws arrangements.
4. Different arrangements of dws are compared with each other. First attempts to determine the size of Weiss domains are due to Landau and Lifshitz (1935) and (Kittel and Galt, 1956).

Several authors have given extended presentations of the state-of-the-art (Hubert and Schäfer, 1998; Hubert, 1974; Chikazumi, 1997; and Kronmüller and Fähnle, 2003). The subdivision of ferro- or ferrimagnetic materials into domains establishing a global demagnetized state results form the magnetostatic energy. For example, the magnetostatic energy of a platelet magnetized perpendicular to the surface per unit surface area is given by $\frac{1}{2}\mu_0 M_{\mathrm{s}}^2 \cdot T$, where T denotes the thickness of the platelet. By means of the formation of domains magnetized parallel or antiparallel to the easy directions this magnetostatic energy can be drastically reduced. On the other hand, however, owing to the formation of domains the total wall energy increases. Therefore an equilibrium domain width exists where the total magnetic Gibbs free energy corresponds to a minimum. In general, the magnetostatic stray field energy is reduced by the formation of so-called closure domains at the surface of the specimen. The type of closure domain is governed by the quality parameter

$$Q = \frac{2K_1}{\mu_0 M_{\mathrm{s}}^2} \tag{153}$$

For $Q > 1$ the closure structure of these hard magnetic materials is governed by the stray field energy, whereas for $Q < 1$ the magnetization deviates from the easy directions and the magnetocrystalline energy determines the energy of closure domains. Several examples of laminar domain patterns are shown in Figure 18 where the Landau structure for $Q < 1$ and the Kittel structure for $Q > 1$ are presented. Of special interest are Landau-type structures with vortices as shown in Figure 19. In the case of laminar domain patterns the total energy per unit area is given by

$$\phi_{\mathrm{tot}} = \gamma_{\mathrm{B}} \frac{T}{D} + \phi_{\mathrm{cl}} \cdot D \tag{154}$$

The first term on the right side of equation (154) corresponds to the specific dw energy, increasing with decreasing domain width D, and the second term corresponds to the energy per

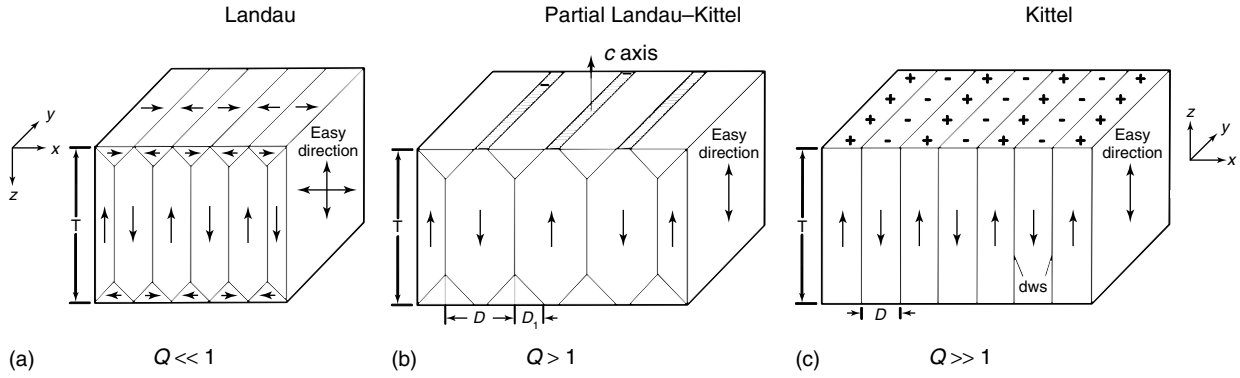

Figure 18. Characteristic laminar domain pattern of platelets for different Q-parameters. (a) Landau structure in ⟨100⟩-α-Fe platelets. (b) Partial Landau–Kittel structure for intermediate Q values (Co). (c) Open Kittel structure for hard magnetic uniaxial crystals with $Q \geq 1$ (FeNdB) (Kronmüller and Fähnle (2003)). (Reproduced with permmission from Cambridge University Press.)

unit area of the closure domains. The equilibrium domain width is obtained from a minimization of ϕ_{tot} with respect to D, giving

$$D = \sqrt{\frac{\gamma_{\text{B}}\, T}{\phi_{\text{cl}}}} \tag{155}$$

Without considering the details of the calculation of ϕ_{el} the results are the following ones:

1. Landau structure of α-Fe with easy directions perpendicular and in-plane. In this case, the closure domain energy is determined exclusively by the magnetoelastic energy, which leads to

$$D = \sqrt{\frac{\gamma_{\text{B}} T}{\frac{9}{16} c_{11} \lambda_{100}^2}} \tag{156}$$

2. Landau structure of a uniaxial soft magnetic materials ($Q \leq 1$) with closure domains magnetized in hard direction

$$D = \sqrt{\frac{\gamma_{\text{B}} T}{\frac{1}{2} K_1}} \tag{157}$$

3. Kittel structure in hard magnetic materials ($Q \geq 1$), with easy direction perpendicular to the platelet.

$$D = \sqrt{\frac{\gamma_{\text{B}} T}{\left(\frac{1.7}{4\pi}\right) M_{\text{s}} J_{\text{s}}}} \tag{158}$$

Equations (156–158) may be used to determine relevant magnetic parameters. For example, from equation (157) we derive:

$$K_1 = 64AT/D^4;\ \gamma_{\text{B}} = 32AT/D^2;\ \delta_{\text{B}} = \frac{\pi}{8} D^2/T \tag{159}$$

So far we have considered domain patterns with discrete orientation of magnetization in the bulk and in the closure domains. In soft magnetic materials, however, the transition from the Kittel structure to the Landau structure with vanishing stray fields takes place continuously as discussed by Hubert and Schäfer (1998) as well as Kronmüller and Fähnle (2003).

In order to describe this process Williams, Bozorth and Shokley (1949) introduced an effective permeability μ^* that takes care of the fact that in materials $Q \leq 1$ the magnetization inclines parallel to the surface not taking care of the easy directions in order to reduce the surface charges. This effect may be taken into account by introducing the effective permeability

$$\mu^* = 1 + \frac{J_{\text{s}}^2}{2\mu_0 K_1} = 1 + Q^{-1} \tag{160}$$

If equation (160) is introduced into equation (158) by replacing μ_0 by $\mu_0 \mu^*$ for a rotation angle of 45° in this closure domains the domain width is given by

$$D = \sqrt{\frac{\gamma_{\text{B}}\, T(1 + Q^{-1})}{\frac{1.7}{4\pi} M_{\text{s}} J_{\text{s}}}} \tag{161}$$

Equations (161) describes fairly well the transition from the Kittel structure ($Q \geq 1$) to the Landau structure ($Q \leq 1$).

6.2 Landau structures with vortices

Domain patterns with vortex structures exist mainly in thin films where the geometry and the distribution of easy directions allows a reduction of the stray field energy only by the formation of vortices at the crossing points of the dws. Typical examples are shown in Figure 19.

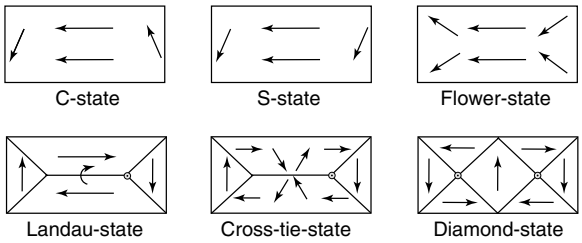

Figure 19. Typical domain patterns in rectangular platelets with vortices in the case of low remanence configurations ($Q \leq 1$) (Kronmüller and Fähnle (2003)). (Reproduced with permmission from Cambridge University Press.)

According to Feldtkeller and Thomas (1965), a vortex corresponds to a region where the magnetization rotates by 360° around a singular point where the magnetization is oriented perpendicular to the film. This configuration is due to the fact that an in-plane magnetization rotating by 360° in the center of the configuration leads to a singularity of the exchange energy because $(\nabla\gamma_i)^2$ becomes infinite. To avoid this singularity the magnetization rotates out of the plane thus producing stray field energy, however, avoiding the singularity of exchange energy. Figure 20 shows the four domain Landau structures in a square platelet with the vortex in the center and Figure 21 shows the spin distribution in the center of the vortex. Different attempts have been made in order to describe the distribution of magnetization within the vortex (Feldtkeller, 1965; Usov and Peschany, 1993, 1994).

These authors use the Ritz method assuming a functional distribution of J_s and minimizing the total magnetic energy. Feldtkeller' s Ansatz for the angle ϑ between $\boldsymbol{J}_s$ and the

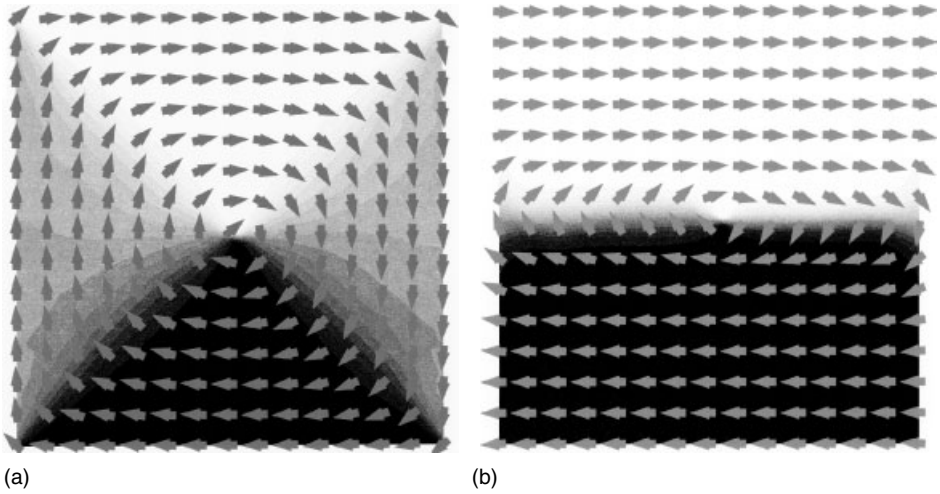

Figure 20. Four and two-domain Landau structures in a square platelet with vortex in the center for Permalloy (a) and Co (b) (Goll, Schütz and Kronmüller, 2003). (Reproduced from Goll *et al*., 2003, with permission from the American Physical Society. © 2003.)

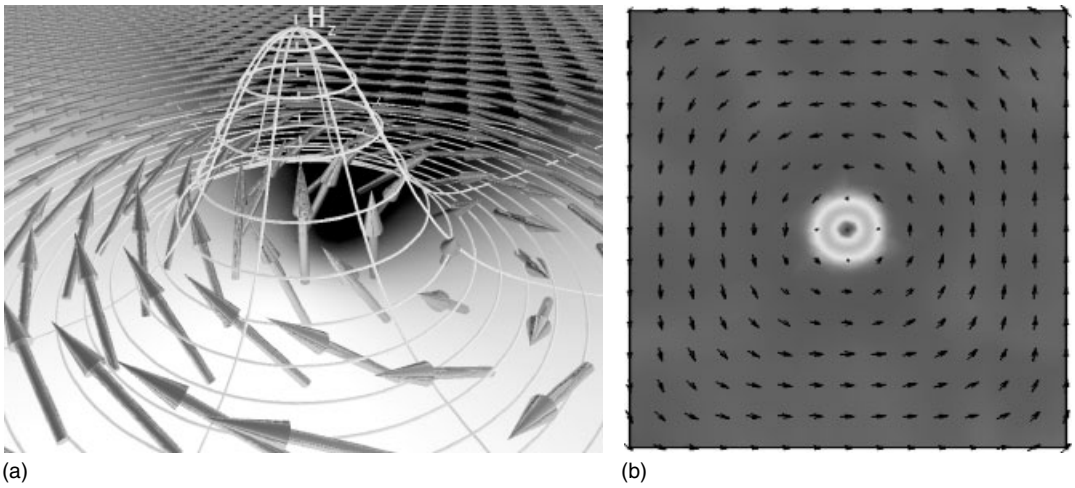

Figure 21. Distribution of magnetization in the center of a vortex. (Courtesy of S. Macke.)

vortex axis is given by $\vartheta(r) \propto \cos[\exp(-2\beta^2 r^2)]$, whereas Usov uses

$$\sin\vartheta = \frac{2\,b\,r}{b^2 + r^2}, \quad \text{for } 0 < r < b, \qquad (162)$$
$$\sin\vartheta = 0 \qquad \text{for } b < r < R$$

where R denotes the radius of the platelet. The parameters β and b in the Feldtkeller and the Usov model have to be determined from the minimization of the total energy. Figure 22 shows the distribution of the reduced z-component, M_z/M_s for the Feldkeller and the Usov model in the case of permalloy. The vortex radius in the case of the model Feldtkeller (1965) varies between 1.5 l_s and 3 l_s for film thicknesses ranging between zero and 20 l_s. Similar results were obtained by Usov and Peschany (1993, 1994) with variation from 2.2 to 4.5 l_s.

Numerical calculations by the finite element technique give further information on the details of the vortex structure. In particular, it turns out that there exists a negative M_z component for distances larger than the vortex radius (see Figure 23). This negative component is of the order of 2% for a platelet of thickness of 25 nm and vanishes nearly for thicknesses $< l_s$.

It is of interest to compare the vortex energy with the total magnetic energy stored in a square platelet of dimensions $250 \times 250 \times 25\,\text{nm}^{-3}$. For permalloy with $A = 13\,\text{pJ m}^{-1}$, $J_s = 1\,\text{T}$, $K_1 = 5.0 \times 10^2\,\text{J m}^{-3}$, $l_s = 5.7\,\text{nm}$ the total magnetic energy of the platelet, composed of ϕ_{ex}, ϕ_k and ϕ_s is 19.83×10^{-18} J, whereas the total magnetic energy

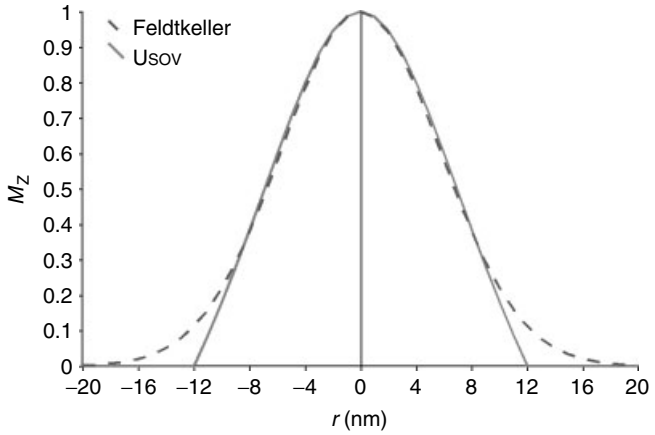

Figure 22. Distribution of M_z/M_s for the Feldtkeller and the Usov Ansatz for permalloy for a film thickness of 5 nm $\approx 1.5 l_s$. (Courtesy of D. Goll and S. Macke.)

stored in the vortex kernel (vortex extension limited by the radius where $m_z = 0$) amounts only to 5.63×10^{-18} J. From these results it becomes obvious that in macroscopic domain patterns the energy stored in vortex arrangements remains rather small in comparison to the dw energies of nm, μm, and cm dimensions. Therefore vortices determine the spin arrangement only in particles of small dimensions.

Many investigations on-line structures in domain walls have been performed on the basis of micromagnetism such as Néel lines, in Bloch walls and Bloch lines and Hubble domains (Thiaville *et al.*, 1991; Miltat, Thiaville and Trouilloud, 1989).

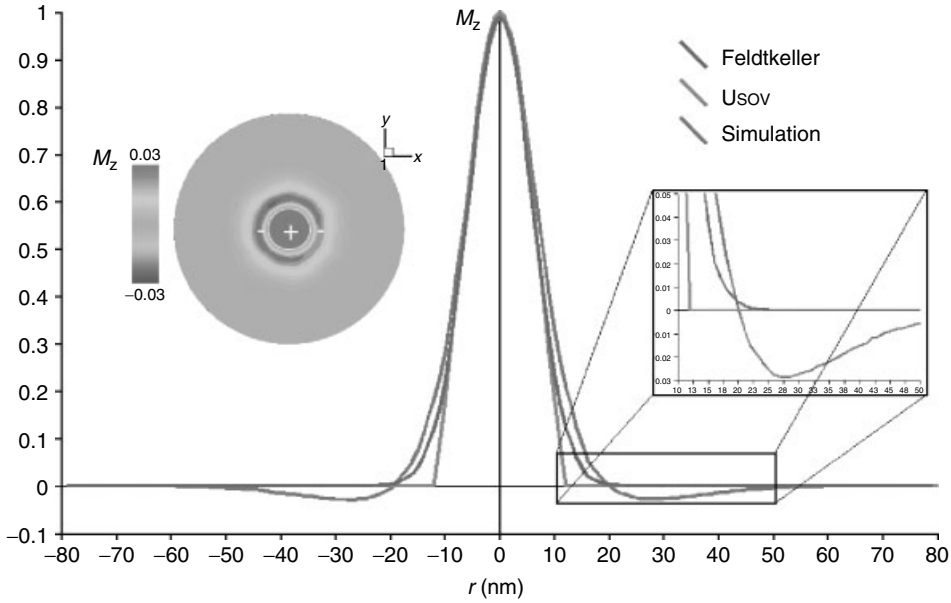

Figure 23. Distribution of M_z/M_s according to numerical calculations with the FEM technique. The negative M_z-component outside the vortex core is shown for a larger scale by the inset. (Courtesy of D. Goll and S. Macke.)

7 MICROMAGNETISM OF DYNAMIC MAGNETIZATION PROCESSES

7.1 The Landau–Lifshitz–Gilbert (LLG) equation

The micromagnetic theory of dynamic magnetization processes deals with the problems of reducing energy losses, with small switching times in demagnetization processes of small particles and thin films and the calculation of resonance frequencies and spin-wave spectra. A first description of the time-dependent motion of magnetic moments is due to Bloch (1932) who considered uncoupled and undamped magnetic moments. Equations for the damped motion of the magnetic polarization at first were published by Landau and Lifshitz (1935).

Starting from the classical mechanical equation for the rotational motion of a rigid body, $\mathrm{d}\boldsymbol{P}/\mathrm{d}t = \boldsymbol{L}$, where $\boldsymbol{P}$ is the angular momentum and $\boldsymbol{L}$ the torque acting on the body, the equation of motion of the magnetic polarization is obtained by using the magneto-mechanical analogue $\boldsymbol{J}_\mathrm{s} = \gamma \boldsymbol{P}$ and inserting the magnetic torque $\boldsymbol{L} = [\boldsymbol{J}_\mathrm{s} \times \boldsymbol{H}_\mathrm{eff}]$, which gives for the undamped rotational motion

$$\mathrm{d}\boldsymbol{J}_\mathrm{s}/\mathrm{d}t = \gamma\,[\boldsymbol{J}_\mathrm{s} \times \boldsymbol{H}_\mathrm{eff}] \tag{163}$$

Here γ denotes the gyromagnetic ratio, $\gamma = -g\,|e|\,/2m = -1.1051g$ $(\mathrm{sA/m})^{-1}$. Landau and Lifshitz have expanded equation (163) by introducing a damping term according to

$$\frac{\mathrm{d}\boldsymbol{J}_\mathrm{s}}{\mathrm{d}t} = \gamma_\mathrm{L}\ [\boldsymbol{J}_\mathrm{s} \times \boldsymbol{H}_\mathrm{eff}]\ - \frac{\alpha_\mathrm{L}}{J_\mathrm{s}}\ [\boldsymbol{J}_\mathrm{s} \times [\boldsymbol{J}_\mathrm{s} \times \boldsymbol{H}_\mathrm{eff}]] \tag{164}$$

Dividing equation (164) by μ_0 and introducing M_s the equation of motion of the spontaneous magnetization is obtained

$$\frac{\mathrm{d}\boldsymbol{M}_\mathrm{s}}{\mathrm{d}t} = \gamma_\mathrm{L}\ [\boldsymbol{M}_\mathrm{s} \times \boldsymbol{H}_\mathrm{eff}] - \frac{\alpha_\mathrm{L}}{M_\mathrm{s}}\ [\boldsymbol{M}_\mathrm{s} \times [\boldsymbol{M}_\mathrm{s} \times \boldsymbol{H}_\mathrm{eff}]] \tag{165}$$

The first term on the right side of equation (165) describes a precessional rotation of $\boldsymbol{M}_\mathrm{s}$ with frequency $\omega = -\gamma H_\mathrm{eff}$. The minus sign in ω means that in the case of a positive effective field the precessional motion takes place anticlockwise. The second term rotates $\boldsymbol{M}_\mathrm{s}$ toward the direction of the effective field, that is, after some time the precessional motion of $\boldsymbol{M}_\mathrm{s}$ finally stops (Figure 24). Equation (165) describes a motion of $\boldsymbol{M}_\mathrm{s}$, which accelerates with increasing damping parameter α_L. Gilbert (1955) pointed out that equation (165) can only be used for small damping. In order to describe the strong damping in thin films (Gilbert and Kelly, 1955) Gilbert

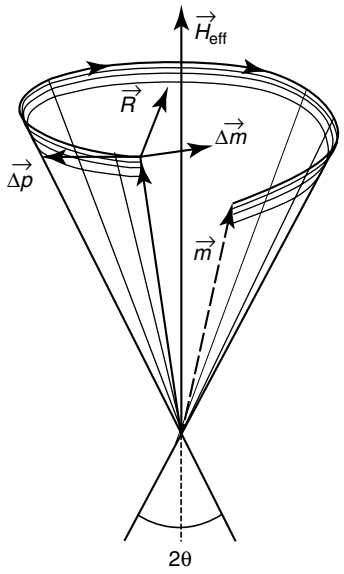

Figure 24. Precessional movement of magnetization around the effective field showing the directions of precessional and damped component.

(1955) proposed an alternative equation, which is written as

$$\frac{\mathrm{d}\boldsymbol{M}_\mathrm{s}}{\mathrm{d}t} = \gamma_\mathrm{G}\ [\boldsymbol{M}_\mathrm{s} \times \boldsymbol{H}_\mathrm{eff}] + \frac{\alpha_\mathrm{G}}{\boldsymbol{M}_\mathrm{s}}\left[\boldsymbol{M}_\mathrm{s} \times \frac{\mathrm{d}\boldsymbol{M}_\mathrm{s}}{\mathrm{d}t}\right] \tag{166}$$

The subscripts L and G in equations (165) and (166) point to the Landau–Lifshitz (LL) and the Gilbert equation. In order to compare the LL and the Gilbert equation the term $\mathrm{d}\boldsymbol{M}_\mathrm{s}/\mathrm{d}t$ on the right side of equation (166) is replaced by the Gilbert equation itself. This leads to the so-called Landau–Lifshitz–Gilbert (LLG) equation:

$$\frac{\mathrm{d}\boldsymbol{M}_\mathrm{s}}{\mathrm{d}t} = \frac{\gamma_\mathrm{G}}{(1+\alpha_\mathrm{G}^2)}\,[\boldsymbol{M}_\mathrm{s} \times \boldsymbol{H}_\mathrm{eff}] + \frac{\alpha_\mathrm{G}\gamma_\mathrm{G}}{(1+\alpha_\mathrm{G}^2)M_\mathrm{s}}\ [\boldsymbol{M}_\mathrm{s} \times [\boldsymbol{M}_\mathrm{s} \times \boldsymbol{H}_\mathrm{eff}]] \tag{167}$$

where the following replacements have taken place

$$\gamma_\mathrm{L} \to \frac{\gamma_\mathrm{G}}{1+\alpha_\mathrm{G}^2}; \quad \alpha_\mathrm{L} \to \frac{\alpha_\mathrm{G}\ \gamma_\mathrm{G}}{1+\alpha_\mathrm{G}^2} \tag{168}$$

The LL and the LLG equation have a similar form, however, the dependences of the precessional and of the damping terms on the parameters $\gamma_{\mathrm{L,G}}$ and $\alpha_{\mathrm{L,G}}$ are quite different.

This becomes obvious if we consider the dependence of the precessional and of the damping term on the $\alpha_{\mathrm{L,G}}$ parameters as presented in Figure 25. The precessional term $\boldsymbol{P} \propto [\boldsymbol{M}_\mathrm{s} \times \boldsymbol{H}_\mathrm{eff}]$, remains constant in the case of the LL equation and decreases in the case of the LLG equation. The damping term increases linearly with α_L in the case

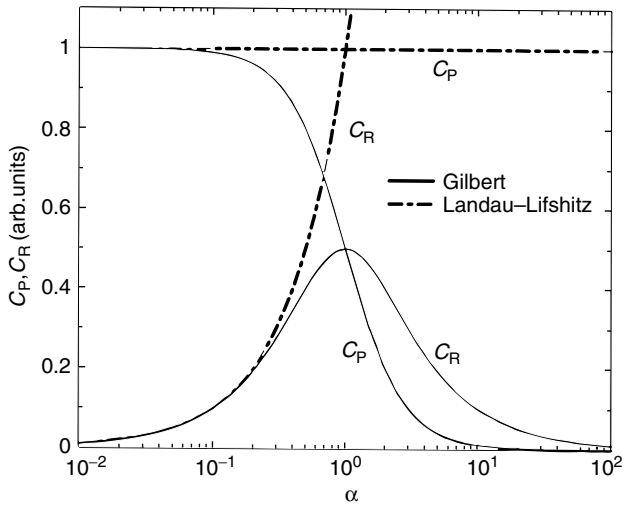

Figure 25. Components of $\mathrm{d}\boldsymbol{M}/\mathrm{d}t$ as a function of α. Precession $C_\mathrm{P} \propto \boldsymbol{M}_\mathrm{s} \times \boldsymbol{H}_\mathrm{eff}$ and damping term $C_\mathrm{R} \propto [\boldsymbol{M}_\mathrm{s} \times [\boldsymbol{M}_\mathrm{s} \times H_\mathrm{eff}]]$ in arbitrary units for the Landau–Lifshitz equation (LL) and the Gilbert equation (LLG). (Reproduced with permmission from Cambridge University Press.)

of the LL equation and runs through a maximum for the LLG equation. It is of interest that in the case of the LLG equation the precession as well as the damping vanishes for large α_G values. This behavior is expected from a physical point of view, whereas the LL equation leads to an unphysical behavior.

7.2 Landau–Lifshitz–Gilbert equations in Cartesian and spherical polar coordinates

7.2.1 Cartesian coordinates

For numerical and analytical calculations it is useful to formulate the LLG equations in terms of reduced dimensionless properties defined as:

$$\tau = \omega t = \gamma H_\mathrm{N} t, \;\; \boldsymbol{h}_\mathrm{eff} = \frac{\boldsymbol{H}_\mathrm{eff}}{H_\mathrm{N}}, \;\; \boldsymbol{m}_\mathrm{s} = \frac{\boldsymbol{M}_\mathrm{s}}{M_\mathrm{s}}$$
$$H_\mathrm{N} = 2K_1/J_\mathrm{s}, \quad \omega = \gamma H_\mathrm{N} \tag{169}$$

where $\boldsymbol{H}_\mathrm{eff}$ is given by equation (80). The motion of the three components m_x, m_y and m_z of $\boldsymbol{m}_\mathrm{s}$ then is described by the following differential equations:

$$\frac{\mathrm{d}\boldsymbol{m}_i}{\mathrm{d}\tau} = \frac{1}{1+\alpha^2}\left[m_j \mid h_{\mathrm{eff},k} \mid -m_\mathrm{k} h_{\mathrm{eff},j}\right] - \frac{\alpha}{1+\alpha^2}\left[m_j\left\{m_i h_{\mathrm{eff},j} - m_j h_{\mathrm{eff},i}\right\} - m_k\left\{m_\mathrm{k} h_{\mathrm{eff},i} - m_i h_{\mathrm{eff},k}\right\}\right] \tag{170}$$
$$i = 1, 2, 3;\; j, k \text{ by cyclic transformation}$$

The differential equation for m_j and m_k are obtained by cyclic transformation. The components of the effective field are obtained from equations (80) and are especially simple in the case of a homogeneous precessional motion, where the exchange field vanishes and $h_{\mathrm{eff},i}$ is given by

$$h_{\mathrm{eff},i} = \frac{1}{H_\mathrm{N}}\left\{-\frac{1}{J}\frac{\partial \phi'_\mathrm{k}}{\partial \gamma_i} + H_{\mathrm{s},i} + H_{\mathrm{ext},i}\right\} \tag{171}$$

$$\text{with} \qquad \boldsymbol{H}_\mathrm{s} = -\begin{pmatrix} N_{xx} & M_\mathrm{s} \\ N_{yy} & M_\mathrm{s} \\ N_{zz} & M_\mathrm{s} \end{pmatrix} \tag{172}$$

if we deal with a specimen of ellipsoidal shapes and demagnetization factors N_{ii}.

7.2.2 Spherical coordinates

In order to get rid of the constraint $\sum_{i=1}^{3} \gamma_i^2 = 1$ spherical coordinates θ and φ (Figure 26) according to equation (71) are introduced. The Gilbert equation (166) then is writen as

$$-\frac{\mathrm{d}\theta}{\mathrm{d}t}\,\sin\theta = -\gamma_\mathrm{G}\, H_{\mathrm{eff},\varphi} + \alpha_\mathrm{s}\,\frac{\mathrm{d}\varphi}{\mathrm{d}t}\sin\theta \tag{173}$$

$$\frac{\mathrm{d}\varphi}{\mathrm{d}t}\,\sin\,\theta = \gamma_\mathrm{G}\, H_{\mathrm{eff},\theta} \;\pm\; \alpha_\mathrm{G}\frac{\mathrm{d}\theta}{\mathrm{d}t}$$
$$\text{with } H_{\mathrm{eff},\varphi} = -\frac{1}{J_\mathrm{s}}\,\frac{\partial \phi_\mathrm{tot}}{\partial \varphi}; \quad H_{\mathrm{eff},\theta} = -\frac{1}{J_\mathrm{s}}\frac{\partial \phi_\mathrm{to}}{\partial \theta} \tag{174}$$

Here $\mathrm{d}\theta/\mathrm{d}t$ described the relaxation of the magnetization into the equilibrium state and $\mathrm{d}\varphi/\mathrm{d}t$ describes the precessional rotation around the orientation of $\boldsymbol{H}_\mathrm{eff}$.

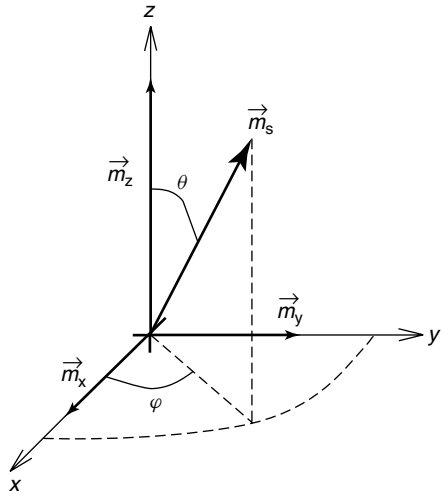

Figure 26. Definition of spherical coordinates θ and φ of the reduced magnetization $\boldsymbol{m} = \boldsymbol{M}/\boldsymbol{M}_\mathrm{s}$.

In the particular case of homogeneous precession in an uniaxial spherical particle the LLG equations are given by ($\boldsymbol{h}_{\text{eff}} = \boldsymbol{h}_{\text{k}} + \boldsymbol{h}_{\text{ext}}$).

$$\frac{\mathrm{d}\theta}{\mathrm{d}\tau} = -\frac{\alpha_{\text{G}}}{1+\alpha_{\text{G}}^2}\ \sin\theta(\cos\theta + h_{z,\text{ext}})$$
$$\frac{\mathrm{d}\varphi}{\mathrm{d}\tau} = \frac{1}{1+\alpha_{\text{G}}^2}\ \left(\cos\ \theta + h_{z,\text{ext}}\right) \tag{175}$$

Here the magnetostatic stray field exerts no torque on the magnetization because it is always oriented antiparallel to the magnetization.

In the case of a thin platelet, the stray field may not be neglected. With demagnetization factors $N_{xx} = N_{yy}$ and N_{zz}, $\boldsymbol{H}_{\text{s}}$ is written as

$$\boldsymbol{H}_{\text{s}} = -M_{\text{s}} \begin{pmatrix} N_{xx} & \sin\theta & \cos\varphi \\ N_{yy} & \sin\theta & \sin\varphi \\ N_{zz} & \cos\theta & \end{pmatrix} \tag{176}$$

and the LLG equations for a uniaxial crystal are given by

$$\sin\theta\frac{\mathrm{d}\varphi}{\mathrm{d}\tau} = \frac{1}{1+\alpha_{\text{G}}^2}\left[F_1 + \alpha_{\text{G}}F_2\right]$$
$$\frac{\mathrm{d}\theta}{\mathrm{d}\tau} = \frac{1}{1+\alpha_{\text{G}}^2}\left[-F_2 + \alpha_{\text{G}}F_1\right] \tag{177}$$

with

$$\begin{aligned} F_1 = {} & [-(k_x + n_{xx})\ \cos^2\varphi - (k_y + n_{yy})\sin^2\varphi \\ & + (k_z + n_{zz})]\sin\theta\cos\theta \\ & + (h_{\text{ext},x}\cos\varphi + h_{\text{ext},y}\sin\varphi)\cos\theta - h_{\text{ext},z}\sin\theta \\ F_2 = {} & \left[(k_x + n_{xx}) - (k_y + n_{yy})\right]\sin\theta\sin\varphi\cos\varphi \\ & - h_{\text{ext},x}\ \sin\varphi + h_{\text{ext},y}\cos\varphi \end{aligned} \tag{178}$$

Here the vectors $\boldsymbol{k}$ are given by

$$\boldsymbol{k} = \begin{pmatrix} 1 \\ 1 \\ 0 \end{pmatrix}, \quad k = \begin{pmatrix} 0 \\ 1 \\ 1 \end{pmatrix} \tag{179}$$

for in-plane and out of plane direction of $\boldsymbol{H}_{ext}$, respectively. The tensor n_{ii} is related to the demagnetization tensor $\boldsymbol{N}$ by

$$\boldsymbol{n} = \frac{1}{Q}\begin{pmatrix} N_{xx} & & \\ & N_{yy} & \\ & & N_{zz} \end{pmatrix} \tag{180}$$

where $Q = 2K_1/(\mu_0 M_{\text{s}}^2)$ denotes the so-called quality factor.

7.3 Magnetization dynamics by spin-polarized electrical currents

In papers by Slonczewski (1996, 1999) and Berger (1996) it has been shown that spin-polarized electrical currents exert torques on $\boldsymbol{M}_{\text{s}}$ producing spin waves at microwave frequencies. This effect is due to the indirect exchange interaction of s electrons with d or f electrons, which are responsible for the spin ordering in transition or rare-earth metals. Similar to the Heisenberg model the s–d and s–f interaction is described by the Hamiltonian

$$H_{\text{s,f,d}} = -2J_{\text{s,f}} \cdot \boldsymbol{s} \cdot \boldsymbol{S} \tag{181}$$

where s denotes the spin of the conduction electrons and S that of the d or f electrons and J_{sd} corresponds to the sd or sf exchange integral. In a continuum theoretical micromagnetic description the current-induced phenomena are described by an extended LLG equation (neglecting the damping term)

$$\begin{aligned} \frac{\partial \boldsymbol{M}_{\text{s}}}{\partial t} = {} & \gamma\ [\boldsymbol{M}_{\text{s}} \times \boldsymbol{H}_{\text{eff}}] + \frac{\propto}{M_{\text{s}}}\left[\boldsymbol{M}_{\text{s}} \times \frac{\mathrm{d}\boldsymbol{M}_{\text{s}}}{\mathrm{d}t}\right] \\ & - \frac{\sigma_j}{M_{\text{s}}^2}\boldsymbol{M}_{\text{s}} \times \left[\boldsymbol{M}_{\text{s}} \times (j \cdot \nabla)\boldsymbol{M}_{\text{s}}\right] \\ & - \xi\frac{\sigma_j}{M_{\text{s}}}\left[\boldsymbol{M}_{\text{s}} \times (j \cdot \nabla)\boldsymbol{M}_{\text{s}}\right] \end{aligned} \tag{182}$$

where j denotes the spin polarized current. The parameter σ_j according to Slonczewski (1996), Berger (1996) and Krüger *et al*. (2007) is defined as

$$\sigma_j = \frac{\epsilon\mu_B}{eM_s(1+\xi^2)} \tag{183}$$

where e denotes the spin polarization efficiency (Slonczewski, 1996; Berger, 1996) and $\xi = \tau_{\text{ex}}/\tau_{\text{sf}}$ the ratio of exchange and spin-flip relaxation times. On the basis of equation (182) a nonlinear theory of microwave generation in magnetic nanocontacts has been developed (Slavin and Kabos, 2005) and the role of current-induced torques for the motion of domain walls has been considered by several authors. There exists an increasing number of publications on this subject dealing with theoretical (Tatara and Kono, 2004; Li and Zhang, 2004; Waintal and Viret, 2004; Thiaville, Nakatami, Miltat and Vernic, 2004; Thiaville, Nakatami, Miltat and Suzuki, 2005) and experimental investigations (Grollier *et al*., 2003; Tsoi, Fontana and Parkin, 2003; Kläui *et al*., 2003, 2005 Kimura, Otami, Tsukagoshi and Aoyagi, 2003; Yamaguchi *et al*., 2004; Vernier *et al*., 2004). The idea to manipulate dws by electrical currents in order to improve the functions of spintronic devices has been outlined by Versluijs, Bari and Coey (2001) and Allwood, Xiong, Cooke and Locatelli (2002).

7.4 Applications of the LLG equations

7.4.1 Effective domain wall mass

As shown in Section 4.1.1 a static 180° dw in a uniaxial crystal is fully described by the rotation angle φ within the dw plane with normal parallel to the z axis. In the case of a moving dw, the spontaneous magnetization due to its precessional rotation has to be described by the rotation angle φ as well as by the angle θ with respect to the dw normal. As shown by Doering (1948), Walker and Dillon (1963), and Slonczewski (1972) at small velocities the wall energy is given by

$$\gamma_B = 4\sqrt{A\ (K_1 + \frac{1}{2}\mu_0 M_s^2 \sin^2\theta)} \tag{184}$$

From a solution of the LLG equation the angle θ is found to increase linearly with velocity v of the dw leading to a quadratic dependence of γ_B on velocity v. Thus γ_B may be written as

$$\gamma_B(v) = \gamma_B(0) + \frac{1}{2} m_w v^2$$
$$\text{with} \quad \gamma_B(0) = 4\sqrt{A\ K_1} \quad \text{and} \tag{185}$$

$$m_w = \frac{1}{2}\mu_0 \gamma_B(0) / \left(A\gamma_G^2\right) = \frac{2\pi\mu_0}{\delta_B \gamma_G^2} \tag{186}$$

A detailed analysis shows that the wall mass is a consequence of the stray field energy resulting from the precessional rotation of $\boldsymbol{M}_s$ within the dw. No simple explicit result exists for two-dimensional dws as they exist in thin films. In particular the role of Bloch lines in dws has been considered by Malozemoff and Slonczewski (1979) and O'Dell (1981).

7.4.2 Switching times in spherical particles

An analytical solution of the LLG equation has been obtained for spheres with uniaxial anisotropy and an external field applied antiparallel to the positive easy direction, which also is parallel to the spontaneous magnetization. In the case of a homogeneous rotation process in a sphere the demagnetization field is always strictly antiparallel to $\boldsymbol{M}_s$ and therefore no torque is exerted on $\boldsymbol{M}_s$ by the demagnetization field. The effective field in reduced units of H_N is given by

$$\boldsymbol{h}_{eff} = \frac{\boldsymbol{H}_{eff}}{H_N} = \begin{pmatrix} -m_x \\ -m_y \\ H_{z,ext}/H_N \end{pmatrix} \tag{187}$$

In terms of spherical coordinates as defined in Figure 26 the LLG equation are given by equations (175). Kikuchi (1956) has integrated equations (175) for $h_{z,ext} = -1$ and given the implicit solution for the time-dependent z-component $m_z = \cos\theta$:

$$\tau = -\frac{1+\alpha_G^2}{4\alpha_G} \times \left[\ln\left(\frac{(m_z(\tau)+1)(m_0-1)}{(m_z(\tau)-1)(m_0+1)} \right) - \frac{2}{m_z(\tau)-1} + \frac{2}{m_0-1} \right] \tag{188}$$

where m_0 corresponds to the z-component of $\boldsymbol{m}$ at $\tau = 0$. For $m_0 = 1$ the torque on $\boldsymbol{m}$ vanishes and no precession would take place. Figure 27 shows the time dependence of $m_z(\tau)$ as determined numerically from equation (188) for $m_0 = 0.99$. Figure 27 shows two time ranges. In a range I strongly dependent on m_0 the magnetization m_z doesn't change strongly. The time τ_R, elapsing until m_z becomes zero is given by

$$\tau_R = \frac{1+\alpha_G^2}{4\alpha_G}\left[\ln\frac{1+m_0}{1-m_0} - \frac{2}{m_0-1} - 2\right] \tag{189}$$

In a range II m_z changes its orientation by almost 180°. The corresponding switching time is given by

$$\tau_s = 2\frac{1+\alpha_G^2}{\alpha_G} \tag{190}$$

Figure 28 shows the characteristic times τ_R and τ_s as a function of the damping constant α_G. Both characteristic times show a minimum at $\alpha_G = 1$, however, their absolute values differ by a factor of 20, depending on the chosen value of m_0. According to the results τ_s always is rather

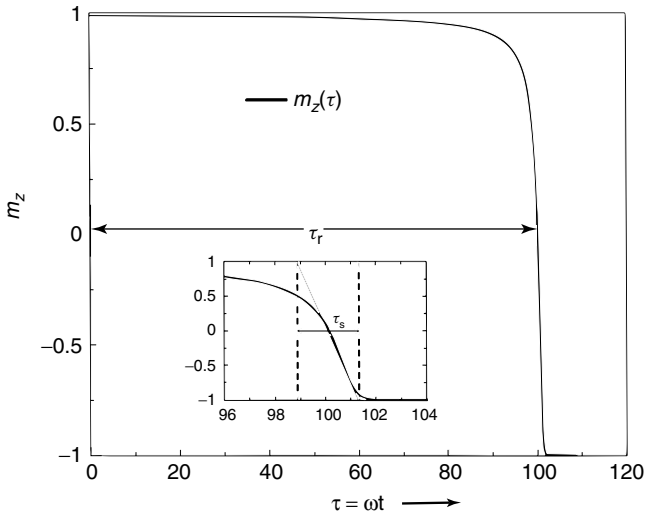

Figure 27. Time evaluation of m_z of a sphere in a reversed field $H_{ext} = -H_N$ for $\alpha = 1$ and $m_0 = 0.99n$ (Kikuchi, 1956) with definition of τ_R and τ_s. (Reproduced with permmission from Cambridge University Press.)

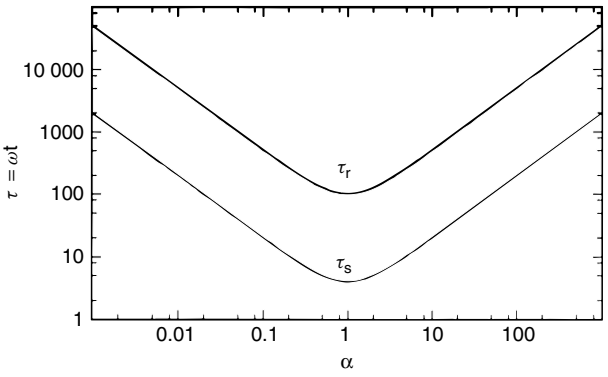

Figure 28. Characteristic switching times τ_R and τ_s of a sphere as a function of α for $m_0 = 0.99$ and $H_{ext} = -H_N$ (Kronmüller and Fähnle (2003)). (Reproduced with permmission from Cambridge University Press.)

small. To reduce the total switching time lower m_0 values and optimum α-values are required. Actually the measured α-values are much lower than the $\alpha = 1$ and are rather of the order of 0.001–0.05.

7.4.3 Switching times in thin platelets and small parallelepipeds

Whereas in spherical particles the magnetic stray fields play no role, in the case of platelets the stray fields cannot be anymore neglected. With the stray field given by equations (27–28) the LLG equations are given by

$$\begin{aligned}\frac{\mathrm{d}\varphi}{\mathrm{d}\tau} &= \frac{1}{1+\alpha_G^2}\left[\left\{1-\frac{1}{Q}(N_\parallel - N_\perp)\cos^2\varphi\right\}\cos\theta\right.\\ &\quad \left. + k_{ext,z} - \frac{1}{Q}(N_\parallel - N_\perp)\sin\varphi\cos\varphi\right]\\ \frac{\mathrm{d}\theta}{\mathrm{d}\tau} &= \frac{-1}{1+\alpha_G^2}\left[\alpha_G\left\{1-\frac{1}{Q}(N_\parallel - N_\perp)\cos^2\varphi\right\}\right.\\ &\quad \times \sin\theta\cos\theta + \alpha_G h_{ext,z} - \sin\theta\\ &\quad \left. -\frac{1}{Q}(N_\perp - N_\parallel)\sin\theta\sin\varphi\cos\varphi\right] \qquad (191)\end{aligned}$$

The demagnetization factors $N_\parallel$ and $N_\perp$ of square parallelepipeds are obtained from Aharoni's results (Aharoni, 1998c). In equation (191) $N_\parallel$ are the demagnetization factors parallel to the in-plane edges of the square platelet and $N_\perp$ corresponds to that perpendicular to the platelet plane.

Switching times haven been determined for square platelets of edge length 12.5 nm and varying thickness with aspect ratios 0.02:1 (cubic particles). The materials investigated are FePt and Co at room temperature with the following material parameters for FePt: $K_1 = 6.6 \times 10^6\,\mathrm{J\,m^{-3}}$, $J_s = 1.43\,\mathrm{T}$, $A = 10\,\mathrm{pJ\,m^{-1}}$ (Hai *et al.*, 2003) and for Co: $K_1 = 0.4 \cdot 10^6\,\mathrm{J\,m^{-3}}$, $J_s = 1.8\,\mathrm{T}$, $A = 13\,\mathrm{pJ\,m^{-1}}$. The ground state of platelets with in-plane easy axis parallel to the edges corresponds to the so-called butterfly state. The reversal of magnetization therefore starts at the corners of the square where $\boldsymbol{J}_s$ reveals a slight inhomogeneity. Figure 29 shows the dependence of the switching time as a function of the damping parameter α for different aspect ratios p of the square platelets. These results were obtained from a numerical solution of equations (191). The inversely applied magnetic field of $1.5H_k$ is strictly parallel to the edges of the square. With decreasing aspect ratio the minimum switching time shifts to smaller α-values, and also τ_s as a whole decreases. The increase of τ_s for larger α-values, $\alpha > \alpha_{min}$, is due to the strongly damped aperiodic relaxation process of $\boldsymbol{M}_s$. For $\alpha < \alpha_{min}$, the switching time again increases owing to reversal processes, which are governed by the precessional process with many precessions before reversal takes place (Goll, Schütz and Kronmüller, 2006).

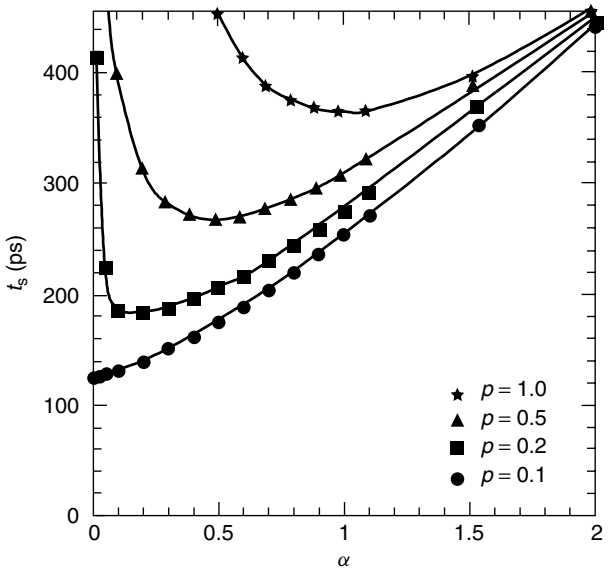

Figure 29. Dependence of the switching time on the damping parameter α for different aspect ratios of a square platelet of Cobalt of edge length 12.5 nm obtained by applying a magnetic field of $H_{ext} = -1.5H_k$ to the remanent quasi-homogeneous equilibrium state (flower state). (Courtesy of D. Goll and S. Macke.)

Figure 29 shows the switching time τ_s as a function of α for the case allowing inhomogeneous rotational processes using the FEM = Finite Element Method method. In this case the reversal process starts from the corners of the platelets by the displacement of a domain wall (Néel walls in thin films) moving to the center of the platelet.

It is of interest to note that the switching times in the case of the flower state are larger than in the case where the field is applied under a misalignment angle of 5° to an ideally

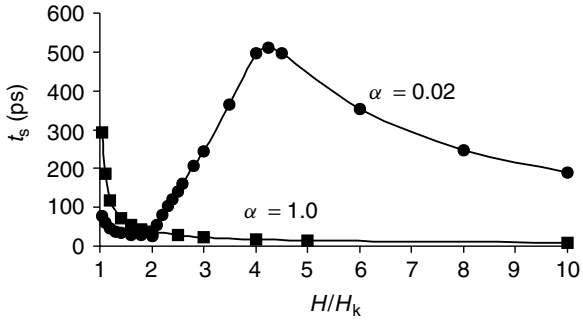

Figure 30. Field dependence of the switching time of a square Cobalt platelet of edge length 12.5 nm (aspect ratio 0.1 and $\alpha = 1$ and 0.01). (Reproduced from D. Goll, G. Schütz and H. Kronmüller: 'Analysis of switching times of inhomogenous magnetization processes in thin platelets', *Physica B* **372**, 2006, copyright © 2006, with permission from Elsevier.)

homogeneous state. This result is due to the fact that the inhomogeneities of $\boldsymbol{J}_s$ at the corners are smaller than 5°.

Another interesting feature of the switching times is their field dependence. Figure 30 shows τ_s for Co as a function of H_{ext}/H_N for $p = 0.01$ and $\alpha = 0.02$ and $\alpha = 1.0$. As for large applied fields $H_{ext} > 1.5H_N$ the switching process takes place quasi–homogeneously the LLG equation is solved assuming homogeneous rotation of $\boldsymbol{M}_s$. For small α-values we may distinguish three stages of τ_s. In stage I up to $H_{ext}/H_N = 2.0$, τ_s decreases. In stage II $2 < \alpha < 4$, τ_s increases up to a maximum value at $H_{ext}/H_N \approx 4$. For larger fields, stage III, τ_s decreases monotonously over the whole field range. Also $Nd_2Fe_{14}B$ show a similar field dependence of τ_s. In the case of large damping parameters the switching time decreases throughout.

The existence of the three field stages is found to be related to the different types of ringing modes as shown in Figure 31 for the three stages. In stage I the ringing amplitude are rather large and therefore the configuration with $\langle J_x \rangle = 0$ is achieved at small times. At larger fields the ringing amplitudes become small leading to larger τ_s values. For large α values τ_s also decreases monotonously over the whole field range.

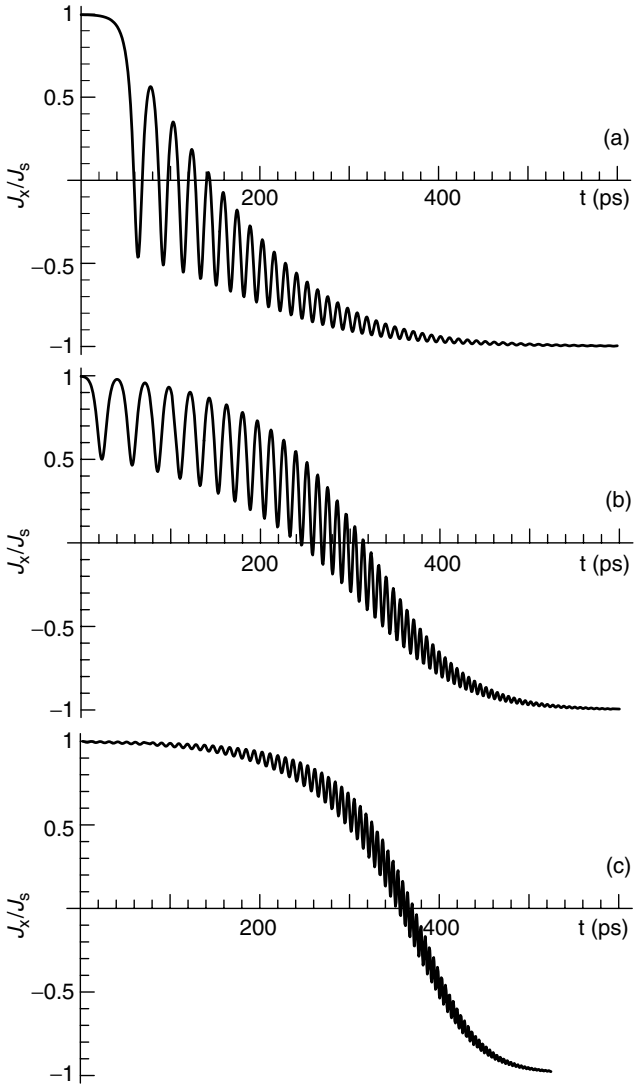

Figure 31. Time dependence of the in-plane x-component of $\boldsymbol{M}_s$ for $\alpha = 0.02$ of the three stages shown for Cobalt in Figure 30. (Reproduced from D. Goll, G. Schütz and H. Kronmüller: 'Analysis of switching times of inhomogenous magnetization processes in thin platelets', *Physica B* **372**, 2006, copyright © 2006, with permission from Elsevier.)

7.4.4 Dynamic nucleation field

Within the framework of the Stoner–Wohlfarth theory (Stoner and Wohlfarth, 1948) and its extension by Kronmüller, Durst and Martinek (1987) the static field follows a hyperbolic curve described by equation (28). An important feature of the asteroid is the rise of the nucleation field for misalignment angles around 90°. Taking into account the precessional movement of $\boldsymbol{M}_s$ it turns out that the nucleation field depends on the damping constant α and the field rate dH_{ext}/dt. Numerical calculations are due to Leineweber and Kronmüller (1999) and Fidler *et al.* (2001). Results obtained for a sphere of $Nd_2Fe_{14}B$ with a rather small radius of 4.2 nm (single-domain particle) with the material parameters $K_1 = 4.3 \times 10^6\,\mathrm{J\,m^{-3}}$, $K_2 = 6.5 \times 10^5\ \mathrm{J/m^{-3}}$, $A = 7.7\,\mathrm{pJ\,m^{-1}}$, $J_s = 1.61\,\mathrm{T}$, $H_N(0) = 5.34 \cdot 10^6\,\mathrm{A\,m^{-1}}$, $\gamma = 2.21 \times 10^5$ 1/sA are shown in Figure 32 for infinite switching field rates. Owing to the precession of $\boldsymbol{M}_s$ the nucleation field over the whole angular range, from $\varphi = 0$ to $\psi = 90°$ is reduced and the reduction is the larger the larger the damping constant α. In particular for angles of $\psi = 90°$ the nucleation field is reduced by nearly a factor of 2, whereas for $\psi = 0°$ no reduction takes place.

7.4.5 Thermal fluctuations and dynamics of magnetization processes

In magnetic recording it is generally accepted that the data stored remain in their state and can be read out reproducibly over many years. Actually, however, the magnetic configuration of a magnetic bit corresponds only to a special minimum of many possible local minima of the Gibbs free energy. Magnetic stability can only be achieved if thermal fluctuations are too weak to overcome the energy barrier to neighboring minima. Pioneering investigations are due to Néel (1949) and Brown (1963, 1979) who gave a first insight into the reversal of magnetization of small particles by thermal fluctuations. According to Brown thermal effects can be included in the LLG equation by adding a stochastically fluctuating field $H_\mathrm{f}(t)$ to the effective field H_eff. The statistical properties of this random field are the following ones:

$$\langle H_{\mathrm{f,i}}(t)\rangle = 0$$
$$\langle H_{\mathrm{f,i}}(t) H_{\mathrm{f,j}}(t+t')\rangle = \mu\delta_{ij}\delta(t') \qquad (192)$$

Equation (192) is a consequence of the fluctuation dissipation theorem (Brown, 1963; Chantrell, Hannany, Wongsam and Lyberatos, 1998), which guarantees that the fluctuating fields are uncorrelated in space and time. The parameter μ corresponds to a temperature dependent constant, which corresponds to the variance of the Gaussian variable $\boldsymbol{H}_\mathrm{f}$ and is given by

$$\mu = \frac{2k_\mathrm{B}T\alpha}{|\gamma_0|M_\mathrm{s}V} \qquad (193)$$

where V denotes the volume of the particle or the discretization volume of finite elements (see also **Magnetization Dynamics Including Thermal Fluctuations: Basic Phenomenology, Fast Remagnetization Processes and Transitions Over High-energy Barriers, Volume 2** and **Magnetization Dynamics: Thermal-driven Noise in Magnetoresistive Sensors, Volume 2**). Inserting $\boldsymbol{H}_\mathrm{f}$ into the LLG equation we obtain a Langevin-type equation for the motion of $\boldsymbol{M}_\mathrm{s}$:

$$\frac{\mathrm{d}\boldsymbol{M}_\mathrm{s}}{\mathrm{d}t} = \frac{\gamma_\mathrm{G}}{1+\gamma_\mathrm{G}^2}\left[\boldsymbol{M}_\mathrm{s}\times(\boldsymbol{H}_\mathrm{eff}+\boldsymbol{H}_\mathrm{f})\right] - \frac{\alpha_\mathrm{G}\gamma_\mathrm{G}}{(1+\alpha_\mathrm{G}^2)\boldsymbol{M}_\mathrm{s}} \qquad (194)$$
$$\times\left[\,\boldsymbol{M}_\mathrm{s}\times\left[\,\boldsymbol{M}_\mathrm{s}\times(\boldsymbol{H}_\mathrm{eff}+\boldsymbol{H}_\mathrm{f})\,\right]\right] \qquad (195)$$

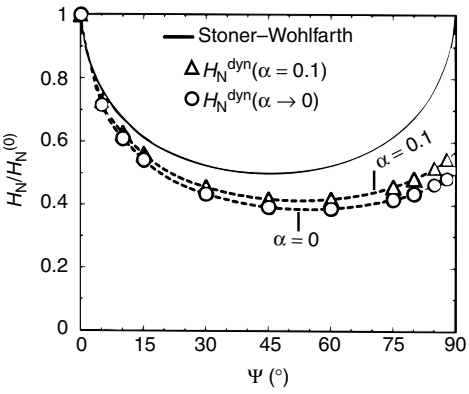

Figure 32. Dynamic nucleation field of a spherical Stoner–Wohlfarth particle of $Nd_2Fe_{14}B$ (diameter 8.4 nm) $H_\mathrm{N}^\mathrm{dyn}$ determined for infinite switching field rates as a function of orientation ψ of H_ext with respect to the easy axis (−) Stoner–Wohlfarth result, $(-0-0-\alpha=0)$, $(-\triangle-\triangle-\alpha=0.1)$. (Reproduced with permmission from Cambridge University Press.)

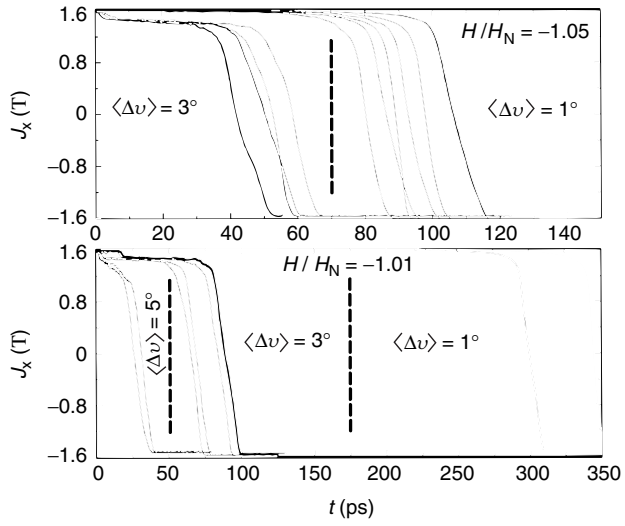

Figure 33. Switching curves of a sphere (diameter 8.4 nm) of $Nd_2Fe_{14}B$ for different applied fields and different strengths $\langle\Delta\vartheta\rangle$ of thermally induced fluctuations. (Reproduced with permmission from Cambridge University Press.)

Thermal excitations described by $\boldsymbol{H}_{\mathrm{f}}$ cause a deviation of $\boldsymbol{M}_{\mathrm{s}}$ from the local equilibrium direction determined by $\boldsymbol{H}_{\mathrm{eff}}$. The effect of $\boldsymbol{H}_{\mathrm{f}}$ in the damping term of equation (194) may be neglected because its effect is of higher order than that of the first term. Equation (194) describes of course the gyromagnetic damped precessional motion of $\boldsymbol{M}_{\mathrm{s}}$, but also the thermally driven spectral noise exerted in small magnetic particles, for example, magnetic dots. Problems of this kind are treated in **Magnetization Dynamics Including Thermal Fluctuations: Basic Phenomenology, Fast Remagnetization Processes and Transitions Over High-energy Barriers, Volume 2** and **Magnetization Dynamics: Thermal-driven Noise in Magnetoresistive Sensors, Volume 2**. A further important effect of $\boldsymbol{H}_{\mathrm{f}}$ is the thermally reduced coercive field of hard magnetic materials as well as the reduction of the switching times by thermal fluctuations (Chantrell, Hannany, Wongsam and Lyberatos, 1998; Leineweber and Kronmüller, 1999; Kronmüller, Leineweber and Bachmann, 2000).

As discussed in Section 7.4.2 in the case of an ideal homogeneously magnetized particle a precession of $\boldsymbol{M}_{\mathrm{s}}$ only takes place if the magnetic field is applied under a misalignment angle θ. Owing to the action of $\boldsymbol{H}_{\mathrm{f}}$ misalignments of $\boldsymbol{M}_{\mathrm{s}}$ occur by thermally activated spin waves. At a temperature T the average misalignment for $T < T_{\mathrm{C}}/2$ is given by $\langle \Delta\theta \rangle = \sqrt{2}(T/T_0)^{3/4}$, where T_0 is the characteristic temperature of Bloch's $\mathrm{T}^{3/2}$ law ($T_0 \approx T_{\mathrm{C}}$). Figure 33 shows switching curves for average misalignment angles $\langle \Delta\theta \rangle$ of $1^\circ, 3^\circ$, and 5° under ideally oriented applied fields of $H_{\mathrm{ext}} = -1.01 H_{\mathrm{N}}$ and $-1.05 H_{\mathrm{N}}$ for the hard magnetic alloy $\mathrm{Nd_2Fe_{14}B}$ (Kronmüller and Fähnle, 2003). These results have been obtained by the dynamic finite element method assuming a Boltzmann distribution $p(\Delta\theta) \propto \exp\left[-\Delta\theta/\langle\Delta\theta\rangle\right]$for the probability of the local misalignment within each cell of the FEM grid. According to Figure 33 the switching relaxation times are considerably reduced by thermal fluctuations. Owing to the assumption of uncorrelated statistical fluctuations switching curves determined successively show a moderate fluctuation.

ACKNOWLEDGMENTS

The author gratefully acknowledges stimulating discussions with D. Goll and S. Macke.

REFERENCES

Aharoni, A. (1973). Asymmetry in domain walls. *Physica Status Solidi (a)*, **18**, 661–667.

Aharoni, A. (1975). Two-dimensional domain walls in ferromagnetic films I - III. *Journal of Applied Physics*, **46**, 408–916, 1783–1786.

Aharoni, A. (1996). *Introduction to the Theory of Ferromagnetism*, Chapman & Hall: London, New York, Tokyo, Melbourne, Madras.

Aharoni, A. (1997). Angular dependence of nucleation by curling in a prolate spheroid. *Journal of Applied Physics*, **82**, 1281–1287.

Aharoni, A. (1998a). Curling nucleation eigenvalue in a prolate spheroid. *IEEE Transactions on Magnetics*, **34**, 2175–2176.

Aharoni, A. (1998b). Periodic walls in very thin films. *Journal of Physics: Condensed Matter*, **10**, 9495–9505.

Aharoni, A. (1998 c). Demagnetization factors for rectangular ferromagnetic prisms. *Journal of Applied Physics*, **83**, 3422–3434.

Aharoni, A. and Jacubovics, J.P. (1990). Structure and energy of 90° walls in thin ferromagnetic films. *IEEE Transactions on Magnetics*, **26**, 2810–2815.

Aharoni, A. and Shtrikman, S. (1958). Magnetization curve of the infinite cylinder. *Physical Review B*, **109**, 1522–1528.

Akulov, N.S. (1928–1931). Zur Theorie der Magnetisierungskurve von Einkristallen. *Zeitschrift fur Physik*, **67**, 794–807.

Allwood, D.A., Xiong, G., Cooke, M.D. and Locatelli, A. (2002). Submicrometer ferromagnetic NOT gate and shift register. *Science*, **296**, 2003–2006.

Barkhausen, H. (1919). Zwei mit Hilfe der neuen Verstärker entdeckte Erscheinungen. *Physische Zeitschrift*, **20**, 401–403.

Becker, R. (1930). Zur Theorie der Magnetisierungskurve. *Zeitschrift fur Physik*, **62**, 253–269.

Becker, R. (1932). Elastic tensions and magnetic characteristics. *Physische Zeitschrift*, **33**, 905–913.

Becker, R. (1934). Über die Magnetostriktionvon ferromagnetischen Ellipsoiden. *Zeit-schrift für Physik*, **87**, 547–559.

Becker, R. and Döring, W. (1939). *Ferromagnetism*, Springer: Berlin.

Berger, L. (1996). Emission of spin waves by a magnetic multilayer by a current. *Physical Review B*, **54**, 9353–9358.

Birss, P.R. (1964). *Symmetry and Magnetism*, Wohlfarth, E.P. (Ed.), North Holland: Amsterdam.

Bitter, F. (1931). On inhomogeneities in the magnetization of ferromagnetic materials. *Physical Review*, **41**, 507–513.

Bloch, F. (1932). Zur Theorie des Austauschproblems und der Remanenzerscheinungen der Ferromagnetika. *Zeitschrift fur Physik*, **67**, 794–807.

Bonet, E., Wernsdorfer, W., Barbara, B., *et al.* (1999). Three-dimensional magnetization reversal measurements in nanoparticles. *Physical Review Letters*, **83**, 4188.

Brown, W.F. Jr. (1940). Theory of the approach to ferromagnetic saturation. *Physical Review*, **58**, 736–743.

Brown, W.F. Jr. (1941). The effect of dislocation on magnetization near saturation. *Physical Review*, **60**, 139–147.

Brown, W.F. Jr. (1945). Virtues and weaknesses of the domain concept. *Reviews of Modern Physics*, **17**, 15–19.

Brown, W.F. Jr. (1962). *Magnetostatic Principles in Ferromagnetism*, North Holland: Amsterdam.

Brown, W.F. Jr. (1963). *Micromagnetics*, Wiley, Interscience: New York, London.

Brown, W.F. Jr. and La Bonte, A.E. (1965). Structure and energy of one-dimensional domain walls ferromagnetic thin films. *Journal Applied Physics*, **36**, 1380–1386.

Brown, W.F. Jr. (1966). *Magnetoelastic Interaction, Springer Tracts in Natural Philosophy*, Truesdell, C. (Ed.), Springer-Verlag: Berlin, Heidelberg, New York, Vol. 9.

Brown, W.F. Jr. (1979). Thermal fluctuations of fine ferromagnetic particles. *IEEE Transactions on Magnetics*, **15**, 1196–1208.

Chantrell, R.W., Hannany, J.D., Wongsam, M. and Lyberatos, A. (1998). High-speed switching in magnetic recording media. *IEEE Transactions on Magnetics*, **34**, 349–354.

Chikazumi, S. (1997). *Physics of Ferromagnetism*, Clarendon Press: Oxford.

Dietze, H-D. and Thomas, H. (1961). Bloch- und Néelwände in dünnen magnetischen Schichten. *Zeitschrift fur Physik*, **163**, 523–534.

Dirac, P.A.M. (1928). The quantum theory of the electron. *Proceedings of the Royal Society*, **117A**, 610–624.

Doering, W. (1948). Über die Trägheit der Wände zwischen Weissschen Bezirken. *Zeitschrift fur Naturforschung*, **3a**, 373–379.

Domann, M., Grimm, H. and Kronmüller, H. (1979). The high-field magnetization curve of amorphous ferromagnetic alloys. *Journal of Magnetism and Magnetic Materials*, **13**, 81–84.

Fähnle, M. (1981). Micromagnetic theory of phase transitions in inhomogeneous ferromagnets. *Physical Status Solidi B*, **106**, 519–528.

Fähnle, M. and Kronmüller, H. (1978). Influence of spacially random magnetostatic, magnetocrystalline, magnetostrictive and exchange fluctuations on law of approach to ferromagnetic saturation of amorphous alloys. *Journal of Magnetism and Magnetic Materials*, **8**, 149–156.

Fähnle, M. and Kronmüller, H. (1980). Micromagnetic theory of phase transitions in inhomogeneous ferromagnets II. Applications. *Physical Status Solidi B*, **98**, 212–228.

Feldtkeller, E. (1965). Mikromagnetisch stetige und unstetige Magnetisierungs-konfigurationen. *Zeitschrift für an-gewandte Physik*, **19**, 530–536.

Feldtkeller, E. and Thomas, H. (1965). Struktur und Energie von Blochlinien in dünnen ferromagnetischen Schichten. *Physik der Kondensiterten Materie*, **4**, 8–14.

Fidler, J., Schrefl, T., Scholz, W. *et al*. (2001). Micromagnetzic simulation of magnetic reversal in rotational magnetic fields. *Physica B*, **306**, 112–116.

Frei, E.H., Strikman, S. and Treves, D. (1957). Critical size and nucleation of ideal ferromagnetic particles. *Physical Review*, **106**, 446–458.

Gans, R. (1932). Regarding the magnetic behaviour of isotropic ferromagnets. *Annalen der Physik*, **152**, 28–44.

Gilbert, T.L. (1955). A Lagrangian formulation of the gyromagnetic equation of the magnetization field. *Physical Review*, **100**, 1253.

Gilbert, T.L. and Kelly, J.M. (1955). Anomalous rotational damping in ferromagnetic sheets, *Proceedings Conference on Magnetism and Magnetic Materials, American Institute of Electrical Engineers*, New York, pp. 253–263.

Goll, D., Berkowitz, A.E. and Bertram, H.N. (2004). Critical sizes for ferromagnetic spherical hollow particles. *Physical Review B*, **70**, 184432.

Goll, D., Schütz, G. and Kronmüller, H. (2003). Critical thickness for high-remanent single-domain configurations in square ferromagnetic thin platelets. *Physical Review B*, **67**, 094414-1–094414-8.

Goll, D., Schütz, G. and Kronmüller, H. (2006). Analysis of switching times of inhomogeneous magnetization processes in thin platelets. *Physica B*, **372**, 273–276.

Grimm, H. and Kronm̈ller, H. (1980). Magnetic polarization of amorphous alloys in the approach to ferromagnetic saturation. *Journal of Magnetism and Magnetic Materials*, **15–18**, 1411–1412.

Grimm, H. and Kronmüller, H. (1983). Investigation of structural defects in the amorphous ferromagnetic alloy $Fe_{40}Ni_{40}P_{14}B_6$. *Physical Status Solidi B*, **117**, 663–674.

Grollier, J., Boulenc, P., Cros, V., *et al*. (2003). Switching a spin valve back and forth by current-induced domain wall motion. *Applied Physics Letters*, **83**, 509–511.

Hai, N.H., Dempsey, N.M., Veron, M., *et al*. (2003). An original route for the preparation of hard FePt. *Journal of Magnetism and Magnetic Materials*, **257**, L139–L145.

Heisenberg, W. (1928). Zur Theorie des Ferromagnetismus. *Zeitschrift fur Physik*, **49**, 619–636.

Hertel, R. (2002). Thickness dependence of magnetization structures in thin permalloy rectangles. *Zeitschrift Fur Metallkunde*, **93**, 957–962.

Hertel, R. and Kronmüller, H. (2002). Finite element calculations on the single domain limit of a ferromagnetic cube – a solution to an mu – MAG standard problem no. 3. *Journal of Magnetism and Magnetic Materials*, **238**, 185–199.

Herzer, G., Fähnle, M., Egami, T. and Kronmüller, H. (1980). Micromagnetic theory of phase transitions in inhomogeneous ferromagnets III. Non-local Landau–Ginzburg theory. *Physical Status Solidi B*, **101**, 713–721.

Herzer, G., Fernengel, W. and Adler, E. (1986). On the theory of nucleation fields in uniaxial ferromagnets. *Journal of Magnetism and Magnetic Materials*, **58**, 48–54.

Hock, St. and Kronmüller, H., (1987). *Proceedings of the 5th International Conference on Magnetic Anisotropy and Coercivity in RE Transition Metal Alloys*, Herget, C., Kronmüller, H. and Poerschke, P. (Eds.), DPG-GmbH: Bad Honnef, p. 275.

Holstein, T. and Primakoff, H. (1940). Field dependence of the intrinsic domain magnetization of a ferromagnet. *Physical Review*, **58**, 1098–1113.

Holz, A. and Hubert, A. (1969). Wandstrukturen in dünnen magnetischen Schichten. *Zeitschrift fur Angewandte Physik*, **20**, 145–152.

Hubert, A. (1974). *Theorie der Domänenwände in Geordneten Wänden*, Springer: Berlin, Heidelberg, New York.

Hubert, A. and Schäfer, R. (1998). *Magnetic Domains*, Springer: Berlin, Heidelberg, New York.

Jiles, D. (1990). *Introduction to Magnetism and Magnetic Materials*, Chapman & Hall: London, New York, Tokyo, Melbourne, Madras.

Kasuya, T. (1956). A theory of metallic ferromagnetism and antiferromagnetism on Zener's model. *Progress of Theoretical Physics*, (Kyoto) **16**, 45–57.

Kikuchi, R. (1956). On the minimum of magnetization reversal time. *Journal of Applied Physics*, **27**, 1352–1357.

Kimura, T., Otami, Y., Tsukagoshi, K. and Aoyagi, Y. (2003). *Journal of Applied Physics*, **94**, 07947.

Kirchner, R. and Döring, W. (1968). Structure and energy of a Néel wall. *Journal of Applied Physics*, **39**, 855–863.

Kittel, C. (1949). Physical theory of ferrimagnetic domains. *Reviews of Modern Physics*, **21**, 541–583.

Kittel, C. and Galt, J.K. (1956). Ferromagnetic domain theory. *Solid State Physics*, **3**, 437–565.

Kittel, C. and Herring, C. (1951). On the theory of spin waves in ferromagnetic media. *Physical Review*, **81**, 869–880.

Kläui, M., Vaz, C.A.F., Bland, J.A.C., *et al*. (2003). Domain wall motion induced by spin polarized currents in ferromagnetic ring structures. *Applied Physics Letters*, **83**, 105–107.

Kläui, M., Vaz, C.A.F., Bland, J.A.C., *et al*. (2005). Controlled and reproducible domain wall displacement by current pulses injected into ferromagnetic ring structures. *Physical Review Letters*, **94**, 106601.

Kléman, M. (1980). Dislocations and magnetism. In *Dislocations in Solids*, Nabarro, F.R.N. (Ed.), North Holland: Amsterdam, pp. 349–402, Vol. 5.

Köster, E. (1967) Verformungs- und Temperaturabhängigkeit der Magnetisierungsprozesse in Nickeleinkristallen. II. Blochwandverschiebungen und Drehungen der spontanen Magnetisierung in ⟨001⟩- Nickeleinkristallen. *Physica Status Solidi*, **19**, 655–671.

Kröner, E. (1958). *Kontinuumstheorie der Versetzungen und Eigenspannungen*, Springer-Verlag: Berlin, Göttingen, Heidelberg.

Kronmüller, H. (1959). Das magnetische Einmündungsgesetz bei plastisch verformten Nickel- und Nickel-Kobalt-Einkristallen. *Zeitschrift fur Physik*, **154**, 1314–1318.

Kronmüller, H. (1967). Contribution of dislocations to magnetocrystalline energy and their effect on rotational hysteresis process. *Journal of Applied Physics*, **38**, 1314–1318.

Kronmüller, H. (1979). Micromagnetism in amorphous alloys. *IEEE Transactions on Magnetics*, **15**, 1218–1225.

Kronmüller, H. (1981). Micromagnetism and microstructures of amorphous alloys. *Journal of Applied Physics*, **52**, 1859–1864.

Kronmüller, H. (1985). The nucleation fields of uniaxial ferromagnetic crystals. *Physical Status Solidi B*, **130**, 197–203.

Kronmüller, H. (1987). Theory of nucleation in inhomogeneous ferromagnets. *Physical Status Solidi B*, **144**, 385–396.

Kronmüller, H. (1991). Micromagnetic background. In *Hard Magnetic Materials*, Grandjean, F. and Long, G.J. (Eds.), Kluwer: Dordrecht, p. 461.

Kronmüller, H., Durst, K-D. and Martinek, G. (1987). Angular dependence of the coercive field in sintered $Fe_{77}Nd_{15}B_8$ magnets. *Journal of Magnetism and Magnetic Materials*, **69**, 149–157.

Kronmüller, H. and Fähnle, M. (1980). Micromagnetic theory of phase transitions in inhomogeneous ferromagnets. *Physical Status Solidi B*, **97**, 513–520.

Kronmüller, H. and Fähnle, M. (2003). *Micromagnetization and the Microstructure of Ferromagnetic Solids*, Cambridge University Press: Cambridge.

Kronmüller, H., Fähnle, M., Domann, M., *et al*. (1979). Magnetic properties of amorphous ferromagnetic alloys. *Journal of Magnetism and Magnetic Materials*, **13**, 53–70.

Kronmüller, H., Leineweber, T. and Bachmann, M. (2000). Intrinsic dynamic and quasistatic magnetization processes in small particles, *16th IMACS World Congress (2000 IMACS)* Lausanne.

Kronmüller, H., Lenge, L. and Habermaier, H-U. (1984). Investigation of the approach to ferromagnetic saturation in sputtered amorphous $Fe_{80-x}Ni_xB_{70}$ films. *Physics Letters A*, **101**, 439–442.

Kronmüller, H. and Seeger, A. (1961). Die Einmündung in die ferromagnetische Sättigung. II. Theorie des Einmündungsgesetzes in plastisch verformten kubisch-flächenzentrierten Einkristallen. *Journal of Physics and Chemistry of Solids*, **18**, 93–115.

Kronmüller, H. and Ulner, J. (1977). Micromagnetic theory of amorphous ferromagnets. *Journal of Magnetism and Magnetic Materials*, **6**, 52–56.

Krüger, B., Pfannkuche, D., Bolte, M., *et al*. (2007). Current-driven domain wall dynamics in curved ferromagnetic nanowires. *Physical Review B*, **75**, 0544211–0544219.

La Bonte, A.E. (1969). Two-dimensional Bloch-type domain walls in ferromagnetic films. *Journal of Applied Physics*, **40**, 2450–2458.

Landau, L.D. and Lifshitz, E. (1935). On the theory of the dispersion of magnetic permeability in ferromagnetic bodies. *Physikalische Zeitschrift der Sowjetunion*, **8**, 153–169.

Landau, L.D. and Lifshitz, E.M. (1971). Elektrodynamik der Kontinua. Akademie-Verlag: Berlin, p. 173–196.

Leineweber, T. and Kronmüller, H. (1999). Dynamics of magnetization states. *Journal of Magnetism and Magnetic Materials*, **192**, 575–590.

Lenge, L. and Kronmüller, H. (1986). Low-temperature magnetization of sputtered amorphous FeNiB films. *Physical Status Solidi B*, **95**, 621–633.

Li, Z. and Zhang, S. (2004). Domain wall dynamics and spin-wave excitations with spin transfer torques. *Physical Review Letters*, **92**, 207203.

Lilley, B.A. (1950). Energies and widths of domain boundaries in ferromagnetics. *Philosophical Magazine*, **41**, 792–813.

Lubersky, F.E. and Morelock, C.R. (1964). Magnetization reversal of almost perfect whiskers. *Journal of Applied Physics*, **35**, 2055–2058.

Malozemoff, A.R. and Slonczewski, J.C. (1979). *Magnetic Domain Walls in Bubble Materials*, Academic Press: New York.

Miltat, J., Thiaville, A. and Trouilloud, P.L. (1989). Néel line structures and energies in uniaxial ferromagnets with quality factor $Q > 1$. *Journal of Magnetism and Magnetic Materials*, **82**, 297–308.

Morrish, A.H. (1965). *The Physical Principles of Magnetism*, John Wiley & Sons: New York.

Néel, L. (1949a). Influence des fluctuations thermiques sur l' alimentation des grains ferromagnétiques très fins. *Comptes Rendus*, **228**, 664–666.

Néel, L. (1949b). Théorie du trainage magnétique des ferromagnétiques en grains fins avec applications aux terres cuites. *Annales de Géophysique*, **5**, 99–136.

Néel, L. (1950). Théorie du trainage magnétique des substances massive dans le domaine de Rayleigh. *Journal de Physique et le Radium*, **11**, 49–61.

Néel, L. (1955a). Theoretical remarks on ferromagnetism at low temperatures. In *Progress in Low-Temperature Physics*, Gorter C.J. (Ed.), North Holland: Amsterdam, pp. 347–350.

Néel, L. (1955b). Energie des parois de Bloch dans les couches minces. *Comptes Rendus de l' Academie des Sciences (Paris)*, **241**, 533–537.

Néel, L., Pauthenet, R., Rimet, G. and Giron, V.S. (1960). On the law of magnetization of ferromagnetic single crystals and polycrystal – applications to uniaxial compounds. *Journal of Applied Physics*, **31**, S27–S28.

O'Dell, T.H. (1981). *Ferromagnetodynamics. The Dynamics of Magnetic Bubbles, Domains, and Domain Walls*, Wiley: New York.

Riedel, H. and Seeger, A. (1971). Micromagnetic treatment of Néel walls. *Physical Status Solidi B*, **46**, 377–384.

Rieder, G. (1959). Eigenspannungen in unendlich geschichteten und elastisch anisotropen Medien, insbesondere in Weissschen Bezirken und geschichteten Platten. Verhandlungen der Braunschweigischen Wissenschaftlichen Gesellschaft, Vol. XI, pp. 20–61.

Ruderman, M.A. and Kittel, C. (1954) Indirect exchange coupling of nuclear magnetic moments by conduction electrons. *Physical Review*, **96**, 99–102.

Slavin, A.N. and Kabos, P. (2005). Approximate theory of microwave generation in a current-driven magnetic nanoconstant magnetized in an arbitrary direction. *IEEE Transactions on Magnetics*, **41**, 1264–1273.

Seeger, A. and Kronmüller, H. (1960). Die Einmündung in die ferromagnetische Sättigung. I. Allgemeine Theorie des Einflusses innerer Spannungen auf das Einmündungsgesetz mit Anwendungen auf Zwischengitteratome und abgeschreckte Metalle. *Journal of Physics and Chemistry of Solids*, **12**, 298–313.

Sixtus, K.J. and Tonks, L. (1931). Propagation of large Barkhausen discontinuities. *Physical Review*, **37**, 930–938.

Stoner, E.C. and Wohlfarth, E.P. (1948). A mechanism of magnetic hysteresis heterogeneous alloys. *Philosophical Transactions of the Royal Society of London, Series A*, **240**, 594–644.

Slonczewski, I.C. (1996) Current-driven excitation of magnetic multilayers. *Journal of Magnetism and Magnetic Materials*, **159**, L1–L7.

Slonczewski, J.C. (1999) Excitation of spin waves by an electric current. *Journal of Magnetism and Magnetic Materials*, **195**, L261–L268.

Slonczewski, I.C. (1972). Dynamics of magnetic domain walls. *International Journal of Magnetism*, **2**, 85–97.

Tatara, G. and Kono, H. (2004). Theory of current-driven domain wall motion: spin transfer versus momentum transfer. *Physical Review Letters*, **92**, 086601.

Thiaville, A., Hubert, A. and Schäfer, R. (1991). An isotropic description of the new-found gradient- related magnetooptical effect. *Journal of Applied Physics*, **69**, 4551–4555.

Thiaville, A., Nakatami, Y., Miltat, J. and Suzuki, Y. (2005). Micromagnetic understanding of current-driven domain wall motion in patterned nanowires. *Europhysics Letters*, **69**, 990–996.

Thiaville, A., Nakatami, Y., Miltat, J. and Vernic, N. (2004). Domain wall motion by spin-polarized current: a micromagnetic study. *Journal of Applied Physics*, **95**, 7049–7051.

Thirion, C., Wernsdorfer, W., Kläui, M., *et al*. (2006). Anisotropy engineering in Co nanodiscs fabricated using perpatterned silicon pillars. *Nanotechnology*, **17**, 1960–1963.

Tsoi, M., Fontana, R.E. and Parkin, S.S.P. (2003). Magnetic domain wall motion triggered by an electric current. *Applied Physics Letters*, **83**, 2617–2619.

Umakoshi, Y. and Kronmüller, H. (1981). Observations of dislocations in deformed iron single crystals by means of high-field susceptibility measurements. *Physical Status Solidi A*, **66**, 509–520.

Usov, N.A. and Peschany, S.E. (1993). Magnetization curling in a fine cylindrical particle. *Journal of Magnetism and Magnetic Materials*, **118**, L290–L294.

Usov, N.A. and Peschany, S.E. (1994). Vortex state in a short ferromagnetic cylinder. *The Physics of Metals and Metallography*, **78**, 591–599.

Vasquez, M., Fernengel, W. and Kronmüller, H. (1989). Approach to magnetic saturation in rapidly quenched amorphous alloys. *Physical Status Solidi A*, **115**, 547–553.

Vernier, N., Allwood, D.A., Atkinson, D., *et al*. (2004). Domain wall propagation in magnetic nanowires by spin-polarized current injection. *Europhysics Letters*, **65**, 526–532.

Versluijs, J.J., Bari, M.A. and Coey, J.M.D. (2001). Magnetoresistance of half-metallic oxide nano-contacts. *Physical Review Letters*, **87**, 026601.

Waintal, X. and Viret, M. (2004). Current induced distortion of a magnetic domain wall. *Europhysics Letters*, **65**, 427–433.

Walker, L.R., unpublished, reported by Dillon, J.F. (1963). In *Magnetism*, Rado, G.T. and Suhl, H. (Eds.), Academic Press: New York, pp. 450–454, Vol. III.

Weiss, P. (1907). L' hypothese de champs moléculaire et la propritée ferromagnetique. *Journal de Physique et le Radium*, **6**, 661–690.

Williams, H.J., Bozorth, R.M. and Shokley, W. (1949). Magnetic domain patterns on single crystals of silicon-iron. *Physical Review*, **75**, 155–178.

Yamaguchi, A., Ono, T., Nasu, S., *et al*. (2004). Real space observation of current-driven domain wall motion in submicron magnetic wires. *Physical Review Letters*, **92**, 077205.

Yosida, K. (1957). Magnetic properties of Cu-Mn alloys. *Physical Review*, **106**, 893–898.

Zener, C. (1951a). Introduction between the d-shells in the transition metals. *Physical Review*, **81**, 440–444.

Zener, C. (1951b). Introduction between the d-shells in the transition metals. 3. Calculation of the Weiss factors in Fe, Co and Ni. *Physical Review*, **83**, 299–301.

FURTHER READING

Callen, E.R. and Callen, H.B. (1960). Anisotropic magnetization. *Journal of Physics and Chemistry of Solids*, **16**, 310–328.

Danan, M.H. (1958). Comparaison des lois d' approche a la saturation déduites de mesures d' imatation et de mesures de susceptibilities differentielles. *Comptes Rendus de l'Acadedmie des Sciences (Paris)*, **246**, 1182–1185.

Gilbert, T.L. (2004). A phenomenological theory of damping in ferromagnetic materials. *IEEE Transactions on Magnetics*, **40**, 3443–3449.

Kronmüller, H., Durst, K.D. and Sagawa, M. (1980). Analysis of the magnetic hardening mechanism in RE-FeB permanent magnets. *Journal of Magnetism and Magnetic Materials*, **74**, 291–302.

Lederman, M., O'Barr, L. and Schultz, S. (1995). Experimental study of individual submicron cylinders. *IEEE Transactions on Magnetics*, **31**, 3793–3795.

Miltat, J. and Kléman, M. (1973). Magnetostrictive displacements around a domain wall junction: elastic field calculation and application to X-ray topography. *Philosophical Magazine*, **28**, 1015–1033.

Néel, L. (1944). Effets des cavités et des inclusions sur le champ coércitif. *Cahiers de Physique*, **25**, 21–44.

Redjdal, M., Kakay, A., Ruane, M.F. and Humphrey, F.B. (2002a). Cross-tie walls in thin permalloy films. *IEEE Transactions on Magnetics*, **38**, 2471–2473.

Redjdal, M., Kakay, A., Ruane, M.F. and Humphrey, F.B. (2002b). Magnetic domain wall transitions based on chirality change and vortex position in thin permalloy (TM) films. *Journal of Applied Physics*, **91**, 8278–8280.

Zener, C. (1954). Classical theory of the temperature dependence of magnetic anisotropy energy. *Physical Review*, **96**, 1335–1337.

Numerical Micromagnetics: Finite Difference Methods

Jacques E. Miltat[1] and Michael J. Donahue[2]

[1] *Université Paris XI Orsay and CNRS, Orsay, France*
[2] *National Institute of Standards and Technology, Gaithersburg, MD, USA*

The first two-dimensional numerical simulation of a domain wall structure was published in 1969. In his celebrated work, LaBonte (1969), showed that the structure of a domain wall in an infinite magnetically soft thin film with thickness in the 100 nm range was neither Bloch nor Néel type, but somehow a mixture of both. Some 35 years later, numerical micromagnetics has become ubiquitous and rather unavoidable a tool in the study of magnetic nanostructures. Rather unexpectedly, LaBonte's pioneering work remains modern because of the immense progress made in the elaboration and observation of magnetic nanostructures. Suffice it to say that three-dimensional numerical micromagnetics unravels much hidden complexity and yet firm underlying logics in the wall structures and magnetization distribution within faceted iron nanocrystals, in agreement with the most demanding experiments (Hertel *et al*., 2005). The present chapter deals with numerical micromagnetics using finite difference methods and is organized as follows. Section 1 captures the essentials of micromagnetics, a continuum theory of ferro- or ferrimagnetic bodies, and thus provides the necessary background for the understanding of the following sections. Sections 2 and 3 are devoted to numerical implementations of the micromagnetic continuum theory with primacy given to the field acting on the magnetization and energy, respectively. Section 4 addresses the issue of accuracy in the time domain. Lastly, on the basis of a single but demanding example, a brief comparison between the two approaches is attempted in Section 5.

Handbook of Magnetism and Advanced Magnetic Materials. Edited by Helmut Kronmüller and Stuart Parkin. Volume 2: *Micromagnetism*. ISBN: 978-0-470-02217-7.

1 BACKGROUND

If solely referring to the number of lattice sites in a micron-size magnetic element with thickness in the range of a few nanometers, it becomes immediately clear that fully *ab initio* methods aimed at defining the local value of the magnetic moment and its direction are out of reach. Micromagnetics is a continuum theory of ferro or ferrimagnetic materials, which allows for the computation of magnetization distributions in samples of arbitrary shape (Brown, 1963; Aharoni, 1996; Hubert and Schäfer, 1998). Its basic assumptions consist in considering the magnetization modulus to remain constant ($\mathbf{M} = M_s\mathbf{m}$, $\mathbf{m}\cdot\mathbf{m} = 1$) and all vector quantities (the magnetization $\mathbf{M}$, the exchange $\mathbf{H}_{\text{exch}}$, and demagnetizing $\mathbf{H}_{\text{d}}$ fields, especially) to vary slowly at the atomic scale.

The components of **m** are the direction cosines of the magnetization **M**. Micromagnetics is based on the one hand on the notion of an effective field acting on the magnetization (Brown, 1963; Miltat, 1994; Aharoni, 1996; Hubert and Schäfer, 1998; Kronmüller and Fähnle, 2003), on the other hand on an equation depicting magnetization dynamics known as the *Landau–Lifshitz* or *Landau–Lifshitz–Gilbert* (*LLG*) equation, depending on the exact formulation of damping. According to Brown's theory (Brown, 1963), the effective field is the functional derivative of the energy density ε, w.r.t. magnetization:

$$\mathbf{H}_{\text{eff}} = -\frac{1}{\mu_0 M_{\text{s}}}\frac{\delta\varepsilon}{\delta\mathbf{m}} \tag{1}$$

As shown earlier in this volume (see also **General Micromagnetic Theory, Volume 2**), the effective field usually contains contributions stemming from the exchange, anisotropy, applied field or Zeeman, and demagnetizing energy densities, namely

$$\begin{aligned}\mathbf{H}_{\text{eff}} &= -\frac{1}{\mu_0 M_{\text{s}}}\frac{\delta\varepsilon}{\delta\mathbf{m}} \\ &= \frac{2A}{\mu_0 M_{\text{s}}}\nabla^2\mathbf{m} - \frac{1}{\mu_0 M_{\text{s}}}\frac{\delta\varepsilon_K}{\delta\mathbf{m}} + \mathbf{H}_{\text{app}} + \mathbf{H}_{\text{d}}\end{aligned} \tag{2}$$

corresponding to the following micromagnetic energy:

$$\begin{aligned}E = \int_{\text{V}} \Big[& A\,(\boldsymbol{\nabla}\mathbf{m})^2 + \varepsilon_K - \mu_0 M_{\text{s}}\left(\mathbf{H}_{\text{app}}\cdot\mathbf{m}\right) \\ & -\frac{1}{2}\mu_0 M_{\text{s}}\left(\mathbf{H}_{\text{d}}\cdot\mathbf{m}\right)\Big]\mathrm{d}^3 r\end{aligned} \tag{3}$$

where, A is the exchange constant (units $\mathrm{J\,m^{-1}}$), ϵ_K the anisotropy energy density (units $\mathrm{J\,m^{-3}}$), $\mathbf{H}_{\text{app}}$ and $\mathbf{H}_{\text{d}}$ the applied and demagnetizing field (units $\mathrm{A\,m^{-1}}$), respectively. As noted as early as 1949 by Kittel (1949), the exchange energy may, by combining the constraint $\mathbf{m}^2 = 1$ with the vector relation $|\nabla f|^2 = \nabla\cdot(f\nabla f) - f\nabla^2 f$, be expressed in either of the following forms:

$$\begin{aligned}E_{\text{exch}} &= \int_{\text{V}} \left[A\,(\boldsymbol{\nabla}\mathbf{m})^2\right]\mathrm{d}^3 r \\ &= -\int_{\text{V}} \left[A\mathbf{m}\cdot\left(\frac{\partial^2\mathbf{m}}{\partial x^2} + \frac{\partial^2\mathbf{m}}{\partial y^2} + \frac{\partial^2\mathbf{m}}{\partial z^2}\right)\right]\mathrm{d}^3 r\end{aligned} \tag{4}$$

Additional energy terms may be included in the energy, for example, terms arising from magnetostriction, or longer range exchange coupling across nonmagnetic spacer layers in spin valves (Kools, Rijks, de Veirman and Coehoorn, 1995; Wei and Bertram, 1996); such terms will not be considered in the following.

When considering an energy density functional solely involving exchange and magnetostatic interactions (the ideally soft magnetic material limit), dimensional arguments soon lead to the definition of a characteristic length known as the (*magnetostatic*) *exchange length*

$$\Lambda = \sqrt{\frac{2A}{\mu_0 M_{\text{s}}^2}} \tag{5}$$

a quantity labeled l_s in **General Micromagnetic Theory, Volume 2**. The exchange length rarely exceeds a few nanometers in 3d ferromagnetic materials or their alloys, thereby imposing severe constraints on the mesh size in numerical simulations.

The effective field (see equation (2)) exerts a torque on the magnetization that is proportional to $\mathbf{M}\times\mathbf{H}$. In full analogy with classical mechanics, the rate of change of the magnetization – angular momentum – is, in the absence of damping, equal to the torque, namely

$$\frac{\mathrm{d}}{\mathrm{d}t}\mathbf{m}(t) = -\gamma_0\left[\mathbf{m}(t)\times\mathbf{H}_{\text{eff}}(t)\right] \tag{6}$$

It follows from equation (6) that as long as the torque is zero, the angular momentum is conserved. For a free electron, γ_0 is equal to $\approx 2.21\times 10^5\,\mathrm{A^{-1}ms^{-1}}$. Still in the absence of damping, magnetization motion reduces to a precession of the magnetization around the effective field, with frequency:

$$\omega_0 = \gamma_0\mathbf{H}_{\text{eff}} \tag{7}$$

that is, $\approx$28 MHz/(mT) in units of $\mu_0\mathbf{H}_{\text{eff}}$ for a free electron spin.

Gilbert damping (Gilbert, 1955, 1956, 2004) is most simply introduced by adding to the effective field an Ohmic type dissipation term, namely

$$\mathbf{H}_{\text{eff}} = \mathbf{H}_{\text{eff}} - \alpha\frac{1}{\gamma_0 M_{\text{s}}}\frac{\mathrm{d}\mathbf{M}}{\mathrm{d}t} \tag{8}$$

where, α is the (dimensionless) Gilbert damping parameter. Introducing equation (8) into equation (6) leads to the so-called LLG equation,

$$\frac{\mathrm{d}\mathbf{m}}{\mathrm{d}t} = -\gamma_0\left(\mathbf{m}\times\mathbf{H}_{\text{eff}}\right) + \alpha\left[\mathbf{m}\times\frac{\mathrm{d}\mathbf{m}}{\mathrm{d}t}\right] \tag{9}$$

or its numerically more tractable and mathematically equivalent form

$$\left(1+\alpha^2\right)\frac{\mathrm{d}\mathbf{m}}{\mathrm{d}t} = -\gamma_0\left[\mathbf{m}\times\mathbf{H}_{\text{eff}} + \alpha\left[\mathbf{m}\times\left(\mathbf{m}\times\mathbf{H}_{\text{eff}}\right)\right]\right] \tag{10}$$

Given a magnetization distribution $\mathbf{m}(\mathbf{r},\mathbf{t}) = \mathbf{M}(\mathbf{r},\mathbf{t})/M_{\text{s}}$, the LLG equation specifies the magnetization distribution at

time $t + \mathrm{d}t$ provided due respect of boundary conditions is maintained. Alternatively, if a sole magnetization distribution at equilibrium is sought for, the only condition that needs to be satisfied reads:

$$\mathbf{m} \times \mathbf{H}_{\text{eff}} = \mathbf{0} \tag{11}$$

Because the exchange energy involves the square of the gradient of the magnetization components, its variation gives rise not only to the exchange contribution to the effective field in equation (2) but also to boundary conditions (BCs). BCs that arise from the sole symmetry breaking of exchange interactions at surfaces are referred to as *free* BCs. Their mathematical expression in the continuum limit reads

$$A\left(\mathbf{m} \times \frac{\partial \mathbf{m}}{\partial \mathbf{n}}\right) = 0 \tag{12}$$

which is equivalent to the Neumann BC

$$\frac{\partial \mathbf{m}}{\partial \mathbf{n}} = 0 \tag{13}$$

since $\mathbf{m}^2 = 1$. In the presence of surface anisotropy, energy density

$$\varepsilon_{K\text{S}} = K_{\text{S}}\left(1 - (\mathbf{n}\cdot\mathbf{m})^2\right) \tag{14}$$

and interlayer exchange, energy density

$$\varepsilon_{\text{J}} = J_1\left(1 - \mathbf{m}\cdot\mathbf{m}'\right) + J_2\left(1 - \left(\mathbf{m}\cdot\mathbf{m}'\right)^2\right) \tag{15}$$

where $\mathbf{m}'$ defines the exchange-bias direction at the interface with the ferro- or ferrimagnetic body, BCs may be expressed (Labrune and Miltat, 1995) either as

$$2A\left(\mathbf{m} \times \frac{\partial \mathbf{m}}{\partial \mathbf{n}}\right) - 2K_{\text{S}}\left(\mathbf{m}\cdot\mathbf{n}\right)\left(\mathbf{m} \times \mathbf{n}\right) - J_1\left(\mathbf{m} \times \mathbf{m}'\right) - 2J_2\left(\mathbf{m} - \mathbf{m}'\right)\left(\mathbf{m} \times \mathbf{m}'\right) = 0 \tag{16}$$

or as

$$\frac{\partial \mathbf{m}}{\partial \mathbf{n}} = \frac{K_{\text{S}}}{A}\left(\mathbf{m}\cdot\mathbf{n}\right)\left(\mathbf{n} - \left(\mathbf{m}\cdot\mathbf{n}\right)\mathbf{m}\right) - \left(\frac{J_1}{2A} + \frac{J_2}{A}\left(\mathbf{m}\cdot\mathbf{m}'\right)\right)\left(\left(\mathbf{m}\cdot\mathbf{m}'\right)\mathbf{m} - \mathbf{m}'\right) \tag{17}$$

See also references Brown (1963), Rado and Weertman (1959) and Guslienko and Slavin (2005).

Altogether, as long as the exchange parameter A is independent of position $\mathbf{r}$, a magnetization continuum owing to micromagnetics is at zero temperature governed by the set of equations:

$$\begin{aligned}
\mathbf{m} &= \mathbf{m}(\mathbf{r}, t)\\
\mathbf{H}_{\text{eff}} &= \mathbf{H}_{\text{eff}}(\mathbf{r}, t)\\
\mathbf{H}_{\text{d}} &= \mathbf{H}_{\text{d}}(\mathbf{r}, t)\\
\mathbf{H}_{\text{eff}} &= \frac{2A}{\mu_0 M_{\text{s}}}\nabla^2\mathbf{m} + \mathbf{H}_{\text{app}} + \mathbf{H}_{\text{d}} - \frac{1}{\mu_0 M_{\text{s}}}\frac{\delta\varepsilon_K}{\delta\mathbf{m}}\\
\frac{\partial \mathbf{m}}{\partial \mathbf{n}} &= \frac{K_{\text{S}}}{A}\left(\mathbf{m}\cdot\mathbf{n}\right)\left[\mathbf{n} - \left(\mathbf{m}\cdot\mathbf{n}\right)\mathbf{m}\right]\\
&\quad - \left[\frac{J_1}{2A} + \frac{J_2}{A}\left(\mathbf{m}\cdot\mathbf{m}'\right)\right]\left[\left(\mathbf{m}\cdot\mathbf{m}'\right)\mathbf{m} - \mathbf{m}'\right]
\end{aligned} \tag{18}$$

augmented with the LLG equation of magnetization motion (9) or the equilibrium condition (11).

In case the exchange constant would be position dependent, an additional term would appear in the exchange components of the effective field. In the following, the exchange constant is assumed to remain constant, that is, a sole function of the ferro- or ferrimagnetic material composition. It has also been implicitly assumed that the system under study was free of surface-specific damping. On the other hand, the saturation magnetization, the anisotropy as well as the damping constant may be modulated according to position without introducing modifications in the set of equations (18).

This chapter considers the finite difference approach to solving these equations, where the magnetization is sampled on a uniform rectangular mesh at points $(x_0 + i\Delta_x, y_0 + j\Delta_y, z_0 + k\Delta_z)$. The computational cell is centered about the sample point with dimensions $\Delta_x \times \Delta_y \times \Delta_z$. The main advantages of the finite difference approach are ease of implementation, simplicity of meshing, efficient evaluation of the demagnetizing energy (via, e.g., fast Fourier transform (FFT) methods), and the accessibility of higher-order methods. A main disadvantage of this approach is that sampling curved boundaries with a rectangular mesh results in a 'staircase-type' approximation to the geometry, which can produce significant errors in the computation. Corrections for this artifact are possible (Parker, Cerjan and Hewett, 2000; Porter and Donahue, 2001; García-Cervera, Gimbutas and Weinan E, 2003), but are not discussed in the present text. The next two sections present two approaches to the problem of discretizing the continuous equations discussed in the preceding text. The first, Section 2, treats equation (2) as fundamental, and focuses primarily on computing an accurate value of $\mathbf{H}_{\text{eff}}$ directly from $\mathbf{m}$. We call this the field-based approach. The alternative energy-based approach, presented in Section 3, is directed first at computing the micromagnetic energy, equation (3). The effective field $\mathbf{H}_{\text{eff}}$, which is needed in the LLG equation (9), is computed from the energy

via the discrete analog of equation (1). The $\mathbf{H}_{\text{eff}}$ computed in this manner is the field value averaged across the corresponding discretization cell. Results using the two methods on a sample problem are compared in Section 5.

2 FINITE DIFFERENCE MICROMAGNETICS: FIELD-BASED APPROACH

As stated in the preceding text, in a field-based approach (Labrune and Miltat, 1995; Albuquerque, 2002; Toussaint *et al*., 2002), one is seeking a numerical solution to the LLG equation (18) on the basis of a direct evaluation of the effective field components under the constraint of problem specific BCs. In this approach, the energy (density) plays a role only to the extent that the effective field is the gradient of the former.

Looking at equation (18) it is immediately seen that a number of derivatives will require evaluation, namely first- and second-order derivatives of the magnetization components in order to define the divergence of the magnetization ($\nabla\cdot\mathbf{m}$) and the components of the exchange field ($\nabla^2\mathbf{m}$), respectively. The magnetization components along boundaries also need to be evaluated in order to define surface charges ($\mathbf{m}\cdot\mathbf{n}$) that do contribute to the demagnetizing field. BCs need to be incorporated in the evaluation of the effective field without loss of accuracy. Finally, solution of the LLG equation does require both stability and accuracy. This section is organized as follows: in a first step we describe the various steps to be taken in order to provide a numerical estimate of the demagnetizing field. In the next step, starting with an evaluation of the exchange field in the bulk, it is first shown how BCs may be included without too heavy a cost in accuracy, at least for so-called free BCs. The third step explains how general BCs may be introduced. Because the problem of an accurate solution of the LLG equation is common to both the field-based and energy-based finite difference methods, it is treated separately (see Section 3).

2.1 Demagnetizing field evaluation

For a magnetization continuum, the demagnetizing field, in full similarity to electrostatics, arises from volume and surface charges

$$\begin{aligned} \lambda_{\text{V}} &= -\mu_0 M_{\text{s}}\,(\nabla\cdot\mathbf{m})\,, \qquad \text{in the volume} \\ \sigma_{\text{S}} &= +\mu_0 M_{\text{s}}\,(\mathbf{m}\cdot\mathbf{n})\,, \qquad \text{at free surfaces} \end{aligned} \tag{19}$$

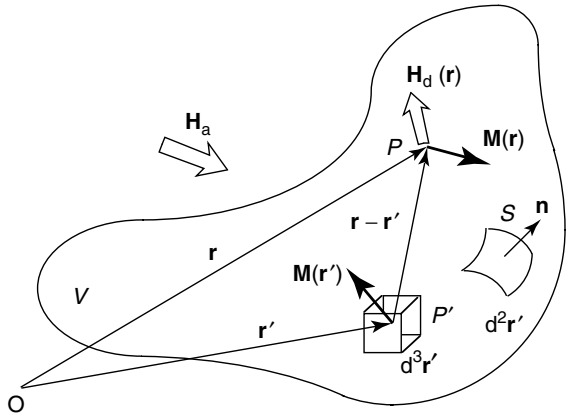

Figure 1. Geometry attached to equation (20).

and derives from the scalar potential expressed as follows:

$$\begin{aligned} \mathbf{H}_{\text{d}}(\mathbf{r}) &= -\nabla\Phi_{\text{d}}(\mathbf{r}) \\ \Phi_{\text{d}}(\mathbf{r}) &= \frac{1}{4\pi\mu_0}\left[\int_V \frac{\lambda_{\text{V}}(\mathbf{r}')}{|\mathbf{r}-\mathbf{r}'|}\,\text{d}^3r' + \int_S \frac{\sigma_{\text{S}}(\mathbf{r}')}{|\mathbf{r}-\mathbf{r}'|}\,\text{d}^2r'\right] \end{aligned} \tag{20}$$

Figure 1 illustrates the geometrical relations between vectors in equation (20).

It follows from equations (19) and (20) that the demagnetizing field may be directly expressed as

$$\begin{aligned} \mathbf{H}_{\text{d}}(\mathbf{r}) = \frac{1}{4\pi\mu_0}\Bigg[&\int_V \frac{(\mathbf{r}-\mathbf{r}')\,\lambda_{\text{V}}(\mathbf{r}')}{|\mathbf{r}-\mathbf{r}'|^3}\,\text{d}^3r' \\ &+ \int_S \frac{(\mathbf{r}-\mathbf{r}')\,\sigma_{\text{S}}(\mathbf{r}')}{|\mathbf{r}-\mathbf{r}'|^3}\,\text{d}^2r'\Bigg] \end{aligned} \tag{21}$$

$\mathbf{H}_{\text{d}}$ derives from the energy density

$$\varepsilon_{\text{demag}} = -\frac{1}{2}\mu_0\,(\mathbf{H}_{\text{d}}\cdot\mathbf{M}) = -\frac{1}{2}\mu_0 M_{\text{s}}\,(\mathbf{H}_{\text{d}}\cdot\mathbf{m}) \tag{22}$$

where the $1/2$ prefactor stems from the fact that $\mathbf{M}$ is the source of $\mathbf{H}_{\text{d}}$.

Four remarks ought to be made here. First, charges must sum up to zero because of the fundamentally dipolar nature of magnetism. Second, contrary to the Zeeman contribution to the total energy, the magnetostatic energy, obtained through summation over the volume and external surface of the element of the energy density equation (22), is necessarily positive or nil. It follows that, in a soft magnetic material, where the magnetostatic energy becomes the leading term, energy may only be minimized by the pole avoidance principle. This means that, whenever possible, the magnetization will tend to be parallel to external boundaries and adopt configurations satisfying $\nabla\cdot\mathbf{m} = 0$ in the volume. Clearly, this may only be achieved at the expense of exchange energy

as well as anisotropy energy when present. Third, because of the long-range decay of magnetostatic interactions, large errors are inevitably made when truncation of the integrals is attempted. Last, but not least, one easily recognizes in the integrals of equation (20) a convolution product. Therefore, from a numerical point of view, much of the computation load may be relieved via an extensive use of FFTs.

Decomposing the magnetic volume into cells (index i', j', k') with *constant* magnetization divergence and the outer surface into tiles (index l', m', n') with *constant* charge density (see Figure 2) immediately leads to an easy and yet accurate numerical estimate of the demagnetizing field at location $\mathbf{r}$. Equation (21) then reduces to a finite sum, namely,

$$\mathbf{H}_{\mathrm{d}}(\mathbf{r}) = \frac{1}{4\pi\mu_0}\sum_{i',j',k'}\left[\lambda_{\mathrm{V}}(i',j',k')\int_{V'(i',j',k')}\frac{(\mathbf{r}-\mathbf{r}')}{|\mathbf{r}-\mathbf{r}'|^3}\,\mathrm{d}^3r'\right] + \frac{1}{4\pi\mu_0}\sum_{l',m',n'}\left[\sigma_{\mathrm{S}}(l',m',n')\int_{S'(l',m',n')}\frac{(\mathbf{r}-\mathbf{r}')}{|\mathbf{r}-\mathbf{r}'|^3}\,\mathrm{d}^2r'\right] \tag{23}$$

where $\mathbf{r}'$ now spans either the volume of cell i', j', k' or the area of tile l', m', n'. The integrals in equation (23) therefore reduce to purely geometrical coefficients that only need to be computed once. Equation (23) may thus be rewritten as follows

$$\mathbf{H}_{\mathrm{d}}(\mathbf{r}) = \frac{1}{4\pi\mu_0}\sum_{i',j',k'}\lambda_{\mathrm{V}}(i',j',k')\,C_{\mathrm{V}}(\mathbf{r},i',j',k') + \frac{1}{4\pi\mu_0}\sum_{l',m',n'}\sigma_{\mathrm{S}}(l',m',n')\,C_{\mathrm{S}}(\mathbf{r},l',m',n') \tag{24}$$

Note that such a decomposition is achieved if the magnetization is assumed to be a trilinear function of the coordinates

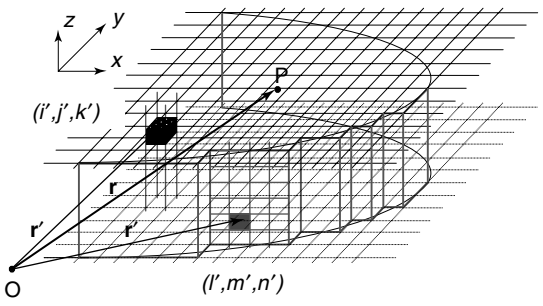

Figure 2. The demagnetizing field at point P($\mathbf{r}$) is built-up from contributions arising from volume cells with constant magnetization divergence and surface tiles with constant charge density. In this drawing, the physical frontier consists in the top and bottom planes, and the continuous rim boundary (in black). The numerical rim boundary is staircase-like (light gray).

x, y, z within the magnetic volume while being constant over the area of a tile. All interaction coefficients C_{V} and C_{S} are definite integrals with kernels $\frac{x-x'}{|\mathbf{r}-\mathbf{r}'|^3}$, $\frac{y-y'}{|\mathbf{r}-\mathbf{r}'|^3}$, $\frac{z-z'}{|\mathbf{r}-\mathbf{r}'|^3}$ for the x, y, and z demagnetizing field components, respectively. For instance, the x component of the demagnetizing field arising from a volume cell is given by equation (24) with

$$C_{\mathrm{V}}^{x} = \int_{x_1'}^{x_2'}\int_{y_1'}^{y_2'}\int_{z_1'}^{z_2'}\frac{x-x'}{|\mathbf{r}-\mathbf{r}'|^3}\mathrm{d}x'\mathrm{d}y'\mathrm{d}z' \tag{25}$$

Similarly, the z component of the demagnetizing field arising from a tile parallel to the xy plane is given by equation (24) with

$$C_{\mathrm{S}xy}^{z} = \int_{x_1'}^{x_2'}\int_{y_1'}^{y_2'}\frac{z-z'}{|\mathbf{r}-\mathbf{r}'|^3}\mathrm{d}x'\mathrm{d}y' \tag{26}$$

For parallepipedic volume cells and rectangular surface tiles, all interaction coefficients may be evaluated with the help of the integrals listed in Appendix A. H^{111} integrals apply to constant divergence volume cells, whereas H^{110}, H^{011}, and H^{101} integrals apply to tiles parallel to the xy, yz, and xz planes, respectively.

Lastly, for both a regular meshing and a regular sampling of the field (volume cells centers or apexes seem natural choices), translational invariance of the interaction coefficients allows for the use of FFTs in the evaluation of the demagnetizing field (Eastwood, Hockney and Lawrence, 1980; Hockney and Eastwood, 1981; Yuan and Bertram, 1992; Berkov, Ramstöck and Hubert, 1993; Ramstöck, Leibl and Hubert, 1994). FFTs considerably reduce the computational load in numerical micromagnetics. However, because the magnetization distribution is not usually periodic, zero-padding techniques need to be implemented (Press, Teukolsky, Wetterling and Flannery, 2001). Further discussion on the use of FFTs in numerical micromagnetics is deferred to Section 3.4. We note in closing this section that a direct evaluation of the field at the apexes of the volume cells leads to weak divergences of the demagnetizing field (Shtrickman and Treves, 1960). It has been shown both numerically (Rave, Ramstöck and Hubert, 1998) and analytically (Thiaville, Tomáš and Miltat, 1998) that the log-type divergence of the demagnetizing field along the edges and at the apices of a uniformly magnetized parallelepiped are balanced via tiny rotations of the magnetization close to boundaries that take place over distances smaller than the exchange length. Methods relying on the direct evaluation of the demagnetizing field therefore practically restrict the choice of the field sampling points to cell centers.

2.2 Derivatives evaluation

Consider a regular, differentiable one-dimensional scalar function $f(x)$ sampled at regular intervals, a (see Figure 3a). Second-order Taylor expansion readily yields expressions for the first and second central derivatives that are widely used in numerics, namely $\frac{\mathrm{d}f}{\mathrm{d}x} = \frac{f_{i+1}-f_{i-1}}{2a}$ and $\frac{\mathrm{d}^2 f}{\mathrm{d}x^2} = \frac{f_{i+1}-2f_i+f_{i-1}}{a^2}$, respectively.

However, the numerical derivation of the structure of a simple Bloch wall using such expressions soon reveals that second-order Taylor expansion leads to restricted accuracy. Fourth-order expansion has actually been found to prove much superior (Trouilloud and Miltat, 1987; Miltat, Thiaville and Trouilloud, 1989; Berkov, Ramstöck and Hubert, 1993; Labrune and Miltat, 1995). Taylor expansion of function $f(x)$ around $x = x_i$ reads as follows:

$$f(x) = \sum_{k=0}^{\infty} \frac{(x-x_i)^k}{k!} f^{(k)}(x_i) = \sum_{k=0}^{\infty} \frac{(x-x_i)^k}{k!} f_i^{(k)} \tag{27}$$

where, $f^{(k)}(x) = f(x)$ if $k = 0$ and $\frac{\mathrm{d}^k f}{\mathrm{d}x^k}$ otherwise. Application of equation (27) to nearest and next nearest neighbors to grid point i and truncation to the fourth order yields a set of four equations, namely

$$\begin{bmatrix} -2a & \frac{(-2a)^2}{2!} & \frac{(-2a)^3}{3!} & \frac{(-2a)^4}{4!} \\ -a & \frac{(-a)^2}{2!} & \frac{(-a)^3}{3!} & \frac{(-a)^4}{4!} \\ +a & \frac{(+a)^2}{2!} & \frac{(+a)^3}{3!} & \frac{(+a)^4}{4!} \\ +2a & \frac{(+2a)^2}{2!} & \frac{(+2a)^3}{3!} & \frac{(+2a)^4}{4!} \end{bmatrix} \begin{bmatrix} f_i^{(1)} \\ f_i^{(2)} \\ f_i^{(3)} \\ f_i^{(4)} \end{bmatrix} = \begin{bmatrix} f_{i-2} - f_i \\ f_{i-1} - f_i \\ f_{i+1} - f_i \\ f_{i+2} - f_i \end{bmatrix} \tag{28}$$

The set of linear equations (28) provide numerical estimates for the first, second, third, and fourth derivatives of f at grid point i. In particular, the general form of the first and second derivative based on second nearest-neighbors expansion reads

$$\begin{aligned} f_i^{(1)} &= \frac{f_{i-2} - 8f_{i-1} + 8f_{i+1} - f_{i+2}}{12a} \\ f_i^{(2)} &= \frac{-f_{i-2} + 16f_{i-1} - 30f_i + 16f_{i+1} - f_{i+2}}{12a^2} \end{aligned} \tag{29}$$

respectively.

2.3 Boundary conditions implementation: 'free' boundary conditions

Expressions in the preceding text cease to be valid when the grid point becomes closest or next-to-closest to the boundary of the magnetic volume. Specific, accuracy preserving expansions need to be worked out. The general principle in the present approach is to replace equations that are missing because of the lack of grid point(s) outside the magnetic volume by equations including explicit reference to BCs, equation (17).

Consider first a point second to closest to boundary (see Figure 3b). Grid point $i + 2$ is missing for this particular geometry. However, defining x_R as the right boundary coordinate along the x axis, the last equation in equation (28) may, assuming $f^{(1)}(x_R)$ to be known along the boundary, be

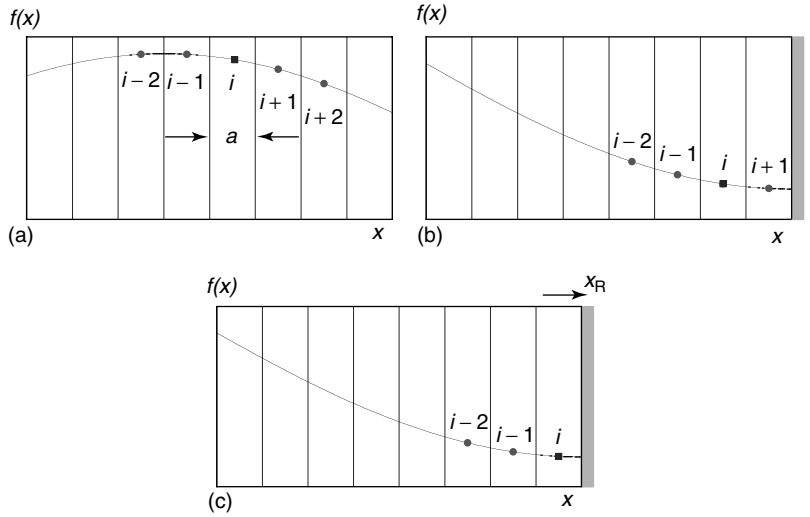

Figure 3. Mesh geometry. (a) Function of the sole scalar x. (b) Mesh points second to closest to boundary. (c) Mesh points closest to boundary.

replaced by

$$f^{(1)}(x_{\mathrm{R}}) = f_i^{(1)} + (x_{\mathrm{R}} - x_i) f_i^{(2)} + \frac{1}{2!}(x_{\mathrm{R}} - x_i)^2 f_i^{(3)} + \frac{1}{3!}(x_{\mathrm{R}} - x_i)^3 f_i^{(4)} \quad (30)$$

which is a result stemming directly from the derivation of Taylor's expansion (27), namely

$$f^{(1)}(x) = \sum_{k=1}^{\infty} \frac{(x - x_i)^{k-1}}{(k-1)!} f^{(k)}(x_i) \quad (31)$$

For the geometry depicted in Figure 3(b), $x_{\mathrm{R}} - x_i = 3a/2$ and equation (28) becomes

$$\begin{bmatrix} -2a & \frac{(-2a)^2}{2!} & \frac{(-2a)^3}{3!} & \frac{(-2a)^4}{4!} \\ -a & \frac{(-a)^2}{2!} & \frac{(-a)^3}{3!} & \frac{(-a)^4}{4!} \\ +a & \frac{(+a)^2}{2!} & \frac{(+a)^3}{3!} & \frac{(+a)^4}{4!} \\ 1 & \left(\frac{+3a}{2}\right) & \frac{(+3a/2)^2}{2!} & \frac{(+3a/2)^3}{3!} \end{bmatrix} \begin{bmatrix} f_i^{(1)} \\ f_i^{(2)} \\ f_i^{(3)} \\ f_i^{(4)} \end{bmatrix} = \begin{bmatrix} f_{i-2} - f_i \\ f_{i-1} - f_i \\ f_{i+1} - f_i \\ f^{(1)}(x_{\mathrm{R}}) \end{bmatrix} \quad (32)$$

Similarly, for a point closest to boundary (see Figure 3c), grid points $i+1$ and $i+2$ are missing. The two first equations of equation (28) now need to be replaced by a single equation, while the two remaining equations need to be truncated to the third order. For the geometry illustrated in Figure 3(c), the minimal set of equations now reads

$$\begin{bmatrix} -2a & \frac{(-2a)^2}{2!} & \frac{(-2a)^3}{3!} \\ -a & \frac{(-a)^2}{2!} & \frac{(-a)^3}{3!} \\ 1 & \left(\frac{+a}{2}\right) & \frac{(+a/2)^2}{2!} \end{bmatrix} \begin{bmatrix} f_i^{(1)} \\ f_i^{(2)} \\ f_i^{(3)} \end{bmatrix} = \begin{bmatrix} f_{i-2} - f_i \\ f_{i-1} - f_i \\ f^{(1)}(x_{\mathrm{R}}) \end{bmatrix} \quad (33)$$

where, $x_{\mathrm{R}} - x_i = a/2$. In both cases, the first and second derivatives are fully determined provided $f^{(1)}(x_{\mathrm{R}})$ is known along the boundary. The implementation of BCs is, however, not unique. For instance, equation (33) could include four internal mesh points instead of only three. Donahue and Porter (2004) have evaluated the accuracy of several numerical schemes allowing for the evaluation of the exchange energy equation (4) and the enclosed derivatives. Their general conclusion is that the so-called 12-neighbors scheme, that is, 4 neighbors along each axis of the Euclidian space, is accuracy preserving up to order 4, at least for 'free' BCs. The derivation in the preceding text belongs to the '12-neighbors' class.

Equation (32) or equation (33) may be applied *mutatis mutandis* to the left boundary $x = x_{\mathrm{L}}$. Altogether, equation (28) and equations akin to equations (32) and (33) fully specify the first, second, and third derivatives of function $f(x)$ within the interval $]x_{\mathrm{L}}, x_{\mathrm{R}}[$, provided boundary values of the first derivatives versus x are known. For 'free' BCs, $f^{(1)}(x_{\mathrm{L}}) = f^{(1)}(x_{\mathrm{R}}) \equiv 0$, or more generally, $\frac{\partial m_{x_{\mathrm{S}}}}{\partial x} = \frac{\partial m_{y_{\mathrm{S}}}}{\partial x} = \frac{\partial m_{z_{\mathrm{S}}}}{\partial x} = 0$ for a flat boundary perpendicular to x located at position x_{S}. Generalization to three dimensions in the Euclidian space proves straightforward. Even for 'free' BCs, however, an evaluation of the relevant magnetization components along boundaries is still required in order to compute the contribution of surface charges to the demagnetizing field. Referring to Figure 3(c), Taylor expansion (equation (27)) up to, for example, the third order yields

$$f(x_{\mathrm{R}}) = f_i + (x_{\mathrm{R}} - x_i) f_i^{(1)} + \frac{1}{2!}(x_{\mathrm{R}} - x_i)^2 f_i^{(2)} + \frac{1}{3!}(x_{\mathrm{R}} - x_i)^3 f_i^{(3)} \quad (34)$$

where i here is the index of the mesh point closest to boundary. Assuming a constant charge density for the surface element centered on x_{R}, the surface charge $+\mu_0 M_{\mathrm{s}}\,(\mathbf{m}\cdot\mathbf{n})$ is simply $+\mu_0 M_{\mathrm{s}} m_{x_{\mathrm{R}}}$ with $m_x(x) = f(x)$ in equation (34). Here also, generalization to three dimensions in the Euclidian space is straightforward.

Summarizing at this point, knowing the distribution $\mathbf{m}(\mathbf{r})$ inside a magnetic volume bounded by flat boundaries, all necessary derivatives of the magnetization components as well as estimates of surface charges are available through Taylor expansion and explicit use of BCs reading $\frac{\partial \mathbf{m}}{\partial \mathbf{n}} = 0$ in the case of 'free' BCs. High accuracy (up to $O(h^4)$) may be preserved in this process.

As an example, the magnetization distribution within a soft and thin rectangular platelet is displayed in Figure 4. The initial state was uniformly magnetized along the diagonal of the rectangle. At remanence, the magnetization becomes essentially uniform and parallel to the element's long edges, thus avoiding both volume and surface charges along the most part of the latter. Close to the extremities, however,

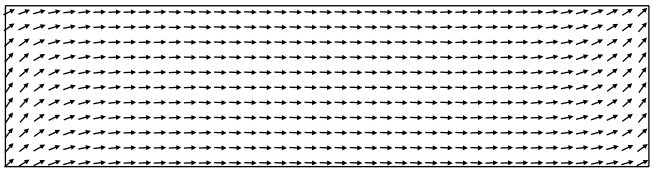

Figure 4. Magnetization distribution characteristic of a so-called S-state in a thin-film element: the magnetization keeps parallel to the long edges of the element, thus avoiding both volume and surface charges along the most part of the latter. Close to the extremities, however, a gradual bending of the magnetization distribution allows for a decrease of surface charges along the element short edges at the expense of exchange and volume magnetostatic energy. $Ni_{80}Fe_{20}$ like materials parameters (exchange constant: $A = 1.3 \times 10^{-11}\,\mathrm{J\,m^{-1}}$, saturation magnetization $M_{\mathrm{s}} = 800\,\mathrm{kA\,m^{-1}}$); dimensions: $500 \times 125 \times 3\,\mathrm{nm}^3$; Meshing: $256 \times 64 \times 1$ (one-layer-of-cells type simulation).

the magnetization distribution is bending in such a way as to allow for a decrease of surface charges along the element short edges at the expense of exchange and volume magnetostatic energy. Actually, in submicron size thin soft magnetic elements, the number of possible magnetization states becomes discrete (Yuan, Bertram, Smyth and Schultz, 1992; Zheng and Zhu, 1997; Rave and Hubert, 2000; Miltat, Albuquerque and Thiaville, 2001; Hertel, 2002). The magnetization state shown in Figure 4 is called an *S state*. Platelets displaying S states may be found in four variants according to the direction of the magnetization in the main section of the element ($\approx +x$ or $\approx -x$), and the magnetization component along the element short edges ($+y$ or $-y$). Reversing the magnetization rotation direction close to one extremity would lead to a so-called C state with, again, four possible variants characterized by a single energy.

Although the thickness in that particular element remains smaller than the exchange length for the material considered (3 vs 5.68 nm), the decomposition of the element into three layers of cells reveals interesting features of the magnetization distribution at equilibrium. The minute splay

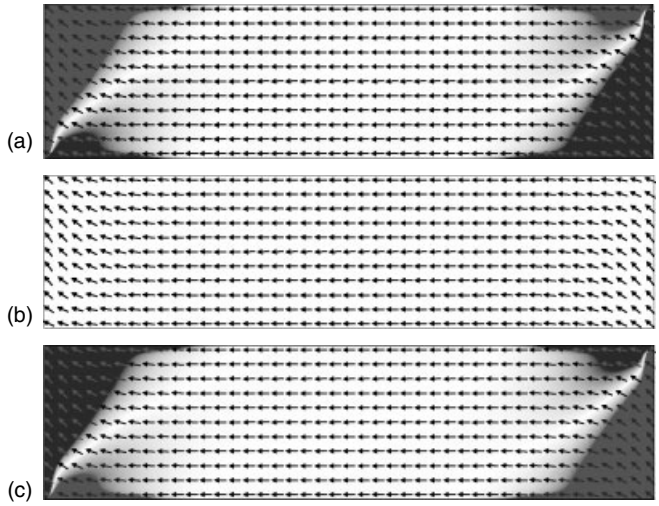

Figure 5. Magnetization distribution characteristic of a so-called S state in a thin-film element owing to three-dimensional micromagnetics. Close to the upper left boundary, the in-plane magnetization is fanning-in, leading to positive volume charges; in the top and bottom computation cell-layers (a and c respectively), the z-component (out-of-plane) of the magnetization is positive and negative, respectively. The fanning-out of the magnetization along the normal to the magnetic element allows for charge compensation between the in-plane and out-of-plane magnetization distributions, leading to an overall reduction of both the exchange and demagnetizing field energy. The magnetization distribution around the bottom right corner behaves symmetrically (in-plane fanning-out, out-of-plane fanning-in). $Ni_{80}Fe_{20}$ like materials parameters (exchange constant: $A = 1.3 \times 10^{-11}\,\mathrm{J\,m^{-1}}$, saturation magnetization $M_s = 800\,\mathrm{kA\,m^{-1}}$); dimensions: $500 \times 125 \times 3\,\mathrm{nm}^3$; meshing: $511 \times 127 \times 3$.

across the thickness of the magnetization displayed in Figure 5 actually leads to a decrease of both the exchange and the magnetostatic energies (see the caption of Figure 5 for details). Figure 5 emphasizes the stringent need for rather small mesh sizes (a relatively small fraction of the exchange length) if the fine features of the magnetization distribution are to be revealed with a satisfying accuracy.

2.4 Boundary conditions implementation: extended boundary conditions

Additional work needs to be performed when dealing with general boundary conditions (17). General BCs are expressed in terms of boundary values for the magnetization. Boundary magnetization values (refer to equation (34)) are functions of derivatives defined at given mesh points that themselves depend on specific derivatives along boundaries (see equations (32) and (33)). It ensues that for each boundary point where an estimate of a boundary derivative is required, an implicit equation needs to be solved. Consider again the boundary point in Figure 3(b) or (c). The requested boundary derivatives read as $\frac{\partial m_x(x_R)}{\partial x}$, $\frac{\partial m_y(x_R)}{\partial x}$, $\frac{\partial m_z(x_R)}{\partial x}$. In components form, neglecting the J_2 biquadratic exchange term, extended BCs for the right boundary (normal along $+x$) read as

$$\begin{aligned}
\frac{\partial m_x^R}{\partial x} &= \frac{K_S}{A} m_x^R \left[1 - m_x^{R2}\right] - \frac{J_1}{2A}\left[\left(\mathbf{m}^R \cdot \mathbf{m}'\right) m_x^R - m_x'\right] \\
\frac{\partial m_y^R}{\partial x} &= -\frac{K_S}{A} m_x^{R2} m_y^R - \frac{J_1}{2A}\left[\left(\mathbf{m}^R \cdot \mathbf{m}'\right) m_y^R - m_y'\right] \\
\frac{\partial m_z^R}{\partial x} &= -\frac{K_S}{A} m_x^{R2} m_z^R - \frac{J_1}{2A}\left[\left(\mathbf{m}^R \cdot \mathbf{m}'\right) m_z^R - m_z'\right]
\end{aligned} \tag{35}$$

where $\mathbf{m}^R = \mathbf{m}(x_R)$. Combined with relations akin to (34) and (32) or (33), equation (35) provides a set of nonlinear equations (third order in the general case) in the variables m_x^R, m_y^R, m_z^R that may easily be solved via, for example, Newton's method. A proper numerical implementation ensures that extended BCs are strictly equivalent to 'free' BCs if $K_S = J_1 = 0$.

2.5 Energy

The energy to be evaluated embodies the exchange, anisotropy, Zeeman, and demagnetizing field energies that sum up to the total energy expressed in equation (3). Additional energy terms do arise from extended BCs, namely $E_{K_S} = \int_S \varepsilon_{K_S}\,\mathrm{d}S$ and $E_J = \int_S \varepsilon_J\,\mathrm{d}S$. Owing to the numerical scheme outlined in the preceding text, both the magnetization and the effective field are meant to be continuous functions of position sampled at regularly spaced volume

mesh points. The magnetization also needs to be evaluated at the center of surface tiles in order to satisfy to BCs and allow for the computation of surface charge densities. Whenever the magnetization is evaluated, its unit norm ($\mathbf{m}\cdot\mathbf{m} = 1$) must be enforced.

2.5.1 Zeeman, anisotropy, and exchange energy

Consider the right-hand expression of the exchange energy in equation (4). Its discrete counterpart reads as

$$E_{\text{exch}} = -A\, V_{\text{Cell}} \sum_{i,j,k} \left[\langle \mathbf{m} \rangle \cdot \left(\left\langle \frac{\partial^2 \mathbf{m}}{\partial x^2} \right\rangle + \left\langle \frac{\partial^2 \mathbf{m}}{\partial y^2} \right\rangle + \left\langle \frac{\partial^2 \mathbf{m}}{\partial z^2} \right\rangle \right) \right] \tag{36}$$

where, $\langle \mathbf{V} \rangle$ is the average value of $\mathbf{V}$ within a given cell. As discussed in Section 3, however, the cell-averaged value of any variable is equal to its value at cell center, be it a volume cell or a surface tile, to order 2, because all nearest order corrective terms sum up to zero. Although higher-order corrections may be worked out, such corrective actions have almost no incidence on the numerical estimate of the relevant energy, as exemplified in Figure 6(a). The same conclusion holds true for the estimate of the Zeeman (applied field) and anisotropy energies as demonstrated in Sections 3.1 and 3.2, respectively. Similar arguments also apply to energy terms linked to specific BCs for which the energy densities in the continuum limit are given by equations (14) and (15).

2.5.2 Demagnetizing field (or magnetostatic) energy

In the present field-based scheme, quantities that are constant per cell or tile are the magnetization divergence and the surface charge density. It is therefore natural to seek an expression for the energy that embodies these quantities. An expression for the energy is readily available if assuming the scalar potential equation (20) to be known (up to this point, only the field has been evaluated at discrete points). If either the magnetization divergence or the surface charge density is piecewise constant, the scalar potential is not. Therefore,

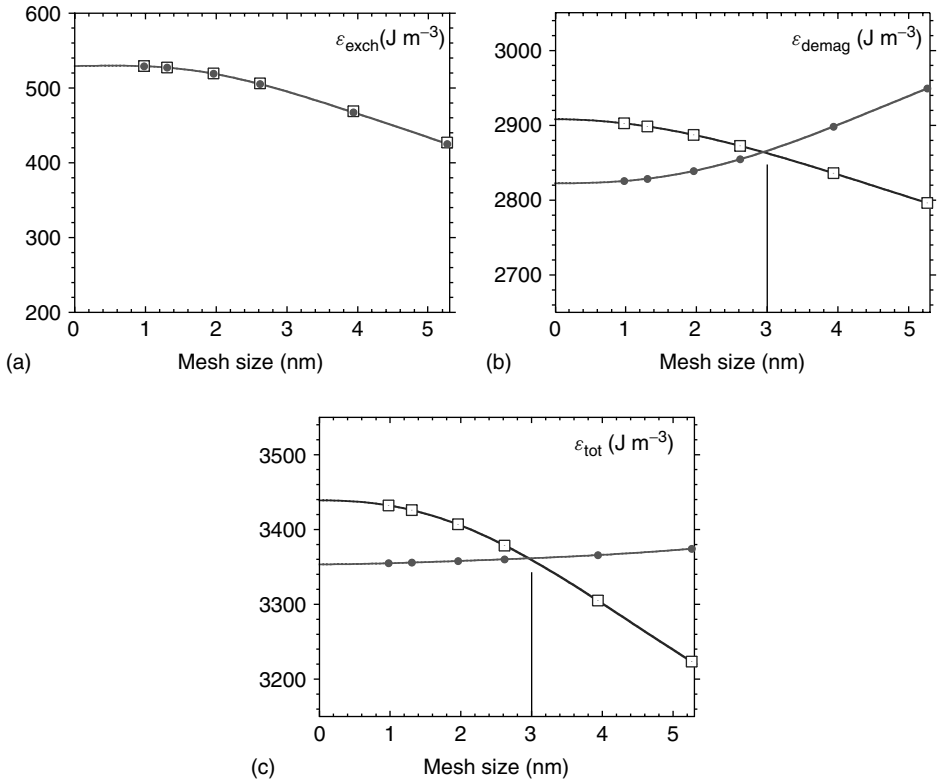

Figure 6. Energy per unit volume versus in-plane mesh size for the S-state magnetization distribution shown in Figure 4. (a) Exchange, (b) magnetostatic, and (c) total energy per unit volume. Open and full symbols refer to direct and cell-averaged summation, respectively. The magnetostatic energy is approximated by equations (41) and (38) for direct and cell-averaged summation, respectively. The fitting curves should be viewed as mere guides to the eye. $Ni_{80}Fe_{20}$ like materials parameters (exchange constant: $A = 1.3 \times 10^{-11}\,\text{J m}^{-1}$, saturation magnetization $M_s = 800\,\text{kA m}^{-1}$); dimensions: $500 \times 125 \times 3\,\text{nm}^3$; one-layer-of-cells type simulation.

the transcription of the continuous energy expression

$$E_{\text{demag}} = \frac{1}{2}\int_V \lambda_V(\mathbf{r})\Phi_d(\mathbf{r})\,d^3r + \frac{1}{2}\int_S \sigma_S(\mathbf{r})\Phi_d(\mathbf{r})\,d^2r \tag{37}$$

into a discrete summation requests the evaluation of the average value of the potential $\langle\Phi_d\rangle$ over each cell or tile (see Section 3.4 where a similar procedure is applied to the evaluation of the average field within a cell). Equation (37) thus becomes

$$E_{\text{demag}} = \frac{1}{2}\sum_{i,j,k}\left[\lambda_V(i,j,k)\langle\Phi_d(i,j,k)\rangle\right] + \frac{1}{2}\sum_{l,m,n}\left[\sigma_S(l,m,n)\langle\Phi_d(l,m,n)\rangle\right] \tag{38}$$

where,

$$\begin{aligned} &4\pi\mu_0 V_{\text{Cell}}\langle\Phi_d(i,j,k)\rangle \\ &= \sum_{i',j',k'}\lambda_V(i',j',k')\int_{V(i,j,k)} d^3r \int_{V(i',j',k')}\frac{1}{|\mathbf{r}-\mathbf{r}'|}\,d^3r' \\ &+ \sum_{l',m',n'}\sigma_S(l',m',n')\int_{V(i,j,k)} d^3r \int_{S(l',m',n')}\frac{1}{|\mathbf{r}-\mathbf{r}'|}\,d^2r' \end{aligned} \tag{39}$$

for volume cells, and

$$\begin{aligned} &4\pi\mu_0 S_{\text{Tile}}\langle\Phi_d(l,m,n)\rangle \\ &= \sum_{i',j',k'}\lambda_V(i',j',k')\int_{S(l,m,n)} d^2r \int_{V(i',j',k')}\frac{1}{|\mathbf{r}-\mathbf{r}'|}\,d^3r' \\ &+ \sum_{l',m',n'}\sigma_S(l',m',n')\int_{S(l,m,n)} d^2r \int_{S(l',m',n')}\frac{1}{|\mathbf{r}-\mathbf{r}'|}\,d^2r' \end{aligned} \tag{40}$$

for surface tiles. Cell or tile average scalar potential evaluation requires integrals of type F^{222}, F^{221} plus circular permutations, F^{220} plus circular permutations, where $F^{000} = \frac{1}{r}$, $F^{100} = \int F^{000}dx$, $F^{110} = \int F^{000}\,dx\,dy$, and so on, (Hubert and Schäfer, 1998). All necessary integrals are tabulated in Appendix B. For instance, the contribution of a tile belonging to the ($xy \equiv [110]$) surface to the averaged potential within a volume cell ($\equiv [111]$) involves the F^{221} integral, and so on. All interaction integrals are positive definite so that interactions between charges of similar sign, whether volume or surface, contribute positively to the energy, whereas interactions between opposite sign charges contribute negatively.

Although potential theory is the only approach to energy evaluation consistent with the present field-based model, a rough estimate of the magnetostatic energy may still be gained from the numerical equivalent of equation (3), namely

$$E_{\text{demag}} = -\frac{1}{2}\mu_0 V_{\text{Cell}}\sum_{i,j,k}(\mathbf{H}_d(i,j,k))\cdot(\mathbf{M}(i,j,k)) \tag{41}$$

where it is implicitly assumed that the magnetization and the demagnetizing field are constant within each volume cell.

Results pertaining to the S state in Figure 4 are displayed in Figure 6. The exchange energy per unit volume versus mesh size (Figure 6a) is seen to depend very little on the use or not of cell-averaged variables in equation (36). Convergence of the exchange energy, on the other hand is only attained for rather small mesh sizes. Markedly different behaviors for the demagnetizing field energy are obtained when using cell-averaged potential theory (equation (38)) or the rough estimate (41) (Figure 6b). In both cases, small mesh sizes are required in order to define the asymptotic value of the magnetostatic energy thus following a trend similar to that of the exchange energy. More surprising at first sight is the fact that both estimates of the magnetostatic energy do not converge to the same value for a vanishing mesh size. It ought to be noted that the best agreement between the two kinds of estimates is obtained for cubic cells (size 3 nm, here). It may therefore be concluded that the rough estimate (41) becomes particularly poor for cell aspect ratios markedly departing from unity. The total energy per unit volume versus mesh size consistent with the assumptions of the present numerical model is shown as full symbols in Figure 6(c). It appears relatively independent of mesh size although this result is physically meaningless: only the respective asymptotic values (Rave, Fabian and Hubert, 1998) of the energy contributions are representative of the physical reality. The exchange and magnetostatic energies actually display opposite curvature convergence behaviors, pointing at a subtle change in the balance between exchange and magnetostatic interactions with decreasing mesh size.

3 FINITE DIFFERENCE MICROMAGNETICS: ENERGY-BASED APPROACH

In an energy-based approach, the magnetic energy is given primacy and is computed directly from the discretized magnetization, whereas the effective field is derived from the resultant energy. The effective field obtained in this manner is a cell-averaged field. This method is obviously convenient if one is interested in finding equilibrium magnetization patterns via direct energy minimization (using, e.g., conjugate-gradient methods), but also has the advantage that the energy, being an integral quantity, has less

variation than the field and is therefore more easily approximated. As noted in Section 2.1, the demagnetizing field can diverge at corners of a sample, yet this logarithmic divergence is integrable, so that the energy contained in any discretization cell remains finite. This effect is seen also in Figure 6(b), where the result using equation (41) leads to an incorrect result, even in the small cell limit. Although the discretization in this example is sufficient to represent variations in the magnetization, it does not pick up variations in the demagnetizing field along the film normal (Parker, Cerjan and Hewett, 2000; Donahue, Porter, McMichael and Eicke, 2000). To correct for this one has to either move to a multilayer simulation or use a potential averaging approach as in equation (38) or as discussed in this section.

3.1 Zeeman energy

As stated before, Zeeman energy is the magnetostatic energy from the interaction of a given magnetization state with an external field,

$$E_{\mathrm{Z}} = -\mu_0 \int_V \mathbf{M}\cdot\mathbf{H}_{\mathrm{app}}\,\mathrm{d}^3 r \tag{42}$$

Here $\mathbf{H}_{\mathrm{app}}$ includes fields directly applied, and also fields resulting from currents inside the device, that is,

$$\mathbf{H}_{\mathrm{current}} = \frac{1}{4\pi}\int_V \mathbf{J}(\mathbf{r}') \times \frac{\mathbf{r}-\mathbf{r}'}{|\mathbf{r}-\mathbf{r}'|^3}\,\mathrm{d}^3 r' \tag{43}$$

Assuming that both $\mathbf{M}$ and $\mathbf{H}_{\mathrm{app}}$ are twice differentiable, we can write

$$\mathbf{M}(\mathbf{r}) = \mathbf{M}(\mathbf{r}_i) + B\,(\mathbf{r}-\mathbf{r}_i) + O(\|\mathbf{r}-\mathbf{r}_i\|^2) \tag{44}$$

$$\mathbf{H}_{\mathrm{app}}(\mathbf{r}) = \mathbf{H}_{\mathrm{app}}(\mathbf{r}_i) + C\,(\mathbf{r}-\mathbf{r}_i) + O(\|\mathbf{r}-\mathbf{r}_i\|^2) \tag{45}$$

where B and C are the 3×3 matrices corresponding to the partial derivatives of $\mathbf{M}$ and $\mathbf{H}_{\mathrm{app}}$, respectively, and $\mathbf{r}_i$ is an arbitrary point suitably close to $\mathbf{r}$. Consider this simple approximation to the Zeeman energy:

$$E_{\mathrm{Z}} \approx -\mu_0 \sum_i \mathbf{M}(\mathbf{r}_i)\cdot\mathbf{H}_{\mathrm{app}}(\mathbf{r}_i)|V_i| \tag{46}$$

where the index i runs over all cells in the simulation, $\mathbf{r}_i$ denotes the center of the rectangular cell i, and $|V_i|$ is the volume of cell i. Given equations (44) and (45), we estimate the error in equation (46) as

$$\left| E_{\mathrm{Z}} - (-\mu_0)\sum_i \mathbf{M}(\mathbf{r}_i)\cdot\mathbf{H}_{\mathrm{app}}(\mathbf{r}_i)|V_i| \right|$$

$$\leq \mu_0 \sum_i \left| \int_{V_i} \mathbf{M}(\mathbf{r})\cdot\mathbf{H}_{\mathrm{app}}(\mathbf{r}) - \mathbf{M}(\mathbf{r}_i)\cdot\mathbf{H}_{\mathrm{app}}(\mathbf{r}_i)\,\mathrm{d}^3 r \right| \tag{47}$$

$$\leq \mu_0 \sum_i \left| \int_{V_i} \mathbf{M}(\mathbf{r}_i)^{\mathrm{T}} C\,(\mathbf{r}-\mathbf{r}_i) + \mathbf{H}_{\mathrm{app}}(\mathbf{r}_i)^{\mathrm{T}} B\,(\mathbf{r}-\mathbf{r}_i) + O(\|\mathbf{r}-\mathbf{r}_i\|^2)\,\mathrm{d}^3 r \right| \tag{48}$$

where T denotes the vector transpose. Since $\mathbf{r}_i$ is at the center of the rectangular cell V_i,

$$\int_{V_i} (\mathbf{M}(\mathbf{r}_i)^{\mathrm{T}} C + \mathbf{H}_{\mathrm{app}}(\mathbf{r}_i)^{\mathrm{T}} B)(\mathbf{r}-\mathbf{r}_i)\,\mathrm{d}^3 r = 0 \tag{49}$$

because the integrand is an odd function with respect to $\mathbf{r}_i$. Thus we see that

$$\left| E_{\mathrm{Z}} - (-\mu_0)\sum_i \mathbf{M}(\mathbf{r}_i)\cdot\mathbf{H}_{\mathrm{app}}(\mathbf{r}_i)|V_i| \right|$$

$$\leq \mu_0 \sum_i \int_{V_i} O(\|\mathbf{r}-\mathbf{r}_i\|^2)\,\mathrm{d}^3 r \tag{50}$$

$$\leq O(\Delta^2)|V| \tag{51}$$

where $|V| = \sum_i |V_i|$ is the total volume of the space, and Δ is the maximum cell dimension.

In this approximation, all of the $\mathbf{M}(\mathbf{r}_i)\cdot\mathbf{H}_{\mathrm{app}}(\mathbf{r}_i)$ terms are weighted equally. Higher-order methods can be obtained by varying the weights, similar to the well-known Simpson's rule (Davis and Rabinowitz, 1984; Stoer and Bulirsch, 1993).

The discretized field expression derived from this approximation to the energy is simply

$$\mathbf{H}_{\mathrm{Z},i} = \mathbf{H}_{\mathrm{app}}(\mathbf{r}_i) \tag{52}$$

3.2 Magnetocrystalline anisotropy energy

Magnetocrystalline anisotropy energy models the preferential magnetization orientation in a material, and depends chiefly on the crystalline structure of the material. For uniaxial materials the energy is given by

$$E_{K,\mathrm{uniaxial}} = -\int_V K_1(\mathbf{m}\cdot\mathbf{u})^2\,\mathrm{d}^3 r \tag{53}$$

where K_1 is the material anisotropy coefficient (in $\mathrm{J\,m^{-3}}$), $\mathbf{m}$ is the unit magnetization direction ($\mathbf{M}/M_{\mathrm{s}}$), and $\mathbf{u}$ is the (unit)

anisotropy axis. If K_1 is positive, then $\mathbf{u}$ is the easy axis, while if K_1 is negative then $\mathbf{u}$ is normal to the easy plane. For some materials, a second term $K_2 \sin^4 \phi$ is important, where K_2 is a second anisotropy coefficient and ϕ is the angle between $\mathbf{m}$ and $\mathbf{u}$. This equation should be modified at material interfaces and defects (Moschel, Hyman, Zangwill and Stiles, 1996).

For cubic materials with crystal axes oriented parallel to the coordinate axes, the energy takes the form

$$E_{K,\text{cubic}} = \int_V K_1(m_x^2 m_y^2 + m_y^2 m_z^2 + m_z^2 m_x^2) + K_2(m_x^2 m_y^2 m_z^2)\, \mathrm{d}^3 r \tag{54}$$

For a rotated crystal orientation, m_x should be replaced with the projection of $\mathbf{m}$ onto the first coordinate axis, m_y with the projection onto the second (orthogonal) axis, and m_z with the projection onto the remaining axis.

If we assume that $\mathbf{m}$, $\mathbf{u}$, K_1, and K_2 are twice differentiable, at least within each cell, then we can expand the integrands in equations (53) and (54) in the manner of equations (44) and (45) and obtain an analogous discrete approximation for the magnetocrystalline anisotropy energy. In the uniaxial case this is

$$E_{K,\text{uniaxial}} \approx -\sum_i K_1(\mathbf{r}_i)\ (\mathbf{m}(\mathbf{r}_i)\cdot\mathbf{u}(\mathbf{r}_i))^2\, |V_i| \tag{55}$$

and for the cubic we have

$$E_{K,\text{cubic}} \approx \sum_i \big[K_1(\mathbf{r}_i)\left(\mathbf{m}_x^2(\mathbf{r}_i)\mathbf{m}_y^2(\mathbf{r}_i) + \mathbf{m}_y^2(\mathbf{r}_i)\mathbf{m}_z^2(\mathbf{r}_i) + \mathbf{m}_x^2(\mathbf{r}_i)\mathbf{m}_z^2(\mathbf{r}_i)\right) + K_2(\mathbf{r}_i)\ \left(\mathbf{m}_x^2(\mathbf{r}_i)\mathbf{m}_y^2(\mathbf{r}_i)\mathbf{m}_z^2(\mathbf{r}_i)\right)\big]|V_i| \tag{56}$$

Using the same argument as in the Zeeman energy section, these approximations are also seen to be of order Δ^2.

The discretized field expressions derived from the discretized energies are

$$H_{K,\text{uniaxial},i} = 2K_1(\mathbf{r}_i)\ (\mathbf{m}(\mathbf{r}_i)\cdot\mathbf{u}(\mathbf{r}_i))\,\mathbf{u}(\mathbf{r}_i)/\mu_0 M_\text{s} \tag{57}$$

$$H_{K,\text{cubic},i} = -2\,D(\mathbf{r}_i)\mathbf{m}(\mathbf{r}_i)/\mu_0 M_\text{s} \tag{58}$$

where D is the diagonal matrix with entries

$$D_{11} = K_1(\mathbf{r}_i)\left(m_y^2(\mathbf{r}_i) + m_z^2(\mathbf{r}_i)\right) + K_2(\mathbf{r}_i)m_y^2(\mathbf{r}_i)m_z^2(\mathbf{r}_i) \tag{59}$$

$$D_{22} = K_1(\mathbf{r}_i)\left(m_x^2(\mathbf{r}_i) + m_z^2(\mathbf{r}_i)\right) + K_2(\mathbf{r}_i)m_x^2(\mathbf{r}_i)m_z^2(\mathbf{r}_i) \tag{60}$$

$$D_{33} = K_1(\mathbf{r}_i)\left(m_x^2(\mathbf{r}_i) + m_y^2(\mathbf{r}_i)\right) + K_2(\mathbf{r}_i)m_x^2(\mathbf{r}_i)m_y^2(\mathbf{r}_i) \tag{61}$$

3.3 Exchange energy

As noted in Section 1, the exchange energy may be represented using either of the expressions in equation (4). In practice, the latter relation,

$$E_\text{exch} = -\int_V A\,\mathbf{m}\cdot\left(\frac{\partial^2\mathbf{m}}{\partial x^2} + \frac{\partial^2\mathbf{m}}{\partial y^2} + \frac{\partial^2\mathbf{m}}{\partial z^2}\right)\mathrm{d}^3 r \tag{62}$$

is somewhat easier to work with and is the form used in the following discussion.

The first step in providing a numerical approximation to equation (62) is to find a discrete form for the second derivative operator. As mentioned in Section 2.2, the simplest approximation, which holds if $\mathbf{m}$ is four times differentiable, is

$$\frac{\partial^2\mathbf{m}}{\partial x^2}(\mathbf{r}) = \frac{1}{\Delta_x^2}\big(\mathbf{m}(\mathbf{r}+\Delta_x\hat{x}) - 2\mathbf{m}(\mathbf{r}) + \mathbf{m}(\mathbf{r}-\Delta_x\hat{x})\big) + O(h^2) \tag{63}$$

where Δ_x is the discretized cell dimension along the $\hat{x}$ direction. The analogous equations for $\partial^2\mathbf{m}/\partial y^2$ and $\partial^2\mathbf{m}/\partial z^2$ (involving Δ_y and Δ_z), lead to a seven point approximation to the integrand in equation (62), involving $\mathbf{M}$ at the point $\mathbf{r}_i$ and its six closest neighbors:

$$E_\text{exch} \approx -\sum_i |V_i| A \sum_j \mathbf{m}(\mathbf{r}_i)\cdot\big(\mathbf{m}(\mathbf{r}_i+\boldsymbol{\epsilon}_j) - \mathbf{m}(\mathbf{r}_i)\big)/|\boldsymbol{\epsilon}_j|^2 \tag{64}$$

Here $\mathbf{r}_i + \boldsymbol{\epsilon}_j$, varying over j, specifies each of the six nearest neighbors to $\mathbf{r}_i$ in the discretized mesh. By the same argument used in the previous two sections, this estimate will be of $O(\Delta^2)$. The corresponding expression for the discretized exchange field is

$$H_\text{exch} = \frac{2A}{\mu_0 M_\text{s}} \sum_j \big(\mathbf{m}(\mathbf{r}_i+\boldsymbol{\epsilon}_j) - \mathbf{m}(\mathbf{r}_i)\big)/|\boldsymbol{\epsilon}_j|^2 \tag{65}$$

One may be tempted to replace $\mathbf{m}(\mathbf{r}_i)\cdot\mathbf{m}(\mathbf{r}_i)$ in equation (64) with $|\mathbf{m}|^2 = 1$, obtaining

$$E_\text{exch} \approx -\sum_i |V_i| A \sum_j \big(\mathbf{m}(\mathbf{r}_i)\cdot\mathbf{m}(\mathbf{r}_i+\boldsymbol{\epsilon}_j) - 1\big)/|\boldsymbol{\epsilon}_j|^2 \tag{66}$$

or to drop the '-1' altogether, which shifts E_exch by a constant amount without affecting the exchange field. Either way, however, leads to numerical problems because the term $\mathbf{m}(\mathbf{r}_i)\cdot\mathbf{m}(\mathbf{r}_i+\boldsymbol{\epsilon}_j)$ effectively loses significant precision in the common case where $\mathbf{m}(\mathbf{r}_i)$ and $\mathbf{m}(\mathbf{r}_i+\boldsymbol{\epsilon}_j)$ are nearly parallel. This can be seen by realizing that $\mathbf{m}(\mathbf{r}_i)\cdot\mathbf{m}(\mathbf{r}_i+\boldsymbol{\epsilon}_j) = \cos\theta$, where θ is the angle between $\mathbf{m}(\mathbf{r}_i)$ and

$\mathbf{m}(\mathbf{r}_i + \boldsymbol{\epsilon}_j)$, and $\cos\theta \approx 1 - \theta^2/2$. The torque depends on the component perpendicular to $\mathbf{m}(\mathbf{r}_i)$, which is represented by the θ^2 term. If $|\theta| \ll 1$, then when stored with a finite number of digits the expression $1 - \theta^2/2$ loses a great deal of the precision in θ^2. On the other hand, if one first subtracts $\mathbf{m}(\mathbf{r}_i)$ from $\mathbf{m}(\mathbf{r}_i + \boldsymbol{\epsilon}_j)$ as in equation (64) then the dot product will be between two nearly perpendicular vectors, and precision is significantly retained (Donahue, Porter, McMichael and Eicke, 2000).

Large angles between neighboring spins $\mathbf{m}(\mathbf{r}_i)$ and $\mathbf{m}(\mathbf{r}_i + \boldsymbol{\epsilon}_j)$ also cause problems, but of a rather different nature. Here the problem arises because equation (64) always underestimates the exchange energy, and the larger the neighboring spin angle θ, the larger the underestimate. As a result, magnetization configurations with regions of high exchange energy that are located between grid points tend to have overall smaller total exchange energy than otherwise identical configurations shifted so that the points of high exchange energy are on or near grid points. This can cause artificial, discretization-induced pinning of high exchange energy structures such as vortices (Donahue and McMichael, 1997) or induce a Peierl's like friction for Bloch points motion (Thiaville *et al*., 2003). Figure 7 illustrates this problem on a small, vortex bearing thin plate. In this example, maximum pinning is 18 mT, which occurs with an in-plane cell size of just under 7 nm. Moreover, the pinning is found to be non-monotonic with Δ, at first worsening as Δ is decreased, only abating after the vortex core is resolved.

A related issue can occur in undermeshed 180° Néel walls (Donahue, 1998). If the angle between neighboring spins across the center of the wall is too large, then the wall demagnetizing field can overwhelm the coarse mesh–weakened exchange field and force the Néel wall to collapse into a structure where the entire wall is squeezed between adjacent spins, as illustrated in Figure 8(a). The problem is fixed when a sufficiently fine mesh is used, as in Figure 8(b).

Simulations in Figures 7 and 8 were performed using the OOMMF public code (Donahue and Porter, 1999).

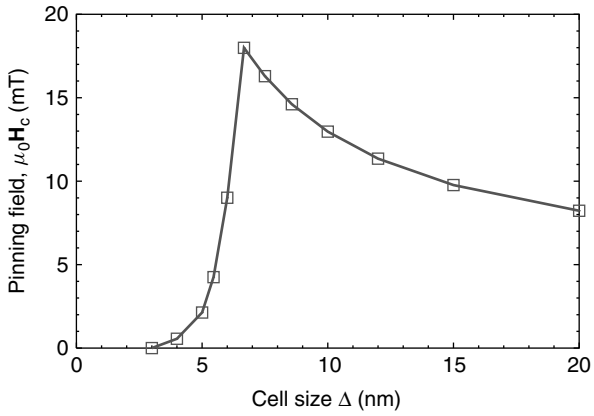

Figure 7. Discretization-induced vortex pinning fields for a $120 \times 120 \times 3\,\text{nm}^3$ $Ni_{80}Fe_{20}$ ($M_s = 800\,\text{kA m}^{-1}$, $A = 13\,\text{pJ m}^{-1}$, $K = 0\,\text{J m}^{-3}$) plate, as a function of in-plane discretization cell size (one-layer-of-cells type simulations). Initial zero-field magnetization configuration is an equilibrium-centered vortex state. Field is applied in plane, parallel to plate edge, and gradually increased until vortex jumps from one discretization cell to the next.

3.4 Self-magnetostatic energy

Self-magnetostatic, or demagnetization energy, is the energy associated with dipole–dipole magnetostatic interactions of material within itself. It is described by

$$E_{\text{demag}} = -\frac{\mu_0}{2} \int_V \mathbf{M} \cdot \mathbf{H}_{\text{d}}\, \mathrm{d}^3 r \tag{67}$$

where the demagnetization field $\mathbf{H}_{\text{d}}$ at position r is

$$\mathbf{H}_{\text{d}}(\mathbf{r}) = -\frac{1}{4\pi} \int_V \nabla \cdot \mathbf{M}(\mathbf{r}') \frac{\mathbf{r} - \mathbf{r}'}{|\mathbf{r} - \mathbf{r}'|^3}\, \mathrm{d}^3 r' + \frac{1}{4\pi} \int_S \hat{\mathbf{n}}(\mathbf{r}') \cdot \mathbf{M}(\mathbf{r}') \frac{\mathbf{r} - \mathbf{r}'}{|\mathbf{r} - \mathbf{r}'|^3}\, \mathrm{d}^2 r' \tag{68}$$

Equation (68) is identical to equation (21) and displayed here anew for convenience. Note that E_{demag} involves long-range interactions, and in terms of $\mathbf{M}$ requires integration over $V \times V$.

If we let $\mathbf{g}(\mathbf{r}) = \mathbf{r}/|\mathbf{r}|^3$, then integration by parts allows one to rewrite equation (68) as

$$\mathbf{H}_{\text{d}}(r) = -\frac{1}{4\pi} \int_V \nabla \mathbf{g}(\mathbf{r} - \mathbf{r}') \mathbf{M}(\mathbf{r}')\, \mathrm{d}^3 r' \tag{69}$$

From this formulation it is clear that an approximation to $\mathbf{M}$ of the form (44) is sufficient to produce an approximation to $\mathbf{H}_{\text{d}}$ of second order, and moreover that at this level of

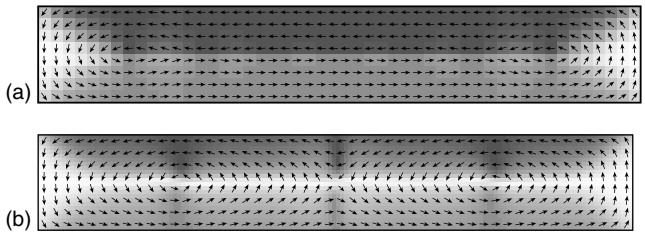

Figure 8. Néel wall in $750 \times 120 \times 30\,\text{nm}^3$ $Ni_{80}Fe_{20}$ rectangle, equilibrium states. (Same material parameters as quoted in Figure 7.) (a) Wall collapses in coarse grid simulation ($\Delta = 15\,\text{nm}$), as compared to (b) fully resolved wall using fine grid ($\Delta = 5\,\text{nm}$). Shade indicates x-axis component of the magnetization. Multilayer cubic cells used in both simulations.

approximation the linear portion of $\mathbf{M}$ can be ignored. Thus we have

$$\mathbf{H}_{\mathrm{d}}(\mathbf{r}) = -\frac{1}{4\pi}\sum_i \int_{V_i} \nabla \mathbf{g}(\mathbf{r}-\mathbf{r}')\mathbf{M}(\mathbf{r}_i')\,\mathrm{d}^3 r' + O(\Delta^2) \tag{70}$$

$$= \frac{1}{4\pi}\sum_i \int_{S_i} \hat{\mathbf{n}}(\mathbf{r}')\cdot\mathbf{M}(\mathbf{r}_i')\frac{\mathbf{r}-\mathbf{r}'}{|\mathbf{r}-\mathbf{r}'|^3}\,\mathrm{d}^2 r' + O(\Delta^2) \tag{71}$$

This shows that, to second order, the demagnetization field at point $\mathbf{r}$ can be computed by treating each cell in the discretization as a uniformly magnetized block. Likewise, second-order accuracy can be maintained in equation (67) by replacing $\mathbf{M}$ in each cell with its value at the center, so we have

$$E_{\mathrm{demag}} \approx -\frac{\mu_0}{8\pi}\sum_{i,j}\int_{V_i}\mathbf{M}(\mathbf{r}_i)\cdot\int_{S_j}\mathbf{M}(\mathbf{r}_j')\cdot\hat{\mathbf{n}}(\mathbf{r}')\frac{\mathbf{r}-\mathbf{r}'}{|\mathbf{r}-\mathbf{r}'|^3}\,\mathrm{d}^2 r'\,\mathrm{d}^3 r \tag{72}$$

$$\approx -\frac{\mu_0}{8\pi}\sum_{i,j}\mathbf{M}^{\mathrm{T}}(\mathbf{r}_i)\left(\int_{V_i}\int_{S_j}\frac{\mathbf{r}-\mathbf{r}'}{|\mathbf{r}-\mathbf{r}'|^3}\hat{\mathbf{n}}^{\mathrm{T}}(\mathbf{r}')\,\mathrm{d}^2 r'\,\mathrm{d}^3 r\right)\mathbf{M}(\mathbf{r}_j) \tag{73}$$

This can be rewritten as

$$E_{\mathrm{demag}} \approx \frac{\mu_0}{2}\sum_{i,j}|V_i|\,\mathbf{M}^{\mathrm{T}}(\mathbf{r}_i)N(\mathbf{r}_i,\mathbf{r}_j)\mathbf{M}(\mathbf{r}_j) \tag{74}$$

where $N(\mathbf{r}_i,\mathbf{r}_j)$ is the 3×3 matrix arising from the fivefold integration in equation (73) divided by $-4\pi|V_i|$. The term $(\mu_0|V_i|/2)\,\mathbf{M}^{\mathrm{T}}(\mathbf{r}_i)N(\mathbf{r}_i,\mathbf{r}_j)\mathbf{M}(\mathbf{r}_j)$ is seen to be the (exact) magnetostatic energy arising between uniformly magnetized cells at positions $\mathbf{r}_i$ and $\mathbf{r}_j$. It is clear from the definition that N depends only on the difference $\mathbf{r}_i-\mathbf{r}_j$, so $N(\mathbf{r}_i,\mathbf{r}_j) = N(\mathbf{r}_i-\mathbf{r}_j) = N_{i-j}$.

If we compute the effective demagnetization field from equation (74), we obtain

$$\mathbf{H}_{\mathrm{d},i} = -\sum_j N_{i-j}\mathbf{M}_j \tag{75}$$

Note that as elsewhere in Section 3, $\mathbf{H}_{\mathrm{d},i}$ is computed from the energy expression (73) rather than the field expression (71), so that $\mathbf{H}_{\mathrm{d},i}$ can be interpreted as being the average value for the demagnetization field in cell i arising from a cell j having uniform magnetization $\mathbf{M}_j$.

We must now compute N_i. It follows from the magnetic reciprocity theorem (Brown, 1963) that N_i must be symmetric. (Newell, Williams and Dunlop, 1993 also discuss additional properties of N_i). This means that the 3×3 matrix N_i holds only six independent entries,

$$N_i = \begin{bmatrix} N_{xx,i} & N_{xy,i} & N_{xz,i} \\ N_{xy,i} & N_{yy,i} & N_{yz,i} \\ N_{xz,i} & N_{yz,i} & N_{zz,i} \end{bmatrix} \tag{76}$$

The entries, $N_{xx,i}$, and so on, can be evaluated analytically (Schabes and Aharoni, 1987; Newell, Williams and Dunlop, 1993; Fukushima, Nakatani and Hayashi, 1998). First, define

$$f(x,y,z) = \frac{1}{2}y(z^2-x^2)\sinh^{-1}\left(\frac{y}{\sqrt{x^2+z^2}}\right) + \frac{1}{2}z(y^2-x^2)\sinh^{-1}\left(\frac{z}{\sqrt{x^2+y^2}}\right) - xyz\arctan\left(\frac{yz}{xR}\right) + \frac{1}{6}(2x^2-y^2-z^2)R \tag{77}$$

$$g(x,y,z) = xyz\sinh^{-1}\left(\frac{z}{\sqrt{x^2+y^2}}\right) + \frac{1}{6}y(3z^2-y^2)\sinh^{-1}\left(\frac{x}{\sqrt{y^2+z^2}}\right) + \frac{1}{6}x(3z^2-x^2)\sinh^{-1}\left(\frac{y}{\sqrt{x^2+z^2}}\right) - \frac{1}{2}y^2z\arctan\left(\frac{xz}{yR}\right) - \frac{1}{2}x^2z\arctan\left(\frac{yz}{xR}\right) - \frac{1}{6}z^3\arctan\left(\frac{xy}{zR}\right) - \frac{xyR}{3} \tag{78}$$

where $R=\sqrt{x^2+y^2+z^2}$, and $\sinh^{-1}$ is the inverse hyperbolic sine, $\sinh^{-1}(x)=\log(x+\sqrt{1+x^2})$. Note that $f(x,y,z)$ and $g(x,y,z)$ are identical to $F^{022}(x,y,z)$ and $F^{112}(x,y,z)$ defined in Appendix B. They describe magnetostatic interactions between parallel and perpendicular charged tiles, respectively. Then

$$4\pi\Delta_x\Delta_y\Delta_z N_{xx,i} = 8f(x_i,y_i,z_i) - 4\sum_{v\in A}f(v) + 2\sum_{v\in B}f(v) - \sum_{v\in C}f(v) \tag{79}$$

$$4\pi\Delta_x\Delta_y\Delta_z N_{xy,i}(x,y,z) = 8g(x_i,y_i,z_i) - 4\sum_{v\in A}g(v) + 2\sum_{v\in B}g(v) - \sum_{v\in C}g(v) \tag{80}$$

where A is the set of 'nearest neighbors' to (x_i,y_i,z_i), B is the set of next nearest neighbors, and C is the set of corners

of the 3×3 cube about (x_i, y_i, z_i):

$$A = \{(x_i \pm \Delta_x, y_i, z_i), (x_i, y_i \pm \Delta_y, z_i), (x_i, y_i, z_i \pm \Delta_z)\} \tag{81}$$

$$B = \{(x_i \pm \Delta_x, y_i \pm \Delta_y, z_i), (x_i \pm \Delta_x, y_i, z_i \pm \Delta_z), (x_i, y_i \pm \Delta_y, z_i \pm \Delta_z)\} \tag{82}$$

$$C = \{(x_i \pm \Delta_x, y_i \pm \Delta_y, z_i \pm \Delta_z)\} \tag{83}$$

so that $|A| = 6$, $|B| = 12$, and $|C| = 8$. The other four elements of N_i are computed analogously, by permuting x, y, z and Δ_x, Δ_y, Δ_z, with $N_{yy,i}$ and $N_{zz,i}$ using equation (79) and $N_{xz,i}$ and $N_{yz,i}$ using equation (80).

If we let ϕ represent the operator on f and g in the right-hand side of equations (79) and (80), we see that $\phi/|V|^2$ is a second-order discrete approximation to the differential operator $-\partial^6/\partial x^2 \partial y^2 \partial z^2$ (Abramowitz and Stegun, 1970). If we define ψ_x/Δ_x^2 to be the second-order discrete approximate to $-\partial^2/\partial^2 x$, $\psi_x(f)(x) = -f(x - \Delta_x, y, z) + 2f(x, y, z) - f(x + \Delta_x, y, z)$ (and likewise ψ_y and ψ_z), we see that ϕ can be decomposed as $\psi_x \circ \psi_y \circ \psi_z$. This admits a relatively efficient approach to the evaluation of N_{xx} for the entire range of (x, y, z) of interest. First, evaluate f at each point on the mesh. Then, evaluate $\psi_z(f)$ at each point on the mesh, which can be done essentially in place. If there are n points in the mesh, evaluating $\psi_z(f)$ requires $2n$ subtractions. Then, evaluate ψ_y on the new values, and finally ψ_x, for a total of $6n$ subtractions (as compared to $26n$ additions/subtractions in a direct implementation of equation (79)). The other five terms of N_i can be evaluated using the same method.

As can be seen from equation (75), $\mathbf{H}_{\mathrm{d},i}$ is a discrete (three dimensional) convolution of N_i with $\mathbf{M}_i$, so it can be computed efficiently using FFT techniques (Stockham, 1966). A few details of the application of the FFT in this case bear mentioning (Donnelly and Rust, 2005a,b).

The basics of the technique are to take the FFT of the N_i and $\mathbf{M}_i$ sequences, say $\tilde{N}_k$ and $\tilde{\mathbf{M}}_k$, multiply these together pointwise to obtain $\tilde{\mathbf{H}}_{\mathrm{d},k}$, and then take the inverse FFT of $\tilde{\mathbf{H}}_{\mathrm{d},k}$ to obtain $\mathbf{H}_{\mathrm{d},i}$. Since the FFT and inverse FFT can be computed with operation count of $O(n \log n)$ (where n is the size of the set $\{i\}$), the computation of the entire set $\{\mathbf{H}_{\mathrm{d},i}\}$ can be computed in $O(n \log n)$, as opposed to $O(n^2)$ resulting from a direct evaluation of equation (75).

However, the magnetization data in equation (75) should be interpreted as being finite in extent but lying in an infinite space. Since convolution by FFT produces a cyclic (periodic) convolution, the magnetization data need to be zero-padded to double length in each of the x, y, and z directions to remove wraparound artifacts. Note that this results in an eightfold increase in the number of points. The interaction coefficient sequence N_i also needs to be extended to this size, however, it is not zero-padded but rather is extended through the origin into 'negative' territory, where, following the usual FFT conventions, index $-i = (-i_x, -i_y, -i_z)$ is stored at the index corresponding to $(n_x - i_x, n_y - i_y, n_z - i_z)$.

Since the interaction coefficient sequence N_i is determined by the geometry of the problem, the FFT of this sequence, $\tilde{N}_k$, can be computed once during program initialization and saved for subsequent use. Moreover, the various symmetries of the terms N_{xx}, N_{xy}, and so on (Newell, Williams and Dunlop, 1993), and the fact that these sequences are real (as opposed to complex), result in the transformed sequences $\tilde{N}_{xx,k}$, $\tilde{N}_{xy,k}$, and so on, having the same symmetries and also being purely real. As a result, only one octant of $\tilde{N}_k$ needs to be stored and that storage can be as real (as opposed to complex) values.

The $\mathbf{M}_i$ sequence is also real; this property can be used to accelerate the FFT by almost a factor of 2 and reduce the storage requirements for $\tilde{\mathbf{M}}_k$ by half. ($\tilde{\mathbf{M}}_k$ is complex valued, but is conjugate symmetric with respect to the origin, so only one half-space needs to be stored.) The fact that large portions of the zero-padded $\mathbf{M}_i$ array are zero can also be used to significantly speed up the FFT.

3.5 Boundary conditions

As discussed in Sections 2.3 and 2.4, at grid points where the stencil for an expression extends beyond the boundaries of the part being simulated, the stencil will need to be adjusted. Typically this involves replacement of missing magnetization values (i.e., points corresponding to stencil values outside the part boundary) with relations involving BCs and possibly additional points inside the part. These considerations apply not just to part boundaries but across any interface where the magnetization fails to fulfill the smoothness requirements for the given expression. We consider in this subsection only the 'free' BCs arising in the case of no surface anisotropy. As discussed in Sections 1 (equations (14)–(17)) and 2.4, other constraints are possible.

In general, BCs may influence any of the energy terms. However, for the second-order relations discussed here (Section 3), only the exchange energy is directly affected. Indeed, expressions (46) and (52) for the Zeeman term, expressions (55–58) for anisotropy, and (74) and (75) for demagnetization may be used unaltered at boundaries or in situations where $\mathbf{M}$ is discontinuous across cell faces.

However, examination of equation (64) reveals that the formula is undefined at boundaries; for example, if $\mathbf{r}_i$ is on the leftmost edge of the discretized mesh, then $\mathbf{r}_i - \Delta_x \hat{x}$ is outside the mesh, so we have no value for $\mathbf{m}$ there.

The most common solution to this problem is to introduce a 'ghost' spin at the missing location, with value the same

as the nearest spin inside the boundary, that is define $\mathbf{m}(\mathbf{r}_i - \Delta_x\hat{x}) = \mathbf{m}(\mathbf{r}_i)$. Here we implicitly assume that the boundary runs along the discretization cell surfaces, and is therefore exactly halfway between $\mathbf{r}_i - \Delta_x\hat{x}$ and $\mathbf{r}_i$. With this definition, the interpolated magnetization $\mathbf{m}(\mathbf{r})$ satisfies the usual Neumann BC $\partial\mathbf{m}/\partial\mathbf{n} = \mathbf{0}$. This approach is sometimes referred to as using 'mirror boundary conditions', because the magnetization is in some sense reflected across the boundary. It should be noted that this simple scheme for defining the value of the ghost spin only works for the second-order method. The relations are more complicated when higher-order methods are involved (Donahue and Porter, 2004). Also, the computed value for the field (65) at the edge spin $\mathbf{r}_i$ is only first-order accurate in Δ_x. However, the boundary region has narrow width Δ_x, so in the energy computation (64) a factor of Δ_x is introduced into the $|V_i|$ term; therefore the computed value for the total energy remains second order in Δ_x (Donahue and Porter, 2004).

The usual artifact of applying an incorrect BC is a loss in accuracy arising from a reduction in method order. This effect is shown in Figure 9, where a uniform magnetization spiral is impressed upon a one-dimensional rod. The magnetization pattern is not relaxed but rather held fixed while the exchange energy is computed for different discretization scales. For this reason the usual 'free' BCs, $\partial\mathbf{m}/\partial\mathbf{n} = \mathbf{0}$ do not hold. To obtain full method accuracy it is necessary to apply the correct boundary conditions, which in this case are of the Dirichlet type.

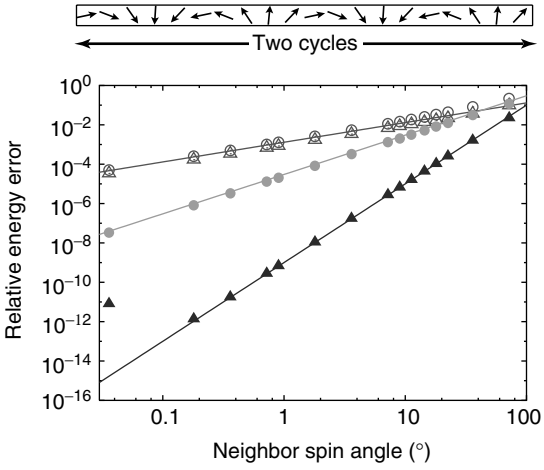

Figure 9. One-dimensional convergence study of exchange energy on an impressed magnetization spiral. Horizontal axis is the (constant) angle between neighboring spins, i.e. 720° divided by the number of spins. Circles represent second-order exchange method discussed in Section 3.3, triangles are a fourth-order method presented in Donahue and Porter (2004). Open symbols (top line) are results using 'free' boundary condition, $\partial\mathbf{m}/\partial\mathbf{n} = \mathbf{0}$; these show only first-order convergence because the magnetization spiral does not obey this boundary condition. Closed symbols (bottom two lines) use the correct Dirichlet boundary conditions and recover the quoted convergence rates, second and fourth order, respectively. The leftmost point on the lowest curve shows the limit of numeric accuracy imposed by round-off errors.

4 SOLVING THE LLG EQUATION

When attempting to solve the LLG equation, accuracy needs to be preserved both in space and time. To look for time accuracy monitoring tools that might easily be implemented in a given code, let us first take the vector product of the right-hand side of the LLG equation (9) with $\mathrm{d}\mathbf{m}/\mathrm{d}t$. One gets

$$\mathbf{h}_{\mathrm{eff}} \cdot \frac{\mathrm{d}\mathbf{m}}{\mathrm{d}\tau} = \alpha \left(\frac{\mathrm{d}\mathbf{m}}{\mathrm{d}\tau} \right)^2 \tag{84}$$

where, $\tau = \gamma_0 M_s t$, $\mathbf{m} = \mathbf{M}/M_s$, $\mathbf{h}_{\mathrm{eff}} = \mathbf{H}_{\mathrm{eff}}/M_s$. Equation (84) is local. Alternatively, starting from the general expression of the system's free energy functional, its rate of change may, provided the applied field be time independent, be written as (Brown, 1963)

$$\frac{\mathrm{d}\int \varepsilon_{\mathrm{T}}}{\mathrm{d}\tau} = -\mu_0 M_s^2 \int \left(\mathbf{h}_{\mathrm{eff}} \cdot \frac{\mathrm{d}\mathbf{m}}{\mathrm{d}\tau} \right) \tag{85}$$

There exists no local counterpart to this expression, owing to the nonlocal nature of magnetostatic interactions. It follows from equations (84) and (85) that the damping parameter is related to the rate of change of the total free energy and the rate of change of the magnetization through

$$\alpha = -\frac{1}{\mu_0 M_s^2} \left[\frac{\int \mathrm{d}\varepsilon_{\mathrm{T}}/\mathrm{d}\tau}{\int (\mathrm{d}\mathbf{m}/\mathrm{d}\tau)^2} \right] \tag{86}$$

As expected, the damping parameter may stay positive only if the overall energy decreases as time elapses. Two numerical equivalents to this important relation may be written down, namely

$$\langle \alpha \rangle = \frac{\gamma_0 \Delta t}{\mu_0 M_s} \left[\frac{-\sum_{i=1}^{N} \Delta\varepsilon_i}{\sum_{i=1}^{N} \Delta\mathbf{m}_i^2} \right] \tag{87}$$

where i is the node index, N the total node number, and the reduced time has been replaced by the physical time step in the calculation, and

$$\alpha_{\mathrm{MS}} = N \frac{\gamma_0 \Delta t}{\mu_0 M_s} \left[\frac{-\sum_{i=1}^{N} \Delta\varepsilon_i}{\left(\sum_{i=1}^{N} \Delta\mathbf{m}_i \right)^2} \right] \tag{88}$$

which represents a transcription of equation (86) for the average magnetization, that is, for the macrospin equivalent to the magnetization distribution. Because of Schwartz' inequality, one always finds

$$\alpha_{\mathrm{MS}} \geq \langle \alpha \rangle \tag{89}$$

This seemingly innocuous relation contains a deep meaning: any experiment that measures the time evolution of some average of the magnetization distribution is bound to yield a value larger than the true Gilbert damping parameter. On the other hand, it turns out that equation (87) provides an extremely sensitive tool when evaluating the accuracy of the numerical time integration of the LLG equation (Albuquerque, Miltat and Thiaville, 2001). Note in passing that the variational form $\Delta\varepsilon_i = -\mathbf{H}_{\mathrm{eff},i} \cdot \Delta\mathbf{M}_i$ provides the most accurate estimate of the energy change within the time step Δt.

A typical calculation of the kind is illustrated in Figure 10 dealing with the effect of a spin-polarized current flowing through a submicron size elliptical element. Momentum transfer from the conduction electrons to the magnetization induces magnetization motion for large enough current densities and may lead to the existence of precessional states (Slonczewski, 1996; Sun, 2000; Miltat, Albuquerque, Thiaville and Vouille, 2001; Stiles, Xiao and Zangwill, 2004; Stiles and Miltat, 2006, references therein; and see also **Theory of Spin-transfer Torque, Volume 2**). Shortly after switching the current on, magnetization motion proves undistinguishable whether using a semi-implicit Crank–Nicholson integration scheme or the fourth-order explicit Runge–Kutta algorithm (Figure 10a). At longer times, however, magnetization trajectories would prove somewhat different. Energy dissipation, on the other hand, as monitored via equation (87), proves distinctively different (Figure 10b) for the two time integration schemes. The Runge–Kutta algorithm leads to a numerical damping parameter equal to the nominal value in this calculation to a better than 10^{-6} relative accuracy for the 25 fs time step considered. Rather large fluctuations in the numerical damping parameter $\langle \alpha \rangle$ are seen to arise from the implicit integration scheme in spite of its unconditional stability. Generally speaking, $\langle \alpha \rangle$ is seen to be significantly depressed whenever the magnetization becomes stationary, a result ascribed to residual numerical noise in the solution of a large set of linear equations (sparse matrix) by means of iterative methods. Such considerations become particularly important when dealing with long time integrations such as requested in spin-transfer problems.

5 COMPARING METHODS

Numerical methods outlined in Sections 2 and 3 do differ in the order of approximations for exchange interactions and

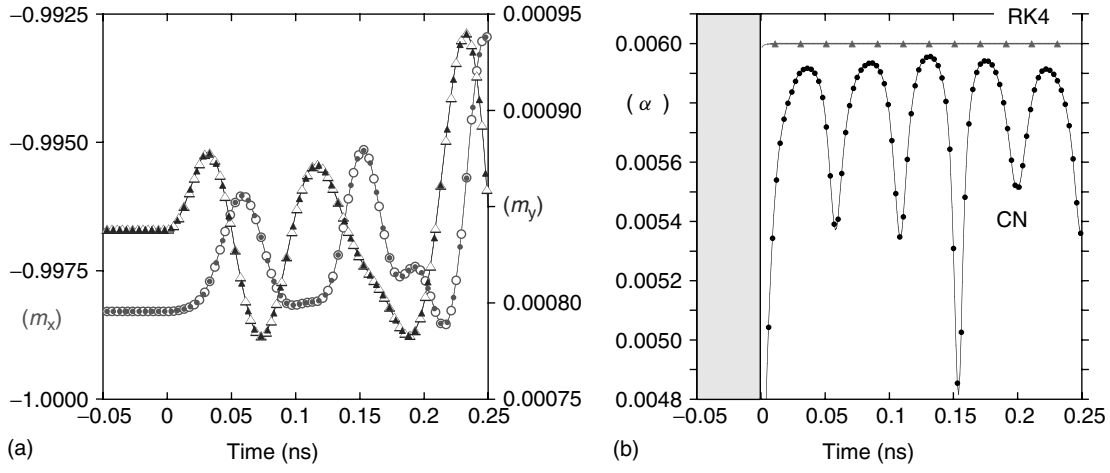

Figure 10. Onset of magnetization motion under the influence of a spin-polarized current flowing across a submicron size elliptical element. The magnetization distribution at rest is stabilized by a field applied along the ellipse long axis and equal to $1.5H_K$, where H_K is the shape anisotropy field of the elliptical platelet. Current density: $J = 0.5\,\mathrm{A\,\mu m^{-2}}$ flowing from time $t = 0$ on. A tiny constant field ($80\,\mathrm{A\,m^{-1}}$ or 1 Oe) is applied along the short ellipse axis, hence the nonzero value of the average m_y component prior to current application. (a) Element-averaged magnetization components versus time along the long (m_x) and short (m_y) elliptical axes, respectively. Open symbols refer to the Crank–Nicholson solution with an implicit character restricted to exchange interactions; full symbols refer to a fourth-order Runge–Kutta time integration. (b) Volume-averaged damping parameter (equation (87)) owing to the semi-implicit Crank–Nicholson (time step 12.5 fs) or explicit fourth-order Runge–Kutta (time step 25 fs) time integration schemes. Co-like materials parameters (exchange constant: $A = 1.3 \times 10^{-11}\,\mathrm{J\,m^{-1}}$, saturation magnetization $M_s = 1500\,\mathrm{kA\,m^{-1}}$, damping coefficient $\alpha = 0.006$); dimensions: $170 \times 80 \times 2.5\,\mathrm{nm}^3$; one-layer-of-cells type simulation.

BCs. More significantly, perhaps, they differ in the evaluation of the demagnetizing field, direct evaluation at nodes in the first case, field averaged over the cell volume in the second. The approach described in Section 3 uses constant magnetization cells, that is, zero-order expansion for the magnetization $\mathbf{m}(\mathbf{r})$. Note, however, that cell averaging, or indeed more complex integration approaches, may equally be applied to cells with a constant divergence (first-order expansion for the magnetization). The real question that arises from the different modeling options is the degree of coherence in approximation levels. Magnetization dynamics raises an additional issue, namely, is there a best numerical implementation for the LLG equation? In other words, should a mapping of the magnetization and the effective field onto the nodes of a regular mesh be preferred to motion involving a cell-averaged magnetization and a cell-averaged field or vice versa? The point being that in general, $\langle \mathbf{m}(t) \times \mathbf{H}_{\text{eff}}(t) \rangle \neq \langle \mathbf{m}(t) \rangle \times \langle \mathbf{H}_{\text{eff}}(t) \rangle$. We do not provide general answers to these questions in the following but, rather, analyze the convergence proper to each approach when dealing with the reversal of a rectangular platelet under the action of a slightly off-axis magnetic field applied at time $t = 0$. The specifics of the test problem considered here, which is the second part of μMAG Problem No. 4 (Micromagnetic Modeling Activity Group, 2005), are shown in Figure 11. At time $t = 0$ a uniform field is applied in-plane at 190° counterclockwise from the positive x axis. The applied field causes the spins in the middle portion of the sample to rotate clockwise, and the spins on either end to rotate counterclockwise. The differing rotation directions results from the relative angle of the applied field with respect to the initial position of the spins in the middle of the plate in contrast to the spins at the ends, but the origin of the motion is perhaps not immediately obvious. The damping parameter α is relatively small, so the spin evolution is dominated by precessional motion. In the middle part of the sample, $\mathbf{H} \times \mathbf{m}$ is directed upward ($+z$), so the initial motion of the spins in the middle is up and out of the film plane. In response, a large opposing demagnetization field is generated directed into the film plane ($-z$). Precession about this demagnetizing field results in the clockwise rotation of these spins, as seen in Figure 11(b). At the ends, the initial spin motion is in the $-z$ direction, the resulting demagnetizing field points along $+z$, and so the rotation of the spins at either end is counterclockwise.

After approximately 0.16 ns, the respective rotations generate two 360°-character domain walls, one on either end (Figure 11c), which are gradually pushed off the sample as the center domain expands (Figure 11d). As the walls are forced off the ends, the confined geometry leads to very tight magnetization structures containing vortices and cross-ties

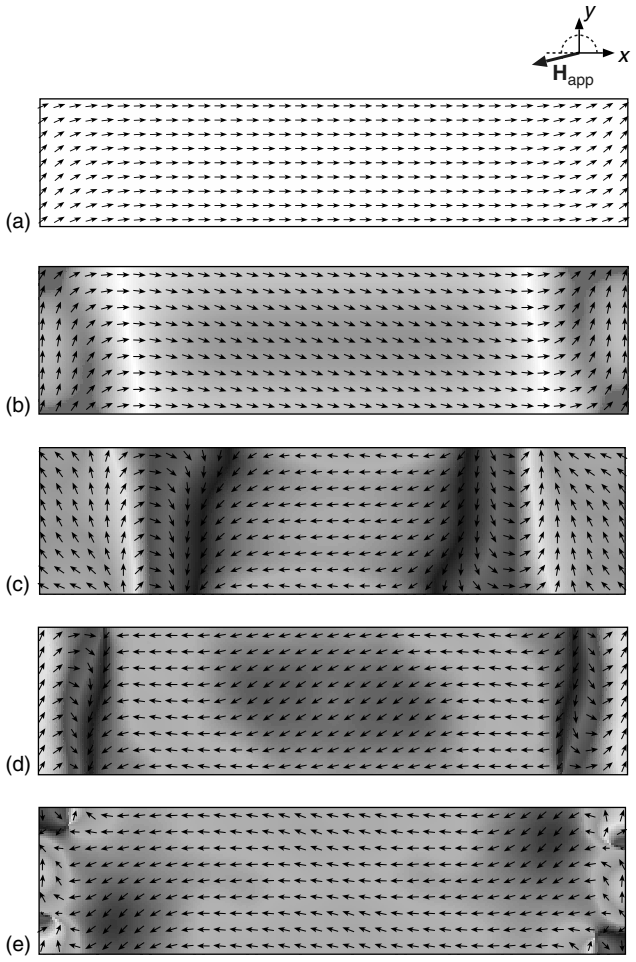

Figure 11. Magnetization states for μMAG Problem 4b (Micromagnetic Modeling Activity Group, 2005). Sample is a $Ni_{80}Fe_{20}$ slab with dimensions $500 \times 125 \times 3\,\text{nm}^3$, material parameters $A = 13\,\text{pJ m}^{-1}$, $M_s = 800\,\text{kA m}^{-1}$, $K = 0\,\text{J m}^{-3}$, $\alpha = 0.02$, $\gamma_0 = 2.211 \times 10^5\,\text{m A}^{-1}\text{s}^{-1}$. Dynamic simulation, starting in a zero-field equilibrium 'S'-state (a). At time $t = 0$ fs a uniform applied field, $\mu_0 \mathbf{H}_{\text{app}} = (-35.5, -6.3, 0)$ mT, is instantaneously applied. By 60 fs (b), domain rotation has begun. Large angle (≈360°) domain walls are formed by 160 fs (c), which are slowly pushed outwards (450 fs, (d)) and off the ends by 520 fs (e). In (b), the shade indicates the z-component of the magnetization, which is $+z$ (out of the page) in the central region, and $-z$ (into the page) at the ends. In (c–e), shade indicates in-plane magnetization angle. These images taken from a simulation using the energy-based method, with $255 \times 63 \times 1$ cell count.

(also called *antivortices*), which require a very fine mesh to properly resolve (Figures 11e and 12).

These effects are reflected in the simulation results displayed in Figures 13 and 14. The simulations all agree fairly well until some time after 0.4 ns, corresponding to the annihilation of the 360° domain walls. After that, although the features described in Figures 11 and 12 prove qualitatively similar in all simulations, discretization effects are clearly

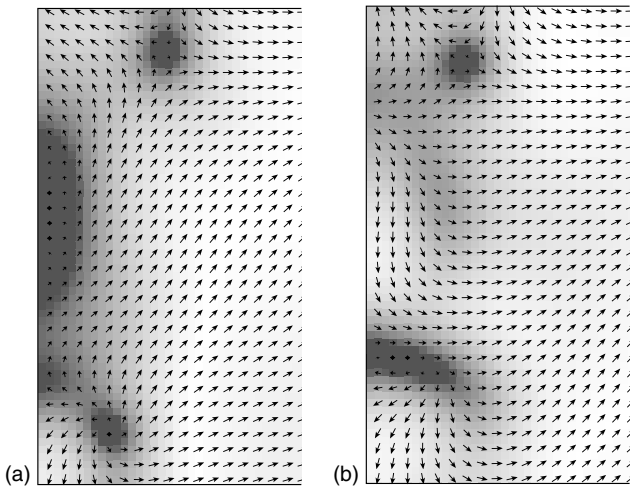

Figure 12. Details at left edge of simulation in Figure 11, at times $t = 500$ fs (a) and $t = 520$ fs (b). Cross-tie (or antivortex) at top and distorted vortex at bottom form from ends of 360° wall. The half-vortex visible in the middle of the left edge in (a) is a remanent of the 360° wall, which is pushed off the edge by 520 fs (b) as the cross-tie and distorted vortex move inward. Shade indicates the z-component of the magnetization, which is primarily out of the page ($+z$).

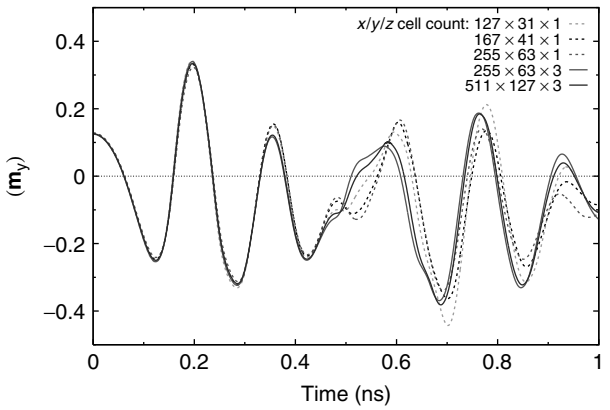

Figure 13. Average m_y versus time results for test problem from Figure 11 using the field-based method of Section 2, with different $x/y/z$ cell counts as indicated. In-plane counts 127×31 yields $\approx$4 nm square cells, $167 \times 41 \approx 3$ nm square cells, $255 \times 63 \approx 2$ nm square cells. Single-layer simulations (z cell count $= 1$) appear to converge toward a different limit than the multilayer simulations (z cell count $= 3$).

evident, especially in the field-based simulations shown in Figure 13. In this figure, the single-layer simulations do not appear to be converging toward the same limit as the three-layer simulations, although the $127 \times 31 \times 1$ solution proves rather close to the converged $500 \times 125 \times 3$ energy-based solution (see Figure 15). Whether this result is purely coincidental is hard to say. We note, however, that the most compact set of initial $\langle \mathbf{m}_y \rangle$ values including both approaches

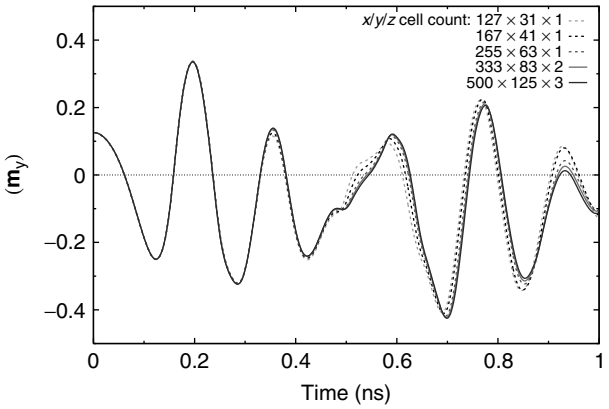

Figure 14. Average m_y versus time results for test problem from Figure 11 using energy-based method of Section 3, with various $x/y/z$ cell counts as indicated. Single-layer and multilayer simulations converge to same limit. Single-layer $500 \times 125 \times 1$ results (not shown) are indistinguishable from multilayer $500 \times 125 \times 3$ results.

is obtained for the extreme meshing conditions, with $\langle \mathbf{m}_y \rangle = 0.12472109$ (field-based), 0.12526786 (energy-based) for the $127 \times 31 \times 1$ discretization, and 0.12567210 (field-based) and 0.12599484 (energy-based) for the $\approx$1 nm cubic mesh size. The larger variability in initial conditions in the field approach is undoubtedly responsible in part for the sizable differences in time integration observed at later times and it is not even certain that three layers suffice for full convergence. In contrast, the results from the energy-based approach shown in Figure 14 do in this test manifest only minor z-layer discretization effects and appear to converge in a relatively straightforward manner. As noted in the preceding text, this is probably more due to the effect of using a cell-averaged demagnetizing field as opposed to any intrinsic property of the energy-based approach, and presumably indicates that the midplane (midcell) demagnetizing field samples are not generally truly representative of the field profile through the thickness of the film (cell), an effect alluded to earlier.

The important point from this comparison, as seen in Figure 15, is that both methods converge toward similar limits, and either way a very small cell size is required to approach that limit. It must be stressed that the cell size required here, $\approx$1 nm, is much smaller than the exchange length for this material, which by equation (5) is about 5.7 nm. This illustrates the importance of always checking for discretization effects in micromagnetic simulations, especially in confined geometries with small magnetic structures such as vortices and cross-ties. We note in closing that a subtle influence of the approximation order in the exchange interactions and BCs may not at this stage be ruled out.

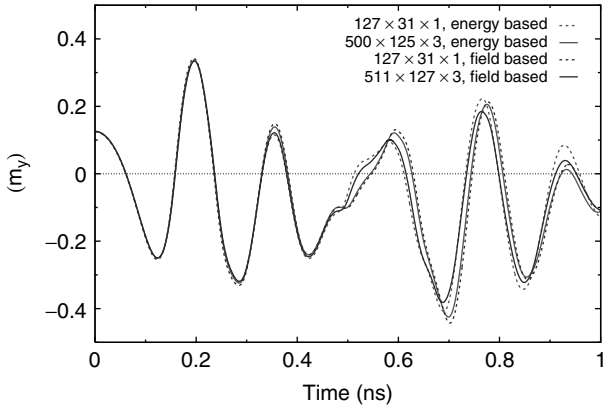

Figure 15. Test problem results comparing field-based (dark gray curves) and energy-based (light gray curves) approaches. Cell count $500 \times 125 \times 3$ corresponds to discretizing with 1 nm cubes.

6 CONCLUSION

This short review of finite difference methods applied to micromagnetics provides the reader with all the necessary ingredients to develop his or her own code. Different approximations have been discussed for exchange interactions and BCs. Ways to include general BCs have also been indicated. The appendices provide all required integrals for the definition of magnetostatic interaction coefficients due to one's own choice regarding discretization. Provided care is taken in the choice of a proper meshing and time integration step, the field- or energy-based methods described in the preceding text lead to comparable meshing sensitivity as evidenced in Figure 15. On the whole, numerical micromagnetics relying on finite difference methods has reached a high maturity level. As already stated, however, available data do not show convergence toward a single $\langle \mathbf{m}_y \rangle(t)$ trajectory for this particular problem. Lastly, if finite difference methods prove extremely efficient in terms of computation time due to an extensive use of FFTs, they display excessive discretization artifacts when dealing with curved geometries. Although that dependence needs to be quantified more precisely, work continues on the issue and practical solutions are expected in the near future.

ACKNOWLEDGMENTS

J. M. is most indebted to André Thiaville for an insightful reading of the manuscript. He also gratefully acknowledges support from the European Community programs FET-IST, under Contract No. FP6-510993 MAGLOG, and Structuring the ERA, under Contract No. MRTN-CT-2006-035327 SPINSWITCH.

REFERENCES

Abramowitz, M. and Stegun, I.A. (Eds.) (1970). *Handbook of Mathematical Functions*, U.S. NBS: Washington.

Aharoni, A. (1996). *Introduction to the Theory of Ferromagnetism*, Oxford University Press.

Albuquerque, G. (2002). *Magnetization Precession in Confined Geometry: Physical and Numerical Aspects*, Ph.D. Thesis (in English), Paris-Sud University, Orsay. http://tel.ccsd.cnrs.fr/documents/archives0/00/00/21/75/.

Albuquerque, G., Miltat, J. and Thiaville, A. (2001). Self-consistency based control scheme for magnetization dynamics. *Journal of Applied Physics*, **89**, 6719–6721.

Berkov, D.V., Ramstöck, K. and Hubert, A. (1993). Solving micromagnetic problems – towards an optimal numerical-method. *Physical Status Solidi A*, **137**, 207–225.

Brown, W.F. (1963). *Micromagnetics*, Interscience Publishers.

Davis, P.J. and Rabinowitz, P. (1984). *Methods of Numerical Integration*, Academic Press: Orlando.

Donahue, M.J. (1998). A variational approach to exchange energy calculations in micromagnetics. *Journal of Applied Physics*, **83**, 6491–6493.

Donahue, M.J. and McMichael, R.D. (1997). Exchange energy representations in computational micromagnetics. *Physica B*, **233**, 272–278.

Donahue, M.J. and Porter, D.G. (1999). *OOMMF User's Guide, Version 1.0*, Interagency Report NISTIR 6376, National Institute of Standards and Technology, Gaithersburg.

Donahue, M.J. and Porter, D.G. (2004). Exchange energy formulations for 3D micromagnetics. *Physica B*, **343**, 177–183.

Donahue, M.J., Porter, D.G., McMichael, R.D. and Eicke, J. (2000). Behavior of muMAG standard problem No. 2 in the small particle limit. *Journal of Applied Physics*, **87**, 5520–5522.

Donnelly, D. and Rust, B. (2005a). The fast Fourier transform for experimentalists, part I: concepts. *Computing in Science and Engineering*, **7**(2), 80–88.

Donnelly, D. and Rust, B. (2005b). The fast Fourier transform for experimentalists, part II: convolutions. *Computing in Science and Engineering*, **7**(4), 92–95.

Eastwood, J., Hockney, R. and Lawrence, D. (1980). P3M3DP – The 3-dimensional periodic particle-particle-particle-mesh program. *Computer Physics Communications*, **19**, 215–261.

Fukushima, H., Nakatani, Y. and Hayashi, N. (1998). Volume average demagnetizing tensor of rectangular prisms. *IEEE Transactions on Magnetics*, **34**, 193–198.

García-Cervera, C.J., Gimbutas, Z. and Weinan E (2003). Accurate numerical methods for micromagnetics simulations with general geometries. *Journal of Computational Physics*, **184**, 37–52.

Gilbert, T.L. (1955). A Lagrangian formulation of the gyromagnetic equation of the magnetization field. *Physical Review*, **100**, 1243.

Gilbert, T.L. (1956). *Formulation, Foundations and Applications of the Phenomenological Theory of Ferromagnetism*, Ph.D. Thesis, Illinois Institute of Technology, Chicago.

Gilbert, T.L. (2004). A phenomenological theory of damping in ferromagnetic materials. *IEEE Transactions on Magnetics*, **40**, 3443–3449.

Guslienko, K.Yu. and Slavin, A.N. (2005). Boundary conditions for magnetization in magnetic nanoelements. *Physical Review B*, **72**, 014463.

Hertel, R. (2002). Thickness dependence of magnetization structures in thin Permalloy rectangles. *Zeitschrift fur Metallkunde*, **93**, 957–962.

Hertel, R., Fruchart, O., Cherifi, S., *et al*. (2005). Three-dimensional magnetic flux-closure patterns in mesoscopic Fe islands. *Physical Review B*, **72**, 214409.

Hockney, R. and Eastwood, J. (1981). *Computer Simulation Using Particles*, McGraw-Hill: New York.

Hubert, A. and Schäfer, R. (1998). *Magnetic Domains*, Springer-Verlag: Berlin.

Kittel, C. (1949). Physical theory of ferromagnetic domains. *Reviews of Modern Physics*, **21**, 541–583.

Kools, J.C.S., Rijks, Th.G.S.M., de Veirman, A.E.M. and Coehoorn, R. (1995). On the ferromagnetic interlayer coupling in exchange-biased spin-valve multilayers. *IEEE Transactions on Magnetics*, **31**, 3918–3920.

Kronmüller, H. and Fähnle, M. (2003). *Micromagnetism and the Microstructure of Ferromagnetic Solids*, Cambridge University Press.

LaBonte, A.E. (1969). Two-dimensional Bloch-type domain walls in ferromagnetic films. *Journal of Applied Physics*, **40**, 2450.

Labrune, M. and Miltat, J. (1995). Wall structures in ferro/antiferromagnetic exchange-coupled bilayers: a numerical micromagnetic approach. *Journal of Magnetism and Magnetic Materials*, **151**, 231–245.

Micromagnetic Modeling Activity Group (μMAG) at the National Institute of Standards and Technology, Gaithersburg, http://www.ctcms.nist.gov/∼rdm/mumag.org.html.

Miltat, J. (1994). domains and domain walls in soft magnetic materials, mostly. In *Applied Magnetism*, Gerber, R., Wright, C.D. and Asti, G. (Eds.), Kluwer: Dordrecht, pp. 221–308.

Miltat, J., Albuquerque, G. and Thiaville, A. (2001). An introduction to micromagnetics in the dynamic regime. In *Spin Dynamics in Confined Magnetic Structures I*, Hillebrands, B. and Ounadjela, K. (Eds.), Springer-Verlag: Berlin, Heidelberg, pp. 1–33.

Miltat, J., Albuquerque, G., Thiaville, A. and Vouille, C. (2001). Spin transfer into an inhomogeneous magnetization distribution. *Journal of Applied Physics*, **89**, 6982–6984.

Miltat, J., Thiaville, A. and Trouilloud, P. (1989). Néel lines structures and energies in uniaxial ferromagnets with quality factor $Q > 1$. *Journal of Magnetism and Magnetic Materials*, **82**, 297–308.

Moschel, A., Hyman, R.A., Zangwill, A. and Stiles, M. (1996). Magnetization reversal in ultrathin films with monolayer-scale surface roughness. *Physical Review Letters*, **77**, 3653–3656.

Newell, A.J., Williams, W. and Dunlop, D.J. (1993). A generalization of the demagnetizing tensor for nonuniform magnetization. *Journal of Geophysical Research-Solid Earth*, **98**, 9551–9555.

Parker, G.J., Cerjan, C. and Hewett, D.W. (2000). Embedded curve boundary method for micromagnetic simulations. *Journal of Magnetism and Magnetic Materials*, **214**, 130–138.

Porter, D.G. and Donahue, M.J. (2001). Generalization of a two-dimensional micromagnetic model to non-uniform thickness. *Journal of Applied Physics*, **89**, 7257–7259.

Press, W.H., Teukolsky, S.A., Wetterling, W.T. and Flannery, B.P. (2001). *Numerical Recipes in Fortran 77: The Art of Scientific Computing*, Cambridge University Press.

Rado, G.T. and Weertman, J.R. (1959). Spin-wave resonance in a ferromagnetic metal. *Journal of Physics and Chemistry of Solids*, **11**, 315–333.

Ramstöck, K., Leibl, T. and Hubert, A. (1994). Optimizing stray field computations in finite-element micromagnetics. *Journal of Magnetism and Magnetic Materials*, **135**, 97–110.

Rave, W., Fabian, K. and Hubert, A. (1998). Magnetic states of small cubic particles with uniaxial anisotropy. *Journal of Magnetism and Magnetic Materials*, **190**, 332–348.

Rave, W. and Hubert, A. (2000). Magnetic ground state of a thin-film element. *IEEE Transactions on Magnetics*, **36**, 3886–3899.

Rave, W., Ramstöck, K. and Hubert, A. (1998). Corners and nucleation in micromagnetics. *Journal of Magnetism and Magnetic Materials*, **183**, 329–333.

Schabes, M.E. and Aharoni, A. (1987). Magnetostatic interaction fields for a 3-dimensional array of ferromagnetic cubes. *IEEE Transactions on Magnetics*, **23**, 3882–3888.

Shtrickman, S. and Treves, D. (1960). On the resolution of Brown's paradox. *Journal of Applied Physics*, **31**, S72–S73.

Slonczewski, J.C. (1996). Current-driven excitation of magnetic multilayers. *Journal of Magnetism and Magnetic Materials*, **159**, L1–L7.

Stiles, M.D. and Miltat, J. (2006). Spin-transfer torque and dynamics. In *Spin Dynamics in Confined Magnetic Structures III*, Hillebrands, B. and Thiaville, A. (Eds.), Springer-Verlag, Berlin, Heidelberg, pp. 225–308.

Stiles, M.D., Xiao, J. and Zangwill, A. (2004). Phenomenological theory of current-induced magnetization precession. *Physical Review B*, **69**, 054408.

Stockham, T.G. (1966). High speed convolution and correlation. *Joint Computer Conference Proceedings*, **28**, 229–233.

Stoer, J. and Bulirsch, R. (1993). *Introduction to Numerical Analysis*, Springer-Verlag: New York.

Sun, J.Z. (2000). Spin-current interaction with a monodomain magnetic body: a model study. *Physical Review B*, **62**, 570–578.

Thiaville, A., Garciá, J.M., Dittrich, R., *et al*. (2003). Micromagnetic study of Bloch-point-mediated vortex core reversal. *Physical Review B*, **67**, 094410.

Thiaville, A., Tomáš, D. and Miltat, J. (1998). On corner singularities in micromagnetics. *Physical Status Solidi A*, **170**, 125–135.

Tomáš, D. (1999). *Modelling of Micromagnetic Structures*, Ph.D. Thesis (in English), Paris-Sud University, Orsay and Charles University, Prague.

Toussaint, J-C., Marty, A., Vukadinovic, N., *et al*. (2002). A new technique for ferromagnetic resonance calculations. *Computational Materials Science*, **24**, 175–180.

Trouilloud, P. and Miltat, J. (1987). Néel lines in ferrimagnetic garnet epilayers with orthorhombic anisotropy and canted magnetization. *Journal of Magnetism and Magnetic Materials*, **66**, 194–212.

Wei, D. and Bertram, H.N. (1996). Interlayer coupling and surface roughness in GMR spin valves. *IEEE Transactions on Magnetics*, **32**, 3434–3436.

Yuan, S.W. and Bertram, H.N. (1992). Fast adaptive algorithms for micromagnetics. *IEEE Transactions on Magnetics*, **28**, 2031–2036.

Yuan, S.W., Bertram, H.N., Smyth, J.F. and Schultz, S. (1992). Size effects of switching fields of thin Permalloy particles. *IEEE Transactions on Magnetics*, **28**, 3171–3173.

Zheng, Y. and Zhu, J-G. (1997). Switching field variation in patterned submicron magnetic film elements. *Journal of Applied Physics*, **81**, 5471–5473.

APPENDICES

A DEMAGNETIZING FIELD: USEFUL INTEGRALS

For parallepipedic volume cells and rectangular surface tiles, defining $\rho = \sqrt{(u^2 + v^2 + w^2)}$, $L_u = \frac{1}{2}\ln(\frac{\rho+u}{\rho-u})$, $P_u = \arctan(\frac{vw}{u\rho})$, and L_v, L_w, P_v, P_w through permutation in the variables u, v, w, all interaction coefficients allowing for a direct evaluation of the demagnetizing field at any position in space (except corners) may be evaluated with the help of the following integrals (Tomáš, 1999):

$$
\begin{aligned}
H_u^{111} &= \iiint \frac{u}{\rho^3}\mathrm{d}u\mathrm{d}v\mathrm{d}w = +uP_u - vL_w - wL_v \\
H_v^{111} &= \iiint \frac{v}{\rho^3}\mathrm{d}u\mathrm{d}v\mathrm{d}w = +vP_v - wL_u - uL_w \\
H_w^{111} &= \iiint \frac{w}{\rho^3}\mathrm{d}u\mathrm{d}v\mathrm{d}w = +wP_w - uL_v - vL_u \\
H_u^{110} &= \iint \frac{u}{\rho^3}\mathrm{d}u\mathrm{d}v = -L_v \\
H_v^{110} &= \iint \frac{v}{\rho^3}\mathrm{d}u\mathrm{d}v = -L_u \\
H_w^{110} &= \iint \frac{w}{\rho^3}\mathrm{d}u\mathrm{d}v = +P_w \\
H_u^{011} &= \iint \frac{u}{\rho^3}\mathrm{d}v\mathrm{d}w = +P_u \\
H_v^{011} &= \iint \frac{v}{\rho^3}\mathrm{d}v\mathrm{d}w = -L_w \\
H_w^{011} &= \iint \frac{w}{\rho^3}\mathrm{d}v\mathrm{d}w = -L_v \\
H_u^{101} &= \iint \frac{u}{\rho^3}\mathrm{d}u\mathrm{d}w = -L_w \\
H_v^{101} &= \iint \frac{v}{\rho^3}\mathrm{d}u\mathrm{d}w = +P_v \\
H_w^{101} &= \iint \frac{w}{\rho^3}\mathrm{d}u\mathrm{d}w = -L_u
\end{aligned}
\tag{A1}
$$

B POTENTIAL: USEFUL INTEGRALS

Defining $\rho = \sqrt{(u^2 + v^2 + w^2)}$, $L_u = \frac{1}{2}\ln(\frac{\rho+u}{\rho-u})$, $Q_u = u\arctan(\frac{vw}{u\rho})$, and L_v, L_w, Q_v, Q_w through permutation in the variables u, v, w, the necessary integrals for the computation of the cell- or tile-averaged scalar potential are as follows (Tomáš, 1999):

$$
\begin{aligned}
F^{220} &= \frac{1}{2}u(v^2 - w^2)L_u + \frac{1}{2}v(u^2 - w^2)L_v \\
&\quad -uvQ_w + \frac{1}{6}\rho(2w^2 - u^2 - v^2) \\
F^{202} &= \frac{1}{2}w(u^2 - v^2)L_w + \frac{1}{2}u(w^2 - v^2)L_u \\
&\quad -wuQ_v + \frac{1}{6}\rho(2v^2 - w^2 - u^2) \\
F^{022} &= \frac{1}{2}v(w^2 - u^2)L_v + \frac{1}{2}w(v^2 - u^2)L_w \\
&\quad -vwQ_u + \frac{1}{6}\rho(2u^2 - v^2 - w^2) \\
F^{211} &= uvwL_u + \frac{1}{6}w(3u^2 - w^2)L_v + \frac{1}{6}v(3u^2 - v^2)L_w \\
&\quad -\frac{1}{6}u(uQ_u + 3vQ_v + 3wQ_w) - \frac{1}{3}\rho vw \\
F^{112} &= uvwL_w + \frac{1}{6}v(3w^2 - v^2)L_u + \frac{1}{6}u(3w^2 - u^2)L_v \\
&\quad -\frac{1}{6}w(wQ_w + 3uQ_u + 3vQ_v) - \frac{1}{3}\rho uv \\
F^{121} &= uvwL_v + \frac{1}{6}u(3v^2 - u^2)L_w + \frac{1}{6}w(3v^2 - w^2)L_u \\
&\quad -\frac{1}{6}v(vQ_v + 3wQ_w + 3uQ_u) - \frac{1}{3}\rho wu
\end{aligned}
$$

$$
\begin{aligned}
F^{221} &= \frac{1}{6}uw(3v^2 - w^2)L_u + \frac{1}{6}vw(3u^2 - w^2)L_v \\
&\quad + \frac{1}{24}(6u^2v^2 - u^4 - v^4)L_w \\
&\quad - \frac{1}{6}uv(uQ_u + vQ_v + 3wQ_w) \\
&\quad + \frac{1}{24}\rho(2w^3 - 3w(u^2 + v^2)) \\
F^{212} &= \frac{1}{6}wv(3u^2 - v^2)L_w + \frac{1}{6}uv(3w^2 - v^2)L_u \\
&\quad + \frac{1}{24}(6w^2u^2 - w^4 - u^4)L_v \\
&\quad - \frac{1}{6}wu(wQ_w + uQ_u + 3vQ_v) \\
&\quad + \frac{1}{24}\rho(2v^3 - 3v(w^2 + u^2)) \\
F^{122} &= \frac{1}{6}vu(3w^2 - u^2)L_v + \frac{1}{6}wu(3v^2 - u^2)L_w \\
&\quad + \frac{1}{24}(6v^2w^2 - v^4 - w^4)L_u \\
&\quad - \frac{1}{6}vw(vQ_v + wQ_w + 3uQ_u) \\
&\quad + \frac{1}{24}\rho(2u^3 - 3u(v^2 + w^2)) \\
F^{222} &= \frac{1}{24}u(6v^2w^2 - v^4 - w^4)L_u \\
&\quad + \frac{1}{24}v(6w^2u^2 - w^4 - u^4)L_v \\
&\quad + \frac{1}{24}w(6u^2v^2 - u^4 - v^4)L_w \\
&\quad - \frac{1}{6}uvw(uQ_u + vQ_v + wQ_w) \\
&\quad + \frac{1}{60}\rho(u^4 + v^4 + w^4 - 3(u^2v^2 + v^2w^2 + w^2u^2))
\end{aligned}
\tag{B1}
$$

All of these integrals are equal to their counterparts in Hubert and Schäfer (1998). The F^{200} integral in Hubert and Schäfer (1998) proves, however, erroneous; it should read: $F^{200} = uL_u - \rho$.

Numerical Methods in Micromagnetics (Finite Element Method)

Thomas Schrefl[1], Gino Hrkac[1], Simon Bance[1], Dieter Suess[2], Otmar Ertl[2] and Josef Fidler[2]

[1] *University of Sheffield, Sheffield, UK*
[2] *Vienna University of Technology, Vienna, Austria*

1 INTRODUCTION

The design and development of magnetic materials and devices requires a precise understanding of both the influence of a material's microstructure on the macroscopic magnetic properties and the influence of the magnetostatic interactions on the functional behavior of a device. A prominent example for the former is the remanence enhancement in exchange spring permanent magnets (Kneller, 1991), while an example for the latter is the case of single pole write heads in perpendicular magnetic recording (Kanai *et al*., 2005). In the following we review these two examples and explain why the finite element method (FEM) is an effective technique to treat these systems quantitatively.

Both the calculation of the remanence and coercivity of permanent magnets and the simulation of perpendicular magnetic recording involve realistic physical models. The calculation of the magnetic properties of permanent magnets needs a model of the grain structure that takes into account the grain size distribution as well as the shape of the grains. The simulation of perpendicular magnetic recording needs a computer model that takes into account the size, the shape, and the relative motion of the magnetic objects in a recording system. The FEM has been widely used to calculate magnetic fields in magnetic circuits, electric motors, and magnetoelectric devices (Preis *et al*., 1992). The strength of the FEM is its flexibility to model complex geometries and to refine the finite element mesh locally where higher accuracy of the solution is needed. The FEM is a well-established tool that has been used in science and engineering over many decades. Finite element mesh generators that perform the task of dividing complex objects into a computational grid are commercially and freely available (Schneiders, 2007).

In nanocrystalline permanent magnets (Manaf, Leonowicz, Davies and Buckley, 1991; Goll, Seeger and Kronmuller, 1998) exchange interactions between the grains cause a strong coupling between the magnetic moments with the effective coupling range being larger than the grain size. Although the crystallites are randomly oriented the remanence will be larger than expected from the Stoner–Wohlfarth theory (Stoner and Wohlfarth, 1948). When the magnet is saturated all the magnetic moments point parallel to the saturation field. Upon decreasing the external field, the magnetocrystalline anisotropy causes the magnetization in the center of the grains to rotate parallel to its easy axis. However, next to the grain boundaries exchange coupling with the neighboring grain that may have

Handbook of Magnetism and Advanced Magnetic Materials. Edited by Helmut Kronmüller and Stuart Parkin. Volume 2: *Micromagnetism*. ISBN: 978-0-470-02217-7.

a different anisotropy direction hinders the rotation of the magnetic moments. In a band along the grain boundaries, the magnetic moments remain oriented in a direction that is close to the direction of the saturation field (Schrefl, Fischer, Fidler and Kronmuller, 1994c). Owing to the interplay of exchange interactions and magnetocrystalline anisotropy the magnetic moments will deviate from their local easy axis next to the grain boundaries, giving rise to remanence enhancement. Remanence enhancement occurs in single-phase, nanocrystalline permanent magnets but can be considerably increased in so-called exchange spring permanent magnets, where magnetically soft grains are strongly exchange coupled to magnetically hard grains. In the remanent state, the magnetization direction in the soft magnetic grains is mostly governed by exchange interactions with the neighboring hard magnetic grains. This keeps the magnetization close to the direction of the saturation field. With increasing size of the soft magnetic grains magnetostatic interactions become dominant, vortices form within the soft magnetic grains, and remanence enhancement breaks down (Schrefl and Fidler, 1998). This example clearly shows that the macroscopic magnetic properties arise from the interplay between the intrinsic magnetic properties and the magnet's microstructure. Upon changing the microstructure (grain size, grain shape), the macroscopic properties change. The remanence and the coercivity will have different values although there is little or no change in the chemical composition of the magnet. This change of the macroscopic magnetic properties arises from a different local arrangement of the magnetic moments for different microstructures.

The directions of the magnetic moments can be calculated numerically by minimizing the total Gibbs' free energy of the system (Brown, 1963a). In the physical model, the intrinsic magnetic properties change from grain to grain. In the mathematical model, this is reflected by coefficients in the governing equations that vary locally in space. The grain structure of a magnet can be modeled by a set of polyhedra. Within a grain, the magnetic moments are not uniform. The interplay between exchange interactions and the magnetocrystalline anisotropy cause a nonuniform magnetization distribution. In order to resolve the magnetization distribution on a subgrain level, the computational grid has to be smaller than a grain. A polyhedral grain can be easily subdivided into tetrahedrons. Within the framework of the FEM discrete equations can be formulated on irregular, tetrahedral grids. The problem of finding the magnetization distribution of the remanent state is transformed into an algebraic minimization problem with the help of the FEM. The algebraic minimization problem is usually solved with an iterative method like the Newton method or the conjugate gradient method (Gill, Murray and Wright, 1993). These iterative schemes start from an initial state and proceed in steps toward a local minimum close to the initial state. A magnet has many magnetization states that correspond to a local minimum of the Gibbs' free energy. Thus, in order to compute the remanent state, a sequence of local minima must be computed. Luckily, for the saturated state the magnetization configuration is known since all magnetic moments can be assumed parallel to the external field if the external field is high. Therefore for the first calculation, a high external field is applied, the initial magnetization is assumed to be parallel to the field, and the magnetization configuration of the corresponding local minimum is calculated by solving the algebraic minimization problem. The external field is decreased and the corresponding magnetic state is calculated. This process is repeated until the remanent state (zero external field) is reached. According to Kinderlehrer and Ma (1994), the successive minimization of the total Gibbs' free energy for different external fields is a valid means to calculate the hysteresis loop of a ferromagnetic material. Alternatively, the Landau–Lifshitz–Gilbert (LLG) equation of motion (Gilbert, 1955; Landau and Lifshitz, 1935) for the magnetization can be solved for a time varying external field. This method shows the dynamic response of the magnetization upon application of an external field. The finite element and a proper time discretization method resolve the magnetization in time and in space. Such dynamic micromagnetic simulations are especially important for application where the external field changes fast, as the hysteresis properties are not only dependent on the field strength but also on the frequency of the field (He *et al*., 1996). Generally, the coercivity increases with increasing rate of change of the external field.

With data rates in the gigahertz regime, the rate of change of the external field and its influence on the coercive field play a major role in magnetic recording (Weller and Moser, 1999). Therefore, in magnetic recording simulation the locally acting external field as function of time has to be taken into account. The magnetic field seen by the data layer is created by the moving write head. In perpendicular recording, the magnetostatic interactions among the write pole of the head, the return pole of the head, and the soft underlayer (SUL) lead to the write field which is perpendicular to the recording media. The data layer itself can be seen as being placed in the 'air gap' of a magnetic circuit being composed of the write pole and the SUL. This is in contrast to conventional longitudinal recording where only the fringing field of the air gap can be used for writing. Thus, the maximum write field is higher than in longitudinal recording. The write field can switch highly coercive grains, which in turn enables a higher bit density. In order to optimize the field gradient, or to tilt the field angle for low field switching according to the Stoner–Wohlfarth angular dependence of the switching field, different soft magnetic

shield can be placed next to the write pole (Liu *et al*., 2005). The write field profile and the write field dynamics arise from the complex interaction of different magnetic parts with a particular shape. Again the FEM provides an easy way to model the complex geometries of the different parts involved in perpendicular recording systems (Scholz and Batra, 2005; Takano, 2005). The write field as a function of time as seen be the data layer grains is the result of magnetization dynamics in the yoke of the write head, which is driven by the magnetic field from the current coils and the magnetostatic interactions between the moving write head and the hard disk medium (Schrefl *et al*., 2005). A common numerical method to treat the interactions between distinct parts is the boundary element method (BEM) (Fetzer, Kurz and Lehner, 1997). Hybrid FEMs/BEMs can be used to effectively simulate the recording process taking into account the relative motion of the head with respect to the hard disk medium (Schrefl, Schabes, Suess and Stehno, 2004).

2 MAGNETOSTATIC FIELD CALCULATION

The FEM is useful technique to break down a complicated object into smaller, easily manageable parts. The basic idea of the FEM is to build a complicated object from, or to divide it into, smaller, simple blocks. Whereas it is impossible to describe a physical process for the complicated object, it can easily be done for the simple building block, the so-called FE. The process of creating a mesh, subdividing an object into triangles, tetrahedrons, or hexahedra, and the reformulation of the partial differential equation is called *finite element discretization*. For magnetic field problems, we can mostly use finite element libraries as black box solvers, however, additional input and software development is required if we want to solve the micromagnetic equations. In this section, we will look at the basic concept of the FEM and review the different formulations for the calculation of the magnetostatic field. We will also discuss various techniques to treat the so-called open boundary problem. In order to solve a partial differential equation uniquely, either the solution or its derivative has to be known at the boundary of the problem domain. This is not possible in computational micromagnetics. If we want to calculate the magnetic field inside a magnet, Maxwell's equations only give a jump condition for the magnetic scalar or magnetic vector potential at the magnet's boundary. Special methods are required to take into account the regularity of the potential, the potential vanishes proportional to r^{-1} as r approaches infinity. The application of the FEM to discretize the magnetic Gibbs' free energy will be discussed in Section 3.1.

The FEM is a numerical technique to solve partial differential equations. However, historically the FEM was developed for solving variational problems. The approximation of a minimization problem with a mesh of triangles goes back the Schellbach in the year 1851 (Schellbach, 1851). He proposed a finite element-like solution to the problem of finding a surface with minimum area that is enclosed by a given curve. Experimentally, this problem can be solved easily by putting a wire frame in soap and looking at the resulting 'soap bubble'. The soap wants to reduce the surface tension and forms an area with minimal surface. Schellbach created a mesh of triangles to interpolate the shape of the surface. In a second step, the nodes (corners of the triangles) were moved to minimize the surface area. An early example of the FEM in civil engineering is the design of the roof for Munich 1972 Olympics arena in the late 1960s (Leonhardt and Schlaich, 1972).

2.1 Finite element discretization

A predecessor of the FEM is the Ritz method (Ritz, 1909). Within the framework of the Ritz method a variational problem is solved as follows:

- start from a functional $f(v)$ which has to be minimized (or maximized). The function $u(\mathbf{r})$ is a minimizer (or maximizer) of $f(v)$ if

$$f(v) \geqslant f(u) \text{ for all } v, (\text{or } f(v) \leqslant f(u) \text{ for all } v) \quad (1)$$

- express $u(\mathbf{r})$ by a set of N unknown parameters u_i. If u is a minimizer (or maximizer) of f, we have to satisfy

$$\frac{\partial}{\partial u_i} f(u) = 0, \ i = 1, \ldots, N \quad (2)$$

- solving equation (2) yields an approximation for the minimizer (or maximizer) u of f.

The Ritz method was used by Brown, in order to calculate the magnetostatic energy for a given magnetization distribution (Brown, 1962). We will discuss Brown's method in Section 2.2.1. Now let us continue with the discussion of the FEM.

Within the framework of the FEMs special functions are used to approximate $u(\mathbf{r})$: The minimizer (or maximizer) u is expanded with a set basis functions, $\varphi_i(\mathbf{r})$,

$$u(\mathbf{r}) = \sum_{i=1}^{N} u_i \varphi_i(\mathbf{r}) \quad (3)$$

The basis functions have only local support and are defined by the help of a mesh of FE. If $\mathbf{r}_i$ denotes the vector from the origin to node i, the FE basis functions have the following properties

$$\varphi_i(\mathbf{r}_j) = \delta_{ij} = \begin{cases} 1 \text{ if } i = j \\ 0 \text{ if } i \neq j \end{cases} \tag{4}$$

Using equations (3) and (4), we see that the value of u at node point i is

$$u(\mathbf{r}_i) = u_i \tag{5}$$

It is possible to treat the problem in terms of these globally defined basis functions. However, for practical reasons it is helpful to treat the problem on the level of a single FE. This makes it easy to solve the problem computationally. The governing equations need to be implemented for one element only. For all the other elements of the finite element mesh, the same functions or subroutines can be called.

2.1.1 The linear tetrahedral finite element

Suppose we subdivide the problem domain V into tetrahedral finite elements and let the total number of tetrahedrons be E. If we refer to a particular finite element with the index e, V_e is the volume (domain) of element e. The vertices of a tetrahedron are numbered locally by the index α that runs from 1 to 4. Figure 1 shows a simple finite element mesh composed of three tetrahedrons. Then we can approximate the solution locally, say on element e by

$$u(\mathbf{r}) = \sum_{\alpha=1}^{4} u_\alpha \varphi_\alpha(\mathbf{r}) \tag{6}$$

The functions $\varphi_\alpha(\mathbf{r})$ are called *shape functions* for the finite element V_e. For the case of simplicity we can restrict ourselves to linear basis functions that are defined as follows

$$\varphi_\alpha(\mathbf{r}_\beta) = \delta_{\alpha\beta}, \quad \sum_{\alpha=1}^{4} \varphi_\alpha(\mathbf{r}) = 1 \tag{7}$$

$$\varphi_\alpha(x, y, z) = a_\alpha + b_\alpha x + c_\alpha y + d_\alpha z, \ \alpha = 1, 2, 3, 4 \tag{8}$$

where $\mathbf{r}$ denotes the vector to the point with the coordinates x, y, and z. Equation (7) uniquely defines the coefficients a_α, b_α, c_α, and d_α (Kikuchi, 1986)

$$a_1 = \frac{1}{6V_e} \begin{vmatrix} x_2 & y_2 & z_2 \\ x_3 & y_3 & z_3 \\ x_4 & y_4 & z_4 \end{vmatrix} \tag{9}$$

$$b_1 = -\frac{1}{6V_e} \begin{vmatrix} 1 & y_2 & z_2 \\ 1 & y_3 & z_3 \\ 1 & y_4 & z_4 \end{vmatrix} \tag{10}$$

$$c_1 = -\frac{1}{6V_e} \begin{vmatrix} x_2 & 1 & z_2 \\ x_3 & 1 & z_3 \\ x_4 & 1 & z_4 \end{vmatrix} \tag{11}$$

$$d_1 = -\frac{1}{6V_e} \begin{vmatrix} x_2 & y_2 & 1 \\ x_3 & y_3 & 1 \\ x_4 & y_4 & 1 \end{vmatrix} \tag{12}$$

where x_α, y_α, and z_α denote the coordinates of node α. The other constants follow form the cyclic permutation of the

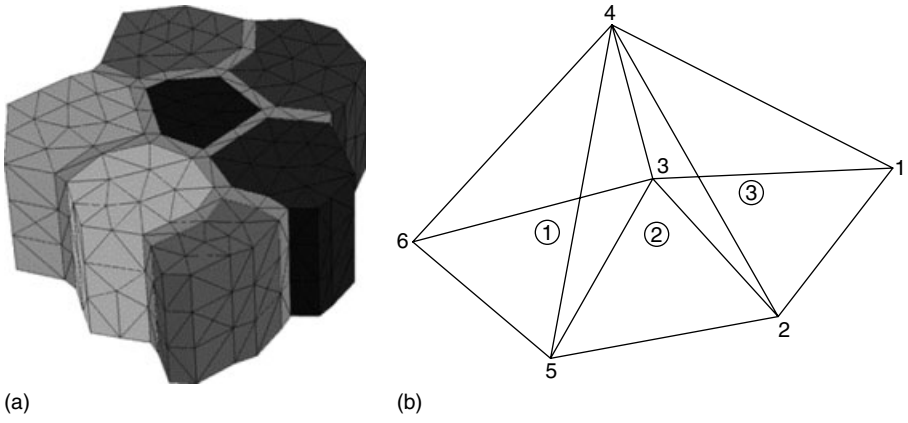

Figure 1. (a) Finite element mesh of the grains in a recording media. Both the grains and the grain boundary phase are subdivided into tetrahedral finite elements. (b) Numbering of nodes and elements in a tetrahedral finite element mesh.

indices 1, 2, 3, and 4. The volume of the element, V_e, can be calculated from

$$6V_e = \begin{vmatrix} 1 & x_1 & y_1 & z_1 \\ 1 & x_2 & y_2 & z_2 \\ 1 & x_3 & y_3 & z_3 \\ 1 & x_4 & y_4 & z_4 \end{vmatrix} \tag{13}$$

Equation (7) has some important consequences. We see that the vector $\mathbf{r}$ can be expressed by the following sum of the shape functions on the finite element

$$\mathbf{r} = \sum_{\alpha=1}^{4} \mathbf{r}_\alpha \varphi_\alpha(\mathbf{r}) \tag{14}$$

or

$$\begin{aligned} x &= \sum_{\alpha=1}^{4} x_\alpha \varphi_\alpha(x, y, z), \quad y = \sum_{\alpha=1}^{4} y_\alpha \varphi_\alpha(x, y, z), \\ z &= \sum_{\alpha=1}^{4} z_\alpha \varphi_\alpha(x, y, z) \end{aligned} \tag{15}$$

Given equation (6), we can easily calculate the gradient of u. This becomes important when we will derive the magnetic field from the magnetic potential. The derivative of u with to x, y, and z can be written as

$$\begin{aligned} \frac{\partial u}{\partial x} &= \sum_{\alpha=1}^{4} u_\alpha \frac{\partial \varphi_\alpha(x, y, z)}{\partial x}, \quad \frac{\partial u}{\partial y} = \sum_{\alpha=1}^{4} u_\alpha \frac{\partial \varphi_\alpha(x, y, z)}{\partial y}, \\ \frac{\partial u}{\partial z} &= \sum_{\alpha=1}^{4} u_\alpha \frac{\partial \varphi_\alpha(x, y, z)}{\partial z} \end{aligned} \tag{16}$$

or

$$\nabla u = \sum_{\alpha=1}^{4} u_\alpha \nabla \varphi_\alpha(\mathbf{r}) \tag{17}$$

Since the basis functions φ_α are linear functions in space within a finite element, the derivative of u are constant within an element. From (8) we can calculate the derivatives of the basis functions

$$\frac{\partial \varphi_\alpha}{\partial x} = b_\alpha, \frac{\partial \varphi_\alpha}{\partial y} = c_\alpha, \frac{\partial \varphi_\alpha}{\partial z} = d_\alpha \tag{18}$$

2.1.2 Approximation of the solution

We can think of f being the energy functional of a problem. The total energy splits into a sum over all elements

$$f(v) = \sum_{e=1}^{E} f^{(e)}(v) \tag{19}$$

where $f^{(e)}$ is the contribution from element V_e to the total energy. Now, the minimizer (or maximizer) of f is expanded with the finite element basis functions. Substituting v in (19) with the right-hand side of equation (3) transforms the variational problem into an algebraic minimization problem. The unknown coefficients u_i correspond to values of the solution at node point $\mathbf{r}_i$ and can be determined by solving

$$\frac{\partial}{\partial u_i} \sum_{e=1}^{E} f^{(e)}(u_1, \ldots, u_N) = 0, \ i = 1, \ldots, N \tag{20}$$

Interchanging the derivation and summation gives

$$\sum_{e=1}^{E} \frac{\partial f^{(e)}(u_1, \ldots, u_N)}{\partial u_i} = 0, \ i = 1, \ldots, N \tag{21}$$

Equation (21) leads to a system of equations that determine the values of u at the node points of the finite element mesh, u_i. The left-hand side of equation (21) is a sum over all the elements of the finite element mesh. Once it is clear how to derive the contributions of one element toward the equations, the contributions from all the other elements can be calculated in a similar way. Computationally this means that the subroutine/function that computes the contribution of an element will be called E times, one time for each element, and the results of the function call are assembled to the global system of equations (see Section 2.2.2). The above-mentioned approach of splitting the total energy of a system into a sum of contributions from each finite element is used in finite element micromagnetic solvers. A well-known example is the finite element solver MAGPAR (Scholz *et al.*, 2003) that computes equilibrium configurations of the magnetization by energy minimization over a set of tetrahedrons.

2.1.3 Notation

In the remainder of this chapter, we use the following conventions for symbols and indices. The indices i and j refer to a node of the finite element mesh. They run from 1 to the total number of nodes, N. The indices l and k refer to the Cartesian coordinates x, y, and z and thus run from 1 to 3. A spatial scalar field $u(\mathbf{r})$ or a vector field $\mathbf{m}(\mathbf{r})$ can be represented on an finite element mesh. u_i is the value of u at the node i with the coordinates $\mathbf{r}_i$, $u_i = u(\mathbf{r}_i)$. The set of all u_i, with $i = 1$ to N, will be the vector $\underline{u}$ over all nodes of the finite element mesh. Similarly, $\mathbf{m}_i$ refers to the vector $\mathbf{m}$ at node i of the finite element mesh. It is the value of the vector field $\mathbf{m}(\mathbf{r})$ at point $\mathbf{r}_i$. The l-th component of the vector $\mathbf{m}$ at node i is given by m_{il}. The vector $\underline{\mathbf{m}}$ has $3N$ components and is the collection of all

m_{il}, $\underline{\mathbf{m}} = (m_{11}, m_{12}, m_{13}, \ldots, m_{il}, \ldots, m_{N3})$. The Greek indices α and β denote the nodes of a given finite element with index e. In tetrahedral finite elements, α and β run from 1 to 4. The finite element basis functions are denoted by φ_i. There are N finite element basis functions, one for each node. The basis function with a Greek subindex, φ_α, is an abbreviation for the basis function at node α of element e, $\varphi_\alpha = \varphi_\alpha^{(e)}$. We use the superscript (e) to denote a quantity given on finite element e. For example, $M_\mathrm{s}^{(e)}$ is the local value of the spontaneous magnetization within finite element e. Matrices are given by uppercase bold-face letters. The transpose of a matrix is denoted by the superscript T. Local matrices, the so-called element matrices, will have the superscript (e). For example, the element stiffness matrix, $\mathbf{K}^{(e)}$, is a 4×4 matrix with the matrix elements $K_{\alpha\beta}^{(e)}, \alpha, \beta = 1, \ldots, 4$.

2.2 The magnetostatic boundary value problem

First, let us consider a ferromagnetic body with spontaneous magnetization, M_s, and a given magnetization distribution

$$\mathbf{M}(\mathbf{r}) = M_\mathrm{s}\mathbf{m}(\mathbf{r}), \text{ with } |\mathbf{m}| = 1 \tag{22}$$

The magnetostatic energy (stray field energy) of the ferromagnetic body with volume V is

$$\Phi_\mathrm{s} = -\frac{\mu_0}{2}\int_V \mathbf{M}\cdot\mathbf{H}_\mathrm{s}\,\mathrm{d}V \tag{23}$$

where μ_0 is the permeability of vacuum. The self-demagnetizing field (stray field), $\mathbf{H}_\mathrm{s}$, may be directly calculated from Maxwell's equations. We split the total magnetic field into a three parts

$$\mathbf{H} = \mathbf{H}_\mathrm{s} + \mathbf{H}_\mathrm{current} + \mathbf{H}_\mathrm{eddy} \tag{24}$$

The stray field, $\mathbf{H}_\mathrm{s}$, is created by the magnetic volume charge density,

$$\rho_\mathrm{m} = -\nabla\cdot\mathbf{M} \tag{25}$$

and the magnetic surface charge density,

$$\sigma_\mathrm{m} = \mathbf{M}\cdot\mathbf{n} \tag{26}$$

where $\mathbf{n}$ denotes the surface normal at the boundary of V. These virtual charges are useful for the calculation of the stray field from a given magnetization distribution. $\mathbf{H}_\mathrm{current}$ is the magnetic field created by a given current distribution. Examples are the current through the driving coil of the write head or the current through the sensing element of a read head. It can be calculated by Bio–Savart's law

$$\mathbf{H}_\mathrm{current}(\mathbf{r}) = \frac{1}{4\pi}\int_V \mathbf{j}\times\frac{\mathbf{r}-\mathbf{r}'}{|\mathbf{r}-\mathbf{r}'|^3}\,\mathrm{d}V' \tag{27}$$

where the integral is over the conductor with a current density $\mathbf{j}$. Finally, in conducting magnets we also may want to include a field, $\mathbf{H}_\mathrm{eddy}$, generated by the eddy currents. Equation (24) splits the magnetic field into its nonrotational part, $\mathbf{H}_\mathrm{s}$, and into its solenoidal part, $\mathbf{H}_\mathrm{current} + \mathbf{H}_\mathrm{eddy}$, which can be written as

$$\nabla\times\mathbf{H}_\mathrm{s} = 0 \tag{28}$$

$$\nabla\cdot(\mathbf{H}_\mathrm{current} + \mathbf{H}_\mathrm{eddy}) = 0 \tag{29}$$

The magnetic induction, $\mathbf{B}$, and the magnetic field are related by

$$\mathbf{B} = \mu_0(\mathbf{H} + \mathbf{M}) \tag{30}$$

Using (28) we can write the stray field as gradient of a magnetic scalar potential

$$\mathbf{H}_\mathrm{s} = -\nabla U \tag{31}$$

Building the divergence of equation (30) and using $\nabla\cdot\mathbf{B} = 0$, we obtain $\nabla\cdot\mathbf{H} = -\nabla\cdot\mathbf{M}$, which can be rewritten with the help of equations (24), (29), and (31) as

$$\nabla^2 U = -\rho_\mathrm{m} \tag{32}$$

Outside the magnet $\mathbf{M} = 0$ we have

$$\nabla^2 U = 0 \tag{33}$$

At the magnet's boundary the following interface conditions hold

$$U^{(\mathrm{in})} = U^{(\mathrm{out})} \tag{34}$$

$$\left(\nabla U^{(\mathrm{in})} - \nabla U^{(\mathrm{out})}\right)\cdot\mathbf{n} = \sigma_\mathrm{m} \tag{35}$$

Equations (34) and (35) follow from the requirement that at the boundary of the magnet the component of $\mathbf{H}$ parallel to the surface and the component of $\mathbf{B}$ perpendicular to the surface are continuous, respectively. Assuming that the magnetic potential is regular at infinity,

$$U(\mathbf{r}) \to \frac{1}{|\mathbf{r}|} \quad \text{for } |\mathbf{r}| \to \infty \tag{36}$$

the solution of equations (32–35) is

$$U(\mathbf{r}) = \frac{1}{4\pi}\left(\int_V \frac{\rho_\mathrm{m}(\mathbf{r}')}{|\mathbf{r}-\mathbf{r}'|}\,\mathrm{d}V' + \oint_{\partial V} \frac{\sigma_\mathrm{m}(\mathbf{r}')}{|\mathbf{r}-\mathbf{r}'|}\,\mathrm{d}S'\right) \tag{37}$$

Numerically, the direct calculation of the magnetic scalar potential (37) on a grid of N grid points leads to a computational effort proportional to N^2. This is undesirable, especially when the computation of the magnetic potential is part of an iterative procedure to determine the magnetization distribution $\mathbf{M}(\mathbf{r})$ and many evaluations of the integrals in equation (37) are required. This is the case in numerical micromagnetics. In energy minimization methods, variants of the Newton method or the conjugate gradient method are used. These are iterative techniques and the magnetic potential has to be evaluated at every iteration step, in order to calculate the magnetostatic energy or its gradient. In dynamic micromagnetics, the magnetostatic field has to be evaluated at least once per time step. Therefore, methods are required that scale better than N^2. Traditionally, fast Fourier transform methods are applied in micromagnetics to evaluate the integral (37) (Mansuripur and Giles, 1988). However, Fourier transform techniques require a regular grid. Alternatively, equations (32–36) can be solved with the FEM that reduces the computational effort since special linear solvers for multiple right-hand sides can be used to solve the discretized equations.

In Sections 2.2.1 and 2.2.2, we show how the magnetic scalar potential can be computed using the FEM. As mentioned earlier, the FEM is the most suitable method for solving variational problems. In Section 2.2.1, we derive a variational problem that is equivalent to the equations (32–36). The finite element discretization of the variational problem leads to a system of linear equations for the magnetic scalar potential at the nodes of the finite element mesh. In Section 2.2.2, we discuss how this system of equations can be easily found by first formulating the equation for a single finite element and then assembling the contributions of all elements. The efficient implementation in a computer code using matrix–vector multiplication is discussed in Section 2.2.3.

2.2.1 Magnetic scalar potential formulation

A convenient way to find the finite element equations for the numerical solution of equations (32)–(36) is to derive an equivalent variational problem. For a given magnetization distribution $\mathbf{M}(\mathbf{r})$, the magnetostatic energy can be evaluated by maximizing the functional (Brown, 1962)

$$\Phi_\mathrm{s,H} = -\frac{\mu_0}{2}\int \mathbf{h}^2 \mathrm{d}V - \mu_0 \int_V \mathbf{M}\cdot\mathbf{h}\,\mathrm{d}V \tag{38}$$

with respect to the vector function $\mathbf{h}$, which is required to be regular at infinity and nonrotational everywhere. In equation (38) the first integral is over the entire space and the second integral is over the volume of the ferromagnet. In order to achieve the irrationality, we can derive $\mathbf{h}$ from a potential u, which is a continuous function in space: $\mathbf{h} = -\nabla u$. We now express u in terms of the finite element basis functions as in equation (3). Maximizing $\Phi_\mathrm{s,H}$ with respect to the coefficients u_i will give the finite element approximation to the stray field energy. With increasing numbers of basis functions in the expansion (3) $\Phi_\mathrm{s,H}$ comes closer to the stray field energy. In the limit of large N, $\Phi_\mathrm{s,H}$ will be equal to the stray field energy, Φ_s, and u will be equal to the magnetic scalar potential U.

In order to compute the system of equations (2) for u_i, let us first consider a single finite element. Substituting the finite element ansatz (6) into equation (38) and using equation (17) to express the gradient will give the energy function for the finite element V_e

$$\Phi_\mathrm{s,H}^{(e)} = -\frac{\mu_0}{2}\int_{V_e}\left(\sum_{\alpha=1}^{4} u_\alpha \nabla\varphi_\alpha\right)^2 \mathrm{d}V + \mu_0 \int_{V_e} \mathbf{M}\cdot\left(\sum_{\alpha=1}^{4} u_\alpha\nabla\varphi_\alpha\right)\mathrm{d}V \tag{39}$$

In order to maximize $\Phi_\mathrm{s,H}^{(e)}$with respect to u_α, we have to solve

$$\frac{\partial\Phi_\mathrm{s,H}^{(e)}}{\partial u_\beta} = 0 \quad \text{for } \beta = 1,\ldots,4 \tag{40}$$

Applying the chain rule to the first integral on the right-hand side of equation (39) gives

$$\frac{\partial\Phi_\mathrm{s,H}^{(e)}}{\partial u_\beta} = -\mu_0\int_{V_e}\left(\sum_{\alpha=1}^{4} u_\alpha\nabla\varphi_\alpha\right)\cdot\nabla\varphi_\beta \mathrm{d}V + \mu_0\int_{V_e}\mathbf{M}\cdot\nabla\varphi_\beta\,\mathrm{d}V \tag{41}$$

which gives a linear system of equations for u_α

$$\mathbf{K}^{(e)}\mathbf{u} = \mathbf{g}^{(e)} \tag{42}$$

where $\mathbf{K}^{(\mathrm{e})}$ is a 4×4 matrix, the so-called element stiffness matrix, with the matrix elements

$$K_{\alpha\beta}^{(e)} = \int_{V_e}\nabla\varphi_\alpha\cdot\nabla\varphi_\beta\,\mathrm{d}V \qquad \alpha = 1,\ldots,4 \text{ and } \beta = 1,\ldots,4 \tag{43}$$

and $\mathbf{g}^{(e)}$ is a column vector, the so-called element load vector, with the entries

$$g_\beta^{(e)} = \int_{V_e} \mathbf{M} \cdot \nabla \varphi_\beta \, \mathrm{d}V \;\; \beta = 1, \ldots, 4 \tag{44}$$

In order to compute the element stiffness matrix and the load vector, the integrals in equations (43) and (44) can be evaluated exactly. Since the basis function is linear on the finite element, the integrand in equation (43) is constant and we obtain for the matrix elements of the element stiffness matrix

$$K_{\alpha\beta}^{(e)} = \left(\nabla \varphi_\alpha \cdot \nabla \varphi_\beta\right) V_e$$
$$\alpha = 1, \ldots, 4 \text{ and } \beta = 1, \ldots, 4 \tag{45}$$

For evaluating the element load vector in a micromagnetic simulation, we also interpolate the magnetization vector linearly in each tetrahedron. For element V_e we obtain

$$\mathbf{M}(\mathbf{r}) = M_\mathrm{s}^{(e)} \sum_{\alpha=1}^{4} \mathbf{m}_\alpha \varphi_\alpha(\mathbf{r}) \tag{46}$$

In composite magnetic material the spontaneous magnetization, M_s, may vary in space. There we allow M_s to change from element to element and denote the local spontaneous magnetization with $M_\mathrm{s}^{(e)}$. The integrand in equation (44) varies linearly in space and thus can be evaluated exactly with the midpoint rule

$$g_\beta^{(e)} = M_\mathrm{s}^{(e)} V_e \left(\frac{1}{4}\sum_{\alpha=1}^{4} \mathbf{m}_\alpha\right) \cdot \nabla \varphi_\beta \;\; \beta = 1, \ldots, 4 \tag{47}$$

2.2.2 *Assembling*

Once we have computed the stiffness matrix and the load vector for all finite elements, we can assemble them to the global system of equations for values of the magnetic potential at the nodes of the finite element mesh, u_i. Neighboring finite elements share common nodes. In order to form the global system of equations, we have to add the local contributions associated with these common nodes. For example, in Figure 1, element 2 and element 3 share the nodes with the node numbers 2, 3, and 4. We add entries of the element stiffness matrix to the global system matrix and we add entries of the element load vector to the right-hand side of the equation.

If we give numbers to each node of the tetrahedral mesh, each finite element V_e is uniquely defined by the numbers of its four vertices. Element 2 consists of the four vertices 2, 3, 4, and 5. If we know the coordinates of the four vertices of an element the geometry of the element is defined and we can compute the shape functions, the derivatives of the shape functions, and the element stiffness matrices. These quantities depend on the geometry only and need to be computed only once at the beginning of the simulations.

The element connectivity of an element is the sequence consisting of its four node numbers. The element connectivity defines a mapping $(e, \alpha) \to i$ from the local node α of element e to the global node i. The assembly process can be defined with the help of the connectivity matrix

$$C_{i\alpha}^{(e)} = \begin{cases} 1 \text{ if the global node } i \text{ corresponds to the} \\ \quad \text{local node } \alpha \text{ on element } e \\ 0 \text{ otherwise} \end{cases} \tag{48}$$

The entries of the right-hand side vector of the global system of equations can be formally written as

$$g_i = \sum_{e=1}^{E} \sum_{\alpha=1}^{4} C_{i\alpha}^{(e)} g_\alpha^{(e)} \tag{49}$$

The matrix elements of the stiffness matrix can be formally written as

$$K_{ij} = \sum_{e=1}^{E} \sum_{\alpha,\beta=1}^{4} C_{i\alpha}^{(e)} K_{\alpha\beta}^{(e)} C_{j\beta}^{(e)} \tag{50}$$

The stiffness matrix is a sparse matrix. Its sparsity pattern reflects the structure of the finite element mesh. K_{ij} is nonzero only if node i and node j are connected with an edge.

In the following equation, we denote vectors that gather nodal values by underlining the symbol. Then, the system of equations to calculate the magnetic potential at the nodes of the finite element mesh is

$$\mathbf{K}\underline{u} = \underline{g} \tag{51}$$

where $\underline{u}$ is a vector containing all the nodal values u_i of the magnetic scalar potential. The energy function given by equation (38) forms the basis for the derivation of the linear system of equations for the potential values. The first integral on the right-hand side of equation (38) is in integral over the entire space. Therefore, we have to mesh the ferromagnet and a large region in the exterior of the ferromagnet. In principle, the finite element mesh has to be extended over a wide region outside the ferromagnet, which will increase the total number of equations and complicates the finite element mesh generation. In Section 2.2.4, we will discuss methods to overcome this problem.

2.2.3 Divergence and gradient operators

The linear system of equations (51) is the discrete form of Poisson equation for the magnetic scalar potential. The matrix–vector product of the left-hand side represents the Laplace operator on the irregular finite element grid, whereas the right-hand side represents the divergence of the magnetization. For ease of computation, it will be convenient to compute the right-hand side of equation (51) by a simple matrix–vector multiplication. Similarly, once we have solved the system of linear equation, it will be helpful to calculate the magnetic field on all nodes of the finite element mesh by the multiplication of a matrix with the vector $\underline{u}$. From equations (25) and (32) we see that the right-hand side of (51) corresponds to the divergence of the magnetization. In order to compute the magnetic field, we need the gradient of the magnetic potential. Therefore, let us have a look how we can represent the divergence of a vector field and the gradient of a scalar field on a finite element mesh by matrix–vector multiplications.

Before we derive a matrix–vector representation for the divergence of the magnetization vector on the finite element grid, $\nabla \cdot \mathbf{M}(\mathbf{r})$, we have to define the representation of the vector field $\mathbf{M}(\mathbf{r})$ on the finite element mesh. In micromagnetics we assume that the magnitude of $\mathbf{M}(\mathbf{r})$ is a function of temperature, T, only and does not change with the magnetic field

$$|\mathbf{M}(\mathbf{r})| = M_\mathrm{s}(T, \mathbf{r}) \tag{52}$$

However, the spontaneous magnetization M_s may change with space. For example, this is the case in composite magnets (Kneller, 1991; Schrefl, Fidler and Kronmüller, 1994a,b; Fischer and Kronmuller, 1996; Fischer, Leineweber and Kronmuller, 1998; Suess *et al*., 2005; Victora and Shen, 2005) where magnetically hard and soft phases are combined. After the generation of the finite element mesh we assign $M_\mathrm{s}(T, \mathbf{r})$ to the different finite elements according to the distribution of the different phases. Therefore, it is sufficient to store the unit vector $\mathbf{m}(\mathbf{r})$. Similar to $\underline{u}$, we define a vector $\underline{\mathbf{m}}$ of length $3N$ that contains the unit magnetization vectors $\mathbf{m}_i$ at the nodal points of the mesh. If the index l denotes the Cartesian component of $\mathbf{m}_i$, $\underline{\mathbf{m}}$ can be explicitly written as

$$\underline{\mathbf{m}} = (m_{11}, m_{12}, m_{13}, \ldots, m_{il}, \ldots, m_{N3})^\mathrm{T} \tag{53}$$

Here and in the remainder of the chapter, we denote the transpose of a matrix with the superscript T. Using this definition we can rewrite the equation for the element load vector (47)

$$g_\beta^{(e)} = \sum_{\alpha=1}^{4} \sum_{l=1}^{3} D_{\beta\alpha l}^{(e)} m_{\alpha l} \;\; \beta = 1, \ldots, 4 \tag{54}$$

The matrix elements of the matrix are

$$D_{\beta\alpha l}^{(e)} = \frac{M_\mathrm{s}^{(e)} V_e}{4} \frac{\partial \varphi_\beta}{\partial x_l} \text{ for } \alpha = 1, \ldots, 4 \text{ and } \beta = 1, \ldots, 4 \tag{55}$$

Similar to the stiffness matrix we can assemble the element contributions and obtain

$$\underline{g} = \mathbf{D}\underline{\mathbf{m}} \tag{56}$$

The above product of the $N \times 3N$ matrix $\mathbf{D}$ with the unit magnetization vector over the mesh represents the divergence of the magnetization distribution, $\nabla \cdot \mathbf{M}(\mathbf{r})$. Here, N is the number of nodes within the ferromagnet.

Similarly, we can derive a product of a $3N \times N$ matrix with the magnetic scalar potential over the mesh that will give the magnetic field on each node of the finite element mesh. The solution of (51) gives the magnetic potential at the nodes of the finite element mesh. Using equation (17) we can calculate the gradient of the potential in every finite element and calculate the magnetic field in every element. Since we used a linear interpolation for the magnetic scalar potential within a tetrahedron, the magnetic field will be constant within a particular finite element and discontinuous at element boundaries. A common practice is to smooth the field to the nodes of the finite element mesh (Zienkiewicz, Lyness and Owen, 1977). In order to extrapolate the magnetic field to the nodes of the mesh, we look at the stray field energy of the system. First we define a magnetic moment at each node of the finite element mesh that is evaluated by spatial averaging

$$\boldsymbol{\mu}_i = \left(\frac{1}{4} \sum_{e=1}^{E} \sum_{\alpha=1}^{4} C_{i\alpha}^{(e)} M_\mathrm{s}^{(e)} V_e \right) \mathbf{m}_i \tag{57}$$

The vector $\mathbf{m}_i$ is the unit vector parallel to the magnetization at node point i and the combined terms in brackets have the dimensions of a magnetic moment. The product $M_\mathrm{s}^{(e)} V_e$ is the magnitude of the magnetic moment of element e. We assign one quarter of a tetrahedron's magnetic moment to node i, if one vertex of the tetrahedron has the global number i. With this definition of the magnetic moment on each node of the finite element mesh, the magnetostatic energy (23) can be rewritten as

$$\Phi_\mathrm{s} = -\frac{\mu_0}{2} \underline{\boldsymbol{\mu}}^\mathrm{T} \mathbf{I} \underline{\mathbf{H}}_\mathrm{s} \tag{58}$$

where $\mathbf{I}$ is the identity matrix, $\underline{\boldsymbol{\mu}}$ and $\underline{\mathbf{H}}_\mathrm{s}$are vectors over the finite element mesh that contain the magnetic moments and

the stray field at the node points, respectively. Alternatively, we can write

$$\Phi_s = -\frac{\mu_0}{2}\underline{\mathbf{m}}^T \mathbf{L}\underline{\mathbf{H}}_s \tag{59}$$

with the $N \times N$ matrix $\mathbf{L}$ defined as

$$L_{ij} = \delta_{ij}\left|\boldsymbol{\mu}_i\right| \tag{60}$$

The matrix $\mathbf{L}$ is a diagonal matrix with the moduli of the magnetic moment at the nodes of the finite element mesh as matrix entries.

In order to derive a matrix–vector equation for $\underline{\mathbf{H}}_s$, we compare equation (59) with the usual formulation of the magnetostatic energy which is given by the sum of the magnetostatic energy contributions from each finite element

$$\begin{aligned}\Phi_s &= \sum_{e=1}^{E}\Phi_s^{(e)}, \text{ with } \Phi_s^{(e)} = -\frac{\mu_0}{2}\int_{V_e}(\mathbf{M}\cdot\mathbf{H}_s)\,\mathrm{d}V \\ &= \frac{\mu_0}{2}\int_{V_e}(\mathbf{M}\cdot\nabla u)\,\mathrm{d}V\end{aligned} \tag{61}$$

Within each element we use the magnetic potential to evaluate the stray field, $\mathbf{H}_s$.

Using the finite element expansion for $\mathbf{M}$ and u, we obtain

$$\begin{aligned}\Phi_s^{(e)} &= \frac{\mu_0}{2}\int_{V_e} M_s^{(e)}\left(\sum_{\alpha=1}^{4}\mathbf{m}_\alpha\varphi_a\right)\cdot\left(\sum_{\beta=1}^{4}u_\beta\nabla\varphi_\beta\right)\mathrm{d}V \\ &= \frac{\mu_0}{2}\sum_{l=1}^{3}\sum_{\alpha,\beta=1}^{4} m_{\alpha l}G_{\alpha l\beta}^{(e)}u_\beta\end{aligned} \tag{62}$$

Using the midpoint rule for the integration of over the element V_e we obtain

$$G_{\alpha l\beta}^{(e)} = \frac{M_s^{(e)}V_e}{4}\frac{\partial\varphi_\beta}{\partial x_l} \text{ for } \alpha = 1,\ldots,4 \text{ and } \beta = 1,\ldots,4 \tag{63}$$

for the matrix elements. After summation over all finite elements, equation (62) will have the same structure as equation (59). By comparison we get $\mathbf{L}\underline{\mathbf{H}}_s = -\mathbf{G}\underline{u}$ or

$$\underline{\mathbf{H}}_s = -\mathbf{L}^{-1}\mathbf{G}\underline{u} \tag{64}$$

The $3N \times N$ matrix **G,** which is computed by assembling the element contributions in equation (63), relates the potential values with the stray field values at the nodes of the finite element mesh.

The matrix to compute the right-hand side of the linear system of equations (divergence operator), the system matrix itself (stiffness matrix), and the matrix to compute the stray field from the potential (gradient operator) are all sparse. Using sparse matrix storage techniques and sparse matrix algebra (Saad, 2003), the stray field can be computed efficiently. The matrices depend only on the geometry of the finite element mesh and thus have to be computed only once at the beginning of the simulation. The linear system of equations can be solved by sparse Gaussian elimination with partial pivoting. The matrix factorization needs to be done only once. Special reordering schemes (Amestoy, Davis and Duff, 2004) reduce the number of nonzeros in the factorization and thus lead to fast direct linear equation solvers (Davis, 2005; Schenk and Gärtner, 2004). For successive field computations on an irregular grid, the stray field can be computed faster and with less computational effort by the use of the FEM than by direct evaluation of equation (37).

2.2.4 *The open boundary problem*

In order to impose the regularity of the magnetic potential, equation (36), the finite element mesh has to be extended over a large region outside the magnetic particles. As a rule of thumb the distance between the boundary of the external mesh and the particle should be at least five times the extension of the particle (Chen and Konrad, 1997). Various other techniques have been proposed to reduce the size of the external mesh or to avoid a discretization of the exterior space. Here we review those methods for open boundary problems that have been successfully used in finite element micromagnetics and discuss the implementation of a hybrid FEM/BEM (Fredkin and Koehler, 1990) to calculate the magnetostatic interactions between distinct magnetic bodies.

The use of asymptotic boundary conditions (Yang and Fredkin, 1998) reduces the size of the external mesh compared to truncation. At the external boundary Robbin conditions are applied, which are derived from a series expansion of the solution of the Laplace equation for U outside the magnet and give the decay rate of the potential at a certain distance from the sample (Khebir, Kouki and Mittra, 1990). A similar technique that considerably reduces the size of the external mesh is the use of space transformations to evaluate the integral over the exterior space in equation (38). Among the various transformations proposed to treat the open boundary problem, the parallelepipedic shell transformation (Brunotte, Meunier and Imhoff, 1992), which maps the external space into shells enclosing the parallelepipedic interior domain, has proved to be the most suitable in micromagnetic calculations. The method can be easily incorporated into standard finite element programs transforming the derivatives of the nodal basis functions. This method was applied in static three-dimensional micromagnetic simulations of the magnetic properties of

nanocrystalline permanent magnets (Schrefl, Fischer, Fidler and Kronmuller, 1994c; Fischer and Kronmuller, 1996).

An alternative approach for treating the so-called open boundary problem is a hybrid FEM/BEM (Koehler, 1997; Fredkin and Koehler, 1990). The basic concept of this method is to split the magnetic scalar potential into two parts $U = U_1 + U_2$, where the potential U_1 is assumed to solve a closed boundary value problem. Then the equations for U_2 can be derived from equations (32–35), which hold for the total potential $U = U_1 + U_2$. The potential U_1 accounts for the divergence of the magnetization and U_2 is required to meet the boundary conditions at the surface of the particle. The latter also carries the magnetostatic interactions between distinct magnetic particles. The potential U_1 is defined to solve Poisson's equation inside the ferromagnetic regions and is set to zero in the exterior space

$$\nabla^2 U_1(\mathbf{r}) = \nabla \cdot \mathbf{M}(\mathbf{r}) \qquad \text{for } \mathbf{r} \in V \tag{65}$$

$$U_1 = 0 \qquad \text{for } \mathbf{r} \notin V \tag{66}$$

with V being the volume of the ferromagnetic regions. At the surface of the magnets, natural boundary conditions hold for U_1

$$\nabla U_1 \cdot \mathbf{n} = \mathbf{M} \cdot \mathbf{n} \qquad \text{for } \mathbf{r} \in \partial V \tag{67}$$

Since the total potential $U = U_1 + U_2$ must fulfill equations (32–36) and, U_2 must satisfy the Laplace equation

$$\nabla^2 U_2(\mathbf{r}) = 0 \tag{68}$$

everywhere in space and fulfill the boundary conditions

$$\left(\nabla U_2^{(\text{in})} - \nabla U_2^{(\text{out})}\right) \cdot \mathbf{n} = 0 \tag{69}$$

and

$$U_2^{(\text{in})} - U_2^{(\text{out})} = U_1^{(\text{in})} \tag{70}$$

A standard FEM may be used to solve equations (65) and (67). Fortunately, equations (68–70) describe the magnetic scalar potential of a dipole layer with moment U_1 at the surface ∂V. The scalar potential of such a dipole layer is known and is given by the double layer integral

$$U_2(\mathbf{r}) = \frac{1}{4\pi} \oint_{\partial V} U_1(\mathbf{r}') \nabla' \frac{1}{|\mathbf{r} - \mathbf{r}'|} \cdot \mathbf{n}' \mathrm{d}S' \tag{71}$$

over the dipole density times the derivative of the Green's function (Jackson, 1999). In principle, U_2 can be evaluated everywhere within the magnetic bodies using (71). However, instead of the direct computation of U_2 discretizing (71), we evaluate U_2 at the boundary and then we solve (68) within V using the known boundary values of U_2 as Dirichlet conditions. To compute U_2 on ∂V, we have to take the limit $\mathbf{r} \to \partial V$ of the surface integral from inside V

$$U_2(\mathbf{r}) = \frac{1}{4\pi} \oint_{\partial V} U_1(\mathbf{r}') \nabla' \frac{1}{|\mathbf{r} - \mathbf{r}'|} \cdot \mathbf{n}' \, \mathrm{d}S' + \left(\frac{\Omega(\mathbf{r})}{4\pi} - 1\right) U_1(\mathbf{r}) \tag{72}$$

where $\Omega(\mathbf{r})$ is the solid angle subtended by ∂V at point $\mathbf{r}$. We discretize (72) using piecewise linear functions to interpolate U_1 on a triangular surface mesh. The values of U_2 on the surfaces of the magnets follow from a matrix–vector product

$$\underline{U}_2 = \mathbf{B} \underline{U}_1 \tag{73}$$

The boundary element matrix, $\mathbf{B}$, depends only on the geometry of the problem and has to be computed only once for a given finite element mesh. $\mathbf{B}$ is a fully populated $M \times M$ matrix that relates the M boundary nodes with each other. In order to evaluate the matrix elements of $\mathbf{B}$, let us construct a surface mesh with F triangles and M nodes. The dipole density U_1 is expanded with linear basis function. Within the triangle S_e the expansion is

$$u_1(\mathbf{r}) = \sum_{\alpha=1}^{3} u_{1\alpha} \varphi_\alpha(\mathbf{r}) \tag{74}$$

with φ_α being linear basis functions on a triangle (Kikuchi, 1986), which can be defined similar to the tetrahedral basis functions in equation (7). First, let us evaluate the integral on the right-hand side of (72) for each node point $\mathbf{r}_i$ of the surface mesh. The integral splits into a sum of integrals over triangles

$$I(\mathbf{r}_i) = \sum_{e=1}^{F} I^{(e)}(\mathbf{r}_i) \tag{75}$$

The contribution of triangle S_e to the integral is

$$I^{(e)}(\mathbf{r}_i) = \frac{1}{4\pi} \oint_{S_e} \left(\sum_{\alpha=1}^{3} u_{1\alpha} \varphi_\alpha(\mathbf{r}')\right) \nabla' \times \frac{1}{|\mathbf{r}_i - \mathbf{r}'|} \cdot \mathbf{n}' \mathrm{d}S' \tag{76}$$

Interchanging the summation and integration, we obtain

$$I^{(e)}(\mathbf{r}_i) = \sum_{\alpha=1}^{3} B_{i\alpha}^{(e)} u_{1\alpha} \tag{77}$$

$B_{i\alpha}^{(e)}$ is the contribution of the local node α of triangle S_e to the matrix element B_{ij} of the boundary matrix.

$$B_{i\alpha}^{(e)} = \frac{1}{4\pi} \oint_{S_e} \varphi_\alpha(\mathbf{r}') \nabla' \frac{1}{|\mathbf{r}_i - \mathbf{r}'|} \cdot \mathbf{n}' \mathrm{d}S' \tag{78}$$

Using the element connectivities of the triangular mesh, we can define a mapping from the triangle number and the local node number $(e, \alpha) \rightarrow j$ to the global numbers of the finite element mesh. Similar to the assembly process for the element stiffness matrix (see Section 2.2.2) we can assemble the boundary matrix

$$B_{ij} = \sum_{e=1}^{F} \sum_{\alpha=1}^{3} C_{j\alpha}^{(e)} B_{i\alpha}^{(e)} + \left(\frac{\Omega(\mathbf{r}_i)}{4\pi} - 1 \right) \delta_{ij} \tag{79}$$

Here $C_{j\alpha}^{(e)}$ is the connectivity matrix as defined in equation (48) and $\Omega(\mathbf{r}_i)$ is the solid angle subtended by the surface of the mesh at the node $\mathbf{r}_i$. Lindholm (1984) gives analytic formulae for the evaluation of the integrals in (78).

Since the hybrid FEM/BEM does not introduce any approximations, the method is accurate and effective. The use of the BEM easily treats the magnetostatic interactions between distinct magnetic particles and requires no mesh outside the magnetic particles. Süß and coworkers (1999) applied the hybrid FEM/BEM, in order to simulate the effect of magnetostatic interactions on the reversal dynamics of magnetic nanoelements. This was also successfully used for the computation of the magnetostatic interactions between the write head, the SUL, and the data layer in perpendicular magnetic recording (Schrefl *et al*., 2005).

In summary, we have to perform the following procedure to compute the demagnetizing field. Prior to the time integration of the LLG equation we assemble the system matrices **K**, **D**, and **G**, and compute the Cholesky factorization of the finite element stiffness matrix **K**. This setup phase also involves the computation of the boundary matrix **B**. This matrix is fully populated. Therefore, we apply one of the matrix compression techniques introduced in Section 2.3 to sparsify the matrix. Generally, we are interested on the dynamic response of a system over a time span which is about two orders of magnitude larger than intrinsic precession time. Thus, the CPU time of the setup phase is only a small fraction of the total CPU time. At each iteration step during the time integration, we have to perform the following steps to update the magnetostatic field:

1. Compute the right-hand side of equation (65) (divergence of the magnetization) by matrix–vector multiplication (equation (56)).
2. Solve the linear system for U_1 using the Cholesky factors of the system matrix.
3. Compute the matrix–vector product to obtain U_2 at the boundary of the magnetic bodies (equation (73)).
4. Solve the linear system for U_2 in the interior of the magnets using the Cholesky factors of the system matrix.
5. Sum U_1 and U_2 and build the gradient of the magnetic potential by the matrix–vector multiplication (equation (64)).

All operations in the above-mentioned algorithm are of linear complexity. Thus, the hybrid FEM/BEM provides a means to compute the magnetostatic field of irregularly shaped, spatially distinct magnets efficiently. In Section 4.1, we will discuss how this method can be extended for problems involving the relative motion of ferromagnets while keeping almost optimal scaling of the algorithm.

Long and coworkers (2006) compared the accuracy of the hybrid FE/BE algorithm with the direct computation of the magnetic potential from its surface charges and volume charges (equation (37)). The comparison was done for a granular magnetic recording media, whereby each grain was subdivided into about 148 tetrahedral finite elements. With this mesh density the error of the finite element solution was less than 0.3% when compared with the direct evaluation of the magnetic scalar potential.

One drawback of the above-mentioned scheme is that the linear system of equations that gives U_1 is indefinite. Thus special linear solvers suitable for indefinite systems (Davis, 2005) have to be applied to solve for U_1. An alternative hybrid FEM/BEM was proposed by Garcia-Cervera and Roma (2006). In their method, the potential U_1 is defined by a closed Dirichlet problem. U_1 solves the Poisson equation within the magnet with the boundary condition $U_1 = 0$ at the magnet's surface. Again the Laplace equation holds for the potential U_2 in the entire space. U_2 will be continuous at the magnet's surface, but its normal derivative will show a jump. Then U_2 is given by the single layer integral over the surface of the magnet. The integral is over the product of a virtual charge density times the free space Green's function. The virtual charge density is the normal derivative of U_1 minus the magnetic surface charge. This method has been applied in combination with an adaptive grid refinement technique for the simulation of the magnetic domain configuration in NiFe nanoelements (Garcia-Cervera and Roma, 2006).

2.2.5 *Magnetic vector potential formulation*

In the previous sections, we discussed the calculation of the stray field by using a magnetic scalar potential. We started from a variational problem stated by Brown (1962) that gives the scalar potential by maximizing a function that approximates the magnetostatic energy. This formulation and its finite element implementation are most useful in dynamic micromagnetic simulations where the magnetostatic field has

to be evaluated at each time step. In static micromagnetics, we want to find the magnetization distribution that minimizes the total Gibbs' free energy of a magnetic system. For energy minimization, we do not necessarily need to know the stray field but we need the total energy and its gradient at each iteration step. For this purpose, it is useful to reformulate the magnetostatic boundary value problem as a minimization problem.

The magnetostatic boundary value problem can be reformulated as a minimization problem using a magnetic vector potential. For a given magnetization distribution $\mathbf{M}(\mathbf{r})$, the magnetostatic energy can be evaluated by minimizing the functional (Brown, 1962)

$$\Phi_{\mathrm{s,B}} = \frac{1}{2\mu_0}\int \mathbf{b}^2 \mathrm{d}V - \int_V \mathbf{M}\cdot\mathbf{b}\,\mathrm{d}V + \frac{\mu_0}{2}\int_V \mathbf{M}^2\,\mathrm{d}V \quad (80)$$

with respect to a vector field $\mathbf{b}$, that is required to be regular at infinity and solenoidal. If minimized with respect to $\mathbf{b}$, the functional $\Phi_{\mathrm{s,B}}$ becomes equal to the magnetostatic energy, Φ_{s}, and $\mathbf{b}$ becomes equal to the magnetic induction $\mathbf{B}$. In order to impose the constraint that $\mathbf{b}$ is solenoidal, we express $\mathbf{b}$ in terms of a magnetic vector potential $\mathbf{b} = \nabla \times \mathbf{A}'$. The unknown vector function $\mathbf{A}'$ can now be expanded with the finite element basis functions defined in (7)

$$\mathbf{A}'(\mathbf{r}) = \sum_{i=1}^{N} \mathbf{A}'_i \varphi_i(\mathbf{r}) \quad (81)$$

Now the magnetic vector potential is computed by an algebraic minimization problem. If minimized with respect to the $3N$ coefficients, A_{xi}, A_{yi}, and A_{zi}, $\Phi_{\mathrm{s,B}}$ reduces to the stray field energy and $\mathbf{A}'$ becomes equal to the magnetic vector potential $\mathbf{A}$, $\mathbf{B} = \nabla \times \mathbf{A}$. Numerical techniques similar to those discussed in the previous sections can be applied for the finite element computation of the magnetic vector potential. Brown's method in combination with the linear nodal tetrahedral elements for the Cartesian components of the magnetic vector potential leads to the same algebraic system of equations as the standard finite element discretization (Demerdash, Nehl and Fouad, 1980) of the corresponding partial differential

$$\nabla \times \nabla \times \mathbf{A} = \nabla \times \mathbf{M} \quad (82)$$

The vector potential formulation for the solution of the magnetostatic boundary value problem is especially useful in static micromagnetic simulations (Asselin and Thiele, 1986). Then the functional $\Phi_{\mathrm{s,B}}$ is used to represent the magnetostatic energy. We simply add $\Phi_{\mathrm{s,B}}$ to the other micromagnetic energy terms. Now we can expand both the magnetic vector potential and the magnetization with the FE bases functions that will give an algebraic minimization problem for the equilibrium configuration of the magnetization and the magnetic vector potential that corresponds to the stray field of the equilibrium state. The total energy will be minimized with respect to both magnetization and magnetic vector potential, in order to compute the equilibrium magnetic states. This method has been applied for the calculation of remanence and coercivity in nanocomposite permanent magnets (Schrefl, Fidler and Kronmüller, 1994b).

2.3 Matrix compression techniques

The application of the FEM/BEM as explained in Section 2.2.4 has many advantages. Only the magnetic bodies of the considered domains need to be discretized, open boundary problems pose no additional difficulties, and problems including motion can be treated in a nice way (Kurz, Fetzer, Lehner and Rucker, 1999; Schrefl, Schabes, Suess and Stehno, 2004). However, the application of the FEM/BEM leads to dense matrices. The storage requirements and computational costs for matrix–vector multiplication are of $O(M^2)$, where M is the number of unknowns, respectively the number of boundary nodes. Clearly we will run into problems if we increase the size of the model, because of limitations regarding computational power. One has optimal efficiency if the computational amount of work is $O(M)$. For many situations characterized by a sparse system matrix, one knows optimal solution algorithms. Examples are multigrid or algebraic multigrid methods (Kaltenbacher *et al.*, 2001; Sun and Monk, 2006). In this chapter, we discuss method to obtain nearly optimal efficiency for the computation of the boundary element matrix and the evaluation of the matrix–vector product (73).

Different methods were used to sparsify matrices from boundary element discretization and to achieve an efficiency close to the optimum in BEMs. Among the various methods are multipole expansion schemes, panel clustering methods, wavelet transforms, and methods based on the singular value decomposition of blocks of the interaction matrix. Originally, fast BEMs were introduced for the fast evaluation of capacities and electrostatic forces in interconnects. An overview on the history of the different acceleration schemes is given in Ramaswamy, Ye, Wang, and White (1999). In micromagnetics fast integration methods are traditionally used for modeling granular recording media (Miles and Middleton, 1991) or the fast evaluation of dipole fields (Koehler, 2005). Most of these methods (Blue and Scheinfein, 1991; Brown, Schulthess, Apalkov and Visscher, 2004) aim at the direct calculation of the magnetic field or magnetic potential from its volume and surface charges (see equation (37)). Here, we focus on fast methods to evaluate boundary integrals for

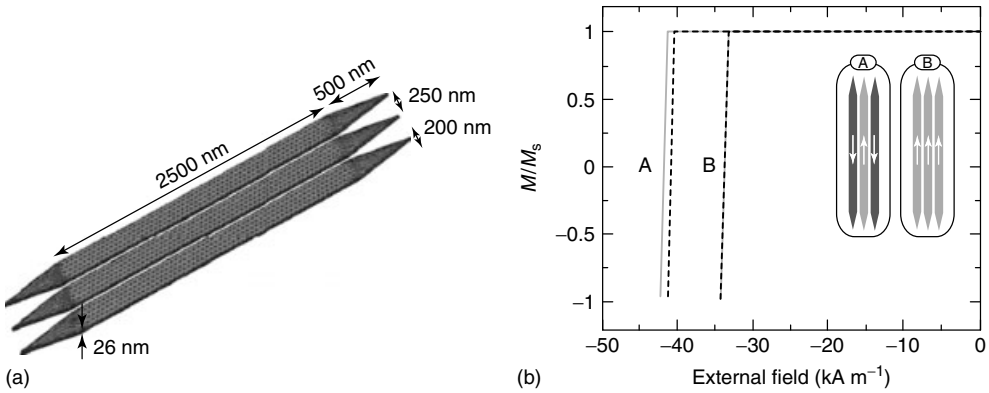

Figure 2. (a) Finite element surface mesh of three interaction NiFe nanoelements. (b) Computed demagnetization curves for the center element for different magnetization configurations of its neighbors. The solid curves use the exact boundary element matrix, the dashed curves use a wavelet compression of the boundary element matrix. In A, the magnetostatic interaction field stabilizes the center element, in B, the magnetostatic interaction field decreases the switching field.

use in hybrid FEM/BEM. All of these methods use the concept of grouping neighboring surface triangles into clusters as proposed originally by Hackbusch and Nowak (1989).

2.3.1 *Wavelet transform*

In numerical methods for partial differential equations, wavelet bases may be used to expand the unknown function such as the magnetization or the magnetic potential. An example for this approach in micromagnetics is the work of Hines, Ridley, and Roberts (2003) and Ridley, Spargo, Hines, and Roberts (2003). Here, we follow a different approach as applied in the computation of capacitance of high speed interconnects (Zheng, Li and Qian, 1999). Rather than expanding the potential with a wavelet basis we first compute the full interaction matrix. Treating the matrix like a two-dimensional discrete image, it is possible to sparsify the matrix applying a wavelet transform (Press, Teukolsky, Vetterling and Flannery, 1997). The matrix–vector product (73) can be evaluated in the wavelet basis. A sparse matrix is obtained after setting small elements of the transformed matrix to zero. Only about 15% nonzero entries remain, which significantly reduces the storage requirements and computation time for the evaluation of the surface integral.

This method was applied to calculate the magnetization reversal mechanisms in magnetic nanoelements (Schrefl, Scholz, Suss and Fidler, 2001). *In situ* observations of magnetization reversal using transmission electron microscopy predict a spread in the switching field due to magnetostatic interactions (Kirk, Chapman and Wilkinson, 1997). Figure 2 shows the surface mesh for three NiFe elements that are 200 nm wide, 3500 nm long and 26 nm thick. The center-to-center spacing is 250 nm. The original boundary element matrix of the system consists of 1.1×10^7 elements. After transformation and thresholding the matrix contains 1.9×10^6 nonzero entries, giving a sparsity of 83%. The demagnetization curve of the center element was calculated for a pair of switched or unswitched neighbors. The magnetization of the neighboring elements was fixed assuming a small uniaxial anisotropy parallel to the long axis. Figure 2 compares the numerically calculated demagnetization curves obtained with the conventional BEM and with wavelet-based matrix compression. In configuration A, the magnetostatic interaction field of the switched neighbors stabilizes the center element. In configuration B, the interaction field of the neighbors favors the reversal of the center element. This comparison shows that the wavelet-based matrix compression method provides accurate results. The spread in the switching field of 8 kA m^{-1} agree well with experimental data obtained on the very same magnetic nanostructures (Kirk, Chapman and Wilkinson, 1997).

2.3.2 *The Barnes and Hut tree code*

Tree codes are algorithms to calculate forces between a large number of particles. They arrange the particles in a hierarchy of clusters, and compute the interaction at a given point by summing over multipole expansions of these groups. In this way the computational requirements can be reduced to a $O(M \log M)$-scaling. A famous implementation of this method is the so-called Barnes and Hut (1986) tree code for the gravitational interaction between stars and galaxies. The domain, which surrounds all particles, is hierarchically partitioned into a sequence of cubes, where each cube contains eight siblings, each with half the side length of the parent cube. These cubes form the nodes of an oct-tree structure. The tree is constructed such that each cube contains either exactly one particle, or is parent to further cubes, in which case the parent cube carries the total mass of all the particles that lie inside this cube. The computation of the

forces at a point **r** proceeds by walking through the tree, and summing up appropriate contributions to the force from the tree elements. The gravitational force of a cell is added if the distance between **r** and the center of mass of the cell is larger than a certain threshold. If a cell fulfills this criterion, the tree walk along this branch can be terminated. Otherwise it is 'opened', and the walk is continued with all its siblings. We can use the same idea to speed up the computation of the surface integral in the hybrid FEM/BEM. The first term of the right-hand side of equation (72) is the potential of a dipole sheet with the dipole density $\mathbf{p} = U_1\mathbf{n}$ (Jackson, 1999). Instead of mass and gravitational potential, we have dipole strength and magnetic potential. After triangulation of the surface into a set of triangles, the surface integral over the surface ∂V can be approximated by a sum over dipoles. There is one dipole per triangle and the dipole strength is U_1 times the triangle area. Using the Barnes and Hut algorithm (Barnes and Hut, 1986), we group the dipoles to clusters and build a tree structure. Then the surface integral can be evaluated by walking through the tree. Dipoles far away from the field point will be grouped together and represented by a larger dipole in the center of the cluster. If the field point is very close to a triangle, the integral over the triangle will be evaluated analytically. As opposed to the wavelet method of Section 2.3.1, the tree code requires only a short setup phase. The matrix–vector product (73) can be evaluated without building the full matrix.

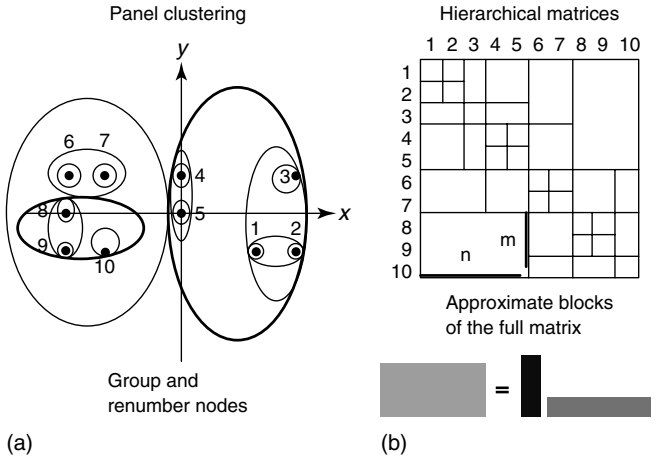

Figure 3. (a) The nodes are renumbered and grouped together so that the nodes with consecutive numbers are located next to each other and form a cluster. (b) Corresponding block structure of the interaction matrix. The large off-diagonal blocks can be approximated by low-rank matrices. (Reproduced from S. Kurz, O. Rain & S. Rjasanow: 'The Adaptive Cross-Approximation Technique for the 3-D Element Method', *IEEE Transactions on Magnetics*, **38**, (2002) copyright © IEEE 2002, with permisison of the IEEE.)

2.3.3 Hierarchical matrices

The idea of clustering the triangles of the surface mesh allows the storage of the boundary matrix in compressed form. The compressed matrix is sparse in a sense that only few data are needed for its representation. The matrix–vector multiplication is of almost linear complexity (Grasedyck and Hackbusch, 2003). Originally, the discretization of boundary integral leads to a large dense matrix that has no explicit structure. However, by suitable renumbering and permuting the boundary nodes, the dense matrix can be written in a block structure so that each block describes the interaction between two clusters of boundary nodes. If the two clusters are far apart, then the corresponding block matrix can be approximated by low-rank matrices. The corresponding two clusters are called *admissible*. If the $n \times m$ matrix **A** is a block matrix that describes the interaction of two admissible clusters, then it can be approximated by the product of two smaller matrices with the dimensions $n \times k$ and $k \times m$

$$A_{nm} = \sum_{i=1}^{k} B_{nk} C_{km} \tag{83}$$

For admissible clusters, k will be much smaller than n and much smaller than m. Therefore both, the storage for the block matrix and CPU time evaluating the product of the block matrix–vector with a vector is only $O(k(n+m))$ instead of $O(nm)$. The renumbering of the nodes is done by geometrical criterions. Consecutive boundary node numbers will be assigned to nodes located close to each other. These nodes are combined in a cluster. Each cluster pair corresponds to a block in the renumbered boundary matrix. Two admissible clusters appearing as a large off-diagonal block matrix can be approximated by a product of two smaller matrices. The off-diagonal blocks represent the far field interactions between nodes.

Figure 3 gives an example for the panel clustering and the block structure for a set of 10 nodes. The cluster with the nodes (8,9,10) and the cluster with the node (1,2,3,4,5) form a pair of admissible clusters. The corresponding block matrix appears in the lower left corner of the boundary matrix.

As with the tree code, there is no need to compute the full matrix in order to evaluate the matrix–vector product (73). First, the boundary nodes are renumbered and arranged into a cluster tree. Then, low-rank approximation of the off-diagonal block matrices can be computed using adaptive cross approximation (Kurz, Rain and Rjasanow, 2002; Grasedyck, 2005; Bebendorf and Grzhibovskis, 2006). This iterative algorithm computes the factorization (83) of the block matrix into two smaller matrices with a complexity of $O(k^2(n+m))$.

We compared the CPU time required for the setup phase and for the evaluation of the boundary integral using the tree code and the hierarchical matrices for matrix compression. The tree code requires the least memory and has the shortest setup phase. The calculation of the tree takes only a quarter of the CPU time that is required to the build the hierarchical matrix. However, the evaluation of the matrix–vector product by walking the tree takes considerable more time than the multiplication of the hierarchical matrix with a vector.

Figure 4 compares the CPU time for matrix–vector multiplication. The CPU time for multiplying the full matrix with a vector scales like M^2, where M is the number of boundary nodes. Whereas both the tree code hierarchical matrix method show an almost linear increase of the CPU time with increasing M, the hierarchical matrix method clearly outperforms the tree code in terms of the slope of the curve. Thus for computationally intensive problems such as magnetic recording simulations that take into account the mutual interactions between the recording head and the data layer, the hierarchical matrix method is the method of choice for matrix sparsification.

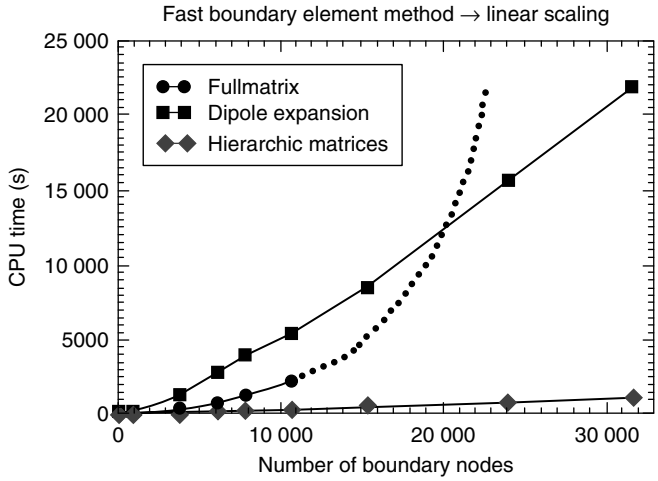

Figure 4. CPU time for the matrix–vector multiplication for different representations of the boundary element matrix.

2.3.4 Multipole expansion

Traditionally, also multipole methods are used to accelerate the BEM. Again this method was originally introduced to speed up the boundary element solution of three-dimensional electrostatic problems (Buchau, Huber, Rieger and Rucker, 2000; Bachthold, Korvink and Baltes, 1996; Nabros and White, 1991). Again we start from a suitable hierarchical clustering of the surface triangles of the boundary mesh. In order to evaluate the surface integral for group of triangles that is located at a large distance, we replace the charge distribution on those triangles by carefully chosen multipoles in the center of a sphere that encloses the triangle cluster. Outside the sphere the multipoles create the same potential field as the original charge distribution. Conventional integration is applied in the near-field of the triangle. Multipole expansion was successfully used to accelerate the evaluation of the surface integral in the hybrid FEM/BEM for micromagnetics (Liu *et al.*, 2006). In this work, almost linear efficiency was achieved with the multipole accelerated hybrid FEM/BEM for simulating the write processes in perpendicular magnetic recording media.

Buchau and coworkers (2003) compared the different boundary acceleration techniques in combination with a hybrid FEM/BEM for nonlinear magnetostatic problems. As compared to the hierarchical matrices, the use of multipole expansion leads to a higher compression rate of the boundary element matrix at the same accuracy. However, the computation of the matrix–vector product was about one order of magnitude faster using a hierarchical matrix.

3 FINITE ELEMENT MICROMAGNETICS

The basic objectives of micromagnetic simulations are the calculation of bulk magnetic properties or the simulation of dynamic magnetization processes. For the optimization and characterization of hard or soft magnetic materials, micromagnetic calculations help understand the correlation between the physical/chemical microstructure and the magnetic properties. In magnetic recording, the simulation of magnetization reversal gives insight into the data rate and area density limits of hard disk storage. Both static micromagnetic calculations and dynamic micromagnetic simulations start from the total Gibbs' free energy of the magnetic system. For the calculation of static hysteresis properties, the total Gibbs' free energy is minimized with respect to the direction cosines of the magnetization for subsequently changing external field. For the simulation of dynamic magnetization processes, the equation of motion is solved for the magnetization vector. The leading term in the equation of motion is the torque term, given by the cross product of the magnetization with the effective field. The effective field is the variational derivative of the total Gibbs' free energy density. A detailed discussion of the micromagnetic energy contributions and the associated effective field terms is given by H. Kronmüller in General Micromagnetic Theory Chapter 1 of Volume II of this Handbook (Kronmüller, 2007). In the following sections, we first discuss the micromagnetic energy contributions and the competitive effects of the different

energy terms on the magnetization configuration upon minimization. Then we introduce the finite element discretization of the energy terms, which leads to a matrix–vector representation of the total Gibbs' free energy and of the effective field. Finally, we briefly discuss time integration techniques for the LLG equation of motion.

3.1 Static hysteresis properties

The minimization of the total Gibbs' free energy of a ferromagnet gives an equilibrium configuration of the magnetization $\mathbf{M}(\mathbf{r})$. Starting from a well defined initial state, initial magnetization curves, hysteresis loops, or recoil curves can be computed by the subsequent calculation of equilibrium states for varying external field. Let us consider the magnetization in a configuration that is a local minimum of the total Gibbs' free energy. A small change in the external field leads to a shift in the position of the local minimum. The total energy can decrease if the magnetization moves toward a new local minimum, which will be attained in the subsequent minimization step. This process is related with a reversible change in the magnetization. The local minimum of the current magnetization state is separated by an energy barrier from any other possible minimum of the system. The barrier height decreases with increasing opposing external field. An irreversible switching event occurs when the energy barrier vanishes. Then the magnetization configuration can relax toward another minimum of the system. This relation of the energy landscape with the quasi-static hysteresis loop obtained in micromagnetic simulations was originally addressed by Schabes (1991).

3.1.1 Total magnetic Gibbs' free energy

Energy minimization methods start from the total Gibbs' free energy

$$\Phi_\mathrm{t} = \Phi_\mathrm{A} + \Phi_\mathrm{K} + \Phi_\mathrm{S} + \Phi_\mathrm{H} \tag{84}$$

which is the sum of the exchange energy, the magnetocrystalline anisotropy energy, the stray field energy, and the Zeeman energy. The energy contributions depend on the magnetization $\mathbf{M}(\mathbf{r})$. Within the framework of micromagnetics, we assume that $|\mathbf{M}(\mathbf{r})| = M_\mathrm{s}$ is a function of temperature only and does not depend on the magnetic field $\mathbf{H}$. Therefore we write the magnetization contributions in terms of the unit vector of the magnetization, $\mathbf{m}(\mathbf{r})$. Any search for a local minimum of the energy with respect to $\mathbf{m}(\mathbf{r})$ has to fulfill the constraint $|\mathbf{m}(\mathbf{r})| = 1$. Upon minimization, the different energy contributions have different effects on the magnetization. The minimization of the ferromagnetic exchange energy

$$\begin{aligned}\Phi_\mathrm{A} &= \int_V \left(A\left((\nabla m_x)^2 + \left(\nabla m_y\right)^2 + (\nabla m_z)^2\right)\right) \mathrm{d}V \\ &= \int_V A \sum_{l=1}^{3} (\nabla m_l)^2 \mathrm{d}V\end{aligned} \tag{85}$$

keeps neighboring magnetic moments parallel to each other. Here m_x, m_y, and m_z are the Cartesian components of $\mathbf{m}(\mathbf{r})$ and A is the ferromagnetic exchange constant. The minimization of the magnetocrystalline anisotropy energy aligns the magnetization along certain crystallographic directions. In uniaxial materials, the magnetocrystalline anisotropy energy is given by

$$\begin{aligned}\Phi_\mathrm{K,uniaxial} = \int_V &\left(K_1\left(1 - (\mathbf{m}\cdot\mathbf{k})^2\right)\right. \\ &\left. + K_2\left(1 - (\mathbf{m}\cdot\mathbf{k})^2\right)^2\right) \mathrm{d}V\end{aligned} \tag{86}$$

whereas in cubic materials

$$\begin{aligned}\Phi_\mathrm{K,cubic} = \int_V &\left(K_1\left(\gamma_1^2\gamma_2^2 + \gamma_1^2\gamma_3^2 + \gamma_2^2\gamma_3^2\right)\right. \\ &\left. + K_2\gamma_1^2\gamma_2^2\gamma_3^2\right) \mathrm{d}V\end{aligned} \tag{87}$$

In equations (86) and (87), K_1 and K_2 are the magnetocrystalline anistropy constants, $\mathbf{k}$ is the unit vector parallel to the magnetocrystalline easy axis, and γ_l is the projection of the magnetization vector on the cubic axis l. In a minimization problem, we may safely neglect terms in the total energy that do not depend on the magnetization. Thus, in the case of vanishing K_2 we may rewrite the first term on the right-hand side of equation (86)

$$\Phi'_\mathrm{K,uniaxial} = -\int_V K_1 (\mathbf{m}\cdot\mathbf{k})^2 \mathrm{d}V \tag{88}$$

The minimization of the stray field energy

$$\Phi_\mathrm{s} = -\frac{\mu_0}{2}\int_V M_\mathrm{s}(\mathbf{H}_\mathrm{s}\cdot\mathbf{m})\,\mathrm{d}V \tag{89}$$

causes the formation of magnetic domains. The minimization of the Zeeman energy rotates the magnetization parallel to the magnetic field, which might be created by an impressed current in a coil or wire,

$$\Phi_\mathrm{H} = -\mu_0\int_V M_\mathrm{s}(\mathbf{H}_\mathrm{current}\cdot\mathbf{m})\,\mathrm{d}V \tag{90}$$

3.1.2 Algebraic minimization

In order to compute the hysteresis loop, we have to minimize the total Gibbs' free energy for different values of the applied field. To accomplish this task, we first discretize the total Gibbs' free energy using the FEM. When the unit vector of the magnetization is expanded with the finite element basis functions

$$\mathbf{m}(\mathbf{r}) = \sum_{i=1}^{N} \mathbf{m}_i \varphi(\mathbf{r}) \tag{91}$$

the energy functional $\Phi_\mathrm{t} = \Phi_\mathrm{t}(\mathbf{M}(\mathbf{r}))$ reduces to an energy function with the nodal values of the unit magnetization vector as unknowns

$$\begin{aligned}\Phi_\mathrm{t} &= \Phi_\mathrm{t}(\mathbf{m}_1, \mathbf{m}_2, \ldots, \mathbf{m}_N) \\ &= \Phi_\mathrm{t}(m_{11}, m_{12}, m_{13}, \ldots, m_{il}, \ldots, m_{N3})\end{aligned} \tag{92}$$

where N is the total number of nodes in the finite element mesh of the magnetic region and l denotes the Cartesian component of $\mathbf{m}$. The minimization of equation (92) with respect to the $3N$ variables, m_{il}, subject to the constraint

$$|\mathbf{m}_i| = \sqrt{m_{i1}^2 + m_{i2}^2 + m_{i3}^2} = 1 \text{ for } i = 1, \ldots, N \tag{93}$$

gives an equilibrium distribution of the magnetization. To satisfy the constraint, equation (93), polar coordinate θ_i, ϕ_i for the unit vector of the magnetization at node i can be introduced such that

$$m_{i1} = \sin\theta_i \cos\phi_i, \;\; m_{i2} = \sin\theta_i \sin\phi_i, \;\; m_{i3} = \cos\theta_i \tag{94}$$

An alternative approach (Koehler, 1997; Chen, Fredkin and Koehler, 1993) to fulfill the constraint (93) is to normalize the unit magnetization vector in the discrete energy function, equation (92), by replacing m_{il} with $m_{il}/|\mathbf{m}_i|$. In both cases, resulting algebraic minimization problem can be solved using a conjugate gradient method (Gill, Murray and Wright, 1993). Conjugate gradient-based minimization techniques require computation of the gradient of the energy, in order to select the search directions. Using polar coordinates, the gradient of the energy can be expressed as

$$\begin{aligned}\frac{\partial \Phi_\mathrm{t}}{\partial \theta_i} &= \sum_{l=1}^{3} \frac{\partial \Phi_\mathrm{t}}{\partial m_l} \frac{\partial m_l}{\partial \theta_i}, \\ \frac{\partial \Phi_\mathrm{t}}{\partial \phi_i} &= \sum_{l=1}^{3} \frac{\partial \Phi_\mathrm{t}}{\partial m_l} \frac{\partial m_l}{\partial \phi_i} \text{ for } i = 1, \ldots, N\end{aligned} \tag{95}$$

After finite element discretization, the total energy of the system in case of uniaxial anistropy may be written in matrix–vector notation

$$\begin{aligned}(\Phi_\mathrm{A} + \Phi'_{\mathrm{K,uniaxial}}) + \Phi_\mathrm{s} + \Phi_\mathrm{H} = \frac{1}{2}\underline{\mathbf{m}}^\mathrm{T}\mathbf{F}_\mathrm{AK}\underline{\mathbf{m}} + \frac{1}{2}\underline{\mathbf{m}}^\mathrm{T}\mathbf{F}_\mathrm{s}\underline{\mathbf{m}} \\ - \underline{\mathbf{F}}_\mathrm{H}^\mathrm{T} \cdot \underline{\mathbf{m}}\end{aligned} \tag{96}$$

where $\underline{\mathbf{m}}$ is the vector containing the nodal values of the unit vector of the magnetization, as introduced in equation (53). The matrix $\mathbf{F}_\mathrm{AK}$ takes into account the exchange energy, Φ_A, and the uniaxial magnetocrystalline anisotropy, $\Phi'_{\mathrm{K,uniaxial}}$. The matrix $\mathbf{F}_\mathrm{AK}$ is sparse, as both energy terms depend only locally on the magnetization. It makes sense to combine both the exchange energy and the magnetocrystalline anisotropy energy into a single term, because the matrix $\mathbf{F}_\mathrm{AK}$ is a function of the finite element basis functions and needs to be computed only once at the beginning of the simulation. The stray field depends on the magnetization distribution over the entire magnetic system. Using equations (31), (37), and (89), the stray field energy can be written as two-fold volume integral over the magnetic particles. As a consequence the demagnetization matrix, $\mathbf{F}_\mathrm{s}$, becomes fully populated. Del Vecchio, Hebbert and Schwee (1989) used equations (95) and (96) to calculate magnetization processes in thin films.

Now we derive the entries of the matrix $\mathbf{F}_\mathrm{AK}$, which is used for the calculation of the sum of the exchange energy and magnetocrystalline anisotropy energy. We use the same approach that is applied to calculate the finite element stiffness matrix in Section 2.2.2. We first compute the energies of one tetrahedron and then sum up the contributions of all finite elements. The exchange energy and the magnetocrystalline anisotropy energy depend only locally on the magnetization. The energies can be computed by summation of the contributions from the finite elements. On the finite element V_e, the exchange energy is given by

$$\begin{aligned}\Phi_A^{(e)} = \int_{V_e} A \sum_{l=1}^{3} \left(\sum_{\alpha}^{4} m_{\alpha l} \nabla \varphi_\alpha \right) \\ \times \left(\sum_{\beta=1}^{4} m_{\beta l} \nabla \varphi_\beta \right) \mathrm{d}V\end{aligned} \tag{97}$$

or in matrix–vector notation

$$\Phi_A^{(e)} = \frac{1}{2} \sum_{k,l=1}^{3} \sum_{\alpha,\beta=1}^{4} m_{\alpha l} F_{\mathrm{A},\alpha k \beta l}^{(e)} m_{\beta l} \tag{98}$$

with the 12×12 matrix

$$F^{(e)}_{\mathrm{A},\alpha k\beta l} = 2A^{(e)} \left(\int_{V_e} \nabla\varphi_\alpha \cdot \nabla\varphi_\beta \mathrm{d}V \right) \delta_{kl} = 2A^{(e)} K^{(e)}_{\alpha\beta} \delta_{kl} \tag{99}$$

$A^{(e)}$ is the local exchange constant in element V_e and $K^{(e)}_{\alpha\beta}$ are the elements of the element stiffness matrix, equation (45). The indices α and β are over the vertices of the tetrahedron and the indices l and k are over the Cartesian coordinates. The uniaxial anisotropy energy of the finite element V_e is given by

$$\begin{aligned} \Phi'^{(e)}_{\mathrm{K,uniaxial}} &= -K^{(e)}_1 \int_{V_e} \left(\sum_{\alpha=1}^{4} \mathbf{m}_\alpha \varphi_\alpha \mathbf{k} \right)^2 \mathrm{d}V \\ &= -K^{(e)}_1 \int_{V_e} \sum_{\alpha,\beta=1}^{4} \sum_{k,l=1}^{3} \left(m_{\alpha l} \varphi_\alpha k^{(e)}_l \right) \\ &\quad \times \left(m_{\beta k} \varphi_\beta k^{(e)}_k \right) \mathrm{d}V \end{aligned} \tag{100}$$

Where $K^{(e)}_1$ is the local magnetocrystalline anisotropy constant in element V_e and $k^{(e)}_l$ is the l-th Cartesian component of the uniaxial anisotropy direction within the finite element. In matrix–vector form equation (100) can be written

$$\Phi'^{(e)}_{\mathrm{K,uniaxial}} = \frac{1}{2} \sum_{k,l=1}^{3} \sum_{\alpha,\beta=1}^{4} m_{\alpha l} F^{(e)}_{\mathrm{K},\alpha k\beta l} m_{\beta l} \tag{101}$$

with the 12×12 matrix

$$F^{(e)}_{\mathrm{K},\alpha k\beta l} = -2K^{(e)}_1 k^{(e)}_l k^{(e)}_k \int_{V_e} \varphi_\alpha \varphi_\beta \mathrm{d}V \tag{102}$$

The integral in equation (102) can be evaluated analytically (Chen, Fredkin and Koehler, 1993)

$$\int_{V_e} \varphi_\alpha \varphi_\beta \mathrm{d}V = (1 + \delta_{\alpha\beta}) \frac{V_e}{20} \tag{103}$$

In a finite element simulation program, the global matrix $\mathbf{F}_{\mathrm{AK}}$ takes into account all local energies. It can be obtained by assembling its finite element contributions $\mathbf{F}^{(\mathrm{e})}_{\mathrm{AK}} = \mathbf{F}^{(e)}_{\mathbf{A}} + \mathbf{F}^{(e)}_{\mathbf{K}}$.

The Zeeman energy can be written by the dot product, $\Phi_{\mathrm{H}} = -\underline{\mathbf{F}}^{\mathrm{T}}_{\mathrm{H}} \cdot \underline{\mathbf{m}}$. The vector $\underline{\mathbf{F}}_{\mathrm{H}}$contains the magnetic field generated by imposed currents at the nodes of the finite element mesh multiplied by the modulus of the local magnetic moment at the nodes

$$(\underline{\mathbf{F}}_{\mathrm{H}})_{ik} = |\boldsymbol{\mu}_i| H_{\mathrm{current},ik} \tag{104}$$

Here the index i runs over all nodes of the finite element mesh, and the index k denotes the Cartesian component of the magnetic field produced by imposed currents. An example is the field exerted on the yoke of the write head created by the write current through the coils during magnetic recording (Schrefl, Schabes, Suess and Stehno, 2004).

The use of the matrix–vector formulation, which is given by equation (96), to compute the total magnetic Gibbs' free energy helps to program micromagnetic solvers. The parallelization of the solver is easy, as the parallelization of matrix–vector operations is straightforward using scientific programming environments (Scholz *et al.*, 2003).

3.2 Dynamics micromagnetics

In Section 3.1, we have shown how the micromagnetic energy contributions can be computed by simple matrix–vector products once a magnetic particle has been discretized by the FEM. The problem of computing the equilibrium states of a magnetic structure then reduces to an algebraic minimization problem. Here, we show how the partial differential equation that describes the magnetization dynamics can be transformed into a system of ordinary differential equations. Only sparse matrices are required to compute the right-hand side of the equations.

The time evolution of the magnetization $\mathbf{M}(\mathbf{r})$ in a ferromagnetic body is given by the LLG equation (Brown, 1963b)

$$\frac{\partial \mathbf{M}}{\partial t} = -\frac{|\gamma|}{1+\alpha^2} \mathbf{M} \times \mathbf{H}_{\mathrm{eff}} - \frac{\alpha}{M_{\mathrm{s}}} \frac{|\gamma|}{1+\alpha^2} \mathbf{M} \times (\mathbf{M} \times \mathbf{H}_{\mathrm{eff}}) \tag{105}$$

where γ is the gyromagnetic ratio, α is the Gilbert damping constant, and $\mathbf{H}_{\mathrm{eff}}$ is the effective field. The effective field is defined as the negative variational derivative of the total Gibbs' free energy density, E_{t}, with respect to the magnetization

$$\mathbf{H}_{\mathrm{eff}}(\mathbf{r}) = -\frac{1}{\mu_0} \frac{\delta E_{\mathrm{t}}}{\delta \mathbf{M}(\mathbf{r})} \tag{106}$$

with the total Gibbs free energy being the integral of E_{t} over the ferromagnetic body

$$\Phi_{\mathrm{t}} = \int_V E_{\mathrm{t}} \mathrm{d}V \tag{107}$$

Similar to the total energy the effective field splits into the exchange field $\mathbf{H}_{\mathrm{A}}$, the anisotropy field $\mathbf{H}_{\mathrm{K}}$, the stray field

$\mathbf{H}_s$, and an applied magnetic field $\mathbf{H}_{\text{current}}$. The exchange field is given by

$$\mu_0 \mathbf{H}_A = \frac{2A}{M_s^2} \Delta \mathbf{M} \tag{108}$$

and the anisotropy field is given by

$$\mu_0 \mathbf{H}_K = \frac{2K_1}{M_s} (\mathbf{m} \cdot \mathbf{k}) \mathbf{k} \tag{109}$$

where A is the exchange constant, K_1 is the uniaxial anistropy constant, and $\mathbf{k}$ is the anisotropy direction. The total effective field is

$$\mathbf{H}_{\text{eff}} = \mathbf{H}_A + \mathbf{H}_K + \mathbf{H}_s + \mathbf{H}_{\text{current}} \tag{110}$$

It is the sum of the exchange field, the anisotropy field, the stray field, and the applied field created by imposed currents. Here we assume small ferromagnetic bodies so that the eddy currents and the magnetic fields created by eddy currents, $\mathbf{H}_{\text{eddy}}$, can be neglected (Kanai, Matsubara, Muraoka and Nakamura, 2001). The components of the exchange field are proportional to the Laplacian of the magnetization. Thus equation (105) has a spatial derivation on its right-hand side and is a partial differential equation. It has to be solved together with an equation that gives the stray field for a certain magnetization distribution. In order to solve the time evolution of the magnetization, we have to solve a system of integro-differential equations.

In the previous sections, we already discussed discretization methods for the effective computation of the stray field. Now we will show how we can discretize the partial differential equation (105). Before going into much detail, let us see how we will proceed for the numerical computation of magnetization dynamics. The main steps are illustrated in Figure 5. First, we discretize the LLG equation and the magnetostatic boundary value problem for a magnetic scalar potential using a hybrid FEM/BEM. This leads to a system of ordinary differential equations. The system of ordinary differential equations describes the dynamics of the magnetic moments at the nodes of the finite element mesh. There are three equations per nodes for the Cartesian components of the magnetic moment. The motion of the magnetic moments is coupled by the exchange field and by the stray field. Together with the anisotropy field and an applied field these files give the total effective field. Similar to the magnetic moments we can define the effective field at the nodes of the finite element mesh. The system of ordinary differential equations is nonlinear. Because the system is stiff (Nakatani, Uesaka and Hayashi, 1989) we need a backward differentiation method for its discretization. This leads to a nonlinear system of equation that has to be solved at each time step. A proper

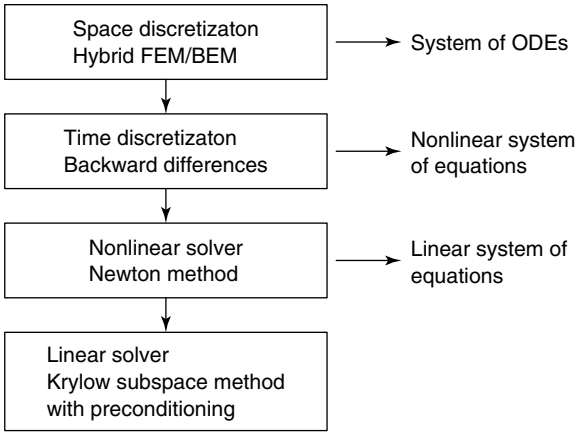

Figure 5. Space and time discretization of the LLG equation. The space discretization transforms the problem into a system of ordinary differential equations. At each time step, a nonlinear system of equations has to be solved which is solved by the Newton–Rapson method. Each Newton step requires the solution of a linear system of equations which is done by a Krylow subspace method (Saad, 2003).

method to solve the nonlinear system is the Newton method that in turn gives a linear system of equation that has to be solved at each Newton step. For the solution of the linear system of equations matrix-free Krylov subspace methods are most appropriate.

In the following text, we will discuss two different methods to evaluate the effective field numerically. The first method uses a physical interpretation of the finite element discretization of the total Gibbs free energy. We assume that a magnetic moment is associated with each node of the finite element mesh as discussed in the paragraph following equation (57). Following the same reasoning, it is possible to define the effective field at the nodes of the finite element mesh. The second method is purely mathematical and uses the concept of mass lumping (Vacus and Monk, 2001) that is commonly used in finite element simulation.

The magnetization $\mathbf{M}(\mathbf{r})$ is a continuous vector field in space. To represent the magnetization distribution, we can subdivide the ferromagnetic body into N distinct control volumes V_i with magnetization $\mathbf{M}_i$. The control volumes have the following properties

$$V = \sum_{i=1}^{N} V_i \text{ and } V_i \cap V_j = 0 \tag{111}$$

Then the effective field at point $\mathbf{r}_i$ can be approximated by

$$\mu_0 \mathbf{H}_{\text{eff}}(\mathbf{r}_i) = \mu_0 \mathbf{H}_{\text{eff},i} \approx -\frac{1}{V_i} \frac{\partial \Phi_t}{\partial \mathbf{M}_i} \tag{112}$$

In equation (112), V_i is the volume surrounding point $\mathbf{r}_i$. In limit of large N, the size each control volume goes to zero and the above equation is exact (Gardiner, 1996). There is also a physical interpretation of this result. Multiplying V_i with $\mathbf{M}_i$ gives the magnetic moment at point $\mathbf{r}_i$. So the effective field can also be written as

$$\mu_0 \mathbf{H}_{\mathrm{eff},i} = -\frac{\partial \Phi_\mathrm{t}}{\partial \boldsymbol{\mu}_i} = -\frac{1}{|\boldsymbol{\mu}_i|}\frac{\partial \Phi_\mathrm{t}}{\partial \mathbf{m}_i} \tag{113}$$

where $\boldsymbol{\mu}_i$ is the magnetic moment at point $\mathbf{r}_i$ and $\mathbf{m}_i$ is the unit vector of the magnetization at point $\mathbf{r}_i$. Now let us consider the finite element discretization of the unit vector of the magnetization $\mathbf{m}(\mathbf{r})$ with linear basis function on a tetrahedral mesh as introduced in Section 2.1 and let the nodes of the finite element mesh coincide with the points $\mathbf{r}_i$. Then equation (113) defines the effective field at the nodes of the finite element mesh. Making use of the matrix–vector notation for the micromagnetic energy (96) we can write the effective field as matrix–vector products

$$\mu_0 \underline{\mathbf{H}}_\mathrm{eff} = -\mathbf{L}^{-1}\mathbf{F}_{AK}\underline{\mathbf{m}} - \mu_0 \mathbf{L}^{-1}\mathbf{G}\underline{\mu} + \mu_0 \underline{\mathbf{H}}_\mathrm{current} \tag{114}$$

where the vector $\underline{\mathbf{H}}_\mathrm{eff}$ is a vector over all nodes of the FE mesh whose definition is similar to the definition of $\underline{\mathbf{m}}$ in equation (53). Here we used equation (64) for the calculation of the stray field $\mathbf{H}_\mathrm{s}$.

Now we will show how to derive the effective field using the FEM. The effective field can be derived using a procedure called *mass lumping* (Vacus and Monk, 2001). The exchange field is given by equation (108). In order to calculate the components of the exchange field, we use the Galerkin method. First, we multiply equation (108) with the saturation magnetization M_s. Secondly, we multiply the resulting equation with test functions φ_i and integrate over the problem domain. This gives a set of $3N$ equations for $H_{\mathrm{A},il}$ where the index i denotes the node number and the index l denotes the Cartesian component of the exchange field. Starting with

$$\int_V M_\mathrm{s}\varphi_i \mu_0 \mathbf{H}_\mathrm{A}\mathrm{d}V = \int_V \varphi_i 2A\Delta\mathbf{m}\,\mathrm{d}V \;\; i = 1, \ldots, N \tag{115}$$

where the integral is over the ferromagnetic body, we now expand both the exchange field with the finite element basis functions (see equation (4)). Within the framework of the Galerkin method the test functions of (115) are identical with the basis functions. On the right-hand side we can reduce the second derivative in space to a first derivative in space using an integration by parts. Then we obtain

$$\int_V M_\mathrm{s}\varphi_i \left(\sum_{j=1}^{N} \mu_0 H_{\mathrm{A},jl}\varphi_j\right)\mathrm{d}V = -2\int_V A\nabla\varphi_i \nabla m_l\,\mathrm{d}V + 2\oint_{\partial V} \varphi_i A\frac{\partial m_l}{\partial n}\,\mathrm{d}S \tag{116}$$

The index i denotes the node number and runs from 1 to N, the index l denotes the Cartesian component of the exchange field and runs from 1 to 3. The second term on the right-hand side of (116) vanishes as the normal derivative of the magnetization components $\partial m_l/\partial n$ vanish according to Brown (1963a). The left-hand side can be written as sum of contributions over the finite elements

$$\int_V M_\mathrm{s}\varphi_i \left(\sum_{j=1}^{N} \mu_0 H_{\mathrm{A},jl}\varphi_j\right)\mathrm{d}V = \sum_{e=1}^{E}\int_{V_e} M_\mathrm{s}^{(e)}\varphi_\alpha \left(\sum_{\beta=1}^{4} \mu_0 H_{\mathrm{A},\beta l}\varphi_\beta\right)\mathrm{d}V \tag{117}$$

The expansion coefficients $H_{\mathrm{A},\beta l}$ are the nodal values of the Cartesian components of the exchange field at the nodes of the tetrahedron. Thus we can write

$$\int_V M_\mathrm{s}\varphi_i \left(\sum_{j=1}^{N} \mu_0 H_{\mathrm{A},jl}\varphi_j\right)\mathrm{d}V = \sum_{e=1}^{E}\sum_{\beta=1}^{4}\left[M_\mathrm{s}^{(e)}\int_{V_e}\varphi_\alpha\varphi_\beta \mathrm{d}V\right]\mu_0 H_{\mathrm{A},\beta l} \tag{118}$$

where we assume that the saturation magnetization, $M_\mathrm{s}^{(e)}$, is constant on each element e. The element matrix

$$M_{\alpha\beta}^{(e)} = \int_{V_e}\varphi_\alpha\varphi_\beta\,\mathrm{d}V \tag{119}$$

is called *mass matrix*. Unfortunately, the matrix contains off-diagonal terms that would require the solution of a linear system of equations to evaluate the exchange field. However, we can compute the value of the exchange field at the nodes of the finite element mesh directly from the right-hand side of equation (116) using mass-lumping technique that is widely used in finite element computation. The matrix elements of $M_{\alpha\beta}^{(e)}$ are given by equation (103). We now approximate $M_{\alpha\beta}^{(e)}$ with a diagonal matrix

$$\widetilde{M}_{\alpha\gamma}^{(e)} = \delta_{\alpha\gamma}\sum_{\beta=1}^{4} M_{\alpha\beta}^{(e)} \tag{120}$$

The diagonal elements of $\widetilde{M}^{(e)}_{\alpha\alpha}$ are the sum of the corresponding rows of the mass matrix. Using (103) we obtain

$$\widetilde{M}^{(e)}_{\alpha a} = \frac{V_e}{20}\sum_{\beta=1}^{4}(1+\delta_{\alpha\beta}) = \frac{V_e}{20}(2+1+1+1) = \frac{V_e}{4} \quad (121)$$

With mass lumping, equation (116) can be written as follows

$$\sum_{e=1}^{E}\sum_{\beta=1}^{4}\left[M_{\mathrm{s}}^{(e)}\frac{V_e}{4}\right]\delta_{\alpha\beta}\mu_0 H_{\mathrm{A},\beta l} = -2\sum_{e=1}^{E}A^{(e)}\int_{V_e}\nabla\varphi_\alpha\sum_{\beta=1}^{4}\nabla\varphi_\beta m_{\beta l}\,\mathrm{d}V \quad (122)$$

Here we expanded the direction cosine of the magnetization, m_l, on the right-hand side of with the finite element basis function and we replaced the integral over the problem domain V with a sum over the integrals over the finite elements V_e. $A^{(e)}$ denotes the local exchange constant within element e. Using the element matrix $F_A^{(e)}$, which was introduced in equation (99) when we calculated the exchange energy, we obtain

$$\sum_{e=1}^{E}\sum_{\beta=1}^{4}\left[M_{\mathrm{s}}^{(e)}\frac{V_e}{4}\right]\delta_{\alpha\beta}\mu_0 H_{\mathrm{A},\beta k} = -F^{(e)}_{A\alpha k\beta l}m_{\beta l} \quad (123)$$

The term in brackets on the left-hand side gives the magnetic moments at the nodes of the finite element mesh. Using the diagonal matrix $\mathbf{L}$, which contains the moduli of the magnetic moments at the nodes (see equation (60)) we obtain

$$\mu_0\mathbf{L}\underline{\mathbf{H}}_{\mathrm{A}} = -\mathbf{F}_{\mathrm{A}}\underline{\mathbf{m}} \quad (124)$$

through assembling the finite element contributions. Thus we can write the exchange field at the finite element mesh as

$$\mu_0\underline{\mathbf{H}}_{\mathrm{A}} = -\mathbf{L}^{-1}\mathbf{F}_{\mathrm{A}}\underline{\mathbf{m}} \quad (125)$$

The last equation has the very same structure as equation (114).

In the last paragraph, we demonstrated the derivation of the exchange field using mass lumping. This method is especially useful when we want to calculate the exchange field in exchange spring magnets or in exchange spring recording media (Suess *et al*., 2005). These magnets are composed of exchange coupled magnetically hard and soft phases. Let us assume that the total volume of the magnet V splits into two exchange-coupled volumes V_1 and V_2 with $V = V_1 \cup V_2$. Further, we denote the saturation magnetization and the exchange constant in V_1 with $M_{\mathrm{s}1}$ and A_1 and in volume V_2 with $M_{\mathrm{s}2}$ and A_2. Then the volume integral on the right-hand side of equation (116) splits into two integrals over the volumes V_1 and V_2, and the surface integral split into a surface integral over the common interface of the two subvolumes, ∂V_{12}, and the two surface integrals on the outer boundaries of the two subvolumes, ∂V_1 and ∂V_2. If $\mathbf{n}_{12}$ denotes the normal vector at the interface pointing from V_1 into V_2 we obtain

$$\begin{aligned}\int_V M_{\mathrm{s}}\varphi_i\left(\sum_{j=1}^{N}\mu_0 H_{\mathrm{A},jl}\varphi_j\right)\mathrm{d}V &= -2\int_{V_1}A_1\nabla\varphi_i\nabla m_l\,\mathrm{d}V \\ -2\int_{V_2}A_2\nabla\varphi_i\nabla m_l\,\mathrm{d}V &+ 2\oint_{\partial V_1}A\varphi_i\frac{\partial m_l}{\partial n}\,\mathrm{d}S \\ +2\oint_{\partial V_2}A\varphi_i\frac{\partial m_l}{\partial n}\,\mathrm{d}S &+ 2\oint_{\partial V_{12}}\varphi_i\left(A_1\frac{\partial m_l}{\partial n_{12}} - A_2\frac{\partial m_l}{\partial n_{12}}\right)\mathrm{d}S\end{aligned} \quad (126)$$

Now we make use of the boundary conditions and the interface conditions, in order to evaluate the surface integrals in equation (126). Using variational calculus, Brown (1963a) showed that $\partial m_l/\partial n = 0$ holds on the surface of a magnet. Similarly, Kronmüller and coworkers (1976) showed that at a materials interface the product of the normal derivative with the exchange constant is continuous. Therefore the interface condition

$$A_1\frac{\partial m_l}{\partial n_{12}} - A_2\frac{\partial m_l}{\partial n_{12}} = 0 \quad \text{on } \partial V_{12} \quad (127)$$

holds. Using the boundary conditions and the interface conditions the surface integrals in equation (126) vanish. Therefore, the exchange field in composite magnets can be derived similar to the exchange field in single-phase magnets by using equations (122–125). In particular, equation (125), which gives the exchange field at the nodes of the finite element mesh, is also valid for composite magnets.

Using the arguments in the preceding text, we can think of individual magnetic moments sitting on the nodes of the finite element mesh. Similarly, we have the vector of the effective field at each node point. We transformed the partial differential equation (105) in a system of ordinary differential equations

$$\frac{\partial\boldsymbol{\mu}_i}{\partial t} = -\frac{|\gamma|}{1+\alpha^2}\boldsymbol{\mu}_i\times\mathbf{H}_{\mathrm{eff},i} - \frac{\alpha}{|\boldsymbol{\mu}_i|}\frac{|\gamma|}{1+\alpha^2}\boldsymbol{\mu}_i \times(\boldsymbol{\mu}_i\times\mathbf{H}_{\mathrm{eff},i}) \quad \text{for } i = 1,\ldots,N \quad (128)$$

However, we do not store the magnetic moment $\boldsymbol{\mu}$ at the node, but interpolate the unit vector of the magnetization $\mathbf{m}$ on the finite element grid. In order to arrive at an equation that is more suitable for computation, we multiply both sides

of equation (128) by the factor $\mu_0/(|\gamma||\boldsymbol{\mu}_i|)$

$$\frac{\partial \mathbf{m}_i}{\partial t'} = -\frac{1}{1+\alpha^2}\mathbf{m}_i \times \mathbf{h}_{\text{eff},i} - \frac{\alpha}{1+\alpha^2}\mathbf{m}_i \times (\mathbf{m}_i \times \mathbf{h}_{\text{eff},i}) \text{ for } i = 1, \ldots, N \tag{129}$$

The index i runs from 1 to the total number of nodes in the finite element mesh. In equation (129), we also introduced the reduced effective field $\mathbf{h}_{\text{eff}} = \mu_0 \mathbf{H}_{\text{eff}}$. As a consequence, all terms in equation (129) are in the order of $O(1)$ which facilitates the numerical solution.

Here we introduced a reduced time

$$t' = \frac{|\gamma|}{\mu_0} t \tag{130}$$

which leads to time steps in the order of $\Delta t' = 10^{-2}$ in the numerical solution scheme. Instead of using the fully populated matrix $\mathbf{F}_s$ to compute the stray field, we can apply the FEM. First, the magnetostatic boundary value problem for the magnetic scalar potential (equations (32–35)) is solved. Secondly, the stray field is computed from the potential using sparse matrix operators on the finite element grid (see equation (64)).

Standard library methods for the solution of stiff ordinary differential equations can be used to solve (129). An example is the backward differentiation scheme as implemented in the CVODE package (Cohen and Hindmarsh, 1996). The package solves an initial value problem for a system of ordinary differential equation given in the following form

$$\frac{\mathrm{d}y_i}{\mathrm{d}t} = f_i(y_1, y_2, \ldots, y_L, t), \; i = 1, \ldots, L \tag{131}$$

Here y_i are the components of the vector $\underline{\mathbf{m}}$ (the collection of the unit vectors of the magnetization vector over all nodes of the finite element mesh, see equation (53). The functions f_i are the components of the right-hand side of the LLG equation as given in (129). The total number of unknowns, L, is three times the number of nodes in the finite element mesh. The user needs to provide an initial state, y_i for $i = 1$ to L at time $t = 0$, and a subroutine for the evaluation of the right-hand side f_i. The computation of the right-hand side involves several steps. Every time the user supplied function for the evaluation of the right-hand side is called, the y_i are treated as components of unit magnetization vectors. Then corresponding effective field is computed using (114) and the right-hand side of (129) is evaluated.

Figure 5 summarizes schematically the approach for the numerical solution of the LLG equation (129). Such an equation cannot be solved directly. However, applying a hierarchy of numerical methods, the problem can be broken down to the solution of a system of linear equations. All but the first task of the following list is done within the time integration package CVODE.

Most of the computation time in finite element programs is spent in solving linear equations. A good choice of the numerical method can shorten the time to solution drastically. The special structure of the system matrices arising from finite element discretization can be used to speed up the simulations. It is used for preconditioning the linear system that has to be solved at each Newton step during time integration (Cohen and Hindmarsh, 1996). We can provide an approximate Jacobian matrix that contains all the short-range interactions (exchange interactions, magnetocrystalline anisotropy, external field) but neglects the long-range magnetostatic interactions. This method speeds up the time integration by orders of magnitude (Suess *et al*., 2002).

4 EXAMPLES

4.1 Write field dynamics in perpendicular recording

Multiscale finite element simulation of the write process in perpendicular media span a length scale of three orders of magnitude (Schrefl *et al*., 2005). The coupled system or partial differential equations for magnetization dynamics (129) is solved simultaneously for the head, the data layer, and the SUL during the motion of the head. All magnetostatic interactions between head, data layer, and SUL are concurrently taken into account. Finite element micromagnetics is combined with fast boundary element techniques to calculate the magnetostatic interactions between the recording head, the data layer, and the SUL in perpendicular magnetic recording. The FEM is highly suitable to model the physical microstructure of the media such as realistic grain shapes and intergranular phases. The fast boundary method provides an efficient and accurate means to simulate the mutual interactions between the moving magnetic parts.

A common approach to include moving parts into electromagnetic finite element simulations is the use of sliding grids and Mortar elements (Buffa, Maday and Rapetti, 2001). An alternative approach is the use of hybrid FEM/BEM techniques (Kurz, Fetzer, Lehner and Rucker, 1999). For magnetic recording simulations, FEMs/BEMs have the advantage that no mesh is needed between the different magnetic parts. In order to avoid the recomputation of the matrix elements of the matrix $\mathbf{B}$ at each time step due to the movement of the head, the superposition principle for the magnetic field is used. The finite element mesh of the entire recording system is split according to the real-world objects. For each object (head, data layer, SUL) its self-demagnetizing field is calculated using the hybrid FEM/BEM (Fredkin

and Koehler, 1990). The magnetic field is the sum of the self-demagnetizing field and the interaction field from other objects. In order to illustrate the computation of the interaction field, let us list the steps required to compute the head field:

1. We compute the magnetic scalar potential created by the head magnetization at the surface of a virtual box, which encloses the data layer. This so-called field box moves together with the head. Therefore the corresponding interaction matrix has to be computed only once.
2. A fast Poisson solver (Swartzentrauber and Sweet, 1979) is used to evaluate the potential within the field box at high spatial resolution on a regular grid.
3. Numerical derivation gives the head field within the field box which is then interpolated at the nodes of the mesh of the data layer.

The above-mentioned procedure, illustrated in Figure 6, is applied for all mutual magnetostatic interactions between the head, data layer, and SUL.

In perpendicular recording, the total write field acting on the data layer is the sum of the field created by the magnetic surface and volume charges in the pole tip of the head and the field created by magnetic surface and volume charges

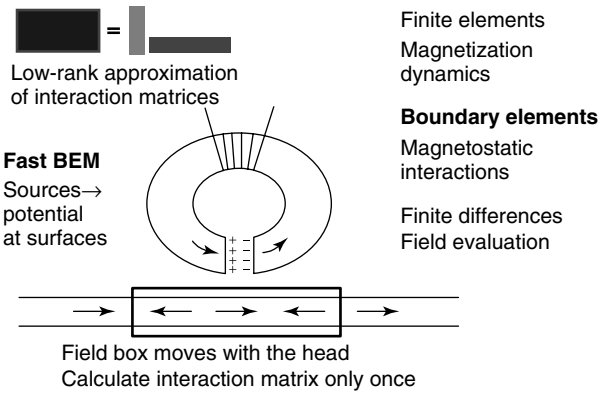

Figure 6. In magnetic recording simulation different numerical methods are combined, in order to achieve optimal performance. The finite element method is used to calculate the magnetization dynamics within the head and within the data layer. A boundary integration technique is used to calculate the magnetostatic interactions between the different parts. Large blocks of the interaction matrix are represented by low-rank approximations, in order to reduce the storage requirements and to speed up the matrix–vector multiplication. Instead of evaluating the potential from the head directly on the nodes of the data layer, the potential is evaluated at the surface of a field box that moves together with the head. Then, a fast Poisson solver is used to evaluate the magnetic scalar potential within the field box. The interaction field is interpolated from the regular grid of the field box onto to nodes of the finite element mesh of the data layer and added to the self-demagnetizing field of the layer.

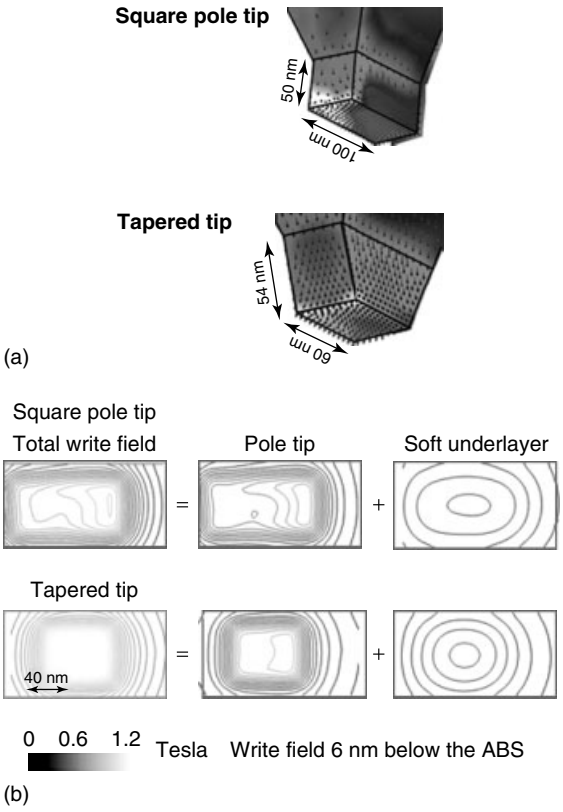

Figure 7. (a) Magnetization distribution in the pole tip of a single pole head. (b) Contour plots of the perpendicular write field. The write field is the sum of the magnetic field created by the pole tip magnetization and the magnetic field created by the soft underlayer magnetization. The magnetization configuration in the square pole tip (top) is a twisted flower state. In the tapered pole tip (bottom) is more uniform than in the square pole tip which in turn increases the perpendicular write field component.

in the SUL. Figure 7 compares the write field contributions for a write head with a square pole tip and a write head with a tapered pole tip. In the square pole tip the interplay of magnetostatic and exchange interaction lead to the formation of a twisted flower state (Hertel and Kronmuller, 2002) at maximum write current. A significant component of the magnetization is parallel to the air bearing surface (ABS) forming a vortex-like state with the center located off axis. In the tapered pole tip, the magnetization aligns almost parallel at an angle of 90° to the ABS at maximum current. For the tapered pole tip the magnetic surface charge density, $\sigma_m = \mathbf{M} \cdot \mathbf{n}$, is higher than for the square pole tip. As a consequence both the perpendicular write field component and the field gradient are higher for the tapered pole tip. Figure 7(b) gives the total write field as sum of the pole tip field and the SUL field. The results show that the tapered pole tip improves both the gradient of the pole tip field and the gradient of the SUL field. The head field gradient is smaller for the SUL field than

for the pole tip field. This result underlines the fundamental differences between the SUL and pole contributions to the total write flux. While the contributions from the pole are generated by a lithographically defined object, the gradients for the SUL contributions are created along a moving domain boundary in the SUL.

A fundamental limit of the data rate in magnetic recording is given by the intrinsic reversal time of the magnetization in head. The reversal speed of the magnetization in pole tip determines the head field rise time. Figure 8(a) compares the write current and the write field as a function of time. The delay between zero crossing of the current and reaching the maximum write field is about 0.8 ns. The time profile of the write field is governed by two characteristic timescales: (i) reversal of the pole tip by vortex motion and (ii) saturation of the pole tip and alignment of the SUL magnetization. Figure 8(b) shows the pole tip magnetization (top) and the corresponding write field (bottom) 0.3, 0.65, and 0.8 ns after zero crossing of the current. The pole tip reversal occurs by vortex motion. After annihilation of the vortex an end domain, which reduces the surface charges, remains for about 0.2 ns. Finally, the pole tip becomes saturated and the maximum write field of 1.2 T is reached.

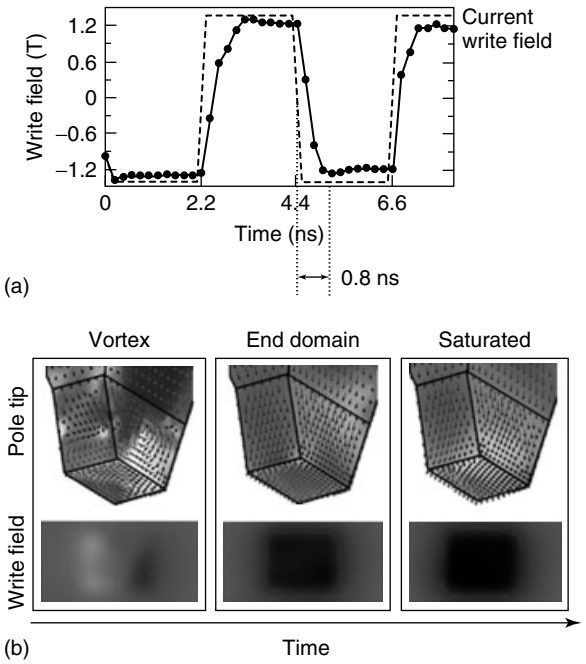

Figure 8. Write field dynamics. (a) Total write field as a function of time at a distance of 6 nm below the ABS. (b) Pole tip magnetization and total write field (color coded) as a function of time. The color code in the pole tip maps the magnetization component parallel to the down track direction (long axis parallel to the ABS). The color code for the write field maps the perpendicular write field component.

4.2 Recording on exchange spring media

The area density of magnetic recording is limited by the so-called superparamagnetic effect (Charap, Lu and He, 1997). With decreasing particle size the particle may switch spontaneously. An increase of the magnetocrystalline anisotropy leads to particles that cannot be switched with the write field. A soft magnetic layer exchange coupled with the hard magnetic grains reduces the switching field with hardly any effect on the thermal stability (Suess *et al*., 2005; Victora and Shen, 2005). Exchange spring media opens the possibility to reach area densities up to 1 Tbit in.$^{-2}$ with conventional perpendicular recording.

Exchange spring media for magnetic recording makes use of the exchange coupling between different magnetic phases at the nanoscale. Similar to nanocomposite permanent magnets, the exchange interactions between a magnetically hard phase and a magnetically soft phase lead to novel magnetic properties that can be tuned by changing the intrinsic magnetic properties of the different phases (Schrefl and Fidler, 1999), by changing the volume fraction of the different phases (Schrefl, Fischer, Fidler and Kronmuller, 1994c), and by changing the strength of the exchange interaction between the different phases (Fukunaga, Kuma and Kanai, 1999). Whereas in permanent magnets we want to increase the remanence while keeping a high coercive field, in recording media we want to reduce the switching field, while keeping a high energy barrier. In permanent magnets, the soft phase increases the remanence and the exchange interactions with the hard phase provides a high coercive field. In domain wall–assisted recording (Dobin and Richter, 2006) the soft magnetic helps to nucleate a reversed domain, the exchange interactions help propagate the reversed domain into the hard magnetic phase, and the hard magnetic phase provides a high thermal stability.

Finite element micromagnetic simulations show that the reversal mode induced by the external write field significantly differs from uniform rotation. A nucleus with oblique magnetization is formed within the soft magnetic part of the grain that helps the reversal of the hard magnetic layer. The switching field is given by the critical value of the external field that is required to expand the nucleus into the hard magnetic phase. In the limit of a thick soft magnetic layer, the switching field of a composite grain corresponds to the domain wall propagation field. Whereas the domain wall propagation field is proportional to the change (gradient) of the domain wall energy, the energy barrier for thermal switching is given by the domain wall energy in the hard phase. Thus, the bilayers can be optimized in order to achieve a high thermal stability without an increase of coercive field. In grains with identical

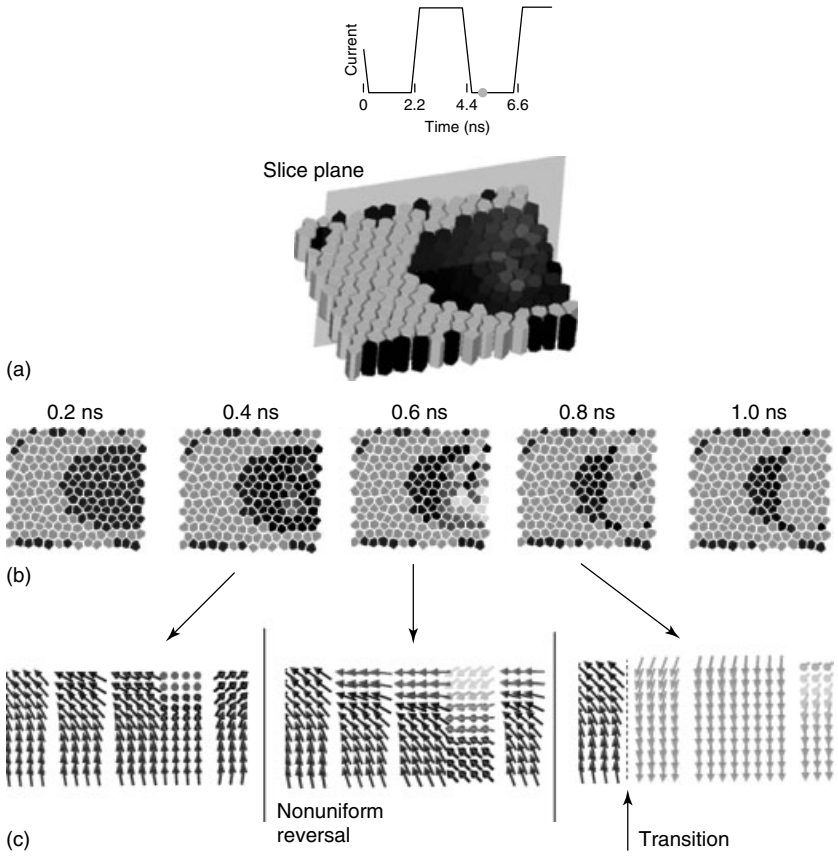

Figure 9. Evolution of the bit pattern during recording on exchange spring media. (a) Write current profile and data layer magnetization 0.4 ns after zero crossing of the current. (b) Top view of the data layer as function of time. (c) Magnetization in a slice through the data layer. The color code maps the perpendicular component of the magnetization. The total layer thickness is 14 nm. The thickness of the soft layer (on top the hard layer) is 5.3 nm, the average magnetic polarization is 0.5 T.

size and coercivity, an optimized bilayer reaches an energy barrier exceeding those of optimized single-phase media by more than a factor of two.

Figure 9 shows the formation of a bit pattern during recording on an exchange spring media. The hard magnetic layer with a thickness of 8.7 nm is perfectly exchange coupled to a soft magnetic layer with a thickness of 5.3 nm. The cross-sectional view clearly shows that switching of the individual grains is nonuniform. If the write field exceeds the critical field for the expansion of the nucleus into the hard phase, the media grains below the pole tip become fully reversed.

4.3 Thermal stability of exchange spring media

In order to estimate the thermal stability of exchange spring media, we have to calculate the energy barrier of composite grain. A micromagnetic system will be close to a local minimum of the total magnetic Gibbs' free energy. Thermal fluctuations of the magnetization cause the magnetization to wander around this minimum. Occasionally, the system will reach a region next to a saddle point. The system may cross the energy barrier and move into the basin of attraction of a different energy minimum. A small single-phase grain reverses by uniform rotation. The energy barrier for uniform rotation is $E_\mathrm{b} = KV$, where K is a uniaxial anisotropy constant that includes the contributions of the magnetocrystalline anisotropy and the shape anisotropy and V is the volume of the grain. The relaxation time is the inverse of probability per unit time for crossing the barrier E_b. It can be approximated using the Néel-Brown theory (Brown, 1963b; Neel, 1949) to

$$\tau = f_0^{-1} e^{E_\mathrm{b}/k_\mathrm{b}T} \tag{132}$$

The attempt frequency, f_0, depends on material parameters, like anisotropy, particle shape, and damping (Braun, 1994). Its value, which ranges from $f_0 = 10^9$ to $f_0 = 10^{12}$ Hz, sets the timescale for thermally assisted magnetization reversal. The Boltzmann constant is $k_\mathrm{B} = 1.3806505(24) \times 10^{-23}\,\mathrm{J\,K^{-1}}$, and T is the temperature.

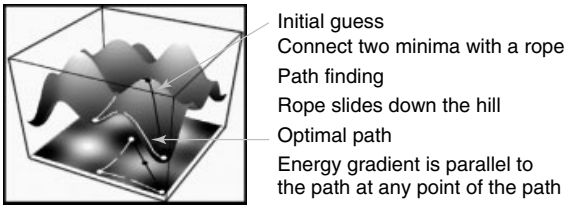

Figure 10. Elastic band method for the computation of the optimal path between two local minima. The left-hand side shows energy landscape of two interacting magnetic particles (Chen, Zhang and Bertram, 1992). The initial path connects the initial state (both particles magnetized up in the center of the graph) with the state final state (both particle magnetized down in the front corner of the graph). This path is changed iteratively until the energy gradient is parallel to the path at any point of the path. This is an optimal path connecting the initial state and the final state via a saddle point. (Reproduced from W. Chen., S. Zhang & H.N. Bertram: 'Energy barriers for thermal reversal of interacting single domain particles'. *Journal of Applied Physics*, **71**, (1992), copyright © 1992 American Institute of Physics, with permission from the AIP.)

In a composite grain of similar size, the magnetization reversal process is nonuniform. Numerical methods are required to calculate the energy barrier. In order to illustrate how the barrier can be obtained numerically, let us start with a simplified system. Figure 10 shows the energy landscape for two interacting magnetic particles (Chen, Zhang and Bertram, 1992). Thermal fluctuations drive the micromagnetic system from the stable region in the center (both particles magnetized up) to another stable region at the corner (both particles magnetized down). The path with the smallest energy barrier is chosen since the population probability decreases exponentially with the energy of the system. To calculate the crossing point with the lowest energy, one needs to find the relevant saddle points between the two stable regions. Starting from an initial guess for the path that connects two local minima of the system, a highly probable path is found by moving the points along the path according to an algorithm that resembles tensioning an elastic band across a mountain. Variants of elastic band methods are commonly used to calculate transition rates in chemical physics (Henkelman and Jonsson, 2000). These so-called string or elastic band methods have been successfully applied for calculating micromagnetic energy barriers by E, Ren and Vanden-Eijnden (2002) and Dittrich *et al*. (2002). Once the energy barrier is calculated, the Neel-Brown theory can be used to calculate the transition probability for energy barrier crossing. Whereas the Neel–Brown theory is commonly used in magnetic recording (Sharrock, 1994), it is interesting to note that in some micromagnetic systems the transition probability follows a Weibull distribution (Kronmüller, Leineweber and Hertel, 2000).

The path connecting the initial state of the system with its final state is represented by a set of images, which are

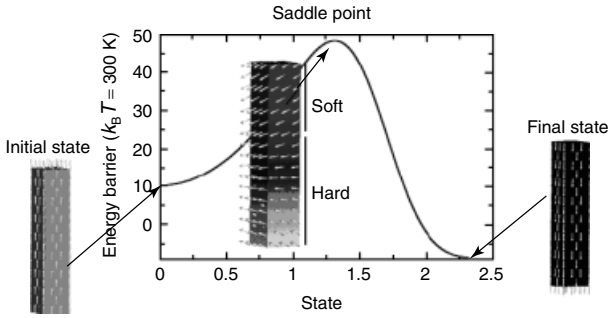

Figure 11. Energy along the minimum energy path for thermally activated switching of a composite grain. The grain is exposed to the mean interaction field of the recording layer that is composed of the demagnetizing field and the intergrain exchange interaction field. Therefore, the energy of the initial state is higher than the energy of the final state. The magnetization configuration of the saddle point configuration is nonuniform.

a small subset of all the magnetic states along the path. The magnetization configuration of an image is represented by the vector $\underline{\mathbf{m}}$, see equation (53), on the finite element grid. A sequence of magnetic states can be constructed in such a way as to form a discrete representation of a path from the initial magnetization state to the final magnetization state. The simplest case of the initial path is a straight-line interpolation in the configuration space between the initial state and the final state (see Figure 10). An optimization algorithm is then applied until at any point along the path the gradient of the energy is only pointing along the path. This path is called *minimum energy path* and means that the energy is stationary for any degree of freedom perpendicular to the path. The set of images along the minimum energy path will be visited during thermally activated reversal of the system.

The elastic band method was applied to calculate the minimum energy path for thermally activated reversal of a composite grain from an exchange spring medium. The interaction field acting in the grain is taken into account using a mean-field approach (Suess *et al*., 2005). It is the sum of the exchange field between the neighboring grains and the demagnetizing field of the film. The comparison of the magnetization configuration of the saddle point (Figure 11) and the intermediate states during recording (Figure 9) shows that the magnetization reversal is nonuniform for both thermally induced switching and field induced switching.

REFERENCES

Amestoy, P.R., Davis, T. A. and Duff, I.S. (2004). Algorithm 837: AMD, an approximate minimum degree ordering algorithm. *ACM Transactions on Mathematical Software*, **30**, 381–388.

Asselin, P. and Thiele, A.A. (1986). On the field Lagrangians in micromagnetics. *IEEE Transactions on Magnetics*, **22**, 1876–1880.

Bachthold, M., Korvink, J.G. and Baltes, H. (1996). Enhanced multipole acceleration technique for the solution of large Poisson computations. *IEEE Transactions on Computer-Aided Design of Integrated Circuits and Systems*, **15**, 1541–1546.

Barnes, J. and Hut, P. (1986). A hierarchical $\mathcal{O}(N \log N)$ force calculation algorithm. *Nature*, **324**, 446–449.

Bebendorf, M. and Grzhibovskis, R. (2006). Accelerating Galerkin BEM for linear elasticity using adaptive cross approximation. *Mathematical Methods in the Applied Sciences*, **29**, 1721–1747.

Blue, J.L. and Scheinfein, M.R. (1991). Using multipoles decreases computation time for magnetostatic self-energy. *IEEE Transactions on Magnetics*, **27**, 4778–4780.

Braun, H-B. (1994) Kramers's rate theory, broken symmetries, and magnetization reversal. *Journal of Applied Physics*, **76**, 6310–6315.

Brown, W.F. Jr. (1962). Nucleation fields of an infinitely long square ferromagnetic prism. *Journal of Applied Physics*, **33**, 3026–3031.

Brown, W.F. Jr. (1963a). *Micromagnetics*, Wiley: New York.

Brown, W.F. Jr. (1963b). Thermal fluctuations of a single domain particle. *Physical Review*, **130**, 1677–1686.

Brown, G., Schulthess, T.C., Apalkov, D.M. and Visscher, P.B. (2004). Flexible fast multipole method for magnetic simulations. *IEEE Transactions on Magnetics*, **40**, 2146–2148.

Brunotte, X., Meunier, G. and Imhoff, J-F. (1992). Finite element modeling of unbounded problems using transformations: a rigorous, powerful and easy solution. *IEEE Transactions on Magnetics*, **28**, 1663–1666.

Buchau, A., Huber, C.J., Rieger, W. and Rucker, W. M. (2000). Fast BEM computations with the adaptive multilevel fast multipole method. *IEEE Transactions on Magnetics*, **36**, 680–684.

Buchau, A., Rucker, W.M., Rain, O., *et al*. (2003). Comparison between different approaches for fast and efficient 3-D BEM computations. *IEEE Transactions on Magnetics*, **39**, 1107–1110.

Buffa, A., Maday, Y. and Rapetti, F. (2001). A sliding mesh-mortar method for a two dimensional eddy currents model of electric engines. *Mathematical Modelling and Numerical Analysis*, **35**, 191–228.

Charap, S.H., Lu, P-L. and He, Y. (1997). Thermal stability of recorded information at high densities. *IEEE Transactions on Magnetics*, **33**, 978–983.

Chen, W., Fredkin, D.R. and Koehler, T.R. (1993). A new finite element method in micromagnetics. *IEEE Transactions on Magnetics*, **29**, 2124–2128.

Cohen, S.D. and Hindmarsh, A.C. (1996). CVODE, a stiff/nonstiff ODE solver in C. *Computers in Physics*, **10**, 138–143.

Chen, Q. and Konrad, A. (1997). A review of finite element boundary techniques for static and quasi-static electromagnetic field problems. *IEEE Transactions on Magnetics*, **33**, 663–676.

Chen, W., Zhang, S. and Bertram, H.N. (1992). Energy barriers for thermal reversal of interacting single domain particles. *Journal of Applied Physics*, **71**, 5579–5584.

Davis, T.A. (2005). Algorithm 849: a concise sparse cholesky factorization package. *ACM Transactions on Mathematical Software*, **31**, 587–591.

Del Vecchio, R.M., Hebbert, R.S. and Schwee, L.J. (1989). Micromagnetics calculation for two-dimensional thin film geometries using a finite element formulation. *IEEE Transactions on Magnetics*, **25**, 4322–4329.

Demerdash, N.A., Nehl, T.W. and Fouad, F.A. (1980). Finite element formulation and analysis of three dimensional magnetic field problems. *IEEE Transactions on Magnetics*, **16**, 1092–1094.

Dittrich, R., Schrefl, T., Suess, D., *et al*. (2002). A path method for finding energy barriers and minimum energy paths in complex micromagnetic systems. *Journal of Magnetism and Magnetic Materials* , **250**, 12–19.

Dobin, A.Y. and Richter, H.J. (2006). Domain wall assisted magnetic recording. *Applied Physics Letters*, **89**, 062512.

E, W., Ren, W. and Vanden-Eijnden, E. (2002). String method for the study of rare events. *Physical Review B*, **66**, 052301.

Fetzer, J., Kurz, S. and Lehner, G. (1997). The coupling of boundary elements and finite elements for nondestructive testing applications. *IEEE Transactions on Magnetics*, **33**, 677–681.

Fischer, R. and Kronmuller, H. (1996). Static computational micromagnetism of demagnetization processes in nanoscaled permanent magnets. *Physical Review B: Condensed Matter*, **54**, 7284–7294.

Fischer, R., Leineweber, T. and Kronmuller, H. (1998). Fundamental magnetization processes in nanoscaled composite permanent magnets. *Physical Review B: Condensed Matter*, **57**, 10723–10732.

Fischer, R., Schrefl, T., Kronmuller, H. and Fidler, J. (1996). Grain-size dependence of remanence and coercive field of isotropic nanocrystalline composite permanent magnets. *Journal of Magnetism and Magnetic Materials*, **153**, 35–49.

Fredkin, D.R. and Koehler, T.R. (1990). Hybrid method for computing demagnetizing fields. *IEEE Transactions on Magnetics*, **26**, 415–417.

Fukunaga, H., Kuma, J. and Kanai, Y. (1999). Effect of strength of intergrain exchange interaction on magnetic properties of nanocomposite magnets. *IEEE Transactions on Magnetics*, **35**, 3235–3240.

Garcia-Cervera, C.J. and Roma, A. M. (2006). Adaptive mesh refinement for micromagnetics simulations. *IEEE Transactions on Magnetics*, **42**, 1648–1654.

Gardiner, C.W. (1996). *Handbook of Stochastic Methods: for Physics, Chemistry and the Natural Sciences*, Springer.

Gilbert, T.L. (1955). A Lagrangian formulation of gyromagnetic equation of the magnetization field. *Physical Review*, **100**, 1243.

Gill, P.E., Murray, W. and Wright, M.H. (1993). *Practical Optimization*, Academic Press: London.

Goll, D., Seeger, M. and Kronmuller, H. (1998). Magnetic and microstructural properties of nanocrystalline exchange coupled PrFeB permanent magnets. *Journal of Magnetism and Magnetic Materials*, **185**, 49–60.

Grasedyck, L. (2005). Adaptive recompression of H-matrices for BEM. *Computing*, **74**, 205–223.

Grasedyck, L. and Hackbusch, W. (2003). Construction and arithmetics of H-matrices. *Computing*, **70**, 295–334.

Hackbusch, W. and Nowak, Z.P. (1989). On the fast matrix multiplication in the boundary element method by panel clustering. *Numerische Mathematik*, **54**, 463–491.

He, L., Doyle, W.D., Varga, L., *et al*. (1996). High-speed switching in magnetic recording media. *Journal of Magnetism and Magnetic Materials*, **155**, 6–12.

Henkelman, G. and Jonsson, H. (2000). Improved tangent estimate in the nudged elastic band method for finding minimum energy paths and saddle points. *Journal of Chemistry and Physics*, **113**, 9978–9985.

Hertel, R. and Kronmuller, H. (2002). Finite element calculations on the single-domain limit of a ferromagnetic cube – a solution to muMAG standard problem no. 3. *Journal of Magnetism and Magnetic Materials*, **238**, 185–199.

Hines, G.V., Ridley, P.H.W. and Roberts, G.W. (2003). *Adaptive Wavelet Methods for Micromagnetics*, University of Wales, Bangor – Department of Mathematics, preprint 03.04, http://www.informatics.bangor.ac.uk/public/math/research/preprints/03/compam03.html#03.04.

Jackson, J.D. (1999). *Classical Electrodynamics*, Wiley: New York.

Kaltenbacher, M., Reitzinger, S., Schinnerl, M. *et al*. (2001). Multigrid methods for the computation of 3D electromagnetic field problems. *Compel: The International Journal for Computation and Mathematics in Electrical and Electronic Engineering*, **20**, 581–594.

Kanai, Y., Greaves, S.J., Yamakawa, K. *et al*. (2005). A single-pole-type head design for 400 gb/in2 recording. *IEEE Transactions on Magnetics*, **41**, 687–695.

Kanai, Y., Matsubara, R., Muraoka, H. and Nakamura, Y. (2001). Numerical study of a narrow-track single-pole head useful for GHz response and large field strength requirements. *IEEE Transactions on Magnetics*, **37**, 1357–1359.

Khebir, A., Kouki, A.B. and Mittra, R. (1990). Asymptotic boundary for finite element analysis of three-dimensional transmission line discontinuities. *IEEE Transactions. on Microwave Theory and Techniques*, **38**, 1427–1431.

Kikuchi, N. (1986) *Finite Element Methods in Mechanics*, Cambridge University Press: New York.

Kinderlehrer, D. and Ma, L. (1994). Computational hysteresis in modeling magnetic systems. *IEEE Transactions on Magnetics*, **30**, 4380–4382.

Kirk, K.J., Chapman, J.N. and Wilkinson, C.D.W. (1997). Switching fields and magnetostatic interactions of thin film magnetic nanoelements. *Applied Physics Letters*, **71**, 539–541.

Kneller, E.F. (1991). The exchange-spring material: a new material principle for permanent magnets. *IEEE Transactions on Magnetics*, **27**, 3588–3600.

Koehler, T.R. (1997). Hybrid FEM-BEM method for fast micromagnetic calculations. *Physica B*, **233**, 302–307.

Koehler, T.R. (2005). The mean field plus approximation. *Journal of Magnetism and Magnetic Materials*, **292**, 1–10.

Kronmüller, H. (Ed.) (2007). *General Micromagnetic Theory*, John Wiley and Sons Ltd.

Kronmüller, H. and Hilzinger, H-R. (1976). Incoherent nucleation of reversed domains in Co5Sm permanent magnets. *Journal of Magnetism and Magnetic Materials*, **2**, 3–10.

Kronmüller, H., Leineweber, T. and Hertel, R. (2000). *Intrinsic dynamics of magnetization processes in small particles*. In *16th IMACS World Congress*, Deville, M. and Owens, R. (Eds.), IMACS: Lausanne, Switzerland, ISBN 3-9522075-1-9.

Kurz, S., Fetzer, J., Lehner, G. and Rucker, W.M. (1999). Numerical analysis of 3D eddy current problems with moving bodies using BEM-FEM coupling. *Surveys on Mathematics for Industry*, **9**, 131–150.

Kurz, S., Rain, O. and Rjasanow, S. (2002). The adaptive cross-approximation technique for the 3-D boundary-element method. *IEEE Transactions on Magnetics*, **38**, 421–424.

Landau, L. and Lifshitz, E. (1935). On the theory of magnetic permeability in ferromagnetic bodies. *Physik Zeits Sowjetunion*, **8**, 153.

Leonhardt, F. and Schlaich, J. (1972). Structural design of roofs over the sports arenas for the 1972 Olympic Games: some problems of prestressed cable net structures. *The Structural Engineering and Mechanics*, **50**, 113–119.

Lindholm, D.A. (1984). Three-dimensional magnetostatic fields from point-matched integral equations with linearly varying scalar sources. *IEEE Transactions on Magnetics*, **MAG-20**, 2025–2032.

Liu, Z.J., Li, J.T., Long, H.H., *et al*. (2005). Distribution of slanted write field for perpendicular recording heads with shielded pole. *IEEE Transactions on Magnetics*, **41**, 2908–2910.

Liu, Z.J., Long, H.H., Ong, E.T., *et al*. (2006). Dynamic simulation of high-density perpendicular recording head and media combination. *IEEE Transactions on Magnetics*, **42**, 943–946.

Long, H.H., Ong, E.T., Liu, Z.J. and Li, E.P. (2006). Fast Fourier transform on multipoles for rapid calculations of magnetostatic fields. *IEEE Transactions on Magnetics*, **42**, 295–300.

Manaf, A., Leonowicz, M., Davies, H.A. and Buckley, R.A. (1991). Effect of grain size and microstructure on magnetic properties of rapidly solidified Fe82.4Nd13.1B4.5 alloy. *Journal of Applied Physics*, **70**, 6366–6368.

Mansuripur, M. and Giles, R. (1988). Demagnetizing field computation for dynamic simulation of the magnetization reversal process. *IEEE Transactions on Magnetics*, **24**, 2326–2328.

Miles, J.J. and Middleton, B.K. (1991). A hierarchical micromagnetic model of longitudinal thin film media. *Journal of Magnetism and Magnetic Materials*, **95**, 99–108.

Nabros, K. and White, J. (1991). FastCap: a multipole accelerated 3-D capacitance extraction program. *IEEE Transactions on Computer-Aided Design of Integrated Circuits and Systems*, **10**, 1447–1459.

Nakatani, Y., Uesaka, Y. and Hayashi, N. (1989). Direct solution of the Landau-Lifshitz-Gilbert equation for micromagnetics. *Japanese Journal of Applied Physics*, **28**, 2485–2507.

Neel, L. (1949). Théorie du traînage magnétique des ferromagnétiques en grains fins avec applications aux terres cuites. *Annals of Géophysics*, **5**, 99–136.

Preis, K., Bardi, I., Biro, O., *et al*. (1992) Different finite element formulations of 3D magnetostatic fields. *IEEE Transactions on Magnetics*, **28**, 1056–1059.

Press, W.H., Teukolsky, S.A., Vetterling, W.T. and Flannery, B.P. (1997). *Numerical Recipes in Fortran 77: The Art of Scientific Computing*, Cambridge University Press.

Ramaswamy, D., Ye, W., Wang, X. and White, J. (1999). Fast algorithms for 3-D simulation. *Journal of Modeling and Simulation of Microsystems*, **1**, 77–82.

Ridley, P.H.W., Spargo, A.W., Hines, G.V. and Roberts, G.W. (2003). Modeling a perpendicular recording medium using a variational method. *Journal of Applied Physics*, **93**, 7453–7455.

Ritz, W. (1909). Über eine neue methode zur Lösung gewisser variations probleme der mathematischen physik. *Journal für die Reine und Angewandte Mathematik*, **135**, 1–61.

Saad, Y. (2003). *Iterative Methods for Sparse Linear Systems*, SIAM: Philadelphia.

Schabes, M.E. (1991). Micromagnetic theory of non-uniform magnetization processes in magnetic recording particles. *Journal of Magnetism and Magnetic Materials*, **95**, 249–288.

Schellbach, K. (1851). Probleme der variationsrechnung. *Journal für die Reine und Angewandte Mathematik*, **41**, 293–363.

Schenk, O. and Gärtner, K. (2004). Solving unsymmetric sparse systems of linear equations with PARDISO. *Journal of Future Generation Computer Systems*, **20**, 475–487.

Schneiders, R. (2007). *Mesh Generation and Grid Generation on the Web*, last accessed, January 2007 http://www-users.informatik.rwth-aachen.de/∼roberts/meshgeneration.html.

Scholz, W. and Batra, S. (2005). Micromagnetic simulation of headfield and write bubble dynamics in perpendicular recording. *IEEE Transactions on Magnetics*, **41**, 2839–2844.

Scholz, W., Fidler, J., Schrefl, T., *et al*. (2003). Scalable parallel micromagnetic solvers for magnetic nanostructures. *Computational Material Science*, **28**, 366–383.

Schrefl, T. and Fidler, J. (1998). Modelling of exchange-spring permanent magnets. *Journal of Magnetism and Magnetic Materials*, **177**, 970–975.

Schrefl, T. and Fidler, J. (1999). Finite element modeling of nanocomposite magnets. *IEEE Transactions on Magnetics*, **35**, 3223–3228.

Schrefl, T., Fidler, J. and Kronmüller, H. (1994a). Nucleation fields of hard magnetic particles in 2D and 3D micromagnetic calculations. *Journal of Magnetism and Magnetic Materials*, **138**, 15–30.

Schrefl, T., Fidler, J. and Kronmüller, H. (1994b). Remanence and coercivity in isotropic nanocrystalline permanent magnets. *Physical Review B*, **49**, 6100–6110.

Schrefl, T., Fischer, R., Fidler, J. and Kronmuller, H. (1994c). Two- and Three-dimensional calculation of remanence enhancement of rare-earth based composite magnets (invited). *Journal of Applied Physics*, **76**, 7053–7058.

Schrefl, T., Schabes, M.E., Suess, D. and Stehno, M. (2004). Dynamic micromagnetic write head fields during magnetic recording in granular media. *IEEE Transactions on Magnetics*, **40**, 2341–2343.

Schrefl, T., Schabes, M.E., Suess, D., *et al*. (2005). Partitioning of the perpendicular write field into head and SUL contributions. *IEEE Transactions on Magnetics*, **41**, 3064–3066.

Schrefl, T., Scholz, W., Suss, D. and Fidler, J. (2001). Computational micromagnetics: prediction of time dependent and thermal properties. *Journal of Magnetism and Magnetic Materials*, **226**, 1213–1219.

Sharrock, M.P. (1994). Time dependence of switching fields in magnetic recording media (invited). *Journal of Applied Physics*, **76**, 6413–6418.

Stoner, E.C. and Wohlfarth, E.P. (1948). A mechanism of magnetic hysteresis in heterogeneous alloys. *Philosophical Transactions of the Royal Society* , **240**, 599–642.

Suess, D., Schrefl, T., FÄhler, S., *et al*. (2005). Exchange spring media for perpendicular recording. *Applied Physics Letters*, **87**, 012504.

Suess, D., Tsiantos, V., Schrefl, T., *et al*. (2002) Time resolved micromagnetics using a preconditioned finite element method. *Journal of Magnetism and Magnetic Materials* , **248**, 298–311.

Sun, J. and Monk, P. (2006). An adaptive algebraic multigrid algorithm for micromagnetism. *IEEE Transactions on Magnetics*, **42**, 1643–1647.

Süß, D., Schrefl, T., Fidler, J. and Chapman, J.N. (1999). Micromagnetic simulation of the long-range interaction between NiFe nano-elements using BE-method. *Journal of Magnetism and Magnetic Materials* , **196**(197), 617–619.

Swartzentrauber, P.N. and Sweet, R.A. (1979). Algorithm 541: efficient fortran subprograms for the solution of separable elliptic partial differential equations. *ACM Transactions on Mathematical Software*, **5**, 352–364.

Takano, K. (2005). Micromagnetic-FEM models of a perpendicular writer and reader. *IEEE Transactions on Magnetics*, **41**, 696–701.

Vacus, O. and Monk, P. (2001). Accurate discretization of a nonlinear micromagnetic problem. *Computer Methods in Applied Mechanics and Engineering*, **190**, 5243–5269.

Victora, R.H. and Shen, X. (2005). Composite media for perpendicular magnetic recording. *IEEE Transactions on Magnetics*, **41**, 537–542.

Weller, D. and Moser, A. (1999). Thermal effect limits in ultrahigh-density magnetic recording. *IEEE Transactions on Magnetics*, **35**, 4423–4439.

Yang, B. and Fredkin, D.R. (1998). Dynamical micromagnetics by the finite element method. *IEEE Transactions on Magnetics*, **34**, 3842–3852.

Zheng, J., Li, Z-F. and Qian, X-N. (1999). An efficient solver for the three-dimensional capacitance of the interconnects in high speed digital circuit by the multiresolution method of moments. *IEEE Transactions on Advanced Packaging*, **22**, 9–15.

Zienkiewicz, O.C., Lyness, J. and Owen, D.R.J. (1977). Three-dimensional magnetic field determination using a scalar potential – a finite element solution. *IEEE Transactions on Magnetics*, **13**, 1649–1656.

Magnetization Dynamics Including Thermal Fluctuations: Basic Phenomenology, Fast Remagnetization Processes and Transitions Over High-energy Barriers

Dmitri V. Berkov
Innovent Technology Development, Jena, Germany

1 DETERMINISTIC LLG EQUATION AND TREATMENT OF THE ENERGY DISSIPATION IN MICROMAGNETICS

1.1 Origin and limitations of the standard LLG equation

An equation of motion for the magnetization of a ferromagnet, known as the Landau–Lifshitz equation

Handbook of Magnetism and Advanced Magnetic Materials. Edited by Helmut Kronmüller and Stuart Parkin. Volume 2: *Micromagnetism*. ISBN: 978-0-470-02217-7.

$$\frac{\mathrm{d}\mathbf{M}}{\mathrm{d}t} = -\gamma_0 \cdot [\mathbf{M} \times \mathbf{H}^{\mathrm{eff}}] - \gamma_0 \cdot \frac{\lambda}{M_{\mathrm{S}}} \cdot [\mathbf{M} \times [\mathbf{M} \times \mathbf{H}^{\mathrm{eff}}]] \quad (1)$$

has been introduced 1935 by L.D. Landau and E.M. Lifshitz in their pioneering work (Landau and Lifshitz, 1935) devoted to the phenomenological evaluation of the permeability tensor of ferromagnets.

The first term in (1) describes the magnetization precession of the total effective field and can be derived in frames of a general phenomenological theory which is based on the assumption that for low temperatures and slowly (in space in time) varying magnetization the magnitude of the magnetization vector $\mathbf{M} = M_{\mathrm{S}}$ is conserved. The latter statement, in turn, follows from the assumption that the equilibrium value of M_{S} is fixed by the exchange interaction, which is assumed to be the strongest interaction in a ferromagnet, which is definitely the case for all 'normal' ferromagnetic materials. Comparison of the equation (1) with the precession equation for a 'free' magnetic moment in the small damping limit provides the value $\gamma_0 = g|e|/2m_{\mathrm{e}}c$ which is the so-called gyromagnetic ratio. The g-factor in this definition, being $g = 2$ for a free electron, may slightly vary around this value dependent on the concrete material. Usually at least the combination $\gamma_0 M_{\mathrm{S}}$ may be measured with a high accuracy using FMR, so that the treatment of the first term in (1) is quite straightforward.

In contrast to the precession term, the handling of the energy dissipation processes in ferromagnets turned out to be a highly complicated issue. The double vector product term in (1) was chosen in the original paper (Landau

and Lifshitz, 1935) basing on the purely phenomenological reason that energy dissipation processes (i) should drive the magnetization toward the effective field direction (in the minimal energy state the magnetization is directed along $\mathbf{H}^{\text{eff}}$), but (ii) the magnetization magnitude M_S should still remain constant. The second term in (1) obviously satisfies these both conditions, being directed toward the effective field and perpendicular to the magnetization.

It was pointed already by the authors of (Landau and Lifshitz, 1935) themselves that the damping form suggested by (1) is by neither the only possible nor the most general one. First of all, it can be seen by a sole inspection of this equation that *if* we understand the coefficient before the damping term λ in a usual way, that is, as a parameter whose value is proportional to the intensity of the energy dissipation processes in our system, then (1) cannot be used to describe the magnetization motion for moderate and large damping. The reason for this limitation can be seen immediately if we consider the overdamped regime ($\lambda \geq 1$) where the magnetic moment motion is dominated by the dissipation term. In this case, the basic equation (1) predicts that the magnetization relaxation is getting *faster* when the damping value *increases* which is in a strong contradiction with a physical picture of damping.

This circumstance was realized already by Landau and Lifshitz themselves, who have pointed out that their equation may be used in the precession-dominated regime ($\lambda \ll 1$) only. The first phenomenological equation which qualitatively, reasonably describes the magnetization motion in the whole dissipation range was suggested by Gilbert (1955):

$$\frac{\mathrm{d}\mathbf{M}}{\mathrm{d}t} = -\gamma_0 \left[\mathbf{M} \times \left(\mathbf{H}^{\text{eff}} - \frac{\alpha}{M_S} \cdot \frac{\mathrm{d}\mathbf{M}}{\mathrm{d}t} \right) \right] \tag{2}$$

Gilbert has derived this equation starting with the equation of the undamped magnetization precession rewritten in the Lagrangian formalism. In this formalism, the damping can be rigorously added to the system using the so-called Rayleigh dissipation function (Landau Lifshitz, 1981). Transforming the resulting equation back to the force-torque form, Gilbert arrived at the equation (2), where the damping is represented by the second term in the round parenthesis with α being the damping constant.

The dissipation term form introduced in the Gilbert formulation of the magnetization dynamics can also be understood in the following way. First, the energy damping is supposed to slow down the precession of the magnetic moment, so the term describing the energy dissipation can be added directly to the effective field which is responsible for the moment precession and defines its frequency via $\omega = \gamma_0 H^{\text{eff}}$. Second, the magnitude of this term should be proportional to the relaxation speed, analogously to a standard (e.g., hydrodynamical) viscous damping. And finally, the added damping term should still conserve the magnetization magnitude. All these three conditions are satisfied by the dissipation term (2), which is called the *Gilbert* damping. It is straightforward to show (Kikuchi, 1956) that this formulation leads to the intuitively expected dependence of the switching time (relaxation speed) on the damping α, where the switching time is large both for small damping (precession-dominated regime, the moment performs many precession cycles before switching) and large damping (magnetic moment does not precess, but moves slowly owing to a large α value).

The Gilbert equation in its native form (2) is highly inconvenient to use, because it contains the time derivative of the magnetization on both sides. Fortunately, it can be easily cast into an explicit form ($\mathrm{d}\mathbf{M}/\mathrm{d}t$ on the left-hand side only) by multiplying both sides by the vector $\mathbf{M}$, transforming the double vector products using the standard vector algebra rule and utilizing the conservation of the magnetic moment magnitude as $(\mathbf{M}\cdot\mathbf{M}) = M_S^2$. The final result

$$\frac{\mathrm{d}\mathbf{M}}{\mathrm{d}t} = -\frac{\gamma_0}{1+\alpha^2} \cdot [\mathbf{M} \times \mathbf{H}^{\text{eff}}] - \frac{\gamma_0}{M_S} \cdot \frac{\alpha}{1+\alpha^2} \cdot [\mathbf{M} \times [\mathbf{M} \times \mathbf{H}^{\text{eff}}]] \tag{3}$$

has the form of the Landau–Lifshitz equation (1) if we replace the gyromagnetic ratio γ_0 by $\gamma_0/(1+\alpha^2)$ and put $\alpha = \lambda$. It is also evident that in the small damping limit both equations coincide if $\alpha = \lambda$, as it should be.

Summarizing, we point out that the two most widely used equations for the description of the damped magnetization motion are formally equivalent. However, the physics involved in the definition of the damping coefficient is quite different: Whereas in the Gilbert form (2) the value of the damping parameter α can be assumed to be proportional to the intensity of the energy dissipation processes which slow down the magnetic moment motion, for the Landau–Lifshitz form it is true only in the small damping limit. Although this issue has been discussed in the past several times (see in addition to the original papers of Landau *et al*. and Gilbert, e.g., also comments in Kikuchi (1956) and Mallinson (1987)), everybody who is familiar with the contemporary literature will surely agree that recalling them once more will at least not harm. The difference mentioned in the preceding text tends to be forgotten simply because for the overwhelming majority of applications (including, but limited to the magnetic random access memory (MRAM) technology and high density storage media) the case of the small damping is of major interest. However, this circumstance detracts no way from the importance of the physical meaning of the parameters entering into these equations.

We conclude this subsection with the following important remark. As soon as we have introduced the restriction $\mathbf{M} = M_S$, the magnetization is allowed only to rotate so that *any* magnetization change $\Delta\mathbf{M}$ should be perpendicular to $\mathbf{M}$ itself. Hence, one can gain the impression, that the equation (1) (or its equivalent forms) is the most general form of the equation of motion in this situation: from a purely mathematical point of view (1) can be considered as an expansion of the magnetization time derivative (which should lie in the plane perpendicular to the magnetization) over the two vectors $[\mathbf{M} \times \mathbf{H}]$ and $[\mathbf{M} \times [\mathbf{M} \times \mathbf{H}]]$ which form an orthogonal basis in this plane. Coefficients γ and λ can then be viewed simply as the expansion coefficients of an arbitrary allowed magnetization change in this basis. However, from the physical point of view the equation (1) and its analogues contain a much stronger assumption than the trivial statement about the existence of such an expansion. Namely, the form (1) means that the expansion coefficients are *time-independent scalar* variables, so that the magnetization motion including damping can be described on a phenomenological level with two *scalar* parameters whose values do *not* depend on the instantaneous magnetization configuration. As we shall see in the subsequent text, this is not necessarily true. However, in many cases the combined Landau–Lifshitz–Gilbert (LLG) equation (3) provides a convenient and at least semiquantitatively adequate description of the damped magnetization precession.

Concluding this subsection, we would like to briefly mention possible extensions of the standard LLG-equation (3) to the case, when the magnetization magnitude is *not* conserved, which may be particularly interesting for temperatures not very far from the Curie point. One of the possibilities to account for a change of the magnetization *value* on the mesoscopic level is the insertion into the LLG equation of the *longitudinal* relaxation term. This question was discussed already by Aharoni in the 1980s. For the recent development, including a more detailed discussion of possible forms of such an additional term, other physical problems concerning this topic (e.g., calculation of the corresponding relaxation time) and some simulation results obtained with such a generalized LLG equation, we refer the reader to the publications (Garanin, 1997; Smith, 2002; Grinstein and Koch, 2003; Garanin and Chubykalo-Fesenko, 2004).

1.2 To the possibility of alternative forms of the damping term

Rigorous *evaluation* of the damping constant entering the LLG equation is one of the most complicated problems of the modern solid-state magnetism not only due to a large variety of the damping mechanisms in ferromagnets, but also because in most cases it is really difficult to separate the contributions of these mechanisms to the energy dissipation rate measured experimentally (e.g., using FMR). To the mechanisms mentioned in the preceding text belong the spin-lattice relaxation (magnon-phonon interaction), two-and many-magnon processes, magnon-impurity interactions, magnon scattering on the surface and interface defects and so on, we refer the interested reader to the contributions in the Volume 1 of this Handbook.

For this reason, aphenomenological approach which could provide nontrivial conclusions about the form of the damping term and supply methods for the evaluation of the damping value beyond the simplest LLG phenomenology, but still valid for a relatively broad class of the energy dissipation processes is in principle highly desirable. However, a development of such an approach is a delicate matter, requiring careful analysis of each step of a corresponding 'general' procedure.

As an example of a such an attempt we would like to analyze a recently developed and meanwhile widely cited approach of Safonov and Bertram (2003) and references therein, who suggested to use the *normal mode analysis* of a magnetic system coupled to a thermal bath. Up to a certain level such an analysis can be performed without specifying the concrete energy dissipation mechanism, but merely employing general assumptions concerning the Hamilton function, which describes the interaction between the magnetization and thermal reservoir.

In the simplest case of a uniformly magnetized ferromagnetic particle, the normal mode analysis starts with the Taylor expansion of the magnetic energy density E/V over small magnetization variations M_x and M_y

$$\frac{E}{V} = \frac{H_{0x}}{2M_S} M_x^2 + \frac{H_{0y}}{2M_S} M_y^2 \tag{4}$$

near the equilibrium moment orientation $\mathbf{M}_0$, whereby the $0z$-axis is directed along $\mathbf{M}_0$. Dimensionless coefficients before the squares of magnetization components $M_{x(y)}$ in (4) can be written in the form $H_{0x(y)}/M_S$, where parameters $H_{0x(y)}$ (which describe the curvature of the energy surface for the equilibrium magnetization state) have the dimension of a field [1].

Any equation of motion which describes the magnetization precession in terms of components M_x and M_y leads to the coupling of their time-dependencies and is thus unsuitable for the identification of the system normal modes. For this reason, Safonov and Bertram proceed by introducing the (complex-valued) functions $a(t) \sim M_x + iM_y$ and $a^*(t) \sim M_x - iM_y$. These functions are fully

analogous to the corresponding quantum-mechanical operators which increase/reduce the z projection of the angular momentum, but the formalism developed by Safonov and Bertram is a purely classical one. The functions $a(t)$ are required to describe the interaction of a magnetic system with a thermal bath, because they appear in the corresponding interaction term of a Hamiltonian; this is the reason why this intermediate transformation should be explicitly introduced. The second transformation $a(t) \sim uc(t) + vc^*(t)$ and $a^*(t) \sim uc^*(t) + vc(t)$ diagonalizes the Hamilton function, which becomes H: $\omega_0 c^* c$, with $\omega_0 = \gamma\sqrt{H_{0x}H_{0y}}$ being the FMR frequency of our system. Equation of motion for these new 'coordinates' are uncoupled, that is, $\dot{c}(t) = -i\omega_0 c(t)$ and $\dot{c}^*(t) = i\omega_0 c^*(t)$.

At the next step the interaction between the *normal modes* of the magnetization oscillations and a thermal bath described *as a set of harmonic oscillators* is introduced via the insertion of a linear coupling between functions $a(t)$ and the thermal bath normal modes b_k into the system Hamiltonian (see Safonov and Bertram, 2003 for details):

$$H \sim E_{\text{mag}} + E_{\text{bath}} + \sum\nolimits_k \left[G_k(ab_k^* + a^* b_k) + F_k(ab_k + a^* b_k^*)\right] \tag{5}$$

where E_{mag} and E_{bath} are the energies of a magnetic system and thermal bath only.

Transformation of the interaction term to the variables $c(t)$ and $c^*(t)$, solution of the resulting dynamic equations for the thermal bath modes b_k and substitution of the expression for b_k into the dynamic equations for $c(t)$ leads to the equation

$$\frac{\mathrm{d}c}{\mathrm{d}t} = -i(\omega_0 + \Delta\omega)c - \eta c + f(t) \tag{6}$$

which describes a damped harmonic oscillator under the influence of a random force (noise) $f(t)$. The damping constant η in this formalism

$$\eta = \pi \left|\tilde{G}_k\right|^2 D(\omega_0) \tag{7}$$

is proportional to (i) the squared interaction coefficient $\tilde{G}_k = uG_k + vF_k$ of a magnetic system with the bath normal mode having the same frequency ω_0 as the undisturbed magnetic system and (ii) the density of states $D(\omega_0)$ of a thermal bath at this frequency.

An important conclusion which can be drawn from the consideration in the preceding text is that in this phenomenological model the magnetization damping present in the Gilbert or Landau–Lifshitz equation of motion for the components of the system magnetization $\mathbf{M}(t)$

$$\frac{\mathrm{d}\mathbf{M}}{\mathrm{d}t} = -\gamma_0 \left[\mathbf{M} \times \left(\mathbf{H}^{\text{eff}} - \frac{\hat{\alpha}}{M_{\text{S}}} \cdot \frac{\mathrm{d}\mathbf{M}}{\mathrm{d}t}\right)\right] \tag{8}$$

cannot be reduced anymore to a scalar variable, but is a tensor

$$\hat{\alpha} = \frac{\eta}{\omega_0^2} \begin{pmatrix} H_{0x} & 0 & 0 \\ 0 & H_{0y} & 0 \\ 0 & 0 & 0 \end{pmatrix} \tag{9}$$

where the diagonal components of this tensor are proportional to the parameters $H_{0\text{x(y)}}$ characterizing the energy surface curvature near the equilibrium magnetization state (expression (9) may be verified by rewriting M_x and M_y via the functions $c(t)$ and $c*(t)$ and substituting the resulting expressions into (8), thus arriving at the equation (6)). This tensor reduces to a scalar only for a symmetric energy minimum with $H_{0\text{x}} = H_{0y}$, which is rather an exception.

The formalism outlined in the preceding text can be extended to magnetic systems with arbitrarily nonhomogeneous equilibrium magnetization configuration (Bertram, Safonov and Jin, 2002). After the discretization of a ferromagnetic body into N finite elements the eigenmodes of its magnetization state can be identified using the equation of motion *without* damping $\dot{\mathbf{M}}_i = -\gamma[\mathbf{M}_i \times \mathbf{H}_i^{\text{eff}}]$. Expanding the system state magnetization vector $\mathbf{T} = (\mathbf{M}_1, \ldots, \mathbf{M}_i, \ldots, \mathbf{M}_N)$ the near the equilibrium state one obtains a set of coupled equations $\dot{T} = -\gamma\hat{\mathbf{H}}\cdot\mathbf{T}$ where tensor $\hat{\mathbf{H}}$ consists of corresponding effective field components. Diagonalization of this tensor provides the eigenvectors $\mathbf{c}_i$, which give the spatial distribution of the i-th eigenmode and eigenvalues, which are proportional to the mode oscillation frequencies ω_i. Further analysis proceeds then as in the simplest case discussed in the preceding text.

However, the procedure sketched in the preceding text, which leads to the conclusion that the damping in the LLG equation *should* be a tensor, is incorrect, as shown by Smith (2002). Taking into account that the question about the form of the phenomenological damping term is crucially important for micromagnetic calculations, we shall briefly reproduce here the argumentation of Smith, replacing his simple illustrative example by an even simpler one.

To find out where is the flaw in the argumentation of Bertram and Safonov, we consider the simplest possible mechanical system with more than one eigenmode, that is, two particles of equal masses m, each of which is attached to a wall via a spring with the stiffness constant k. Particles are placed in the *isolated* reservoirs filled with a fluid with

different viscosities (this is the only difference between the particles) and coupled via a spring with the stiffness k_c. If particle coordinates x_1 and x_2 in the mechanical equilibrium are set to zero, the corresponding equations of motion are

$$m\ddot{x}_1 = -\eta_1\dot{x}_1 - kx_1 + k_c(x_2 - x_1) + F_1^L \tag{10}$$

$$m\ddot{x}_2 = -\eta_2\dot{x}_2 - kx_2 - k_c(x_2 - x_1) + F_2^L \tag{11}$$

Here, the friction coefficients η_1 and η_2 are different owing to different fluid viscosities. Random thermal forces F^{L} responsible for the Brownian motion of the particles are obviously *uncorrelated* (because the reservoirs with the particles are isolated from each other), δ correlated in time and their mean-square values are proportional to the system temperature T.

The determination of the system normal modes should be performed in a standard way, using the equations (10) and (11) without dissipative and fluctuation forces. In this very simple case, it is enough to add and subtract these equations in order to find out that the normal modes are $x_+^{\mathrm{n}} = (x_1 + x_2)/\sqrt{2}$ and $x_-^{\mathrm{n}} = (x_1 - x_2)/\sqrt{2}$, so that the transformation matrix U between the vector of the particle coordinates $\mathbf{x}$ and the normal modes of our system $\mathbf{x}^{\mathrm{n}}$ (i.e., $\mathbf{x} = U\cdot\mathbf{x}^{\mathrm{n}}$) is

$$U = \frac{1}{\sqrt{2}}\begin{bmatrix} 1 & 1 \\ 1 & -1 \end{bmatrix} \tag{12}$$

Next, we apply this transformation to the initial equations of motion system, (10) and (11), written in the matrix form

$$M\ddot{\mathbf{x}} = -\mathrm{H}\dot{\mathbf{x}} + K\mathbf{x} + F^{\mathrm{L}} \tag{13}$$

where the mass and friction matrices are diagonal ($M = diag(m, m)$, $\mathrm{H} = diag(\eta_1, \eta_2)$), and the stiffness matrix K has both diagonal $K_{11} = K_{22} = -(k + k_c)$ and off-diagonal elements $K_{12} = K_{21} = k_c$. The transformation to the normal modes proceeds in the usual way: we insert the unit matrix in the form $I = U\cdot U^{\mathrm{T}}$ into the matrix-vector products into the equation (13) and multiply it by the matrix U^{T} from the left. Using the relation $U^{\mathrm{T}}\mathbf{x} = \mathbf{x}^{\mathrm{n}}$ and performing the matrix multiplications $\tilde{M} = U^{\mathrm{T}}MU = M$, $\tilde{\mathrm{H}} = U^{\mathrm{T}}\mathrm{H}U$, $\tilde{K} = U^{\mathrm{T}}KU$, we arrive at the *equations of motion for the normal modes*:

$$\begin{bmatrix} m & 0 \\ 0 & m \end{bmatrix}\cdot\begin{bmatrix} \ddot{x}_+^{\mathrm{n}} \\ \ddot{x}_-^{\mathrm{n}} \end{bmatrix} = -\frac{1}{2}\begin{bmatrix} \eta_1 + \eta_2 & \eta_1 - \eta_2 \\ \eta_1 - \eta_2 & \eta_1 + \eta_2 \end{bmatrix}\cdot\begin{bmatrix} \dot{x}_+^{\mathrm{n}} \\ \dot{x}_-^{\mathrm{n}} \end{bmatrix} + \begin{bmatrix} -k & 0 \\ 0 & -(k + 2k_c) \end{bmatrix}\cdot\begin{bmatrix} x_+^{\mathrm{n}} \\ x_-^{\mathrm{n}} \end{bmatrix} + \begin{bmatrix} F_+^{\mathrm{n,L}} \\ F_-^{\mathrm{n,L}} \end{bmatrix} \tag{14}$$

where the vector of fluctuation forces $\mathbf{F}^{\mathrm{n,L}} = U^{\mathrm{T}}\cdot\mathbf{F}^{\mathrm{L}}$ now contains the corresponding forces for the normal modes defined as $F_+^{\mathrm{n,L}} = (F_1^{\mathrm{L}} + F_2^{\mathrm{L}})/\sqrt{2}$, $F_-^{\mathrm{n,L}} = (F_1^{\mathrm{L}} - F_2^{\mathrm{L}})/\sqrt{2}$.

It can be immediately seen from equation (14) that the equations of motion for the normal modes which include the damping term are *correlated* owing to the non-diagonal character of the transformed damping matrix $\tilde{\mathrm{H}} = U^{\mathrm{T}}\mathrm{H}U$. This means that the simple phenomenological addition of the *uncoupled* damping terms like the term $-\eta\cdot c$ in (6) is incorrect. This term in (6) results from writing the equations of motion for the coupled system 'magnetic body + thermal bath' directly in terms of the normal modes (see (5)), which hence turns out to be incorrect at least when the coupling of these modes and correlation properties of corresponding random (fluctuation) forces are important. The conclusion (9) about the obligatory tensor form of the damping in the LLG equation, being a direct consequence of the *uncoupled* damping of *normal modes*, is for this reason erroneous. A detailed extension of this discussion to the case of micromagnetic equations can be found in (Smith, 2002).

Another very important point is that the addition of *uncoupled* fluctuation forces into the equations of motion for *the normal modes* (instead of using corresponding equations for real particles) as it is done in equation (6) is also physically incorrect. Namely, if thermal forces acting on the *normal modes* would be indeed uncorrelated, then the corresponding forces acting on *real* particles (obtained via the backward transformation as $\mathbf{F}^L = U\cdot\mathbf{F}^{\mathrm{n,L}}$) would be correlated, which is completely unphysical. This is evident at least in the case considered in the preceding text where particles are placed into *separate isolated* reservoirs. Taking into account that the random (Brownian) forces are caused by the chaotic motion of the fluid molecules, any correlations between these forces in two separate isolated fluid volumes are obviously absent.

The discussion in the preceding text should remind the reader, that although normal modes of the system are doubtlessly a very useful physical concept, one should not forget that initially dynamical equations must be written for real particles (magnetic moments) where the physical meaning of various terms in such equations can be directly examined.

The last comment in order is that the argumentation line presented here does *not* mean that the tensor form of the damping term is *forbidden*. As already mentioned by Smith (2002), this only means that any conclusion about the specific

form of the damping should be based on the consideration of the corresponding physical mechanism responsible for the energy dissipation.

2 STOCHASTIC LLG EQUATION: CHOICE OF THE STOCHASTIC CALCULUS

2.1 General introduction to the solution of SDEs

Equation-of-motion simulations of the remagnetization dynamics *including* thermal fluctuations require, in contrast to the case $T = 0$, the solution of stochastic differential equations (SDE), which is by far more difficult. A simple example of such stochastic (Langevin) equations arising in the theory of stochastic processes is the equation of motion for a particle in a viscous medium under the influence of a deterministic force F_{det} and thermal fluctuations represented via the random (or Langevin) force ξ_{L}(η denotes the friction coefficient)

$$\dot{x} = \frac{1}{\eta} F_{\mathrm{det}}(t) + a(x,t)\cdot\xi_{\mathrm{L}}(t) \tag{15}$$

$\xi_{\mathrm{L}}(t)$ is usually assumed to be a random Gaussian variable, δ correlated in time:

$$\langle \xi(t) \rangle = 0, \quad \langle \xi(0)\cdot\xi(t) \rangle = 2D\cdot\delta(t) \tag{16}$$

with the noise power $D \sim T$. The 'good' function $a(x,t)$ contains the coordinate- and time-dependencies of the noise characteristics.

The problem with the equations of this kind is that they can *by no means* be interpreted as the 'usual' differential equations (DE). Namely, any attempt to integrate equation (15) as an ordinary DE leads to the integral

$$W(t) = \int_0^t \xi(t')\cdot \mathrm{d}t' \tag{17}$$

which obviously represents a random process, because its integrand is a random variable. From the correlation properties (16) it follows that $W(t)$ is the standard Wiener process (Brownian motion) Gardiner (1997). This process is *not* differentiable – the ratio $(W(t+\Delta t) - W(t))/\Delta t$ diverges in the limit $\Delta t \to 0$ almost surely. Because the derivative $\mathrm{d}W/\mathrm{d}t = \xi(t)$ does not exist, in the usual sense the equation (16) including this derivative *does not exist* also and hence cannot be interpreted as a 'normal' ordinary DE.

The proper way to assign a mathematically correct meaning to the equations like (15) is to introduce the differential of the Wiener process $\mathrm{d}W$ (which is usually viewed by a physicist as a replacement of the product $\xi(t)\mathrm{d}t$) and to define the corresponding integral

$$I = \int a(x,t)\cdot \mathrm{d}W(t) \tag{18}$$

analogously to the standard Riemann–Stieltjes integrals as the limit of partial sums

$$\begin{aligned} I &= \lim_{n\to\infty} \sum_{i=1}^{n} a(x(\tau_i), \tau_i)\cdot \Delta W(\Delta t_i) \\ &= \lim_{n\to\infty} \sum_{i=1}^{n} a(x(\tau_i), \tau_i)\cdot [W(t_i) - W(t_{i-1})] \end{aligned} \tag{19}$$

with the points τ_i where the integrand values are evaluated lie inside the interval $[t_{i-1}, t_i]$.

This limit, being understood in the mean-square sense (see any handbook on stochastic calculus) is convenient enough to develop the complete analysis of such *stochastic* integrals. The real problem is that (in a heavy contrast to the standard analysis) this limit itself – and not just the values of partial sums in (19) – *depends on the choice of the intermediate points* τ_i (see Chapter 3 in Gardiner (1997) for a simple but impressive example).

The only way to cope with this problem is to introduce some standard choices of the intermediate points and to find the best choice from the physical point of view. The two standard choices – (i) $\tau_i = t_{i-1}$ coincide with the *left* points of the intervals (*Ito* stochastic calculus) and (ii) $\tau_i = (t_{i-1} + t_i)/2$ are in the *middle* of the intervals (*Stratonovich* interpretation) – lead to *different* solutions if the noise in a stochastic equation is *multiplicative* – that is, the random term is *multiplied* by some function of the system variables. In this case, usually the *Stratonovich* interpretation provides physically correct results, recovering, for example, some important properties of physical random processes obtained using more general methods (Gardiner, 1997).

In micromagnetics, the most common way to include thermal fluctuation effects into the consideration is the addition of the so-called 'fluctuation field' to the deterministic effective field in equation (LLG). This leads to the *stochastic* LLG equation (Brown, 1963b) for the magnetic moment motion.

$$\begin{aligned} \frac{\mathrm{d}\mathbf{M}}{\mathrm{d}t} &= -\gamma\cdot[\mathbf{M}\times(\mathbf{H}^{\mathrm{det}} + \mathbf{H}^{\mathrm{fl}})] - \lambda\cdot\frac{\gamma}{M_{\mathrm{S}}} \\ &\quad \cdot[\mathbf{M}\times[\mathbf{M}\times(\mathbf{H}^{\mathrm{det}} + \mathbf{H}^{\mathrm{fl}})]] \end{aligned} \tag{20}$$

Here, the *deterministic* effective field $\mathbf{H}^{\mathrm{det}}$ acting on the magnetization includes all the standard micromagnetic contributions (external, anisotropy, exchange and magnetodipolar interaction field). Analogous to the random force in

the mechanical equation (15), Cartesian components of the fluctuation field $\mathbf{H}_i^{\mathrm{fl}}$ are usually assumed to be δ correlated in space and time (Brown, 1963b)

$$\langle H_{\xi,i}^{\mathrm{fl}} \rangle = 0 \quad \langle H_{\xi,i}^{\mathrm{fl}}(0) \cdot H_{\psi,j}^{\mathrm{fl}}(t) \rangle = 2D \cdot \delta(t) \cdot \delta_{ij} \cdot \delta_{\xi\psi} \tag{21}$$

where i, j are the discretization cell (magnetic moment) indices and $\xi, \psi = x, y, z$. The noise power D evaluated using the fluctuation-dissipation theorem (see subsequent text for a detailed discussion) is proportional to the system temperature T and depends on γ and the damping constant λ:

$$D = \frac{\lambda}{1+\lambda^2} \cdot \frac{kT}{\gamma M_{\mathrm{S}} \Delta V} \tag{22}$$

We note in passing that the fluctuation field $\mathbf{H}^{\mathrm{fl}}$ in the dissipation term of (20) can be omitted by rescaling correspondingly the noise power D (Garcia-Palacios and Lazaro, 1998; Braun, 2000). We shall use this possibility below by comparing the Ito and Stratonovich interpretations of the LLG equations.

The noise in the Langevin equations 20 is *multiplicative*, because in the vector products the random field projections are *multiplied* by the magnetic moment projections. This fact was pointed out already in the pioneering paper of Brown (1963b), who suggested to use for this reason the Stratonovich interpretation of the equation.

Analytic solution of (20) is possible only in a few simplest cases, so that really interesting magnetic systems can be studied only numerically. For such simulations, the choice of the stochastic calculus is, in principle, of *primary* importance, because different numerical integration schemes converge to different stochastic integrals: The Euler and the simple implicit methods converge to the Ito solution, Heun and Milstein schemes – to the Stratonovich limit (McShane, 1974) and Runge-Kutta methods can converge to both types of the stochastic integrals (including the in-between cases) depending on their coefficients (Rümelin, 1982). Most authors (see, e.g., Garcia-Palacios and Lazaro, 1998; Scholz, Schrefl and Fidler, 2001; Berkov, Gorn and Görnert, 2002) and commercial micromagnetic packages (advanced recording model (ARM), LLG, MicroMagus) use the Heun, Runge-Kutta or modified Bulirsch–Stoer methods converging to the Stratonovich solution, but several groups employ the Ito-converging Euler (Zhang and Fredkin, 2000; Lyberatos and Chantrell, 1993) method and implicit schemes (Nakatani, Uesaka, Hayashi and Fukushima, 1997). These last papers were criticized in Garcia-Palacios and Lazaro (1998) where it has been claimed that only the Stratonovich interpretation ensures the physically correct solution of (20).

Fortunately, we could show that for *standard* micromagnetic models (where $|\mathbf{M}| = M_{\mathrm{S}} = Const$) both Ito and Stratonovich stochastic calculi provide identical results, so that the only criterion by the choice of the integration method is its efficiency by the solution of the LLG stochastic equation for the particular system under study. In the next subsection, we address this question in more detail because of its methodical importance.

2.2 Equivalence of Ito and Stratonovich stochastic calculus for standard micromagnetic models

In this subsection, we shall prove that for the system in which the dynamics is described by the stochastic equation (20) the Ito and Stratonovich versions of the stochastic calculus are equivalent *if the magnetization magnitude (or the magnitude of the discretization cell/single particle) is assumed to be constant* [2]. This is true for many magnetic system models including the classical Heisenberg and related models, spin glasses, fine magnetic particle systems (Dotsenko, 1993; Hansen and Morup, 1998), and in standard micromagnetics (Brown, 1963a).

First, we repeat that the fluctuation field in the dissipation term of (20) that can be omitted by rescaling correspondingly the noise power D (Garcia-Palacios and Lazaro, 1998; Braun, 2000). Thus we can restrict ourselves to the study of a simpler equation

$$\begin{aligned} \frac{\mathrm{d}\mathbf{m}_i}{\mathrm{d}\tau} = &- \left[\mathbf{m}_i \times (\mathbf{h}_i^{\mathrm{eff}} + \mathbf{h}_i^{\mathrm{fl}})\right] \\ &- \lambda \cdot \left[\mathbf{m}_i \times \left[\mathbf{m}_i \times \mathbf{h}_i^{\mathrm{eff}}\right]\right] \end{aligned} \tag{23}$$

To proceed, we recall that by the transition between the Ito and Stratonovich forms of a stochastic differential equation the additional drift term appears: if one adds to a SDE system

$$\frac{\mathrm{d}x_i}{\mathrm{d}t} = A_i(\mathbf{x}, t) + \sum_k B_{ik} \xi_k \tag{24}$$

the *deterministic* drift $D \sum_{jk} B_{jk} (\partial B_{ik} / \partial x_j)$, then the *Ito* solution of this new system

$$\frac{\mathrm{d}x_i}{\mathrm{d}t} = A_i(\mathbf{x}, t) + D \sum_{jk} B_{jk} \frac{\partial B_{ik}}{\partial x_j} + \sum_k B_{ik} \xi_k \tag{25}$$

is equivalent to the *Stratonovich* solution of the initial system (24) (Kloeden and Platen, 1995).

For the LLG equation written in Cartesian coordinates the matrix $\mathbf{B}$ is $B_{ik} = \sum_j \varepsilon_{ijk} m_j$, and the additional drift term reduces to $\mathrm{d}\mathbf{m}_i / \mathrm{d}\tau = -2D\mathbf{m}_i$. This drift is directed *along* the magnetic moment $\mathbf{m}_i$ trying to change its *magnitude*, which is forbidden by the model. Hence, this term *must* be discarded, which leads to the equivalence of the Ito and Stratonovich schemes.

The same result can be obtained (and understood) in a much simpler way rewriting the LLG equation using spherical coordinates (θ, ϕ) of the moment unit vector $\mathbf{m}$ (Cartesian coordinates of magnetic moments are *not* independent: owing to the conservation of a moment magnitude they are subject to the restriction $m_{x,i}^2 + m_{y,i}^2 + m_{z,i}^2 = 1$). In spherical coordinates the part containing the fluctuation (stochastic) field part of (23) which is of interest for us reads (Brown, 1963b; Braun, 2000).

$$\frac{\mathrm{d}\theta}{\mathrm{d}\tau} = h_{\varphi}^{fl}, \quad \frac{\mathrm{d}\varphi}{\mathrm{d}\tau} = -\frac{1}{\sin\theta} h_{\theta}^{fl} \tag{26}$$

so that the matrix $\mathbf{B}$ responsible for the drift mentioned in the preceding text is

$$B = \begin{pmatrix} B_{\theta\theta} & B_{\theta\varphi} \\ B_{\theta\varphi} & B_{\varphi\varphi} \end{pmatrix} = \begin{pmatrix} 0 & 1 \\ -1/\sin\theta & 0 \end{pmatrix} \tag{27}$$

and this drift is exactly zero: $D\sum_{jk} B_{jk}(\partial B_{ik}/\partial x_j) = 0$ ($i, j, k = 1, 2$ and $x_1 = \theta, x_2 = \phi$). Hence, we arrive at the same result that Stratonovich and Ito stochastic integrals are equivalent in this case, which means that *for stochastic dynamics of models with rigid dipoles* (*dipoles with constant magnitudes*) *there is no difference between the Ito and Stratonovich solutions of corresponding stochastic differential equations* (Berkov and Gorn, 2002).

It is interesting to see why the opposite statement made in Garcia-Palacios and Lazaro (1998) is incorrect. Using the Fokker–Planck equation (FPE) which describes the evolution of the probability distribution of the magnetization orientation $P(\mathbf{m}, t)$, the authors of Garcia-Palacios and Lazaro (1998) have shown that an additional drift term $\partial(\mathbf{m}P)/\partial\mathbf{m}$ appears in the FPE derived from the *Ito* interpretation of the Langevin equation. But this term should be excluded from the FPE because it leads to the probability density drift *along* the magnetization vector which would change the moment magnitude (this can be most easily seen in *spherical* coordinates (m, θ, ϕ) where this term reduces to $\partial(mP)/\partial m$).

To support our conclusion about the equivalence of the Ito and Stratonovich integrals for models with constant magnetic moment magnitudes, we have performed numerical experiments simulating equilibrium (density of states) and nonequilibrium (time dependent magnetization relaxation) properties of a disordered system of magnetic dipoles. We have solved the stochastic LLG equation (20) using methods converging either to its Ito (Euler scheme) or Stratonovich (drift-modified Euler and Heun schemes) solutions. Results obtained by all these methods coincide within the statistical accuracy, confirming that Ito and Stratonovich calculi lead, for these systems, to the same physical results despite that the noise in the stochastic LLG equation is *multiplicative*.

However, we point out that the proof in the preceding text *heavily relies* on the *conservation* of the moment magnitude. Hence for models where this is *not* the case – for example, by simulations of the heat assisted magnetic recording (HAMR) or for models attempting to relax the local restriction $\mathbf{M} = M_S = \text{Const}$ (see preceding text) – one should pay close attention to the choice of a numerical method used to solve equation (20).

3 STOCHASTIC LLG EQUATION: THERMAL NOISE CORRELATIONS

3.1 Thermal fluctuations for a single magnetic moment

3.1.1 Introduction

As it was stated in Section 2, the 'standard' way to take into account the thermal fluctuations of the magnetization in micromagnetic simulations is the inclusion of the 'fluctuation field' $\mathbf{H}^{fl}$ into the basic equation (20), which we write out here for a single magnetic moment $\boldsymbol{\mu}$ once more to have it at hand:

$$\frac{\mathrm{d}\boldsymbol{\mu}}{\mathrm{d}t} = -\gamma\cdot\left[\boldsymbol{\mu}\times(\mathbf{H}^{det}+\mathbf{H}^{fl})\right] - \lambda\cdot\frac{\gamma}{\mu}\cdot\left[\boldsymbol{\mu}\times\left[\boldsymbol{\mu}\times(\mathbf{H}^{det}+\mathbf{H}^{fl})\right]\right] \tag{28}$$

Components of the this field $\mathbf{H}_i^{fl}$ are supposed to have δ correlation in space and time

$$\langle H_{\xi,i}^{fl}\rangle = 0 \;\langle H_{\xi,i}^{fl}(0)\cdot H_{\psi,j}^{fl}(t)\rangle = 2C\cdot\delta(t)\cdot\delta_{ij}\cdot\delta_{\xi\psi} \tag{29}$$

where i, j are the discretization cell (or magnetic moment) indices and $\xi, \psi = x, y, z$. The proportionality coefficient before the δ functions in (29) is the noise power C, which can be evaluated as (when the random field is present in both terms on the right-hand side of (20))

$$C = \frac{\lambda}{1+\lambda^2}\cdot\frac{kT}{\gamma\mu} = \frac{\lambda}{1+\lambda^2}\cdot\frac{kT}{\gamma M_S V_p} \tag{30}$$

In the last equality we have used the relation $\mu = M_S V_p$ between the particle magnetic moment μ, saturation magnetization of the particle material M_S and the particle volume V_p.

The question of main interest is whether the properties (29) and (30), introduced by Brown (1963b) for a single-domain particle – actually for a single magnetic moment surrounded by a thermal bath – would survive for a typical micromagnetic system, where complicate interactions between the magnetic moments of the finite elements used to discretize a continuous problem are present.

We start the discussion of this principal problem with the statement that it actually contains two separate question:

1. Whether the correlations between random field components *can be really treated as δ -functional ones* and
2. Whether *the noise power can be evaluated using the universal expression like* (30) which contains *only* the system temperature T, the gyromagnetic ratio γ, the damping constant λ and the magnitude of the cell magnetic moment $\mu = M_S \Delta V$, and thus does not depend on any interaction details and other features of the concrete system under study.

To answer these questions for a micromagnetic system, we first recall how the δ correlations (29) of the random noise are introduced for a single magnetic particle, how the power of this noise (30) can be obtained for this simplest case, and discuss a physical sense of the expression (30).

First of all, in case of a single particle (single magnetic moment) we are not interested in *spatial* correlation properties of the noise. The statement that temporal correlations of the random field components are δ functional is an *assumption* based explicitly on the properties of that physical component of a thermal bath which is responsible for the appearance of thermal fluctuations. The most common point of view is that thermal fluctuations are mainly due to the interactions with phonons. In this case, we are interested in the correlation time associated with typical phonons, which contribute to thermal bath fluctuations. If we study the properties of our system at room temperature, which is of the same order of magnitude as the Debye temperature of typical materials, then we are speaking about phonons with the wavelength about several interatomic distances; typical life time of such room-temperature phonons is about a picosecond or less, so for remagnetization processes on time scales much larger than that we can safely accept the temporal correlation function $\delta(t)$ in (29). We note in passing that for the description of the magnetization dynamics on a much shorter time scales the phenomenology (20) is not valid anyway, because the equilibrium between various subsystems of a magnetic body (electrons, phonons, magnons etc.) cannot be reached. We also point out that the logic presented above to justify the δ-functional character of temporal noise correlations fails for systems at low temperatures, where the decay time of the characteristic (long-wave) phonons may be more than several nanoseconds, especially in pure materials.

3.1.2 *Derivation of the relation between the noise power and system properties for a mechanical Brownian motion*

Let us now examine the derivation of the relation (30). Usually it is quoted as a consequence of a so-called fluctuation-dissipation theorem (see subsequent text), but in many cases it can be obtained in a much simpler way, which also make the physical sense of this relation more transparent. To illustrate this point, we start with the mechanical Brownian motion of a 'normal' free particle described by the Langevin equation

$$m\frac{\mathrm{d}^2 x}{\mathrm{d}t^2} = -\eta\frac{\mathrm{d}x}{\mathrm{d}t} + F^{\mathrm{fl}}(t) \tag{31}$$

where the first term on the right is the friction force and the second term represents the Langevin (fluctuating) force, which has by the assumptions outlined above zero-mean value and the correlation properties $\langle F^{\mathrm{fl}}(0)\cdot F^{\mathrm{fl}}(t)\rangle = 2C\cdot\delta(t)$. Introducing the particle velocity $v = \mathrm{d}x/\mathrm{d}t$, we obtain for v from the equation above a simple first-order differential equation

$$\frac{\mathrm{d}v}{\mathrm{d}t} + \frac{\eta}{m}v = \frac{1}{m}F^{\mathrm{fl}}(t) \tag{32}$$

which explicit solution

$$v(t) = v(0)e^{-\eta t/m} + \frac{1}{m}\int_0^t e^{-\eta(t-t')/m}F^{\mathrm{fl}}(t')\,\mathrm{d}t' \tag{33}$$

allows the straightforward evaluation of the mean-square velocity: writing the velocities for two different time moments $v(t_1)$ and $v(t_2)$ using (33), multiplying these quantities and taking the thermal average, we obtain the expression for the product $\langle v(t_1)v(t_2)\rangle$ which contains only the correlation function $\langle F^{\mathrm{fl}}(t_1)\cdot F^{\mathrm{fl}}(t_2)\rangle = 2C\cdot\delta(t_1 - t_2)$ (all other terms are zero because the velocity values are not correlated with the values of the random force). Putting $t_1 = t_2$ and using the basic property of the δ function, we finally obtain the desired result $\langle v^2\rangle = C/2\eta m$. On the other hand, in the *thermal equilibrium* the average kinetic energy of the particle is $\langle E_K\rangle = m\langle v^2\rangle/2 = kT/2$, so that $\langle v^2\rangle = kT/m$. Equating these two expressions for the mean square of the particle velocity, we obtain the desired result

$$C = \eta\cdot kT \tag{34}$$

which connects the noise power C with the friction coefficient η and system temperature T. Note that by derivation of this relation we have used only the fact that the system (particle) is in a thermodynamical equilibrium with the surrounding thermal bath.

For a particle which moves in an external potential and hence possesses the energy $V(x)$ the situation is more complicate, because no general analytical solution of the corresponding Langevin equation

$$\eta\frac{\mathrm{d}x}{\mathrm{d}t} = -\nabla V(x) + F^{\mathrm{fl}}(t) \tag{35}$$

is available in (35) we have neglected the inertial term for simplicity, which means that we are interested in times much larger than the velocity equilibration time $t_p = m/\eta$. In this situation, the relation between the noise power C and the system features can be established using another principal equation of the theory of stochastic processes – the FPE.

The FPE describes the temporal and spatial evolution of the probability density $w(x,t)$ which gives the probability $w(x,t)\cdot dx\cdot dt$ to find the particle inside the region $[x; x+dx]$ during the time interval $[t; t+dt]$. This equation can be derived in many ways; the most transparent general method to obtain the FPE starts from the so-called Chapman–Kolmogorov (also called *Smoluchovski*) equation. From a physical point of view, this latter equation simply states that the conditional probability $P(x_1,t_1|x_3,t_3)$ to find the particle at x_1 at the time t_1, *if* its position at the time t_3 was x_3, can be obtained by integrating the product of conditional probabilities for the transitions $(x_1,t_1)\to(x_2,t_2)$ and $(x_2,t_2)\to(x_3,t_3)$ over all intermediate particle positions x_2. The derivation of the FPE from the Chapman–Kolmogorov equation is conceptually very simple (see, e.g., Gardiner, 1997) and assumes only the existence of the limits

$$A(x,t) = \lim_{\Delta t\to 0}\frac{\langle x(t+\Delta t)-x(t)\rangle}{\Delta t}$$
$$B(x,t) = \frac{1}{2}\lim_{\Delta t\to 0}\frac{\langle (x(t+\Delta t)-x(t))^2\rangle}{\Delta t} \qquad (36)$$

The resulting FPE reads in a general case

$$\frac{\partial w(x,t)}{\partial t} = -\frac{\partial}{\partial x}[A(x,t)\cdot w(x,t)] + \frac{\partial^2}{\partial x^2}[B(x,t)\cdot w(x,t)] \qquad (37)$$

Here, the first term on the right describes the systematic particle *drift* due to the potential force $F_{pot}(x) = -\nabla V(x)$ and the second term is responsible for the particle *diffusion* due to thermal fluctuations. For each concrete system the limits (36) can be evaluated from the corresponding Langevin equation (Coffey, Kalmykov and Waldron, 2004) in conceptually the same manner as the mean square of the particle velocity was derived from (32). For the simple system described by the equation (35) the result is

$$A = -\nabla V(x)/\eta, \quad B(x) = Const = C/\eta^2 \qquad (38)$$

(C is the noise power from the correlation function $\langle F^{fl}(t_1)\cdot F^{fl}(t_2)\rangle = 2C\cdot\delta(t_1-t_2)$ of the random force) so that the FPE (37) has the form of a standard diffusion equation

$$\frac{\partial w(x,t)}{\partial t} = \frac{\partial}{\partial x}\left[\frac{1}{\eta}\frac{\partial V}{\partial x}\cdot w(x,t)\right] + \frac{C}{\eta^2}\cdot\frac{\partial^2 w(x,t)}{\partial x^2} \qquad (39)$$

which means that the noise power C is equal to the diffusion coefficient.

To establish now the required relation between the noise power and other system properties, we use the statement that in the equilibrium state (where the time derivative $\partial w/\partial t = 0$ the probability distribution function should be given by the (normalized) Boltzmann exponent $w(x) = N\exp(-V(x)/kT)$. Substitution of this expression into the right-hand side of the FPE (39) gives the equation, which is worth to be explicitly written out:

$$\frac{d^2V}{dx^2}\left(\eta - \frac{C}{kT}\right) - \frac{1}{kT}\cdot\left(\frac{dV}{dx}\right)^2\left(\eta - \frac{C}{kT}\right) = 0 \qquad (40)$$

The equation (40) should be satisfied for an arbitrary potential $V(x)$ which leads exactly to the same relation $C = \eta\cdot kT$ between the random noise power and system parameters as the result (34) for a free particle. Now we have proved that this relation *does not* depend on the concrete potential $V(x)$, and thus represent a very general statement. Again, the only physical assumption used to derive this formula was the statement that *the system is in a thermodynamical equilibrium*, so that the Boltzmann distribution for the probability density $w(x,t)$ could be used.

3.1.3 FPE and noise power evaluation for a single magnetic moment

The FPE can be derived for a single magnetic moment in the same way as in the preceding text for a mechanical particle. The resulting equation is, however, much more complicate due to the following reasons: (i) we deal here with a *rotational* diffusion and (ii) the precession term (which is the counterpart of the inertial term in mechanics) in the corresponding Langevin equation (20) cannot be neglected, because this would lead to a *qualitatively* incorrect description of the magnetization dynamics for the overwhelming majority of physically interesting systems.

The first derivation of the corresponding FPE was presented (up to our knowledge) by Brown (1963b), who used the 'physical' or 'intuitive' method, employing the continuity equation for the distribution density $w(\theta,\phi)$ of the magnetic moment directions. This equation relates the time derivative of $w(\theta,\phi)$ and its flux on the (θ,ϕ) sphere, whereby the diffusion term is added to the flux in a phenomenological way using the similarity with the equation describing the mechanical rotational diffusion. The rigorous derivation of this FPE, which uses the functional analysis methods can be found in the Appendix of Garanin (1997). Another derivation of the same FPE from the Langevin equation (20) which employs the relations (known from the general rules of stochastic calculus) between the coefficients of the Langevin

equation and corresponding terms from FPE is contained in Garcia-Palacios and Lazaro (1998). The structure of the resulting equation

$$\frac{\partial w(\mathbf{m},t)}{\partial t} = -\nabla_{\mathbf{m}}\Big\{\gamma[\mathbf{m}\times\mathbf{H}^{\text{eff}}]w - \gamma\cdot\lambda\cdot[\mathbf{m}\times[\mathbf{m}\times\mathbf{H}^{\text{eff}}]]w + D_{\text{rot}}[\mathbf{m}\times[\mathbf{m}\times\nabla_{\mathbf{m}}]]w\Big\} \tag{41}$$

is obviously inherited from the Langevin equation in the LLG form (20) which the FPE (41) has been derived from: the first term in the curved parenthesis describes the drift of the probability density due to the precession term in (20), the second term corresponds to the drift due to the damping torque and the third (diffusion) term also has the structure of the damping term in the original LLG. The operator $\nabla_{\mathbf{m}}$ acting on the vectors on the right-hand side of (41) means the divergence over the components of the vector $\mathbf{m}$, so that, for example, in Cartesian coordinates $\nabla_{\mathbf{m}}\mathbf{a} \equiv \sum_i \partial a_i/\partial m_i (i = x, y, z)$. The coefficient before the rotational diffusion term, expressed in terms of the quantities entering into the LLG equation (20), is

$$D_{\text{rot}} = \gamma^2(1+\lambda^2)\cdot C \tag{42}$$

where C is the noise power of the fluctuating field $\mathbf{H}^{\text{fl}}$.

The procedure for the calculation of the noise power using this FPE is fully analogous to that described in the preceding text for the mechanical translational diffusion. Namely, we substitute the equilibrium probability density $w(x) = N\exp(-V(\theta,\varphi)/kT)$ into the equation (41) with zero left-hand side ($\partial w/\partial t = 0$). Taking into account the effective field definition $\mathbf{H}^{\text{eff}} = -\partial V/\partial\mathbf{m}$ we arrive after a very tedious, but straightforward differentiation at the relation similar to (40), which in this case can be satisfied only if

$$D_{\text{rot}} = kT\cdot\frac{\gamma\lambda}{\mu} \tag{43}$$

Equating the two expression (42) and (43) for D_{rot}, we arrive at the final result which establish the relation (30) between the noise power C and the system parameters:

$$C = \frac{\lambda}{1+\lambda^2}\cdot\frac{kT}{\gamma\mu} = \frac{\lambda}{1+\lambda^2}\cdot\frac{kT}{\gamma M_{\text{S}} V_{\text{p}}} \tag{44}$$

As in the corresponding relation (34) for the mechanical translational Brownian motion, the noise power is proportional to the system temperature kT and to the friction constant λ. Also, fully analogous to the mechanical noise power (34), the value of C in (44) does *not* depend on the concrete potential $V(\theta,\phi)$ acting on the magnetic moment, which can be understood as a first hint that this result will remain unchanged for a system of *interacting* magnetic moments also. The appearance of the gyromagnetic ratio γ in the denominator is due to its presence as a common factor for both drift terms in the initial FPE (41), so that after the substitution of an equilibrium Boltzmann probability density and differentiation it appears in the equality (43). The factor $(1+\lambda^2)$ in the denominator reflects the special structure of the LLG (28), where the fluctuating field $\mathbf{H}^{\text{fl}}$ has been added *both* to the precession and dissipation terms. It is also possible to use an alternative form of this equation – with $\mathbf{H}^{\text{fl}}$ added to the precession term *only*, in which case the factor $(1+\lambda^2)$ in the relation (45) is absent (Garcia-Palacios and Lazaro, 1998).

One aspects of this relation deserve a special discussion, namely, the inverse proportionality of the noise power C to the total particle magnetic moment μ, or – taking into account that the saturation magnetization of the particle material M_{S} is constant – to the particle volume V_{p}. In other words, the noise power, or the dispersion of the fluctuation field $\sigma_{\text{fl}}^2 = \langle(\mathbf{H}^{\text{fl}})^2\rangle decreases$ linearly with the increasing particle volume. This dependence can be understood on an intuitive level in the following way. Let us consider a small magnetic particle consisting of N atoms with magnetic moments $\boldsymbol{\mu}_i$. For each atomic magnetic moment the equation of motion (we neglect damping to simplify the discussion) can be written as

$$\frac{\mathrm{d}\boldsymbol{\mu}_i}{\mathrm{d}t} = -\gamma\cdot\big[\boldsymbol{\mu}_i\times(\mathbf{H}^{\text{det}} + \mathbf{H}_i^{\text{fl}})\big] \tag{45}$$

Here, we have assumed that the particle is so small deterministic effective fields are approximately equal for all elementary moments. Thermal fluctuation field $\mathbf{H}_i^{\text{fl}}$ randomly varies from one atom to another. To obtain the equation of motion for the total particle magnetic moment $\boldsymbol{\mu}_{\text{tot}} = \sum_{i=1}^{N}\boldsymbol{\mu}_i$, we have to sum the equations (45) over all particle atoms:

$$\sum_i \frac{\mathrm{d}\boldsymbol{\mu}_i}{\mathrm{d}t} = \frac{\mathrm{d}\boldsymbol{\mu}_{\text{tot}}}{\mathrm{d}t} = -\gamma\cdot\sum_i\big[\boldsymbol{\mu}_i\times\mathbf{H}^{\text{det}}\big] - \gamma\cdot\sum_i\big[\boldsymbol{\mu}_i\times\mathbf{H}_i^{\text{fl}}\big] \tag{46}$$

Taking into account the independence of $\mathbf{H}^{\text{det}}$ on the elementary moment index, the first sum on right-hand side immediately transforms to $[\boldsymbol{\mu}_{\text{tot}}\times\mathbf{H}^{\text{det}}]$. Situation with the second (random field) term is more complicate, because $\mathbf{H}_i^{\text{fl}}$ is a random quantity. Using again the assumption that the particle is small enough to ensure that due to the exchange interaction atomic magnetic moments are nearly parallel, we

can write the elementary moment on the second sum as $\boldsymbol{\mu}_i = \boldsymbol{\mu}_{\text{tot}}/N$ and factor the i-independent total moment out of the sum. Then the equation (46) takes the desired form of the Langevin equation for the total moment

$$\begin{aligned}\frac{\mathrm{d}\boldsymbol{\mu}_{\text{tot}}}{\mathrm{d}t} &= -\gamma\cdot\left[\boldsymbol{\mu}_{\text{tot}}\times\mathbf{H}^{\text{det}}\right] - \gamma\cdot\left[\frac{\boldsymbol{\mu}_{\text{tot}}}{N}\times\sum_i \mathbf{H}_i^{\text{fl}}\right] \\ &= -\gamma\cdot\left[\boldsymbol{\mu}_{\text{tot}}\times(\mathbf{H}^{\text{det}}+\mathbf{H}_{\text{tot}}^{\text{fl}})\right] \end{aligned} \tag{47}$$

if we *define* the fluctuation field $\mathbf{H}_{\text{tot}}^{\text{fl}}$ acting on the total moment as

$$\mathbf{H}_{\text{tot}}^{\text{fl}} = \frac{1}{N}\sum_{i=1}^{N}\mathbf{H}_i^{\text{fl}} \tag{48}$$

The relation (48) between the total and elementary thermal fields means that the dispersion of the total fluctuation field σ_{tot}^2 can be evaluated as

$$\sigma_{\text{tot}}^2 = \frac{1}{N^2}\cdot\sum_{i=1}^{N}\sigma_i^2 = \frac{1}{N^2}\cdot N\sigma_{\text{at}}^2 = \frac{1}{N}\cdot\sigma_{\text{at}}^2 \tag{49}$$

where we have used the assumption that all fluctuation fields are random *independent* variables with *equal* dispersions $\sigma_i^2 = \sigma_{\text{at}}^2 \forall i = 1,\ldots,N$. The dispersion of the fluctuating field on a single atom σ_{at}^2 does not depend on the system volume, so the equality (49) explains why the dispersion of the total fluctuation field $\mathbf{H}_{\text{tot}}^{\text{fl}}$ which appears in the LLG equation (28) is inversely proportional to the number of elementary magnetic moments in the system, that is, to the system volume.

The relation (30) can also be understood as the statement that with increasing particle volume the importance of thermal fluctuation decreases, in accordance with an intuitive picture of Brownian motion.

Already here we would like to point out, that the increase of the noise power (30) with the decreasing particle volume just discussed has serious consequences for numerical micromagnetic simulations. The random field $\mathbf{H}^{\text{fl}}$ present in the LLG equation of motion is the *main factor*, which limits the simulation time step when an algorithm with the built-in adaptive step-size control is used (which should always be the case). The reason is quite simple: fluctuation field, being a random process, is *not* a smooth function of time and space, which naturally strongly diminishes the efficiency of any numerical integrator. It can be even shown that the order of a numerical integration scheme applied to a stochastic equation is usually a *square root* of the order of the same scheme applied to an ordinary differential equation (Kloeden and Platen, 1995). Hence, the growth of the mean fluctuation field amplitude with the decreasing discretization cell volume (entering into (30) instead of the particle volume) enforced by the relation (30) leads to the *decrease* of the integration time step in micromagnetic simulations on finer grids, which should be always kept in mind by estimating simulation time basing on the data obtained on coarser grids.

3.2 Noise correlations for an interacting system: general theory

The most interesting question concerning the random field concept used to simulate magnetization dynamics under the influence of thermal fluctuations is the following: can the random field components on different spatial locations (different discretization cells) still be considered as *independent* (uncorrelated) random variables, despite the strong interactions between magnetic moments? The hand-waving argument that this interaction should not influence the correlation properties of random fields, because all the interaction kinds are already included in the deterministic part of the effective field $\mathbf{H}^{\text{det}}$ cannot be considered as fully satisfactory. For example, in a system of interacting particles moving in a viscous media, random forces acting on different particles should be treated as correlated ones to ensure correct statistical properties of such systems (see, e.g., Ermak and McCammon, 1978). For this reason, we have to resort to a general theory which allows to evaluate noise correlations in interacting many-particle systems in a rigorous way.

This theory operates with the so-called *thermodynamically* conjugate variables (Landau and Lifshitz, 1980) (which should not be confused with the conjugate variables known from quantum mechanics) and we repeat here briefly the major points of this concept to make this review self-contained. In short, we consider a system which state is fully characterized by a set of N variables $\{\mathbf{x} = x_1, x_2, \ldots, x_N\}$ chosen so that their values at equilibrium are zero: $\mathbf{x}_0 = 0$. If the system fluctuates, that is, the values of system variables deviate from these equilibrium values and change with time, then the time derivatives $\mathrm{d}x_i/\mathrm{d}t$ can be expressed as functions of instantaneous values of $\mathbf{x}(t)$ as $\dot{x}_i = f_i(\mathbf{x})$. If the deviations from the equilibrium are small, we can expand the functions f_i around $\mathbf{x} = 0$ and maintain only the first order terms in small quantities x_i (at equilibrium in the absence of thermal fluctuations $\dot{x}_i = 0$), obtaining a system of first-order differential equations describing the relaxation of the system variables to their equilibrium values as

$$\frac{\mathrm{d}x_i}{\mathrm{d}t} = \sum_k \Lambda_{ik}x_k, \text{ where } \Lambda_{ik} = \frac{\partial f_i}{\partial x_k} \tag{50}$$

To account for thermal fluctuations, we introduce into (50) random forces $\xi_i(t)$ which are assumed to be responsible for

the fluctuations of the system variables:

$$\frac{\mathrm{d}x_i(t)}{\mathrm{d}t} = \sum_k \Lambda_{ik} x_k(t) + \xi_i(t) \tag{51}$$

Assuming that the correlation times of these forces are much less than all characteristic system relaxation times, we can write the correlation functions $K_{\mathrm{ik}}(t)$ of the random forces as $\langle \xi_i(0)\xi_k(t)\rangle = 2C_{ik}\cdot\delta(t)$. The problem is to calculate the correlation coefficients C_{ik} in order to obtain from the system (51) correct statistical properties of the system fluctuations.

It turns out that the correlation matrix C_{ik} can be expressed in the simplest way when the system (51) is rewritten in terms of *thermodynamically conjugate variables* $\{\mathbf{X} = X_1, X_2, \ldots, X_N\}$ defined as derivatives of the system entropy S over the 'initial' variables $\mathbf{x}$: $X_i = -\partial S/\partial x_i$. Near the equilibrium the difference between the system entropy S and its maximum (equilibrium) value $S_{\max}$ can be expanded over small deviations x_i: $S - S_{\max} = -\frac{1}{2}\sum_{i,k}\beta_{ik}x_i x_k$, so that thermodynamically conjugate variables X_i are linear functions of $\{\mathbf{x}\}$:

$$X_i = -\frac{\partial S}{\partial x_i} = \beta_{ik}x_k, \quad \text{or} \quad \mathbf{X} = \hat{\boldsymbol{\beta}}\mathbf{x} \tag{52}$$

where $\hat{\beta} = \{\beta_{ik}\}$. Substituting $\mathbf{x} = \hat{\beta}^{-1}\mathbf{X}$ into the sum on the right-hand side of (51), we obtain the stochastic equations for thermal fluctuations of our system near its equilibrium state in the form

$$\begin{aligned}\frac{\mathrm{d}\mathbf{x}}{\mathrm{d}t} &= -\hat{\Lambda}\mathbf{x} + \boldsymbol{\xi} = -(\hat{\Lambda}\cdot\hat{\beta}^{-1})\mathbf{X} + \boldsymbol{\xi} \\ &= -\hat{\Gamma}\cdot\mathbf{X} + \boldsymbol{\xi}, \ \text{or} \end{aligned} \tag{53}$$

$$\frac{\mathrm{d}x_i}{\mathrm{d}t} = -\sum_k \Gamma_{ik}X_k + \xi_i \tag{54}$$

with the matrix $\hat{\Gamma} = \{\Gamma_{ik}\}$ defined as $\hat{\Gamma} = \hat{\Lambda}\hat{\beta}^{-1}$.

The usefulness of these transformations becomes apparent when we express the correlation coefficients of the random forces C_{ik} in terms of matrices $\hat{\Lambda}$, $\hat{\Gamma}$, and $\hat{\beta}$. Corresponding derivation for the many-variable case is quite tedious, so we restrict ourselves to the system characterized by a single variable x and its conjugate $X = -\partial S/\partial x = \beta x$. Such a system is described by the relaxation equation

$$\frac{\mathrm{d}x}{\mathrm{d}t} = -\Lambda x(t) + \xi(t) \tag{55}$$

The temporal correlation function of x defined as $\varphi(t - t') = \langle x(t)x(t')\rangle$ may depend on the difference $t - t'$ only (stationary fluctuations) and can be easily found multiplying (55) by $x(t')$, performing statistical averaging $\langle\cdots\rangle$ and taking into account that the values of $x(t')$ and $\xi(t)$ are uncorrelated. The result is $\varphi(t) = \langle x^2\rangle\exp(-\lambda|t|) = (1/\beta)\exp(-\Lambda|t|)$, where the mean square of x was evaluated from its probability distribution $w(x)\ \exp\{S(x)\}$ using the above mentioned quadratic expansion $S - S_{\max} = -(\beta/2)x^2$ near its maximum.

Denoting the Fourier transform (FT) of $x(t)$ as $\tilde{x}(\omega)$, we rewrite the definition of $\phi(t)$ as

$$\begin{aligned}\varphi(t - t') &= \langle x(t)x(t')\rangle \\ &= \frac{1}{(2\pi)^2}\iint \langle\tilde{x}(\omega)\tilde{x}(\omega')\rangle e^{-i(\omega t + \omega' t')}\mathrm{d}\omega\mathrm{d}\omega' \end{aligned} \tag{56}$$

The statement that the CF $\varphi(t - t')$ may depend on the time *difference* only (see above) requires that the FT product in (56) has the form $\langle\tilde{x}(\omega)\tilde{x}(\omega')\rangle = 2\pi\cdot P_x(\omega)\cdot\delta(\omega + \omega')$. Here $P_x(\omega)$ is the spectral power of $x(t)$ and is, according to (56), the Fourier transform of its correlation function $\varphi(t) = \langle x(t)x(0)\rangle$ (Wiener–Khinchin theorem). For $\varphi(t) = (1/\beta)\exp(-\Lambda|t|)$ the simple integration gives $P_x(\omega) = 2\Lambda/\beta(\omega^2 + \Lambda^2)$.

Now we apply the same method to calculate the correlation function of the random force. Expressing $\xi(t)$ via its FT $\tilde{\xi}(\omega)$, (due to (55) we have $\tilde{\xi}(\omega) = (\Lambda - i\omega)\tilde{x}(\omega)$), and using the definition $K(t - t') = \langle\xi(t)\xi(t')\rangle$, we obtain

$$\begin{aligned}K_\xi(t - t') &= \frac{1}{(2\pi)^2}\iint \langle\tilde{\xi}(\omega)\tilde{\xi}(\omega')\rangle e^{-i(\omega t + \omega' t')}\mathrm{d}\omega\mathrm{d}\omega' \\ &= \frac{1}{(2\pi)^2}\iint (\lambda - i\omega)(\lambda - i\omega')\langle\tilde{x}(\omega) \\ &\quad \times \tilde{x}(\omega')\rangle e^{-i(\omega t + \omega' t')}\mathrm{d}\omega\mathrm{d}\omega' \\ &= \frac{1}{2\pi}\int (\lambda^2 + \omega^2)P_x(\omega)e^{-i\omega t}\mathrm{d}\omega \end{aligned} \tag{57}$$

where by the last transformation the property $\langle\tilde{x}(\omega)\tilde{x}(\omega')\rangle = 2\pi\cdot P_x(\omega)\cdot\delta(\omega + \omega')$ was used. Equation (57) means that the spectral power of the random noise fluctuations $P_\xi(\omega)$ is related to the spectral power $P_x(\omega)$ of the x-fluctuations via $P_\xi(\omega) = (\omega^2 + \Lambda^2)P_x(\omega)$. Hence the random force spectrum $P_\xi(\omega) = 2\Lambda/\beta$ is frequency independent, as it should be for the quantity with the CF $K(t) = \langle\xi(t)\xi(0)\rangle = (2\lambda/\beta)\cdot\delta(t)$.

In terms of the conjugate variable the relaxation equation for a single-variable system reads $\mathrm{d}x/\mathrm{d}t = -\Gamma\cdot X(t) + \xi(t)$, so that $\tilde{\xi}(\omega) = \Gamma\cdot\tilde{X}(\omega) - i\omega\tilde{x}(\omega)$. The procedure identical to (57) results in the relation $P_\xi(\omega) = \omega^2 P_x(\omega) + \Gamma^2 P_X(\omega)$ between the spectral powers of the random noise, $x(t)$ and its conjugate $X(t)$. The spectrum $P_X(\omega) = 2\beta\Lambda/(\omega^2 + \Lambda^2)$ can be found from the equation $\mathrm{d}X/\mathrm{d}t = -\Lambda X(t) + \xi(t)/\beta$ for $X(t)$ (it follows from (55) and $X = \beta x$). Combining $P_x(\omega)$

and $P_X(\omega)$ into the noise spectrum $P_\xi(\omega)$ and using the relation $\Gamma = \Lambda/\beta$ (analogue of matrix relation $\hat{\Gamma} = \hat{\Lambda}\hat{\beta}^{-1}$), we obtain $P_\xi(\omega) = 2\Gamma$, so that $\langle \xi(t)\xi(0)\rangle = 2\Gamma\cdot\delta(t)$.

The whole exercise presented in the preceding text makes real sense only for the many-variable case (random noise correlations as a function of Γ can be obtained for a single-variable system immediately from the equation $\mathrm{d}x/\mathrm{d}t = -\Lambda x(t) + \xi(t)$ and the relation $\Gamma = \Lambda/\beta$). For a system described by *many* variables, however, we need a set of CF's $\varphi_{ik}(t) = \langle x_i(t)x_k(0)\rangle$ and their FT's $P_{ik}^{(x)}(\omega)$. The *system* of differential equations for these CF's $\mathrm{d}\varphi_{ik}(t)/\mathrm{d}t = \sum_l \lambda_{il}\varphi_{ik}(t)$ is transformed into the system of linear algebraic equations for $P_{ik}^{(x)}(\omega)$. Solving this and analogous system for spectral powers $P_{ik}^{(X)}(\omega)$ of the conjugates, using of the relations between the FT's of noise components, initial and conjugate variables $\tilde{\xi}_i(\omega) = \sum_k \Gamma_{ik}\tilde{X}_k(\omega) - i\omega\tilde{x}_i(\omega)$ (which follows from $\mathrm{d}x_i/\mathrm{d}t = -\sum_k \Gamma_{ik}X_k(t) + \xi_i(t)$) we obtain the result $P_{ik}^{(\xi)}(\omega) = \Gamma_{ik} + \Gamma_{ki}$. Hence the required correlation properties of the random noise components are

$$\langle \xi_i(t)\xi_k(0)\rangle = (\Gamma_{ik} + \Gamma_{ki})\cdot\delta(t) \tag{58}$$

which is a direct generalization of the single-variable relation $\langle \xi(t)\xi(0)\rangle = 2\Gamma\cdot\delta(t)$.

The simplicity of the relation (58) which gives the correlation coefficients of the random noise matrix directly in terms of the elements of $\hat{\Gamma}$-matrix is the reason to use equation (54) where the stochastic motion of a system near its equilibrium state is described using the *conjugate* variables $\{\mathbf{X}\}$.

The relation (58) can be used to derive correlation properties of the random noise in a very important particular case, which includes also micromagnetic models. To do this, we begin with the important remark that our starting point, namely the relaxation equations (50) for the system variables are *not* the equation of motion derived from some physical formalism (like Newton laws or Lagrange mechanics), but are merely a direct consequence of the mathematical assumption that the relaxation rates $\mathrm{d}x_i/\mathrm{d}t$ of the system variables near its equilibrium state can be expanded in terms of small deviations $\{\mathbf{x}\}$ from their equilibrium values. Equations (50) maintain only the first-order terms of this expansion.

For many physical system the expansion coefficients Γ_{ik} may be given in a more specific form, which allows further progress by evaluating the correlation matrix $\langle \xi_i\xi_k\rangle = (\Gamma_{ik} + \Gamma_{ki})$. First we note, that the entropy change by the system deviation from its equilibrium state may be expressed via the *minimal work* $A_{\min}$ required to transfer the system from equilibrium into the state with the entropy S as $S - S_{\max} = -A_{\min}/kT$ (see, e.g., Landau and Lifshitz, 1980). This allows us to calculate conjugate variables as derivatives of this work: $X_i = -\partial S/\partial x_i = (1/kT)\cdot(\partial A_{\min}/\partial x_i)$.

Further, for a wide class of physical systems this minimal work $A_{\min}$ is equal to the energy difference $E - E_0$ between the system energy in the equilibrium state E_0 and in the given state E, which can be also expanded near the equilibrium state as

$$E - E_0 = \frac{1}{2} + \sum_{i.k} a_{ik}x_i x_k \tag{59}$$

so that

$$X_i = \frac{1}{kT}\frac{\partial A_{\min}}{\partial x_i} = \frac{1}{kT}\frac{\partial E}{\partial x_i} = \frac{1}{kT}\sum_k a_{ik}x_k \tag{60}$$

which means that the matrix $\{\beta_{ik}\}$ from the definition (52) in this case is $\hat{\beta} = \hat{a}/kT$.

If the deterministic motion of the system can be described by the Newtonian equations with the inertial term neglected, that is, in the form $\eta_i\cdot\mathrm{d}x_i/\mathrm{d}t = F_i$, then, evaluating the forces as $F_i = -\partial E/\partial x_i = -\sum_k a_{ik}x_k$, introducing particle mobilities as inverses of the corresponding friction coefficients $\kappa_i = 1/\eta_i$, and adding random forces to the right-hand side of the equation of motions, we obtain these equations in the form

$$\frac{\mathrm{d}x_i}{\mathrm{d}t} = -\kappa_i\sum_k a_{ik}x_k + \xi_i \tag{61}$$

where the random forces ξ_i are related to the forces F_i used in (35) via $\xi_i = F_i/\kappa_i$. Comparing this system to the relaxation equations (51), we find that in this case $\hat{\Gamma} = \hat{\kappa}_{\mathrm{diag}}\hat{a}$, where the diagonal matrix $\hat{\kappa}_{\mathrm{diag}}$ contains mobilities κ_i on its main diagonal. Substituting $\hat{\Gamma} = \hat{\kappa}_{\mathrm{diag}}\hat{a}$ and $\hat{\beta} = \hat{a}/kT$ into the definition of the matrix $\hat{\Gamma} = \hat{\Lambda}\hat{\beta}^{-1}$, we arrive at the important result

$$\hat{\Gamma} = kT\cdot\hat{\kappa}_{\mathrm{diag}} \tag{62}$$

This means that for a system where (i) the minimal work required to bring it out of the equilibrium is equal to the corresponding energy change and (ii) the relaxation of the system coordinates can be expressed via the damped equations of motion, the correlation matrix of random forces acting on different variables

$$\begin{aligned}\langle \xi_i(t)\xi_k(0)\rangle &= (\Gamma_{ik} + \Gamma_{ki})\cdot\delta(t)\\ &= 2\kappa_i\cdot kT\cdot\delta_{ik}\cdot\delta(t)\end{aligned} \tag{63}$$

is *diagonal*. This property is *independent* on the specific expression of the interaction energy $E\{\mathbf{x}\}$ between the particles, which means that for such a system random noise components are uncorrelated despite the presence of an interparticle interaction.

3.3 Noise correlations for an interacting system: application to micromagnetic simulations

Using the formalism developed above, we shall rigorously demonstrate in this subsection that *physical* correlations between the random fields on *different* cells or between the random field components on *one and the same* cell are absent.

The formalism from the previous subsection may be applied directly to micromagnetic Langevin dynamics simulations of magnetization fluctuations in a thermodynamic equilibrium. Although the situation in micromagnetics is slightly more complicate than for systems discussed in Section 3.2 (due to the presence of a *precessional* term), a complete description of random field correlation properties is nevertheless possible.

For a micromagnetic system the variables $\{\mathbf{x}\}$, which determine its state are the magnetization projection. Here we consider a system which is already discretized into finite elements (cells) and denote the projections of the magnetization inside the i-th cell as $M_i^\alpha, \alpha = x, y, z$. The most important step now is the establishing of the corresponding conjugate variables. Comparing the definition of the deterministic effective field

$$\mathbf{H}_i^{\text{det}} = -\frac{1}{\Delta V_i}\frac{\partial E}{\partial \mathbf{M}_i}, \text{ or}$$
$$H_{i,\alpha}^{\text{det}} = -\frac{1}{\Delta V_i}\frac{\partial E}{\partial M_i^\alpha}(\alpha = x, y, z) \tag{64}$$

appearing in the LLG equation for a discretized system

$$\frac{\mathrm{d}\mathbf{M}_i}{\mathrm{d}t} = -\gamma\cdot\Big[\mathbf{M}_i \times (\mathbf{H}_i^{\text{det}} + \mathbf{H}_i^{\text{fl}})\Big] - \lambda\cdot\frac{\gamma}{M_{\text{S}}}\cdot\Big[\mathbf{M}_i \times \Big[\mathbf{M}_i \times (\mathbf{H}_i^{\text{det}} + \mathbf{H}_i^{\text{fl}})\Big]\Big] \tag{65}$$

with the definition (60) of the conjugate variables $X_i = (1/kT)(\partial E/\partial x_i)$, we immediately see that the variable X_i^α conjugate to the projection M_i^α is simply proportional to the corresponding effective field projection:

$$X_i^\alpha = -\frac{\Delta V_i}{kT}\cdot H_{i,\alpha}^{\text{det}} \tag{66}$$

The direct consequence of this proportionality is the absence of correlations between the random field projection on *different* discretization cells, because in the LLG equation of motion for the magnetization of the i-th cell only the effective field projections *for the same cell* (and hence – conjugate variables with the same index i) do appear. This means that the matrix elements $\Gamma_{ik}^{\alpha\beta}$ from the system (54) with different cell indices $i \neq k$ are automatically zero, ensuring the absence of intercell correlations according to (58).

To find out, whether any correlations between the random field components on *one and the same* cell do exist, some technical work should be done. To simplify the treatment, we assign to each cell its own coordinate system with the $0z$-axis parallel to the equilibrium direction of the cell moment. The quadratic energy expansion around the equilibrium magnetization state

$$E - E_0 = \frac{1}{2}\sum_{i,j}\sum_{\alpha,\beta=x,y} a_{ik}\cdot\Delta M_i^\alpha \Delta M_j^\beta \tag{67}$$

will then include small deviations $\Delta M_i^\alpha \ll M_i^z \approx M_{\text{S}}$ (from zero) of the x and y magnetization components only, because the magnitude of the cell magnetic moment should be conserved. The deterministic effective field evaluated according to (64) will have on each cell also only x and y components $H_i^{x(y)}$ which will be of same order of magnitude as ΔM_i^α. Writing the LLG equations of motion (65) for ΔM_i^x and ΔM_i^y, neglecting the terms $\Delta M_i^{x(y)}\cdot H_{i,z}^{\text{fl}}$ which are small compared to $M_i^z\cdot H_{i,x(y)}^{\text{fl}}$ (because $\Delta M_i^\alpha \ll M_i^z$) and linearizing the resulted equations with respect to small deviations $\Delta M_i^x \equiv M_i^x$ and $\Delta M_i^y \equiv M_i^y$, we obtain the system

$$\frac{1}{\gamma M_{\text{S}}}\frac{\mathrm{d}M_i^x}{\mathrm{d}t} = +(H_{i,\text{det}}^y + H_{i,\text{fl}}^y) + \lambda(H_{i,\text{det}}^x + H_{i,\text{fl}}^x) \tag{68}$$

$$\frac{1}{\gamma M_{\text{S}}}\frac{\mathrm{d}M_i^y}{\mathrm{d}t} = -(H_{i,\text{det}}^x + H_{i,\text{fl}}^x) + \lambda(H_{i,\text{det}}^y + H_{i,\text{fl}}^y) \tag{69}$$

It is evident from these equations that the coefficients $\Gamma_{ik}^{\alpha\beta}$ for $\alpha \neq \beta$ obey the relation $\Gamma_{ii}^{xy} = -\Gamma_{ii}^{yx}$, so that the cross-correlation coefficients of the fluctuation field projections on the given cell are identically zero: $C_{ii}^{xy} = C_{ii}^{yx} \sim (\Gamma_{ii}^{xy} + \Gamma_{ii}^{yx}) = 0$. This property, being obtained in our specific coordinate system, should remain the same in any other coordinates due to the space isotropy. *Hence there are no physical correlations neither between the random fields on different cells nor between the random field components on one and the same cell*. This result was obtained also in Chubykalo *et al*. (2003) with a somewhat more complicated method.

Note that this statement does not apply to artificial (having nonphysical nature) correlations between the random fields on different cells that appear due to the finite-element discretization of an initially continuous problem. This topic is discussed in the next subsection.

* * *

A very interesting theme is the discussion of the correlation properties of the random thermal fields in micromagnetics

from a point of view of the fluctuation-dissipation theorem (FDT). Due to the space limitations we preferred not to include this topic into the current review, because it requires a careful and detailed discussion supplemented by a substantial amount of the readers theoretical knowledge. A very transparent and clear discussion of this topic at a high scientific level can be found in Smith (2001).

4 DISCRETIZATION EFFECTS IN DYNAMIC MICROMAGNETIC SIMULATION

4.1 Discretization effects for $T = 0$

In this subsection, we discuss the influence of a finite-element representation of the continuous micromagnetic problem (discretization) on the magnetization dynamics observed in numerical simulations performed *without* taking into account thermal fluctuations, that is, for $T = 0$.

To demonstrate the importance of the discretization effects we have chosen the following problem: we study the switching dynamics of a nanoelement with lateral sizes $L_x \times L_z = 400 \times 600\,\text{nm}$, thickness $h = 5\,\text{nm}$ (our $0xz$-plane coincides with the element plane), $M_S = 1000\,\text{G}$ and exchange stiffness $A = 10^{-6}\,\text{erg cm}^{-1}$. To simplify our task, we have set the magnetocrystalline anisotropy to zero. The switching of this element is simulated integrating the LLG equation (1) using an optimized Bulirsch–Stoer algorithm with the adaptive step-size control. We start from the S-type remanent state applying at $t = 0$ the external field $\mathbf{H} = H_z\mathbf{e}_z$ with $H_z = -200\,\text{Oe}$; this field is well beyond the corresponding quasistatic switching field $H_{sw} \approx -80\,\text{Oe}$. To study the discretization effects *s*imulations were done for five sequentially refined grids ($N_x \times N_z = 40 \times 60, 60 \times 90, 80 \times 120, 120 \times 180, 200 \times 300$) with the same (1:1) aspect ratio of the grid cell.

The switching process for the most interesting low damping case $\lambda = 0.01$ is shown in Figure 1(a) (grid $N_x \times N_z = 120 \times 180$): it starts with the reversal of closure domains near the short element borders, proceeds via the reversal of the central domain and is completed by the 'flip' of narrow domains near the long sides.

To emphasize the importance of the discretization effects we have compared results for several grids listed above. In Figure 1(b) we present corresponding $m_x(t)$ dependencies, because in our geometry the influence of the discretization effects can be most clearly seen on this projection. It can be clearly seen that the remagnetization curves do *not* converge to any limiting curve up to the finest grid $N_x \times N_z = 200 \times 300$. The effect is even *qualitative*, as it can be seen from the comparison of final states (m_x-gray-scale maps on the right in Figure 1(b)) for all discretizations $N_x \times N_z \leq 120 \times 180$ and for $N_x \times N_z = 200 \times 300$.

This discrepancy can not be attributed to an insufficient discretization of the interaction (energy) terms, because already for a moderate grid $N_x \times N_z = 80 \times 120$ the cell sizes $\Delta_x = \Delta_z = 5\,\text{nm}$ are smaller than our characteristic micromagnetic length $l_{\text{dem}} = (A/M_S^2)^{1/2} = 10\,\text{nm}$. We have also verified starting from the grid $N_x \times N_z = 60 \times 90$ quasistatic hysteresis loops did not change when the grid was refined further.

The reason for a significant modification of the switching process by the grid refinement is a strong influence

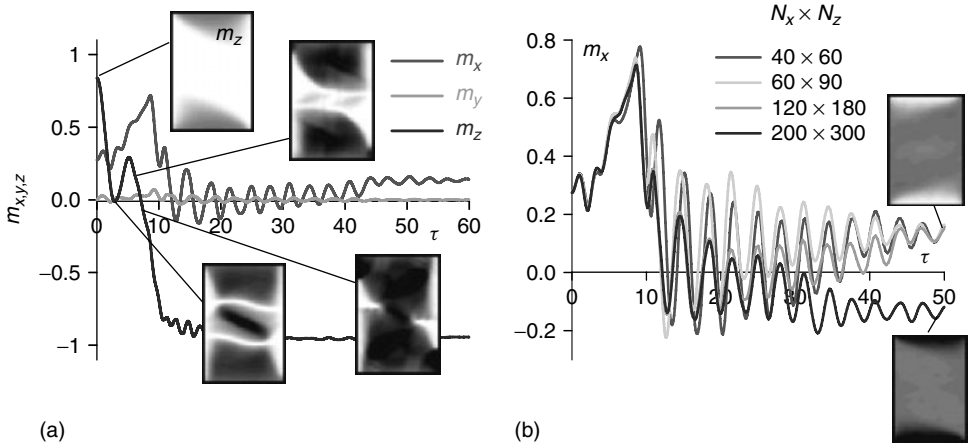

Figure 1. Switching of a thin 'soft' magnetic element ($400 \times 600 \times 5\,\text{nm}$) with a *low* damping ($\lambda = 0.01$) in a field $H_z = -200\,\text{Oe}$ starting from the S-type remanent state: (a) time-dependencies of all magnetization projections for the discretization $N_x \times N_z = 120 \times 180$($m_z$-grey-scale maps for several times $\tau = t\gamma M_S$ are shown). (b) m_x time dependencies simulated using various grids as shown in the legend. (Reproduced from D.V. Berkov *et al*., 2002. © 2002 with permission from IEEE.)

of magnetic excitations with a short wavelength. For the static case, it is sufficient to discretize the system using the mesh size somewhat smaller than the characteristic (exchange or demagnetizing) magnetic length of the material. For dynamics it is, generally speaking, not true. Even if the mesh is fine enough to represent all the features of the starting magnetization state, during the remagnetization process magnons with the wavelengths shorter than the grid cell size may play an important role, so that magnons with decreasing wavelengths appear when the remagnetization proceeds. As soon as the grid is unable to support these magnons, simulations became inadequate (Berkov, 2002a). This means that in such situations *dynamical* simulations on a given lattice are valid up to some *maximal* time duration.

The problem emphasized in this subsection requires further thorough investigation, because recently the so-called spin-injection driven magnetization dynamics was predicted theoretically and discovered experimentally (see the review of Miltat, Albuquerque and Thiaville, 2001 in this Volume). It has been shown that when the magnetization dynamics is excited by a spin polarized current, both (i) large deviations of the magnetization from its equilibrium position and (ii) quasichaotic magnetization dynamics (where spatial variations of the magnetization are very fast) are possible and even represent quite common features of corresponding remagnetization processes. This rapidly developing topic with potentially very rich applications makes the study of numerical artifacts due to the interplay of the discretization grid with short-wavelength magnons really important.

For systems with *larger* dissipation the effect demonstrated above may be absent due to a much smaller decay times of the short-wave magnons (so that they do not play any significant role by switching).

4.2 Influence of the discretization on the random field correlations

We proceed with the consideration of discretization effects on the magnetization dynamics simulated at finite temperatures, that is, with the fluctuation field $\mathbf{H}^{\mathrm{fl}}(\mathbf{r}, t)$ included into the LLG equation. The standard assumption (29) that this field is δ correlated in space and time may become invalid due to the following effect: as pointed above, by discretizing a continuous magnetic film we exclude all magnons with the wavelength smaller than the grid cell size $\Delta = \min(\Delta x, \Delta z)$. However, these magnons can still have a mean free path *much larger* than the grid cell size, thus causing substantial correlations especially of the exchange fields on neighboring cells. Although these excitations cannot be included into simulations on the given grid explicitly, it is possible to take them into account as an additional contribution to the fluctuation field $\mathbf{H}^{\mathrm{fl}}$ with the corresponding correlation properties.

To compute the correlation function (CF) of the effective field produced by such short-wave magnons, we have first performed simulations (with the white noise only) solving LLG equations at the grid which was finer than the 'actual' grid intended to be used for final simulations. Then from the total effective field produced at this fine grid all contributions with the wavelength *larger* than the cell sizes of the 'actual' grid Δ were cut out, so that only magnons with short wavelengths $\lambda_{\mathrm{mag}} \leq \Delta$ remained. Afterwards magnetic field generated by these short-wave magnons was calculated and averaged over all subcells inside the given cell of the actual simulation grid. Finally, the correlation properties of *this averaged field* were evaluated (Berkov and Gorn, 2004).

The resulting CF has a quite complicated form both in space (Figure2a) and time (Figure 2b) and can be roughly described as exponentially decaying oscillations. Both the

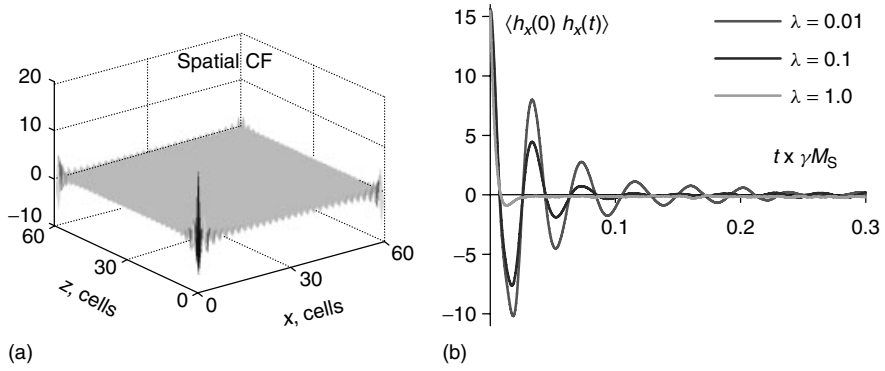

Figure 2. Correlation functions (CF) of the x component of the random field $\mathbf{H}^{\mathrm{fl}}$ resulting from the short-wave magnons. (a) 2D spatial CF, (b) Temporal CF on one and the same cell for various dissipation constants λ. (Reproduced from Berkov *et al*., 2004, with permission from Elsevier. © 2004.)

time and space oscillation periods are determined by the corresponding properties of the magnons with the shortest wavelength available for the 'actual' grid. The *space* decay length depends mainly on the 'quasistatic' magnetic system parameters like the saturation magnetization and exchange constant, whereas the decay *time* is determined by the damping λ.

To take into account the influence of the short-wave magnons which are cut off by the given grid, one should, strictly speaking, perform simulations on this grid by solving the SDE system (20) with both the standard white noise term and an additional colored noise with correlations imposed by *the field of these short-wave magnons*. For this purpose it is necessary to implement an algorithm, which could generate a Gaussian random noise with any given correlation function.

Several methods for generation of such a noise are available. Matrix methods (James, 1980) can generate random sequences with arbitrary given CF, but are very time and storage consuming. Linear Langevin equation (Garcia-Ojalvo and Sancho, 1994) or the so-called 'physical' methods (simulation of a simplified system without long-range interactions) are fast, but can generate only noise with monotonously or regularly oscillating exponentially decreasing CFs. These methods may be in principle applied to micromagnetic systems, because correlations caused by the short-wave magnons are mostly oscillating and exponentially decreasing.

However, correlation functions like those shown above still exhibit significant irregularities, which cannot be reproduced by 'physical' method. In this case, some version of a spectral method (Romero and Sancho, 1999) should be used, because this method can generate arbitrarily correlated random numbers. The method is based on the usage of the temporal and spatial FT of the required correlation function which after the multiplication with the so-called anticorrelated (in the Fourier space) random numbers gives the Fourier image of the random number field with requested correlations. Their inverse FT provides the requested random numbers themselves (Romero and Sancho, 1999). The important disadvantage of the method is that the complete correlation matrix should be stored (for a spatially 2D system our the dimension of the this matrix would be $N_x \times N_z \times L_t$, where L_t is the number of time steps), requiring large memory resources. For this reason, in most cases the usage of so-called 'external storage' of the Fourier transform is unavoidable (Press, Teukolsky, Vetterling and Flannery, 1992).

4.3 Discretization and the density of magnon states

Finite-element discretization of a micromagnetic system *qualitatively* affects the spectral power its thermal excitations, so this question should be addressed here in detail. To present the main point as transparent as possible, we consider a simplest model: a square region of an extended thin film (periodic boundary conditions are assumed) in an external field perpendicular to the film plane and neglect anisotropy and magnetodipolar interactions.

A spectrum of *equilibrium* thermal magnetic excitations can be efficiently computed using the Langevin dynamics (Berkov and Gorn, 2005). Starting from the saturated state along the external field we integrate the SDEs (20) till the total energy does not change systematically with time (equilibrium is reached). From this time moment we save the trajectories of every cell magnetization during a sufficiently long time (which depends on the desired accuracy and

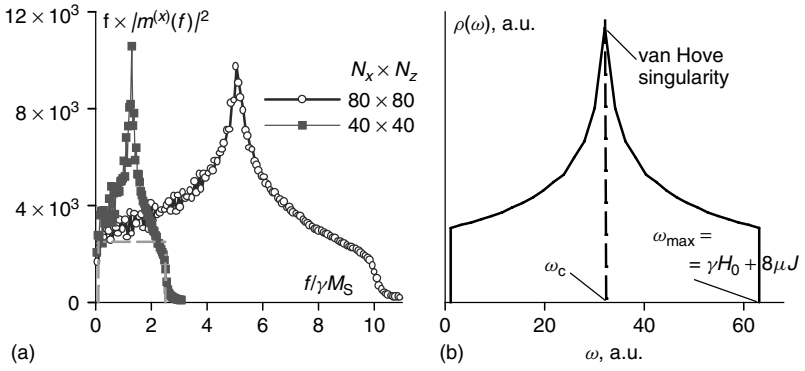

Figure 3. (a) Power spectrum of m_x-oscillations for various discretizations. Cusps are the manifestations of the magnon DoS singularity (right panel). The dashed rectangle represents the spectrum expected in the limit of very fine discretization for a low frequency region available for the 40×40 discretization; (b) density of magnon states for the model (70). The cusp by $\omega_c = \omega_{min} + \omega_{max})/2$ is the van Hove singularity common for all 2D models with the cosine like $\omega(\mathbf{k})$ dependence. (Reproduced from Berkov *et al*., 2005, with permission from Elsevier. © 2005.)

frequency resolution of the spectral power finally obtained). Finally we perform the temporal FT of these trajectories and averaging over several thermal noise realizations.

Corresponding results for a thin-film region with lateral sizes 400×400 nm, thickness $h = 5$ nm, $M_S = 1000$ G, $A = 10^{-6}$ erg cm^{-1} placed in an external field $H_{ext} = 100$ Oe are presented in Figure 3(a), where oscillation power spectra of m_x projection at $T = 10$ K are shown for two different discretizations. The most striking features of these spectra are (i) sharp cusps in the middle and (ii) a shift of this cusp towards higher frequencies when the grid is refined.

This result can be easily understood as follows. After the in-plane discretization of the film into $N_x \times N_y$ cells with the sizes Δx and Δy and volumes ΔV the system energy $E = E_{\text{ext}} + E_{\text{exch}}$ is converted into the sum over cells i, j

$$E = -\mu \sum_{i,j=1}^{N_{x(y)}} \mathbf{m}_{ij} \mathbf{H}_{ij}^{\text{ext}} - \frac{1}{2} J \mu^2 \sum_{\langle i,j \rangle} (\mathbf{m}_i \mathbf{m}_j) \qquad (70)$$

where μ is the cell magnetic moment. The exchange constant J in (70) depends on the exchange stiffness A and the grid cell parameters as

$$J = \frac{A}{M_S^2 \cdot \Delta V} \left(\frac{1}{\Delta x^2} + \frac{1}{\Delta y^2} \right) \qquad (71)$$

As usual, the total oscillation power for the given frequency ω in a thermal equilibrium is directly proportional to the number of modes contributing to this frequency, that is, to the magnon density of states $\rho(\omega)$. For a typical *lattice* model described by the energy (70) this density of states is well known. Namely, the quadratic expansion of (70) over small magnetization deviations from the ground state (small temperature or large external field limit) leads to the eigenfrequencies $\omega_{pq} = \gamma \cdot (H_{\text{ext}} + \mu J \cdot f_{pq})$ depending on the eigenmodes wave vector indices p and q via the sum of cos functions as $f_{pq} = 2 \cdot (2 - \cos(2\pi p / N_x) - \cos(2\pi q / N_z))$, which is common for all 2D lattice models with the nearest-neighbors harmonic interaction. If the eigenfrequencies depend on the wave vectors in a cosine like manner, then the density of states (Figure 3b) contains the famous van Hove singularity in its middle, which is clearly visible in both spectra in Figure 3(a) as a cusp. The spectrum shift toward higher frequencies when the discretization is refined follows simply from the fact that the eigenfrequencies $\omega_{pq} = \gamma \cdot H_{\text{ext}} + \mu J \cdot f_{pq})$, being proportional to the exchange constant J, increase according to (71) as an inverse square of a cell size when a mesh is refined.

The actual excitation spectrum of a real system (which we attempt to simulate) also contains such a cusp (a real system is discrete at the atomic level) but for frequencies determined by the interatomic distances and thus absolutely unavailable for simulations. This means that the correct spectrum of the continuous thin film model in the frequency region available for micromagnetic simulations is nearly flat as shown by the dashed rectangle in Figure 3(a). Hence, in order to obtain adequate results for equilibrium system properties using such simulations, one should either work in the frequency region where the spectrum is still approximately flat ($\omega \ll \omega_c$) or use a *colored* noise to correct the excitation spectrum of the corresponding lattice model.

5 MAGNETIZATION RELAXATION OVER HIGH ENERGY BARRIERS

For system with high energy barriers $\Delta E \gg kT$ direct simulation of the magnetic moment trajectories using the Langevin dynamics is fairly impossible. Such simulations simply mimic the time-dependent system behavior so that the simulation time necessary to overcome the barrier *exponentially* growths with its height following the Arrhenius–Van't Hoff law (probability to overcome the barrier is $p \sim \exp(-\Delta E / T)$)–exactly as for real systems.

Nevertheless, methods for numerical simulations allowing to study transitions over large barriers are highly desirable from the practical point of view: they are the only way to predict the long-time stability of the information storage devices. To evaluate the transition probability p over such barriers we must in the first place find the *lowest* saddle point between the two metastable state of interest. Its height gives us the corresponding energy barrier ΔE between these states, allowing to estimate p from the Arrhenius–Van't Hoff law. Analytical methods for the saddle-point search exist only for relatively simple magnetic systems (Braun, 1994, 2000; Klik and Gunther, 1990). In principle, such a saddle point can be found by solving a system of nonlinear equations $\partial E / \partial x_i = 0$ (where x_i denote the variables of a system configuration space), because at a saddle point *all* energy derivatives $\partial E / \partial x_i$ should be zero, but neither an energy maximum nor a minimum should be achieved. However, general methods for the solution of such systems are not available, and there exist even arguments that there will never be any (Press, Teukolsky, Vetterling and Flannery, 1992). For this reasons numerical methods based on other principles are required.

5.1 Time-temperature scaling method

The time-temperature scaling method (Xue and Victora, 2000) quantifies the rough idea that in some cases simulations of the transition over high energy barriers involving

macroscopically long waiting times at *low* temperatures can be replaced by simulations over the same energy barrier, but at a much *higher* temperature so that the transition time (and hence – the simulation time) is much smaller and is accessible for simulations.

To make this idea applicable in numerical simulations, we need the quantitative relation between the time and temperature scales. To establish such a relation, we start from the simplest version of the Arrhenius–Van't Hoff law which states that the average transition time τ_{av} depends on the energy barrier height ΔE and the system temperature T mainly exponentially via their ratio as

$$\tau_{\mathrm{av}} = \frac{1}{\nu_0} \exp\left(\frac{\Delta E}{kT}\right) \tag{72}$$

where the prefactor is defined using the so-called 'attempt frequency' ν_0. If the temperature dependence of this frequency is weak compared to the exponent $\exp(-\Delta E/kT)$ then the product $kT{\cdot}\log(\tau_{\mathrm{av}}{\bullet}\nu_0)$ remains constant for the transition over this barrier. This means that if a transition over some barrier takes on average a long time τ_{long} at a (low) temperature T_{long}, then in order to observe the same transition during a desired short time τ_{short} we need to increase the temperature up to the value $T_{\mathrm{s/l}}$ which is related to the quantities introduce above via

$$T_{\mathrm{s/l}} \log(\nu_0 \tau_{\mathrm{short}}) = T_{\mathrm{long}} \log(\nu_0 \tau_{\mathrm{long}}) \tag{73}$$

To calculate from this equation, the scaled temperature $T_{s/l}$ which we should use in simulations if we would like to reduce our simulation time from the inaccessible value τ_{long} down to τ_{short}, we need to determine the attempt frequency ν_0 for the system under study. Analytical formulae for ν_0 are available only for the simplest systems like a single-domain particle (Brown, 1963b). For this reason Xue and Victora (2000) have proposed the following trick. They have introduced a new time τ_{ref} which is much larger than the short time τ_{short} (which we would like to use for final simulations), but still small enough so that simulations during this time are possible and the desired transition occurs during the time τ_{ref} at some intermediate temperature T_{ref}. The first step for the determination of the attempt frequency ν_0 (and hence – the temperature $T_{\mathrm{s/l}}$) is the simulation of a system at the temperature T_{ref} during the time τ_{ref}, whereby some physical property of the system is determined or some dynamical process in the system is recorded. Then one should perform several simulation runs at different temperatures during the short time τ_{short} and *find the temperature* $T_{\mathrm{s/r}}$ for which the process recorded at T_{ref} during the time τ_{ref} *proceeds as similar as possible* to the process observed during the short time τ_{short}. This means, that the corresponding times and temperatures are connected via the same relation as (73), namely

$$T_{\mathrm{s/r}} \log(\nu_0 \tau_{\mathrm{short}}) = T_{\mathrm{ref}} \log(\nu_0 \tau_{\mathrm{ref}}) \tag{74}$$

This latter relation can be used to extract the attempt frequency ν_0, because all other quantities here are known. Determination of ν_0 from (74) and its substitution into (73) leads to the following expression for the required high simulation temperature $T_{\mathrm{s/l}}$:

$$T_{\mathrm{s/l}} = T_{\mathrm{long}} + (T_{\mathrm{s/r}} - T_{\mathrm{ref}}) \cdot \frac{T_{\mathrm{long}} \log(\tau_{\mathrm{long}}/\tau_{\mathrm{short}})}{T_{\mathrm{ref}} \log(\tau_{\mathrm{ref}}/\tau_{\mathrm{short}})} \tag{75}$$

Simulations at this temperature during the time τ_{short} should now reproduce the behavior of the system under study at the low temperature T_{long} during the time τ_{long} which is exponentially larger than τ_{short} due to the relation (73).

Xue and Victora have applied their algorithm to the simulations of the hysteresis loops at various field sweep rates R (which served as inverse time scales τ_{short} etc.). A remarkable agreement between the two numerically calculated loops for the sweep rates 0.5 and 50 Oe nsec^{-1} was obtained and the loop measured experimentally at $R = 50\,\mathrm{Oe\,sec^{-1}}$ (i.e., nine orders of magnitude slower) could be successfully predicted (Xue and Victora, 2000). They have also simulated the process of a bit decay in magnetic recording media (Xue and Victora, 2001) over a macroscopically long time scale, which is highly interesting for the development of high-density magnetic storage.

Concluding this subsection, we note that the method outlined above probably is not able to reproduce correctly the magnetization dynamics for a system with *low* dissipation, when the precession term in the LLG equation is really important (results of Xue and Victora were obtained on systems with moderate damping). The reason is that actual simulations in this method are performed at temperatures much higher that the actual system temperature, so that the relation between the random (fluctuation) field and the deterministic field is wrong. Another limitation of this formalism is the usage of the relation (72), which is valid only when the entropic contribution to the transition probability (curvature of the energy landscape in the vicinity of a saddle point and energy minima) can be neglected.

5.2 Rigorous evaluation methods for the energy barrier height

In this subsection, we describe general numerical methods for the evaluation of the energy barrier height between the two metastable states. All methods aim to evaluate some

kind of an optimal trajectory between these states and the required energy barrier can then be calculated as the barrier along this trajectory. The transition probability between the energy minima in question can then be evaluated using the general transition-rate theory (Hoenggi, Talkner and Borkovec, 1990), whereby the features of the energy surface near critical points may be also taken into account.

5.2.1 *Minimization of a thermodynamical action (Onsager–Machlup functional)*

General idea

This method is based on the search for the *most probable transition path* between the two energy minima by minimizing the corresponding *thermodynamical action* derived from the path-integral formulation of the problem. The underlying idea (Onsager and Machlup, 1953) can be explained considering a system of N particles with coordinates $x_i (i = 1, \ldots, N)$ and the interaction energy $V(\mathbf{x})(\mathbf{x} = (x_1, \ldots, x_N))$ in a viscous fluid. Langevin equations for this system are

$$\dot{x}_i = -\frac{\partial V(\mathbf{x})}{\partial x_i} + \xi_i(t), \quad i = 1, \ldots, N \tag{76}$$

where we have neglected the inertial term for simplicity and absorbed the friction constant into the time scaling. Langevin forces ξ_i are again assumed to be independent Gaussian δ-correlated random variables: $\langle \xi_i(0)\xi_j(t)\rangle = 2D\delta_{ij}\delta(t)$.

Due to these simple correlation properties the probability of some *particular* noise realization $\{\xi_i(t)\}, i = 1, \ldots, N$ for the time period $[0, t_\mathrm{f}]$ is (Onsager and Machlup, 1953); (Bray and McKane, 1989)

$$P[\boldsymbol{\xi}(t)] = A \exp\left[-\frac{1}{4D}\int_0^{t_\mathrm{f}} \sum_i \xi_i^2(t)\mathrm{d}t\right] \tag{77}$$

Rewriting the system (76) as $\xi_i(t) = \mathrm{d}x_i/\mathrm{d}t + \partial V(\mathbf{x})/\partial x_i$ and introducing the Jacobian $J[\mathbf{x}(t)]$ of the transformation $\mathbf{x} \to \boldsymbol{\xi}$, we immediately obtain that the probability to observe a *given trajectory* $\mathbf{x}(t)$ for the transition $A \to B$ during the time t_f $(\mathbf{x}_A(0) \to \mathbf{x}_B(t_\mathrm{f}))$ is

$$P[\mathbf{x}(t)] \sim J[\mathbf{x}] \exp\left[-\frac{S(\mathbf{x}(t), t_\mathrm{f})}{4D}\right] \tag{78}$$

where the *thermodynamical action* $S(\mathbf{x}(t))$ is defined as

$$S(\mathbf{x}(t), t_\mathrm{f}) = \int_0^{t_\mathrm{f}} \mathrm{d}t \sum_i \left(\frac{\mathrm{d}x_i}{\mathrm{d}t} + \frac{\partial V(\mathbf{x})}{\partial x_i}\right)^2 \tag{79}$$

It is obvious that the trajectory which minimizes the action $S(\mathbf{x}(t))$ provides the most probable (optimal) transition trajectory $\mathbf{x}_\mathrm{opt}(t)$, along which the energy barrier for this transition can be found: $\Delta E(A \to B) = E_\mathrm{max}(\mathbf{x}_\mathrm{opt}) - E_A$. The minimization of the functional $S(\mathbf{x}(t))$ can be performed using various numerical methods which employ the discretization of the transition path $\mathbf{x}(t)$ thus reducing the task of minimizing (79) to the problem of the minimization of a many-variable function (see Berkov, 1998 for detail).

Unfortunately, the minimization of the functional (79) by itself, being technically quite complicate, does *not* represent a main problem when searching for an optimal physical transition path. The main problem is the presence of many 'false' local minima of the functional (79), that is, the existence of many trajectories between the states A and B *which minimize* (79) *but do not provide any information about the corresponding energy barriers*.

To explain why this is almost always the case we note that for *any* path for which the conditions $\mathrm{d}x_i/\mathrm{d}t = \pm\partial V(\mathbf{x})/\partial x_i$ are fulfilled (the plus/minus sign correspond to the downhill/uphill trajectory parts) provides an extremum to the action (79) (Bray and McKane, 1989). This means that the extremal trajectories for the action functional (79) go *along the gradient lines* of the energy surface.

On a very simple 2D energy landscape shown in Figure 4(a) *both* the solid line $M_1 \to M_2$ and the dashed line $M_1 \to P_2 \to M_2$ deliver local extrema to the action for the transition $M_1 \to M_2$, because both paths proceed along the gradient lines of the energy surface. Moreover, these both extrema are local *minima* of the action; in fact, they were obtained by minimizing (79) with the potential shown in Figure 4 as a gray-scale map simply starting from different initial trajectories. However, the solid line trajectory passes through the saddle point, giving the correct energy barrier height (the 'true' optimal trajectory), whereas the dashed line $M_1 \to P_2 \to M_2$ goes via the energy *maximum* supplying no useful information whatsoever ('false' optimal trajectory). The next example shown in Figure 4(b) demonstrates that even the *value* of the action (given by the sum of heights which an optimal trajectory has to climb over) along the 'false' optimal path $(M_1 \to P_2 \to M_2)$ may be smaller than the corresponding value along the 'true' optimal trajectory. Hence without a *reliable* algorithm able to distinguish between these two kinds of optimal paths the whole method is absolutely useless, because the number of 'false' optimal trajectories exponentially growth with the complexity of system.

An apparently straightforward possibility to discriminate between these two cases is the analysis of the *curvature tensor* of the energy surface at the points where the energy along the optimal trajectory has local *maxima*: if the corresponding matrix of the second energy derivatives has exactly *one*

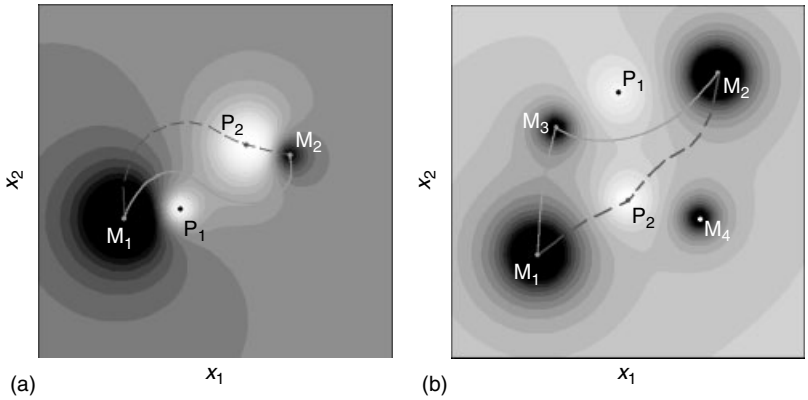

Figure 4. (a) 'True' (solid line) and 'false' (dashed line) optimal trajectories for a simple energy landscape. (b) An example of an energy landscape, where the action (79) along the 'false' optimal path $M_1 \to P_2 \to M_2$ may be even smaller than along the 'true' path $M_1 \to M_3 \to M_2$ (see text for details). (Reproduced from Berkov *et al.*, 1998, with permission from Elsevier. © 1998.)

negative eigenvalue, then this point indeed corresponds to a transition saddle. This method, however, is not sufficiently reliable due to a discrete representation of the continuous trajectory and a finite accuracy by the determination of an 'optimal' path. An alternative algorithm based on small 'jumps' away from the trajectory point with the highest energy in a random direction and subsequent minimization of the system energy starting from this new position, is described in detail in (Berkov, 1998).

Another problem arises due to the presence of the transition time t_f in the action (79) as the upper integral limit, which should be known in advance to set the time step and/or the number of time slices in the discretized action version; this transition time is of course not known. Fortunately, the barrier *height* determined from the discretized action turned out to depend on the t_f-value only slightly. For this reason sufficiently accurate results could be obtained by minimizing the discretized action using the small constant time step and simply doubling the number of time slices until the relative difference between the two barriers heights obtained for the subsequent action minimizations becomes less than a certain small threshold.

Implementation for magnetic systems

To apply this method to systems of interacting magnetic moments we have to start with the magnetic counterpart to the Langevin equation (76), namely, with the stochastic Landau–Lifshitz–Gilbert equation of motion for magnetic moments (20). The precession term in this equation affects, of course, the optimal transition *trajectory*, but does not change the system energy and hence it is reasonable to assume that it does not change the barrier *height* for this transition (see also our discussion of the string method below). For this reason we neglect the precession term in (20) and obtain the equation of motion for the magnetization unit vectors $\mathbf{m}_i$

$$\frac{\mathrm{d}\mathbf{m}_i}{\mathrm{d}t} = -\Big[\mathbf{m}_i \times \Big[\mathbf{m}_i \times (\mathbf{h}_i^{\mathrm{det}} + \mathbf{h}_i^{\mathrm{fl}})\Big]\Big] = -\mathbf{m}_i \cdot (\mathbf{m}_i \cdot \mathbf{h}_i^{\mathrm{tot}}) + \mathbf{h}_i^{\mathrm{tot}} \tag{80}$$

where all constants are again absorbed in the time unit, the total field is $\mathbf{h}^{\mathrm{tot}} = \mathbf{h}^{\mathrm{det}} + \mathbf{h}^{\mathrm{fl}}$ and the normalization $m_i = 1$ was used by the last transformation.

The conservation of the magnetic moment magnitude enforces the transition to spherical coordinates (θ, ϕ) of $\mathbf{m}$, because only the random field components perpendicular to $\mathbf{m}$ should be taken into account. Transforming all vectors to the new coordinates with the z'-axis along $\mathbf{m}$ and the x'-axis in the meridian plane of the initial spherical coordinates (so that in the initial system $m_x = \sin\theta\cos\varphi$, $m_y = \sin\theta\sin\varphi$, $m_z = \cos\theta$), we obtain equations of motion for the magnetization angles

$$\frac{\partial\theta_i}{\partial t} = -\frac{\partial E\{\Omega\}}{\partial\theta_i} + h^{\mathrm{fl}}_{i,x'},$$
$$\sin\theta_i \cdot \frac{\partial\phi_i}{\partial t} = -\frac{1}{\sin\theta_i} \cdot \frac{\partial E\{\Omega\}}{\partial\phi_i} + h^{\mathrm{fl}}_{i,y'} \tag{81}$$

where $h^{\mathrm{fl}}_{x'}$ and $h^{\mathrm{fl}}_{y'}$ are Cartesian components of the fluctuation field $\mathbf{h}^{\mathrm{fl}}$ in the new coordinate system. Deterministic effective field $\mathbf{h}^{\mathrm{det}}$ is already contained in corresponding angular derivatives of the magnetic energy E{Ω} (where {Ω} denotes the set of all angles (θ_i, φ_i)), which may include also the interaction energy of any kind (i.e., exchange, dipolar, RKKY, etc.).

The system (81) is fully analogous to (76) so that under the same assumptions (Langevin field components are independent Gaussian δ-correlated random variables) the magnetization path in the Ω space which minimizes the

thermodynamical action S for a magnetic system

$$S[\Omega(t)] = \int_0^{t_f} \mathrm{d}t \sum_i \left[\left(\frac{\mathrm{d}\theta_i}{\mathrm{d}t} + \frac{\partial E\{\Omega\}}{\partial \theta_i} \right)^2 + \left(\sin\theta_i \cdot \frac{\mathrm{d}\phi_i}{\mathrm{d}t} + \frac{1}{\sin\theta_i} \cdot \frac{\partial E\{\Omega\}}{\partial \phi_i} \right)^2 \right] \qquad (82)$$

provides the information about the energy barrier separating the states Ω_A and Ω_B.

Application for magnetic nanocomposites

With this method we have calculated the distribution of the energy barriers in a system of single-domain magnetic particles (embedded in a nonmagnetic matrix) with the uniaxial anisotropy and magnetodipolar interaction between the particles. The most intriguing question for this system is the influence of the magnetodipolar interaction on the distribution density of the energy barriers $\rho(E)$ (Hansen and Morup, 1998; Dormann, Fiorani and Tronc, 1999), which controls both the reversible and irreversible thermodynamics of the system. To solve this question, we have computed $\rho(E)$ for various volume concentrations of the magnetic phase, thus varying the interaction strength.

Calculations were performed for systems with high ($\beta = 2K/M_S^2 = 2.0$), moderate ($\beta = 0.5$) and low ($\beta = 0.2$) single-particle anisotropies. The energy barrier distributions were accumulated from $N_{conf} = 8$ realizations of the particle disorder; for each configurations about $N_{trans} = 200$ transitions between metastable states were analyzed. Corresponding results are shown in Figure 5 were the distribution of the reduced energy barriers $\varepsilon = E/M_S^2 V$ are presented.

First of all, it can be seen that for low particle concentrations ($\leq 1\%$)$\rho(\varepsilon)$ consists of the relatively narrow peak positioned at the value corresponding to the energy barrier $\varepsilon_{sp} = \beta/2$ for a single particle moment flip, as it should be for a weakly interacting system. The position of this single-particle flip barrier is shown both in Figure 5 with the dashed line. As expected, with increasing concentration the energy barrier density broadens, but for the systems with the low and high anisotropy this broadening occurs in a qualitatively different ways. For the high-anisotropy case (Figure 5, right column) the broadening of $\rho(\varepsilon)$ with increasing concentration is accompanied by its shift toward *lower* energy barriers, so that already for moderate particle concentration ($\geq 4\%$) almost all barriers lie below the value for a single particle.

For the system of particles with the low anisotropy (Figure 5, left column) barriers both higher *and* lower than a single particle barrier arise. However, the overall

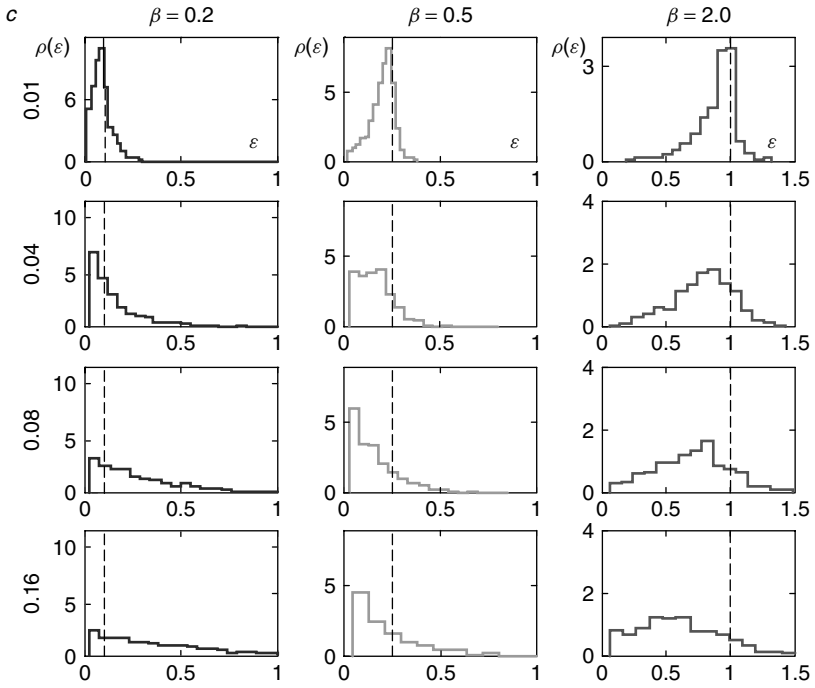

Figure 5. Density of the energy barriers for transitions between randomly chosen energy minima in a disordered magnetic particle system with the low ($\beta = 0.2$, left column), moderate ($\beta = 0.5$, middle column) and high ($\beta = 2.0$, right column) single-particle anisotropies for various particle volume fractions c. Dashed lines show positions of the energy barriers for a single particle with the corresponding anisotropy.

energy barrier spectrum clearly shifts toward *higher* energies with increasing particle concentration. Detailed physical explanation of this behavior can be found in Berkov (2002b).

It is also important to keep in mind that different transitions cause different moment changes. The key question is whether the magnitude of the moment changes is *correlated* with the height of the corresponding energy barrier. If, for example, the moment change tends to zero when the energy barrier height for this particular transition decreases, small energy barriers would not play any significant role in the system thermodynamics, because corresponding magnetization changes would be nearly undetectable. For this reason we need a 2D *mutual* distribution of the energy barriers and moment changes $\rho(E,\Delta m)$. Corresponding contour plots for a system with the low anisotropy $\beta = 0.2$ and two different concentrations are shown in Figure 6. For the low concentration $c = 0.01$ the density $\rho(E, \Delta m)$ consists of a single sharp peak positioned near the point ($\varepsilon = 0.1$, $\Delta m = 2.0$), which corresponds to a single-particle flip. From $\rho(E, \Delta m)$ for the high concentration $c = 0.16$ it can be seen that, although the moment changes for the low barriers are concentrated at somewhat smaller values than Δm for the higher ones, they do *not* tend to zero. Hence all transitions provide approximately equivalent contributions to the system thermodynamics.

5.2.2 The string method

General idea

To explain the main idea of the string method (Ren and Vanden-Eijnden, 2002), we start with the same basic equation

$$\dot{x}_i = -\nabla V(\mathbf{x}) + \xi_i(t), \quad i = 1, \ldots, N \tag{83}$$

as for the action minimization method. It is intuitively clear, that for a system which time evolution is described by this

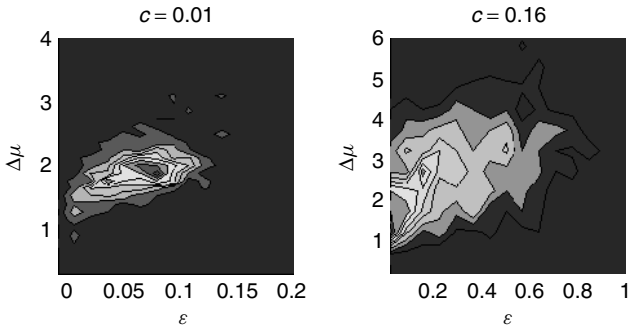

Figure 6. Mutual 2D distribution density $\rho(E, \Delta m)$ of the energy barriers and moment changes for dilute ($c = 0.01$, left panel) and concentrated ($c = 0.16$, right panel) system of magnetic particles with $\beta = 0.2$. (Reproduced from D.V. Berkov *et al.*, 2002. © 2002 with permission from IEEE.)

equation, the path $\phi_{opt}(\mathbf{x})$ which connects the two given metastable states A and B of the potential $V(\mathbf{x})$ and goes via a saddle point with the minimal energy barrier, satisfies the condition

$$(\nabla V)_\perp(\phi_{\text{opt}}) = 0 \tag{84}$$

In this notation $(\nabla V)_\perp(\phi)$denotes the component of the energy gradient, which is perpendicular to a curve ϕ. The physical sense of the statement (84) is that at any point of the optimal transition path the energy gradient is perpendicular to this path, with other words, the transition path proceeds along the energy gradient lines (see also our discussion of the action minimization method given above). A rigorous proof of this statement can be found in (Freidlin and Wentzell, 1998).

Although the equation (84) is only the necessary, but by no means the sufficient condition that the path ϕ goes through the lowest energy barrier between A and B (see, e.g., Figure 4a, where for the dashed line curve the condition $(\nabla V)_\perp(\phi) = 0$ is also fulfilled everywhere), this equation provides a useful hint how to find ϕ_{opt} starting from some arbitrary path ϕ: one can simply 'move' this path with the 'velocity'$\mathbf{u} = (\nabla V)_\perp(\phi)$which is normal to the path curve, until the stationary state of the system (given by the condition $\mathbf{u} = 0$) is reached.

To implement this idea, it is necessary to introduce some parameterization of a path ϕ, so that the coordinates of a point along the curve ϕ (in the N-dimensional configuration space of our system) are represented as functions of some parameter α: $x_1 = x_1(\alpha), \ldots, x_N = x_N(\alpha)$. Then, treating the evolution of ϕ with the velocity $\mathbf{u} = (\nabla V)_\perp(\phi)$ as a 'motion' in a fictitious time t, so that the instantaneous position of the path is given by the functions $\phi(\alpha, t) = (x_1(\alpha, t), \ldots, x_N(\alpha, t))$, we can write the corresponding 'dynamical' equation for $\phi(\alpha, t)$ as (Ren and Vanden-Eijnden, 2002)

$$\frac{\partial \phi(\alpha, t)}{\partial t} = -(\nabla V)_\perp(\phi) = -[\nabla V(\phi) - (\nabla V, \mathbf{e}_\tau)\mathbf{e}_\tau] \tag{85}$$

where the vector $\mathbf{e}_\tau$ is the unit tangent vector ϕ and thus its components at the curve point characterized by the parameter value α are

$$e_\tau^{(l)} = \frac{1}{\|\mathbf{x}_\alpha\|} \cdot \frac{\partial x^{(l)}(\alpha, t)}{\partial \alpha}, \quad \|x_\alpha\| = \sqrt{\sum_{l=1}^{N} \left(\frac{\partial x^{(l)}}{\partial \alpha} \right)^2} \tag{86}$$

so that the expression in the square brackets on the right-hand side of (85) is, as required, the component of the energy gradient vector normal to ϕ.

Numerical solution of (85) requires the discretization of the path ϕ using some concrete parametrization. A significant advantage of the string method is that this parametrization can be chosen arbitrarily basing on the considerations of either simplicity, or stability of a numerical method used to integrate (86), or required accuracy for the energy barrier value etc. The simplest choice is the 'natural' parametrization of a curve using the parameter α equal to its normalized arclength. In this case for a path starting at the point A with the coordinates $(x_A^{(1)}, \ldots, x_A^{(N)})$ and ending at $B(x_B^{(1)}, \ldots, x_B^{(N)})$ we have $\alpha(A) = 0$ and $\alpha(B) = 1$. Starting from some smooth curve between A and B, we discretize it into $K+1$ points equally spaced along the curve (for this kind of parametrization!) where the k-th point along the curve with coordinates $\mathbf{x}_k$ is characterized by the parameter value $\alpha_k = k/K (k = 0, \ldots, K)$. Calculating the derivatives of the coordinates as functions of α by some finite-difference approximation method, we compute the components of the unit tangent vector (86) for the given position of a string (at the given 'time' t) and make a 'time' step integrating numerically equations (85).

Application to micromagnetic systems

By implementation of this formalism for a micromagnetic system we encounter the same question as in the action minimization method: the dissipation term in the stochastic LLG-equation indeed represents the gradient of the micromagnetic energy (or, to be more precise, projection of this gradient into the hyperplane normal to all magnetic moment vectors), but the precession term does not. In their paper (Ren and Vanden-Eijnden, 2003) devoted to the usage of the string method in micromagnetism E *et al*. mention that they could prove that the local minima and saddle points remain the same after neglecting the precession term (unfortunately, this result is cited in (Ren and Vanden-Eijnden, 2003) as 'unpublished').

E *et al*. have demonstrated the applicability of the string method to micromagnetism in the papers (Ren and Vanden-Eijnden, 2002, 2003), where they have studied the remagnetization of a thin Permalloy nanoelement ($200 \times 200 \times 10\,\mathrm{nm}^3$ nanoelement, discretized in-plane only) choosing the two remanent S states with opposite magnetization orientations as initial and final states of the transition over a barrier (an external field was assumed to be absent). They could show that there exist at least two possible paths for this transition. The first path correspond to the magnetization switching via the intermediate S states (rotated by 90° relative to the initial and final S states) flower state, flower states (which were identified as saddle points) and the C state which was the lowest energy minimum visited during the transition process. The second transition path corresponded to the formation of the two vortices, which propagation through the nanoelement governed the switching process. The energy barriers for this second path were found to be significantly higher than for the first one. Another example briefly considered in (Ren and Vanden-Eijnden, 2003) deals with the remagnetization of a rectangular prism with a square cross-section ($200 \times 50 \times 50\,\mathrm{nm}^3$, discretized in 3D), where also two possible transition paths for the switching between the two states with the magnetization oriented (on average) along the two opposite directions of the long prism axis have been found.

From the methodical point of view, the string method has two significant advantages compared to the action minimization. First, a thermodynamical action itself already contains the first derivatives of the system energy (forces or torques). Hence its minimization with any method employing the *derivatives* of the function to be minimized (and only such methods provide a reasonable convergence speed) requires the evaluation of second derivatives of the system energy, that is, its Hessian matrix. By the string method which is based on the 'equation of motion' like (85), only the first energy derivatives are required, so that computational cost should be lower and the stability of the method higher than for the action minimization. The second important issue is the appearance of many undesired local maxima of the action, as discussed in the previous subsection. In the string method these maxima will probably play no significant role, because each point of the string is moved according to the equation (85) in the direction toward *lower* values of the system energy, so that it is highly unlikely that the string gets stuck at some 'false' metastable state like that shown in Figure 4, because such a 'false' path always goes through at least one energy *maximum*.

5.2.3 The elastic band method

Description of the method

The elastic band method, belonging to the so-called 'chain-of-states' method for searching the saddle points in complicate energy landscapes, is closely related to the string method discussed above. The main initial idea (exactly as in the discretized version of a string method) was to represent the continuous path in the configuration space of a system under study as a number of discrete states $\{\mathbf{S}_k\}(kd = 0, \ldots, K)$ and to build up an 'object function' of a type

$$Q = \sum_{k=1}^{K} V\{\mathbf{S}_k\} + \kappa \sum_{k=1}^{K-1} (\mathbf{S}_k - \mathbf{S}_{k-1})^2 \qquad (87)$$

Keeping the initial ($k = 0$) and final ($k = K$) states fixed and minimizing this function with respect to the set of states $\{\mathbf{S}_k | k = 1, \ldots, K-1\}$ should, on the one hand, lead to the decrease of the energies of the states involved (given by the terms $V\{\mathbf{S}_k\}$ in the first sum). On the other hand, the second sum should prevent the neighboring states (along the path) to

'run away' from each other (because the terms $(\mathbf{S}_k - \mathbf{S}_{k-1})^2$ give the distances between the states in the configuration space), thus keeping the discretized path reasonably smooth. Together these two tendencies should provide the sequence of closely positioned states (second sum) with the energy being as low as possible (first sum), which from the qualitative point of view obviously corresponds to the path over a saddle point between the fixed initial and final states. The method was named an 'elastic band' method, because the second term in (87) exactly corresponds to the energy of elastic bands (springs) with zero natural length and elastic constant κ 'built in between' the neighboring states of the chain $\{\mathbf{S}_k\}$.

In practice, this idea does not work really well: if the elastic constant κ is chosen too large (elastic term dominates) then the chain of states tends to 'round the corners' of the energy landscape, trying to reduce the length of the chain (distances between the neighboring states) on the cost of increasing the potential energy of the chain states. If κ is too small, then the elastic term is not able to prevent the states from sliding into the potential minima (initial and final states), so that the saddle point can be located with a reasonable accuracy. The region of intermediate κ values where the saddle point position of a continuous transition path is reproduced by the chain (87) well enough, is usually very narrow or may even not exist (see an excellent review contained in Jónsson, Mills and Jacobsen, 1998). For this reason the elastic band method, introduced in the middle of the 1980th, was considered as unreliable a decade long.

The solution of both problems was suggested by Mills and Jonsson (1994) (see Jónsson, Mills and Jacobsen, 1998 for a detailed explanation), who noted that both effects were due to the 'too physical' understanding of the model (87). Namely, by the minimization of the object function (87) both the potential (due to the first sum) and elastic (second sum) forces were fully taken into account using the straightforward differentiation of the object function Q. By its constructed Q fully mimics the energy of a set of 'particles' (states) connected via springs with elastic constants κ and moving in a potential landscape V. But the actual purpose of this function is quite different from simply imitating the behavior of the physical system just described: Q should be constructed so that the chain of 'particles' (states) reproduces as good as possible the *optimal continuous* path between the two given energy minima, which goes from the starting to the final state *along the gradient lines* of the potential $V\{\mathbf{x}\}$. Hence, Q fulfills its purpose well enough if (i) the first term would move the states *perpendicular* to the gradient lines (grad(V) is normal to the optimal path, see above) and (ii) the second term would produce only the force *parallel* to the path (to ensure that the states stay close to each other, it is sufficient to apply a force along the line connecting the states). For this reason we can *separate* the effects of the first (potential) and the second (elastic) terms by taking into account (i) only that projection of the potential force which is *perpendicular* to the path and (ii) only that projection of the elastic force which is *parallel* to the path.

This leads to the 'nudged elastic band'(NEB) model with the 'equation of motion' for the state i in the form similar to that of (85)

$$\frac{\partial \mathbf{S}_k}{\partial t} = -[\nabla V - (\nabla V, \mathbf{e}_\tau)\mathbf{e}_\tau]_{\mathbf{S}_k} + (\mathbf{F}_k^{\mathrm{el}}, \mathbf{e}_\tau)\mathbf{e}_\tau \qquad (88)$$

where the first term in square brackets is fully analogous to the corresponding term in equation (85) thus 'moving' each state in the direction normal to the transition path and the second term represents the tangential projection of the elastic force $\mathbf{F}^{\mathrm{el}}$ (derivative of the second sum in (87)) which takes care that the states remain close to each other in the configuration space. During to the fact that the two terms on the right-hand side of (88) are perpendicular to each other, that is, fully decoupled, there exist now a wide range of the elastic constants κ where the position of the saddle point along the transition path can be reproduced with a nearly arbitrary accuracy just by increasing the number of states used to discretize a path.

Finally, we note that the quality of decoupling of the two force contributions in (88) and thus – the quality of the saddle point determination and the stability of the method as a whole – crucially depend on the calculation accuracy of the tangent vector direction $\mathbf{e}_\tau$. For this reason large effort has been devoted to the development of improved method for the tangent determination for discretized curves (Jonsson and Henkelmaan, 2000).

Micromagnetic simulations using the elastic band method

Up to our knowledge, first application of the NEB method to micromagnetic simulations is due to Dittrich *et al*., (2002,2003a,b), Dittrich, 2003 and Dittrich, Thiaville, Miltat and Schrefl (2003). In their first paper, Dietrich *et al*. (Dittrich *et al*., 2002) describe their concrete implementation of the general NEB algorithm for micromagnetics, which involves a transition to the spherical coordinates of magnetic moment (as really independent variables, see the discussion above) and a proper finite-difference approximation of the tangent vector for the discretized transition path.

In this first study Dittrich *et al*. (2002) noted that for some simple systems the method works well even without the spring force, that is, without the second term in (88). This means that one can sometimes obtain a good approximation to a saddle-point path simply by moving the states of the discretized initial guess for the transition path along the energy gradient projection perpendicular to the instantaneous trajectory configuration (we note in passing that this simplified method has nothing to do anymore with the

'NEB'). In particular, in Dittrich *et al*. (2002) the energy barriers calculated numerically for the system of two interacting single-domain particles with uniaxial anisotropies were found to agree well with the analytical results available for this system. The ability of the method to find energy barriers for (i) a coherent switching of a small ($5 \times 5 \times 1\,\mathrm{nm}^3$) rectangular nanoelement, (ii) a switching of an elongated slab (typical cross-section size 13 nm, length 70 nm) via the domain wall motion, and (iii) magnetization reversal of a piece of a granular magnetic media was also demonstrated.

Later Dittrich *et al*. have implemented also a complete elastic band method (Dittrich *et al*., 2003a), including the second (elastic) term into their 'equation of motion' for the states in the chain. As expected, they have observed that for every concrete problem there exist a broad range of the elastic constant values where the height and position of a saddle point is reproduced with a sufficiently high accuracy, although for each new problem this region must be found afresh. With this improved algorithm Dittrich *et al*. could rigorously evaluate energy barriers arising due to the shape anisotropy in triangular and square nanoplatelets, investigate the increase of the energy barrier in a ferromagnetic grain coupled to an antiferromagnet (a promising candidate for a high-density recording media with improved thermal stability) and identify several possible reversal modes in a MRAM cell (Dittrich *et al*.,2003a,b; Dittrich, Thiaville, Miltat and Schrefl, 2003).

More details about micromagnetic simulations performed with this method can be found in the contribution **Numerical Methods in Micromagnetics (Finite Element Method), Volume 2** of T. Schrefl to this volume.

An interesting topic which has been pursued by several research groups in the last few years is the applicability of the Monte-Carlo (MC) methods (Binder, 1986) for dynamic micromagnetic simulations at finite temperatures. The major *advantage* of modern MC schemes when applied to the magnetization transition between various metastable states is evident: The corresponding computation time does *not* depend exponentially on the height of the energy barrier separating these states, as it is the case for the Langevin dynamics. However, there exist also several principal problems by the dynamical application of the MC methods. The two most serious of them are: (i) the difficulty to establish a relation between a MC step and a physical time and (ii) proper inclusion of the magnetization precession, which is also a highly nontrivial task, because the precession does not lead to the change of the system energy and hence does not affect the probability to accept a MC step. Recent methodical progress on this area can be found in Nowak, Chantrell and Kennedy (2000), Chubykalo *et al*. (2003), and Cheng, Jalil, Lee and Okabe (2005, 2006) and is reviewed in the contribution of U. Nowak to this volume.

NOTES

[1] Note however, that the effective field itself $\mathbf{H}^{\mathrm{eff}} = (1/V)\cdot\partial E/\partial\mathbf{M}$ is of course zero at equilibrium – up to the component along the magnetization vector which can be neglected because the magnetization magnitude is assumed to be constant

[2] The *deterministic* Landau–Lifshitz–Gilbert equation conserves the moment magnitude anyway. However this is *not* automatically the case for its stochastic analogue.

ACKNOWLEDGMENTS

The author greatly acknowledges many useful discussions on the topics treated in this chapter with J. Miltat, N. Smith, M. Stiles, A. Slavin, T. Schrefl, and U. Nowak.

REFERENCES

Berkov, D.V. (1998). Numerical calculation of the energy barrier distribution in disordered many-particle system: the path integral method. *Journal of Magnetism and Magnetic Materials*, **186**, 199.

Berkov, D.V. (2002a). Fast switching of magnetic nanoparticles: simulation of thermal noise effects using the Langevin dynamics. *IEEE Transactions on Magnetics*, **MAG-38**, 2489.

Berkov, D.V. (2002b). Density of energy barriers in fine magnetic particle systems. *IEEE Transactions on Magnetics*, **MAG-38**, 2637.

Berkov, D.V. and Gorn, N.L. (2002). Thermally activated processes in magnetic systems consisting of rigid dipoles: equivalence of the Ito and Stratonovich stochastic calculus. *Journal of Physics: Condensed Matter*, **14**, L1.

Berkov, D.V. and Gorn, N.L. (2004). Micromagnetic simulations using Langevin dynamics: studying thermal field correlations. *Journal of Magnetism and Magnetic Materials*, **272–276**, Part 1, 687.

Berkov, D.V. and Gorn, N.L. (2005). Stochastic dynamic simulation of fast remagnetization processes: recent advances and applications. *Journal of Magnetism and Magnetic Materials*, **290–291**, 442.

Berkov, D.V., Gorn, N.L. and Görnert, P. (2002). The Langevin-dynamics simulation of interacting fine magnetic particle system. *Journal of Magnetism and Magnetic Materials*, **226**, 1936.

Bertram, H.N., Safonov, V.L. and Jin, Z. (2002). Thermal magnetization noise, damping fundamentals, and mode analysis: application to a thin film GMR sensor. *IEEE Transactions on Magnetics*, **38**, 2514.

Binder, K. (Ed.) (1986) *Monte-Carlo Methods in Statistical Physics*, Springer-Verlag: Berlin.

Braun, H-B. (1994). Kramer's rate theory, broken symmetries and magnetization reversal. *Journal of Applied Physics*, **76**, 6310.

Braun, H-B. (2000). Stochastic magnetization dynamics in magnetic nanostructures: from Neel-Brown to soliton-antisoliton creation. In *Structure and Dynamics of Heterogeneous Systems*, Entel, P. and Wolf, D. (Eds.), World Scientific, Singapore.

Bray, A.J. and McKane, A.J. (1989). Instanton calculation of the escape rate for activation over a potential barrier driven by colored noise. *Physical Review Letters*, **62**, 493.

Brown, W.F. (1963a). *Micromagnetics*, Wiley: New York.

Brown Jr., W.F. (1963b). Thermal fluctuations of a single domain particle. *Physical Review*, **130**, 1677.

Cheng, X.Z., Jalil, M.B.A., Lee, H.K. and Okabe, Y. (2005). Time-quantifiable Monte Carlo method for simulating a magnetization-reversal process. *Physical Review*, **B72**, 094420.

Cheng, X.Z., Jalil, M.B.A., Lee, H.K. and Okabe, Y. (2006). Mapping the Monte Carlo scheme to Langevin dynamics: A Fokker-Planck approach. *Physical Review Letters*, **96**, 067208.

Chubykalo, O. , Smirnov-Rueda, R., Gonzalez, J.M., *et al*. (2003). Brownian dynamics approach to interacting magnetic moments. *Journal of Magnetism and Magnetic Materials*, **266**, 28.

Chubykalo, O., Nowak, U., Smirnov-Rueda, R., *et al*. (2003). Monte Carlo technique with a quantified time step: Application to the motion of magnetic moments. *Physical Review*, **B67**, 064422.

Coffey, W.T., Kalmykov, Yu.P. and Waldron, J.T. (2004). *The Langevin Equation (With Applications to Stochastic Problems in Physics, Chemistry and Electrical Engineering)*, World Scientific.

Dittrich, R. (2003). *Finite Element Computation of Energy Barriers in Magnetic Systems*, Ph.D. Thesis, Vienna University of Technology.

Dittrich, R., Schrefl, T., Forster, H., *et al*. (2003a). Energy barriers in magnetic random access memory elements. *IEEE Transactions on Magnetics*, **39**, 2839.

Dittrich, R., Schrefl, T., Suess, D., *et al*. (2003b). Thermally induced magnetization reversal in AFC media, *Journal of Applied Physics*, **93**, 7405.

Dittrich, R., Schrefl, T., Suess, D., *et al*. (2002). A path method for finding energy barriers and minimum energy paths in complex micromagnetic systems. *Journal of Magnetism and Magnetic Materials*, **250**, L12.

Dittrich, R., Thiaville, A., Miltat, J. and Schrefl, T. (2003). A rigorous micromagnetic computation of configurational anisotropy energies in nanoelements. *Journal of Applied Physics*, **93**, 7891.

Dotsenko, V.S. (1993). Physics of the spin-glass state. *Physics - Usp. (USA)*, **36**, 455.

Dormann, J.L., Fiorani, D. and Tronc, E. (1999). On the models for interparticle interaction in nanoparticle assemblies: comparison with experimental results. *Journal of Magnetism and Magnetic Materials*, **266**, 28.

E, W., Ren, W. and Vanden-Eijnden, E. (2002). String method for the study of rare events. *Physical Review*, **B66**, 052301.

E, W., Ren, W. and Vanden-Eijnden, E. (2003). Energy landscape and thermally activated switching of submicron-sized ferromagnetic elements. *Journal of Applied Physics*, **93**, 2275.

Ermak, D.L. and McCammon, J.A. (1978). Brownian dynamics with hydrodynamic interaction. *Journal of Chemical Physics*, **69**, 1352.

Freidlin, M.I. and Wentzell, A.D. (1998). *Random Perturbations of Dynamical Systems*, Springer: New York.

Garanin, D.A. (1997). Fokker-Planck and Landau-Lifshitz-Bloch equations for classical ferromagnets. *Physical Review*, **B55**, 3050.

Garanin, D.A. and Chubykalo-Fesenko, O. (2004). Thermal fluctuations and longitudinal relaxation of single-domain magnetic particles at elevated temperatures. *Physical Review*, **B70**, 212409.

Gardiner, S. (1997). *Handbook on Stochastic Processes*, Springer-Verlag: Berlin.

Garcia-Ojalvo, J. and Sancho, J.M. (1994). Colored noise in spatially extended systems. *Physical Review*, **E49**, 2769.

Garcia-Palacios, J.L. and Lazaro, F.J. (1998). Langevin-dynamics study of the dynamical properties of small magnetic particles. *Physical Review*, **B58**, 14937.

Gilbert, T.L. (1955). A Lagrangian formulation of gyromagnetic equation of the magnetization field. *Physical Review*, **100**, 1243.

Grinstein, G. and Koch, R.H. (2003). Coarse graining in micromagnetics. *Physical Review Letters*, **90**, 207201.

Hansen, M.F. and Morup, S. 1998. Models for the dynamics of interacting magnetic nanoparticles. *Journal of Magnetism and Magnetic Materials*, **184**, 262.

Henkelmaan, G. and Jonsson, H., (2000). Improved tangent estimate in the nudged elastic band method for finding minimum energy paths and saddle points. *Journal of Chemical Physics*, **113**, 9978.

Hoenggi, P., Talkner, P. and Borkovec, M. (1990). Reaction-rate theory: fifty years after Kramers. *Reviews of Modern Physics*, **62**, 251.

James, F. (1980). Monte Carlo theory and practice. *Reports on Progress in Physics*, **43**, 1145.

Jónsson, H., Mills, G. and Jacobsen, K.W. (1998). Nudged elastic band method for finding minimum energy paths of transitions. In *Classical and Quantum Dynamics in Condensed Phase Simulations*, Berne, B.J., Ciccotti, G. and Coker, D.F. (Eds.), World Scientific.

Kikuchi, R. (1956). On the minimum of magnetization reversal time. *Journal of Applied Physics*, **27**, 1352.

Klik, I. and Gunther, L. (1990). Thermal relaxation over a barrier in single domain ferromagnetic particles. *Journal of Applied Physics*, **67**, 4505.

Kloeden, P.E. and Platen, E. (1995). *Numerical Solution of Stochastic Differential Equations*, Springer-Verlag: Berlin.

Landau, L.D. and Lifshitz, E.M. (1935). On the theory of the dispersion of magnetic permeability in ferromagnetic bodies. *Physikalische Zeitschrift der Sowjetunion*, **8**, 153.

Landau, L.D. and Lifshitz, E.M. (1980). *Statistical Physics (Part 1)*, Butterworth-Heinemann.

Landau, L.D. and Lifshitz, E.M. (1981). *Mechanics*, Butterworth-Heinemann.

Lyberatos, A. and Chantrell, R.W. (1993). Thermal fluctuations in a pair of magnetostatically coupled particles. *Journal of Applied Physics*, **73**, 6501.

Mallinson, J.C. (1987). On damped gyromagnetic precession. *IEEE Transactions on Magnetics*, **23**, 2003.

McShane, E.J. (1974). *Stochastic Calculus and Stochastic Models*, Academic Press: New York.

Mills, G. and Jonsson, H. (1994). Quantum and thermal effects in H_2 dissociative adsorption: evaluation of free energy barriers in multidimensional quantum systems. *Physical Review Letters*, **72**, 1124.

Miltat, J., Albuquerque, G. and Thiaville, A. (2001). An introduction to micromagnetics in the dynamical regime. In *Spin Dynamics in Confined Magnetic Structures I*, *Topics in Applied Physics*, Hillebrands, B. and Ounadjela, K. (Eds.), Springer-Verlag: Berlin, Vol. 83.

Nakatani, Y., Uesaka, Y., Hayashi, N. and Fukushima, H. (1997). Computer simulation of thermal fluctuation of fine particle magnetization based on Langevin equation. *Journal of Magnetism and Magnetic Materials*, **168**, 347.

Nowak, U., Chantrell, R.W. and Kennedy, E.C. (2000). Monte Carlo simulation with time step quantification in terms of Langevin dynamics. *Physical Review Letters*, **84**, 163.

Onsager, L. and Machlup, S. (1953). Fluctuations and irreversible processes. *Physical Review*, **91**, 1505.

Press, W.H., Teukolsky, S.A., Vetterling, W.T. and Flannery, B.P. (1992). *Numerical Recipes in Fortran: The Art of Scientific Computing*, Cambridge University Press.

Romero, A.H. and Sancho, J.M. (1999). Generation of short and long range temporal correlated noises. *Journal of Computational Physics*, **156**, 1.

Rümelin, W. (1982). Numerical treatment of stochastic differential equations. *SIAM Journal on Numerical Analysis*, **19**, 604.

Safonov, V.L. and Bertram, H.N. (2003). Linear stochastic magnetization dynamics and microscopic relaxation mechanisms. *Journal of Applied Physics*, **94**, 529.

Scholz, W., Schrefl, T. and Fidler, J. (2001). Micromagnetic simulations of thermally activated switching in fine particles. *Journal of Magnetism and Magnetic Materials*, **233**, 296.

Smith, N. (2001). Modelling of thermal magnetization fluctuations in thin-film magnetic devices. *Journal of Applied Physics*, **90**, 5768.

Smith, N. (2002). Fluctuation–dissipation considerations for phenomenological damping models for ferromagnetic thin films. *Journal of Applied Physics*, **92**, 529.

Xue, J. and Victora, R.H. (2000). Micromagnetic predictions for thermally assisted reversal over long time scales. *Applied Physics Letters*, **77**, 3432.

Xue, J. and Victora, R.H. (2001). Micromagnetic predictions of bit decay caused by thermal fluctuations over long time scale. *Journal of Applied Physics*, **89**, 6985.

Zhang, K. and Fredkin, D.R. (2000). Thermal relaxation of clusters of interacting Stoner-Wohlfarth particles. *Journal of Applied Physics*, **87**, 4795.

FURTHER READING

Advanced Recording Model, package for micromagnetic simulations, Euxine technologies, http://www.euxine.com.

Brown, G., Novotny, M.A. and Rikvold, P.A. (2001). Thermal magnetization reversal in arrays of nanoparticles. *J. Appl. Phys.*, **89**, 7588.

Chikazumi, S. (1997). *Physics of Ferromagnetism*, Clarendon Press.

Feng, X. and Fischer, P.B. (2001). Coarse-graining Landau-Lifshitz damping. *J. Appl. Phys.*, **80**, 6988.

Feynman, R.P. and Hibbs, A.R. (1965). *Quantum Mechanics and Path Integrals*, McGraw-Hill: New York.

Hubert, A. and Schäfer, R. (1998). *Magnetic Domains: The Analysis of Magnetic Microstructures*, Springer-Verlag.

Kittel, C. (1953). *Introduction to Solid State Physics*, John Wiley & Sons: New York.

Landau, L.D. and Lifshitz, E.M. (1975). *The Classical Theory of Fields*, Pergamon Press: Oxford.

Landau, L.D. and Lifshits, E.M. (1985). *Electrodynamics of Continuous Media*, Elsevier Science.

Lee, K.J., Park, N.Y. and Lee, T.D. (2001). Numerical study of spin relaxation by thermal fluctuation: effect of shape anisotropy. *J. Appl. Phys.*, **89**, 7460.

Martinez, E., Lopez-Diaz, L. Torres, L. and Alejos, O. (2003). Temperature dependence of spontaneous magnetization using a continuous model, *IEEE Transactions on Magnetics*, **39**, 2522.

McKane, A.J., Luckock, H.C. and Bray, A.J. (1990). Path integrals and non-Markov processes I and II. *Phys. Rev.*, **A41**, 644.

O'Grady, K. and Laider, H. (1999). The limits of magnetic recording – media considerations. *J. Magn. Magn. Mat.*, **200**, 616.

Safonov, V.L. and Bertram, H.N. (2002). Thermal magnetization noise in a thin film. *Phys. Rev.*, **B65**, 172417.

Scheinfein, R. Landau-Lifshitz-Gilbert Micromagnetics Simulator, http://www.llgmicro.com.

Suhl, H. (1998). Theory of the magnetic damping constant. *IEEE Transactions on Magnetics*, **MAG-34**, 1834.

Thiaville, A., Miltat, J. and Ben Youssef, J. (2001). Dynamics of vertical Bloch lines in bubble garnets: experiments and theory. *Europ. Phys. J. B*, **23**, 37.

Wohlfarth, E.P. and Stoner, E.C. (1948). A mechanism of magnetic hysteresis in heterogeneous alloys. *Phil. Trans. Roy. Soc. (London), Ser. A*, **240**, 599.

Nonlinear Magnetization Dynamics in Nanomagnets

Claudio Serpico[1], Giorgio Bertotti[2], Isaak D. Mayergoyz[3] and Massimiliano d'Aquino[4]

[1] *Università di Napoli "Federico II", Napoli, Italy*
[2] *Istituto Nazionale di Ricerca Metrologica, Torino, Italy*
[3] *UMIACS University of Maryland, College Park, MD, USA*
[4] *Università di Napoli "Parthenope", Napoli, Italy*

1 INTRODUCTION

The theoretical study of magnetization dynamics has been the focus of considerable research for many years (Landau and Lifshitz, 1935; Gilbert, 1955, 2004; Kikuchi, 1956; Callen, 1958; Mallinson, 1987; Wigen, 1994). Traditionally, this study has been driven by the ferromagnetic resonance problems (Damon, 1953; Suhl, 1957; Walker, 1957; Skrotskii and Alimov, 1959a) in which the main part of magnetization is pinned by a strong constant magnetic field, whereas only a small transverse component of magnetization executes resonance motions caused by radiofrequency (rf) fields. These small magnetization motions are studied by linearizing the magnetization dynamics equation and, for this reason, the literature on magnetization dynamics has been mostly concerned with the linear magnetization dynamics studies. Recently, new directions of research have emerged that deal with large motions of magnetization and require the analysis of the nonlinear dynamics magnetization. These new directions are mainly connected to the recent advance in magnetic storage technologies. The enormous increase in data storage density and transfer rate has required the design and the realization of magnetic devices in the nanoscale spatial range. In these devices, the magnetization dynamics modes are usually approximately spatially uniform but undergo motions which appreciably deviate from equilibrium. The study of nonlinear quasi-coherent magnetization motion is particularly relevant in such research as fast precessional switching (Acremann *et al*., 2000; Bauer, Fassbender, Hillebrands and Stamps, 2000; Crawford, Kabos and Silva, 2000; Schumacher *et al*., 2003) of magnetization in thin films and magnetization dynamics induced by spin-polarized current injection (Berger, 1996; Slonczewski, 1996; Sun, 2000; Grollier *et al*., 2001; Kiselev *et al*., 2003; Rippard *et al*., 2004), and ferromagnetic resonance in nanomagnets and ultrathin magnetic films.

In this chapter, we will systematically apply and review the methods and concepts of nonlinear dynamical system theory relevant to the analysis of large magnetization motions governed by the commonly used magnetization evolution equation: Landau–Lifshitz equation. Precessional and damping switchings of magnetization and nonlinear ferromagnetic

Handbook of Magnetism and Advanced Magnetic Materials. Edited by Helmut Kronmüller and Stuart Parkin. Volume 2: *Micromagnetism*. ISBN: 978-0-470-02217-7.

dynamics driven rf field are treated as very important applications. However, many results obtained for those applications are of considerable interest in their own right. The chapter is organized as follows.

Sections 2 and 3 deal with the theoretical aspects of Landau–Lifshitz dynamics. First, the Landau–Lifshitz equation is introduced as dynamical generalization of micromagnetic Brown's equation and its general property are considered. Then, Landau–Lifshitz dynamics is treated as a nonlinear dynamical system defined on a sphere and the problem of equilibria and geometric representation of dynamics is discussed. Special attention is paid to the conservative Landau–Lifshitz dynamics and analytical expressions are derived for this dynamics in terms of elliptic-type integrals.

Sections 4 deals with precessional and damping magnetization switchings. Analytical treatment of the damping switching and the precessional switching for uniaxial magnetic particle is illustrated in details and a comparison of the two switching techniques is presented in terms of switching speed. Then, a novel approach, based on the averaging technique, to the analysis of magnetization relaxation to equilibrium is presented. This approach is and results in a differential equation for the free energy.

In Section 5, we will address the problem of the existence of spatially uniform magnetization modes under far-from-equilibrium conditions driven from an external rf field. In the case of systems with uniaxial rotational symmetry subject to a circularly polarized rf, remarkable conclusions can be drawn (Skrotskii and Alimov, 1959a,b; Khapikov, 1992; Träxler, Just and Sauermann, 1996). Indeed, the presence of rotational symmetry has far-reaching consequences because the equivalent dynamical system on the unit sphere is reduced to autonomous form and the basic physical aspects of the dynamics can be recast into corresponding topological and geometric properties of the phase portraits of the Landau–Lifshitz equation (Bertotti, Serpico and Mayergoyz, 2001). The phase portraits of the dynamics and the associated bifurcation diagrams exhibit an extremely rich and interesting structure, and provide some nontrivial predictions concerning periodic and quasiperiodic types of dynamical response as well as nonlinear ferromagnetic resonance mechanisms.

2 MICROMAGNETICS AND LANDAU–LIFSHITZ EQUATION

2.1 Fundamental equations

2.1.1 Brown's equations and their dynamical generalization

The study of magnetization dynamics in ferromagnetic media is based micromagnetic Brown's equations and their dynamical generalizations (Brown, 1962, 1963; Aharoni, 1996; Bertotti, 1998; Hubert and Schäefer, 1998; Kronmueller and Faehnle, 2003; Landau and Lifshitz, 1984). This material has been broadly discussed in another chapter (**General Micromagnetic Theory, Volume 2**) of this handbook and here we shall limit ourselves to a brief introduction of the main equations.

Micromagnetics is an highly nonlinear continuum theory which takes into account effects on rather different spatial scales: short-range exchange forces and long-range magnetostatic effects. The state of the ferromagnetic body is described by the magnetization vector field $\mathbf{M}(\mathbf{r})$ which, for temperature considerably below the Curie temperature, satisfies the following condition

$$|\mathbf{M}(\mathbf{r})| = M_{\mathrm{s}}(T) \tag{1}$$

which means that the magnitude of $\mathbf{M}(\mathbf{r})$ is spatially uniform and equal to the saturation magnetization $M_{\mathrm{s}}(T)$ at the given temperature T. The constraint expressed in equation (1) reflects the fact that, at the smallest spatial scale compatible with the continuum hypothesis, the strong exchange interaction prevails over all other types of force.

The direction of $\mathbf{M}(\mathbf{r})$ is in general nonuniform and, at equilibrium, is determined by minimizing an appropriate Gibbs–Landau free energy functional $G_{\mathrm{L}}(\mathbf{M}(.);\ \mathbf{H}_{\mathrm{a}})$ (Brown, 1962, Brown, 1963; Aharoni, 1996; Landau and Lifshitz, 1984). The minimization of $G_{\mathrm{L}}(\mathbf{M}(.);\ \mathbf{H}_{\mathrm{a}})$ under the constraint given by equation (1), leads to the Brown's equations:

$$\mathbf{M} \times \mathbf{H}_{\mathrm{eff}} = 0 \tag{2}$$

where the effective field $\mathbf{H}_{\mathrm{eff}}$ is defined as (minus) the variational derivative of the free energy functional with respect to the magnetization vector field: $\mathbf{H}_{\mathrm{eff}} = -\delta G_{\mathrm{L}}/\delta\mathbf{M}$. The effective field $\mathbf{H}_{\mathrm{eff}}$ takes into account all the information about the geometry and the magnetic properties of the system. When magnetoelastic effects are neglected, it is given by:

$$\mathbf{H}_{\mathrm{eff}} = \mathbf{H}_{\mathrm{a}}(t) + \mathbf{H}_{\mathrm{S}} + \mathbf{H}_{\mathrm{EX}} + \mathbf{H}_{K} \tag{3}$$

where $\mathbf{H}_{\mathrm{a}}(t)$ is the applied field, $\mathbf{H}_{\mathrm{S}}$ is the magnetostatic (demagnetizing) field produced by the magnetization $\mathbf{M}(\mathbf{r})$, $\mathbf{H}_{\mathrm{EX}} = (2A/\mu_0 M_{\mathrm{s}}^2)\nabla^2\mathbf{M}$ is the exchange field (A is the exchange stiffness constant and μ_0 is the vacuum permeability) (Bertotti, 1998), which describes exchange forces which tend to oppose magnetization nonuniformities, and $\mathbf{H}_K$ is the crystal anisotropy field, a purely local term which depends on the magnetization vector at the point considered and on some constants characterizing the local anisotropy. In the case of uniaxial materials, it has the following form

$$\mathbf{H}_K(\mathbf{M}) = \mathrm{H}_K(\mathbf{e}_K \cdot \mathbf{M}/M_{\mathrm{s}})\mathbf{e}_K \tag{4}$$

where H_K is an anisotropy parameter, and $\mathbf{e}_K$ is the unit vector along the easy axis direction.

The minimization of $G_L(\mathbf{M}(.);\ \mathbf{H}_a)$ also leads to boundary conditions on $\mathbf{M}(\mathbf{r})$ which, in the simplest case, are

$$\frac{\partial \mathbf{M}}{\partial \mathbf{n}} = 0 \tag{5}$$

at the body surface ($\mathbf{n}$ denotes the surface normal unit vector). This condition is expected when no surface anisotropy is present which is the case we shall treat here.

It is also important to underline two additional assumptions implicitly contained in the equation in the preceding text. First, the use of magnetostatic field $\mathbf{H}_S$ implies that we are in fact neglecting any propagation effect, which means that the electromagnetic wavelength must be much larger than the linear dimensions of the body under study. Second, eddy currents have been neglected and thus no eddy currents term has been included in $\mathbf{H}_{\text{eff}}$.

When $\mathbf{M} \times \mathbf{H}_{\text{eff}} \neq 0$, the system is not at equilibrium and evolves according to some appropriate dynamic equation. The most used dynamic equation is the Landau–Lifshitz equation (Landau and Lifshitz, 1935) based on the idea that in a ferromagnetic body the effective field $\mathbf{H}_{\text{eff}}$ induces a precession of the local magnetization $\mathbf{M}(\mathbf{r}, t)$ of the form

$$\frac{\partial \mathbf{M}}{\partial t} = -\gamma \mathbf{M} \times \mathbf{H}_{\text{eff}} \tag{6}$$

where $\gamma > 0$ is the absolute value of the gyromagnetic ratio. Equation (6) gives rise to magnetization dynamics in which the value of the saturation magnetization $M_s = |\mathbf{M}|$ is locally preserved, because $\partial|\mathbf{M}|^2/\partial t = 2\mathbf{M}\cdot\partial\mathbf{M}/\partial t = 0$. In this respect, equation (6) is consistent with the fundamental micromagnetic constraint (1). However, this equation cannot describe any approach to equilibrium, because $\mathrm{d}G_L/\mathrm{d}t = -\mathbf{H}_{\text{eff}}\cdot\partial\mathbf{M}/\partial t = 0$, which means that the dynamics is nondissipative.

Energy relaxation mechanisms can be taken into account by additional phenomenological terms, chosen through heuristic considerations. In their original paper, Landau and Lifshitz (1935) introduced an equation of the following form

$$\frac{\partial \mathbf{M}}{\partial t} = -\gamma_L \mathbf{M} \times \mathbf{H}_{\text{eff}} - \frac{\alpha_L \gamma_L}{M_s} \mathbf{M} \times (\mathbf{M} \times \mathbf{H}_{\text{eff}}) \tag{7}$$

where γ_L is a gyromagnetic-type constant and α_L is a dimensionless damping parameter. The value of α_L is always very small, of the order of $10^{-4}/10^{-3}$. The parameter γ_L is usually assumed to be equal to the gyromagnetic ratio γ. In addition to the Landau–Lifshitz equation, another equation broadly used in the description of magnetization dynamics is the one proposed by Gilbert (1955, 2004):

$$\frac{\partial \mathbf{M}}{\partial t} = -\gamma_G \mathbf{M} \times \left(\mathbf{H}_{\text{eff}} - \frac{\alpha_G}{\gamma_G M_s} \frac{\partial \mathbf{M}}{\partial t} \right) \tag{8}$$

where again γ_G is a gyromagnetic constant and α_G a dimensionless damping constant. The Gilbert form is equivalent to subtracting from the effective field a viscouslike term proportional to the time derivative of magnetization and this type of dissipative terms can be introduced by using the method Rayleigh dissipation function in the framework of Lagrangian dynamics (Gantmacher, 1975; Gilbert, 1955, 2004).

By using appropriate algebraic manipulations (Aharoni, 1996), equation (8) can be transformed in the following form:

$$\frac{\partial \mathbf{M}}{\partial t} = -\frac{\gamma_G}{1+\alpha_G^2} \mathbf{M} \times \mathbf{H}_{\text{eff}} - \frac{\alpha_G \gamma_G}{(1+\alpha_G^2) M_s} \mathbf{M} \times (\mathbf{M} \times \mathbf{H}_{\text{eff}}) \tag{9}$$

from which it is clear that equations (7) and (8) are mathematically equivalent to provided that:

$$\alpha_G = \alpha_L = \alpha, \qquad \gamma_G = \gamma_L (1+\alpha^2) \tag{10}$$

The above relations shows that the two gyromagnetic constants γ_L and γ_G cannot be simultaneously equal to the gyromagnetic ratio γ. In addition, while in equation (7) the damping term is proportional to α_L, the damping term in equation (9) is a nonmonotonic function of α_G which, after reaching a maximum at $\alpha_G = 1$, monotonically decreases. This is the behavior physically expected for large damping parameters.

These facts suggest that equations (7) and (8) are not physically equivalent, and this raises the interesting question of which is the most appropriate magnetization dynamics equation. This issue acquires particular relevance whenever α is expected to be a nontrivial function of the state of the system. In fact, this issue is part of the more general and relatively open problem of what are the limits under which the phenomenological introduction of damping is acceptable and is in agreement with microscopic models of spin dynamics (Callen, 1958; Suhl, 1998). It is also important to notice that the difference between equations (7) and (8) are of second order in the damping parameters and accordingly, for typical values of α_G and α_L, are expected to be quantitatively not very relevant. In the rest of this chapter, we describe magnetization dynamics by means of equation (8). We take $\gamma_G = \gamma$ and we will denote α_G simply as α. We refer to this equation as the Landau–Lifshitz–Gilbert (LLG) equation.

2.1.2 Spatially uniform solutions

In this chapter, we investigate magnetization dynamics in nanomagnets in which the magnetization is expected to be, with good approximation, spatially uniform. LLG equation admits indeed spatially uniform solutions under the following conditions: (i) the ferromagnetic body is of ellipsoidal shape; (ii) no surface anisotropy is present, so equation (5) is valid at the body surface; (iii) the parameters (e.g., anisotropy constants, anisotropy axis direction) which characterize the local anisotropy field $\mathbf{H}_K$ are spatially uniform; (iv) the applied field $\mathbf{H}_\mathrm{a}$ is spatially uniform; (v) the initial distribution of magnetization is spatially uniform.

The first condition guarantees that internal demagnetizing fields is spatially uniform. Indeed, $\mathbf{H}_\mathrm{S}$ inside uniformly magnetized ellipsoidal bodies is spatially uniform and can be expressed in terms of the demagnetizing factors. By choosing a system of unit vectors ($\mathbf{e}_x$, $\mathbf{e}_y$, $\mathbf{e}_z$) along the principal axes of the ellipsoid, one obtains:

$$\mathbf{H}_\mathrm{S}(\mathbf{M}) = -N_x M_x \mathbf{e}_x - N_y M_y \mathbf{e}_y - N_z M_z \mathbf{e}_z \qquad (11)$$

where N_x, N_y, N_z are the demagnetizing factors and $N_x + N_y + N_z = 1$ (Osborne, 1945). The second condition is necessary because the presence of surface anisotropy could produce pinning of magnetization at the body surface, which could induce spatial magnetization nonuniformities. The third condition guarantees that the anisotropy field $\mathbf{H}_K$ is spatially uniform when $\mathbf{M}$ is spatially uniform.

Under these conditions, the effective field associated with a spatially uniform magnetization state is itself spatially uniform and can be written as:

$$\mathbf{H}_\mathrm{eff}(\mathbf{M}, t) = \mathbf{H}_\mathrm{a}(t) + \mathbf{H}_K(\mathbf{M}) - N_x M_x \mathbf{e}_x - N_y M_y \mathbf{e}_y - N_z M_z \mathbf{e}_z \qquad (12)$$

This result is tantamount of the fact that the LLG equation admits spatially uniform solutions. Indeed, consider the initial-value problem for equation (8) under the condition of spatially uniform initial distribution: $\mathbf{M}(\mathbf{r}, t = 0) = \mathbf{M}_0$. It can be readily verified that a spatially uniform vector field $\mathbf{M}(t)$ is the unique solution of LLG equation (8), provided that it is the solution of the ordinary differential equation:

$$\frac{\mathrm{d}\mathbf{M}}{\mathrm{d}t} = -\gamma \mathbf{M} \times \left(\mathbf{H}_\mathrm{eff}(\mathbf{M}, t) - \frac{\alpha}{\gamma M_\mathrm{s}} \frac{\mathrm{d}\mathbf{M}}{\mathrm{d}t} \right) \qquad (13)$$

with the initial condition $\mathbf{M}(t = 0) = \mathbf{M}_0$.

Once we have recognized this important property of LLG magnetization dynamics in ellipsoidal particles, the issue of stability of spatially uniform modes naturally arises. The question is whether small nonuniform perturbations of the initial uniform magnetization distribution would increase during the time evolution or would remain small. The quantitative theory for studying this issue has not been completely established yet. The problem has been investigated in detail for certain particular cases such as nucleation theory, magnetostatic mode analysis and spin-wave analysis (Brown, 1963; Aharoni, 1996; Suhl, 1956, 1957; Walker, 1957). In qualitative terms, the smaller the magnetic body the more stable the spatially uniform solutions are expected to be. In this respect, in the remaining part of this article, we assume that the dimensions of the body are small enough that magnetization state can be considered as, with good approximation, spatially uniform. As a final remark, we also observe that the analysis presented can be also applied to nonspheroidal nanomagnets (as thin films or cubes) if one can assume *a priori* that the magnetization is spatially uniform within the magnetic body (and this again is physically reasonable for very small bodies). In this case, one can prove that equations (11) and (12) are still valid, provided that the left-hand sides of these two equations are interpreted as the spatial averaged (over the magnetic body) magnetostatic field and effective field, respectively (Aharoni, 1996). In conclusion, one can write the LLG equation in uniformly magnetized nonspheroidal bodies equation as the ordinary differential equation (13).

2.1.3 LLG equation in dimensionless form

It is useful to rewrite the LLG equation in dimensionless form to reveal the natural scales in the problem. In this respect, fields and magnetization are naturally measured in units of M_s. Accordingly, we introduce the dimensionless vectors $\mathbf{m} = \mathbf{M}/M_\mathrm{s}$ and $\mathbf{h}_\mathrm{eff} = \mathbf{H}_\mathrm{eff}/M_\mathrm{s}$. In addition, a natural timescale is provided by $(\gamma M_\mathrm{s})^{-1}$ and thus we normalize the time as $t \to \gamma M_\mathrm{s} t$ (in permalloy, with $\gamma = 2.2 \times 10^5\,\mathrm{A^{-1}\,m\,s^{-1}}$ and $M_\mathrm{s} = 8 \times 10^5\,\mathrm{A\,m^{-1}}$, one finds $\gamma M_\mathrm{s} = 176\,\mathrm{GHz}$, that is, $(\gamma M_\mathrm{s})^{-1} \simeq 6\,\mathrm{ps}$). By using these normalizations equation (13) can be written as follows:

$$\frac{\mathrm{d}\mathbf{m}}{\mathrm{d}t} = -\mathbf{m} \times \left(\mathbf{h}_\mathrm{eff}(\mathbf{m}, t) - \alpha \frac{\mathrm{d}\mathbf{m}}{\mathrm{d}t} \right) \qquad (14)$$

where $\mathbf{h}_\mathrm{eff}(\mathbf{m}, t) = \mathbf{H}_\mathrm{eff}/M_\mathrm{s} = \mathbf{h}_\mathrm{a}(t) + \mathbf{h}_\mathrm{S}(\mathbf{m}) + \mathbf{h}_K(\mathbf{m})$, $\mathbf{h}_\mathrm{a}(t) = \mathbf{H}_\mathrm{a}(t)/M_\mathrm{s}$, $\mathbf{h}_\mathrm{S}(\mathbf{m}) = \mathbf{H}_\mathrm{S}(\mathbf{M})/M_\mathrm{s}$, and $\mathbf{h}_K(\mathbf{m}) = \mathbf{H}_K(\mathbf{M})/M_\mathrm{s}$. According to equation (11) one has that

$$\mathbf{h}_\mathrm{S}(\mathbf{m}) = -N_x m_x \mathbf{e}_x - N_y m_y \mathbf{e}_y - N_z m_z \mathbf{e}_z \qquad (15)$$

Regarding the anisotropy field, we assume that it has the form as in equation (4) and thus we have

$$\mathbf{h}_K(\mathbf{m}) = \kappa (\mathbf{e}_K \cdot \mathbf{m}) \mathbf{e}_K \qquad (16)$$

where $\kappa = \mathrm{H}_K/M_\mathrm{s}$ is the normalized anisotropy constant (if K_1 is the physical anisotropy constant $\kappa = 2K_1/\mu_0 M_\mathrm{s}^2$, this dimensionless constant is often denoted by Q and it is referred to as *quality factor* (Kronmueller and Faehnle, 2003; Hubert and Schäefer, 1998)). If we further assume that $\mathbf{e}_K$ is along one of Cartesian unit vectors, the normalized effective field can be written in the following simple form:

$$\mathbf{h}_\mathrm{eff} = -D_x m_x \mathbf{e}_x - D_y m_y \mathbf{e}_y - D_z m_z \mathbf{e}_z + \mathbf{h}_\mathrm{a}(t) \quad (17)$$

where the parameters D_x, D_y, D_z include the effects of both demagnetizing fields and crystal anisotropy fields. In the case that $\mathbf{e}_K = \mathbf{e}_x$, they are given by:

$$D_x = N_x - \kappa, \quad D_y = N_y, \quad D_z = N_z \quad (18)$$

In the sequel, except when otherwise specified, we assume that the parameters D_x, D_y, D_z are ordered as follows:

$$D_x \leq D_y \leq D_z \quad (19)$$

which can be always achieved by an appropriate permutation of the Cartesian axes. When inequality (19) is fulfilled then the axis $\mathbf{e}_x$ is the easy axis of the magnetic particle.

The free energy associated with the magnetic body is expressed in normalized form as:

$$g_\mathrm{L}(\mathbf{m}; \mathbf{h}_\mathrm{a}) = \frac{G_\mathrm{L}(\mathbf{M}; \mathbf{H}_\mathrm{a})}{\mu_0 M_\mathrm{s}^2 V} = \frac{1}{2} D_x m_x^2 + \frac{1}{2} D_y m_y^2 + \frac{1}{2} D_z m_z^2 - \mathbf{h}_\mathrm{a}(t) \cdot \mathbf{m} \quad (20)$$

where V is the volume of the body and $G_\mathrm{L}(\mathbf{M}; \mathbf{H}_\mathrm{a})$ is the micromagnetic free energy. The effective field is related to the energy through the expression:

$$\mathbf{h}_\mathrm{eff} = -\frac{\partial}{\partial \mathbf{m}} g_\mathrm{L}(\mathbf{m}; \mathbf{h}_\mathrm{a}) \quad (21)$$

where $\partial/\partial\mathbf{m}$ denotes the gradient with respect to $\mathbf{m}$. Equation (14) can be transformed in the following equivalent form

$$\frac{\mathrm{d}\mathbf{m}}{\mathrm{d}t} = -\frac{1}{1+\alpha^2}\mathbf{m} \times \mathbf{h}_\mathrm{eff}(\mathbf{m}, t) - \frac{\alpha}{1+\alpha^2}\mathbf{m} \times (\mathbf{m} \times \mathbf{h}_\mathrm{eff}(\mathbf{m}, t)) \quad (22)$$

which is the normalized version of equation (9).

2.2 General aspect of LLG dynamics

2.2.1 Conservation of magnetization amplitude

It can be readily seen, by dot multiplication of both sides of equation (14) by $\mathbf{m}$, that the quadratic form $m_x^2 + m_y^2 + m_z^2$ is an integral of motion of LLG dynamics. By taking into account equation (1) and the normalization introduced in the previous section, one can conclude that under all circumstances

$$m_x^2 + m_y^2 + m_z^2 = 1 \quad (23)$$

which means that equation (14) defines a dynamical system evolving on the surface of the unit sphere. The evolution of this dynamical system proceeds along the lines of the vector field:

$$\mathbf{v}(\mathbf{m}, \alpha, t) = -\frac{1}{1+\alpha^2}\mathbf{m} \times \mathbf{h}_\mathrm{eff}(\mathbf{m}, t) - \frac{\alpha}{1+\alpha^2}\mathbf{m} \times (\mathbf{m} \times \mathbf{h}_\mathrm{eff}(\mathbf{m}, t)) \quad (24)$$

given by the right-hand side of equation (22). These lines are tangential to the unit sphere for all $\mathbf{m}$, α and t.

In the interesting particular case where the applied field is constant ($\mathrm{d}\mathbf{h}_\mathrm{a}/\mathrm{d}t = 0$), the dynamical system defined by equation (14) or (22) is autonomous, since the effective field does not depend explicitly on time anymore. Accordingly, the vector field in equation (24) is stationary: $\mathbf{v} = \mathbf{v}(\mathbf{m}, \alpha)$. The fact that the evolution of magnetization is driven by a stationary vector field tangential to the unit sphere has some remarkable consequences of a topological nature:

- There must exist equilibrium states for the system (points where $\mathbf{v} = 0$), because a stationary vector field on the sphere necessarily has singular points (Perko, 1996). In general, singular points of a vector field can be either zeros or poles where the magnitude of the vector field tends to infinity. However, the LLG vector field $\mathbf{v}$ is continuous and, consequently, it cannot have poles.
- The number of equilibria is at least two and is even under all circumstances. This conclusion is derived from Poincaré index theorem (Perko, 1996), which asserts that the number of nodes, foci, and centers minus the number of saddles of any autonomous dynamics on the sphere is equal to two. The distinctive qualitative features of saddles, nodes, foci, and centers are shown in Figures 1(a–d) (see Perko, 1996; Wiggins, 1990; Hubbard and West, 1995 for more details on the classifications of equilibria in nonlinear dynamical systems).
- Chaos is precluded, because the phase space is two dimensional (Wiggins, 1990; Hubbard and West, 1995).

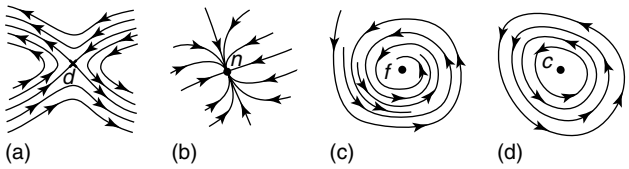

Figure 1. Qualitative sketches of magnetization dynamics on small portions of the unit sphere in neighborhoods of equilibrium points of different nature. (a) Saddle equilibrium; (b) stable node (the sketch for the unstable node can be obtained by inverting the arrows); (c) stable focus (the sketch for the unstable focus can be obtained by inverting the arrows); (d) center (this kind of equilibrium is generally present only in conservative (undamped) systems).

This is the consequence of the generalized version of the Poincaré-Bendixson theorem, which states that on two-dimensional manifolds the only possible steady states are either stationary states associated with equilibria or self-oscillations (periodic steady states) associated with limit cycles of the dynamics. The distinctive features of limit cycles are shown in Figure 14.

2.2.2 *Energy balance in LLG dynamics*

The equation describing the time evolution of the free energy can be readily obtained from the LLG equation written in the form (14). Dot multiplication of both sides of the equation by $\mathbf{h}_{\text{eff}}(\mathbf{m}, t) - \alpha \mathrm{d}\mathbf{m}/\mathrm{d}t$ yields $(\mathbf{h}_{\text{eff}}(\mathbf{m}, t) - \alpha \mathrm{d}\mathbf{m}/\mathrm{d}t) \cdot \mathrm{d}\mathbf{m}/\mathrm{d}t = 0$. Then, by using the fact that $\mathbf{h}_{\text{eff}} = -\partial g_{\text{L}}/\partial \mathbf{m}$, one arrives at the energy balance equation:

$$\frac{\mathrm{d}}{\mathrm{d}t} g_{\text{L}}(\mathbf{m}; \mathbf{h}_{\text{a}}) = -\alpha \left| \frac{\mathrm{d}\mathbf{m}}{\mathrm{d}t} \right|^2 - \mathbf{m} \cdot \frac{\mathrm{d}\mathbf{h}_{\text{a}}}{\mathrm{d}t} \tag{25}$$

The two terms on the right-hand side respectively represent the power dissipated because of intrinsic damping and the power supplied through the action of the time-varying applied field.

When the applied field is constant, the energy balance equation is reduced to the simpler form:

$$\frac{\mathrm{d}g_{\text{L}}}{\mathrm{d}t} = -\alpha \left| \frac{\mathrm{d}\mathbf{m}}{\mathrm{d}t} \right|^2 \tag{26}$$

which has the following important consequences:

- The dynamics of the system is such that the free energy $g_{\text{L}}(\mathbf{m}(t); \mathbf{h}_{\text{a}})$ is always a decreasing function of time.
- The time derivative of $g_{\text{L}}(\mathbf{m}(t); \mathbf{h}_{\text{a}})$ is zero only when $\mathrm{d}\mathbf{m}/\mathrm{d}t = 0$, namely, when the system reaches equilibrium points. Since equilibrium points are stationary points for the energy, the dynamics is directed away from energy maxima and toward energy minima.
- No self-oscillations (periodic solutions) are admissible. Indeed, the necessary condition for the existence of a nonconstant periodic solution is that $g_{\text{L}}(\mathbf{m}(t); \mathbf{h}_{\text{a}})$ is a periodic (nonmonotone) function of time. This requirement is in contradiction with the monotone time decrease implied by equation (26).

The considerations in the preceding text also apply to the case when $\mathbf{h}_{\text{a}}(t)$ has only a transient variation and, after a finite interval of time, becomes a constant vector (this is the typical case in magnetization switching under pulsed field). When the applied field becomes constant the energy balance expressed by equation (26) precludes the appearance of self-oscillations in the system dynamics: the magnetization will always evolve toward one of the stable equilibria. In the case of coexisting stable equilibria, which will be the final equilibrium state is determined by the applied field history and by the initial magnetization state.

On the other hand, when the vector field $\mathbf{v}(\mathbf{m}, \alpha, t)$ is not stationary, LLG dynamics becomes much more complicated, and quasiperiodic or chaotic solutions may appear (Wigen, 1994; Alvarez, Pla and Chubykalo, 2000).

We should mention here that there is a special case of nontransient and periodic variation of the applied field in which magnetization dynamics can, nevertheless, be reduced to autonomous form. This is the case when the magnetic body has uniaxial symmetry and the applied field is time harmonic and circularly polarized. By taking advantage of the symmetry of the problem, one can introduce a reference frame in which the applied field is constant and the dynamics is reduced to an autonomous dynamical system on the unit sphere (Bertotti, Serpico and Mayergoyz, 2001; Bertotti, Mayergoyz and Serpico, 2006b). This case is treated in details in Section 5.

3 MAGNETIZATION DYNAMICS ON THE UNIT SPHERE

3.1 Equilibria

3.1.1 *The general problem*

The first step in the analysis of magnetization dynamics is the determination of the equilibrium points and the study of their stability. We will focus our attention on the study of equilibria in the case of constant applied field. Equilibrium states are found by solving the equation:

$$\mathbf{m} \times \mathbf{h}_{\text{eff}} = 0 \tag{27}$$

under the constraint $|\mathbf{m}| = 1$. Notice that due to the viscous-like nature of damping in LLG dynamics (damping proportional to $\mathrm{d}\mathbf{m}/\mathrm{d}t$), the equilibrium states are not affected by the value of α and thus the problem of finding equilibria can be formulated in terms of the free energy only. If we take into account the constraint $|\mathbf{m}| = 1$, equation (27) can be rewritten in spherical coordinates as two scalar equations:

$$\frac{\partial g_{\mathrm{L}}}{\partial \theta} = 0, \frac{\partial g_{\mathrm{L}}}{\partial \phi} = 0 \tag{28}$$

which means that LLG equilibria are always critical points of the free energy $g_{\mathrm{L}}(\mathbf{m}; \mathbf{h}_{\mathrm{a}})$ with $\mathbf{m}$ restricted to vary on the unit sphere. In this respect, equilibria can be classified as energy maxima (which will be indicated with the label 'u'), energy minima (indicated by the letter 's') and energy saddles (indicated by the letter 'd'). If the magnetic body is invariant with respect to the angle ϕ, the second equation in equation (28) can be ignored. This is the case corresponding to the Stoner–Wohlfarth model (Stoner and Wohlfarth, 1948) reviewed briefly below. For more general magnetic systems, it is necessary to consider some appropriate extension of the Stoner–Wohlfarth theory. In this respect, a rather general approach is to solve the following system of equations:

$$\mathbf{h}_{\mathrm{eff}}(\mathbf{m}) = \lambda \mathbf{m}, \qquad |\mathbf{m}|^2 = 1 \tag{29}$$

which is equivalent to four scalar equations for the four unknowns represented by λ and the three components of $\mathbf{m}$. This approach was proposed in Donahue and Porter (2002) and leads to the determination of *two*, *four*, or *six* equilibrium points, depending on the value and the orientation of the applied field. This treatment is, however, based on the assumption of uniaxial crystalline anisotropy. A comprehensive treatment of equilibrium magnetization states in uniformly magnetized particles for an arbitrary crystalline anisotropy can be found in Thiaville (2000).

The classification of equilibria in terms of the free energy is also instrumental for the understanding of their stability properties under constant applied field. In this case, according to equation (26), if the system is not at equilibrium, magnetization motion is such that the free energy decreases in time for $\alpha > 0$ and remains constant for $\alpha = 0$. Thus, for $\alpha > 0$, the dynamics will always bring magnetization away from energy maxima and toward energy minima. On the other hand, for $\alpha = 0$ the magnetization will keep on precessing around an energy minimum or maximum if it is initially close to it. We conclude that for $\alpha > 0$ energy maxima are unstable nodes or foci and energy minima are stable nodes or foci of the dynamics (see Figure 1b and c, respectively). Conversely, for $\alpha = 0$ energy maxima and minima are all centers of the dynamics (see Figure 1d). The energy saddles are also unstable. Indeed, in any neighbor of a saddle there are magnetization states with energy lower than the energy of the saddle. Thus, in the case $\alpha > 0$, magnetization will be directed away from the saddle. In the case $\alpha = 0$ the magnetization trajectories follow Constant-energy lines and since the dynamics around the saddle is like the one depicted in Figure 1(a), almost all trajectories tend to go away from the saddle.

3.1.2 Stoner–Wohlfarth model

The Stoner–Wohlfarth theory applies to spheroidal particles with rotational symmetry. We assume that the symmetry axis and the magnetocrystalline easy axis are both along the x axis. This implies that $N_y = N_z$ and $\mathbf{e}_K = \mathbf{e}_x$, and parameters D_x, D_y, D_z are given by:

$$D_x = N_x - \kappa, \quad D_y = D_z = D_\perp \tag{30}$$

where the notation '$\perp$' indicates the direction perpendicular to $\mathbf{e}_x$. By using the latter equations and the condition $|\mathbf{m}|^2 = 1$, the free energy of the particle (20) can be easily recast in the following form:

$$g_{\mathrm{L}}(\mathbf{m}; \mathbf{h}_{\mathrm{a}}) = -\frac{1}{2}(D_\perp - D_x)m_x^2 + \frac{1}{2}D_\perp - \mathbf{h}_{\mathrm{a}} \cdot \mathbf{m} \tag{31}$$

where $D_\perp - D_x$ is a positive quantity. We observe that, for symmetry reasons, at equilibrium, the magnetization lies in the plane defined by the easy axis $\mathbf{e}_x$ and the applied field $\mathbf{h}_{\mathrm{a}}$. By introducing the spherical angle θ between $\mathbf{m}$ and $\mathbf{e}_x$, one has $m_x = \cos\theta$ and equation (31) can be transformed into:

$$g_{\mathrm{L}}(\theta; \mathbf{h}_{\mathrm{a}}) = \frac{1}{2}D_x + \frac{1}{2}\kappa_{\mathrm{eff}} \sin^2\theta - h_{ax}\cos\theta - h_{a\perp}\sin\theta \tag{32}$$

where

$$\kappa_{\mathrm{eff}} = D_\perp - D_x \tag{33}$$

is the effective anisotropy constant, h_{ax} and $h_{a\perp}$ are the components of the applied field parallel and perpendicular to the x–axis, respectively. The equilibria can be found by means of the first of equation (28) which, after simple algebraic manipulations, becomes

$$\frac{h_{a\perp}}{\sin\theta_0} - \frac{h_{ax}}{\cos\theta_0} = \kappa_{\mathrm{eff}} \tag{34}$$

For given values of h_{ax} and $h_{a\perp}$, equation (34) returns the angles θ_0 such that the free energy has an extremum. It is interesting to notice that equation (34) can be transformed

into a polynomial equation. Indeed, after appropriate algebraic manipulations, one readily derives the following quartic equation in $m_x = \cos\theta$:

$$h_{a\perp}^2 m_x^2 = (h_{ax} + \kappa_{\text{eff}} m_x)^2 (1 - m_x^2) \tag{35}$$

which admits either two real solutions or four real solutions depending on the values of the parameters $h_{ax}, h_{a\perp}, \kappa_{\text{eff}}$. Each of these solutions corresponds to a stable or unstable equilibrium.

Qualitatively speaking, one can easily see from equation (32) that for small values of the applied field (e.g., consider the case $h_{ax} = 0, h_{a\perp} = 0$) the anisotropy energy prevails and the free energy has two minima (near the states $\mathbf{m} = \pm\mathbf{e}_x$) while, for sufficiently strong applied fields, the linear term $-\mathbf{h}_a \cdot \mathbf{m}$ prevails and the free energy has only one minima characterized by a magnetization direction approximately aligned with the applied field. Thus, there exists a region around the origin of the control plane $(h_{ax}, h_{a\perp})$ in which there are two minima of the free energy whereas, outside this region, there is only one minimum.

A more systematic study of energy maxima and minima can be carried out by computing $\partial^2 g_{\text{L}}/\partial\theta^2$ at the equilibria, that is, at values θ_0 which are solutions of equation (34). This is given by:

$$\left.\frac{\partial^2 g_{\text{L}}}{\partial\theta^2}\right|_{\theta_0} = \frac{\kappa_{\text{eff}} \cos^3\theta_0 + h_{ax}}{\cos\theta_0} = \frac{h_{a\perp} - \kappa_{\text{eff}} \sin^3\theta_0}{\sin\theta_0} \tag{36}$$

The boundary between the region with two minima and region with one minima is a bifurcation line which can be found by searching equilibria with $\partial^2 g_{\text{L}}/\partial\theta^2 = 0$, that is, inflection points. These points correspond to the critical condition expected when a minima disappears (this process correspond to the so-called saddle-node bifurcation (Kuznetsov, 1995)). By using this condition in equation (36), one arrives to the parametric representation of the bifurcation line which is referred to as the *Stoner–Wohlfarth astroid*:

$$\begin{cases} h_{ax} = -\kappa_{\text{eff}} \cos^3\theta_0 \\ h_{a\perp} = \kappa_{\text{eff}} \sin^3\theta_0 \end{cases} \tag{37}$$

which can be expressed in implicit form by the following equation:

$$h_{ax}^{2/3} + h_{a\perp}^{2/3} = \kappa_{\text{eff}}^{2/3} \tag{38}$$

The Stoner–Wohlfarth asteroid is the curve labeled as A_{sw} in Figure 2.

The Stoner–Wohlfarth asteroid has remarkable geometrical properties which permit one to graphically derive the directions of admissible magnetization equilibria. To discuss these proprieties, we first notice that the equation (34), which gives magnetization equilibria, can be interpreted in the following way: given an equilibrium state $\mathbf{m}$, that is, assigned the value θ_0, this equation gives the set of excitation conditions $(h_{ax}, h_{a\perp})$ which produce such $\mathbf{m}$. Since (34) is linear in $(h_{ax}, h_{a\perp})$, this set is a straight line in the $(h_{ax}, h_{a\perp})$ plane, and it has slope $\text{tg}\theta_0$. This line touches the Stoner–Wohlfarth asteroid in the point of the (h_{ax}, h_{ay}) plane given by equation (37). One can easily check that the tangent to the asteroid, at the point given by the angle θ_0, is given by

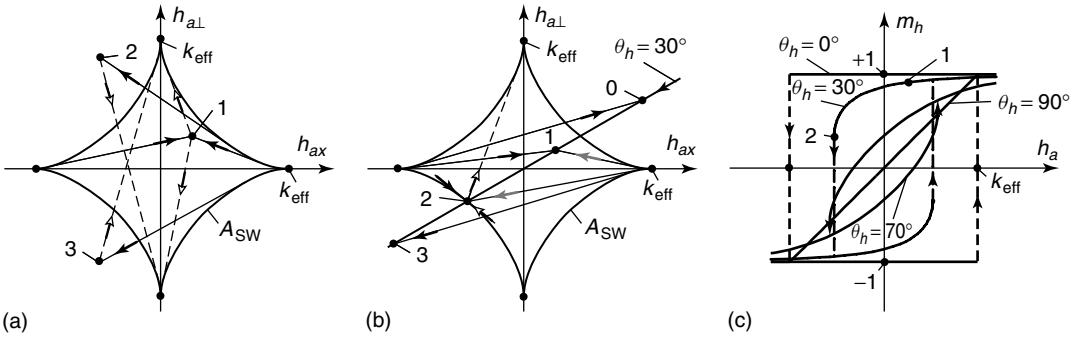

Figure 2. Illustration of Stoner–Wohlfarth tangent construction and hysteresis loops of m_h versus h_a. (a) Points 1, 2, 3 in the control plane and associated tangent lines to the Stoner–Wohlfarth asteroid. Black arrows and white arrows along the tangent lines represent stable and unstable equilibria, respectively. (b) The applied field point $(h_{ax}, h_{a\perp})$ moves along the straight line, with slope $\theta_h = 30°$, going through points 0, 1, 2, 3. This line represents applied fields $h_{ax} = h_a \cos\theta_h$, $h_{a\perp} = h_a \sin\theta_h$ with decreasing amplitude h_a and fixed direction. The evolution of magnetization is given by the black arrows (stable equilibrium) which are obtained by the tangent construction. Notice that when the field point is inside the asteroid, there is a second stable equilibrium, which is represented with a gray arrow. At the point 2 (where all equilibria are represented), the equilibrium represented by the black arrow annihilates with an unstable equilibria (white arrow) and the magnetization 'jumps' toward the remaining stable equilibrium. (c) Hysteresis loop in the plane (m_h, h_a) for different values of θ_h; m_h is the component of $\mathbf{m}$ along the direction of $\mathbf{h}_a$. The points 1 and 2 correspond to the points 1, 2 in (b). Jumps of magnetization are represented by dashed lines.

$dh_{a\perp}/dh_{ax} = (dh_{a\perp}/d\theta)(d\theta/dh_{ax}) = \mathrm{tg}\theta_0$. This means that the straight line (34), for $\theta = \theta_0$, is a tangent at the point of the Stoner–Wohlfarth asteroid which corresponds to θ_0. This geometrical property suggests the following construction: given a point in the control plane we can draw the tangent lines to the asteroid emanating from this point. The slope of each of these lines identifies a possible magnetization equilibrium. According to equation (37), the upper half of the asteroid corresponds to $0 < \theta_0 < \pi$, while the lower half corresponds to $-\pi < \theta_0 < 0$. Thus, tangent lines to the upper half correspond to magnetization equilibrium directions pointing upward, while tangent lines to the lower half correspond to magnetization equilibrium directions pointing downward (see Figure 2a). One also can see that, while only two tangent lines can be drawn from points external to the asteroids (see points 2, 3 in Figure 2a), four tangents can be drawn from points inside it (see points 1 in Figure 2a). Each of these tangents may identify either a stable or an unstable state and the stability can be discussed using equation (36). Let us use the last expression in this equation. One can see that when a tangent to the asteroid drawn from the point $(h_{ax}, h_{a\perp})$ touches the upper half of the asteroid $(0 < \theta_0 < \pi, \sin\theta_0 > 0)$ the corresponding equilibrium is an energy minimum $(\partial^2 g_L/\partial\theta^2|_{\theta_0} > 0)$ or an energy maximum $(\partial^2 g_L/\partial\theta^2|_{\theta_0} < 0)$ depending on if $h_{a\perp} > \kappa_{\mathrm{eff}} \sin^3\theta_0$ (i.e., $(h_{ax}, h_{a\perp})$ is above the tangency point) or $h_{a\perp} < \kappa_{\mathrm{eff}} \sin^3\theta_0$ (i.e., $(h_{ax}, h_{a\perp})$ is below that the tangency point), respectively. On the other hand, when the tangent line touches the lower half of the asteroid $(-\pi < \theta_0 < 0,\ \sin\theta_0 < 0)$, the opposite occurs, and the equilibrium is an energy minimum or an energy maximum depending if $h_{a\perp} < \kappa_{\mathrm{eff}} \sin^3\theta_0$ or $h_{a\perp} > \kappa_{\mathrm{eff}} \sin^3\theta_0$, respectively. According to this rule, only one stable equilibrium exists when the applied field point $(h_{ax}, h_{a\perp})$ is outside the asteroid. Conversely, two stable equilibria exist when $(h_{ax}, h_{a\perp})$ is inside the asteroid (see Figures 2a and b).

The asteroid properties discussed in the preceding text are the basis for the analysis of magnetization process taking place when the applied field is slowly varied over time. This variation has to occur on a time scale much larger than the timescale of the transient necessary to let magnetization relax to a stable equilibrium state. This condition corresponds to static hysteresis processes. Let us consider the case when $\mathbf{h}_a$ oscillates between opposite values along a fixed direction. The $\mathbf{m}$ orientation at each point is obtained by the tangent construction discussed in the preceding text. Inside the asteroid two orientation are possible, and the one which is actually realized depends on past history (see Figure 2b). If the field oscillation were all contained inside the asteroid, the magnetization would reversibly oscillate around the orientation initially occupied. A qualitatively different behavior occurs when the field amplitude is large enough to cross the asteroid boundary. The state occupied by the system may lose stability when the field point $(h_{ax}, h_{a\perp})$ exits the asteroid and the magnetization jumps discontinuously to a new equilibrium state (see point 2 in Figure 2b). This irreversible jumps are also referred to as Barkhausen jumps. In Figure 2(b) it is shown the magnetization half cycle where the field intensity decrease from positive to negative values. The process related to the increasing-field half cycle can be easily derived by symmetry. The hysteresis process can be clearly shown by representing the component $m_h = \cos(\theta_0 - \theta_h)$ of $\mathbf{m}$ along the applied field direction (θ_h is the angle between $\mathbf{h}_a$ and $\mathbf{e}_x$). By using different values of θ_h, one obtains static hysteresis loops as drawn in Figure 2(c). Note, in particular, that no loop at all is obtained when the field is exactly perpendicular to the anisotropy axis ($\theta_h = 90^\circ$).

3.1.3 Equilibria when one component of the applied field is zero

In many cases relevant to applications, one can assume that the applied field $\mathbf{h}_a$ lies in one of the coordinate planes, namely, that one of the Cartesian components of $\mathbf{h}_a$ is zero. In this situation, the analysis of equilibria can be substantially simplified. In the following, we will assume that $h_{az} = 0$, but the theory can be extended to the other cases by an appropriate reorientation of the Cartesian axes. In the case $h_{az} = 0$, by using the fact that $m_z^2 = 1 - m_x^2 - m_y^2$, m_z can be eliminated from the expression of the free energy, equation (20). This leads to the following formula:

$$g_L(\mathbf{m}; \mathbf{h}_a) = -\frac{D_z - D_x}{2} \times \left[(m_x - a_x)^2 + k^2 \left(m_y - a_y\right)^2 - p_0^2\right] \quad (39)$$

where:

$$a_x = -\frac{h_{ax}}{D_z - D_x}, a_y = -\frac{h_{ay}}{D_z - D_y}, k^2 = \frac{D_z - D_y}{D_z - D_x} \quad (40)$$

$$p_0^2 = a_x^2 + a_y^2 + \frac{D_z}{D_z - D_x} \quad (41)$$

Equation (39) is written in a particularly simple form because it already includes the constraint $|\mathbf{m}|^2 = 1$. This form permits one to readily recognize the nature of equilibria, namely, whether they are energy maxima, minima, or saddles.

Let us start our discussion by writing the equation for equilibria. By using the constants defined in equation (40) and (41), the components of equation (27) along the three

Cartesian axes can be written as

$$\left(D_z - D_y\right) m_z \left(m_y - a_y\right) = 0 \tag{42}$$

$$-\left(D_z - D_x\right) m_z \left(m_x - a_x\right) = 0 \tag{43}$$

$$\left(D_z - D_x\right) m_y \left(m_x - a_x\right) - \left(D_z - D_y\right) m_x \left(m_y - a_y\right) = 0 \tag{44}$$

Due to the form of equations (42–44), it is convenient to divide equilibria in two families: equilibria with $m_z \neq 0$ and equilibria with $m_z = 0$.

- Equilibrium points with $m_z \neq 0$
  In this case, equations (42–43) immediately lead to $m_x = a_x$ and $m_y = a_y$. The value of m_z can be then determined from the constraint $|\mathbf{m}| = 1$. This leads to two equilibrium points:

$$m_x = a_x, m_y = a_y, m_z = \pm\sqrt{1 - a_x^2 - a_y^2} \tag{45}$$

  which are symmetric with respect to the (m_x, m_y) plane. Notice that solutions of this type are possible only when the field lies inside the region confined by:

$$a_x^2 + a_y^2 = 1 \tag{46}$$

  that is:

$$\frac{h_{ax}^2}{\left(D_z - D_x\right)^2} + \frac{h_{ay}^2}{\left(D_z - D_y\right)^2} = 1 \tag{47}$$

  The expression (39) of the free energy shows that these equilibria are always energy maxima.
- Equilibrium points with $m_z = 0$
  This class of equilibria is characterized by the condition $m_x^2 + m_y^2 = 1$. Thus, their positions on the unit circle of the (m_x, m_y) plane can be described by the angle coordinate ϕ_0: $m_x = \cos\phi_0$, $m_y = \sin\phi_0$. The angle ϕ_0 associated with the equilibrium points is obtained by solving equation (44) rewritten in the form:

$$\left(D_y - D_x\right) \sin\phi_0 \cos\phi_0 + h_{ax} \sin\phi_0 - h_{ay} \cos\phi_0 = 0 \tag{48}$$

  In order to interpret the meaning of equation (48), it is useful to express the system free energy $g_{\mathrm{L}}(\mathbf{m}; \mathbf{h}_{\mathrm{a}})$ (see equation (20)) for $m_z = 0$ in terms of the angle ϕ_0:

$$g_{\mathrm{L}}\left(m_z = 0, \phi_0; \mathbf{h}_{\mathrm{a}}\right) = \frac{1}{2} D_x + \frac{1}{2}\left(D_y - D_x\right) \sin^2\phi_0 - h_{ax} \cos\phi_0 - h_{ay} \sin\phi_0 \tag{49}$$

  This energy expression is identical to equation (32) considered in the Stoner–Wohlfarth model, with $(D_y - D_x)$, h_{ay}, and ϕ_0 playing the role of κ_{eff}, $h_{a\perp}$ and θ_0, respectively. Equation (48) coincides with the equation $\partial g_{\mathrm{L}}/\partial\phi_0 = 0$. It can be inferred from this fact that all the results known for the Stoner–Wohlfarth model can be extended to the equilibrium points characterized by $m_z = 0$. In particular, one immediately concludes that there will be either four equilibrium points, two of which will be energy minima, or two equilibrium points, one of which will be an energy minimum. The bifurcation line where the number of energy minima changes from one to two or vice versa is given by the asteroid curve in the (h_{ax}, h_{ay}) control plane shown in Figure 3:

$$h_{ax}^{2/3} + h_{ay}^{2/3} = \left(D_y - D_x\right)^{2/3} \tag{50}$$

In conclusion, there are four qualitative different situations, separated by the two bifurcation lines given by equations (47) and (50) (see Figure 3).

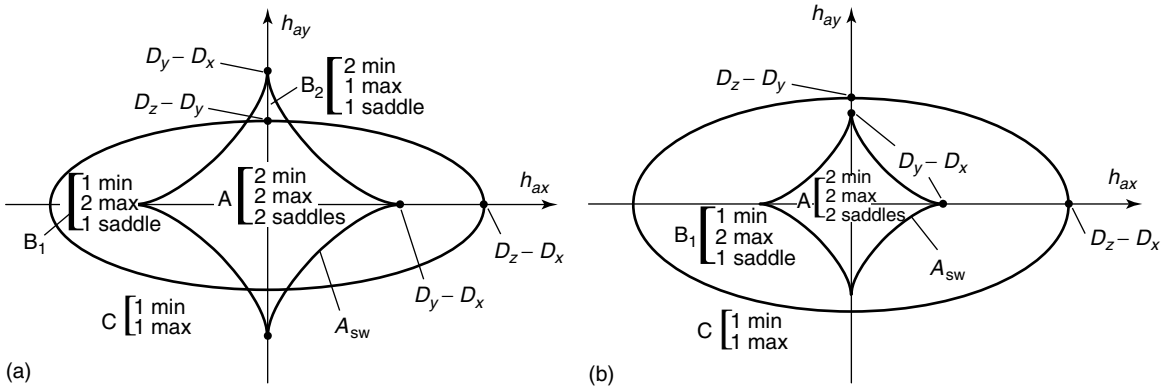

Figure 3. Bifurcation lines in the (h_{ax}, h_{ay}) control plane. (a) $D_z - D_y < D_y - D_x$; (b) $D_z - D_y > D_y - D_x$. The label A_{sw} indicates Stoner–Wohlfarth asteroid.

- Region A, 6 equilibrium points: 2 minima, 2 maxima, 2 saddles
- Region B_1, 4 equilibrium points: 1 minimum, 2 maxima, 1 saddle
- Region B_2, 4 equilibrium points: 2 minima, 1 maximum, 1 saddle
- Region C, 2 equilibrium points: 1 minimum, 1 maximum.

In this classification, the number of saddles has been indirectly determined on the basis of Poincaré index theorem: the number of maxima and minima minus the number of saddles must be equal to two. Let us notice that for certain values of the parameters D_x, D_y and D_z the region B_2 may not exist (see Figure 3b). The condition for the existence of region B_2 is that $D_y - D_x > D_z - D_y$.

3.2 Geometrical and analytical descriptions of conservative LLG dynamics

3.2.1 Unit-circle representation

As we have already discussed in a previous section (see Section 3.1.3), due to the viscouslike nature of the damping, equilibria of the system are given by critical points of the free energy $g_L(\mathbf{m}; \mathbf{h}_a)$. In addition, since the damping constant α is usually a small quantity, on short timescales, LLG dynamics is approximately conservative. In this respect, detailed information of the nature of dynamics can be obtained from the configuration of constant-energy lines, that is, the lines given by $g_L(\mathbf{m}; \mathbf{h}_a) = g_0$ on the unit sphere. It turns out that, in the case when one of the components of the applied field is zero (in the following we will assume $h_{az} = 0$), it is possible to give a two-dimensional representation of constant-energy lines. Indeed, by taking into account equation (39) and setting the energy equal to g_0 we end up with the equation:

$$(m_x - a_x)^2 + k^2 \left(m_y - a_y\right)^2 = p^2 \tag{51}$$

where:

$$p^2 = a_x^2 + k^2 a_y^2 + \frac{D_z - 2g_0}{D_z - D_x} \tag{52}$$

Equation (51) shows that the projection of magnetization trajectories on the (m_x, m_y) plane is described by a family of self-similar elliptic curves with aspect ratio k (which, according to equation (40), depends only on the anisotropy factors), all centered at the point (a_x, a_y). The family of ellipses is generated by varying the free energy value g_0 within an appropriate interval. Indeed, for a given value of $\mathbf{h}_a$, the constant g_0 controls the size of the ellipses through equation (52). It must be underlined that the only admissible portions of the ellipses are obtained by taking those parts of equation (51) which lie inside the circle $m_x^2 + m_y^2 \leq 1$. Although this representation involves only two components of magnetization, information on the third component m_z can be immediately obtained by using that $m_z^2 = 1 - (m_x^2 + m_y^2)$. For example, $m_z = \pm 1$ when $(m_x, m_y) = (0, 0)$ while $m_z = 0$ when (m_x, m_y) lies on the unit circle. The unit-circle representation can be interpreted as a top view of the unit sphere. In this sense, only the upper hemisphere $m_z > 0$ is immediately represented. However, when the applied field lies in the (x,y) plane, the free energy has a mirror symmetry with respect to the (m_x, m_y) plane and this implies that constant-energy lines (or parts of the same constant-energy line) with given energy g_0, belonging to different hemispheres, are projected into the same ellipse (or portion of ellipse) in the (m_x, m_y) plane. In other terms, the unit circles representation consists of lines, each of which represents two constant-energy (conservative) trajectories or two parts of the same trajectory with opposite values of m_z. The ellipses originating from the energy saddles (bold lines passing through the point indicated with d) are either homoclinic trajectories, that is, trajectories starting and ending on a saddle equilibrium, or heteroclinic trajectory, that is, trajectories starting from a saddle equilibrium and ending at a different saddle equilibrium. Trajectories, homoclinic, and heteroclinic, passing through saddles are also referred to as separatrices because they create a natural partition of the phase portrait into different 'central regions' (regions spanned by a continuum of nested closed lines on the unit sphere). Examples of unit-circle representation are reported in Figure 4(a–c). The three figures correspond to zero applied field, field applied along x axis, and field applied along y axis, respectively.

3.2.2 Integrability of conservative dynamical equations

We already mentioned in Section 3.2.1 that the family of trajectories with constant energy gives important information about LLG dynamics on short timescale owing to the fact that the damping constant is normally a small parameter. In this section, we show that conservative LLG dynamics can be studied analytically. The starting point for the analytical solution of the conservative dynamics is equation (51), which shows that the projection of the magnetization trajectory onto the (m_x, m_y) plane is an arc of the ellipse. Therefore, the trajectory can be expressed in the parametric form:

$$m_x = a_x - p\cos u, \quad m_y = a_y + \frac{p}{k}\sin u \tag{53}$$

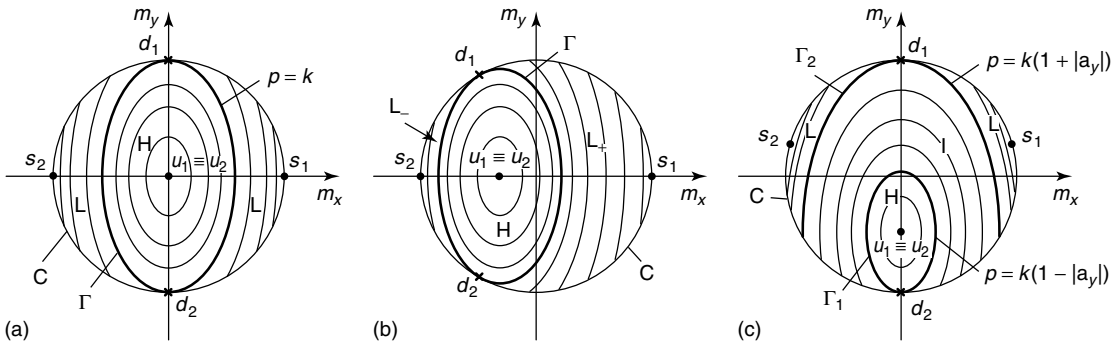

Figure 4. Sketches of the unit-circle representation for three different values of $\mathbf{h}_a$: (a) $\mathbf{h}_a = 0$, (b) $\mathbf{h}_a = h_{ax}\mathbf{e}_x$, (c) $\mathbf{h}_a = h_{ay}\mathbf{e}_y$. Magnetization trajectories are obtained from the intersection of the ellipses given by equation (51) with the unit circle $m_x^2 + m_y^2 \leq 1$. The following notation is used to indicate equilibrium points: 's' denotes energy minima, 'u' denotes energy maxima, and 'd' denotes energy saddles. The thicker lines (indicated by Γ) denote separatrices (homoclinic and heteroclinic trajectories). Letters H, L, I are used to label 'central regions': H denotes 'high-energy regions', L denotes 'low-energy regions', and I denotes 'intermediate energy regions'.

where the connection between the parametric variable u and time is to be determined. Equation (53) implies that the remaining magnetization component m_z will be given by:

$$m_z = \pm\sqrt{1 - (a_x - p\cos u)^2 - (a_y + (p/k)\sin u)^2} \quad (54)$$

By inserting equation (53) into the x component of equation (14) with $\alpha = 0$, one finds:

$$\frac{\mathrm{d}u}{\mathrm{d}t} = k\,(D_z - D_x)\,m_z \quad (55)$$

Since m_z depends on u only, one obtains the desired equation for $u(t)$ by using the method of separation of variables:

$$\frac{\mathrm{d}u}{\sqrt{1 - (a_x - p\cos u)^2 - \left(a_y + (p/k)\sin u\right)^2}} = k\,(D_z - D_x)\,\mathrm{d}t \quad (56)$$

where the '$\pm$' signs are no longer indicated because the last equation is to be interpreted as an equation for multibranch analytical functions in the complex plane.

Equation (56) is solvable in terms of elliptic integrals. This can be shown by carrying out the substitution $w = \tan(u/2)$, which transforms equation (56) into the equation:

$$\frac{\mathrm{d}w}{\sqrt{P(w)}} = \frac{k}{2}\,(D_z - D_x)\,\mathrm{d}t \quad (57)$$

where $P(w)$ represents the fourth-order polynomial:

$$P(w) = \left(1 + w^2\right)^2 - \left[a_x(1 + w^2) - p(1 - w^2)\right]^2 - \left[a_y(1 + w^2) + (2p/k)w\right]^2 \quad (58)$$

Equation (57) is precisely of the form permitting integration in terms of elliptic integrals and elliptic functions (Hancock, 1958; Smirnov, 1989). However, the integration is based on the knowledge of the roots of the polynomial $P(w)$, which are generally given by rather complicated formulas.

3.2.3 Solution under zero field

The study of equation (56) in all its complexity is carried out in Bertotti, Mayergoyz and Serpico (2006a), here we limit ourselves to the case of zero applied field, which gives some first insight into the properties of conservative magnetization dynamics. This case is simple enough to be solved without excessive technical complications. Under zero field, conservative LLG equation (see equation (14) with $\alpha = 0$, and equation (17) with $\mathbf{h}_a = 0$) becomes formally identical to Euler equation for the angular momentum of a rigid body (Landau and Lifshitz, 1976). The unit-circle representation of conservative magnetization trajectories is, in this case, the one in Figure 4(a): the unit sphere is partitioned into four central regions, two symmetric high-energy regions (indicated by H and projected into the same region of the unit circle) and two symmetric low-energy energy regions (indicated by L). The magnetization components (equations (53) and (54)) can be expressed as functions of $w = \sin u$ only, since $a_x = a_y = 0$ (see equation (40)) and one finds that:

$$m_x = \mp p\sqrt{1 - w^2}, \quad m_y = \frac{p}{k}w,$$
$$m_z = \pm\frac{k'p}{k}\sqrt{w_0^2 - w^2} \quad (59)$$

where:

$$w_0 = \frac{k}{k'p}\sqrt{1 - p^2} \quad (60)$$

$k'^2 = 1 - k^2$, and p^2 is linearly related to the system energy through equation (52), which for zero field is reduced to:

$$p^2 = \frac{D_z - 2g_0}{D_z - D_x} \tag{61}$$

By making the change of variable $w = \sin u$ in equation (56), one obtains the following equation:

$$\frac{\mathrm{d}w}{\sqrt{\left(1 - w^2\right)\left(1 - k_H^2 w^2\right)}} = \Omega_H \mathrm{d}t \tag{62}$$

where:

$$k_H = \frac{1}{w_0} = \frac{k'p}{k}\frac{1}{\sqrt{1 - p^2}} \tag{63}$$

$$\Omega_H = k\sqrt{1 - p^2}\,(D_z - D_x) \tag{64}$$

The solution of equation (62) is the Jacobi 'sin-type' elliptic function (Hancock, 1958):

$$w = \mathrm{sn}\,(\Omega_H t, k_H) \tag{65}$$

By inserting equation (65) into equation (59) and by using Jacobi elliptic function transformation rules one obtains the magnetization components:

$$m_x = \mp p\,\mathrm{cn}\,(\Omega_H t, k_H) \tag{66}$$

$$m_y = \frac{p}{k}\mathrm{sn}\,(\Omega_H t, k_H) \tag{67}$$

$$m_z = \pm\sqrt{1 - p^2}\mathrm{dn}\,(\Omega_H t, k_H) \tag{68}$$

One finds two sets of solutions, depending on the choice made for the sign of m_z. The corresponding sign of m_x is determined by using LLG equation. Equations (66)–(68) depend on the energy g_0 of the conservative motion through the parameter p defined by equation (61). The parameter p has an intuitive geometrical meaning. As shown by equation (51), it measures the size of the ellipse along which the magnetization motion takes place. The energy of the system takes values in the interval (see equation (39)):

$$\frac{D_x}{2} \le g_0 \le \frac{D_z}{2} \tag{69}$$

that is, $0 \le p^2 \le 1$. When g_0 is varied in this interval, the first two equations in equation (59) generate the unit-circle representation of the conservative phase portrait shown in Figure 4(a). The energy maxima ('u_1', 'u_2' in in Figure 4a) correspond to $p = 0$, where the constant-energy ellipse given by equation (51) is reduced to a point, whereas $p = 1$ represents the energy minima ('s_1', 's_2' in Figure 4a), where the ellipse is tangent to the unit circle from outside. The heteroclinic separatrix trajectories (bold lines Γ connecting the two saddles 'd_1', 'd_2' in Figure 4a) divide the portrait into the high-energy (H) and low-energy (L) regions.

- *Region H:* This region actually consists of two separate regions symmetric with respect to the (m_x, m_y) plane. The system energy varies in the interval $D_y/2 \le g_0 \le D_z/2$, that is:

$$0 \le p^2 \le k^2 \tag{70}$$

According to equation (63), $0 \le k_H \le 1$ in this region, so one immediately concludes from equations (66)–(68) that the magnetization motion is a precessional motion about the hard z axis. By taking into account the properties of Jacobi elliptic functions, one obtains for the precession period:

$$T_{g_0} = \frac{4\mathbf{K}(k_H)}{\Omega_H} \tag{71}$$

where $\mathbf{K}(k_H)$ represents the complete elliptic integral of the first kind (Hancock, 1958; Smirnov, 1989).

- *Region L:* This region consists of two regions symmetric with respect to the (m_y, m_z) plane, in which the energy varies in the interval $D_x/2 \le g_0 \le D_y/2$. Therefore:

$$k^2 \le p^2 \le 1 \tag{72}$$

which implies $1 \le k_H \le \infty$. The nature of the corresponding magnetization motions is made clear by observing that the role of cn and dn Jacobi functions is exchanged when their modulus exceeds 1. By using known transformation rules for Jacobi functions one can write equations (66)–(68) in the equivalent form:

$$m_x = \mp p\mathrm{dn}\,(\Omega_L t, k_L) \tag{73}$$

$$m_y = \frac{1}{k'}\sqrt{1 - p^2}\mathrm{sn}\,(\Omega_L t, k_L) \tag{74}$$

$$m_z = \pm\sqrt{1 - p^2}\mathrm{cn}\,(\Omega_L t, k_L) \tag{75}$$

where:

$$\Omega_L = k_H \Omega_H = k'p\,(D_z - D_x) \tag{76}$$

$$k_L = \frac{1}{k_H} = \frac{k}{k'p}\sqrt{1 - p^2} \tag{77}$$

It can be verified that $0 \leq k_L \leq 1$, so equations (73)–(75) describe a precessional motion about the x axis. The precession period is:

$$T_{g_0} = \frac{4\mathbf{K}(k_L)}{\Omega_L} \tag{78}$$

In the following two sections, we discuss in some detail the solution of equation (56) under a nonzero field in two cases of particular physical interest, namely, when the field is perpendicular or parallel to the easy axis of the system.

4 NONLINEAR MAGNETIZATION DYNAMICS UNDER CONSTANT AND PULSED APPLIED FIELDS

The problem of nonlinear magnetization dynamics under constant and pulsed applied fields arises especially in magnetization switching of magnetic particles and thin films. This topic has received considerable attention in connection with the enormous advances in the magnetic storage technologies and spintronics (Bauer, Fassbender, Hillebrands and Stamps, 2000; Mallinson, 2000).

Traditionally, the study of magnetization reversal has been carried out by using the classical Stoner–Wohlfarth model (Stoner and Wohlfarth, 1948). As we have discussed in Section 3.1.2, this model is static in nature and does not take into account any magnetization dynamics. However, in the frequency range relevant to magnetic storage applications, magnetization precession has a crucial influence on magnetization dynamics and therefore has to be appropriately taken into account. Despite the nonlinear nature of the dynamics it is possible to develop a systematic and rigorous analysis of the LLG equation by using the methods of nonlinear dynamical system theory. These techniques have been outlined in the previous sections of this article and turn out very effective in the analysis of magnetization switching. In particular, these techniques yield detailed information about the parameters which enter in the design of devices (e.g., critical fields for switching, pulse duration, frequency of precessional motion, relaxation time in 'ringing' processes).

4.1 Switching under rectangular field pulses

4.1.1 Damping switching in uniaxial magnetic body

The traditional mode of switching in uniaxial particles (damping switching; Mallinson, 2000) is shown in Figure 5(a). The switching is realized by applying a field opposite to the initial magnetization orientation. If the field

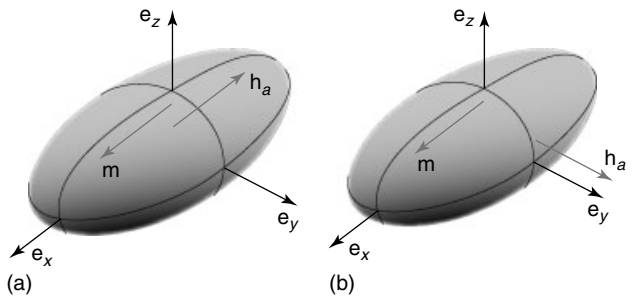

Figure 5. (a) Damping switching mode of operation. the applied field is opposite to the initial magnetization; (b) Precessional switching mode of operation: the applied field is orthogonal to the initial magnetization.

is strong enough, the initial state becomes unstable and the magnetization relaxes toward the energy minimum in the direction of the applied field. We analyze this mechanism by using the LLG equation in the Landau–Lifshitz form (see equation (22)):

$$\frac{\mathrm{d}\mathbf{m}}{\mathrm{d}t} = -\frac{1}{1+\alpha^2}\mathbf{m} \times \mathbf{h}_{\text{eff}} - \frac{\alpha}{1+\alpha^2}\mathbf{m} \times (\mathbf{m} \times \mathbf{h}_{\text{eff}}) \tag{79}$$

Exact analytical solutions of this equation can be obtained in the special case where the magnetic body exhibits uniaxial symmetry and the external field is applied exactly along the symmetry axis, which we choose as the x axis (see Figure 5a). Under these assumptions, the effective field is given by the formula:

$$\mathbf{h}_{\text{eff}} = -D_\perp(m_y\mathbf{e}_y + m_z\mathbf{e}_z) - D_x m_x \mathbf{e}_x + h_{ax}\mathbf{e}_x \tag{80}$$

where $D_\perp = D_y = D_z$ and h_{ax} is assumed to be constant during the pulse duration. Kikuchi (1956) considered a similar problem for an isotropic ferromagnetic sphere, where the effective field is defined by the formula:

$$\mathbf{h}_{\text{eff}} = -\mathbf{m}/3 + h_{ax}\mathbf{e}_x \tag{81}$$

The difference in the mathematical forms of equations (80) and (81) leads to a profound difference in the physics of magnetization switching. In the case of equation (81), there exists an infinite set of equilibrium states for $h_{ax} = 0$ and no critical field is required to switch from one equilibrium state to another. In contrast, in the case of equation (80) there are only two equilibrium states for $h_{ax} = 0$, namely, $m_x = \pm 1$, and the switching from one equilibrium state to the other is only possible if the applied field h_{ax} exceeds some critical field. The problem when the effective field is given by equation (80) has been treated in Mallinson (2000), and Leineweber and Kronmueller (1999) where the analysis is based on the solution of the LLG equation

in spherical coordinates. Our approach will exploit the rotational symmetry of the problem (the treatment below closely follows the one in Bertotti, Mayergoyz, Serpico and Dimian (2003)).

When the effective field is given by equation (80), the LLG equation becomes invariant with respect to rotations of coordinate axes y and z around the x axis. As a result of this rotational symmetry, it is expected that $\mathrm{d}m_x/\mathrm{d}t$ depends only on the x component of $\mathbf{m}$. Indeed, by using simple algebra, one finds that:

$$(\mathbf{m}\times\mathbf{h}_{\mathrm{eff}})\cdot\mathbf{e}_x = 0,$$
$$[\mathbf{m}\times(\mathbf{m}\times\mathbf{h}_{\mathrm{eff}})]\cdot\mathbf{e}_x = -\kappa_{\mathrm{eff}}\left(\tfrac{m_x+h_{ax}}{\kappa_{\mathrm{eff}}}\right)(1-m_x^2) \qquad (82)$$

where $\kappa_{\mathrm{eff}} = D_\perp - D_x$ (as in equation (33) of the Stoner–Wohlfarth theory). From equation (22) and the first of equation (82), we derive the following equation:

$$\frac{1}{\kappa_{\mathrm{eff}}}\frac{\mathrm{d}m_x}{\mathrm{d}t} = \frac{\alpha}{1+\alpha^2}\left(m_x + \frac{h_{ax}}{\kappa_{\mathrm{eff}}}\right)\left(1-m_x^2\right) \qquad (83)$$

Equation (83) shows that the magnetization switching from the state $m_x = 1$ to the state $m_x = -1$ (or vice versa) is driven exclusively by damping: in the conservative case ($\alpha = 0$) the x component of magnetization simply remains constant. In this sense, this switching can be regarded as 'damping' switching. On the other hand, the equation shows that anisotropy affects the switching only in the form of scale factors for field and time. Indeed, if one expresses equation (83) in terms of the rescaled time $\kappa_{\mathrm{eff}}t$ and rescaled field $h_{ax}/\kappa_{\mathrm{eff}}$, anisotropy disappears completely from the description. This means that damping switching will follow a law of correspondent states when represented in terms of these rescaled variables.

It seems from equation (83) that no switching is possible if the magnetization is initially in the equilibrium state $m_x = 1$. However, owing to thermal effects, the vector $\mathbf{m}$ slightly fluctuates around the above equilibrium state. As a result, the value of m_x at the instant when the applied field is turned on will be slightly different from 1 and the switching process is initiated. This argument justifies the solution of equation (83) with the initial condition:

$$m_x(t=0) = m_{x0} \qquad (84)$$

where m_{x0} is close to 1. It is apparent from equation (83) that if $h_{ax} < -\kappa_{\mathrm{eff}}$, then $\mathrm{d}m_x/\mathrm{d}t < 0$ and the switching to the equilibrium state $m_x = -1$ will proceed for any m_{x0}. On the other hand, if $h_{ax} \geq -\kappa_{\mathrm{eff}}$, then, for m_{x0} sufficiently close to 1, $\mathrm{d}m_x/\mathrm{d}t > 0$ and no switching is possible. This clearly reveals that κ_{eff} plays the role of critical switching field. In the sequel, it is assumed that $h_{ax} < -\kappa_{\mathrm{eff}}$.

By separating variables in equation (83), we obtain:

$$\int_{m_{x0}}^{m_x}\frac{\mathrm{d}m_x}{(1-m_x^2)(m_x - |h_{ax}|/\kappa_{\mathrm{eff}})} = \frac{\alpha\kappa_{\mathrm{eff}}}{1+\alpha^2}t \qquad (85)$$

and, after integration:

$$t = \frac{1+\alpha^2}{2\alpha(\kappa_{\mathrm{eff}}-|h_{ax}|)}\ln\frac{1-m_{x0}}{1-m_x} + \frac{1}{2(\kappa_{\mathrm{eff}}+|h_{ax}|)} \times \ln\frac{1+m_{x0}}{1+m_x} + \frac{\kappa_{\mathrm{eff}}}{\kappa_{\mathrm{eff}}^2 - h_{ax}^2}\ln\frac{|h_{ax}|-\kappa_{\mathrm{eff}}m_x}{|h_{ax}|-\kappa_{\mathrm{eff}}m_{x0}} \qquad (86)$$

By using the last equation, the minimal pulse time needed for switching can be found. Indeed, if the duration of the field pulse is such that a negative value of m_x is reached, then the magnetization will be in the basin of attraction of the reversed state $m_x = -1$, and the switching will be achieved. Thus, the minimal pulse duration T_{ds} (ds stands for damping switching) can be found by substituting $m_x = 0$ in equation (86):

$$T_{\mathrm{ds}} = \frac{1+\alpha^2}{\alpha}\left[\frac{\ln(1-\cos\phi_0)}{2(\kappa_{\mathrm{eff}}-|h_{ax}|)} + \frac{\ln(1+\cos\phi_0)}{2(\kappa_{\mathrm{eff}}+|h_{ax}|)} + \frac{\kappa_{\mathrm{eff}}}{\kappa_{\mathrm{eff}}^2 - h_{ax}^2}\ln\frac{|h_{ax}|}{|h_{ax}|-\kappa_{\mathrm{eff}}\cos\phi_0}\right] \qquad (87)$$

where ϕ_0 is the angle formed by the initial magnetization with the x axis. For the typical case of small ϕ_0, the minimal pulse time T_{ds} given by equation (87) is very close to the actual switching time at which m_x reaches a value almost equal to -1. Indeed, equation (83) shows that m_x decreases much faster when it is close to zero than when it is close to its initial equilibrium value. This conclusion is supported by the calculations shown in Figure 6, made by using equation (86). It is interesting to notice that T_{ds} tends to infinity both for $\alpha \to 0$ and $\alpha \to \infty$. Indeed, for $\alpha \to 0$, we have conservative dynamics and the system oscillates around the initial state. While for $\alpha \to \infty$, as a result of the viscous nature of Gilbert damping, dynamics become slower and slower. In addition, one can easily see that the minimum of T_{ds} as function of α, is obtained for $\alpha = 1$, which is the optimum value of damping to achieve fast damping switching. However, most materials used in applications have a damping constant appreciably smaller than 1.

Figure 7 presents the field dependence of the inverse pulse time $1/T_{\mathrm{ds}}$ calculated from equation (87). The curves are approximately linearly dependent on the field except for field values very close to the critical field κ_{eff}. Indeed, for small values of the initial angle ϕ_0, the first term in the right-hand side of equation (87) is dominant. By neglecting the two

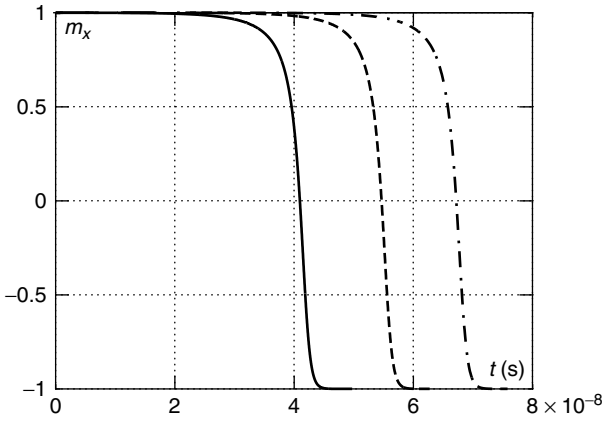

Figure 6. Evolution of m_x with time (measured in s) calculated from equation (86), with $m_{x0} = \cos\phi_0$. Continuous line: $\phi_0 = 1^\circ$; dashed line: $\phi_0 = 0.3^\circ$; dash-dotted line: $\phi_0 = 0.1^\circ$. Parameter values: $\alpha = 0.01$, $\kappa_{\rm eff} = 0.25$, $h_{ax} = -1.2\kappa_{\rm eff}$, $(\gamma M_{\rm s})^{-1} = 6\,{\rm ps}$ (permalloy).

other terms, one obtains the approximate law:

$$\frac{1}{T_{\rm ds}} \simeq \frac{\alpha}{(1+\alpha^2)\ln(\sqrt{2}/\phi_0)}(|h_{ax}| - \kappa_{\rm eff}) \qquad (88)$$

which is indeed linear in the field. Equation (88) shows that the dynamic (short-time) coercivity appreciably exceeds the static coercivity $\kappa_{\rm eff}$. This behavior is similar to that observed in Thornley (1975), Doyle and He (1993), and Rizzo, Silva and Kos (2000).

The switching time given by equations (87) and (88) depends on the value of the initial angle ϕ_0. The expected value of this angle can be evaluated by using statistical mechanics arguments. If the fluctuations are so weak that no thermally induced switching can occur within the timescale of observation of ϕ_0, then, one can approximate the behavior of $g_{\rm L}(\mathbf{m}; \mathbf{h}_{\rm a} = 0)$ around $\phi_0 = 0$ by a parabolic potential well. This leads to the following distribution function:

$$\rho(\phi_0) \approx c\phi_0 \exp\left[\frac{\mu_0 M_{\rm s}^2 \kappa_{\rm eff} V}{2k_{\rm B}T}\phi_0^2\right] \qquad (89)$$

where $k_{\rm B}$ is Boltzmann constant, T is the temperature, c is an appropriate normalization constant, μ_0 is vacuum permeability, and V is the volume of the magnetic body. For a permalloy film with dimensions 0.1 µm, 0.1 µm, 10 nm at room temperature ($T = 300^\circ K$), the expected value of ϕ_0 is in the order of $\sqrt{k_{\rm B}T/(\mu_0 M_{\rm s}^2 \kappa_{\rm eff} V)} \approx 0.8^\circ$.

4.1.2 *Precessional switching in uniaxial magnetic body and comparison with damping switching*

In this section, we will present an alternative technique to obtain the switching of a nanomagnet which is commonly

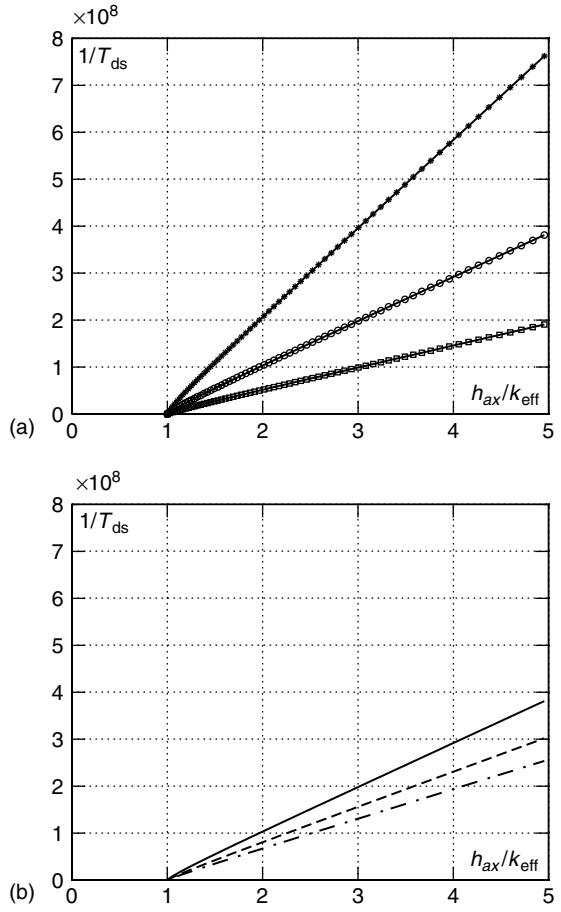

Figure 7. Inverse of minimum pulse duration $1/T_{\rm ds}$ (measured in s^{-1}) versus ratio between applied field and critical switching field $\kappa_{\rm eff}$, calculated from equation (87)) for damping switching ($\alpha = 0.01$, $(\gamma M_{\rm s})^{-1} = 6\,{\rm ps}$ (permalloy)). (a) $1/T_{\rm ds}$ versus $h_{ax}/\kappa_{\rm eff}$ for $\phi_0 = 1^\circ$ and different values of $\kappa_{\rm eff}$: '□': $\kappa_{\rm eff} = 0.125$; '○': $\kappa_{\rm eff} = 0.25$; '∗': $\kappa_{\rm eff} = 0.5$. (b) $1/T_{\rm ds}$ versus $h_{ax}/\kappa_{\rm eff}$ for $\kappa_{\rm eff} = 0.25$ and different values of ϕ_0: continuous line: $\phi_0 = 1^\circ$; dashed line: $\phi_0 = 0.3^\circ$; dash-dotted line: $\phi_0 = 0.1^\circ$.

referred to as *precessional switching*. The mode of operation of precessional switching is depicted in Figure 5(b). The magnetization is initially along the easy axis and a field approximately orthogonal to the easy axis is applied on the magnetic body. The field produces a torque which tilts the magnetization from its initial position and drives a precessional oscillation. Magnetization reversal is realized by switching the field off when the magnetization is close to its reversed orientation.

We notice that, while in damping switching the role of dissipation is crucial, precessional switching is accomplished by controlling the magnetization precession within a time interval which is usually so short that the role of dissipation is negligible. This type of switching can be considerably faster and it may require lower applied fields in comparison

with traditional switching. However, the switching is realized only if the field pulse duration is accurately controlled in such a way that the field is switched off precisely when the magnetization is close to its reversed orientation.

For the sake of comparison with damping switching we will consider precessional switching in a spheroidal particle rotationally symmetric with respect to the anisotropy easy axis $\mathbf{e}_x$ (Mayergoyz, Dimian, Bertotti and Serpico, 2005). The case of generic ellipsoidal particle can be treated by means of appropriate generalization of the following derivation (Bertotti, Mayergoyz and Serpico, 2006a). Owing to the uniaxial symmetry of the system, the effective field (17) can be written in the following form:

$$\mathbf{h}_{\text{eff}} = -D_{\perp}(m_x\mathbf{e}_x + m_y\mathbf{e}_y) - D_x m_x\mathbf{e}_x + h_{ax}\mathbf{e}_x + h_{ay}\mathbf{e}_y \tag{90}$$

where $D_{\perp} = D_y = D_z$. It is interesting to notice that the expression (90) can be written as $\mathbf{h}_{\text{eff}} = (D_{\perp} - D_x)m_x\mathbf{e}_x + h_{ax}\mathbf{e}_x + h_{ay}\mathbf{e}_y - D_{\perp}\mathbf{m}$, and the last term $D_{\perp}\mathbf{m}$ is proportional to $\mathbf{m}$ and thus has no effect on the torque $\mathbf{m} \times \mathbf{h}_{\text{eff}}$. For this reason, in the case of uniaxial particles, one can assume the following alternative expression of the effective field

$$\mathbf{h}_{\text{eff}} = \kappa_{\text{eff}} m_x\mathbf{e}_x + h_{ax}\mathbf{e}_x + h_{ay}\mathbf{e}_y \tag{91}$$

where, as in the previous section, $\kappa_{\text{eff}} = D_{\perp} - D_x$ (see equation (33)). The magnetic free energy corresponding to the above effective field has the form:

$$g_{\text{L}}(\mathbf{m}; \mathbf{h}_{\text{a}}) = -\frac{\kappa_{\text{eff}}}{2}m_x^2 - h_{ax}m_x - h_{ay}m_y \tag{92}$$

It can be easily observed that in the case of zero applied field there are two stable equilibria $\mathbf{m} = \pm\mathbf{e}_x$ surrounded by two energy wells separated by the boundary $m_x = 0$ (the circle corresponding to $m_x = 0$ on the unit sphere has the role of the separatrix between the two energy well). Since the dissipation results in the decrease in magnetic free energy, it can be concluded that the time evolution of magnetization within each energy well inevitably leads to the stable equilibrium inside this well. Thus, the essence of the precessional switching is to move the magnetization by the applied pulsed magnetic field from one energy well to another. As soon as the target potential well is reached, the applied field can be switched off and magnetization will relax to a new equilibrium as a result of damping.

In the following, we analyze the dynamics in the time interval when the field is applied. In this interval, we assume that the effect of damping is negligible and thus we solve conservative LLG equation.

By using conservation of the free energy (92) and $m_x^2 + m_y^2 + m_z^2 = 1$, one can easily prove that magnetization

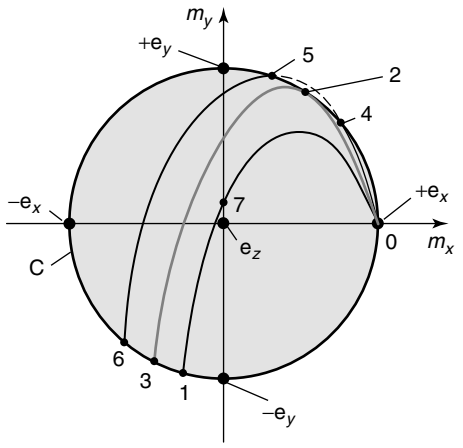

Figure 8. Unit-circle representation of trajectories for precessional switching in uniaxial particle.

trajectories in the (m_x, m_y) plane, starting from the point $(m_x = 1, m_y = 0)$ (point ('0' in Figure 8), are described by the following equation

$$-\frac{\kappa_{\text{eff}}}{2}m_x^2 - h_{ax}m_x - h_{ay}m_y = -\frac{\kappa_{\text{eff}}}{2} - h_{ax} \tag{93}$$

Thus, on the (m_x, m_y) plane, the precessional magnetization motion occurs along the parabola (93) that is confined within the unit disk $m_x^2 + m_y^2 \leq 1$. The fact that, in the present case, we do not have arcs of ellipses (as it is generally the case according to the discussion in Section 3.2.1), is a consequence of the rotational symmetry of the magnetic body.

Several examples of parabolic magnetization trajectories on (m_x, m_y) plane are shown in Figure 8.

Next, we want to investigate the different types of parabolic trajectories that can be generated by (93) in a function of the values of h_{ax} and h_{ay}. Our purpose is to find the region in the (h_{ax}, h_{ay}) control plane which corresponds to trajectories of the family (93) which, starting from the point $(m_x = 1, m_y = 0)$ and remaining inside the unit circle

$$m_x^2 + m_y^2 = 1 \tag{94}$$

eventually enters in the $m_x < 0$ half circle (e.g., trajectory '0-7-1' in Figure 8) . A necessary condition for this is that the trajectories admit an intersection with the line $m_x = 0$ with $|m_y \leq 1|$. By substituting $m_x = 0$ in (93) we arrive to the following equation:

$$m_y = \frac{(h_{ax} + \kappa_{\text{eff}}/2)}{h_{ay}} \tag{95}$$

From the last equation one obtains that the intersection of the parabola (93) with the line $m_x = 0$ occurs inside the unit

circle ($m_y \leq 1$) under the following condition

$$\left|h_{ax} + \frac{\kappa_{\text{eff}}}{2}\right| \leq |h_{ay}| \tag{96}$$

The region in the (h_{ax}, h_{ay}) control plane corresponding to the inequality (96) is represented in gray in Figure 9(a).

Next, we have to analyze the conditions on (h_{ax}, h_{ay}) to rule out situations like the one corresponding to the trajectory 0-4-5-6 sketched in Figure 8 in which the parabola passing through the point ($m_x = 1, m_y = 0$) (point '0' in the figure) corresponds to two disjoint pieces of magnetization trajectories (0-4 and 5-6). In this condition, there can be no precessional switching since the magnetization evolution starting from $\mathbf{e}_x$ remains trapped in the half plane $m_x > 0$ (between the points 0 and 4 in Figure 8). The family of parabolas similar to 0-7-1 and the family of parabolas similar to 0-4-5-6 are separated by the critical trajectories 0-2-3 which is tangent to the $m_x > 0$ portion of the unit circle. This case corresponds to values of (h_{ax}, h_{ay}) for which there is a saddle point in 2 and the initial state $\mathbf{e}_x$ is on the corresponding homoclinic trajectory 0-2-3. Small deviations from this critical condition lead to trajectories consisting of one piece of parabola (for instance, trajectory 0-7-1 in Figure 8) or to trajectories consisting of two disjoint pieces of the same parabola (for instance, trajectory 0-4 and 5-6 in Figure 8). Let us investigate the conditions under which we have the critical case.

By imposing the condition of tangency of the curves represented by equations (94) and (93), one arrives at the following relation:

$$\kappa_{\text{eff}} m_x m_y + h_{ax} m_y - h_{ay} m_x = 0 \tag{97}$$

At point 2 (Figure 8), three equations (94), (93), and (97) are satisfied. These three equations define the curve h_{ay} versus h_{ax} that separates the values of h_{ax} and h_{ay} which correspond to the first and second classes of parabolic trajectories, respectively. This h_{ay} versus h_{ax} curve can be easily found in parametric form by introducing the polar angle ϕ_0 such that:

$$m_x = \cos\phi_0, \qquad m_y = \sin\phi_0 \tag{98}$$

By substituting (98) into (93) and (97) and solving these equations with respect to h_{ax} and h_{ay}, we arrive at the following parametric equation for the 'separating' curve:

$$\begin{aligned} h_{ax} &= -\kappa_{\text{eff}} \cos\phi_0 \cos^2(\phi_0/2), \\ h_{ay} &= \kappa_{\text{eff}} \sin\phi_0 \sin^2(\phi_0/2) \end{aligned} \tag{99}$$

(similar formulas were derived by using different reasoning in Porter, 1998). We observe that, by varying the parameter ϕ_0 in equation (99) in the interval $[-\pi/2, \pi/2]$, we

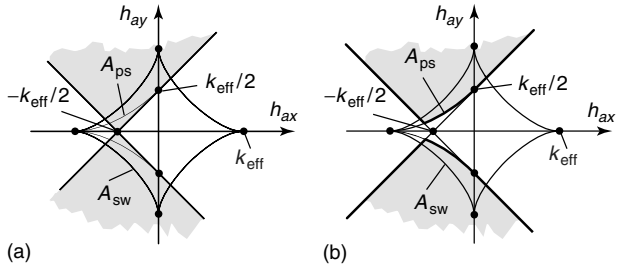

Figure 9. Regions in the (h_{ax}, h_{ay}) control plane related to the conditions for precessional switching. The curves labeled by A_{sw} and A_{ps} correspond to the Stoner–Wohlfarth model asteroid (see equation (37)) and to equation (99), respectively. (a) The shaded region correspond to equation (96)). (b) The shaded region correspond to the condition of precessional switching.

generate two arcs of the asteroid (curve A_{ps} in Figures 9a and b) which are inside the Stoner–Wohlfarth asteroid (curve A_{sw} in Figures 9a and b). These two arcs of the asteroid along with the vertical segment, defined by conditions $h_{ax} = 0$ and $-\kappa_{\text{eff}}/2 \leq h_{ay} \leq \kappa_{\text{eff}}/2$, define the boundary of a closed region in the control plane (h_{ax}, h_{ay}) completely inside the Stoner–Wohlfarth asteroid. When the applied field is inside this region, according to the discussion in the preceding text, there is an intersection of the parabolic trajectory (93) with $m_x > 0$ portion of the unit circle and the trajectory starting from $\mathbf{e}_x$ remains trapped in the $m_x > 0$ half plane (like trajectory $0 - 4$ in Figure 8b). By removing the above region from the gray region corresponding to condition (96) (see Figure 9a), one obtains the switching region for precessional switching in Stoner–Wohlfarth particles depicted in Figure 9(b).

Now we will focus on the duration of the applied field pulse which guarantees successful switching. In this respect, we will assume that magnetization evolves on a trajectory similar to trajectory '0-7-1' in Figure 8. To find the evolution of magnetization, one can consider that the x component of LLG equation, in this case, reads

$$\frac{\mathrm{d}m_x}{\mathrm{d}t} = h_{ay} m_z \tag{100}$$

By using (93) and the condition $m_z^2 = 1 - m_x^2 - m_y^2$, one can expressed m_z^2 as a fourth-order polynomial in m_x. Thus in this case, by using equation (100), the time windows for switching the field off is $t_7 < t < t_1$, where:

$$t_7 = -\int_1^0 \frac{\mathrm{d}m_x}{|h_{ay} m_z(m_x)|} \tag{101}$$

and

$$t_1 - t_7 = -2\int_0^{m_{x2}} \frac{\mathrm{d}m_x}{|h_{ay} m_z(m_x)|} \tag{102}$$

and $m_x = 1$, $m_x = 0$ and $m_x = m_{x2}$ correspond to points 0, 7, and 1 in Figure 8, respectively. The value of m_{x2} can be found by solving simultaneous equations (94) and (93).

Let us determine the duration of the field pulse necessary to switching in the case of applied field along the y axis ($\mathbf{h}_\mathrm{a} = h_{ay}\mathbf{e}_y$). In the case of Stoner–Wohlfarth particle it can be shown that, after appropriate integration of equation (56), m_y can be expressed in the following form:

$$m_y(t) = \frac{D}{2h_{ay}}\mathrm{sn}^2(h_{ay}t, k_s) \tag{103}$$

where $\mathrm{sn}(u, k)$ is the 'sin-type' Jacobi elliptic function of argument u and modulus k, and $k_s = D/(2h_{ay})$. It can be readily inferred that m_x will reach the value -1 after one period of the function $\mathrm{sn}^2(h_{ay}t, k_s)$ (which is half of the period of the function $\mathrm{sn}(h_{ay}t, k_s)$). This period can be expressed, in physical units, as

$$T_\mathrm{ps} = \frac{1}{\gamma M_\mathrm{s}}\frac{2K(k_s)}{h_{ay}} \tag{104}$$

where $K(k)$ is the complete elliptic integral of the first kind of modulus k.

It has been previously discussed that in the case of precessional switching the field pulse duration must be tuned with attention, in the sense that complete switching is achieved only if the field is switched off in a certain time window. No such timing is required for damping switching, because any field pulse of duration exceeding the minimum time T_ds will lead to switching. Precessional switching is thus more difficult to realize. On the other hand, it has clear advantages with respect to damping switching, because the critical field is lower and the switching time is much shorter. In fact, it is instructive to compare switching times for precessional and damping switching for the same value of the ratio r_c between applied fields and corresponding critical fields, that is, $h_{ay}/\kappa_\mathrm{eff}$ for damping switching and $2h_{ay}/\kappa_\mathrm{eff}$ for precessional switching. For T_ps, we will use the formulas for Stoner–Wohlfarth particles, since they were obtained for the same symmetry assumed for damping switching, namely, uniaxial symmetry around the $\mathbf{e}_x$ direction. One can express the ratio $T_\mathrm{ps}/T_\mathrm{ds}$ in the form:

$$\frac{T_\mathrm{ps}}{T_\mathrm{ds}} = \frac{\alpha}{1+\alpha^2}F(r_\mathrm{c}) \tag{105}$$

where the function $F(r_\mathrm{c})$ is obtained from equations (87) and (104). The graph of the function $F(r_\mathrm{c})$ is shown in Figure 10 for different values of the angle ϕ_0 involved in damping switching. It is clear from this figure and equation (105) that precessional switching is (for $\alpha \ll 1$) approximately $1/\alpha$ times faster than damping switching. For applied fields close to their respective critical fields (i.e., r_c close to 1), this difference is even more pronounced.

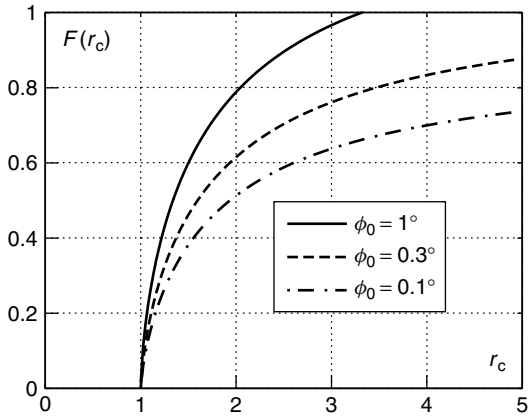

Figure 10. Comparison between precessional and damping switching times. Plot of the function $F(r_\mathrm{c}) = T_\mathrm{ps}/T_\mathrm{ds}$ versus the ratio r_c between applied field and corresponding critical field, that is, $h_{ay}/\kappa_\mathrm{eff}$ for damping switching and $2h_{ay}/\kappa_\mathrm{eff}$ for precessional switching. The function is plotted for different values of the initial angle ϕ_0 characterizing damping switching. Continuous line: $\phi_0 = 1^\circ$; dashed line: $\phi_0 = 0.3^\circ$; dash-dotted line: $\phi_0 = 0.1^\circ$.

4.2 Relaxation to equilibrium

The analysis of magnetization relaxation to equilibrium is instrumental for the interpretation of the 'ringing' phenomena (Back *et al.*, 1998, 1999; Schumacher *et al.*, 2003; Kaka and Russek, 2002) that occur in precessional switching whenever the magnetization is not exactly in the desired equilibrium state at the moment the external field is switched off. The relaxation process exhibits two distinct timescales: the fast timescale of precessional dynamics and the relatively slow timescale of relaxation dynamics controlled by the damping constant α. The free energy g_L varies significantly only on the slow timescale. In other words, the free energy is a 'slow' variable whose dynamics is not obscured by 'ringing' and thus reveals the actual rate of relaxation to equilibrium. For this reason, it is desirable to derive the differential equation for the free energy and use it for relaxation studies instead of the Landau–Lifshitz equation. It turns out that this equation can be derived by using the averaging technique. This technique is conceptually related to the Poincaré–Melnikov method presented in Section 5.2.3 in the description of magnetization dynamics driven by time-harmonic fields.

Our starting point for the analysis of relaxation toward equilibrium is equation (26), discussed in Section 2.2.2:

$$\frac{\mathrm{d}g_\mathrm{L}}{\mathrm{d}t} = -\alpha\left|\frac{\mathrm{d}\mathbf{m}}{\mathrm{d}t}\right|^2 \tag{106}$$

This equation shows that the magnetization dynamics under constant applied field is such that the free energy is monotonically decreasing until some equilibrium state is reached. Since the damping constant is a small quantity, $\alpha \ll 1$, the magnetization dynamics during one period of the precessional motion closely mimics the conservative dynamics corresponding to $\alpha = 0$. The free energy is decreased appreciably only over many precession periods and remains practically constant during one period. For this reason, no essential information on relaxation is lost if equation (26) is averaged over one precession period and the conservative solution is used for $\mathrm{d}\mathbf{m}/\mathrm{d}t$. By denoting the averaged energy as $\overline{g}_{\mathrm{L}}$, we have:

$$\frac{\mathrm{d}\overline{g}_{\mathrm{L}}}{\mathrm{d}t} = -\frac{\alpha}{T_{\overline{g}_{\mathrm{L}}}} \int_0^{T_{\overline{g}_{\mathrm{L}}}} \left| \frac{\mathrm{d}\mathbf{m}_{\overline{g}_{\mathrm{L}}}}{\mathrm{d}t} \right|^2 \mathrm{d}t \tag{107}$$

where $\mathbf{m}_{\overline{g}_{\mathrm{L}}}(t)$ corresponds to the conservative dynamics with energy $\overline{g}_{\mathrm{L}}$ and $T_{\overline{g}_{\mathrm{L}}}$ is the associated precession period. Explicit expressions for these quantities have been derived in Section 3.2. Each precession trajectory is fully determined by the value of its free energy, so the right-hand side of equation (107) is a function of energy only and equation (107) can be solved by the method of separation of variables.

Let us apply this approach to the description of 'ringing' phenomena. The derivations in the sequel are valid for arbitrary values of D_x, D_y, D_z and uniaxial symmetry is not assumed. We denote by g_{off} the energy of the system immediately after the external field has been switched off. We assume that the field pulse is such that magnetization switching is guaranteed. This means that after the field is switched off the system is inside the energy region around the final equilibrium state of interest (see Figure 8). In terms of energy, this means that $D_x/2 < g_{\mathrm{off}} < D_y/2$. This energy value represents the initial condition for the integration of equation (107). The solution is obtained once the right-hand side of equation (107) is explicitly calculated. This can be done by introducing the variable w (see equation (59)) and by taking advantage of the fact that $|\mathrm{d}\mathbf{m}/\mathrm{d}t|^2 = |\mathrm{d}\mathbf{m}/\mathrm{d}w|^2 |\mathrm{d}w/\mathrm{d}t|^2$. By using equation (59) one finds:

$$\left| \frac{\mathrm{d}\mathbf{m}}{\mathrm{d}w} \right|^2 = \frac{p^2}{1-w^2} + \frac{k'^2}{k^2} \frac{w_0^2 p^2}{w_0^2 - w^2} \tag{108}$$

where w_0 and p^2 are respectively given by equations (60) and (61), with $\overline{g}_{\mathrm{L}}$ in the place of g_0. It can be verified that $w_0^2 < 1$ in the zero-field energy region under study. The derivative $\mathrm{d}w/\mathrm{d}t$ is obtained from equations (62)–(64):

$$\frac{\mathrm{d}w}{\mathrm{d}t} = \pm k' p \left(D_z - D_x\right) \sqrt{\left(1-w^2\right)\left(w_0^2 - w^2\right)} \tag{109}$$

Therefore:

$$\left| \frac{\mathrm{d}\mathbf{m}}{\mathrm{d}t} \right|^2 \mathrm{d}t = k' p^3 w_0^2 \left(D_z - D_x\right) \times \left(\sqrt{\frac{1-w^2/w_0^2}{1-w^2}} + \frac{k'^2}{k^2} \sqrt{\frac{1-w^2}{1-w^2/w_0^2}} \right) \frac{\mathrm{d}w}{w_0} \tag{110}$$

By inserting equation (110) into equation (107), the integral in the latter equation can be reduced to canonical elliptic integrals of the first and second kind. By taking into account that the variable w spans the interval $(0, w_0)$ four times in one precession period and by using equation (78) for $T_{\overline{g}_{\mathrm{L}}}$, one obtains the desired equation for the energy:

$$\frac{\mathrm{d}\overline{g}_{\mathrm{L}}}{\mathrm{d}t} = -\alpha \left(D_z - 2\overline{g}_{\mathrm{L}}\right) \left[\left(2\overline{g}_{\mathrm{L}} - D_x\right) + \left(D_y - D_x\right) \times \frac{\mathbf{E}(k_{\mathrm{L}}(\overline{g}_{\mathrm{L}})) - \mathbf{K}(k_{\mathrm{L}}(\overline{g}_{\mathrm{L}}))}{\mathbf{K}(k_{\mathrm{L}}(\overline{g}_{\mathrm{L}}))} \right] \tag{111}$$

where $\mathbf{K}$ and $\mathbf{E}$ respectively represent the complete elliptic integrals of the first and second kind, while:

$$k_{\mathrm{L}}^2 = w_0^2 = \frac{D_z - D_y}{D_y - D_x} \frac{2\overline{g}_{\mathrm{L}} - D_x}{D_z - 2\overline{g}_{\mathrm{L}}} \tag{112}$$

Equation (111) is a first-order separable differential equation that can be solved numerically. However, a useful approximate analytical solution can be obtained by observing that $k_{\mathrm{L}}^2 < 1$ during the entire relaxation. Hence, the elliptic integrals $\mathbf{K}$ and $\mathbf{E}$ can be expressed in simpler form by using the expansions:

$$\mathbf{K}(k_{\mathrm{L}}) = \frac{\pi}{2} \left(1 + \frac{k_{\mathrm{L}}^2}{4}\right) + \mathcal{O}(k_{\mathrm{L}}^4) \tag{113}$$

$$\mathbf{E}(k_{\mathrm{L}}) = \frac{\pi}{2} \left(1 - \frac{k_{\mathrm{L}}^2}{4}\right) + \mathcal{O}(k_{\mathrm{L}}^4) \tag{114}$$

As a result, equation (111) is reduced to:

$$\frac{\mathrm{d}\overline{g}_{\mathrm{L}}}{\mathrm{d}t} = -\alpha \left(2\overline{g}_{\mathrm{L}} - D_x\right) \left(D_{yz} - 2\overline{g}_{\mathrm{L}}\right) \tag{115}$$

where $D_{yz} = (D_y + D_z)/2$. Equation (115) can be easily integrated by the method of separation of variables. The result is:

$$\overline{g}_{\mathrm{L}}(t) = \frac{D_x}{2} + \frac{\left(D_{yz} - D_x\right)\left(g_{\mathrm{off}} - D_x/2\right)}{\left(2g_{\mathrm{off}} - D_x\right) + \left(D_{yz} - 2g_{\mathrm{off}}\right) \exp\left[2\alpha \left(D_{yz} - D_x\right) t\right]} \tag{116}$$

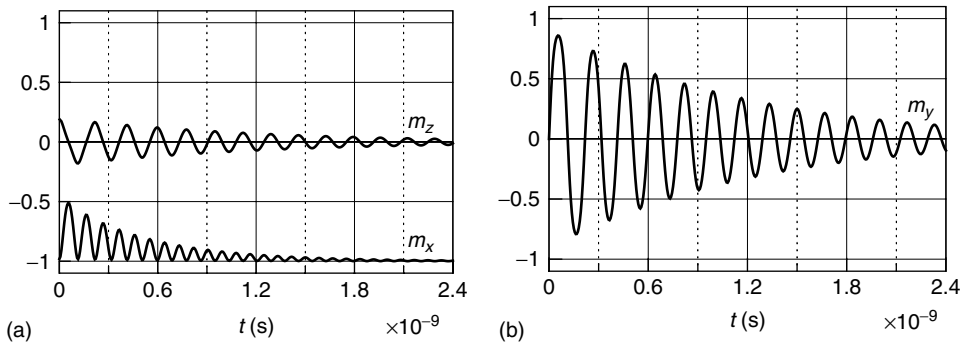

Figure 11. Magnetization components versus time obtained by numerical integration of LLG equation. Parameters: $\alpha = 0.01$, $D_x = -0.05$, $D_y = 0$, $D_z = 1$, $g_{\text{off}} = -0.005$, $(\gamma M_s)^{-1} = 6\,\text{ps}$.

Figure 11 shows an example of magnetization relaxation to equilibrium, computed by direct numerical integration of the LLG equation (equations (14) and (17). The system is a thin film with in-plane anisotropy along the x axis ($D_x = -0.05$, $D_y = 0$, $D_z = 1$). The magnetization is initially inside the central energy region around $m_x = -1$. The energy varies in this region from $g_{\text{L}} = D_y/2 = 0$ (energy of heteroclinic trajectories) down to $g_{\text{L}} = D_x/2 = -0.025$ (energy minimum at $m_x = -1$). The initial energy is $g_{\text{off}} = -0.005$, relatively close to the upper boundary of the region. By inserting the numerically computed magnetization components in the equation for the free energy (equation (20)), one obtains the time behavior of the instantaneous energy $g_{\text{L}}(t)$. The result is shown by the continuous line in Figure 12. The wavy behavior of the energy reflects the precessional magnetization dynamics taking place on the fast timescale. The dashed line represents the averaged energy $\overline{g}_{\text{L}}(t)$ obtained by numerical integration of equation (111).

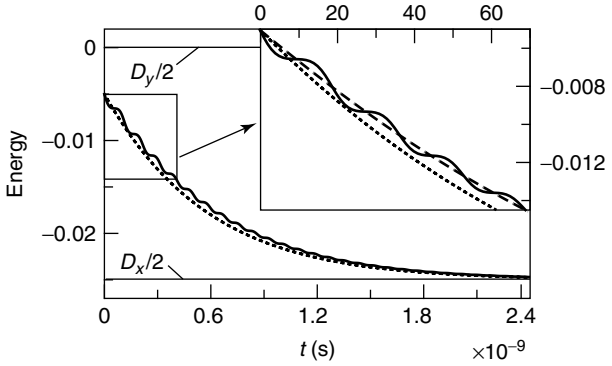

Figure 12. Comparison between numerically and analytically computed energy relaxation to equilibrium. Continuous line: numerical integration of LLG equation; dashed line (omitted in the main diagram for the sake of clarity but shown in the inset): numerical integration of equation (111); dotted line: equation (116). Parameters: $\alpha = 0.01$, $D_x = -0.05$, $D_y = 0$, $D_z = 1$, $g_{\text{off}} = -0.005$, $(\gamma M_s)^{-1} = 6\,\text{ps}$.

Finally, the dotted line represents the approximate analytical solution given by equation (116). It is apparent that the description of the relaxation in terms of the averaged energy $\overline{g}_{\text{L}}(t)$ leads to quite accurate results. The analytical approximation is quite satisfactory as well, if one takes into account that the initial value of the elliptic-integral modulus k_{L} is as large as $k_{\text{L}} \simeq 0.89$.

We remark in conclusion that the averaging technique discussed in this section is general and can be applied to relaxation phenomena under nonzero field as well, provided that one has sufficient information about the solution $\mathbf{m}_{g_0}(t)$ of the conservative dynamics for the field considered.

5 NONLINEAR MAGNETIZATION DYNAMICS UNDER CIRCULARLY POLARIZED FIELD

5.1 LLG dynamics in rotationally invariant systems

In nanometer-scale magnetic bodies, appropriately applied microwave fields can drive spatially uniform magnetization motions very far from static equilibrium conditions. In this situation, it is not possible to treat the problem through linearization of the equations of motion around a reference static equilibrium state and one has to study the magnetization dynamics taking fully into account nonlinear effects such as nonlinear resonance, bifurcations, quasiperiodic, or even chaotic dynamics. In this section, we consider nanomagnets with uniaxial anisotropy and subject to circularly polarized microwave applied fields. The problem is rotationally invariant around the disk axis and this permits one to analytically determine all admissible single-domain dynamical regimes (Bertotti, Serpico and Mayergoyz, 2001). The possibility of deriving exact solutions of the nonlinear problem is very important since give the possibility to treat, by

perturbation techniques, magnetization dynamics in far-from-equilibrium conditions (Bertotti, Mayergoyz and Serpico, 2001a). In this respect, it is appropriate here to mention that in recent times there has been increasing interest in situations (e.g., precessional switching; Kaka and Russek, 2002 or spin-transfer-driven magnetization dynamics; Kiselev *et al*., 2003, and Rippard *et al*., 2004) where the magnetization of nanomagnetic elements is forced to execute large motions.

5.1.1 LLG equation in the rotating frame

We consider here a spheroidal particle with symmetry axis along the z axis. In this section, we do not assume that inequality (19) is necessarily valid. By subscript '$\perp$' we will denote components of vectors in the plane orthogonal to the z axis. The magnetostatic field $\mathbf{h}_S$ is given by

$$\mathbf{h}_S = -N_z m_z - N_\perp \mathbf{m}_\perp \tag{117}$$

where the $N_x = N_y = N_\perp$ $(N_z + 2N_\perp = 1)$. As we have done previously, we also assume that the crystal anisotropy is uniaxial, with the anisotropy axis along the z direction:

$$\mathbf{h}_K = \kappa m_z \mathbf{e}_z \tag{118}$$

The external field consists of the constant component $h_{az}\mathbf{e}_z$ directed along the symmetry axis and the circularly polarized rf component $\mathbf{h}_{a\perp}(t)$ in the perpendicular plane (see Figure 13), that is,

$$\mathbf{h}_a(t) = \mathbf{h}_{a\perp}(t) + h_{az}\mathbf{e}_z \tag{119}$$

where

$$\mathbf{h}_{a\perp}(t) = h_{a\perp}\left(\cos\omega t\,\mathbf{e}_x + \sin\omega t\,\mathbf{e}_y\right) \tag{120}$$

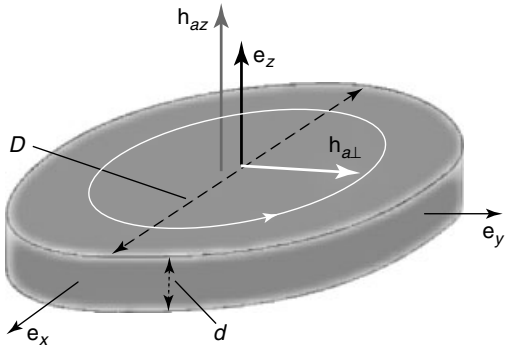

Figure 13. Sketch of uniaxial nanomagnet subject to circularly polarized microwave fields.

The free energy of the system is

$$g_L(\mathbf{m};\mathbf{h}_a) = \frac{1}{2}\left(N_z m_z^2 + N_\perp m_\perp^2\right) - \frac{1}{2}\kappa m_z^2 - \mathbf{h}_a\cdot\mathbf{m} \tag{121}$$

and the effective field can be written as

$$\mathbf{h}_{\text{eff}} = -\frac{\partial g_L}{\partial \mathbf{m}} = \mathbf{h}_{a\perp} + (h_{az} + \kappa_{\text{eff}} m_z)\,\mathbf{e}_z - N_\perp \mathbf{m} \tag{122}$$

where:

$$\kappa_{\text{eff}} = \kappa + N_\perp - N_z \tag{123}$$

Under these conditions, we want to study LLG equation, which is reported below for the reader's commodity:

$$\frac{\mathrm{d}\mathbf{m}}{\mathrm{d}t} - \alpha\mathbf{m}\times\frac{\mathrm{d}\mathbf{m}}{\mathrm{d}t} = -\mathbf{m}\times\mathbf{h}_{\text{eff}} \tag{124}$$

The system under study is characterized by the parameters $(\alpha, \kappa_{\text{eff}})$, whereas the excitation conditions are described by the control parameters $(\omega, h_{az}, h_{a\perp})$.

The dynamical system on the unit sphere described by equation (124) is nonautonomous, because $\mathbf{h}_{\text{eff}}$ explicitly depends on time through the external field $\mathbf{h}_{a\perp}(t)$. However, the nontrivial complications usually encountered in the analysis of nonautonomous systems can be circumvented by taking advantage of the rotational symmetry of the problem. This becomes evident when one considers the form of equation (124) in the rotating frame of reference in which the external field is stationary. In this frame, which is rotated at the angular frequency ω around the $\mathbf{e}_z$ axis, the magnetization derivative is transformed as follows:

$$\left[\frac{\mathrm{d}\mathbf{m}}{\mathrm{d}t}\right]_{\text{lab frame}} = \left[\frac{\mathrm{d}\mathbf{m}}{\mathrm{d}t}\right]_{\text{rot frame}} - \omega\mathbf{m}\times\mathbf{e}_z \tag{125}$$

Therefore, in the rotating-frame equation (151) takes the form:

$$\frac{\mathrm{d}\mathbf{m}}{\mathrm{d}t} - \alpha\mathbf{m}\times\frac{\mathrm{d}\mathbf{m}}{\mathrm{d}t} = -\mathbf{m}\times(\mathbf{h}_{\text{eff}} - \omega\mathbf{e}_z + \alpha\omega\mathbf{m}\times\mathbf{e}_z) \tag{126}$$

The field $\mathbf{h}_{\text{eff}}$ is still given by equation (122), but $\mathbf{h}_{a\perp}$ is now time independent by construction. On the other hand, no new time dependence appears as a result of the transformation to the rotating frame, as all the parameters of the problem are invariant with respect to rotations about the symmetry axis. Thus, no explicit time dependence is present anymore in the right-hand side of equation (126). In other words, the transformation to the rotating frame brings the dynamics to autonomous form.

In equation (126), the role of 'effective' energy is played in by the quantity:

$$\tilde{g}_{\mathrm{L}}\left(\mathbf{m};\mathbf{h}_{\mathrm{a}}\right)=g_{\mathrm{L}}\left(\mathbf{m};\mathbf{h}_{\mathrm{a}}\right)+\omega m_z \tag{127}$$

This can be shown by introducing the associated effective field

$$\tilde{\mathbf{h}}_{\mathrm{eff}}\equiv\frac{-\partial\tilde{g}_{\mathrm{L}}}{\partial\mathbf{m}}=\mathbf{h}_{\mathrm{eff}}-\omega\mathbf{e}_z \tag{128}$$

and by writing equation (126) in the form:

$$\frac{\mathrm{d}\mathbf{m}}{\mathrm{d}t}=-\mathbf{m}\times\tilde{\mathbf{h}}_{\mathrm{eff}}+\alpha\mathbf{m}\times\left(\frac{\mathrm{d}\mathbf{m}}{\mathrm{d}t}-\omega\mathbf{m}\times\mathbf{e}_z\right) \tag{129}$$

where all the contributions proportional to the damping parameter have been collected into a single term. Whenever damping is negligible one has that $\tilde{\mathbf{h}}_{\mathrm{eff}}\cdot\mathrm{d}\mathbf{m}/\mathrm{d}t=0$, that is, $\tilde{g}_{\mathrm{L}}$ is conserved.

When α is nonzero, the effective energy $\tilde{g}_{\mathrm{L}}$ is no longer constant along the magnetization trajectories. One obtains from equation (129) that $\tilde{g}_{\mathrm{L}}$ changes at the rate:

$$\frac{\mathrm{d}\tilde{g}_{\mathrm{L}}}{\mathrm{d}t}\equiv-\tilde{\mathbf{h}}_{\mathrm{eff}}\cdot\frac{\mathrm{d}\mathbf{m}}{\mathrm{d}t}=-\alpha\left(\frac{\mathrm{d}\mathbf{m}}{\mathrm{d}t}-\omega\mathbf{m}\times\mathbf{e}_z\right)\cdot\frac{\mathrm{d}\mathbf{m}}{\mathrm{d}t} \tag{130}$$

The right-hand side of equation (189) can be negative and positive, depending on the orientation of $\mathbf{m}$. This means that the dynamics in the rotating frame is not a mere relaxation toward minima of the effective free energy, and one cannot exclude (as it was discussed in the case of constant applied field) that the presence of periodic steady states (limit cycles) in which the energy has a periodic variation in time (see Figure 14). This latter kind of steady state in the rotating frame corresponds to quasiperiodic solution in the lab frame.

Let us also underline that the term in equation (129) proportional to α can be often treated as a perturbation to the undamped dynamics controlled by the effective energy $\tilde{g}_{\mathrm{L}}$, owing to the fact that $\alpha\ll 1$ for all systems of physical interest. This perturbative approach is particularly useful in the study of limit cycles.

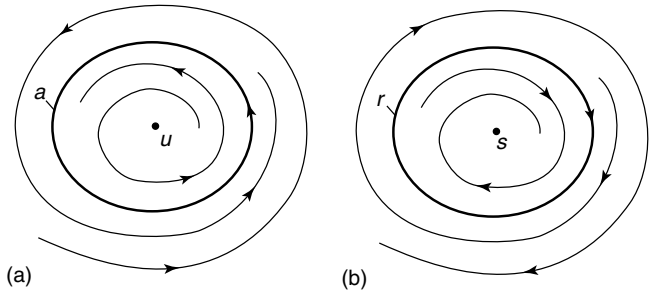

Figure 14. Schematic representation of limit cycles. (a) Stable limit cycle (a, i.e., attractive) surrounding unstable focus; (b) unstable limit cycle (r, i.e., repulsive) surrounding stable focus.

The study of LLG dynamics in the rotating frame of reference can be conveniently carried out by introducing the spherical-angle state variables (θ,ϕ), representing the angle of $\mathbf{m}$ with respect to $\mathbf{e}_z$ $(0\le\theta\le\pi)$ and the lag angle of $\mathbf{m}_\perp$ with respect to $\mathbf{h}_{\mathrm{a}\perp}$ $(-\pi\le\phi\le\pi)$, respectively. In other words, we express the magnetization as:

$$\begin{aligned}\mathbf{m}&=m_{a\perp}\mathbf{e}_a+m_{b\perp}\mathbf{e}_b+m_z\mathbf{e}_z\\&=\sin\theta\cos\phi\mathbf{e}_a-\sin\theta\sin\phi\mathbf{e}_b+\cos\theta\mathbf{e}_z\end{aligned} \tag{131}$$

where $(\mathbf{e}_a,\mathbf{e}_b,\mathbf{e}_z)$ is a right-handed Cartesian set of unit vectors for the rotating frame, of which $\mathbf{e}_a$ is directed along $\mathbf{h}_{\mathrm{a}\perp}$. The minus sign in the expression for $m_{b\perp}$ is due to the fact that ϕ represents the angle by which the magnetization *lags* the field. Equation (129) in spherical coordinates reads

$$\begin{aligned}\frac{\mathrm{d}\theta}{\mathrm{d}t}-\alpha\sin\theta\frac{\mathrm{d}\phi}{\mathrm{d}t}&=\frac{1}{\sin\theta}\frac{\partial\tilde{g}_{\mathrm{L}}}{\partial\phi}-\alpha\omega\sin\theta\\&=h_{a\perp}\sin\phi-\alpha\omega\sin\theta\end{aligned} \tag{132}$$

$$\begin{aligned}\alpha\frac{\mathrm{d}\theta}{\mathrm{d}t}+\sin\theta\frac{\mathrm{d}\phi}{\mathrm{d}t}&=\frac{\partial\tilde{g}_{\mathrm{L}}}{\partial\theta}=h_{a\perp}\cos\phi\cos\theta\\&\quad-\left(h_{az}-\omega+\kappa_{\mathrm{eff}}\cos\theta\right)\sin\theta\end{aligned} \tag{133}$$

where $\tilde{g_{\mathrm{L}}}(\theta,\phi)$ is the effective free energy expressed in spherical coordinates.

Spherical coordinates are quite a natural reference system to represent magnetization evolution on the sphere and they are very convenient to derive analytical formulas. However, the ensuing description of magnetization dynamics is not always completely transparent in the vicinity of the sphere poles where the angle ϕ is undefined. For this reason, especially in phase portraits where limit cycles are present, it is useful to introduce the stereographic projection of the unit sphere on the plane. The stereographic coordinates w_x and w_y are connected to the Cartesian coordinates by the following relations:

$$w_x=\frac{m_x}{1+m_z}\qquad w_y=\frac{m_y}{1+m_z} \tag{134}$$

where $\mathbf{w}=w_x\mathbf{e}_x+w_y\mathbf{e}_y$. The main properties of this transformation are the following: angles between intersecting lines are preserved (conformal transformation) Schwerdtfeger, 2001; $\mathbf{m}=+\mathbf{e}_z$ is projected into the origin of the plane; the north hemisphere ($m_z>0$) is projected inside the unit circle; the south hemisphere ($m_z<0$) is projected outside the unit circle; $\mathbf{m}=-\mathbf{e}_z$ is projected into infinity. In order to have a complete picture of the phase portrait, we also consider the stereographic projection which projects the

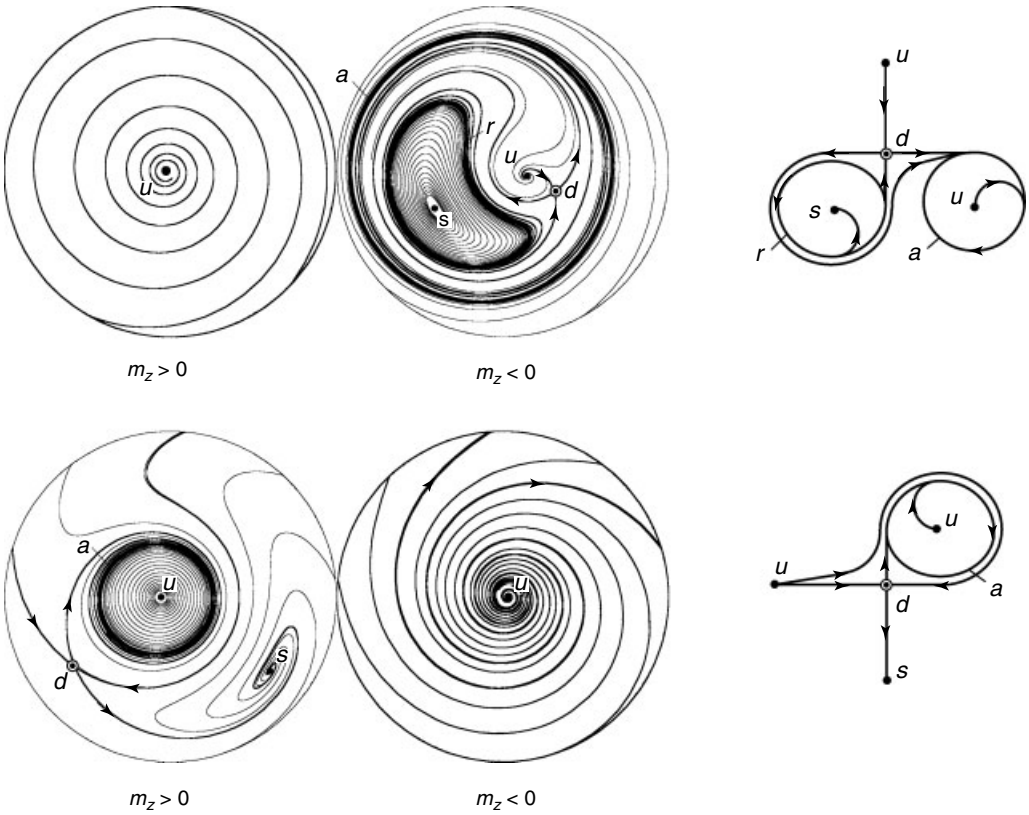

Figure 15. Examples of phase portraits of LLG dynamics in the rotating frame of reference. Each phase portrait is represented in terms of joint stereographic projections of $m_z > 0$ and $m_z < 0$ hemispheres onto the unit circle. The point of contact of the $m_z > 0$ and $m_z < 0$ circles corresponds to $m_{a\perp} = 1$, that is, magnetization fully aligned along the rf field $\mathbf{h}_{a\perp}$. s: stable node; u: unstable node; d: saddle; a: stable limit cycle; r: unstable limit cycle. System parameters: $\alpha = 0.1$, $\kappa_{\text{eff}} = -1$. Field frequency: $\omega = 0.5$. Upper portrait: $h_{az} = -0.2$, $h_{a\perp} = 0.08$. Lower portrait: $h_{az} = 0.8$, $h_{a\perp} = 0.08$. Simplified graphical representation of phase portraits is given on the right.

south hemisphere into the unit circle and the north hemisphere outside the unit circle. This is simply given by the transformation: $w_x = m_x/(1 - m_z)$ and $w_y = m_y/(1 - m_z)$. Two examples of phase portraits represented by means of stereographic projection are reported in Figure 15.

5.1.2 Topological aspects

Equation (126) (LLG equation in the rotating frame of reference) describes an autonomous dynamical system evolving on the surface of the unit sphere $|\mathbf{m}|^2 = 1$. For this reason the topological aspects discussed in Section 2.2.1. By using the rotating frame of reference and the consequent autonomous character of the dynamics permits one to study its properties in geometric terms, through the phase portrait (Wiggins, 1990; Hubbard and West, 1995; Perko, 1996; Hale and Kocak, 1991) of the equation (see Figure 15 for an example). In particular we can arrive to the following conclusions:

- *Existence of fixed points:* The phase portrait on the sphere must necessarily contain a nonzero number of fixed points for which $\mathrm{d}\mathbf{m}/\mathrm{d}t = 0$ (Perko, 1996). These fixed points occur in the rotating frame of reference. In the laboratory frame, each of them results in a magnetization mode in which the magnetization precesses about the symmetry axis in synchronism with the external field. These rotating modes will be termed **P** modes. Therefore, one reaches the remarkable conclusion that a certain number of **P** modes must necessarily exist *for any value* of the control parameters $\left(\omega, h_{a\parallel}, h_{a\perp}\right)$. Interestingly, in a **P** mode the system response to a time-harmonic excitation (see equation (120)) is itself time harmonic, with no generation of higher-order harmonics, despite the inherent strongly nonlinear character of the dynamics. These **P** modes can be also seen as magnetization modes that are frequency and phase locked to the external microwave field.
- *Number of fixed points:* By using the Poincaré index theorem (Perko, 1996) (see also Section 2.2.1). one can infer that the number of **P** modes is at least two and is even under all circumstances. Following this result, one can classify LLG phase portraits for rotationally

invariant systems according to the number and nature of their fixed points as follows:
- phase portraits with two fixed points: two nodes or foci;
- phase portraits with four fixed points: three nodes or foci + 1 saddle;
- ...

The nature of a fixed point (node, focus, or saddle) can be determined through the analysis of its stability. This aspect will be discussed in Section 5.2.2.

- *Presence of limit cycles:* The fact that the effective energy is not always decreasing as a function of time (see equation (189)) gives rise to the possibility of existence of periodic steady state (limit cycles, see Figure 14 for a sketch). Limit cycles in the rotating frame correspond to quasiperiodic solutions in the laboratory frame, named **Q** modes, which results from the combination of the frequency of the limit cycle (generated by the system itself) and the frequency of the external field. These **Q** modes can be also seen as magnetization modes that are *not* frequency or phase locked to the external microwave field.
- *Nonexistence of chaos:* Chaos is precluded, because the phase space is two dimensional (Wiggins, 1990). The onset of chaotic phenomena is not compatible with the simultaneous presence of rotational symmetry and uniform magnetization. Only when one or both of these requirements are relaxed, chaotic phenomena may appear (Wigen, 1994; Alvarez, Pla and Chubykalo, 2000).

5.2 P modes, Q modes, and ferromagnetic resonance

*5.2.1 Periodic modes (**P** modes)*

By setting $\mathrm{d}\theta/\mathrm{d}t = \mathrm{d}\phi/\mathrm{d}t = 0$ in equations (132) and (133) one obtains the equations for the fixed points of the dynamics in the rotating frame:

$$h_{a\perp} \sin\phi_0 = \alpha\omega \sin\theta_0 \tag{135}$$

$$h_{a\perp} \cos\phi_0 \cos\theta_0 = (h_{az} - \omega + \kappa_{\mathrm{eff}} \cos\theta_0) \sin\theta_0 \tag{136}$$

By taking the ratio of the corresponding sides of equations (135) and (136), one obtains:

$$\alpha\omega \cot\phi_0 = \frac{h_{az} - \omega}{\cos\theta_0} + \kappa_{\mathrm{eff}} \tag{137}$$

Then, by dividing both sides of equation (136) by $\cos\theta_0$ and summing the square of the two sides of the equation with the squares of the corresponding sides of (135), one obtains

$$\frac{h_{a\perp}^2}{\sin^2\theta_0} = \left(\frac{h_{az} - \omega}{\cos\theta_0} + \kappa_{\mathrm{eff}}\right)^2 + (\alpha\omega)^2 \tag{138}$$

For later use it is convenient to introduce the quantity:

$$\nu_0 = \alpha\omega \cot\phi_0 \tag{139}$$

By using ν_0 equations (137) and (138) can be rewritten as

$$\nu_0 = \frac{h_{az} - \omega}{\cos\theta_0} + \kappa_{\mathrm{eff}} \tag{140}$$

$$\nu_0^2 = \frac{h_{a\perp}^2}{\sin^2\theta_0} - \alpha^2\omega^2 \tag{141}$$

The convenience in using ν_0 comes from the following considerations. The angle ϕ_0 is in one-to-one correspondence with ν_0 because $0 \le \phi_0 \le \pi$ under all circumstances. In fact, equation (135) shows that $\sin\phi_0 \ge 0$ for all **P** modes, because $h_{a\perp}$, α, ω, and $\sin\theta_0$ are all positive quantities by definition. In other words, in a **P** mode the magnetization always lags the field. The plane $(\cos\theta_0, \nu_0)$ is the natural plane for the representation of **P** modes. A generic **P** mode will be located in the region $-1 \le \cos\theta_0 \le 1$, $-\infty < \nu_0 < \infty$, that is, $0 \le \theta_0 \le \pi$, $0 \le \phi_0 \le \pi$.

By solving equations (140) and (141), one obtains the values of $(\cos\theta_0, \nu_0)$ for the various **P** modes existing under given excitation conditions $(\omega, h_{az}, h_{a\perp})$. In practise this can be done by solving equation (138) which can be seen as the following fourth order equation in m_z:

$$\frac{h_{a\perp}^2}{1 - m_z^2} = \left(\frac{h_{az} - \omega}{m_z} + \kappa_{\mathrm{eff}}\right)^2 + (\alpha\omega)^2 \tag{142}$$

which, after simple manipulation can be written as

$$(1 + \Omega^2)m_z^4 + 2b_z m_z^3 + [b_\perp^2 + b_z^2 - (1 + \Omega^2)]m_z^2 - 2b_z m_z - b_z^2 = 0 \tag{143}$$

where

$$\Omega = \frac{\alpha\omega}{\kappa_{\mathrm{eff}}}, \quad b_z = \frac{h_{az} - \omega}{\kappa_{\mathrm{eff}}}, \quad b_\perp = \frac{h_{a\perp}}{\kappa_{\mathrm{eff}}} \tag{144}$$

Equation (143) will admit either two or four real roots which correspond to the coexistence of two or four periodic solution of original LLG equation. It is interesting to notice that equation (143) reduces to equation (35) obtained for the Stoner–Wohlfarth model, by considering the limit $\omega \to 0$, and replacing m_x with m_z. This is consistent with the view that the **P** mode theory is a special dynamical generalization

of the Stoner–Wohlfarth model (Magni, Bertotti, Serpico and Mayergoyz, 2001).

In order to find the excitation conditions corresponding to a given **P** mode $(\cos\theta_0, \nu_0)$ one can use the same equations (140) and (141), written in the form

$$h_{az} = (\nu_0 - \kappa_{\text{eff}})\cos\theta_0 + \omega \tag{145}$$

$$h_{a\perp} = \sqrt{\left(1 - \cos^2\theta_0\right)\left(\nu_0^2 + \alpha^2\omega^2\right)} \tag{146}$$

Given a particular **P** mode solution of equations (140) and (141), its rotating-frame components defined by equation (131) can be expressed in terms of $\cos\theta_0$ only, by using equations (135) and (136) to eliminate ϕ_0:

$$m_{a\perp} = \left(\frac{h_{az} - \omega}{\cos\theta_0} + \kappa_{\text{eff}}\right)\frac{\sin^2\theta_0}{h_{a\perp}} \tag{147}$$

$$m_{b\perp} = -\frac{\alpha\omega\sin^2\theta_0}{h_{a\perp}} \tag{148}$$

$$m_z = \cos\theta_0 \tag{149}$$

It important to stress that **P** mode solutions correspond to spatial uniform periodic solutions of the original LLG equation. If we denote a **P** mode in the lab frame with $\mathbf{m}_0(t)$, we immediately have that

$$\frac{\mathrm{d}\mathbf{m}_0}{\mathrm{d}t} = \omega\mathbf{e}_z \times \mathbf{m}_0(t) \tag{150}$$

which comes from the fact that $\mathbf{m}_0(t)$ is uniformly rotating unit vector around the z axis with angular frequency ω. If we substitute (150) into the original LLG equation:

$$\frac{\mathrm{d}\mathbf{m}_0}{\mathrm{d}t} - \alpha\mathbf{m}_0 \times \frac{\mathrm{d}\mathbf{m}_0}{\mathrm{d}t} = -\mathbf{m}_0 \times \mathbf{h}_{\text{eff}0} \tag{151}$$

we end up with the following condition

$$\mathbf{m}_0(t) \times (\mathbf{h}_{\text{eff}0}(t) - \omega\mathbf{e}_z + \alpha\omega\mathbf{m}_0(t) \times \mathbf{e}_z) = 0 \tag{152}$$

where $\mathbf{h}_{\text{eff}0}(t)$ is the effective field associated to $\mathbf{m}_0(t)$. Equation (152) implies that the following condition is verified at each time instant

$$\left[\mathbf{h}_{\text{eff}0}(t) - \omega\mathbf{e}_z + \alpha\omega\mathbf{m}_0(t) \times \mathbf{e}_z\right] = \lambda_0\mathbf{m}_0(t) \tag{153}$$

where λ_0 is a constant depending on $(\cos\theta_0, \nu_0)$. If we pass now to the rotating reference frame and express **m** through equations (147–149), one can prove that λ_0 has the following simple expression:

$$\lambda_0 = \nu_0 - N_\perp \tag{154}$$

Equation (153) is particularly useful in the discussion of stability of **P** mode.

5.2.2 *P mode stability*

The results obtained in the previous section do not say anything about the fact that a given **P** mode may or may not be physically realizable. Only the modes that are dynamically stable will survive for long times and will be experimentally observable. Dynamical stability can be studied by perturbing the **P** mode solution and by analyzing the ensuing time behavior of the perturbation. To be completely general, this analysis should be carried out for arbitrary space-time dependent perturbations compatible with the boundary conditions of the problem. In the present section, this analysis is limited to spatially uniform perturbations only. Physically this means that we are going to consider magnetic particles so small that exchange forces rule out the appearance of space nonuniformities, however, small. The problem of stability of **P** modes against spatially nonuniform perturbations is treated in details in Bertotti, Mayergoyz and Serpico (2001a, 2006b).

Under the assumption of space uniformity, a given **P** mode will be dynamically stable if the corresponding fixed point of the rotating-frame dynamics is stable. Stability is studied by standard methods (Hubbard and West, 1995; Kuznetsov, 1995), by linearizing equation (126) around the **P** mode fixed point. Nevertheless, it is instructive to start our analysis in the lab frame. Let us denote a **P** mode in the lab frame by $\mathbf{m}_0(t)$ (which is periodic with period $2\pi/\omega$). We want to study the dynamics of $\mathbf{m}(t)$ in the vicinity of the periodic solution $\mathbf{m}_0(t)$. In other terms, we consider magnetization states

$$\mathbf{m}(t) = \mathbf{m}_0(t) + \Delta\mathbf{m}(t) \tag{155}$$

with

$$|\Delta\mathbf{m}(\mathbf{r}, t)| \ll |\mathbf{m}_0(t)| = 1 \tag{156}$$

If we substitute equation (155) into LLG equation (124), and neglect all terms which are second or higher order in the components of the vector $\Delta\mathbf{m}$, we arrive to the following linearized LLG equation.

$$\frac{\partial}{\partial t}\Delta\mathbf{m} - \alpha\mathbf{m}_0 \times \frac{\partial}{\partial t}\Delta\mathbf{m} - \alpha\Delta\mathbf{m} \times \frac{\mathrm{d}}{\mathrm{d}t}\mathbf{m}_0 = -\Delta\mathbf{m} \times \mathbf{h}_{\text{eff}0} - \mathbf{m}_0 \times \Delta\mathbf{h}_{\text{eff}} \tag{157}$$

where

$$\Delta\mathbf{h}_{\text{eff}} = D_x\Delta m_x\mathbf{e}_x + D_y\Delta m_y\mathbf{e}_y + D_z\Delta m_z\mathbf{e}_z \tag{158}$$

Equation (157) can be put in the following simpler form:

$$\frac{\partial}{\partial t}\Delta\mathbf{m} - \alpha\mathbf{m}_0 \times \frac{\partial}{\partial t}\Delta\mathbf{m} = -\Delta\mathbf{m} \times \left(\mathbf{h}_{\text{eff}0} - \alpha\frac{\mathrm{d}}{\mathrm{d}t}\mathbf{m}_0\right) + \mathbf{m}_0 \times \Delta\mathbf{h}_{\text{eff}} \tag{159}$$

Now by using equations (150) and (152), we can write equation (159) as

$$\frac{\partial}{\partial t}\Delta\mathbf{m} - \alpha\mathbf{m}_0 \times \frac{\partial}{\partial t}\Delta\mathbf{m} = -\Delta\mathbf{m} \times (\lambda_0\mathbf{m}_0 + \omega\mathbf{e}_z) + \mathbf{m}_0 \times \Delta\mathbf{h}_{\text{eff}} \tag{160}$$

From this last equation and equation (150) one immediately derive that

$$\mathbf{m}_0(t)\cdot\frac{\partial}{\partial t}\Delta\mathbf{m} = +\Delta\mathbf{m}\cdot\mathbf{m}_0(t) \times \omega\mathbf{e}_z = -\Delta\mathbf{m}\cdot\frac{\mathrm{d}}{\mathrm{d}t}\mathbf{m}_0 \tag{161}$$

which implies that

$$\frac{\partial}{\partial t}\left[\Delta\mathbf{m}(t)\cdot\mathbf{m}_0(t)\right] = 0 \tag{162}$$

namely, that, at each instant of time the components of perturbation in the direction of $\mathbf{m}_0(t)$ are constant. This means that, as far as small perturbations around periodic solution are concerned, we can limit ourselves to the components of $\Delta\mathbf{m}(t)$ orthogonal to $\mathbf{m}_0(t)$. In this respect, it is convenient to introduce in the plane perpendicular to $\mathbf{m}_0$ the following uniformly rotating unit vectors:

$$\mathbf{e}_1 \propto (\mathbf{e}_z \times \mathbf{m}_0) \times \mathbf{m}_0 \tag{163}$$

$$\mathbf{e}_2 \propto \mathbf{e}_z \times \mathbf{m}_0 \tag{164}$$

where the symbol '$\propto$' has the meaning of 'being directed along'.

Let us express $\Delta\mathbf{m}$ as

$$\Delta\mathbf{m}(t) = \Delta m_1(t)\mathbf{e}_1(t) + \Delta m_2(t)\mathbf{e}_2(t) \tag{165}$$

We observe that studying magnetization dynamics in the reference frame ($\mathbf{m}_0$, $\mathbf{e}_1$, $\mathbf{e}_2$) is tantamount of studying the dynamics in the rotating reference frame previously introduced.

Let us now substitute equation (165) into (160), and take into account that

$$\frac{\mathrm{d}\mathbf{e}_1(t)}{\mathrm{d}t} = \omega\mathbf{e}_z \times \mathbf{e}_1(t), \qquad \frac{\mathrm{d}\mathbf{e}_2(t)}{\mathrm{d}t} = \omega\mathbf{e}_z \times \mathbf{e}_1(t) \tag{166}$$

after appropriate manipulation one arrives to the following equation

$$\frac{\mathrm{d}}{\mathrm{d}t}\begin{pmatrix}\Delta m_1\\ \Delta m_2\end{pmatrix} + \begin{pmatrix}0 & \alpha\\ -\alpha & 0\end{pmatrix}\begin{pmatrix}\Delta m_1\\ \Delta m_2\end{pmatrix} = \begin{pmatrix}-\alpha\omega\cos\theta_0 & -(\nu_0 - N_\perp)\\ (\nu_0 - N_\perp) & -\alpha\omega\cos\theta_0\end{pmatrix}\begin{pmatrix}\Delta m_1\\ \Delta m_2\end{pmatrix} + \begin{pmatrix}0 & 1\\ -1 & 0\end{pmatrix}\begin{pmatrix}\Delta h_{\text{eff1}}\\ \Delta h_{\text{eff2}}\end{pmatrix} \tag{167}$$

where Δh_{eff1} and Δh_{eff2} are the projections of $\Delta\mathbf{h}_{\text{eff}}$ (see equation (158)) along the two directions $\mathbf{e}_1(t)$ and $\mathbf{e}_2(t)$. Let us now analyze the form of this two components. The anisotropy part of $\Delta\mathbf{h}_{\text{eff}}$, it is given by

$$\Delta\mathbf{h}_{\text{eff,AN}} = \mathbf{e}_1(t)(\mathbf{e}_1(t)\cdot\mathbf{e}_z)\kappa\Delta m_z \tag{168}$$

and by taking into account that

$$\mathbf{e}_1(t)\cdot\mathbf{e}_z = \sin\theta_0,\ \Delta m_z = \Delta m_1 \sin\theta_0 \tag{169}$$

one obtains that

$$(\Delta\mathbf{h}_{\text{eff,AN}})_{1,2} = \begin{pmatrix}\kappa\sin^2\theta_0 & 0\\ 0 & 0\end{pmatrix}\cdot\begin{pmatrix}\Delta m_1\\ \Delta m_2\end{pmatrix} \tag{170}$$

It is interesting to notice that, due to the symmetry and despite the time-varying nature of the basis ($\mathbf{e}_1$, $\mathbf{e}_2$), the part of $\Delta\mathbf{h}_{\text{eff}}$ related to anisotropy is time independent.

The magnetostatic part of $\Delta\mathbf{h}_{\text{eff}}$ is given by

$$\Delta\mathbf{h}_{\text{M}} = -N_\perp\Delta\mathbf{m}_\perp - N_z\Delta m_z\mathbf{e}_z = -N_\perp\Delta\mathbf{m} + (N_\perp - N_z)\,\Delta m_z\mathbf{e}_z \tag{171}$$

thus,

$$\Delta h_{\text{M1}} = -N_\perp\Delta m_1 + (N_\perp - N_z)\sin^2\theta_0\Delta m_1,$$
$$\Delta h_{\text{M2}} = -N_\perp\Delta m_2 \tag{172}$$

By using these results one finds that equation (174) is simply reduced to

$$\begin{pmatrix}1 & \alpha\\ -\alpha & 1\end{pmatrix}\frac{\partial}{\partial t}\begin{pmatrix}\Delta m_1\\ \Delta m_2\end{pmatrix} = \begin{pmatrix}-\alpha\omega\cos\theta_0 & -\nu_0\\ \nu_0 - \kappa_{\text{eff}}\sin^2\theta_0 & -\alpha\omega\cos\theta_0\end{pmatrix}\begin{pmatrix}\Delta m_1\\ \Delta m_2\end{pmatrix} \tag{173}$$

which coincides with the equation that would be obtained by linearizing LLG equation in the rotating reference frame in spherical coordinates (see equations (132 and 133)) around a given **P** mode and making the following correspondence $\Delta\theta = \Delta m_1$, $\sin\theta_0\Delta\phi = \Delta m_2$.

Equation (172) can be put in the following explicit form

$$\frac{\mathrm{d}}{\mathrm{d}t}\begin{pmatrix}\Delta m_1\\ \Delta m_2\end{pmatrix} = A_0\begin{pmatrix}\Delta m_1\\ \Delta m_2\end{pmatrix} \tag{174}$$

where:

$$A_0 = \frac{1}{1+\alpha^2}\begin{pmatrix}1 & -\alpha\\ \alpha & 1\end{pmatrix}\begin{pmatrix}-\alpha\omega\cos\theta_0 & -\nu_0\\ \nu_0 - \kappa_{\text{eff}}\sin^2\theta_0 & -\alpha\omega\cos\theta_0\end{pmatrix} \tag{175}$$

and the pair $(\cos\theta_0, \nu_0)$ identifies the particular **P** mode considered. Stability is controlled by the eigenvalues of the matrix A_0. More precisely, let us calculate the determinant of A_0:

$$\det A_0 = \frac{1}{1+\alpha^2}\left(\nu_0^2 - \kappa_{\text{eff}}\sin^2\theta_0\,\nu_0 + \alpha^2\omega^2\cos^2\theta_0\right) \quad (176)$$

its trace:

$$\text{tr}A_0 = -\frac{2\alpha}{1+\alpha^2}\left(\nu_0 - \frac{\kappa_{\text{eff}}\sin^2\theta_0}{2} + \omega\cos\theta_0\right) \quad (177)$$

and the characteristic frequency $\omega_0^2 = \det A_0 - (\text{tr}A_0)^2/4$:

$$\omega_0^2 = \frac{1}{\left(1+\alpha^2\right)^2}\left[\left(\nu_0 - \frac{\kappa_{\text{eff}}\sin^2\theta_0}{2} - \alpha^2\omega\cos\theta_0\right)^2 - \left(1+\alpha^2\right)\frac{\kappa_{\text{eff}}^2\sin^4\theta_0}{4}\right] \quad (178)$$

Then, **P** mode stability can be classified as follows (Hubbard and West, 1995).

- $\det A_0 < 0$. Saddle-type fixed point.
- $\det A_0 > 0$ and $\omega_0^2 < 0$. Node-type fixed point:
  - $\text{tr}A_0 < 0$: stable node;
  - $\text{tr}A_0 > 0$: unstable node.
- $\det A_0 > 0$ and $\omega_0^2 > 0$. Focus-type fixed point:
  - $\text{tr}A_0 < 0$: stable focus;
  - $\text{tr}A_0 > 0$: unstable focus.

The difference between a node and a focus is not relevant to the rest of our analysis: we will use the term node in a generic sense, to denote either of them. The symbols (s), (u), and (d) will be used to denote stable nodes, unstable nodes, and saddles, respectively. A given **P** mode represents a physically realizable mode only when it is of (s) type ($\det A_0 > 0$ and $\text{tr}A_0 < 0$).

Stability results acquire a transparent form in the $(\cos\theta_0, \nu_0)$ **P** mode plane. Stability is controlled by the equations $\det A_0 = 0$ and $(\text{tr}A_0 = 0, \det A_0 > 0)$, where $\det A_0$ and $\text{tr}A_0$ are given by equations (176) and (177), respectively. These equations can be solved in order to obtain ν_0 as a function of $\cos\theta_0$. The results are as follows.

- $\det A_0 = 0$:

$$\nu_0 = \frac{\kappa_{\text{eff}}\sin^2\theta_0}{2} \pm \sqrt{\frac{\kappa_{\text{eff}}^2\sin^4\theta_0}{4} - \alpha^2\omega^2\cos^2\theta_0} \quad (179)$$

The above two values are real in the interval:

$$\cos^2\theta_0 \le \left(\sqrt{1+\frac{\alpha^2\omega^2}{\kappa_{\text{eff}}^2}} - \left|\frac{\alpha\omega}{\kappa_{\text{eff}}}\right|\right)^2 \quad (180)$$

- $(\text{tr}A_0 = 0, \det A_0 > 0)$:

$$\nu_0 = \frac{\kappa_{\text{eff}}\sin^2\theta_0}{2} - \omega\cos\theta_0 \quad (181)$$

By inserting equation (181) into equation (176) one finds that $\det A_0 \ge 0$ for

$$\cos^2\theta_0 \ge \left(\sqrt{1+\frac{\omega^2\left(1+\alpha^2\right)}{\kappa_{\text{eff}}^2}} - \left|\frac{\omega\sqrt{1+\alpha^2}}{\kappa_{\text{eff}}}\right|\right)^2 \quad (182)$$

Figure 16 shows the lines $\det A_0 = 0$ and $(\text{tr}A_0 = 0, \det A_0 > 0)$ calculated from equations (179) and (181) for a thin film with negligible crystal anisotropy. These lines divide the **P** mode plane into three regions associated with stable nodes (**S**), unstable nodes (**U**), and saddles (**D**). Physically realizable modes are only those located in the region **S**.

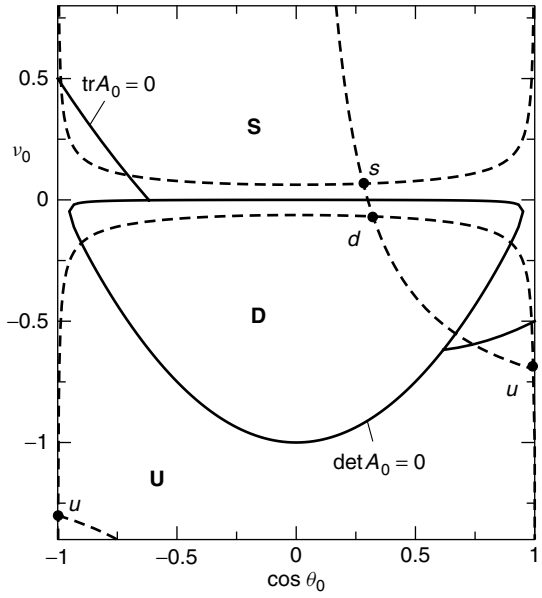

Figure 16. Representation of **P** modes in $(\cos\theta_0, \nu_0)$ plane. Continuous lines: $\det A_0 = 0$ and $(\text{tr}A_0 = 0, \det A_0 > 0)$. **P** modes lying inside region **D** are saddles of the rotating-frame dynamics, while those outside **D** are stable nodes (region **S**) or unstable nodes (region **U**). Broken lines: equation (140) for $h_{a\parallel} = 0.8$ and equation (141) for $h_{a\perp} = 0.08$. Solid points: intersection points representing the four **P** modes associated with $h_{a\parallel} = 0.8$, $h_{a\perp} = 0.08$ (see bottom phase portrait in Figure 15). System parameters: $\alpha = 0.1$, $\kappa_{\text{eff}} = -1$. Field frequency: $\omega = 0.5$.

These results take a more complex form in the field control plane $(h_{a\parallel}, h_{a\perp})$. Because there are two or four **P** modes associated with any given point of this plane, the functions $\det A_0$ and $\mathrm{tr}A_0$ will take the form of twofolded or fourfolded sheets when represented in this plane. According to Poincaré index theorem, when four **P** modes are present one of them is necessarily a saddle characterized by $\det A_0 < 0$. Therefore, the control plane region admitting four **P** modes coincides with the region where $\det A_0 < 0$ for one of the **P** modes. By substituting equation (179) into equations (145) and (146), one obtains a parametric representation of the boundary ($\det A_0 = 0$) between the two and four **P** mode regions, with $\cos\theta_0$ as the independent variable (see Figure 17). By similar considerations, one can determine the line ($\mathrm{tr}A_0 = 0, \det A_0 > 0$) (broken line in Figure 17) by substituting equation (181) into equations (145) and (146). The $\det A_0 < 0$ region can be construed as the dynamic generalization of Stoner–Wohlfarth asteroid region (Stoner and Wohlfarth, 1948; Bertotti, 1998). Indeed, it can be verified that this region coincides with the usual asteroid region in the limit $\omega \to 0$.

Equations (140) and (141) are invariant under the transformation: $\cos\theta_0 \to -\cos\theta_0$, $\nu_0 \to -\nu_0$, $\kappa_{\mathrm{eff}} \to -\kappa_{\mathrm{eff}}$. Given a **P** mode solution of the original equations, this transformation gives a corresponding **P** mode solution for the case where the effective anisotropy takes the opposite value. Equations (176) and (177) show that $\mathrm{tr}A_0 \to -\mathrm{tr}A_0$ and $\det A_0 \to \det A_0$ as a result of the above transformation. This means that when the sign of anisotropy is reversed stable **P** modes are changed into unstable ones and vice versa while the $\det A_0 = 0$ and $\mathrm{tr}A_0 = 0$ lines remain unaltered. These rules permit one to extend known results to systems with effective anisotropy of opposite sign. In addition, equation (176) shows that $\det A_0 > 0$ whenever ν_0 and κ_{eff} have opposite signs. Therefore the saddle point can exist only provided ν_0 and κ_{eff} have identical sign. This means that for the saddle points we have $0 \le \phi_0 < \pi/2$ when $\kappa_{\mathrm{eff}} > 0$ and $\pi/2 < \phi_0 \le \pi$ when $\kappa_{\mathrm{eff}} < 0$.

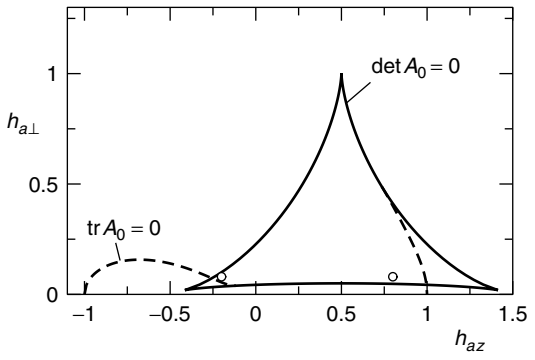

Figure 17. Representation of $\det A_0 = 0$ line and ($\mathrm{tr}A_0 = 0$, $\det A_0 > 0$) line in $(h_{a\parallel}, h_{a\perp})$ control plane. System parameters: $\alpha = 0.1$, $\kappa_{\mathrm{eff}} = -1$. Field frequency: $\omega = 0.5$. Small empty circles represent location of the two phase portraits shown in Figure 15.

It is worth remarking that the mentioned connection between fixed-point stability and anisotropy sign reflects a more general property of LLG dynamics (equations (132) and (133)), namely, the fact that reversing the sign of the effective anisotropy is essentially equivalent to reversing the direction of time. Indeed, equations (132) and (133) are invariant under the transformation: $\theta \to \pi - \theta$, $\phi \to \pi - \phi$, $\kappa_{\mathrm{eff}} \to -\kappa_{\mathrm{eff}}$, $t \to -t$, from which the **P** mode symmetries just discussed can be derived as a particular case.

5.2.3 *Quasiperiodic modes (**Q** modes)*

In order to be physically realizable, a **P** mode must be a stable node of the rotating-frame dynamics. When no **P** mode is stable, there will exist (at least) one attracting limit cycle in the dynamics (Poincaré-Bendixson theorem) (Perko, 1996). A limit cycle represents a periodic magnetization motion along a closed path on the unit sphere. This conclusion holds in the rotating reference frame. In the laboratory frame, the periodic motion along the limit cycle has to be combined with the rotation of the reference frame and this results in a quasiperiodic magnetization mode (**Q** mode) (see Figure 18). The quasiperiodicity arises because the external field and the limit-cycle periods are usually not commensurable.

The following argument proves that **Q** modes are necessarily present under appropriate conditions. Let us consider the case of small rotating field amplitudes, $h_{a\perp} \to 0$, where $\sin\theta_0 \to 0$ and $\cos\theta_0 \to \pm 1$. By making use of equations (140) and (141), one can write equations (176) and (177) in the approximate form:

$$\det A_0 \simeq \frac{1}{1+\alpha^2}\left(\nu_0^2 + \alpha^2\omega^2\right) \tag{183}$$

$$\mathrm{tr}A_0 \simeq -\frac{2\alpha}{1+\alpha^2}\left(\kappa_{\mathrm{eff}} \pm h_{a\parallel}\right) \tag{184}$$

Only two **P** modes are possible, because $\det A_0 > 0$. Furthermore, the sign of $\mathrm{tr}A_0$ is opposite to that of κ_{eff} for both modes in the interval $|h_{a\parallel}| < |\kappa_{\mathrm{eff}}|$. Therefore, in this interval both **P** modes are unstable for any system with negative effective anisotropy and a **Q** mode will necessarily appear.

This formal result has an intuitive physical interpretation. Let us assume that $\kappa_{\mathrm{eff}} < 0$ and that initially only the constant positive field $h_{a\parallel} < |\kappa_{\mathrm{eff}}|$ is applied, that is, $h_{a\perp} = 0$. In this case, no time-dependent driving field is present. In the laboratory frame, there exists a continuous set of static, marginally stable equilibrium states characterized by fixed

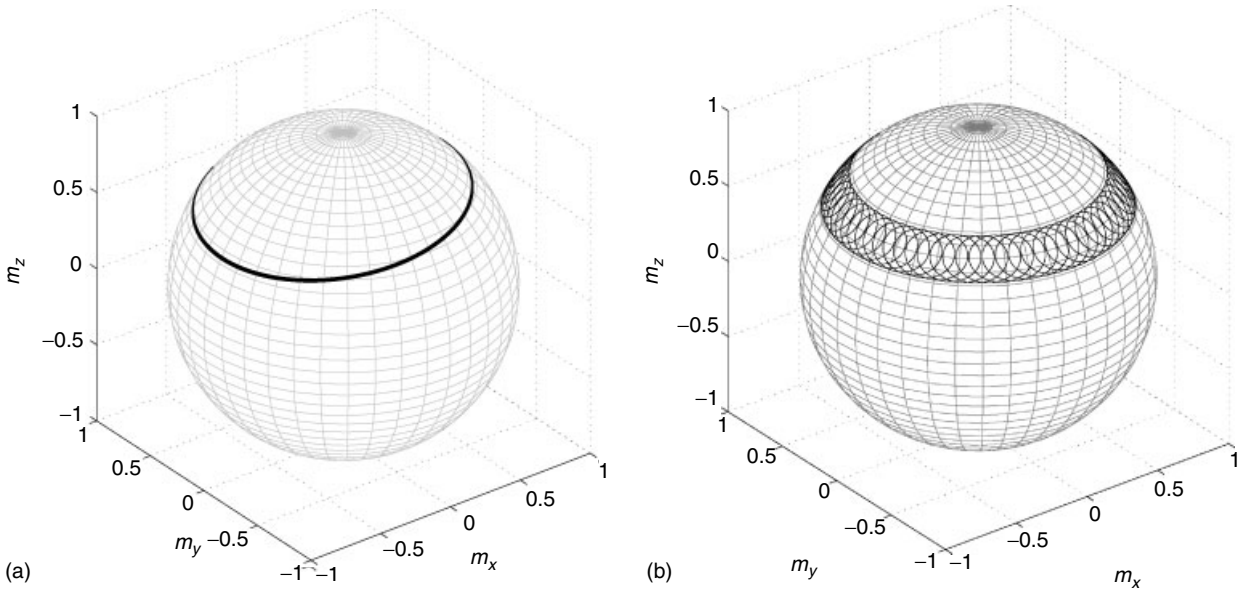

Figure 18. Representation on unit sphere of quasiperiodic motion (**Q** mode) in the rotating reference frame (a) and in the laboratory reference frame (b). In the rotating reference frame the **Q** mode appear as a limit cycle. System parameters: $\alpha = 0.1$, $\kappa_{\text{eff}} = -1$. Field frequency: $\omega = 0.5$. Field amplitude: $h_{a\parallel} = 0.8$, $h_{a\perp} = 0.08$.

$\cos\theta$ and arbitrary ϕ. In fact, by expressing the energy of the system (equation (121)) in terms of θ and ϕ one finds:

$$g_{\text{L}}\left(\theta, \phi; h_{a\parallel}, h_{a\perp}\right) = \frac{N_\perp}{2} - \frac{\kappa_{\text{eff}}}{2}\cos^2\theta - h_{a\parallel}\cos\theta - h_{a\perp}\sin\theta\cos\phi \tag{185}$$

When $\kappa_{\text{eff}} < 0$ and $h_{a\perp} = 0$ the energy is independent of ϕ and assumes its minimum value for $\cos\theta = h_{a\parallel}/|\kappa_{\text{eff}}|$. In the rotating frame, this continuous set of states results in a limit cycle of period $2\pi/\omega$. When the small rotating field $h_{a\perp}$ is applied, the set of equivalent static states is changed into a quasiperiodic motion. In fact, the rotating field is not strong enough to force the magnetization into synchronous rotation. The magnetization follows the field only for a small part of each rotation period and then periodically falls off synchronism. The result is a **Q** mode characterized by a slow average **m** precession around the symmetry axis, accompanied by a notation of frequency ω. Only when $h_{a\perp}$ exceeds a certain threshold, **m** gets locked to the field and the **Q** mode is destroyed in favor of a stable **P** mode.

In general, one expects that both stable (denoted by (a), i.e., attracting) and unstable (denoted by (r), i.e., repelling) limit cycles may be present in the dynamics (see Figure 15). The problem of theoretically predicting the number and the location of limit cycles for a given dynamical system is of extraordinary mathematical difficulty. However, when dissipation is small (that is, $\alpha \ll 1$ in equation (129)) some insight can be obtained (Serpico, d'Aquino, Bertotti and Mayergoyz, 2004) by a perturbative approach known as the Poincaré–Melnikov method for slightly dissipative systems (Perko, 1996; Guckenheimer and Holmes, 1997) (this method is discussed in detail in Bertotti, Mayergoyz and Serpico (2006a) where it is applied to spin-torque driven magnetization dynamics). Here, we simply present the key elements permitting one to apply the method to rotationally invariant LLG dynamics.

The starting point of our discussion is the equation for the undamped dynamics obtained by taking $\alpha = 0$ in equation (129):

$$\frac{\text{d}\mathbf{m}}{\text{d}t} = -\mathbf{m} \times \tilde{\mathbf{h}}_{\text{eff}} \tag{186}$$

This equation shows that the effective energy $\tilde{g}_{\text{L}}$ defined by equation (127) is an integral of motion for the undamped dynamics, because $\tilde{\mathbf{h}}_{\text{eff}} \cdot \text{d}\mathbf{m}/\text{d}t = 0$. Thus the magnetization trajectories coincide with the closed level curves of the $\tilde{g}_{\text{L}}$ function. From equations (121) and (127) one finds that $\tilde{g}_{\text{L}}(\mathbf{m}; \mathbf{h}_{\text{a}})$ can be expressed as:

$$\tilde{g}_{\text{L}}(\mathbf{m}; \mathbf{h}_{\text{a}}) = \frac{1}{2}N_\perp - \frac{1}{2}\kappa_{\text{eff}} m_z^2 - (h_{az} - \omega)m_z - h_{a\perp}m_{a\perp} \tag{187}$$

Therefore, the line $C(\tilde{g}_0)$ of constant energy $\tilde{g}_0$ is described by the equation:

$$\kappa_{\text{eff}} m_z^2 + 2(h_{az} - \omega)m_z + 2h_{a\perp}m_{a\perp} = N_\perp - 2\tilde{g}_0 \tag{188}$$

When α is nonzero, the effective energy $\tilde{g}_L$ is no longer constant along the magnetization trajectories. One obtains from equation (129) that $\tilde{g}_L$ changes at the rate:

$$\frac{\mathrm{d}\tilde{g}_{\mathrm{L}}}{\mathrm{d}t} \equiv -\tilde{\mathbf{h}}_{\mathrm{eff}} \cdot \frac{\mathrm{d}\mathbf{m}}{\mathrm{d}t} = -\alpha \left(\frac{\mathrm{d}\mathbf{m}}{\mathrm{d}t} - \omega \mathbf{m} \times \mathbf{e}_z \right) \cdot \frac{\mathrm{d}\mathbf{m}}{\mathrm{d}t} \quad (189)$$

Thus, whenever $\alpha \ll 1$ the energy $\tilde{g}_{\mathrm{L}}$ will be a slowly varying function of time and magnetization trajectories will be only slightly distorted with respect to the undamped ones. Let us now consider a limit cycle of the dissipative dynamics. According to the previous reasoning, the corresponding closed trajectory will be close to a certain trajectory $C(\tilde{g}_0)$ of the undamped dynamics. By definition, the limit cycle represents a periodic motion, so the energy of the system will also be periodic when calculated along the limit cycle. This means that the time integral of the right-hand side of equation (189) along the limit cycle will be zero. Since the limit cycle is very close to the undamped trajectory $C(\tilde{g}_0)$ we can calculate this integral along the undamped trajectory without making an appreciable error. By also taking into account that equation (186) holds for the undamped motion and that $\tilde{\mathbf{h}}_{\mathrm{eff}} = \mathbf{h}_{\mathrm{eff}} - \omega \mathbf{e}_z$, we conclude that the integral of the right-hand side of equation (189) along the limit cycle will be approximately equal to $-\alpha M(\tilde{g}_0)$, where:

$$M(\tilde{g}_0) = -\oint_{C(\tilde{g}_0)} (\mathbf{m} \times \mathbf{h}_{\mathrm{eff}}) \cdot \mathrm{d}\mathbf{m} \quad (190)$$

Therefore, it is expected that $M(\tilde{g}_0) \simeq 0$ for a limit cycle. This heuristic reasoning can be given a rigorous mathematical formulation by invoking Poincaré–Melnikov method (Perko, 1996; Guckenheimer and Holmes, 1997). In particular, one can prove that in the limit of small damping the equation $M(\tilde{g}_0) = 0$ represents the *necessary and sufficient condition* for the existence of a limit cycle. The limit cycle is stable or unstable depending on whether $\mathrm{d}M/\mathrm{d}\tilde{g}_0$ is respectively positive or negative at the point where $M(\tilde{g}_0) = 0$. Therefore, the knowledge of the undamped dynamics is sufficient to predict the number and location of limit cycles, provided the damping constant α is sufficiently small.

The Melnikov function $M(\tilde{g}_0)$ can be studied by analytical or numerical methods under quite general conditions because $\mathbf{h}_{\mathrm{eff}}$ (equation (122)) and $\tilde{g}_{\mathrm{L}}$ (equation (127)) are all known functions of $\mathbf{m}$. There is no need to determine the precise time dependence $\mathbf{m}(t)$ for the undamped magnetization motion in order to calculate the Melnikov function: it is enough to know the geometrical shape of the unperturbed trajectories, that is, the constant $\tilde{g}_{\mathrm{L}}$ lines given by equation (188). Figure 19 illustrates the example where this method is applied to the thin film with negligible crystal anisotropy considered in Figure 15. The Melnikov function is calculated from equations (122), (127), and (190) for all energies

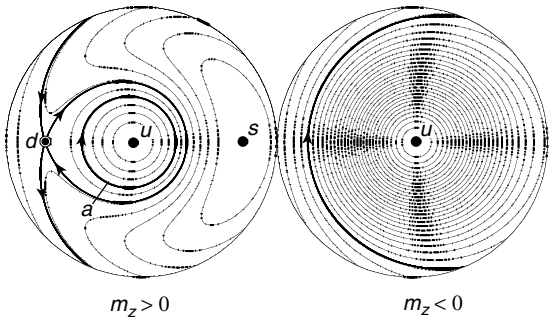

Figure 19. Phase portrait for nondissipative system. Trajectories are given by lines of constant effective energy $\tilde{g}_L(\mathbf{m}; \mathbf{h}_a) = \tilde{g}_0$ (see equations (121) and (127)). s: $\tilde{g}_{\mathrm{L}}$ minimum; u: $\tilde{g}_{\mathrm{L}}$ maxima; d: $\tilde{g}_{\mathrm{L}}$ saddle. System parameters: $\alpha = 0$, $\kappa_{\mathrm{eff}} = -1$. Field frequency: $\omega = 0.5$. Field amplitude: $h_{a\parallel} = 0.8$, $h_{a\perp} = 0.08$. Trajectory labeled by a is stable limit cycle present in dissipative dynamics in the limit of small damping α, as predicted by Melnikov theory (compare with bottom phase portrait in Figure 15).

in the interval $\tilde{g}_d \leq \tilde{g}_0 \leq \tilde{g}_u$, where $\tilde{g}_d$ and $\tilde{g}_u$ represent the energies of the d and u stationary points in the $m_z > 0$ hemisphere in Figure 19. One finds that: $M(\tilde{g}_d) < 0$; $M(\tilde{g}_u) = 0$ (indeed, the Melnikov function is zero by definition for every energy extremum); $\mathrm{d}M/\mathrm{d}\tilde{g}_0|_{\tilde{g}_0 = \tilde{g}_u} < 0$ (this means that the energy maximum is going to be an unstable focus of the dissipative dynamics). These boundary properties imply that there must exist at least one additional $M(\tilde{g}_0)$ zero inside the interval $\tilde{g}_d < \tilde{g}_0 < \tilde{g}_u$. In fact, one finds just one additional zero. The corresponding trajectory is labeled by a in Figure 19. This trajectory is going to be a stable limit cycle of the dissipative dynamics for sufficiently small α. The comparison with Figure 15 shows that this limit cycle is indeed present in the dynamics even when α is as large as 0.1.

5.2.4 Nonlinear ferromagnetic resonance

The field region close to the right-hand corner of the region $\det A_0 < 0$ in Figure 17 is where ferromagnetic resonance phenomena occur (Wigen, 1994; Gurevich and Melkov, 1996). In typical ferromagnetic resonance experiments, the large dc field $h_{az} > 0$ is initially applied to the system. The ensuing **P** mode coincides with the saturation state along the positive $\mathbf{e}_z$ axis. Then the microwave field of amplitude $h_{a\perp}$ and angular frequency ω is switched on. The resonance experiment is carried out by slowly decreasing the field h_{az} while keeping $h_{a\perp}$ and ω constant. Resonance occurs when the Larmor frequency associated with the effective field becomes equal to the rotating field frequency ω. In dimensionless notation, this means that $h_{az} + \kappa_{\mathrm{eff}} \simeq \omega$.

The resonance becomes manifest when one considers the power p absorbed by the **P** mode under fixed $h_{a\perp}$ and

variable h_{az}. By using equations (148) and (141) one obtains:

$$p \equiv \mathbf{h}_{a\perp} \cdot \frac{\mathrm{d}\mathbf{m}_\perp}{\mathrm{d}t} = \alpha\omega^2 \sin^2\theta_0 = \frac{\alpha\omega^2 h_{a\perp}^2}{\nu_0^2 + \alpha^2\omega^2} \qquad (191)$$

When the microwave field is small, the angle θ_0 is small as well and one can use equation (140) under the approximation $\cos\theta_0 \simeq 1$ to express ν_0 in terms of h_{az}. Under this approximation, equation (191) yields:

$$p = \frac{\alpha\omega^2 h_{a\perp}^2}{(h_{az} + \kappa_{\mathrm{eff}} - \omega)^2 + \alpha^2\omega^2} \qquad (192)$$

We obtain the lorentzian line shape typical of linear resonant behavior. The absorbed power is maximum for $h_{az} + \kappa_{\mathrm{eff}} = \omega$, as previously anticipated, and the linewidth is $\alpha\omega$. When progressively larger microwave field amplitudes are considered, large precessional motions set in and the approximation $\cos\theta_0 \simeq 1$ is no longer acceptable. To deal with this nonlinear regime, we can make use of equations (140)–(141) to express h_{az} as a function of $\cos\theta_0$ for the **P** mode under consideration. One finds:

$$h_{az} = \omega - \kappa_{\mathrm{eff}} \cos\theta_0 \pm \cos\theta_0 \sqrt{\frac{h_{a\perp}^2}{\sin^2\theta_0} - \alpha^2\omega^2} \qquad (193)$$

Equations (191) and (193) give the parametric representation of the absorbed power $p(h_{az})$ under nonlinear conditions, with $\cos\theta_0$ as the independent variable. An example is shown in Figure 20 for the case of a thin-film disk with negligible crystal anisotropy ($\kappa_{\mathrm{eff}} = -1$). The initial condition, where $\cos\theta_0 \simeq 1$ and h_{az} is very large, corresponds to choosing the branch with the positive sign in equation (193). This is the correct branch to consider when $\cos\theta_0$ is decreased from $\cos\theta_0 = 1$ down to $\sin^2\theta_0 = h_{a\perp}^2/\alpha^2\omega^2$, where the square root in equation (193) vanishes. This is where the absorbed power is maximum. From here, the branch with the negative sign in equation (193) must be considered for $\cos\theta_0$ increasing from the minimum resonance value back to $\cos\theta_0 = 1$. As shown in Figure 20, the absorbed power profile gets increasingly distorted under increasing rf field amplitude. According to equation (191), the state of maximum absorbed power always corresponds to $\nu_0 = 0$. From equations (140) and (141) one finds that this condition is described by the equation:

$$h_{a\perp} = \frac{\alpha\omega}{|\kappa_{\mathrm{eff}}|} \sqrt{\kappa_{\mathrm{eff}}^2 - (h_{az} - \omega)^2} \qquad (194)$$

which is the curved dashed line shown in Figure 20.

When κ_{eff} is negative and large enough, the distortion of the absorbed power profile can become so important that the system becomes unstable and hysteretic jumps appear in the absorbed power. This phenomenon has been observed indeed and is known in the literature as 'foldover' (Seagle, Charap and Artman, 1985; Fetisov, Patton and Sygonach, 1999). Foldover effects are properly understood by using the bifurcation analysis presented in Section 5.2.2. Let us consider the representation of **P** modes in the $(h_{az}, h_{a\perp})$ field control plane. During the resonance experiment, the **P** mode under study moves from right to left along a horizontal line in the control plane, as shown in Figure 20. If this line crosses the boundary of the $\det A_0 < 0$ region (point A in Figure 20), a saddle-node pair of additional **P** modes is created. The **P** mode motion executed by the system is destroyed at point B in Figure 20 by a second saddle-node bifurcation involving the saddle previously created at point A. Consequently, the system becomes unstable and jumps to a different **P** mode motion of definitely smaller amplitude. If the field h_{az} is now increased, the newly attained **P** mode evolves under the action of the field until it is destroyed by the saddle-node bifurcation at point A in Figure 20 where the system jumps back to the original **P** mode. It is clear from this analysis that the $h_{a\perp}$ threshold beyond which foldover

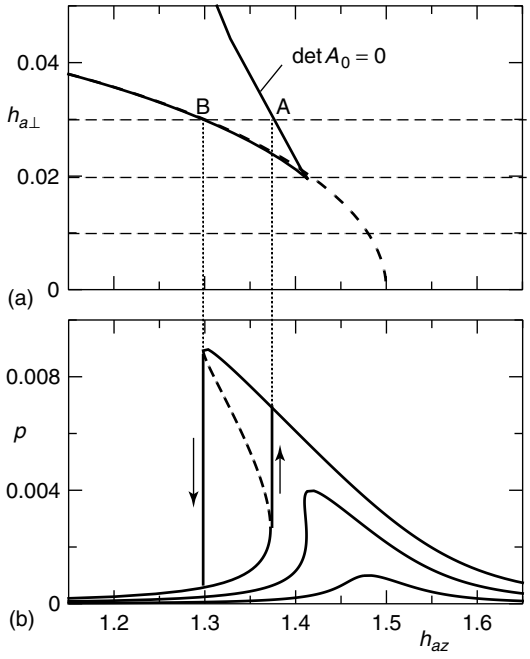

Figure 20. (a) Magnified view of right-hand corner of $\det A_0 < 0$ region for the thin-film disk shown in Figure 17. Horizontal dashed lines: field history for resonance experiments under rf field amplitudes $h_{a\perp} = 0.01, 0.02, 0.03$. Curved dashed line: $\nu_0 = 0$ nonlinear resonance condition (equation (194)). *A* and *B*: saddle-node bifurcation points where instability in system response may occur. (b) Absorbed power (equations (191) and (193)) for $h_{a\perp} = 0.01, 0.02, 0.03$ with representation of foldover jumps taking place for the highest rf field amplitude at points A and B. System parameters: $\alpha = 0.1$, $\kappa_{\mathrm{eff}} = -1$. Field frequency: $\omega = 0.5$.

becomes possible coincides with the ordinate of the lower right-hand tip of the $\det A_0 < 0$ region. That is the point where the two roots of the equation $\det A_0 = 0$ coincide. This means that $\kappa_{\text{eff}} \sin^2\theta_0 = 2\alpha\omega\cos\theta_0$ (see equation (176)), which yields:

$$\cos\theta_0 = \sqrt{1 + \frac{\alpha^2\omega^2}{\kappa_{\text{eff}}^2}} - \frac{\alpha\omega}{|\kappa_{\text{eff}}|}, \nu_0 = \alpha\omega\cos\theta_0 \quad (195)$$

Substitution of this result into equation (141) leads to the following expression for the threshold for foldover:

$$h_{a\perp}^2 = \frac{4\,(\alpha\omega)^3}{|\kappa_{\text{eff}}|} \frac{\sqrt{1 + \frac{\alpha^2\omega^2}{\kappa_{\text{eff}}^2}}}{\left(\frac{\alpha\omega}{|\kappa_{\text{eff}}|} + \sqrt{1 + \frac{\alpha^2\omega^2}{\kappa_{\text{eff}}^2}}\right)^2} \quad (196)$$

This exact result is the generalization of the estimate $h_{a\perp}^2 \simeq 3.08(\alpha\omega)^3/|\kappa_{\text{eff}}|$ obtained for the thin-film geometry by Anderson and Suhl (1955) through an approximate linear analysis.

ACKNOWLEDGMENTS

This work has been partially supported by the BURC 2003 Grant provided by Regione Campania (Italy) and by MIUR-PRIN Project N.2006098315.

REFERENCES

Acremann, Y., Back, C.H., Buess, M., *et al*. (2000). Imaging precessional motion of the magnetization vector. *Science*, **290**, 492–495.

Aharoni, A. (1996). *Introduction to the Theory of Ferromagnetism*, Oxford University Press: Oxford.

Alvarez, L.F., Pla, O. and Chubykalo, O. (2000). Domain wall diodes in ferromagnetic planar nanowires. *Physical Review B*, **61**, 11613–11617.

Anderson, P.W. and Suhl, H. (1955). Instability in the motion of ferromagnets at high microwave power levels. *Physical Review*, **100**, 1788–1789.

Back, C.H., Allenspach, R., Weber, W., *et al*. (1999). Minimum field strength in precessional magnetization reversal. *Science*, **285**, 864–867.

Back, C.H., Weller, D., Heidmann, J., *et al*. (1998). Magnetization reversal in ultrashort magnetic field pulses. *Physical Review Letters*, **81**, 3251–3254.

Bauer, M., Fassbender, J., Hillebrands, B. and Stamps, R.L. (2000). Switching behavior of a stoner particle beyond the relaxation time limit. *Physical Review B*, **61**, 3410–3416.

Berger, L. (1996). Emission of spin waves by a magnetic multilayer traversed by a current. *Physical Review B*, **54**, 9353–9358.

Bertotti, G. (1998). *Hysteresis in Magnetism*, Academic Press: Boston.

Bertotti, G., Mayergoyz, I.D. and Serpico, C. (2001). Spin-wave instabilities in large-scale nonlinear magnetization dynamics. *Physical Review Letters*, **87**, 217203.

Bertotti, G., Mayergoyz, I.D., Serpico, C. and Dimian, M. (2003). Comparison of analytical solutions of landau-lifshitz equation for "damping" and "precessional" switchings. *Journal of Applied Physics*, **93**, 6811–6813.

Bertotti, G., Mayergoyz, I.D. and Serpico C. (2006a). Nonlinear magnetization dynamics. switching and relaxation phenomena. In *The Science of Hysteresis*, *Elsevier Series in Electromagnetism*, Bertotti, G. and Mayergoyz, I.D. (Eds.), Elsevier: Amsterdam, pp. 435–565, Vol. 2.

Bertotti, G., Mayergoyz, I.D. and Serpico, C. (2006b). Nonlinear magnetization dynamics. magnetization modes and sin waves under rotating fields. In *The Science of Hysteresis, Elsevier Series in Electromagnetism*, Bertotti, G. and Mayergoyz, I.D. (Eds.), Elsevier: Amsterdam, pp. 567–642, Vol. 2.

Bertotti, G., Serpico, C. and Mayergoyz, I.D. (2001). Nonlinear magnetization dynamics under circularly polarized field. *Physical Review Letters*, **86**, 724–727.

Brown, W.F. (1962). *Magnetostatic Principles in Ferromagnetism*, North Holland: Amsterdam.

Brown, W.F. (1963). *Micromagnetics*, Krieger Publishing Company: New York.

Callen, H.B. (1958). A ferromagnetic dynamical equation. *Journal of Physics and Chemistry of Solids*, **4**, 256–270.

Crawford, T.M., Kabos, P. and Silva, T.J. (2000). Coherent control of precessional dynamics in thin film permalloy. *Applied Physics Letters*, **76**, 2113–2115.

Damon, R.W. (1953). Relaxation effects in the ferromagnetic resonance. *Reviews of Modern Physics*, **25**, 239–245.

Donahue, M.J. and Porter, D.G. (2002). Analysis of switching in uniformly magnetized bodies. *IEEE Transactions on Magnetics*, **38**, 2468–2470.

Doyle, W.D. and He, L. (1993). The effect of dc bias fields on the switching speed in magnetic particulate media. *IEEE Transactions on Magnetics*, **29**, 3634.

Fetisov, Y.K., Patton, C.E. and Sygonach, V.T. (1999). Nonlinear ferromagnetic resonance and foldover in yttrium iron garnet thin films – inadequacy of the classical model. *IEEE Transactions on Magnetics*, **35**, 4511–4521.

Gantmacher, F.R. (1975). *Lectures in Analytical Mechanics*, Mir Publications: Moscow.

Gilbert, T.L. (1955). A Lagrangian formulation of the gyromagnetic equation of the magnetization field. *Physical Review*, **100**, 1243.

Gilbert, T.L. (2004). A phenomenological theory of damping in ferromagnetic materials. *IEEE Transactions on Magnetics*, **40**, 3443–3449.

Grollier, J., Cros, V., Hamzic, A., *et al*. (2001). Spin-polarized current induced switching in co/cu/co pillars. *Applied Physics Letters*, **78**, 3663–3665.

Guckenheimer, J. and Holmes, P. (1997). *Nonlinear Oscillations, Dynamical Systems, and Bifurcations of Vector Fields*, Springer-Verlag: New York.

Gurevich, A.G. and Melkov, G.A. (1996). *Magnetization Oscillations and waves*, CRC Press: Boca Raton.

Hale, J. and Kocak, H. (1991). *Dynamics and Bifurcations*, Springer-Verlag: Berlin.

Hancock, H. (1958). *Elliptic Integrals*, Dover: New York.

Hubbard, J.H. and West, B.H. (1995). *Differential Equations: A Dynamical Systems Approach*, Springer-Verlag: New York.

Hubert, A. and Schäefer, R. (1998). *Magnetic Domains*, Springer-Verlag: Berlin.

Kaka, S. and Russek, S.E. (2002). Precessional switching of submicrometer spin valves. *Applied Physics Letters*, **80**, 2958–2960.

Khapikov, A.F. (1992). Dynamics of the magnetization reversal of a cylinder in an alternating magnetic field. *JETP Letters*, **55**, 352–356.

Kikuchi, R. (1956). On the minimum of magnetization reversal time. *Journal of Applied Physics*, **27**, 1352–1357.

Kiselev, S.I., Sankey, J.C., Krivorotov, I.N., *et al*. (2003). Microwave oscillations of a nanomagnet driven by a spin-polarized current. *Nature*, **425**, 380–383.

Kronmueller, H. and Faehnle, M. (2003). *Micromagnetism and the Microstructure of Ferromagnetic Solids*, Cambridge University Press: Cambridge.

Kuznetsov, Y.A. (1995). *Elements of Applied Bifurcation Theory*, Springer-Verlag: New York.

Landau, L.D. and Lifshitz, E.M. (1935). Theory of the dispersion of magnetic permeability in ferromagnetic bodies. *Physikalische Zeitschrift der Sowjetunion*, **8**, 153–169.

Landau, L.D. and Lifshitz, E.M. (1976). *Mechanics*, Pergamon Press: Oxford.

Landau, L.D. and Lifshitz, E.M. (1984). *Electrodynamics of Continuous Media*, Pergamon Press: Oxford.

Leineweber, T. and Kronmueller, H. (1999). Dynamics of magnetisation states. *Journal of Magnetism and Magnetic Materials*, **42**, 575–590.

Magni, A., Bertotti, G., Serpico, C. and Mayergoyz, I.D. (2001). Dynamic generalization of stoner-wohlfarth model. *Journal of Applied Physics*, **89**, 7451–7453.

Mallinson, J.C. (1987). On damped gyromagnetic precession. *IEEE Transactions on Magnetics*, **23**, 2003–2004.

Mallinson, J.C. (2000). Damped gyromagnetic switching. *IEEE Transactions on Magnetics*, **36**, 1976–1981.

Mayergoyz, I.D., Dimian, M., Bertotti, G. and Serpico, C. (2005). Critical fields and pulse durations for precessional switching of perpendicular media. *Journal of Applied Physics*, **97**, 10E509.

Osborne, J.A. (1945). Demagnetizing factors of general ellipsoid. *Physical Review*, **67**, 351–357.

Perko, L. (1996). *Differential Equations and Dynamical Systems*, Springer-Verlag: New York.

Porter, D.G. (1998). Analytical determination of the LLG zero-damping critical switching Field. *IEEE Transactions on Magnetics*, **34**, 1663–1665.

Rippard, W.H., Pufall, M.R., Kaka, S., *et al*. (2004). Direct-current induced dynamics in cofe/nife point contacts. *Physical Review Letters*, **92**, 027201.

Rizzo, N.D., Silva, T.J. and Kos, A.B. (2000). Nanosecond magnetization reversal in high coercivity thin films. *IEEE Transactions on Magnetics*, **36**, 159–165.

Schumacher, H.W., Chappert, C., Sousa, R.C., *et al*. (2003). Quasiballistic magnetization reversal. *Physical Review Letters*, **90**, 017204.

Schwerdtfeger, H. (2001). *Geometry of Complex Numbers*, Dover: New York.

Seagle, D.J., Charap, S.H. and Artman, J.O. (1985). Foldover in yig. *Journal of Applied Physics*, **57**, 3706–3708.

Serpico, C., d'Aquino, M., Bertotti, G. and Mayergoyz, I.D. (2004). Quasiperiodic magnetization dynamics in uniformly magnetized particles and films. *Journal of Applied Physics*, **95**, 7052–7054.

Skrotskii, G.V. and Alimov, Y.I. (1959a). Ferromagnetic resonance in a circularly polarized magnetic field of arbitrary amplitude. *Soviet Physics JETP*, **35**, 1035–1037.

Skrotskii, G.V. and Alimov, Y.I. (1959b). Effect of specimen shape on ferromagnetic resonance in a strong radio-frequency field. *Soviet Physics JETP*, **36**, 899–901.

Slonczewski, J.C. (1996). Current-driven excitation of magnetic multilayers. *Journal of Magnetism and Magnetic Materials*, **159**, L1–L7.

Smirnov, V. (1989). *Cours de Mathématiques Supérieures*, Mir Publications: Moscow.

Stoner, E.C. and Wohlfarth, E.P. (1948). A mechanism of magnetic hysteresis in heterogeneous alloys. *Philosophical Transactions of the Royal Society, Series A*, **240**, 599–642.

Suhl, H. (1956). The nonlinear behavior of ferrites at high microwave signal levels. *Proceedings of IRE*, **44**, 1270–1284.

Suhl, H. (1957). The theory of ferromagnetic resonance at high signal powers. *Journal of Physics and Chemistry of Solids*, **1**, 209–227.

Suhl, H. (1998). Theory of the magnetic damping constant. *Journal of Magnetism and Magnetic Materials*, **34**, 1834–1838.

Sun, J.Z. (2000). Spin-current interaction with a monodomain magnetic body: a model study. *Physical Review B*, **62**, 570–578.

Thiaville, A. (2000). Coherent rotation of magnetization in three dimensions: a geometric approach. *Physical Review B*, **61**, 12221–12232.

Thornley, R.F.M. (1975). Pulse response of recording media. *Journal of Magnetism and Magnetic Materials*, **11**, 1197.

Träxler, T., Just, W. and Sauermann, H. (1996). Dynamics of homogeneous magnetizations in strong transverse driving fields. *Zeitschrift fur Physik B*, **99**, 285–295.

Walker, L.R. (1957). Magnetostatic modes in ferromagnetic resonance. *Physical Review*, **105**, 390–399.

Wigen, P.E. (Ed.) (1994). *Nonlinear Phenomena and Chaos in Magnetic Materials*. World Scientific Publishing: Singapore.

Wiggins, S. (1990). *Introduction to Applied Nonlinear Dynamical Systems and Chaos*, Springer-Verlag: New York.

Classical Spin Models

Ulrich Nowak
University of York, York, UK

1 INTRODUCTION

Classical spin models bridge the gap between a full electronic description of a magnetic material and conventional micromagnetism where magnetic properties are calculated on the basis of a continuum theory for the energy of a system. While quantum effects are obviously neglected, classical spin models take into account the discrete nature of matter, so that they allow for an investigation of magnetic particles in the nanometer regime where a continuum theory would fail. The fact that magnetic structures are described on an atomic level makes it possible to investigate ferromagnets (FMs) as well as antiferromagnets (AFMs) or even heterostructures composed of both of them. Methods exist for the calculation of thermal equilibrium properties and, to some extent, also for nonequilibrium properties. Classical spin models are thus particularly suited to the study of thermal effects. On the other hand, numerical calculations with an atomic resolution are restricted to system sizes of the order of 10^7 spins so that only systems sizes of the order of some 10 nm can be treated numerically (at the moment). However, magnetic materials are controllable down to the nanometer scale, leading to a fundamental interest in the understanding of the magnetism of small ferromagnetic particles or heterostructures (Schneider and Blügel, 2005). This interest is even amplified by the broad variety of industrial applications in pure magnetic as well as spin electronic devices. For theoretical investigations numerical methods are thus desirable, especially methods that are capable of treating realistic magnetic model systems including heterostructures and the effects of thermal activation.

This chapter focuses on classical spin models, physical principles as well as numerical methods. Section 2 deals with the basics of classical spin Hamiltonians, thermal averages, and the equation of motion – the Landau–Lifshitz–Gilbert (LLG) equation. In Section 3 the two most established numerical methods in this context are discussed, namely Monte Carlo methods (Binder and Heermann, 1997) and Langevin dynamics simulations (Lyberatos and Chantrell, 1993). Special emphasis is laid on the relation between these different methods, which leads to time-quantified Monte Carlo methods (Nowak, Chantrell and Kennedy, 2000). Sections 4 and 5 are an introduction to two topics which are typical for a modeling within the framework of classical spin models, namely thermally activated switching in nanoparticles (Nowak, 2001) and exchange bias (EB) (Nogués and Schuller, 1999), an effect arising in compound systems of ferro- and antiferromagnetic materials. Section 6 concludes this article.

Handbook of Magnetism and Advanced Magnetic Materials. Edited by Helmut Kronmüller and Stuart Parkin. Volume 2: *Micromagnetism*. ISBN: 978-0-470-02217-7.

2 THEORETICAL CONCEPTS

2.1 Classical spin models

A classical spin model is the classical limit of a quantum mechanical, localized spin model – the Heisenberg model (Heisenberg, 1928) (see Steevens, 1963; Anderson, 1963; Levy, 2000, for the theoretical background). The Hamiltonian of a classical spin model describing a magnetic system may contain contributions from exchange interactions, crystalline anisotropies, the external magnetic field, and dipole–dipole interactions. There might also be other contributions (e.g., a magnetovolume coupling) which, for the sake of simplicity, will not be considered in the following. An appropriate Hamiltonian may then be written in the form

$$\mathcal{H} = \mathcal{H}_{\text{exc}} + \mathcal{H}_{\text{anis}} + \mathcal{H}_{\text{field}} + \mathcal{H}_{\text{dipol}} \tag{1}$$

Within the framework of the classical Heisenberg model the exchange energy is expressed as

$$\mathcal{H}_{\text{exc}} = -\sum_{\langle ij \rangle} J_{ij} \mathbf{S}_i \cdot \mathbf{S}_j \tag{2}$$

where the $\mathbf{S}_i = \boldsymbol{\mu}_i / \mu_s$ are three-dimensional magnetic moments reduced to unit length. This part represents the exchange of the magnetic moments and it is often (but not necessarily) restricted two nearest-neighbor interactions with a unique exchange coupling constant J. For $J > 0$ this part of the Hamiltonian leads to ferromagnetic order while for $J < 0$ it can lead to antiferromagnetic order if the lattice structure allows for antiferromagnetic order without frustration effects.

The simplest example for a crystalline anisotropy is

$$\mathcal{H}_{\text{anis}} = -d_z \sum_i S_{iz}^2 \tag{3}$$

which is a uniaxial anisotropy favoring the z axis as easy axis of the system for positive anisotropy constant d_z. Of course, other anisotropy terms describing any crystalline, stress, or surface anisotropies could also be considered.

The Zeeman energy is

$$\mathcal{H}_{\text{field}} = -\mathbf{b} \cdot \sum_i \mathbf{S}_i \tag{4}$$

describing the coupling of the moments to an external magnetic field with $\mathbf{b} = \mu_s \mathbf{B}$. Here, μ_s is the absolute value of the magnetic moment which for an atomic moment is of the order of a Bohr magneton.

The dipole–dipole coupling of the magnetic moments leads to an energy

$$\mathcal{H}_{\text{dipole}} = -w \sum_{i<j} \frac{3(\mathbf{S}_i \cdot \mathbf{e}_{ij})(\mathbf{e}_{ij} \cdot \mathbf{S}_j) - \mathbf{S}_i \cdot \mathbf{S}_j}{r_{ij}^3} \tag{5}$$

with $w = \mu_s^2 \mu_0 / 4\pi a^3$ when the spins are on a regular lattice with spacing a. The atomic magnetic moments are handled in a point dipole approximation. The r_{ij} are the normalized distances between moments i and j and the $\mathbf{e}_{ij}$ are unit vectors in the direction of $\mathbf{r}_{ij}$. Since the dipole–dipole interaction of two moments depends on their distance vector, the dipolar energy contribution will depend on the shape of the sample. Dipoles try to be aligned, minimizing free surface charges, which leads to shape anisotropy and to the fact that domain structures may minimize the energy of the system. Hence, dipole–dipole coupling is the microscopic origin of the magnetostatic stray field energy.

Classical spin models are in some sense 'between' a full quantum mechanical first-principles description and a micromagnetic continuum approach. But they can also be interpreted as the discretized version of a micromagnetic continuum model, where the charge distribution for a single cell of the discretized lattice is approximated by a point dipole (Berkov, Ramstöck and Hubert, 1993; Hubert and Schäfer, 1998). Also, for certain magnetic systems their description in terms of a lattice of magnetic moments is based on the mesoscopic structure of the material, especially when a particulate medium is described (Chantrell, Lyberatos and Wohlfarth, 1986; Nowak, Rüdiger, Fumagalli and Güntherodt, 1996; Nowak, 1997; Nowak, Heimel, Kleinefeld and Weller, 1997; Chantrell, Walmsley, Gore and Maylin, 2000; Verdes *et al*., 2002). In this case it is assumed that one grain or particle can be described by a single magnetic moment. Therefore, the size of the particles and the temperature must be small enough so that internal degrees of freedom are not relevant for the special problem under consideration.

When compared, the use of classical spin models for the description of magnetic materials has advantages as well as disadvantages. The main disadvantage is that owing to the atomic resolution the system size is clearly restricted to a nanoscale (at the moment to the order of, say, 10^7 spins, steadily increasing with computational power). But the advantages are (i) realistic lattice structures and interactions can be taken into account without assuming a continuous magnetization (Vedmedenko *et al*., 2004), (ii) finite temperatures can be taken into account without cutting the spin-wave spectra because of the discretization (Berkov, 2007), (iii) the form and the parameters of the Hamiltonian can be derived from first-principles calculations (see e.g., Mryasov, Nowak, Guslienko and Chantrell, 2005), and (iv) the modeling of

para-, ferri-, ferro- or antiferromagnets, and even heterostructures composed of several of these different materials is straightforward.

Hence typical magnetic systems for a description using classical spin models are nanostructures or systems with very narrow domain walls (Garanin, 1991; Kazantseva, Wieser and Nowak, 2005), especially when thermal excitations are relevant (Garanin, 1997; Nowak, 2001), and magnetic heterostructures including antiferromagnetic components (Malozemoff, 1987; Nowak *et al*., 2002b).

2.2 Thermodynamics and the equation of motion

In order to calculate thermodynamic equilibrium properties one has to calculate thermal averages for the properties of interest. For instance, in a canonical ensemble the temperature-dependent reduced magnetization becomes

$$\mathbf{m}(T) = \frac{1}{N}\left\langle \sum_i \mathbf{S}_i \right\rangle = \frac{1}{N}\mathrm{Tr}\,\frac{1}{Z} e^{-\mathcal{H}/k_\mathrm{B}T} \sum_i \mathbf{S}_i \qquad (6)$$

where $\langle \ldots \rangle$ denotes a thermal average and $Z = \mathrm{Tr}\, e^{-\mathcal{H}/k_\mathrm{B}T}$ is the canonical partition function (see, e.g., Reif, 1965). For N classical spins the calculation of the trace would involve an integral over phase space, that is, integrals over N unit spheres. This high-dimensional integral can usually not be calculated exactly for realistic magnetic systems. Instead either approximations have to be used, the most famous one being the mean-field approximation (Wagner, 1972; Levy, 2000) or numerical techniques like Monte Carlo methods.

Moreover, one often is interested in nonequilibrium properties. Then, the basic equation of motion for magnetic moments coupled to a heat bath is the LLG equation (Landau and Lifshitz, 1935; Gilbert, 1955; Brown, 1963a) with Langevin dynamics. For electronic magnetic moments it can be written in the form

$$\dot{\mathbf{S}}_i = -\frac{\gamma}{(1+\alpha^2)\mu_s}\mathbf{S}_i \times \left(\mathbf{H}_i(t) + \alpha\, \mathbf{S}_i \times \mathbf{H}_i(t)\right) \qquad (7)$$

where $\gamma = 1.76 \times 10^{11}(\mathrm{T\,s})^{-1}$ is the absolute value of the gyromagnetic ratio and $\mathbf{H}_i(t) = \boldsymbol{\zeta}_i(t) - \partial\mathcal{H}/\partial\mathbf{S}_i$. The thermal noise $\boldsymbol{\zeta}_i(t)$ obeys

$$\langle \boldsymbol{\zeta}_i(t) \rangle = 0 \qquad (8)$$

$$\langle \zeta_{i\eta}(t)\zeta_{j\theta}(t') \rangle = \delta_{i,j}\delta_{\eta,\theta}\delta(t-t')2\alpha k_\mathrm{B}T\mu_s/\gamma \qquad (9)$$

i and j denote once again the sites of the lattice and η and θ the Cartesian components. The first part of equation (7) describes the spin precession, which can be derived from Heisenberg's equation of motion in the classical limit, while the second part includes the relaxation of the moments. α is a dimensionless parameter describing phenomenologically the strength of the coupling to the heat bath. Note, that this microscopic coupling parameter is not necessarily identical with the usual macroscopic damping parameter (Chubykalo, Nowak, Chantrell and Garanin, 2006) but we will, nevertheless, refer to α as damping parameter in the following. As a consequence of the fluctuation dissipation theorem, α governs the relaxation aspect of the coupling to the heat bath as well as the fluctuations via the strength of the thermal noise (Lyberatos and Chantrell, 1993; Chubykalo *et al*., 2003b; Berkov, 2007). The assumption of uncorrelated noise on an atomic level is a simplification reflecting the lack of knowledge regarding the fundamental physical mechanisms involved in the coupling between spins and heat bath. The microscopic understanding of damping is an outstanding challenge for current research (Smith and Arnett, 2001; Safonov and Bertram, 2002; Rebei and Parker, 2003). However, the strength of the noise in equation (9) ensures correct thermal averages.

One can solve the LLG equation easily for an isolated spin coupled to an external field $\mathbf{B}$, neglecting the thermal fluctuations. Then the first term in equation (7) leads to a spin precession with the precession time $\tau_p = 2\pi(1+\alpha^2)/(\gamma B)$. The second part describes a relaxation of the spin from an initial state into local equilibrium on the relaxation timescale $\tau_r = \tau_p/\alpha$. In other words, α sets the relation between the timescales of precession and relaxation. In the high damping limit, which in the following will turn out to be important in connection with Monte Carlo simulations, mainly the second term of the LLG equation is relevant and the time can be rescaled by the factor $(1+\alpha^2)\mu_s/(\alpha\gamma)$. Hence, this factor should completely describe the α and γ dependence of any timescale in the high damping limit.

The LLG equation is a stochastic equation of motion. Starting repeatedly from identical initial conditions will lead to different trajectories in phase space because of the influence of noise. Hence, averages have to be taken in order to describe the system appropriately. The basis for the statistical description of an ensemble of systems where each one is described by a Langevin equation is the corresponding Fokker–Planck (FP) equation. This is a differential equation for the time evolution of the probability distribution in phase space (Coffey, 1996). In his pioneering work Brown (1963b) developed a formalism for the description of thermally activated magnetization reversal on the basis of the FP equation which led to a low-temperature asymptotic formula for the escape rates in simple magnetic systems (for an overview see Coffey, 1996). The solution of the FP equation will converge to equilibrium properties, that is to the same values defined by equation (6).

However, realistic calculations for systems with many degrees of freedom need computational approaches. The two basic methods for the simulation of classical spin systems are Langevin dynamics and Monte Carlo methods. The following section is devoted to these methods, especially to their relation which will lead to time-quantified Monte Carlo methods.

3 NUMERICAL METHODS

3.1 Langevin dynamics simulations

The basic numerical approach for the description of thermally activated spin dynamics is the direct numerical integration of equation (7). Instead of solving the corresponding FP equation, one calculates trajectories in phase space following the underlying equation of motion. In order to obtain results in the sense of a thermodynamic average one has to calculate many of these trajectories starting with the same initial conditions, taking an average over these trajectories for the quantities of interest. This method is referred to as *Langevin dynamics simulation* (Lyberatos and Chantrell, 1993).

The LLG equation with Langevin dynamics is a stochastic differential equation with multiplicative noise. For this kind of differential equation a problem arises which is called the *Itô–Stratonovich dilemma* (Greiner, Strittmatter and Honerkamp, 1988). As a consequence, different time discretization schemes may with decreasing time step converge to different results (see Wolf, 1998, for a discussion of the different discretization schemes from a physical point of view). As was pointed out by García-Palacios and Lázaro (1998) the multiplicative noise in the Langevin equation was treated in Brown's original work – and also in subsequent publications – by means of the Stratonovich interpretation. Hence, in order to obtain numerical results that are comparable to these approaches via the FP equation one has to use adequate methods. Note, that the simplest method for the integration of first-order differential equations, the Euler method, converges to an Itô interpretation of the Langevin equation. The simplest appropriate discretization scheme leading to a Stratonovich interpretation is the Heun method (Greiner, Strittmatter and Honerkamp, 1988; Wolf, 1998; García-Palacios and Lázaro, 1998; Nowak, 2001) which is described in the following [1].

For simplicity, the Heun discretization scheme is introduced here for a one-dimensional problem. We consider a first-order differential equation with multiplicative noise,

$$\dot{x}(t) = f\Big(x(t), t\Big) + g\Big(x(t), t\Big)\zeta(t) \tag{10}$$

where $\zeta(t)$ represents a noise with a distribution of moments $\langle\zeta(t)\rangle = 0$ and $\langle\zeta(t)\zeta(t')\rangle = D\delta(t-t')$. The time variable is discretized in intervals Δt so that $t_n = n\Delta t$ and $x_n = x(t_n)$. Then, owing to Heun's method equation (7) becomes

$$\begin{aligned} x_{n+1} = x_n &+ \frac{1}{2}\Big(f(x_n, t_n) + f(\overline{x}_{n+1}, t_{n+1})\Big)\Delta t \\ &+ \frac{1}{2}\Big(g(x_n, t_n) + g(\overline{x}_{n+1}, t_{n+1})\Big)\tilde{\zeta}_n \end{aligned} \tag{11}$$

This method is a predictor–corrector method where the predictor $\overline{x}_{n+1}$ is calculated from an Euler integration scheme,

$$\overline{x}_{n+1} = x_n + f(x_n, t_n)\Delta t + g(x_n, t_n)\tilde{\zeta}_n$$

$\tilde{\zeta}_n$ are random numbers with a distribution characterized by the two first moments $\langle\tilde{\zeta}_n\rangle = 0$ and $\langle\tilde{\zeta}_n\tilde{\zeta}_m\rangle = D\Delta t\delta_{n,m}$, which can be achieved by use of random numbers with a Gaussian distribution, $p(\zeta) \sim \exp(-\zeta^2/2\sigma)$, with width $\sigma = D\Delta t$. The generalization of the scheme in the preceding text to equation (7) is straightforward.

3.2 Monte Carlo methods

Monte Carlo methods are well established in the context of equilibrium thermodynamics, where mainly Ising-type models have been investigated because of the broad variety of applications of this class of models in statistical physics (Stauffer, Hehl, Winkelmann and Zabolitzky, 1993; Binder and Heermann, 1997). However, in the context of magnetic materials the use of Ising models is restricted to the modeling of materials with a very large uniaxial anisotropy (Kirby, Shen, Hardy and Sellmyer, 1994; Lyberatos, Earl and Chantrell, 1996; Nowak, Heimel, Kleinefeld and Weller, 1997), while more realistic models have to include finite anisotropies.

Within a Monte Carlo approach trajectories in phase space are calculated following a master equation (Reif, 1965) for the time development of the probability distribution $P_s(t)$ in phase space,

$$\frac{\mathrm{d}P_s}{\mathrm{d}t} = \sum_{s'}(P_{s'}w_{s'\to s} - P_s w_{s\to s'}) \tag{12}$$

Here, s and s' denote different states of the system and the w are the transition rates from one state to another one which have to fulfill the condition (Reif, 1965)

$$\frac{w_{s\to s'}}{w_{s'\to s}} = \exp\left(\frac{E(S) - E(S')}{k_\mathrm{B}T}\right) \tag{13}$$

The master equation describes exclusively the coupling of the system to the heat bath. Hence, only the irreversible part of the dynamics of the system is considered including the relaxation and the fluctuations, but not the energy conserving part of the equation of motion – the precession. Instead, only a random-walk-like motion due to the coupling to the heat bath can appear. We will discuss the connection to Langevin dynamics later and continue with a general description of Monte Carlo algorithms for vector spin models, as far as they are different from algorithms for Ising models due to their continuum degrees of freedom.

Even though for Ising systems (Swendsen and Wang, 1987) as well as for Heisenberg systems (Wolff, 1989) cluster algorithms exist, which – depending on the details of the problem – can equilibrate a system much faster, we restrict ourselves to the simple case of single-spin-flip dynamics since here, the connection to a realistic dynamical behavior of the system is more straightforward. For the Ising model there exists no equation of motion and the master equation in connection with a single-spin-flip dynamics governs the so-called Glauber dynamics (Glauber, 1963), which is thought to describe a qualitatively realistic dynamic behavior. For a system of classical magnetic moments the situation is different due to the existence of an equation of motion – the LLG equation.

A single-spin-flip algorithm is performed in the following way: at the beginning one single spin from the lattice is chosen either randomly or in some systematic order and a trial step of this selected spin is made (possible choices for trial steps will be described in detail in the subsequent text). Then the change of the energy of the system is computed according to equation (1). Finally the trial step is accepted, for instance with the heat bath probability,

$$w_{s\to s'} = \frac{w_0}{1+\exp\left(\frac{E(S')-E(S)}{k_{\mathrm{B}}T}\right)} \tag{14}$$

which is one possible choice among others satisfying the condition in equation (13) for any arbitrary constant w_0. Scanning the lattice and performing the procedure explained in the preceding text once per spin (on average) is called *one Monte Carlo step* (MCS). It defines a quasitime scale of the simulation. The connection to real time will be discussed later on.

The way the trial step is chosen is of importance for the validity and efficiency of the algorithm as well as for the physical interpretation of the dynamic behavior of the algorithm (Hinzke and Nowak, 1999). For an Ising system the trial step is naturally a spin flip. For a Heisenberg spin there are many choices. One possible trial step is a small deviation from the former state. For a spin this could be a random movement of the spin with uniform probability distribution within a given opening angle around the former spin direction. Here, each spin can only move by a limited step size and hence, in a model with a uniaxial anisotropy, it has to overcome the anisotropy energy barrier for a complete reversal. This might be a realistic choice for many model systems. But if one is, for instance, interested in the crossover from Heisenberg to Ising-like behavior with increasing anisotropy, one has to allow also for larger steps which are able to overcome a given anisotropy energy barrier. Otherwise the dynamics of the system would freeze and in a system with very large anisotropy (Ising limit) no spin flip would occur at all (Hinzke and Nowak, 1999).

Another possible trial step that circumvents this problem is a step with a uniform distribution in the entire phase space. Here, an arbitrary spin direction that does not depend on the initial direction of the spin is chosen at random. This step samples the whole phase space efficiently and a single spin is not forced to overcome the anisotropy energy barrier. Instead it is allowed to change from one direction to any other one instantaneously. Both of these trail steps are allowed choices in the sense that the corresponding algorithms lead to correct equilibrium properties since they fulfill two necessary conditions: they are ergodic and symmetric.

Ergodicity requires that the whole phase space can be sampled by an algorithm. An example for an nonergodic algorithm is one that performs only Ising-like trial steps, $S_z \to -S_z$, in a Heisenberg model. Here, starting from some initial direction the spin can only reach two positions out of the whole phase space which would be a unit sphere for a Heisenberg spin. Nevertheless, one is allowed to perform such reflection steps as long as one uses *also* other trial steps that guarantee ergodicity. These ideas lead to combinational algorithms which – depending on the problem – can be very efficient (Hucht, Moschel and Usadel, 1995; Hinzke and Nowak, 1999).

The second condition that has to be fulfilled by any algorithm is a symmetry condition: for the probability to do a certain trial step it must be $p_t(s \to s') = p_t(s' \to s)$. Otherwise equation (13) is not fulfilled since the probabilities to perform certain trial steps contribute to the transition rates. The symmetry condition would for instance be violated in a Heisenberg system if one chooses new trial spin directions by simply generating three random numbers as S_x, S_y, and S_z coordinates within a cube and normalizing the resultant vector to unit length. Then before normalization the random vectors are homogeneously distributed within the cube and after the normalization they have some nonuniform probability distribution on the unit sphere which is higher along the diagonal directions of the cube. Hence, trial steps from any other direction into the diagonal direction are more probable then vice versa and the algorithm yields wrong results. A description, how to choose unit vectors

with random directions and a constant probability distribution correctly can be found in the book of Vesely (1993).

3.3 Time-quantified Monte Carlo simulations

In general, Monte Carlo methods do not allow for an interpretation of the results in terms of a realistic dynamics. Only recently, a time-quantified Monte Carlo method was introduced (Nowak, Chantrell and Kennedy, 2000; Smirnov-Rueda *et al*., 2000; Chubykalo *et al*., 2003a; Cheng, Jalil, Lee and Okabe, 2006) and it was shown that at least the dynamics of a high damping scenario can indeed be simulated by a Monte Carlo simulation since here the exact knowledge of the precessive motion of the spins is not necessary. The main idea of time-quantified Monte Carlo methods is to compare the fluctuations that are established in the Monte Carlo simulation within one MCS with the fluctuations that are established within a given timescale associated with the linearized stochastic LLG equation (Ettelaie and Moore, 1984; Smirnov-Rueda *et al*., 1999).

Following the original work (Nowak, Chantrell and Kennedy, 2000), we start with a calculation of the magnetization fluctuations in the Langevin equation. Close to a local energy minimum one can expand the energy of a system given that first-order terms vanish as

$$E \approx E_0 + \frac{1}{2}\sum_{i,j} A_{ij} S_i S_j \tag{15}$$

where S_i are now variables representing small deviations from equilibrium. Let us consider a single spin only with a uniaxial anisotropy (anisotropy constant d_z, see equation (3)) and a field $\mathbf{b} = \pm b_z \hat{\mathbf{z}}$, which is also aligned with the easy axis (a more general calculation can be found in Chubykalo *et al*., 2003b). In this system, we find equilibrium along the z axis, leading to variables S_x and S_y describing small deviations from the equilibrium position $\mathbf{S} = \pm\hat{\mathbf{z}}$. The energy increase ΔE associated with fluctuation in S_x and S_y is then simply

$$\Delta E \approx \frac{1}{2}\left(A_{xx} S_x^2 + A_{yy} S_y^2\right) \tag{16}$$

with $A_{xx} = A_{yy} = 2d_z + b_z$. Rewriting the LLG equation in the linearized form without the thermal fluctuations,

$$\begin{aligned} \dot{S}_x &= L_{xx} S_x + L_{xy} S_y \\ \dot{S}_y &= L_{yx} S_x + L_{yy} S_y \end{aligned} \tag{17}$$

we can identify the matrix elements

$$\begin{aligned} L_{xx} = \ L_{yy} \ &= -\frac{\alpha\gamma}{(1+\alpha^2)\mu_s}(2d_z + b_z) \\ L_{xy} = -L_{yx} &= \frac{\gamma}{(1+\alpha^2)\mu_s}(2d_z + b_z) \end{aligned}$$

As shown in Lyberatos, Berkov and Chantrell (1993) the correlation function for the variables describing small deviations from equilibrium can be expressed in the form

$$\langle S_i(t) S_j(t')\rangle = \mu_{ij}\delta_{ij}\delta(t - t') \tag{18}$$

Here, i and j denote the Cartesian components and Dirac's δ function is an approximation for exponentially decaying correlations on timescales $t - t'$ that are larger than the timescale of the exponential decay τ_r. The covariance matrix μ_{ij} can be calculated from the system matrices A_{ij} and L_{ij} as (Lyberatos, Berkov and Chantrell, 1993)

$$\mu_{ij} = -k_\mathrm{B} T\left(L_{ik} A_{kj}^{-1} + L_{jk} A_{ki}^{-1}\right)$$

For our problem this yields

$$\begin{aligned} \mu_{xx} &= \mu_{yy} = 2k_\mathrm{B} T \frac{\alpha\gamma}{(1+\alpha^2)\mu_s} \\ \mu_{xy} &= \mu_{yx} = 0 \end{aligned} \tag{19}$$

Integrating the fluctuating quantities $S_x(t)$ and $S_y(t)$ over a finite time interval Δt, equations (18) and (19) yield

$$\langle \overline{S}_x^2\rangle = \langle \overline{S}_y^2\rangle = 2k_\mathrm{B} T \frac{\alpha\gamma}{(1+\alpha^2)\mu_s}\Delta t \tag{20}$$

representing the fluctuations of $S_x(t)$ and $S_y(t)$ respectively, averaged over a time interval Δt.

For comparison, we now calculate the fluctuations $\langle S_x^2\rangle$ which are established within one MCS of a Monte Carlo simulation (Nowak, Chantrell and Kennedy, 2000). We select an algorithm where the trial step of the Monte Carlo algorithm is a random deviation of the magnetic moment from its former direction up to a certain maximum opening angle. In order to achieve this efficiently one first constructs a random vector with constant probability distribution within a sphere of radius R by use of the rejection method (Vesely, 1993). This random vector is then added to the initial moment and subsequently the resulting vector is again normalized. Note that the probability distribution following from this trial step is nonuniform but isotropic, so that the symmetry condition mentioned in the previous subsection is guaranteed.

For this algorithm the probability distribution for trial steps of size $r = \sqrt{S_x^2 + S_y^2}$ is $p_t = 3\sqrt{R^2 - r^2}/(2\pi R^3)$ for $0 < r < R$. The acceptance probability using a heat bath

algorithm is $w(r) = 1/(1 + \exp(\Delta E(r^2)/k_\mathrm{B}T))$. Assuming that the spin is close to its (local) equilibrium position, as before, $\Delta E(r^2)$ for small r can be taken from equation (16). In order to calculate the fluctuations within one MCS we have to integrate over that part of the phase space that can be reached within one MCS,

$$\langle S_x^2 \rangle = \int_0^{2\pi} \mathrm{d}\varphi \int_0^R r\ \mathrm{d}r\ \frac{r^2}{2}\ w(r)\, p_t(r) = \frac{R^2}{10} - \mathcal{O}\left(\frac{(2d_z + b_z)R^4}{k_\mathrm{B}T}\right) \tag{21}$$

where the last line is an expansion for small R leading to the validity condition

$$R \ll \frac{k_\mathrm{B}T}{(2d_z + b_z)} \tag{22}$$

By equalizing the fluctuations within a time interval Δt of the LLG equation and one MCS we find the relation

$$R^2 = \frac{20 k_\mathrm{B} T \alpha \gamma}{(1 + \alpha^2)\mu_s} \Delta t \tag{23}$$

for the trial step width R (Nowak, Chantrell and Kennedy, 2000). Equation (23) now relates one MCS, performed using an algorithm as explained before, with a real time interval of the Langevin equation. In this equation $(\alpha\gamma/(1 + \alpha^2)\mu_s)\Delta t$ is simply the reduced time of the LLG equation, rescaled in the high damping limit where only the second part of equation (7) is relevant. The more interesting result of equation (23) is the temperature dependence since it turns out that there is no trivial assignment of one MCS to a fixed time interval. Instead, the larger the temperature, the larger the trial steps of the Monte Carlo algorithm in order to allow for the appropriate fluctuations.

In principle, equation (23) gives the possibility to choose the trial step width for a Monte Carlo simulation in such a way that one MCS corresponds to some microscopic time interval, but there are of course restrictions for possible values of the trial step width and also for the validity of the algorithm: R must be small enough so that the truncated expansion in equation (21) is a good approximation. On the other hand R should not be too small since otherwise the Monte Carlo algorithm needs too much computation time to sample the phase space. Therefore, either one chooses such a value for Δt so that R takes on reasonable values or one chooses a reasonable constant value for R and uses equation (23) to calculate Δt as the real time interval associated with one MCS. Furthermore, effects from spin precession are neglected so that in general only the high damping limit with a purely diffusive spin motion can be simulated. Also, since the derivation in the preceding text started from a linearized equation of motion (equation (17)) and since the energy expression (equation (15)) is an expansion, equation (23) can only be valid close to equilibrium.

For any numerical method, analytically solvable models are important as test tools for the evaluation of the numerical techniques. Originally, (Nowak, Chantrell and Kennedy, 2000) the goal was a comparison of characteristic timescales for the thermally activated reversal obtained numerically with those following from an analytical treatment of isolated Stoner–Wohlfarth particles with a uniaxial anisotropy and a field at an oblique angle to the easy axis (Coffey *et al.*, 1998c). The results are shown in Figure 1.

Here, an ensemble of isolated single-domain particles is considered where each particle is represented by a magnetic moment with energy

$$E(\mathbf{S}) = -d_z S_z^2 - \mu_s \mathbf{B}\cdot\mathbf{S} \tag{24}$$

The material parameters are those for a 20-nm Co particle. Both of the simulations, Monte Carlo as well as Langevin dynamics, start with the magnetic moments in positive z direction. The magnetic field which is well below the Stoner–Wohlfarth limit for athermal reversal has a negative z component so that the magnetization will reverse after some time. The time that is needed for the z component of the magnetization to change its sign averaged over a large number of runs ($N = 1000$) is the numerically obtained characteristic time τ. During a simulation for temperatures which are low as compared to the energy barrier, the system is in the metastable, initial state for a very long time, while the time needed for the magnetization reversal itself is

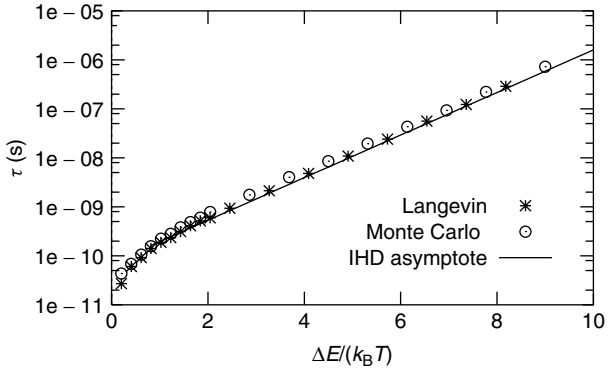

Figure 1. Characteristic times versus inverse temperature. Comparison of the intermediate to high damping asymptote with results from Langevin dynamics and Monte Carlo simulations with time quantification. (Reprinted figure with permission from *Physical Review Letters*, **84**, 1, 163, 2000. Copyright 2000 by the American Physical Society.)

rather short. In this case the characteristic time τ should be comparable to the escape time following from an analytical calculation via the FP equation.

The time-quantified Monte Carlo simulations in Figure 1 were done with an algorithm using a trial step according to equation (23) with $\Delta t \approx 6 \times 10^{-12}\,\mathrm{s}$ and $\alpha = 1$. The magnetic field is $|\mathbf{B}| = 0.2\,\mathrm{T}$ with an angle of 27° to the easy axis. The results for $\tau(T)$ are compared with results from Langevin dynamics simulations using the Heun method as described before and with analytical results obtained in the intermediate to high damping (IHD) limit (Coffey *et al*., 1998a,b,c). This asymptote has the general form of a thermal activation law, namely

$$\tau = \tau_0 e^{\Delta E / k_\mathrm{B} T} \tag{25}$$

The explicit expressions for τ_0 and ΔE were derived in Coffey *et al*. (1998a,b,c). The validity condition for the IHD formula is $\alpha \Delta E / k_\mathrm{B} T \gg 1$ which has been satisfied in the case presented here.

From Figure 1 it is clear that the Langevin dynamics data agree very well with the analytical asymptote in the preceding text. For higher temperatures, $k_\mathrm{B} T > \Delta E$, the asymptote is no longer appropriate. Here, the numerical data for τ tend to zero for $T \to \infty$ as one expects. The Monte Carlo data deviate slightly but the agreement is remarkable – especially taking into account the simple form of equation (23) underlying this algorithm and also considering the fact that there is no adjustable parameter in all our simulations and formulae.

Figure 2 shows how the time-quantified Monte Carlo methods converges in the high damping limit. The data were obtained for the same parameter values as before and $\Delta E / k_\mathrm{B} T = 3.3$. The figure shows that for increasing damping constant α the Monte Carlo data converge to the IHD formula and to the data from Langevin dynamics simulation for large α.

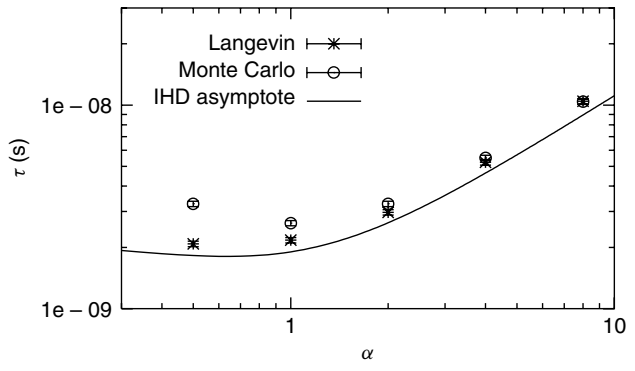

Figure 2. Characteristic time versus damping constant: comparison of the intermediate to high damping asymptote with Langevin dynamics and Monte Carlo simulations. (Reprinted figure with permission from *Physical Review Letters*, **84**, 1, 163, 2000. Copyright 2000 by the American Physical Society.)

Even though the Monte Carlo time step quantification by equation (23) was derived originally only for the simple system which we considered here (Nowak, Chantrell and Kennedy, 2000), it turned out to be successfully applicable to more complicated, interacting spin systems also (Hinzke and Nowak, 2000a,b; Chubykalo *et al*., 2003a,b; Cheng, Jalil, Lee and Okabe, 2006). However, one should note that the method rests on a comparison with Langevin dynamics. Here, the coupling to the heat bath is added phenomenologically to the equation of motion leading to a damping constant α, the microscopic evaluation of which is still missing.

4 THERMALLY ACTIVATED MAGNETIZATION REVERSAL

4.1 Introduction

The understanding of thermally activated spin dynamics is a major challenge for the knowledge of magnetic systems and devices. The pioneering work of Brown (1963b) represents the basis for the understanding of thermally activated dynamic processes in isolated single-domain particles. The basic idea is that the energy barrier ΔE separating two (meta)stable magnetic states of a nanoparticle can be overcome by thermal activation on a certain timescale which can be calculated within the framework of Langevin dynamics. In the limit of low temperatures the escape time τ follows a thermal activation law (see equation (25)), where the prefactor as well as the energy barrier depend on the mechanism of the reversal. As a solvable example, Brown considered an ensemble of isolated magnetic moments with a uniaxial anisotropy. Each single particle of the ensemble is described as one superspin of constant length. The superspin is thought to represent the magnetic moment of a whole particle since it was assumed that if the particle is sufficiently small it is always homogeneously magnetized and its microscopic, internal degrees of freedom can be neglected. After the original work of Brown, extensive calculations were performed in order to calculate the energy barrier as well as the prefactor asymptotically for various model systems (Aharoni, 1969; Braun, 1993; Coffey *et al*., 1998a; García-Palacios and Svedlindh, 2000; Chantrell, Walmsley, Gore and Maylin, 2000).

Experiments on isolated, magnetic particles have confirmed this approach. Wernsdorfer *et al*. measured the switching time of isolated nanometer-sized particles (Wernsdorfer

et al., 1996b, 1997b), and wires (Wernsdorfer *et al*., 1996a, 1997a). For sufficiently small particles (Wernsdorfer *et al*., 1997b) agreement was found with the theoretical predictions of Brown (1963b). For larger particles (Wernsdorfer *et al*., 1996b) and wires (Wernsdorfer *et al*., 1996a, 1997a) activation volumes were found which were much smaller than the corresponding particle and wire volumes. Obviously, different reversal mechanisms can dominate the thermally activated switching behavior of nanoparticles depending on their geometry and size, such as coherent rotation, nucleation, and curling.

These modes may appear in different limits of a cylindrical geometry. Coherent rotation and nucleation can be modeled in the one-dimensional limit by a simple spin chain – a model which is very useful since it was treated analytically and asymptotic results for the energy barriers as well as for the escape rates are available (Braun, 1993; 1994a,b). We will discuss this model in the following text. A three-dimensional model for an extended nanowire is discussed in the last subsection in connection with curling.

Let us start with a chain of magnetic moments of length L (number of spins) with periodical boundary conditions defined by the Hamiltonian

$$\mathcal{H} = \sum_i \Big[- J\mathbf{S}_i \cdot \mathbf{S}_{i+1} - d_z (S_i^z)^2 + d_x (S_i^x)^2 - \mu_s B S_i^z \Big] \tag{26}$$

This is a discretized version of the one-dimensional model for a magnetic nanowire considered by Braun (1993). For $d_z, d_x > 0$ the z axis is the easy axis and the x axis the hard axis of the system. These anisotropy terms may contain contributions from shape anisotropy as well as crystalline anisotropies (Braun, 1994a). In the interpretation as shape anisotropy, this single-ion anisotropy is assumed to imitate the influence of a dipolar interaction of strength $w = d_z/\pi$ (Braun, 1993). Nevertheless, an exact numerical treatment of the dipolar interactions is possible (Hinzke and Nowak, 2000b; Nowak, 2001; Nowak *et al*., 2005; Wieser, Usadel and Nowak, 2006).

4.2 Coherent rotation

In the case of small chain length the magnetic moments rotate coherently, minimizing the exchange energy while overcoming the energy barrier due to the anisotropy of the system. Owing to the hard-axis anisotropy the rotation is mainly in the yz plane. As long as all spins are mostly parallel, they can be described as one effective magnetic moment which behaves like the one-spin model described before. The corresponding energy barrier ΔE is the same as that of a Stoner–Wohlfarth particle since the additional hard axis does not change the energy of the optimal path in phase space from one minimum to the other. The escape time was calculated from the FP equation in the large damping limit (Braun, 1994b). The results is a thermal activation law (equation (25)) where the energy barrier is now proportional to the system size L,

$$\Delta E_{\mathrm{cr}} = L d_z (1-h)^2 \tag{27}$$

while the explicit form of the prefactor transformed into the units used here is

$$\tau_{\mathrm{cr}} = \frac{2\pi(1+\alpha^2)}{\alpha\gamma B_{\mathrm{c}}} \times \frac{\sqrt{d(1+h)/(1-h+d)}}{1-h^2-d+\sqrt{(1-h^2+d)^2+4d(1-h^2)/\alpha^2}} \tag{28}$$

We introduced the coercive field $B_{\mathrm{c}} = 2d_z/\mu_s$ and the reduced quantities $h = \mu_s B/(2d_z)$ and $d = d_x/d_z$. The first term in equation (28) is the microscopic relaxation time of one spin in the field B_{c} (see Section 2.1), while the second term includes corrections following from the details of the model. The equation in the preceding text should hold for low temperatures $k_{\mathrm{B}}T \ll \Delta E_{\mathrm{cr}}$ and obviously for $B < B_{\mathrm{c}}$ since otherwise the energy barrier is zero, leading to a spontaneous reversal without thermal activation. Note, however, that recently deviations were found for increasing system size, suggesting that even for a coherent rotation the internal degrees of freedom lead to longitudinal fluctuations which are not contained in a single-spin description (Hinzke and Nowak, 2000a; Nowak *et al*., 2005; Chubykalo, Nowak, Chantrell and Garanin, 2006).

4.3 Soliton–antisoliton nucleation

With increasing system size nucleation must become energetically favorable since here the energy barrier is a constant, while it is proportional to the system size in the case of coherent rotation. For the spin chain under consideration, switching by soliton–antisoliton nucleation was proposed (Braun, 1994a) for sufficiently large system size. Here, the nucleation process initiates a pair of domain walls which splits the system into domains with opposite directions of magnetization parallel to the easy axis (for graphical representations see Hinzke, Nowak and Usadel, 2000; Nowak, 2001). These two domain walls pass the system in the subsequent reversal process. Owing to the hard-axis anisotropy the spin rotation is once again mainly in the yz plane. Since these two domain walls necessarily have opposite helicities within this easy plane they were called a *soliton–antisoliton pair*.

The energy barrier ΔE_{nu} which has to be overcome during this nucleation process is

$$\Delta E_{\mathrm{nu}} = 4\sqrt{2Jd_z}\left(\tanh R - hR\right) \tag{29}$$

with $R = \operatorname{arccosh}(\sqrt{1/h})$ (Braun, 1994a). For vanishing magnetic field this energy barrier has the form $\Delta E_{\mathrm{nu}}(h = 0) = 4\sqrt{2Jd_z}$ which represents the well-known energy of two Bloch walls (Hubert and Schäfer, 1998). As usual, the corresponding escape time obeys a thermal activation law, where the prefactor has been calculated for various limits (Braun, 1994a). The prefactor obtained in the overdamped limit (equation (5.4) in Braun, 1994a) in our units is

$$\tau_{\mathrm{nu}} = \frac{2\pi(1+\alpha^2)}{\alpha\gamma B_{\mathrm{c}}} \frac{(\pi k_{\mathrm{B}}T)^{1/2}(2J)^{1/4}}{16L\, d_z^{3/4}|E_0(R)| \tanh R^{3/2} \sinh R} \tag{30}$$

As in equation (28) the left part is the microscopic relaxation time of a spin in the coercive field B_{c}. The eigenvalue $E_0(R)$ has been calculated numerically (Braun, 1994a). In the limit $h \to 1$ it is $|E_0(R)| \approx 3R^2$. The $1/L$ dependence of the prefactor reflects the size dependence of the probability of nucleation. The larger the system the more probable is the nucleation process and the smaller is the timescale of the relaxation. Furthermore, the prefactor has a remarkable $\sqrt{k_{\mathrm{B}}T}$ dependence.

We should note that all the results in the preceding text are for systems with periodic boundary conditions (or rings), which restricts the applicability to finite nanowires where nucleation processes may start at the ends of the sample. Therefore, the case of open boundaries was also considered, analytically (Braun, 1999, 2000) as well as numerically (Hinzke and Nowak, 2000b). Even though the prefactor of the thermal activation law could not be obtained up to now, it was shown (Braun, 1999) that the energy barrier is just halved in that case, due to the fact that in systems with open boundaries the nucleation can set in at only one end. Hence, solitons and antisolitons do not necessarily emerge pairwise. In the case of two solitons (or two antisolitons) nucleating simultaneously at both ends, these cannot annihilate easily in the later stage of the reversal process due to their identical helicity. Instead a 360° domain wall remains in the system.

Let us now investigate the intermediate temperature range. Owing to the larger thermal fluctuations as compared to the sole soliton–antisoliton nucleation several nuclei may grow simultaneously, also depending on system size. Obviously, depending on the nucleation probability many nuclei may arise during the time period of the reversal process (for graphical representations see again Hinzke, Nowak and Usadel, 2000; Nowak, 2001). This multiple nucleation process was investigated mainly in the context of Ising models where it is called *multidroplet nucleation* (a review is given by Rikvold and Gorman, 1994).

The characteristic time τ_{mn} for the multidroplet nucleation can be estimated with respect to the escape time for a single nucleation process with the aid of the classical nucleation theory (Becker and Döring, 1935). Here, the following scenario is assumed: in the first stage many nuclei of critical size arise within the same time interval. Later these nuclei expand with a certain domain wall velocity v and join each other. This leads to a change of magnetization

$$\Delta M(t) = \int_0^t \frac{(2vt')^D}{\tau_{\mathrm{nu}}}\,\mathrm{d}t' \tag{31}$$

after a time t in D dimensions. The characteristic time when half of the system ($L^D/2$) is reversed is then given by (Rikvold and Gorman, 1994; Hinzke and Nowak, 2000a)

$$\tau_{\mathrm{mn}} = \left(\frac{L}{2v}\right)^{\frac{D}{D+1}} \left((D+1)\tau_{\mathrm{nu}}^*\right)^{\frac{1}{D+1}} \exp\frac{\Delta E_{\mathrm{nu}}}{(D+1)k_{\mathrm{B}}T} \tag{32}$$

The domain-wall velocity in a spin chain following the LLG equation for small fields is (Wieser, Nowak and Usadel, 2004)

$$v = \frac{\gamma B}{\alpha} \tag{33}$$

Hence for the one-dimensional system under consideration the characteristic time is given by

$$\tau_{\mathrm{mn}} = \sqrt{\frac{\alpha L \tau_{\mathrm{nu}}}{\gamma B}} \exp\frac{\Delta E_{\mathrm{nu}}}{2k_{\mathrm{B}}T} \tag{34}$$

This means that the (effective) energy barrier for the multidroplet nucleation is reduced by a factor 1/2, and the characteristic time no longer depends on the system size since τ_{nu}^* for the soliton–antisoliton nucleation has a $1/L$ dependence (see equation (30)).

All the different reversal mechanisms mentioned in the previous sections can occur within the same model system – the spin chain – depending on the system size among other parameters. The crossover from coherent rotation to soliton–antisoliton nucleation was studied in Braun (2000) for a periodic system. Here, the value L_{c} of the chain length below which only uniform solutions of the Euler–Lagrange equations of the problem exist (coherent rotation) was calculated to be

$$L_{\mathrm{c}} = \pi\sqrt{\frac{2J}{d_z(1-h^2)}} \tag{35}$$

For vanishing magnetic field this crossover length scale is $L_c = \pi\sqrt{2J/d_z}$, a value that is clearly related to the Bloch wall width $\delta = \sqrt{J/2d}$ (Hubert and Schäfer, 1998), because of the fact that two domains walls have to fit into the system during the nucleation process. For a chain with open boundary conditions the crossover length scale is halved since here only one domain wall has to fit into the system (Braun, 2000). One can understand this result from a slightly different point of view also, namely by comparing the energy barrier of soliton–antisoliton nucleation (equation (29)) with that of coherent rotation (equation (27)). This results in a very similar condition for the crossover from coherent rotation to nucleation (Hinzke and Nowak, 2000a), which can also be generalized to higher dimensions (Hinzke and Nowak, 1998).

For even larger system size, multiple nucleation becomes probable. Comparing the escape time for soliton–antisoliton nucleation with the characteristic time for multiple nucleation, one gets for the intersection of these two times the crossover condition (Hinzke and Nowak, 2000a)

$$L_{\mathrm{sm}} = \sqrt{\frac{\gamma B \tau_{\mathrm{nu}} L_{\mathrm{sm}}}{\alpha}}\, \exp\frac{\Delta E_{\mathrm{nu}}}{2k_{\mathrm{B}}T} \tag{36}$$

The corresponding time L_{sm}/v is the time that a domain wall needs to cross the system. In other words, as long as the time needed for the nucleation event itself is large as compared to the time needed for the subsequent reversal by domain-wall motion, one single nucleus determines the characteristic time. In the opposite case many nuclei will appear during the time needed for the first soliton–antisoliton pair to cross the system, resulting in multidroplet nucleation. These considerations are comparable to calculations in Ising models (Rikvold, Tomita, Miyashita and Sides, 1994).

Figure 3 summarizes the system size dependence of the reduced characteristic time (Hinzke and Nowak, 2000a). Results from Monte Carlo simulations are shown as well as the appropriate asymptotes described in the preceding text for two different temperatures. For small system sizes the spins rotate coherently. Here the energy barrier (equation (27)) is proportional to the system size leading to an exponential increase of τ with system size. Following equation (28) the prefactor of the thermal activation law should not depend on L but, as already mentioned in the preceding text, numerically one finds slight deviations from the asymptotic expressions due to longitudinal magnetization fluctuations (Nowak *et al.*, 2005; Chubykalo, Nowak, Chantrell and Garanin, 2006). In the region of soliton–antisoliton nucleation the energy barrier does not depend on the system size but the prefactor varies as $1/L$ (see equations (29) and (30)). Interestingly, this leads to a decrease of the characteristic time with increasing system size. Therefore, there

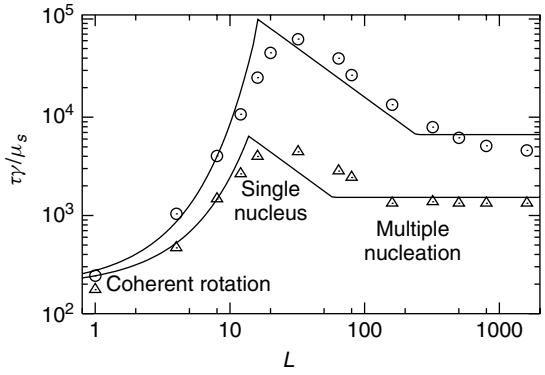

Figure 3. Reduced characteristic time versus system size for $k_{\mathrm{B}}T = 0.024J$ (triangles) and $k_{\mathrm{B}}T = 0.016J$ (circles). $h = 0.75$. Solid lines are piecewise the appropriate asymptotes and the data are from Monte Carlo simulations. (Reprinted from *Phys. Rev. B.*, Vol. 61, 6734, 2000. Copyright 2000 by the American Physical Society.)

is a maximal characteristic time – the maximum of the stability of the particle – close to that system size where the crossover from coherent rotation to nucleation occurs. This decrease ends where multidroplet nucleation sets in, following equation (36). For still larger systems the characteristic time has a constant value which is given by equation (34). Qualitatively the same behavior can be found in the particle size dependence of the dynamic coercivity which is the coercive field one observes during hysteresis on a given timescale τ: solving the equation describing the thermal activation in the three regimes explained in the preceding text for $h(L)$ at constant τ one finds an increase of the dynamic coercivity in the coherent rotation regime, a decrease in the nucleation regime, and at the end a constant value for multiple nucleation. These findings are qualitatively in agreement with measurements of the size dependence for the dynamic coercivity of barium ferrite recording particles (Chang, Zhu and Judy, 1993).

4.4 Curling

In the previous subsections we considered a model which even though it is one-dimensional shows properties that are far from being trivial since different switching mechanisms can occur. Many of the findings obtained from this model are relevant for real magnetic nanowires, as long as those are thin enough to be effectively one-dimensional. Nevertheless, for a realistic description of magnetic nanoparticles one needs three-dimensional models and one has to consider the dipole–dipole interaction. In the following we will discuss the degree to which the physics of the switching process changes when one considers a three-dimensional model

including dipole–dipole interaction. Only few numerical results exist so far, some of them we discuss in the following.

Considering the mathematical form of the dipole–dipole interaction in equation (5) one notes that dipoles tend to align, with that trying to build up closed loops or vortices. On the other hand, a loop has an enhanced exchange energy. Therefore to calculate the spin structure of an extended magnetic system is a complicated optimization problem. Even a sufficiently small magnetic nanostructure which, in equilibrium, is in a single-domain state, could reverse its magnetization by more complicated modes than coherent rotation or nucleation. A characteristic length scale below which it is energetically unfavorable for the system to break the long-range order and split into domains is the so-called *exchange length* δ_x (Hubert and Schäfer, 1998). Like the Bloch wall width $\delta = \sqrt{J/2d}$ mentioned earlier, it is a characteristic length scale for a given material. For a spin model it can be derived in the following way: a twist of the direction of the spins by an angle of π over a length scale l (number of spins) costs an exchange energy of

$$\begin{aligned}\Delta E_x &= -J \sum_{i=1}^{l} (1 - \mathbf{S}_i \cdot \mathbf{S}_{i+1}) \\ &\approx -J \sum_{i=1}^{l} \frac{(\theta_i - \theta_{i+1})^2}{2} \approx \frac{J\pi^2}{2l}\end{aligned} \tag{37}$$

assuming constant changes of the angle θ from one spin to the next one (which can also be shown to be the wall profile with the minimum energy by a solution of the corresponding Euler–Lagrange equations). The dipolar field energy of a chain of parallel-oriented dipoles can be expressed via Riemann's ζ function using

$$\zeta(3) = \sum_{i=1}^{\infty} \frac{1}{i^3} \approx 1.202 \tag{38}$$

Hence, the gain of dipolar energy of a chain of l spins can roughly be estimated to be at most $3wl\zeta(3)$, where $w = \mu_s^2 \mu_0 / 4\pi a^3$ is the strength of the dipole–dipole coupling (see equation (5) and also (Hucht, Moschel and Usadel, 1995) for a similar calculation in two dimensions). A comparison of the energies yields the exchange length (measured as number of atoms)

$$\delta_x = \pi \sqrt{\frac{J}{6\zeta(3)w}} \tag{39}$$

Note that in a continuum theory the dipolar energy is estimated from formulae for the magnetostatic energy of ellipsoids (Hubert and Schäfer, 1998). The results deviate slightly since the factor $3\zeta(3)$ is replaced by π. We prefer the expression in the preceding text derived directly for a spin model.

Let us now consider a nanowire, that is either a cylindrical system or an extremely elongated ellipsoid. As long as the thickness of the particle is smaller than the exchange length, the magnetization will be homogeneous in the planes perpendicular to the long axis so that the system behaves effectively one-dimensionally (Braun, 1999). For thicknesses larger than the exchange length, reversal modes may occur where the magnetization is nonuniform in the perpendicular planes, for example curling (Aharoni, 1996) (for graphical representations see Nowak, 2001).

The existence of the crossover from nucleation to curling was investigated by simulations of cylindrical systems (Hinzke and Nowak, 2000b; Nowak, 2001). Here, for the first time fast Fourier transformation (FFT) methods for the calculation of the dipolar fields were combined with Monte Carlo simulations with quantified time step. These methods allowed for a statistical investigation of particle sizes of up to 32 768 spins in three dimensions. A systematic numerical determination of the corresponding energy barriers and characteristic times is nevertheless still missing.

5 SIMULATION OF ANTIFERROMAGNETS: EXCHANGE BIAS

For compound materials consisting of an FM in contact with an AFM a shift of the hysteresis loop along the magnetic field axis can occur, which is called *exchange bias* (*EB*). Often, this shift is observed after cooling the entire system in an external magnetic field below the Néel temperature T_N of the AFM. For reviews on EB the reader is referred to the articles by Nogués and Schuller (1999) and Stamps (2000). Although EB has been well known since many years (Meiklejohn and Bean, 1956, 1957) its microscopic origin is still discussed controversially.

A detailed understanding of EB can only be achieved by an understanding of the antiferromagnetic spin structure so that classical spin models are the common starting point for microscopic models of EB. In an early approach by Malozemoff (1987, 1988a,b), EB is attributed to the formation of domain walls in the AFM, perpendicular to the FM/AFM interface due to interface roughness. These domain walls are supposed to occur during cooling in the presence of the magnetized FM and to carry a small net magnetization at the FM/AFM interface (see Figure 4a). This interface magnetization is furthermore supposed to be stable during the reversal of the FM, consequently shifting the hysteresis loop. However, the formation of domain walls in the AFM

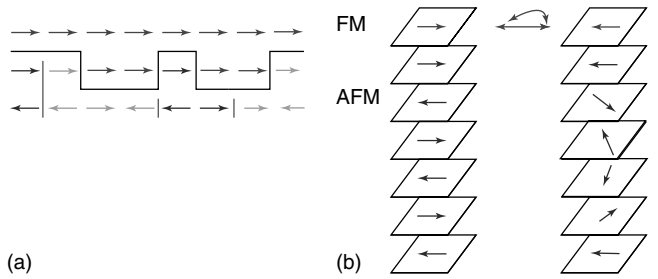

Figure 4. (a) Sketch of the model after Malozemoff (1987, 1988a,b) which shows the FM on top of the AFM in a domain configuration. (b) Sketch of the model Mauri, Siegmann, Bagus and Kay (1987). During reversal of the FM a spring is wound up in the AFM. (Reprinted from *Journal of Magnetism and Magnetic Materials*, Vol 240, 2002, Pages 243–247. Copyright 2002, with permission from Elsevier.)

only due to interface roughness is energetically unfavorable and its occurrence and stability have never been proved.

Alternative approaches have been developed. In a model introduced by Mauri, Siegmann, Bagus and Kay (1987) EB is obtained through a mechanism in which a domain-wall forms in the AFM parallel to the interface while the magnetization of the FM rotates (see Figure 4b). In contrast to experimental findings this mechanism works only for uncompensated interfaces where the interface layer of the AFM is such that is carries a net magnetization. Furthermore the interface is assumed to be perfectly flat since otherwise it would be effectively compensated by roughness. An extension by Koon (1998) for compensated interfaces where the model of Mauri was combined with a spin-flop coupling was later on proved to show no EB (Schulthess and Butler, 1998, 1999). To obtain EB Schulthess and Butler had to assume uncompensated AFM spins at the interface. However, their occurrence and stability during a magnetic hysteresis loop was not explained.

In a recent experiment Miltényi *et al*. (2000) showed that it is possible to strongly influence EB in Co/CoO bilayers by diluting the antiferromagnetic CoO layer, that is by inserting nonmagnetic substitutions ($Co_{1-x}Mg_xO$) or defects ($Co_{1-y}O$) not at the FM/AFM interface but rather throughout the volume part of the AFM. In the same letter in was shown that a corresponding theoretical model, the domain-state (DS) model, investigated by Monte Carlo simulations shows a behavior very similar to the experimental results. It was argued that EB has its origin in a DS in the AFM which triggers the spin arrangement and the FM/AFM exchange interaction at the interface. Later it was shown that a variety of experimental facts associated with EB can be explained within this DS model (Nowak, Misra and Usadel, 2001, 2002; Nowak *et al*., 2002b; Keller *et al*., 2002; Misra, Nowak and Usadel, 2003, 2004; Beckmann, Nowak and Usadel, 2003, 2006; Scholten, Usadel and Nowak, 2005; Spray and Nowak, 2006). The importance of defects for the EB effect was also confirmed by experiments on $Fe_xZn_{1-x}F_2$/Co bilayers (Shi, Lederman and Fullerton, 2002) and by experiments (Mewes *et al*., 2000; Mougin *et al*., 2001) where it was shown that it is possible to modify EB by means of irradiating an FeNi/FeMn system by He ions in presence of a magnetic field. Depending on the dose of the irradiation and the magnetic field present at the time of irradiation, it was possible to manipulate both the magnitude and even the direction of the EB field. Further support for the relevance of domains in EB systems is given by a direct spectroscopic observation of AFM domains (Nolting *et al*., 2000; Ohldag *et al*., 2001). In the following we focus on the DS model.

5.1 Domain-state model

The DS model for EB (Miltényi *et al*., 2000) consists of t_{FM} monolayers of FM and t_{AFM} monolayers of diluted AFM. The FM is exchange coupled to the topmost layer of the AFM. The geometry of the model is sketched in Figure 5.

The system is described by a classical Heisenberg model with nearest-neighbor exchange on a simple cubic lattice with exchange constants J_{FM} and J_{AFM} for the FM and the AFM respectively, while J_{INT} stands for the exchange constant between FM and AFM. For simplicity we assume that the values of the magnetic moments of FM and AFM are identical (included in the magnetic field energy B). The Hamiltonian of the system is then

$$\begin{aligned}\mathcal{H} = &-J_{\mathrm{FM}} \sum_{\langle i,j \rangle} \boldsymbol{S}_i \cdot \boldsymbol{S}_j - \sum_i \left(d_z S_{iz}^2 + d_x S_{ix}^2 + \boldsymbol{S}_i \cdot \boldsymbol{B} \right) \\ &-J_{\mathrm{AFM}} \sum_{\langle i,j \rangle} \epsilon_i \epsilon_j \boldsymbol{\sigma}_i \cdot \boldsymbol{\sigma}_j - \sum_i \epsilon_i \left(k_z \sigma_{iz}^2 + \boldsymbol{\sigma}_i \cdot \boldsymbol{B} \right) \\ &-J_{\mathrm{INT}} \sum_{\langle i,j \rangle} \epsilon_j \boldsymbol{S}_i \cdot \boldsymbol{\sigma}_j \end{aligned} \tag{40}$$

where $\mathbf{S}_i$ denote normalized spins at sites of the FM layer and $\boldsymbol{\sigma}_i$ denote normalized spins at sites of the AFM.

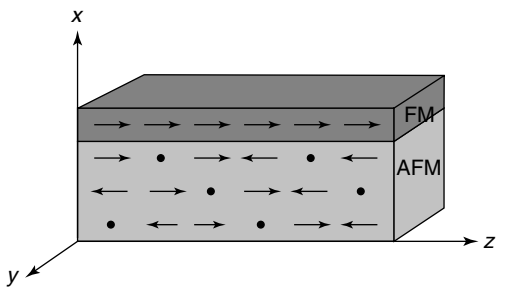

Figure 5. Sketch of the DS model with one FM layer and three diluted AFM layers. The dots mark defects. The easy axis of both FM and AFM is the z axis.

The first line of the Hamiltonian describes the energy of the FM with the z axis as its easy axis (anisotropy constant $d_z > 0$). The dipolar interaction is approximated in the model by an additional anisotropy term (anisotropy constant $d_x = -0.1 J_{\mathrm{FM}}$ in the present case) which includes the shape anisotropy, leading to a magnetization which is preferentially in the y–z plane. The second line is the contribution from the AFM also having its easy axis along z direction. The AFM is diluted, that is a fraction p of sites is left without a magnetic moment ($\epsilon_i = 0$) while the other sites carry a moment ($\epsilon_i = 1$). The last term describes the interaction of the FM with the interface AFM monolayer.

Equation (40) suggests a simple ground state argument for the strength of the bias field. Assuming that all spins in the FM remain parallel during field reversal and that some net magnetization of the interface layer of the AFM remains constant during the reversal of the FM a simple calculation gives the usual estimate for the bias field,

$$t_{\mathrm{FM}} B_{\mathrm{EB}} = J_{\mathrm{INT}} m_{\mathrm{INT}} \tag{41}$$

where m_{INT} is the stable part of the interface magnetization of the AFM (per spin) which is responsible for the EB. For an ideal uncompensated and totally stable interface one would expect $m_{\mathrm{INT}} = 1$. As is well known, this estimate leads to a much too high bias field, while for an ideal compensated interface, on the other hand, one would expect $m_{\mathrm{INT}} = 0$ and, hence, $B_{\mathrm{EB}} = 0$. Experimentally, however, often there is on the one hand no big difference between compensated and uncompensated interfaces and on the other hand, it is found that B_{EB} is much smaller than $J_{\mathrm{INT}}/t_{\mathrm{FM}}$, rather of the order of a few percent of it. The solution of this puzzle is that m_{INT} is neither constant during field reversal nor is it a simple known quantity (Keller *et al*., 2002; Nowak *et al*., 2002b) and we discuss this quantity in the following.

5.2 Results from Monte Carlo simulation

Apart from the mean-field work by Scholten, Usadel and Nowak (2005) mainly Monte Carlo methods were used to investigate the DS model. Some of them focused on the Ising limit for the AFM (Nowak, Misra and Usadel, 2001; Nowak *et al*., 2002b; Beckmann, Nowak and Usadel, 2003, 2006; Spray and Nowak, 2006) while others used the full Heisenberg Hamiltonian of the previous subsection (Nowak, Misra and Usadel, 2002; Misra, Nowak and Usadel, 2003). In the latter case a heat bath algorithm with single-spin-flip dynamics was used where the trial step of the spin update consisted of two steps: firstly a small variation within a cone around the former spin direction, followed, secondly, by a total spin flip. This twofold spin update is ergodic and symmetric and can take care of a broad range of anisotropies, from very soft spins up to the high anisotropy (Ising) limit. To observe the domain structure of the AFM one has to guarantee that typical length scales of the domain structure fit into the system and typical system sizes were a lateral extension of 128×128 and a thickness of $t_{\mathrm{FM}} = 1$ and t_{AFM} ranging from 3 to 9. Periodical boundary conditions were used within the film plane and open boundary conditions perpendicular to it.

The main quantities monitored were the thermal averages of the z component of the magnetic moment for each individual monolayer normalized to the magnetic moment of the saturated monolayer. In simulations the system is first cooled from above to below the ordering temperature of the AFM. During cooling the FM is initially magnetized along the easy z axis resulting in a nearly constant exchange field for the AFM monolayer at the interface. Also, the system is cooled in the presence of an external magnetic field, the cooling field. In addition to the exchange field from the ordered FM this field acts on the AFM also. When the desired final temperature is reached, a magnetic field along the easy axis is applied and reduced in small steps down to a certain minimum value and afterward raised again up to the initial value. This corresponds to one cycle of the hysteresis loop. A hysteresis loop obtained as described in the preceding text is depicted in Figure 6. Results for the magnetization of the

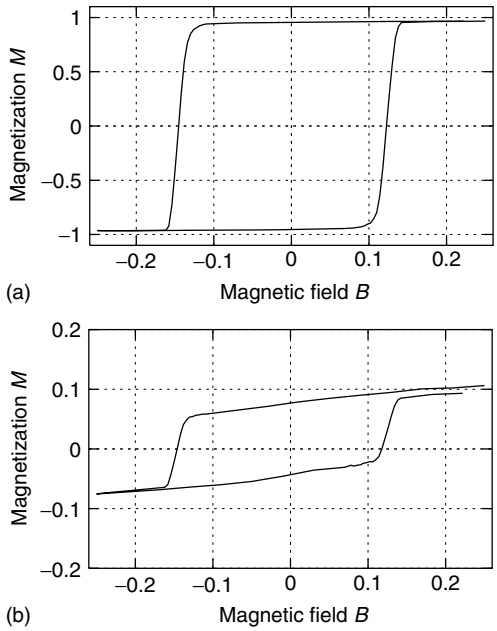

Figure 6. Simulated hysteresis loops of the DS model as explained in the text. Dilution $p = 0.4$, $k_{\mathrm{B}}T = 0.1 J_{\mathrm{FM}}$, positive interface coupling, $J_{\mathrm{INT}} = |J_{\mathrm{AFM}}|$. AFM anisotropy $k_z = J_{\mathrm{FM}}/2$. The cooling field was $B_{\mathrm{c}} = 0.25 J_{\mathrm{INT}}$. The magnetic moment of the FM (a) and the interface monolayer of the AFM (b) normalized to its saturation value is shown. (Reprinted from *Journal of Magnetism and Magnetic Materials*, Vol 240, 2002, Pages 243–247. Copyright 2002, with permission from Elsevier.)

FM (a) as well as that of the AFM interface monolayer (b) are shown. Exchange biasing is clearly observed.

An analysis of the magnetization curve of the interface layer gives an interesting insight into the nature of EB. After the field cooling procedure the AFM interface carries a magnetization. A part of this AFM interface magnetization is stable during hysteresis and leads to the fact that the magnetization curve of the interface layer of the AFM is shifted upward. This irreversible part of the interface magnetization of the AFM acts as an additional effective field on the FM, resulting in EB. Note that the interface magnetization of the AFM also displays hysteresis as a result of the exchange coupling to the FM. This means that the whole interface magnetization of the AFM consists of a reversible part leading to an enhanced coercivity and an irreversible part leading to EB.

In experiments, usually the magnetization of the whole FM/AFM bilayer is measured. The corresponding sample magnetization loop might not only be shifted horizontally but also vertically. The vertical shift contains contributions from the volume part of the AFM as well as from its interface. The volume magnetization of the AFM is induced by the cooling field and hence not shifted when the cooling field is zero and shifted upward when it is finite. The interface contribution depends on the sign of the interface coupling and may be positive, as in our calculation or even negative for negative interface coupling (Nogués, Leighton and Schuller, 2000; Keller *et al*., 2002; Nowak *et al*., 2002b).

With the following two sketches we wish to illustrate on a more microscopic basis where the interface magnetization of the AFM comes from, including its partitioning in reversible and irreversible parts. Figure 7(a) shows spin configurations in a small portion of the interface monolayer of the AFM after field cooling. The simulated system size is $64 \times 64 \times 10$ with only one FM monolayer. For simplicity, this simulation was performed in the Ising limit for the AFM ($k_z \to \infty$). The dilution p of the AFM is 50%, nevertheless the spins are much more connected than it appears from the sketch via the third dimension.

Obviously, the AFM is in a DS, where a domain is defined as a region of undisturbed antiferromagnetic order. The reason for the domain formation and, consequently, for the lack of long-range order is the interface magnetization which couples to the exchange field coming from the FM and the external field (both pointing up) lowering the energy of the system. The interface magnetization follows from two contributions. Examples for both are indicated via the circles. One contribution comes from parallel spin pairs in the domain walls (*domain-wall magnetization*), all pointing up in our example (Figure 7a), that is, into the direction of the exchange field of the FM and the external field. A second contribution comes from an imbalance of the number of defects of the two antiferromagnetic sublattices

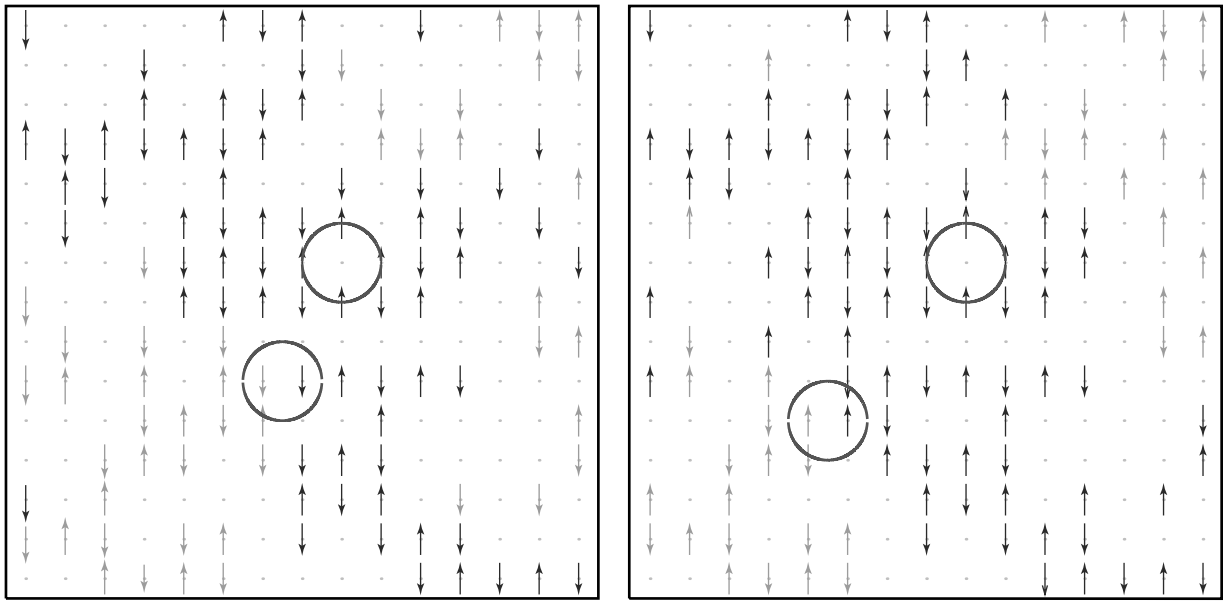

Figure 7. Snapshots of spin configurations in a small portion of the interface monolayer of the AFM after field cooling with the external field and the FM magnetization pointing upward (a) and after reversal of the FM (b). The interface coupling is assumed to be positive. The gray shading distinguishes different AFM domains. The circles mark sources of magnetization, wall magnetization as well as volume magnetization.

(*volume magnetization*). The imbalance of the number of defects of the two antiferromagnetic sublattices also leads to a net magnetization within a domain which couples to the exchange field of the FM and the external field. The reason for the imbalance is that the domain structure is not random. Rather, it is an optimized structure arising during the initial cooling procedure with as much magnetization as possible coupling to the exchange field of the FM and the external field, following the energy minimization principle.

However, an AFM interface magnetization alone cannot lead to EB. Only the irreversible part of it (during hysteresis) may lead to EB. Figure 7(b) shows, for comparison, spin configurations in the same portion of the interface monolayer of the AFM after reversal of the FM. Clearly, the major part of the domain structure did not change during reversal of the FM. However, there are rearrangements on smaller length scales, leading mainly to the fact that the domain-wall magnetization changes its sign. In Figure 7(b) all of the spin pairs within domain walls are pointing down following the reversed FM and the external field.

However, the volume magnetization coming from the defects remains frozen. The stability of the domain structure stems from the fact that the domain walls are pinned at defects sites as well as between pairs of spins which are aligned with the field. Hence, during a movement of the domain-wall energy barriers may have to be overcome by thermal activation. This explains why a large domain in general will stay in a metastable state on exponentially long timescales, while rearrangements on a shorter length scale are possible, of course depending on the temperature and the material parameters of the AFM.

Many of the essential properties of diluted AFMs, the occurrence of DSs, metastability, remnant magnetization, and slow relaxation, among others, have been investigated before, even though not in the context of EB (for reviews on diluted AFMs see Kleemann, 1993; Belanger, 1998, for a detailed discussion of the connection between diluted AFMs and EB systems see Nowak *et al*., 2002b).

Important features of EB systems found experimentally (Keller *et al*., 2002) have their counterpart in the simulations (Nowak *et al*., 2002b), such as the order of magnitude of EB fields, the shape of hysteresis curves, the dilution dependence of EB, its temperature dependence, the training effect, and the occurrence of positive EB. Other properties of EB systems, which were successfully investigated within the framework of the DS model are the dependence of EB on thickness of the AFM (Nowak, Misra and Usadel, 2001; Ali *et al*., 2003), the dependence on the anisotropy of the AFM in Nowak, Misra and Usadel (2002), the influence of ion irradiation (Misra, Nowak and Usadel, 2003) asymmetric reversal modes (Beckmann, Nowak and Usadel, 2003), properties of the AFM domain structures (Misra, Nowak and Usadel, 2004), the enhanced coercivity (Scholten, Usadel and Nowak, 2005), the cooling field dependence (Beckmann, Nowak and Usadel, 2003), and the influence of interface roughness (Spray and Nowak, 2006). However, finally one should note that most of the AFMs used in EB systems have a polycrystalline structure (Stiles and McMichael, 1999; Suess *et al*., 2003), which so far was not taken into account by the DS model. Work following these lines is still missing and would certainly contribute to the further understanding of EB.

6 CONCLUSIONS AND OUTLOOK

Within the framework of classical spin models it is possible to investigate magnetic properties of a variety of different materials, as for example, ferri-, ferro-, or antiferromagnets, and even heterostructures composed of several different materials. Simulation techniques for the investigation of thermal equilibrium properties exist and – to some extent – also for nonequilibrium situations.

However, classical spin models neglect quantum effects and, furthermore, one expects certain limits for the validity of the stochastic LLG equation regarding its short-time spin dynamics as well as the form of the damping which still suffers from a lack of microscopic understanding. A mathematical formulation of damping (Smith and Arnett, 2001; Safonov and Bertram, 2002; Rebei and Parker, 2003) as well as a systematic construction and parameterization of classical spin model Hamiltonians (Mryasov, Nowak, Guslienko and Chantrell, 2005) for certain given materials on the basis of first-principles calculation remain a challenge for current research.

NOTE

[1] The fact that the noise is multiplicative in the LLG equation has been questioned, since the parameter space is the unit sphere, so that the relevant random-field term (giving rise to a torque) and the magnetization derivative are restricted to the tangent plane. The use of a Heun scheme might thus not be mandatory.

REFERENCES

Aharoni, A. (1969). Effect of a magnetic field on the superparamagnetic relaxation time. *Physical Review*, **177**, 793.

Aharoni, A. (1996). Comment on Kramer's rate theory, broken symmetries, and magnetization reversal. *Journal of Applied Physics*, **80**, 3133.

Ali, M., Marrows, C.H., Al-Jawad, M., *et al*. (2003). Antiferromagnetic layer thickness dependence of the IrMnCo exchange bias system. *Physical Review B*, **68**, 214420.

Anderson, P.W. (1963). Exchange in insulators: superexchange, direct exchange, and double exchange. In *Magnetism: A Treatise on Modern Theory and Materials*, Rado, G.T. and Suhl, H. (Eds.), Academic Press: New York, Vol. 1.

Becker, R. and Döring, W. (1935). Kinetische Behandlung der Keimbildung in übersättigten Dämpfen. *Annalen der Physik (Leipzig)*, **24**, 719.

Beckmann, B., Nowak, U. and Usadel, K.D. (2003). Asymmetric reversal modes in ferromagnetic/antiferromagnetic multilayers. *Physical Review Letters*, **91**, 187201.

Beckmann, B., Usadel, K.D. and Nowak, U. (2006). Cooling field dependence of asymmetric reversal modes for ferromagnetic/antiferromagnetic multilayers. *Physical Review B*, **74**, 054431.

Belanger, D.P. (1998). Experiments on the random field Ising model. In *Spin Glasses and Random Fields*, Young, A.P. (Ed.), World Scientific: Singapore.

Berkov, D.V. (2007). Magnetization dynamics including thermal fluctuations. In *Handbook of Magnetism and Advanced Magnetic Materials*, Kronmüller, H. and Parkin, S. (Eds.), John Wiley & Sons: Chichester, Vol. 2.

Berkov, D.V., Ramstöck, K.R. and Hubert, A. (1993). Solving micromagnetic problems. *Physica Status Solidi A*, **137**, 207.

Binder, K. and Heermann, D.W. (1997). *Monte Carlo Simulation in Statistical Physics*, Springer-Verlag: Berlin.

Braun, H.B. (1993). Thermally activated magnetization in elongated ferromagnetic particles. *Physical Review Letters*, **71**, 3557.

Braun, H.B. (1994a). Fluctuations and instabilities of ferromagnetic domain-wall pairs in an external magnetic field. *Physical Review B*, **50**, 16485.

Braun, H.B. (1994b). Kramer's rate theory, broken symmetries, and magnetization reversal. *Journal of Applied Physics*, **76**, 6310.

Braun, H.B. (1999). Nucleation in ferromagnetic nanowires – magnetostatics and topology. *Journal of Applied Physics*, **85**, 6172.

Braun, H.B. (2000). Stochastic magnetization dynamics in magnetic nanostructures: from Néel-Brown to soliton-antisoliton creation. In *Structure and Dynamics of Heterogenous Systems*, Entel, P. and Wolf, D.E. (Eds.), World Scientific: Singapore.

Brown, W.F. (1963a). *Micromagnetics*, John Wiley & Sons: New York.

Brown, W.F. (1963b). Thermal fluctuations of a single-domain particle. *Physical Review*, **130**, 1677.

Chang, T., Zhu, J-G. and Judy, J.H. (1993). Method for investigating the reversal properties of isolated barium ferrite fine particles utilizing MFM. *Journal of Applied Physics*, **73**, 6716.

Chantrell, R.W., Lyberatos, A. and Wohlfarth, E. (1986). The coefficient of magnetic viscosity II: the time dependent magnetisation of interacting fine particle materials. *Journal of Physics F*, **16**, L145.

Chantrell, R.W., Walmsley, N., Gore, J. and Maylin, M. (2000). Calculation of the susceptibility of interacting superparamagnetic particles. *Physical Review B*, **63**, 024410.

Cheng, X.Z., Jalil, M.B.A., Lee, H.K. and Okabe, Y. (2006). Mapping the Monte Carlo scheme to Langevin dynamics: a Fokker-Planck approach. *Physical Review Letters*, **96**, 067208.

Chubykalo, O., Nowak, U., Chantrell, R.W. and Garanin, D. (2006). Dynamic approach for micromagnetics close to the Curie temperature. *Physical Review B*, **74**, 094436.

Chubykalo, O., Nowak, U., Smirnov-Rueda, R., *et al*. (2003a). The Monte Carlo technique with quantified time step: application to the motion of magnetic moments. *Physical Review B*, **67**, 64422.

Chubykalo, O., Smirnov-Rueda, R., Wongsam, M.A., *et al*. (2003b). Brownian dynamics approach to interacting magnetic moments. *Journal of Magnetism and Magnetic Materials*, **266**, 28.

Coffey, W.T. (1996). *The Langevin Equation*, World Scientific: Singapore.

Coffey, W.T., Crothers, D.S.F., Dorman, J.L., *et al*. (1998a). Effect of an oblique magnetic field on the superparamagnetic relaxation time. II. Influence of the gyromagnetic term. *Physical Review B*, **58**, 3249.

Coffey, W.T., Crothers, D.S.F., Dorman, J.L., *et al*. (1998b). Range of validity of Kramer's escape rates for non-axially symmetric problems in superparamagnetic relaxation. *Journal of Physics: Condensed Matter*, **10**, 9093.

Coffey, W.T., Crothers, D.S.F., Dorman, J.L., *et al*. (1998c). Thermally activated relaxation time of a single domain ferromagnetic particle subjected to a uniform field at an oblique angle to the easy axis: comparison with experimental observations. *Physical Review Letters*, **80**, 5655.

Ettelaie, R. and Moore, M.A. (1984). Comparison of Langevin and Monte Carlo dynamics. *Journal of Physics A: Mathematical and General*, **17**, 3505.

Garanin, D.A. (1991). Dynamics of elliptic domain walls. *Physica A*, **178**, 467.

Garanin, D.A. (1997). Fokker-Planck and Landau-Lifshitz-Bloch equation for classical ferromagnets. *Physical Review B*, **55**, 3050.

García-Palacios, J.L. and Lázaro, F.J. (1998). Langevin-dynamics study of the dynamical properties of small magnetic particles. *Physical Review B*, **58**, 14937.

García-Palacios, J.L. and Svedlindh, P. (2000). Langevin-dynamics study of the dynamical properties of small magnetic particles. *Physical Review Letters*, **85**, 3724.

Gilbert, T.L. (1955). A Lagrangian formulation of the gyromagnetic equation of the magnetization field. *Physical Review*, **100**, 1243.

Glauber, R.J. (1963). Time-dependent statistics of the Ising model. *Journal of Mathematical Physics*, **2**, 294.

Greiner, A., Strittmatter, W. and Honerkamp, J. (1988). Numerical integration of stochastic differential equation. *Journal of Statistical Physics*, **51**, 95.

Heisenberg, W. (1928). Zur Theorie des Ferromagnetismus. *Zeitschrift fur Physik*, **49**, 619.

Hinzke, D. and Nowak, U. (1998). Magnetization switching in a Heisenberg model for small ferromagnetic particles. *Physical Review B*, **58**, 265.

Hinzke, D. and Nowak, U. (1999). Monte Carlo simulation of magnetization switching in a Heisenberg model for small ferromagnetic particles. *Computer Physics Communications*, **121–122**, 343.

Hinzke, D. and Nowak, U. (2000a). Magnetic relaxation in a classical spin chain as model for nanowires. *Physical Review B*, **61**, 6734.

Hinzke, D. and Nowak, U. (2000b). Magnetization switching in nanowires: Monte Carlo study with fast Fourier transformation for dipolar fields. *Journal of Magnetism and Magnetic Materials*, **221**, 365.

Hinzke, D., Nowak, U. and Usadel, K.D. (2000). Thermally activated magnetization reversal in classical spin chains. In *Structure and Dynamics of Heterogenous Systems*, Entel, P. and Wolf, D.E. (Eds.), World Scientific: Singapore.

Hubert, A. and Schäfer, R. (1998). *Magnetic Domains*, Springer-Verlag: Berlin.

Hucht, A., Moschel, A. and Usadel, K.D. (1995). Monte-Carlo study of the reorientation transition in Heisenberg models with dipolar interaction. *Journal of Magnetism and Magnetic Materials*, **148**, 32.

Kazantseva, N., Wieser, R. and Nowak, U. (2005). Transition to linear domain walls in nanoconstrictions. *Physical Review Letters*, **94**, 37206.

Keller, J., Miltényi, P., Beschoten, B., *et al*. (2002). The domain state model for exchange bias II: experiment. *Physical Review B*, **66**, 14431.

Kirby, R.D., Shen, J.X., Hardy, R.J. and Sellmyer, D.J. (1994). Magnetization reversal in nanoscale magnetic films with perpendicular anisotropy. *Physical Review B*, **49**, 10810.

Kleemann, W. (1993). Random-field induced antiferromagnetic, ferroelectric and structural domains states. *International Journal of Modern Physics B*, **7**, 2469.

Koon, N.C. (1998). Calculations of exchange bias in thin films with ferromagnetic/antiferromagnetic interfaces. *Physical Review Letters*, **78**, 4865.

Landau, D.L. and Lifshitz, E. (1935). On the theory of the dispersion of magnetic permeability in ferromagnetic bodies. *Physikalische Zeitschrift der Sowjetunion*, **8**, 153.

Levy, L-P. (2000). *Magnetism and Superconductivity*, Springer-Verlag: Berlin.

Lyberatos, A., Berkov, D.V. and Chantrell, R.W. (1993). A method for the numerical simulation of the thermal magnetization fluctuations in micromagnetics. *Journal of Physics: Condensed Matter*, **5**, 8911.

Lyberatos, A. and Chantrell, R.W. (1993). Thermal fluctuations in a pair of magnetostatistically coupled particles. *Journal of Applied Physics*, **73**, 6501.

Lyberatos, A., Earl, J. and Chantrell, R.W. (1996). Model of thermally activated magnetization reversal in rare-earth-transition-metal compounds. *Physical Review B*, **53**, 5493.

Malozemoff, A.P. (1987). Random-field model of exchange anisotropy at rough ferromagnetic-antiferromagnetic interfaces. *Physical Review B*, **35**, 3679.

Malozemoff, A.P. (1988a). Heisenberg-to-Ising crossover in a random-field model with uniaxial anisotropy. *Physical Review B*, **37**, 7673.

Malozemoff, A.P. (1988b). Mechanism of exchange anisotropy. *Journal of Applied Physics*, **63**, 3874.

Mauri, D., Siegmann, H.C., Bagus, P.S. and Kay, E. (1987). Simple model for thin ferromagnetic films exchange coupled to an antiferromagnetic substrate. *Journal of Applied Physics*, **62**, 3047.

Meiklejohn, W.H. and Bean, C.P. (1956). New magnetic anisotropy. *Physical Review*, **102**, 1413.

Meiklejohn, W.H. and Bean, C.P. (1957). New magnetic anisotropy. *Physical Review*, **105**, 904.

Mewes, T., Lopusnik, R., Fassbender, J., *et al*. (2000). Suppression of exchange bias by ion irradiation. *Applied Physics Letters*, **76**, 1057.

Miltényi, P., Gierlings, M., Keller, J., *et al*. (2000). Diluted antiferromagnets in exchange bias: Proof of domain state model. *Physical Review Letters*, **84**, 4224.

Misra, A., Nowak, U. and Usadel, K.D. (2003). Control of exchange bias by diluting the antiferromagnetic layer. *Journal of Applied Physics*, **93**, 6593.

Misra, A., Nowak, U. and Usadel, K.D. (2004). Structure of domains in an exchange bias model. *Journal of Applied Physics*, **95**, 1357.

Mougin, A., Mewes, T., Jung, M., *et al*. (2001). Local manipulation and reversal of the exchange bias field by ion irradiation in FeNi/FeMn double layers. *Physical Review B*, **63**, 60409.

Mryasov, O.N., Nowak, U., Guslienko, K. and Chantrell, R.W. (2005). Temperature dependent magnetic properties of FePt: effective spin Hamiltonian model. *Europhysics Letters*, **69**, 805.

Nogués, J., Leighton, C. and Schuller, I.K. (2000). Correlation between antiferromagnetic interface coupling and positive exchange bias. *Physical Review B*, **61**, 1315.

Nogués, J. and Schuller, I.K. (1999). Exchange bias. *Journal of Magnetism and Magnetic Materials*, **192**, 203.

Nolting, F., Scholl, A., Stöhr, J., *et al*. (2000). Direct observation of the alignment of ferromagnetic spins by antiferromagnetic spins. *Nature*, **405**, 767.

Nowak, U. (1997). Micromagnetic simulation of nanoscale films with perpendicular anisotropy. *Journal of Applied Physics*, **81**, 5579.

Nowak, U. (2001). Thermally activated reversal in magnetic nanostructures. In *Annual Reviews of Computational Physics IX*, Stauffer, D. (Ed.), World Scientific: Singapore, p. 105.

Nowak, U., Chantrell, R.W. and Kennedy, E.C. (2000). Monte Carlo simulation with time step quantification in terms of Langevin dynamics. *Physical Review Letters*, **84**, 163.

Nowak, U., Heimel, J., Kleinefeld, T. and Weller, D. (1997). Domain dynamics of magnetic films with perpendicular anisotropy. *Physical Review B*, **56**, 8143.

Nowak, U., Misra, A. and Usadel, K.D. (2001). Domain state model for exchange bias. *Journal of Applied Physics*, **89**, 7269.

Nowak, U., Misra, A. and Usadel, K.D. (2002). Modeling exchange bias microscopically. *Journal of Magnetism and Magnetic Materials*, **240**, 243.

Nowak, U., Mryasov, O.N., Wieser, R., *et al*. (2005). Spin dynamics of magnetic nanoparticles: beyond Brown's theory. *Physical Review B*, **72**, 172410.

Nowak, U., Rüdiger, U., Fumagalli, P. and Güntherodt, G. (1996). Dependence of magnetization reversal on the crystallite size in

MnBi thin films: experiment, theory, and computer simulation. *Physical Review B*, **54**, 13017.

Nowak, U., Usadel, K.D., Miltényi, P., *et al*. (2002). The domain state model for exchange bias I: theorie. *Physical Review B*, **66**, 14430.

Ohldag, H., Scholl, A., Nolting, F., *et al*. (2001). Spin reorientation at the antiferromagnetic NiO(001) surface in response to an adjacent ferromagnet. *Physical Review Letters*, **86**, 2878.

Rebei, A. and Parker, G. (2003). Fluctuation and dissipation of coherent magnetization. *Physical Review B*, **67**, 104434.

Reif, F. (1965). *Fundamentals of Statistical and Thermal Physics*, McGraw-Hill Book Company: New York.

Rikvold, P.A. and Gorman, B.M. (1994). Recent results on the decay of metastable phases. In *Annual Reviews of Computational Physics I*, Stauffer, D. (Ed.), World Scientific: Singapore, p. 149.

Rikvold, P.A., Tomita, H., Miyashita, S. and Sides, S.W. (1994). Metastable lifetimes in a kinetic Ising model: dependence on field and system size. *Physical Review E*, **49**, 5080.

Safonov, V. and Bertram, N. (2002). Thermal magnetization noise in a thin film. *Physical Review B*, **65**, 172417.

Schneider, C.M. and Blügel, S. (Eds.) (2005). *Magnetism Goes Nano*. Lecture Notes of the 36th Spring School of the IFF Jülich, Forschungs-zentrum Jülich GmbH: Jülich.

Scholten, G., Usadel, K.D. and Nowak, U. (2005). Coercivity and exchange bias of ferromagnetic/antiferromagnetic multilayers. *Physical Review B*, **71**, 64413.

Schulthess, T.C. and Butler, W.H. (1998). Consequences of spin-flop coupling in exchange biased films. *Physical Review Letters*, **81**, 4516.

Schulthess, T.C. and Butler, W.H. (1999). Coupling mechanisms in exchange biased films. *Journal of Applied Physics*, **85**, 5510.

Shi, H.T., Lederman, D. and Fullerton, E.E.C. (2002). Exchange bias in $Fe_xZn_{1-x}F_2$/Co bilayers. *Journal of Applied Physics*, **91**, 7763.

Smirnov-Rueda, R., Chubykalo, O., Nowak, U., *et al*. (2000). Real time quantification of Monte Carlo steps for different time scales. *Journal of Applied Physics*, **87**, 4798.

Smirnov-Rueda, R., Hannay, J.D., Chubykalo, O., *et al*. (1999). Simulation of magnetic relaxation by a Monte Carlo technique with correlations and quantified time steps. *IEEE Transactions on Magnetics*, **35**, 3730.

Smith, N. and Arnett, P. (2001). White-noise magnetization fluctuations in magnetoresistive heads. *Applied Physics Letters*, **78**, 1448.

Spray, J. and Nowak, U. (2006). Exchange bias in ferromagnetic/antiferromagnetic bilayers with imperfect interfaces. *Journal of Physics D*, **39**, 4536.

Stamps, R.L. (2000). Mechanisms for exchange bias. *Journal of Physics D*, **33**, R247.

Stauffer, D., Hehl, F.W., Winkelmann, V. and Zabolitzky, J.G. (1993). *Computer Simulation and Computer Algebra*, Springer-Verlag: Berlin.

Steevens, K.W.H. (1963). Spin hamiltonians. In *Magnetism: A Treatise on Modern Theory and Materials*, Rado, G.T. and Suhl, H. (Eds.), Academic Press: New York, Vol. 1.

Stiles, M.D. and McMichael, R.D. (1999). Model for exchange bias in polycrystalline ferromagnet-antiferromagnet bilayers. *Physical Review B*, **59**, 3722.

Suess, D., Kirschner, M., Schrefl, T., *et al*. (2003). Exchange bias of polycrystalline antiferromagnets with perfectly compensated interfaces. *Physical Review B*, **67**, 54419.

Swendsen, R.H. and Wang, J.S. (1987). Nonuniversal critical dynamics in Monte Carlo simulations. *Physical Review Letters*, **58**, 86.

Vedmedenko, E.Y., Kubetzka, A., von Bergmann, K., *et al*. (2004). Domain wall orientation in magnetic nanowires. *Physical Review Letters*, **92**, 077207.

Verdes, C., Ruiz-Diaz, B., Thompson, S., *et al*. (2002). Computational model of the magnetic and transport properties of interacting fine particles. *Physical Review B*, **65**, 174417.

Vesely, F. (1993). *Computational Physics*, Universitätsverlag: Wien.

Wagner, D. (1972). *Introduction to the Theory of Magnetism*, Pergamon Press: Oxford.

Wernsdorfer, W., Doudin, B., Mailly, D., *et al*. (1996a). Nucleation of magnetization reversal in individual nanosized nickel wires. *Physical Review Letters*, **77**, 1873.

Wernsdorfer, W., Hasselbach, K., Sulpice, A., *et al*. (1996b). Dynamical measurement of domain-wall nucleation and annihilation in individual amorphous Co particles. *Physical Review B*, **53**, 3341.

Wernsdorfer, W., Hasselbach, K., Benoit, A., *et al*. (1997a). Measurements of magnetization switching in individual nickel nanowires. *Physical Review B*, **55**, 11552.

Wernsdorfer, W., Orozco, E.B., Hasselbach, K., *et al*. (1997b). Experimental evidence of the Néel-Brown model of magnetization reversal. *Physical Review Letters*, **78**, 1791.

Wieser, R., Nowak, U. and Usadel, K.D. (2004). Domain wall mobility in nanowires: transverse vs. vortex walls. *Physical Review B*, **69**, 64401.

Wieser, R., Usadel, K.D. and Nowak, U. (2006). Thermodynamic behavior of nano-magnets with vortex configuration. *Physical Review B*, **74**, 094410.

Wolf, D.E. (1998). Stochastic differential equations. In *Advances in Computer Simulation*, Kondor, I. and Kertész, J. (Eds.), Springer: Heidelberg, p. 104.

Wolff, U. (1989). Collective Monte Carlo updating for spin systems. *Physical Review Letters*, **62**, 361.

Magnetization Configurations and Reversal in Small Magnetic Elements

Mathias Kläui[1] and Carlos António Fernandes Vaz[2]

[1] *Universität Konstanz, Konstanz, Germany*
[2] *University of Cambridge, Cambridge, UK*

1 INTRODUCTION

The recent surge of interest in the magnetism of small elements stems from a combination of three factors: firstly, the continuous development in the techniques for deposition of thin metal films and, in particular, molecular-beam epitaxy, which allows for the growth of metal structures virtually free of impurities and with controllable crystallinity; secondly, the development of electron beam lithography in the context of semiconductor technology, which has been subsequently co-opted for the structuring of metal elements, either by direct lithography or by metal deposition through a lithographically defined mask; and finally, the simultaneous development of magnetic characterization techniques, which have become ever more sensitive and are able to operate on shorter timescales and with greater spatial resolution. The happy confluence of these three trends has created the ideal conditions for a fruitful and rapid exploration of the magnetism of small magnetic structures, in particular, of their equilibrium and dynamic properties. A constant motivation throughout has been the potential for device applications that fit in with the current trend of miniaturization in magneto- and microelectronic technology.

It is in this context that we attempt here to review some of the aspects of the magnetism of small elements; this would seem a thankless task given the large body of work devoted to this subject, but we hope that, by focusing on the equilibrium static properties and quasiequilibrium dynamics of small elements, a broad picture of the recent achievements in this area may be uncovered, and also that a general understanding of the physics governing the magnetic properties of systems in the nano- and mesoscale, for which the shape of the element plays a critical role, may be exposed. With this purpose in mind, we propose to discuss the magnetism of small elements based on soft magnetic materials (*3d* transition ferromagnets and alloys), and we shall also limit ourselves largely to in-plane magnetized elements, that is, those for which the magnetic anisotropies are relatively small. The present chapter is organized as follows. In Section 2, we mention briefly some of the experimental techniques which have been used for the magnetic characterization of the magnetic structures mentioned in later sections. In Section 3, we consider the different magnetic energy terms which govern the magnetic behavior of materials on a macroscopic scale and which are implemented in micromagnetic simulators. In the next

Handbook of Magnetism and Advanced Magnetic Materials. Edited by Helmut Kronmüller and Stuart Parkin. Volume 2: *Micromagnetism*. ISBN: 978-0-470-02217-7.

sections, we introduce single domain systems (Section 4) and then move to the magnetism of mesoscopic elements (Section 5), characterized by magnetic states of nonuniform magnetization and which we distinguish from the multidomain states that one encounters in large elements (discussed briefly in Section 6). From the magnetostatics, we move to the magnetodynamics and discuss next the magnetization reversal of small elements (Section 7). In Section 8, we provide a brief summary of our overview.

2 CHARACTERIZATION TECHNIQUES

An impressive array of experimental techniques has been developed recently that aim at the detection and measurement of magnetic signals in small structures and thin films. This is particularly true of imaging techniques, whose increased spatial and time resolutions have made possible the study of both the detailed static spin configuration and the dynamic properties (down to the picosecond range) of small elements. Here, we only introduce the experimental techniques, which can give information about the magnetic configuration of small structures or thin films. While the available experimental techniques can be classified in many ways, we distinguish here between imaging and magnetometric techniques, which allow respectively a more direct or indirect access to the spin structure of magnetic systems.

Imaging techniques directly return information about the spatial magnetization distribution. These include, in order of increasing spatial resolution, scanning Kerr microscopy (SKM), based on the magneto-optic Kerr effect (MOKE), which has been used for the imaging of both continuous magnetic films and of small structures (Heidkamp and Erskine, 2000). Although the spatial resolution is limited to a few micrometers (in some cases extended to the submicrometer range (Stotz and Freeman, 1997)), when associated with stroboscopic techniques, it allows for time resolutions down to the sub-nanosecond (Ballentine, Hiebert, Stankiewicz and Freeman, 2000; Acremann *et al*., 2001; Hicken *et al*., 2002; Choi and Freeman, 2005). Scanning Hall effect microscopy (Bekaert *et al*., 2002) can achieve similar spatial resolutions, and is based on the Hall voltage generated by a miniaturized Hall probe that measures the stray field originating from the sample. Magnetic force microscopy (MFM) is based on the interaction of a magnetic tip with the stray field and magnetic charges issuing from the sample (Grütter, Mamin and Rugar, 1992; Hubert, Rave and Tomlinson, 1997). As such, it has the disadvantage that tip-sample interaction may disturb the magnetic pattern of soft magnetic materials (Memmert, Müller and Hartmann, 2000, 2001; García, Thiaville and Miltat, 2002), and, in some instances, it is even known to assist in the switching of the magnetization (Ohkubo, Kishigami, Yanagisawa and Kaneko, 1991; Manalis *et al*., 1995; Li *et al*., 2002). An additional complication is the fact that the stray field is not uniquely defined (Vellekoop, Abelmann, Porthun and Lodder, 1998). The spatial resolution of MFM is of the order of 50 nm, but it is a very slow technique (scanning times of the order of minutes). Better spatial resolution is provided by magnetic transmission X-ray microscopy (MTXM) (Fischer *et al*., 2001; Kang *et al*., 2005) and photoemission electron microscopy (PEEM) (Schneider *et al*., 1997; Schönhense, 1999; Locatelli *et al*., 2002; Scholl *et al*., 2002; Hopster and Oepen, 2005), with spatial resolution (currently) of $\sim$30 nm; its acquisition times are of the order of a few minutes, but ultrafast PEEM in conjunction with stroboscopic techniques have time resolutions in the sub-nanosecond range (Kuksov *et al*., 2004). Scanning electron microscopy with polarization analysis (Spin-SEM or SEMPA) (Scheinfein *et al*., 1989; Unguris, Scheinfein, Celotta and Pierce, 1990; Allenspach, 1994) has a spatial resolution of the order of 20 nm, and techniques with even higher spatial resolutions ($\leq$10 nm) include Lorentz microscopy (Chapman, 1984) and electron holography (Dunin-Borkowski *et al*., 2000). The ultimate imaging technique, as far as spatial resolution is concerned, is spin-polarized scanning tunneling microscopy (Wulfhekel and Kirschner, 1999; Bode, Pietzsch, Kubetzka and Wiesendanger, 2001), with subatomic resolution, but acquisition times tend to be long.

In magnetometric techniques, we include those techniques which give information about the magnetization structure, but which cannot determine unequivocally what such configuration may be. In order of increasing sensitivity, VSM (vibrating sample magnetometer), AGFM (alternating gradient magnetometer), and SQUID (superconducting quantum interference device), allow the measurement of *M-H* characteristics over arrays of small elements, but usually they are encumbered by the presence of the large diamagnetic contribution of the substrate. MOKE (Bader, 1991; Qiu and Bader, 1998) and its variants (Vavassori *et al*., 1999; Guedes *et al*., 2000) are surface-sensitive techniques (with probing depth of the order of the skin depth of the material under study, around 20 nm for most metals) and have been extensively used for the magnetic characterization of thin films and arrays of structures; it combines high sensitivities with fairly simple setups and typical spot sizes are of the order of 100 µm. Other techniques that require arrays of elements for sufficient signal-to-noise ratios include (polarized) neutron scattering (Fitzsimmons *et al*., 2004), ferromagnetic resonance (FMR) (Goglio *et al*., 1999; Giesen *et al*., 2005; Martyanov *et al*., 2005), and Brillouin light scattering (BLS) (Demokritov, Hillebrands and Slavin, 2001; Gubbiotti *et al*., 2002), the latter two probing directly the spin-wave spectra of the small structures. Recent developments include a microfocus BLS setup, with spatial

resolution of the order of 300 nm (Demidov *et al*., 2004). Hall effect magnetometry (Oral, Bending and Henini, 1996; Rahm *et al*., 2001; Schuh *et al*., 2001; Wunderlich *et al*., 2001; Steiner and Nitta, 2004) has also been employed, where individual microscopic elements are measured by placing them directly onto the Hall probe, allowing therefore a spatial discrimination of the order of or better than 1 μm; magnetoresistance (MR) is also a very powerful technique, which has the advantage that the signal does not decrease with decreasing size of the element and which is usually based on the anisotropic MR effect (Hong and Giordano, 1995; Aumentado and Chandrasekhar, 1999; Wegrowe *et al*., 1999); it has been used, for example, to probe the magnetization structure in nanometer-sized constrictions (Kläui *et al*., 2003b, 2004d) and also for studies of atomic contacts (García, Muñoz and Zhao, 1999; Gabureac, Viret, Ott and Fermon, 2004; Montero *et al*., 2004). Extraordinary Hall effect has been employed in perpendicularly magnetized structures as a very sensitive technique for the study of the magnetic configurations and magnetization dynamics in small structures, offering good time resolution but rather involved data analysis (Webb, 1990; Ravelosona *et al*., 2002; Belmeguenai, Devolder and Chappert, 2005). Micro-SQUID probes were developed by Mailly, Chapelier and Benoit (1993) and Wernsdorfer (2001) to probe the switching properties of nanometer-sized particles, and also rely on the placement of the nanoparticle onto the micro-SQUID junction; it combines high spatial discrimination with the extreme sensitivity of SQUID junctions. In general terms, these techniques allow the study of both static and dynamic properties, such as coercivities, magnetic anisotropies, magnetic moment, and spin-wave dynamics, and as such provide information that is critical for a complete characterization of the system. This is important because, for thin films and small structures, we may expect changes in the magnetic properties with respect to the bulk material, and also because the effect of interaction between elements or the effect of the physical shape of the element also strongly affects the magnetic properties of the system.

A more detailed description of these techniques can be found in volume 3 of this series.

3 MAGNETIC ENERGY TERMS IN MICROMAGNETISM

In small elements, as in bulk materials and thin films, the static and dynamic magnetic properties are determined by the relative contribution of the different magnetic energy terms to the free energy, namely, exchange, magnetostatic, magnetic anisotropy, and the Zeeman energy (if an external field is present). However, the sensitivity of the magnetic dipolar energy to the shape of the element changes dramatically the relative importance of the different energy terms in small structures, where boundaries constitute a significant portion of the whole system. In fact, while the magnetostatic energy term favors states of magnetic flux closure, and therefore multidomain states or states of nonuniform magnetization, such states come at a significant cost in exchange energy, since now regions of nonuniform magnetization (such as domain walls) occupy a large portion of the overall system. As the size of the element is reduced, the exchange energy becomes dominant, and, below a critical dimension, the single domain state is the lowest in energy. We can therefore speak of three magnetic regimes characterized by different types of equilibrium states (Vaz *et al*., 2006): the *multidomain* state regime, for elements with dimensions typically above $\sim$2 μm, which exhibit equilibrium states with magnetic domains of uniform magnetization; the *nonuniform* magnetic state regime, for sizes in the range $\sim$0.2–2 μm, where the states of lowest energy correspond to complicated magnetic configurations which are a result of a delicate balance between the different energy terms and which cannot be described by individual magnetic domains (Vaz *et al*., 2005); and the *quasiuniform* regime, for sizes below $\sim$200 nm, which is characterized by magnetic states that closely resemble the uniform state (Barbara, 2005). These boundaries are not rigid, however, and depend strongly on the strength of the magnetic anisotropy, among other factors, but our view is that they are qualitatively correct for most *3d* cubic and polycrystalline magnetic materials.

While the sensitivity of the magnetic energy to the shape of the element opens an endless range of possibilities for the study of small structures, in practice, we may expect that simple magnetic states may be more stable in highly symmetric structures, such as circles, squares, rings, ellipses, or wires. These structures have in fact received the bulk of the attention in this research area, partly because of their potential for technological applications, where simple and reproducible magnetic states with fast magnetic switching are key.

3.1 Exchange energy

This is the energy term which is at the origin of ferromagnetic order. Its microscopic origin is related to a combination of the Pauli exclusion principle and the Coulomb repulsive interaction between ions. Depending on the particular atomic arrangement, it may lead to several magnetic spin arrangements, such as ferromagnetism (Fe, Co, Ni, Gd, Dy, CrO_2, etc.), antiferromagnetism (Cr, FeO, CoO, NiO, FeMn, etc.), ferrimagnetism (γ-Fe_2O_3, Fe_3O_4, $Y_3Fe_5O_{12}$, etc.), helicoidal magnetism (Ho, Er), and so on. (Keffer, 1966; Gautier, 1982; Hurd, 1982; Pierre, 1982). Here we shall consider

only ferromagnetic materials, but ferrimagnets are susceptible to an identical analysis; the case of antiferromagnetism requires a special treatment, since these materials exhibit properties that are quite different from those of ferromagnets (Nagamiya, Yosida and Kubo, 1955; Fawcett, 1988; Fawcett *et al*., 1994; Aeppli, 2004).

The exchange energy is minimum when all spins are aligned parallel to each other, and, therefore, as far as this energy term is concerned, states of uniform magnetization are the lowest in energy. Although the strength of the exchange interaction is very high (of the order of $k_B T_c$, where T_c is the Curie temperature) it is, however, a short range interaction, such that, over large samples, other magnetic energy terms may be comparable or larger. This marks the transition from a state of uniform to a state of nonuniform magnetization; this transition has received particular attention over the years due to its practical implications for the manufacture of permanent magnets and particulate recording media. In fact, one could say that nanomagnetism is a field that dates from the early 1930s, when Frenkel and Dorfman (1930) first estimated the critical size for a single domain particle.

It is worth noting that, although the 3*d* transition metals are itinerant systems due to the high electron hopping frequency, the orbital bands responsible for the magnetic order (the 3*d* bands) are fairly localized such that the description of the exchange energy by the Heisenberg Hamiltonian is a good approximation. In fact, it has been suggested that the band structure of ferromagnets remains largely unaltered at temperatures above the Curie temperature, suggesting that the paramagnetic phase is not a result of the collapse of the band exchange spliting, but is rather due to spin disorder introduced by thermal agitations (Korenman, 1983). A unified description of localized and itinerant magnetism has been provided in the context of the generalized spin-fluctuation picture developed by Moriya (1985).

Although magnetic order arises ultimately from the electron spin (of the 3*d* bands in the case of the 3*d* transition metals and from the 4*f* orbitals in the case of the 4*f* transition metals), it is usually sufficient to consider a continuum approximation when the size of the magnetic system is much larger that the atomic dimensions; in this case, the Heisenberg Hamiltonian gives for the excess exchange energy for cubic or isotropic materials due to inhomogeneous spin configurations (Landau and Lifshitz, 1935; Carr, 1966; Kittel, 1987) (See also **General Micromagnetic Theory, Volume 2**):

$$E_{\text{ex}} = A \int_{\Omega} (\nabla \mathbf{m})^2 \, \mathrm{d}v \tag{1}$$

where A is the exchange constant, $\mathbf{m} = \mathbf{M}/M_s$ is the magnetization unit vector (M_s is the saturation magnetization) and Ω is the volume.

3.2 Magnetostatic self-energy

This is the classical interaction energy between magnetic dipoles. It is a long-range term and the source of most complications as far as magnetic configurations are concerned. There are several ways in which this term can be represented; perhaps the most common is to note that, in the absence of electric currents and in the static case, Maxwell's equations give $\nabla \times \mathbf{H} = 0$, that is, $\mathbf{H}$ is irrotational and therefore can be written as the gradient of a potential ϕ whose source is given by the fictitious magnetic charge distribution $\nabla^2 \phi = -\nabla \cdot \mathbf{H} = \nabla \cdot \mathbf{M}$ (Jackson, 1975; Brown, 1962). Although a solution for ϕ can be written explicitly, its calculation is often very difficult:

$$\phi(\mathbf{r}) = -\frac{1}{4\pi} \int_{\Omega} \frac{\nabla \cdot \mathbf{M}(\mathbf{r}')}{|\mathbf{r} - \mathbf{r}'|} \, \mathrm{d}v + \frac{1}{4\pi} \int_{\partial\Omega} \frac{\mathbf{n} \cdot \mathbf{M}(\mathbf{r}')}{|\mathbf{r} - \mathbf{r}'|} \, \mathrm{d}s \tag{2}$$

where $\mathbf{n}$ is the unit vector perpendicular to the volume surface $\partial\Omega$. The field $\mathbf{H}_d = -\nabla\phi$ is called the *magnetic dipolar field* and it tends to oppose the direction of magnetization (inside the magnetized body); the magnetostatic energy is given by

$$E_{\text{MS}} = \frac{\mu_0}{2} \int_{\Omega} \mathbf{H}_d \cdot \mathbf{M} \, \mathrm{d}v \tag{3}$$

This is the energy term that is responsible for the existence of magnetic domains: it favors states of closed flux magnetization and therefore competes directly with the exchange energy term. Only in simple cases it is possible to express the magnetostatic energy analytically: in single domain particles with very regular geometries, thin films, and infinite wires. Since it is a global term, it is the most difficult and lengthy energy term to calculate in micromagnetic simulations.

3.2.1 Demagnetizing factor

The calculation of the magnetostatic energy is significantly simplified in the case of uniform magnetized states, for which the first term of (2) is zero. It is often easier to calculate the magnetostatic energy than the dipolar field explicitly, and we call the ratio between this energy and the factor $\mu_0 M_s^2/2$ the *magnetometric demagnetizing factor*, or demagnetizing factor for short. The usefulness of these expressions is that we may compare the energy of the uniform state with that of other nonuniform configurations and determine the phase diagram separating the regions of stability for each of the magnetic states. This requires, however, that energy expressions for the other states are available and also a knowledge of what other magnetic states may be stable. Good guesses are based on the symmetry of the element, but more accurate knowledge can be obtained from the results

of micromagnetic simulations. While the demagnetizing factors for ellipsoids have been made available for a long time (Maxwell, 1891), a useful presentation of the results have been provided by Osborn (1945) and Stoner (1945) along the revolution axes and for a range of particular cases. The case of cylinders and disks has also been considered extensively (Joseph, 1966; Kaczér and Klem, 1976; Hegedus, Kadar and Torre, 1979; Aharoni, 1981; Chen, Brug and Goldfarb, 1991; Goode and Rowlands, 2003; Beleggia *et al*., 2005), including approximate expressions for the limiting cases of wires and disks (Joseph, 1966, 1976). The case of a flat square prism has also been considered by Joseph (1976), while the demagnetizing factor for rings have been studied by several authors (Kaczér and Klem, 1976; Hegedus, Kadar and Torre, 1979; Chen, Brug and Goldfarb, 1991; Vaz, Athanasiou, Bland and Rowlands, 2006).

3.3 Magnetic anisotropy

Magnetic anisotropy refers to variations in the magnetic energy with the spatial orientation of the magnetization. From a microscopic perspective, several terms can be distinguished, such as the intrinsic magnetocrystalline anisotropy, the magnetoelastic anisotropy, surface anisotropy, field-induced anisotropy (all of which originate microscopically from the spin-orbit coupling), growth-induced (morphology related) anisotropy, exchange anisotropy, and so forth. However, from a macroscopic perspective, we may collect all the energy contributions with a given symmetry into a single *effective anisotropy* when discussing its effect on the equilibrium or dynamic behavior of the magnetization configuration. This is useful on many counts. For example, one often deals with polycrystalline materials, which consist of small crystallites randomly oriented with respect to each other such that no anisotropy is present, that is, the material behaves as an isotropic material. In weakly anisotropic materials, this is a good description if the crystallite size is of the order of the exchange length of the material or smaller, but for larger crystallite sizes local deviations of the magnetization may occur; in the other extreme, for very small elements composed of a small number of crystallites, it may be possible that the magnetic anisotropy no longer averages to zero, and an effective magnetocrystalline anisotropy may remain, which needs to be taken into account (New, Pease and White, 1996; Ross *et al*., 2000; Spargo, Ridley, Roberts and Chantrell, 2002).

Phenomenologically, one can write the magnetic anisotropy energy in terms of the direction cosines of the magnetization consistent with the magnetic symmetry of the system. For a cubic system, the general expression is of the form:

$$E_{\text{cub}} = \int_{\Omega} \left(K_1 \sum_{i>j} \alpha_i^2 \alpha_j^2 + K_2 \alpha_1^2 \alpha_2^2 \alpha_3^2 + K_3 \sum_{i>j} (\alpha_i^2 \alpha_j^2)^2 + \ldots \right) \mathrm{d}v \tag{4}$$

where K_1, K_2, and so on are the effective anisotropy constants.

3.4 Zeeman energy

This energy term corresponds to the dipole interaction with an external magnetic field. For a uniform field, its effect is that of exerting a torque on the dipole moment when this is aligned along directions different from that of the external field. The expression for this energy term is given by

$$E_{\text{Zeeman}} = -\mu_0 \int_{\Omega} \mathbf{H}_0 \cdot \mathbf{M} \, \mathrm{d}v \tag{5}$$

3.5 Lengthscales in magnetism

The preceding expressions for the magnetic energy terms allows one, in principle, to calculate the equilibrium states that minimize the Landau free energy of the system, given by

$$G(\mathbf{H}, T) = U - TS - \mu_0 \int_{\Omega} \mathbf{H_0} \cdot \mathbf{M} \, \mathrm{d}v \tag{6}$$

where S is the entropy, T the temperature, and U the internal energy of the system (which includes the previously mentioned magnetic energy terms and is a functional of the magnetization configuration); the last term is the Zeeman energy term. Such a calculation is, in general, very complicated, and here we shall consider only the equilibrium state at zero temperature. This approximation is justified if the energy barriers that have to be overcome during switching are much higher than the thermal energy (i.e., temperature) of the system. In this case, it is possible to calculate numerically the magnetic equilibrium state as a function of applied fields in the continuum approximation (*micromagnetism* (Brown, 1963; Aharoni, 1996)); while in principle the equilibrium configurations can be calculated analytically from Brown's equation (Brown, 1963); in practice such calculations can only be carried out in some special cases. When the atomic structure of the system cannot be neglected, the spins have to be treated individually and quantum effects have to be taken into account (Hilzinger and Kronmüller, 1972, 1973;

Wernsdorfer, 2001). We consider here systems where micromagnetics should still hold (See also **General Micromagnetic Theory, Volume 2**), and we shall limit ourselves to quasistatic equilibrium processes, that is, we assume that the applied magnetic field changes slowly compared to the magnetization dynamics.

A case that can be solved analytically is that of a system that acts like a macrospin, that is, a system with uniformly aligned magnetization (single domain particle). As discussed in the preceding text, this state is favored by the exchange interaction but comes at a cost of magnetostatic energy. We can obtain an estimate of the dimensions of a magnetic particle below which it is a single domain by comparing the order of magnitude of the exchange energy ($\sim Al$) and magnetostatic energy ($\sim \mu_0 M_s^2 l^3/2$); this gives the characteristic *exchange length* $l_s = (2A/\mu_0 M_s^2)^{1/2}$, below which twisting of the magnetization is energetically unfavorable; this also follows from the scaling of the energy terms (Schabes and Bertram, 1988; Hertel, 2004). For larger particles, another characteristic lengthscale which is of importance is the *domain wall width*, $l_k = (A/K)^{1/2}$, which gives an indication of the strength of the anisotropy energy with respect to the exchange energy (and therefore determines the width of the domain wall separating magnetic domains in multidomain states). In this context, it is worth mentioning a third parameter corresponding to the ratio between the magnetic anisotropy constant and the magnetostatic energy, $Q = 2K/\mu_0 M_s^2$, called the *quality factor*. This is an important parameter in perpendicularly magnetized films (See also **Alternative Patterning Techniques: Magnetic Interactions in Nanomagnet Arrays, Volume 3**).

4 SINGLE DOMAIN SYSTEMS WITH UNIFORM MAGNETIZATION

When analyzing a magnetic system, we are firstly interested in the stable equilibrium magnetization configurations, that is, the directions of the spins in the system for a given set of external parameters. From this information, key properties, such as the switching fields, can be deduced. In general, due to the large number of degrees of freedom, such an analysis has to be carried out using numerical techniques. A more easily accessible case is a single domain system, where the magnetization configuration can be described by a single angle of a macrospin. We start with the description of such a system, where instructive analytical calculations are possible, to illustrate how the different energy terms discussed in the preceding text govern the magnetic behavior.

4.1 Theory of single domain systems: the Stoner–Wohlfarth model

If a system is in a single domain state in equilibrium and the spins rotate uniformly during reversal, then it can be described by a macrospin model. While single domain systems may reverse by inhomogeneous modes, such as curling (Aharoni, 1996; Frei, Shtrikman and Treves, 1957; Kronmüller and Fähnle, 2003) (see Section 7.3), we start here with a system with a uniform magnetization at all times.

The simplest classical model describing single domain systems with coherent rotation was developed by Stoner and Wohlfarth (1948), and Néel (1947) and is commonly referred to as the *Stoner–Wohlfarth model*. The aim of this model is to analytically calculate the equilibrium directions of the magnetization for a given anisotropy and a given applied field (and field history). Further, for a magnetic field applied along a given direction, one can calculate the field value at which the magnetization reverses.

Since spatial variations do not have to be taken into account in this model, the exchange energy does not play a role and the magnetic switching is governed by the interplay between the Zeeman energy and the effective anisotropy. In line with the original calculations (Stoner and Wohlfarth, 1948), we restrict ourselves here to the two-dimensional case, which is easier to understand intuitively (many experimental thin film systems can be described to a first approximation by the two-dimensional mode). The theory has, however, been extended to three dimensions by Thiaville (Thiaville, 1998, 2000) to deal with systems such as clusters (Jamet *et al.*, 2001).

Well below the Curie temperature, the magnetization vector can be assumed to be of constant length, so that the problem of finding the magnetization direction angle θ that minimizes the energy for a given applied field $\mathbf{H}$ with the direction ϕ can be mathematically formulated as follows:

$$E(\mathbf{h}) = \min[F(\mathbf{m}(\theta)) - 2\mathbf{h} \cdot \mathbf{m}(\theta)] \tag{7}$$

Here $\mathbf{m} = \mathbf{M}/M_s$ is the normalized magnetization direction vector, $F(\mathbf{m})$ is the anisotropy energy density divided by the anisotropy constant K and $\mathbf{h} = \mu_0 \mathbf{H} M_s/2K$ is the reduced applied field. In polar coordinates, $\mathbf{m} = (\cos\theta, \sin\theta)$ and the orthogonal vector is $\mathbf{e} = (-\sin\theta, \cos\theta)$. In equilibrium

$$\frac{\mathrm{d}E}{\mathrm{d}\theta} = \frac{\mathrm{d}F}{\mathrm{d}\theta} - 2\mathbf{h} \cdot \mathbf{e} = 0 \tag{8}$$

and whether the position is a stable minimum or not can be determined by the second derivative:

$$\frac{\mathrm{d}^2E}{\mathrm{d}\theta^2} = \frac{\mathrm{d}^2F}{\mathrm{d}\theta^2} + 2\mathbf{h} \cdot \mathbf{m} \tag{9}$$

This determines the equilibrium magnetization direction for a given field. Now, one is interested in the critical field where the solution becomes unstable, that is, when the second derivative is zero (saddle point). Using both equations to solve for the x and y components of the critical field $\mathbf{h_c}$ one obtains

$$\mathbf{h_c} = \frac{1}{2}\left(\frac{\mathrm{d}F}{\mathrm{d}\theta}\mathbf{e} - \frac{\mathrm{d}^2F}{\mathrm{d}\theta^2}\mathbf{m}\right) \tag{10}$$

For a twofold anisotropy $F = K_t \sin^2\theta$ this gives

$$h_{c,x}(\theta) = \cos^3\theta \tag{11}$$

$$h_{c,y}(\theta) = \sin^3\theta \tag{12}$$

For a given magnetization direction defined by θ, one obtains a critical field strength and field direction where the energy of the system has a saddle point. Hence, if a field larger than the critical field is applied, there is only one stable direction for the magnetization. If one considers, *M-H* hysteresis loop measurements, the magnetization exhibits an irreversible jump at the critical field. For the twofold anisotropy, a polar plot of $\mathbf{h_c}$ (Stoner–Wohlfarth asteroid) is shown in Figure 1. The aim, which was to express the critical field as a function of the applied field direction $\mathbf{h_c}(\phi)$, has not been reached yet as only $\mathbf{h_c}(\theta)$ has been determined. The relationship between the two angles is given by

$$\phi = \arctan(h_{c,y}(\theta)/h_{c,x}(\theta)) \tag{13}$$

In the case of twofold anisotropy, this can be solved follows: $\theta = \arctan(\tan^{1/3}\phi)$. $\theta(\phi)$ can then be introduced into equations (11) and (12) and the well-known formula for the dependence of the switching field on the angle of the applied field is obtained (Kronmüller and Fähnle, 2003):

$$h_c(\phi) = (\sin^{2/3}\phi + \cos^{2/3}\phi)^{-3/2} \tag{14}$$

While there is an explicit formula for the switching fields, the hysteresis loops in general have to be calculated numerically. For the case of twofold anisotropy, the result is shown in Figure 2. Further information and explanations can be found in Slonczewski (1956), Wernsdorfer (2001), Kronmüller and Fähnle (2003).

Now we consider the case of a fourfold anisotropy, where a general analytical expression for the switching field $\mathbf{h_c}$ as a function of the angle of the applied field cannot be calculated (even though analytical expressions for fields applied close to the hard and easy axes can be derived (Kläui, 2003)).

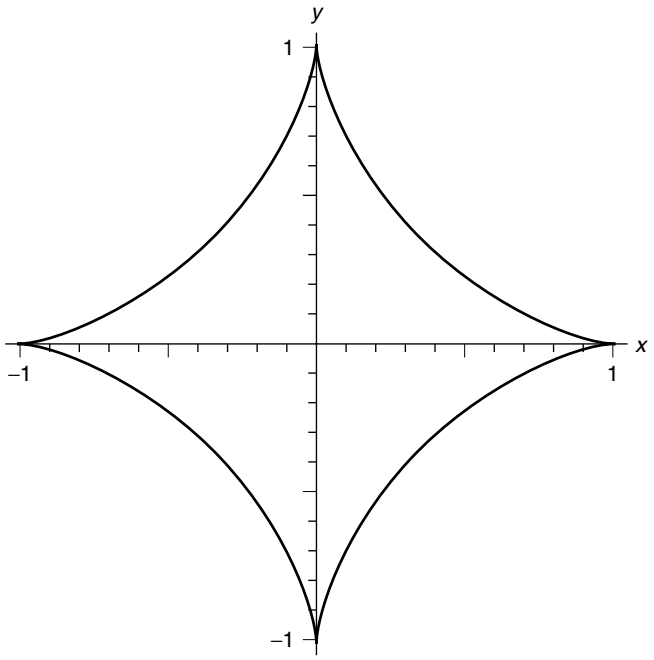

Figure 1. Plot of the critical fields (solid line) for a twofold anisotropy.

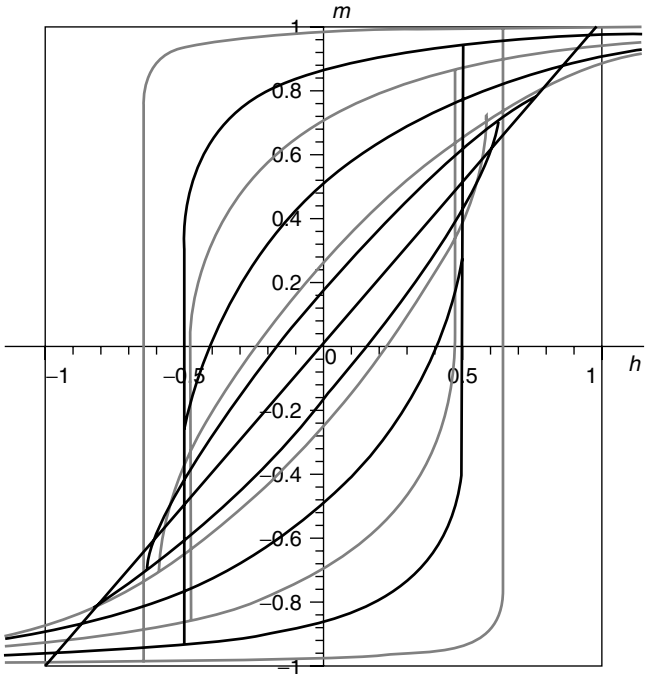

Figure 2. Longitudinal *M-H* hysteresis loops for 0 (innermost line through the origin, hard axis), 5, 10, 30, 45, 60, 85, and 90 (outermost square loop, easy axis) degrees away from the hard axis for the case of a twofold anisotropy.

In the case of the fourfold anisotropy, $F = K_1 \sin^2 2\theta$, and inserting this expression into equation (10), we obtain

$$h_{c,x}(\theta) = \frac{-5}{4}\cos 3\theta - \frac{3}{4}\cos 5\theta \tag{15}$$

$$h_{c,y}(\theta) = \frac{5}{4}\sin 3\theta - \frac{3}{4}\sin 5\theta \tag{16}$$

Again, *M-H* measurements along the easy or hard axis show jumps at the critical field. For other angles, more complicated multistep switching occurs corresponding to transitions between different local energy minima, which are due to the presence of two easy axes in the fourfold anisotropy case (Wernsdorfer, 2001). The angular dependence of the switching fields is presented in Figure 3.

Owing to the additional energy minima, the interpretation of these graphs is not as straightforward as in the case of a twofold anisotropy (an in-depth description on how to interpret them can be found in Thiaville (1998), and Wernsdorfer (2001)).

The preceding results provide a framework with which to interpret experimental data. Firstly, if a system exhibits a simple uniaxial (twofold) or cubic (effectively, a fourfold anisotropy in two dimensions) anisotropy and we know the saturation magnetization, we can deduce the anisotropy constants. In general, however, more than one anisotropy term is present in real systems and the anisotropy energy terms can be expanded in a power series of $m_x^a m_y^b m_z^c$ with $a + b + c = 2, 4, 6$ etc. Calculations of the switching fields for different anisotropies indicate, in fact, that there is not necessarily a simple map between the switching fields and the anisotropies, meaning that the switching fields can be calculated from the anisotropies, but not necessarily vice versa, which is usually the desired case.

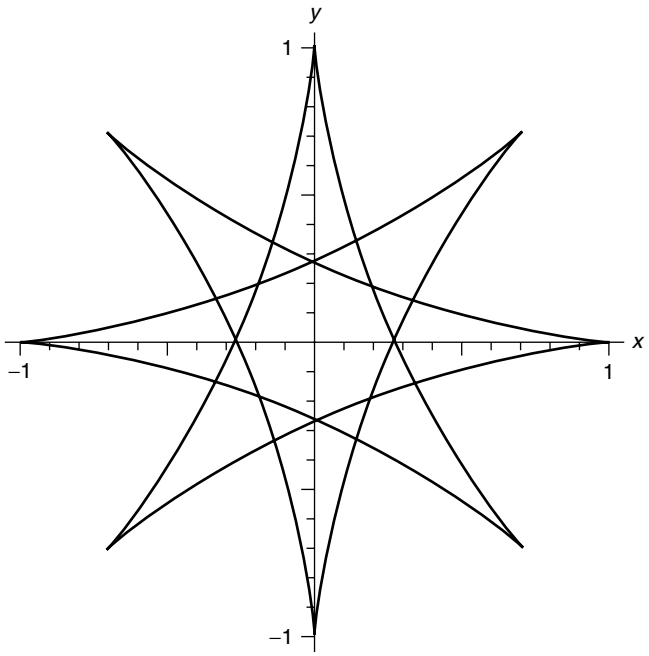

Figure 3. Plot of the critical fields (solid line) for a fourfold anisotropy.

4.2 Experimental observations of single domain systems

Structures which reverse via coherent rotation are promising for applications (Prinz, 1999, 1998) as this switching process can occur on very short timescales (Schumacher *et al*., 2003). Coherent rotation is predominantly found in small particles where the exchange energy dominates. For the fabrication of small magnetic elements, top-down and bottom-up approaches have been put forward (Martín *et al*., 2003; Terris and Thomson, 2005). Top-down patterning using standard lithographic methods allows us to fabricate structures easily down to lateral sizes of around 50 nm (Martín *et al*., 2003). For these sizes, one can simply engineer the shape anisotropy by varying the element geometry, but such top-down fabricated structures often do not exhibit the properties expected of single domain particles that reverse via coherent rotation. In particular, the angular dependence of the switching fields fits the Stoner–Wohlfarth behavior only for angles close to the hard axis, where the effects of defects, domain formation, and, in general, twisting of the spins away from the single domain configurations are not very significant (Wernsdorfer *et al*., 1995a,b). Even though some structures show an angular dependence of the switching fields, which is, for some directions, similar to the Stoner–Wohlfarth asteroids magnetic, relaxation experiments revealed a nucleation volume that is much smaller than the physical volume (Fruchart *et al*., 1999; Wernsdorfer *et al*., 1995a,b) and most of the larger elements display complicated domain structures (Section 6). The bottom-up technique has been shown to be more fruitful for the fabrication of single domain particles. In particular, clusters fabricated by laser ablation or in dedicated cluster sources have been shown to be uniform in size with up to some 1000 atoms and with diameters of a few nanometers (Jamet *et al*., 2001), and these exhibit well-defined anisotropies. Although small, these clusters are essentially three-dimensional in shape, whereas the thin film elements discussed earlier are flat.

It should be mentioned that measurements on such small structures are extremely challenging. In particular, since the anisotropies of these elements can be randomly oriented, individual structures need to be measured with extremely high magnetic sensitivity. A powerful technique that is well suited for such measurements is the μ-SQUID technique

pioneered by Mailly, Chapelier and Benoit (1993) and Wernsdorfer (2001), which is capable of determining the angular dependence of the switching fields for comparison with calculated Stoner–Wohlfarth asteroids.

The first systems for which clear coherent rotation was observed with this technique were BaFeO nanoparticles with a pronounced twofold anisotropy (Wernsdorfer *et al*., 1997a) and Co nanoparticles (Bonet *et al*., 1999; Jamet *et al*., 2001), which were fabricated in a matrix using a laser vaporization and inert gas condensation source. An example of the angular dependence of the switching field distribution of such a particle with twofold anisotropy is shown in Figure 4. The measured asteroid follows very closely the theoretical asteroid (Figure 1). While we do not discuss thermal effects here, it should be pointed out that they have been studied and lead to a reduction in the switching fields with increasing temperature (Wernsdorfer, 2001).

Alternatively, nanodisks have been fabricated by depositing magnetic material on top of prepatterned nanopillars (Kläui *et al*., 2002a). In this approach for the fabrication of small circular elements with diameters down to a few nanometers, Au colloids with diameters down to 5 nm are used as etch masks (Lewis and Ahmed, 1999). After patterning of the semiconductor substrate into nanopillars, the metal nanodisk layers are grown with molecular-beam epitaxy (Kläui *et al*., 2002a). A scanning electron microscopy (SEM) image and a scanning transmission electron microscopy (STEM) image of such fabricated structures are shown in Figure 5. In the STEM image, a clear contrast between the silicon pillar, the cobalt, and the gold-capping layer is visible.

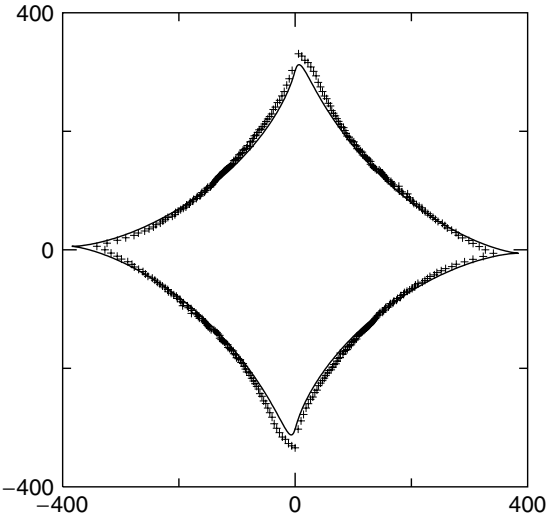

Figure 4. Stoner–Wohlfarth asteroid for a Co particle with a twofold anisotropy: comparison between experiment (crosses) and theory (solid line). Both scales are in mT ($1\,\mathrm{mT} \approx 800\,\mathrm{Am}^{-1}$). (Reprinted figure with permission from Bonet *et al*., *Phys. Rev. Lett.* **83**, 4188 (1999). Copyright 1999 by the American Physical Society.)

In Figure 6, three examples of measurements of the angular switching field dependence are shown (cold-mode measurement, for details see Wernsdorfer (2001)). These were taken on three individual 30-nm wide pillars with a 15-nm-thick Co nanodisk on top (Thirion *et al*., 2006). Figure 6 (a) shows an example of a dominant twofold anisotropy, which is very similar to the previously discussed case of a pure twofold anisotropy (see Figure 1).

The fit in Figure 6(a) (solid line) was obtained by rotating the twofold anisotropy term and invoking a three-dimensional model to account for a tilting between the μ-SQUID and the plane of the nanodisk. In (b), a particle with a dominant fourfold anisotropy is shown, which exhibits an asteroid that is very similar to that of a pure fourfold anisotropy (Figure 3). The particles are round, so no in-plane shape anisotropy is expected, and the magnetocrystalline anisotropy of fcc Co is cubic, so a perfect crystal should have a purely cubic anisotropy (in Jamet *et al*. (2001) high-resolution images revealed small Co elements in the fcc phase). For a thin film system, the anisotropy is then reduced to a fourfold anisotropy in the plane. In nanoclusters and other small particles, this cubic magnetocrystalline anisotropy had always been superseded by surface or defect-induced strong uniaxial (twofold) anisotropy terms (Wernsdorfer, 2001; Jamet *et al*., 2001). As seen in Figure 6(b), there are nanodisks that exhibit a nearly perfect fourfold anisotropy, meaning that, in some of these nanodisks, the anisotropy is governed by the magnetocrystalline anisotropy with an extracted anisotropy constant that is very similar to what has been measured on fcc Co films (Krams *et al*., 1992). Thus, in these structures, defects (in the magnetic film such as stacking faults, local oxidation etc., and shape deviations from a perfectly round disk) are less important. When defects are artificially introduced, for instance, by letting the sample oxidize in air, the twofold anisotropies start to dominate and all nanodisks exhibit asteroids such as the one in Figure 6(a). Thus, by measuring the anisotropies, the quality of the nanodisks can be judged and consequently the relation between fourfold magnetocrystalline and defect-induced twofold anisotropy can be used as a quality-gauge tool.

For the case of a mixed cubic and uniaxial anisotropy, as shown in Figure 6(c), the simulated asteroid does not reproduce the measured asteroid very well, which points to the already mentioned difficulty that there is no easy way to extract the anisotropy constants for an arbitrary measured asteroid. Since we have restricted ourselves to a combination of fourfold and twofold anisotropies, neglecting any other anisotropies and higher-order terms, the discrepancy is not surprising.

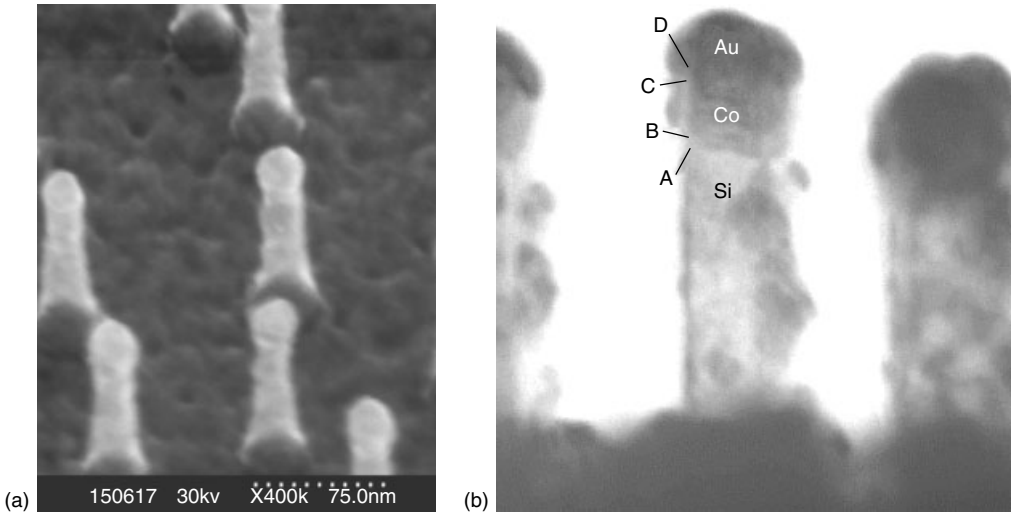

Figure 5. (a) SEM image of Si pillars after etching and removal of the 30-nm large gold colloids but before the metal deposition shows a nanopillar with a round top. (b) Bright field STEM image of a single 30-nm wide nanopillar with Au(6 nm)/Cu(2 nm)/Co(15 nm) deposited on top, showing a clear contrast between the different layers (the materials were identified using electron energy loss spectroscopy, EELS: A, silicon; B, C, cobalt, and D, gold). (Reprinted from Fabrication & Magnetic properties of patterned epitaxical nanodots. *Microelectron. Eng.*, **61**, 593. M. Kläui *et al*.)

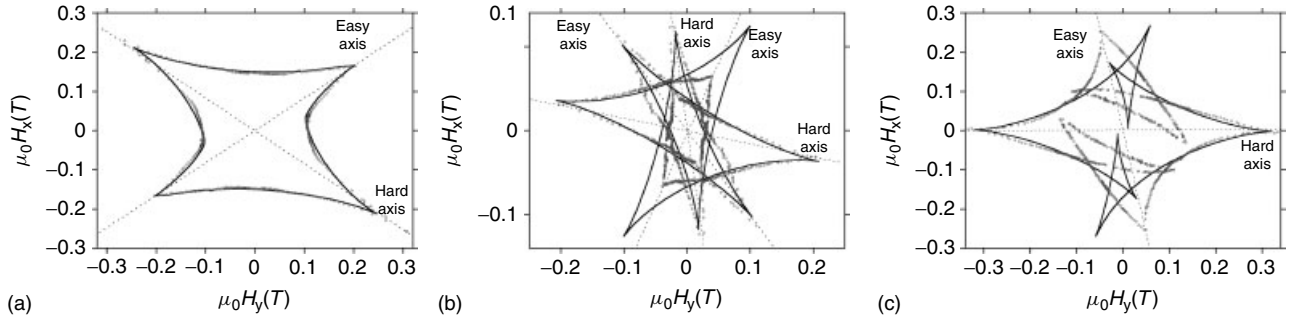

Figure 6. Stoner–Wohlfarth asteroids measured for different nanodisks of the same sample (30-nm-wide dots with 15-nm thick Co on Si pillars). (a) Measured (circles) and simulated (full line) asteroid with a dominant twofold anisotropy. (b) Measured and simulated asteroid with a dominating fourfold anisotropy. (c) Asteroid corresponding to a mixed fourfold and twofold anisotropy with different strengths and different easy and hard axis directions. (C. Thirion, W. Wernsdorfer, M. Klaui, C.A.F. Vaz, P. Lewis, H. Ahmed, J.A.C. Bland and D. Mailly in Nanotechnology 17, 1960–1963 (2006) IOP Publishing Ltd.)

Thus, we see that while the basics of the Stoner–Wohlfarth model are easy to grasp, the calculations even for the two simplest cases of a twofold and a fourfold anisotropy are already difficult and not always analytically solvable. Comparison to experimental observations shows good agreement for some systems, but the limitations of the model become already apparent for slightly more complicated systems.

5 NONUNIFORM STATES

For particle sizes above a critical dimension, one expects the uniform state to become energetically unfavorable due to the contribution of the magnetostatic energy term; magnetic configurations that lower the latter energy tend to be states that minimize magnetic flux leakage from the sample, while simultaneously conforming with the topology of the element (Tchernyshyov and Chern, 2005). Such states have been studied theoretically for many decades in the context of the critical size for single domain particles (Aharoni, 1996), but the recent development of imaging techniques has allowed the direct probing of the magnetic configuration of small elements, particularly those fabricated from thin films, since most techniques are only sensitive to the surface spin distribution. In this case, one often assumes that the magnetization does not vary with thickness (ultrathin film regime),

which in thin films is valid when the film thickness is smaller or comparable to the exchange length. In small elements, one expects this to be valid, but the presence of perpendicular interface anisotropies or large surface roughness, for instance, may lead to nonuniform distributions of the magnetization along the out-of-plane direction.

In this section, we are interested in describing the different magnetic states that occur in small elements in the size range from around 200 nm up to around 2 μm, where multidomain states have not yet set in. These states are characterized by relatively complicated spin configurations where the magnetization tends to vary over the whole element and does not lend to a simple analytical description, except in some cases. This complexity is a result of the fine balance between the different energy terms, exchange, magnetostatic, and anisotropy, and is intimately connected with the physical shape of the element (via the magnetostatic energy contribution). Often, several magnetic states are local minima of the total energy and in principle can be stabilized and observed if the energy barrier separating the different minima is higher than the thermal or other excitations.

Of the geometries that have been most studied, disks and cylinders, prisms, ellipses, and wires are among the most widespread. The advantage of such geometries is that they are simple enough to have cylindrical or Cartesian symmetry (and therefore one expects relatively simple equilibrium magnetic states) while still containing just enough complexity to make them ideal choices for the study of the magnetism of small elements. Next, we consider each of these geometries separately, with particular focus on the equilibrium properties. However, we shall also include some discussion of the steady-state magnetization dynamics, such as spin-wave modes (See also **Magnetic Modes in Circular Thin Film Elements, Experiment and Theory, Volume 2**, **Spin Waves: History and a Summary of Recent Developments, Volume 1**, **Spin Structures and Spin Wave Excitations, Volume 3**, and **Investigation of Spin Waves and Spin Dynamics by Optical Techniques, Volume 3** for a more detailed discussion).

5.1 Disks

The disk geometry is the simplest of the planar geometries described here, but this simplicity can be misleading. While to first order it can be approximated by a very flat ellipsoid, it turns out that such an approximation is not a very accurate one, as far as the magnetostatic energy density is concerned (it is underestimated) (Pardavi-Horvath, 1999). Topologically, the edges of the disk introduce singularities in the magnetic potential, and theoretically the ground state of such elements is not the uniform state (Usov, 1993), although for small enough structures the deviations from the uniform state are negligible (Brown, 1969; Aharoni, 1996). As the size of the disk increases, the magnetostatic energy density contribution also increases (linearly with thickness for in-plane magnetized elements) up to a point where the uniform state is no longer the lowest in energy. The theoretical determination of such nonuniform equilibrium states is not possible, since the Brown equation for such a general case is too difficult to be solved analytically; the states we know are the result of either good guesses (such as the vortex state), or the result of micromagnetic simulations and experimental observation.

Stable magnetic nonuniform states at remanence for in-plane magnetized disks with low anisotropy include the vortex state (Cowburn *et al*., 1999; Schneider, Hoffmann and Zweck, 2000; Zhu and Zheng, 2002; Vaz *et al*., 2003), the C-state (Guslienko *et al*., 2002; Ha, Hertel and Kirschner, 2003; Wei *et al*., 2003), the S-state (Guslienko *et al*., 2002; Ha, Hertel and Kirschner, 2003), the triangle state (Zhu and Zheng, 2002; Guslienko *et al*., 2002; Vaz *et al*., 2005), and the diamond state (Prejbeaunu *et al*., 2002; Zhu and Zheng, 2002; Vaz *et al*., 2005) (see Figure 7). The C, S, and triangle states have a relatively large remanence and can be seen as deviations from the uniform state in order to accommodate the larger contribution of the magnetostatic energy. The C and S states have been predicted to be stable for small diameters and are therefore difficult to resolve experimentally (and it is likely that the uniform state ascribed to high remanence states in disks may be in fact often either of these states); effectively, only for the C-state we are aware of experimental observation in submicrometer $Ni_{80}Fe_{20}$ circular elements (Heumann, Uhlig and Zweck, 2005; Acremann *et al*., 2006). At larger diameters (0.4–2 μm), the triangle state has been predicted from micromagnetic simulations (Zhu and Zheng, 2002; Guslienko *et al*., 2002) and observed experimentally in Co polycrystalline disks 2 μm in diameter (Vaz *et al*., 2005) (see Figure 7c). This is a metastable state which is stabilized by energy barriers separating it from states lower in energy (Vaz *et al*., 2005, 2006). It is characterized by a buckling of the magnetization, and, like the previous two states, by the presence of two 'edge vortices' where a strong stray field is present. The diamond and the vortex state are states of almost zero remanence; the vortex state consists of a circular distribution of the magnetization and is characterized by the presence of a vortex core in the middle of the disk. The diamond state consists of two vortices that resemble a seven-domain configuration in square elements (Figure 7b); however, the magnetization is not uniform in any region except in the inner part of the disk, which is, in any case, not bounded by sharp domain walls (this inner domain resembles a rhombus). Again, the diamond state is not that of lowest

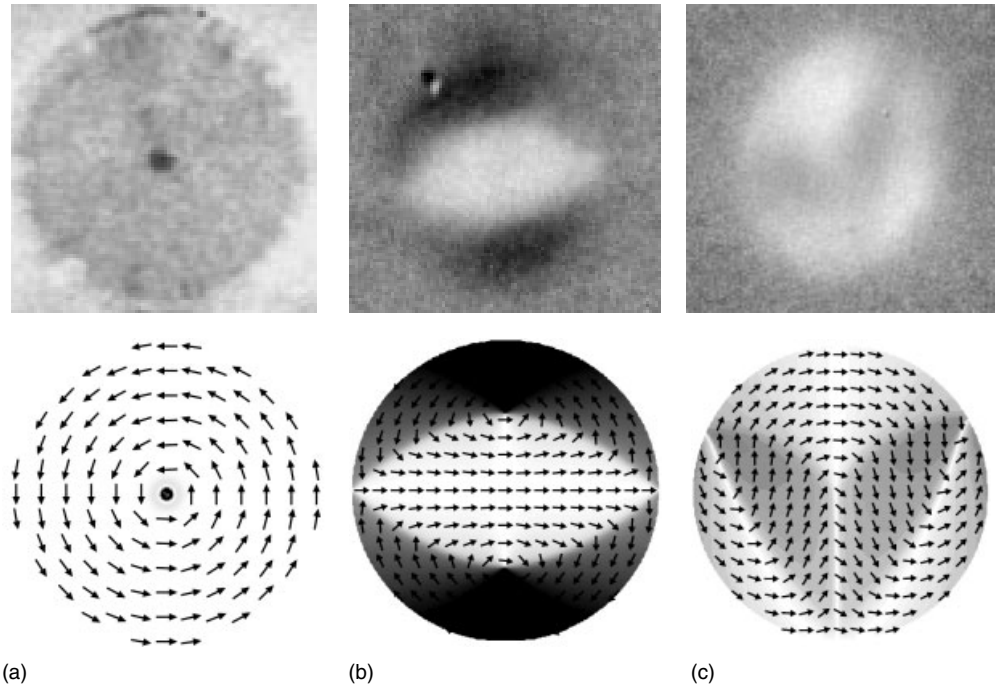

Figure 7. Experimental observation of magnetic states in disk elements and comparison with the results of micromagnetic simulations: (a) Vortex state, showing the out-of-plane magnetization component at the vortex core (MFM, $Ni_{80}Fe_{20}$, 1 μm diameter, 50 nm thick (Reprinted figure with permission from Science AAAS, T. Shinjo, *Science* **289**:930, 2000. Copyright 2000 AAAS.); (b) Diamond state (PEEM, fcc Co, 1.65 μm diameter, 29 nm thick (Vaz *et al*., 2005); (c) triangle state (PEEM, polycrystalline Co, 1.65 μm diameter, 19 nm thick (Vaz *et al*., 2005)). In (b) and (c), the magnetic contrast is along the horizontal direction.

energy, but may be stabilized by the presence of energy barriers separating it from the vortex state (Vaz *et al*., 2005, 2006), and may be nucleated in the process of the magnetization relaxation from the saturated state (Mattheis, Berkov and Gorn, 1999; Prejbeaunu *et al*., 2002).

The vortex state has attracted much attention since it is the ground state of disk elements over a wide range of diameters and thicknesses; the phase boundary for the ground state between the vortex and the uniform state has been well studied theoretically (Jubert and Allenspach, 2004; Vaz, Athanasiou, Bland and Rowlands, 2006) and experimental results also give an idea of the relative stability range (Cowburn *et al*., 1999; Prejbeaunu *et al*., 2002); also, schemes devised to control the circulation of the magnetization have been suggested (Schneider, Hoffmann and Zweck, 2001; Taniuchi, Oshima, Akinaga and Ono, 2005). An interesting aspect of the vortex state is the core at its center, where the large exchange energy cost due to the large twisting of the spins leads to a configuration where the magnetization points along the out-of-plane direction, at a cost of magnetostatic energy. The balance between these two contributions determines the size of the vortex core, which is of the order of the exchange length of the material (Feldtkeller and Thomas, 1965; Usov and Kurkina, 2002; Jubert and Allenspach, 2004; Vaz, Athanasiou, Bland and Rowlands, 2006). The very small out-of-plane component of the magnetization has been observed experimentally (Shinjo *et al*., 2000; Raabe *et al*., 2000; Wachowiak *et al*., 2002; Okuno *et al*., 2002) (see Figure 7a). This is indeed another striking example of the manifestation of the fine balance between these two energy contributions.

The magnetization dynamics of disk elements has also been addressed in the literature; here we mention the steady-state spin-wave dynamics, which has been probed by FMR (Buess *et al*., 2004; Raabe *et al*., 2005; Novosad *et al*., 2005) and BLS (Demokritov, Hillebrands and Slavin, 2001; Novosad *et al*., 2002; Gubbiotti *et al*., 2002; Gubbiotti *et al*., 2006). These experimental results give information about the spectral and spatial components of the spin wave modes and show the existence of both azimuthally and radially excited modes, which are determined largely by the topology of the element (Buess *et al*., 2004; Raabe *et al*., 2005). Other modes of excitation, which occur at much lower frequencies, correspond to the resonant displacement of the vortex core of the disk in the vortex state (Novosad *et al*., 2005), or the gyrotropic mode corresponding to a spiral motion of the magnetization at the vortex core as it approaches the equilibrium position (Park *et al*., 2003). Similar type of excitations

are observed by means of electric current driven excitations, such as the resonant excitation of a vortex wall in nanowires reported by Saitoh, Miyajima, Yamaoka and Tatara (2004).

It is also important to mention the effect of magnetocrystalline anisotropy on the magnetic configuration of disk elements. For in-plane magnetized elements, its effect for low values of the anisotropy is that of distorting the magnetic configuration that is observed in the isotropic case. For example, for fcc Co disk elements, the ground state consists of a hybrid between the vortex state and the quadrant, or Landau–Lifshitz, state: it resembles the vortex state close to the periphery of the disk (in order to minimize the stray field), while close to the center the magnetization becomes uniform along the four directions of easy magnetization, separated by sharp domain walls (Vaz *et al*., 2003, 2004b), again an instructive example of the balance between the three energy terms, anisotropy, exchange, and magnetostatic. This is also apparent when plotting the domain wall width as a function of the radial coordinate, which shows a plateau at small values (corresponding to a value close to the expected domain wall width) and reverts to the geometrical limit (as in the vortex state) for values close to the disk radius; this has been called a *geometrically constrained domain wall*, in analogy with identical geometrical constraints in other magnetic structures (Bruno, 1999; Jubert, Allenspach and Bischof, 2004; Kläui *et al*., 2003b, 2005a). An identical type of distortion on the vortex state due to the presence of a small uniaxial anisotropy has been studied numerically by (Jubert and Allenspach, 2004). It is worth pointing out that the presence of anisotropy tends to favor the uniform state over the vortex state (Jubert and Allenspach, 2004; Vaz, Athanasiou, Bland and Rowlands, 2006). Another state which is favored in disks with strong uniaxial anisotropy is the bidomain state, as observed in 34-nm Fe(110)/GaAs(110) epitaxial elements 1–4 μm in diameter (Pulwey, Zölfl, Bayreuther and Weiss, 2002) (in the same study, a Landau–Lifshitz state for Fe(100) disks with cubic anisotropy is reported, but the details of the domain wall cannot not be resolved from the MFM images obtained). Another situation occurs when a perpendicular magnetic anisotropy is present; in this case, the magnetization may no longer be confined to the plane of the element and other magnetic states may occur. The relative importance of the perpendicular magnetic anisotropy is measured by the *quality factor* Q (see Section 3.5). For quality factors close to or larger than one, perpendicular states of the magnetization are favored; this can be a simple uniform state, but other low-energy states are possible, such as the bubble state, bidomain states, or other more complex configurations (Hehn *et al*., 1997; Ohno, Miyajima, Shigeto and Shinjo, 1999; Eames and Dahlberg, 2002; Skidmore, Kunz, Campbell and Dan Dahlberg, 2004; Komineas, Vaz, Bland and Papanicolaou, 2005; Kageyama and Suzuki, 2006). A review covering perpendicularly magnetized elements is given in **Alternative Patterning Techniques: Magnetic Interactions in Nanomagnet Arrays, Volume 3**.

5.2 Rings

A geometry that has received much attention recently is the ring geometry. It differs from the disk geometry in that it has a lower energy vortex state due to the absence of the energetically costly vortex core (Zhu, Zheng and Prinz, 2000; Rothman *et al*., 2001); one consequence of this is that the vortex state is more stable compared to the uniform state (in addition, the presence of extra surfaces in the inner hole also results in an increase in the magnetostatic energy of the uniform state (Vaz, Athanasiou, Bland and Rowlands, 2006)). However, it was observed experimentally that such structures are able to attain a high remanence state, called the *onion state* (Rothman *et al*., 2001; Li *et al*., 2001; Kläui *et al*., 2003a), in which the magnetization in each half of the ring has an opposite sense of circulation. This is a metastable equilibrium state, made more stable by energy barriers introduced by defects and irregularities (such as edge roughness) and in fact the switching field from the onion to the vortex state can be quite high (Rothman *et al*., 2001). Such magnetic states have been observed experimentally with SEMPA and PEEM (Kläui, Vaz, Lopez-Diaz and Bland, 2003, Kläui *et al*., 2003a) (see Figure 8a). While the vortex state in these structures is quite simple, the details of the onion state are more subtle (Figures 8b and c). The region separating the two oppositely magnetized halves constitutes a domain wall, which is either a vortex or a transverse wall (Kläui *et al*., 2003a), in accordance with what is predicted for wires (McMichael and Donahue, 1997; Nakatani, Thiaville and Miltat, 2005). The presence of one or the other type of wall is determined by the interplay between the magnetostatic and exchange energy; for thick and wide rings, the magnetostatic energy dominates and vortex walls are favored (these lead to a nearly complete flux closure of the magnetization), while for thin and narrow rings the exchange energy dominates and transverse walls are favored (in such case, the energy gain in reducing the stray field would not compensate for the increase in exchange energy due to a large twisting of the spins in a narrow region). Phase diagrams separating the regions of stability for the domain wall type in the onion state have been reported for polycrystalline Co (Kläui *et al*., 2004b) and $Ni_{80}Fe_{20}$ (Laufenberg *et al*., 2006) ring elements. In the limit of very wide rings, we recover the disk geometry and magnetic configurations that are characteristic of disk elements (Kläui *et al*., 2006).

In some instances, the observation of 360° domain walls has been reported in rings with diameters from 360 to 520 nm

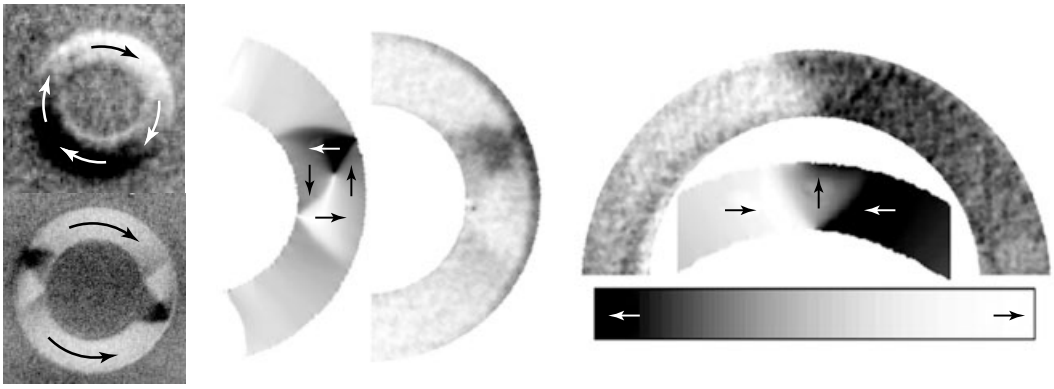

Figure 8. (a) PEEM images of rings in the vortex state (top) and in the onion state (bottom, exhibiting vortex walls). The rings are 30-nm-thick $Ni_{80}Fe_{20}$, 2.7 μm outer diameter, 530 nm wide, and the magnetic contrast is approximately along the vertical direction. (b) Detail of vortex wall in a polycrystalline Co ring (34 nm thick, 350 nm wide, 1.65 μm outer diameter) and (c) of a transverse wall (10 nm thick, 260 nm wide, 1.65 μm outer diameter) imaged by PEEM and compared with the results of micromagnetic simulations (Kläui *et al*., 2004b).

and widths from 30 to 200 nm, and such states have been termed *twisted states* (Zhu and Zhu, 2003; Castaño *et al*., 2003; Castaño *et al*., 2004). These occur at the transition from onion to vortex state when two transverse walls with opposite senses of rotation, although attracted to each other due to dipolar coupling, are prevented from annihilating by the exchange energy associated with the required large spin twisting involved in this proess. (Castaño *et al*., 2003); it turns out that such walls are fairly stable against a wide range of applied external fields (Castaño *et al*., 2004). In addition, other more complicated states were also observed in such ring structures, such as states consisting of two 360° domain walls (Castaño *et al*., 2003) and double-vortex walls in very thick rings (Park *et al*., 2006).

The effect of magnetic anisotropy on the properties of ring elements has been less studied; in part, this is because the magnetic behavior is dominated by the exchange and magnetostatic energies (shape), while other magnetic anisotropies are expected to introduce only small perturbations to the isotropic case. This happens to be the case for narrow rings and for small anisotropies; for instance, for 34-nm-thick fcc Co(001) rings with 1.7 μm outer diameter, it is observed that the magnetic state of 250-nm-wide rings is not affected by the magnetic anisotropy, while 400-nm-wide rings in the onion state show the presence of local domains pointing along directions of easy magnetization (Kläui *et al*., 2003a). From the magnetic switching behavior of fcc Co rings (16–29 nm thick, 1.65 μm outer diameter), it is observed that the magnetic easy axis of fcc Co becomes a direction of 'hard' magnetization for the ring structure; this is a consequence of the fact that in rings in the onion state the magnetization close to the end-wall point along the hard axis, making this magnetic direction easier to switch than when the onion state points along the hard axis direction (Vaz *et al*., 2004a); this behavior is in agreement with the results of micromagnetic simulations (Lopez-Diaz, Rothman, Kläui and Bland, 2001b).

The spin dynamics of ring elements have also been probed with FMR (Giesen *et al*., 2005; Neudecker *et al*., 2006), time-resolved MOKE (Neudecker *et al*., 2006), and BLS (Schultheiss *et al*., 2006). For the ring widths studied, azimuthal modes in the onion state are evident, along with other excitation modes that are associated with the head-to-head walls. Micro-BLS results (Schultheiss *et al*., 2006) suggest that, at the transverse wall of the onion state, the spin quantization is predominantly caused by the inhomogeneities of the local internal field, similar to what is observed in transversally magnetized stripes (Jorzick *et al*., 1999).

In addition to circular rings, other toroidal structures were also investigated, such as elliptical rings (Castaño, Ross and Eilez, 2003; Jung *et al*., 2004), and 'window-frame'-type structures (Vavassori *et al*., 2003; Zhu, Grütter, Metlushko and Ilic, 2003; Wei *et al*., 2004; Libál *et al*., 2005; Adeyeye, Singh and Goolaup, 2005). The motivation using elliptical rings is that of creating easy direction of magnetization (shape anisotropy) and therefore to constrain the onion state to point along one direction (Castaño, Ross and Eilez, 2003). It is found that, upon saturation along the long axis, twisted states are not easily formed, while, upon saturation along the short axis, such metastable states are often observed (Castaño, Ross and Eilez, 2003). In the case of 'window-frame'-type of structures, the magnetic states resemble those observed for ring structures, except for the presence of two additional states at remanence when the field is applied along the side of the square, one close to saturation (with two transverse walls at those sides perpendicular to the direction of the applied magnetic field) and a horseshoe type of state, with one head-to-head and one tail-to-tail wall on one side of

the square (Vavassori *et al*., 2003; Zhu, Grütter, Metlushko and Ilic, 2003).

Besides thin magnetic films, other types of structures, such as spin valves and pseudo-spin valves (the former have an antiferromagnetic pinning layer to set a unidirectional easy axis, while the latter do not) have been investigated with a view to using each element as a memory bit, which could be read by electrical means using the giant MR effect (Castaño, Morecroft, Jung and Ross, 2005; Morecroft, Castaño, Jung and Ross, 2006).

5.3 Square and rectangle (bar) elements

Again, the equilibrium magnetic states observed in these types of structures reflect the Cartesian symmetry of this geometry and are also determined by the size and particular aspect ratio of the element. For square elements, and bars with lengths comparable to the width, with dimensions below $\sim$100 nm, we expect equilibrium states such as the flower and the leaf states (magnetization parallel or diagonal to the edge direction, respectively), which correspond to small deviations from the uniform state (Usov and Peschany, 1994a; Cowburn and Welland, 1998; Goode and Rowlands, 2005); micromagnetic studies show that the flower state is expected to be the equilibrium state at larger thicknesses, while the leaf state is the equilibrium state at small thicknesses (Cowburn and Welland, 1998). For more elongated structures, the equilibrium state is expected to be a mixture of the flower and the leaf state, and resembles the S-state found in larger elements (Tartakovskaya, Tucker and Ivanov, 2001; Goode and Rowlands, 2005).

For larger elements, for which the magnetostatic energy term becomes dominant, we find, in addition to the high remanence S- and C-states, the flux closure quadrant (Landau–Lifshitz) or the seven-domain states (Kirk, Chapman and Wilkinson, 1997; Dunin-Borkowski, McCartney, Kardynal and Smith, 1998; Gomez *et al*., 1999a; Schneider *et al*., 2004) (see Figure 9). These zero remanence states are characterized by the presence of uniform magnetic domains separated by 90° Néel domain walls; as a consequence, such states could be classified as multidomain states, but given the critical role played by the shape of the element in small square and bar elements in determining the equilibrium state, we prefer to see it as another example of a nonuniform magnetic state, determined by the fine balance between the magnetostatic and exchange energy terms. We note that, besides the cost in exchange energy, there is also some magnetostatic energy associated with these Néel walls. The high remanence states such as the S- and the C-state have been studied numerically (Gadbois and Zhu, 1995; Zheng and Zhu, 1997; Fidler *et al*., 2004; Kronmüller, Goll, Hertel and Schütz, 2004) and experimentally (Chapman *et al*., 1998; Dunin-Borkowski, McCartney, Kardynal and Smith, 1998; Dunin-Borkowski *et al*., 2000; Kirk *et al*., 2001; García, Thiaville and Miltat, 2002; Shi, Li and Tehrani, 2002; Liu, Chapman, McVitie and Wilkinson, 2004a). These states are in fact quite similar and they correspond to a central uniform spin configuration, which is terminated by end domains, where the magnetization runs parallel to the edge; the C-state corresponds to the case when both edge domains point in different directions, while the S-state corresponds to the case when they point along the same direction (see Figure 9). Another type of edge domain, which is observed in elongated rectangles after saturation in an applied field, consists of a 'squeezed' vortex which sits toward one corner of the element with the largest domain pointing in the direction of the average magnetization (Kirk, Chapman and Wilkinson, 1997; Dunin-Borkowski, McCartney, Kardynal and Smith, 1998; Gomez *et al*., 1999a; Shi *et al*., 1999; Kirk *et al*., 2001); also, cross-tie domain walls are observed in thick $Ni_{80}Fe_{20}$ elements (Gomez *et al*., 1999a,b; Shigeto *et al*., 2002). For larger elements (typically above 5 μm), multidomain configurations set in (Seynaeve *et al*., 2001; Hirohata *et al*., 2002). These elongated elements have received much attention because they constitute an obvious choice for memory elements; the shape asymmetry introduces an effective (shape) magnetic anisotropy and therefore an increase in thermal stability; however, the presence of such edge domains has been shown to cause irreproducibilities in the magnetic switching (Zheng and Zhu, 1997), which is detrimental for applications; in fact, modifications in the edge structure, such as pointed ends, have been suggested in order to make the switching process more reproducible (Schrefl, Fidler, Kirk and Chapman, 1997; Yu *et al*., 1999; Herrmann, McVitie and Chapman, 2000; Liu, Chapman, McVitie and Wilkinson, 2004a).

The spin dynamics of square and rectangular elements have also been studied numerically (Fidler *et al*., 2004) and experimentally by BLS (Chérif, Dugautier, Hennequin and Moch, 1997; Gubbiotti *et al*., 2000; Chérif, Roussigné and Moch, 2002; Jorzick *et al*., 2002) and time-resolved MOKE (Park *et al*., 2003; Perzlmeier *et al*., 2005). The experimental BLS studies mentioned were performed under an applied magnetic field and show that the spin wave frequencies, determined mostly by the dipolar field, are sensitive to the lateral confinement imposed by the element (in a similar fashion as observed in wire structures); Jorzick *et al*. (2002), in particular, have shown that spatially localized spin waves arise in square elements as a consequence of the potential well created by the inhomogeneous internal magnetic field within the element. The numerical study of Fidler *et al*. (2004), on the other hand, has shown that the spin-wave spectrum for the S-state in square elements is distinct from

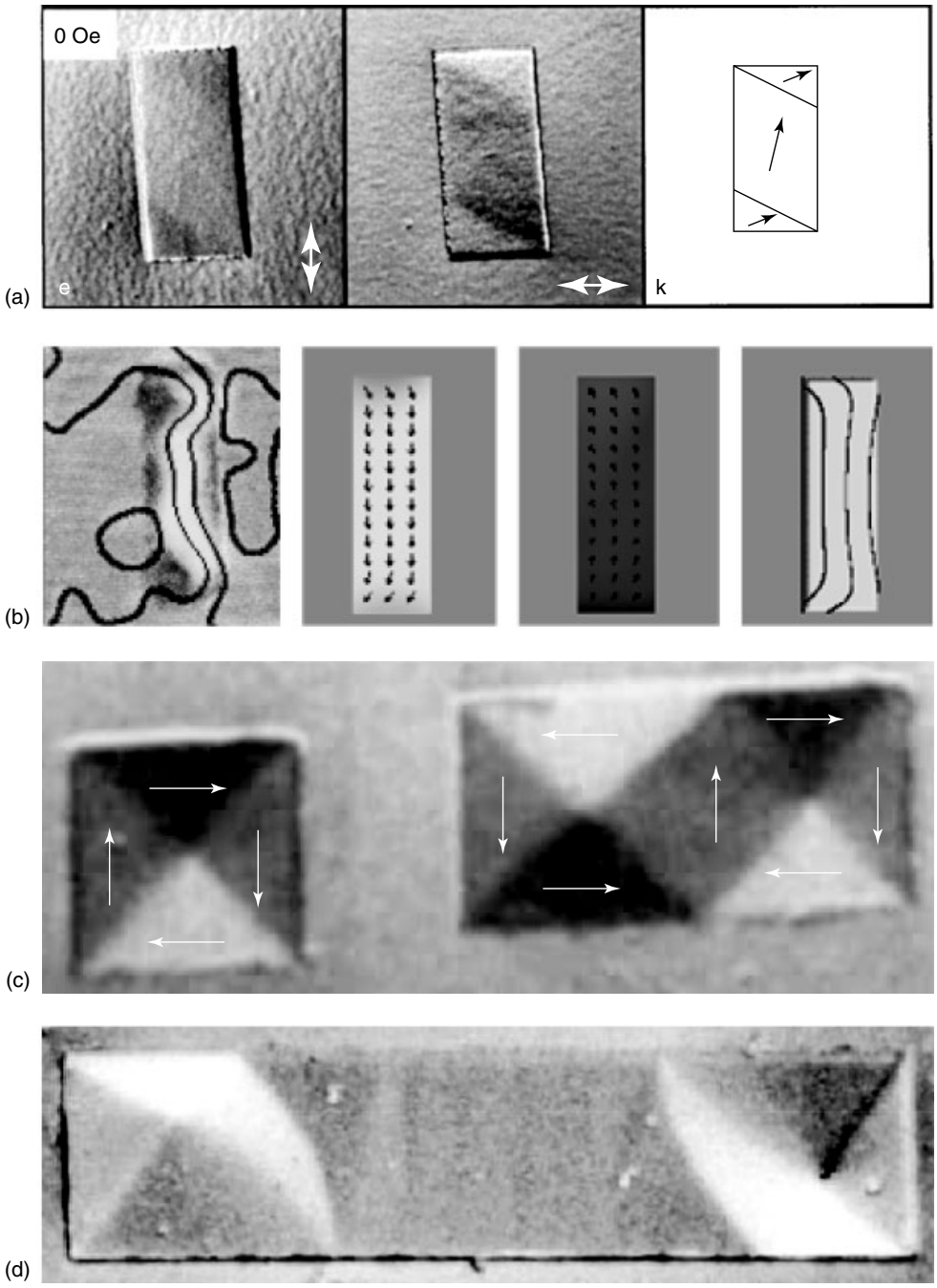

Figure 9. Magnetic images of remanent states of square and rectangular elements; (a) Lorentz image (Foucault mode) of a $2 \times 4\,\mu m^2$ NiFe(8 nm)/Cu(2.5 nm)/NiFe(6 nm) element in the S-state (Reprinted with permission from Institute of Physics, Direct Observation of Magnetization . . . , *Journal of Applied Physics*, **83**, 5321. Copyright 1998, American Institute of Physics.); (b) from left to right: electron holography image of a $60 \times 200\,nm^2$ Co(10 nm)/Au(5 nm)/Ni(10 nm) element in the C-state; micromagnetic simulations for the Co and Ni magnetization; simulations of the holographic phase contours for the composite Co/Au/Ni structure (Reproduced by permission of Blackwell Publishing from R.E. Dunin-Borkowski, M.R. McCartney, B. Kardynal, S.S.P. Parkin, M.R. Scheinfein and D.J. Smith, (2000). Off-axis electron holography of patterned magnetic nanostructures, *J. Microsc.* **200**, 187.); (c) Lorentz microscopy image (Foucault mode) of a $1 \times 1\,\mu m^2$ and $2 \times 1\,\mu m^2$ NiFe(20 nm) elements in the quadrant, and seven-domain state, respectively, and (d) Lorentz microscopy image (Foucault mode) of a $4 \times 1\,\mu m^2$ NiFe(26 nm) showing a state of high remanence with vortex end walls. (Reproduced by permission of Taylor and Francis Ltd. (http://www.tandf.co.uk/journals) from K.J. Kirk, (2000). Nanomagnets for sensors and data storage, *Contemporary Physics*, **41**, 61.)

that of the C-state: as a consequence of the larger effective fields present in the C-state, the eigenfrequencies for this state are shifted to higher frequencies. Park *et al*. (2003) have studied the spin dynamics of square elements in the quadrant (Landau–Lifshitz) state,which was found to exhibit two types of excitations, one corresponding to the precession of the magnetization about the local demagnetizing field in each quadrant and the other localized in the domain walls.

5.4 Ellipses

The motivation behind the study of elliptical elements lies in the introduction of magnetic (shape) anisotropy, while avoiding the formation of edge domains and their negative influence on the reproducibility of the magnetic switching (Liu, Chapman, McVitie and Wilkinson, 2004a). Hybrids between bars and ellipses, such as bars with tapered ends, have also been studied with the same goal in mind (see previous paragraph). Understandably, most studies on elliptical elements focus on ellipses with large aspect ratios, and the magnetic states found in micrometer and submicrometer size ellipses depend on the applied magnetic field direction: after saturation along the long axis, they tend to remain in the uniform state, while when the field is applied along the short axis, a larger variety of magnetic states are observed, including the vortex state, the diamond state, the triangle state, and the uniform state magnetized along the long axis (Bedrossian, Gibbons and Cerjan, 1997; Fernandez, Gibbons, Wall and Cerjan, 1998; Usov, Chang and Wei, 2001; Liu, Chapman, McVitie and Wilkinson, 2004a; Liu, Chapman, McVitie and Wilkinson, 2004b; Felton *et al*., 2004; Buchanan *et al*., 2005). The spin dynamics of the diamond state in elliptical NiFe dots has been studied recently by Buchanan *et al*. (2005) and by Gubbiotti *et al*. (2005) using BLS and it is observed that the frequency modes depend strongly on the dot eccentricity and direction of the magnetic field.

5.5 Wires

These consist of structures where the length is much larger than the width, and therefore the relevant geometrical parameters are the width and thickness. A large body of work has been devoted to the study of wire structures and a number of fabrication techniques have allowed the fabrication of magnetic wires with widths ranging from a few nanometers to several micrometers. Depending on the fabrication process, planar wires, or wires with circular cross section can be fabricated (namely, by electrodeposition using porous membranes as templates (Whitney, Jiang, Searson and Chien, 1993; Lederman, O'Barr and Schultz, 1995; Ferré *et al*., 1997)). Here we cite some studies as a way of illustrating the distinctive magnetic properties exhibited by wire structures (see also **Domain Wall Propagation in Magnetic Wires, Volume 2**).

The study of monolayer thick bcc Fe wires grown on W(110) has provided much insight into the magnetism of two-dimensional structures (Pratzer *et al*., 2001; Pratzer and Elmers, 2003; Kubetzka, Pietzsch, Bode and Wiesendanger, 2003). Such two-dimensional Fe wires have a very strong uniaxial anisotropy along the direction perpendicular to the wire axis (due to the Fe/W(110) lattice mismatch), and are observed to form magnetic domains along the direction orthogonal to the wire length (Pratzer *et al*., 2001; Pratzer and Elmers, 2003; Kubetzka, Pietzsch, Bode and Wiesendanger, 2003). Spin-polarized STM studies of such domains allowed the determination of the wall width down to the subatomic resolution; for a 1-ML Fe wire, 17 nm wide, the domain wall width was determined to be 0.6 ± 0.2 nm, while for a 2-ML Fe/W(110) stripe, 8.5 nm wide, it was found to be 3.8 ± 0.2 nm. Such sharp domain walls for the monolayer wire are energetically more favorable than extended domain walls since, for such thicknesses, the exchange and anisotropy energies dominate over the magnetostatic energy (Braun, 1994). In general, one expects that, in comparison to bulk materials, atomically thin narrow nanowires may present new and exciting properties, such as effects due to quantum confinement and strongly modified electronic properties (Himpsel, 1995).

Arrays of wider Ni wires, 70–130 nm wide, have been grown on grooved InP(001) substrates (Jorritsma and Mydosh, 1998) by deposition at non-normal angles; this method explores the etching anisotropy of InP(001) with respect to specific etchants (Jorritsma, Gijs, Kerkhof and Stienen, 1996). Jorritsma and Mydosh (1998) have found that the Ni wires thus fabricated change the magnetization easy axis from longitudinal to transverse to the wire direction with decreasing temperature, an effect they attribute to the stress due to thermal expansion mismatch between Ni and InP.

The term *nanowires* is virtually a synonym for electrodeposited structures; they can vary in width from tens to a few hundreds of nanometers (Whitney, Jiang, Searson and Chien, 1993; Lederman, O'Barr and Schultz, 1995; Ferré *et al*., 1997). A number of seminal experiments have measured individual nanowires using highly sensitive micro-SQUID junctions (Wernsdorfer *et al*., 1996a); they have also been used to study domain wall MR effects, an effect which seems to be particularly large in Co and Ni nanowires and attributed to the spin accumulation effect (Ebels *et al*., 2000).

More conventionally, arrays of wires have been fabricated by standard lithography techniques, with widths varying from $\sim$100 nm to tens of μm (Adeyeye *et al*., 1996, 1997a,b). The coercivity is found to decrease with increasing wire width (Adeyeye *et al*., 1996); this is explained by a buckling

of the magnetization perpendicular to the length of the wire, creating perpendicular domains that do not move and block the reverse domain from propagating during magnetization reversal (Kryder *et al*., 1980), an effect that becomes more pronounced with decreasing wire width (see also Sections 7.3 and 7.4). The effect of magnetic interaction between micrometer wide wires has also been addressed, and shows that magnetic interactions between wires become unimportant for distances above the wire width (Adeyeye *et al*., 1997a); this behavior is characteristic of small elements and a critical factor as far as the design of high density storage media is concerned (Kläui, Vaz, Bland and Heyderman, 2005). In this context, the small stray field provided by flux closure states is very advantageous.

The magnetic states sustained by wire elements do not consist only of the uniform state, with the magnetization along the wire axis (in the absence of strong transverse anisotropies). Effectively, either as a consequence of applied transverse magnetic fields, or of fields applied in the direction opposite to the wire magnetization, reverse domains can be sustained along the wire. This has been observed in Co nanowires (Ebels *et al*., 2000; García, Thiaville and Miltat, 2002). In flat wires, the region separating such opposite domains constitute 180° domain walls, and their character can be either transverse or vortex, as already mentioned (McMichael and Donahue, 1997; Nakatani, Thiaville and Miltat, 2005); experimental observation of such wall structures in straight wires has been reported in the literature (Yamaguchi *et al*., 2004; Kläui *et al*., 2005b). Under applied fields close to the 'hard axis' of the wire, edge domains consisting of Néel walls parallel to the wire were observed in $Ni_{80}Fe_{20}$ wires 2–10 μm wide and 10–30 nm thick, giving rise to hysteretic behavior in rotational hysteresis measurements (Mattheis, Ramstöck and McCord, 1997); this is a result of the stray field at the wire edges when the magnetization points away from the wire axis. For wires with strong transverse anisotropies, the ground state is either the transverse uniform state or an open-stripe domain structure, depending on the wire thickness and width (Prejbeaunu *et al*., 2001).

5.6 Pillars

By pillars, we refer to structures whose aspect ratio (thickness/lateral size) is of the order of unity. The magnetic states in these structures can be quite complex, since now the magnetization will vary along the three spatial directions; in the case of cylindrical elements, some states preserve the cylindrical symmetry but have a radial magnetization distribution that varies across the element thickness. We lose the simplicity characteristic of thin elements, but it may be possible that the additional complexity results in properties that can be harnessed for applications or other studies. Since three-dimensional imaging is not possible as yet (see however, (Hertel *et al*., 2005)), these magnetic states may be deduced either from their *M-H* characteristics or from their surface signature when imaged by the usual imaging techniques; these results can also be confirmed by the results of micromagnetic simulations. Equilibrium magnetic states depend on the element geometry, but they tend to form states such as the flower, vortex, uniform, bidomain, and bubble states (Rave, Fabian and Hubert, 1998; Maicas *et al*., 2002; Hertel and Kronmüller, 2002; Ross *et al*., 2002; Kronmüller, Goll, Hertel and Schütz, 2004; Usov and Peschany, 1994b; Komineas, Vaz, Bland and Papanicolaou, 2005; Moutafis *et al*., 2006). For example, the uniform and flower states are states of high magnetic moment, characterized by an almost uniform magnetization; in the flower state, local deviations of the magnetization are a result of the inhomogeneous dipolar field (the uniform state is likely to occur in systems with strong magnetic anisotropies or in systems with high aspect ratios (Huang *et al*., 2000)). The vortex, bidomain, and bubble states are states of small total magnetic moment, and in which the magnetization varies strongly along all directions in space; for example, the vortex state resembles the center of a vortex state of a disk, where the vortex core constitutes a large portion of the magnetic state, and therefore a sizeable remanence may be expected for this magnetic state. Bubble states are expected to occur in systems with a large quality factor and consist of two circular domains pointing in opposite directions and also, in this case, the magnetization varies along the out-of-plane direction (Komineas, Vaz, Bland and Papanicolaou, 2005; Moutafis *et al*., 2006) such states are stable under no applied magnetic field (as opposed to bubble states in continuous films) and have been observed experimentally in cylindrical Ni dots (Skidmore, Kunz, Campbell and Dan Dahlberg, 2004), Co dots (Hehn *et al*., 1997; Kageyama and Suzuki, 2006), and $Ni_{80}Fe_{20}$ dots (Eames and Dahlberg, 2002).

6 MULTIDOMAIN STATES

As usually defined, multidomain states are magnetic states characterized by the presence of more than one region where the magnetization is uniform. The driving force behind the splitting into domains is the long-range magnetic dipolar interaction, which acts to minimize magnetic 'pole charges' at the sample surface. Strictly speaking, in an ideal crystal one would expect, if not an absolute energy minimum, at least a small number of magnetic configurations with similar energies separated by intrinsic energy barriers such that the system may fall into one such state and remain there in the absence of disturbances. As the size of the system is reduced,

we would expect such energy degeneracy to be lifted, and the resulting energy differences to be sufficient to drive the system into the ground state, through energy gradients or thermal excitations. It is this distinction that has led us to consider magnetic states such as the quadrant state in small elements as a nonuniform state rather than a multidomain state; for larger elements, other multidomain states are stable other than the quadrant state. A large body of work has been built up over several decades specifically dedicated to the understanding of equilibrium magnetic domain structures in samples larger than those discussed in this chapter; the most extensive discussion of such work to date is that of Hubert and Schäfer (1998) and will not be discussed here (a shorter overview can be found in Kleman (1982)).

One major complication in studying magnetic configurations in real samples is the presence of imperfections that act as extrinsic pinning sites for the magnetization and that tend to stabilize nonequilibrium magnetic configurations (Kleman, 1982). If the energy barrier separating these states is much larger than that of external excitations, such states may be considered as metastable equilibrium states, otherwise they give rise to thermal relaxation effects; in particular, the stability of such states depends strongly on the temperature. Another effect of these pinning sites is to give rise to magnetic configurations that are much more complicated than those expected for perfect crystals due partly to the randomness associated with defects. Since the incorporation of pinning in micromagnetism is difficult, there are very few studies of extrinsic contributions to the magnetic configurations. We give a couple of examples to drive this point home. In Figure 10(a), we show an MFM image at remanence of an array of 25-nm-thick NiFe square elements obtained by Gubbiotti *et al*. (2000); we see that, while we expect the ground state to be the quadrant state, many elements exhibit more complicated domain structures that may be metastable (and vanish under small applied fields) but, nevertheless, are accessible after saturation or other field histories (Uhlig, Li, Han and Shi, 2002; Liou *et al*., 2001); this is an important consideration for practical applications that require well-defined domain configurations for reliable operation. Another example is shown in Figure 10(b) for 15-nm-thick bcc Fe(001) elements imaged by Lorentz microscopy (at remanence after saturation along the easy axis) by Gu *et al*. (1997); here, the puzzling behavior is the breaking into magnetic domains as the size of the element decreases, which at first sight seems counterintuitive. However, the size of the elements is fairly large, and, for the larger square, edge domains are observed, which presumably arise from edge imperfections, and these may help stabilize this large single domain.

In general, since the range of magnetic configurations increases with the size of the element, it follows that a vast number of complex spin arrangements is possible for larger systems (Hubert and Schäfer, 1998). One practical advantage of smaller elements is that the accessible magnetic states are much more limited.

7 SWITCHING

So far, we have discussed the stable equilibrium magnetization configurations that are found in small magnetic structures. The next step is the dynamic description of how such state a magnetic system approaches equilibrium. The equilibrium is given by a local energy minimum of the corresponding thermodynamic potential (e.g., the Landau Free Energy, equation (6) (Bertotti, 1998)). Here, We take the case where the equilibrium condition is changed by varying the applied field (Zeeman energy). But, changes of other energy terms can also occur, such as changes in the magnetic anisotropies when the temperature is varied.

We limit ourselves here to quasistatic reversal, which means that the field is ramped much more slowly than the dynamics of the magnetization. Depending on the materials and systems considered, the rates of change where the reversal can be described as quasistatic vary. For the materials considered here, this means slew rates of less than approximately $80\,\mathrm{kAm^{-1}\,s^{-1}}$. In the quasistatic case, the magnetic system is thus always in equilibrium as the external conditions change (e.g., the field is ramped). Dynamic switching, where the field changes are on a timescale that is comparable to the magnetization dynamics, is treated in **Magnetic Modes in Circular Thin Film Elements, Experiment and Theory, Volume 2**. We limit our discussion to magnetic field-induced switching, but other reversal schemes, such as those based on current-induced magnetic switching have been proposed (Katine *et al*., 2000; Grollier *et al*., 2002; Wegrowe *et al*., 2002; Kläui *et al*., 2005c) and are discussed in detail in **Theory of Spin-transfer Torque, Volume 2**, **Microwave Generation in Magnetic Multilayers and Nanostructures, Volume 2**, **Spin Angular Momentum Transfer in Magnetoresistive Nanojunctions, Volume 5**, and **Current Induced Domain-wall Motion in Magnetic Nanowires, Volume 2**.

7.1 Theoretical treatment of dynamical behavior

To determine the magnetization dynamics, we start with the quantum mechanical Heisenberg equation for the time evolution of the spin operator

$$i\hbar\frac{\mathrm{d}}{\mathrm{d}t}\langle\hat{\mathbf{S}}(t)\rangle = \langle[\hat{\mathbf{S}}(t), \hat{\mathcal{H}}(\hat{\mathbf{S}}(t))]\rangle \tag{17}$$

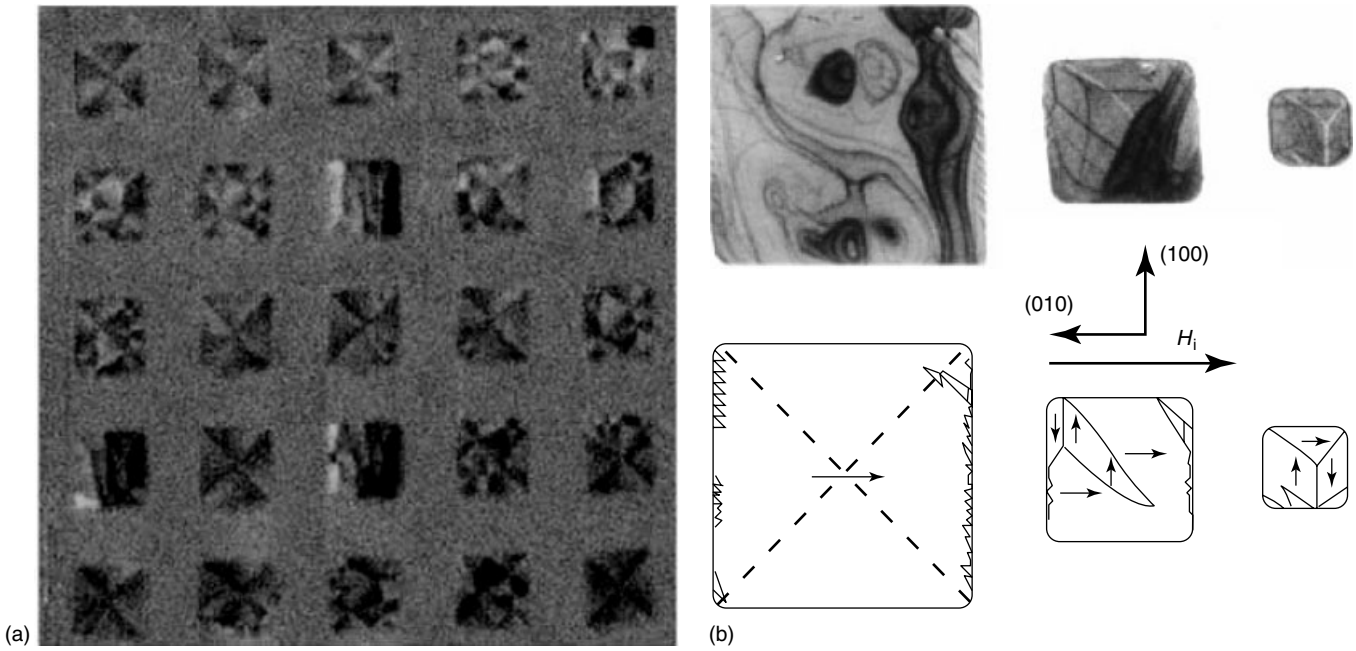

Figure 10. (a) MFM image of an array of 25-nm NiFe squares, 2 µm in size, at remanence. (Reprinted with permission from American Institute of Physics, Finite size effects in patterened magnetic permalloy films. *Journal of Applied Phys.* **87**, 5633. Copyright 2000, American Institute of Physics.) (b) Lorentz microscopy image (Fresnel mode) of 15-nm bcc Fe(001) squares (55, 30, 12 µm in size), at remanence. (Reprinted figure with permission from American Physical Society, *Phys Rev. Lett.* **78**, 1158 (1997) E. Gu *et al*. Copyright 1997 by the American Physical Society.)

with $\hat{\mathbf{S}}$ the spin operator and $\hat{\mathcal{H}}$ the Hamiltonian, which is here proportional to $\hat{\mathbf{S}} \cdot \hat{\mathbf{H}}_{\text{eff}}$ with $\hat{\mathbf{H}}_{\text{eff}}$ the effective magnetic field (Nalwa, 2002). Magnetic moments behave like angular momenta, since they observe the quantum mechanical bracket relations $[S_x, S_y] = i\hbar S_z$, etc. For an electron spin, the former is related to the latter by

$$\mathbf{m}_{\text{spin}} = \gamma\hbar\mathbf{S} = (\hbar q_e/m_e)\mathbf{S} \tag{18}$$

with q_e and m_e the electron mass. Evaluating equation (17) using the bracket relations and the Ehrenfest theorem to transform to the classical magnetization yields for the time evolution (Nalwa, 2002)

$$\frac{\partial \mathbf{m}}{\partial t} \equiv \dot{\mathbf{m}} = \gamma \mathbf{m} \times \mathbf{H}_{\text{eff}} \tag{19}$$

The change in angular momentum is given by the torque $\boldsymbol{\Gamma} = \mathbf{m} \times \mathbf{H}_{\text{eff}}$ exerted on it by the field $\mathbf{H}_{\text{eff}}$ and this describes the gyroscopic precession. From equation (5) with $\mathbf{H}_0$ now replace by $\mathbf{H}_{\text{eff}}$, it follows that $dE/dt = 0$, i.e., the energy is conserved. Hence, equation (19) cannot describe a system which is changing its energy such as a system approaching equilibrium. To introduce energy dissipation, Brown (1963) used the analogy to classical mechanics, where the force responsible for energy dissipation (friction) is proportional to the generalized velocities. In this case, the generalized coordinates are the Cartesian components of the magnetization $\mathbf{m}$ and the general forces are the components of $\mathbf{H}_{\text{eff}}$. Introducing this into equation (19) yields

$$\dot{\mathbf{m}} = \mathbf{m} \times (\gamma \mathbf{H}_{\text{eff}} - \alpha \dot{\mathbf{m}}) \tag{20}$$

where α is the phenomenological dimensionless proportionality factor for the damping. This equation is known as *Gilbert's equation*. Another formulation of this equation was given by *Landau* and *Lifshitz*:

$$\dot{\mathbf{m}} = \gamma_{\text{LL}} \mathbf{m} \times \mathbf{H}_{\text{eff}} - \alpha_{\text{LL}} \mathbf{m} \times (\mathbf{m} \times \mathbf{H}_{\text{eff}}) \tag{21}$$

It should be noted that γ_{LL} and γ from equation (20) are different (Bertotti, 1998; Heinrich, 2005). To a first approximation, all dissipation processes can be assumed to be included in the phenomenological damping factor α. In general, α is not very well known, and intensive research is being carried out to understand its microscopic origins (Buess, Haug, Scheinfein and Back, 2005; Heinrich, 2005).

7.2 Uniform reversal of single domain systems by coherent rotation

Equations (20) and (21) are directly applicable for single domain particles where the spins stay aligned during the reversal, which is called *reversal by coherent rotation* (Section 4.1). Here, we can simply evaluate these equations for a single (macro)spin. Analytical solutions have long been available (Gilette and Oshima, 1958; Kikuchi, 1956) and, more recently, numerical studies have been performed (Serpico, Mayergoyz and Bertotti, 2003; Fidler and Schrefl, 2000). These studies were also extended to include the response of single domain particles to short field pulses (Bauer, Fassbender, Hillebrands and Stamps, 2000). The results of two (macro)spin calculations are shown in Figure 11. In Figure 11(a), it can be seen that the magnetization direction starts to rotate toward the $-y$ direction, since the acting field component is in the $-z$ direction. It then turns toward $+z$ and continues to precess around the field direction and spirals due to the damping toward the field direction. Whereas in Figure 11(a) the damping constant is 0.2, it has a more realistic smaller value of 0.02 in Figure 11(b). This reduced damping leads to many more precessions of the magnetization around the field direction, before the magnetization has spiraled toward its equilibrium direction along the field direction. Experimentally, such switching trajectories have been observed for pulsed reversal (Schumacher *et al.*, 2003).

7.3 Nonuniform reversal of single domain systems

As pointed out before, there are geometries for which the remanent magnetization configuration is a single domain state, but where the reversal does not take place via coherent rotation, such as larger ellipsoidal elements with a constant demagnetization factor. In general, coherent rotation is only one possible reversal mode (Aharoni, 1996; Frei, Shtrikman and Treves, 1957; Kronmüller and Fähnle, 2003) and occurs only if the critical switching field for this mode is lower than for any other reversal mode. We consider now another possible reversal mode, which, for certain geometries, leads to a lower critical switching field than that attained by coherent rotation.

An example is a long cylinder, where the shape anisotropy favors the magnetization to lie along the cylinder axis to form a single domain state. If the radius of the cylinder is larger than the exchange length l_s, then a reversal via the so-called curling mode is favorable (Lederman, O'Barr and Schultz, 1995). The curling mode is strictly only applicable to ellipsoids of revolution (Aharoni, 1996; Kronmüller and Fähnle, 2003), but has been extended to describe approximately the reversal in other regularly shaped elements (Aharoni, 1999). In this mode, the magnetization reverses by forming a vortex structure where the magnetization lies parallel to the cylinder wall forming concentric circles around the cylinder axis. Analytically, the angular dependence of the switching

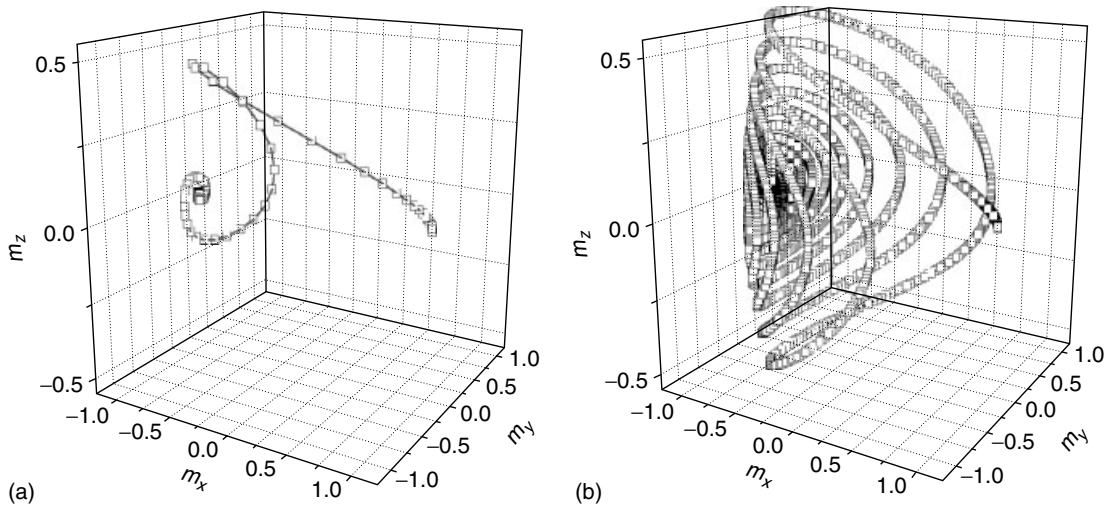

Figure 11. The trajectory (spin directions) of single domain permalloy ($Ni_{80}Fe_{20}$) systems are shown during the reversal from $m_x = 1$ (spin pointing along the positive x-direction) to the field direction (5° away the $-x$ direction toward $-z$ as visible in the final direction of the spin) for a damping of $\alpha = 0.2$ (a) and $\alpha = 0.02$ (b). The anisotropies are equivalent to those of a particle with aspect ratio 10:10:1 (x:y:z) and the field strength is x-component $-63.8\,\mathrm{kAm^{-1}}$; z-component $-5.6\,\mathrm{kAm^{-1}}$.

fields can be calculated for ellipsoids of revolution for a field applied along the direction of the long axis of the ellipsoid and is then given by Aharoni (1997):

$$H_{\text{curl}} = \frac{M_s}{2} \frac{a_x a_z}{\sqrt{a_z^2 \sin^2\theta + a_x^2 \cos^2\theta}} \tag{22}$$

with θ the angle between the applied field and the long axis of the ellipsoid, $a_{x,z} = 2N_{x,z} - k/S^2$, $N_{x,z}$ the demagnetization factors, $S = R/l_s$, and R the minor semiaxes of the ellipsoid. The parameter k is a monotonically decreasing function of the aspect ratio of the ellipsoid with values ranging from $k = 1.079$ for an infinite cylinder to $k = 1.379$ for a sphere (Aharoni, 1986). As an example, the switching fields for a long cylinder for various values of S are shown in Figure 12. For $S<1$ the switching field for coherent rotation reversal is lower and switching occurs by coherent rotation. It should be pointed out that, in contrast to the mode of coherent rotation, the curling mode is limited to these geometries and cannot be analytically extended to cope with any three-dimensional anisotropy functions, but approximate calculations have been proposed (Aharoni, 2000; Ishii, 1991).

In addition to reversal by the curling mode, some authors (Kronmüller and Fähnle, 2003) consider the buckling mode, while for others the existence of further modes is more contentious (Aharoni, 1996). The buckling mode is obtained by starting from the uniform mode and modulating the magnetization direction in sinusoidal fashion along the cylinder axis. The extra exchange energy is then compensated by the reduced stray field energy due to alternating surface charges. Only for a small geometry range can this mode have a lower critical switching field (Aharoni, 1996; Kronmüller and Fähnle, 2003). Such a reversal mode has also been reported to occur in wire structure (Adeyeye *et al*., 1996, Kryder *et al*., 1980) (see also Section 5.5).

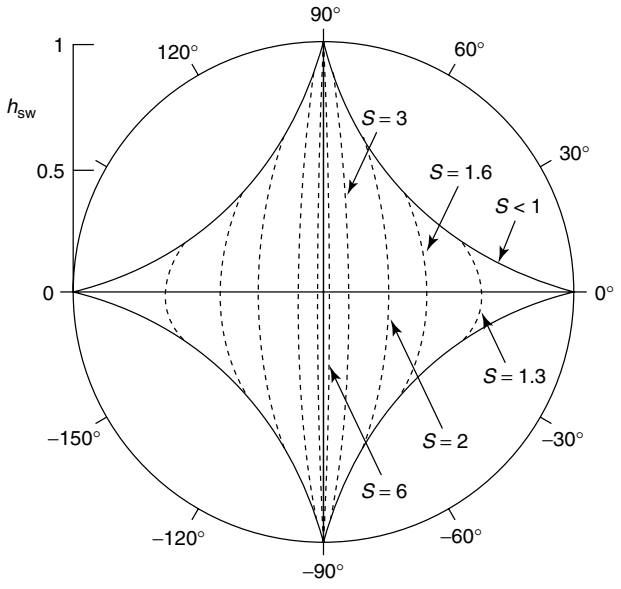

Figure 12. Angular dependence of the switching fields of the curling mode calculated according to equation (22) for an infinite cylinder. (Reproduced by permission of Wiley-Interscience from W. Wernsdorfer, (2001). Classical and quantum magnetization reversal studied in nanometer-sized particles and clusters. *Adv. Chem. Phys.*, **118**, 99.)

7.4 Experimental evidence for nonuniform reversal modes

As theoretically discussed in Sections 4 and 7.3, reversal via coherent rotation is reserved for a limited set of systems. Most magnetic structures exhibit more complicated reversal modes. One of these modes is reversal by curling as theoretically treated in the previous section. This reversal mode was predicted to prevail in long wire structures, where the wire radius is larger than the exchange length. The calculated dependence of the switching fields is compared with measured values for Ni wires with different radii in Figure 13.

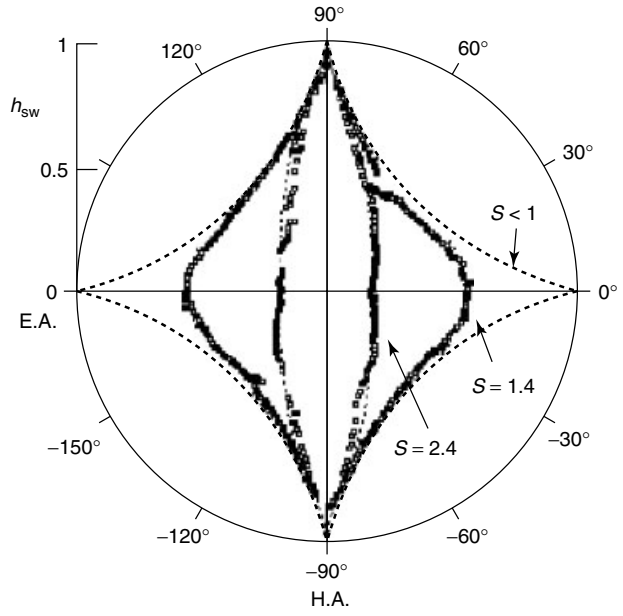

Figure 13. Angular dependence of the experimentally measured switching fields of two Ni wires with diameters of 45 and 92 nm corresponding to S = 1.4 and S = 2.4 (squares) and theoretical values (dotted line). The switching fields are normalized by 124 mT (99 kAm^{-1}) and 280 mT (224 kAm^{-1}) respectively. (Reproduced by permission of Wiley-Interscience from W. Wernsdorfer, (2001). Classical and quantum magnetization reversal studied in nanometer-sized particles and clusters. *Adv. Chem. Phys.*, **118**, 99.)

It should be pointed out that the curling mode as developed theoretically (Aharoni, 1996) does not describe the complete reversal. It rather describes points of instability where the reversal sets in, from which the angular dependence of the switching fields can be predicted, for example. Dynamic measurements on wires have often yielded a nucleation volume that is much smaller than the wire volume (Wernsdorfer *et al*., 1996a,b, 1997b). This points to a more inhomogeneous reversal that starts in part of the wire and then propagates along the wire to completely reverse it and not to a reversal taking place uniformly along the wire. This picture is also supported by theoretical calculations and micromagnetic simulations (Ferré *et al*., 1997; Braun, 1999). This already points to the limits of the applicability of the reversal modes discussed above.

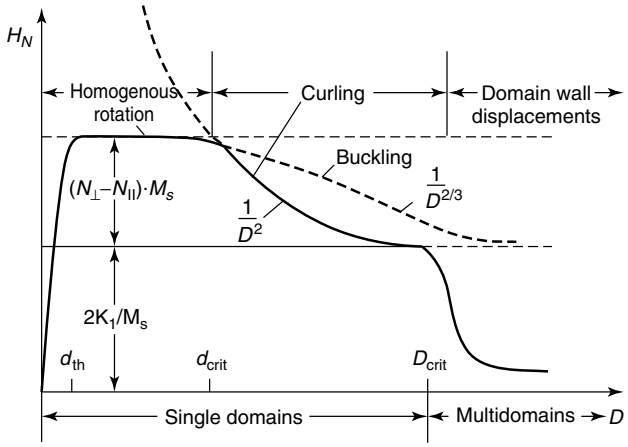

Figure 14. Schematic of switching fields of the different reversal modes as a function of particle diameter. The type of magnetic configuration is also shown in the bottom axis (single domain or multidomain, which includes nonuniform configurations here). (Helmut Kronmüller, Manfred Fähnle, Micromagnetism and the Microstructure of Ferromagnetic Solids, (2003), Figure 6.12. Cambridge University Press.)

7.5 Size range for magnetization reversal by coherent rotation, curling, and buckling

Now that the main different reversal modes in single domain systems have been discussed, a brief review of the applicability of the theory is appropriate (Schmidts, Martinek and Kronmüller, 1992).

An experimental example of a measurement where the limits of the applicability of the single domain theory becomes clear was already carried out by Kneller and Luborsky (1963) who measured the coercivity and remanence of Fe particles as a function of size. This result is shown schematically in Figure 14. A maximum switching field is observed for particle size between d_{th} and d_{crit}, while below d_{th} the coercivity is reduced due to thermal excitations (superparamagnetism (Aharoni, 1996; Bean, 1955; Bean and Livingstone, 1959)) (and we may also expect that the classical 0 K theory discussed here is not applicable for very small systems, where quantum effects play a significant role, as for example, in molecular magnets (Hilzinger and Kronmüller, 1972; Hilzinger and Kronmüller, 1973; Wernsdorfer, 2001)).

In the region where the coercivity is maximum, the switching fields usually agree with the theories of coherent rotation for single domain systems presented in Section 4.1 (Aharoni, 1986). The switching field for coherent (homogeneous) rotation of an ellipsoidal particle, $H_N = 2K_1/M_s + (N_\perp - N_\parallel)M_s$, is due to the superposition of the material anisotropy K_1 (e.g., magnetocrystalline) and the shape anisotropy, represented by the demagnetizing factors $N_\perp$ and $N_\parallel$ (Kronmüller and Fähnle, 2003).

At d_{crit}, the transition from reversal by coherent rotation to curling and buckling occurs (see Kronmüller and Fähnle (2003); Frei, Shtrikman and Treves (1957) for details). D_{crit} is the diameter above which domain formation sets in, which is of the order of l_k (Section 3.5). Such magnetization configurations then experience a very inhomogeneous reversal. Next, we will expand on such nonhomogeneous reversal modes including the reversal of structures that also exhibit nonhomogeneous magnetization configurations, such as those discussed in Sections 5 and 6.

7.6 Inhomogeneous reversal

For inhomogeneous magnetization configurations such as nonuniform and multidomain magnetization configurations, the reversal can be expected to be inhomogeneous. We discuss here transitions between some of the nonuniform magnetization configurations presented in Sections 5 and 6.

The details of the actual switching processes shown here were obtained from micromagnetic simulations (see also **Numerical Micromagnetics: Finite Difference Methods, Volume 2** and **Numerical Methods in Micromagnetics (Finite Element Method), Volume 2**), since they allow direct access to the magnetization configurations, which are more instructive than *M-H* curves for example. Furthermore, single shot nanometer and picosecond scale space- and time-resolved measurements are very difficult. While there are some measurements of the dynamical switching processes, these have been primarily measured for larger structures using fast-pulsed fields and not for the quasistatic reversal we treat here This is because most dynamic measurements are pump probe (Schumacher *et al*., 2003; Beach *et al*., 2005) which are more suited to repeatable dynamic reversal than

to quasistatic reversal that can contain stochastic features. Where both simulations and experiments have been carried out, micromagnetic simulations have been shown to give a good indication of the dynamics of the reversal process, and this is in particular true when the original and final magnetic state as well as the switching fields agree with the experimental results.

Since in larger elements the effective field is inhomogeneous, the magnetic states as well as the reversal are inhomogeneous. We have seen that we can categorize the magnetic states into two broad categories, nonuniform and multidomain states containing domain walls. Since the reversal depends on the initial and the final magnetization configuration, there are a large number of combinations that lead to a large number of different reversals. Thus, it is not possible here to discuss the details of all the different reversal modes for all geometries. But, similar to the categorization of the states, we can categorize the reversal according to the fundamental processes that occur most frequently: (i) rotation of spins (coherent or noncoherent), (ii) nucleation of domains and domain walls, (iii) propagation of domain walls, and (iv) annihilation of domain walls. We emphasize, however, that the boundaries between these categories are not strict.

We start with a case where the initial and final states are simple and do not deviate much from the single domain state, such as the S-state (see Figure 9) and for which we expect a rather simple reversal. When an opposite field is applied to this S-state, the magnetization switches to the opposite S-state at a critical switching field. For a certain geometry ($500 \times 125 \times 3\,\mathrm{nm}^3$ NiFe), this is the micromagnetic standard problem #4, which is a test case for micromagnetic calculations but also relevant for applications, where elements of this size are often considered. Solutions have been variously calculated (Kronmüller, Fischer, Hertel and Leineweber, 1997; Kronmüller and Hertel, 2000; Albuquerque, Miltat and Thiaville, 2001; McMichael, Donahue, Porter and Eicke, 2001; Tsiantos, Suess, Schrefl and Fidler, 2001) and can involve intermediate states that are more inhomogeneous than the initial and final S-state. The magnetization configurations during such a reversal are shown in Figure 15. We see that first the area at the edges of the bar reverses, since there the torque on the magnetization by a reverse field is largest. In the center, the magnetization is still pointing in the original direction. The area where the spins have reversed then expands to cover the whole sample and the opposite S-state is attained. Depending on the size of the element, this reversal can involve very inhomogeneous states in larger elements, but, as the size decreases, the reversal becomes more homogeneous until the coherent rotation process is obtained for single domain particles. In larger elements, such as the one discussed in the preceding text, intermediate states occur that resemble multidomain states, even though the domains are transient features where the size

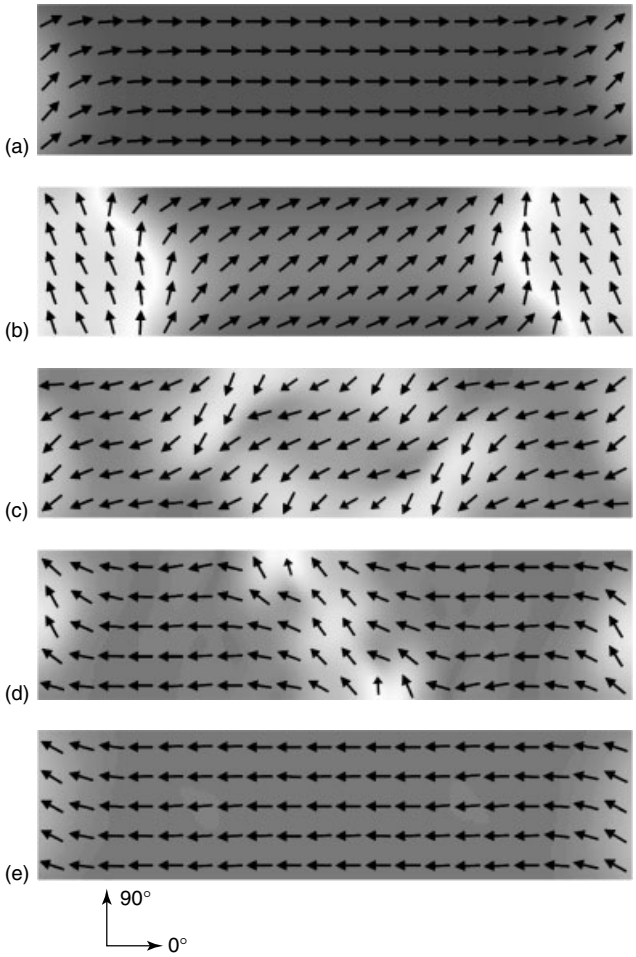

Figure 15. Magnetization configurations during the transition from the S-state to the opposite S-state in a $500 \times 125\,\mathrm{nm}^2$ NiFe element with 3 nm thickness. A field of 250 Oe ($\approx 20\,\mathrm{kA\,m^{-1}}$) is applied along 170°. (a) S-state at remanence; (b) after the field is applied, first the areas at the borders start to reverse; (c), (d) during the switching, different inhomogeneous states are attained; (e) the opposite S-state.

and the angle between them changes very quickly. These have also been observed experimentally (Choi *et al*., 2001; Hiebert, Lagae and De Boeck, 2003).

For the more complicated processes involving domain walls, we can concentrate on one geometry, which exhibits transitions involving all the processes mentioned above. A suitable choice is the ring geometry, since it exhibits well-defined and well-understood states with and without domain walls that have been discussed in Section 5.2. We recall briefly the magnetic states, observed in rings: (i) the flux closure vortex state, which does not contain domain walls; (ii) the onion state, characterized by the presence of a head-to-head and a tail-to-tail wall (see Figure 8). The *M-H* hysteresis loop of such a ring exhibits a double switching (open circles in Figure 16).

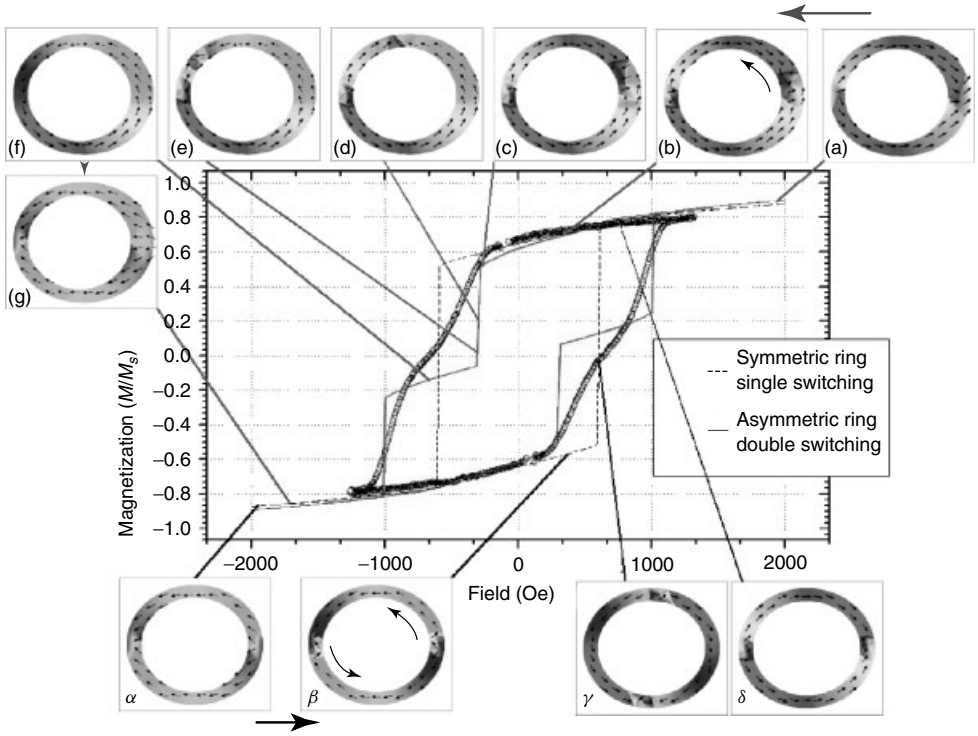

Figure 16. Dotted line with a single jump: Calculated hysteresis loops of a symmetric ring (outer diameter $D_{\text{ext}} = 1625\,\text{nm}$, width $W = 170\,\text{nm}$, thickness $t = 34\,\text{nm}$ fcc Co); Solid line with a double jump: Calculated hysteresis loops of an asymmetric ring (outer diameter $D_{\text{ext}} = 1625–1750\,\text{nm}$, width $W = 170–220\,\text{nm}$, thickness $t = 34\,\text{nm}$ fcc Co); open circles: Experimental data for an array of such rings (from Rothman *et al*., 2001). The calculated magnetization configurations for the onion-to-vortex transition are shown in insets (a)–(f) (color code as in Figure 17). (g) Shows the reverse onion state. It is found that the symmetric ring switches directly from the onion to the reverse onion configuration (insets $\alpha - \delta$). (Reprinted figure with permission from Rothman *et al*., *Phys. Rev. Lett.* **86**, 1098 (2001). Copyright 2001 by the American Physical Society.)

Here, we detail the physical processes occurring during the reversals. A double switching is observed in the experiment and, if asymmetries are present in the ring, as in all experiments, the simulations also yield a double switching (solid line) (Rothman *et al*., 2001). Let us concentrate on the first transition from a state containing domain walls to one without. After relaxing the field from positive saturation, the onion state is formed (first with a transverse domain wall Figure 16(a) and then, as the field is relaxed to zero, with a vortex domain wall (b), depending on the geometry (Kläui *et al*., 2004b, 2004d)). After reversing the field, both walls feel a force with a direction that depends on the wall position with respect to the field direction (Kläui *et al*., 2002c). Since one wall is, in general, more strongly pinned than the other, a transition into a vortex state takes place when the other wall has de-pinned (in the direction of the black arrow in Figure 16b) and has moved toward the pinned wall (Figure 16c–e), resulting in the annihilation of both walls (Figure 16f). The simulated switching field for the onion-to-vortex transition, $H_{C1} = 350$ Oe ($\approx 28\,\text{kA}\,\text{m}^{-1}$), falls well within the distribution of the experimental values (Rothman *et al*., 2001).

There is direct evidence for this reversal mechanism since in some rings the domain walls were pinned during their propagation somewhere around the perimeter of the ring and such states (similar to Figure 16d) have been observed (Welp *et al*., 2003; Zhu, 2002). Furthermore, by using a notch to selectively pin one of the domain walls, we have been able to make use of this switching process in order to control the domain wall propagation and thereby select the circulation direction of the resulting vortex state (Kläui *et al*., 2002c).

This transition from a state with domain walls (onion state) to one without (vortex state) exhibits the typical features of transitions characterized by the propagation and annihilation of domain walls. Here, two domain walls annihilate each other, while in other cases domain walls can also be annihilated by simply being pushed outside the magnetic element. Examples are the transition from a multidomain Landau state (Figure 9) to a quasiuniform S-state when a field is applied to a rectangular bar (García *et al*., 2002; Chapman *et al*., 1998), or transitions from more complicated multidomain states to quasiuniform states in rectangles and squares (Gomez *et al*., 1999a; Gu *et al*., 1998). In discs, the transition from the vortex to the S-state or C-state takes place via the displacement and the annihilation

of the vortex core, which is annihilated (expelled) at one of the edges. In wide rings, where the 'vortexcore' state (Kläui *et al*., 2003a) is present, the reversal from the vortexcore state to the onion state takes place by a similar expulsion of the vortex core (Kläui *et al*., 2004a; Kläui, Vaz, Lopez-Diaz and Bland, 2003).

In simulations, an asymmetry had to be introduced into the ring (variation of the ring width) to reproduce the onion-to-vortex transition. In the *M-H* loop of a perfectly symmetric ring (dotted line in Figure 16), only one transition is observed: the ring switches directly from one state containing domain walls (onion state) to the opposite onion state that contains the same number of domain walls, without falling into the vortex state. The switching mechanism in this case is surprisingly simple and close to domain wall motion. The two walls start to move simultaneously in the same rotational direction so that they chase each other around the perimeter of the ring as seen in the insets $\alpha - \delta$ of Figure 16. The onion state is completely switched when the walls have reached the opposite side. Even though this transition is not easily observed with a quasistatic field, it can be induced using pulsed fields (Lopez-Diaz, Kläui, Rothman and Bland, 2001a), varying size and geometry (Zhu *et al*., 2006) or by using fields that are not exactly applied opposite the wall positions (Uhlig and Zweck, 2004). This transition from a state containing domain walls (onion state) to another containing domain walls (reversed onion state) is one of the simplest cases of such a reversal containing domain wall propagation, since here no domain walls have to be nucleated or annihilated. Of course, in such transitions, the number of domain walls does not have to be constant and may in fact involve the nucleation and/or annihilation of domain walls in addition to domain wall motion.

The process we discuss next is that of domain wall nucleation. An example where this occurs is the second transition in Figure 16 (solid line), from the vortex state (Figure 16f) with no domain walls to the onion state (Figure 16g) that contains two domain walls (Kläui *et al*., 2002b). In Figure 17, the magnetization configurations during the reversal are shown as well as the configuration before and after the switching: Figure 17(a) shows the ring in the vortex state at zero field. As the applied field is increased, the spins rotate slightly but the ring remains in the vortex state as seen in Figure 17(b). At the critical field, a reverse domain is nucleated at the edge of the ring (indicated by the black arrow in Figure 17c). This domain then grows in size and the walls gradually propagate along the perimeter of the ring and outwards (Figures 17d–e) until the onion state is attained (Figure 17f). The calculated switching field H_{C2} at around 1000 Oe ($\approx 80\,\mathrm{kAm^{-1}}$) (solid line in Figure 16) again falls within the observed switching field distribution (open circles in Figure 16). Other reversals that contain such processes

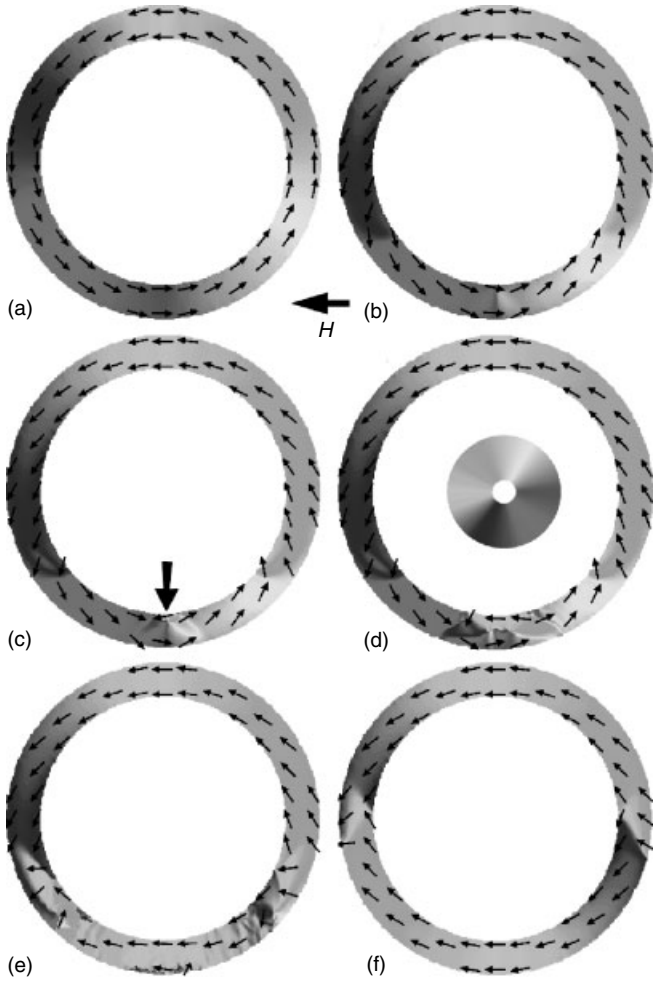

Figure 17. Magnetization configurations during the vortex-to-onion transition. (a) Vortex state at remanence; (b) just before switching; (c), (d), (e) during the switching; (f) onion state. Figures (a), (b), and (f) are equilibrium states, whereas (c), (d), and (e) are snapshots of the dynamics of the reversal. The direction of the applied field is indicated by arrows and the color code for the magnetization directions is presented.

are, for example, the formation of the Landau states and other multidomain states in rectangular bars: when an applied field is reduced from saturation, and an opposite field is applied, domain walls are nucleated at the edges (García *et al*., 2002; Gu *et al*., 1998). Such a nucleation also occurs in other transitions, such as the transition in a disc from the S-state to the vortex state, which occurs by the nucleation of a vortex core at the edge. The core then moves to the center and thereby reverses half of the disc to form the vortex state (Cowburn *et al*., 1999; Wernsdorfer, 2001; Fernandez, Gibbons, Wall and Cerjan, 1998).

A combination of domain wall nucleation, propagation, and annihilation can be found in wires with diameters above the range where reversal by coherent rotation or curling takes

place. The reversal then occurs by the nucleation of a domain wall at one end, the propagation of the domain wall along the wire, which thereby reverses the complete wire, and the final annihilation of the domain wall when it has reached the opposite end (Fidler *et al*., 2002; Ono *et al*., 2001). Wires are discussed in more detail in **Domain Wall Propagation in Magnetic Wires, Volume 2**.

It should be pointed out that, for example, in the case of strong wall pinning (where the field for domain wall propagation is higher than that for domain nucleation), the reversal can be dominated by the nucleation of a large number of reverse domains with only little wall propagation rather than by the nucleation and propagation of a single domain wall (Rosenbusch, Lee, Lauhoff and Bland, 1997). In general, the fields at which a certain process sets in governs the type of reversal.

In summary, the inhomogeneous reversal can be characterized by the interplay of different processes, which can be seen as the building blocks of the actual reversal: (i) rotation of spins, (ii) nucleation of domains, domain walls/vortices, (iii) propagation of domain walls/vortices, and (iv) annihilation of domain walls/vortices. One consequence of these different kinds of processes is that the different switching fields have different temperature dependences (Kläui *et al*., 2004c). For example, the nucleation field of a reverse domain is much less temperature dependent than the domain wall propagation field (Kläui *et al*., 2004c). Furthermore, the different processes also depend differently on defects, such as edge irregularities. This leads, for instance, to a larger switching field distribution for the domain wall depinning and propagation field than for the nucleation of a reverse domain field (Kläui *et al*., 2004c).

There are innumerable reversal routes for small magnetic elements, many of which can be very intricate. But the reversal is most often composed of the processes that we discussed, with each process being individually influenced by intrinsic as well as extrinsic factors.

8 CONCLUSIONS

We have attempted in this chapter to present the general types of magnetization configurations and the reversal processes in small magnetic elements. While it is not possible to give an exhaustive overview of such a vast and fast moving field, we hope that we have nonetheless discussed the most important aspects and provided instructive examples, from which an extrapolation to other systems may be possible.

Theoretically, the systems considered here can be modeled within the micromagnetics framework. This means that the magnetic properties can be described using a classical continuum approximation, which limits us to systems that are large enough so that quantum effects do not play a significant role and small enough so that computational cost is not prohibitive. This size regime between a few nanometers and a few micrometers is extremely relevant for applications. At the same time, such systems exhibit novel physical properties that are distinctly different from the bulk magnetic properties, due to their reduced dimensions (2-D films, 1-D wires, 0-D dots), and because an appreciable fraction of the atoms is located at surfaces or interfaces.

The different energy terms that are relevant in determining the magnetization configurations have been discussed:

(1) For very small systems, *the exchange energy* dominates, favoring single domain states, which can be described by a macrospin. Such systems are described theoretically by the analytical Stoner–Wohlfarth theory. At zero field, the equilibrium magnetization directions are governed by the *anisotropy energy* due to the electronic structure, strain, or other symmetry-breaking effects. Experimental examples of systems that exhibit a range of anisotropies and behave as single domain structures have been presented.

(2) For larger structures, the stray field becomes important and the *magnetostatic self-energy* governs the magnetization configurations. To minimize the stray field, the spins align themselves with the periphery of the element and thus the shape strongly influences the magnetic states. Elements tend to exhibit magnetization configurations that are commensurate with the geometry, such as the vortex state in a disc or a ring and Landau states in rectangular elements. Adding anisotropies yields states that are governed by the interplay between the three energy terms, such as the combination of the vortex and the quadrant state in a disc with a fourfold anisotropy.

(3) When external fields are applied, the *Zeeman energy* starts to play a role by trying to align the magnetization with the field direction. This leads to the concept of magnetic reversal, when elements change their magnetization configuration in response to the field. Theoretically, the reversal can be described within the micromagnetics theory by the Landau–Lifshitz–Gilbert equation, which describes the precession of the magnetization around the applied field direction and includes a phenomenological damping term that accounts for energy dissipation and which forces the magnetization to align with the applied field direction. For single domain systems, these two terms manifest themselves in a superposition of precession and damping that leads to a spiral motion of the spin direction toward the equilibrium position. For more complicated magnetization configurations, inhomogeneous reversal occurs. While the reversal routes can be intricate, they can be broken down into elementary processes for which we give a number of examples.

It is the intricate interplay between these different micromagnetic energy terms that leads to the rich magnetostatic and magnetodynamic behavior observed in small magnetic structures.

ACKNOWLEDGMENTS

We are indebted to a number of people for invaluable help. We would like to thank Professor H. Kronmüller for providing Figure 14. Dr W. Wernsdorfer has kindly helped us revise the section on single domain particles and provided Figures 4, 6, 12, and 13. Dr L. Lopez-Diaz has calculated the data for Figures 11 and 15, has provided valuable micromagnetics insights, and helped with proofreading. We are also very grateful to Professor T. Shinjo, Professor J. N. Chapman, Dr R. E. Dunin-Borkowski, Professor K. J. Kirk, and Dr G. Gubbiotti for kindly allowing us to reproduce here selected figures from their published work. We are also deeply grateful to Professor B. Hillebrands for allowing us to discuss unpublished results. Dr T. Moore has kindly proofread the chapter, for which we are very thankful. It is also a pleasure to acknowledge the contribution of our colleagues and collaborators, from whom we have learned and profited much during these formative years.

M. Kläui is greatly indebted to Professor U. Rüdiger and C. A. F. Vaz to Professor J. A. C. Bland for continuous support.

REFERENCES

Acremann, Y., Buess, M., Back, C.H., *et al*. (2001). Ultrafast generation of magnetic fields in a Schottky diode. *Nature*, **414**, 51.

Acremann, Y., Strachan, J.P. Chembrolu, V., *et al*. (2006). Time-resolved imaging of spin transfer switching: beyond the macrospin concept. *Physical Review Letter*, **96**, 217202.

Adeyeye, A.O., Bland, J.A.C., Daboo, C. and Hasko, D.G. (1997). Magnetostatic interactions and magnetization reversal in ferromagnetic wires. *Physical Review B*, **56**, 3265.

Adeyeye, A.O., Singh, N. and Goolaup, S. (2005). Spin state evolution and magnetic anisotropy of elongated $Ni_{80}Fe_{20}$ nanorings. *Journal of Applied Physics*, **98**, 094301.

Adeyeye, A.O., Bland, J.A.C., Daboo, C., *et al*. (1996). Size dependence of the magnetoresistance in submicron FeNi wires. *Journal of Applied Physics*, **79**, 6120.

Adeyeye, O., Lauhoff, G., Bland, J.A.C., *et al*. (1997). Magnetoresistance behavior of submicron $Ni_{80}Fe_{20}$ wires. *Applied Physics Letters*, **70**, 1046.

Aeppli, G. (2004). The ubiquity of antiferromagnetism in strange solids. *Journal of Magnetism and Magnetic Materials*, **272–276**, 7.

Aharoni, A. (1981). Magnetostatic energy of a saturating cylinder. *Journal of Applied Physics*, **52**, 6840.

Aharoni, A. (1986). Perfect and imperfect particles. *IEEE Transactions on Magnetics*, **22**, 478.

Aharoni, A. (1996). *Introduction to the Theory of Ferromagnetism*, Clarendon Press: Oxford.

Aharoni, A. (1997). Angular dependence of nucleation by curling in a prolate spheroid. *Journal of Applied Physics*, **82**, 1281.

Aharoni, A. (1999). Curling reversal mode in nonellipsoidal ferromagnetic particles. *Journal of Applied Physics*, **86**, 1041.

Aharoni, A. (2000). Surface anisotropy in ferromagnetic prolate spheroids. *Journal of Applied Physics*, **87**, 5526.

Albuquerque, G., Miltat, J. and Thiaville, A. (2001). Self-consistency based control scheme for magnetization dynamics. *Journal of Applied Physics*, **89**, 6719.

Allenspach, R. (1994). Ultrathin films: magnetism on the microscopic scale. *Journal of Magnetism and Magnetic Materials*, **129**, 160.

Aumentado, J. and Chandrasekhar, V. (1999). Magnetoresistance of single-domain ferromagnetic particles. *Applied Physics Letters*, **74**, 1898.

Bader, S.D. (1991). SMOKE. *Journal of Magnetism and Magnetic Materials*, **100**, 440.

Ballentine, G.E., Hiebert, W.K., Stankiewicz, A. and Freeman, M.R. (2000). Ultrafast microscopy and numerical simulation study of magnetization reversal dynamics in permalloy. *Journal of Applied Physics*, **87**, 6830.

Barbara, B. (2005). Single-particle nanomagnetism. *Solid State Sciences*, **7**, 668.

Bauer, M., Fassbender, J., Hillebrands, B. and Stamps, R.L. (2000). Switching behavior of a Stoner particle beyond the relaxation time limit. *Physical Review B*, **61**, 3410.

Beach, G.S.D., Nistor, C., Knutson, C., *et al*. (2005). *Nature Materials*, **4**, 741.

Bean, C.P. (1955). Hysteresis loops of mixtures of ferromagnetic micropowders. *Journal of Applied Physics*, **26**, 1381.

Bean, C.P. and Livingstone, J.D. (1959). Superparamagnetism. *Journal of Applied Physics*, **30**, 120S.

Bedrossian, P.J., Gibbons, M.R. and Cerjan, C.J. (1997). Domain topology of micron-scale, ferromagnetic pancakes. *Materials Research Society Symposium Proceedings*, **475**, 277.

Bekaert, J., Buntinx, D., van Hasendonck, C., *et al*. (2002). Non-invasive magnetic imaging and magnetization measurement of isolated mesoscopic Co rings. *Applied Physics Letters*, **81**, 3413.

Beleggia, M., De Graef, M., Millev, Y.T., *et al*. (2005). Demagnetization factors for elliptic cylinders. *Journal of Physics D: Applied Physics*, **38**, 3333.

Belmeguenai, M., Devolder, T. and Chappert, C. (2005). Magnetization switching assisted by out-of-plane ultrafast pulsed field in high perpendicular anisotropy nanostructures. *Journal of Magnetism and Magnetic Materials*, **290–291**, 514.

Bertotti, G. (1998). *Hysteresis in Magnetism*, Academic Press: San Diego.

Bode, M., Pietzsch, O., Kubetzka, A. and Wiesendanger, R. (2001). Imaging magnetic nanostructures by spin-polarized scanning

tunneling spectroscopy. *Journal of Electron Spectroscopy and Related Phenomena*, **114–116**, 1055.

Bonet, E., Wernsdorfer, W., Barbara, B., *et al*. (1999). Three-dimensional magnetization reversal measurements in nanoparticles. *Physical Review Letters*, **83**, 4188.

Braun, H-B. (1994). Fluctuations and instabilities of ferromagnetic domain-wall pairs in an external magnetic field. *Physical Review B*, **50**, 16485.

Braun, H-B. (1999). Nucleation in ferromagnetic nanowires – magnetostatics and topology. *Journal of Applied Physics*, **85**, 6172.

Brown, W.F. Jr. (1962). *Magnetostatic Principles in Ferromagnetism*, North-Holland Publishing: Amsterdam.

Brown, W.F. Jr. (1963). *Micromagnetics*, Interscience Publishers: New York.

Brown, W.F. Jr. (1969). The fundamental theorem of the theory of fine ferromagnetic particles. *Annals of the New York Academy of Sciences*, **147**, 463.

Bruno, P. (1999). Theory of interlayer exchange coupling. In *Magnetische Schichtsysteme in Forschung und Anwendung*, Volume 2 of Vorlesungsmanuskripte des 30. IFF-Ferienkurses, Schriften des Forschungszentrums Jülich, p. B8.1.

Buchanan, K.S., Roy, P.E., Grimsditch, M., *et al*. (2005). Soliton-pair dynamics in patterned ferromagnetic ellipses. *Nature Physics*, **1**, 172.

Buess, M., Haug, T., Scheinfein, M.R. and Back, C.H. (2005). Micromagnetic dissipation, dispersion, and mode conversion in thin permalloy platelets. *Physical Review Letters*, **94**, 127205.

Buess, M., Höllinger, R., Haug, T., *et al*. (2004). Fourier transform imaging of spin vortex eigenmodes. *Physical Review Letters*, **93**, 077207.

Carr, W.J. Jr. (1966). Secondary effects in ferromagnetism. In *Encyclopedia of Physics*, Flügge, S. (Ed.), Springer-Verlag, p. 274, Vol. 18/2.

Castaño, F.J., Morecroft, D., Jung, W. and Ross, C.A. (2005). Spin-dependent scattering in multilayered magnetic rings. *Physical Review Letters*, **95**, 137201.

Castaño, F.J., Ross, C.A. and Eilez, A. (2003). Magnetization reversal in elliptical-ring nanomagnets. *Journal of Physics D: Applied Physics*, **36**, 2031.

Castaño, F.J., Ross, C.A., Eilez, A., *et al*. (2004). Magnetic configurations in 160-520-nm-diameter ferromagnetic rings. *Physical Review B*, **69**, 144421.

Castaño, F.J., Ross, C.A., Frandsen, C., *et al*. (2003). Metastable states in magnetic nanorings. *Physical Review B*, **67**, 184425.

Chapman, J.N. (1984). The investigation of magnetic domain structures in thin foils by electron microscopy. *Journal of Physics D*, **17**, 623.

Chapman, J.N., Aitchison, P.R., Kirk, K.J., *et al*. (1998). Direct observation of magnetization reversal processes in micron-sized elements of spin-valve material. *Journal of Applied Physics*, **83**, 5321.

Chen, D-X., Brug, J.A. and Goldfarb, R.B. (1991). Demagnetizing factors for cylinders. *IEEE Transactions on Magnetics*, **27**, 3601.

Chérif, S.M., Dugautier, C., Hennequin, J-F. and Moch, P. (1997). Brillouin light scattering by magnetic surface waves in dot-structured permalloy layers. *Journal of Magnetism and Magnetic Materials*, **175**, 228.

Chérif, S.M., Roussigné, Y.E. and Moch, P. (2002). Finite-size effects in arrays of permalloy square dots. *IEEE Transactions on Magnetics*, **38**, 2529.

Choi, B.C. and Freeman, M.R. (2005). Nonequilibrium spin dynamics in laterally defined magnetic structures. In *Ultrathin Magnetic Structures III*, Bland, J.A.C. and Heinrich, B. (Eds.), Springer-Verlag: Berlin, p. 211.

Choi, B.C., Belov, M., Hiebert, W.K., *et al*. (2001). Ultrafast magnetization reversal dynamics investigated by time domain imaging. *Physical Review Letters*, **86**, 728.

Cowburn, R.P. and Welland, M.E. (1998). Micromagnetics of the single-domain state of square ferromagnetic nanostructures. *Physical Review B*, **58**, 9217.

Cowburn, R.P., Koltsov, D.K., Adeyeye, A.O., *et al*. (1999). Single-domain circular nanomagnets. *Physical Review Letters*, **83**, 1042.

Demidov, V.E., Demokritov, S.O., Hillebrands, B., *et al*. (2004). Radiation of spin waves by a single micrometer-sized magnetic element. *Applied Physics Letters*, **85**, 2866.

Demokritov, S.O., Hillebrands, B. and Slavin, A.N. (2001). Brillouin light scattering studies of confined spin waves: linear and nonlinear confinement. *Physics Reports*, **348**, 441.

Dunin-Borkowski, R.E., McCartney, M.R., Kardynal, B. and Smith, D.J. (1998). Magnetic interactions within patterned cobalt nanostructures using off-axis electron holography. *Journal of Applied Physics*, **84**, 374.

Dunin-Borkowski, R.E., Mccartney, M.R., Kardynal, B., *et al*. (2000). Off-axis electron holography of patterned magnetic nanostructures. *Journal of Microscopy*, **200**, 187.

Eames, P. and Dahlberg, E.D. (2002). Characterization of domain states in submicron sized permalloy particles with perpendicular anisotropy. *Journal of Applied Physics*, **91**, 7986.

Ebels, U., Radulescu, A., Henry, Y., *et al*. (2000). Spin accumulation and domain wall magnetoresistance in 35 nm Co wires. *Physical Review Letters*, **84**, 983.

Fawcett, E. (1988). Spin-density-wave antiferromagnetism in chromium. *Reviews of Modern Physics*, **60**, 209.

Fawcett, E., Alberts, H.L., Galkin, V.Yu., *et al*. (1994). Spin-density-wave antiferromagnetism in chromium alloys. *Reviews of Modern Physics*, **66**, 25.

Feldtkeller, E. and Thomas, H. (1965). Struktur und Energie von Blochlinien in dünnen ferromagnetischen Schichten. *Physik der Kondensiterten Materie*, **4**, 8.

Felton, S., Gunnarsson, K., Roy, P.E., *et al*. (2004). MFM imaging of micron-sized permalloy ellipses. *Journal of Magnetism and Magnetic Materials*, **280**, 202.

Fernandez, A., Gibbons, M.R., Wall, M.A. and Cerjan, C.J. (1998). Magnetic domain structure and magnetization reversal in submicron-scale Co dots. *Journal of Magnetism and Magnetic Materials*, **190**, 71.

Ferré, J., Ounadjela, K., George, J.M., *et al*. (1997). Magnetization processes in nickel and cobalt electrodeposited nanowires. *Physical Review B*, **56**, 14066.

Fidler, J. and Schrefl, T. (2000). Micromagnetic modelling – the current state of the art. *Journal of Physics D*, **33**, R135.

Fidler, J., Schrefl, T., Scholz, W., *et al*. (2004). Magnetostatic spin waves in nanoelements. *Physica B*, **343**, 200.

Fidler, J., Schrefl, T., Tsiantos, V.D., *et al*. (2002). Micromagnetic simulation of the magnetic switching behaviour of mesoscopic and nanoscopic structures. *Computation Materials Science*, **24**, 163.

Fischer, P., Eimüller, T., Schütz, G., *et al*. (2001). Element-specific imaging of magnetic domains at 25 nm spatial resolution using soft x-ray microscopy. *Review of Scientific Instruments*, **72**, 2322.

Fitzsimmons, M.R., Bader, S.D., Borchers, J.A., *et al*. (2004). Neutron scattering studies of nanomagnetism and artificially structured materials. *Journal of Magnetism and Magnetic Materials*, **271**, 103.

Frei, H., Shtrikman, S. and Treves, D. (1957). Critical size and nucleation field of ideal ferromagnetic particles. *Physical Review*, **106**, 446.

Frenkel, J. and Dorfman, J. (1930). Spontaneous and induced magnetisation in ferromagnetic bodies. *Nature*, **126**, 274.

Fruchart, O., Nozières, J.P., Wernsdorfer, W., *et al*. (1999). Enhanced coercivity in submicrometer-sized ultrathin epitaxial dots with in-plane magnetization. *Physical Review Letters*, **82**, 1305.

Gabureac, M., Viret, M., Ott, F. and Fermon, C. (2004). Magnetoresistance in nanocontacts induced by magnetostrictive effects. *Physical Review B*, **69**, 100401(R).

Gadbois, J. and Zhu, J-G. (1995). Effect of edge roughness in nanoscale magnetic bar switching. *IEEE Transactions on Magnetics*, **31**, 3802.

García, N., Muñoz, M. and Zhao, Y-W. (1999). Magnetoresistance in excess of 200% in ballistic Ni nanocontacts at room temperature and 100 Oe. *Physical Review Letters*, **82**, 2923.

García, J.M., Thiaville, A. and Miltat, J. (2002). MFM imaging of nanowires and elongated patterned elements. *Journal of Magnetism and Magnetic Materials*, **249**, 163.

García, J.M., Thiaville, A., Miltat, J., *et al*. (2001). Quantitative interpretation of magnetic force microscopy images from soft patterned elements. *Applied Physics Letters*, **79**, 656.

García, J.M., Thiaville, A., Miltat, J., *et al*. (2002). MFM imaging of patterned permalloy elements under an external applied field. *Journal of Magnetism and Magnetic Materials*, **242–245**, 1267.

Gautier, F. (1982). Itinerant magnetism. In *Magnetism of Metals and Alloys*, Cyrot, M. (Ed.), North-Holland, p. 1.

Giesen, F., Podbielski, J., Korn, T. and Grundler, D. (2005). Multiple ferromagnetic resonance in mesoscopic permalloy rings. *Journal of Applied Physics*, **97**, 10A712.

Giesen, F., Podbielski, J., Korn, T., *et al*. (2005). Hysteresis and control of ferromagnetic resonances in rings. *Applied Physics Letters*, **86**, 112510.

Gilette, P.R. and Oshima, K. (1958). Magnetization reversal by rotation. *Journal of Applied Physics*, **29**, 529.

Goglio, G., Pignard, S., Radulescu, A., *et al*. (1999). Microwave properties of metallic nanowires. *Applied Physics Letters*, **75**, 1769.

Gomez, R.D., Luu, T.V., Pak, A.O., *et al*. (1999a). Domain configurations of nanostructured permalloy elements. *Journal of Applied Physics*, **85**, 6163.

Gomez, R.D., Luu, T.V., Pak, A.O., *et al*. (1999b). Domain wall motion in micron-sized permalloy elements. *Journal of Applied Physics*, **85**, 4598.

Goode, D.A. and Rowlands, G. (2003). The demagnetizing energies of a uniformly magnetized cylinder with an elliptic cross-section. *Journal of Magnetism and Magnetic Materials*, **267**, 373.

Goode, D.A. and Rowlands, G. (2005). Analytical magnetic distributions and Stoner-Wohlfarth theory for near-uniformly magnetised rectangular nanomagnets. *Journal of Magnetism and Magnetic Materials*, **295**, 197.

Grollier, J., Lacour, D., Cros, V., *et al*. (2002). Switching the magnetic configuration of a spin valve by current induced domain wall motion. *Journal of Applied Physics*, **92**, 4825.

Grütter, P., Mamin, H.J. and Rugar, D. (1992). Magnetic force microscopy (MFM). In *Scanning Tunneling Microscopy II*, Springer Series in Surface Sciences 28, Wiesendanger, R. and Güntherodt, H-J. (Eds.), Springer-Verlag: Berlin, p. 151.

Gu, E., Ahmad, E., Bland, J.A.C., *et al*. (1998). Micromagnetic structures and microscopic magnetization-reversal processes in epitaxial Fe/GaAs(001) elements. *Physical Review B*, **57**, 7814.

Gu, E., Ahmad, E., Gray, S.J., *et al*. (1997). Micromagnetism of epitaxial Fe(001) elements on the mesoscale. *Physical Review Letters*, **78**, 1158.

Gubbiotti, G., Albani, L., Carlotti, G., *et al*. (2000). Finite size effects in patterned magnetic permalloy films. *Journal of Applied Physics*, **87**, 5633.

Gubbiotti, G., Carlotti, G., Nizzoli, F., *et al*. (2002). Magnetic properties of submicron circular permalloy dots. *IEEE Transactions on Magnetics*, **38**, 2532.

Gubbiotti, G., Carlotti, G., Okuno, T., *et al*. (2005). Spin dynamics in thin nanometric elliptical permalloy dots: a brillouin light scattering investigation as a function of dot eccentricity. *Physical Review B*, **72**, 184419.

Gubbiotti, G., Madami, M., Tacchi, S., *et al*. (2006). Normal mode splitting in interacting arrays of cylindrical permalloy dots. *Journal of Applied Physics*, **91**, 08C701.

Guedes, I., Zaluzec, N.J., Grimsditch, M., *et al*. (2000). Magnetization of negative magnetic arrays: elliptical holes on a square lattice. *Physical Review B*, **62**, 11719.

Guslienko, K.Yu., Novosad, V., Otani, Y., *et al*. (2002). Magnetization reversal due to vortex nucleation, displacement, and annihilation in submicron ferromagnetic dot arrays. *Physical Review B*, **65**, 024414.

Ha, J.K., Hertel, R. and Kirschner, J. (2003). Micromagnetic study of magnetic configurations in submicron permalloy disks. *Physical Review B*, **67**, 224432.

Hegedus, C.J., Kadar, G. and Torre, E.D. (1979). Demagnetization matrices for cylindrical bodies. *Journal of the Institute of Mathematics and its Applications*, **24**, 279.

Hehn, M., Ounadjela, K., Ferré, R., *et al*. (1997). Reorientational magnetic transition in mesoscopic cobalt dots. *Applied Physics Letters*, **71**, 2833.

Heidkamp, M. and Erskine, J.L. (2000). High-speed high spatial resolution magneto-optic Kerr effect polarimeter/microscope for studies of ultrathin magnetic structures. *Review of Scientific Instruments*, **71**, 3141.

Heinrich, B. (2005). Spin relaxation in magnetic metallic layers and multilayers. In *Ultrathin Magnetic Structures III*, Bland, J.A.C. and Heinrich, B. (Eds.), Springer-Verlag: Berlin Heidelberg, p. 143.

Herrmann, M., McVitie, S. and Chapman, J.N. (2000). Investigation of the influence of edge structure on the micromagnetic behavior of small magnetic elements. *Journal of Applied Physics*, **87**, 2994.

Hertel, R. (2004). *Untersuchung Magnetischer Strukturen in Weichmagnetischen Schichten mit der Methode der Finiten Elemente*, Ph.D. Thesis, University of Stuttgart.

Hertel, R. and Kronmüller, H. (2002). Finite element calculations on the single-domain limit of a ferromagnetic cube – a solution to μMAG standard problem No. 3. *Journal of Magnetism and Magnetic Materials*, **238**, 185.

Hertel, R., Fruchart, O., Cherifi, S., *et al*. (2005). Three-dimensional magnetic-flux-closure patterns in mesoscopic Fe islands. *Physical Review B*, **72**, 214409.

Heumann, M., Uhlig, T. and Zweck, J. (2005). True single domain and configuration-assisted switching of submicron permalloy dots observed by electron holography. *Physical Review Letters*, **94**, 077202.

Hicken, R.J., Hughes, N.D., Moore, J.R., *et al*. (2002). Magneto-optical studies of magnetism on pico and femtosecond time scales. *Journal of Magnetism and Magnetic Materials*, **242–245**, 559.

Hiebert, W.K., Lagae, L. and De Boeck, J. (2003). Spatially inhomogeneous ultrafast precessional magnetization reversal. *Physical Review B*, **68**, 20402.

Hilzinger, H.R. and Kronmüller, H. (1972). Spin configuration and intrinsic coercive field of narrow domain walls in Co_5R-compounds. *Physica Status Solidi B*, **54**, 593.

Hilzinger, H.R. and Kronmüller, H. (1973). Analytical derivation of spin configuration and intrinsic coercive field of a narrow domain wall. *Physica Status Solidi B*, **59**, 71.

Himpsel, F.J. (1995). Quantized electronic states in nanostructures. *Journal of Electron Spectroscopy and Related Phenomena*, **75**, 187.

Hirohata, A., Xu, Y.B., Bland, J.A.C., *et al*. (2002). Influence of crystalline structures on the domain configurations in controlled mesoscopic ferromagnetic wire junctions. *Journal of Applied Physics*, **91**, 7308.

Hong, K. and Giordano, N. (1995). Approach to mesoscopic magnetic measurements. *Physical Review B*, **51**, 9855.

Hopster, H. and Oepen, H.P. (Eds.) (2005). *Magnetic Microscopy of Nanostructures*, Nanoscience and Nanotechnology, Springer-Verlag: Berlin.

Huang, M., Abraham, M.C., Savas, T.A., *et al*. (2000). Magnetic force microscopy study of interactions in 100 nm period nanomagnet arrays. *Journal of Applied Physics*, **87**, 5108.

Hubert, A. and Schäfer, R. (1998). *Magnetic Domains*, Springer-Verlag: Berlin.

Hubert, A., Rave, W. and Tomlinson, S.L. (1997). Imaging magnetic charges with magnetic force microscopy. *Physica Status Solidi B*, **204**, 817.

Hurd, C.M. (1982). Varieties of magnetic order in solids. *Contemporary Physics*, **23**, P469.

Ishii, Y. (1991). Magnetization curling in an infinite cylinder with a uniaxial magnetocrystalline anisotropy. *Journal of Applied Physics*, **70**, 3765.

Jackson, J.D. (1975). *Classical Electrodynamics*, *Second Edition*, John Wiley & Sons: New York.

Jamet, M., Wernsdorfer, W., Thirion, C., *et al*. (2001). Magnetic anisotropy of a single cobalt nanocluster. *Physical Review Letters*, **86**, 4676.

Jorritsma, J., Gijs, M.A.M., Kerkhof, J.M. and Stienen, J.G.H. (1996). General technique for fabricating large arrays of nanowires. *Nanotechnology*, **7**, 263.

Jorritsma, J. and Mydosh, J.A. (1998). Temperature-dependent magnetic anisotropy in Ni nanowires. *Journal of Applied Physics*, **84**, 901.

Jorzick, J., Demokritov, S.O., Hillebrands, B., *et al*. (2002). Spin wave wells in nonellipsoidal micrometer size magnetic elements. *Physical Review Letters*, **88**, 047204.

Jorzick, J., Demokritov, S.O., Mathieu, C., *et al*. (1999). Brillouin light scattering from quantized spin waves in micron-size magnetic wires. *Physical Review B*, **60**, 15194.

Joseph, R.I. (1966). Ballistic demagnetising factor in uniformly magnetized cylinders. *Journal of Applied Physics*, **37**, 4639.

Joseph, R.I. (1976). Demagnetising factor in nonellipsiodal samples – a review. *Geophysics*, **41**, 1052.

Jubert, P-O. and Allenspach, R. (2004). Analytical approach to the single-domain-to-vortex transition in small magnetic disks. *Physical Review B*, **70**, 144402.

Jubert, P-O., Allenspach, R. and Bischof, A. (2004). Magnetic domain walls in constrained geometries. *Physical Review B*, **69**, 220410.

Jung, W., Castaño, F.J., Ross, C.A., *et al*. (2004). Elliptical-ring magnetic arrays fabricated using zone-plate-array lithography. *Journal of Vacuum Science and Technology B*, **22**, 3335.

Kaczér, J. and Klem, Z. (1976). The magnetostatic energy of coaxial cylinders and coils. *Physical Status Solidi B*, **35**, 235.

Kageyama, Y. and Suzuki, T. (2006). Temperature dependence of magnetic domain structures of single-crystal Co thin films and particles. *Journal of Applied Physics*, **99**, 8Q506.

Kang, B-S., Kim, D-H., Anderson, E., *et al*. (2005). Polarization-modulated magnetic soft-x-ray transmission microscopy. *Journal of Applied Physics*, **98**, 093907.

Katine, J.A., Albert, F.J., Buhrman, R.A., *et al*. (2000). Current-driven magnetization reversal and spin-wave excitations in Co/Cu/Co pillars. *Physical Review Letters*, **84**, 3149.

Keffer, F. (1966). Spin waves. In *Encyclopedia of Physics*, Flügge, S. (Ed.), Springer-Verlag: Berlin, p. 1, Vol. 18/2.

Kikuchi, R. (1956). On the minimum of magnetization reversal time. *Journal of Applied Physics*, **27**, 1352.

Kirk, K.J., Chapman, J.N. and Wilkinson, C.D.W. (1997). Switching fields and magnetostatic interactions of thin film magnetic nanoelements. *Applied Physics Letters*, **71**, 539.

Kirk, K.J., Scheinfein, M.R., Chapman, J.N., *et al*. (2001). Role of vortices in magnetization reversal of rectangular NiFe elements. *Journal of Physics D: Applied Physics*, **34**, 160.

Kittel, C. (1987). *Quantum Theory of Solids*, *Second Edition*, John Wiley & Sons: New York.

Kläui, M.M. (2003). *Nanomagnetism of High-symmetry Structures*, Master's Thesis, University of Cambridge.

Kläui, M., Vaz, C.A.F., Bland, J.A.C. and Heyderman, L.J. (2005). Domain wall coupling and collective switching in interacting mesoscopic ring magnet arrays. *Applied Physics Letters*, **86**, 32504.

Kläui, M., Vaz, C.A.F., Lopez-Diaz, L. and Bland, J.A.C. (2003). Vortex formation in narrow ferromagnetic rings. *Journal of Physics: Condensed Matter*, **15**, R985.

Kläui, M., Lewis, P.A., Vaz, C.A.F., *et al*. (2002a). Fabrication and magnetic properties of prepatterned epitaxial nanodots. *Microelectronic Engineering*, **61**, 593.

Kläui, M., Lopez-Diaz, L., Rothman, J., *et al*. (2002b). Switching properties of free-standing epitaxial ring magnets. *Journal of Magnetism and Magnetic Materials*, **240**, 7.

Kläui, M., Vaz, C.A.F., Bland, J.A.C., *et al*. (2002c). Controlled magnetic switching in single narrow rings probed by magnetoresistance measurements. *Applied Physics Letters*, **81**, 108.

Kläui, M., Vaz, C.A.F., Bland, J.A.C., *et al*. (2003a). Direct observation of spin configurations and classification of switching processes in mesoscopic ferromagnetic rings. *Physical Review B*, **68**, 134426.

Kläui, M., Vaz, C.A.F., Rothman, J., *et al*. (2003b). Domain wall pinning in narrow ferromagnetic ring structures probed by magnetoresistance measurements. *Physical Review Letters*, **90**, 97202.

Kläui, M., Vaz, C.A.F., Bland, J.A.C., *et al*. (2004a). Multistep switching phase diagram of ferromagnetic ring structures. *Journal of Applied Physics*, **95**, 6639.

Kläui, M., Vaz, C.A.F., Bland, J.A.C., *et al*. (2004b). Head-to-head domain-wall phase diagram in mesoscopic ring magnets. *Applied Physics Letters*, **85**, 5637.

Kläui, M., Vaz, C.A.F., Bland, J.A.C., *et al*. (2004c). Switching processes and switching reproducibility in ferromagnetic ring structures. *Applied Physics Letters*, **84**, 951.

Kläui, M., Vaz, C.A.F., Wernsdorfer, W., *et al*. (2004d). Domain wall behaviour at constrictions in ferromagnetic ring structures. *Physica B*, **343**, 343.

Kläui, M., Ehrke, H., Rüdiger, U., *et al*. (2005a). Direct observation of domain-wall pinning at nanoscale constrictions. *Applied Physics Letters*, **87**, 102509.

Kläui, M., Jubert, P-O., Allenspach, R., *et al*. (2005b). Direct observation of domain-wall configurations transformed by spin currents. *Physical Review Letters*, **95**, 026601.

Kläui, M., Vaz, C.A.F., Bland, J.A.C., *et al*. (2005c). Controlled and reproducible domain wall displacement by current pulses injected into ferromagnetic ring structures. *Physical Review Letters*, **94**, 106601.

Kläui, M., Rüdiger, U., Vaz, C.A.F., *et al*. (2006). Magnetic states in wide annular structures. *Journal of Applied Physics*, **99**, 08G308.

Kleman, M. (1982). Magnetisation processes in ferromagnets. In *Magnetism of Metals and Alloys*, Cyrot, M. (Ed.), North-Holland, p. 535.

Kneller, E.F. and Luborsky, F.E. (1963). Particle size dependence of coercivity and remanence of single-domain particles. *Journal of Applied Physics*, **34**, 656.

Komineas, S., Vaz, C.A.F., Bland, J.A.C. and Papanicolaou, N. (2005). Bubble domains in disc-shaped ferromagnetic particles. *Physical Review B*, **71**, 060405(R).

Korenman, V. (1983). Magnetovolume effects in the local-band theory of ferromagnetism: pressure dependence of t_c in iron and nickel. *Physica B*, **119**, 21.

Krams, P., Lauks, F., Stamps, R.L., *et al*. (1992). Magnetic anisotropies of ultrathin Co(001) films on Cu(001). *Physical Review Letters*, **69**, 3674.

Kronmüller, H. and Fähnle, M. (2003). *Micromagnetism and the Microstructure of Ferromagnetic Solids*, Cambridge University Press.

Kronmüller, H., Fischer, R., Hertel, R. and Leineweber, T. (1997). Micromagnetism and the microstructure in nanocrystalline materials. *Journal of Magnetism and Magnetic Materials*, **175**, 177.

Kronmüller, H. and Hertel, R. (2000). Computational micromagnetism of magnetic structures and magnetisation processes in small particles. *Journal of Magnetism and Magnetic Materials*, **215–216**, 11.

Kronmüller, H., Goll, D., Hertel, R. and Schütz, G. (2004). Critical thicknesses of domain formations in cubic particles and thin films. *Physica B*, **343**, 229.

Kryder, M., Kie, A., Mazzeo, N., *et al*. (1980). Magnetic properties and domain structures in narrow NiFe stripes. *IEEE Transactions on Magnetics*, **16**, 99.

Kubetzka, A., Pietzsch, O., Bode, M. and Wiesendanger, R. (2003). Spin-polarized scanning tunneling microscopy study of 360° walls in an external magnetic field. *Physical Review B*, **67**, 020401(R).

Kuksov, A., Schneider, C.M., Oelsner, A., *et al*. (2004). Investigating magnetization dynamics in permalloy microstructures using time-resolved x-ray photoemission electron microscope. *Journal of Applied Physics*, **95**, 6530.

Landau, L.D. and Lifshitz, E.M. (1935). On the theory of the dispersion of magnetic permeability in ferromagnetic bodies. *Physikalische Zeitschrift der Sowjetunion*, **8**, 153.

Laufenberg, M., Backes, D., Bührer, W., *et al*. (2006). Observation of thermally activated domain wall transformations. *Applied Physics Letters*, **88**, 052507.

Lederman, M., O'Barr, R. and Schultz, S. (1995). Experimental study of individual ferromagnetic sub-micron cylinders. *IEEE Transactions on Magnetics*, **31**, 3793.

Lewis, P. and Ahmed, H. (1999). Patterning of silicon nanopillars formed with a colloidal gold etch mask. *Journal of Vacuum Science and Technology B*, **17**, 3239.

Li, S.P., Lew, W.S., Bland, J.A.C., *et al*. (2002). Intrinsic anisotropy-defined magnetization reversal in submicron ring magnets. *Journal of Applied Physics*, **92**, 7397.

Li, S.P., Peyrade, D., Natali, M., *et al*. (2001). Flux closure structures in cobalt rings. *Physical Review Letters*, **86**, 1102.

Libál, A., Grimsditch, M., Metlushko, V., *et al*. (2005). Control of magnetic vortex chirality in square ring micromagnets. *Journal of Applied Physics*, **98**, 083904.

Liou, S.H., Sabiryanov, R.F., Jaswal, S.S., *et al*. (2001). Magnetic domain patterns of rectangular and elliptic arrays of small permalloy elements. *Journal of Magnetism and Magnetic Materials*, **226–230**, 1270.

Liu, X., Chapman, J.N., McVitie, S. and Wilkinson, C.D.W. (2004a). Reversal mechanisms and metastable states in magnetic nanoelements. *Journal of Applied Physics*, **96**, 5173.

Liu, X., Chapman, J.N., McVitie, S. and Wilkinson, C.D.W. (2004b). Introduction and control of metastable states in elliptical and rectangular magnetic nanoelements. *Applied Physics Letters*, **84**, 4406.

Locatelli, A., Cherifi, K.S., Heun, S., *et al*. (2002). X-ray magnetic circular dichroism imaging in a low energy electron microscope. *Surface Review and Letters*, **9**, 171.

Lopez-Diaz, L., Kläui, M., Rothman, J. and Bland, J.A.C. (2001a). Precessional switching in narrow ring nanomagnets. *Physica B*, **306**, 211.

Lopez-Diaz, L., Rothman, J., Kläui, M. and Bland, J.A.C. (2001b). Vortex formation in magnetic narrow rings: the role of magnetocrystalline anisotropy. *Journal of Applied Physics*, **89**, 7579.

Maicas, M., Rivero, M.A., López, E., *et al*. (2002). Micromagnetic structures in square magnetic nanodots. *Journal of Magnetism and Magnetic Materials*, **242–245**, 1024.

Mailly, D., Chapelier, C. and Benoit, A. (1993). Experimental observation of persistent currents in a GaAs-AlGaAs single loop. *Physical Review Letters*, **70**, 2020.

Manalis, S., Babcock, K., Massie, J., *et al*. (1995). Submicron studies of recording media using thin-film magnetic scanning probes. *Applied Physics Letters*, **66**, 2585.

Martín, J.I., Nogués, J., Liu, K., *et al*. (2003). Ordered magnetic nanostructures: fabrication and properties. *Journal of Magnetism and Magnetic Materials*, **256**, 449.

Martyanov, O.N., Yudanov, V.F., Lee, R.N., *et al*. (2005). Ferromagnetic resonance investigation of collective phenomena in two-dimensional periodic arrays of Co particles. *Applied Physics A*, **81**, 679.

Mattheis, R., Berkov, D. and Gorn, N. (1999). Magnetic reversal in ultra-thin nanoshaped magnetic dots: numerical simulations and Kerr observation. *Journal of Magnetism and Magnetic Materials*, **198–199**, 216.

Mattheis, R., Ramstöck, K. and McCord, J. (1997). Formation and annihilation of edge walls in thin-film permalloy strips. *IEEE Transactions on Magnetics*, **33**, 3993.

Maxwell, J.C. (1891). *A Treatise on Electricity and Magnetism*, *Third Edition*, Clarendon Press: Oxford. Vol. 2.

McMichael, R.D. and Donahue, M.J. (1997). Head to head domain wall structures in thin magnetic strips. *IEEE Transactions on Magnetics*, **33**, 4167.

McMichael, R.D., Donahue, M.J., Porter, D.G. and Eicke, J. (2001). Switching dynamics and critical behavior of standard problem No. 4. *Journal of Applied Physics*, **89**, 7603.

Memmert, U., Müller, A.N. and Hartmann, U. (2000). Probes for magnetic force microscopy imaging of soft magnetic samples. *Measurement Science and Technology*, **11**, 1342.

Montero, M.I., Dumas, R.K., Liu, G., *et al*. (2004). Magnetoresistance of mechanically stable Co nanoconstrictions. *Physical Review B*, **70**, 184418.

Morecroft, D., Castaño, F.J., Jung, W. and Ross, C.A. (2006). Angular dependence of the giant magnetoresistance in multilayer rings with different contact configurations. *Journal of Applied Physics*, **99**, 08T104.

Moriya, T. (1985). *Spin Fluctuations in Itinerant Electron Magnetism*, Volume 56 of Solid-State Sciences, Springer-Verlag.

Moutafis, C., Komineas, S., Vaz, C.A.F., *et al*. (2006). Vortices in ferromagnetic elements with perpendicular anisotropy. *Physical Review B*, **74**, 214406.

Nagamiya, T., Yosida, K. and Kubo, R. (1955). Antiferromagnetism. *Advances in Physics*, **4**, 1.

Nakatani, Y., Thiaville, A. and Miltat, J. (2005). Head-to-head domain walls in soft nano-strips: a refined phase diagram. *Journal of Magnetism and Magnetic Materials*, **290–291**, 750.

Nalwa, H.S. (2002). *Magnetic Nanostructures*, American Scientific Publishers: Stevenson Ranch.

Néel, L. (1947). Le champ coercitif d'une poudre ferromagnétique cubique à grains anisotropes. *Comptes Rendus*, **224**, 1550.

Neudecker, I., Kläui, M., Perzlmaier, K., *et al*. (2006). Spatially resolved dynamic eigenmode spectrum of Co rings. *Physical Review Letters*, **96**, 057207.

New, R.M.H., Pease, R.F.W. and White, R.L. (1996). Lithographically patterned single-domain cobalt islands for high-density magnetic recording. *Journal of Magnetism and Magnetic Materials*, **155**, 140.

Novosad, V., Fradin, F.Y., Roy, P.E., *et al*. (2005). Magnetic vortex resonance in patterned ferromagnetic dots. *Physical Review B*, **72**, 024455.

Novosad, V., Grimsditch, M., Guslienko, K.Yu., *et al*. (2002). Spin excitations of magnetic vortices in ferromagnetic nanodots. *Physical Review B*, **66**, 052407.

Ohkubo, T., Kishigami, J., Yanagisawa, K. and Kaneko, R. (1991). Submicron magnetizing and its detection based on the point magnetic recording concept. *IEEE Transactions on Magnetics*, **27**, 5286.

Ohno, H., Miyajima, H., Shigeto, K. and Shinjo, T. (1999). Dot-arrays of Co/Pt multilayers with perpendicular magnetic anisotropy. *Journal of Magnetism and Magnetic Materials*, **198–199**, 225.

Okuno, T., Shigeto, K., Ono, T., *et al*. (2002). MFM study of magnetic vortex cores in circular permalloy dots: behavior in external field. *Journal of Magnetism and Magnetic Materials*, **240**, 1.

Ono, T., Ooka, Y., Kasai, S., *et al*. (2001). Magnetization reversal and electric transport in ferromagnetic nanowires. *Materials Science and Engineering B*, **84**, 126.

Oral, A., Bending, S.J. and Henini, M. (1996). Real-time scanning hall probe microscopy. *Applied Physics Letters*, **69**, 1324.

Osborn, J.A. (1945). Demagnetizing factors of the general ellipsoid. *Physical Review*, **67**, 351.

Pardavi-Horvath, M. (1999). Shape and size effects in nanostructured 2D magnetic systems. *Journal of Magnetism and Magnetic Materials*, **198–199**, 219.

Park, J.P., Eames, P., Engebretson, D.M., *et al*. (2003). Imaging of spin dynamics in closure domain and vortex structures. *Physical Review B*, **67**, 020403(R).

Park, M.H., Hong, Y.K., Choi, B.C., *et al*. (2006). Vortex head-to-head domain walls and their formation in onion-state ring elements. *Physical Review B*, **73**, 094424.

Perzlmaier, K., Buess, M., Back, C.H., *et al*. (2005). Spin-wave eigenmodes of permalloy squares with a closure domain structure. *Physical Review Letters*, **94**, 57202.

Pierre, J. (1982). Magnetism of rare earth metals and intermetallic compounds. In *Magnetism of Metals and Alloys*, Cyrot, M. (Ed.), North-Holland, p. 245.

Pratzer, M. and Elmers, H.J. (2003). Domain wall energy in quasi-one-dimensional Fe/W(110) nanostripes. *Physical Review B*, **67**, 094416.

Pratzer, M., Elmers, H.J., Bode, M., *et al*. (2001). Atomic-scale magnetic domain walls in quasi-one-dimensional Fe nanostripes. *Physical Review Letters*, **87**, 127201.

Prejbeaunu, I.L., Buda, L.D., Ebels, U., *et al*. (2001). Domain structures in epitaxial $(10\bar{1}0)$ Co wires. *IEEE Transactions on Magnetics*, **37**, 2108.

Prejbeaunu, I.L., Natali, M., Buda, L.D., *et al*. (2002). In-plane reversal mechanisms in circular Co dots. *Journal of Applied Physics*, **91**, 7343.

Prinz, G.A. (1998). Magnetoelectronics. *Science*, **282**, 1660.

Prinz, G.A. (1999). Magnetoelectronics applications. *Journal of Magnetism and Magnetic Materials*, **200**, 57.

Pulwey, R., Zölfl, M., Bayreuther, G. and Weiss, D. (2002). Magnetic domains in epitaxial nanomagnets with uniaxial or fourfold crystal anisotropy. *Journal of Applied Physics*, **91**, 7995.

Qiu, Z.Q. and Bader, S.D. (1998). Kerr effect and surface magnetism. In *Nonlinear Optics in Metals*, Bennemann, K.H. (Ed.), Oxford University Press, p. 1.

Raabe, J., Pulwey, R., Sattler, R., *et al*. (2000). Magnetization pattern of ferromagnetic nanodisks. *Journal of Applied Physics*, **88**, 4437.

Raabe, J., Quitmann, C., Back, C.H., *et al*. (2005). Quantitative analysis of magnetic excitations in Landau flux-closure structures using synchrotron-radiation microscopy. *Physical Review Letters*, **94**, 217204.

Rahm, M., Bentner, J., Biberger, J., *et al*. (2001). Hall-magnetometry on ferromagnetic micro-rhombs. *IEEE Transactions on Magnetics*, **37**, 2085.

Rave, W., Fabian, K. and Hubert, A. (1998). Magnetic states of small cubic particles with uniaxial anisotropy. *Journal of Magnetism and Magnetic Materials*, **190**, 332.

Ravelosona, D., Cayssol, F., Wunderlich, J., *et al*. (2002). Dynamics of magnetization reversal in a mesoscopic wire. *Journal of Magnetism and Magnetic Materials*, **249**, 170.

Rosenbusch, P., Lee, J., Lauhoff, G. and Bland, J.A.C. (1997). Magnetisation reversal in thin Cu/Ni/Cu/Si(001) films. *Journal of Magnetism and Magnetic Materials*, **172**, 19.

Ross, C.A., Chantrell, R., Hwang, M., *et al*. (2000). Incoherent magnetization reversal in 30-nm Ni particles. *Physical Review B*, **62**, 14252.

Ross, C.A., Haratani, S., Castaño, F.J., *et al*. (2002). Magnetic behavior of lithographically patterned particle arrays. *Journal of Applied Physics*, **91**, 6848.

Rothman, J., Kläui, M., Lopez-Diaz, L., *et al*. (2001). Observation of a bi-domain state and nucleation free switching in mesoscopic ring magnets. *Physical Review Letters*, **86**, 1098.

Saitoh, E., Miyajima, H., Yamaoka, T. and Tatara, G. (2004). Current-induced resonance and mass determination of a single magnetic domain wall. *Nature*, **432**, 2004.

Schabes, M.E. and Bertram, H.N. (1988). Magnetization processes in ferromagnetic cubes. *Journal of Applied Physics*, **64**, 1347.

Scheinfein, M.R., Unguris, J., Kelley, M.H., *et al*. (1989). Improved low-energy diffuse scattering electron-spin polarization analyzer. *Review of Scientific Instruments*, **61**, 2501.

Schmidts, H.F., Martinek, G. and Kronmüller, H. (1992). Recent progress in the interpretation of nucleation fields of hard magnetic particles. *Journal of Magnetism and Magnetic Materials*, **104**, 1119.

Schneider, M., Hoffmann, H. and Zweck, J. (2000). Lorentz microscopy of circular ferromagnetic permalloy nanodisks. *Applied Physics Letters*, **77**, 2909.

Schneider, M., Hoffmann, H. and Zweck, J. (2001). Magnetic switching of single vortex permalloy elements. *Applied Physics Letters*, **79**, 3113.

Schneider, C.M., Frömter, R., Ziethen, C., *et al*. (1997). Magnetic domain imaging with a photoemission microscope. *Materials Research Society Symposium Proceedings*, **475**, 381.

Schneider, C.M., Kuksov, A., Krasyuk, A., *et al*. (2004). Incoherent magnetization rotation observed in subnanosecond time-resolving x-ray photoemission electron microscopy. *Applied Physics Letters*, **85**, 2562.

Scholl, A., Ohldag, H., Nolting, F., *et al*. (2002). X-ray photoemission electron microscopy, a tool for the investigation of complex magnetic structures. *Review of Scientific Instruments*, **73**, 1362.

Schönhense, G. (1999). Imaging of magnetic structures by photoemission electron microscopy. *Journal of Physics: Condensed Matter*, **11**, 9517.

Schrefl, T., Fidler, J., Kirk, K.J. and Chapman, J.N. (1997). Domain structures and switching mechanisms in patterned magnetic elements. *Journal of Magnetism and Magnetic Materials*, **175**, 193.

Schuh, D., Biberger, J., Bauer, A., *et al*. (2001). Hall-magnetometry on ferromagnetic dots and dot arrays. *IEEE Transactions on Magnetics*, **37**, 2091.

Schultheiss, H., Nembach, H.T., Weber, M.C., *et al*. (2006). Space resolved dynamics in small magnetic rings. (unpublished).

Schumacher, H.W., Chappert, C., Sousa, R.C., *et al*. (2003). Quasiballistic magnetization reversal. *Physical Review Letters*, **90**, 17204.

Serpico, C., Mayergoyz, I.D. and Bertotti, G. (2003). Analytical solutions of Landau-Lifshitz equation for precessional switching. *Journal of Applied Physics*, **93**, 6909.

Seynaeve, E., Rens, G., Volodin, A.V., *et al*. (2001). Transition from a single-domain to a multidomain state in mesoscopic ferromagnetic Co structures. *Journal of Applied Physics*, **89**, 531.

Shi, J., Li, J. and Tehrani, S. (2002). Thermal fluctuation effects on quasistatic magnetic switching of patterned $Ni_{81}Fe_{19}$ elements. *Journal of Applied Physics*, **91**, 7458.

Shi, J., Tehrani, S., Zhu, T., *et al*. (1999). Magnetization vortices and anomalous switching in patterned NiFeCo submicron arrays. *Applied Physics Letters*, **74**, 2525.

Shigeto, K., Okuno, T., Mibu, K., *et al*. (2002). Magnetic force microscopy observation of antivortex core with perpendicular magnetization in patterned thin film of permalloy. *Applied Physics Letters*, **80**, 4190.

Shinjo, T., Okuno, T., Hassdorf, R., *et al*. (2000). Magnetic vortex core observation in circular dots of permalloy. *Science*, **289**, 930.

Skidmore, G.D., Kunz, A., Campbell, C.E. and Dan Dahlberg, E. (2004). Micromagnetic domain structures in cylindrical nickel dots. *Physical Review B*, **70**, 012410.

Slonczewski, J.C. (1956). Theory of magnetic hysteresis in films and its applications to computers. Research Memorandum, IBM Research Center Poughkeepsie, 003.111.224.

Spargo, A.W., Ridley, P.H.W., Roberts, G.W. and Chantrell, R.W. (2002). Influences of granular microstructure on the reversal mechanism of Co nanoelements. *Journal of Applied Physics*, **91**, 6923.

Steiner, M. and Nitta, J. (2004). Control of magnetization states in microstructured permalloy rings. *Applied Physics Letters*, **84**, 939.

Stoner, E.C. (1945). The demagnetizing factors for ellipsoids. *Philosophical Magazine, Series 7*, **36**, 803.

Stoner, E.C. and Wohlfarth, E.P. (1948). A mechanism of magnetic hysteresis in heterogeneous alloys. *Philosophical Transactions of the Royal Society of London, Series A*, **240**, 599.

Stotz, J.A.H. and Freeman, M.R. (1997). A stroboscopic scanning solid immersion lens microscope. *Review of Scientific Instruments*, **68**, 4468.

Taniuchi, T., Oshima, M., Akinaga, H. and Ono, K. (2005). Vortex-chirality control in mesoscopic disk magnets observed by photoelectron emission microscopy. *Journal of Applied Physics*, **97**, 10J904.

Tartakovskaya, E.V., Tucker, J.W. and Ivanov, B.A. (2001). Self-consistent theory and simulation of quasiuniform states in thin rectangular magnetic nanoparticles. *Journal of Applied Physics*, **89**, 8348.

Tchernyshyov, O. and Chern, G-W. (2005). Fractional vortices and composite domainwalls in flat nanomagnets. *Physical Review Letters*, **95**, 197204.

Terris, B.D. and Thomson, T. (2005). Nanofabricated and self-assembled magnetic structures as data storage media. *Journal of Physics D: Applied Physics*, **38**, R199.

Thiaville, A. (1998). Extensions of the geometric solution of the two dimensional coherent magnetization rotation model. *Journal of Magnetism and Magnetic Materials*, **182**, 5.

Thiaville, A. (2000). Coherent rotation of magnetization in three dimensions: a geometrical approach. *Physical Review B*, **61**, 12221.

Thirion, C., Wernsdorfer, W., Kläui, M., *et al*. (2006). Anisotropy engineering in Co nanodiscs fabricated using prepratterned silicon pillars. *Nanotechnology*, **17**, 1960.

Tsiantos, V.D., Suess, D., Schrefl, T. and Fidler, J. (2001). Stiffness analysis for the micromagnetic standard problem No. 4. *Journal of Applied Physics*, **89**, 7600.

Uhlig, W.C., Li, H., Han, B.S. and Shi, J. (2002). Controlled magnetisation reversal in patterned Co nanostructures. *Journal of Applied Physics*, **91**, 6943.

Uhlig, T. and Zweck, J. (2004). Direct observation of switching processes in permalloy rings with Lorentz microscopy. *Physical Review Letters*, **93**, 47203.

Unguris, J., Scheinfein, M.R., Celotta, R.J. and Pierce, D.T. (1990). Scanning electron microscopy with polarisation analysis: studies of magnetic microstructure. In *Chemistry and Physics of Solid Surfaces VIII*, Domb, C. and Green, M.S. (Eds.), Springer-Verlag: Berlin, p. 239.

Usov, N.A. (1993). On the concept of a single-domain nonellipsoidal particle. *Journal of Magnetism and Magnetic Materials*, **125**, L7.

Usov, N.A., Chang, C-R. and Wei, Z-H. (2001). Nonuniform magnetization structures in thin soft type ferromagnetic elements of elliptical shape. *Journal of Applied Physics*, **89**, 7591.

Usov, N.A. and Kurkina, L.G. (2002). Magnetodynamics of vortex in thin cylindrical platelet. *Journal of Magnetism and Magnetic Materials*, **242–245**, 1005.

Usov, N.A. and Peschany, S.E. (1994a). Flower state micromagnetic structures in a fine parallelepiped and a flat cylinder. *Journal of Magnetism and Magnetic Materials*, **135**, 111.

Usov, N.A. and Peschany, S.E. (1994b). Flower state micromagnetic structure in fine cylindrical particles. *Journal of Magnetism and Magnetic Materials*, **130**, 275.

Vavassori, P., Grimsditch, M., Novosad, V., *et al*. (2003). Metastable states during magnetization reversal in square permalloy rings. *Physical Review B*, **67**, 134429.

Vavassori, P., Metlushko, V., Osgood, R.M. III, *et al*. (1999). Magnetic information in the light diffracted by a negative dot array of Fe. *Physical Review B*, **59**, 6337.

Vaz, C.A.F., Athanasiou, C., Bland, J.A.C. and Rowlands, G. (2006). Energetics of magnetic ring and disk elements: uniform versus vortex state. *Physical Review B*, **73**, 054411.

Vaz, C.A.F., Kläui, M., Bland, J.A.C., *et al*. (2006). Fundamental magnetic states of disk and ring elements. *Nuclear Instruments and Methods in Physics Research B*, **246**, 13.

Vaz, C.A.F., Kläui, M., Bland, J.A.C., *et al*. (2004a). Effect of the magnetocrystalline anisotropy on the magnetic behaviour of ring elements. *Journal of Applied Physics*, **95**, 6732.

Vaz, C.A.F., Lopez-Diaz, L., Kläui, M., *et al*. (2004b). Observation of a geometrically constrained domain-wall in epitaxial fcc Co small disks. *Journal of Magnetism and Magnetic Materials*, **272–276**, 1674.

Vaz, C.A.F., Kläui, M., Heyderman, L.J., *et al*. (2005). Multiplicity of magnetic domain-states in circular elements probed by photoemission electron microscopy. *Physical Review B*, **72**, 224426.

Vaz, C.A.F., Lopez-Diaz, L., Kläui, M., *et al*. (2003). Direct observation of remanent magnetic states in epitaxial fcc Co small disks. *Physical Review B*, **67**, 140405(R).

Vellekoop, B., Abelmann, L., Porthun, S. and Lodder, C. (1998). On the determination of the internal magnetic structure by magnetic force microscopy. *Journal of Magnetism and Magnetic Materials*, **190**, 148.

Wachowiak, A., Wiebe, J., Bode, M., *et al*. (2002). Direct observation of internal spin structure of magnetic vortex cores. *Science*, **298**, 577.

Webb, B.C. (1990). Anomalous hall effect measurements of domain writing and erasure in magneto-optic thin-films. *IEEE Transactions on Magnetics*, **26**, 1715.

Wegrowe, J-E., Fabian, A., Guittienne, Ph., *et al*. (2002). Exchange torque and spin transfer between spin polarized current and ferromagnetic layers. *Applied Physics Letters*, **80**, 3775.

Wegrowe, J-E., Kelly, D., Frank, A., *et al*. (1999). Magnetoresistance of ferromagnetic nanowires. *Physical Review Letters*, **82**, 3681.

Wei, D.H., Hsu, Y.J., Lin, C-C., *et al*. (2004). Layer-and lateral-resolved magnetization studies using photoemission electron microscopy. *Journal of Magnetism and Magnetic Materials*, **282**, 49.

Wei, Z-H., Lai, M-F., Chang, C-R., *et al*. (2003). Nonuniform micromagnetic states in thin permalloy disk. *IEEE Transactions on Magnetics*, **39**, 2675.

Welp, U., Vlasko-Vlasov, V.K., Hiller, J.M., *et al*. (2003). Magnetization reversal in arrays of Co rings. *Physical Review B*, **68**, 544081.

Wernsdorfer, W. (2001). Classical and quantum magnetization reversal studied in nanometer-sized particles and clusters. *Advances in Chemical Physics*, **118**, 99.

Wernsdorfer, W., Hasselbach, K., Benoit, A., *et al*. (1995a). Measurement of the dynamics of the magnetization reversal in individual single-domain Co particles. *Journal of Magnetism and Magnetic Materials*, **151**, 38.

Wernsdorfer, W., Hasselbach, K., Mailly, D., *et al*. (1995b). DC-SQUID magnetization measurements of single magnetic particles. *Journal of Magnetism and Magnetic Materials*, **145**, 33.

Wernsdorfer, W., Doudin, B., Mailly, D., *et al*. (1996a). Nucleation of magnetization reversal in individual nanosized nickel wires. *Physical Review Letters*, **77**, 1873.

Wernsdorfer, W., Hasselbach, K., Sulpice, A., *et al*. (1996b). Dynamical measurement of domain-wall nucleation and annihilation in individual amorphous Co particles. *Physical Review B*, **53**, 3341.

Wernsdorfer, W., Bonet, E., Hasselbach, K., *et al*. (1997a). Macroscopic quantum tunneling of magnetization of single ferrimagnetic nanoparticles of barium ferrite. *Physical Review Letters*, **79**, 4014.

Wernsdorfer, W., Hasselbach, K., Benoit, A., *et al*. (1997b). Measurements of magnetization switching in individual nickel nanowires. *Physical Review B*, **55**, 11552.

Whitney, T.M., Jiang, J.S., Searson, P.C. and Chien, C.L. (1993). Fabrication and magnetic properties of arrays of metallic nanowires. *Science*, **261**, 1316.

Wulfhekel, W. and Kirschner, J. (1999). Spin-polarized scanning tunneling microscopy on ferromagnets. *Applied Physics Letters*, **75**, 1944.

Wunderlich, J., Ravelosona, D., Chappert, C., *et al*. (2001). Influence of geometry on domain wall propagation in a mesoscopic wire. *IEEE Transactions on Magnetics*, **37**, 2104.

Yamaguchi, A., Ono, T., Nasu, S., *et al*. (2004). Real-space observation of current-driven domain wall motion in submicron magnetic wires. *Physical Review Letters*, **92**, 77205.

Yu, J., Ruediger, U., Thomas, L., *et al*. (1999). Micromagnetics of mesoscopic epitaxial (110) Fe elements with nanoshaped ends. *Journal of Applied Physics*, **85**, 5501.

Zheng, Y. and Zhu, J-G. (1997). Switching field variation in patterned submicron magnetic film elements. *Journal of Applied Physics*, **81**, 5471.

Zhu, X. (2002). *Magnetic Force Microscopy Studies of Submicron and Nanoscale Magnet Arrays*, Ph.D. Thesis, McGill University.

Zhu, X., Grütter, P., Metlushko, V. and Ilic, B. (2003). Control of domain patterns in square shaped nickel rings. *Journal of Applied Physics*, **93**, 7059.

Zhu, J-G. and Zheng, Y. (2002). The micromagnetics of magnetoresistive random access memory. In *Spin Dynamics in Confined Magnetic Structures I*, Topics in Applied Physics, Hillebrands, B. and Ounadjela, K. (Eds.), Springer-Verlag, p. 289.

Zhu, J-G., Zheng, Y. and Prinz, G.A. (2000). Ultrahigh density vertical magnetoresistive random access memory. *Journal of Applied Physics*, **87**, 6668.

Zhu, X. and Zhu, J-G. (2003). A vertical MRAM free of write disturbance. *IEEE Transactions on Magnetics*, **39**, 2854.

Zhu, F.Q., Chern, G.W., Tchernyshyov, O., *et al*. (2006). Magnetic bistability and controllable reversal of asymmetric ferromagnetic nanorings. *Physical Review Letters*, **96**, 027205.

Magnetic Properties of Systems of Low Dimensions

Rolf Allenspach
IBM Research, Zurich Research Laboratory, Rüschlikon, Switzerland

1 INTRODUCTION

To a large extent, size and geometry govern magnetic domain patterns in large ferromagnetic specimens: it is the long-range magnetic dipolar interaction that is responsible for the occurrence of magnetic domains, and this interaction is determined by an integration over the entire volume of the sample. In this chapter, small objects rather than bulk ferromagnets will be discussed. The topic is closely related to the chapter by Kläui and Vaz (2007). Their chapter covers the range from very small nanometer-sized particles to micrometer-sized objects, with an extensive discussion of the underlying energy terms relevant for a micromagnetic understanding, with a description of the single-domain (SD) particle and its magnetization reversal, and a brief overview on multidomain (MD) states in larger geometries.

In this chapter, a different route is taken. The focus is on well-defined magnetic elements mainly of micrometer size, specifically on their domain structures and their domain walls. In particular, the effects that are related to the presence of boundaries, edges, and constrictions are described, and how they are influenced by geometry of the system is studied. An important aspect is the presence of anisotropy. So far most studies, both experimental and theoretical, have been done in systems in which anisotropy is essentially negligible. In this chapter, emphasis is given to a system in which anisotropy is a key factor in determining domain patterns. We are interested in the size-dependent properties of these domain patterns, and illustrate them in phase diagrams spanning a wide range of length scales and thicknesses. Even though magnetization reversal is closely linked to domain patterns, it is not discussed here – for the sake of brevity. The approach taken is the one of an experimentalist: we concentrate on experimental findings and use micromagnetic simulations to elucidate the physics underlying the observations.

Size effects not only determine domain patterns, but also affect domain walls. The finite, small size of a magnetic element confines the domain wall to a narrow environment, and thereby modifies domain-wall profiles and types in a controlled way. This geometrical tunability is a new aspect of domain walls that is starting to be exploited in alternative schemes to move domain walls, such as in spin-transfer torque devices, as described in the chapters by Ono (2007) and Thomas and Parkin (2007).

In both of these topics, 'low dimensional' is synonymous to 'small in size'. Magnetism in low-dimensional systems, however, has an additional important aspect that extends beyond a mere comparison of simulated micromagnetic patterns with their experimental counterparts. 'Low dimensional' has a specific thermodynamic meaning: effects that require a description in a three-dimensional framework are excluded. Typical properties in ferromagnets relating to this type of dimensionality are phase transitions. As cooperative

Handbook of Magnetism and Advanced Magnetic Materials. Edited by Helmut Kronmüller and Stuart Parkin. Volume 2: *Micromagnetism*. ISBN: 978-0-470-02217-7.

phenomena, they are described by order parameters and critical exponents. It is not intended to provide a comprehensive report of the physics of phase transitions in low-dimensional ferromagnets. Instead, phase transitions are approached from a microscopic viewpoint by classifying the phases and their transitions according to domain patterns and their origin. This specific topic thus embraces two seemingly disparate fields of condensed matter physics: micromagnetism and critical phenomena.

Even by limiting this chapter to these three topics, it would be a hopeless task to aim for an all-embracing review. The theme of low-dimensional ferromagnets is therefore presented by means of examples: Three specific systems illustrate low-dimensional phase transitions, domain patterns, and domain walls. Section 2 is devoted to ultrathin, perpendicularly magnetized Fe/Cu films. Their rich variety of stripe-domain phases provide new insight into the microscopic aspects of phase transitions in two dimensions. Small elements of a ferromagnet with in-plane magnetization and tunable anisotropy are discussed in Section 3. The Co/Cu system exhibits a wide range of different domain patterns that distinctly depend on the lateral size and thickness of the elements. Finally, in Section 4, geometric confinement is extended from domains to domain walls. Domain walls in small $Fe_{20}Ni_{80}$ elements exhibit complex spin arrangements that strongly deviate from the wall types commonly encountered in magnetic thin films, and they can be modified and tuned by changing the size of the element and by introducing constrictions.

2 PHASES AND PHASE TRANSITIONS

This section deals with dimensionality in a thermodynamic sense: effects in ferromagnets that are two-dimensional (2D) rather than three-dimensional (3D) are considered. Hence aspects in magnetic films that relate magnetic properties to cooperative phenomena and their phase transitions are discussed. Phase transitions are characterized by a specific set of parameters, such as order parameters and critical exponents. Note that by restricting ourselves to 2D effects, we do not necessarily limit the system size: the important quantity is the correlation length. For a system to be regarded as 2D, the only requirement is that the correlation length has to be bigger than one of the system extensions.

The prototypical system for the investigation of 2D phase transitions is a magnetic film. In fact, the development of many theories describing phase transitions was inspired by ferromagnetic model systems. The nature of the phase transition and many of its properties are determined by magnetic anisotropies. For vanishing anisotropy, the isotropic Heisenberg model describes reality best, whereas for large uniaxial anisotropy, it is the Ising model. Both these limiting cases (and also intermediate ones) have been investigated in detail in a variety of magnetic films. In almost all studies, the goal was to deduce the critical exponent that describes the approach of the magnetization to Curie temperature, T_C. Experimentally, the critical exponents vary widely, covering the entire range from the mean-field-approximation value to the exponent characteristic of the Ising model. A few model systems exist that seem to be magnetically simple enough to exhibit unequivocal behavior. A prominent one is an ultrathin Fe film, only one or two monolayers (MLs) thick, grown on W(110) (Elmers, Hauschild and Gradmann, 1996). This system, with its uniaxial in-plane anisotropy, essentially behaves as a 2D Ising system. Critical exponents are very close to those expected for the Ising system, and the universality hypothesis has been experimentally confirmed with high accuracy, even with a magnetic field applied (Back *et al*., 1995).

Although such studies test and confirm very fundamental assumptions in theories of cooperative phenomena, they do not provide insight into the microscopic aspects of phase transitions. Length scales, in particular, enter only through the scaling hypothesis, and the order parameter – magnetization – is a macroscopic quantity. The investigation of microscopic aspects of phase transitions is experimentally demanding. At T_C, the spontaneous magnetization vanishes, and temporal fluctuations may become relevant. On the theoretical side, the situation is of similar complexity. For instance, even for the simplest model – the 2D Ising system – no exact solution for the transition in an external field is known.

In the past few years, however, remarkable progress has been made in the understanding of the microscopic aspects of these phases and their transitions. Most of the progress comes from the investigation of Ising systems, realized in perpendicularly magnetized ferromagnetic films. These films exhibit two characteristics that make a microscopic investigation rewarding: the existence of a specific domain state, a regular array of stripe domains, and the occurrence of a spin-reorientation transition, in which the magnetization changes direction. Theoretically, the challenge comes from the fact that a strong short-range interaction – the exchange – competes with a weak long-range interaction, the dipole–dipole interaction. 2D systems with short-range attraction and long-range repulsion are widespread and include – besides the ferromagnets – for instance, polymers, gels, self-assembled MLs, and ferrofluidics. In the following text, some recent investigations of the microscopic properties of phases and phase transitions in perpendicularly magnetized ferromagnets are summarized; but the implications might eventually go beyond this class of materials. In these investigations micromagnetism is relevant, but equally

important is an understanding of the topology and critical phenomena.

2.1 Perpendicular magnetization and the spin-reorientation transition

Domain patterns in perpendicularly magnetized films have been investigated theoretically almost since the first realistic micromagnetic approaches appeared. Kittel (1946) considered the case in which the thickness of the ferromagnet is much larger than the domain size, so that the magnetostatic interaction of the two surfaces could be safely neglected. He concluded that the domain width in a regular array of stripe domains increases with the square root of the film thickness, provided that the relevant material constants, such as magnetization and anisotropy, remain the same. This result was extended to films for which the thickness is comparable with the domain width (Málek and Kamberský, 1958), and later on, the influence of an applied magnetic field was also considered (Kooy and Enz, 1960). All these approaches were essentially based on analytical micromagnetic models, complemented where necessary by partial solving of the problems numerically.

Garel and Doniach (1982) looked at the domain pattern from a different perspective. They realized that stripe domains and their transformation in a magnetic field could be described as a phase transition. A 2D Ginzburg–Landau model was applied, and a first-order transition to a hexagonal bubble phase was predicted, followed by a further transition to the uniform, saturated state. Close to the critical temperature, stripe or bubble melting was predicted to occur. Here, dimensionality embraced micromagnetism: it was explicitly mentioned that because of the long-range character of magnetic dipolar forces the dimensionality becomes relevant.

The formation of the stripe-domain phase results from a competition between a short-range interaction – the exchange that tends to align neighboring spins – and the long-range dipolar interaction favoring antiparallel alignment between distant spins. By application of a magnetic field, the stripe pattern can be transformed into various domain arrangements, such as bubbles, mazes, chevrons, or labyrinths (Molho *et al.*, 1987). The extrapolation of these thick films to the ultrathin limit is not straightforward, and the analogy to smectic liquid crystals was pointed out (Sornette, 1987). In their pioneering paper, Yafet and Gyorgy (1988) finally calculated that a stripe-domain configuration is also the ground state in zero magnetic field in the ultrathin limit, provided that the ratio of anisotropy and magnetostatic energy is close to 1. Numerical simulations (Kaplan and Gehring, 1993) confirmed that the stripe-domain phase is very close to but slightly lower in energy than the checkerboard configuration (Czech and Villain, 1989) and suggested that an irregular domain pattern as observed in ultrathin Co/Au(111) films (Allenspach, Stampanoni and Bischof, 1990) is consistent with this model. Whereas, originally, the magnetization in the walls between the stripes was assumed to vary like a cosine function (Yafet and Gyorgy, 1988), it was recently stated that this profile is modified by the long-range dipolar interaction, and hence the magnetization modulation depends on the stripe width (Kisielewski, Maziewski, Polyakova and Zablotskii, 2004).

Ultrathin film systems with stripe domains often exhibit an additional interesting characteristic: a spin-reorientation transition. In films with perpendicular magnetization, a reorientation of the spin is the natural consequence of the shape anisotropy winning over surface anisotropy at large thickness or at high temperature. The easy magnetization axis changes and the spins reorient, as shown in Figure 1. Only if the Curie temperature happens to be below the reorientation temperature, does the perpendicular magnetization exist up to the paramagnetic phase. Both cases exist and will be illustrated.

Figure 1 illustrates the microscopic features of a spin reorientation in a 5.3-ML fcc-Fe/Cu(001) film (1 ML = 0.18 nm) with increasing temperature (Allenspach and Bischof, 1992),

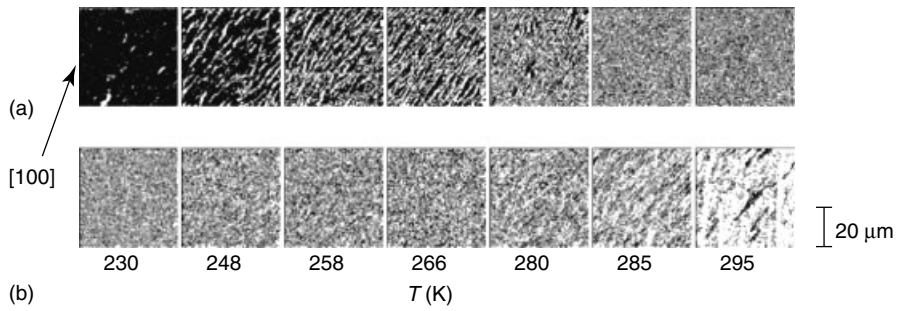

Figure 1. Evolution of the domain pattern in 5.3-ML fcc Fe on Cu(001) with temperature. (a) Out-of-plane magnetization component, (b) in-plane magnetization component. Stripe domains are formed and stripe narrowing occurs with increasing temperature before the magnetization reorients into the plane. (Reproduced from Allenspach and Bischof, 1992, with permission from the American Physical Society. © 1992.)

determined experimentally by spin-polarized scanning electron microscopy (spin-SEM) (Allenspach, 2000). Below $T = 230\,\mathrm{K}$, the film is perpendicularly magnetized and in an SD state. With increasing temperature, irregularly shaped, reversed domains nucleate, growing in number as the temperature increases further. These domains elongate and start to form a stripe-domain pattern, with stripes running along the crystallographic [100] direction. At even higher temperatures, the distance between stripes narrows. Finally, the magnetization reorients into the plane, and an irregular domain pattern forms.

The observation of a stripe pattern qualitatively confirmed the predictions by Yafet and Gyorgy (1988). The stripe period, however, remained unexplained: it should only be accessible to the experiment if the perpendicular anisotropy and the magnetostatic energy (or shape anisotropy) nearly cancel each other. Otherwise, the stripe period should grow beyond typical sample sizes and hence an SD state should be observed. Moreover, the observation of stripe narrowing with temperature contradicted theory (Seul and Wolfe, 1992). However, if finite-temperature spin fluctuations are taken into account (Kashuba and Pokrovsky, 1993; Abanov, Kalatsky, Pokrovsky and Saslow, 1995), the stripe phase is much more abundant and becomes the preferred ground state as long as exchange exceeds a certain value (MacIsaac, Whitehead, Robinson and De'Bell, 1995). Moreover, with increasing temperature, disorder should occur, and the phase transforms from a 2D smectic crystal phase to a nematic phase, and eventually to a fourfold symmetric phase called a tetragonal liquid (Abanov, Kalatsky, Pokrovsky and Saslow, 1995). This transition is a distinct feature of a 2D melting process and is absent in thick magnetic films (Vaterlaus *et al*., 2000). Monte Carlo simulations (Booth, MacIsaac, Whitehead and De'Bell, 1995) arrive at essentially the same conclusion. However, whether the intermediate nematic phase exists or a first-order phase transition occurs remains elusive.

A detailed experimental investigation of the evolution of the striped phase going beyond Allenspach and Bischof (1992) has been recently performed, again in the fcc-Fe/Cu(001) system (Portmann, Vaterlaus and Pescia, 2003). By choosing a smaller thickness of the ferromagnet, the Curie temperature T_C drops below the reorientation temperature and hence the stripe phase can be followed up to the paramagnetic phase (see Figure 2). Far below T_C, stripes are observed to be meandering around a preferential orientation and to exhibit specific defects. Experimentally, four different types of dislocations have been identified, which are in agreement with the topological defect classification (Abanov, Kalatsky, Pokrovsky and Saslow, 1995). At higher temperature, orientational melting occurs, and the domain phase transforms into a more symmetric labyrinth phase in which the stripes terminate preferentially in square corners, confirming the prediction of the tetragonal liquid phase. This fourfold symmetry is not unexpected as it reflects the crystalline symmetry of the Fe/Cu(001) system. It is still a matter of debate whether the transition from the stripe phase to the tetragonal phase is a continuous transition going through a nematic phase or a first-order phase transition. The most recent Monte Carlo simulations and analytical modeling favor a weak first-order transition, based on the calculated scaling of the specific heat (Cannas, Stariolo and Tamarit, 2004). Strikingly, at even higher temperature, the tetragonal order is lost again, and a lower symmetry phase reoccurs with reduced stripe width before the paramagnetic phase is reached (Portmann, Vaterlaus and Pescia, 2003).

The microscopic mechanisms of both the melting and the inverse melting process are quite intricate. In the melting process, the stripes emit fingers and branches orthogonal to the stripe direction, that is, a transverse instability (Molho *et al*., 1987) promotes the loss of orientational ordering. A similar evolution of disorder has been observed in thick garnet films (Seul and Wolfe, 1992). There, the stripe phase transformed through a sequence of highly regular patterns, such as undulations and chevrons, into a phase characterized by disclination defects. The labyrinthine phase in garnets, on the other hand, displays hexagonal

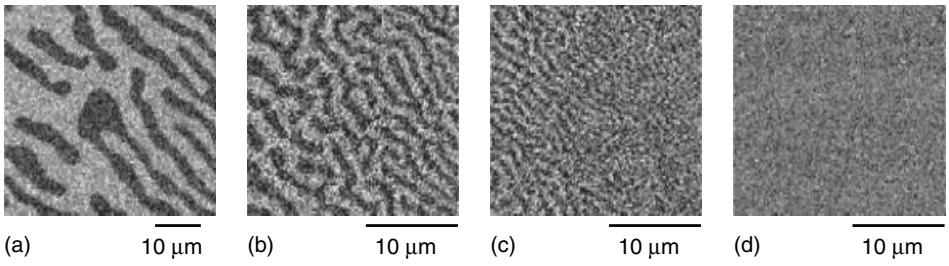

Figure 2. The four domain phases in perpendicularly magnetized ultrathin fcc-Fe/Cu(001) films upon approaching the paramagnetic phase, measured by spin-SEM. The film thickness is 1.89 ML. (a) Stripe phase at $T = 210\,\mathrm{K}$; (b) labyrinth tetragonal liquid phase at $T = 268\,\mathrm{K}$; (c) reentrant stripe phase at $T = 283\,\mathrm{K}$; (d) paramagnetic phase at $T = 313\,\mathrm{K}$. Note that the image size varies as indicated by the scale bars. (Reproduced from Portmann, Vaterlaus and Pescia, 2003, with permission from Nature Publishing Group.)

rather than tetragonal symmetry, controlled by the crystalline orientation, and is reached by a dynamic relaxation that is nonexponential and compatible with the expectations for a glassy state (Reimann, Richter and Rehberg, 2002). The inverse melting process in Fe/Cu(001) goes through repetitive steps of detaching short stripe-domain segments from knee-bend domains to arrive at smooth and straight stripe domains. Here – as in the transition from the stripe phase to the tetragonal liquid phase – the strength of the long-range dipolar interaction might play an important role. This interaction effectively leads to a transverse compressive force on the stripes and, depending on its strength, a crossover from defect-mediated stripe melting (or freezing) to spin disorder is predicted to occur (Stoycheva and Singer, 2000).

Very recently, it was shown that the approach to the paramagnetic phase contains a dynamic component (Portmann, Vaterlaus and Pescia, 2006): the stripe domains become mobile in a narrow temperature interval of a few Kelvin around T_C (see Figure 3). Stripe sections have been observed to displace on a timescale of seconds, locally keeping a high degree of orientational order. This stripe mobility exists upon both annealing and cooling through T_C. These observations are in marked contrast to the phase transition in an in-plane-magnetized thin-film system (Kerkmann, Pescia and Allenspach, 1992), and it has been argued that they are related to a dynamical singularity associated with the liquid-to-glass transition in stripes (Portmann, Vaterlaus and Pescia, 2006). First hints of the existence of a dynamic domainlike behavior near or even above the Curie temperature in perpendicularly magnetized ultrathin Fe/Ni(111) films were already drawn from susceptibility measurements in a detailed investigation of the spin-reorientation transition (Arnold, Pappas and Venus, 1999). The real-space observation of the dynamic aspects of this phase transition goes a step further: it provides new experimental insight into the microscopic nature of 2D phase transitions, against which theories and models can be tested.

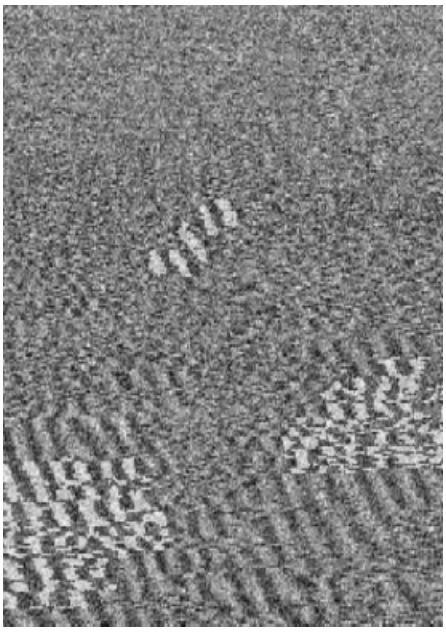

Figure 3. Transition from the paramagnetic to the stripe-domain phase observed by spin-SEM in a fcc-Fe/Cu(001) film of 1.96-ML thickness. The temperature is around room temperature and decreases by 3 K while successive line scans are taken from top to bottom. Image width: 18 µm. The contrast of some of the areas that indicate stripe mobility has been enhanced. (Reproduced from Portmann, Vaterlaus and Pescia, 2006, with permission from the American Physical Society. © 2006.)

2.2 The stripe-domain width

The geometrical and topological classification presented previously describes phase transitions in a rather qualitative manner. Phase transitions, however, are characterized by experimentally verifiable quantitative parameters, such as the scaling lengths and critical exponents. One important parameter of the stripe-domain phase is the average width D of the stripes. In the past decade, several experimental studies were performed to determine the domain width upon approaching the spin reorientation or the ferro- to paramagnetic phase transition. The first determination of the domain size during spin reorientation was done in Co/Au(111) films (Allenspach and Stampanoni, 1992), followed soon after by a systematic study of the evolution of the domain width with the film thickness on a wedge-type sample (Speckmann, Oepen and Kirschner, 1995). It was found that at constant temperature the domain size decreases exponentially upon approaching the spin-reorientation thickness (see Figure 4a). Close to the spin-reorientation thickness, this observation was in line with the prediction (Kaplan and Gehring, 1993) that the domain width D depends on film thickness t according to the functional dependence $D = 0.955\, t \exp(\sigma_w/(4\, M_s^2\, t))$, where σ_w is the domain-wall energy and M_s is the saturation magnetization.

In the Fe/Ni/Cu(001) system, both the thickness and the temperature dependence of D are experimentally accessible. In both cases, D exhibits an exponential dependence (Won *et al.*, 2005; see Figure 4b). The Fe/Ni system is particularly attractive because – for appropriate Fe and Ni thicknesses – anisotropies and demagnetization energies can be balanced in such a way that the spin-reorientation temperature, T_R, is below or above T_C (Zhao *et al.*, 2004). Interestingly, if $T_C < T_R$, the exponential dependence of the domain width on temperature is preserved up to an

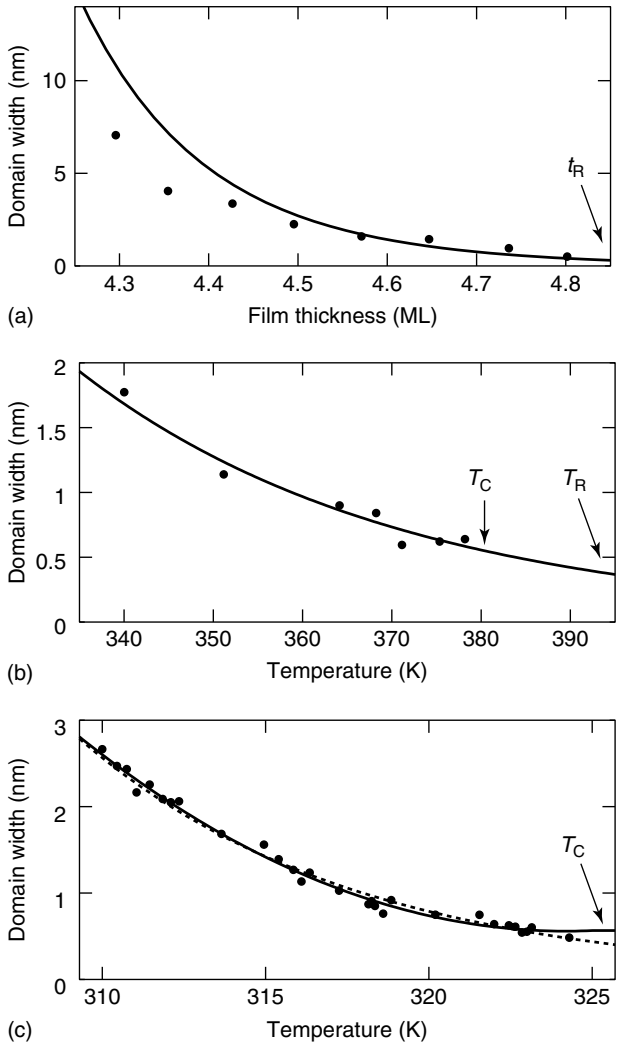

Figure 4. Domain width upon approaching the phase transition. (a) Width versus Co film thickness in the Co/Au(111) system. The reorientation transition takes place at $t_R \approx 4.9$ ML (1 ML = 0.2 nm). The exponential fit follows the model of Kaplan and Gehring (1993), with the only fit parameter being the interface anisotropy. From Speckmann, Oepen and Kirschner (1995). (b) Width versus temperature in the Fe/Ni/Cu(001) system, with 2.7 ML Fe and 5.4 ML Ni (1 ML = 0.18 nm). In this system, $T_C < T_R$, with $T_C \approx 380$ K and $T_R \approx 395$ K. The exponential fit extrapolates through T_C up to T_R. From Won *et al.* (2005). (c) Width versus temperature in Fe on Cu(001), with a Fe thickness of 1.95 ML (1 ML = 0.18 nm). At this thickness, no reorientation transition takes place. T_C is estimated to be 325.7 K. From Portmann, Vaterlaus and Pescia (2006). The solid line gives a quadratic power-law fit, the dashed line the best exponential fit for comparison.

extrapolated T_R, which means that the domain width at T_C remains finite. Similarly, an exponential behavior has also been found in exchange-coupled layers if the anisotropy and interlayer coupling are taken into account (Wu *et al.*, 2004). In the Fe/Cu(001) system, the stripe-domain width has been fitted by a power-law dependence upon approaching T_C, $D \sim D_C + (T_C - T)^2$, keeping a finite width D_C at the transition temperature (Portmann, Vaterlaus and Pescia, 2006; see Figure 4c). The differences to an exponential dependence, however, are minute, and future experiments will have to show whether this is significant. Conceptually, such a phase transition can always be described by a power-law series, and at zero temperature reality is accurately described by an exponential dependence. Hence both approaches tackle the problem from a different perspective: micromagnetics in the case of the exponential dependence and critical phenomena in the case of the power-law dependence.

In summary, the stripe-domain phase is a commonly observed domain pattern in perpendicularly magnetized ferromagnets, in the entire range from ultrathin to thick films. The prerequisite for their existence in micrometer-thick specimens is that the anisotropy is so large that closure domains are energetically avoided. From a purist's point of view, all these systems are strictly low dimensional: for an infinitely extended film, any finite width is sufficient to describe the system as being 2D. Many of the phenomena described occur in specimens of any thickness. It is the competition between attractive short-range and repulsive long-range interactions that leads to the stripe phase and to even more complex modulated phases and the formation of structures on mesoscopic length scales. Nevertheless, significant differences are observed between an ultrathin and a thick film. The reentrant behavior of the stripe phase and its mobility close to the Curie temperature have only been observed in ultrathin films of Fe/Cu(001). It remains a matter for future work to clarify, both theoretically and experimentally, whether these effects are specific to this system or a general feature of ultrathin ferromagnets. The most prominent difference between ultrathin and thick films is the width of the stripe domains. Only in ultrathin films, a strong dependence of the stripe width on the temperature – even far away from the phase-transition temperature – has been observed. This observation is not limited to the Fe/Cu(001) system and has also been theoretically described. In thick films, stripe narrowing is explicitly excluded (Seul and Wolfe, 1992) or considered to be negligible as long as the temperature is not too close to T_C (Molho *et al.*, 1987). Only very close to T_C is the stripe width not frozen and can adjust with temperature. In ultrathin films, fluctuations are much more prominent and extend the critical temperature range. In this respect, the situation is similar to in-plane-magnetized ultrathin films (Kerkmann, Pescia and Allenspach, 1992). The investigation of phase transitions using microscopic imaging has led to new insight into such very fundamental, truly low-dimensional magnetic properties.

3 SIZE DEPENDENCE OF DOMAIN PATTERNS

In this section, effects related to the geometrical dimensions of a ferromagnet are considered. In this respect, 'low dimensional' can be regarded as being synonymous to 'small in size'. Size aspects govern magnetic domain patterns. Hence magnetic domain patterns and their variations with changing size are discussed here. While the exchange interaction tends to keep all spins aligned and thus favors a uniform SD state, the long-range magnetostatic interaction tries to avoid stray fields emanating from the ferromagnetic element. The balance of these two energies is responsible for the existence of an inhomogeneous magnetization distribution: domains and domain walls, or – alternatively – rapidly varying magnetization distributions such as vortices. This balance depends on the size and the geometry. If the sample size becomes smaller than the width of a typical domain wall, this state is replaced by a more uniform magnetization distribution. The transition from a uniform to a nonuniform state is thus determined by the exchange and the magnetostatic energy. The magnetic patterns observed in the nonuniform state, however, are largely governed by magnetic anisotropy. Although this holds for systems with arbitrary anisotropy axis, we restrict ourselves here to systems with in-plane magnetization. The domain patterns in ferromagnets with perpendicular magnetization direction have been discussed in the preceding section, in the context of the stripe-domain phase.

A wealth of studies have been performed to investigate domain patterns in small in-plane-magnetized elements, with the vast majority of the work having been done in NiFe alloys with negligible magnetocrystalline anisotropy (Cowburn *et al*., 1999; Gomez *et al*., 1999; Hubert and Rührig, 1991; Barthelmess, Pels, Thieme and Meier, 2004). Of particular interest, is the transition from the nearly SD state to the nonuniform state with increasing thickness and lateral size of the element. In small disks, domain patterns with well-defined walls are absent because anisotropy is negligible. The nonuniform magnetization distribution corresponds to a circular magnetization arrangement with a centered, narrow core having perpendicular magnetization, the vortex state (Shinjo *et al*., 2000). If the shape of the element deviates from a disk, deviations from both SD and vortex states occur. For the SD state, the geometrical dependencies lead to an effective configurational anisotropy (Schabes and Bertram, 1988), which can stabilize alternative patterns such as leaf states (Cowburn and Welland, 1998a), flower states (Schabes and Bertram, 1988), or even more complex twisted flower states (Hertel and Kronmüller, 2002).

This section discusses domain patterns in a system with nonvanishing magnetocrystalline in-plane anisotropy. We restrict ourselves to one particular model system, namely, epitaxial fcc Co/Cu, rather than providing a comprehensive review of domain formation in such systems. We will vary the thickness t and lateral size L of the elements in a wide range to obtain a complete phase diagram of domain patterns in the (t, L) space. Some regions of this phase diagram have been investigated before, with a focus on small t (Stamm *et al*., 1998) and on the magnetization reversal after an SD state has been set (Oepen, Lutzke and Kirschner, 2002). Epitaxial Co on MgO was also studied, with the emphasis on domain states in elements having small L and large t (Kazakova, Hanson, Blomquist and Wäppling, 2001). Similar patterns are encountered in other epitaxial systems that exhibit nonnegligible magnetocrystalline anisotropy, such as bcc Fe/GaAs(001) (Pulwey, Zölfl, Bayreuther and Weiss, 2003).

Epitaxial Co films grown on stepped Cu(001) substrates exhibit a complex magnetocrystalline anisotropy: because the substrate is miscut from the (001) direction, a uniaxial step anisotropy is superimposed on the cubic anisotropy required by the fourfold symmetry of the Cu(001) substrate (Berger, Linke and Oepen, 1992). The ratio of uniaxial anisotropy K_u to fourfold cubic anisotropy K_1 can be adjusted by the film thickness or the miscut angle, which is equivalent to changing the average step distance. For typical miscut angles of a few degrees, K_u is not larger than a few percent of K_1. Nevertheless it can be accurately determined by analyzing the shape of the hysteresis loop (Weber, Allenspach and Bischof, 1997), and it is responsible for the occurrence of quantum size oscillations in magnetic anisotropy (Weber *et al*., 1996b). Here, we will consider Co/Cu elements miscut by 1° with respect to the (001) direction. The step-edge direction runs along $[1\bar{1}0]$, leading to a vicinal Co(1 1 81) system with an average step distance of 10 nm. The thickness dependence of K_u and K_1 has been determined on continuous films (Weber *et al*., 1996a). At small thickness, the easy magnetization axis is parallel to the step-edge direction. At a thickness of 3.1 nm, the uniaxial anisotropy changes sign. This leads to a switching of the easy magnetization direction by 90° from the $[1\bar{1}0]$ to the [110] direction. Correspondingly, the intermediate axis switches from [110] to $[1\bar{1}0]$. The evolution of the anisotropy constants K_u and K_1 as a function of thickness is shown at the top of Figure 5.

Patterning of the elements can be done in various ways. The approach taken most often is fabrication by lithographic means (either optical or electron beam), which requires the use of photoresists and lift-off techniques (For a review of techniques used to deposit magnetic materials, see Ross, 2001). In ultrathin films, that is, films of a few atomic layers, this technique is applicable only if the films are protected against the ambient atmosphere. Moreover, it is

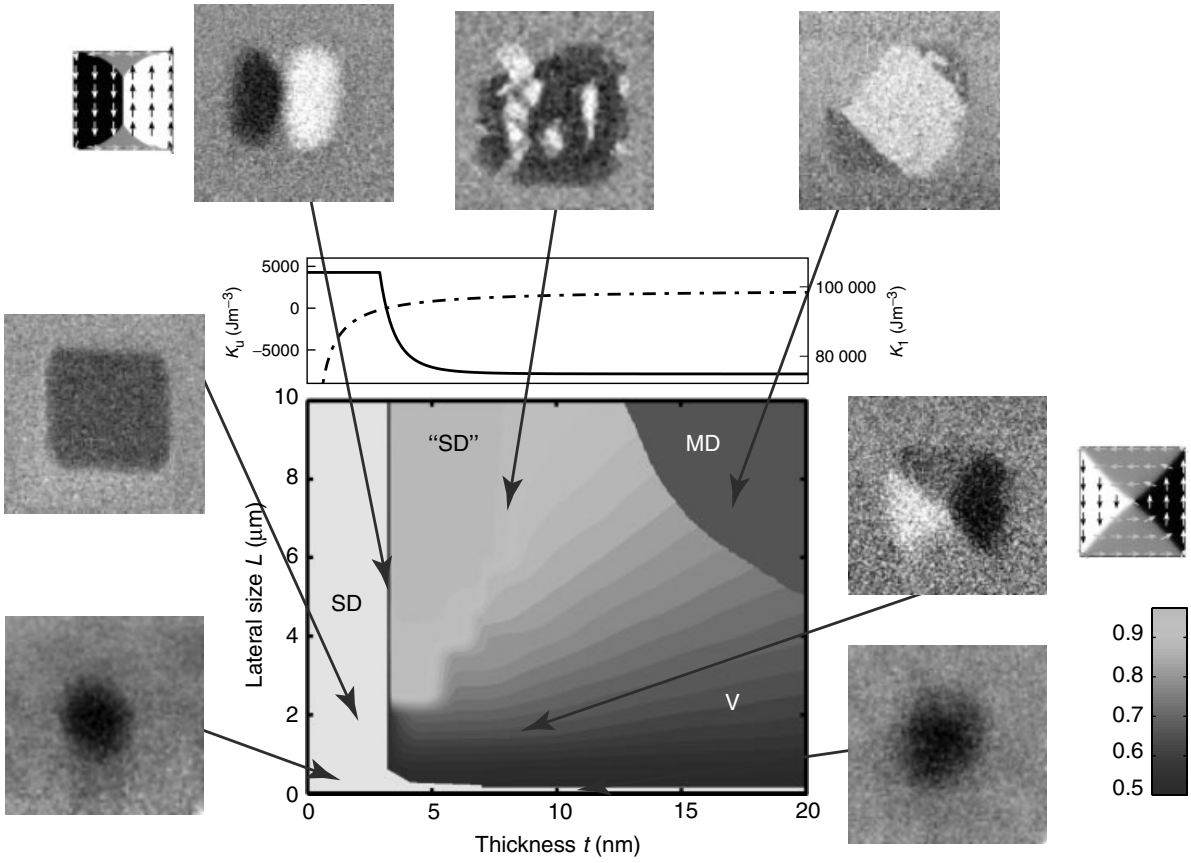

Figure 5. Phase diagram of the lowest-energy configurations in stepped Co/Cu(001) elements. At the top, the evolution of uniaxial (K_u, straight line) and cubic (K_1, dash-dotted line) anisotropy with thickness used in the micromagnetic simulations is shown. The experimental domain patterns were determined by spin-SEM; the arrows point to the thicknesses t and lengths L of the elements. The micromagnetic simulations have been performed on a narrow grid of (t, L) parameters. Two simulations are shown next to the experimental patterns with the same (t, L) parameters. The contour lines plot $\langle M_x^2 \rangle = \int (M_x/M_s)^2 \, dV$ as a measure of the deviations from the perfectly symmetric vortex state. States are classified as single-domain (SD), vortex (V), and multidomain (MD) states. A true, uniform SD state with $\langle M_x^2 \rangle = 0$ (for $t < 3.1$ nm) exists in the region labeled SD. The region labeled V exhibits $\langle M_x^2 \rangle$ values between 0.5 and 0.98 (see bar at the right). A gradual transition from a perfect V to an almost uniform state labeled "SD" (with $\langle M_x^2 \rangle$ close to 1) is observed for large L (>6 μm) near $t \approx 5$ nm.

often observed that the edges of lithographically produced elements exhibit altered magnetic properties. Hard pinning centers responsible for incomplete magnetization reversal are frequently ascribed to such material issues. To study the intrinsic magnetic properties of ultrathin uncovered structures, a different approach is used here: the patterns are produced by a nanostencil deposition technique in which the elements are fabricated by evaporation through thin Si-nitride shadow masks (Zahl, Bammerlin, Meyer and Schlittler, 2005), thus avoiding the use of lithographic steps during fabrication. Square elements, having variable edge lengths between 500 nm and 10 μm and thicknesses between 0.5 and 20 nm, were epitaxially grown using standard deposition parameters (Weber, Allenspach and Bischof, 1997) and in field-free environment. For smaller elements (250 to <500 nm), stencil masks produced by optical interference lithography have been employed, restricting the shape to circular or elliptical disks.

The experimental work is compared with micromagnetic simulations carried out with the OOMMF code (Donahue and Porter, 1999). A new module was added to the 3D solver package to take the complex anisotropy term relevant for stepped Co films into account. The material parameters used in the simulations were the literature values of fcc Co, with a saturation magnetization $M_s = 1424\,\mathrm{kAm^{-1}}$ and an exchange constant $A = 30 \times 10^{-12}\,\mathrm{Jm^{-1}}$. For each thickness, the anisotropy constants K_u and K_1 as given at the top of Figure 5 were used. A wide range of parameters for the thickness and lateral size was simulated to arrive at a full phase diagram of the minimum energy domain state versus the thickness and lateral size of the element. Different starting configurations for the simulations often resulted

in different converged final states. Therefore, for each set of parameters, a variety of domain states were calculated. Comparison of converged states always included the uniform SD state and the flux-closed vortex state as starting configurations. At small lateral sizes, flower, leaf, and buckle states were included, whereas at large sizes, diamond states were tested.

As with all micromagnetic simulations, it cannot be guaranteed that the global energy minimum has been reached. The same problem is faced in experiments: it is unclear to what extent the as-grown, the remanent, or the demagnetized state should be considered for such studies. All elements have been demagnetized by an alternating field of sufficient strength to overcome the anisotropy barriers. Although there is no proof for either the simulations or the experiment that the lowest-energy configuration has indeed been attained, we are confident that the trend is correctly reproduced.

Figure 5 shows a representative selection of magnetic configurations obtained experimentally. Different patterns are observed depending on the thickness and lateral size: an SD state, vortex (V) states gradually approaching a flux-closed Landau state, and MD states. To facilitate a comparison of this wide variety of states with the simulation results, each simulated pattern is characterized by the averaged square of the magnetization component along the easy magnetization axis for the ultrathin Co film (the $[1\bar{1}0]$ direction), $\langle M_x^2 \rangle = \int (M_x/M_s)^2 \, dV$. Accordingly, an SD state is described by $\langle M_x^2 \rangle = 0$ or $\langle M_x^2 \rangle = 1$ depending on the easy axis direction, whereas a perfect V state has $\langle M_x^2 \rangle = 0.5$. The details of the phase diagram are discussed next.

For elements with small lateral size L (typically below 500 nm), a transition from an SD to a V state is observed with increasing thickness. This SD-to-V transition is characterized by the balance of magnetostatic energy in the SD state with the sum of the exchange and anisotropy energy in the V state. The thinner the element, the smaller its demagnetizing energy, and, correspondingly, the transition is shifted to larger L. This SD-to-V transition has been investigated before in $Fe_{20}Ni_{80}$ with negligible anisotropy. Qualitatively the experimentally observed trend with size and thickness was reproduced by numerical simulations even though the simulations predict the transition to occur at smaller L than what was experimentally observed (Cowburn *et al.*, 1999). The authors remarked, however, that the calculation should be considered as a lower limit rather than an actual representation of the boundary. This discrepancy is not caused by numerical instabilities or inaccuracies of the finite-difference method used in the simulation, as proved by studies that compared the numerical simulations with an analytical description of the SD-to-V transition (Jubert and Allenspach, 2004; Vaz, Athanasiou, Bland and Rowlands, 2006). The analytical description and the simulations agreed, but the discrepancy with the experiment remained and could also not be attributed to a possible weak anisotropy. A likely explanation is that roughness at the element edges could be responsible for the discrepancy (Jubert and Allenspach, 2004). Including this roughness will indeed shift the SD-to-V transition, albeit not sufficiently (Vaz, Athanasiou, Bland and Rowlands, 2006).

For very small square elements, additional stable configurations exist, which are characterized by small deviations from the SD state (Cowburn and Welland, 1998b; Pulwey, Zölfl, Bayreuther and Weiss, 2003). They allow the demagnetization energy to be reduced significantly by letting the spins align themselves parallel to the element edges, without introducing a complete vortex with its prohibitively large exchange and anisotropy energy. In our stepped Co/Cu system, the buckle or C state is the lowest-energy state for a narrow band of parameters near the SD-to-V boundary for $L < 200$ nm. No leaf state (Cowburn and Welland, 1998b) exists because the configurational anisotropy is too small to keep a diagonal magnetization against K_u and K_1. Experimentally, this region is not accessible: the smallest elements investigated have a length $L = 250$ nm and a circular shape, which suppresses the occurrence of these states.

At very small thicknesses, the magnetostatic energy is small. Flux closure is not required and the SD state prevails irrespective of the lateral size (Stamm *et al.*, 1998). As K_u is large, deviations from the uniform state are virtually absent. A first phase transition occurs at $t \approx 3$ nm, at which the cost in demagnetization energy for the SD state becomes larger than the exchange and anisotropy energy for the V state. The observed configuration is strongly influenced by anisotropy. Although the pattern is still derived from a V configuration, it is more reminiscent of a two-domain state with triangular closure domains at the edges. Compared with a fully symmetric vortex, the two triangular domains in which the magnetization points along the intermediate axis are shrunk, and $\langle M_x^2 \rangle$ is increased from 0.5 for a perfect vortex to $\approx$0.8. This leads to an appreciable reduction of the anisotropy energy and overcompensates the energy cost of the newly formed 180° domain wall. Only at $t = 3.1$ nm, where K_u vanishes, a perfect fourfold symmetry of the vortex is regained, and hence $\langle M_x^2 \rangle = 0.5$. At larger thickness, K_u changes sign, interchanging the role of the easy and the intermediate magnetization axes. A second phase transformation back to a more uniform state occurs, rotated by 90° with respect to the direction at small thickness. As the magnetostatic energy of this SD state increases with increasing t, a distortion towards a V state occurs. The deviations from the fourfold symmetry are less pronounced than at small t. This argument is somewhat oversimplified, because in reality the demagnetization energy scales with t/L rather than with t. As a result, the demagnetization energy

of the SD configuration increases with decreasing L. Correspondingly, the SD state at $t \approx 4.5$ nm becomes increasingly less stable for smaller L and eventually disappears.

Squares with very large lateral size ($L \approx 10\,\mu$m) exhibit additional phase transitions with increasing thickness (see Figure 5): Starting from an SD state, a crossover to a V-type configuration takes place, which reverts to an almost uniform SD state before reaching – via some V component as characterized by a reduction in $\langle M_x^2 \rangle$ – a MD configuration. The cost of the additional domain-wall energy is compensated by the gain in magnetostatic energy, while anisotropy plays only a minor role at this transition. Correspondingly, the V-to-MD transition was also observed in low-anisotropy permalloy elements (Gomez *et al*., 1999). However, in various magnetic force microscopy studies, it remained a matter of debate whether the observed patterns have to be interpreted as signatures of MD or of V states (Fernandez, Gibbons, Wall and Cerjan, 1998; Van Bael, Temst, Moshchalkov and Bruynseraede, 1999; Kazakova, Hanson, Blomquist and Wäppling, 2001). In the Co elements considered here, the MD state is experimentally already attained for thicknesses well below those calculated. These irregularly shaped domain patterns are reminiscent of the irregular domains observed in extended in-plane films after demagnetization (Oepen *et al*., 1990). Only in thicker elements straight domain walls are observed, finally approaching the 3D world of micromagnetics. It is worth mentioning that at even larger L, a further transition has been reported in a system with fourfold anisotropy. In 15-nm-thick Fe(001) elements on GaAs, a transition from the MD state to an essentially SD state is observed upon increasing L to $\approx$50 μm (Gu *et al*., 1997). This transition was ascribed to the competition of in-plane dipolar and anisotropy energies, and in essence marks the transition to the uniformly magnetized infinitely extended film, containing a few irregular closure domains at the element edges.

In summary, a very rich phase diagram of domain states in stepped Co/Cu(001) elements exists: with varying lateral size and thickness of the element, distinct configurations are identified, in particular SD, V, and MD patterns. This complex behavior is caused by the complex anisotropy and its thickness dependence. It results from the competition between the uniaxial step-induced anisotropy, the cubic anisotropy, and the magnetostatic stray-field energy. Anisotropy favors a uniform magnetization pattern, whereas a reduction of magnetostatic energy requires a flux-closure pattern. Micromagnetic simulations and experimental observations largely agree. Simulations find marginal deviations from the perfectly uniform magnetization distribution in the region of the phase diagram labeled as SD. The SD-to-V boundary at small lateral size is, as in earlier studies, qualitatively reproduced by simulations or by an analytical approach, whereas the V-to-MD transition at large lateral size is shifted to reduced thicknesses. Apart from these minor discrepancies, Figure 5 proves that micromagnetic simulations have become an essential tool to calculate magnetization patterns in large elements, extending well into the micrometer length scale, thanks to the amazing increase in computing power in the past few years.

The Co/Cu model system shows that anisotropy is crucial for the type of domain patterns observed. As uniaxial anisotropy is determined by the miscut or the step distance of the substrate, these crystallographic aspects determine the domain pattern in an adjustable and tunable manner. The conclusion that the SD state prevails regardless of size, shape, and magnetic history (Stamm *et al*., 1998) is only valid in the narrow parameter space of the phase diagram in which the thickness vanishes. However, it is remarkable that thanks to the tunability of anisotropy stable SD configurations can be induced and V states avoided at much larger thicknesses, as is required for certain technological applications such as magnetic random-access memories.

This discussion completely ignores thermal effects. Ultrathin films, however, in general show a pronounced temperature dependence of their magnetic properties, as for instance, described in Section 2: fluctuations of domain patterns have been observed near the Curie temperature. Moreover, if SD particles become small enough, superparamagnetic behavior is observed (Bean and Livingston, 1959): the anisotropy energy is so small that thermal fluctuations can overcome this barrier and reverse the magnetization spontaneously. In Co/Cu(001) elements, we have observed ferromagnetic instabilities. The magnetization in 300-nm dots that are only a few ML thick begins to fluctuate on the timescale of the spin-SEM experiment (see Figure 6). Hence, even though ultrasmall elements are in an SD state at low temperature, this state is prone to time-dependent magnetization switching. This precludes an application of these dots as magnetic bits for 'nanorecording', as was suggested earlier (Stamm *et al*., 1998).

4 CONFINED DOMAIN WALLS

4.1 Domain walls in small elements

The concept of a magnetic domain wall is a direct consequence of the theory of magnetic domains proposed 100 years ago by Weiss (1907). On the typical length scale encountered in a ferromagnet, this transition is a continuous rotation from the magnetization direction in one domain to the direction in the adjacent one, because it extends over many lattice constants. Soon after Bloch (1932) realized this fact, Landau and Lifshitz (1935) introduced a variational approach to calculate the first domain-wall width and

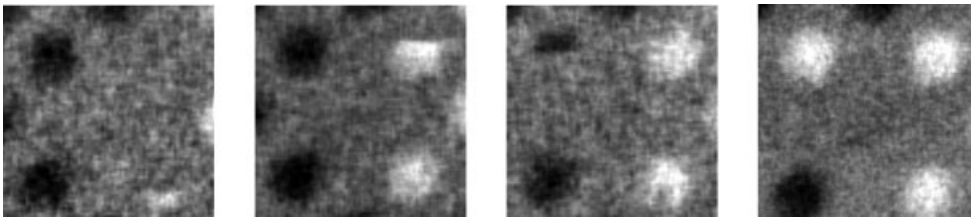

Figure 6. Magnetization fluctuations in 300-nm Co dots on slightly miscut Cu(001), measured by spin-SEM. The four images from left to right were taken consecutively. No magnetic field was applied. The in-plane magnetization component M_y along the page is shown, coded as white for magnetization along $+y$ and black along $-y$; magnetization along $\pm x$ appears gray. All dots except the one at the lower left corner switch within the timescale of the experiment (about 4 h). The top left dot, for instance, switched from $-y$ to $\pm x$ and to $+y$. The abrupt gray scale change along the x direction within a dot indicates a magnetization switching from one line scan to the next.

wall profile. Only two material parameters are involved, the exchange constant A and the anisotropy energy K. The magnetization then varies as $\tanh(x/w_0)$, with w_0 being a convenient definition of the wall width, $w_0 = \sqrt{(A/K)}$.

This prototypical one-dimensional (1D) Bloch wall is rarely observed because it requires an infinite sample or very large anisotropy energy, as otherwise the dipolar magnetic energy cannot be neglected. In a finite system, boundaries such as edges and surfaces are important, and dipolar contributions need to be taken into account. In a thin film with in-plane anisotropy, for instance, the magnetization within a Bloch wall would point out of plane, adding an appreciable amount of surface demagnetizing energy to the total wall energy. Néel (1955) proposed an alternative domain-wall type, for which the magnetization rotates entirely within the plane. This wall has an internal magnetostatic energy but no surface energy, and is energetically favored in thin films. A detailed analytical description of the Néel wall profile is complex. Its main features are a narrow core, in which the magnetization rotates rapidly, and a long tail of several micrometers in length, which is characterized by a gradual change of the magnetization direction. The core width depends on the uniaxial anisotropy and the shape anisotropy energy $1/2\,\mu_0\,M_s^2$, with $w_{\text{core}} = c\sqrt{(A/(K + 1/2\,\mu_0\,M_s^2))}$, where c is a proportionality constant of the order of 1 (Riedel and Seeger, 1971).

But even for this more complex case, the width of a domain wall is solely determined by intrinsic material parameters. Only very recently, it has become clear that the width of a wall could depend on the dimensions of the sample. In particular, very narrow domain walls could exist in nanoscopic elements. A first experimental observation of a wall width of a few nanometers was explained by a pronounced increase of the exchange or by the breakdown of the micromagnetic continuum approach on the atomic scale (Pratzer *et al.*, 2001). On the other hand, it was suggested that a domain wall can be much narrower than w_0 if the angle of rotation across the wall is small (Ding, Wulfhekel and Kirschner, 2002). However, the domain-wall width is reduced in small dimensions even if both these arguments are not applicable. An example of such a confined magnetic domain wall is shown in Figure 7 for an epitaxial Co element of 300-nm diameter and 10-nm thickness. On these length scales, continuum micromagnetics still perfectly describes the physics. The wall is a 180° Néel wall, that is, the magnetization rotates by a large angle. A line profile across the wall gives a wall width of about 50 nm. Compared with an extended film, this value is roughly a factor of 4 smaller than the width of the unconstrained wall (Berger and Oepen, 1992). Because the material parameters such as magnetization, anisotropy, and exchange are largely the same, the wall width is reduced for geometrical reasons: it decreases when the lateral size of the element shrinks. This reduction is caused by a modification of the magnetic dipolar energy contribution at the element edges, as discussed in the next paragraph in more detail.

A systematic study of the geometry dependence of the Néel wall width has been done in lithographically fabricated

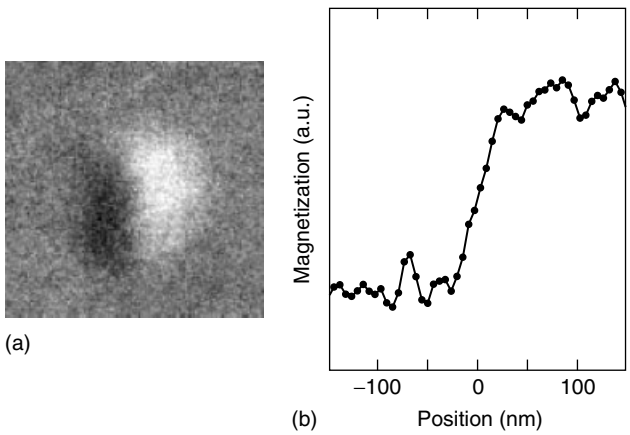

Figure 7. (a) In-plane magnetization image of an individual epitaxial 300-nm-diameter Co dot on Cu(001), with a thickness of 10 nm, fabricated using the nanostencil method (Zahl, Bammerlin, Meyer and Schlittler, 2005) and measured *in situ* by spin-SEM. The dot decays into a multidomain state containing two antiparallel regions with a 180° domain wall in between. (b) Line scan across the wall taken along the horizontal axis. The wall width is about 50 nm.

micrometer-sized structures. In 20-nm-thick $Fe_{20}Ni_{80}$ rectangular elements, a 180° Néel wall has been pinned at the center by a narrow notch. The width of the element has been systematically varied between 1 and 4 μm, and the domain-wall profile has been measured (Jubert, Allenspach and Bischof, 2004). Without notch, a well-defined two-domain state would not be the lowest-energy state of the element. The dimensions of the notch, however, can be chosen such that the wall width is not affected by the presence of the notch. Figure 8 shows that the finite width of the element leads to wall confinement. The domain-wall width decreases with shrinking element size, on length scales larger than a micrometer. The limiting value in the infinitely extended 10-nm-thick film could not be determined experimentally because it was not possible to stabilize a 180° Néel wall after demagnetization in an alternating field. In somewhat thicker films, long tails with an extension of several micrometers were reported (Suzuki, Wilts and Patton, 1968; Wong and Laughlin, 1996). In a small element, these tails are limited by the element width, leading to a modified profile and a reduced width of the Néel wall core. Micromagnetic simulations confirm the experimentally observed trend, but quantitative deviations remain. Similar discrepancies have been found in studies of small disks (Vaz *et al*., 2003). Their origin remains unclear. It has been proposed that exchange is underestimated in the simulations (Jubert, Allenspach and Bischof, 2004). The observed wall-width reduction originates in the tails of the wall: they are cut at the element edges. Hence, the magnetostatic charges that are present in the tails need to be redistributed within the entire Néel wall. This rearrangement of charges is rather intricate and not fully understood theoretically (Holz and Hubert, 1969). Such a wall-width reduction on a micrometer scale is only expected to occur in Néel walls. Bloch walls are uncharged: wall tails are absent, and hence no energy is gained by confining the wall on these length scales.

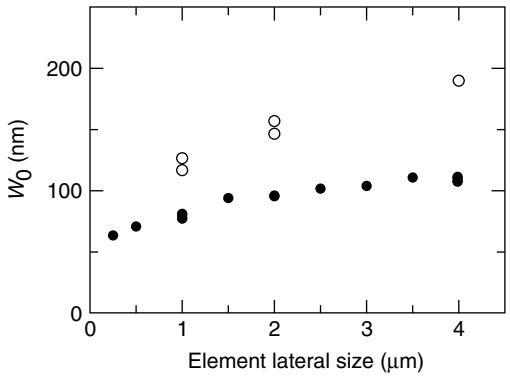

Figure 8. Domain-wall width versus element width for rectangular $Fe_{20}Ni_{80}$ elements with a thickness of 20 nm, for a 180° Néel wall. The experimental results (empty circles) are obtained from spin-SEM; the simulations (filled circles) are calculated with the OOMMF code. (Reproduced from Jubert, Allenspach and Bischof, 2004, with permission from the American Physical Society. © 2004.)

At length scales smaller than the exchange length, the continuum micromagnetic approximation is no longer appropriate. The discreteness of the atomic lattice and hence of the spin distribution becomes important. This was recognized a long time ago (Hilzinger and Kronmüller, 1973). For narrow domain walls, it was calculated that the coercive field should depend on the exact position of the wall with respect to the atomic positions in the crystal lattice, but the effect should be on the order of a few percent only. In a recent study, a drastic influence of the orientation of magnetic domain walls in Fe nanowires was observed (Vedmedenko *et al*., 2004). Regardless of the wire orientation, the domain walls are oriented along two crystallographic directions (see Figure 9). Most walls run along the $[1\bar{1}1]$ direction, and in some cases a $[3\bar{3}1]$ direction is observed. Neither orientation

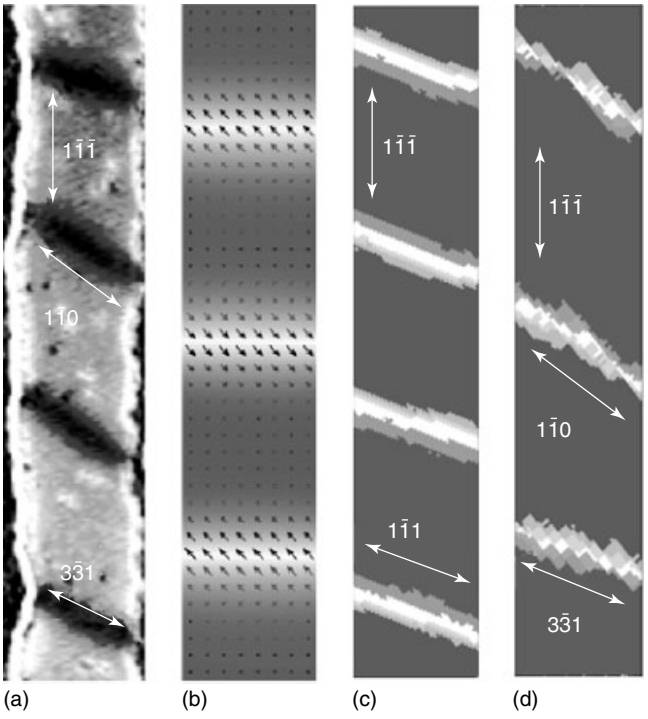

Figure 9. Domain walls in a Fe/W(110) nanowire section, with a thickness of 2 ML and a width of 20 nm. (a) Image taken by spin-polarized scanning tunneling microscopy; the domain walls appear dark, with orientations along the $[1\bar{1}0]$ and the $[3\bar{3}1]$ directions. (b) Micromagnetic continuum simulation with isotropic exchange. The domain walls (bright) run perpendicular to the nanowire direction to minimize the wall length. (c–d) Monte Carlo simulation on a discrete lattice; in (c) the exchange was taken to be identical along all nearest neighbors, while in (d), lattice relaxation was taken into account, with the largest exchange coupling taken along the $[1\bar{1}0]$ direction. (Reproduced from Vedmedenko, Kubetzka and Bergmann, 2004, with permission from the American Physical Society. © 2004.)

can be reconciled with a micromagnetic simulation in which a uniform exchange constant is assumed. Monte Carlo simulations on the discrete lattice, however, are able to reproduce the experimental result. The wall orientation is determined by the atomic lattice and the strength of the exchange constant between neighboring atoms along different directions. In contrast to what is expected in continuum micromagnetics, magnetic anisotropy and magnetostatic energy play only a minor role in the wall orientation.

4.2 Domain walls at constrictions

The examples shown in Figures 7 and 8 illustrate that scaling of the element size down to (sub)micrometer dimensions leads to appreciable effects on the domain-wall width. Micromagnetically, this is a straightforward extension of what happens when going from a bulk ferromagnet to a thin film. The existence of magnetic dipolar energy contributions at the surface favors the transition from a Bloch to a Néel wall, and, similarly, the existence of boundaries at which the tail of the Néel wall is cut off leads to a redistribution of magnetic charges across the entire domain wall. A further rearrangement is expected if additional geometrical changes are introduced, such as notches or protrusions. Interestingly, this more complex geometry recently gained more attention by theoreticians than the simpler case of a small element.

Using a 1D analytical approach, Bruno predicted that Bloch walls shrink in constrictions that are smaller in size than the width of the unconstrained wall (Bruno, 1999). He suggested that this geometrically constrained wall should be considered as a new wall type, different from both a Bloch and a Néel wall. This work was inspired by the intriguing result that the magnetoresistance in Ni nanocontacts reached values of 280%, and it was speculated that the domain-wall width depends on the contact size (García, Muñoz and Zhao, 1999). Shortly afterwards, world record magnetoresistance values have been announced (Chopra and Hua, 2002; Hua and Chopra, 2003), but a critical evaluation came to the conclusion that artifacts due to magnetostrictive, magnetostatic, and magnetomechanical effects can mimic ballistic magnetoresistance (Egelhoff *et al*., 2004).

In the limit of very small constrictions, Bruno calculated that the wall width is determined solely by geometry and not by the material parameters. The wall width can be as small as the constriction diameter. Such a narrow wall costs exchange energy density. The total wall energy, however, can yet be lowered with a larger energy density, because the wall is confined to a smaller volume. Dipolar effects are neglected in this model and it is assumed that the wall remains planar and of Bloch type even within the constriction. However, classical Monte Carlo simulations and micromagnetic modeling have shown that the Bloch wall is only stable at large constriction. When the constriction is made smaller, a crossover to a vortex wall takes place before finally a Néel configuration is energetically preferred at very small constrictions (Labaye, Berger and Coey, 2002). Micromagnetic modeling showed that the domain walls are not straight but rather 2D (Jubert and Allenspach, 2005) or even 3D (Molyneux, Osipov and Ponizovskaya, 2002) configurations which bend outside the constriction area. Thus, while the phenomenon of a geometrically constrained domain wall is well described by the analytical model, the restriction to 1D fails to predict the wall-width reduction quantitatively. A direct comparison of the analytical model to micromagnetic simulations is given in Figure 10. In contrast to the analytical model, the simulations do not show scaling: it is the constriction size and not the ratio of constriction to element size that matters (Jubert and Allenspach, 2005). The origin of this discrepancy stems from the assumption of the analytical model that the wall remains planar, thus having a length extending throughout the element if the wall is positioned outside the constriction.

Experimentally, Bloch walls with decreased width have been observed by spin-polarized scanning tunneling microscopy (STM) in epitaxial Fe stripes which self-organize on W(110) substrates: the unconstrained wall width is 6 nm, the wall pinned at the constriction of about 1 nm in size

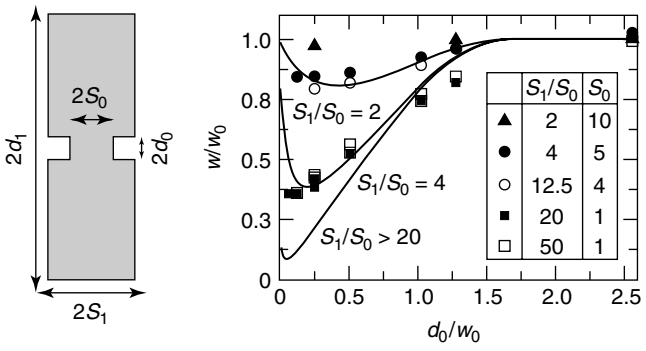

Figure 10. (a) Schematic description of a thin rectangular magnetic element with width $2d_1$ and length $2S_1$ containing a constriction characterized by its width $2d_0$ and its length $2S_0$. (b) Evolution of the domain-wall width versus constriction dimension d_0 for various values of S_0 and S_1 as given in the inset, calculated by micromagnetic simulations with the OOMMF code. Both axes are normalized with the unconstrained Bloch wall width, $w_0 = \sqrt{(A/K)}$. The lines give the wall-width variations calculated with Bruno's analytical model for three ratios of S_1/S_0. (Reproduced from Jubert and Allenspach, 2005 © 2005, with permission from Elsevier.)

is reduced to 2 nm (Pietzsch, Kubetzka, Bode and Wiesendanger, 2000). Pinning of an in-plane domain wall at a lithographically fabricated NiFe constriction has been observed by magnetic force microscopy in a search for increased magnetoresistance effects (Miyake *et al*., 2002). Even though the wall width was found to be reduced, no evidence of a substantial ballistic magnetoresistance was observed. Comparison with simulations is difficult in this case because the wall is a head-to-head domain wall. A systematic study to correlate the constriction geometry to the wall width has been performed on 180^o Néel walls (Jubert, Allenspach and Bischof, 2004). These walls were stabilized in thin $Ni_{80}Fe_{20}$ elements containing a constriction by employing a rectangular shape, which favors an antiparallel two-domain state. This configuration with a 180° Néel wall positioned in the constriction is obtained after demagnetization by an alternating magnetic field. Without constriction, an SD prevails. The 2D magnetization pattern (and hence the domain-wall profile) in the constriction was determined by spin-SEM and compared with micromagnetic simulations (see Figure 11).

The profile across the wall is shown in Figure 11(e). The agreement with the calculated profile is excellent. A symmetric Néel wall with its two distinct features can be identified: a core region with a rapid magnetization rotation, which can be approximated by a hyperbolic tangent function, and long tails extending over large distances.

The wall is somewhat more complex, though. A close-up of the constriction region illustrates that it is 2D and asymmetric (see Figure 12). The magnetization rotates by 180° at the constriction, but for topological reasons differently at the two constriction edges. Exchange forces the spins to remain as closely aligned as possible with each other, and hence the rotation occurs over a longer distance in the outer part of the turn. The small intermediate domain nucleated at one constriction edge results from the fact that low-angle Néel walls are energetically favored over large-angle walls, and thus energy can be gained by replacing a 180° domain wall by two 90° walls (Holz and Hubert, 1969). A micromagnetic simulation successfully reproduces all these features (see Figure 12). The same energy argument also applies to a Bloch wall. Hence, a Bloch wall is also, in general, a 2D object. However, it remains symmetric at the constriction edges because the magnetization rotates in planes perpendicular to the film surface (Jubert and Allenspach, 2005).

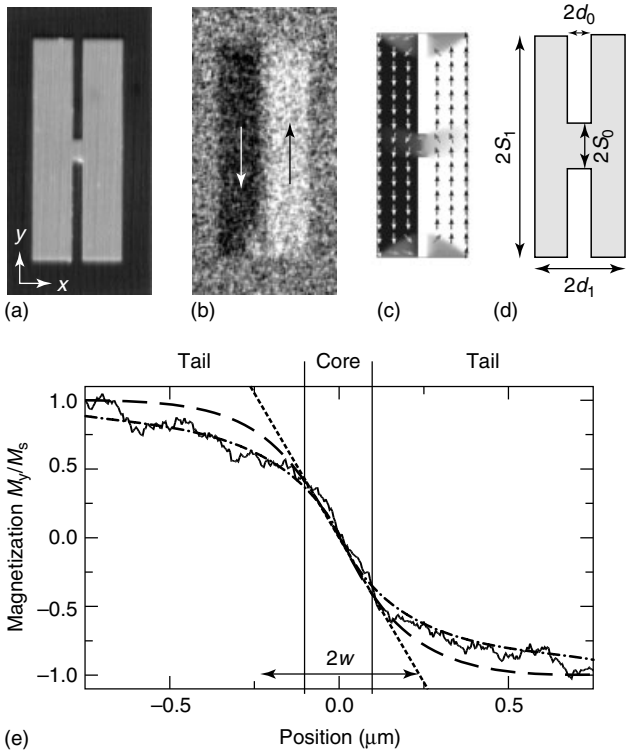

Figure 11. $Fe_{20}Ni_{80}$ rectangle 10 μm × 4 μm in size containing a constriction with $d_0 = 225$ nm and $S_0 = 500$ nm; thickness 7.5 nm. (a) Topographic image and (b) magnetization configuration after demagnetization as determined by spin-SEM. The arrows indicate the magnetization direction. (c) Micromagnetic simulation for an element having the same dimensions. (d) Schematic defining the element and constriction parameters. (e) Domain-wall profile across the constriction. The experimental profile is compared with the simulation (dash-dotted line) and a hyperbolic tangent function (dashed line). (Reproduced from Jubert, Allenspach and Bischof, 2004, with permission from the American Physical Society. © 2004.)

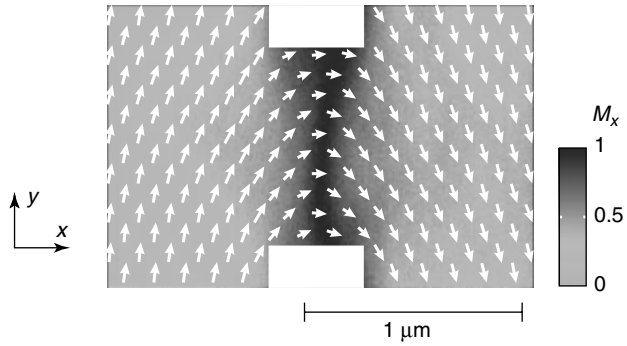

Figure 12. Magnetization configuration in a 7.5-nm-thick $Fe_{20}Ni_{80}$ rectangular element containing a constriction, measured by spin-SEM. Only the center part of the 10 μm × 4 μm rectangle is shown, exhibiting a two-domain state with magnetization along $+y$ (to the left of the constriction) and $-y$ (to the right). The gray scale represents the magnetization component M_x, the arrows give the in-plane magnetization direction as determined from the measured M_x and M_y components. The wall configuration is asymmetric with respect to the top and bottom edges, with a wider wall exhibiting a triangular domain with magnetization along $+x$ at the top constriction. The constriction dimensions are $d_0 = 225$ nm and $S_0 = 500$ nm, as defined in Figure 11(d). (Adapted from Allenspach and Jubert, 2006.)

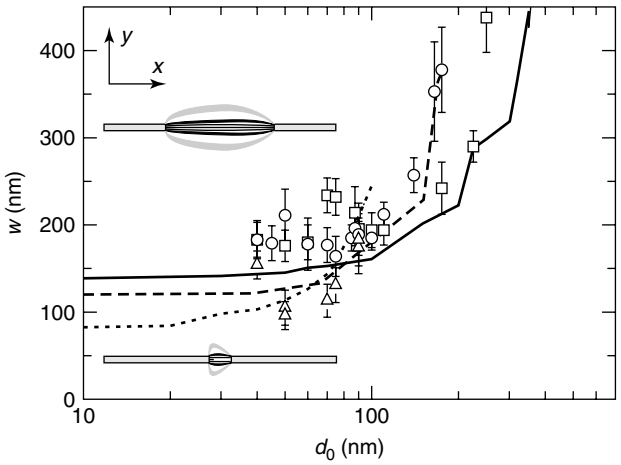

Figure 13. Domain-wall width w versus constriction dimension d_0 in $Fe_{20}Ni_{80}$ with $S_0 = 100\,\text{nm}$ (triangles, dotted line), 250 nm (circles, dashed line), and 500 nm (squares, solid line). Dots are experimental values and lines are micromagnetic simulations. The element is 7.5-nm thick, with a lateral size of $10\,\mu\text{m} \times 4\,\mu\text{m}$. Two simulated domain walls with fixed d_0 but varying S_0 show the outward bending of the wall. (Reproduced from Jubert, Allenspach and Bischof, 2004, with permission from the American Physical Society. © 2004.)

By varying the constriction dimensions, the wall width can be modified continuously over a wide range. Figure 13 presents the evolution of the wall width as a function of the constriction width d_0, with the constriction length S_0 as a parameter. For small d_0, the domain-wall width w is almost constant. As d_0 becomes larger than about 100 nm, w increases strongly with d_0. The minimum value of w attained at small d_0 depends on S_0, with w being smaller for smaller S_0. The increase of w for larger d_0 is steeper for smaller S_0. The domain-wall widths determined from the simulated micromagnetic patterns reproduce the experimental trend very well. The 2D nature of the patterns helped us understand the observed wall-width variations in a quantitative way.

Far from the constriction edges, the 180° Néel wall width is determined by the material parameters and the extension of the element, as discussed in Section 4.1. The width of this wall is defined to be w_0. If the wall is located in a constriction, however, it is affected by the constriction parameters. The magnetization is forced to lie parallel to the constriction edges, because the dipolar energy can be minimized in this way. Hence, the wall width locally corresponds to d_0. Such a small wall width cannot be maintained throughout the constriction if $2d_0 < w_0$ because the cost in exchange energy is too large. Hence, the wall deforms in the constriction, adopting a 2D shape with outward deformation (see lower inset in Figure 13). The situation is completely analogous to the case of the Bloch wall presented in Figure 10. For large S_0, the wall profile in the constriction center is unaffected as the deformation is restricted to the region near the edges. In this case, the measured wall width is almost constant, $w \approx w_0$ (see upper inset in Figure 13). For small S_0, on the other hand, the wall width at the center is reduced, $w < w_0$. Keeping it at a width w_0 would require a very rapid wall variation along the constriction and hence cost excessive exchange energy. Accordingly, a reduction of w is observed below a threshold value of $S_0 \approx 250\,\text{nm}$.

The opposite limit of $2d_0 > w_0$ can be understood along the same lines. Again, the wall attains a 2D shape, but bends inward instead of outwards. For small S_0, the wall at the center becomes wider rather than narrower, $w > w_0$. For large S_0, the confinement is again limited to the constriction edges, and correspondingly the increase of w is shifted to larger d_0. In the limit of d_0 approaching S_0, the domain-wall-type changes completely: the domain formed at the constriction edge visible in Figure 12 expands toward the center of the constriction, leading to a splitting of the 180° Néel wall into two 90° Néel walls, as was observed experimentally (Jubert, Allenspach and Bischof, 2004).

These experiments demonstrate that domain-wall dimensions and profiles can be tailored by constriction geometry. For the same material properties, the wall width can be varied in a wide range. It is strongly confined in small and narrow constrictions, but stretched for wide constrictions owing to significant dipolar energy contributions at the constriction edges. For specific constriction geometries, even the wall type can be changed. These observations are not limited to the prototypical 180° Néel walls considered here. 90° Néel walls in T-shaped junctions exhibit the same behavior: the wall width pinned at the contact region strongly depends on the contact dimensions (Haug *et al.*, 2005).

In conclusion, magnetic domain walls in small elements can be strongly affected by two geometrical approaches, by the lateral dimensions of the element, and by constrictions. Lateral confinement causes Néel walls to shrink because of a redistribution of demagnetization versus exchange energy, while Bloch walls are not affected. Constrictions influence both Néel and Bloch walls: wall profiles can be reduced or expanded in width and attain a complex 2D topology, and wall types can be modified. This geometrical tunability offers an additional handle on a domain wall. It is possible to tailor domain walls without resorting to changing the material parameters. This might become important for future applications in which logical bits are represented as individual domain walls (Allwood *et al.*, 2002; Parkin, 2004). In such concepts, geometrical effects are also successfully used to inject domain walls (Thomas *et al.*, 2005) or to favor a propagation direction, because the pinning and de-pinning of a domain wall depends on the geometry (Hirohata *et al.*, 2000; Allwood, Xiong and Cowburn, 2004; Himeno, Kasai

and Ono, 2005). The examples presented demonstrate that experiments, micromagnetic simulation and – where available – analytical models agree reasonably well. Some discrepancies remain and are not yet resolved, even on length scales at which continuum micromagnetics is still applicable. Theoretically, also the thermal effects are still largely unexplored. A recent study predicts an interesting change in wall profile because of thermal activation (Kazantseva, Wieser and Nowak, 2005).

ACKNOWLEDGMENTS

The unpublished experimental data on small epitaxial Co/Cu elements in Sections 3 and 4 have been acquired together with Samy Boukari and Andreas Bischof, the simulations were done in collaboration with Pierre-Olivier Jubert.

REFERENCES

Abanov, Ar., Kalatsky, V., Pokrovsky, V.L. and Saslow, W.M. (1995). Phase diagram of ultrathin ferromagnetic films with perpendicular anisotropy. *Physical Review B*, **51**, 1023–1038.

Allenspach, R. (2000). Spin-polarized scanning electron microscopy. *IBM Journal of Research and Development*, **44**, 553–570.

Allenspach, R. and Bischof, A. (1992). Magnetization direction switching in Fe/Cu(100) epitaxial films: temperature and thickness dependence. *Physical Review Letters*, **69**, 3385–3388.

Allenspach, R. and Jubert, P.-O. (2006). Magnetic domain walls in nanowires. *Materials Research Society Bulletin*, **31**, 395–399.

Allenspach, R. and Stampanoni, M. (1992). Magnetic domain imaging of epitaxial thin films by spin-polarized scanning electron microscopy. *Materials Research Society Symposium Proceedings*, **231**, 17–26.

Allenspach, R., Stampanoni, M. and Bischof, A. (1990). Magnetic domains in thin epitaxial Co/Au(111) films. *Physical Review Letters*, **65**, 3344–3347.

Allwood, D.A., Xiong, G., Cooke, M.D., *et al*. (2002). Submicrometer ferromagnetic NOT gate and shift register. *Science*, **296**, 2003–2006.

Allwood, D.A., Xiong, G. and Cowburn, R.P. (2004). Domain wall diodes in ferromagnetic planar nanowires. *Applied Physics Letters*, **85**, 2848–2850.

Arnold, C.S., Pappas, D.P. and Venus, D. (1999). Domain formation near the reorientation transition in perpendicularly magnetized, ultrathin Fe/Ni bilayer films. *Journal of Applied Physics*, **85**, 5054–5059.

Back, C.H., Würsch, Ch., Vaterlaus, A., *et al*. (1995). Experimental confirmation of universality for a phase transition in two dimensions. *Nature*, **378**, 597–600.

Barthelmess, M., Pels, C., Thieme, A. and Meier, G. (2004). Stray fields of domains in permalloy microstructures – measurements and simulations. *Journal of Applied Physics*, **95**, 5641–5645.

Bean, C.P. and Livingston, J.D. (1959). Superparamagnetism. *Journal of Applied Physics*, **30**, 120S–129S.

Berger, A., Linke, U. and Oepen, H.P. (1992). Symmetry-induced uniaxial anisotropy in epitaxial cobalt films grown on Cu(1113). *Physical Review Letters*, **68**, 839–842.

Berger, A. and Oepen, H.P. (1992). Magnetic domain walls in ultrathin fcc Co films. *Physical Review B*, **45**, 12596–12599.

Bloch, F. (1932). Zur Theorie des Austauschproblems und der Remanenzerscheinung der Ferromagnetika. *Zeitschrift für Physik*, **74**, 295–335.

Booth, I., MacIsaac, A.B., Whitehead, J.P. and De'Bell, K. (1995). Domain structures in ultrathin magnetic films. *Physical Review Letters*, **75**, 950–953.

Bruno, P. (1999). Geometrically constrained magnetic domain wall. *Physical Review Letters*, **83**, 2425–2428.

Cannas, S.A., Stariolo, D.A. and Tamarit, F.A. (2004). Stripe-tetragonal first-order phase transition in ultrathin magnetic films. *Physical Review B*, **69**, 092409/1–092409/4.

Chopra, H.D. and Hua, S.Z. (2002). Ballistic magnetoresistance over 3000% in Ni nanocontacts at room temperature. *Physical Review B*, **66**, 020403/1–020403/3.

Cowburn, R.P., Koltsov, D.K., Adeyeye, A.O., *et al*. (1999). Single-domain circular nanomagnets. *Physical Review Letters*, **83**, 1042–1045.

Cowburn, R.P. and Welland, M.E. (1998a). Micromagnetics of the single-domain state of square ferromagnetic nanostructures. *Physical Review B*, **58**, 9217–9220.

Cowburn, R.P. and Welland, M.E. (1998b). Phase transitions in planar magnetic nanostructures. *Applied Physics Letters*, **72**, 2041–2043.

Czech, R. and Villain, J. (1989). Instability of two-dimensional Ising ferromagnets with dipole interaction. *Journal of Physics: Condensed Matter*, **1**, 619–627.

Ding, H.F., Wulfhekel, W. and Kirschner, J. (2002). Ultra sharp domain walls in the closure domain pattern of Co(0001). *Europhysics Letters*, **57**, 100–106.

Donahue, M.J. and Porter, D.G. (1999). *OOMMF User's Guide*, Version 1.0, http://math.nist.gov/oommf/ National Institute of Standards and Technology: Gaithersburg.

Egelhoff, W.F. Jr., Gan, L., Ettedgui, H., *et al*. (2004). Artifacts in ballistic magnetoresistance measurements. *Journal of Applied Physics*, **95**, 7554–7559.

Elmers, H.-J., Hauschild, J. and Gradmann, U. (1996). Critical behavior of the uniaxial ferromagnetic monolayer Fe(110) on W(110). *Physical Review B*, **54**, 15224–15233.

Fernandez, A., Gibbons, M.R., Wall, M.A. and Cerjan, C.J. (1998). Magnetic domain structure and magnetization reversal in submicron-scale Co dots. *Journal of Magnetism and Magnetic Materials*, **190**, 71–80.

García, N., Muñoz, M. and Zhao, Y.-W. (1999). Magnetoresistance in excess of 200% in ballistic Ni nanocontacts at room temperature and 100 Oe. *Physical Review Letters*, **82**, 2923–2926.

Garel, T. and Doniach, S. (1982). Phase transitions with spontaneous modulation – the dipolar Ising ferromagnet. *Physical Review B*, **26**, 325–329.

Gomez, R.D., Luu, T.V., Pak, A.O., *et al*. (1999). Domain configurations of nanostructured permalloy elements. *Journal of Applied Physics*, **85**, 6163–6165.

Gu, E., Ahmad, E., Gray, S.J., *et al*. (1997). Micromagnetism of epitaxial Fe(001) elements on the mesoscale. *Physical Review Letters*, **78**, 1158–1161.

Haug, T., Back, C.H., Raabe, J., *et al*. (2005). Magnetic domain walls in T-shaped permalloy microstructures. *Applied Physics Letters*, **86**, 152503/1–152503/3.

Hertel, R. and Kronmüller, H. (2002). Finite element calculations on the single-domain limit of a ferromagnetic cube – a solution to μMAG standard problem no. 3. *Journal of Magnetism and Magnetic Materials*, **238**, 185–199.

Hilzinger, H.R. and Kronmüller, H. (1973). Analytical derivation of spin configuration and intrinsic coercive field of a narrow domain wall. *Physica Status Solidi B*, **59**, 71–77.

Himeno, A., Kasai, S. and Ono, T. (2005). Current-driven domain-wall motion in magnetic wires with asymmetric notches. *Applied Physics Letters*, **87**, 243108/1–243108/2.

Hirohata, A., Xu, Y.B., Yao, C.C., *et al*. (2000). Domain wall trapping in controlled submicron ferromagnetic elements. *Journal of Applied Physics*, **87**, 4727–4729.

Holz, A. and Hubert, A. (1969). Wandstrukturen in dünnen magnetischen Schichten. *Zeitschrift für Angewandte Physik*, **26**, 145–152.

Hua, S.Z. and Chopra, H.D. (2003). 100,000% ballistic magnetoresistance in stable Ni nanocontacts at room temperature. *Physical Review B*, **67**, 060401/1–060401/4.

Hubert, A. and Rührig, M. (1991). Micromagnetic analysis of thin-film elements. *Journal of Applied Physics*, **69**, 6072–6077.

Jubert, P.-O. and Allenspach, R. (2004). Analytical approach to the single-domain-to-vortex transition in small magnetic disks. *Physical Review B*, **70**, 144402/1–144402/5.

Jubert, P.-O. and Allenspach, R. (2005). Modifying Bloch walls by constrictions. *Journal of Magnetism and Magnetic Materials*, **290–291**, 758–760.

Jubert, P.-O., Allenspach, R. and Bischof, A. (2004). Magnetic domain walls in constrained geometries. *Physical Review B*, **69**, 220410-R/1–220410-R/4.

Kaplan, B. and Gehring, G. (1993). The domain structure in ultrathin magnetic films. *Journal of Magnetism and Magnetic Materials*, **128**, 111–116.

Kashuba, A.B. and Pokrovsky, V.L. (1993). Stripe domain structures in a thin ferromagnetic film. *Physical Review Letters*, **70**, 3155–3158.

Kazakova, O., Hanson, M., Blomquist, P. and Wäppling, R. (2001). Arrays of epitaxial Co submicron particles: critical size for single-domain formation and multidomain structures. *Journal of Applied Physics*, **90**, 2440–2446.

Kazantseva, N., Wieser, R. and Nowak, U. (2005). Transition to linear domain walls in nanoconstrictions. *Physical Review Letters*, **94**, 037206/1–037206/4.

Kerkmann, D., Pescia, D. and Allenspach, R. (1992). Two-dimensional magnet at Curie temperature: epitaxial layers of Co on Cu(100). *Physical Review Letters*, **68**, 686–689.

Kisielewski, M., Maziewski, A., Polyakova, T. and Zablotskii, V. (2004). Wide-scale evolution of magnetization distribution in ultrathin films. *Physical Review B*, **69**, 184419/1–184419/7.

Kittel, C. (1946). Theory of the structure of ferromagnetic domains in films and small particles. *Physical Review*, **70**, 965–971.

Kläui, M. and Vaz, C.A.F. (2007). Magnetization configurations and reversal in small magnetic elements. In *Handbook of Magnetism and Advanced Magnetic Materials*, Kronmüller, H. and Parkin, S. (Eds.), John Wiley & Sons: Chichester, Vol. 2.

Kooy, C. and Enz, U. (1960). Experimental and theoretical study of the domain configuration in thin layers of $BaFe_{12}O_{19}$. *Philips Research Reports*, **15**, 7–29.

Labaye, Y., Berger, L. and Coey, J.M.D. (2002). Domain walls in ferromagnetic nanoconstriction. *Journal of Applied Physics*, **91**, 5341–5346.

Landau, L.D. and Lifshitz, E. (1935). On the theory of the dispersion of magnetic permeability in ferromagnetic bodies. *Physikalische Zeitschrift der Sowjetunion*, **8**, 153–169.

MacIsaac, A.B., Whitehead, J.P., Robinson, M.C. and De'Bell, K. (1995). Striped phases in two-dimensional dipolar ferromagnets. *Physical Review B*, **51**, 16033–16045.

Málek, Z. and Kamberský, V. (1958). On the theory of the domain structure of thin films of magnetically uni-axial materials. *Czechoslovak Journal of Physics*, **8**, 416–421.

Miyake, K., Shigeto, K., Mibu, K., *et al*. (2002). Geometrical confinement of a domain wall in a nanocontact between two NiFe wires. *Journal of Applied Physics*, **91**, 3468–3470.

Molho, P., Porteseil, J.L., Souche, Y., *et al*. (1987). Irreversible evolution in the topology of magnetic domains. *Journal of Applied Physics*, **61**, 4188–4193.

Molyneux, V.A., Osipov, V.V. and Ponizovskaya, E.V. (2002). Stable two-and three-dimensional geometrically constrained magnetic structures: the action of magnetic fields. *Physical Review B*, **65**, 184425/1–184425/6.

Néel, L. (1955). Énergie des parois de Bloch dans les couches minces. *Comptes Rendus de l' Académie des sciences Paris*, **241**, 533–536.

Oepen, H.P., Benning, M., Ibach, H., *et al*. (1990). Magnetic domain structure in ultrathin cobalt films. *Journal of Magnetism and Magnetic Materials*, **86**, L137–L142.

Oepen, H.P., Lutzke, W. and Kirschner, J. (2002). Magnetization reversal in ultrathin Co/Cu(001)-microstructures. *Journal of Magnetism and Magnetic Materials*, **251**, 169–177.

Ono, T. (2007). Domain wall propagation in magnetic wires. In *Handbook of Magnetism and Advanced Magnetic Materials*, Kronmüller, H. and Parkin, S. (Eds.), John Wiley & Sons: Chichester, Vol. 2.

Parkin, S.S.P. (2004). *Shiftable Magnetic Shift Register and Method of Using the Same*. US Patent 6 834 005.

Pietzsch, O., Kubetzka, A., Bode, M. and Wiesendanger, R. (2000). Real-space observation of dipolar antiferromagnetism in magnetic nanowires by spin-polarized scanning tunneling spectroscopy. *Physical Review Letters*, **84**, 5212–5215.

Portmann, O., Vaterlaus, A. and Pescia, D. (2003). An inverse transition of magnetic domain patterns in ultrathin films. *Nature*, **422**, 701–704.

Portmann, O., Vaterlaus, A. and Pescia, D. (2006). Observation of stripe mobility in a dipolar frustrated ferromagnet. *Physical Review Letters*, **96**, 047212/1–047212/4.

Pratzer, M., Elmers, H.J., Bode, M., *et al*. (2001). Atomic-scale magnetic domain walls in quasi-one-dimensional Fe nanostripes. *Physical Review Letters*, **87**, 127201/1–127201/4.

Pulwey, R., Zölfl, M., Bayreuther, G. and Weiss, D. (2003). Transition of magneto-crystalline anisotropy and domain structure in epitaxial Fe(001) nanomagnets. *Journal of Applied Physics*, **93**, 7432–7434.

Reimann, B., Richter, R. and Rehberg, I. (2002). Glasslike relaxation of labyrinthine domain patterns. *Physical Review E*, **65**, 031504/1–031504/4.

Riedel, H. and Seeger, A. (1971). Micromagnetic treatment of Néel walls. *Physical Status Solidi B*, **46**, 377–384.

Ross, C.A. (2001). Patterned magnetic recording media. *Annual Review of Materials Research*, **31**, 203–235.

Schabes, M.E. and Bertram, H.N. (1988). Magnetization processes in ferromagnetic cubes. *Journal of Applied Physics*, **64**, 1347–1357.

Seul, M. and Wolfe, R. (1992). Evolution of disorder in two-dimensional stripe patterns: smectic instabilities and dislocation unbinding. *Physical Review Letters*, **68**, 2460–2463.

Shinjo, T., Okuno, T., Hassdorf, R., *et al*. (2000). Magnetic vortex core observation in circular dots of permalloy. *Science*, **289**, 930–932.

Sornette, D. (1987). Undulation instability in stripe domain structures of "bubble" materials. *Journal de Physique, Paris*, **48**, 151–163.

Speckmann, M., Oepen, H.P. and Kirschner, J. (1995). Magnetic domain structures in ultrathin Co/Au(111): on the influence of film morphology. *Physical Review Letters*, **75**, 2035–2038.

Stamm, C., Marty, F., Vaterlaus, A., *et al*. (1998). Two-dimensional magnetic particles. *Science*, **282**, 449–451.

Stoycheva, A.D. and Singer, S.J. (2000). Stripe melting in a two-dimensional system with competing interactions. *Physical Review Letters*, **84**, 4657–4660.

Suzuki, T., Wilts, C.H. and Patton, C.E. (1968). Lorentz microscopy determination of domain-wall width in thick ferromagnetic films. *Journal of Applied Physics*, **39**, 1983–1986.

Thomas, L. and Parkin, S. (2007). Current induced domain-wall motion in magnetic nanowires. In *Handbook of Magnetism and Advanced Magnetic Materials*, Kronmüller, H. and Parkin, S. (Eds.), John Wiley & Sons: Chichester, Vol. 2.

Thomas, L., Rettner, C., Hayashi, M., *et al*. (2005). Observation of injection and pinning of domain walls in magnetic nanowires using photoemission electron microscopy. *Applied Physics Letters*, **87**, 262501/1–262501/3.

Van Bael, M.J., Temst, K., Moshchalkov, V.V. and Bruynseraede, Y. (1999). Magnetic properties of submicron Co islands and their use as artificial pinning centers. *Physical Review B*, **59**, 14674–14679.

Vaterlaus, A., Stamm, C., Maier, U., *et al*. (2000). Two-step disordering of perpendicularly magnetized ultrathin films. *Physical Review Letters*, **84**, 2247–2250.

Vaz, C.A.F., Athanasiou, C., Bland, J.A.C. and Rowlands, G. (2006). Energetics of magnetic ring and disk elements: uniform versus vortex state. *Physical Review B*, **73**, 054411/1–054411/9.

Vaz, C.A.F., Lopez-Diaz, L., Kläui, M., *et al*. (2003). Direct observation of remanent magnetic states in epitaxial fcc Co small disks. *Physical Review B*, **67**, 140405-R/1–140405-R/4.

Vedmedenko, E.Y., Kubetzka, A., von Bergmann, K., *et al*. (2004). Domain wall orientation in magnetic nanowires. *Physical Review Letters*, **92**, 077207/1–077207/4.

Weber, W., Allenspach, R. and Bischof, A. (1997). Determining magnetic anisotropies from hysteresis loops. *Applied Physics Letters*, **70**, 520–522.

Weber, W., Bischof, A., Allenspach, R., *et al*. (1996a). Structural relaxation and magnetic anisotropy in Co/Cu(001) films. *Physical Review B*, **54**, 4075–4079.

Weber, W., Bischof, A., Allenspach, R., *et al*. (1996b). Oscillatory magnetic anisotropy and quantum well states in Cu/Co/Cu(100) films. *Physical Review Letters*, **76**, 3424–3427.

Weiss, P. (1907). L'hypothèse du champ moléculaire et la propriété ferromagnétique. *Journal de Physique et le Radium*, **6**, 661–690.

Won, C., Wu, Y.Z., Choi, J., *et al*. (2005). Magnetic stripe melting at the spin reorientation transition in Fe/Ni/Cu(001). *Physical Review B*, **71**, 224429/1–224429/5.

Wong, B.Y. and Laughlin, D.E. (1996). Direct observation of domain walls in NiFe films using high-resolution Lorentz microscopy. *Journal of Applied Physics*, **79**, 6455–6457.

Wu, Y.Z., Won, C., Scholl, A., *et al*. (2004). Magnetic stripe domains in coupled magnetic sandwiches. *Physical Review Letters*, **93**, 117205/1–117205/4.

Yafet, Y. and Gyorgy, E.M. (1988). Ferromagnetic strip domains in an atomic monolayer. *Physical Review B*, **38**, 9145–9151.

Zahl, P., Bammerlin, M., Meyer, G. and Schlittler, R.R. (2005). All-in-one static and dynamic nanostencil atomic force microscopy/scanning tunneling microscopy system. *Review of Scientific Instruments*, **76**, 023707/1–023707/5.

Zhao, H.W., Won, C., Wu, Y.Z., *et al*. (2004). Magnetic phase transition and spin-reorientation transition of Cu/Ni/Fe/Cu(001) studied by photoemission electron microscopy. *Physical Review B*, **70**, 024423/1–024423/6.

Domain Wall Propagation in Magnetic Wires

Teruo Ono
Kyoto University, Uji, Japan

1 DOMAIN WALL PROPAGATION BY AN EXTERNAL MAGNETIC FIELD

1.1 Detection of domain wall propagation using GMR effect

Recent developments in nanolithography techniques have made it possible to prepare well-defined dots and wires; magnetism in mesoscopic systems has become an updated topic from both the scientific and technological points of view. The process of magnetization reversal in a single-domain ferromagnetic structure is fundamental in magnetism, and it has been of considerable interest to theorists and experimentalists since the pioneering work of Néel. An understanding of this problem is of fundamental importance for the magnetization reversal in complex systems, such as assemblies of fine particles, thin films, and bulk materials. The process of magnetization reversal is also very important in practical applications such as hard disk drive (HDD) magnetoresistive random access memory (MRAM) and so on.

Nucleation and propagation of a magnetic domain wall are two important processes in magnetization reversal. These processes can be clearly seen in the magnetic wire with submicron width. As shown in Figure 1(a), in very narrow ferromagnetic wires, the magnetization is restricted to be directed parallel to the wire axis due to the magnetic shape anisotropy. When the external magnetic field is applied against the magnetization, a magnetic domain wall nucleates at the end of the wire and the magnetization reversal proceeds by the propagation of this domain wall through the wire (Figure 1b and 1c). However, it is very difficult to detect the propagation of the domain wall, because the change in magnetic moments in this process is very small due to the small volume of the magnetic wire.

Here, the principle of how to detect the domain wall propagation in magnetic wires using the magnetoresistance gaint magnetoresistance (GMR) effect is described. The GMR effect is the change in electrical resistance caused by the change of the magnetic structure in magnetic multilayers (Baibich *et al*., 1988). This means that the magnetic structure of the system can be detected by resistance measurements. Consider the GMR system shown in Figure 2, which is composed of magnetic, nonmagnetic, and magnetic layers. The resistance is largest for the antiparallel magnetization configuration (Figure 2a), and it is smallest for the parallel configuration (Figure 2d). During the magnetization reversal of one of the two magnetizations (Figure 2b and 2c), the total resistance of the system is given by the sum of the resistances of the parallel magnetization part and the antiparallel magnetization part. Thus, the resistance of this system, R, is given by

$$R = \frac{x}{L} R_{\uparrow\uparrow} + \frac{L - x}{L} R_{\uparrow\downarrow} \tag{1}$$

where x is the position of the domain wall, L is the length of the wire, $R_{\uparrow\uparrow}$ is the resistance for parallel configuration, and $R_{\uparrow\downarrow}$ is the resistance for antiparallel configuration. Therefore,

Handbook of Magnetism and Advanced Magnetic Materials. Edited by Helmut Kronmüller and Stuart Parkin. Volume 2: *Micromagnetism*. ISBN: 978-0-470-02217-7.

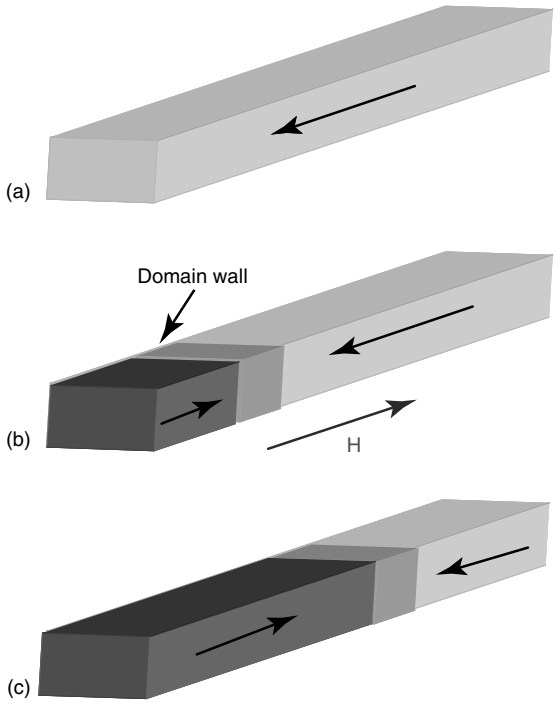

Figure 1. Schematic illustration of the magnetization reversal process in a magnetic wire.

the position of the domain wall can be determined by the resistance measurements.

The above idea has been demonstrated experimentally (Ono, Miyajima, Shigeto and Shinjo, 1998). The samples were prepared using lift-off techniques. $Ni_{81}Fe_{19}$(20 nm)/Cu(10 nm)/$Ni_{81}Fe_{19}$(5 nm) trilayer film was deposited on the patterned mask by electron-beam evaporation in a vacuum of 1×10^{-8} Torr. The wire with trilayered structure was obtained after the resist mask was removed. Owing to the large Cu-layer thickness, the interlayer exchange coupling between the thin and thick NiFe layers is negligible. The magnetoresistance measurements were performed at 300 K. The magnetic field was applied along the axis of the wires. Resistance was determined using a four-point dc technique. As seen in Figure 3, the samples have four current–voltage terminals where the voltage is probed over a distance of 20 μm. Furthermore, the samples have an artificial neck (0.35-μm width) introduced at one-third of the distance from one voltage probe in order to monitor the magnetic domain wall propagation.

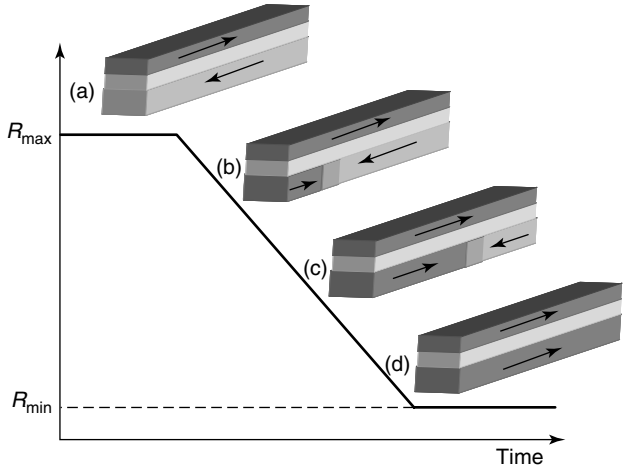

Figure 2. Schematic explanation for the detection of the domain wall propagation in magnetic wires using the magnetoresistance effect.

Figure 4 shows the resistance of the trilayer system as a function of the external magnetic field. Prior to the measurement, a magnetic field of 100 Oe was applied in order to achieve magnetization alignment in one direction. Then, the resistance was measured in steps of 1 Oe as the field was swept toward the counter direction. The result of the magnetoresistance measurement displays essentially four very sharp leaps. The first and second leaps correspond to the magnetization reversal of the thin NiFe layer, whereas the third and fourth leaps correspond to the magnetization reversal of the thick NiFe layer.

The magnetization reversal takes place in the sample as follows: As long as the counter field is smaller than the critical field, the magnetizations of both thin and thick NiFe layers align parallel, and the resistance shows the lowest value. As the applied magnetic field exceeds 5 Oe, the resistance abruptly jumps and maintains a constant value up to 10 Oe. Then, exceeding 10 Oe, the resistance abruptly jumps again and maintains the largest value up to 22 Oe. The result indicates

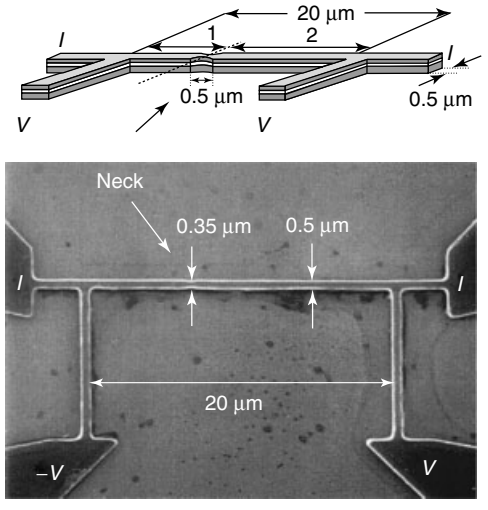

Figure 3. SEM image and schematic illustration of the sample. The sample consists of a $Ni_{81}Fe_{19}$(20 nm)/Cu(10 nm)/$Ni_{81}Fe_{19}$(5 nm). (Reproduced from Ono *et al.*, 1998, with permission from the American Physical Society. © 1998.)

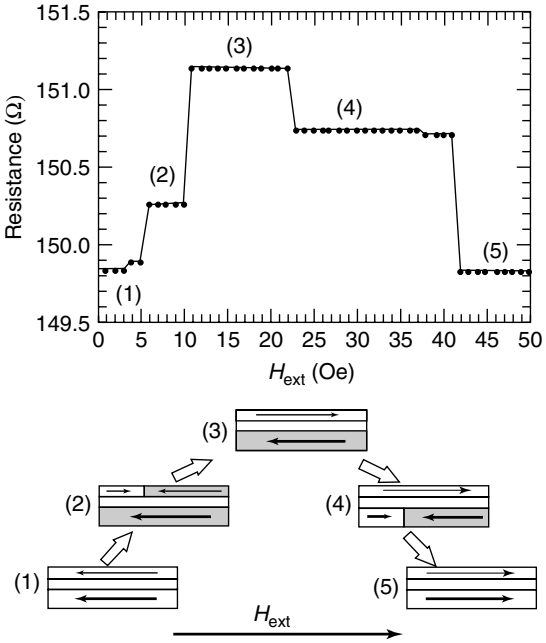

Figure 4. Resistance as a function of the external magnetic field at 300 K. The magnetic domain structures inferred from the resistance measurement and the direction of the external field are schematically shown. (Reproduced from Ono *et al.*, 1998, with permission from the American Physical Society. © 1998.)

that the antiparallel magnetization alignment is realized at an external field between 11 and 22 Oe, where the resistance shows the largest value. The ratio of the resistance changes at the first and second leaps is 1:2. This means that one-third of the total magnetization of the thin NiFe layer changes its direction at the first leap in Figure 4, since the GMR change is directly proportional to the switching layer magnetization. The ratio, 1:3, corresponds to the ratio of the length between one voltage probe and the neck to the overall length of the wire between the voltage probes. Therefore, in this case, a magnetic domain wall nucleates in the shorter part of the wire (left side of the scanning electron microscopy (SEM) image in Figure 3) and propagates to the neck, where it is pinned up to 10 Oe. The second leap, upon exceeding 10 Oe, corresponds either to de-pinning of the magnetic domain wall from the neck or to nucleation and propagation of another magnetic domain wall on the other side of the neck (right side of the SEM image in Figure 3). These two possibilities cannot be distinguished from the result shown in Figure 4. Since the ratio of the resistance changes at the third and fourth leaps is also 1:2, the magnetization reversal of the thick NiFe layer takes place in the same manner as in the thin NiFe layer described in the preceding text.

It was shown that a magnetic domain wall can be trapped by the artificial structure introduced into the wire. This is an example of the control of the magnetization reversal process by controlling the shape of mesoscopic magnets. Though the nucleation position of the domain wall could not be determined in the above experiments, it has been reported that one can inject a domain wall from one end of a wire by breaking its symmetry (Shigeto, Shinjo and Ono, 1999). It should be noted that the GMR method corresponds to a very highly sensitive magnetization measurement. For the sample investigated in the preceding text, the sensitivity is as high as 10^{-13} emu (10^7 spins). The method, in principle, can be applied to smaller samples as long as the resistance of the samples can be measured and the relative sensitivity increases with decreasing sample volume.

1.2 Domain wall velocity measurements

Sixtus and Tonks (1931) first measured the domain wall velocity in bulk magnetic wires. Figure 5 shows a schematic diagram of the circuit for velocity measurements. Under a homogeneous magnetic field, a magnetic domain wall is nucleated by adding a local magnetic field, which is produced by an adding coil. The domain wall traveling along the wire from left to right produces successive voltage surges in two search coils, which are placed around the wire at a known separation. The velocity of the domain wall can be calculated from the time interval of the voltage surges and the separation of the coils. The domain wall velocity, obtained experimentally, was discussed in terms of the dissipation of the magnetic energy by eddy currents.

The GMR detection method described in Section 1.1 has an advantage in dynamic measurements because of its simplicity. Here, velocity measurements of a single-domain wall propagating in a magnetic nanowire are presented (Ono *et al.*, 1999). Because the GMR detection method provides information on the domain wall position, as shown in equation (1),

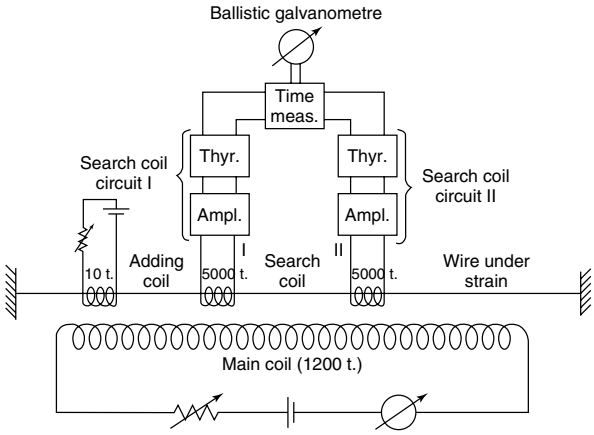

Figure 5. Schematic diagram of the circuit for velocity measurements by Sixtus and Tonks (1931). (Reproduced from Sixtus & Tonks 1931, with permission from the American Physical Society. © 1931.)

the domain wall velocity, $v = \mathrm{d}x/\mathrm{d}t$, can be determined by the time-domain measurements, and v is given by

$$v = \frac{\mathrm{d}x}{\mathrm{d}t} = \frac{L}{R_{\uparrow\downarrow} - R_{\uparrow\uparrow}} \frac{\mathrm{d}R}{\mathrm{d}t} \tag{2}$$

Thus, the GMR method can offer the time variation of velocity. This is an advantage over the experiments on bulk magnetic wires by Sixtus and Tonks, where only the average velocity of a domain wall can be obtained during the propagation in bulky scale (Sixtus and Tonks, 1931).

The samples for the domain wall velocity measurements have trilayer structures of $Ni_{81}Fe_{19}$(40 nm)/Cu(20 nm)/$Ni_{81}Fe_{19}$(5 nm). The width of the wire is 0.5 μm and the sample has four current–voltage terminals where the voltage is probed over a distance of 2 mm. The magnetic field was applied along the wire axis. The resistance was determined using a four-point dc technique. An electrical current flowing in a sample was supplied by a battery (1.5 V) to minimize the noise from a current source. The magnitude of the electrical current was adjusted by using a proper resistance in the circuit. The typical current was 100 μA. The voltage across two voltage probes was monitored by a differential preamplifier and a digital oscilloscope. The current passing through the electromagnet was also monitored by the digital oscilloscope, so as to obtain both resistance and applied magnetic field during the magnetization reversal, simultaneously.

Figure 6 shows the resistance change of the trilayer system at 77 K as a function of the applied magnetic field. Prior to the measurement, a magnetic field of 500 Oe was applied in order to align the magnetization in one direction. Then, the resistance was measured at 10 ms intervals with the sweeping field toward the counter direction at the sweeping rate of 20 Oe s^{-1}. Provided that the counter field is smaller than a critical field (70 Oe), both magnetizations in two NiFe layers are aligned in parallel, and the resistance takes the smallest value. When the applied magnetic field exceeds 70 Oe, the resistance increases and remains at the largest value until the field reaches 120 Oe, and then the resistance abruptly decreases to the smallest value. The result indicates that the antiparallel magnetization alignment is realized in the field range between 80 and 120 Oe, where the resistance shows the largest value. The change in resistance at 80 and 120 Oe is attributed to the magnetization reversals of the 5-nm-thick NiFe and 40-nm-thick NiFe layers, respectively. Since we did not find any measured point during the magnetization reversal of the 40-nm-thick NiFe in Figure 6, it is concluded that the magnetization reversal of the 40-nm-thick NiFe is completed within 10 ms. On the other hand, the magnetization reversal of the 5-nm-thick NiFe proceeds gradually with increasing applied magnetic field. This indicates that the magnetization reversal of the 5-nm-thick NiFe takes place by the pinning and de-pinning of the magnetic domain wall. Hereafter, we focus on the magnetization reversal of the 40-nm-thick NiFe.

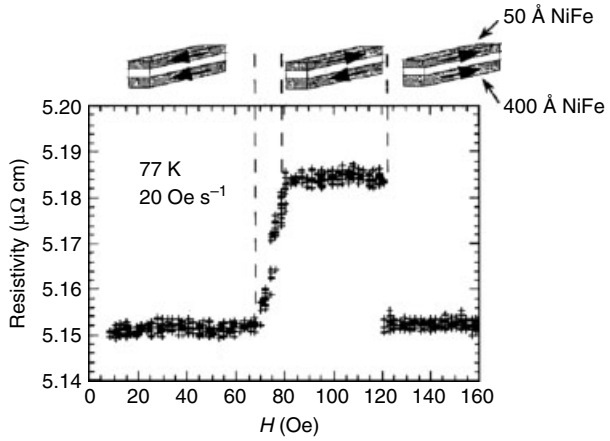

Figure 6. Resistance as a function of the external magnetic field at 77 K. The resistance was measured at 10 ms intervals while sweeping the field toward the counter direction at the sweeping rate of 20 Oe s^{-1}. The magnetic domain structures inferred from the resistance measurement are schematically shown. (Reproduced from T. Ono, H. Miyajima, K. Shigeto, K. Mibu, N. Hosoito, and T. Shinjo, *Science*, **284** (1999), with permission from AAAS.)

Figure 7 shows an experimental result on the time variation of the resistance during the magnetization reversal of the 40-nm-thick NiFe layer. The data were collected at 40-ns intervals. The linear variation of resistance with time

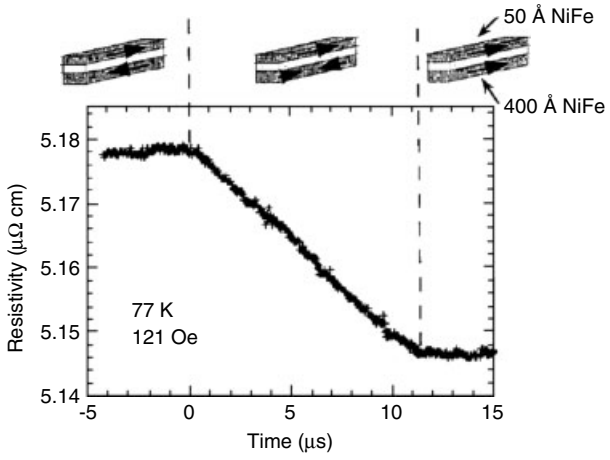

Figure 7. Time variation of the resistance during the magnetization reversal of the 40-nm-thick NiFe layer at 77 K, which was collected at 40 ns intervals. The applied magnetic field simultaneously monitored by digital oscilloscope was 121 Oe. As the sweeping rate of the applied magnetic field was 20 Oe s^{-1}, the variation of the applied magnetic field during magnetization reversal is less than 2×10^{-5} Oe, that is, the applied magnetic field is regarded as constant during the measurements. (Reproduced from T. Ono, H. Miyajima, K. Shigeto, K. Mibu, N. Hosoito, and T. Shinjo, *Science*, **284** (1999), with permission from AAAS.)

in Figure 7 indicates that the propagation velocity of the magnetic domain wall is constant during the magnetization reversal of the 40-nm-thick NiFe layer. The propagation velocity of the magnetic domain wall at the applied field of 121 Oe is estimated to be 182 m s^{-1}, which is calculated from the separation (2 mm) of the two voltage probes and the time (11 μs) the wall traveled across it. Since the sweeping rate of the applied magnetic field was 20 Oe s^{-1}, the variation of the applied magnetic field during magnetization reversal is less than 2×10^{-5} Oe, that is, the applied field is regarded as constant during the measurements.

Since the reversal field of the 40-nm-thick NiFe varied in every measurement, ranging from 90 to 140 Oe, the wall velocities at various magnetic fields were obtained by repeating the measurements. The result at 100 K is shown in Figure 8. The wall velocity depends linearly on the applied magnetic field, and it is described as $v = \mu(H - H_0)$, where v is the wall velocity, H the applied magnetic field, μ so-called wall mobility, and it was obtained that $\mu = 2.6$ (m s^{-1} Oe^{-1}) and $H_0 = 38$ (Oe). Here, we utilized the statistical nature of the magnetization reversal field to obtain the external magnetic field dependence of the domain wall velocity. A similar but more sophisticated experiment was performed by Himeno *et al*. (2004). They set two Cu wires to cross the magnetic wire at the ends of the wire, which produced a pulsed local magnetic field by a flow of pulsed electric current. This pulsed local magnetic field can nucleate a domain wall at the end of the magnetic wire under a given external magnetic field. This enables us to determine the domain wall velocity as a function of the external magnetic field in a controlled manner.

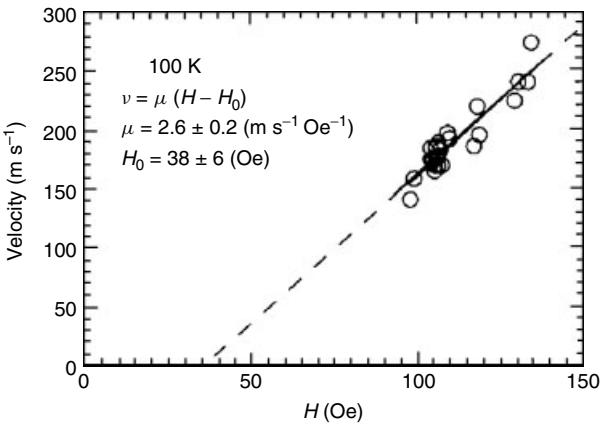

Figure 8. Dependence of domain wall velocity v on amplitude H of the applied magnetic field at 100 K. The wall velocity depends linearly on the applied magnetic field and is described as $v = \mu(H - H_0)$, where $\mu = 2.6$ (m s^{-1} Oe^{-1}) and $H_0 = 38$ (Oe). (Reproduced from T. Ono, H. Miyajima, K. Shigeto, K. Mibu, N. Hosoito, and T. Shinjo, *Science*, **284** (1999), with permission from AAAS.)

Magneto-optic Kerr effect magnetometer in micron-scale spatial resolution, together with the pulsed magnetic field, offers another approach to measure a domain wall velocity. It has been reported that very high domain wall velocity over 1000 m s^{-1} was realized for a single-layer 5-nm-thick $Ni_{80}Fe_{20}$ wire with 200 nm in width (Atkinson *et al*., 2003). The result has been reproduced well by the micromagnetics simulation by considering the corrugation of the magnetic wire (Nakatani, Thiaville and Miltat, 2003).

2 DOMAIN WALL PROPAGATION BY AN ELECTRIC CURRENT

Figure 9(a) illustrates a domain wall between two domains in a magnetic wire; the arrows show the direction of magnetic moments. The magnetic domain wall is a transition region of the magnetic moments between domains, and the direction of moments gradually changes in the domain wall. What will happen if an electric current flows through a domain wall? Suppose a conduction electron passes though the domain wall from left to right. During this travel, the spin of conduction electron follows the direction of local magnetic

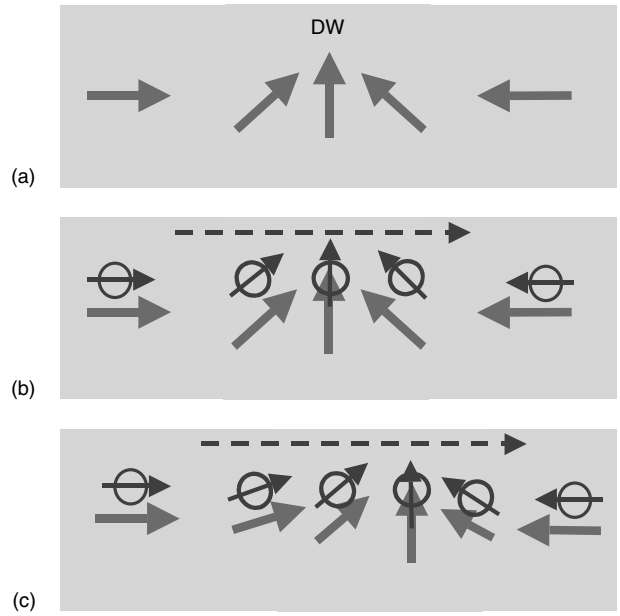

Figure 9. Schematic illustration of current-driven domain wall motion; (a) a domain wall between two domains in a magnetic wire. The arrows show the direction of magnetic moments. The magnetic domain wall is a transition region of the magnetic moments between domains, and the direction of moments gradually changes in the domain wall. (b) The spin of conduction electron follows the direction of local magnetic moments because of the s–d interaction. (c) As a reaction, the local magnetic moments rotate in the reverse direction, and in consequence, the electric current displaces the domain wall.

moments because of the s–d interaction (Figure 9b). As a reaction, the local magnetic moments rotate in the reverse direction (Figure 9c), and, in consequence, the electric current can displace the domain wall (Berger, 1984, 1992). This current-driven domain wall motion provides a new strategy to manipulate a magnetic configuration without the assistance of a magnetic field, and will improve drastically the performance and functions of recently proposed spintronic devices, whose operation is based on the motion of a magnetic domain wall (Allwood *et al*., 2002; Versluijs, Bari and Coey, 2001). Reports on this subject have been increasing in recent years from both theoretical (Tatara and Kohno, 2004; Li and Zhang, 2004; Zhang and Li, 2004; Waintal and Viret, 2004; Thiaville, Nakatani, Miltat and Vernie, 2004; Thiaville, Nakatani, Miltat and Suzuki, 2005) and experimental (Grollier *et al*., 2003; Tsoi, Fontana and Parkin, 2003; Klaui *et al*., 2003; Kimura, Otani, Tsukagoshi and Aoyagi, 2003; Yamaguchi *et al*., 2004; Lim *et al*., 2004; Vernier *et al*., 2004; Yamanouchi, Chiba, Matsukura and Ohno, 2004; Saitoh, Miyajima, Yamaoka and Tatara, 2004; Klaui *et al*., 2005) points of view because of its scientific and technological importance. However, many important results cannot be reviewed here owing to limitations of space. In this section, only the result of direct observation of the current-driven domain wall motion in a microfabricated magnetic wire is presented (Yamaguchi *et al*., 2004). Magnetic force microscopy (MFM) is used to show that a single-domain wall can be displaced back and forth by positive and negative pulsed currents.

An L-shaped magnetic wire with a round corner, as schematically illustrated in Figure 10, was prepared for the experiments. One end of the L-shaped magnetic wire is connected to a diamond-shaped pad, which acts as a domain wall injector (Shigeto, Shinjo and Ono, 1999), and the other end is sharply pointed to prevent a nucleation of a domain wall from this end (Schrefl, Fidler, Kirk and Chapman, 1997). L-shaped magnetic wires of 10-nm-thick $Ni_{81}Fe_{19}$ were fabricated onto thermally oxidized Si substrates by means of an e-beam lithography and a lift-off method. The width of the wire is 240 nm.

In order to introduce a domain wall positioned in the vicinity of the corner, the direction of the external magnetic field was tilted from the wire axis in the substrate plane as shown in Figure 10. In the initial stage, a magnetic field of +1 kOe was applied in order to align the magnetization in one direction along the wire. Then, a single-domain wall was introduced by applying a magnetic field of −175 Oe. After that, the MFM observations were carried out in the absence of a magnetic field. The existence of the single-domain wall in the vicinity of the corner was confirmed as shown in Figure 11(a). The domain wall is imaged as a bright contrast, which corresponds to the stray field from positive

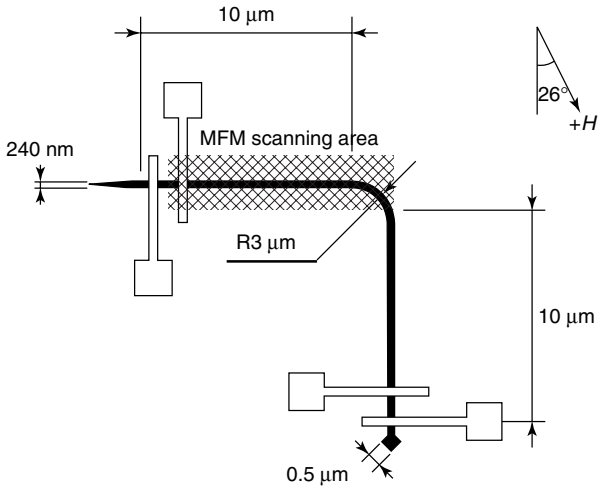

Figure 10. Schematic illustration of a top view of the sample. One end of the L-shaped wire is connected to a diamond-shaped pad, which acts as a domain wall injector, and the other end is sharply pointed to prevent a nucleation of a domain wall from this end. The wire has four electrodes made of Cu. MFM observations were performed for the hatched area at room temperature. (Reproduced from Yamaguchi *et al*., 2004, with permission from the American Physical Society. © 2004.)

magnetic charge. In this case, a head-to-head domain wall is realized as illustrated schematically in Figure 11(d). The position and the shape of the domain wall were unchanged after several MFM scans, indicating that the domain wall was pinned by a local structural defect, and that a stray field from the probe was too small to change the magnetic structure and position of the domain wall.

After the observation of Figure 11(a), a pulsed current was applied through the wire in the absence of a magnetic field. The current density and the pulse duration were $7.0 \times 10^{11}\,\mathrm{A\,m^{-2}}$ and 5 μs, respectively (The values of the current density here are different from those in Yamaguchi *et al*., (2004). In Yamaguchi *et al*., (2004), the current density has been calculated using the pulsed voltage applied to the sample with the sample resistance at room temperature. However, it was found in the following study that the sample resistance, when the current-driven domain wall motion occurred, was much higher than the sample resistance at room temperature. Thus, the values of the current density in Yamaguchi *et al*., (2004) were inaccurate. The current density presented here was calculated using the value of the pulsed current, which was directly measured). Figure 11(b) shows the MFM image after an application of the pulsed current from left to right. The domain wall, which had been in the vicinity of the corner (Figure 11a), was displaced from right to left by the application of the pulsed current. Thus, the direction of the domain wall motion is opposite to the current direction. Furthermore, the direction of the domain

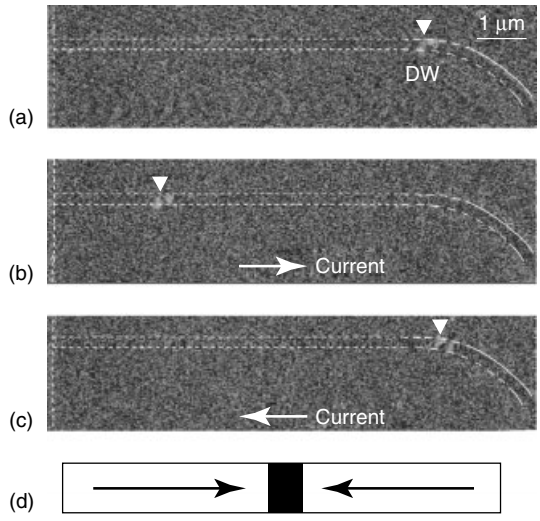

Figure 11. (a) MFM image after the introduction of a head-to-head domain wall. The domain wall is imaged as a bright contrast, which corresponds to the stray field from positive magnetic charge. (b) MFM image after an application of a pulsed current from left to right. The current density and pulse duration are $7.0 \times 10^{11}\,\mathrm{A\,m^{-2}}$ and 5 μs, respectively. DW is displaced from right to left by the pulsed current. (c) MFM image after an application of a pulsed current from right to left. The current density and pulse duration are $7.0 \times 10^{11}\,\mathrm{A\,m^{-2}}$ and 5 μs, respectively. The domain wall is displaced from left to right by the pulsed current. (d) Schematic illustration of a magnetic domain structure inferred from the MFM image. The domain wall has a head-to-head structure.

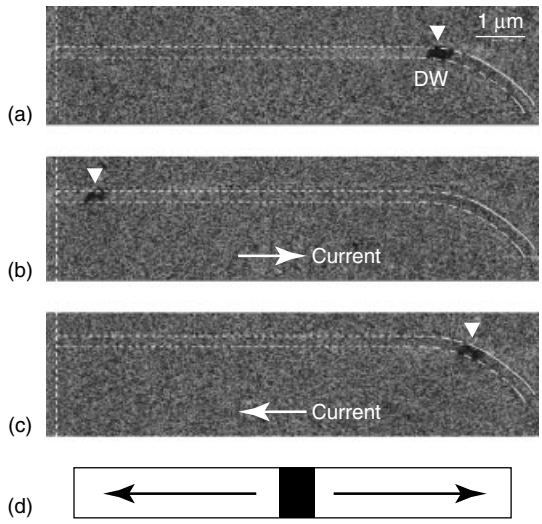

Figure 12. (a) MFM image after the introduction of a tail-to-tail domain wall. The domain wall is imaged as a dark contrast, which corresponds to the stray field from negative magnetic charge. (b) MFM image after an application of a pulsed current from left to right. The current density and pulse duration are $7.0 \times 10^{11}\,\mathrm{A\,m^{-2}}$ and 5 μs, respectively. DW is displaced from right to left by the pulsed current. (c) MFM image after an application of a pulsed current from right to left. The current density and pulse duration are $7.0 \times 10^{11}\,\mathrm{A\,m^{-2}}$ and 5 μs, respectively. The domain wall is displaced from left to right by the pulsed current. (d) Schematic illustration of a magnetic domain structure inferred from the MFM image. The domain wall has a tail-to-tail structure.

wall motion can be reversed by switching the current polarity as shown in Figure 11(c). These results are consistent with the spin transfer mechanism (Berger, 1984, 1992).

The same experiments for a domain wall with different polarities, a tail-to-tail domain wall, were performed to examine the effect of a magnetic field generated by the current (Oersted field). The tail-to-tail domain wall was generated by the following procedure. A magnetic field of −1 kOe was applied in order to align the magnetization in the direction opposite to that in the previous experiment. Then, a tail-to-tail domain wall (DW) was introduced by applying a magnetic field of +175 Oe. The introduced DW is imaged as a dark contrast in Figure 12(a), which indicates that a tail-to-tail domain wall is formed as schematically illustrated in Figure 12(d). Figure 12(a–c) show that the direction of the tail-to-tail DW displacement is also opposite to the current direction. The fact that both head-to-head and tail-to-tail domain walls are displaced opposite to the current direction indicates clearly that the domain wall motion is not caused by the Oersted field.

Figure 13(a–k) are successive MFM images with one pulsed current applied between each consecutive image. The current density and the pulse duration were $7.0 \times 10^{11}\,\mathrm{A\,m^{-2}}$ and 0.5 μs, respectively. Each pulse displaced the domain wall opposite to the direction of the current. The difference in the displacement for each pulse is possibly due to the pinning by randomly located defects. The average displacement per pulse did not depend on the polarity of the pulsed current. The average domain wall displacement per pulse as a function of the pulse duration under the condition of constant current density of $7.0 \times 10^{11}\,\mathrm{A\,m^{-2}}$ is shown in Figure 14. The average domain wall displacement is proportional to the pulse duration, which indicates that the domain wall has a constant velocity of $3.0\,\mathrm{m\,s^{-1}}$. It was also confirmed that the domain wall velocity increases with the current density.

It was shown that the domain wall position in the wire can be controlled by tuning the intensity, the duration and the polarity of the pulsed current, and thus the current-driven domain wall motion has the potential for the spintronic device application. However, there are several issues posed to its practical applications. The most important of these issues is the reduction of the high current density required for the current-driven domain wall motion. Recent experiments indicated that, in some cases, the high current density results in the considerable Joule heating of the sample (Yamaguchi *et al*., 2005). Though the lower threshold current density of $10^{9}\,\mathrm{A\,m^{-2}}$ has been reported for ferromagnetic semiconductor (Ga, Mn)As, the Curie temperature of this

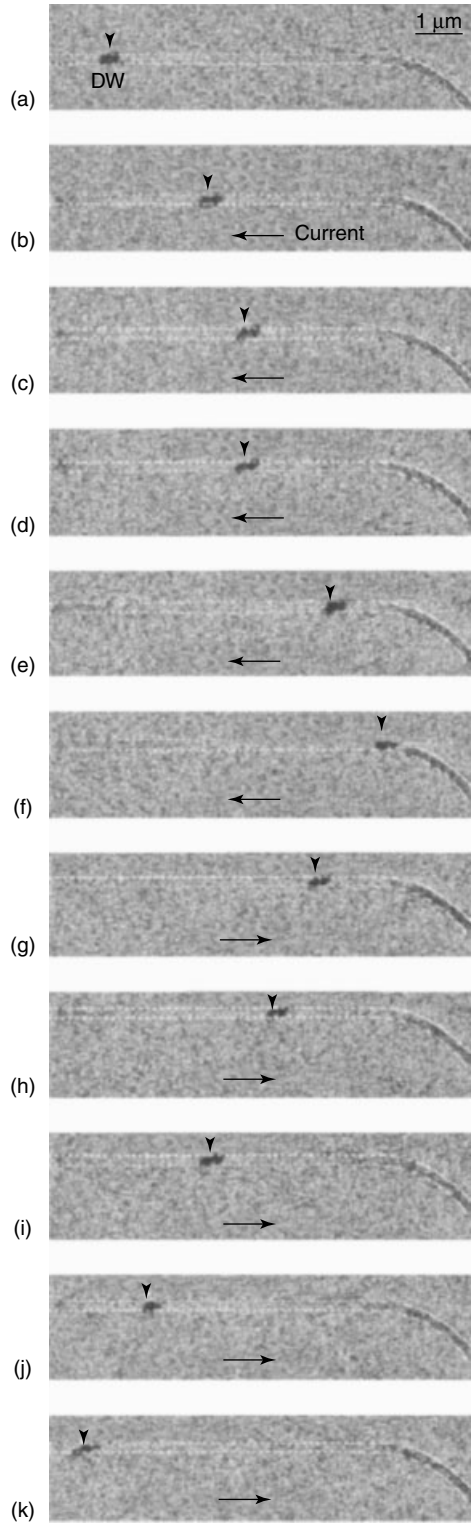

Figure 13. Successive MFM images with one pulse applied between each consecutive image. The current density and the pulse duration were 7.0×10^{11} A m^{-2} and 0.5 μs, respectively. Note that a tail-to-tail domain wall is introduced, which is imaged as a dark contrast. (Reproduced from Yamaguchi *et al*., 2004, with permission from the American Physical Society. © 2004.)

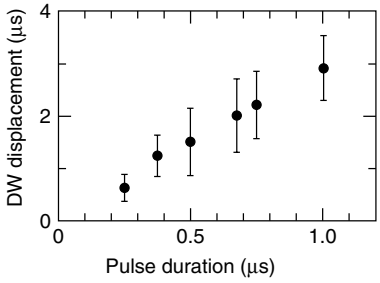

Figure 14. Average domain wall displacement per pulse as a function of the pulse duration under a condition of constant current density of 7.0×10^{11} A m^{-2}. (Reproduced from Yamaguchi *et al*., 2004, with permission from the American Physical Society. © 2004.)

material is below room temperature (Yamanouchi, Chiba, Matsukura and Ohno, 2004). Thus, it is indispensable to explore a way to reduce the threshold current density for ferromagnetic metals from the viewpoint of practical applications.

REFERENCES

Allwood, D.A., Xiong, G., Cooke, M.D., *et al*. (2002). Submicrometer ferromagnetic not-gate and shift register. *Science*, **296**, 2003.

Atkinson, D., Allwood, D.A., Xiong, G., *et al*. (2003). Magnetic domain-wall dynamics in a submicrometre ferromagnetic structure. *Nature Materials*, **2**, 85–87.

Baibich, M.N., Broto, J.M., Fert, A., *et al*. (1988). Gaint magnetoresistance of (001)Fe/(001)Cr magnetic superlattices. *Physical Review Letters*, **61**, 2472.

Berger, L. (1984). Exchange interaction between ferromagnetic domain wall and electric current in very thin metallic films. *Journal of Applied Physics*, **55**, 1954.

Berger, L. (1992). Motion of a magnetic domain wall traversed by fast-rising current pulses. *Journal of Applied Physics*, **71**, 2721.

Grollier, J., Boulenc, P., Cros, V., *et al*. (2003). Switching a spin valve back and forth by current-induced domain wall motion. *Applied Physics Letters*, **83**, 509.

Himeno, A., Ono, T., Nasu, S., *et al*. (2004). Propagation velocity measurement of a magnetic domain wall in a submicron magnetic wire. *Journal of Magnetism and Magnetic Materials*, **272-276**, 1577–1578.

Kimura, T., Otani, Y., Tsukagoshi, K. and Aoyagi, Y. (2003). Suppressed pinning field of a trapped domain wall due to direct current injection. *Journal of Applied Physics*, **94**, 07947.

Klaui, M., Vaz, C.A.F., Bland, J.A.C., *et al*. (2003). Domain wall motion induced by spin polarized currents in ferromagnetic ring structures. *Applied Physics Letters*, **83**, 105.

Klaui, M., Vaz, C.A.F., Bland, J.A.C., *et al*. (2005). Controlled and reproducible domain wall displacement by current pulses injected into ferromagnetic ring structures. *Physical Review Letters*, **94**, 106601.

Li, Z. and Zhang, S. (2004). Domain-wall dynamics and spin-wave excitations with spin-transfer torques. *Physical Review Letters*, **92**, 207203.

Lim, C.K., Devolder, T., Chappert, C., *et al*. (2004). Domain wall displacement induced by subnanosecond pulsed current. *Applied Physics Letters*, **84**, 2820.

Nakatani, Y., Thiaville, A. and Miltat, J. (2003). Faster magnetic walls in rough wires. *Nature Materials*, **2**, 521–523.

Ono, T., Miyajima, H., Shigeto, K. and Shinjo, T. (1998). Magnetization reversal in submicron magnetic wire studied by using giant magnetoresistance effect. *Applied Physics Letters*, **72**, 1116–1117.

Ono, T., Miyajima, H., Shigeto, K., *et al*. (1999). Propagation of a magnetic domain wall in a submicrometer magnetic wire. *Science*, **284**, 468–470.

Saitoh, E., Miyajima, H., Yamaoka, T. and Tatara, G. (2004). Current-induced resonance and mass determination of a single magnetic domain wall. *Nature*, **432**, 203.

Schrefl, T., Fidler, J., Kirk, K.J. and Chapman, J.N. (1997). Domain structures and switching mechanisms in patterned magnetic elements. *Journal of Magnetism and Magnetic Materials*, **175**, 193.

Shigeto, K., Shinjo, T. and Ono, T. (1999). Injection of a magnetic domain wall into a submicron magnetic wire. *Applied Physics Letters*, **75**, 2815–2817.

Sixtus, K.J. and Tonks, L. (1931). Propagation of large barkhausen discontinuities. *Physical Review*, **37**, 930.

Tatara, G. and Kohno, H. (2004). Theory of current-driven domain wall motion: spin transfer versus momentum transfer. *Physical Review Letters*, **92**, 086601.

Thiaville, A., Nakatani, Y., Miltat, J. and Suzuki, Y. (2005). Micromagnetic understanding of current-driven domain wall motion in patterned nanowires. *Europhysics Letters*, **69**, 990.

Thiaville, A., Nakatani, Y., Miltat, J. and Vernie, N. (2004). Domain wall motion by spin-polarized current: a micromagnetic study. *Journal of Applied Physics*, **95**, 7049.

Tsoi, M., Fontana, R.E. and Parkin, S.S.P. (2003). Magnetic domain wall motion triggered by an electric current. *Applied Physics Letters*, **83**, 2617.

Vernier, N., Allwood, D.A., Atkinson, D., *et al*. (2004). Domain wall propagation in magnetic nanowires by spin-polarized current injection. *Europhysics Letters*, **65**, 526.

Versluijs, J.J., Bari, M.A. and Coey, J.M.D. (2001). Magnetoresistance of half-metallic oxide nanocontacts. *Physical Review Letters*, **87**, 026601.

Waintal, X. and Viret, M. (2004). Current-induced distortion of a magnetic domain wall. *Europhysics Letters*, **65**, 427.

Yamaguchi, A., Nasu, S., Tanigawa, H., *et al*. (2005). Effect of joule heating in current-driven domain wall motion. *Applied Physics Letters*, **86**, 012511.

Yamaguchi, A., Ono, T., Nasu, S., *et al*. (2004). Real-space observation of current-driven domain wall motion in submicron magnetic wires. *Physical Review Letters*, **92**, 077205.

Yamanouchi, M., Chiba, D., Matsukura, F. and Ohno, H. (2004). Current-induced domain-wall switching in a ferromagnetic semiconductor structure. *Nature*, **428**, 539.

Zhang, S. and Li, Z. (2004). Roles of nonequilibrium conduction electrons on the magnetization dynamics of ferromagnets. *Physical Review Letters*, **93**, 127204.

Current Induced Domain-wall Motion in Magnetic Nanowires

Luc Thomas and Stuart Parkin
IBM Almaden Research Center, San José, CA, USA

1 INTRODUCTION

Over the past several years, there has been renewed interest in understanding the interaction between spin-polarized current and magnetic domain walls (DWs), a phenomenon that was first studied more than 20 years ago in macroscopic magnetic thin films. Although there are several possible ways in which current can interact with domain walls, perhaps the most interesting interaction is that in which spin angular momentum from spin-polarized current can result in motion of the domain wall. Current passing through almost any magnetic material readily becomes spin polarized through spin-dependent electron scattering processes. Since motion of a domain wall requires reversal of magnetic moments, and, since spin angular momentum is conserved, the transfer of spin angular momentum from the current to the magnetic system can result in domain-wall excitation or movement, both precessional and translational.

Handbook of Magnetism and Advanced Magnetic Materials. Edited by Helmut Kronmüller and Stuart Parkin. Volume 2: *Micromagnetism*. ISBN: 978-0-470-02217-7.

Advances in lithographic techniques now allow the study of domain walls in confined magnetic nanostructures with lateral dimensions as small as a few tens of nanometers. Moreover, the magnetic configurations of such structures can be engineered by properly shaping them. Thus, whereas earlier studies involved complex patterns of several domain walls, it is now possible to study the current-induced motion of a single domain wall by injecting a wall into a nanopatterned magnetic device.

In this chapter, we review recent theoretical developments and experiments related to the current-driven motion of domain walls in magnetic nanowires. This is a challenging task, since this field of research is still in its infancy and yet the field is developing at a rapid pace. Note that several aspects of the current-induced motion of domain walls from spin momentum transfer are closely related to that of the current-induced excitation and switching of magnetization in spin-valve and magnetic tunnel junction structures. These latter phenomena are reviewed extensively elsewhere in this encyclopedia.

In the first part of this chapter, we briefly review the structure of DWs in magnetic nanowires. We then discuss theoretical models, which have been developed to describe the interaction of spin-polarized current with such DWs, and discuss some of the consequences and predictions of these models.

The second part of this chapter is devoted to firstly, a review of various experimental procedures and techniques, including the fabrication of magnetic nanodevices and useful DW detection techniques. Secondly, the manipulation of DWs using magnetic fields is discussed in some detail since this is very helpful in appreciating the significantly different consequences of their manipulation by current.

Finally, we review experiments on the current-driven motion of DWs.

In the final part of this chapter, we briefly discuss possible applications of the phenomena described in this chapter to potential magnetic memory and logic devices.

2 THEORY AND SIMULATIONS

2.1 Domain walls in nanowires

Magnetic DWs have been studied in bulk samples and thin films for nearly a century. DWs have structures which range from the simplest Bloch wall, which can be described analytically by a one-dimensional model, to complex two- and three-dimensional structures. There are several excellent reviews of this topic including, for example, Hubert and Schafer's comprehensive textbook (Hubert and Schäfer, 2000). In this section, we discuss the most common DW structures found in soft magnetic nanowires, the so-called head-to-head (or tail-to-tail) DWs. We also describe Bloch walls, which can be found in nanowires formed from materials with large perpendicular magnetic anisotropy.

2.1.1 Head-to-head domain walls in soft magnetic nanowires

Macroscopic magnetic structures will typically form flux-closed magnetic domain structures, which lower their energy. In sufficiently narrow nanowires made from soft magnetic materials, for example, submicron-wide permalloy ($Ni_{81}Fe_{19}$) wires, flux-closed domain structures are no longer energetically favored. Rather, owing to the nanowire's magnetic shape anisotropy, magnetic domains are aligned along the nanowire's length, with magnetizations pointing toward (or away) from each another. These domains are separated by head-to-head (or tail-to-tail) DWs.

The structure of head-to-head DWs was first studied using micromagnetic simulations by McMichael and Donahue (1997). They found two distinct DW structures: the transverse (T) wall and the vortex (V) wall. Simulated magnetization maps for these two wall structures are shown in Figure 1(g) and (h). Which of these two DWs has the lowest energy depends on the width w and thickness t of the wire: the (w, t) boundary between these two states was found numerically to be given by:

$$t \cdot w = C\delta^2$$

where the exchange length δ is given by $\delta^2 = \frac{A}{\mu_0 M_s^2}$ (1)

For permalloy ($M_s = 800\,\mathrm{emu\,cm^{-3}}$, $A = 1.3 \times 10^{-6}\,\mathrm{erg\,cm^{-1}}$), the exchange length is very short at about $\delta = 4\,\mathrm{nm}$ and the numerical constant C was determined to be 128. This phase diagram has been refined recently by Nakatani, Thiaville and Miltat (2005), who have identified an intermediate magnetic state between the T and V walls, as an asymmetric transverse wall.

Note that the relative stability of T and V walls was also studied by calculating the energy of the V wall as a function of the position of the vortex core with respect to the center of the nanowire (Youk *et al*., 2006). When the V wall is the lowest energy state, its energy is minimized when its core is at the center of the wire, whereas when the T wall has the lower energy, the V wall's energy is minimized when its core is at one edge of the nanowire. Interestingly, the authors also identified metastable configurations in which the vortex core is offset from the center of the wire.

The DW width is a critical parameter for both field and current-driven DW motion. However, this quantity is not well defined, since the magnetization of both T and V walls varies significantly across the width of a nanowire, as shown in Figure 1. In Nakatani, Thiaville and Miltat (2005), the DW width parameter Δ was estimated by fitting the DW magnetization profile with that derived for a 1D Bloch wall, namely:

$$\begin{aligned} \theta(x) &= 2\arctan[e^{x/\Delta}] \\ m_x &= \cos[\theta(x)] = \tanh\frac{x}{\Delta} \\ m_y &= \sin[\theta(x)] = \frac{1}{\cosh\frac{x}{\Delta}} \end{aligned} \quad (2)$$

where $m_{x,y}$ are the two in-plane components of the magnetization normalized to the saturation value, and θ is the angle between the local magnetization direction and the nanowire's long axis x (i.e., the easy magnetization direction). This profile describes the transverse wall form quite well, providing that Δ is allowed to vary across the nanowire's width (i.e., the direction y), as shown by the solid lines in Figure 1(a)–(c). By contrast, these expressions do not account for the V wall's profile. Nakatani, Thiaville and Miltat (2005) extracted a width for the V wall by fitting the profile of the longitudinal magnetization averaged across the width of the nanowire (Figure 1c and f). For both V and T walls, the DW width parameter Δ was found to depend only weakly on the wire thickness, but to scale with the wire width w, according to the approximate relations (Nakatani, Thiaville and Miltat, 2005):

$$\Delta_{TW} = \frac{w}{\pi} \quad \Delta_{VW} = \frac{3w}{4} \quad (3)$$

The V wall is significantly wider than the T wall. Note that the actual length scale over which most of the magnetization change occurs is $\pi\Delta$, which is much larger than that given by equation (3) (Malozemoff and Slonczewski, 1979).

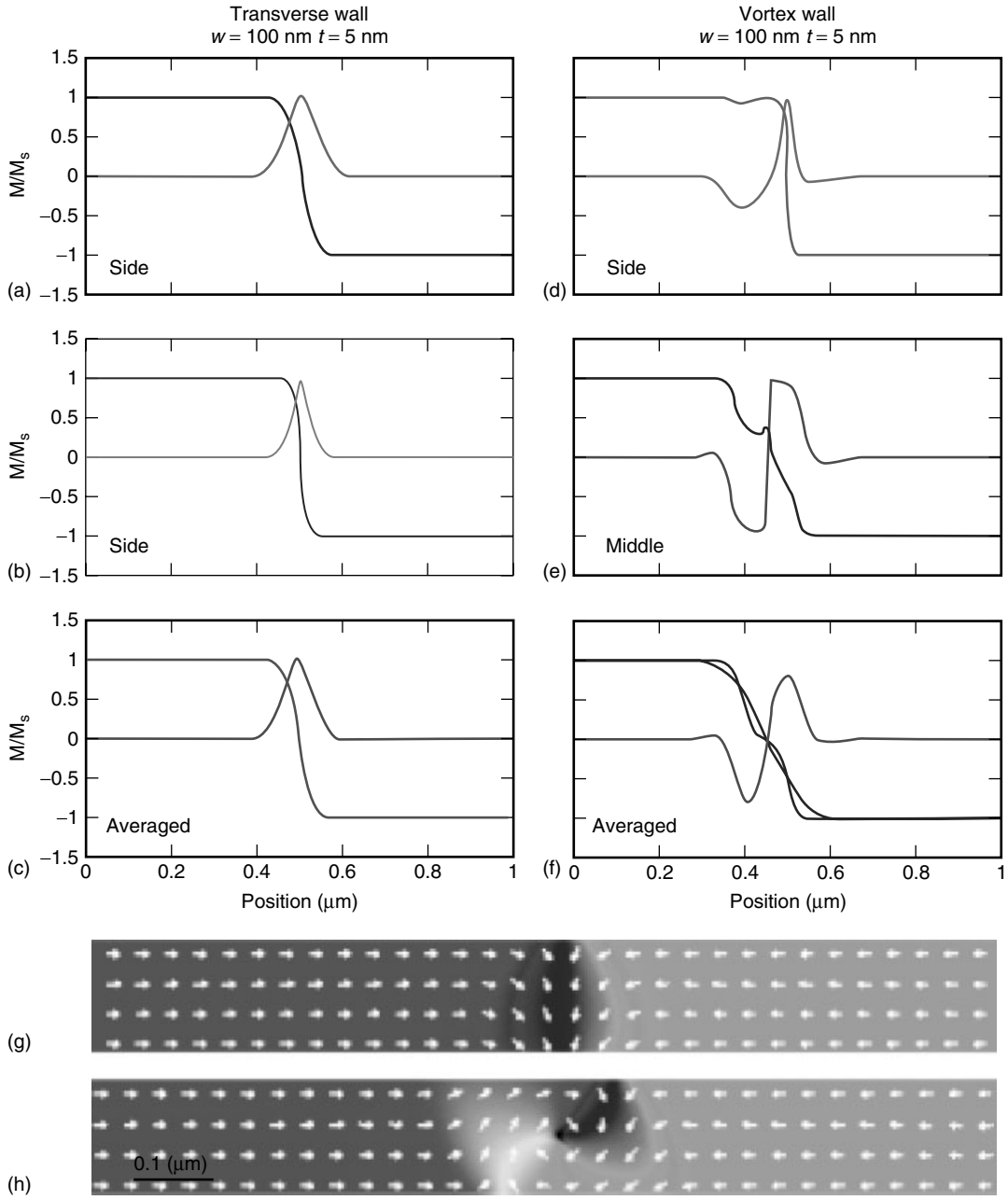

Figure 1. Calculated structures of transverse (T) and vortex (V) head-to-head DWs derived from micromagnetic simulations. Profiles of the longitudinal (dark gray) and transverse (medium gray) magnetizations along the nanowire's length are shown at different positions across the nanowire's width: T wall: top and bottom edges; V wall: topside and center. The profiles of the magnetization averaged over the width of the nanowire for both the T and V walls are also shown. Fits to the analytical 1D Bloch wall, equation (2), are shown in all cases for the T wall, but only for the averaged longitudinal magnetization for the V wall. For the T wall, the magnetization profile has roughly the same form across the width of the wire, although the DW width varies significantly. By contrast, the magnetization profiles are quite different for the V wall at the edges and at the center of the wire.

The DW width can be deduced in several other ways. For example, as discussed in Section 3.4.3, the DW velocity is proportional to Δ in small magnetic fields. The dynamical DW width derived in this way is in good agreement with that obtained from the 1D DW expression of equation (2) for the transverse wall, but this is not the case for the V wall. Indeed, since the V wall moves more slowly than the T wall, the dynamical DW width is actually smaller for the V than for the T wall. As shown by Nakatani, Thiaville and Miltat (2005), a better agreement with the dynamical DW width is

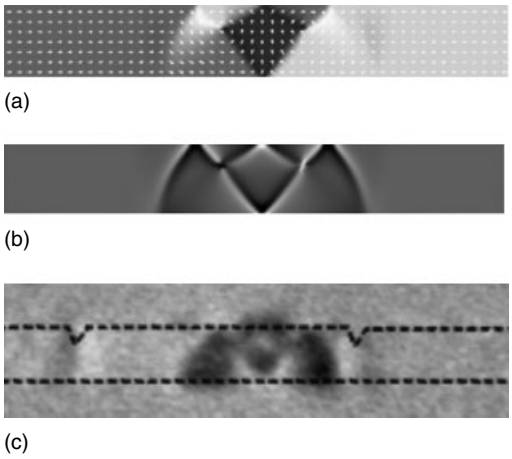

Figure 2. (a) Magnetization distribution of a two-vortex wall calculated from micromagnetic simulations of a permalloy nanowire (200 nm wide, 40 nm thick). The middle map (b) shows the divergence of the magnetization for comparison with the MFM image (c) of such a two-vortex wall measured in a 40-nm-thick, 300-nm-wide permalloy nanowire. The dotted lines show the edges of the nanowires as determined by AFM.

found by using a definition of the DW width proposed by Thiele (1973a), in which the inverse DW width is given by:

$$\Delta^{-1} = \frac{1}{2wtM_S^2}\int_V \left(\frac{\partial \vec{M}}{\partial x}\right)^2 \mathrm{d}V \qquad (4)$$

Another experimental method of estimating the DW width, which is relevant to many of the experimental results discussed in this chapter, is from the anisotropic magnetoresistance (AMR) of the DW (see Section 3.3.1).

More complex head-to-head DW structures than either the T or the V DW can also be found in magnetic nanowires, depending on their size and the aspect ratio of their cross section. Figure 2 shows an example of a DW found in sufficiently thick nanowires. Flux-closed domain structures, which can be seen in the figure at the upper edge of the nanowire, form so as to reduce the magnetostatic energy of the DW. Two-vortex DWs of opposite chirality can be seen in the figure. We have observed this wall structure using magnetic force microscopy (MFM) imaging in permalloy nanowires more than 20 nm thick. Florez, Krafft and Gomez (2005) have reported similar structures in permalloy wires, 40 nm thick.

In narrow wires with circular or square cross sections, a vortex wall can also appear, with the vortex core parallel to the long axis of the wire. This structure has been described by Thiaville and Nakatani as a Bloch-point wall (Thiaville and Nakatani, 2006).

An interesting methodology for categorizing these different DW structures was proposed recently by Youk *et al.* (2006), Tchernyshyov and Chern (2005), and Chern, Youk and Tchernyshyov (2006). They describe the DWs as composite objects built from a certain number of topological defects characterized by a winding number n. Vortices in the bulk of the wire have $n = 1$ and antivortices, $n = -1$, whereas edge defects present in the transverse wall have winding numbers $n = \pm 1/2$. The vortex DW wall is built from one bulk defect (the vortex itself) and two edge defects $n = -1/2$, and the transverse wall from two edge defects $n = \pm 1/2$. For any DW structure, the total topological charge, including both edge and bulk defects, must be zero. The authors propose that the DW dynamics can be described by the creation, propagation, and annihilation of these topological defects.

As an illustration, magnetic domain structures in U-shaped nanowires of various widths, formed from 10- and 20-nm-thick CoFe films are shown in Figure 3. These images are measured in zero magnetic field by photoemission electron microscopy (PEEM). The gray scale reflects the projection of the nanowire's in-plane magnetization along the vertical axis of the image (see Section 3.3 for more details). The nanowire's magnetization is first saturated along this direction with a large magnetic field (1 kOe). After this field is reduced to zero, the magnetization is aligned along the arms of the U-shaped structure so that a DW is nucleated in the curved portion of the U. In the narrowest wires (200 nm wide), the DWs have a T structure, clearly identified by the single black triangle-shaped region. For intermediate widths, the PEEM images clearly show an asymmetric transverse wall structure (see, e.g., the 400-nm-wide/20-nm-thick or the 600-nm-wide/10-nm-thick nanowires). When the wide width is increased, V walls can clearly be identified by the alternating black/white regions (e.g., the 600-nm-wide/20-nm-thick wire). Note that for the same 600 nm width, the 10-nm-thick wire still exhibits an asymmetric T wall structure, whereas the 20-nm-thick wire already shows the V structure, following the trend shown by the phase boundary of equation (1). The 800-nm-wide wires show more complex domain patterns, with ripples starting to appear along the arms of the wire.

Similar experiments have been reported by Klaui *et al.* (2004) who used PEEM microscopy to study the DW structure in cobalt rings, whose thicknesses were varied between 2 and 38 nm, and whose widths were varied from 100 to 730 nm. A clear phase boundary between T and V walls was observed as a function of the ring dimensions. However, this transition did not agree with that anticipated by equation (1). The T wall was observed for dimensions where the V wall should be more stable. This discrepancy is a consequence of the metastability of the two wall structures. Even though the V has lower energy, an energy barrier prevents the transformation of the T wall into the V wall.

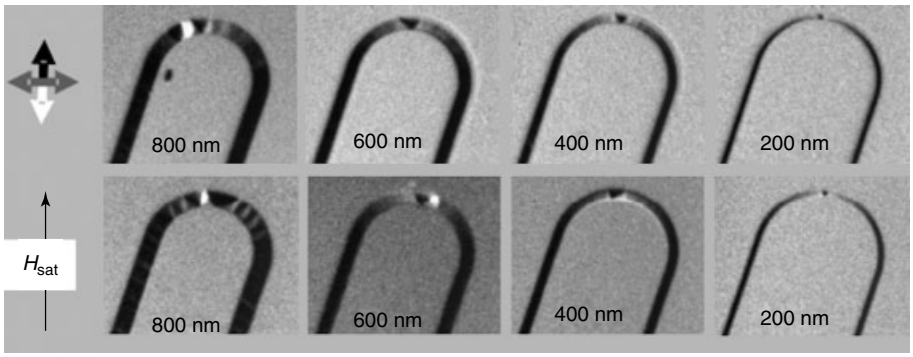

Figure 3. PEEM images of the magnetic domain structure of U-shaped CoFe nanowires with different widths and a thickness of 10 nm (upper) or 20 nm (lower). The samples were first saturated along the direction indicated by the arrow, and the images were taken in remanence.

It turns out that the T wall is favored by the DW injection process (using a large transverse field), so T walls are observed for a wide range of ring sizes.

2.1.2 Other types of walls

Head-to-head DWs are only stable in nanowires with strong shape anisotropy and/or uniaxial anisotropy along the nanowire's direction. In the presence of significant crystalline anisotropy in the in-plane transverse or out-of-plane directions, other domain patterns can be observed even for submicron wires. For example, Schrefl, Fidler, Kirk and Chapman (1997) have reported flux-closed domain patterns in NiFe elements as narrow as 200 nm in which the domains' magnetization is aligned transverse to the nanowire's direction. This was unexpected in nominally soft NiFe, but was explained by a strong stress-induced anisotropy. For materials such as Pt/Co/Pt trilayers with strong perpendicular anisotropy ($\sim 10^7\,\mathrm{erg\,cm^{-3}}$), the domains' magnetization is oriented along the out-of-plane anisotropy direction. In such nanowires, the DWs are nearly ideal Bloch walls (Wunderlich *et al*., 2001; Cayssol *et al*., 2004), with widths as small as 5 nm. In the case of (Ga,Mn)As epilayers, in-plane cubic anisotropy has been reported (Tang, Kawakami, Awschalom and Roukes, 2003), giving rise to 90° DWs (Holleitner *et al*., 2004; Honolka *et al*., 2005; Tang *et al*., 2004; Tang and Roukes, 2004) albeit in large structures (100 µm wide).

2.2 Theoretical models of current-driven domain-wall motion

2.2.1 Early work

The interplay between magnetization and charge carriers in metallic ferromagnets has been studied for several decades. The first reported interaction of current on DWs in such materials was due to eddy-current losses (Williams, Shockley and Kittel, 1950). The DW mobility in macroscopic samples at low fields was found to be almost two orders of magnitude smaller than that expected from calculations by Landau and Lifshitz, which took into account magnetic relaxation.

The influence of an electric current flowing within a ferromagnet, or in the vicinity of it, was first studied in the 1970s by Carr (1974a,b), Emtage (1974), and Charap (1974), and independently by Berger (1974), Partin, Karnezos, deMenezes and Berger (1974). These authors found that in materials for which the current flow is sensitive to the magnetization, for example, because of the Hall effect or magnetoresistance, the presence of a DW would, in turn, affect the current distribution. For example, in the case of a 180° DW, the reversal of the magnetization is associated with reversal of the Hall electric field. The nonuniform current distribution can be modeled by a uniform current on which an eddy-current loop concentric with the center of the DW is superimposed. This current loop thus creates a magnetic field, which exerts a net force on the DW in the direction of the drift velocity of the carriers and, thereby, can lead to DW motion. This mechanism was called *self-induced DW drag* or *hydromagnetic domain drag*. The force on the DW can be written, following Berger's notation, as:

$$F_x = 2M_s\mu_e^{-1}(R_1 J - v_w) \quad \mu_e = \frac{\pi^3 \rho}{8.4 t M_s} \tag{5}$$

where J is the current density perpendicular to the wall, R_1 is the anomalous Hall constant, v_w is the wall velocity, μ_e is the wall mobility, as limited by eddy currents, (which is different from the intrinsic wall mobility, which is related to damping), and t is the film thickness. Since the net force on the DW increases with the sample thickness it vanishes for very thin wires.

Because magnetic fields extend over fairly long distances, the DW drag mechanism can also occur if the current does not flow directly through the DW, but rather through a

neighboring over or underlayer, such as a semiconducting (Carr, 1974b; Charap, 1974) or a permalloy (Carr, 1974a; Emtage, 1974) layer. This is particularly applied to the motion of DWs in magnetic bubble materials, which were made of high-resistivity oxides, and which were the subject of much of this early work.

Note that all these theories describe 180° DWs, for which the current is perpendicular to the magnetization direction both in the domains and in the DW. In this case, the Hall electric field reverses across the DW, irrespective of the DW structure. This is not the case for head-to-head DWs, for which current and magnetization are parallel everywhere except within the DW.

This first mechanism derives solely from electromagnetic effects. The influence of the carrier spins was recognized a few years later by Berger (1978). He proposed that the s–d exchange interaction between the conduction electrons and the localized magnetic moments could influence the DW dynamics in two different ways. The first contribution, which Berger called *s–d exchange drag* (Berger, 1984), is a viscous force on the DW which is proportional to the current. This term arises from the difference between the spin-dependent reflection coefficients of the conduction electrons at the DW. The second contribution is an 'exchange torque' related to the transfer of spin angular momentum from the s conduction electrons to the localized magnetization (Berger, 1978, 1986). This mechanism is analogous to the spin-transfer torque proposed by Slonczewski in magnetic heterostructures in which magnetic layers are separated by thin metal or insulating layers (Slonczewski, 1996).

2.2.2 *Recent results: two types of torques*

In the past few years, new experimental results on the interaction between electric current and magnetic DWs have triggered a flurry of theoretical studies (Shibata, Tatara and Kohno, 2005; Bazaliy, Jones and Zhang, 1998; Tatara and Kohno, 2004; Tatara *et al*., 2006; Zhang and Li, 2004; Li and Zhang, 2004a,b; He, Li and Zhang, 2005; Barnes and Maekawa, 2005; Thiaville, Nakatani, Miltat and Vernier, 2004; Thiaville, Nakatani, Miltat and Suzuki, 2005; Waintal and Viret, 2004; Xiao, Zangwill and Stiles, 2006; Dugaev *et al*., 2006; Tserkovnyak, Skadsem, Brataas and Bauer, 2006; Tatara, Vernier and Ferre, 2005; Ohe and Kramer, 2006). In most cases, theorists follow a two-step approach. First, they calculate the current-induced torque on the magnetization from the spin-polarized s conduction electrons in the limit of static magnetic moments, since the magnetization dynamics are slow compared to those of the electrons. Second, the influence of the current-related torque on the DW dynamics is studied by solving the Landau–Lifshitz–Gilbert (LLG) equation of motion, usually by approximating the DW structure, so as to obtain analytical expressions.

The influence of the current on the magnetization dynamics is often treated by including two spin-torque terms proportional to the gradient of the magnetization in the LLG equation. In the case of homogeneous magnetic material, and assuming the current is flowing in the x direction, the LLG equation can be written as (Thiaville, Nakatani, Miltat and Suzuki, 2005):

$$\frac{\partial \vec{m}}{\partial t} = -\gamma\, \vec{m} \times \vec{H} + \alpha\, \vec{m} \times \frac{\partial \vec{m}}{\partial t} - u \frac{\partial \vec{m}}{\partial x} + \beta u\, \vec{m} \times \frac{\partial \vec{m}}{\partial x} \quad (6)$$

where m is the magnetization normalized to the saturation value, H is the micromagnetic effective field, γ is the gyromagnetic factor, and α is the Gilbert damping constant. For permalloy films, α is of the order of 0.01 (Nibarger, Lopusnik and Silva, 2003; Nibarger, Lopusnik, Celinski and Silva, 2003)

The first two terms on the right-hand side of equation (6) are the usual precessional and damping terms, respectively, and the last two terms describe the interaction with the current.

The first current contribution is derived in the adiabatic limit. In the adiabatic limit, which, *a priori*, is justified for sufficiently wide DWs, the conduction electrons spin orientation follows the local magnetization direction. The magnitude of the adiabatic spin torque, which can be derived directly from the conservation of spin angular momentum, is given by:

$$u = \frac{g \mu_B J P}{2 e M_s} \quad (7)$$

where g is the Lande factor ($\sim$2), J is the current density, P is the spin polarization of the current, $\mu_B = 0.927 \times 10^{-20}$ emu, the Bohr magnetron, and $e = 1.6 \times 10^{-19}$ C, the electron charge. For permalloy, for which $M_s = 800\,\mathrm{emu\,cm^{-3}}$, and assuming $P = 0.4$, $u = 1\,\mathrm{m\,s^{-1}}$ when $J = 3.5 \times 10^6\,\mathrm{A\,cm^{-2}}$. Note that the polarization is sometimes replaced by the Slonczewski function (Slonczewski, 1996) $g(P)$.

The second contribution of the current is often dubbed the *nonadiabatic spin-torque* or β *term*. As shown by equation (6), it behaves as a spatially varying magnetic field which is proportional to the gradient of the magnetization. The magnitude of the nonadiabatic term is given by the dimensionless constant β, which is of the order of the damping constant α. Both the origin and the magnitude of the 'β term' is under much debate.

Zhang and Li (2004) have proposed a model in which there is a slight mistracking between the electron spin and the local magnetization direction. This generates a nonequilibrium

spin accumulation across the DW, which relaxes by spin-flip scattering toward the magnetization direction. This model leads to both adiabatic and nonadiabatic spin-torque terms (there are also two small terms proportional to the time derivative of the magnetization, which slightly modify the gyromagnetic ratio and the damping constant). The magnitude of the nonadiabatic term is written as $\beta = \tau_{ex}/\tau_{sf}$, where τ_{ex} is the relaxation time associated with the s–d exchange energy $J_{ex}(\tau_{ex} = \hbar/SJ_{ex})$ and τ_{sf} is the spin-flip relaxation time. Numerical estimates are obtained by assuming that $J_{ex} \sim 1\,\text{eV}$, $S = 2$, and $\tau_{sf} \sim 1\,\text{ps}$, giving $\beta \sim 0.01$. Note that this model assumes the DW width to be much larger than the length scale of the transverse spin accumulation (only a few nanometers), such that the nonadiabatic contribution does not vanish even for very wide DWs.

Xiao, Zangwill and Stiles (2006) cast doubt on the existence of this nonadiabatic contribution. They find that although there is a transverse spin accumulation across the DW, the spin current follows the magnetization adiabatically unless the DW width is extremely small. In the narrow wall limit, the nonadiabatic spin torque is nonlocal and oscillatory in space.

Tatara and Kohno (2004) have also calculated the two current interaction terms shown in equation (2), in both the narrow and wide DW limits. In their model, the relevant length scale is the Fermi wavelength (a few angstrom). In the wide DW limit, they obtain a spin-transfer-torque term dubbed *spin transfer* with the same form as that shown in equations (6) and (7). In the narrow DW limit, they derive a forcelike term called *momentum transfer*, which plays the same role as the β term integrated over the DW. This momentum transfer is very similar to the s–d *exchange drag* proposed by Berger (1984) and is a function of the DW resistance R_{DW}. The momentum transfer per unit cross-sectional area of the DW is written as:

$$F_{el} = neR_{DW}J(tw) = \frac{R_{DW}}{R_0}J(tw) = \frac{\rho_{DW}}{R_0}J\Delta \qquad (8)$$

where J is the current density, t and w are the wire thickness and width, respectively, n is the electron density, R_0 is the ordinary Hall coefficient ($1/R_0 = ne$), and $\rho_{DW} = R_{DW}tw/\Delta$, is the DW resistivity, where Δ is the DW width.

The linak between the nonadiabatic spin torque and DW resistance is also mentioned by Zhang and Li (2004). Although they do not explicitly discuss this relationship, it is interesting to consider the relationship between the momentum transfer force (8) and the β term. It can be seen from the LLG equation (6) (and more obviously from the integrated form (13)) that the β term indeed plays the same role as the magnetic field force term. It follows that the β-term-related force (per unit cross-sectional area) can be written as:

$$F_\beta = \frac{2M_s}{\gamma\Delta}\beta u \qquad (9)$$

By equating this with equation (8), it follows that

$$\beta = \frac{\gamma\Delta^2 e}{g\mu_B P}\frac{\rho_{DW}}{R_0} \qquad (10)$$

Interestingly, if the DW resistivity decreases as $1/\Delta^2$, as predicted by the Levy–Zhang model on DW magnetoresistance (Levy and Zhang, 1997), β will be roughly constant, independent of the DW width. In order to obtain a numerical estimate, we consider the DW resonance experiments of Saitoh, Miyajima, Yamaoka and Tatara (2004), which will be discussed later in this chapter. The sample is a permalloy nanowire, with a thickness $t = 45\,\text{nm}$ and a width $w = 70\,\text{nm}$. The DW has a transverse structure such that the DW width can be estimated as $\Delta \sim 22\,\text{nm}$ (as discussed in Section 2.1). We assume a spin polarization $P \sim 0.5$, and a Hall resistance $R_0 \sim 1.3 \times 10^{-10}\,\text{C m}^{-3}$ for permalloy (as measured, e.g., by Freitas and Berger (1985)). The DW resistance is reported to be $R_{DW} = 0.26\,\text{m}\Omega$, such that the DW resistivity is about $3.7 \times 10^{-11}\,\Omega\text{m}$. From equation (10), this leads to $\beta \sim 0.4$.

In a recent paper, Berger has developed the relationship between nonadiabatic spin torque (exchange drag in his terminology) and DW resistance further so as to describe in a single scaling plot experimental results for DW velocity, DW resistance, and critical current for DW depinning (Berger, 2006).

In both Tatara and Kohno and Zhang and Li's models, in the absence of the β term, there is an intrinsic threshold current for irreversible DW motion, even in an ideal wire without any DW pinning sites. Below this threshold value, the DW only moves short distances while the current is applied, but moves back to its original position after the current is turned off (note that this is not the case if there is an irreversible deformation of the DW's structure or if DW pinning is taken into account). Barnes and Maekawa (2005) argue that this intrinsic pinning does not exist (Barnes, 2006; Tatara Takayama and Kohno, 2006). In their model, the ground state in the presence of current corresponds to the DW moving at a constant velocity u, without any tilt or distortion. This corresponds to massless motion and in the ideal case (no roughness), there is no threshold current for DW motion: the DW starts moving, albeit very slowly, as soon as the current is nonzero. The discrepancy arises from the means of introducing damping into the LLG equation. Whereas, both the Gilbert $\left(\alpha\vec{m} \times \frac{\partial\vec{m}}{\partial t}\right)$ and the Landau–Lifshitz $\left(\frac{\alpha\gamma}{1+\alpha^2}\vec{m} \times \vec{m} \times \vec{H}\right)$ formulations are

equivalent in the absence of current, this is no longer the case when the current interaction terms are included. When the adiabatic spin-torque term is added to the LLG equation in its Gilbert or Landau–Lifshitz forms, the resulting equation differs by a term $\alpha u\, \vec{m} \times \frac{\partial \vec{m}}{\partial x}$. In other words, in the second case, the adiabatic spin torque includes a β term, with $\beta = \alpha$.

In a recent extension of their work, Tatara *et al*. (2006) have made a distinction between the nonadiabatic spin torque (i.e., momentum transfer) defined by equation (8) and the β term. The implication of both the adiabatic and nonadiabatic spin torques on the DW dynamics will be discussed in more detail in Section 2.2.3, in the framework of the semianalytical one-dimensional model.

Several recent papers cast doubts about the previous description and find that the current-induced torques cannot be written as a simple function of the magnetization gradient. Xiao, Zangwill and Stiles (2006) find that in the very narrow DW limit, the nonadiabatic torque oscillates across the DW, and extends over a length scale much larger than the DW width. Other authors find that the nonadiabaticity of the conduction electrons lead to the precession of their spins (Waintal and Viret, 2004), in turn generating spin waves which influence the DW motion (Ohe and Kramer, 2006). A recent study focused on GaMnAs also shows that the spin-orbit coupling increases the reflection of the carriers (holes in this case) at the DW, leading to spin accumulation and the enhancement of the nonadiabatic spin torque (Nguyen, Skadsem and Brataas, 2007).

Although thermal effects are not included in most theories, a few authors have addressed thermally assisted processes. Tatara, Vernier and Ferre (2005) find that in a rigid wall approximation, thermally activated wall motion occurs below the zero-temperature threshold value, and the DW velocity varies exponentially with the spin current. They also find that the velocity exhibits a 'universal behavior' in the sense that it does not depend on the pinning potential or the material parameters. In their model, thermal fluctuations are simply introduced as the transition rate over an energy barrier, which is derived from the transverse anisotropy. Recently, Duine, Nunez and Mac Donald (2007) have developed a more complete description of thermally activated processes by deriving the Langevin equations of the nonzero temperature motion of a rigid DW. They find that at nonzero temperatures, the DW velocity varies linearly with current, even without a β term.

2.2.3 *Analytical descriptions: one-dimensional model and vortex model*

Although DWs are complex three-dimensional objects, it is very useful to develop models that allow for an analytical or semianalytical description of the DW dynamics. The most widely used approach is the so-called one-dimensional (1D) model, which was developed in the 1970s and has been described in detail by Malozemoff and Slonczewski in their comprehensive book about magnetic bubbles (Malozemoff and Slonczewski, 1979). The model assumes that the DW has the 1D profile given by equation (2), such that the magnetization varies only in the direction perpendicular to the DW (here the x direction). It is also assumed that the static profile is essentially preserved during the DW motion, although the DW width is allowed to change. The dynamical DW structure is described by (in spherical coordinates):

$$\theta(x,t) = \pm 2 \arctan\left(\mathrm{e}^{\frac{x-q(t)}{\Delta}}\right)$$
$$\psi(x,t) = \Psi(t) \tag{11}$$

where q is the position of the DW center, Ψ is the tilt angle of the DW magnetization away from its equilibrium position (see Figure 4), and Δ is the DW width parameter. The latter is written as:

$$\Delta_0 = \sqrt{\frac{A}{K_0}}\Delta = \frac{\Delta_0}{\sqrt{1 + \frac{K}{K_0}\sin^2(\Psi)}} \tag{12}$$

where A is the exchange constant (erg cm^{-1}). K_0 is the magnitude of the uniaxial anisotropy that defines the magnetization direction in the magnetic domains, and K is the magnitude of the uniaxial transverse anisotropy. In the head-to-head configuration, the transverse anisotropy is that within the plane perpendicular to the wire's long axis. The magnitude of the transverse anisotropy can also be written as an anisotropy field $H_k = 2K/M_s$, where M_s is the saturation magnetization of the material. This profile was originally derived for the 1D Bloch wall. It also gives a good description of the Néel wall and the head-to-head transverse wall, provided that the axes are properly defined (see Figure 4 for the T wall). Qualitative agreement with experiments is also obtained for more complex wall structures such as the head-to-head vortex wall (Thomas *et al*., 2006).

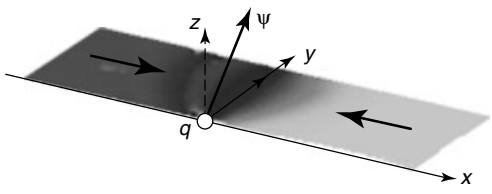

Figure 4. Transverse DW showing the definition of the variables of the 1D model: q (position of the center of mass of the DW) and Ψ (tilt angle of the DW's magnetization out of the plane of the nanowire).

In this model, the LLG equation (6) can be integrated over the static DW profile and the dynamics are described by two time-dependent variables q (DW position) and Ψ (domain distortion). The DW width Δ depends on Ψ such that it is also time dependent unless $K_0 \gg K$. For simplicity, we assume that Δ is not time dependent in the following discussion.

The LLG equation including the current-related terms can be rewritten as:

$$\begin{aligned}(1+\alpha^2)\dot{\Psi} &= -\frac{\gamma}{2M_s}\left(\frac{\partial\sigma}{\partial q}\right) - \frac{\gamma\alpha}{2}H_k \sin(2\Psi) + \frac{(\beta-\alpha)u}{\Delta} \\ (1+\alpha^2)\dot{q} &= -\frac{\alpha\gamma\Delta}{2M_s}\left(\frac{\partial\sigma}{\partial q}\right) + \frac{\gamma\Delta}{2}H_k \sin(2\Psi) + (1+\alpha\beta)u\end{aligned} \tag{13}$$

The DW potential energy $\sigma(q)$ includes the contributions from an external field and from position-dependent energy terms arising, for example, from defects in the nanowire. The field term is simply written as $\sigma(q) = -2M_s Hq$. The influence of roughness or pinning may be approximated by potential wells or barriers, which depend only on q.

It was pointed out long ago (Malozemoff and Slonczewski, 1979) that equation (13) resembles Hamilton's equations of motion for two canonical conjugate variables q and $2M_s\Psi/\gamma$, that is the position and its conjugate momentum. Following this analogy, the DW mass (Döring mass) can be defined as:

$$m_D = \frac{2M_s}{\gamma^2 \Delta H_k} S \tag{14}$$

S is the cross section of the nanowire. These equations can be solved analytically in many cases, yielding useful expressions for both the critical current and the DW velocity. As discussed earlier, the physics of the current-driven DW motion depend strongly upon the presence or absence of the β contribution. Without the β term and in zero magnetic field ($\partial\sigma/\partial q = 0$), there is an intrinsic critical current, below which the DW only moves transiently. This critical current is readily calculated by finding stationary solutions of equation (13). The stationary solution, such that $\dot{\Psi} = 0$ and $\dot{q} = v = 0$, only exists if u is smaller than a critical value, given by:

$$u_c = \frac{\gamma \Delta H_k}{2} \tag{15}$$

Note that u_c depends only on the magnetic material parameters, unless there is extremely large pinning (Tatara and Kohno, 2004). In permalloy nanowires (or other soft materials where crystalline anisotropy can be neglected), the transverse anisotropy field H_k is proportional to the shape anisotropy in the plane perpendicular to the long axis of the wire. Note that this anisotropy field is also the key parameter in models of field-driven DW motion. For example, the Walker breakdown field is directly proportional to H_k (Malozemoff and Slonczewski, 1979). If the current is smaller than this critical value, the velocity decreases rapidly (over a few nanoseconds) and the DW stops. However, when the current is reduced to zero (for example, at the end of a current pulse), the DW moves back to its initial position. On the contrary, for currents higher than this critical value, the wall can move irreversibly over long distances. In this regime, the instantaneous velocity oscillates strongly in time, in a way reminiscent of the field-driven DW motion above the Walker limit. The average velocity can be written as:

$$v = \frac{\sqrt{u^2 - u_c^2}}{1+\alpha^2} \tag{16}$$

The situation is very different when the β term is taken into account. Indeed, for an ideal wire without pinning, irreversible DW motion occurs as soon as the current is nonzero, and the terminal velocity is simply $v = \beta u/\alpha$. Therefore, in this case, the critical current becomes extrinsic, and is dependent on the magnitude of any pinning (i.e., will be related to roughness and defects).

The two key parameters of the model are the DW width Δ and the transverse anisotropy field H_k. It is essential to estimate realistic values in order to attempt a quantitative (or even qualitative) description of experiments or simulations. The DW width is readily defined for a head-to-head transverse wall, as described in Section 2.1.1. Its definition becomes slightly more ambiguous for a vortex wall, where the 'physical' DW width, largely dominated by the tails of the DW does not account for the field-driven DW dynamics. Much better agreement is obtained using the so-called dynamical DW width defined by Thiele (see Section 2.1.1), in which the (small) vortex core has larger 'weight' than the (large) tails of the DW. The transverse anisotropy H_k, which prevents the rotation of the DW's magnetization out of the plane of the wire, is somewhat more delicate. In permalloy nanowires with head-to-head transverse walls, the transverse anisotropy is directly related to the shape anisotropy of the cross section of the wire. For small values of Ψ (only small out-of-plane rotation of the wall's magnetization), calculating H_k from the shape anisotropy appears reasonable. However, for large values of Ψ, the DW's magnetization does not rotate coherently out of plane. Lower energy paths are possible, which involve deformations of the wall structure, for example, by nucleation of an antivortex. In such a case, the effective value of H_k is smaller than that calculated from the shape anisotropy. Thus, if the dynamics involves high Ψ values, the value of H_k obtained from the shape anisotropy does not provide a good quantitative description. For example, the Walker breakdown field, which is directly proportional to H_k

in the 1D model, is significantly overestimated. Another strategy is to find other methods to estimate H_k, for example, from the value of the Walker breakdown field found from micromagnetic simulations. However, *a contrario*, this value might not account for the low Ψ dynamics. The definition of H_k becomes even more problematic in the case of a vortex wall, for which the 1D approximation is certainly not correct. However, we have shown (Thomas *et al*., 2006) that the 1D model can still be useful in describing the DW dynamics, provided that H_k can be estimated from micromagnetic simulations.

Examples of DW trajectories obtained by numerical integration of equation (13) are shown in Figure 5. We chose values of the parameters to match the properties of the nanowire described in the following paragraph using micromagnetic simulations ($\Delta = 48$ nm, $H_k = 1600$ Oe). The damping constant is $\alpha = 0.01$. The first two panels show the time evolution of the variables q and Ψ for a constant current corresponding to $u = 100\,\mathrm{m\,s^{-1}}$, calculated for different values of the β term. Since u is smaller than the critical value $u_c = 675.8\,\mathrm{m\,s^{-1}}$ given by equation (15), the DW motion stops after a transient time for $\beta = 0$. Similarly, Ψ saturates to a constant value given by $\sin(2\Psi) = -2u/(\gamma\Delta H_k)$ (stationary solution of equation (13)). If $\beta \neq 0$, the DW moves at a constant velocity after a transient time, the terminal velocity is given by $\beta u/\alpha$ and Ψ saturates at a value

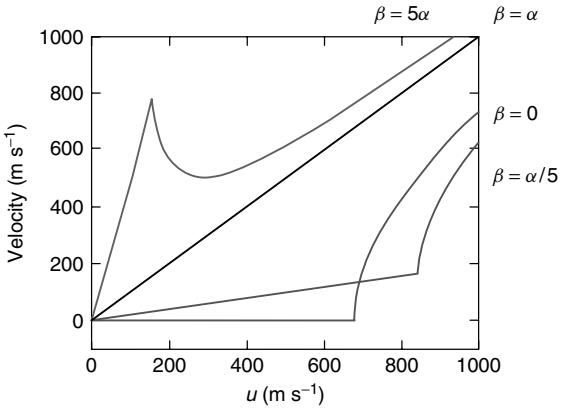

Figure 6. Averaged DW velocity calculated within the 1D model for the same set of parameters as in Figure 4, for different values of the ratio β/α.

$\sin(2\Psi) = -2u(1-\beta/\alpha)/(\gamma\Delta H_k)$. Figure 5 shows the time evolution of q and Ψ for $\beta = 0$ and different values of u. For values smaller than the critical current, the behavior is that described in the preceding text. Above the critical value (see curve for $u = 800\,\mathrm{m\,s^{-1}}$), the DW keeps moving continuously and its motion becomes precessional, in a fashion similar to the field-driven motion mechanism above the Walker breakdown field. The angle Ψ increases as the DW magnetization rotates continuously form one in-plane direction to the

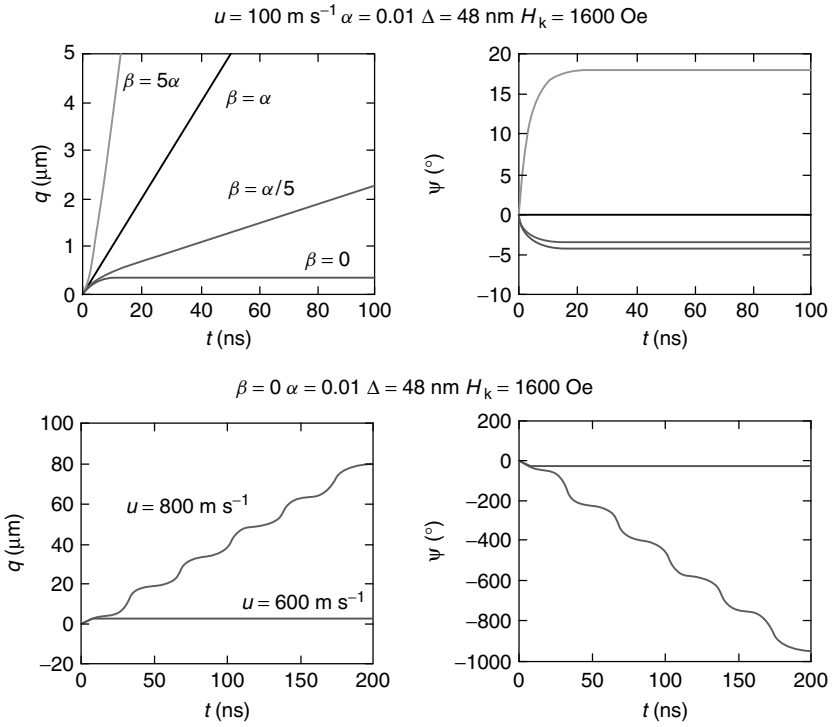

Figure 5. Time dependence of the DW position q and tilt angle Ψ calculated using equation (13) for the parameters indicated in the figure.

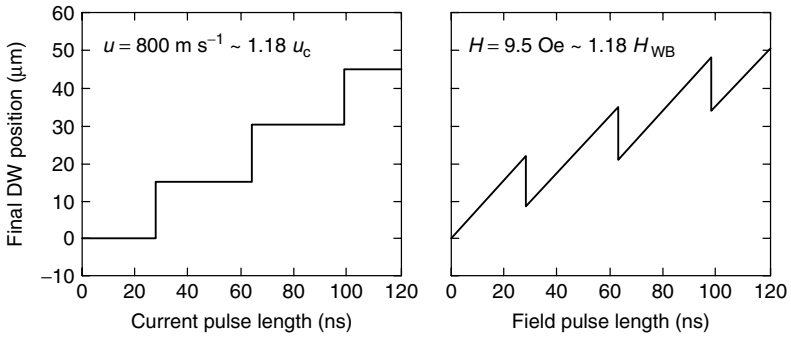

Figure 7. Final DW position after a current or field pulse, calculated using the same parameters as in Figure 4, for $\beta = 0$.

other, and the DW velocity oscillates accordingly. Note that the DW velocity is a maximum when the DW magnetization rotates across the out-of-plane direction ($\Psi = \pm\pi/2$), contrary to the field case, for which the velocity drops (and even reverses). Time-averaged terminal velocity curves are shown in Figure 6 as a function of u, for different ratios of β/α.

An interesting feature of the current-driven motion for zero-β is that for $u > u_c$, the DW displacement after current pulses appears to be quantized. The DW moves only by multiples of $\pi\Delta/\alpha$. This peculiar property follows from the DW's relaxation toward its equilibrium state, $\Psi = 0$, after the current is turned off. The same DW relaxation also occurs at the end of a field pulse, leading to a discontinuity of the DW position as a function of the pulse length rather than a quantized position. This can be understood from equation (13). Let us assume that the DW moves in the stationary regime with either field ($\dot{q} = v = \gamma\Delta H/\alpha$, $\sin(2\Psi) = 2H/(\alpha H_k)$) or current ($\dot{q} = v = 0$, $\sin(2\Psi) = -2u/(\gamma\Delta H_k)$). After the field and current are turned off, the equations of motion are the same. The DW velocity is simply proportional to $\sin(2\Psi)$. Therefore, in the field case, since Ψ is positive, the DW velocity remains positive and decreases to zero. On the contrary, in the current case, $\sin(2\Psi)$ is negative, such that the velocity become negative when the current is turned off, and the DW moves back to its original position. If u is larger than the critical current u_c, the relaxation after the pulse will be either backward (if $\Psi < \pi/2 \pmod{\pi}$) or forward (if $\Psi > \pi/2 \pmod{\pi}$). The DW's final position is shown in Figure 7 as a function of the length of a current or field pulse, for the same parameters used previously.

Note that because of this relaxation mechanism, the critical current given by equation (15) is only correct for dc currents. For current pulses, irreversible DW motion only occurs if the pulse is long enough for Ψ to exceed $\pi/2$. If not, the DW goes back to its original position even if $u > u_c$. As a result, the critical current varies as the inverse of the pulse length.

The addition of a magnetic field and/or pinning potential to equation (13) yields many interesting results. For example, the depinning from a potential well is very different depending on the depth of the pinning potential, the value of the β term and the external magnetic field. This leads to different expressions for the depinning current in different regimes, as described by Tatara *et al*. (2006).

Thiaville and Nakatani (2006) have studied in detail the comparison between the 1D model and micromagnetic simulations for the case of field-driven DW dynamics. To paraphrase their conclusions, 'it is very helpful for a qualitative understanding, and it becomes quantitative at really small sizes, a few exchange lengths.'

A different approach is clearly needed to describe complex wall structures such as the head-to-head vortex wall. A more general description of the steady state DW motion has been proposed by (Thiele, 1973a,b) and extended by Thiaville, Nakatani, Miltat and Suzuki (2005) to include both contributions from the current. Thiele's approach has been used successfully to describe quantitatively the dynamics of a vortex located in a small elliptical disk, driven either by magnetic field (see, e.g., the recent papers Novosad *et al*., 2005; Buchanan *et al*., 2005) or spin-polarized current (Shibata *et al*., 2006). However, a quantitative description of a moving DW using this framework is still lacking, although first attempts have been published recently (He, Li and Zhang, 2006a).

2.2.4 *Micromagnetic simulations*

Micromagnetic simulations are extremely useful to explore DW dynamics because realistic DW structures can be studied without limitations, and in particular, transformations of the DW structure can be described without approximation. Moreover, nonuniform fields (such as the Oersted field from the current) or nonuniform current distributions can be readily included. In addition, roughness and pinning can be easily introduced.

Several authors have published results of micromagnetic simulations of current-driven DW motion for both vortex and transverse DW structures (Thiaville, Nakatani, Miltat and Vernier, 2004; Thiaville, Nakatani, Miltat and Suzuki, 2005;

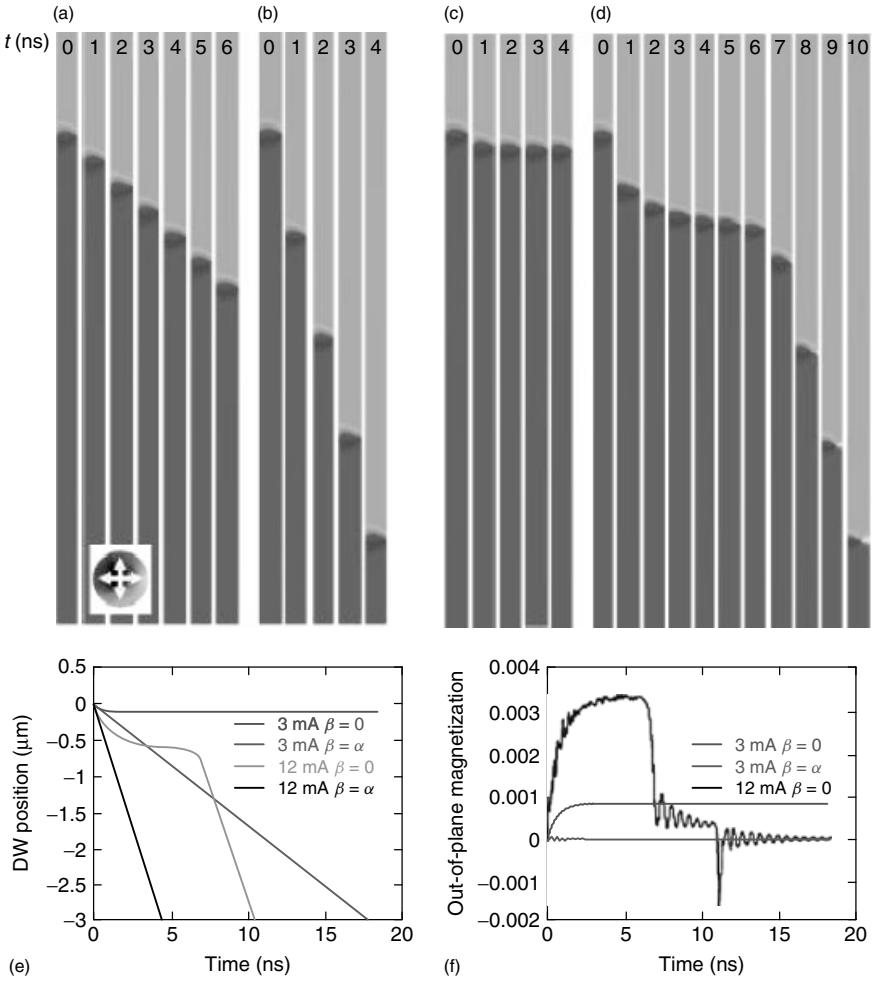

Figure 8. Micromagnetic simulations of the motion of a transverse DW in a permalloy nanowire, 150 nm wide, and 5 nm thick, for $I = 3$ and 12 mA. Top panels, from left to right: magnetization maps for $I = 3$ mA, $\beta = \alpha$ (a, left), $I = 12$ mA, $\beta = \alpha$ (b), $I = 3$ mA, $\beta = 0$ (c) and $I = 12$ mA, $\beta = 0$ (d, right). Bottom panels: Time dependence of the DW position (e) and the out of plane magnetization (f) in all four cases.

He, Li and Zhang, 2006a,b). There are also a few recent reports of the field-driven DW motion in similar structures (Thiaville and Nakatani, 2006; Nakatani, Hayashi, Ono and Miyajima, 2001; Nakatani, Thiaville and Miltat, 2003; Porter and Donahue, 2004).

Examples of micromagnetic simulations of the current-driven propagation of DWs for different nanowires (5 and 20 nm thick, 150 nm wide, 4 μm long) are shown in Figures 8 and 9. These calculations were performed using the LLG micromagnetic simulator code developed and commercialized by Mike Scheinfein. Standard parameters for permalloy are used, and the Gilbert damping constant is set at $\alpha = 0.01$. The cell size is $5 \times 5 \times 5$ and $5 \times 5 \times 10\,\text{nm}^3$ for 5- and 20-nm-thick wires, respectively. Fixed boundary conditions are applied at both ends of the nanowire to pin the magnetization along the wire axis. Note that the Oersted field is included in the simulations.

The first example (Figure 8) shows the time evolution of a transverse wall (the most stable structure for a nanowire of these dimensions), for two different current values (3 and 12 mA), and for the cases $\beta = 0$ (adiabatic torque only, b) and $\beta = \alpha$ (a). Note that the current is turned on instantaneously at time zero. In the latter case ($\beta = \alpha$), as discussed earlier in the framework of the 1D model, the DW propagates without distortion, at a constant velocity, directly proportional to the current.

On the contrary, when $\beta = 0$, there is an intrinsic threshold current (whose value is given by equation (15)). Below this value, at $I = 3$ mA, the DW only moves during the first nanosecond after the current is turned on. The DW velocity is a maximum at $t = 0$ and then drops progressively to zero as an out-of-plane magnetization component develops (proportional to Ψ in the one-dimensional model) as shown in the bottom panel of Figure 8. The DW displacement

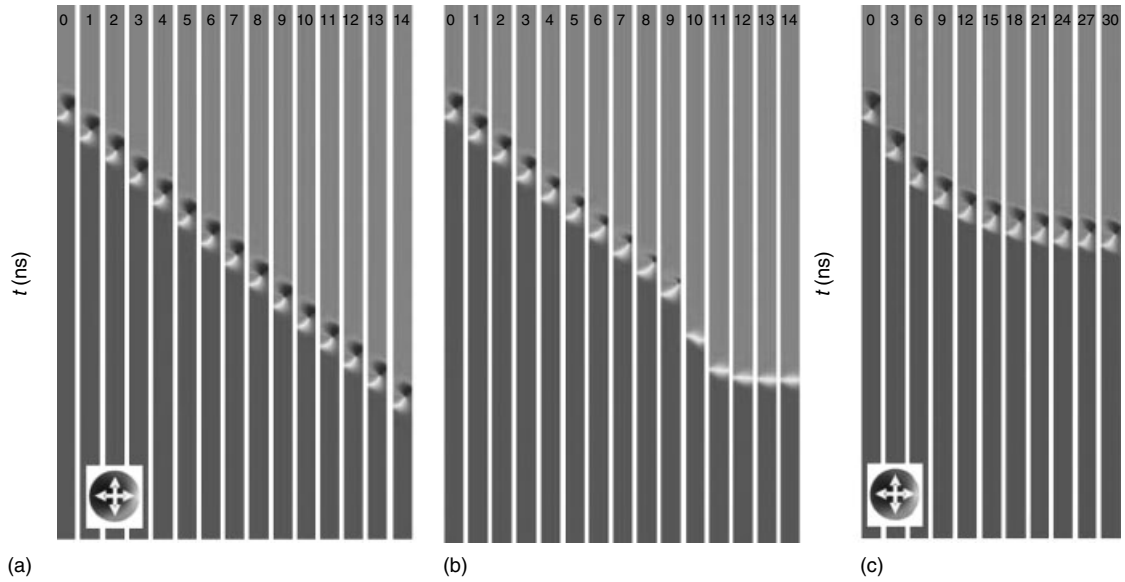

Figure 9. Micromagnetic simulations of the motion of a vortex DW in permalloy nanowires (a and b) width 150 nm, thickness 5 nm, current 3 mA, $\beta = \alpha$ and $\beta = 0$, respectively (c) width 150 nm, thickness 20 nm, current 9 mA, $\beta = 0$.

is completely reversible: if the current is turned off, the DW moves back to its initial position (not shown). On the contrary, for $I = 12$ mA (above the threshold current), the DW motion is irreversible. The first stage of the motion is qualitatively similar to the low-current case: the DW starts moving at its maximum velocity and then slows down. However, the displacement is much larger than in the low-current case. More importantly, the out-of-plane component is also larger, and the DW is not in dynamical equilibrium: an antivortex is nucleated at the right side of the wire, and its propagation across the width of the nanowire is associated with a strong increase of the DW velocity (note that just above the threshold current, the nucleation of the antivortex is extremely slow, on the order of tens of nanoseconds). Once the antivortex is expelled at the left side of the wire, the DW recovers the same structure as its initial state, except its magnetization has been rotated by 180°. If the current is maintained then the DW motion is periodic, and the DW structures oscillates between T walls with left- and right-handed orientations, and the DW velocity oscillates between high and low values as antivortices penetrate and are expelled from the nanowire. If the current is turned off, the DW will relax to an equilibrium state without current, namely an undistorted left or right-handed T wall, such that it can move either forward or backward after the current is turned off, depending upon its state at this time. Note that the current density needed to reach this regime is very high, on the order of 1.6×10^9 A cm^{-2}.

The second example (Figure 9) shows the case of a vortex wall for $I = 3$ mA, and for $\beta = \alpha$ (a) and $\beta = 0$ (b). Results are very similar to the T wall case. In the first case ($\beta = \alpha$), the DW moves at roughly constant velocity. Contrary to the field-driven motion, the DW velocity is not related to the DW structure, and the V and T walls move at the same velocity $v = \beta u/\alpha$. In the second case ($\beta = 0$), the DW structure is distorted as the vortex core is progressively pushed to the side and finally expelled from the nanowire. Note that for smaller currents, a dynamical equilibrium would be reached, in which the V wall would stop moving, as described below for the 20-nm-thick wire case. However, in the case shown here, the current is larger than the threshold for the V wall, but smaller than that for the T wall; therefore, the V wall is transformed into a T wall and then follows the same behavior as that described before. Since the V wall is very unstable for these dimensions (see equation (1)), this transformation can occur at very low current (<1 mA, about 1.3×10^8 A cm^{-2}). Similar results have been described by He *et al*. for a 128-nm-wide, 8-nm-thick nanowire (He, Li and Zhang, 2006a,b). They concluded that the V wall has a smaller critical current that the T wall.

For wire dimensions such that the V wall is the stable structure, the threshold current of the V wall increases, and may even exceed that of the T wall. As shown in Figure 9(c) for a 20-nm-thick wire (with $\beta = 0$), at 9 mA (current density of 3×10^8 A cm^{-2}) a dynamical equilibrium is reached and the DW stops moving. Larger current (∼15 mA) are required to overcome this dynamical equilibrium and achieve irreversible motion. Interestingly, if the initial state is a T wall, a current of 9 mA is sufficient to drive the T wall ∼2 μm, before it is transformed into a V wall and eventually stops (not shown). Note that the timescale is much slower for this larger structure.

Note that the details of the propagation mechanism above the threshold current depend on both the size of the structure and the magnitude of the current, in the same way as the DW propagation mechanism for fields larger than the Walker breakdown field. When the current (or similarly the magnetic the field) increases, higher energy routes become possible. In the example shown in Figure 8, an antivortex is nucleated. For larger structures, more complex scenarios can occur (reversal of the vortex core magnetization, nucleation, and annihilation of one or more vortices, etc.).

3 EXPERIMENTS

3.1 Device fabrication

3.1.1 Lithography techniques

Submicron-sized magnetic wires can be fabricated by various lithography techniques, such as focused ion beam (FIB), optical lithography, and electron-beam lithography. Other methods, which are not discussed here include nanoimprint and interference lithography.

FIB lithography is essentially a one-step process: the nanostructure is drawn from a plain film by milling the magnetic material locally with a high-energy ion beam (typically, Ga^+ ions accelerated at $\sim$30 keV). The ion current can be tuned to achieve high resolution (Xiong, Allwood, Cooke and Cowburn, 2001). Large currents (a few nanoamperes) are used to mill wide areas, whereas much smaller currents (a few picoamperes) are used to define finer features of the structure. This multistep approach ensures that critical cuts are made in as short a time as possible, thus reducing blurring due to stage drift. Resolutions down to about 20 nm can be achieved. Fairly complex structures can be fabricated, such as tracks for DW logic (Allwood *et al*., 2002b). However, it is not simple to make electric contacts to the nanostructure without adding an additional electron-beam lithography step. One method is to use the magnetic material itself as a contact, by leaving small bridges between the nanostructures themselves and a larger outer structure. In the example shown in Figure 10(a), a large area permalloy element ($10 \times 0.1\,mm^2$) was first fabricated by magnetron sputter deposition through a metal shadow mask. The nanowire was then patterned using a multistep FIB milling process. A 6.6 nA beam was used to cut two 5-μm-wide trenches perpendicular to the wire's long axis (see inset of Figure 10a). Much lower current beams (11 and 4 pA) were then used to precisely shape the nanowire. This method has a major disadvantage for studies of DW propagation. Since the nanowires are connected at both ends by magnetic material, it is difficult to control the nucleation and injection of a single DW. To solve this problem, the magnetic nanowire can be isolated completely form the outer structure during milling, both electrically and magnetically. The ends of the nanowires can be shaped to favor or suppress DW nucleation. Electrical connections can be restored by using the FIB to deposit a metal locally by reduction of an organometallic vapor (Thomas *et al*., 2005). In the example shown in Figure 10(b), small Pt contacts were deposited at both ends of the wire.

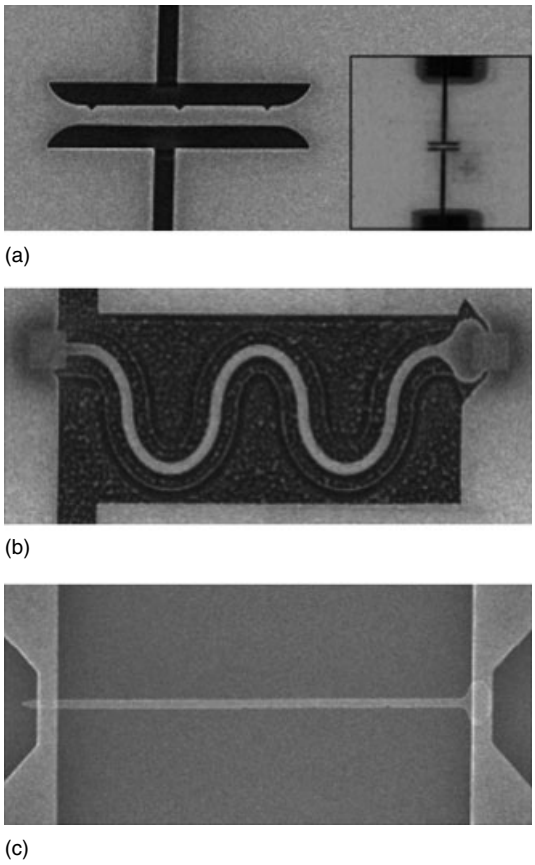

Figure 10. Examples of nanowires fabricated by FIB (a and b) and electron-beam lithography (c). (Courtesy of Charles Rettner.)

FIB lithography allows the fabrication of only one device at a time, and thus it is not practical for systematic studies of nanowires with different sizes and shapes. It is also worth noticing that FIB lithography is not suitable for all materials. For example, the giant magnetoresistance (GMR) of spin-valve structures patterned by FIB is strongly reduced, which is likely related to damage at the edges of the device (Katine, Ho, Ju and Rettner, 2003).

Conventional optical and electron-beam lithography techniques are more convenient to fabricate nanowires and their electric contacts in successive lithographic steps. Both liftoff and ion milling methods have been successfully used to fabricate magnetic nanowires. An example of a nanowire fabricated by electron-beam lithography and ion milling is

shown in Figure 10(c). The nanowire was first patterned from an extended film. Its ends were tapered to favor the nucleation and propagation of a DW from one end of the device. The nonmagnetic metallic contacts at either end were added in a second step.

These film-based methods usually produce 'flat' nanowires whose widths are much larger than their thicknesses. The layout in the sample plane can be changed easily, and complex structures have been fabricated. Nanowire shapes are most often designed to accommodate constraints such as the measurement technique (Hall crosses for Hall-effect detection), the control of the DW injection and pinning (L- or U-shaped structures, rings, etc.).

3.1.2 Nanoporous templates – electroplating

Electroplating is also a powerful (and inexpensive) technique to fabricate nanowires. In this approach, the first step is the fabrication of a template with pores of appropriate diameter. These templates can be track-etched polycarbonate membranes, anodized alumina films (Whitney, Jiang, Searson and Chien, 1993) or photoresist patterned by electron-beam lithography techniques (Duvail *et al*., 1998). The pores in the template are then filled by electrodeposition. This leads to an array of nanowires that can be studied in the template or after dissolution of the template. Several methods have been reported to make electric contacts to a single nanowire, either in the template or after dissolution. These methods include monitoring the resistance during the deposition so as to stop after only one nanowire becomes electrically connected (Wegrowe *et al*., 1998) and depositing contacts in a later step using electron-beam or optical lithography (Vila, Piraux, George and Faini, 2002).

Nanowires prepared by electrodeposition are usually cylinders, with a roughly circular cross section and potentially very high aspect ratios (length/diameter up to $\sim$1000). Bent nanowires have also been fabricated by centrifugation, after dissolution of the membrane and suspension in a liquid (Tanase, Silevitch, Chien and Reich, 2003).

Although nanowires fabricated by electrodeposition have been used to study DW magnetoresistance (Ebels *et al*., 2000) or magnetization reversal (Wernsdorfer *et al*., 1996), there are no reports as yet of current-driven DW motion in such samples. However, multilayered nanopillars made by electrodeposition have been used to study current-driven magnetization reversal (Wegrowe *et al*., 2004, 1999).

3.2 Materials

The list of materials used for current-driven DW motion studies is surprisingly short. The majority of experiments use permalloy ($Fe_{81}Ni_{19}$). There are also a few reports on other soft magnetic materials (CoFe and Ni), on hard magnetic materials with perpendicular magnetization (epitaxial Pt/Co/Pt multilayers), on diluted magnetic semiconductors (epitaxial GaMnAs) as well as one or two studies on nanowires formed from spin-valve structures.

There are several requirements for materials suitable for the study of current-driven DW motion in nanowires. First, their magnetic properties must be well behaved, so as to allow for well-defined DWs on the submicron scale. Soft magnetic materials are well suited, since long exchange lengths and large wall widths make them less sensitive to local structural defects. The crystalline quality becomes more important for harder materials. Second, the resistivity must be small to limit losses and Joule heating. Third, the spin polarization must be high so as to enhance spin-transfer efficiency. Fourth, in order to detect the DW motion by electrical means, materials with significant magnetoresistance (AMR, GMR, or anomalous Hall resistance) are most useful.

These constraints have so far precluded the exploration of very many materials. This means that the detailed influence of material parameters, such as the saturation magnetization and the magnetic anisotropy, have not yet been studied in detail.

3.3 Detection of domain walls in nanowires

In this section, we describe some of the experimental techniques that have been used to probe DWs in nanowires. General principles and technical details can be found elsewhere. Here we emphasize the main aspects of these different measurement techniques in the specific context of probing DWs in nanowires, and address some of their advantages and drawbacks. It is important to note that different techniques are useful for measuring different DW properties. For example, some measurement methods such as the magneto-optical Kerr effect (MOKE) and GMR (Parkin and Wessels, 1995) are sensitive to the magnetization of the magnetic domains, from which the presence of DWs and their location can be inferred. By contrast, other methods, such as the AMR probe the presence of the DW itself but lack sensitivity to its position. Therefore, depending on the characteristics and the sensitivity of the measurement technique, modifications of the DW structure or motion over small distances can be detected or be completely overlooked. This can result in significant ambiguities, for example, in the definition of the critical current for DW motion.

Another key aspect of the measurement method is the capability to acquire enough statistics to account for stochastic variations in the motion of the DW. For example, many microscopy techniques are slow. Thus, even though these

techniques have sufficient spatial resolution to access the static DW structure before and after its motion, the limited number of experiments which can be performed in a reasonable time may not allow for the measurement of all possible configurations. On the other hand, techniques such as time-resolved MOKE require a large number of repetitions of nominally the same DW motion to achieve adequate signal to noise, and so can lead to misleading results if fluctuations in this motion are important.

3.3.1 Electrical measurements

Magnetoresistance measurements are very convenient to detect DWs in nanowires. The AMR and GMR effects are most commonly used (Parkin and Wessels, 1995). There are also several experimental studies based on the ordinary and anomalous Hall effects (HE). These techniques, which are based on electrical measurements, are fast, allowing for extensive and systematic studies of current-driven DW motion.

Anisotropic magnetoresistance (AMR)

The resistivity of ferromagnetic metals typically exhibits AMR, whereby it depends on the angle θ between the magnetization and the electric current direction in the material, according to the relation:

$$\rho(\theta) = \rho_\perp + \delta\rho\cos^2(\theta) \quad \text{with} \quad \delta\rho = \rho_\parallel - \rho_\perp \tag{17}$$

The normalized AMR ratio is defined as $\delta\rho/\rho_{av} = \delta\rho/(\rho_\parallel/3 + 2\rho_\perp/3)$. This effect, which arises from spin-orbit coupling, can exceed 5% for some Ni–Fe and Co–Ni alloys at room temperature (and can be much larger at lower temperatures). The AMR values of many 3d transition-metal alloys are listed in the review paper of McGuire and Potter (1975).

The presence of a DW in a nanowire, which exhibits AMR, changes the nanowire's resistance because the magnetization within the DW deviates from the wire's long axis and thus from the current direction. In order to estimate the magnitude of the signal, consider the case of two head-to-head domains separated by a DW of width Δ with a magnetization profile following the 1D Bloch wall of equation (2). When no DW is present, and the magnetization lies parallel to the nanowire's long axis, the resistance is simply:

$$R_{\text{sat}} = \frac{\rho_\parallel L}{wt} \tag{18}$$

where L, w, and t are the length, width and thickness of the wire, respectively. When a DW is present within the nanowire, its resistance becomes:

$$R_{\text{DW}} = \int_{-L/2}^{L/2} \rho[\theta(x)]\frac{\mathrm{d}x}{wt} \tag{19}$$

Thus, the contribution of the DW to the nanowire's resistance, in the limit $L \gg \Delta$ is:

$$R_{\text{DW}} - R_{\text{sat}} = \frac{-\delta\rho 2\Delta}{wt} \tag{20}$$

The signal from the DW is directly proportional to the AMR ratio and the DW width. In permalloy, to a first approximation, the DW width scales with the nanowire's width $\Delta \propto w$ (see Section 2.1.1). Therefore, the DW contribution to the resistance is of the order of $\delta\rho/t$ and is independent of the wire width. Note that since the AMR signal arises from the DW itself, its relative contribution to the total nanowire resistance decreases as $1/L$, and can become quite small in long wires. It can also be easily washed out by drifts in the nanowire resistance over time (e.g., owing to small changes in temperature).

An important characteristic of the AMR signal is that it does not depend on the position of the DW (in uniform, homogeneous nanowires). Thus, the AMR signal detects the presence, or absence, of a DW between the electrical contacts used to probe the nanowire's resistance.

An example of the magnetoresistance (MR) hysteresis loop of a straight NiFe nanowire, 300 nm wide and 10 nm thick, is shown in Figure 11(a). The distance between the electrical contacts is 4 μm. One end of the nanowire has a tapered tip, to prevent DW nucleation, and the other end is attached to a large nucleation pad to assist DW injection (see Section 3.4.1). Note that these pads have very different shapes in Figure 11(a) and (b). A triangular notch is patterned on one side of the wire, which acts as a pinning center for the DW. A magnetic field H is applied parallel to the nanowire's long axis. When the magnetization is saturated along this axis, so that it is parallel to the current flow, the resistance is highest. When the field is decreased to $H = -25$ Oe a DW is injected into the nanowire and is trapped at the pinning site. This results in a sharp drop of resistance by $\sim$0.2 Ω. The resistance level decreases further by $\sim$30% as the field becomes more negative. This may be because the DW is moved further into the notch or because the DW becomes wider as it is stretched away from the notch. This will depend on the detailed structure of the DW (whether V or T and its chirality). When the field exceeds ~ -25 Oe, the DW is driven from the pinning site to the other end of the nanowire outside the region between the contacts and the resistance reverts back to the saturation value. Note that since the AMR is only sensitive to the presence of the DW between the contacts, no signal is detected in these quasistatic

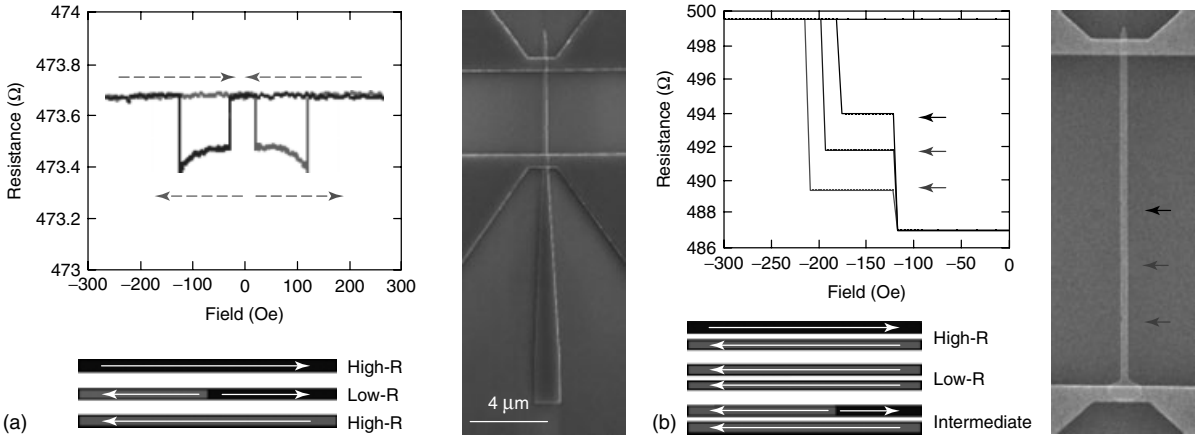

Figure 11. Examples of magnetoresistance curves obtained when the propagation of a DW along the nanowire is probed by AMR in a NiFe nanowire (a) or GMR in a spin-valve nanowire, which has the basic structure of NiFe/Cu/CoFe/Ru/CoFe/IrMn (b).

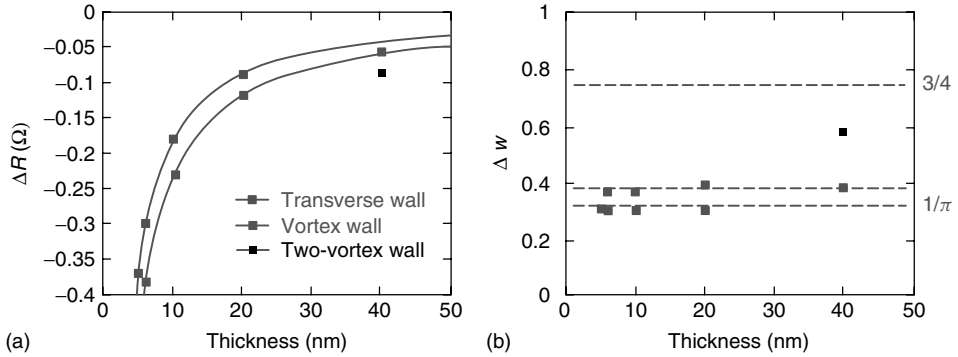

Figure 12. (a) DW resistance, for three different DW structures, in a permalloy nanowire of width 20 nm, as a function of the nanowire thickness t, calculated from micromagnetic simulations. (b) Ratio of the DW widths, obtained from equation (20), to the nanowire width (symbols), and comparison with values obtained from fits of the magnetization profile to the 1D Bloch wall model profile.

measurements if the DW is not trapped between the contacts after injection but rather propagates directly to the end of the wire.

Although the signal is rather small, the AMR is highly sensitive to details of the DW structure. For example, since the AMR signal depends on the DW width, V and T walls can be distinguished. The AMR signals calculated from micromagnetic simulations for three different DW structures in 100-nm-wide NiFe wires are shown in Figure 12, as a function of the wire thickness. Values of resistivity of 30 μΩcm and an AMR ratio of 1% are used. Interestingly, the V wall exhibits a signal about 30% larger than the T wall and the double-V wall shows an even larger signal. The calculated values vary inversely with nanowire thickness, as expected from equation (20). The DW widths can be estimated from this same equation (Figure 12b). Interestingly, the ratio of the DW width to the nanowire width (Δ/w) is nearly independent of thickness for the V and T walls. For the T wall, Δ/w is $\sim 1/\pi$, as proposed by Nakatani, Thiaville and Miltat (2005). However, for the V wall, Δ/w is ∼0.4, which is much smaller than that obtained by fitting the magnetization profile to the 1D Bloch wall profile, that is, 3/4.

Experimentally, we find that the AMR signal does not depend much on the wire width, in good agreement with equation (20). The comparison between nanowires with different thicknesses is less conclusive since both the nanowire resistivity and the AMR ratio vary with thickness. However, different wall structures can be well resolved (Hayashi *et al.*, 2006b). The AMR signatures of four different DWs trapped at a notch in a 300-nm-wide, 10-nm-thick permalloy nanowire are shown in Figure 13.

In summary, AMR is a powerful technique to probe the presence of DWs in magnetic nanowires. The main drawbacks of AMR measurements are the small output signal, the lack of sensitivity to DW displacement, and the limited choice of magnetic materials with large enough AMR ratios.

Note that AMR is not the only contribution to the resistance of the DW. Spin-dependent scattering across the DW can also contribute to its resistance (Levy and

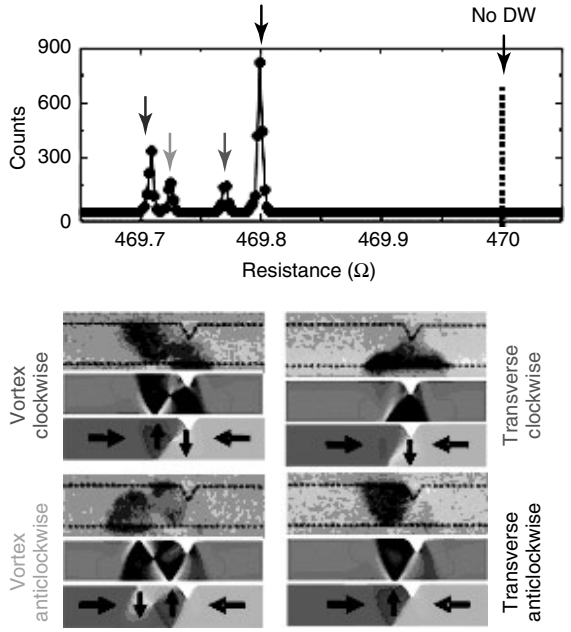

Figure 13. Histogram of measurements of the resistance of a permalloy nanowire (10 nm thick and 300 nm wide) after injection of a DW in a series of repeated experiments. The four peaks in the histogram correspond to four different DW structures. The DW structure, corresponding to each resistance value, was determined by MFM imaging and reproduced by micromagnetic simulations. For all four DW structures are shown the MFM image (top), the corresponding magnetization map from micromagnetic simulation (bottom) and the map of the divergence of the magnetization (middle). (Reproduced from Masamitsu Hayashi, Luc Thomas, Charles Rettner, Rai Moriya, Xin Jiang, and Stuart S.P. Parkin, *Phys. Rev. Lett.* **97**, 207205 (2006), copyright © by the American Physical Society, with permission from APS.)

Zhang, 1997). This latter effect is often termed the *intrinsic DW resistance*. Although the resistance of DWs has been extensively studied in the past decade (Marrows, 2005), the intrinsic contribution is usually smaller than the AMR in 3d transition-metal nanowires (∼0.1 to 1% of the resistivity). Indeed, in permalloy nanowires, we find that the AMR can largely account for the DW resistance in wires wider than ∼100 nm. Large intrinsic DW effects have been reported in nanoconstrictions in permalloy nanowires although it is difficult to rule out contributions from magnetoelastic effects. Intrinsic contributions to the DW resistance in GaMnAs wires have also been reported (Ruster *et al*., 2003).

Giant magnetoresistance

GMR is observed in multilayered structures in which two or more ferromagnetic layers are separated by thin nonmagnetic metallic spacer layers (Parkin and Wessels, 1995; Parkin, 1994). The current can flow either parallel or perpendicular to these layers. These geometries are often termed *current-in-plane* (*CIP*) and *current perpendicular to plane* (*CPP*), respectively. Few GMR measurements of DW motion have been reported although both the CIP (Ono, Miyajima, Shigeto and Shinjo, 1998; Ono *et al*., 1999a; Grollier *et al*., 2002, 2003, 2004; Lim *et al*., 2004.) and CPP (Zambano and Pratt, 2004) geometries have been used, typically with a spin-valve structure (Parkin and Wessels, 1995; Parkin *et al*., 2003). One magnetic layer, nominally in a single domain state, acts as a *reference* layer, and the DW motion is observed in a second magnetic layer, the *free* layer, where the two layers are separated by a thin Cu layer (Parkin, 1994). Although GMR values of more than 70% are found in Co/Cu multilayers at room temperature (Parkin, Li and Smith, 1991), typical GMR effects in spin-valve structures useful for DW studies are much smaller (∼1–5%). However, the GMR signals are much larger than the AMR signal from a DW in a permalloy nanowire, since the GMR arises from the magnetic domains and not from the DW alone. This also means that the GMR signal is sensitive to the precise position and thus the motion of a DW along a nanowire.

A typical example is illustrated in Figure 11(b), in which the resistance hysteresis loops of a 200-nm-wide spin-valve nanowire formed from a NiFe/Cu/CoFe/Ru/CoFe/IrMn structure are shown. In the field range shown, only the magnetization of the free layer (a 20-nm-thick NiFe layer) reverses. When the free layer's moment is completely switched from being parallel to antiparallel to the reference layer (an NiFe layer exchange biased by an antiferromagnetic IrMn layer) the resistance of the device changes by ∼12 Ω, which is nearly 100 times larger than the AMR signal (0.2 Ω) for a permalloy nanowire device with similar resistance. In the example shown in Figure 11(b) the nanowire was fabricated with three notches of different depths along one side of the nanowire (as shown in the scanning electron micrograph (SEM) in Figure 11b) so that the DW is trapped successively at these pinning sites. This accounts for the resistance plateaus in the figure.

While GMR appears well suited to the study of the motion of DWs in nanowires, the necessary use of additional magnetic and nonmagnetic layers causes severe problems. In particular, the shunting of current through the nonmagnetic spacer layer, which is typically much more conducting than the other layers in the stack, results in an inhomogeneous current distribution through the stack. This may lead to Oersted fields from the current within the magnetic layer in which the DWs move. A second, perhaps even more important problem, is the interaction of the fringing fields from the DWs with the reference layer moment through magnetic dipolar interactions (Gider, Runge, Marley and Parkin, 1998; Thomas, Samant and Parkin, 2000; Thomas *et al*., 2000). Moreover, any inhomogeneities in the reference layer (either magnetic or structural) will likely lead to pinning centers for the DWs in the free layer, again through dipolar fields. A

third significant problem is that the current densities needed to move DWs in transition-metal ferromagnetic materials are often so high that the device becomes significantly heated, so that the exchange bias is weakened (typical blocking temperatures are ∼500 K) and the reference layer moment is no longer magnetically stabilized. Notwithstanding these problems, GMR has a particular advantage in that, since the GMR effect derives largely from spin-dependent interface scattering (Parkin, 1992, 1993), many different free layer ferromagnetic materials can be studied by inserting ultrathin layers at the interface with the Cu spacer layer which give high GMR (Parkin, 1993).

Hall effect

The Hall effect is also a powerful technique to study DW motion. For materials with magnetization perpendicular to the sample plane, for example, CoPt alloys or multilayers and GaMnAs, the anomalous hall effect (AHE) provides a direct measurement of the DW position (Wunderlich *et al*., 2001; Yamanouchi, Chiba, Matsukura and Ohno, 2004). Indeed, just as for GMR, the AHE is proportional to the net magnetization (within the Hall cross), although the signal can be even larger. For example, in epitaxial GaMnAs nanowires, a change in resistance of more than 400 Ω has been reported (although at low temperatures) (Wunderlich *et al*., 2001). This large signal allows the detection of DWs moving over distances as short as 10 nm (Ravelosona *et al*., 2005).

The Hall effect is also observed for samples magnetized in plane when the magnetization is not exactly parallel to the current, as a consequence of the AMR. Although the effect is quite small in metallic samples (Berger, 1991a; Sato *et al*., 2000; Gopalaswamy and Berger, 1991), a giant planar Hall effect has been reported in GaMnAs films magnetized in plane (Tang, Kawakami, Awschalom and Roukes, 2003) and this effect has been used to detect a single DW (Honolka *et al*., 2005; Tang *et al*., 2004; Tang, Masmanidis and Kawakami, 2004). Hall-effect-based measurements require the device to be patterned in a Hall-cross geometry, thus limiting the flexibility of the device structure. Moreover, DWs can be strongly pinned at the cross, as shown by Wunderlich *et al*. (2001).

3.3.2 Optical measurements

The magneto-optical Kerr effect (MOKE) has been used to probe DW motion (Lee *et al*., 2000; Cowburn, Allwood, Xiong and Cooke, 2002; Allwood *et al*., 2002a; Atkinson *et al*., 2003; Vernier *et al*., 2004; Beach *et al*., 2005, 2006; Yamanouchi, Chiba, Matsukura and Ohno, 2004; Yamanouchi *et al*., 2006). However, using conventional optics, the spatial resolution of MOKE is limited by the wavelength of the light used, typically to about 0.5 μm. This makes it difficult to detect DWs directly. However, it is possible to detect the magnetization of magnetic domains, and thereby detect the presence and position of a DW in nanowires even as narrow as 120 nm (Vernier *et al*., 2004). Even though the size of the light source is diffraction limited, the motion of DWs can be detected over much shorter distances, that is, within the light spot, when the signal to noise ratio of the Kerr detection scheme is high enough, for example, by using pump-probe MOKE experiments. The main advantages of MOKE detection are its application to a wide range of magnetic materials and, perhaps most importantly, the fact that it does not perturb the magnetic structure.

3.3.3 Magnetic microscopy techniques

High-resolution magnetic microscopy is extremely useful to unambiguously measure a DW's structure. As discussed in paragraph 3.3.1, resistance measurements can be very sensitive to the DW structure, but can only be fully interpreted in conjunction with magnetic microscopy images. The Kerr effect can be used to image magnetic structures, either by scanning a beam of light across the sample or by using an optical microscope. The latter has been used to study injection and pinning of DWs in permalloy nanowires, as narrow as 500 nm wide (Yokoyama *et al*., 2000).

MFM is an elegant and simple technique, with a resolution of ∼25 nm, which is good enough to well resolve the structure of many DWs. However, it has very serious drawbacks. First, by contrast with the MOKE effect, MFM probes not the magnetization but rather the dipole fields generated by inhomogeneities in the magnetization. For samples magnetized in plane these fields are approximately proportional to the divergence of the magnetization. This means that it can be difficult to resolve the structure of complex DW structures from an MFM image without the aid of micromagnetic simulations. Second and more important is the interaction between the MFM magnetic tip and the sample, which is often large enough to perturb the magnetic structure of the sample. The field from the tip can both distort and cause transformations in the structure of DWs (Lacour *et al*., 2004) and can also drag DWs along a nanowire even if the DWs are trapped at pinning centers. Clearly, it is preferable to use MFM magnetic tips with the lowest possible magnetic moments, as discussed in several studies (Saitoh, Miyajima, Yamaoka and Tatara, 2004; Yamaguchi *et al*., 2004). Examples of MFM images of T and V DWs trapped at a notch are shown in Figure 13. Also shown are maps of the divergence of the magnetization computed for these DW structures using micromagnetic simulations, which are in good agreement with the experimental measurements. Another example is shown in Figure 2 in which the MFM image of a double-V structure is compared with the simulated

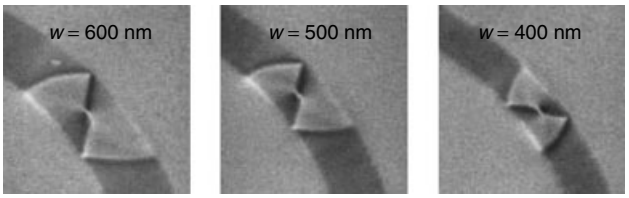

Figure 14. MFM images of a vortex DW in 40-nm-thick FeCoNi nanowires with widths of 400, 500, and 600 nm.

structure. Figure 14 shows MFM images of V walls located in curved nanowires with different widths. In these cases the nanowires are relatively thick (40 nm), so that the vortex core polarity can be resolved even though the core dimensions ($\sim$5 nm radius) are much smaller than the experimental resolution. Note that the core appears as the white signal in the middle of the V wall.

In homogeneous nanowires with smooth edges and surfaces DWs can be moved in fields of just a few oersteds so that even low moment MFM tips can destabilize such DWs. Even though a DW may appear stable in consecutive MFM images, the structure observed may have been modified by the proximity of the tip even before the first image was taken. Moreover, the signal measured with low moment MFM tips is quite small, particularly for thin magnetic layers ($<$10 nm). MFM provides the most useful results for strongly pinned DWs or DWs in nanowires with large propagation fields.

Scanning tunneling microscopy (STM) has atomic lateral resolution and does not perturb the magnetic structure. STM has been used successfully to image the vortex core in Fe islands (Wachowiak *et al*., 2002) and has potential for the study of DW motion.

Other magnetic imaging techniques include PEEM and various X-ray microscopy techniques, which are typically most useful when carried out at a synchrotron, which can provide energy resolved photon fluxes of high intensity. PEEM is sensitive to the projection of the magnetization in the X-ray incidence plane, and has a spatial resolution below 100 nm. Examples of PEEM images of magnetic domain structures are shown in Figures 3 and 15. V and T wall structures can readily be identified. A particular advantage of PEEM is its elemental selectivity, which can be used to detect the magnetization of individual layers in multilayered structures. Other advantages are that PEEM is nonperturbative, and it is suitable for time-resolved measurements of magnetization dynamics in submicron structures (Choe *et al*., 2004). PEEM can be used to study samples grown on any substrate, provided the capping layer is thin enough. However, PEEM is sensitive only to the surface of the sample ($\sim$10–20 Å), which can be both good and bad. For example, PEEM can measure very thin samples but, on the other hand, surface contamination can significantly affect the measurement. Since PEEM is an electron microscopy technique, imaging in the presence of magnetic fields is not possible. Moreover, large voltages (15 to 20 kV) are required which risks electrical discharges, which can damage the sample. This means that it is also difficult to apply electric currents to the samples *in situ*.

Transmission X-ray microscopy and scanning transmission X-ray microscopy (STXM) can also be used for imaging magnetic nanostructures both in the time and spatial domains (Puzic *et al*., 2005; Van Waeyenberge *et al*., 2006). The spatial resolution is higher than that of PEEM and it is much easier to apply magnetic fields and electric current to the sample. However, these techniques require special samples grown on thin transparent membranes. This can be an issue for current-driven DW motion studies, for which the dissipation of heat through the substrate from Joule heating of the wire may be important.

Electron microscopy techniques are also suitable for imaging DWs in nanowires with high spatial resolution. Transmission electron microscopy in the Lorentz mode has been used successfully to study magnetization processes in permalloy and Co nanowires with widths as small as 100 nm (Schrefl, Fidler, Kirk and Chapman, 1997). Spin-resolved scanning electron microscopy (spin-SEM, or SEMPA) is also nonperturbative and has very high lateral resolution ($\sim$20 nm). This technique has been used successfully to image the DW structure in nanoconstrictions (Jubert, Allenspach, and Bischof, 2004) and the DW displacement induced by current pulses in nanowires (Klaui *et al*., 2005b, Jubert *et al*., 2006). By combining high-resolution images of the two in-plane components of the magnetization, Klaui *et al*. (Klaui *et al*., 2005b) have shown the progressive distortion of a vortex wall and its eventual transformation into a transverse wall as a result of the injection of several current pulses. Note that spin-SEM has the same drawbacks as other electron microscopy based techniques such as PEEM, for example the surface sensitivity (such that capping layers cannot be used or need to be removed in-situ) and the difficulty of using magnetic fields while imaging. Recently, high-resolution electron holography was used to study the structure of DWs trapped in constrictions (Klaui *et al*., 2005a).

3.3.4 Time-resolved experiments

Time-resolved measurements are extremely useful to study the dynamics of DW propagation. Measurements using the Kerr effect (Atkinson *et al*., 2003; Beach *et al*., 2005), GMR (Ono *et al*., 1999a,b), and AMR (Hayashi *et al*., 2006a) have been reported. In all cases reported so far, reasonable signal to noise ratios could only be achieved by signal averaging over very many repeated measurements. However, with improved detection sensitivity all of these techniques have the potential for single-shot detection. Other techniques

offer the potential for time-resolved measurements of current-driven DW motion, for example, PEEM (Choe *et al*., 2004), STXM (Puzic *et al*., 2005), or inductive measurements (Silva, Lee, Crawford and Rogers, 1999). However, all these methods rely upon a pump-probe approach, which is rather inconvenient for the measurement of irreversible processes such as DW motion. Indeed, the sample must be reset to an identical initial state before each measurement, and the motion must be reasonably reproducible in order to obtain useful results. An important technical point is that the sample reset must be relatively fast to collect data in a reasonable amount of time. This can be difficult if even modest fields are required for this process.

3.4 Field-driven domain-wall motion in magnetic nanowires

Understanding and controlling the field-driven motion of DWs in nanowires is an important preliminary step to studying their current-driven dynamics.

The simplest way to create a DW in a magnetic nanowire is to first saturate its magnetization along its long axis and then in a second step to apply a smaller magnetic field in the opposite direction. The magnetization reversal process has been studied both experimentally (Schrefl, Fidler, Kirk and Chapman, 1997) and numerically (Nakatani, Hayashi, Ono and Miyajima, 2001) in nanowires with square ends. In these cases the magnetization reversal originates from closure domains at the ends of the nanowire, which expand as the magnetization rotates rotate toward the applied field. The field associated with the nucleation of the reversed domain can be large, since it must overcome the shape anisotropy of the wire. This field decreases as the inverse of the wire width and can reach several hundred oersteds in submicron-wide permalloy or Co nanowires (Shigeto *et al*., 2000).

Since the field required to nucleate a DW in a nanowire is generally much larger than the field needed to propagate a DW along the wire, once a DW is created it will be swept along the length of the wire. Different schemes can be used to circumvent this problem and generate a single DW in a nanowire whose field- and current-driven motion can subsequently be studied. All these schemes enable the independent control of the three critical steps of field-driven DW motion (i) DW nucleation, (ii) DW injection into the nanowire, and (iii) DW propagation along the nanowire. These will be discussed in the following paragraphs.

3.4.1 Nucleation and injection of domain walls

Three methods have been proposed to nucleate DWs in soft magnetic nanowires.

Nucleation pad

Shigeto, Shinjo and Ono (1999) first introduced the technique of using a nucleation pad attached to one end of a nanowire to generate a DW in the wire. The pad's lateral dimensions are much larger than the wire width, typically of the order of or larger than 1 μm. Various pad shapes have been used including squares, diamonds, and ellipses. Owing to the pad's size and shape, the field required to nucleate a DW inside the pad is smaller than that needed to nucleate a DW within the nanowire itself. If the shape of the pad favors a flux-closed structure, a DW may reside in the pad at remanence. Cowburn *et al*. (Cowburn, Allwood, Xiong and Cooke, 2002) studied a 1-μm-sized square pad attached to a 100-nm-wide, 5-nm-thick permalloy wire. DW propagation was probed by MOKE at different positions along the nanowire. The reversal field of the nanowire alone, when terminated with square ends, exhibits a reversal field of ∼180 Oe. When the nucleation pad is attached to the nanowire, the reversal field is reduced significantly to ∼40 Oe. The same principle means that by shaping the end of the nanowire, for example to a point, so as to increase the local shape anisotropy, the nucleation field for a DW can be significantly increased (Schrefl, Fidler, Kirk and Chapman, 1997).

The nucleation of a DW in the pad does not guarantee that it can be injected into the nanowire. The junction between the wire and the pad is a local energy minimum, and a magnetic field is required to move the DW into the wire. This injection field depends on the dimensions and shape of the nucleation pad and the nanowire. The injection field typically decreases for wider wires. However, it can be quite large for wire widths below 500 nm. For example, in experiments reported by Yokoyama *et al*. (2000), the injection field with a diamond-shaped nucleation pad is ∼60 Oe for a 500-nm-wide, 20-nm-thick permalloy wire. Without the nucleation pad, the injection field is slightly higher (about 85 Oe). For 2-μm-wide nanowires, these fields are reduced to ∼25 and ∼35 Oe, respectively.

The relatively high value of the injection field makes it difficult to inject a DW into a nanowire without the DW moving along the length of the nanowire. The DW will move along the nanowire when the field exceeds a critical propagation field, which is determined by any defects in the nanowire, such as edge or surface roughness. For smooth wires, the propagation field may be as small as a few oersteds, which is much smaller than the injection field in most cases. Therefore, nucleation pads do not solve the problem of the controlled injection of a DW into the nanowire, unless there is significant pinning along the nanowire. One way to solve this problem is to fabricate an artificial pinning center within the nanowire. The distinction between nucleation, injection, and propagation fields is illustrated in Figure 15, in which PEEM imaging was used to study field-driven DW injection in a

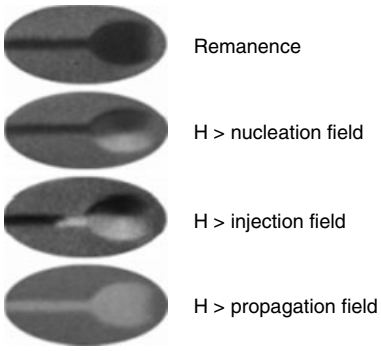

Figure 15. PEEM images of the domain structure of a 20-nm-thick, 250-nm-wide permalloy nanowire, measured at remanence after application of magnetic fields of various amplitudes (Thomas *et al*., 2005). The elliptical pad is ∼1.7 µm long, 1 µm wide. (Reproduced from L. Thomas, C. Rettner, M. Hayashi, M.G. Samant, S.S.P. Parkin, A. Doran, and A. Scholl: 'Observation of injection and pinning of domain walls in magnetic nanowires using photoemission electron microscopy', *Applied Physics Letters* **87**, (2005) copyright © 2006 American Institute of Physics, with permission from the AIOP.)

permalloy nanowire (Thomas *et al*., 2005). Note that DWs can also be injected from a nucleation pad into a nanowire without an artificial pinning site if sufficiently short field pulses are used, such that the DW does not have time to fully propagate along the nanowire (Beach *et al*., 2005). This is only possible if the applied field can be changed on a short timescale determined by the DW propagation speed.

Nonlinear nanowire shape

The second scheme for DW nucleation uses a shaped nanowire whose remanent state after saturation along a particular orientation of an external magnetic field exhibits one or several DWs. Numerous shapes are possible including U- or L-shaped wires (Thomas *et al*., 2006; Yamaguchi *et al*., 2004, 2006a), zig-zag wires (Klaui *et al*., 2005b; Taniyama, Nakatani, Namikawa and Yamazaki, 1999; Taniyama, Nakatani, Yakabe and Yamazaki, 2000), and rings (Rothman *et al*., 2001; Klaui *et al*., 2005b; Laufenberg *et al*., 2006b). An example of DW nucleation is shown in Figure 16 for an L-shaped wire. In this case a saturation field, high enough to overcome the nanowire's shape anisotropy, is applied at ∼45° to the two straight legs of the nanowire. The magnetization in both legs of the nanowire rotates toward the field to reach an angle defined by the ratio of the external field and the shape anisotropy field. When the field is reduced to zero, the magnetization rotates back toward the wire's axis (the easy direction of the shape anisotropy), so nucleating a DW near the bend. This method is attractive because it generates a DW highly reproducibly, even in smooth nanowires without any pinning centers. However, its main drawback is that it requires a large external field, big enough to overcome the wire's shape anisotropy.

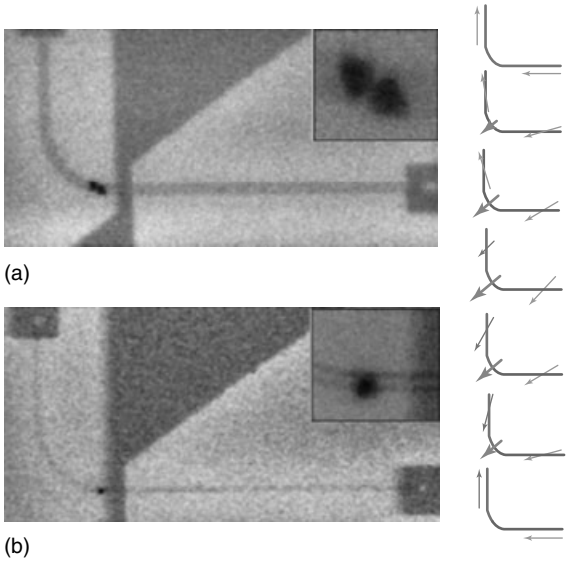

Figure 16. Schematic of the field-induced injection of a DW into the bend of a L-shaped nanowire by applying an external field at ∼45° to the two straight legs of the nanowire. MFM measurements at remanence after the injection of a DW into 20-nm-thick permalloy nanowires with widths of (a) 300 and (b) 100 nm, respectively. Magnified images of the DWs are shown in the inset.

Nucleation line

The third technique to nucleate a DW in nanowire uses a separate conducting wire situated above or below and approximately perpendicular to the magnetic nanowire (Hayashi *et al*., 2006a,b; Himeno, Kasai and Ono, 2005; Himeno *et al*., 2005). A current is passed through this wire, which generates a localized Oersted field which is used to reverse the magnetization of a section of the nanowire immediately adjacent to the conducting wire (see Figure 17). Thus two DWs are created. The Oersted field will cause the DWs to move along the nanowire away from the conducting wire a short distance till the Oersted field is decreased below the propagation field of the nanowire. This method is very attractive because it allows the local application of significant local fields of several hundred oersteds on the nanosecond timescale at a very high repetition rate compared to an external electromagnet. On the other hand the current needed to nucleate the DW may be quite high, particularly for thick nanowires with square aspect ratios, so that heating or electromigration may be an issue.

3.4.2 Domain-wall pinning and depinning from local pinning sites

Once a DW is nucleated and injected into a nanowire, it will move along the wire if an applied magnetic field exceeds the propagation field. The propagation field arises from local pinning centers associated, for example, with roughness or defects in the nanowire. For permalloy, it is strongly

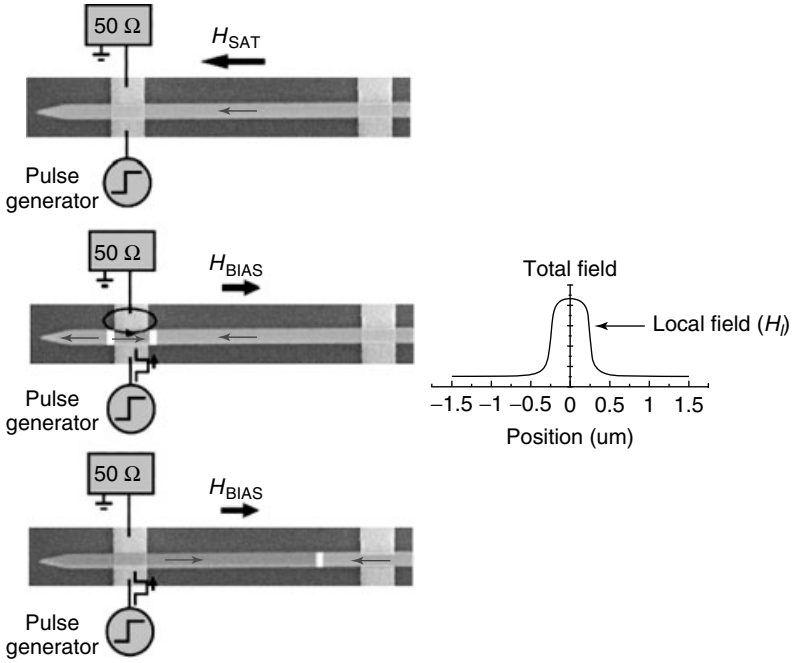

Figure 17. A schematic diagram showing DW injection using a local Oersted field generated in a nearby current lead. (Courtesy of Masamitsu Hayashi.)

dependent on the quality of the samples, and can take values from a few (Faulkner *et al*., 2004) to tens of oersteds (Yamaguchi *et al*., 2004). Note that the propagation field typically depends on the DW position along the nanowire. This means that the observed propagation field for motion of the DW over a given length will depend both on the initial DW position and this length.

Artificial pinning sites can be provided by fabricating appropriately shaped local modifications of the nanowire. In soft nanowires, quite a variety of designs can be used to successfully pin DWs. These include notches, humps, constrictions, or crosses, which lead to potential wells (attractive) or potential barriers (repulsive) of various widths and depths. Pinning centers can also be provided by creating local modifications of the nanowire using, for example, ion bombardment (Holleitner *et al*., 2004) or possibly localized oxidation, localized thermal annealing treatments or by using atomic force microscopes to physically or chemically modify the nanowire (Schumacher *et al*., 2001). It is also possible to use magnetic materials deposited under, on, or near the nanowire to change the magnetic properties of the nanowire in localized regions. One example is the use of magnetically hard CoSm pads on permalloy nanowires (Nagahama, Mibu and Shinjo, 2000). DW pinning has been carried out by varying the thickness of GaMnAs nanowires (Yamanouchi, Chiba, Matsukura and Ohno, 2004) and by using a Hall-cross geometry (Pt/Co/Pt layers by Wunderlich *et al*. 2001) for perpendicularly magnetized nanowires.

The depinning field from a symmetric V-shaped notch is roughly proportional to the notch depth (Yokoyama *et al*., 2000; Himeno *et al*., 2003; Faulkner *et al*., 2004; Klaui *et al*., 2005a). For permalloy wires, depinning fields can reach several hundred oersteds. Values as high as ∼1 kOe have been reported at low temperature in permalloy nanorings (Klaui *et al*., 2003a) and in CoFe nanowires at room temperature (Tsoi, Fontana and Parkin, 2003).

A very important point is that the depth of a pinning potential depends on details of the DW's structure and may, for example, be quite different for T and V walls and even for the same wall if it is of clockwise or counterclockwise chirality. Moreover, since the structure of a DW may evolve with time, for example, because of forces on the DW from current or field, the pinning potential itself may change with time and even during the transit time of a DW across the potential. This makes the notion of DW pinning very complex!

Another point is that the depinning field of a DW from a notch (or protuberance) may depend on the direction of motion of a DW. For example, the propagation field of DWs in nanowires with highly asymmetrically shaped protuberances (Himeno, Kasai and Ono, 2005; Allwood, Xiong and Cowburn, 2004) was found to differ by a factor of two depending on the direction of DW motion. However, even if the pinning site is symmetric, for example a V-shaped notch, the DW depinning fields to either side of the notch may be quite different. This can be because the DW may not

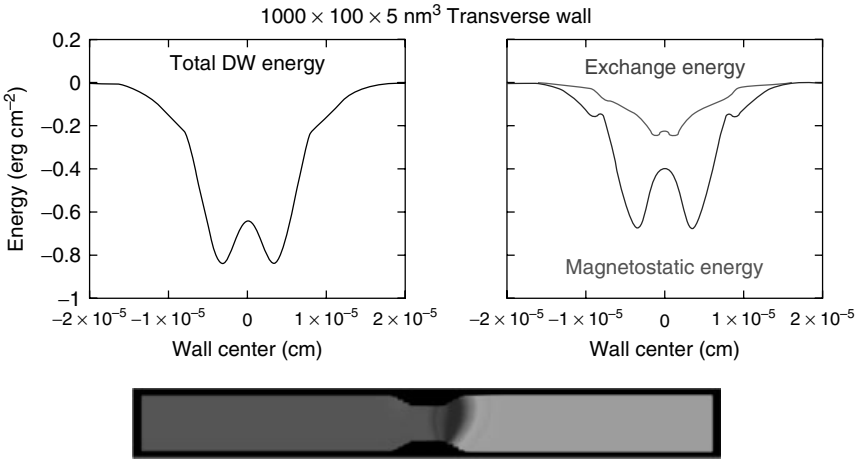

Figure 18. Micromagnetic simulations of the energy landscape of a DW pinned at a notch.

reside in the center of the notch but rather to one side, as discussed later in more detail.

Micromagnetic calculations are very helpful in understanding the pinning of DWs in pinning sites such as notches (see, e.g., a symmetric notch in Figure 18). The pinning potential is determined as follows. First, a stable DW structure is prepared at a specific location, either inside or outside the notch. This state is relaxed in zero field until equilibrium is reached. This equilibrium state is in general a metastable state. Second, a magnetic field is applied so that the DW moves along the nanowire, either away from or across the notch. The magnitude of the field is chosen to be large enough to overcome the pinning potential but is as small as possible so as to ensure that the DW follows the lowest energy trajectory. The latter is encouraged by using a large damping constant (e.g., $\alpha = 1$). The potential energy landscape for the DW is then obtained from the total energy of the system minus the Zeeman energy. The DW position is then calculated from the net longitudinal magnetization of the nanowire. In general, boundary conditions are used to fix the direction of the magnetization of the nanowire at either end along the long axis of the nanowire. Thus the DW energy will be modified when too close to the ends of the nanowire. For the example shown in Figure 18 the nanowire has a width and thickness of 100 and 5 nm, respectively, so that the stable state of the DW in the nanowire is a T wall. There are two minima in the pinning potential at either side of the notch. By considering the contributions of the exchange and magnetostatic energies to the total potential, it is clear that the DW pinning is associated with two main factors (i) the reduction of the DW volume within the notch (i.e., due to the reduced width of the nanowire) and (ii) the reduction of the DW energy when the nanowire's edges are not parallel to the nanowire's long axis. The exchange energy is minimized when the DW volume is reduced. However, the magnetostatic energy plays the more dominant role and, in particular, accounts for the energy minima when the DW sits within either of the two wedged portions of the nanowire, which define the edges of the notch. It should be emphasized that the magnetostatic energy is the dominant contribution to the energy for both V and T head-to-head DWs, accounting for ~80–90% of the wall's energy (McMichael and Donahue, 1997). Thus, the pinning potential is dominated by magnetostatic rather than volumetric effects in the head-to-head DW case, in contrast to the theoretical prediction for a Bloch wall trapped at a nanconstriction (Bruno, 1999).

The pinning potential becomes more complex for thicker wires, as illustrated in Figure 19. The nanowire width and notch shape are the same as before, except that the nanowire

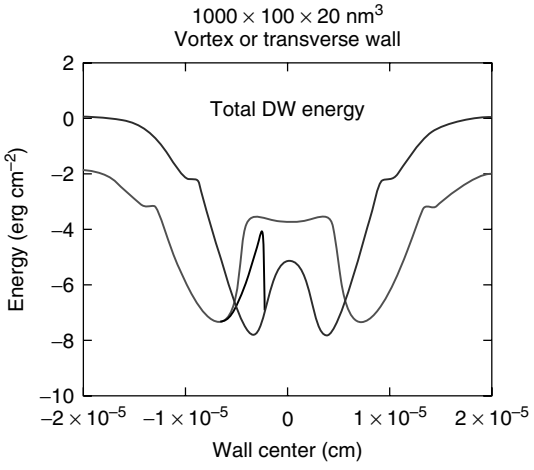

Figure 19. Micromagnetic calculations of the energies of a V (medium gray) and a T (dark gray) DW pinned at a notch of the same form as that shown in Figure 18. The black curve shows the energy of the DW when it transforms from a V to a T wall as it enters the notch.

thickness is increased from 5 to 20 nm. In this case, the stable state outside the notch is a V wall. In these simulations, the initial state was either a V or a T wall centered in the notch and the DW was moved away from the notch to the left or right with magnetic fields to calculate the potential. The pinning potential exhibits the same features as for the thinner wire, with two minima at either side of the notch, for both the V and T DWs. However, there is an additional shallow local minimum in the middle of the notch for the V wall. This example is interesting because the structure of the DW with the lower energy is different within (T wall) and outside the notch (V wall). This leads to a change of the wall structure when the V wall moves across the notch, as illustrated by the black curve in Figure 19. The energy barrier for this transformation is indeed smaller than that needed to move the vortex wall across the notch.

It is quite typical that there are significant variations in the DW pinning and depinning processes in repeated experiments, leading to, for example, variations in depinning fields. As discussed earlier, one reason is that there may be several metastable structures of a DW trapped at a notch, each with a different pinning potential (Hayashi *et al*., 2006b). A particularly interesting example is shown in Figure 20 for the case of a DW injected and trapped at an artificial pinning site in a permalloy nanowire, 10 nm thick and 300 nm wide. Four distinct DW states are found, whose structures, as determined from MFM images, correspond to two V walls and two T walls, one of each with a clockwise and the other with a counterclockwise chirality. Note that the DWs are pinned at the left side of the notch in the images because they were injected from the left side. Each of these DWs is a metastable state with a corresponding pinning potential and associated depinning fields, which can be well reproduced by micromagnetic calculations. Interestingly, even though the notch is symmetric, the pinning potential is quite asymmetric for one chirality of the T and V DW. Similar results have been reported by Miyake *et al*. (2005) for a nanocontact much narrower (∼15 nm) than the example shown in Figure 20.

3.4.3 Time-resolved experiments

Field-driven DW dynamics were studied in detail in the 1970s with regard to magnetic bubble memory applications, as extensively reviewed by Malozemoff and Slonczewski (1979). As mentioned in paragraph 2.2.3, a 1D theory of DW motion was developed to account for Bloch-like DWs. Many of the results of this theory, however, also apply to more complex DW structures.

In an ideal situation without pinning, the motion of a DW along a magnetic nanowire has distinct characteristics depending on the strength of the applied field. The motion

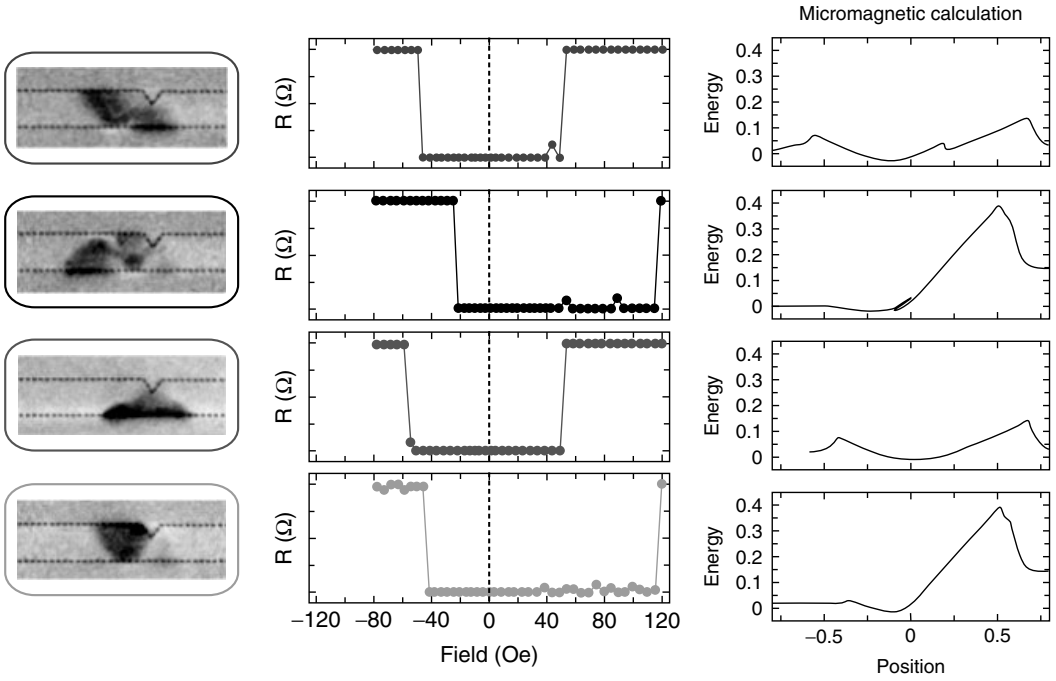

Figure 20. Measured depinning fields from a notch for DWs with metastable T and V structures, in a 10-nm-thick, 300-nm-wide permalloy nanowire. Also shown are the corresponding energy landscapes calculated from micromagnetic simulations. (Reproduced from Masamitsu Hayashi, Luc Thomas, Charles Rettner, Rai Moriya, Xin Jiang, and Stuart S.P. Parkin, *Phys. Rev. Lett.* **97**, 207205 (2006), copyright © by the American Physical Society, with permission from APS.)

can be described analytically within the 1D model. In a first regime, at low fields, the DW velocity increases at short times to attain a steady value. In this stationary regime, the velocity increases linearly with field, according to the relation:

$$v(H) = \frac{\gamma \Delta}{\alpha} H \tag{21}$$

When the field exceeds a certain threshold value, the so-called Walker breakdown field, the average DW velocity drops sharply. Above this field, the DW moves in a complex manner, and its velocity oscillates in time. When the field is increased further, the average velocity is again proportional to the field, although the wall mobility is strongly reduced compared to the low-field value. The velocity in this second regime depends on field according to the relation:

$$v(H) = \frac{\gamma \Delta}{\alpha + \alpha^{-1}} H \tag{22}$$

When pinning is included, the DW only moves along the nanowire when the field exceeds a critical value H_c. Depending on the nature of the potential (whether it is conservative or nonconservative), the DW velocity can be written (Malozemoff and Slonczewski, 1979; Baldwin and Culler, 1969), for $|H| > H_c$, as:

$$v(H) \propto \frac{(H^2 - H_c^2)}{H}$$
$$\text{or} \qquad v(H) \propto H - H_c \qquad \text{respectively} \tag{23}$$

Only a few experimental studies have explored the time-resolved motion of DWs in nanowires. Ono *et al*. (1999b) have used GMR measurements to probe the propagation of a DW in a trilayer structure NiFe (40 nm)/Cu (20 nm)/NiFe (5 nm). The nanowire was 500 nm wide and extremely long (2 mm). The DW motion in the 40-nm-thick layer was probed on the microsecond timescale, for magnetic fields between 100 and 150 Oe. The DW velocity was found to increase linearly with field above a threshold field ($\sim$35–40 Oe). The wall velocity v was between 150 and 250 m s^{-1}, corresponding to wall mobilities v/H of about 2.6 m s^{-1} Oe^{-1}. Atkinson *et al*. (2003) performed a similar study on a single layer permalloy nanowire (5 nm thick, 200 nm wide) using time-resolved MOKE experiments. The wire was much shorter (about 50 µm) than that used in the study of Ono *et al*. and the DW motion was probed on much shorter timescales (20–500 ns). These authors also found that the DW velocity increased linearly with field for fields above $\sim$25 Oe. However, the DW mobility was more than 10 times higher ($\sim$38 m s^{-1} Oe^{-1}). These two experiments were performed in relatively high fields, compared to the expected Walker breakdown fields. Moreover, in both cases the propagation fields were large. Nevertheless, these authors interpreted their data using the theory in the low-field regime, (equation (21)) in which the velocity is proportional to field. They deduced extraordinarily high values of the Gilbert damping constant, namely, $\alpha = 0.63$ (Ono *et al*., 1999b) and $\alpha = 0.053$ (Atkinson *et al*., 2003), in both cases much higher values than those found in thin permalloy films (0.01–0.02) (Nibarger, Lopusnik and Silva, 2003; Nibarger, Lopusnik, Celinski and Silva, 2003).

Recent experiments by Beach *et al*. (2005) and our work (Hayashi *et al*., 2006a) suggest that these surprisingly high damping constants (i.e., small DW mobilities) more likely indicate DW motion in the high-field regime above the Walker threshold field, in which equation (21) is not valid. Indeed, in the high-field regime, the velocity also increases linearly with field, but is lowered by a factor α^2 compared to the low-field regime (see equations (21) and (22)). Clear evidence of the Walker breakdown was observed in the work of both Beach *et al*. (2005) and Hayashi *et al*. (2006a), with a field dependence of the velocity following the textbook behavior (as shown, e.g., in Figure 22). The Walker breakdown field was found to be only a few oersteds, and the data are consistent with reasonable values of the Gilbert damping constant. Note that we have recently reported the experimental observation of periodic oscillations of the DW structure, as predicted above the Walker breakdown (Hayashi *et al*., 2007b).

The experiments discussed above address the ballistic (or viscous) regime for DW motion, for which the DW dynamics can be described by the Landau–Lifshitz–Gilbert equation at zero temperature. Thermally activated processes allow for DW motion below the critical field H_c. This has been observed in nanowires made with thin Pt/Co/Pt trilayers and two regimes have been identified. The thermally activated regime is characterized by a wall velocity written as (Wunderlich *et al*., 2001; Ravelosona *et al*., 2005):

$$v(H, T) = v_0 \exp\left(\frac{-2M_s V(H_c - H)}{k_B T}\right) \tag{24}$$

where k_B is the Boltzmann constant and T the temperature, H and H_c are the applied and propagation fields, respectively, and V is the activation volume. In the creep regime, the DW velocity is written as (Cayssol *et al*., 2004):

$$v(H, T) = v_0 \exp\left(\frac{-U_c (H_c/H)^{1/4}}{k_B T}\right) \tag{25}$$

with U_c and H_c are the scaling energy and the critical field, respectively. In this creep regime, the wall velocity was found to vary as the inverse of the wire width, and to decrease for larger wire roughness (Cayssol *et al*., 2004). Both regimes are characterized by very small DW velocities ($\ll$1 m s^{-1}).

3.5 Current-induced domain-wall motion

3.5.1 Experimental considerations

The first studies of current-driven DW motion were performed by Berger *et al*. in extended permalloy films. In these studies (and also in the more recent work of Gan *et al*. (2000)), the DWs have 180° Bloch, Néel, or cross-tie DW structures, the current flows in the direction perpendicular both to the wall and the magnetization within the domains, and there is no pinning besides the local defects responsible for the film's coercivity. Several DWs are probed at the same time, in contrast to recent experiments on magnetic nanowires, which probe single DWs. For nanowire samples with perpendicular anisotropy, the current is also perpendicular to both the wall and to the domain magnetization direction, as in extended films. However, for head-to-head DWs in nanowires, the current is perpendicular to the wall but parallel to the magnetization in the domains. These different geometries must be taken into account in experiments, which probe the current-induced motion of DWs since, for example, the role of the self-field (Oersted field) and the hydromagnetic domain drag are different.

Current-induced DW experimental studies can be separated into two broad categories, current-induced DW propagation and current-induced DW depinning. In the first category, the position of the DW in a nanowire is probed before and after the application of the current. Thus, the critical current for DW motion and the DW displacement direction and distance can be inferred. When current pulses are used, the DW velocity can also be determined. In the second category, the field to depin DW is measured as a function of the applied current.

3.5.2 Current-induced domain-wall motion in zero field

From an experimental viewpoint, current-induced DW motion occurs above a critical current density J_c. As mentioned earlier, this is an important parameter both for comparing experiment with theory and for potential technological applications. It is unfortunate that the magnitude of J_c is often ambiguous, making comparison between data and theory difficult.

1. Uncertainties with regard to the definition of the critical current
   (a) What is the experimental definition of the critical current?
   The experimental definition of the critical current depends on the type of measurement and the sensitivity of the experimental technique. Indeed, the critical current for DW motion over micron-sized distances can be quite different from that needed to change the DW structure within a notch or move a DW over very short distances between neighboring pinning sites. For example, in the early work by Salhi and Berger (1994), wall motion was detected by Kerr microscopy, such that 'the critical current density is determined by finding the smallest value for which a sequence of 600 pulses produces a detectable wall displacement'. Given the resolution of the setup, this corresponds to an overall displacement of about 12 μm (or 20 nm/pulse, assuming all pulses induce the same DW displacement, which is far from certain). By contrast, in a recent report by Ravelosona *et al*. (2005), DW motion over a few tens of nanometers can be detected directly in a Hall cross, owing to the high sensitivity of the AHE effect. In summary, the experimental definition of the critical current is as vague as 'the minimum current for some measurable change to take place'.
   (b) Joule heating
   The current densities used in most experiments are large (see Table 1) and Joule heating is significant. This temperature increase can play a significant role in current-induced DW dynamics, as discussed later. Here we only address experimental consequences of the heating of the nanowire. In particular, current pulse generators often deliver constant voltage pulses rather than constant current pulses so that the current delivered depends on the load resistance. While, for dc or long current pulses this is easily corrected by directly measuring the actual current delivered to the nanowire, this correction becomes more difficult for short current pulses. The temperature of a nanowire can increase by many hundreds of degrees on the nanosecond timescale depending on the amount of Joule heating. This is obviously more significant the larger the current and the higher the resistivity of the nanowire (and the electrical contacts to the nanowire). Thus, the resistivity of permalloy nanowires, for example, can easily increase by a factor of 2 or 3 in 1 or 2 ns, and similarly decrease on very short timescales so that these temperature changes cannot be detected by dc measurements after the current pulses are applied. Thus, it is very important to carry out time-resolved resistance measurements. The change in the nanowire resistance due to heating can lead to incorrect values of critical currents for DW motion, if it is not properly taken into account. For example, this effect accounts for a reduction of the critical current density by a factor of 2 between the values published by Yamaguchi *et al*. (2004, 2005).

Table 1. Compilation of values of the critical current density for DW motion in various nanowires. Note that some experiments are performed at low temperature.

Material	Thickness (nm)	Width (nm)	Wall type	Current (dc or pulse length)	Type of experiment	Critical current $J_c(10^7\,A\,cm^{-2})$	References
NiFe	28–45	3.5 mm	180 NW	<2 μs	P	1–1.4 (nc)	Freitas and Berger (1985)
NiFe	14 < t < 86	3 mm	180	1 μs	P	2.3–360 (nc)	Hung and Berger (1988)
NiFe	120 < t < 740	3.5 mm	180	50–300 ns	P	0.01–1 (nc)	Salhi and Berger (1994)
NiFe	102–161	20 μm	180 BW	10 ns (rt)	P	2.5–4.3 (nc)	Gan *et al*. (2000)
NiFe	40	200	HH	dc	S	1 (with field)	Kimura *et al*. (2003)
NiFe	34	400	HH	dc	S	7 (with field)	Klaui *et al*. (2003b)
NiFe	5	120	HH	dc	S	7	Vernier *et al*. (2004)
NiFe	30	<1 μm	HH	dc	S	1.1	Lepadatu and Xu (2004)
Ni	30					2.2	
NiFe	10	240	HH	0.3–1 μs	P	11 (nc)	Yamaguchi *et al*. (2004)
						6.7 (c)	Yamaguchi *et al*. (2006b)
NiFe	40	300	HH	20 ns (rt)	P	7.5 (nc)	Florez, Krafft and Gomez (2005)
NiFe	5–35	200	HH	20 μs	S	05–13 (nc)	Klaui *et al*. (2005c)
NiFe	10	500	HH	10 μs	P	22 (nc)	Klaui *et al*. (2005b)
CoFe	10	100	HH	dc	S	1 (with field)	Tsoi, Fontana and Parkin (2003)
NiFe	10–113	110–275	HH	5 μs	P	3.9–7.7 (c)	Yamaguchi *et al*. (2006a)
NiFe	35	110	HH	10 μs	S	27.5 (c)	Laufenberg *et al*. (2006b)
NiFe	10	300	HH	10–100 ns	P	10 (c)	Hayashi *et al*. (2007a)
NiFe	10	300	HH	4 ns	S	30 (c)	Hayashi *et al*. (2006b)
SV		1000	HH	dc	P–S	2.6	Grollier *et al*. (2002)
SV	10	300	HH	dc	P–S	<0.8	Grollier *et al*. (2003)
SV	5	300	HH	0.4–2 ns	P–S	<0.8 (full sw) <0.27 (2 μm)	Lim *et al*. (2004)
MnGaAs	17–25	20 000	180 BW	100 ms	P	0.008	Yamanouchi, Chiba, Matsukura and Ohno (2004)
Pt/Co/Pt	0.5	200	180 BW	dc	P	<1	Ravelosona *et al*. (2005)

P: DW propagation experiment; S: switching experiment; dc: dc current; rt: rise time of the current pulse for exponentially shaped pulses; c/nc: values corrected/ not corrected for resistance change induced by Joule heating.

There is another more subtle consequence of the resistance increase during the application of current pulses to a nanowire. Indeed, both the rate of change and the magnitude of the temperature rise from Joule heating depend strongly on the thermal conductivity of the nanowire to the substrate. The timescale of the resistance increase can vary by 1 or 2 orders of magnitude depending on the thermal conductivity of the seed layers on which the nanowire is prepared, the quality of the nanowire/seed layer interface and the substrate material. For short pulses compared to this thermal timescale, the current becomes time dependent. Therefore, the actual value of the critical current for DW motion can depend on the relative timescales of heating and that of the DW dynamics.

(c) Inhomogeneous current flow

For nanowires with varying width or for multilayered structures, such as spin valves, the definition of the current density is ambiguous. In the case of nanowires with notches, the current density reaches its maximum value in the narrowest part of the wire. However, in many cases, the DW is not trapped in the middle of the notch, but rather to one side of the notch, so that it is not clear which nanowire width should be used to calculate the critical current density. For the case of spin-valve stacks, a large fraction of the current flows in the nonmagnetic spacer. The structure studied by Grollier *et al*. is one example (Grollier *et al*., 2003). The spin-valve stack used was composed of CoO (3)/Co (7)/Cu (10)/NiFe (5)/Au (3), where the thicknesses are given in nanometers and DW motion was studied in the NiFe layer. If the current density is assumed to be uniform throughout all the layers then the critical current density reported by Grollier *et al*. in zero field was $\sim 8 \times 10^6\,A\,cm^{-2}$. On the other hand, if one assumes reasonable values of the conductivity of each layer, the critical current density in the NiFe layer is only $\sim 1.8 \times 10^6\,A\,cm^{-2}$,

which is nearly five times smaller! It is interesting to note that, in either case these critical current densities are surprisingly low compared to other studies of current-induced DW motion. Similarly, when a magnetic nanowire is prepared on a seed layer (e.g., for improved film quality) or with a cap layer (e.g., to prevent oxidation or to aid in the fabrication of nanowire devices), some of the current may flow through these layers and affect the determination of the critical current density in the magnetic layer itself.

(d) Parasitic magnetic fields and self-field
The field dependence of the critical current for DW motion will be discussed in more detail in Section 3.5.4. However, for weakly pinned DWs and nanowires with small propagation fields, parasitic magnetic fields such as the remanent field of an electromagnet, or the self-field from current passing through the electrical leads to the sample can easily influence critical current measurements. The self-field from the current passing through the magnetic nanowire itself can also play a significant role. For straight nanowires, its influence is often neglected because there is no net field along the nanowire direction, assuming uniform current flow. However, there will be strong highly nonuniform components of the currents self-field in directions transverse to the nanowire. Even though the average value should be zero in the ideal case, it is difficult to rule out 'wall streaming' effects, which were described by Berger in several publications (Salhi and Berger, 1994; Berger, 1992): the local inhomogeneous fields associated with a current pulse can shake the DW significantly and assist its motion by effectively reducing the local pinning. In any case, for inhomogeneous current flows, for example, in spin-valve stacks, as mentioned above, there will be a net nonzero contribution of the Oersted field in the direction transverse to the nanowire within the magnetic layer in which the DW is moved.

2. Critical current density in zero field
Values of the critical current density measured in zero fields for various magnetic nanowires are complied in Table 1. Most of these data were obtained for permalloy nanowires. Very few experimental results have been reported for other materials. It is interesting that much smaller current densities have been reported in nanowires formed from GaMnAs, Pt/Co/Pt and spin-valve-based structures than for permalloy nanowires, although all of these experiments are subject to detailed interpretation.
Results reported for permalloy nanowires by different groups vary significantly, perhaps not surprising considering the wide variety of techniques and geometries used in these studies and the uncertainty in the measurement of J_c. Some general conclusions can be drawn from these data, which are plotted in Figure 21 as a function of the sample thickness:

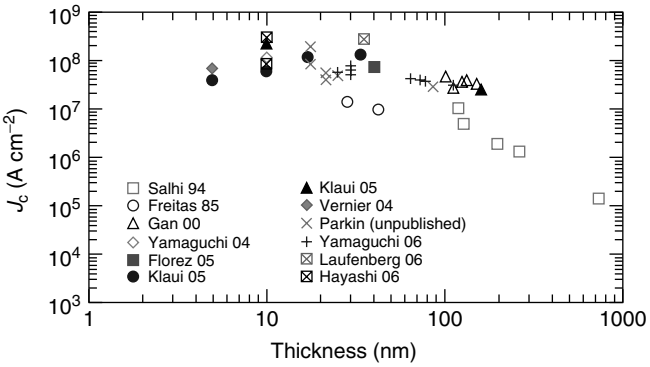

Figure 21. Critical current for DW motion in permalloy structures reported in the literature as listed in Table 1, plotted as a function of the sample thickness.

(a) Shorter current pulses allow the use of higher current densities before breakdown of the nanowire. The dependence of the critical current density on pulse length has been investigated by several groups. Pulse lengths between 50 and 300 ns were explored in Salhi and Berger (1994) and between 0.4 and 2 ns in Lim *et al.* (2004). In both cases, no significant variation in J_c was found.

(b) The wire width does not seem to play a significant role. In particular, 180° DWs in large structures and head-to-head walls in narrow wires exhibit very similar critical current densities. However, in all these experiments, the aspect ratio of the nanowire's cross section is about the same, the width always being much larger than the thickness.

(c) The wire thickness seems to play a more important role. For films thicker than about 50 nm, Salhi and Berger (1994) have observed that J_c decreases as $1/t^2$ (in the 120–740 nm range). This dependence is explained by current-induced distortions of the Bloch wall. For wires thinner than about 40 nm, J_c is between 5 and 30×10^7 A cm^{-2}, if the current is corrected for the resistance increase during the pulse. There is no clear dependence of J_c in this thickness range when considering all the available experimental data. However, Klaui *et al.* (2005c) have reported a significant increase, from 5.0×10^7 A cm^{-2} for 5-nm-thick to 1.3×10^8 A cm^{-2} for 35-nm-thick permalloy nanowires. Note that these experiments were performed at low temperature.

(d) There is no clear correlation between J_c and the wall structure. In particular, head-to-head DWs in narrow wires and 180° DWs in large structures exhibit very similar values.

(e) Surprisingly, the magnitude of the DW pinning does not appear to play any significant role on the critical current density. Data summarized in Figure 21 show results for both strongly pinned DWs (with depinning fields up to 200 Oe) and extended films, with propagation fields of a few oersteds. Different theories of DW motion arrive at different conclusions as to whether J_c is intrinsic or extrinsic. To date experimental results seem rather inconclusive. Indeed, there have been two apparently contradictory attempts to find a scaling rule for different magnetic nanowire samples. In the first case (Yamaguchi *et al*., 2006a), Ono's group plot J_c versus the transverse anisotropy times the DW width $H_k\Delta$ for permalloy nanowires. A roughly linear variation is observed, as given by equation (15) which describes an intrinsic critical current, in the presence of adiabatic spin torque, without a β term. By contrast, Berger presents a different scaling law (Berger, 2006), in which the DW mobility is plotted versus the aspect ratio of the wire (itself a function of the DW width) and includes different magnetic materials. His conclusion is that exchange drag (i.e., momentum transfer or nonadiabatic spin torque) can largely account for the various results, which means that the critical current is in fact extrinsic (i.e., only related to coercivity or pinning).

3. DW propagation direction and distance

Experimental results for samples made with 3d metals (NiFe, CoFe, Ni, Pt/Co/Pt) show consistently that DWs move along the electron flow (or opposite to the current direction) at zero or low fields, in agreement with the spin-torque model. The direction of DW motion is also opposite to the current direction for GaMnAs, even though the carriers in this system are holes (Yamanouchi, Chiba, Matsukura and Ohno, 2004). Two other important experimental findings agree with spin-torque models. First, the DW motion direction reverses with the current polarity. Second, head-to-head and tail-to-tail DWs move in the same direction with current, so that simple field-driven mechanisms can be ruled out.

Even though the overall propagation is along the electron flow, the propagation distance can vary significantly, both for a single wall over repeated experiments and for several walls during the same current excitation. This was first reported by Berger, who observed that only a subset of walls in the field of view of a Kerr microscope moved during a current pulse (Freitas and Berger, 1985). This behavior was explained by local variations of the coercivity and/or the presence of a parasitic field. Gan *et al*. (2000) also observed significant variations of wall motion in large structures (20 μm wide). The distribution of the DW propagation distance was significantly different, and in some cases, DWs moved backwards (opposite to the electron flow). Moreover, portions of the same wall sometimes moved in opposite directions.

Experiments on current-induced DW motion in nanowires exhibit similarly strong variations. For example, Yamaguchi *et al*. (2004) report that five identical current pulses applied to a V wall result in motion of the DW of 2.2, 0.9, 0, 1.9, and 1.1 μm, respectively. In our own experiments we have also observed wide variations in DW motion direction and distance in many cases. Occasionally, DWs are found to move opposite to the electron flow, particularly when DWs are depinned from a notch.

These fluctuations could be related to local variations of the DW pinning strength, as was invoked for larger structures. However, DWs can be moved repeatedly across exactly the same position in a nanowire and thus, it should be possible to correlate the DW displacement induced by a current pulse with position in the nanowire. There is no evidence of such an effect in Yamaguchi's paper. Another possibility is that the DW structure may evolve during motion, as was observed in experiments by (Klaui *et al*., 2005b; Jubert *et al*., 2006), who report a gradual decrease of the displacement of a V DW when consecutive pulses are injected across it. The DW eventually stops after a few pulses. High-resolution imaging with SEMPA revealed that the DW structure was modified by the current pulses, which caused the DW to evolve from a V to a T wall structure. Such a systematic variation of the DW displacement with successive pulses has not been observed in other studies (Yamaguchi *et al*., 2004; Gan *et al*., 2000).

Many other results are not fully understood. For example, Lim *et al*. (2004) have observed a reversal of the DW propagation direction when the current increases above some threshold value.

3.5.3 Domain-wall velocity

The first measurements of current-driven DW velocity were obtained by simply dividing the observed DW displacement after the current pulsed had been applied by the current pulse length, for microsecond long current pulses. However as discussed in the preceding text, the DW displacement often exhibits significant fluctuations over repeated experiments. It is unclear whether such estimates of the DW velocity are meaningful.

In several reports, it was shown that the DW displacement scales approximately with the pulse length (Yamaguchi *et al*., 2004; Klaui *et al*., 2005b; Jubert *et al*., 2006) giving a more reliable measurement of the wall velocity. In both studies, the current density was slightly higher than J_c and long pulses were used, between 0.3 and 1 µs in Yamaguchi *et al*. (2004), and 1 order of magnitude larger (10 µs) in Yamaguchi *et al*. (2004) and Klaui *et al*. (2005b). The measured velocities were very small, of the order of $3-5\,\mathrm{m\,s^{-1}}$ and $0.1-0.5\,\mathrm{m\,s^{-1}}$, respectively.

Interestingly, DW velocities estimated by dividing the DW displacement by the current pulse length are much higher when short pulses (nanoseconds long) are used. For example, Lim *et al*. (2004) reported switching a spin-valve nanowire in zero field with pulses as short as 0.4 ns and concluded that the DW moves >20 µm in less than 1 ns. The corresponding DW velocity of about $20\,\mathrm{km\,s^{-1}}$ seems much too high to be meaningful. It may suggest a more complex mechanism of DW motion, perhaps involving DW motion long after the end of the current pulse. Such overshooting and a DW inertia effect have been observed in the context of field-driven motion of magnetic bubbles (Malozemoff and Slonczewski, 1979). We have also performed experiments using pulse lengths between 0.5 and 100 ns. In some cases, we have observed DW displacements of ∼1 µm for current pulse lengths of 1 ns, with an associated 'velocity' of up to $1000\,\mathrm{m\,s^{-1}}$. Importantly, we do not observe any clear linear scaling of the DW displacement with the pulse length for these long pulses (note that the data vary widely). This also suggests that the mechanism of DW motion is more complex for short excitations.

Recently, the DW velocity in permalloy nanowires has been measured more accurately by time-resolved measurements, in the presence of a combination of field and current (Hayashi *et al*., 2006a; Beach *et al*., 2006) as well as current alone (Hayashi *et al*., 2007a). Both measurements were 'time-of-flight' experiments, in which the velocity is obtained by dividing a distance traveled by the DW by the time the DW takes to move between two points along the nanowire. In both cases, data were averaged over a large number of repetitions. The distance was between different positions of the laser spot in the Kerr measurements by Beach *et al*. (2006) and between two electrical contacts in the AMR studies by Hayashi *et al*. (2006a, 2007a).

In the presence of field and current, the DW velocity is affected differently depending on the relative magnitude of the field and current and the current polarity (Hayashi *et al*., 2006a) (see Figure 22). When the electron flow is along the direction of the field-driven motion, the DW velocity is enhanced by up to $\sim 100\,\mathrm{m\,s^{-1}}$. The Walker breakdown field is not significantly affected, at least not for the current densities investigated. By contrast, when the electron flow is opposite to the direction of field-driven motion, the DW velocity is reduced. The DW motion can even be stopped (or slowed below the experimental detection limit) – when the field is smaller than ∼25 Oe (2.5 times the Walker breakdown field). Note that in the case of a moving DW, there does not seem to be a critical current: the velocity varies continuously with the current density, and even small currents influence the DW velocity.

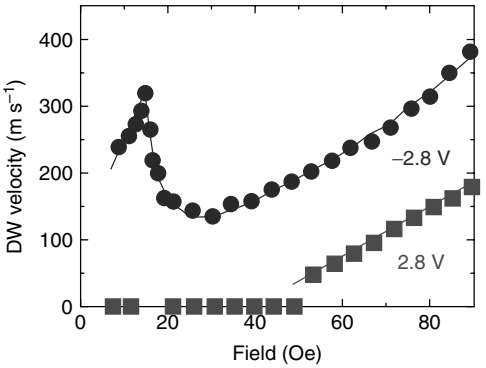

Figure 22. DW velocity determined by time-resolved AMR measurements in a 10-nm-thick, 200-nm-wide permalloy nanowire, in the presence of current flowing in both directions. The current density is $\sim 1.4 \times 10^8\,\mathrm{A\,cm^{-2}}$. (Reproduced from figure 2(c) in M. Hayashi, L. Thomas, C. Rettner, R. Moriya, and S.S.P. Parkin, 'Direct observation of the coherent precession of magnetic domain walls propagating along permalloy nanowires', *Nature Physics* **3**, 21 (2007).)

DW motion driven by current only was also reported. In this case, the DW motion was only detected for current densities higher than $\sim 7-10 \times 10^7\,\mathrm{A\,cm^{-2}}$. Motion was along the electron flow. The DW velocity increases with the current, from $\sim 80\,\mathrm{m\,s^{-1}}$ at the threshold current up to about $150\,\mathrm{m\,s^{-1}}$. Note that the DW velocity saturates for the highest current densities investigated, although the origin of this effect is not clear. Interestingly, such high velocities (more than 2 orders of magnitude larger than those reported by Yamaguchi and Klaui) approach and may even exceed the rate of spin angular momentum transfer given by the parameter u (equation (15)) (Hayashi *et al*., 2007b).

Finally, we briefly mention experiments performed on the current-induced motion of DWs in GaMnAs nanowire structures by Ohno's group (Yamanouchi, Chiba, Matsukura and Ohno, 2004; Yamanouchi *et al*., 2006) (similar data were also published recently by Tang, Kawakami, Awschalom and Roukes, 2006) but only in combination with a magnetic field). Ohno *et al*. report DW motion, driven by current only, with DW velocities spanning more than 5 orders of magnitude up to $22\,\mathrm{m\,s^{-1}}$. Two different regimes are observed: the DW velocity increases roughly linearly with the current density for currents above a threshold current (between 3.5 and $5.5 \times 10^5\,\mathrm{A\,cm^{-2}}$ depending upon the temperature). The data

are consistent with the spin-transfer efficiency expected from equation (15) (albeit slightly larger), once the temperature dependence of the magnetization and the spin polarization are taken into account. A second subthreshold regime is observed, in which the DW velocities are between 10^{-5} and $1\,\mathrm{m\,s^{-1}}$, which is interpreted as DW creep.

3.5.4 Field dependence of the critical current

The field dependence of the critical current has been studied by several groups. In most of these experiments, the DW is first pinned at either a defect (Thomas *et al*., 2006; Laufenberg *et al*., 2006b; Grollier *et al*., 2004; Lim *et al*., 2004), or a notch (Florez, Krafft and Gomez, 2005; Hayashi *et al*., 2006b; Klaui *et al*., 2005c) or at a cross (Ravelosona *et al*., 2005). In one report (Vernier *et al*., 2004), a quite different experimental method was used: the propagation field along a nanowire is measured while dc currents of both polarities are applied. All these studies show some consistent trends:

- The critical current for DW depinning decreases when the field is increased.
- DW motion occurs along the field direction, except for very small fields.
- The polarity dependence of the depinning current is weak. The strongest effect of the current is a reduction of the depinning field independent of the current polarity.
- Both linear and nonlinear field dependences of the critical current have been reported.

We have studied the field dependence of the critical current for depinning a DW from a notched pinning site, with widely varying pinning strengths, in NiFe wires with various different dimensions (see e.g., Hayashi *et al*., 2006b). Our results show very little dependence on the current polarity, in agreement with other studies. In most cases, the critical current exhibits a strongly nonlinear variation with field. We observe two distinct regimes. In a low-field regime, the critical current depends only weakly on the notch pinning strength (as measured by the depinning field) and the magnetic field. By contrast, in a high-field regime, the field dependence is much stronger. An illustration of these two regimes is shown in Figure 23, for permalloy nanowires with different notches. Note that for these experiments, two DWs were nucleated on either side of the wire. Current-driven depinning most likely causes annihilation of these two DWs.

3.5.5 Subcritical domain-wall transformations and metastability

The role of metastable DW states was first noted by Berger (1992). He pointed out that in some thickness range, Bloch and Neel walls are nearly degenerate. Thus, only a small torque is needed to rotate the wall's magnetization from one DW state to the other, resulting in a reduced critical current.

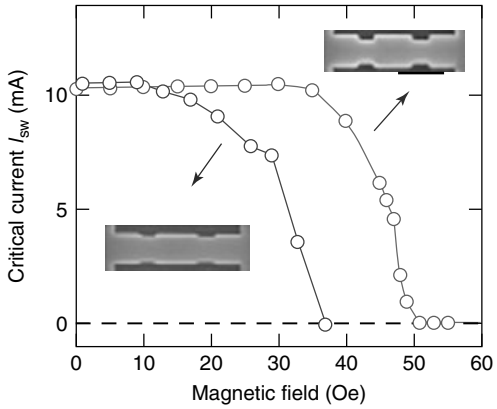

Figure 23. Field dependence of the critical dc current for depinning DWs in 18-nm-thick, 315-nm-wide, permalloy nanowires.

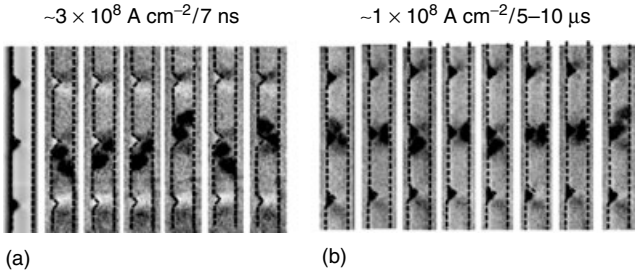

Figure 24. DW transformations measured by MFM in 20-nm-thick, 300-nm-wide permalloy nanowires upon successive application of current pulses.

Current-driven DW changes can take place below the critical value or depinning. For example, in the work of Florez, Krafft and Gomez (2005), it was observed that the wall structure was modified even though the DW was still trapped within the notched pinning site. We have also observed this behavior, both using MFM and AMR experiments. Examples of the modification of the DW structure upon application of current pulses are shown in Figure 24. The NiFe nanowire is 300 nm wide and 20 nm thick. In the first set of experiments (a), the DW retains its V structure, but the V chirality is reversed. In the second set of images (b), the original V DW is transformed into a T wall, which remains stable for a few pulses before transforming back to into a V wall (with a reversed chirality). The detailed mechanisms responsible for this behavior are not fully understood. However, these experiments suggest that the electric current allows the magnetic system to access metastable states, even if the energy barriers separating these states are often very high (for example, $\sim 6 \times 10^{-11}$ erg in the

example of Figure 19). Thermally activated transformations are also possible if the energy barrier is smaller. For example, transformation from a T to a V DW was observed at ∼550 K by Laufenberg *et al*. (2006a) in 7-nm-thick, 730-nm-wide permalloy nanorings. This corresponds to an energy barrier of $\sim 8.0 \times 10^{-14}$ erg.

Current-driven depinning also exhibits significant stochastic variations, particularly in low fields. In repeated experiments, the probability for DW depinning varies significantly. In other words, the critical current at a given field can vary widely. This can partly be related to the multiple metastable DW states at a notch.

3.5.6 Dynamical effects

Most experiments published so far have used dc currents or long pulses (microseconds). Little is known on possible dynamical effects driven by shorter pulses or alternating current. Until recently, there were only a few experimental reports on the influence of the pulse length for nanosecond-long current pulses. Salhi and Berger (1994) studied the influence of a series of square pulses with lengths between 50 and 300 ns on the critical current, and they did not observe any dependence. The same insensitivity to pulse length has been reported by Lim *et al*. (2004) for a spin-valve nanowire, for much shorter pulses (between 0.4 and 2 ns).

However, Berger has proposed several interesting dynamical effects related to current pulses or ac currents. For example, in the case of pulses with fast rise-times and slow fall-times, he proposed a 'wall streaming' mechanism in which the DW can escape a pinning potential on the trailing edge of the pulse (Salhi and Berger, 1994; Berger, 1992). He also proposed several other notions such as the existence of a 'Ferro–Josephson' effect (Berger, 1986) where the precession of the DW driven by the current generates a dc voltage across the DW, following a mechanism quite similar to the Josephson effect in superconducting junctions. In a further development, he showed that the combination of a hard-axis, high-frequency field and a dc current could lead to the locking of the DW precession frequency with the ac field. This would give rise to steps in the current dependence of this induced voltage, similar to Shapiro steps in Josephson junctions (Berger, 1991b). Finally, he also showed that ac currents could generate oscillations of a DW, with a resonance frequency of ∼10–100 MHz (Berger, 1996).

In a recent experiment, the influence of a small ac excitation has been studied by Saitoh *et al*. in a U-shaped permalloy nanowire (Saitoh, Miyajima, Yamaoka and Tatara, 2004). The authors observed a peak in the device resistance as a function of the frequency of the ac current in the MHz range. The peak frequency could be tuned between ∼5 and 25 MHz by varying the applied magnetic field. Interestingly, the peak was observed even though the excitation is extremely small (about two orders of magnitude smaller than the dc critical current). These data are understood in terms of a current-driven resonance of the DW in the parabolic potential created by the applied field. This interpretation is supported by a model by Tatara, Saitoh, Ichimura and Kohno (2005). The authors propose that this behavior results from momentum transfer (or nonadiabatic spin torque) rather than spin transfer. Even though the momentum transfer (proportional to the DW resistance in Tatara's model) is very small, it is amplified at resonance and becomes dominant. The authors also suggest that the amplitude of the DW displacement is very large (∼10 μm), although there is no direct evidence to support this claim.

We have reported recently that the current-driven motion from a local pinning potential is indeed very sensitive to the pulse length (Thomas *et al*., 2006). We have shown that the probability of depinning a DW from a local pinning site oscillates with the length of the current pulse, with a period of a few nanoseconds (see Figure 25). Importantly, both head-to-head and tail-to-tail DWs exhibited the same behavior. These oscillations of depinning probability lead to strong oscillations in the critical current. We have shown that this behavior is related to the current-induced precession of the DW trapped in a pinning potential. When the pulse length is close to a multiple of half the precession period, the amplitude of the DW oscillation is amplified after the end of the current pulse, in turn leading to DW depinning. Importantly, this is a subthreshold behavior, which occurs for currents smaller than the dc critical current. Moreover, in this depinning regime, we showed that the DW displacement is against the electron flow, opposite to the propagation direction above threshold. This behavior can be accounted for within the framework of the 1D model described in Section 2.2.3. Even though the DW in the experiment was a vortex wall, we were able to achieve a good qualitative description of the experimental results Yamanouchi *et al*., (2006).

3.5.7 Thermal effects: current-induced heating and nucleation of domain walls

As already emphasized, the high critical current density required to achieve current-induced DW motion in most samples induces significant Joule heating. The effect of temperature on the current/ DW interaction is not fully understood. One obvious effect is the decrease of magnetization and anisotropy of the magnetic material. According to equation (15), this should help to reduce the intrinsic critical current, since J_c is proportional to $M_s H_k$, and H_k is an anisotropy field which is itself proportional to M_s. However, the polarization of the current should also be reduced, which should compensate at least partially the gain from

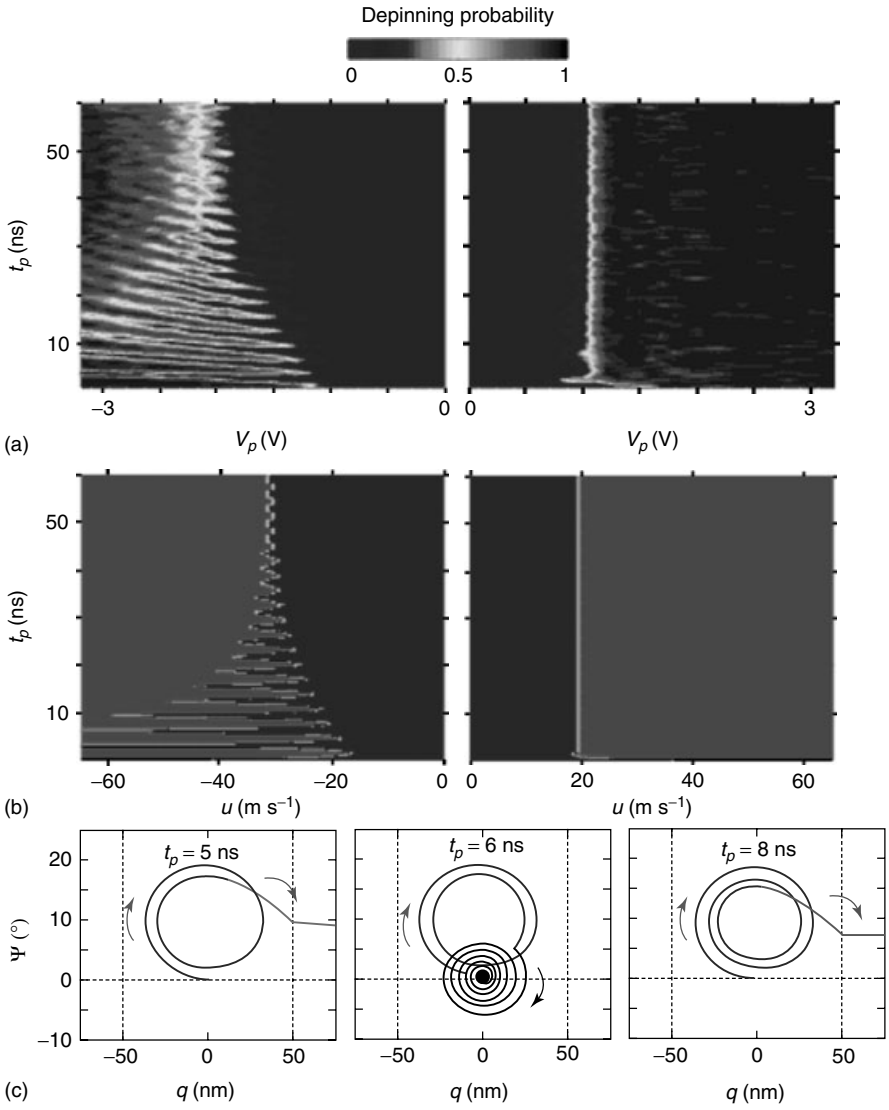

Figure 25. Oscillatory depinning of a DW as a function of the current pulse length. Experiments (a), calculations (b), and schematic explanation of the mechanism (c). (From Thomas *et al*. (2006).)

the reduction of M_s. Moreover, spin-wave excitations can be amplified by the spin torque and lead to chaotic behavior, thus preventing DW motion.

In a recent report on permalloy nanorings, Laufenberg *et al*. (2006b) observed a slight increase of the critical current with temperature between 4 and 300 K, from ∼2 to 2.8×10^8 A cm^{-2}. This variation is opposite to that of the DW depinning field, which decreases with temperature. The authors conclude that the spin-transfer efficiency decreases with temperature, although the origin of such a variation is not clear. In this temperature range, far below the Curie temperature for permalloy, the magnetic properties exhibit little variation. The authors propose to explain this decrease in efficiency by thermally excited spin waves, which couple with the current flow, effectively absorbing some spin angular momentum. Results are opposite for GaMnAs structures for which the critical current decreases by ∼50% when the temperature increases between 100 and 107 K, as the spin-torque efficiency increases owing to the temperature dependence of the magnetization and spin polarization (Yamanouchi *et al*., 2006).

Temperature effects were also addressed by Yamaguchi *et al*. (2005) in a much higher temperature range. It was shown that spontaneous DW nucleation occurs in permalloy nanowires when the current density exceeds 7.5×10^7 A cm^{-2}. The authors suggest that this phenomenon occurs because the temperature exceeds the Curie temperature for NiFe during the pulse, thus leading to the breakdown of the nanowire into a multidomain state. We have observed similar effects in many nanowires. Interestingly

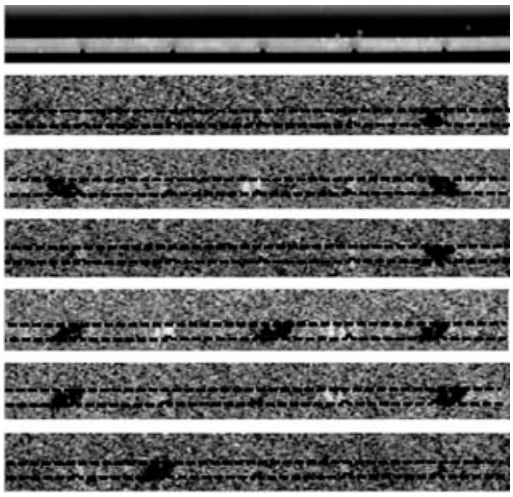

Figure 26. MFM images measured from a 10-nm-thick, 300-nm-wide permalloy nanowire, upon successive application of 3-ns-long current pulses, with a current density of $\sim 7 \times 10^8\,\mathrm{A\,cm^{-2}}$ (value not corrected for resistance increase due to heating).

in the example shown in Figure 26, DWs are nucleated, whereas preexisting DWs are essentially unaffected by the current pulse. This suggests that DW generation can occur below the Curie temperature, for example, because of the reversal of the magnetization in one or several portions of the nanowire, thereby generating pairs of DWs. In the many cases where we have observed this behavior, the ends of the nanowires are not reversed, and the DWs always appear in pairs, thus supporting this interpretation. Micromagnetic simulations that include thermal effects also suggest that the spin torque amplifies magnetization fluctuations and can thereby eventually lead to the complete reversal of parts a nanowire.

Interestingly, Shibata *et al*. find by theoretical calculations that, above a current threshold, the ground state of a ferromagnet becomes a multidomain state with several DWs (Shibata, Tatara and Kohno, 2005). The threshold for nucleation is given by (using the notation of Section 2.2.3):

$$u_{\mathrm{nuc}} = \gamma \Delta H_{\mathrm{k0}} \left(1 + \sqrt{\frac{H_{\mathrm{k}}}{H_{\mathrm{k0}}}}\right) \tag{26}$$

where H_{k0} and H_{k} are the longitudinal and transverse anisotropy fields, respectively. If $u_{\mathrm{nuc}} < u_{\mathrm{c}}$ (u_{c} the intrinsic critical current given by equation (13)), that is if $H_{\mathrm{k}} > 8H_{\mathrm{k0}}$, the multidomain state is stable, and this could appear as the spontaneous nucleation of multiple DWs in a nanowire, as observed experimentally. An estimate of the current density required to reach this nucleation regime is found to be $\sim 3 \times 10^9\,\mathrm{A\,cm^{-2}}$ for Co. For permalloy, this value could be lower, particularly since Joule heating would contribute to a reduction of the magnetization, since permalloy has a lower Curie temperature than Co.

4 OUTLOOK

The observation that current can induce motion in DWs has a long history dating back more than 25 years. Indeed, it was appreciated long ago that there are several ways in which current can interact with DWs, including the notion that the transfer of spin angular momentum from current to DWs can perturb a DW. However, there were few experiments on this important interaction perhaps because it is only dominant in magnetic structures on the nanoscale, and is thus is obscured by other effects in larger structures. As the capability to make ever smaller high quality structures has evolved over the past years it has become possible to fabricate structures in which single DWs can be controllably injected and whose motion can be probed following or even during the application of nanosecond-long current and field pulses. These experimental studies have clearly demonstrated that spin-polarized current does result in the motion of DWs along magnetic nanowires. Moreover, short current pulses, whose length is matched with the precessional frequency of a DW, can resonantly excite the precession of the DW. While there are a number of open questions, as discussed briefly at the end of the last section, the notion of moving DWs with current is not only of considerable scientific interest, but suggests a number of interesting technological applications.

More than a quarter of a century ago there was considerable interest in the possibility of building magnetic memory devices by storing information in the form of magnetic domains or bubbles in single-crystalline garnet thin films. In this original planar magnetic memory the bubbles were defined and moved by magnetic fields created on chip. Much creative and imaginative work was expended to develop ingenious structures to reliably manipulate magnetic domains in these materials, as discussed in several review articles and papers (see, e.g., Malozemoff and Slonczewski, 1979; de Leeuw, Van Den Doel and Enz, 1980; Bar'yakhtar, Ivanov and Chetkin, 1985; Schneider, 1975; Pugh, Critchlow, Henle and Russell, 1981; Eschenfelder, 1980). In this chapter we focused the discussion on the motion of head-to-head DWs in magnetic nanowires. One problem with manipulating such types of DWs by magnetic fields is that head-to-head and their counterpart tail-to-tail walls move in opposite direction in the presence of a magnetic field. This problem can be solved by using spin momentum transfer from current to move DWs since the current becomes repolarized over very short distances (e.g., the spin relaxation length can be as short as $\sim 5\,\mathrm{nm}$ in permalloy (Bass and Pratt, 2007)). Thus current moves head-to-head and tail-to-tail DWs in permalloy and other transition metals in the *same* direction. This distinctive feature of current-induced DW motion allows the possibility of interesting new device technologies not previously possible with field manipulation. One of the more interesting

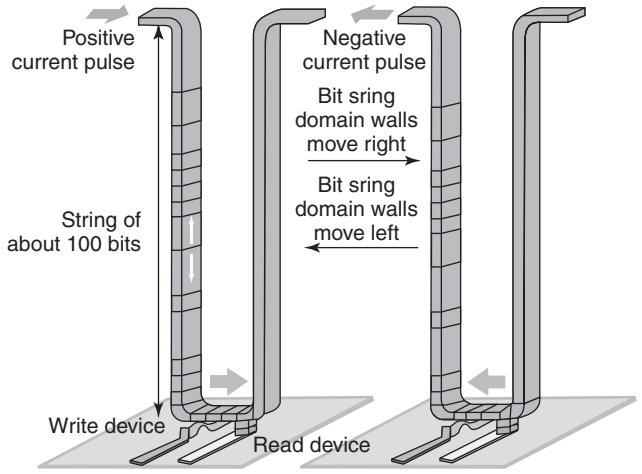

Figure 27. Schematic of the magnetic racetrack memory device.

of these devices is the magnetic racetrack memory (MRM) (Parkin, 2004).

The magnetic racetrack memory promises a nonvolatile solid-state data-storage device that combines the very low cost of conventional magnetic hard-disk drives with the high reliability and high performance of nonvolatile solid-state memory. The MRM concept is that of a magnetic shift register in which individual spintronic reading and writing elements, formed using conventional CMOS technology, are married to magnetic 'racetracks' in which 10 to 100 nanoscale bits are stored as magnetic domains (schematically shown in Figure 27). The racetracks are vertical columns of magnetic material, formed in the third dimension, perpendicular to a plane of CMOS logic elements and devices formed on a silicon substrate. Each of these columns is addressed by a single read and write element whereby the magnetic domains in the racetrack are moved, by nanosecond-long current pulses using current-induced motion of DWs, to the read and write devices. Since the racetracks are formed in the third dimension the footprint of each racetrack in the CMOS logic plane is very small and therefore the cost should be low. Indeed the goal of the MRM is to store $\sim$100 data bits in the same area of a silicon wafer that one data bit in conventional solid-state memories would occupy. Since the cost of a CMOS memory or logic device is largely determined by the area of the silicon wafer the proposed magnetic shift memory has the potential to be $\sim$100 times cheaper per bit than conventional solid-state memory and so comparable in cost to a HDD. At the same time the proposed solid-state memory will have the reliability and integrity of conventional solid-state memories. Thus, the proposed spintronic magnetic shift memory will have a previously unrealized combination of extremely low cost, high reliability, and excellent performance as compared to flash drives and HDDs.

The magnetic racetrack is just one example of a possible new technology which takes advantage of the new physics of current-driven DW motion, which has just begun to be fully appreciated and understood in the past few years. As discussed throughout this chapter, however, many aspects of current-driven DW motion remain unanswered. The most fundamental question is the detailed theoretical description of the current-magnetization interaction. Of particular interest is the understanding of the role of nonadiabatic contributions to the current–magnetization interaction. There is considerable debate over the existence and nature of this contribution, and, consequently whether there is an intrinsic threshold current for DW motion in uniform, homogeneous magnetic nanowires.

Another important question is the maximum possible speed of DWs driven by current alone. Many experimental studies, mostly in permalloy but also in GaMnAs, have indicated extremely low current-driven DW velocities. These velocities are so small that they are difficult to rationalize within today's theoretical models. Clearly, further experimental and theoretical studies are called for. Systematic studies of the relationship between the critical current needed to move a DW as well as the DW velocity and the intrinsic material parameters of the magnetic material (e.g., magnetization, anisotropy, and spin polarization of the current) will likely lead to a much improved understanding of the basic mechanisms involved in the current–DW interaction.

A particularly interesting question is the magnitude of the current required to sustain the motion of a DW along a nanowire and whether this is largely determined by the spin polarization of the current and the magnetization of the magnetic domains or whether other factors may play a significant role. The answer to this important question will determine how useful current-induced DW motion will be for technological applications. From both a technological and a scientific perspective, the understanding and control of the DW structure and the interaction between DWs is both challenging and interesting.

The renewed interest in DW dynamics in magnetic nanostructures has already revealed new physical phenomena and the considerable activity in this field promises exciting future discoveries.

ACKNOWLEDGMENTS

We would like to thank our colleagues at the Almaden Research Center for their contribution to this work: Masamitsu Hayashi, Rai Moriya, Charles Rettner, Xin Jiang, Yaroslaw Bazaliy, Bastiaan Bergman, Brian Hughes and Kevin Roche. We are also grateful to Pierre-Olivier Jubert and Michael Scheinfein for their helpful comments on the

manuscript. This work was partly supported by the Defense Microelectronics Activity.

REFERENCES

Allwood, D.A., Vernier, N., Xiong, G., *et al*. (2002a). Shifted hysteresis loops from magnetic nanowires. *Applied Physics Letters*, **81**, 4005.

Allwood, D.A., Xiong, G., Cooke, M.D., *et al*. (2002b). Submicrometer ferromagnetic NOT gate and shift register. *Science*, **296**, 2003.

Allwood, D.A., Xiong, G. and Cowburn, R.P. (2004). Domain wall diodes in ferromagnetic planar nanowires. *Applied Physics Letters*, **85**, 2848.

Atkinson, D., Allwood, D.A., Xiong, G., *et al*. (2003). Magnetic domain-wall dynamics in a submicrometre ferromagnetic structure. *Nature Materials*, **2**, 85.

Baldwin, J.A. and Culler, G.J. (1969). Wall-pinning model of magnetic hysteresis. *Journal of Applied Physics*, **40**, 2828.

Barnes, S.E. (2006). Comment on theory of current-driven domain wall motion: spin transfer versus momentum transfer. *Physical Review Letters*, **96**, 189701.

Barnes, S.E. and Maekawa, S. (2005). Current-spin coupling for ferromagnetic domain walls in fine wires. *Physical Review Letters*, **95**, 107204.

Bar'yakhtar, V.G., Ivanov, B.A. and Chetkin, M.V. (1985). Dynamics of domain walls in weak ferromagnets. *Soviet Physics Uspekhi*, **28**, 563.

Bass, Jack. and Pratt, William.P. Jr. (2007). Spin-diffusion lengths in metals and alloys, and spin-flipping at metal/metal interfaces: an experimentalist's critical review, *Journal of Physics: Condensed Matter*, **19**, 183201.

Bazaliy, Y.B., Jones, B.A. and Zhang, S-C. (1998). Modification of the Landau-Lifshitz equation in the presence of a spin-polarized current in colossal- and giant-magnetoresistive materials. *Physical Review B*, **57**, R3213.

Beach, G.S.D., Knutson, C., Nistor, C., *et al*. (2006). Nonlinear domain-wall velocity enhancement by spin-polarized electric current. *Physical Review Letters*, **97**, 057203.

Beach, G.S.D., Nistor, C., Knutson, C., *et al*. (2005). Dynamics of field-driven domain-wall propagation in ferromagnetic nanowires. *Nature Materials*, **4**, 741.

Berger, L. (1974). Prediction of a domain-drag effect in uniaxial, non-compensated, ferromagnetic metals. *Journal of Physics and Chemistry of Solids*, **35**, 947.

Berger, L. (1978). Low-field magnetoresistance and domain drag in ferromagnets. *Journal of Applied Physics*, **49**, 2156.

Berger, L. (1984). Exchange interaction between ferromagnetic domain-wall and electric-current in very thin metallic-films. *Journal of Applied Physics*, **55**, 1954.

Berger, L. (1986). Possible existence of a Josephson effect in ferromagnets. *Physical Review B*, **33**, 1572.

Berger, L. (1991a). Galvanomagnetic voltages in the vicinity of a domain-wall in ferromagnetic thin-films. *Journal of Applied Physics*, **69**, 1550.

Berger, L. (1991b). Prediction of Shapiro steps in the dc voltage across a magnetic domain-wall traversed by a dc current and exposed to high-frequency magnetic-fields. *Journal of Applied Physics*, **69**, 4683.

Berger, L. (1992). Motion of a magnetic domain-wall traversed by fast-rising current pulses. *Journal of Applied Physics*, **71**, 2721.

Berger, L. (1996). Current-induced oscillations of a Bloch wall in magnetic thin films. *Journal of Magnetism and Magnetic Materials*, **162**, 155.

Berger, L. (2006). Analysis of measured transport properties of domain walls in magnetic nanowires and films. *Physical Review B*, **73**, 014407.

Bruno, P. (1999). Geometrically constrained magnetic wall. *Physical Review letters*, **83**, 2425.

Buchanan, K.S., Roy, P.E., Grimsditch, M., *et al*. (2005). Soliton-pair dynamics in patterned ferromagnetic ellipses. *Nature Physics*, **1**, 172.

Carr, W.J. (1974a). Force on domain-wall due to perturbation of current in a magnetoresistive overlayer. *Journal of Applied Physics*, **45**, 3115.

Carr, W.J. (1974b). Propagation of magnetic domain-walls by a self-induced current distribution. *Journal of Applied Physics*, **45**, 394.

Cayssol, F., Ravelosona, D., Chappert, C., *et al*. (2004). Domain wall creep in magnetic wires. *Physical Review Letters*, **92**, 107202.

Charap, S.H. (1974). Interaction of a magnetic domain-wall with an electric-current. *Journal of Applied Physics*, **45**, 397.

Chern, G.W., Youk, H. and Tchernyshyov, O. (2006). Topological defects in flat nanomagnets: the magnetostatic limit. *Journal of Applied Physics*, **99**, 08Q505.

Choe, S.B., Acremann, Y., Scholl, A., *et al*. (2004). Vortex core-driven magnetization dynamics. *Science*, **304**, 420.

Cowburn, R.P., Allwood, D.A., Xiong, G. and Cooke, M.D. (2002). Domain wall injection and propagation in planar Permalloy nanowires. *Journal of Applied Physics*, **91**, 6949.

Dugaev, V.K., Vieira, V.R., Sacramento, P.D., *et al*. (2006). Current-induced motion of a domain wall in a magnetic nanowire. *Physical Review B: Condensed Matter and Materials Physics*, **74**, 054403.

Duine, R.A., Nunez, A.S. and Mac Donald, A.H. (2007). Thermally Assisted Current-Driven Domain Wall Motion. *Physics Review Letter*, **98**, 056605.

Duvail, J.L., Dubois, S., Piraux, L., *et al*. (1998). Electrodeposition of patterned magnetic nanostructures. *Journal of Applied Physics*, **84**, 6359.

Ebels, U., Radulescu, A., Henry, Y., *et al*. (2000). Spin accumulation and domain wall magnetoresistance in 35 nm Co wires. *Physical Review Letters*, **84**, 983.

Emtage, P.R. (1974). Self-induced drive of magnetic domains. *Journal of Applied Physics*, **45**, 3117.

Eschenfelder, A.H. (1980). *Magnetic Bubble Technology*, Springer-Verlag: Berlin.

Faulkner, C.C., Cooke Michael, D., Allwood, D.A., *et al*. (2004). Artificial domain wall nanotraps in Ni[sub 81]Fe[sub 19] wires. *Journal of Applied Physics*, **95**, 6717.

Florez, S.H., Krafft, C. and Gomez, R.D. (2005). Spin-current-induced magnetization reversal in magnetic nanowires with constrictions. *Journal of Applied Physics*, **97**, 10C705.

Freitas, P.P. and Berger, L. (1985). Observation of s-d exchange force between domain walls and electric current in very thin Permalloy films. *Journal of Applied Physics*, **57**, 1266.

Gan, L., Chung, S.H., Aschenbach, K.H., *et al*. (2000). Pulsed-current-induced domain wall propagation in Permalloy patterns observed using magnetic force microscope. *IEEE Transactions on Magnetics*, **36**, 3047.

Gider, S., Runge, B-U., Marley, A.C. and Parkin, S.S.P. (1998). The magnetic stability of spin-dependent tunneling devices. *Science*, **281**, 797.

Gopalaswamy, S. and Berger, L. (1991). Observation of galvano-magnetic voltages at a magnetic domain-wall in Ni-Fe films. *Journal of Applied Physics*, **70**, 5825.

Grollier, J., Lacour, D., Cros, V., *et al*. (2002). Switching the magnetic configuration of a spin valve by current-induced domain wall motion. *Journal of Applied Physics*, **92**, 4825.

Grollier, J., Boulenc, P., Cros, V., *et al*. (2003). Switching a spin valve back and forth by current-induced domain wall motion. *Applied Physics Letters*, **83**, 509.

Grollier, J., Boulenc, P., Cros, V., *et al*. (2004). Spin-transfer-induced domain wall motion in a spin valve. *Journal of Applied Physics*, **95**, 6777.

Hayashi, M., Thomas, L., Bazaliy, Y.B., *et al*. (2006a). Influence of current on field-driven domain wall motion in Permalloy nanowires from time resolved measurements of anisotropic magnetoresistance. *Physical Review Letters*, **96**, 197207.

Hayashi, M., Thomas, L., Rettner, C. *et al*. (2006b). Dependence of current and field driven depinning of domain walls on their structure and chirality in Permalloy nanowires. *Physical Review Letters*, **97**, 207205.

Hayashi, M., Thomas, L., Rettner, C., *et al*. (2007a). Current driven domain wall velocities exceeding the spin angular momentum transfer rate in Permalloy nanowires. *Physical Review Letters*, **98**, 037204.

Hayashi, M., Thomas, L., Rettner, C., *et al*. (2007b). Direct observation of the coherent precession of magnetic domain walls propagating along Permalloy nanowires. *Nature Physics*, **3**, 21.

He, J., Li, Z. and Zhang, S. (2005). Current-driven domain-wall depinning. *Journal of Applied Physics*, **98**, 016108.

He, J., Li, Z. and Zhang, S. (2006a). Current-driven vortex domain wall dynamics by micromagnetic simulations. *Physical Review B*, **73**, 184408.

He, J., Li, Z. and Zhang, S. (2006b). Effects of current on vortex and transverse domain walls. *Journal of Applied Physics*, **99**, 08G509.

Himeno, A., Kasai, S. and Ono, T. (2005). Current-driven domain-wall motion in magnetic wires with asymmetric notches. *Applied Physics Letters*, **87**, 243108.

Himeno, A., Okuno, T., Kasai, S., *et al*. (2005). Propagation of a magnetic domain wall in magnetic wires with asymmetric notches. *Journal of Applied Physics*, **97**, 066101.

Himeno, A., Ono, T., Nasu, S., *et al*. (2003). Dynamics of a magnetic domain wall in magnetic wires with an artificial neck. *Journal of Applied Physics*, **93**, 8430.

Holleitner, A.W., Knotz, H., Myers, R.C., *et al*. (2004). Pinning a domain wall in (Ga,Mn)As with focused ion beam lithography. *Applied Physics Letters*, **85**, 5622.

Honolka, J., Masmanidis, S., Tang, H.X., *et al*. (2005). Domain-wall dynamics at micropatterned constrictions in ferromagnetic (Ga,Mn)As epilayers. *Journal of Applied Physics*, **97**, 063903.

Hubert, A. and Schäfer, R. (2000). *Magnetic Domains*, Springer-Verlag: Berlin.

Hung, C.Y. and Berger, L. (1988). Exchange forces between domain-wall and electric-current in Permalloy-films of variable thickness. *Journal of Applied Physics*, **63**, 4276.

Jubert, P.-O., Allenspach, R. and Bischof, A. (2004). Magnetic domain walls in constrained geometries. *Physics Review B*, **69**, 220410.

Jubert, P.-O., Kläui, M., Bischof, A., *et al*. (2006). Velocity of vortex walls moved by current. *Journal of Applied Physics*, **99**, 08G523.

Katine, J.A., Ho, M.K., Ju, Y.S. and Rettner, C.T. (2003). Patterning damage in narrow trackwidth spin-valve sensors. *Applied Physics Letters*, **83**, 401.

Kimura, T., Otani, Y., Yagi, I., *et al*. (2003). Suppressed pinning field of a trapped domain wall due to current injection. *Journal of applied Physics*, **94**, 7266.

Klaui, M., Ehrke, H., Rudiger, U., *et al*. (2005a). Direct observation of domain-wall pinning at nanoscale constrictions. *Applied Physics Letters*, **87**, 102509.

Klaui, M., Jubert, P.O., Allenspach, R., *et al*. (2005b). Direct observation of domain-wall configurations transformed by spin currents. *Physical Review Letters*, **95**, 026601.

Klaui, M., Vaz, C.A.F., Bland, J.A.C., *et al*. (2005c). Controlled and reproducible domain wall displacement by current pulses injected into ferromagnetic ring structures. *Physical Review Letters*, **94**, 106601.

Klaui, M., Vaz, C.A.F., Bland, J.A.C., *et al*. (2003a). Domain wall pinning and controlled magnetic switching in narrow ferromagnetic ring structures with notches (invited). *Journal of Applied Physics*, **93**, 7885.

Klaui, M., Vaz, C.A.F., Bland, J.A.C., *et al*. (2003b). Domain wall motion induced by spin polarized currents in ferromagnetic ring structures. *Applied Physics Letters*, **83**, 105.

Klaui, M., Vaz, C.A.F., Bland, J.A.C., *et al*. (2004). Head-to-head domain-wall phase diagram in mesoscopic ring magnets. *Applied Physics Letters*, **85**, 5637.

Lacour, D., Katine, J.A., Folks, L., *et al*. (2004). Experimental evidence of multiple stable locations for a domain wall trapped by a submicron notch. *Applied Physics Letters*, **84**, 1910.

Laufenberg, M., Backes, D., Buhrer, W., *et al*. (2006a). Observation of thermally activated domain wall transformations. *Applied Physics Letters*, **88**, 046602.

Laufenberg, M., Buhrer, W., Bedau, D., *et al*. (2006b). Temperature dependence of the spin torque effect in current-induced domain wall motion. *Physical Review Letters*, **97**, 046602.

Lee, W.Y., Yao, C.C., Hirohata, A., *et al*. (2000). Domain nucleation processes in mesoscopic Ni80Fe20 wire junctions. *Journal of Applied Physics*, **87**, 3032.

de Leeuw, F.H., Van Den Doel, R. and Enz, U. (1980). Dynamic properties of magnetic domain walls and magnetic bubbles. *Reports on Progress in Physics*, **43**, 689.

Lepadatu, S. and Xu, Y.B. (2004). Direct observation of domain wall scattering in patterned Ni80Fe20 and Ni nanowires by current-voltage measurements. *Physical Review Letters*, **92**, 127201.

Levy, P.M. and Zhang, S.F. (1997). Resistivity due to domain wall scattering. *Physical Review Letters*, **79**, 5110.

Li, Z. and Zhang, S. (2004a). Domain-wall dynamics driven by adiabatic spin-transfer torques. *Physical Review B*, **70**, 064708.

Li, Z. and Zhang, S. (2004b). Domain-wall dynamics and spin-wave excitations with spin-transfer torques. *Physical Review Letters*, **92**, 207203.

Lim, C.K., Devolder, T., Chappert, C., *et al*. (2004). Domain wall displacement induced by subnanosecond pulsed current. *Applied Physics Letters*, **84**, 2820.

Malozemoff, A.P. and Slonczewski, J.C. (1979). *Magnetic Domain Walls in Bubble Material*, Academic Press: New York.

Marrows, C.H. (2005). Spin-polarised currents and magnetic domain walls. *Advances in Physics*, **54**, 585.

McGuire, T.R. and Potter, R.I. (1975). Anisotropic magnetoresistance in ferromagnetic 3d alloys. *IEEE Transactions on Magnetics*, **11**, 1018.

McMichael, R.D. and Donahue, M.J. (1997). Head to head domain wall structures in thin magnetic strips. *IEEE Transactions on Magnetics*, **33**, 4167.

Miyake, K., Shigeto, K., Yokoyama, Y., *et al*. (2005). Exchange biasing of a Neel wall in the nanocontact between NiFe wires. *Journal of Applied Physics*, **97**, 014309.

Nagahama, T., Mibu, K. and Shinjo, T. (2000). Electric resistance of magnetic domain wall in NiFe wires with CoSm pinning pads. *Journal of Applied Physics*, **87**, 5648.

Nakatani, Y., Hayashi, N., Ono, T. and Miyajima, H. (2001). Computer simulation of domain wall motion in a magnetic strip line with submicron width. *IEEE Transactions on Magnetics*, **37**, 2129.

Nakatani, Y., Thiaville, A. and Miltat, J. (2003). Faster magnetic walls in rough wires. *Nature Materials*, **2**, 521.

Nakatani, Y., Thiaville, A. and Miltat, J. (2005). Head-to-head domain walls in soft nano-strips: a refined phase diagram. *Journal of Magnetism and Magnetic Materials*, **290**, 750.

Nguyen, A.K., Skadsem, H.J. and Brataas, A. (2007). Giant current-driven domain wall mobility in (Ga,Mn)As. *Physics Review Letter*, **98**, 146602.

Nibarger, J.P., Lopusnik, R., Celinski, Z. and Silva, T.J. (2003). Variation of magnetization and the Lande g factor with thickness in Ni-Fe films. *Applied Physics Letters*, **83**, 93.

Nibarger, J.P., Lopusnik, R. and Silva, T.J. (2003). Damping as a function of pulsed field amplitude and bias field in thin film Permalloy. *Applied Physics Letters*, **82**, 2112.

Novosad, V., Fradin, F.Y., Roy, P.E., *et al*. (2005). Magnetic vortex resonance in patterned ferromagnetic dots. *Physical Review B*, **72**, 094442.

Ohe, J. and Kramer, B. (2006). Dynamics of a domain wall and spin-wave excitations driven by a mesoscopic current. *Physical Review Letters*, **96**, 027204.

Ono, T., Miyajima, H., Shigeto, K., *et al*. (1999a). Propagation of the magnetic domain wall in submicron magnetic wire investigated by using giant magnetoresistance effect. *Journal of Applied Physics*, **85**, 6181.

Ono, T., Miyajima, H., Shigeto, K., *et al*. (1999b). Propagation of a magnetic domain wall in a submicrometer magnetic wire. *Science*, **284**, 468.

Ono, T., Miyajima, H., Shigeto, K. and Shinjo, T. (1998). Magnetization reversal in submicron magnetic wire studied by using giant magnetoresistance effect. *Applied Physics Letters*, **72**, 1116.

Parkin, S.S.P. (1992). Dramatic enhancement of interlayer exchange coupling and giant magnetoresistance in $Ni_{81}Fe_{19}$/Cu multilayers by addition of thin Co interface layers. *Applied Physics Letters*, **61**, 1358.

Parkin, S.S.P. (1993). Origin of enhanced magnetoresistance of magnetic multilayers: spin-dependent scattering from magnetic interface states. *Physical Review letters*, **71**, 1641.

Parkin, S.S.P. (1994). In *Ultrathin Magnetic Structures*, Heinrich, B. and Bland, J.A.C. (Eds.), Springer-Verlag: Berlin, p. 148, Vol. II.

Parkin, S.S.P. (1995). In *Annual Review of Materials Science*, Wessels, B.W. (Ed.), Annual Reviews: Palo Alto, p. 357, Vol. 25.

Parkin, S.S.P. (2004) USA Patent No. 6,834,005 (2003-06-10 (filed).

Parkin, S.S.P., Jiang, X., Kaiser, C., *et al*. (2003). Magnetically engineered spintronic sensors and memory. *Proceedings of the IEEE*, **91**, 661.

Parkin, S.S.P., Li, Z.G. and Smith, D.J. (1991). Giant magnetoresistance in antiferromagnetic Co/Cu multilayers. *Applied Physics Letters*, **58**, 2710.

Partin, D.L., Karnezos, M., deMenezes, L.C. and Berger, L. (1974). Nonuniform current distribution in neighborhood of a ferromagnetic domain-wall in cobalt at 42k. *Journal of Applied Physics*, **45**, 1852.

Porter, D.G. and Donahue, M.J. (2004). Velocity of transverse domain wall motion along thin, narrow strips. *Journal of Applied Physics*, **95**, 6729.

Pugh, E.W., Critchlow, D.L., Henle, R.A. and Russell, L.A. (1981). Solid state memory development in IBM. *IBM Journal of Research and Development*, **25**, 585.

Puzic, A., Van Waeyenberge, B., Chou, K.W., *et al*. (2005). Spatially resolved ferromagnetic resonance: imaging of ferromagnetic eigenmodes. *Journal of Applied Physics*, **97**, 10E704.

Ravelosona, D., Lacour, D., Katine, J.A., *et al*. (2005). Nanometer scale observation of high efficiency thermally assisted current-driven domain wall depinning. *Physical Review Letters*, **95**, 117203.

Rothman, J., Klaui, M., Lopez-Diaz, L., *et al*. (2001). Observation of a bi-domain state and nucleation free switching in mesoscopic ring magnets. *Physical Review Letters*, **86**, 1098.

Ruster, C., Borzenko, T., Gould, C., *et al*. (2003). Very large magnetoresistance in lateral ferromagnetic (Ga,Mn)As wires with nanoconstrictions. *Physical Review Letters*, **91**, 216602.

Saitoh, E., Miyajima, H., Yamaoka, T. and Tatara, G. (2004). Current-induced resonance and mass determination of a single magnetic domain wall. *Nature*, **432**, 203.

Salhi, E. and Berger, L. (1994). Current-induced displacements of Bloch Walls in Ni-Fe films of thickness 120-740 Nm. *Journal of Applied Physics*, **76**, 4787.

Sato, H., Hanada, R., Sugawara, H., *et al*. (2000). Local magnetization rotation in NiFe wire monitored by multiple transverse probes. *Physical Review B*, **61**, 3227.

Schneider, J. (1975). Amorphous GdCoCr films for bubble domain applications. *IBM Journal of Research and Development*, **19**, 587.

Schrefl, T., Fidler, J., Kirk, K.J. and Chapman, J.N. (1997). Domain structures and switching mechanisms in patterned magnetic elements. *Journal of Magnetism and Magnetic Materials*, **175**, 193.

Schumacher, H.W., Ravelosona, D., Cayssol, F., *et al*. (2001). Propagation of a magnetic domain wall in the presence of AFM fabricated defects. *IEEE Transactions on Magnetics*, **37**, 2331.

Shibata, J., Nakatani, Y., Tatara, G., *et al*. (2006). Current-induced magnetic vortex motion by spin-transfer torque. *Physical Review B*, **73**, 020403.

Shibata, J., Tatara, G. and Kohno, H. (2005). Effect of spin current on uniform ferromagnetism: domain nucleation. *Physical Review Letters*, **94**, 076601.

Shigeto, K., Okuno, T., Shinjo, T., *et al*. (2000). Magnetization switching of a magnetic wire with trilayer structure using giant magnetoresistance effect. *Journal of Applied Physics*, **88**, 6636.

Shigeto, K., Shinjo, T. and Ono, T. (1999). Injection of a magnetic domain wall into a submicron magnetic wire. *Applied Physics Letters*, **75**, 2815.

Silva, T.J., Lee, C.S., Crawford, T.M. and Rogers, C.T. (1999). Inductive measurement of ultrafast magnetization dynamics in thin-film Permalloy. *Journal of Applied Physics*, **85**, 7849.

Slonczewski, J.C. (1996). Current-driven excitation of magnetic multilayers. *Journal of Magnetism and Magnetic Materials*, **159**, L1.

Tanase, M., Silevitch, D.M., Chien, C.L. and Reich, D.H. (2003). Magnetotransport properties of bent ferromagnetic nanowires. *Journal of Applied Physics*, **93**, 7616.

Tang, H.X., Kawakami, R.K., Awschalom, D.D. and Roukes, M.L. (2003). Giant planar hall effect in epitaxial (Ga,Mn)As devices. *Physical Review Letters*, **90**, 107201.

Tang, H.X., Kawakami, R.K., Awschalom, D.D. and Roukes, M.L. (2006). Propagation dynamics of individual domain walls in Ga1-xMnxAs microdevices. *Physical Review B*, **74**, 041310.

Tang, H.X., Masmanidis, S., Kawakami, R.K., *et al*. (2004). Negative intrinsic resistivity of an individual domain wall in epitaxial (Ga,Mn)As microdevices. *Nature*, **431**, 52.

Tang, H.X. and Roukes, M.L. (2004). Electrical transport across an individual magnetic domain wall in (Ga,Mn)As microdevices. *Physical Review B*, **70**, 205213.

Taniyama, T., Nakatani, I., Namikawa, T. and Yamazaki, Y. (1999). Resistivity due to domain walls in Co zigzag wires. *Physical Review Letters*, **82**, 2780.

Taniyama, T., Nakatani, I., Yakabe, T. and Yamazaki, Y. (2000). Control of domain structures and magnetotransport properties in patterned ferromagnetic wires. *Applied Physics Letters*, **76**, 613.

Tatara, G. and Kohno, H. (2004). Theory of current-driven domain wall motion: spin transfer versus momentum transfer. *Physical Review Letters*, **92**, 086601.

Tatara, G. and Kohno, H. (2006). Comment on Theory of current-driven domain wall motion: spin transfer versus momentum transfer – reply. *Physical Review Letters*, **96**, 189702.

Tatara, G., Saitoh, E., Ichimura, M. and Kohno, H. (2005). Domain-wall displacement triggered by an ac current below threshold. *Applied Physics Letters*, **86**, 232504.

Tatara, G., Takayama, T., Kohno, H., *et al*. (2006). Threshold current of domain wall motion under extrinsic pinning, beta-term and non-adiabaticity. *Journal of the Physical Society of Japan*, **75**, 064708.

Tatara, G., Vernier, N. and Ferre, J. (2005). Universality of thermally assisted magnetic domain-wall motion under spin torque. *Applied Physics Letters*, **86**, 252509.

Tchernyshyov, O. and Chern, G.W. (2005). Fractional vortices and composite domain walls in flat nanomagnets. *Physical Review Letters*, **95**, 197204.

Thiaville, A. and Nakatani, Y. (2006). In *Spin Dynamics in Confined Magnetic Structures III*, Springer-Verlag: Berlin, pp. 161, Vol. 101.

Thiaville, A., Nakatani, Y., Miltat, J. and Suzuki, Y. (2005). Micromagnetic understanding of current-driven domain wall motion in patterned nanowires. *Europhysics Letters*, **69**, 990.

Thiaville, A., Nakatani, Y., Miltat, J. and Vernier, N. (2004). Domain wall motion by spin-polarized current: a micromagnetic study. *Journal of Applied Physics*, **95**, 7049.

Thiele, A.A. (1973a). Steady-state motion of magnetic domains. *Physical Review Letters*, **30**, 230.

Thiele, A.A. (1973b). Excitation spectrum of magnetic domain-walls. *Physical Review B*, **7**, 391.

Thomas, L., Hayashi, M., Jiang, X., *et al*. (2006). Oscillatory dependence of current-driven magnetic domain wall motion on current pulse length. *Nature*, **443**, 197.

Thomas, L., Luning, J., Scholl, A., *et al*. (2000). Oscillatory decay of magnetization induced by domain-wall stray fields. *Physical Review Letters*, **84**, 3462.

Thomas, L., Rettner, C., Hayashi, M., *et al*. (2005). Observation of injection and pinning of domain walls in magnetic nanowires using photoemission electron microscopy. *Applied Physics Letters*, **87**, 262501.

Thomas, L., Samant, M.G. and Parkin, S.S.P. (2000). Domain-wall induced coupling between ferromagnetic layers. *Physical Review Letters*, **84**, 1816.

Tserkovnyak, Y., Skadsem, H.J., Brataas, A. and Bauer, G.E.W. (2006). Current-induced magnetization dynamics in disordered itinerant ferromagnets. *Physical Review B*, **74**, 144405.

Tsoi, M., Fontana, R.E. and Parkin, S.S.P. (2003). Magnetic domain wall motion triggered by an electric current. *Applied Physics Letters*, **83**, 2617.

Van Waeyenberge, B., Puzic, A., Stoll, H., *et al*. (2006). Magnetic vortex core reversal by excitation with short bursts of an alternating field. *Nature*, **444**, 461.

Vernier, N., Allwood, D.A., Atkinson, D., *et al*. (2004). Domain wall propagation in magnetic nanowires by spin-polarized current injection. *Europhysics Letters*, **65**, 526.

Vila, L., Piraux, L., George, J.M. and Faini, G. (2002). Multiprobe magnetoresistance measurements on isolated magnetic nanowires. *Applied Physics Letters*, **80**, 3805.

Wachowiak, A., Wiebe, J., Bode, M., *et al*. (2002). Direct observation of internal spin structure of magnetic vortex cores. *Science*, **298**, 577.

Waintal, X. and Viret, M. (2004). Current-induced distortion of a magnetic domain wall. *Europhysics Letters*, **65**, 427.

Wegrowe, J.E., Dubey, M., Wade, T., *et al*. (2004). Spin transfer by spin injection between both interfaces of a Ni nanowire. *Journal of Applied Physics*, **96**, 4490.

Wegrowe, J.E., Gilbert, S.E., Kelly, D., *et al*. (1998). Anisotropic magnetoresistance as a probe of magnetization reversal in individual nano-sized nickel wires. *IEEE Transactions on Magnetics*, **34**, 903.

Wegrowe, J.E., Kelly, D., Jaccard, Y., *et al*. (1999). Current-induced magnetization reversal in magnetic nanowires. *Europhysics Letters*, **45**, 626.

Wernsdorfer, W., Doudin, B., Mailly, D., *et al*. (1996). Nucleation of magnetization reversal in individual nanosized nickel wires. *Physical Review Letters*, **77**, 1873.

Whitney, T.M., Jiang, J.S., Searson, P.C. and Chien, C.L. (1993). Fabrication and magnetic-properties of arrays of metallic nanowires. *Science*, **261**, 1316.

Williams, H.J., Shockley, W. and Kittel, C. (1950). Studies of the propagation velocity of a ferromagnetic domain boundary. *Physical Review*, **80**, 1090.

Wunderlich, J., Ravelosona, D., Chappert, C., *et al*. (2001). Influence of geometry on domain wall propagation in a mesoscopic wire. *IEEE Transactions on Magnetics*, **37**, 2104.

Xiao, J.A., Zangwill, A. and Stiles, M.D. (2006). Spin-transfer torque for continuously variable magnetization. *Physical Review B*, **73**, 054428.

Xiong, G., Allwood, D.A., Cooke, M.D. and Cowburn, R.P. (2001). Magnetic nanoelements for magnetoelectronics made by focused-ion-beam milling. *Applied Physics Letters*, **79**, 3461.

Yamaguchi, A., Nasu, S., Tanigawa, H., *et al*. (2005). Effect of Joule heating in current-driven domain wall motion. *Applied Physics Letters*, **86**, 012511.

Yamaguchi, A., Ono, T., Nasu, S., *et al*. (2004). Real-space observation of current-driven domain wall motion in submicron magnetic wires. *Physical Review Letters*, **92**, 077205.

Yamaguchi, A., Ono, T., Nasu, S., *et al*. (2006a). Erratum: real-space observation of current-driven domain wall motion in submicron magnetic wires (vol 92, pg 077205, 2004). *Physical Review Letters*, **96**, 179904.

Yamaguchi, A., Yano, K., Tanigawa, H., *et al*. (2006b). Reduction of threshold current density for current-driven domain wall motion using shape control. *Japanese Journal of Applied Physics Part 1-Regular Papers Brief Communications and Review Papers*, **45**, 3850.

Yamanouchi, M., Chiba, D., Matsukura, F. and Ohno, H. (2004). Current-induced domain-wall switching in a ferromagnetic semiconductor structure. *Nature*, **428**, 539.

Yamanouchi, M., Chiba, D., Matsukura, F., *et al*. (2006). Velocity of domain-wall motion induced by electrical current in the ferromagnetic semiconductor (Ga,Mn)As. *Physical Review Letters*, **96**, 096601.

Yokoyama, Y., Suzuki, Y., Yuasa, S., *et al*. (2000). Kerr microscopy observations of magnetization process in microfabricated ferromagnetic wires. *Journal of Applied Physics*, **87**, 5618.

Youk, H., Chern, G.W., Merit, K., *et al*. (2006). Composite domain walls in flat nanomagnets: the magnetostatic limit. *Journal of Applied Physics*, **99**, 08B101.

Zambano, A.J. and Pratt, W.P. (2004). Detecting domain-wall trapping and motion at a constriction in narrow ferromagnetic wires using perpendicular-current giant magnetoresistance. *Applied Physics Letters*, **85**, 1562.

Zhang, S. and Li, Z. (2004). Roles of nonequilibrium conduction electrons on the magnetization dynamics of ferromagnets. *Physical Review Letters*, **93**, 127204.

The Motion of Domain Walls in Nanocircuits and its Application to Digital Logic

Russell P. Cowburn
Imperial College London, London, UK

1 INTRODUCTION

Spintronics describes the concept of attempting to use both the charge and the spin on the electron in microelectronic devices (Prinz, 1998; Wolf *et al*., 2001). One of the most highly sought after functionalities in microelectronics is non-volatility, that is, the ability to retain memory even when power is removed. This is particularly true as the popularity of mobile electronic communication and computing devices grows. In principle, ferromagnetic materials could provide this functionality because of the hysteresis, and hence memory, that accompanies most ferromagnets. Unfortunately, no suitable room-temperature ferromagnetic semiconductor material has yet been identified (Dietl *et al*., 2000); the most common ferromagnetic materials are metals. The aim of this research has been to see how far we can push the properties of basic ferromagnetic metallic alloys, which are usually considered to have relatively simple magnetic and electrical properties, toward highly functional devices that mimic and complement the digital logic functions of semiconductor microelectronics. Obtaining complex functionality from these simple materials will only be possible in nanoscale devices: in the bulk, the magnetic response of the alloy considered here would be purely linear. This work in many ways exemplifies the principle of nanotechnology: not simply a more miniature version of what we could already do, but rather making use of the unique behavior that develops when dimensions are reduced to the nanometer scale in order to make devices that have no larger-scale equivalent.

Handbook of Magnetism and Advanced Magnetic Materials. Edited by Helmut Kronmüller and Stuart Parkin. Volume 2: *Micromagnetism*. ISBN: 978-0-470-02217-7.

2 DOMAIN-WALL PROPAGATION AND NUCLEATION

All of the devices described in this chapter are based upon magnetic nanowires made from the common ferromagnetic alloy permalloy ($Ni_{80}Fe_{20}$). Magnetic nanowires are nanometer-sized magnetic structures, which are artificially fabricated using laboratory-scale versions of the lithographic techniques commonly used in microchip manufacture. In particular, the work in this chapter uses either electron beam lithography (EBL) or focused ion beam (FIB) milling (Xiong, Allwood, Cooke and Cowburn, 2001). A typical process will involve the deposition of a thin magnetic film, either using thermal evaporation or sputter deposition, followed by the

exposure of a computer-generated pattern. The pattern is exposed by rastering either a focused electron beam or a focused gallium beam. A development and pattern-transfer step then transfers the exposed image onto the deposited magnetic metal. The ability to create high-definition shapes of precisely the designer's choosing is extremely important, since the underlying principle at work throughout this research is that magnetic properties may be artificially modified by changing the shape and size of the nanostructure. This principle is not commonly seen on the macroscopic scale: the coercivity and anisotropy of a bulk material are usually intrinsic properties, which do not depend strongly on the shape of the sample. On the nanometer scale, however, the local demagnetizing fields are of comparable strength to the exchange fields (the quantum mechanical interaction responsible for ferromagnetism). A rich interplay results, which leads to magnetic properties being strongly dependent on shape and size.

Magnetic properties throughout this chapter are measured using a high-sensitivity laser probe (Cowburn, Koltsov, Adeyeye and Welland, 1998) based on the magneto-optical Kerr effect (MOKE) (Hubert and Schaeffer, 1998). The Kerr effect causes the polarization state of light to be slightly modified when it is reflected from a magnetic surface by an amount that is proportional to the component of magnetization in a given direction. Although the polarization rotations are small (typically 1° if all of the light is focused onto magnetic material, and proportionately less if the nanostructure is smaller than the focused beam size), MOKE is an excellent highly localized magnetometry.

Figure 1 shows two typical nanowires used in this chapter (see Cowburn, Allwood, Xiong and Cooke, 2002 for experimental details and Ono *et al*., 1999 for further examples of domain-wall nucleation and propagation). Shown are localized hysteresis loop measurements made at different positions along the length of the wire. One sees a coercivity of around 200 Oe in the case of Figure 1(a) and a coercivity of around 40 Oe in the case of Figure 1(b). What is striking is that the only difference between these two cases is that in Figure 1(b) the end of the nanowire has been formed into a large island area, known as an *injection pad*. The reason that their coercivities differ by a factor of 5 is because the magnetization reversal mechanism is altered by the presence or absence of the injection pad. In the structure without a pad, magnetization reversal occurs by the nucleation of a new reverse domain, probably close to the end of the nanowire where the demagnetizing fields are strongest, followed by a rapid propagation of the domain wall associated with the newly nucleated domain along the length of the nanowire. The limiting step for this process is the nucleation of the reverse domain, a highly energetic process. The strength of the reversed magnetic field required to force this nucleation is therefore quite high (200 Oe). In the structure with a pad, however, the new domain can easily nucleate inside the large pad because its thickness-to-width ratio (which determines the shape anisotropy) is lower. Once the reverse domain has been nucleated, the associated domain wall is free to move from the pad into the nanowire and propagate along it, effecting reversal of the complete wire. Domain-wall propagation in such nanowires is a very low energy process and so can still occur even at the much lower field at which the nucleation process occurred.

We assign the name *nucleation field* (H_n) to the coercivity reported in Figure 1(a) (200 Oe), that is, the field that must be applied to induce magnetization reversal if no domain wall is introduced artificially from any other source. We also define the term *propagation field* (H_p), which is the field that must be applied to move an existing domain wall along a nanowire. We might be tempted to say from Figure 1(b) that H_p is 40 Oe for this nanowire. In fact, however, even Figure 1(b) is still nucleation limited, albeit at a lower value inside the large pad. Figure 2 shows a different means of accessing H_n and H_p in a nanowire. In this case, we apply a magnetic field which is oriented along the wire axis for most of its sweep, but which rotates to 45° toward the extrema of the loop. This guarantees the starting magnetization state in both arms of the L-shaped nanowire as the applied field sweeps back toward zero. We generate such an applied field sequence by controlling the current in two pairs of coils, which apply fields in the X (nanowire axis) and Y (transverse) directions. If we choose the relative signs of the X and Y fields such that the 45° pulse is tangential to the corner of the L-shaped nanowire, then no domain wall exists in the wire and so the coercivity corresponds to a nucleation-limited reversal. In this case we measure H_n as 205 Oe, virtually identical to the case of Figure 1. If we now reverse the sign of the Y field, the 45° pulse becomes perpendicular to the corner, resulting in a single domain wall being created there. The coercivity now corresponds to the propagation field, since reversal in the main length of the wire is achieved simply by pushing that already-created domain wall around the corner and along the wire. Remarkably, we find a value of just 3 Oe for H_p. The coercivity of the nanowire has been modified by a factor of 65 simply by the presence or absence of a single domain wall.

3 DOMAIN-WALL CONDUITS

When the ratio between H_p and H_n is substantial, we describe the magnetic nanowires as *domain-wall conduits*. This is because if one applies a magnetic field H in the range $H_p < H < H_n$, then the nanowire will accept any domain wall introduced to it and propagate it along the wire, but will not reverse if no domain wall is given. For the nanowires

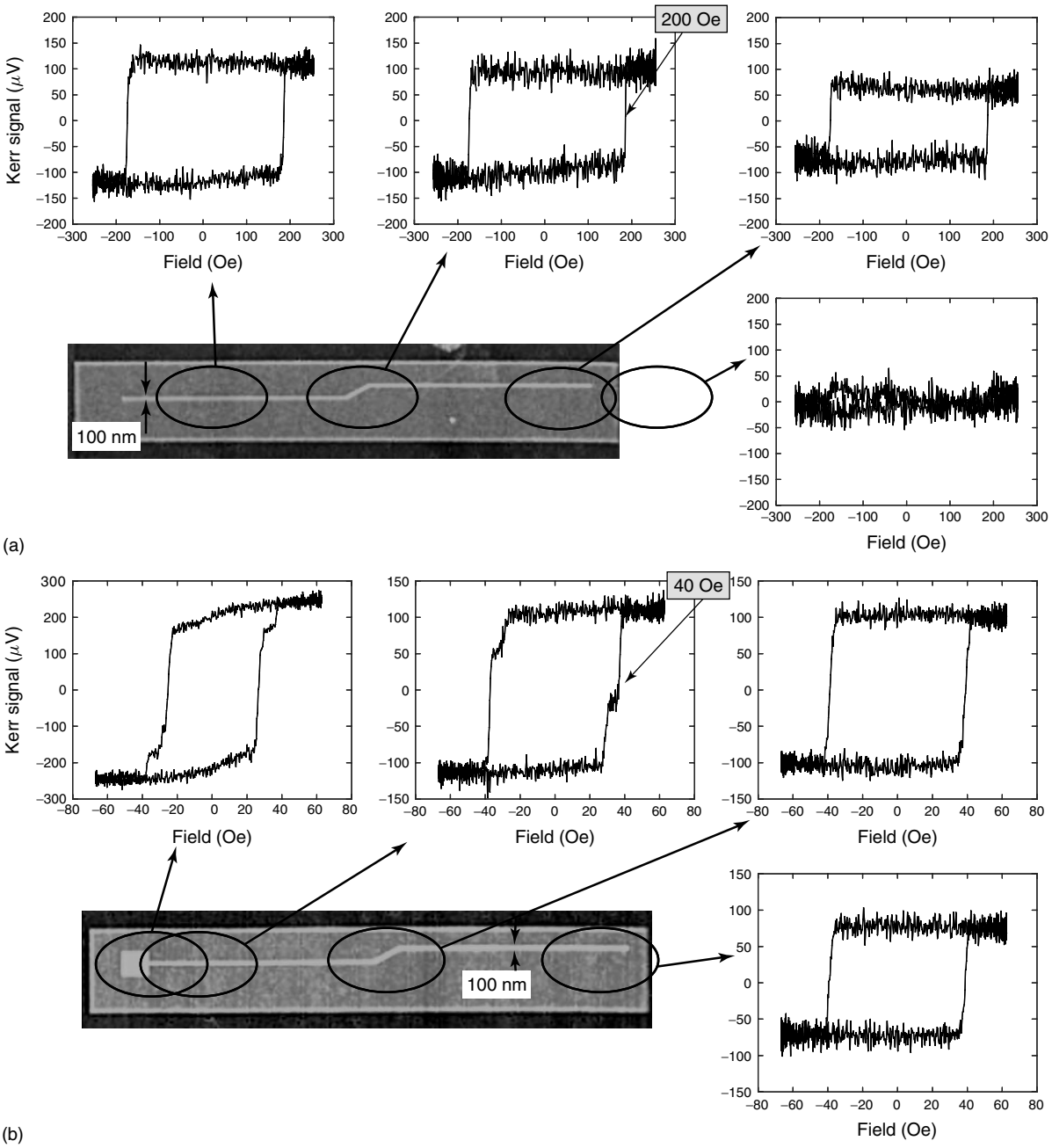

Figure 1. MOKE measurements of two 100-nm-wide 5-nm-thick permalloy nanowires. The ellipses shows approximately the averaging volume of the MOKE measurements. (Reused with permission from R.P. Cowburn, D.A. Allwood, G. Xiong and M.D. Cooke, *Applied Physics Letters*, **91**, 6949 (2002) © 2002, American Institute of Physics.)

shown here, this range is very large (any field between 3 and 205 Oe in the case of Figure 2 will result in domain-wall-conduit behavior). There is thus a parallel between electrical conductors and domain-wall conduits: an electrical conductor transports the electrical potential applied at one end to the other by a flow of electrons; a domain-wall conduit transports the magnetization direction applied at one end to the other by the flow of a single domain wall. Interestingly, electrical conduction results in losses due to the resistance of the conductor; the potential at the far end will always be slightly different from the potential at the near end. Although there are also losses in the transport of a domain wall through spin-wave emission by the wall as it moves, these energy losses are exactly compensated by the energy absorbed from the externally applied magnetic field H. The externally applied magnetic field therefore has a parallel to a power supply,

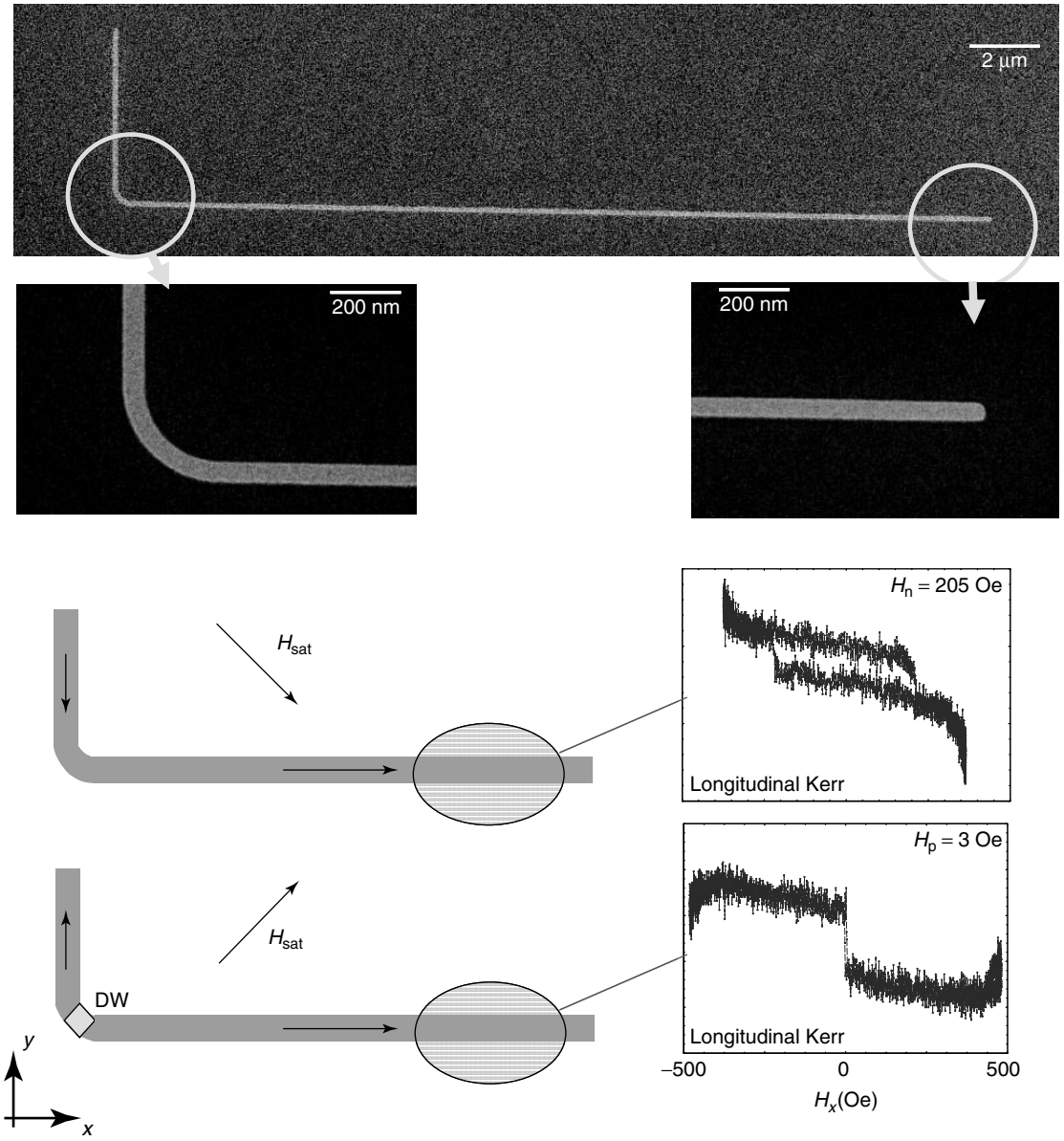

Figure 2. Domain nucleation and domain-wall propagation in a 120-nm-wide, 8-nm-thick permalloy nanowire.

and the domain-wall conduit should be considered as being an active component that can draw on that power supply, rather than the simpler, passive two-terminal component that is an electrical conductor. The propagation field is loosely analogous to a contact potential: it is the offset field that must be overcome before domain-wall conduction will occur. The nucleation field is loosely analogous to breakdown: it is the strength of field at which the magnetization state of the domain-wall conduit no longer relates to the input, but is overridden by the externally applied magnetic field or power supply.

Domain-wall conduits allow us to propagate magnetization states from one place to another, and so for spintronic applications it is natural to assign those magnetization states to Boolean states, allowing us to move information. We define a Boolean '1' as being when the magnetization direction is parallel to the direction in which information flows, and a Boolean '0' as being when the magnetization direction is antiparallel to the direction in which information flows. This may seem a little complex and the question may be asked: why not simply use 'right is 1, left is 0'. The answer is because of the possibility of using the nanowires in more complex geometries than simple straight lines. What will happen if we turn a corner, or, moreover, turn two 90° corners? The U-turn would have introduced a data inversion if we had used a simple fixed-space definition of

Boolean state. Clearly this would be undesirable. By using the direction of flow of information as the basis direction we can turn corners without affecting the data.

There is an additional complexity in propagating information through nanowire domain-wall conduits, caused by the vector nature of magnetization. Figure 3 demonstrates the problem. Suppose we wish to propagate a data sequence made up of 1s and 0s. Domain walls in nanowires carry a magnetic charge, due to the divergence of magnetization in the wall. Walls that lie between the two heads of the magnetization arrows are called *head-to-head* domain walls and carry a positive magnetic charge (since the magnetization has a positive divergence in the vicinity of the wall). Conversely, walls that lie between the two tails of the magnetization arrows are called *tail-to-tail* domain walls and carry a negative magnetic charge. When a magnetic field is applied to the domain wall, positive walls move in the direction of the field, but negative walls move against the direction of the field. Consequently, any data pattern that is more complex than simply all 1s will not propagate correctly, rather, the 1s will expand and annihilate the 0s.

A new approach to solving this problem is the use of spin-momentum transfer, in which a spin-polarized electrical current is used to drive the domain walls through the nanowire (Berger, 1984; Vernier *et al*., 2004; Lim *et al*., 2004; Yamaguchi *et al*., 2004). Spin-momentum transfer through a domain wall does not depend on the sign of the charge carried by the wall, and so all walls move in the same direction. However, this phenomenon is relatively weak and is not yet well understood. While it may provide an interesting solution in the future, at this stage we continue to use externally applied magnetic fields to propagate information.

The solution is to use a magnetic field that rotates in the plane of the nanowire and to impose a minimum spacing on the domain walls. If we require that positive and negative walls are always separated by at least two 90° corners, then although they will move in opposite directions for a given applied field, both of these directions will be the correct direction of information flow. Moreover, once separated by this degree, they will always remain so and will not catch up and annihilate. The only other constraint is that nanowires should only turn corners in one sense: the same as the sense of rotation of the applied magnetic field. So if the field is rotating in an anticlockwise direction, then all corners should turn left, as viewed from the direction of propagation of the domain walls. If the network requires a right-hand turn, then it is simply necessary to perform three left-hand turns instead. Once these constraints are obeyed, it is possible to build an arbitrary network of nanowires and to propagate information reliably through it. It is interesting to note that the combination of a fixed rotating field sense (or chirality) combined with having only a single sense of corner defines a propagation direction around the network. In electronic systems, it is usually necessary to have a semiconductor element such as a diode or transistor before inputs can be isolated from outputs. This result is the first indication that we are achieving a higher level of functionality from the magnetic nanowires than a simple metal would suggest was possible. It is also of enormous practical importance, since one of the frequent failures that one observes in new-concept nanoelectronic devices is the inability to achieve input–output isolation and hence to define an information flow direction through a network.

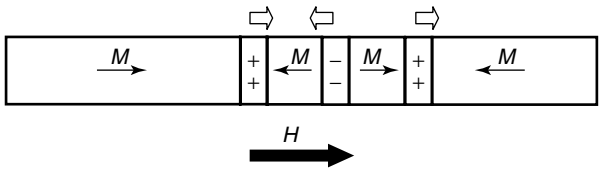

Figure 3. The problem of propagating a data pattern in a nanowire under an externally applied magnetic field, H. The white arrows show the direction of motion of the different domain walls.

A consequence of using a rotating field to propagate domain walls of both signs is that the domain-wall conduits become synchronous. Rising edges always propagate half a rotating field cycle before falling edges, and every 90° corner introduces a 90° phase shift into the signal. This presents both challenges and opportunities for the design of spintronic circuits based on domain-wall-carrying nanowires. The greatest challenge is that conventional microelectronic design tools assume that signals propagate through interconnect asynchronously and at a fraction of the speed of light. It will be difficult to use these tools in this new world where entire clock cycles of delay can be introduced simply by the choice of interconnect routing. On the positive side, the synchronous delay associated with each corner means that there is a large amount of embedded memory automatically distributed around the network. New architectural concepts will be required to exploit this memory, but it is noteworthy that one of the challenges facing microelectronics in the future is how to reduce the separation and resulting bottleneck between logic and memory. A further benefit, which will be expanded in more detail toward the end of this chapter, is that shift registers are extremely simple to realize in domain-wall logic – they are largely just lengths of interconnect.

4 LOGIC ELEMENTS

Now that we have interconnect for magnetic logic signals which can be used in near-arbitrary networks and hence move information to wherever we choose, the next step is to find ways of acting on that information in order to

perform computations. Any Boolean logic function can be realized once a two-input function (e.g., AND, OR) and an inverter (NOT) are available, simply by combinations of these basic functions. In addition, two architectural elements are required, namely, a fan-out structure, which creates two identical copies of a single signal without any loss in signal strength, and a crossover junction, which allows two perpendicular signal paths to cross without interference. In principle, once these four basic elements are available in domain-wall logic, any other circuit can be constructed.

4.1 The NOT gate

Figure 4 shows the design we have adopted for the NOT gate. See Allwood *et al*. (2002) for experimental detail. Since data are encoded by the direction of magnetization, the inverter function (which maps a 1 to a 0 and a 0 to a 1) is implemented by forcing a 180° rotation on the magnetization. The simplest way to achieve this is through a cusp structure. As the nanowire turns through the first quarter cycle of the cusp, the magnetization attempts to remain parallel to the nearest edge in order to minimize its potential energy. The magnetization therefore rotates with the cusp. During the second quarter cycle of the cusp, the magnetization continues rotating, with the result that the magnetization on the input side of the cusp is rotated 180° with respect to that on the output side. What makes this structure so useful is that it not only works statically, as described here, but also dynamically. That is to say that if a domain wall is incident upon the input side, corresponding to a transition edge in the data, the first half of the cusp looks like an anticlockwise corner and so the domain wall is carried into it by the external rotating magnetic field. Once in the central stub section, the domain wall finds that the second half of the cusp *also* looks like an anticlockwise corner and, so, is also pushed around it by the next quarter cycle of the rotating field, emerging on the other side of the cusp. It is a defining topological feature of a cusp that as one moves through it, both halves appear to have the same chirality.

The simplest way to test a NOT gate is by connecting its output to its input and thus forming a ring oscillator, as shown experimentally in Figure 4. While in microelectronics this would result in a high-frequency oscillation, the frequency of which would be determined by the propagation delay on the gate, the synchronous nature of domain-wall logic leads to a slightly different result. Figure 5 shows the equivalent electronic circuit. The half-cycle synchronous delay associated with propagating the domain wall through the cusp (or, put another way, because 1s and 0s propagate half a clock cycle apart in this architecture, the output of the NOT function must change half a cycle after its input) is shown as a $T/2$ delay, where T is the period of the rotating field. Additionally, there is a further delay of T due to the synchronous

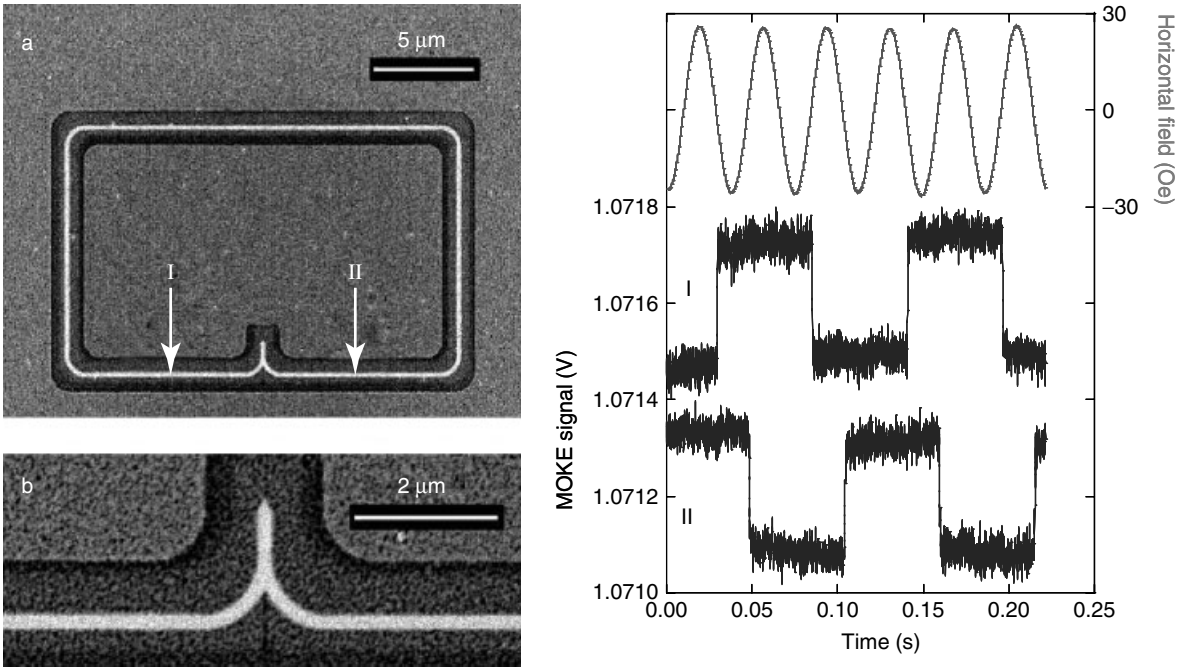

Figure 4. A NOT gate in a closed loop to form a synchronous ring oscillator. The bright white shade is 5-nm-thick permalloy. Signal measurements are made by MOKE at the two positions I and II. The device is bathed in an in-plane rotating magnetic field, one component of which is plotted.

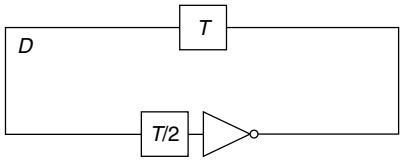

Figure 5. The equivalent electronic circuit for the synchronous ring oscillator shown in Figure 4. The square blocks are delay elements; T is the periodic time of the rotating magnetic field.

way in which the domain walls will move through the loop connecting the output to the input. The total loop time is therefore $3T/2$, which simple analysis shows will lead to a self-sustained oscillation with a periodicity of $3T$.

Figure 4 shows the result of measuring the magnetization on firstly the input arm I, and then the output arm II of the NOT gate while the entire chip is bathed in a rotating magnetic field. All of the expected features are visible. There is a half clock-cycle delay between the rising edge on the input of the gate and the corresponding falling edge on the output of the gate. The periodicity of the result is also seen to be three times the rotating field frequency, as expected. Although in this experiment we do not see the domain wall directly, the response periodicity of $3T$ is the sign that everything is functioning correctly. See Zhu *et al*. (2005) for direct magnetic force microscopy images of the domain wall moving around the loop and through the gate.

This simple circuit can be used to demonstrate how the chirality of the rotating field imposes an information propagation direction on the data. Figure 6 shows similar data to those shown in Figure 4, except that the applied field was stopped half way through the experiment and its sense of rotation reversed. It can be seen that when the applied field was rotating anticlockwise, the signal at the left-hand side of the NOT gate was leading the signal at the right-hand side by half a cycle, meaning that data were flowing from left to right through the NOT gate. Once the applied field was switched to clockwise rotation, the signal at the left-hand side of the NOT gate lagged that at the right-hand side by half a cycle, showing that data were flowing from right to left. The mirror symmetry of the cusp shape means that, in principle, either end can act as input, but a definite direction is, nevertheless, imposed by the sense of rotation of the applied field.

Once simple nanowires are formed into more complex shapes such as NOT gates, the ideality of the conduit begins to fail. For example, as the domain wall passes from the first quarter turn of the cusp to the second quarter turn, there is an instant when the wall cannot be considered to be in a well-defined conduit, and a complex micromagnetic pattern emerges. Consequently, the propagation field is augmented by the structural discontinuities in the logic gate. It is important to assess whether this increase in H_p is sufficiently large to reduce the available margin between H_p and H_n in which conduit behavior occurs. We do this by measuring the two-dimensional operating margin plot shown in Figure 7. The rotating field is expressed as an arbitrary ellipse with principle axes aligned along the X and Y directions, and measurements are made for different sizes and shapes of the

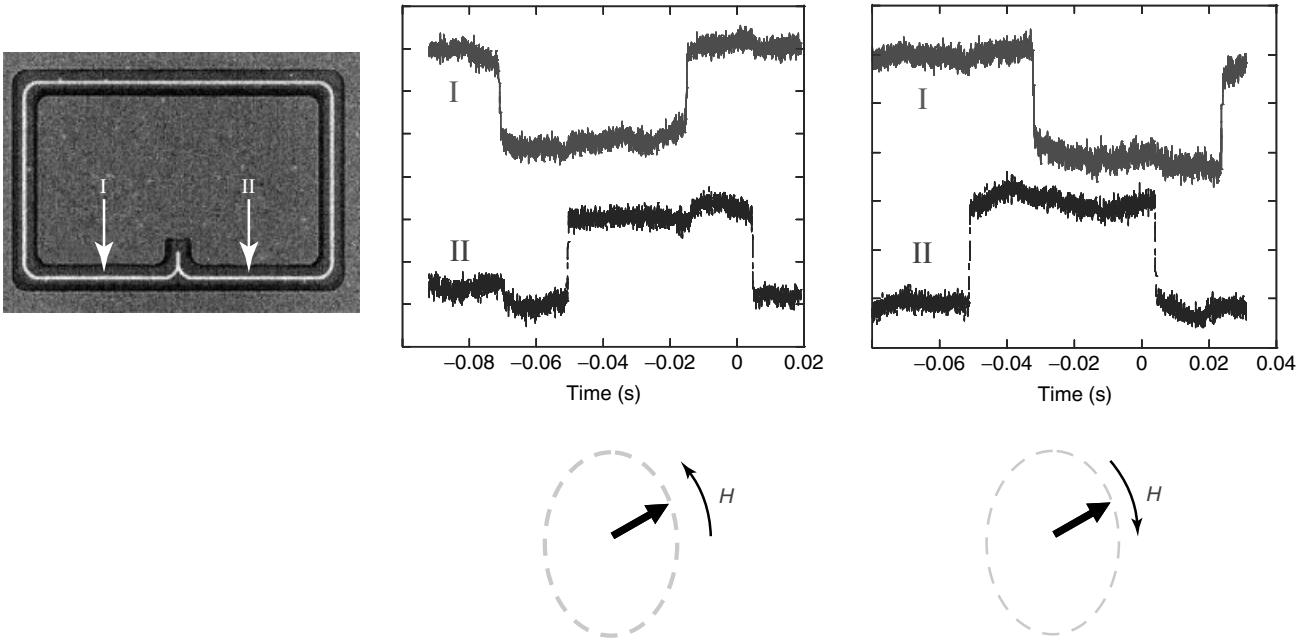

Figure 6. A NOT gate in a closed loop operated under two different senses of rotating field. The signal traces are made by MOKE at points I and II.

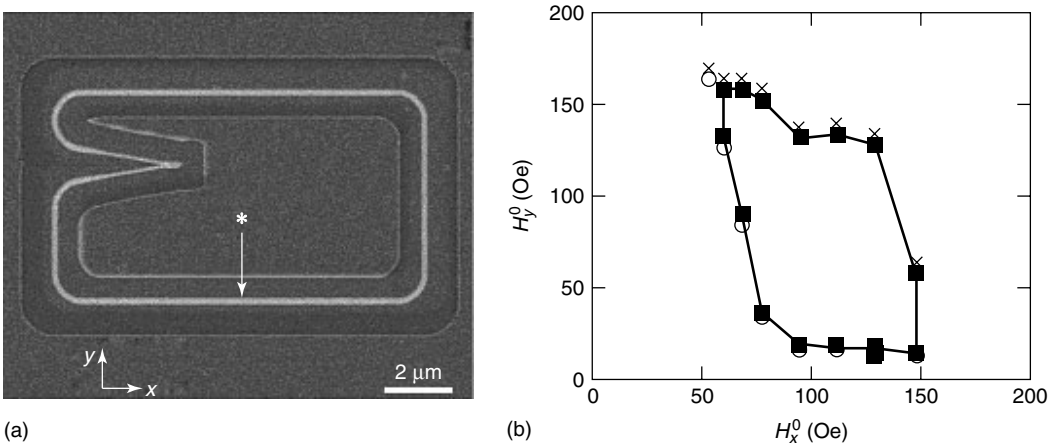

Figure 7. (a) An optimized NOT gate and (b) its operating margin phase diagram. The rotating magnetic field is described as an ellipse with major axis strengths $H^0{}_x$ and $H^0{}_y$. All field values inside the closed loop are found to operate the device correctly. (Reused with permission from D.A. Allwood, Gang Xiong, M.D. Cooke, C.C. Faulkner, D. Atkinson and R. Cowburn, *Journal of Applied Physics*, **95**, 8264 (2004). © 2004, American Institute of Physics.)

field locus as to whether the circuit functions or not. One sees in Figure 7 a well-defined enclosed operating area. Outside the top right of the operating area, the applied field is too strong and nucleation occurs in the NOT gate. This is observed experimentally by the periodicity of the response changing from $3T$ to T, as the gate begins switching in step with the applied field, regardless of the incoming data value. Outside the bottom left of the operating area, the applied field is too weak and domain walls are unable to propagate through the structural discontinuities of the cusp. Close to the boundary one sees occasional dephasing of the response, meaning that the device skipped a cycle as a domain wall became trapped; further away from the boundary (closer to the origin), there is no response at all, since domain walls are unable to move. See Allwood *et al*. (2004) for further discussion on NOT-gate operating margins and optimization of the shape of NOT gates.

The size of the operating margin (i.e., the area within the operating area) is important for two reasons. Firstly, it defines the fabricational fault tolerance of the gate, since small changes to the gate shape will most likely shift the operating area: we assume that the larger the margin was to start with, the more it can be shifted without device failure. Secondly, when we come to combine different types of gate, it is necessary to overlay their different operating areas and limit the applied field to areas that are common to all devices. This process is usually easier if the individual margins are large to start with.

4.2 The AND/OR gate

Figure 8 shows the structure used to perform either the AND or the OR function. See Faulkner *et al*. (2003) for further experimental details. Two nanowires are brought together through a shallow angle to a nodal point. A small amount of tapering is applied to the wire width immediately before the nodal point. The principle of operation is that for a domain wall to pass from one of the input arms to the output arm it must reverse a volume of spins in the node; if there is a domain wall coming down each arm at that instant, together they can reverse the center far more easily than a single wall could. Thus, there are two propagation fields for the device: H_{p1} that is the field required to propagate a single domain wall down an input arm and through to the output, and H_{p2} that is the field required to propagate a domain wall down both inputs arms and through to the output. We can set up these two conditions (plus a control experiment of no domain walls, which leads to the nucleation field for the gate being measured) by making different structures with different numbers of injection pads (Figure 8 shows one example where a single domain wall is injected). As in the case of the NOT gate, we measure the two-dimensional operating area phase diagram (see Figure 8). It is clear from this figure that $H_{\mathrm{p2}} < H_{\mathrm{p1}} < H_{\mathrm{n}}$. Just as there was a certain field range H such that $H_{\mathrm{p}} < H < H_{\mathrm{n}}$ in which a magnetic nanowire could be considered to be a domain-wall conduit, similarly there is a certain field range in which the two-input nanowire junction can be considered to be a logic gate. If we limit the applied field to the range $H_{\mathrm{p2}} < H < H_{\mathrm{p1}}$ then we describe the junction as being AND-like. This means that the applied field is strong enough to switch the output if each input supplies a domain wall, but not strong enough if only one input (or no inputs) supplies a domain wall. We use the term *AND* in the description of this gate because, like the true AND gate, it requires both inputs to act before the output will change. We say 'like', because this condition is

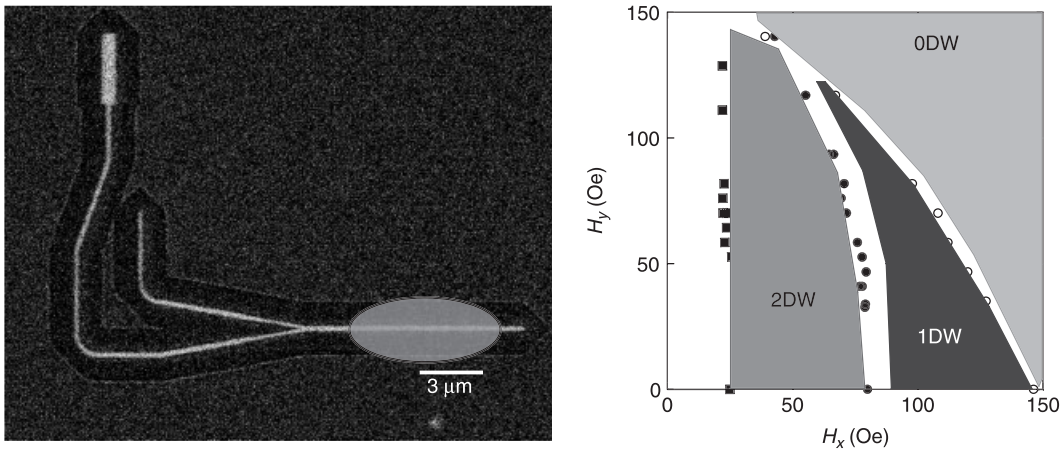

Figure 8. An AND gate and its operating margin phase diagram. Externally applied field strengths lying within the 2 DW region can only reverse the gate if two domain walls are injected into it. The 1 DW region can reverse if either one or two domain walls are injected. The 0 DW region can reverse even without artificial injection of domain walls (nucleation).

Input A	Input B	Output
0	0	0
0	1	Previous state
1	0	Previous state
1	1	1

AND-like

Input A	Input B	Output
0	0	0
0	1	0
1	0	0
1	1	1

AND

Input A	Input B	Output
0	0	0
0	1	Oscillates
1	0	Oscillates
1	1	1

OR-like

Input A	Input B	Output
0	0	0
0	1	1
1	0	1
1	1	1

OR

Figure 9. The Boolean truth tables for AND-like, OR-like, AND, and OR functions.

not enough to fully implement the Boolean AND function. Figure 9 shows the truth tables for the AND-like gate and compares it with the true AND function. The problem occurs for the case where the output is high and one of the inputs goes low. In a true AND gate, this would be enough to take the output low; in the AND-like gate, the output remains in its existing state. There is thus an undesirable hysteresis in the AND-like gate, although this may have some application in an alternative architecture which can take advantage of the memory associated with that hysteresis.

Similarly, if we limit the applied field to the range $H_{\mathrm{p2}} < H_{\mathrm{p1}} < H < H_{\mathrm{n}}$ then we describe the junction as being OR like. This means that the applied field is strong enough to switch the output if either (or both) input supplies a domain wall. As with the AND-like gate, this is close but not exactly the same as the true Boolean OR function. In this case, the failure occurs when one input is high and the other is low. A true OR gate would have a high output in this case; in the OR-like gate the output actually oscillates freely with the applied field (see Figure 9).

The OR-like and AND-like gates can be converted into a true Boolean function simply by adding a bias to the applied rotating field. Assuming the gates are oriented along the X direction, we simply shift the ellipse of the locus of the rotating field by $-\Delta H_x$. This means that the X component of the rotating field now sweeps between $H_x - \Delta H_x$ at its positive extreme and $-H_x - \Delta H_x$ at its negative extreme. We then arrange that $H_{\mathrm{p2}} < (H_x - \Delta H_x) < H_{\mathrm{p1}}$ and $H_{\mathrm{p1}} < (H_x + \Delta H_x) < H_{\mathrm{n}}$, that is, the gate is AND-like in positive fields and OR-like in negative fields. Together these conditions make a true AND gate. What is attractive about this scheme is that if the gate is simply reflected about its Y axis, the effective sign of ΔH_x is reversed, and the gate becomes OR-like in positive fields and AND-like in negative fields, which is the same as a true OR gate. Thus, by simply adding a single global bias to the rotating field, we can have both AND gates and OR gates in the same circuit, without having to localize the bias to the gate in question. AND gates result when the gate is oriented such that information flows in the opposite direction to the bias, and OR gates result when oriented such that information flows in the direction of the bias. A working experimental demonstration of the true AND gate will be given later in this chapter.

4.3 Fan-out gate

Figure 10 shows the structure used to perform the fan-out operation. It is essentially the AND/OR gate reversed such that domain walls flow into the single terminal and out through the two terminals. When the incoming domain wall meets the nodal junction it splits into two walls, each being half the original

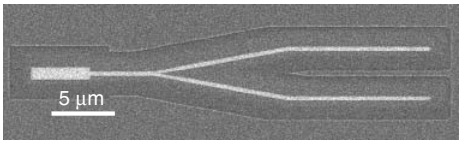

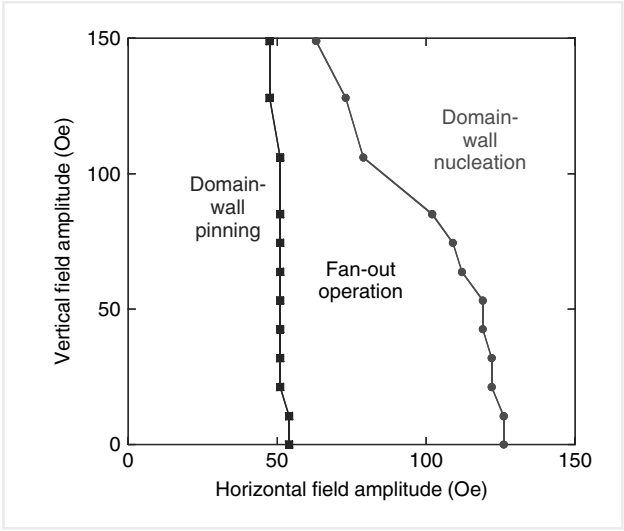

Figure 10. The fan-out gate with its operating margin phase diagram.

length. As these two walls pass along the tapered output arms, their length increases gradually until the full length has been restored. The energy of a domain wall is proportional to its length, and so work must be done to achieve this expansion. This energy is taken from the applied field and is manifested as a small increase in propagation field during the expansion. Figure 10 shows the operating margin diagram for the fan-out gate. It is a relatively robust gate, with large margins. Interestingly, the symmetry of the operating space follows the symmetry of the device: *Y*-axis fields have very little influence on its operation, since both the magnetization and the information flow directions are along the *X* axis.

That a fan-out gate is possible demonstrates the fact that domain walls are actually kink solitons (Bar'yakhter, Chetkin, Ivanov and Gadetskii, 1994). There is no equivalent to 'half-strength' domain walls and so there is no dilution of signal when it is split into two copies, as would be the case in a simple linear system. Rather, the extra energy that is needed is absorbed from the applied field and two full-strength signals emerge. From an electronic systems point of view, this shows that domain-wall logic possesses the equivalent of *gain*, since the domain-wall solitons are able to absorb from the applied field power supply whatever energy is required firstly to overcome losses and secondly to amplify the signal level through the fan-out gate. Gain is usually only associated with active semiconductor devices, once again demonstrating the high level of functionality present in the magnetic nanowire system.

4.4 Crossover gate

When two signal paths need to cross without interference in conventional microelectronics, a via is used to route one signal up to a higher level. A similar system could be envisaged in domain-wall logic, although the via would have to be a sloped ramp rather than a straight column to ensure that the domain wall could propagate under the action of an in-plane rotating field. It is possible, however, to cross two signal paths in domain-wall logic in the same plane, without any magnetic separation of the two, by using the crossover gate. If the via is analogous to a motorway flyover, then the crossover gate parallels a traffic-light-controlled crossroad. Figure 11 shows the structure used. A small taper is applied to each nanowire before contacting the central node to minimize the size of the central area where the domain-wall conduit is badly defined. The domain wall will experience a certain pinning force at this point due to its momentary loss of sidewalls; there will thus again be an operating area phase diagram for the device. There should never be a collision between two domain walls, providing the two signal paths approach each other at right angles, ensuring that domain walls in one arm always arrive one-quarter of a rotating field cycle before the other arm.

To date, the crossover gate is the structure with the smallest operating margin, largely due to the high propagation field created by the central node. It is hoped that in future developments the margin can be increased.

5 NANOCIRCUITS CONTAINING MULTIPLE GATES

As explained earlier in this chapter, the challenge in moving from single gates to different gates operating in the same nanocircuit is that there can only be one applied rotating

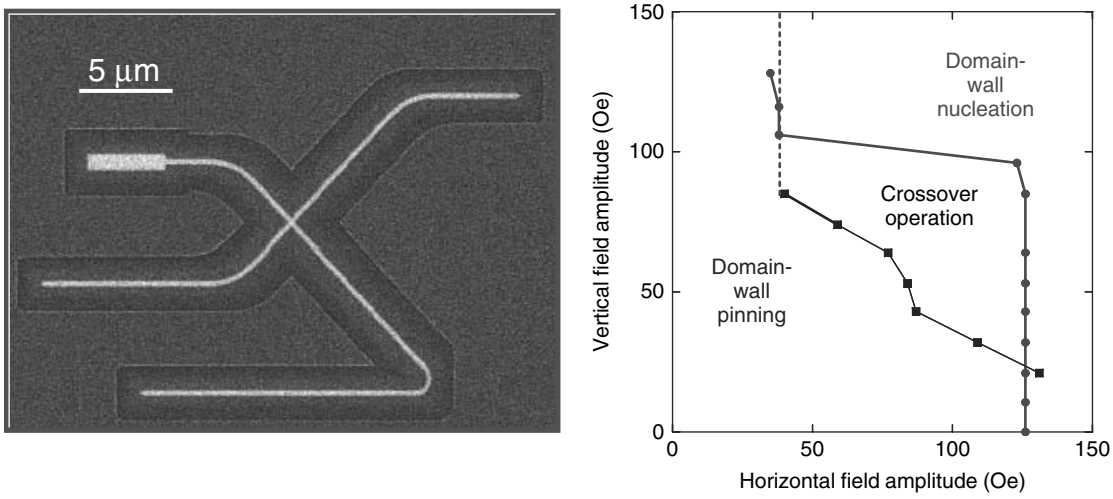

Figure 11. The crossover gate with its operating margin phase diagram.

field locus (since the field is applied globally to the entire chip) and this must lie within the operating margins of *all* the different types of gates in the circuit. At present, there is a common overlap area to the four types of gates, but it is very small. Future development will focus on increasing the size of the common overlap. Nevertheless, the overlap is currently large enough to allow a variety of combinations of gates to be demonstrated.

Figure 12 demonstrates the ability to concatenate multiple gates of the same function. Eleven NOT gates are formed into a loop (Allwood *et al.*, 2002). The measured circuit response shows a periodicity of $13T$ (T is the periodicity of the rotating field). This is exactly what would be expected: there is a loop delay time of $11/2T$ due to the $T/2$ delay introduced by each of the 11 NOT gates, and then there is an extra T delay for the closed loop, making a total loop delay of $13/2T$, and hence an oscillating periodicity of $13T$. It is noteworthy that in order to obtain a good signal-to-noise ratio from the MOKE measurements, we usually average many cycles (just like a cathode-ray oscilloscope). The response shown in Figure 12 was averaged approximately 100 000 times. This means that the single domain wall in the nanocircuit performed over 1 000 000 transits through a NOT gate. The fact that the transitions in the response remained sharp despite extensive signal averaging shows that there was no dephasing of the response at all during that time. In other words, it is highly probable that all 1 000 000 NOT operations were achieved successfully. Once again, we see the solitonic nature of the domain wall: unless the domain wall has a mechanism for compensating energy losses, it would not be possible for the same single wall to undergo this many logic operations.

Figure 13 shows the first combination of two different types of gate within the same circuit: a NOT gate is combined with a crossover gate by putting an extra twist into the feedback loop. The measured response is seen to be an

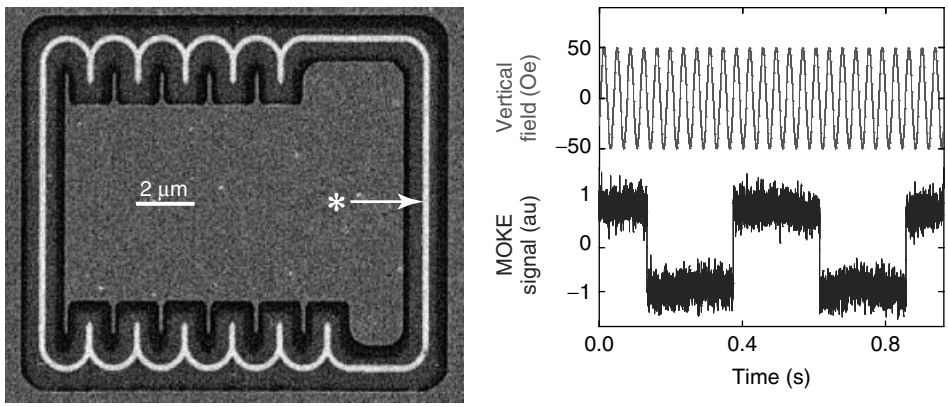

Figure 12. Eleven NOT gates connected to form a serial shift register. A MOKE measurement at the asterisked point shows a synchronous oscillation at 1/13th of the rotating field frequency (one component of which is plotted).

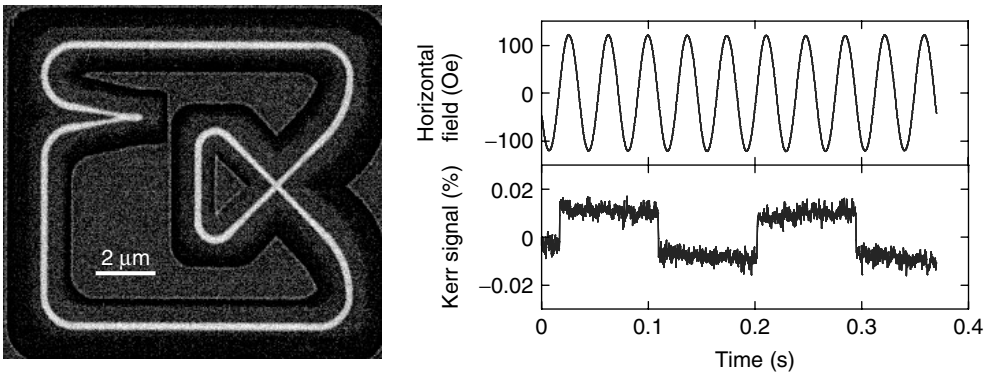

Figure 13. A NOT gate and a crossover gate combined in the same nanocircuit and operating under the same externally applied magnetic field. One component of the rotating magnetic field is shown, along with the signal response within the loop, as measured by MOKE.

oscillation with a periodicity of $5T$. Recall that in Figure 4, a single NOT gate in a closed loop usually gives a response periodicity of only $3T$. The change in periodicity is the sign that the domain wall is executing the crossover junction correctly, and is not taking a short cut at the crossover gate by turning right or left when it should be going straight on. By going straight on, it incurs an extra full minor loop on top of the existing major loop and hence the total delay due to the full closed loop increases from T to $2T$. When added to the $T/2$ delay due to the NOT gate itself, the loop delay time becomes $5/2T$, and hence the expected response periodicity is $5T$, as observed.

Figure 14 shows another combination of two different types of gate within the same circuit, except this time it is a NOT gate combined with several fan-out gates. A simple $3T$ ring oscillator is formed around the NOT gate, but a fan-out gate is inserted into the loop in order to extract a copy of the response. This signal is then split into two copies, and each of those is split again to make four copies of the original ring oscillator signal. MOKE measurements localized to each of the four outputs show that, indeed, the $3T$ signature can be seen on each. Multiple fan-out operations are one way of amplifying the total volume of magnetic material switching to make final detection easier, as well as being an integral part of any logic circuit.

There is an additional way to fan-out signals, and that is to use the central stub of the NOT gate, which carries a copy of the input signal. This signal is accessed simply by extending the length of the stub into a full nanowire. Figure 15 shows an example of a ring oscillator connected to a serial-in, parallel-out shift register formed from a chain of NOT gates with accessible stubs. The ring oscillator in this case is simply providing a convenient signal to trace through the shift register. The shift in the MOKE signal as we move the laser probe from one nanowire to the next shows the correct operation.

The twists on the end of the nanowires perform an important role by preventing domain walls from reflecting and reentering the system. Depending on the precise shape of the end of a nanowire, a domain wall may or may not

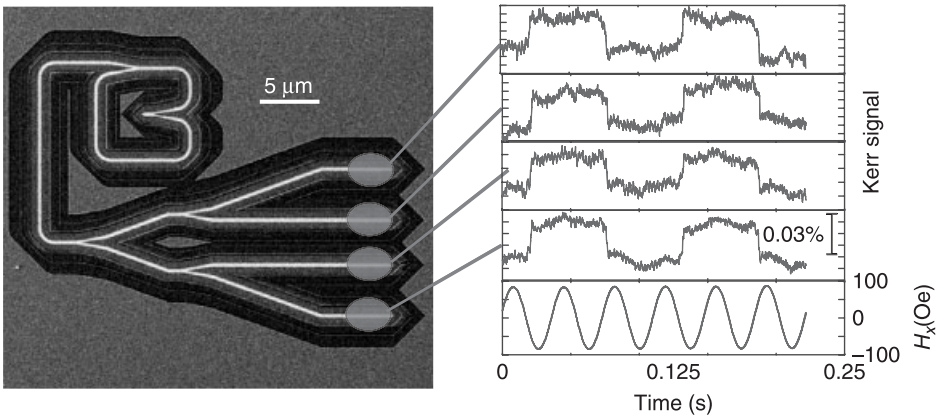

Figure 14. A NOT gate combined with four fan-out gates. MOKE measurements show four identical copies of the signal expected inside the NOT-gate ring oscillator.

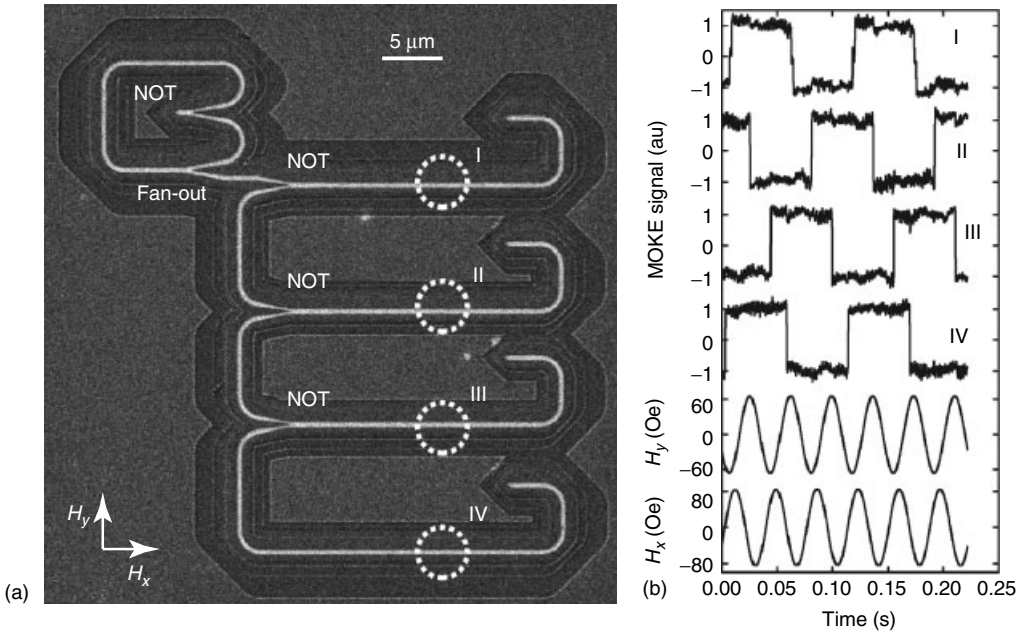

Figure 15. A nanocircuit which uses the central stub of the NOT gate to replicate the input signal. (Reused with permission from D.A. Allwood, *Applied Physics Letters*, **89**, 10254 (2006). © 2006. American Institute of Physics.)

annihilate. If it does not annihilate, it will be backpropagated half a clock cycle later and may interfere with the correct operation of the logic gates. If annihilation at the end of the conduit cannot be guaranteed, the conduit can be correctly terminated by ensuring that there are two 90° corners between its end and the final logic element. The 180° turn forms what we refer to as a *domain-wall black hole*: should a domain wall enter into it and not annihilate at the end, the rotating field will be unable to backpropagate it through the double corner, since these corners are of the wrong chirality. In the rotating field scheme, whatever goes into a black hole never reemerges.

We now move to the next level of integration and begin to combine three different types of gate within a single nanocircuit. Figure 16 shows the combination of NOT gates, fan-out gates, and a single AND gate. We know it is an AND gate and not an OR gate because of the sign of the bias that was applied to the rotating field. The bottom-left NOT gate forms a ring oscillator in order to generate a local signal, which can be traced through the circuit. A fan-out gate copies that signal out of the closed loop and then a second fan-out forms two identical copies. One of these copies is routed directly into the AND gate, while the second copy is inverted in a NOT gate. The primary function of this is to generate two dephased signals, which will cycle the AND gate through the four states of its truth table. We have sketched in Figure 16 the expected signals incident upon the AND gate. We then move the laser probe to the output of the AND gate and make an experimental measurement of its output. Figure 16 shows a $3T$ period signal, but with a nonsymmetrical mark–space ratio. This is exactly what would be expected from an AND gate being cycled through its truth table. Three of the four possible input states involve at least one 0, and so the output remains low for these three states. Only in the fourth state, when both inputs go to 1 would we expect to see the output go high. The three-element circuit thus functions correctly, and has also provided a useful test bed for cycling the AND gate through all of its states.

The final step is then to replace the second NOT gate in this circuit with a crossover gate, as shown in Figure 17, in order to form a nanocircuit that contains at least one example of each of the four basic gates. See Allwood *et al*. (2005) for experimental details. In this case we test the ring oscillator and the two fan-outs first by making a measurement in the bottom right-hand corner, work out what the signals should now be at the input to the AND gate, and then measure its output. The only difference in the operation of these circuits is that there is a longer phase delay between the two signals entering the AND gate: in Figure 16 the second NOT gate introduces a half clock–cycle delay, while in Figure 17 the minor loop with crossover introduces a one clock–cycle delay.

In principle, now that the four basic elements have all been demonstrated to work together in the same nanocircuit, domain-wall logic could be used to construct any digital logic circuit of arbitrary complexity. In practice, further work needs to be done to augment the size of the operating margin of the complete circuit in order to reintroduce the

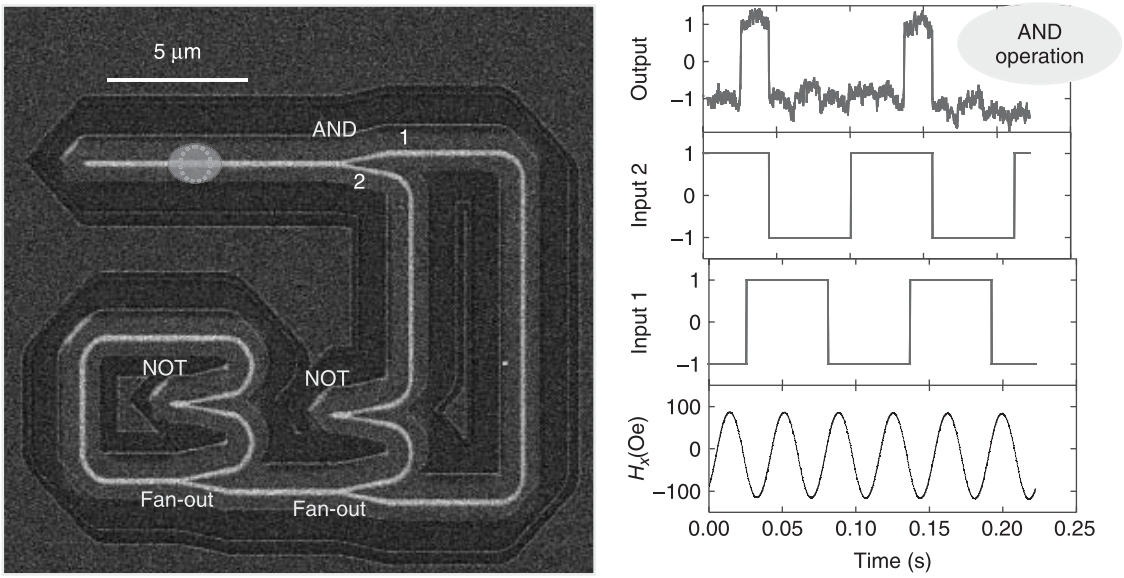

Figure 16. A nanocircuit containing three different types of gate: NOT gates, fan-out gates and an AND gate. The two signal incident upon the AND gate are shown schematically, along with an experimental measurement of the output of the AND gate as it is cycled through its four states.

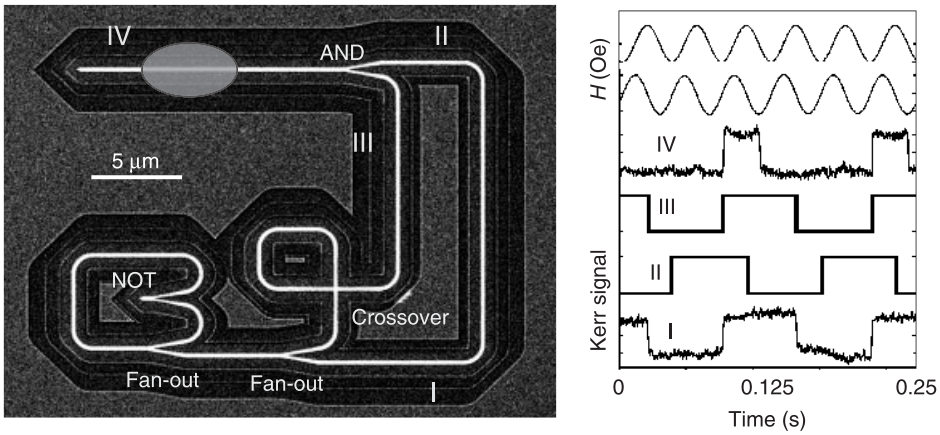

Figure 17. A nanocircuit containing the four basic gates: NOT, AND, crossover, and fan-out.

fabricational fault tolerance that is already present in the large margins of the individual gates. Further understanding is also required about the precise influence of synchronous interconnect on large circuits.

6 DATA INPUT–OUTPUT

The recently developed technology of magnetic random access memory (MRAM) (Engel *et al*., 2005) has already solved most of the engineering issues involved in interfacing between a soft ferromagnetic layer and an underlying CMOS system. Specifically, in MRAM, data writing is achieved by passing an electrical current through a conductor placed close to the magnetic element, allowing the magnetic field generated around the current to nucleate a reverse domain in the magnetic nanostructure. Data reading is achieved by the use of a magnetic tunnel junction (MTJ) (Moodera *et al*., 1995) in which the electrical resistance of two magnetic layers separated by a thin film of insulator is found to depend strongly on the relative magnetization directions. By fixing the magnetization direction of one layer, it becomes a reference against which the magnetization direction of the other layer may be measured. Signal levels large enough to interface directly with CMOS transistors are achieved by this method. We intend to piggyback off these developments for interfacing signals between the magnetic system and conventional electronics. Domain-wall logic can be considered as an

extension to MRAM. In MRAM, the data storing magnetic layer is very simple and is only used to store a single bit of information. The concepts developed in magnetic logic can be used to extend the functionality of that storage layer, allowing data to be processed as well as stored.

We have developed an alternative data input method, which may be important if three-dimensional structures are implemented in domain-wall logic. One of the major limitations to creating ultrahigh-density three-dimensional microelectronic circuits is the cost of making connections to the multiple layers. A useful strategy for realizing the ultrahigh data density of three-dimensional structures without increasing the cost is to attempt to find a way in which the input and output to the three-dimensional structure is maintained in two dimensions. Figure 18 shows a device we have developed which allows this to be done with domain-wall logic. See Allwood *et al*. (2005) for further experimental details. The figure shows a chain of eight NOT gates, where one gate has had its central stub enlarged. This reduces the shape anisotropy in that stub and hence reduces its nucleation field a little. Consequently, if the *globally applied* rotating magnetic field is modulated in amplitude slightly, it is possible to cause nucleation in the NOT gate with the elongated pad, thus forcing its data state to the direction of the global field. Importantly, the strength of modulation needed to achieve this is not so strong as to lie outside the operating margin of all the other gates in the chain, and so they continue to work normally. Thus, by modulating the global field, we can write data directly into the serial shift register and then shift that same data throughout the rest of the shift register. In this case, the globally applied rotating magnetic field is not only serving as a power supply and clock, as it does in all other domain-wall circuits, but it is also acting as a serial input data channel. Figure 18 shows a working demonstration of this experiment, where we have written the data sequence 11010 into the shift register by modulating the rotating field. This writing sequence is applied only once. An hour later, we then begin cycling the rotating field without modulation and use the MOKE laser probe to read the serial data circulating around the shift register. We see the sequence 11010 repeatedly, as it goes around the circular shift register. We have thus succeeded in injecting data into the nanoscale storage ring, although the source of field modulation was 1 cm away from the chip itself. As a control experiment, we show also in Figure 18 a straight trace, obtained during reading when the 11010 sequence had not been previously written. The reason that we do not see a 10T periodic signal as might be expected based on earlier results is that there is an even number of NOT gates in this loop, which prevents it from acting as a ring oscillator.

This result is significant because it demonstrates the ability to write data into nanoscale storage rings from a distance. This immediately opens up the possibility of a three-dimensional data storage cube, in which all magnetic field generation and sensing is performed on the bottom CMOS layer, but where data can be remotely targeted to specific parts of the three-dimensional volume simply according to where one places the NOT gate with the enlarged stub. Such a device would have the storage density of a three-dimensional device but the fabricational cost structure of a two-dimensional device. This idea is explored further later in this chapter.

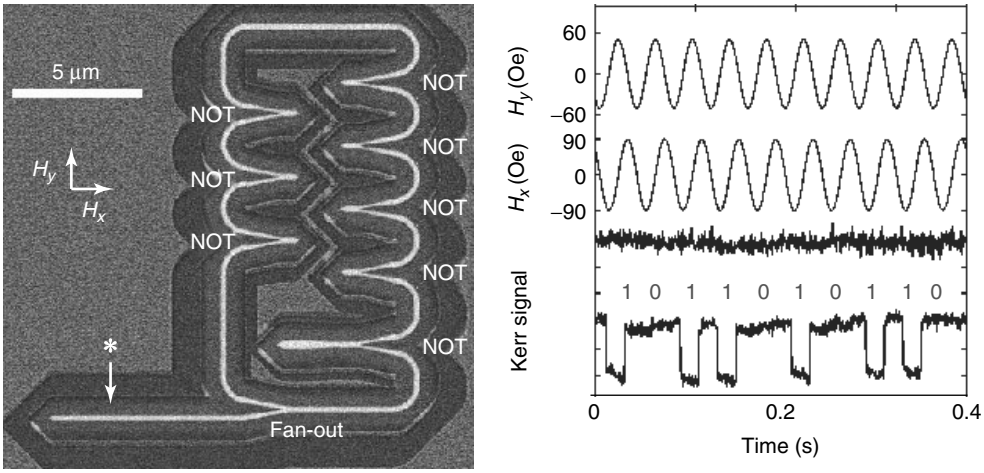

Figure 18. A serial shift register formed from eight NOT gates, with the central stub of one NOT gate enlarged to form a data input element. The data sequence 11010 is written into the shift register by modulating the rotating magnetic field. The signal traces show the recovered data sequence circulating around the shift register, as well as a flat trace showing the result when the writing sequence is not performed.

7 DOMAIN-WALL SPEED

Modern microprocessors run at clock frequencies in excess of 1 GHz and it is important to understand how domain logic compares against this target. All of the results presented so far in this chapter have been at very low frequencies. This is not a fundamental limit, but rather reflects the convenience of using a large iron-cored electromagnet during laboratory testing. There are two speed limitations inherent in domain-wall logic. Firstly, domain walls propagate by the precession of the spins in the center of the wall around the local effective magnetic field. The speed of propagation is thus ultimately limited by the gyromagnetic precession frequency. However, the speed will also depend upon the degree to which precession is damped through energy losses, which can be both material and geometry dependent. In particular, at the beginning of this work, it was not clear to what degree nanoscale confinement in the nanowire would increase damping. It is important that the domain-wall propagation speed should be fast enough to maintain the synchronous nature of the system: a domain wall must have had time to propagate as far as it needs to within a given quadrant of the rotating field phase.

The second limitation comes from how quickly the externally applied magnetic field can be rotated. If it were generated from a microwave strip line, then tens of gigahertz would be possible. However, this would require the line to terminate in a 50 Ω load, which would dissipate very large amounts of power, making the power dissipation from the chip uncompetitive. The alternative method for generating the rotating field is to use microfabricated coils. These can be highly efficient if made thick enough (the power dissipation could be as low as 1 W cm^{-2}, 100 times lower than the dissipation limit of silicon). However, the inductance of such coils limits their frequency. It would not be possible to generate rotating field frequencies much higher than 10 MHz across an extended area, although very high frequencies could be achieved if only covering a few square millimeters.

Thus, different constraints apply depending on the size of the chip. Small chips can operate quickly if the domain-wall propagation speed is high enough. Large chips will always be limited by the generation of the rotating field, and so domain-wall speed (unless very slow) is less important.

Figure 19 summarizes the experiments we have performed to measure the domain-wall propagation speed through a simple nanowire. See Atkinson *et al*. (2003) for further experimental details. The nanowires are fabricated directly onto the top of a microwave strip line, through which we can launch current pulses with sub-nanosecond rise times. These current pulses lead to a magnetic field pulse across the width of the strip line, which is used to accelerate a domain wall from one end of a nanowire of known length to the other. The domain wall is introduced to the starting end of the straight 'racetrack' by a perpendicular wire, and the MOKE laser probe is placed at the other end of the nanowire in order to detect the arrival of the domain wall. We assume that the domain wall has very little inertia and will stop propagating virtually as soon as the applied field pulse terminates. We continually test this assumption by repeating experiments with two pulses of half the original width to see if the results remain unchanged. In most magnetic systems this assumption is found to hold. Equally importantly, we also test that we are indeed measuring domain-wall propagation and are not nucleating a reversal by the pulsed field by changing the bias field applied to the injecting arm to prevent it from injecting a domain wall. When we do this, all switching in the racetrack is also seen to stop, proving that it was indeed the injected domain wall that was responsible for the reversal. We measure speed by applying different widths of pulse and finding the probability of switching at the far end of the nanowire as a function of pulse width. From the 50% probability point, we can determine the average time

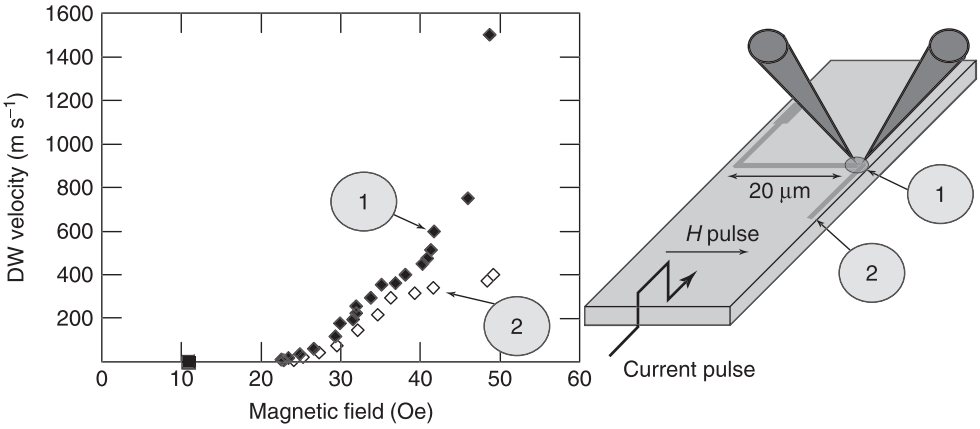

Figure 19. A measurement of the domain-wall propagation speed in a magnetic nanowire fabricated on the back of a microwave strip line.

required for the domain wall to cover the racetrack, and since we know its length, we can calculate its speed. We repeat this process for different amplitudes of pulsed field, and hence can measure the domain-wall speed as a function of the field strength (Figure 19). The domain wall is found to move with speeds of up to $1000\,\mathrm{m\,s^{-1}}$ for fields of the strength that would be applied in logic devices. Importantly, we note slight differences in result at the highest speeds, depending on whether we place the laser probe at the end of the race track or a little further down a perpendicular extension to the race track. This indicates that there is some dynamic 'bouncing' of the wall as it attempts to navigate the corner. One thousand meters per second is $1\,\mu\mathrm{m\,ns^{-1}}$ and most logic gates are $1\,\mu\mathrm{m}$ or less in length and so transit times of around 1 ns could be expected. This is reasonably competitive with microelectronic speeds, although not with the very fastest. Across-chip clock frequencies of up to 200 MHz could probably be made to work, which would not be fast enough for the very fastest applications, but would certainly be fast enough for some applications.

Alternative experimental methods for obtaining domain-wall velocities in nanowires have been described by Ono *et al*. (1999), in which a giant magneto resistance trilayer is formed from the nanowire under test and two other layers, allowing the resistance of the trilayered nanowire to serve as a probe of the fraction of the nanowire that has magnetically reversed and hence the position of the domain wall. (See also **Domain Wall Propagation in Magnetic Wires, Volume 2**.)

8 SCALABILITY

The successful uptake of any new microelectronic technology often depends upon its scaling properties. The capital costs of deploying new technologies are so high that a financial return can only be made if the technology continues to be used for several years. During that time, the definition of lithography will continue to improve and so the technology must be capable of continuing to operate as its dimensions are reduced. The way in which magnetic devices sometimes struggle with scaling is that thermal fluctuations usually depend upon the product KV, where K is the magnetic anisotropy and V is the volume of magnetic material corresponding to a single data bit. As lithographic feature sizes are reduced, V falls and so to restabilize the device it is necessary to increase K. This is usually possible, either by a change of magnetic material, or in the case of domain-wall device simply by changing the thickness-to-width ratio of the nanowires, leading to an increase in the shape anisotropy. However, the strength of magnetic field, which must be applied to operate the device usually scales with K, and so the result is a device which is stable but which requires a stronger magnetic field to operate it. In some technologies (e.g., hard disk drives and MRAM) it can be difficult to achieve those increased levels of magnetic field, either because of magnetic saturation or because of power dissipation.

We have analyzed the scaling limitations in domain-wall logic. We have addressed two specific questions, namely: (i) how should the thickness of the nanowire be scaled as the width is reduced; (ii) will the domain wall always be a small object, or will it become so extended in small nanowires that we can no longer make useful logic gates?

Regarding the first of these, we have identified two different scaling regimes. In the first instance, where structures are being scaled from the current 200-nm-width downwards, the thickness should be scaled with F as the width of the wire is also scaled with F (F is the minimum feature size of the lithography). This keeps the thickness-to-width ratio of the nanowires constant, and so the shape anisotropy field also remains constant. Consequently, the strength of applied rotating field required to operate the device should remain unchanged. During this first scaling regime, the power-delay product (see the next section for a definition) will reduce with F^3, since it is proportional only to the volume if the applied field amplitude remains constant. The limit of this scaling regime comes when the power-delay product becomes comparable to a few tens of $k_\mathrm{B}T$, where k_B is Boltzmann's constant and T is room temperature. At this point, thermal fluctuations begin to disrupt the data, and so it is necessary during further scaling to avoid any extra reduction in the power-delay product. We do this by switching to the second scaling regime in which the thickness of the nanowires is scaled with $F^{-1/2}$ while the width continues to scale with F, that is, the thickness rises as the width of the nanowire falls. The power-delay product should then remain roughly unchanged with this scaling law, while the strength of field needed to drive the device rises. Since the applied magnetic field does not have to be localized to a small volume, it is possible to generate relatively large fields without excessive current densities. Generating magnetic fields over extended areas is much more energy efficient than generating them in localized areas, since in the former case the thickness of the conductors can be increased almost arbitrarily without loss of contribution of the magnetic flux. We therefore do not anticipate a premature limit to scaling caused by this rise in driving field.

Regarding the domain-wall width (i.e., measured along the long axis of the nanowire), we have used micromagnetic simulations (Web: math.nist.gov/oommf/) to calculate the domain-wall profile in a nanowire as a function of the size of the nanowire. Figure 20 shows the result. At the current width of 200 nm, the plot shows that the domain wall should

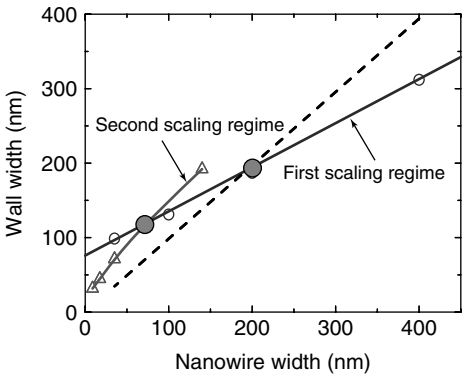

Figure 20. Domain-wall width (measured along the long axis of the nanowire) as a function of nanowire width for the two scaling regimes.

be approximately 200 nm wide, that is, it can be considered to be a square object. During the first scaling regime, the domain-wall width shrinks less rapidly than the width of the nanowire, and so the domain wall becomes slightly rectangular, but not excessively so: at the limit of the first scaling regime at (70-nm-wide nanowires), the domain wall is only 110 nm wide. During the second scaling regime, the increase in shape anisotropy causes the domain wall to become shorter again and the growth in elongation ceases. By the time the nanowire is 32 nm wide, the domain wall is 50 nm, meaning that it remains roughly a rectangle with an aspect ratio of 1.5 throughout the entire second scaling regime.

9 POTENTIAL APPLICATIONS OF DOMAIN-WALL LOGIC

Domain-wall logic is not a contender for a wholesale replacement of CMOS microelectronics. CMOS is a highly mature technology with many advantages, and still has many years of scaling available to it. However, a strong trend in microelectronics, which is expected to apply to the relationship between CMOS and many other areas of nanotechnology in the future, is to combine multiple technologies on a single platform: the system on chip (SoC). Mature economies usually break into a large number of specialists each doing what he or she does best. The same principle applies to complex microelectronic devices. In this context, domain-wall logic brings another item to the menu of available technologies. So what does domain-wall logic do well?

- It gives high level of functionality to relatively simple structures. To implement an AND gate in CMOS would take six transistors; domain-wall logic achieves it simply by bringing two nanowires together. Similarly, the other high-level properties that have been highlighted in this chapter, such as input–output isolation and signal/power gain are all intrinsic to the nanowire and do not have to be explicitly created.
- The power dissipation per logic gate is extremely low. Microelectronic engineers usually measure dissipation from a gate by the power-delay product, that is to say the product of how much power is dissipated multiplied by how long the gate takes to process a single function. The units of this quantity are energy, corresponding to the energy dissipated during the evaluation of the function performed by the gate. CMOS power-delay product depends on the size of the devices. To compare like with like, we therefore take the 200-nm minimum feature size CMOS value of 10^{-2} pJ (Waser, 2003). On very general magnetic grounds, we can say that an upper bound for the power-delay product for domain-wall logic is $2M_{\mathrm{s}}VH$, where M_{s} is the saturation magnetization of the magnetic material, V is the volume of magnetic material in a gate and H is the amplitude of the applied field. Applying the parameters for a typical 200-nm domain-wall logic gate gives 10^{-5} pJ, that is, 1000 times lower than the equivalent CMOS device. Because of the inefficiencies inherent in the generation of high-speed magnetic fields (see the preceding text), this does not necessarily mean that domain-wall logic chips will not consume much power. What it does mean, however, is that the waste heat will be generated from the global field generator and not from the logic devices themselves. This is of particular relevance if one comes to stack the devices into three-dimensional neural-like circuits. The two key technical difficulties to doing this in CMOS are (i) distributing the power and clock to everywhere inside the volume of network and (ii) extracting the waste heat from the center of the network so that the device does not melt. We believe that domain-wall logic is an excellent choice of primitive for three-dimensional architectures.
- Nonvolatility comes as standard. In a world of mobile computing and portable (or even wearable) devices, the concept of 'instant on' is becoming increasingly important. Users accept that devices cannot be expected to operate when there is no power. However, as soon as power becomes available, users want the device to be ready, and not have to undergo a long boot process, or to have forgotten what it was doing when the power last failed. Since there are currently very few nonvolatile memory technologies available which can be embedded directly into CMOS, a data transfer process is usually required between a high-speed, volatile memory register in the heart of the CMOS logic and an off-chip

low-speed, nonvolatile store where the state variables of the system are stored. With domain-wall logic, all of this becomes redundant. Providing that the rotating field is properly controlled so that it stops gracefully as power fails and does not apply intermediate levels of field leading to data corruption, the domain-wall logic circuit should simply stop and retain all of its state variables. As soon as the power returns, the logic continues from where it left off.

- Domain-wall logic can make use of redundant space on top of CMOS. Because no complex heterostructures are required, the logic elements can sit in a single layer fabricated as a back end of line process after the CMOS has been laid down. This can improve the efficiency of the underlying CMOS by farming out some space-consuming task to the domain-wall logic on top. Since this space was never accessible to CMOS itself anyway, it all counts as a gain.
- Being metals, the basic computational elements of domain-wall logic are automatically radiation hard, and so are suitable for use in space or in military applications.
- Domain-wall logic is very good at forming high-density shift registers. These could be used as nonvolatile serial memory. Serial memory is used for storing entire files, and so does not require high-speed random access. The hard disk drive and NAND flash devices (e.g., as used to store the photographs in a digital camera) are examples of nonvolatile serial memory. Both of these devices are currently two-dimensional in form. Shift registers made from domain-wall logic elements have the potential to be stacked into three dimensions without incurring extra wiring complexity, since data and power can be transmitted remotely through magnetic fields, as demonstrated earlier in this chapter. In a hard disk drive the data are stored as rows of magnetic domains, and this would remain the same in a domain-wall logic serial memory. What would differ is that in a hard disk the domains are mechanically rotated on their disk underneath a static sensor, while in domain-wall logic the domains themselves would move under the action of an externally applied magnetic field along static domain-wall conduits, potentially stacked into an ultrahigh-density three-dimensional array.

The weaknesses of domain-wall logic have already been described throughout this chapter, but are in summary (i) limited operational speed and (ii) unconventional synchronous interconnect. Whether the latter should be regarded as an advantage or a disadvantage is open to debate, since it is the same property that makes domain-wall logic so suitable for high-density serial memory. Nevertheless, interfacing with conventional design tools remains a challenge.

10 CONCLUSION

While bulk magnetic alloys usually exhibit very simple linear properties, structuring on the nanoscale introduces more complex, nonlinear behavior that can be used for a new generation of spintronic devices. In particular, the coercivity of the magnetic material, which is usually an intrinsic property in the bulk, becomes very dependent on whether the magnetization reversal mechanism is limited by domain nucleation or by domain-wall propagation. We have demonstrated modifications to the coercivity of as much as a factor of 65 simply by whether a domain wall is artificially injected or not. The huge ratio between the domain-wall propagation field and domain nucleation field that exists in magnetic nanowires has allowed us to introduce the concept of the domain-wall conduit, in which the nanowire can be considered to be a highly efficient conductor for domain walls. If information is encoded by the domains, then domain-wall conduits allow that information to be moved around an arbitrary network, and the possibility of building computational devices emerges. Furthermore, we have shown that by precisely modifying the shape of the nanowire, we can exert topological control over the information and hence implement Boolean NOT gates, AND gates, fan-out gates, and crossover gates. These four basic elements can then be interconnected to form fully functioning nanoscale logic circuits. We have demonstrated, among others, a functioning circuit that contains at least one example of each of these basic gates all operating together in the same circuit. From here, in principle, any digital logic circuit could now be implemented without transistors.

We have discussed the strengths and weaknesses of domain-wall logic as compared to other mainstream digital technologies and concluded that, like most nanoscale devices, domain-wall logic is not a one-stop replacement for all areas of digital logic, but rather should be used selectively to perform the functions that it does best. We have highlighted, in particular, the benefits of forming three-dimensional shift registers from domain-wall logic elements for the purpose of ultrahigh-density data storage.

ACKNOWLEDGMENTS

This chapter draws heavily on work performed by current and past researchers in my research team: Dan Allwood, Dorothee Petit, Dan Read, Del Atkinson, Gang Xiong, Colm Faulkner, and Vanessa Jausovec. I express my thanks to all of them.

This work is supported by Ingenia Holdings Ltd. The work and results reported in this publication were obtained with research funding from the European Community under

the Sixth Framework Programme, contract number 510993: MAGLOG. The views expressed are solely those of the authors, and the other contractors and/or the European Community cannot be held liable for any use that may be made of the information contained herein. The support of European Community Framework 5, contract number HPRN-CT-2002-00318 'Ultraswitch' is acknowledged.

REFERENCES

Allwood, D.A., Xiong, G., Cooke, M.D., *et al*. (2004). Characterization of submicrometer ferromagnetic NOT gates. *Journal of Applied Physics*, **95**, 8264.

Allwood, D.A., Xiong, G., Faulkner, C.C., *et al*. (2002). Submicrometer ferromagnetic NOT gate and shift register. *Science*, **296**, 2003–2006.

Allwood, D.A., Xiong, G., Faulkner, C.C., *et al*. (2005). Magnetic domain-wall logic. *Science*, **309**, 1688.

Atkinson, D., Allwood, D.A., Xiong, G., *et al*. (2003). Magnetic domain-wall dynamics in a submicrometre ferromagnetic structure. *Nature Materials*, **2**, 85.

Bar'yakhter, V.G., Chetkin, M.V., Ivanov, B.A. and Gadetskii, S.N. (1994). *Dynamics of Topological Magnetic Solitons*, Springer-Verlag: Berlin.

Berger, L. (1984). Magnetostriction of Pd-Fe alloys. *Journal of Applied Physics*, **55**, 1954–1956.

Cowburn, R.P., Allwood, D.A., Xiong, G. and Cooke, M.D. (2002). Domain wall injection and propagation in planar permalloy nanowires. *Journal of Applied Physics*, **91**, 6949–6951.

Cowburn, R.P., Koltsov, D.K., Adeyeye, A.O. and Welland, M.E. (1998). Probing submicron nanomagnets by magneto-optics. *Applied Physics Letters*, **73**, 3947–3949.

Dietl, T., Ohno, H., Matsukura, F., *et al*. Zener model description of ferromagnetism in zinc-blende magnetic semiconductors. *Science*, **287**, 1019.

Engel, B.N., Akerman, J., Butcher, B., *et al*. (2005). A 4-Mb toggle MRAM based on a novel bit and switching method. *IEEE Transactions on Magnetics*, **41**, 132–136.

Faulkner, C.C., Allwood, D.A., Cooke, M.D., *et al*. (2003). Controlled switching of ferromagnetic wire junctions by domain wall injection. *IEEE Transactions on Magnetics*, **39**, 2860.

Hubert, A. and Schaeffer, R. (Eds.) (1998). *Magnetic Domains: The Analysis of Magnetic Microstructures*, Springer Verlag: New York, ISBN 3-540-64108-4.

Lim, C.K., Devolder, T., Chappert, C., *et al*. (2004). Domain wall displacement induced by subnanosecond pulsed current. *Applied Physics Letters*, **84**, 2820.

Moodera, J.S., Kinder, L.R., Wong, T.M., *et al*. (1995). Large magnetoresistance at room temperature in ferromagnetic thin film tunnel junctions. *Physical Review Letters*, **74**, 3273–3276.

Ono T., Miyajima H., Shigeto K., *et al*. (1999). Propagation of a magnetic domain wall in a submicrometer magnetic wire. *Science*, **284**(5413), 468–470.

Prinz, G.A. (1998). Magnetoelectronics. *Science*, **282**, 1660.

Vernier, N., Allwood, D.A., Atkinson, D., *et al*. (2004). Domain wall propagation in magnetic nanowires by spin-polarized current injection. *Europhysics Letters*, **65**, 526.

Waser, R. (Ed.) (2003). *Nanoelectronics and Information Technology*, Wiley VCH: Weinheim, p. 330.

Web: math.nist.gov/oommf/, 2006.

Wolf, S.A., Awschalom, D.D., Buhrman, R.A., *et al*. (2001). Spintronics: a spin-based electronics vision for the future. *Science*, **294**, 1488.

Xiong, G., Allwood, D.A., Cooke, M.D. and Cowburn, R.P. (2001). Magnetic nanoelements for magnetoelectronics made by focused ion beammilling. *Applied Physics Letters*, **79**, 3461–3463.

Yamaguchi, A., Ono T., Nasu, S., *et al*. (2004). Real-space observation of current-driven domain wall motion in submicron magnetic wires. *Physical Review Letters*, **92**, 077205.

Zhu, X., Allwood, D.A., Xiong, G., *et al*. (2005). Spatially resolved observation of domain-wall propagation in a submicron ferromagnetic NOT-gate. *Applied Physics Letters*, **87**, 062503.

Guided Spin Waves

Riccardo Hertel
Research Center Jülich, Jülich, Germany

1 INTRODUCTION

Considering the breathtaking progress in nanomagnetism over the last decades, it is remarkable that the role assigned to magnetic elements in technological applications has hardly evolved away from the mere storage of information. This also holds for modern magnetoelectronic devices such as the nonvolatile magnetic random access memory (MRAM) (Wolf *et al*., 2001). There, ferromagnetic patterned elements act as bistable systems to store a unit of information, that is, '1' or '0', depending on their magnetization state. Once the magnetically stored information is read (e.g., using the tunnel-magnetoresistance effect), it is elaborated by other means, like integrated electronic circuits. One of the purposes of this chapter is to present a concept that allows to read, transmit, and elaborate magnetically stored information in a purely ferromagnetic system. This could be achieved with spin waves propagating along wave guides and, in particular, by using the phase of the spin waves. In fact, it is demonstrated that the phase of propagating spin waves can be manipulated by introducing magnetic domain walls in the wave guides. If the presence or absence of a domain wall in a magnetic strip is used as an elementary unit to store information, the phase-shift effect induced by the domain walls gives the possibility of using propagating spin waves to read this information. By exploiting constructive and destructive interference effects, logical operations can be performed with spin waves. The concept of spin-wave logics proposed in this chapter could be the first step toward the development of a new generation of programmable logic devices that may be able to both store information and perform logical operations.

The chapter is structured as follows. First, in Section 2, the basics of the theory of micromagnetism and of the numerical method are presented. In Section 3, the possibility of splitting and merging spin waves is discussed. The effect of a domain wall on a propagating spin wave is described in Section 4. It is shown that the phase of a spin wave changes when it runs through a domain wall. In Section 5, how spin-wave-based logical devices could be realized by using the effects presented in the previous sections is discussed. Spin-wave guides can be combined in a simple way in order to obtain programmable devices that can perform basic logical operations such as AND, OR, NOT, NXOR. Finally, Section 6 briefly discusses Berry-phase effects of magnons in a ferromagnetic ring. Such Berry-phase effects have recently been related to the effect of the domain-wall-induced phase shift in propagating spin waves described in this chapter.

1.1 Magnetic ringing

The field-driven magnetization reversal of a magnetic thin-film element is connected with the release of energy.

Handbook of Magnetism and Advanced Magnetic Materials. Edited by Helmut Kronmüller and Stuart Parkin. Volume 2: *Micromagnetism*. ISBN: 978-0-470-02217-7.

The Zeeman energy depends on the relative orientation of the sample's magnetization and the direction of the external field. In the simple case of a homogeneously magnetized nanostructure with volume V and saturation magnetization M_s, the energy difference between the magnetization state oriented antiparallel to an external magnetic field H and the one oriented parallel to the field, that is, between the initial and the final state, is $\Delta E = 2\mu_0 H M_s V$.

On its path from the initial, antiparallel state toward the final equilibrium state with homogeneous magnetization parallel to the external field, the magnetic system dissipates this energy difference.

Phenomenologically, the dissipation of energy occurring during the dynamic magnetization process is described by the damping constant α in the Landau–Lifshitz–Gilbert (LLG) equation. However, this intrinsic damping is generally not sufficient to dissipate the entire amount of energy within the typical time of a magnetization reversal process, which for submicron-sized thin-film elements is usually on the subnanosecond time scale. Therefore, immediately after the reversal, a magnetic thin-film element remains in an energetically excited state, which decays relatively slowly to its equilibrium state, typically within a few nanoseconds. In thin-film elements, the residual energy is converted into magnetostatic spin waves (Choi, Belov, Ballentine and Freeman, 2001). These spin waves are known as *magnetic ringing*. The magnetic ringing may persist for several nanoseconds after the magnetization reversal (Acremann *et al.*, 2001; Koch, Deak and Abraham, 1998). An example of such a dynamical magnetization reversal process and the magnetic ringing occurring after the magnetic switching is shown in Figure 1. Some snapshots of the simulated magnetic reversal process in a Permalloy thin-film element exposed to an external in-plane magnetic field are shown in Figure 1(a)–(d). As can be seen in Figure 1(e), the x component of the magnetization switches almost completely into the field direction after only 300 ps, but the y component displays pronounced oscillations that decay only after about 2 ns. The occurrence of spin waves can be seen in the out-of-plane magnetization component (cf. Figure 1(f)–(h)), which displays a noisy modulation of the magnetic structure. These spin waves contain a considerable amount of exchange energy and stray field energy. The specifications of this example are chosen according to the μMAG Standard Problem No. 4 (McMichael, 2000) and are described in the sketch in Figure 1. As far as the material properties are concerned, the saturation polarization is $J_s = \mu_0 M_s = 1\,\mathrm{T}$, the exchange constant is $A = 1.3 \cdot 10^{-11}\,\mathrm{Jm}^{-1}$, and the damping constant is $\alpha = 0.02$.

1.2 Using spin waves

Obviously, the magnetic ringing is undesirable from a technological point of view. The long-lasting perturbation of the

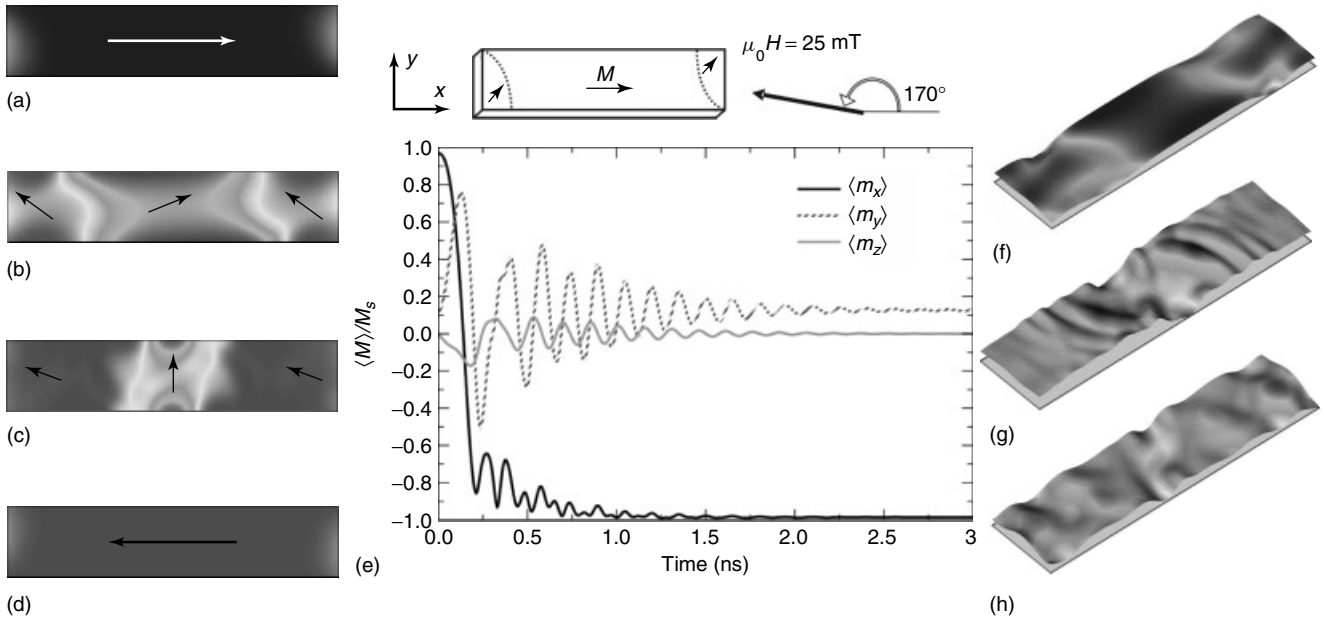

Figure 1. Simulated magnetization reversal in a thin-film element (Permalloy, 500 nm × 125 nm × 3 nm). (a)–(d) Snapshots of the reversal process at different times after applying the field; (a) 0 ps, (b) 145 ps, (c) 402 ps, and (d) 1170 ps. The gray scale represents the x component of the magnetization. (f)–(h) Out-of-plane component of the magnetization (magnified) at (f) 402 ps, (g) 1170 ps, (h) 1577 ps. (e) Volume-averaged components of the normalized magnetization as a function of time. The initial magnetization state and the applied external field are sketched on top of frame (e).

magnetization after the reversal represents a disturbing noise, which should be avoided if a magnetic thin-film element is to be used as a switch to store information. For application purposes, the ideal magnetic thin-film element should switch as quickly as possible from a '1' to a '0' without any noise and perturbation. In order to suppress the spin waves (i.e., the ringing), the intrinsic damping of the material can be increased (Bailey, Kabos, Mancoff and Russek, 2001), thereby dissipating the Zeeman energy difference directly into heat. However, a damping that is too large would lead to a slower, 'viscous' magnetization reversal (Kikuchi, 1956). Therefore, considerable effort has been made to find alternative ways to switch the magnetization, particularly with a technique known as *precessional switching* (Gerrits *et al*., 2002), with which a fast magnetization reversal and suppression of spin waves can be achieved. This precessional switching process is, however, difficult to realize. Magnetic field pulses have to be applied in the film plane perpendicular to the magnetization direction. The shape of these field pulses must be chosen carefully within small margins to ensure a well-defined reversal process. A detailed discussion of the precessional switching mechanism goes beyond the scope of this chapter. Rather than presenting advanced concepts of magnetization switching, the central question of the concept discussed in this chapter is the following: 'Can spin waves be used instead of considering them as a disturbing, collateral effect that occurs when a magnetic nanostructure switches'? An appealing aspect of this idea is that spin waves occur in a natural way in ferromagnetic thin films, as can obviously be recognized by the fact that it is difficult to suppress them. It has recently been suggested (Hertel, Wulfhekel and Kirschner, 2004) that spin waves may be used as carriers of information, and, in particular, that it should be possible to evaluate this information by exploiting the *phase* of spin waves.

This work is entirely based on micromagnetic computer simulations. Although the accuracy and the predictive power of modern micromagnetic algorithms has recently evolved to a point where such simulations can be regarded as reliable computer experiments, a real experimental verification of the new effects reported in this chapter would be desirable to confirm these predictions.

2 MICROMAGNETISM AND NUMERICAL METHOD

The theoretical, analytic study of spin waves in ferromagnetic materials is a vast subject of research (Hillebrands and Ounadjela, 2002; Akhiezer, Baryachtar and Peletminsky, 1968; Damon and Eshbach, 1961; Hurben and Patton, 1996). By using simplifying assumptions and by linearizing the dynamic equations, numerous modes have been studied analytically. In the nonlinear regime, the occurrence of solitons has been reported (Slavin, Demokritov and Hillebrands, 2002) and studied analytically.

Although the analytic theory of spin waves provides important information and helps in understanding the qualitative behavior of spin waves, it frequently suffers from serious limitations. These limitations are due to the simplifications required to make the problem analytically treatable, including, for example, the assumption of infinite extension of the material or other simplifying approximations, the validity of which is often doubtful. Particularly in the case of nanostructured materials, where finite-size effects are known to have a decisive impact on the magnetic properties, some of these approximations are questionable. In fact, even the calculation of realistic *static* magnetization structures in nanostructured ferromagnets – which certainly represent a simpler case compared to the treatment of the magnetization dynamics of spin waves – can generally only be obtained by means of numerical simulations.

Computational micromagnetism gives the possibility of investigating dynamic magnetization processes in nanostructured materials on time and length scales that are difficult to access experimentally. Micromagnetic simulations provide detailed information on the dynamics of the whole three-dimensional magnetization field in the sample. In the simulations, a patterned element of a given material, size, and shape can be exposed, for example, to an external field pulse and the response of the magnetization can be modeled by integrating the equation of motion. The correctness of such calculations has been firmly ensured in the last years by cross checking the results obtained with different codes and by directly comparing experimental observations with micromagnetic simulations. The fundamental equation that is used in micromagnetic simulations to describe the magnetization dynamics is the Landau–Lifshitz–Gilbert equation.

2.1 The Landau–Lifshitz–Gilbert equation

In the theory of micromagnetism, magnetization is represented as a continuous, directional field $\boldsymbol{M}(\boldsymbol{r}, t)$ with constant magnitude, $|\boldsymbol{M}| = M_s$. The task of dynamic micromagnetic simulation consists in the calculation of the spatiotemporal evolution of the magnetization field $\boldsymbol{M}(\boldsymbol{r}, t)$ in a ferromagnet. The Gilbert equation

$$\frac{\mathrm{d}\boldsymbol{M}}{\mathrm{d}t} = -\gamma\,(\boldsymbol{M} \times \boldsymbol{H}_{\mathrm{eff}}) + \frac{\alpha}{M_s}\left(\boldsymbol{M} \times \frac{\mathrm{d}\boldsymbol{M}}{\mathrm{d}t}\right) \qquad (1)$$

is the equation of motion of the magnetization $\boldsymbol{M}(\boldsymbol{r}, t)$, where $\boldsymbol{H}_{\text{eff}}$ is the effective field, γ is the gyromagnetic ratio, and α is a phenomenological damping constant. The effective field is generally a complicated function of the magnetization distribution of the sample. This is discussed in more detail in the next paragraphs. The Gilbert equation can be rewritten into an explicit form, which is known as the *Landau–Lifshitz–Gilbert (LLG) equation*

$$\frac{\mathrm{d}\boldsymbol{M}}{\mathrm{d}t} = -\frac{\gamma}{1+\alpha^2}(\boldsymbol{M} \times \boldsymbol{H}_{\text{eff}}) - \frac{\alpha\gamma}{M_s(1+\alpha^2)}[\boldsymbol{M} \times (\boldsymbol{M} \times \boldsymbol{H}_{\text{eff}})] \tag{2}$$

Analytic solutions of the Gilbert equation are usually only possible in the macro-spin approximation (Kikuchi, 1956), where the magnetic structure of the sample is assumed to be homogeneous throughout the reversal process. Usually, the macro-spin approximation is only valid for special cases or for very small magnetic particles of up to about 10 nm size (Wernsdorfer, Orozco and Hasselbach, 1997). The macro-spin approximation is, in any case, not suitable for describing magnetization waves. To calculate the dynamics of the inhomogeneous, three-dimensional vector field of the magnetization, numerical methods are required, with which the LLG equation is integrated in time.

2.2 Effective field terms

The energy of a ferromagnet depends on its magnetic structure (Brown, 1963). In a static equilibrium state, the magnetization field $\boldsymbol{M}(\boldsymbol{r})$ arranges in such a way as to minimize the total energy. This minimum can either be a local or a global one, depending on the magnetic history of the sample.

The most important contributions to the total energy are usually the ferromagnetic exchange energy, the dipolar or magnetostatic energy, the magnetocrystalline anisotropy energy and the Zeeman energy in an external magnetic field. These energy terms are briefly described in the next paragraphs. A more detailed discussion of the micromagnetic energy terms and of the LLG equation can be found in textbooks on micromagnetism (Brown, 1963; Hubert and Schäfer, 1998; Aharoni, 1996; Kronmüller and Fähnle, 2003).

The effective field $\boldsymbol{H}_{\text{eff}}$ is defined as the negative variational derivative of the micromagnetic energy density e with respect to the magnetization,

$$\mu_0 \boldsymbol{H}_{\text{eff}} = -\frac{\partial e}{\partial \boldsymbol{M}} \tag{3}$$

It is therefore sufficient to introduce the energy terms that contribute to the total micromagnetic energy density, from which the effective field can then be derived according to equation (3). In most cases, a discussion of the energy terms is also more instructive than a derivation of the various effective field terms.

2.2.1 Exchange energy

The characteristic property of ferromagnetic materials is their tendency to keep neighboring magnetic moments parallel to each other. The short-range exchange interaction prevents strong inhomogeneities of the magnetization on small length scales. In other words, any increase in inhomogeneity of the magnetization field increases the exchange energy. The simplest and, in most cases, perfectly sufficient representation of the exchange energy density is given by

$$e_{\text{exc}} = \sum_{i=x,y,z} A \cdot (\nabla m_i)^2 \tag{4}$$

where A is the exchange constant and $\boldsymbol{m} = \boldsymbol{M}/M_{\text{s}}$ is the reduced or normalized magnetization (Aharoni, 1996). This expression can also be derived from a Taylor expansion of the Heisenberg term assuming small-angle deviations between neighboring moments (Kronmüller and Fähnle, 2003).

2.2.2 Magnetostatic energy

Each magnetic moment in a ferromagnetic sample represents a magnetic dipole and therefore contributes to a total magnetic field $\boldsymbol{H}_{\text{s}}$ inside the sample. The energy connected with this field is known as the *stray field energy* or the *magnetostatic energy*. The local stray field energy density depends on the orientation of the magnetic moments with respect to this field,

$$e_{\text{st}} = -\frac{\mu_0}{2}\boldsymbol{H}_{\text{s}} \cdot \boldsymbol{M} \tag{5}$$

In the literature, different terms are used for the field $\boldsymbol{H}_{\text{s}}$. It is called the *magnetic stray field*, the *dipolar field*, the *demagnetizing field*, or the *magnetostatic field*. The factor $1/2$ in equation (5) is required for self-energy terms. This energy contribution arises from the long-range magnetostatic interaction between the magnetic moments in the sample. It can be shown that the total stray field energy, which results from a volume integration of equation (5), is always positive definite (Brown, 1962; Aharoni, 1996). The consideration of the stray field energy therefore always increases the total energy of the system, for any arrangement of the magnetization. In order to minimize the stray field energy of a ferromagnet, the sources of the field $\boldsymbol{H}_{\text{s}}$ have to be minimized. This is known as *Brown's pole avoidance principle* (Brown, 1962).

The stray field $\boldsymbol{H}_s(\boldsymbol{r})$ at one point $\boldsymbol{r}$ results, in principle, from a summation of the form

$$\boldsymbol{H}_s(\boldsymbol{r}) = \frac{1}{4\pi}\left(\sum_i \frac{\boldsymbol{\mu}_i}{|\boldsymbol{r}-\boldsymbol{r}_i|^3} - 3\cdot\frac{(\boldsymbol{\mu}_i\cdot\boldsymbol{r})\cdot\boldsymbol{r}}{|\boldsymbol{r}-\boldsymbol{r}_i|^5}\right) \tag{6}$$

which extends over all the magnetic moments inside the sample.

The magnetic dipole moments $\boldsymbol{\mu}_i$ can be assumed to be localized on an atomic length scale. It is not practicable to perform a calculation of the stray field in mesoscopic particles by means of the summation over these point dipoles. In the framework of micromagnetism, such dipolar sums are therefore not considered. A possible approximation consists in locating 'effective' dipoles at the (more or less arbitrarily chosen) sites of discretization points, and performing the summation only over these points. However, this approximation can be problematic because it implicitly assigns a physical meaning to a numerical entity, and this could result in large numerical errors. It has been shown that these errors can be reduced by using multipoles rather than dipoles at the discretization points (Blue and Scheinfein, 1991). However, these multipoles have to be extended to quite high orders to achieve accurate results, as was shown by applying the fast multipole method (FMM) to micromagnetic problems (Seberino and Bertram, 2001). The micromagnetic calculation of demagnetizing fields involves a transition from the discrete sum (equation (6)) to a continuum integration. By converting the sum (equation (6)) over the individual magnetic dipoles into an integral over the sample volume (Brown, 1963), the stray field can be obtained from

$$\begin{aligned}\boldsymbol{H}_s(\boldsymbol{r}) = &-\frac{1}{4\pi}\int \frac{(\boldsymbol{r}-\boldsymbol{r}')\rho(\boldsymbol{r}')}{|\boldsymbol{r}-\boldsymbol{r}'|^3}\,\mathrm{d}V' \\ &+\frac{1}{4\pi}\oint \frac{(\boldsymbol{r}-\boldsymbol{r}')\sigma(\boldsymbol{r}')}{|\boldsymbol{r}-\boldsymbol{r}'|^3}\,\mathrm{d}S'\end{aligned} \tag{7}$$

where $\boldsymbol{n}$ is the surface normal vector. The magnetic charges $\rho = -\nabla\cdot\boldsymbol{M}$ and $\sigma = \boldsymbol{M}\cdot\boldsymbol{n}$ are the sources of the demagnetizing field.

2.2.3 Magnetocrystalline anisotropy

The magnetocrystalline anisotropy energy results from the crystalline structure of a ferromagnet. According to the crystal symmetry, the direction of the magnetization favors energetically an alignment toward certain axes. In the simplest case of a uniaxial magnetocrystalline anisotropy, the energy density connected with this term is to the first nonvanishing order given by

$$e_{an} = K_u\left[1-(\boldsymbol{m}\cdot\boldsymbol{k})^2\right] \tag{8}$$

where K_u is the uniaxial anisotropy constant and $\boldsymbol{k}$ is a unit vector parallel to the easy axis. The easy axis represents the preferential orientation of the magnetization in the crystal.

In the present study, only ideally soft-magnetic materials are considered, that is, ferromagnets with vanishing magnetocrystalline anisotropy.

2.2.4 Further energy terms

If a ferromagnet is exposed to an externally applied magnetic field $\boldsymbol{H}_{ext}$, its energy obviously depends on the orientation of the magnetization with respect to the field. The Zeeman energy of the system is simply

$$e_{ext} = -\mu_0\boldsymbol{H}_{ext}\cdot\boldsymbol{M} \tag{9}$$

Further energy terms that may be relevant in certain cases are the surface anisotropy and the energy connected with magnetoelastic effects. These energy terms are discussed in detail elsewhere (Brown, 1963; Hubert and Schäfer, 1998; Aharoni, 1996; Kronmüller and Fähnle, 2003). Magnetoelastic effects can be ignored in most practical cases. The consideration of the latter would require the solution of additional differential equations, thus remarkably complicating the overall calculation.

2.3 Finite-element micromagnetics

The numerical integration of the Landau–Lifshitz–Gilbert equation (2) requires the calculation of the effective field $\boldsymbol{H}_{eff}$. The effective field results from the local energy densities described in the preceding text. In this study, the numerical calculation of the effective fields and of the magnetic structure is performed with the finite-element method (FEM).

A relatively extended description of the finite-element formulation is given in the next few paragraphs. The readers who are not interested in these numerical details are invited to skip these paragraphs and proceed with Section 3, where propagating spin waves in thin magnetic strips are discussed.

Although the basic concepts required for the development of a micromagnetic finite-element algorithm have been published in a number of papers (Schrefl, 1999a,b; Yang and Fredkin, 1996, 1998; Chen, Fredkin and Koehler, 1993; Koehler and Fredkin, 1992; Hertel, 2001), it seems that they are generally not well known, unlike the better-known *finite difference (FD) method* (Berkov, Ramstöck and Hubert, 1993). Obviously, a complete description of the mathematics and the numerics of the FEM and the boundary element method (BEM) cannot be covered in a single article. Therefore, only the most essential ingredients of a micromagnetic FEM–BEM formulation are presented.

2.3.1 Discretization

An important property of the FEM is given by its spatial discretization scheme, which differs significantly from the simpler and more frequently used FD scheme. The latter uses a regular grid of cubic or prism-shaped discretization cells. In the FEM, the sample's volume is subdivided into tetrahedral elements of irregular size, shape, and orientation. This allows the approximation of the shape of magnetic elements of general geometry, for example, with curved boundaries, in a more precise way compared to FD schemes, where a staircase approximation (Garcia-Cervera, Gimbutas and Weinan, 2003) is required (cf. Figure 2). In this chapter, the propagation of spin waves in a ring-shaped magnetic thin-film element is discussed. For the modeling of ring shapes, the geometrical flexibility connected with the FEM is of major importance in order to rule out numerical errors and spurious effects as they may arise from a 'staircase' approximation.

The vertex points of the finite elements, that is, the nodes (cf. Figure 3), are the set of discretization points at which all the required values are calculated, like the effective fields, the magnetization, and the magnetic scalar potential. The discretization points are connected to each other by means of linear interpolation functions within each element.

The shape functions $\eta_i^{(n)}(\boldsymbol{r})$ are part of the FEM discretization scheme. They are linear functions of the form

$$\eta_i^{(n)}(\boldsymbol{r}) = a_i + b_i x + c_i y + d_i z \tag{10}$$

where the coefficients are defined for each node i of an element (n) so that

$$\eta_i^{(n)}(\boldsymbol{r}_j) = \delta_{ij} \tag{11}$$

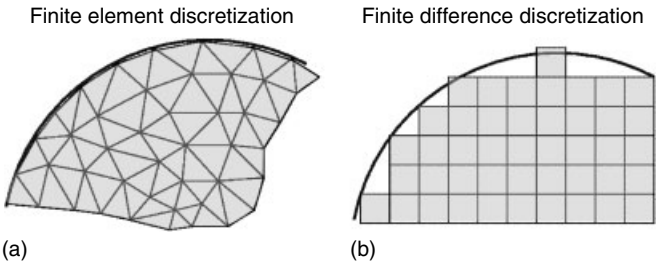

Figure 2. Schematic representation of the smoother approximation of the boundaries with finite elements (a) and a coarser staircase approximation with a regular grid (b). In practice, a finer grid of cubic cells would be used to reduce the errors resulting from the staircase approximation. However, even if the stair steps are infinitely small, the approximation with finite differences leads to a systematic error since the length of the boundary is not considered correctly.

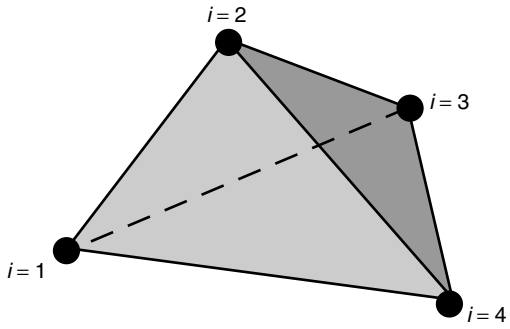

Figure 3. Tetrahedral finite elements are used as discretization cells. In these elements, the discretization points are located at the nodes, that is, the corner points of the elements. Linear shape functions $\eta_i^{(n)}(\boldsymbol{r})$ are defined for each node i of each element n.

The name 'shape functions' indicates that the values of the coefficients only depend on the shape of the finite element. In equation (11), $\boldsymbol{r}_j$ is the position of the node j of the element and δ_{ij} is the Kronecker symbol. If $\boldsymbol{r}$ is outside the element n, the shape functions $\eta_i^{(n)}(\boldsymbol{r})$ are zero. By using these shape functions, a piecewise linear representation of the discretized functions is achieved in the whole computational region. Inside the element n, which contains a point $\boldsymbol{x}$, a piecewise linear representation $\tilde{f}$ of a function f can be written as

$$f(\boldsymbol{x}) \simeq \tilde{f}(\boldsymbol{x}) = \sum_{i=1}^{4} \eta_i^{(n)}(\boldsymbol{x})\alpha_i \tag{12}$$

where $\alpha_i = f(\boldsymbol{x}_i)$ and $\boldsymbol{x}_i$ are the positions of the nodes of the vertices i.

2.3.2 Calculation of the demagnetizing field

While the numerical calculation of most of the contributions of the effective field is quite straightforward, a complicated task consists in solving the long-range magnetostatic interaction. Instead of evaluating the integral (7) for each discretization point in the sample in order to calculate $\boldsymbol{H}_\mathrm{s}(\boldsymbol{r})$, an equivalent way of calculating the stray field consists in introducing a scalar potential U that solves Poisson's equation $\Delta U = \nabla \cdot \boldsymbol{M}$. From this potential, the demagnetizing field (or stray field) is obtained as the gradient field $\boldsymbol{H}_\mathrm{s} = -\nabla U$. The stray field $\boldsymbol{H}_\mathrm{s}$ can usually be obtained much faster by solving Poisson's equation than by performing the integration according to equation (7). A combination of the FEM and the BEM is applied to calculate the potential U. This hybrid FEM–BEM scheme (Fredkin and Koehler, 1990) is an elegant and precise Greens function method.

In the first step, the potential U is split in two parts $U = U_1 + U_2$. Outside the sample, U_2 is zero. With ordinary

finite-element techniques (i.e., the Galerkin method), it is relatively easy to solve Poisson's equation

$$\Delta U_1 = -\rho \tag{13}$$

with the Neumann boundary condition

$$\left.\frac{\partial U_1}{\partial \boldsymbol{n}}\right|_{in} - \left.\frac{\partial U_1}{\partial \boldsymbol{n}}\right|_{out} = \sigma \tag{14}$$

However, the solution of this problem is not unique. Any potential U_3 with continuous derivatives at the boundary that satisfies Laplace's equation $\Delta U_3 = 0$ could be added to U_1 and the result would still represent a solution of the Poisson equation with Neumann boundary conditions. To obtain a unique solution for the potential $U = U_1 + U_2$, one has to solve the Laplace equation $\Delta U_2 = 0$ for U_2 with the correct Dirichlet boundary conditions. These Dirichlet boundary conditions for U_2 are unique once the values of U_1 are known at the boundary. Solving Laplace's equation for U_2 is numerically as unproblematic as solving Poisson's equation for U_1. The difficulty lies rather in finding the correct Dirichlet boundary conditions that make U_2 and finally U the unique solution. Assuming that a solution for U_1 with correct Neumann boundary conditions has been found, the next task consists in calculating the values of U_2 at the boundary of the sample.

Introducing the Greens function

$$G = \frac{1}{|\boldsymbol{r} - \boldsymbol{r'}|} \tag{15}$$

the scalar potential U for a given magnetization vector $\boldsymbol{M}$ fulfills the equation

$$U = \int \boldsymbol{M} \cdot (\nabla G)\, \mathrm{d}V \tag{16}$$

A further relationship that is required is

$$\Delta G = -4\pi\delta(\boldsymbol{r} - \boldsymbol{r'}) \tag{17}$$

where $\delta(\boldsymbol{r})$ is the Dirac δ-function. Integrating equation (13) and equation (17) over the sample volume V and applying Greens' theorem yields

$$-\oint U_1 \frac{\partial G}{\partial \boldsymbol{n}}\, \mathrm{d}S = 4\pi \int U_1 \delta(\boldsymbol{r})\, \mathrm{d}V - 4\pi \int \boldsymbol{M} \cdot (\nabla G)\, \mathrm{d}V \tag{18}$$

Here, the Neumann boundary condition (14) has been used. Insertion of equation (16) results in

$$-\oint U_1 \frac{\partial G}{\partial \boldsymbol{n}}\, \mathrm{d}S = 4\pi \int U_1 \delta(\boldsymbol{r})\, \mathrm{d}V - 4\pi (U_1 + U_2) \tag{19}$$

If $\boldsymbol{r}$ is inside the integration volume, the integral over the δ-function is, by definition,

$$\int U_1 \delta(\boldsymbol{r} - \boldsymbol{r'})\, \mathrm{d}V' = U_1(\boldsymbol{r}) \tag{20}$$

In the case that the point $\boldsymbol{r}$ is located at the boundary, the solid angle Ω subtended at that point is important. Outside the magnetic region, U_1 is equal to zero, while inside it has a finite value. Hence, if $\boldsymbol{r}$ is at the surface of the integration volume, the integration over the δ-function is weighted with a factor $\Omega/4\pi$.

$$\int U_1 \delta(\boldsymbol{r})\, \mathrm{d}V = \frac{\Omega}{4\pi} U_1 \tag{21}$$

For any point $\boldsymbol{r}$ located at the boundary, this finally yields

$$U_2(\boldsymbol{r}) = \frac{1}{4\pi} \oint U_1(\boldsymbol{r'}) \frac{\partial G}{\partial \boldsymbol{n}}\, \mathrm{d}S' + \left(\frac{\Omega}{4\pi} - 1\right) U_1(\boldsymbol{r}) \tag{22}$$

Hence, the values U_2 at the boundary can be calculated from the values U_1 at the boundary by integrating over the sample surface (Lindholm, 1984). Having obtained the Dirichlet boundary values of U_2 from the surface integration performed with the BEM, the Laplace equation $\Delta U_2 = 0$ can be solved with the FEM. This hybrid FEM–BEM scheme yields accurate solutions for $U = U_1 + U_2$, and hence for the stray field $\boldsymbol{H}_\mathrm{s} = -\nabla U$.

The somewhat lengthy equations of this section may create the impression that this method to calculate $\boldsymbol{H}_\mathrm{s}$ is complicated and time-consuming. But, in fact, the numerical calculation can be performed quickly and precisely. The numerical implementation of this hybrid FEM–BEM scheme is, on the other hand, quite an ambitious undertaking compared to the implementation of the fast Fourier transform method (FFT) used in FD schemes.

2.3.3 Calculation of the exchange field

Besides the calculation of the stray field $\boldsymbol{H}_\mathrm{s}$, determining the effective field of the ferromagnetic exchange $\boldsymbol{H}_\mathrm{exc}$ also represents a nontrivial task in finite-element micromagnetic simulations. The three Cartesian components H^x_exc of the exchange field can be calculated from

$$H^{(i)}_\mathrm{exc} = \frac{2A}{\mu_0 M_\mathrm{s}} \Delta m_i \tag{23}$$

where $i = x, y, z$. For the calculation of $H^{(i)}_\mathrm{exc}$, the Galerkin method is used to convert the Laplace operator on the right-hand side of equation (23) into a set of linear equations, as explained below. A very similar procedure is also applied for solving the Poisson equation for the potential U, but here the

situation is simpler, mainly because the BEM is not required for the calculation of the exchange field. Equation (23) has to be solved in the whole ferromagnet, that is, for every discretization point. The Galerkin method makes use of test functions w in the sense that the problem is reformulated as follows: If

$$\int w \cdot H_x \,\mathrm{d}V = \int w \cdot \frac{2A}{\mu_0 M_\mathrm{s}} \Delta \boldsymbol{m}_x \,\mathrm{d}V \tag{24}$$

holds for *any* test function w, then $H_\mathrm{exc}^{(i)}$ is a solution of equation (23). This is known as the *weak form* of equation (23). In equation (24), the x component has been chosen for i without loss of generality, and the subscript 'exc' has been dropped.

Integrating by parts yields

$$\begin{aligned}\int_\Omega w \cdot H_x \,\mathrm{d}V &= -\frac{2A}{\mu_0 M_\mathrm{s}} \int_\Omega \nabla w \cdot \nabla m_x \,\mathrm{d}V \\ &\quad + \frac{2A}{\mu_0 M_\mathrm{s}} \oint_{\partial\Omega} w \cdot \nabla m_x \,\mathrm{d}\boldsymbol{S} \qquad (25) \\ &= -\frac{2A}{\mu_0 M_\mathrm{s}} \int_\Omega \nabla w \cdot \nabla m_x \,\mathrm{d}V \qquad (26)\end{aligned}$$

where the Brown condition $\partial m_x / \partial \boldsymbol{n}|_{\partial\Omega} = \boldsymbol{0}$ for the derivatives of the magnetization at the particle boundary $\partial\Omega$ has been used (Brown, 1940), Ω is the particle volume and $\boldsymbol{n}$ is the surface normal vector. The integration over the volume Ω can be transformed into a sum of integrations over the N finite elements:

$$\sum_{n=1}^{N} \int_{\Omega_n} w \cdot H_x \,\mathrm{d}V = \sum_{n=1}^{N} -\frac{2A}{\mu_0 M_\mathrm{s}} \int_{\Omega_n} \nabla w \cdot \nabla m_x \,\mathrm{d}V \tag{27}$$

In each element n, the test functions w, the exchange field H_x and the magnetization components m_i can be represented using the set of aforementioned shape functions according to equation (12). Inserting this expansion into equation (24) leads to an enormous sum:

$$\begin{aligned}&\sum_{n=1}^{N} \sum_{k=1}^{4} \sum_{l=1}^{4} w_k h_x^l \int_{\Omega_n} \eta_k^{(n)} \eta_l^{(n)} \,\mathrm{d}V \\ &\quad = \sum_{n=1}^{N} \sum_{k=1}^{4} \sum_{j=1}^{4} -\frac{2A}{\mu_0 M_\mathrm{s}} w_k m_x^j \int_{\Omega_n} \nabla \eta_k^{(n)} \nabla \eta_j^{(n)} \,\mathrm{d}V \qquad (28)\end{aligned}$$

In this equation, $\{w_k\}$ are the values of the test functions at the nodes k, $\{h_x^l\}$ are the values of the x component of the exchange field at the nodes l, and $\{m_x^j\}$ are the x component of the normalized magnetization at the nodes j. Since equation (28) must be valid for any arbitrary test function w, a comparison of coefficients w_k can be performed. This transforms this huge sum into a large set of linear equations. The matrix $\underline{\underline{A}}$ of this set of linear equations is very sparse, meaning that by far most of the elements of this matrix are zero. By using special indexing methods (Press, Flannery, Teukolsky and Vetterling, 1986), it is possible to store only the nonvanishing elements of the matrix, thus saving a large amount of computer memory. The fact that the matrix of this set of linear equations is very sparse allows to efficiently solve the set of equations iteratively by using the conjugate gradient method. Note that for such large, sparse systems of linear equations, iterative solutions are always much faster and more accurate than any result that could be achieved by trying to calculate the inverse matrix $\underline{\underline{A}}^{-1}$. In fact, an inversion of $\underline{\underline{A}}$ is not possible in practical cases because the inverse matrix $\underline{\underline{A}}$ would generally not be a sparse matrix any more and could therefore not even be stored if the typical rank n is in the order of several tens of thousands. The integrals containing the shape functions η in equation (28) need to be performed only once at the beginning of the calculation.

Compared to the exchange field, the remaining contributions to the effective field, that is, the effective fields of the magnetocrystalline anisotropy and the Zeeman field are much simpler to calculate.

2.3.4 *Integration of the Landau–Lifshitz equation*

For the algorithm to be fast, it is imperative that the procedures to calculate the effective fields are programmed in an efficient way, since these calculations have to be performed several thousands of times during the simulation of a realistic dynamic magnetization process. In every time step, the contributions to the effective fields are calculated according to the current magnetization distribution $\boldsymbol{M}(\boldsymbol{r}, t)$, and the total effective field $\boldsymbol{H}_\mathrm{eff}$ is updated at each nodal point of the finite-element mesh. These values of $\boldsymbol{H}_\mathrm{eff}$ then enter the LLG equation, which is used to determine the next configuration of the magnetization $\boldsymbol{M}(\boldsymbol{r}, t)$. In the numerical form, the time derivative of the magnetization is replaced by a difference quotient,

$$\frac{\mathrm{d}\boldsymbol{M}}{\mathrm{d}t} \longrightarrow \frac{\Delta \boldsymbol{M}}{\Delta t} \tag{29}$$

so that the magnetization after a time step Δt reads

$$\begin{aligned}\boldsymbol{M}(t + \Delta t) &= \boldsymbol{M}(t) + \Delta \boldsymbol{M} \\ &= \boldsymbol{M}(t) - \Delta t \cdot \left[\frac{\gamma}{1+\alpha^2} \boldsymbol{M} \times \boldsymbol{H}_\mathrm{eff} \right. \\ &\quad \left. + \frac{\alpha\gamma}{M_\mathrm{s}(1+\alpha^2)} \boldsymbol{M} \times (\boldsymbol{M} \times \boldsymbol{H}_\mathrm{eff}) \right] \qquad (30)\end{aligned}$$

The numerical integration of equation (30) can be quite problematic. Purely explicit integration schemes that only use the previously calculated values at the time t to determine $\Delta \boldsymbol{M}$ show poor stability properties. To improve the stability of the integration of the differential equation, implicit schemes can be applied, which also use the values of the effective fields at the time $(t + \Delta t)$. However, these methods require the calculation of a large Jacobian matrix. For the code used in this study, the best results for the time integration have been obtained with a semi-implicit Adams backward difference (BDF) scheme (Hindmarsh, 1983). In this scheme, the size of the time steps is calculated adaptively and is typically in the subpicosecond range.

With this general purpose micromagnetic algorithm, the dynamics of the magnetization can be simulated for virtually arbitrary shapes. In the study reported in this chapter, the code has been applied to investigate the propagation of spin waves in submicron-sized ferromagnetic strips.

3 PROPAGATING SPIN WAVES

The first point that has to be addressed in order to study whether spin waves can be used to carry and to manipulate information consists in ensuring a controlled propagation of spin waves. The spin waves occurring after a magnetic switching process as shown in Figure 1 consist of a large number of spin-wave modes with different propagation direction, wave number, phase, and amplitude. These spin waves may be reflected several times at the boundary, thus leading to an incoherent noise.

The simplest idea for a controlled propagation of spin waves is to use a thin and narrow ferromagnetic strip as a waveguide (Slavin, Demokritov and Hillebrands, 2002). In this geometry, the spin waves enter on one side of the strip and propagate along the strip line until they reach the opposite end. The geometric confinement enforces a one-dimensional propagation of spin waves. Figure 4 illustrates such a simple case of a flat magnetic strip (Permalloy, 360 nm × 36 nm × 6 nm) that acts as a waveguide for spin waves. The equilibrium magnetic structure of this thin platelet at zero field is simple: in order to minimize the magnetostatic energy, the magnetization aligns along the strip axis, owing to the element's shape anisotropy. The sample is homogeneously magnetized, apart from some small deviations (known as *flower state*, Schabes and Bertram, 1988) at the particle's end (cf. Figure 4a), which are unimportant for the present study. To generate propagating spin waves in this strip, a percussional perturbation is applied at one end of the sample. In an experiment, such a sudden and localized perturbation of the equilibrium structure could be achieved, for example, by applying a short and strong electric current pulse in a small region, running perpendicularly through the strip. When an electric current flows through a ferromagnet, it is spin-polarized. Owing to the spin-transfer-torque effect (Berger, 1996; Slonczewski, 1996), a sufficiently strong spin-polarized electric current can exert a considerable torque on the magnetization, thus leading to the generation of spin waves. In these simulations, the procedure is simpler. By lifting the magnetization by 10° out of the plane in a small region at one end of the slab, the demagnetizing energy and the exchange energy is locally increased.

When the system is released, spin waves are emitted from the perturbed region. The spin waves propagate through the strip and reach the opposite end after some time. In our example, after about 100 ps. Contrary to the magnetic ringing in the previous case, these spin waves have a well-defined propagation direction along the film strip. Instead of a noisy perturbation resulting from the superposition of several spin waves, plane waves are now propagating along the strip. Although, as in the case of magnetization ringing, several spin-wave modes with frequencies in the range of several gigahertz are generated, the wave vector of these spin waves is now parallel to the magnetic strip and the spin waves have a well-defined phase. To detect the arrival of the spin waves at the opposite end of the strip, a 'seismographic' record can be plotted that displays the out-of-plane component of

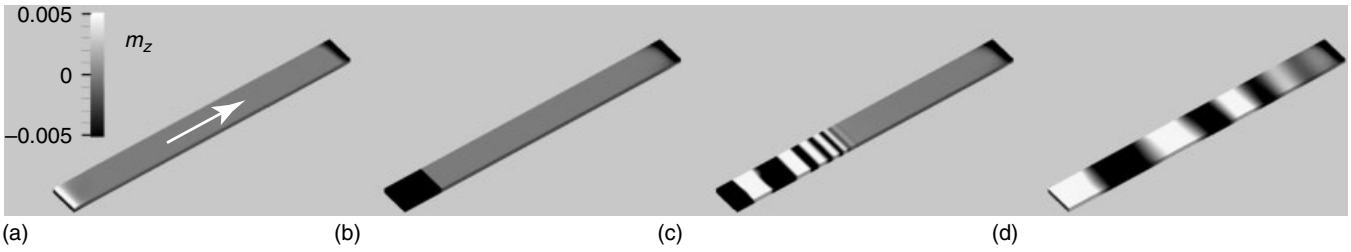

Figure 4. Wave propagation in a magnetic nano-strip. The gray scale displays the out-of-plane component. (a) Initial, zero field state. The arrow depicts the in-plane magnetization. (b) The initial state is perturbed by locally lifting the magnetization out of the film plane (black region on the left). (c) and (d) Snapshots of the spin-wave propagation in zero field at $t = 27$ ps (c) and $t = 298$ ps (d) after the system is released.

the magnetization as a function of time at a selected point on the strip (cf. Figure 5). Experimentally, the spin waves could be detected using the giant-magnetoresistance effect (Baibich *et al*., 1988; Binasch, Grünberg, Saurenbach and Zinn, 1989). The spectrum of spin waves that is generated immediately after the release of the system contains a broad range of frequencies. Owing to dispersion, the short-wavelength, high-frequency oscillations propagate faster than spin waves of lower frequencies. The first signal in the seismograph is a series of small spikes, indicating the onset of small, high-frequency oscillations. These spikes are followed by a stronger signal that displays an almost harmonic oscillation.

Besides transmitting spin waves in a controlled fashion with such waveguides, it is also possible to split the signal transported by a spin wave. The propagation of spin waves in a Y-shaped magnetic thin-film element is a simple example for this. At zero field, the magnetization in the magnetic 'nano-tuning fork' shown in Figure 6 is aligned parallel to the branches. When the system is perturbed at the broader end of the sample in the same way as was done before, spin waves are generated that propagate toward the junction, where they split symmetrically into the two branches. Similarly, spin waves arriving from two branches can be merged into one strip. This can lead to different interference effects, depending on the phase of the spin waves. In order to use spin waves for logical operations, such a splitting and merging of the signal is essential.

4 DOMAIN-WALL-INDUCED PHASE SHIFTS

The mere propagation of spin waves only allows to guide a signal along a magnetic strip. However, if the *phase* of a

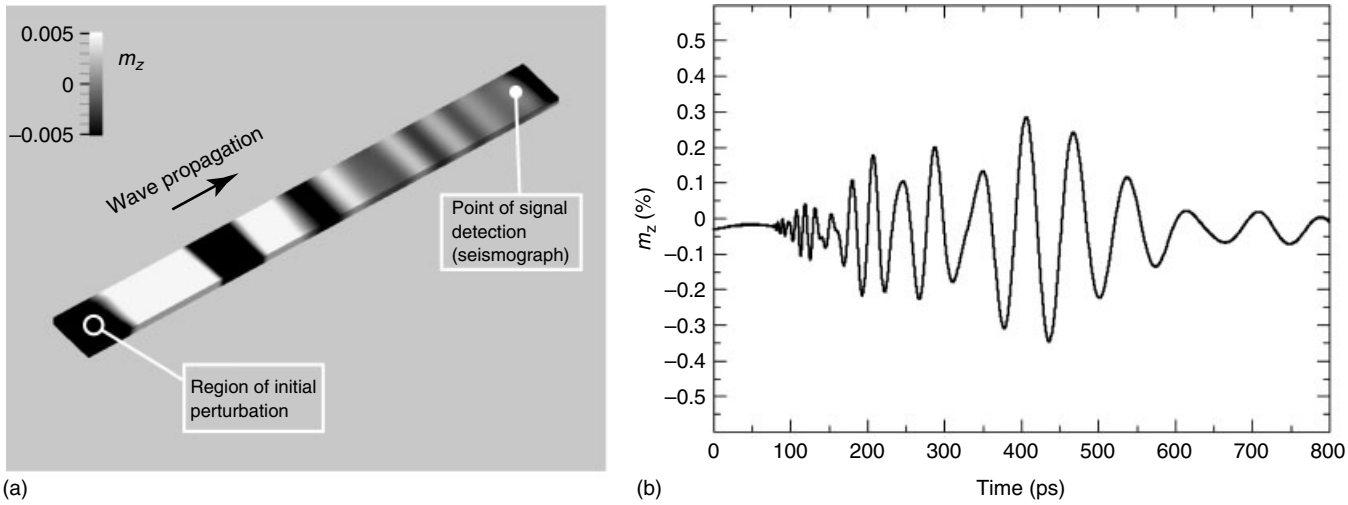

Figure 5. Spin waves generated at one end of a magnetic strip can be recorded with a magnetic 'seismograph' displaying the out-of-plane magnetization component as a function of time at one point on the opposite end.

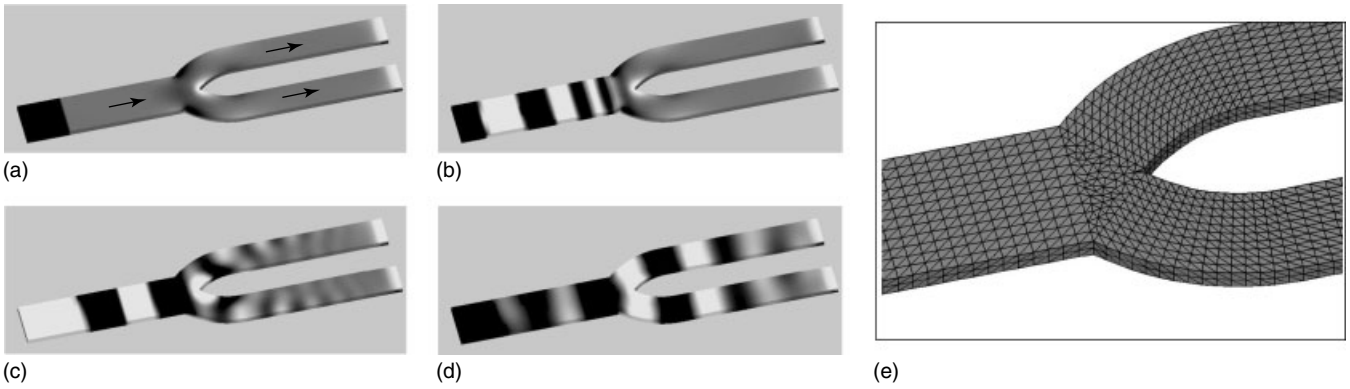

Figure 6. Four images of a Permalloy 'tuning fork' with propagating spin waves. The frames (a)–(d) are at 0, 40, 100, and 215 ps after the release, respectively. A part of the finite-element mesh is shown in frame (e) to illustrate the smooth approximation of the curved boundary. The length of the nanomagnetic tuning fork is 353 nm and its film thickness is 6 nm.

spin wave can be modified in a controlled way, it becomes feasible to perform logical operations with propagating spin waves. The principle of such logical devices is discussed in more detail in the next section. In the following text, it is shown that a spin wave changes its phase when it passes through a magnetic domain wall.

To study the influence of a domain wall on propagating spin waves, the numerical experiment on the propagation of spin waves in a magnetic strip shown in Figure 4 is repeated with different initial conditions. Instead of the homogeneously magnetized magnetic ground state, a bi-domain state with a 180° head-to-head wall in the middle is used as the static magnetic configuration in the nano-strip before generating the spin waves. In the case of a head-to-head domain configuration in magnetic strips, transverse domain walls occur if the sample is sufficiently narrow and thin (McMichael and Donahue, 1997; Kläui, Vaz *et al.*, 2004a). In larger strips, the transverse wall is replaced by a vortex-type domain wall (McMichael and Donahue, 1997). In the micromagnetic simulation, the transverse domain wall develops automatically if appropriate initial conditions are chosen. The position of the domain wall in the strip can be pinned by introducing small notches at the boundary, which attract the transverse domain walls (Kläui, Vaz and Wernsdorfer, 2004b). In the example shown in Figure 7(a), the strip does not contain such notches and the domain-wall position is not stable. In fact, the strip is a single-domain particle in the strict sense that the only stable magnetization state is the homogeneous one. Therefore, the 180° head-to-head domain wall eventually propagates toward one end of the sample and dissolves. The motion of the domain wall is very slow compared to the speed of the spin waves. In this example, it takes about 10 ns until the domain wall exits the sample. Hence, the magnetization state with a 180° domain wall can be regarded as stable on the timescale connected with the propagation of spin waves.

By lifting the magnetization slightly out of the plane at one end of the slab again and letting the system relax, spin waves are generated that run along the strip. When they meet the domain wall, no reflection is visible. Plane wave fronts are restored after the spin wave has run through the domain wall. The spin wave seems to pass unhindered through the domain wall (cf. Figure 7(c and d)).

As in the previous case, a 'seismograph' of the z component at a point at the opposite end of the slab can be recorded to display the arrival of the spin waves. The characteristics of the oscillation of the z component as a function of time are very similar to the case of a homogeneously magnetized slab. A comparison of the seismographs obtained in the two cases, however, reveals an interesting difference concerning the low-frequency oscillations. If the spin wave has run through the domain wall, the *phase* of these oscillations is shifted by about $\pi/2$ with respect to the case of homogeneous magnetization (Figure 8a). The main signal, that is, the envelope of the oscillation, arrives after the same time as in the homogeneous case and is therefore not slowed down by the domain wall. According to the simulations, the domain wall is transparent for spin waves, but the presence of a domain wall changes the phase of spin waves. This phase shift depends strongly on the wavelength. The short, high-frequency oscillations appear to be unaffected by the domain wall, while the low-frequency oscillations with larger

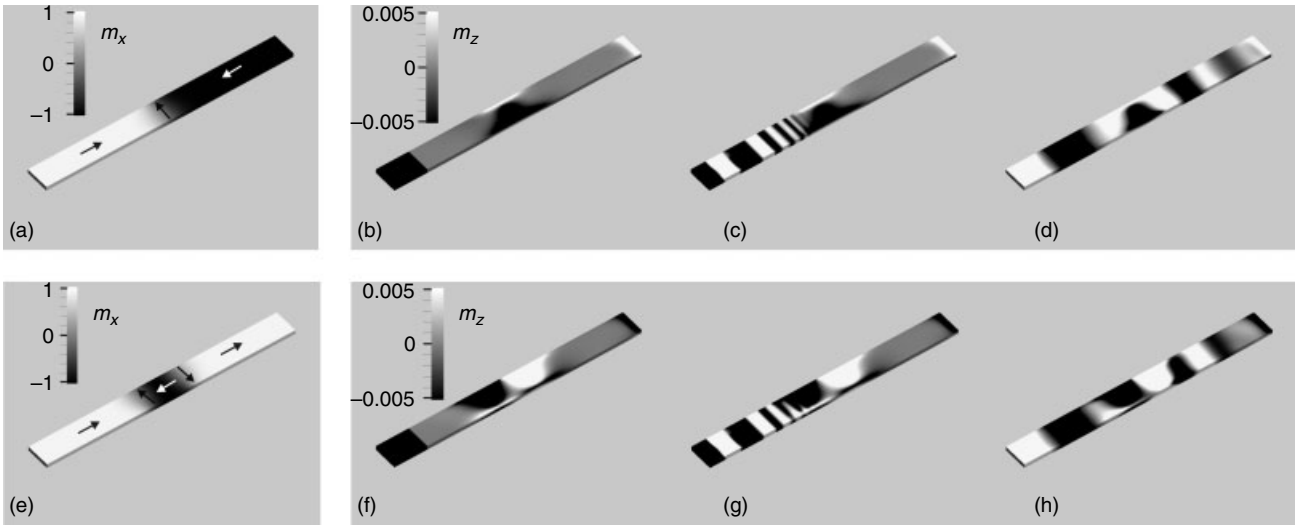

Figure 7. Wave propagation in a strip with a 180° domain wall (a–d) and with a 360° domain wall (e–h). The gray scale in frames (a) and (e) shows the in-plane magnetization along the strip, the other frames display the out-of-plane components like those in Figure 5. The snapshots are taken at $t = 0$ ps (b) and (f); 27 ps (c) and (g); and 298 ps (d) and (h).

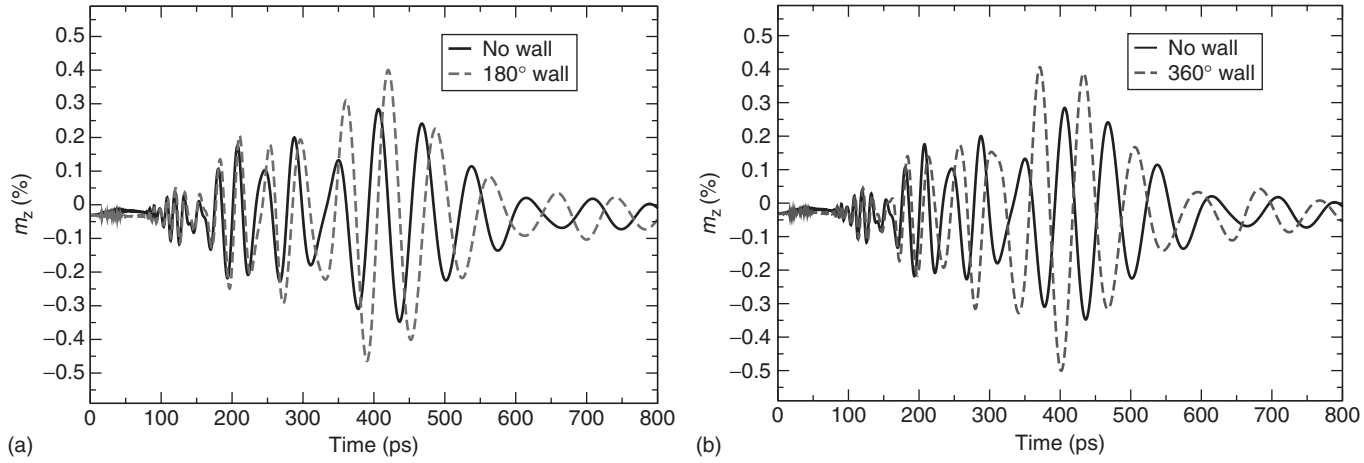

Figure 8. Magnetic seismographs recorded at the opposite end of the strip in the case of a 180° wall (a) and a 360° wall (b). The oscillations are compared with the signal obtained without domain wall, as shown in Figure 5(b).

wavelength that carry the main signal are phase shifted by $\Delta\Phi \simeq \pi/2$. In addition to the wavelength, simulations on other strip geometries show that the film thickness also has a strong influence on the value of the phase shift. This is probably related to the sensitive dependence of the domain-wall width on the film thickness. However, more detailed studies are required to systematically investigate the correlation between the phase shift and quantities like domain-wall width, magnetocrystalline anisotropy, film thickness, lateral width of the strip, and so on. Simulations with different values of the Gilbert damping parameter indicate that the phase shift effect is not sensitive to α.

The surprising phase-shift effect can also be probed with a 360° domain wall (cf. Figure 7(e–h)). This leads to a doubling of the phase shift and the main oscillations now shift by $\Delta\Phi \simeq \pi$ with respect to the homogeneous strip (cf. Figure 8b). While in the simulations a 360° domain wall can be prepared relatively easily by choosing suitable initial conditions for the calculation, such a magnetic structure is more difficult to obtain experimentally. Interestingly, 360° domain walls in thin magnetic nanorings have recently been observed by means of magnetic force microscopy, and it seems to be possible to generate and to remove 360° domain walls experimentally in a controlled way by means of an external magnetic field (Castano, Ross and Frandsen, 2003).

The phase shift induced by a magnetic domain wall in propagating spin waves has recently been calculated analytically for the case of a 180° Bloch wall (Bayer, Schultheiss, Hillebrands and Stamps, 2005). This study was stimulated by the micromagnetic simulations discussed in the preceding text, which predicted such an effect (Hertel, Wulfhekel and Kirschner, 2004). Similar to the present study, Bayer, Schultheiss, Hillebrands and Stamps (2005) find that a Bloch wall does not lead to the reflection or absorption of a spin wave and that a phase shift is obtained, depending on the wave vector of the spin wave. It can be assumed that the present case of a Néel wall is comparable to the situation with a Bloch wall studied by Bayer, Schultheiss, Hillebrands and Stamps (2005).

The possibility of manipulating the phase of spin waves, demonstrated here by means of magnetic domain walls, in combination with the ability to split and to merge spin waves propagating along thin magnetic strips, paves the way to interference experiments with spin waves. These interference effects could represent the working principle of programmable devices performing logical operations with spin waves, which is discussed in the next section.

5 SPIN-WAVE LOGICS

Phase differences of spin waves can be studied with magnetic ring structures, with which spin waves can be split into two branches. If the spin waves propagating in the branches acquire a phase difference with respect to each other, the phase shift should lead to characteristic interference effects when the waves are merged on the opposite side of the ring. The concept to split a wave on a ring and to use interference effects to probe the phase is similar to the Aharonov–Bohm effect (Aharonov and Bohm, 1959). A model for a spin-wave interferometer is an elongated ring with two small plates on opposite sides, as shown in Figure 9. One of the outer plates is used to excite spin waves and the other to measure the signal after the spin waves have traveled through the ring.

In a first example, the static magnetic structure in the ring is the so-called *onion state* (Rothman, Kläui and Lopez-Diaz, 2001). This is an almost homogeneous structure with the magnetization locally aligned parallel to the strip

and to the branches in order to reduce magnetic surface charges (cf. Figure 9(a and b)). In this configuration, the magnetization direction is essentially parallel to the direction of propagation of the spin waves.

If spin waves are generated on one of the outer platelets, the spin waves propagate toward the junction, where they are split symmetrically on the two branches and eventually merge on the opposite side. This process is shown in Figure 10(a)–(d). In this ring geometry, some high-frequency, edge-localized spin-wave modes are observed, which did not occur in the case of a straight bar. These modes, which are apparently connected with the curvature of the branches, dissipate very quickly so that they are almost completely attenuated before they reach the opposite side of the ring. Apart from these additional modes at the edge, the excitation spectrum consists of almost plane waves. When the branches meet again, the wave fronts merge with the same phase. The arrival of the spin waves at the opposite end can again be displayed with a 'seismograph'. The spectrum is similar to the previous case of a single strip.

To study the influence of a domain wall on the phase of the spin waves, a 360° domain wall is inserted in one of the branches, and the simulation is repeated with this structure. The result is shown in Figure 10(e)–(h). The spectrum of the signal that arrives on the opposite side is significantly different from the previous case with a homogeneously magnetized ring (cf. Figure 11a). While the fast excitations of short wavelength are essentially the same as before, the central low-frequency oscillation is much more strongly damped in the case with a 360° domain wall. This strong

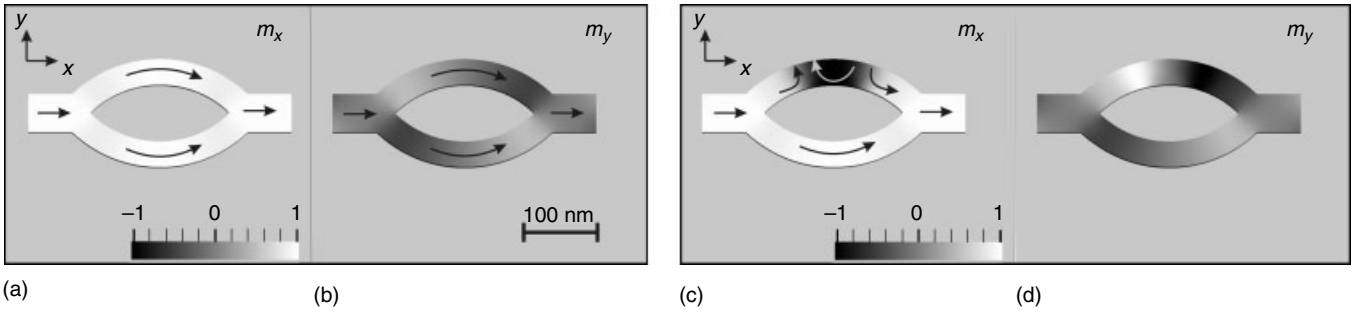

Figure 9. Two magnetization states in a flat, elongated ring structure. (a) and (b) Quasihomogeneous 'onion state'. The magnetization is oriented in the x-direction, with some small deviations in the ring branches. (c) and (d) Inhomogeneous state with a 360° wall in one branch of the ring.

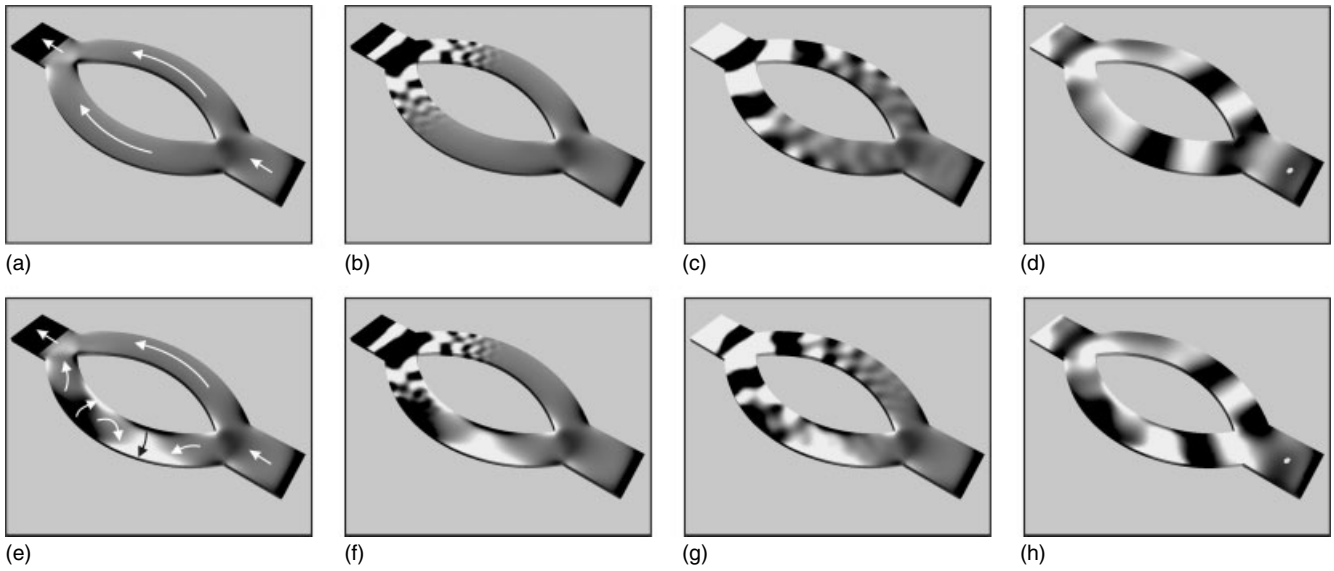

Figure 10. Propagating spin waves in a ring-shaped element. Top row, onion state; bottom row, ring with 360° wall. The gray scale shows the out-of-plane component, like in the previous examples. The arrows in frames (a) and (e) depict the in-plane magnetization structure. Snapshots of the dynamic relaxation process are taken at 0 ps (a) and (e); 27 ps (b) and (f); 67 ps (g); 90 ps (c); 298 ps (d) and (h). The white point in the frames (d) and (h) indicates the region where the seismograph of Figure 11(a) is recorded.

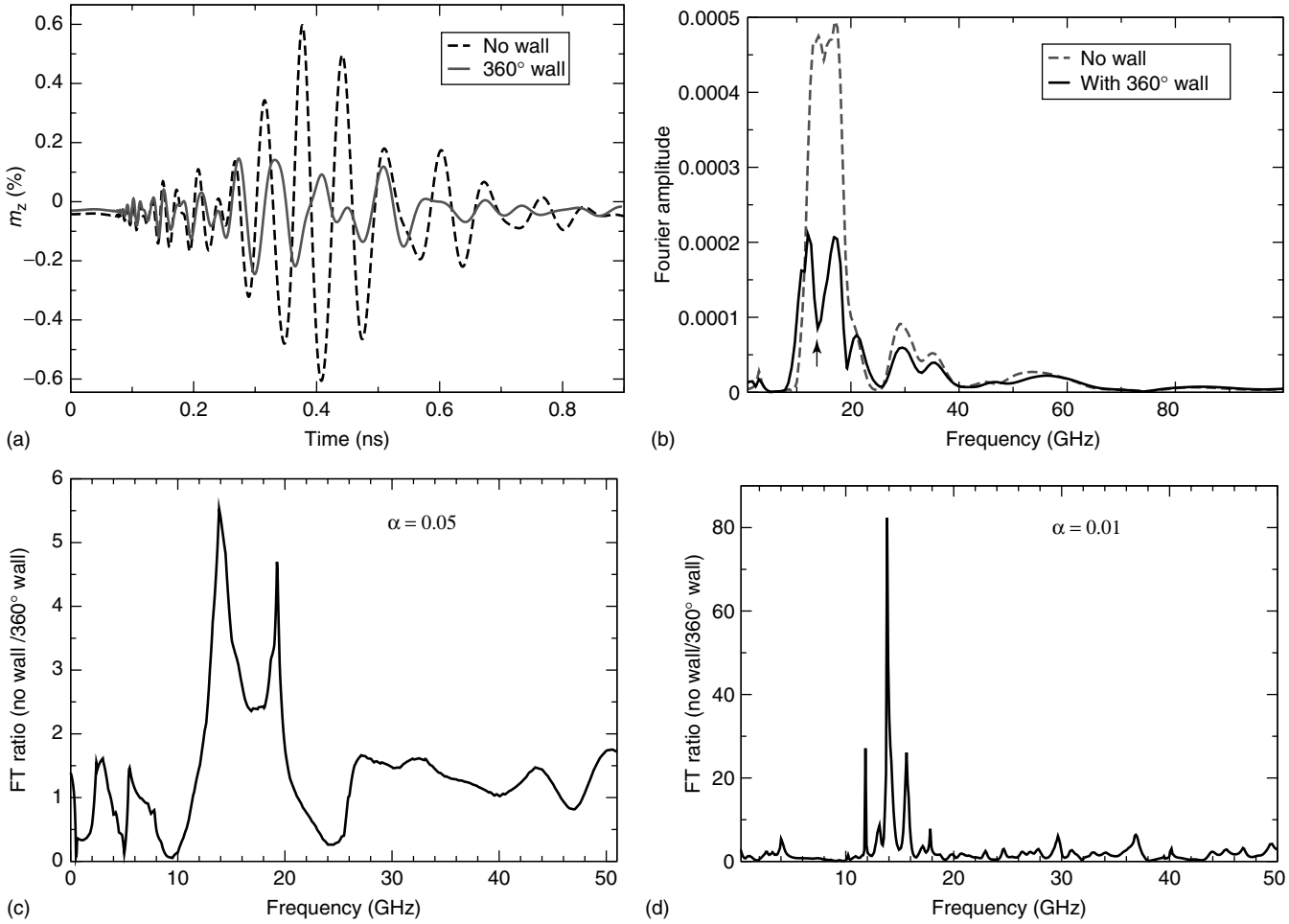

Figure 11. (a) Seismographs of the spin waves arriving at the opposite end of the ring in the case of the onion state and in the inhomogeneous state with a 360° wall. (b) Fourier transforms of the signals from frame (a). (c) Ratio of the Fourier amplitudes from frame (b). (d) Ratio of Fourier transforms as shown in frame (c) in the case of lower damping ($\alpha = 0.01$).

attenuation results from destructive interference when the spin waves merge (Figure 10h).

Since the phase shift depends on the frequency, there is a small range of frequencies in the spectrum of the excitations that matches the condition of opposite phase almost exactly. This can best be seen by analyzing the Fourier spectra of the magnetic seismographs for both cases. The arrow in Figure 11(b) points at the frequency that is most strongly damped by the presence of the domain wall. This results in a peak at about 14 GHz when the ratio of the Fourier components of these two cases is plotted, cf. Figure 11(c). This data refers to the case shown in the simulation, where a relatively large damping constant $\alpha = 0.05$ was used. A lower value of α (0.01) leads to a reduction of the line width of the Fourier components. In this case, the ratio of the Fourier components displays a much sharper peak at 14 GHz (Figure 11d). The spin waves with this frequency are almost completely filtered out by the ring with a 360° domain wall. Therefore, the spin interferometer can also be considered as a spin-wave filter for one characteristic frequency. If the signal is carried with this frequency, the ratio of the signal without a domain wall to the one with a 360° domain wall is very large, in our case of the order of 80.

If we assume that a 360° domain wall can be inserted and removed in the branches, this magnetic ring can be regarded as a spin-wave-based logical device that performs a disjunctive exclusive OR (NXOR) operation. This is illustrated in Figure 12. The input signal consists in placing domain walls acting as phase-shifting units into the branches, and the probing is obtained by letting a spin wave of suitable frequency run through the ring, which is either transmitted or blocked by the device.

This NXOR switch is the most simple type of a spin-wave-based logical device. Other logical operations can be achieved by combining such rings, as sketched in Figure 13. In the switches, phase shifters are inserted or removed,

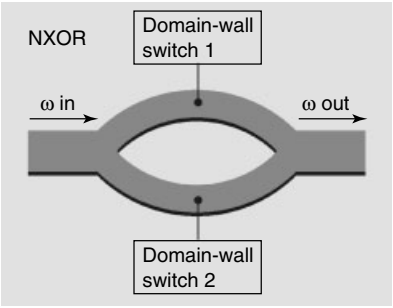

Domain wall in branch 1	Domain wall in branch 2	Signal out
0	0	1
1	0	0
0	1	0
1	1	1

Figure 12. The property of the ring to block the propagation of spin waves of a certain frequency depending on the presence or absence of domain walls in the ring branches can – in principle – be used for logical operations. In this example, the ring acts like a disjunctive, exclusive OR switch (NXOR).

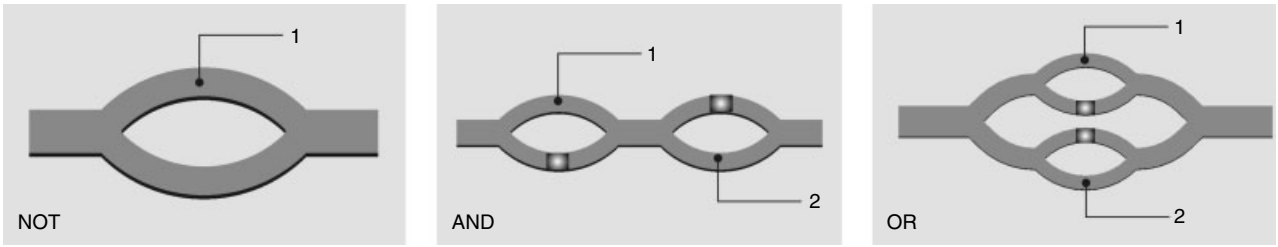

Figure 13. Other logical operations based on spin-wave propagation can be performed by combining rings. The switches 1 and 2 in these schematics are regions where a 360° wall is inserted or removed. The larger dots in the AND and in the OR sketch represent fixed phase-shifting units (360° walls).

according to the signal that is to be probed, in the same way as was done in the NXOR switch when a domain wall was inserted or removed in one branch.

6 BERRY-PHASE EFFECTS IN FERROMAGNETIC RINGS

Because of the similarity of the effects, it may be suspected that the domain-wall-induced phase shift in spin waves occurring in an elongated magnetic ring has a similar origin as the Berry phase (Berry, 1984, 1985) that an electron wave acquires due to the magnetic vector potential in the Aharonov–Bohm effect.

Effects connected with a Berry phase or a Hannay angle (Hannay, 1985) in propagating spin waves are related to the precessional motion of the magnetization around the effective field (Braun and Loss, 1996). This is illustrated in an example for a Berry-phase effect in a thin ferromagnetic ring with vortex magnetization in the plane (cf. Figure 14b). In this case, the dispersion relation of spin waves propagating along the ring does not depend on the sense of propagation being parallel $(\boldsymbol{k}_1, \omega_1)$ or antiparallel $(\boldsymbol{k}_2, \omega_2) = (-\boldsymbol{k}_1, \omega_1)$ to the local magnetization direction. Micromagnetic simulations confirm the occurrence of standing spin-wave patterns in such a case, which can be decomposed in sets of identical spin waves with opposite sense of propagation.

If the magnetization is lifted out of the plane by means of an external field applied perpendicular to the ring plane (cf. Figure 14c), the degeneracy is lifted (Ivanov and Zaspel, 2005). The quasistanding spin waves resulting in this case display a slow and constant motion of the nodal points of the oscillations; either clockwise or counterclockwise, depending on the sign of the external field. To understand this effect, it is important to note that – according to the LLG equation – the precession of the magnetization in an effective field always has the same sense of rotation (Figure 14a). If spin waves propagate parallel to the direction of the effective field, this precession is perpendicular to the propagation direction. By lifting the effective field out of the ring plane, the precessional motion of the magnetization obtains a component along the propagation direction, which is either in the same or in the opposite sense, thereby lifting the degeneracy of clockwise and counterclockwise propagation. A mechanical analogy for this is Foucault's pendulum: The oscillation of the pendulum can be decomposed in two circular components with opposite sense of rotation. During one day, the pendulum is adiabatically transported on a circular orbit due to the rotation of the earth. If the pendulum is at the equator, the rotation axis of the earth is perpendicular to the rotation axis. In this case, the clockwise and the counterclockwise oscillations are degenerate. This corresponds in our case to the effective field lying in the film plane. A chirality of the system is imposed in both cases:

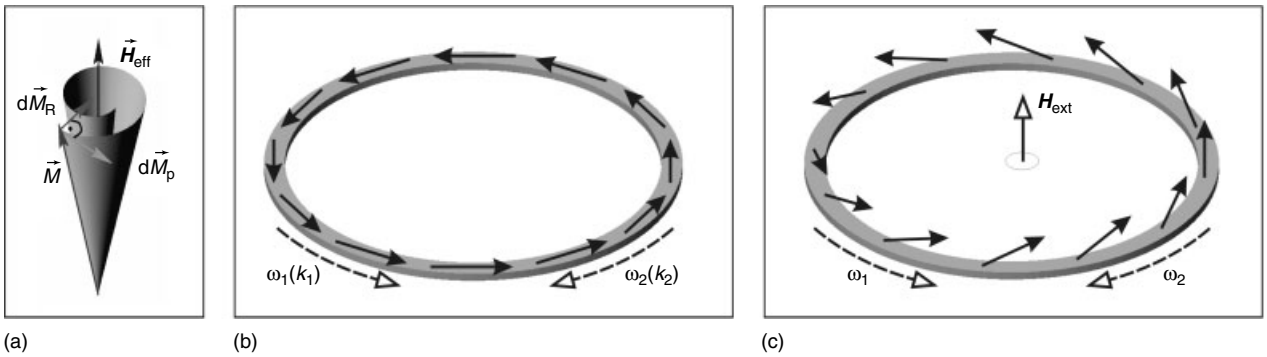

Figure 14. (a) Schematics of the magnetization dynamics described by the LLG equation. (b) Thin magnetic ring with vortex configuration. Spin waves propagating parallel ($\boldsymbol{k}_1$) or antiparallel ($\boldsymbol{k}_2$) to the magnetization direction are degenerate. (c) The degeneracy can be lifted by tilting the magnetization out of the ring plane with an external magnetic field.

the sense of rotation of the earth is constant, as is the sense of rotation of the magnetization in the precessional motion around the effective field. If Foucault's pendulum is located at a latitude away from the equator, the earth's slow rotation is superimposed on the circular components of the swinging pendulum, and the degeneracy of these oscillations is lifted. Hence, the plane of oscillation slowly rotates with respect to the surface. In the case of spin waves, this would correspond to the situation when the precession axis has a component perpendicular to the propagation direction, that is, when the average magnetization is lifted out of the ring plane.

Apart from this simple example, which only serves to present the basic idea of Berry phases in magnons, thorough analytical studies on this topic have been reported very recently by Bruno (2004) and Dugaev, Bruno, Canals and Lacroix (2005). These studies confirm the effect of a phase shift of a spin wave running through a domain wall, as predicted by the simulations. They provide an explanation for the phase shift in terms of a Berry-phase effect. The study of Berry phases in magnons is a new topic in magnetism, which has been elaborated analytically to a good extent. Further numerical and possibly experimental work is required to establish a more comprehensive picture of such effects in magnetism.

7 CONCLUSION

Thin ferromagnetic strips can serve as waveguides for propagating spin waves. Micromagnetic finite-element simulations show that such waveguides can be used to split and merge spin waves coherently. If a propagating spin wave meets a 180° head-to-head or a 360° domain wall, it runs through it without being scattered. However, the domain-wall changes the phase of the spin wave. By manipulating the phase of the spin waves, constructive and destructive interferences can be generated. This could be the working principle of a new type of programmable logical devices based on spin-wave propagation. Of course, the technical applicability of such devices is questionable, and it is doubtful whether this new concept for logical devices could ever compete with the advanced electronic technology that has been developed in the last decades. Compared to the recently proposed concept of magnetic logics based on domain-wall motion (Allwood *et al*., 2002), however, the spin-wave-based logics presented here would have the advantage of a nondestructive read-out process and a faster signal propagation. Probably more important than these technical issues is the fact that an interesting and fundamental effect in magnetism has been revealed by micromagnetic simulations, that is, the interaction of spin waves with domain walls. This has stimulated a number of interesting analytical studies, including Berry-phase effects in magnons, and will hopefully also trigger experimental investigations on this effect.

ACKNOWLEDGMENTS

I would like to thank Prof. A. S. Arrott for reading the manuscript and for several helpful suggestions.

Note: Since this chapter was written, a number of interesting developments have been reported in the literature. Remarkable examples for this are the recent works of Choi, Lee, and Kim (2006) and Choi, Lee, Guslienko and Kim (2007).

REFERENCES

Acremann, Y., Buess, M., Back, C.H., *et al*. (2001). Ultrafast generation of magnetic fields in a Schottky diode. *Nature*, **414**, 51–54.

Aharoni, A. (1996). *Introduction to the Theory of Ferromagnetism*, Oxford Science Publications, Clarendon Press: Oxford.

Aharonov, Y. and Bohm, D. (1959). Significance of electromagnetic potentials in the quantum theory. *Physical Review*, **115**(5), 485–491.

Akhiezer, A.I., Baryachtar, V. and Peletminsky, S. (Eds.) (1968). *Spin Waves*, North-Holland: Amsterdam.

Allwood, D.A., Xiong, G., Cooke, M.D., *et al*. (2002). Submicrometer ferromagnetic NOT gate and shift register. *Science*, **296**, 2003–2006.

Baibich, M.N., Broto, J.M., Fert, A., *et al*. (1988). Giant magnetoresistance of (001) Fe / (001) Cr magnetic superlattices. *Physical Review Letters*, **61**(21), 2472.

Bailey, W., Kabos, P., Mancoff, F. and Russek, S. (2001). Control of magnetization dynamics in $Ni_{81}Fe_{19}$ thin films through the use of rare-earth dopants. *IEEE Transactions on Magnetics*, **37**(4), 1749–1754.

Bayer, C., Schultheiss, H., Hillebrands, B. and Stamps, R.L. (2005). Phase Shift of Spin Waves Travelling through a 180° Bloch-Domain Wall. *IEEE Transactions on Magnetics*, **41**(10), 3094–3096.

Berger, L. (1996). Emission of spin waves by a magnetic multilayer traversed by a current. *Physical Review B*, **54**(13), 9353–9358.

Berkov, D., Ramstöck, K. and Hubert, A. (1993). Solving micromagnetic problems. *Physical Status Solidi A*, **137**, 207–225.

Berry, M.V. (1984). Quantal phase factors accompanying adiabatic changes. *Proceedings of the Royal Society of London Series A*, **392**, 45–57.

Berry, M.V. (1985). Classical adiabatic angles and quantal adiabatic phase. *Journal of Physics A: Mathematical and General*, **18**, 15–27.

Binasch, G., Grünberg, P., Saurenbach, F. and Zinn, W. (1989). Enhanced magnetoresistance in layered magnetic structures with antiferromagnetic interlayer exchange. *Physical Review B*, **39**(7), 4828–4830.

Blue, L.J. and Scheinfein, M.R. (1991). Using multipoles decreases computation time for magnetostatic self-energy. *IEEE Transaction on Magnetics*, **27**(6), 4778–4780.

Braun, H-B. and Loss, D. (1996). Berry's phase and quantum dynamics of ferromagnetic solitons. *Physical Review B*, **53**(6), 3237–3255.

Brown, W.F. Jr. (1940). Theory of the approach to magnetic saturation. *Physical Review*, **58**, 736–743.

Brown, W.F. Jr. (1962). *Magnetostatic Principles in Ferromagnetism*, North-Holland publishing company: Amsterdam.

Brown, W.F. Jr. (1963). *Micromagnetics*, Interscience Publishers, John Wiley & Sons: New York, London.

Bruno, P. (2004). Nonquantized Dirac monopoles and strings in the Berry phase of anisotropic spin systems. *Physical Review Letters*, **93**(24), 247202.

Castano, F.J., Ross, C.A., Frandsen, C., *et al*. (2003). Metastable states in magnetic nanorings. *Physical Review B*, **67**, 184425.

Chen, W., Fredkin, D.R. and Koehler, T.R. (1993). A new finite element method in micromagnetics. *IEEE Transaction on Magnetics*, **29**(3), 2124–2128.

Choi, B.C., Belov, M., Ballentine, G. and Freeman, M. (2001). Ultrafast magnetization reversal dynamics investigated by time domain imaging. *Physical Review Letters*, **86**(4), 728–731.

Choi, S., Lee, K.-S. and Kim S.-K. (2006). Spin wave interference. *Applied Physics Letters*, **89**, 062501.

Choi, S., Lee, K.-S., Guslienko, K.Yu. and Kim, S.-K. (2007) Strong radiation of spin waves by core reversal of a magnetic vortex and their wave behaviors in magnetic nanowire waveguides. *Physical Review Letters*, **98**, 087205.

Damon, R.W. and Eshbach, J.R. (1961). Magnetostatic modes of a ferromagnet slab. *Journal of Physics and Chemistry of Solids*, **19**(3–4), 308–320.

Dugaev, V.K., Bruno, P., Canals, B. and Lacroix, C. (2005). Berry phase of magnons in textured ferromagnets. *Physical Review B*, **72**(2), 024456.

Fredkin, D.R. and Koehler, T.R. (1990). Hybrid method for computing demagnetizing fields. *IEEE Transaction on Magnetics*, **26**(2), 415–417.

Garcia-Cervera, C.J., Gimbutas, Z. and Weinan, E. (2003). Accurate numerical methods for micromagnetic simulations with general geometries. *Journal of Comparative Physiology*, **184**(1), 37–52.

Gerrits, T., van den Berg, H., Hohlfeld, J., *et al*. (2002). Ultrafast precessional magnetization reversal by picosecond magnetic field pulse shaping. *Nature*, **418**, 509–512.

Hannay, J.H. (1985). Angle variable holonomy in adiabatic excursion of an integrable hamiltonian. *Journal of Physics A: Mathematical and General*, **18**, 221–230.

Hertel, R. (2001). Micromagnetic simulations of magnetostatically coupled nickel nanowires. *Journal of Applied Physics*, **90**(11), 5752–5758.

Hertel, R., Wulfhekel, W. and Kirschner, J. (2004). Domain-wall induced phase shifts in spin waves. *Physical Review Letters*, **93**, 257202.

Hillebrands, B. and Ounadjela, K. (Eds.) (2002). *Spin Dynamics in Confined Structures I*, Springer, Cambridge, New York.

Hindmarsh, A.C. (1983). Odepack, a systematized collection of ode solvers. In *Scientific Computing*, Stepleman, R.S., Carver, M., Peskin, R., *et al.* (Eds.), North Holland: Amsterdam, pp. 55–64.

Hubert, A. and Schäfer, R. (1998). *Magnetic Domains – The Analysis of Magnetic Microstructures*, Springer: Berlin, New York, Heidelberg.

Hurben, M.J. and Patton, C.E. (1996). Theory of magnetostatic spin waves for in-plane magnetized anisotropic films. *Journal of Magnetism and Magnetic Materials*, **163**(36–39), 39–69.

Ivanov, B.A. and Zaspel, C.E. (2005). High-frequency modes in vortex-state nanomagnets. *Physical Review Letters*, **94**(2), 0207205.

Kikuchi, R. (1956). On the minimum of magnetization reversal time. *Journal of Applied Physics*, **27**(11), 1352–1357.

Kläui, M., Vaz, C.A.F., Bland, J.A.C., *et al*. (2004a). Head-to-head domain-wall phase diagram in mesoscopic ring magnets. *Applied Physics Letters*, **85**(23), 5637–5639.

Kläui, M., Vaz, C.A.F., Wernsdorfer, W., *et al*. (2004b). Domain wall behaviour at constrictions in ferromagnetic ring structures. *Physica B*, **343**(1–4), 343–349.

Koch, R.H., Deak, J.G., Abraham, W., *et al*. (1998). Magnetization reversal in micron-sized magnetic thin films. *Physical Review Letters*, **81**(20), 4512–4515.

Koehler, T.R. and Fredkin, D.R. (1992). Finite element methods for micromagnetics. *IEEE Transaction on Magnetics*, **28**(2), 1239–1244.

Kronmüller, H. and Fähnle, M. (2003). *Micromagnetism and the Microstructure of Ferromagnetic Solids*, Cambridge University Press: Cambridge, New York.

Lindholm, D.A. (1984). Three-dimensional magnetostatic fields from point-matched integral equations with linearly varying scalar sources. *IEEE Transaction on Magnetics*, **20**(5), 2025–2032.

McMichael, R.D. (2000). *Standard problem #4*, µMAG Micromagnetic Modeling Activity Group, http://www.ctcms.nist.gov/~rdm/mumag.html.

McMichael, R.D. and Donahue, M.J. (1997). Head to head domain wall structures in thin magnetic strips. *IEEE Transaction on Magnetics*, **33**(5), 4167–4169.

Press, W.H., Flannery, B.P., Teukolsky, S.A. and Vetterling, W.T. (1986). *Numerical Recipes: the Art of Scientific Computing*, Cambridge University Press: Cambridge, New York.

Rothman, J., Kläui, M., Lopez-Diaz, L., *et al*. (2001). Observation of a bi-domain state and nucleation free switching in mesoscopic ring magnets. *Physical Review Letters*, **86**(6), 1098–1101.

Schabes, M.E. and Bertram, H.N. (1988). Magnetization processes in ferromagnetic cubes. *Journal of Applied Physics*, **64**(3), 1347–1357.

Schrefl, T. (1999a). Finite elements in numerical micromagnetism part I: granular hard magnets. *Journal of Magnetism and Magnetic Materials*, **207**(1–3), 45–65.

Schrefl, T. (1999b). Finite elements in numerical micromagnetism part II: patterned magnetic elements. *Journal of Magnetism and Magnetic Materials*, **207**(1–3), 66–77.

Seberino, C. and Bertram, H. (2001). Concise, efficient three-dimensional fast multipole method for micromagnetics. *IEEE Transactions on Magnetics*, **37**(3), 1078–1086.

Slavin, A.N., Demokritov, S.O. and Hillebrands, B. (2002). Nonlinear spinwaves in one- and two-dimensional magnetic waveguides. In *Spin Dynamics in Confined Magnetic Structures I*, *Topics in Applied Physics*, Hillebrands, B. and Ounadjela, K. (Eds.), Springer, pp. 35–62, Vol. 83.

Slonczewski, J.C. (1996). Current-driven excitations of magnetic multilayers. *Journal of Magnetism and Magnetic Materials*, **159**, L1–L7.

Wernsdorfer, W., Orozco, E.B., Hasselbach, K., *et al*. (1997). Experimental evidence of the Néel-Brown model of magnetization reversal. *Physical Review Letters*, **78**(9), 1791–1794.

Wolf, S.A., Awschalom, D.D., Buhrman, R.A., *et al*. (2001). Spintronics: A Spin-based Electronics Vision for the Future. *Science*, **294**, 1488–1495.

Yang, B. and Fredkin, D.R. (1996). Dynamical micromagnetics of a ferromagnetic particle: numerical studies. *Journal of Applied Physics*, **79**(8), 5755–5757.

Yang, B. and Fredkin, D.R. (1998). Dynamical micromagnetics by the finite element method. *IEEE Transaction on Magnetics*, **34**(6), 3842–3852.

Micromagnetism–Microstructure Relations and the Hysteresis Loop

Dagmar Goll
Max-Planck-Institut für Metallforschung, Stuttgart, Germany

1 INTRODUCTION

Magnetic materials are widely used in many (modern) application fields ranging from electrical engineering, car industry, and energy technique to sensor systems, high-density recording, and applications in medicine and biology. For technological progress in these fields and for an application-oriented magnet design, the characteristic magnetic properties of the hysteresis loop are of great importance. Their steady improvement brings about, in particular, a continuous miniaturization of magnetic devices (hard magnetic materials) and a continuous reduction of energy losses during energy transmission (soft magnetic materials) leading to innovations in many new application fields and consequently to a rapid growth of the worldwide market.

Modern high-quality magnets are based on both optimized microstructures (including defect structures) and compounds with outstanding intrinsic material parameters, such as the spontaneous polarization $J_s = \mu_0 M_s$ (spontaneous magnetization M_s, vacuum permeability $\mu_0 = 4\pi \times 10^{-7}\,\mathrm{Vs\,Am^{-1}}$), the magnetocrystalline anisotropy constants K_1 and K_2, and the magnetostriction λ. Optimized microstructures are composed of amorphous regions and/or ensembles of small magnetic grains with length scales varying from nanometer to centimeter. These extrinsic magnetic properties can be controlled by the choice of the alloy composition from the phase diagram (including small amounts of additives) and by the processing route as, for example, sintering, rapid quenching, sputtering, or molecular beam epitaxy (including thermal and mechanical treatments). The detailed analysis of microstructure–magnetic property relationships by means of different high-resolution electron microscopy techniques and magnetic hysteresis loop measurements in combination with the theory of micromagnetism allows a quantitative interpretation of magnetization processes responsible for magnetic softening/hardening. This provides general rules for a successful specific tailoring of optimized characteristic magnetic properties of the hysteresis loop in the whole ferromagnetic (or ferrimagnetic) temperature range.

In the following text, the micromagnetism–microstructure correlation and its influence on the characteristic magnetic properties of the hysteresis loop is reviewed. The following three sections give a survey of the basic characteristics of the hysteresis loop (Section 2), microstructure (Section 3), and

Handbook of Magnetism and Advanced Magnetic Materials. Edited by Helmut Kronmüller and Stuart Parkin. Volume 2: *Micromagnetism*. ISBN: 978-0-470-02217-7.

micromagnetism and magnetization processes (Section 4). In Sections 5 and 6 the micromagnetism–microstructure relations are discussed for hard and soft magnetic materials. In Section 7, the micromagnetism–microstructure relations are investigated in the approach to saturation. In Section 8, it is demonstrated how the detailed knowledge of the micromagnetism–microstructure correlation can be used for a systematic design of high-performance magnets.

2 HYSTERESIS LOOP

The macroscopic magnetic properties of a ferromagnet are characterized by the hysteresis loop and determine the suitability of magnetic materials for a given application. The hysteresis loop is obtained by applying a magnetic field $\mu_0 H$ to the specimen and measuring the ensuing change of the magnetic polarization J in field direction. Starting from the initial demagnetized state ($J = \mu_0 H = 0$ T) the polarization increases with increasing field and finally reaches the saturation polarization ($J = J^{\mathrm{sat}}$). When the magnetizing field is reduced to zero from the saturated state the sample remains magnetized. This polarization at zero field is called remanence J_r. It can be returned to zero by applying a reverse magnetic field of strength $\mu_0 H_\mathrm{c}$ known as the coercive field which is, therefore, the measure for the magnet's resistance against demagnetizing fields. Further increase of the reversed applied field magnetizes the sample to saturation in the opposite direction ($J = -J^{\mathrm{sat}}$). A large spontaneous polarization J_s is a prerequisite for high J_r values, whereas a large magnetocrystalline anisotropy constant may result in large coercivities. In principle, ferromagnetic substances can be classified into soft and hard magnetic materials depending on how easily the material can be (de)magnetized as illustrated in Figure 1.

Hard magnets provide stable permanent magnetic fields (after exposure to a magnetic field) and create surface poles without continuous expenditure of electrical energy. They are characterized by high coercivity ($\mu_0 H_\mathrm{c} \approx 0.1$–$4$ T, $H_\mathrm{c} \approx 80$–$3200\,\mathrm{kA\,m^{-1}}$), high remanence, and a high maximum energy product ($(BH)_{\max} \approx 10$–$500\,\mathrm{kJ\,m^{-3}}$). The maximum energy product represents the magnetic energy per unit volume which can be maximally stored by a hard magnet, thereby specifying the performance or strength of a permanent magnet. $(BH)_{\max}$ is defined as the maximum rectangular area within the $B(H) = \mu_0 H + J$ hysteresis loop in the second quadrant. The theoretical upper limit of $(BH)_{\max}$ is given by $(BH)^{\mathrm{theo}}_{\max} \approx J_\mathrm{r}^2/(4\mu_0)$ as long as the condition $\mu_0 H_\mathrm{c} > 0.5 J_\mathrm{r}$ is fulfilled. Typical hard magnetic materials are based on RE-TM compounds, hard ferrites, AlNiCo, and CoPt/FePt.

Soft magnetic materials enable amplification of the flux produced by an electrical current considerably, therefore being important in any application involving a change in magnetic induction. They are characterized by low coercivity ($\mu_0 H_\mathrm{c} \approx 0.2\,\mu\mathrm{T}$–$1.25\,\mathrm{mT}$, $H_\mathrm{c} \approx 0.16$–$1000\,\mathrm{A\,m^{-1}}$), high (initial) permeability $\mu_\mathrm{i} = \mathrm{d}B/\mathrm{d}(\mu_0 H)$ or (initial) susceptibility $\chi_0 = \mathrm{d}M/\mathrm{d}H = \mu_\mathrm{i} - 1$ ($\mu_\mathrm{i} \approx \chi_0 \approx 10^5$–$10^6$ for $H \to 0$) which describe the response of magnetic materials to a small magnetic field, therefore indicating how much magnetic induction B is generated by the material in a given magnetic field strength H and low high-frequency losses. The characteristics usually go along with low conductivity and small magnetostriction which describes the change of the shape of a ferromagnetic specimen during the magnetization process. Soft magnets are based on Fe, Fe–Si, Fe–Ni (permalloy), Fe–Co ((su)permendur), soft ferrites, and metallic glasses.

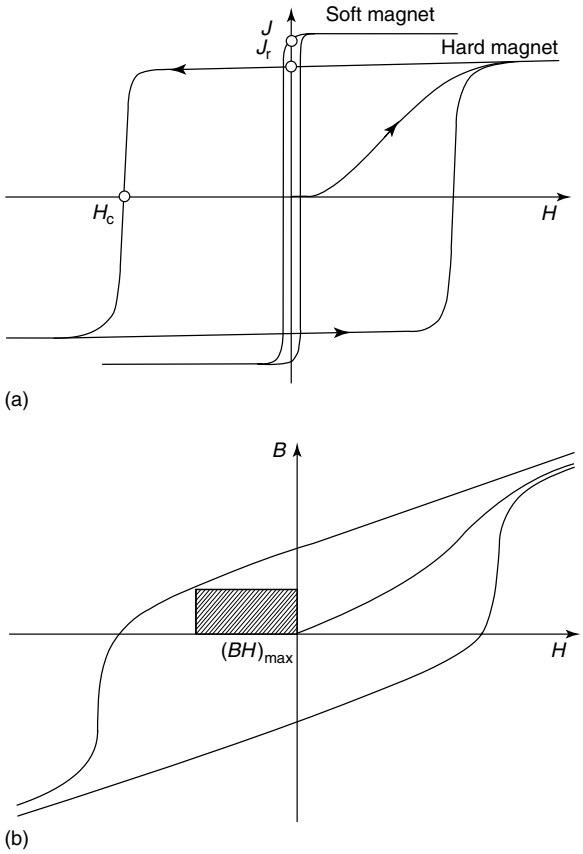

Figure 1. Characteristic magnetic properties: (a) $J(H)$ hysteresis loop with coercivity H_c and remanence J_r for typical soft and hard magnetic materials. (b) $B(H)$ hysteresis loop with the maximum energy product, that is, the maximum rectangular area within the loop in the second quadrant.

In addition to hard and soft magnetic materials, there exists a number of sophisticated magnetic materials with unusual properties like giant magnetostriction (see also **Magnetostrictive Materials and Magnetic Shape Memory Materials, Volume 4**), giant magnetoresistance, and giant magnetoimpedance.

3 MICROSTRUCTURE

Depending on whether the atoms of a magnet are arranged spatial periodically in crystal lattices or randomly, the magnetic material is crystalline or amorphous. Whereas in the former case, the distances between nearest neighbors are constant (short-range atomic order) and a base lattice is regularly repeated (long-range atomic order), in the latter case only short-range ordering occurs. Therefore, the interference pattern of crystalline magnets resulting from X-ray, electron, or neutron diffraction is sharp and reflects the symmetry of the crystal lattice. In contrast, only diffuse interference patterns are observed for amorphous magnets for small diffraction angles. In general, all solids are of a finite extension and show unavoidable disordering in the volume. These deviations from the ideal crystalline or amorphous structure (ideal microstructure) are called defect structures (real microstructure) and result in inhomogeneities of the intrinsic material parameters which influence the magnetic properties of the material decisively.

3.1 Crystalline magnets

A crystalline magnet whose crystal lattice shows perfect translational periodicity is called a single crystal. Correspondingly, a polycrystal consists of many single crystalline grains of different orientations. Depending on whether the grain size is on the micrometer or nanometer scale the polycrystalline magnets are microcrystalline or nanocrystalline, respectively. The defect structures in crystalline magnets are classified according to their geometrical extensions into point defects (zero dimensional), dislocations (one dimensional), planar defects (two dimensional), and volume defects (three dimensional). Single crystalline magnets contain only point defects and dislocations; in polycrystalline magnets planar defects may additionally occur. Volume defects such as pores or cracks are macroscopic defects and will not be taken into account in this article.

Point defects (Figure 2a) are atomic defects such as vacancies, self-interstitials, impurity interstitials, substitutional impurity atoms, or atomic disorder in ordered alloys resulting in lattice distortions.

Dislocations mostly appear as edge and screw dislocations or as a mixture of both. An edge dislocation (Figure 2b) is characterized by an additional net plane which ends within the bulk of the crystal. The line direction **l** of the inner edge of this half-plane is perpendicular to the Burgers vector **b** described by the distance between net planes. A screw dislocation (Figure 2c) corresponds to a shear deformation where one part of the crystal is displaced by a nearest neighbor distance with respect to the other part. The line direction **l** and the Burgers vector **b** are parallel to each other. The stress fields of dislocations are of long-range type and vary as $1/r$.

Planar defects may appear abruptly as it is the case for phase boundaries and twin boundaries or are of one or several atomic widths as it is the case for stacking faults, antiphase boundaries in intermetallics, and grain boundaries. At a phase boundary (Figure 3a) between two different phases the intrinsic material parameters change abruptly. When the lattices between the two phases match perfectly the phase boundary is called coherent, otherwise incoherent. Two phase boundaries may form precipitations as in $Sm_2(Co,Cu,Fe,Zr)_{17}$ permanent magnets (Figure 3c) where a three-phase precipitation nanostructure develops in a self-organized process during a complex annealing procedure and consists of Fe-rich cells, Cu-rich cell walls, and Zr-rich lamellae. At a twin boundary (Figure 3b) two grains are grown together at a common interface and the lattice periodicity is interrupted at the interface without displacement of the lattice atoms. Stacking faults (Figure 4a) occur when in close-packed lattices the stacking sequence is disturbed, for example, ABCACABC instead of ABCABCA. When the stacking fault is not extended over the whole grain

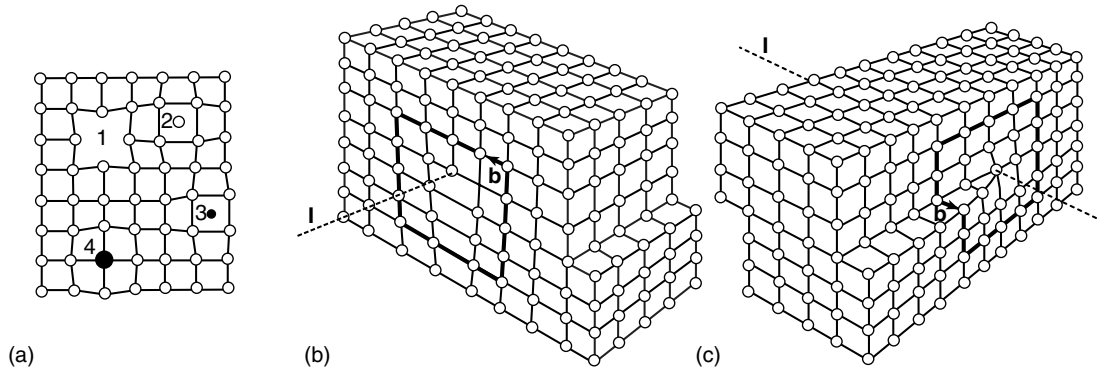

Figure 2. Schematic models of point defects and dislocations: (a) Point defects (1: vacancy, 2: self-interstitial, 3: impurity interstitial, 4: substitutional impurity atom), (b) edge dislocation (**l** $\perp$ **b**), and (c) screw dislocation (**l**$\|$**b**).

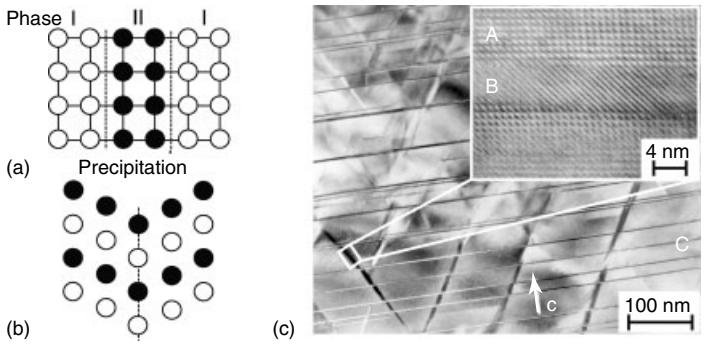

Figure 3. Abrupt planar defects: (a) Atomic configuration of a phase boundary. (b) Atomic configuration of a twin boundary. (c) Phase boundaries leading to precipitations in $Sm_2(Co,Cu,Fe,Zr)_{17}$ micrometer-scaled hard magnetic grains (A: Fe-rich 2:17 cells, B: Cu-rich 1:5 cell walls, C: Zr-rich lamellae). (Reproduced from D. Goll, H. Kronmüller, and H.H. Stadelmaier: Micromagnetism and the microstructure of high-temperature permanent magnets, *J Applied Physics*, **96** (2004), copyright © 2004 American Institute of Physics, with permission from the AIP.)

but ends along a line, the limiting line corresponds to an incomplete dislocation where the length of the Burgers vector is smaller than the distance between net planes. Antiphase boundaries (Figure 4b) are characterized by an abrupt change in the lattice of multiatomic alloys so that atoms of the same kind become neighbored.

For grain boundaries between single crystalline grains of different orientations there exists a variety of atomic structures. For a small twist angle θ between the orientations of two neighboring grains the interface is a low-angle grain boundary based on a regular dislocation structure. In the easiest case, a linear array of edge dislocations of distance d compensates the twist angle θ ($b/d = 2\sin\theta/2 \approx \theta$) as illustrated in Figure 5(a). An array of screw dislocations or mixed arrays result in more complex low-angle grain boundaries. For larger misorientation angles ($\theta > 15^\circ$), high-angle grain boundaries occur where the regular arrangement of dislocations is missing and the boundary region of about 2 nm in size is strongly disturbed. In the case of complete disorder the structure of the grain boundary becomes amorphous (Figure 5b). This intergranular film is independent of the orientation of the grains and can be regarded as a cement that holds the grains together. In the case of thermal equilibrium, high-angle grain boundaries may show some kind of periodicity in the strongly disturbed boundary region (Figure 5c). As an example for grain boundaries, in Figure 6 three different kinds of nanostructures are shown for $RE_2Fe_{14}B$ (RE = Nd, Pr) based permanent magnets where grain boundaries between grains of different orientations and different phases.

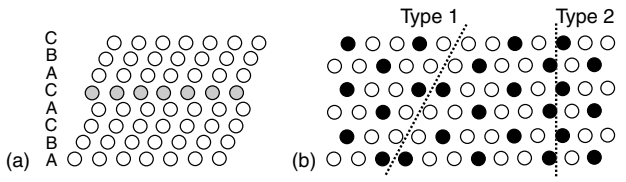

Figure 4. Extended planar defects: (a) Stacking fault (intrinsic, when one plane is missing; extrinsic, when one plane is added). (b) Two types of antiphase boundaries of hexagonal $SmCo_5$ showing the changes of nearest neighbor interactions.

3.2 Amorphous magnets

Amorphous magnets are also called glassy or noncrystalline magnets. The ideal amorphous state and also the liquid state of the melt are characterized by statistical intrinsic fluctuations of the mass density, known as free or antifree volumes (Cohen and Turnbull, 1959; Egami, Maeda and Vitek, 1980), and therefore by intrinsic fluctuations of the intrinsic material parameters, especially of the exchange energy and the local magnetic anisotropy. The free volumes result from vacant spaces between topologically disordered atoms. The intrinsic fluctuations lead to inhomogeneities in the orientation of the spontaneous polarization. All deviations from this are considered as defect structures in the amorphous material. The defect structures in amorphous magnets result from atomic rearrangements during the quenching process which lead to a chemical short-range order, to magnetic aftereffects, or to agglomerations of the free or antifree volumes providing internal stress sources therefore being restricted to magnetorestrictive amorphous materials. The quenched-in defect structures are the reason for the metastable character of the amorphous state. They can be classified into intrinsic defects which are stable below the crystallization temperature and extrinsic defects which recover during an annealing treatment below the crystallization temperature.

Especially the formation of chemical short-range order without loss of the topological amorphous state has its origin in magnetic annealing effects and the tendency for crystallization of the amorphous metastable state. Within small clusters of chemically ordered regions atomic metal–metal pairs of different metal atoms (e.g., Ni–Fe) may exist

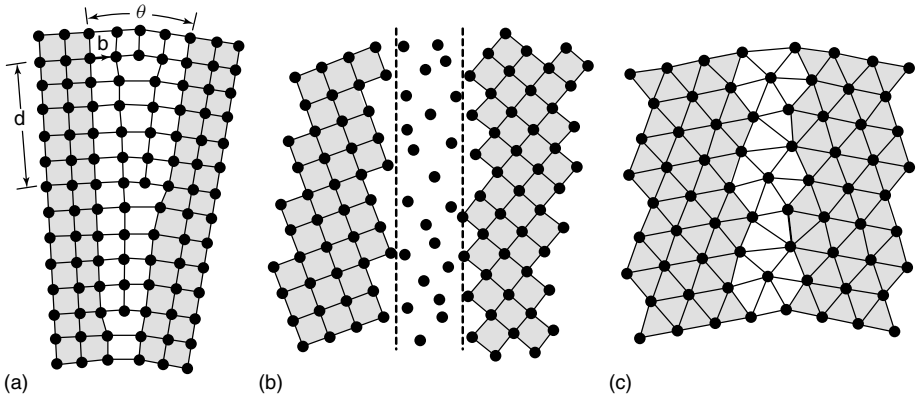

Figure 5. Grain boundaries: (a) Low-angle grain boundary of parallel edge dislocations with constant distances d compensating the twist angle θ between two grains misoriented relative to each other. (b) High-angle grain boundary (amorphous case). (c) High-angle grain boundary (thermal equilibrium).

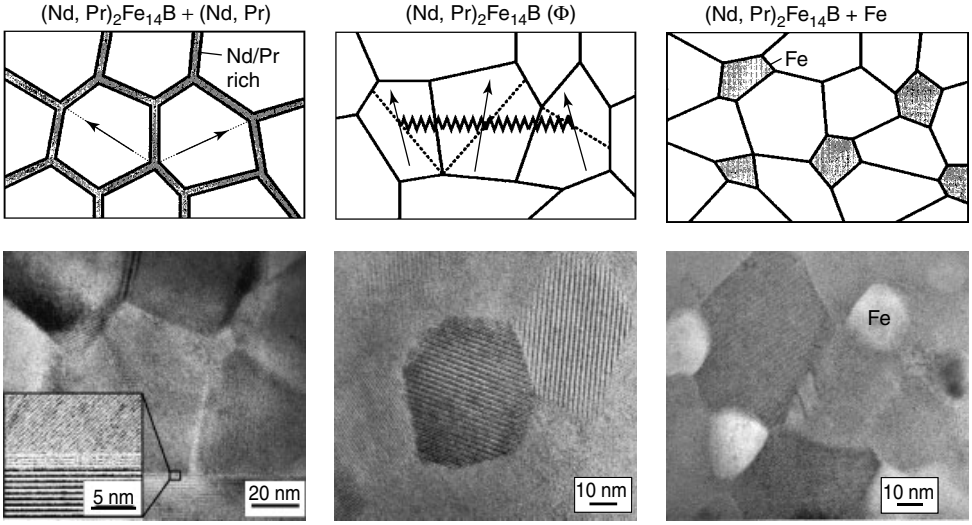

Figure 6. Grain boundaries between grains of different orientations and different phases exemplary for nanocrystalline $RE_2Fe_{14}B$ (RE = Nd,Pr) based permanent magnets. $RE_2Fe_{14}B$+(Nd,Pr) (high-coercivity magnet): Decoupled magnet where the hard magnetic $RE_2Fe_{14}B$ grains are magnetically isolated by the overstoichiometric RE which forms an amorphous paramagnetic interlayer that holds the grains together. $RE_2Fe_{14}B$ (high-coercivity, high-remanence magnet): Stoichiometric magnet where the hard magnetic $RE_2Fe_{14}B$ grains are in direct contact with each other. The exchange interaction in between induces a magnetic texture. $RE_2Fe_{14}B$+Fe (high-remanence magnet): Composite magnet with overstoichiometric Fe resulting in additional soft magnetic Fe grains which are exchange coupled to the hard magnetic $RE_2Fe_{14}B$ grains (exchange hardening) (Goll, Seeger and Kronmüller, 1998; Goll and Kronmüller, 2000).

which are aligned parallel to the spontaneous polarization, thus, giving rise to an induced magnetocrystalline anisotropy (Luborsky and Walter, 1977; Fujimori, Obi, Masumoto and Saito, 1976).

On the other hand, agglomerations of free or antifree volumes created during rapid quenching of the melt are rather stable with respect to annealing treatments and therefore cannot be removed completely from the material (Kronmüller, 1981b). They have their origin in the partial instability of the free volumes below the melting point. Relaxations of the dispersed free volumes by themselves result in quasi-point defects with short-range elastic stress fields varying as $1/r^3$ (Figure 7a). By a relaxation of the atomic network, the vacancy clusters may collapse locally and therefore generate planar defects which are equivalent to dislocation dipoles exerting short-range elastic stress fields varying as $1/r^2$ (Figure 7b). If the arrangement of the quasidislocation dipoles is correlated with a gradient in density along one direction, then uncompensated poles exist over large distances and also generate long-range elastic stress fields varying as $1/r$ (Figure 7c).

Local structural relaxation effects may result in magnetic aftereffects which are thermally activated processes. As shown in Figure 8(a), by a small displacement of the free

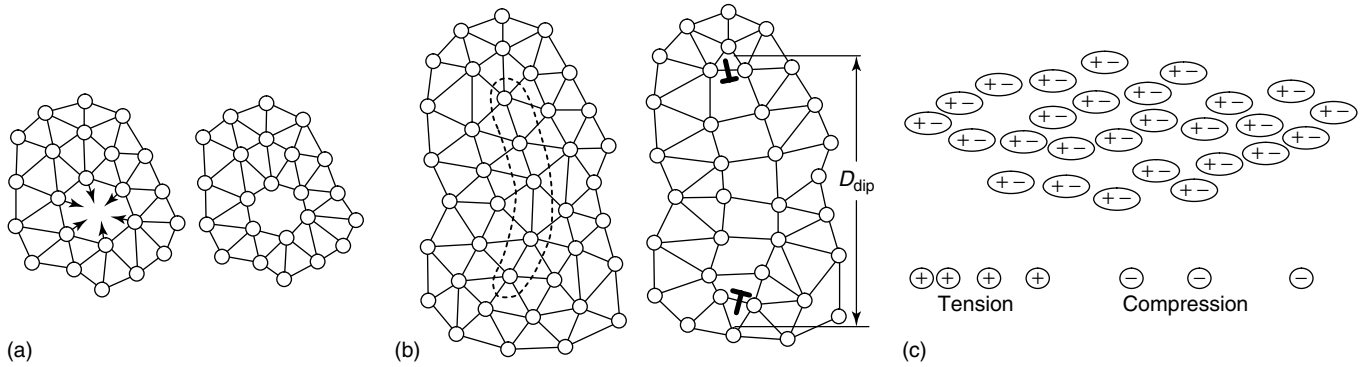

Figure 7. Agglomerations of free or antifree volumes: (a) Vacancy type defect in the unrelaxed and relaxed network model. (b) Two-dimensional model of a quasidislocation dipole formed by agglomerated free volumes. (c) Long-range stresses due to an inhomogeneous arrangement of dislocation dipoles.

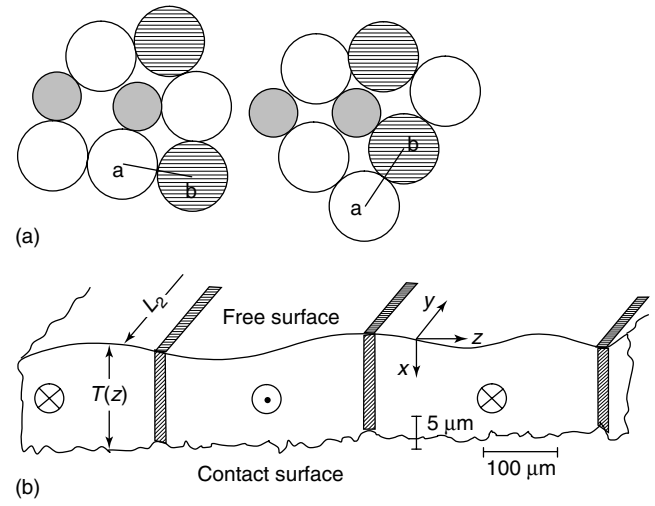

Figure 8. (a) Structural reorientation of the atom pair a–b by means of the free volume. (b) Amorphous ribbon with fluctuating thickness $T(y, z)$ showing a large surface roughness on the contact surface (wavelength $\lambda \approx 10\,\mu m$) and a weak surface roughness on the free surface (wavelength $\lambda \approx 100\,\mu m$).

volume the atom-pair axes are reoriented. Such reorientations lead to a decrease of the magnetic energy depending on the orientation of the spontaneous polarization and the atom-pair axes.

The surface irregularities due to the natural surface roughness of rapidly quenched amorphous magnets can be regarded as macroscopic defect structures. The thickness fluctuations of the ribbons are due to the uneven surface of the roller as well as inhomogeneous solidification processes on the free surface (Becker, 1981; Wang and Kronmüller, 1982). Whereas the contact surface between the ribbon and the roller according to Figure 8(b) reveals a large surface roughness, on the free surface only a weak surface roughness is observed.

4 MICROMAGNETISM AND MAGNETIZATION PROCESSES

The theory of micromagnetism (see also **General Micromagnetic Theory, Volume 2**) developed by Landau and Lifshitz (1935) and Brown (1940) is a rather effective tool for the description of magnetization processes (including magnetic domain patterns) (see also **Magnetization Configurations and Reversal in Small Magnetic Elements, Volume 2**) and characteristic properties of the hysteresis loop of ferromagnetic materials. The validity of this continuum theory ranges on a length scale which is large compared to typical atomic distances but small in comparison to macroscopic sample dimensions. With the theory of micromagnetism, the orientation of the spontaneous polarization J_s can be determined as a function of position r and external field H_{ext} by minimizing Gibbs total energy and solving the resulting micromagnetic equations.

4.1 Single-domain particles

Single-domain particles are homogeneously magnetized particles. The hysteresis loop of a single-domain particle corresponds to a rectangular loop (Figure 9a) when the magnetic field is applied parallel to the easy axis. For a certain opposite field, the nucleation field H_N, the magnetization of the particle switches spontaneous irreversibly into the opposite direction. The nucleation field depends on the type of nucleation mode that initiates the reversal of the magnetization. The three most important nucleation modes are coherent rotation, curling, and buckling. They are represented in Figure 9(c–e) for an infinite cylinder. The coherent rotation mode corresponds to homogeneous rotation of the magnetization and is characterized by vanishing exchange energy but magnetic stray field components. The curling mode corresponds to a

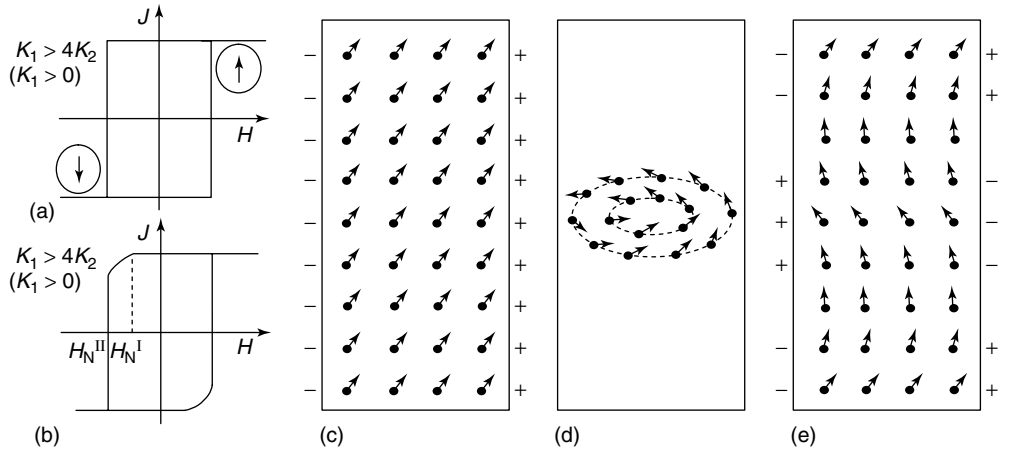

Figure 9. Hysteresis loop of a single-domain particle with easy axis parallel to the applied field: (a) $4|K_2| < |K_1|$ and (b) $4|K_2| > |K_1|$. Nucleation modes of an infinite cylinder (Frei, Shtrikman and Treves, 1957): (c) homogeneous rotation, (d) curling, and (e) buckling.

magnetization orientation perpendicular to the radial vector, that is, there exists no radial component of the magnetization anywhere in the particle, and is characterized by a vanishing stray field energy but nonvanishing exchange energy. The buckling mode corresponds approximately to homogeneous rotation for each cross section with sinusoidal variation of the amplitude along the cylinder axis where the alternating surface charges lead to an increase of the exchange energy which, however, is overcompensated by the gain in stray field energy.

The reversal process is governed by the nucleation mode with the smallest nucleation field. Therefore, the buckling mode is not important in practice.

For a single-domain particle of rotational-ellipsoidal shape and demagnetization factors $N_{||}$ and $N_\perp$ parallel and perpendicular to the easy axis the nucleation field H_N is obtained as eigenvalue of the linearized micromagnetic equations (with constant material parameters J_s, K_1, and A) (Aharoni and Shtrikman, 1958; Brown, 1963; Frei, Shtrikman and Treves, 1957):

$$H_N^{\text{coherent}} = \frac{2K_1}{J_s} - (N_{||} - N_\perp)\frac{J_s}{\mu_0}$$
$$H_N^{\text{curling}} = \frac{2K_1}{J_s} - N_{||}\frac{J_s}{\mu_0} + 2\pi k\frac{A}{R^2 J_s} \qquad (1)$$

with $k = 1.08$ for an infinite cylinder and $k = 1.38$ for a sphere. In other words, whereas the coherent rotation mode is independent of the particle size R, the nucleation field in the case of the curling mode decreases with increasing particle size. This means that for small single-domain particles, nucleation takes place by the coherent rotation process and for larger single-domain particles by the curling process. The critical particle diameter D_{crit} for which the nucleation field of both processes becomes equal is given by

$$D_{\text{crit}} = 2\sqrt{\pi k}\sqrt{\frac{2\mu_0 A}{N_\perp J_s^2}} \qquad (2)$$

A completely different reversal behavior occurs when the anisotropy constant K_2 gains in influence ($4|K_2| > |K_1|$) (Figure 9b). Then the magnetization rotates reversibly out of the easy axis at $H_N^{\text{I}} = H_N^{\text{coherent}}$ and the instability field for irreversible demagnetization is (Kronmüller, 1985; Herzer, Fernengel and Adler, 1986)

$$H_N^{\text{II}} = \frac{8K_2}{3\sqrt{3}J_s}\left(1 + \frac{K_1 + J_s^2(N_\perp - N_{||})/\mu_0}{2K_2}\right)^{3/2} \qquad (3)$$

4.2 Multidomain particles

A multidomain particle is subdivided into homogeneously magnetized domains, in which the magnetization is oriented along an easy axis. The transition region between two domains, which ranges over several lattice planes, is called domain wall. Domain formation reduces the stray field energy, whereby the gain in stray field energy is larger than the exchange energy and magnetocrystalline anisotropy energy needed for domain wall formation, because the magnetic moments in the walls are oriented neither parallel to each other nor along an easy axis. The resulting domain configuration always corresponds to a minimum total magnetic energy.

In the case of 180° domain walls separating two domains with magnetization direction oriented antiparallel to each other, two different types of domain walls may occur – Bloch walls producing surface charges and Néel walls producing volume charges (Figure 10a). The energy of the two wall

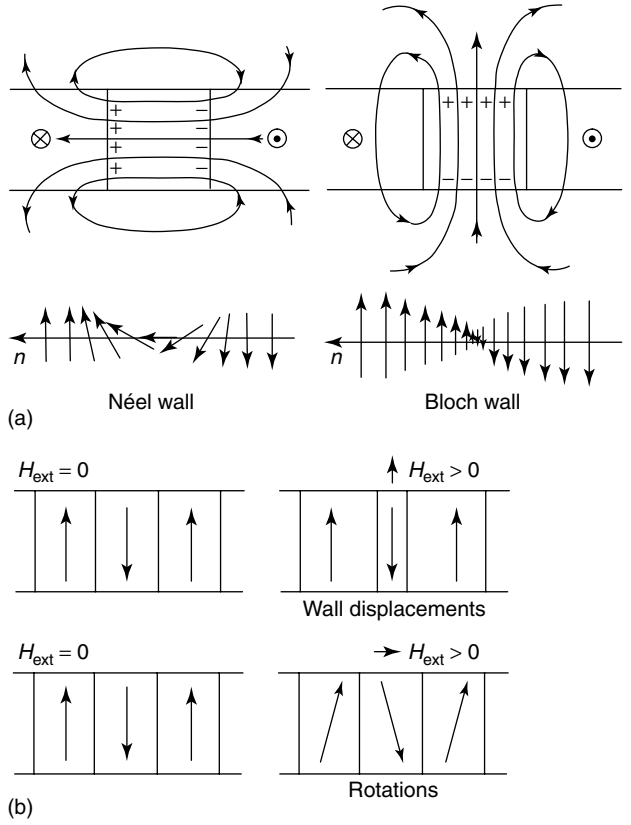

Figure 10. (a) Magnetization distribution in a Néel wall and a Bloch wall. (b) Two types of magnetization processes (wall displacements and rotations of the magnetization) due to the application of an external magnetic field.

types depend decisively on the particle dimensions. In the case of a macroscopic sample (sample dimension $\gg$ domain wall thickness), the Bloch wall is stray field free as its surface charges can be neglected. In the case of a thin film (sample dimension $\ll$ domain wall thickness), the Néel wall is stray field free as its volume charges can be neglected. According to the theory of micromagnetism the wall energy γ and the wall thickness δ are for the stray field free wall given by

$$\gamma = 4\sqrt{AK_1} \quad \text{and} \quad \delta = \pi\sqrt{A/K_1} \tag{4}$$

In general, the wall of the smallest stray field energy is energetically preferred. The critical particle dimension for which the Bloch and Néel wall become energetically equal is given by $D_{\text{crit}} = 0.14\sqrt{A/K_1}$ (Hubert, 1974) where the exchange length $l_{\text{K}} = \sqrt{A/K_1}$ is a measure for the distance over which a inhomogeneity in a homogeneous magnetization distribution is lowered to $1/e$.

By applying an external magnetic field a multidomain particle can be magnetized by two types of magnetization processes, wall displacements and rotations (Figure 10b). In the case of wall displacements, the applied field leads to a force on the domain wall so that domains which are oriented in field direction start growing at the expense of the other domains. In the case of rotations, the applied field leads to a torque $J_{\text{s}} \times H$ on the magnetization resulting in a magnetization rotation into field direction. When the magnetic field is applied perpendicular (parallel) to a lamellar domain structure, rotations (wall displacements) are dominating resulting in flat-type (more rectangular-shaped) hysteresis loops with small (large) $J_{\text{r}}/J_{\text{s}}$ ratios.

4.3 Critical particle sizes for single domain behavior

As long as the gain in stray field energy is smaller than the wall energy needed, domain formation does not occur and the single-domain state is energetically favored. This is the case for particle sizes smaller than a critical diameter D_{crit} (Kittel, 1946). For middle-hard and hard magnetic materials, the magnetic energies of the single-domain state (stray field energy) and the two-domain state (stray field energy and wall energy) become equal at $D^{\text{sd}}_{\text{crit}}$ so that the single-domain state becomes unstable and transforms into the two-domain state. For a particle of ellipsoidal shape, from the energy balance of the two states at $D^{\text{sd}}_{\text{crit}}$ (a, b: short, long axis of an ellipsoid)

$$\frac{1}{2\mu_0} N_{||} J_{\text{s}}^2 \frac{4\pi}{3} a^2 b = \pi a b \gamma_{\text{B}} + \alpha \frac{1}{2\mu_0} N_{||} J_{\text{s}}^2 \frac{4\pi}{3} a^2 b \tag{5}$$

the critical particle diameter follows as

$$D^{\text{sd}}_{\text{crit}} = 2a = \frac{3\gamma_{\text{B}}\mu_0}{N_{||}(1-\alpha)J_{\text{s}}^2} \tag{6}$$

The parameter α denotes a factor by which the stray field energy of the two-domain state is reduced compared to the single-domain state. For a spherical particle where $N_{||} = 1/3$ and $\alpha = 0.47 \approx 1/2$ (Goll, Berkowitz and Bertram, 2004) the critical particle diameter is given by $D^{\text{sd}}_{\text{crit}} = 18\gamma_{\text{B}}\mu_0/J_{\text{s}}^2$. For platelets with $N_{||} \approx 1$, D_{crit} turns out to be a factor of 3 smaller than for spherical particles. For needle-type particles with $N_{||} \ll 1$ the critical particle diameter becomes largest which makes them important for magnetic recording systems. For hollow spherical particles characterized by an inner and an outer particle diameter ($\varepsilon = D^{\text{i}}/D^{\text{o}}$) the critical particle diameter also increases for increasing ε ratios. For soft magnetic materials at D_{crit} the single-domain state transforms into a vortex state.

To guarantee thermal stability of single-domain particles for time intervals of decades the particle size must be larger than the critical diameter $D^{\text{theor}}_{\text{crit}}$. Otherwise, reversion of the polarization J_{s} is induced by the thermal fluctuation energy kT of the thermally excited spin system. According to

Néel (1950) the lifetime of a ferromagnetic particle of volume V follows an Arrhenius law $\tau = \tau_0 \exp(K_{\text{eff}} V/(kT))$ where $K_{\text{eff}} = K_1 + 1/(2\mu_0)(N_\perp - N_{||})J_s^2$ is the effective anisotropy constant of an ellipsoidal particle and τ_0 denotes the resonance relaxation time of the spin system which is approximately given by $\tau_0^{-1} = \gamma H_{\text{eff}}/(2\pi)$ (γ: gyromagnetic ratio, $H_{\text{eff}} = 2K_{\text{eff}}/J_s$). For a hard magnetic particle as FePt ($K_{\text{eff}} = 6.6 \times 10^6\,\text{J m}^{-3}$, $\tau_0 = 3.1 \times 10^{-12}\,\text{s}$) the lifetime amounts to $\tau = 0.1\,\text{s}$ for $D = 3\,\text{nm}$ and to $\tau = 10^{10}$ s for $D = 3.9\,\text{nm}$. For a soft magnetic particle as Fe ($K_{\text{eff}} = 4.6 \times 10^4\,\text{J m}^{-3}$, $\tau_0 = 6.7 \times 10^{-10}\,\text{s}$) the lifetime is given by $\tau = 0.1\,\text{s}$ for $D = 14.8\,\text{nm}$ and by $\tau = 10^{10}$ s for $D = 19.6\,\text{nm}$. In any case, there exists a very narrow range of diameters where the transition from a thermally unstable to a thermally stable state takes place.

5 HARD MAGNETIC MATERIALS: MICROMAGNETISM AND MICROSTRUCTURE

The RE-TM intermetallics (RE–Fe–B: $Nd_2Fe_{14}B$, $Pr_2Fe_{14}B$; Sm–Co: $SmCo_5$, $Sm_2(Co,Cu,Fe,Zr)_{17}$; Sm–Fe: $Sm_2Fe_{17}N_3$, $Sm_2Fe_{15}Ga_2C_2$) (see also **Rare-earth Nanocrystalline and Nanostructured Magnets, Volume 4**; **Dilute Magnetic Oxides and Nitrides, Volume 4**) are the most promising hard magnetic materials at present where the high spontaneous polarization J_s and Curie temperature T_C of the transition metals (TM = Fe, Co) are combined with high magnetocrystalline anisotropy K_1 of the rare-earth metals (RE = Nd, Pr, Sm) resulting in exceptional intrinsic magnetic properties ($J_s > 1.2$ T, $T_C > 250\,^\circ\text{C}$, $K_1 > 10^6\,\text{J m}^{-3}$). The highest $(BH)_{\max}$ values are currently supplied by the ternary intermetallics $RE_2Fe_{14}B$ (RE = Nd, Pr) ($(BH)_{\max} = 450\,\text{kJ m}^{-3}$) at room temperature and by the quinary intermetallic $Sm_2(Co,Cu,Fe,Zr)_{17}$ ($(BH)_{\max} = 100\,\text{kJ m}^{-3}$ at $400\,^\circ\text{C}$) at elevated temperatures. Hard ferrites of the type $(Ba/Sr)Fe_{12}O_{19}$ (Kojima, 1982) are considered as ceramic hard magnets with a low crystal symmetry which results in a high (uniaxial) magnetocrystalline anisotropy ($K_1 = 0.3\,\text{MJ m}^{-3}$, $J_s = 0.47$ T, $T_C = 450\,^\circ\text{C}$, $(BH)_{\max} = 23\,\text{kJ m}^{-3}$). AlNiCo magnets (Mc Currie, 1982) owe their hard magnetic properties to the shape anisotropy of small elongated ferromagnetic FeCo particles precipitated in a weakly magnetic AlNi matrix ($K_1 = 0.04\,\text{MJ m}^{-3}$, $J_s = 1.2$ T, $T_C = 860\,^\circ\text{C}$, $(BH)_{\max} = 45\,\text{kJ m}^{-3}$). FePt and CoPt based permanent magnets (Buschow, 1997) ($(BH)_{\max} = 200\,\text{kJ m}^{-3}$) reveal their high (uniaxial) magnetocrystalline anisotropies ($6.6\,\text{MJ m}^{-3}$ and $4.9\,\text{MJ m}^{-3}$, respectively) from an ordered face-centered tetragonal phase (L_{10} phase) which develops at lower temperatures from a disordered face-centered cubic phase.

Hard magnets are manufactured by two principle processing routes – sintering (see also **Rare-earth Transition-metal Magnets, Volume 4**) and melt spinning (see also **Rare-earth Nanocrystalline and Nanostructured Magnets, Volume 4**) (instead of spinning sometimes mechanical alloying or HDDR (hydrogenation, disproportionation, desorption, and recombination) are used). Sintering leads to anisotropic (textured) microcrystalline magnets with multidomain particles of size 1–20 μm whose easy axes are oriented along one direction. Sintered magnets have to be after-treated by sawing or grinding. Melt spinning results in isotropic nanocrystalline magnets with single-domain particles of size 10–200 nm whose easy axes are isotropically distributed. The nanocrystalline ribbons can be powderized and bonded with epoxy to form isotropic polymer bonded magnets of any final shape without expensive after-treatments. For nanocrystalline permanent magnets three different types of nanostructures can be distinguished: high-coercivity magnets where the grains are magnetically decoupled by a paramagnetic intergranular film; high-remanence–high-coercivity magnets where the hard magnetic grains are magnetically coupled by exchange interactions which induce a magnetic texture; and high-remanence magnets with a mixture of hard and soft magnetic grains where in addition to the effect of exchange coupling between the grains the large polarization of the soft magnetic grains also enhances the remanence by exchange hardening. All three types of nanostructures can be realized for $(Nd,Pr)_2Fe_{14}B$ based magnets by a suitable choice of the chemical composition from the phase diagram as shown in Figure 6 ($(Nd,Pr)_2Fe_{14}B$ + (Nd,Pr): decoupled magnets, $(Nd,Pr)_2Fe_{14}B$: stoichiometric magnets, $(Nd,Pr)_2Fe_{14}B$ + Fe: composite magnets). Another type of nanostructure develops in a self-organized process during a complex annealing procedure in $Sm_2(Co,Cu,Fe,Zr)_{17}$ which is illustrated in Figure 3(c) with the cell walls providing effective planar pinning sites for domain walls which may result in exceptional coercivity values up to elevated temperatures.

Owing to economic aspects, hard ferrites account for half the value of all permanent magnets worldwide. The other half of the market is mostly for RE magnets with their maximum energy products up to 15 times larger than for ferrites. Until now, sintering has been the commercially most important process. However, melt spinning combined with polymer bonding is gaining in importance, especially in the case of $RE_2Fe_{14}B$ (RE = Nd, Pr).

5.1 Coercivity

The large coercive fields of permanent magnets and, therefore, the magnetic hardening are alternatively accomplished by two basic mechanisms – reversal of the magnetization

by nucleation of reversed domains (nucleation mechanism) or reversal of the magnetization by displacement of pinned domain walls (pinning mechanism). For both hardening mechanisms the coercivity can be well described in the framework of the theory of micromagnetism by the universal relation (Kronmüller, 1987; Sagawa und Hirosawa, 1987; Kronmüller and Fähnle, 2003)

$$\mu_0 H_c = \mu_0 \alpha \frac{2K_1}{J_s} - N_{\text{eff}} J_s \tag{7}$$

where the parameters α and N_{eff} which may in turn depend on the intrinsic material parameters include the influence of the microstructure on the coercivity. The microstructure is the reason for Brown's paradox (Brown, 1945), that is, the experimentally realized coercivities as shown in Figure 11(a) in general amount a factor of $3-5$ smaller than the ideal nucleation field $\mu_0 H_N = 2K_1/J_s$ of a spherical single-domain particle whose magnetization is reversed by an irreversible homogeneous rotation process ($\alpha = 1$, $N_{\text{eff}} = 0$ in equation (7)).

Depending on the particle size the effect of the microstructure on the coercivity can be quite different (Figure 11b). Whereas in the case of nucleation hardening (single-domain range) crystal imperfections reduce the coercivity, in the case of pinning hardening (multidomain range) imperfections increase the coercivity due to the pinning effect of the domain walls. It is nowadays generally accepted that in $(Nd,Pr)_2Fe_{14}B$, $SmCo_5$ and conventional ferrite magnets the nucleation mechanism governs the coercivity, whereas in $Sm_2(Co,Cu,Fe,Zr)_{17}$ type magnets domain wall pinning processes are dominant.

For both hardening mechanisms, the demagnetization factor N_{eff} is due to the locally enhanced stray fields occurring at edges and corners of the grains which cannot be described by the demagnetizing factors $N_\perp$ and $N_{||}$ any more.

5.1.1 Nucleation

Nucleation is initiated in inhomogeneous boundary regions and occurs only for magnets consisting of single-domain nanoparticles or of micrometer-scaled multidomain particles with a small defect density. The latter particles behave (once saturated) like single-domain particles until reaching the coercivity as their nucleation field is much larger than the macroscopic demagnetizing field. In the case of nucleation hardening the microstructural parameter $\alpha = \alpha_K \alpha_\psi \alpha_{ex}$ can be subdivided into three parameters.

a Nucleation in magnetically inhomogeneous regions (parameter α_K): The crystal structure of the hard magnetic grains is not perfect throughout the grains. There exist surface

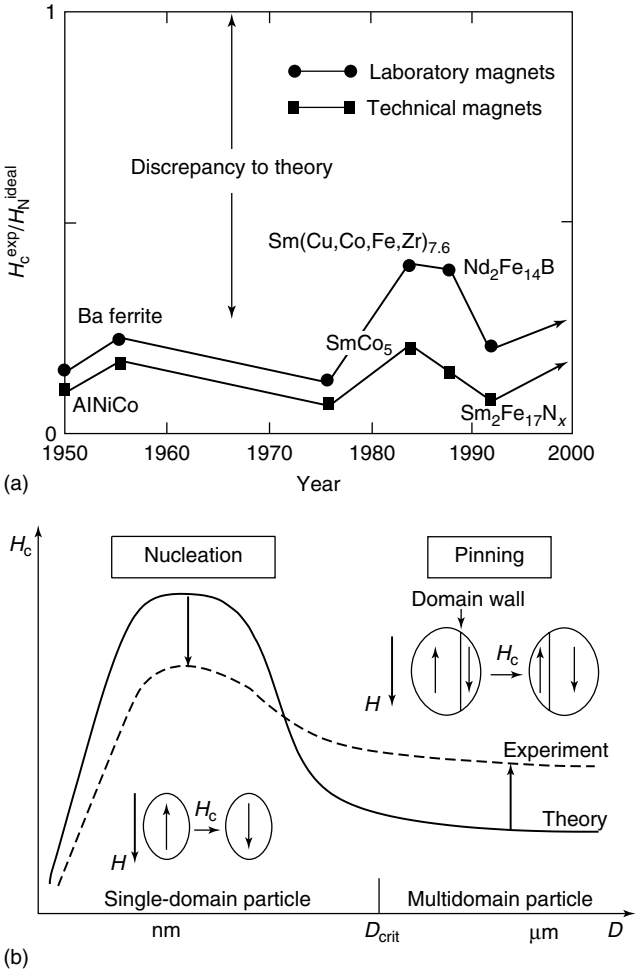

Figure 11. (a) Brown's paradox: The experimentally realized coercivities amount to a factor of $3-5$ smaller than the ideal nucleation field. (b) Schematic representation of the coercive field as a function of the particle size D (———ideal magnet with perfect particles, - - - - real magnet with imperfect particles).

regions where the atomic lattice is distorted by stresses and/or the stoichiometry has changed due to diffusion processes, especially when different phases are neighbored. As a consequence, the crystal anisotropy is locally reduced in the surface regions leading to a reduction of the nucleation field by a factor α_K (as the inhomogeneous regions influence K_1 much stronger than J_s or A, the two latter parameters can be regarded as constants). For the one-dimensional model potential

$$K_1(z) = K_1(\infty) - \frac{\Delta K}{\cosh^2(z/r_0)} \tag{8}$$

which is illustrated in Figure 12(a–b) for a planar grain boundary, the microstructural parameter α_K has been calculated analytically by Kronmüller (1987) from the

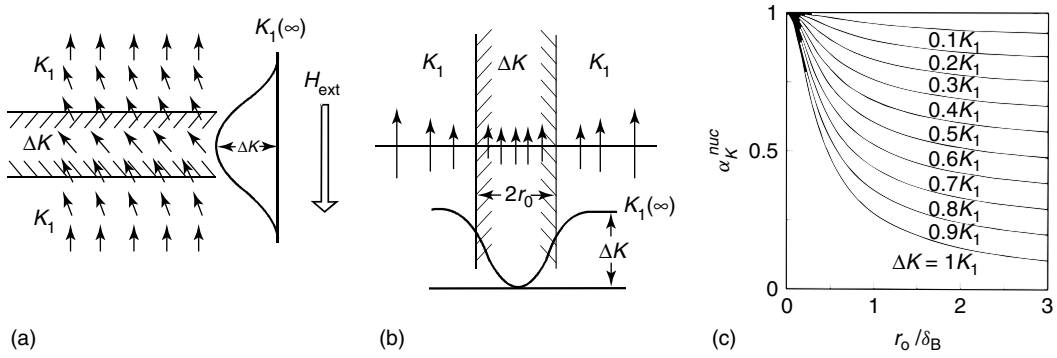

Figure 12. Nucleation of a reversed domain within a planar intergranular phase of reduced anisotropy of width $2r_0$: (a) Stripe perpendicular to the direction of the applied field. (b) Stripe parallel to the direction of the applied field. (c) Microstructural parameter α_K as a function of r_0/δ_B for different ΔK.

micromagnetic equations

$$\alpha_K = 1 - \frac{\delta_B^2}{4\pi^2 r_0^2}\left(1 - \sqrt{1 + \frac{4\pi^2 r_0^2}{\delta_B'^2}}\right)^2$$

$$= \begin{cases} 1 - \pi^2 \dfrac{\delta_B^2}{\delta_B'^4} r_0^2 & \text{for} \quad r_0 \ll \delta_B \\ \dfrac{1}{\pi}\dfrac{\delta_B^2}{\delta_B'}\dfrac{1}{r_0} + \dfrac{K_1 - \triangle K}{K_1} & \text{for} \quad 2\pi r_0 \geq \delta_B \\ \dfrac{K_1 - \triangle K}{K_1} & \text{for} \quad r_0 \gg \delta_B \end{cases} \qquad (9)$$

where $K_1 = K_1(\infty)$ is the anisotropy constant inside the grain, ΔK denotes the relative reduction at the grain surface, $2r_0$ describes the extension of the magnetic defect, $\delta_B = \pi\sqrt{A/K_1(\infty)}$ is the wall width of the perfect crystal and $\delta_B' = \pi\sqrt{A/\Delta K}$ corresponds to a fictitious wall width of a material with anisotropy ΔK. For $\Delta K \approx K_1$ the three limiting cases are given by $\alpha_K = 1 - \pi^2 r_0^2/\delta_B^2$, $\alpha_K = \delta_B/(\pi r_0)$, and $\alpha_K = 0$.

The nucleation field in the first limit corresponds approximately to the ideal nucleation field and in the third limit to the nucleation field of the inhomogeneous (soft magnetic region). For the second limit the nucleation field writes

$$H_N = \frac{2K_1}{J_s}\frac{\delta_B}{\pi r_0} - \frac{N_{eff} J_s}{\mu_0} = \frac{\gamma_B}{2J_s}\frac{1}{r_0} - \frac{1}{\mu_0} N_{eff} J_s \qquad (10)$$

where $\gamma_B = 4\sqrt{AK_1}$ describes the wall energy per unit area. In Figure 12(c), α_K is presented as a function of r_0/δ_B and for ΔK as a parameter.

b Nucleation field of misaligned grains (parameter α_ψ): If the magnetic field is applied under an angle ψ_0 with respect to the negative c axis of a uniaxial single-domain particle the nucleation field is reduced by a factor α_ψ. Owing to the misalignment the hysteresis loop shows deviations from the ideal rectangular shape as shown in Figure 13(a). The spontaneous polarization starts immediately to rotate reversibly until the rotation angle reaches the critical angle θ_N (Stoner and Wohlfarth, 1948; Kronmüller, Durst and Martinek, 1987)

$$\theta_N = \arctan\sqrt[3]{\tan\psi_0} + \frac{2}{3}\frac{K_2}{K_1 + (N_{||} - N_\perp)J_s^2/(2\mu_0)} \qquad (11)$$

where the spontaneous polarization rotates irreversibly into a direction near to the direction of the applied field. The microstructural parameter α_ψ has been determined by Stoner–Wohlfarth for $K_2 = 0$ (Stoner and Wohlfarth, 1948) and by Kronmüller for $|K_1| > 4|K_2|$ (Kronmüller, Durst and Martinek, 1987) and is given by

$$\alpha_\psi = \frac{H_N(\psi_0)}{H_N(0)} = \frac{1}{\left\{(\cos\psi_0)^{2/3} + (\sin\psi_0)^{2/3}\right\}^{3/2}} \times \left[1 + \frac{2K_2}{K_1 + (N_{||} - N_\perp)J_s^2/(2\mu_0)}\frac{(\tan\psi_0)^{2/3}}{1 + (\tan\psi_0)^{2/3}}\right] \qquad (12)$$

The condition $|K_1| > 4|K_2|$ is fulfilled for $Nd_2Fe_{14}B$, $SmCo_5$, and Sm_2Co_{17} for $T < T_C$. The angular dependence of the microstructural parameter α_ψ is shown in Figure 13(b) for a spherical $Nd_2Fe_{14}B$ particle at room temperature. Accordingly, the nucleation field shows a minimum for a misorientation angle $\psi_0 \approx 45^\circ$. This minimum nucleation field H_N^{min} has been derived explicitly by Martinek and Kronmüller (1990)

$$H_N^{min} = \frac{1}{2\sqrt{2}J_s}\left[K_1 + \frac{K_2}{4}\left(W - \frac{K_1}{K_2} + 3\right)\right] \times \sqrt{W\left(\frac{K_1}{K_2} + 1\right) - \left(\frac{K_1}{K_2}\right)^2 - \frac{2K_1}{K_2} + 3} \qquad (13)$$

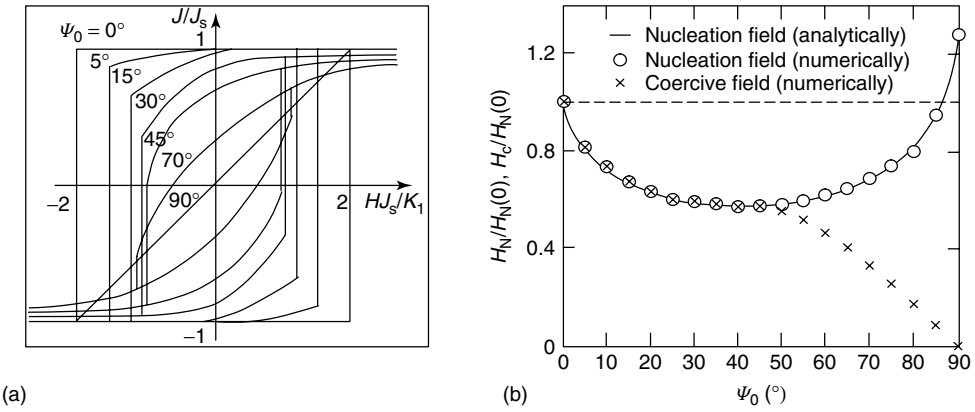

Figure 13. (a) Hysteresis loops of a single-domain particle as a function of the misorientation angle ψ_0 (after E.C. Stoner and E.P. Wohlfarth, Philosophical Transactions of the Royal Society of London, 1948, 240, pp 599–642, with permission from The Royal Society). For $\psi_0 = 90^\circ$ magnetization reversal takes place by reversible rotations ($H_c(90^\circ) = 0$). (b) Angular dependence of the nucleation field and the coercive field of a $Nd_2Fe_{14}B$ sphere in reduced units ($\alpha_\psi = H_N/H_N(0)$).

with

$$W = \pm\sqrt{\left(\frac{K_1}{K_2} + 1\right)^2 + 8} \tag{14}$$

where the + sign holds for $K_2 > 0$ and $K_1 > -2K_2$ and the − sign for $K_2 < 0$ and $K_1 > 0$. For small $|K_2|$ values ($|K_2| < 0.25\,|K_1|$) the minimum nucleation field of a spherical particle is approximately given by

$$H_N^{\min} \approx \frac{K_1 + K_2}{J_s} \tag{15}$$

Also presented in Figure 13(b) is the corresponding angular dependence of the coercive field $H_c/H_N(0)$ which coincides with the angular dependence of the nucleation field only for $\psi_0 < \pi/4$, but decreases for $\psi_0 > \pi/4$ according to $H_c = K_1/J_s \sin(2\psi_0)$ as then nucleation takes place in the third quadrant.

In the case of isotropic (decoupled) magnets with an isotropic distribution of easy axes, the average of all misalignment angles ψ_0 has to be taken for α_ψ. As $\langle\alpha_\psi\rangle$ is of the order of 0.53 in the range $30^\circ < \psi_0 < 60^\circ$ which corresponds approximately to the minimum value $\alpha_\psi^{\min} \approx 0.5$ at $\psi_0 = \pi/4$ in equation (7), α_ψ can be replaced by $\alpha_\psi^{\min} = (K_1 + K_2)/(2K_1) \approx 0.5$ or $\alpha_\psi(2K_1/J_s)$ by $H_N^{\min}$.

c Nucleation field of exchange-coupled grains (parameter α_{ex}): In the case of exchange coupling between the grains, the coercivity is further reduced as compared to exchange-decoupled grains. Possible sources contributing to this decrease of H_c are the random-anisotropy effect and strongly misaligned grains. The random-anisotropy effect (see Section 6.1) results in a reduction of the effective anisotropy constant. This effect becomes important if the grain size D is smaller than the domain wall width $\delta_B = \pi(A/K_1)^{1/2}$. However, as in the case of hard magnetic materials the condition $D < \delta_B$ is not fulfilled ($\delta_B < 5$ nm, $D \approx 10$–20 nm) so far, the random-anisotropy effect cannot become effective. In the case of strongly misaligned grains ($\pi/4 \le \psi_0 \le \pi/2$) the coercivity decreases to zero with increasing misalignment angle ψ_0 (Figure 13b) and magnetization reversal of those grains takes place mainly by reversible rotations. Due to the exchange coupling the strongly misaligned grains induce a rotation of the spontaneous polarization J_s within the neighboring grains so that the magnetization reversal is enhanced even in well-oriented grains since the critical angle θ_N is reached already for smaller fields. The reversal process in exchange-coupled grains, therefore, is a collective process where a cluster of grains becomes demagnetized by the grain of largest misalignment. As the average coercive field of strongly misaligned grains is of the order of $0.25(2K_1/J_s)$ the microstructural parameter α_{ex} is approximately given by 0.5.

d Micromagnetic analysis of nucleation processes: The micromagnetic analysis of nucleation processes and of the temperature dependence of the coercivity starts from equation (7). In general, the grains with the smallest H_c values, that is, the grains characterized by $\alpha_\psi^{\min}$, with $H_N^{\min} = \alpha_\psi^{\min} H_N$ equation (7) can be rewritten as

$$\mu_0 H_c = \alpha_K \alpha_{ex} \mu_0 H_N^{\min} - N_{eff} J_s \tag{16}$$

Consequently, if the dominant process for the magnetization reversal is the nucleation of reversed domains, plotting the temperature dependent $\mu_0 H_c(T)/J_s(T)$ values versus the temperature dependent $\mu_0 H_N^{\min}(T)/J_s(T)$ values yields a straight line. The slope and axis intersection of the straight

line correspond to the microstructural parameters $\alpha_K\alpha_{ex}$ and N_{eff}, respectively, in the case of temperature independent microstructural parameters. Hereby, $\mu_0 H_c(T)/J_s(T)$ results from hysteresis loop measurements at different temperatures in the ferromagnetic temperature range, whereas $\mu_0 H_N^{min}(T)/J_s(T)$ is determined by the intrinsic material parameters J_s, K_1, and K_2 well known from single crystals.

The validity of the nucleation model has been demonstrated for a large number of different permanent magnets. Figure 14 shows exemplarily the $\mu_0 H_c/J_s$ versus $\mu_0 H_N^{min}/J_s$ plots for sintered $SmCo_5$ and $BaFe_{12}Fe_{19}$ (Figure 14a–b) and for different types of nanocrystalline $Pr_2Fe_{14}B$ based magnets (Figure 14c) (Goll, Seeger and Kronmüller, 1998; Goll and Kronmüller, 2003; Kronmüller and Fähnle, 2003). In all cases a linear relationship is obtained. With the assumption $\alpha_{ex} = 1$ for sintered and decoupled magnets and $\alpha_{ex} \leq 1/2$ for exchange-coupled magnets, α_K values between 0.3 and 0.8 are received from the measured $\alpha_K\alpha_{ex}$ values which correspond to a width of the inhomogeneity region of $0.3\delta_B < 2r_0 < \delta_B$. For example, in the case of $SmCo_5$ with $\alpha_K = 0.33$ and $\alpha_{ex} = 1$, $2r_0$ approximately amounts to 1 nm. In the case of nanocrystalline $Pr_2Fe_{14}B$ based permanent magnets, there exists a large range of the values for $\alpha_K\alpha_{ex}$. For decoupled $Pr_2Fe_{14}B$ + Pr with overstoichiometric Pr for which $\alpha_{ex} = 1$ can be assumed, α_K values of 0.8 are obtained, whereas the exchange-coupled stoichiometric $Pr_2Fe_{14}B$ magnets and composite $Pr_2Fe_{14}B$+Fe magnets with overstoichiometric Fe show $\alpha_K\alpha_{ex}$ values between 0.06 and 0.32. The reduced values of $\alpha_K\alpha_{ex}$ reflect a reduction in coercivity and may be attributed to the small anisotropy constant of α-Fe and to the parameter α_{ex} which reduces the $\alpha_K\alpha_{ex}$ values by at least 50% due to exchange coupling between the grains inducing collective demagnetization processes of clusters of grains. Concerning the N_{eff} values large values of $N_{eff} \geq 1$ are obtained for sintered magnets, whereas the values of nanocrystalline permanent magnets range from 0 to 0.2 for exchange-coupled magnets up to 0.8 for decoupled magnets. The reasons for small N_{eff} values are both a more spherical grain shape and the fact that the locally enhanced stray fields are drastically reduced owing to the smoothing effect of the exchange interaction at the grain boundaries. It is noteworthy that for the bonded magnets nearly the same microstructural parameters are observed as for their fully dense counterpart. The validity of the nucleation model was also successfully tested for $Nd_2Fe_{14}B$, $Sm_2Fe_{17}N_x$ and $Sm_{2+\delta}Fe_{14}Ga_2C_2$-based permanent magnets (Bauer, Seeger, Zern and Kronmüller, 1996; Kronmüller and Fähnle, 2003).

5.1.2 Pinning

Pinning is connected with the existence of magnetic inhomogeneities inside the grains acting as pinning centers for domain wall motion. The pinning centers are most effective when the whole wall area is involved as is the case for planar defects or precipitations. Such defects are called repulsive (attractive) for domain walls when their wall energy is larger (smaller) than the wall energy of the surrounding matrix. In the case of pinning, hardening the microstructural parameter $\alpha = \alpha_{K,pin}\alpha_{\psi,pin}$ is a measure for the pinning strength and can be subdivided into two parameters. The parameter $\alpha_{\psi,pin}$ denotes the misorientation of the grains and is given by $\alpha_{\psi,pin} = 1/\cos\psi_0$ (Kronmüller, Durst and Sagawa, 1988) where ψ_0 is again the angle between the applied field and the negative c axis.

a Pinning by phase boundaries: At the phase boundary $z = z_0$, the intrinsic material parameters J_s, K_1, and A change abruptly from the parameters of the magnetic softer

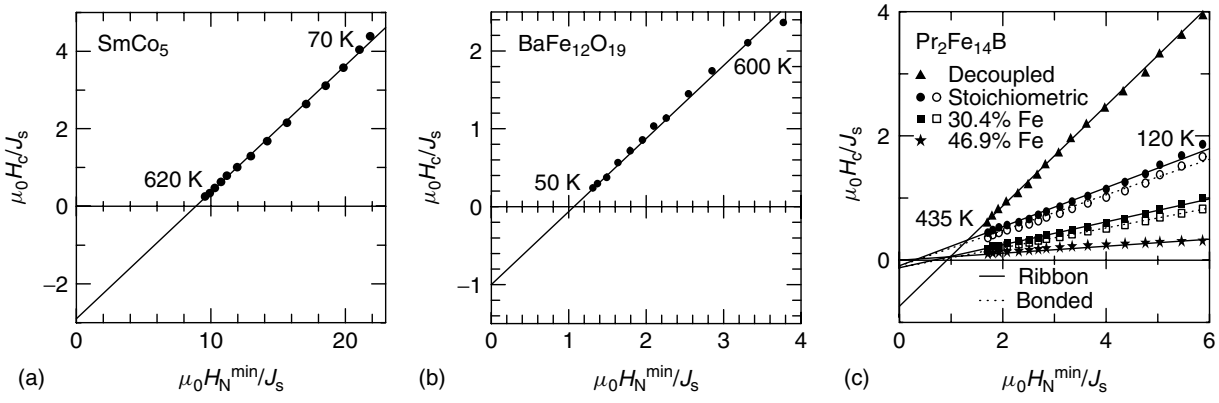

Figure 14. Plots of $\mu_0 H_c/J_s$ versus $\mu_0 H_N^{min}/J_s$ to determine the microstructural parameters $\alpha_K\alpha_{ex}$ and N_{eff}: (a) $SmCo_5$ sintered magnet ($\alpha_K = 0.33$, $N_{eff} = 2.9$), (b) Ba-ferrite sintered magnet ($\alpha_K = 0.94$, $N_{eff} = 1.0$), and (c) $Pr_2Fe_{14}B$ melt-spun magnets: decoupled ($\alpha_K = 0.8$, $N_{eff} = 0.74$), stoichiometric ($\alpha_K\alpha_{ex} = 0.32$, $N_{eff} = 0.09$), composite (30.4% Fe) ($\alpha_K\alpha_{ex} = 0.18$, $N_{eff} = 0.12$), composite (46.9% Fe) ($\alpha_K\alpha_{ex} = 0.06$, $N_{eff} = 0.0$).

phase I to the parameters of the magnetic harder phase II. A domain wall characterized by the azimuthal angle φ_0 of J_s at z_0 is pushed by an applied magnetic field against the phase boundary and moves spontaneously from phase I into phase II when the coercivity is reached (Figure 15). Minimizing the total energy of this domain wall configuration results in the coercivity (Kronmüller and Goll, 2002)

$$\mu_0 H_c = \mu_0 \frac{2K_1^{II}}{J_s^{II}} \frac{1 - \varepsilon_K \varepsilon_A}{(1 + \sqrt{\varepsilon_A \varepsilon_J})^2} \tag{17}$$

$$\cos \varphi_0^{crit} = \frac{\sqrt{\varepsilon_A \varepsilon_J} - 1}{\sqrt{\varepsilon_A \varepsilon_J} + 1} \tag{18}$$

with the ratios $\varepsilon_A = A^I/A^{II}$, $\varepsilon_K = K_1^I/K_1^{II}$, and $\varepsilon_J = J_s^I/J_s^{II}$. The coercive field vanishes for $\varepsilon_K \varepsilon_A = 1$ and particularly for $\varepsilon_A = \varepsilon_K = 1$, that is, if phase I and phase II are equivalent with respect to K_1 and A. For $\varepsilon_J \varepsilon_A = 1$ the critical angle becomes $\varphi_0^{crit} = \pi/2$, that is, equal parts of the 180° domain wall are located in phase I and phase II. If phase I corresponds to a soft magnetic phase ($\varepsilon_K = 0$), H_c is given by

$$\mu_0 H_c = \mu_0 \frac{2K_1^{II}}{J_s^{II}} \frac{1}{(1 + \sqrt{\varepsilon_A \varepsilon_J})^2} \tag{19}$$

In hard magnetic materials large spontaneous polarizations and Curie temperatures guarantee large energy products and excellent temperature stability. The suitable condition therefore is $\varepsilon_J = \varepsilon_A = 1$ for which the coercive field writes

$$\mu_0 H_c = \mu_0 \frac{2K_1^{II}}{J_s^{II}} (1 - \varepsilon_K) \tag{20}$$

and becomes maximum for $\varepsilon_K = 0$, then corresponding to one-quarter of the ideal nucleation field.

b Pinning by narrow planar defects: A narrow planar defect is composed of N individual crystal planes of distance d. Its extension $r_0 = N\,d$ is smaller than the domain wall width and each plane is characterized by a local anisotropy constant K_1^i and a local exchange constant $A_{i,i+1}$. For calculating the coercive field the domain wall is divided into three regions as illustrated in Figure 15(b). Then the unperturbed regions I and III (anisotropy constant K_1, exchange constant A) can be treated by the continuum theory of micromagnetism (Kronmüller, 1973; Friedberg and Paul, 1975), whereas in region II which contains the defect, the individual crystal planes are treated by the discrete Heisenberg model (Hilzinger and Kronmüller, 1975; Hilzinger, 1977). Minimizing the total energy of this planar configuration leads to the following coercivity

$$\mu_0 H_c = \mu_0 \frac{\pi}{3\sqrt{3}} \frac{2K_1}{J_s} \alpha_{\psi,pin} \frac{d}{\delta_B} \left| \sum_{i=1}^{N-1} \left(\frac{A}{A_{i,i+1}} - \frac{K_1^i}{K_1} \right) \right|$$

$$- N_{eff} J_s = \mu_0 \alpha_{\psi,pin} \alpha_{K,pin} \frac{2K_1}{J_s} - N_{eff} J_s \tag{21}$$

If the material parameters of all perturbed layers are identical ($K_1^i = K_1^*$, $A_{i,i+1} = A^*$) equation (21) results in

$$\mu_0 H_c = \mu_0 \frac{\pi}{3\sqrt{3}} \alpha_{\psi,pin} \frac{Nd}{\delta_B} \left| \frac{A}{A^*} - \frac{K_1^*}{K_1} \right| \frac{2K_1}{J_s} - N_{eff} J_s \tag{22}$$

and the parameter $\alpha_{K,pin}$ increases linearly with increasing r_0/δ_B (Figure 17).

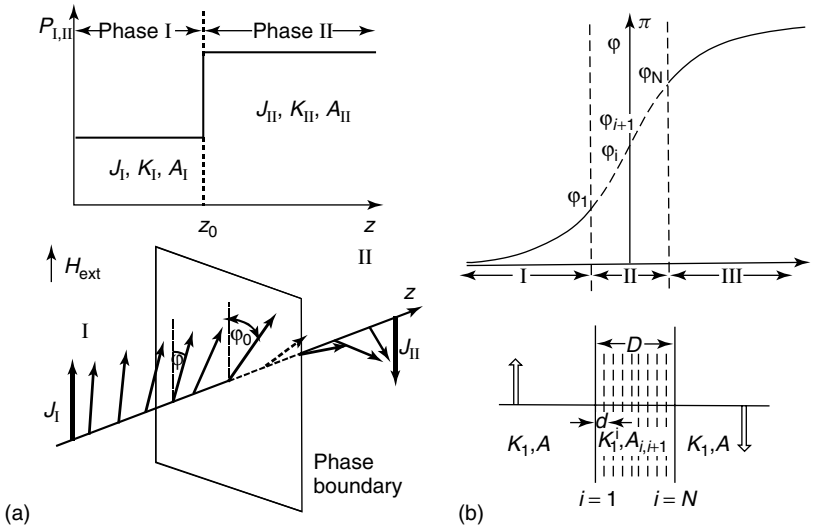

Figure 15. (a) Micromagnetic model of an ideal phase boundary with abrupt changes of the material constants and spin configuration of a domain wall pressed against the phase boundary. (b) Discrete model of a domain wall interacting with a narrow planar defect of N net planes.

c Pinning by extended planar defects: If the extension of the planar defect r_0 is larger than the domain wall width δ_B the coercive field is given by

$$\mu_0 H_c = \mu_0 \frac{1}{2J_s} \alpha_{\psi,\mathrm{pin}} \left. \frac{\mathrm{d}\gamma_B(z)}{\mathrm{d}z} \right|_{\max} - N_{\mathrm{eff}} J_s \qquad (23)$$

where $\left. \mathrm{d}\gamma_B(z)/\mathrm{d}z \right|_{\max}$ describes the maximum slope of the wall energy $\gamma_B(z) = 4\sqrt{AK_1(z)}$. For a linear change of $\gamma_B(z)$ between two phases I and II $\left. \mathrm{d}\gamma_B(z)/\mathrm{d}z \right|_{\max}$ is given by $\left|\gamma_{II} - \gamma_I\right| / r_0$. For the model potential of equation (8) the coercivity given by equation (23) results in

$$\begin{aligned} \mu_0 H_c &= \mu_0 \frac{2K_1(\infty)}{J_s} \frac{2\delta_B}{3\pi r_0} \alpha_{\psi,\mathrm{pin}} - N_{\mathrm{eff}} J_s \\ &= \mu_0 \frac{\gamma_B}{3J_s} \frac{1}{r_0} \alpha_{\psi,\mathrm{pin}} - N_{\mathrm{eff}} J_s \end{aligned} \qquad (24)$$

with $\alpha_{K,\mathrm{pin}} = 2\delta_B/(3\pi r_0)$, that is, with increasing r_0/δ_B, the parameter $\alpha_{K,\mathrm{pin}}$ decreases according to a $1/r_0$ law (Figure 17).

d Domain wall bowing: If a planar defect is interrupted, domain walls can bow and pass the inhomogeneity when the applied field reaches a critical value. According to Kronmüller and Hilzinger (1976) in the case of an interruption length d_{il} and one-dimensional bowing processes, the coercivity is given by

$$\mu_0 H_c = \mu_0 \frac{\pi}{\sqrt{2} J_s^{\mathrm{defect}}} \gamma^{\mathrm{matrix}} \frac{1}{d_{il}} \qquad (25)$$

e Micromagnetic analysis of pinning processes: In the case of high-temperature $Sm_2(Co,Cu,Fe,Zr)_{17}$ hard magnets, the temperature dependence of H_c is narrowly connected to the magnetic material parameters of the cell 2:17 and the cell wall 1:5 phases. Information about these material parameters is obtained from the analysis of the distribution of the five elements Co, Sm, Fe, Cu, Zr within the cells and the cell walls which has been performed by high-resolution energy dispersive X-ray (EDX) measurements (Goll, Kleinschroth, Sigle and Kronmüller, 2000; Goll, Kronmüller and Stadelmaier, 2004).

A quantitative description of $H_c(T)$ starts from equation (17). With the temperature dependencies of the intrinsic material parameters J_s, K_1, and A for the cell 2:17 (index I) and the cell wall 1:5 (index II)

$$\begin{aligned} J_s^{\mathrm{I,II}}(T) &= c_J^{\mathrm{I,II}}(1 - T/T_C^{\mathrm{I,II}})^{\beta}; \\ K_1^{\mathrm{I,II}}(T) &= c_K^{\mathrm{I,II}}(1 - T/T_C^{\mathrm{I,II}})^{3\beta}; \\ A^{\mathrm{I,II}}(T) &= c_A^{\mathrm{I,II}}(1 - T/T_C^{\mathrm{I,II}})^{2\beta} \end{aligned} \qquad (26)$$

where β denotes the critical exponent ($\beta = 0.5$: molecular field theory, $\beta = 0.365$: Heisenberg model) and $c_x^{\mathrm{I,II}}$ is

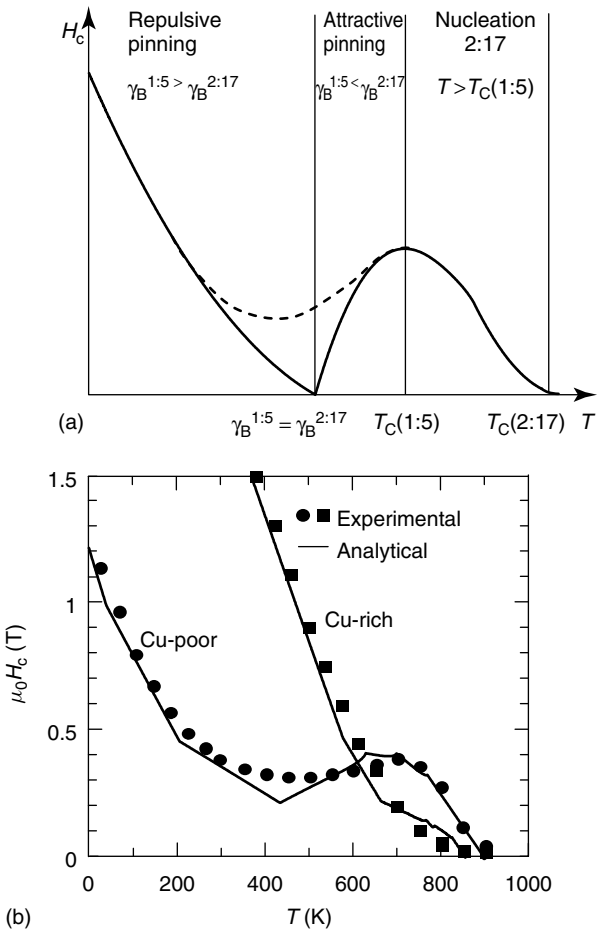

Figure 16. (a) Schematic temperature dependence $H_c(T)$ according to equation (27) showing the three ranges of repulsive and attractive pinning as well as the high-temperature nucleation range. (b) Conventional (Cu-rich cell walls) and anomalous (Cu-poor cell walls) $H_c(T)$ behavior of $Sm_2(Co,Cu,Fe,Zr)_{17}$ magnets.

related to the material constants at $T = 0$, the coercivity can be rewritten as (Kronmüller and Goll, 2003)

$$\begin{aligned} \mu_0 H_c(T) = \mu_0 \frac{2c_K^{\mathrm{II}}}{c_J^{\mathrm{II}}} \left(1 - \frac{T}{T_C^{\mathrm{II}}}\right)^{2\beta} \\ \times \frac{1 - \varepsilon_{KA} \left(\frac{1 - T/T_C^{\mathrm{I}}}{1 - T/T_C^{\mathrm{II}}}\right)^{5\beta}}{\left[1 + \left\{\varepsilon_{AJ} \left(\frac{1 - T/T_C^{\mathrm{I}}}{1 - T/T_C^{\mathrm{II}}}\right)^{3\beta}\right\}^{1/2}\right]^2} \end{aligned} \qquad (27)$$

with the parameters $\varepsilon_{KA} = c_K^{\mathrm{I}} c_A^{\mathrm{I}} / c_K^{\mathrm{II}} c_A^{\mathrm{II}}$ and $\varepsilon_{AJ} = c_A^{\mathrm{I}} c_J^{\mathrm{I}} / c_A^{\mathrm{II}} c_J^{\mathrm{II}}$. The expression allows a quantitative discussion of the temperature dependence of H_c (Figure 16a) As in general $\varepsilon_{KA} < 1$, $\varepsilon_{AJ} > 1$ and $T_C^{\mathrm{I}} > T_C^{\mathrm{II}}$ holds, two crossover temperatures exist. At low temperatures ($\varepsilon_A \varepsilon_K < 1$, $\varepsilon_A \varepsilon_J \approx 1$) H_c is determined by repulsive pinning at the cell walls leading

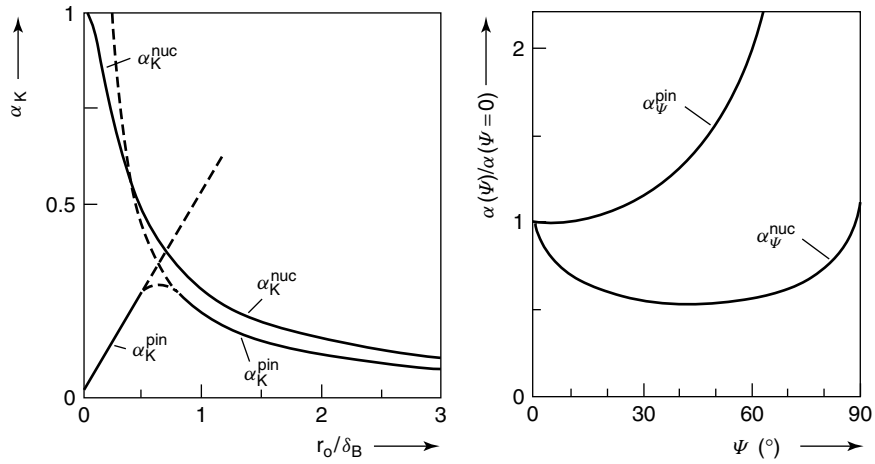

Figure 17. (a) Comparison of the α_K parameters for pinning and nucleation in planar defects of width r_0 as a function of r_0/δ_B (Kronmüller, Durst and Sagawa, 1988). (b) Comparison of the α_ψ parameters for pinning and nucleation as a function of the misorientation angle ψ_0. (Kronmüller *et al*., 1988/1987.)

to a monotonous decrease of H_c with increasing temperature. At intermediate temperatures repulsive pinning changes into attractive pinning in the cell walls at $\varepsilon_{KA} < 1$, $\varepsilon_{AJ} = 1$ with K_1^{II} becoming smaller than K_1^{I} because $T_C^{I} > T_C^{II}$ holds. In this temperature range, the indices I and II have to be exchanged in equations (26) and (27) and $H_c(T)$ may increase up to a maximum value at $T = T_C^{I}$. At the Curie temperature of the cell wall phase, the matrix pyramids become single-domain particles being magnetically isolated by thin paramagnetic cell walls. Accordingly, for higher temperatures the coercive field is determined by the nucleation field $(2K_1^{2:17}/J_s^{2:17})\alpha$ of the 2:17 cells and therefore decreases.

In Figure 16(b) by the superposition of the three $H_c(T)$ curves for varying parameters ε_{KA} and ε_{AJ} and average Curie temperatures the experimental result of a positive and a negative temperature gradient dH_c/dT could be nicely explained (Goll, Kronmüller and Stadelmaier, 2004).

5.1.3 Comparison of the hardening mechanisms

The type of hardening mechanism can be determined in principle from the temperature dependence of the coercivity. In Figure 17, the microstructural parameters α_K and α_ψ are compared with each other for the nucleation and pinning mechanism. Whereas for $\alpha_K > 0.3$ nucleation is the only reversal mechanism which may occur, for $\alpha_K < 0.3$ nucleation and pinning may take place. Consequently, the maximum coercivity of pinning-hardened magnets amounts to 30% of the ideal nucleation field. In the case of the microstructural parameter α_ψ, with increasing misorientation angle α_ψ increases for pinning-hardened magnets and shows a minimum at $\psi_0 = 45^\circ$ for nucleation hardened magnets. Another distinguishing feature is the initial magnetization curve. Whereas for pinning-hardened magnets the magnetization increases rather slowly for small applied fields due to the pinning of domain walls, the magnetization increases rapidly for nucleation hardened magnets consisting of multidomain particles in the thermally demagnetized state. As a consequence, in the latter case the saturation is achieved for smaller fields.

5.1.4 Others

In the phenomenological nucleus expansion model ('global model') (Givord and Rossignol, 1996) a preformed nucleus of reversed polarization expands due to thermal activation within the lifetime of the reversed nucleus which follows an Arrhenius equation $\tau = \tau_0 \exp(-\Delta E/kT)$ where τ_0 is of the order of 10^{-11} s and $\Delta E(t) = kT \ln(t/\tau_0) \approx 25\,kT$ ($t \approx 1$–10^3 s) corresponds to the activation enthalpy necessary for the spontaneous expansion of the nucleus by overcoming the magnetic enthalpy. If the nucleus is characterized by its surface area s, its volume v, and its domain wall energy γ_B', at the coercive field H_c the energy balance between ΔE and the magnetic enthalpy consisting of domain wall energy, magnetostatic energy of the external field at H_c and the demagnetization energy is given by

$$s\gamma_B' - J_s H_c v - \frac{1}{\mu_0} N_{eff} J_s^2 v = 25kT \qquad (28)$$

As the nucleus forms in perturbed regions the specific wall energy γ_B' of the nucleus can be related to the ideal wall energy γ_B of the perfect crystal by $\gamma_B' = \alpha_B \gamma_B = 4\sqrt{AK_1}\alpha_B$ with the microstructural parameter $\alpha_B < 1$. Similarly, the

nucleus surface can be related to the nucleus volume by $s = \alpha_s v^{2/3}$ where α_s corresponds to a geometrical factor given by $\alpha_s = (36\pi)^{1/3} = 4.84$ for a sphere and by $\alpha_s = (\pi \cot\theta)^{1/3}/\cos\theta$ for a cone with apex angle θ. With these substitutions the following expression can be derived from equation (28) for the coercivity

$$\mu_0 H_c = \mu_0 \frac{\alpha_s \alpha_B \gamma_B}{J_s v^{1/3}} - J_s N_{eff} - \mu_0 \frac{25kT}{v J_s} \qquad (29)$$

As the nucleus volume is related to the wall width $\delta_B = \pi\sqrt{AK_1}$ as $v = \alpha_v^3 \delta_B^3$ equation (29) can be rewritten as

$$\mu_0 H_c = \mu_0 \frac{\alpha_s \alpha_B}{\alpha_v} \frac{1}{J_s} \frac{\gamma_B}{\delta_B} - J_s N_{eff} - \mu_0 \frac{25kT}{v J_s}$$
$$= \mu_0 \frac{2K_1}{J_s} \frac{2\alpha_s \alpha_B}{\pi \alpha_v} - J_s N_{eff} - \mu_0 H_f \qquad (30)$$

with the thermal fluctuation field $\mu_0 H_f = \mu_0 25kT/(vJ_s)$ which corresponds to 5–10% of the coercive field. The microstructural parameters α_s and α_B can be obtained from plotting $\mu_0(H_c + H_f)/J_s$ versus $\mu_0 \gamma_B/(J_s^2 v^{1/3})$ where H_c, v, and H_f are received experimentally and J_s and γ_B are given by the intrinsic material parameters. In Figure 18(a) (Becher, Seeger and Bauer, 1998) the temperature dependence of the activation volume of different types of magnets is shown. Figure 18(b) (Becher, *et al.* 1998) shows the plots from which the microstructural parameters $\alpha_s\alpha_B$ and N_{eff} can be derived. From equation (30) it becomes obvious that the coercivity due to nucleus expansion is described by the same type of equation as in the case of nucleation. The only difference between the two models seems to be that the nucleation model is based on the micromagnetic equations, whereas the nucleus expansion model starts from an empirical energetic approach which corresponds just to the integrated micromagnetic equations. Although the parameters α_s, α_B, and α_v can be identified with the parameters α_K and α_{ex} as $4\alpha_s\alpha_B/\pi\alpha_B \equiv \alpha_K\alpha_{ex}$ it has to be noted that the nucleus expansion model turns out to be incompatible with the real microstructure. As the measured activation volumes v are of the order of $300\,\text{nm}^3$ the grain boundaries would extend over a width of $5\delta_B \approx 20\,\text{nm}$. In contrast, according to the nucleation model the reversal of the polarization starts in regions of width 0.5–2 nm which is in excellent agreement with the real microstructure. Furthermore, the microstructural parameters α_s, α_B, and α_v are less defined. In particular, their temperature dependence is unknown and can only be quantified by further assumptions on the nucleus shape (González *et al.*, 1994). Naturally, the thermal fluctuation field can also be introduced into the nucleation model as a further term which reduces the nucleation field. However, normally the thermal fluctuation field can be neglected as it corresponds only to 5–10% of the coercivity and the micromagnetic energy terms are dominating.

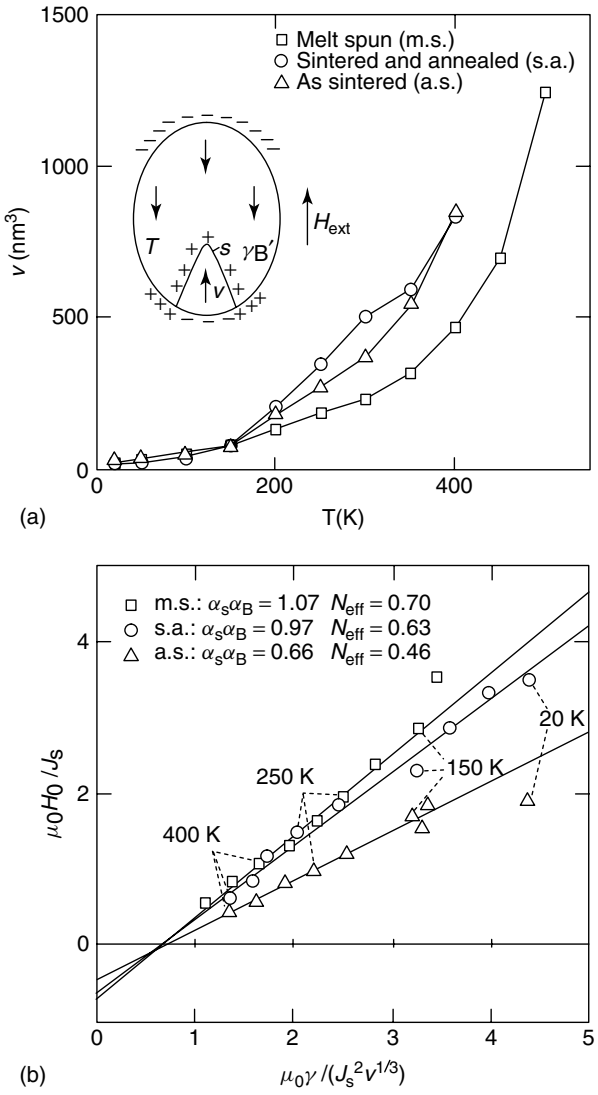

Figure 18. (a) Temperature dependence of the activation volume of three different types of $Nd_2Fe_{14}B$ based magnets. The inset illustrates the spike-type nucleus of volume v, surface area s, and wall energy γ'_B (Becher, Seeger and Bauer, 1998). (b) Corresponding plots to determine $\alpha_s\alpha_B$ and N_{eff} according to the global model (Becher, Seeger and Bauer, 1998).

5.2 Remanence and $(BH)_{max}$

Depending on the degree of the texture the remanence varies between $J_r \approx J_s$ in the case of a perfect orientation of the easy axes along one direction and $J_r = 0.5 J_s$ in the case of an isotropic orientation of the easy axes and magnetically decoupled grains. In the case of exchange-coupled grains, a magnetic texture is induced within a region

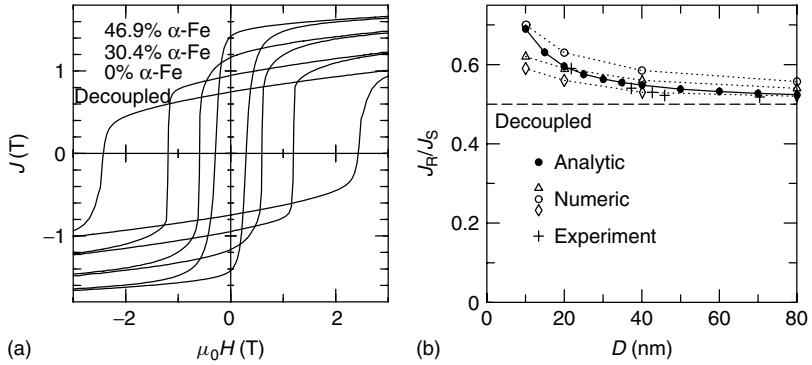

Figure 19. (a) Remanence enhancement in nanocrystalline stoichiometric and composite $Pr_2Fe_{14}B$ + α-Fe isotropic magnets compared to a nanocrystalline decoupled $Pr_2Fe_{14}B$ + Pr isotropic magnet (Goll, Seeger and Kronmüller, 1998). The corresponding nanostructures are shown in Figure 6. (b) Grain-size dependence of the reduced remanence of $Nd_2Fe_{14}B$ according to equation (31) in comparison with numerical (Δ, $\circ$: directly contacted grains; *diamond*: $A_{gb} = A/10$ (width of grain boundaries: 3 nm) and experimental results. (Reproduced from D. Goll: 'Micromagneticism and microstructure – tailoring of high performance magnets', *Z Metallkunde* **93**, (2002) 1009–1017, with permission of Carl Hanser Verlag.)

of $\delta_B = \pi(A/K_1)^{0.5} = \pi l_K$ at the grain boundaries with the texture axis parallel to the direction of the applied field involving a significant remanence enhancement compared to decoupled magnets (Figure 19a). The influence of the exchange coupling on the remanence can be expressed analytically by using a simple micromagnetic model which describes the exchange coupling between two neighboring grains in analogy to a Bloch wall. From minimizing the total magnetic Gibbs energy the remanence of stoichiometric magnets is obtained as

$$J_r \approx \frac{1}{2} J_s + 1.5 \frac{J_s}{D} l_K \tag{31}$$

Here, the first term (*Stoner–Wohlfarth* term) denotes the decoupled contribution to the remanence, whereas the second one describes the remanence enhancement effect due to exchange coupling at the grain boundaries. Accordingly, J_r of an exchange-coupled single-phase magnet is determined by the average grain size D and the intrinsic material parameters J_s, K_1, and A of the grains. For a given material, the remanence enhancement increases with decreasing grain sizes. In Figure 19(b) (Goll, 2002), the grain-size dependence of the reduced remanence according to equation (31) is compared for $Nd_2Fe_{14}B$ to that calculated numerically for a three-dimensional ensemble of hard magnetic exchange coupled grains as well as to the experimental data obtained by Manaf, Buckley, Davies and Leonowicz (1991). Consequently, for an efficient remanence (and therefore $(BH)_{max}$) enhancing effect, the grain size should be smaller than 20 nm. In composite magnets the remanence (and therefore $(BH)_{max}$) is further increased as the large spontaneous polarization of α-Fe ($J_s = 2.15$ T) significantly intensifies the magnetic texturing effect (Figure 19a). For a complete exchange hardening of the soft magnetic grains, it is imperative that the grain size of the soft magnetic grains is of the order of twice the Bloch wall width δ_B of the hard magnetic phase.

6 SOFT MAGNETIC MATERIALS: MICROMAGNETISM AND MICROSTRUCTURE

Crystalline soft magnetic materials (see also **Advanced Soft Magnetic Materials for Power Applications, Volume 4**) as permalloy, sendust, Fe–Si-transformer steel and MnZn ferrites are characterized by a low magnetocrystalline anisotropy and a low magnetostriction (at least for a certain temperature). In order to achieve large initial susceptibilities (or initial permeabilities) and small coercivities in these materials, defect structures should be reduced as much as possible. As some of these materials have a low critical shear stress, plastic deformations are serious sources for deteriorating the soft magnetic properties.

Amorphous soft magnetic materials (see also **Amorphous Alloys, Volume 4**; **Soft Magnetic Bulk Glassy and Bulk Nanocrystalline Alloys, Volume 4**) are mainly based on transition metal–metalloids with compositions near $(Fe, Co, Ni)_{80}(B, Si, C)_{20}$ and are commonly divided into two major groups: iron-based and Co-based alloys. The Fe-based amorphous alloys (e.g., $Fe_{67}Co_{18}B_{14}Si$) are based on inexpensive raw materials, have a high saturation polarization ($J_s =$ 1.1–1.8 T), but their magnetostriction ($\lambda_s \approx 30 \times 10^{-6}$) is large which limits their soft magnetic behavior. By adding Ni, for example, $Fe_{40}Ni_{40}P_{14}B_6$ or $Fe_{40}Ni_{40}B_{20}$, the saturation polarization and at the same time the magnetostriction become smaller. The Co-based amorphous alloys, for example, $Co_{71}Fe_1Mo_1Mn_4Si_{14}B_9$ reveal nearly zero magnetostriction ($\lambda_s < 3 \times 10^{-7}$), therefore offering a superior

soft magnetic behavior, but their saturation polarization is by a factor of 2 lower than that of the Fe-based materials. Amorphous alloys are produced mainly by rapid quenching ($\sim 10^6\,\mathrm{K\,s^{-1}}$) from the melt or by either sputtering or evaporation. They allow a wide range of property variation, for example, the initial permeability can be varied continuously from $\mu_i \approx 1000$ to $\mu_i \approx 300\,000$. Disadvantages of all amorphous alloys are their thermal instability and a low Curie temperature.

Nanocrystalline soft magnetic materials (see also **Soft Magnetic Materials – Nanocrystalline Alloys, Volume 4**) consist of ultrafine grains with an average size of ∼5–15 nm which are embedded in an amorphous matrix. They are prepared by crystallization of amorphous melt-spun ribbons (with the addition of Cu and Nb) during annealing. The volume ratio of the nanocrystalline phase can be controlled by the annealing temperature and ranges between 50 and 80%. The most widely investigated alloy is $Fe_{73.5}Cu_1Nb_3Si_{13.5}B_9$ (Yoshizawa, Oguma and Yamauchi, 1988; Herzer, 1996) which combines the highest achievable permeabilities ($\mu_i \approx 200\,000$) with the simultaneously highest saturation polarizations ($J_s \approx 1.2$–1.3 T) and which is also characterized by vanishing anisotropy (due to exchange softening) and a near zero magnetostriction ($\lambda_s < 1 \times 10^{-7}$). Nanocrystalline soft magnets are more stable above room temperature and have a larger remanence as compared to amorphous Co-based soft magnets, whereas the large electrical resistivity ($\rho = 100$–$130\,\mu\Omega$cm) and the low losses are of the same order. The only drawback of nanocrystalline soft magnets is the severe embrittlement upon crystallization.

In Figure 20(a) the typical initial permeabilities and saturation polarizations are presented for amorphous, nanocrystalline, and crystalline soft magnetic alloys with nonzero magnetostriction.

6.1 Coercivity and permeability

In soft magnetic materials the domain walls interact with a large number of (statistically distributed) defects, for example, for a dislocation density of $10^{10}\,\mathrm{cm^{-2}}$ there are 10^4 dislocations within a domain wall of cross section $10^{-6}\,\mathrm{cm^2}$, and the interaction force has to be determined by statistical methods. The quantities which have to be determined by statistics are coercive field H_c and the initial susceptibility χ_0 (or initial permeability μ_i) and the Rayleigh constant α_R of the Rayleigh (1887) law $J = \chi_0\mu_0 H + \alpha_R(\mu_0 H)^2$ which describes the reversible (first term) and the irreversible (second term) part of magnetization at small fields. Initial permeability and coercivity obey a reciprocal relationship so that materials with low coercivity necessarily have a high initial permeability and vice versa.

In soft magnetic materials the coercivity sensitivity depends on the grain size D. According to Figure 20(b), good soft magnetic properties are received for amorphous magnets for nanocrystalline magnets with grain sizes smaller than 20 nm and for (micro)crystalline magnets with very large grain sizes $D > 100\,\mu$m.

6.1.1 Models

The models of the statistical pinning potential (Kronmüller, 1970; Kronmüller and Fähnle, 2003) and of the random anisotropy (Alben, Becker and Chi, 1978; Herzer, 1990) are effective tools to describe the hysteresis loops of soft magnetic materials.

a Statistical pinning potential: The defects in soft magnetic materials cause a statistically fluctuating Bloch-wall potential or field of force as shown in Figure 21(a) which is the reason for irreversible domain wall movements and therefore for

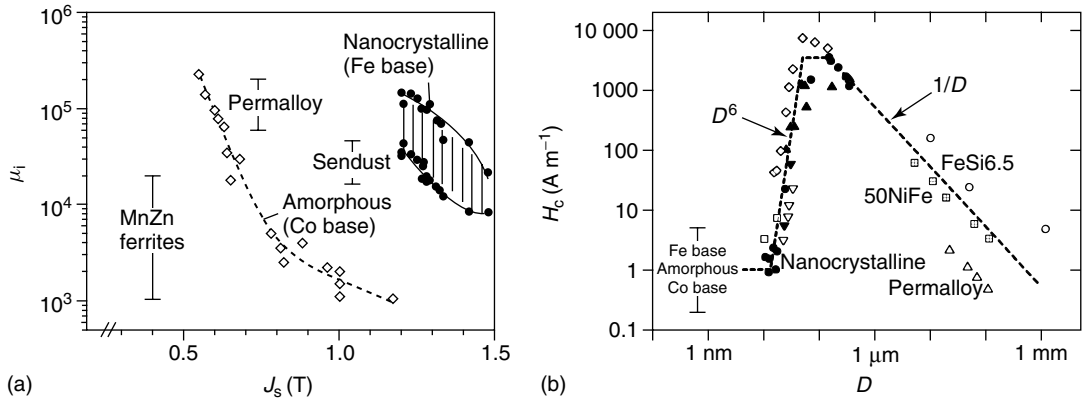

Figure 20. (a) Typical initial permeabilities μ_i and saturation polarizations J_s for a variety of soft magnetic materials (Petzold, 2002). (Reproduced from Petzold *et al*., 2002, with permission from Elsevier. © 2002.) (b) Dependence of the coercivity H_c on the grain size D for soft magnetic materials showing the amorphous, nanocrystalline, and microcrystalline regions (Herzer, 1995). (Reproduced from Herzer *et al*., 1999, with permission from Elsevier. © 1999.)

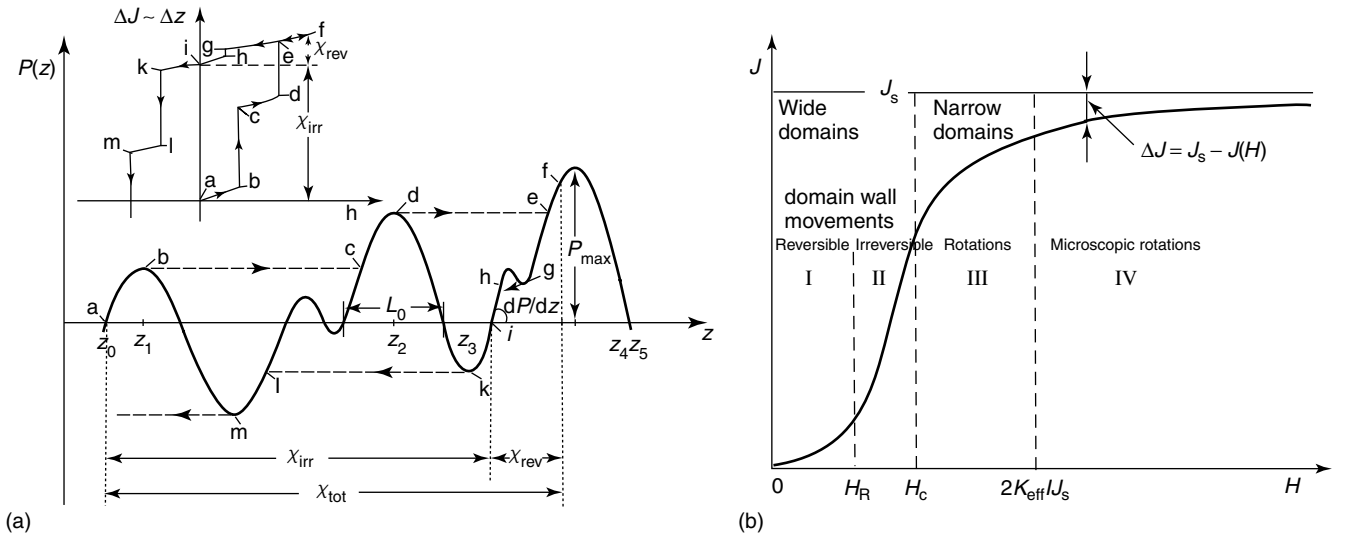

Figure 21. (a) Characteristic parameters of the statistical field of force acting on a domain wall. The broken line indicates reversible and irreversible displacements of the domain wall. With increasing (decreasing) field, a domain wall moves from a to f (f to m). The inset shows schematically the corresponding hysteresis loop resulting from the reversible (χ_{rev}) and irreversible (χ_{irr}) magnetization processes. (b) Schematic magnetization curve with four characteristic regions of magnetization processes.

the hysteresis loop. By applying a magnetic field a domain wall is reversibly displaced in its potential valley and reaches a force maximum at a certain field value, then performing a spontaneous irreversible Barkhausen jump (Barkhausen, 1919) to the next higher force maximum, and so on. According to Figure 21(b), four characteristic regions of magnetization processes can be distinguished as a function of the applied magnetic field. In region I ($0 < H < H_{\mathrm{R}}$, $H_{\mathrm{R}} < 0.1H_{\mathrm{c}}$) magnetization occurs by displacements of domain walls which can be described by Rayleigh's law. In region II ($0.1H_{\mathrm{c}} < H < H_{\mathrm{c}}$) magnetization takes place by large irreversible Barkhausen jumps and the permeability reaches its maximum value. In region III ($H_{\mathrm{c}} < H < 2K_{\mathrm{eff}}/J_{\mathrm{s}}$) narrow domain regions as closure domains are magnetized parallel to the applied field by domain wall displacements and by rotational processes. In region IV ($H > 2K_{\mathrm{eff}}/J_{\mathrm{s}}$) magnetization approaches to saturation and occurs by microscopic reversible rotations in regions of inhomogeneous spin states around defect structures. Similarly, the coercivity can be regarded as the field strength for which demagnetization via large Bloch wall jumps over force maxima become possible.

In a quantitative description, the total force acting on a rigid domain wall is given by the sum extending over all defects

$$P(z) = \sum_j p(z - z_j) \tag{32}$$

where $p(z - z_j)$ describes the individual force of a defect at position z_j acting on a domain wall at position z and z is the coordinate parallel to the domain wall normal. According to Figure 21(a) the statistical field of force $P(z)$ is characterized by the averages of the wavelength $2L_0$ which is defined as twice the distance between neighboring zero positions of $P(z)$ and which is independent of the defect density, of the maximum $P_{\max}$ and of the reciprocal slopes $1/R = 1/(\mathrm{d}P/\mathrm{d}z)$ at $P(z) = 0$. When the total force $P(z)$ obeys a Gaussian distribution function f, the probability of finding an interaction force between P and $P + \mathrm{d}P$ or a slope $R = \mathrm{d}P/\mathrm{d}z$ between R and $R + \mathrm{d}R$ is given by

$$f(P) = \frac{1}{\sqrt{2\pi}\,B_0} \exp\left(-\frac{P^2}{2B_0}\right);$$
$$f(R) = \frac{1}{\sqrt{2\pi}\,B_1} \exp\left(-\frac{R^2}{2B_1}\right) \tag{33}$$

where B_0 and B_1 are the correlation functions which are related to the individual interaction forces as follows:

$$B_0 = \frac{F_{\mathrm{B}}N}{L_3} \int_{-L_3/2}^{L_3/2} \left[p^2(z) - \langle p(z)\rangle^2\right] \mathrm{d}z;$$
$$B_1 = \frac{F_{\mathrm{B}}N}{L_3} \int_{-L_3/2}^{L_3/2} \left\{\left[\frac{\mathrm{d}\,p(z)}{\mathrm{d}\,z}\right]^2 - \left\langle\frac{\mathrm{d}\,p(z)}{\mathrm{d}\,z}\right\rangle^2\right\} \mathrm{d}\,z \tag{34}$$

with F_{B} the domain wall area, L_3 the domain wall distance, and N the defect density. In this case, the characteristic parameters of the statistical potential are correlated with the

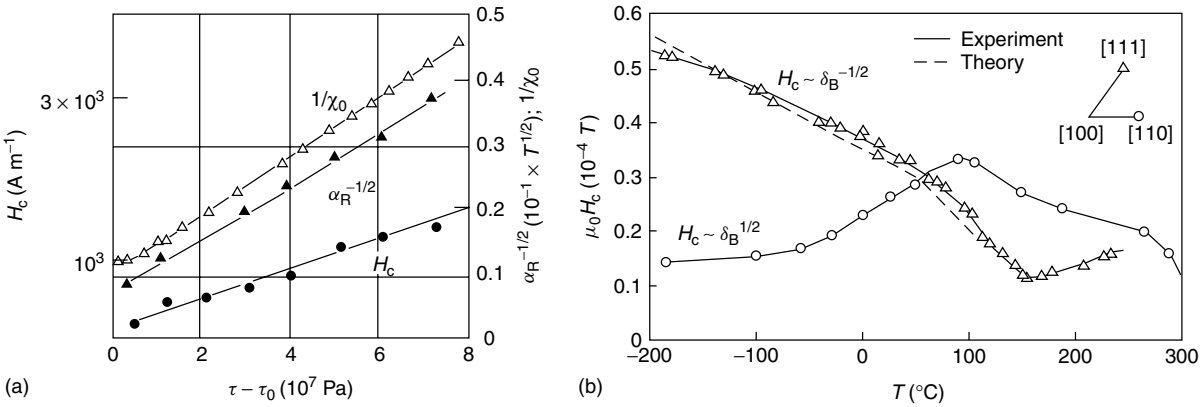

Figure 22. (a) Dependence of H_c, χ_0, and α_R on the dislocation density N of a plastically deformed Ni single crystal. N is related to the applied flow stress τ by $\tau-\tau_0=0.36\,Gb(Nl)^{1/2}$ (τ_0: initial flow stress, G: shear modulus, b: Burgers vector, l: dislocation line strength interacting with a domain wall) (Kronmüller, 1972). (Reproduced from H. Kronmüller: 'Magnetic techniques for the study of dislocations in ferromagnetic materials' in *Internat J Nondestr. Testing*, **3** (1972) 315–350, with permission from Taylor & Francis Ltd, www.informaworld.com.) (b) Temperature dependence of the coercive field of Ni single crystals owing to dislocations ($\propto \delta_B^{1/2}$) in the as-grown crystal and to dislocation dipoles ($\propto \delta_B^{-1/2}$) after heavy neutron irradiation. The broken line corresponds to the theoretical prediction for $H_c(T)$ of dislocation dipoles (Kronmüller, 1966). (Reproduced from H. Kronmüller: 'Magnetisierungskurve der Ferromagnetike' in A. Seeger (ed): *Moderne Probleme der Metallphysik*, vol. 2 (Springer, Berlin, 1966), with permission of Spruigner Science and Business Media.)

correlation functions in the following way:

$$\overline{2L_0}=2\pi\sqrt{\frac{B_0}{B_1}};\quad \overline{\frac{1}{R}}=\sqrt{\frac{\pi}{2B_1}};\quad \overline{P}_{\max}=\sqrt{\frac{B_0}{2\pi}} \tag{35}$$

and the relationship of the coercive field H_c as well as of the initial susceptibility χ_0 and the Rayleigh constant α_R to these parameters is obtained as

$$\mu_0 H_c=\frac{\mu_0\sqrt{\pi}}{J_s F_B\left|\cos\varphi_0\right|}\overline{P}_{\max}\sqrt{\frac{\ln L_3}{2L_0}};$$

$$\chi_0=\frac{(2J_s\cos\varphi_0)^2 F_B}{\mu_0 L_3}\overline{\frac{1}{R}};\quad \alpha_R=\frac{\left|2J_s\cos\varphi_0\right|^3 F_B^2}{(2\mu_0\pi)^2}\frac{L_0}{L_3}\frac{1}{(\overline{P}_{\max})^3} \tag{36}$$

where φ_0 is the angle between the applied field and J_s within the domains. The combination of equation (35) with equation (36) leads to the following relations between H_c, χ_0, and α_R

$$\frac{\chi_0 H_c}{J_s}=\frac{\sqrt{\pi}}{2\mu_0}\left|\cos\varphi_0\right|\frac{L_0}{L_3}\left(\ln\frac{L_3}{2L_0}\right)^{1/2};$$

$$\mu_0\frac{\alpha_R H_c}{\chi_0}=\frac{8}{3\sqrt{\pi}}\left(\ln\frac{L_3}{2L_0}\right)^{1/2};$$

$$\frac{\chi_0^2}{J_s\alpha_R}=\frac{3\pi}{16}\frac{L_0}{L_3}\left|\cos\varphi_0\right| \tag{37}$$

where the average wavelength is approximately given by $2L_0\approx 2\delta_B$. From equations (34, 35, 36) the dependence of H_c, χ_0, and α_R on the defect density is predicted as $H_c\propto N^{1/2}$, $\chi_0\propto 1/N^{1/2}$, and $\alpha_R\propto 1/N$ which has been tested successfully for plastically deformed Ni single crystals as shown in Figure 22(a) where the interaction force is proportional to the magnetoelastic stresses of the domain wall.

b Random anisotropy: In an ensemble of exchange-coupled grains (size D, volume fraction v) with a random distribution of the easy directions the polarization cannot abruptly follow the changes of the easy direction. Within a range of the exchange length $l_K=\sqrt{A/K_1}$ the polarization rotates into the direction of the easy axis. For $l_K>D$ the polarization is not able to follow the easy axes of the individual grains, but is increasingly forced to align parallel by exchange interaction. Consequently, for $l_K>D$ an averaging over the $N=v(l_K/D)^3$ grains lying within the volume $(l_K)^3$ takes place and the resulting effective anisotropy constant $\langle K\rangle$ and effective exchange length l_K^{eff} are given by

$$\langle K\rangle\approx v\frac{K_1}{\sqrt{N}}=\sqrt{v}K_1\left(\frac{D}{l_K^{\text{eff}}}\right)^{3/2}=v^2\frac{K_1^4}{A^3}D^6$$

$$=v^2K_1\left(\frac{D}{\delta_B}\right)^6\pi^6;\quad l_K^{\text{eff}}=\sqrt{\frac{A}{\langle K\rangle}} \tag{38}$$

For example, for grain sizes $D\approx l_K/3\approx 10$–15 nm the magnetocrystalline anisotropy K_1 is reduced by 3 orders of magnitude to a few joule per cubic meter and the effective exchange length l_K^{eff} becomes 2 orders of magnitude larger than the exchange length l_K. In nanocrystalline $Fe_{73.5}Cu_1Nb_3Si_{13.5}B$ indeed wide domain widths of

approximately 2 µm could be observed by high-resolution Kerr effect studies (Schäfer, Hubert and Herzer, 1991). If additionally a significant macroscopic anisotropy K_u exists resulting from shape anisotropy, induced anisotropy, or magnetoelastic anisotropy the total averaged anisotropy can be written as (Herzer and Varga, 2000)

$$\langle K \rangle = K_u + \frac{1}{2} v \sqrt{K_u K_1} \left(\frac{D}{l_K^{eff}} \right)^3 \tag{39}$$

The expressions for the random anisotropy, which are valid for uniaxial and cubic crystals, can be used to determine χ_0 and H_c of nanocrystalline soft magnetic materials.

6.1.2 Application to (single-)crystalline materials

In (single-)crystalline soft magnetic materials dislocations, dislocation dipoles and point defects or impurity atoms act as pinning centers for domain walls. Dislocations have a magnetostrictive interaction with domain walls due to the elastic interaction energy of the magnetostrictive elastic stresses of the domain wall and the longer-range elastic stresses of the dislocations. In many cases, the dislocation structure of plastically deformed materials is composed of dislocation dipoles which may be formed by cyclic deformation or by agglomerations of vacancies or interstitial atoms.

For dislocations, dislocation dipoles, and point defects the temperature dependence of H_c and χ_0 is determined by the intrinsic material parameters J_s, K_1, A, and the magnetostriction λ_s. In the case of individual dislocations the temperature dependence of H_c and χ_0 is given by

$$H_c(T) \propto \frac{\lambda_s}{J_s} \left(\frac{A}{K_1} \right)^{1/4} \sqrt{N} \propto \delta_B^{1/2};$$
$$\chi_0(T) \propto \frac{J_s^2}{\lambda_s} \left(\frac{A}{K_1} \right)^{1/4} \frac{1}{\sqrt{N}} \propto \delta_B^{1/2} \tag{40}$$

with the same dependence of H_c and χ_0 on δ_B, that is, the pinning effect decreases with decreasing wall width δ_B. However, with increasing magnetostriction λ_s and dislocation density N, χ_0 decreases, whereas H_c increases. The Rayleigh constant α_R is independent of δ_B and its temperature dependence on the magnetic material parameters is given by $\alpha_R \propto J_s^3/(\lambda_s^2 N)$. As according to equation (36) α_R is inversely proportional to L_3, with increasing domain wall density α_R increases. In the case of dislocation dipoles (and point defects), the temperature dependence of H_c follows the law

$$H_c(T) \propto \frac{\lambda_s}{J_s} \left(\frac{K_1}{A} \right)^{1/4} \sqrt{N} \propto \delta_B^{-1/2} \tag{41}$$

and the interaction force increases with decreasing wall width δ_B. The initial susceptibility χ_0 decreases according to a $\delta_B^{3/2}$ law with decreasing wall width δ_B.

For Ni single crystals the $\delta_B^{1/2}$ and the $\delta_B^{-1/2}$ dependence of H_c has been measured as illustrated in Figure 22(b). The temperature dependence of H_c in as-grown single crystals is owing to dislocations as main pinning centers and to dislocation dipoles after heavy neutron irradiation. As K_1 increases with decreasing temperature, H_c decreases in the case of dislocations and increases in the case of dislocation dipoles with decreasing temperature.

6.1.3 Application to nanocrystalline materials

In nanocrystalline soft magnetic materials, the macroscopic magnetocrystalline anisotropy reveals very small or virtually zero due to the random-anisotropy effect. For grains with diameters smaller than the wall width, the hysteresis loops typically show an enhanced remanence ($J_r/J_s > 0.90$) and the coercivity H_c and the initial susceptibility χ_0 are closely related to $\langle K \rangle$ by

$$H_c = P_c \frac{\langle K \rangle}{J_s} \propto D^6; \quad \chi_0 = P_\chi \frac{J_s^2}{\mu_0 \langle K \rangle} \propto D^{-6} \tag{42}$$

with the parameters $P_c = 0.96$ and $P_\chi = 0.33$ for uniaxial grains and $P_c = 0.94$ and $P_\chi = 0.33$ for cubic grains and $K_1 > 0$. For the Rayleigh constant α_R a D^{-12} law holds due to equations (37). In Figure 23 the D^6, D^{-6} and D^{-12}-law for H_c, χ_0, and α_R have been tested for different nanocrystalline iron-based alloys (Herzer, 1997).

In nanocrystalline magnets, the magnetization process takes place by domain wall displacements for $D < l_K^{eff}$ and by rotational processes for $D > l_K^{eff}$: The selfconsistency conditions for domain wall displacements and rotational processes respectively are given by

$$\frac{\chi_0 H_c \mu_0}{J_s} = \frac{\sqrt{\pi}}{2} v \frac{\delta_B}{L_3} \left(\ln \frac{L_3}{2\delta_B} \right)^{1/2};$$
$$\frac{\chi_0 \mu_0 H_c}{J_s} = P_c P_\chi \approx 0.32 \tag{43}$$

where in the first relation v corresponds to the relative volume and the domain walls are oriented parallel to the applied field and the second relation holds for uniaxial and cubic symmetry. By plotting $\chi_0 H_c \mu_0 / J_s$ the type of magnetization processes can be analyzed as shown in

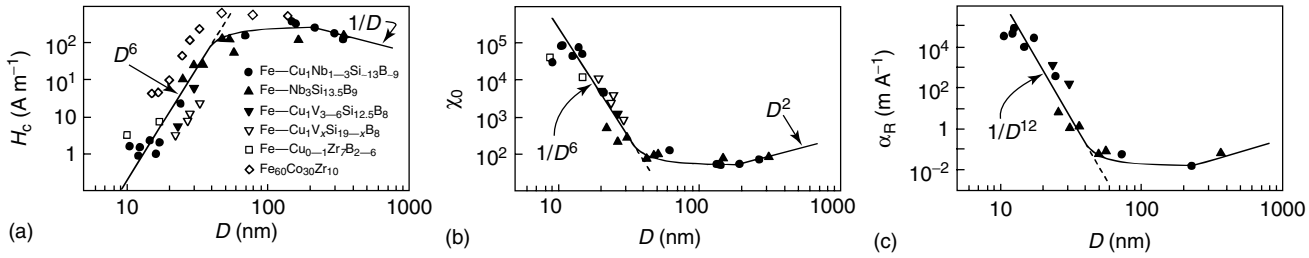

Figure 23. Coercivity H_c (a), initial susceptibility χ_0 (b), and Rayleigh constant α_R (c) of nanocrystalline iron-based alloys as a function of the grain size D showing the predicted D^6, D^{-6}, and D^{-12}-dependencies. (Reproduced from Herzer 1997, with permission from Elsevier. © 1997.)

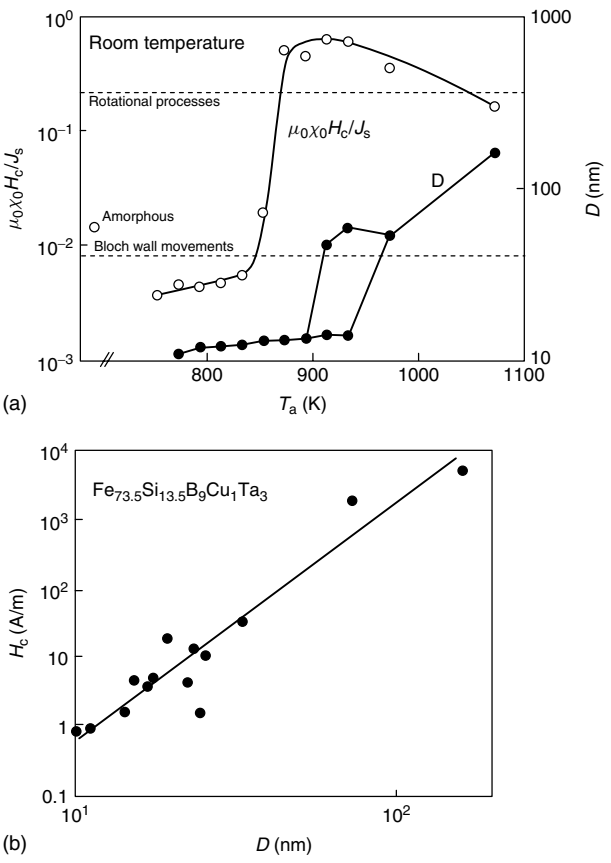

Figure 24. (a) $\mu_0\chi_0H_c/J_s$ as a function of the grain size controlled by the annealing temperature compared with predictions for domain wall displacements and rotational processes (Hofmann, Reininger and Kronmüller, 1992). (b) Dependence of the coercivity on the grain size D for $Fe_{73.5}Si_{13.5}Nb_3Cu_1B_9$ with uniaxial induced anisotropy ($H_c = 2.9 \times 10^{-4} d^{3.35}$ A m^{-1}). (Reproduced from Murillo & González 2000, with permission from Elsevier. © 2000.)

Figure 24(a) for nanocrystalline $Fe_{73.5}Si_{13.5}Nb_3Cu_1B_6$ (Hofmann, Reininger and Kronmüller, 1992). For annealing temperatures $T_A < 850$ K ($D < l_K^{eff}$) domain wall displacements occur, whereas for $T_a > 900$ K ($D > l_K^{eff}$) rotational processes take place.

For grains with diameters significantly larger than the wall width ($D \gg l_K^{eff}$, $D > 100$ nm) domains can be formed within the grains and H_c and χ_0 are given by Kronmüller and Hilzinger (1976)

$$H_c = \frac{2\gamma_B}{J_s \cos\varphi_0}\frac{1}{D}; \quad \chi_0 = \frac{2}{3}\frac{J_s^2 \cos\varphi_0 D^2}{4\pi\mu_0\gamma_B L_3} \qquad (44)$$

where φ_0 is the angle between the applied field and the polarization within the domains. Then the magnetization process takes place by the bowing of domain walls at grain boundaries. In Figure 23 for large D the $1/D$ and D^2 law for H_c and χ_0 have been obtained for different nanocrystalline iron-based alloys.

In the case of an appreciable macroscopic-induced anisotropy, according to equation (39), H_c obeys a D^3 law which has been experimentally confirmed by Murillo and González (2000) and by Suzuki, Herzer and Cadogan (1998) as shown in Figure 24(b).

6.1.4 Application to amorphous materials

In amorphous alloys at least five pinning effects for domain walls may contribute to the total coercivity (Kronmüller, 1981a; Kronmüller and Fähnle, 2003). These contributions are intrinsic fluctuations (H_c^i) which give rise to a lower limit of the coercivity, short-range-ordered effects (H_c^{cl}) and relaxation effects (H_c^{rel}) both of which may be minimized by a suitable annealing treatment, surface effects (H_c^{surf}) which can be minimized by extremely smooth surfaces and internal stress sources (H_c^{σ}) interacting with domain walls which can only be reduced significantly by using nonmagnetostrictive alloys. Within the framework of the statistical potential theory the contributions due to statistically distributed types of pinning centers add quadratically whereas the effect of relaxation processes has to be added linearly because each domain wall is submitted to a stabilization energy with wavelength $2L_0$. Thus, the total coercivity is given by

Kronmüller (1981a)

$$H_c^{\text{total}} = \left[(H_c^{\sigma})^2 + (H_c^{\text{surf}})^2 + (H_c^{\text{cl}})^2 + (H_c^{\text{i}})^2\right]^{1/2} + H_c^{\text{rel}} \tag{45}$$

In the special case where the contribution of the pinning due to surface irregularities is larger than all other contributions, the different terms add linearly as the wavelength of the surface pinning is much larger ($\approx$10 µm) than that of the intrinsic fluctuations (<0.5 µm). In the following text, the five contributions are ordered with increasing influence on H_c.

a Intrinsic fluctuations: The intrinsic fluctuations of exchange interactions and local anisotropies due to the non-periodic atomic arrangement may act as pinning centers for domain walls. In general, the statistical fluctuations of an intrinsic material parameter $P(\mathbf{r})$ is the sum of the volume average $\langle P(\mathbf{r})\rangle$ and the fluctuating part $\delta P(\mathbf{r})$ of the parameter

$$P(\mathbf{r}) = \langle P(\mathbf{r})\rangle + \delta P(\mathbf{r}) \tag{46}$$

If a domain wall is exposed to fluctuations of the local anisotropy energy $\delta K(r)$ and of the exchange energy $\delta A(r)$ the resulting intrinsic coercive field is given by Kronmüller (1981b)

$$\mu_0 H_c^{\text{i}} = \frac{\sqrt{\pi}}{M_s}\frac{\sqrt{\rho_M}\langle\Omega\rangle}{\sqrt{2F_B\delta_B}} \times \left(\frac{8}{15}\langle\delta K^2\rangle + \frac{11}{15}\langle\delta A^2\rangle\frac{\pi^4}{\delta_B^4}\right)^{1/2}\left(\ln\frac{L_3}{2L_0}\right)^{1/2} \tag{47}$$

where ρ_M corresponds to the density of magnetic ions and $\langle\Omega\rangle$ to the average atomic volume. For statistical independent fluctuations $\langle\delta K^2\rangle$ and $\langle\delta A^2\rangle$ may be replaced by $\langle K^2\rangle$ and $\langle A^2\rangle$. Depending on the material parameters $\mu_0 H_c^{\text{i}}$ of amorphous soft magnetic materials amounts to 10^{-7}–10^{-4} mT (e.g., Fe: $\mu_0 H_c^{\text{i}} = 3.2\times10^{-5}$ mT).

b Clusters of chemical short-range-ordered regions: The formation of chemical short-range-ordered clusters which are characterized by the number n_{cl} of atoms per cluster results in an enhancement of the intrinsic coercive field by a factor $\sqrt{n_{\text{cl}}}$ (Kronmüller, 1981a)

$$\mu_0 H_c^{\text{cl}} = \mu_0 H_c^{\text{i}}\sqrt{n_{cl}} \tag{48}$$

Depending on the material parameters $\mu_0 H_c^{\text{cl}}$ is smaller than 10^{-4} mT.

c Surface irregularities: The natural surface roughness of amorphous ribbons may also influence the coercivity. A planar domain wall of lateral extension L_2 in y direction (Figure 8b) moving through a ribbon of thickness $T(z)$ therefore changes its domain wall area as a function of position z. Its total energy and the force exerted on it may be written as

$$\phi_\gamma(z) = \gamma_B L_2\langle T(z)\rangle;$$
$$P^{\text{surf}}(z) = -\gamma_B L_2\frac{\mathrm{d}}{\mathrm{d}z}\langle T(z)\rangle \tag{49}$$

where $\langle T(z)\rangle$ corresponds to the statistical average of T in y direction and γ_B is the specific wall energy. For a sinusoidal z dependence $\langle T(z)\rangle = \langle T\rangle + \Delta T\sin(2\pi z/\lambda)$ (λ: wavelength of the surface irregularities, ΔT: amplitude of the surface irregularities) the surface coercive field is given by Kronmüller (1981a)

$$\mu_0 H_c^{\text{surf}} = \frac{\pi}{M_s}\frac{\Delta T}{\langle T\rangle}\gamma_B\sqrt{\rho_s}\sqrt{\frac{L_2}{2\lambda}\ln\left(\frac{L_3}{2L_0}\right)} \propto \frac{1}{\langle T\rangle} \tag{50}$$

where $\rho_s \leq \lambda^2$ denotes the number of surface pinning centers per unit area. The increase of H_c^{surf} with decreasing $\langle T\rangle$ after several surface pretreatments is shown in Figure 25(a). The increase is largest for grinding with glasspaper and smallest for electropolished samples. $\mu_0 H_c^{\text{surf}}$ normally amounts to 10^{-4}–10^{-3} mT.

d Relaxation effects: Domain wall mobility is furthermore affected by the magnetic aftereffects. As the relaxations are thermally activated, the mobility of the domain walls becomes time dependent. The reorientation of atom-pair axes within the domain wall into energetically more favorable orientations results in a stabilization of the domain wall. The additional field required to overcome this statistical force field is the time-dependent coercive field of relaxation (Kronmüller, 1981a)

$$\mu_0 H_c^{\text{rel}}(t) = \text{const}\frac{\varepsilon_p^2\rho_p}{kT}(1 - \mathrm{e}^{-t/\tau}) \tag{51}$$

where ρ_p is the atom-pair density reorienting with a relaxation time τ and ε_p is the interaction energy of atom pairs with the spontaneous polarization. If the displacement of domain walls can be described by the statistical potential theory H_c^{rel} can be derived from the fundamental relation

$$\chi_0(t)H_c(t) \approx \frac{J_s\delta_B}{L_3} \tag{52}$$

Accordingly, a relaxation $\Delta\chi$ of the initial susceptibility χ_0 is related to an increase ΔH_c of the coercive field as given by

$$H_c^{\text{rel}}(t) = \Delta H_c(t) = -\frac{\Delta\chi(t)}{\chi_0}H_c(0) \tag{53}$$

where $H_c(0)$ is the unrelaxed coercivity. As experimentally the relative relaxation $\Delta\chi/\chi_0$ was found to vary from 0.05 to

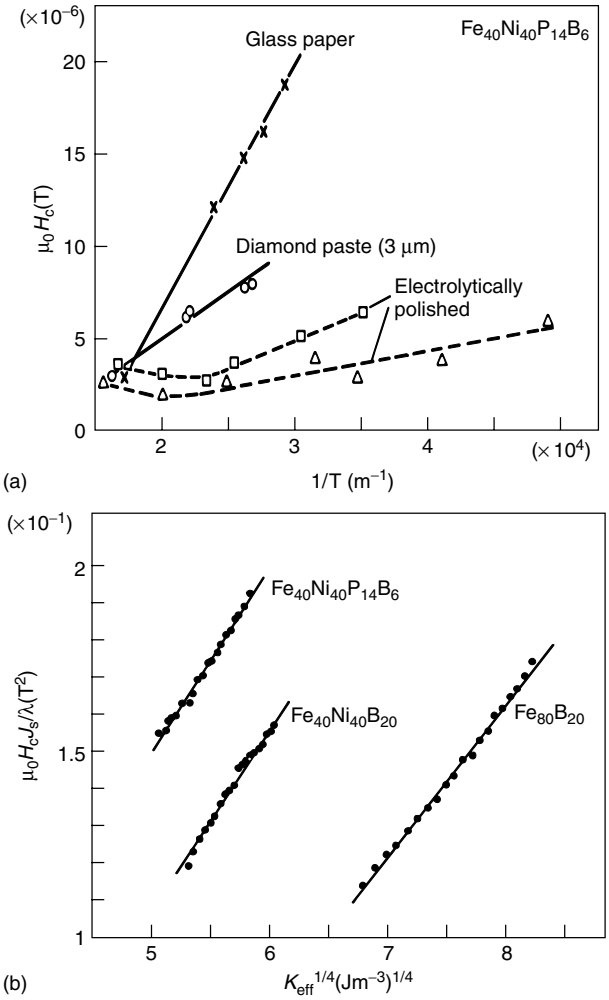

Figure 25. (a) Coercivity H_c of $Fe_{40}Ni_{40}P_{14}B_6$ as a function of the ribbon thickness T after different types of surface treatments. The slopes increase with increasing degree of roughness. (Reproduced from Kronmüller 1981, with permission from Elsevier. © 1981.) (b) Temperature dependence of H_c for magnetostrictive Fe–Ni-based alloys in the temperature range 100–310 K. (Reproduced from Gröger & Kronmüller 1981, with permission from Elsevier. © 1981.)

1.0 (Allia, Mazzetti and Vinai, 1980; Moser and Kronmüller, 1980) H_c^{rel} may contribute significantly to the total coercive field ($\mu_0 H_c^{rel} = 10^{-5}$–$10^{-3}$ mT).

e Internal stresses: In magnetostrictive materials elastic stress sources are the dominant pinning centers, therefore, governing the coercive field. With increasing magnetostriction λ_s the coercivity H_c increases and χ_0 decreases. For quasidislocation dipoles, which are the main sources of elastic stresses, the coercive field is given by

$$\mu_0 H_c^{\sigma} \propto \frac{\lambda_s}{J_s}\left(\frac{K_1}{A}\right)^{1/4} \tag{54}$$

This relation has been tested in Figure 25(b) for various nickel–iron based amorphous alloys showing the predicted temperature dependence of H_c (Gröger and Kronmüller, 1981). It has been shown (Kronmüller, Lenge and Habermeier, 1984) that elastic dipoles of extensions 1–10 nm are present in amorphous alloys with a high density of 10^{18} m^{-3}. Depending on the material parameters and the defect density $\mu_0 H_c^{\sigma}$ amounts to 10^{-3}–10^{-2} mT.

6.2 High-frequency behavior and losses

When a soft magnetic material is subjected to a time-varying magnetic field $H(t)$ various energy dissipation mechanisms occur so that part of the energy injected into the system by the external field is irrevocably transformed into heat. In a cyclic field of frequency f the loss per cycle, that is, the energy per unit volume converted into heat, is given by

$$W = \int H \frac{\mathrm{d}B}{\mathrm{d}t}\mathrm{d}t \tag{55}$$

The loss per unit time is called power loss $P = f \times W$ [W m^{-3}]. The total power loss P at frequency f is the sum of the (static) hysteresis loss P_h due to defect structures interacting with domain walls, the classical (eddy current) loss P_{cl} due to the specimen geometry and the excess (eddy current) loss P_{exc} (formerly called anomalous loss) due to the existence of magnetic domains. The frequency dependence of the three contributions to the total power loss per cycle are shown in Figure 26(a). When the material is (de)magnetized under sinusoidal induction rate, the total power loss P is given by Bertotti (1998) and Bertotti (2006)

$$P = P_h + P_{cl} + P_{exc}; \quad P_h = 4k_{hyst}B^{\beta}f;$$
$$P_{cl} = \frac{\pi^2\sigma d^2}{6}(Bf)^2; \quad P_{exc} = k_{exc}\sqrt{\sigma}(Bf)^{3/2} \tag{56}$$

where σ is the electrical conductivity of the material and B the amplitude of magnetic induction. k_{hyst} and β include the structural aspects which affect domain wall pinning and magnetization reversal, k_{exc} includes microstructural effects as grain-size fluctuations or wavelengths of stresses. The eddy current losses give rise to changes in the shapes of the hysteresis loops as shown in Figure 26(a).

The hysteresis loss is the power loss obtained when the field is cycled slowly under quasistatic conditions. It is (like the coercivity) directly related to structural disorder in the material which provides sources for domain wall pinning. The hysteresis loss is a consequence of the fact that magnetization proceeds through Barkhausen jumps of domain walls which are unpinned from defects by the pressure of the external field. Each wall jump results in an

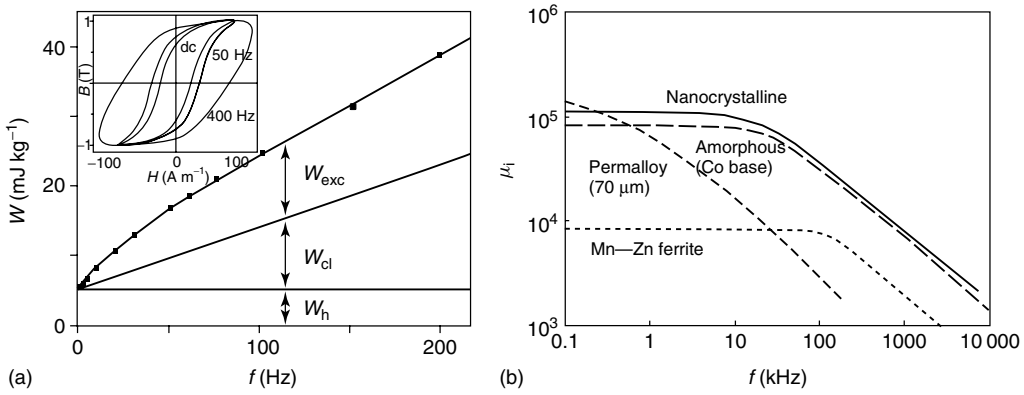

Figure 26. (a) Separation of the total power loss per cycle into its components (W_h: hysteresis loss, W_{cl}: classical loss, W_{ex}: excess loss) as a function of frequency f for grain-oriented Fe-3wt%Si (specimen thickness 0.3 mm). The inset shows typical dynamical hysteresis loops for nonoriented Fe-3wt%Si (specimen thickness 0.35 mm) (quasistatic (dc), 50 Hz, 400 Hz). (Reproduced from Bertotti 2006, with permission from Elsvier. © 2006.) (b) Magnetic initial permeability μ_i as a function of frequency f for different soft magnetic materials (Hilzinger and Tenbrink, 2001). (Reproduced from Hilzinger & Tenbrinck, 2006, with permission from Elsevier. © 2006.)

induction change which induces local eddy currents which in turn dissipate a finite amount of energy as heat. The sum over all jumps results in the hysteresis loss. The amount of energy which is dissipated during individual wall jumps is determined by the height of the energy barrier created by the pinning obstacle. As a general rule, the smaller the coercivity, the smaller is the hysteresis loss. According to equation (56) the hysteresis loss is independent of the electrical conductivity σ and of the sample thickness d when pinning effects are volume effects (however, when the surface of the sample acts as relevant pinning source, the hysteresis loss increases with decreasing thickness of the sample). The hysteresis loss per cycle ($W_h = P_h/f$), which is equivalent to the area enclosed by the quasistatic hysteresis loop, is furthermore independent of the frequency f.

The classical loss is always present in metallic soft magnetic materials. It is obtained from solving Maxwell's equations for a homogeneous conducting medium with no structural inhomogeneities and no magnetic domains (Bozorth, 1993). The boundary conditions which are given by the system geometry determine the distribution of eddy currents in the specimen and the ensuing heat dissipation. The classical loss can be minimized by reducing both the electrical conductivity σ and the specimen thickness d. Therefore, magnetic cores of devices are never made of bulk soft magnetic materials.

The excess loss results from the large-scale motion of domain walls in the specimen. Around the moving domain walls eddy currents tend to concentrate. The influence of excess losses significantly depends on the size and arrangement of magnetic domains. For a regular arrangement of longitudinal domains the expression for the excess loss in equation (56) simplifies to $P_{exc} = 1.63(2L/d)P_{cl}$ (d: specimen thickness, L: average domain width) (Bishop, 1976). The finer the domain structure, the smaller is the excess loss. The excess loss can be neglected when the domain width is much smaller than the specimen thickness or when magnetization changes homogeneously by rotation as is the case for flat-type hysteresis loops with small J_r/J_s ratios (for hysteresis loops with large J_r/J_s ratios where the magnetization process takes place by domain wall displacements excess eddy current losses do occur).

The initial permeability μ_i is independent of the frequency for low frequencies, whereas for high frequencies μ_i approaches unity (Figure 26b) The frequency at which μ_i starts to decrease depends on the magnetic material and has its origin in the occurence of resonance effects, for example, dimensional resonance due to the sample geometry, magnetic resonance due to the rotation of the magnetization against the action of the anisotropy field or due to the resonant oscillation of domain walls.

Especially amorphous and nanocrystalline alloys reveal low losses and a high permeability even at elevated frequencies which is essentially related to the facts that they are produced as thin ribbons and that their electrical resistivity is high, both reducing eddy current losses.

7 APPROACH TO SATURATION: MICROMAGNETISM AND MICROSTRUCTURE

The approach to saturation of a ferromagnetic hysteresis loop is known as the region of quasisaturation where the angle between the spontaneous polarization J_s and the applied field H is very small. In this region the hysteresis loop can be regarded as fully reversible and the field dependence of the

polarization can be generally written as (Kronmüller, 1959; Kronmüller and Fähnle, 2003)

$$J(H,T) = J_s - \sum_{i=1}^{6} \frac{a_{i/2}}{H^{i/2}} + \Delta J_{SW} + \chi_p \mu_0 H \qquad (57)$$

that is the approach to saturation is determined by intrinsic and extrinsic properties.

Intrinsic properties are magnetocrystalline anisotropies, spin waves, and the Pauli paramagnetic susceptibility χ_p. In (nano) crystalline magnets the magnetocrystalline anisotropy results in a a_2/H^2 term and a a_3/H^3 term. For uniaxial anisotropy, Danan (1958) derived for the coefficients $a_2 = 4K_1^2/(15J_s^2)$ and $a_3 = 16K_1^3/(105J_s^3)$. For cubic anisotropy, Akulov (1931), Gans (1932), and Becker and Döring (1939) found for the coefficients $a_2 = 8K_1^2/(105J_s^2)$ and $a_3 = 192K_1^3/(5005J_s^3)$. In amorphous magnets, local fluctuations of the magnetocrystalline anisotropy give rise to a $a_{1/2}/H^{1/2}$ term at small fields and a a_2/H^2 term at large fields. The spin-wave contribution ΔJ_{SW} for a quadratic dispersion law of the spin-wave energy spectrum can be derived according to Holstein and Primakoff (1940) as

$$\begin{aligned}\Delta J_{SW} &= -J_s \left(\frac{T}{T_0}\right)^{3/2} + \Delta J_{para} \\ &= -J_s \left(\frac{T}{T_0}\right)^{3/2} + C(T) f_{HP}\end{aligned} \qquad (58)$$

where the first term corresponds to the well-known Bloch's $T^{3/2}$ law and the second term takes care of the spin-wave paraeffect which results from the reduction of the number of magnons by an applied magnetic field. The characteristic temperature T_0 and the function $C(T)$ are related to the spin-wave stiffness constant D_{sp} of the magnon energy spectrum $\epsilon_k = D_{sp}k^2$ (k: spin-wave wave vector) and f_{HP} is the Holstein–Primakoff function

$$\begin{aligned} k_B T_0 &= D_{sp} \left(\frac{J_s(0)}{0.117\mu_B}\right)^{2/3}; \\ C(T) &= \left(\frac{\mu_B^{3/2} k_B}{2\pi}\right) \frac{\mu_0}{(2D_{sp})^{3/2}} T; \\ f_{HP} &= 3\sqrt{\mu_0 H} + \sqrt{J_s(0)} \frac{\mu_0 H + J_s(0)}{J_s(0)} \sin^{-1} \\ &\quad \times \left(\frac{J_s(0)}{\mu_0 H + J_s(0)}\right)^{1/2} \end{aligned} \qquad (59)$$

with k_B Boltzmann's constant and $J_s(0)$ the spontaneous polarization at $T \to 0$. The enhanced Pauli paramagnetism of the band structure gives rise to the linear term $\chi_p \mu_0 H$.

Extrinsic properties are due to magnetoelastic stress sources which produce inhomogeneous spin states. The corresponding deviations from saturation are determined by the geometry of the defect, the range of the spin inhomogeneity, and the interaction between defects. Typical spin distributions around point defects, dislocations, and dislocation dipoles are shown in Figure 27. Point defects with stress fields varying as $\sigma \propto 1/r^3$ give rise to a $a_{1/2}/H^{1/2}$ term. Straight dislocation dipoles with stress fields $\sigma \propto 1/r^2$ lead to a a_1/H term as long as the distance D between the two dislocations is smaller than the exchange length $l_H = \sqrt{2A/(J_s H)}$. Otherwise, the two dislocations act as two single straight (opposite) dislocations exhibiting a $\sigma \propto 1/r$ dependence of the stress field which gives rise to a a_2/H^2 term. Nonmagnetic spherical inclusions of radius r_0 result in a $a_{1/2}/H^{1/2}$ term for $r_0 < l_H$ and in a $a_{3/2}/H^{3/2}$ term for $r_0 > l_H$.

In general, in the high-field region the paraeffect becomes important whereas in the lower field region the microstructural effects are prevailing. For hard magnetic materials the influence of the microstructural effects can be neglected compared to the influence of the magnetocrystalline anisotropy.

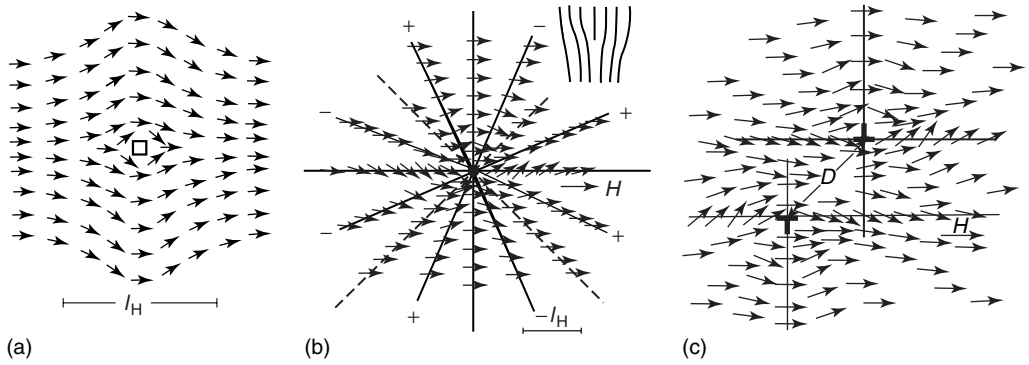

Figure 27. Spin distribution around (a) a vacancy type defect, (b) an isolated quasidislocation, and (c) a quasidislocation dipole.

The law of approach to saturation can be used to analyze the defect structures in (nano)crystalline magnets and especially in amorphous magnets where conventional techniques as X-ray or neutron diffraction or transmission electron microscopy fail due to the nonperiodic structure. The analysis of the field dependence also opens the possibility to determine the temperature dependence of the spontaneous polarization $J_s(T, 0) = J_s[1 - (T/T_0)^{3/2}]$ at zero magnetic field after separation of the microstructural effects and the paraeffect.

In order to determine the microstructural terms, $J(T, H)$ has to be plotted as a function of $1/H^{n/2}$. Figure 28 shows the result of such plots for amorphous $Fe_{40}Ni_{40}P_{14}B_6$ and $Fe_{40}Ni_{40}B_{20}$. In the case of $Fe_{40}Ni_{40}P_{14}B_6$ the approach to saturation is described by a a_1/H term for $\mu_0 H < 0.2\,\mathrm{T}$. In contrast, $Fe_{40}Ni_{40}B_{20}$ follows a a_1/H law in the field range $0.01 \leq \mu_0 H \leq 0.03\,\mathrm{T}$ and obeys a a_2/H^2 law for $0.03\,\mathrm{T} \leq \mu_0 H \leq 0.2\,\mathrm{T}$. The steep increase in the $J(H, T)$ versus $1/H^{n/2}$ diagrams for $\mu_0 H > 0.2\,\mathrm{T}$ for both materials is due to the spin-wave term. For an analysis of this region the spin-wave contribution to $J(H, T)$ can be eliminated by extrapolating the microstructural effects to higher fields ($1/H_n \to 0$). In Figure 29(a) the paraeffect ΔJ_{para} is represented as a function of the Holstein–Primakoff function f_{HP} for $Fe_{40}Ni_{40}P_{14}B_6$. It follows from this that the paraeffect depends linearly on f_{HP}. From the slopes of the straight lines the functions $C(T)$ given in equation (59) are obtained. The magnetoelastic origin of the inhomogeneity terms becomes obvious in Figure 29(b) where in rapidly quenched or plastically deformed materials the $1/H$ term is predominant proving the presence of quasidislocation dipoles, whereas in nearly nonmagnetostrictive alloys as $Co_{58}Ni_{10}Fe_5Si_{11}B_{16}$ the $1/H$ term is rather small.

It should be noted that perfect single crystals can be saturated completely when the magnetic field is applied parallel to an easy or heavy direction of the crystal. In the case of orientation parallel to an easy axis the field strength necessary to reach ferromagnetic saturation is rather small as the movement of the domain walls is not impeded. In the case of orientation parallel to a heavy axis ferromagnetic saturation is reached for $\mu_0 H = 2\mu_0 K_1/J_s$ by reversible rotations.

8 TAILOR-MADE HIGH-PERFORMANCE MAGNETS

According to Sections 5 and 6, both hard and soft magnetic materials are strongly dependent not only on intrinsic material parameters but also on the special types of microstructures. Actually the deviations from the ideal lattice in many cases are responsible for certain outstanding properties. The

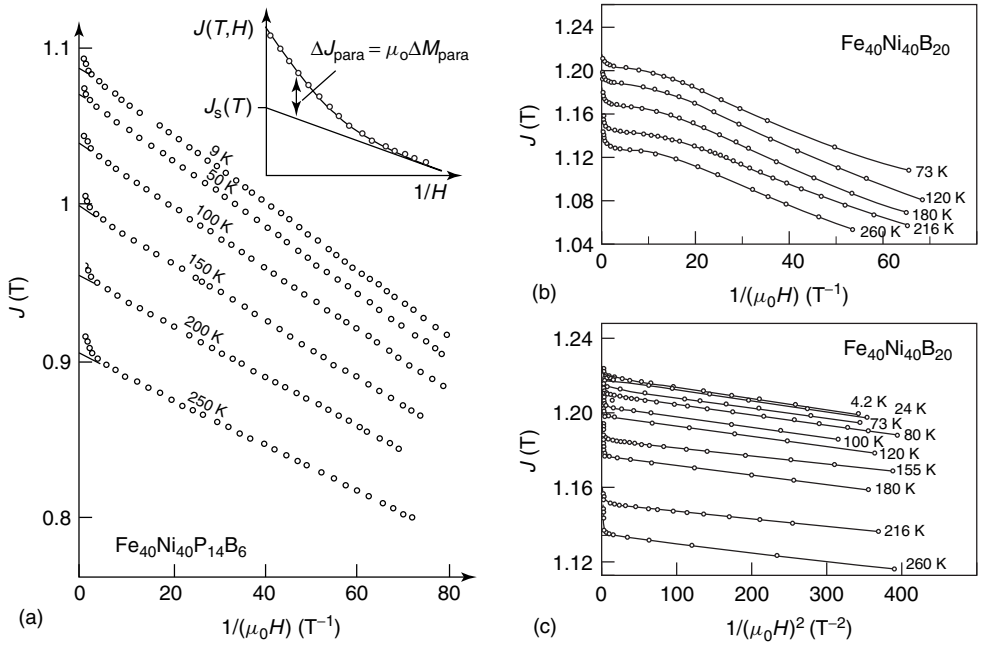

Figure 28. Field dependence of the polarization $J(T, H)$ at different temperatures of (a) amorphous $Fe_{40}Ni_{40}P_{14}B_6$ as a function of $1/(\mu_0 H)$ (Kronmüller and Grimm, 1977), (Reproduced from Kronmüller & Grimm 1977, with permission from Elsevier. © 1977.) (b) amorphous $Fe_{40}Ni_{40}B_{20}$ as a function of $1/(\mu_0 H)$ (Domann, Grimm and Kronmüller, 1979), (Reproduced from Domann *et al.*, 1979, with permission from Elsevier. © 1979.) and (c) amorphous $Fe_{40}Ni_{40}B_{20}$ as a function of $1/(\mu_0 H)^2$. (Reproduced from Kronmüller *et al.*, 1979, with permission from Elsevier. © 1979.)

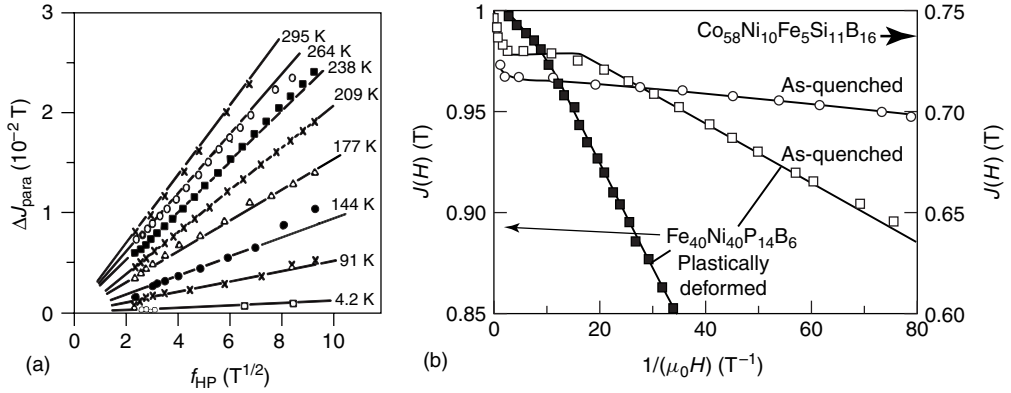

Figure 29. (a) The paraeffect $\Delta J_{para} = \Delta J - a_1 H$ for $Fe_{40}Ni_{40}P_{14}B_6$ at different temperatures as a function of the Holstein–Primakoff function f_{HP}. (Reproduced from Kronmüller *et al.*, 1979, with permission from Elsevier. © 1979.) (b) Polarization $J(H)$ as a function of $1/(\mu_0 H)$ for different amorphous alloys (Grimm and Kronmüller, 1983). (Reproduced from H. Grimm & H. Kronmüller, *Phys. Stat. Sol (b)*, **117** (1983), with permission from Wiley VCH.)

detailed knowledge of the micromagnetism–microstructure correlation can be used for a systematic design of high-performance magnets. In particular, nanocrystalline and nanostructured magnets allow a wide variation of microstructures and therefore offer a new opportunity for tailoring extremely hard and extremely soft magnetic materials. Using suitable additives the grain sizes as well as the magnetic properties and the chemical composition of the grain boundaries can be tailored on an atomic scale.

8.1 Optimization of hard and soft magnets

With nanocrystalline hard magnets based on $RE_2Fe_{14}B$, magnets with definite properties of the hysteresis loop can be designed due to the fact that small deviations from the stoichiometry and small amounts of certain additives may lead to drastic changes in the magnetic properties. In Figure 30(a) it is illustrated how the room temperature magnetic properties change with increasing Fe content for melt-spun $Pr_2Fe_{14}B$ magnets. The increasing Fe content not only results in an enhancement of the remanence but also in a decrease of the coercivity. However, as long as the condition $\mu_0 H_c > 0.5 J_r$ is fulfilled, $(BH)_{max}$ increases. Otherwise, $(BH)_{max}$ is limited by irreversible demagnetization processes.

With nanocrystalline soft magnets based on $Fe_{73.5}Cu_1Nb_3Si_{13.5}B_9$ the magnetic properties of the hysteresis loop can be controlled only in part by the grain-size effect. If the grain size is small enough, the composition and the volume fraction of the individual phases take over the control of the soft magnetic properties. Soft magnetic applications require not only highest permeability but also lowest coercivity. A well defined shape of the hysteresis loop with a well defined level of permeability adjusted to the particular application is equally important. A wide spectrum of properties can be tailored by magnetic field annealing which induces a uniaxial anisotropy with easy axis parallel to the direction of the magnetic field applied during the heat treatment. As an example, Figure 30(b) shows the hysteresis loops after different heat treatments with and without magnetic field. Accordingly, almost perfect rectangular (flat shaped) hysteresis loops are obtained for magnetic fields along (tranverse) to the magnetic path in the application, whereas a more round shaped hysteresis loop is obtained by conventional annealing without a magnetic field. Field induced anisotropies K_u are due to atomic pair ordering which minimizes the spin-orbit coupling energy. K_u directly controls the soft magnetic properties, for example, after tranverse field annealing the permeability is constant up to saturation and is given by $\mu = J_s^2/(2\mu_0 K_u)$ and after longitudinal field annealing low induced anisotropies facilitate domain refinement resulting in reduced excess losses.

A further important aspect many applications look for is a small temperature coefficient of the magnetic properties over a large temperature range. Especially, for nanostructured $Sm_2(Co,Cu,Fe,Zr)_{17}$ hard magnets depending on the compostion and on the annealing parameters the temperature dependence of the coercivity H_c can be easily changed according to Section 5.1.2 from the conventional monotonic to the recently developed nonmonotonic behavior showing coercivities up to 1 T even at 400 °C. For nanocrstalline soft magnets a very temperature stable behavior of the permeability is guaranteed as the averaging out of the magnetocrystalline anisotropy by exchange interaction is effective over a large temperature range.

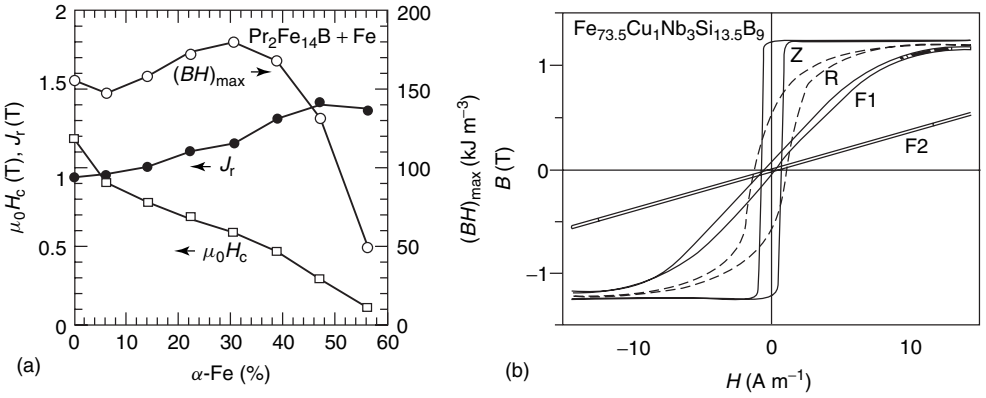

Figure 30. (a) Magnetic properties of nanocrystalline composite $Pr_2Fe_{14}B$ permanent magnets as a function of excess α-Fe. For an iron excess of 30.4 vol%, J_r amounts to 1.17 T, that is, an increase of 51% as compared to the decoupled value of 0.78 T and $(BH)_{max}$ is measured to be 180.7 kJ m^{-3}. (Reproduced from Goll *et al*., 1998, with permission from Elsevier. © 1998.) (b) Hysteresis loops of nanocrystalline $Fe_{73.5}Cu_1Nb_3Si_{13.5}B_9$ soft magnets annealed without (R) and with a magnetic field applied parallel (Z) and tranverse (F2) ($K_u \approx 20\,\mathrm{J\,m^{-3}}$, $\mu \approx 30 \times 10^3$) to the magnetic path. Sample F1 ($K_u \approx 6\,\mathrm{J\,m^{-3}}$, $\mu \approx 100 \times 10^3$) was first crystallized and then annealed in a transverse field. (Reproduced from Herzer, 1996, with permission from Elsevier. © 1996.)

8.2 Computational micromagnetism

A rather successful tool for a quantitative and also predictive treatment of the complex microstructure–property relationship are numerical micromagnetic finite-element simulations (see also **Numerical Methods in Micromagnetics (Finite Element Method), Volume 2**) which may provide general rules for the design of optimized magnets. Simulations of magnetization processes of ensembles of grains are obtained from a minimization of the magnetic free enthalpy G with respect to the orientation of the spontaneous polarization J_s:

$$\delta G = \delta \int (\phi_A + \phi_K + \phi_S + \phi_H)\,\mathrm{d}V = 0 \qquad (60)$$

where G is composed of four contributions: exchange energy $\phi_A = A(\nabla\varphi)^2$, crystal anisotropy $\phi_K = K_1 \sin^2\varphi + K_2 \sin^4\varphi$, stray field energy $\phi_S = -1/2 H_s J_s$ and magnetostatic energy $\phi_H = -H_{ext} J_s$ (φ: angle between easy axis and J_s, H_s: stray field which follows from a scalar potential U by $H_s = -\nabla U$ and U obeys Poisson's equation $\Delta U = (1/\mu_0)\,\mathrm{div} J_s$). The minimization is usually performed by using the finite-element technique (FEM). For three-dimensional numerical simulations a cubic model particle composed of polyhedral regular or irregular grains is taken into consideration. In the model particle, the average grain size and the magnetic material parameters of the grains and grain boundaries can be modified which enables a systematic study of the main influences on the characteristic properties of the hysteresis loop.

As an example, Figure 31 shows the orientation of the spontaneous polarization J_s of the remanent state for a model composite permanent magnet composed of 35 irregular grains with an average grain diameter of 10 nm and with easy axes distributed isotropically. Fifty-one percent of the grains are soft magnetic α-Fe grains which are embedded in 49% hard magnetic grains of $Nd_2Fe_{14}B$ (Fischer, Schrefl, Kronmüller and Fidler, 1995). At the grain boundaries the orientation of J_s changes smoothly within a region of width δ_B from one easy direction to another one. Under the assumption of a perfect exchange coupling between the grains, Figure 32(a) illustrates the dependence of J_r and $\mu_0 H_c$ on the grain size D. Both quantities decrease with increasing grain size and J_r and H_c can be fitted empirically by the following logarithmic laws (Fischer, Schrefl, Kronmüller and Fidler, 1996)

$$J_r = J_{sat}\left(0.84 - 0.085 \ln \frac{D}{\delta_B^{hard}}\right);$$
$$H_c = H_N^{(0)}\left(0.22 - 0.041 \ln \frac{D}{\delta_B^{hard}}\right) \qquad (61)$$

with $H_N^{(0)} = 2K_1^{hard}/J_s$ and $J_{sat} = J_s^{hard} v^{hard} + J_s^{soft} v^{soft}$ where the upper indices refer to the saturation polarizations and volume fractions of the hard and soft magnetic phases. It turns out that for grain sizes of 20 nm ($5\delta_B^{hard}$) the coercivity amounts to $H_c \approx 0.15 H_N^{(0)}$ and the remanence is considerably larger than the isotropic value of $0.5 J_s$. Figure 32(b) shows the numerical results for J_r, H_c, and $(BH)_{max}$ as a function of the α-Fe content in comparison with experimental data. Whereas for J_r a fairly well agreement is obtained, the theoretical predictions for H_c and $(BH)_{max}$ are appreciably larger than the experimental values. In the case of $(BH)_{max}$ this is due to the fact that for the experimental results the condition $\mu_0 H_c > 0.5 J_r$ is only valid for α-Fe concentrations smaller

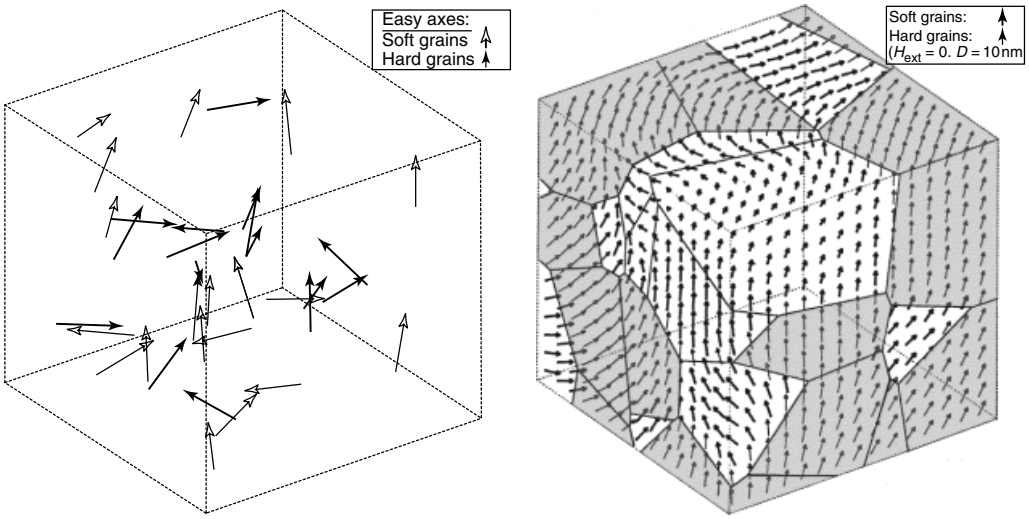

Figure 31. Configurations of the easy axes and of the remanent polarization of 35 irregular grains of average diameter 10 nm within a cube with a volume fraction of 51% α-Fe (*dark*) and 49% $Nd_2Fe_{14}B$ (*light*). (Reproduced from Fischer *et al*., 1995, with permission from Elsevier. © 1995.)

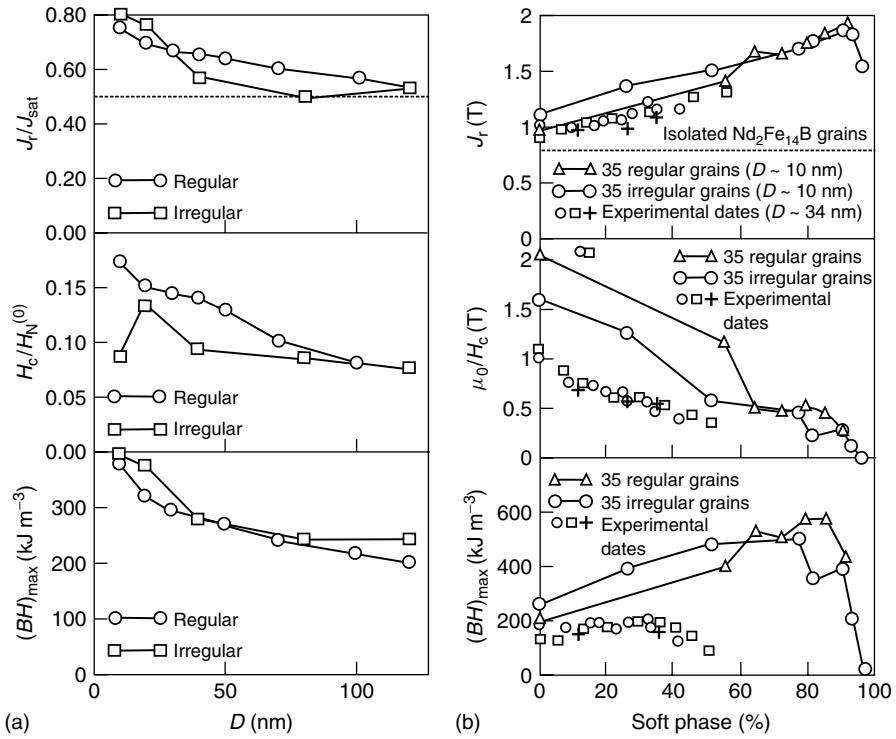

Figure 32. (a) J_r, $\mu_0 H_c$ and $(BH)_{max}$ for the irregular configuration of Figure 31 and a regular dodecahedral grain structure as a function of mean grain size D (Fischer, Schrefl, Kronmüller and Fidler, 1996). (b) Numerical results for J_r, $\mu_0 H_c$ and $(BH)_{max}$ as a function of the α-Fe content in comparison with experimental results. (Reproduced from Fischer *et al*., 1996, with permission from Elsevier. © 1996.)

than 30%, whereas the numerical results fulfill this condition up to 50%. The observed discrepancy between numerical and experimental results can be explained by modifying the intrinsic material parameters within the grain boundaries. Owing to the atomic disorder within grain boundaries it can be assumed that especially A and K_1 have reduced values within the grain boundaries. Figure 33(a) shows the influence of the reduction of these two parameters on the demagnetization curve for a cube of 64 grains of average diameter 20 nm (Fischer and Kronmüller, 1998). For the simulation

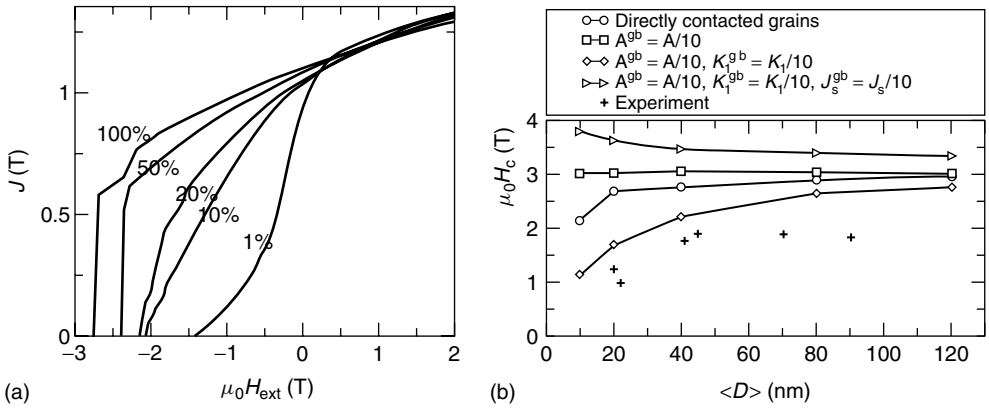

Figure 33. (a) Demagnetization curves for an assembly of 64 $Nd_2Fe_{14}B$ grains (average grain diameter 20 nm) and an intergranular phase of reduced anisotropy and exchange constant (thickness 3 nm). (Reproduced from Fischer & Kronmüller 1998, with permission from Elsevier. © 1998.) (b) Coercive field as a function of the mean grain diameter $\langle D \rangle$ and grain boundaries of width 3 nm and reduced material parameters in comparison with experimental results (Fischer and Kronmüller, 1998).

3 nm grain boundaries are assumed where A and K_1 suffer a steplike reduction. With decreasing A and K_1 within the grain boundaries $\mu_0 H_c$ and J_r also decrease. If the parameter $f = A^{gb}/A = K_1^{gb}/K_1$ (gb: grain boundary) is introduced, $\mu_0 H_c$ and J_r obey the following relations

$$\frac{H_c}{H_N^{(0)}} = 0.304 + 0.098 f; \frac{J_r}{J_{sat}} = 0.646 + 0.036 f \qquad (62)$$

A further interesting property is the dependence of the coercive field on the average grain diameter $\langle D \rangle$ (Figure 33b). Here it turns out that the experimental results obtained by Manaf, Buckley, Davies and Leonowicz (1991) for nanocrystalline $Nd_{13.2}Fe_{79.6}B_6Si_{1.2}$ can only be received in numerical simulations by modifying A and K_1 within the grain boundaries. Figure 34 shows the corresponding magnetization reversal process for an individual grain separated from neighboring grains by grain boundaries with reduced values of A and K_1 (Fischer and Kronmüller, 1998). Obviously, magnetization reversal primarily nucleates within the grain boundaries, whereas in the grain the polarization starts to rotate reversibly into the direction of the applied field.

8.3 Future visions and limits

Further progress in the fields of extremely hard and extremely soft magnetic materials is possible if one succeeds to develop materials with optimal property spectra where magnetic, electrical, mechanical, corrosive, and thermal properties are optimized simultaneously. The development of outstanding multiproperty materials requires interdisciplinary research activities where the development of intrinsic properties as well as investigations of the microstructure and of local chemical compositions are carried out.

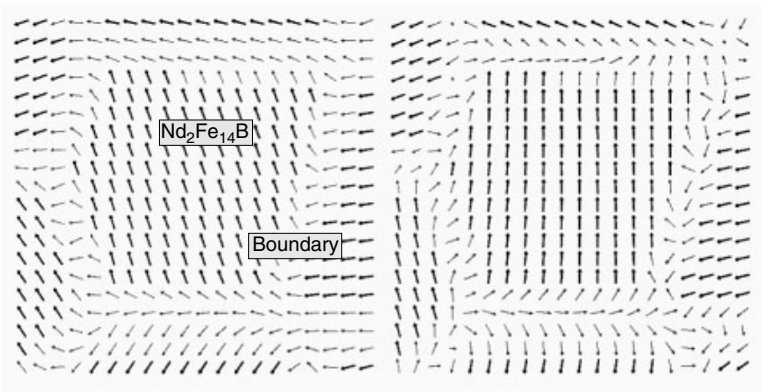

Figure 34. Magnetization distribution at the remanent state and at the overcritical state (field to the right, $\mu_0 H = 0.6$ T) just before magnetization reversal. The strong arrows indicate the magnetic moments within the bulk of the grains. (Reproduced from Fisher & Kronmüller 1998, with permission from Elsevier. © 1998.)

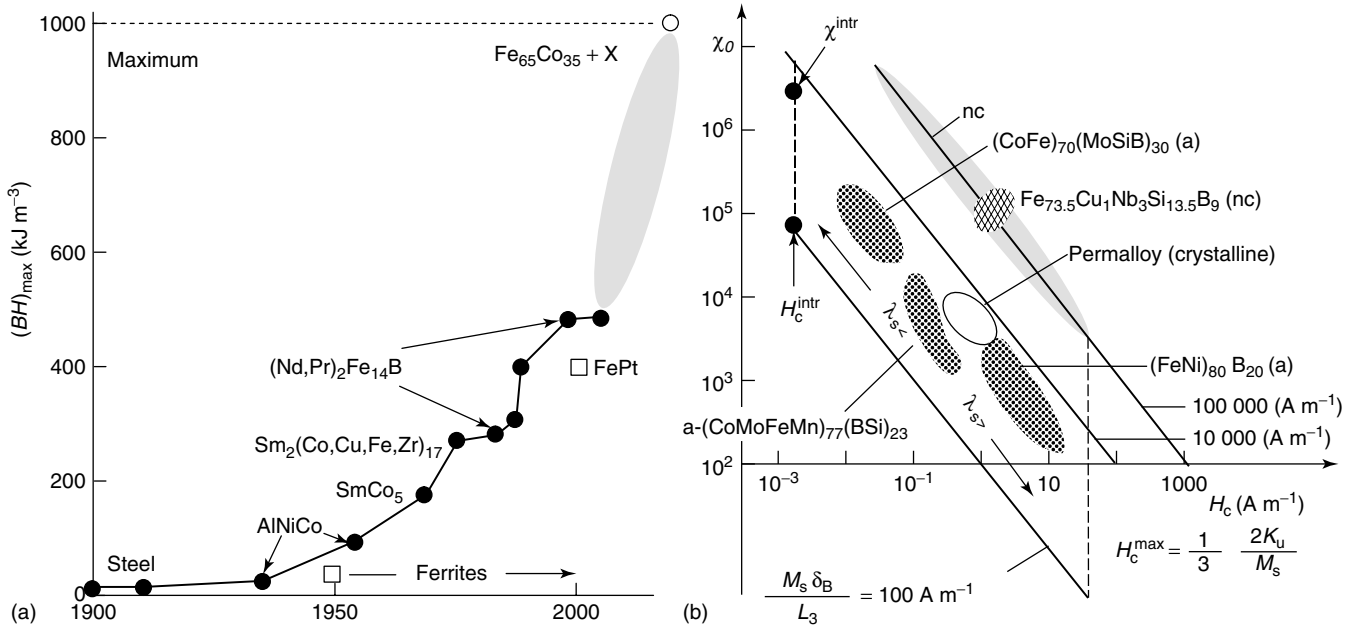

Figure 35. (a) Progress in improving $(BH)_{max}$ of hard magnetic materials over the last century. The shaded region covers hypothetical FeCo-based alloys which are magnetically hardened by additives X. (b) Upper and lower bounds for χ_0 and H_c of soft magnetic materials based on the fundamental relation $\chi_0 H_c = M_s \delta_B / L_3$.

High-coercivity materials are currently based on the intermetallic compounds $Nd_2Fe_{14}B$, $SmCo_5$, and Sm_2Co_{17}. Deficiencies of these compounds are the low Curie temperature of $Nd_2Fe_{14}B$ ($T_C = 312\,^\circ$C) and the low spontaneous polarization of $SmCo_5$ (1.05 T) and Sm_2Co_{17} (1.25 T). This allows applications only up to 100 °C for the $Nd_2Fe_{14}B$ systems and the maximum energy products of the SmCo systems are a factor of 2–3 smaller at room temperature than that of $Nd_2Fe_{14}B$. To achieve Curie temperatures of the order of 450 °C far more additives have to be investigated in the $Nd_2Fe_{14}B$ system. Figure 35(a) presents the development of the maximum energy product $(BH)_{max}$ during the last century. The shaded region shows the progress, which could be still achieved if a FeCo-based magnet with a large spontaneous polarization of 2.45 T could be realized by introducing strong planar pinning centers.

High-permeability materials require large spontaneous polarization, vanishing magnetocrystalline anisotropy, and vanishing magnetostriction. A further breakthrough for these materials could be achieved if nanocrystalline alloys with a larger spontaneous polarization; however, still a low magnetostriction could be found. The spontaneous polarization of the presently used Finemet of 1.25 T could be raised to 1.5 T by using a FeZrB alloy. Also the Curie temperature would be improved and could be further raised by adding Co. The upper and lower bounds for χ_0 and H_c of soft magnetic materials can be derived from the self-consistence relationship of equation (37) which can be approximately written as $\chi_0 \approx M_s \delta_B / (H_c L_3)$ as the square root of the logarithm $\sqrt{\ln(L_3/2L_0)}$ does not depend sensitively on $L_3/(2L_0)$ and is of the order of 2 ($L_3 \approx 100\delta_B - 1000\delta_B$). For ratios δ_B/L_3 varying between 10^{-3} and 10^{-1} and $M_s = 10^5$ A m^{-1} the bounds are given by $100\,\mathrm{A\,m^{-1}} < M_s\delta_B/L_3 < 10^4\,\mathrm{A\,m^{-1}}$. According to Figure 35(b) the CoFe- and NiFe-based amorphous and crystalline alloys lie between these two limits, whereas nanocrystalline FeSiNbCuB alloys are located at $M_s\delta_B/L_3 = 100\,\mathrm{kA\,m^{-1}}$ due to the random-anisotropy effect resulting in domain wall widths of a factor of 5–10 larger than in amorphous alloys. The fine shaded region shows the future possible improvement by using optimized nanocrystalline soft magnets. The absolute lower and upper limits of H_c and χ_0, respectively, are expected for ideal amorphous materials with $K_1 \to 0$ and $\lambda_s \to 0$.

REFERENCES

Aharoni, A. and Shtrikman, S. (1958). Magnetization curve of the infinite cylinder. *Physical Review*, **109**, 1522–1528.

Akulov, N.S. (1931). über den Verlauf der Magnetisierungskurve in starken Feldern. *Zeitschrift für Physik*, **69**, 822–831.

Alben, R., Becker, J.J. and Chi, M.C. (1978). Random anisotropy in amorphous ferromagnets. *Journal of Applied Physics*, **49**, 1653–1658.

Allia, P., Mazzetti, P. and Vinai, F. (1980). Magnetic aftereffects and structural instabilities in amorphous soft magnetic materials. *Journal of Magnetism and Magnetic Materials*, **19**, 281–283.

Barkhausen, H. (1919). Two with help of new repeating rediscovered appearances by H Barkhausen – the silence during unmagnetising of iron. *Physikalische Zeitschrift*, **20**, 401–403.

Bauer, J., Seeger, M., Zern, A. and Kronmüller, H. (1996). Nanocrystalline NdFeB permanent magnets with enhanced remanence. *Journal of Applied Physics*, **80**, 1667–1673.

Becker, J.J. (1981). Effects of surface treatment and thinning on magnetic properties of rapidly quenched amorphous alloy ribbons. *Journal of Applied Physics*, **52**, 1905–1907.

Becker, R. and Döring, W. (1939). *Ferromagnetismus*, Springer: Berlin.

Becher, M., Seeger, M., Bauer, J., *et al*. (1998). Magnetic viscosity measurements on nanocrystalline NdFeB and PrFeB magnets. In *Proceedings of 10th International Symposium on Magnetic Anisotropy and Coercivity in Rare-Earth Transition Metal Alloys*, Schultz, L. and Müller, K.H. (Eds.), Werkstoff-Informationsgesellschaft: Frankfurt, pp. 307–316.

Bertotti, G. (1998). *Hysteresis in Magnetism*, Academic Press: Boston.

Bertotti, G. (2006). Magnetic losses. In *Encyclopedia of Materials: Science and Technology*, Buschow, K.H.J., Cahn, R.W., Flemings M.C., *et al*. (Eds.), Elsevier, pp. 4798–4804.

Bishop, J.E.L. (1976). The influence of a random domain size distribution on the eddy-current contribution to hysteresis in transformer steel. *Journal of Physics D: Applied Physics*, **9**, 1367–1377.

Bozorth, R.M. (1993). *Ferromagnetism*, IEEE Press: New York.

Brown, W.F. Jr. (1940). Theory of the approach to magnetic saturation. *Physical Review*, **58**, 736–743.

Brown, W.F. Jr. (1945). Virtues and weaknesses of the domain concept. *Reviews of Modern Physics*, **17**, 15–19.

Brown, W.F. Jr. (1963). *Micromagnetics*, Intersience Publishers, John Wiley & Sons: New York, London.

Buschow, K.H.J. (1997). Magnetism and processing of permanent magnetic materials. In *Handbook of Magnetic Materials*, Buschow, K.H.J. (Ed.), North Holland: Amsterdam, pp. 463–593, Vol. 10.

Cohen, M.H. and Turnbull, D. (1959). Molecular transport in liquids and glasses. *Journal of Chemical Physics*, **31**, 1164–1169.

Danan, M.H. (1958). *Colloque Nationale de Magnétisme*, Weiss P. (Ed.), Centre national de la recherche scientifique: Paris.

Domann, M., Grimm, H. and Kronmüller, H. (1979). High-field magnetization curve of amorphous ferromagnetic alloys. *Journal of Magnetism and Magnetic Materials*, **13**, 81–84.

Egami, T., Maeda, K. and Vitek, V. (1980). Structural defects in amorphous solids – a computer-simulation study. *Philosophical Magazine A*, **41**, 883–901.

Fischer, R. and Kronmüller, H. (1998). The role of grain boundaries in nanoscaled high-performance magnets. *Journal of Magnetism and Magnetic Materials*, **184**, 166–172.

Fischer, R., Schrefl, T., Kronmüller, H. and Fidler, J. (1995). Phase distribution and computed magnetic properties of high-remanent composite materials. *Journal of Magnetism and Magnetic Materials*, **150**, 329–344.

Fischer, R., Schrefl, T., Kronmüller, H. and Fidler, J. (1996). Grain size dependence of remanence and coercive field of isotropic nanocrystalline composite permanent magnets. *Journal of Magnetism and Magnetic Materials*, **153**, 35–49.

Frei, E.H., Shtrikman, S. and Treves, D. (1957). Critical size and nucleation field of ideal ferromagnetic particles. *Physical Review*, **106**, 446–454.

Friedberg, R. and Paul, D. (1975). New theory of coercive force of ferromagnetic materials. *Physical Review Letters*, **34**, 1234–1237.

Fujimori, H., Obi, Y., Masumoto, T. and Saito, H. (1976). Soft ferromagnetic properties of some amorphous alloys. *Materials Science and Engineering*, **23**, 281–284.

Gans, R. (1932). Regarding the magnetic behaviour of isotropic ferromagnetics. *Annalen der Physik*, **15**, 28–44.

Givord, D. and Rossignol, M.F. (1996). Coercivity. In *Rare-earth Ion Permanent Magnets*, Coey, J.M.D. (Ed.), Clarendon Press: Oxford, pp. 218–285.

Goll, D. (2002). Micromagnetism and microstructure – tailoring of high-performance magnets. *Zeitschrift für Metallkunde*, **93**, 1009–1017.

Goll, D., Berkowitz, A.E. and Bertram, H.N. (2004). Critical sizes for ferromagnetic spherical hollow nanoparticles. *Physical Review B*, **70**, 184432.

Goll, D., Kleinschroth, I., Sigle, W. and Kronmüller, H. (2000). Melt-spun precipitation-hardened $Sm_2(Co, Cu, Fe, Zr)_{17}$ magnets with abnormal temperature dependence of coercivity. *Applied Physics Letters*, **76**, 1054–1056.

Goll, D. and Kronmüller, H. (2000). High-performance permanent magnets. *Naturwissenschaften*, **87**, 423–438.

Goll, D. and Kronmüller, H. (2003). Coercivity mechanism in nanocrystalline and bonded magnets. In *Bonded Magnets*, Hadjipanayis, G.C. (Ed.), Kluwer Academic Publishers: Netherlands, pp. 115–127.

Goll, D., Kronmüller, H. and Stadelmaier, H.H. (2004). Micromagnetism and the microstructure of high-temperature permanent magnets. *Journal of Applied Physics*, **96**, 6534–6545.

Goll, D., Seeger, M. and Kronmüller, H. (1998). Magnetic and microstructural properties of nanocrystalline exchange coupled PrFeB permanent magnets. *Journal of Magnetism and Magnetic Materials*, **185**, 49–60.

González, J.M., Giri, A.K., De Julian, C., *et al*. (1994). Experimental comparison and analysis of coercivity models. *Europhysics Letters*, **28**, 143–148.

Grimm, H. and Kronmüller, H. (1983). Investigation of structural defects in the amorphous ferromagnetic alloy $Fe_{40}Ni_{40}P_{14}B_6$. *Physical Status Solidi B*, **117**, 663–674.

Gröger, B. and Kronmüller, H. (1981). The effect of internal stresses on the magnetization curve of amorphous ferromagnetic FeNi-alloys. *Applied Physics*, **24**, 287–297.

Herzer, G. (1990). Grain-size dependence of coercivity and permeability in nanocrystalline ferromagnets. *IEEE Transactions on Magnetics*, **26**, 1397–1402.

Herzer, G. (1995). Soft magnetic nanocrystalline materials. *Scripta Metallurgica et Materialia*, **33**, 1741–1756.

Herzer, G. (1996). Nanocrystalline soft magnetic materials. *Journal of Magnetism and Magnetic Materials*, **158**, 133–136.

Herzer, G. (1997). Nanocrystalline soft magnetic alloys. In *Handbook of Magnetic Materials*, Buschow, K.H.J. (Ed.), North Holland: Amsterdam, pp. 415–462, Vol. 10.

Herzer, G., Fernengel, W. and Adler, E. (1986). On the theory of nucleation fields in uniaxial ferromagnets. *Journal of Magnetism and Magnetic Materials*, **58**, 48–54.

Herzer, G. and Varga, L.K. (2000). Exchange softening in nanocrystalline alloys. *Journal of Magnetism and Magnetic Materials*, **215**, 506–512.

Hilzinger, H.R. (1977). The influence of planar defects on the coercive field of hard magnetic materials. *Applied Physics*, **12**, 253–260.

Hilzinger, H.R. and Kronmüller, H. (1975). Investigation of bloch-wall-pinning by antiphase boundaries in RCo_5-compounds. *Physics Letters A*, **51**, 59–60.

Hilzinger, H.R. and Tenbrink, J. (2001). Soft magnetic materials: applications. In *Encyclopedia of Materials: Science and Technology*, Buschow, K.H.J., Cahn, R.W., Flemings, M.C., *et al*. (Eds.), Elsevier, pp. 8679–8684.

Hofmann, B., Reininger, T. and Kronmüller, H. (1992). Influence of the microstructure on the magnetization processes in nanocrystalline $Fe_{73.5}Cu_1Nb_3Si_{13.5}B_9$. *Physical Status Solidi A*, **134**, 247–261.

Holstein, T. and Primakoff, H. (1940). Field dependence of the intrinsic domain magnetization of a ferromagnet. *Physical Review*, **58**, 1098–1113.

Hubert, A. (1974). *Theorie der Domänenwände in Geordneten Medien*, Springer: Berlin.

Kittel, C. (1946). Theory of the structure of ferromagnetic domains in films and small particles. *Physical Review*, **70**, 965–971.

Kojima, H. (1982). Fundamental properties of hexagonal ferrites with magnetoplumbite structure. In *Ferromagnetic Materials*, Wohlfarth, E.P. (Ed.), North Holland: Amsterdam, pp. 305–392, Vol. 3.

Kronmüller, H. (1959). Das magnetische Einmündungsgesetz bei plastisch verformten Nickel- und Nickel-Kobalt-Einkristallen. *Zeitschrift für Physik*, **154**, 574–600.

Kronmüller, H. (1966). Magnetisierungskurve der Ferromagnetika. In *Moderne Probleme der Metallphysik*, Seeger, A. (Ed.), Springer: Berlin, pp. 24–156, Vol. 2.

Kronmüller, H. (1970). Statistical theory of Rayleigh's law. *Zeitschrift für Angewandte Physik*, **30**, 9–13.

Kronmüller, H. (1972). Magnetic techniques for the study of dislocations in ferromagnetic materials. *International Journal of Nondestructive Testing*, **3**, 315–350.

Kronmüller, H. (1973). Domain wall behavior – microstructure and micromagnetism. *AIP Conference Proceedings*, **10**, 1006–1025.

Kronmüller, H. (1981a). Theory of the coercive field in amorphous ferromagnetic alloys. *Journal of Magnetism and Magnetic Materials*, **24**, 159–167.

Kronmüller, H. (1981b). Micromagnetism and microstructure of amorphous alloys. *Journal of Applied Physics*, **52**, 1859–1864.

Kronmüller, H. (1985). The nucleation fields of uniaxial ferromagnetic crystals. *Physical Status Solidi B*, **130**, 197–203.

Kronmüller, H. (1987). Theory of nucleation fields in inhomogeneous ferromagnets. *Physical Status Solidi B*, **144**, 385–396.

Kronmüller, H., Durst, K.D. and Martinek, G. (1987). Angular dependence of the coercive field in sintered $Fe_{77}Nd_{15}B_8$ magnets. *Journal of Magnetism and Magnetic Materials*, **69**, 149–157.

Kronmüller, H., Durst, K.D. and Sagawa, M. (1988). Analysis of the magnetic hardening mechanism in RE-FeB permanent magnets. *Journal of Magnetism and Magnetic Materials*, **74**, 291–302.

Kronmüller, H. and Fähnle, M. (2003). *Micromagnetism and the Microstructure of Ferromagnetic Solids*, Cambridge University Press, Cambridge.

Kronmüller, H. and Goll, D. (2002). Micromagnetic theory of the pinning of domain walls at phase boundaries. *Physica B*, **319**, 122–126.

Kronmüller, H. and Goll, D. (2003). Analysis of the temperature dependence of the coercive field of Sm_2Co_{17} based magnets. *Scripta Materialia*, **48**, 833–838.

Kronmüller, H. and Grimm, H. (1977). High-field suszeptibility and spin-wave spectrum of $Fe_{40}Ni_{40}P_{14}B_6$-alloys. *Journal of Magnetism and Magnetic Materials*, **6**, 57–60.

Kronmüller, H. and Hilzinger, H-R. (1976). Incoherent nucleation of reversed domains in Co_5Sm permanent magnets. *Journal of Magnetism and Magnetic Materials*, **2**, 3–10.

Kronmüller, H., Lenge, N. and Habermeier, H-U. (1984). Investigation of the approach to ferromagnetic saturation in sputtered amorphous $Fe_{80-x}Ni_xB_{20}$ films. *Physics Letters A*, **101**, 439–442.

Kronmüller, H., Fähnle, M., Domann, M., *et al*. (1979). Magnetic properties of amorphous ferromagnetic alloys. *Journal of Magnetism and Magnetic Materials*, **13**, 53–70.

Landau, L. and Lifshitz, E. (1935). On the theory of the dispersion of magnetic permeability in ferromagnetic bodies. *Physikalische Zeitschrift der Sowjetunion*, **8**, 153–169.

Luborsky, F.E. and Walter, J.L. (1977). Magnetically induced anisotropy in amorphous alloys of Fe-Ni-P-B. *IEEE Transactions on Magnetics*, **13**, 1635–1638.

Manaf, A., Buckley, R.A., Davies, H.A. and Leonowicz, M. (1991). Enhanced magnetic properties in rapidly solidified NdFeB based alloys. *Journal of Magnetism and Magnetic Materials*, **101**, 360–362.

Martinek, G. and Kronmüller, H. (1990). Influence of grain orientation on the coercive field in Fe-Nd-B permanent magnets. *Journal of Magnetism and Magnetic Materials*, **86**, 177–183.

Mc Currie, R.A. (1982). The structure and properties of AlNiCo permanent magnets. In *Ferromagnetic Materials*, Wohlfarth, E.P. (Ed.), North Holland: Amsterdam, pp. 107–188, Vol. 3.

Moser, N. and Kronmüller, H. (1980). Magnetic aftereffects in amorphous ferromagnetic alloys $Co_{70.4}Fe_{4.6}Si_{15}B_{10}$, $Fe_{40}Ni_{40}B_{20}$ and $Fe_{40}Ni_{40}P_{14}B_6$. *Journal of Magnetism and Magnetic Materials*, **19**, 275–277.

Murillo, N. and González, J. (2000). Effect of the annealing conditions and grain size on the soft magnetic character of FeCu(Nb/Ta)SiB nanocrystalline alloys. *Journal of Magnetism and Magnetic Materials*, **218**, 53–59.

Néel, L. (1950). Theorie du trainage magnetique des substances massives dans le domaine de Rayleigh. *Journal de Physique et le Radium*, **11**, 49–61.

Petzold, J. (2002). Advantages of softmagnetic nanocrystalline materials for modern electronic applications. *Journal of Magnetism and Magnetic Materials*, **242**, 84–89.

Rayleigh, L. (1887). On the behavior of iron and steel under the operation of feeble magnetic forces. *Philosophical Magazine*, **23**, 225–245.

Sagawa, M. and Hirosawa, S. (1987). Coercivity and microstructure of R-Fe-B sintered permanent magnets. *Journal de physique (Paris), Colloques*, **49**, 617–622.

Schäfer, R., Hubert, A. and Herzer, G. (1991). Domain observation on nanocrystalline material. *Journal of Applied Physics*, **69**, 5325–5327.

Stoner, E.C. and Wohlfarth, E.P. (1948). A mechanism of magnetic hysteresis in heterogeneous alloys. *Philosophical transactions of the Royal Society of London*, **240**, 599–642.

Suzuki, K., Herzer, G. and Cadogan, J.M. (1998). The effect of coherent uniaxial anisotropies on the grain-size dependence of coercivity in nanocrystalline soft magnetic alloys. *Journal of Magnetism and Magnetic Materials*, **177–181**, 949–950.

Wang, Y.J. and Kronmüller, H. (1982). The influence of surface conditions on the magnetic properties in amorphous alloys $Fe_{40}Ni_{40}B_{20}$ and $Co_{58}Ni_{10}Fe_5Si_{11}B_{16}$. *Physical Status Solidi A*, **70**, 415–421.

Yoshizawa, Y., Oguma, S. and Yamauchi, K. (1988). New Fe-based soft magnetic alloys composed of ultrafine grain structure. *Journal of Applied Physics*, **64**, 6044–6046.

Modeling of Nonlinear Behavior and Hysteresis in Magnetic Materials

David C. Jiles and Yevgen Melikhov
Cardiff University, Cardiff, UK

1 INTRODUCTION

Material properties, including magnetic properties, depend on a number of factors operating on different length scales so that often the situation is beyond a description based on simple theories with one or two equations. Even though progress is still being made to make computer-aided design simulators for materials more realistic, much more is still needed before a material with the desired performance can be designed from first principles. Reliable accurate theoretical models are needed which can provide enough predictive accuracy. For magnetic materials, a model accurately describing hysteresis loops should be the foundation of such computer-aided design tools. Many magnetic properties such as coercivity, remanence, susceptibility, and energy loss can then be determined from the modeled hysteresis loop.

There were many attempts in the past to develop analytical models that accurately describe actual experimental magnetization data. Models have been suggested to describe the magnetization of ferromagnetic materials. However, only some of these have had prolonged success. These include the Preisach model (Preisach, 1935), the Stoner–Wohlfarth model (Stoner and Wohlfarth, 1948, 1991), the Globus model (Globus, 1962, 1975), and the Jiles–Atherton model (Jiles and Atherton, 1986). A detailed review on these models has been given by Liorzou, Phelps and Atherton (2000). Before these models can be used in a meaningful way, one has to be aware of the strengths and weaknesses of each model, since none of these is capable of giving a truly comprehensive description of the many magnetic processes that take place in a magnetic material.

2 DEVELOPMENT OF HYSTERESIS THEORIES AND CONCEPTS

The phenomenon of hysteresis arises most often as a result of cooperative behavior of a large number of identical interacting elements (Vicsek, 2001). The most familiar examples occur in ferromagnetism, but similar behavior occurs in ferroelectrics (Chen and Montgomery, 1980), ferroelastics (Tuszynski, Mroz, Kiefte and Clouter, 1988), and mechanics,

Handbook of Magnetism and Advanced Magnetic Materials. Edited by Helmut Kronmüller and Stuart Parkin. Volume 2: *Micromagnetism*. ISBN: 978-0-470-02217-7.

particularly fatigue. For a long time, theory and modeling of hysteresis in magnetic materials was a subject for the specialist investigator. However, in recent years, the widespread accessibility and increasing capability of computers has made modeling available to a much wider range of investigators, so that this area of study has become of much broader interest.

In order to improve materials on a systematic basis, it is necessary to have an understanding of the underlying physics of the magnetization process and, in particular, the relationship between structure and properties of magnetic materials. This understanding can then be used to direct research along directions that are likely to be successful in identifying materials with the desired properties. Another reason for modeling the magnetic properties is in the design of devices, using computer-aided design methods, whereby the performance of materials with different properties can be assessed and compared. These techniques can be used to identify suitable materials properties for particular applications and can show how devices are likely to perform. This approach means that much of the expense in designing and constructing devices could be eliminated through the use of computer-aided modeling techniques so that design changes and optimization are performed on a computer and the final construction is then based on the ideal design including an accurate description of the magnetic properties.

The magnetic modeling methods that are in use today are quite diverse and the choice of model depends crucially on the length scale of interest. Ultimately these models depend on the presence of magnetization (magnetic moment per unit volume) in certain localized volumes of materials. This magnetic moment per unit volume can be represented in terms of a net magnetic moment per atom, although in many cases, the magnetic moment is not actually localized on the atomic/ionic cores, but instead, is caused by itinerant electrons. The models that we will consider here range from first principles calculations at the level of discrete magnetic moments, such as those of Landau, Lifshitz, and Gilbert, to methods that can be used to model whole magnetic components of devices on the macroscopic scale such as the Preisach model.

3 MODELING OF NONLINEAR MAGNETISM AT THE DISCRETE LEVEL

From the time of ampere and oersted, it was known that on the macroscopic scale, a magnetic dipole moment of fixed magnitude m would rotate under a magnetic field H with torque Λ according to the equation

$$\Lambda = \mu_0 m \times H \tag{1}$$

This same concept, the general torque equation, can be applied at the atomistic scale, or at the level of discrete magnetic moments of fixed magnitude, but variable orientation. This approach can be used to describe the behavior of an individual magnetic moment. The behavior of the entire material can then be determined by integrating the same process over the entire solid. The rate of change of magnetization M with time depends on the torque

$$\frac{\partial M}{\partial t} = -\gamma \Lambda \tag{2}$$

where γ is the gyromagnetic ratio. In the absence of damping a magnetic moment that is not initially aligned with the total field will precess around the field direction with a resonance frequency ω_0, which depends on the strength of the field and the magnitude of the moment

$$\omega_0 = \gamma \, \mu_0 \, H \tag{3}$$

In the complete absence of damping, this precession will continue for infinite time as shown in Figure 1(a). In practice, there is always some damping in solids and therefore for light damping (long time constant) there will be some precessional motion, and some rotational motion toward the field direction as shown in Figure 1(b). The time taken to do this will depend on the damping coefficient. At high levels of damping (short time constant), the precessional component of the motion is suppressed because the moment reaches its final equilibrium orientation before precession has taken place, as shown in Figure 1(c).

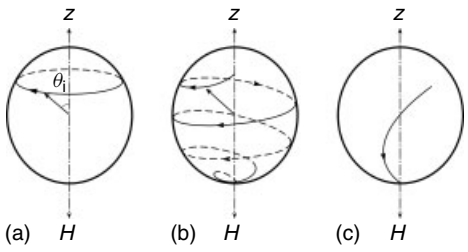

Figure 1. The motion of magnetic moment under the action of a magnetic field depends crucially on the level of damping. (a) No damping results in precession, (b) light damping results in a spiraling motion of the magnetic moment into the field direction, and (c) heavy damping results in a rotation of the moment into the field direction with no precession.

3.1 The Landau–Lifschitz–Gilbert model

The preceding equations describe the behavior of magnetic moments in isolation. In a magnetic material, there are interactions between the moments, so that magnetism in solids is a cooperative process. Therefore, the preceding equation must be modified when dealing with moments in a solid to take into account these interactions. Landau and Lifshitz (1935) and Landau (1967) suggested the following modification

$$\frac{\partial M}{\partial t} = -\gamma \Lambda - \frac{4\pi \lambda_{\mathrm{d}}}{M^2}(M \times M \times H) \tag{4}$$

where λ_{d} is the damping coefficient and the second term on the right-hand side of the equation is the damping term which restrains, effectively slows down, the rotation of the moments under the action of a field. There is no direct experimental verification of the damping term, but the existence of such a term in bulk materials is reasonable from a theoretical standpoint.

A crucial question arises over the exact form of the magnetic field H that should be used in this equation. For an isolated magnetic moment in free space, this will be just the classical magnetic field obtained from Maxwell's equations. However, in view of the magnetic interactions that exist within a material, this total field must also include any other interactions that give rise to a turning force on a dipole. An obvious and well-known example of this is the exchange interaction, which is not included in the classical description of the magnetic field under Maxwell's equations.

The damping coefficient in the model equation is treated as an adjustable parameter, since there appears to be no obvious way to determine this from first principles. A value is used that is consistent with experimental data and this is then used to determine the behavior of an array consisting of a large number of individual magnetic moments under the action of an applied field. The model does not explicitly include temperature in the calculations, although one can argue that the damping coefficient is temperature dependent. However, this provides only one rather arbitrary way of including temperature effects in the model.

Subsequently Gilbert considered the problem from a continuum perspective, and developed a modified form of the equation (Gilbert, 1955, 2004). The Gilbert form of the equation, as shown in the following text, is now used more often than the Landau–Lifshitz form of the equation:

$$\frac{\partial M}{\partial t} = -\gamma \mu_0 M \times H + \frac{\alpha}{M}\left(M \times \frac{\partial M}{\partial t}\right) \tag{5}$$

where α is damping parameter.

In principle, the Landau–Lifshitz–Gilbert (LLG) model can be used either at the atomistic scale or at the 'micromagnetic' continuum scale with the unit cells being much smaller than a single domain. The model is really directed toward volumes smaller than a single domain. Practical applications of the model are made at length scales much greater than the atomistic. Individual 'moments' are defined for the purposes of the model at the level of typically 50 nm and each of these moments is treated as an indivisible unit. This can be justified if there is coherent rotation of the atomic moments occurring over the volume occupied by these moments. The model is suitable for time-dependent calculations of the reorientation of magnetic moments under the action of a field. It has the advantage over other models of not requiring the moments within a domain to be parallel, in fact as shown in Figure 2 it calculates the optimum orientations of moments, which in general are not necessarily parallel.

The results of calculations based on the LLG model can be averaged to provide hysteresis curves of materials as shown in Figure 3. The model can be extended beyond the range of the single domain into simulations of multidomain specimens through the use of finite element methods. This approach, known as *computational micromagnetics*, enables both micro- and macroscale calculations to be incorporated into a single model simulation (Kronmuller, Fischer, Hertel and Leineweber, 1997; Fidler and Schrefl, 2000). This allows microstructure of a material to be included in the simulation and in this way it is possible to combine the advantage of exact theoretical equations developed for a small number of interacting magnetic moments with applications to practical materials.

4 MODELING OF NONLINEAR MAGNETISM BY DOMAIN ROTATION

Some aspects of hysteresis can be described in terms of a model of the rotation of magnetization. This takes no account of the details of the individual moments below the single domain in scale and therefore unlike the LLG model, it does not try to account for the differences in orientations of individual magnetic moments within the domain.

Within domains, the model considers the competing effects of anisotropy and magnetic field on the orientation of moments as shown in Figure 4. The domains themselves can have random alignments or they can be textured (meaning preferred orientation) or they can be even completely aligned in certain directions, although this would be a relatively trivial case requiring nothing more than a calculation of moment orientations within one single-domain particle.

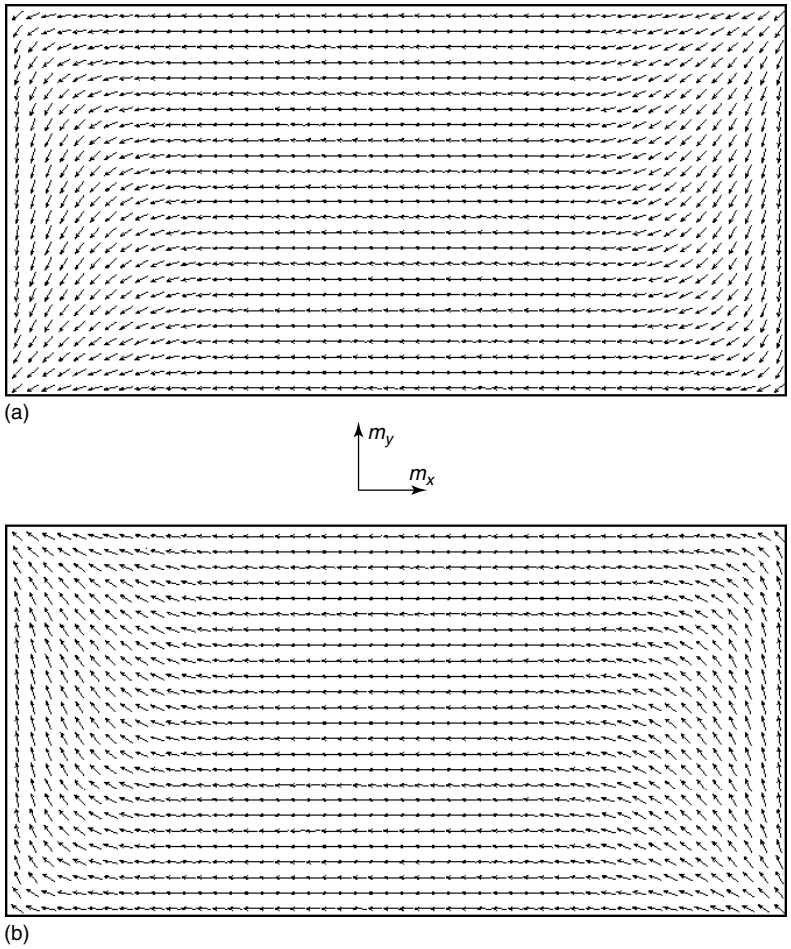

Figure 2. Solution of the Landau–Lifshitz–Gilbert equation for an array of magnetic moments representing a thin film of permalloy of dimensions 2 μm by 0.5 μm. (After R.D. McMichael, http://www.ctcms.nist.gov/~rdm/mumag.org.html.) For the purposes of calculation, each individual magnetic moment occupies an area of 0.05 μm ×0.05 μm. The solution shows the remanent state after the magnetization had been saturated along the long axis (a) and after the magnetization had been saturated along the short axis (b). (With special thanks to Dr Robert D McMichael.)

4.1 The Stoner–Wohlfarth model

The Stoner–Wohlfarth model takes as its basis an array of single-domain particles that can reorient their magnetization by coherent rotation of all moments within the domain. The model considers a dispersion of single-domain magnetic particles in some other unspecified matrix material. The model in its original formulation assumed that there were no magnetic interactions between the particles. In other words, the distribution of the particles was so dilute that each particle was effectively isolated and could not be influenced by the orientation of any other particles. This assumption can be changed, and in fact, it has been changed by others, although including such interactions adds greatly to the computational complexity of the model. The model in its original formulation also assumed axial anisotropy. This is the simplest type of anisotropic calculation to make. Other forms of anisotropy such as cubic can be included (Lee and Bishop, 1966).

The basic idea of the model is to consider the reorientation of a magnetic moment within a single-domain particle in which the applied field is at some arbitrary angle to the anisotropic easy axis. In the case of the uniaxial easy axis along the field direction (Figure 5), this results in a bimodal switching behavior with resultant coercive fields in the forward and reverse directions. In the other extreme case, where the magnetic field is applied along the anisotropic hard axis, this results in a magnetization curve with no coercivity (Figure 6). In general, the domains will be oriented at an arbitrary angle relative to the field and such domains will have properties that lie between these two extremes (Figure 7). A material may be considered to consist of an assembly of domains, each at different angles to the field direction (Figure 8). The overall magnetization of the multidomain

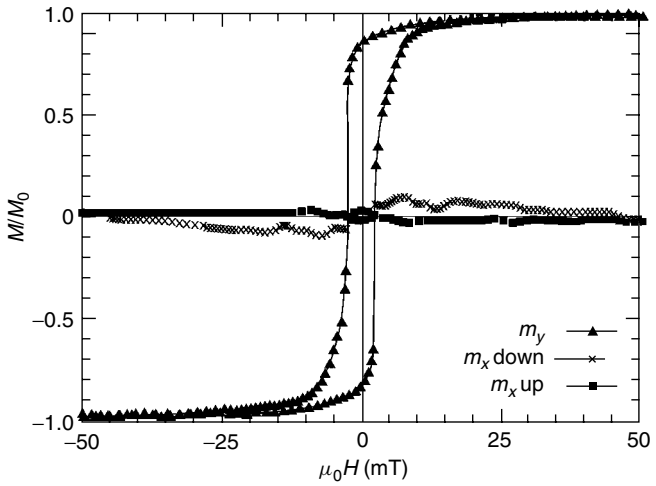

Figure 3. Calculated magnetization curve for the 2 mm $\times$0.5 mm permalloy film shown in Figure 2. 'm_y' shows the component of magnetization along the long axis.

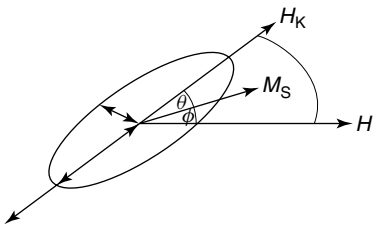

Figure 4. Rotation of magnetization M_S of an isolated single domain under the competing effects of magnetic field H and anisotropy H_K.

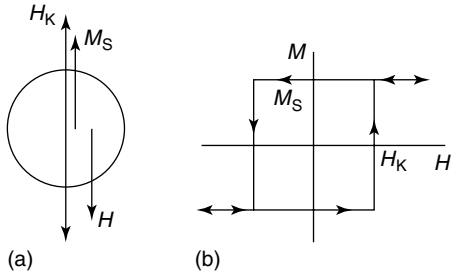

Figure 5. (a) Rotation of the direction of magnetization M_S of a single-domain particle with uniaxial anisotropy, oriented with its easy axis H_K along the direction of the applied field H, and (b) its corresponding magnetization curve.

sample is then the vector sum of all of the magnetic moments of the domains divided by the total volume as shown in Figure 9.

The turning force on a magnetic moment due to the applied field depends on the vector product of magnetic moment with magnetic field. The turning force on the magnetic

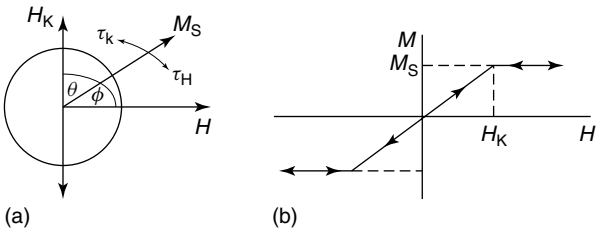

Figure 6. (a) Rotation of the direction of magnetization M_S of a single domain particle with uniaxial anisotropy, oriented with its easy axis H_K perpendicular to the direction of the applied field H, and (b) its corresponding magnetization curve (note absence of hysteresis).

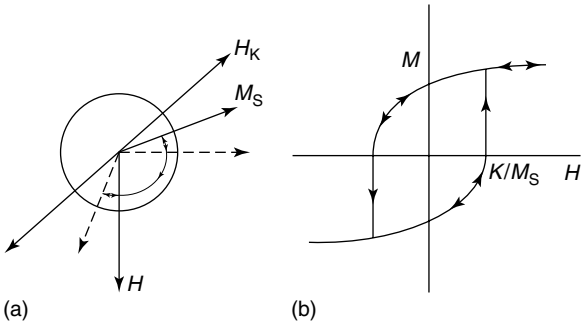

Figure 7. (a) Rotation of the direction of magnetization M_S of a single domain particle with uniaxial anisotropy, oriented with its easy axis H_K at an arbitrary angle to the direction of the applied field H, and (b) its corresponding magnetization curve.

moment due to anisotropy is the derivative of the energy with respect to angle. The Stoner–Wohlfath model determines the equilibrium orientation of magnetization by equating these terms. For a particle with uniaxial anisotropy, the equilibrium orientation is given by

$$\mu_0 H M_S \sin\phi - 2K_1 \sin\theta\cos\theta - 4K_2 \sin^3\theta\cos\theta = 0 \quad (6)$$

where ϕ is the angle of the magnetization M_S relative to the field H, K_1 and K_2 are the first and second anisotropy coefficients, respectively, and θ is the angle of the magnetization relative to the magnetic easy axis. From the Stoner–Wohlfarth model, it is possible to calculate the saturation field H_S needed to rotate the magnetization of the most difficult domain oriented at 90° to the field direction,

$$H_S = \frac{2K_1 + 4K_2}{\mu_0 M_S} \quad (7)$$

It is also possible to calculate the coercivity of the domains based on the switching field needed to reorient the domain aligned antiparallel to the field,

$$H_C = \frac{2K_1}{\mu_0 M_S} \quad (8)$$

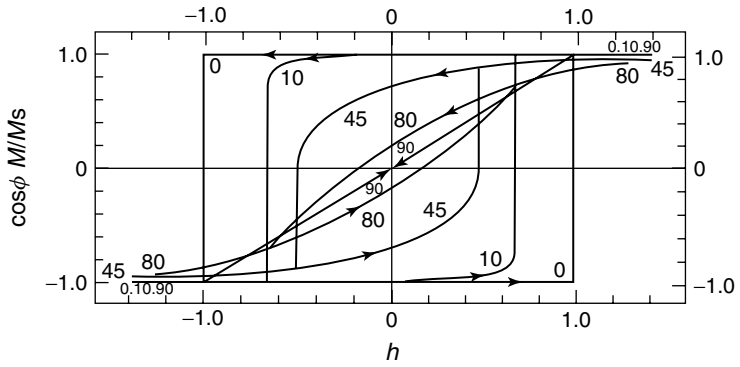

Figure 8. Magnetization curves obtained using the Stoner–Wohlfarth model for domains with uniaxial anisotropy oriented with different directions of the easy axis relative to the applied field. The field axis is shown in units of 'reduced field' h, whereby $h = 1$ corresponds to a field strength of $K/(\mu_0 M_S)$, where K is the anisotropy coefficient and M_S is saturation magnetization. The magnetization axis shows the component of magnetization along the field direction, normalized relative to the saturation magnetization M_S.

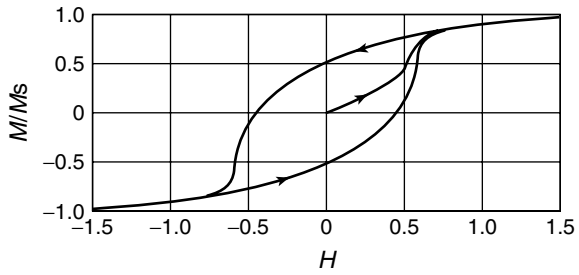

Figure 9. A composite hysteresis curve obtained by summing the elementary magnetization curves for a randomly distributed orientation of easy axes.

The model has been widely used for describing the dependence of magnetic properties of materials on anisotropy and texture. In addition, many of the original ideas behind the model have been developed and extended and have found applications in fine particle systems (Spratt, Bissell, Chantrell and Wohlfarth, 1988; Chantrell, 1997).

5 MODELING OF NONLINEAR MAGNETISM BY DOMAIN BOUNDARY MOVEMENT

In multidomain samples, much of the magnetization change occurs in the domain boundary regions and therefore it is of great interest to know and understand what changes are occurring at the boundary in order to describe and predict the properties of such materials. The importance of domain boundary motion has been recognized by many investigators including (Becker, 1932; Kersten, 1943, 1956; Neel, 1944, 1959; Globus, 1962, 1975; Globus and Duplex, 1966, 1969; Globus, Duplex and Guyot, 1971; Globus and Guyot, 1972; Guyot and Globus, 1973; Escobar, Valenzuela and Magana, 1983; Escobar, Magana and Valenzuela, 1985) and more recently by Bertotti (1988). The main idea in the treatment of domain boundary motion is to separate the motion into two components: reversible and irreversible. In most respects, this separation is somewhat artificial, since both processes take place together in multidomain materials. However, the physics of the situation can be more easily analyzed if these processes are separated. Irreversible processes necessarily cause energy dissipation and lead to coercivity and hysteresis while reversible processes do not.

The motion of domain walls can further be divided into two types: flexible wall motion and rigid wall motion. The higher the surface energy of the domain walls, the greater the tendency to move in planar fashion, particularly if the pinning sites that restrain the domain wall are weaker. On the other hand, domain walls with lower surface energy will tend to bend first, particularly if the pinning sites are stronger. In practice, components of both types of movement occur together.

5.1 The Becker–Doring model

In the case of planar wall motion, much of the early modeling was developed by Becker, who was particularly concerned with the movement of domain walls interacting with regions of inhomogeneous strain, such as dislocations. Simplifying assumptions need to be made in order that an analytical solution can be obtained. Assuming a simplified periodically varying internal potential through which the domain walls move, an expression for the initial susceptibility χ_{in} for a material of a volume V composed of 180° domain walls of thickness δ can be derived in terms of the amplitude and

wavelength of the periodic potential,

$$\chi_{\text{in}} = \frac{2\ A\ l^2\ \mu_0\ M_S^2\ \cos^2\theta}{3\pi^2\ \lambda_S\ \sigma_0\ V\ \delta} \tag{9}$$

where θ is the angle of the domain magnetization relative to the applied magnetic field, A is the cross-sectional area of the wall, l is the periodicity of the internal potential with amplitude $E_{\max} = 3\ \lambda_S\ \sigma_0/2$ due to periodically varying stress of amplitude σ_0 in a material of magnetostriction λ_S. The critical field, or local coercivity, occurs when the domain wall moves over one of the local maxima in the slope of the potential and is therefore given by

$$H_C = \frac{\pi\ E_{\max}\ \delta}{l\ \mu_0\ M_S\ \cos\theta} \tag{10}$$

5.2 The Kersten–Néel model

Models have been developed by Néel and Kersten in the case of domain wall bending as shown in Figure 10. Kersten, in particular, was concerned with the movement of domain walls that were pinned by 'inclusions', which meant simply inhomogeneous volumes within the material. In this case, equations can be derived for the initial susceptibility for small deformations of the domain wall

$$\chi_{\text{in}} = \frac{\mu_0 M_S^2\ l^3 h(\cos\theta_1 - \cos\theta_2)^2}{3\gamma_\pi V} = \frac{\mu_0 M_S^2\ l^2 h(\cos\theta_1 - \cos\theta_2)^2}{3\gamma_\pi L} \tag{11}$$

where l is the spacing between the pinning sites, L is the length of the domain, γ_π is the domain wall energy per unit area, V is a volume of a material, and h is the length of the section of domain wall as shown. For the local coercivity

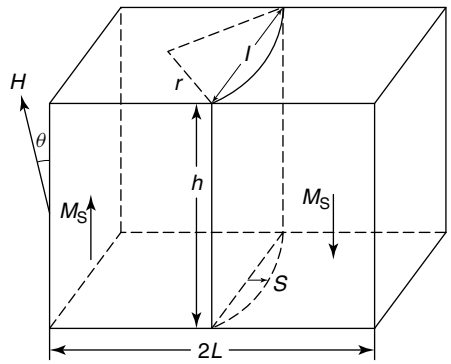

Figure 10. Deformation of a domain wall under the action of an applied magnetic field.

or critical field H_C above which the domain wall will break away from the pining site

$$H_C = \frac{\gamma_\pi\ \cos\phi_{\text{crit}}}{\mu_0\ M_S\ l\ (\cos\theta_1 - \cos\theta_2)} \tag{12}$$

where θ_1 and θ_2 are the angles of the magnetization relative to the magnetic field on either side of the domain wall.

5.3 The Globus–Guyot model

In the case of ferrites in which the defects are mostly confined to grain boundaries, the domain walls will be pinned principally at the grain boundaries and therefore the behavior can be modeled assuming that the domain walls move simply by bending like an elastic membrane as described by Globus (1962). The Globus model depends on equations for deformation of the domain walls similar to those of Kersten. For the purposes of modeling, an approximation is made in which the grains are assumed to be spherical. Most applications of ferrites are for higher frequency magnetic field and therefore the domain walls can be considered to vibrate under the action of a time-dependent field.

Under the action of a 'weak' applied magnetic field, the domain walls deform but remain fixed on the grain boundaries. From this it was predicted that the permeability depended linearly on the grain diameter. Comparison with experiment yielded good agreement (Globus and Duplex, 1966). Further studies showed that wall motion components dominate in ferrites, while rotational processes, which are dependent on anisotropy but not grain size, are of secondary importance in these materials (Globus and Duplex, 1969). The equation governing the deformation of the magnetic domain walls are described by Globus, Duplex, and Guyot (1971). Although the model was developed originally to describe the properties of ferrites, it was later shown to be valid for spinels and garnets. Dissipative processes resulting from translation of the domain walls at higher field strengths were added to the model subsequently by Guyot (Globus and Guyot, 1972; Guyot and Globus, 1973).

The most comprehensive treatment of the underlying theory of this model, including most of the equations, has been given by Escobar, Valenzuela and Magana (1983) and Escobar, Magana and Valenzuela (1985). Accordingly, the initial susceptibility due to domain wall bending is

$$\chi_{\text{in}} = \frac{\mu_0\ M_S^2\ D}{\gamma_\pi} \tag{13}$$

where M_S is saturation magnetization, γ_π is the domain wall surface energy, and D is the grain diameter. The value of the

critical field for the unpinning of domain walls is

$$H_C = \frac{2\ f}{\mu_0\ M_S\ D} \tag{14}$$

where f is the pinning force per unit length on the domain wall along the grain boundary, which is assumed to be independent of the applied field.

5.4 The statistical pinning theory model

If the force $f(z - z_J)$ between a defect at position z_J in a ferromagnetic material and a domain wall at position z moving perpendicular to z is introduced, the total force $F(z) = \sum_{J=1}^{N} f(z - z_J)$ of all defects N interacting with the domain wall could be taken into account using statistical methods. Such model was elaborated by Kronmuller and others (Kronmuller, 1992), and allowed computing the properties of the initial magnetization curve and the parameters of the hysteresis loop in the Rayleigh region $M = \chi_{in}\, H + \alpha_R\, \mu_0\, H^2$:

$$\begin{aligned} H_C &= \frac{1}{\mu_0 M_S A|\cos\phi|}\left(\frac{B_0}{2}\right)^{1/2}\left(\ln\frac{L_3}{2L_0}\right)^{1/2} \\ \chi_{in} &= \frac{\mu_0 A(2M_S\cos\phi)^2}{L_3}\left(\frac{\pi}{2B_1}\right)^{1/2} \\ \alpha_R &= \frac{\mu_0 A^2|2M_S\cos\phi|^3}{2\pi}\frac{L_0}{L_3}\frac{1}{B_0} \end{aligned} \tag{15}$$

where L_0 is the distance between two adjacent defects, L_3 and A are the domain wall length and area, respectively, ϕ is the angle between the applied field and magnetization. B_0 and B_1 are correlation functions, which are directly proportional to the number of defects N and are related to the individual interaction force $f(z - z_J)$ of a defect.

5.5 The stochastic process model

Domain wall modeling concepts can be through the use of domain wall eddy current dissipation (Bertotti, 1988) and stochastic process models, in which the domain wall moves through a randomly fluctuating potential (Alessandro, Beatrice, Bertotti and Montorsi, 1990; Bertotti, Mayergoyz, Basso and Magni, 1999). The randomness of the potential seen by the domain walls can be quantified using two independent parameters, which represent mathematically the physical properties of the potential in terms of an average amplitude and an average fluctuation wavelength.

If H_C is a randomly fluctuating function of position, then it will also be a randomly fluctuating function of the flux Φ. Local maxima in H_C represent pinning sites in the material, and for large displacements of domain walls, there will be a correlation length ζ which represents the range of interaction of domain walls with pinning sites. These effects can be described if it is assumed that the local coercivity H_C obeys a Langevin equation of the form

$$\frac{dH_C}{d\Phi} + \frac{H_C - \langle H_C\rangle}{\zeta} = \frac{dW}{d\Phi} \tag{16}$$

where now the 'flux' Φ is the measure of displacement of domain walls, instead of the position, $W(\Phi)$ is a randomly fluctuating ('white noise') function whose average value will be zero, and ζ is the interaction length, or correlation length, for domain walls with pinning sites. Eventually with some additional limiting assumptions the equation reduces to

$$\frac{d\dot{\Phi}}{dt} + \frac{1}{\tau}(\dot{\Phi} - \mu_0\, A\ \dot{M}) = -\frac{1}{\sigma\ G}\frac{dH_C}{dt} \tag{17}$$

where A is cross-sectional area of the domain wall, G is a dimensionless parameter, τ is a characteristic relaxation time, and σ is the electrical conductivity.

The motion of domain walls through the internal randomly fluctuating potential, leads to discontinuous changes in magnetization. These discontinuous processes are manifested as Barkhausen noise (Schlesinger, 2001), which is closely connected with the existence of hysteresis. Hysteresis is found to be a direct result of discontinuous, dissipative processes occurring over small volumes which when summed together produce the familiar hysteresis over larger volumes. The Barkhausen emissions are fractal in nature, which means that the structure of the Barkhausen emissions is independent of the scale. A review of the theory behind domain wall dynamics and the Barkhausen effect has been given by Jiles (2000).

The domain boundary models are best applied to multidomain materials in which the movement of magnetic domain boundaries is the principal magnetization mechanism. This means mostly bulk soft magnetic materials with low anisotropy and with large density of inhomogeneities either in the form of strains (dislocations) or inclusions (particles of a second phase).

6 MODELING OF NONLINEAR MAGNETISM BY SWITCHING MECHANISMS

A model for description of hysteresis based on switching mechanisms such as the Barkhausen effect was proposed by Preisach (1935). This assumes that a material is composed of an assembly of elemental volumes that each have

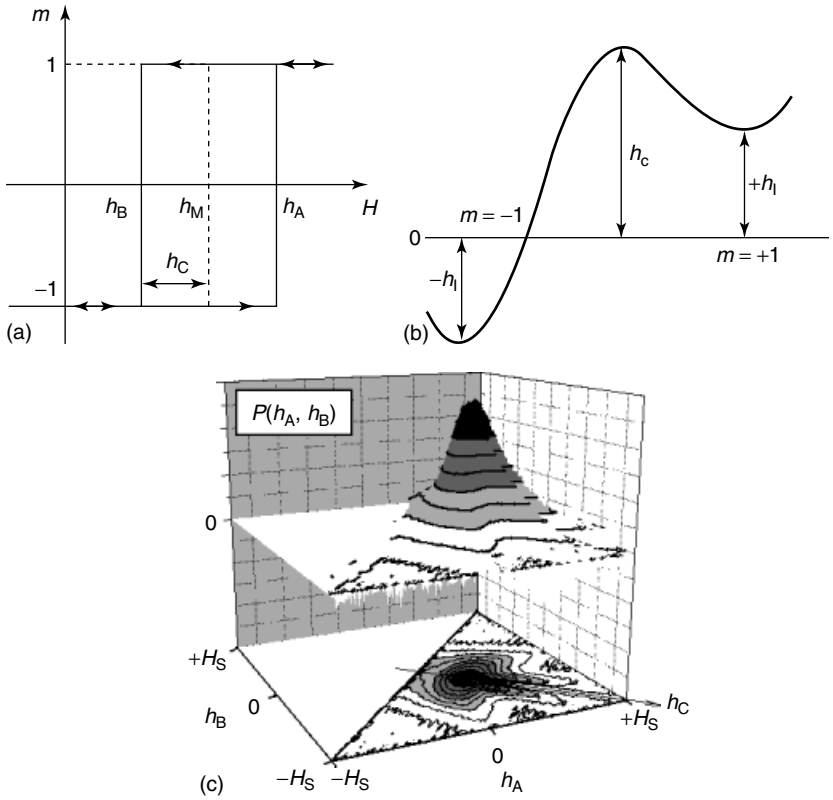

Figure 11. (a) Magnetization curve for an elementary hysteresis loop and (b) its energetic representation as an elementary metastable two-level subsystem, where the two states $m = \pm 1$ (represented by local minima) are divided by a barrier. Differences between extrema and energy level 0 are shown in units of magnetic field. (c) An example of a 3D plot of a Preisach function $P(h_A, h_B)$ and its corresponding contour plot.

a characteristic pair of switching fields (forward and reverse coercivities) from which the local magnetization curve of the elemental volume can be represented by a rectangular hysteresis loop. The following possibilities are allowed: (i) the width of the elementary loops have a certain distribution function, whereby loops with zero width can occur; (ii) the elementary local hysteresis loops can have their midpoints offset from zero field, which is known as a *bias field*. It is evident that the magnetic state of such local regions will be field-history dependent. All of the above considerations will therefore result in magnetic hysteresis.

6.1 The classical Preisach model

The classical Preisach model (CPM), (Preisach, 1935; Mayergoyz, 1986, 1991) is based on the assumption that a ferromagnetic material consists of a large number of elemental switching volumes. Each fragment is described by an elementary rectangular hysteresis loop, which has two field parameters, the critical or the coercive field of the free fragment h_C, and the bias field, or offset field, h_I. It is useful and convenient to introduce the switching field parameters h_A and h_B (Figure 11(a)):

$$h_A = h_I + h_C, h_B = h_I - h_C \tag{18}$$

The meaning of the switching fields is the following: if the external magnetic field is increased to H_1, all elemental switching volumes whose switching field h_A was lower or equal to the external field $h_A \leq H_1$ would switch their magnetization up; if the magnetic field is decreased to H_2, all elemental switching volumes whose switching field h_B was higher or equal to the external field $h_B \geq H_2$ would be switched down. The magnetization of all other elemental switching volumes will depend on previous history of changes of the external magnetic field.

Introducing the plane defined by the switching fields h_A, h_B. Each elemental switching volume has its own point on that plane and that point is unique for each volume. It is possible to assume, from the physical point of view, that h_C may be nonnegative only $h_C \geq 0$, that is, the half of the plane, $h_A \geq h_B$, will be meaningful only. A probability distribution function of the elemental switching volumes with

the switching fields h_A, h_B or Preisach function $P(h_A, h_B)$ may be defined in the plane of the Preisach variables h_A, h_B. It is necessary to stress that by definition and from the physical meaning of the probability distribution function, the values of the Preisach function $P(h_A, h_B)$ are nonnegative on the whole plane $h_A \geq h_B$ (Figure 11(c)):

$$P(h_A, h_B) \geq 0 \tag{19}$$

It is possible to show (Mayergoyz, 1991) that the half of the plane $h_A \geq h_B$ is always divided into two parts, $S^{(+)}$ and $S^{(-)}$, by a staircase line $L(t)$ (where t is time), which represents the history of the changes of the external magnetic field (Figure 12). All elemental switching volumes in the part $S^{(+)}$ are switched up and have the magnetization '+1', all elemental switching volumes in the part $S^{(-)}$ have the magnetization '−1'.

Introducing a simple hysteresis operator $\gamma(h_A, h_B)$ defined on the plane h_A, h_B:

$$\gamma(h_A, h_B)H(t) = Q(h_A, h_B) = \begin{cases} +1, & \text{if} \quad (h_A, h_B) \in S^{(+)} \\ -1, & \text{if} \quad (h_A, h_B) \in S^{(-)} \end{cases} \tag{20}$$

According to the CPM, the total magnetization of the system with hysteresis can be written in the form:

$$\begin{aligned} M(t) &= M_S \iint_{h_A \geq h_B} P(h_A, h_B)\gamma(h_A, h_B)H(t)\, \mathrm{d}h_A\, \mathrm{d}h_B \\ &= M_S \iint_{h_A \geq h_B} P(h_A, h_B)\, Q(h_A, h_B)\, \mathrm{d}h_A\, \mathrm{d}h_B \\ &= M_S \iint_{S^{(+)}} P(h_A, h_B)\, \mathrm{d}h_A\, \mathrm{d}h_B - M_S \\ &\quad \times \iint_{S^{(-)}} P(h_A, h_B)\, \mathrm{d}h_A\, \mathrm{d}h_B \end{aligned} \tag{21}$$

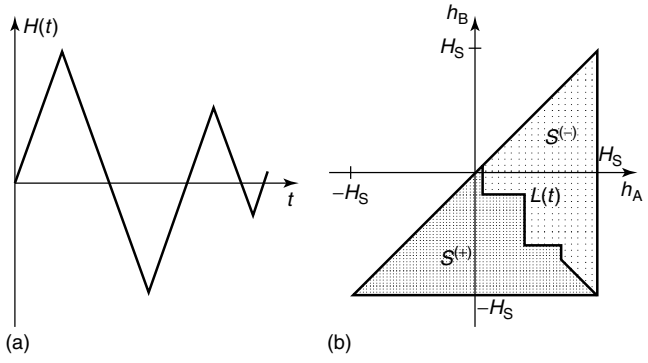

Figure 12. (a) A history of changes of the external magnetic field and (b) its representation by a staircase line $L(t)$ in the plane of the switching fields h_A, h_B. The staircase line $L(t)$ divides the Preisach plain into two areas $S^{(+)}$ and $S^{(-)}$. H_S is magnetic field at which magnetic saturation of sample is achieved.

where M_S represents saturation magnetization of the specimen.

The magnetization always reaches a saturation point, which means that any increase of the external magnetic field H after some field H_S will not influence the total magnetization of the system any further. This means, taking into account equations (19) and (21), that in such regions where $h_A \geq H_S$ or $h_B \leq -H_S$, the Preisach function is strictly equal to zero $P(h_A, h_B) = 0$. For the geometric interpretation of the CPM, it is possible to look only at the Preisach triangle which is defined by these inequalities: $-H_S \leq h_A \leq H_S, -H_S \leq h_B \leq H_S, h_A \geq h_B$.

Starting from the demagnetized state, which assumes equality of numbers of the switched up and switched down elemental volumes, together with the symmetry of the $P(h_A, h_B)$ function along the $h_A = -h_B$ line, the Preisach triangle will be divided as shown in Figure 13(a).

Increase of the external magnetic field now results in the initial magnetization curve or virgin curve (Figure 13(b)). After the saturation field H_S is achieved, all elemental volumes will be switched up and the system will be saturated. Next gradual decrease of the external magnetic field to the negative value of the saturation magnetic field $-H_S$ gives first the remanent magnetization M_R (Figure 13(c)), then the coercive field H_C, and finally a negative saturation state.

The basic properties of the CPM and the fundamental representation theorem will be mentioned here briefly. A detailed description of the properties and the proof of the theorem may be found in Mayergoyz (1986, 1991).

Staircase line $L(t)$, the prehistory of the material: The interface $L(t)$ between the regions $S^{(+)}$ and $S^{(-)}$ has a staircase shape. Moreover, past extreme values of the external magnetic field may be found on this line as h_A, h_B coordinates of the vertices of each 'step'.

W*iping-out property*: Each local input maximum wipes out the vertices of $L(t)$ whose h_A coordinates are below this maximum, and each local minimum wipes out the vertices whose h_B coordinates are above this minimum. It is worth noting that the wiping-out property is usually fulfilled in real magnetic materials.

Congruency property: All minor hysteresis loops corresponding to back-and-forth variations of the external magnetic field between the same two consecutive extreme values are congruent. Unlike the wiping-out property, the congruency property is not fulfilled very often for real magnetic materials.

Symmetry of the CPM: The symmetry property may be written as

$$P(h_A, h_B) = P(-h_B, -h_A) \tag{22}$$

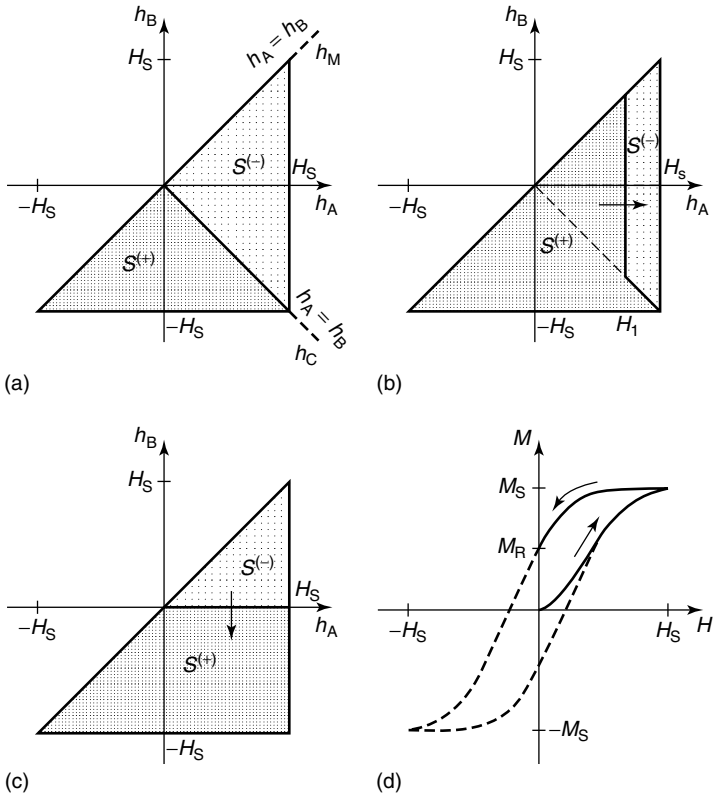

Figure 13. The Preisach triangle in the plane of the switching fields (a) at the demagnetized state, (b) for the initial curve, and (c) at the remanent magnetization. (d) Hysteresis curve corresponding to the (a)–(c) paths.

Representation theorem: The wiping-out property and the congruency property constitute the necessary and sufficient conditions for a hysteresis nonlinearity to be represented by the CPM on a set of monotonically increasing field amplitudes.

To use the CPM one needs first to check the wiping-out and congruency properties and then to define the Preisach function $P(h_A, h_B)$. It is difficult to determine the analytical form of the $P(h_A, h_B)$ even in cases where it is possible to describe the system by the CPM. However, the numerical form, in a matrix formulation, of $P(h_A, h_B)$ may be found without any difficulties. For this purpose, the discretization of the external magnetic field is employed in which, the coordinates h_A and h_B describe a mesh over the Preisach triangle. Assuming that the Preisach function is a constant over any single cell (meaning the average value for the cell) and finding the variation of the magnetization connected with this cell, one may find the average value of $P(h_A, h_B)$ for the cell. Such changes in magnetization can be determined if a set of symmetric minor loops or a set of first-order transition (reversal) curves is used.

Starting from the demagnetized state, the two nearest symmetric minor loops were measured (Figure 14); the loop

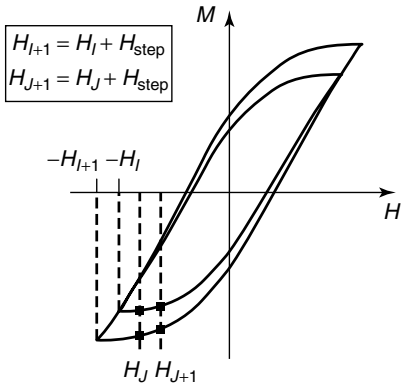

Figure 14. Two neighboring measured symmetrical minor loops used for experimental identification of the Preisach function.

with the larger amplitude of the external magnetic field is measured after the loop with the smaller amplitude. Let us consider the ascending branches of both loops. The maximum fields H_I and $H_{I+1} = H_I + H_{step}$ are the h_B coordinates for the loops; during the measurement of each loop, the h_A coordinate is varied only.

The integrated or local coercive field distribution function $P(h_C)$ (Basso, Bertotti, Infortuna and Pasquale, 1995) may

be constructed from the Preisach function $P(h_A, h_B)$:

$$P(h_C) = \int_0^{H_S} P(h_C, h_I)\, dh_I \tag{23}$$

This function gives the probability of finding all elemental volumes whose coercive field is equal to h_C.

Knowing the probability distribution function $P(h_A, h_B)$, it is possible to follow magnetization M as a function of the external magnetic field H by using equation (21) if the system is describable by the CPM. This procedure is known as *backward transformation*.

6.2 Variations of the Preisach model

The *moving Preisach model*, presented by Della Torre (1966), is the extension of the CPM when the Preisach function is modified to have magnetization dependence:

$$M(t) = M_S \iint_{h_A \geq h_B} P(h_A + \alpha M, h_B + \alpha M) \times \gamma(h_A, h_B) H(t)\, dh_A\, dh_B \tag{24}$$

where α is a mean field parameter that is material dependent. The moving model obeys congruency and wiping-out properties; however, congruency in this case is substituted by skew-congruency, where loops are congruent if they are bounded by the two skewed lines with $H + \alpha M = \text{const}$. The identification procedure for the moving Preisach model requires detection of α first and then finding the Preisach function in a standard way (Della Torre, 1991). The *complete moving hysteresis model* is a further extension of the moving Preisach model where, instead of a single square elementary magnetic hysteresis loop for each elemental volume, a more complicated elementary magnetic hysteresis loop with a parameter squareness S was introduced and this elementary loop was divided into fully irreversible and fully reversible components. This allowed both the locally reversible and irreversible components of the magnetization to be computed even for asymmetrical magnetizing processes (Vajda, Della Torre and Pardavi-Horvath, 1992; Vajda and Della Torre, 1993).

Another modification of the CPM with the Preisach function having magnetization dependence is called the *product model* (Kadar, 1987), which can be presented in the form:

$$\frac{dM}{dH} = R(M)\left[\beta + \int Q(h_A, h_B) dh_A\right] \tag{25}$$

where β represents a reversible component (reversible susceptibility when $M = 0$), $Q(h_A, h_B)$ is the residual Preisach function with the symmetrical properties of the classical Preisach function, and $R(M)$ is a noncongruency function,

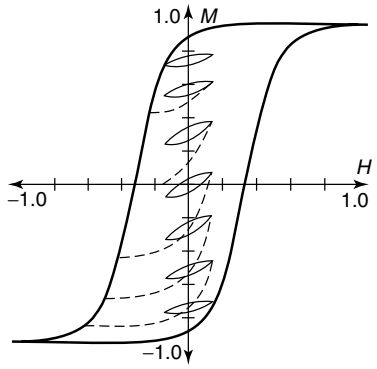

Figure 15. Nonlinear congruency property for the product model. In the classical Preisach model, the 'heights' of the minor loops ΔM, which are bounded by two vertical lines $H = \text{const}$, are equal. In case of product model, these 'heights' follow a nonlinear function. (Reproduced from from G. Kadar and E. Della Torre: 'Hysteresis modelling: I. Noncongruency', *IEEE Transactions on Magnetics* **23** (1987), © IEEE 1987, with permission from the IEEE.)

which has to be an even function of M, should have a maximum at $M = 0$ and should approach zero as M approaches saturation $\pm M_S$, such as $R(M) = 1 - (M M_S)^2$. The product model obeys wiping-out property (see Figure 15); however, congruency becomes nonlinear such that the 'height' of the minor loops ΔM which are bounded by two vertical lines $H = \text{const}$ is a nonlinear function (Kadar and Della Torre, 1987).

The wiping-out property is equivalent to the immediate formation of a stable hysteresis loop after only one cycle of field variation back and forth (see Figure 16). But in reality, accommodation occurs often in ferromagnetic materials. Accommodation, which is a gradual drifting of the minor hysteresis loop toward an equilibrium loop when the magnetic field is cycled between two limiting values, can be described by the modified Preisach models as was shown by Kadar and Della Torre (Della Torre and Kadar, 1987; Della Torre, 1994). In a *Preisach model for accommodation*, it is

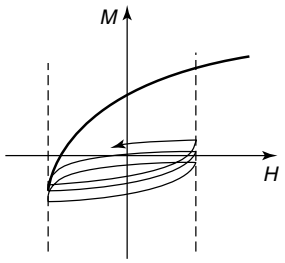

Figure 16. Accommodation, a gradual drifting of the minor hysteresis loop, which is cycled between two fields toward an equilibrium loop, as described by the *Preisach model for accommodation*. (Reproduced from E. Della Torre: 'A Preisach model for accommodation', *IEEE Transactions on Magnetics* **30** (1994), © IEEE 1994, with permission from the IEEE.)

assumed that the interaction field h_I of a hysteron can be changed, or equivalently that the elementary hysteresis loops can be 'moved'. It is also assumed that when a hysteron moves, its magnetization may either remain the same as it was or it may reverse into the opposite state. If it remains in the same magnetized state, it dilutes the neighboring hysterons. This situation is modeled by assuming that $Q(h_A, h_B)$ from equation (20) can be a constant value different from ± 1. Introducing the replacement factor $\xi, 0 \leq \xi < 1$, it is possible to take into account the accommodation of the minor loop.

6.3 The time-dependent Preisach model

In order to describe the dynamic hysteresis loops by the Preisach model, an elementary hysteresis loop $Q(h_A, h_B)$ from equation (20) was modified to include time $Q(h_A, h_B; t)$, so its time rate of change is proportional to the difference between the actual external field and the switching fields according to

$$\frac{\partial Q(h_A, h_B; t)}{\partial t} = \begin{cases} k\,[H(t) - h_A], & \text{when} \quad H(t) > h_A \\ k\,[H(t) - h_B], & \text{when} \quad H(t) < h_B \end{cases} \tag{26}$$

where k is an additional model parameter (Bertotti, 1992a; Bertotti and Pasquale, 1992b). This *rate-dependent Preisach model* allowed computing dynamic hysteresis loops and successfully interpreting dynamic losses per cycle per unit mass as a function of magnetizing frequency for soft magnetic materials, such as, for example, nonoriented SiFe steel. The similar idea of modifying an elementary hysteresis loop was also realized in Lu *et al*. (2003). For faster computations, keeping in mind engineering applications, another rate-dependent model, called the *external dynamic Preisach model*, was proposed in Fuzi (1999), where magnetization was computed by the CPM with modified input field, delayed with respect to the actual field strength. An example of the dynamic hysteresis loop computed by the external dynamic Preisach model is presented in Figure 17.

Krasnoselskii and Pokrovskii (1983) separated the basis of the model from its physical meaning and developed a general mathematical tool for description of hysteresis, be it magnetic, electric, mechanical, or any other general type of hysteretic phenomenon. Since then, a number of extensions of this model have been tried and applied for different purposes, but all of these are still derivatives of the original classical Preisach magnetic model.

6.4 The temperature-dependent Preisach model

Static energetic representation of a hysteron in which two minima and a barrier between them exist (see Figure 11(b)),

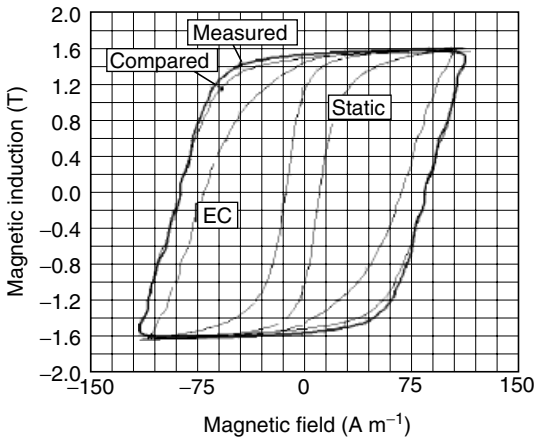

Figure 17. Static, eddy current and dynamic magnetizing loops computed by the external dynamic Preisach model and compared with the measured dynamic loop for the grain-oriented silicon iron steel sheet magnetized in rolling direction under field-control condition with frequency 250 Hz. (Reproduced from Janos Fuzi: 'Computationally efficient rate dependent hysteresis model', *COMPEL* **18**:3 (1999), with permission from Emerald Group Publishing.)

can be expanded if temperature T and time t are introduced (Mitchler, Dan Dahlberg, Wesseling and Roshko, 1996).

Without temperature if a hysteron is in a local minimum, the energy barrier will prevent the magnetization switching into the state with a global minimum energy. With finite temperature, jump into the global minimum can occur spontaneously by thermal activation, with the characteristic time

$$\tau = \tau_0 \exp\left(\frac{W}{k_B T}\right) \tag{27}$$

where τ_0^{-1} is a microscopic attempt frequency and W represents the height of the barrier, which will lead to the evolution of $Q(h_A, h_B)$, from equation (20) with time and to the appearance of the superparamagnetic state. As an example, a graphical representation of field cooling (FC) magnetic measurement is shown in Figure 18(a) and zero field cooling (ZFC) in Figure 18(b) (Song and Roshko, 2000).

Successful application of the proposed model, that is, the construction of the FC and ZFC curves, isothermal-remanent moment (IRM), thermo-remanent moment (TRM), and hysteresis loops at various temperatures, was done for ferromagnetic perovskites, such as $La_{0.95}Mg_{0.05}MnO_3$ and $La_{0.5}Sr_{0.5}CoO_3$ (Zhao *et al*., 2001) and $SrRuO_3$ (Roshko and Huo, 2001), for ferromagnetic nanoparticles embedded in a nonmagnetic matrix, such as Fe nanoparticles in alumina (Roshko, Viddal, Ge and Gao, 2004), and in others. In these studies, the Preisach function for particulate ferromagnetic materials can be decomposed into two distributions of the h_C and h_I fields, such as, for example, in

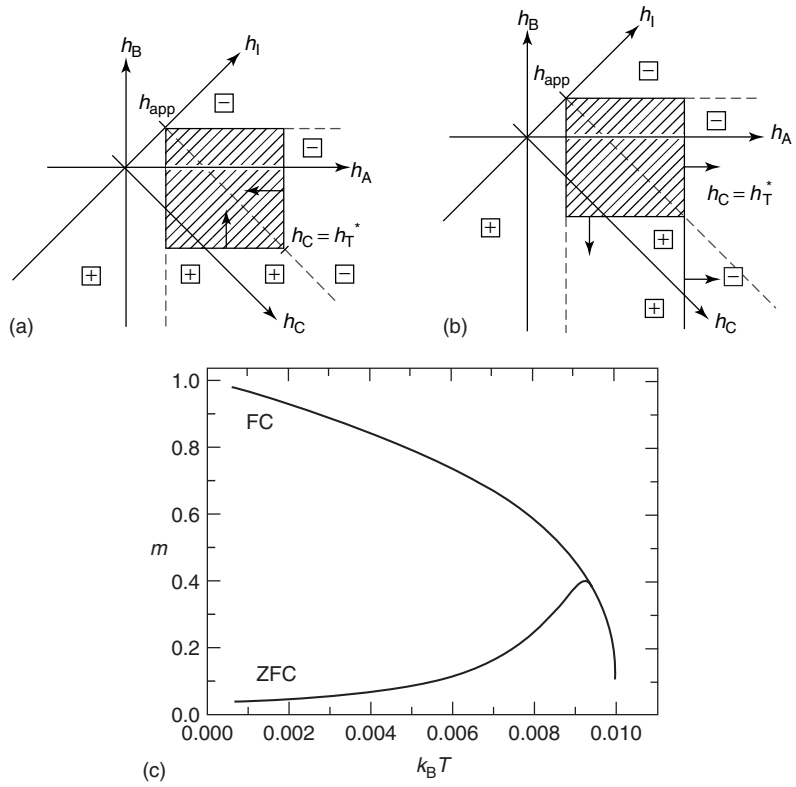

Figure 18. (a) Subsystem states at temperature T after cooling in an applied field h_{app} (FC). (b) Subsystem states at temperature T in an applied field h_{app} after cooling in zero field (ZFC). (The shaded region is superparamagnetic and arrows show boundary evolution of this region with time). (c) Temperature dependence of the field-cooled (FC) and zero field-cooled (ZFC) moment. (Reproduced from T. Song and R.M. Roshko: 'A Preisach model for systems with magnetic order', *Physica B*, **275** (2000), copyright © Elsevier 2000, with permission of Elsevier.)

Zhao *et al*. (2001):

$$P(h_C, h_I) = \frac{1}{2\pi\sigma_C\sigma_I h_C} \exp\left[-\frac{(\log(h_C/h_{CM}))^2}{2\sigma_C^2} - \frac{h_I^2}{2\sigma_I^2}\right] \tag{28}$$

All parameters in this Preisach function are functions of temperature and are proportional to $(1 - T/T_C)^\Gamma$ with Curie temperature T_C and critical exponent Γ.

7 MODELING OF NONLINEAR MAGNETISM BY ENERGY DISSIPATION

Theoretical description of bulk magnetic properties such as coercivity, remanence, permeability, and hysteresis loss, encounters other problems that make it difficult, if not impossible, to simply scale up the predictions of models that are based on consideration of one or two domains. Therefore, a more general approach is needed in order to develop equations that represent the average behavior of the materials. These models necessarily use statistical thermodynamic principles to describe the resulting magnetization behavior of a very large number of magnetic domains. The earliest thermodynamic approaches were developed for the simplest systems, specifically paramagnets. Paramagnets have the simplicity of being magnetically homogeneous, unlike ferromagnets. Later models were developed for ferromagnets without including hysteresis, and finally hysteresis models were developed. The classical model for magnetism on this scale is the Langevin–Weiss model which considers an array of magnetic moments in thermal equilibrium at a particular temperature.

7.1 The Jiles–Atherton model

The Langevin–Weiss approach was used as the basis for developing a model of hysteresis (Jiles and Atherton, 1986). The model of hysteresis that was developed in this way depends on statistical mechanics and is most relevant on the mesoscopic scale. It works well for materials with low

anisotropy for which the main mechanism is domain boundary movement. It can be used for simple anisotropies such as axial and planar anisotropies with minor modifications. For highly anisotropic materials it can still be used with the understanding that a simple analytic anhysteretic equation cannot in general be developed for anisotropic materials and therefore the mathematical approximations become less realistic, the greater the anisotropy and the larger the number of magnetic easy directions.

The orientations of the magnetic moments are distributed statistically and integrating the distribution of moments over all possible orientations leads to an equation for the bulk magnetization. The form of this equation depends on the restrictions imposed by anisotropy, so, for example, different solutions are obtained depending on whether the magnetic moments experience axial anisotropy, planar anisotropy, or are in a completely isotropic environment (Jiles, Lee, Kenkel and Metlov, 2000).

The extension of the Langevin–Weiss theory used to describe ferromagnetic materials incorporates a coupling among magnetic moments acting as a strong magnetic field to align the magnetic moments in a domain parallel to each other. To quantify this coupling, a mean field is invoked, which is proportional to the bulk magnetization M, so that the effective field is $\tilde{H} = H + \alpha M$. This mean field approach to describing the interactions needs to be applied with some caution, but recent work by Chamberlin (2000) has shown that the mean field approach is viable for clusters of spins on the nanoscopic scale.

7.2 Description of the anhysteretic magnetization

In the absence of energy dissipation, all energy supplied to the material is equal to the change in magnetostatic energy in the material. This is the anhysteretic magnetization. Instead of considering details of the coupling between each individual magnetic moment, a mean field approximation is used to represent the interdomain coupling. By replacing the classical magnetic field H with the effective magnetic field $H + \alpha M$, which includes coupling to the magnetization, an equation for the anhysteretic magnetization of a ferromagnetic material can be obtained as follows:

$$M = M_{\mathrm{S}} L\left(\frac{\mu_0\, m\, (H + \alpha M)}{k_{\mathrm{B}} T}\right) \tag{29}$$

where $L(x)$ is the anhysteretic function, $x = \frac{\mu_0\, m\, \tilde{H}}{k_{\mathrm{B}}\, T}$, and $\tilde{H} = H + \alpha M$ is the effective field which includes both the applied field and the self-coupling field. The exact form of the function $L(x)$ depends on the anisotropy of the material: for isotropic materials the anhysteretic function is the Langevin function:

$$M = M_{\mathrm{S}} \{\coth(x) - 1/x\} \tag{30}$$

for materials exhibiting axial anisotropy the anhysteretic function is a hyperbolic tangent,

$$M = M_{\mathrm{S}} \tanh(x) \tag{31}$$

and for materials exhibiting planar anisotropy

$$M = \frac{k_{\mathrm{B}}\, T}{\mu_0} \frac{\mathrm{d}}{\mathrm{d}\tilde{H}} \log Z = M_{\mathrm{S}} \frac{I_0'(x)}{I_0(x)} \tag{32}$$

where Z is the statistical partition function and

$$I_0(x) = \sum_{s=0}^{\infty} \frac{1}{(s!)^2} \left(\frac{x}{2}\right)^{2s} \tag{33}$$

and

$$I_0'(x) = \sum_{s=1}^{\infty} \frac{s}{(s!)^2} \left(\frac{x}{2}\right)^{2s-1} \tag{34}$$

An extension to cover other more complicated anisotropies was made (Ramesh, Jiles and Roderick, 1996), in which the energy of a magnetic moment with anisotropic perturbation was calculated in three dimensions and therefore different kinds of anisotropic materials could be described. This allows an increasing range of magnetic materials in which anisotropy and texture play a significant role to be modeled, for example, hard magnetic materials.

Following the development of the generalized anhysteretic function (Jiles, Ramesh, Shi and Fang, 1997; Fang *et al.*, 1998a,b)

$$M_{\mathrm{aniso}} = M_{\mathrm{S}} \frac{\sum\limits_{\text{all moments}} \mathrm{e}^{-E/k_{\mathrm{B}}T} \cos\theta}{\sum\limits_{\text{all moments}} \mathrm{e}^{-E/k_{\mathrm{B}}T}} \tag{35}$$

where θ is the angle between the direction of the magnetization M and the direction of the applied field, and E is the energy of the magnetic moment m

$$E = \mu_0 \langle m \rangle (H + \alpha M) + E_{\mathrm{aniso}} \tag{36}$$

where E_{aniso} is the anisotropic component of energy which depends on the structure of the material. For example, in the case of cubic anisotropy,

$$E_{\mathrm{aniso}} = K_1 \sum_{i \neq j}^{3} \cos^2\theta_i \cos^2\theta_j \tag{37}$$

with the normal convention on symbols. In this description, only the first anisotropy coefficient K_1 was used since this approximation in most cases provides a sufficiently accurate description of the different magnetization curves along different directions. A texture coefficient f_{text}, which is a statistical evaluation of the volume fraction of the textured portion of a material, was also introduced. The anhysteretic magnetization M_{an} can then be given as

$$M_{\text{an}} = f_{\text{text}}\, M_{\text{aniso}} + (1 - f_{\text{text}})\, M_{\text{iso}} \tag{38}$$

where M_{aniso} is the anisotropic anhysteretic magnetization contribution, and M_{iso} is the isotropic anhysteretic magnetization contribution. For more complicated textured materials, there may be several different texture orientations such that each particular direction has a proportion of the grains oriented along it. The anisotropic contribution of each part must be calculated separately and the net anisotropic portion of the anhysteretic magnetization is the weighted sum of the components of magnetization of these orientations along the direction of the applied field.

From this description of the thermodynamic anhysteretic magnetization, it is possible to develop a description of hysteresis through consideration of energy dissipation mechanisms. The irreversible and reversible components of magnetization can be described separately in the mathematical formulation, although physically they are not separate. The two components of magnetization can then be combined to give an equation for the total magnetization.

7.3 Extension to hysteresis

In the case of hysteresis, the energy supplied to the material appears either as magnetostatic energy or hysteresis loss. The magnetostatic energy in the material is the energy difference between input energy and the energy loss due to processes such as domain wall pinning. One of the assumptions of the model is that the energy loss is proportional to the change in magnetization. Although this was derived from the domain wall motion under the action of a magnetic field, it is not limited to magnetization by domain wall motion and therefore the model applies to any situation in which the energy loss is proportional to the change in magnetization as could occur also under domain rotation.

An equation for the irreversible change in magnetization is obtained,

$$\frac{\mathrm{d}M_{\text{irr}}}{\mathrm{d}H} = \frac{M_{\text{an}} - M_{\text{irr}}}{\delta\, k - \alpha(M_{\text{an}} - M_{\text{irr}})} \tag{39}$$

where the directional parameter δ takes $+1$ when H increases in the positive direction ($\mathrm{d}H/\mathrm{d}t > 0$), and -1 when H increases in the negative direction ($\mathrm{d}H/\mathrm{d}t < 0$), ensuring that the pinning always opposes the change in magnetization.

During magnetization, there is also a reversible component of magnetization that can result from reversible domain wall bowing, reversible translation of domain walls, or reversible domain rotation. For the purposes of modeling, the reversible component M_{rev} of magnetization was assumed to be proportional to the difference between the anhysteretic magnetization M_{an} and irreversible magnetization M_{irr}, with a constant of proportionality, the reversibility coefficient c, which represents the fraction of magnetization change that is reversible. Hence, the total magnetization M is the sum of reversible magnetization and irreversible magnetization:

$$M = M_{\text{irr}} + M_{\text{rev}} = (1 - c)\, M_{\text{irr}} + c\, M_{\text{an}} \tag{40}$$

where the constant coefficient c ranges from 0 (completely irreversible magnetization) to 1 (completely reversible magnetization). The model equation for the total magnetization, which includes both irreversible and reversible magnetization, is then

$$\frac{\mathrm{d}M}{\mathrm{d}H} = (1 - c)\frac{(M_{\text{an}} - M)}{\delta k - \alpha(M_{\text{an}} - M)} + c\frac{\mathrm{d}M_{\text{an}}}{\mathrm{d}H} \tag{41}$$

Solutions of this equation with a suitable anhysteretic function give a typical sigmoid-shaped hysteresis loop as shown in Figure 19. By changing the values of the hysteresis parameters, this model is able to predict the magnetization of both soft and hard magnetic materials.

The anhysteretic and hysteresis equations represent the component of magnetization along the field direction. Therefore, the calculated resultant magnetization M is the component of magnetization parallel to the direction of the applied field. As a result, although the model equation for hysteresis remains basically the same, there is a significant difference in the modeled magnetic properties along different field directions due to the differences in the anhysteretic magnetization along different directions.

7.4 Extension to describe the effects of stress

The effects of stress on magnetization of materials can also produce very significant changes. The incorporation of these effects into a more general model, which includes magnetic field and temperature, has been achieved. The key to this is to provide a description under which both magnetic field and stress can be treated as similar. An equation for the stress equivalent field has been identified (Sablik, Kwun, Burkhardt

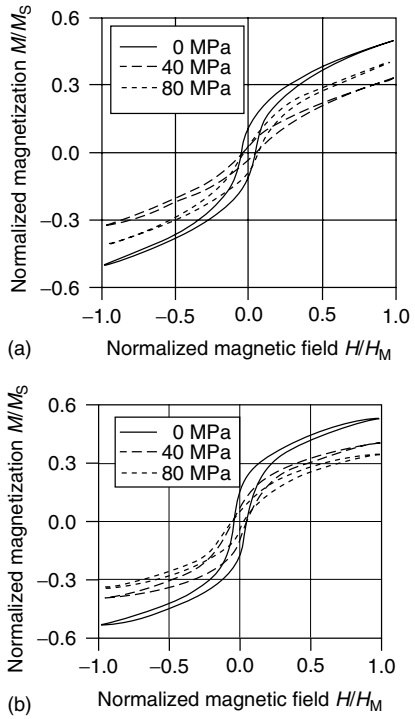

Figure 19. (a) Hysteresis measurements and (b) Jiles–Atherton model simulations of an amorphous $Co_{77}B_{23}$ ribbon, at different levels of applied tensile stress. (Hauser *et al*., 2005.) (Reproduced from H. Hauser, D.C. Jiles, Y. Melikhov, L. Li, and R. Grossinger: 'An approach to modeling the dependence of magnetization on magnetic field in the high field regime', *Journal of Magnetism and Magnetic Materials*, 2005, copyright © Elsevier 2005, with permission from Elsevier.)

and Jiles, 1987; Sablik and Jiles, 1988),

$$H_\sigma = \frac{3}{2}\frac{\sigma}{\mu_0}\left(\frac{\partial\lambda}{\partial M}\right)_T \tag{42}$$

$$H_\sigma(\theta) = \frac{3}{2}\frac{\sigma}{\mu_0}(\cos^2\theta - \nu\sin^2\theta)\left(\frac{\partial\lambda}{\partial M}\right)_T \tag{43}$$

where λ is magnetostriction, ν is Poisson ratio, and θ is angle between stress and measured magnetic field.

Variable stress also has effects that go beyond those that are described by the above equation. In fact, the application of stress causes unpinning of domain walls, and this effect can be described by a law of approach to the anhysteretic (Jiles, 1995; Jiles and Devine, 1995). This is given by the following equation for the change in irreversible component of magnetization $M_{\rm irr}$ with elastic energy W

$$\frac{{\rm d}M_{\rm irr}}{{\rm d}W} = \frac{1}{\xi}(M_{\rm an} - M_{\rm irr}) \tag{44}$$

where ξ is a coefficient with dimensions of energy per unit volume, and adding on the reversible component gives the

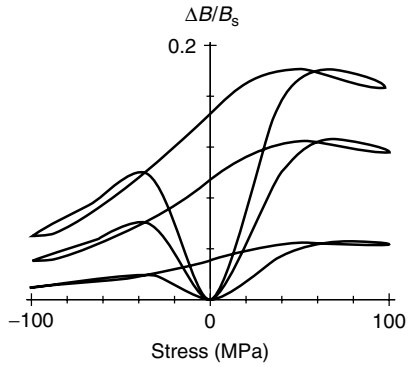

Figure 20. The calculated variation of magnetic induction with stress at fields of 26, 80, and $132\,{\rm A\,m^{-1}}$. The specimen was demagnetized and then subjected to an applied stress of up to 100 MPa, either in tension of compression. (After D. Jiles: Theory of the Magnetomechanical effect, *Journal of Physics D: Applied Physics* **28**, 1995, with permission from IOP Publishing Ltd.)

change in the total magnetization,

$$\frac{{\rm d}M}{{\rm d}W} = \frac{1}{\xi}(M_{\rm an} - M) + c\frac{{\rm d}M_{\rm an}}{{\rm d}W} \tag{45}$$

The anhysteretic is itself stress dependent because of the contribution of H_σ to the effective field, so the law of approach really contains two components: a reversible component that represents the change in the anhysteretic with stress, and an irreversible component which represents the change in the displacement of the magnetization from the prevailing stress dependent anhysteretic as shown in Figure 20.

7.5 Extension to describe time dependence

The effects of the frequency of the magnetic field on magnetization can also be included in this model (Jiles, 1994). In this case, the effects of eddy currents add to the dissipation and so result in higher coercivity and hysteresis loss.

$$\begin{aligned}&\left(\frac{\mu_0{\rm d}^2}{2\rho\beta}\frac{{\rm d}H}{{\rm d}t}\right)\left(\frac{{\rm d}M}{{\rm d}H}\right)^2 \\ &+\left(\frac{G{\rm d}w\mu_0 H_0}{\rho}\right)^{1/2}\left(\frac{{\rm d}H}{{\rm d}t}\right)^{1/2}\left(\frac{{\rm d}M}{{\rm d}H}\right)^{3/2} \\ &+\left[k\delta - \alpha\left(M_{\rm an}(H) - M(H) + k\delta c\frac{{\rm d}M_{\rm an}}{{\rm d}H_{\rm e}}\right)\right]\left(\frac{{\rm d}M}{{\rm d}H}\right) \\ &-\left[M_{\rm an}(H) - M(H) + k\delta c\frac{{\rm d}M_{\rm an}}{{\rm d}H_{\rm e}}\right] = 0\end{aligned} \tag{46}$$

Other approaches to the frequency dependence of magnetization are needed for insulating materials, in which eddy currents do not play a major role. This has been described previously for the case of high-frequency ferrites

(Jiles, 1993). The differential equation governing the magnetization in this case is

$$\frac{\mathrm{d}^2}{\mathrm{d}t^2}M(t) + 2\eta\frac{\mathrm{d}}{\mathrm{d}t}M(t) + \omega_\mathrm{n}^2 M(t) = \omega_\mathrm{n}^2 M_\infty(H) \qquad (47)$$

The extension to the basic model as given in the above equations, describes magnetic properties in terms of a multidomain structure that makes it widely applicable. The physical basis of this model is adjustable to cover the case of anisotropic and textured structures. This eliminates the need for the isotropic approximation and expands the applicability of this model to more complicated situations.

The differential magnetic susceptibility depends on the displacement of the prevailing magnetization from the anhysteretic magnetization. The anhysteretic magnetization is a function of the energy of the moments within a domain. To include anisotropic effects into the model, the anisotropy energy must be incorporated into the total energy of the moments.

The general equation for hysteresis can be solved with the incorporation of the appropriate anisotropic, textured, or stress-dependent anhysteretic magnetization, M_an. This gives the magnetization curves along particular directions. An advantage of this model is that the basic hysteresis equation remains the same, as do the hysteresis coefficients, so that the only change has been the incorporation of different forms of anisotropy into the equation for the anhysteretic.

8 SUMMARY

This paper has described the underlying basis for hysteresis models that can be used to describe the magnetic properties of materials. These provide a diverse range of modeling capabilities that span length scales from the discrete atomistic scale through nanoscopic and continuum/microscopic up to the macroscopic everyday scale of devices and components. Effects of anisotropy, stress, frequency of excitation, compacting processing, chemical composition, and heat treatment have been incorporated in these models. Experimental results and simulation data have shown that these effects have an impact on the magnetic properties and that these effects can be described and understood through the various hysteresis models.

LIST OF SYMBOLS

A	Cross-sectional area
a	Domain density parameter – Jiles–Atherton model
B_0, B_1	Correlation functions
c	Reversibility coefficient – Jiles–Atherton model
D	Diameter of grains/crystallites – Globus model
d	Dimensional parameter (diameter) – eddy current model
E	Energy
E_aniso	Anisotropy energy
E_max	Amplitude of internal potential
$F(z)$	Total force of all defects interacting with a domain wall
f	Pinning force per unit length – Globus model
f_text	Texture parameter – Jiles–Atherton model
$f(z - z_J)$	Individual interaction force of a defect
G	Dimensionless eddy current parameter – Bertotti model
H	Magnetic field
$\tilde{H}$	Effective magnetic field
H_0	Internal effective field due to potential
H_C	Coercive field
H_K	Anisotropy field
H_S	Saturating field
H_σ	Stress equivalent field
h	Length along domain wall perpendicular to direction of bending
h_A	Switching field – Preisach model
h_B	Switching field – Preisach model
h_C	Critical or the coercive field of the free fragment – Preisach model
h_I	Offset field, or bias field, for elemental switching volumes in Preisach model
$I(x)$	Bessel function series
K, K_1, K_2	Anisotropy coefficient
k	Pinning parameter (or dissipation parameter) – Jiles–Atherton model
k	Rate proportionality parameter – Preisach model
k_B	Boltzmann's constant
L	Length
L_0	Distance between two adjacent defects
L_3	Domain wall length
$L(x)$	anhysteretic function with $x = \frac{\mu_0 m\tilde{H}}{k_\mathrm{B}T}$ and $\tilde{H} = H + \alpha M$ – Jiles–Atherton model
$L(t)$	Staircase line which divides areas $S^{(+)}$ and $S^{(-)}$ – Preisach model
l	Length between domain wall pinning sites
M	Magnetization
M_R	Remanent magnetization
M_S	Saturation magnetization

M_{an}	Anhysteretic magnetization
M_{aniso}	Anisotropic anhysteretic magnetization – Jiles–Atherton model
M_{irr}	Irreversible component of magnetization
M_{iso}	Isotropic anhysteretic magnetization – Jiles–Atherton model
M_{rev}	Reversible component of magnetization
M_{∞}	Quasi static or equilibrium magnetization
m	Magnetic moment
N	Number of defects
$P(h_A, h_B)$	Preisach distribution function – Preisach model
$P(h_C, h_I)$	Preisach distribution function – Preisach model
$P(h_C)$	Integrated or local coercive field distribution function – Preisach model
$Q(h_A, h_B)$	Elementary hysteresis loop – Preisach model
$Q(h_A, h_B; t)$	Modified elementary hysteresis loop – Preisach model
$R(M)$	Noncongruency function – Preisach model
S	Squareness of the hysteresis loop
$S^{(+)}$ and $S^{(-)}$	Areas in the Preisach plain – Preisach model
T	Temperature
T_C	Curie temperature
t	Time
V	Volume
$W(\Phi)$	White noise function
W	Dimensional parameter (width) – eddy current model
W	Energetic barrier value – Preisach model
W	Elastic energy – Jiles–Atherton model
Z	Thermodynamic partition function
α	Damping parameter – Landau–Lifshitz–Gilbert model
α	Mean field coupling coefficient
α_R	Rayleigh constant
β	Shape parameter
β	Reversible component – Preisach model
χ	Susceptibility
χ_{in}	Initial susceptibility
δ	Domain wall thickness
δ	Directional parameter (± 1)
Φ	Magnetic flux
ϕ	Angle
Γ	Critical power
γ	Gyromagnetic ratio
γ_π	Domain wall energy per unit area
$\gamma(h_A, h_B)$	Hysteresis operator – Preisach model
η	Damping coefficient for harmonic motion
Λ	Torque
λ	Magnetostriction
λ_S	Saturation magnetostriction
λ_d	Damping coefficient – Landau–Lifshitz–Gilbert model
μ_0	Permeability of free space
ν	Poisson's ratio
θ	Angle
ρ	Resistivity
σ	Stress
σ_0	Stress amplitude
σ_C	Standard deviation of coercive field distribution – Preisach model
σ_I	Standard deviation of interaction field distribution – Preisach model
ζ	Correlation (or interaction) length – Bertotti model
τ	Time constant
ω_0	Resonance frequency
ω_n	Natural resonance frequency for harmonic motion
ξ	Decay coefficient – Law of approach
ξ	Replacement factor – Preisach model
ξ	Magnetization-elastic stress coefficient – Jiles–Atherton model

REFERENCES

Alessandro, B., Beatrice, C., Bertotti, G. and Montorsi, A. (1990). Domain-wall dynamics and Barkhausen effect in metallic ferromagnetic materials: 1. Theory and 2. Experiment. *Journal of Applied Physics*, **68**, 2901–2915.

Basso, V., Bertotti, G., Infortuna, A. and Pasquale, M. (1995). Preisach model study of the connection between magnetic and microstructural properties of soft magnetic materials. *IEEE Transactions on Magnetics*, **31**, 4000–4005.

Becker, R. (1932). Elastische spannungen und magnetische Eigenschaften. *Physikalische Zeitschrift*, **33**, 905–913.

Bertotti, G. (1988). General-properties of power losses in soft ferromagnetic materials. *IEEE Transactions on Magnetics*, **24**, 621–630.

Bertotti, G. (1992a). Dynamic generalization of the scalar Preisach model of hysteresis. *IEEE Transactions on Magnetics*, **28**, 2599–2601.

Bertotti, G. and Pasquale, M. (1992b). Physical interpretation of induction and frequency dependence of power losses in soft magnetic materials. *IEEE Transactions on Magnetics*, **28**, 2787–2789.

Bertotti, G., Mayergoyz, I.D., Basso, V. and Magni, A. (1999). Functional integration approach to hysteresis. *Physical Review E*, **60**, 1428–1440.

Chamberlin, R.V. (2000). Mean-field cluster model for the critical behaviour of ferromagnets. *Nature*, **408**, 337–339.

Chantrell, R.W. (1997). Hysteresis particulate materials. In *Magnetic Hysteresis in Novel Magnetic Materials*, Hadjipanayis, G.C. (Ed.), Kluwer: Dordrecht.

Chen, P.J. and Montgomery, S.T. (1980). A macroscopic theory for the existence of the hysteresis and butterfly loops in ferroelectricity. *Ferroelectrics*, **23**, 199–208.

Della Torre, E. (1966). Effect of interaction on the magnetization of single-domain particles. *IEEE Transactions on Audio and Electroacoustics*, **AU-14**, 86–92.

Della Torre, E. (1991). Existence of magnetization-dependent Preisach model. *IEEE Transactions on Magnetics*, **27**, 3697–3699.

Della Torre, E. (1994). A Preisach model for accommodation. *IEEE Transactions on Magnetics*, **30**, 2701–2707.

Della Torre, E. and Kadar, G. (1987). Hysteresis modelling: II. Accommodation. *IEEE Transactions on Magnetics*, **23**, 2823–2825.

Escobar, M.A., Magana, L.F. and Valenzuela, R. (1985). Effect of the grain size distribution on the magnetization curve. *Journal of Applied Physics*, **57**, 2142–2146.

Escobar, M.A., Valenzuela, R. and Magana, L.F. (1983). Analytical prediction of the magnetization curve and the ferromagnetic hysteresis loop. *Journal of Applied Physics*, **54**, 5935–5940.

Fang, X., Jiles, D.C. and Shi, Y. (1998a). Modelling of magnetic properties of Nd-Dy-Fe-B particulate composites with different compacting processes. *Journal of Magnetism and Magnetic Materials*, **187**, 79–82.

Fang, X., Shi, Y. and Jiles, D.C. (1998b). Modelling of magnetic properties of heat treated Dy-doped and Ti-C-doped NdFeB particles bonded in isotropic and anisotropic arrangements. *IEEE Transactions on Magnetics*, **34**, 1291–1293.

Fidler, J. and Schrefl, T. (2000). Micromagnetic modelling – the current state of the art. *Journal of Physics D: Applied Physics*, **33**, R135–R156.

Fuzi, J. (1999). Computationally efficient rate dependent hysteresis model. *COMPEL-The International Journal for Computation and Mathematics in Electrical and Electronic Engineering*, **18**, 445–457.

Gilbert, T.L. (1955). Lagrangian formulation of the gyromagnetic equation of the magnetization field. *Physical Review*, **100**, 1243.

Gilbert, T.L. (2004). A phenomenological theory of damping in ferromagnetic materials. *IEEE Transactions on Magnetics*, **40**, 3443–3449.

Globus, A. (1962). Influence de la dimension des parois sur la permeabilite initiale. *Comptes Rendus de l' Academie des Sciences*, **255**, 1709.

Globus, A. (1975). Universal hysteresis loop for soft ferromagnetic material, *Proceedings of the European Physical Society, 2nd Conference on Soft Magnetic Material*, Cardiff, p. 233.

Globus, A. and Duplex, P. (1966). Separation of susceptibility mechanisms for ferrites of low anisotropy. *IEEE Transactions on Magnetics*, **2**, 441–445.

Globus, A. and Duplex, P. (1969). Initial susceptibility of ferrimagnetic materials and topography of domain walls. *Physica Status Solidi*, **31**, 765–774.

Globus, A., Duplex, P. and Guyot, M. (1971). Determination of initial magnetization curve from crystallites size and effective anisotropy field. *IEEE Transactions on Magnetics*, **7**, 617–622.

Globus, A. and Guyot, M. (1972). Wall displacement and bulging in magnetization mechanisms of the hysteresis loop. *Physica Status Solidi B*, **52**, 427–431.

Guyot, M. and Globus, A. (1973). Determination of the domain wall energy from hysteresis loops in YIG. *Physica Status Solidi B*, **59**, 447–454.

Hauser, H., Jiles, D.C., Melikhov, Y., *et al*. (2005). An approach to modeling the dependence of magnetization on magnetic field in the high field regime. *Journal of Magnetism and Magnetic Materials*, **300**, 273–283.

Jiles, D.C. (1993). Frequency dependence of hysteresis curves in non-conducting magnetic materials. *IEEE Transactions on Magnetics*, **29**, 3490–3492.

Jiles, D.C. (1994). Frequency dependence of hysteresis curves in conducting magnetic materials. *Journal of Applied Physics*, **76**, 5849–5855.

Jiles, D.C. (1995). Theory of the magnetomechanical effect. *Journal of Physics D: Applied Physics*, **28**, 1537–1546.

Jiles, D.C. (2000). Dynamics of domain magnetization and the Barkhausen effect. *Czechoslovak Journal of Physics*, **50**, 893–924.

Jiles, D.C. and Atherton, D.L. (1986). Theory of ferromagnetic hysteresis. *Journal of Magnetism and Magnetic Materials*, **61**, 48–60.

Jiles, D.C. and Devine, M.K. (1995). The law of approach as a means of modelling the magnetomechanical effect. *Journal of Magnetism and Magnetic Materials*, **140–144**, 1881–1882.

Jiles, D.C., Lee, S.J., Kenkel, J. and Metlov, K.L. (2000). Superparamagnetic magnetization equation in two dimensions. *Applied Physics Letters*, **77**, 1029–1031.

Jiles, D.C., Ramesh, A., Shi, Y. and Fang, X. (1997). Application of the anisotropic extension of the theory of hysteresis to the magnetization curves of crystalline and textured magnetic materials. *IEEE Transactions on Magnetics*, **33**, 3961–3963.

Kadar, G. (1987). On the Preisach function of ferromagnetic hysteresis. *Journal of Applied Physics*, **61**, 4013–4015.

Kadar, G. and Della Torre, E. (1987). Hysteresis modelling: I. Noncongruency. *IEEE Transactions on Magnetics*, **23**, 2820–2822.

Kersten, M. (1943). *Underlying Theory of Ferromagnetic Hysteresis and Coercivity*, Hirzel: Leipzig.

Kersten, M. (1956). Uber die Bedeutung der Versetzungsdichte fur die Theorie der Koerzitivkraft rekristallisierter Werkstoffe. *Zeitschrift fur Angewandte Physik*, **8**, 496–502.

Krasnoselskii, M.A. and Pokrovskii, A.V. (1983). *Systems with Hysteresis*, Nauka: Moscow.

Kronmuller, H. (1992). Coercivity and domain wall pinning. In *Concise Encyclopedia of Magnetic & Superconducting Materials*, Evetts, J. (Ed.), Pergamon Press: Oxford, pp. 72–82.

Kronmuller, H., Fischer, R., Hertel, R. and Leineweber, T. (1997). Micromagnetism and the microstructure in nanocrystalline materials. *Journal of Magnetism and Magnetic Materials*, **175**, 177–192.

Landau, L.D. (1967). In *Collected Papers*, Ter Haar, D. (Ed.), Gordon and Breach: New York, pp. 101–114.

Landau, L.D. and Lifshitz, E.M. (1935). On the theory of the dispersion of magnetic permeability in ferromagnetic bodies. *Physikalische Zeitschrift der Sowjetunion*, **8**, 153–169.

Lee, E.W. and Bishop, J.E.L. (1966). Magnetic behaviour of single-domain particles. *Proceedings of the Physical Society*, **89**, 661–675.

Liorzou, F., Phelps, B. and Atherton, D.L. (2000). Macroscopic models of magnetization. *IEEE Transactions on Magnetics*, **36**, 418–428.

Lu, M., Leonard, P.J., Marketos, P., *et al*. (2003). A simple dynamic Preisach hysteresis model for FeSi materials. *International Journal of Modern Physics B*, **17**, 2325–2331.

Mayergoyz, I.D. (1986). Mathematical models of hysteresis. *Physical Review Letters*, **56**, 1518–1521.

Mayergoyz, I.D. (1991). *Mathematical Models of Hysteresis*, Springer-Verlag: New York.

Mitchler, P.D., Dan Dahlberg, E., Wesseling, E.E. and Roshko, R.M. (1996). Henkel plots in a temperature and time dependent Preisach model. *IEEE Transactions on Magnetics*, **32**, 3185–3194.

Neel, L. (1944). Les lois de l'aimantation et de la subdivision en domaines elementaires d'un monocristal de fer. *Journal de Physique et le Radium*, **5**, 265–276.

Neel, L. (1959). Sur les effets des interactions entre les domaines elemetaires ferromagnetique: bascule et reptation. *Journal de Physique et le Radium*, **20**, 215–221.

Preisach, F. (1935). Uber die magnetische nachwrikung (on magnetic aftereffect). *Zeitschrift fur Physik*, **94**, 277–302.

Ramesh, A., Jiles, D.C. and Roderick, J. (1996). A model of anisotropic anhysteretic magnetization. *IEEE Transactions on Magnetics*, **32**, 4234–4236.

Roshko, R.M. and Huo, D.L. (2001). A Preisach characterization of the Barkhausen spectrum of a canonical ferromagnet $SrRuO_3$. *Physica B*, **306**, 246–250.

Roshko, R.M., Viddal, C.A., Ge, S. and Gao, M. (2004). A Preisach analysis of remanence isoterms for nanoparticles of Fe in alumina. *IEEE Transactions on Magnetics*, **40**, 2137–2139.

Sablik, M.J. and Jiles, D.C. (1988). A model for hysteresis in magnetostriction. *Journal of Applied Physics*, **64**, 5402–5404.

Sablik, M.J., Kwun, H., Burkhardt, G.L. and Jiles, D.C. (1987). Model for the effect of tensile and compressive stress on ferromagnetic hysteresis. *Journal of Applied Physics*, **61**, 3799–3801.

Schlesinger, M.F. (2001). Physics in the noise. *Nature*, **411**, 641.

Song, T. and Roshko, R.M. (2000). A Preisach model for systems with magnetic order. *Physica B*, **275**, 24–27.

Spratt, G.W.D., Bissell, P.R., Chantrell, R.W. and Wohlfarth, E.P. (1988). Static and dynamic experimental studies of particulate recording media. *Journal of Magnetism and Magnetic Materials*, **75**, 309–318.

Stoner, E.C. and Wohlfarth, E.P. (1948). A mechanism of magnetic hysteresis in heterogeneous alloys. *Philosophical Transactions of the Royal Society of London*, **A240**, 599–642.

Stoner, E.C. and Wohlfarth, E.P. (1991). *IEEE Transactions on Magnetics*, **27**, 3475–3518.

Tuszynski, J.A., Mroz, B., Kiefte, H. and Clouter, M.J. (1988). Comments on the hysteresis loop in ferroelastic LiCsSO4. *Ferroelectrics*, **77**, 111–120.

Vajda, F. and Della Torre, E. (1993). Characteristics of the complete moving hysteresis model. *Journal of Applied Physics*, **73**, 5833–5835.

Vajda, F., Della Torre, E. and Pardavi-Horvath, M. (1992). Analysis of reversible magnetization-dependent Preisach models for recording media. *Journal of Magnetism and Magnetic Materials*, **115**, 187–189.

Vicsek, T. (2001). A question of scale. *Nature*, **411**, 421.

Zhao, J.H., Song, T., Kunkel, H.P., *et al*. (2001). Preisach analysis of two ferromagnetic perovskites: $La_{0.95}Mg_{0.05}MnO_3$ and $La_{0.5}Sr_{0.5}CoO_3$. *Journal of Applied Physics*, **89**, 7248–7250.

Magnetization Dynamics: Thermal-driven Noise in Magnetoresistive Sensors

Jian-Gang Zhu
Carnegie Mellon University, Pittsburgh, PA, USA

1 INTRODUCTION

Since the discovery of giant magnetoresistance (GMR) effect in Fe/Cr multilayers (Baibich *et al*., 1988), various magnetoresistive flux sensor-based thin-film multilayer structures have rapidly been developed into a variety of commercial applications. One of the most significant applications is the read heads for hard disk drives (HDDs), which has directly enabled the rapid growth of disk drive capacities over the last 10 years (Zhu, 2003). The large magnetoresistance in either the metallic magnetoresistive multilayer structures or the magnetic tunnel junctions can provide a high read back signal level, quickly replacing conventional anisotropic magnetoresistive (AMR) read heads, which had replaced inductive read heads earlier. The large magnetoresistive ratio has substantially enhanced the signal-to-electronic noise ratio of the read head, enabled the use of very low magnetic moment media in the longitudinal recording configuration, and facilitated the rapid area-density increase for HDDs in the past decade.

In all the magnetoresistive field sensors, magnetization rotation in the multilayer sensing stack driven by the magnetic flux produces a change in the resistance of the stack via magnetoresistive effect. In HDDs, the lateral dimension of the read sensor in a head has been rapidly decreasing and is below 100 nm at present. Thermally excited fluctuation of magnetization rotation in the sensor stack gives rise to voltage noise via the same magnetoresistive effect. If the head noise is dominated by this thermal magnetic noise, known as *mag-noise*, increasing the magnetoresistive effect will not enhance the signal-to-noise ratio (SNR) of the head. Therefore, understanding the mag-noise becomes critical since it could be the ultimate limit of the SNR in magnetoresistive sensors (Zhu, 2003).

In this chapter, we shall discuss a mechanism that results in stochastic oscillation of the magnetization orientation in magnetoresistive sensors, especially in magnetoresistive read heads used in HDD applications.

2 MAGNETORESISTIVE HEADS

Figure 1 shows a typical, magnetoresistive head design currently used in a HDD for data retrieval. The sensor stack is either a spin valve sensing current flowing in the plane (CIP) or a magnetic tunnel junction sensing current flowing perpendicular to the plane (CPP). In the CIP spin valve head, the sensing stack is a magnetic multilayer structure that consists of a free layer, an interlayer of normal metal

Handbook of Magnetism and Advanced Magnetic Materials. Edited by Helmut Kronmüller and Stuart Parkin. Volume 2: *Micromagnetism*. ISBN: 978-0-470-02217-7.

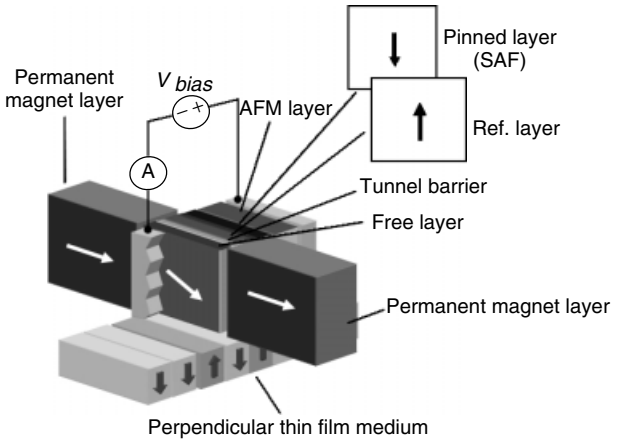

Figure 1. Schematic drawing of a typical tunneling magnetoresistive head with abutted permanent magnets for domain stabilization.

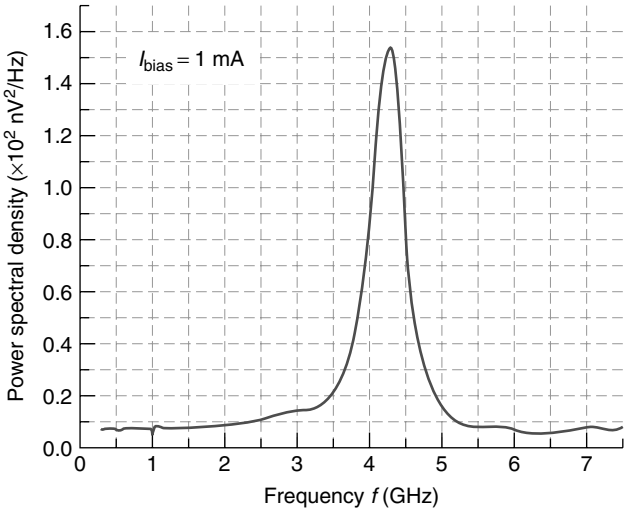

Figure 2. Measured power spectral density of a tunneling magnetoresistive head with a nominal resistance of 48 Ω. The physical track width of the head is 120 nm, with similar stripe height. The measurement was performed at 1-mA sensing current and no external magnetic field was applied. The electronic noise power spectral density, obtained by saturating the magnetic free layer with a large magnetic field along the magnetization direction of the permanent magnet, has been subtracted.

(Cu is always used), a synthetic antiferromagnetic trilayer, and an antiferromagnetic layer. The magnetic moment in the free layer rotates in response to the magnetic field arising from the recorded transitions in a disk medium, performing the function of sensing. The synthetic antiferromagnetic trilayer is a pair of ferromagnetic layers sandwiching a thin metallic layer, usually $Co_{90}Fe_{10}$/Ru/$Co_{90}Fe_{10}$. The magnetic moments of the two $Co_{90}Fe_{10}$ layers are coupled by a strong antiparallel, interlayer exchange coupling and are forced to orient perpendicular to the air-bearing surface (ABS) by the exchange bias field arising from the interface with the antiferromagnetic layer. The free layer, the normal metal interlayer, and the adjacent $Co_{90}Fe_{10}$ layer form a giant magnetoresistive trilayer, whose resistance depends on the relative orientation of the magnetic moments of the layers. In a magnetic tunnel junction head, often referred to as a *tunneling magnetoresistive* (*TMR*) *head*, the normal metal interlayer is replaced by an insulative tunnel barrier that is so thin that spin-dependent electron tunneling occurs. A pair of thin-film permanent magnets is abutted to the sensor stack in the horizontal direction to ensure a single domain configuration in the free layer. The width of the spin valve sensor stack is about 100 nm in present HDDs with similar dimension in height. The free layer is usually a $Co_{90}Fe_{10}$/$Ni_{81}Fe_{19}$ composite layer with a typical thickness of 1/3 nm, respectively.

3 MAG-NOISE AND ITS POWER SPECTRAL DENSITY

Owing to the small volumetric dimension of the free layer, its magnetization rotation can be excited by thermal energy. Figure 2 shows an experimentally measured voltage noise power spectral density (NPSD) of a typical TMR head in its quiescent state (the state with no external field present). This phenomenon was first reported by Smith and Arnett by measuring the noise power of a CIP spin valve head and they referred to this type of noise as *mag-noise* (Smith and Arnett, 2001, 2002; Smith *et al*., 2003).

The NPSD shown in Figure 2 arises from the dynamics of the magnetization in the free layer, excited by thermal fluctuations (Bertram, Jin and Safonov, 2002; Zhu, 2002; Zhou, Roesler and Zhu, 2002; Zhang and Lederman, 2002; Brown, 1978). In the absence of both an external magnetic field and thermal excitation, the magnetization is locally aligned with the effective magnetic field. Thermal excitation causes the magnetization to deviate away from the local equilibrium direction. When the deviation occurs, magnetization gyrates around the local equilibrium direction while the deviation angle decreases, a motion referred to as *damping*. Both gyromotions can be described by the Landau-Lifshitz-Gilbert equation (Bertram and Zhu, 1992; Gilbert, 1956):

$$\frac{\mathrm{d}\hat{m}}{\mathrm{d}t} = -\gamma \hat{m} \times \vec{h} + \alpha \frac{\mathrm{d}\hat{m}}{\mathrm{d}t} \times \hat{m} \tag{1}$$

where $\hat{m}$ is magnetization unit vector, $\vec{h}$ is total effective magnetic field, and γ is the gyromagnetic ratio. The first term in the equation describes the gyromotion of the magnetization vector, and the second term the damping motion. This particular vector form of the damping

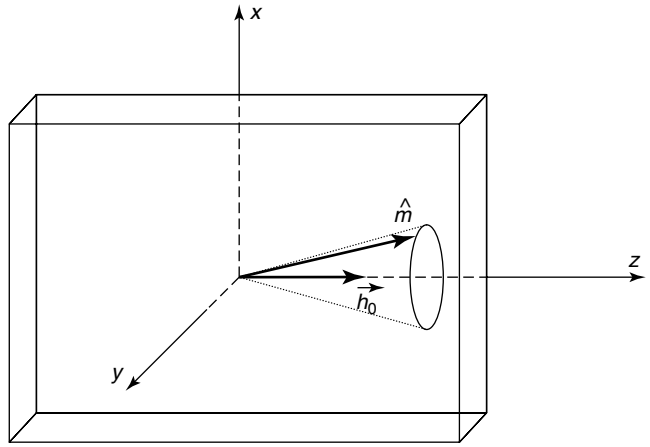

Figure 3. Magnetization gyromotion around its equilibrium direction, z axis, with $\vec{h}_0$ representing the stabilization field provided by the permanent-magnet layers abutted at the side edges of the free layer.

motion was first proposed by Gilbert (1956) and α is known as the *Gilbert damping constant*. In the following discussion, we shall basically follow the derivation given by Smith (2001), though, in a much more simplified manner.

Assuming that the magnetization in the free layer is uniform and that the thermally excited magnetization deviation from the equilibrium direction is small, the magnetization unit vector can be written as below following the coordinates given by Figure 3.

$$\begin{aligned}\hat{m} &= m_x\hat{e}_x + m_y\hat{e}_y + m_z\hat{e}_z \\ &\approx m_x\hat{e}_x + m_y\hat{e}_y + 1\cdot\hat{e}_z\end{aligned} \tag{2}$$

and the field can be written as

$$\begin{aligned}\vec{h} &= h_x\hat{e}_x + h_y\hat{e}_y + h_z\hat{e}_z \\ &= \left(h_{T,x} - D_x m_x\right)\hat{e}_x + \left(h_{T,y} - D_y m_y\right)\hat{e}_y + h_0\hat{e}_z\end{aligned} \tag{3}$$

where $h_{\mathrm{T},x}$ and $h_{\mathrm{T},y}$ are the effective random thermal fields along x and y directions, respectively; D_x and D_y are the effective demagnetizing factors along x and y directions, respectively; and h_0 is the stabilization field. Thus, equation (1) becomes

$$\begin{aligned}&\begin{bmatrix}1 & \alpha\\ -\alpha & 1\end{bmatrix}\begin{bmatrix}\dot{m}_x\\ \dot{m}_y\end{bmatrix} \\ &\quad= \begin{bmatrix}0 & -\gamma\left(h_0 + D_y\right)\\ \gamma\left(h_0 + D_x\right) & 0\end{bmatrix}\begin{bmatrix}m_x\\ m_y\end{bmatrix} + \gamma\begin{bmatrix}h_{T,y}\\ -h_{T,x}\end{bmatrix}\end{aligned} \tag{4}$$

Assume that the reference layer magnetization is 'fixed' along the x axis, through the strong interlayer exchange coupling between the pinned and the reference layers and the strong exchange bias field provided by the antiferromagnetic layer. The magnetoresistance is, then, only a function of m_x; eliminating m_x and $\dot{m}_y$ in the above equations, we have

$$\begin{aligned}&\ddot{m}_x + \eta\dot{m}_x + \omega_0^2 m_x \\ &\quad= \frac{\gamma}{1+\alpha^2}\left(\sqrt{1+\alpha^2}\,\omega_y h_{\mathrm{T},x} + \alpha\dot{h}_{\mathrm{T},x} + \dot{h}_{\mathrm{T},y}\right)\end{aligned} \tag{5}$$

where the resonance frequency is

$$\omega_0 = \sqrt{\omega_x\omega_y} \tag{6}$$

and

$$\omega_x = \frac{\gamma\left(h_0 + D_x\right)}{\sqrt{1+\alpha^2}} \tag{7}$$

$$\omega_y = \frac{\gamma\left(h_0 + D_y\right)}{\sqrt{1+\alpha^2}} \tag{8}$$

and

$$\eta = \frac{\alpha\left(\omega_x + \omega_y\right)}{\sqrt{1+\alpha^2}} \tag{9}$$

Equation (5) has the form of a damped harmonic oscillator. The following statistic properties of the random thermal fields on the right-hand side can be derived using the fluctuation-dissipation theorem (Brown, 1963; Kubo, 1966; Smith, 2002; Zheng, Bertram and Dakroub, 2002):

$$\lim_{\tau_0\to\infty}\frac{1}{2\tau_0}\int_{-\tau_0}^{\tau_0} h_{\mathrm{T},x}(\tau)h_{\mathrm{T},x}(\tau - t)\,\mathrm{d}\tau = \frac{2k_{\mathrm{B}}T\alpha}{M_{\mathrm{s}}V\gamma}\delta(t) \tag{10}$$

$$\lim_{\tau_0\to\infty}\frac{1}{2\tau_0}\int_{-\tau_0}^{\tau_0} h_{\mathrm{T},y}(\tau)h_{\mathrm{T},y}(\tau - t)\,\mathrm{d}\tau = \frac{2k_{\mathrm{B}}T\alpha}{M_{\mathrm{s}}V\gamma}\delta(t) \tag{11}$$

and

$$\lim_{\tau_0\to\infty}\frac{1}{2\tau_0}\int_{-\tau_0}^{\tau_0} h_{\mathrm{T},x}(\tau)h_{\mathrm{T},y}(\tau - t)\,\mathrm{d}\tau = 0 \tag{12}$$

where k_{B} is the Boltzmann constant, T is the absolute temperature, and V and M_s are the volume and the saturation magnetization of the free layer, respectively. Since the power spectral density (PSD) for m_x is defined as

$$\begin{aligned}&PSD_{m_x}(\omega) \\ &\quad= \int_{-\infty}^{+\infty}\left(\lim_{\tau_0\to\infty}\frac{1}{2\tau_0}\int_{-\tau_0}^{\tau_0} m_x(\tau)m_x(\tau - t)\,\mathrm{d}\tau\right)e^{-j\omega t}\,\mathrm{d}t\end{aligned} \tag{13}$$

one obtains

$$PSD_{m_x}(\omega) = \frac{2k_B T\alpha\gamma}{M_s V\left(1+\alpha^2\right)}\left(\frac{\omega_y^2+\omega^2}{\left(\omega_0^2-\omega^2\right)^2+\eta^2\,\omega^2}\right) \quad (14)$$

The above expression can also be rewritten as follows:

$$PSD_{m_x}(\omega) \approx PSD_{m_x}(0)\cdot\left(\frac{\omega_0^4}{\left(\omega_0^2-\omega^2\right)^2+\frac{PSD_{m_x}(0)}{PSD_{m_x}(\omega_0)}\omega_0^2\,\omega^2}\right) \quad (15)$$

where $\omega_y \gg \omega_0$, true for all magnetoresistive read heads, has been assumed. The measured PSD is then:

$$PSD_{V_x}(\omega) = PSD_{m_{x_x}}(\omega) \times I_{\text{bias}}^2 \Delta R^2 \quad (16)$$

where ΔR is the full amplitude of the magnetoresistance change of the read sensor stack.

Figure 4 shows a voltage spectral comparison between an experimentally measured NPSD of a CIP spin valve read head and the analytical expression given by equations (14) and (16) assuming $\alpha = 0.0185$. Such agreement has been found for a variety of spin valve and TMR heads without any exception, and the assumed values of α are all in the vicinity of $\alpha = 0.019$. This fact validates that the Gilbert damping form in equation (1) does indeed give a correct description of the dynamic damping motion of the magnetization vector, at least in metallic magnetic thin films.

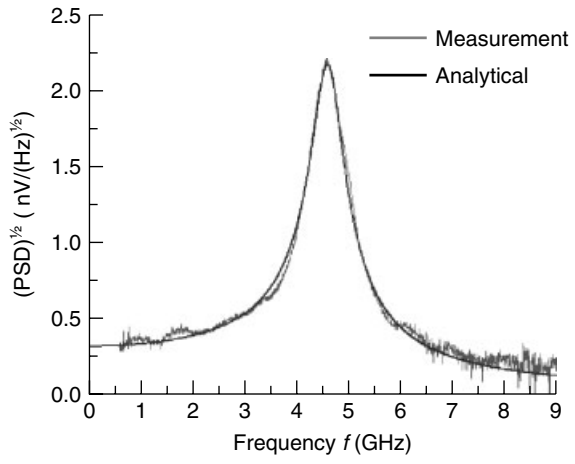

Figure 4. Comparison between an experimentally measured voltage spectral density of a CIP spin valve head (black) and the analytical expression of equations (14) and (16) (gray), assuming the Gilbert damping constant $\alpha = 0.0185$. The excellent agreement indicates the validity of the Gilbert damping form in metallic magnetic thin films.

4 MICROMAGNETIC MODELING AND SIMULATION ANALYSIS

Micromagnetic models have been developed to simulate the thermally activated magnetization processes in small-dimension magnetic devices, including the spin valve read heads (Zhu, 2002; Zheng, Bertram and Dakroub, 2002; Heinonen and Cho, 2004; Akimoto *et al*., 2005). Here, a rather comprehensive method developed for modeling spin valve read heads is described. Although the model is for specific spin valve sensors, it is quite representative for all types of applications involving small thin-film magnetic devices.

In this model, each of the three magnetic layers in the sensor stack is discretized into a layer of square mesh cells as shown in Figure 5. Within each mesh cell, the magnetization is assumed to be uniform. The volumetric energy density of each mesh cell, E, is calculated by summing up the following energy contributions: the local magnetic anisotropy energy, E_a, including magnetocrystalline anisotropy energy and anisotropy induced because of deposition in a magnetic field; the ferromagnetic exchange energy within the layer, E_{ex}; the magnetostatic energy, E_m, including interlayer interactions; the interlayer exchange energy, $E_{\text{int-ex}}$; the interfacial exchange pinning energy between the pinned layer and the antiferromagnetic layer, E_{pin}; and the Zeeman energy due to the field external to the sensor stack, E_Z. The effective magnetic field within each mesh cell, $\vec{H}$, is then calculated by taking a negative gradient of the energy density with respect to the local magnetization, $\vec{M}$ (Brown, 1978; Bertram and Zhu, 1992).

$$\vec{H} = -\frac{\partial E}{\partial \vec{M}} = -\left(\frac{\partial E}{\partial M_x}\hat{e}_x + \frac{\partial E}{\partial M_y}\hat{e}_y + \frac{\partial E}{\partial M_z}\hat{e}_z\right) \quad (17)$$

where

$$E = E_a + E_{ex} + E_m + E_{\text{int-ex}} + E_{pin} + E_Z \quad (18)$$

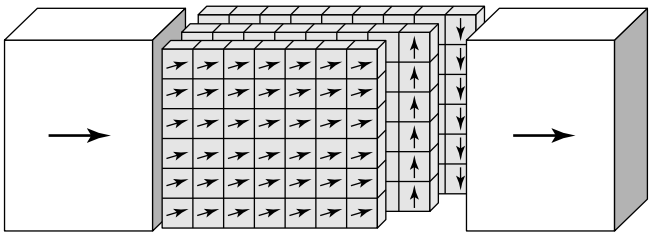

Figure 5. Schematic drawing of the modeling mesh of a magnetoresistive read head structure. Each of the three magnetic layers is discretized into a two-dimensional mesh of cells. The magnetization within each cell is assumed to be uniform and its orientation at any instant follows the Landau-Lifshitz-Gilbert equation (equation (1)).

The orientation of the magnetization in each mesh cell is assumed to follow the Landau-Lifshitz-Gilbert equation, equation (1) (Brown, 1978; Bertram and Zhu, 1992). If N is the total number of mesh cells in the stack, there are $3N$ coupled, nonlinear first-order differential equations. The thermal excitation is modeled by adding a random thermal field, $\vec{h}_{\mathrm{T}}$, to the effective field $\vec{H}$, for each mesh cell. The thermal field is completely random in orientation from cell to cell. The magnitude of the random thermal fields follows a Gaussian distribution with the variance determined by the fluctuation-dissipation theorem (Brown, 1979; Lyberatos, Berkov and Chantrell, 1993; Koch, Woods, Kirtley and Sun, 2001).

$$\overline{h_{\mathrm{T}}^2} = \frac{2k_{\mathrm{B}}T\alpha}{\gamma M_{\mathrm{s}}\Delta V\Delta t} \tag{19}$$

where ΔV is the volume of each mesh cell and Δt is the time duration over which the chosen random fields are kept unchanged. A different set of random fields is chosen every Δt period. The value of Δt is chosen to be in the range of 20–100 ps. The simulation results are insensitive to any value chosen within this region for modeling metallic magnetic thin films. The simulation time step for integrating the coupled differential equations needs to be significantly smaller than the random field duration, Δt.

Figures 6(a–c) show a set of simulation results for a CIP spin valve head. Figure 6(a) shows a snap shot of the thermally excited gyromagnetic motion of the magnetization in the free layer (the angle has been amplified by a factor of 10). Figure 6(b) shows the time domain waveform of the voltage signal and Figure 6(c) shows the corresponding noise voltage spectral density. The spatially nonuniform magnetization gyromotion in the free layer due to the nonuniform magnet fields, including both the magnetic field from the side-abutted permanent magnets and the demagnetization field from the edges, gives rise to multiple peaks, which have also been observed experimentally. In other words, the smaller peak at a higher frequency in the calculated spectrum is due to a nonzero, higher-order magnetostatic mode in the thermally excited spin wave (usually, ferromagnetic resonance only refers to the uniform rotation mode).

Micromagnetic modeling of thermal-driven noise in magnetoresistive sensors can also provide very useful insights on various characteristics of magnetoresistive heads. Here is one example. Figure 7 shows a calculated magnetization configuration at the quiescent state for both the free layer and the abutted permanent magnetic layer via micromagnetic simulation. The permanent-magnet film, consisting of closely packed CoPt magnetic grains, is also modeled. In the permanent-magnet layer, each magnetic grain has a relatively strong uniaxial magnetocrystalline anisotropy, with a single easy axis, the c axis of the hcp crystalline structure, lying in the film plane. However, the easy axes are oriented randomly from grain to grain, resulting in a rippling magnetization configuration, often referred to as

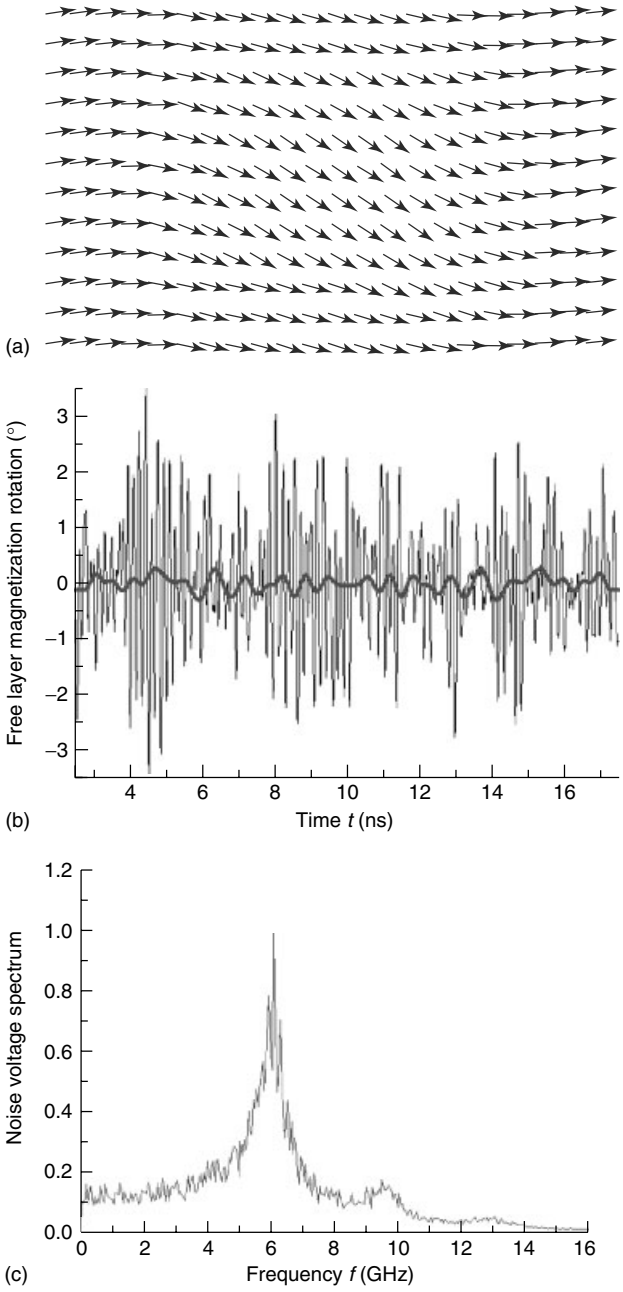

Figure 6. (a) A snap shot of magnetization rotation by thermal excitation in the free layer. The magnetization angles are exaggerated by a factor of 10 in this plot for visualization. The temperature in the free layer is assumed to be 60°C. (b) The angle of magnetization rotation, averaged over the entire free layer, is plotted as a function of time. The thicker curve in the center is the result of passing through a 2-GHz bandwidth low-pass filter. (c) The corresponding voltage spectral density of the modeled spin valve head.

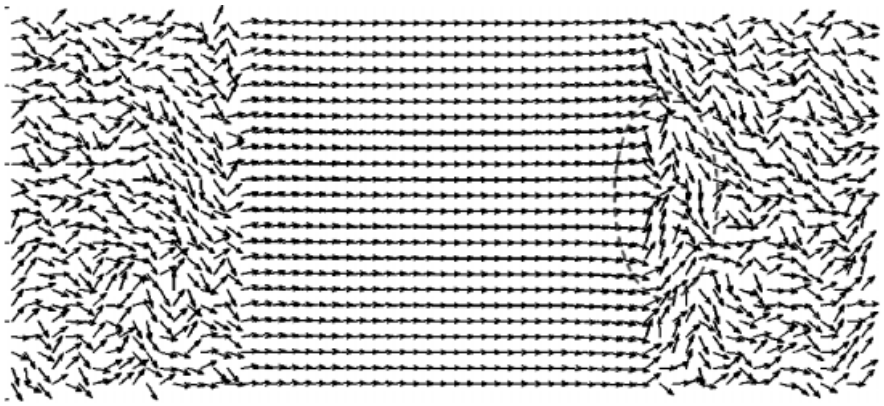

Figure 7. Calculated microscopic magnetization configurations in the free layer and abutted permanent-magnet (PM) layer for a CIP spin valve head. A CoPt film with a thickness of 30 nm has been assumed for the PM layer with a grain size of 10 nm. The physical track width of the free layer is assumed to be $w = 300$ nm and stripe height $h = 240$ nm.

magnetization ripples, as shown in the figure. The magnetization ripple results in microscale variations of the magnetic field provided by the permanent-magnet layer at the abutted junctions. This microscale bias field variation could be responsible for the often-observed head-to-head variation of various performance characteristics, such as read-track width variation, even for heads produced from the same wafer. The microscale variation of the field can also yield spatial variation of thermally excited magnetization oscillation in the free layer. Figure 8 shows the simulated magnetization oscillations at three different locations using the permanent-magnet magnetization configuration shown in Figure 7 and the color scale shows the rms value of the vertical magnetization component in the spatial map of the free layer. A locally weak field from the permanent magnetic layer at the right edge results in a significantly larger oscillation amplitude in the nearby region than elsewhere in the free layer. The calculated PSDs in the three corresponding locations show that the resonance frequency corresponding to the weak biased region at the right edge is significantly lower than that

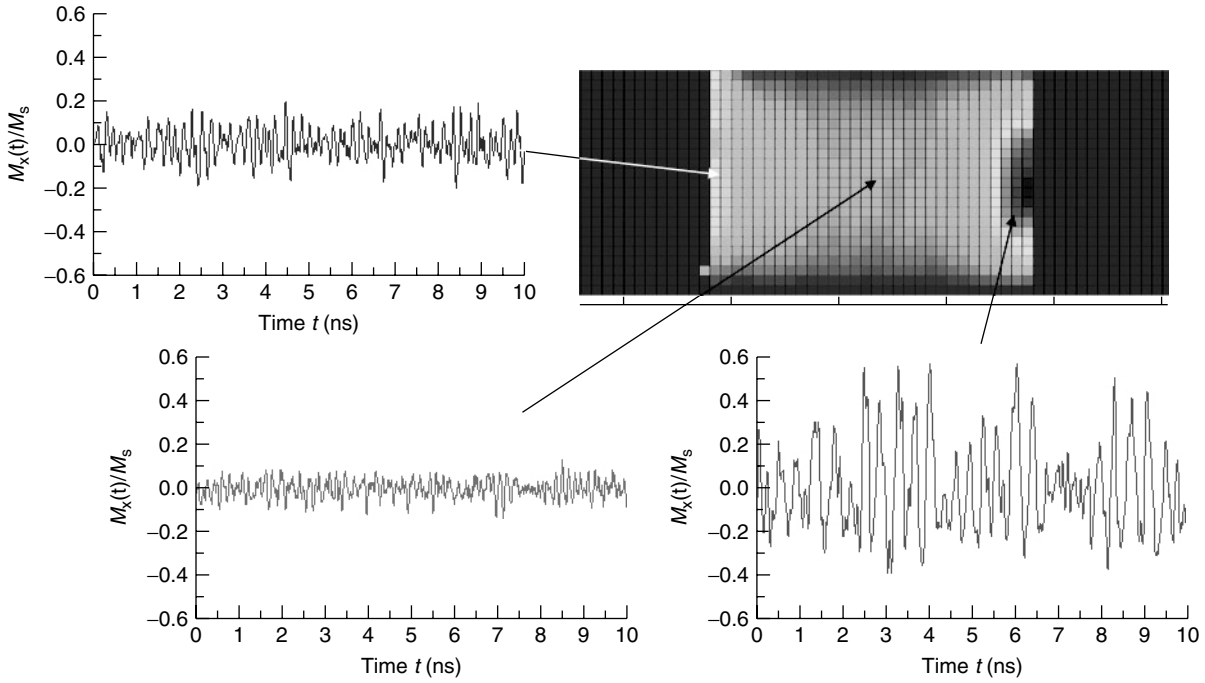

Figure 8. Simulated thermally excited magnetization oscillations at three different locations of the free layer with the permanent-magnet layer magnetization configuration shown in Figure 7. The color scale in the spatial color map (upper right) shows the rms amplitude of the oscillation.

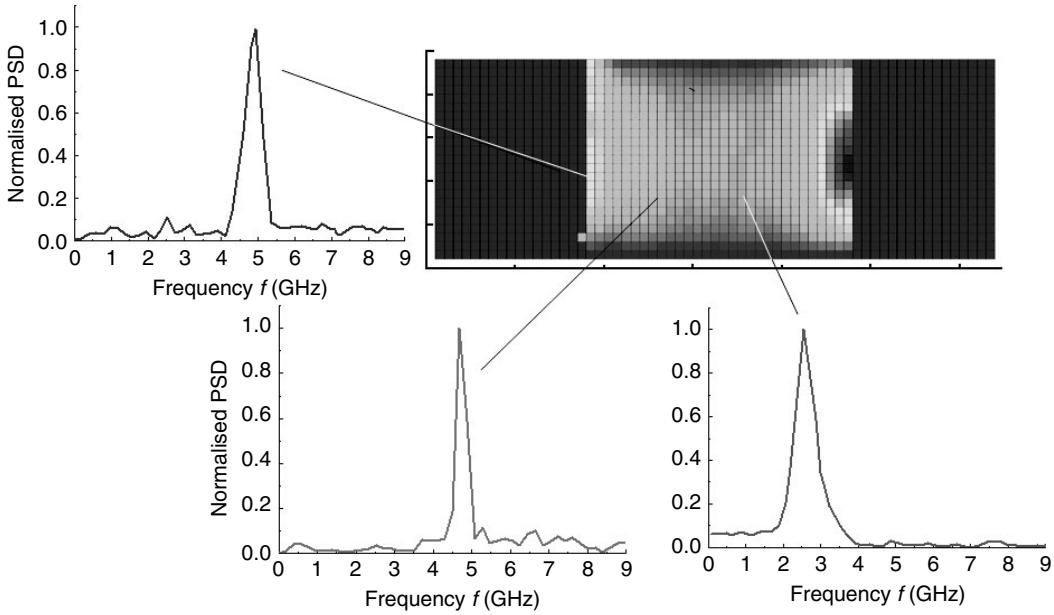

Figure 9. Calculated power spectral density of the magnetization oscillation at the three locations indicated in Figure 8. The weak biased region at the right edge of the free layer results in a significantly lower resonance frequency than the single resonance frequency elsewhere.

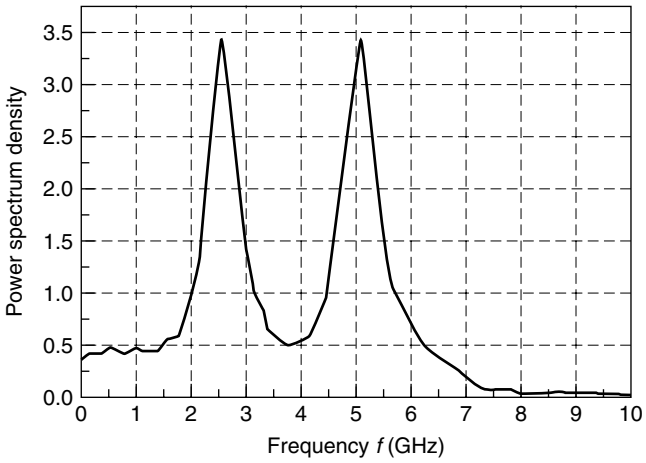

Figure 10. Calculated output voltage spectral density (au) from the micromagnetic simulation of the spin valve head presented in Figures 6–8.

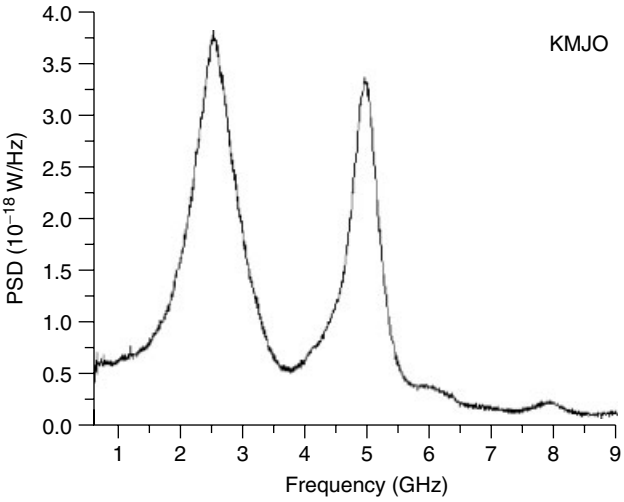

Figure 11. Experimentally measured power spectral density of a CIP spin valve head with abutted permanent-magnet stabilization. The higher peak at the lower frequency yields a high mag-noise level below 1 GHz.

elsewhere in the free layer, as shown in Figure 9. The head output voltage PSD is shown in Figure 10, clearly showing two distinctive resonance peaks. The lower-frequency peak results in a relatively high noise level in the frequency region below 1 GHz.

The predicted phenomenon has actually been often observed for spin valve heads, especially the ones with relatively large stripe heights. Figure 11 shows the measured NPSD of a spin valve head that exhibits the same features as the calculated one shown in Figure 10. The two heads have the same track width, stripe height, and magnetic layers.

5 THERMAL EXCITATION OF REFERENCE LAYER

The excellent predictability of micromagnetic simulation has provided many insights on the mag-noise characteristics of various types of magnetoresistive read heads (Zhou, Zhu and Kim, 2003), including the effect of thermally excited magnetization rotation in the reference/pinned synthetic

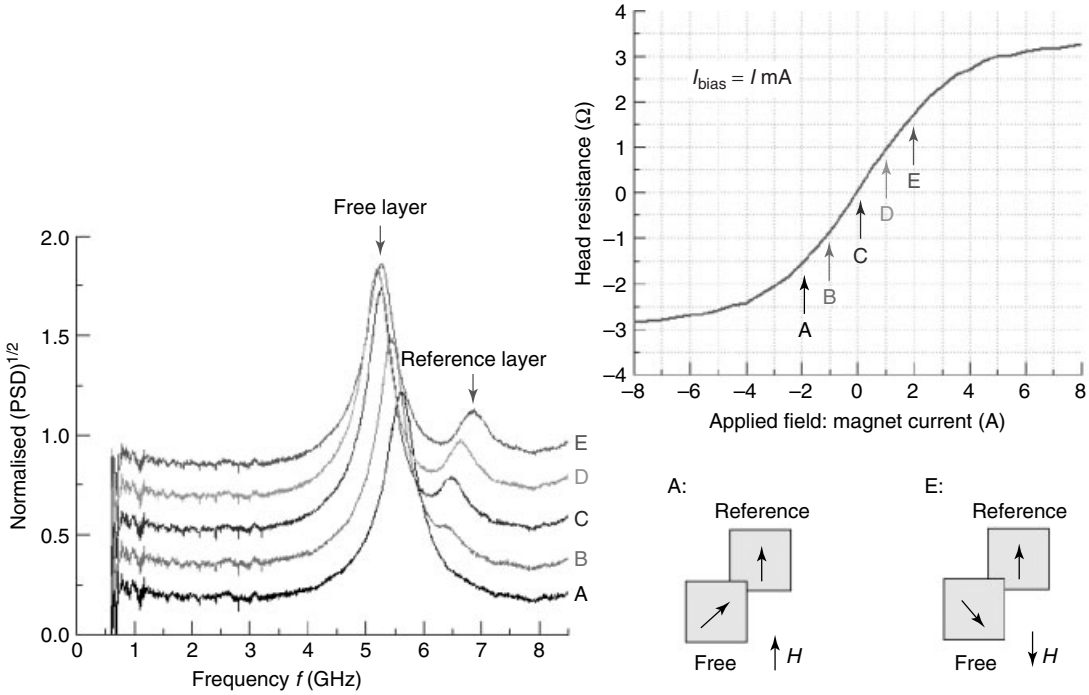

Figure 12. Experimentally measured power spectral densities of a magnetic tunnel junction head with abutted permanent-magnet stabilization at various fields applied perpendicular to the air-bearing surface, as indicated by the accompanying transfer curve. The baselines of the spectra were shifted vertically for visualization. The slight rising of the spectra below 2 GHz is magnetic in nature and is likely due to the acoustic mode of the ferromagnetic resonance of the synthetic antiferromagnet reference layer structure (Morrish, 2001).

antiferromagnet structure at insufficient exchange pinning fields (Heinonen and Cho, 2004; Akimoto, Mukouyama, Kanai and Uehara, 2006). Since the magnetization in the reference layer is usually at a 90° angle with respect to that in the free layer, the magnetoresistive output voltage can be written as

$$V \approx I_{\text{bias}} \cdot \Delta R \cdot \left(m_{x,\text{free}} + m_{z,\text{ref}}\right) \tag{20}$$

where $m_{x,\text{free}}$ and $m_{z,\text{ref}}$ are essentially the magnetization rotation angles away from equilibrium orientation in the free and reference layers, respectively. Assuming negligible coupling between the free and reference layers and small fluctuation angles, the variance of the output voltage can be written as

$$\begin{aligned}\overline{V^2} &\approx I_{\text{bias}}^2 \cdot \Delta R^2 \cdot \left(\overline{m_{x,\text{free}}^2} + \overline{m_{z,\text{ref}}^2} + 2 \cdot \overline{m_{x,\text{free}} \cdot m_{z,\text{ref}}}\right) \\ &= I_{\text{bias}}^2 \cdot \Delta R^2 \cdot \left(\overline{m_{x,\text{free}}^2} + \overline{m_{z,\text{ref}}^2}\right)\end{aligned} \tag{21}$$

Thus, the PSD of the output voltage can be written as the following:

$$PSD_V(\omega) = I_{\text{bias}}^2 \cdot \Delta R^2 \cdot \left(PSD_{m_x,\text{free}}(\omega) + PSD_{m_z,\text{ref}}(\omega)\right) \tag{22}$$

where $PSD_{mx,\text{free}}(\omega)$ and $PSD_{mz,\text{ref}}(\omega)$ are the PSDs of magnetization components in the free and reference layers, respectively.

Figure 12 shows a series of measured PSD curves for a magnetic tunnel junction head at a series of magnetic field values as indicated by the accompanied transfer curve. The field is applied perpendicular to the ABS of the head. As shown in the figure, the satellite peak to the right of the main peak in the voltage spectral densities shifts toward higher frequencies while increasing its magnitude when the applied field changes from the same direction as the reference layer magnetization to the opposite direction. The reference layer is a part of the exchange-biased synthetic antiferromagnet trilayer. The fact that the opposite frequency shifts for the two resonant peaks under the applied field indicates that the two peaks arise from separate magnetic layers. The satellite peak off the main resonance peak is, therefore, likely due to the thermally excited ferromagnetic resonance of the reference trilayer structure.

6 SUMMARY

Thermally excited magnetization precession results in magnetization oscillation in the magnetic layer(s) of magnetoresistive read heads in HDDs. The magnetization oscillation

behaves like a random-force-driven damped oscillator. Experimentally measured PSDs show excellent agreement with the formulation derived from the gyromagnetic equation with the Gilbert damping. The measured damping constant has been found to be around $\alpha = 0.019$ for the $Ni_{81}Fe_{19}/Co_{90}Fe_{10}$ composite free layer in all measured CIP spin valve heads. Micromagnetic modeling has become an excellent tool in the study of various noise spectral characteristics in spin valve heads. Combining micromagnetic modeling with spectral measurements of the read heads, many microscale "defects" in the heads could be diagnosed and understood.

ACKNOWLEDGMENTS

The author would like to thank Dr Yuchen Zhou, Ms Nayoung Kim, and Ms Veronica J. Yusz for the experimental measurements presented in this article. The author would also like to thank Professor H. Neal Bertram for many enlightening discussions on the subject and Mr H. Akimoto for insightful communication on the thermal excitation of the reference layer structure in spin valve heads. The research results presented and the writing of this article were made possible by the ABB endowed chair fund and the support from the Data Storage Systems Center at Carnegie Mellon University.

REFERENCES

Akimoto, H., Kanai, H., Uehara, Y., *et al*. (2005). Analysis of thermal magnetic noise in spin-valve GMR heads by using micromagnetic simulation. *Journal of Applied Physics*, **97**, 10N705.

Akimoto, H., Mukouyama, N., Kanai, H. and Uehara, Y. (2006). Analysis of the thermal magnetic noise spectrum of TMR heads by micromagnetic simulation. *Journal of the Magnetics Society of Japan*, **30**, 82–85.

Baibich, M.N., Broto, J.M., Fert, A., *et al*. (1988). Giant magnetoresistance of (001)Fe/(001)Cr magnetic superlattices. *Physical Review Letters*, **61**(21), 2472.

Bertram, H.N., Jin, Z. and Safonov, V.L. (2002). Experimental and theoretical studies of thermal magnetization noise in GMR head. *IEEE Transactions on Magnetics*, **38**(1), 38–44.

Bertram, H.N. and Zhu, J.-G. (1992). Fundamental magnetization processes in thin-film recording media. In *Solid State Physics*, Ehrenreich, H. and Turnbull, D. (Eds.), Academic Press, pp. 271–371, Vol. 46.

Brown, W.F. (1963). Thermal fluctuations of a single-domain particle. *Physical Review*, **130**(5), 1677–1686.

Brown, W.F. (1978). *Micromagnetics*, R. E. Krieger: Huntington, New York.

Brown, W.F. (1979). Thermal fluctuation of fine ferromagnetic particles. *IEEE Transactions on Magnetics*, **15**(5), 1196–1208.

Gilbert, T.L. (1956). Relaxation damping in ferromagnetic materials. *Bulletin of the American Physical Society*, **1**, 189.

Heinonen, O. and Cho, H.S. (2004). Thermal magnetic noise in tunneling readers. *IEEE Transactions on Magnetics*, **40**(4), 2227–2232.

Koch, R., Woods, S.I., Kirtley, J.R. and Sun, S. (2001). *Abstract DA02 from the 46th Annual Conference on Magnetism and Magnetic Materials*, Seattle, WA, November 12–16.

Kubo, R. (1966). The fluctuation-dissipation theorem. *Reports on Progress in Physics*, **29**, 255.

Lyberatos, A., Berkov, D.V. and Chantrell, R.W. (1993). A method for the numerical simulation of the thermal magnetization fluctuations in micromagnetics. *Journal of Physics: Condensed Matter*, **5**, 8911–8920.

Morrish, A.H. (2001). *The Physical Principles of Magnetism*, IEEE Press, pp. 607–624.

Smith, N. (2001). Modeling of thermal magnetization fluctuations in thin-film magnetic devices. *Journal of Applied Physics*, **90**(11), 5768–5773.

Smith, N. (2002). Fluctuation-dissipation considerations for phenomenological damping models for ferromagnetic thin films. *Journal of Applied Physics*, **92**(7), 3877–3885.

Smith, N. and Arnett, P. (2001). White noise magnetization fluctuation in magnetoresistive heads. *Applied Physics Letters*, **78**, 1448.

Smith, N. and Arnett, P. (2002). Thermal magnetization noise in spin valves. *IEEE Transactions on Magnetics*, **38**(1), 32–37.

Smith, N., Synogatch, V., Mauri, D., *et al*., (2003). Thermal magnetization fluctuation in CoFe spin-valve devices. *Journal of Applied Physics*, **91**(10), 7454–7457.

Zhang, J. and Lederman, M. (2002). Analysis of magnetic noise in lead overlaid giant magnetoresistive read heads. *Journal of Applied Physics*, **91**(10), 7285–7287.

Zheng, J., Bertram, H.N. and Dakroub, H. (2002). Experimental measurements and analysis of thermal magnetization noise in GMR sensors. *IEEE Transactions on Magnetics*, **38**(5), 2265–2267.

Zhou, Y., Roesler, A. and Zhu, J.-G. (2002). Experimental observations of thermally excited ferromagnetic resonance and mag-noise spectra in spin valve heads. *Journal of Applied Physics*, **91**(10), 7276–7278.

Zhou, Y., Zhu, J.-G. and Kim, N. (2003). Thermally excited ferromagnetic resonance as a diagnostic tool for spin valve heads. *Journal of Applied Physics*, **93**(10), 8579–8581.

Zhu, J.-G. (2002). Thermal magnetic noise and spectra in spin valve heads. *Journal of Applied Physics*, **91**(10), 7273–7275.

Zhu, J.-G. (2003). New heights for hard disk drives. *Materials Today*, **6**, 22–31.

Magnetic Modes in Circular Thin Film Elements, Experiment and Theory

Christian H. Back and Matthias Buess
Universität Regensburg, Regensburg, Germany

1 INTRODUCTION

In the last several years high-frequency-confined spin-wave eigenmodes of micrometer-sized magnetic elements have been systematically studied for the straightforward case of elements possessing an almost mono domain state (Hiebert *et al*., 1997; Demokritov and Hillebrands, 2002; Jorzick *et al*., 1999; Wu *et al*., 2002; Gubbiotti *et al*., 2003; Novosad *et al*., 2002). Only in recent years, the experimental analysis of modes confined to inhomogeneous magnetized ferromagnetic elements has been tackled. The excitations exhibit added complexity when the ground-state magnetization configuration is the flux-closed magnetic vortex whose inner core supports perpendicular magnetization components on a nanometer length scale (Shinjo *et al*., 2000; Raabe *et al*., 2000; Wachowiak *et al*., 2002).

Let us consider applying a short magnetic field pulse to a magnetic element. At the positions where the field is not aligned with the ground-state magnetization direction, there will be a torque and $\boldsymbol{M}$ will start a precessional motion, according to the Landau–Lifshitz–Gilbert (LLG) equation. However, dynamics are strongly affected by the finite size of the element and the existence of boundaries. This results in various eigenmodes whose spatial distribution and frequency depend on the shape and size of the element. A connection to acoustic eigenmodes of macroscopic plates can be drawn and the similarities and differences will be discussed.

Handbook of Magnetism and Advanced Magnetic Materials. Edited by Helmut Kronmüller and Stuart Parkin. Volume 2: *Micromagnetism*. ISBN: 978-0-470-02217-7.

2 EXPERIMENTAL TECHNIQUE

Time-resolved Kerr microscopy is a frequently used method to study the spin dynamics of thin-film systems in the time domain. It combines high temporal resolution of 150 fs with a spatial resolution of 300 nm for the setup used in the experiments described in the following text. To observe the precessional response of a spin system in the time domain, the magnetization has to be tipped off the equilibrium position. This has been done by laser-induced unpinning in ferromagnetic/antiferromagnetic system (Ganping *et al*., 1999), by using the temperature dependence of the anisotropy (van Kampen *et al*., 2002) or by optical current generation at a Schottky barrier (Acremann *et al*., 2001). We use the magnetic field generated in a lithographically produced microcoil. A Ti-sapphire laser operating at a repetition rate of 80 MHz triggers the current pulse by an optical switch (Hiebert *et al*., 1997). The excitation of the motion is monitored by a probe pulse aimed at measuring the perpendicular component of the magnetization $\boldsymbol{M}$. The probe pulse is frequency doubled to enhance the optical resolution and focused onto the sample. The detector analyzes the polarization of the reflected laser spot. A Wollaston prism splits the beam into two orthogonal linear polarization

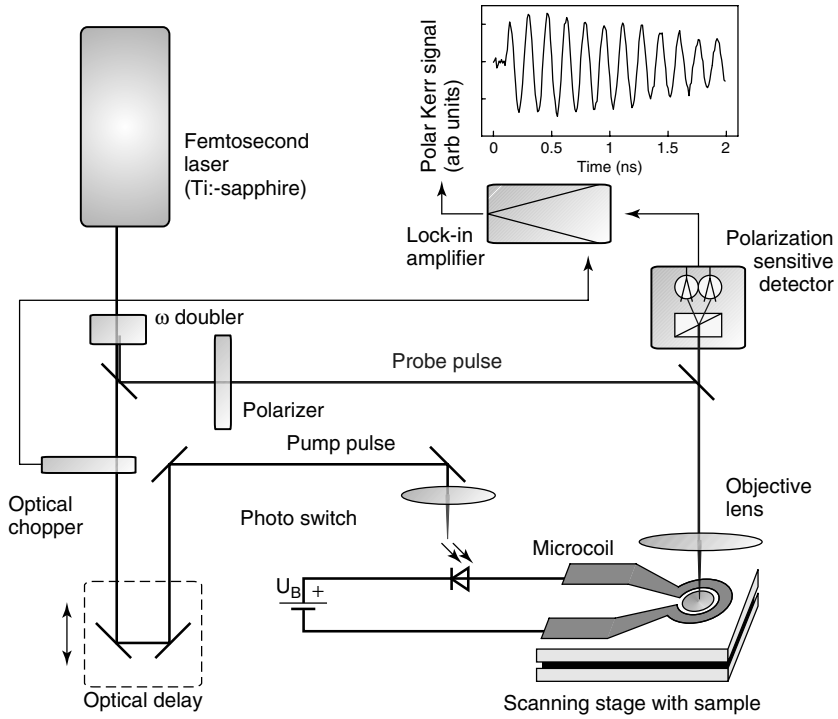

Figure 1. Diagram of the experimental setup using a microcoil. The probe pulse triggers an electric pulse by a photo switch that produces a magnetic field pulse in the microcoil, where the sample is located. The sample can be scanned under the lens of the microscopy by a piezo stage.

components whose intensity is detected in photodiodes. The polar magneto-optic Kerr effect induces a rotation of the plane of polarized light due to the perpendicular magnetization component. The time position is defined by the delay time between the field pulse and the measurement pulse. This is achieved by an optical delay line that changes the length of the pump beam path. The pump beam is mechanically chopped at kilohertz frequency and lock-in technique is used for detection of the small Kerr rotation. A piezo scanning stage moves the sample with respect to the microscope laterally and the vertical positioning is used to control and adjust the working distance (focus) of the lens. Figure 1 shows a diagram of the setup.

3 RADIAL EXCITATION FOR A CIRCULAR VORTEX-STATE PLATELET

The idealized magnetic element is a thin circular platelet with small aspect ratio d/R. Its ground state is the closed flux vortex state which can be best described in circular coordinates: $M_0(r, \varphi, z) = M_s \cdot (0, 1, 0)$

We consider the Landau–Lifshitz equation of motion

$$\frac{\partial \boldsymbol{M}}{\partial t} = \gamma \boldsymbol{M} \times \frac{\delta \mathcal{E}[\boldsymbol{M}]}{\delta \boldsymbol{M}(\boldsymbol{r})} \tag{1}$$

where the negative derivative of the energy functional $\mathcal{E}[\boldsymbol{M}]$ represents the effective field acting onto $\boldsymbol{M}$. In a 'back of the envelope' model we consider exclusively the external pulse field and the dipolar interaction inside the sample. For the circularly symmetric sample, no anisotropies are introduced. Generally, exchange interaction tends to align neighboring spins and establishes long-range ferromagnetic order. Here, the circulating flux configuration is the ground state for the sample and can be explained by dipolar interaction alone. In addition, micromagnetic simulations have been conducted to explore this limit and show that the exchange interaction will become relevant for smaller samples and higher modes. In the size regime we examined, no deviations of the modal frequencies from the dipolar dominated model are observed. Therefore, exchange interaction can be neglected [1] for the size range of our platelets, which is much bigger than the exchange length and the optical resolution of the experiment. As a consequence, the central region with the vortex core pointing out of plane will not be modeled. More detailed theories have been established using more general boundary conditions and a description of the core region ((Ivanov and Zaspel, 2005; Zivieri and Nizzoli, 2005) and references therein) but are not needed here to explain our experimental data.

The dipolar energy is expressed by the magnetic charge density.

$$\mathcal{E}_\mathrm{d} = \frac{\mu_0}{8\pi} \iint \frac{\rho_\mathrm{M}(\boldsymbol{r})\, \rho_\mathrm{M}(\boldsymbol{r}')}{|\boldsymbol{r} - \boldsymbol{r}'|} \mathrm{d}\boldsymbol{r}\, \mathrm{d}\boldsymbol{r}' \tag{2}$$

We estimate the deviation from the ground-state configuration to be smaller than 5%, so that the component of $\boldsymbol{M}$ along φ is assumed to remain equal to the ground-state value $M_{0\varphi} = M_\mathrm{s}$ for all times and the derivatives in φ direction are neglected to lowest order. The energy functional describing the total dipolar energy now reads

$$\begin{aligned}\mathcal{E}_\mathrm{d}[\boldsymbol{M}] = {} & \frac{\mu_0}{8\pi} \iint \frac{\partial_z^\mathrm{r} M_\mathrm{z}(\boldsymbol{r}) \partial_z^{\mathrm{r}'} M_\mathrm{z}(\boldsymbol{r}')}{|\boldsymbol{r} - \boldsymbol{r}'|} \mathrm{d}\boldsymbol{r}\, \mathrm{d}\boldsymbol{r}' \\ & + \frac{\mu_0}{8\pi} \iint \frac{\nabla_\parallel^\mathrm{r} \cdot \boldsymbol{M}_\parallel(\boldsymbol{r}) \nabla_\parallel^{\mathrm{r}'} \cdot \boldsymbol{M}_\parallel(\boldsymbol{r}')}{|\boldsymbol{r} - \boldsymbol{r}'|} \mathrm{d}\boldsymbol{r}\, \mathrm{d}\boldsymbol{r}' \end{aligned} \tag{3}$$

where $\parallel$ indicates the vector components parallel to the plane and z is the coordinate perpendicular to it. We use the identity

$$\left(\partial_z^\mathrm{r}\, \partial_z^{\mathrm{r}'} + \nabla_\parallel^\mathrm{r} \cdot \nabla_\parallel^{\mathrm{r}'}\right) \frac{1}{|\boldsymbol{r} - \boldsymbol{r}'|} = 4\pi\, \delta(\boldsymbol{r} - \boldsymbol{r}') \tag{4}$$

and homogeneous $\boldsymbol{M}$ along the z-direction to write

$$\begin{aligned}\mathcal{E}_\mathrm{d}[\boldsymbol{M}] = {} & \frac{\mu_0\, d}{2} \int_\mathrm{disk} M_\mathrm{z}^2(r)\, \mathrm{d}\boldsymbol{r} \\ & + \frac{\mu_0\, d^2}{8\pi} \int_\mathrm{disk} \int_\mathrm{disk} \frac{\nabla_\mathrm{r} \boldsymbol{M}_\mathrm{r}(r) \nabla_\mathrm{r} \boldsymbol{M}_\mathrm{r}(r')}{|\boldsymbol{r} - \boldsymbol{r}'|} \mathrm{d}\boldsymbol{r}\, \mathrm{d}\boldsymbol{r}' \end{aligned} \tag{5}$$

where $\nabla_\mathrm{r} \boldsymbol{M}_\mathrm{r} = \frac{1}{r} \frac{\partial}{\partial r}(r M_\mathrm{r}(r))$. Equation (5) contains only integrals over the disk area and is a perturbative expression. The first term is the energy arising from M_z appearing during the motion. It is of order $d\, R^2$ and contributes an effective field of the order $d\, R^2/(d\, R^2) \approx 1$. The next term in M_z would contribute a field of the order d/R and is neglected because, as $d \ll R$, it would only provide a minor correction. Thus, the field acting on $\boldsymbol{M}$ by virtue of the lowest-order term in M_z amounts to the standard demagnetizing field $-M_\mathrm{z}$ pointing in the direction opposite to M_z. This is the field of a perpendicularly magnetized plate with infinite radius. The finite radius introduces corrections of the order d/R which are neglected here. The second term is due to a radial component appearing during the motion. Its functional derivative is the radial field $H_\mathrm{r}[M_\mathrm{r}]$

$$H_\mathrm{r}[M_\mathrm{r}] = \frac{d}{4\pi} \frac{\partial}{\partial r} \int_\mathrm{disk} \frac{1}{|\boldsymbol{r} - \boldsymbol{r}'|} \frac{1}{r'} \frac{\partial}{\partial r'} (r' M_{\mathrm{r}'})\, \mathrm{d}r' \tag{6}$$

which is a linear functional of M_r. Notice that it is of the order d/R. However, if neglected, no precessional motion develops, in contrast to the experiment. Thus, within this perturbative approach, it makes sense to neglect the contribution of order d/R of the effective field along z, but it makes no sense to neglect the contribution of the same order d/R to the radial field. With all relevant fields specified, we obtain the system of coupled linear equations

$$\frac{\partial M_\mathrm{r}}{\partial t} = -\gamma_0 M_\mathrm{s} (H_\mathrm{ext} - M_\mathrm{z}) \tag{7}$$

$$\frac{\partial M_\varphi}{\partial t} = 0 \tag{8}$$

$$\frac{\partial M_\mathrm{z}}{\partial t} = +\gamma_0 M_\mathrm{s} H_\mathrm{r}[M_\mathrm{r}] \tag{9}$$

Generally, the Landau–Lifshitz (LL) equations couple different components. By taking the second derivative of 7 and inserting into 9, the LL equations can be decoupled to

$$\frac{\partial^2 M_\mathrm{r}}{\partial t^2} = -\gamma_0 M_\mathrm{s} \frac{\partial H_\mathrm{ext}}{\partial t} + (\gamma_0 M_\mathrm{s})^2 H_\mathrm{r}[M_\mathrm{r}] \tag{10}$$

$$M_\mathrm{z}(r, t) = \frac{1}{\gamma_0 M_\mathrm{s}} \sum_i \dot{c}_i(t) M_\mathrm{r}^i(r) + H_\mathrm{ext}(\boldsymbol{r}, t) \tag{11}$$

Equation (10) shows explicitly that the problem cannot be reduced to a standard wave equation. Equation (11) allows M_z to be straightforwardly calculated once M_r is known. We seek a solution of equation (10) with the separation ansatz $M_\mathrm{r}(r, t) = \sum_i c_i(t) M_\mathrm{r}^i(r)$. The radial functions $M_\mathrm{r}^i(r)$ are the solutions of the eigenvalue equation

$$H_\mathrm{r}[M_\mathrm{r}^i] = -N_\mathrm{r}^i M_\mathrm{r}^i \tag{12}$$

Inserting the separation ansatz in equation (10) leads to a set of decoupled ordinary differential equations for the coefficients c_i

$$\ddot{c}_i + \omega_i^2 c_i = -\gamma_0 M_\mathrm{s} \left(H_\mathrm{ext}(r),\, M_\mathrm{r}^i(r)\right) \dot{H}_\mathrm{ext}(t) \tag{13}$$

where the eigenfrequencies ω_i are related to the sought for eigenvalues N_r^i by the relation

$$N_\mathrm{r}^i = \frac{\omega_i^2}{\gamma_0^2 M_\mathrm{s}^2} \tag{14}$$

We use the scalar product $(a, b) = \int_0^R a(r) b(r) 2\pi r\, \mathrm{d}r$ and the external field pulse is written as $H_\mathrm{ext}(t) H_\mathrm{ext}(\boldsymbol{r})$. As equation (13) is the equation of motion of a classical undamped forced harmonic oscillator, it can be solved exactly, provided eigenmodes and eigenvalues are known, so that the coefficients c_i and thus $M_\mathrm{z}(r, t)$ can be calculated

analytically:

$$c_i = -\gamma_0 M_s \Big(H_{ext}(r), M_r^i(r) \Big) \int_{-\infty}^{\infty} H_{ext}(\tau)\, G(t,\tau)\, d\tau \quad (15)$$

with the Greens function $G(t,\tau) = \frac{1}{\omega_i} \sin(\omega_i (t-\tau))$. The ideal case of $H_{ext}(t) \propto \delta(t)$ can be solved at a glance and produces a solution equivalent to imposing a finite value to M_r at $t = 0$. The key elements of this problem are the eigenmodes $M_r^i(r)$. To determine them, we first notice that the integral in equation (6) diverges for $r = 0$ unless $M_r|_{r=0}$ is zero. This establishes the first boundary condition: the radial component of the magnetization must vanish in the center of the disk. Next, we notice that the exact solution of the eigenvalue equation for a disk with infinite radius is (see (Buess *et al.*, 2005))

$$N_r = \frac{1}{2}\, dk_r \quad (16)$$

and $M_r \propto J_1(k_r r)$, J_1 being the first-order Bessel function and k_r being the in-plane radial wave vector labeling the low energy excitations with frequency $\omega \propto \sqrt{k_r}$. When the disk has a finite radius, $H_r[M_r]$ contains a contribution arising from the magnetic charge ρ_M building up at $r = R$ in virtue of abrupt change of M_r from $M_r(R)$ to zero. This contribution diverges the unless $M_r|_{R=0} = 0$. This establishes the second boundary condition [2]. Thus, within our two dimensional model, the appearance, during the motion, of a finite radial component M_r at the center of the disk or at the boundary $r = R$ is associated with an infinite magnetostatic energy, so that pinning $M_r|_{0,R} = 0$ must be introduced to avoid this divergence. By virtue of the vanishing of M_r at $r = R$, the operator $H_r[M_r]$ defined on a disk with finite radius becomes a hermitic one. In the spirit of the Ritz variational principle, $J_1(k_r)$ are 'good' eigenfunctions for finite R as well, provided k_r is chosen to fulfill the boundary condition $J_1(k_r)|_{r=R} = 0$. This produces a discrete set of eigenvalues N_r^i and a complete orthonormal basis set M_r^i on the disk. In this approximation, the frequencies ω_i of the eigenmodes can be calculated as

$$\omega_i^2 = \frac{1}{2}\gamma_0^2 M_s^2 dk_r = \frac{1}{2}\gamma_0^2 M_s^2 \frac{d}{R}\, x_{1i} \quad (17)$$

where x_{1i} is the i-th zero of the J_1 Bessel function. In the next section, this relation is put to the test by comparing with the experimental data.

4 FOURIER TRANSFORM IMAGING OF THE EIGENMODES

In this section, the multimode excitation spectrum measured by time-resolved Kerr microscopy is analyzed.

The samples are single 15-nm thick ferromagnetic permalloy disks with diameters of 3 µm, 4 µm, and 6 µm and are produced by e-beam evaporation. The details are described in (Buess *et al.*, 2004). A Cu microcoil was prepared that surrounds the sample with an inner diameter of 8 µm and an outer diameter of 12 µm. In the ground state the magnetic elements exhibit a flux-closure vortex configuration (Raabe *et al.*, 2000). This state is perturbed by a short magnetic field pulse perpendicular to the sample plane, that is used to tip $\boldsymbol{M}$ off the equilibrium direction. This magnetic field pulse exerts a torque onto the local magnetization vector that launches the precessional motion of the magnetization.

4.1 Time-domain measurement

A current pulse of about 100 ps rise time launched into the microcoil provides the perpendicularly oriented magnetic tipping field pulse exciting the spin precessional motion (Hiebert *et al.*, 1997; Acremann *et al.*, 2000; Buess *et al.*, 2003) of the ferromagnetic microstructures under examination. The magnetic response of the individual disks is examined by recording a time-resolved movie with a high spatial resolution of 300 nm. The maximum strength of the field pulse is less than $\approx$4000 A m^{-1} (50 Oe) and is estimated by the current through the microcoil. This leads to a small deviation from the ground state. Figure 2 shows a stroboscopic sequence of polar Kerr microscopy images obtained during and after the application of the field pulse for a disk with 3 µm radius. The time interval between each image is 30 ps. The image contrast is produced by the z-component of the magnetization vector undergoing a spatially nonuniform motion. Notice that our experiment measures changes of M_z with respect to the ground state configuration. Therefore, the image of the initial state (the first image) shows no contrast. Despite the complexity of the sequence, one recognizes an overall periodicity of the motion with maxima (bright) and minima (dark) of M_z recurring after a characteristic time of the order of 350 ps. The modal structure of the motion is not immediately apparent from Figure 2 but will emerge from the Fourier transformation (FT) analysis. Note that in this regime of small deviations from the ground state, the in-plane tangential component of the magnetization vector is, to first order, unaffected by the motion. The radial component M_r (not measured in the present experiment) is connected to $M_z(t)$ by the relation $\dot{M}_r \propto M_z$ and has a phase difference of $\pi/2$, so that the magnetization vector performs an elliptical precessional path as shown in (Acremann *et al.*, 2000). Thus, in this linear limit, it is sufficient to consider only one component in order to have the full knowledge of the modal structure. We have measured here only the component that

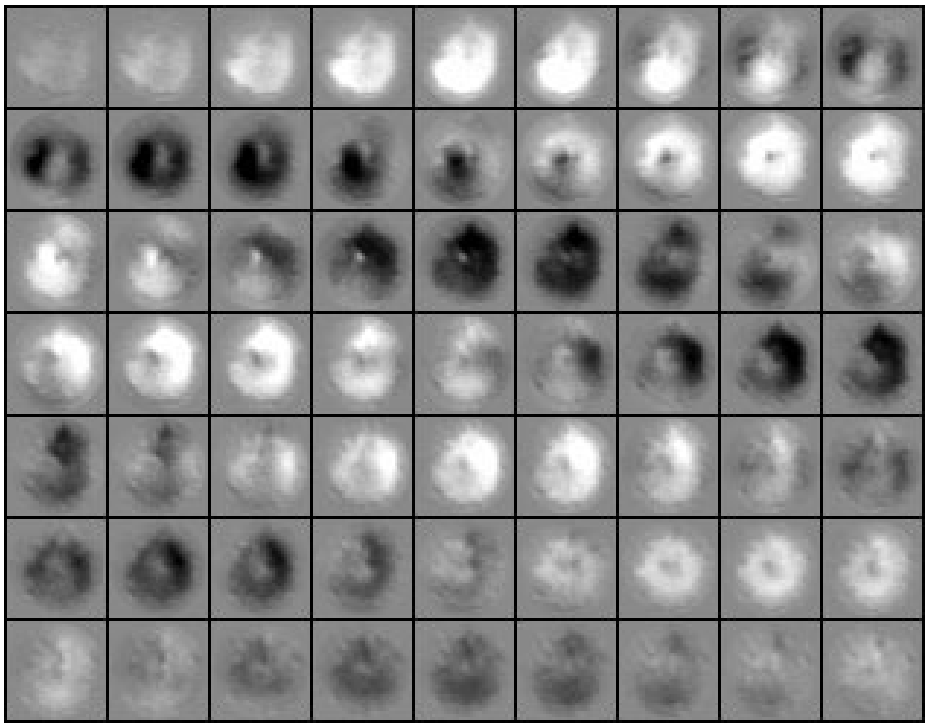

Figure 2. Temporal evolution of the precessional motion. $M_z(t) - M_z(t = 0)$ – that is, the difference between the value of the z-component of the magnetization vector before application of the pulse and after application of the pulse – is imaged as a function of the time elapsed after the magnetic field pulse. Notice that some images show a central spot, which is clearly distinguishable from the surroundings. This feature will be discussed in connection with Figure 10. From such a sequence one may extract an overall periodicity corresponding to the strongest excited mode. The spin motion, however, is not uniform, but is the superposition of a number of modes. (Reprinted with permission from M. Buess *et al*., *Phys. Rev. Lett.*, **93**, 077207 (2004).)

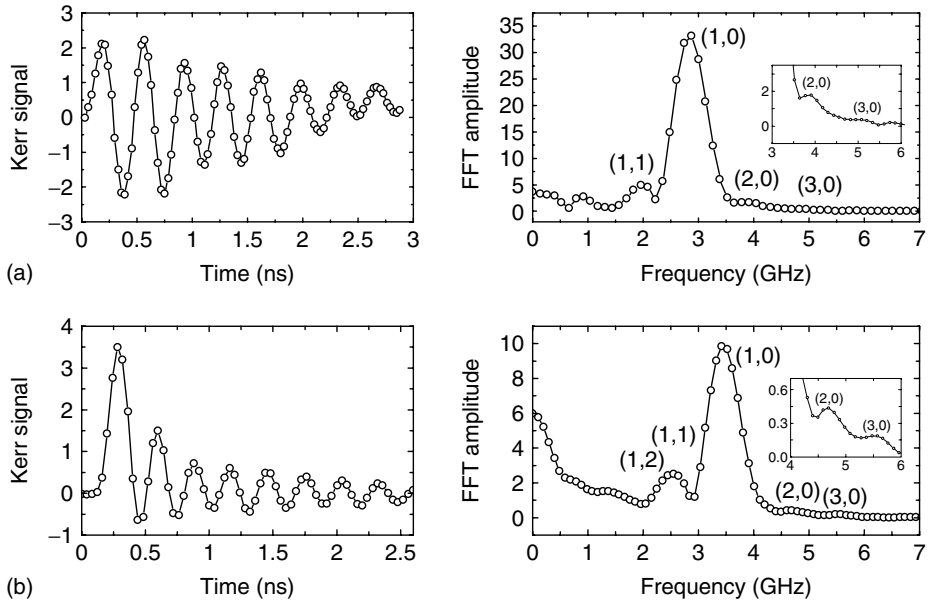

Figure 3. Spatially averaged signal (left) and Fourier transform amplitude (on the right). The insets show the same frequency domain data enlarged, to depict the small peaks at higher frequency more clearly. (a) Data from 6-μm disk (b) from 4-μm disk. The labeling of the maxima is explained later in Section 4.6.

could be detected with the greatest precision, namely, the one perpendicular to the disk (M_z).

4.2 Spatially averaged signal

The information of the spatio-temporal data presented in the last section cannot be understood at first view. In the first approach, we spatially average the signal over each frame in the data of Figure 3 and plot it as a function of delay time. This is the same result that we would get by using a laser spot of the size of the element. The oscillating signal of the 6 µm-diameter disk is shown in Figure 3(a) (left) with its FT amplitude (on the right). The dominant peak at 2.9 GHz is easily identified in the FT amplitude and recognized as the (almost uniform) precessional motion of the magnetization. No clear indication of other modes can be seen. For a different sample, a 4-µm-diameter disk, the averaged signal is shown in Figure 3(b) in the time domain (on the left) and the frequency domain (on the right). The principal peak for this smaller disk is found at a higher frequency of 3.4 GHz in agreement with Section 3 where the frequency is found to be proportional to the square root of the wave vector. A smaller peak at 2.5 GHz is also prominent.

4.3 Mode images by local Fourier transform

One of the difficulties in identifying the dynamical eigenmodes is that the excitation by, for example, a short magnetic field pulse results in a complicated spin motion where several modes are superposed in an intricate way. This difficulty is circumvented by using a phase-sensitive FT technique. Frequency domain analysis of the time sequenced images reveals resonances corresponding to the eigenmodes defined by the lithographically produced elements.

A detailed view of the various eigenmodes driving the spin motion in Figure 2 is obtained by Fourier transforming the time-domain signal recorded at each location into the frequency domain. This is referred to as the local FT. Of each FT, not only the amplitude – as in Ref. (Park *et al*., 2003; Hicken *et al*., 2003) – is retained but also the phase. The location of the maximum of these resonances can be determined with an accuracy of 0.2 GHz (corresponding to the separation of data points in the FT). The typical width of the resonance curves is 0.5–1.0 GHz. The values of the resonance frequencies have been accurately reproduced by an analytical calculation based on Ref. (Buess *et al*., 2003) and by a micromagnetic simulation (see Section 5, (LLG)).

Images of the amplitude (top) and the phase (bottom) at resonance of various eigenmodes are displayed in Figure 4. One recognizes two types of modes: some are organized into concentric rings with circular nodes having the spectral weight and phase distribution Figure 4(a–c) obeying the axial symmetry of the ground state as $M_s = 860\,\mathrm{kA\,m^{-1}}$. The modes in Figure 4(d) and (e) instead, have one and two diametric nodes, respectively, and break the axial symmetry. The various nodal lines are easily identified because at their spatial location the spectral weight is small and the phase jumps by π.

4.4 Axially symmetric (radial) modes

Fourier amplitude (left) and -phase (right) images of the three low-lying axially symmetric modes are displayed in Figure 4(a–c). The left-hand side of each image shows the result of the micromagnetic calculation, the right hand side is amplitude (or phase) of the FT of the experimental time-domain images. The modes can be classified according to the number of nodes: the fundamental and highest-amplitude mode has a node only in the center of the disk and at its border ($n = 1$: 4a). The phase is uniform over the disk. The next mode has a node at approximately half distance between the core and the boundary ($n = 2$: 4b). Going across the node the temporal phase changes by π, just as in any standing wave. Finally, we observe a third mode with two nodes within the disk ($n = 3$: 4c) and with π phase jump across each node. This modal structure is well described by the first-order Bessel function $J_1(k_n r)$, where k_n assumes discrete values determined by the boundary conditions and r is the radius. Such modes are natural basis functions in a circular membrane (Sparks, 1970). The frequencies can be calculated by an analytical model described in Sections 3 and 4.9.

4.5 Nonaxially symmetric (azimuthal) modes

Only axially symmetric modes are expected if the tipping pulse is uniform over the disk and all geometries are perfectly axially symmetric. Symmetry breaking modes, instead, require a nonuniform tipping pulse or a deviation of the sample from a perfect cylindrical shape. Our computation of the field configuration arising from the single turn coil reveals that the tipping pulse has a sizable gradient in the plane of the vortex, owing to the coil opening toward the leads. The maximum difference in tipping field amplitude reaches 30%. As revealed by our micromagnetic simulation (LLG), this asymmetry is capable of exciting nonaxially symmetric modes. Figure 4(d) shows Fourier amplitude (top) and Fourier phase (bottom) of a single-node, nonaxially symmetric mode at 2.08 GHz. The lowest lying nonaxially symmetric mode is imaged in Figure 4(e) (top: amplitude, bottom:

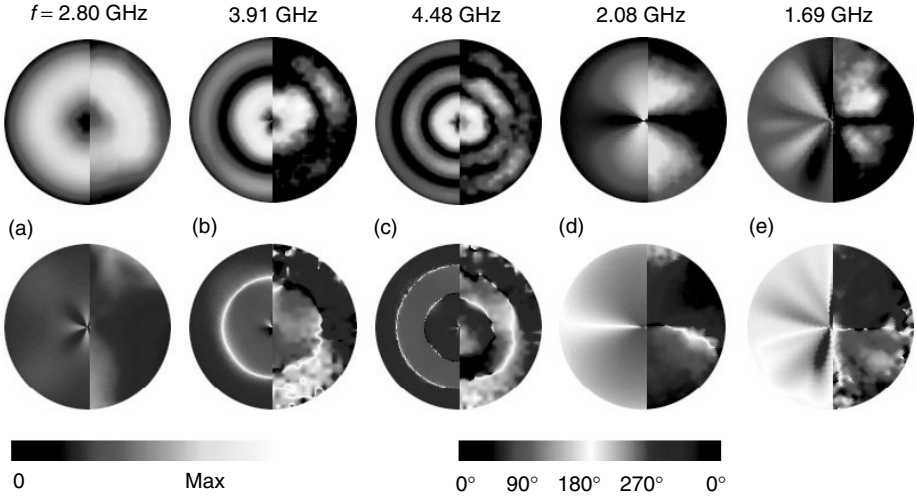

Figure 4. Images of the eigenmodes for a disk with radius $R = 3\,\mu$m. FT of Figure 2 at each location results in a spectrum with five resonances. The top row shows the absolute value of the Fourier amplitude at resonance and the bottom row shows the phase. The modal maps are composed from two half-images: the left from the micromagnetic simulation, the right from the experiment. (a–c) Axially symmetric modes showing concentric nodes ($n = 1, 2, 3$, $m = 0$). Mode (a) has the largest spectral weight, that is, it is dominating the motion and is responsible for the overall periodicity apparent from Figure 2(b) and (c) are higher modes with regions exhibiting different phases. (d–e) These modes have nodal lines going across the image. (d) exhibits one azimuthal node (1,1) and (e) two azimuthal nodes (1,2). This mode consists of four regions, oscillating in pairs in phase. Note that across the nodal lines the phase changes by 180°. A Hamming cutoff window was used to obtain the fast Fourier transform (FFT) data from the 3.33 ns long scans. The half-images from the time-domain micromagnetic simulation data (see Section 5) were obtained using the same procedure. (Reprinted with permission from M. Buess *et al.*, *Phys. Rev. B*, **71**, 104415 (2005).)

phase). This mode has two mutually orthogonal radial nodal lines (top). While passing through each node, the phase changes by π (bottom). We observe, for the single-node nonaxial mode, a systematic striking behavior, illustrated in Figure 5 for a 6 µm (top) and 3 µm-diameter disk (bottom). The Fourier amplitude is shown on the left of Figure 5(a) and (c), the Fourier phase on the right, and the reconstructed time sequences in Figure 5(b) and (d). The phase changes in both cases – in particular in Figure 5(c) – almost continuously along a circular path surrounding the center are in contrast to Figure 5(a). Correspondingly, the time-domain sequences in Figure 5(b) and (d) reveal that this mode is traveling along a circular trajectory surrounding the core. We explain this motion by noticing that the symmetry of this problem allows the existence of *two* mutually orthogonal degenerate single-node modes which can be simultaneously excited, their relative weight depending on the actual geometry of the tipping pulse. Superposition of such modes can produce the observed 'circularly polarized' eigenmode – just as, by analogy, linearly polarized light can be superposed to yield circular polarization. In this specific sample, the optical micrographs reveal that the 3 µm disk is rather displaced from the coil center whereas the 6 µm-disk is not: this explains why the 'circularly polarized' mode is more pronounced in Figure 5(c) and (d) than in Figure 5(a) and (b).

4.6 Wave vectors and boundary conditions

We first relate the nodal structure of the modes to a $\boldsymbol{k}$-vector and construct experimental dispersion relations. The modal structure observed in Figure 4 requires the introduction of polar coordinates r, φ in the plane of the disk. We define the wave vector $\boldsymbol{k} = (k_\mathrm{r}, k_\varphi)$ of a spin excitation by introducing an orthogonal set of basis functions suitable for the two-dimensional vortexlike spin configuration. $m_\mathrm{r}(r, \varphi) \sim \mathrm{J}_1(k_\mathrm{r} r)\exp(ik_\varphi \varphi)$. It can be shown that the radial part is an exact solution for infinite radius (Buess *et al.*, 2005). These functions are the analog for circular geometries of plane waves in Cartesian geometries. The 2π periodicity in φ requires $k_\varphi^m = 0, \pm 1, \pm 2, \ldots$, with the index $m = 0, \pm 1, \pm 2, \ldots$ counting the number of diametric nodes.

The boundary conditions at $r = 0$ and at $r = R$ (Kakazei *et al.*, 2004; Buess *et al.*, 2003) establish a set of possible values for k_r: $k_\mathrm{r}^n = \frac{x_n}{R}$, x_n indicating the zeroes of the Bessel functions J_1; $n \in \mathcal{N}$ counts the number of circular antinodes. $n = 1$ corresponds to the state with nodes at $r = R$ and $r = 0$. From Figure 4 – counting the nodes and their location – one can read out the mode numbers (n, m) of the measured modes. We can now construct the experimental dispersion relations f versus $(n, m = 0)$ (radial modes, Figure 6a) and f versus $(n = 1, m)$ (azimuthal modes, Figure 6b). We observe a positive dispersion (monotonically increasing) for

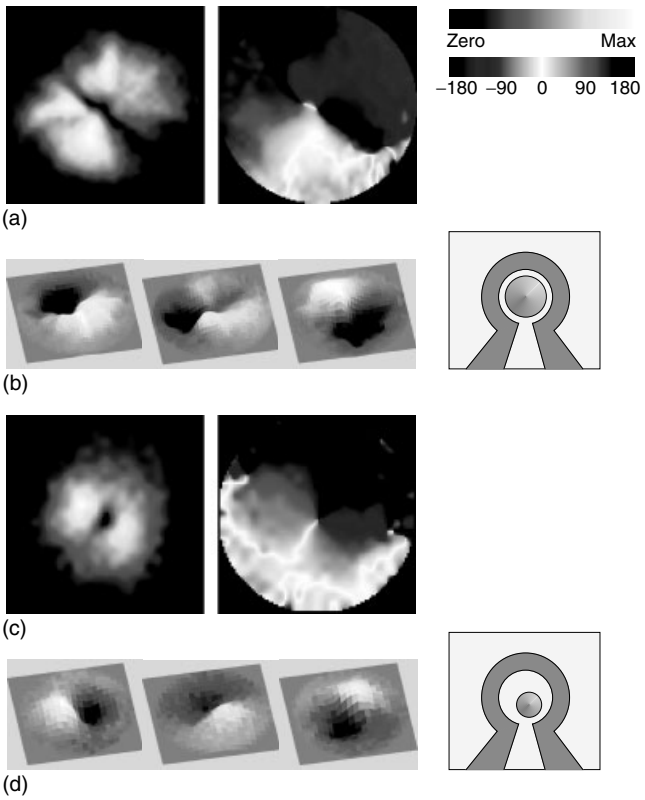

Figure 5. Single-node symmetric mode ($n = 1, m = 1$). (a) On the left the amplitude and on the right the phase of the mode from the 6 µm-diameter disk at 1.9 GHz are displayed. This corresponds to the sample show in the rightmost illustration. The mode consists of two regions divided by a node and oscillating with equal Fourier amplitude, but roughly opposite phase. Three images of the temporal evolution of this mode by back transformation are given in (b). Time interval between the middle (right) image and the left image: 120 (270) ps. (c) The single-node nonaxially symmetric mode in a 3 µm disk occurs at 2.8 GHz. The node is barely visible (left) and the phase (right) changes gradually along a trajectory surrounding the core center. Correspondingly, the temporal sequence obtained by back transformation – given in (d) after a time interval of 125 and 250 ps consists of a bright dark doublet rotating around the disk center. The respective illustration on the right indicates that the magnetic sample (bright) is off centered, which may explain the difference in the excitation of the two samples.

the axially symmetric modes $m = 0$ and negative dispersion (monotonically decreasing) for the modes with $m \neq 0$.

4.7 Negative dispersion

For the time being, we notice that the classification has revealed the surprising result of negative dispersion for the azimuthal quantization direction. The frequency of the two-node eigenmode (1,2) is lower than the one of the single-node eigenmode (1,1) which in turn is lower than the fundamental (1,0) mode. The energy and the frequency decrease as the number of nodes increase. Micromagnetic simulations (LLG; OOMMF) reproduce both values and sequence very accurately. In a simple view, one might consider the dynamic magnetostatic stray field produced by the precessing magnetization. When increasing the node number along the azimuthal direction this stray field and thus the total effective field is reduced, leading to decreasing frequency with increasing node number. This explanation works until the exchange interaction dominates and the frequency starts to increase again. Thus, the observed modes are analogous to magnetostatic backward volume modes which can show negative dispersion, albeit in a circular structure. A more detailed theory is presented in Section 4.9.

An important result is the existence of two distinct types of dynamical modes, one with positive dispersion and one with negative dispersion. Negative dispersion – the lowering of the frequency with increasing wave vector – is occasionally measured in light optics for negative index media (Pendry and Smith, 2004; Pendry and Smith, 2003), special photonics crystals (Parimi *et al*., 2004; Kosaka *et al*., 1998), and media with inverted population (Chiao, 1993). The references (Damon and Eshbach, 1960; Fletscher and Kittel, 1960; Sparks, 1970; Dillon, 1960; Gubbiotti *et al*., 2003; Park *et al*., 2002; Bayer *et al*., 2004; Demokritov *et al*., 2001; Kakazei *et al*., 2004; Perzlmaier *et al*., 2005) quoted here (the list is by no means exhaustive) indicate that this should be a quite general phenomenon, not limited to the geometry and size investigated in the present chapter, when the excitation spectrum is dominated by magnetostatic modes. As suggested by Fletcher and Kittel more than 40 years ago (Fletscher and Kittel, 1960), a possible way to qualitatively explain this phenomenon is to consider the magnetostatic energy associated with the excited modes. In Buess *et al*. (2005), it is shown that the magnetostatic energy, which Fletcher and Kittel refer to, are the diagonal elements of our matrix. These diagonal elements are exactly the Coulomb energy of the effective magnetic charge $\frac{1}{r}\frac{\partial}{\partial r} r \psi_{n,m}(r, \varphi)$. They are also indicated in Figure 6 and are clearly quite close to the 'true' eigenfrequencies, confirming the qualitative suggestion by Fletcher and Kittel. The negative dispersion means that when the magnetic charge distribution is partitioned by introducing diametric nodes, the Coulomb energy (and thus the frequency) *decreases*.

4.8 Comparison with acoustic membranes

An analogy can be drawn with eigenmodes of acoustic membranes which resonate in such a way that adding a circular or a diametric node inevitably produces an increase of the vibrational frequency. Chladni's law for sound in a circular membrane (Rayleigh, 1945; Rossing, 1982) states

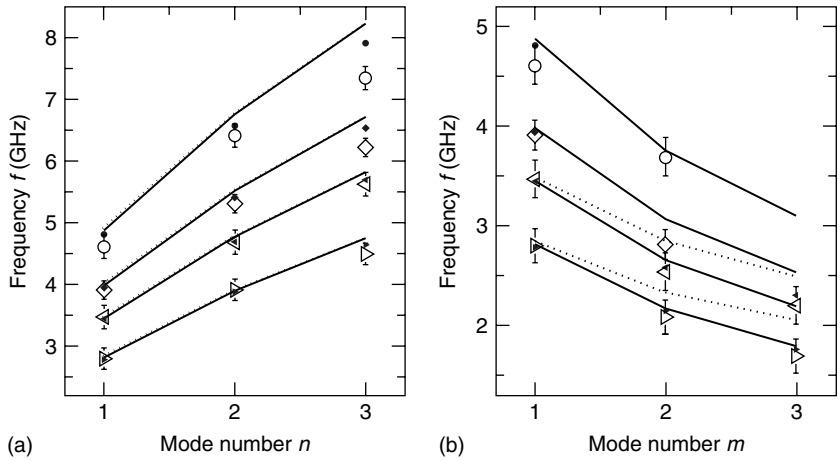

Figure 6. Dispersion relations. (a) The frequency for modes of the type $(n, m = 0)$ as a function of the radial mode number n: $R = 1\,\mu$m; ○, 1.5 µm; ⋄, 2 µm; △, 3 µm; ▽ are displayed as open symbols. The error bars are $\pm\frac{df}{2}$. (b) the frequency for modes of the type $(n = 1, m)$ as a function of the azimuthal mode number m. The corresponding data points of the micromagnetic simulation based on the LLG code LLG, are diagramed as full symbols. Results from the variational model as discussed in the Section 4.9 are represented as solid and the dotted lines. The dotted line is calculated by the diagonal elements and the solid line from the full matrix eigenvalues. (Reprinted with permission from M. Buess *et al*., *Phys. Rev. B*, **71**, 104415 (2005).)

that $f \propto (m + 2n)^2$. This phenomenon is a consequence of the positive dispersion of ordinary waves. It has been shown by imaging the modes and analyzing their corresponding frequencies in Section 4 that Chladni's law is violated by spin excitations in small circular ferromagnetic disks with a vortexlike ground-state configuration. This violation is due to the particular laws governing spin dynamics: in ordinary standing waves residing on a membrane, the change of frequency due to diametric modes is related to the matrix elements of the angular part of the Laplace operator, which scales with the square of the angular momentum, m^2. The relevant operator for spin systems contains the Coulomb interaction, which behaves quite differently with m, as discussed in the preceding text.

4.9 Advanced variational theory

We expand our analytical model from Section 3 to include modes containing diametric nodal lines in order to construct a more thorough theoretical model that also comprises the azimuthal dependence (φ) of the magnetization $\boldsymbol{m}(r, \varphi)$.

In the following text, we suggest a quantitative model that essentially accounts for all the experimental dispersion curves measured, including the lowering of the frequency f with m and the size dependence. We point out that for moderate field pulse excitations and large magnetic elements (e.g., several tens of microns) the highly degenerate excitation spectrum is dominated by magnetostatic modes (Tamaru *et al*., 2002). When the size of the elements is reduced or higher-order modes are excited, the exchange interactions can, in general, no longer be ignored and the dynamic response gradually changes from a purely magnetostatic to an exchange dominated one (Jorzick *et al*., 2002; Park *et al*., 2003; Demokritov *et al*., 2001).

As shown previously in Section 3 the relevant operator governing the dipolar modes is the dimensionless in-plane radial field given by $h_r[m_r]$. The eigenfrequencies of the various modes are related to the eigenvalues N_r of the equation $h_r[m_r] = -N_r m_r$ by the relation $\omega^2 = (\gamma M_s)^2 N_r$. These results were already used to calculate modes with circular nodal lines in a 6 µm Cobalt disk (Buess *et al*., 2003). Here, they are generalized to include modes with diametric nodes as well. The matrix $[h]_{nn',m} = \langle \psi_{n,m}, h_r \psi_{n',m} \rangle$ is evaluated within the trial space consisting of the orthonormal basis functions

$$\psi_{n,m} = \frac{1}{\sqrt{\pi} R\, J_2(x_{1n})} \mathrm{J}_1(k_n r)\, e^{im\varphi} \tag{18}$$

on the disk with radius R (Jackson, 1999). The variational approach comprises a mixing of several radial basis functions $\mathrm{J}_1(k_n r)$ by keeping the azimuthal dependence $e^{im\varphi}$ (the symmetry) fixed. Using a set of 15 basis functions $n, n' = 1, \ldots 15$ within each sector m was found to give good convergence. The details of this calculation are provided in (Buess *et al*., 2005). The $m = 0$ sector provides the eigenvalues for the modes with circular nodes. The $m = 1, 2, \ldots$ sectors provide the eigenvalues for modes with $1, 2, \ldots$ diametric nodes. The frequencies resulting from the matrix diagonalization are plotted as dotted lines in Figure 6. The agreement with the experimental data is remarkable, taking into account that the calculation is a fully analytical one with no

adjustable parameters. In particular, the negative dispersion for the modes with diametric nodes is also well reproduced.

4.10 Size dependence

The time evolution of individual micron-sized permalloy disks with vortex structure has been recorded at time intervals of 25–40 ps and the excitation spectrum has been extracted as described in the preceding text for each magnetic element. In this section, the size dependence of the modal frequencies is analyzed.

The frequencies f^* corresponding to the maxima of the resonance peaks are used for constructing the experimental dispersion curves in Figure 6. The corresponding frequency data (local FT) was used to identify the mode numbers (n, m) and to justify the peak positions f^* where the amplitude was weak (see average spectra in Figure 3). Figure 6 shows all obtained experimental and simulated mode frequencies for different sample sizes together with calculated values.

4.11 Scaling

Our analytical calculations (see equation 17 and (Buess *et al.*, 2005)) suggest a simple scaling law that should be obeyed by all modes, provided they are of magnetostatic origin: all frequencies for different radii should fall onto one single function when $f(n,m)\left(\frac{R}{d}\right)^{1/2}$ is plotted as a function of n at fixed m (radial modes) or m at fixed n (azimuthal modes), this function being only dependent on the number of diametric and circular nodes. The agreement is excellent (see Figure 6). The largest deviations from this scaling law are observed for small radii, where the exchange interaction is expected to become more important. We recall that the frequency depends only on a symmetry function $s(n,m)$ and the aspect ratio of the disk ($f \sim \sqrt{\frac{d}{R}}\, s(n,m)$) for both kind of modes. This is quite a universal behavior for these idealized magnetostatic thin-film vortex structures. The symmetry function reads

$$s(n,m) = \frac{\gamma_0 M_\mathrm{s}}{2\pi}\left(N_{n,m}\right)^{1/2} \tag{19}$$

and uses the eigenvalues of $N^{(15)}_{n,m} = -\{\mathrm{spec}([h]^{(15)}_{\tilde{n}\tilde{n}',m})\}_n$ in (Buess *et al.*, 2005).

4.12 Variational eigenmodes

In Section 4.9 and (Buess *et al.*, 2005) the demagnetizing factors N_r have been calculated by a variational theory where the matrix representation of the radial dipolar operator $\hat{h}_\mathrm{r}$ has been calculated for a given basis system. To each $m = 0, 1, 2\ldots$ belongs a 15×15 matrix $[h]_{nn',m}$ with

$$[h]_{nn',m} = \left\langle \psi_{n,m}, \hat{h}_\mathrm{r}\, \psi_{n',m} \right\rangle \tag{20}$$

The diagonalized matrix $[d] = [s^{-1}][h][s]$ provides the eigenvalues $-N_\mathrm{r}^\mathrm{eig}(n,m)$ and with $(2\pi f)^2 = (\gamma_0 M_\mathrm{s})^2 N_\mathrm{r}$ we obtain the solid lines in Figures 6 and 7. In addition, the transformation matrix $[s]$ contains the coordinates of the optimized eigenfunctions that belong to the eigenvalues. Consequently, we have not only obtained the demagnetizing factors and the resulting frequencies but also an optimized radial part for the eigenmodes. The most striking fact is that the difference between the shape of the basis functions and the optimized functions increases for higher m. This is in correspondence with the deviations of the frequencies in Figure 7 (dotted and solid lines).

To compare the radial dependence of the experimental data with the results of the theory, the frequency domain data (Figure 4) is displayed as line scans of the FT amplitude as a function of distance to the disk center. Figure 9(a) shows this for the experimental data of the 6 µm-diameter disk and Figure 9(b) for a micromagnetic simulation (see Section 5). The FT amplitudes of the modes $(n,m) = (1,1)$, (1,0), (2,0), (3,0) are normalized to unity and plotted. In general, the agreement with the simulation and the theory (Figure 9) is good. It can be seen that the shape of the (1,1) mode differs from the one of the (1,0) mode. The more simple approach (diagonal values of $[h]_{nn',m}$) use the same radial functions J_1 for both modes, but when the optimized radial parts (belonging to the eigenvalues of $[h]_{nn',m}$) are compared

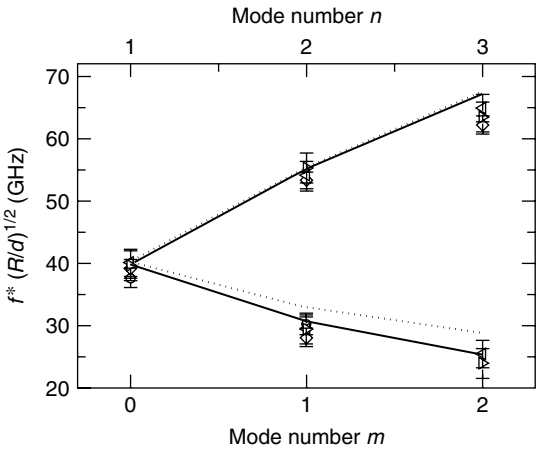

Figure 7. Scaling. When $f(n,m)\left(\frac{R}{d}\right)^{1/2} \doteq \tilde{f}$ is plotted versus m at fixed n or versus n at fixed m, all data points for different radii fall onto one single dispersion curve $\tilde{f}(m)$ and $\tilde{f}(n)$. The symbol and line attributes are the same as in Figure 6. (Reprinted with permission from M. Buess *et al.*, *Phys. Rev. B*, **71**, 104415 (2005).)

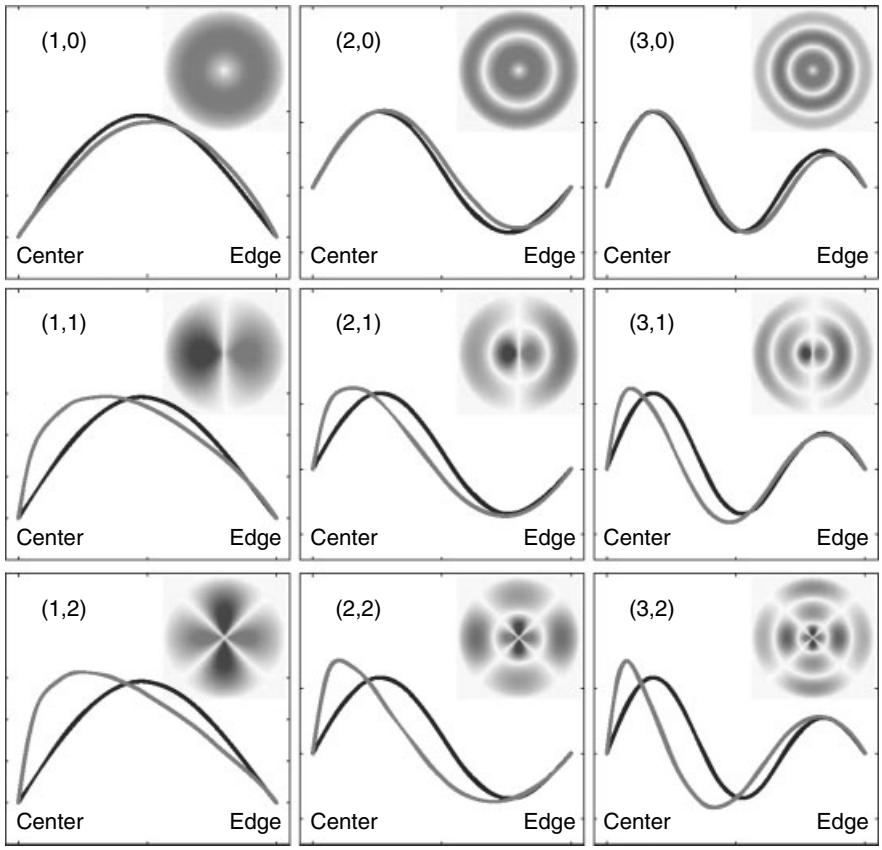

Figure 8. Optimized variational radial parts eigenfunctions (gray lines) compared to Bessel J_1 basis functions (black). For increasing azimuthal mode number m the optimized functions consistently are shifted towards the disk center. The insets show the spatial distribution of M_r amplitude at maximal excursion. The dynamical motion of $\boldsymbol{M}$ forms an elliptical trajectory. Except for ($n = 1$, $m = 0$) the amplitude has regions of both positive and negative sign.

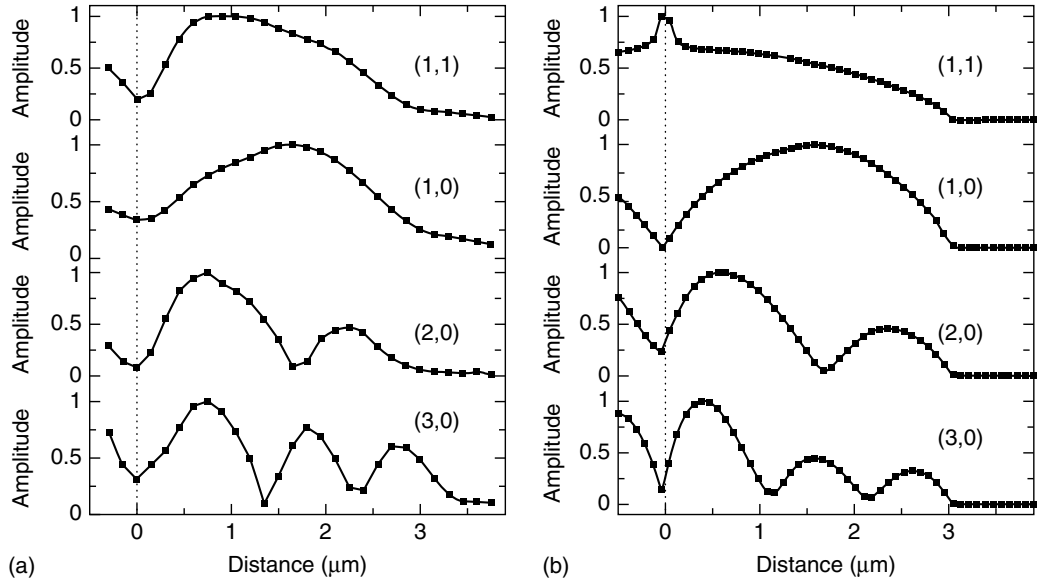

Figure 9. In (a) the FT amplitude for line scans through the center of the disk is extracted from the experimental data for the 6-μm-diameter disk for different modes labeled by (m,n). (b) shows the corresponding data for the micromagnetic simulation.

with the data, they clearly show the same trend: the amplitude is shifted toward the center for $m > 0$.

The curve from the micromagnetic simulation for the mode (1,1) deviates clearly from the experimental one. The reasons are the following: Theoretical considerations ((Ivanov and Zaspel, 2005; Zivieri and Nizzoli, 2005) and references therein) and some experimental data show that the azimuthal mode consists of two modes: one is traveling clockwise and the other anticlockwise around the center. With a real vortex core pointing out of the axis of the film, the frequencies of the two modes are slightly different. The effect grows for smaller disks and its analysis is beyond the scope of this chapter. In fact one of the two modes has high and the other a low amplitude in the center. Note, the limited resolution in the experiment of 300 nm.

4.13 Motion of the vortex core

We now proceed to the motion of the well-defined, circular element seen in some of the images of Figure 2 to reside in the vicinity of the center of the disk. From line scans across the image, this circular element appears as a clear peak (see insets in the bottom part of Figure 10) with a width of the order of the spatial resolution. The location of its maximum can be determined with an accuracy of about 0.2 µm and is seen to move with time (Figure 10a). Furthermore, its z-magnetization is oscillating with time (Figure 10b, circles). Most strikingly, at some times, the 'core' assumes negative M_z values, that is, it is oppositely magnetized with respect to the immediate surroundings (Figure 10b, triangles). Notice that the eigenmodes in this dipolar dominated regime are expected to have zero amplitude at the center of the disk (see Section 3). Thus, we do not have an immediate explanation for the negative M_z magnetization at the center, except that it indicates 'core' switching at some instances. In the ground state, the core of perpendicular magnetization extends over some 10 nm (Shinjo *et al*., 2000; Raabe *et al*., 2000; Wachowiak *et al*., 2002). As our experiment measures deviations from the ground state, the initial state is contrastless but a core dynamics would give rise to a contrast in the M_z component. However, our experiment collects the signal within a spot of 300 nm diameter, and it is not obvious that we can indeed observe the much smaller core. On the other side, our experiment is sensitive to minute ($<2^\circ$) deviations from the ground state. Thus, a reversal of the core magnetization would result in a 30 times stronger Kerr signal and would appear as a strong contrast even with our 'poor' spatial resolution. Notice that our micromagnetic simulations, which include the excitation of nonradially symmetric modes by a nonuniform pulse, appear to reveal this most remarkable process as well. The presence of eigenmodes breaking the axial symmetry of the ground state is thought to be essential for the operation of core switching (Gaididei *et al*., 2003). In fact, we have observed that the central region of the vortex changes its sign with time, suggesting that core switching have taken place.

A more detailed understanding of the generation of azimuthal modes may lead to a concept for controlled ultrafast switching of the vortex core.

5 MICROMAGNETIC SIMULATIONS

In principle, micromagnetic computer simulations solve the Landau–Lifshitz–Gilbert equations (e.g., in the form of equation 21) for each cell of a two- or three-dimensional grid. The effective fields comprise all required interactions acting on the individual cells that also depend on the magnetization $\boldsymbol{M}(r', t)$ of the other cells.

To support our data two different programs were used: LLG (LLG) and OOMMF (OOMMF). The LLG micromagnetics simulator is a three-dimensional simulation tool that integrates the Landau–Lifshitz–Gilbert (LLG) equations. Sample geometries and material parameters, temporally and spatially varying parameters like external fields can be set. The revolution in computer technology has enabled enough calculational power to achieve the relevant cell sizes and time steps for realistic results. There are many publications (Park *et al*., 2002; Hiebert *et al*., 1997; Buess *et al*., 2004) that demonstrate the excellent predictive abilities of the LLG equations of motion in the picosecond time regime for describing magnetization dynamics. The advantage of employing micromagnetic simulations is that all global or position-dependent parameters of the modeled system can be set and the magnetization and energies can be monitored. Unwanted artifacts of the experiment (noise, deviations from ideal system, resolution etc.) are not present. Comparison of the experiment with simulations can justify the proposed bottom lines or yield new results.

Figure 11 is an overview of results for a 4-µm-sized circular platelet with of 15-nm thickness. For the micromagnetic simulation, the sample was divided into $10.6\,\text{nm} \times 10.6\,\text{nm} \times 15.0\,\text{nm}$ pixels in a 375×375 array. The saturation magnetization, exchange stiffness, gyromagnetic frequency, and damping constant are $860\,\text{kA m}^{-1}$ ($860\,\text{emu cm}^3$), $13{\cdot}10^{-12}\,\text{J m}^{-1}$ ($1.3\,\text{micro-erg cm}^{-1}$), $176\,\text{GHz T}^{-1}$ ($17.6\,\text{MHz Oe}^{-1}$), and 0.008, respectively. The equations of motion were integrated in 0.4 ps steps from $t = 0$ to $t = 20$ ns. The data were stored for the entire array and for the average value of each magnetization component. The black line with squares in Figure 11 is the amplitude spectrum of the M_z component averaged over the disk region $S_{\text{ft av}}$. FT was performed by taking the first 6.2 ns of the data and using a Hamming windowing filter. The

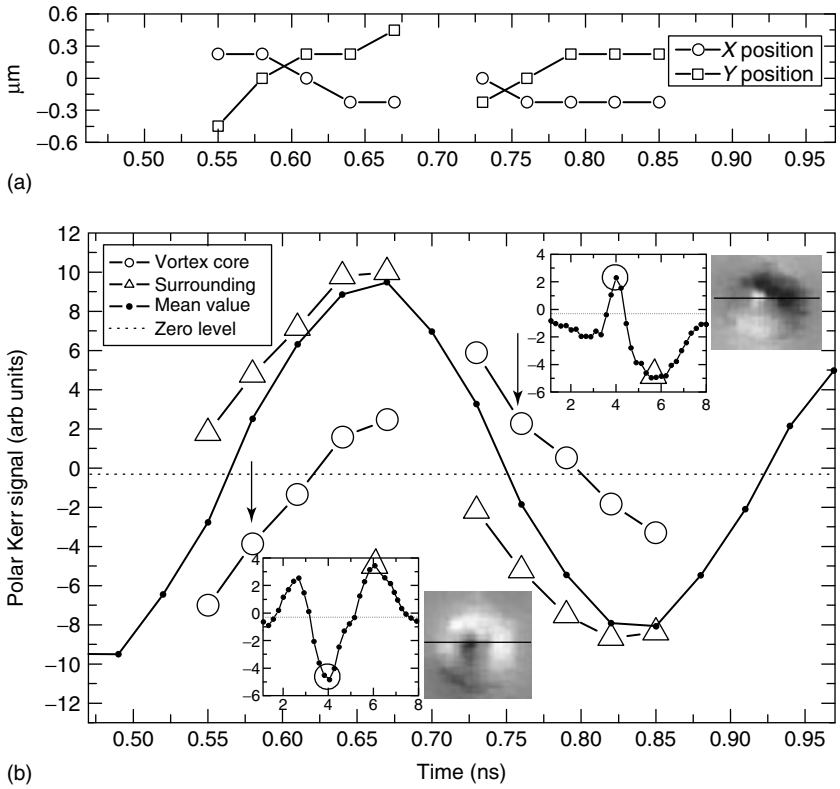

Figure 10. The core region. (a): Plot of the coordinates of the central part with respect to the geometrical image center ($X = 0, Y = 0$), in units of µm. (b): The continuous line indicates the average signal over the disk, and provides us with a check of the zero line (dotted), obtained from the nonmagnetic surroundings. The triangles give the strength of the magnetization surrounding the core, as derived from line scans of the images of the type indicated. The circles give the strength of the magnetization in the core region, which can be seen to become negative and positive. The signal also deviates systematically from the zero line expected for axially symmetric dipolar modes. The data from the line scans shown are marked with arrows. (Reprinted with permission from M. Buess *et al.*, *Phys. Rev. Lett.*, **93**, 077201 (2004).)

fundamental mode (1,1) is dominant and the higher radial modes (2,1), (3,1) . . . are clearly visible. A broad peak is visible below the fundamental mode that is composed of the azimuthal modes $m = 1, 2, 4$ belonging to order $n = 1$. The corresponding local FT modal images (amplitude and phase) are displayed for all peak positions and allow the classification of radial and azimuthal numbers (n,m).

In addition to the average amplitude spectra $S_{\mathrm{ft\ av}} = \mathrm{abs}(\mathrm{FT}(\mathrm{av}(data)))$ where the data was spatially averaged before FT, we can also consider the spatial averaging *after* FT $S_{\mathrm{av\ ft}} = \mathrm{av}(\mathrm{abs}(\mathrm{FT}(data)))$. This is most effective for modes that have regions of different sign because $S_{\mathrm{ft\ av}}$ is compensated fully or partially, though $S_{\mathrm{ft\ av}}$ shows a clear peak. Generally $0 \leq S_{\mathrm{ft\ av}} \leq S_{\mathrm{av\ ft}}$. The dark gray line with circles in Figure 12 is the spatially averaged data after FT $S_{\mathrm{av\ ft}}$.

Notice that $S_{\mathrm{ft\ av}}$ and $S_{\mathrm{av\ ft}}$ are identical for the fundamental modes, as the phase is uniform over the disk in contrast to the other modes. In particular, three modes in the broad low-frequency part are resolved. Moreover, additional modes (n,1) – which show a change of sign across the central line – appear just between the radially symmetric modes (n,0) and ($n - 1$,0).

In summary, we have studied the excitation spectrum of simple magnetic vortex-state structures with high accuracy and have identified several eigenmodes of the system. The spatial distribution and the frequency of the measured eigenmodes can be accounted for by a linear model based purely on dipolar interactions. Micromagnetic simulations show excellent agreement with our experimental findings. The argument developed in the preceding text shows that introducing spatial nodes does not necessarily mean that the frequency increases as expected not only for a large class of phenomena, such as ordinary waves, but also for quantum-mechanical systems, like the hydrogen atom or the harmonic oscillator. In smaller magnetic disks, the exchange interaction should become more important, and it is expected to change the sign of the dispersion (Fletscher and Kittel, 1960) for

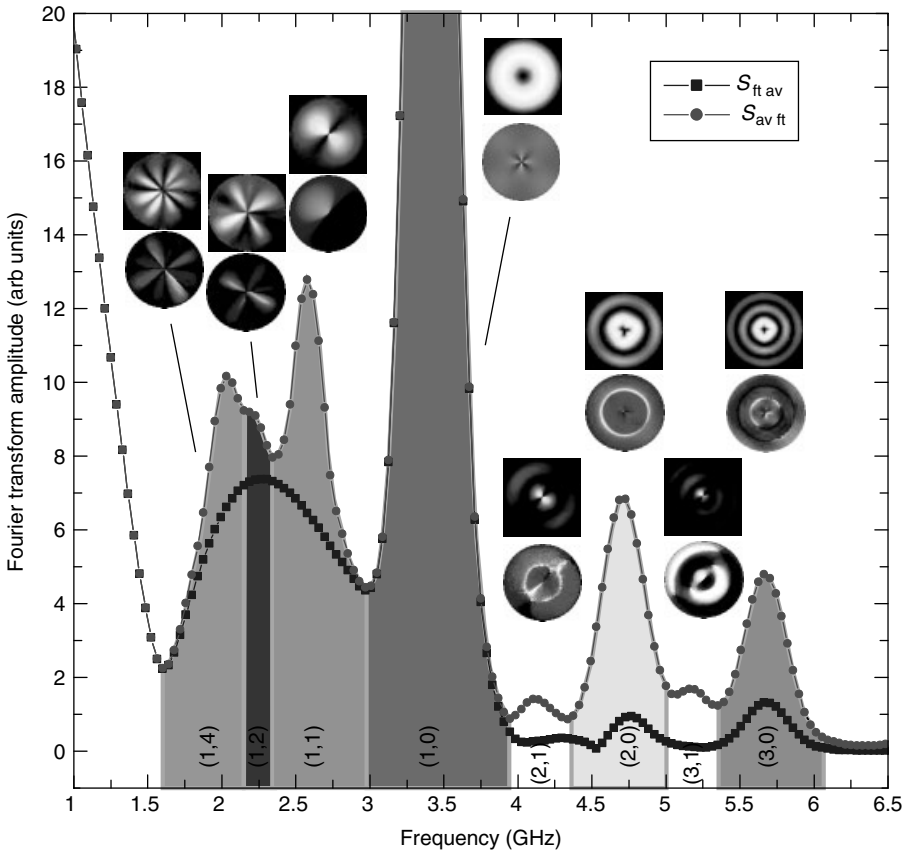

Figure 11. Overview of data obtained by a micromagnetic simulation.

higher m. We can envisage the realization of a new type of junction between elements having opposite dispersion, in analogy to the boundary between left-handed and right-handed photonic crystals (Pendry and Smith, 2004; Pendry and Smith, 2003).

Recall that a spatial asymmetry in the field pulse is needed in order to obtain modes with lower-than-radial symmetry. The low-frequency azimuthal peak in the average amplitude spectra should not be visible at all if the modes had perfect symmetry $e^{im\varphi}$. However, the asymmetry introduced by the field pulse slightly shapes the modes resulting in a nonzero amplitude for these frequencies. The next section uses this data and focuses on the temporal evolution of the modes and compares with the results on the experimental data of the 4 µm platelet.

6 MICROMAGNETIC DISSIPATION, DISPERSION, AND MODE CONVERSION

In the preceding sections of this chapter, the first term of the LLG equation (21), the precessional motion, was investigated by a series of time-resolved Kerr measurements of thin permalloy circular platelets. The focus was on the frequency and the spatial distribution of Fourier amplitude and phase of the observed eigenmodes.

$$\frac{\partial \boldsymbol{M}}{\partial t} = \gamma \boldsymbol{M} \times \frac{\delta \mathcal{E}[\boldsymbol{M}]}{\delta \boldsymbol{M}(\boldsymbol{r})} + \frac{\alpha}{M} \boldsymbol{M} \times \frac{\partial \boldsymbol{M}}{\partial t} \tag{21}$$

In contrast, the succeeding part deals with the second term of equation (21) that accounts for the energy dissipation, an empirical term added to account for the tendency of the system to turn toward an equilibrium state.

6.1 Earlier work

In the precessional regime, optical (Hiebert *et al.*, 1997; Acremann *et al.*, 2000; Buess *et al.*, 2004; Barman *et al.*, 2003; Park *et al.*, 2002) and soft X-ray (Choe *et al.*, 2004; Stoll *et al.*, 2004) pump-probe experiments were employed to examine magnetization dynamics excited by short magnetic field pulses, typically triggered by a laser pulse. Time-dependent measurements are nearly ideal for determining the modal frequencies, the mode structure (Buess *et al.*, 2004;

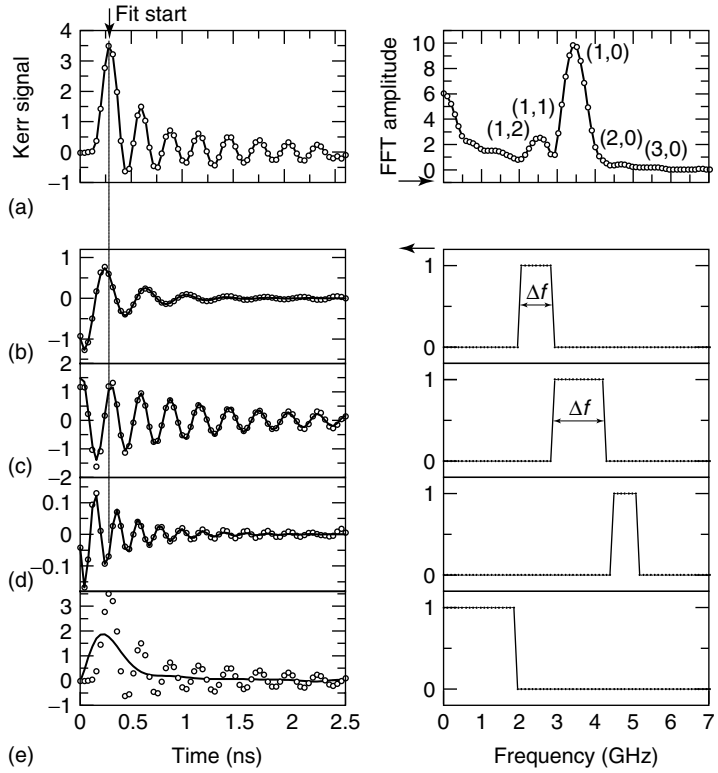

Figure 12. Fourier filtering: Experimental data. (a) shows the average perpendicular magnetization component on the left and its Fourier transform on the right. (b)–(d) By applying the filters on the right before back transformation into the time domain, the temporal evolution (circles) for different modes can be extracted. The solid lines show the fits with $M_i(t) = \sin(2\pi f_i t + \varphi_i)\exp(-t/\tau_i)$ (see text). Δf is the width of the filter. (e) The low-frequency parts up to 2 GHz belong to the transient response on the pulse. (Reprinted with permission from Buess *et al*., *Phys. Rev. Lett.*, **94**, 127205 (2005).)

Hiebert *et al*., 1997; Park *et al*., 2002) and the phenomenological damping parameter (Hiebert *et al*., 2003; Back *et al*., 1999; Tudosa *et al*., 2004; Barman *et al*., 2003) which can be directly compared to measurements using ferromagnetic resonance (FMR) (Celinski and Heinrich, 1991; Ebels *et al*., 2002). When measurements of the damping parameter extracted from quasilinear time-domain measurements do not agree with FMR measurements (Back *et al*., 1999; Tudosa *et al*., 2004; Dobin and Victora, 2004), explanations typically invoke sample and field inhomogeneities (Dobin and Victora, 2004; Belov *et al*., 2004) and higher-order magnon scattering.

In order to probe damping mechanisms typical of the intrinsically nonlinear LLG regime, the modes excited in micron scale permalloy circular platelets presented in the previous sections are examined. Micron-sized disks are ideal systems to study mode excitation, mode conversion, and damping since the small size of the disks provides many well-defined excitations (Buess *et al*., 2004; Gubbiotti *et al*., 2003; Guslienko and Slavin, 2000; Buess *et al*., 2005) within the frequency range easily characterized by stroboscopic time-resolved scanning Kerr microscopy – typically 0–10 GHz (Hiebert *et al*., 1997; Acremann *et al*., 2000; Buess *et al*., 2004; Barman *et al*., 2003; Park *et al*., 2002).

6.2 Eigenmodes of the system

The spin-wave spectrum described in the previous sections was obtained by the resonances of the averaged spectrum and the frequency domain analysis of time sequenced images. Here, we examine mode dispersion and energy channeling between modes which lead to an apparent increase in damping for certain modes.

Our experimental analysis is performed based on the data of a single 4-μm-diameter, 15 nm thick, permalloy disk exhibiting a vortex ground state. Following excitation using a perpendicular magnetic tipping pulse, polar Kerr data are recorded at 40 ps intervals. These data are images encompassing a field of view of 6.5 μm square. A typical trace of the polar Kerr signal as a function of time averaged over the whole element is shown in Figure 12(a) (left frame). Its FT is shown in Figure 12(a) (right frame), and the observed peaks are used to identify the modes. The excited modes

are labeled (*n*,*m*) as in the preceding text; *n* counts the number of axially symmetric nodes and *m* counts the number of azimuthal nodes. We identify the fundamental ((1,0), 3.5 GHz), the second ((2,0), 4.7 GHz), and the third ((3,0), 5.6 GHz) radial modes possessing zero, one, and two additional radial nodes, respectively. We can also identify the dipolar ((1,1), 2.5 GHz) and quadrupolar ((1,2), 2.2 GHZ) azimuthal modes which possess one and two nodes along the equilibrium direction of $\boldsymbol{M}$, respectively. The higher-order azimuthal modes decrease in energy for $m = 0$, 1, 2, consistent with backward volume mode excitations where the $\boldsymbol{k}$-vector is parallel to the magnetization $\boldsymbol{M}$ (Damon and Eshbach, 1960; Buess *et al*., 2004; Buess *et al*., 2005), whereas for the radial modes the opposite is true; $\boldsymbol{k}$ is perpendicular to $\boldsymbol{M}$. The Fourier spectrum does not consist of discrete sharp peaks at the modal frequencies, but of peaks with a finite width (up to 0.7 GHz FWHM). We previously identified these excitations as eigenmodes based upon the linearized LLG equation and the scalar magnetic potential in Section 4.9. The peaks observed in the frequency spectrum as well as those computed from the full LLG equations are not delta functions in frequency due to the presence of dispersion, suggesting that perhaps our earlier terminology might have been misleading. Owing to the finite sampling length and the resulting need of windowing, simple analysis in the frequency domain is not sufficient to illuminate the decay rates and mode conversion. The entire (dispersed) peak contains information about the time evolution of a given mode.

6.3 Linearized equation of motion including damping

We will recall briefly the relevant equations for the precession frequency for this geometry and a decay constant based on a linear, single-α approach: $M_\mathrm{r} = M_\mathrm{s} m_\mathrm{r}$; $M_\varphi = M_\mathrm{s}(1 - O(m_\varphi^2))$; $M_\mathrm{z} = M_\mathrm{s} m_\mathrm{z}$ where m_r and m_z are the direction cosines of the magnetization perturbations, and, $m_\mathrm{r} \ll 1$ and $m_\mathrm{z} \ll 1$. We consider thin micron-sized disks with a ground-state circulating flux-closure configuration ($m_\mathrm{r} = 0$, $m_\varphi = 1, m_\mathrm{z} = 0$), subject to the linearized Landau–Lifshitz–Gilbert equation:

$$\begin{aligned} \dot{m}_\mathrm{r} &= \gamma_0 m_\mathrm{z} N_\mathrm{z} M_\mathrm{s} + \alpha \dot{m}_\mathrm{z} \\ \dot{m}_\mathrm{z} &= -\gamma_0 m_\mathrm{r} N_\mathrm{r} M_\mathrm{s} - \alpha\, \dot{m}_\mathrm{r} \end{aligned} \tag{22}$$

Here, M_s is the saturation magnetization, γ_0 is the absolute value of the gyromagnetic ratio multiplied by μ_0. $N_\mathrm{z} = 1$ is the demagnetizing factor for thin film shape and N_r is defined for a given mode, as defined in Sections 3 and 4.9. N_r is proportional to the averaged effective field for that mode. Inserting oscillatory solutions $\sim e^{i\omega t}$ leads to the result for the decay time τ and the precession frequency f:

$$\tau = \frac{2(1+\alpha^2)}{\alpha\gamma_0 M_\mathrm{s}(N_\mathrm{r} + N_\mathrm{z})} \tag{23}$$

$$2\pi f \cong \gamma_0 M_\mathrm{s} \sqrt{\frac{N_\mathrm{r} N_\mathrm{z}}{(1+\alpha^2)}} \tag{24}$$

With $N_\mathrm{z} = 1$ and in the limit $\alpha \ll 1$ we obtain $\tau = \frac{2}{\alpha\gamma_0 M_\mathrm{s}(N_\mathrm{r}+1)}$ and $2\pi f = \gamma_0 M_\mathrm{s} N_\mathrm{r}^{\frac{1}{2}}$. Thus to evaluate our experimental data, we need to extract the experimental frequencies f and the decay times τ.

6.4 Fourier filtering

In our implementation, the spatially averaged Kerr signal $K(t)$ is used to compute the complex Fourier spectra $S(f)$ as

$$S(f_n) = \frac{1}{N} \sum_{m=1}^{N-1} K(t_m) H(t_m) e^{-2\pi i m n/N} \tag{25}$$

where N is the number of data points of the temporal signal which when acquired over a fixed time interval Δt determines the maximum Fourier frequency in the spectrum and the resolution in the frequency domain and $H(t)$ is the Hamming window function. Windowing is used to reduce the artifacts from the finite sampling length. It is better to extract the damping parameter in the time domain as shown in Figure 14 rather than from the width of the transformed peak, in contrast to FMR, where the time signals are essentially of infinite duration.

We can now back-transform a modal peak after applying a band-pass filter $F(f)$ to the Fourier spectra $S(f)$ since the data are ordered in frequency and the modes are obviously well separated. To compare with the original temporal data, the inverse FT has to be normalized by $H(t)$ in the time domain as

$$M_k(t_m) = \frac{1}{H(t_m)} \Re \sum_{n=1}^{N-1} S(f_n) F_k(f_n)\, e^{2\pi i m n/N} \tag{26}$$

allowing different modal components $M_k(t)$ of $K(t)$ in the time domain to be analyzed. If modal damping were to obey an exponential decay, an effective decay time, τ for each mode can be defined.

6.5 Time-dependent Fourier transform

An alternative method to the Fourier filtering (FF) described in the last section is presented here. Time-dependent Fourier transform (TDF) aims at displaying time and frequency information in the same two-dimensional plot. This is achieved by analyzing only a small section of the time-domain data, a window of length t_{win}. This window is shifted over the whole data and as a function of time displacement Δt, slice by slice of a two-dimensional spectrum is generated by FT. The result is a map of the Fourier amplitude (or phase) as a function of frequency and time displacement Δt. The principle is well known and used for signal processing of audio signals (this is also what a spectrum analyzer of a hi-fi system does: it produces a momentary spectrum of the amplitude of different frequency bands).

TDF should therefore be useful for analyzing the evolution of different frequency components (eigenmodes) in the data of excited ferromagnetic permalloy platelets. It can be described by a formula which is very similar to equation (25):

$$S(f_n, \Delta t) = \frac{1}{N} \sum_{m=1}^{N-1} K(t_m) \tilde{H}_{t_{\text{win}}}(t_m - \Delta t)\, e^{-2\pi i m n/N} \quad (27)$$

For the window function $\tilde{H}_{t_{\text{win}}}$ a Hanning window of length t_{win} is used ($\tilde{H}_{t_{\text{win}}}(t) = 0$ for $t \leq 0$ or $t \geq t_{\text{win}}$). Hence, the FT of $K(t)$ is merely applied in the range $\Delta t \leq t \leq \Delta t + t_{\text{win}}$. The parameter t_{win} is very critical: by construction of S, the frequency resolution is determined by the length t_{win} of the examined signal as $\Delta f = 1/t_{\text{win}}$. In addition, a value $S(f_n, \Delta t)$ corresponds to a range t_{win} within the time domain and therefore determines the time resolution t_{win} of $S(f_n, \Delta t)$. Obviously there is a trade-off between frequency and temporal resolution. The higher the frequency resolution, the smaller the temporal resolution and vice versa. This is important for interpreting the spectra. Figure 13 shows this method applied to the averaged M_z data of the micromagnetic simulation. A window length t_{win} of 2.8 ns was used for the data of 20 ns total length. The Fourier amplitude $S(f_n, \Delta t)$ is plotted on a logarithmic scale. Notice that the amplitude changes by 12 orders of magnitude. The amplitude of the modal peaks above 3 ns drops exponentially and shows an almost perfect linear fit in Figure 13(c). The decay times have been evaluated as $\tau_{(1,0)} = 1.30$ ns, $\tau_{(2,0)} = 1.29$ ns and $\tau_{(3,0)} = 1.30$ ns with errors 0.01 ns. These values are discussed in the subsequent text.

What about the azimuthal modes visible in the spectra of Figure 5 at a frequency below 3 ns? This peak decays much faster and the evaluated decay time is of the order of the time resolution $\Delta t = 0.36$ ns, therefore limited by the TDF window length t_{win}. When t_{win} is decreased, the modes are no longer separated well by the reduced frequency resolution. However, the time evolution of these modes can be analyzed with the FF method as described in the next section. This shows that the TDF method is complementary to FF: a different aspect is that it does not matter for TDF that the higher radial modes are 3 orders of magnitude smaller in amplitude than the fundamental one. The peaks are well separated in frequency and there is no mixing of different frequency components. However, in FF, the small amplitude of the *higher* modes leads to bigger errors for these modes. Hence TDF is used for the evaluation of the radial modes only when we have analysed the whole spectrum with (FF) as shown in the next section.

6.6 Results and discussion

Figure 12(a) shows the averaged Kerr data $K(t)$ (left) and its Fourier transform amplitude $S(f)$ (right). The right side of Figure 12(b)–(e) show the filters $F(f)_k$ used in equation (2) to obtain the modes (1,0), (2,0), the azimuthal mode and the low-frequency residuals corresponding to the modal magnetization curves $M_k(t)$ (left), respectively. Fits to our data using an exponentially decaying sine function (solid lines in Figure 12(b)–(e), left frame) lead to the decay times $\tau_{\text{exp}}^{\text{fit}}$ displayed in Table 1. For the nonradially symmetric azimuthal modes, there are some peculiarities: from the frequency domain data, the peak positions for the (1,1)- and (1,2)-modes are known and a superposition of these modes is seen in the Fourier spectrum from 2 to 2.8 GHz; this is referred to as the *azimuthal peak*. Note that the amplitude of the two components is determined by the spatial and temporal shape of the field pulse. The resulting value obtained by mode filtering and damped-oscillation fit is displayed as $\tau_{\text{exp}}^{\text{fit}}$. This demonstrates the significant result that the symmetry breaking azimuthal modes ($\tau_{\text{azim}} = 0.37$ ns) decay three times faster than the fundamental mode ($\tau_{(1,0)} = 1.1$ ns) for windows whose widths $\Delta f/f_0$ are as good as constant (0.31 versus 0.37 for the azimuthal and fundamental peak, respectively). This is a surprising result, because the calculated $\tau_{\alpha=0.008}^{\text{calc}}$ for all modes is constant within the experimental errors, as the decay constant depends weakly on N_r in $N_z + N_r = 1 + N_r \cong 1$ [3]. Thus, additional mode damping due to energy transfer or mode conversion must occur. Furthermore, despite the large error bar, we observed a significant difference for the decay of the modes (1,0) and (2,0). It is fortuitous to note that the higher radial modes have very small amplitude. Consequently, the decay times of the filtered signals have bigger error for the modes (2,0). The decay time for the mode (3,0) cannot be determined accurately. The error bar was obtained by analyzing the resulting

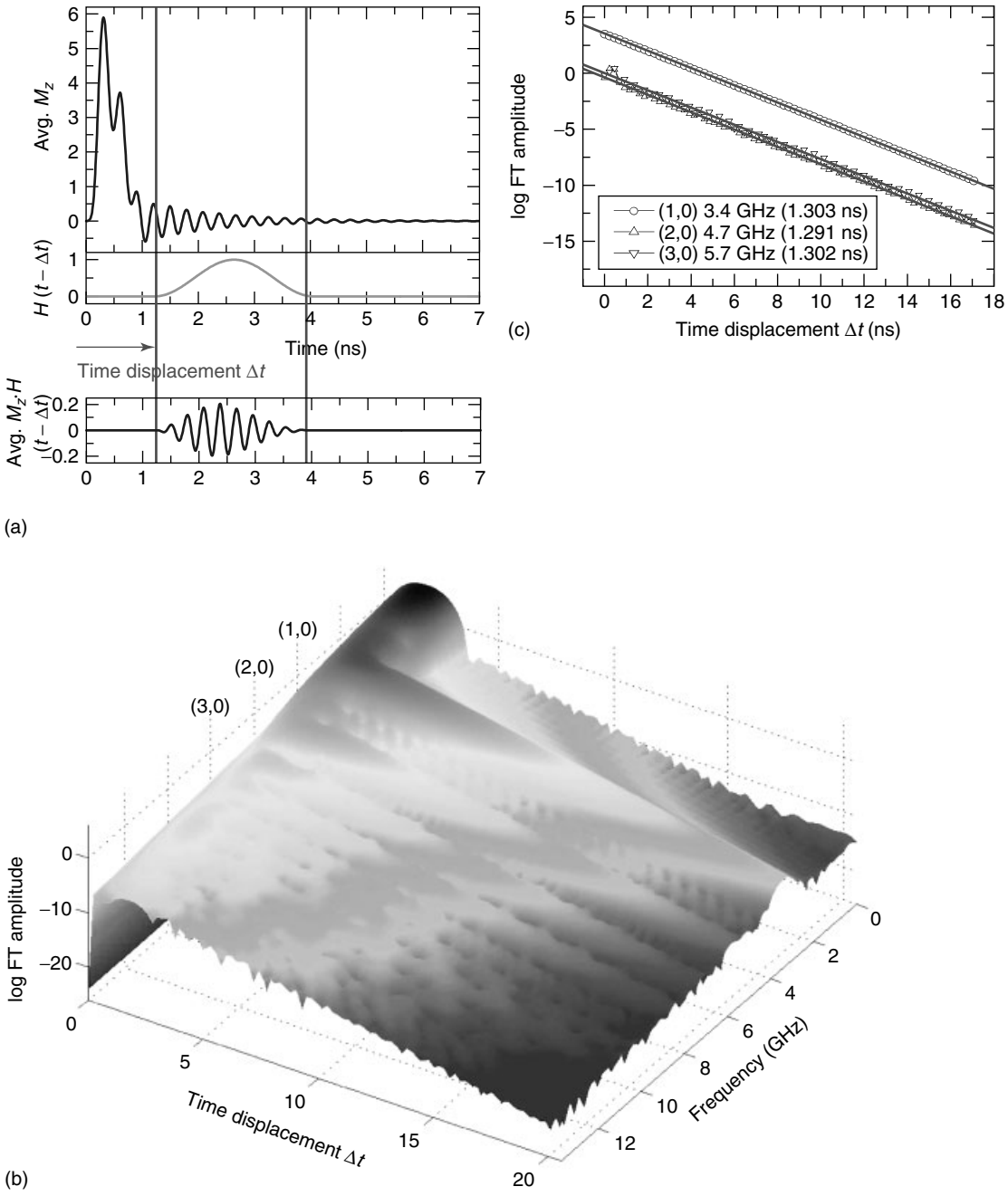

Figure 13. Time-dependent Fourier transform for the 4 µm data of the micromagnetic simulation (see Section 5). (a) Illustration of time-dependent windowing. The spatially averaged M_z is multiplied by the window function H with time displacement Δt before Fourier transformation. (b) The Fourier amplitude as a function of frequency and time displacement Δt is displayed on a logarithmic scale. (c) The time evolution of the modes is analyzed by plotting the amplitude at peak position of the first three radial modes. The decay times of the exponentially decaying values are evaluated as 1.30, 1.29, and 1.30 ns.

decay time by varying the parameters of the filtering process. Unfortunately, experimentally, we cannot separate the effect of the damping of each independent mode from energy that is coupled (nonlinearly) between the modes. However, there are many publications (Buess *et al*., 2004; Park *et al*., 2002; Hiebert *et al*., 1997) that demonstrate the excellent predictive abilities of the LLG equations of motion in the picosecond time regime for describing magnetization dynamics. The advantage of employing micromagnetic simulations is that energies can be monitored and global or position-dependent

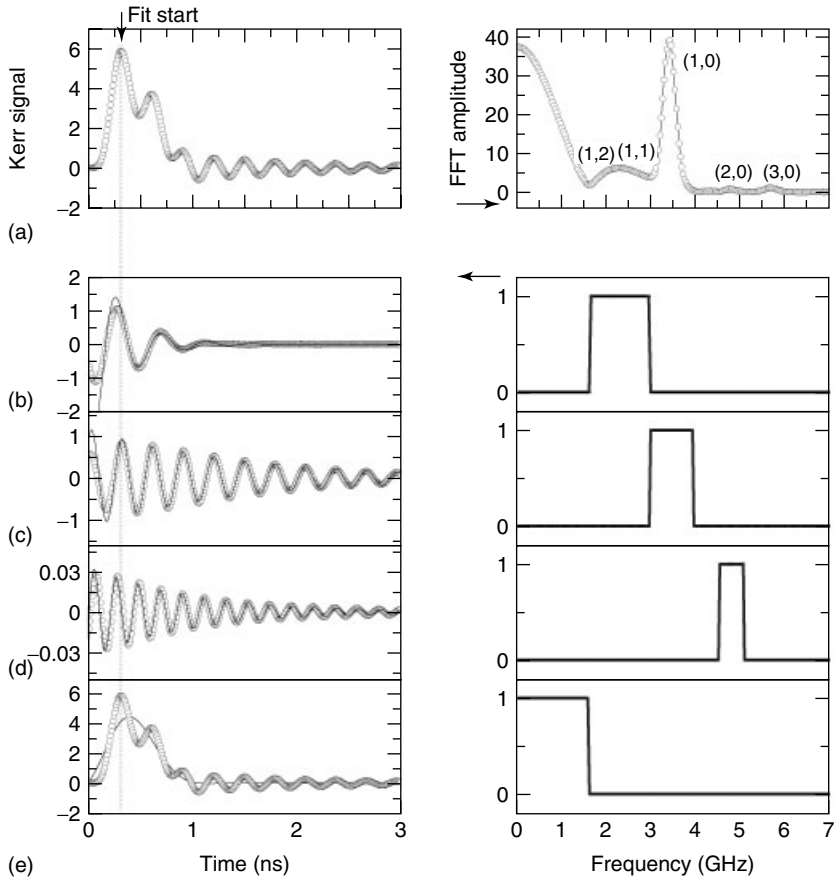

Figure 14. Fourier filtering: Micromagnetic simulation. The same modes are extracted from the computed average M_z component as in Figure 1. The good qualitative agreement with the simulation supports the findings in Figure 1. (Reprinted with permission from M. Buess *et al.*, *Phys. Rev. Lett.*, **94**, 127205 (2005).)

Table 1. Compilation of all relevant parameters for each of the eigenmodes (m,n). The peak frequencies f_{exp} and f_{sim} are obtained from the absolute-FT spectra of the 4-μm disk data and from the micromagnetic simulation, respectively. $N_{\mathrm{r,sim}}$ is calculated from f_{sim} and leads to the values $\tau^{\mathrm{calc}}_{\alpha=0.008}$ (see text). The decay times $\tau^{\mathrm{fit}}_{\mathrm{exp}}$ and $\tau^{\mathrm{fit}}_{\mathrm{sim}}$ are derived by the Fourier filtering (FF) method presented in this section. The decay times $\tau^{\mathrm{TDF}}_{\mathrm{sim}}$ are obtained by Time-dependent Fourier transform (TDF).

Mode (m,n)	f_{exp} [GHz]	f_{sim} [GHz]	$N_{\mathrm{r,sim}}$	$\tau^{\mathrm{calc}}_{\alpha=0.008}$ [ns]	$\tau^{\mathrm{fit}}_{\mathrm{exp}}$ [ns]	$\tau^{\mathrm{fit}}_{\mathrm{sim}}$ [ns]	$\tau^{\mathrm{TDF}}_{\mathrm{sim}}$ [ns]
(1,2)	2.2±0.1	2.21±0.05	0.0053	1.308	0.37±0.1	0.31±0.1	0.45±0.1	
(1,1)	2.5±0.1	2.58±0.05	0.0068	1.306			0.44±0.1	
(1,0)	3.4±0.1	3.41±0.05	0.013	1.299	1.1±0.2		1.3±0.1	1.30±0.01
(2,0)	4.7±0.1	4.71±0.05	0.024	1.283	0.6±0.4		1.4±0.3	1.29±0.01
(3,0)	5.6±0.1	5.67±0.05	0.035	1.270			1.0±0.3	1.30±0.01

parameters can be set. We have reproduced the details of the modal structure including the nonradially symmetric modal response for excitations in circular platelets of permalloy. Shown in Figure 14(a) are the computed LLG (LLG) averaged M_z data (left) and its Fourier amplitude $S(f)$ (right). Figures 14(b)–(d) show the filters $F(f)_k$ used in equation (2) (right frame) to obtain the modes (1,0), (2,0) and the azimuthal modes peak, corresponding to the modal magnetization curves $M_k(t)$ (left frame), respectively. At first glance one observes that in Figure 14 the position of the resonances

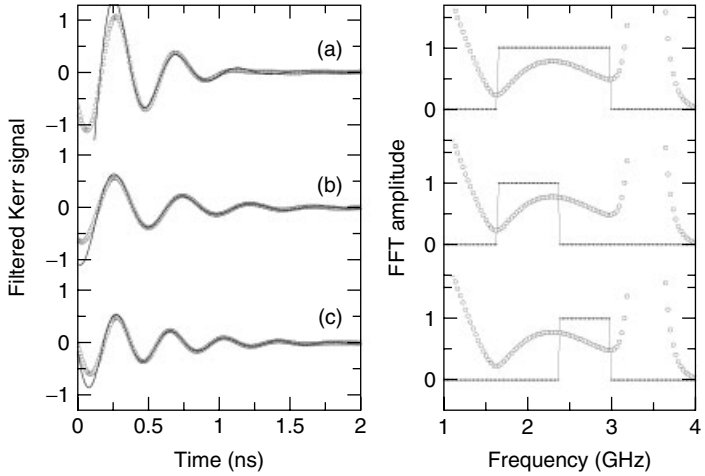

Figure 15. Fourier filtering: Azimuthal mode separation. Detailed analysis of the azimuthal peak in Figure 14(b). The left side shows the filtered signals (circles) with fit (solid), and on the right the filters (circles) and FT of the original curve (solid). We find that the decay time for the whole peak in (a) (0.31 ns) is composed of the two components (b) and (c) with 0.44 and 0.45 ns.

as well as their relative strength is very similar to the data in Figure 12. We also observe that the decay times of the individual modes show the same trend as in Figure 12: fits to our data (see Table 1) demonstrate good agreement in the decay times with the experimental values. Also included in the table are the $N_{\mathrm{r,sim}}$ calculated by equation (24) from the values f_{sim} and the resulting $\tau^{\mathrm{calc}}_{\alpha=0.008}$ by equation (23). Again, the symmetry breaking azimuthal modes decay much faster than the fundamental mode. Finally, in the simulation it was possible to separate the azimuthal peak into the two modes. For this purpose, the average amplitude over the local FT of the magnetic movie was used to determine the separation frequency of 2.35 GHz between the two modes. In Figure 15 the two different filtered and back-transformed components are displayed. The resulting τ^{fit} of 0.44 and 0.45 ns are corrected values and are 45% bigger than the decay time for the total azimuthal peak. However, it quantifies the effect of increased decay rate by superposition of the two overlapping peaks. This is still quite a small correction when compared to the longer decay times of the radial modes. And again we see the same trend on the modes (2,0) and (3,0) as in the experiment, which differ from the calculated values $\tau^{\mathrm{calc}}_{\alpha=0.008}$ (equation 23) only within the uncertainty. Since the LLG simulations use a single phenomenological damping parameter we can immediately rule out different damping of one mode over another as the cause for the extra observed damping in the low-frequency modes. Rather, we can see that since energy is conserved and the global energy loss is governed by α, that mode–mode coupling must channel energy from the low-frequency modes toward the higher frequency modes. Scattering must be consistent with solutions to the nonlinear wave equation and energy conservation (i.e., scattering to higher frequency modes must also reduce the amplitude if the scattering is in one direction in k space).

We conclude that we have presented a method to extract the decay rates for different modes from a single average precession component. For the low-frequency modes we find an increased damping whose possible origin lies in mode conversion. For the radial modes, we find a behavior as expected from the linearized LLG equation. These two important features are closely reproduced in the micromagnetic simulation where the phenomenological Gilbert damping model is implemented with a single α. This demonstrates that for confined single-material ferromagnetic structures no additional theory of dissipation is necessary for exact reproduction of such intricate experimental results: The single α straightforward LLG is all that is required to understand and explain the physics. These measurements are the first clear demonstration that mode–mode coupling plays a significant role in magnetization dynamics, and the data demonstrate how mode conversion could be construed as damping.

NOTES

[1] For modes smaller than 1 μm and higher mode numbers, the stronger effect of exchange interaction leads to deviations between theory and micromagnetic simulation.

[2] Of course, magnetic fields are, strictly speaking, only singular at boundaries in the two-dimensional limit which we have adopted here. In practice, boundaries have a finite thickness and although the fields might become large they remain finite at two-dimensional surfaces. In the present case, $H_{\mathrm{r}}\,|_{z=0,r\to R-\to}\,-2\pi M_{\mathrm{r}}(R)$).

[3] In principle, the sum of the demagnetizing factors adds up to exactly one. However, in our approximation we directly set $N_z = 1$ for a thin-film disk and calculate N_r.

REFERENCES

Acremann, Y., Back, C.H., Buess, M., *et al*. (2000). Imaging precessional motion of the magnetization vector. *Science*, **290**, 492.

Acremann, Y., Buess, M., Back, C.H., *et al*. (2001). Ultrafast generation of magnetic fields in a schottky diode. *Nature*, **414**, 51.

Back, C.H., Allenspach, R., Weber, W., *et al*. (1999). Field strength in precessional magnetization reversal. *Science*, **285**, 864.

Barman, A., Kruglyak, V.V., Hicken, R.J., *et al*. (2003). Anisotropy, damping, and coherence of magnetization dynamics in a 10 mum square ni81fe19 element. *Applied Physics Letters*, **82**, 3065.

Bayer, C., Park, J.P., Wang, H., *et al*. (2004). Spin waves in an inhomogeneously magnetized stripe. *Physical Review B*, **69**, 134401.

Belov, M., Liu, Z., Sydora, R.D., *et al*. (2004). Modal oscillation control in internally patterned $ni_{80}fe_{20}$ thin film microstructures. *Physical Review B*, **69**, 094414.

Buess, M., Acremann, Y., Kashuba, A., *et al*. (2003). Pulsed precessional motion on the "back of an envelope". *Journal of Physics: Condensed Matter*, **15**, R1093.

Buess, M., Hollinger, T., Haug, T., *et al*. (2004). Fourier transform imaging of spin vortex eigenmodes. *Physical Review Letters*, **93**, 077207.

Buess, M., Knowles, T.P.J., Hollinger, R., *et al*. (2005). Excitations with negative dispersion in a spin vortex. *Physical Review B*, **71**, 104415.

Celinski, Z. and Heinrich, B. (1991). Ferromagnetic resonance linewidth of fe ultrathin films grown on a bcc cu substrate. *Journal of Applied Physics*, **70**, 5935.

Chiao, R.Y. (1993). Superluminal (but causal) propagation of wave packets in transparent media with inverted atomic population. *Physical Review A*, **48**, R34.

Choe, S-B., Acremann, Y., Scholl, A., *et al*. (2004). Vortex core–driven magnetization dynamics. *Science*, **304**, 420.

Damon, R. and Eshbach, J. (1960). Magnetostatic modes of a ferromagnetic slab. *Journal of Applied Physics*, **31**, 104S.

Demokritov, S.O. and Hillebrands, B. (2002). In *Spinwaves in Laterally Confined Magnetic Structures Spin Dynamics in Confined Magnetic Structures I*, Hillebrands, B. and Ounadjela, K. (Eds.), Springer-Verlag: Berlin, p. 65.

Demokritov, S.O., Hillebrands, B., Slavin, A.N., *et al*. (2001). Brillouin light scattering studies of confined spin waves: linear and non-linear confinement. *Physics Reports*, **348**, 441.

Dillon, J.F., Jr. (1960). Magnetostatic modes in disks and rods. *Journal of Applied Physics*, **31**, 1605.

Dobin, A.Yu. and Victora, R.H. (2004). Surface roughness induced extrinsic damping in thin magnetic films. *Physical Review Letters*, **92**, 257204.

Ebels, U., Buda, L.D., Ounadjela, K., *et al*. (2002). In *Small Amplitude Dynamics of Nonhomogeneous Magnetization Distributions Spin Dynamics in Confined Magnetic Structures I*, Hillebrands, B. and Ounadjela, K. (Eds.), Springer-Verlag: Berlin, p. 167.

Fletcher, P.C. and Kittel, C. (1960). Considerations on the propagation and generation of magnetostatics waves and spin waves. *Physical Review*, **120**, 2004.

Gaididei, Y., Kamppeter, T., Mertens, F.G., *et al*. (2003). Switching between different vortex states in two-dimensional easy-plane magnets due to an ac magnetic field. *Physical Review B*, **61**, 9449.

Ganping, Ju., Nurmikko, A.V., Farrow, R.F.C., *et al*. (1999). Ultrafast time resolved photoinduced magnetization rotation in a ferromagnetic/antiferromagnetic exchange coupled system. *Physical Review Letters*, **82**, 3705.

Gubbiotti, G., Carlotti, G., Okuno, T., *et al*. (2003). Brillouin light scattering investigation of dynamic spin modes confined in cylindrical permalloy dots. *Physical Review B*, **68**, 1844091.

Guslienko, K.Yu. and Slavin, A.N. (2000). Spin-waves in cylindrical magnetic dot arrays with in-plane magnetization. *Journal of Applied Physics*, **87**, 6337.

Hicken, R.J., Barman, A., Kruglyak, V.V., *et al*. (2003). Optical ferromagnetic resonance studies of thin film magnetic structures. *Journal of Physics D: Applied Physics*, **36**, 2183.

Hiebert, W.K., Lagae, L., De Boeck, J., *et al*. (2003). Spatially inhomogeneous ultrafast precessional magnetization reversal. *Physical Review B*, **68**, 020402(R).

Hiebert, W.K., Stankiewicz, A., Freeman, M.R., *et al*. (1997). Direct observation of magnetic relaxation in a small permalloy disk by time-resolved scanning kerr microscopy. *Physical Review Letters*, **79**, 1134.

Ivanov, B.A. and Zaspel, C.E. (2005). High frequency modes in vortex-state nanomagnets. *Applied Physics Letters*, **94**, 027205.

Jackson, J.D. (1999). *Classical Electrodynamics*, *Third Edition*, John Wiley & Sons: New York, London, Sydney, p. 115.

Jorzick, J., Demokritov, S.O., Hillebrands, B., *et al*. (1999). Spin-wave quantization and dynamic coupling in micron-size circular magnetic dots. *Applied Physics Letters*, **75**, 3859.

Jorzick, J., Demokritov, S.O., Hillebrands, B., *et al*. (2002). Spin wave wells in nonellipsoidal micrometer size magnetic elements. *Physical Review Letters*, **88**, 047204.

Kakazei, G.N., Wigen, P.E., Yu, K., *et al*. (2004). Spin-wave spectra of perpendicularly magnetized circular submicron dot arrays. *Applied Physics Letters*, **85**, 443.

van Kampen, M., Jozsa, C., Kohlhepp, J.T., *et al*. (2002). All-optical probe of coherent spin waves. *Physical Review Letters*, **88**, 227201.

Kosaka, H., Kawashima, T., Tomita, A., *et al*. (1998). Superprism phenomena in photonics crystals. *Physical Review B*, **58**, R10096.

The LLG code can be found at http://llgmicro.home.mindspring.com/.

Novosad, V., Grimsditch, M., Guslienko, K.Yu., *et al*. (2002). Spin excitations of magnetic vortices in ferromagnetic nanodots. *Physical Review B*, **66**, 052407.

The OOMMF code can be found at http://math.nist.gov/oommf/.

Parimi, P.V., Lu, W.T., Vodo, P., *et al*. (2004). Negative refraction and left-handed electromagnetism in microwave photonic crystal. *Physical Review Letters*, **92**, 127401.

Park, J.P., Eames, P., Engebretson, D.M., *et al*. (2002). Spatially resolved dynamics of localized spin-wave modes in ferromagnetic wires. *Physical Review Letters*, **89**, 277201.

Park, J.P., Eames, P., Engebretson, D.M., *et al*. (2003). Imaging of spin dynamics in closure domain and vortex structures. *Physical Review B*, **67**, 020403(R).

Pendry, J.B. and Smith, D.R. (2003). Comment on "wave refraction in negative-index media: always positive and very inhomogeneous". *Physical Review Letters*, **90**, 029703.

Pendry, J.B. and Smith, D.R. (2004). Reversing light with negative refraction. *Physics Today*, **57**, 37.

Perzlmaier, K., Buess, M., Back, C.H., *et al*. (2005). Spin-wave eigenmodes of permalloy squares with closure domain structure. *Physical Review Letters*, **94**, 057202.

Raabe, J., Pulwey, R., Sattler, R., *et al*. (2000). Magnetization pattern of ferromagnetic nanodisks. *Journal of Applied Physics*, **88**, 4437.

Rayleigh, L. (1945). *The Theory of Sound*, *Vol.1, Second Edition*, revised and enlarged, Dover Publications: New York, pp. 306–394.

Rossing, T.D. (1982). Chladni's law for vibrating plates. *American Journal of Physics*, **50**, 271.

Shinjo, T., Okuno, T., Hassdorf, R., *et al*. (2000). Magnetic vortex core observation in circular dots of permalloy. *Science*, **289**, 930.

Sparks, M. (1970). Magnetostatic modes in an infinite circular disk. *Solid State Communications*, **8**, 731.

Stoll, H., Puzic, A., van Waeyenberge, B, *et al*. (2004). High-resolution imaging of fast magnetization dynamics in magnetic nanostructures. *Applied Physics Letters*, **84**, 3328.

Tamaru, S., Bain, J.A., van de Veerdonk, R.J.M., *et al*. (2002). Imaging of quantized magnetostatic modes using spatially resolved ferromagnetic resonance. *Journal of Applied Physics*, **91**, 8034.

Tudosa, I., Stamm, C., Kashuba, A.B., *et al*. (2004). The ultimate speed of magnetic switching in granular recording media. *Nature*, **428**, 831.

Wachowiak, A., Wiebe, J., Bode, M., *et al*. (2002). Direct observation of internal spin structure of magnetic vortex cores. *Science*, **298**, 577.

Wu, J., Schmool, D.S., Hughes, N.D., *et al*. (2002). Picosecond large angle reorientation of the magnetization in $Ni_{81}Fe_{19}$ cc circular thin-film elements. *Journal of Applied Physics*, **91**, 278.

Zivieri, R. and Nizzoli, F. (2005). Theory of spin modes in vortex-state ferromagnetic cylindrical dots. *Physical Review B*, **71**, 014411.

Nonlinear Multidimensional Spin-wave Excitations in Magnetic Films

Sergej O. Demokritov[1] and Andrei N. Slavin[2]

[1] *University of Münster, Münster, Germany*
[2] *Oakland University, Rochester, MI, USA*

1 INTRODUCTION

The concept of small-amplitude, lowest-lying dynamic eigenmodes of magnetic media called *spin waves* was introduced by Bloch (1930). Early experimental evidence for the existence of spin waves came from measurements of thermodynamic properties, but the first direct observation was made through ferromagnetic resonance (FMR) (Griffiths, 1946) and then through light scattering (Fleury, Porto, Cheesmman and Guggenheim, 1966). In the quantum-mechanical approach the spin-wave quanta (magnons) are similar to the quanta of light (photons) or those of acoustic waves (phonons).

Spin waves provide the basis for describing the spatial and temporal evolution of the magnetization distribution in a magnetic sample under the general assumption that locally the length of the magnetization vector is constant. The length of the magnetization vector is conserved, if, first, the system is in a thermodynamic equilibrium described by a temperature far below the Curie temperature and, second, if no topological anomalies, like vortices, are present. The latter is fulfilled for samples in a single-domain state, that is, samples that are magnetized to saturation by an external applied magnetic field. Then the dynamics of the magnetization vector is described by the Landau–Lifshitz torque equation (Landau and Lifshitz, 1935)

$$\frac{\mathrm{d}\vec{M}}{\mathrm{d}t} = -|\gamma|\vec{M} \times \vec{H}_{\mathrm{eff}} \tag{1}$$

where $\vec{M} = \vec{M}_0 + \vec{m}(\vec{r}, t)$ is the total magnetization, $\vec{M}_0$ and $\vec{m}(\vec{r}, t)$ are the vectors of saturation and variable magnetization, correspondingly, $|\gamma|$ is the modulus of the gyromagnetic ratio for the electron spin ($|\gamma|/2\pi = 2.8\,\mathrm{MHz\,Oe^{-1}}$), and $\vec{H}_{\mathrm{eff}} = -\delta W/\delta\vec{M}$ is the effective magnetic field calculated as a variational derivative of the energy function W, where all the relevant interactions in the magnetic substance have been taken into account (see, e.g., Lvov, 1994; Wigen, 1994; Cottam, 1994). If the amplitude of the variable magnetization $\vec{m}(\vec{r}, t)$ is small compared to the saturation magnetization $\vec{M}_0$, that is, if the angle of magnetization precession is small, one can develop a solution for the variable magnetization in a series of plane waves of magnetization (having a

Handbook of Magnetism and Advanced Magnetic Materials. Edited by Helmut Kronmüller and Stuart Parkin. Volume 2: *Micromagnetism*. ISBN: 978-0-470-02217-7.

three-dimensional wave vector $\vec{k}$) or spin waves,

$$\vec{m}(\vec{r}, t) = \sum_k \vec{m}_k(t) \exp(i\vec{k}\vec{r}) \tag{2}$$

Thus, spin waves can be obtained as a solution of equation (1), if the nonlinearity is neglected. Theoretical estimations and experiment show that it can be done if the mean amplitude of the precession is less than 1°.

However, both $\vec{M}$ and $\vec{H}_{\text{eff}}$ are time dependent, and since one has the product of these quantities on the right-hand side of equation (1), this equation is intrinsically nonlinear. This nonlinearity should be taken into account if higher values of the angle of magnetization precession are allowed. From the quantum-mechanic point of view, the nonlinearity describes the interaction between the magnons.

Depending on the particular properties of the described phenomena, the interaction can be either attractive or repulsive. In the framework of a crude but very useful approximation, the nonlinearity can be taken into account by considering the properties of spin waves that are dependent on their amplitude, as is shown in the following sections.

There are several methods of spin-wave excitation in magnetic films. First, spin waves of the frequency ω_k can be excited linearly ($\omega_k = \omega_s$) by a microwave magnetic field of a strip-line antenna when an input microwave electromagnetic signal of the frequency ω_s is supplied to the antenna. A strip-line antenna of the width w and aperture (or length) l can effectively excite spin waves having the wave number component in the direction perpendicular to the antenna aperture in the interval $0 < k < 2\pi/w$, while the range of propagation directions (or the interval of the wave number components parallel to the antenna aperture) is determined by the antenna length l. The magnitude of the wave number of the linearly excited spin wave is determined by the frequency of the input electromagnetic signal ω_s and by the spin-wave dispersion relation $\omega_k(k)$ in a magnetic film.

Second, pairs of contrapropagating spin waves can be excited (or amplified) parametrically by a weakly localized electromagnetic pumping (effective wave number of the pumping $k_p \simeq 0$) having frequency ω_p twice as large as the frequency of the excited spin waves. This process obeys the conservation laws $\omega_p = 2\omega_k$, $k_p \simeq 0 = \mathbf{k} + (-\mathbf{k})$. The magnitude of the wave number of the excited spin-wave pair is determined by the k dependence of the threshold of parametric excitation in a magnetic film (see chapter 10 of Gurevich and Melkov (1996) for details). If a spin-wave packet with a definite carrier wave number k is excited linearly by a strip-line antenna and experiences parametric interaction with the microwave field of double-frequency pumping, this wave packet is amplified and a contrapropagating wave packet with a carrier wave number $-k$ is parametrically excited. This situation is discussed in detail in Section 5.

Third, recently, it has been discovered theoretically (Slonczewski, 1996; Berger, 1996; Slonczewski, 1999) and confirmed experimentally (Tsoi *et al.*, 1998; Kiselev *et al.*, 2003) that there is yet another method of spin-wave excitation in metallic magnetic films due to transfer of the angular momentum of spin-polarized charge carriers. This method of spin-wave excitation is very efficient and leads to very large amplitudes of the excited spin waves, and the nonlinear properties of spin waves play a very important role in this new excitation mechanism. The nature and properties of the spin-wave modes excited by spin-polarized current in metallic ferromagnetic films are discussed in the last section of this chapter.

Finally, very recently an optical approach for spin-wave excitation based on the spin–momentum transfer effect has been developed. It takes advantage of circularly polarized, short laser pulses. A direct transfer of the photon angular momentum to spins in solid states can be used for coherent excitation and absorption of spin waves with frequencies about 100 GHz (Kimel *et al.*, 2004; Hansteen, Kimel, Kirilyuk and Rasing, 2005).

Spin waves in magnetic samples comprise an excellent testing ground to study general properties of nonlinear waves. In many aspects, nonlinear phenomena in magnetic systems supporting spin waves are more easily accessible compared to nonlinear processes in, for example, optics or plasma physics.

First, the nonlinearity in magnetic systems is rather large compared to optical nonlinearities, and this makes the generation of nonlinear waves and wave packets rather easy in experiment. Second, spin waves with velocities in the range of a few kilometers per second are relatively slow compared to the electromagnetic waves in optics or plasma. Therefore, the observation of propagating waves puts less demand on the time resolution of the experimental setup. All these properties of spin waves in bulk magnetic samples were successfully used in early experiments on nonlinear spin-wave dynamics (see, e.g., Lvov, 1994).

Spin waves at microwave frequencies propagating in monocrystalline *ferrite films* and, in particular, in yttrium iron garnet ($Y_3Fe_5O_{12}$, YIG) films with very low losses, characterized by a very narrow FMR linewidth of $2\Delta H_K = 0.4$ Oe at 10 GHz, provide an especially good opportunity to study the general properties of nonlinear wave phenomena. An important advantage of ferrite films as a medium for experimental investigations of nonlinear wave dynamics is the fact that the wave process in the film is directly accessible from the surface for characterization by either inductive probes or magneto-optical methods. For example, using

the recently developed space- and time-resolved Brillouin light-scattering (BLS) technique in YIG films one can visualize and study linear and nonlinear processes involving slow waves (spin waves) by scattering fast waves (light) on slow waves as on a quasistationary diffraction grating. This experimental approach allows us to perform such unique experiments, as direct observation of wave tunneling through a potential barrier created by a local inhomogeneity in the bias magnetic field with the appropriate spatial and temporal resolution (Demokritov *et al*., 2004).

An additional advantage of ferrite films as a medium for experimental investigation of nonlinear waves is the fact that the nonlinear and dispersive characteristics of spin waves in ferrite films can be controlled by changing the magnitude and orientation of the bias magnetic field. Figure 1 shows a typology for different orientations between the in-plane wave vector $\vec{k}$ and the magnetization $\vec{M}_0$ (Damon and Eshbach, 1961). Three different geometries are shown. If $\vec{k}$ and $\vec{M}_0$ are both in the film plane and if $\vec{k}$ is perpendicular to $\vec{M}_0$, the so-called magnetostatic surface wave (MSSW) exists. If $\vec{k}$ and $\vec{M}_0$ are collinear in the film plane, a mode with negative dispersion, the so-called backward-volume magnetostatic spin-wave (BVMSW) mode exists with the group velocity antiparallel to the wave vector. Finally, if the magnetization is perpendicular to the film plane, the existing modes are the so-called forward-volume magnetostatic spin-wave (FVMSW) modes.

A wide variety of nonlinear wave phenomena, like parametric and kinetic instabilities of spin waves, auto-oscillations, chaotic dynamics, strange attractors, formation, propagation, and collision of 'bright' and 'dark' spin-wave envelope solitons, nonlinear diffraction, self-focusing of spin-wave packets, and tunneling of these packets through potential barriers can be observed in ferrite films at moderate input microwave power levels of less than 1 W (see, e.g., Wigen, 1994; Cottam, 1994; Büttner *et al*., 2000; Demokritov, Hillebrands and Slavin, 2001).

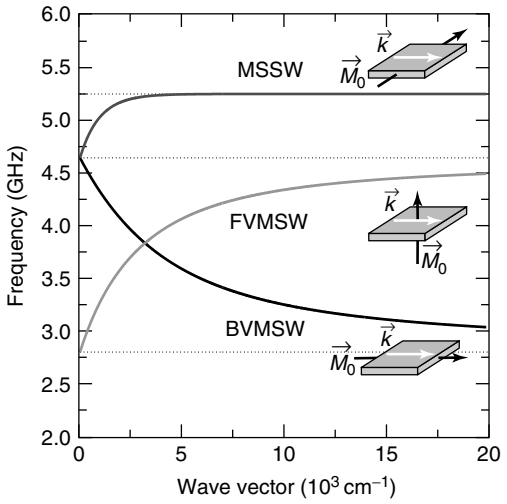

Figure 1. Typology of magnetostatic spin-wave modes for different directions of the magnetization, $\vec{M}_0$, and the in-plane wave vector, $\vec{k}$. MSSW: magnetostatic surface spin waves; FVMSW: forward-volume magnetostatic spin waves; BVMSW: backward-volume magnetostatic spin waves.

Here we present a review of the experimental investigations of nonlinear spin waves in magnetic films, performed using the novel magneto-optical method of space- and time-resolved BLS (Büttner *et al*., 2000).

The outline of the review is as follows. After this introduction (Section 1), in Section 2 we give a theoretical description of nonlinear spin-wave dynamics in magnetic films using the classical Hamiltonian formalism for spin waves in an unbounded ferromagnet (Lvov, 1994), in combination with the dipole-exchange theory of the spin-wave spectrum in magnetic films (see Slavin, 1994, and Chapter 2 in Cottam, 1994) and the elements of the spin-torque theory of spin-wave excitation (Slavin and Kabos, 2005).

Section 3 describes the space- and time-resolved BLS technique – an important tool for the investigation of magnetic dynamics – and compares it with the other techniques for experimental investigation of spin waves.

The following sections describe experiments on the excitation of nonlinear spin-wave modes in magnetic films performed by different experimental methods.

Section 4 is devoted to the experimental study of nonlinear spin-wave excitations generated by an external microwave signal. Here the advantages of the BLS experimental technique are clearly demonstrated by the observation of a two-dimensional counterpart of spin-wave envelope solitons – spin-wave bullets. It is interesting to note that formation of wave bullets was predicted in optics (Silberberg, 1990), but the first experimental observation of this effect has been reported for the system of spin waves using the BLS experimental technique (Bauer *et al*., 1998).

Section 5 describes the experimental study of nonlinear spin-wave excitations, either self-generated from noise in active rings containing ferrite-film delay line and external amplifier or parametrically generated or/and amplified by a weakly localized double-frequency microwave pumping. The experiments described in this section prove that one-dimensional spin-wave solitons and two-dimensional spin-wave bullets are the intrinsic nonlinear excitations of a finite-width spin-wave waveguide and an infinite in-plane magnetic film, respectively. The experiments also show that the combination of an active ring with parametric pumping allows us to observe novel nonlinear symmetry-breaking spin-wave excitations having a rather unusual Möbius topology.

Section 6 demonstrates that the general ideas about nonlinear spin waves formulated in the theoretical Section 2 and illustrated experimentally for spin waves in ferrite films in Sections 3–5 remain in force even in the case when spin-wave modes are excited by the spin torque created by spin-polarized direct current in a very thin magnetic film made of a ferromagnetic metal. It turns out that a large-amplitude, standing spin-wave mode excited by spin-polarized current in an in-plane magnetized metallic film is a two-dimensional standing spin-wave bullet, similar to the propagating spin-wave bullets studied in Sections 3–5.

The conclusions are given in Section 7.

2 THEORETICAL DESCRIPTION OF SPIN WAVES IN MAGNETIC FILMS

It this section we give a brief outline of the general theory of nonlinear spin waves in magnetic films. We consider both the situation when a spin wave or a spin-wave packet propagating in a dielectric ferromagnetic film is linearly excited by a microwave magnetic field $\vec{h}_{\rm s}(\vec{r},t)=\vec{h}_{\rm s}(\vec{r})\exp(i\omega_{\rm s}t)$ and then interacts parametrically with the double-frequency ($\omega_{\rm p}=2\omega_{\rm s}$) microwave pumping $\vec{h}_{\rm p}(\vec{r},t)=\vec{h}_{\rm p}(\vec{r})\exp(i\omega_{\rm p}t)$ (see Bagada, Melkov, Serga and Slavin, 1997; Melkov *et al*., 2000; Serga *et al*., 2005; Melkov *et al*., 2001), and the recently discovered effect of microwave spin-wave excitation in a metallic ferromagnetic film by a spin-polarized direct current traversing the film (Slavin and Kabos, 2005; Slavin and Tiberkevich, 2005).

To describe magnetization dynamics in the presence of a spin-polarized current, the equation of motion for the magnetization $\vec{M}$ in a magnetic film (equation (1)) can be written in the form that includes the spin-transfer torque $\vec{T}_I$ (Slonczewski, 1996; Berger, 1996; Slonczewski, 1999):

$$\frac{{\rm d}\vec{M}}{{\rm d}t}=-|\gamma|\vec{M}\times\vec{H}_{\rm eff}+\vec{T}_I \tag{3}$$

where $|\gamma|=g\mu_{\rm B}/\hbar$ is the modulus of the gyromagnetic ratio for the electron spin; g is the spectroscopic Lande factor; $\mu_{\rm B}=e\hbar/2m_e$ is the Bohr magneton; e and m_e are the modulus of the electron charge and the electron mass, respectively; and $\hbar=h/2\pi$, where h is the Planck constant.

The first term on the right-hand side of equation (3) represents the traditional torque, with $\vec{H}_{\rm eff}=-\delta W/\delta\vec{M}$ being the effective magnetic field in the magnetic film. The free energy W includes, first of all, the Zeeman energy of magnetization interaction with the external magnetic field $h_{\rm e}$, which consists of the external bias magnetic field $\vec{H}_{\rm e}$ and the microwave fields of the input signal $\vec{h}_{\rm s}$ and microwave pumping $\vec{h}_{\rm p}$. It also includes the energies of the dipole–dipole interaction, exchange interaction, and crystallographic anisotropy, together with the Zeeman energy of interaction with the inhomogeneous Oersted field $\vec{H}_{\rm I}(\vec{r})$ created by the spin-polarized current. The explicit expression for the energy W in a magnetic film of a finite thickness L is given in Slavin (1994); Wigen (1994). For simplicity, we will not consider anisotropy and interaction with the field $\vec{H}_{\rm I}(\vec{r})$, which have only a limited influence on the generation of the spin waves.

The second term on the right-hand side of equation (3)

$$\vec{T}_I=\frac{\alpha_I}{M}\vec{M}\times[\vec{M}\times\vec{p}] \tag{4}$$

represents the Slonczewski–Berger torque (Slonczewski, 1996; Berger, 1996; Slonczewski, 1999) of polarized current exerted on the magnetization $\vec{M}$ of the magnetic film, where $\vec{p}$ is a unit vector in the direction of spin polarization of the direct current traversing the magnetic film, while:

$$\alpha_I=\sigma S_{\rm c}J=\sigma I \tag{5}$$

is a linear function of the current density J and the area $S_{\rm c}$ of the contact or a linear function of the magnitude of spin-polarized current I. We would like to stress that the last term in equation (3) is nonconservative and depending on the direction (sign) of the current can contribute to either positive or negative magnetic dissipation in the magnetic film. The modulus of the quantity σ is defined in Slonczewski (1996) as

$$\sigma=\epsilon\frac{g\mu_{\rm B}}{2eMS_{\rm c}L} \tag{6}$$

where ϵ is the spin-polarization efficiency defined in Slonczewski (1996), μ_0 is the magnetic permeability of free space, and L is the magnetic film thickness.

We shall consider solution of equation (3) in the coordinate system where axis z is parallel to the direction of the static saturation magnetization $\vec{M}_0$ ($\vec{e}_z||\vec{M}_0$) in the magnetic film. We shall represent vectors $\vec{M}$ and $\vec{p}$ in equations (3) and (4) as sums of components perpendicular and parallel to the unit vector $\vec{e}_z$:

$$\vec{M}=\vec{m}_\perp+M_z\vec{e}_z;\quad \vec{m}_\perp=m_x\vec{e}_x+m_y\vec{e}_y;$$
$$M_z^2=M_0^2-|\vec{m}_\perp|^2 \tag{7}$$
$$\vec{p}=\vec{p}_\perp+p_z\vec{e}_z;\quad \vec{p}_\perp=p_x\vec{e}_x+p_y\vec{e}_y \tag{8}$$

To consider approximate dynamic solutions of equation (3) in the magnetic film we first find the equilibrium orientation θ of the internal bias magnetic field $\vec{H}$ (and the static magnetization $\vec{M}_0$) in this layer (relative to the plane of the layer) in the absence of current ($\alpha_I=0$) from the usual

electrodynamic boundary conditions for a single magnetic layer:

$$H_e \cos\theta_e = H\cos\theta;$$
$$H_e \sin\theta_e = (H + 4\pi M_z)\sin\theta \tag{9}$$

for given magnitude H_e and orientation θ_e of the external bias magnetic field.

In the following equation we also assume that $p_\perp \ll p_z$ and $m_\perp \ll M_z$. In this case, the expression for the spin-transfer torque equation (4) can be substantially simplified to give

$$\vec{T}_I = \frac{\alpha_I}{M}[\vec{M}(\vec{p}\vec{M}) - \vec{p}M^2] \cong \frac{\alpha_I}{M} p_z M_z \vec{m}_\perp - \alpha_I M \vec{p}_\perp \tag{10}$$

If $p_\perp \ll p_z$ the influence of the second term in equation (10) on the magnetization dynamics is not very significant. For large enough values of current, this term can change only the equilibrium orientation of $\vec{M}_0$, while the first term in equation (10) describes either negative or positive current-dependent dissipation, with sign depending on the current direction. Thus, when describing excitation of spin waves by spin-polarized current, we neglect the second term in equation (10) and write the expression for the spin-transfer torque $\vec{T}_I$ of equation (3) in the simple form

$$\vec{T}_I \cong \frac{\alpha_I}{M} p_z M_z \vec{m}_\perp \tag{11}$$

At first we shall consider a spatially uniform problem, that is, we will neglect spatial localization of the microwave field of parametric pumping and of the spin-polarized current. In this spatially uniform case, it is natural to represent the magnetization as a sum of plane waves propagating in the magnetic film:

$$\vec{m}_\perp(\vec{r}) = \sum \vec{m}_{k\perp} \exp(-i\vec{k}\vec{r}) \tag{12}$$

where $\vec{r}$ is the coordinate vector in the plane of the film and $\vec{k}$ is the wave vector of the excited spin-wave mode directed in the plane of the film at the angle φ to the projection of the bias magnetic field.

Using all these assumptions, we perform in the equation of motion equation (3) the usual series of Holstein–Primakoff and Bogolyubov transformations. First, we introduce the circularly polarized variables a_k:

$$m_k^+ = (m_k^-)^* = m_{kx} + i m_{ky}$$
$$= \sqrt{2|\gamma|M_0}\left(a_k - \frac{|\gamma|}{4M_0}\sum_{k_1,k_2} a_{k_1}^* a_{k_2} a_{k+k_1-k_2}\right) \tag{13}$$

$$M_z = M_0 - |\gamma| \sum_{k_1,k_2} a_{k_1}^* a_{k_2} \tag{14}$$

Next, we introduce the elliptically polarized dimensionless variables b_k :

$$a_k = \sqrt{\frac{M_0\omega_k}{|\gamma|A_k}}(u_k b_k + v_k b_{-k}^*) \tag{15}$$

(for details see Wigen (1994) p. 215–216). The coefficients of the last $u - v$ transformation for the case of spin waves in a magnetic film magnetized at an arbitrary internal angle θ have the form (Wigen, 1994)

$$u_k = \sqrt{\frac{A_k + \omega_k}{2\omega_k}},$$
$$v_k = \frac{B_k}{|B_k|}\sqrt{\frac{A_k - \omega_k}{2\omega_k}} \tag{16}$$

where

$$2A_k = 2\Omega_k + \omega_M \cos^2\theta + \omega_M P(kL)[1 - \cos^2\theta(1 + \cos^2\varphi)] \tag{17}$$

$$B_k = A_k - \Omega_k - \omega_M P(kL)\sin^2\varphi + i(\omega_M/2)P(kL)\sin\theta\sin 2\varphi \tag{18}$$

$$\omega_k^2 = A_k^2 - |B_k|^2 = \Omega_k[\Omega_k + \omega_M F(kL)] \tag{19}$$

$$\Omega_k = \omega_H + (2\gamma A/M_0)k^2 \tag{20}$$

$$F(kL) = (1 - P(kL)\cos^2\varphi)\cos^2\theta + P(kL) \times\left[\sin^2\theta + \frac{\omega_M}{\Omega_k}(1 - P(kL))\cos^2\theta\sin^2\varphi\right] \tag{21}$$

$$P(kL) = 1 - \frac{1 - \exp(-kL)}{kL} \tag{22}$$

where $\omega_M = |\gamma|M_z$, $\omega_H = |\gamma|H$, and H and θ are the magnitude and direction of the internal bias field $\vec{H}$, respectively, found from the boundary conditions (equation (9)), φ is the angle of wave propagation in the film plane; and A is the exchange constant.

In this chapter we will not discuss in detail the process of linear excitation of spin waves by the microwave magnetic field $\vec{h}_s(\vec{r}, t)$ of a strip-line antenna, which is extensively described in literature (see e.g., Chapter 5 in Stancil, 1993), and will only discuss either the spin waves that are excited by parametric pumping or spin-polarized direct current, or the waves propagating in a magnetic film sufficiently far from the input strip-line antenna.

The resulting equation for the amplitude of the spin wave written in the wave number space has the form:

$$\frac{\mathrm{d}b_k}{\mathrm{d}t} = -i\omega_k b_k - iV_{k,-k}h_\mathrm{p}b^*_{-k} - i\sum_{k+k_1=k_2+k_3} T_{k,k_1,k_2,k_3}b^*_{k_1} \times b_{k_2}b_{k_3} - \Gamma_k b_k + \sigma I\sum_{k_1}\frac{M_{k_1 z}}{M_0}b_{k-k_1} \tag{23}$$

where ω_k is the linear spin-wave frequency given by equation (19), $V_{k,-k}$ is the coupling coefficient between the parametrically excited contrapropagating spin waves b_k, b^*_{-k}, and the microwave pumping defined by equation (7) in Melkov *et al*. (2001), h_p is the amplitude of the quasiuniform parametric pumping field, T_{k,k_1,k_2,k_3} is the coefficient of four-wave interaction between spin waves defined in Lvov (1994), Slavin (1994), and Γ_k is the phenomenologically introduced dissipation parameter of spin waves. In the following text we shall consider several particular cases of the general equation (23).

First of all we shall consider excitation of the spin-wave mode in a very thin layer of a ferromagnetic metal by spin-torque $\vec{T}_I$ defined by equation (11). The spin-polarized direct current creating this torque is localized in the circular contact having the radius R_c in the film plane. This situation is realized in the recent experiments conducted by Kiselev *et al*. (2003, 2004); Rippard *et al*. (2004a,b). In these experiments, the thickness L of the magnetic film ("free" layer) is rather small, usually smaller than the exchange length $l_\mathrm{ex} = \sqrt{2A/M_0^2}$ in the ferromagnetic metal, while the in-plane radius of the current-carrying region (nanocontact), R_c, is substantially larger than both the layer thickness and the exchange length $R_\mathrm{c} > l_\mathrm{ex} > L$. In such a situation the nanocontact plays the role of an antenna and excites a spectrally narrow packet of spin waves localized near $\vec{k} = 0$ and having a spectral width in the k space of the order of $\Delta k \sim 2\pi/R_\mathrm{c} \ll 2\pi/L$. Although this wave packet can be considered spectrally narrow compared to the characteristic wave number $k_L \sim 2\pi/L$, the absolute values of spin-wave wave numbers in the packet $k \sim 2\pi/R_\mathrm{c}$ are sufficiently large, so the exchange interaction creates a dominant contribution to the spin-wave spectrum. At the same time, the in-plane anisotropy of the spin-wave spectrum, equation (19) caused by the dynamic dipole–dipole terms (of the order of $kL \sim L/R_\mathrm{c}$) could be ignored, and only the static demagnetization and exchange interaction should be taken into account in the spin-wave dispersion equation. This leads to the following simple approximate expression for the spin-wave dispersion law:

$$\omega_k = \omega_0 + Dk^2 \tag{24}$$

where $\omega_0^2 = \omega_H(\omega_H + \omega_M\cos^2\theta)$ is the spin-wave frequency and spin-wave dispersion $D = \partial^2\omega_k/\partial k^2 = (A/M_0)(\partial\omega_0/\partial H)$ calculated at $k = 0$. Since the excited packet of spin waves is spectrally narrow we can also replace the four-wave coupling coefficient T_{k,k_1,k_2,k_3} and the damping rate Γ_k in equation (23) by their values at $k = 0$: $N \equiv T_{0,0,0,0}$, $\Gamma = \Gamma_0$.

Using the above simplifications and performing the inverse Fourier transformation in equation (23) one derives the Ginzburg–Landau equation for the amplitude of the excited spin-wave mode in the coordinate space $b(\vec{r}, t) = \sum_{\vec{k}} b_k(t)\exp(i\vec{k}\vec{r})$:

$$\frac{\partial b}{\partial t} = -i[\omega_0 b - D\Delta b + N|b|^2 b] - \Gamma b + f(r/R_\mathrm{c})\sigma I b - f(r/R_\mathrm{c})\sigma I|b|^2 b \tag{25}$$

where r is the two-dimensional position vector in the film plane, Δ is radial part of the Laplace operator written in cylindrical coordinate system, and $f(r/R_\mathrm{c})$ is a dimensionless function that describes distribution of the current across the nanocontact area.

Second, we shall consider the case when a spectrally narrow ($\Delta k \ll k_0$) spin-wave packet is linearly excited by an external signal $\vec{h}_\mathrm{s}(\vec{r}, t)\exp(i\omega_\mathrm{s}t)$ created by a microwave pulse having the carrier frequency ω_s and the duration τ and supplied to a strip-line antenna of width w in a rather thick ferromagnetic film $w \geq L \gg l_\mathrm{ex}$. In this case the characteristic carrier wave number $k_0 \leq 2\pi/w$ of the excited spin-wave packet is determined by the carrier frequency ω_s of the input signal, while the spectral width Δk of the excited spin-wave packet is determined by the input pulse duration τ. In the case of a thick ferrite film, the contribution of the exchange interaction to the spin-wave dispersion could be ignored, and the spin-wave spectrum can be described by equation (19) with the exchange constant $A = 0$.

Using the spectral narrowness ($\Delta k \ll k_0$) of the spin-wave packet, we can again assume that the coupling and damping coefficients in equation (23) do not depend on k, $T_{k,k_1,k_2,k_3} \to N \equiv T_{k_0,k_0,k_0,k_0}$, $\Gamma_k \to \Gamma \equiv \Gamma_{k_0}$ and approximate the nonexchange spin-wave dispersion law equation (19) by its Taylor expansion near the point $\vec{k} = \vec{k}_0 = k_0\vec{z}$:

$$\omega_k = \omega_\mathrm{s} + v_\mathrm{g}\Delta k_z + \frac{1}{2}D\Delta k_z^2 + \frac{1}{2}S\Delta k_y^2 \tag{26}$$

where $v_\mathrm{g} = \partial\omega/\partial k_z|_{k_{0z}}$ is the group velocity, $D = \partial^2\omega/\partial k_z^2|_{k_{0z}}$ and $S = \partial^2\omega/\partial k_y^2|_{k_{0z}}$ are the dispersion and diffraction coefficients. For simplicity, we assumed that the central wave vector $\vec{k}_0$ lies along one of the 'principal directions' of the dispersion law (i.e., either parallel or perpendicular to

the direction of the in-plane bias magnetic field $\vec{H}$), so the cross term $\partial^2\omega/\partial k_z \partial k_y|_{k_{0z}}$ vanishes. It should be stressed that, in contrast with equation (24), the approximate dispersion equation (26) contains the term with group velocity (linear in Δk), because the Taylor expansion is performed near a nonzero central (or carrier) wave vector. Introducing a dimensionless slow-varying amplitude of the spin-wave packet envelope:

$$U(y,z,t) = \sum_{|\Delta\vec{k}|\ll k_0} b_{\vec{k}_0+\Delta\vec{k}}(t)\exp(i\Delta\vec{k}\vec{r} + i\omega_0 t) \qquad (27)$$

and performing the inverse Fourier transformation in equation (23), we can obtain the so-called (2+1)-dimensional nonlinear Schrödinger equation (NSE) for the spin-wave packet envelope U (see e.g., Lvov, 1994; Slavin, 1994):

$$i\left(\frac{\partial U}{\partial t} + v_g\frac{\partial U}{\partial z}\right) + \frac{1}{2}D\frac{\partial^2 U}{\partial z^2} + \frac{1}{2}S\frac{\partial^2 U}{\partial y^2} - N|U|^2U = -i\Gamma U \qquad (28)$$

The coefficients v_g, D, S, and N in equation (28) have been calculated for different directions of spin-wave propagation in Chapter 9 of Wigen (1994). A more rigorous calculation of the nonlinear coefficient N is reported in Wigen, 1994 using a classical Hamiltonian formalism for spin waves in magnetic films.

Finally, we shall consider the case when a spectrally narrow spin-wave packet, linearly excited by a strip-line antenna in a ferrite film and propagating far from the antenna, interacts with a quasiuniform magnetic field $\vec{h}_p$ of a double-frequency ($\omega_p = 2\omega_s$) microwave pumping. As a result of such parametric interaction, an additional idle spin-wave packet with opposite wave vectors $-\vec{k}_0 \pm \Delta\vec{k}$ will be generated, that is, in this case the spin waves are localized near two points $\pm\vec{k}_0$ of the k space. Therefore, one can introduce two slow-varying envelopes $U_{1,2}$ for the description of partial spin-wave packets:

$$U_{1,2}(y,z,t) = \sum_{|\Delta\vec{k}|\ll k_0} b_{\pm\vec{k}_0+\Delta\vec{k}}(t)\exp(i\Delta\vec{k}\vec{r} + i\omega_0 t) \qquad (29)$$

The inverse Fourier transformation of equation (23) gives the following system of equations for the spin-wave packet envelopes $U_{1,2}$:

$$i\left(\frac{\partial U_1}{\partial t} + v_g\frac{\partial U_1}{\partial z} + \omega_r U_1\right) + \frac{D}{2}\frac{\partial 2U_1}{\partial z2} + \frac{S}{2}\frac{\partial 2U_1}{\partial y2} - N\left(|U_1|^2 + 2|U_2|^2\right)U_1 = iVh_p(z,t)\,U_2^* \qquad (30)$$

$$-i\left(\frac{\partial U_2^*}{\partial t} - v_g\frac{\partial U_2^*}{\partial z} + \omega_r U_2^*\right) + \frac{D}{2}\frac{\partial^2 U_2^*}{\partial z2} + \frac{S}{2}\frac{\partial^2 U_2^*}{\partial y2} - N\left(|U_2|^2 + 2|U_1|^2\right)U_2^* = -iV^*\,h_p^*\,(z,t)\,U_1 \qquad (31)$$

where the coefficients of nonlinear self-modulation inside the packets $T_{k_0k_0,k_0k_0}$ and $T_{-k_0-k_0,-k_0-k_0}$, as well as the coefficient of nonlinear cross-modulation between the packets $T_{-k_0k_0,-k_0k_0}$ were assumed to be equal to each other $N = T_{k_0k_0,k_0k_0} = T_{-k_0-k_0,-k_0-k_0} = T_{-k_0k_0,-k_0k_0}$.

The system of equations (30) and (31) gives a good description of the process of interaction of two-dimensional nonlinear spin-wave packets propagating in a magnetic film with a quasiuniform microwave magnetic field h_p of a double-frequency parametric pumping.

3 EXPERIMENTAL TECHNIQUES FOR INVESTIGATION OF SPIN-WAVE EXCITATIONS

There are several experimental approaches for the investigation of linear and nonlinear spin-wave processes. The classical approach of microwave spectroscopy has the important advantage of its simplicity. The input microwave signal is supplied to the input antenna, which converts it in a spin-wave packet in the sample. After some propagation time, the packet is detected by the output antenna placed on the sample several millimeters apart from the input one. The characteristics of the output microwave signal (duration, delay time, shape, phase, frequency spectrum etc.) can then be measured and analyzed. The duration of the detected signal, for example, can be brought into connection with the length of the packet along its propagation direction. Using an additional antenna or an open resonator placed between the input and output antennae, one can manipulate the wave packets in the magnetic medium and study their amplification. The disadvantage of the described technique is lack of spatial resolution. One can study the wave packet only at the position of the output antenna. The propagation and development of the packet between the antennae, which is of particular importance for nonlinear phenomena, cannot be studied by means of this technique. Similar problems arise if one tries to investigate two-dimensional effects. Since the antenna integrates the detected signal over its length, important information about the transverse length of the packet is being lost. An inductive scanning probe based on a small wire loop sensitive to the magnetic field caused by the spin waves during their propagation (Vlannes, 1987) brought limited success. Recent attempts to overcome this drawback made Scott, Kostylev, Kalinikos and Patton (2005) raise a hope that the inductive probe approach

would establish a competitive technique for time- and space-resolved observation of spin-wave modes. Direct observation of spin precession is possible by optical probing using the magneto-optical Faraday or Kerr effects (Geisau, Netzelmann, Rezende and Pelzl, 1990; Hiebert, Stankiewicz and Freeman, 1997). By applying a stroboscopic technique, one can measure the time dependence of different components of the magnetization. However, since the measurements are performed in the time domain, the upper frequency limit of such techniques is 3–7 GHz (Perzlmaier *et al*., 2005).

BLS is an optical spectroscopic method for investigation of excitations with frequencies in the GHz regime. From the point of view of classical electrodynamics, the BLS process can be understood as follows: Owing to magneto-optical effects a moving phase grating is created in the medium by a spin wave; this grating propagates with the phase velocity of the spin wave. Light is Bragg-reflected from the phase grating with its frequency Doppler-shifted by the spin-wave frequency.

The quantum-mechanic understanding of the BLS process is illustrated in Figure 2. A photon of energy $\hbar\omega_I$ and momentum $\hbar\vec{q}_I$ interacts with the elementary quantum of spin waves $(\hbar\omega, \hbar\vec{q})$, which is the magnon. The scattered photon gains an increase in energy and momentum:

$$\hbar\omega_S = \hbar(\omega_I + \omega) \tag{32}$$

$$\hbar\vec{q}_S = \hbar(\vec{q}_I + \vec{q}) \tag{33}$$

if a magnon is absorbed as a result of the scattering process. From equation (33) it is evident, that the wave vector $\vec{q}_S - \vec{q}_I$, transferred in the scattering process, is equal to the wave vector $\vec{q}$ of the spin wave. It can be chosen in the experiment by variation of the scattering angle. If spin waves with wave vectors much smaller than the wave vector of the light are under investigation, the small-angle scattering geometry should be used. On the contrary, the backscattering geometry corresponds to the maximum transferred wave vector, $2|\vec{q}_I|$. A magnon can also be created by energy and momentum transfer from the photon, which in the scattered state has the energy $\hbar(\omega_I - \omega)$ and momentum $\hbar(\vec{q}_I - \vec{q})$. For finite temperatures ($T \gg \hbar\omega/k_B \approx 1K$) both processes have about the same probability.

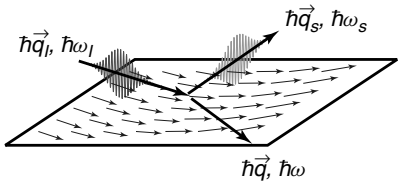

Figure 2. Brillouin light-scattering process from spin waves (magnons). The wave vectors of the incident and the scattered photons as well as that of the magnon are shown. The array of arrows schematically illustrates the orientation of magnetic moments in a spin wave.

However, since for a spin-wave mode propagating in a film the conservation conditions are fulfilled only for the two in-plane components of the wave vector, $\vec{q}_\parallel$. The third component perpendicular to the film, q_x, is not well defined by the conservation law because of a finite width of the film, which results in an essential uncertainty in the wave vector due to the uncertainty principle. Furthermore, if the excitation is not an infinitive plane wave, but a bound, localized state comprising many magnons (soliton or bullet; see the following sections), the in-plane components of the wave vector do not conserve as well. The uncertainty in q_x is, apparently, inversely proportional to the size of the excitation ξ, $\delta q_\parallel \approx 2\pi/\xi$. Thus, it should be taken into account, if $(\vec{q}_S - \vec{q}_I)_\parallel \xi \approx 2\pi$. This effect is of particular importance if excitations in nanocontacts are under investigation.

During the last decades, BLS has developed to a very versatile tool to investigate spin waves in magnetic films with the wave vector in the interval of $0–10^6\,\mathrm{cm}^{-1}$, both thermally driven and excited using an external source (Demokritov, Hillebrands and Slavin, 2001). The tandem Fabry–Pérot interferometer designed by Sandercock is currently widely used as a fairly standard solution (Sandercock, 1978) for the BLS studies. The frequency resolution of the technique of about 200 MHz is usually determined by the flatness of the mirrors of the interferometer, which should be of the highest quality, and their alignment. For example, a typical flatness of the mirrors over the diameter of 50–70 mm is specified as 25–30 nm. For the alignment, an active stabilization procedure continuously analyzing the shape and the measured frequency position of the reference laser beam is obligatory (Hillebrands, 1999). As a result of such a resolution, the detection of waves with frequencies below 1 GHz is questionable. The upper frequency limit of the waves accessible for the BLS technique is determined by the free spectral range of the interferometer, which can hardly be made above 300 GHz, since the distance between mirrors in this case should be below 0.5 mm.

The advantages of the BLS as a technique for investigation of spin waves are (i) high-frequency resolution in the GHz regime and the potential to investigate spin waves with different absolute values and orientations of their wave vectors; (ii) a wide dynamic range, that is, the possibility of detecting both low-amplitude thermal spin waves and high-amplitude spin waves, excited by an external source; and (iii) high spatial resolution defined by the size of the laser beam, which can be focused down to 300 nm in diameter (Perzlmaier *et al*., 2005).

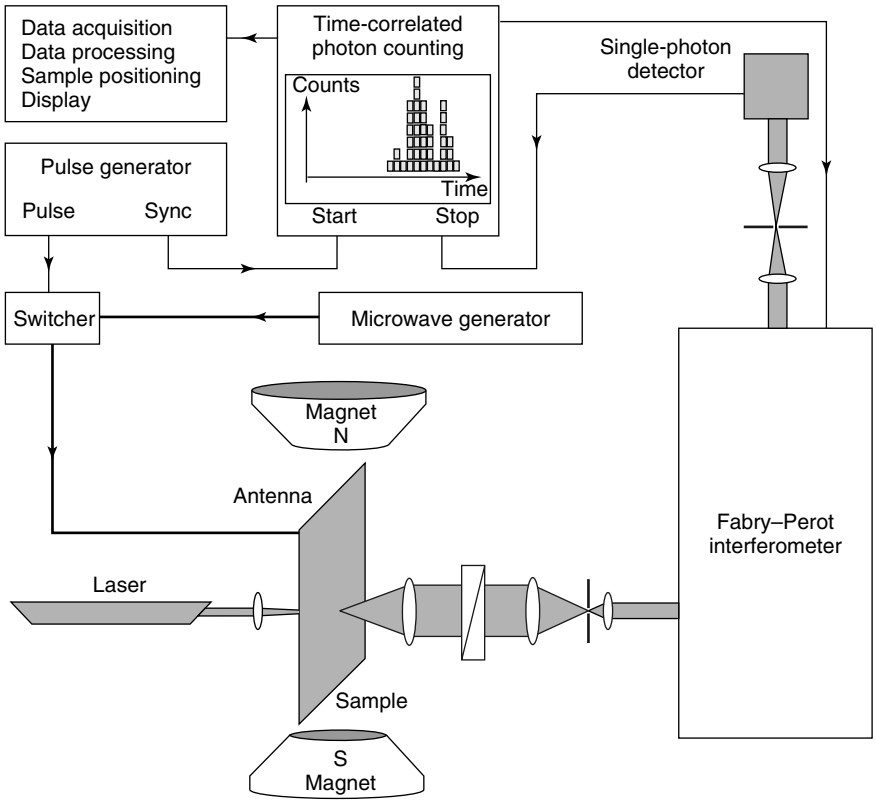

Figure 3. Schematic layout of the Brillouin light-scattering setup in the forward-scattering geometry with space and time resolution. (For a discussion of the components see the main text).

To investigate magnetic excitations simultaneously with spatial and temporal resolutions, an experimental technique based on a standard BLS setup has been developed. It is schematically shown in Figure 3. Similar to the microwave technique, spin waves are generated by an input antenna attached to the sample. The spatial distribution of the wave intensity is measured by scanning the laser beam across the sample, which is performed by a motorized sample mount. Spin waves are effectively excited in a wave vector interval $|\vec{q}| < 300\,\mathrm{rad/cm}$, with the upper bound imposed by the width of the antenna. Thus the light scattered into the forward direction is usually detected to achieve a high sensitivity in this low-wave-vector regime.

Temporal resolution is added by using a time-correlated single-photon counting method similar to time-of-flight measurements in, for example, mass spectroscopy. A pulse generator generates pulses of typically 10–30 ns duration with a repetition rate of typically 1 MHz. The pulse is sent to a microwave switching device to create a pulsed microwave field and to generate a spin-wave pulse. The same pulse is also used to start a 24-bit reference counter counting the output pulses of a 4 GHz time base. If the spin-wave pulse crosses the laser spot, light is inelastically scattered. The scattered light passes through the interferometer and is detected by a single-photon detector. The output signal of the detector is used to stop the reference counter. The counter content is now a measure of the elapsed time between the launch of the spin-wave pulse and the arrival at the position of the laser spot. A cell of a memory array addressed by the content of the counter is incremented by one and the procedure is repeated. After accumulating a large number of events, the content of the memory array represents the temporal variation of the light-scattering cross section (which is proportional to the spin-wave intensity) at the current position of the laser spot. By repeating the procedure for different positions of the laser spot on the sample, two-dimensional maps of the spin-wave intensity are constructed for different values of delay time. The data is arranged in a digital video animation with each frame representing the spatial distribution of the spin-wave intensity for a given delay time. The entire system is built on the basis of a digital signal processing device, which is placed on a PCI computer board. The device can handle up to 2×10^7 events per second continuously. A lower limit of about 1–2 ns on the time resolution is imposed to keep the obtained frequency uncertainty of the at a reasonable level. Typical accumulation times are 5 s per position of the laser spot. A complete measurement of a two-dimensional spin-wave intensity pattern in a film with a sampling area of

$2 \times 6\,\text{mm}^2$ and a mesh size of 0.1 mm takes a little more than 2 h including dead times caused by sample positioning. Using a similar approach, spin waves of different frequencies can be detected simultaneously with a time and space resolution.

The experiments described in the following text usually combine the microwave technique with the BLS one. To investigate nonlinear excitations, high-amplitude spin precession is excited by an external microwave source. To minimize the applied microwave power, media with low damping constants are usually used. As mentioned in the preceding text, rare-earth garnets demonstrate an extremely low damping, YIG ($Y_3Fe_5O_{12}$) having the lowest damping. Excitations with a precession angle of several degrees can be excited in YIG films. Bismuth-substituted-iron garnet ($Lu_{0.96}Bi_{2.04}Fe_5O_{12}$, BIG) films are also an attractive magnetic media for nonlinear studies. Although the dissipation parameter is larger in BIG, this material generates a much higher BLS signal due to its higher magneto-optical activity for green light, commonly used for BLS experiments.

4 NONLINEAR SPIN-WAVE MODES EXCITED BY EXTERNAL MICROWAVE SIGNAL

It has been shown in Section 2 that an intrinsically nonlinear equation of motion for the magnetization Landau and Lifshitz (1935) in the limit of weak nonlinearity can be reduced to the NSE equation (28) describing the evolution of spectrally narrow nonlinear spin-wave packets. The stable or quasistable solutions of this equation describe natural nonlinear spin-wave excitations existing in a magnetic film, and these excitations form a new *nonlinear* basis for the description of microwave dynamics of magnetization in magnetic films.

The most well known of those solutions is a one-dimensional temporal envelope soliton solution, which can be interpreted as a bound state of a large number of linear spin waves (or magnons) (Kosevich, Ivanov and Kovalev, 1988). In contrast to linear wave packets, which spread while propagating in a dispersive medium, the temporal soliton is stable: it preserves its shape during propagation. Moreover, the theory predicts that two solitons can undergo a head-to-head collision without destroying each other (Büttner *et al*., 1999). One distinguishes bright and dark solitons. An envelope dark soliton can be understood as a stable propagating dip in a carrier wave of otherwise constant amplitude in a nonlinear medium. In real experiments, one-dimensional spin-wave envelope solitons can be observed either in the quasi-one-dimensional geometry of a spin-wave waveguide – a narrow strip of a YIG film having a width that is smaller than the characteristic wavelength of transverse modulational instability in the medium (see Demokritov, Hillebrands and Slavin, 2001 for details) – or in the two-dimensional geometry of a wide YIG film where the Lighthill criterion (Lighthill, 1965) of modulational instability in the transverse direction is not fulfilled (e.g., the case of a perpendicularly magnetized YIG film (see Chapter 9 in Wigen (1994)).

In a two-dimensional geometry when the Lighthill criterion is fulfilled in both in-plane directions, it is possible to observe the formation of quasistable two-dimensional self-focused spin-wave packets – wave bullets – that are two-dimensional spatio-temporal analogs of solitons. We would like to stress that bullets existing in a two-dimensional case are only quasistable and do not survive collisions with other bullets (see Demokritov, Hillebrands and Slavin, 2001); nevertheless, they play a very important role in the nonlinear spin-wave dynamics of magnetic films. In fact, bullets give us a convincing example of the general importance of magnetic systems for nonlinear physics. The possibility of 'light bullets', that is, stable optical wave pulses strongly localized in space and time by self-focusing, which is stabilized by saturation of nonlinearity at high wave amplitudes, has been suggested by Silberberg (1990). There exists, however, no clear experimental evidence for this effect in optics, likely because in optical fibers diffraction is much stronger than dispersion and, therefore, both effects cannot be observed simultaneously. On the contrary, the first experimental observation of bullets has been performed in magnetic films (Bauer *et al*., 1998; Büttner *et al*., 1999). The success is mainly based on the fact that the dispersion law of spin waves can be easily manipulated in experiment by changing the magnitude and direction of the bias magnetic field applied to the magnetic film.

The most interesting geometry to study nonlinear spin-wave processes in magnetic films is the case of an in-plane magnetized ferrite (YIG) film. While the exchange-dominated spin-wave spectrum (24) of a very thin metallic film is approximately isotropic in the film plane, in the case of a relatively thick YIG film, the spin-wave dispersion equation (26) is strongly anisotropic in the film plane.

For backward-volume magnetostatic (nonexchange) waves (BVMSW) propagating along the direction of the bias magnetic field in a thick ferrite film, the nonlinear coefficient N is negative, while the coefficients D and S describing dispersion and diffraction are both positive (see Chapter 9 in Wigen (1994)). Thus the Lighthill criterion (Lighthill, 1965) for modulational instability is fulfilled in both in-plane directions ($SN < 0$, $DN < 0$), and the BVMSW are susceptible to both self-modulation in the direction of propagation (z) and self-focusing in the transverse direction (y).

In the case of a sinusoidal input signal supplied to a relatively short input antenna situated on a wide ferrite-film sample, the excited dipolar spin waves are monochromatic, and they propagate in a relatively wide angle in the transverse

(y) direction. These monochromatic waves are not affected by dispersion, but owing to the presence of different directions of wave vectors in the excited beam they are strongly affected by diffraction. Owing to the competition between diffraction and nonlinearity, transverse modulational instability develops, and this leads to stationary self-focusing of the wave beam and to the formation of spatial spin-wave envelope solitons (Boyle *et al*., 1996; Bauer *et al*., 1997; Büttner *et al*., 2000). This effect can be described by a one-dimensional reduction of the NSE equation (28) with $\partial U/\partial t = 0$ and $D = 0$.

In the opposite case, when a wave packet propagates in a narrow strip of a ferrite film (spin-wave waveguide), where the strip width is smaller than the wavelength of the transverse modulational instability (see equations (28) and (29) in Demokritov, Hillebrands and Slavin (2001) for details), the packet is not affected by diffraction, but, owing to the presence of many different spectral components in the packet, it is strongly affected by dispersion. The competition between dispersion and nonlinearity leads to a longitudinal self-modulation of the wave packet and to the formation of 'bright' temporal spin-wave envelope solitons (see, e.g., Kalinikos, Kovshikov and Slavin, 1983; Chen, Tsankov, Nash and Patton, 1994 and references therein).

The properties of MSSW propagating perpendicular to the direction of the bias magnetic field are very different. MSSW modes are modulationally stable and can only form 'dark' spin-wave solitons (Chen, Tsankov, Nash and Patton, 1993). Formation of 'bright' and 'dark' temporal envelope solitons can also be described by a one-dimensional reduction of the NSE equation (28); only in this case we should assume that $S = 0$.

The effects of longitudinal and transverse self-modulation can be observed simultaneously if a pulsed input signal excites a two-dimensional wave packet of BVMSW modes in a wide YIG film sample. In this case, modulational instability takes place in both in-plane directions and leads to a spatio-temporal self-focusing of the wave packet and to initial stages of the wave collapse, when the whole energy of the packet is concentrated in a small spatial region (Bauer *et al*., 1998). The full $(2 + 1)$-dimensional NSE is necessary for the theoretical description of this effect.

Finally, when a two-dimensional linear or nonlinear spin-wave packet propagates in a ferrite film and interacts with a weakly spatially localized field of microwave pumping (Bagada, Melkov, Serga and Slavin, 1997; Melkov *et al*., 2000; Serga *et al*., 2005) the full system of equations (30) and (31) (or its one-dimensional reduction) are needed to describe this interesting and complicated nonlinear wave process.

In this section we shall describe experiments where one- and two-dimensional nonlinear spin-wave packets – solitons and bullets – were excited by an external input microwave pulse launched in the film by a strip-line antenna.

4.1 Bright temporal and spatial solitons

Observation of bright temporal spin-wave envelope solitons in magnetic films using the microwave technique has been reported in Kalinikos, Kovshikov and Slavin (1983) and Kalinikos, Kovshikov and Slavin (1988, 1994) for different orientations of the static magnetization, corresponding to different spin-wave modes. These works have shown that it is in fact possible to create in YIG films nonlinear wave packets, possessing many properties intrinsic to solitons. For example, after some formation time, spin-wave envelope solitons propagate with a constant width. Moreover, it was also shown that the measured phase profile inside the wave packet is flat and corresponds to that of a theoretical soliton solution of equation (28) with $S = 0$.

The first attempt to observe bright spatial solitons of dipolar spin waves in magnetic films was undertaken by Boyle *et al*. (1996). This paper reports the BLS study of the stationary self-channeling of dipolar spin waves in rear-earth garnet films, although the indication of the initial stages of self-focusing was also present in the reported data.

A clear evidence of nonlinear self-focusing of dipolar spin-wave beams and creation of spatial solitons was presented in Bauer *et al*. (1997), where BVMSW beams in a $Lu_{2.04}Bi_{0.96}Fe_5O_{12}$ (BIG) waveguide (width 2 mm) were studied. One of the results was the appearance of a snakelike structure in the beam propagation path, which is caused by the interaction of transverse waveguide modes (Büttner *et al*., 1998). Different width modes of the waveguide, excited by the microwave antenna, propagate with different phase velocities. They interfere with each other creating a snakelike pattern in the spin-wave intensity in the waveguide.

To exclude the effect of self-focusing on measurements, a wide BIG sample (width 18 mm) was used (Büttner *et al*., 2000). The input power in this experiment was varied from $P_{\text{in}} = 10$ mW (linear case) up to $P_{\text{in}} = 600$ mW (nonlinear case). In Figure 4(a) and (b), the measured spin-wave intensity distribution is shown for different values of the input power. The intensity maps are corrected for attenuation, and the data is normalized to the maximum intensity in each map.

In the linear case, as displayed in Figure 4(a), the spin-wave amplitude changes slightly due to the effect of the diffraction, which causes a beam divergence during propagation, so that the spin-wave intensity is distributed over a wider range with increasing distance from the antenna.

In the nonlinear case, the propagation of the spin waves is very different (Figure 4b). The beam no longer diverges. It

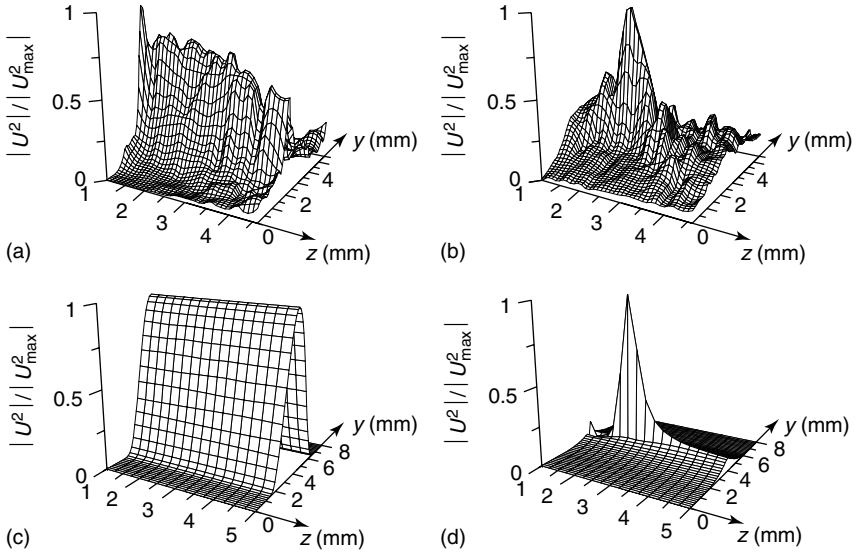

Figure 4. Stationary self-focusing of BVMSW beams in a wide BIG sample. (a) and (b) Experimental distributions of the spin-wave normalized intensity in the film plane for the linear ($P_{in} = 10$ mW) and nonlinear ($P_{in} = 600$ mW) regime, respectively. A clear self-focusing maximum is seen at the point ($z = 2.5$ mm, $y = 3$ mm) in the nonlinear regime. (c) and (d) Results of numerical calculations. (From Büttner *et al*., 2000.)

converges to a small diameter while the spin-wave amplitude increases and a clear focus of spin-wave intensity is observed at the point $z = 2$ mm, $y = 2$ mm. This is the result of the competition between diffraction and nonlinearity, and it can be qualitatively interpreted as the formation of a spatial soliton of a higher order (Agrawal, 1994). In the nonlinear regime, the formation of a narrow wave channel of constant amplitude parallel to the propagation direction z was not observed in these experiments, probably because of the fact that the spatial attenuation in the film is large, and it can play a significant role in the beam-shaping process. Since the spin-wave beam loses energy because of dissipation during propagation, the beam finally diverges when its amplitude becomes so small that the diffraction effect dominates as is the case for $z > 2.6$ mm in Figure 4(b).

4.2 Dark temporal and spatial solitons

As already mentioned, an envelope dark soliton is a stable dip in a carrier wave of otherwise constant amplitude. The dispersion broadening of such a dip is stopped by the influence of nonlinearity, and the actual profile of the completely formed dark soliton, as well as the phase modulation of the carrier wave across the soliton, is a result of a fine dynamic balance between the influences of nonlinearity and dispersion. The characteristic feature of such a dark soliton is a nonzero jump in the phase of its carrier wave as one crosses the dip (Remoissenet, 1999; Slavin, 1995). In the case of a black soliton, if the maximum depth of its dip is equal to the amplitude of the carrier wave, this phase shift is exactly equal to 180°. Thus, to obtain a single dark soliton from an initial wave profile, the phase modulation of the carrier wave should be performed before it enters the nonlinear medium. Without such a modulation, one or several *couples* of dark solitons can be created (Chen, Tsankov, Nash and Patton, 1993; Nash, Kabos, Patton and Staudinger, 1996; Slavin, Kivshar, Ostrovskaya and Benner, 1999). In this case, the phase jumps of successive solitons are added, and the net phase shift across the entire output signal is equal to an integer multiple of 360°.

To create an appropriate phase modulation of the wave, the experimental setup schematically shown in Figure 5 was applied (Serga *et al*., 2004). A similar experimental technique was used in a more-detailed study of dark spin-wave solitons presented in Bischof, Slavin, Benner and Kivshar (2005). Its main difference from a standard setup for investigation of, for example, bright solitons is that the input signal is composed of two coherent rectangular microwave pulses with controlled mutual phase shift in the range $(0, 2\pi)$. The combined pulse is amplified by a power amplifier with controlled gain and is sent to a short-circuited microstrip antenna attached to a strip of a single-crystal YIG film. The input peak power of the microwave signal P_{in} was varied in the range from 0.2 up to 50 mW. The second antenna is used for the detection of the spin-wave packets after their propagation along the YIG film. As shown in Figure 5, the antennae are situated transverse to the long side of the YIG sample and are separated by 8 mm. The sample was magnetized by a static magnetic field of $H_0 = 1745$ Oe applied in the film plane and transverse to the

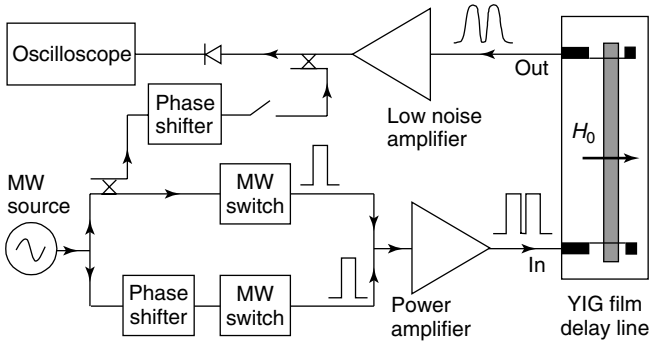

Figure 5. Experimental setup for creation of dark temporal solitons. The YIG film is shown by a shaded rectangle (from Serga *et al*., 2004). (For a discussion of the rest of the components see the main text).

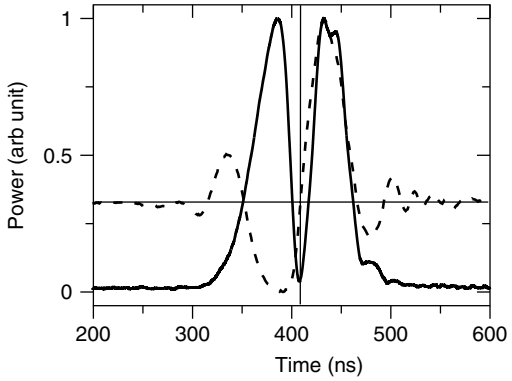

Figure 6. Normalized output signal formed from a nonlinear input rectangular pulse with a dip, demonstrating the formation of a black soliton (solid line). To obtain the black soliton, a phase adjustment between two parts of the initial pulse by 50° was introduced to compensate for the induced nonlinear phase shift. The dashed line shows the result of interference of the black soliton signal with a monochromatic reference signal, illustrating the 180° phase shift over the soliton. (From Serga *et al*., 2004.)

long edge of the strip. In this geometry, MSSW were excited. Such waves have a monotonic dispersion curve $\omega(k)$ with negative dispersion, $D < 0$, and nonlinearity, $N < 0$. The positive product $ND > 0$ (Lighthill, 1965) allows MSSW wave packets to form dark envelope solitons while traveling between the antennae. To analyze the phase jump inside the output signal, the interference between the output signal and a reference signal from the same microwave source was recorded.

Owing to the spin-wave dispersion in the film, the output pulse is broadened and the two initially rectangular pulses forming it acquire bell-like profiles. The width of the central dip decreases with increasing power, providing clear evidence of the dark-soliton formation. However, the dip does not reach the zero level: the intensity at the dip is increasing with increasing power. It means that a 'gray' soliton is created at the initial phase modulation of 180°. This effect is connected with the excitation-induced nonlinear phase modulation (Slavin, Kivshar, Ostrovskaya and Benner, 1999). To obtain a fully 'black' soliton having zero amplitude at the center of the dip, the excitation-introduced phase shift is compensated by the external phase shifter. The envelope shape of the output signal for this case is shown in Figure 6. Thus, an artificial precompensation of the nonlinear phase shift enables one to observe the generation of a single, fundamental black spin-wave envelope soliton having a 180° phase jump.

A similar technique combining two microwave pulses with a phase shift can be used for the formation of dark spatial solitons. Instead of mixing two microwave pulses at one antenna, as was done for the preceding studies of temporal dark solitons, the formation of a spatial dark soliton has been realized by using two axially aligned microstrip antennae (shown by the vertical stripes in Figure 7) attached to the surface of a wide YIG film. Two long (300 ns) coherent microwave pulses with a 180° phase shift between them were supplied to the antennae. Two-dimensional propagating spin waves have been studied using the space-resolved BLS technique. As seen in Figure 7 the antennae excite two almost-parallel beams of MSSW. As a result of a destructive interference of the beams an initial gap is created between them even in the linear case (Figure 7a). This gap plays the role of a soliton seed. Increasing the beam power leads to a sharpening of the gap (see Figure 7b) between them. At the same time, the depth of the gap remains at a constant value. Remarkably and contrary to the linear case, the nonlinear gap preserves its shape for a long propagation distance, as seen in Figure 7(b).

4.3 Spatio-temporal self-focusing: spin-wave bullets

In the experiments discussed in the preceding text, either narrow YIG films were used or stationary effects of the spin-wave propagation were studied. For the investigation of two-dimensional spatio-temporal self-focusing, the propagation of relatively short spin-wave packets in a large YIG film (thickness 7 μm, width 18 mm, length 26 mm) has been studied (Bauer *et al*., 1998). The static magnetic field $H =$ 2098 Oe was applied parallel to the propagation direction. Thus, the BVMSW geometry was realized. The carrier frequency was chosen to be $\omega_s/2\pi = 7970$ MHz, which results in a carrier wave vector $k_{0z} = 50\,\mathrm{cm}^{-1}$.

Figure 8 shows the distribution of the spin-wave intensities for the preceding parameters and for two different input powers: $P_{\mathrm{in}} = 10$ mW in the linear (Figure 8a) and $P_{\mathrm{in}} =$ 460 mW in the nonlinear regime (Figure 8b). The data are

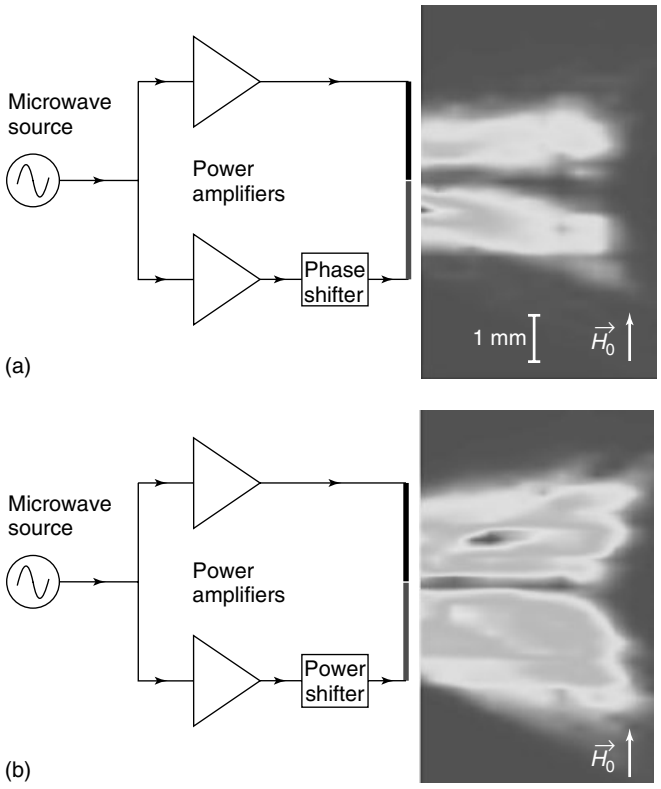

Figure 7. Formation of the dark spatial soliton in a wide YIG sample. Frames (a) and (b) show the normalized two-dimensional distributions of the intensity of spin waves measured in the linear and nonlinear cases, respectively. The orientation of the magnetic field corresponds to the MSSW geometry (Serga, Demokritov and Hillebrands, unpublished).

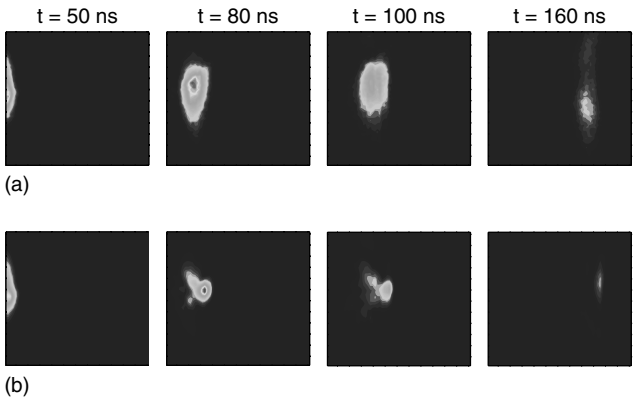

Figure 8. Nonstationary self-focusing of a two-dimensional BVMSW packet. The figure shows the spin-wave intensity distribution in the film created by the propagating pulse of duration 29 ns in a false-color presentation for linear ($P_{\text{in}} = 10$ mW, (a)) and nonlinear ($P_{\text{in}} = 460$ mW, (b)) regimes. Four panels correspond to four successive moments after the moment of a pulse launch from the antenna, as indicated in the figure. Spatio-temporal self focusing is clearly seen for $T = 80$ ns in the nonlinear regime. (Adapted from Bauer *et al*., 1998.)

shown in the false-color presentation. In the linear case, diffraction and dispersion cause a broadening of the initial wave packet both perpendicular to and along the propagation direction, while its amplitude decreases due to dissipation. The propagation of the wave packets in the nonlinear case is quite different. Here the initial high-amplitude wave packet starts to converge, and its amplitude is increasing. Theory predicts that in the two-dimensional case a stable equilibrium between dispersion, diffraction, and nonlinearity is not possible, and nonlinear self-focusing of the wave packets with high-enough initial energy should lead to a wave collapse, that is, all the energy of the packet will be concentrated at one spatial point. In a real medium with dissipation, the complete wave collapse is, of course, avoided, as the wave packet loses its energy. Therefore, in a certain interval of propagation distances, nonlinear collapse is stabilized by dissipation, and a quasistable, strongly localized two-dimensional wave packet, a *spin-wave bullet*, is formed, as predicted in Silberberg (1990).

The effect of bullet formation is further illustrated in Figure 9, where the width of the packet perpendicular to (L_y) and along (L_z) the propagation direction and the peak amplitude of the nonlinear wave packet are shown as functions of the propagation time. For $25\,\text{ns} < t < 40\,\text{ns}$ the packet enters the range of measurement. After the packet enters the measurement region, L_y and L_z rapidly decrease ($40\,\text{ns} < t < 50\,\text{ns}$), while simultaneously the peak intensity P_{peak} increases with a minimum in width and a maximum in intensity at $t = 70$ ns, where a *spin-wave bullet* is formed. For $t > 70$ ns the amplitude of the bullet decays because of the dissipation while L_y and L_z stay constant. At $t > 100$ ns the amplitude is so small that the spatio-temporal focusing effect vanishes and the bullet starts to broaden.

Figure 10 shows the evolution of the spin-wave bullet sizes with increasing input power. It is clear that both in-plane sizes of the bullet decrease with increasing power and become closer to each other. This is a typical behavior of a two-dimensional wave packet approaching the collapse point (see, e.g., Berge, 1998).

5 SELF-GENERATION AND PARAMETRIC EXCITATION OF NONLINEAR SPIN-WAVE MODES

In Section 4 it was shown that spin-wave solitons and bullets are formed from different input microwave signals supplied to the magnetic film from an external source. We would like to stress that the profiles of the formed solitons and bullets are determined by the amplitude of the input signal

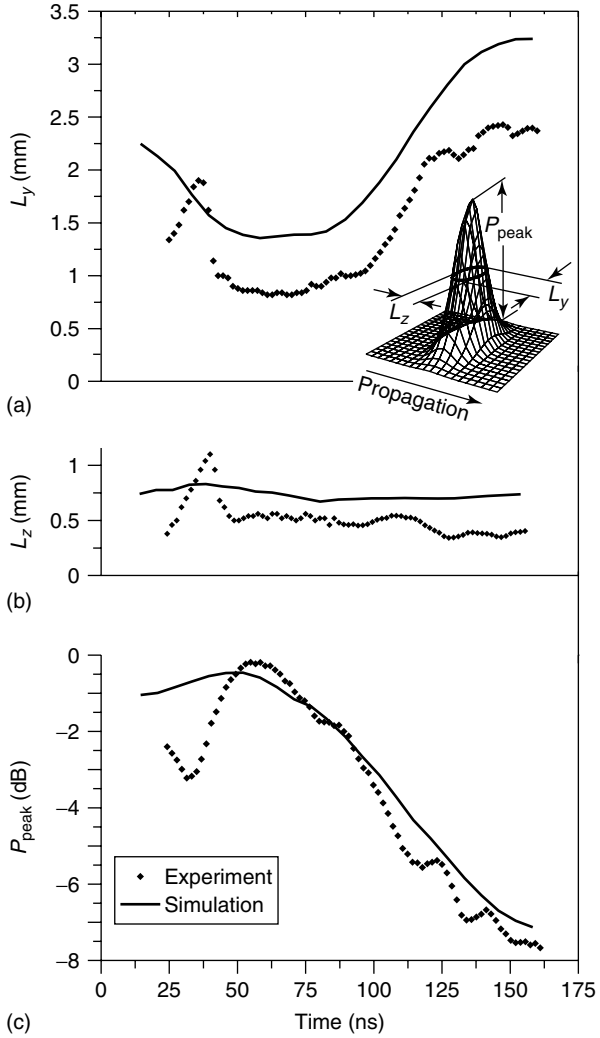

Figure 9. Time evolution of the transverse (L_y) and the longitudinal (L_z) width of the spin-wave packet and the packet amplitude in the nonlinear regime. The symbols show the result of the experiment, the straight line shows the result of a simulation based on the numerical solution of the two-dimensional nonlinear Schrödinger equation. (From Bauer *et al*., 1998.)

and the nonlinear, dispersive, and diffractive parameters of the film and are not closely related to the shape of the excitation signal. In other words, solitons and bullets are the natural intrinsic nonlinear excitation of a nonlinear dispersive medium, and any initial condition of a sufficiently high-amplitude will be reduced to these intrinsic nonlinear excitations in the the process of its evolution in such a medium.

In this section we present an additional experimental confirmation of this fact and demonstrate that spin-wave solitons and bullets can be generated *without any external signal*, directly from the internal noise existing in an active ring. We also demonstrate that spin-wave bullets can be generated

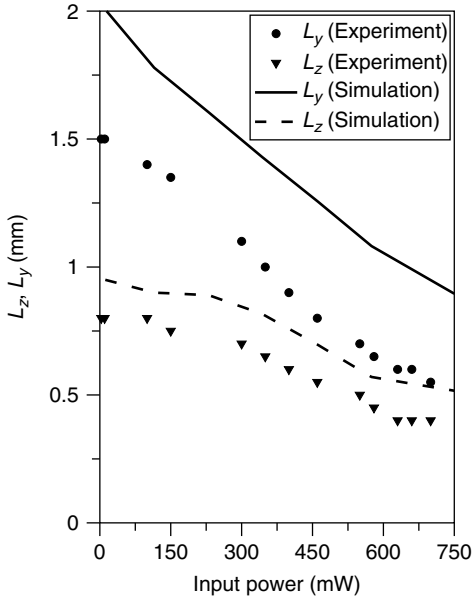

Figure 10. Widths L_y and L_z of the dipolar spin-wave packet of half-maximum power measured at the focal point (point of the maximum peak power) shown as functions of the input power P_{in}. Symbols: experiment, lines: numerical simulation based on the solution of the nonlinear Schrödinger equation. (From Bauer *et al*., 1998.)

and amplified parametrically, if a microwave pumping of a double frequency is supplied to the magnetic film.

The experiments on self-generation of spin-wave bullets in active rings and their amplification by parametric pumping are of particular importance. As mentioned in the preceding text, the two-dimensional spin-wave bullets, formed as a result of the competition between the effects of nonlinearity, dispersion, diffraction, and linear dissipation are, in contrast with one-dimensional solitons, only quasistable and do not survive collisions with other bullets (Büttner *et al*., 1999). Therefore, it is very interesting to compare the properties of solitons and bullets generated from external input pulses (Section 4) with properties of self-generated solitons and bullets (discussed in the following text).

5.1 Self-generation of quasi-one-dimensional solitons

A magnetic ring for soliton self-generation is usually based on a ferromagnetic film connected to an external amplifier that closes the self-generation ring and provides the energy to compensate the losses in the ring. The amplifier operates in the linear regime and has a wide frequency band of amplification. Therefore, the magnetic film is the only source of nonlinear effects in the ring. As discussed in the previous sections, changing the mutual orientation of the applied field

and the wave vector of the spin wave, one can realize the BVMSW or MSSW geometry. BVMSW, having a positive dispersion coefficient D and a negative nonlinear coefficient N, supports the formation of bright solitons. MSSW, with negative D and N, supports the formation of dark solitons. The self-generation of both bright and dark solitons will be discussed in this subsection.

An active ring consisting of just a magnetic film and an amplifier cannot create solitons, since the self-generation in such a system tends to become chaotic. To stabilize the self-generation of spin-wave solitons, the time-gating Kalinikos, Kovshikov and Patton (1998b, 1998a) and frequency-filtering (Kalinikos, Scott and Patton, 2000; Scott, Kalinikos and Patton, 2001) techniques have been proposed.

The first approach takes advantage of a microwave pulse switch, introduced between the film and the amplifier. The switch periodically closes the ring for a certain period, thus, providing conditions for circulation of a microwave packet of a finite width. If the period of switching is equal to a round-trip circulation time, the frequency spectrum of the wide-band signal allowed by the amplifier and the magnetic film only becomes narrower due to survival of the resonant ring harmonics, which can propagate in the ring only in that particular time window. With successive circulation, the amount of these harmonics is decreased owing to the dispersion effect. Finally, at a given signal amplitude the competition between the dispersion and the four-wave nonlinear interaction results in the longitudinal modulational instability, which is responsible for the energy transition from one frequency mode to neighboring resonant modes and the soliton formation.

The self-generation of magnetic bright solitons was first performed using the time-gating technique in Kalinikos, Kovshikov and Patton (1998b). The ring based on the YIG film in the BVMSW geometry (the applied field is parallel to the wave vector) has a round-trip time $T_s = 100\,\text{ns}$. By adjusting the switching period to match T_s and increasing the gain of the amplifier, the self-generation of a series of narrow wave packets was achieved. By measuring the waveform of the packets and the phase profile inside each packet, the self-generation of bright solitons due to nonlinear interaction of the propagating resonant BVMSW modes was confirmed. From the theoretical point of view, this nonlinear process causes soliton formation if the frequency spacing between neighboring resonance modes, Δf, determined by $T_s : \Delta f = 1/T_s = 10\,\text{MHz}$, is smaller than twice the modulational instability frequency f_m of the waves, $\Delta f < 2f_m$. The latter can be estimated from the NSE (28) with $S = 0$ (see also Remoissenet, 1999) : $f_m = U v_g \sqrt{(|N/D|)}/\pi$, where U is, as usual, the dimensionless amplitude of the spin-wave packet envelope. For the experimental conditions given in Kalinikos, Kovshikov and Patton (1998b) $f_m = 43\,\text{MHz}$. Thus, the preceding condition is in fact fulfilled.

As already mentioned, the self-generation of dark spin-wave solitons can be achieved through MSSW geometry (Kalinikos, Kovshikov and Patton, 1998a). Another key difference from the above described case of bright-soliton generation is that the active ring was periodically broken for a short period of time (switched off) by the switcher. One expects that the dark-soliton pulses will be formed from the dips created by the interruption of the wave circulation. By adjusting the experimental conditions, the circulation time and the frequency spacing between the modes were chosen to be the same as for the experiments with the bright solitons: $T_s = 100\,\text{ns}$, $\Delta f = 1/T_s = 10\,\text{MHz}$. In order to obtain the self-generation, the gain of the amplifier was tuned to compensate the losses and to achieve continuous microwave self-generation. Second, the period of the interruption was adjusted to coincide with T_s. Finally, the soliton duration was varied to obtain the waveform packets and the phase profile inside each packet that correspond to dark solitons. The measured phase characteristic demonstrates two 180° jumps of the phase within each dark wave packet. As discussed in the previous section, this is unambiguous evidence that dark solitons were formed as a pair. This experimental observation is corroborated by theory, predicting the generation of a pair of dark solitons from a dip created by the amplitude modulation only (see, e.g., Kivshar and Luther-Davies, 1998).

5.2 Self-generation of spin-wave bullets

In this subsection, the self-generation of spin-wave bullets from thermal noise in a wide YIG film will be discussed. Characteristics of the self-generated bullets will be compared with those of spin-wave bullets formed from coherent input wave packets.

The realization of the active ring structure for bullet self-generation (Serga, Demokritov, Hillebrands and Slavin, 2004) is similar to that for soliton self-generation with time gating (Kalinikos, Kovshikov and Patton, 1998b, 1998a). As the medium for propagation of the wave packets, a relatively wide YIG film (lateral dimensions $26 \times 18\,\text{mm}$, thickness $d = 7\,\mu\text{m}$) is chosen. A standard delay-line structure consisting of two parallel strip-line antennae is placed on the sample. As is usually the case for bullet studies, the lateral dimensions of the sample are intentionally chosen to be much larger than the length of the input antenna and the distance between the antennae, thus creating the conditions for the existence of a two-dimensional (unrestricted in plane) spin-wave process. The applied field $H_0 = 1735\,\text{Oe}$ is applied parallel to the

propagation direction. Thus, the BVMSW geometry is realized. The two antennae are connected through a microwave switch and a high-gain, wide-band microwave amplifier. The signal from the spin-wave packet is collected at Antenna 2 and, after amplification, brought back into the film by Antenna 1, closing the ring. The microwave switch is used as a mode selector, for details see the following text.

As described in the previous sections, the propagation of two-dimensional spin-wave packets is described by the two-dimensional NSE (28): One should, however, consider Γ as the combined relaxation parameter, comprising the damping in the film, losses in the antennae, and the parameter characterizing the gain of the amplifier ($\Gamma_a < 0$). Let us emphasize again that dissipation plays an important role in the formation of spin-wave bullets. Without dissipation the ongoing self-focusing effect would result in a collapse of the self-focusing packet Sulem and Sulem, 1999. However, the presence of even a weak linear dissipation in the medium stops the self-focusing and results in the formation of a quasistable spin-wave bullet (or bullet of BVMSW) (Bauer *et al*., 1998). On the other hand, the dissipation should be small enough to allow for a sufficient time span for developing the nonlinear two-dimensional instability.

The YIG film with the strip-line antennae forms a transmission line for two-dimensional BVMSW wave packets, but no external coherent input signal was applied to the antennae. Instead, the transmission line is connected to a microwave switch and a wide-band microwave amplifier, closing the active ring. This transmission line plays the role of a resonator in a feedback loop of a standard microwave generator (Tuan and Parekh, 1985). The resonance frequencies of a ring are determined by the phase matching condition

$$k_{nz}(\omega)l + \phi = 2\pi n \tag{34}$$

where n is an integer, l is a distance between the antennae, and ϕ is the additional phase shift associated with the electronic part of the ring. The main qualitative difference between the the soliton-generation experiment and the experiment with a wide film is due to the fact that the wide YIG film sample allows for the generation of substantially two-dimensional BVMSW packets that are affected not only by dispersion, but also by diffraction. To achieve the stable generation of a train of spin-wave packets, it is necessary to fulfill several conditions similar to those necessary for soliton generation (Kalinikos, Kovshikov and Patton, 1998b; Scott, Kalinikos and Patton, 2001). The only additional condition is that Δf should be smaller than the doubled instability frequencies corresponding to the both longitudinal and transverse instabilities. Besides, in two dimensions there exists an additional mechanism of self-limitation associated with diffraction and the partial collapse of the strongly self-focused bullet that manifests itself for large, necessary values of the external amplification gain coefficient.

The time-gating technique described in the preceding text was applied to reach a stable generation of two-dimensional nonlinear wave packets. The switch is opened once during each propagation period of the packet over the ring ($T_0 = 190$ ns) for a time (about $\tau_b = 20$ ns), which is larger than the expected duration of the generated bullet. For small amplification gains, the synchronization of the switch is crucial: a variation of the modulation period, T_0, by more than ± 3 ns leads to a breakdown of the self-generation process.

The described experimental microwave setup allows one to generate a train of short (about 20 ns duration) two-dimensional spin-wave packets and to measure their carrier frequency, duration, and propagation time by monitoring the microwave signals at the input and output antennae of the transmission line. To monitor the propagation of the nonlinear wave packets, the space- and time-resolved BLS technique in the forward geometry is used. As described in the previous sections the BLS technique provides the two-dimensional distribution of the spin-wave intensity $I(y, z)$ (proportional to the squared amplitude of the local dynamic magnetization in the film, $|U|^2$) of the propagating wave packet with a spatial resolution of 0.1 mm and a temporal resolution of 2 ns.

Two series of intensity distributions corresponding to two different values of the external amplification gain at different propagating times as indicated are shown in Figure 11. The first series of profiles (Figure 11a) corresponds to a relatively low value of the amplification gain, yielding a peak power of the generated wave packet at the Antenna 1 of about $P_1 = 1$ mW. This power is not sufficient to cause a pronounced transverse nonlinear self-focusing of the generated wave packet, and a spin-wave bullet is not formed. Nevertheless, the propagating wave packet is almost stationary along most of its propagation path. Here the regime of nonlinear compensation of the dispersive and diffractive spread of the wave packet is achieved. Such a propagation regime was not observed for the coherent excitation of BVMSW packets (Bauer *et al*., 1998) where the propagating packet was either self-focusing or exhibited a relatively strong diffraction spreading. The multiple-pass circulation of the packet in the ring is responsible for the observed stabilization of the wave packet size in this weakly nonlinear regime.

The second series of profiles (Figure 11b) corresponds to a relatively high value of the amplification gain yielding a peak power of the generated wave packet at the input antenna of $P_1 = 220$ mW. Here the generated wave packet is clearly self-focusing in both in-plane directions, and a bullet is formed. The experimentally measured parameters of

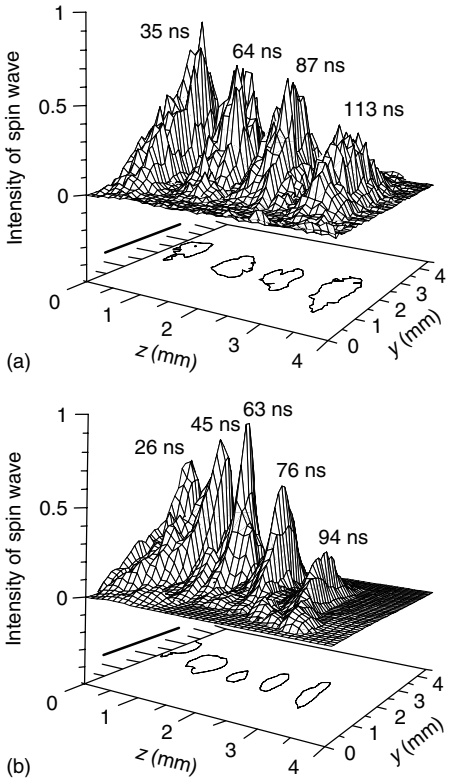

Figure 11. Spatio-temporal self-focusing of two-dimensional self-generated BVMSW packets. The upper part of the panels shows the spin-wave intensity distributions of the packet at successive instants of time, as indicated, after the launch of the packet. The lower part presents the cross sections of the propagating pulse at half-maximum power. Panels (a) and (b) correspond to quasilinear ($P_1 = 1\,\text{mW}$) and strongly nonlinear ($P_1 = 220\,\text{mW}$) spin-wave packets, respectively. The black stripe in the lower part of the panels indicates the position of the antenna. (From Serga, Demokritov, Hillebrands and Slavin, 2004.)

this bullet (width, length, peak power) are very close to the parameters of a BVMSW bullet formed under coherent excitation by an external input microwave pulse. For example, the minimal transverse size of the bullet observed in Bauer *et al*. (1998) is 0.6 mm, while the minimum transverse size of the bullet observed in the self-generation experiment is 0.65 mm, as it show in Figure 12.

5.3 Amplification and parametric generation of spin-wave bullets

The preceding results demonstrate that spin-wave bullets can be self-generated from noise. This proves that, similar to solitons in quasi-one-dimensional systems, wave bullets are intrinsic multidimensional excitations of the nonlinear medium with dispersion, diffraction, and dissipation. It is known (Bagada, Melkov, Serga and Slavin, 1997; Kolodin *et al*., 1998; Melkov *et al*., 2000) that, in a quasi-one-dimensional spin-wave waveguide, parametric interaction of the spin-wave packet with an external pumping may result in a substantial amplification of the initial packet and, in some cases, the parametric generation of a phase-conjugated wave packet propagating in the opposite direction. Therefore, it is important to study parametric interaction of two-dimensional linear and nonlinear spin-wave packets (Serga *et al*., 2005).

Advantages and disadvantages of magnetic films as a medium for nonlinear wave studies, with respect to, for example, optical media, were already discussed in this review. An additional advantage of the magnetic films is the fact that it is possible to realize an effective parametric interaction of a propagating wave packet (having a carrier wave vector $\mathbf{k}$ and frequency ω) with nonstationary (pulsed) electromagnetic pumping (Melkov *et al*., 1999). The conservation laws for such a parametric interaction process have the form

$$\omega + \omega' = \omega_\text{p}, \quad \mathbf{k} + \mathbf{k}' = \mathbf{k}_\text{p} \tag{35}$$

where ω_p, ω, ω' and $\mathbf{k}_\text{p}$, $\mathbf{k}$, $\mathbf{k}'$ are the carrier angular frequencies and carrier wave numbers of the electromagnetic pumping pulse, initial spin-wave packet, and the 'idle' spin-wave packet formed in the interaction process, respectively.

We will see in the following text that from the point of view of parametric amplification the properties of two-dimensional bullets are very similar to those of one-dimensional solitons. In fact, the parametric interaction of a two-dimensional linear spin-wave packet with parametric pumping leads to the formation of pronounced two-dimensional spin-wave bullets from both amplified, forward-propagating and reversed, phase-conjugated packets. These results might be surprising, taking into account the finite width of the studied wave packets in wave vector space and the strong anisotropy of the spin-wave spectrum in a tangentially magnetized magnetic film (see Büttner *et al*., 2000 for details).

The setup for spin-wave amplification experiments is shown in Figure 13. Spin waves were excited in a single-crystal YIG film of 5 μm thickness, $4.1 \times 30\,\text{mm}^2$, using a microstrip antenna of 25 μm width and 2 mm length. The lateral dimensions of the film ($4.1 \times 30\,\text{mm}^2$) were chosen much larger than the characteristic size of a spin-wave bullet (0.2–0.8 mm). The magnetic field H_0 was applied in the film plane along the long side of the film (z axis in Figure 13). As discussed in the preceding text, this geometry corresponds to the excitation of BVMSW. The input BVMSW packets were excited by rectangular electromagnetic pulses of duration 30 ns supplied by a rectangular dielectric resonator with an opening in the middle. The film went through the opening, and the resonator

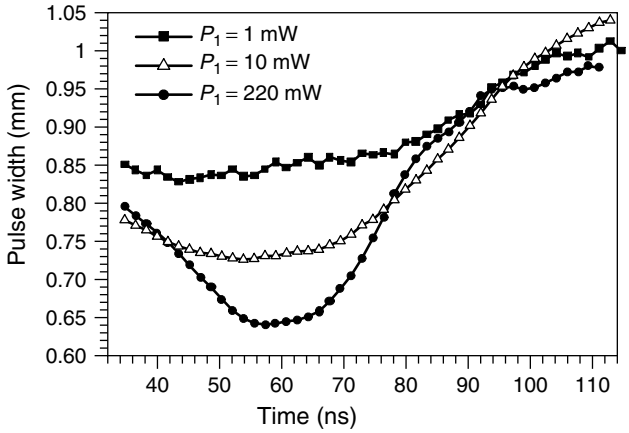

Figure 12. Evolution of the transverse width of the spin-wave packet, L_y, with propagation time t at different amplification gains illustrating the bullet self-generation. (From Serga, Demokritov, Hillebrands and Slavin, 2004.)

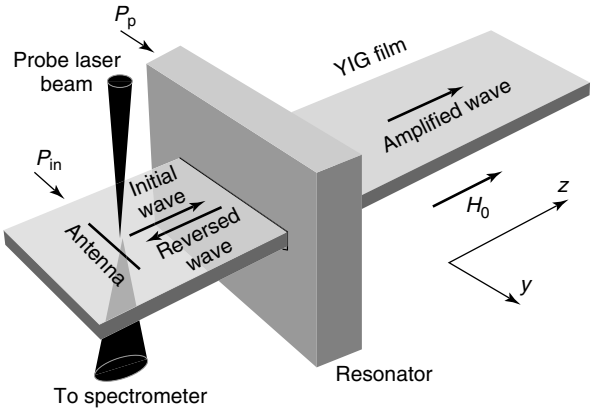

Figure 13. Experimental setup for parametric amplification of spin-wave bullets. Leads feeding the antenna and the resonator are not shown. (From Serga, Demokritov, Hillebrands and Slavin, 2004.)

was placed at a distance of 2.5 mm from the antenna (see Figure 13). The pumping microwave field was parallel to the applied magnetic field. The pumping pulse was supplied to the dielectric resonator at the time when the propagating wave packet was close to the center of the resonator. As a result of the parametric interaction, the forward-propagating amplified and the backward-propagating amplified, reversed, and phase-conjugated spin-wave packets were formed.

A series of maps, showing the two-dimensional distribution of the spin-wave intensities $I(z, y)$ is shown in Figure 14. Figure 14(a) demonstrates the evolution of a two-dimensional wave packet of duration $\tau = 30$ ns after it has been launched from the antenna and until it reaches the pumping area. As seen in Figure 14, the packet spreads along the transverse (y) direction during propagation because of the strong diffraction in the film. The spreading of the packet is

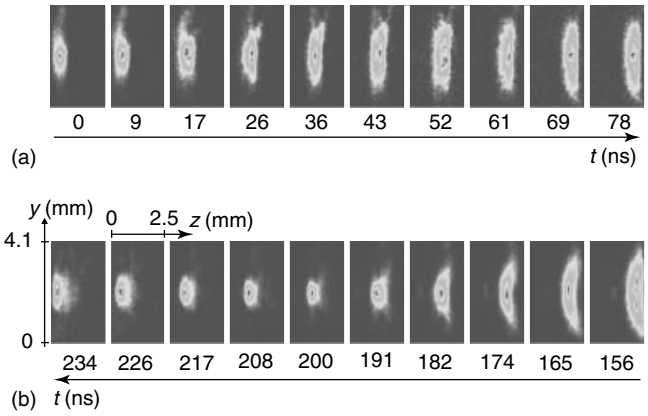

Figure 14. The spatial distributions of the spin-wave intensity captured at successive moments of time both for incident (a) and for reversed (b) spin-wave packets. $P_{in} = 146$ mW, measured by means of time- and space-resolved BLS. (From Serga, Demokritov, Hillebrands and Slavin, 2004.)

illustrated in Figure 15(a), showing its width versus the propagation distance. The three curves correspond to different values of the input power.

Figure 14(b) demonstrates the propagation and evolution of the reversed ($\mathbf{k}' = -\mathbf{k}$) wave packet formed as a result of the parametric interaction. It is clear that the reversed packet experiences a strong nonlinear two-dimensional self-focusing, which leads to the formation of a pronounced spin-wave bullet (see frames corresponding to 191, 200, and 208 ns). The evolution of the bullet width L_y in this reverse propagation is shown by curve (2) in Figure 15(c).

One can see from Figure 14 that the reversed packet undergoes a wave-front reversal (phase conjugation). In fact, frames corresponding to 69 and 78 ns illustrate that the wave packet has a concave front. On the other hand, the reversed packet (165 and 174 ns) has a convex front. Note the reversal of the propagation direction between Figure 14(a) and (b). As seen from Figure 15(d) the front-reversal process due to phase conjugation is more profound for linear, low-power input packet.

Figure 15(b) demonstrates that spin-wave bullet formation also takes place in the forward-propagating amplified wave packet after its interaction with the pumping. However, the bullet formation in the forward-propagating spin-wave packet takes place at a larger distance from the pumping resonator than in the case of the reversed wave packet (1.5 mm compared to 1.0 mm) and the width of the formed bullet L_y is larger (0.3–0.4 mm compared to 0.22–0.25 mm). These differences are connected with the fact that two mechanisms contribute to bullet formation from the reversed packet. The first mechanism is the nonlinear self-focusing effect, characteristic for the four-wave nonlinearity in a focusing medium and responsible for bullet self-formation. The second

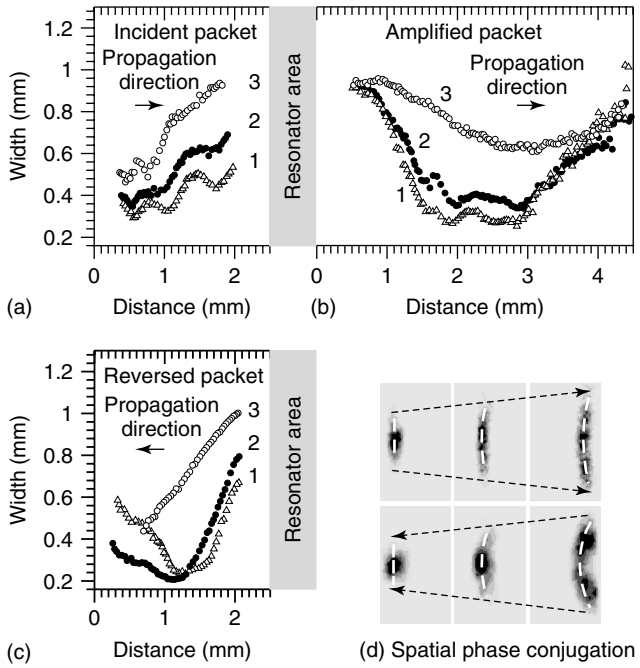

Figure 15. Frames (a) and (b) demonstrate the evolution of the transverse width L_y of the spin-wave packet before its interaction with pumping and after its parametric amplification, respectively. Frame (c) shows the evolution of the width, L_y, of the reversed spin-wave packet. Curves (1), (2), and (3) correspond to the input powers P_{in} of 226 mW (strongly nonlinear), 146 mW (nonlinear), and 22 mW (linear), respectively. Frame (d) illustrates the two-dimensional phase conjugation and front-reversal process of a linear (22 mW) wave packet due to interaction with the pumping. (From Serga, Demokritov, Hillebrands and Slavin, 2004.)

mechanism is the linear self-focusing effect, characteristic for the process of two-dimensional phase conjugation and wave-front reversal (Zeldovich, Pilipetskii and Shkunov, 1985). This linear focusing effect can be observed separately if the power of the input signal is low enough (see curve (3) for $P_{\text{in}} = 22$ mW in Figure 15c). It is clear that curve (3) demonstrating the linear focusing effect has a substantially smaller slope than curves (1) and (2), demonstrating the formation of nonlinear bullets. Thus, owing to the combined action of linear and nonlinear effects the focusing and compression of the reversed wave packet is more pronounced than that of the forward-propagating amplified wave packet, although the amplitude of the forward packet is larger.

As discussed in the previous sections, for description of the parametric interaction of a two-dimensional spin-wave packet with pumping, one needs to use a system of two coupled NLS equations for the envelopes of forward-propagating and reversed wave packets (see equations (30) and (31)). The above described processes of spin-wave packet propagation and interaction with parametric pumping were modeled numerically using those equations. It was assumed that the input linear wave packet has the following profile:

$$U_1^2(y, z, t = 0) = U_0^2 \cosh^{-2}\left[\frac{2(z - z_0)}{L_{z0}}\right] \cos^2\left[\frac{\pi(y - y_0)}{L_{y0}}\right] \tag{36}$$

where L_{y0} and L_{z0} were the same as in the experiment (Figure 15). The initial amplitude of the input pulse U_0 was chosen to be smaller than the minimum threshold of four-wave nonlinearity $U_{\text{th}} = \sqrt{\omega_r / N}$ (see Slavin and Benner, 2003) to guarantee the linear regime of the input wave packet propagation before interaction with pumping. The pumping field of $h_{\text{p}} = 60$ Oe was assumed to be uniform in space and was acting for 40 ns starting at the time when the maximum of the input propagating pulse was at a distance of 3 mm from the antenna.

The two-dimensional distributions of the normalized spin-wave intensity $|U(y, z)/U_0|^2$ calculated for three different times (before, immediately after, and 30 ns after the end of the pumping pulse) are shown in Figure 16(a–c), correspondingly. The numerical model correctly reproduces all the qualitative features of the observed parametric interaction process: Immediately after the interaction with pumping, two counterpropagating wave packets (Figure 16b) are formed from the initial linear wave packet (Figure 16a). This is followed by the formation of bullets in both forward-propagating and reversed wave packets (Figure 16c). Note that the numerical results corroborate the experimental observation that self-focusing of the reversed spin-wave bullet is stronger than self-focusing of the forward-propagating packet.

Thus, the results presented in this section confirm the fact that spin-wave bullets are two-dimensional intrinsic excitations of a nonlinear diffractive and dispersive medium with dissipation. Bullets demonstrate their self-generation from the thermal noise. Besides they can be generated parametrically in magnetic films from linear input wave packets. They are formed from both the forward-propagating and reversed wave packets, and their properties are similar to the properties of wave bullets generated by an external coherent microwave pulse, described in the previous section.

5.4 Self-generation of symmetry-breaking nonlinear spin-wave excitations

In the previous section, solitons and bullets self-generated in active rings have been discussed. The phase matching condition equation (34) was considered as a fundamental condition for the existence of an excitation in a ring. For linear excitations that fill the entire ring, the phase matching condition is the consequence of the unambiguous definition of the wave phase in each particular point of the ring.

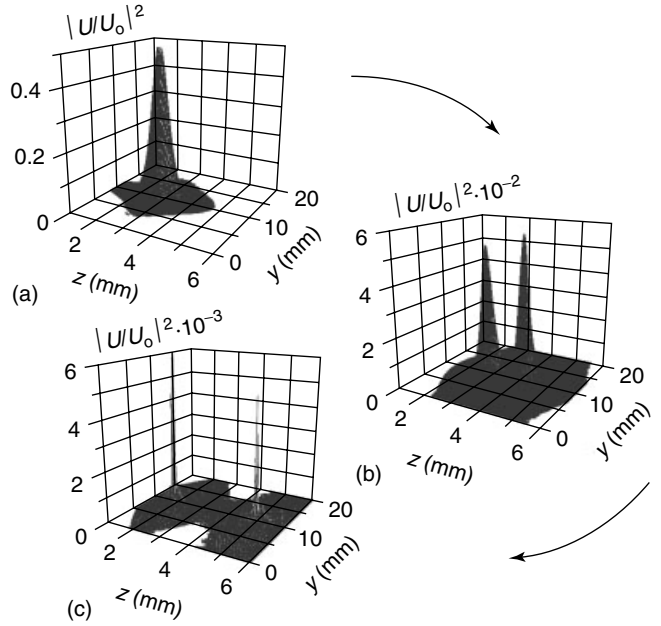

Figure 16. Numerical modeling of bullet formation by parametrically amplified and conjugated spin-wave packets. Frame (a) shows the initial spin-wave packet. Frame (b) shows the amplified and conjugated spin-wave packets just after their parametric interaction with an electromagnetic pumping. In frame (c) a pronounced two-dimensional compression of both spin-wave packets is seen. (From Serga, Demokritov, Hillebrands and Slavin, 2004.)

For nonlinear, localized excitations, the phase matching condition can be broken, since at a given instant of time the phase of such an excitation is defined in the interval of its localization. Thus, the phase matching should be considered as an additional symmetry, which can be broken for some excitations. Although the preceding considerations seem to be very simple, the symmetry-breaking spin-wave excitations have been discovered theoretically (Carr, Clark and Reinhardt, 2000) and experimentally (Demokritov *et al*., 2003) only very recently.

In their pioneering work, Carr, Clark and Reinhardt (2000) have analyzed the solutions of a nonlinear wave equation with attractive nonlinearity in a box with infinitely high walls and, equivalently, in a ring. It was found that the general solution can be described by multisoliton modes, and the modes can be classified by the number of solitons comprising a particular mode. There are, however, two classes of such modes if one takes into account the symmetry connected with the phases of the particular solitons building those modes. The first class covers the nonlinear modes having one-to-one correspondence with the linear solutions. In fact, there is a direct connection between the mode number of a linear mode and its mirror symmetry with respect to the center of the box: odd and even modes are symmetric and antisymmetric, respectively. The standing wave with two half wavelengths fitting the box is antisymmetric with respect to the box center. This linear mode corresponds to a two-soliton nonlinear mode. The nonlinear mode belonging to the first class is also antisymmetric, that is, the phases of the two solitons are opposite. The second class covers the nonlinear modes, having no one-to-one correspondence to linear modes. These modes are called *symmetry-breaking modes*. For example, contrary to the discussed linear mode, there exists a nonlinear mode consisting of two solitons with the same phase, which is symmetric with respect to the box center.

The preceding approach can be adapted for envelope solitons. One needs, however, to define the phase of soliton-like wave packets. In fact, let us consider a one-dimensional spin-wave packet propagating in an unconfined magnetic medium. The dynamic magnetization $m(x,t)$ describing the packet can be written as $m(x,t) = f(x - v_g t)\exp(i\varphi(x,t))$ with $\varphi(x,t) = 2\pi\nu t - kx - \varphi_a(x)$, where f is the envelope function and $\varphi_a(x)$ is an additional phase chirp due to nonlinear effects. One can characterize a propagating soliton by its phase as a whole, for example, at the maximum point of the envelope function: $\varphi(t) = \varphi(x,t)$ for $x = v_g t$. Since the group velocity of a wave can differ from the phase velocity (this is usually the case for spin waves) the defined phase is time dependent, that is, it changes constantly while the soliton is propagating.

As a model system for experimental study of the symmetry-breaking modes, an active nonlinear ring based on spin-wave propagation in a narrow magnetic YIG film waveguide was constructed (see Figure 17). A magnetic field of 1870 Oe is applied parallel to the direction of the spin-wave propagation, realizing the BVMSW geometry corresponding to the waves with an attractive nonlinearity. Therefore, one can expect that the nonlinear eigenmode spectrum of the ring consists of sets of soliton-like wave packets (Carr, Clark and Reinhardt, 2000). A YIG film of 7 μm thickness, 1.5-mm width, and 40-mm length, forms a waveguide. Two short-circuited microstrip antennae for the excitation and detection of spin waves are attached to the film at a distance $l = 8$ mm apart from each other. A linear electronic amplifier, which connects the output and input antennae, compensates the damping of the waves and maintains unidirectionality of the ring, its gain is chosen in such a way that the system is below the self-generation threshold if the phase-sensitive amplifier discussed in the following text is disabled. In the linear regime, that is, for low gains, the ring shows a series of resonant eigenmodes with frequencies in the interval 7.25–7.30 GHz, spaced by $\Delta\nu = 3.2$ MHz, and wave vectors $k = 100$–$150\,\mathrm{cm}^{-1}$. The exact frequencies of the modes are determined by the phase matching condition: $kl = 2\pi n$ with integer n. The time for a full circuit around the ring is $T_0 = 310$ ns.

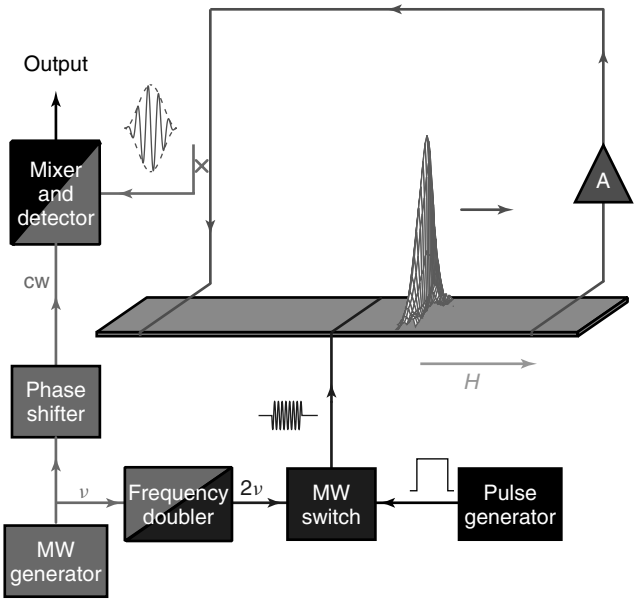

Figure 17. Schematic layout of the active ring for observation of nonlinear symmetry-breaking modes. The ring consists of the film, two antennae, and the linear microwave amplifier (A). Nonlinear modes of the ring are filtered using parametric pumping at double frequency at the position of the center antenna (as described in the text). The ring and the microwave components working at frequency ν are shown in red. The components working at frequency 2ν are shown in blue. The directional coupler, the phase shifter, and the mixer with detector are used for phase-sensitive detection of the modes by mixing them with a continuous wave (CW) reference signal. (From Demokritov *et al*., 2003.)

For the investigation of nonlinear eigenmodes of the ring, it is necessary to have a selection mechanism to individually address each eigenmode. One widely employed approach is the use of a critical threshold mechanism: only the mode with the largest amplification gain is generated at the expense of all others (Agrawal, 1994). Another approach is the use of phase-selective amplifiers, which allows only the modes having a well-defined preset phase at the location of the amplifier in the ring to exist in the active ring. To achieve phase-selective amplification, the technique of parametric parallel pumping is used. A sufficiently strong microwave field with frequency 2ν can parametrically amplify a spin-wave packet of frequency ν (Bagada, Melkov, Serga and Slavin, 1997; Kolodin *et al*., 1998). The pumping microwave field is sent to a microstrip resonator attached to the film centered between the two antennae as shown in Figure 17. For a narrow pumping area, that is, if $k\delta \ll 2\pi$, where δ is the width of the pumping area, the amplification gain is phase sensitive (Melkov *et al*., 2001). Figure 18 illustrates the phase dependence of such an amplification: waves having phases $\pi/4 + n\pi$ with respect to the pumping field are amplified most efficiently. Using this amplification, one

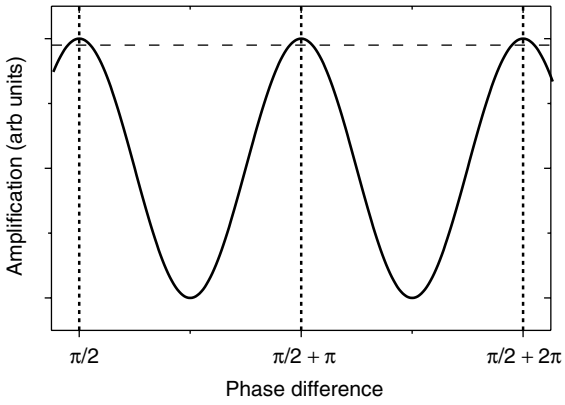

Figure 18. Amplification coefficient of the parametric amplifier as a function of the difference between the phase of the spin wave and the pumping field.

needs to compensate the losses in the ring as shown in the figure by the horizontal dash line. Only the modes having their phases close to the maxima of the amplification coefficient will survive in the ring.

In the experiment, the amplification of the electronic amplifier is chosen in such a way that no nonlinear modes are observed without parametric pumping. Then, the pumping is applied as a single microwave pulse with the duration $\tau = 15{-}35$ ns. Such a pumping results in the creation of a single soliton-shaped microwave packet circulating in the ring. Figure 19 showing the signal detected by the output antenna illustrates the development of the packet in the ring. The packet circulates in the ring with the period T_0, and its amplitude is slowly decreasing. As seen in Figure 19,

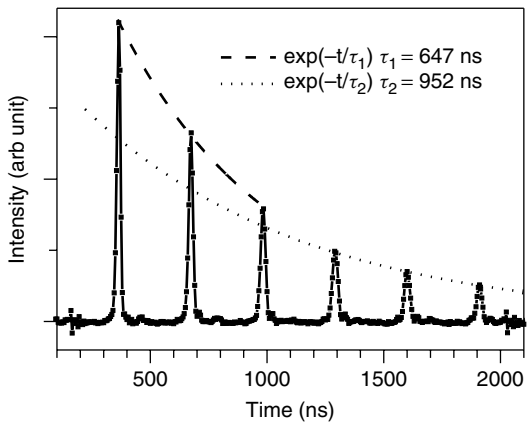

Figure 19. Waveform of a nonlinear wave packet created in the ring by a single pumping pulse. The decay of the packet intensity is due to damping in the magnetic film, which is partially compensated by the electronic amplifier. The soliton nature of the packet is confirmed by a smaller decay time (τ_1) of the packet amplitude with respect to that (τ_2) of the linear packets. (Demokritov, Serga and Hillebrands, unpublished.)

the decay of the amplitude during the first rounds is much faster than that for the small amplitude, confirming the soliton nature of the pulse. More exact analysis of Figure 19 also shows that the wave packet increases its width while decreasing its intensity as one expects from the soliton theory (Remoissenet, 1999). Thus, based on the preceding discussion, one can conclude that the created wave packet has soliton properties, at least during the first two rotations over the ring when the intensity of the wave packet is large enough. By applying pumping pulses periodically, one can keep the intensity of the packet in the soliton regime constant.

Figure 20 illustrates the waveforms of the detected eigenmodes with the curve (a) showing the waveform of the pumping field as a reference. By sweeping the frequency in a narrow interval of 20 MHz, several nonlinear eigenmodes are subsequently observed. Without phase analysis, all modes detected at different frequencies are undistinguishable and consist of a series of soliton-like pulses spaced in time by the time interval T_0 (curve b). The phase-detection technique reveals, however, two different types of single-soliton modes. First, there are soliton modes that keep their phase after traveling around the ring, as demonstrated by the curve (c). They are labeled 'N' for 'normal solitons', since they do not break the phase matching condition. Second, there are soliton modes with the phase difference of π between the two subsequent detections of the soliton, as demonstrated by the curve (d). These modes need to travel twice about the ring to meet the initial phase condition. Since they remind one of the well-known Möbius strip, they are labeled 'M' for 'Möbius mode'. The waveform of the M mode can be reversed by changing the continuous wave (CW) reference phase as shown by the curve (e). Both normal and Möbius modes are observed alternatively at different carrier frequencies, ν_N and ν_M, with $\nu_N - \nu_M = 1.6\,\text{MHz}$, that is, $\Delta\nu/2$. The physical nature of the N modes is easily understood: a soliton is propagating about the ring with the closed-loop phase shift of $2\pi n$. Each of these normal soliton modes has a counterpart among the linear excitations. In a Möbius mode the soliton acquires a phase shift of $2\pi(n + 1/2)$ per loop, that is it breaks the phase matching condition. For this reason it cannot have a counterpart among the linear modes.

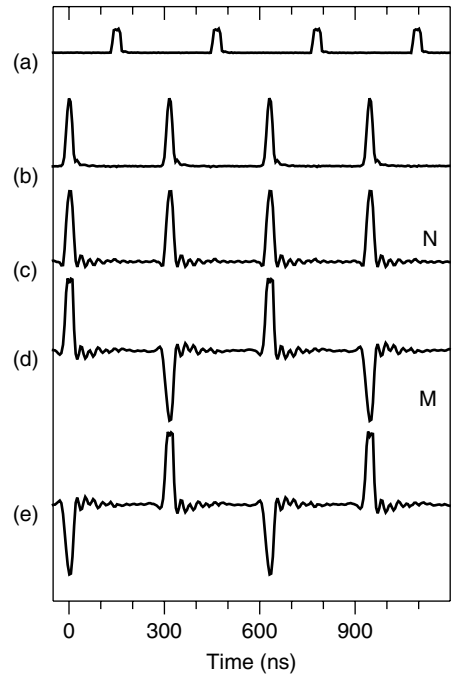

Figure 20. Waveforms of the one-soliton modes observed in the ring, $T_p = T_0$; (a) waveform of the pumping field, (b) waveform of a nonlinear mode obtained without phase-sensitive detection, (c) and (d) waveforms of normal and Möbius modes detected using phase sensitive detection, respectively, (e) is the same as (d) with the phase of the reference wave shifted by π. (From Demokritov *et al*., 2003.)

The possible existence of Möbius modes, that is, eigenmodes with a phase shift per loop that is different from an integer multiple of 2π has not been considered by Carr, Clark and Reinhardt (2000). Instead, soliton modes comprising several solitons and the mutual phase relations between those solitons are discussed in Carr, Clark and Reinhardt (2000). Eigenmodes consisting of several soliton-like wave packets can be also found in the experiment. This happens if the repetition period of the pumping pulses, T_p is a fraction of T_0. Figures 21 and 22 illustrate the cases $T_p = T_0/2$ and $T_p = T_0/3$, that is, a mode with two/three equally spaced solitons rotating in the loop. Similar to Figure 20, the top curves demonstrate the pumping waveforms, while the other curves are the measured waveforms of the different modes detected by phase analysis. The numbers adjacent to the curves in Figure 21 numerate the corresponding values of the mode frequencies in units of GHz. The two vertical dashed lines indicate the time interval T_0, which each of the solitons needs to complete the loop. For $T_p = T_0/2$ one observes two normal modes and one Möbius mode. Although the two normal modes are not completely degenerate, their frequency separation is much smaller than $\delta\nu$. The difference between the Möbius mode and both the normal modes, $\nu_N - \nu_M$, is close to $\Delta\nu/2 = 1.6\,\text{MHz}$. By sweeping the frequency, alternating normal and Möbius modes appear, as demonstrated by the curve at 7.2687 GHz, which, with respect to the observed signal, is identical to the curve at 7.2855 GHz, but separated from the latter in frequency by the amount $\Delta\nu$. As seen in Figure 22, two normal modes and two Möbius modes are found for $T_p = T_0/3$. Again, alternating normal and Möbius modes are observed with the same frequency interval. To summarize these findings: The phase sensitivity of the parametric pumping process constitutes a phase selection rule for the allowed eigenmodes of the ring. The modes with

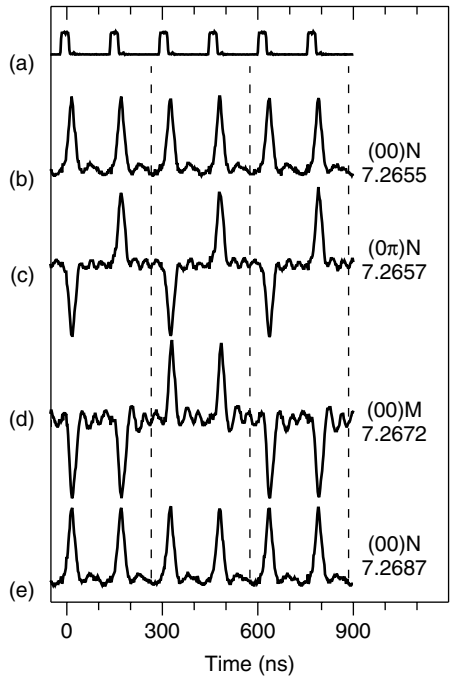

Figure 21. Waveforms of the two-soliton modes observed in the ring, $T_p = T_0/2$; (a) waveform of the pumping field, (b), (c), (d), and (e) waveforms of different modes with the numbers being the frequency of each mode in units of GHz (from Demokritov *et al*., 2003). (The mode nomenclature is explained in the text).

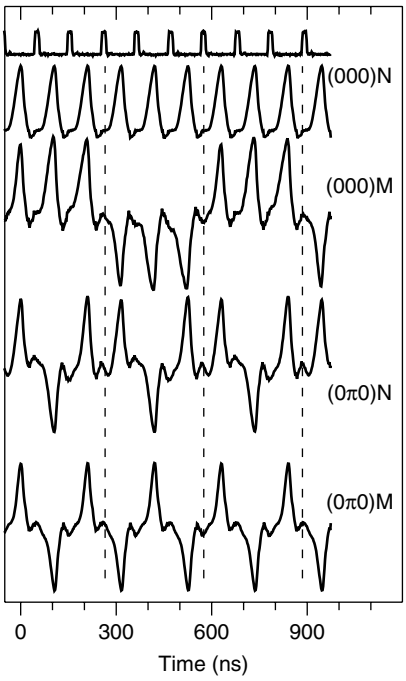

Figure 22. Waveforms of the three-soliton modes observed in the ring, $T_p = T_0/3$; waveforms of the pumping field and of the observed modes (from Demokritov *et al*., 2003). (The mode nomenclature is explained in the text).

phase shifts per loop of $2\pi n$ and $\pi + 2\pi n$ can survive in the ring.

In order to classify the multisoliton modes found, the soliton phase relative to the phase of an arbitrary chosen soliton, which we set to zero without loss of generality, is quoted. A soliton having the same phase will be indicated by '0', one with a phase difference of π, by 'π'. The suffixes 'N' and 'M' for normal and Möbius modes are added. For $T_p = T_0$ only two one-soliton modes exist, a normal mode, (0)N, and a Möbius mode, (0)M. In the case of two-soliton modes one finds, using combinatorics, four possible combinations: (00)N, (0π)N, (00)M, and (0π)M. However, the last two modes are physically identical, as they can be transferred into each other by shifting the origin of the timescale by $T_0/2$. According to Carr, Clark and Reinhardt (2000) some of the N eigenmodes are expected to have broken symmetry, since they cannot evolve monotonously from their linear counterparts. It is found that the (00)N mode has a linear counterpart, while the ($0\,\pi$)N mode has the predicted broken symmetry. A similar analysis for $T_p = T_0/3$ predicts the existence of four nonequivalent three-soliton modes: (000)N, ($0\pi 0$)N, (000)M, and ($0\pi 0$)M. All these modes are observed in the experiment, as demonstrated in Figure 22.

As a conclusion to this section, one should point out that the observation of the symmetry-breaking nonlinear modes is of fundamental importance for nonlinear physics. It opens a new way to create nonlinear objects with new symmetry properties forbidden for linear excitations. As a generalization of the observed Möbius solitons, one can imagine fractal solitons, acquiring the phase shift per loop of $\pi/3$, $2\pi/3$, and so on.

6 STANDING SPIN-WAVE BULLET GENERATED BY SPIN-POLARIZED CURRENT

In the previous sections we discussed nonlinear dynamics of one- and two-dimensional spin-wave packets that were linearly excited by a microwave input signal or self-generated in an active ring containing ferrite (YIG) film, or parametrically excited by the microwave field of double-frequency pumping.

In this section we demonstrate that the nonlinear properties of two-dimensional spin-wave bullets play a critically important role in the process of spin-wave excitation by a spin torque created by spin-polarized current traversing a thin in-plane magnetized film made of a ferromagnetic metal.

It was theoretically predicted (Slonczewski, 1996; Berger, 1996) and experimentally observed (Tsoi *et al*., 1998; Rippard, Pufall and Silva, 2003; Rippard *et al*., 2004a,b; Kiselev

et al., 2003) that spin-polarized current passing through a thin magnetic film ('free' layer of a magnetic layered structure) can excite microwave magnetization oscillations in this layer. A *spatially uniform nonlinear* theory explaining many experimentally observed features of this phenomenon was developed in a series of theoretical papers (Slonczewski, 1999; Rezende, de Aguiar and Azevedo, 2005; Slavin and Kabos, 2005; Bertotti *et al*., 2005). Although it was clear from experiments that the excitation of microwave oscillations has a threshold character (i.e., it is observed for sufficiently large currents $I > I_{\rm th}$), and that the frequency of the excited spin-wave mode is close to the natural FMR frequency of the system, the exact nature of the dynamic mode excited at the threshold in a magnetic nanocontact was not determined in Slonczewski (1999), Rezende, de Aguiar and Azevedo (2005), Slavin and Kabos (2005), Bertotti *et al*. (2005). This is especially true in the case of current-driven nanocontacts (Tsoi *et al*., 1998; Rippard, Pufall and Silva, 2003; Rippard *et al*., 2004a,b) where magnetic layers are not bound in plane, and there are no lateral reflective boundaries that could create an effective magnetic resonator (like in the case of nanopillars, Kiselev *et al*. (2004)).

The most complete theoretical analysis of the nature of the spin-wave eigenmode excited by spin-polarized current in a nanocontact geometry was performed by Slonczewski (1999). He developed a *spatially nonuniform linear* theory of spin-wave excitations in a nanocontact, where the 'free' ferromagnetic layer is infinite in plane, while the spin-polarized current traversing this layer has a finite cross section, $S = \pi R_{\rm c}^2$, where $R_{\rm c}$ is the contact radius. Considering a perpendicularly magnetized nanocontact and using a linearized Landau–Lifshitz equation, Slonczewski was able to show that in the *linear* case the lowest threshold of excitation by spin-polarized current is achieved for an exchange-dominated cylindrical spin-wave mode having frequency determined by equation (24) with wave number $k = k_0 \simeq 1.2/R_{\rm c}$ and traveling out of the region of current localization Slonczewski, 1999. Here ω_0 is the FMR frequency and D is the spin-wave dispersion coefficient determined by the exchange interaction and dependent on the direction of the bias magnetic field (see equation (26)).

It was also shown that the threshold current $I_{\rm th}$ in such a geometry consists of two additive terms: the first one arises from the radiative loss of energy carried by the propagating spin wave out of the region of current localization, while the second one is caused by the usual energy dissipation in the current-carrying region:

$$I_{\rm th}^{\rm lin} \simeq 1.86 \frac{D}{\sigma R_{\rm c}^2} + \frac{\Gamma(H)}{\sigma} \qquad (37)$$

Here, the spin-polarization efficiency σ is given by equation (6) and $\Gamma(H)$ is the spin-wave damping, dependent on the bias magnetic field H. We note that the preceding results of the linear analysis are valid for an arbitrary magnetization orientation if one uses the appropriate expressions for the frequency ω_0 and spin-wave dispersion coefficient D.

For a typical nanocontact of radius $R_{\rm c} \sim 20$–30 nm, the radiative losses are about 1 order of magnitude larger than the direct energy dissipation and should make the main contribution to the threshold current. This result, however, contradicts experimental observations (see, e.g., Rippard, Pufall and Silva, 2003): the experimentally measured magnitude of the threshold current in an in-plane magnetized nanocontact is much smaller than the value predicted by equation (37), although the dependence of this current on the magnetic field H is satisfactory described by this equation.

In this section, following Slavin and Tiberkevich (2005), it is shown that in an in-plane magnetized magnetic film the competition between the nonlinearity and exchange-related dispersion leads to the formation of a stationary two-dimensional self-localized nonpropagating spin-wave mode – standing spin-wave bullet. This bullet is very similar in its structure to the propagating self-localized spin-wave bullets observed on YIG films and discussed in detail in the previous sections of this chapter. The frequency of this standing spin-wave 'bullet' is shifted *below* the spectrum of linear spin waves by the nonlinearity and, therefore, this nonlinear mode has an evanescent character with vanishing radiative losses, which leads to a substantial decrease of its threshold current $I_{\rm th}$ in comparison with the linear propagating mode (equation (37)).

It was demonstrated in Section 2 that the equation describing the amplitude $b(r, t)$ of a spin-wave mode excited by spin-polarized current I in a free layer on an in-plane magnetized magnetic nanocontact can be written in the form of equation (25), where $\omega_0 \equiv \sqrt{\omega_H(\omega_H + \omega_M)}$ is the linear FMR frequency ($\omega_H \equiv \gamma H$, $\omega_M \equiv 4\pi\gamma M_0$, and γ is the gyromagnetic ratio), $D = (2\gamma A/M_0)(\omega_H + \omega_M/2)/\omega_0$ is the dispersion coefficient for spin waves (A is the exchange stiffness), Δ is the two-dimensional Laplace operator in the film plane, $N = -\omega_H\omega_M(\omega_H + \omega_M/4)/\omega_0(\omega_H + \omega_M/2)$ is the coefficient describing nonlinear frequency shift, and $\Gamma \equiv \alpha_{\rm G}(\omega_H + \omega_M/2)$ is the spin-wave damping rate ($\alpha_{\rm G}$ is the dimensionless Gilbert damping parameter). The dimensionless function $f(x)$ describes the spatial distribution of the spin-polarized current. The dimensionless spin-wave amplitude b is connected with the z component of the magnetization by the equation $|b|^2 = (M_0 - M_z)/2M_0$. Equation (25) differs from equation (9) in Slonczewski (1999) (which resulted in the solution (37)) by the presence of two additional nonlinear terms: the term containing the coefficient N and describing a nonlinear frequency shift of

the excited mode, and the last term describing the current-induced positive nonlinear damping that stops the increase of the amplitude of the excited mode at relatively large currents. Also, since the equation (25) was obtained as a Taylor expansion, it is literally correct only for sufficiently small spin-wave amplitudes $|b| < 1$.

Without damping and current terms ($\Gamma = 0$, $I = 0$) equation (25) coincides with the well-known $(2 + 1)$-dimensional NSE (see Akhmediev and Ankiewicz (1997) and equation (28)) written in a cylindrical coordinate system where dispersion and diffraction coefficients are equal to each other, $S = D$, because of the axially symmetric character of the exchange-dominated spin-wave spectrum of a very thin magnetic 'free' layer. In the considered case of an in-plane magnetized film, the nonlinear coefficient N is negative, and the nonlinearity and dispersion satisfy the well-known Lighthill criterion $ND < 0$ (Lighthill, 1965), and the NSE has a nonlinear self-localized radially symmetric standing solitonic solution (or the solution in the form of a *standing spin-wave bullet*)

$$b(t, r) = B_0 \psi(r/\ell) e^{-i\omega t} \tag{38}$$

where the dimensionless function $\psi(x)$, having maximum value of 2.2 at $x = 0$, describes the profile of the bullet. This function is the localized solution of the equation

$$\psi'' + \frac{1}{x}\psi' + \psi^3 - \psi = 0 \tag{39}$$

which has to be found numerically (see e.g., Chiao, Garmire and Townes, 1964; Silberberg, 1990).

In equation (38), B_0, ℓ, and ω are the characteristic amplitude, characteristic size, and frequency of the bullet, respectively. Among these three parameters only one is independent. Taking the amplitude B_0 as an independent parameter, we can express the two other parameters as

$$\omega = \omega_0 + N B_0^2, \quad \ell = \frac{\sqrt{|D/N|}}{B_0} \tag{40}$$

We would like to stress that the frequency of the spin-wave bullet lies *below* the linear frequency ω_0 of the FMR (see equation (40), and note that $N < 0$), that is, outside the spectrum of linear spin waves. This is the main reason for the self-localization of the spin-wave bullet, as the effective wave number of the spin-wave mode with the frequency given in equation (40) is purely imaginary. It also follows from equation (38) and the Taylor expansion condition $|b| < 1$, that the maximum magnitude of B_0 for which the perturbative approach is still correct is $B_0 = 0.46$.

It is well known (Akhmediev and Ankiewicz, 1997) that the bulletlike solutions of $(2 + 1)$-dimensional NSE are unstable with respect to the small perturbations: the wave packets having the bullet shape (38) but amplitudes smaller than B_0 decay because of the dispersion spreading, while the wave packets having amplitudes higher than B_0 collapse because of the nonlinearity. At the same time, equation (25) with both Gilbert dissipation Γ and current I is a two-dimensional analog of a Ginzburg–Landau equation that is known to have stable localized solutions Aranson and Kramer, 2002. In the particular case of an in-plane magnetized nanocontact, the current-induced terms in equation (25) might stabilize spin-wave bullets and might prevent them from both dispersion spreading and nonlinear collapse. One can assume that for a small damping rate Γ and current I the full nonconservative equation (25) can have a bulletlike solution, only slightly different from the exact solution, equation (38), of the conservative NSE equation.

In was shown in Slavin and Tiberkevich (2005) that equation (25), indeed, has a *stable* bullet solution if the bullet amplitude B_0 satisfies the following equation

$$\frac{\sigma I}{\Gamma} = \frac{1.86}{\eta_2(q B_0) - B_0^2 \eta_4(q B_0)} \tag{41}$$

where

$$q \equiv \sqrt{\left| \frac{N}{D/R_c^2} \right|} \tag{42}$$

is the parameter describing the strength of nonlinearity relative to exchange-originated dispersion for the nanocontact of radius R_c, and the function $\eta_n(q B_0)$ is defined as

$$\eta_n(q B_0) \equiv \int_0^\infty f(x/q B_0) \psi^n(x) x \, dx \tag{43}$$

This equation implicitly defines the amplitude B_0 (and, therefore, frequency ω and size ℓ) of the stationary bullet as a function of the system parameters ($\sigma I/\Gamma$ and q). On the other hand, equation (41) can be interpreted as an equation that defines a current magnitude, I, which is necessary to support a stationary spin-wave bullet of amplitude B_0.

The dependence of the normalized bias current $\zeta(B_0) = I(B_0)/I_{\min}$ (where $I_{\min} \equiv \Gamma/\sigma$) for two values of the nonlinearity factor q is shown in Figure 23 for the case of a steplike current distribution ($f(x) = 1$ if $x < 1$ and $f(x) = 0$ otherwise). This dependence has a clear minimum corresponding to the amplitude $B_0 = B_{\text{th}}$ of a bullet formed at the threshold of microwave generation by spin-polarized current. Note that the normalized current $\zeta(B_0)$ shown in Figure 23 was denoted as 'supercriticality' ζ in the spatially uniform theory (Slavin and Kabos, 2005). Note, also, that all the presented formalisms are technically not applicable in the shaded area

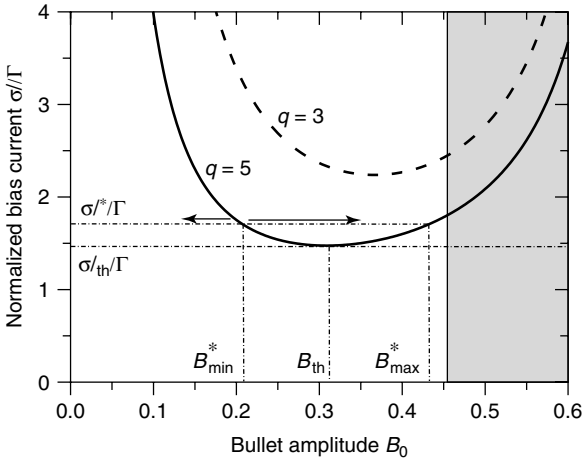

Figure 23. Dependence (41) of the normalized current $\zeta = \sigma I/\Gamma$ on the bullet amplitude B_0 for two values of the nonlinearity factor q: solid line $-q = 5$, dashed line $-q = 3$. Dash-dotted lines indicate the threshold current I_{th}, threshold bullet amplitude B_{th}, and low (B^*_{min}) and high (B^*_{max}) bullet amplitudes for a certain supercritical current $I^* > I_{th}$. The shaded area to the right of the vertical line $B_0 = 0.46$ indicates the region where our perturbative approach is not valid.

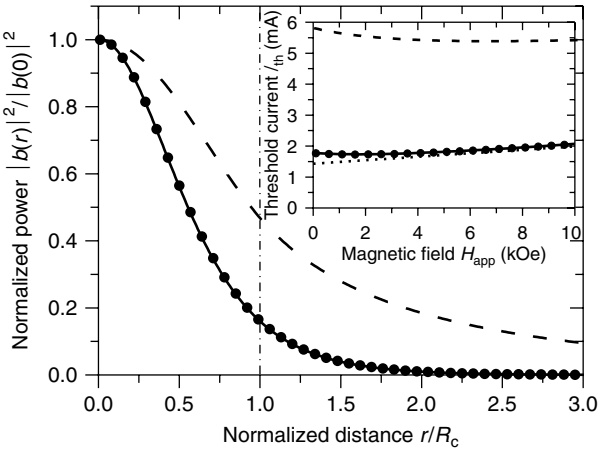

Figure 24. Normalized profiles of the spin-wave mode generated by spin-polarized current at the threshold: solid line – bullet profile (38), circles – result of the numerical solution of equation (25), dashed line – profile of the linear eigenmode calculated from the *linearized* equation (25). The vertical dash-dotted line shows the region of current localization. The inset shows the dependence of the threshold current I_{th} on the applied magnetic field H_{app}: solid line – nonlinear bullet equation (41), dashed line – Slonczewski-like linear mode (37). Dotted line – numerical fit $I\,(\mathrm{mA}) = 1.43 + 0.056\,H_{app}(\mathrm{kOe})$ to the experimental data from. (From Rippard, Pufall and Silva, 2003.)

in the right part of Figure 23 where the Taylor expansion condition $b < 1$ is violated.

The analytical result, equation (41), is heavily based on the assumption that the profile of the spin-wave mode generated at the threshold is approximately the same as the profile of a stationary bullet, equation (38). To check the validity of this assumption, equation (25) was solved numerically. The results of comparison of the spin-wave excitation profiles at the threshold obtained for a typical set of experimental parameters (Rippard, Pufall and Silva, 2003) from the analytical solution equation (38) (solid line) and numerical solution of equation (25) (black dots) are shown in Figure 24.

One clearly sees that the numerical profile of the nonlinear eigenmode is practically indistinguishable from the approximate 'bulletlike' profile, so the 'bullet' model works exceptionally well in this case. For comparison, the spatial profile of the Slonczewski-like (Slonczewski, 1999) linear spin-wave mode is also presented in Figure 24 (dashed line). The amplitude of this linear mode at the threshold is vanishingly small, $|b(r)|^2 \to 0$.

The inset of Figure 24 demonstrates the dependence of the threshold current on the applied magnetic field. One can see that the bullet model gives quantitative description of the threshold current experimentally measured in Rippard, Pufall and Silva (2003) and agrees with experiment much better than the linear threshold equation (37).

Figure 25 demonstrates the comparison of the predictions of the 'bullet' model with the results of the experiment (see

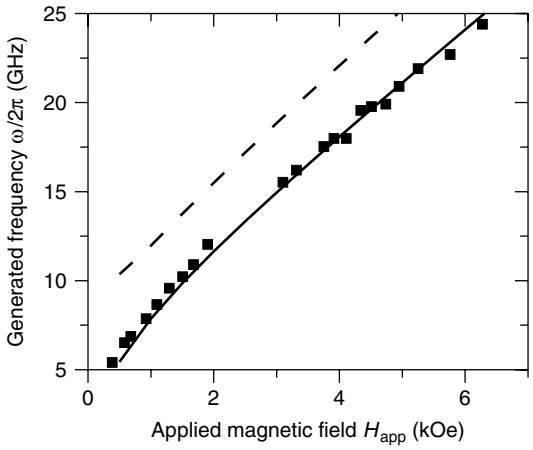

Figure 25. Dependence of the frequency ω, generated at the threshold on the applied magnetic field H_{app}. Solid line – frequency of the nonlinear bullet equation (40), dashed line – frequency of the linear mode (24), symbols – experimental data. (From Rippard *et al*., 2004a.)

Figure 2a in Rippard *et al*. (2004a)) for the magnitude of the spin-wave frequency generated at the threshold as a function of the applied magnetic field. It is again clear that the 'bullet' model gives a quantitative description of the experiment.

We need to mention that the stable bullet solution described above was obtained for the case of the *in-plane*-magnetized magnetic nanocontact. Similar results can be

obtained for the nanocontacts magnetized at such angles to their plane that the nonlinear frequency shift coefficient N is still negative and the Lighthill criterion $ND < 0$ is satisfied (see Figure 8 in Slavin and Kabos (2005) showing the angular dependence of the nonlinear frequency shift coefficient N).

In the case of larger magnetization angles, when $N > 0$ and the Lighthill criterion is not fulfilled, the mechanism of spin-wave self-localization and standing bullet formation described above does not work, and the spin-wave mode excited at the threshold is, most likely, a *propagating* exchange-dominated nonlinear spin wave similar to the one described by the linear solution for a normally magnetized 'free' layer (Slonczewski, 1999). We note, however, that the experiments (Rippard, Pufall and Silva, 2003) show that the measured threshold currents for *normally* magnetized films, for which $ND > 0$ and no standing spin-wave bullets are possible, are also somewhat lower than the values predicted by the linear model (Slonczewski, 1999).

An attempt to create a spatially nonuniform *nonlinear* model of spin-wave excitation by spin-polarized current in a normally magnetized magnetic nanocontact was undertaken in Hoefer *et al*. (2005). Unfortunately, the theoretical results obtained in Hoefer *et al*. (2005) failed to give a quantitative description of the experiments (Rippard *et al*., 2004a,b) for practically reasonable values of the polarization efficiency $\varepsilon = 0.2–0.3$. A qualitative agreement with experiments was obtained in Hoefer *et al*. (2005) for two *different* and rather unrealistic values of $\varepsilon : \varepsilon = 0.8$ in Figure 3 and $\varepsilon = 0.5$ in Figure 4 of Hoefer *et al*. (2005). Thus, the nature of the spin-wave mode excited by spin-polarized direct current in a normally magnetized magnetic nanocontact remains an open question that requires additional investigation.

7 CONCLUSION

In conclusion, stable one-dimensional spin-wave envelope solitons and quasistable two-dimensional spin-wave bullets are, indeed, the natural, intrinsic nonlinear excitations of the dynamic magnetization in magnetic films. The shape and properties of these nonlinear spin-wave modes are practically independent of the method of their excitation and are determined by the dispersive, diffractive, and nonlinear properties of the film. Spin-wave bullets, being unstable in a lossless medium, can be temporarily stabilized by linear dissipation and can propagate for significant distances of several millimeters without substantially changing their shape. Propagating spin-wave solitons and bullets can be self-generated from noise in active rings containing ferrite films and can be parametrically generated and amplified.

The detailed study of the properties of these self-generated nonlinear modes performed using the BLS technique led to experimental discovery of the novel type of symmetry-breaking nonlinear wave excitations – Möbius solitons.

Finally, we demonstrated theoretically that the lowest threshold of spin-wave excitation in an *in-plane* magnetized magnetic nanocontact driven by spin-polarized current is achieved for a two-dimensional nonlinear self-localized spin wave mode – *standing spin-wave bullet*, stabilized by the combined influence of the natural and current-induced nonlinear dissipation.

Thus, the two-dimensional nonlinear self-localization of spin-wave packets, discovered in our previous work for spin waves propagating in ferrite films, turned out to be very important in the process of excitation of nonpropagating evanescent spin-wave modes by spin-polarized current in ultrathin metallic ferromagnetic films.

We believe that the summarized results demonstrate the general nature of multidimensional nonlinear wave excitations described by the NSE (28) and the Ginzburg–Landau equation (25) and will be interesting and important for the investigation of nonlinear wave dynamics in other (e.g., optical) physical systems.

REFERENCES

Agrawal, G.P. (Ed.) (1994). *Nonlinear Fiber Optics*, Academic Press: Boston.

Akhmediev, N.N. and Ankiewicz, A. (Eds.) (1997). *Solitons. Nonlinear Pulses and Beams*. Chapman & Hall: London.

Aranson, I.S. and Kramer, L. (2002). The world of the complex Ginzburg-Landau equation. *Reviews of Modern Physics*, **74**, 99.

Bagada, A.V., Melkov, G.A., Serga, A.A. and Slavin, A.N. (1997). Parametric interaction of dipolar spin wave solitons with localized electromagnetic pumping. *Physical Review Letters*, **79**, 2137.

Bauer, M., Büttner, O., Demokritov, S.O., *et al*. (1998). Observation of spatiotemporal self-focusing of spin waves in magnetic films. *Physical Review Letters*, **81**(17), 3769–3772.

Bauer, M., Mathieu, C., Demokritov, S.O., *et al*. (1997). Direct observation of two-dimensional self-focusing of spin waves in magnetic films. *Physical Review B*, **56**(14), 8483–8486.

Berge, L. (1998). Wave collapse in physics: principles and applications to light and plasma waves. *Physics Reports*, **303**, 259–370.

Berger, L. (1996). Emission of spin waves by a magnetic multilayer traversed by a current. *Physical Review B*, **54**, 9353–9358.

Bertotti, G., Serpicio, C., Mayergoyz, I.D., *et al*. (2005). Magnetization switching and microwave oscillations in nanomagnets driven by spin-polarized currents. *Physical Review Letters*, **94**, 127206.

Bischof, B., Slavin, A.N., Benner, H. and Kivshar, Yu. (2005). Generation of spin-wave dark solitons with phase engineering. *Physical Review B*, **71**, 104424.

Bloch, F. (1930). On the theory of ferromagnetism. *Zeitschrift fur Physik*, **61**, 206.

Boyle, J.W., Nikitov, S.A., Boardman, A.D., *et al*. (1996). Nonlinear self-channeling and beam shaping of magnetostatic waves in ferromagnetic films. *Physical Review B*, **53**(18), 12173–12181.

Büttner, O., Bauer, M., Demokritov, S.O., *et al*. (1999). Collisions of spin wave envelope solitons and self-focused spin wave packets in magnetic films. *Physical Review Letters*, **82**(21), 4320–4323.

Büttner, O., Bauer, M., Demokritov, S.O., *et al*. (2000). Linear and nonlinear diffraction of dipolar spin waves in yttrium iron garnet films observed by space- and time-resolved Brillouin light scattering. *Physical Review B*, **61**(17), 11576–11587.

Büttner, O., Bauer, M., Mathieu, C., *et al*. (1998). Mode beating of spin wave beams in ferrimagnetic $Lu_{2.04}Bi_{0.96}Fe_5O_{12}$ films. *IEEE Transactions on Magnetics*, **34**, 1381.

Carr, L.D., Clark, C.W. and Reinhardt, W.P. (2000). Stationary solutions of the one-dimensional nonlinear Schrödinger equation. II. Case of attractive nonlinearity. *Physical Review A*, **62**, 063611.

Chen, M., Tsankov, M.A., Nash, J.M. and Patton, C.E. (1993). Microwave magnetic-envelope dark solitons in yttrium iron garnet thin films. *Physical Review Letters*, **70**, 1707.

Chen, M., Tsankov, M.A., Nash, J.M. and Patton, C.E. (1994). Backward-volume-wave microwave-envelope solitons in yttrium iron garnet films. *Physical Review B*, **49**(18), 12773–12790.

Chiao, R.Y., Garmire, E. and Townes, C.H. (1964). Self-trapping of optical beams. *Physical Review Letters*, **13**, 479.

Cottam, M.G. (Ed.) (1994). *Linear and Nonlinear Spin Waves in Magnetic Films and Superlattices*, World Scientific: Singapore.

Damon, R.W. and Eshbach, J.R. (1961). Magnetostatic modes of ferromagnetic slab. *Journal of Physics and Chemistry of Solids*, **19**(3/4), 308.

Demokritov, S.O., Hillebrands, B. and Slavin, A.N. (2001). Brillouin light scattering studies of confined spin waves: linear and nonlinear confinement. *Physics Reports*, **348**, 442–489.

Demokritov, S.O., Serga, A.A. and Hillebrands, B., unpublished.

Demokritov, S.O., Serga, A.A., Andre, A., *et al*. (2004). Tunneling of dipolar spin waves through an region of inhomogeneous magnetic field. *Physical Review Letters*, **93**(4), 047201.

Demokritov, S.O., Serga, A.A., Demidov, V.E., *et al*. (2003). Experimental observation of symmetry-breaking nonlinear modes in an active ring. *Nature*, **426**, 159–162.

Fleury, P.A., Porto, S.P.S., Cheesmman, L.E. and Guggenheim, H.J. (1966). Light scattering by spin waves in FeF_2. *Physical Review Letters*, **17**(2), 84–87.

Geisau, O.V., Netzelmann, U., Rezende, S.M. and Pelzl, J. (1990). Inhomogeneous ferromagnetic resonance absorption in ferrites detected by photothermal deflections. *IEEE Transactions on Magnetics*, **26**, 1471.

Griffiths, J.H. (1946). Anomalous high-frequency resistance of ferromagnetic metals. *Nature*, **158**(4019), 670.

Gurevich, A.G. and Melkov, G.A. (Eds.) (1996). *Magnetization Oscillations and Waves*, CRC Press.

Hansteen, F., Kimel, A., Kirilyuk, A. and Rasing, Th. (2005). Femtosecond photomagnetic switching of spins in ferrimagnetic garnet films. *Physical Review Letters*, **95**, 047402.

Hiebert, J.H., Stankiewicz, A. and Freeman, M.R. (1997). Direct observation of magnetic relaxation in a small permalloy disk by time-resolved scanning Kerr microscopy. *Physical Review Letters*, **79**, 1134.

Hillebrands, B. (1999). Progress in multipass tandem Fabry–Perot interferometry: I. A fully automated, easy to use, self-aligning spectrometer with increased stability and flexibility. *The Review of Scientific Instruments*, **70**(3), 1589–1598.

Hoefer, M.A., Ablowitz, M.J., Ilan, B., *et al*. (2005). Theory of magnetodynamics induced by spin torque in perpendicularly magnetized thin films. *Physical Review Letters*, **95**, 267206.

Kalinikos, B.A., Kovshikov, N.G. and Patton, C.E. (1998a). Observation of self-generation of dark envelope solitons for spin waves in ferromagnetic films. *JETP Letters*, **68**(2), 229–233.

Kalinikos, B.A., Kovshikov, N.G. and Patton, C.E. (1998b). Self-generation of microwave magnetic envelope soliton trains in yttrium iron garnet thin films. *Physical Review Letters*, **80**(19), 4301–4304.

Kalinikos, B.A., Kovshikov, N.G. and Slavin, A.N. (1983). Observation of spin-wave solitons in ferromagnetic films. *JETP Letters*, **38**(7), 413–417.

Kalinikos, B.A., Kovshikov, N.G. and Slavin, A.N. (1988). Envelope solitons and modulation instability of dipole-exchange magnetization waves in yttrium iron garnet films. *JETP Letters*, **67**(2), 303–312.

Kalinikos, B.A., Scott, M.M. and Patton, C.E. (2000). Self-generation of fundamental dark solitons in magnetic films. *Physical Review Letters*, **84**(20), 4697–4700.

Kimel, A.V., Kirilyuk, A., Tsvetkov, A.A., *et al*. (2004). Laser-induced ultrafast spin reorientation in the antiferromagnet $TmFeO_3$. *Nature*, **429**, 850.

Kiselev, S.I., Sankey, J.C., Krivorotov, I.N., *et al*. (2003). Microwave oscillations of a nanomagnet driven by a spin-polarized current. *Nature*, **425**, 380.

Kiselev, S.I., Sankey, J.C., Krivorotov, I.N., *et al*. (2004). Current-induced nanomagnet dynamics for magnetic fields perpendicular to the sample plane. *Physical Review Letters*, **93**, 036601.

Kivshar, Yu.S. and Luther-Davies, B. (1998). Dark optical solitons: physics and applications. *Physics Reports*, **298**, 81.

Kolodin, P.A., Kabos, P., Patton, C.E., *et al*. (1998). Amplification of microwave magnetic envelope solitons in thin yttrium iron garnet films by parallel pumping. *Physical Review Letters*, **80**(9), 1976–1979.

Kosevich, A.M., Ivanov, B.A. and Kovalev, A.S. (Eds.) (1988). *Nonlinear Magnetization Waves: Dynamic and Topological Solitons*, Naukova Dumka: Kiev.

Landau, L. and Lifshitz, E. (1935). On the theory of magnetic permeability in ferromagnetic bodies. *Physikalische Zeitschrift der Sowjetunion*, **8**, 153.

Lighthill, M.J. (1965). Waves in nonlinear dispersive systems. *Journal of the Institute of Mathematics and its Applications*, **1**, 269.

Lvov, V.S. (Ed.) (1994). *Wave Turbulence Under Parametric Excitation*, Springer.

Melkov, G.A., Serga, A.A., Slavin, A.N., *et al*. (1999). Parametric interaction of magnetostatic waves with a nonstationary local

pump. *Journal of Experimental and Theoretical Physics*, **89**, 1189.

Melkov, G.A., Serga, A.A., Tiberkevich, V.S., *et al*. (2000). Wave front reversal of a dipolar spin wave pulse in a nonstationary three-wave parametric interaction. *Physical Review Letters*, **84**, 3438–34441.

Melkov, G.A., Serga, A.A., Tiberkevich, V.S., *et al*. (2001). Nonadiabatic interaction of a propagating wave packet with localized parametric pumping. *Physical Review E*, **63**, 066607.

Nash, J.M., Kabos, P., Patton, C.E. and Staudinger, R. (1996). Phase properties of microwave magnetic envelope dark solitons in yttrium iron garnet thin films. *Journal of Applied Physics*, **79**(8), 5367.

Perzlmaier, K., Buess, M., Back, C.H., *et al*. (2005). Spin-wave eigenmodes of permalloy squares with a closure domain structure. *Physical Review Letters*, **94**, 057202.

Remoissenet, M. (Ed.) (1999). *Waves Called Solitons: Concepts and Experiments*, Springer: Berlin.

Rezende, S.M., de Aguiar, F.M. and Azevedo, A. (2005). Spin-wave theory for the dynamics induced by direct currents in magnetic multilayers. *Physical Review Letters*, **94**, 037202.

Rippard, W.H., Pufall, M.R. and Silva, T.J. (2003). Quantitative studies of spin-momentum-transfer-induced excitations in Co'Cu multilayer films using point-contact spectroscopy. *Applied Physics Letters*, **82**, 1260–1262.

Rippard, W.H., Pufall, M.R., Kaka, S., *et al*. (2004a). Current-driven microwave dynamics in magnetic point contacts as a function of applied field angle. *Physical Review B*, **70**, 100406.

Rippard, W.H., Pufall, M.R., Kaka, S., *et al*. (2004b). Direct-current induced dynamics in $Co_{90}Fe_{10}$ =$Ni_{80}Fe_{20}$ point contacts. *Physical Review Letters*, **92**, 027201.

Sandercock, J.R. (1978). Light scattering from surface acoustic phonons in metals and semiconductors. *Solid State Communications*, **26**(8), 547.

Scott, M.M., Kalinikos, B.A. and Patton, C.E. (2001). Self-generation of bright microwave magnetic envelope soliton trains in ferrite films through frequency filtering. *Applied Physics Letters*, **78**(7), 970–972.

Scott, M.M., Kostylev, M.P., Kalinikos, B.A. and Patton, C.E. (2005). Excitation of bright and dark envelope solitons for magnetostatic waves with attractive nonlinearity. *Physical Review B*, **71**, 174440.

Serga, A.A., Andre, A., Demokritov, S.O., *et al*. (2004). Black soliton formation from phase-adjusted spin wave packets. *Journal of Applied Physics*, **95**(11), 6607–6609.

Serga, A.A., Demokritov, S.O. and Hillebrands, B., unpublished.

Serga, A.A., Demokritov, S.O., Hillebrands, B. and Slavin, A.N. (2004). Self-generation of two-dimensional spin-wave bullets. *Physical Review Letters*, **92**(11), 117203.

Serga, A.A., Hillebrands, B., Demokritov, S.O., *et al*. (2005). Parametric generation of forward and phase-conjugated spin-wave bullets in magnetic films. *Physical Review Letters*, **94**, 167202.

Silberberg, Y. (1990). Collapse of optical pulses. *Optics Letters*, **15**, 1282.

Slavin, A.N. (1994). "Bright" and "dark" spin wave envelope solitons in magnetic films. *IEEE Transactions on Magnetics*, **30**, 37.

Slavin, A.N. (1995). Influence of the carrier signal phase on the formation of "Dark" spin wave envelope solitons in magnetic films. *IEEE Transactions on Magnetics*, **31**, 3479.

Slavin, A.N. and Benner, H. (2003). Formation and propagation of spin-wave envelope solitons in weakly dissipative ferrite waveguides. *Physical Review B*, **67**, 174421.

Slavin, A.N. and Kabos, P. (2005). Approximate theory of microwave generation in a current-driven magnetic nanocontact magnetized in an arbitrary direction. *IEEE Transactions on Magnetics*, **41**, 1264.

Slavin, A.N., Kivshar, Y.S., Ostrovskaya, E.A. and Benner, H. (1999). Generation of spin-wave envelope dark solitons. *Physical Review Letters*, **82**(12), 2583–2586.

Slavin, A.N. and Tiberkevich, V.S. (2005). Spin wave mode excited by spin-polarized current in a magnetic nano-contact is a standing self-localized wave bullet. *Physical Review Letters*, **95**, 237201.

Slonczewski, J.C. (1996). Current driven excitation of magnetic multilayers. *Journal of Magnetism and Magnetic Materials*, **159**, L1–L7.

Slonczewski, J.C. (1999). Excitation of spin waves by an electric current. *Journal of Magnetism and Magnetic Materials*, **195**, L261–L268.

Stancil, D.D. (Ed.) (1993). *Theory of Magnetostatic Waves*, Springer: New York.

Sulem, C. and Sulem, P-L. (Eds.) (1999). *The Nonlinear Schrödinger Equation: Self-Focusing and Wave Collapse*, Springer: Berlin.

Tsoi, M., Jansen, A.M.G., Bass, J., *et al*. (1998). Excitation of a magnetic multilayer by an electric current. *Physical Review Letters*, **80**, 4281–4284.

Tuan, H.S. and Parekh, J.P. (1985). Q-factor for an MSW delay-line based oscillator. *Circuits Systems and Signal Processing*, **4**, 221.

Vlannes, N.P. (1987). Experimental study of microwave magnetostatic waves in thin-film yttrium-iron-garnet with a new magnetic-induction probe. *Journal of Applied Physics*, **61**, 416–426.

Wigen, P.E. (Ed.) (1994). *Nonlinear Phenomena and Chaos in Magnetic Materials*, World Scientific: Singapore.

Zeldovich, B.Ya., Pilipetskii, R.F. and Shkunov, V.V. (Eds.) (1985). *Principles of Phase Conjugation*, Springer: Berlin.

Theory of Spin-transfer Torque

Mark D. Stiles
National Institute of Standards and Technology, Gaithersburg, MD, USA

1 INTRODUCTION

The observation of giant magnetoresistance (Baibich *et al*., 1988; Binasch, Grünberg, Saurenbach and Zinn, 1989) in multilayers of magnetic metals separated by nonmagnetic metals established that electric current in these magnetic multilayers is spin polarized. Eight years later, Slonczewski (1996) and Berger (1996) showed that the angular momentum carried by the spin-polarized current between the magnetic layers exerts torques on the magnetizations. They predicted that when the current is large enough, these *spin-transfer* torques can cause reversal and precession of the magnetization. This prediction has been confirmed in a number of laboratories and in a number of different sample geometries including mechanical point contacts (Tsoi *et al*., 1998; Ji, Chien and Stiles, 2003), lithographically defined point contacts (Myers *et al*., 1999; Rippard, Pufall and Silva, 2003), electrochemically grown nanowires (Wegrowe *et al*., 1999), manganite junctions (Sun, 1999), lithographically defined nanopillars (Katine *et al*., 2000; Grollier *et al*., 2001; Mancoff and Russek, 2002; Urazhdin, Birge, Pratt and Bass, 2003; Özyilmaz *et al*., 2003; Lee *et al*., 2004b; Hayakawa *et al*., 2004; Covington *et al*., 2004; Jiang *et al*., 2004), tunnel junctions (Liu, Zhang, Freitas and Martins, 2003; Huai *et al*., 2004; Fuchs *et al*., 2004; Deac *et al*., 2004), and semiconductor structures (Moriya, Hamaya, Oiwa and Munekata, 2004).

There has been a great deal of research both exploring the variety of behaviors exhibited by these systems and testing the possible explanations that have been offered. Some of these efforts are described in **Spin Angular Momentum Transfer in Magnetoresistive Nanojunctions, Volume 5**, **Microwave Excitations in Spin Momentum Transfer Devices, Volume 5**, and **Spin-transfer in High Magnetic Fields and Single Magnetic Layer Nanopillars, Volume 5**. Spin-transfer torques are not only interesting scientifically but are also potentially important in some commercial applications. In existing implementations of magnetic random access memory (MRAM), bits are switched by the magnetic fields caused by current pulses. This method of switching severely constrains the fabrication of the bits because the magnetic fields are not well localized. The possibility that the bits could be directly addressed and switched by a polarized current is one promising application of spin-transfer torques. Another possible application is based on using the rapid precession observed in these multilayers under suitable conditions. The high frequency oscillating resistance suggests the use of these systems as current controlled high-frequency oscillators (see also **Microwave Generation in Magnetic Multilayers and Nanostructures, Volume 2** for more details). On the other hand, in read heads with perpendicular current flow, precession interferes with the operation of the heads by creating an unwanted noise source. Thus, for some applications, it is desirable to

Handbook of Magnetism and Advanced Magnetic Materials. Edited by Helmut Kronmüller and Stuart Parkin. Volume 2: *Micromagnetism*.

understand how to optimize these effects and for others how to minimize them.

Giant magnetoresistance is the dependence of the resistance of a magnetic multilayer on the orientation of the magnetizations in neighboring ferromagnetic layers (see also **Enhanced Magnetoresistance, Volume 1**). Thus, it provides a mechanism for inferring the relative orientations of the magnetizations in a multilayer simply by measuring the resistance. When spin transfer torques change the magnetic configuration of the structure, the resistance of the structure changes as well. To detect these torques, typically one layer, called the *free layer*, responds to the spin-transfer torques, and the other, called the *fixed layer*, is constructed in a way so that it does not. Thus, when the current rotates the magnetization of the free layer, the resistance of the multilayer changes. In the precessing state, a constant input current gives a rapidly varying voltage owing to the time variation in the resistance.

All of the devices studied share some common geometrical attributes, starting with the fact that the current flows perpendicularly to the magnetic layers. Spin-transfer torques are interfacial (see subsequent text) so the free layer is kept thin, usually 3–6 nm thick, because the current necessary to move the magnetization from its ground state is proportional to this thickness. Typically, the fixed layer is much thicker than the free layer so it responds less strongly to the current-induced torques. Cross-sectional dimensions are commonly on the order of 100 nm because of the high current density necessary to move the magnetization. There are two reasons. First, the heating generated by this current density needs to be tied to a relatively large heat sink. Second, the torques due to the current-induced magnetic field become less important as the cross-sectional area decreases.

Tsoi *et al*. observed spin-transfer torques using a point contact to a magnetic multilayer in a high applied magnetic field (Tsoi *et al*., 1998). The signature of a spin-transfer torque in their measurement was the observation of peaks in the differential resistance, peaks that appeared only for one direction of current flow. These peaks were interpreted as evidence of a precessing state. Shortly thereafter, measurements on lithographically defined samples, point contacts by Myers *et al*. (1999) and nanopillars by Katine *et al*. (2000), showed both a similar peak, asymmetric in the current, in high applied magnetic fields, and hysteretic switching between parallel and antiparallel states at lower fields. The crossover field between these behaviors is roughly the zero-current coercive field. The switching was attributed to spin-transfer torques because the behavior was asymmetric. For large currents of electrons flowing from the fixed layer to the free layer, the parallel state was stable, whereas for large currents in the opposite direction, the antiparallel state was stable. If the current-induced switching were due to the magnetic fields produced by the current, the stable state in high currents would be independent of the direction of current flow.

High-frequency measurements of resistance provided more data to interpret the origin of the peak in the differential resistivity at high fields and currents. Urazhdin, Birge, Pratt and Bass (2003) showed that rapid fluctuations between two states with different resistances give rise to peaks in the differential resistance. The dwell times in each state depended strongly on current, so that with increasing current there was a rapid transition from spending most of the time in the low-resistance state to spending most of the time in the high-resistance state. This rapid and reversible rise in the resistance leads to a peak in the differential resistance. Shortly thereafter, measurements at still higher frequencies by Kiselev *et al*. (2003) and Rippard *et al*. (2004a) demonstrated the existence of precession for currents and fields close to the peak, but not clearly associated with it. They observed sharp peaks in the power spectrum density, a measure of the frequency dependent resistance in the devices, characteristic of precession. In some cases, these peaks were extremely sharp, with dimensionless quality factors, $Q \approx 18\,000$ (Rippard *et al*., 2004b). Krivorotov *et al*. (2004) observed the precession through real-time measurements of the resistance and even measured the few precession periods the system undergoes on the way to reversal in lower applied fields.

Finite sample temperatures add additional complications. For low applied fields, the hysteretic switching depends on the measurement time, or the rate at which the field or current is swept (Myers *et al*., 2002). The observed two-level switching is also strongly temperature dependent. There have been a number of studies of this and the associated low frequency noise (Tsoi *et al*., 1998; Myers *et al*., 2002; Urazhdin, Birge, Pratt and Bass, 2003; Fabian *et al*., 2003; Pufall *et al*., 2004). Sometimes the power spectrum density has the Lorentzian form expected for two-level switching, but frequently the low frequency noise has a more general form.

A number of experiments have tested qualitative and quantitative predictions of the models used to describe these systems. The dependence of the switching currents on the thicknesses of the layers confirm that the spin-transfer torque is interfacial (Albert *et al*., 2002). The dependence of the switching current on the angle of the applied field relative to the easy axis of the free layer shows the expected increases as the field becomes perpendicular (Mancoff *et al*., 2003). Comparisons between calculated and measured 'phase diagrams' (Katine *et al*., 2000; Kiselev *et al*., 2004; Koch, Katine and Sun, 2004) in which the behavior of the system is measured as a function of current and applied field show that the models qualitatively reproduce the measurements. For devices that are symmetric, the asymmetric behavior that typically is a signature of the spin-transfer torque becomes symmetric in current, as expected (Tsoi, Sun and Parkin, 2004). Studies of the material dependence show

the expected reduction of switching currents with decreasing saturation magnetization (Pufall, Rippard and Silva, 2003). By choosing appropriate and different materials for each magnetic layer, it is possible to make a device in which the state with antiparallel magnetizations has the lowest resistance, the so called *inverse giant magnetoresistance*. Studies of spin-transfer torques using these material systems (AlHajDarwish *et al*., 2004) show that the stability of the parallel and antiparallel states depends mainly on the properties of the fixed layer, and only weakly on those of the free layer. Again, this result is consistent with the theoretical models described in the subsequent text.

The rest of the chapter describes the theoretical developments put forth to predict and explain the observed behavior. Section 2, reviews spin transport in systems with collinear magnetizations. These calculations show how the current in the nonmagnetic layers becomes spin polarized and what determines how large the polarization is in different devices. However, the magnetizations must be noncollinear for spin-transfer torques to play a role. To understand these torques, it is necessary to calculate the behavior of individual electrons scattering from interfaces with their spin noncollinear with the magnetization, as described in Section 3. Section 4 combines the transport calculations and the scattering calculations to give calculations of the torque as a function of the device geometry and the orientations of the magnetization. The consequences of these torques on the dynamics is briefly discussed in Section 5.

2 COLLINEAR TRANSPORT

The theory of spin transport near interfaces started with Aronov (1976). A macroscopic theory was described by Johnson and Silsbee (1987) and van Son, van Kempen and Wyder (1987) and derived from the Boltzmann equation by Valet and Fert (1993). The history of these developments is discussed in a review article by Žutić, Fabian and Das Sarma (2004). This section discusses charge and spin transport in magnetic multilayers with collinear magnetizations, starting with a single interface between a ferromagnet and a nonmagnet. The results for single interfaces combine to give results for more complicated structures, including the structure of principle interest in this chapter, two ferromagnetic layer separated by a nonmagnetic layer embedded in a nonmagnetic host. The differences in the transport for parallel and antiparallel magnetizations of the two layers gives the giant magnetoresistance.

The negative charge of the electron is a potential source of confusion. For example, charge currents move oppositely to number (and spin) currents. Additionally, the electron's magnetic moment is opposite to its spin, leading to several more possibilities for confusion (Jonker, Hanbicki, Pierce and Stiles, 2004). In this chapter, these issues are addressed by avoiding charge and magnetization and working instead with number densities and currents and spin densities and currents. Multiplying the number current by $-e$ gives the charge current; e is positive by convention. Similarly, multiplying the spin density by $g\mu_B/\hbar$ gives the magnetization density. For free electrons, $g_e \approx -2.002319$. In transition-metal ferromagnets, in which the orbital moment is largely quenched, the g-values are close to -2. In the examples discussed in the subsequent text, one of the magnetic layers has its magnetization in the $-\hat{\mathbf{z}}$ direction, so that the spin density is in the $\hat{\mathbf{z}}$ direction. Majority electrons, referred to as 'spin up', have their spins aligned parallel to the spin density and minority electrons, referred to as 'spin down', antiparallel. The symbols $\uparrow$ and $\downarrow$ refer to majority and minority electrons, respectively.

The main quantities of interest in this section are the spin accumulation and the spin current. The spin accumulation is the excess spin density above the equilibrium amount for each material. For the nonmagnetic material, this is just the spin density itself. The spin current is the net flow of spins. Consider an isolated interface between a nonmagnet and a ferromagnet with a constant and uniform current consisting of electrons flowing from the nonmagnetic layer perpendicularly to the interface into the ferromagnetic layer. Figure 1 shows the behavior of the spin accumulation and the spin current. Far from the interface, both behave as they would in bulk materials. There is no spin accumulation in either material and the spin current is zero in the nonmagnetic material. In the ferromagnet on the other hand, the conductivity for majority electrons, $\sigma_\uparrow$ is greater than that for minority electrons, so the current density is spin polarized. More current is carried by majority electrons compared to minority electrons, $j_\uparrow > j_\downarrow$. The difference

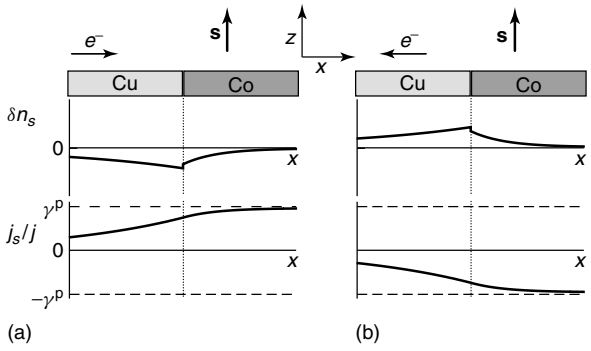

Figure 1. Spin accumulation (δn_s) and spin current (j_s) for electron flow from a nonmagnet into a ferromagnet (a) and vice versa (b). γ^{p} is the polarization of the current in the ferromagnet far from any interfaces. The magnetization in the ferromagnet, **M**, is along the $-\hat{\mathbf{z}}$ direction so that the ferromagnetic spin density **s** is along the $\hat{\mathbf{z}}$ direction.

in the spin dependence of the bulk conductivities between the ferromagnet and nonmagnet means that more majority electrons are extracted from the interface region into the ferromagnet than are delivered to it from the nonmagnet. Thus, a deficit of majority electrons builds up near the interface. Similarly, there is an accumulation of minority electrons near the interface because fewer are extracted into the ferromagnet than are delivered from the nonmagnet.

When the density of spins varies spatially, as it does here, with an excess of minority spins and a deficit of majority spins accumulating near the interface, the spins diffuse in a direction to reduce this variation. Thus, majority electron diffuse into the interface region and minority electrons diffuse away from it. The diffusion of these spins gives rise to the spatially varying parts of the spin current seen in Figure 1. In each material, the spin current for the majority electrons is given by

$$\mathbf{j}_\uparrow = (\sigma_\uparrow/e)\mathbf{E} - D_\uparrow \nabla \delta n_\uparrow \tag{1}$$

where $\delta n_\uparrow$ is the excess density of majority electrons, and $D_\uparrow$ is the spin-dependent diffusion constant, which, like the conductivity $\sigma_\uparrow$, is different in each material. The diffusion constants and the conductivities are related through the Einstein relation $e^2\sigma_\uparrow = D_\uparrow \mathcal{N}_\uparrow$ where $\mathcal{N}_\uparrow$ is the spin-dependent density of states. The density of states also relates the accumulation of each spin to a spin-dependent chemical potential $\delta n_\uparrow = \mathcal{N}_\uparrow \mu_\uparrow$.

The transport equations for majority and minority spins can be combined into an equation describing the net spin current and spin accumulation. The screening length in metals is on the atomic scale, so there is no charge accumulation in the interior of a conductor. This justifies setting $\delta n_\downarrow = -\delta n_\uparrow$ except across interfaces where dipole layers are possible. Summing the transport equations for majority, equation (1), and minority spins, solving for the electric field $\mathbf{E}$ in terms of the current $\mathbf{j}$, and inserting the result into the difference of the two transport equations gives

$$\mathbf{j}_s = \gamma^{\mathrm{p}}\mathbf{j} - D_s \nabla \delta n_s \tag{2}$$

where $\mathbf{j}_s = \mathbf{j}_\uparrow - \mathbf{j}_\downarrow$ and $\delta n_s = \delta n_\uparrow - \delta n_\downarrow$. The first term on the right-hand side of equation (2) is zero in nonmagnets, and gives the current polarization in the bulk of the ferromagnet with $\gamma^{\mathrm{p}} = (\sigma_\uparrow - \sigma_\downarrow)/(\sigma_\uparrow + \sigma_\downarrow)$. The second term describes the net diffusion of spins with $D_s = (D_\uparrow\sigma_\uparrow + D_\downarrow\sigma_\downarrow)/(\sigma_\uparrow + \sigma_\downarrow)$.

The system reaches the steady state shown in Figure 1 because spin-flip scattering, which reduces the number of excess spins by coupling their angular momentum with the lattice, cuts off a limitless increase. The net spin accumulation δn_s decays with a characteristic spin-flip scattering time τ_{sf}

$$\frac{\mathrm{d}\delta n_s}{\mathrm{d}t} = -\nabla\cdot\mathbf{j}_s - \frac{\delta n_s}{\tau_{\mathrm{sf}}} \tag{3}$$

The first term on the right-hand side describes the net flow of spins into and out of a region and the second describes the reduction in the spin density due to spin-flip scattering. In steady state, the left-hand side vanishes so that equations (2) and (3) can be combined to give a diffusion equation for spins. The spin diffusion length $l_{\mathrm{sf}} = \sqrt{D_s\tau_{\mathrm{sf}}}$ is the characteristic length scale in this diffusion equation, it varies from several nanometers in alloys such as $Ni_{80}Fe_{20}$ to around 500 nm in Cu. In Figure 1, the spin accumulation in both materials decays exponentially away from the interface with the spin diffusion length appropriate for each material.

Spin-flip scattering provides an important source of angular momentum for the current carrying electrons. As noted in the preceding text, the current flowing in from the nonmagnet does not carry angular momentum toward the interface, but the current flowing in the ferromagnet does carry angular momentum away from the interface. The angular momentum coupled from the lattice through spin-flip scattering is the source of the difference between the angular momentum flowing in the two leads.

Equations (2) and (3) describe all of the results in Figure 1 except the discontinuity in the spin accumulation at the interface. This discontinuity arises because the interface has a spin-dependent resistance, R_σ associated with it (Schep *et al.*, 1998; Stiles and Penn, 2000; Xia *et al.*, 2001; Bauer, Schep, Xia and Kelly, 2002). For each spin, the current across the interface is related to a discontinuity in the spin chemical potential, described in the preceding text, across the interface

$$R_\uparrow \mathbf{j}_\uparrow\cdot\hat{\mathbf{n}} = \mu_\uparrow^{\mathrm{NM}} - \mu_\uparrow^{\mathrm{FM}} \tag{4}$$

As there is a 'natural' polarization to the bulk current given by γ^{p}, so is there a natural polarization to the spin current through the interface given by $\gamma^{\mathrm{I}} = (R_\downarrow - R_\uparrow)/(R_\downarrow + R_\uparrow)$. The apparent sign reversal comes from the definition in terms of resistances rather than conductances. Whenever the polarization of the current, j_s/j, in the bulk of a material is different from the polarization of the conductivity γ^{P}, there must be a spatially varying spin density to generate a diffusive contribution to the spin density to compensate. Similarly, whenever the polarization of the current crossing an interface differs from the polarization of the interface conductance, γ^{I}, there must be a discontinuity in the spin chemical potential across the interface.

Figure 1(b) shows that when the current direction changes, the spin accumulation and spin currents both change signs. In this case, more majority and fewer minority electrons enter

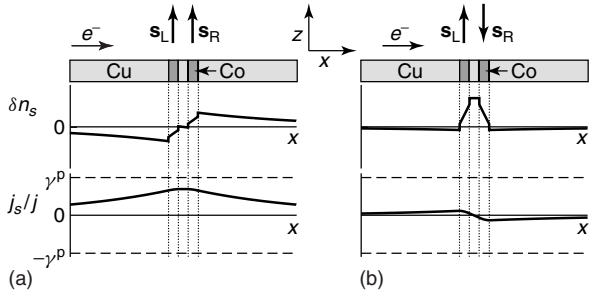

Figure 2. Spin accumulation (δn_s) and spin current (j_s) for electron flow through two ferromagnetic layers embedded in a nonmagnetic host and separated by a thin nonmagnetic spacer layer. The magnetizations of the two layers are parallel along the $\hat{\mathbf{z}}$ direction on the left side and antiparallel on the right. γ^{p} is the polarization of the current in the bulk ferromagnet far from any interfaces.

the interface region than leave it. Hence, there is a positive spin accumulation and a net diffusion of majority electrons away from the interface and minority spins into it.

These ideas describing spin transport through and near interfaces provide the basis for understanding more complicated structures. For example, consider the case of two finite ferromagnetic layers separated by a nonmagnetic spacer layer and embedded in a nonmagnetic host as depicted in Figure 2. Far from the layers, there is no spin current or spin accumulation in the nonmagnetic host. For parallel magnetizations, as depicted to the left, there are more majority electrons flowing through the layers than minority electrons. This flow of electrons leads to minority electrons accumulating to the left of the layers and diffusing to the left and majority electrons accumulating to the right and diffusing to the right. The result is a positive spin current in both cases. The polarization of the current is less than the polarization of the interface conductance, so there are substantial discontinuities in the spin accumulation across the interfaces.

On the other hand, when the two magnetizations are antiparallel, the current flowing through the layers is largely unpolarized, provided the layers are thin compared to the appropriate spin diffusion lengths. The unpolarized current flowing through the ferromagnetic layers requires substantial gradients in the spin accumulation to provide the diffusive spin currents to compensate the bulk-like spin currents. Also, since the current is much less polarized than the interface conductances, there are substantial discontinuities in the spin accumulation as well. This situation leads to an interesting result. In the case of parallel magnetizations, the current flowing through the spacer layer is highly polarized, but the spin accumulation is close to zero. On the other hand, for antiparallel alignment, the spin current in the spacer layer is close to zero but there is substantial spin accumulation.

Figure 2 provides an explanation (Baibich *et al.*, 1988) for giant magnetoresistance. When the magnetizations are parallel, the current carrying electrons are polarized so that more of them flow through the low-resistance majority channel. This polarization of the current lowers the average resistance of the structure and provides a short circuit as compared to the antiparallel case. In the antiparallel case, the current remains largely unpolarized so that close to half of the electrons are forced to flow through the higher resistance minority channel in each layer.

It should be clear from Figure 2 that the spin current depends on the sample geometry, including the leads. In most samples, the leads only have the same cross-sectional area as the rest of the sample for a length much shorter than the spin diffusion length. Then, the structure widens out quickly. In one-dimensional drift–diffusion calculations, this widening is typically modeled by asserting that the spin accumulation goes to zero at the widening point, but the spin current is finite there. This approximation is motivated by the large density of states in the wide part of the sample. Three-dimensional calculations of the transport (Berger, 2004; Hamrle, Kimura, Yang and Otani, 2005) bear out this picture qualitatively, but quantitative differences remain.

There are several key points from this discussion that are important for understanding spin-transfer torques. Spin-dependent conductivities in ferromagnetic layers and spin-dependent conductances at interfaces with ferromagnetic layers lead to spin-polarized current flowing through the nonmagnetic layers in these structures. Spin-flip scattering couples angular momentum from the lattice into the electron system, allowing for apparent nonconservation of angular momentum within the electron system itself. Finally, the spin polarization of the current at particular points in the structure is not a local property. It depends on everything upstream and downstream within a few spin diffusion lengths. It also depends strongly on the alignment of the magnetizations in close-by layers.

3 SPIN-DEPENDENT INTERFACIAL SCATTERING

3.1 Spin currents for noncollinear magnetizations

The last section describes transport in devices with collinear magnetizations, but torques only occur when the magnetizations are noncollinear. Treating the noncollinear case requires understanding the behavior of spins currents at interfaces when the spins are not collinear with the magnetization of the ferromagnet. This section splits the discussion of this behavior into three subsections. The present subsection, Section 3.1, defines spin current in a noncollinear system and describes its equation of motion. Section 3.2 describes the scattering of individual electrons at interfaces as a function

of their spin direction. The result is a torque on the electron spin and a reaction torque on the magnetization. Finally, Section 3.3 describes the behavior of the collection of electrons carrying current. The sum of the reaction torques from the electron spins gives the spin transfer torque for the chosen spin current. These descriptions provide boundary conditions that can be used to generalize the results of the previous section to the case of noncollinear magnetizations. This generalization is taken up Section 4.

When the magnetizations are collinear it is possible to treat the spin accumulation as a scalar and the spin current as a vector. In the presence of noncollinear magnetizations, it is necessary to treat the spin accumulation as a vector to account for variations in the direction of the spins and the spin current as a tensor to account for both the direction of the spins and the direction they are moving. Classically the spin current carried by an individual electron is the outer product of its spin and velocity $(\hbar/2)\hat{\mathbf{s}} \otimes \mathbf{v}$ as illustrated in Figure 3(a). More generally, these quantities are given by the expectation values of the spin operator $\mathbf{S}$ and the velocity operator $\hat{\mathbf{v}}$

$$\mathbf{s}(\mathbf{r}) = \sum_{i\sigma\sigma'} \psi^*_{i\sigma}(\mathbf{r})\, \mathbf{S}_{\sigma,\sigma'}\, \psi_{i\sigma'}(\mathbf{r})$$

$$\mathbf{Q}(\mathbf{r}) = \sum_{i\sigma\sigma'} \mathrm{Re}\left[\psi^*_{i\sigma}(\mathbf{r})\, \mathbf{S}_{\sigma,\sigma'} \otimes \hat{\mathbf{v}}\, \psi_{i\sigma'}(\mathbf{r})\right] \tag{5}$$

In these sums, the index i refers to occupied states, and the index σ to the spinor components of the states. In general, the total spin current need not factor into an outer product of a spin direction and a vector current, but in systems like those considered in the previous section, it does

$$\mathbf{Q} = (\hbar/2)\, \hat{\mathbf{s}} \otimes \mathbf{j}_s = (\hbar/2) P\, \hat{\mathbf{s}} \otimes \mathbf{j} \tag{6}$$

where $\hat{\mathbf{s}}$ is a unit vector in the direction of the spin density. The last form in equation (6) writes the difference of currents carried by each spin as a polarization P times the number current.

The equation of motion for the spin density can be derived in the same way as the familiar continuity equation for the number density

$$\frac{\partial n}{\partial t} = -\boldsymbol{\nabla}\cdot\mathbf{j} \tag{7}$$

which is derived from the commutator of the operator for the number density with the Hamiltonian. The number operator commutes with all terms except the kinetic energy, which gives the right-hand side. The expression shows that the time rate of change of the number of electrons in a volume is given by the net rate of flow of electrons into the volume. For the spin density this procedure gives

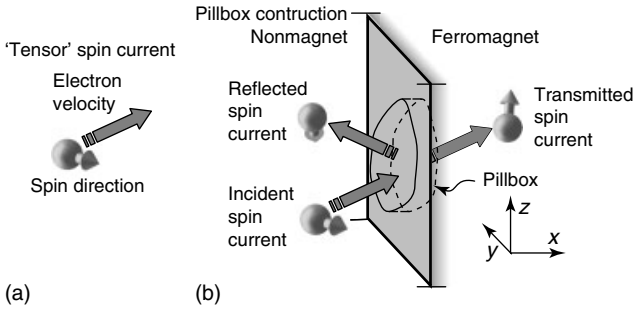

Figure 3. (a) An electron moving in one direction with its spin in another illustrating a tensor spin current. (b) A pillbox around interface for computing the interfacial torque.

$$\frac{\partial \mathbf{s}}{\partial t} = -\boldsymbol{\nabla}\cdot\mathbf{Q} + \mathbf{n}_{\mathrm{ext}} - \alpha\hat{\mathbf{s}} \times \frac{\partial \mathbf{s}}{\partial t} - \hat{\mathbf{s}}\frac{\delta s}{\tau_{\mathrm{sf}}} \tag{8}$$

where $\boldsymbol{\nabla}\cdot\mathbf{Q} = \partial_k Q_{ik}$, summing over the repeated index k. The first term on the right-hand side is similar to the right-hand side of equation (7). It is a contribution to the time rate of change of the spin density given by the net flow of spin into that volume. Unlike the case for the number density, there are other terms that can change the spin density. The second term on the right-hand side of equation (8) comes from the terms in the Hamiltonian in which the energy depends on the orientation of the spin density, terms like the Zeeman interaction with an external field, the magnetocrystalline anisotropy, and the magnetostatic interaction between the magnetizations at different points. These terms tend to cause precession of the spin density around its equilibrium direction and are combined into the effective torque; the last two terms are phenomenological representations of more complicated interactions. The first of these is the damping that tends to reduce the magnitude of the precession and the second is the spin-flip scattering described in equation (3). With just the second and third terms on the right-hand side, equation (8) is the familiar Landau–Lifshitz–Gilbert equation written in terms of the spin density instead of the magnetization. The last term is an addition for cases in which the magnitude of the spin density is allowed to vary owing to flowing current. The first term is the spin-transfer torque of interest in this chapter.

There are two contributions to the spin-transfer term in equation (8), as there are two contributions to the spin current. One contribution to the spin current is carried by all of the electrons and exists whenever the spin density (or magnetization) varies spatially even if there is no current flow. The gradient of this contribution to the spin current gives the micromagnetic exchange interaction discussed in chapter **General Micromagnetic Theory, Volume 2**.

The second contribution is carried by nonequilibrium carriers near the Fermi energy. It only exists in the presence of a current and is the contribution of interest in this chapter. The rest of the chapter deals only with the spin current carried by the nonequilibrium electrons close to the Fermi energy; the contribution from the spin current due to the spatially varying magnetization is included in the torque, $\mathbf{n}_{\text{ext}}$, as is generally done in micromagnetics.

The remainder of the $-\nabla\cdot\mathbf{Q}$ term in equation (8) is the spin-transfer torque and has two important manifestations. The manifestation of principle interest in this chapter is an interfacial contribution in multilayers that is discussed in the subsequent text. There is an additional contribution for spatially varying spin densities in bulk materials originally studied by Berger (1978, 1979). When the spin-density direction varies spatially it exerts a torque on the spins carried along with the current as they move through the variation. These spins tend to rotate to stay aligned with the magnetization. If they stayed perfectly aligned, the spin current would have the form $(\hbar/2)P\hat{\mathbf{u}}(\mathbf{r})\otimes\mathbf{j}$, where $\hat{\mathbf{u}}(\mathbf{r})$ is the local direction of the spin density. Then, the reaction torque on the spin density is $-(\hbar/2)P(\mathbf{j}\cdot\nabla)\hat{\mathbf{u}}(\mathbf{r})$ (Berger, 1984, 1986; Bazaliy, Jones and Zhang, 1998; Ansermet, 2004) for a constant current. If the spins carried by the current do not adiabatically follow the direction of the magnetization, there can be an additional torque of the form $\xi(\hbar/2)P\hat{\mathbf{u}}(\mathbf{r})\times(\mathbf{j}\cdot\nabla)\hat{\mathbf{u}}(\mathbf{r})$ (Waintal and Viret, 2004; Zhang and Li, 2004; Thiaville, Nakatani, Miltat and Suzuki, 2005). However, calculations of this latter quantity are still in a preliminary state.

The rest of this chapter focuses on the interfacial spin-transfer torque of importance in magnetic multilayers (Slonczewski, 1996; Waintal, Myers, Brouwer and Ralph, 2000; Xia *et al*., 2002; Stiles and Zangwill, 2002a). To understand the origin of this torque, it is useful to integrate the spin-transfer torque $-\nabla\cdot\mathbf{Q}$ over the volume of a pillbox surrounding the interface between a nonmagnetic metal and a ferromagnetic metal, as illustrated in Figure 3(b). The volume integral gets converted into the difference in the flux between the two surfaces. For a spin-current incident from the nonmagnetic metal, the net flux can be written as a torque on the enclosed magnetization

$$\mathbf{N}_{\text{c}} = (\mathbf{Q}^{\text{in}} - \mathbf{Q}^{\text{tr}} + \mathbf{Q}^{\text{ref}})\cdot A\hat{\mathbf{x}} \approx \mathbf{Q}^{\text{in}}_{\perp}\cdot A\hat{\mathbf{x}} \qquad (9)$$

where 'in', 'tr', and 'ref' refer to the incident, transmitted and reflected spin currents, respectively. The equality in this equation is the difference in the fluxes through the two interfaces and is an exact result. The approximate result, which states that the transverse component of the incident spin current is absorbed by the ferromagnet at the interface, is developed in the rest of this section.

3.2 Torque due to individual electrons

The behavior of individual electron spins in magnetic multilayers is determined by their interaction with the spin polarized electronic structure of the ferromagnetic metals. Modeling the details of the spin transport requires a model for this electronic structure, which is complicated (Fulde, 1995; Held and Vollhardt, 1998; Yang, Savrasov and Kotliar, 2001) because it is a balance of intra-atomic exchange and correlation effects with interatomic hybridization. In isolated atoms, electrons occupy states in partially filled levels in such a way so as to maximize the total spin (Hund's first rule). Maximizing the spin reduces the Coulomb repulsion between the electrons because parallel spins are naturally kept away from each other by the Pauli exclusion principle. Within partially filled atomic levels, the orbital energies of the different states are the same so there is no penalty for developing this polarization. In solids, the atomic levels hybridize with levels on neighboring atoms forming bands and removing the degeneracy of the states within a level. Since the degeneracy is lifted, there is now a cost for developing a spin polarization as each flipped spin has to be put into a higher energy state. Typically, the Coulomb energy gain from developing a spin polarization is less than that cost, so most solids remain unpolarized. However, in Fe, Co, and Ni, among others, the energy gain is sufficient for ferromagnetism to develop.

Two approaches are commonly used to describe the electronic structure of ferromagnets in the context of magnetic multilayers. One is based on models used to describe magnetic impurities in nonmagnetic hosts (Langreth and Wilkins, 1972). In these models, the d levels on the impurity are treated as localized states that form a local moment. This model ignores the hybridization of the levels forming the moment. In the most common treatment of this model, the local moment becomes a well-defined object in its own right. The moment is then weakly coupled to the moment of the conduction electron spins. This model is referred to as the 's-d' model or the local moment model.

The other approach, adopted in this chapter, is based on the local spin-density approximation (LSDA) (Kohn and Sham, 1965; von Barth and Hedin, 1972; Gunnarsson and Lundqvist, 1976; Jones and Gunnarsson, 1989). This approach was developed for computing the total electronic energy of systems. In metallic solids, it works very well for calculations of properties such as cohesive energies, equilibrium lattice constants, and the magnetic moments (Moruzzi, Janak and Williams, 1978). Alternatively, this method can be thought of as an approximation for the electronic structure in which the interatomic hybridization is treated exactly, but the interactions between the electrons are treated in mean-field theory. This approach does a reasonable job describing the Fermi surfaces of the transition metals.

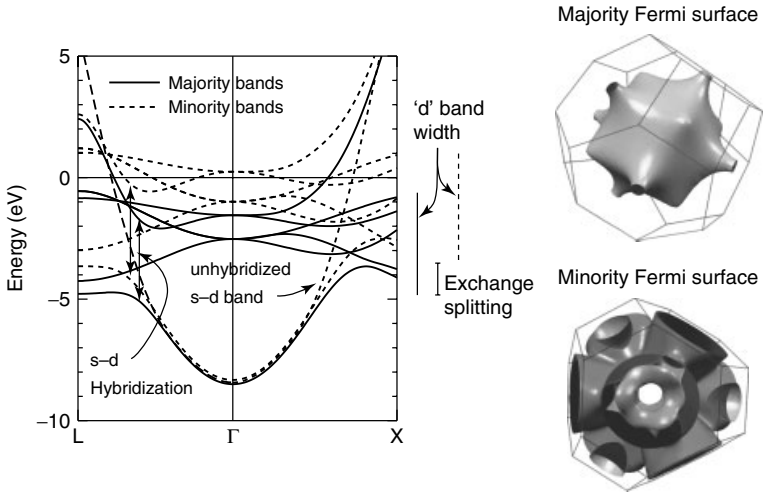

Figure 4. The band structures and Fermi surfaces of face-centered cubic Co. The solid (dotted) curves give the majority (minority) bands along two high symmetry directions through the Brillouin zone center, Γ. The thin dashed curve shows the s-p band if it were not hybridized with the d bands. The bars to the right of the bands show the width of the d bands and the exchange splitting between the majority and minority bands. The arrows in the band structure plots give the width of the gap caused by the hybridization between the s-p and d bands of the same symmetry. The Fermi surfaces are by permission from Choy *et al*. (1995). (Fermi surfaces reproduced from Choy, T.-S., Naset, J., Chen, J., Hershfield, S., and Stanton, C.J. The Fermi Surface Database, 1995, http://www.phys.ufl.edu/fermisurface/.)

Since the transport behavior is dominated by the properties of the electrons at the Fermi energy, this approach is adopted in the rest of this chapter. Calculated band structures and Fermi surfaces for majority and minority electrons in face-centered cubic Co are shown in Figure 4. The fact that the bandwidth of the d-derived states as well as the s-d hybridization are larger than the exchange splitting highlight the importance of treating the hybridization of the d states.

Either approach can describe much of the physics of these systems, largely because so much is unknown about the details of the systems. For example, the spin-dependent conductivity would be difficult to calculate directly even if the details of all of the defects causing the scattering were known. Since these details are not known, the conductivities are usually taken from experiment, allowing either model to correctly describe that aspect of the behavior. However, there are some processes where the details of the Fermi surfaces matter and the two models give different results. As discussed below, the spin-transfer process is an example where this difference is important. Figure 4 shows that when the hybridization of the d-electrons is taken into account, the Fermi surfaces of the majority and minority electrons are quite different. In local moment models, the two Fermi surfaces are almost identical.

Two different aspects of the exchange interaction are discussed in this chapter, the exchange interaction that gives rise to the moments and the micromagnetic exchange. The latter aspect is the additional energy that arises when the direction of the moment varies in space. In this chapter, the magnetization of the layers is generally assumed to be uniform, so references to the exchange interaction refer to the aspect giving rise to the moment. References to micromagnetic exchange refer to the spatially varying aspect.

When electrons scatter from interfaces between a nonmagnetic metal and a ferromagnetic metal, the exchange interaction in the ferromagnet leads to scattering that depends on the spin of the electron. For electrons with moments parallel to the magnetization in the ferromagnet, the reflection amplitude, $R_\uparrow$, is different from the reflection amplitude for electrons with moments antiparallel, $R_\downarrow$. For multilayers with collinear magnetizations, spin-dependent reflection leads to a spin-dependent interface resistance (Schep *et al*., 1998; Stiles and Penn, 2000; Xia *et al*., 2001; Bauer, Schep, Xia and Kelly, 2002). The transmission amplitudes, $T_\uparrow$ and $T_\downarrow$ are similarly spin dependent.

The reflection amplitudes for electrons with moments misaligned with respect to the magnetization can be computed directly from the reflection amplitudes for collinear moments. As discussed in the preceding text, the magnetization is assumed to be in the $-\hat{\mathbf{z}}$-direction so that the ferromagnetic spin density is in the $\hat{\mathbf{z}}$-direction. Then, the spin state of an electron spin pointing in the direction specified by the polar angle θ and azimuthal angle ϕ is given by a coherent superposition of majority- and minority-spin states

$$|\theta, \phi\rangle = \cos(\theta/2)\, e^{-i\phi/2}\, |\uparrow\rangle + \sin(\theta/2)\, e^{i\phi/2}\, |\downarrow\rangle \quad (10)$$

So, an electron in the nonmagnet with a spin pointing in the θ, ϕ direction with wave vector k can be described by the wave function $e^{ikx}\, |\theta, \phi\rangle$. Since quantum mechanics is linear,

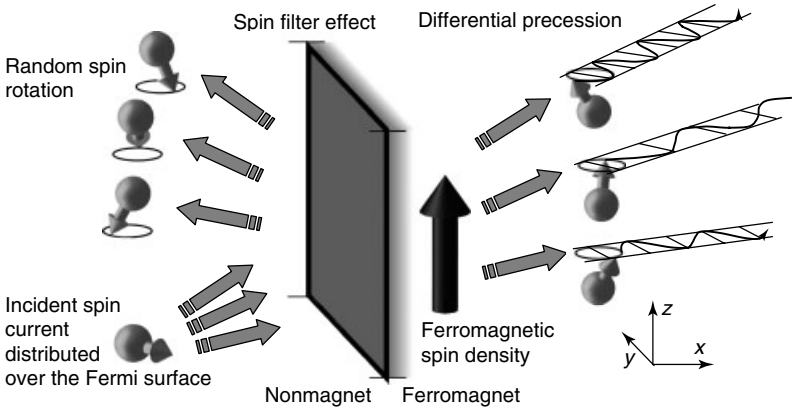

Figure 5. Mechanisms contributing to absorption of incident transverse spin current. Electrons incident from the nonmagnet (lower left) are distributed over states represented here by three different incident directions. All of these electrons are in the same spin state, which is transverse to the ferromagnetic spin density. The reflected electron spins have predominantly minority character and their transverse components are distributed over many directions (random spin rotation) because of the variation over the Fermi surface of the phases of the reflection amplitudes. The transmitted electron spins precess as they go into the ferromagnet because the wave vectors for the majority and minority components are different. Electrons with different initial conditions precess at different rates, leading to classical dephasing (differential precession).

the majority, and minority components of the wave function reflect as they would in the absence of any coherence. The reflected wave function is thus

$$e^{-ikx}\left[R_\uparrow \cos(\theta/2)\, e^{-i\phi/2}\,|\uparrow\rangle + R_\downarrow \sin(\theta/2)\, e^{i\phi/2}\,|\downarrow\rangle\right] \quad (11)$$

The reflected spin is rotated with respect to its incident direction and is pointing in the direction specified by $\tan(\theta'/2) = |R_\downarrow/R_\uparrow|\tan(\theta/2)$ and $\phi' = \phi + \mathrm{Im}[\ln(R_\uparrow^* R_\downarrow)]$. Such rotations are sketched in Figure 5.

Physically, the reflected electron spin precesses during its interaction with the exchange field present in the ferromagnet. Similar effects occur for transmitted electrons with one additional complication. When the electrons go through the ferromagnet they continue to interact with the exchange field and precess around it. This precession manifests itself through the different wave vectors for the two components of the wave function

$$\begin{aligned} &e^{-ik_\uparrow x} T_\uparrow \cos(\theta/2)\, e^{-i\phi/2}\,|\uparrow\rangle \\ &\quad + e^{-ik_\downarrow x} T_\downarrow \sin(\theta/2)\, e^{i\phi/2}\,|\downarrow\rangle \end{aligned} \quad (12)$$

As for the reflected wave function, there is rotation owing to the relative amplitudes and phases of $T_\uparrow$ and $T_\downarrow$. In addition, the different components accumulate additional relative phase from the factor $\exp[i(k_\uparrow - k_\downarrow)x]$ as they propagate. This phase factor describes the precession around the magnetization as the spin propagates through the ferromagnet. There is no such precession for the reflected wave function. In a local moment model, the spatial frequency of the precession is much slower than it is when more realistic Fermi surfaces are considered. Realistic Fermi surfaces give spatial precession periods on the order of several lattice constants.

When the interaction of the spin with the magnetization causes the spin to precess, there is a reaction torque from the spin on the magnetization. This reaction torque is the current-induced torque described in equation (9). The second part of that equation expresses an approximate numerical result for the size of the torque. One of the mechanisms for this result is seen from the following simple argument based on a particular limit (Waintal, Myers, Brouwer and Ralph, 2000), in which the reflection probability for majority electrons is zero and for minority electrons is one. Although this simple behavior is not general, it does occur for some electrons (Stiles, 1996). For a ferromagnetic spin density along $-\hat{\mathbf{z}}$ and an interface normal in the $\hat{\mathbf{x}}$ direction, consider an incident electron with its spin in the $\hat{\mathbf{x}}$ direction. The spin currents on the faces of the pillbox of Figure 3 as in equation (9) are

$$\begin{aligned} \mathbf{Q}_{\mathrm{in}} &= \frac{\hbar}{2}\hat{\mathbf{x}} \otimes v\hat{\mathbf{x}} \\ \mathbf{Q}_{\mathrm{refl}} &= \frac{\hbar}{4}(-\hat{\mathbf{z}}) \otimes (-v\hat{\mathbf{x}}) \\ \mathbf{Q}_{\mathrm{trans}} &= \frac{\hbar}{4}\hat{\mathbf{z}} \otimes v\hat{\mathbf{x}} \end{aligned} \quad (13)$$

This combination gives a current-induced torque of $\mathbf{N}_{\mathrm{c}} = \hat{\mathbf{x}} A v\hbar/2$. There are two features of this result. First, there is no torque along the direction of the magnetization. This is a general result and simply reflects the fact that the component of the spin along the magnetization is conserved during the scattering process. The second feature is that the component of the spin transverse to the magnetization is absorbed by the

magnetization. The mechanism for the torque in this simple model is the spatial separation of the majority and minority components of the wave function. The transverse component of the spin current arises from the interference of these two components of the wave function. When they cease overlapping, the transverse component of the spin current vanishes. The two components of the wave function are separated by the exchange interaction, the ultimate cause for the spin dependence of the reflection amplitudes and hence the torque.

The result that the transverse spin current is absorbed at the interface is exact only for this special limit of complete spatial separation. However, it holds approximately for many transition metal interfaces. Explaining this approximate result requires a discussion of the distribution of electrons that carry a current.

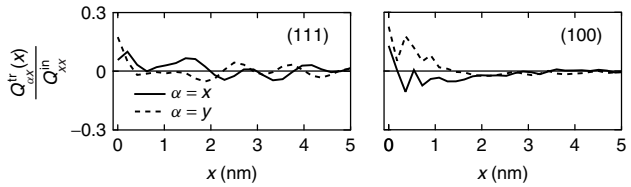

Figure 6. Decay of transverse transmitted spin current as a function of distance from the interface for two orientations of Co/Cu. For a unit incident transverse polarization, the solid curve in each panel is $Q_{xx}(x)$. The dotted curve in each panel is $Q_{yx}(x)$. Asymptotically, the spin current shows decaying oscillatory behavior. The oscillation is due to the precession (see equation (12)) and the decay is due to increasing cancellation of the precession from different parts of the Fermi surface. The amplitude of the asymptotic behavior is smaller for the (111) case than for the (100) case due to the details of the Fermi surface of Co.

3.3 Torque due to an ensemble of electrons

Collinear transport is described in Section 2 using the language of the drift-diffusion approximation in terms of densities and currents, ignoring the behavior of individual electrons. Determining the boundary conditions at the interfaces between different materials requires summing over the behavior of the individual electrons. The electrons carrying the current are spread over the entire Fermi surface and have different properties.

Equation (11) shows that the electron spins rotate when they reflect. First-principles calculations (Xia *et al.*, 2002; Stiles and Zangwill, 2002a; Zwierzycki *et al.*, 2005) show that these rotations vary rapidly over the Fermi surface. A schematic of this distribution of rotations is shown in Figure 5. For most interfaces that have been studied, there is a tendency for a polarization to develop along the direction of the magnetization; either majority or minority reflection is greater on average. However, in all cases, the transverse component of the reflected spin current sums to a value close to zero. Thus, $\mathbf{Q}^{\mathrm{ref}}$ in equation (9) has only a small transverse component.

These same calculations show a similar, but not as complete cancellation of the transmitted transverse spin current. However, the transmitted electrons are rapidly precessing due to the evolving phase difference $\exp[i(k_\uparrow - k_\downarrow)x]$ for the two spin components of the wave function for each electron. The difference in wave vector varies rapidly over the Fermi surface. Thus, there is an increase in the dephasing and concomitant decrease in the transverse component as a function of penetration into the ferromagnet. This precession is illustrated schematically in Figure 5 and the net precession and decay of the spin current is illustrated in Figure 6. If the spin current is considered several layers into the ferromagnet, the transmitted current has only a small transverse component. The small transverse part of the transmitted and reflected spin currents means that the transverse part of the incident spin current is largely transferred to the ferromagnetic magnetization. This result is the approximate second half of equation (9).

Quantitative calculations like those in Figure 6 require keeping track of the distributions of electrons on either side of the interface. One approach is a fully coherent calculation (Zwierzycki *et al.*, 2005; Edwards, Federici, Mathon and Umerski, 2005). Such calculations have the drawback that including all of the coherent multiple scattering between interfaces involves significant computational effort. These coherent effects are not observed experimentally, presumably because disorder in the samples averages them out. An alternate approach, adopted in this chapter, is a generalization of the Boltzmann equation. The Boltzmann equation describes the evolution of the distribution function for electrons when the spatial variations in the system are slow enough that the electrons in a small region can be described as if they were in an infinite bulk region with similar material properties. Coherence between electrons at different wave vectors or positions is ignored. In magnetic multilayers, this approximation can only be valid away from interfaces. However, distributions in two regions away from the interfaces can be joined together through boundary conditions calculated quantum mechanically.

In the ferromagnet, the distribution function $f_s(\mathbf{r}, \mathbf{k})$, depends on position $\mathbf{r}$, wave vector $\mathbf{k}$, and band index (not indicated). The magnetization provides the natural quantization direction and there is a separate function for each spin $s = \uparrow, \downarrow$. Any spin component transverse to this direction tends to rapidly vanish due to dephasing effects similar to those discussed in the preceding text for spin currents injected into a ferromagnet.

In the nonmagnetic layers on the other hand, there is neither a natural quantization direction, nor the rapid

dephasing that is present in ferromagnets. In this case, it is necessary to generalize the Boltzmann equation to keep track of the coherence between electrons in different spin states on each part of the Fermi surface. This can be done by generalizing the two distribution functions to 2×2 distribution matrices

$$f_{s,s'}(\mathbf{r}, \mathbf{k}, t) = f(\mathbf{r}, \mathbf{k}, t)\delta_{s,s'} + \sum_{\alpha=x,y,z} f_\alpha(\mathbf{r}, \mathbf{k}, t)[\sigma_\alpha]_{s,s'} \qquad (14)$$

where σ_α, are Pauli spin matrices ($\alpha = x, y, z$). This construction allows the electron spins to point in arbitrary directions. The four functions that characterize the distribution matrices give the densities and currents

$$\begin{aligned} n_0 + \delta n &= \sum_{\mathbf{k}} f(\mathbf{k}) \qquad j_\beta = \sum_{\mathbf{k}} f(\mathbf{k}) v_\beta(\mathbf{k}) \\ s_\alpha &= \frac{\hbar}{2}\sum_{\mathbf{k}} f_\alpha(\mathbf{k}) \qquad Q_{\alpha\beta} = \frac{\hbar}{2}\sum_{\mathbf{k}} f_\alpha(\mathbf{k}) v_\beta(\mathbf{k}) \end{aligned} \qquad (15)$$

where v_β is a component of the velocity of the state at $\mathbf{k}$, and n_0 is the equilibrium density. Moments of the Boltzmann equation give the drift-diffusion equations in the nonmagnet as shown for the collinear case by Valet and Fert (1993).

The construction in equation (14) is based on including the coherence between majority- and minority-spin states, but only for states at the same point on the Fermi surface. Thus, the possibility of such a construction in ferromagnets depends on the model for the electronic structure of the ferromagnet. Calculations based on local moment models (Heide, 2001; Heide, Zilberman and Elliott, 2001; Zhang, Levy and Fert, 2002; Shpiro, Levy and Zhang, 2003; Hitchon, Chantrell and Rebei, 2004), typically include coherence between majority and minority states because there is little difference between the Fermi surfaces of the majority and minority transport electrons. On the other hand, for realistic models of the electronic structure, such a construction is not possible because states with the same energy do not generally have the same wave vector. Thus Boltzmann equation and drift-diffusion calculations based on realistic band structures do not allow for transverse spins in ferromagnets. It is possible to extend the Boltzmann equation so as to include the coherence that is left out of the Boltzmann equation; this is done in the first-principles calculations (Stiles and Zangwill, 2002a; Zwierzycki *et al.*, 2005). However, it is difficult to include scattering in calculations with coherence between non-overlapping Fermi surfaces.

In the Boltzmann equation, the boundary conditions for each electronic state are determined by the spin-dependent reflection and transmission amplitudes shown in equations (11) and (12). The boundary conditions for reflection can be expressed in terms of four real reflection parameters

$$\begin{aligned} \mathrm{R}_\uparrow &= |R_\uparrow|^2 \qquad \mathrm{R}_\perp = \mathrm{Re}[R_\downarrow^* R_\uparrow] \\ \mathrm{R}_\downarrow &= |R_\downarrow|^2 \qquad \mathrm{R}_\times = \mathrm{Im}[R_\downarrow^* R_\uparrow] \end{aligned} \qquad (16)$$

The two parameters on the left are the reflection probabilities for the majority and minority components, respectively. They determine the reflected number current and the reflected longitudinal spin current. The two quantities on the right, which are not probabilities as they can be negative, determine the reflected transverse spin current. $\mathrm{R}_\perp$ describes reflection of a spin along the same azimuthal axis as the incident state. A negative value implies rotation by 180°. $\mathrm{R}_\times$ describes reflection along an axis rotated by $\pm 90^\circ$. The boundary conditions for transmission are described by the transmission probabilities for majority and minority electrons. Since these models do not include transverse spins in the ferromagnet, any such spins that are transmitted are assumed to be absorbed by the magnetization at the interface. Similarly, the incident electrons from the ferromagnet are assumed to be collinear with the magnetization, so those process are described the majority and minority transmission and reflection probabilities alone.

The transformation from the Boltzmann equation to the drift-diffusion equation requires appropriate averages over these reflection parameters. The result that the incident transverse spin current is absorbed at the interface is equivalent to stating that $\mathrm{R}_\perp$ and $\mathrm{R}_\times$ average to zero. Then, the boundary conditions for transport in multilayers with noncollinear magnetizations are that the transverse spin current and accumulation in the ferromagnet are both zero and the transverse spin accumulation and current in the nonmagnet are proportional to each other

$$\mathbf{Q}_\perp \cdot \hat{\mathbf{n}} = B\mathbf{s}_\perp \qquad (17)$$

The $\perp$ subscript indicates the transverse component. The constant of proportionality is a constant with units of velocity $B = A_{\mathrm{FS}}/(8\pi^3\hbar\mathcal{N})$, where A_{FS} is the Fermi surface area of the nonmagnetic material projected onto a plane in the interface direction.

The spin-transfer torque described here is due to the spin current carried by nonequilibrium carriers at the Fermi energy. Although the spin-transfer torque is interfacial, it is typically treated as spread uniformly throughout the free layer because the free layer is thin enough that the micromagnetic exchange interaction tends to keep the magnetization aligned. It is interesting to see how this comes about in detail. The interfacial spin-transfer torque needs to be balanced by another interfacial torque so as to prevent a diverging response. This balancing torque comes from

the micromagnetic exchange. Normally, the micromagnetic exchange has the boundary condition that the normal gradient of the magnetization vanishes $(\hat{\mathbf{n}} \cdot \nabla)\mathbf{s}(\mathbf{r}) = 0$. This condition is simply the requirement that the interfacial torque vanish. In the presence of an interfacial spin-transfer torque, the gradient is nonzero at the interface. Since the magnetization is differentiable, a finite derivative at the interface gives a finite derivative into the layer. This rotation of the magnetization effectively 'spreads' the interfacial spin-transfer torque over the thin layer. As mentioned after equation (8), the micromagnetic exchange torque can be understood as the gradient of a spin current carried by all of the electrons in the Fermi sea. A finite normal gradient corresponds to a discontinuous spin current. At the interface, both the transport spin current and the micromagnetic spin current are discontinuous. In fact, the total spin current is continuous. At the interface, the incident spin current carried by the nonequilibrium carriers at the Fermi energy is converted into a 'quasiequilibrium' spin current carried by all of the electrons. This conversion is what effectively spreads the interfacial spin-transfer torque over the thickness of the film.

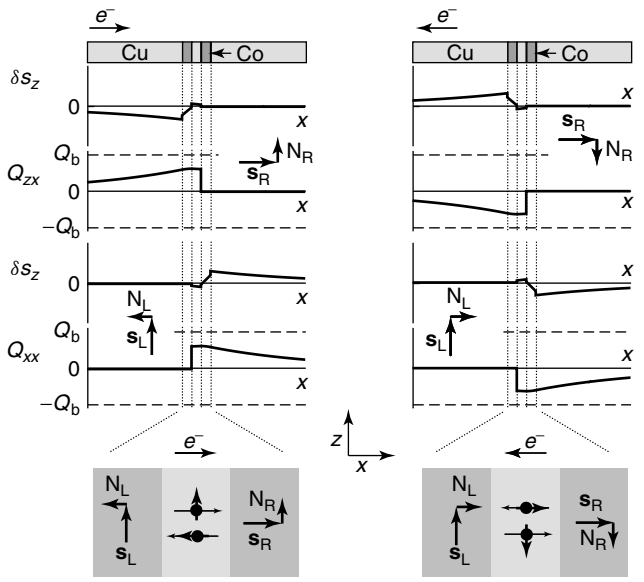

Figure 7. Spin accumulation (δs_α) and spin current ($Q_{\alpha x}$) for electron flow through two ferromagnetic layers embedded in a nonmagnetic host and separated by a thin nonmagnetic spacer layer. The magnetizations of the two layers are perpendicular to each other, for purposes of illustration both are in the plane of the figure. On the left side, the current flows in the $\hat{\mathbf{x}}$ direction and on the right in the $-\hat{\mathbf{x}}$ direction. Q_b is the magnitude of the spin current in the bulk ferromagnet far from any interfaces. The transverse component of the spin current is discontinuous at each interior interface giving rise to torques on the magnetizations of each layer. The directions of the torques are indicated for each of the interfaces. The bottom panel gives a cartoon of the spin current in the spacer layer.

4 NONCOLLINEAR TRANSPORT AND TORQUE

With the boundary condition derived in the previous section, it is now possible to compute the transport for multilayers with noncollinear magnetizations. Such calculations have been undertaken with a variety of different approaches, including the Keldysh formalism (Edwards, Federici, Mathon and Umerski, 2005), the Boltzmann equation (Stiles and Zangwill, 2002b; Shpiro, Levy and Zhang, 2003), the drift-diffusion approximation (Berger, 1998; Grollier *et al*., 2003; Fert *et al*., 2004; Stiles, Xiao and Zangwill, 2004; Barnas *et al*., 2005), random matrix theory (Waintal, Myers, Brouwer and Ralph, 2000), and circuit theory (Brataas, Nazarov and Bauer, 2000; Brataas, Bauer and Kelly, 2006). Although the calculations differ in detail, they all find qualitatively similar results. Here, we describe the physics in the language of the drift-diffusion approach.

A calculation of the spin current and spin accumulation in a magnetic multilayer with perpendicular magnetizations is shown in Figure 7. The behavior is closely related to that shown in Figure 2. Consider the component of spin along $\hat{\mathbf{z}}$, aligned with the spin density in the left layer. Far to the left of the sample, the spin current is unpolarized, but it becomes polarized due to the spin-dependent conductivity of the ferromagnetic layer as described in Section 2. More majority electrons go through the left layer leading to backward diffusion of minority spins in the left lead and a positive spin current. This spin current continues unchanged through the thin spacer layer but goes to zero at the left interface of the right ferromagnet. At this interface, the spins are transverse to the spin density in that layer and the transverse spin current is absorbed as described in Section 3. The abrupt change in the spin current gives a current-induced torque on the right ferromagnet at its left interface.

When the component of the spin along $\hat{\mathbf{z}}$ goes to zero at this interface, components along $\hat{\mathbf{x}}$ are generated by the spin-dependent reflection. The reflected electrons are predominantly antiparallel to the spin density in the right ferromagnetic layer and move away from the interface toward the left ferromagnet. When they hit the right interface of the left ferromagnet, they are again transverse to the spin density and that component of the spin density gets absorbed at that interface. Again, this discontinuity in the spin current give rise to a current-induced torque.

An interesting result of this calculation is that the torques tend to make the two magnetizations pinwheel after each other, apparently violating conservation of angular momentum. This apparent violation is resolved by the role of spin-flip scattering, which couples angular momentum from the

lattice into the electron system, which is then absorbed by the magnetization. Another interesting feature of this figure is that in the spacer layer, the spin-current direction is not aligned with the spin accumulation, but rather is almost perpendicular. Such a result is not entirely unexpected because the spin current is related to the gradient of the spin accumulation rather than the accumulation itself.

The calculation shown in Figure 7 gives the torque and the resistance of the multilayer for a particular magnetic configuration. Similar calculations give the torque and magnetoresistance as a function of angle, see Figure 8. Related calculations done by a number of authors (Vedyayev *et al*., 1997; Slonczewski, 2002; Stiles and Zangwill, 2002b; Huertas-Hernando, Bauer and Nazarov, 2002; Kovalev, Brataas and Bauer, 2002; Bauer, Tserkovnyak, Huertas-Hernando and Brataas, 2003; Manschot, Brataas and Bauer, 2004a,b; Xiao, Zangwill and Stiles, 2004) give similar results. If the spin-current incident on the free layer were independent of the relative orientation of the magnetizations of the two layers and given by $(\hbar/2)\mathcal{P}\,\hat{\mathbf{s}}_0 \otimes \mathbf{j}$, then the torque would be

$$\frac{\mathbf{N}_c}{A} = \frac{\hbar}{2}(\mathbf{j}\cdot\hat{\mathbf{x}})\;\mathcal{P}\;\left[\hat{\mathbf{s}}_0 - (\hat{\mathbf{s}}_0\cdot\hat{\mathbf{s}})\hat{\mathbf{s}}\right] \tag{18}$$

where $\hat{\mathbf{s}}$ is the directions of the ferromagnetic spin density for the free layer. The last factor is simply the transverse part of the spin current. It is more frequently written in terms of the equivalent triple product form, $\hat{\mathbf{s}}\times(\hat{\mathbf{s}}_0\times\hat{\mathbf{s}})$. The magnitude of this vector is $\sin\theta$, where θ is the relative angle between the magnetization $\hat{\mathbf{s}}$ and the direction of the spin current $\hat{\mathbf{s}}_0$. This form of the torque is frequently used in simulations of the magnetic dynamics.

However, calculations show that the spin current *does* depend on the relative angle of the magnetizations, but the changes to equation (18) are simple. The direction of the torque remains the same if $\hat{\mathbf{s}}_0$ is taken to be the direction of the fixed layer magnetization. This replacement works because the direction of spin current is generally some combination of $\hat{\mathbf{s}}$ and $\hat{\mathbf{s}}_0$. Since $\hat{\mathbf{s}}$ does not have a component that is transverse to itself, only the contribution along $\hat{\mathbf{s}}_0$ remains. After that replacement, the rest of the changes in the behavior found in these calculations are captured simply by letting the polarization $\mathcal{P}$ be a function of the relative angle θ between the two magnetizations see Figure 8.

For multilayers with equivalent magnetic layers, Slonczewski (2002) derived an analytic formula for $\mathcal{P}$ by combining a density matrix description of the spacer layer with a circuit theory (Brataas, Nazarov and Bauer, 2000). Extensions of the formula for arbitrary magnetic layers

$$\mathcal{P}(\theta) = \left[\frac{q_+}{B_0 + B_1\cos\theta} + \frac{q_-}{B_0 - B_1\cos\theta}\right] \tag{19}$$

have been described by a number of authors (Kovalev, Brataas and Bauer, 2002; Xiao, Zangwill and Stiles, 2004; Fert *et al*., 2004; Manschot, Brataas and Bauer, 2004a). The four parameters (B_0, B_1, q_+, and q_-) in this expression can be written in terms of layer thicknesses, resistivities, spin diffusion lengths, and so on. The ratio q_-/q_+ depends on the asymmetry between the free layer and the fixed layer and goes to zero for symmetric systems (Slonczewski, 2002). The ratio B_1/B_0 goes to zero when the polarization of the current is independent of the relative angle between the magnetizations. Calculations show that this behavior only occurs in unphysical limits. Xiao, Zangwill and Stiles (2004) have compared solutions of a Boltzmann equation with equation (19) and found very good agreement.

It is difficult to directly compare the form of the torque in equation (19) with experiment because the torque is not directly measurable in the experiment; the only experimental observable is the time-dependent resistance. It is possible to use equation (19) to predict the dynamics, and then to predict the time-dependent resistance to compare with experiment, such simulations are described briefly in Section 5. However, such a comparison requires correctly knowing and treating all of the other factors that contribute to the dynamics. More direct comparisons can be made between the measured and calculated resistances as a function of the relative angle between the magnetizations (Pratt, W.P. Jr. Private Communication), (Urazhdin, Loloee and Pratt, 2005). The measurements show clear deviation from simple $\sin^2(\theta/2)$ behavior. However, the deviations tend to be smaller than those calculated (Manschot, Brataas and Bauer, 2004a) with the models that give results like equation (19).

The torque in equations (18) and (19) is zero for parallel and antiparallel alignments of the magnetization. The existence of transitions out of these configurations is then due to instabilities developing in the configurations as the current is varied, see Sun (2000); Bazaliy, Jones and Zhang

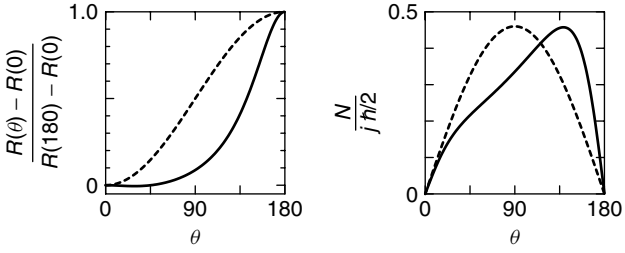

Figure 8. The angular dependence of the torque and magnetoresistance as a function of the relative angle of the two magnetizations. The dashed curves show the simple forms frequently used in micromagnetic simulations, $\sin^2(\theta/2)$ and $\mathcal{P}\sin\theta$ for the relative magnetoresistance and the torque, respectively.

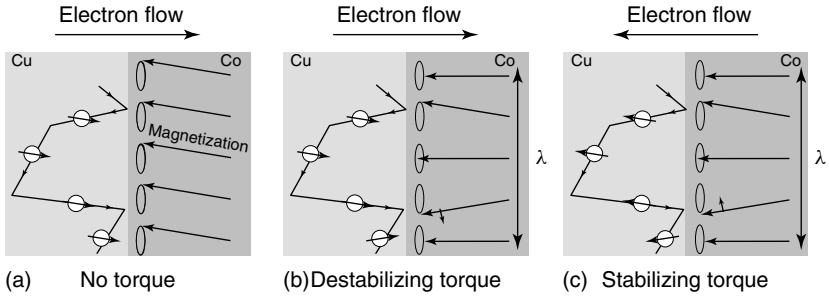

Figure 9. Spin-transfer torque due to lateral diffusion. Each panel shows an electron diffusing in a nonmagnet and reflecting twice from the interface with a ferromagnet. After it scatters, it is oriented *on average* either parallel or antiparallel to the magnetization depending on the direction of the electron flow, see Figure 1. In (a), the ferromagnetic magnetization is uniform laterally so that when the electron scatters the second time, it is aligned with the magnetization and there is no reorientation of either. The electron flow is from the nonmagnet into the ferromagnet, so the accumulated spins are minority spins. In (b), there is a nonuniform magnetization, and the diffusing minority spin is not aligned with the magnetization the second time it scatters. The magnetization exerts a torque on it and it exerts a torque on the magnetization which tends to amplify the spin wave. In (c), the electron flow is in the opposite direction so the diffusing spins are majority spins. In this case, the torque in the second scattering event tends to reduce the amplitude of the nonuniform spin wave.

(2004). For appropriate directions of current flow, the spin-transfer torque tends to amplify small deviations away from the collinear configuration and damping tends to diminish them. For large enough currents, the spin-transfer torque dominates and the system becomes unstable.

A different origin of the instability has been proposed by Berger and studied by a number of authors (Berger, 1996, 1997, 1999, 2002; Tsoi and Tsoi, 2001; Heide, 2001; Tsoi *et al*., 2004). Here, the longitudinal spin accumulation in the ferromagnet drives the instability rather than the transverse spin current. As the current through the structure increases, the spin accumulation eventually becomes large enough that it is possible to flip a spin from minority to majority and excite a magnon. This process is most clearly seen when the spin accumulation is described in terms of a spin-dependent chemical potential. In Berger's model, a particular magnon mode, possibly the uniform mode, gets macroscopically populated through stimulated emission. This instability then gives rise to reversal with a particular critical current density. Tserkovnyak, Brataas and Bauer (2003) have shown that a model without direct magnon excitation but including spin pumping (see below) can give the same critical current density.

When the magnetization varies in space, there are additional considerations. If the magnetization varies along the direction of the current flow, there are torques on the magnetization as the spins in the current precess around the varying magnetizations, as mentioned in Section 3. If the magnetization varies in the plane of the interface, lateral diffusion of spins can tend to increase or decrease these variations depending on the direction of the current flow. If the net electron flow is from a nonmagnet into a ferromagnet, the spins that accumulate in the nonmagnet are, on average, antiparallel to the spin density in the ferromagnet. If the spin density is not uniform, locally, the spins tend to align opposite to the local spin density. These electrons are diffusing, so there is a good chance that some of them diffuse laterally and scatter again from the interface at some different point. If the direction of the spin density at the point is different, the electron, on average, exerts a torque on the magnetization at that point. When the electron flow is from the nonmagnet into the ferromagnet, more minority spins are diffusing, and the torque tends to amplify the variations away from the average, see Figure 9. On the other hand, for electron flow from the ferromagnet into the nonmagnet, more of the diffusing spins are aligned with the spin density, and the resulting torque tends to reduce variations away from the average.

These torques due to lateral diffusion have been discussed (Polianski and Brouwer, 2004; Stiles, Xiao and Zangwill, 2004) in the context of instabilities in single ferromagnetic films and (Brataas, Tserkovnyak and Bauer, 2006) in the context of trilayers. For single films, these calculations show that for the current densities studied experimentally in these systems, nonuniform modes can become unstable. Instabilities have been observed in point contact experiments with single films (Ji, Chien and Stiles, 2003; Chen, Ji, Chien and Stiles, 2004) and also in lithographically defined single films (Özyilmaz *et al*., 2004). The critical currents are close to those found in the calculations and the field dependence of the critical currents is also similar. However, there are still details of the experimental results that are not explained by the calculations.

Finally, before discussing the dynamics that result from the spin transfer torque, there is a correction to the boundary condition, equation (17), when the magnetization is time dependent

$$\mathbf{Q}_\perp \cdot \hat{\mathbf{n}} = B\mathbf{s}_\perp + B'\hat{\mathbf{u}} \times \dot{\hat{\mathbf{u}}} \tag{20}$$

where $\hat{\mathbf{u}}$ is the direction of the magnetization and $\dot{\hat{\mathbf{u}}}$ is its time derivative. This additional term describes the phenomenon called *spin pumping*, an effect originally proposed by Berger (1996, 2001), developed by Tserkovnyak, Brataas and Bauer (2002, 2005) and computed in a number of different models (Tserkovnyak, Brataas and Bauer, 2002; Mills, 2003; Šimánek and Heinrich, 2003; Šimánek, 2003). The two terms in equation (20) are closely related. The first term describes the spin current discontinuity that gives rise to a torque and causes the magnetization to move and the second is the spin current that results from a moving magnetization. Both phenomena are controlled by related parameters

$$B' = \frac{A_{\mathrm{FS}}}{(2\pi)^3}\frac{\hbar}{2} = \frac{\hbar^2}{2}\mathcal{N}B \tag{21}$$

where A_{FS} is projected area of the Fermi surface in the nonmagnet.

Equation (20) shows that even in the absence of a current, a moving magnetization drives a spin current in the nonmagnetic material. When this spin current is absorbed through spin-flip scattering or scattering from another ferromagnetic layer, the spin-pumping process acts like a form of interfacial damping. These effects have been observed in line-width measurements in ferromagnetic resonance (Urban, Woltersdorf and Heinrich, 2001; Mizukami, Ando and Miyazaki, 2002; Ingvarsson *et al*., 2002; Lubitz, Cheng and Rachford, 2003; Heinrich *et al*., 2003; Lenz *et al*., 2004).

5 DISCUSSION

This chapter describes the physics that leads to spin-transfer torques in magnetic multilayers. When the magnetizations of the layers are not collinear with each other, the spin-polarized currents transfer angular momentum to the magnetizations near the interfaces, giving rise to spin-transfer torques. These torques can be computed using a combination of quantum-mechanical calculations of the behavior of spins at interfaces and semiclassical transport calculations to describe the flow of spins in the multilayers.

Quantum-mechanical calculations of spins at interfaces show that a combination of spatial separation of spin components coupled with classical dephasing leads to the approximate absorption of the transverse spin current at the interfaces. This result means that independent of their orientation when approaching the interface, the spins are on average collinear with the magnetization when they leave the interface. In effect, any component of the incoming spins that is transverse to the magnetization is transfered to the magnetization. The angular momentum along the magnetization direction is conserved.

The results of the quantum-mechanical calculations are inserted into semiclassical transport calculations as boundary conditions. These calculations determine the degree of the spin polarization at the interfaces. They show that currents become spin polarized through the combination of spin-dependent conductivities and interface conductances together with spin-flip scattering. Spin-flip scattering couples angular momentum between the electron system and the lattice. The spin-transfer torque couples angular momentum between the electron system and the magnetization.

The transport calculations are done for fixed magnetizations, even when the magnetizations are time dependent. This approximation is justified by a separation of timescales. A typical precession period for the magnetization is about 10^{-9} s and the transit time for a ballistic Fermi surface electron to go through the device (about 100 nm) is about 10^{-13} s. Even though the transport is not ballistic, this difference in timescales argues that treating the electrons as moving through a fixed magnetization should be a good first approximation.

The result of the semiclassical transport calculations is an expression for the spin-transfer torque as a function of the angle between the two magnetizations, equations (18) and (19). These equations summarize the results of the calculations described in this chapter. It is difficult to directly compare this result with experiment. Experimentally, it is the consequences of the torque that are readily measured, for example, the critical currents for switching between parallel and antiparallel configurations. To compare with such experiments, the calculated torque is inserted into the equation of motion for the magnetization, the Landau–Lifshitz–Gilbert equation, and used to compute the dynamics. There are several approaches to such computations.

The simplest approach is to assume that the magnetization of each layer is separately uniform. The model based on this assumption is called the *macrospin model*. The simplicity of the resulting equation of motion lends itself to analytic determination of critical currents (Bazaliy, Jones and Zhang, 2001, 2004; Xi and Shi, 2004) and detailed exploration of behavior as a function of field and current (Katine *et al*., 2000; Kiselev *et al*., 2004; Koch, Katine and Sun, 2004; Xiao, Zangwill and Stiles, 2005). However, the assumption of a uniform magnetization is not always justified. Relaxing this approximation gives a full micromagnetic model. Such calculations (Miltat, Albuquerque, Thiaville and Vouille, 2001; Li and Zhang, 2003; Zhu and Zhu, 2004; Lee *et al*., 2004a,b; Zhu, Zhu and White, 2004; Berkov and Gorn, 2005a,b; Montigny and Miltat, 2005) treat the detailed spatial variation of the magnetization, but the results are sensitive to many of the details of the samples. Since many of these details, like grain sizes, local anisotropies, the detailed shape,

and so on are not measured, it is hard to make definitive comparisons between these calculations and measurements.

A final complication of the comparison between theory and experiment is that experiments are typically done at finite temperature and calculations are most simply done at zero temperature. Under the influence of temperature, transitions between different configurations become statistical rather than deterministic. Several different approaches have been used to analyze the statistics of the switching events (Myers *et al*., 2002; Koch, Katine and Sun, 2004; Li and Zhang, 2004; Apalkov and Visscher, 2005). The most straightforward approach to including thermal effects is to include a fluctuating field in macrospin simulations (Russek *et al*., 2005; Xiao, Zangwill and Stiles, 2005). Such simulations give a reasonably good account of the effects of temperature if allowance is made for the difference in the timescales used in experiments and those achievable in the simulations.

Comparisons between theory and experiment generally give qualitative, but not quantitative agreement. One of the most straightforward predictions of the torque in equations (18) and (19) when inserted into the macrospin model is that the critical currents for the transitions between parallel and antiparallel alignment are determined by the slopes of the torque as a function of angle for 0° and 180° relative angles. Since transport calculations generally give a very different polarization of the current for the two alignments, the critical current for the parallel to antiparallel transition is expected to be larger in magnitude than that for the reverse transition. Although there is wide variation seen experimentally, the trend is that this difference is smaller than what is expected from theory. It is not clear whether this disagreement points to errors in the calculation of the torque or deviations of the reversal process from that expected for a macrospin. Other disagreements between macrospin calculations and experiment appear to explainable by micromagnetic calculations. These are discussed in more detail in other chapters in the volume.

REFERENCES

Albert, F.J., Emley, N.C., Myers, E.B., *et al*. (2002). Quantitative study of magnetization reversal by spin-polarized current in magnetic multilayer nanopillars. *Physical Review Letters*, **89**, 226802-1–226802-4.

AlHajDarwish, M., Kurt, H., Urazhdin, S., *et al*. (2004). Controlled normal and inverse current-induced magnetization switching and magnetoresistance in magnetic nanopillars. *Physical Review Letters*, **93**, 157203-1–157203-4.

Ansermet, J.P. (2004). Classical description of spin wave excitation by currents in bulk ferromagnets. *IEEE Transactions on Magnetics*, **40**, 358–360.

Apalkov, D.M. and Visscher, P.B. (2005). Slonczewski spin-torque as negative damping: Fokker-Planck computation of energy distribution. *Journal of Magnetism and Magnetic Materials*, **286**, 370–374.

Aronov, A.G. (1976). Spin injection in metals and polarization of nuclei. *JETP Letters*, **24**, 32–34.

Baibich, M.N., Broto, J.M., Fert, A., *et al*. (1988). Giant magnetoresistance of (001) Fe/(001) Cr magnetic superlattices. *Physical Review Letters*, **61**, 2472–2475.

Barnas, J., Fert, A., Gmitra, M., *et al*. (2005). From giant magnetoresistance to current-induced switching by spin transfer. *Physical Review B*, **72**, 024426-1–024426-12.

von Barth, U. and Hedin, L. (1972). A local exchange-correlation potential for the spin polarized case. *Journal of Physics C: Solid State Physics*, **5**, 1629.

Bauer, G.E.W., Schep, K.M., Xia, K. and Kelly, P.J. (2002). Scattering theory of interface resistance in magnetic multilayers. *Journal of Physics D: Applied Physics*, **35**, 2410–2414.

Bauer, G.E.W., Tserkovnyak, Y., Huertas-Hernando, D. and Brataas, A. (2003). Universal angular magnetoresistance and spin torque in ferromagnetic/normal metal hybrids. *Physical Review B*, **67**, 094421-1–094421-4.

Bazaliy, Y.B., Jones, B.A. and Zhang, S.C. (1998). Modification of the Landau-Lifshitz equation in the presence of a spin-polarized current in colossal-and giant-magnetoresistive materials. *Physical Review B*, **57**, R3213–R3216.

Bazaliy, Y.B., Jones, B.A. and Zhang, S.C. (2001). Towards metallic magnetic memory: how to interpret experimental results on magnetic switching induced by spin-polarized currents. *Journal of Applied Physics*, **89**, 6793–6795.

Bazaliy, Y.B., Jones, B.A. and Zhang, S.C. (2004). Current-induced magnetization switching in small domains of different anisotropies. *Physical Review B*, **69**, 094421-1–094421-19.

Berger, L. (1978). Low-field magnetoresistance and domain drag in ferromagnets. *Journal of Applied Physics*, **49**, 2156–2161.

Berger, L. (1979). Domain drag effect in the presence of variable magnetic-field or variable transport current. *Journal of Applied Physics*, **50**, 2137–2139.

Berger, L. (1984). Exchange interaction between ferromagnetic domain wall and electric current in very thin metallic films. *Journal of Applied Physics*, **55**, 1954.

Berger, L. (1986). Possible existence of a Josephson effect in ferromagnets. *Physical Review B*, **33**, 1572.

Berger, L. (1996). Emission of spin waves by a magnetic multilayer traversed by a current. *Physical Review B*, **54**, 9353–9358.

Berger, L. (1997). Multilayers as spin-wave emitting diodes. *Journal of Applied Physics*, **81**, 4880–4882.

Berger, L. (1998). Spin-wave emitting diodes and spin diffusion in magnetic multilayers. *IEEE Transactions on Magnetics*, **34**, 3837–3841.

Berger, L. (1999). Generation of dc voltages by a magnetic multilayer undergoing ferromagnetic resonance. *Physical Review B*, **59**, 11465–11470.

Berger, L. (2001). Effect of interfaces on Gilbert damping and ferromagnetic resonance linewidth in magnetic multilayers. *Journal of Applied Physics*, **90**, 4632–4638.

Berger, L. (2002). Interaction of electrons with spin waves in the bulk and in multilayers (invited). *Journal of Applied Physics*, **91**, 6795–6800.

Berger, L. (2004). Influence of current leads on critical current for spin precession in magnetic multilayers. *Journal of Magnetism and Magnetic Materials*, **278**, 185–194.

Berkov, D. and Gorn, N. (2005a). Transition from the macrospin to chaotic behavior by a spin-torque driven magnetization precession of a square nanoelement. *Physical Review B*, **71**, 052403-1–052403-4.

Berkov, D. and Gorn, N. (2005b). Magnetization precession due to a spin-polarized current in a thin nanoelement: numerical simulation study. *Physical Review B*, **72**, 094401-1–094401-15.

Binasch, G., Grünberg, P., Saurenbach, F. and Zinn, W. (1989). Enhanced magnetoresistance in layered magnetic-structures with antiferromagnetic interlayer exchange. *Physical Review B*, **39**, 4828–4830.

Brataas, A., Bauer, G.E.W. and Kelly, P.J. (2006) Non-collinear magnetoelectronics. *Physics Reports*, **427**, 157.

Brataas, A., Nazarov, Y.V. and Bauer, G.E.W. (2000). Finite-element theory of transport in ferromagnet-normal metal systems. *Physical Review Letters*, **84**, 2481–2484.

Brataas, A., Tserkovnyak, Y. and Bauer, G.E.W. (2006). Current-induced macrospin vs spin-wave excitations in spin valves. *Physical Review B*, **73**, 014408.

Chen, T.Y., Ji, Y., Chien, C.L. and Stiles, M.D. (2004). Current-driven switching in a single exchange-biased ferromagnetic layer. *Physical Review Letters*, **93**, 026601-1–026601-4.

Choy, T-S., Naset, J., Chen, J., *et al*. (1995) *The Fermi Surface Database*, http://www.phys.ufl.edu/fermisurface/.

Covington, M., AlHajDarwish, M., Ding, Y., *et al*. (2004). Current-induced magnetization dynamics in current perpendicular to the plane spin valves. *Physical Review B*, **69**, 184406-1–184406-8.

Deac, A., Redon, O., Sousa, R.C., *et al*. (2004). Current driven resistance changes in low resistance x area magnetic tunnel junctions with ultra-thin Al-O-x barriers. *Journal of Applied Physics*, **95**, 6792–6794.

Edwards, D.M., Federici, F., Mathon, J. and Umerski, A. (2005). Self-consistent theory of current-induced switching of magnetization. *Physical Review B*, **71**, 054407-1–054407-16.

Fabian, A., Terrier, C., Guisan, S.S., *et al*. (2003). Current-induced two-level fluctuations in pseudo-spin-valve (Co/Cu/Co) nanostructures. *Physical Review Letters*, **91**, 257209-1–257209-4.

Fert, A., Cros, V., George, J.M., *et al*. (2004). Magnetization reversal by injection and transfer of spin: experiments and theory. *Journal of Magnetism and Magnetic Materials*, **272–276**, 1706–1711.

Fuchs, G.D., Emley, N.C., Krivorotov, I.N., *et al*. (2004). Spin-transfer effects in nanoscale magnetic tunnel junctions. *Applied Physics Letters*, **85**, 1205–1207.

Fulde, P. (1995). *Electron Correlations in Molecules and Solids*, Springer-Verlag: New York.

Grollier, J., Cros, V., Hamzić, A., *et al*. (2001). Spin-polarized current induced switching in Co/Cu/Co pillars. *Applied Physics Letters*, **78**, 3663–3665.

Grollier, J., Cros, V., Jaffrès, H., *et al*. (2003). Field dependence of magnetization reversal by spin transfer. *Physical Review B*, **67**, 174402-1–174402-8.

Gunnarsson, O. and Lundqvist, B.I. (1976). Exchange and correlation in atoms, molecules, and solids by spin-density functional formalism. *Physical Review B*, **13**, 4274–4298.

Hamrle, J., Kimura, T., Yang, T. and Otani, Y. (2005). Three-dimensional distribution of spin-polarized current inside (Cu/Co) pillar structures. *Physical Review B*, **71**, 094434-1–094434-7.

Hayakawa, J., Ito, K., Fujimori, M., *et al*. (2004). Current-driven switching of exchange biased spin-valve giant magnetoresistive nanopillars using a conducting nanoprobe. *Journal of Applied Physics*, **96**, 3440–3442.

Heide, C. (2001). Spin currents in magnetic films. *Physical Review Letters*, **8719**, 197201-1–197201-4.

Heide, C., Zilberman, P.E. and Elliott, R.J. (2001). Current-driven switching of magnetic layers. *Physical Review B*, **6305**, 064424-1–064424-7.

Heinrich, B., Tserkovnyak, Y., Woltersdorf, G., *et al*. (2003). Dynamic exchange coupling in magnetic bilayers. *Physical Review Letters*, **90**, 187601-1–187601-4.

Held, K. and Vollhardt, D. (1998). Microscopic conditions favoring itinerant ferromagnetism: Hund's rule coupling and orbital degeneracy. *European Physical Journal B*, **5**, 473–478.

Hitchon, W.N.G., Chantrell, R.W. and Rebei, A. (2004). *Spin Accumulation in Ferromagnets*. cond-mat/0407051.

Huai, Y.M., Albert, F., Nguyen, P., *et al*. (2004). Observation of spin-transfer switching in deep submicron-sized and low-resistance magnetic tunnel junctions. *Applied Physics Letters*, **84**, 3118–3120.

Huertas-Hernando, D., Bauer, G.E.W. and Nazarov, Y.V. (2002). Theory of the angular magneto resistance in CPP spin valves. *Journal of Magnetism and Magnetic Materials*, **240**, 174–176.

Ingvarsson, S., Ritchie, L., Liu, X.Y., *et al*. (2002). Role of electron scattering in the magnetization relaxation of thin Ni81Fe19 films. *Physical Review B*, **66**, 214416-1–214416-5.

Ji, Y., Chien, C.L. and Stiles, M.D. (2003). Current-induced spin-wave excitations in a single ferromagnetic layer. *Physical Review Letters*, **90**, 106601-1–106601-4.

Jiang, Y., Abe, S., Ochiai, T., *et al*. (2004). Effective reduction of critical current for current-induced magnetization switching by a Ru layer insertion in an exchange-biased spin valve. *Physical Review Letters*, **92**, 167204-1–167204-4.

Johnson, M. and Silsbee, R.H. (1987). Thermodynamic analysis of interfacial transport and of the thermomagnetoelectric system. *Physical Review B*, **35**, 4959–4972.

Jones, R.O. and Gunnarsson, O. (1989). The density functional formalism, its applications and prospects. *Reviews of Modern Physics*, **61**, 689–746.

Jonker, B.T., Hanbicki, A.T., Pierce, D.T. and Stiles, M.D. (2004). Spin nomenclature for semiconductors and magnetic metals. *Journal of Magnetism and Magnetic Materials*, **277**, 24–28.

Katine, J.A., Albert, F.J., Buhrman, R.A., *et al*. (2000). Current-driven magnetization reversal and spin-wave excitations in Co/Cu/Co pillars. *Physical Review Letters*, **84**, 3149–3152.

Kiselev, S.I., Sankey, J.C., Krivorotov, I.N., *et al*. (2003). Microwave oscillations of a nanomagnet driven by a spin-polarized current. *Nature*, **425**, 380–383.

Kiselev, S.I., Sankey, J.C., Krivorotov, I.N., *et al*. (2004). Current-induced nanomagnet dynamics for magnetic fields perpendicular to the sample plane. *Physical Review Letters*, **93**, 036601-1–036601-4.

Koch, R.H., Katine, J.A. and Sun, J.Z. (2004). Time-resolved reversal of spin-transfer switching in a nanomagnet. *Physical Review Letters*, **92**, 088302-1–088302-4.

Kohn, W. and Sham, L.J. (1965). Self-consistent equations including exchange and correlation effects. *Physical Review*, **140**, A1133.

Kovalev, A.A., Brataas, A. and Bauer, G.E.W. (2002). Spin transfer in diffusive ferromagnet-normal metal systems with spin-flip scattering. *Physical Review B*, **66**, 224424-1–224424-8.

Krivorotov, I.N., Emley, N.C., Garcia, A.G.F., *et al*. (2004). Temperature dependence of spin-transfer-induced switching of nanomagnets. *Physical Review Letters*, **93**, 166603-1–166603-4.

Langreth, D.C. and Wilkins, J.W. (1972). Theory of spin resonance in dilute magnetic alloys. *Physical Review B*, **6**, 3189.

Lee, K.J., Deac, A., Redon, O., *et al*. (2004a). Excitations of incoherent spin-waves due to spin-transfer torque. *Nature Materials*, **3**, 877–881.

Lee, K.J., Liu, Y., Deac, A., *et al*. (2004b). Spin transfer effect in spin-valve pillars for current-perpendicular-to-plane magnetoresistive heads (invited). *Journal of Applied Physics*, **95**, 7423–7428.

Lenz, K., Tolinski, T., Lindner, J., *et al*. (2004). Evidence of spin-pumping effect in the ferromagnetic resonance of coupled trilayers. *Physical Review B*, **69**, 144422-1–144422-7.

Li, Z. and Zhang, S. (2003). Magnetization dynamics with a spin-transfer torque. *Physical Review B*, **68**, 024404-1–024404-10.

Li, Z. and Zhang, S. (2004). Thermally assisted magnetization reversal in the presence of a spin-transfer torque. *Physical Review B*, **69**, 134416-1–134416-6.

Liu, Y.W., Zhang, Z.Z., Freitas, P.P. and Martins, J.L. (2003). Current-induced magnetization switching in magnetic tunnel junctions. *Applied Physics Letters*, **82**, 2871–2873.

Lubitz, P., Cheng, S.F. and Rachford, F.J. (2003). Increase of magnetic damping in thin polycrystalline Fe films induced by Cu/Fe overlayers. *Journal of Applied Physics*, **93**, 8283–8285.

Mancoff, F.B., Dave, R.W., Rizzo, N.D., *et al*. (2003). Angular dependence of spin-transfer switching in a magnetic nanostructure. *Applied Physics Letters*, **83**, 1596–1598.

Mancoff, F.B. and Russek, S.E. (2002). Spin-current-induced magnetotransport in Co-Cu-Co nanostructures. *IEEE Transactions on Magnetics*, **38**, 2853–2855.

Manschot, J., Brataas, A. and Bauer, G.E.W. (2004a). Nonmonotonic angular magnetoresistance in asymmetric spin valves. *Physical Review B*, **69**, 092407-1–092407-4.

Manschot, J., Brataas, A. and Bauer, G.E.W. (2004b). Reducing the critical switching current in nanoscale spin valves. *Applied Physics Letters*, **85**, 3250–3252.

Mills, D.L. (2003). Ferromagnetic resonance relaxation in ultrathin metal films: the role of the conduction electrons. *Physical Review B*, **68**, 014419-1–014419-10.

Miltat, J., Albuquerque, G., Thiaville, A. and Vouille, C. (2001). Spin transfer into an inhomogeneous magnetization distribution. *Journal of Applied Physics*, **89**, 6982–6984.

Mizukami, S., Ando, Y. and Miyazaki, T. (2002). Effect of spin diffusion on Gilbert damping for a very thin permalloy layer in Cu/permalloy/Cu/Pt films. *Physical Review B*, **66**, 104413-1–104413-9.

Montigny, B. and Miltat, J. (2005). Micromagnetic simulations of current-induced microwave excitations. *Journal of Applied Physics*, **97**, 10 C708-1–10C708-3.

Moriya, R., Hamaya, K., Oiwa, A. and Munekata, H. (2004). Current-induced magnetization reversal in a (Ga,Mn)As-based magnetic tunnel junction. *Japanese Journal of Applied Physics Part 2 Letters Express Letter*, **43**, L825–L827.

Moruzzi, V.L., Janak, J.F. and Williams, A.R. (Eds.) (1978). *Calculated Electronic Properties of Metals*, Pergamon Press: New York.

Myers, E.B., Albert, F.J., Sankey, J.C., *et al*. (2002). Thermally activated magnetic reversal induced by a spin-polarized current. *Physical Review Letters*, **89**, 196801-1–196801-4.

Myers, E.B., Ralph, D.C., Katine, J.A., *et al*. (1999). Current-induced switching of domains in magnetic multilayer devices. *Science*, **285**, 867–870.

Özyilmaz, B., Kent, A.D., Monsma, D., *et al*. (2003). Current-induced magnetization reversal in high magnetic fields in Co/Cu/Co nanopillars. *Physical Review Letters*, **91**, 067203-1–067203-4.

Özyilmaz, B., Kent, A.D., Sun, J.Z., *et al*. (2004). Current-induced excitations in single cobalt ferromagnetic layer nanopillars. *Physical Review Letters*, **93**, 176604-1–176604-4.

Polianski, M.L. and Brouwer, P.W. (2004). Current-induced transverse spin-wave instability in a thin nanomagnet. *Physical Review Letters*, **92**, 026602-1–026602-4.

Pufall, M.R., Rippard, W.H., Kaka, S., *et al*. (2004). Large-angle, gigahertz-rate random telegraph switching induced by spin-momentum transfer. *Physical Review B*, **69**, 214409-1–214409-5.

Pufall, M.R., Rippard, W.H. and Silva, T.J. (2003). Materials dependence of the spin-momentum transfer efficiency and critical current in ferromagnetic metal/Cu multilayers. *Applied Physics Letters*, **83**, 323–325.

Rippard, W.H., Pufall, M.R., Kaka, S., *et al*. (2004a). Direct-current induced dynamics in Co90Fe10/Ni80Fe20 point contacts. *Physical Review Letters*, **92**, 027201-1–027201-4.

Rippard, W.H., Pufall, M.R., Kaka, S., *et al*. (2004b). Current-driven microwave dynamics in magnetic point contacts as a function of applied field angle. *Physical Review B*, **70**, 100406-1–100406-4.

Rippard, W.H., Pufall, M.R. and Silva, T.J. (2003). Quantitative studies of spin-momentum-transfer-induced excitations in Co/Cu multilayer films using point-contact spectroscopy. *Applied Physics Letters*, **82**, 1260–1262.

Russek, S.E., Kaka, S., Rippard, W.H., *et al*. (2005). Finite-temperature modeling of nanoscale spin-transfer oscillators. *Physical Review B*, **71**, 104425-1–104425-6.

Schep, K.M., van Hoof, J.B.A.N., Kelly, P.J., *et al*. (1998). Theory of interface resistances. *Journal of Magnetism and Magnetic Materials*, **177**, 1166–1167.

Shpiro, A., Levy, P.M. and Zhang, S.F. (2003). Self-consistent treatment of nonequilibrium spin torques in magnetic multilayers. *Physical Review B*, **67**, 104430-1–104430-17.

Šimánek, E. (2003). Gilbert damping in ferromagnetic films due to adjacent normal-metal layers. *Physical Review B*, **68**, 224403-1–224403-10.

Šimánek, E. and Heinrich, B. (2003). Gilbert damping in magnetic multilayers. *Physical Review B*, **67**, 144418-1–144418-12.

Slonczewski, J.C. (1996). Current-driven excitation of magnetic multilayers. *Journal of Magnetism and Magnetic Materials*, **159**, L1–L7.

Slonczewski, J.C. (2002). Currents and torques in metallic magnetic multilayers. *Journal of Magnetism and Magnetic Materials*, **247**, 324–338.

van Son, P.C., van Kempen, H. and Wyder, P. (1987). Boundary resistance of the ferromagnetic-nonferromagnetic metal interface. *Physical Review Letters*, **58**, 2271–2273.

Stiles, M.D. (1996). Spin-dependent interface transmission and reflection in magnetic multilayers. *Journal of Applied Physics*, **79**, 5805.

Stiles, M.D. and Penn, D.R. (2000). Calculation of spin-dependent interface resistance. *Physical Review B*, **61**, 3200–3202.

Stiles, M.D., Xiao, J. and Zangwill, A. (2004). Phenomenological theory of current-induced magnetization precession. *Physical Review B*, **69**, 054408-1–054408-15.

Stiles, M.D. and Zangwill, A. (2002a). Anatomy of spin-transfer torque. *Physical Review B*, **66**, 014407-1–014407-14.

Stiles, M.D. and Zangwill, A. (2002b). Noncollinear spin transfer in Co/Cu/Co multilayers (invited). *Journal of Applied Physics*, **91**, 6812–6817.

Sun, J.Z. (1999). Current-driven magnetic switching in manganite trilayer junctions. *Journal of Magnetism and Magnetic Materials*, **202**, 157–162.

Sun, J.Z. (2000). Spin-current interaction with a monodomain magnetic body: a model study. *Physical Review B*, **62**, 570–578.

Thiaville, A., Nakatani, Y., Miltat, J. and Suzuki, Y. (2005). Micromagnetic understanding of current-driven domain wall motion in patterned nanowires. *Europhysics Letters*, **69**, 990–996.

Tserkovnyak, Y., Brataas, A. and Bauer, G.E.W. (2002). Enhanced Gilber damping in thin ferromagnetic films. *Physical Review Letters*, **88**, 117601-1–117601-4.

Tserkovnyak, Y., Brataas, A. and Bauer, G.E.W. (2003). Dynamic stiffness of spin valves. *Physical Review B*, **67**, 140404-1–140404-4.

Tserkovnyak, Y., Brataas, A., Bauer, G.E.W. and Halperin, B.I. (2005) Nonlocal magnetization dynamics in ferromagnetic hybrid nanostructures. *Reviews of Modern Physics*, **77**, 1375.

Tsoi, M., Jansen, A.G.M., Bass, J., *et al*. (1998). Excitation of a magnetic multilayer by an electric current. *Physical Review Letters*, **80**, 4281–4284.

Tsoi, M.V. and Tsoi, V.S. (2001). Fluctuation model of current-driven magnon excitation. *JETP Letters*, **73**, 98–102.

Tsoi, M., Sun, J.Z. and Parkin, S.S.P. (2004). Current-driven excitations in symmetric magnetic nanopillars. *Physical Review Letters*, **93**, 036602-1–036602-4.

Tsoi, M., Sun, J.Z., Rooks, M.J., *et al*. (2004). Current-driven excitations in magnetic multilayer nanopillars from 4.2 K to 300 K. *Physical Review B*, **69**, 100406-1–100406-4.

Urazhdin, S., Birge, N.O., Pratt, W.P. and Bass, J. (2003). Current-driven magnetic excitations in permalloy-based multilayer nanopillars. *Physical Review Letters*, **91**, 146803-1–146803-4.

Urazhdin, S., Loloee, R. and Pratt, W.P. (2005). Noncollinear spin transport in magnetic multilayers. *Physical Review B*, **71**, 100401-1–100401-4.

Urban, R., Woltersdorf, G. and Heinrich, B. (2001). Gilbert damping in single and multilayer ultrathin films: role of interfaces in nonlocal spin dynamics. *Physical Review Letters*, **8721**, 217204-1–217204-4.

Valet, T. and Fert, A. (1993). Theory of the perpendicular magnetoresistance in magnetic multilayers. *Physical Review B*, **48**, 7099–7113.

Vedyayev, A., Ryzhanova, N., Dieny, B., *et al*. (1997). Angular variation of giant magnetoresistance for current perpendicular to the plane of the layers. *Physical Review B*, **55**, 3728–3733.

Waintal, X., Myers, E.B., Brouwer, P.W. and Ralph, D.C. (2000). Role of spin-dependent interface scattering in generating current-induced torques in magnetic multilayers. *Physical Review B*, **62**, 12317–12327.

Waintal, X. and Viret, M. (2004). Current-induced distortion of a magnetic domain wall. *Europhysics Letters*, **65**, 427–433.

Wegrowe, J.E., Kelly, D., Jaccard, Y., *et al*. (1999). Current-induced magnetization reversal in magnetic nanowires. *Europhysics Letters*, **45**, 626–632.

Xi, H.W. and Shi, Y.M. (2004). High frequency magnetization rotation induced by a dc spin-polarized current in magnetic nanostructures. *Journal of Applied Physics*, **96**, 1585–1590.

Xia, K., Kelly, P.J., Bauer, G.E.W., *et al*. (2001). Interface resistance of disordered magnetic multilayers. *Physical Review B*, **6305**, 064407-1–064407-4.

Xia, K., Kelly, P.J., Bauer, G.E.W., *et al*. (2002). Spin torques in ferromagnetic/normal-metal structures. *Physical Review B*, **65**, 220401-1–220401-4.

Xiao, J., Zangwill, A. and Stiles, M.D. (2004). Boltzmann test of Slonczewski's theory of spin-transfer torque. *Physical Review B*, **70**, 172405-1–172405-4.

Xiao, J., Zangwill, A. and Stiles, M.D. (2005). Macrospin models of spin transfer dynamics. *Physical Review B*, **72**, 014446-1–014446-13.

Yang, I., Savrasov, S.Y. and Kotliar, G. (2001). Importance of correlation effects on magnetic anisotropy in Fe and Ni. *Physical Review Letters*, **8721**, 216405-1–216405-4.

Zhang, S., Levy, P.M. and Fert, A. (2002). Mechanisms of spin-polarized current-driven magnetization switching. *Physical Review Letters*, **88**, 236601-1–236601-4.

Zhang, S. and Li, Z. (2004). Roles of nonequilibrium conduction electrons on the magnetization dynamics of ferromagnets. *Physical Review Letters*, **93**, 127204-1–127204-4.

Zhu, X.C. and Zhu, J.G. (2004). Angular dependence of the microwave excitation by direct current. *Journal of Applied Physics*, **95**, 7318–7320.

Zhu, X.C., Zhu, J.G. and White, R.M. (2004). Spin transfer excited regular and chaotic spin waves in current perpendicular to plane spin valves. *Journal of Applied Physics*, **95**, 6630–6632.

Žutić, I., Fabian, J. and Das Sarma, S. (2004). Spintronics: fundamentals and applications. *Reviews of Modern Physics*, **76**, 323–410.

Zwierzycki, M., Tserkovnyak, Y., Kelly, P.J., *et al*. (2005). First-principles study of magnetization relaxation enhancement and spin transfer in thin magnetic films. *Physical Review B*, **71**, 064420-1–064420-11.

Microwave Generation in Magnetic Multilayers and Nanostructures

William H. Rippard and Matthew R. Pufall
National Institute of Standards and Technology, Boulder, CO, USA

1 INTRODUCTION

The states of magnetic devices are typically controlled and manipulated through applied magnetic fields. The magnetization states of the magnetic elements can be controlled through quasistatic fields, as in the case of magnetic switching, or through time-varying applied fields, as is done in precessional switching (Kaka and Russek, 2002; Gerrits *et al*., 2002) and ferromagnetic resonance (FMR) (Sparks, 1964). In 1996, it was predicted that the magnetization states of thin-film magnetic elements could be similarly controlled through the use of a spin-polarized dc current through the spin-transfer effect (Slonczewski, 1996; Berger, 1996). At that time, typical device dimensions were large enough so that the spin-transfer torque (STT) was much smaller than the torques resulting from applied fields and device anisotropy fields. Hence, the STT did not appreciably alter device performance. However, as device dimensions shrink to below $\approx$100 nm, the STT can be of similar strength to those associated with magnetic fields, and the spin-transfer effects can drastically alter the behavior of the magnetic devices. More specifically, spin-transfer effects have been shown to lead to quasistatic hysteretic switching (Myers *et al*., 1999; Katine *et al*., 2000), high-frequency telegraph switching (Urazhdin, Birge, Pratt and Bass, 2003; Pufall *et al*., 2004), and coherent precessional dynamic excitations (Kiselev *et al*., 2003; Rippard *et al*., 2004a,b). These new effects may find applications in terms of current-induced switching in future generation magnetic random access memory (MRAM) elements and magnetic recording technologies and may enable magnetic nanostructures to be used as *active* circuit elements: for example, high-frequency nanoscale oscillators, mixers, and detectors. However, these same effects may also prove to be problematic in terms of decreasing stability and increasing noise in nanoscale magnetic sensors such as hard-disk read heads (Smith, 2004).

Many of the initial spin-transfer research efforts have focused on characterizing and understanding spin torque–induced switching behaviors of a patterned magnetic element in fields on the order of the device's coercive field. In the case of larger applied fields, these same devices showed anomalies in their transport properties (peaks in the differential resistance of the device for certain values of the dc current I_{dc}), which were often taken as evidence of the onset of spin-transfer-induced dynamics in these structures (Katine *et al*., 2000). Analogous high-field measurements were also performed with mechanical point contacts, which showed similar transport anomalies at high current densities. Although there was one early measurement that showed a relationship between the transport through the

Handbook of Magnetism and Advanced Magnetic Materials. Edited by Helmut Kronmüller and Stuart Parkin. Volume 2: *Micromagnetism*.

devices and externally applied microwave signals (Tsoi *et al*., 2000), the evidence that the spin torque effect led to coherent microwave precession in these devices remained only indirect until relatively recently (Kiselev *et al*., 2003; Rippard *et al*., 2004a).

Here, we give an overview of the work performed at the National Institute of Standards and Technology (NIST) in studying these coherent precessional dynamics induced in magnetic nanostructures and compare these dynamics in lithographically patterned nanopillar devices and nanocontact devices. In general, the precessional frequency of the magnetic oscillators can be tuned over a range of several gigahertz by varying the dc current applied to the device. The oscillation frequencies also depend on the applied magnetic field, resulting in a nanoscale oscillator that can be tuned from a few gigahertz to greater than 40 GHz. For nanocontact devices, the linewidths of these excitations can be as narrow as a few megahertz. This gives quality factors for the excitations of more than 18 000 at the highest frequencies. As the direction of the field applied to the devices is changed from parallel to perpendicular to the film plane, the power output from the structures increases by several orders of magnitude. For nearly out-of-plane fields, the high-frequency voltage output from the device can be a significant fraction of the maximum voltage expected from the giant magnetoresistance (GMR) effect. The nanoscale oscillators also display a number of attributes that make them attractive for potential technological applications. These include the ability to frequency modulate the devices, phase lock them to external reference signals, and electronically control their phase relative to that of an input signal.

2 SPIN-TRANSFER DYNAMICS

The fundamental concept behind the spin-transfer effect is the transfer of angular momentum from spin-polarized current carrying electrons to the magnetization of a ferromagnetic film. The result of this transfer of angular momentum is that the polarized electron current exerts a torque on the magnetization of the ferromagnetic film, generally referred to as the *spin-transfer torque*. The STT can either add to the intrinsic damping, thereby stiffening the system, or can counteract the dampening in the system, leading to current-induced switching or coherent steady-state precessional dynamics. Here, we will concentrate on the spin-transfer-induced precessional dynamics and generally compare the measured behaviors to those initially predicted by Slonczewski (1999), who described the dynamic behavior of the free layer magnetization $\vec{m}_{\text{free}}$ by

$$\frac{\mathrm{d}\vec{m}_{\text{free}}}{\mathrm{d}t} = -\mu_0\gamma\vec{m}_{\text{free}} \times \vec{H}_{\text{eff}} - \mu_0\gamma\alpha\vec{m}_{\text{free}} \times (\vec{m}_{\text{free}} \times \vec{H}_{\text{eff}}) + \frac{\varepsilon J_{\text{inj}}\hbar}{el_z 2}\frac{\gamma}{M_{\text{s1}}}\vec{m}_{\text{free}} \times (\vec{m}_{\text{free}} \times \vec{m}_{\text{fixed}}) \quad (1)$$

where $\vec{m}_{\text{fixed}}$ is the magnetization of the fixed layer, γ is the gyromagnetic ratio, α is the phenomenological damping term, J_{inj} is the current density through the device, and l_z is the thickness of the free layer. The first term in equation (1) describes typical Larmor precession of the magnetization about the total effective field; the second is the phenomenological damping term which acts to return the magnetization to lie parallel with the total effective field; and the third describes spin-transfer-induced torque, the sign of which is determined by the direction of current flow through the device and can be either positive or negative. By comparing the functional forms of the second and third terms we can see that, for the correct sign of current flow, the STT can counteract that associated with intrinsic damping in the system. For certain ranges of current and applied field, this leads to coherent steady-state precessional motion of the free layer magnetization.

The magnitude of the STT is proportional to the current density passed through the device and, in order for the spin-transfer effects to become significant, high current densities are required. Typical critical currents associated with switching and precessional dynamics are on the order of 10^6–10^7 A cm^{-2}, depending on the device geometry and materials under study. Devices generally have critical dimensions of about 100 nm, so that such high current densities can be achieved with only moderate applied currents of a few milliamperes. Such small dimensions are also required to ensure that the spin-transfer effects dominate over the oersted fields generated by the applied current itself (Katine, Albert and Buhrman, 2000). Experiments have been performed with patterned magnetic pillar structures (Katine *et al*., 2000; Koch, Sun and Katine, 2004; Deac *et al*., 2005; Mancoff *et al*., 2003; Ozyilmaz *et al*., 2003; Urazhdin, Birge, Pratt and Bass, 2003; Kaka *et al*., 2005a; Sun *et al*., 2002; Tulapurkar *et al*., 2004), nanowires (Fabian *et al*., 2003), small electrical contacts made either to or between macroscopic magnetic layers (Rippard *et al*., 2004a; Myers *et al*., 1999), mechanical point contacts (Tsoi *et al*., 2000; Ji, Chien and Stiles, 2003; Pufall, Rippard and Silva, 2003), and patterned magnetic tunnel junctions (Huai *et al*., 2004; Fuchs *et al*., 2005). There is now very good evidence that the spin-transfer effect can be used to induce both switching and precessional motion of the magnetization in the devices in all cases, although the details may vary between the different device geometries.

Cross-sectional views of the typical nanopillar and nanocontact devices we discuss here are shown in Figure 1, along

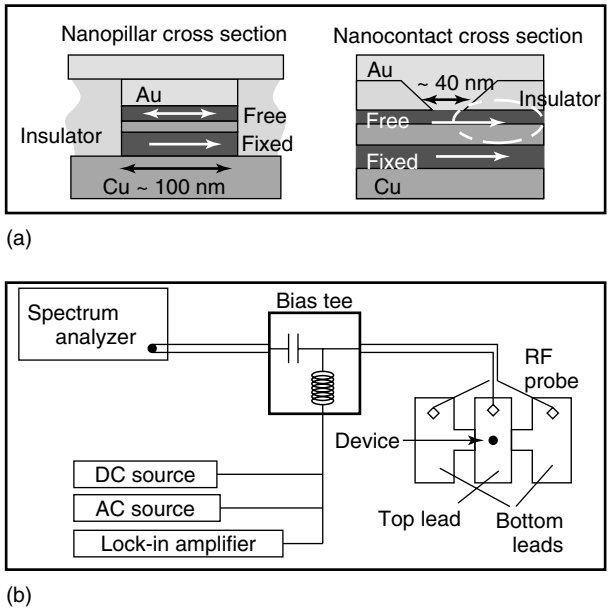

Figure 1. (a) Cross-sectional schematics of both the nanopillar and nanocontact device geometries. (b) Measurement schematic. The bias tee defines the high- and low-frequency legs of the circuit. A spectrum analyzer or a sampling oscilloscope measures the device output. In many measurements, an amplifier is located between the spectrum analyzer and the bias tee.

with a schematic of the measurement geometry. For either device geometry a spin-valve stack such as Ta (5 nm)/Cu (50 nm)/FM1 (20 nm)/Cu (3.5 nm)/FM2 (5 nm)/Cu (1.2 nm)/Au (2.5 nm), where FM is a ferromagnetic material, is first sputter deposited onto an oxidized Si substrate. The thick bottom Cu layer acts as a current shunt to reduce local heating in the active area of the device. To fabricate nanopillar devices, this mesa is then patterned and ion milled to form a pillar structure typically having either an elliptical or elongated hexagonal shape with dimensions of roughly 100 nm (Katine, Albert and Buhrman, 2000). A thick Au layer is used to make electrical contact to the device. Alternatively, a nanocontact device is fabricated by simply making a roughly 50-nm-diameter electrical contact to the top of the spin-valve mesa, which is roughly $8\,\mu\text{m} \times 24\,\mu\text{m}$ on a side. In both cases, the top contact is lithographically patterned into a coplanar waveguide structure and contacted with high-frequency 50 Ω probes. The thicker FM1 layer is typically $Co_{90}Fe_{10}$ while the thinner FM2 layer is typically $Ni_{80}Fe_{20}$. Hence, in these devices the thicker FM1 ('fixed') layer will have a critical current roughly eight times that of the thinner FM2 ('free') layer because of its increased thickness and larger saturation magnetization.

For both device structures the device resistance can range from less than 5 Ω to greater than 30 Ω depending on the materials in use and the lateral dimensions of the structure. The maximum resistance change associated with the GMR effect is typically about 200 mΩ. The structures are contacted with microwave probes and a dc current I_{dc} is passed through the device, along with about a 10 μA ac current, so that both the dc and differential resistances of the device can be simultaneously measured. We use the convention that positive currents correspond to electrons flowing from the free layer into the fixed layer. The devices are current biased so that changes in the relative alignment between FM1 and FM2 result in a voltage across the device through the GMR effect. The output from the device is measured through the high-frequency leg of the measurement circuit by use of either a spectrum analyzer or sampling oscilloscope (Figure 1b). Typically the signal from the device is amplified by 30 dB before measurement. In all cases this is divided out of the presented data. The losses associated with the impedance mismatch between the low resistance device and the 50 Ω load (measurement circuitry) are not taken into account but are expected to be substantial. The measurement circuit has a bandwidth of 0.1 GHz to ≈35 GHz. All measurements discussed here were performed at room temperature. Owing to ohmic heating the device temperature is slightly higher (≈10 °C) than the system temperature (Krivorotov *et al.*, 2004).

2.1 Nanopillar devices

Explicit measurements of coherent spin torque–induced dynamics were first performed in nanopillar devices by a group at Cornell University (Kiselev *et al.*, 2003) and soon afterwards in nanocontact devices by the group at NIST (Rippard *et al.*, 2004a). The evolution of the magnetization dynamics in a typical nanopillar device as a function of current for three different fields applied in the plane of the film is shown in Figure 2(a–c). The individual plots show the current dependence of the microwave precessional frequency f for a given applied field with the power associated, with the precession shown in a linear color scale. Individual spectral traces from the three different fields are shown in the line traces below the two-dimensional plots. The particular device shown here is a nanopillar structure with an elongated hexagonal shape (see Figure 2c) having dimensions of $120\,\text{nm} \times 60\,\text{nm}$, where both FM1 and FM2 are Co films.

As seen in Figure 2(a), precessional dynamics begin to occur in the device at $I_{dc} = 6.5$ mA. The spectral measurements indicate that the device response is composed of a number of harmonically related excitation frequencies and a low-frequency broadband response. Simulations suggest that the precessional magnetization trajectories in this geometry are elliptical in shape and that a number of harmonics will be present. In this case four harmonics can be observed. For

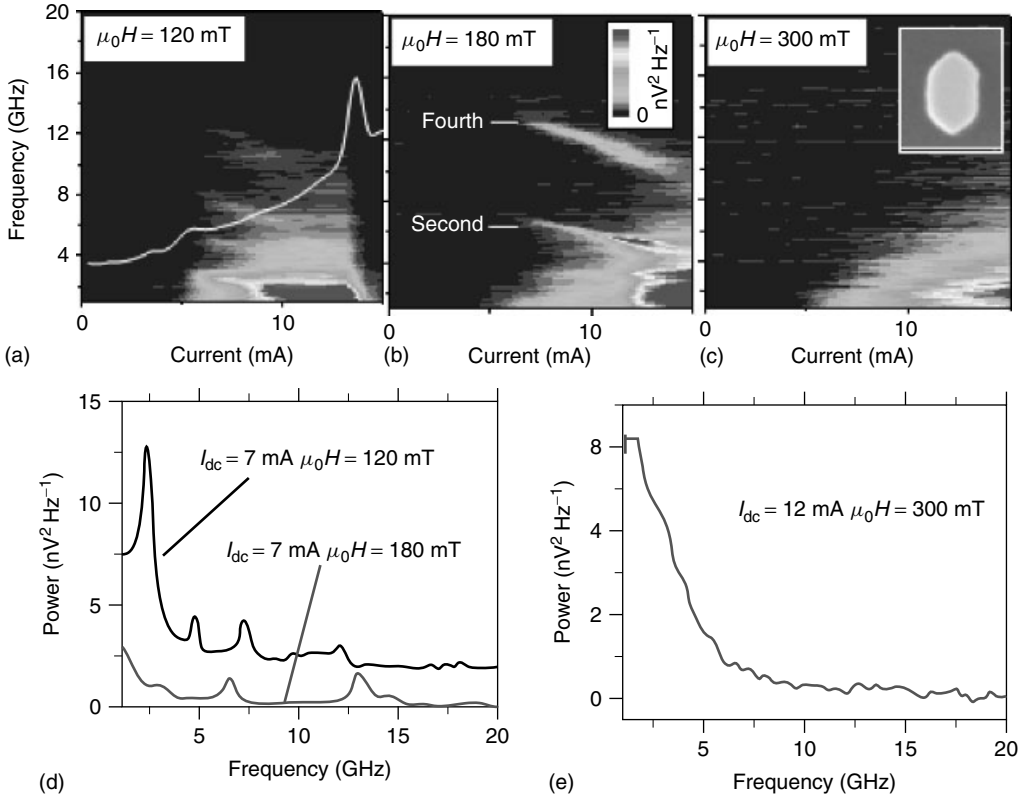

Figure 2. (a–c) Plots showing the spectral output of a nanopillar device as a function of I_{dc} for three different applied fields. The amplitude of the power spectral density is shown in a linear color scale from 0 to 7 $nV^2\,Hz^{-1}$. The corresponding dV/dI_{dc} curve is plotted for the data in (a). A plan view micrograph of the elongated hexagonal (60 nm × 120 nm) ion mill mask used to laterally pattern the nanopillar is shown in the inset of (c). The overlay in (a) shows the differential resistance curve of the device as a function of I_{dc}, and has maximum and minimum values of 17.7 and 16.2 Ω, respectively. (d–e) Spectral traces corresponding to individual current bias point in plots (a–c) showing various harmonically related signals along with the broadband low-frequency output as discussed in the text. In (d) the plots are offset for clarity.

precessional motion of the free layer which is perfectly symmetric about the easy axis of the device, only even-harmonic signals should be observed owing to the signal being generated through the GMR effect, which creates a signal roughly proportional to the cosine of the angle between the fixed and free layer magnetization directions. In most cases, however, odd harmonics are measured as well, indicating that there is some misalignment between the time-averaged magnetization directions of the two ferromagnetic layers. This is perhaps due to a slight misalignment between the applied field direction and the easy axis of the device but could also result from a relative splaying of the layers owing to either the oersted fields generated by the current or the spin-transfer effect itself.

As the current through the device increases, the frequency of oscillation decreases (red shifts) and the linewidth of the oscillations also increases. (The excitation linewidth is taken as the full-width-at-half-maximum (FWHM) of the spectral peak, as determined from a Lorentzian fit to the power spectral density.) The red shift in frequency with I_{dc} agrees well with theoretical expectations based on single-domain simulations of the Slonczewski model, as discussed in the previous sections of this volume and elsewhere (Russek *et al*., 2005; Kiselev *et al*., 2003; Xiao, Zangwill and Stiles, 2005; Berkov and Gorn, 2005; Lee *et al*., 2004; Bertotti *et al*., 2005). The increase in linewidth indicates that, in this geometry, the excitations become less coherent with increasing current. At currents above $I_{dc} = 8.5$ mA for a 120 mT applied field, the linewidths of the spectral peaks become roughly equal to the oscillation frequency and it is no longer possible to clearly identify a distinct oscillation frequency. At still higher currents, the various harmonic signals merge and only a low-frequency broadband response is measured. Above $I_{dc} = 14$ mA, no significant microwave output from the device is measured.

Both the onset and cessation of the precessional dynamics are correlated with features in the differential resistance curve which overlays the plot in Figure 2(a). The largest peaks in these curves are typically correlated with the onset or cessation of the large low-frequency broadband background,

as is the case here. These peaks in the differential resistance curve indicate that the device goes through abrupt and reversible changes in resistance at particular values of I_{dc}. The details of the heights and widths of these peaks in dV/dI_{dc} vary from device to device and can typically be taken as indicating only that the state of the device has been significantly changed at these current values. The overall quasiparabolic shape of the differential resistance curve is due to a combination of ohmic heating in the structure and a change in the average projection of the free layer magnetization onto that of the fixed layer.

As the applied field is increased the frequency of oscillation increases and the even-power harmonics become more pronounced than the odd harmonic signals, indicating that precession of the free layer is more symmetric with respect to the direction of the fixed layer (Figure 2b and d). The precessional oscillations again begin for $I_{dc} = 6.5\,\text{mA}$ and red shift with increasing current. At high-enough currents the spectral signals again become indistinct and only a broad low-frequency signal is measured. As the field is further increased to $\mu_0 H = 0.3\,\text{T}$ (Figure 2c), no distinct spectral frequency can be observed at any current and only the broadband low-frequency signals are measured. This same qualitative behavior is reported in the initial work at Cornell University (Kiselev *et al*., 2003), although the details vary slightly.

The evolution of the coherent spectral signals generally agrees with single-domain simulations based on the theory of Slonczewski (1996), although significant discrepancies between the experimental data and the model also exist (Russek *et al*., 2005; Kiselev *et al*., 2003; Xiao, Zangwill and Stiles, 2005; Berkov and Gorn, 2005; Lee *et al*., 2004; Bertotti *et al*., 2005). Perhaps the most manifest difference is that the single-domain simulations suggest that the precessional motion should neither simply cease nor evolve into a low-frequency broadband signal as the current through the device increases. Instead, numerical integration of equation (1) shows that the precessional modes change from in-plane precession to trajectories in which the time-averaged magnetization $\langle \boldsymbol{M}_{\mathbf{free}} \rangle$ has a component along the direction perpendicular to the plane of the film. In this regime, the frequency of precession is predicted to increase with increasing I_{dc} (blue shift) with current. Typically, this blue-shifting mode is not observed experimentally, but instead a broadband low-frequency output is measured.

The cause of this broadband signal can be understood by measuring the device output in the time domain. An example of this is shown in Figure 3. The time traces show that this broadband microwave signal results from the device undergoing random telegraph switching. As seen in the figure, the dwell times the device spends in the particular states are functions of current, resulting in a spectral signature that changes with I_{dc}, as seen in Figure 2. Initial studies indicated that the

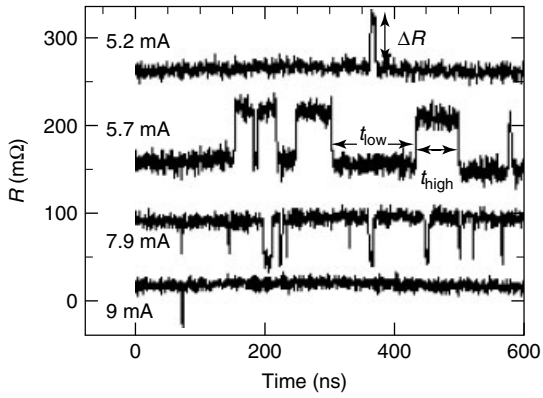

Figure 3. Time-domain measurements showing random telegraph noise occurring in a nanopillar device for several different current values (the curves are offset for clarity). For low currents the device has large dwell times in the low resistance state, whereas for high current values the device has large dwell time in the high resistance state. This switching behavior yields the broadband low-frequency signals discussed in the preceding text. The functional forms of the spectra are expected to be either Lorentzian or f^{-1}, depending on the details of the switching characteristics. (Reproduced from Pufall *et al*., 2004, with permission from the American Physical Society. © 2004.)

switching was between full parallel and antiparallel alignment and that the switching rates ranged between roughly 1 kHz and 1 MHz and the authors proposed an effective temperature model to explain their results (Urazhdin, Birge, Pratt and Bass, 2003; Fabian *et al*., 2003; Wegrowe, 2003). Further investigations found that the states between which the magnetization of the device switches are more complicated and do not necessarily correspond to parallel and antiparallel alignment. Instead, the states can correspond to only partial alignment and the switching rates can exceed 1 GHz (Pufall *et al*., 2004). Switching between numerous states can even occur, depending on the strength and direction of the applied field (Covington *et al*., 2004). The details of the switching behavior are determined largely by whether the applied field is greater than or less than the coercive field of the device under study. We note that this switching behavior can occur even in fields larger than the coercive field of the device. This means that, in the absence of the spin-transfer effect, there exists only one stable energy state for the device – the state having the magnetization pointing in the direction of the applied field. Evidently, the STT allows the device to access states that would not be stable in its absence.

At present, we do not have a full understanding of the states between which the device is switching. It has been suggested that the devices are switching between a static or switched state and a precessional state, or two different precessional states (Li and Zhang, 2003). This is certainly possible. However, spectral measurements show no evidence of a precessional state. This indicates that either the

frequency of any precessional motion, if present, has to be low enough to be overwhelmed by the low-frequency signal associated with the telegraph noise or that the amplitude of the precession is small enough to be below the noise floor of the measurements. Neither of these possibilities seems particularly suitable to explain the observed results. More recent simulations suggest that the two states are associated with the creation and annihilation of vortex states in the devices (Lee *et al*., 2004; Berkov and Gorn, 2005). More detailed comparisons with the experimental observations are still needed in order to verify this possibility. Here, we give an overview of the coherent precessional excitations induced by the spin-transfer effect and we will not discuss this switching behavior in any detail. We instead refer the interested reader to the references just mentioned.

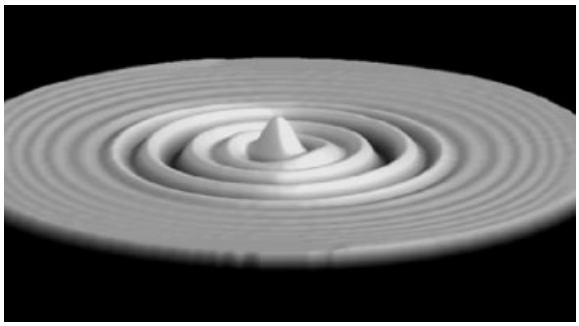

Figure 4. Micromagnetic modeling of the nanocontact geometry. The simulation assumes a dc current of 5 mA injected into a 50-nm area at the center of a 1-μm NiFe disk. The plot shows the local value of m_x in the excited region directly underneath the contact as well as spin waves radiating away from the contact area. The vertical axis is in arbitrary units.

2.2 Nanocontact devices

Throughout much of the remaining part of the chapter, we will concentrate on the precessional dynamics induced in nanocontact devices (see Figure 1b) in which a small ($\approx$50 nm) electrical contact is made to a larger (about 10 μm × 20 μm) magnetic spin-valve structure. The devices discussed will be composed of spin valves having FM1 as $Co_{90}Fe_{10}$ and FM2 as $Ni_{80}Fe_{20}$. In this device geometry, the current is not as well confined to the active area underneath the electrical contact, as in nanopillar devices. Hence, the current densities required to induce a dynamical response are expected to be slightly higher, as the continuous film will act as a slight current shunt away from the device area. However, there are several advantages to this device geometry: the edge defects associated with the patterning of the devices will be mitigated; there is no parasitic dipole coupling between the layers; the device area will be free from oxides that will be present on the sides of the patterned magnetic devices; and the devices are easier to fabricate (particularly for integrated arrays). These topics will be discussed in more detail in the following text.

One potentially important difference between the two device configurations is that in the nanocontact geometry the area undergoing magnetic precession is directly coupled to the surrounding magnetic film through the exchange interaction. As was pointed out by Slonczewski (1999), this naturally leads to spin-wave radiation away from the contact area into the surrounding film. Hence, the nanopillar and nanocontact device geometries have very different boundary conditions, which may play an important role in the nature of the dynamic excitations. An example of a simulated excitation in a nanocontact device, which was obtained using the object oriented micromagnetic framework (OOMMF) program (Donahue and Porter, 2005), is shown in Figure 4. The simulation here assumes a localized current source (40-nm diameter contact) into a 1-μm NiFe/Cu/CoFe disk with an out-of-plane applied magnetic field (1.1 T). As seen in the figure, even though the current is locally injected, the induced excitations have an effectively extended nature and may result in dynamical excitations that are significantly different from those excited in nanopillar devices. More recent theoretical work has even suggested that the exchange coupling between the region directly excited by the STT and the surrounding film in the nanocontact geometry can lead to excitations having fairly complicated mode profiles even directly underneath the contact area (Hoefer *et al*., 2005). The differences between the measured behaviors of the spin-transfer-induced excitations in the two device geometries will be discussed in more detail in the following text.

2.2.1 *In-plane fields*

We will first discuss the dynamics for fields applied in the plane of the film (the same field geometry described in the preceding text for the nanopillar devices). In Figure 5(a) we show the differential resistance of the device as a function of I_{dc}. The curve is similar to those observed for nanopillar devices. There is a quasiparabolic background, on top of which is a small peak in the curve, which occurs here at $I_{dc} = 4$ mA. The spectral output of the device is shown for several values of I_{dc} as indicated in Figure 5(b). For low currents no spectral peaks are observed. At $I_{dc} = 4$ mA, a spectral peak emerges at a frequency of $f = 7.9$ GHz. As seen in the figure, the oscillation frequency red shifts with increasing current, as was observed in the nanopillar devices. The power in the peak initially increases with I_{dc}. However, at higher currents the power output continually decreases until no spectral peaks are observed, as shown by the $I_{dc} = 9$ mA data.

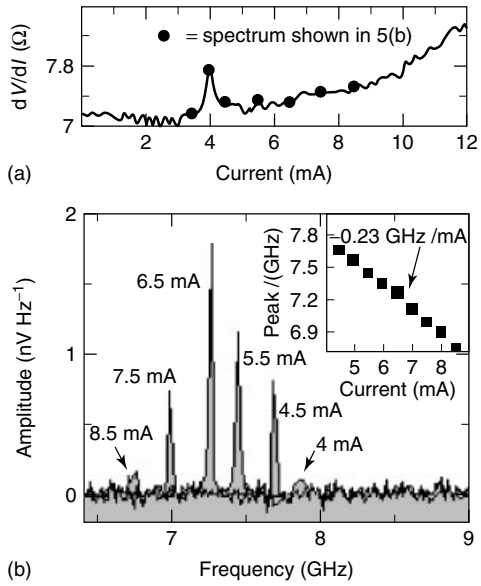

Figure 5. (a) dV/dI_{dc} versus I_{dc} with $\mu_0 H = 0.1\,\mathrm{T}$. (b) High-frequency spectra taken at several different values of current through the device corresponding to the symbols in (a). The inset shows the linear variation of f with I_{dc}. (Reproduced from Rippard *et al*., 2004a, with permission from the American Physical Society. © 2004.)

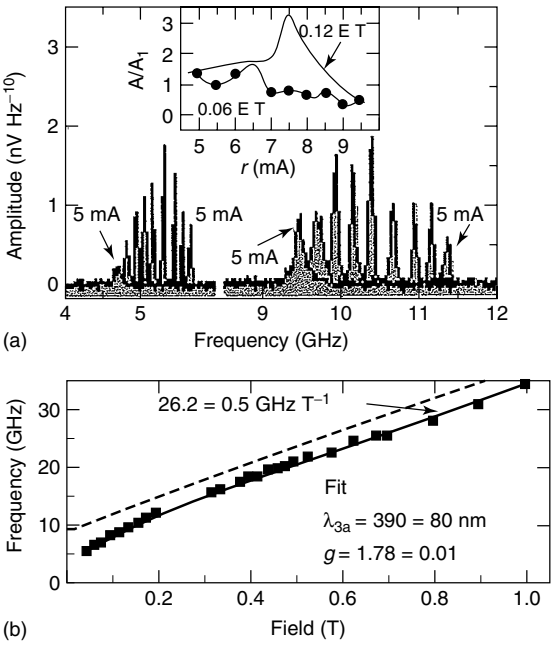

Figure 6. (a) High-frequency spectra for currents from 5 to 9 mA taken in 0.5 mA steps with $\mu_o H = 0.06\,\mathrm{T}$ showing the fundamental response and another at twice that frequency (inset). Amplitude ratios of the peaks as a function of I_{dc} for two different fields. (b) Measured frequency at onset as a function of $\mu_0 H$ along with fit (solid line). The dashed line corresponds to the excitation frequencies predicted by Slonczewski (1999) using the deflated value of $g = 1.8$. Error bars (FWHM) are smaller than the data points. (Reproduced from Rippard *et al*., 2004a, with permission from the American Physical Society. © 2004.)

The oscillation frequency, determined by fitting Lorentzian functions to the spectra, depends linearly on the injected current, as shown in Figure 5(b) (inset). The strength of this red shift depends on the magnitude of the applied field and varies from approximately $0.2\,\mathrm{GHz\,mA^{-1}}$ at low fields ($\approx$50 mT) to approximately $1\,\mathrm{GHz\,mA^{-1}}$ at higher fields of $\approx$0.8 T. For this field geometry, devices can typically be tuned over a range of several gigahertz by varying the current through the device for a fixed field magnitude. As shown in Figure 6(a), both first and second harmonic signals are often observed in these devices, as was the case with the nanopillar structures. Here, the existence of a first-harmonic signal cannot be attributed to a misalignment between the layers being induced by the applied *field*, as the fields are much larger than the film coercivities of a few millitesla. Instead, the misalignment is more likely caused by the applied current either through the generated oersted fields or the spin torque itself.

The frequency of oscillation can also be controlled by the strength of the applied field, as shown in Figure 6(b). The data plotted correspond to the highest precession frequency (lowest current) for a given applied field (see Figure 5(b)). As seen in the figure, the precessional frequency can be tuned from a few gigahertz to greater than 35 GHz by varying the applied field from 50 mT to 1 T, giving an average field tunability of roughly $26\,\mathrm{GHz\ T^{-1}}$. A very similar variation of the oscillation frequency with the applied field is found for nanopillar devices (Kiselev *et al*., 2003). No spectral peaks are measured above $\mu_0 H > 1\,\mathrm{T}$ ($f = 35\,\mathrm{GHz}$). However, this does not necessarily indicate the cessation of precessional dynamics. Measurement of dynamic excitations above 35 GHz is beyond the bandwidth of our present measurement system. The drop in signal strength at these highest frequencies occurs in all measurement geometries and is due to the bandwidth limitation of the measurement system. Furthermore, the signals in Figure 5 correspond to first-harmonic peaks and the strength of the second harmonic signal quite probably increases at high applied fields, as precession becomes more symmetric about the field direction (i.e., the direction of the fixed layer). In fact, output from the devices above 100 GHz is quite possible in the present measurements.

Determination of the precessional mode being excited is clearly of interest. The nanopillar devices are typically small enough to behave largely as single-domain particles and the precessional frequencies at the onset of oscillations are reasonably well described by the standard Kittel equation for FMR (Kittel, 1986). Both of these point to the uniform precession of the free layer in the nanopillar devices, at least at the onset of precession. Recent micromagnetic modeling

results suggest that this single-domain behavior breaks down for currents slightly above the critical current (Lee *et al*., 2004; Montigny and Miltat, 2006, private communication; Berkov and Gorn, 2005). In the nanocontact devices, the mode or the wavelength of the excitation is less clear. Slonczewski (1999) initially predicted that the excitation wavelength would be set by the localized nature of the current passing through the layers and that the device size would roughly equal half of the wavelength of the excited mode.

In order to investigate the excitation wavelength, we fit the data shown in Figure 6(b) to the Kittel equation for in-plane spin-wave generation excluding dipole effects:

$$f(H) = \left(g\mu_B\mu_0/h\right)\left((H + H_{sw} + H_k + M_{eff})\right. \\ \left.\times\ (H + H_{sw} + H_k)\right)^{1/2} \quad (2)$$

where $H_{sw} = Dk^2/(g\mu_B\mu_0)$, D is the exchange stiffness, g is the Landé factor, k is the magnon wave number, M_{eff} is the effective magnetization, H_k is the anisotropy field, μ_0 is the permeability of free space, h is Planck's constant, and μ_B is the Bohr magneton (Kittel, 1986). Equation (2) is strictly valid only in the limit of small-amplitude precession, a limit that is likely not met in the present experiments. We include this fitting procedure as a comparison to the behavior predicted by Slonczewski (1999) and as a beginning point for a discussion of the modes excited in the nanocontact structures.

In fitting the data, k and g are treated as free parameters while fixed values of $\mu_0 M_{eff} = 0.8\,\mathrm{T}$ and $\mu_0 H_k = 0.4\,\mathrm{mT}$ are used, as determined from magnetometry measurements. The fit yields $g = 1.78 \pm 0.01$ and a magnon wavelength of $\lambda = 390 \pm 80\,\mathrm{nm}$. From both the above fit and the linear portion of the data for $\mu_0 H > 0.4\,\mathrm{T}$ we determine $g = 1.78 \pm 0.01$, which is smaller than the accepted value of $g = 2$. This discrepancy is not unexpected. Numerical simulations of the Landau–Lifshitz–Gilbert (LLG) equation show that fitting equation (2) to data corresponding to large-angle precession will give an apparently suppressed value of g. As we will discuss in more detail in the following text, the precessional angles in these devices can be quite large.

The wavelength determined from the fit is much larger than the contact diameter, in contrast to the initial predictions. Although given the above considerations the wavelength determined from the fit can be taken only as a guide, the data do indicate that the excitations approximate the uniform precessional mode, that is, the uniform FMR mode, and that the excitation frequency is not dominated by the spin-wave exchange energy H_{sw}. For comparison, assuming a 40-nm electrical contact, an excitation wavelength predicted by Slonczewski would yield a value of about $\mu_0 H_{sw} = 0.14\,\mathrm{mT}$, making the predicted frequencies (shown as the dashed line in Figure 6b) clearly higher than those observed experimentally. Similar values for g and λ were measured for devices having CoFe as the free layer, although the oscillation frequencies were higher, in accordance with the larger value of the CoFe saturation magnetization.

2.2.2 *Out-of-plane fields*

The dynamics excited by the spin-transfer effect change dramatically with the direction of the applied field. First, we will discuss the dynamics when the field is applied perpendicular to the plane of the films. In this geometry, the applied field will pull the magnetizations of both ferromagnetic layers at least partially out of the plane of the film. The calculated canting angles for both CoFe and NiFe for several different field strengths and angles are shown in Figure 7. This figure shows that over the field range of interest (0.5–1 T) the NiFe layer is canted at a significantly larger angle than the CoFe, particularly for applied values on the order of 1 T.

An example of the evolution of the precessional dynamics as a function of current for an out-of-plane field of $\mu_0 H = 0.9\,\mathrm{T}$ is shown in Figure 8(a). As can be seen in the figure, the oscillation frequencies increase (blue shift) with increasing I_{dc} for this geometry and field range. More complicated behavior is also observed; for example, there are discrete jumps in the precessional frequency with current. These jumps are not typically hysteretic in the current or applied field, although some devices do show hysteretic characteristics at this extreme field angle. The cause of the discontinuous evolution of frequency with current is not

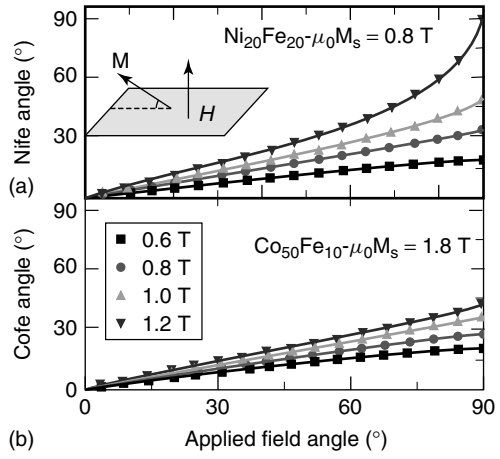

Figure 7. Schematic diagram to define the angles discussed in the text. The plot gives the calculated static angle between the two layers as a function of the angle of the applied field for several different field strengths.

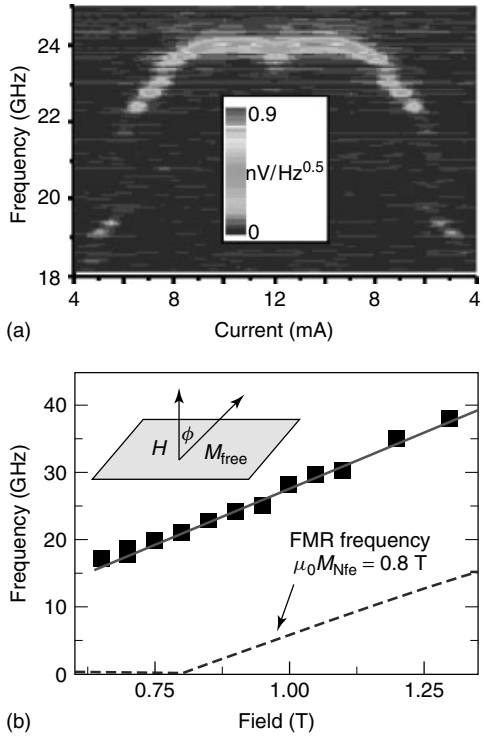

Figure 8. (a) Plot of f as a function of I_{dc} with the amplitude shown in a linear color scale, as shown in the inset. Discretization in the plot results from measuring the frequency spectra in 500 μA intervals. (b) f versus H for H applied out of plane. Data correspond to the highest f. The error bars (FWHM) are smaller than the data points. The fit to the data is discussed in the text. The dashed line gives the calculated FMR precessional frequencies. (Reproduced from Rippard *et al*., 2004a, with permission from the American Physical Society. © 2004.)

certain, although simulations suggest that it might be caused by an abrupt reorientation of the 'fixed' layer, which will be discussed in more detail in the following text.

In Figure 8(b), we plot the excitation frequency as a function of the applied field strength. For clarity, we again plot only the highest measured precession frequency for each given applied field value. The precession frequency is found to vary linearly with a slope of roughly 32 GHz T^{-1}. The data are fit with the Kittel equation for circular magnetization precession about the axis perpendicular to the plane of the film, which correspond to the trajectories predicted by the single-domain simulations

$$f(H) = \left(g\mu_B\mu_0/h\right)\left(H - M_{eff}\cos(\phi)\right) \qquad (3)$$

where ϕ is the angle of precession with respect to the field direction, θ_H. The data are fit using g and ϕ as free parameters to match the slope and intercept of the data, respectively. From the fit we find $g = 2.1 \pm 0.01$ and a precession angle $\phi = 80^\circ$, indicating that these are large-angle precessional modes. For comparison, the dashed line in the figure represents the corresponding small-angle modes typically observed in FMR experiments. The origin of the significant offset between the two curves is the greatly reduced demagnetization factor ($M_{eff}\cos(\phi)$) associated with the large-angle precessional modes. This results in relatively large total applied effective fields as compared to those associated with small precessional angles. As was the case of in-plane applied fields, these precessional excitations can be considered as very large-angle versions of FMR excitations (Bertotti *et al*., 2005), although such modes cannot be accessed through the application of time-varying fields used in FMR experiments (Suhl, 1958).

2.2.3 *Intermediate field angles*

There are clear differences between the precessional dynamics in the two geometries discussed in the preceding text. For the in-plane case, the precessional frequencies linearly decrease with the current through the device, and the frequency of precession evolves in a continuous manner. In the out-of-plane geometry the evolution of the dynamics with current is more complicated. Overall, the excitation frequencies increase with increasing I_{dc}, and there are discontinuous jumps in the excitation frequency as the current through the device is changed. In the following text, we investigate the evolution of the precessional motion as a function of both I_{dc} and $\mu_0 H$ as the direction of the applied field is changed from in-plane to out-of-plane.

In Figure 9, we show the device oscillation frequencies as a function of I_{dc} for several field angles θ_H, given relative to the film plane, for a constant field $\mu_0 H = 0.8$ T. For in-plane fields, the frequency output linearly red shifts with current, as is generally observed in these devices for in-plane fields, as discussed in the preceding text. As the angle of the applied field is increased, the excitations typically appear over a wider range of currents, and the dependence of the frequency f on I_{dc} becomes more complicated. For the data at $\theta_H = 35^\circ$ a linear red shift is found for low currents. However, at $I_{dc} = 5$ mA the slope of the curve $\mathrm{d}f/\mathrm{d}I_{dc}$ changes sharply and, although the current-induced red shift persists, f deviates significantly from a linear dependence on current. As the angle is increased, this initial sharp change in slope becomes an abrupt jump in the excitation frequency, as shown by the data for $\theta_H = 45^\circ$, defining two distinct frequency branches in the f versus I_{dc} curve. For $\theta_H = 55^\circ$ the precession frequency initially decreases but then blue shifts with current for $I_{dc} > 5$ mA. At this angle, as I_{dc} reaches 6.625 mA the excited mode becomes poorly defined (the excitation linewidth is several gigahertz wide and the amplitude strongly decreases), and we were not

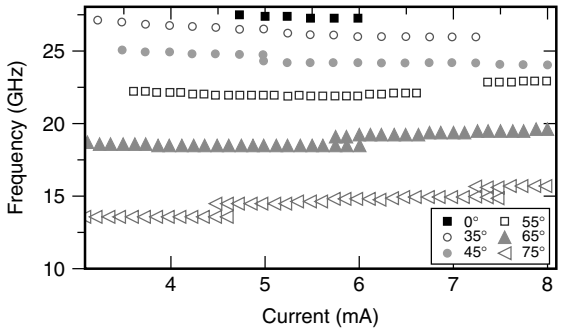

Figure 9. Frequency versus current for several different field angles for $\mu_0 H = 0.8$ T. The FWHM of the spectra are smaller than the data points. Both increasing and decreasing I_{dc} scans are shown but are not visible on this scale range. (Reproduced from Rippard *et al.*, 2004b, with permission from the American Physical Society. © 2004.)

able to uniquely determine f for 6.75 mA $< I_{dc} <$ 7.25 mA. However, as the current increases further the mode again becomes well defined and blue shifts with current.

As the field angle is increased, we again see abrupt jumps in the frequency of the oscillations with increasing current, although the jumps in f are now to higher frequencies instead of to lower frequencies. For instance, for $\theta_H = 65^\circ$ the oscillation frequency red shifts for currents below 6 mA, whereas for higher currents the oscillations abruptly shift to a higher frequency and show a blue shift with increasing current. At higher angles similar multiple jumps in f with I_{dc} are still seen but with the frequency now showing an *overall* blue shift on each of the individual branches of the curves (see $\theta_H = 75^\circ$). However, the frequency does not typically vary linearly, or even monotonically, with I_{dc} over the entire range of the individual branches of these curves. For instance, for the middle branch of the $\theta_H = 75^\circ$ data, f shows a blue shift at low current but a red shift for $I_{dc} > 6.75$ mA. This same discontinuous evolution of frequency with I_{dc} described in the preceding text occur over the range of fields studied (0.5–1.1 T) although the particular current and angle at which two frequency branches are delineated, as well as the detailed dependence of f on I_{dc} over a particular branch, vary with H. For a given angle, f can be tuned, on average, over a range of several gigahertz by varying I_{dc}.

As shown in Figure 9 for $\theta_H = 65^\circ$ and $I_{dc} \approx 5.75$ mA, the frequency output of the device at fixed current and field can be multivalued. This is not hysteretic behavior with f depending on the direction of current sweep. Rather multiple nonharmonically related peaks are observed in the spectral output of the device at this particular current and field. Individual time-sequenced spectra typically show that the powers in the individual peaks change significantly from scan to scan with the power associated with one of the frequencies increasing or decreasing at the expense or benefit of the other. We attribute this to the device hopping between distinct precessional trajectories with different oscillation frequencies. Often each individual peak in a multipeak spectrum has a linewidth less than 50 MHz, indicating that the individual modes are still well defined. In some cases, this hopping behavior is not explicitly observed and is likely due to our $\approx$100 ms spectral acquisition time that limits direct detection of this switching behavior to situations in which one of the precessional states has a dwell time of that order or longer.

The reason for the discontinuous evolution of the precessional frequency with current is not clear, but simulations suggest that it may result from the 'fixed' layer undergoing a reorientation. As no additional precessional modes are observed, it appears that the 'fixed' layer is not entering a precessional state at these frequency jumps. However, other measurements do indicate that there may be precessional motion occurring in the 'fixed' layer over small ranges of $\mu_0 H$ and θ_H. This is shown in Figure 10. In this case, three nonharmonically related spectral peaks occur over a wide range of current. In addition to the main spectral peak there are also peaks symmetrically located at 500 MHz above and below the main peak. The upper and lower sideband peaks are not symmetric in power and only the lower sideband appears in the two-dimensional plot on this color scale. However, both are visible in the line trace in Figure 10(b). This is very reminiscent of a spectral peak undergoing frequency modulation, in which sideband signals appear at frequencies different from that of the main signal (this will be discussed in more detail in the following text). However, in this case, no modulation source is applied, and the two sidebands are symmetric in frequency but not in power. The cause of these sideband signals is not certain, although it possibly results from excitation or reorientation of the 'fixed' layer. The frequency of the modulation signal is quite low and does not correspond to the difference in the precessional excitation frequencies of the two layers induced by the spin-transfer effect, at least according to single-domain modeling using equation (1). However, this may result from a 'scissoring' mode between the two layers. This 'self-modulation' behavior typically occurs for fields of about 0.5–0.6 T applied approximately 60° to the film plane.

2.2.4 *Oscillator output power*

Up to this point, we have focused largely on the dependence of the precession frequency on the strength and direction of the applied field. We will now focus on the power associated with the different mode structures and the linewidths of the excitations. In general, we find that the linewidths of the devices are quite narrow having FWHM values of a few megahertz to a few tens of megahertz. For certain field geometries we have found that the measured voltage output

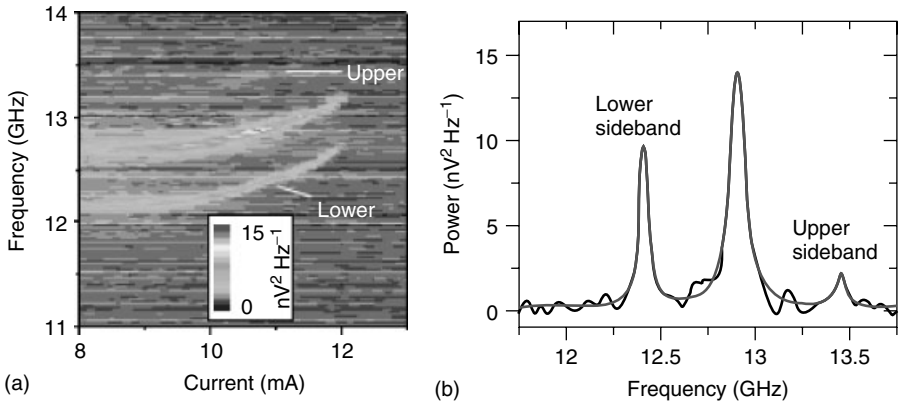

Figure 10. (a) Plot showing the spectral output from a device with $\mu_0 H = 0.5\,\mathrm{T}$ applied at 60° away from the film plane. The main peak has both an upper and lower sideband, reminiscent of frequency modulation. (b) Spectral trace for $I_{\mathrm{dc}} = 11\,\mathrm{mA}$ along with a fit (solid line).

associated with the precessional dynamics can be as much as one-third of the maximum voltage obtainable from the GMR effect.

For a particular field strength and angle the device output power can be a strong function of I_{dc}, Figure 11(a). The power output does not generally scale as I^2 as it would for a constant precession angle and a constant average orientation between $\boldsymbol{M}_{\mathrm{free}}$ and $\boldsymbol{M}_{\mathrm{fixed}}$. Instead, the output power depends more strongly on the particular frequency branch of the excitation, consistent with the relative directions of the fixed and free layers significantly changing when a jump in frequency occurs. Shown in Figure 11(b) is the *maximum* integrated power output of a device versus applied field angle. In general, the current yielding the maximum power output varies with $\mu_0 H$ and θ_H. For this device this current varies between $I_{\mathrm{dc}} = 5$ and 7 mA over the range of fields and angles studied. Hence, normalizing the data by I^2 does not significantly affect the trend in the plot. The maximum power output of the device varies by roughly 2 orders of magnitude, from about 1 pW to 0.1 nW, as the field is changed from in-plane to out-of-plane. This general trend is in accordance with the device output power resulting from the GMR effect, in which the instantaneous resistance of the device is proportional to $\boldsymbol{M}_{\mathrm{free}} \cdot \boldsymbol{M}_{\mathrm{fixed}}$. When the two magnetization directions are parallel, the change in the projection of $\boldsymbol{M}_{\mathrm{free}}$ onto $\boldsymbol{M}_{\mathrm{fixed}}$ during one precessional cycle is relatively small when compared to when they are nearly perpendicular, for a given angle of precession (see Figure 11c). Hence for fields applied perpendicular to the film plane, which will tend to splay $\boldsymbol{M}_{\mathrm{free}}$ relative to $\boldsymbol{M}_{\mathrm{fixed}}$, a larger change ΔR is expected for a given precessional angle, which will in turn lead to a larger output signal from the device.

For simple circular precession, the GMR signal should follow $\Delta R = \Delta R_{\mathrm{max}} \sin(\gamma) \sin(\phi)$ where ΔR_{max} is the maximum GMR signal, γ is the angle between the time-averaged values of $\langle \boldsymbol{M}_{\mathrm{fixed}} \rangle$ and $\langle \boldsymbol{M}_{\mathrm{free}} \rangle$ (generally different

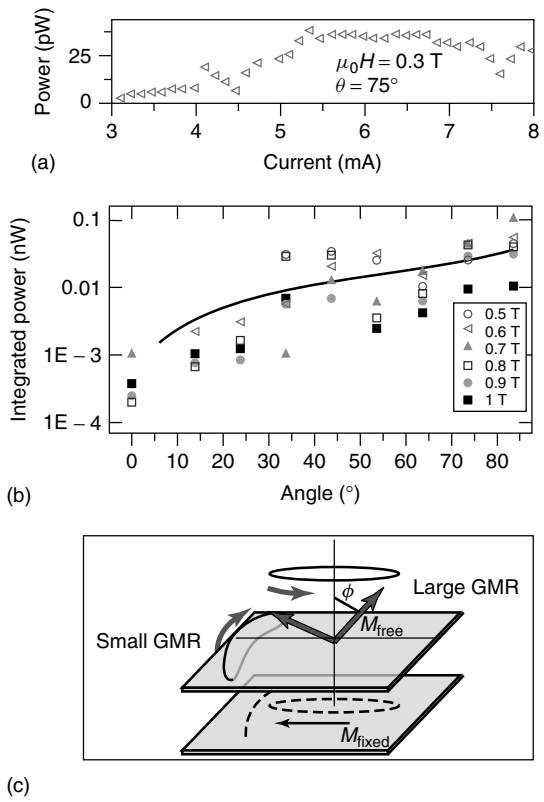

Figure 11. (a) Integrated output power (area under spectral peak) versus I_{dc}. For currents having multiple frequencies the powers in both peaks are included. Data correspond to those of the same symbol in Figure 8(a). (b) Maximum integrated power output versus field angle for several different fields. The line shows the calculated functional form of the power assuming a constant circular precessional angle and $\mu_0 H = 0.8\,\mathrm{T}$. (c) Schematic diagram showing the projection of $\boldsymbol{M}_{\mathrm{free}}$ onto $\boldsymbol{M}_{\mathrm{fixed}}$ (dashed lines) for two different geometries. For similar precessional angles, the change in the projection is much larger for geometries where the two layers are skewed with respect to one another. (Reproduced from Rippard *et al.*, 2004b, with permission from the American Physical Society. © 2004.)

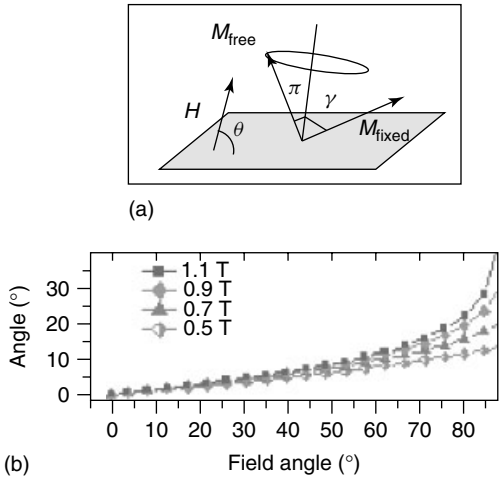

Figure 12. (a) Schematic defining the variables discussed in the text. (b) Calculated value of the angle γ, the angle between $\boldsymbol{M}_{\text{fixed}}$ and the time-averaged value of $\boldsymbol{M}_{\text{free}}$.

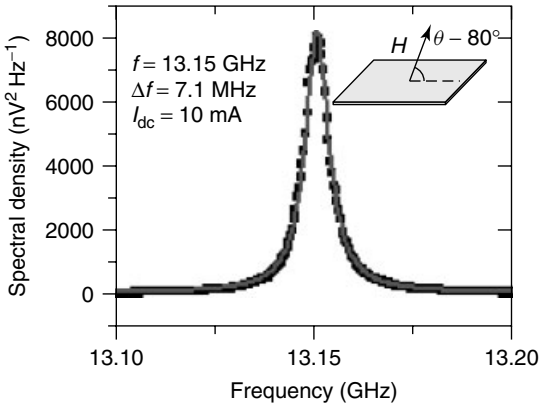

Figure 13. Plot showing the particularly strong output power from a device with $\mu_0 H = 0.6\,\text{T}$, applied 80° away from the film plane, along with a Lorentzian fit. The integrated power in the peak converts to 0.8 mV peak-to-peak signal.

from θ_H, Figure 12b), and ϕ is the precession angle (inset Figure 12a). Hence, for a constant precession angle the device power output should increase with θ_H and roughly scale as $\sin(\gamma)$ at fixed current, over the range of fields and angles studied here. While the measured power output does increase with θ_H, its dependence on angle at fixed H does not follow such a simple relation (solid line in Figure 11b). For instance, the power output generally does not simply increase with H at a given applied field angle, indicating that the excited trajectories are more complicated functions of H and I_{dc}.

The largest power outputs measured are significant fractions of the maximum possible through the GMR effect. In Figure 13, we show the output from a device with $\mu_0 H = 0.65\,\text{T}$ applied 80° out of the film plane and $I_{\text{dc}} = 10\,\text{mA}$. For this particular geometry the integrated output power in the out-of-plane geometry is roughly 1 nW, corresponding to a peak-to-peak voltage of 0.8 mV. This is about 30% of the maximum voltage obtainable through the GMR effect in this device, which has a $\Delta R_{\text{max}} = 230\,\text{m}\Omega$. The voltage measured by the spectrum analyzer represents only a fraction of the signal being generated at the device itself owing to the finite resistance of the device structure and imperfect microwave coupling between the device and the off-chip measurement circuitry. A simple circuit analysis shows that the voltage measured at the spectrum analyzer is

$$V_{\text{spectrum analyzer}} = V_{\text{device}} \left(\frac{Z_{\text{load}}}{Z_{\text{device}} + Z_{\text{load}}} \right) \qquad (4)$$

where Z_{device} is the device impedance and Z_{load} is the impedance of the load circuit (Johnk, 1988). For the 15 Ω device discussed here this indicates that only roughly three-fourths of the actual device output is measured by the spectrum analyzer, assuming that the high-frequency impedance of the device is equal to its dc value. Taking this into account, the peak in Figure 13 corresponds to approximately half of the total possible output from the device, that is, precessional angles of approximately 60°. The additional, and possibly significant, losses due to imperfect coupling between the on-chip and off-chip transmission lines are not included in this model.

2.2.5 *Comparison between linewidth, power, and frequency evolution*

A more complete comparison between the linewidth, power, and their dependencies on current and field are discussed in the following text. In Figure 14, we show the detailed evolution of the precessional frequency, as functions of both I_{dc} and magnetic field strength, for $\theta_H = 75°$. As seen in Figure 14 the precession frequency does not have a simple dependence on either of these parameters. Overall, the precessional frequencies vary from roughly 11 to 24 GHz as the applied field is swept from 0.5 to 1.1 T. The evolution of the dynamics with current is more complicated. However, we can easily observe that the precession red shifts with increasing current at low applied fields and that the oscillations change to blue shifting with increasing I_{dc} as the applied field is increased. The most striking features in the surface plot are the well-defined places where the precessional frequency evolves in a discontinuous manner with either current, applied field, or both, as indicated by the solid lines in the figure. The positions of the steps vary fairly continuously with both field and current, forming a surface consisting of several plateaus separated by steps (when multiple spectral

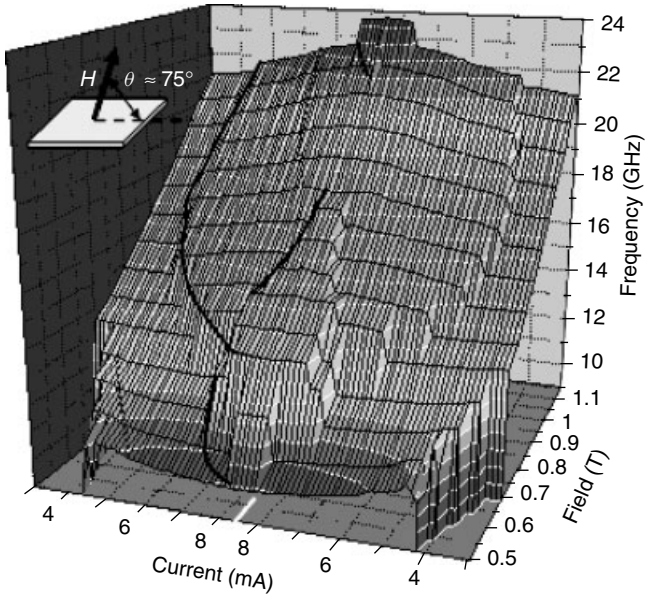

Figure 14. Surface plot showing the evolution of the precession frequency with both current and applied field for an applied field angle of 75°. At the lowest currents and applied fields no precessional dynamics are measured, which appears as the vertical sidewall in the plot. The surface includes data from both increasing and decreasing current scans. The lines discussed in the text are shown only on the increasing current scan for clarity and serve only as visual guides.

peaks are present, see Figure 9, only the peak with the largest integrated power is included in the plot). Within these individual plateaus the evolution of the precessional frequency with current and field is typically very smooth and continuous. However, there are also regions in which the oscillation frequency goes through more rapid changes in one of these variables, as indicated by the dashed lines in the plot. These features, although not as dramatic as the steplike features described in the preceding text, are still distinct from the typical evolution of the dynamics. At the lowest fields and currents no spectral signals are measured for this angle of applied field. For the purposes of this surface plot, the frequency of precession is taken to be zero when no spectral peak is measured, which results in the artificial appearance of a large step where the precessional dynamics first appear.

The overall behavior of the dynamics generally agrees with numerical simulations of equation (1). Simulations of this measurement geometry indicate a red-shifting behavior at low fields and a blue-shifting behavior at higher fields. However, the discontinuous jumps have not been observed in the simulations, nor have the smaller ridges. The jumps may result from the 'fixed' layer undergoing a reorientation or precessional oscillations itself, as discussed in the preceding text. They may also result from the free layer precession changing from a quasiuniform mode to some other normal mode, although the change in frequency associated with the jump are smaller than one would expect for this behavior (McMichael and Stiles, 2005). Other somewhat complicated behavior is also found in the measurements. For instance, for $\mu_0 H = 0.70\,\mathrm{T}$ the oscillations show complex behaviors as I_{dc} is swept from about 7.5 to 8.5 mA. After the discontinuous jump with current, the precession frequency increases, and then decreases, before increasing once again. Such a complicated frequency dependence on current has not been found from numerical integration of equation (1), assuming a constant damping value (Russek *et al.*, 2005; Xiao, Zangwill and Stiles, 2005).

As shown by the plots in Figure 15(a–b), the device output power and the oscillation linewidth vary a great deal over the range of currents and fields studied here. The oscillation linewidth varies from below 5 MHz to greater than 100 MHz while the output power varies from the picowatt to nanowatt range. As seen in the two plots, the parameters giving the higher output power are not simply correlated with the oscillations having larger linewidths. For instance, for fields between 0.6 and 0.8 T the highest powers are found for currents between $I_{\mathrm{dc}} = 7.5$–$8.5\,\mathrm{mA}$, while the oscillations over this region have linewidths of only a few megahertz.

Clear correlations exist between the excitation linewidth and the frequency surface plot. Most notably, a large gradient in the frequency surface (i.e., f varies strongly with either current of applied field) is generally correlated with a corresponding increase in the measured linewidth. This is expected with any tunable oscillator. Noise in any parameter that changes the oscillation frequency will also cause the oscillation linewidth to broaden. Treating fluctuations in the applied field and I_{dc} as independent sources of noise, the simplest description of the noise contribution to the excitation linewidths is

$$\Delta f = \left(\left(\frac{\partial f}{\partial H} \right)^2 (\Delta H)^2 + \left(\frac{\partial f}{\partial I_{\mathrm{dc}}} \right)^2 (\Delta I_{\mathrm{dc}})^2 \right)^{1/2} \qquad (5)$$

where ΔH is the fluctuation of the magnetic field during the measurement interval $\approx 10\,\mathrm{s}$ and ΔI_{dc} is the noise in the current through the device due to Johnson noise, shot noise, and noise in the current source itself. We measure $\Delta(\mu_0 H) = 0.05\,\mathrm{mT}$ and estimate $\Delta I_{\mathrm{dc}} = 1\,\mu\mathrm{A}$. For a typical value of $\mathrm{d}f/\mathrm{d}H = \gamma = 26\,\mathrm{GHz\ T^{-1}}$, the field-noise-induced linewidth amounts to 1.3 MHz, which is approximately equal to the narrowest peaks that we regularly measure. This indicates that the linewidths are limited by the noise in the measurement system and that the linewidths of the oscillations themselves could be substantially narrower than their measured values.

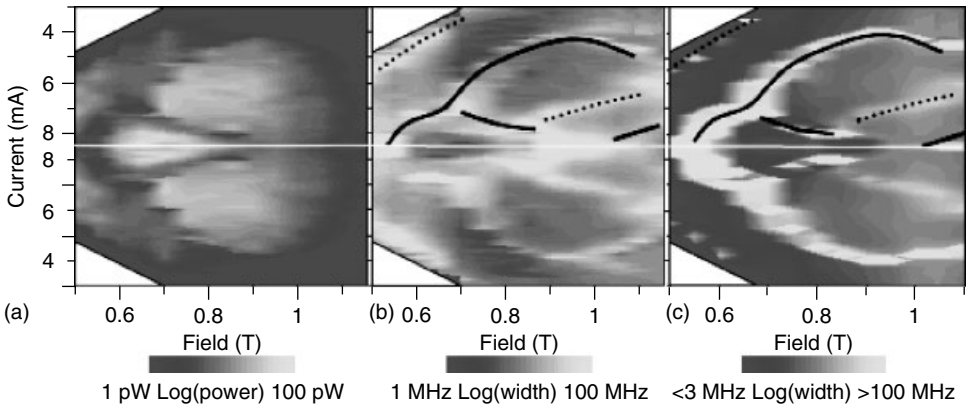

Figure 15. (a) Two-dimensional plot showing the device output power as discussed in the text with the power shown in a logarithmic color scale. (b) Analogous plot of the measured linewidth over the same parameters with the linewidth (FWHM) shown in a logarithmic color scale. (c) Analogous plot of the 'calculated linewidth' over the same range of parameters shown in a logarithmic color scale. In all cases, data from both the increasing and decreasing current scans are included so that the plots are symmetric about the highest bias current. The different lines in (b) and (c) correspond to the analogous lines in Figure 13 and serve only as visual guides for the purpose of comparison.

To directly compare the measured linewidths to the model outlined in the preceding text we have numerically differentiated the surface plot and constructed the resulting calculated noise-induced linewidths in Figure 15(c) using equation (5). Over most of the surface the differentiation process is well defined. However, at the discontinuous jumps in frequency this is not the case and the resulting values for the linewidths will be too large. Hence, at these locations the measured linewidths and calculated 'noise linewidth' can be compared only qualitatively. There are several clear correlations between regions having high measured linewidths and regions having large calculated linewidths. The correlation is particularly strong when there is a discontinuous jump in the oscillation frequency in either current or applied field where the gradient of the frequency surface is strongest. These locations are shown as dashed lines in the figures. Similarly, strong correlation occurs between regions having measured linewidths on the order of a few megahertz, and regions having narrow linewidths in the calculation. These measurements indicate that the largest linewidths result at least partially from a very strong variation of the precession frequency with either current or field and noise fluctuations in these two variables. Similarly, the narrowest measured linewidths are seemingly also limited by systematic noise and may not reflect the actual linewidth of the oscillations themselves.

However, the correlation between the calculated and measured linewidths is not complete. For instance, the calculations give a region of very narrow linewidth for $I_{dc} = 8-8.5$ mA and an applied field of 0.9–1 T, whereas the measured linewidths over this region are actually fairly large. This is also somewhat the case at the lowest fields and current values between 6 and 7 mA. This indicates that the linewidths are not always dominated by the noise characteristics of the current and field but can also perhaps result from instabilities of the magnetization trajectories. Of course, thermal effects will, in general, prevent the magnetization from following a perfectly exact and closed trajectory, which will act to give a finite linewidth to the spectral peaks. However, the data here suggest that, at least for the narrowest peaks, thermal effects are not the dominant source of linewidth broadening in the nanocontact devices.

2.2.6 *Linewidth comparison in nanopillars and nanocontacts*

It is interesting to compare the linewidths in typical nanopillar devices to those of nanocontact devices. At first glance one might expect the nanocontact devices to have broader spectral signals. The region undergoing precession is attached to a continuous ferromagnetic film, which will result in spin waves being shed away from the contact area. This is a loss mechanism and could lead to a broadening of the excitation linewidth. However, as shown in the preceding text, the oscillations associated with the nanocontact devices are typically significantly narrower than those associated with the nanopillar geometry. The room-temperature oscillation linewidths of nanopillar devices typically range from a few hundred megahertz up to several gigahertz, whereas the nanocontact oscillations have linewidths typically ranging from a few megahertz to a several tens of megahertz (see Figures 2 and 15).

The cause of this discrepancy is not presently clear, but there are a number of possibilities. In the pillar structures, the edges of the device structure are formed by lithographically defining a mask in the shape of the desired structure and then ion milling through the magnetic layers to form a pillar.

As with any lithographic process, this will naturally lead to shape defects in the edge of the device. Further processing will also oxidize the sides of the pillar structures. Each of these is expected to broaden the oscillation linewidths. This edge roughness will naturally lead to local variations in the demagnetizing fields. Thus, the magnetization at the edges of a laterally patterned structure will tend to oscillate at slightly different frequencies than the magnetization in the middle of the structure and cause linewidth broadening. This is further exacerbated by defects and perhaps nonuniform oxidation along the device sides. These effects result in the nonuniform precession of the magnetization throughout the device structure and the excitation of incoherent spin waves leading to broadened linewidths (Lee *et al*., 2004; Berkov and Gorn, 2005). In the nanocontact devices there is no patterning of the ferromagnetic film close to the device area, and so the problems associated with devices edges will be lessened, if not resolved. Of course the contact itself will have some edge defects, but these local defects will tend to be washed out by the diffusive nature of the current flowing through the device.

However, it is difficult to attribute the narrow linewidths in the nanocontact geometry solely to the lack of edge defects and oxidation. Single-domain simulations of pillar devices innately lack any of the issues associated with edge defects and preclude the possibility of spin-wave excitations and nonuniform precession. However, thermal effects can be included in the simulations through the use of a fluctuating thermal field term that is proportional to $(T/V)^{1/2}$, where T is temperature and V is the device volume (Brown, 1963; Zhu, 2002). The effect of the thermal field is to perturb the precessional trajectories from being perfectly repeating, which will act to broaden the spectral linewidths. The strength of the thermal field is inversely proportional to the device volume and broadens the oscillation linewidths as the device dimensions are decreased, as shown in Figure 16 (Russek *et al*., 2005). Simulations of devices having dimensions of $50\,\text{nm} \times 50\,\text{nm}$, the nominal size of the nanocontacts discussed here, give linewidths on the order of 1 GHz for room-temperature precession. Hence, in the nanocontact geometry the precessional motion appears to be stabilized against these thermal effects, as compared to the pillar structure. Recent experimental work shows that the linewidths in nanopillar devices are significantly narrowed by reduced temperatures, indicating that thermal effects are at least partially responsible for their comparatively increased linewidths (Sankey *et al*., 2005). This stabilization in nanocontact devices possibly results from the exchange interaction between the precessing magnetization and the surrounding film. It is also possible that the effective volume of the precessing magnetization in the nanocontact geometry is much larger than the contact size, as was discussed in Figure 6, rendering the oscillations more stable against thermal effects. Resolving this question will significantly increase our understanding of the similarities and differences between the two device geometries.

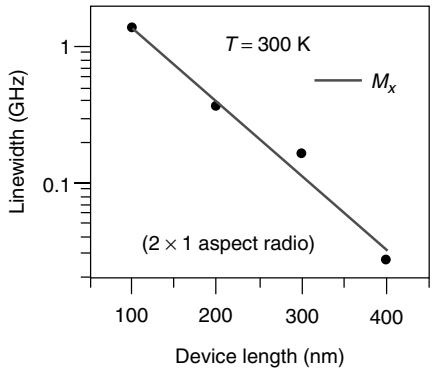

Figure 16. Plot showing the simulated linewidth vs device size for a set of 5-nm-thick $Ni_{80}Fe_{20}$ rectangular devices at room temperature. A 2:1 aspect ratio is used in all simulations. The line is an exponential fit, which gives an 82-nm decay length. (Reproduced from Russek *et al*., 2005, with permission from the American Physical Society. © 2005.)

In the preceding text, we have largely concentrated on the present understanding and experimental results of the spin-transfer-induced excitations in terms of their frequencies, linewidths, and output powers. Although there are still a number of unresolved issues, the excitation frequencies can generally be understood as very large-angle precessional motion approximating the uniform (FMR) mode. The linewidths in the oscillations depend on the device geometry and vary with the particular field and current applied to the device. For the nanocontact devices, the linewidths are typically a few tens of megahertz but can be larger, particularly when the oscillation frequency strongly depends on current or field. The narrowest linewidths are a few megahertz, which appears not to represent the intrinsic linewidth of the devices but instead reflects noise in the measurement system. The device output can be tuned by several orders of magnitude by controlling the geometry between the fixed and free layers, as expected from the GMR effect. At present, the output from the devices is still relatively low for microwave applications, although the device output power is a very significant fraction of that available through the GMR effect. The maximum signals to date are about 1 mV peak to peak. Of course, efforts to increase the ΔR_{max} in these devices are underway, either through the TMR effect, through materials engineering, or alternative device geometries such as coherent arrays (Kaka *et al*., 2005b; Mancoff, Rizzo, Engel and Tehrani, 2005). Impedance matching the devices to the measurement circuitry is also expected to significantly increase the measured output power.

2.3 Modulation effects

These spin-transfer-based nanoscale oscillators have several features making them attractive for potential applications. The devices are back-end CMOS compatible, they have nanoscale 'footprints', the devices are frequency agile, and they do not rely on any particular substrate material. The most obvious potential application for these devices would be as high-frequency clock oscillators or as microwave sources for on-chip signals. However, these devices would have a greater number of potential applications if the oscillation frequencies can be modulated allowing for transmission and reception of information and spectral analysis of microwave signals. In addition, many applications would also require the devices to be phase locked or referenced to either other devices or an external reference signal, such as is done in phase-locked loops and radio communications applications. In the following sections, we discuss recent work investigating these behaviors in the spin-transfer-based oscillators.

2.3.1 Frequency modulation

The measurement setup for the following modulation and phase-locking experiments is shown in Figure 17. The system consists of high- and low-frequency branches defined by the bias tee. A power splitter is inserted into the high-frequency branch and a tunable microwave source is coupled into one leg of the power splitter. This will modulate the current through the device so that

$$I = I_{\mathrm{dc}} + \Delta I_{\mathrm{ac}} \cos\left(2\pi f_{\mathrm{mod}} t\right) \tag{6}$$

where f_{mod} is the frequency of the injected current. Since our devices are not matched to the 50 Ω impedance of the measurement circuitry, we must in general calculate the magnitude ΔI_{ac} using the voltage output from the microwave source and a simple microwave circuit analysis (Johnk, 1988). In this measurement, part of the signal from the microwave source is also parasitically input directly into the spectrum analyzer/oscilloscope. Hence, the signal measured by the spectrum analyzer or oscilloscope will be composed of a signal from the microwave source along with the output from the spin-transfer oscillator. These two different signals are easily distinguished as long as the input frequency is far from the device oscillation frequency, but care needs to be taken with the frequencies that are close to one another or identical.

The spectral output from a typical device when biased only with a dc current is shown in Figure 18 for $\mu_0 H = 0.7\,\mathrm{T}$ and $\theta_H = 80^\circ$. The frequency increases roughly linearly from $I_{\mathrm{dc}} = 6$–$8\,\mathrm{mA}$, and then increases at a more gradual rate up to $I_{\mathrm{dc}} = 9.5\,\mathrm{mA}$. To examine the effects of an ac current on the resonance, the device is first biased to a fixed current and an additional 40 MHz ac current is applied through the power splitter, generating a time-varying resonance frequency, that is, frequency modulation (FM). In Figure 19(a), the spectral outputs at $I_{\mathrm{dc}} = 8.5\,\mathrm{mA}$ are shown for two input ac current amplitudes. The spectra generally show that, with increasing modulation current amplitude ΔI_{ac}, more power is driven into sidebands positioned at $f = f_{\mathrm{center}} \pm n40\,\mathrm{MHz}$ (the sideband order $n = 1, 2, \ldots$), with the specific sideband magnitudes depending on the variation of the precession frequency with current. For example, at a bias point in the linear region of the f versus I_{dc} curve, such as $I_{\mathrm{dc}} = 7.5\,\mathrm{mA}$, the upper and lower sidebands of a given order have approximately the same amplitude. However, when the device is biased at $I_{\mathrm{dc}} = 8.5\,\mathrm{mA}$, where the frequency does not have simple linear dependence on current (Figure 18), the upper and lower sidebands have significantly different magnitudes and vary differently with ΔI_{ac}.

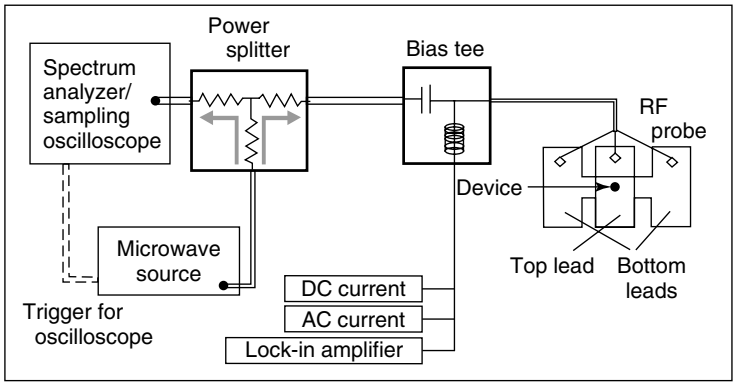

Figure 17. Schematic diagram showing the measurement setup used to allow high-frequency modulation of the current through the device. When a sampling oscilloscope is used in the measurements, the oscilloscope is referenced to a 10 MHz signal from the microwave generator to which the high-frequency output from the generator is phase locked. The arrows show the parallel paths, the signal from the generator follows.

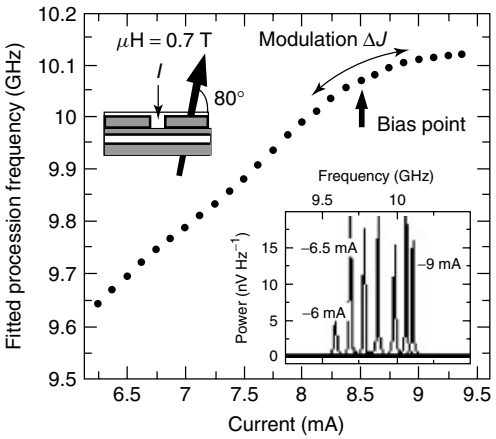

Figure 18. Frequency of spin-transfer-induced precession in a nanocontact as a function of dc bias current. Schematic shows sample measurement geometry. Inset: Spectral output of nanocontact for several dc currents, showing variation of frequency and amplitude with current (Pufall *et al*., 2005). (Reproduced from Pufall *et al*., 2005, with permission from the American Physical Society. © 2005.)

Multiple Lorentzian functions were simultaneously fit to the spectra for $I_{dc} = 8.5\,\text{mA}$ to determine the spectral peak positions and amplitudes for different magnitudes of the modulation current ΔI_{ac} (see Figure 19(b–d)). The upper and lower sideband amplitudes of a given order vary in markedly different ways as a function of ΔI_{ac}. For example, for the first-order sidebands ($f = f_0 \pm 40\,\text{MHz}$, Figure 19c), the upper sideband is larger in magnitude at a given ΔI_{ac} and peaks at a higher ΔI_{ac} than the lower sideband. In contrast, for the second-order sidebands ($f = f_0 \pm 80\,\text{MHz}$, Figure 19d), the lower sideband is larger in magnitude for low ΔI_{ac}, with the upper sideband becoming larger for $\Delta I_{ac} > 0.75\,\text{mA}$. Finally, the central peak (the 'carrier' frequency f_0, see Figure 19b) red shifts significantly with ΔI_{ac}. As will be shown, these effects are due to the nonlinear shape of the f versus I_{dc} transfer curve in the neighborhood of 8.5 mA.

The general form for the output signal from an oscillator is

$$V(I,t) = \text{Re}(V_0 \exp(i\theta(I,t))) \tag{7}$$

where the phase angle is defined as

$$\theta(I,t) = 2\pi \int_0^t f\left(I\left(t'\right)\right) \mathrm{d}t' \tag{8}$$

When $f(I) = \text{constant} = f_0$, the phase angle is simply $2\pi f_0 t = \omega_0 t$, and the oscillator output spectrum is a single peak at f_0. For typical frequency-modulation systems, the frequency varies linearly with the modulation parameter. With such a linear f versus I_{dc} characteristic of slope b, the current will have the form $I(t) = I_{dc,0} + \Delta I_{ac}\cos(2\pi f_{mod} t)$ and the phase angle becomes

$$\theta(I,t) = \omega_0 t + \beta \sin(\omega_{mod} t) \tag{9}$$

in which $\omega_0 = 2\pi f(I_{dc,0})$, $\omega_{mod} = 2\pi f_{mod}$, and the modulation factor $\beta \equiv f_{dev}/f_{mod} \equiv b\Delta I_{ac}/f_{mod}$. The resulting expression for $V(I,t)$ can be expanded in a Bessel series given by

$$V(I,t) = V_0 \mathrm{e}^{i(\omega_0 t + \beta \sin(\omega_{mod} t))} = V_0 \mathrm{e}^{i\omega_0 t} \sum_{l=-\infty}^{\infty} J_l(\beta)\, e^{il\omega_{mod} t} \tag{10}$$

This expression shows the familiar result that the output spectrum has peaks at f_0, $f_0 \pm f_{mod}$, $f_0 \pm 2f_{mod}$, . . . , $f_0 \pm lf_{mod}$, and that the amplitude of the lth sideband is proportional to $J_l(\beta)$ for linear FM. The calculated FM spectrum and a function of drive amplitude is shown in Figure 20, showing that as the modulation amplitude is increased more power is taken from the peak at the center or carrier frequency f_0, and driven into the modulation sidebands (Couch, 2001).

For many values of field and field angle, the precession frequency of the spin-transfer oscillators does not linearly depend on I_{dc} but instead follows a higher-order polynomial in current near the bias point, as is the case for $I_{dc} = 8.5\,\text{mA}$ in Figure 18. This function $f(I)$ can be expanded as a Taylor series of order n:

$$f(I, I_{dc,0}) = \sum_n \frac{1}{n!} \left.\frac{\partial^n f}{\partial I^n}\right|_{I=I_{dc,0}} \left(I - I_{dc,0}\right)^n \tag{11}$$

With this form for $f(I)$, a sinusoidal input current of the form $I(t) = I_{dc,0} + \Delta I_{ac}\cos(2\pi f_{mod} t)$ results in a power series in $\Delta I_{ac}\cos(\omega_{mod} t)$:

$$f(I_{dc,0}, \Delta I_{ac}, t) = f(I_{dc,0}) + \sum_{n=1}^{\infty} \frac{1}{n!} \left.\frac{\partial^n f}{\partial I^n}\right|_{I=I_{dc,0}} \times (\Delta I_{ac}\cos(\omega t))^n \tag{12}$$

This results in several modifications to the linear FM expression (equation 10). First, each factor $\cos^k(\omega_{mod} t)$ can be expanded as a series in $\cos(m\omega_{mod} t)(m \le k)$:

$$\cos^n(\omega t) = \frac{1}{2^n}\binom{n}{n/2} + \frac{1}{2^{n-1}} \sum_{k=0}^{n/2-1} \binom{n}{k} \times \cos\left[(n-2k)\,\omega t\right];\, n \text{ even} \tag{13}$$

$$= \frac{1}{2^{n-1}} \sum_{k=0}^{n-1/2} \binom{n}{k} \times \cos\left[(n-2k)\,\omega t\right];\, n \text{ odd}$$

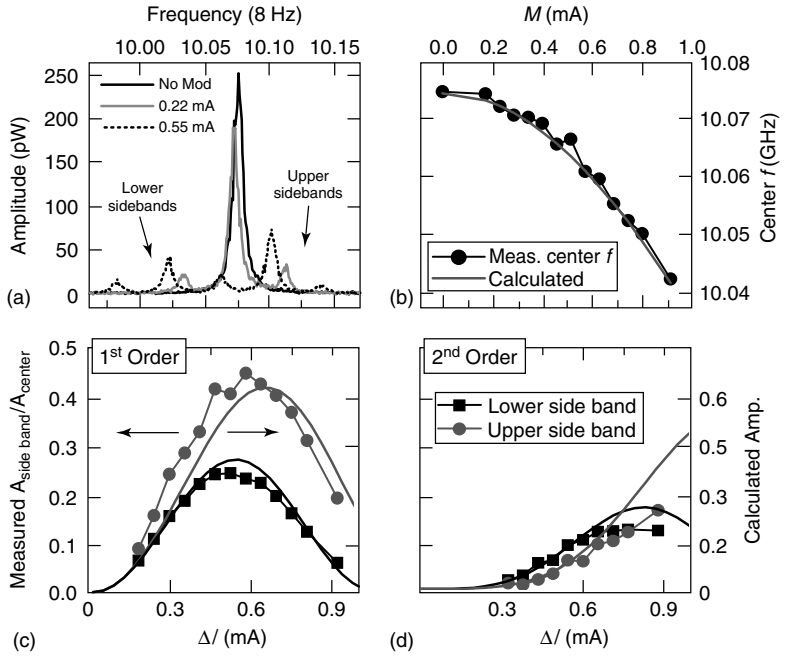

Figure 19. (a–d) Effects of injected ac current on spin-transfer resonance, at a dc current bias of $I_{dc} = 8.5\,\text{mA}$, $f_{mod} = 40\,\text{MHz}$. Solid lines in (b)–(d) are sideband amplitudes, calculated as described in the text. (a) Spectral output of device for several input modulation amplitudes ΔI_{ac}, showing sideband changes and shift of center frequency versus ΔI_{ac}. (b) Shift of center frequency versus ΔI_{ac}. (c) Variation of upper and lower first-order sideband amplitudes versus ΔI_{ac}. (d) Variation of upper and lower second-order sideband amplitudes versus ΔI_{ac}. Right scales show calculated sideband amplitudes and left scale, measured sideband amplitudes. (Reproduced from Pufall *et al.*, 2005, with permission from the American Physical Society. © 2005.)

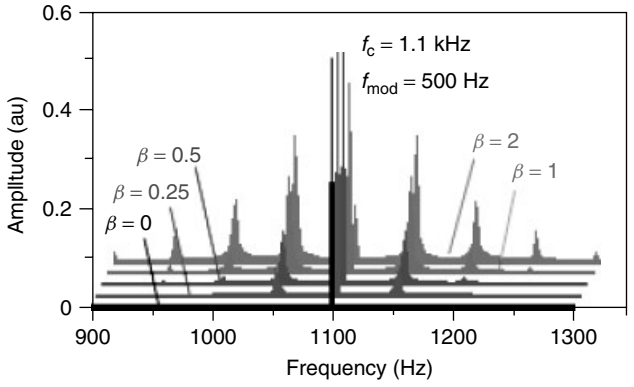

Figure 20. Simulated FM curves from equation (9), showing growth of sideband amplitudes with increasing $\beta = f_{dev}/f_{mod}$. Carrier frequency $f = 1.1\,\text{kHz}$, $f_{mod} = 50\,\text{Hz}$. Traces are offset for clarity.

Upon substitution of this expansion into the expression for $\theta(t)$ (equation (8)), one finds that a series in $\sin(m\omega_{mod}t)(m \leq n$, the order of the polynomial) now replaces the single sinusoidal term in equation (10). In addition, each even power in the cosine power series also contributes a term linear in t. These terms collectively are the source of the shift of the carrier (center) frequency, reflecting the fact that a sinusoidal drive shifts the average frequency of the device away from $f(I_{dc,0})$ when the frequency dependence on current is not symmetric about the bias point.

Each harmonic of ω_{mod} can be individually rewritten as a Bessel series, as in equation (10). The expression for $V(I_0, \Delta I, t)$ is then a product of Bessel functions with the number of factors set by the order of the polynomial. For example, the third-order expression is

$$V(I_0, \Delta I, t) = \text{Re}\left\{V_0 e^{iA_0 t} \sum_{l=-\infty}^{\infty} \sum_{m=-\infty}^{\infty} \sum_{p=-\infty}^{\infty} \times J_l(A_1)\, J_m(A_2)\, J_p(A_3)\, e^{i(l+2m+3p)\omega_{mod}t}\right\} \tag{14}$$

in which the A_n are linear combinations of the Taylor coefficients, and A_0 is a sum of $\omega_0 = 2\pi f(I_0)$ with contributions from even powers in the Taylor expansion. The A_i are, in general, functions of $I_{dc,0}$, ΔI, and ω_{mod}, and are generalizations of the modulation factor $\beta = f_{dev}/f_{mod}$ in linear FM in equation (10). This sum has terms proportional to $\sin(A_0 t)$, $\sin(A_0 t \pm \omega_{mod}t)$, $\sin(A_0 t \pm 2\omega_{mod}t)$, $\sin(A_0 t \pm 3\omega_{mod}t)$, . . . describing a carrier at a (shifted) frequency $A_0/2\pi$, plus sidebands at integer harmonics of f_{mod}. The

amplitude of a given sideband is a sum of terms such that the sum of the indices $l + 2m + 3p$ is equal to the order of the sideband, that is, $\pm 1, \pm 2$, and so on. Since the indices l, m, p can be either positive or negative, a large number of terms contribute to the amplitude of a given order. Furthermore, Bessel functions with negative indices can themselves be negative (since $J_m(x) = (-1)^m J_m(x)$), and so can produce an amplitude asymmetry between the upper and lower sidebands of a given order.

The computed center frequency shift and sideband amplitudes as functions of drive amplitude are shown as solid lines in Figure 19(b–d), determined using a fifth-order Taylor series expansion about $I_{dc,0} = 8.5\,\text{mA}$. As seen in the figure, the above expressions accurately describe both the red shift of the center frequency and also the relative variations of the sideband amplitudes with the modulation current, up to a constant amplitude factor. The model describes the amplitude difference between the upper and lower sidebands of a given order and also the crossover in their relative magnitudes (for linear FM, the magnitudes of the upper and lower sidebands of a given order are equal). The overall magnitudes of the calculated sidebands (but not the carrier frequency amplitude) are too large by a factor of 1.5, a factor that varies with bias point. This possibly results from nonlinearities in the current–voltage transport characteristics of the device, or from nonlinear amplitude modulation effects not included in the model. The amplitude of the output signal is not constant with current (Figure 18 inset), and on average decreases away from $I_{dc,0}$, which acts to decrease the amplitudes of the sidebands.

Note that these observed FM effects are not simply electrical, that is, the result of signal mixing due to a nonlinear current–voltage relation, but rather correspond to periodic variations in the precessional trajectory of the free layer magnetization. Simulated trajectories of a $100\,\text{nm} \times 100\,\text{nm}$ device for both zero and nonzero modulation amplitudes over one-half period of the modulation are shown in Figure 21 for an applied field $\mu_0 H = 0.7\,\text{T}$ at 80° to the film plane. In this configuration, the simulations predict a roughly linear dependence of frequency on current. The trajectory for nonzero modulation has a larger width in the z direction (perpendicular to the film plane). The modulation drives the magnetization periodically more into and out of the plane, expanding and contracting the cone of precession. This decreases and increases the demagnetizing field, which in turn modulates the net effective field and the precession frequency. The projection onto the y–z plane shows that the average value of the magnetization perpendicular to the plane oscillates at the modulation frequency.

These results show that the spin-transfer-based oscillators can be frequency modulated by modulating the current through the device. The spectral output from the devices can

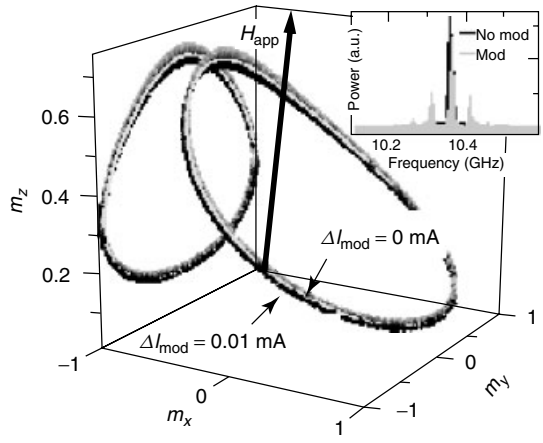

Figure 21. Plot of computed single-domain magnetization trajectory with (grayscale symbols) and without (light gray line) injected ac current modulation, over one modulation period. Color scale on trajectory denotes phase of ac modulation, from gray (ac current at minimum) to black (ac current at maximum). Axes are in units of the saturation magnetization. Trajectories also projected onto y–z plane to show spreading of the orbit in the z direction with drive. Simulations shown are at $T = 0\,\text{K}$, to more easily show the trajectory. AC current values differ from measured values owing to a different slope of calculated f versus I_{dc} curve and uncertainties in the absolute scaling of I_{dc} in the model. Inset: Fourier transforms of x component of trajectories showing frequency sidebands generated during modulation. (Reproduced from Pufall *et al.*, 2005, with permission from the American Physical Society. © 2005.)

largely be understood by the standard frequency-modulation analysis that includes a nonlinear dependence of frequency on I_{dc}. The data indicate that the large-angle precessional modes of the magnetization induced by spin transfer are stable and tolerant of significant (current-induced) perturbations. Further measurements have shown that the devices can be modulated at frequencies approaching that of the current-induced precession. This indicates that the precessional dynamics are not only robust to a large bandwidth of modulation inputs, but that the devices are able to respond to very rapid changes in current. These results indicate that the oscillators may be amenable to high-bandwidth, on-chip transmission and reception applications as well as rapid on-chip spectral analysis of a wide range of frequencies.

2.3.2 *Injection locking*

As mentioned in the preceding text, in many electronics applications oscillators must be phase referenced to a secondary signal. Most modern circuits accomplish this through the use of phase-locked loops. We investigate the ability of these spin-transfer oscillators to phase lock to an external signal using the simpler method of injection locking. In this synchronization scheme, the current through the device is modulated at a frequency close to, but distinct from, the

natural oscillation frequency of the oscillator, inducing the device to sympathetically oscillate at the drive frequency. This general feature of nonlinear oscillators is exploited in many modern technologies such as wireless communications, the American power grid, various power combining architectures, and phased array antennae networks (Strogatz, 2003). We find that the spin-transfer-based oscillators studied here can similarly be injection locked to signals up to several hundred megahertz away from their natural oscillation frequencies and, over this locking range, the phase of the oscillator can be electronically tuned over a range of roughly $\pm 90^{\circ}$ relative to the injected signal.

The output of a nanocontact device as a function of I_{dc} is shown in Figure 22(a) along with the corresponding differential resistance curve (Figure 22b). The small feature in the $\mathrm{d}V/\mathrm{d}I_{\mathrm{dc}}$ curve at 6.25 mA corresponds to the onset of oscillations in the f versus I_{dc} response. The power associated with the oscillations is shown in Figure 22(c) and is represented in a linear color scale in the top part of the figure. In Figure 22(d) and (e), we show the analogous data when an ac current $I_{\mathrm{ac}}^{(\mathrm{rms})} = 410\,\mu\mathrm{A}$ at 10.86 GHz (f_{drive}) is added to I_{dc}. In our measurement, part of this ac signal is parasitically shunted to the spectrum analyzer used to acquire the data, and produces a background signal at 10.86 GHz in Figure 22(d). We have found that in this configuration the spectrum analyzer lacks sufficient dynamic range to repeatably subtract this parasitic background, and so we are unable to directly measure the device output at this particular frequency using this method. At low currents the oscillation frequency is slightly pulled toward the drive frequency f_{drive}. As I_{dc} is increased the deviation between the driven and nondriven frequencies increases as the spin-transfer oscillations are pulled closer to the drive frequency. At $I_{\mathrm{dc}} = 7.4$ mA the device locks to the drive frequency, as we will explicitly show below, and remains so until $I_{\mathrm{dc}} = 7.8$ mA. At larger currents the device oscillation frequency is distinct from the drive frequency but is again pulled toward f_{drive}. Over the locking range of the oscillator a dc-rectified voltage V_{rect} is measured (see Figure 22(f)). This gives indirect evidence of injection locking of the oscillator to the input signal (Tsoi *et al.*, 2000).

When locked, the oscillator is expected to take on the noise characteristics of the injected signal (Razavi, 2004). A frequency stability of $f/\Delta f > 10^9$ is expected in the present case as determined by the microwave source, allowing measurement of the signal using stroboscopic sampling techniques. Direct measurement of the oscillator synchronization is done in the time domain using a sampling oscilloscope instead of the spectrum analyzer (see Figure 17). The oscilloscope is triggered from a 10 MHz signal that is phase referenced to the microwave generator. The signal measured by the oscilloscope is again composed of both a background signal from the microwave generator and the output from the spin-transfer device. To determine the device output, the background signal is first measured with no current running through the device. A second measurement is then taken with I_{dc} through the device and the background signal is subtracted, leaving the device output. Typically about 1000 averages are acquired for each time trace. In principle, this measurement is equivalent to the one using a spectrum analyzer.

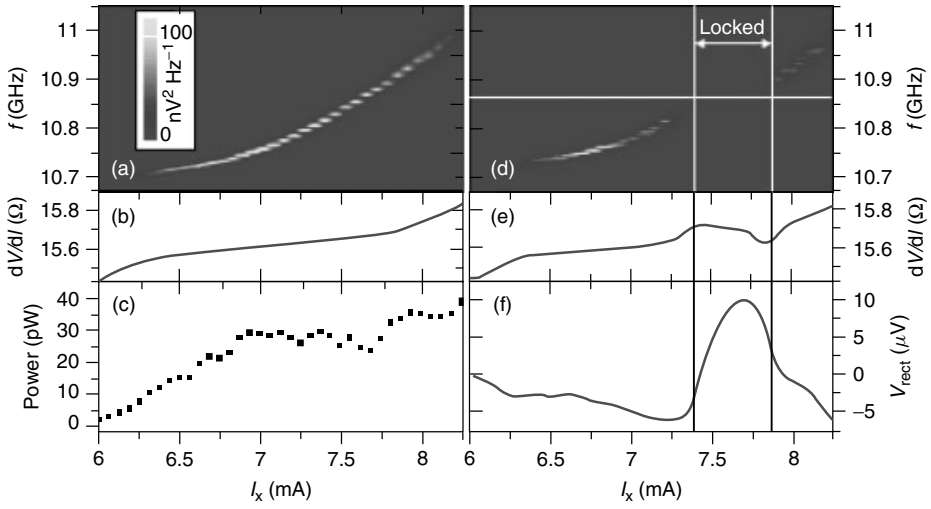

Figure 22. (a) Plot of f versus I_{dc} with amplitude shown in a linear color scale from 0 (black) to 100 $\mathrm{nV^2\,Hz^{-1}}$(light) with (b) corresponding $\mathrm{d}V/\mathrm{d}I_{\mathrm{dc}}$ curve without ac drive. Inset: Device and measurement schematic. (c) Device output power versus I_{dc} without ac drive signal in the same color scale. (d and e) Same as in (a and b) but with an ac drive at 10.86 GHz, 410 $\mu\mathrm{A}^{\mathrm{rms}}$. (f) Plot of V_{rect} versus I_{dc}. Vertical lines indicate the region of locking (Rippard *et al.*, 2005). (Reproduced from Rippard *et al.*, 2005, with permission from the American Physical Society. © 2005.)

However, the dynamic range of the sampling oscilloscope is larger ($1{:}2^{15}$) than that of the spectrum analyzer, permitting repeatable subtraction of the background signal. Such a stroboscopic measurement technique gives a null result unless the output from the device is phase synchronous with the injected microwave signal (i.e., the trigger signal) throughout the entire measurement interval of several minutes.

As indicated in Figure 22(d), the oscillator is locked to the injected signal for $I_{dc} = 7.6\,\text{mA}$. A time trace corresponding to this locked state is shown in Figure 23(a) along with a sinusoidal fit. The fact that we are able to measure the signal in the time domain explicitly shows that the oscillator is phase locked to the injected signal. A fit to the data yields an oscillation frequency of 10.86 GHz and a peak voltage of 44 μV. A spectral measurement of the device output without an ac bias for $I_{dc} = 7.6\,\text{mA}$ is shown in Figure 23(b). The spectral signal is equivalent to a peak voltage of 51 μV, in good agreement with the time-domain signal. Spectral measurements indicate that no significant power is generated at other frequencies (0–40 GHz). The deviation of the signal from a sinusoid is likely the result of imperfect synchronization between the trigger and the injected signal, as similar deviations from a sinusoid are obtained when the microwave generator output is directly measured.

The effect of varying the dc current through the locking range is shown in Figure 24(a). The device is locked to an ac current of $I_{ac}^{rms} = 410\,\mu\text{A}$ at 10.86 GHz and the time-domain signal is measured as I_{dc} is varied from 7.2 to 7.8 mA. As seen in the figure, the phase of the spin-transfer oscillator varies relative to that of the injected signal, allowing electronic phase control of the devices. Over the locking range the phase of the device varies by roughly $\pm 90^\circ$, as shown in Figure 24(b). No time-domain signals are observed outside this range, indicating that the signal is no longer phase coherent with the injected signal, as shown by the $I_{dc} = 7.85\,\text{mA}$ data.

We compare our results to the model of Adler (1973), which treats the oscillator as an active nonlinear circuit element coupled to an RLC circuit. Although simple, this analysis has been found to describe the locking characteristics of a range of oscillator circuits such as those based on diodes, transistors, and klystrons, to name a few (York, 1998 and references therein). The basic result of the analysis is

$$f_{drive} - f_o = \Delta f_{lock} \sin(\phi);\ \Delta f_{lock} = \frac{\Delta f}{2}\frac{V_{inj}}{V_{osc}} \qquad (15)$$

where Δf_{lock} defines the locking range of the device, Δf is the free-running oscillation linewidth, f_o is the free-running oscillation frequency, V_{inj} is the injected ac voltage across the device, V_{osc} is the oscillator voltage output, and ϕ is the phase difference between the oscillator and injected signal. Equation (15) has a solution for $f_{drive} = f_o \pm \Delta f_{lock}$, and over that range the phase of the oscillator relative to the injected signal varies from $-90^\circ < \phi < 90^\circ$, in agreement with the data in Figure 24. This result is derived under the limit that the addition of the injected signal does not significantly alter the output amplitude of the oscillator. In our devices, this criterion is met as long as the oscillator output (amplitude and linewidth) does not depend too strongly on the dc bias current over the locking range. This is often the case, as it is for the data presented here (see Figure 22c). In other cases, significant deviations from the 180° phase shift and the simple linear dependence of the locking range on the injected signal strength are found, as expected when significant power variation is included in the model (Fukumoto, Nakajima and Nakajima, 1983).

The dependence of the oscillation frequency on dc current for several different ac injection amplitudes is shown in Figure 25(a). ΔI_{ac} is estimated using standard microwave circuit analysis and taking the RF device resistance as equivalent to its dc value with no complex components (Johnk, 1988). As was seen in Figure 22, when the device is biased outside of the locking range, the spectral measurements indicate that the oscillation frequency is pulled toward the injected ac signal. The measured frequency is pulled only

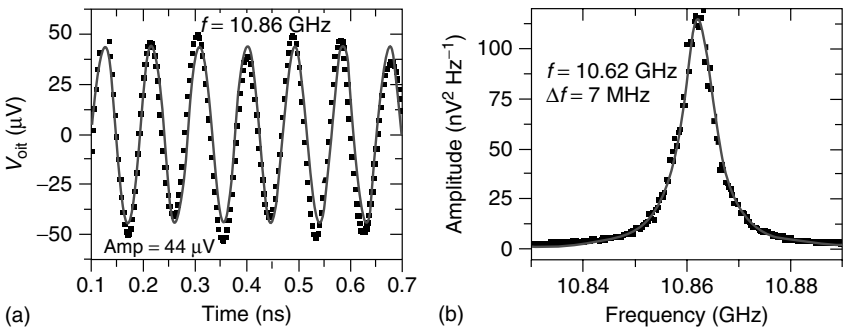

Figure 23. (a) Time-domain measurement of device output at $I_{dc} = 7.6\,\text{mA}$ along with a sinusoidal fit (line). (b) Spectral measurement of the device output with the same bias I_{dc} along with a fit to a Lorentzian function. (Reproduced from Rippard *et al.*, 2005, with permission from the American Physical Society. © 2005.)

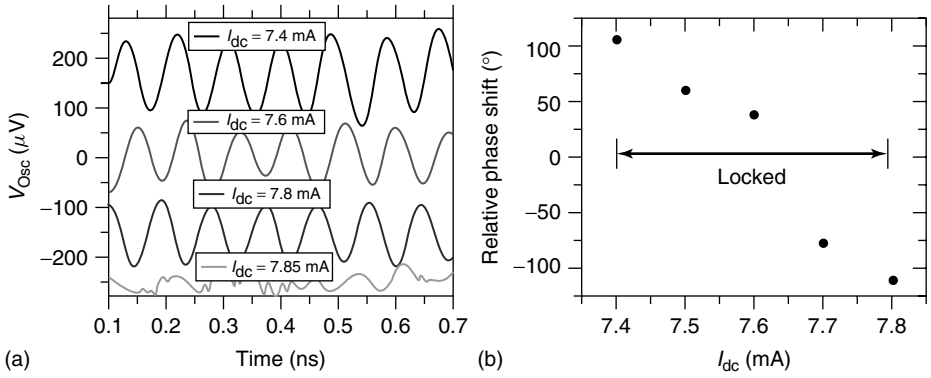

Figure 24. (a) Time-domain measurements of the device output as a function of dc current bias. The data are offset for clarity. (b) Relative phase shift between the device output and the external drive signal. An overall phase of 100° has been subtracted from the data. (Reproduced from Rippard *et al*., 2005, with permission from the American Physical Society. © 2005.)

slightly from its nondriven value far from the locking region. However, when the device is just outside of the locking range, the effect of the frequency pulling is much more significant, with the measured frequency continuously approaching the injection frequency.

This is not a frequency-modulation effect. In modulation schemes, the frequency of the mixed signal is independent of the amplitude of the modulation signal, at least for a linear f versus I_{dc} relationship, as discussed in the preceding text. As seen in Figure 25(a) this is not the case. Instead, the measurements are consistent with the oscillator quasilocking to the injection signal. When the oscillator is close to but outside the locking range, the device undergoes periods of being locked to the injected signal, punctuated by periods when the oscillator undergoes rapid phase slips and oscillates at frequencies different from f_{drive} (Razavi, 2004). The closer the oscillator is to the locking range, the longer the time between these periods of rapid phase change. The result is that the device oscillates not at a single frequency but over a range of frequencies, which appears as the pulling effect shown in Figure 25(a).

In Figure 25(b), the full locking range ($2\Delta f_{lock}$) is shown more explicitly as a function of the drive amplitude. The locking range is taken as the difference between the nondriven device oscillation frequencies at the minimum and maximum dc currents at which the device locks to the injected signal. The device is taken to be locked to the injected signal when more than 90% of the oscillator signal is at the injection frequency. The locking range varies approximately linearly with drive amplitude with a slope of $16\,\mathrm{MHz\,mV^{-1}}$. From equation (15), the full locking range is expected to be linear with a slope of $\Delta f / V_{osc}$ and intersect the origin. The predicted slope can only be estimated since the quantity depends explicitly upon the device output. Whereas the cabling and other component insertion losses can be measured, the coupling coefficient between our low impedance devices and a $50\,\Omega$ microwave line must be calculated. For the device investigated here having $\Delta f = 7\,\mathrm{MHz}$ we estimate that equation (15) predicts a slope of $42\,\mathrm{MHz\,mV^{-1}}$. The remaining discrepancy is possibly accounted for by a difference between the dc device resistance used in our estimate and the actual device impedance at 10.86 GHz.

The quantitative difference between the slope predicted by equation (15) and the measured value is not constant but instead varies with the device studied and the measurement geometry. To date, the values have always been within a factor of 5. For other devices in the same measurement geometry and a given injection amplitude, devices having larger linewidths and lower output powers lock over a wider range of frequencies in accordance with equation (15). In general, the devices can be locked to signals up to several hundred megahertz away from their natural oscillation frequency. The fit to the data indicates that a drive of finite amplitude, $1 \pm 0.2\,\mathrm{mV}$, is required to lock the device. This is in contrast to the predictions of equation (15). We have not yet determined the cause of the nonzero intercept, but it may reflect additional intrinsic losses in the nanocontact devices due to magnon radiation away from the device area (Slonczewski, 1999).

Close to the locking range, spectral measurements of the oscillations are predicted to yield $f = f_{drive} \pm ((f_o - f_{drive})^2 - \Delta f_{lock}^2)^{0.5}$ (Razavi, 2004). The line in Figure 25(a) shows this dependence for the data with $I_{ac}^{rms} = 330\,\mu\mathrm{A}$. As seen in the figure, this qualitatively describes the data close to the locking region. However, as the device frequency gets farther away from the locking regime, the measured frequency pulling is significantly larger than that predicted by the simple model used here. This discrepancy likely results from the amplitude effects that are not taken into account in the simple oscillator model (see Figure 22c).

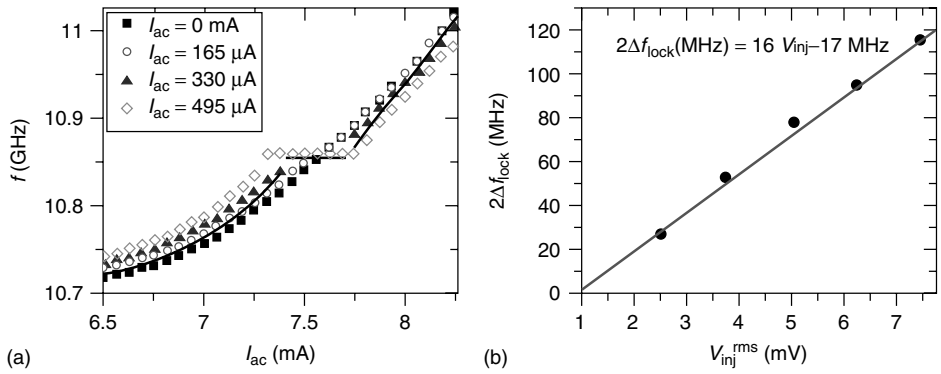

Figure 25. (a) Plot showing the f versus I_{dc} relation for several different amplitudes of drive at 10.86 GHz. The solid line is the predicted oscillation frequency for the drive of 330 μA, as discussed in the text. (b) Plot showing the locking range as a function of ac drive amplitude (ac voltage across the device) along with a linear fit to the data. (Reproduced from Rippard *et al*., 2005, with permission from the American Physical Society. © 2005.)

3 SUMMARY

As we have shown, the spin-transfer effect can result in a variety of coherent precessional dynamics in magnetic nanostructures. The precessional frequencies depend on both the current and magnetic field and can be tuned over a wide range of frequencies. Present measurements have demonstrated output frequencies up to about 40 GHz, but we expect to be able to generate even higher frequencies. The frequency dependence on magnetic field can be largely understood in terms of large-angle FMR precessional modes. The frequency dependence on the applied current is generally in agreement with the predictions of Slonczewski, although there are significant discrepancies between the theory and experiment. The device output power can be tuned over several orders of magnitude by varying the direction and strength of the applied field. The largest powers occur for nearly out-of-plane applied fields, which is consistent with the predicted magnetization trajectories and the GMR effect. The largest powers can be significant fractions of the maximum available through the GMR effect, and with improved impedance matching, the signals are expected to be nearly equivalent to the maximum values. The linewidths of the excitations can be quite narrow, leading to quality factors commonly in excess of 10^4. The narrowest linewidths are about 2 MHz and are presently limited by the fluctuations in the applied magnetic field and current noise.

The devices show attributes that are promising for potential applications. The spin-transfer oscillators can be frequency modulated at rates approaching the natural oscillation frequency of the device. This potentially allows the devices to be used in localized wireless communication architectures as well as in on-chip high-speed spectral analysis. The oscillators can be injection locked to an external reference signal up to several hundred megahertz away from their natural oscillation frequencies. Over the locking range, the phase of the device can be tuned relative to that of the injection signal by approximately $\pm 90^\circ$. These measurements demonstrate the potential for spin-transfer-based oscillators in practical microwave circuits that require synchronization of multiple oscillators (such as in timing circuits, signal tracking and reception, and signal demodulation) and phase control of multiple oscillators (such as directional beam steering, phased array detection, and localized coherent manipulation of quantum states).

ACKNOWLEDGMENTS

This work was supported by the NIST nanomagnetodynamics program, the NIST Office of Microelectronics Programs, the NIST Advanced Technology Program, and the DARPA SpinS program. We gratefully acknowledge S. Kaka, T. Silva, S. Russek, and J. Katine, with whom much of the experimental work was performed. We also acknowledge M. Stiles and R. McMichael for helpful discussions and S. Wolf for motivating the work on injection locking, as well as R. Goldfarb, A. McCallum, D. Smith, and C. Weil for helpful commentary on this manuscript.

REFERENCES

Adler, R. (1973). A study of locking phenomena in oscillators. *Proceedings of the IEEE*, **61**, 1380–1385.

Berger, L. (1996). Emission of spin waves by a magnetic multilayer traversed by a current. *Physical Review B*, **54**, 9353–9358.

Berkov, D. and Gorn, N. (2005). Magnetization precession due to a spin polarized current in a thin nanoelement: a numerical simulation study. *Physical Review B*, **72**, 094401-4. lanl.Cond-mat/0503754.

Bertotti, G., Serpico, C., Mayergoyz, I., *et al*. (2005). Magnetization switching and microwave oscillations in nanomagnetic

driven by spin-polarized currents. *Physical Review Letters*, **94**, 127206-1–127206-4.

Brown, W. (1963). Thermal fluctuations of a single-domain particle. *Physical Review*, **130**, 1677–1686.

Couch, L.W. (2001). *Digital and Analog Communication Systems*, Prentice Hall: Upper Saddle River.

Covington, M., AlHajDarwish, M., Ding, Y., *et al*. (2004). Current-induced magnetization dynamics in current perpendicular to the plane spin valves. *Physical Review B* **69**(18), 184406.

Deac, A., Lee, K., Liu, Y., *et al*. (2005). Spin transfer effects in exchange-biased spin-valves for current-perpendicular-to-plane magnetoresistive heads. *Journal of Magnetism and Magnetic Materials*, **290**, 42–47.

Donahue, M. and Porter, D. (2005). The simulation code can be found along with supporting documentation at http://math.nist.gov/oommf/.

Fabian, A., Terrier, C., Guisan, S., *et al*. (2003). Current-induced two-level fluctuations in pseudo-spin-valve (Co/Cu/Co) nanostructures. *Physical Review Letters*, **91**, 257209-1–257209-4.

Fuchs, G.D., Krivorotov, I.N., Braganca, P.M., *et al*. (2005). Adjustable spin torque in magnetic tunnel junctions with two fixed layers. *Applied Physics Letters*, **86**, 152509-1–152509-3.

Fukumoto, K., Nakajima, M. and Nakajima, M. (1983). Mathematical representation of microwave oscillator characteristics by use of the Rieke diagram. *IEEE Transactions on Microwave Theory and Techniques*, **83**, 954–959.

Gerrits, T., Van den Berg, H., Hohlfeld, J., *et al*. (2002). Ultrafast precessional magnetization reversal by picosecond magnetic field pulse shaping. *Nature*, **418**, 509–512.

Hoefer, M., Ablowitz, M., Ilan, B., *et al*. (2005). Theory of magnetodynamics by spin torque in perpendicularly magnetized thin films. *Physical Review Letters*, **95**, 267206-4. http://amath.colorado.edu/activities/preprints/.

Huai, Y., Albert, F., Nguyen, P., *et al*. (2004). Observation of spin-transfer switching in deep submicron-sized and low-resistance magnetic tunnel junctions. *Applied Physics Letters*, **84**, 3118–3120.

Ji, Y., Chien, C. and Stiles, M. (2003). Current-induced spin-wave excitations in a single ferromagnetic layer. *Physical Review Letters*, **90**, 106601-1–106601-4.

Johnk, C.T.A. (1988). *Engineering Electromagnetic Fields and Waves*, *Second Edition*, John Wiley & Sons: New York.

Kaka, S. and Russek, S. (2002). Precessional switching of submicrometer spin valves. *Applied Physics Letters*, **80**, 2958–2960.

Kaka, S., Pufall, M., Rippard, W., *et al*. (2005a). Spin transfer switching of spin valve nanopillars using nanosecond pulsed currents. *Journal of Magnetism and Magnetic Materials*, **286**, 375–380.

Kaka, S., Pufall, M., Rippard, W., *et al*. (2005b). Mutual phase-locking of microwave spin torque nano-oscillators. *Nature*, **437**, 389–392.

Katine, J., Albert, F. and Buhrman, R. (2000). Current-induced realignment of magnetic domains in nanostrucutred Cu/Co multilayer pillars. *Applied Physics Letters*, **76**, 354–356.

Katine, J., Albert, F., Buhrman, R., *et al*. (2000). Current-driven magnetization reversal and spin wave excitations in Co/Cu/Co pillars. *Physical Review Letters*, **84**, 4212–4215.

Kiselev, S., Snakey, J., Krivorotov, I., *et al*. (2003). Microwave oscillations of a nanomagnet driven by a spin-polarized current. *Nature*, **425**, 380–383.

Kittel, C. (1986). *Introduction to Solid State Physics*, *Sixth Edition*, John Wiley & Sons: New York.

Koch, R., Sun, J. and Katine, J. (2004). Time-resolved reversal of spin-transfer switching in a nanomagnet. *Physical Review Letters*, **92**, 088302-1–088302-4.

Krivorotov, I., Emley, N., Garcia, A., *et al*. (2004). Temperature dependence of spin-transfer-induced switching of nanomagnets. *Physical Review Letters*, **93**, 16603-1–16603-4.

Lee, K.J., Deac, A., Redon, O., *et al*. (2004). Excitation of incoherent spin-waves due to spin–transfer torque. *Nature Materials*, **3**, 877–881.

Li, Z. and Zhang, S. (2003). Magnetization dynamics with a spin-transfer torque. *Physical Review B*, **68**, 024404-1–024404-10.

Mancoff, F., Rizzo, N., Engel, B. and Tehrani, S. (2005). Phase-locking in double-point-contact spin-transfer devices. *Nature*, **437**, 393–395.

Mancoff, F., Dave, R., Rizzo, N., *et al*. (2003). Angular dependence of spin-transfer switching in a magnetic nanostructure. *Applied Physics Letters*, **83**, 1596–1598.

McMichael, R. and Stiles, M. (2005). Magnetic normal modes of nano-elements. *Journal of Applied Physics*, **97**(1–3), 10J901.

Montigny, B. and Miltat, J. (2006). Micromagnetic simulations of current-induced microwave excitations. *Journal of Applied Physics*, **97**, Art. No. 10C708.

Myers, E., Ralph, D., Katine, J., *et al*. (1999). Current-induced switching of domains in magnetic multilayer devices. *Science*, **285**, 867–870.

Ozyilmaz, B., Kent, A., Monsma, D., *et al*. (2003). Current-induced magnetization reversal in high magnetic fields in Co/Cu/Co nanopillars. *Physical Review Letters*, **91**, 067203-1–067203-4.

Pufall, M., Rippard, W. and Silva, T. (2003). Materials dependence of the spin-momentum transfer efficiency and critical current in ferromagnetic metal/Cu multilayers. *Applied Physics Letters*, **83**, 325–325.

Pufall, M., Rippard, W., Kaka, S., *et al*. (2004). Gigahertz-rate random telegraph switching induced by spin-momentum transfer. *Physical Review B*, **69**, 214409-1–214409-5.

Pufall, M., Rippard, W., Kaka, S., *et al*. (2005). Frequency modulation of spin-transfer oscillators. *Applied Physics Letters*, **86**, 082506-1–082586-3.

Razavi, B. (2004). A study of injection locking and pulling in oscillators. *IEEE Journal of Solid State Circuits*, **39**, 1415–1424.

Rippard, W.H., Pufall, M.R., Kaka, S., *et al*. (2004a). Direct-current induced dynamics in $Co_{90}Fe_{10}/Ni_{80}Fe_{20}$ point contacts. *Physical Review Letters* **92**, 27201-1–27201-4.

Rippard, W.H., Pufall, M.R., Kaka, S., *et al*. (2004b). Current-driven microwave dynamics in magnetic point contacts as a function of applied field angle. *Physical Review B* **70**, 100406-1–100406-4.

Rippard, W.H., Pufall, M.R., Kaka, S., *et al*. (2005). Injection locking and phase control of spin transfer nano-oscillators. *Physical Review Letters*, **95**, 067203-1–067203-4.

Russek, S.E., Kaka, S., Rippard, W.H., *et al*. (2005). Finite-temperature modeling of nanoscale spin-transfer oscillators. *Physical Review B*, **71**, 104425-1–104425-6.

Sankey, J., Krivorotov, I., Kiselev, S., *et al*. (2005). Linewidths for magnetic precession drive by dc spin-polarized currents. *Physical Review B*, **72**, 224427-4. lanl.Cond-mat, 0505733.

Slonczewski, J. (1996). Current-driven excitation of magnetic multilayers. *Journal of Magnetism and Magnetic Materials*, **159**, L1–L7.

Slonczewski, J. (1999). Excitation of spin waves by an electric current. *Journal of Magnetism and Magnetic Materials*, **195**, L261–L268.

Smith, N. (2004). Basic considerations for magnetization dynamics in the combined presence of spin-transfer torques and thermal fluctuations. xxx.lanl.Cond-mat 0406486.

Sparks, M. (1964). *Ferromagnetic-Relaxation Theory*, McGraw-Hill: New York.

Strogatz, S. (2003). *Sync: The Emerging Science of Spontaneous Order*, Hyperion: New York, Vol. 51.

Suhl, H. (1958). Origin and use of instabilities in ferromagnetic resonance. *Journal of Applied Physics*, **29**, 416–421.

Sun, J., Monsma, D.J., Abraham, D.W., *et al*. (2002). Batch-fabricated spin-injection magnetic switches. *Applied Physics Letters*, **81**, 2202–2204.

Tsoi, M., Jansen, A., Bass, J., *et al*. (2000). Generation and detection of phase-coherent current-driven magnons in magnetic multilayers. *Nature*, **406**, 46–48.

Tulapurkar, A., Devolder, T., Yagami, K., *et al*. (2004). Sub-nanosecond magnetization reversal in magnetic nanopillars by spin angular momentum transfer. *Applied Physics Letters*, **85**, 5358–5360.

Urazhdin, S., Birge, N., Pratt, W. and Bass, J. (2003). Current-driven magnetic excitations in permalloy-based multilayer nanopillars. *Physical Review Letters*, **91**, 146803-1–146803-4.

Wegrowe, J-E. (2003). Magnetization reversal and two-level fluctuations by spin injection in a ferromagnetic metallic layer. *Physical Review B*, **68**, 214414-1–214414-4.

Xiao, J., Zangwill, A. and Stiles, M. (2005). Macrospin models of spin transfer dynamics. *Physical Review B*, **72**, 014446-13.

York, R. (1998). Injection- and phase-locking techniques for beam control. xxx.lanl.Cond-mat/0504142.

Zhu, J-G. (2002). Thermal magnetic noise and spectra in spin valve heads. *Journal of Applied Physics*, **91**, 7273–7275.

FURTHER READING

Krivorotov, I.N., Emley, N.C., Sankey, J.C., *et al*. (2005). Time domain measurements of nanomagnet dynamics driven by spin-transfer torques. *Science*, **307**, 228–231.

York, R.A. (1993). Nonlinear analysis of phase relationships in quasi-optical arrays. *IEEE Transactions on Microwave Theory and Techniques*, **41**, 1799–1809.

Spin Structures and Spin Wave Excitations

Igor A. Zaliznyak
CMPMSD, Brookhaven National Laboratory, Upton, NY, USA

1 INTRODUCTION AND OUTLINE

Technological progress of recent years clearly brings to the forefront the ever-increasing importance of magnetism and magnetic materials in the everyday life. Detailed understanding of microscopic atomic structure and origins of magnetic phenomena now appears as key to further advances in diverse fields of science and technology. Although studies of magnetic structures and excitations form a rapidly expanding area of modern science offering new discoveries and surprises without an end in sight, a large body of experimental material and theoretical work accumulated over the past half a century can be understood in the framework of a simple microscopic description based on semiclassical treatment of systems of localized spins of magnetic ions. This article presents a brief survey of common types of spin structures and excitations found in magnetic crystals that can be described in the framework of such a semiclassical spin-wave approach. Experimental examples of neutron scattering studies, as best known to the author, are presented for each type, and discussed in the context of an up-to-date presentation of the linear spin-wave theory, perhaps, at the undergraduate level.

The article is organized as follows. The introductory second section outlines the fundamental connection between magnetism and the electronic spins from which it arises, spin interactions that are at the origin of cooperative magnetic phenomena are discussed in the third section, the fourth and the fifth sections present survey of different spin structures and spin-wave excitations, respectively, and the last section gives a brief summary.

Handbook of Magnetism and Advanced Magnetic Materials. Edited by Helmut Kronmüller and Stuart Parkin. Volume 3: *Novel Techniques for Characterizing and Preparing Samples*. © 2007 John Wiley & Sons, Ltd. ISBN: 978-0-470-02217-7.

2 MAGNETISM AND SPIN

Magnetism of many-electron condensed matter systems is a cooperative macroscopic quantum phenomenon originating from the fundamental relationship between the magnetic moment $\boldsymbol{M}$ and the angular momentum $\boldsymbol{J}$,

$$\boldsymbol{M} = \gamma \boldsymbol{J} \tag{1}$$

where, γ is the so-called gyromagnetic ratio (Einstein and De Haas, 1915; Barnett, 1935). This expression is a counterpart of the famous equivalence relation between the magnetic field $\mathbf{H}$ acting on the electron and the rotation with angular velocity $\boldsymbol{\Omega}_L = \frac{|e|}{2m_e c}\mathbf{H}$ known as *Larmor's theorem*, where, e and m_e are the electron's charge and mass and c is the velocity of light in vacuum. If a system interacts with an anisotropic environment, such as an atom in crystal's electric field, $\boldsymbol{M}$ and $\boldsymbol{J}$ might be not co-aligned and the gyromagnetic ratio becomes a tensor quantity, $\gamma_{\alpha\beta}$.

The magnetic moment associated with the Ampere's molecular electric current produced by an electron moving in an atomic orbit can already be derived semiclassically from

the Biot–Savart law,

$$\boldsymbol{\mu}_{le} = -\frac{\mu_{\mathrm{B}}}{\hbar}\left[\mathbf{r}_e \times \mathbf{p}_e\right] = -\frac{\mu_{\mathrm{B}}}{\hbar}\mathbf{l}_e = -\frac{|e|}{2m_{\mathrm{e}}c}\mathbf{l}_e \qquad (2)$$

This establishes the gyromagnetic ratio for the orbital motion, $\gamma_l = -\frac{|e|}{2m_{\mathrm{e}}c}$. This ratio is negative, so the electron's orbital magnetic moment is opposite to its orbital angular momentum. The magnetism of moving electric charges, however, is grossly insufficient for explaining magnetic properties of matter, such as magnetism of the lodestone (magnetite) known since ancient times, which is why it was one of the longest-standing problems in the history of science (Mattis, 1965). Magnetic fields produced by orbital Ampere currents, like artificial magnetic fields from electromagnets, are of electrodynamic origin. They are caused by nonrelativistic motion of electric charges and therefore contain a relativistically small factor, $\sim\alpha \approx 1/137$. The energy of magnetic interaction between two magnetic dipoles associated with Ampere orbital currents of two electrons at a distance $r = 1\,\text{Å}$, each carrying 1 Bohr magneton, $\mu_{\mathrm{B}} = |e|\hbar/(2m_{\mathrm{e}}c) = 0.927{\cdot}10^{-20}$ erg/Gs,

$$V(\mathbf{r}) = -\left\{\frac{8\pi}{3}\,(\boldsymbol{\mu}_1{\cdot}\boldsymbol{\mu}_2)\;\delta\,(\mathbf{r}) - \frac{(\boldsymbol{\mu}_1{\cdot}\boldsymbol{\mu}_2)}{r^3} + \frac{3\,(\boldsymbol{\mu}_1{\cdot}\mathbf{r})\;(\boldsymbol{\mu}_2{\cdot}\mathbf{r})}{r^5}\right\} \qquad (3)$$

is only $\sim \mu_{\mathrm{B}}^2/(k_{\mathrm{B}}r^3) \approx 0.6\,\text{K}$. This is way too small compared with the entropy contribution to the free energy to explain the existence of magnetism at room temperature and above. In addition, a simple theorem, established independently by N. Bohr and J. H. van Leeuwen, in fact prohibits magnetism in a system of classical electrons in thermal equilibrium (Mattis, 1965).

Therefore, fundamentally, room temperature magnetism could not be described by classical electrodymanics and was only explained with the devise of quantum mechanics in the early twentieth century. It is a consequence of the existence of an additional quantum degree of freedom of an electron, its spin (Compton, 1921; Uhlenbeck and Goudsmith, 1925). In quantum mechanics the electron at rest still possesses a quantum of 'internal' angular momentum, $\hbar\mathbf{s}_e$ ($\hbar$ is the Planck's constant), described by the spin angular momentum operator $\mathbf{s}_e$ of magnitude $\mathrm{s}_e = 1/2$,

$$\mathbf{s}_e^2 = s_e(s_e+1) = \frac{3}{2},\ \left[s_e^x, s_e^y\right] = is_e^z,\ \ etc \qquad (4)$$

There is also a magnetic moment of magnitude $\mu_{se} = \mu_{\mathrm{B}}\,(1 + \alpha/2\pi - \cdots) \approx 1.001\mu_{\mathrm{B}}$ associated with the electron's spin (Abragam and Bleaney, 1986). It is aligned opposite to spin angular momentum,

$$\boldsymbol{\mu}_{se} = -g_s\mu_{\mathrm{B}}\mathbf{s}_e = \gamma_s{\cdot}\left(\frac{1}{2}\hbar\mathbf{s}_e\right), \quad \gamma_s = -g_s\frac{|e|}{2m_{\mathrm{e}}c} \qquad (5)$$

where $g_s \approx 2.002$ is Lande g factor and γ_s is spin gyromagnetic ratio for the free electron which, like γ_l, is also negative. Neglecting a $\approx 0.1\%$ relativistic correction, $\gamma_s = 2\gamma_l$. In addition to the orbital angular momentum $\boldsymbol{L}$, magnetic moment of a many-electron atom is determined by its total spin,

$$\mathbf{S} = \sum_e \mathbf{s}_e \qquad (6)$$

where the summation can be restricted only to $2S$ unpaired electrons. Magnetism of condensed matter systems is usually described in terms of interactions between these atomic spins and resulting spin structures and excitations. Within the spin-S ground-state (GS) multiplet of a Hund's atom, electronic spins in the incomplete shell can be expressed as $\mathbf{s}_e = \pm\frac{1}{2S}\mathbf{S}$, with plus sign for the majority and minus for the minority electrons.

For an atomic system with total angular momentum $\boldsymbol{J} = \boldsymbol{L} + \boldsymbol{S}$, atomic gyromagnetic ratio in equation (1) is a combination of γ_s and γ_l and in many cases can be calculated using simple Lande-type formulae (Abragam and Bleaney, 1986). Larmor's equivalence between magnetic field and rotation can be seen in that additional term in the free energy resulting from magnetic field $\mathbf{H}$ and the term arising from Larmor rotation with frequency $\boldsymbol{\Omega}_L = \gamma{\cdot}\mathbf{H}$ are exactly equal,

$$F_M = -\mathbf{M}{\cdot}\mathbf{H} = -\gamma\,\mathbf{J}{\cdot}\frac{\boldsymbol{\Omega}_L}{\gamma} = -\mathbf{J}{\cdot}\boldsymbol{\Omega}_L \qquad (7)$$

and can be interchanged as a matter of convenience. This fundamental equivalence immediately leads to the Lagrangian of spin rotations,

$$L = \frac{1}{2}\chi\left(\frac{\boldsymbol{\Omega}}{\gamma} - \mathbf{H}\right)^2 \qquad (8)$$

which is at the origin of the powerful macroscopic description of long-wavelength, low-energy excitations in magnetic systems with finite magnetic susceptibility χ and in the presence of a magnetic field, in the framework of spin hydrodynamics (Andreev, 1978).

3 SPIN INTERACTIONS AND SPIN HAMILTONIAN

Strong interaction between electronic spins leading to magnetism in condensed matter results from a combination of the electrostatic Coulomb repulsion between electrons and a quantum-mechanical coupling between electron spin and coordinate wave functions established by the Pauli principle

which prohibits electrons with the same orbital wave function from also having parallel spins. Hence, a many-electron wave function minimizing the Coulomb energy corresponds to a particular mutual spin alignment of interacting electrons. As was first established by Heisenberg and Dirac (Dirac, 1926; Heisenberg, 1926, 1928) within the first-order approximation of the perturbation theory the electrostatic Coulomb interaction in the many-electron system can be expressed in the form of a spin Hamiltonian,

$$H = \sum_{e,e'} J_{ee'} \left(\mathbf{s}_e \cdot \mathbf{s}_{e'} + \frac{1}{4} \right) \tag{9}$$

which became known as the *Heisenberg exchange interaction*. Expression in brackets, up to a sign, is just a permutation operator for two electrons, tagged e and e', expressed through their spins. The strength of such direct exchange interaction between two electrons occupying orbital states with wave functions ψ_1 and ψ_2 is given by the overlap integral,

$$J_{ee'} = -\int \psi_1{}^*(\mathbf{r}_e)\ \psi_2{}^*(\mathbf{r}_{e'}) \times \frac{e^2}{r_{ee'}}\ \psi_1(\mathbf{r}_{e'})\ \psi_2(\mathbf{r}_e)\ \mathrm{d}^3\mathbf{r}_e\ \mathrm{d}^3\mathbf{r}_{e'} \tag{10}$$

which measures the frequency with which two electrons exchange their orbital states (Bethe and Jackiw, 1997). For the localized orthogonal orbitals the integral is always positive (Bethe and Jackiw, 1997; Yosida, 1998) and the direct exchange coupling is negative, $J_{ee'} < 0$, favoring parallel, ferromagnetic alignment of electronic spins. This type of interaction is at the origin of the Hund's rule requiring that electrons in an unfilled atomic shell maximize their total spin, and is also involved in the ferromagnetism of 3d metals (Fe, Ni, Co) and other materials. In very few cases, though, straightforward direct exchange is the leading cause of ferromagnetism. In fact, contribution of electron–nuclei Coulomb interaction to the direct electron exchange coupling between two atoms can actually make this coupling positive (e.g., when electron's wave functions have large overlap close to the nuclei), favoring antiparallel, antiferromagnetic spin alignment (Van Vleck, 1945).

In addition to direct exchange, there are a number of indirect exchange mechanisms contributing to coupling between atomic spins in condensed matter systems. The leading cause of the antiferromagnetism in magnetic insulators is the superexchange interaction resulting from the hybridization of wave functions of magnetic 3d ions with those of the intervening nonmagnetic anions (Kramers, 1934; Anderson, 1959). In the second-order perturbation theory, virtual electron hopping between the anion and the cation orbitals lowers the energy of the localized electrons. Depending on the electronic and orbital configuration and the resulting hopping matrix elements, direct exchange on the anion site may either lead to antiferromagnetic, or ferromagnetic superexchange (Kanamori, 1959). While in insulators with localized electrons superexchange interaction is short-range, typically acting only between the nearest cations bonded by an anion, in semiconductors where anion states form band superexchanges interaction can be long range, extending to distant neighbors (White, 1983). In addition to superexchange, electron hopping through anion site between 3d cations with two degenerate states, such as in Mn^{3+}/Mn^{4+} mixed valence systems, can facilitate ferromagnetic coupling, which is known as *double exchange* (Zener, 1951, 1959). Finally, in metals, direct exchange between the localized 3d electrons and itinerant conduction electrons leads to a long-range indirect RKKY interaction whose sign depends on the distance between 3d sites and on the density of delocalized itinerant electrons (Kasuya, 1956; Yosida, 1957).

In view of the fact that spin of each unpaired electron of a Hund's atom is (within the ground-state multiplet) proportional to the total spin $\boldsymbol{S}$, in most cases spin Hamiltonian of a system of magnetic atoms in a crystal can, to a good approximation, be written as,

$$H = \sum_{j \neq j'} J_{jj'} \mathbf{S}_j \cdot \mathbf{S}_{j'} + \sum_j D \left(S_j^z \right)^2 - \sum_{j,\beta} \gamma_\beta H_\beta S_j^\beta \equiv H_E + H_A + H_Z \tag{11}$$

The first term here is the Heisenberg exchange including all direct and indirect exchange interactions, the second term describes the simplest, second-order uniaxial spin anisotropy resulting from electron interaction with the crystal electric field, $\sim A(L^z)^2$, and mediated by the relativistic spin-orbit coupling, $\sim\lambda(\boldsymbol{LS})$, and the third term is Zeeman energy in magnetic field $\mathbf{H}$. The sum is over all atoms tagged by an index j.

While isotropic Heisenberg exchange does select the mutual spin alignment in the GS spin structure, it has a full O(3) spherical symmetry with respect to spin rotations and therefore does not establish any particular spin orientation with respect to positions of atoms (on the lattice) in the coordinate space. Continuum of GS spin configurations that are related by simultaneous rotation of all spins is allowed. Symmetry of the order parameter in the exchange structure can be understood by moving every spin to a single point without changing its direction. As a result, there might be just one spin group with coinciding spin directions as in the ferromagnet, two groups corresponding to two sublattices with opposite spins, this occurs in antiferromagnets and ferrimagnets, a star of n groups of similar spins with C_n

rotational symmetry corresponding to n sublattices in a commensurate spiral magnet, a circle (or ellipse) filled with continuum of spin directions, such as in the incommensurate spin spiral, and so on, see Figures 4 and 5. A complete classification of exchange spin structures was given in Andreev and Marchenko (1980).

Anisotropic interactions sensitive to spin direction with respect to atomic positions arise from several sources. First and perhaps most important is the electron spin interaction with crystal electric field mediated by spin-orbit coupling which was mentioned above. Although spin-orbit interaction is a relativistic, electrodynamic effect, it is an intra-atomic interaction and is only small on an atomic energy scale. With $\lambda \sim 100-1000$ K and more, it is still very significant on the energy scale of condensed matter systems. Crystal-field effects are most pronounced in rare earths and in systems where the atom's orbital moment is unquenched and contributes significantly to the atomic magnetization. In rare earths strong spin-orbit coupling leads to the fine structure of atomic multiplets where total angular momentum $\boldsymbol{J}$ is a good quantum number and magnetism exists in the ground-state $\boldsymbol{J}$ multiplet. In most cases, magnetic moment of an atom can still be described by an effective spin and using equation (1), perhaps with anisotropic gyromagnetic tensor $\gamma_{\alpha\beta}$. Anisotropic spin interaction with crystal electric field on the same site can be described by a single-ion spin Hamiltonian, which is usually expressed in terms of Stevens operators $O_l^m(\mathbf{S})$ (Abragam and Bleaney, 1986; Jensen and Mackintosh, 1991),

$$H_A = \sum_{l \le S} \sum_{m=0}^{2l} B_{2l}^m O_{2l}^m(\mathbf{S}) \tag{12}$$

of which only $O_2^0(\mathbf{S}) = 3(S^z)^2 - S(S+1)$ was included in equation (11). B_{2l}^m are the crystal-field parameters, which, in principle, can be obtained from an *ab initio* calculation of charge distribution in the crystal. These parameters determine spin orientations with respect to the crystal axes and magnetic field. In the absence of magnetic field and for the uniaxial anisotropy of equation (11), spins can minimize their energy by aligning parallel to z axis when the anisotropy constant is negative, $D < 0$, (easy-axis anisotropy) and by being perpendicular to the z axis when D is positive (easy-plane anisotropy).

Electron hopping (i.e., the orbital hybridization) between the cation and surrounding anions can lead to a transferred spin anisotropy, which is determined by the electric field at the anion site. In addition, an account for spin-orbit interaction may add anisotropic part to the exchange interaction, resulting in two-spin anisotropy, $\mathrm{H}_A = \sum_{\alpha,\beta} D_{jj'}^{\alpha\beta} S_j^\alpha S_{j'}^\beta$, $\alpha, \beta = x, y, z$. Another small source of anisotropic two-spin coupling is the magnetic dipole interaction, equation (3). The structure of the diagonal part of anisotropic exchange is similar to equation (3) and is often called the *pseudodipole interaction*. The off-diagonal part is the antisymmetric exchange of Dzyaloshinskii (1958)–Moriya (1960) and is usually written in the form,

$$\mathrm{H}_{\mathrm{DM}} = \mathbf{D}_{jj'} \cdot [\mathbf{S}_j \times \mathbf{S}_{j'}] \tag{13}$$

This interaction is at the origin of weak ferromagnetism of antiferromagnets, Figure 2(b), and incommensurate spiral spin structures such as shown in Figure 4. An expression for vector $\mathbf{D}$ can be derived in the perturbation theory and depends on the matrix elements of the orbital angular momentum of the interacting atoms. Its direction in the crystal can often be determined from the symmetry of atomic orbitals with respect to the line segment connecting spins j and j'. If there is inversion symmetry with respect to the center of this bond, $\mathbf{D}$ vanishes. For $S = 1/2$ ions such as Cu^{2+}, single-ion spin Hamiltonian resulting from the crystal field is just a constant and only two-ion spin anisotropy is possible.

In metals and systems with itinerant electrons, the anisotropy of indirect exchange mediated by these electrons can arise not only from their spin-orbital coupling to the crystal field, but also from the spin and wave vector dependent electron scattering due to Fermi surface anomalies, which is sensitive to the spin polarization of electron bands.

4 SPIN STRUCTURES

While spin Hamiltonian of equation (11) is clearly oversimplified, for example, it assumes localized spins and only includes uniaxial single-ion spin anisotropy, it properly describes a great variety of important cases, some of which are discussed in the subsequent text. It also appears that with some notable exceptions, such as often found in one-dimensional (1D) and two-dimensional (2D) and/or frustrated spin systems where the GS is disordered (Mermin and Wagner, 1966a,b; Haldane, 1983; Chandra and Doucot, 1988), spin structures and excitations of this Hamiltonian can be correctly predicted by adopting a semiclassical description of spin based on $1/S$ expansion. This approach, which is justified for large spins, is known as the *spin-wave theory* (Anderson, 1952; Nagamiya, 1967; Nagamiya, Nagata and Kitano, 1962).

The starting point for spin-wave calculation is finding the GS spin configuration that has the lowest energy, E_{GS}, for classical spins, that is, treating spin operators in equation (11) as classical vector variables. This neglects all fluctuations and is essentially a mean-field approximation. For a system of N identical spins S on a Bravais crystal lattice and without

anisotropy and magnetic field ($D = H = 0$), the general solution for the classical GS of equation (11) is a coplanar spin spiral (Yoshimori, 1959; Villain, 1959; Kaplan, 1959, 1961),

$$\mathbf{S}_j = \mathbf{S}_\mathbf{Q} e^{i\mathbf{Q}\cdot\mathbf{r}_j} + \mathbf{S}^*_\mathbf{Q} e^{-i\mathbf{Q}\cdot\mathbf{r}_j} \tag{14}$$

GS spin configuration is thus specified by the order parameter $\mathbf{S}_\mathbf{Q}$, which is simply a Fourier transform of spin structure. This includes ferromagnetic ($\mathbf{Q} = 0$ and all spins are parallel) and antiferromagnetic (there are two spin positions in the lattice, with $\mathbf{Q}\mathbf{r}_j = 0$ and $\mathbf{Q}\mathbf{r}_j = \pi$, i.e., there are two sublattices with antiparallel spins) collinear spin structures, see Figure 1. In a collinear structure $\mathbf{S}_\mathbf{Q}$ in (14) is a real vector of length $S/2$. In a noncollinear spiral spin structure, $\mathbf{S}_\mathbf{Q}$ is a complex vector satisfying conditions $\mathbf{S}^2_\mathbf{Q} = 0$ and $2\left(\mathbf{S}_\mathbf{Q}\cdot\mathbf{S}^*_\mathbf{Q}\right) = S^2$ that ensure that all spins have equal length S. Consequently, its real and imaginary parts are two mutually perpendicular vectors of length $S/\sqrt{2}$. They define the plane to which all spins are confined. Spins follow circularly polarized rotation in this plane, which propagates in the direction of wave vector $\mathbf{Q}$ and with the rotation angle given by $\mathbf{Q}\mathbf{r}_j$. All spins in a plane perpendicular to $\mathbf{Q}$ are co-aligned. Unlike circularly polarized electromagnetic wave, which is transverse, in the absence of anisotropic interactions spin plane in the exchange spin spiral may have arbitrary orientation with respect to the propagation vector $\mathbf{Q}$ (and the crystal lattice).

If spin ordering wave vector $\mathbf{Q}$ is commensurate with some reciprocal lattice vector $\boldsymbol{\tau}$, that is, there exists a whole number n such that $n\mathbf{Q} = \boldsymbol{\tau}$, then only n different values of spin rotation angle (mod 2π) are possible on the lattice and the spin structure is the commensurate spiral with finite repeat period. In this case there are only n different spin orientations in the crystal and one can divide the spin system into n sublattices with co-aligned spins and define a superlattice with a larger unit cell which contains all differently aligned spins. A simple example is spin structure in a 2D antiferromagnet on triangular lattice. It is a commensurate spin spiral with propagation vector $\mathbf{Q} = (1/3, 1/3)$ consisting of three sublattices directed at 120° to each other, see Figure 5(c). While sublattice description is straightforward, it entails significant complications for spin-wave calculations and for understanding the structure and behavior of spin order parameter and excitations. Existence of n spin species requires n equations of motion; an enlarged unit cell corresponds to a proportionally smaller Brillouin zone into which dispersion of all excitations existing in the system have to be folded. It also implies a number of extinction rules for nuclear Bragg peak intensities prohibiting unphysical peaks, which would be at fractional positions in the real lattice. Finally, sublattice description is not possible for incommensurate spirals.

While in some cases introducing spin sublattices is unavoidable, in many situations spin structure is a weakly distorted exchange spiral (14) and can be best described in terms of the nuclear lattice on which the spin Hamiltonian, for example (11), is defined. In this description all spins in the ordered structure are treated equally, without subdividing them into sublattices. The lattice unit cell is not increased to incorporate translational symmetry breaking by spin order. The corresponding folding of the nuclear Brillouin zone is also avoided. Instead, additional (magnetic) Bragg peaks corresponding to spin superlattices are indexed in the paramagnetic (nuclear) Brillouin zone. For a Bravais lattice there is a single branch of spin-wave excitations, whose properties are determined by spin structure.

A general procedure for finding the GS structure of classical spin Hamiltonian (11) on a simple Bravais lattice was developed in Nagamiya (1967), Nagamiya, Nagata, and Kitano (1962), Yoshimori (1959), Villain (1959), and Kaplan (1959, 1961) and recently discussed in Zaliznyak and Zhitomirsky (1995a,b), Zaliznyak (2003), and Zhitomirsky and Zaliznyak (1996). One has to minimize a function of N classical vector variables $\mathbf{S}_j$, subject to N constraints of equal length, $\mathbf{S}^2_j = S^2$. Employing Lagrange multipliers and switching to Fourier representation, which takes advantage of lattice translational symmetry, the following system of equations for spin configuration, minimizing spin Hamiltonian (11) under the equal-spin constraint is obtained,

$$N J_\mathbf{q}\mathbf{S}_\mathbf{q} + \mathbf{e}_z D S^z_\mathbf{q} - \sum_{\mathbf{q}'} \lambda_{\mathbf{q}'}\mathbf{S}_{\mathbf{q}-\mathbf{q}'} = \frac{\gamma}{2}\mathbf{H}\delta_{\mathbf{q},0},$$
$$\sum_{\mathbf{q}'} \mathbf{S}_{\mathbf{q}'}\cdot\mathbf{S}_{\mathbf{q}-\mathbf{q}'} = S^2\delta_{\mathbf{q},0} \tag{15}$$

Here $\mathbf{e}_z$ is the unit vector along z axis, $\delta_{\mathbf{q},\mathbf{q}'}$ is a 3D Kronekker symbol, and $\mathbf{S}_\mathbf{q}$, $\lambda_\mathbf{q}$ and $J_\mathbf{q}$ are the lattice Fourier transforms of spin $\mathbf{S}_j$, Lagrange multiplier λ_j and exchange coupling $J_{jj'}$ lattice fields, for example,

$$J_\mathbf{q} = \sum_{\mathbf{r}_{jj'}} J_{jj'} e^{-i\,\mathbf{q}\cdot\mathbf{r}_{jj'}} = J_{-\mathbf{q}},\ J_{jj'} = \frac{1}{N}\sum_\mathbf{q} J_\mathbf{q} e^{i\,\mathbf{q}\cdot\mathbf{r}_{jj'}} \tag{16}$$

Result (14) follows immediately from equations (15). In the absence of anisotropy and magnetic field, the GS energy per spin is $E_{GS}/N = J_\mathbf{Q} S^2$, so the ordering wave vector $\mathbf{Q}$ corresponds to the minimum of the Fourier transform of exchange interaction, $J_\mathbf{Q} = \min\{J_\mathbf{q}\}$. When magnetic field $\mathbf{H}$ is turned on in the absence of spin anisotropy ($D = 0$), spins simply tilt toward field, forming a cone. $\mathbf{S}_\mathbf{Q}$ and the plane of spin spiral component align perpendicular to the field, and

the net magnetization, $\gamma \mathbf{S_0} = \chi \mathbf{H}$, is parallel to it. The same simple structure is realized when there is uniaxial anisotropy but the magnetic field is parallel to its axis, although for easy-axis spin anisotropy ($D < 0$) it occurs only for fields above spin-flop transition field, $H > H_{\rm sf} \sim \mathrm{S}\sqrt{|D|J}$. The balance between exchange and Zeeman energy determines spin-canting (cone) angle α, $\sin\alpha = H/H_{\rm s}$, which is valid up to the saturation field, $H_{\rm s} = 2S(J_0 + J_{\rm Q} + D)$. Above $H_{\rm s}$, $\sin\alpha = 1$ and spins are aligned parallel to the magnetic field.

In the general case, when both anisotropy and magnetic field are present, the situation is significantly more complicated. In addition to straightforward spin canting toward magnetic field as in the simple cases mentioned above, a noncollinear classical spin spiral also becomes distorted. This distortion, known as 'bunching', is described by the appearance of Fourier harmonics at integer multiples, $n\mathbf{Q}$, of the spin structure ordering wave vector $\mathbf{Q}$, that is, at $\boldsymbol{S}_{2\mathbf{Q}}$, $\boldsymbol{S}_{3\mathbf{Q}}$, and so on, in addition to $\boldsymbol{S}_{\rm Q}$. When such distortion is weak, for example, for small D and H, it can be calculated using perturbative harmonic expansion, $\lambda_{\mathbf{q}} = \sum_n \lambda_n \delta_{\mathbf{q},n\mathbf{Q}}$, $\mathbf{S_q} = \sum_n \mathbf{S}_{n\mathbf{Q}} \delta_{\mathbf{q},n\mathbf{Q}}$, where $\lambda_{n\neq 0} \sim O\left(\sqrt{\frac{D}{J}}, \frac{\gamma H}{J}\right) \cdot \lambda_{|n|-1}$ and $\left|S_{n\mathbf{Q}}\right| \sim O\left(\lambda_{|n|-1}\right)$ (Zaliznyak, 2003). Alternatively, it can be obtained by considering perturbative corrections to spiral winding angle in the real-space spin structure, $\delta\theta_j = \sum_n \alpha_n \cos\left(n\mathbf{Q}\mathbf{r}_j\right) + \beta_n \sin\left(n\mathbf{Q}\mathbf{r}_j\right)$, where the coefficients α_n and β_n are of the order $\sim O\left(\left(\frac{D}{J}\right)^{\frac{n}{2}}, \left(\frac{\gamma H}{J}\right)^n\right)$ (Zaliznyak and Zhitomirsky, 1995a,b).

Squares of the absolute value of Fourier components of spin density, $|\mathbf{S_Q}|^2$, $|\mathbf{S}_{2\mathbf{Q}}|^2$, and so on, are proportional to the intensity of magnetic Bragg reflections associated with spin order at the corresponding wave vectors, $\mathbf{Q}$, $2\mathbf{Q}$, and so on, which are measured in experiment, for example, by magnetic neutron diffraction (Izyumov and Ozerov, 1970; Zaliznyak and Lee, 2005; see also **X-ray and Neutron Scattering by Magnetic Materials, Volume 1**). For spin structures on a simple Bravais lattice discussed above, where there is only one spin in the crystal unit cell, $\mathbf{S_Q}$ is simply given by the magnitude of that spin S. Higher harmonics, which result from distortion of exchange spin structure, for small distortions can be calculated following the procedure described in the preceding text, see for example Zaliznyak and Zhitomirsky (1995a,b) and Zheludev *et al*. (1998, 1999). For non-Bravais crystal lattices with several spins in the unit cell, $\mathbf{S_Q}$ is the Fourier transform of the spin density of the entire unit cell. When there is more than one atom in the unit cell of the crystal, the above procedure of finding spin GS has to be modified by introducing several spin species. While this situation is actually more common in real materials, it leads to some computational complications, resulting in a system of linear equations for the order parameters of different spin species (Izyumov and Ozerov, 1970). Nevertheless, the result in principle is not much different from that for Bravais lattice. In fact, spin structures can often be easily understood by simply considering bond energies contributing to the Hamiltonian (11).

Some examples of spin structures found in different materials are shown in Figure 1 through Figure 4. The simplest, ferromagnetic structure, most commonly occurs in metals, such as 3d metals of the iron group, Figure 1(a). While electron states in metals form bands and applicability of the localized spin description is questionable, experiments do indicate existence of localized magnetic moments in metals of the iron group and their alloys, persisting well above the Curie temperature (Schurer, Sawatzky and van der Woude, 1971; Brown *et al*., 1982; Lynn, 1975, 1984). This can be visualized by adopting a simple approximate picture called the s–d model, where electrons of the incomplete d shell are localized, while valence s electrons are involved in metallic cohesion and are collectivized and described by Bloch wave functions (Zener, 1959, 1951). They provide long-range indirect exchange between the localized d electrons. First-principle local spin density functional calculations (Liechtenstein, Katsnelson, Antropov and Gubanov, 1986) indicate that effective Heisenberg localized spin Hamiltonian can indeed be used for describing 3d metals, and give effective exchange parameters for iron and nickel which agree well with experimental values. However, experimentally determined magnetic moments in ferromagnetic 3d metals, $\mu_{\rm Fe} \approx 2.2$, $\mu_{\rm Co} \approx 1.7$, $\mu_{\rm Ni} \approx 0.6$, are noticeably smaller than corresponding expected free-atom values arising from spin of unpaired 3d electrons, $S_{\rm Fe} = 2$, $S_{\rm Co} = 3/2$, $S_{\rm Ni} = 1$, which shows that simplistic s–d model is at best a very coarse approximation.

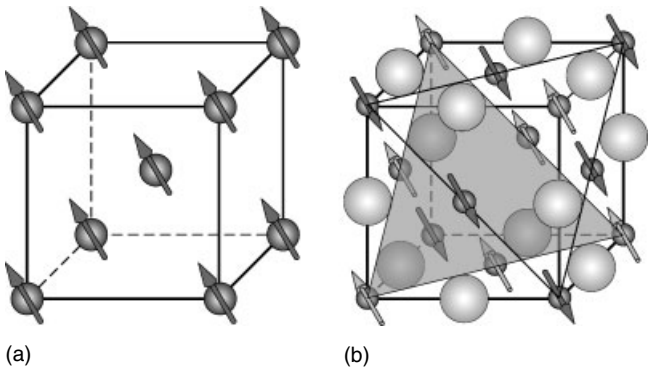

Figure 1. (a) Ferromagnetic spin alignment on the body-centered cubic (bcc) lattice found in simple metals (Fe, Ni, Co, . . .). (b) Antiferromagnetic spin structure on the NaCl-type face-centered cubic (fcc) lattice found in metal monoxides such as FeO, NiO, CoO, MnO. Small darker spheres with arrows show metal ions and their spins, larger spheres are oxygen anions. Structure consists of ferromagnetic sheets perpendicular to (111) diagonal of the cubic unit cell (shown semitransparent in the figure), staggered antiferromagnetically.

Transition-metal monoxides with simple fcc crystal lattice adopt antiferromagnetic spin structure shown in Figure 1(b) (Shull, Strauser and Wollan, 1951). It is driven by strong antiferromagnetic superexchange through 180° M–O–M (M = Fe, Ni, Co, Mn) bond. Propagation vector of such structure is Q = (1/2, 1/2, 1/2), in reciprocal lattice units of the cubic lattice shown in the figure. Spin alignment, however, is different in different oxides, although except for CoO spins tend to be confined to [111] planes. Antiferromagnetic order at T_N is usually accompanied by a slight trigonal distortion arising from magnetostriction associated with anisotropic spin interactions, which makes the symmetry of the crystal consistent with that of the spin structure, (Kugel, Hennion and Carabatos, 1978; Tomiyasu, Inami and Ikeda, 2004; Barbier *et al*., 2004; Goodwin, Tucker, Dove and Keen, 2006). NiO has the highest Neel temperature in the series, $T_N^{(NiO)} \approx 524\,K$, $T_N^{(CoO)} \approx 298\,K$, $T_N^{(FeO)} \approx 198\,K$, $T_N^{(MnO)} \approx 118\,K$.

Apart from simple ferro- and antiferromagnetism shown in Figure 1, there are collinear spin structures where both parallel and antiparallel spin alignments coexist, giving rise to an uncompensated net ferromagnetic, or more precisely ferrimagnetic moment. This can result from existence of atoms with different spins within the unit cell, such as Fe^{3+} and Fe^{2+}, which do not compensate each other when aligned antiferromagnetically, or from the combination of ferro- and antiferromagnetic spin alignment in the spin structure. In fact, both possibilities are realized in magnetite, Fe_3O_4, which is a prototypical ferrimagnet known as *lodestone* since ancient times, Figure 2(a). At room temperature the unit cell of magnetite contains three Fe_3O_4 formula units and 24 spins in total, which are unequally distributed between 8 tetrahedrally coordinated A sites (populated by Fe^{3+}, S = 2) and 16 octahedrally coordinated B sites (equally populated by 8 Fe^{3+}, S = 2 and 8 Fe^{2+}, S = 5/2). Antiferromagnetic superexchange J_{AB} between A and B sites passing through ≈125° A–O–B bond leads to the antiparallel alignment of A and B spins within the unit cell. Unequal population of A and B sites results in the ferrimagnetic structure. Already large unit cell is not further increased by spin structure, and magnetic Bragg reflections appear on top of nuclear Bragg peaks (Shull, Wollan and Koehler, 1951). Despite small value of the superexchange coupling, $J_{AB} \approx 2.35\,meV \approx 27\,K$ (Alperin, Steinsvoll, Nathans and Shirane, 1951), magnetite orders at very high temperature, $T_C \approx 858\,K$. This can be expected for large Fe^{2+}/Fe^{3+} spins and is consistent with spin-wave calculations (Mills, Kenan and Milford, 1966).

In the rhombohedral structure of hematite, Fe_2O_3, (and escolaite, Cr_2O_3) there are four Fe^{3+} (S = 2) ions in the unit cell and two types of bonds between them. In the antiferromagnetic structure below $T_N \approx 950\,K$ spins coupled by the superexchange passing through oxygen anions align antiferromagnetically, while those coupled directly are co-aligned, Figure 2(b). Once again spin order does not break lattice translational symmetry and magnetic and nuclear Bragg peaks overlap (Nathans, Pickart, Alperin and Brown, 1964). Superexchange bond, which couples spins from different sublattices, passes through two oxygen triangles that are rotated by 60° with respect to each other and thus lacks

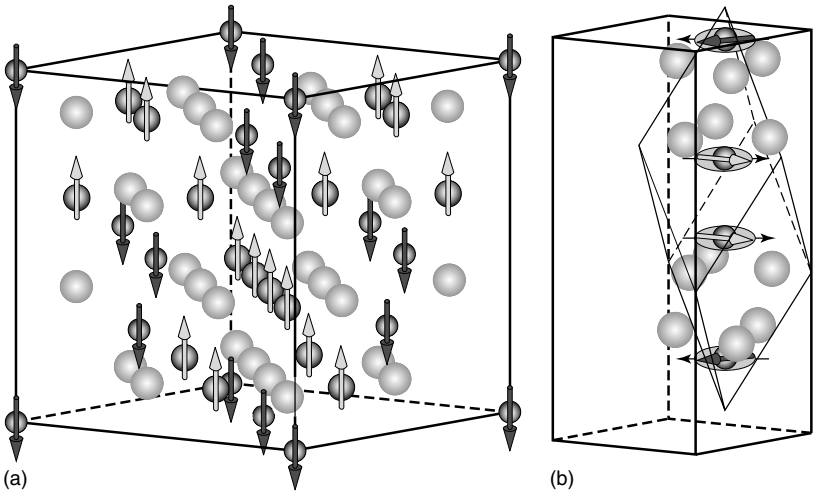

Figure 2. (a) Ferrimagnetic spin structure of magnetite, Fe_3O_4. The unit cell contains 32 O^{2-} anions (larger light-shaded spheres) and 24 Fe cations (smaller dark spheres). 8 Fe^{3+} ions (S = 2) with co-aligned magnetic moments $\approx 4\,\mu_B$ occupy tetrahedrally coordinated sites (down arrows), while 16 octahedrally coordinated sites are occupied by an equal mixture of 8 Fe^{3+} and 8 Fe^{2+} (S = 5/2, $\mu \approx 5\,\mu_B$) ions aligned in the opposite direction (up arrows), resulting in net ferromagnetic moment $\approx 4\,\mu_B$ per unit cell, or $\approx 1/6\,\mu_B$ per iron. (b) Weak ferromagnetism in hematite, Fe_2O_3. Nearly antiferromagnetic spins are shown slightly tilted in the basal plane, resulting in small ferromagnetic moment. Both hexagonal and the rhombohedral unit cell with four Fe^{3+} ions and oxygens bridging them are shown.

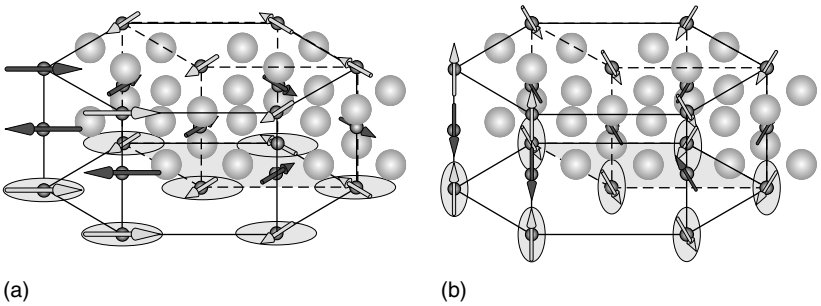

Figure 3. Triangular spin ordering in quasi-one-dimensional ABX_3 hexagonal perovskites; magnetic ordering wave vector is $Q = (1/3, 1/3, 1)$. Dark spheres with arrows show 3d metal ions and their spin. Anions (X) bridging 3d ions (B) in the chains at the corners one unit cell (dashed lines) and providing the exchange coupling are also shown (larger light spheres). (a) Easy-plane anisotropy does not distort 120° spin structure, simply forcing the plane of spin spiral to lie in the $a-b$ basal plane. (b) Easy-axis anisotropy $||\, c$ axis not only forces spin plane to be perpendicular to the basal plane, but also distorts perfect 120° triangular ordering (e.g., in $CsNiCl_3$ the angle between the spin direction in the neighbor chains is ≈119°).

inversion symmetry. This allows DM anisotropic contribution to superexchange, with **D** vector parallel to the threefold rotation axis (z axis). As a result, spins from different sublattices can lower their energy by slightly canting toward each other and producing a weak ferromagnetic component in the basal plane, perpendicular to z axis. The same weak ferromagnetism is also found in many other materials, for example, $MnCO_3$ and $CoCO_3$ (Borovik-Romanov, 1959).

Perhaps, the simplest noncollinear exchange spin structure is a 120° triangular spin ordering occurring in an antiferromagnet on the two-dimensional triangular lattice. It is also an example of the commensurate spin spiral with propagation vector $\mathbf{Q} = (1/3, 1/3)$. Such spin ordering is found in many magnetically quasi-one-dimensional perovskites of ABX_3 family (A = Cs, Rb, K, . . .; B = Ni, Mn, V, . . .; X = Cl, Br, I, . . .) with hexagonal crystal structure. In these compounds antiferromagnetic spin chains consisting of 3d metal sites and running along the hexagonal C_6 axis are arranged on the triangular lattice in the basal plane and form a 120° triangular spin structure in this plane, Figure 3. Easy-plane anisotropy found, for example, in $CsMnBr_3$ and $CsVBr_3$ does not distort 120° exchange structure, simply forcing all spins into the basal plane (Eibshutz, Sherwood, Hsu and Cox, 1972; Inami *et al*., 1995). In the case of easy-axis anisotropy (e.g., in $CsNiCl_3$, $RbNiCl_3$, $CsMnI_3$), spins lie in a plane containing the z axis. Triangular spin ordering of ideal spiral structure is distorted and spin opening angle is less than 120° (Yelon and Cox, 1972, 1973). In $CsMnI_3$, where it is only 100°, magnetic Bragg peak corresponding to third order harmonics of spin spiral structure, $3\mathbf{Q} = (1, 1, 1)$, is readily observed (Harrison, Collins, Abu-Dayyeh and Stager, 1991).

An example of the incommensurate spiral spin structure resulting from Dzyaloshinskii–Moriya interaction is found in quasi-2D $S = 1/2$ antiferromagnet $Ba_2CuGe_2O_7$ shown in Figure 4 (Zheludev *et al*., 1996, 1998, 1999). Absence of the inversion symmetry of the antiferromagnetic bond between nearest-neighbor spins on the centered square lattice in the basal plane allows uniform antisymmetric DM exchange with vector **D** perpendicular to (001) z axis. The spin interaction energy is minimized when all spins are perpendicular to **D**, in which case exchange energy per bond is $2J\cos\varphi + D\sin = \sqrt{4J^2 + D^2}\cos(\varphi - \alpha)$, where J is the antiferromagnetic isotropic Heisenberg superexchange,

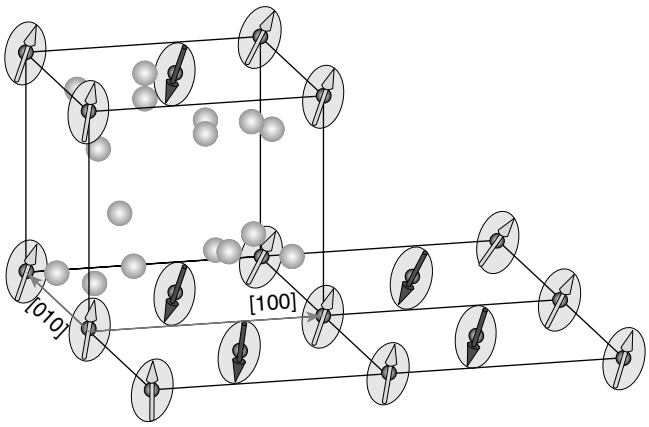

Figure 4. Spiral spin structure in quasi-2D antiferromagnet $Ba_2CuGe_2O_7$. Cu^{2+} ions (dark spheres) with $S = 1/2$ spins (arrows) form ideal square lattice in the $a-b$ plane. Larger, light-shaded spheres show oxygens in one unit cell. Noncentrosymmetric tetragonal crystal structure (space group $P\underline{4}2_1m$) gives rise to Dzyaloshinskii–Moriya interaction which favors spiral spin arrangement with spins confined in $[1, -1, 0]$ xz plane (x axis is directed along the diagonal of the square) and magnetic propagation vector $(1 + \varsigma, \varsigma, 0)$ with $\varsigma \approx 0.0273$. This means that interacting nearest-neighbor spins along the diagonal of the square unit cell rotate by $\alpha = 360^\circ \cdot \varsigma \approx 9.8^\circ$ in xz plane with respect to their antiparallel alignment in the simple collinear antiferromagnetic structure with $\mathbf{Q} = (1, 0, 0)$.

$\alpha = -\arctan(D/J)$ and φ is the angle between the spins. The energy is a minimum for $\varphi = \pi + \alpha$ and the GS spin structure is an incommensurate spin spiral with propagation vector $\mathbf{Q} = (1 + \varsigma, \varsigma, 0)$, $\varsigma = \alpha/(2\pi)$, shown in Figure 4. In this case not only spin alignment, but also spiral propagation vector are both determined by weak anisotropic interactions, and therefore both are equally strongly sensitive to magnetic field (Zheludev *et al.*, 1997).

5 SPIN-WAVE EXCITATIONS

Spin waves are usually understood in the framework of semiclassical description and can be visualized as small oscillations of classical spin vectors around their equilibrium positions in the GS spin structure, as shown in Figure 5. Their wavelike spatial composition results from the translational symmetry of the system. Frequencies of spin-wave oscillations can be calculated from spin Hamiltonian, for example, equation (11), by writing torque equations of motion for classical spins (Mattis, 1965). Such an approach relies entirely on classical mechanics and can be most generally pursued employing Poisson brackets formalism (Dzyaloshinskii and Volovick, 1979). Spin waves are normal modes of the linearized equations of motion. They involve small spin deviations that are perpendicular to the equilibrium spin direction. Hence, spin waves are transversely polarized, with two mutually orthogonal linear polarizations of spin oscillations possible. A circular spin precession around its equilibrium position can have two possible directions, clockwise and counterclockwise; one is shown in Figure 5(a) for a spin wave in ferromagnetic structure.

In an antiferromagnetic spin structure, precession of two sublattices can have the same, Figure 5(b), or the opposite sense, Figure 5(c). In the sublattice description, where the magnetic superlattice contains two spin species, these correspond to two distinct, in-phase and antiphase, spin-wave modes. In the extended, paramagnetic Brillouin zone (BZ) description, where there is only one spin-wave branch for spins on a Bravais lattice, these two modes correspond to spin waves having different wave vectors, $\mathbf{q}$ and $\mathbf{q} \pm \mathbf{Q}$, where $\mathbf{Q}$ is the antiferromagnetic ordering wave vector. For a three-sublattice antiferromagnetic spin structure on a triangular lattice there are two possible choices of sublattice(s) rotating in the 'wrong' sense. Hence, there are three spin-wave modes, Figure 5(d). In general, the total number of spin-wave modes in the sublattice description equals the number of sublattices. For a Bravais nuclear lattice, multiple modes arise from folding of the dispersion surface of a single mode defined in the large nuclear Brillouin zone into a small BZ of magnetic superlattice. Hence, their number is equally given by the volume ratio of these BZ.

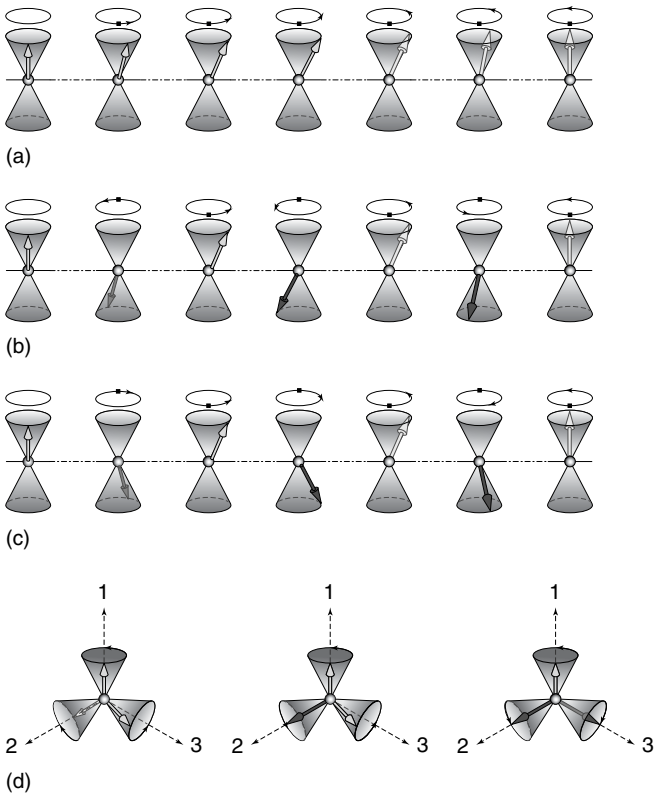

Figure 5. Spin waves in different spin structures. Each spin undergoes precession about its equilibrium direction sweeping out the surface of a cone over a period $2\pi/\omega(q)$, where $\omega(q)$ is frequency of spin wave and q is the wave vector. (a) Ferromagnet, (b) in phase, and (c) antiphase mode in two-sublattice antiferromagnet, (d) in phase and two antiphase (left to right) modes in three-sublattice antiferromagnet on triangular lattice. A half-period of spin-wave oscillation spanning six spins is shown in (a) and (b, c), corresponding to spin wave with wave vector equal to 1/12 of reciprocal lattice unit in the direction of propagation. Antiphase mode in (c) corresponds to wave vector 7/12 in the extended paramagnetic Brillouin zone description.

In quantum-mechanical description of spins, elementary quanta of spin excitation in spin systems, which by virtue of equation (1) are also elementary magnetic excitations, are known as *magnons*. In quantum mechanics, states of an isolated spin system on a lattice are specified by the total spin of the system, S_{tot}, its z component, S^z_{tot}, and wave vector $\mathbf{q}$, which determines the eigenvalue of the lattice translation operator, $\mathrm{T}_{\mathbf{r}}$,

$$\mathrm{T}_{\mathbf{r}} \left|\mathbf{q}, S_{\text{tot}}, S^z_{\text{tot}}\right\rangle = e^{i\mathbf{q}\cdot\mathbf{r}} \left|\mathbf{q}, S_{\text{tot}}, S^z_{\text{tot}}\right\rangle \tag{17}$$

A GS for an isotropic saturated ferromagnet is $\left|0, NS, S^z_{\text{tot}}\right\rangle$, $-NS < S^z_{\text{tot}} < NS$. For an antiferromagnet it is $|0, 0, 0\rangle$ (this implies sublattice description; ordered GS is doubly degenerate). In many cases this set of quantum numbers is sufficient for describing low-energy states of the

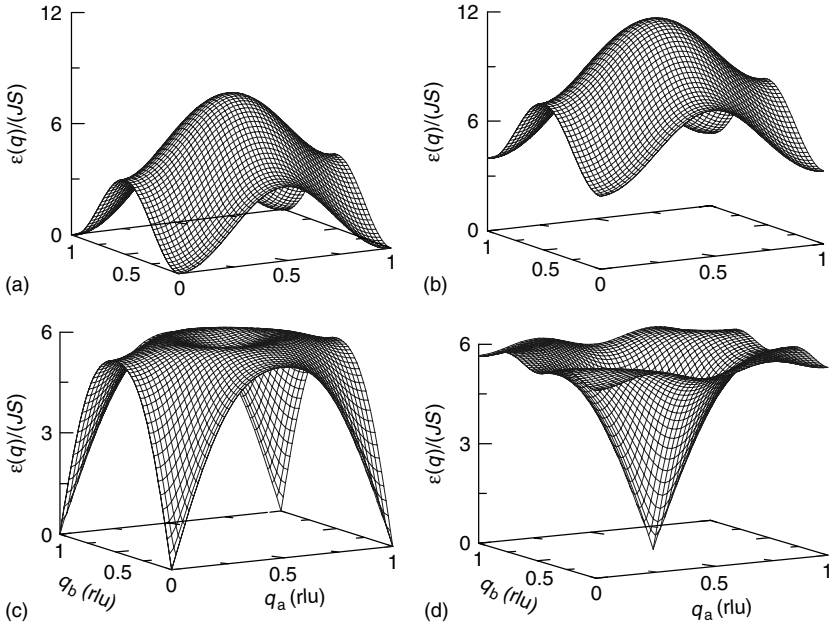

Figure 6. Cuts of the spin-wave dispersion surface in a ferromagnet, $J_a = J_b = J_c = J < 0$, (a), (b) and an antiferromagnet, $J_a = J_b = J_c = J > 0$, (c), (d) on a three-dimensional (3D) Bravais cubic lattice by an (h,k,l_0) reciprocal lattice plane with $l_0 = 0$ (a and c) and $l_0 = 0.5$ (b and d). Wave vector is measured in reciprocal lattice units (rlu), $q_a = h$, $q_b = l$. (a) Spin structure of a ferromagnet has propagation vector Q = (0, 0, 0) and magnetic Bragg peak positions coincide with nuclear structure Bragg peaks at the corners of the Brillouin zone. A cosine-like dispersion is quadratic in q around these points. (b) Dispersion for Q = (h, k, 0.5) does not pass through Q = 0 magnetic ordering vector and has a gap. (c) Dispersion in Q = (h, k, 0) zone does not pass through Q = (1/2, 1/2, 1/2) magnetic ordering vector of an antiferromagnet but still softens for the uniform mode at Q = 0 and has no gap. (d) Dispersion in Q = (h, k, 1/2) zone cuts through the Goldstone mode with sine-like dispersion linear in the vicinity of magnetic ordering vector Q = (1/2, 1/2, 1/2).

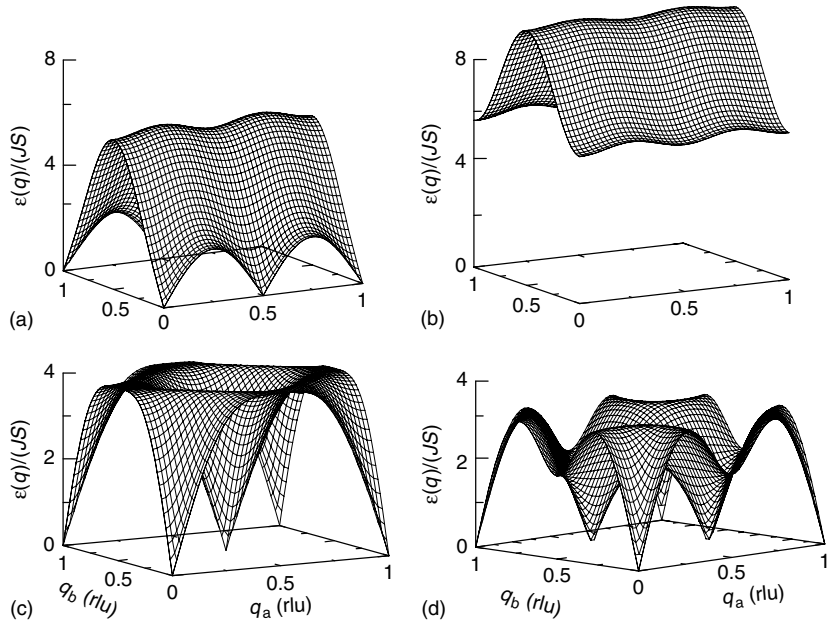

Figure 7. (a, b) Spin-wave dispersion in an antiferromagnet on the 3D cubic Bravais lattice with $J_a = -J_b = -J_c = J > 0$, that is ferromagnetic layers in b–c plane stacked antiferromagnetically along a. (a) cut by a (h,k,0) reciprocal lattice plane showing a Goldstone mode with sine-like dispersion along a arising from magnetic ordering vector Q = (0.5, 0, 0). (b) cut by a (h,k,0.5) plane containing neither Q = 0 nor Q = (0.5, 0, 0) and therefore no soft modes. (c) Spin-wave dispersion in a 2D antiferromagnet on a square lattice. There are two soft modes, at Q = 0 and at the magnetic ordering vector Q = (1/2, 1/2). (c) Spin waves in a triangular lattice antiferromagnet. In addition to soft mode at Q = 0, there are two Goldstone modes at two equivalent spin ordering wave vectors, Q = (1/3, 1/3) and Q = (2/3, 2/3).

system, which can differ from the GS by having a nonzero $\mathbf{q}$ and by the value of the total spin, that is, $\Delta S^z_{\text{tot}} = 0, \pm 1$. Therefore, quantum magnons describing these states are specified by wave vector, $\mathbf{q}$, and spin, $S = 1$, $S^z = 0, \pm 1$, quantum numbers. Clearly, there are three magnon polarizations in quantum theory, as opposed to only two for transverse spin waves in classical description. However, in systems where semiclassical description is valid, for example, for $S >> 1$, and spin order is well developed, only two magnons corresponding to semiclassical spin waves are relevant.

Except for few specific important cases, full quantum-mechanical treatment of spin Hamiltonian presents insurmountable difficulties (Mattis, 1965; see also **Magnetism of Low-dimensional Systems: Theory, Volume 1**, **Spin Waves: History and a Summary of Recent Developments, Volume 1**). The most successful approximate approach to treating quantum spins is the spin-wave theory, which starts from a semiclassical approximation and is based on a perturbative expansion in $1/S$. Semiclassical magnons obtained in the leading, first-order perturbation of spin-wave theory are just classical spin waves.

In spin-wave theory spins are quantized by expanding deviations from their equilibrium directions in the classical spin structure in a series of Bose creation–annihilation operators, using for example, Holstein–Primakoff transformations (Holstein and Primakoff, 1940). Energies of spin excitations and quantum corrections to spin structure can then be calculated using perturbation theory for a system of interacting bosons. A rather complete nonlinear spin-wave theory accounting for second and higher order perturbation corrections has been developed for the isotropic Heisenberg Hamiltonian; some examples are found in Dyson (1956), Chubukov (1984), Rastelli, Reatto, and Tassi (1985), Ohyama and Shiba (1993, 1994), and Veillette, James and Essler (2005), (see also **Spin Waves: History and a Summary of Recent Developments, Volume 1**).

Spin-wave calculations proceed by transforming every spin operator to its own coordinate system with z axis pointing along the spin direction in the classical GS spin structure. For a coplanar exchange spiral (14), such coordinate transformation is achieved by a rotation through an angle $\mathbf{Q}\mathbf{r}_j$. Then, in order to obtain the first $1/S$ correction to classical approximation, in the standard perturbation scheme spin operators are expressed through boson operators, a^+, a, by employing the truncated Holstein-Primakoff transformation, $S^z_j = S - a^+a$, $S^+_j \approx a\sqrt{2S}$, $S^-_j \approx a^+\sqrt{2S}$. The first-order corrections in such a linear, or harmonic spin-wave theory appear in the form of quadratic boson Hamiltonian describing a system of quantum oscillators, which correspond to quantized classical spin waves. Applying this procedure to Hamiltonian (11) for spin spiral without harmonic distortions, the following boson equivalent is obtained, (Zhitomirsky and Zaliznyak, 1996),

$$\mathrm{H} = \sum_{\mathbf{q}} \left\{ \left(A_{\mathbf{q}} + C_{\mathbf{q}}\right)\ a^+_{\mathbf{q}} a_{\mathbf{q}} + \frac{1}{2} B_{\mathbf{q}} \left(a_{\mathbf{q}} a_{-\mathbf{q}} + a^+_{\mathbf{q}} a^+_{-\mathbf{q}} \right) \right\} \tag{18}$$

where

$$\begin{aligned} A_{\mathbf{q}} &= -2SJ_{\mathbf{Q}} + S\cos^2\alpha\left(J_{\mathbf{q}} + D\right) \\ &\quad + S\left(1 + \sin^2\alpha\right)\frac{J_{\mathbf{q}+\mathbf{Q}} + J_{\mathbf{q}-\mathbf{Q}}}{2} \\ B_{\mathbf{q}} &= -S\cos^2\alpha\left(J_{\mathbf{q}} + D - \frac{J_{\mathbf{q}+\mathbf{Q}} + J_{\mathbf{q}-\mathbf{Q}}}{2}\right), \\ C_{\mathbf{q}} &= S\sin\alpha\left(J_{\mathbf{q}+\mathbf{Q}} - J_{\mathbf{q}-\mathbf{Q}}\right) \end{aligned}$$

$A_{\mathbf{q}}$ and $B_{\mathbf{q}}$ are even, while $C_{\mathbf{q}}$ is an odd function of $\mathbf{q}$. Equation (18) is diagonalized by the standard Bogolyubov transformation (which leaves odd-$\mathbf{q}$ terms unchanged), resulting in the Hamiltonian of uncoupled harmonic oscillators, $\mathrm{H} = \sum_{\mathbf{q}} \left\{ \varepsilon\left(\mathbf{q}\right)\left(a^+_{\mathbf{q}} a_{\mathbf{q}} + \frac{1}{2}\right) - \frac{1}{2}A_{\mathbf{q}} \right\}$. The constant term $\sum_{\mathbf{q}} \frac{1}{2}\left(\varepsilon\left(\mathbf{q}\right) - A_{\mathbf{q}}\right)$ gives $1/S$ quantum correction to the classical GS energy. The energy of semiclassical magnons is $\varepsilon\left(\mathbf{q}\right) = \sqrt{A^2_{\mathbf{q}} - B^2_{\mathbf{q}}} + C_{\mathbf{q}}$, or,

$$\begin{aligned} \varepsilon\left(\mathbf{q}\right) = 2S \Bigg(&\sqrt{\left(\frac{J_{\mathbf{q}+\mathbf{Q}} + J_{\mathbf{q}-\mathbf{Q}}}{2} - J_{\mathbf{Q}}\right)} \\ &\times \sqrt{\left(\frac{J_{\mathbf{q}+\mathbf{Q}} + J_{\mathbf{q}-\mathbf{Q}}}{2}\sin^2\alpha + \left(D + J_{\mathbf{q}}\right)\cos^2\alpha - J_{\mathbf{Q}}\right)} \Bigg) \end{aligned} \tag{19}$$

According to Goldstone's theorem, breaking of the continuous symmetry of the Hamiltonian in the GS must entail a zero energy mode(s) in the excitation spectrum. Such modes appear in the spin-wave dispersion of equation (19) at $\mathbf{q} = 0$ and at $\mathbf{q} = \mathbf{Q}$, the latter only has zero energy in the absence of anisotropy and magnetic field.

Dispersion of spin-wave excitations in different spin structures on simple Bravais lattices calculated using equation (19) for $H = D = 0$ and for nearest-neighbor spin interaction are shown in Figures 6 and 7. Fourier transformed exchange is obtained by summing over the neighbor bonds, $J_{\mathbf{q}} = \sum_{\mathbf{d}} 2J_{\mathbf{d}} \cos\left(\mathbf{q}\cdot\mathbf{d}\right)$, which for a simple cubic lattice is just $J_a \cos 2\pi q_a + J_b \cos 2\pi q_b + J_c \cos 2\pi q_c$. For a ferromagnet, where $\mathbf{Q} = 0$, this expression simply has to be shifted upwards by $J_0 = J_a + J_b + J_c$ to obtain the spin-wave spectrum shown in Figure 6(a,b). There is a Goldstone mode with quadratic dispersion at $\mathbf{q} = 0$.

Inelastic neutron scattering provides a direct way of studying spin waves in most magnetic materials. Magnetic neutron scattering cross-section is directly proportional to the dynamic spin susceptibility and exhibits sharp, delta

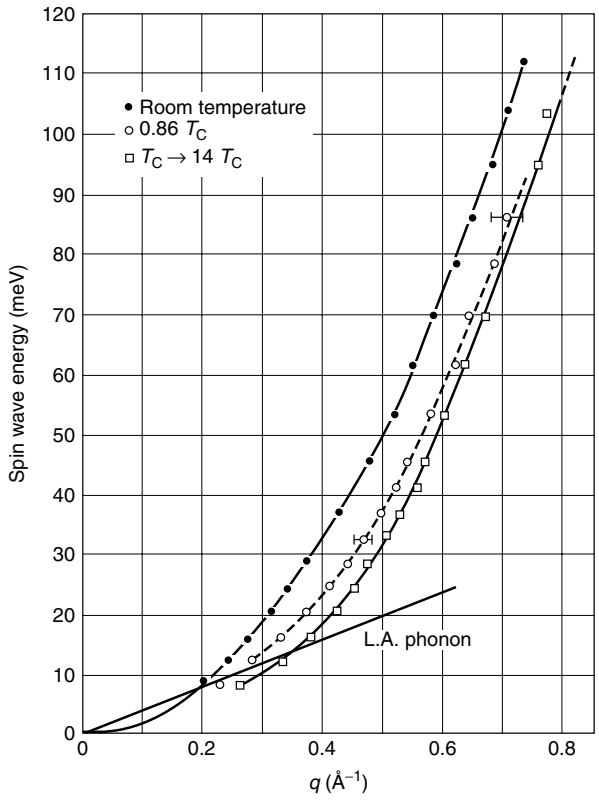

Figure 8. Dispersion of spin waves in Fe with 12 at% of Si at several temperatures, measured by J. W. Lynn using unpolarized inelastic neutron scattering (Lynn, 1975, 1984). With increasing temperature, spin-wave energy somewhat softens, but, outside a small hydrodynamic region, spin-waves neither disappear nor their dispersion renormalizes to zero as $T \rightarrow T_C$, indicating existence of localized spins. (Reprinted figure from permission from J.W. Wynn *et al*., 1975 with permission from the American Physical Society. © 1975.)

function-like peaks at spin-wave energies (Izyumov and Ozerov, 1970; Zaliznyak and Lee, 2005; see also **X-ray and Neutron Scattering by Magnetic Materials, Volume 1**). Quadratic spin-wave dispersion measured by J. W. Lynn in ferromagnetic iron is shown in Figure 8. Spin waves persisting at elevated temperatures, up to and above the Curie temperature, indicate existence of localized spins. Quadratic in q dispersion is, in fact, a very general consequence of the existence of net ferromagnetic moment in the spin system, and therefore it is also observed in ferrimagnets (Alperin, Steinsvoll, Nathans and Shirane 1951).

In antiferromagnets and helimagnets (spin spirals) spin-wave dispersion of Goldstone modes is linear. For an antiferromagnet on a Bravais cubic lattice, cuts of the dispersion surface by planes perpendicular to [001] direction intercept only one Goldstone mode at a time, Figure 6(c,d). The situation is different in ferro-antiferromagnet, which is made of ferromagnetic sheets in $b-c$ plane coupled antiferromagnetically along a, Figure 7(a,b). The antiferromagnetic, sine-like dispersion is pronounced along a axis, while ferromagnetic dispersion in $b-c$ plane is only modified to produce linear spectrum of a Goldstone mode in the vicinity of the ordering wave vector, $\mathbf{Q} = (1/2, 0, 0)$.

A sine-like dispersion of spin waves in the prototypical antiferromagnet NiO measured by Hutchings and Samuelsen (1972) is shown in Figure 9. Data in the figure is indexed in the reduced Brillouin zone of magnetic superlattice, which contains a number of modes whose dispersions coincide.

Spin-wave dispersion in a 2D antiferromagnet on square lattice is shown in Figure 7(c). Such system attracted considerable attention after antiferromagnetism was discovered in the undoped parent materials of high-temperature superconducting cuprates, La_2CuO_4 (Vaknin *et al*., 1987) and $Y_2BaCu_3O_{6+x}$, (Tranquada *et al*., 1988) where weakly coupled layers of Cu^{2+} ions form square lattice in the basal $a-b$ plane of the tetragonal crystal structure. Exchange coupling through 180° Cu–O–Cu bond is extremely strong, reaching ∼0.23 meV in chain cuprates (Zaliznyak *et al*., 2004). Hence, spin excitations are the most energetic eigenmodes and are crucial to understanding properties of cuprate materials. Recent advent of high-power pulsed spallation neutron sources utilizing time-of-flight spectroscopy enabled direct experimental observation of such excitations. Spectacular data on spin excitations in La_2CuO_4 reported in Coldea *et al*. (2001) was successfully described by spin waves, using effective localized spin Hamiltonian with superexchange and additional cyclic exchange induced by electron itinerancy. Similar measurements of high-energy excitations in superconducting $Y_2BaCu_3O_{6+x}$ reported in Stock *et al*. (2005) can also be reasonably well interpreted within the spin-wave framework. These finding are quite surprising in view of the quantum nature of Cu^{2+} spins ($S = 1/2$) and the low-dimensional (2D) character of these systems, undermining the mean-field approach.

Spin-wave dispersion in a 2D antiferromagnet on triangular lattice is shown in Figure 7(d). In addition to $\mathbf{q} = 0$ and $\mathbf{q} = \mathbf{Q} = (1/3, 1/3)$, there is also a Goldstone mode at $\boldsymbol{\tau} - \mathbf{Q} = (2/3, 2/3) = 2\mathbf{Q}$, $\boldsymbol{\tau} = (1, 1)$ is a reciprocal lattice vector. This coincidence (up to $\boldsymbol{\tau}$) between $\mathbf{Q}$ and $2\mathbf{Q}$ makes purely 2D triangular lattice a singular case. For one, harmonic expansion reduces to a single relation and cannot be used to describe bunching of triangular spin structure in magnetic field. Second, spin-wave calculations up to a second order in $1/S$ reveal dramatic modification of spin-wave spectrum (Starykh, Chubukov and Abanov, 2006). These complications are absent in quasi-1D hexagonal ABX_3 antiferromagnets with nearly triangular 120° spin structures, (Eibshutz, Sherwood, Hsu and Cox, 1972; Inami *et al*., 1995; Yelon and Cox, 1972, 1973) where leading interaction is the in-chain exchange perpendicular to triangular lattice and the

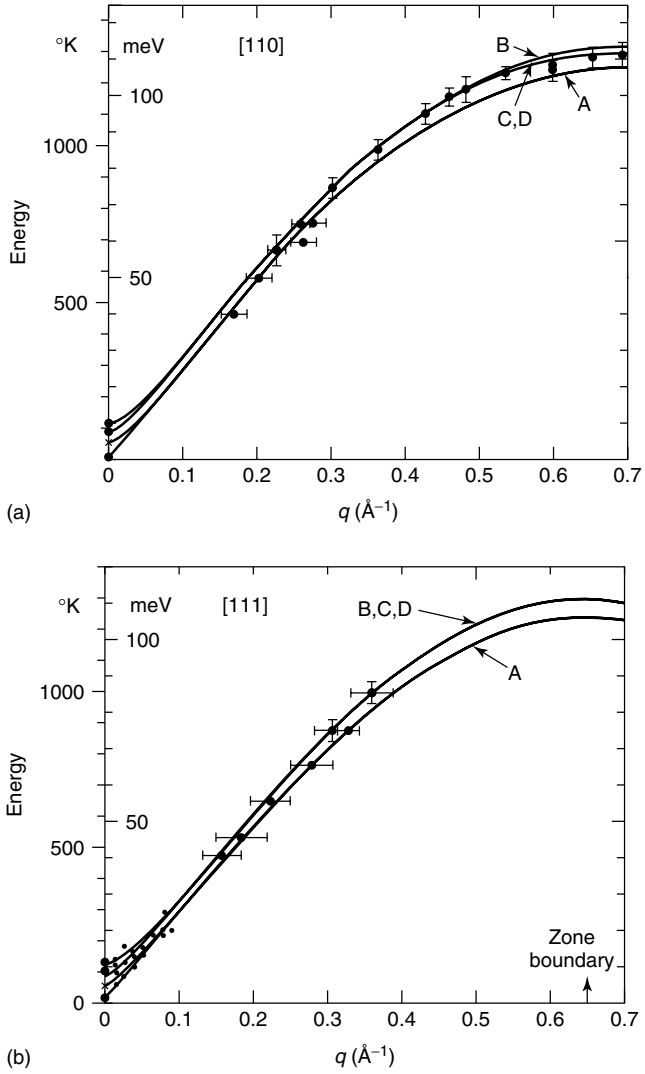

Figure 9. Dispersion of spin waves in antiferromagnetic NiO at $T = 78$ K, (a) along (110) and (b) along (111) reciprocal lattice directions, measured by Hutchings and Samuelsen (1972). Wave vector is indexed in small Brillouin zone of magnetic superlattice with 4 × times enlarged unit cell, such that magnetic ordering wave vector is $Q = (1, 1, 1)$. Different curves marked A, B, C, and D show spin-wave calculation for different magnetic domains corresponding to four possible symmetrically equivalent directions of Q in the cubic lattice. (Reprinted figure from M.T. Hutchings *et al*., 1972 with permission from the American Physical Society. © 1972.)

ordering wave vector is essentially 3D, $\mathbf{Q} = (1/3, 1/3, 1) \neq 2\mathbf{Q} = (2/3, 2/3, 0)$. Numerous neutron scattering studies of spin excitations in these materials indicate that for spin $S > 1$ they are reasonably well described by linear spin-wave theory. Some experimental examples presented in Inami *et al*. (1995) are reproduced in Figure 10. Resemblance of the data with dispersion of equation (19) shown in Figure 7(d) is clearly identifiable.

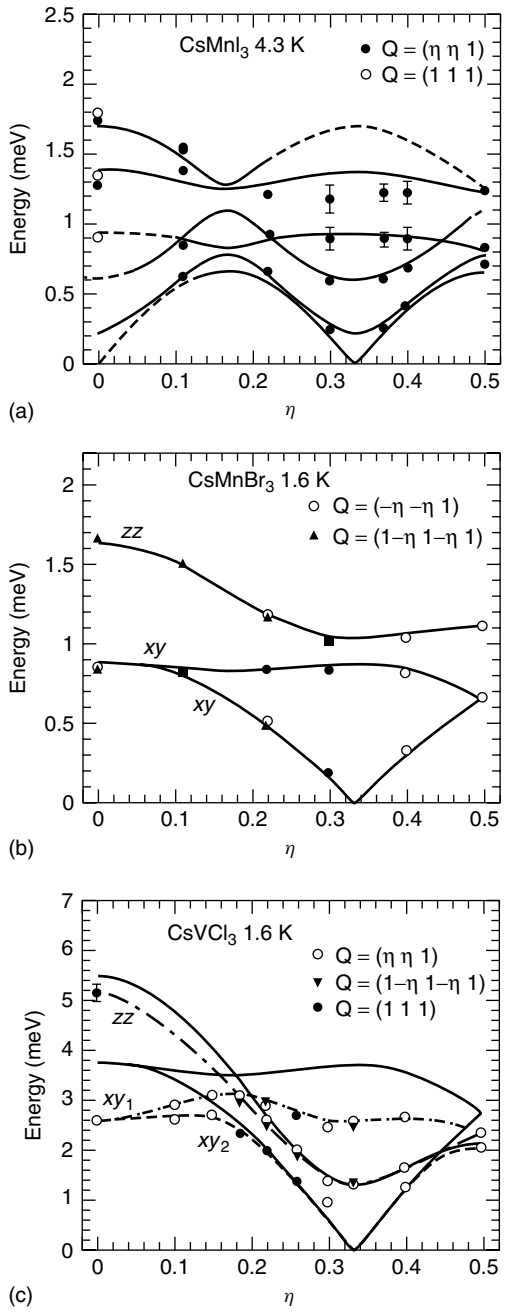

Figure 10. Spin-wave dispersion in the a–b basal plane in several hexagonal quasi-1D antiferromagnets with 120° triangular spin structure measured by Inami *et al*. (1995). (Reprinted figure from A. Zheludev *et al*., 1999, with permission from the American Physical Society. © 1999.)

Perhaps, the most spectacular success of applying spin-wave description to excitations in a spin system is presented in Figure 11. It reproduces spin-wave spectrum in Dzyaloshinskii–Moriya spiral magnet $Ba_2CuGe_2O_7$, whose structure is shown in Figure 4 and was discussed above, measured by Zheludev *et al*. (1998, 1999). Antisymmetric

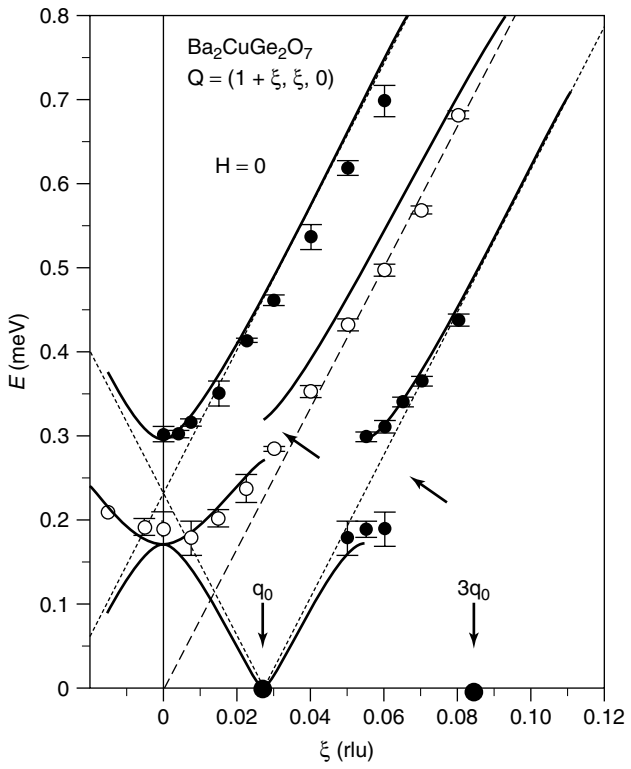

Figure 11. Dispersion of spin waves in Dzyaloshinskii–Moriya spiral spin structure found in $Ba_2CuGe_2O_7$ in zero magnetic field, measured at $T = 0.35\,\mathrm{K}$ by Zheludev *et al*. (1998, 1999). The filled circles on the abscissa axis show positions of the observed magnetic Bragg peaks at Q and 3Q. The solid curves are parameter-free theoretical curves resulting from spin-wave theory calculation. (Reprinted figure with permission from A. Zheludev *et al*., *Phys. Rev. B* Vol 59, 11432. © 1999 by the American Physical Society.)

DM exchange in this material is accompanied by a two-ion anisotropy, and the resulting spin GS is an incommensurate bunched spiral, with clearly observable magnetic Bragg peaks corresponding to third harmonics, $3\mathbf{Q}$, of the ordering wave vector $\mathbf{Q}$. Distortion of spin spiral results in appearance of discontinuities in the spin-wave dispersion at wave vectors $n\mathbf{Q}$, which are clearly observed in experiment.

6 SUMMARY

Although magnetism is rooted in the quantum-mechanical nature of electron's spin, spin structures and excitations in a great variety of magnetic materials can be successfully understood and often accurately described on the basis of semiclassical treatment of a localized spin Hamiltonian. Dispersion of spin excitations predicted by spin-wave theory agrees surprisingly well with neutron scattering experiment even for ordered spin systems with $S = 1/2$, where $1/S$ expansion is clearly not a good approximation. The fundamental reason for this is perhaps simply the fact that while the mapping of spin operators to bosons employed in different flavors of spin-wave theory might not be entirely correct, the fundamental nature of spin excitations as coupled oscillators on a lattice is captured correctly. The resulting equations of motion and corresponding boson Hamiltonian are therefore also correct. However, they may involve effective interaction parameters which can differ significantly from those in the original spin Hamiltonian and which are prescribed by the spin-wave approximation. Therefore, while reasons for the success of semiclassical spin-wave description might be superficial, similar to the Weiss theory of ferromagnetism, it provides a very useful parameterization for describing spin structures and excitations in magnetic materials, for example, in the form of equation (18).

REFERENCES

Abragam, A. and Bleaney, B. (1986). *Electron Paramagnetic Resonance of Transition Ions*, Dover Publications: New York.

Alperin, H.A., Steinsvoll, O., Nathans, R. and Shirane, G. (1951). *Physical Review*, **154**, 508.

Anderson, P.W. (1952). An approximate quantum theory of the antiferromagnetic ground state. *Physical Review*, **86**, 694.

Anderson, P.W. (1959). New approach to the theory of superexchange interactions. *Physical Review*, **115**, 2.

Andreev, A.F. (1978). *Soviet Physics JETP*, **47**(2), 411.

Andreev, A.F. and Marchenko, V.I. (1980). Symmetry and the macroscopic dynamics of magnetic materials. *Soviet Physics Uspekhi*, **23**, 21.

Barbier, A., Mocuta, C., Neubeck, W., *et al*. (2004). Surface and bulk spin ordering of antiferromagnetic materials: NiO(111). *Physical Review Letters*, **93**, 257208.

Barnett, S.J. (1935). Gyromagnetic and electron-inertia effects. *Reviews of Modern Physics*, **7**, 129.

Bethe, H.A. and Jackiw, R. (1997). *Intermediate Quantum Mechanics*, Addison-Wesley: Reading, MA.

Borovik-Romanov, A.S. (1959). *JETP*, **9**, 539.

Brown, P.J., Capellmann, H., Deportes, J., *et al*. (1982). *Journal of Magnetism and Magnetic Materials*, **30**, 243.

Chandra, P. and Doucot, B. (1988). Possible spin-liquid state at large S for the frustrated square Heisenberg lattice. *Physical Review B*, **38**, 9335.

Chubukov, A.V. (1984). *Journal of Physics C*, **17**, L991.

Coldea, R., Hayden, S.M., Aeppli, G., *et al*. (2001). Spin waves and electronic interactions in $La_2Cu\,O_4$. *Physical Review Letters*, **86**, 5377.

Compton, A.H. (1921). Possible Magnetic Polarity of Free Electrons. *Journal of the Franklin Institute*, **192**, 144.

Dirac, P.A.M. (1926). On the theory of quantum mechanics. *Proceedings of the Royal Society*, **112A**, 661.

Dyson, F.J. (1956). General theory of spin-wave interactions. *Physical Review*, **102**, 1217–1230.

Dzyaloshinskii, I. (1958). A thermodynamic theory of "weak" ferromagnetism of antiferromagnetics. *Journal of Physics and Chemistry of Solids*, **4**, 241.

Dzyaloshinskii, I.E. and Volovick, G.E. (1979). *Annals of Physics*, **125**, 67.

Eibshutz, M., Sherwood, R.C., Hsu, F.S.L. and Cox, D.E. (1972). *AIP Conference Proceedings*, **17**, 864.

Einstein, A. and De Haas, W.J. (1915). Experimenteller nachweis der ampereschen molekularströme (experimental proof of Ampere's molecular currents). *Verhandlungen der Deutschen physikalischen Gesellschaft*, **17**, 152–170, 203.

Goodwin, A.L., Tucker, M.G., Dove, M.T. and Keen, D.A. (2006). The magnetic structure of MnO at 10K from neutron total scattering. *Physical Review Letters*, **96**, 047409.

Haldane, F.D.M. (1983). Nonlinear field theory of large-spin Heisenberg antiferromagnets: semiclassically quantized solitons of the one-dimensional easy-axis Néel state. *Physical Review Letters*, **50**, 1153–1156.

Harrison, A., Collins, M.F., Abu-Dayyeh, J. and Stager, C.V. (1991). Magnetic structures and excitations of CsMnI3: a one-dimensional Heisenberg antiferromagnet with easy-axis anisotropy. *Physical Review B*, **43**, 679.

Heisenberg, W. (1926). Many-body problem and resonance in quantum mechanics. *Zeitschrift fur Physik*, **38**, 441.

Heisenberg, W. (1928). Zur Theorie des Ferromagnetismus. *Zeitschrift fur Physik*, **49**, 619.

Holstein, T. and Primakoff, H. (1940). Field dependence of the intrinsic domain magnetization of a ferromagnet. *Physical Review*, **58**, 1098.

Hutchings, M.T. and Samuelsen, E.J. (1972). Measurement of spin-wave dispersion in NiO by inelastic neutron scattering and its relation to magnetic properties. *Physical Review B*, **6**, 3447.

Inami, T., Kakurai, K., Tanaka, H., *et al*. (1995). Magnetic excitations in quasi-one-dimensional hexagonal ABX_3-type antiferromagnets. *Physica B*, **213–214**, 167.

Izyumov, Yu.A. and Ozerov, R.P. (1970). *Magnetic Neutron Diffraction*, Plenum Press: New York.

Jensen, J. and Mackintosh, A.R. (1991). *Rare Earth Magnetism*, Clarendon Press: Oxford.

Kanamori, J. (1959). Superexchange interaction and symmetry properties of electron orbitals. *Journal of Physics and Chemistry of Solids*, **10**, 87.

Kaplan, T.A. (1959). Classical spin-configuration stability in the presence of competing exchange forces. *Physical Review*, **116**, 888–889.

Kaplan, T.A. (1961). Some effects of anisotropy on spiral spin-configurations with application to rare-earth metals. *Physical Review*, **124**, 329.

Kasuya, T. (1956). A theory of metallic ferromagnetism and antiferromagnetism on zeners model. *Progress of Theoretical Physics*, **16**, 45.

Kramers, H.A. (1934). *Physica*, **1**, 191.

Kugel, G.E., Hennion, B. and Carabatos, C. (1978). Low-energy magnetic excitations in wustite ($Fe_{1-x}O$). *Physical Review B*, **18**, 1317.

Liechtenstein, A., Katsnelson, M.I., Antropov, V.P. and Gubanov, V.A. (1986). Local spin density functional approach to the theory of exchange interactions in ferromagnetic metals and alloys. *Journal of Magnetism and Magnetic Materials*, **67**, 65.

Lynn, J.W. (1975). Temperature dependence of the magnetic excitations in iron. *Physical Review B*, **11**, 2624.

Lynn, J.W. (1984). Breakdown of dynamic scaling analysis in isotropic ferromagnets. *Physical Review Letters*, **52**, 775.

Mattis, D.C. (1965). *The Theory of Magnetism*, Harper & Row: New York.

Mermin, N.D. and Wagner, H. (1966a). Absence of ferromagnetism or antiferromagnetism in one- or two-dimensional isotropic heisenberg models. *Physical Review Letters*, **17**, 1133–1136.

Mermin, N.D. and Wagner, H. (1966b). Absence of ferromagnetism or antiferromagnetism in one- or two-dimensional isotropic heisenberg models. *Physical Review Letters*, **17**, 1307.

Mills, R.E., Kenan, R.P. and Milford, F.J. (1966). Green's-function theory of ferrimagnetism, with an application to magnetite. *Physical Review*, **145**, 704–717.

Moriya, T. (1960). Anisotropic superexchange interaction and weak ferromagnetism. *Physical Review*, **120**, 91.

Nagamiya, T. (1967). In *Solid State Physics*, Seitz, F., Turnbull, D. and Ehrenreich, H. (Eds.), Academic Press: New York, p. 305, Vol. 20.

Nagamiya, T., Nagata, T. and Kitano, Y. (1962). Magnetization process of a screw spin system. *Progress of Theoretical Physics*, **27**, 1253.

Nathans, R., Pickart, S.J., Alperin, H.A. and Brown, P.J. (1964). Polarized-neutron study of hematite. *Physical Review*, **136**, A1641.

Ohyama, T. and Shiba, H. (1993). Nonlinear excitations in quasi-one-dimensional triangular antiferromagnets. *Journal of the Physical Society of Japan*, **62**, 3277.

Ohyama, T. and Shiba, H. (1994). Spin dynamics and quantum fluctuations in quasi-one-dimensional triangular antiferromagnets: magnetic field effects. *Journal of the Physical Society of Japan*, **63**, 3454.

Rastelli, E., Reatto, L. and Tassi, A. (1985). Quantum fluctuations in helimagnets. *Journal of Physics C*, **18**, 353.

Schurer, P.J., Sawatzky, G.A. and van der Woude, F. (1971). Localized versus itinerant description of ferromagnetism in iron. *Physical Review Letters*, **27**, 586–589.

Shull, C.G., Strauser, W.A. and Wollan, E.O. (1951). Neutron diffraction by paramagnetic and antiferromagnetic substances. *Physical Review*, **83**, 333–345.

Shull, C.G., Wollan, E.O. and Koehler, W.C. (1951). Neutron scattering and polarization by ferromagnetic materials. *Physical Review*, **84**, 912–921.

Starykh, O.A., Chubukov, A.V. and Abanov, A.G. (2006). Flat spin-wave dispersion in a triangular antiferromagnet. *Physical Review B*, **74**, 180403.

Stock, C., Buyers, W.J.L., Cowley, R.A., *et al*. (2005). From incommensurate to dispersive spin-fluctuations: the high-energy

inelastic spectrum in superconducting $YBa_2Cu_3O_{6.5}$. *Physical Review B*, **71**, 024522.

Tomiyasu, K., Inami, T. and Ikeda, N. (2004). Magnetic structure of CoO studied by neutron and synchrotron x-ray diffraction. *Physical Review B*, **70**, 184411.

Tranquada, J.M., Cox, D.E., Kunnmann, W. (1988). Neutron-diffraction determination of antiferromagnetic structure of Cu Ions in $YBa_2Cu_3O_{6+x}$ with x=0.0 and 0.15. *Physical Review Letters*, **60**, 156.

Uhlenbeck, G. and Goudsmith, S. (1925). *Naturwiss*, **13**, 953.

Vaknin, D., Sinha, S.K., Moncton, D.E., *et al*. (1987). Antiferromagnetism in La_2CuO_{4-y}. *Physical Review Letters*, **58**, 2802.

Van Vleck, J.H. (1945). Survey of the theory of ferromagnetism. *Reviews of Modern Physics*, **17**, 27.

Veillette, M.Y., James, A.J. and Essler, F.H. (2005). Spin dynamics of the quasi-two-dimensional spin-1/2 quantum magnet Cs_2CuCl_4. *Physical Review B*, **72**, 134429.

Villain, J. (1959). La structure des substances magnetiques. *Journal of Physical Chemistry*, **11**, 303.

White, R.M. (1983). *Quantum Theory of Magnetism*, Springer-Verlag: Berlin.

Yelon, W.B. and Cox, D.E. (1972). Magnetic ordering in $RbNiCl_3$. *Physical Review B*, **6**, 204.

Yelon, W.B. and Cox, D.E. (1973). Magnetic transitions in $CsNiCl_3$. *Physical Review B*, **7**, 2024.

Yoshimori, A. (1959). A New Type of Antiferromagnetic Structure in the Rutile Type Crystal. *Journal of the Physical Society of Japan*, **14**, 807.

Yosida, K. (1957). Magnetic properties of Cu-Mn alloys. *Physical Review*, **106**, 893.

Yosida, K. (1998). *Theory of Magnetism*, Springer-Verlag: Berlin.

Zaliznyak, I.A. (2003). Heisenberg magnet with modulated exchange. *Physical Review B*, **68**, 134451.

Zaliznyak, I.A. and Lee, S-H. (2005). *Modern Techniques for Characterizing Magnetic Materials*, Zhu, Y. (Ed.), Springer: Hidelberg, New York.

Zaliznyak, I.A., Woo, H., Perring, T.G., *et al*. (2004). Spinons in the strongly correlated copper oxide chains in $SrCuO_2$. *Physical Review Letters*, **93**, 087202.

Zaliznyak, I.A. and Zhitomirsky, M.E. (1995a). cond-mat/0306370.

Zaliznyak, I.A. and Zhitomirsky, M.E. (1995b). *JETP*, **81**,(3), 579.

Zener, C. (1951). Interaction between the d-Shells in the transition metals. II. Ferromagnetic compounds of manganese with perovskite structure. *Physical Review*, **82**, 403.

Zener, C. (1959). Interaction between the d shells in the transition metals. *Physical Review*, **81**, 440.

Zheludev, A., Shirane, G., Sasago, Y., *et al*. (1996). Spiral phase and spin waves in the quasi-two-dimensional antiferromagnet $Ba_2CuGe_2O_7$. *Physical Review B*, **54**, 15163.

Zheludev, A., Maslov, S., Shirane, G., *et al*. (1997). Field-induced commensurate-incommensurate phase transition in a Dzyaloshinskii-Moriya spiral antiferromagnet. *Physical Review Letters*, **78**, 4857.

Zheludev, A., Maslov, S., Shirane, G., *et al*. (1998). Experimental Evidence for Kaplan-Shekhtman-Entin-Wohlman-Aharony interactions in $Ba_2CuGe_2O_7$. *Physical Review Letters*, **81**, 5410.

Zheludev, A., Maslov, S., Shirane, G., *et al*. (1999). Magnetic anisotropy and low-energy spin waves in the Dzyaloshinskii-Moriya spiral magnet $Ba_2CuGe_2O_7$. *Physical Review B*, **59**, 11432.

Zhitomirsky, M.E. and Zaliznyak, I.A. (1996). Static properties of a quasi-one-dimensional antiferromagnet in a magnetic field. *Physical Review B*, **53**, 3428.

Domain States Determined by Neutron Refraction and Scattering

Axel Hoffmann and Gian P. Felcher
Argonne National Laboratory, Argonne, IL, USA

1 INTRODUCTION

One of the most significant contributions to the understanding of condensed matter made by neutron scattering has been the determination of the magnetic structure of materials. Neutron interaction with matter consists of a 'nuclear' term, resulting from the interaction between the neutron and the each of the nuclei of the atoms, and a magnetic term, due to the interaction between neutron magnetic moment or spin and the magnetic moments in the solids. For a magnetic material like iron, the two interactions have comparable size. The interaction length is also very small, being comparable to the radius of the nucleus, which is smaller by a factor of 10^{-4} than the size of the atom. This means that neutrons may penetrate deeply in matter, sampling a large, and statistically significant volume or area of the material. On the other hand most of the information obtained, in the form of a diffraction or scattering pattern, may require a substantial amount of material because the weakness of interaction is compounded with the limited neutron fluxes emitted from present day sources.

Typical neutron wavelengths are of the order of a few angstroms, comparable to the distance between atoms in a crystalline structure. This explains why neutron diffraction has been a primary tool to determine magnetic structures of single crystals or even polycrystalline samples. Consider for simplicity a ferromagnetic single crystal in which only one magnetic domain is present. In this case, the magnetic structure is identical to the crystalline structure; the intensity of each diffraction peak is composed of a term due to the neutron–nucleus interaction and a magnetic term of the crystalline unit cell. The magnetic intensities diffracted in a given Bragg reflection depend on the angle between the direction of the magnetization and the direction of the momentum transfer of that Bragg reflection. From the diffracted intensities, the collective direction of the magnetic moments aligned in the domain can be obtained. Further information can be obtained if, in addition, the spin of the neutron is known both before and after scattering. For instance, if the polarization axis of the incident neutron beam is parallel to the magnetization, the scattered neutron has the original spin state; but if the two axes are perpendicular, the scattered neutron can have a reversed spin state.

In the case of an antiferromagnetic structure the net magnetization is zero, but still magnetic Bragg reflections are observable, since the crystal may be thought of as being divided in magnetic sublattices, each with its own orientation. For an antiferromagnet, diffraction lines of solely magnetic origin may appear, giving a detailed account of the antiferromagnetic structure. These diffraction lines correspond to lattice planes that in fact have a net magnetization. Even

Handbook of Magnetism and Advanced Magnetic Materials. Edited by Helmut Kronmüller and Stuart Parkin. Volume 3: *Novel Techniques for Characterizing and Preparing Samples*. ISBN: 978-0-470-02217-7.

for antiferromagnets, selection rules for intensity and polarization permit, with few exceptions, the determination of the direction of the moments in each sublattice (Bacon, 1975; see also **X-ray and Neutron Scattering by Magnetic Materials, Volume 1**).

Domains are quite common in various physical or chemical systems. They are generally stabilized by competing interactions on different length scales, which in the magnetic case are generally exchange (short-range) and magnetostatic (long-range) interactions (Seul and Andelman, 1995). Within this review we will focus our discussion on magnetic domains, that is, magnetically ordered regions with different orientations of the magnetization. We would also like to note that the techniques discussed in this chapter are also useful to investigate different domain structures, such as the ones occurring due to phase separation in complex oxides, where regions with different magnetic order (i.e., ferromagnetic metallic and antiferromagnetic insulating) coexist. An in depth discussion of these types of domains is beyond the scope of this chapter and the interested reader is referred to a recent review by Dagotto, Hotta and Moreo (2001).

Figure 1 shows how a ferromagnetic material may break down into domains, when the material is in a magnetic field that is weaker than the saturating field. Each domain is characterized by a different orientation of the magnetization. When no magnetic field is applied, in each domain the magnetization is aligned along one of the directions of easy magnetization allowed by the symmetry of the crystal (Birss, 1964). From the *intensities* of the Bragg reflections it is then possible to reconstruct *statistics of the domains*, that is, the fraction of the volume of the sample occupied by domains with each allowed magnetization direction. This is one of the earliest information provided by neutron scattering (Bacon, 1975). Another information that can be obtained from the *width of the Bragg reflections* is the average *size of the domains*. This is because the width of a magnetic Bragg reflection is inversely proportional to the domain size. To be practically detectable in conventional diffraction, the domain size should not exceed 100 nm. Besides the simple relationships between domains and scattered neutrons, one can ask the question if it is possible to obtain further information about domains from neutron scattering experiments? Since in conventional diffraction neutrons determine the pair correlation of atomic moments as a function of their distance, it is natural to ask if they could also be used to measure the pair correlation of the magnetization in adjacent magnetic domains. Unfortunately in general this type of information is difficult to obtain; and some of the reasons will be outlined here. However, such difficulties can be more easily surmounted for samples consisting of very well ordered magnetic nanostructures, or with systems of reduced dimensionality. We note that investigations of nanomagnetic systems with X rays and neutrons have been recently reviewed by Kortright *et al*. (1999) and Fitzsimmons *et al*. (2004), respectively.

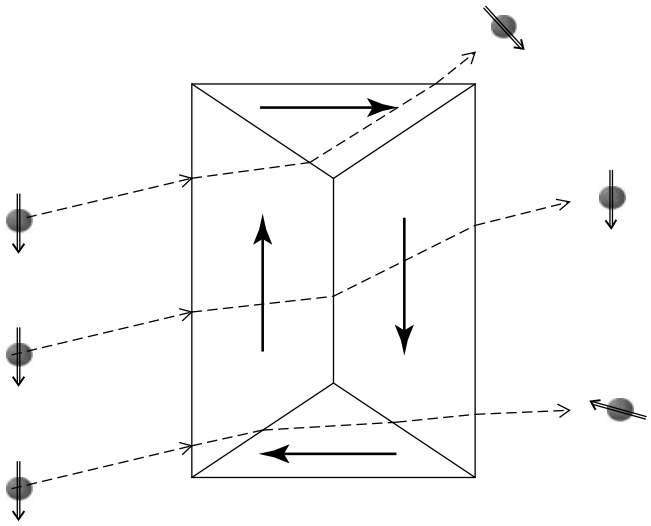

Figure 1. Simple example of a flux-closure domain pattern ('Landau pattern'). Depicted are three different neutron trajectories illustrating the effects of polarized neutron refraction and precession.

1.1 Refraction and scattering

So far we discussed that neutrons can give information about domains via scattering. As we will see in detail later, neutron refraction can also play an important role in the investigation of magnetic domains. Early on it was discovered that a well-collimated beam of thermal neutrons diverges when it is passed through finely divided material. This is attributed to scattering and refraction occurring at each individual particle (Weiss, 1951). Until now we have only considered scattering. In the forward direction, scattering does not depend on the detailed crystalline nature of the material, but only on the size of the grains. The grains scatter the neutrons in a cone with an angular width of $\sim\lambda/d$, where d is the particle's size. The difference between refraction and scattering depends on the difference between the phase change in traversing the particle diameter and the phase change in traversing the same path length in vacuum. A neutron that passes through a slab of material is not scattered by it, but its wavelength inside it is changed by a small amount, which is proportional to the refractive index. If along the flight path the difference in phase is appreciably less than one wavelength, the scattering theory has to be applied, otherwise we apply the refraction theory. For instance in a diamond slab neutrons of 4 Å wavelength experience a lag of one period, with respect to vacuum, after 9 μm. Thus the question as to how the neutron is modified after crossing a slab of material arises. In order

to measure the difference of phase change in the flight path within the medium versus that in vacuum, an interferometric measurement is required. The primary beam needs to be split in two components, the first traveling in vacuum and the second in the medium. Then the phase shift of the neutron in the medium appears as a shift of the interference pattern after the two beams are recombined (Werner and Klein, 1987).

The trajectory of a neutron through an assembly of ferromagnetic domains can be described in a similar way. However, it is much easier to verify magnetic – rather than material – refraction effects. Let us assume that the neutron beam is initially polarized in a certain direction (Figure 1). Within each magnetic domain in which the magnetic induction $\vec{B}$ is not parallel to the initial polarization, the neutron spin precesses around $\vec{B}$. Upon exiting the domain, the spin of the outgoing neutron is rotated by a phase defined by the size of $\vec{B}$ and by the time spent in the domain. This phase shift is equal to the phase shift described above for the neutron passing through a material particle. However, in the magnetic case there is no need for interferometry or a reference beam, because the polarization of the incoming beam is defined by a neutron polarizer and the polarization of the outgoing beam is sorted out by a neutron polarization analyzer.

Are refraction effects important in assessing sizes and orientations of domains? A full rotation of the neutron spin takes place, for an ordinary ferromagnetic material, over a length of a few micrometers. Domains of that size scatter neutrons of wavelength of a few angstroms at angles too small for an easy identification of the scattered neutrons, versus those that are simply transmitted through the sample. Separation between the scattered and transmitted components becomes appreciable for domains below 100 nm: here, refractive effects may be considered in the first instance as unimportant, and the intensity of the neutrons that have interacted with the sample may be treated on the basis of the scattering processes. Conversely, for micrometer-size domains, scattering processes have been neglected and information on the domains has been obtained on the basis of the polarization of the neutrons exiting the sample. The need of reconciling these two points of view has arisen recently in the study of domains in nanostructured materials.

This chapter is organized as follows. In Section 2 we discuss in detail different neutron scattering techniques, such as diffraction, depolarization, and grazing incidence reflectivity, from which information about domain structures can be obtained. Following this we will present in Section 3 several science issues involving magnetic domains, which are suitable to neutron investigations. First we discuss basic domain structures in homogeneous materials, and then we show how modified magnetic domain behavior can come about through confinement or coupling between dissimilar materials. Finally, Section 4 gives a brief summary of this chapter.

2 TECHNIQUES

2.1 Diffraction

In classic magnetostatics the Zeeman interaction energy between a magnetic moment $\vec{\mu}$ and a magnetic field $\vec{B}$ is fully described by the Hamiltonian:

$$E = \vec{\mu} \cdot \vec{B} \tag{1}$$

Starting from this term allows determining both the rotation and translation forces, which the field exerts on the magnetic moment. Thus the torque, $-(\partial E/\partial \zeta)$, where ζ is the angle between $\vec{\mu}$ and $\vec{B}$, leads to the well-known Larmor precession of the magnetic moment around $\vec{B}$ in the limit of constant $\vec{B}$. This relation remains valid for the interaction of the magnetic moment of the neutron inside a magnetic material, provided that the neutron is treated as a quantum particle, $\mu_N \hat{\sigma}$, where μ_N is the neutron magnetic moment and $\hat{\sigma}$ are the Pauli's matrices. Thus in principle this equation can be used directly to study magnetic materials; the neutrons probe the distribution of $\vec{B}$ inside the sample and one could subsequently find appropriate models to reproduce the observed $\vec{B}$ configuration. However, since it is most customary to describe magnetism in terms of atomic magnetic moments, it is preferable to express $\vec{B}(\vec{r})$ by the distribution of the magnetic moment density $\vec{M}(\vec{r})$. The Fourier transformation of the magnetostatic expression reduces to:

$$\vec{B}(\vec{q}) = 4\pi \vec{M}_{\perp}(\vec{q}) \tag{2}$$

where $\vec{M}_{\perp}$ is the component of the magnetic moment density perpendicular to the neutron momentum transfer $\hbar\vec{q}$ of the neutrons, where the absolute value of the scattered wave vector $\vec{q}$ is given by

$$|\vec{q}| = \frac{4\pi \sin\theta}{\lambda} \tag{3}$$

Here θ is the half of the scattering angle and λ the neutron wavelength. The vectors $\vec{q}$ considered here are only those corresponding to a Bragg reflection of the crystalline and magnetic crystal. The term *magnetic crystal* is used for any magnetically ordered crystal. In ferromagnetic crystals the magnetic moments of all equivalent magnetic atoms in the crystalline cell are equal and point in the same direction. These restrictions do not apply for the much wider choice of ferri- or antiferromagnetic configurations (Opechowski and Guccione, 1965). From a crystallographic point of view, a ferromagnetic crystal is distinct from an antiferromagnetic one because only the former allows the (000) reflection, or the scattering in the forward direction. In all cases, the orientation of the magnetic moments (in absence of an external

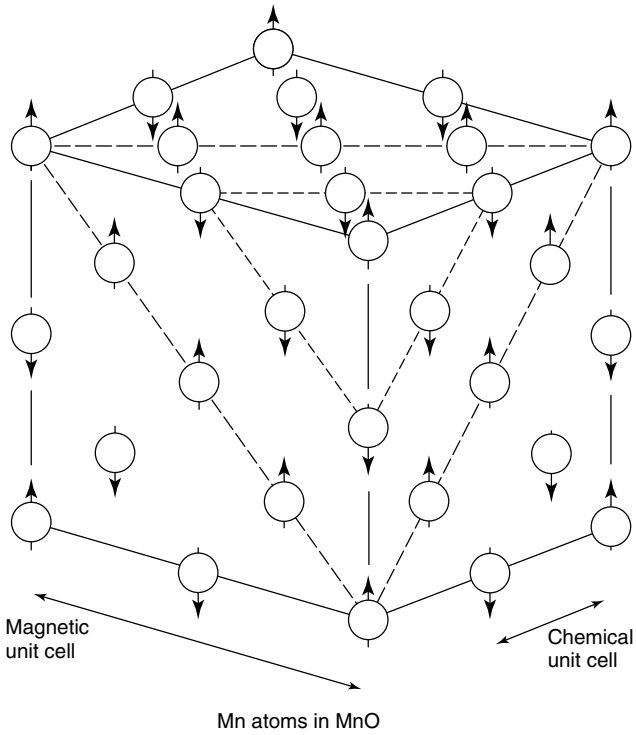

Figure 2. Antiferromagnetic structure of MnO. (Reprinted figure from *Phys. Rev.* Vol. 83, 333 (1951), © 1951 by the American Physical Society.)

magnetic field, which would distort the symmetry) is quite restricted, because certain symmetry operations do not have the result of turning a spin onto itself. In addition, the symmetry of the magnetic crystal is often lower than that of the crystal structure on which it resides; however, the magnetoelastic forces are often too weak to create a detectable distortion of the crystalline lattice. As a result of these effects, in the same single crystal, more than one magnetic domain is possible. By examining the Bragg reflections it is possible to establish what is the population of different domains. A typical example is indicated in Figure 2, illustrating the magnetic structure of the face-centered-cubic oxides of transition elements (Shull, Strauser and Wollan, 1951). The magnetic cell, represented here as a cube with twice the size of the crystalline cell, is distinguished by a propagation axis along the [111] direction. Since the cubic crystal has four equivalent [111] directions, four types of domains are possible (T domains). In addition, we have to consider the direction of the magnetic moments, that in Figure 2 are represented as collinear and parallel to the [001] axis. For each of the [111] propagation axis, we can choose three [001] equivalent directions (S domains). In total, a single crystal of MnO can split into $4 \times 3 = 12$ magnetic domains. The study of antiferromagnetic domain structures and symmetries remained largely of academic interest until the 1980s, when their importance

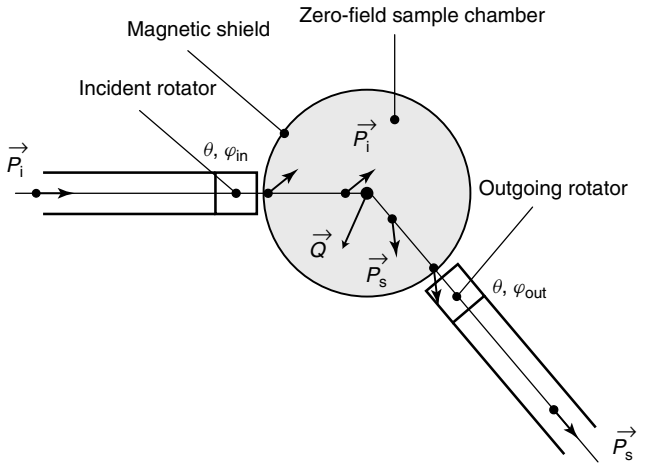

Figure 3. Simple schematic of a neutron scattering experiment with full polarization analysis. Schematic based on the description in Brown, Forsyth and Tasset (1993). (Reproduced from Brown *et al*., 1993, with permission from The Royal Society, London. © 1993.)

in affecting the magnetism of adjacent ferromagnets was recognized (Mauri, Siegmann, Bagus and Kay, 1987).

The most complete diffraction equipment hitherto constructed to study the domain population in zero applied field includes a device, named *Cryopad*, and hitherto has been limited to antiferromagnets (Brown, Forsyth and Tasset, 1993). This device is set in a conventional diffractometer such as schematically represented in Figure 3, and allows spherical polarimetry to be carried out in a neutron scattering experiment. The incoming monochromatic neutron beam is polarized axially, in the direction parallel to its propagation direction. At the entrance of the Cryopad region, the orientation of the neutron spin is turned in a direction characterized by the angular coordinates θ, φ_{in}. After this is accomplished, the neutron enters a region of zero magnetic field. In this region, the orientation of the neutron spin remains unaltered, except during the process of being diffracted by the sample. The sample, at the center of the gray area of Figure 3, consists of a single crystal oriented to reflect neutrons with a certain momentum transfer $\vec{q}$. Along the flight path of the diffracted neutrons, at the exit of the zero-field chamber, magnetic circuits can be tuned to bring the polarization of the diffracted beam in the direction of its propagation: the tuning is tested by a polarization analyzer. This technique has been called *spherical polarimetry* because the polarization axis of the incident and diffracted beams are uniquely and separately determined. In contrast, in conventional uniaxial polarimetry (Moon, Riste and Koehler, 1969) the polarization of the incident and the diffracted radiation are analyzed with respect to a fixed and common axis. The technique is being now used extensively to determine the magnetic structure of complex antiferromagnets (see, for instance,

Zaharko *et al*., 2003) because antiferromagnets are systems for which it is difficult to alter the domain population.

The equations that relate the scattered polarization to the incident polarization and to the physics of the scattering process have been developed by Blume (1963). The polarization P_s of the neutrons scattered by a Bragg reflection with scattering vector $\vec{k}$ from an ordered magnetic structure may be written in terms of the magnetic interaction vector $\vec{M}_\perp$ as:

$$\begin{aligned}\vec{P}_s I = {} & \vec{P}_i N N^* + \vec{M}_\perp N^* + \vec{M}_\perp^* N + I[\vec{P}_i \times \vec{M}_\perp^* N \\ & - \vec{P}_i \times \vec{M}_\perp N^*] + \vec{M}_\perp[\vec{P}_i \cdot \vec{M}_\perp^*] + \vec{M}_\perp^*[\vec{P}_i \cdot \vec{M}_\perp] \\ & - \vec{P}_i[\vec{M}_\perp \cdot \vec{M}_\perp^*] + i[\vec{M}_\perp \times \vec{M}_\perp^*] \end{aligned} \quad (4)$$

In equation (4), I is proportional to the scattered intensity

$$\begin{aligned} I = {} & N N^* + N \vec{P}_i \cdot \vec{M}_\perp^* + N^* \vec{P}_i \cdot \vec{M}_\perp \\ & + \vec{M}_\perp \cdot \vec{M}_\perp^* + \vec{P}_i \cdot \vec{M}_\perp \times \vec{M}_\perp^* \end{aligned} \quad (5)$$

P_i is the incident polarization, N is the nuclear structure factor, and $\vec{M}_\perp$ the magnetic structure factor of the crystalline cell. Equations (4) and (5) may seem quite complicated. However, each term identifies separate and well-defined features of the magnetic structure. For instance, the last terms in equations (4) and (5) are present only if the magnetic structure is noncollinear. For collinear structures, equations (4) and (5) greatly simplify when $\vec{P} || \vec{M}_\perp$. The last terms become important for spiral structures, because they define the direction of propagation of the spiral and its chirality.

Real depolarization of the scattered beam is an indication that a mixed state consisting of more than one magnetic domain is present (see Section 2.2). The ability to distinguish such depolarization from rotation of the polarization away from the unique axis of the conventional technique is one of the features that make zero-field polarimetry very powerful. The different types of antiferromagnetic domains that can occur in antiferromagnetic structures may be classified into configuration domains, 180° and chirality domains, and orientation domains. The type and number of domains that occur depend on the relative symmetries of the paramagnetic and the ordered magnetic phases. In general, if the order of the paramagnetic space group is p and that of the magnetic group is m, the number of different domains is p/m. In a multidomain sample, the quantity $P_s I$ is given by the vector sum of the contributions from the individual domains weighted by their domain fractions. In general, it is easy to distinguish the domain population in the case of 180° and chiral domains. For more complex structures the intensities usually suffice to give the indication of the domain population, if the structures are collinear. A similar approach to diffraction may be possible using resonant X-ray scattering. In general, X-ray magnetic scattering is relatively weak in comparison to charge scattering, becoming sizable only in the proximity of electronic resonances. As a matter of fact, by tuning the wavelength of the X rays it is possible to use element specific resonant scattering, which enables one to obtain magnetic information related to a specific element. For more information about resonant X-ray techniques the reader is referred to **Synchrotron Radiation Techniques Based on X-ray Magnetic Circular Dichroism, Volume 3**.

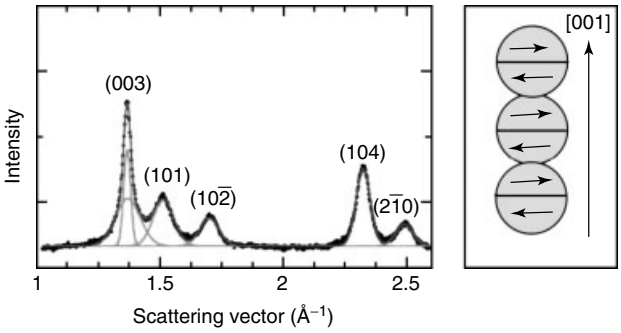

Figure 4. Diffraction of antiferromagnetic α-Fe_2O_3 particles. The (003) and (101) are purely magnetic; the relative sharpness of (003) indicates the presence of magnetic correlations along the [001] direction. (Reprinted figure from *Phys. Rev. B.* Vol. 72, 214406 (2003). © 2003 by the American Physical Society.)

Information on the size of domains can be obtained from the width of the diffraction lines. A representative example of an experiment in this direction is presented in Figure 4, which represents the diffraction pattern from an assembly of α-Fe_2O_3 nanoparticles of 10 nm diameter (Frandsen *et al*., 2005). Each particle is antiferromagnetic and the spins are confined to lie in the low-anisotropy (001) plane. The selective broadening of the (003) and (101) reflections indicates an exchange coupling between particles in the [001] direction. This preferential coupling occurs for assemblies freshly prepared by a solgel method; it disappears by regrinding the sample.

For an assembly of ferromagnetic domains a special 'diffraction' line is broadened, the (000) reflection; that is to say that small-angle scattering takes place around the transmitted beam. Small-angle scattering from domains is easy to detect: Figure 5 shows its earliest observation (Hughes, Burgy, Heller and Wallace, 1949). The beam transmitted through a block of saturated iron has the same shape as the beam without sample. When no magnetic field is applied to iron, the transmitted beam appears much broader. It is tempting to derive, from the increase of the width, the average domain size. Actually, the interpretation of the small-angle scattering is conceptually simpler than the analysis of the broadening of Bragg reflections at finite $\vec{q}$, because it does not depend on the detailed crystalline structure of the sample, that is, as in the case of strain broadening of the Bragg reflection. However, there are

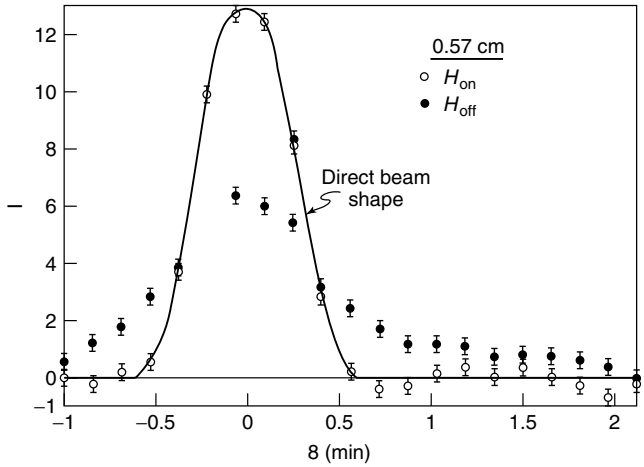

Figure 5. Small-angle scattering of thermal neutrons (wavelength 2.2 ± 0.5 Å) from a block of unmagnetized iron. (Reprinted figure from *Phys. Rev.* Vol. 75, 565 (1949) © 1949 by the American Physical Society.)

genuine difficulties. In its simplest treatment, scattering is assumed to be a minor perturbation of the incident beam; in other words, most of the beam is transmitted through the sample as if no interaction had taken place. This condition is definitely not fulfilled here, since in the scattering pattern of unmagnetized iron no features are recognizable as belonging to the transmitted beam. Multiple scattering then must have taken place, and the broadening is much larger than that due for the single scattering event. Correspondingly, the domain size uncritically inferred from patterns like that presented in Figure 5 is much smaller than the real one. Of course Figure 5 presents the first qualitative observation of magnetic domains; later experiments performed under more exacting conditions were able to provide quantitative information (see, for instance, Löffler, Braun and Wagner, 2000). An inherent difficulty in small-angle scattering is the unambiguous separation of the transmitted from the scattered radiation; a task that becomes progressively more difficult the larger the diameters of the domains are. For domains larger than 100-nm small-angle scattering becomes too hard to detect and alternative techniques have been proposed.

2.2 Neutron beam depolarization

Three-dimensional neutron depolarization is a technique for determining magnetic domain structures in the bulk of magnetic materials for which the typical domain size is in the micrometer range. An experiment consists in determining the change in the polarization of a neutron beam after transmission through a specimen. The polarization change of the neutron beam is related to the micromagnetic state of the medium. The mean magnetic induction results

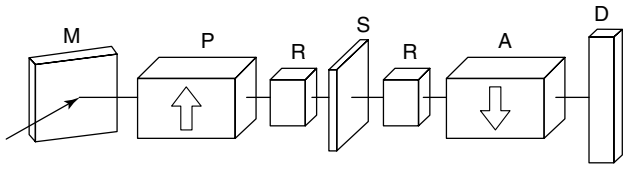

Figure 6. A schematic description of the three-dimensional neutron depolarization system as described by Rekveldt (1973) viewing a continuous wave neutron source. The instrument consists of a monochromator M, a polarizer P, polarization rotators R, a sample S, a polarization analyzer A, and a detector D.

in a net precession of the polarization vector around the mean magnetic induction, while variations in the local magnetic induction result in an effective shortening of the polarization vector, which is called *depolarization*. The neutron depolarization technique in general yields the mean magnetic induction $\vec{B}$, its mean local fluctuation $\Delta\vec{B}$, and the size of the domain (along the neutron's path) over which this fluctuation takes place. This technique has been used to study a variety of topics such as magnetic particulate media and magnetic recording materials (Rekveldt, 1973; Rosman and Rekveldt, 1991; Mitsuda and Endoh, 1985).

A schematic view of a three-dimensional depolarization equipment is given in Figure 6. Most of the instruments have been placed at reactors. A monochromatic beam, of a few angstrom long wavelength, is polarized passing through a polarization cavity. Polarization rotators are placed before and after the sample chamber in order to polarize and analyze the polarization of the beam along three different axes. Each polarization rotator consists of two coils to produce magnetic fields in two directions perpendicular to the transmission direction of the neutron beam. Through the combination of the magnetic fields produced by the coils, the polarization direction can be changed at will. In the sample changer a magnetic field is set on the sample, again in an arbitrary direction. In its handling of the polarization of the neutron, the instrument is quite similar to the Cryopad discussed in Section 2.1. However, here the main difference is that the flight path after the sample is just in transmission geometry. All neutrons have the same flight path at the entrance – before interacting with the sample – as well as at the exit, making polarimetry possible even in the presence of an applied magnetic field.

In a three-dimensional neutron depolarization experiment the polarization vector $\vec{P}$ of a polarized neutron beam is analyzed after transmission through a magnetic sample in all three spatial directions as in spherical polarimetry. The change in $\vec{P}$, caused by Larmor precession of the neutron spin about local magnetic inductions, after passage through a magnetic material can be written in matrix form

$$\vec{P} = \hat{D}\vec{P}_0 \tag{6}$$

In equation (6) $\vec{P}_0$ and $\vec{P}$ are the initial and final polarization vectors respectively, and $\hat{D}$ is the (3×3) depolarization matrix. The elements of $\hat{D}$ are determined experimentally from the measured neutron intensities I_{ij}, where $j = x,\ y,\ z$ represents the direction in which the original beam is polarized and $i = x,\ y,\ z$ represents the spin direction in which the beam is analyzed:

$$D_{ij} = \frac{1 - I_{ij}}{I_s} \tag{7}$$

In equation (7) I_s is the intensity of the fully depolarized beam. The polarization direction transmitted by the analyzer is chosen opposite to that of the polarizer. Therefore, the intensity at the detector is minimal when the polarization direction remains unchanged resulting, under condition of no depolarization, in $D_{ii} = 1$. If the polarization vector rotates π radians, the intensity becomes maximal. The experiment has the beauty and the simplicity of a transport measurement. What remains to be seen is how the matrix $\hat{D}$ can be directly be related to the magnetic structure of the sample in the micrometer range.

In the Larmor approach, the interaction of the polarization vector with a local magnetic induction $\vec{B}$ is described by the equation:

$$\frac{\mathrm{d}\vec{P}(t)}{\mathrm{d}t} = \gamma \left[\vec{P}(t) \times \vec{B}(t)\right] \tag{8}$$

where γ is the gyromagnetic factor of the neutron. The time variable t can be transformed using $t = x/v$ where x is the position variable in the neutron propagation path and v the neutron's velocity. The local magnetic induction can be separated into the mean magnetic induction $\langle\vec{B}\rangle$ and its local fluctuations as experienced by the neutron passing though the material. The mean magnetic induction results in rotation of the polarization vector after transmission through the entire sample. The local fluctuations are responsible for depolarizing the transmitted beam. It is possible to write a correlation function:

$$\alpha_{ij} = \frac{1}{W} \int_W \mathrm{d}^3\vec{r} \int_0^x \mathrm{d}x' \Delta B_i(x, y, z) \Delta B_j(x', y, z) \tag{9}$$

In equation (9), W is a representative subvolume of the medium with size d along the propagation direction of the beam. $\langle d\rangle$, the mean domain size, is supposed to be sufficiently small so that the polarization change in W is small. Within W the magnetization is correlated. In principle, equation (9) also contains terms correlating the magnetization of different domains as seen by the neutron along its path in the x direction. However, a number of assumptions are usually made to permit the evaluation of some physical quantities, such as the mean domain size $\langle d\rangle$. If there is no correlation in the magnetization of different domains, the depolarization matrix element D_{zz} for a magnetic field applied along the z axis becomes:

$$D_{zz} \approx 1 - cL\,\langle d\rangle \left\langle \left(B_s - \overline{B}\right)^2 \right\rangle \lambda^2 \tag{10}$$

In equation (10), c is a constant, λ is the neutron wavelength, L is the total thickness of the sample, and $\langle d\rangle = \sqrt[3]{W}$. This quantity can be derived from the depolarization matrix, if the saturation magnetization and also the magnetization at the field used in the course of the measurements are known. More complex expressions need to be written for systems that are either chemically or magnetically nonhomogeneous.

Neutron depolarization has been used for solving a variety of problems where magnetic domain sizes are of crucial importance. For instance, the compound UGe_2 is both ferromagnetic and superconducting at low temperatures. These two states of matter are considered incompatible with each other. In order to explain the finding, it was suggested that the size of the ferromagnetic domains was less than the coherence length of the superconductor. The latter was estimated to be 20 nm. In a 3D depolarization experiment (Sakarya, van Dijk and Brück, 2005) the average magnetic domain size was found to be of the order of a few micrometers, ruling out that interpretation.

A second example is the investigation of the evolution of the composite structure of iron during the cooling process of carbon steel (Offerman *et al*., 2002). At high temperatures (above 820 °C) the dominant phase is austenite, which has a face-centered-cubic structure and is nonmagnetic. At lower temperatures there is the formation of ferrite, which is body centered and magnetic. This transformation – not only of scientific interest but also of obvious technological importance – has been long studied by neutron depolarization to obtain density and size of the *magnetic* ferrite particles in the course of the cooling process (te Velthuis *et al*., 2001). However, the advent of microbeams at synchrotron light sources permitted a more direct way of observing separately the number and the size of the crystallites. The illuminated volume of material was so small that the diffraction pattern of each crystalline component consisted not of uniform Debye–Sherrer rings but of sequence of spots on the locus of the rings. The number of spots was considered proportional to the density of crystallites in the sample; their intensity proportional to their size. The information that was obtained is presented in Figure 7. The same information in principle could have been obtained by three-dimensional neutron depolarization if the intensity of the source had allowed collimation of the beam to the proper area. Since more powerful neutron sources will be available in the near future, the basic theoretical background

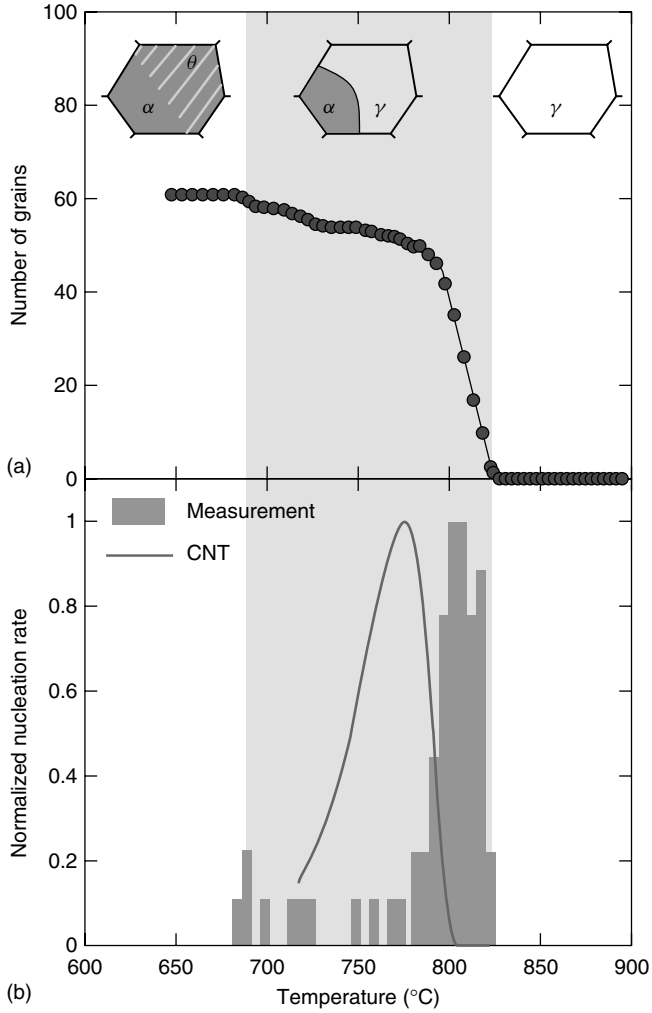

Figure 7. Number of grains of ferrite (α) during cooling of carbon steel. A comparison is made with the classical nucleation theory (CNT). (Reprinted figure with permission from Offerman *et al*., 2002, *Science* **298**:1003–1005. © 2002.)

has been developed in order to evolve neutron depolarization into a tomographic technique (Toperverg, 2002; Badurek, Buchelt, Leeb and Szeywerth, 2003).

2.3 Reflectivity

For the purpose of studying interfaces and surfaces, the neutron-matter interaction and the resulting scattering power may be thought to be in general too weak. This weakness can be overcome by sending the neutron beam at grazing incidence to the surface, in a geometry where the Fresnel reflectivity from the surface cannot be neglected (Werner and Klein, 1987).

In a homogeneous material the neutron–matter interaction may be represented by a smooth pseudopotential whose magnitude is related simply to the scattering density as

$$V^{\pm} = \frac{2\pi h^2}{m} bN + \vec{\mu}\cdot\vec{B} \tag{11}$$

if the neutron spin is aligned parallel (+) or opposite (−) to $\vec{B}$. In equation (11) N is the density of atoms occupying a unit volume, m the neutron mass, and h the reduced Planck constant. In free space ($V = 0$) the component of the incident neutron wave vector normal to the surface is $k_z = 2\pi(\sin\theta_i/\lambda)$ and k_x, k_y are the components in the surface's plane. θ_i is the angle of incidence and λ is the neutron wavelength. In the medium the perpendicular component of the neutron momentum k_{zi} is modified by the optical potential, such that:

$$k_{zi}^{\pm} = \sqrt{k_{z0}^2 - \frac{2m}{h^2}V^{\pm}} \tag{12}$$

Particle and flux conservation at the surface determine the reflectance r and transmittance t. The observable reflectivity R takes the form:

$$R = |r|^2 = \left|\frac{k_{z0} - k_{zi}^{\pm}}{k_{z0} + k_{zi}^{\pm}}\right|^2 \tag{13}$$

For values of $k_{z0}^2 < \left(2m/h^2\right)V^{\pm}$, the neutron wave vector becomes imaginary: the neutron wave decays exponentially in the material and the neutrons are totally reflected. These angles are very small (for 5 Å neutrons the critical angle is less than half a degree). However, at these angles of grazing incidence, surface effects become important. In a neutron reflectivity experiment, the intensity of the neutrons reflected from the surface is measured as a function of the neutron momentum component, which is perpendicular to the surface, $q_z = 2k_{z0}$. Above the critical angle, the reflectivity from a semi-infinite body of homogeneous material decreases as q_z^{-4} (Fresnel reflectivity). Since q_z is a conjugate variable of the depth z from the film surface, a scan over a suitable range of q_z provides excellent information on the chemical and magnetic depth profile $V^{\pm}(z)$ of the film (Lekner, 1987). For instance, if the material is composed of several layers that are periodically repeated, the q^{-4} dependence of the reflectivity is strongly perturbed and maxima occur at the values of $q_{zi} = 2\pi/d$, where d is the repeat distance of the layers. The reflectivity of a periodic multilayer may be easily understood in terms of conventional diffraction: When normalized to the Fresnel reflectivity, the measured reflectivity reduces to a series of peaks whose intensity at large q_z is nearly the square of the scattering length density of the single period. This treatment assumes that the material is chemically and magnetically homogeneous in each plane parallel to the surface.

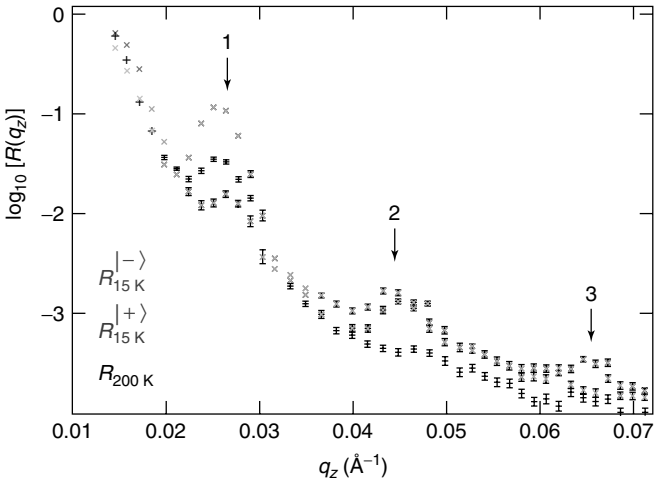

Figure 8. Specular reflectivity of a superlattice composed of a bilayer (LCMO (16 nm)/YBCO (16 nm)) repeated six times: in the paramagnetic region ($T = 200$ K) the indexed diffraction peaks modulating the q^{-4} decay of the reflectivity are well visible. At low temperature, below both $T_C \sim 165$ K and $T_{sc} \sim 75$ K, the reflectivity becomes strongly spin dependent and can be analyzed in terms of a detailed magnetic profile. (Reprinted figure from *Phys. Rev. B.* Vol. 71, 140509® (2005). © 2005 by the American Physical Society.)

For a material with $B \neq 0$, the critical angle is spin dependent; in other words, for neutrons, a ferromagnet is birefringent. Figure 8 presents the reflectivity pattern of a film, composed of the periodic repetition of pairs of layers. At low temperature, one of these is ferromagnetic, the second is a superconductor. In this experiment, the polarization of the incident beam was parallel (R^+) or antiparallel (R^-) to the magnetic field $\vec{H}$ applied to the sample. $\vec{H}$ was in the plane of the sample and was sufficiently high to saturate it. Thus the magnetic induction $\vec{B}$ in the sample was parallel to $\vec{H}$, and no neutron spin flip was expected. This is not generally true in experiments designed to study the magnetization reversal process.

In neutron reflectivity, only uniaxial (and not spherical) polarimetry has been applied. According to this, when the incident neutrons are polarized along an applied magnetic field $\vec{H}$ and the polarization after reflection is analyzed along the same axis, four reflectivities are recorded: R^{++}, R^{+-}, R^{-+}, R^{--}. The first (second) sign refers to the incident (reflected) neutron polarization with respect to $\vec{H}$. For films thinner than the domain-wall thickness, only two-dimensional arrays of domains are possible. In addition, for a majority of magnetic systems shape anisotropy constrains the magnetization to the surface's plane. Specular scattering can give information about the distribution of magnetization directions in lateral domains (Lee *et al.*, 2002). For a single domain, simple and transparent relations link the magnetization to the spin-dependent specular reflectivity. When the direction of magnetization and the applied field are in the film's plane, and $\vec{M}$ is at an angle φ with $\vec{H}$, then:

$$\frac{R^{++}(\varphi) - R^{--}(\varphi)}{R_s^{++}(0^\circ) - R_s^{--}(0^\circ)} = \cos\varphi \tag{14}$$

and:

$$\frac{R^{-+}(\varphi)}{R_s^{-+}(90^\circ)} = \sin^2\varphi \tag{15}$$

provided that the direction of $\vec{M}$ is constant along the thickness of the film. The normalizing quantities, $R_s(0^\circ)$ and $R_s(90^\circ)$, refer to reflectivities measured with $\vec{M}$ saturated and aligned parallel and perpendicular to the neutron polarization, respectively. These relations are valid at all values of q_z above the critical edge for total reflection.

When a film breaks down into lateral domains, the effect on the specular reflectivity depends on the size of the domains. For domains larger than the coherence length the intensities reflected from different domains superimpose incoherently in the specular beam. In this case the terms dependent on φ of equations (14) and (15) can be interpreted as averages across the sample plane. While the term $\langle\cos\varphi\rangle$ may be measured as well by conventional magnetometry, $\langle\sin^2\varphi\rangle$ provides new information leading to the mean square dispersion of the domain orientations $\chi^2 = \langle\cos^2\varphi\rangle - \langle\cos\varphi\rangle^2$. The information on surface magnetic domains as obtained in specular reflectivity is similar to that obtained by observing the magnetic intensities of Bragg reflections from a magnetically ordered solid and consists in providing the statistical distribution of domains. On the other hand, the size of the domains can be determined only if off-specular scattering is detectable.

Any imperfection in the layers parallel to the surface – including domains in the plane of the film – causes some scattering away from the specularly reflected beam, with the geometry illustrated in Figure 9. The scattering may take place in the plane of reflection (defined by the angle of incidence θ_i and reflection θ_f) or else at an angle $\Delta\varphi$ out of the reflection plane. Inhomogeneities in the plane of the film can be represented by a vector $\boldsymbol{\tau}$ with planar projections τ_x and τ_y, where x is chosen in the reflection plane, and y perpendicular to it. When $\boldsymbol{\tau}$ is small in comparison with the incoming wave vector, the laws of conservation of energy and momentum in the plane reduce to:

$$\tau_x = \frac{2\pi}{\lambda}\sin\theta\cdot\Delta\theta; \quad \tau_y = \frac{2\pi}{\lambda}\cdot\Delta\phi \tag{16}$$

where $\Delta\theta$ and $\Delta\phi$ are the observed angles. At grazing incidence fluctuations of $\boldsymbol{\tau}$, which are isotropic in the plane of the film ($\tau_x = \tau_y$), can give scattering at detectable $\Delta\theta$ even

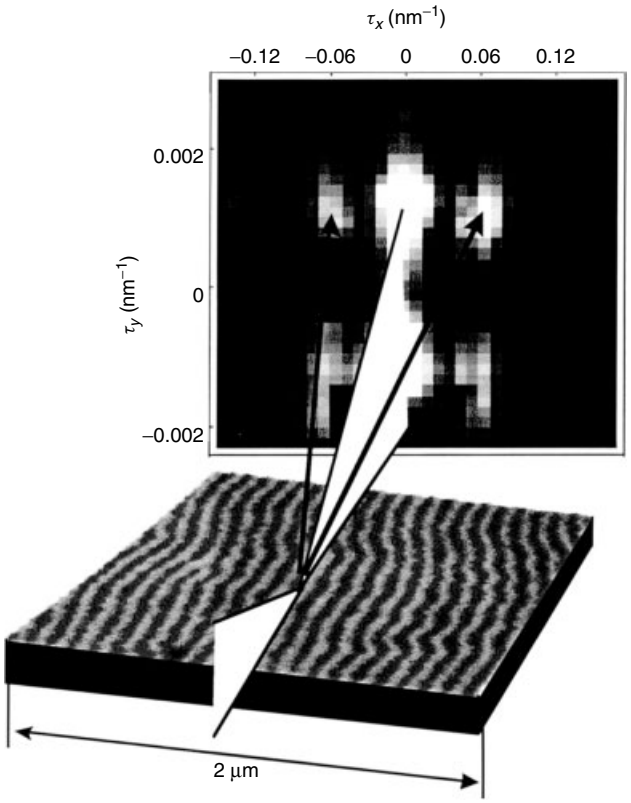

Figure 9. Geometry for scattering at grazing incidence from magnetic stripe domains in a perpendicularly magnetized thin magnetic film. Scattering along τ_y can be observed only because of the large anisotropy of the surface corrugation lengths along x and y. (Reprinted figure from *Physica B: Condensed Matter*, Vol 267–268, Fermon *et al*., © 1999 with permission from Elsevier.)

when $\Delta\phi$ is negligibly small. Reversing the argument, the maximum size of the objects that give rise to lateral scattering (finite $\Delta\phi$ is the same as in transmission geometry and is of the order of a few nanometers). The lateral fluctuations that give rise to a comparable $\Delta\theta$ are instead of the order of a micrometer. The accepted nomenclature is to call the scattering with $\Delta\theta \neq 0$ off-specular reflectivity, while the scattering with $\Delta\phi \neq 0$ is called *scattering at grazing incidence* (Pannetier, Ott, Fermon and Samson, 2003). Most of the experiments carried out on magnetic domains were geared to measure the off-specular reflectivity, integrating the signal along τ_y.

Sizable off-specular reflectivity has been almost universally observed in sputtered samples of magnetic multilayers in the antiferromagnetic state (see also Section 3.3). However, spin-dependent off-specular reflectivity can be observed even in simple systems. Figure 10(a) shows the hysteresis curve of a thin film of ferromagnetic Co covered with CoO. The film has been cooled in a magnetic field through the characteristic temperature at which CoO becomes antiferomagnetic: the effect of field cooling is a displaced hysteresis loop. In addition, a training effect (Hoffmann, 2004) is visible in the repeated hysteresis cycles at low temperature (te Velthuis *et al*., 2000). Except for saturation, a sizable off-specular scattering is observed at all points of the hysteresis cycle. For instance Figure 10(b) shows the spin-dependent intensities of the off-specular scattering obtained at $H = 30$ Oe for the ascending branch of the first hysteresis loop. All the experimental results are well reproduced by calculations based on a simple distribution of the two-dimensional ferromagnetic domains of Co during magnetization reversal (te Velthuis *et al*., 2006). Recently, benchmark neutron experiments have been started on well-defined arrays of nanostructured materials that have been also studied with concurrent techniques such as Kerr microscopy (Lee *et al*., 2003; Theis-Bröhl *et al*., 2005). For these systems it ought to be possible to establish how well the complex scattering patterns obtained by neutron scattering can be interpreted in terms of a statistical ensemble of domains and of their evolution in the presence of a magnetic field.

3 SCIENCE ISSUES

3.1 Homogeneous materials

In order to explain effects, such as different remanent states in ferromagnets, domains were first proposed by Weiss (1907). Subsequently these domains were observed for the first time using a decoration technique by Bitter (1931) and Landau and Lifshitz (1935) were the first to provide a satisfactory explanation. The formation of domains occurs because of the interplay between various energies, such as exchange, anisotropy, magnetostatic, and magnetoelastic energies. In particular magnetostatic energies are important for the understanding of domains in ferromagnets. A magnetization with a component perpendicular to the surface of a ferromagnet, generates magnetic poles and magnetic fields outside of the magnetic material. In general, avoiding these magnetic poles and the concomitant magnetic fields minimizes magnetostatic energies. As shown in Figure 1 the magnetostatic energies can be reduced by the formation of opposite domains and can vanish altogether by the formation of so-called closure domains. It is immediately clear that size and shape, as well as crystalline orientation of the surfaces will influence the domain structures considerably. Some of the basic relationships will be demonstrated below and a much more detailed overview of the properties of ferromagnetic domains can be found in Hubert and Schäfer (1998).

The experimental detection of domains in ferromagnets is based on the fact that each domain has a net nonzero magnetization. This is either measured by detecting the magnetization

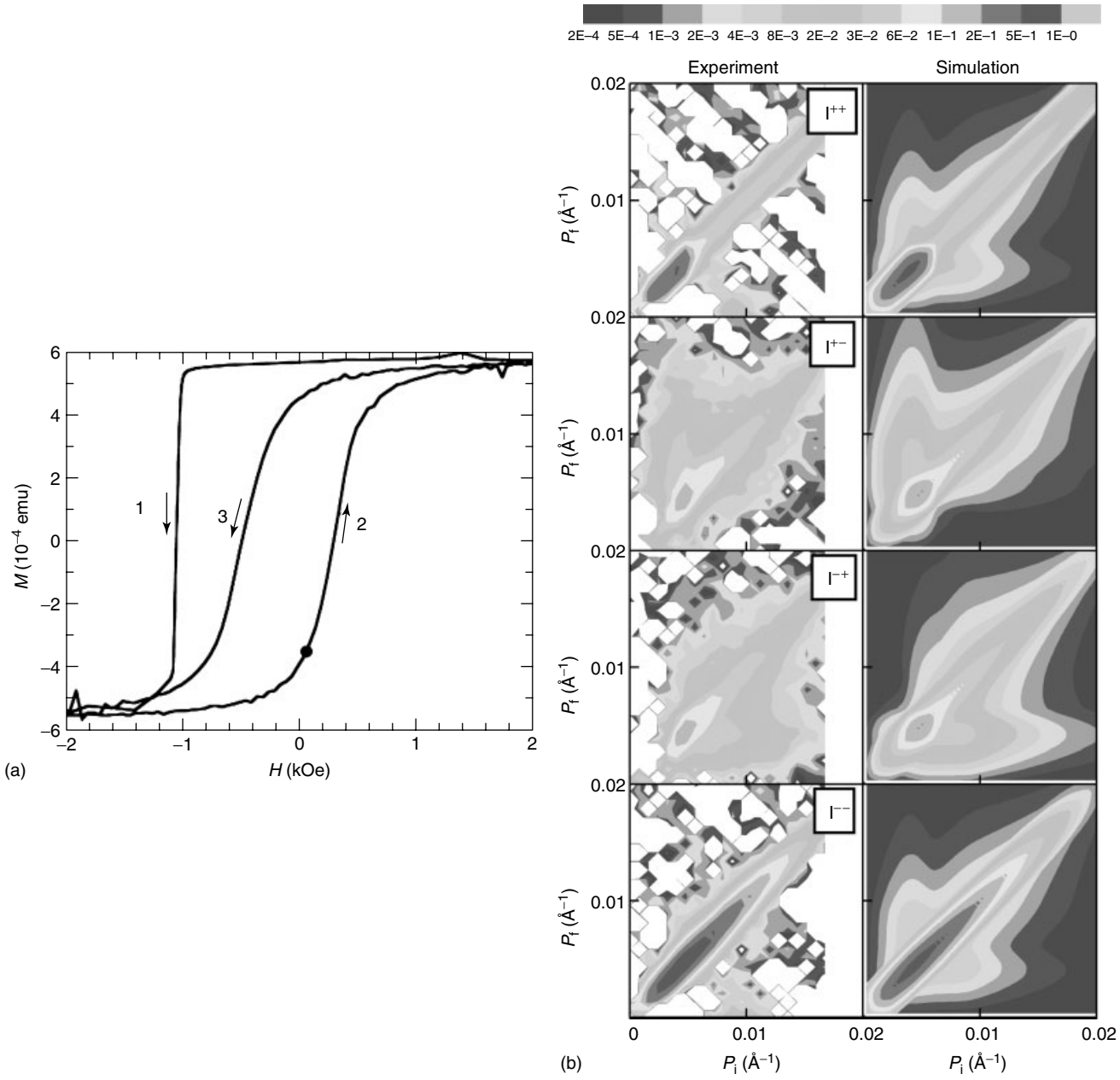

Figure 10. (a) Low-temperature hysteresis loop of a Co/CoO thin film. Cooling in a magnetic field through the ordering temperature of antiferromagnetic CoO causes an exchange bias. A training effect (Hoffmann, 2004) is also visible. (Adapted from te Velthuis *et al*., 2000.) (b) Off-specular neutron reflectivity gives detailed information about size and distribution of the magnetic domains for each point of the hysteresis cycle. Left: Measured spin-dependent reflectivities of the same Co/CoO sample as in (a). The data were collected at $H = 30$ Oe on the ascending curve, marked by a solid dot in (a). $P_i = 2\pi \sin \theta_i$, $P_f = 2\pi \sin \theta_f$. The diagonal line represents the specular scattering. The observed off-specular scattering indicates the presence of finite domains. The spin-flip intensity (I^{+-}, I^{-+}) of the off-specular scattering indicates that the magnetization of these domains is not collinear with the applied magnetic field. Right: simulated off-specular reflectivity based on a simple model for the magnetic domains (te Velthuis *et al*., 2006).

directly or by the stray fields, which occur at the boundaries between domains. The former approach is typically used for scattering (see Section 2) or spectroscopy techniques, while the later is more typical for real space imaging techniques, such as decoration techniques or magnetic force microscopy.

As mentioned in the preceding text, domains form in a ferromagnetic material to balance the different magnetic interactions. From this follows a critical minimum size, below which a magnetic material is single domain since the relatively high increase of exchange energy for a inhomogeneous

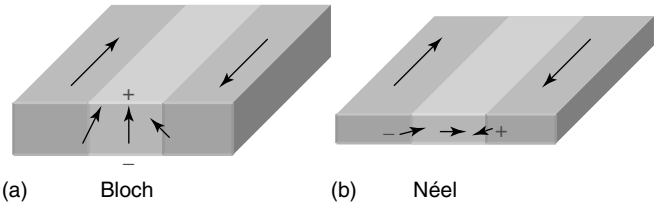

Figure 11. Schematics of Bloch (a) and Néel (b) domain walls. For the Bloch wall the magnetic charges build up at the surface of sample, while for the Néel wall the magnetic charges are contained within the sample.

magnetization state in a small particle is too high (Kittel, 1949). Assuming spherical particles one can determine the following critical radius for low anisotropy

$$r_c = \sqrt{\frac{9A}{\mu_0 M_s^2}\left[\ln\left(\frac{2r_c}{a}\right) - 1\right]} \tag{17}$$

and for high (cubic or uniaxial) anisotropy

$$r_c = \frac{9\sqrt{AK}}{\mu_0 M_s^2} \tag{18}$$

Here A is the exchange stiffness, M_s is the saturation magnetization, a is the lattice constant, and K is the anisotropy constant. The exchange stiffness is given by $A = JS^2/a$, with J being the exchange integral and S the ferromagnetic spin. Typical values for A are $10^{-11}\,\mathrm{J\,m^{-1}}$. In the case of low-anisotropy materials the magnetization forms a so-called vortex state above r_c, while in the case of high anisotropy materials one obtains above r_c well-defined domains with walls separating them.

In general, one can distinguish several types of domain walls in ferromagnetic systems with domains. The two main types of domain walls are Bloch and Néel walls, which are depicted schematically in Figure 11. For a Bloch domain wall the magnetization rotates continuously in the plane of the domain wall. The wall width d_w for the case of opposing domains can be determined from balancing exchange and anisotropy energies (Bloch, 1932):

$$d_w = \pi\sqrt{\frac{A}{K}} \tag{19}$$

One should notice that if the magnetization does not rotate a full 180°, then the domain-wall thickness might also be much less. For example at Co(0001) surfaces, domains have been observed where the relative difference in magnetization direction is about 20° and the domain walls separating these domains are only $1.1 \pm 0.3\,\mathrm{nm}$ wide (Ding, Wulfhekel and Kirschner, 2002).

When the ferromagnetic material becomes very thin, then the magnetic charges associated with the Bloch walls at the surfaces (see Figure 11) create an energetically unfavorable stray field. In this case it may become energetically more favorable to have the magnetization rotate continuously perpendicular to the plane of the domain wall, which is then called a *Néel wall*. Again the width of this wall can be easily determined by balancing exchange and, in this case, magnetostatic energies and in the thin-film limit (O'Handley, 2000) is given by:

$$d_w = \pi\sqrt{\frac{2A}{\mu_0 M_s^2}} \tag{20}$$

Interestingly, since Néel walls have a chirality associated with the sense of magnetization rotation, it is possible for two colliding Néel walls to form a metastable 360° wall, if the individual walls had opposite chirality (Portier and Petford-Long, 2000; Castaño *et al*., 2003).

In general, domain walls are not necessarily just simple Bloch or Néel walls, but the walls can combine aspects of both. For example even films with Bloch walls, may still have Néel caps at their surface. In fact, for films with intermediate thickness one can observe a mixture of Bloch and Néel walls, which is the so-called cross-tie wall (Middlehoek, 1963).

In the following we discuss a few of the typical domain structures that are particularly relevant for thin magnetic films. Magnetic thin films with an anisotropy perpendicular to the film plane tend to form so-called stripe domains in order to minimize magnetostatic energies (see Figure 12a). For the case where the width of the film is much larger than its thickness, the width of the stripe domains can be calculated as (Kittel, 1949):

$$d_d \approx \sqrt{\frac{t\sqrt{KA}}{\mu_0 M_s^2}} \tag{21}$$

where t is the film thickness. Similarly stripes can also be observed for patterned films with in-plane anisotropy, that is, for wires with an anisotropy perpendicular to the wire axis, but in the film plane. In this case the width of the stripes is (O'Handley, 2000):

$$d_d \approx L\sqrt{\frac{\sqrt{KA}}{\mu_0 M_s^2 t}} \tag{22}$$

where L is the width of the wire.

Again in reality the situation can be more complex. The above equations describe the lowest-energy configurations. However, it is also possible that the precise stripe spacing is determined by metastable configurations, which depend

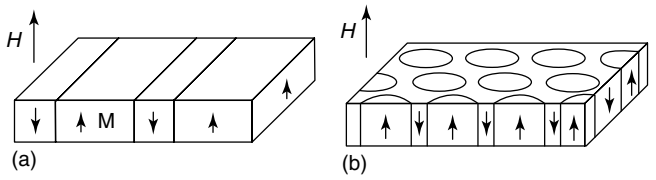

Figure 12. Schematics of stripe (a) and bubble (b) domains. (Reprinted figure from *Phys. Rev. B.* Vol. 26, 325 (1982) © 1982 by the American Physical Society.)

on the magnetic history of the samples (Leaf *et al*., 2006). Furthermore the amount of anisotropy may depend on the film thickness. For example many thin-film systems have a so-called spin reorientation transition, where the anisotropy direction changes as a function of film thickness (Allenspach, 1994). The reason for this is that surface anisotropies can compete with bulk anisotropies and magnetostatic constrains. Therefore, stripe domains close to such a reorientation transition can occur with a complicated wrinkle pattern (Duden and Bauer, 1996). In this case thickness fluctuations can give rise to regions with in-plane and out-of-plane anisotropies, such that the magnetization prefers to be at an intermediate tilt angle with respect to the surface normal. As a consequence the out-of-plane and in-plane magnetization component can set up domain patterns with different length scales, that is, a short-length-scale domain pattern for out of plane (similar to the stripes discussed in the preceding text), while the in-plane component sets up a long-length-scale domain pattern.

Another commonly observed domain pattern is closure domains, which were first suggested by Landau and Lifshitz (1935). Closure domains are more easily obtained in cubic than in uniaxial systems. However, magnetostriction can give rise to strain, which can further complicate the domain structure and actually stabilize stripe domains with reduced elastic strains. In general, closure domains require a minimum sample size and are favored by large magnetization, large sample thickness, small anisotropy, and small wall energy.

Ferromagnetic layers with very high perpendicular anisotropy can develop, in addition to strip domains, so-called bubble domains, which are shown schematically in Figure 12(b) (Malozemoff and Slonczewski, 1979). As the applied field is raised above a critical value there is a transition from stripe to bubble domains (Garel and Doniach, 1982). One interesting consequence of such bubble domains are that small ($<$100 nm) bubble domains can persist to very high field beyond the apparent saturation field obtained from standard magnetometry measurements (Davies *et al*., 2004). Such residual domains can change the magnetization reversal considerably if they are not completely annihilated.

Magnetization reversal can be governed by domain nucleation, domain-wall motion, and magnetization rotation in each domain. In general the reversal can be a complex superposition of all of these mechanisms. Small patterned systems allow looking at simplified model systems, where the reversal is dominated only by a few factors. But even for large samples the field dependence of the hysteresis raises interesting question about the evolution of magnetic domains. For example it is often observed that the value of the magnetization at a given field is reproduced, even if a minor hysteresis loop is applied during the major loop. This observation is referred to as return-point memory. One obvious question is whether this macroscopic return-point memory also corresponds to an identical configuration of magnetic domains. This question was studied by Pierce *et al*. (2003) in Co/Pt thin films with different microstructures using X-ray speckle metrology. They observed that for films with smooth interfaces the nucleation and domain evolution is random and uncorrelated for subsequent hysteresis loops in spite of perfect macroscopic return-point memory. However, for the rougher films the domains show a high degree of correlation during the nucleation, and the correlation becomes reduced further along during the magnetization reversal. This indicates that if there are enough defects present in the magnetic system the nucleation of reversed domains occurs at identical defects, but the motion of domain walls is more random thereafter.

Until now we discussed mainly domains in ferromagnetic systems. While there are also domains possible in antiferromagnetic systems, their behavior tends to be less studied and at the same time very different from ferromagnetic systems. Unlike in ferromagnets, magnetostatic energies are vanishingly small in antiferromagnets and therefore they are not a driving force for domain formation. Furthermore, any gain in configurational entropy is typically not sufficient to overcome the domain-wall energy. Therefore domains in antiferromagnets are generally metastable. However, magnetoelastic interaction, such as piezomagnetism in fluorides (Borovik-Romanov, 1960), may be the dominating energy for domain formation in antiferromagnets. In many cases domains in antiferromagnets may simply originate from random nucleation of long-range order. Applying an external magnetic field during the ordering may influence this domain formation, that is, in MnF_2 fields larger than 150 Oe result in a single-domain state, while smaller fields give rise to multiple domains (Baruchel, Schlenker and Barbara, 1980). In contrast, a field close to that of the spin-flop transition (94 kOe) is required in order to form a single domain at low temperature (Felcher and Kleb, 1996). On the other hand, random defects may also be responsible for establishing a multiple-domain state (Kleemann, 1993). In general, the connection between domains in the antiferromagnet and their macroscopic properties has not been extensively studied. However, domains in antiferromagnets have received increased attention lately

because of their potential role in exchange bias as discussed in more detail subsequently (see Section 3.3).

Owing to the lack of net magnetization for an antiferromagnetically ordered material, the first experimental indications of domains were rather indirect. In a uniaxial antiferromagnet the magnetic susceptibility parallel and perpendicular to the antiferromagnetic anisotropy axis is very different. As a consequence uniaxial antiferromagnets have a spin-flop transition, where the spins suddenly rotate perpendicular to the applied field with a slight canting toward the field in the case where it is applied along the anisotropy axis (Néel, 1936; Foner, 1963). The spin-flop field at which this transition occurs is given by Tanner (1979):

$$H_{\mathrm{f}} = \sqrt{\frac{2K}{\mu_0(\chi_\perp - \chi_{||})}} \tag{23}$$

where K is the anisotropy constant and $\chi_\perp$ and $\chi_{||}$ are the susceptibilities perpendicular and parallel to the anisotropy axis, respectively. This spin-flop transition gives rise to a sudden increase in magnetization. In contrast, for cubic antiferromagnets there is no sudden spin-flop transition (Tanner, 1979). In a cubic antiferromagnet one expects a mixture of domains with spins parallel and perpendicular to the applied field and therefore applying an external field will just result in a spin-flop process via gradual domain-wall motion between these domains (Néel, 1954).

Some antiferromagnetic materials may also have a spin-flip transition as a function of temperature, which typically reflects the temperature evolution of the anisotropy. Examples are Hematite (α-Fe_2O_3), which has the so-called Morin transition at approximately 260 K (Morin, 1950), and chromium, where the direction of the antiferromagnetic spins changes from transverse to longitudinal with respect to the antiferromagnetic ordering vector at 123 K (Werner, Arrott and Kendrick, 1967). As in the case for the field-induced spin-flop discussed in the preceding text, domains in the chromium make this spin-flip transition rather gradual, instead of being first order. Using X-ray microdiffraction it has been recently shown that spin-flipped longitudinal domains nucleate at the domain wall between different transverse domains and subsequently grow gradually until the transverse domains are completely replaced (Evans *et al*., 2002).

Unlike in the case of ferromagnets, the net zero magnetization makes a direct detection of domains in antiferromagnets relatively difficult, which is one of the main reasons they are less studied. However, there are several approaches to directly detect and image antiferromagnetic domains. For example, it is possible that magnetostriction can give rise to strain domains, which are identical to the antiferromagnetic domains (Roth, 1960). In this case, X-ray topography can be used to map out strain domains (Tanner, 1976). It should be noted, however, that the imaging of antiferromagnetic domains via their accompanying strain is only possible in single crystals.

Other possibilities for directly detecting domains are either by utilizing an antiferromagnetic Bragg reflection (reflecting the increased unit cell superstructure) or spectroscopic signatures (i.e., dichroism). Bragg reflections have been used for domain imaging with either polarized neutron diffraction tomography (Schlenker and Baruchel, 1978) or X-ray diffraction microscopy (Evans *et al*., 2002). Examples of imaging with spectroscopic signatures are optical (Eremenko, Kharchenko and Beliy, 1979) or X-ray linear dichroism–based detection (Scholl *et al*., 2000).

Domain structures in antiferromagnets can be much more complex than in ferromagnets, since one can distinguish between domains with different orientations of the ordering vector (T domains, i.e., four different T domains in NiO, which order along (111), see also Section 2.1) and different orientations of the spins along different anisotropy axes (S domains, i.e., for each T domain there are three different S domains, since the anisotropy axes in NiO are the equivalent (112) directions, see also Section 2.1). The nomenclature arises from the fact that T domains are equivalent to different crystallographic twins, while S domains are due to different spin directions. Distinguishing between these different domains may require different approaches. For example, when using neutron scattering T domains can be differentiated by their different Bragg reflections, while S domains can only be detected through polarization selection rules (see Section 2.1).

For completeness we finish the section on homogeneous materials with domains by mentioning that some materials (Tb, Dy, $Tb_{50}Ho_{50}$, $Gd_{60}Y_{40}$, MnP) have a spiral magnetic order. In this case it is also possible to have domains with different chiralities (Palmer, 1975).

3.2 Confined systems

As discussed in the previous section it is clear that geometrical confinement can significantly affect magnetic domain structures. In the following we discuss two types of confined systems, namely, granular systems and well-defined patterned systems, that is, systems obtained via lithography.

Granular systems consist of grains, which are typically sufficiently small to be single domain. In this case the overall magnetic domain behavior is governed by the interactions of the grains. It turns out that at least in the case for ferromagnetic grains as their sizes are reduced, they can start to act collectively, meaning that the domain sizes become bigger than the individual grain sizes. This has

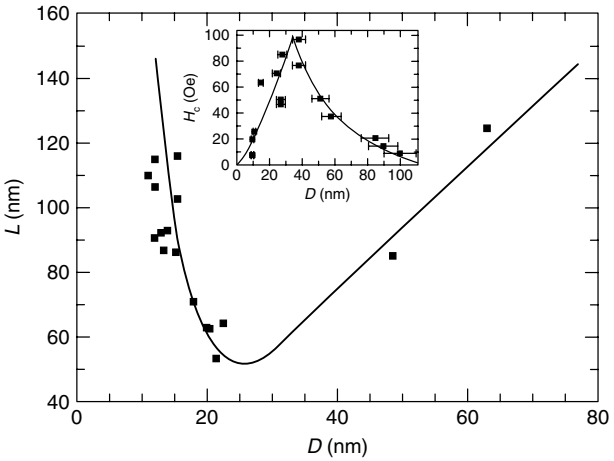

Figure 13. Magnetic correlation length L versus grain size D as determined from small-angle neutron scattering of nanostructured Fe. The inset shows the corresponding coercivity data. (Reprinted figure from *Phys. Rev. Lett.* Vol. 85, 1990 (2000). © 2000 by the American Physical Society.)

been observed by determining magnetic correlations lengths from small-angle neutron scattering (see Figure 13) (Löffler, Braun and Wagner, 2000). The magnetic correlation length is indicative of an average domain size. For large grains the correlation size scales with the grain size, but for very small grains the correlation length increases again. One of the consequences is that in materials with very small grains the crystal anisotropy will be replaced by an effective anisotropy from the superposition of the anisotropies of the magnetically correlated grains. If these grains are randomly oriented, this effective anisotropy can be very small, which makes granular materials very attractive for soft-magnetic applications (Yoshizawa, Oguma and Yamauchi, 1988).

At the same time granular systems can also be used prepare extremely hard magnets. As seen in Section 3.1 there is a critical size below which the magnetization in a grain becomes single domain (see equations (17) and (18)). This also means that the mode of magnetization reversal may change from a domain nucleation and domain-wall motion to either coherent or incoherent rotation. This can give rise to a significant coercivity increase for small grain systems with high crystalline magnetic anisotropy. For example, it has been shown that the coercivity can exceed 10 T for FePt films with grain sizes of 20–30 nm (Shima, Takanashi, Takahashi and Hono, 2004).

Most patterned systems have typical length scales much larger than granular systems. As a consequence, the magnetization of an individual element is often not just a simple single domain. However the limited size often can give rise to very simple domain structures, which tend to 'close the flux' and minimize magnetic strayfields. One of the simplest systems is circular dots, which give rise to a so-called magnetic vortex (Cowburn *et al*., 1999). Similar flux-closure domain configurations can also be observed in other structures, such as rings (Rothman *et al*., 2001; Li *et al*., 2001), rectangular particles (Hubert and Schäfer, 1998), or films with holes. Interestingly, when these systems have a broken in-plane symmetry, that is, either due to shape or magnetocrystalline anisotropy or due to exchange coupling, then the precise remanent domain state may depend on the magnetic history, such as magnitude and direction of previously applied magnetic fields. Examples of such broken symmetries are rectangular patterns (Thomas *et al*., 2000b), elliptical patterns (Vavassori *et al*., 2004), and exchange-biased systems (Sort *et al*., 2005, 2006a).

All the aforementioned examples are systems based on patterned thin films. However 'flux-closure' domain structures can also be observed in other nanopatterned systems. For example flux-closure structures have also been observed for cylindrical Co nanowires with sufficiently large diameter (>50 nm) (Henry *et al*., 2001).

So far there has been only very limited use of scattering techniques for investigating the magnetization behavior in patterned systems. Temst, Van Bael, and Fritzsche (2001) showed that off-specular polarized neutron reflectometry can be used to investigate the field dependence of the magnetization in patterned structures. However, so far there is no detailed information about inhomogeneous magnetization states. In contrast Lee *et al*. (2003) used off-specular neutron scattering to determine the domain structures for magnetic antidot arrays, which have also been suggested for high-density data storage (Cowburn, Adeyeye and Bland, 1997).

In the case of systems with predominantly in-plane anisotropy, flux-closure domain structures, such as a vortex, are stable over a wide range of sizes. But the situation can be markedly different in systems with perpendicular anisotropy, which tend to form stripe domains as discussed in Section 3.1. As long as the lateral size of the pattern is comparable to the stripe width (see equations (21) and (22)), only a few, very simple, well-defined domain patterns are stable consisting of either concentric rings or parallel stripe patterns (Skidmore, Kunz, Campbell and Dahlberg, 2004). But as soon as the lateral dimension of the system becomes larger than $1.5d_d$ the stripe domain patterns become complex and randomly oriented. However, the stripe domains still prefer to be either perpendicular or parallel to the edges of the patterned system.

Aside from confining the possible different domain states, nanostructuring also offers different ways of manipulating domain structures. In bulk systems one generally only investigates how the domain structure is changed by varying external parameters such as applied field and/or temperature. In patterned materials there is also a possibility to change the domain structure through the application of electrical

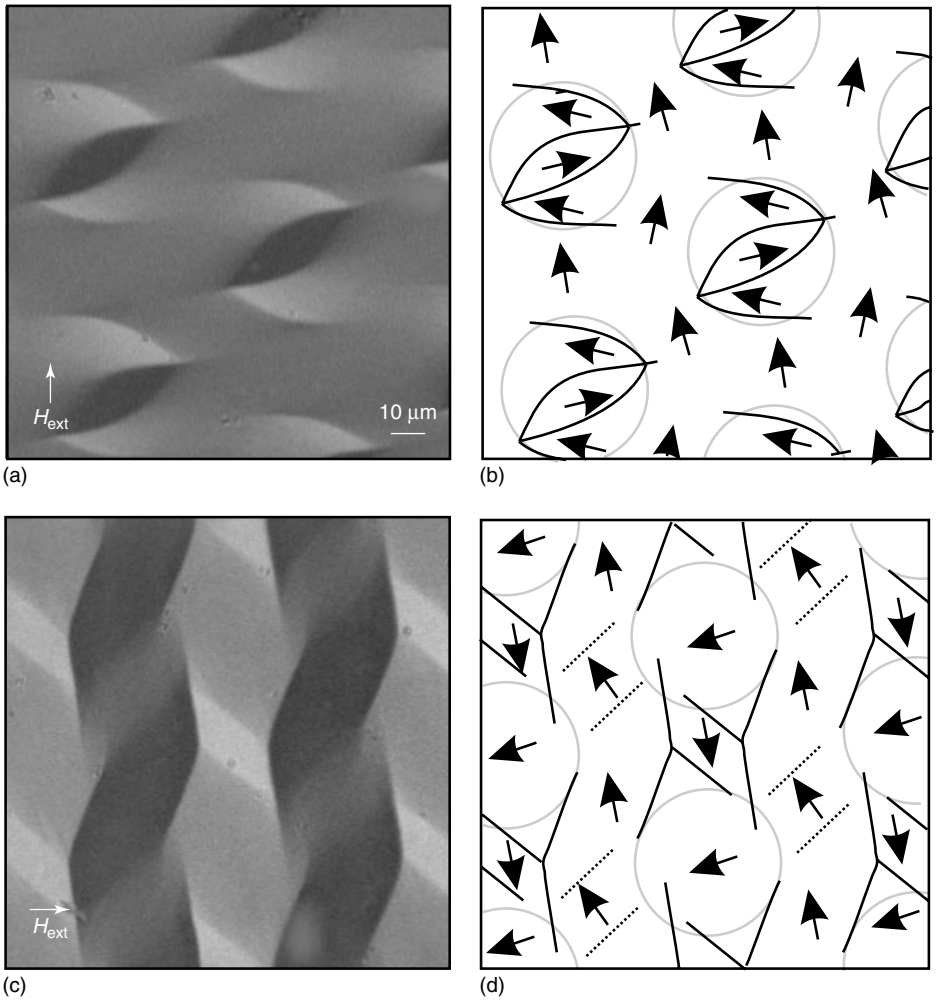

Figure 14. Magneto-optic Kerr microscopy images and deduced domain patterns for FeCoSiB films in which the anisotropies were laterally modified through He-ion irradiation. (Reproduced from J. McCord *et al*., 2005, with permission from American Institute of Physics.)

currents (Gan *et al*., 2000). This current-induced domain-wall motion is either due to spin torque (thin films) (Berger, 1984) and domain drag (thicker films) (Berger, 1978) or due to linear momentum transfer (narrow domain wall) (Tatara and Kohno, 2004).

Recently there have been also approaches using lateral variations of anisotropy to modifying domain patterns besides confining the actual physical size of magnetic systems. The local magnetic anisotropy can be controlled by thickness modulation (Costa-Krämer *et al*., 2003), selective epitaxy (Li *et al*., 2002), or by local ion irradiation (Fassbender, Ravelosona and Samson, 2004). Using a substrate with laterally modulated crystallinity at the surface, Li *et al*. (2002) prepared Ni films with laterally alternating out-of-plane and in-plane anisotropy, which was reflected in a corresponding domain structure. Similarly, Swerts *et al*. (2003) established well-defined domain structures by laterally varying the roughness of the films through regional use of silver buffer layers. Ion irradiation allows changing the microstructure locally (Fassbender, Ravelosona and Samson, 2004), which can be used to tailor both the magnitude of the anisotropy (Chappert *et al*., 1998), as well as the direction (McCord *et al*., 2005). Especially the later possibility of laterally modifying the anisotropy direction allows for the generation of very complex well-defined domain patterns (see Figure 14).

Aside from the static domain patterns in confined magnetic structures, there is an increasing interest in the dynamic behavior of domain patterns and their role for magnetization reversal processes. The dynamic behavior can be complicated, since the magnetization in each domain might show precessional motion, while the domain walls themselves can have excitations analogous to oscillating strings, and intersections of domain walls, such as vortex cores can perform translational motion (Park *et al*., 2003; Perzlmaier *et al*., 2005; Raabe *et al*., 2005; Guslienko *et al*., 2006). Interestingly,

systems with a vortex core (circular disks or squares), may have left or right handedness due to the chirality of the domain pattern and the orientation of the vortex-core magnetization. While in most cases this handedness is unimportant for the static domain patterns, it becomes very important for the dynamic behavior of these systems (Choe *et al*., 2004; Buchanan *et al*., 2005).

3.3 Coupled systems

3.3.1 Antiferromagnetically coupled multilayers

Until now we discussed mainly homogeneous, one-component systems. It is clear that interactions between different magnetic materials can also modify the balance between the different magnetic energies and therefore influence the domain formation considerably. In particular magnetic multilayers were studied extensively in this respect. The interest in magnetic multilayers increased dramatically with the discovery by Grünberg *et al*. (1986) that nonmagnetic layers sandwiched between two ferromagnetic layers can give rise to oscillating ferromagnetic or antiferromagnetic coupling between the ferromagnetic layers depending on the thickness of the nonmagnetic layer (Grünberg *et al*., 1986). Especially the antiferromagnetically coupled multilayers were studied extensively because of the observation of giant magnetoresistance (Baibich *et al*., 1988), which in the meantime has become a key ingredient for many magnetotransport applications (Daugthon, Pohm, Fayfield and Smith, 1999). At the same time antiferromagnetically coupled multilayers are of great basic science interest, since they can be used as model systems for understanding antiferromagnetic behavior in general (Wang *et al*., 1994). Domains in these synthetic antiferromagnetic systems are important for technology driven as well as fundamental science, since the domains may give rise to noise in applications (Hardner, Weissman and Parkin, 1995) and at the same time domains in antiferromagnetic systems have been less studied, as discussed in Section 3.1. Nevertheless, antiferromagnetic coupling may also have beneficial effects for applications, since it can be used for reducing the switching field relative to the thermal stability in antiferromagnetically coupled magnetic recording media (McFayden, Fullerton and Carey, 2006).

Note that in these coupled multilayer systems, there are other possible coupling mechanisms, besides the interlayer exchange coupling. Both structural and magnetic inhomogeneities can result in interlayer coupling. Stray fields due to interface roughness can result in so-called orange peel coupling (Néel, 1962). Similarly stray fields from domains walls can couple the magnetization structure in different ferromagnetic layers (Fuller and Sullivan, 1962; Thomas *et al*., 2000a; Lew *et al*., 2003).

Both polarized neutron (Huang, Felcher and Parkin, 1991; Hahn *et al*., 1994; Borchers *et al*., 1996, 1999; Langridge *et al*., 2000; Nagy *et al*., 2002) as well as X-ray resonant scattering (Idzerda, Chakarian and Freeland, 1999; Spezziani *et al*., 2002; Nefedov *et al*., 2005) have contributed considerably to the present understanding of domains in synthetic antiferromagnetic systems. By analyzing diffuse reflectivity around either the chemical superlattice Bragg reflection or the half-order (antiferromagnetic) Bragg reflections it is possible to obtain information about the ferromagnetically and antiferromagnetically coupled domains respectively (see also Section 2.3).

The first observation of domains in antiferromagnetically coupled multilayers with polarized neutron reflectometry was by Huang, Felcher and Parkin (1991) who studied the Co/Ru system and determined the average domain size to $L_x \approx 4\,\mu$m. Similarly the domain structure was also investigated in Co/Cu (Borchers *et al*., 1999; Langridge *et al*., 2000; Spezziani *et al*., 2002), Fe/Cr (Hahn *et al*., 1994; Nagy *et al*., 2002; Nefedov *et al*., 2005), and $Ni_{80}Fe_{20}$/Ag (Borchers *et al*., 1996) multilayers. In the Co/Cu system it was observed that for the as-prepared samples the domain structures in individual ferromagnetic layers are correlated. However, after subsequent magnetization reversal the domains are uncorrelated (Borchers *et al*., 1999; Langridge *et al*., 2000). This explains directly an experimentally observed decrease of magnetoresistance between the virgin and other remnant configurations. In general, the domain structure in these artificial antiferromagnetic systems is very sensitive to the magnetic history (Hardner, Weissman and Parkin, 1995; Nagy *et al*., 2002). When the domains nucleate after saturation their formation is mostly governed by the competition between Zeeman energy and antiferromagnetic interlayer coupling. This competition can give rise to very small domains ($<1\,\mu$m). On the other hand, during the bulk spin flop, the magnetocrystalline anisotropy becomes very important, resulting in much larger domains ($>10\,\mu$m) (Nagy *et al*., 2002).

Not only the domain structures, but also the domain walls in antiferromagnetically coupled multilayers offer rich research opportunities. This was demonstrated by Hellwig, Berger, and Fullerton (2003) in antiferromagnetically coupled multilayers with perpendicular anisotropy, such that the magnetization is preferentially perpendicular to the interfaces. In this case dipolar interactions also become important and their relative strength with respect to the antiferromagnetic interlayer coupling can be tuned by varying the ferromagnetic layer thickness. Interestingly as long as the antiferromagnetic coupling clearly dominated, the domain walls always had no net magnetization. But when the dipolar coupling became large enough then the domain wall developed a

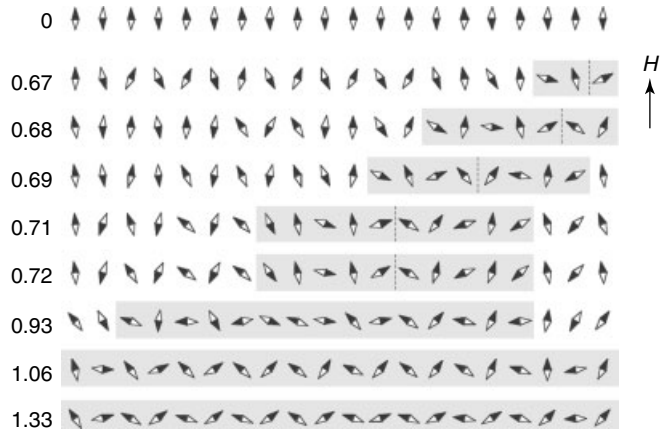

Figure 15. Magnetization direction of each Fe layer in an antiferromagnetically coupled Fe/Cr superlattice as determined with polarized neutron reflectometry. The compass needles indicate the relative direction of the magnetizations in each ferromagnetic layer of the superlattice. The applied fields indicated on the left are normalized by the bulk spin-flop field. (Reprinted figure from *Phys. Rev. Lett.* Vol. 89, 127203 (2002). © 2002 by the American Physical Society.)

striped pattern, by having the domain wall shifted in each ferromagnetic layer. Whether such complex domain walls occur in real antiferromagnets is still an interesting open question.

Besides domain walls, there is another interesting inhomogeneous magnetization structure in synthetic antiferromagnets related to the so-called surface spin flop. As mention in Section 3.1, antiferromagnetic materials can react to an external applied field with a spin-flop transition, where the spins rotate mostly perpendicular to the anisotropy axis. It was realized early on that this transition can be modified at the surface of an antiferromagnet (Mills, 1968; Keffer and Chow, 1973). The experimental verification of this effect was possible only through the use of antiferromagnetically coupled multilayers as model systems for finite antiferromagnets (Wang *et al*., 1994). The actual depth profile of the surface spin flop as a function of applied field has been shown with polarized neutron reflectometry (te Velthuis, Jiang, Bader and Felcher, 2002). Specifically at the surface spin flop, the magnetization of the topmost layers reverses, which gives rise to two antiphase domains as a function of depth into the multilayer. This domain wall moves with increasing field into the center of the superlattice and acts as a nucleation site for the subsequent bulk spin-flop transition (see Figure 15). Furthermore lateral domains can complicate the surface spin-flop effect (Lauter-Pasyuk *et al*., 2002).

The example of the surface spin flop shows that complex noncollinear magnetization structures can occur in multilayers consisting of ferromagnetic layers separated by nonmagnetic spacers because of the intricate balance between different interactions. It should also be noted that noncollinear magnetization structures can be established intentionally during the fabrication of these multilayers. For example, Felcher *et al*. (1998) showed that a helical magnetization structure can be imprinted if the superlattice structure is grown in a continuously rotating field.

3.3.2 Exchange bias

Another extensively studied type of coupled magnetic heterostructures are exchange bias systems (Nogués and Schuller, 1999; Nogués *et al*., 2005). Exchange bias systems were first discovered by Meiklejohn and Bean (1956) and consist of antiferro- and ferromagnetic materials where the coupling between the two gives rise to a symmetry-breaking unidirectional anisotropy resulting in hysteresis loops, which are asymmetrically shifted with respect to the field axis (Meiklejohn and Bean, 1956). This hysteresis loop can be understood intuitively by assuming that the ferromagnet couples only to one sublattice of the antiferromagnet, which remains essentially unaffected by an external field because of the vanishing net magnetization of the antiferromagnet. While this naive model works quantitatively for model systems, which mimic this situation (Jiang *et al*., 2000), it fails to capture many details quantitatively for most real exchange bias systems. In particular the observed loop shift is often several orders of magnitude smaller than theoretically expected (Tsang, Heiman and Lee, 1981). At the same time, exchange bias is observed in systems where the nominal interface of the antiferromagnet is being compensated (Nogués and Schuller, 1999). In this case one would expect that the ferromagnet couples equally to all antiferromagnetic sublattices and thus there should be no net coupling and thus no symmetry breaking. Both observations, the relatively small hysteresis loop shift and the observed bias for compensated antiferromagnetic surfaces, can be possibly reconciled by assuming domains in the antiferromagnet. Domains in the antiferromagnet would reduce the net moment at an uncompensated surface, and at the same time they could generate a net moment at a nominally compensated surface. In either case the bias shift is generally believed to result from a net magnetic moment in the antiferromagnet at the interface. In fact such net magnetizations have been observed recently with polarized neutron reflectometry (Hoffmann *et al*., 2002; Roy *et al*., 2005) and X-ray resonant scattering (Roy *et al*., 2005). Furthermore it has been shown there is a direct correlation between exchange bias and uncompensated spins in the antiferromagnet (Takano *et al*., 1997).

One of the first quantitative theoretical models investigating the role of lateral domains in the antiferromagnet was proposed by Malozemoff (1987). In his model the finite size of the antiferromagnetic domains results in a net moment

simply from a statistical imbalance between the two sublattices. This statistical argument suggests that smaller antiferromagnetic domains give rise to a larger net magnetization per interface area. However, there is so far no direct experimental confirmation of a correlation between exchange bias magnitude and sizes of antiferromagnetic domains.

Another possibility for inhomogeneous magnetization structures in the antiferromagnet of exchange bias structures are domain walls parallel to the interface of the ferromagnet (Mauri, Siegmann, Bagus and Kay, 1987; Stiles and McMichael, 1999), which is very similar to the behavior observed in exchange spring systems discussed further below. Indeed, recent measurements with resonant X-ray reflectivity and polarized neutron reflectivity detected directly such a domain wall parallel to the interface in the uncompensated magnetization of a strained FeF_2 antiferromagnet (Roy *et al*., 2005). However, in this case the domain wall does not necessarily originate from the reversal of the ferromagnetic magnetization, but from different response to external fields of uncompensated moments in the bulk and at the interface of the antiferromagnet. Similarly, Borchers *et al*. (2000) have shown that in Fe_3O_4/NiO the domains in the antiferromagnet depend sensitively on the cooling field, which furthermore underscores the importance of domains in exchange bias systems.

Besides the aforementioned direct observation of domains and domain walls in the antiferromagnet of exchange bias systems, there is also additional indirect evidence of the importance of antiferromagnetic domains. Keller *et al*. (2002) investigated exchange bias as a function of nonmagnetic impurities in the antiferromagnet. They observed that the exchange bias can increase for a moderate concentration of impurities, which could stabilize smaller domains, hence resulting in a larger net moment that couples to the ferromagnet (Nowak *et al*., 2002). However, the situation is more complex, since the precise interfacial microstructure is also very important for determining the influence of impurities in the antiferromagnet on the experimentally observed exchange bias (Shi *et al*., 2003).

Aside from the magnitude of the exchange bias shift, the domain structure in the antiferromagnet may also influence the direction of the shift. Normally the exchange bias shift has the opposite sign of the applied field during field cooling (Nogués and Schuller, 1999). However, a few selected exchange bias systems can exhibit a positive exchange bias shift upon field cooling in very large magnetic fields (Nogués, Lederman, Moran and Schuller, 1996). This crossover from negative to positive exchange bias has been investigated by Kirk, Hellwig, and Fullerton (2002) in model structures based on coupled Co/Pt multilayers, where one of the multilayers was exchange biased by a CoO layer. Interestingly the transition from conventional negative exchange bias to positive exchange bias depends sensitively of the domain structure in the layer responsible for the exchange bias. If the domains in the biasing layer are smaller than those in the biased layer the exchange bias shift changes continuously from negative to positive values. However, if the domains in the biasing layer are larger than typical domains in the biased layer, then the hysteresis loop can become bifurcated with part of the hysteresis loop being biased positively, while the other part is biased negatively. A similar behavior has also recently been observed in a real exchange bias system (Roshchin *et al*., 2005).

Aside from domains in the antiferromagnet, domains in the ferromagnet can also play an important role for exchange bias systems. Some of the unusual aspects of exchange bias systems, such as asymmetries in the magnetization reversal and training effects, can be connected to ferromagnetic domain formation. Using polarized neutron reflectometry Fitzsimmons *et al*. have shown that the magnetization reversal on either side of the hysteresis loops for Fe/Mn_2F (Fitzsimmons *et al*., 2000, 2001) and Fe/Fe_2F (Fitzsimmons *et al*., 2002) can be different, such that with decreasing field the reversal is mostly via a coherent rotation of the magnetization, while for increasing fields the reversal proceeds via domain nucleation and domain-wall motion. More recently it has been shown that this asymmetry in magnetization reversal is a more general consequence due to the competition between different anisotropies in exchange bias systems (Camarero *et al*., 2005). Another unusual property of many exchange bias systems is that after the initial field cooling procedure subsequent hysteresis loops may differ from each other with successively decreasing exchange bias (Hoffmann, 2004). It has been observed that the change in hysteretic behavior is also correlated with domain formation in the ferromagnetic layer (Lee *et al*., 2002; Gierlings *et al*., 2002; Radu *et al*., 2003). For example, Lee *et al*. (2002) observed that domains are differently oriented during different reversals and Radu *et al*. (2003) suggest that after the first reversal interfacial domains form, which remain unchanged during the subsequent reversals. It also should be noted that locally varying exchange coupling can give rise to complex domain structures (Gogol, Chapman, Gilles and Vanhelmont, 2002).

So far we discussed the naturally occurring domains in the ferromagnet. Another aspect of exchange bias systems is that the ferromagnetic layer can be prepared in a well-defined domain configuration in the unbiased state (typically at high temperature), which can be subsequently imprinted into the antiferromagnetic layer. If there are only domains with opposite magnetization orientations, then this can result in two separately shifted subloops (Chien *et al*., 2003). A similar situation exists, when the antiferromagnet owing to its crystalline orientation projects out laterally different field components (Roshchin *et al*., 2005). This idea of

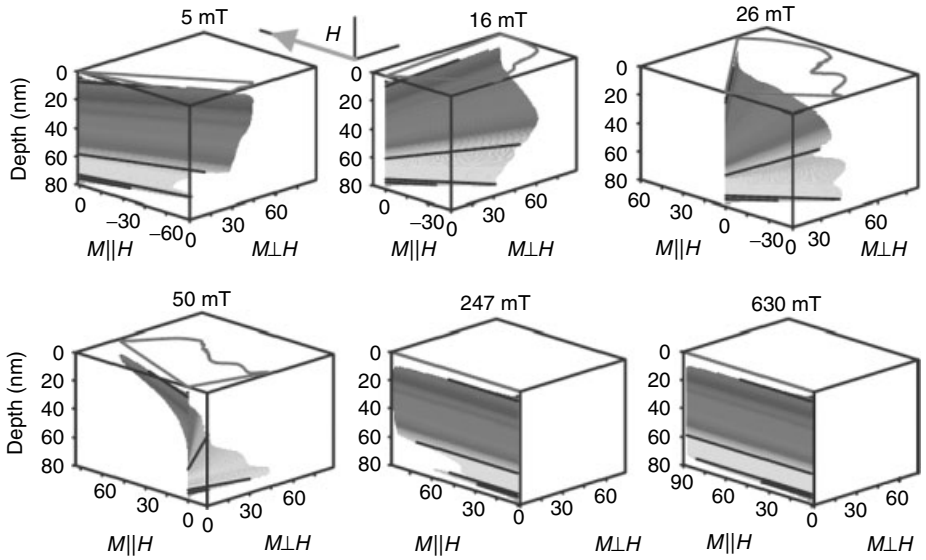

Figure 16. Twist of the magnetization in exchange spring system consisting of a hard magnetic FePt layer (up to the third line from the bottom) and a soft magnetic NiFe layer (upper layers). (Reprinted figure from *Phys. Rev. Lett.* Vol. 88, 067201 (2002). © 2002 by the American Physical Society.)

imprinting magnetization structures can also be utilized to fine tune the shapes of hysteresis loops (Brück *et al*., 2005). More recently, it has also shown that other inhomogeneous magnetization states, such as magnetic vortex states, can be faithfully imprinted into the antiferromagnet (Sort *et al*., 2006a,b).

3.3.3 Exchange spring

Another system of coupled magnetic heterostructures with potential technological applications are exchange spring systems, consisting of coupled hard and soft ferromagnetic materials (Kneller and Hawig, 1991; Fullerton, Jiang and Bader, 1999). For permanent magnet applications the figure of merit is typically the energy product $(BH)_{\max}$, which generally increases with increasing coercivity and increasing saturation magnetization. However, in general, hard magnetic materials have a high anisotropy (thus large coercivity), but relatively low saturation magnetization. At the same time soft-magnetic materials can have a very large saturation magnetization, but typically have a rather low anisotropy. Using hard–soft coupled systems offer the promise of combining the best features of both materials, leading to more powerful permanent magnets.

The limit for improving the energy product in exchange spring systems is determined by how much the interfacial coupling dominates the magnetization behavior of the soft-magnetic component. Once the soft-magnetic layers are thicker than the exchange layer (typically $\approx$10 nm) they can develop a twisted magnetization structure, where the magnetization at the interface is closely aligned with the hard-layer magnetization but away from the interface the magnetization rotates continuously toward the applied magnetic field. Such a twist has been directly observed with polarized neutron reflectometry for $Fe_{55}Pt_{45}/Ni_{80}F_{20}$ bilayer (see Figure 16) (O'Donovan *et al*., 2002). In this particular measurement, the magnetization structure was obtained with high accuracy by combining reflectivity spectra from the front- and backside of the sample, which adds additional constraints to the possible models for fitting the data. Notice that the domain wall extends actually both into the soft and hard magnetic layer.

While the basic behavior of exchange springs can be understood within simple models describing inhomogeneous magnetizations perpendicular to the hard/soft interface, lateral domains may influence the detailed magnetization behavior. For example, in general one would expect only ferromagnetic coupling between the two ferromagnetic constituents of an exchange spring system. However, Vlasko-Vlasov *et al*. (2001) showed that exchange spring systems can also have a biquadratic coupling, meaning that the magnetization in the soft-magnetic layer has a preferred orientation perpendicular to the easy axis of the hard magnetic layer. This effect originates from domains in the hard magnetic layer. In the case of a uniaxial hard magnetic system a partial magnetization reversal of the hard-layer magnetization results in domains with opposite magnetizations. Owing to the high anisotropy, the domains in the hard magnetic layer are in general much smaller than the domains in the soft-magnetic layer. Thus one single soft domain may couple to

multiple hard domains with opposite magnetization. This situation gives rise to a frustration of the interfacial interactions, which then results in the observed biquadratic coupling.

More recent developments show various different interesting aspects of exchange spring systems. For example, contrary to common intuition, a sharp interface between the hard and soft materials does not result in the highest possible energy product. Jiang *et al*. (2004) showed that an intentionally interdiffused (i.e., graded) interface can enhance the energy product, since the field range of reversible magnetization change is significantly extended. Another recent development is an increased interest in lateral exchange spring structures, where the interfacial domain walls change from the Bloch to the Néel type (see also Section 3.1 and Figure 11). The different magnetostatic energies can modify the behavior significantly and depending on the competition between the different interactions there can be the formation of opposite domains or a more coherent magnetization reversal (Fraile Rodríguez *et al*., 2006). Lastly, exchange springs also generated interest for applications beyond the hard magnetic materials, for which they were initially investigated. One new application idea is to use exchange springs, which contain a component with a metamagnetic transition, as possible magnetic recording media, where the switching field can be dramatically reduced by heating past the metamagnetic transition (Thiele, Maat and Fullerton, 2003; Guslienko *et al*., 2004).

3.3.4 Ferromagnet/superconductor hybrids

The last coupled systems to be discussed are ferromagnetic/superconducting hybrids. The interaction between ferromagnets and superconductors has generated a lot of research interest over the years, since the two types of magnetic order are generally mutually exclusive (for a recent review see Lyuksyutov and Pokorovsky, 2005). Their interplay can generate a variety of interesting effects, such as strong vortex pinning (Otani, Pannetier, Nozières and Givord, 1993; Martín, Vélez, Nogués and Schuller, 1997; Morgan and Ketterson, 1998; Van Bael, Temst, Moshchalkov and Bruynseraede, 1999; Martín *et al*., 1999; Hoffmann, Prieto and Schuller, 2000), π phase (Radovic *et al*., 1991; Ryazanov *et al*., 2001), and triplet (Volkov, Bergeret and Efetov, 2003) superconductivity, variations in the superconducting transition temperature (Jiang, Davidovic, Reich and Chien, 1995; Gu *et al*., 2002), and giant magnetoresistance (Peña *et al*., 2005). Most studies ignore the influence of magnetic domain structures or specifically prepare systems with single-domain magnetizations. Nevertheless, there are a few investigations, which specifically target the influence of magnetic domain structures on the superconducting properties of superconducting/ferromagnetic hybrids. Van Bael, Temst, Moshchalkov and Bruynseraede (1999) showed that vortex pinning is stronger for patterned ferromagnetic particles with in-plane single-domain state versus flux-closure state, indicating that the stray field is important. The situation is different for systems where the magnetization of the ferromagnet is perpendicular to the layer, and thus perpendicular to the interface with the superconductor. In this case the formation of a domain state increases the magnetic fields penetrating the superconductor and thus can give rise to increased vortex pinning (Lange, Van Bael, Moshchalkov and Bruynseraede, 2002). However, at the same time the stray field from the magnetic domains can also significantly reduce the superconducting transition temperature (Lange, Van Bael and Moshchalkov, 2003). More recent investigations of Nb thin films grown on ferromagnetic $BaFe_{12}O_{19}$ substrates indicate that the interplay between ferromagnetic domains and superconductivity can be even more complex, resulting in nonmonotonic variations of the superconducting transition temperature as a function of applied magnetic fields (Yang *et al*., 2004). This behavior has been interpreted as evidence for theoretically predicted nucleation of superconductivity at the ferromagnetic domain walls (Aladyshkin *et al*., 2003). Interestingly, so far there has been less investigation into the question how the proximity of a superconductor influences magnetic domain formation. In principle one could expect a strong influence, since the presence of a superconductor changes considerably the magnetostatic energies, which are ultimately often the driving force for domain formation.

4 SUMMARY

From the very beginning of neutron scattering investigations, magnetic materials have been one of the main subjects studied, since neutron scattering is uniquely suited for obtaining atomic-scale magnetic structure. In this chapter we provided an overview about how neutron scattering can also be utilized to obtain information about larger-scale magnetic structures, in particular, magnetic domains. Information about the size, orientation, and population of domains can be determined by neutron diffraction, depolarization, or refraction. Furthermore, neutron scattering can also in principle provide insight about the correlations between domains, similar to its use for studying atomic-scale correlations. However, studies of domain correlations are still in its infancy, but are poised to become more important with the advent of the next generation neutron sources in the near future. Besides introducing the various techniques we also provided a brief overview about different current scientific issues, where magnetic domains play a central role and which lend themselves to neutron investigations. Such a selection of scientific problems from a broad field of research as magnetism has to

be naturally subjective and incomplete; thus we apologize for any oversights. Nevertheless, the examples shown in this chapter should illustrate the role of neutron refraction and scattering in determining magnetic domain states. We are quite confident that based on the solid foundation of the past work, neutrons will continue to play a major role in unraveling magnetic domain structures.

ACKNOWLEDGMENTS

Our research in this field and thus the preparation of this manuscript was financially supported by the US Department of Energy, Basic Energy Sciences, under Contract No. DE-AC02-06CH11357.

REFERENCES

Aladyshkin, A.Y., Budzin, A.I., Fraerman, A.A., *et al*. (2003). Domain-wall superconductivity in hybrid superconductor-ferromagnet structures. *Physical Review B*, **68**, 184508.

Allenspach, R. (1994). Ultrathin films: magnetism on the microscopic scale. *Journal of Magnetism and Magnetic Materials*, **129**, 160–185.

Bacon, G.E. (1975). *Neutron Diffraction*, Clarendon Press: Oxford.

Badurek, G., Buchelt, R.J., Leeb, H. and Szeywerth, R. (2003). Neutron interferometric reconstruction of magnetic domain structures. *Physica B*, **335**, 114–118.

Baibich, M.N., Bobo, J.M., Fert, A., *et al*. (1988). Giant magnetoresistance of (001)Fe/(001)Cr magnetic superlattices. *Physical Review Letters*, **61**, 2472–2475.

Baruchel, J., Schlenker, M. and Barbara, B. (1980). 180 antiferromagnetic domains in MnF_2 by neutron topography. *Journal of Magnetism and Magnetic Materials*, **15–18**, 1510–1512.

Berger, L. (1978). Low-field magnetoresistance and domain drag in ferromagnets. *Journal of Applied Physics*, **49**, 2156–2161.

Berger, L. (1984). Exchange interaction between ferromagnetic domain wall and electric current in very thin metallic films. *Journal of Applied Physics*, **55**, 1954–1956.

Birss, R.R. (1964). *Symmetry and Magnetism*, North Holland: Amsterdam.

Bitter, F. (1931). On inhomogeneities in the magnetization of ferromagnetic materials. *Physical Review*, **38**, 1903–1905.

Bloch, F.E. (1932). Zur theorie des austauschproblems und der remanenzerscheinung der ferromagnetika. *Zeitschrift für Physik A Hadrons and Nuclei*, **74**, 295–335.

Blume, M. (1963). Polarization effects in the magnetic elastic scattering of slow neutrons. *Physical Review*, **130**, 1670–1676.

Borchers, J.A., Dura, J.A., Unguris, J., *et al*. (1999). Observation of antiparallel magnetic order in weakly coupled Co/Cu multilayers. *Physical Review Letters*, **82**, 2796–2799.

Borchers, J.A., Gehring, P.M., Erwin, R.W., *et al*. (1996). Antiferromagnetic interlayer correlations in annealed $Ni_{80}Fe_{20}$/Ag multilayers. *Physical Review B*, **54**, 9870–9882.

Borchers, J.A., Ijiri, Y., Lind, D.M., *et al*. (2000). Detection of field-dependent antiferromagnetic domains in exchange-biased Fe_3O_4/NiO superlattices. *Applied Physics Letters*, **77**, 4187–4189.

Borovik-Romanov, A.S. (1960). Piezomagnetism in antiferromagnetic cobalt and manganese fluorides. *Soviet Physics JETP*, **11**, 786–793.

Brown, P.J., Forsyth, J.B. and Tasset, F. (1993). Neutron polarimetry. *Proceedings of the Royal Society London, Series A*, **442**, 147–160.

Brück, S., Sort, J., Baltz, V., *et al*. (2005). Exploiting length scales of exchange-bias systems to fully tailor double-shifted hysteresis loops. *Advanced Materials*, **17**, 2978–2983.

Buchanan, K.S., Roy, P.E., Grimsditch, M., *et al*. (2005). Soliton-pair dynamics in patterned ferromagnetic ellipses. *Nature Physics*, **1**, 172–176.

Camarero, J., Sort, J., Hoffmann, A., *et al*. (2005). Origin of the asymmetric magnetization reversal behavior in exchange-biased systems: competing anisotropies. *Physical Review Letters*, **95**, 057204.

Castaño, F.J., Ross, C.A., Frandsen, C., *et al*. (2003). Metastable states in magnetic nanorings. *Physical Review B*, **67**, 184425.

Chappert, C., Bernas, H., Ferre, J., *et al*. (1998). Planar patterned magnetic media obtained by ion irradiation. *Science*, **280**, 1919–1922.

Chien, C.L., Gornakov, V.S., Nikitenko, V.I., *et al*. (2003). Hybrid domain walls and antiferromagnetic domains in exchange-coupled ferromagnet/antiferromagnet bilayers. *Physical Review B*, **68**, 014418.

Choe, S-B., Acremann, Y., Scholl, A., *et al*. (2004). Vortex core-driven magnetization dynamics. *Science*, **304**, 420–422.

Costa-Krämer, J.L., Guerrero, C., Melle, S., *et al*. (2003). Pure magneto-optic diffraction by a periodic domain structure. *Nanotechnology*, **14**, 239–244.

Cowburn, R.P., Adeyeye, A.O. and Bland, J.A.C. (1997). Magnetic domain formation in lithographically defined antidot permalloy arrays. *Applied Physics Letters*, **70**, 2309–2311.

Cowburn, R.P., Koltsov, D.K., Adeyeye, A.O., *et al*. (1999). Single-domain circular nanomagnets. *Physical Review Letters*, **83**, 1042–1045.

Dagotto, E., Hotta, T. and Moreo, A. (2001). Colossal magnetoresistant materials: the key role of phase separation. *Physics Reports*, **344**, 1–153.

Daugthon, J.M., Pohm, A.V., Fayfield, R.T. and Smith, C.H. (1999). Applications of spin dependent transport materials. *Journal of Physics D: Applied Physics*, **32**, R169–R177.

Davies, J.E., Hellwig, O., Fullerton, E.E., *et al*. (2004). Magnetization reversal of Co/Pt multilayers: microscopic origin of high-field magnetic irreversibility. *Physical Review B*, **70**, 224434.

Ding, H.F., Wulfhekel, W. and Kirschner, J. (2002). Ultra sharp domain walls in the closure domain pattern of Co(0001). *Europhysics Letters*, **57**, 100–106.

Duden, T. and Bauer, E. (1996). Magnetization wrinkle in thin ferromagnetic films. *Physical Review Letters*, **77**, 2308–2311.

Eremenko, V.V., Kharchenko, N.F. and Beliy, L.I. (1979). Visualization of the 180-degree antiferromagnetic domains by means of new magnetooptical effect. *Journal of Applied Physics*, **50**, 7751–7753.

Evans, P.G., Isaacs, E.D., Aeppli, G., *et al*. (2002). X-ray microdiffraction images of antiferromagnetic domain evolution in chromium. *Science*, **295**, 1042–1045.

Fassbender, J., Ravelosona, D. and Samson, Y. (2004). Tailoring magnetism by light-ion irradiation. *Journal of Physics D*, **37**, R179–R196.

Felcher, G.P. and Kleb, R. (1996). Antiferromagnetic domains and the spin-flop transition of MnF_2. *Europhysics Letters*, **36**, 455–460.

Felcher, G.P., Lohstroh, W., Fritzsche, H., *et al*. (1998). Imprinting magnetic structures. *Applied Physics Letters*, **72**, 2894–2896.

Fermon, C., Ott, F., Gilles, B., *et al*. (1999). Towards a 3D magnetometry by neutron reflectometry. *Physica B*, **267–268**, 162–167.

Fitzsimmons, M.R., Bader, S.D., Borchers, J.A., *et al*. (2004). Neutron scattering studies of nanomagnetism and artificially structured materials. *Journal of Magnetism and Magnetic Materials*, **271**, 103–146.

Fitzsimmons, M.R., Leighton, C., Hoffmann, A., *et al*. (2001). Influence of interfacial disorder and temperature on magnetization reversal in exchange-coupled bilayers. *Physical Review B*, **64**, 104415.

Fitzsimmons, M.R., Leighton, C., Nogués, J., *et al*. (2002). Influence of in-plane crystalline quality of an antiferromagnet on perpendicular exchange coupling and exchange bias. *Physical Review B*, **65**, 134436.

Fitzsimmons, M.R., Yashar, P., Leighton, C., *et al*. (2000). Asymmetric magnetization reversal in exchange-biased hysteresis loops. *Physical Review Letters*, **84**, 3986–3989.

Foner, S. (1963). Antiferromagnetic and ferromagnetic resonance. In *Magnetism*, Rado, G. and Suhl, H. (Eds.), Academic Press: New York, pp. 384–447, Vol. 1.

Fraile Rodríguez, A., Heyderman, L.J., Nolting, F., *et al*. (2006). Permalloy thin films exchange coupled to arrays of cobalt islands. *Applied Physics Letters*, **89**, 142508.

Frandsen, C., Bahl, C.R.H., Lebech, B., *et al*. (2005). Oriented attachment and exchange coupling of α-Fe_2O_3 nanoparticles. *Physical Review B*, **72**, 214406.

Fuller, H.W. and Sullivan, D.L. (1962). Magnetostatic interactions between thin magnetic films. *Journal of Applied Physics*, **33**, 1063–1064.

Fullerton, E.E., Jiang, J.S. and Bader, S.D. (1999). Hard/soft magnetic heterostructures: model exchange-spring magnets. *Journal of Magnetism and Magnetic Materials*, **200**, 392–404.

Gan, L., Chung, S.H., Aschenbach, K.H., *et al*. (2000). Pulsed-current-induced domain wall propagation in permalloy patterns observed using magnetic force microscope. *IEEE Transactions on Magnetics*, **36**, 3047–3049.

Garel, T. and Doniach, S. (1982). Phase transitions with spontaneous modulation–the dipolar Ising ferromagnet. *Physical Review B*, **26**, 325–329.

Gierlings, M., Prandolini, M.J., Fritsche, H., *et al*. (2002). Change and asymmetry of magnetization reversal for a Co/CoO exchange-bias system. *Physical Review B*, **65**, 092407.

Gogol, P., Chapman, J.N., Gilles, M.F. and Vanhelmont, F.W.M. (2002). Domain processes in the magnetization reversal of exchange-biased IrMn/CoFe bilayers. *Journal of Applied Physics*, **92**, 1458–1465.

Grünberg, P., Schreiber, R., Pang, Y., *et al*. (1986). Layered magnetic structures: evidence for antiferromagnetic coupling of Fe layers across Cr interlayers. *Physical Review Letters*, **57**, 2442–2445.

Gu, J.Y., You, C-Y., Jiang, J.S., *et al*. (2002). Magnetization-orientation dependence of the superconducting transition temperature in the ferromagnet-superconductor-ferromagnet system: CuNi/Nb/CuNi. *Physical Review Letters*, **89**, 266805.

Guslienko, K.Y., Chubykalo-Fesenko, O., Myrasov, O., *et al*. (2004). Magnetization reversal via perpendicular exchange spring in FePt/FeRh bilayer films. *Physical Review B*, **70**, 104405.

Guslienko, K.Y., Han, X.F., Keavney, D.J., *et al*. (2006). Magnetic vortex core dynamics in cylindrical ferromagnetic dots. *Physical Review Letters*, **96**, 067205.

Hahn, W., Loewenhaupt, M., Felcher, G.P., *et al*. (1994). Fe/Cr multilayers: effect of annealing on the spin structure and magnetoresistance. *Journal of Applied Physics*, **75**, 3564–3570.

Hardner, H.T., Weissman, M.B. and Parkin, S.S.P. (1995). History dependent domain structures in giant-magnetoresistive multilayers. *Applied Physics Letters*, **67**, 1938–1940.

Hellwig, O., Berger, A. and Fullerton, E.E. (2003). Domain walls in antiferromagnetically coupled multilayer films. *Physical Review Letters*, **91**, 197203.

Henry, Y., Ounadjela, K., Piraux, L., *et al*. (2001). Magnetic anisotropy and domain patterns in electrodeposited cobalt nanowires. *European Physics Journal B*, **20**, 35–54.

Hoffmann, A. (2004). Symmetry driven irreversibilities at ferromagnetic-antiferromagnetic interfaces. *Physical Review Letters*, **93**, 097203.

Hoffmann, A., Prieto, P. and Schuller, I.K. (2000). Periodic vortex pinning with magnetic and nonmagnetic dots: the influence of size. *Physical Review B*, **61**, 6958–6965.

Hoffmann, A., Seo, J.W., Fitzsimmons, M.R., *et al*. (2002). Induced magnetic moments at a ferromagnet-antiferromagnet interface. *Physical Review B*, **66**, 220406(R).

Huang, Y.Y., Felcher, G.P. and Parkin, S.S.P. (1991). Antiferromagnetic and ferromagnetic order in Co/Ru multilayers. *Journal of Magnetism and Magnetic Materials*, **99**, L31–L38.

Hubert, A. and Schäfer, R. (1998). *Magnetic Domains*, Springer-Verlag: Berlin.

Hughes, D.J., Burgy, M.T., Heller, R.B. and Wallace, J.W. (1949). Magnetic refraction of neutrons at domain boundaries. *Physical Review*, **75**, 565–569.

Idzerda, Y.U., Chakarian, V. and Freeland, J.W. (1999). Quantifying magnetic domain correlations in multilayer films. *Physical Review Letters*, **82**, 1562–1565.

Jiang, J.S., Davidovic, D., Reich, D.H. and Chien, C.L. (1995). Oscillatory superconducting transition temperature in Nb/Gd multilayers. *Physical Review Letters*, **74**, 314–317.

Jiang, J.S., Felcher, G.P., Inomata, A., *et al*. (2000). Exchange-bias effect in Fe/Cr(211) double superlattice structures. *Physical Review B*, **61**, 9653–9656.

Jiang, J.S., Pearson, J.E., Liu, Z.Y., *et al*. (2004). Improving exchange-spring nanocomposite permanent magnets. *Applied Physical Letters*, **85**, 5293–5295.

Keffer, F. and Chow, H. (1973). Dynamics of the antiferromagnetic spin-flop transition. *Physical Review Letters*, **31**, 1061–1063.

Keller, J., Miltényi, P., Beschoten, B., *et al*. (2002). Domain state model for exchange bias. II. Experiments. *Physical Review B*, **66**, 014431.

Kirk, T.L., Hellwig, O. and Fullerton, E.E. (2002). Coercivity mechanisms in positive exchange-biased Co films and Co/Pt multilayers. *Physical Review B*, **65**, 224626.

Kittel, C. (1949). Physical theory of ferromagnetic domains. *Review of Modern Physics*, **21**, 541–583.

Kleemann, W. (1993). Random-field induced antiferromagnetic, ferroelectric and structural domain states. *International Journal of Modern Physics B*, **7**, 2469–2507.

Kneller, E.F. and Hawig, R. (1991). The exchange-spring magnet: a new material principle for permanent magnets. *IEEE Transactions on Magnetics*, **27**, 3588–3560.

Kortright, J.B., Awschalom, D.D., Stöhr, J., *et al*. (1999). Research frontiers in magnetic materials at soft X-ray synchrotron radiation facilities. *Journal of Magnetism and Magnetic Materials*, **207**, 7–44.

Landau, L. and Lifshitz, E. (1935). On the theory of the dispersion of magnetic permeability in ferromagnetic bodies. *Physikalische Zeitschrift der Sowjetunion*, **8**, 153–169.

Lange, M., Van Bael, M.J. and Moshchalkov, V.V. (2003). Phase diagram of a superconductor/ferromagnet bilayer. *Physical Review B*, **68**, 174522.

Lange, M., Van Bael, M.J., Moshchalkov, V.V. and Bruynseraede, Y. (2002). Magnetic-domain-controlled vortex pinning in a superconductor/ferromagnet bilayer. *Applied Physics Letters*, **81**, 322–324.

Langridge, S., Schmalian, J., Marrows, C.H., *et al*. (2000). Quantification of magnetic domain disorder and correlations in antiferromagnetically coupled multilayers by neutron reflectometry. *Physical Review Letters*, **85**, 4964–4967.

Lauter-Pasyuk, V., Lauter, H.J., Toperverg, B.P., *et al*. (2002). Transverse and lateral structure of the spin-flop phase in Fe/Cr antiferromagnetic superlattices. *Physical Review Letter*, **89**, 167203.

Leaf, G., Kaper, H., Yan, M., *et al*. (2006). Dynamic origin of stripe domains. *Physical Review Letters*, **96**, 017201.

Lee, D.R., Srajer, G., Fitzsimmons, M.R., *et al*. (2003). Polarized neutron scattering from ordered magnetic domains on a mesoscopic permalloy antidot array. *Applied Physics Letters*, **82**, 82–84.

Lee, W-T., te Velthuis, S.G.E., Felcher, G.P., *et al*. (2002). Ferromagnetic domain distribution in thin films during magnetization reversal. *Physical Review B*, **65**, 224417.

Lekner, J. (1987). *Theory of Reflection*, Martinus Nijhoff Publishers: Dordrecht.

Lew, W.S., Li, S.P., Lopez-Diaz, L., *et al*. (2003). Mirror domain structures induced by interlayer magnetic wall coupling. *Physical Review Letters*, **90**, 217201.

Li, S.P., Lee, W.S., Bland, J.A.C., *et al*. (2002). Microstructures–spin-engineering magnetic media. *Nature (London)*, **415**, 600–601.

Li, S.P., Peyrade, D., Natali, M., *et al*. (2001). Flux closure structures in cobalt rings. *Physical Review Letters*, **86**, 1102–1105.

Löffler, J.F., Braun, H-B. and Wagner, W. (2000). Magnetic correlations in nanostructured ferromagnets. *Physical Review Letters*, **85**, 1990–1993.

Lyuksyutov, I.F. and Pokorovsky, V.L. (2005). Ferromagnet-superconductor hybrids. *Advances in Physics*, **54**, 67–136.

Malozemoff, A.P. (1987). Random-field model of exchange anisotropy at rough ferromagnetic-antiferromagnetic interfaces. *Physical Review B*, **35**, 3679–3682.

Malozemoff, A.P. and Slonczewski, J.C. (1979). *Magnetic Domain Walls in Bubble Materials*, Academic Press: New York.

Martín, J.I., Vélez, M., Hoffmann, A., *et al*. (1999). Artificially induced reconfiguration of the vortex lattice by arrays of magnetic dots. *Physical Review Letters*, **83**, 1022–1025.

Martín, J.I., Vélez, M., Nogués, J. and Schuller, I.K. (1997). Flux pinning in a superconductor by an array of submicrometer magnetic dots. *Physical Review Letters*, **79**, 1929–1932.

Mauri, D., Siegmann, H.C., Bagus, P.S. and Kay, E. (1987). Simple model for thin ferromagnetic films exchange coupled to an antiferromagnetic substrate. *Journal of Applied Physics*, **62**, 3047–3049.

McCord, J., Gemming, T., Schultz, L., *et al*. (2005). Magnetic anisotropy and domain patterning of amorphous films by He-ion irradiation. *Applied Physics Letters*, **86**, 162502.

McFayden, I.R., Fullerton, E.E. and Carey, M.J. (2006). State-of-the-art magnetic hard disk drives. *MRS Bulletin*, **31**, 379–383.

Meiklejohn, W.H. and Bean, C.P. (1956). New magnetic anisotropy. *Physical Review*, **102**, 1413–1414.

Middlehoek, S. (1963). Domain walls in thin Ni-Fe films. *Journal of Applied Physics*, **34**, 1054–1059.

Mills, D.L. (1968). Surface spin-flop state in a simple antiferromagnet. *Physical Review Letters*, **20**, 18–21.

Mitsuda, S. and Endoh, Y. (1985). Neutron depolarization studies on magnetization process using pulsed polarized neutrons. *Journal of the Physical Society of Japan*, **54**, 1570–1580.

Moon, R.M., Riste, T. and Koehler, W.C. (1969). Polarization analysis of thermal-neutron scattering. *Physical Review*, **181**, 920–931.

Morgan, D.J. and Ketterson, J.B. (1998). Asymmetric flux pinning in a regular array of magnetic dipoles. *Physical Review Letters*, **80**, 3614–3617.

Morin, F.J. (1950). Magnetic susceptibility of α Fe_2O_3 and α Fe_2O_3 with added titanium. *Physical Review*, **78**, 819–820.

Nagy, D.L., Bottyán, L., Croonenborghs, B., *et al*. (2002). Coarsening of antiferromagnetic domains in multilayers: the key role

of magnetocrystalline anisotropy. *Physical Review Letters*, **88**, 1572002.

Néel, L. (1936). Propriétés magnétiques de l'état métallique et énergie d'interaction entre atomes magnétiques. *Annales de Physique (Paris)*, **5**, 232–279.

Néel, L. (1954). Ferro- and antiferromagnetism. In *Proceedings of the International Conference on Theoretical Physics*, Science Council of Japan: Kyoto, Tokyo, pp. 701–714.

Néel, L. (1962). Sur un nouveau mode de couplage entre les aimantations de deux couches minces ferromagnétiques. *Comptes Rendus de l'Académie des science*, **255**, 1676–1981.

Nefedov, A., Grabis, J., Bergmann, A., *et al*. (2005). X-ray resonant magnetic scattering by Fe/Cr superlattices. *Superlattices and Microstructure*, **37**, 99–106.

Nogués, J., Lederman, D., Moran, T.J. and Schuller, I.K. (1996). Positive exchange bias in FeF_2-Fe bilayers. *Physical Review Letters*, **76**, 4624–4627.

Nogués, J., Moran, T.J., Lederman, D., *et al*. (1999). Role of interface structure on exchange-biased FeF_2-Fe. *Physical Review B*, **59**, 6984–6993.

Nogués, J. and Schuller, I.K. (1999). Exchange bias. *Journal of Magnetism and Magnetic Materials*, **192**, 203–232.

Nogués, J., Sort, J., Langlais, V., *et al*. (2005). Exchange bias in nanostructures. *Physics Reports*, **422**, 65–117.

Nowak, U., Usadel, K.D., Keller, J., *et al*. (2002). Domain state model for exchange bias. I. Theory. *Physical Review B*, **66**, 014430.

O'Donovan, K.V., Borchers, J.A., Majkrzak, C.F., *et al*. (2002). Pinpointing chiral structures with front-back polarized neutron reflectometry. *Physical Review Letters*, **88**, 067201.

Offerman, S.E., van Dijk, N.H., Siestma, J., *et al*. (2002). Grain Nucleation and growth during phase transformations. *Science*, **298**, 1003–1005.

O'Handley, R.C. (2000). *Modern Magnetic Materials: Principles and Applications*, John Wiley & Sons Ltd: New York.

Opechowski, W. and Guccione, R. (1965). Magnetic Symmetry. In *Magnetism*, Rado, G.T. and Suhl, H. (Eds.), Academic Press: New York, pp. 105–165, Vol. 2a.

Otani, Y., Pannetier, B., Nozières, J.P. and Givord, D. (1993). Magnetostatic interactions between magnetic arrays and superconducting thin films. *Journal of Magnetism and Magnetic Materials*, **126**, 622–625.

Palmer, S.B. (1975). Antiferromagnetic domains in rare earth metals and alloys. *Journal of Physics F: Metal Physics*, **5**, 2370–2378.

Pannetier, M., Ott, F., Fermon, C. and Samson, Y. (2003). Surface diffraction on magnetic nanostructures in thin films using grazing incidence SANS. *Physica B*, **335**, 54–58.

Park, J.P., Eames, P., Engbretson, D.M., *et al*. (2003). Imaging of spin dynamics in closure domain and vortex structures. *Physical Review B*, **67**, 020403(R).

Peña, V., Sefrioui, Z., Arias, D., *et al*. (2005). Giant magnetoresistance in ferromagnet/superconductor superlattices. *Physical Review Letters*, **94**, 057002.

Perzlmaier, K., Buess, M., Back, C.H., *et al*. (2005). Spin-wave eigenmodes of permalloy squares with a closure domain structure. *Physical Review Letters*, **94**, 057202.

Pierce, M.S., Moore, R.G., Sorensen, L.B., *et al*. (2003). Quasistatic X-ray speckle metrology of microscopic magnetic return-point memory. *Physical Review Letters*, **90**, 175502.

Portier, X. and Petford-Long, A.K. (2000). The formation of 360° domain walls in magnetic tunnel junction elements. *Applied Physics Letters*, **76**, 754–756.

Raabe, J., Quitmann, C., Back, C.H., *et al*. (2005). Quantitative analysis of magnetic excitations in Landau flux-closure structures using synchrotron-radiation microscopy. *Physical Review Letters*, **94**, 217204.

Radovic, Z., Ledvij, M., Dobrosavljevic-Grujic, L., *et al*. (1991). Transition temperatures of superconductor-ferromagnet superlattices. *Physical Review B*, **44**, 759–764.

Radu, F., Etzkorn, M., Siebrecht, R., *et al*. (2003). Interfacial domain formation during magnetization reversal in exchange biased CoO/Co bilayers. *Physical Review B*, **67**, 134409.

Rekveldt, M.Th. (1973). Study of ferromagnetic bulk domains by neutron depolarization in three dimensions. *Zeitschrift für Physik A Hadrons and Nuclei*, **259**, 391–410.

Roshchin, I.V., Petracic, O., Morales, R., *et al*. (2005). Lateral length scales in exchange bias. *Europhysics Letters*, **71**, 297–303.

Rosman, R. and Rekveldt, M.Th. (1991). Neutron-depolarization theory in particulate media. *Physical Review B*, **43**, 8437–8449.

Roth, W.L. (1960). Neutron and optical studies of domains in NiO. *Journal of Applied Physics*, **31**, 2000–2011.

Rothman, J., Kläui, M., Lopez-Diaz, L., *et al*. (2001). Observation of a bi-domain state and nucleation free switching in mesoscopic ring magnets. *Physical Review Letters*, **86**, 1098–1101.

Roy, S., Fitzsimmons, M.R., Park, S., *et al*. (2005). Depth profile of uncompensated spins in an exchange bias system. *Physical Review Letters*, **95**, 047201.

Ryazanov, V.V., Oboznov, V.A., Rusanov, A.Y., *et al*. (2001). Coupling of two superconductors through a ferromagnet: evidence for a π junction. *Physical Review Letters*, **86**, 2427–2430.

Sakarya, S., van Dijk, N.H. and Brück, E. (2005). Determination of the magnetic domain size in the ferromagnetic superconductor UGe_2 by three-dimensional neutron depolarization. *Physical Review B*, **71**, 174417.

Schlenker, M. and Baruchel, J. (1978). Neutron techniques for the observation of ferro- and antiferromagnetic domains. *Journal of Applied Physics*, **49**, 1996–2001.

Scholl, A., Stöhr, J., Lüning, J., *et al*. (2000). Observation of antiferromagnetic domains in epitaxial thin films. *Science*, **287**, 1014–1016.

Seul, M. and Andelman, D. (1995). Domain shapes and patterns: the phenomenology of modulated phases. *Science*, **267**, 476–483.

Shi, H., Lederman, D., Dilley, N.R., *et al*. (2003). Temperature-induced sign change of the exchange bias in $Fe_{0.82}Zn_{0.18}F_2$/Co bilayers. *Journal of Applied Physics*, **93**, 8600–8602.

Shima, T., Takanashi, K., Takahashi, Y.K. and Hono, K. (2004). Coercivity exceeding 100∼kOe in epitaxially grown FePt sputtered films. *Applied Physics Letters*, **85**, 2571–2573.

Shull, C.G., Strauser, W.A. and Wollan, E.O. (1951). Neutron diffraction by paramagnetic and antiferromagnetic substances. *Physical Review*, **83**, 333–345.

Skidmore, G.D., Kunz, A., Campbell, C.E. and Dahlberg, E.D. (2004). Micromagnetic domain structures in cylindrical nickel dots. *Physical Review B*, **70**, 012410.

Sort, J., Buchanan, K.S., Novosad, V., *et al*. (2006b). Imprinting vortices into antiferromagnets. *Physical Review Letters*, **97**, 067201.

Sort, J., Hoffmann, A., Chung, S-H., *et al*. (2005). Magnetization reversal in submicron disks: exchange biased vortices. *Physical Review Letters*, **95**, 067201.

Sort, J., Salazar-Alvarez, G., Baró, M.D., *et al*. (2006a). Controlling magnetic vortices through exchange bias. *Applied Physics Letters*, **88**, 042502.

Spezziani, C., Torelli, P., Sacchi, M., *et al*. (2002). Hysteresis curves of ferromagnetic and antiferromagnetic order in metallic multilayers by resonant x-ray scattering. *Physical Review B*, **66**, 052408.

Stahn, J., Chacalian, J., Niedermayer, Ch., *et al*. (2005). Magnetic proximity effect in perovskite superconductor/ferromagnet multilayers. *Physical Review B*, **71**, 140509.

Stiles, M.D. and McMichael, R.D. (1999). Model for exchange bias in polycrystalline ferromagnet-antiferromagnet bilayers. *Physical Review B*, **59**, 3722–3733.

Swerts, J., Temst, K., Van Bael, M.J., *et al*. (2003). Magnetic domain wall trapping by in-plane surface roughness modulation. *Applied Physics Letters*, **82**, 1239–1241.

Takano, K., Kodama, R.H., Berkowitz, A.E., *et al*. (1997). Interfacial uncompensated antiferromagnetic spins: role in unidirectional anisotropy in polycrystalline $Ni_{81}Fe_{19}$/CoO bilayers. *Physical Review Letters*, **79**, 1130–1133.

Tanner, B.K. (1976). *X-Ray Diffraction Topography*, Pergamon Press: London.

Tanner, B.K. (1979). Antiferromagnetic domains. *Contemporary Physics*, **20**, 187–210.

Tatara, G. and Kohno, H. (2004). Theory of current-driven domain wall motion: Spin transfer versus momentum transfer. *Physical Review Letters*, **92**, 086601.

Temst, K., Van Bael, M.J. and Fritzsche, H. (2001). Application of off-specular polarized neutron reflectometry to measurements on an array of mesoscopic ferromagnetic disks. *Applied Physics Letters*, **79**, 991–993.

Theis-Bröhl, K., Toperverg, B.P., Leiner, V., *et al*. (2005). Correlated magnetic reversal in periodic stripe patterns. *Physical Review B*, **71**, 020403.

Thiele, J.U., Maat, S. and Fullerton, E.E. (2003). FeRh/FePt exchange spring films for thermally assisted magnetic recording media. *Applied Physics Letters*, **82**, 2859–2861.

Thomas, L., Luning, J., Scholl, A., *et al*. (2000a). Oscillatory decay of magnetization induced by domain-wall stray field. *Physical Review Letters*, **84**, 3462–3465.

Thomas, L., Parkin, S.P.P., Yu, J., *et al*. (2000b). Micromagnetics of submicron (110) Fe elements. *Applied Physics Letters*, **76**, 766–768.

Toperverg, B.P. (2002). Polarized neutron reflection and off-specular scattering. In *Polarized Neutron Scattering, Series Matter and Materials*, Brückel, Th. and Schweika, W. (Eds.), Schriften des Forschungzentrum Jülich, pp. 247–288, Vol. 12.

Tsang, C., Heiman, N. and Lee, K. (1981). Exchange induced unidirectional anisotropy at FeMn-$Ni_{80}Fe_{20}$ interfaces. *Journal of Applied Physics*, **52**, 2471–2473.

Van Bael, M.J., Temst, K., Moshchalkov, V.V. and Bruynseraede, Y. (1999). Magnetic properties of submicron Co islands and their use as artificial pinning centers. *Physical Review B*, **59**, 14674–14679.

Vavassori, P., Zaluzzec, N., Metlushko, V., *et al*. (2004). Magnetization reversal via single and double vortex states in submicron permalloy ellipses. *Physical Review B*, **69**, 214404.

te Velthuis, S.G.E., Berger, A., Felcher, G.P., *et al*. (2000). Training effects and the microscopic magnetic structure of exchange biased Co/CoO bilayers. *Journal of Applied Physics*, **87**, 5046–5048.

te Velthuis, S.G.E., van Dijk, N.H., Rekveldt, M.Th., *et al*. (2001). Domain size determination of granular ferromagnetic systems with neutron depolarization. *Journal of Applied Physics*, **89**, 1275–1280.

te Velthuis, S.G.E., Felcher, G.P., Welp, U., *et al*. (2006). Magnetic domain configurations in the hysteresis cycle of an exchange-coupled ferromagnetic film (Co/CoO). (unpublished).

te Velthuis, S.G.E., Jiang, J.S., Bader, S.D. and Felcher, G.P. (2002). Spin flop transition in a finite antiferromagnetic superlattice: Evolution of the Magnetic Structure. *Physical Review Letters*, **89**, 127203.

Vlasko-Vlasov, V.K., Welp, U., Jiang, J.S., *et al*. (2001). Field induced biquadratic exchange in hard/soft ferromagnetic bilayers. *Physical Review Letters*, **86**, 4386–4389.

Volkov, A.F., Bergeret, F.S. and Efetov, K.B. (2003). Odd triplet superconductivity in superconductor-ferromagnet mulilayered structures. *Physical Review Letters*, **90**, 117006.

Wang, R.W., Mills, D.L., Fullerton, E.E., *et al*. (1994). Surface spin-flop transition in Fe/Cr(211) superlattices: experiment and theory. *Physical Review Letters*, **72**, 920–923.

Weiss, P. (1907). L'hypothèse du champ moléculaire et la propriété ferromagnétique. *Journal de Physique*, **6**, 661–690.

Weiss, R.J. (1951). Small angle scattering of neutrons. *Physical Review*, **83**, 379–389.

Werner, S.A., Arrott, A. and Kendrick, H. (1967). Temperature and magnetic-field dependence of the antiferromagnetism in pure chromium. *Physical Review*, **155**, 528–539.

Werner, S.A. and Klein, A.G. (1987). Neutron optics. In *Methods of Experimental Physics*, Price, D.L. and Skold, K. (Eds.), Academic Press: New York, pp. 259–337, Vol. 23A.

Yang, Z., Lange, M., Volodin, A., *et al*. (2004). Domain-wall superconductivity in superconductor-ferromagnet hybrids. *Nature Materials*, **3**, 793–798.

Yoshizawa, Y., Oguma, S. and Yamauchi, K. (1988). New Fe-based soft magnetic alloys composed of ultrafine grain structure. *Journal of Applied Physics*, **64**, 6044–6046.

Zaharko, O., Fischer, P., Schenk, A., *et al*. (2003). Zero-field magnetic structure in CeB6 reinvestigated by neutron diffraction and muon spin relaxation. *Physical Review B*, **68**, 214401.

Polarized Neutron Reflectivity and Scattering from Magnetic Nanostructures and Spintronic Materials

Hartmut Zabel[1], Katharina Theis-Bröhl[1] and Boris P. Toperverg[1,2]

[1] *Ruhr-Universität Bochum, Bochum, Germany*
[2] *Petersburg Nuclear Physics Institute RAS, Saint Petersburg, Russia*

1 INTRODUCTION

Artificial magnetic nanostructures are being intensively investigated because of their intriguing magnetic properties and their specific device applications. By reducing the size in one or more directions new magnetic properties have been observed which are not present in the bulk and which are highly usable for device application. With perpendicular stacked magnetic layers a reduction of size in the out-of-plane direction is accomplished. They allow the investigation of collinear and noncollinear exchange coupling between ferromagnetic (F) layers, exchange bias (EB) between F- and antiferromagnetic (AF) layers, confinement and scaling effects of spin-density wave magnetism, and proximity effects between F and superconducting layers. Reducing the size in the lateral direction results in a plethora of different shapes for F nanostructures such as stripes, dots, antidots, rings, squares, rectangles, triangles, and different ellipsoids. The fabrication of these shapes usually requires lithographic processes or, alternatively, self assembly of magnetic nanostructures. The main interest in magnetic nanostructures is the understanding of the domain structure in the ground state, the reversal mechanism in the space and time domain, and the dipolar interaction between these elements. Here we will review magnetic films and heterostructures, magnetic superlattices, and lateral magnetic nanostructures as they have mainly been investigated via polarized neutron scattering and neutron reflectivity (NR).

During the past 10 years polarized NR has played an increasingly important role for the exploration of magneto- and spintronic nanostructures. Well-known systems extensively studied include exchange-coupled magnetic superlattices, exchange spring valves between soft and hard magnetic films, EB systems between F and AF films, magnetic semiconductors and half-metallic ferromagnets. In addition to studies of layered systems, laterally patterned magnetic systems such as stripes and islands on the submicrometer scale are now being intensively analyzed by neutron scattering.

Although neutron scattering is generally known as a *bulk probe* particularly sensitive to magnetic moments and magnetic excitations by virtue of the chargeless but magnetic particle properties, it is the interface sensitivity which turned

Handbook of Magnetism and Advanced Magnetic Materials. Edited by Helmut Kronmüller and Stuart Parkin. Volume 3: *Novel Techniques for Characterizing and Preparing Samples*. ISBN: 978-0-470-02217-7.

out to be most useful in studies of magnetic thin films, multilayers, and lateral magnetic nanotructures. Although the wavelength of cold neutrons can be 1–3 orders of magnitude smaller than the thickness of thin films, the sensitivity is due to the distortion of the neutron wave field near surfaces when potential steps are encountered. The interface sensitivity is exploited in specular NR and off-specular neutron scattering. Often it is advantageous to first fix the neutron polarization vector, that is the neutron magnetic moment with respect to the scattering plane, and to analyze the polarization state of the exit beam before the detector. This variant of neutron reflectivity is called *polarized neutron reflectivity* (*PNR*) and is used mainly for the investigation of magnetic thin films, magnetic superlattices, or any other kind of magnetic heterostructure. Responding to the upsurge of interest in PNR a number of neutron reflectometers for magnetic studies have become available at all major steady-state and pulsed neutron sources around the globe.

A variety of powerful methods are available for the analysis of magnetic nanostructures. In this concert of competing methods, neutron studies have to justify themselves by unique answers to specific questions. Those include:

- magnetic correlation lengths in films and superlattices;
- depth profiles of the magnetization vector;
- quantitative magnetic roughness parameters of buried interfaces;
- magnetic fluctuations and correlations of domain distributions;
- magnetic hysteresis in the presence of superconductivity;
- sensitivity to magnetic induction;
- distinction between different magnetic reversal mechanisms.

In the past PNR was also used for absolute moment determination. This is indeed an important application of PNR, as the cross sections are well known and independent of model assumptions. However, if moments of ultrathin layers are determined other aspects start to play a dominating role, such as growth morphologies, surface roughness, interdiffusion, and so on. In this case, specular and off-specular diffuse scattering has to be analyzed for reliable data analysis and PNR has to be combined with surface science methods. This topic may be revisited in the future when higher intensities and in situ growth capabilities at neutron beam lines become available.

A number of excellent review articles have been published in recent years either focusing on the method of polarized neutron reflectivity (Fermon and Menelle, 1999; Ankner and Felcher, 1999; Majkrzak, 1996; Majkrzak and Donovan, 2006) or on the magnetic film systems (Fitzsimmons *et al*., 2004; Zabel and Theis-Bröhl, 2003; Bland and Vaz, 2005). Here we describe in some detail the method of polarized neutron reflectivity with particular emphasis on the description of perpendicular and lateral micro- anuctures and review recent applications. The distorted wave Born approximation (DWBA) for the description of off-specular diffuse scattering from magnetic domains and nanostructures is described in some detail here for the first time. The outline is as follows. After providing the theoretical framework for PNR, off-specular, and Bragg scattering, experimental considerations for the scattering technique will be discussed. This is followed by a review of NR studies of thin magnetic films, superlattices, and lateral magnetic patterns.

2 METHOD OF POLARIZED NEUTRON REFLECTIVITY

2.1 Unpolarized neutron reflectivity

In the following, we consider first an elastic reflection experiment of unpolarized monochromatic neutrons. Furthermore, we assume that a collimated neutron beam impinges at a glancing angle α_i onto a flat and extended surface separating vacuum (air) and medium (Figure 1). The reflected beam leaves the surface under a glancing angle α_f. In case of specular reflection, the incident and exit angles are identical: $\alpha_i = \alpha_f$. For this reason, we may drop the indices i, f for the moment, but use them again when discussing off-specular scattering. The scattering vector $\boldsymbol{Q}_z$ has the length $Q_z = 2k \sin\alpha$ and points along the z-direction parallel to the surface normal, where $k = 2\pi/\lambda$ is the magnitude of the incident (and/or scattered) wave vector $\boldsymbol{k}$,

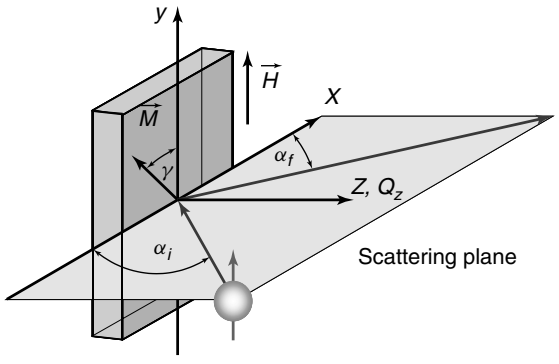

Figure 1. Scattering geometry for polarized neutron reflectivity studies. Neutrons are initially polarized along the y axis. Non-spin-flip reflection is due to the $B_y = |\boldsymbol{B}| \cos\gamma$ projection of the magnetic inductance vector $\boldsymbol{B}$, while $B_x = |\boldsymbol{B}| \sin\gamma$ causes spin-flip reflectivity.

and λ is the neutron wavelength. In vacuum the part of neutron energy corresponding to its propagation in the z-direction is

$$E_z = \frac{\hbar^2 \boldsymbol{Q}_z^2}{8m} \tag{1}$$

where m is the neutron mass. At the interface between vacuum and medium the neutrons experience a potential step of height

$$V = \frac{2\pi\hbar^2}{m} Nb \tag{2}$$

Here N is the atomic number density and b is the coherent scattering length of the neutrons. The product Nb is usually referred to as the scattering length density (SLD). Total reflection occurs for $E_z \leq V$. Thus from equations (1) and (2) one obtains for $E_z = V$ the critical scattering vector for total reflection

$$Q_c = \sqrt{16\pi Nb} \tag{3}$$

Note that total reflection occurs only if the coherent scattering length b is positive, that is if $V > 0$. Then, for $Q < Q_c$ the neutron wave in the medium is exponentially damped within the medium, and for $Q > Q_c$ a Fresnel reflectivity is observed, which drops off with Q^{-4}. In case of thin films, Kiessig fringes are superimposed on the general Fresnel reflectivity due to the constructive (or destructive) interference of the neutron waves reflected from inner and outer interfaces. For multilayers with a chemical periodicity Λ parallel to the z-direction, satellite (Bragg) reflections are observed at positions

$$Q_l \approx \sqrt{Q_c^2 + \left(l\frac{2\pi}{\Lambda}\right)^2} \tag{4}$$

where l is the order of the satellite reflection, and $Q_c \leq (2\pi l/\Lambda)$.

So far unpolarized NR and non-resonant X-ray reflectivity provide essentially the same results. Differences occur due to the fact that the coherent scattering cross section for neutrons is not a smooth function of the atomic number as it is for X rays, and that even different isotopes of the same element can be distinguished. The main difference, however, occurs when investigating magnetic films and multilayers either with PNR or with X-ray resonant magnetic scattering (XRMS). Here we will discuss only PNR, and compare with XRMS later on.

2.2 Basic features of specular polarized neutron reflectivity

Neutrons carry a magnetic moment $\boldsymbol{\mu}$, whose operator

$$\hat{\boldsymbol{\mu}} = \gamma_n \mu_N \hat{\boldsymbol{\sigma}} \tag{5}$$

is proportional to the Pauli spin operator $\hat{\boldsymbol{\sigma}}$ acting in a two-dimensional spin space and being represented by a set of 2×2 matrices: $\hat{\boldsymbol{\sigma}} = \{\hat{\sigma}_x, \hat{\sigma}_y, \hat{\sigma}_z\}$. Here $\gamma_n = -1.913$ is the gyromagnetic ratio of neutron and $\mu_N = e\hbar/2m_p c$ is the nuclear magneton. $\boldsymbol{\mu}$ interacts with the magnetic induction $\boldsymbol{B}$ providing a magnetic (Zeeman) potential for the neutrons. The corresponding operator of magnetic potential energy

$$\hat{V}_m = -(\hat{\boldsymbol{\mu}} \cdot \boldsymbol{B}) \tag{6}$$

is represented by a 2×2 matrix. In general, the magnetic induction $\boldsymbol{B}$ in a magnetic film consists of an external field $\boldsymbol{B}_0$ and a sample magnetization $\boldsymbol{M}$ vectors

$$\boldsymbol{B} = \boldsymbol{B}_0 + \mu_0 \boldsymbol{M} \tag{7}$$

where μ_0 is the permeability of free space.

Usually, the magnetic field is applied parallel to the sample surface, and due to the strong shape anisotropy the magnetization vector $\boldsymbol{M}$ is displayed within the magnetic film plane. Then the first term, $\boldsymbol{B}_0$, is identical inside and outside of the sample and does not contribute to the contrast in the reflection potential. Therefore, it can safely be neglected in the subsequent consideration. This can also be done in the more general case when the vector $\boldsymbol{B}_0$ has an arbitrary direction and the magnetization vector has also a component normal to the surface. The latter contributes to the inductance $\boldsymbol{B}_{\text{ext}}$ outside of the sample. However, the component of the inductance vector $\boldsymbol{B}_z$ normal to the surface is continuous and hence does not make a contrast for magnetic reflection. As a result, considering specular reflection one should neglect the first term in equation (7) and only take into account the neutron interaction with the lateral component $\boldsymbol{M}_L$ of magnetization vector. Below the superscript L will be silently anticipated.

Let us assume that in the z direction a half-infinite sample with a flat surface is in a F, single-domain state. Furthermore, we assume that the incoming monochromatic neutron beam can ideally be polarized collinear with the y axis, as indicated in the schematic outline of the scattering geometry in Figure 1. If the sample is also homogeneously magnetized along the y axis, then the potential energies of the neutron-sample interaction for alternative

polarization directions are the eigenvalues of the interaction operator in equation (6) and they are determined by the equation

$$V_{\pm} = V_n \pm V_m = \frac{2\pi\hbar^2}{m} N(b_n \pm b_m) \tag{8}$$

where V_n is the neutron – nuclei interaction potential, b_n is the nuclear and b_m is the magnetic scattering length, the (+) sign stands for the spin up, that is for neutrons polarized along, and the (−) sign for the spin-down state, that is for the neutrons polarized opposite to the (small) ambient field guiding the polarization directed along the y-axis. If, however, the magnetization makes an angle γ against the y-axis then the matrix of magnetic interaction $\hat{V}_m$ is not diagonal and the 3D Schrödinger equation reads:

$$\left\{-\frac{\hbar^2}{2m}\Delta + \hat{V}(z) - E\right\} |\Psi(\boldsymbol{r})\rangle = 0 \tag{9}$$

where the energy $E = \hbar^2 k^2/2m$ is conserved for elastic scattering. Owing to the fact that $\hat{V}(z)$ depends only on the transverse coordinate z the lateral projection $\boldsymbol{\kappa}$ of the wave vector $\boldsymbol{k}$ is also conserved and the two component wave function $|\Psi(\boldsymbol{r})\rangle$ is factorized into the product $|\Psi(\boldsymbol{r})\rangle = \exp\{i(\boldsymbol{\kappa}\boldsymbol{\rho})\}\,|\Psi(z)\rangle$, where $\boldsymbol{\rho}$ is the lateral projection of the radius-vector $\boldsymbol{r}$. The 2D vector of spin states $|\Psi(z)\rangle$ is represented by a column

$$|\Psi(z)\rangle = \begin{pmatrix} \Psi_+(z) \\ \Psi_-(z) \end{pmatrix} \tag{10}$$

with 2 elements $\Psi_{\pm}$ which denote probability amplitudes to find a neutron with positive, or correspondingly, negative spin projection onto the y-axis. Both spin states of the neutron are partially populated if the interaction matrix

$$\begin{pmatrix} V_{++} & V_{+-} \\ V_{-+} & V_{--} \end{pmatrix} = \frac{2\pi\hbar^2}{m} N \left[\begin{pmatrix} b_n & 0 \\ 0 & b_n \end{pmatrix} + \begin{pmatrix} b_y & b_x \\ b_x & -b_y \end{pmatrix} \right] \tag{11}$$

has non-diagonal elements $V_{\pm\mp} \propto b_x = b_m \sin\gamma$, proportional to the component of magnetic induction perpendicular to the polarization axis. The diagonal elements $V_{\pm\pm} \propto (b_n \pm b_y)$ depend on $b_y = b_m \cos\gamma$, that is on the inductance component parallel to the y-axis. Using equations (10) and (11) the Schrödinger equation in matrix form equation (9) can be explicitly written as a system of two coupled equations

$$\frac{\partial^2}{\partial z^2}\Psi_+(z) + \left[p_0^2 - \frac{2m}{\hbar^2}V_{++}(z)\right]\Psi_+(z) - \frac{2m}{\hbar^2}V_{+-}(z)\Psi_-(z) = 0 \tag{12}$$

$$\frac{\partial^2}{\partial z^2}\Psi_-(z) + \left[p_0^2 - \frac{2m}{\hbar^2}V_{--}(z)\right]\Psi_-(z) - \frac{2m}{\hbar^2}V_{-+}(z)\Psi_+(z) = 0 \tag{13}$$

where $p_0 = Q_z/2 = k\sin\alpha$ is the component of the neutron wave vector normal to the field boundary, and $p_0^2 = k^2 - \kappa^2$ due to the conservation of energy at elastic reflection.

This couple of linear differential equations can readily be solved, but the following first conclusions can be drawn before we present their formal solution in explicit form. When V_{ij} with $i \neq j$ are zero, a set of equations (12) and (13) are decoupled and only non-spin-flip (NSF) scattering occurs, that is the neutrons maintain their spin state upon interaction with the sample.

For NSF scattering, the magnetization vector $\boldsymbol{M}$ has to be oriented along the y axis. Alternatively, if V_{ij} with $i = j$ are zero, the V_{+-} and V_{-+} potentials flip the neutron spin from up to down and vice versa with equal efficiency. The spin-flip (SF) scattering is caused by a magnetization vector $\boldsymbol{M}$ projection M_x onto the x-axis. Thus, by distinguishing between NSF and SF scattering, a quantitative analysis of PNR data yields the x- and y components of $\boldsymbol{M}$, which combine to the magnitude and orientation of the magnetization vector $\boldsymbol{M}$ in the sample plane.

Note that in the configuration shown in Figure 1 only the absolute value of M_x, the magnetization projection, but not its sign, can be determined. In other words, from PNR data one cannot distinguish whether the magnetization is turned to the right or to the left with respect to the polarization analysis axis. This is due to the fact, that in equations (12) and (13) enter only the equal non-diagonal elements $V_{+-} = V_{-+}$. We shall see later that in the more general kinematic case, for example, via a 3D or vector PNR analysis, other matrix elements appear, for example $V_{z\pm}$ and $V_{\pm z}$, allowing a complete projection of the vector $\boldsymbol{M}$.

There are several important points to be noted here

- the effective potentials V_{++} and V_{--} for the y-component contain nuclear and magnetic contributions;
- the potentials V_{+-} and V_{-+} are solely of magnetic origin;
- PNR is not sensitive to any magnetization component parallel to the scattering vector;

- spin and orbital parts, which contribute to the total magnetization of the sample, cannot be distinguished.

Solutions of equations (12) and (13) have been provided by several authors (Felcher *et al.*, 1987; Majkrzak, 1989, 1991), and here we just briefly indicate the main steps leading to the explicit expression for PNR in the simplest case of reflection from a semi-infinite homogeneous film.

For the interaction matrix $V_{ij}(z) = V_{ij}$ constant within the magnetic media the general solution of equations (12) and (13) should, as usual, be written in the form of the superposition of plane waves e^{ipz} and e^{-ipz} with the wave numbers p and the amplitudes to be found. Substitution of this superposition into equations (12) and (13) results in a couple of linear homogeneous algebraic equations with respect to Ψ_+ and Ψ_-

$$[p^2 - p_0^2 + (p_n^2 + p_y^2)]\Psi_+(z) + p_x^2\Psi_-(z) = 0 \quad (14)$$

$$p_x^2\Psi_+(z) + [p^2 - p_0^2 + (p_n^2 - p_y^2)]\Psi_-(z) = 0 \quad (15)$$

where $p_n^2 = 4\pi N b_n$, $p_x^2 = 4\pi N b_x$, and $p_y^2 = 4\pi N b_y$. The couple of equations (14) and (15) may have a nontrivial solution only if its determinant is zero:

$$[(p^2 - p_0^2 + p_n^2) + p_y^2][(p^2 - p_0^2 + p_n^2) - p_y^2] - p_x^4 = 0 \quad (16)$$

This biquadratic equation has two pairs of solutions, $p = p_\pm$ and $p = -p_\pm$, where

$$p_\pm = \sqrt{p_0^2 - [p_n^2 \pm p_m^2]} \quad (17)$$

The first pair with $p = p_\pm$ corresponds to the wave propagation into the medium, while the second one, with $p = -p_\pm$, refers to their propagation in the opposite direction. Amplitudes of these waves will be found from boundary conditions, but now it is important to stress that despite the fact that each of equations (12) and (13) depends on the angle γ, they are only compatible if $p_m^2 = \sqrt{p_x^4 + p_y^4} = 4\pi N b_m$ and the wave numbers in equation (17) are independent of the tilt angle γ. This is the inherent property of the spin 1/2 operator which has only two eigenvalues $\pm 1/2$.

Equation (17) has a transparent physical meaning. Indeed, the neutron wave with the initial wave number p_0 experiences inside the magnetic medium a refraction effect such that the degeneracy with respect to the spin states is lifted. This effect is in analogy with the well-known birefringence in optically active media. For neutrons magnetic media are active due to the Zeeman effect, and spin components of the neutron wave in a magnetic field have different phase velocities $v_\pm = \hbar k_\pm / m$, where $k_\pm = \sqrt{\kappa^2 + p_\pm^2}$, and therefore different refractive indices. Correspondingly, there exist two critical wave numbers of the total reflection

$$p_{c\pm} = \sqrt{p_n^2 \pm p_m^2} \quad (18)$$

and two critical angles $\alpha_{c\pm}$:

$$p_{c\pm} = k \sin\alpha_{c\pm} = \sqrt{4\pi N(b_n \pm b_m)} \quad (19)$$

one for the positive and one for the negative spin projection onto the magnetic inductance direction in the medium. The wave number in and outside the medium and are illustrated in Figure 2.

In contrast to the refraction indices and the wave numbers $p_\pm$, the amplitudes of plane waves inside the magnetic medium vary with the tilt angle γ. Indeed, the general solution for the spin components of the wave function is written as a superposition

$$\Psi_+(z) = t_{++}e^{ip_+z} + t_{+-}e^{ip_-z} + r_{++}e^{-ip_+z} + r_{+-}e^{-ip_-z} \quad (20)$$

$$\Psi_-(z) = t_{-+}e^{ip_+z} + t_{--}e^{ip_-z} + r_{-+}e^{-ip_+z} + r_{--}e^{-ip_-z} \quad (21)$$

of two couples of plane waves with wave numbers satisfying equations (12) and (13) and propagating for $z \geq 0$ with two different phase velocities. The eight amplitudes $t_{\pm\pm}$, $t_{\pm\mp}$, $r_{\pm\pm}$, and $r_{\pm\mp}$ in this equations are to be determined from boundary conditions and hence depend on the initial spin state, which is dictated, in particular, by the angle γ. Owing to equations (14) and (15) not all wave amplitudes are independent, but linked by pairs $t_{-+} = t_{++}\tan(\gamma/2)$, $t_{+-} = -t_{--}\tan(\gamma/2)$, $r_{-+} = r_{++}\tan(\gamma/2)$, and $r_{+-} = -r_{--}\tan(\gamma/2)$. The first two terms in equations (20) and (21) correspond to the propagation of the (transmitted) waves from the front surface into the depth

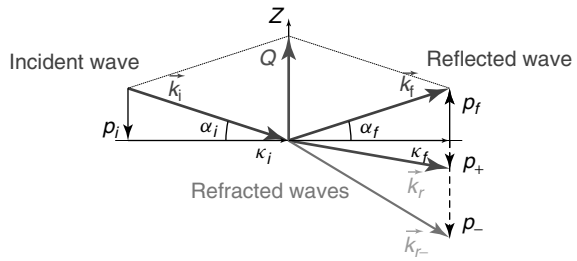

Figure 2. Kinematics of polarized neutron reflection. Owing to the invariance with respect to the lateral shift $\boldsymbol{\kappa}_f = \boldsymbol{\kappa}_i = \boldsymbol{\kappa}$, $p_f = p_i = p_0$, and $\alpha_f = \alpha_i = \alpha$. The wave vector component normal to the surface is split in magnetic medium due to the Zeeman effect.

of the medium. The second couple describes the propagation in the opposite direction, for example, waves reflected from the substrate in the case of the film with finite thickness. For semi-infinite media the latter waves are absent and one should set $r_{\pm\pm} = r_{\pm\mp} = 0$. Then each of the transmitted spin-wave components has to be matched with the corresponding one in free space. For neutrons initially polarized as shown in Figure 1 the spin component with positive spin projection is due to NSF reflection, while those with negative projection may appear due to SF reflection, and for $z \leq 0$ one has:

$$\Psi_+(z) = \mathrm{e}^{ip_0 z} + r_{++}\mathrm{e}^{-ip_0 z} \tag{22}$$

$$\Psi_-(z) = r_{-+}\mathrm{e}^{-ip_0 z} \tag{23}$$

If neutrons are initially polarized opposite to the guiding field, then

$$\Psi_+(z) = r_{+-}\mathrm{e}^{-ip_0 z} \tag{24}$$

$$\Psi_-(z) = \mathrm{e}^{ip_0 z} + r_{--}\mathrm{e}^{-ip_0 z} \tag{25}$$

Matching at $z = 0$ the spin components of the wave function from equations (20) and (21) and their derivatives with the corresponding quantities from either equations (22) and (23), or from equations (24) and (25) one readily obtains a set of equations for the transmission and reflection amplitudes:

$$t_{++} - t_{--}\tan\frac{\gamma}{2} = 1 + r_{++} \tag{26}$$

$$t_{++}\tan\frac{\gamma}{2} + t_{--} = r_{-+} \tag{27}$$

$$p_+ t_{++} - p_- t_{--}\tan\frac{\gamma}{2} = p_0(1 - r_{++}) \tag{28}$$

$$p_+ t_{++}\tan\frac{\gamma}{2} + p_- t_{--} = -p_0 r_{-+} \tag{29}$$

Solution of these equations immediately delivers expressions for the transmission amplitudes. They can be combined into the matrix so that for positive initial polarization one obtains:

$$\begin{pmatrix} t_{++} & t_{+-} \\ t_{-+} & t_{--} \end{pmatrix} = \begin{pmatrix} T_+\cos^2\frac{\gamma}{2} & T_-\sin\frac{\gamma}{2}\cos\frac{\gamma}{2} \\ T_+\sin^2\frac{\gamma}{2} & -T_-\sin\frac{\gamma}{2}\cos\frac{\gamma}{2} \end{pmatrix} \tag{30}$$

where $T_\pm$ are the Fresnel transmission amplitudes

$$T_\pm = \frac{2p_0}{p_0 + p_\pm} = \frac{2p_0}{p_0 + \sqrt{p_0^2 - p_n^2 \mp p_m^2}} \tag{31}$$

For alternative initial polarization one should match the wave function spin component in equations (20) and (21) with the corresponding ones in equations (24) and (25). This results in a set of another four equations similar to equations (26–29)

$$t_{++} - t_{--}\tan\frac{\gamma}{2} = r_{+-} \tag{32}$$

$$t_{++}\tan\frac{\gamma}{2} + t_{--} = 1 + r_{--} \tag{33}$$

$$p_+ t_{++} - p_- t_{--}\tan\frac{\gamma}{2} = -p_0 r_{+-} \tag{34}$$

$$p_+ t_{++}\tan\frac{\gamma}{2} + p_- t_{--} = p_0(1 - r_{--}) \tag{35}$$

Their solutions can also be collected into a matrix

$$\begin{pmatrix} t_{++} & t_{+-} \\ t_{-+} & t_{--} \end{pmatrix} = \begin{pmatrix} T_+\sin\frac{\gamma}{2}\cos\frac{\gamma}{2} & -T_-\sin\frac{\gamma}{2}\cos\frac{\gamma}{2} \\ T_+\sin^2\frac{\gamma}{2} & T_-\cos^2\frac{\gamma}{2} \end{pmatrix} \tag{36}$$

similar to that in equation (30).

Finally, using the equations in the preceding text one obtains a set of explicit expressions for the SF and NSF reflection amplitudes completing a reflectance matrix $\hat{R}$

$$\begin{pmatrix} r_{++} & r_{+-} \\ r_{-+} & r_{--} \end{pmatrix} = \begin{pmatrix} R_+\cos^2\frac{\gamma}{2} + R_-\sin^2\frac{\gamma}{2} & (R_+ - R_-)\cos\frac{\gamma}{2}\sin\frac{\gamma}{2} \\ (R_+ - R_-)\cos\frac{\gamma}{2}\sin\frac{\gamma}{2} & R_+\sin^2\frac{\gamma}{2} + R_-\cos^2\frac{\gamma}{2} \end{pmatrix} \tag{37}$$

In this equation, the amplitudes $R_\pm$ are just eigenvalues of the matrix $\hat{R}$ which is diagonal at $\gamma = 0, \pi$. Owing to equations (26–29) and equations (32–35) $R_\pm = R_\pm^F$, where

$$R_\pm^F = \frac{p_0 - p_\pm}{p_0 + p_\pm} = \frac{p_0 - \sqrt{p_0^2 - p_{c\pm}^2}}{p_0 + \sqrt{p_0^2 - p_{c\pm}^2}} \tag{38}$$

are the Fresnel amplitudes of reflection for neutrons ideally polarized along with, or opposite to the magnetic in-plane induction in the medium, and the critical wave numbers $p_{c\pm}$ are given in equation (19). From equation (38) it immediately follows that if $p_0 \leq p_{c+}$ then $|R_+| = 1$ and neutrons with positive projection of their spins onto the direction of the sample inductance experience the total reflection. If $p_0 \leq p_{c-} \leq p_{c+}$ then $|R_-| = |R_+| = 1$ and neutrons with alternative spin projection are also totally reflected.

With PNR it is possible to measure independently the NSF reflectivities $\mathcal{R}^{++} = |r_{++}|^2$, $\mathcal{R}^{--} = |r_{--}|^2$ and the SF reflectivities $\mathcal{R}^{+-} = \mathcal{R}^{-+} = |r_{\pm\mp}|^2$ which due to equation (37) are explicitly written as

$$\mathcal{R}^{++} = \frac{1}{4}|R_+(1 + \cos\gamma) + R_-(1 - \cos\gamma)|^2 \tag{39}$$

$$\mathcal{R}^{--} = \frac{1}{4}|R_+(1-\cos\gamma) + R_-(1+\cos\gamma)|^2 \quad (40)$$

$$\mathcal{R}^{+-} = \mathcal{R}^{-+} = \frac{1}{4}|R_+ - R_-|^2 \sin^2\gamma \quad (41)$$

Often a simplified version of PNR is used which does not require an analysis of the final spin states of reflected neutrons. Then the measured quantities are:

$$\mathcal{R}^{+} = \mathcal{R}^{++} + \mathcal{R}^{+-} = |R_+|^2 \cos^2\frac{\gamma}{2} + |R_-|^2 \sin^2\frac{\gamma}{2} \quad (42)$$

$$\mathcal{R}^{-} = \mathcal{R}^{--} + \mathcal{R}^{-+} = |R_+|^2 \sin^2\frac{\gamma}{2} + |R_-|^2 \cos^2\frac{\gamma}{2} \quad (43)$$

while one half of their sum,

$$\frac{1}{2}\{\mathcal{R}^{+} + \mathcal{R}^{-}\} = \frac{1}{2}\{|R_+|^2 + |R_-|^2\} = \mathcal{R}_0 \quad (44)$$

determines the reflectivity $\mathcal{R}_0$ of unpolarized neutrons. From the latter equation it is clearly seen that nuclear and magnetic reflection potentials can, in principle, be determined without polarized neutrons. Indeed, the reflectivity curve $\mathcal{R}(p_0)$ should show two plateaus. The one at $p_{c-} \le p_0 \le p_{c+}$, where one half of unpolarized neutrons are reflected. The other half is totally reflected at $p_0 \le p_{c-}$ where $\mathcal{R}_0 = 1$.

In that sense, polarization does not add new insight but allows an independent determination of $|R_+|$ and $|R_-|$. In a particular case $\gamma = 0$, that is when the neutron polarization is collinear with the magnetization direction,

$$\mathcal{R}^{++} = \mathcal{R}^{+} = |R_+|^2, \text{ and } \mathcal{R}^{--} = \mathcal{R}^{-} = |R_-|^2 \quad (45)$$

while $\mathcal{R}^{+-} = \mathcal{R}^{-+} = 0$.

PNR also allows to determine the orientation of the in-plane magnetic induction vector with respect to the neutron polarization axis fixed in the laboratory coordinate system. Indeed, owing to equations (42) and (43) the weights of the positive and negative spin components contributing to the reflectivities $\mathcal{R}^{\pm}$ is controlled by the angle γ, as illustrated in the next section.

2.3 Quantum spin state of neutrons

Here we stress again that there exist only two wave numbers p_{c+} and p_{c-} of the total reflection independent of the angle γ and determined by equation (19). At low angles of incidence α PNR may show two plateaus, at which the reflected intensity does not vary with the wave vector transfer projection $Q_z = 2p_0$. At the first plateau, in accordance with equations (42–43) and equation (38), the values of $\mathcal{R}^{\pm}$ are determined by the angle γ, while at the second one $\mathcal{R}^{\pm} = 1$. Such a behavior is a direct consequence of the splitting of the neutron quantum spin states in a magnetic field of the reflecting medium.

In a recent paper, Radu *et al*. (2005b) have carried out an experiment which provides direct and unambiguous evidence that, indeed, two critical angles $\alpha_{c\pm}$ for the total reflection exist, corresponding to the $\mathcal{R}^{+}$ and to the $\mathcal{R}^{-}$ reflectivity, respectively:

$$Q_c^{\pm} = 2p_{c\pm} = \sqrt{V_n \pm \frac{2m}{\hbar^2}|\boldsymbol{\mu}\|\boldsymbol{B}_s|} \quad (46)$$

The goal was to find a system where the angle between the neutron polarization and direction of the magnetization inside of the film can be fixed and controlled. Then the $\mathcal{R}^{+}$ and $\mathcal{R}^{-}$ reflectivities were measured to determine whether the position of the critical edges changes as a function of the angle γ, or whether the critical edges stay fixed, and only intensity redistributes between reflections $\mathcal{R}^{+}$ and $\mathcal{R}^{-}$ with change of γ. The easiest way to control the angle is to rotate the magnetic film and therefore the magnetization direction with respect to the neutron spin polarization, which remains fixed in space outside of the sample. This requires that the film should have a high remanent magnetization.

As magnetic film, a 100-nm thick Fe layer on a Si substrate was chosen. The results are shown in Figure 3. Two characteristics of the reflectivities are observed: first, the critical edges are fixed and independent of the in-plane rotation angle of the magnetization vector, and second the $\mathcal{R}^{-}$ intensity continuously increases at the expense of the $\mathcal{R}^{+}$ intensity as a function of the γ angle. The plain experimental results as well as a detailed fit unambiguously show that the critical edges Q_c^{+} and Q_c^{-} for total reflection of the two spin states are fixed and are independent of the orientation of the magnetization vector in the film, confirming that the neutron quantum spin states inside of the sample are referred to the quantization axis parallel or antiparallel to the magnetization vector.

The fact that the intensities at the first plateaus in Figure 3 depend on γ in accordance with equations (42) and (43) allows to determine the angle γ, if it is not known in advance. For that purpose it is convenient to use the difference,

$$\mathcal{R}^{+} - \mathcal{R}^{-} = \{|R_+|^2 - |R_-|^2\}\cos\gamma \quad (47)$$

which is directly proportional to $\cos\gamma$. For the same purpose one can also use the so-called spin asymmetry:

$$SA = \frac{\mathcal{R}^{+} - \mathcal{R}^{-}}{\mathcal{R}^{+} + \mathcal{R}^{-}} = \frac{|R_+|^2 - |R_-|^2}{|R_+|^2 + |R_-|^2}\cos\gamma \quad (48)$$

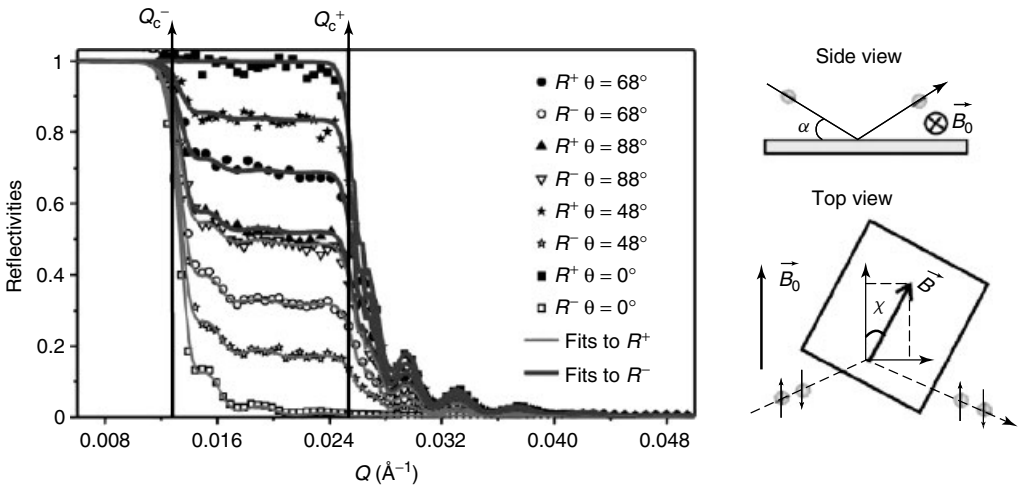

Figure 3. Experimental results of reflectivity curves $\mathcal{R}^+$ and $\mathcal{R}^-$ from a 100-nm-thick Fe film on a Si substrate. The reflectivities are plotted on a linear scale. The two sets of $\mathcal{R}^+$ (solid black symbols) and $\mathcal{R}^-$ (open black symbols) reflectivity curves were measured for four different angles γ (χ in author's (Radu *et al*., 2005b) notations) between the neutron polarization and the film magnetization vector (i.e., the magnetic induction B in the sample plane). The dark gray and light gray lines are the simulated $\mathcal{R}^+$ and $\mathcal{R}^-$ reflectivities, respectively. In panels on the right side, the experimental geometry is shown. The experiment demonstrate that, indeed, the critical edges Q_c^+ and Q_c^- do not depend on the tilt angle. (Reprinted figure with permission from F. Radu *et al*., *Phys Rev. B* Vol. 71, 214423, 2005. © 2005 by the American Physical Society.)

2.4 Phase shift and PNR with total polarization analysis

One can admit that equations (42) and (43) corresponding to the reduced version of PNR, as well as the equation for unpolarized reflectivity equation (44), contain only absolute values $|R_\pm|$ of reflectance amplitudes. On the other hand, below the total reflection edges the wave numbers $p_\pm$ and the amplitudes $R_\pm$ given in equation (38) are complex quantities. The latter ones can be presented as $R_\pm = |R_\pm| \exp(i\chi_\pm)$, where $\chi_\pm$ are phases missing in equations (42–44). They, however, enter the more general equations (39–41) providing at $\gamma \neq 0$ an access to interesting phenomena of the interference between spin states inside a magnetic media.

In order to demonstrate the role of the phases, let us consider the case when the polarization axis is normal to the vector of inductance, that is $\gamma = \pm\pi/2$. Then $\mathcal{R}^{++} = \mathcal{R}^{--}$, $\mathcal{R}^{+-} = \mathcal{R}^{-+}$, and reflectivities

$$\mathcal{R}^{\pm\pm} = \frac{1}{4}|R_+ + R_-|^2 = \frac{1}{4}\{|R_+|^2 + |R_-|^2 + 2|R_+||R_-|\cos\chi_{+-}\} \quad (49)$$

$$\mathcal{R}^{\pm\mp} = \frac{1}{4}|R_+ - R_-|^2 = \frac{1}{4}\{|R_+|^2 + |R_-|^2 - 2|R_+||R_-|\cos\chi_{+-}\} \quad (50)$$

contain the term, proportional to $\cos\chi_{+-}$, where $\chi_{+-} = \chi_+ - \chi_-$. The evolution of the phases $\chi_\pm$ and their difference is sketched in Figure 4(a). For a semi-infinite magnetic media with purely real nuclear SLD, each of the phases turns to zero above the corresponding critical edges, while they reach the maximum value $\chi_\pm = \pi$ at $p_0 = 0$. As a result, within the window $p_{c-} \leq p_0 \leq p_{c+}$ the difference $\chi_{+-} = \chi_+(p_0)$ increases when p_0 decreases. In this range the SF reflectivity, $\mathcal{R}^{\pm\mp}$, also increases and reaches maximum [1] at $p_0 = p_{c-}$, while the NSF reflectivity, $\mathcal{R}^{\pm\pm}$, decreases, but in a way that their sums $\mathcal{R}^{\pm} = \mathcal{R}^{\pm\pm} + \mathcal{R}^{\pm\mp}$ stay almost constant at the level of 0.5, as seen in Figure 4(b). Within the range $p_0 \leq p_{c-} \leq p_{c+}$ one has

$$\mathcal{R}^{\pm\pm} = \cos^2\frac{\chi_{+-}}{2}, \text{ and } \mathcal{R}^{\pm\mp} = \sin^2\frac{\chi_{+-}}{2} \quad (51)$$

This means that due to the constructive interference between spin states, NSF reflectivities at $p_0 \to 0$ increase and tend to one, while SF reflectivities vanish because of destructive interference.

The term containing the phase difference can be separated from other contributions to PNR just by subtraction:

$$\mathcal{R}^{\pm\pm} - \mathcal{R}^{\pm\mp} = |R_+||R_-|\cos\chi_{+-} \quad (52)$$

Therefore, in order to determine both the absolute values and the phase shift one needs to carry out additional measurements with different angles between the polarization axis and the inductance direction.

If neither the angle γ, nor nuclear and magnetic potentials (for instance, in the case of alloys, or complex compounds)

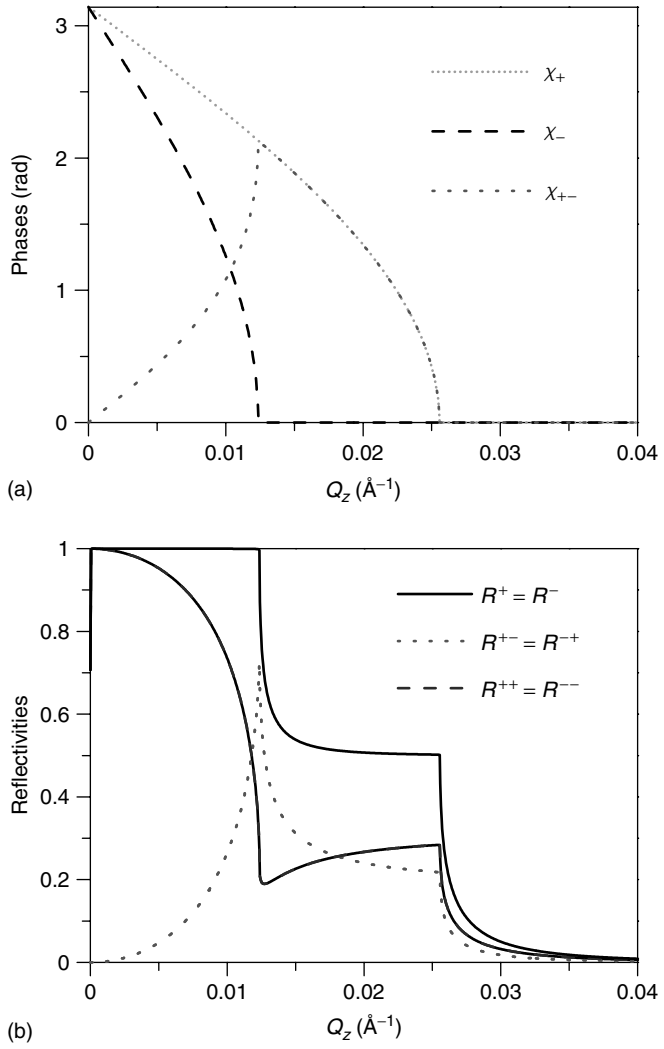

Figure 4. (a): Evolution of phases $\chi_+(Q_z)$, $\chi_-(Q_z)$ of reflection amplitudes $R_\pm = |R_\pm| \exp(i\chi_\pm)$ and the phase difference $\chi_{+-} = \chi_+ - \chi_-$ calculated for reflection from iron. At $Q_z \to 0$ the phases $\chi_\pm \to \pi$. (b): Non-spin-flip (dashed) and spin-flip (dotted) reflectivities calculated for iron with magnetization turned at 90° with respect to the polarization axis. The continuous line shows the sum $R^+ = R^- = R^{++} + R^{+-}$ (middle line in Figure 3). Note the sharp maximum of spin-flip reflectivities at $Q_z = Q_c^-$.

are a priory known, then the parameters can be found via the fitting of data to the theoretical model. For the semi-infinite homogeneous sample the nonlinear fitting routine may be rather stable providing a set of parameters even if only two reflectivities $\mathcal{R}^\pm$ are available. In this case, the phases vary in a restricted range $0 \le \chi^\pm \le \pi$ and are uniquely determined via, for example, the nuclear and magnetic SLDs.

However, this is not the case for more complicated magnetic SLD profiles of interest or even for a single magnetic film of a thickness d placed onto a non-magnetic substrate. In the latter case, all the considerations in the preceding text are valid, and one can easily find the reflection amplitudes $R_\pm$ just by matching the spin components of the wave functions at the outer surface and at the interface with the substrate. This will result in the explicit equation for the reflectances

$$R_\pm = \frac{R_\pm^F + R_{s\pm}^F e^{2i\varphi_\pm}}{1 + R_\pm^F R_{s\pm}^F e^{2i\varphi_\pm}} \tag{53}$$

Here $\varphi_\pm = p_\pm d$, $R_\pm^F$ are the reflection amplitudes from the front face of the sample are given in equation (38), and $R_{s\pm}^F$ are the Fresnel amplitudes for the neutron wave reflected from the interface between the film and the substrate

$$R_{s\pm}^F = \frac{p_\pm - p_s}{p_\pm + p_s} \tag{54}$$

These equations are similar to equation (38), in which the incoming wave number in the vacuum p_0 is substituted by $p_\pm$ in the magnetic film, and $p_s = \sqrt{p_0^2 - p_c^2}$ is the wave number of the neutron propagation in the substrate with the SLD $(Nb)_c = p_c^2/4\pi$.

Traveling through the film from the surface to the substrate each of the neutron spin-wave components now gains the phase factor $\varphi_\pm = p_\pm d$. This leads to interference phenomena manifested in the oscillation of the reflection coefficients (so-called Kiessig fringes). Such oscillations above the total reflection region can be recognized in Figure 3 and are due to the finite thickness of the iron film deposited on a silicon substrate.

Interestingly such oscillations can be observed (te Velthuis, Felcher, Blomquist and Wäppling, 2001; Toperverg, Lauter and Lauter-Pasyuk, 2005a) also in the range $p_{c-} \le p_0 \le p_{c+}$, if the magnetization is not collinear with the polarization axis. In this case, they are due to the interference between different spin components of the neutron wave transmitted into the film and reflected from the substrate. An example of such oscillations is given in Figure 5, where SF and NSF reflectivities are plotted against the wave vector transfer. The experiment (Toperverg, Lauter and Lauter-Pasyuk, 2005a) was carried out on a sample consisting of ^{57}Fe film deposited on a sapphire substrate with the critical wave number $p_c = 8.46 \times 10^{-3}$Å^{-1}. The isotope of iron is chosen due to the fact, that the nominal value for $p_{c+} = 9.35 \times 10^{-3}$Å^{-1} is close to the value of p_c for the substrate, while for the negative spin projection $p_{c-} = i6.13 \times 10^{-3}$Å^{-1} is imaginary. Hence, the positive spin component can totally be reflected from the front face of the sample with almost no account of the interface with the substrate. In contrast, total external reflection of the negative spin component can only be due to the substrate optical potential. But this means that at $p_0 \le p_c$ the negative spin component acquires an additional phase shift with respect to the positive one. In the particular case

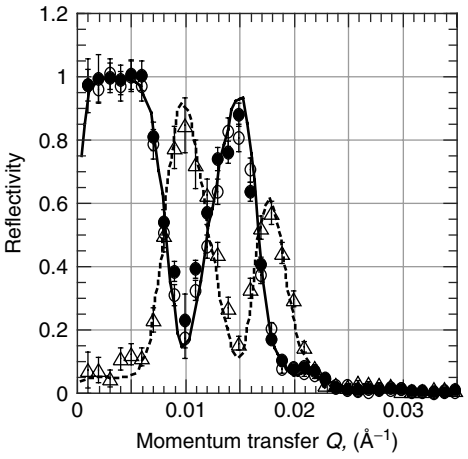

Figure 5. Pseudoprecession oscillations in SF (triangles) and NSF (circles) reflectivities recorded from a ^{57}Fe film magnetized perpendicular to the neutron polarization vector. (Reproduced from Toperverg *et al*., 2005, with permission from Elsevier © 2005.)

of complete compensation, that is if $p_c = p_{c+}$ and $p_{c-} = 0$, the wave number $p_- = p_0$ and $p_+ = p_s$. Then, owing to equation (38) and equation (54) $R_-^F = R_{s+}^F = 0$, while $R_+^F = R_{s-}^F = |R_{s-}^F| \exp(i\chi_s)$. Below the total reflection in accordance with equation (53) this yields $R_+ = \exp(i\chi_s)$ and $R_- = \exp(2i\varphi_0 + i\chi_s)$, where φ_0 is the phase shift due to the film, χ_s is the phase shift due to the substrate, and in equation (51) $\chi_{+-} = -2\varphi_0 = -2p_0 d$.

In Toperverg, Lauter and Lauter-Pasyuk (2005a) the authors argue that at such a reflection the vector of the neutron polarization $\boldsymbol{P}$ rotates around the film inductance $\boldsymbol{B}$ direction for an angle $2\varphi_0$. This phenomenon is called the *Larmor pseudo-precession*.

2.5 Theoretical framework of polarized neutron reflection from multilayers

From the reflected intensities the potential profile along the sample normal can be retrieved and hence PNR provides a tool for layer-by-layer magnetometry (Rücker *et al*., 2002). From general symmetry arguments it follows that equations (39–43) are also valid in the case of any layered structure with collinearly magnetized layers. In this case, each amplitude R_+ and R_- in equations (39–43) can be calculated with a standard Parratt recursion routine (Parrat, 1954), or via the matrix formalism (Born and Wolf, 1975). The net magnetization may certainly make any angle γ with the direction of polarization analysis. Interface roughness, as it occurs in all realistic samples, is best taken into account by a large number of infinitely thin slabs of a gradually varying potential across an interface (Ankner, Majkrzak and Satija, 1993; Schreyer, 1994), or by assuming a specific interface profile, as in the Névot-Croce model (Névot and Croce, 1980).

If, however, the magnetization direction varies as a function of the z coordinate, for example from layer to layer, then equations (39–43) are not valid anymore. This is due to the fact that the reflectivity cannot be characterized by simply a single angle between magnetization and neutron polarization vectors (Toperverg, Rühm, Donner and Dosch, 1999) because of the PNR signal carries an information not only on the total magnetization direction, but also on its vectorial depth profile. This can be illustrated by a simple example of a bilayer with equal layers but with layer inductions $\boldsymbol{B}_1$ and $\boldsymbol{B}_2$ which make a certain angle γ against each other. Then, if $|\boldsymbol{B}_1| = |\boldsymbol{B}_2|$ the net inductance vector $\boldsymbol{B} = \boldsymbol{B}_1 + \boldsymbol{B}_2$ is just the sum of two vectors. However, it is intuitively clear that the reflectivity is sensitive not only to the direction of the vector $\boldsymbol{B}$ but also to the order of $\boldsymbol{B} = \boldsymbol{B}_1$ and $\boldsymbol{B}_2$ in a sequence. Indeed, if for instance, layers are sufficiently thick, so that neutrons can be totally reflected just from the top layer, then namely, the top layer magnetization, but not the net magnetization direction, will determine the reflectivities at the total reflection range. Well above the total reflection, the neutron wave penetrates deep into the system and the role of the bottom-layer magnetization gradually increases for an elevated angle of incidence. This consideration shows that for noncollinear structures the angle γ between the polarization direction and the vector $\boldsymbol{B}$ does not solely determine the behavior of the reflected intensity. Formally, there also exists a direction given by the direct product $[\boldsymbol{B}_1 \times \boldsymbol{B}_2]$. This vector alters its direction if the layers are interchanged and thus it is sensitive to the order of the induction vectors in a sequence.

If the direction of the vector $\boldsymbol{B}(z)$ depends on the z-coordinate, then the way of solving of equations (12) and (13) given in the preceding text has to be reconsidered. In the past, several methods were developed to treat this problem. The earliest matrix formalism was provided by Blundell and Bland (1992), a generalized matrix representation has been described by Radu and Ignatovich (1999) and Rühm, Toperverg and Dosch (1999) have implemented a so-called Supermatrix formalism (Toperverg, Rühm, Donner and Dosch, 1999), and a comprehensive overview of the theoretical treatment of PNR has been provided by Fermon and Menelle (1999).

Usually, in order to analyze experimental data for thin films and multilayers, theoretical reflectivities have to be calculated assuming a potential well structure $V_{ij}(z)$ composed of slabs of constant potential with sharp interfaces. Then a Parratt-type recursion formalism determines all transmitted and reflected amplitudes at each interface. Here we briefly sketch the Parratt routine adjusted for polarized neutron reflection from a sequence of layers with arbitrary arrangement of layer magnetization vectors. This,

so-called superiterative algorithm (Toperverg, 2002a,b) is better suited for numerical calculations (Kentzinger, Toperverg and Rücker, 2003), than those referred to above (Radu and Ignatovich, 1999; Rühm, Toperverg and Dosch, 1999; Fermon and Menelle, 1999).

Following the standard procedure let us divide the slab, as in the preceding text, into slices according to

$$\hat{V}(z) = \sum_{l=1}^{N} \{\hat{V}_{nl} + \hat{V}_{ml}\} \tag{55}$$

where, $\hat{V}_{nl} = \hat{1} V_{nl}$ for $z_{l-1} \leq z < z_l$ and V_{nl} is the nuclear optical potential (if the interaction with the nuclear spin is neglected) of the l^{th} slice, and $\hat{1}$ is the unit matrix in the spin space [2]. The magnetic part of the interaction operator $\hat{V}_{ml} = -\hat{\boldsymbol{\mu}} B_l$ is defined as in the preceding text.

Let us first note, that one can avoid writing down the Schödinger equation (9) in a particular (laboratory) coordinate system as a couple of equations (12) and (13), but instead, represent the solution of equation (9) just above the surface in the following general form

$$|\psi_0(z)\rangle = \{e^{ip_0 z} + e^{-ip_0 z}\hat{R}\}|\Psi_0^i\rangle \tag{56}$$

where $|\Psi_0^i\rangle$ is the initial vector of neutron spin states at the surface, $\hat{R}$ is the 2×2 reflectance matrix transforming spin components of the incoming wave function $|\Psi_0^i\rangle$ into the components of the reflected wave $|\psi_R(0)\rangle = \hat{R}|\Psi_0^i\rangle$.

In the laboratory coordinate system, an explicit expression for the elements $r_{\pm\pm}$ and $r_{\pm\mp}$ of the reflectance matrix $\hat{R}$ and assuming a semi-infinite magnetic sample is given in equation (37).

The boundary conditions at the interfaces between layers can be written in a compact form, if one keeps the interaction potential operator $\hat{V}(z)$ in equation (9) in the vector form of equation (55) independent of the coordinate system and if one applies the algebraic rules of the Pauli operators. To do so, one should just notice that the vector of states $|\psi_l(z)\rangle$ inside any layer l can be written via the vector of initial states $|\Psi^i(0)\rangle$ in the same way as in equation (56) $|\psi_l(z)\rangle = \hat{\mathcal{S}}_l(z)|\Psi_0^i\rangle$, where

$$\hat{\mathcal{S}}_l(z) = \{e^{i\hat{\varphi}_l(z)}\hat{t}_l + e^{-i\hat{\varphi}_l(z)}\hat{r}_l\} \tag{57}$$

and the matrices $\hat{t}_l$ and $\hat{r}_l$ take into account the transformation of the neutron spin-wave components at refraction through and reflection from the interfaces. Here $\hat{\varphi}_l(z) = \hat{p}_l(z - z_{l-1})$ are the phase matrices, and $z_0 = 0$. The wave number matrix $\hat{p}_l = \sqrt{p_0^2 - \hat{p}_{cl}^2}$ is diagonal if the quantization axis is chosen parallel to the vector $\boldsymbol{B}_l$. Then its eigenvalues $p_{l\pm} = \sqrt{p_0^2 - p_{cl\pm}^2}$ are determined by the critical wave numbers $p_{cl\pm}^2 = 4\pi(nb_{nl} \mp nb_{ml})$, where nb_{nl} and nb_{ml} are the nuclear and magnetic scattering length densities within the l^{th} layer. The exponents in equation (57) are generally represented as (Landau and Lifshits, 1977)

$$e^{\pm i\hat{\varphi}_l(z)} = \frac{1}{2}\{[e^{\pm i\varphi_{l+}(z)} + e^{\pm i\varphi_{l-}(z)}] + (\hat{\boldsymbol{\sigma}}\boldsymbol{b}_l)[e^{\pm i\varphi_{l+}(z)} - e^{\pm i\varphi_{l-}(z)}]\} \tag{58}$$

where $\boldsymbol{b}_l = \boldsymbol{B}_l/|\boldsymbol{B}_l|$ and $\varphi_{l\pm} = p_{l\pm}(z - z_{l-1})$. These exponents are also diagonal along with the matrix $\hat{p}_l$.

The transmittance, $\hat{t}_l$, and reflectance, $\hat{r}_l$ matrices are, however, diagonal in the same representation as the matrix $\hat{p}_l$ only for a collinear magnetization arrangement. In general, the components of those matrices are to be found via the continuity conditions for the wave function spin components and their first derivative at subsequent interfaces

$$|\psi_{l+1}(z_{l+1})\rangle = |\psi_l(z_{l+1})\rangle \tag{59}$$

$$|\psi'_{l+1}(z_{l+1})\rangle = |\psi'_l(z_{l+1})\rangle \tag{60}$$

These conditions together with equation (57) immediately deliver the following couple of matrix equations

$$\hat{t}_{l+1} + \hat{r}_{l+1} = e^{i\hat{\varphi}_l}\hat{t}_l + e^{-i\hat{\varphi}_l}\hat{r}_l \tag{61}$$

$$\hat{p}_{l+1}\{\hat{t}_{l+1} - \hat{r}_{l+1}\} = \hat{p}_l\{e^{i\hat{\varphi}_l}\hat{t}_l - e^{-i\hat{\varphi}_l}\hat{r}_l\} \tag{62}$$

where $\hat{\varphi}_l = \hat{p}_l d_l$ is the matrix of the phase shift gained over the layer thickness d_l. The sequence of these coupled equations should, as usual, be completed by adding two more boundary conditions: one for the front interface (usually vacuum) and a second one for the back interface N (usually the substrate):

$$\hat{1} + \hat{R} = \hat{t}_1 + \hat{r}_1 \tag{63}$$

$$p_0(\hat{1} - \hat{R}) = \hat{p}_1(\hat{t}_1 - \hat{r}_1) \tag{64}$$

$$\hat{T} = e^{i\hat{\varphi}_N}\hat{t}_N + e^{-i\hat{\varphi}_N}\hat{r}_N \tag{65}$$

$$\hat{p}_s\hat{T} = \hat{p}_N(e^{i\hat{\varphi}_N}\hat{t}_N - e^{-i\hat{\varphi}_N}\hat{r}_N) \tag{66}$$

where the wave number operator in the substrate is denoted as $\hat{p}_s$.

The set of equations (61–66) look exactly the same as those (Parrat, 1954) for spinless particles and the only difference is that each equation is written as a 2×2 matrix, which actually represents four equations for the matrix elements. However, one may not write them explicitly but rather use general rules of matrix algebra and directly solve the system of equations (61–66) for the reflectance $\hat{r}_l$ matrices and transmittance $\hat{t}_l$ matrices, including $\hat{R}$ and $\hat{T}$.

One of the ways to find a final solution is to apply a customarily used matrix formalism (Born and Wolf, 1975) and express each couple of equations (61–62) as one supermatrix (SM) equation. Then multiplication of supermatrices determined for each layer results in a global supermatrix, linking together $\hat{R}$ and $\hat{T}$ matrices in equations (63–66). This allows to express the elements of $\hat{R}$ and $\hat{T}$ via the elements of the global supermatrix.

Despite of a certain elegancy and transparency for the theoretical analysis, the SM approach is 'ill-conditioned' and may cause numerical problems for a large number and/or large thicknesses of the layers. The source of the problems is indicated in (Toperverg, 2002a) where instead of SM formalism a generalization of the Parratt formalism (Parrat, 1954) was proposed. Such a generalization is based on the same principles, as the SM routine, although it uses another algorithm for calculations. The trick is that the matrix equations (61) and (62) can be immediately solved with respect to the ratio $\hat{R}_l = (\hat{r}_l \hat{t}_l^{-1})$ written as

$$\hat{R}_l = \mathrm{e}^{i\hat{\varphi}_l}\{(\hat{1} - \hat{p}_l^{-1}\hat{p}_{l+1}) + (\hat{1} + \hat{p}_l^{-1}\hat{p}_{l+1})\hat{R}_{l+1}\} \times \{(\hat{1} + \hat{p}_l^{-1}\hat{p}_{l+1}) + (\hat{1} - \hat{p}_l^{-1}\hat{p}_{l+1})\hat{R}_{l+1}\}^{-1}\mathrm{e}^{i\hat{\varphi}_l} \quad (67)$$

These equations can easily be solved via recursion procedures, beginning from the values $\hat{R}_{N+1} = 0$ and ending by finally computing the reflectance matrix $\hat{R} = \hat{R}_0$.

Additionally, one can calculate, if necessary, the transmittance matrices via the recursive solution of the following set of equations

$$\hat{t}_{l+1} = \{\hat{1} + \hat{R}\}^{-1}\{\hat{1} + \mathrm{e}^{i\hat{\varphi}_l}\hat{R}_l\mathrm{e}^{i\hat{\varphi}_l}\}\mathrm{e}^{i\hat{\varphi}_l}\hat{t}_l \quad (68)$$

In this case, the recursion begins with $\hat{t}_0 = \hat{1}$ and ends with $\hat{t}_{N+1} = \hat{T}$. Finally, the reflectance matrices $\hat{r}_l = \hat{R}_l\hat{t}_l$ can also be found via computing the reflectance matrix $\hat{R}_l$ and $\hat{t}_l$. In analogy to the SM approach, this method may be called *Super-Recursion* (*SR*), or Matrix–Recursion (MR) formalism, because it uses recursion routines for solution of coupled matrix equations. The SR formalism allows to compute spin components of the reflectance matrix for arbitrary orientations between magnetization directions in subsequent layers.

In the collinear case, all partial reflectance matrices $\hat{R}_l$ can simultaneously be diagonalized along with the total reflectance matrix $\hat{R}$ via choosing the quantization axis parallel to the sample inductance vector. Then equation (67) reduces to two unlinked sets of equations: one set for eigenvalues R_{l+} and the other for R_{l-} of the reflectance matrices $\hat{R}_l$. Solving these sets of equations one can express the eigenvalues $R_\pm$ of the reflectance matrix $\hat{R}$ via the Fresnel reflectance amplitudes $R^F_{l\pm}$ as given in equation (38) and phases $\varphi_{l\pm}$ for positive and negative spin projections onto the inductance direction. An example of solutions of equation (67) for eigenvalues $R_\pm$ is presented in equation (53).

2.6 Vector polarization analysis

In an arbitrary coordinate system the reflectance matrix $\hat{R}$ contains all four elements $r_{\pm\pm}$ and $r_{\pm\mp}$ which are expressed via the eigenvalues $R_\pm$ and the angle γ as given in equation (37). As soon as those elements are found, one can easily compute the NSF and the SF reflection coefficients: $\mathcal{R}^{\pm\pm} = |r_{\pm\pm}|^2$ and $\mathcal{R}^{\pm\mp} = |r_{\pm\mp}|^2$ as it has been demonstrated in the preceding text in equations (39–41) and in equations (49) and (50) for a single film. However, as it was already pointed out, the reflectivity for the system with noncollinear magnetization arrangement is no longer characterized solely by the angle γ between the net magnetization of the system and the polarization analysis direction. In particular, a SF signal may occur even at $\gamma = 0$ carrying a signature of noncollinearity.

The kinematics depicted in Figure 1 does not exhaust all the capabilities of PNR. Indeed, the classical 3D vector of the neutron polarization $\boldsymbol{P}$ is generally defined as mean value $\boldsymbol{P} = \frac{1}{2}\langle\hat{\boldsymbol{\sigma}}\rangle$ of the neutron spin operator over spin states in the neutron beam. In an arbitrary coordinate system, this vector may have all three Cartesian projections P_x, P_y and P_z being nonzero with $|\boldsymbol{P}| = \sqrt{P_x^2 + P_y^2 + P_z^2} \leq 1$. In the particular case sketched in Figure 1, the polarization vector is initially set along the y axis, and only the projection P_y of the final polarization vector $\boldsymbol{P}$ is assumed to be probed. Two other undetermined components P_z and P_x are, nonetheless, quite important even in the case of reflection from semi-infinite media, or a single magnetic film.

This becomes clear if one admits that the polarization vector of neutrons may not only change its length, but also change direction precessing around a field direction.

The 1D analysis of the polarization vector, which probes neutron spin states along only one direction, cannot unambiguously distinguish between those processes. Then the missing information does not allow to uniquely determine the direction of the vectors $\boldsymbol{B}_l$ in complicated noncollinear structures. In the simplest case covered by equation (37), it is, for example, not possible to discriminate the tilt angle γ from $\gamma + \pi$. This can already be seen from the fact, that equation (37) contains only $\sin^2\frac{\gamma}{2}$ and $\cos^2\frac{\gamma}{2}$, but not $\sin\gamma$. The latter determines whether the magnetization vector in Figure 1 is tilted to the left, or to the right with respect to the y-axis.

The method of 3D vector polarization analysis has been invented by Rekveldt (1971) and Drabkin, Okorokov and

Runov (1972) for spin analysis of neutron spin states in the beam passing through F materials. Later on, the method was extended to small angle by Okorokov and Runov (2001) and inelastic neutron scattering by Tasset (2001), while its application in PNR studies was proposed in Toperverg, Nikonov, Lauter-Passyuk and Lauter (2001).

Here, we consider the general principles of 3D PNR analysis which allows to evaluate all three projections of the outgoing polarization vector by arbitrarily setting the initial polarization vector. The corresponding consideration is based on equations for PNR which can be written down in the tensor form independent of a particular choice of the coordinate system. Such an opportunity is already provided by equation (56), where the reflectance matrix $\hat{R}$ transforms the spin components of the incoming neutron $|\Psi_0^i\rangle$ into the components of reflected wave $|\psi_R(0)\rangle = \hat{R}|\Psi_0^i\rangle$ in the immediate vicinity of the surface. In this range, $|\Psi_0^i\rangle$ is determined by the spin state of the incident polarized neutrons and field conditions on its path to the sample. Observable quantities, for example, spin components of the neutron flux density, are meant as statistical averages over the initial polarized neutron states and over the neutron traces to the sample. Correspondingly, neutrons reflected from the sample propagate trough the analyzing system to the detector. The result of this propagation, analysis, and detection is described by the projection $\langle\Psi_0^f|\psi_R(0)\rangle$ of the reflected vector of neutron states $|\psi_R(0)\rangle$ onto the vector of states $\langle\Psi_0^f|$ possible due to the analyzing system. The latter is also a statistical device, and the reflected flux density has to be considered as a result of statistical averaging of the probability $|\langle\Psi_0^f|\psi_R(0)\rangle|^2$ over the states of the analyzing system and the flight passes taken by the outgoing neutrons. After all averaging, the measurable reflectivity $\mathcal{R}$ is given by the expectation value

$$\mathcal{R} = \overline{|\langle\Psi_0^f|\hat{R}|\Psi_0^i\rangle|^2} = \mathrm{Tr}\{\hat{\rho}^f\hat{R}\hat{\rho}^i\hat{R}^+\} \tag{69}$$

where $\hat{\rho}^i$ and $\hat{\rho}^f$ are the spin-density matrices of incoming and outgoing neutron states at the sample surface

$$\hat{\rho}^i = \overline{|\Psi^i(0)\rangle\langle\Psi^i(0)|} = \frac{1}{2}\left\{1 + (\boldsymbol{P}^i\hat{\boldsymbol{\sigma}})\right\} \tag{70}$$

$$\hat{\rho}^f = \overline{|\Psi^f(0)\rangle\langle\Psi^f(0)|} = \frac{1}{2}\left\{1 + (\boldsymbol{P}^f\hat{\boldsymbol{\sigma}})\right\} \tag{71}$$

Here the 2×2 density matrices are expanded over a set of matrices which includes the unit matrix and three orthogonal Pauli matrices which complete the vector $\hat{\boldsymbol{\sigma}}$. Such the expansion provides a parameterization of the density matrix with the incoming 3D polarization vector, $\boldsymbol{P}^i = \boldsymbol{b}_i|\boldsymbol{P}^i|$, and the 3D vector $\boldsymbol{P}^f = \boldsymbol{b}_f\boldsymbol{P}^f$ of polarization efficiency. The unit vectors $\boldsymbol{b}_i$ and $\boldsymbol{b}_f$ set the directions in which the neutrons are polarized and analyzed, while the absolute values $|\boldsymbol{P}^i| \leq 1$ and $|\boldsymbol{P}^f| \leq 1$ show the degree of the incident neutron beam polarization and efficiency of the analyzing device in corresponding directions.

Parameterizing the 2×2 reflectance matrix $\hat{R} = R(\hat{\boldsymbol{\sigma}})$ in the same manner as in equations (70) and (71) yields an invariant representation:

$$\hat{R} = R + (\boldsymbol{R}\hat{\boldsymbol{\sigma}}) \tag{72}$$

via the complex scalar $R = \frac{1}{2}\mathrm{Tr}\{\hat{R}\}$, and the vector $\boldsymbol{R} = \frac{1}{2}\mathrm{Tr}\{\hat{R}\hat{\boldsymbol{\sigma}}\}$ with three, generally nonzero, complex Cartesian projections R_x, R_y and R_z. These projections, as well as the scalar R, can readily be expressed via the (complex) eigenvalues $R_\pm$ of the matrix $\hat{R}$ and components of the (complex) unit vector $\boldsymbol{r} = \boldsymbol{R}/\sqrt{\boldsymbol{R}^2}$. The latter determines the coordinate system in which the matrix

$$\hat{R} = \frac{1}{2}[(R_+ + R_-) + (\boldsymbol{r}\boldsymbol{\sigma})(R_+ - R_-)] \tag{73}$$

is diagonal. One can also recognize that the scalar R and the length of the vector $\boldsymbol{R}$ are independent of the choice of the coordinate. They are expressed via the matrix invariants: the trace $(R_+ + R_-) = 2R$ and determinant $R^2 - \boldsymbol{R}^2 = R_+R_-/4$ of the matrix $\hat{R}$ so, that $\boldsymbol{R}^2 = (R_+ - R_-)^2/4$.

Note that in a collinear magnetization arrangement the direction of the vector $\boldsymbol{R}$ coincides with that of the inductance. In a more general case, it has all three projections, for example, normal to the surface, and depends on the wave vector transfer. Therefore, the reflectance matrix cannot be diagonalized in any fixed coordinate system independent of Q_z.

One of the advantages of the representation in equation (73) is that it is invariant with respect to the choice of the coordinate system. The other is that one can apply the rules of the Pauli matrix algebra and after substitution of equations (70–72) into equation (69) and calculating the traces, one readily obtains (Toperverg, Rühm, Donner and Dosch, 1999) the following equation for the reflectivity $\mathcal{R} = \mathcal{R}(\boldsymbol{P}^i, \boldsymbol{P}^f)$ in the invariant tensor form:

$$\mathcal{R} = \mathcal{R}(P^i_\mu, P^f_\nu) = \mathcal{R}_0 + \mathcal{R}^i_\mu P^i_\mu + \mathcal{R}^f_\mu P^f_\mu + \mathcal{R}_{\mu\nu}P^i_\mu P^f_\nu \tag{74}$$

where summation over repeating indices μ and ν is assumed. These indices enumerate the Cartesian projections x, y, and z of the vectors $\boldsymbol{P}^i$, $\boldsymbol{P}^f$, $\boldsymbol{\mathcal{R}}^i$, and $\boldsymbol{\mathcal{R}}^f$ as well as of the tensor $R_{\mu\nu}$. Equation (74), together with the procedure for the calculation of the four components of the reflectance matrix $\hat{R}$ (four complex functions R, R_x, R_y, and R_z), totally solves the problem to compute all NSF, $\mathcal{R}^{\pm\pm} = \mathcal{R}(\pm\boldsymbol{P}^i, \pm\boldsymbol{P}^f)$, and SF, $\mathcal{R}^{\pm\mp} = \mathcal{R}(\pm\boldsymbol{P}^i, \mp\boldsymbol{P}^f)$ reflectivities for an arbitrary orientation between the initial polarization and the polarization

analysis directions, and at any distribution of the magnetization directions across the multilayer stack. Equation (74) is exact and general. It is also valid for the transmission coefficient, if one just substitutes the reflectance, $\hat{R}$, for the transmittance, $\hat{T}$, matrices.

The first term in equation (74) is independent of either incoming and outgoing polarization and describes the reflection of unpolarized neutrons. The next two terms are linear with respect to each of the polarization vectors $\boldsymbol{P}^i$ and $\boldsymbol{P}^f$. Together with the first term they determine the reflectivity in the cases when either the neutrons are initially polarized ($\boldsymbol{P}^i \neq 0$), but no analysis (at $\boldsymbol{P}^f = 0$) is assumed, or alternatively, polarization due to reflection of initially unpolarized ($\boldsymbol{P}^i = 0$) neutrons is analyzed. The last term in equation (74) is bilinear with respect to the vectors $\boldsymbol{P}^i$ and $\boldsymbol{P}^f$. It describes that the contribution of the reflection with the evolution of the initial polarization vector caused by magnetic interaction.

The form of equation (74) follows from the basic properties of spin 1/2 particles and can immediately be written down without any preknowledge about a magnetization arrangement in the reflecting system. It uses only the fact that any scalar function of the spin 1/2 operator, for example, $\hat{R} = R(\hat{\boldsymbol{\sigma}})$ in equation (72), is reduced to a linear function (Landau and Lifshits, 1977) of $\hat{\boldsymbol{\sigma}}$.

An explicit expression for the coefficients $\mathcal{R}_0$, $\boldsymbol{\mathcal{R}}^i$, $\boldsymbol{\mathcal{R}}^f$, and $R_{\mu\nu}$ in equation (72) are as follows:

$$\mathcal{R}_0 = \frac{1}{2}\{|R|^2 + |\boldsymbol{R}|^2\} \tag{75}$$

$$\mathcal{R}^i_\mu = \Re\{R^* R_\mu\} + \frac{1}{2}\Im\{[\boldsymbol{R}^* \times \boldsymbol{R}]_\mu\} \tag{76}$$

$$\mathcal{R}^i_\mu = \Re\{R^* R_\mu\} - \frac{1}{2}\Im\{[\boldsymbol{R}^* \times \boldsymbol{R}]_\mu\} \tag{77}$$

$$\mathcal{R}_{\mu\nu} = \frac{1}{2}\{|R|^2 - |\boldsymbol{R}|^2\}\delta_{\mu\nu} + \Re\{R^*_\mu R_\nu\} - \frac{1}{2}\Im\{R^* R_\lambda\}\varepsilon_{\mu\nu\lambda} \tag{78}$$

where $\delta_{\mu\nu}$ is the Kronecker symbol, and $\varepsilon_{\mu\nu\lambda}$ is the Levi–Civita tensor. This tensor is totally antisymmetric with respect to its spatial indices. At first sight the last terms in equations (76–78) violate the reciprocity principle which requires the total invariance of the scattering cross sections with respect to interchange between initial and final states, that is inversion of the scattering process. Owing to this requirement it is expected that $\mathcal{R}^{+-} = \mathcal{R}^{-+}$. In particular, one expects no difference placing the spin analyzer in front, or behind the sample when measuring $\mathcal{R}^{\pm}$. However, due to the last terms in equations (76) and (77), which may exist for noncollinear structures, the first version of the reduced polarization analysis measures reflectivities $\mathcal{R}^{0\pm}$, while the second version provides $\mathcal{R}^{\pm 0} \neq \mathcal{R}^{0\pm}$. From equations (78) and (74) it is also evident that $\mathcal{R}^{+-} \neq \mathcal{R}^{-+}$ if $\boldsymbol{P}^i$ is not collinear with $\boldsymbol{P}^f$ and with the sample magnetization.

Here it is important to recall that polarization and magnetization are pseudovectors which are odd in time, changing sign at time reversal as well as at inversion of the coordinate system. Therefore, the reciprocity principle includes alternation of the magnetization directions in all layers if the initial and final neutron states (including spin states) are interchanged.

The role of the last two terms in equations (76) and (77) can be illustrated by the simplest example of 1D polarization analysis with $\boldsymbol{P}^i$ and $\boldsymbol{P}^f$ parallel with the y-axis, as considered in the preceding text. In this case, the set of equations (74) and (78) reduces to the following form

$$\begin{aligned}\mathcal{R} = \frac{1}{4}\{&|R + R_y|^2(1 + P^i_y)(1 + P^f_y) \\ &+|R - R_y|^2(1 - P^i_y)(1 - P^f_y) \\ &+|R_x - i R_z|^2(1 + P^i_y)(1 - P^f_y) \\ &+|R_x + i R_z|^2(1 - P^i_y)(1 + P^f_y)\}\end{aligned} \tag{79}$$

From this equation it follows that at ideal polarization, that is at $P^i_y = \pm 1$ and $P^f_y = \pm 1$ the difference between $\mathcal{R}^{+-}$ and $\mathcal{R}^{+-}$ is solely due to the term R_z which appears due to noncollinearity in the layer magnetization arrangement.

In the collinear case, the set of equations (75–78) is substantially simplified. In particular, the two last terms in equations (76) and (77) vanish, which distinguish the chirality in the sequence of the layer magnetization vectors. Finally the set of equations (75–78) can be represented via the eigenvalues $R_\pm$ of the reflectance matrix

$$\mathcal{R}_0 = \frac{1}{4}\{|R_+|^2 + |R_-|^2\} \tag{80}$$

$$\mathcal{R}^i_\mu = \mathcal{R}^f_\mu = \frac{b_\mu}{4}\{|R_+|^2 - |R_-|^2\} \tag{81}$$

$$\begin{aligned}\mathcal{R}_{\mu\nu} = \frac{1}{4}\{&(|R_+|^2 + |R_-|^2)b_\mu b_\nu + 2\Re(R^*_+ R_-)(\delta_{\mu\nu} - b_\mu b_\nu) \\ &+2\Im(R^*_+ R_-)\varepsilon_{\mu\nu\lambda} b_\lambda\}\end{aligned} \tag{82}$$

and the projections of the unit vector $\boldsymbol{b}$ pointing in the direction of the net inductance. The first two contributions to the reflectivity, which are due to equations (80) and (81), are symmetric with respect to the interchange of $\boldsymbol{P}^i$ and $\boldsymbol{P}^f$. The tensor $\mathcal{R}_{\mu\nu}$ in equation (82) is decomposed into three orthogonal tensors of different symmetry. The first two terms are symmetric with respect to the interchange of $\boldsymbol{P}^i$ and $\boldsymbol{P}^f$ and acting on the projections of the polarization vectors parallel to $\boldsymbol{b}$ (the first term) and perpendicular (the second term) to $\boldsymbol{b}$. The components of the last tensor in equation (82)

are also perpendicular to $\boldsymbol{b}$, but this tensor is antisymmetric. It contributes to the reflectivity only if all three vectors $\boldsymbol{P}^i$, $\boldsymbol{P}^f$ and $\boldsymbol{b}$ are noncollinear. In contrast to all other contributions, it is sensitive to the sign of $\boldsymbol{b}$. If for example, the vector $\boldsymbol{P}^i$ has the only component P_y^i, while $\boldsymbol{P}^f$ is directed normal to the surface and has the component P_z^f, then this term is proportional to the product $b_x P_y^i P_z^f$ and is sensitive to the sign of the magnetization projection b_x. This allows to determine whether the magnetization vector in Figure 1 is tilted to the left, or to the right with respect to the y axis.

The role of chirality is illustrated in Figure 6 where PNR curves have been calculated for a semi-infinite sample of iron with the magnetization being tilted by $\gamma = +45^\circ$ (Figure 6a) and $\gamma = -45^\circ$ (Figure 6b) with respect to the initial polarization directed along the y axis. The final polarization is analyzed along the z axis normal to the surface. One can clearly see the interchange between the different components of the PNR matrix as the angle γ changes sign.

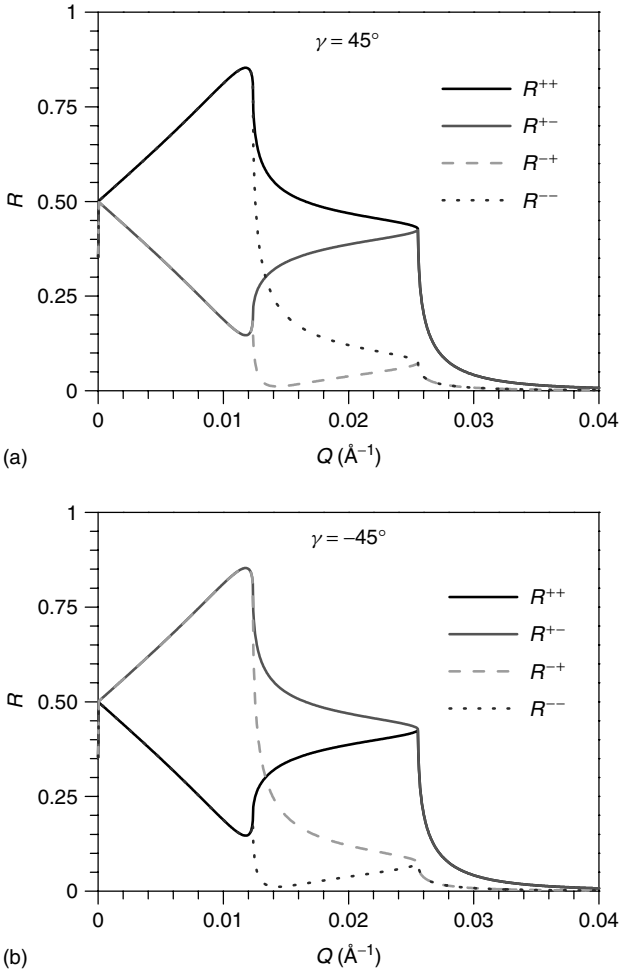

Figure 6. NSF (solid lines) and SF (dashed lines) reflectivities from iron with the magnetization tilted by the angle $\gamma = 45^\circ$ (a) and by the angle $\gamma = -45^\circ$ (b) with respect to the y axis. The initial polarization oriented parallel to the y axis, while the final polarization analyzed is along the z axis.

2.7 Kinematics of off-specular scattering

In the consideration in the preceding text, it was assumed that the surface is laterally infinite and homogeneous. Moreover, we have intentionally ignored the atomic structure of the magnetic media and introduced the optical potential expressed via the SLD, the quantity averaged over a scale much greater than an atomic scale. It is intuitively clear that those approximations are quite reasonable in the range of shallow angles of incidence, $\alpha_i \ll 1$ and reflection $\alpha_f \ll 1$. At these conditions the projection $Q_z = (2\pi/\lambda)(\sin\alpha_i + \sin\alpha_f) \approx 2\pi(\alpha_i + \alpha_f)/\lambda$ of the wave vector transfer $\boldsymbol{Q}$ is much smaller than the reciprocal interatomic spacings. This justifies the continuous medium approximation in the transverse direction, while a crystalline structure can, if necessary, be taken into account via subdividing the medium into a set of atomic scale layers and calculating the reflection coefficient as described in the preceding text.

If at shallow incidence the lateral projection $\boldsymbol{Q}_L = \boldsymbol{\kappa}_f - \kappa_i$ of the vector $\boldsymbol{Q}$ matches a reciprocal vector $\boldsymbol{\tau}_L$ of the crystalline structure, then one may observe so-called grazing incidence neutron Bragg diffraction (GIND) which can, in principle, deliver valuable information (Dosch, 1993) on the atomic and magnetic order in the near surface vicinity. We shall not go into further details of this phenomenon and only mention that it can be described within the framework of the DWBA discussed in the subsequent text. DWBA accounts for optical effects, and in particular, for birefringence of the incident and diffracted neutron waves inside the magnetic medium, while small effects due to lateral crystallinity are treated as a perturbation (Günther, Donner, Toperverg and Dosch, 1998; Toperverg, Rühm, Donner and Dosch, 1999; Toperverg, Lauter-Pasyuk and Lauter, 2005b).

Usually the lateral projection $\lambda_L \approx \lambda$ of the neutron wavelength λ is comparable to the interatomic spacing, and GIND occurs at relatively large angles $\vartheta_y = \vartheta_B$ (Figure 7), where ϑ_B is the angle determined by the Bragg equations $(4\pi/\lambda)\sin(\vartheta_B/2) = \tau_y$ and $(4\pi/\lambda)\cos(\vartheta_B/2) = \tau_x$ via the projections τ_y and τ_x of the 2D reciprocal lattice vectors $\boldsymbol{\tau}_L$. Zeroth order diffraction at $\boldsymbol{\tau}_L = 0$ corresponds to specular reflection, which can be calculated exactly as described in the preceding text where atomic structure was ignored.

Taking into account specular and Bragg reflections, as well as scattering from that lateral heterogeneities of SLD, the cross section of neutron scattering at grazing incidence is conveniently written as a sum of three terms

$$\frac{d\sigma}{d\Omega} = \left(\frac{d\sigma}{d\Omega}\right)_{\text{spec}} + \left(\frac{d\sigma}{d\Omega}\right)_{\text{off-spec}} + \left(\frac{d\sigma}{d\Omega}\right)_{\text{diffuse}} \qquad (83)$$

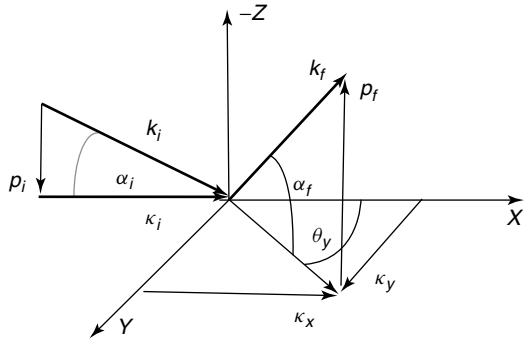

Figure 7. 3D scattering kinematics.

$$\left(\frac{\mathrm{d}\sigma}{\mathrm{d}\Omega}\right)_{\mathrm{spec}} = \mathcal{S}_R \frac{Q_z^2}{4}\mathcal{R}(Q_z)\delta(Q_x)\delta(Q_y) \tag{84}$$

$$\left(\frac{\mathrm{d}\sigma}{\mathrm{d}\Omega}\right)_{\mathrm{off-spec}} = \mathcal{S}_R \sum_{\boldsymbol{\tau}\neq 0} \mathcal{F}(p_0^i, p_0^f; \boldsymbol{\tau}_L)\delta(Q_x - \tau_x) \times \delta(Q_y - \tau_y) \tag{85}$$

Here the first term is the cross section of the specular reflection expressed via the reflection coefficient $\mathcal{R} = \mathcal{R}(Q_z; \boldsymbol{P}^i, \boldsymbol{P}^f)$, the second term corresponds to off-specular Bragg diffraction and contains a combination $\mathcal{F}(p_0^i, p_0^f; \boldsymbol{\tau}_L)$ of structure factors and form-factors. In the Born approximation it depends on the wave vector transfer $Q_z = p_0^f - p_0^i$, while in DWBA it is a function of two separate variables $p_0^i = k\sin\alpha_i$ and $p_0^f = k\sin\alpha_f$. The last term in equation (84) stands for off-specular diffuse scattering which is due to random domains, roughness and so on, and will be thoroughly discussed later.

The normalization factors in equation (84) can be checked via the sum rule: the integral over the solid angle has to be equal to the sample area $\mathcal{S}_R$ illuminated by the neutron beam. In accordance with the previous consideration, below the critical angle of incidence $\mathcal{R} = 1$ and all neutrons impinging onto the sample should be specularly reflected [3].

We shall here not further calculate the second term in equation (83) for diffraction from atomic structures (Günther, Donner, Toperverg and Dosch, 1998; Toperverg, Rühm, Donner and Dosch, 1999; Toperverg, Lauter-Pasyuk and Lauter, 2005b), but instead consider GIND from laterally nano-patterned layered systems (Toperverg *et al*., 2000). In this case, the lateral spacing is assumed to be much larger than the interatomic distances [4] and GIND contributes to the range of angles $\vartheta_y \ll 1$. Then, at $\alpha_i \ll 1$ and $\alpha_f \ll 1$ the Cartesian projections of the the wave vector transfer can be approximated as follows

$$Q_x \approx \frac{\pi}{\lambda}(\alpha_i^2 - \alpha_f^2 - \vartheta_y^2) \tag{86}$$

$$Q_y \approx \frac{2\pi}{\lambda}\vartheta_y \tag{87}$$

$$Q_z \approx \frac{2\pi}{\lambda}(\alpha_f + \alpha_i) \tag{88}$$

From this equation it follows that at $\alpha_i \sim \alpha_f \sim \vartheta_y \ll 1$ the projection $Q_x \ll Q_y \sim Q_z$.

In the low angle approximation the $\delta-$functions, which determine the Bragg peak positions in equation (85), read

$$\delta(Q_y - \tau_y) = \frac{\lambda}{2\pi}\delta(\vartheta_y - \vartheta_B) \tag{89}$$

$$\delta(Q_x - \tau_x) = \frac{\lambda}{2\pi\alpha_B}\{\delta(\alpha_f - \alpha_B) + \delta(\alpha_f + \alpha_B)\} \tag{90}$$

$$\vartheta_B = \pm\lambda\tau_y/2\pi \tag{91}$$

$$\alpha_B = \sqrt{\alpha_i^2 - \vartheta_B^2 \pm \lambda\tau_x/\pi} \tag{92}$$

where the first term in equation (90) corresponds to reflection into the upper hemisphere, while the second one describes reflection below the horizon. Equation (92) determines two branches of GIND, which can exist at $\alpha_i^2 \geq \vartheta_B^2 \pm \lambda\tau_x/\pi$. In a particular case $\tau_y = 0$ these branches can be observed at low angles $\alpha_f \sim \alpha_i \ll 1$ only for the systems with very large spacing $a \sim \lambda/\alpha_i^2$, typically from micrometer up to submillimeter range. For such huge spacings the term ϑ_B^2 in equation (92) does not play a role and can safely be neglected, except for the case when the period in the y direction is by 3–4 orders of magnitude smaller than that along the x axis. In fact, Bragg reflection can also be observed at low α_B if neither one of the two periods is large enough to be detected. This is achieved (Toperverg *et al*., 2000; Theis-Bröhl, Schmitte, Leiner and Zabel, 2003; Theis-Bröhl *et al*., 2003) by turning the 2D lattice around the sample normal so that the projection τ_x of the reciprocal vector $\boldsymbol{\tau}$ becomes sufficient to fit the position of the Bragg peak at $\alpha_f = \alpha_B$ into the accessible window of detected angles.

2.8 Coherence volume and resolution

It is worth to note that both specular and Bragg reflection are essentially coherent phenomena. They both result from the constructive interference of neutron waves scattered at different points of the sample in either specular, or Bragg directions. Scattering in all other directions is suppressed by destructive interference. Such a description assumes that scattered waves are due to the incident monochromatic plane wave which determines their phase relationship. On the other hand, the neutron source is an incoherent device randomly emitting polychromatic neutron waves diverging from different points in the source volume at uncorrelated moments

in time. Observables, for example, scattered flux density, polarization, and so on, are the result of the statistical averaging of the corresponding quantum-mechanical quantities over neutron emittance events. Further devices of the experimental set up, for example, monochromatization and collimation systems select those events with close phases of emittance so that statistical averaging does not totally eliminate the interference phenomena. Such a filtering reduces the statistical source volume to the so-called *source coherence volume*. It can be considered as a fraction of the source emitting neutron waves with approximately fixed phase relationship. The coherence volume is relatively small so that fronts of irradiated divergent spherical waves at some distance are almost flat. All this justifies the plane wave approximation used in the theoretical consideration in the preceding text. It is constrained by residual dephasing which is taken into account via the *resolution function*.

An intimate relation between resolution effects and coherency of the neutron radiation (Sinha, Tolan and Gibaud, 1998) can be illustrated by the following examples. The first one considers GIND from periodically patterned systems, while the second one concerns PNR from a multidomain F film.

If the periods of a lateral pattern in the x and the y directions are not dramatically different, then due to resolution effects the low angle kinematics generally does not render possible to observe diffraction peaks simultaneously for both angles ϑ_y and α_f. Instead, Bragg angles can be resolved only for the x direction, while in the other direction the Bragg condition is obscured by resolution effects. The uncertainty $\Delta Q_y \sim (2\pi/\lambda)\Delta\vartheta_y$ is mainly due to the angular divergence $\Delta\vartheta_y$ in the y direction, where rather relaxed collimation of the beam is usually provided. The uncertainty ΔQ_x is mostly due to the finite collimation $\Delta\alpha_i$ and finite resolution in detection $\Delta\alpha_f$. It can roughly be estimated as

$$\Delta Q_x \sim \frac{\pi}{\lambda}\sqrt{(\alpha_i\Delta\alpha_i)^2 + (\alpha_f\Delta\alpha_f)^2} \ll \Delta Q_y \qquad (93)$$

A strong asymmetry in the lateral resolution implies a strong anisotropy of the area from which a coherent scattering can be observed. This coherence area [5] is substantially extended along the x-axis for a distance $l_x \sim 1/\Delta Q_x$, while it is relatively short in y-direction in which it is estimated as $l_y \sim 1/\Delta Q_y \ll l_x$. If the period of the lateral structure $a \ll l_x$, then the coherence area may comprise a number of unit cells along x axis, but very few, or even none along the y axis, if $l_y \sim a$. Interference of neutron waves will then result in strong Bragg reflections only at $\alpha_f = \alpha_B$ and a smooth line shape along ϑ_y. The latter is determined by the incident beam collimation in the corresponding direction.

Usually the coherence area covers only a small fraction of the sample surface illuminated by the neutron beam. Therefore, an experimentally recorded (specular and off-specular) Bragg reflection is actually an incoherent sum of intensities coherently reflected from different small areas of the sample. It is often silently assumed that the sample is homogeneous over its total surface so that the reflection coefficients from different parts of the sample, alias different coherence areas, are identical. Then incoherent summation over these areas results in the sample area $\mathcal{S}_R$ in equations (84) and (85). This, however, is not always the case, as can be seen from examples depicted in Figure 8. The first illustration shows two orientations of a lateral stripe array. If the stripes are running along the y axis, then one can observe both: specular reflection, and off-specular Bragg peaks. Rotating the sample around its normal efficiently increases the lateral spacing and the Bragg peaks approach the position at the origin. They finally become unresolvable from the specular reflection. At this point, the coherence area may comprise only one stripe, and each of them as well as the interstripe spaces contribute independently to solely specular reflection.

Another typical situation refers to reflection from a continuous magnetic film broken into a multidomain state as illustrated in Figure 9. If the domains are larger than $l_x \gg l_y$, as assumed in Figure 9(a), then each of the domains reflects independently. The reflectivity has to be calculated for different magnetic domains with different magnetization vectors and finally averaged over all possible domain orientations. Such averaging would not affect the intensity of unpolarized neutron reflection, while only PNR delivers an information

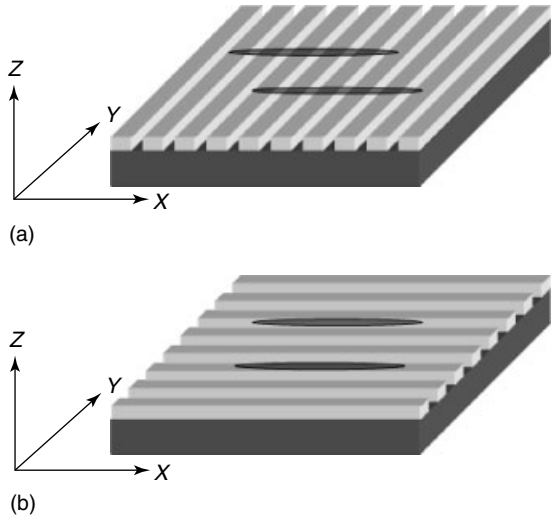

Figure 8. Illustration of the coherence anisotropy. Bragg diffraction can be detected if the coherence ellipse covers a number of stripes (a). Alternatively, each stripe and interstripe spacing contributes to specular reflection and respective intensities are added incoherently (b).

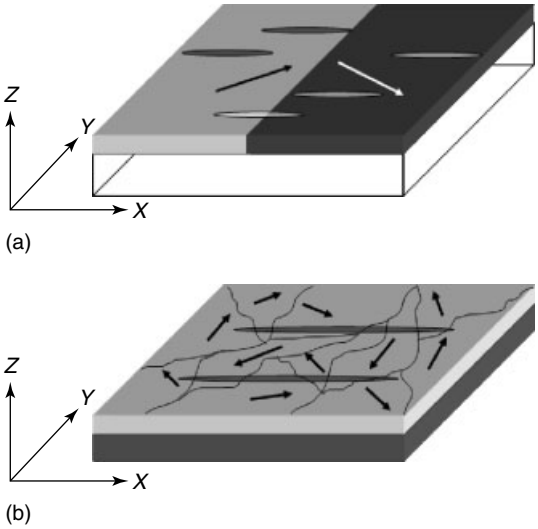

Figure 9. Sketch of lateral magnetic domains with magnetization directions indicated by arrows. In (a) the two large domains are bigger than the coherence area. In most cases, the coherence ellipses are displayed within only one domain, in a few cases the ellipse may cross a common boundary between two of them. In (b) each coherence ellipse covers several domains.

on the magnetization distribution over the reflected surface. Hence, averaging equation (48) one obtains an equation which can be used to find the mean value $\langle \cos\gamma \rangle$ from measurements of the spin asymmetry. This mean value is proportional to the mean magnetization projection onto the polarization analysis axis but it does not allow to discriminate between coherent rotation of the net magnetization for the angle γ and the magnetization reduction due to random domains. For example, SA cannot distinguish between totally demagnetized state and rotation of magnetization perpendicular to the polarization direction, because in both cases $\langle \cos\gamma \rangle = 0$. More certainty can be gained via full 1D-PNR, that is measuring NSF and SF reflectivities. Indeed, averaging of equations (39–41) gives access not only to the mean value $\langle \cos\gamma \rangle$, but also to the mean square $\langle \sin^2\gamma \rangle$. The latter is proportional to the mean square of the magnetization vector projections onto the $x-$axis. Correspondingly, one can determine $\langle \cos^2\gamma \rangle = 1 - \langle \sin^2\gamma \rangle$. In case of a random distribution of domain magnetization directions the dispersion $\Delta = \langle \cos^2\gamma \rangle - \langle \cos\gamma \rangle^2 \neq 0$ is essentially positive. It reaches a maximum value $\Delta_{\max}$ for the totally demagnetized state. In contrast, coherent rotation of the magnetization vector yields $\Delta = 0$. If at the same time $\langle \cos\gamma \rangle = 0$ than sample is in a single-domain state, but with magnetization turned perpendicular to the polarization axis.

As mentioned previously, the 1D polarization analysis cannot distinguish between right and left tilt of the magnetization vector and it is not possible to unambiguously discriminate between rotation of the net magnetization by an angle γ and a multidomain state in which the domain magnetization is equally turned by the angles $\pm\gamma$. This uncertainty is cured by the vector polarization analysis. Owing to the tensorial form of equation (74), corresponding averaging over domain magnetization can easily be performed. Then the limitation of equation (74) is only related to the ratio between characteristic domain sizes and the coherence length. If domains are smaller than the coherence l_x, but still much larger than $l_y \ll l_x$ as sketched in Figure 9(b) then the neutron wave is not only reflected from and transmitted through the mean optical potential, but also scattered in off-specular directions $\alpha_f \neq \alpha_i$. This scattering may be either coherent, as in the case of periodic domain structure, artificial regular patterns and so on, or diffuse, if the domains are randomly distributed over the surface. In all cases, if such scattering is experimentally detected, it serves as a direct evidence in favor of inhomogeneities smaller than l_x. On the other hand, such inhomogeneities, either periodic, or random, also affect the specular reflection reducing the mean value of the reflection potential.

2.9 Cross section of polarized neutron scattering

At shallow incidence angles off-specular scattering, either coherent Bragg reflections or diffuse scattering from lateral inhomogeneities, is usually a much weaker effect than specular reflection. Therefore, it is usually considered within the framework of the perturbation theory as a small correction to the exact solution of the Schrödinger equation for the mean optical potential derived in the preceding text. In most cases, it is sufficient to truncate the perturbation series for the scattering amplitude and take into account only the linear term with respect to the perturbation potential. Such truncation is accomplished either in the Born approximation (BA) or in the DWBA, thoroughly discussed in the next subsections. Here we, however, firstly concentrate on general and independent approximations of the equations for off-specular scattering cross sections of *polarized* neutrons.

Considering a layered systems with a sequence of N layers stacked in the z direction which, in addition, exhibits some lateral inhomogeneity such as a periodic stripe or random domain pattern we decompose the interaction potential in each layer l into two parts

$$\hat{V}(\boldsymbol{\rho}) = \sum_{l=1}^{N} \{\hat{V}_l + \Delta\hat{V}_l(\boldsymbol{\rho})\} \tag{94}$$

Here the main term, $\hat{V}_l = \langle \hat{V}_l(\boldsymbol{\rho}) \rangle_{\mathrm{coh}}$, is independent of the lateral coordinate vector $\boldsymbol{\rho}$, homogeneous across each layer and contributes only to specular reflection and transmission. The choice of the reference potentials $\hat{V}_l$ is constrained

by the condition that after lateral averaging $\langle \Delta \hat{V}_l(\boldsymbol{\rho})\rangle_{\rm coh} = \langle \hat{V}_l(\boldsymbol{\rho}) - \hat{V}_l\rangle_{\rm coh} = 0$. A benefit of such a choice is that it allows to eliminate a contribution to the cross section of specular reflection of the terms linear with respect to $\Delta \hat{V}_l(\boldsymbol{\rho})$. This contribution may cause rather undesirable corrections to the reflectivity which has already been calculated in the preceding text exactly. The terms proportional to $\Delta \hat{V}_l(\boldsymbol{\rho}) = \Delta \hat{V}_l^N(\boldsymbol{\rho}) + \Delta \hat{V}_l^M(\boldsymbol{\rho})$, where $\Delta \hat{V}_l^N(\boldsymbol{\rho})$ and $\Delta \hat{V}_l^M(\boldsymbol{\rho})$ refer to deviations in nuclear and magnetic potentials, are regarded as perturbations to the main potential $\hat{V}_l = \langle \hat{V}_l^N(\boldsymbol{\rho})\rangle_{\rm coh} + \langle \hat{V}_l^M(\boldsymbol{\rho})\rangle_{\rm coh}$ and cause scattering into off-specular directions.

Magnetic off-specular scattering, which is due to the potential deviations $\Delta \hat{V}_l^M(\boldsymbol{\rho}) = -\hat{\boldsymbol{\mu}}\Delta \boldsymbol{B}_l(\boldsymbol{\rho})$, may change the spin state of the incident neutrons, while nuclear scattering leaves them unchanged. Hence the scattering amplitude $F = F(\boldsymbol{k}_i, \boldsymbol{k}_f)$ is represented by the matrix element

$$F(\boldsymbol{k}_i, \boldsymbol{k}_f) = \langle \Psi_0^i | \hat{F}(\boldsymbol{k}_i, \boldsymbol{k}_f; \hat{\boldsymbol{\sigma}}) | \Psi_0^f \rangle \tag{95}$$

of the 2×2 amplitude matrix $\hat{F} = \hat{F}(\boldsymbol{k}_i, \boldsymbol{k}_f; \hat{\boldsymbol{\sigma}})$.

This matrix, as any 2×2 matrix, can formally be decomposed over the orthogonal set of Pauli matrices so that

$$\hat{F} = F_0 + (\hat{\boldsymbol{\sigma}}\boldsymbol{F}) \tag{96}$$

Explicit expressions for the scalar, F_0, and the vector, $\boldsymbol{F}$, components of the scattering amplitude in BA and DWBA are given in corresponding sections in the subsequent text. Here we just mention, that in BA F_0 is due to the nuclear scattering amplitude, while $\boldsymbol{F}$ corresponds to the magnetic scattering amplitude. In DWBA such clear separation of nuclear and magnetic contributions does not hold anymore.

The expansion in equation (96) allows to readily perform an averaging over spin states of the scattering cross section determined by the equation

$$\frac{{\rm d}\sigma}{{\rm d}\Omega} = {\rm Tr}\{\hat{\rho}^f \hat{F} \hat{\rho}^i \hat{F}^+\} \tag{97}$$

which is similar to equation (69).

Substitution of equation (96) and equations (70) and (71) for the density matrices $\hat{\rho}^i$ and $\hat{\rho}^f$ into this equation immediately results in the expression for the scattering cross section,

$$\left(\frac{{\rm d}\sigma}{{\rm d}\Omega}\right) = \Sigma_0 + \Sigma_\mu^i P_\mu^i + \Sigma_\mu^f P_\mu^f + \Sigma_{\mu\nu} P_\mu^i P_\nu^f \tag{98}$$

with the tensor structure being identical to that of equation (74) for the reflection coefficient, if one substitutes the scalar $\mathcal{R}_0$ by Σ_0, the vectors $\boldsymbol{\mathcal{R}}^{i,f}$ in this equation by $\boldsymbol{\Sigma}^{i,f}$ and the tensor $\mathcal{R}_{\mu\nu}$ by tensor $\Sigma_{\mu\nu}$ of scattering cross section. These quantities can be expressed via bilinear combinations of the scalar amplitude F_0 and projections of the amplitude vector $\boldsymbol{F}$ in the same way as $\mathcal{R}_0$, $\boldsymbol{\mathcal{R}}^{i,f}$ and $\mathcal{R}_{\mu\nu}$ are expressed in equations (75–78) via bilinear combinations of the scalar R and projection of the vector $\boldsymbol{R}$. Resulting equations can be used to describe (Toperverg, Nikonov, Lauter-Passyuk and Lauter, 2001) off-specular scattering for arbitrary orientation between directions of incident polarization vector $\boldsymbol{P}^i$ and the vector of polarization analysis $\boldsymbol{P}^f$. These equations are absolutely general and exact. They do not assume any approximations and only exploit the fact that the neutron magnetic moment is associated with its spin 1/2. In particular, they apply either for BA and DWBA providing in the following sections explicit expressions for four complex amplitudes F_0, F_x, F_y, and F_z.

In the most common particular case of a 1D polarization configuration, that is when the incident polarization vector $\boldsymbol{P}^i$ is directed along the y axis and the only projection P_y^f of the outgoing neutron polarization onto the same axis is analyzed, the equation for scattering cross section boils down to the following set of equations for SF and NSF cross sections:

$$\left(\frac{{\rm d}\sigma}{{\rm d}\Omega}\right)_{yy}^{++} = \Sigma_0 + \Sigma_y^i |P_y^i| + \Sigma_y^f |P_y^f| + \Sigma_{yy} |P_y^i||P_y^f| \tag{99}$$

$$\left(\frac{{\rm d}\sigma}{{\rm d}\Omega}\right)_{yy}^{--} = \Sigma_0 - \Sigma_y^i |P_y^i| - \Sigma_y^f |P_y^f| + \Sigma_{yy} |P_y^i||P_y^f| \tag{100}$$

$$\left(\frac{{\rm d}\sigma}{{\rm d}\Omega}\right)_{yy}^{+-} = \Sigma_0 + \Sigma_y^i |P_y^i| - \Sigma_y^f |P_y^f| - \Sigma_{yy} |P_y^i||P_y^f| \tag{101}$$

$$\left(\frac{{\rm d}\sigma}{{\rm d}\Omega}\right)_{yy}^{-+} = \Sigma_0 - \Sigma_y^i |P_y^i| + \Sigma_y^f |P_y^f| - \Sigma_{yy} |P_y^i||P_y^f| \tag{102}$$

Four cross sections Σ_0, Σ_y^i, Σ_y^f, and Σ_{yy} in this set of equations are expressed via various products of four components of the scattering amplitude matrix $\hat{F}$ parameterized in equation (96):

$$\Sigma_0 = \frac{1}{2}\{\langle |F_0|^2 + |F_y|^2 + |F_x|^2 + |F_z|^2\rangle\} \tag{103}$$

$$\Sigma_y^i = \Re\langle F_0^* F_y\rangle + \frac{1}{2}\langle [F_z^* F_x - F_x^* F_z]\rangle \tag{104}$$

$$\Sigma_y^f = \Re\langle F_0^* F_y\rangle - \frac{1}{2}\langle [F_z^* F_x - F_x^* F_z]\rangle \tag{105}$$

$$\Sigma_{yy} = \frac{1}{2}\{\langle |F_0|^2 + |F_y|^2 - |F_x|^2 - |F_z|^2\rangle\} \tag{106}$$

The set of equations (99–102) solves the problem of averaging over spin states separating quantities characterizing a scattering system from instrumental parameters, that is the polarization efficiencies. Indeed, the system of four linear equations (99–102) can easily be solved providing expressions for Σ_0, Σ_y^i, Σ_y^f and Σ_{yy} via combinations of four experimentally measured quantities: two NSF and two SF scattering cross sections. Furthermore, the set of equations (103–106) links together scattering amplitudes calculated below in BA and DWBA for various physical models with experimentally measured cross sections.

On the other hand, the set of equations (103–106) for 1D polarization analysis does not provide all the scope of information which can be gained with polarized neutron off-specular scattering. This is already seen from the fact that equations (103–106) contain seven, generally independent, products of different complex functions F_0, F_x, F_y, and F_z averaged over beam divergency, as well as over possible disorder (domains, roughness, etc.) in the sample. The missing information is, however, available with the complete 3D vector polarization arrangement. Such arrangement would allow to measure all 36, instead of four cross sections in equations (103–106). Aligning $\boldsymbol{P}^i$ and $\boldsymbol{P}^f$ collinear with either x or the z axis one can measure eight additional NSF and SF cross sections diagonal with respect to the Cartesian indices. Another 24 cross section, non-diagonal with respect to x, y and z indices can be measured by setting polarization analysis axis perpendicular to the initial ones. The latter cross sections are not independent and linked via the reciprocity principle. Finally 20 measurable cross sections are, in principle, available altogether to recover all 16 cross sections in equation (98), for example, the scalar Σ_0, six components of two 3D vectors Σ_μ^i and Σ_μ^f, as well as nine components of 3D tensor $\Sigma_{\mu\nu}$ of the second rank. These quantities determined as functions of the incoming and outgoing wave vectors contain all physical information which can be extracted from 3D vector polarization analysis. In the following sections we, however, mainly restrict our consideration to 1D polarization analysis as being well in use in the last decade.

2.10 Off-specular scattering in the Born approximation

In this subsection we, for introductory purpose, concentrate on the most simple approach, that is BA, often used for the description of off-specular scattering of polarized neutrons. In BA optical effects, for example refraction into the mean potential and birefringence due to magnetic interaction are completely ignored. Hence BA is supposed to be valid only far away from the total reflection condition for the incident and scattered neutron waves. Therefore, in case of PNR, BA misses some important polarization effects and may even lead to confusions in the data interpretation. On the other hand, BA allows a simpler discussion of many issues which are common for both BA and DWBA. One of those issues is the general dependency of scattering cross sections on polarization vectors as discussed in the previous section.

In BA the amplitude matrix $\hat{F}(\boldsymbol{k}_i, \boldsymbol{k}_f) = F^N(\boldsymbol{Q}) + \hat{F}^M(\boldsymbol{Q})$ in equations (95–97) is a sum of the unit matrix of nuclear, $F^N(\boldsymbol{Q})$, and the matrix of magnetic, $\hat{F}^M(\boldsymbol{Q})$, scattering. These amplitude matrices in BA depend on the wave vector transfer $\boldsymbol{Q} = \boldsymbol{k}_f - \boldsymbol{k}_i$ and taking into account equation (94) are written as follows:

$$\hat{F}^{N,M}(\boldsymbol{Q}) = -\frac{m}{2\pi\hbar^2}\sum_l \int_{z_{l-1}}^{z_l} \mathrm{d}z\, \mathrm{e}^{i Q_z z} \times \int \mathrm{d}x\, \mathrm{d}y\, \mathrm{e}^{i(Q_x x + Q_y y)} \Delta \hat{V}_l^{N,M}(\boldsymbol{\rho}) \quad (107)$$

where $\boldsymbol{Q}$ has the lateral, Q_x and Q_y, and transverse, $Q_z = p_0^i + p_0^f$, components, $p_0^i = (2\pi/\lambda)\sin\alpha^i$ is the incoming, while $p_0^f = (2\pi/\lambda)\sin\alpha^f$ is the scattered wave vector projection into the normal to the surface.

In BA the first term, $F_0 = F^N(\boldsymbol{Q})$, in equation (96) refers to the nuclear scattering amplitude, while $\boldsymbol{F} = \boldsymbol{b}F^M(\boldsymbol{Q})$ is associated with the magnetic scattering amplitude, and $\boldsymbol{b} = \Delta\boldsymbol{B}(\boldsymbol{Q})/|\Delta\boldsymbol{B}(\boldsymbol{Q})|$ is the unit vector. The scattering amplitude vector $\boldsymbol{F}$ is almost totally displayed within the surface plane. This is due to the fact that in accordance with the Maxwell equations $\boldsymbol{B}(\boldsymbol{Q}) \perp \boldsymbol{Q}$ and the vector $\boldsymbol{Q}$ at glancing angles of incidence and scattering is pointing nearly perpendicular to the surface.

The first terms in equation (103) and equation (106) are responsible for purely nuclear scattering. The three other terms in these equations, as well as the last terms in equation (104) and equation (105) correspond to purely magnetic scattering, while the first terms in the latter equations describe interference between magnetic and nuclear scattering. In BA, $F_z \approx 0$ and therefore the last terms in equations (103–106) can be neglected. Note, this is not the case in DWBA where they may play a role.

The angular brackets in equations (103–106) denote the averaging over the resolution function and hence account for the coherence properties of the neutron radiation. These properties reveal such a strong anisotropy (see, Figures 8 and 9) that even in the case of a pinhole collimation, off-specular scattering in x direction probes lateral length scales exceeding those accessible in the y direction by several orders of magnitude. Moreover, PNR experiments usually use slit-like collimation in z direction, providing simultaneously fine resolution in the Q_x component of the wave vector transfer. On the other hand, almost all neutrons

scattered from large-scale lateral inhomogeneities in the y direction are scattered under unresolved angles. Therefore equation (98) for the scattering cross sections should be integrated over ϑ_y and each term in equations (103–106) is then expressed via the following correlator of the Born partial amplitudes:

$$\langle F_\mu^* F_\nu \rangle = \lambda \int \mathrm{d}y F_\mu^*(Q_z, Q_x; y) F_\nu(Q_z, Q_x; y) \qquad (108)$$

Here μ and ν stand for x, y, z, or 0, and

$$F_\mu(Q_z, Q_x; y) = \sum_l \frac{1}{2\pi} \int \mathrm{d}Q_y \mathrm{e}^{iQ_y y} F_l^\mu(\boldsymbol{Q}) \qquad (109)$$

is the Fourier transform of the corresponding component of the scattering amplitude averaged over Q_y.

Deviations $\Delta\hat{V}_l^N(x, y)$ in the nuclear scattering potential in equation (107) are determined by deviations $\Delta(Nb)_l^N(x, y)$ in nuclear SLDs $(Nb)_l^N(x, y)$ from its mean value $\overline{(Nb)_l^N}$. Decomposition of the SLD into the mean value and deviations is sketched in Figure 10 for the case of a single patterned layer deposited onto a substrate, as depicted in Figure 8. An explicit equations for the amplitude of nuclear scattering from periodic gratings are given in Appendix A. In a more general case of a 2D lateral structure, one can consider the SLD profile in Figure 10 as taken for a fixed y coordinate, bearing in mind that the size of the structural elements along the y axis is much greater than the corresponding width of the coherence ellipsoid [6] in Figure 8.

The particular form of equation (108) is essentially based on the incomparability of coherence ranges in the x and y direction. In fact, the coherence length in the y direction is totally ignored, while in the x direction it is assumed to be very large. If the latter goes to infinity, in the case of nuclear scattering from grating with a period a (see Appendix A) one has the following equations for the first terms in equations (103–106)

$$\langle F_0^* F_0 \rangle = \lambda \int \mathrm{d}y \mathcal{N}_x \mathcal{F}(Q_z, Q_x; y) \frac{2\pi}{a} \sum_\tau \delta(Q_x - \tau) \qquad (110)$$

Here $\mathcal{N}_x = \mathcal{N}_x(y)$ is the number of structural elements and $\tau = 2\pi/a$ in the x direction at fixed y coordinate, while

$$\mathcal{F}(Q_z, Q_x; y) = \left| \sum_l F_l^z(Q_z, y) F_l^L(Q_x, y) \right|^2 \qquad (111)$$

with explicit equations for the transverse, $F_l^z(Q_z, y)$, and lateral, $F_l^L(Q_x, y)$, components of the stripe form-factor given in Appendix A.

In the example of the periodic stripe array sketched in Figure 8 all the functions are independent of the y coordinate and the integral in equation (110) is equal to the length $\mathcal{L}_y$ of the sample in the y direction, while the product $\mathcal{L}_x \mathcal{L}_y = \mathcal{S}$ yields the area factor $\mathcal{S}$ in equation (85), where $\mathcal{L}_x = \mathcal{N}_x a$ is the length of the sample in the x-direction. Owing to the choice of the scattering potential ΔV^N the contribution of the term with $\tau = 0$ in the sum in equation (110) vanishes. Convolution with the resolution function replaces the $\delta-$ by that describes either the line shape of off-specular and specular Bragg reflections.

Note, that starting from the configuration in Figure 8(a) and turning the sample around the normal to the surface by the angle Φ increases efficiently the spacing $a = a_0/\cos\Phi$, where $a_0 = a_1 + a_2$, and decreases τ, that is the distance between Bragg peaks positioned at $Q_x = \tau$. Finally, at $\Phi \to \pi/2$ the Bragg peaks merge the specular reflection at $Q_x = 0$. This effect (Toperverg *et al.*, 2000) will be illustrated in the subsequent text with experimental results (Theis-Bröhl, Schmitte, Leiner and Zabel, 2003; Theis-Bröhl *et al.*, 2003; Theis-Bröhl, 2003). The consideration in the preceding text, however, does not cover a crossover to the limit when the corresponding coherence length becomes comparable with the size of a single structural element as it happens if $\Phi \to \pi/2$. Finally, the specular reflectivity is accounted for as incoherent sum of reflected signals from different stripes and from interstripe spaces. It is a very difficult task to accurately pass the crossover from one regime of averaging to another, while one can match two limiting cases via a weight function controlling respective contributions of coherent and incoherent processes into the measured signal.

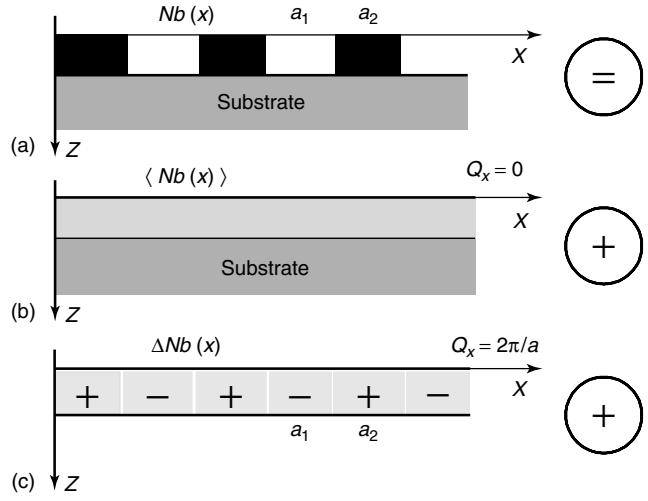

Figure 10. Decomposition of the SLD lateral pattern into a mean layer SLD $\langle Nb \rangle$ (contributing to specular reflection) and SLD deviations $\Delta Nb(x)$, responsible for off-specular diffraction.

Clear discrimination between coherent and incoherent procedures of averaging is especially important for magnetic systems. Magnetic off-specular scattering is due to the potential $\Delta\hat{V}_l^M(\boldsymbol{\rho}) = -(\hat{\boldsymbol{\mu}}\Delta\boldsymbol{B}_l)$ of neutron interaction with deviations $\Delta\boldsymbol{B}_l(\boldsymbol{\rho}) = \boldsymbol{B}_l(\boldsymbol{\rho}) - \overline{\boldsymbol{B}}_l$ of magnetic inductance $\boldsymbol{B}_l = \boldsymbol{B}_l(\boldsymbol{\rho})$ from its mean value $\overline{\boldsymbol{B}}_l = \langle \boldsymbol{B}_l(\boldsymbol{\rho})\rangle_{\rm coh}$ averaged over the coherence range. These deviations have to be classified taking into account the choice of the reference magnetic potential, that is the absolute value and direction of the vector $\overline{\boldsymbol{B}}_l$ pointing along the unit vector $\boldsymbol{b}_l^{\parallel} = \overline{\boldsymbol{B}}_l/|\overline{\boldsymbol{B}}_l|$.

An example of such a classification is shown in Figure 11 for the 'cartoon model' of magnetization distribution over a stripe array in the demagnetized state. The reason for this sort of distribution may be due to the competition between shape anisotropy of the stripes and the sample. This is discussed in the subsequent text in more detail, while for now we concentrate on basic principles of the theoretical description of specular and off-specular PNR from domain patterns such as those shown in Figures 9(b) and 11(c). In the latter figure the stripe magnetization is arranged into two large domains comprising a number of stripes and separated by a domain wall (DW) running across the stripes. In one of the domains the vector $\boldsymbol{B} = \boldsymbol{B}^j$ in each stripe is tilted to the right by the angle γ^j different for even and odd values of the superscript j enumerating the stripes. In the other domain the magnetization is tilted to the left with respect to the shape induced anisotropy directed along the y axis. The mean inductance $\overline{\boldsymbol{B}}$ and, correspondingly, the vector $\boldsymbol{b}^{\parallel}$ is also tilted to the right in one domain and to the left in the other domain by the angles $\overline{\gamma} \approx \pm\pi/2$ as presented in the middle panel. The net inductance of two domains (in the particular example it is zero) may be directed along the y axis, while the alternating vectors of deviations $\Delta\boldsymbol{B}^j(x)$ are directed along and opposite to the stripes, so that the angle $\beta^j = \gamma^j - \overline{\gamma}$ between directions of vectors $\boldsymbol{B}^j$ and $\overline{\boldsymbol{B}}$ alters sign in neighboring stripes, and in Figure 11(c) $\beta^j \approx (-1)^j\pi/2$. In such a configuration of domains the SF specular reflections are accompanied by NSF off-specular Bragg diffraction [7] if the polarization analysis direction is set along the y-axis. At the same time, the deviation angles γ^j decrease the mean value of the magnetic LSD $\overline{(Nb)}^M = (Nb)|\overline{\cos\gamma^j}|$ and the magnetic contribution to the specular reflection is reduced in favor of the off-specular Bragg scattering. If, in particular, $\gamma^j = \pm\pi$, then magnetic scattering does not contribute to specular reflection at all.

Often the angles β^j experience random fluctuations around the mean values $\overline{\beta^j}$ by the angles $\Delta\beta^j(x, y)$. Such fluctuations may be caused by defects, structural roughness, or may develop in a range of parameters where the magnetic structure becomes unstable and tends to rearrange in a more stable domain configuration. These fluctuations reduce both specular and Bragg reflections. By definition the mean value

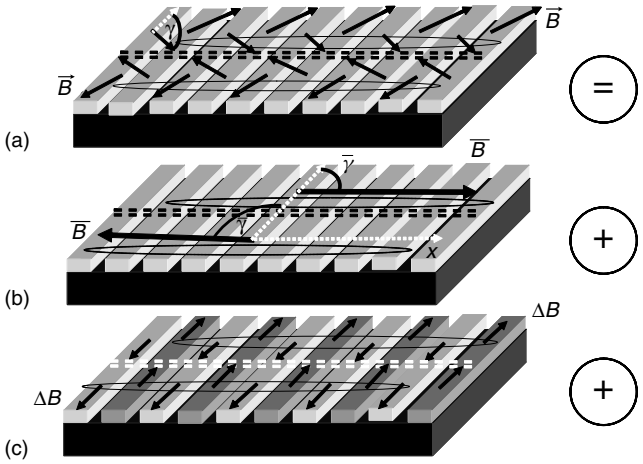

Figure 11. Magnetic domains in striped pattern. Arrows in (a) indicate directions of local inductance $\boldsymbol{B}(x, y)$ within the coherence ellipsoids. In each stripe it is tilted by an angle $\gamma(x, y)$ against the y axis. The wall between two domains is shown by a double dashed line. Thick arrows in (b) represent the mean domain inductance $\overline{\boldsymbol{B}}(y)$ with the tilt angles $\overline{\gamma}(y)$. The lateral distribution over stripe deviations $\Delta\boldsymbol{B}(x, y) = \boldsymbol{B}(x, y) - \overline{\boldsymbol{B}}(y)$ is displayed in (c).

$\overline{\Delta\beta^j} = 0$. However, $\overline{(\Delta\beta^j)^2} \neq 0$, while fluctuations $\Delta\beta^j$ may be correlated so that the mean value $\langle\Delta\beta^j\Delta\beta^{j'}\rangle \neq 0$ for a certain number of neighboring structural elements indexed by $j \neq j'$. If these elements are comprised within the coherence length in the x direction, then such fluctuations cause SF and NSF diffuse off-specular scattering concentrated around each Bragg peak including the one of zeroth order, that is specular reflection.

In the counterexample shown in Figure 9 the domain magnetization is randomly distributed over the layer plane. Then diffuse off-specular scattering is centered around $Q_x = 0$ and its spread over Q_x is determined by their mean size. Both, specular reflection and diffuse scattering may contain NSF and SF components. It is worth to note that random domains with dimensions smaller than the coherence length reduce the mean value $\overline{(Nb)}^M = (Nb)^M\overline{\cos\beta^j}$ of the magnetic SLD and the magnetic contribution to the specular and the Bragg reflections. In particular, the magnetic contribution may vanish if $\overline{\cos\beta^j} = 0$. In this case, random domains mainly scatter in the off-specular directions.

In layered systems the vector $\boldsymbol{b}_l^{\parallel}$ may vary from layer to layer, hence being not necessarily collinear with the direction of the polarization analysis, tilted against this direction by an angle $\overline{\gamma}_l$ and varying also from one coherence spot to another along the layer plane. Within each of such spots the unit vector $\boldsymbol{b}_l^{\parallel}$ together with two other orthogonal unite vectors: $\boldsymbol{b}_l^{\perp} \perp \boldsymbol{b}_l^{\parallel}$, chosen within the layer plane, and $\boldsymbol{b}_l^{\dashv} = [\boldsymbol{b}_l^{\perp} \times \boldsymbol{b}_l^{\parallel}]$, normal to the surface, determines the local Cartesian coordinate system. The vector of the inductance deviations $\Delta\boldsymbol{B}_l = \Delta\boldsymbol{B}_l(x, y)$ can naturally be expanded over

the triad of unit vectors so that,

$$\Delta \boldsymbol{B}_l = \Delta B_l^{\parallel} \boldsymbol{b}_l^{\parallel} + \Delta B_l^{\perp} \boldsymbol{b}_l^{\perp} + \Delta B_l^{\dashv} \boldsymbol{b}_l^{\dashv} \tag{112}$$

where $\Delta B_l^{\parallel} = (\boldsymbol{b}_l^{\parallel} \boldsymbol{B}_l) - \overline{(\boldsymbol{B}_l \boldsymbol{b}_l^{\parallel})}$ describes the deviation of the inductance projection parallel to $\boldsymbol{b}_l^{\parallel}$, while two other terms in the expansion equation (112) correspond to deviations in the local induction directions with respect to its mean orientation within the coherence range. Correspondingly, the scattering amplitude vector of magnetic scattering in equation (96) can be decomposed into three components

$$\boldsymbol{F}(\boldsymbol{Q}) = \sum_l \{F_l^{\parallel} \boldsymbol{b}_l^{\parallel} + F_l^{\perp} \boldsymbol{b}_l^{\perp} + F_l^{\dashv} \boldsymbol{b}_l^{\dashv}\} \tag{113}$$

Here the first term, $F_l^{\parallel} = (\boldsymbol{F}_l \boldsymbol{b}_l^{\parallel})$, is due to longitudinal deviations $\Delta B_l^{\parallel}$. This term, as well as the scalar scattering amplitude represented as a sum

$$F_0(\boldsymbol{Q}) = \sum_l F_l^0 \tag{114}$$

of partial scalar amplitudes $F_l^0 = F_l^0(\boldsymbol{Q})$, do not mix neutron spin states if the quantization axis is chosen along $\boldsymbol{b}_l^{\parallel}$. Hence, in BA the longitudinal components $F_l^{\parallel} = F_l^{\parallel}(\boldsymbol{Q})$, together with $F_l^0 = F_l^N$, which is due to deviations in the nuclear SLD, is responsible for NSF off-specular scattering if the polarization analysis direction is set collinear with the vector $\boldsymbol{b}_l^{\parallel}$. The next two terms in this case mix spin states and create off-specular SF scattering.

Generally, in magnetically inhomogeneous media the inductance vector $\boldsymbol{B}_l = \boldsymbol{B}_l(x, y)$ changes either its direction and its absolute value in accordance with the Maxwell equations. However, in many cases of practical importance the magnetization, and consequently the inductance, are rather homogeneously distributed over relatively large areas, as indicated in Figure 11, while changing their values across relatively narrow regions between those areas. This particularly occurs in continuous films in which narrow DWs separate homogeneously magnetized domains (Figure 9). Each of the latter occupies a substantial volume and, if it is smaller than the coherence ellipsoid, creates quite powerful off-specular scattering. Certainly, DWs also scatter neutrons in off-specular directions. However, this scattering is by several orders of magnitude weaker just due to a very small volume of the sample they occupy. That is why in the first approximation one can safely neglect the DW thickness, set $|\boldsymbol{B}_l| = const$ and equal in each domain to its nominal value, and regard continuity conditions for the magnetic flux components normal to the wall faces. Note, that owing to the continuity conditions across the interfaces between layers the last terms in equations (112) and (113) vanish.

Assuming that the domain magnetization is displayed in the layer plane one concludes that $\Delta B_l^{\parallel} = |\boldsymbol{B}_l|(\cos\beta_l^j - \overline{\cos\beta_l})$, while $\Delta \boldsymbol{B}_l^{\perp} = |\boldsymbol{B}_l| \sin\beta_l^j$, and $\beta_l^j = \beta_l^j(x, y)$ describe deviations $\beta_l^j = \gamma_l^j - \overline{\gamma}_l$ in angles $\gamma_l^j = \gamma_l^j(x, y)$ of the domain magnetization from the mean value $\overline{\gamma}_l(y)$ averaged over domains within the coherence area. Setting $\overline{\gamma}_l = \overline{\gamma}_l(y)$ as a function of only one, for example, the y-coordinate, we, actually, apply the same approximation as in the consideration of nuclear off-specular scattering. This is valid under the assumption that the long axis of the coherence ellipsoid crosses many domains along the x axis, while the short ellipsoid axis is smaller than the domain size in y direction.

Then the amplitudes of magnetic scattering from longitudinal and transverse deviations in BA can be written down explicitly in a form

$$F_l^{\parallel,\perp}(Q_z, Q_x; y) = F_l^z(Q_z, y) \sum_j \mathrm{e}^{i Q_x x_j} \tilde{F}_{lj}^{\parallel,\perp}(Q_x, y) \tag{115}$$

similar to that of equation (A1), in which the transverse form-factor $F_l^z(Q_z, y)$ is determined by equation (A2) in the Appendix A.

The lateral distribution of magnetic inhomogeneities is determined by the functions $\tilde{F}_{lj}^{\parallel}(Q_x, y)$ and $\tilde{F}_{lj}^{\perp}(Q_x, y)$ which can be represented as Fourier transforms

$$\tilde{F}_{lj}^{\parallel,\perp}(Q_x, y) = \int_0^{a_j} \mathrm{d}x\, \mathrm{e}^{i Q_x x} \Delta(Nb)_l^{\parallel,\perp}(x, y) \tag{116}$$

of the longitudinal, $\Delta(Nb)_l^{\parallel}(x, y) = (Nb)_l^M(\cos\beta_l - \overline{\cos\beta_l})$, and transverse, $\Delta(Nb)_l^{\perp}(x, y) = (Nb)_l^M \sin\beta_l$ deviation in magnetic SLD. This equation has exactly the same shape as equation (A3) for the lateral form-factor $F_{lj}^L(Q_x, y)$ of nuclear scattering (see in Appendix A), if one notices that $\Delta(Nb)_l^{\parallel,\perp}(x, y) = (Nb)_l^{\parallel,\perp}(x, y) - \overline{(Nb)_l^{\parallel,\perp}}(y)$ with $(Nb)_l^{\parallel}(x, y) = (Nb)_l^M \cos\beta_l(x, y)$, $(Nb)_l^{\perp}(x, y) = (Nb)_l^M \sin\beta_l(x, y)$, $\overline{(Nb)}_l^{\parallel}(y) = (Nb)_l^M \overline{\cos\beta(y)}$, and $\overline{(Nb)}_l^{\perp}(y) = 0$. Therefore integration in equation (116) results in equations for $F_l^{\parallel,\perp}(Q_x, y)$ which immediately follow from equation (A4) if $\Delta(Nb)_l^m$ in this equation is substituted by $\Delta(Nb)_l^{m\parallel,\perp}$, where the index m enumerates magnetic structural elements in the unit cell along the x axis.

The magnetic unit cells may be different for longitudinal and transverse deviations and either of them may not coincide with the nuclear one. In the example sketched in Figure 11 the integral in equation (116) covers two stripes, where $\Delta(Nb)^{\perp} = \pm(Nb)^M |\sin\beta^j|$, and two interstripe spaces where $\Delta(Nb)^{\perp} = 0$, and the unit cell is doubled with respect to the nuclear one. Longitudinal deviations in

this case are suppressed due to the flux continuity conditions and $\Delta(Nb)^{\parallel} = 0$. For random domains drawn in Figure 9 the structural element coincides with a single domain and both types of deviations are present.

After the coefficients $F_l^{\parallel}$ and $F_l^{\perp}$ in equation (113) are found one can return to the laboratory coordinate system and write down explicitly equations

$$F_x = \sum_l (F_l^{\parallel} \cos\gamma_l + F_l^{\perp} \sin\gamma_l) \tag{117}$$

$$F_y = \sum_l (F_l^{\parallel} \sin\gamma_l + F_l^{\perp} \cos\gamma_l) \tag{118}$$

for F_x and F_y, which together with equation (109) and equation (A1) given in Appendix A for F_0 determine correlators $\langle F_\mu^* F_\nu \rangle$ in equation (108) and finally the scattering cross section in equation (98).

For the case of a single magnetic layer, the first term in equation (98) corresponding to the scattering cross section of unpolarized neutrons is simply a sum,

$$\Sigma_0 = \frac{1}{2}\langle |F^0|^2 + |F^{\parallel}|^2 + |F^{\perp}|^2 + |F^{\dashv}|^2 \rangle \tag{119}$$

of nuclear and all three possible cross sections of magnetic scattering. In BA the last term here vanishes, while the cross sections of scattering on longitudinal and transverse magnetization deviations are given by the equations which follow from equation (110) for $\langle |F_0|^2 \rangle$ if one substitutes $\mathcal{F}(Q_z, Q_x; y)$ in this equation for $\mathcal{F}^{\parallel}(Q_z, Q_x; y)$, or correspondingly, for $\mathcal{F}^{\perp}(Q_z, Q_x; y)$. Equations for the latter quantities can immediately be obtained from equation (111) by substitution the respective magnetic form-factors $F_l^{\parallel,\perp}(Q_x, y)$, given in equation (116), instead of the nuclear one $F_l^L(Q_x, y)$ presented in the Appendix A. The result can be used to evaluate the part of the scattering cross section bilinear with respect to polarizations. In accordance with equation (106) the corresponding equation takes the following shape

$$\Sigma_{yy} = \Sigma_0 - \langle |F_x|^2 + |F_z|^2 \rangle \tag{120}$$

where the last term in BA is neglected.

In contrast to Σ_0, the term Σ_{yy} explicitly depends on the angle $\gamma(y)$. In principle, this angle can also be determined by means of a reduced version of PNR, when either $P^i \neq 0$, but $P^f = 0$, that is incident neutrons are polarized, but no analysis of the final spin state is available, or vice versa, when $P^i = 0$, but $P^f \neq 0$. In both cases, the linear term with respect to P^i, or P^f in equation (98) changes sign if the polarization is flipped. Hence interference between magnetic and nuclear scattering can readily be separated from other contributions. Such interference may contribute into off-specular diffraction if, in accordance to equations (104) and (105), deviations in magnetic and nuclear SLDs are properly correlated. This, unfortunately, is not the case for the example sketched in Figure 11. Correlations, indeed take place for components of magnetic inductance perpendicular to $\overline{\boldsymbol{B}}$. However, according to equation (A4) presented in Appendix A, the nuclear structure factor vanishes at the position of the magnetic superstructure Bragg reflection.

On the other hand, the magnetic structure factor vanishes at the position where the nuclear structure shows a Bragg peak. As a result, the interference term, which is proportional to the real part of the product $\langle F^{\perp}(Q_x, y) F^L(Q_x, y) \rangle$, does not contribute to the Bragg diffraction, as can be seen in Figure 12(a) and (c). In this figure, the results of the calculation in BA are represented in the form of maps of the scattered intensity distribution over the plane with coordinates p_0^i versus p_0^f. For the stripe pattern shown in Figure 11 there are no longitudinal deviations of the magnetization and the magnetic-nuclear interference term affects only the specular SF reflectivity seen as a ridge running along the diagonal in Figure 12(a). The intensity variation along this ridge is calculated exactly, including all interference terms, and together with the NSF reflectivity ridge (Figure 12c) it, in principle, allows the determination of the angle γ. Other parameters of the model and in particular, the magnetization distribution over the stripe array, can be deduced from a quantitative analysis of the intensity distribution between different Bragg diffraction bands seen as curved lines in the maps. There is, however, an appreciable difference between the intensity distributions as calculated in BA (Figure 12a and c) as compared to calculations in DWBA (Figure 12b and d). The differences are visible over a significant area in the maps and are most pronounced for small p_0^i and p_0^f. Only at high values of p_0^i and p_0^f the results of DWBA collapse to those obtained in BA. In this range, the scattered intensity is already reduced due to lateral and transverse form-factors, while superstructure diffraction bands merge with the specular ridge. In conclusion, while BA has an applicability range at high values of p_0^i and p_0^f, it can hardly be used for any quantitative evaluation of data taken with PNR. Moreover, BA may often be misleading even for a qualitative interpretation of experimental results of specular and off-specular scattering from magnetization distributions in thin films and multilayers.

2.11 Distorted wave Born approximation

All general equations which have already been derived in the preceding text for the polarization analysis (e.g.,

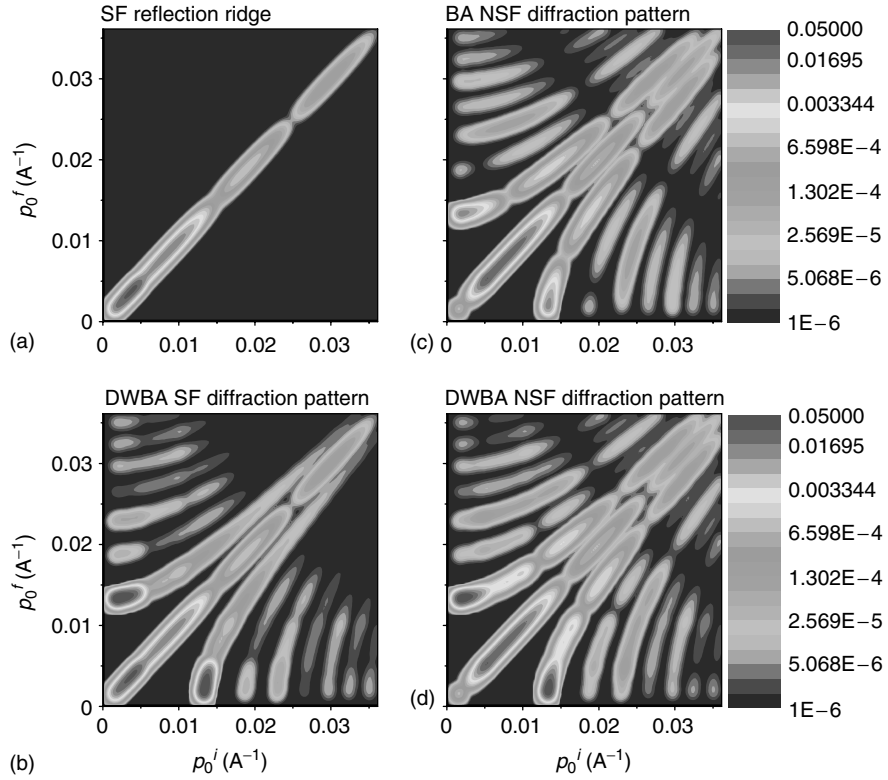

Figure 12. SF (a and b) and NSF (c and d) scattering intensity distribution over incoming, p_0^i versus outgoing, p_0^f wave vector components normal to the surface. Calculations are performed in BA (a and c) and in DWBA (b and d) for the model of a Co/Fe stripe array on a silicon wafer, as depicted in Figure 11. The stripes have a width of 4.75 µm and a height of 270 Å. They are separated by empty space of 0.25 µm. All panels show SF and NSF specular reflection ridges running along diagonals of the maps at $p_0^i = p_0^f$. Sets of Bragg diffraction bands are seen as bent lines in all panels except for the first one. They approach the specular ridge and decay at elevated values of p_0^i and p_0^f where BA becomes valid. High intensity bands correspond to magnetic superstructure due to the antiparallel or antiferromagnetic orientation of the stripe magnetization. Low intensity bands are due to nuclear scattering from the period of the stripe array. Intensity modulation superposed on the specular ridges and the diffraction bands is due to the height of the stripes. Differences in the period of this modulation, as well as absence of SF diffraction in (a) is due to the fact that BA ignores refraction in the mean optical potential. This effect is accounted for in DWBA, as explained in the main text.

equations (98–106)), as well as the discussion concerning the lateral components of structure- and form-factors (lateral averaging, etc.) remain valid and apply also at shallow incidence when the optical effects become important. However, in order to provide a quantitative description of the experimental situation, the equations for the transverse form-factors have substantially to be modified. This will, in particular, result in new polarization effects which are ignored in BA.

DWBA (Mott and Massey, 1965; Sinha, Sirota, Garoff and Stanley, 1988) is also based on the decomposition of the optical potential (equation (94)) into two parts, the averaged optical potential and deviations from the mean. The deviations from the average optical potential are treated as perturbations which cause off-specular scattering. However, the 1D Schödinger equation (9) for the mean potential averaged over those deviations $\hat{\overline{V}}(z) = \langle \hat{V}(\boldsymbol{r}) \rangle_{\text{coh}}$, is solved exactly. The solution $|\Psi(\boldsymbol{r})\rangle$ for layered systems was found in equations (56–58) in the factorized form $|\Psi(\boldsymbol{r})\rangle = \exp(i\kappa_x x + i\kappa_y y)|\psi(z)\rangle$, where

$$|\psi(z)\rangle = \sum_l \hat{\mathcal{S}}_l(z)|\Psi_0\rangle \tag{121}$$

$\kappa_x = \kappa_x^{i,f}$ and $\kappa_y = \kappa_x^{i,f}$ are lateral projections of the incoming and scattered wave vectors $\boldsymbol{k}^{i,f}$ and the $\hat{\mathcal{S}}_l(z) = \hat{\mathcal{S}}_l^{i,f}(z)$ matrices describe the neutron wave propagation inside the l^{th} layer before and after the scattering event on the deviation $\Delta\hat{V}_l$ of the interaction potential.

The $\hat{\mathcal{S}}$ matrices exactly account for refraction and reflection effects in the mean layer potentials, and instead of the equation for the Born amplitude matrix in equation (107)

one has to use the DWBA amplitude matrix in the following form

$$\hat{F}(\boldsymbol{k}^i, \boldsymbol{k}^f) = -\frac{m}{2\pi\hbar^2} \sum_l \int_{z_{l-1}}^{z_l} \mathrm{d}z \int \mathrm{d}\boldsymbol{\rho} \mathrm{e}^{i(Q_x x + Q_y y)} \times \hat{\mathcal{S}}_l^i(z) \Delta \hat{V}_l(x, y) \hat{\mathcal{S}}_l^f(z) \quad (122)$$

Here $\hat{F}(\boldsymbol{k}^i, \boldsymbol{k}^f) = \hat{F}(p_0^i, p_0^f; Q_x, Q_y)$, in contrast to the BA expression in equation (107) depends not only on the transverse wave vector transfer $Q_z = p_0^i - p_0^f$. Owing to the $\hat{\mathcal{S}}$ matrices, it depends also on the incoming, p_0^i, and scattered, p_0^f, wave vector projection normal to the surface.

The substitution of equation (121) into equation (122) results in an expression of the DWBA scattering amplitude matrix,

$$\hat{F}(p_0^i, p_0^f; Q_x, Q_y) = \sum_l \{\hat{F}_l^{tt} + \hat{F}_l^{tr} + \hat{F}_l^{rt} + \hat{F}_l^{rr}\} \quad (123)$$

via the sum of four terms corresponding to all possible partial amplitude matrices $\hat{F}_l^{\tau\rho}$ describing transitions between neutron wave spin components transmitted into and reflected from the layer mean potential. These amplitude matrices are written explicitly as

$$\hat{F}_l^{\tau\rho} = -\frac{m}{2\pi\hbar^2} \int_{z_{l-1}}^{z_l} \mathrm{d}z\, \hat{a}_l^{i\tau} \mathrm{e}^{i\hat{\varphi}_l^{i\tau}(z)} \Delta \hat{V}_l(Q_x, Q_y) \mathrm{e}^{i\hat{\varphi}_l^{f\rho}(z)} \hat{a}_l^{f\rho} \quad (124)$$

where the indices $\tau, \rho = t, r$ enumerate transmission and reflection matrices so that $\hat{a}_l^{it} = \hat{t}_l^i$, $\hat{a}_l^{ft} = \hat{t}_l^f$ are transmittance matrices for incoming and scattered waves, $\hat{a}_l^{ir} = \hat{r}_l^i$, $\hat{a}_l^{fr} = \hat{r}_l^f$ are corresponding reflectance matrices, $\hat{\varphi}_l^{it}(z) = \hat{p}_l^i(z - z_{l-1})$, $\hat{\varphi}_l^{ft}(z) = \hat{p}_l^f(z - z_{l-1})$, $\hat{\varphi}_l^{ir}(z) = -\hat{\varphi}_l^{it}(z)$ and $\hat{\varphi}_l^{fr}(z) = -\hat{\varphi}_l^{ft}(z)$ are phase matrices introduced in equation (57), with $\hat{p}_l^i = \sqrt{(p_0^i)^2 - \hat{p}_{cl}^2}$ and $\hat{p}_l^f = \sqrt{(p_0^f)^2 - \hat{p}_{cl}^2}$. In fact, owing to equations (123) and (124) $\hat{F}^{\tau\rho}$ is a supermatrix whose elements are composed of 2×2 spin matrices.

The DWBA scattering amplitude matrix given in equation (123), as well as each element of the supermatrix in equation (124) can be represented in the same manner as was done in equation (96) for the amplitude matrix in BA. Then substitution of the result into equation (97) yields a set of equations for the scattering cross section in DWBA identical with equations (98–106). In the next step one can use the expansion of the DWBA amplitude vectors $\boldsymbol{F}_l$ over unit vectors, as it has been done in equation (113) for the case of BA, and take into account that either transmission–reflection and phase matrices are diagonal in the representation with the quantization axis parallel to $\boldsymbol{b}_l^{\parallel}$.

This allows to express the scalars, F_l^0, in equation (114) and the corresponding components of the DWBA amplitude vectors $\boldsymbol{F}_l$ in equation (113) in the following compact form (Toperverg, Rühm, Donner and Dosch, 1999; Toperverg, Nikonov, Lauter-Passyuk and Lauter, 2001)

$$F_l^0 = \frac{1}{2}(F_l^{++} + F_l^{--}) \quad (125)$$

$$F_l^{\parallel} = \frac{1}{2}(F_l^{++} - F_l^{--}) \quad (126)$$

$$F_l^{\perp} = \frac{1}{2}(F_l^{+-} + F_l^{-+}) \quad (127)$$

$$F_l^{\dashv} = \frac{i}{2}(F_l^{+-} - F_l^{-+}) \quad (128)$$

In these equations the amplitudes

$$F_l^{++} = \tilde{F}_{l++}^N + \tilde{F}_{l++}^M \quad (129)$$

$$F_l^{--} = \tilde{F}_{l--}^N - \tilde{F}_{l--}^M \quad (130)$$

correspond to nuclear scattering, $\tilde{F}_{l\pm\pm}^N$, and magnetic scattering, $\tilde{F}_{l\pm\pm}^M$, which maintain the neutron spin states after splitting in the mean magnetic field in the layer l. The amplitudes $\tilde{F}_l^{+-} = \tilde{F}_{l+-}^M$ and $\tilde{F}_l^{-+} = \tilde{F}_{l-+}^M$ describe scattering processes, which mix those states.

Owing to equations (123) and (124) each amplitude $\tilde{F}_{l\mu\nu}^{N,M}$, with $\mu = \pm, \nu = \pm$, is represented by the linear combination [8]

$$\tilde{F}_{l\mu\nu}^{N,M} = \frac{1}{2} \sum_{\tau,\rho} a_\mu^{f\tau} F_{l\mu\nu}^{N,M}(Q_{\mu\nu}^{\tau\rho}, Q_x, Q_y) a_\nu^{i\rho} \quad (131)$$

of the Born amplitudes $F_{l\mu\nu}^{N,M}(Q_{\mu\nu}^{\tau\rho}, Q_x, Q_y)$. The latter ones depend on a number of different effective transverse wave vector transfers $Q_{\mu\nu}^{tt} = p_{l\mu}^i + p_{l\nu}^f = -Q_{\mu\nu}^{rr}$, $Q_{\mu\nu}^{tr} = p_{l\mu}^i - p_{l\nu}^f = -Q_{\mu\nu}^{rt}$, relevant to the various matrix elements between transmitted ($\tau, \rho = t$) and reflected ($\tau, \rho = r$) waves with, or without intermixing of the spin states. To shorten the notation for all these wave vector transfers they can be combined in a unique supermatrix $\hat{Q}_z = Q_{\mu\nu}^{\tau\rho}$. In equation (131) the amplitudes $F_{l\mu\nu}^{N,M}(\hat{Q}_z, Q_x, Q_y)$ are decorated by the corresponding amplitudes of transmission, $a_\pm^{it} = t_\pm^i$ and $a_\pm^{ft} = t_\pm^f$, into the layer through its front face, or reflection $a_\pm^{ir} = r_\pm^i$ and $a_\pm^{fr} = r_\pm^f$, from its back interface.

The matrix elements $F_{l\pm\pm}^N$ describe nuclear off-specular scattering of either positive or negative spin components of the neutron wave. They are proportional to the nuclear SLD contrast fluctuations $\Delta\overline{(Nb)_l^N} = (Nb)_l^N - \overline{(Nb)_l^N}$ with respect to its mean value $\overline{(Nb)_l^N}$ and are mostly due to the interfacial roughness, or due to artificial patterning. It

is important to note that $F^N_{l++} \neq F^N_{l--}$ even though SLD and the Born amplitude F^N_l of nuclear scattering given in Appendix A are independent of the spin state. This is a direct consequence of DWBA which describes scattering of neutron waves whose spin states are split due to the Zeeman effect in the mean optical potential. Hence their wave numbers are different. Nuclear scattering, certainly, does not mix those states.

The amplitudes $F^M_{l\pm\pm}$ correspond to off-specular scattering from longitudinal deviations $\Delta(Nb)^{\parallel}_l = \overline{(Nb)^M_l}(b^{\parallel}_l - \langle b^{\parallel}_l\rangle)$ of the projection $b^{\parallel}_l = (\boldsymbol{b}_l\boldsymbol{b}^{\parallel}_l) = \cos\beta_l$ of the local vector $\boldsymbol{b}_l = \boldsymbol{b}_l(x, y)$ onto the direction of $\boldsymbol{b}^{\parallel}_l$ from its mean value $\langle b^{\parallel}_l\rangle = \langle(\boldsymbol{b}_l\boldsymbol{b}^{\parallel}_l)\rangle = \overline{\langle\cos\beta_l\rangle}$ averaged over domains within the coherence range. Scattering from longitudinal magnetic fluctuations also maintains the neutron spin state. Two amplitudes, $F_{l\pm\mp} = F^M_{l\pm\mp}$, are due to fluctuations $\Delta(Nb)^{\pm}_l = (Nb)^M_l[(\boldsymbol{b}_l\boldsymbol{b}^{\perp}_l) \mp i(\boldsymbol{b}_l\boldsymbol{b}^{\dashv}_l)]$ of the field components perpendicular to $\boldsymbol{b}^{\parallel}_l$ and correspond to magnetic scattering which mix the spin states.

Consequently, the calculation in DWBA is reduced to simply a substitution of the Born amplitudes

$$F^{N,M}_{l\mu\nu}(\hat{Q}_z, Q_x, Q_y) = \int \mathrm{d}\boldsymbol{r}\, \mathrm{e}^{i(\hat{Q}_z z + Q_x x + Q_y y)}\Delta(Nb)^{N,M}_{\mu\nu} \tag{132}$$

into equation (131), taking into account that $\Delta(Nb)^N_{\pm\pm} = \Delta(Nb)^N_l$, $\Delta(Nb)^M_{\pm\pm} = \Delta(Nb)^{\parallel}_l$, while $\Delta(Nb)^M_{\pm\mp} = \Delta(Nb)^{\pm}_l$. If $(\boldsymbol{b}_l\boldsymbol{b}^{\dashv}_l) = 0$ then $\Delta(Nb)^M_{\pm\mp} = \Delta(Nb)^{\perp}_l$.

After the DWBA amplitudes have been determined, the lateral averaging can be accomplished in exactly the same way as was done for the BA cross sections in the preceding text. In particular, similar to equation (109) one can define the Fourier transform of equation (132),

$$F^{\lambda}_{l\mu\nu}(\hat{Q}_z, Q_x; y) = \frac{1}{2\pi}\int \mathrm{d}Q_y \mathrm{e}^{-iQ_y y} F^{\lambda}_{l\mu\nu}(\hat{Q}_z, Q_x, Q_y) \tag{133}$$

for each of the three amplitudes indexed by the superscript λ, denoting N, $\parallel$, or $\perp$. Then instead of equation (115) and equation (A1) in Appendix A one has the following set of equations:

$$F^N_l(\hat{Q}_z, Q_x; y) = F^z_l(\hat{Q}_z, y)\sum_j \mathrm{e}^{iQ_x x_j} F^L_{lj}(Q_x, y) \tag{134}$$

$$F^{\parallel,\perp}_l(\hat{Q}_z, Q_x; y) = F^z_l(\hat{Q}_z, y)\sum_j \mathrm{e}^{iQ_x x_j} \tilde{F}^{\parallel,\perp}_{lj}(Q_x, y) \tag{135}$$

These equations differ from the former ones just by the argument of the BA transverse form-factor $F^z_l(Q_z)$, provided in equation (A2) of Appendix A and depending on the transverse projection of the wave vector transfer Q_z. In DWBA Q_z has to be substituted for one of the 16 components of the supermatrix $\hat{\mathcal{Q}}_z = Q^{\tau\rho}_{\mu\nu}$. Then the corresponding results are to be inserted into the sum equation (131) used to calculate the amplitude components determined in equations (125–128), and then in equations (117–118). The latter finally give access to the terms of the cross sections determined in equation (98).

The sketched procedure to determine the scattering amplitudes in DWBA appears cumbersome while comprising all processes of NSF and SF nuclear and magnetic scattering of neutron waves refracted in and reflected from the mean optical potential. However, being well structured the procedure can easily be programmed and, as we shall see, allows to analyze rather complex multilayered systems providing a wealth of information hardly accessible by other means. The effects of each step in DWBA (reflection and transmission amplitudes, birefringence, etc.) can perfectly be classified so that a qualitative interpretation of prominent features detected in properly presented raw data can serve as a solid basis for choosing an adequate theoretical model. The latter, being further refined via, for example, a least square fit routine, would then quantify the information contained in the scattering pattern. Some of those distinct features are illustrated for a few benchmark examples discussed further in the subsequent text.

Before doing so, let us turn back to Figure 12 demonstrating the role of transmission–reflection factors in equation (131) for a simple example of a single periodically patterned film of Co, as sketched in Figure 11. Calculation carried out in BA (Figure 12a and c) and in DWBA (Figure 12b and d) for the same pattern and collected in the maps in Figure 12 show that in BA some essential features are missing. In particular, DWBA calculations for NSF scattering (Figure 12d) reveal noticeable difference as compared to BA results (Figure 12c). Thus, in contrast to BA, the oscillations along diffraction bands in the DWBA map are perfectly in phase with those on the specular ridge, as they should. This improvement of the BA outcome is due to the fact that the transverse form-factor in DWBA depends on the wave numbers $p^i_{\pm}$ and $p^f_{\pm}$ corrected for refraction effects, instead of those in the vacuum used by BA.

However, the most striking result of DWBA is that it provides SF Bragg diffraction. The latter is manifested via strong SF diffraction bands seen in Figure 12(b), which are absent in BA shown in Figure 12(a). This effect is mainly due to the transmission, $t^{i,f}_{\pm}$ and reflection, $r^{i,f}_{\pm}$ amplitudes in equation (131). These amplitudes take into account that the mean magnetic field of the effective layer (sketched in Figure 10b) oriented in accordance with Figure 11(b) not collinear with the polarization analysis axis. In such a

configuration both states with spin projections along and opposite to the mean magnetic field of the neutron wave inside the effective layer are populated. Then each of both spin components is scattered at local (periodic) deviations from the magnetic and nuclear SLD. In short, this example demonstrates that if the mean magnetic field in the layer is noncollinear with the initial polarization, SF off-specular scattering may occur due to *longitudinal* magnetic and *even nuclear* inhomogeneities. Local field projections perpendicular to the direction of the mean magnetic field mix spin states, while those parallel to this direction maintain the neutron spin states, which are split in the mean magnetic field. If the latter is directed perpendicular to the polarization analysis axis, as in Figure 11, then spin states are equally populated and SF scattering intensities $I^{+-} = I^{-+}$. More generally, as we shall see subsequent text for another example, $I^{+-} \neq I^{-+}$, and contribution of magnetic scattering can be separated that arising due to the nuclear scattering.

The role of transmission–reflection amplitudes is not restricted to the mixing of initial neutron spin states in case of noncollinearity between magnetization and polarization directions discussed in the preceding text. These amplitudes may also be responsible for another peculiar and often confusing features observed even for such a simple system as a single F film in a multidomain state. An example of NSF and SF scattering maps from domains in a 200 Å thick Co film on a Si substrate is displayed in a set of maps [9] in Figure 13. In the model system, it was assumed that the domain size is on the average 50 μm, and the domain magnetization is randomly tilted by an angle $\Delta\gamma$ with respect to the mean value averaged over the coherence volume. This mean magnetization itself may vary as a function of the y coordinate yielding an angle $\overline{\gamma}(y)$, as sketched in Figure 9. Short range magnetization fluctuations due to domains reduce the mean magnetic optical potential by a factor $\overline{\cos(\Delta\gamma)}$. In the simulation this value is set to ≈ 0.3. The second effect of these fluctuations is off-specular diffuse scattering, which is due to either magnetization projections perpendicular to the mean magnetization, or due to longitudinal fluctuations. Perpendicular fluctuations are characterized by the mean value $\overline{\sin^2(\Delta\gamma)}$, which here was chosen to be 0.75. For such a choice both perpendicular and longitudinal fluctuations contribute to off-specular scattering. As was mentioned in the preceding text, the contribution of the latter ones is proportional to the dispersion [10] $\tilde{\Delta} = \overline{\cos^2(\Delta\gamma)} - \overline{\cos(\Delta\gamma)}^2 = 0.16$.

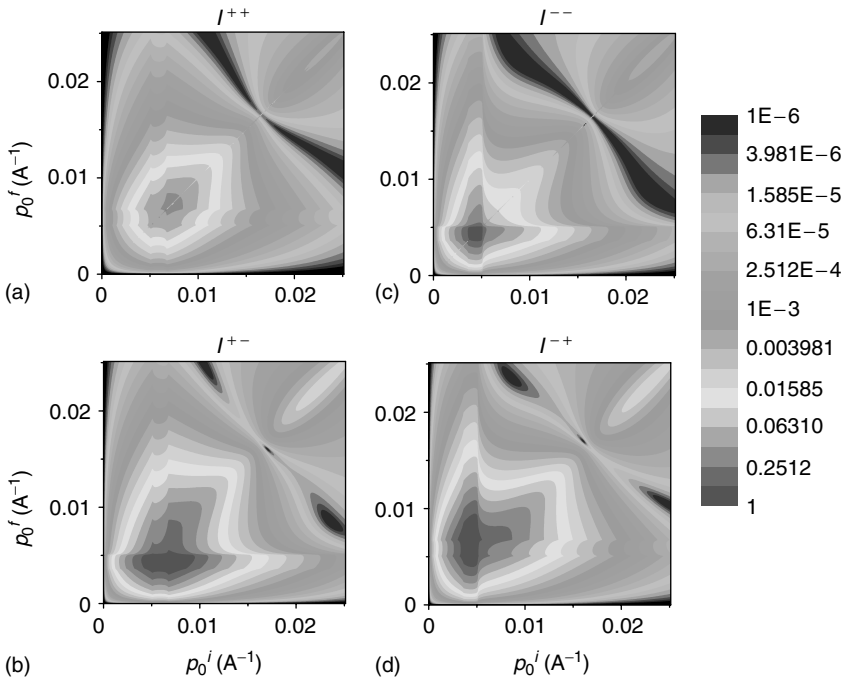

Figure 13. NSF (a) and (c) and SF (b) and (d) off-specular scattering intensity distribution calculated for a ferromagnetic 200 Å thick Co film deposited onto a Si substrate. It is assumed that the Co film is decomposed into a set of random domains with the mean size of 50 μm. The distribution of angles $\Delta\gamma$ between magnetization directions and the y axis is characterized by two parameters: $\langle\cos(\Delta\gamma)\rangle = 0.30$ and $\langle\sin^2(\Delta\gamma)\rangle = 0.75$. The mean magnetization averaged over the coherence length along the x axis is assumed to be independent of the y coordinate and to be collinear with the polarization analysis direction set along the y axis. Specular reflection ridges are eliminated for clarity.

Figure 13(a) and (c) present intensity distributions of NSF diffuse scattering. The dramatic difference between the scattering intensity I^{++} with positive spin projection (a), and I^{--} for negative spin projection (c) demonstrate the sensitivity of the diffuse scattering to the residual magnetization. In the model calculations, the mean magnetization averaged over the coherence range is reduced down to only 30% of its nominal value.

The off-specular diffuse NSF scattering reaches its maximum value at higher angles for neutrons polarized parallel to the mean magnetic magnetization (Figure 13a and b) than for neutrons polarized opposite to it (Figure 13c and d). Such a location of diffuse scattering on the maps is the direct consequence of the particular dependencies of the transmission and reflection amplitudes in equation (131) plotted in Figure 14. There one can clearly recognize a few prominent features. First of all, transmission and reflection amplitudes reveal noticeable singularities at points of the total reflection for this or the other spin components. These singularities substantially enhance the diffuse scattering (up to a factor 16 for a single film). Such enhancement is well known as the *Yoneda effect* (Yoneda, 1963) firstly observed for X-ray scattering from rough surfaces. In the case of off-specular scattering from domains, the neutron field is enhanced in the magnetic film at the critical edges $p_{c\pm}$ and at the critical wave number for the substrate. For our example the neutron field for positive spin projection is enhanced at $p_0 = p_{c+} \approx 6.7 \times 10^{-3}\,\text{Å}^{-1}$, while for both of them at $p_0 = p_s \approx 5.1 \times 10^{-3}\,\text{Å}^{-1}$, that is at the critical wave number for the silicon substrate.

The singularity related to the substrate is quite weak in Figure 14, but it is well expressed in Figure 13(c). This is due to the influence of the transverse form-factor discussed in the subsequent text for a Co film on a sapphire substrate where the effect is even more dramatic. For Co material the nominal magnetic optical potential is almost twice as big as the nuclear one [11]. Therefore, the critical wave number p_{c-} for saturated Co is imaginary and for the negative spin component there is no critical angle for total reflection. Then the first singularity in Figure 14 has to be absent. If, however, the Co film is partially demagnetized due to domains smaller than the coherence range then the mean magnetization may be reduced so that the mean magnetic SLD becomes lower than the nuclear one. Assuming a residual 30% of the nominal magnetization, the critical wave number for the state with negative spin projection is $p_{c-} \approx 3.6 \times 10^{-3}\,\text{Å}^{-1}$ and corresponding singularity is well presented in Figure 14. This figure, certainly, does not provide a full impression on the behavior of the transmission and reflection amplitudes, which are complex quantities. Nonetheless, Figure 14 can qualitatively explain the peculiarities of the diffuse intensity distribution over the maps plotted in Figure 13. For instance,

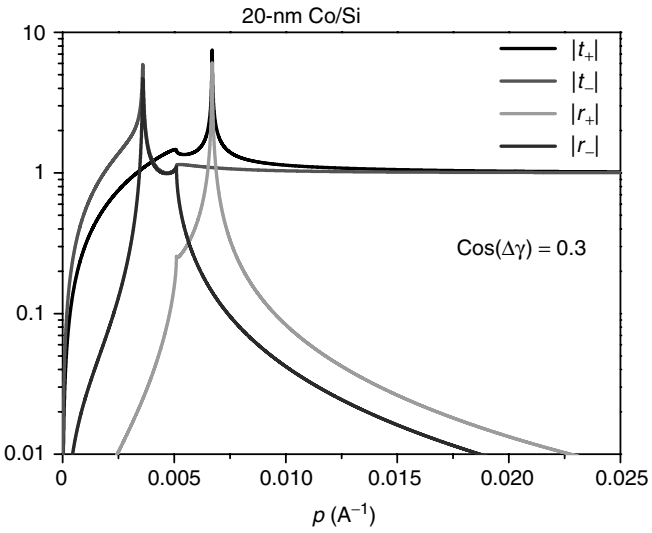

Figure 14. Transmission, $|t_\pm|$, and reflection, $|r_\pm|$ amplitudes of the neutron wave field in the mean optical potentials of the effective ferromagnetic 200 Å thick Co film on a Si substrate.

one can see that the reflection and transmission amplitudes at the critical edges are equal and just this fact doubles the neutron wave field which can be scattered in corresponding off-specular direction. Solely this fact provides an enhancement factor of 16 for the DWBA scattering cross section over the result obtained within BA. In reality, such enhancement factors may reach up to a few orders of magnitude depending on the particular design of the multilayer stack. At the wave numbers smaller than critical edges for the total reflection transmission and reflection amplitudes rapidly decay. This leads to a strong reduction of the scattered intensity when the neutron waves do not penetrate deep into the mean optical potential.

The transmission–reflection amplitudes also explain the substantial asymmetry in the SF scattered intensity distribution as seen in Figure 13. Indeed, SF scattering accounts for the fact that the spin states in the incoming and outgoing neutron waves are inversely populated. As mentioned before we consider here for clarity the case that the mean magnetization is collinear with the neutron polarization axis. Then Figure 13(d) refers to an incoming beam polarized opposite to the magnetization direction (spin-down state) and the corresponding amplitudes t^i and r^i are enhanced only at $p_0^i = p_s$ and at $p_0^i = p_{c-}$. Therefore, each cut of this map at fixed outgoing p_0^f, that is along the abscissa, shows an enhancement of the *incoming* wave field at $p_0^i = p_{c-}$ and at $p_0 = p_s$ (these two singularities are not well resolved in the maps). If at the same time the outgoing neutron is flipped into the up state then the corresponding amplitudes t^f and r^f provide the *scattered* wave field enhancement at $p_0^f = p_{c+}$ and $p_0^f = p_s$. As a result at fixed incoming wave

number p_0^i the scattering intensity reaches a maximum value at $p_0^f = p_{c+}$ and $p_0^f = p_s$. For the I^{+-} in Figure 13(b) the situation is just reversed: the incoming wave reflected from and transmitted into higher optical potential, than its scattered counterpart. Owing to the reciprocity principle both maps in Figure 13(b) and (d) are interchangeable by switching the magnetic field direction. If the magnetic layer is totally demagnetized via formation of small domains so that the mean field becomes zero, then $I^{++} = I^{--}$, $I^{+-} = I^{+-}$, and all maps are perfectly symmetric with respect to interchange p_0^i and p_0^f.

The crucial role of distortions of the incoming and scattered waves is demonstrated in Figure 15. These plots show off-specular scattering maps [12] calculated for a multidomain state of a 200 Å thick cobalt film, deposited onto a sapphire substrate covered with a 2000 Å thick sublayer of titanium. The maps also contain specular reflection ridges running along diagonals of the maps. They were omitted in the previous example for clarity. Specular ridges in the SF channels appear if the mean magnetization averaged over the coherence spot depends on its position on the sample surface. As was mentioned before this is quite a common case due to the strong anisotropy of the coherence ellipsoid whose long axis may cross several domains, while the short one is much smaller than the size of domains. In this case, one can expect quite appreciable fluctuations in angles $\overline{\gamma}(y)$. These fluctuations are characterized by two parameters set-in calculations of the maps in Figure 15 as follows: $\overline{\cos\gamma} = 0.866$ and $\overline{\sin^2\gamma} = 0.125$. Fluctuations on smaller scale cause off-specular scattering, the intensity of which is determined by the domain size (set-in calculations to 5 μm), and by fluctuations $\Delta\gamma$ in angles between domain magnetic moment directions and the magnetization direction of the coherence spot. Calculations in Figure 15 were carried out for $\overline{\cos(\Delta\gamma)} = 0.866$ and $\overline{\sin^2(\Delta\gamma)} = 0.125$.

The maps in Figure 15 display rather rich intensity details, although they possess the same general symmetry properties as the maps plotted in Figure 13. Most of the details are related to the transmission and reflection amplitudes because the film form-factor is kept the same as in the preceding text. The amplitude dependencies plotted in Figure 16, manifest, in contrast to Figure 14, a number of interesting features, which are related to the fact that the Ti nuclear SLD is negative and forms a wide (but shallow) potential well, while the SLD of the sapphire substrate is higher than the SLD of Co for the positive spin projection. Such a SLD profile is responsible for the oscillations of the transmission and reflection amplitudes either above and below the total reflection edge of sapphire. The situation is similar to that discussed above in view of pseudo-precession. Destructive interference of waves passed over the titanium potential well to and reflected from

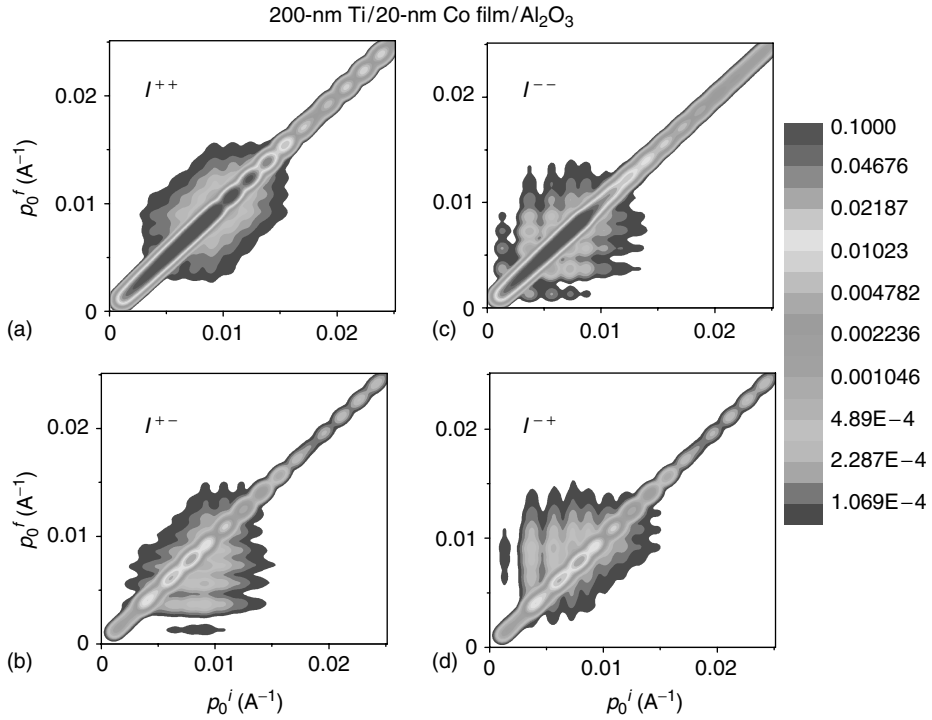

Figure 15. The same as in Figure 13, but for a 200 Å thick multidomain Co layer deposited onto the sapphire substrate covered with a 2000 Å thick titanium sublayer. Maps are calculated for the following set of parameters: $\overline{\cos\gamma} = \overline{\cos(\Delta\gamma)} = 0.866$, $\overline{\sin^2\gamma} = \overline{\sin^2(\Delta\gamma)} = 0.125$.

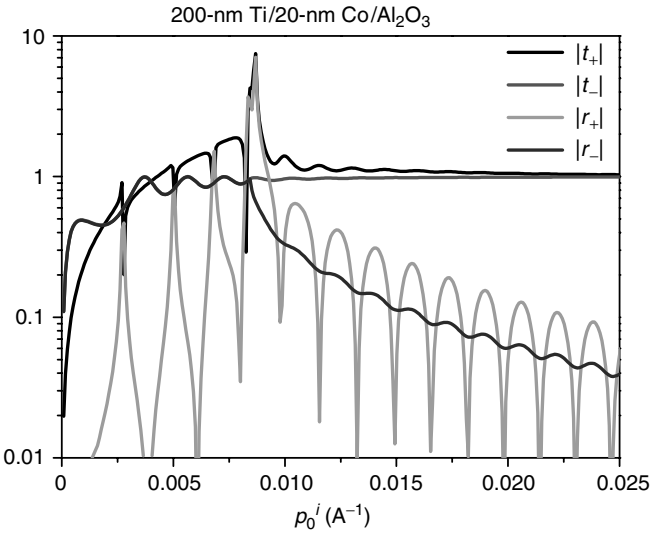

Figure 16. The same as in Figure 14, but for a 200 Å thick Co layer deposited onto a sapphire substrate covered with a 2000 Å thick titanium film with the same set of domain parameters as in Figure 15.

the substrate is expressed in narrow dips in the absolute values $|t^+|$ of the transmission amplitude and antiphase maxima in $|r^+|$ dependence on the wave number p_0^i. Those dips and maxima may exactly compensate each other. However, in equation (131) this compensation is destroyed due to the difference in phases of transmitted and reflected waves, as well as due to the transverse form-factor $F^M(\hat{\mathcal{Q}}_z)$ of the magnetic layer. As a result, the Yoneda wings in the maps of Figure 13 are cut by a set of narrow valleys running either parallel to p_0^i axis or parallel to p_0^f in Figure 15.

In accordance with equation (A2) the transverse form-factor of the film is an oscillating function of the transverse wave vector transfer Q_z with the period matched with the film thickness d. Corresponding oscillations lead to a modulation of scattered intensity along diffraction lines, as was demonstrated in Figure 12. Such a modulation is also present in the maps of Figure 13 where the first minimum in the form-factor $F^M(Q_{\mu\nu}^{\tau\rho})$ is manifested as valleys running across the main diagonal of the maps. Taking a closer look at the maps in the upper row one notices that the locations of the valleys are slightly shifted up in the left and down in the right maps. This shift is due to the difference in refraction effects for neutron waves with positive and negative spin projections. The refraction effects are even better seen in the bottom panels where corresponding valleys are asymmetric. The scattered intensity I^{++} in DWBA is not a function of the unique transverse wave number Q_z, but is rather a bilinear combination of four transverse form-factors $F^M(Q_{++}^{tt})$, $F^M(Q_{++}^{tr})$, $F^M(Q_{++}^{rt})$ and $F^M(Q_{++}^{tt})$. Hence, positions of one set of interference minima for I^{++} and, in particular, for one seen as a valley in Figure 13(a), are determined by the conditions:

$$Q_{++}^{tt} = -Q_{++}^{rr} = p_+^f + p_+^i = n\frac{\pi}{d} \tag{136}$$

if n is an odd number. If n is an even number then the corresponding equations determine the position of the maximum values for matrix elements responsible for transitions between two transmitted or two reflected waves with either the same or different spin states. For the map represented in Figure 13 the scattered intensity I^{--} the valleys run for odd n along the line determined by the equations

$$Q_{--}^{tt} = -Q_{--}^{rr} = p_-^f + p_-^i = n\frac{\pi}{d} \tag{137}$$

while in the maps for I^{+-} and I^{-+} valleys are traced by the equation

$$Q_{+-}^{tt} = -Q_{-+}^{rr} = p_+^f + p_-^i = n\frac{\pi}{d} \tag{138}$$

The scattering processes discussed in the preceding text account for only half of possible transitions described by 16 amplitudes in equation (132). The other half is due to processes which account for transitions between transmitted and reflected waves and depend on off-diagonal components of the wave vector transfers supermatrix $Q_{\mu\nu}^{\tau\neq\rho}$. Transverse form-factors relevant to these processes at odd n show minima if the *anomalous* wave vector transfers

$$Q_{++}^{tr} = -Q_{++}^{rt} = p_+^f - p_+^i = n\frac{\pi}{d} \tag{139}$$

$$Q_{--}^{tr} = -Q_{--}^{rt} = p_-^f - p_-^i = n\frac{\pi}{d} \tag{140}$$

for spin state conserving transitions. If the spin states are changed, then those minima are determined by the equations

$$Q_{+-}^{tr} = -Q_{+-}^{rt} = Q_{-+}^{rt} = -Q_{-+}^{tr} = p_+^f - p_-^i = n\frac{\pi}{d} \tag{141}$$

Related features are not seen in Figure 13. In this case, they are rather week and beyond the range displayed in this figure. Therefore, we will discuss next an example of a thick Co film, where *anomalous* scattering processes dominate [13], as in Figure 17.

In simulations, the mean magnetization was set again along the polarization analysis axis, but in contrast to the previous examples the sample is supposed to be in a multidomain state with a remanence half of the saturation magnetization value. The average size of the domains is set to 50 μm and the magnetic moments of different domains within the coherence volume are randomly tilted so that $\overline{\sin^2 \Delta\gamma} = 0.75$.

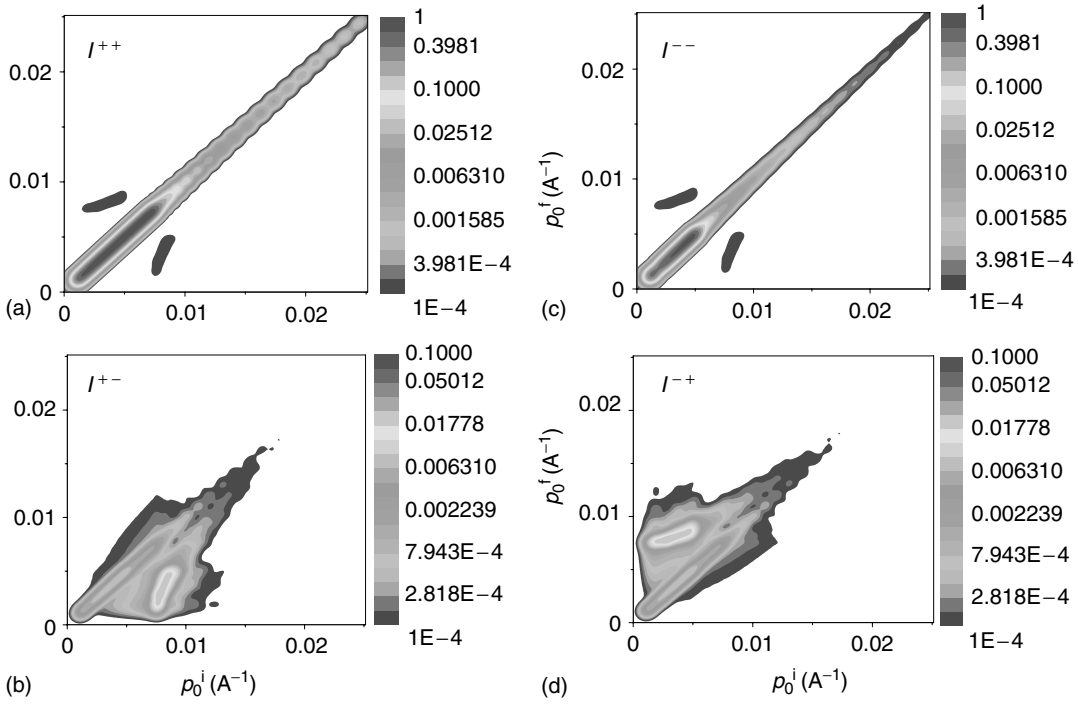

Figure 17. NSF (a and c) and SF (b and d) scattering intensity maps for random magnetic domains in a 2500 Å thick Co film on a Si substrate. Calculations are carried out for the sample in the state relatively close to saturation so that $\overline{\cos \Delta\gamma} = 0.5$, and $\overline{\sin^2 \Delta\gamma} = 0.75$. The mean magnetization is assumed to be perfectly collinear with the polarization analysis axis, while traces of off-specular scattering in the top and specular signal in the bottom panels are due to incomplete polarization efficiency which is set to 99%.

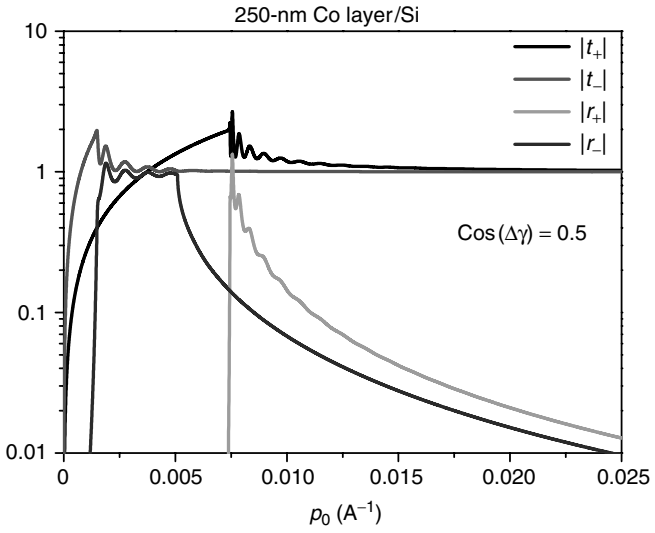

Figure 18. The same as in Figure 16, but for a 2500 Å thick film on Si substrate.

The behavior of the transmission and reflection amplitudes for this case are illustrated in Figure 18 where one can recognize singularities similar to those in Figure 14 and fast total thickness oscillations as in Figure 16. These oscillations in Figure 18 are due to the thick Co layer itself, but not caused by the thick sublayer as in the former case.

Large shifts of the critical edges due to a high magnetization value within a domain provides strong asymmetry in off-specular SF scattering intensity distribution as seen in Figure 17. However, its particular 'banana-like' shape is due to the fact that scattering is mostly contributed by an anomalous process with the wave vector transfers determined by equation (141). This equation for $n = 0$ has the following solutions:

$$p_0^f = \sqrt{(p_0^i)^2 - 2p_{cm}^2} \tag{142}$$

$$p_0^i = \sqrt{(p_0^f)^2 - 2p_{cm}^2} \tag{143}$$

where $p_{cm}^2 = 4\pi (Nb)_m \overline{\cos \Delta\gamma}$ is the critical wave number for the mean magnetic potential and $(Nb)_m$ is the nominal magnetic SLD. The first equation here corresponds to the left, while the second one to the right map in Figure 17. Owing to the large thickness of the film the transverse form-factor at these values has a rather sharp maximum, while the side maxima at $p_+^i - p_-^f = 2\pi n$ are suppressed.

In the preceding discussion, we intentionally concentrated on a few simple examples of single magnetic films in

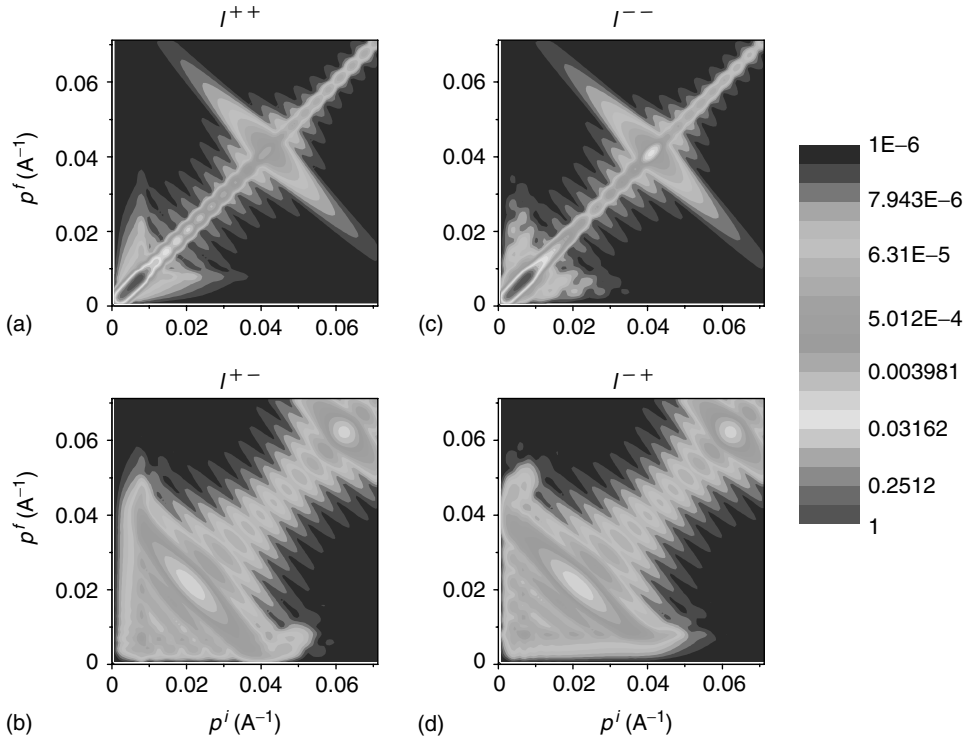

Figure 19. NSF (a) and (c) and SF (b) and (d) scattering intensity maps for magnetic domains in the antiferromagnetically coupled $[^{57}\mathrm{Fe}(67)\mathrm{Cr}(9)]\times 12$ multilayer on sapphire substrate. Calculations are carried out for the model of column-like domains with lateral size of 5 μm and domain magnetization tilted in the neighboring layers to the left and to the right by $\sim 45^\circ$ with respect to the polarization analysis axis. Alternation of the domain magnetization projection perpendicular to this axis result in SF superstructural Bragg sheets in the bottom panels. The mean layer magnetization is assumed to be reduced by the factor $\overline{\cos \Delta\gamma} = 0.5$, so that alternation of the domain magnetization projections onto the y axis causes NSF structural Bragg sheets as seen in the top panels running across the Bragg peak on the specular reflection ridge. The net magnetization is assumed to be perfectly collinear with the polarization and this ridge is only present in NSF channels.

a domain state or with a periodic lateral pattern. These examples show that DWBA provides a deep understanding of the rich details in the NSF and SF scattering maps. Furthermore, DWBA provides a solid framework for correct and quantitative analysis of experimental data, yielding information on the lateral magnetization distribution over the film plane. However, the main advantage of PNR and, in particular, of off-specular scattering is attributed to its sensitivity to the depth profile of the magnetization distribution.

This can already be seen comparing the last three examples for films of different thickness. One more example is still needed to illustrate the case of DWBA for laterally structured periodic multilayers. The magnetization distribution in such system is of a special practical importance, while off-specular scattering of polarized neutrons is a powerful tool to study it in great detail. On the other hand, owing to the transverse periodicity off-specular scattering maps from multilayer structures contain qualitatively new features which need to be discussed separately.

Figure 19 shows an example of a DWBA calculation carried out for a multidomain state of a $[^{57}\mathrm{Fe}(67)\mathrm{Cr}(9)]\times 12$ multilayer deposited onto a sapphire substrate. In this system, atomic spins in neighboring F layers of iron are antiferromagnetically exchange coupled through the metallic chromium spacer layers. Very often, however, F layers are not homogeneously magnetized, but rather fall into a set of lateral domains. Then owing to the exchange coupling the multilayer stack appears to be broken up into lateral domains where magnetic moments are arranged antiferromagnetically across the multilayer. In an applied magnetic field the magnetization of the Fe layers is forced toward the field direction and the system may undergo a transition into the spin-flop phase, as discussed in the subsequent text (Lauter-Pasyuk *et al.*, 2002). In this state the sublayer magnetization, for example, the magnetization in each of the lateral domains, is tiled to the left and to the right with respect to the applied field direction. The net magnetization is directed along the field, while in the sublayers it has alternating projections onto the perpendicular direction to the field.

In Figure 19(a) and (c) we present NSF scattering intensity distributions, which show ridges of specular reflections. Along these ridges one can see the ranges of total reflection at low wave numbers, Kiessig fringes, and Bragg peaks due to the periodicity in the mean optical potential variation across the multilayer stack. Note that in Figure 19(c), corresponding to I^{--}, this peak is stronger than in Figure 19(a), corresponding to I^{++}. This is due to the fact that the nuclear SLD of ^{57}Fe is lower than the magnetic SLD, providing highest optical contrast for reflection of neutrons with negative spin projections onto the field direction. All maps in Figure 19 reveal off-specular scattering justifying that the lateral size of the domains (set to 5 µm) are smaller than the coherence length. Off-specular scattering in the NSF maps may be caused by conformal interfacial roughness and/or deviations from the magnetization projections parallel to the net magnetization. The latter is set along the polarization analysis axis. NSF off-specular scattering is substantially enhanced at the critical edge of the total reflection (Yoneda scattering), and its line shape depends on the spin state of the scattered neutrons. In particular, for I^{++} it is enhanced at $p_0^i \approx p_{c+}$, or $p_0^f \approx p_{c+}$, where p_{c+} is the critical wave number of the total reflection from SLD of ^{57}Fe for neutrons with positive spin projection. For negative projection the critical edge is absent and an enhancement of I^{--} occurs along a set of sheets (Kiessig sheets) determined by equations (140) and (139) with d corresponding to the total thickness of the multilayer. These sheets have similar origin to those in the case of thick Co films discussed in the preceding text. Off-specular scattering is also enhanced along the lines crossing the position of the Bragg peak on the reflectivity ridge. There it forms so-called Bragg sheets along which, in accordance with equations (136) and (137) $Q_z \approx 2\pi/d$, where d is the multilayer period. The extension of the Bragg sheets is mostly determined by the domain size, while their intensity is due to the amplitude of deviations from the mean optical potential and the degree of their conformity through the multilayer stack.

Figure 19(b) and (d) show SF scattering maps In contrast to the NSF maps they do not contain specular ridges. This means that in the model there is no mean magnetization projection onto the direction perpendicular to the polarization analysis axis. But instead, one can see in those maps extensive Bragg (and also Kiessig) sheets running along the lines determined by equation (138) with $n = 1$ and $n = 3$. SF Bragg sheets manifest AF ordering of domain magnetization projections perpendicular to the mean magnetization. Such an ordering doubles the unit cell with respect to the structural cell across the multilayer stack. Owing to nonzero magnetization the intensity distribution I^{+-} and I^{-+} are asymmetric with respect to main diagonal. In particular, one can see strong distortions of the superstructural Bragg sheet when angles of incidence of the incoming or exit beams approach the sample horizon. Close to the critical edges the anomalous scattering becomes very strong resulting in an anomalous Bragg sheet running along the lines determined by equation (141), as was discussed in the example of the thick Co films in the preceding text. In the subsequent text, we present experimental results which use above considerations to interpret data collected from various magnetic films, multilayers, and laterally structured magnetic arrays.

3 EXPERIMENTAL CONSIDERATIONS

As discussed in the preceding text, any y component of a magnetic field distribution or a sample magnetization leads to two critical angles for total neutron reflection with respect to the two possible neutron spin polarizations. If the incident beam is unpolarized, for scattering vectors $\mathbf{Q}_c^- \leq \mathbf{Q} \leq \mathbf{Q}_c^+$, neutrons with polarization parallel to the magnetization are reflected and neutrons with the opposite polarization are transmitted. This property is exploited in supermirrors for polarizing neutron beams, where either the reflected or the transmitted beam can be used for polarizing the incident neutron beam for PNR experiments (Krist *et al*., 1995; Böni, 1997). For practical reasons, it is advantageous to use the transmitted beam and to accept the small absorption. The same scheme is used for the scattered beam if a two-dimensional polarization analysis of the magnetization vector is required.

PNR studies are carried out either in a wavelength or in an angle dispersive mode. In the angle dispersive mode, a monochromator in the incident beam selects a narrow wavelength band of $\Delta\lambda/\lambda = 0.5$ to 5% depending on the resolution required. Instead of a monochromator also a Fermi velocity selector with a continuously tunable wavelength can be placed in the incident beam. However, this requires that an end position for the instrument is available.

In the wavelength dispersive mode the time-of-flight start time is defined by the first chopper, while the second chopper serves for pulse shaping and for eliminating frame overlap problems. In both set-ups supermirrors (SM) and π-spin flip coils (SF_1 and SF_2) are used in the incident and reflected beam for polarizing the beam before the sample and for analyzing the polarization state after the scattering event.

Supermirrors and spin flippers can be integrated into one device if the remanent magnetization of the supermirror is high enough and if its magnetization can be switched from one orientation to the opposite with a pulsed field (Böni, 1997; Böni, Clemens, Senthil Kumar and Pappas, 1999).

The main advantage of the wavelength dispersive mode is a fixed glancing angle to the sample surface. On the other hand, the angle dispersive mode has the advantage of a constant efficiency for the supermirrors and spin flippers, optimized for the particular wavelength used. At steady-state neutron sources both modes of operation are being used, while at pulsed neutron sources only the wavelength dispersive mode is suitable.

A typical setup for a polarized neutron reflectometer is shown in Figure 20. The supermirrors are used in the transmission mode, and in the chosen example the front flipper is turned 'on' to provide a spin-up state, while the back flipper is turned 'off', thus measuring the $(+-)$ cross section in transmission mode of the back analyzer and the $(++)$ cross section in reflection mode. Using two detectors, the $(++)$ and $(+-)$ cross sections can be measured simultaneously. In case of an angle dispersive reflectometer between the source and the first polarizer a monochromater has to be placed, while for wavelength dispersive detection the monochromator is substituted by a chopper system. In Figure 21, the angle dispersive ADAM reflectometer at the Instiut Laue–Langevin is shown in a cut away view.

Instead of taking radial scans in the Q_z direction, that is parallel to the specular ridge, it is often necessary to map out the off-specular diffuse intensity, by using a position-sensitive detector (PSD). The PSD covers the specular reflection as well as collects off-specular intensity.

The simultaneous polarization analysis of the specular and off-specular exit beam requires the use of a wide angle polarization analyzer. Two types of wide angle analyzers are presently being used, either a stack of supermirrors

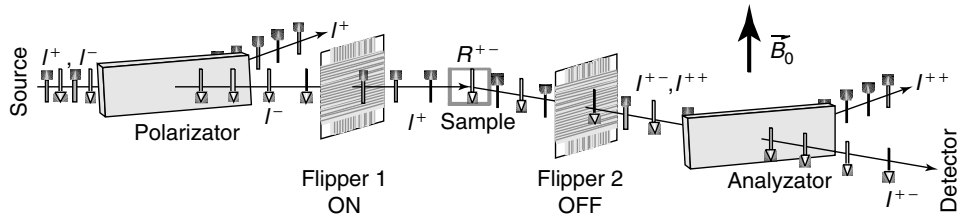

Figure 20. Schematic outline of an angle dispersive neutron reflectometer with polarization analysis. The incident monochromatic and unpolarized beam is polarized by the first supermirror in transmission mode. Spin flippers before and after the sample can change the neutron polarization from up to down and vice versa. The back supermirror analyzes the polarization state of the neutrons after the sample. In the shown configuration with the front spin flipper turned on and the back spin flipper turned off, the SF $R^{+,-}$ reflectivity is measured (Siebrecht, 2001).

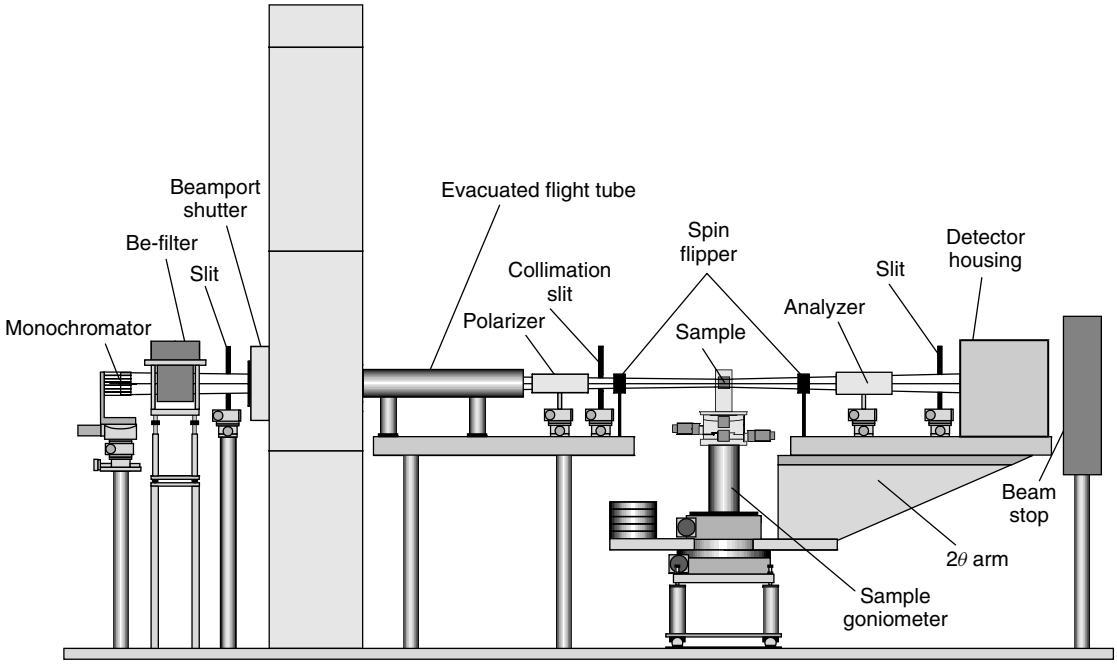

Figure 21. Cut away view of the angle dispersive neutron reflectometer ADAM at the Institut Laue–Langevin, Grenoble.

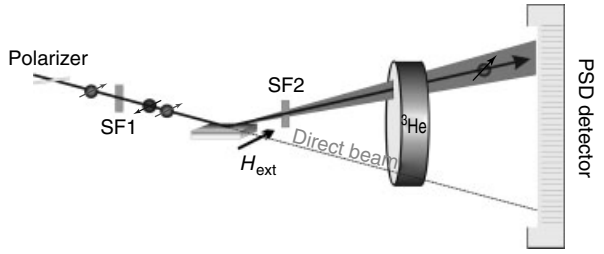

Figure 22. Schematic outline of a scattering experiment using a spin filter for analyzing the polarization of the exit beam and detection with a position-sensitive detector. (Reproduced from M. Wolff *et al*., 2006, with permission from Taylor and Francis. © 2006.)

(Krist, Fritzsche and Mezei, 2002; Syromyatnikov *et al*., 2001) or a polarized ^{3}He transmission spin filter in the exit beam (Zimmer *et al*., 2000; Nickel, Rühm *et al*., 2001). A schematic outline of the scattering geometry with a spin filter analyzer is shown in Figure 22. In recent years, huge progress has been made with respect to lifetime and quality factor of ^{3}He spin filters (Radu, 2005; Wolff *et al*., 2006). While in the past there was some hesitation to use spin filters as a standard tool, recent developments seem to favor the use of spin filters over solid state analyzers. The main advantages being that with polarized ^{3}He spin filters (i) highly divergent beams can be analyzed; and (ii) the analyzing efficiency is homogeneous and predictable with negligible small-angle scattering from the ^{3}He cell. The use of ^{3}He spin filters requires a sophisticated infrastructure for polarizing ^{3}He by optical pumping, which is available at the Institut Laue–Langevin (Grenoble, France) and at the NIST Center for Neutron Research (Gaithersburg, USA), and becomes also available at other neutron sources in the near future. Supermirror stacks are, in contrast, maintenance free, but may cause additional small-angle scattering. Supermirror stacks in reflection mode (Syromyatnikov *et al*., 2001) appear to be operating better than those in transmission mode (Krist, Fritzsche and Mezei, 2002; Syromyatnikov *et al*., 2001).

By designing a neutron reflectometer, three main decisions have to be taken:

- horizontal or vertical scattering plane;
- angle dispersive or wavelength dispersive scattering mode;
- with or without polarization analysis.

For the investigation of magnetic samples, polarization analysis is mandatory. The other two decisions are a question of convenience, floor space available, and investment cost.

Historically, three generations of polarized neutron reflectometers can be distinguished. The first generation of neutron reflectometers were built in the late 1980s, using a polarized beam without polarization analysis (Felcher *et al*., 1987). The second generation of instruments built in the early 1990s included supermirrors for the spin polarization and for spin analysis (Majkrzak, 2001; Siebrecht *et al*., 1997). The third generation starting with the early twenty-first century is equipped with wide angle polarization analyzers, PSD detectors, and an option for grazing incidence small-angle scattering of magnetic in-plane structures (GISANS) (Rücker *et al*., 2001; Pannetiera, Ott, Fermon and Samson, 2003). A fourth generation can be foreseen and developments are taking shape at several places for spin-echo type reflectometers, which accept divergent incident beams (Major *et al*., 2003; Pynn *et al*., 2003). Table 1 provides a non-comprehensive list of typical reflectometers at different neutron sources. Worldwide the total number of polarized and unpolarized neutron reflectometers operational at steady-state and pulsed neutron sources is about 30, and this number is steadily increasing (see http://material.fysik.uu.se/group_members/adrian/reflect.htm for an up-to-date list).

4 PNR INVESTIGATIONS OF MAGNETIC FILMS, HETEROSTRUCTURES, AND SUPERLATTICES

Different magnetic heterostructures are conceivable, such as simple magnetic films on substrates, bilayers, trilayers, or multilayers. These structures are referred to as perpendicular

Table 1. Representative neutron reflectometers with different options are listed.

Name	Affiliation	SP	DM	PA	Reference
ADAM	ILL	Horizontal	a	SM, ^{3}He, PSD	(Siebrecht *et al*., 1997)
AMOR	PSI	Vertical	w	SM	(Clemens *et al*., 2000)
CRISP	ISIS	Vertical	w	SM, PSD	(Felici *et al*., 1988)
D17	ILL	Horizontal	a and w	SM,^{3}He, PSD	(Cubitt and Fragnetto, 2002)
NG7REFL	NIST	Horizontal	a	SM, PSD	(Majkrzak, 2001)
POSY I	IPNS	Horizontal	w	SM, PSD	(Felcher *et al*., 1987)

SP: scattering plane; DM: diffraction mode (wavelength (w) and angle (a)); PA: polarization analysis; PSD: position-sensitive detector; SM: supermirror; ^{3}He: spin filter.

heterostructures as their extension within the plane is 'infinite', but in the perpendicular direction the layer thicknesses can range from a few monatomic layers up to a few hundred nanometers. In contrast, lateral heterostructures usually require some top–down lithographic processing or, alternatively, some bottom up self assembly.

In Figure 23, some typical magnetic heterostructures are sketched. PNR investigations of magnetic heterostructures include the magnetization profile within single magnetic films and in multilayers (Figure 23a); magnetic states and phase transitions in films of magnetic alloys, compounds, and dilute magnetic semiconductor (Figure 23b); magnetization reversal mechanism and domain formation in exchange-biased systems (Figure 23d); twisting effects of the magnetization vector in spring magnets (Figure 23e); and domain states and stripes (Figure 23c). The theoretical framework for the analysis of these magnetic heterostructures is provided in Section 2.5. Experimental results are discussed in the following sections.

PNR has developed into an essential tool for the analysis of artificial magnetic heterostructures with main emphasis on vector magnetization profiles, magnetic domain distributions and fluctuations, magnetization reversal mechanisms, and on correlation effects. Although the competition with XRMS has increased in recent years (Kortright *et al*., 2003), there are some advantages PNR offers that are hard to challenge. Those include the data analysis using the BA or the DWBA, the well-known cross sections, and the purely magnetic SF scattering that has no counterpart in XRMS.

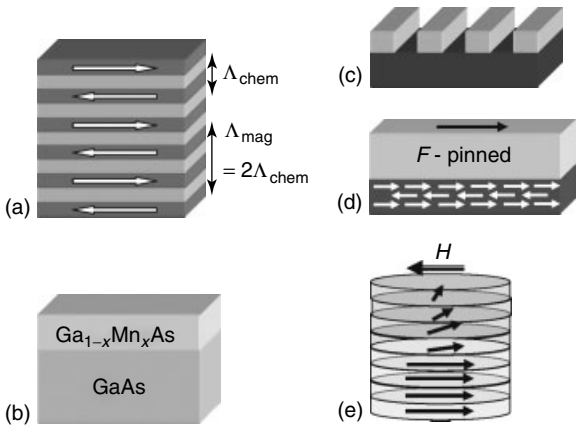

Figure 23. Selection of magnetic nanostructures investigated by polarized neutron reflectivity experiments. (a) Exchange-coupled superlattice with antiferromagnetic order; (b) dilute magnetic semiconductor as spin-aligner in semiconductor heterostructures; (c) laterally patterned magnetic films; (d) bilayer of a ferromagnetic film on an antiferromagnetic substrate with exchange bias at the common interface; (e) spring magnetic consisting of a top soft magnetic layer on a hard magnetic layer, where twisting occurs only in the soft layer and in an opposing external magnetic field.

Thin F films are important objects in many device applications. They are characterized by a certain thickness, interfacial roughness, domain state within the film plane, and magnetization profile normal to the film surface. Furthermore, magnetic films are characterized by their magnetic hysteresis, including coercivity, remanence, saturation, and magnetic anisotropy. A thin film is never standing alone but is supported by a substrate or is sandwiched between other layers. Even in the case of a self supported thin film, the magnetic film will acquire an oxide cover, unless protected by a cap layer. Whether a thin film is investigated on a substrate or as a film embedded in a multilayer depends on the question asked and on the physics to be analyzed. If at all possible, multilayers are preferable over thin films, not only because they increase the probing volume but mainly because they give rise to Bragg reflections due to the artificial periodicity. Bragg reflections represent the Fourier transform of the real structure and are much more sensitive to small perturbations than reflectivity from single films is.

We will discuss recent experimental developments in the analysis of thin magnetic films, magnetic heterostructures, multilayers, and patterned magnetic films. We will not discuss ultrathin magnetic films, as this topic has recently been reviewed by Bland and Vaz (2005). The following sections are not intended to provide a review on the physics of thin magnetic films, heterostructures, and superlattices, but to discuss PNR applications to these systems.

4.1 Thin ferromagnetic films

4.1.1 Magnetic heterostructures

We start our discussion with a PNR study of a thin F layer on a non-magnetic substrate. Figure 24 shows polarized reflectivity scans from a single 2-nm-thick Fe(110) film on top of a 150-nm-thick Nb(110) film grown on a sapphire substrate. The Fe film is protected by a 5-nm-thick Nb capping layer. The measurements were carried out at the ADAM instrument of the Institut Laue–Langevin, Grenoble, in an angle dispersive mode (Zabel and Theis-Bröhl, 2003).

The Fe film is in a F state and the magnetization vector is aligned parallel to the y axis. Two types of oscillations can be observed. The rapid oscillation is due to the total film thickness including all three layers, the wider oscillation originates from the top Nb protecting layer, while the complete oscillation from the 2-nm-thick Fe film is not visible due to the limited Q-range of the scan. Nevertheless, the special sandwich design for the F film provides a very high sensitivity for neutron scattering. The $\mathcal{R}^{++}$ and $\mathcal{R}^{--}$ intensities are strongly split, with a negligible amount of SF scattering, indicative first for the F state of the sample,

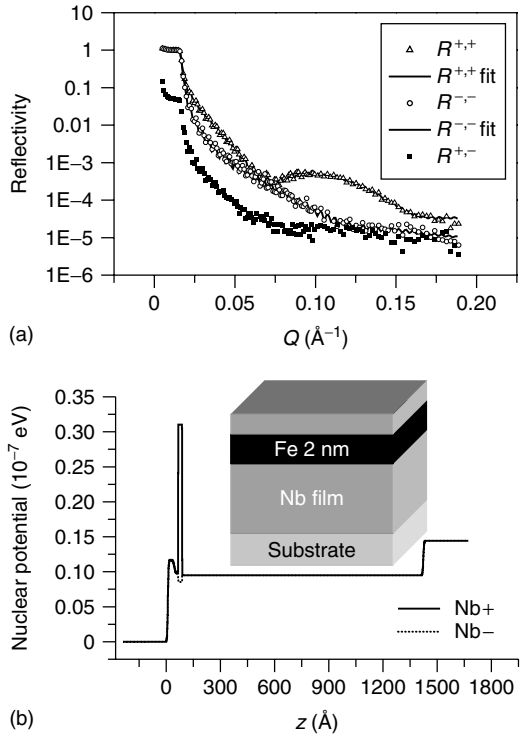

Figure 24. (a) Polarized neutron reflectivities are shown for a ferromagnetic 2-nm thick Fe layer on a non-magnetic Nb film. The intensity splitting between the $\mathcal{R}^{++}$ and $\mathcal{R}^{--}$ reflectivities is a clear sign for the ferromagnetic state of the thin Fe layer. Shown in the lower part of the figure is also the $\mathcal{R}^{+-}$ spin-flip scattering. This scattering is featureless, indicating that any component of the magnetization vector parallel to the x axis is negligible. (b) Nuclear and magnetic profiles for the up and down neutron spin polarization resulting from a fit to the reflectivity curves according to the generalized matrix method. (Reproduced from F. Radu *et al*., 1999, with permission from Elsevier. © 1999.)

and second for the orientation of the magnetization vector being parallel to the y axis. Figure 24(b) shows the nuclear and magnetic density profile resulting from a fit to the $\mathcal{R}^{++}$ and $\mathcal{R}^{--}$ reflectivities, using the generalized matrix method for describing the polarized reflectivity (Radu and Ignatovich, 1999). The profile not only confirms the F state of the Fe layer with a magnetic moment identical to the Fe bulk moment and little interdiffusion at the Fe/Nb interfaces, but also shows that an oxide layer exists at the surface with a slightly enhanced SLD. The solid and dashed lines are the reflectivity profiles for the parallel and antiparallel polarization of the neutrons in relation to the layer magnetization. The antiparallel alignment results in little contrast to the Nb layers, as already recognized by the missing oscillations in the $\mathcal{R}^{--}$ reflectivity curve. The astounding conclusion of this measurement is the very high sensitivity of PNR to thin F layers, corresponding in the present case to only 10^{-3} emu. Obviously this is not the limit and even thinner samples have been investigated in the past (Blundell and Bland, 1992). This is an important result, since PNR provides valuable magnetic information on ultrathin buried films together with structural information as concerns the film thickness, the magnetization profile, and the interfacial roughness.

A number of similar PNR experiments have been performed in the past on magnetic films, in most cases in order to learn about the magnetization profile in buried layers, whenever 'dead' layers are suspected from interdiffusion or interfacial roughness. For instance, Vaz *et al*. (2005) have investigated the magnetization profile of a 5-nm-thick epitaxial Fe layer grown on GaAs(100) with a 1.3-nm-thick AlO_x tunnel barrier and capped with 25 nm Au layer. From the PNR results they conclude that at the interfaces no interdiffusion occurred and that the Fe magnetic moment corresponds to the bulk value in spite of the non-ideal growth properties on the amorphous AlO_x tunnel barrier. Thus, in this case a 'dead' layer does not form at the interface and the full polarization of the Fe layer can be used for spin tunneling into GaAs. The question of a 'dead' layer at the Fe/GaAs interface can also be answered by Mössbauer spectroscopy experiments, using a probing ^{57}Fe layer at the interface (Doi *et al*., 2002). The advantage of PNR over Mössbauer spectroscopy is that no special isotopes are needed nor particular growth conditions to avoid interdiffusion of ^{57}Fe and natural Fe.

Zhengdong *et al*. (2004) have studied the growth of Ni on MgO. When growing metals on oxide surfaces, it can be suspected that an oxide layer forms at the interface. NiO is AF below $T_N = 500$ K and causes an EB when in contact with Ni. This scenario could indeed be observed for Ni grown on MgO(001) after annealing at 573 K. Neutron reflectivity studies have confirmed the existence of a non-magnetic layer at the interface between Ni and MgO with a SLD that matches NiO rather well.

Magnetite (Fe_3O_4) is a highly interesting ferromagnetic oxide with a complex spinel structure. Because of the high moment and half-metallicity it is considered as a suitable material for spintronic applications (Coey and Chien, 2003). Significant values of spin polarization have already been observed in bulk Fe_3O_4 (Bratkovsky, 1998; Kozlowski *et al*., 1993). However, several studies of (001) oriented thin films, usually grown on MgO(001), have exhibited very small magneto-resistive (MR) ratios. These reduced MR values have been attributed to complex magnetic and structural properties at their interfaces. To clarify the magnetic moment of magnetite in thin films grown on MgO, Morall *et al*. (2003) have performed PNR measurements at room temperature, which is far below the Curie temperature of 860 K. For a 5.3-nm-thick film an average magnetic moment of 2.8 μ_B was determined, much less than the expected value of 4 μ_B. The authors could not explain the discrepancy but refer to a

rather high layer roughness of 2.3 nm and a possible reduced Curie temperature. It should be pointed out that for roughness parameters on the order of the film thickness the determination of magnetic moments with the PNR method becomes unreliable.

So far we have discussed F thin films in saturation. The main emphasis of these studies is the depth dependent magnetization profile, which is determined by two reflection coefficients $\mathcal{R}^{++} = \mathcal{R}^{+}$ and $\mathcal{R}^{--} = \mathcal{R}^{-}$. Off-specular and SF scattering is not expected in this case and therefore does not need to be analyzed. The situation is different for F films either in remanence or at the coercive field. If the remanence is less than 100%, magnetic domains are expected which will give rise to new effects thoroughly discussed in the Section 2.11: first the magnetic domains will cause diffuse scattering in case that the domains are smaller than the longitudinal coherence length of the neutron beam, and second the canting of the domain magnetization vectors will cause SF scattering. This effect has recently been studied in some detail by Radu *et al*. (2005a). For this experiment a 2500 Å thick Co film was used, grown by rf-sputtering on a SiO_2 substrate. Growth conditions and substrate choice provided a polycrystalline Co film. A Kerr image taken at a field of 10 Oe, which is comparable to the neutron experimental condition, showed a small-angle ripple domain structure, which is due to the polycrystalline nature of the film combined with the intrinsic magnetocrystalline anisotropy of Co. The magnetization within the ripple domains is partly tilted by the angle $\Delta\gamma$ to the left and to the right with respect to the applied magnetic field (partial spin-flop orientation). The ripple domains are responsible for the reduced remanence observed in the magnetic hysteresis. The neutron intensity maps for all four cross sections from the Co film on Si are shown in Figure 25.

The general features of these maps are well reproduced by DWBA simulations plotted in Figure 17. Off-specular SF scattering is mostly concentrated along the lines determined by equations (141–143), which account for birefringence in the magnetic part of the mean optical potential. These equations allow to experimentally find the mean value $\overline{\cos(\Delta\gamma)}$ averaged over the coherence length. Figure 17 demonstrates that DWBA is able to describe not only the location, but also the absolute intensity of diffuse scattering. The latter is proportional to the mean value $\overline{\sin^2(\Delta\gamma)}$ and fitting the data to the theoretical model one can determine the dispersion $\tilde{\Delta} = \overline{\cos^2(\Delta\gamma)} - \overline{\cos(\Delta\gamma)}^2$, quantifying the domain reversal mechanism, as discussed in the next subsection. On the other hand, some important conclusions on the lateral magnetization distribution in the

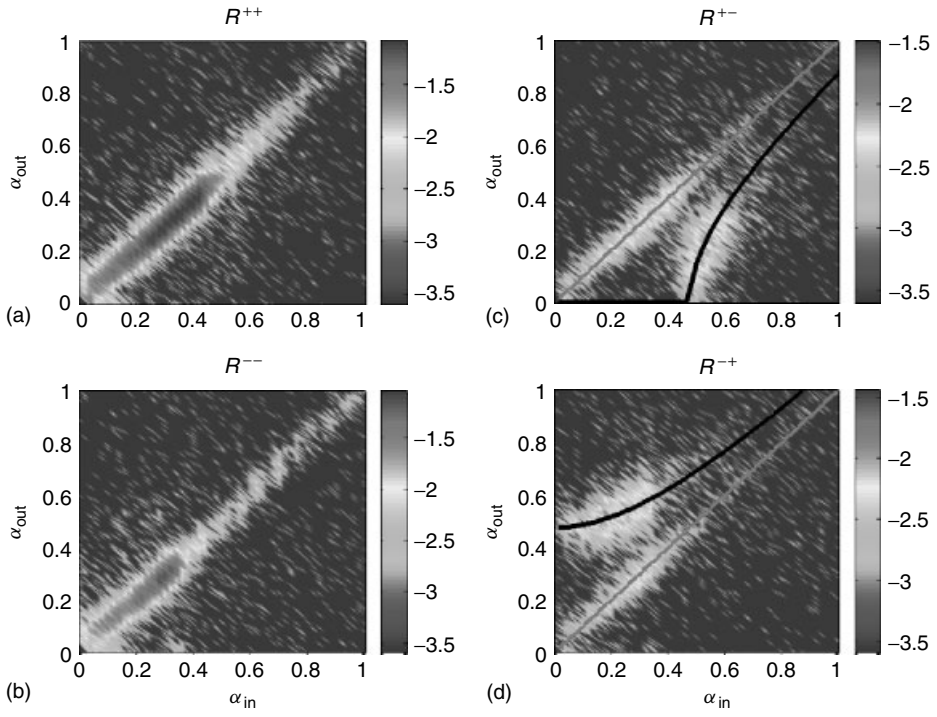

Figure 25. Intensity maps taken from a 2500-Å-thick polycrystalline Co film on a Si substrate. The maps were recorded close to remanence (≈10 Oe). The left column shows intensity maps for the non-spin-flip cross sections $\mathcal{R}^{++}$ (a) and $\mathcal{R}^{--}$ (b), the right column for the spin-flip cross sections $\mathcal{R}^{+-}$ (c) and $\mathcal{R}^{-+}$ (d). The intensities are plotted in terms of exit angles (vertical axis) versus incident angle (horizontal axis). For a discussion of the maps, see main text. (Reproduced from Radu *et al*., with permission from IOP Publishing Ltd, ©.)

domains can already be made even before carrying out a quantitative analysis of the data in Figure 25. First of all one may admit that the intensity distribution in Figure 25(c) and (d) is strongly asymmetric such that (c) becomes identical to (d) if angles of incidence and of scattering are interchanged. Second, almost no off-specular non-spin-flip scattering (Figure 25a and b) is detected. This means that, as explained in the Section 2.11, the ripple domains do not cause any appreciable fluctuations of magnetization projection onto the direction of the mean inductance (e.g., along y axis). This is only possible if the moments in the magnetic domains are tiled to the left and to the right from y axis by about the same angles $\pm\Delta\gamma$, and $\tilde{\Delta} \approx 0$. The other conclusion immediately follows from the SF maps in Figure 25, if one accepts that the intensity along the specular SF reflection ridge (displayed along diagonals) is mainly due to a non-perfect polarization analysis. If corrections for the SF efficiency are applied, the specular SF intensity should vanish and only NSF specular reflection would be left. This means that there is no tilt of the mean magnetization averaged over the coherence length, and $\overline{\gamma} = 0$. At the same time deviations $\Delta\gamma$ due to the ripple domains are not correlated over distances more than the coherence length.

The example in the preceding text shows that investigations of magnetic thin films by PNR provides rich and quantitative statistical information on domain distributions and magnetization fluctuations. An additional twist is gained when studying by PNR the magnetization reversal as a function of applied field. From specular and off-specular scattering the type of reversal (coherent or incoherent) can be distinguished. This has been particularly useful for functionalized thin magnetic films, which are in contact with different F or AF films for the investigation of exchange springs or EB heterostructures, respectively, to be discussed in the next paragraphs.

Exchange springs are magnetic heterostructures consisting of a magnetically soft material in contact with a magnetically hard layer. When the magnetization of the soft layer is reversed in an external field, the spins close to the interface are pinned to the hard magnetic layer, whereas spins further away may be twisted under the action of the external field to form a magnetic spiral, as schematically shown in Figure 23(e). The concept of exchange springs is based on a seminal paper by (Kneller and Hawig, 1991) and has been reviewed in Fullerton, Jiang and Bader (1999). A review of NR studies on exchange-spring heterostructures is provided by Felcher and Hoffmann in this volume (see also **Domain States Determined by Neutron Refraction and Scattering, Volume 3**) and therefore will not be discussed here any further.

4.1.2 Exchange bias

The EB effect refers to a shift of the F hysteresis to negative values when a F system is in contact with an AF system via a common interface and cooled in a positive applied magnetic field through the Néel temperature of the AF system. The EB phenomenon is associated with the interfacial exchange coupling between F and AF spin structures, resulting in a unidirectional magnetic anisotropy (Meiklejohn and Bean, 1956, 1957; Meiklejohn, 1962). The EB effect is essential for the development of magnetoelectronic switching devices (spin valves) and for random access magnetic storage units. Therefore, there is a large interest not only to understand its basic physical mechanism but also to design interfaces with controllable and robust unidirectional anisotropies.

Extensive data have been collected on the EB field H_{EB} and the coercivity field H_c for a large number of bilayer systems, which are reviewed in Berkowitz and Takano (1999), Nogués and Schuller (1999), Stamps (2000a,b), and Kiwi (2001). Because of the asymmetry, the coercivities H_{c1} and H_{c2} for the descending and ascending branches of the hysteresis, respectively, are different. Then $(H_{c1} + H_{c2})/2 = H_{EB}$ is the EB field and $|H_{c1} - H_{c2}| = H_c$ is the coercive field. The details of the EB effect depend crucially on the AF/F combination chosen and on the structure and thickness of the films. However, some characteristic features apply to most systems: (i) H_{EB} and H_c increase as the system is cooled in an applied magnetic field below the blocking temperature $T_B \leq T_N$ of the AF layer, where T_N is the Néel temperature of the AF layer; (ii) the magnetization reversal can be different for the ascending and descending part of the hysteresis loop (Fitzsimmons *et al*., 2000; Radu *et al*., 2002b; Gierlings *et al*., 2002; Lee *et al*., 2002; Radu *et al*., 2003a); (iii) thermal relaxation effects of H_{EB} and H_c indicate that a stable magnetic state is reached only at very low temperatures (Geoghegan, McCormick and Street, 1998; Goodman*et al*., 2000; Radu *et al*., 2002a).

PNR has been instrumental in unraveling the details of the magnetization reversal in EB systems. Using PNR methods statistical information can be gained on the mean magnetization vector, the mean square dispersion of the magnetization in domains, and the reversal mechanism either by rotation or domain wall (DW) motion. This is in contrast to vector magneto-optical Kerr effect (MOKE), which allows to determine the average x and y components of the magnetization vector $\langle M_x \rangle$ and $\langle M_y \rangle$, but not the dispersion $\Delta = \langle \cos^2 \gamma \rangle - \langle \cos \gamma \rangle^2$ (see Section 2.8), where γ denotes the tilt angle of local magnetization averaged over distances greater than the coherence length. Because of this and the possibility to investigate domain formation by off-specular

Table 2. Polarized neutron reflectivity investigations of AF/F bilayers and multilayers which exhibit an exchange bias effect.

EB system (AF/F)	References
CoO/Co	Radu *et al*., 2002a,b; Radu *et al*., 2003a
CoO/Co	te Velthuis *et al*., 2000
CoO/Co	Lee *et al*., 2002
CoO/Co	Gierlings *et al*., 2002
Fe/Cr(211)	te Velthuis, Jiang and Felcher, 2000; Jiang *et al*., 2000
Ru/Co	Steadman *et al*., 2002
MnF_2/Fe	Fitzsimmons *et al*., 2001
MnF_2/Fe	Leighton *et al*., 2001, 2002
FeF_2/Fe	Fitzsimmons *et al*., 2002
$LaFeO_3$/Co	Hoffmann *et al*., 2002
IrMn/CoFe	Paul *et al*., 2004, 2005; Paul, Kentzinger, Rücker and Brückel, 2006
TbFe/GdFe	Hauet *et al*., 2006
FeMn/FeNi	Solina *et al*., 2005
MnPd/Fe	Blomqvist, Krishnana, Srinath and te Velthuis, 2004

diffuse scattering, PNR has been applied to a number of EB systems, which are listed in Table 2.

Two types of EB systems have been studied in the past. The first type consists of F layers in contact with natural antiferromagnets such as oxides (CoO, NiO), fluorides (MnF_2, FeF_2) or itinerant antiferromagnets (FeMn, CoMn, IrMn, etc.). The second type consists of F layers in contact with artificial antiferromagnets, such as AF coupled Fe/Cr or Co/Ru multilayers. In the former case with PNR only the F layer can be investigated but not the pinning AF layer, as the reciprocal lattice vector for the AF superstructure is by far bigger than the scattering vectors usually probed in PNR experiments. However, in the latter case with PNR both, the F layer and the antiferromagnetically coupled (AFC) multilayer can be investigated in the same reflectivity experiment, allowing a correlation between the reversal of magnetization in the F layer and the reaction of the pinning AF coupled multilayer. This resembles the situation of the spring magnets where also both, the soft and hard magnetic films are investigated simultaneously by PNR.

The following paragraphs are not intended to provide a comprehensive overview on EB systems studied with PNR, but to discuss a few illustrative examples to demonstrate the capability of the method. Here we will confine the discussion to CoO/Co, which is the original system for which the EB effect was discovered (Meiklejohn and Bean, 1956) and which has been intensively investigated in the past by PNR methods [14].

In order to enhance the signal, Gierlings *et al*. (2002) have grown a multilayer consisting of CoO/Co bilayers separated by Au spacer layers which magnetically isolate neighboring CoO/Co bilayers and at the same time provide Bragg reflections, which can conveniently be analyzed. The neutron data are shown in Figure 26. They have compared the reversal in the unbiased state above the Néel temperature of CoO ($T_N = 280\,K$) and in the field cooled biased state at 10 K. In the unbiased state they find a magnetization reversal via coherent rotation in the descending as well as in the ascending field direction. However, in the biased state, the reversal in descending fields is clearly characterized by nucleation and DW motion, whereas the reversal in the ascending field remains unaffected. Thus it appears that the EB only affects the magnetization reversal in the direction opposite to the bias field direction. This behavior appears to be typical for the CoO/Co system and has also been observed by other groups (Radu *et al*., 2002b; Radu *et al*., 2003a; Lee *et al*., 2002), and may be different for other systems.

The mean magnetization direction characterized by $\langle\cos\gamma\rangle$ and the dispersion $\Delta = \langle\cos^2\gamma\rangle - \langle\cos\gamma\rangle^2$ [15] was used by Lee *et al*. (2002) for the analysis of the reversal mechanism of a CoO/Co bilayer grown on a sapphire substrate. The dispersion offers a powerful tool for analysis of the domain state of magnetic films without requiring a full analysis of the specular reflectivity profile, provided that the diffuse scattering is negligible and that the magnetic domains are larger than the coherence length of the neutrons such that an incoherent averaging over the magnetic domains is allowed. At the coercivity the magnetization component $M_y = 0$. This can be either the result of a coherent rotation, a domain state with equally populated M_y and $-M_y$ domains, or due to a random distribution of magnetic domains. In the first case $\Delta = 0$, in the second case $\Delta = 1$, and for the third case $\leq \Delta \leq 1$. Thus a finite value of Δ indicates an angular spread of domains. The magnetic hysteresis and the corresponding Δ values are reproduced in Figure 27 ($\Delta = \chi^2$ in the authors notations). At temperatures above the blocking temperature the magnetic hysteresis is symmetric and $H_{EB} = 0$. In this case, the $\Delta \equiv \chi^2$ values are close to one for all scattering

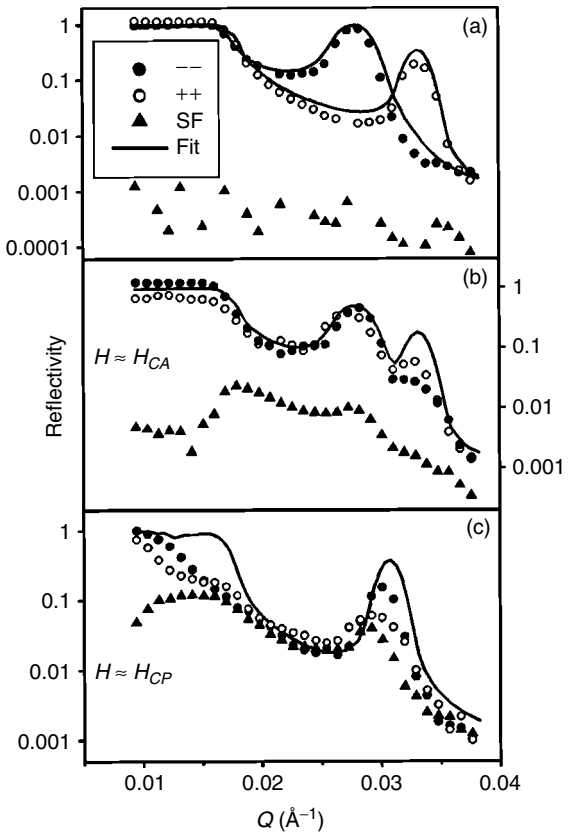

Figure 26. Reflectivity measurements from a CoO/Co/Au multilayer. (a) NSF and SF reflectivities are shown for the sample in saturation. The position of the first Bragg peak is shifted for the $(++)$ and $(--)$ reflectivities due to the different optical potentials. This would also be expressed in different critical scattering vectors, which is, however, here obscured due to the higher potential of the Al_2O_3 substrate for the $(++)$ reflectivity; (b) reflectivities taken in a descending field close to coercivity. The split peaks in both, $(++)$ and $(--)$ reflectivities and the low SF intensity indicates a domain state with parallel and antiparallel domains with respect to the field direction equally populated; (c) reflectivities taken in an ascending field close to the coercive field. All cross section exhibit roughly the same peak position, indicative for a coherent rotation of the magnetization direction into the x direction. (Reprinted figure with permission from M. Gierlings *et al.*, *Phys Rev. B* Vol 65, 092407 (2002). © 2002 by the American Physical Society.)

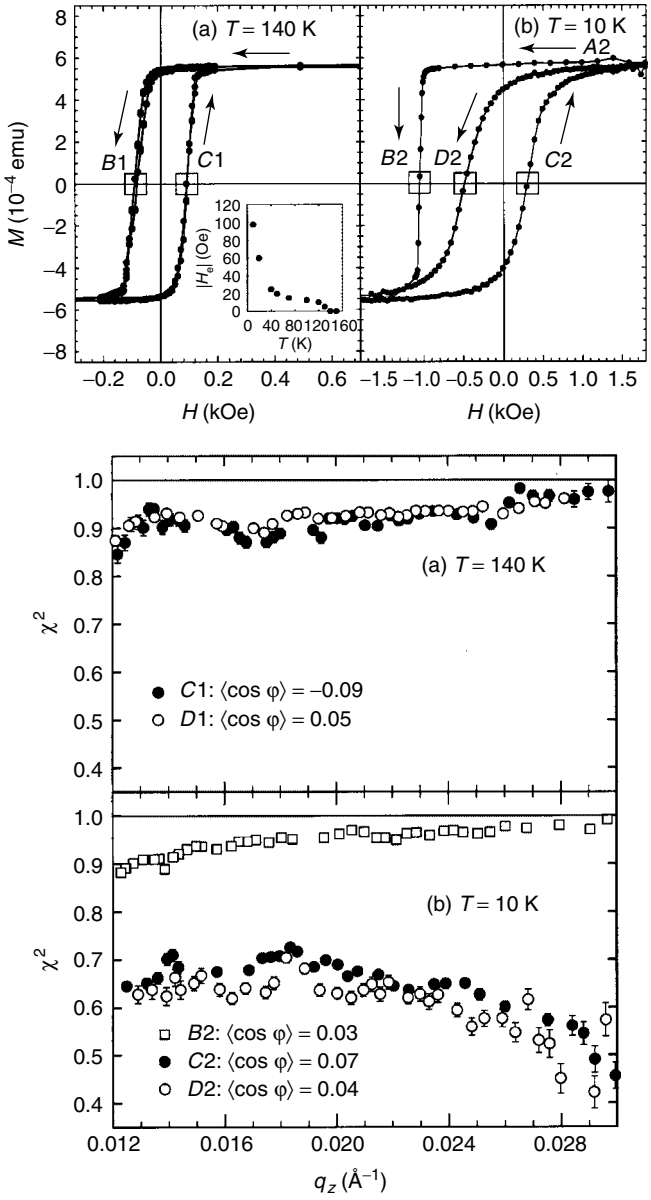

Figure 27. Left panel: Magnetic hysteresis of a CoO/Co bilayer taken at a temperature above the blocking temperature T_b; Right panel: $\chi^2 \equiv \Delta$ values evaluated from PNR measurements taken at the designated remanent points and indicated in the left panel. For temperatures above the blocking temperature, χ^2 is essentially one. After field cooling to 10 K the χ^2 value remains one for the untrained magnetization reversal, but assumes values smaller than one in the trained state, indicative for the development of a angular distribution of domains. (Reprinted figure with permission from W.-T. Lee *et al.*, *Phys. Rev.* Vol. 65, 224417 (2002). © 2002 by the American Physical Society.)

vectors probed, as can be seen in the top right panel of Figure 27. This indicates that for $T > T_B$ the magnetization reversal is characterized by domain nucleation and wall motion. The same behavior is also seen after field cooling below T_B for the first reversal in a descending field. However, after increasing the magnetic field again from negative to positive values, $\Delta \equiv \chi^2$ has clearly dropped below one for all subsequent coercivities in ascending and descending fields. Thus it can be inferred that after the first magnetization reversal of the virgin and field cooled sample, a domain state is created at the CoO/Co interface. This domain state obviously changes the shape of the hysteresis and lowers the EB field.

Radu *et al.* have carried out similar PNR experiments of the magnetization reversal of CoO/Co bilayers, studying not

only the specular reflectivity (Lee *et al*., 2002), but also the off-specular diffuse scattering (Radu *et al*., 2003a). From the spin asymmetry of the specular reflectivity they have evaluated the magnetic hysteresis and compared the neutron results with MOKE measurements. Both hystereses are practically identical (see Figure 28a), neglecting slightly different H_{c1} values due to different temperatures during the MOKE and PNR measurements. Furthermore Radu *et al*. have analyzed the spin flip scattering during the first untrained reversal and during subsequent trained reversals. Similar to Gierlings *et al*. (2002) and Lee *et al*. (2002) they conclude that the first untrained reversal is characterized by nucleation and DW motion. However, all subsequent reversals exhibit some partial coherent rotation. Radu *et al*. emphasize that during the first reversal of the virgin bilayer the CoO/Co interface becomes irreversibly altered, which is manifested mainly in a dramatically enhanced off-specular diffuse scattering in the SF cross sections that cannot be removed even in high magnetic fields. The spin disorder, created during the first reversal can be recognized by the off-specular diffuse SF scattering in Figures 28(d) and (e) and more impressively by the maps shown in Figure 29 for all four cross sections R^{--}, R^{+-}, R^{-+}, R^{++} taken at characteristic points of the hysteresis before and after reversal.

The scattered intensity distribution seen in the maps of Figure 29 can be described in terms of DWBA (Section 2.11). In particular, the asymmetry of the SF off-specular scattering, which is due to a birefringence effect, alters the R^{+-} and R^{-+} maps in the descending and ascending branch of the hysteresis, as it should be in accordance with the reciprocity principle discussed above. The maps in Figure 29 differ from those in Figure 25 in many details [16]. Some of them, for example, the streaks running parallel to the coordinate axis, are not relevant to the physics of the EB system, but are just due to the choice of the sapphire substrate with high optical potential, as explained in the Section 2.11. Those details of the scattered intensity distribution are well reproduced [17] in the maps of Figure 15 calculated in DWBA for the model of F domains. The latter is similar to the one used for the single Co film on the Si substrate. However, the other features carry information which are specific for the EB bilayer system. This is, in particular, the specular SF reflection, which in Figure 29 is much stronger than the off-specular scattering, in contrast to Figure 25.

The presence of *specular spin-flip* intensity may be attributed to the fact that in the trained sample the magnetization within the domains is correlated over distances bigger than the lateral projection of the coherence length. Such long-range correlation lengths occur only because of the interfacial exchange coupling of the F moments to the rigid and frozen-in domains in the AF counterlayer. Without the interfacial exchange coupling the specular SF scattering is expected to be much weaker. The additional and intrinsic disorder is expressed in off-specular scattering and hence in the residual fluctuations of the magnetization vector which persists even in the nominally saturated state.

The restoration of the interface state is only possible by refreshing the field cooling procedure. With PNR the change of the interface is quite obvious. Using the element specificity of the XRMS technique for the investigation of the similar CoO/Fe EB system, it could be shown that the proximity of the F layer induces a small but finite magnetic moment in the AF layer (Radu *et al*., 2006). Furthermore, the F moment in the CoO layer appears to have two components: one is frozen-in and does not follow the applied magnetic field, while the other one follows in phase the F magnetization of the F layer. The 'loose' F component is responsible for the EB field and the shape of the hysteresis after the first reversal has taken place.

4.1.3 Spin valves

Spin valves are functional heterostructures in giant magneto resistance (GMR) and magneto-tunneling resistance (TMR) devices. Two F layers are separated by a non-magnetic layer, one of them being pinned by exchange coupling to an AF layer and the other one is comparatively easy to rotate in an externally applied field. Spin valves play an essential role in GMR heads, in MRAM devices, and in novel AFC hard disks. Analyzing the layer resolved switching is therefore of paramount importance.

Choi *et al*. (2000) have performed a layer selective vector magnetometry study with PNR for analyzing the magnetic configuration of the following layer sequence: Cu/Co/Cu/FeNi/Cu/Co/Cu. The magnetically soft FeNi layer in the middle is exchange coupled to the outer Co layers, acting as a double spin valve system. Instead of one step in the magnetic hysteresis for a single spin valve, two steps are observed. At the first plateau the center FeNi layer reverses by applying a reversing field, then the lower Co layer switches, and saturation is reached when also the upper Co layer is switched. Neutron reflectivity has been used for analyzing the magnetization vectors of the different layers in more detail. The data show that in the plateau region a perfect antiparallel alignment between the Co and the FeNi layers cannot be reached, but that there is always some canting. Layer resolved vector magnetometry provides a much more detailed picture of the reversal mechanism than it is possible with an layer averaging method such as SQUID or VSM.

Toney *et al*. have recently investigated the switching of an AFC trilayer (Toney *et al*., 2005). The upper magnetic layer was a 12-nm-thick $Co_{63}Pt_{11}Cr_{18}B_8$ alloy, while the lower

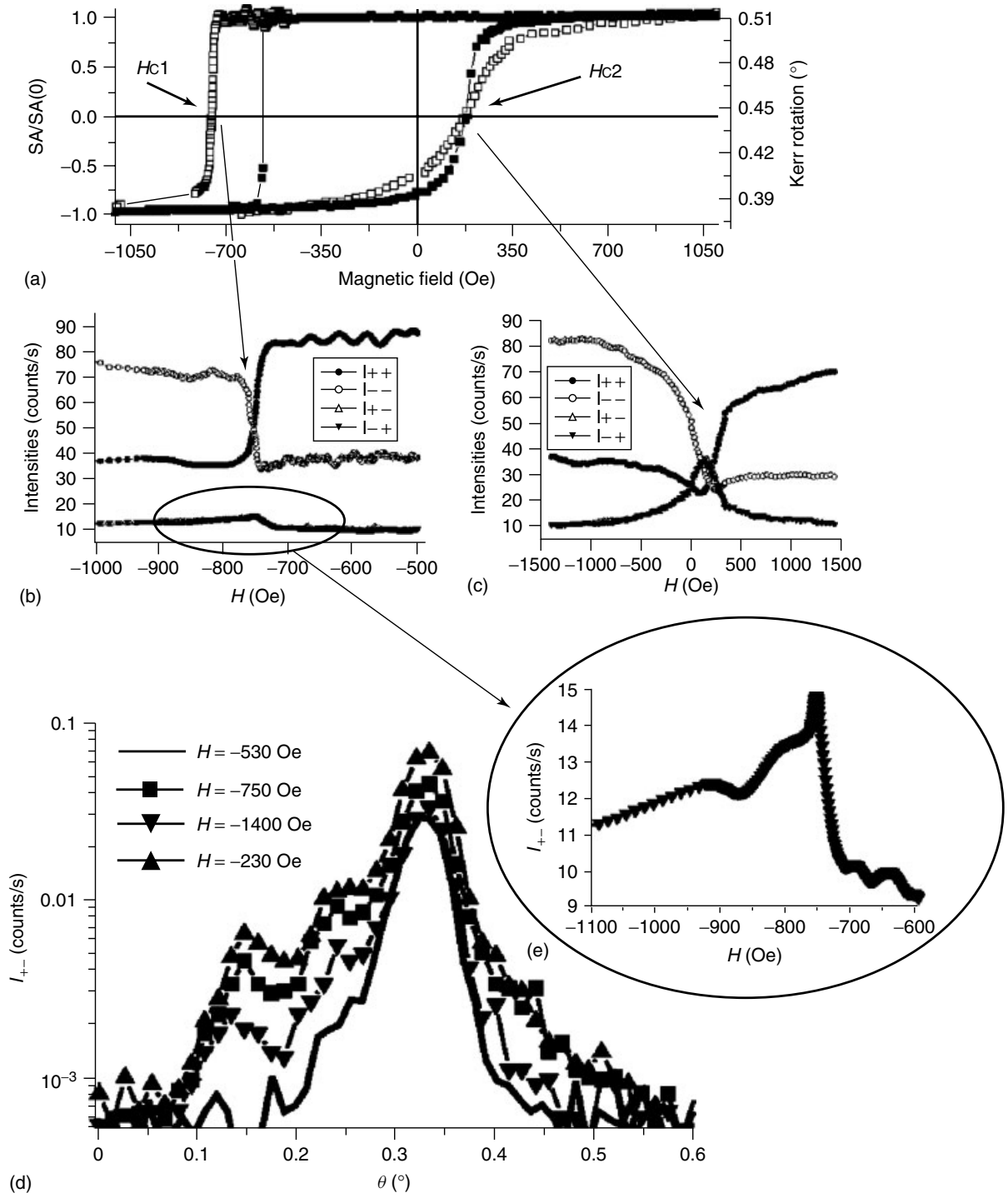

Figure 28. (a) Comparison of MOKE hysteresis loop (full squares) and neutron hysteresis loop (open squares) of a CoO/Co bilayer after field cooling to 50 K (MOKE) and to 10 K (neutrons); (b) and (c) reproduce the specular NSF and SF scattering close to the coercive fields in the descending and ascending branch of the hysteresis; (d) off-specular diffuse spin-flip scattering taken just before magnetization reversal at −530 Oe (line), at $H_{c1} = -750$ Oe (full squares), in saturation at −1400 Oe (down full triangles), and before the second magnetization reversal at −230 Oe (up full triangles); (e) a zoom in from panel (d) showing the weak SF intensity at the first magnetization reversal with a sharp spike from domain wall propagation. The SF scattering at H_{c2} is much more pronounced and indicates a coherent rotation of the magnetization. (Reprinted figure with permission from F. Radu *et al*., *Phys Rev. B* Vol. 67, 134409 (2003). © 2003 by the American Physical Society.)

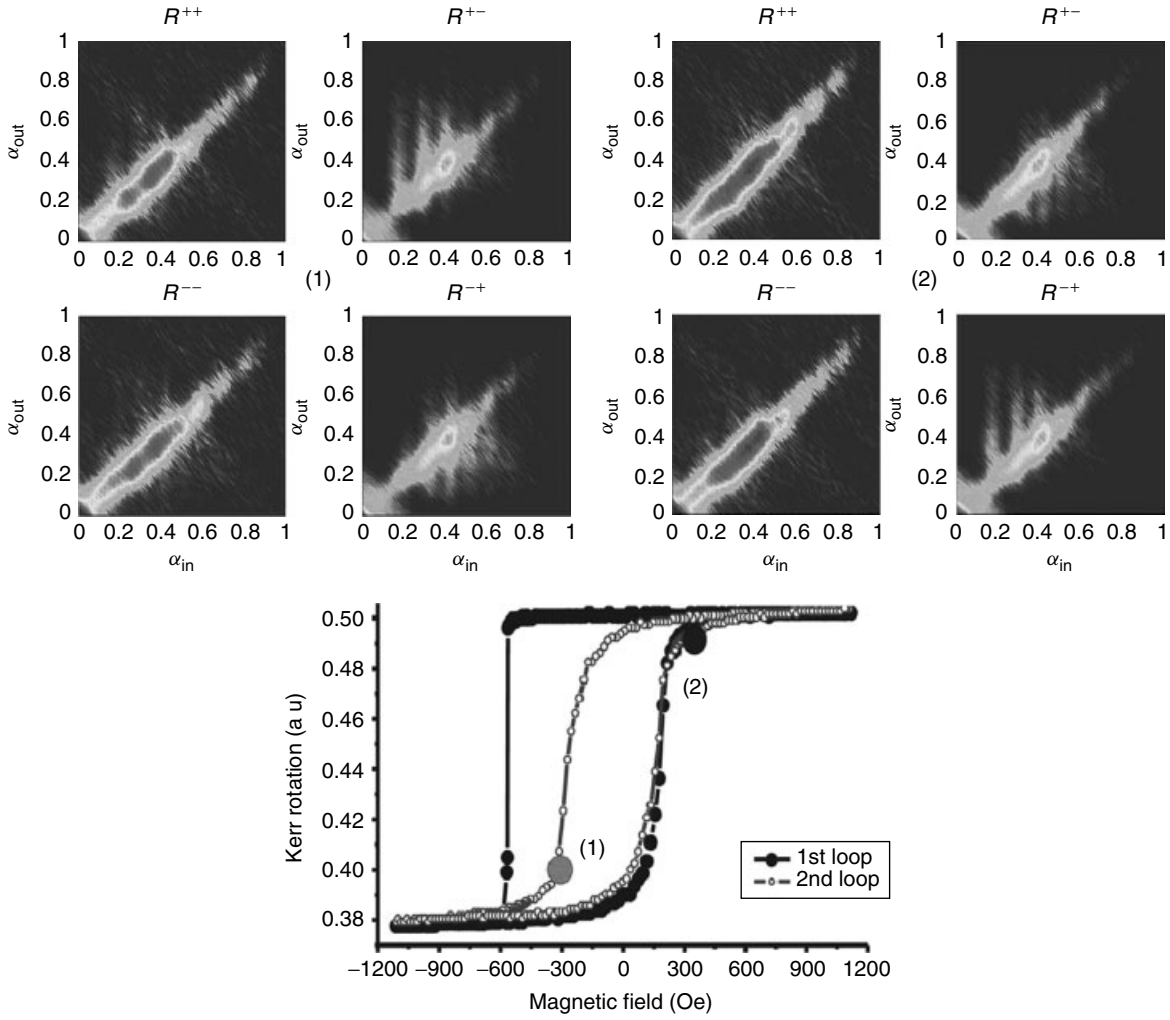

Figure 29. Intensity maps from a CoO/Co bilayer with exchange bias taken with polarized neutrons and using a ^{3}He spin filter for the spin analysis of scattered neutrons. Always four sets for the four different reflectivities are shown: R^{--}, R^{+-}, R^{-+}, R^{++}. The first set shown on the top right panels (taken at point (2) of the hysteresis loop) shows the sample after field cooling through the Néel temperature of CoO in an external field of 2 kOe and after the first reversal has taken place in the ascending branch of the loop. The R^{++} and R^{--} specular intensities are essentially the same as before the first reversal, but the off-specular spin-flip reflectivities R^{+-} and R^{-+} have dramatically changed. Their asymmetry signals a ferromagnetic domain state or spin disorder at the interface between the ferromagnetic and antiferromagnetic layer. The second reversal occurs at a different coercive field than the first reversal (training effect). However, the off-specular spin-flip reflectivities R^{+-} and R^{-+} shown for point (1) in the top left panels remain the same, only the sign has changed, indicating that the interfacial domain disorder is stable but changes orientation with the field direction. The logarithmic intensity color coding is identical for all maps. (Reproduced from F. Radu *et al*., 2003 with permission from Elsevier. © 2003.)

magnetic layer was a 3-nm-thick $Co_{86}Cr_{14}$ alloy separated by a 0.7-nm-thick Ru layer providing a strong AF coupling of the upper and lower layer. The alloy grains in the polycrystalline F layers are supposed to be magnetically decoupled. Magnetization measurements confirm that at large applied fields, the AF coupling is overcome and the magnetization in the F layers is parallel to the field. As the field is reduced, the thinner lower layer first reverses at $H = H_{ex}$ to become antiparallel to the thick upper layer. As the field is further reversed, the upper layer switches and both layers are again parallel to the field. While this explanation of the magnetic reversal is basically correct, the details are revealed by PNR measurements, as shown in the Figure 30. In particular, the PNR measurements provide information about the depth dependence of the magnetization at the different field values and therefore give a more detailed understanding of the reversal process. Detailed analysis shows that the field dependence of the upper layer magnetization during reversal of the lower layer does not follow simple expectations for a layer with magnetically

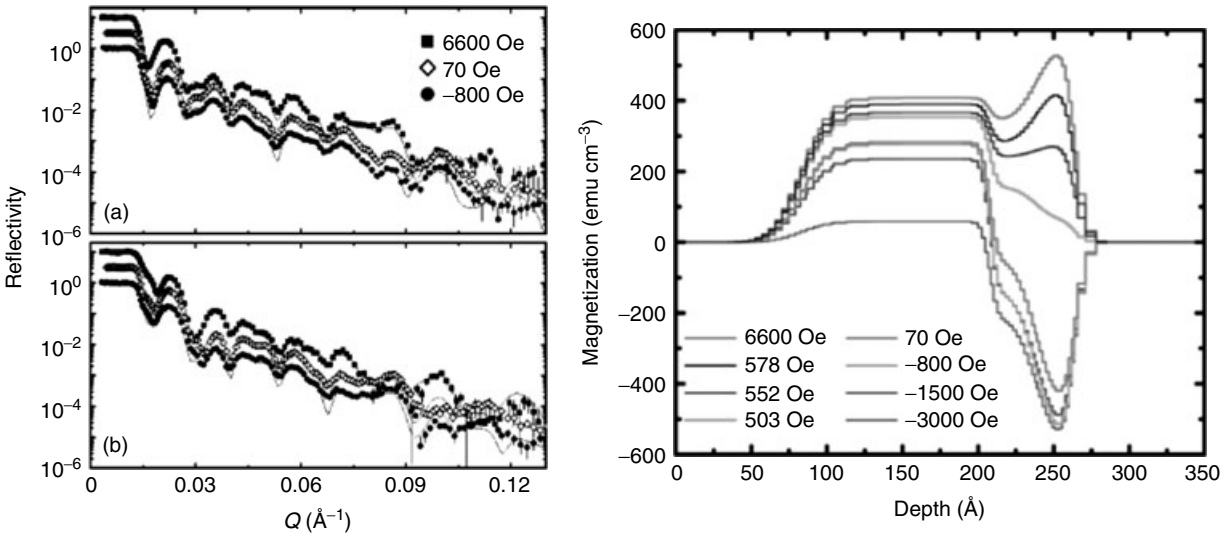

Figure 30. Reflectivity measurements from thick $Co_{63}Pt_{11}Cr_{18}B_8/Ru/Co_{86}Cr_{14}$ trilayer, used for data storage in antiferromagnetically coupled hard disks. (a) R^{++} reflectivity, (b) R^{--} reflectivity and for the respective magnetic field values. In right panel, the magnetization profiles are shown as obtained from best fits to the data. (Reproduced from M.F, Toney *et al*., 2005, with permission from American Institute of Physics. © 2005.)

decoupled grains and high anisotropy that is AFC to the lower layer. Near the reversal field for the lower layer at $H_{ex} \leq 500$ Oe, the magnetization of the upper layer abruptly drops from the saturation value of 400 emu cm^{-3} to approximately 300 emu cm^{-3}, and then gradually decreases as the field is decreased to -3000 Oe. This sudden drop was unexpected from SQUID data and is only revealed by the PNR measurements. The authors conclude that the coupling of the upper and lower layers during reversal may be more complex than previously assumed and may include interactions from DWs in the lower layer. These results have a direct impact on the future design of AFC hard disks.

4.2 Magnetic multilayers

Magnetic multilayers and magnetic superlattices are the most rewarding playground for PNR measurements as short and long-range F- and AF correlation effects can easily be revealed, as well as conformal and non-conformal interface roughnesses and layer resolved reversal processes. In this respect, the PNR method is essentially unrivaled. Resonant magnetic X-ray scattering has become a serious competition in recent years. However, the deeper penetration depth of neutrons and the well-known cross sections remain to be strongholds of PNR. Because of this, a large number of magnetic multilayers have been investigated by PNR since the early 1980s, representative examples are listed in Table 3.

The archetypal magnetic superlattices for which interlayer exchange coupling (IEC) was intensely investigated in the past are Fe/Cr and Co/Cu superlattices. In Fe/Cr superlattices the spin density wave (SDW) magnetism of the Cr spacer layer supports the IEC. At the same time, the SDW magnetism interferes with IEC in case of interfacial defects. The interplay between the ferromagnetism of the Fe layers and the SDW order of the Cr spacer layers adds to the complexity of Fe/Cr superlattices. Co/Cu superlattices are comparatively easy objects as the Cu spacer layer does, at first glance, not inflict further complications. Therefore Co/Cu superlattices with [100], [110], and [111] orientations served as testbeds for studies of the oriental dependence of the period and the strength of the IEC. Although the magnetic and electronic properties of Co/Cu superlattices are straightforward, growth problems have inhibited the observation of an oscillatory IEC in the [111] growth direction.

4.2.1 Co/Cu multilayers

Co/Cu multilayers continue to serve as model systems for exchange coupling, domain states, and interfacial magnetic roughness. In the [111] growth direction, however, Cu antiphase domains develop on the Co(111) surface, giving rise to magnetic pinholes. For a long time the oscillatory IEC was obscured in Co/Cu(111) superlattices due to its inherent weakness and due to the fact that domain wall pinning at structural defects inhibit AF alignment of the F layers. Schreyer *et al*. have finally verified with PNR methods the oscillatory character of the IEC for carefully

Table 3. Representative examples for polarized neutron investigations of magnetic multilayers.

Multilayer	Main scientific focus	References
Co/Cu(111)	IEC	Schreyer *et al*., 1993a,b
Co/Cu	MR	Borchers *et al*., 1999
Co/Cu	MR	Langridge *et al*., 2000
Co/Cu	MR	Toyoshima *et al*., 1999
Fe/Cr(001)	IEC	Schreyer *et al*., 1995a; Schreyer *et al*., 1997
Fe/Cr(001)	IEC	Ankner *et al*., 1997
Fe/Cr	IEC	Pechan *et al*., 1994
Fe/Cr	IEC	Loewenhaupt *et al*., 1993
Fe/Cr(001)	IEC, SDW	Fullerton *et al*., 1996; Fullerton, Bader and Robertson, 1996
Fe/Cr	IEC	Adenwalla, Felcher, Fullerton and Bader, 1996
Fe/Cr(001)	DS	Lauter-Pasyuk *et al*., 2001, 2002
FeCr/Cr(001)	IEC	Siebrecht *et al*., 1999
Fe/Cr(211)	EB	Jiang *et al*., 2000
Fe/Si	IEC	Ankner, Majkrzak and Homma, 1993
Fe/Pd	IEC	Cheng *et al*., 2004
Co/Pd	IEC	Borchers *et al*., 1994
$Co_{0.80}Fe_{0.20}/Al_2O_3$	RM, DS, PT	Bedanta *et al*., 2005
Co/Re	SFT	Charlton, Lederman, Yusuf and Felcher, 1999
Py/Ag	IEC	Borchers *et al*., 1996
Py/Cu	IEC	Borchers *et al*., 1997
Py/Ru	IEC	Su *et al*., 2005
FeCoV/TiZr	MR	Van De Kruijs *et al*., 2001
U/Fe	IEC	Brown *et al*., 2003; Beesley *et al*., 2004
UAs/Co	IEC	Mannix *et al*., 1997
Fe/Ce(H)	IEC	Lohstroh *et al*., 2000
Fe/La(H)	IEC	Lohstroh *et al*., 2001
Fe/V(H)(001)	IEC	Hjörvarsson *et al*., 1997
Fe/V(H)(001)	IEC, PT	Leiner *et al*., 2003
Fe/Nb(H)	IEC	Klose *et al*., 1997
Ho/Y(H)(00.1)	IEC, PT	Leiner, Ay and Zabel, 2004
Gd/W	IEC	Yi Li *et al*., 1997
Co_2MnGe/V	IEC, DS	Bergmann *et al*., 2005
GaMnAs/GaAs	IEC, DS	Kepa *et al*., 2001
GaMnAs/MnAs	MM	Diwekar *et al*., 2004

IEC: interlayer exchange coupling; RM: reversal mechanism; DS: domain structure; MR: magnetic roughness; SDW: spin-density wave; PT: phase transition; MM: magnetic moment; EB: exchange bias; SFT: spin-flop transition.

grown epitaxial Co/Cu(111) (Schreyer *et al*., 1993a). They could clearly identify a half order, albeit weak, Bragg peak signaling AF correlation at the first (Cu thickness 1 nm) and second maximum (Cu thickness 2 nm) of the AF interlayer exchange coupling.

The magnetic arrangement of Co/Cu polycrystalline multilayers has been analyzed by Borchers *et al*. (1999), shown in Figure 31. The Cu spacer was chosen rather thick as to provide only a weak exchange coupling between the adjacent Co layers. The NSF reflectivity curve measured from the Co/Cu multilayer in the as prepared state of the sample shows a half-order AF peak along with a first-order Bragg reflection. The observation of a half-order superstructure reflection provides direct evidence for AF coupling in neighboring layers. Weak SF reflectivity enhanced at the position of the half-order AF periodicity and first order chemical periodicity indicates that the magnetization of the Co layers may not be exactly parallel to the field guiding neutron polarization. Diffuse scattering measured slightly away from the specular ridge indicates that the magnetization is not homogeneous in the lateral direction, but rather is decomposed into a set of F domains. In the domains the magnetic moments keep the antiparallel orientation across the multilayer stack. This alternation appears to be quite perfect as no diffuse scattering contribution at the first-order Bragg peak was detected. In contrast, the intensity of the specular and off-specular half-order superstructure peak is of the same magnitude. From this it can be inferred that the AF order is spread out in the lateral direction over a distance bigger than the coherence length. Indeed, via rocking scans across the half-order AF Bragg position, that is varying Q_x at fixed value of $Q_z = Q_{\mathrm{Bragg}}$, it was found that the diffuse scattering forms Bragg sheets, similar to those

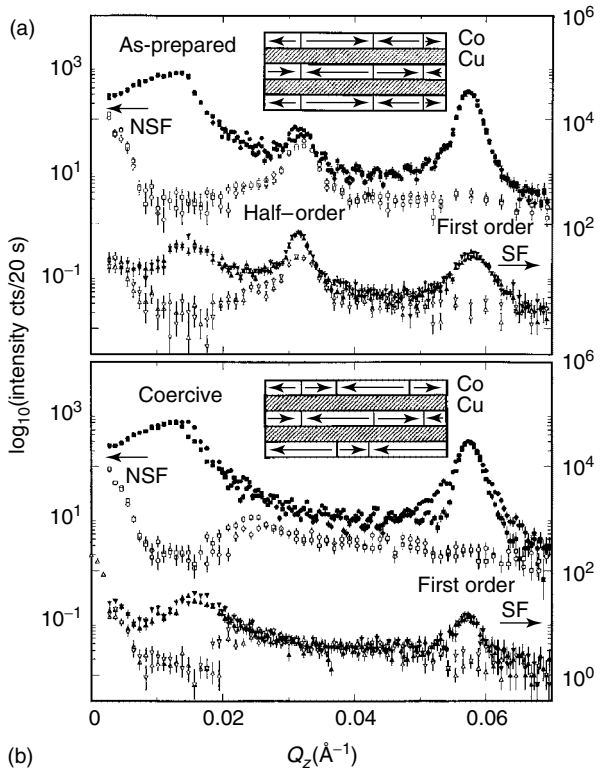

Figure 31. PNR scan from a weakly antiferromagnetically coupled Co/Cu multilayer. Both, specular (solid symbols) and slightly off-specular (open symbols) are shown for all four cross sections. (a) The reflectivity for the as prepared sample. (b) The reflectivity after the sample has been saturated in a high magnetic field and then reduced to the coercive field of 54 Oe, defined by the maximum in the magneto resistance. (Reprinted figure with permission from J.A. Borchers *et al*., *Phys. Rev. Lett.* Vol. 82, 2796 (1999). © 1999 by the American Physical Society.)

depicted in Figure 19 [18]. The lateral size of domains was estimated by the evaluation of the Q_x extension of Bragg sheets within the framework of the BA (Section 2.10).

After applying a magnetic field, the AF coupling is removed and the diffuse scattering is now spread over larger parts of the reciprocal space. Two types of magnetic diffuse scattering can therefore be recognized. One is due to correlated domains giving rise to the Bragg sheets. The other originates from uncorrelated domains. The correlated AF domains yield a diffuse peak in the transverse direction at the half-order position, whose width is inversely proportional to the average lateral domain size. The featureless diffuse scattering is due to uncorrelated magnetic domains and likely from spin disorder at the interfaces.

Langridge *et al*. (2000) have also investigated the magnetic roughness in Co/Cu multilayers. In remanence the half-order peak is widely spread out, indicating an AF domain structure, which is vertically correlated throughout the multilayer. After applying a magnetic field, the AF coupling is removed and the diffuse scattering is now spread over larger parts of the reciprocal space. Two types of magnetic diffuse scattering can therefore be recognized. One is due to correlated domains giving rise to the Bragg sheet. The other one originates from uncorrelated spins at the interfaces. These two parts have been analyzed and quantified in detail in Langridge *et al*. (2000) in the kinematic approximation. The magnetic roughness and how it reveals itself in X-ray and neutron scattering experiments is presently of high interest to experimentalist as well as theorists.

4.2.2 Fe/Cr multilayers

As already mentioned, Fe/Cr superlattices are more complex than other exchange-coupled superlattices owing to the spin-density wave magnetism of the Cr spacer layer. The competition between the interlayer coupling and the antiferromagnetism of Cr often results in a noncollinear coupling, that is the magnetization vectors in adjacent magnetic layers may deviate considerably from F (coupling angle 0°) or AF (coupling angle 180°) alignment. Early studies of Fe/Cr superlattices therefore have concentrated on the exploration of the coupling angle. Adding a biquadratic coupling term to the bilinear exchange coupling predicts under certain conditions a coupling angle of 90°.

However, extensive PNR work has convincingly demonstrated that the coupling angles are neither collinear nor biquadratic but take values in-between. This finding favored Slonczewski's proximity magnetism model (Slonczweski, 1995), which includes both, the interlayer exchange coupling between the Fe layers and the topological antiferromagnetism of the Cr spacer layer together with long-range lateral thickness fluctuations. With this model any angle between 0° and 180° can be realized depending on the relative strength of the F and AF coupling terms J_+ and J_-, respectively (Slonczweski, 1995):

$$E(\phi) = J_+ \left(\frac{\phi}{\pi}\right)^2 + J_- \left(\frac{\pi - \phi}{\pi}\right)^2 \qquad (144)$$

Figure 32 shows a typical result from an exchange coupled [Fe(5.7 nm)/Cr(1.7 nm)]×9 superlattice grown in [001] direction. A magnetic half-order peak can be recognized in the NSF as well as in the SF cross sections. Furthermore, a F component can be discerned at the first-order Bragg peak by the intensity splitting of the R^{++} and R^{--} reflectivities. This unusual reflection pattern, which contains signatures of a F- and an AF orientation of the Fe layers, can be best explained by Fe layer magnetization vectors enclosing an angle of about 50° between adjacent planes, as shown schematically in the lower left corner (Schreyer *et al*., 1995a,b). Nontrivial

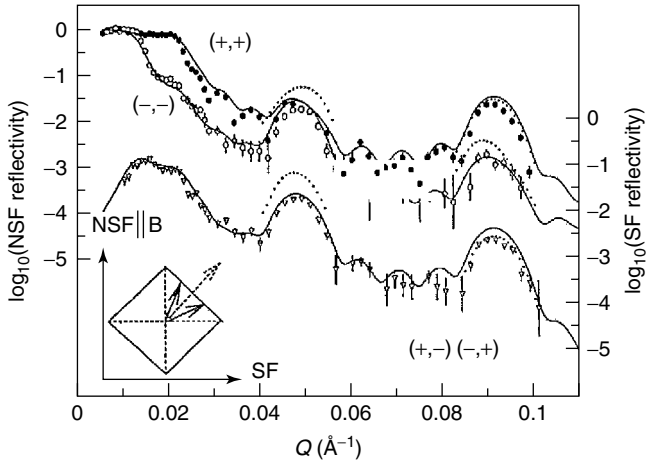

Figure 32. Polarized neutron measurements from a 10 bilayer Fe/Cr superlattice. In all four cross sections a half order Bragg peak can be recognized indicating an antiferromagnetic doubling of the magnetic periodicity, as well as a ferromagnetic splitting of the first-order Bragg peak in the NSF cross sections. From the coexistence of half-order antiferromagnetic peaks and ferromagnetic splitting of the integer Bragg peaks, a noncollinear coupling angle of the magnetization vectors in adjacent Fe layers was discerned. (Reprinted figure with permission from Schreyer *et al*., *Phys Rev. B* Vol 52, 16066 (1995). © 1995 by the American Physical Society.)

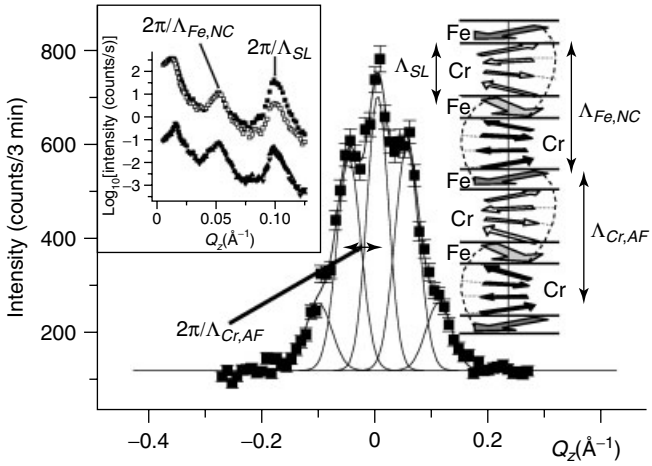

Figure 33. Polarized neutron measurements from Fe/Cr superlattice revealing the correspondence between a twisted Fe magnetization and twisted Cr spin structure. The sample studied is a 200 repeat $Fe_{19}/Cr_{42}(001)$ superlattice. The left inset shows PNR results of all four cross sections. The splitting of the first order Bragg peak together with the presence of a half-order peak in the NSF and SF reflectivities indicates a noncollinear (NC) coupling of the Fe layers with a period twice the superlattice period: $\Lambda_{Fe,NC} = 2\Lambda_{SL}$. The main part shows a scan through the high angle (010) peak in the [00*l*] direction. The bcc forbidden (010) peak is a fingerprint of the commensurate AF Cr spin structure. This peak is surrounded by satellite peaks, which indicate the same doubling of the superlattice period as observed in the PNR measurement at low angles, however, here $\Lambda_{Cr,AF} = 2\Lambda_{SL}$. Thus the AF Cr structure is modulated by the same period as the Fe backbone. The right inset shows a schematic of the Fe and Cr magnetic structures as deduced from the scattering data fulfilling the condition $\Lambda_{Cr,AF} = \Lambda_{Fe,NC} = 2\Lambda_{SL}$. The empty and filled small arrows indicate an opposing sense of rotation of the Cr moments between the NC coupled Fe layers (large arrows). (Reprinted figure with permission from Schreyer *et al*., *Phys Rev. Lett.* Vol. 79, 4914 (1997). © 1997 by the American Physical Society.)

coupling angles were later confirmed by Abbe *et al*. (2004) with nuclear resonant scattering using circular polarized synchrotron radiation.

The interplay between exchange coupling, SDW order, and interface roughness was further investigated for thicker Cr spacer layers. For an ideally flat Fe/Cr interface an antinode of the transverse and incommensurate SDW order is expected to be placed next to the interface. Then the AF Fe–Cr interface coupling is strong and the phase information controlling parallel or antiparallel alignment of successive Fe layers is transmitted through the Cr spacer (Fullerton, Bader and Robertson, 1996). By decreasing the Cr layer thickness below a critical value, the incommensurate SDW order collapses and is replaced by a commensurate AF order with an enhanced Néel temperature (Fullerton *et al*., 1995; Schmitte *et al*., 1999). In Figure 33 polarized neutron data are reproduced for a Fe/Cr superlattice with a Cr thickness of 42 Å (Schreyer *et al*., 1997). The low angle reflectivity measurements again reveal a noncollinearly coupled superlattice, while the high angle data confirm that for this thickness the Cr spin structure is in a commensurate state with AF order. In addition, the superlattice periodicity is imprinted not only on the structure factor of the Fe layers but also on the Cr layers. Thus both, the F and AF layers are modulated by the same superlattice periodicity. Together with the reflectivity data this implies that the Fe as well as the Cr spin structure must be twisted, providing a noncollinear exchange coupling between the Fe layer magnetization vectors. This at first glance surprising noncollinear spin arrangement can be best explained within the frame of the proximity exchange model introduced by Slonczweski (1995), described already above. Assuming that thin Cr layers are in a commensurate SDW state, lateral thickness fluctuations of monatomic high steps require the Cr spin structure to twist counterclockwise on either side of a step in order to couple to a homogeneous Fe layer magnetization. The combination of left and right turning Cr spin springs, representing the spin stiffness of the Cr layer, mediates a noncollinear Fe magnetization.

Further progress on the understanding of Fe/Cr superlattices has been achieved by mapping out the off-specular diffuse scattering in addition to the specular polarized neutron reflectivity (Lauter-Pasyuk *et al*., 2001, 2002). Figure 34 shows the reciprocal-space map [19] taken from a [Fe(6.7 nm)/Cr (0.9 nm)]×12 superlattice in an applied field

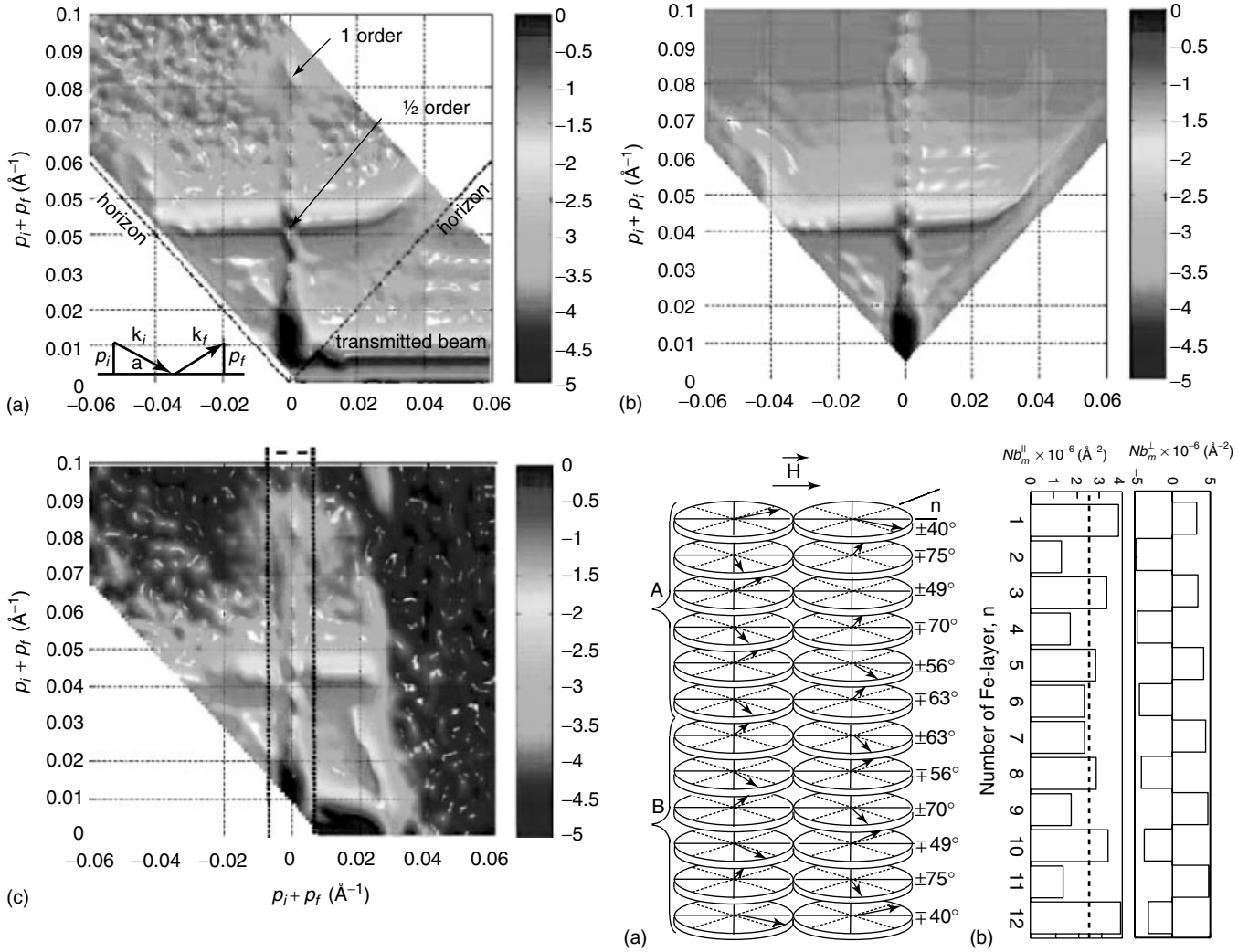

Figure 34. Left panel: (a) Experimental 2D map of the intensity scattered from the Fe/Cr(001) superlattice as a function of the momentum transfer $Q_z = (p_i + p_f)$ versus $(p_i - p_f)$, where p_i and p_f are the components of the incoming and the outgoing wave vector perpendicular to the sample surface, respectively, defined in Figure 2. The logarithmic intensity color scale is shown on the side. The incoming neutrons are in the $(-)$ state. No polarization analysis of the outgoing beam is applied. (b) 2D model fit to the experimental data in (a) using the distorted wave Born approximation. (c) Same map as in (a), however, now recorded with a $(-)$ analyzer turn-on within the region marked by vertical dashed lines. Right panel: (a) Configuration of the magnetization vectors in the Fe layers of the Fe/Cr superlattice in the external field **H** applied in plane along one of the easy axes; dashed lines mark the hard axes. Only Fe layers are shown. The only possible two types of domains (left and right) are depicted. Brackets A and B indicate the two transverse antiphase parts of one lateral domain. The canting angles ϕ_n between $\mathbf{M}_n$ and **H** are shown on the right-hand side. (b) Magnetic parts of the layer resolved neutron scattering length density for the parallel and perpendicular projection of the magnetization with respect to the magnetic field $Nb_m^{\parallel}$ (left) and $Nb_m^{\perp}$ (right), respectively. The dashed line indicates the average value for $Nb_m^{\parallel}$ parallel to the field direction. For more details see text. (Reprinted figure with permission from Lauter-Pasyuk *et al.*, *Phys. Rev. Lett.* Vol. 89, 167203 (2002) © 2002 by the American Physical Society.)

of 19.5 mT. The specular ridge running vertically is crossed by an extensive Bragg sheet at the position of the AF half-order Bragg peak, while no appreciable off-specular scattering is seen around the first-order Bragg peak. Polarization analysis has shown that the specular reflectivity is of completely non-spin-flip nature, while the SF Bragg sheet is produced by in-plane domains with magnetization components normal to the net magnetization and perfect AF correlation across neighboring magnetic layers. The most prominent feature of the NSF reflectivity is the fact that it shows a dip instead of a peak at the position of the half-order AF Bragg peak. The origin of the dip is a stacking fault defect in the mean magnetization distribution over layers as discussed in the subsequent text.

The maps in Figure 34 demonstrate a number of remarkable features due to the optical effects accounted for in DWBA as described in the Section 2.11. One of those effects is the appreciable asymmetry of the maps with respect to an interchange of the incident and scattered wave vectors, as is clearly seen in Figure 34. This effect can be explained as follows: neutrons with the incident momentum enter the sample with one spin state, then undergo a SF process in the sample and leave with a different spin state. Accordingly, the optical potentials and the critical angles for the neutrons entering and exiting the sample are different. From this asymmetry, the mean magnetization averaged over the coherence length can be determined. The intensity of the SF Bragg sheet is, on the other hand, proportional to the mean square fluctuation of the magnetization projection perpendicular to the polarization analysis axis.

This example shows that the off-specular diffuse magnetic and SF scattering is very rich in information, allowing a complete analysis of domain structures and coupling angles in magnetic multilayers. Figure 34(b) shows a calculation of the intensity map, taking into account not only the layer structure of the superlattice but also the magnetic domain structure, displayed in the panel to the right. The calculated map reproduces very well the recorded intensity map, showing that the Fe/Cr superlattice contains a twisted domain state [20]. The canting of the magnetization vectors in each of two possible lateral domains is nonuniform across the multilayer stack. The canting angles are maximal in the end layers due to missing neighbors and therefore weaker exchange coupling. The canting angles progressively relax toward the middle of the multilayer from both sides. The magnetization vectors in the top and bottom layers are tilted in an antiphase fashion, which creates an unavoidable stacking fault in the middle. This is a specific feature of multilayers with an even number of bilayers and by symmetry reasons cannot be avoided in a canted state. The stacking fault causes a dip in the half-order Bragg peak at the specular position due to destructive interference between the neutron waves reflected from the sequence of layers on either side of the stacking fault.

4.2.3 Heusler multilayers

Heusler compounds have attracted recent interest as electrodes in spintronic devices (Hillebrands and Felser, 2006). Due to a half-metallic splitting of the d band at the Fermi level, the spin polarization is predicted to be 100%. The full Heusler compounds have a composition of the type X_2YZ, (X = Co,Ni; Y = Mn, Z = Si,Ge) and a L_{21} structure, which consists of 4 interpenetrating fcc lattices. Only compounds with long-range structural order exhibit a F order parameter. Site disorder has detrimental effects on the polarization, the average magnetic moment, and the Curie temperature. Film growth of ordered Heusler alloys and proper epitaxy to adjacent metal or semiconductor layers is still a challenge. Often a cluster type ferromagnetism is observed below a blocking temperature. Neutron reflectometry has been used to investigate the magnetization profile in the Heusler layers and interlayer coupling effects across non-magnetic interlayers. In particular Bergmann *et al*. have studied the structural and magnetic properties of a series of sputter-deposited [Co_2MnGe/V] multilayers (Bergmann *et al*., 2005). Those measurements have revealed a magnetic phase transition at a Néel temperature T_N that is characterized by an onset of simultaneous F intralayer order in the Co_2MnGe layers and AF interlayer order between adjacent Co_2MnGe layers. In Figure 35 the experimental results obtained by specular PNR and reciprocal-space maps are shown, together with a structural model, which applies to the low temperature coupled state. Above T_N the magnetic layers are in a superparamagnetic state. The observed AF interlayer ordering is attributed to magnetic stray fields arising from the granular Heusler layers. The interlayer dipolar interactions cause a reversible magnetic phase transition of the magnetic clusters with weak AF order between the layers and for thin enough V spacer spacers. For V thicknesses more than 3 nm, the AF coupling vanishes.

The remanent state of the [Co_2MnGe(3 nm)/V(3 nm)] multilayer is particularly interesting as the PNR results reproduced in Figure 35(c) cannot be described by a single-domain state. The half-order AF Bragg peak is seen in the NSF and SF reflectivities, indicating that the AF coupled domains are canted with respect to the polarization axis. At the same time there is a F component clearly visible at the first-order Bragg peak. This requires the AF domains to have a F projection onto the y-axis parallel to the guiding field direction. The specular PNR data can well be simulated using a model, which assumes a coherent AF coupling through the multilayer stack, the AF sublattice having the magnetic moments m_1 and $-m_2$ with $|m_1| = |-m_2|$, respectively. In order to provide both SF and NSF reflections at the AF peak position, the model assumes that the sublattice magnetizations have projections parallel and perpendicular to the applied field.

However, the results of the PNR simulations are based on the hypothesis that the layers are homogeneously magnetized over the neutron coherence area: specular reflectivity does not provide any direct information on the lateral length scales of the film, completely ignoring their crystalline structure and possible large-scale inhomogeneities. A transverse scan of the AF peak in zero field at 15 K as well as the 2D map in Figure 35(a) reveal the presence of magnetic off-specular scattering. In fact, the transverse scan through the half-order AF peak has no resolution-limited Gaussian profile

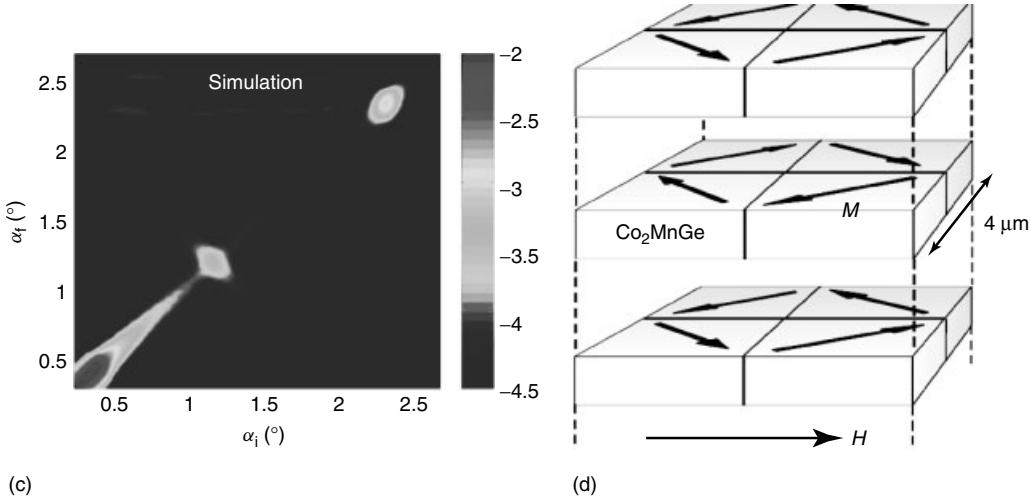

Figure 35. Left column: 2D maps of the specular and off-specular scattering from a Heusler alloy multilayer with a vanadium spacer layer and 50 repeats: Co_2MnGe(3 nm)/V(3 nm). The specular ridge stretches along the diagonal. The angles α_i and α_f refer to the incident an exit angles as defined in Figure 1. The top panel (a) shows the experimental results at remanence and at 15 K and without polarization analysis, the lower panel (b) is a simulation of the scattering pattern with a superiterative-based version of the Distorted Wave Born Approximation as explained in the Section **2.10**. In this simulation the domain state shown in panel (d) was assumed, which obviously can reproduce the data very well. There is a clear AF coupling in this multilayer, expressed by the half-order peak, which also exhibits some streaking due to the breakdown of the magnetic layers in domains. The half order peak is also observed in the specular reflectivity scans shown in panel (c). The AF peak is entirely diffuse, indicating that the domains are smaller than the longitudinal projection of the neutron lateral coherence length. The estimated domain size according to the simulation in (b) is 2.1 μm. (Reprinted figure with permission from A. Bergmann *et al*., *Phys. Rev. B*, Vol. 72, 214403 (2005). © 2005 by the American Physical Society.)

and can well be described by a Lorentzian line shape. This gives a strong hint that the AF peak seen in the specular reflectivity is mainly due to a contribution of off-specular scattering to the specular reflection within the range of their overlap. The presence of magnetic off-specular scattering indicates that the magnetization in the single layers is broken up into domains, the size of which being smaller than the longitudinal projection of the neutron coherence length $L_{\|} = L/\sin\alpha$, where the neutron coherence length L is given by $L = 1/\Delta Q$, and ΔQ is the uncertainty in the wave vector transfer due to experimental resolution. The longitudinal projection of the lateral coherence length is estimated to be about 60 μm. Hence, simulating the specular data only leads to false results for this sample. A complete simulation of both, the specular and off-specular intensity using the superiterative-based version of the distorted wave Born approximation, presented in the Section 2.11, can account for all features of the scattering map. The results are shown in Figure 35(b). In the fit it was assumed that the magnetic films break up into a Landau type of pattern with four possible types of domains with perfect AF coupling and an average lateral size of 2.1 μm with magnetic moments of the layers set to 50% of the bulk value. The model is sketched in Figure 35(d).

The domain state of the Heusler alloy multilayer is particular illustrative for the analysis of PNR data from magnetic multilayers. It clearly shows that a correct picture on the state of the sample can only be gained by recording both, specular and off-specular intensity. For all present and future PNR experiments this has now become a standard.

4.2.4 Tuning of exchange coupling with hydrogen

Usually the IEC is explored by varying the thickness of the mediating paramagnetic layer. A new twist is added if the IEC can be varied solely by changing the electronic properties of the interlayer without changing its thickness. This can be achieved in various ways via alloying, temperature change, photoconductance, and so on, but most effectively, reversibly and nondestructively by loading the interlayer with hydrogen. Hydrogen in metals adds an electron and creates new states at the Fermi level, thereby changing the quantum well states drastically. Change of the interlayer exchange coupling with hydrogen has been demonstrated for Fe/Nb (Klose *et al*., 1997) and Fe/V superlattices (Hjörvarsson *et al*., 1997), and a change from ferro- to AF coupling has been observed by the development of a half-order peak as a function of hydrogen concentration. The development of the half order AF peak as a function of hydrogen concentration is illustrated in Figure 36 for Fe/Nb (Klose *et al*., 1997) and in Figure 37 for Fe/V (Hjörvarsson *et al*., 1997). Interstitial hydrogen in the metal matrix also expands the host lattice. However, the observed IEC effects are more drastic than can be explained by a comparatively small lattice

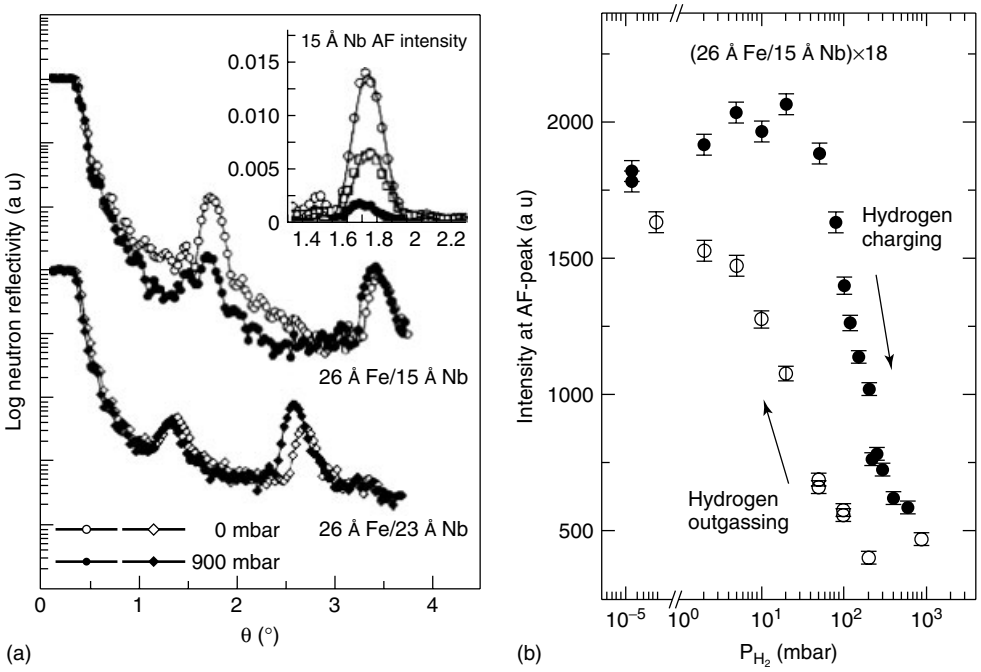

Figure 36. (a) Neutron reflectivity results from two Fe/Nb multilayers with different Nb spacer thicknesses. Both multilayers exhibit antiferromagnetic coupling in remanence and before hydrogen loading as recognized by the half-order peak at the scattering angles $\theta = 1.2^{\circ}$ and 1.5°, respectively. The exchange coupling of the multilayer with a Nb thickness of 15 Å changes with increasing hydrogen concentration and becomes more ferromagnetic. Note that all peaks shift to smaller angles due to the expanding multilayer period upon hydrogen loading. (b) Intensity of the half-order antiferromagnetic peak as a function of the hydrogen concentration for a complete cycle of loading and degassing of the Nb spacer. (Reprinted figure with permission from F. Klose *et al*., *Phys Rev. Lett.* Vol. 78, 1150 (1997). © 1997 by the American Physical Society.)

expansion. In the work of Leiner *et al*. (2003) the concept of IEC was combined with issues of intra- ($J_{\parallel}$) and interlayer ($J_{\perp}$) exchange coupling. By fine tuning the hydrogen concentration, $J_{\perp}$ changes the sign from positive or F exchange coupling to negative or AF exchange coupling. At the crossover point the quasitwo- dimensional magnetic layers are not coupled in the perpendicular direction. With zero coupling, there is no interaction between the magnetic sheets and each layer becomes an isolated two-dimensional magnet. Griffiths (1970) presented the properties of this system as a 'phase diagram' plotting the Curie temperature and the Néel temperature as a function of varying interlayer exchange coupling $J_{\perp}$ (inset of Figure 38). This reveals that as adjacent layers decouple, the critical temperature also drops toward a minimum value at zero coupling. Therefore, according to Griffiths for $J_{\perp} = 0$ the system should display a strongly reduced but finite ordering temperature. This phase diagram could largely be confirmed by Leiner *et al*. (2003) using hydrogen in Fe/V superlattices to effectively decouple the Fe layers. With decreasing $J_{\perp}$ one expects an increasing in-plane fluctuation of the magnetization. This could, however, not yet been observed and remains a challenge for the future.

A significant change of the interlayer exchange coupling was also found in Fe/LaH_x multilayers with varying hydrogen concentration (Lohstroh *et al*., 2001). Even small amounts of additional hydrogen atoms dissolved in metallic LaH_x may invert the sign of the coupling, similar to Fe/V(H), asserting that the main effect is due to a change of the electronic structure of the host lattice. In contrast, in Fe/Ce multilayers the Fe layers are magnetically decoupled, but become weakly coupled when Cerium is hydrogenated. The weak AF coupling can only be discerned by the half-order peak in NR experiments (Lohstroh *et al*., 2000).

Hydrogen in Ho/Y superlattices penetrates preferentially into the Y layers and breaks the coupling between the Ho magnetic spirals from one layer to the next. Without hydrogen and for Y layer thicknesses below 5 nm, the Ho spin spiral penetrates through the Y layer with a fixed phase relationship from one Ho layer to the next. With hydrogen in the Y spacer layer, the Y polarization and the exchange coupling is interrupted. This is because between the compositions of YH_2 and YH_3 a metal insulator transition takes place (Huiberts *et al*., 1996).

With neutron reflectometry at small angles the $(000 + \tau)$ peak was measured as a function of temperature and hydrogen concentration (Leiner, Ay and Zabel, 2004). The integrated intensity of the peak yields the order parameter,

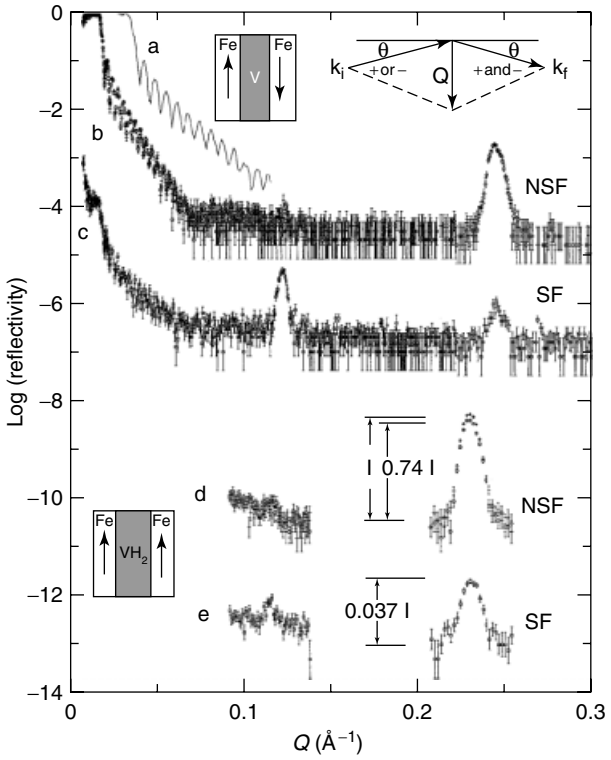

Figure 37. Polarized neutron reflectivity at room temperature for a Fe(3 ML)/V(14 ML) superlattice before and after hydrogen loading. The inset in the upper right corner shows the neutron scattering geometry for the polarized beam. NSF and SF refers to non-spin-flip and spin-flip reflectivity, respectively. After hydrogen loading the half-order peak in the SF channel has vanished. The shift of the first-order Bragg peak to smaller scattering vectors is due to the lattice expansion from the hydrogen in the vanadium spacer. (Reprinted figure with permission from B. Hjörvarsson *et al*., *Phys Rev. Lett.* Vol. 79, 901 (1997). © 1997 by the American Physical Society.)

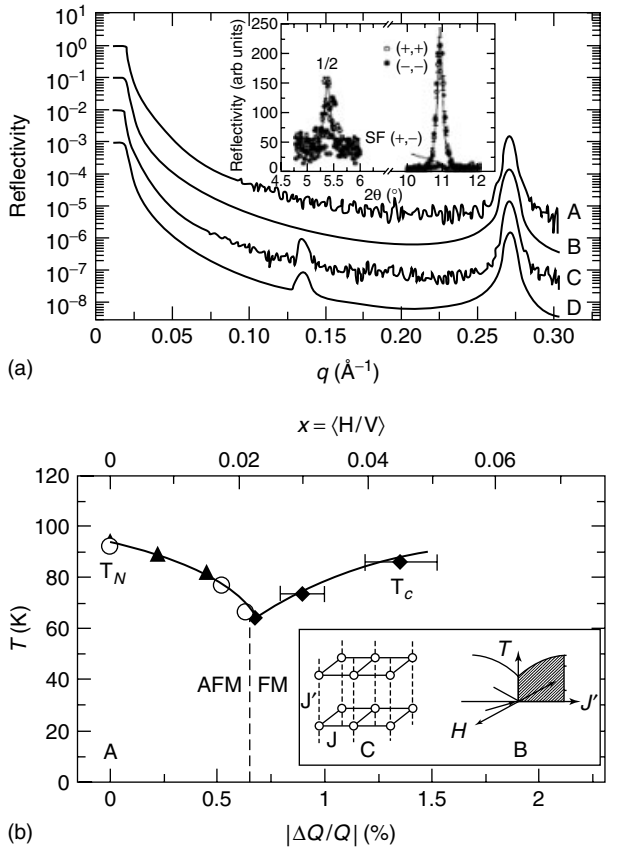

Figure 38. (a) Neutron reflectivity from a Fe(2 ML)/V(13 ML) at high and low temperatures. In the low temperature scan a half-order becomes visible, indicative for an antiferromagnetic coupling of the adjacent Fe layers, separated by V spacer layers. (b) The experimental phase diagram of an iron–vanadium Fe(2 ML)/V(13 ML) multilayer as a function of hydrogen concentration and temperature. Inset: Schematic magnetic phase diagram by Griffiths (1970) of a model system of spins on a cubic lattice (T is the temperature, J' is the interlayer coupling strength and H is the external magnetic field). (Reprinted figure with permission from V. Leiner *et al*., *Phys. Rev. Lett.* Vol. 91, 037202 (2003). © 2003 by the American Physical Society.)

whereas the width contains the information on the coherence length of the spin spiral in Ho. Figure 39 reproduces maps of the $(000 + \tau)$ peak before hydrogen loading and as a function of temperature. The peak is split into several satellite peaks due to the folding of the $(000 + \tau)$ peak with the superlattice reflections. In Figure 40 a radial scan through the τ peak clearly shows that the original splitting of the τ peak into several side peaks diminishes with increasing hydrogen content in the Y spacer layers and a broad τ peak remains, representative for a short Ho spiral in a single layer. Once this state is reached, the Néel temperature for the Ho layer drops dramatically. This is more pronounced for thinner Ho layers. Thus for a Ho(11 ML)/Y(23 ML) superlattice the Néel temperature drops from initially 93 to 75 K with increasing hydrogen concentration. This Néel temperature is identical to the one measured for a single Ho film of the same layer thickness, which is reduced compared to the bulk value of 131 K due to finite size effects.

4.2.5 Dilute magnetic semiconductors

Dilute magnetic semiconductors (DMS) are of tremendous present interest for spintronic applications. They usually consist of II-VI or III-V compounds doped with magnetic ions. The prototype DMS is $Ga_{1-x}Mn_xAs$, which exhibits ferromagnetism for Mn concentrations up to $x \approx 7\%$ and a Curie temperature as high as 170 K (Matsukuraa, Ohnoa and Dietl, 2002). Kepa *et al*. (2001) have studied a superlattice of alternating GaAs and $Ga_{1-x}Mn_xAs$ layers by PNR to investigate the magnetic ordering with a Mn concentration

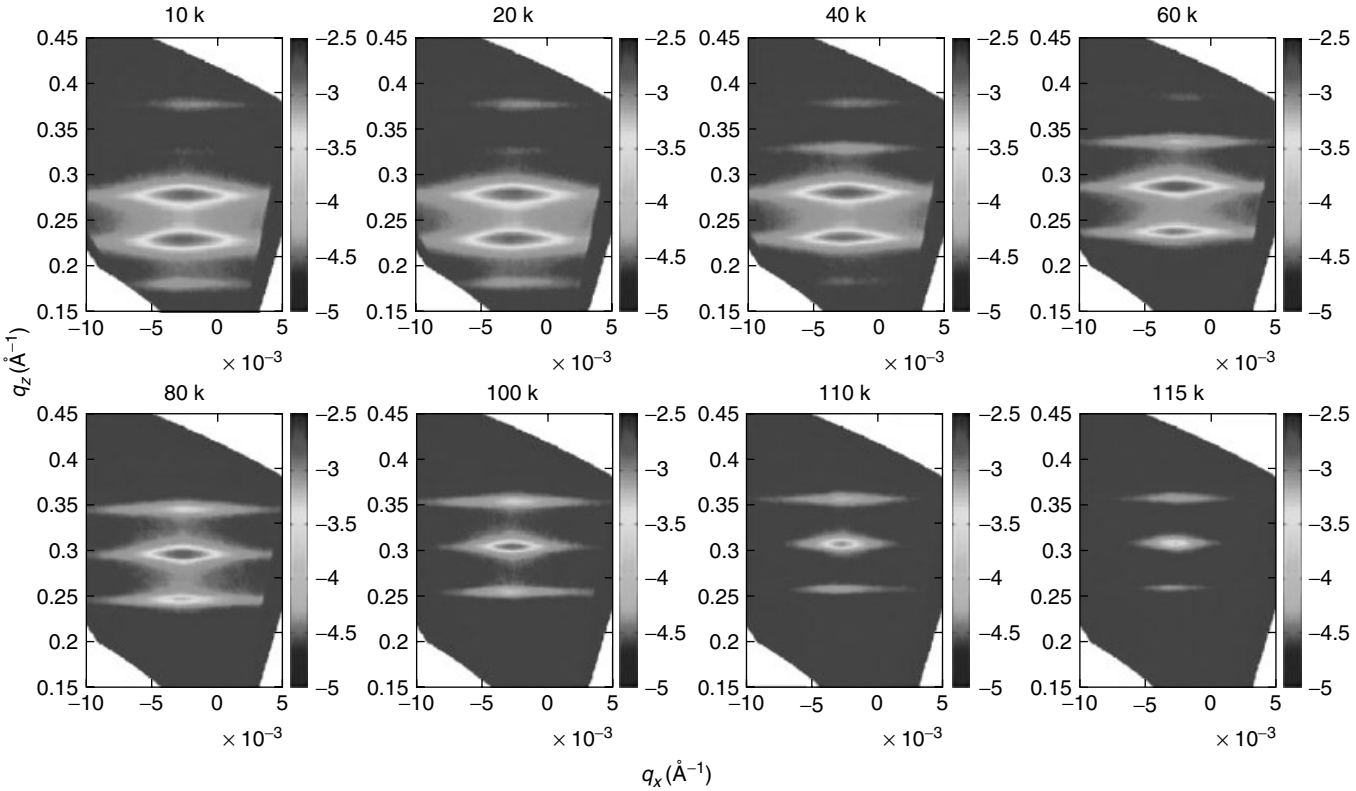

Figure 39. Reciprocal-space maps around the position of the magnetic $(000 + \tau)$ peak of a (Ho(27 ML)/Y(17 ML)) superlattice before hydrogen uptake in the Y spacer layer and for different temperature up to the Neel temperature of 91 K. (Reprinted figure with permission from V. Leiner *et al*., *Phys Rev. B* Vol. 70, 104429 (2004). © 2004 by the American Physical Society.)

of 6% in the magnetic layers. Below the Curie temperature of about 30 K the NSF reflectivities $\mathcal{R}^{++}$ and $\mathcal{R}^{--}$ split at the first-order Bragg reflection, clearly indicating F ordering Figure 41. This ordering persist even in essentially zero field, which is a clear sign for a single-domain state throughout the superlattice. As the single-domain state occurs by zero field cooling, Kepa *et al*. suggest that a long-range interlayer exchange interaction must be responsible for the perfect F alignment of all GaMnAs layers in the superlattice. Modeling of the reflectivities confirm that all Mn atoms contribute to the F single domain state and that Mn is in $S = 5/2$ state.

In contrast to Kepa *et al*. (2001), Kirby *et al*. (2004) have studied single $Ga_{1-x}Mn_xAs$ layers by PNR in the as deposited state and after annealing. The main interest in this work was to analyze the magnetization profile in the GaMnAs layer, which is a direct measure of the Mn-concentration distribution in the z direction. GaMnAs layers are used for spin injection into GaAs and therefore the magnetization or the polarization should be high at the GaMnAs/GaAs interface. Indeed, before annealing the magnetization profile is rather asymmetric with a low Mn concentration at the interface and a high concentration close to the surface. After annealing at 280 °C for 1 h the concentration distribution and magnetization increased and the profile becomes much more homogeneous. Annealing therefore has not only the effect of Mn redistribution in the z direction but also to change the occupancy from interstitial to substitutional sites. PNR yields an amazingly rich insight in the magnetization distribution even for thin alloy films and low concentrations.

Primus *et al*. (2005) have recently studied the magnetization reversal mechanism of $Ga_{1-x}Mn_xAs$ layers on GaAs substrates with PNR methods. A SF peak at the coercive field is observed for one sample, while for a second sample no SF peak is observed. Therefore it is concluded that in the second sample the reversal takes place via 180° domain wall nucleation and propagation, while in the first sample the magnetization reversal may proceed by an incoherent rotation mechanism through 90° domains. Both samples differ in their growth temperature and show different in-plane anisotropies. The first sample exhibits an in-plane biaxial anisotropy, while the second sample has an in-plane uniaxial anisotropy. Thus, magnetic anisotropy and reversal mechanism are intimately related.

A very interesting PNR study has recently been performed by (Diwekar *et al*., 2004) on GaAs films. During MBE

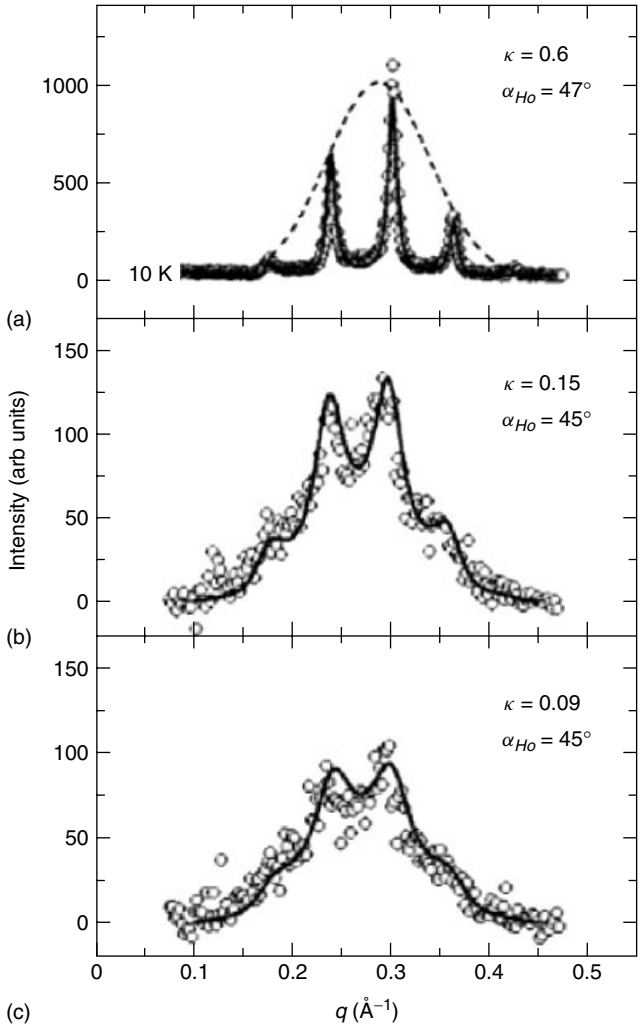

Figure 40. Specular diffraction patterns of a (Ho(11 ML)/Y(23 ML)) superlattice taken for the pristine sample (a) and with two different deuterium concentrations in the yttrium interlayers (b) and (c). Due to the reduced thickness of the individual holmium films the width of the τ peak, plotted as a dashed line in panel (a), is increased. Before hydrogen loading the diffraction pattern shows sharp peaks of an exchange-coupled superlattice. Through exposure to hydrogen at two different pressures, the interlayer correlation is successively lost and the shape of the diffraction pattern approaches the envelope function for the τ peak of an individual thin Ho film. The parameter κ characterizes the interlayer correlation where $\kappa = 1$ defines perfect order. (Reprinted figure with permission from V. Leiner *et al*., *Phys Rev. B* Vol. 70, 104429 (2004). © 2004 by the American Physical Society.)

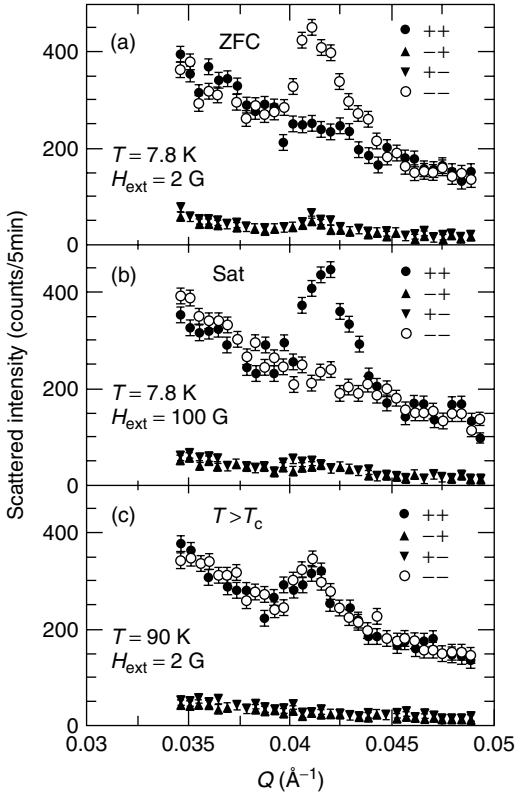

Figure 41. Polarized neutron reflectivity from a GaMnAs/GaAs superlattice. The first-order Bragg peak exhibits the same $\mathcal{R}^{++}$ and $\mathcal{R}^{--}$ splitting after zero field cooling (a) and field cooling (b), showing that the GaMnAs layers are in a ferromagnetic state at low temperatures and that the magnetization vectors in all layers are parallel aligned. The SF reflectivity is negligible. Such a behavior is usually only observed in case of interlayer exchange coupling, which is also invoked here to explain the reflectivity results. In (c) the reflectivity is shown for temperatures above the ordering temperature, where no splitting of the NSF Bragg peak is observed. (Reprinted figure with permission from H. Kepa *et al*., *Phys Rev. B* Vol. 64, 121302 (2001). © 2001 by the American Physical Society.)

growth the GaAs layers were interlaced with partially filled MnAs layers in discrete and periodic distances, forming a digital ferromagnetic heterostructure (DFH). Owing to the alignment of the Mn moments even in a weak external field, the superlattice shows F Bragg peaks below the ordering temperature of about 40 K (see Figure 42). In contrast to the studies by Kepa *et al*. (2001), the DFH exhibits a sizable difference for the saturation and remanent magnetization, which becomes even more pronounced when comparing PNR and SQUID data. The PNR data from the F Bragg peak focus on those magnetic moments which follow the DFH periodicity, while the SQUID data take an average over all moments. This difference indicates that in the superlattices magnetic clusters must be present, which align in the external field even at temperatures far above the spontaneous ordering temperature. Diwekar *et al*. have made another interesting observation. Below 100 K, magnetic moments within each MnAs layer first order locally, but long-range order is developed along the growth direction only below $T_c = 40 < 100$ K. This two-step ordering mechanism can be attributed to fluctuations in the interlayer exchange interactions.

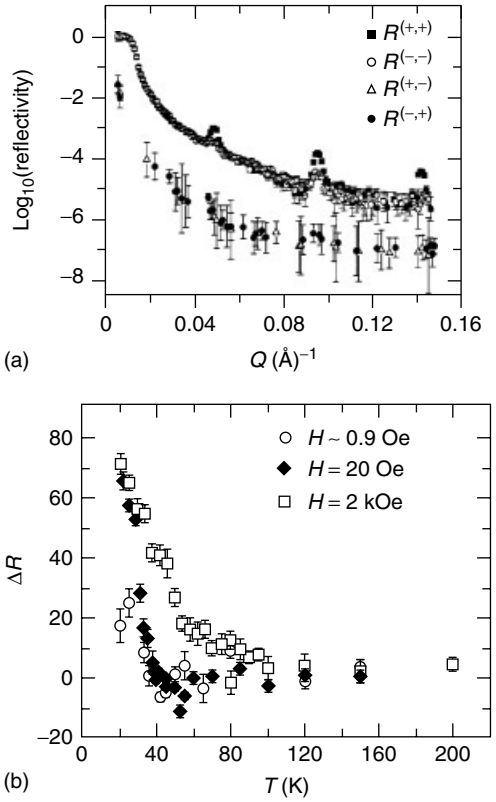

Figure 42. (a) Polarized neutron reflectivity from a digital superlattice of 50 ML GaAs interlaced with a half-filled MnAs layer and repeated 60 times. The half-filled monolayer with Mn atoms provides enough contrast to clearly recognize the superlattice periodicity. (b) Temperature dependence of the magnetization determined from integrated intensity difference $\Delta R = R^{+,+} - R^{-,-}$ between the NSF cross sections at the first-order SL Bragg peak position. The strong field dependence of the data is indicative for a cluster type magnetism. ΔR is only sensitive to magnetization contributions that have the periodicity of the SL. In contrast, magnetometer measurements average over all moments, periodic and random. (Reproduced from M. Diwekar *et al*., with permission from American Institute of Physics. © 2004.)

5 LATERALLY PATTERNED MAGNETIC ARRAYS

Laterally patterned and periodic magnetic arrays have recently attracted much scientific interest because the interplay between exchange and shape anisotropy allows to control the magnetic domain state within the magnetic elements in remanence such as dipoles and vortices, and their spatial separation controls the dipolar interaction and correlation during reversal. A number of experimental techniques has been employed to characterize the domain state and the magnetization reversal of these new lateral nanostructures. Among those PNR may not be the obvious experimental tool because of a combination of low intensity and diminishing scattering volume. Nevertheless, in recent years PNR has been shown to be a rather powerful method for the investigation of some of their fundamental properties. In contrast to imaging methods, such as Kerr microscopy and magnetic force microscopy, neutrons simultaneously probe the whole magnetic array and hence are sensitive to cooperative effects within the array. On the other hand, being a depth sensitive probe, PNR measurements disclose information hidden in buried magnetic layers and interfaces. This may become especially important in the near future when for the information storage in magnetic media the third dimension will be used, for example, via the layer-by-layer patterning in multilayered systems.

Quantitative evaluation of PNR data allows to recover the vectorial magnetization profile and also to receive rather detailed information on magnetization vector fluctuations and correlations within the magnetic array. However, it should be kept in mind that the lateral resolution element, that is the area from which a coherent scattering can be observed, is highly anisotropic and covers only a small fraction of the sample surface illuminated by the neutron beam. The effect of coherent and incoherent summation of the scattering signal from lateral stripe arrays is discussed in Section 2.8 and can be used to obtain information that is complementary to methods which use a different averaging method such as MOKE. Similar to the case of continuous thin magnetic films the complementarity of PNR and MOKE can effectively be used for characterizing the magnetization reversal mechanisms and for discriminating between rotation and domain nucleation.

There are three possible sources of information on the magnetic state in a periodic array as can be seen from a model simulation of a magnetic stripe array in Figure 43: specular neutron reflectivity, Bragg diffraction from the lateral period and off-specular diffuse scattering from domains smaller than the coherence range. The simulations were carried out by use of the DWBA routine described in the Section 2.11 and highlight some particular features not accounted for in Figure 12. The simulations shown in Figure 43 have been performed for an 80-nm-thick Co stripe array (stripe width 3 μm and periodicity 4 μm). The stripes are oriented perpendicular to the scattering plane and parallel to the y-axis. The mean magnetization within the stripes is assumed to be tilted by 25° away from y-axis (i.e., the neutron polarization axis). Furthermore fluctuations are allowed around the mean magnetization orientation. The specular reflection ridge runs along the diagonal, where $\alpha_i = \alpha_f$. In Figure 43 the splitting of the NSF reflectivities $\mathcal{R}^{++}$ and $\mathcal{R}^{--}$ is well visible due to the assumption of a high sample magnetization. SF reflectivities $\mathcal{R}^{+-}$ and $\mathcal{R}^{-+}$ are due to the orientation of the mean magnetization away from the polarization axis of the

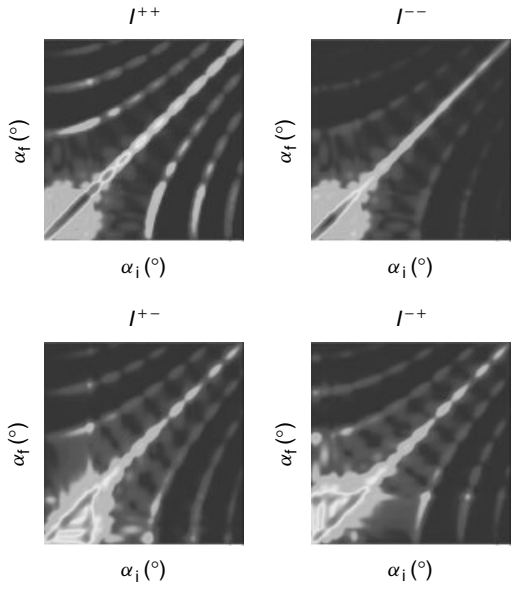

Figure 43. Model simulation of intensity maps of all four cross sections for an 80-nm thick Co stripe array with a stripe width of 3 µm and a periodicity of 4 µm. The mean magnetization is assumed to be oriented about 25° away from the neutron polarization axis which is equivalent to the orientation of the ridge of the stripes. It is further assumed that the stripes are not in a single-domain state but exhibit fluctuations around the mean magnetization within the coherence area.

neutrons. The other two features occur in the intensity maps at $\alpha_i \neq \alpha_f$. The first one is the intensity of Bragg diffraction concentrated along curved lines $\cos\alpha_i - \cos\alpha_f \approx n(\lambda/\Lambda)$, where n denotes the order of diffraction and Λ is the period. It is caused by the periodic variation of nuclear and magnetic potentials across the striped pattern. Equivalent to the specular reflection splitting occurs between the NSF diffraction lines. SF Bragg diffraction in the off-specular scattering range can be observed due to rotation of the stripe magnetization away from the stripe ridge which is assumed to be parallel to the polarization axis of the neutrons. The second feature is a well-structured diffuse intensity observed at low angles of incidence α_i and/or scattering angles α_f. This intensity distribution is asymmetric with respect to the main diagonal in the bottom panels of Figure 43. The I^{+-} off-specular intensity is mostly disposed at $\alpha_f < \alpha_i$, while the I^{-+} off-specular intensity is concentrated at $\alpha_f > \alpha_i$ such that the left image becomes identical to the right one if α_i and α_f are interchanged. Correspondingly, there is also an antisymmetry between the off-specular scattering intensities in the same SF maps if simulated for fields below and above the coercive field. The asymmetry is a direct consequence of optical effects accounted for in DWBA (Section 2.11). NSF diffuse scattering is, in contrast, symmetric. SF and NSF scattering together are sensitive to magnetization fluctuations of both longitudinal and transverse components. Both features are due to the lateral magnetization variation on a scale smaller than the coherence range.

For a complete determination of the magnetization state of a lateral magnetic array it is important to simultaneously evaluate the specular reflectivities, the off-specular Bragg diffractions, and the diffuse scattering. This is due to the fact that the information these different scattering contributions contain are not independent but rather are interrelated. Sometimes, due to a lack of magnetic material in the patterned sample or due to other reasons, it may even be the case that no splitting of the NSF reflectivities can be observed while splitting still occurs along the Bragg diffraction lines in the off-specular scattering range.

Such a case is described by Temst, Van-Bael and Fritzsche (2001) where 20-nm-thick circular Co disks with a diameter of 4 µm are arranged in a 2 × 2 cm large square lattice with a 10 µm period as seen in Figure 44(a). The authors could not observe a splitting at the specular reflectivity but were able to extract qualitative magnetic information from field dependent intensity measurements of all four cross sections at the Bragg positions. From missing SF Bragg diffraction they concluded that the disks pass through a multidomain state during magnetization reversal.

In Figure 45 similar measurements of Temst *et al.* and Fritzsche *et al.* using rectangular bars are shown (Temst *et al.*, 2003a,b; Fritzsche, Van Bael and Temst, 2003). In both cases the bars were saturated in a negative field parallel to the long side of the bars and parallel to the NSF direction [21]. For the PNR experiment, a magnetic field H was applied along the positive NSF axis (x direction in Figure 44b), that is, opposite to the direction of the remanent magnetization.

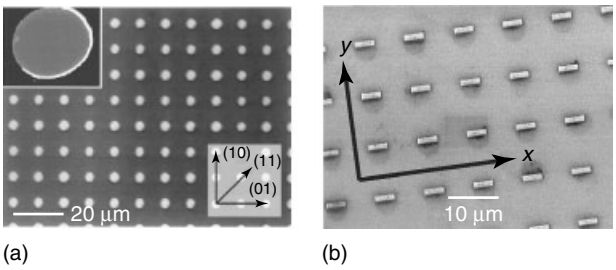

Figure 44. (a) Optical microscopy picture of a periodic array of Co disks on a square lattice with a 10 µm period (Temst, Van-Bael and Fritzsche, 2001). The length of the white bar corresponds to 20 µm. The inset (upper left corner) shows an AFM image of a single disk. In the lower right corner the in-plane directions are defined. (Reproduced from K. Temst *et al.*, with permission from the American Institute of Physics. © 2001.) (b) SEM picture of an array of Co bars (Temst *et al.*, 2003a). The white marker corresponds to 20 µm. (Reproduced from K. Temst *et al.*, 2003, with permission from Elsevier. © 2003.)

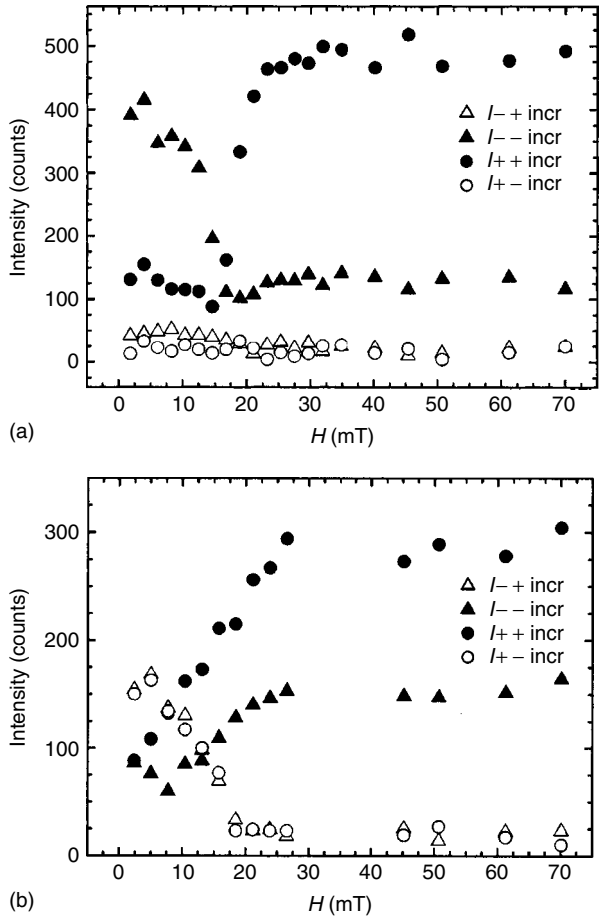

Figure 45. Intensity of the first-order off-specular Bragg peak as a function of decreasing field H applied along the easy axis (a) and along the hard axis of rectangular Co bars (b) (Figure 44b). Prior to this experiment, the bars were saturated along the negative x direction, that is along the easy axis. (Reproduced from K. Temst *et al*., 2003, with permission from Elsevier. © 2003.)

Figure 45(a) shows the intensity of the off-specular first-order Bragg peak as a function of magnetic field. The SF contribution is very small, indicating that there are negligible magnetization components perpendicular to the neutron polarization axis. Figure 45(b) reproduces the NSF and SF Bragg intensities as a function of magnetic field after the sample has been saturated along the easy axis and rotated by 90°, such that the easy axis magnetization is parallel to the SF axis. In this case, a strong SF signal can be observed, since the remanent magnetization is now perpendicular to the neutron polarization. As the field is increased parallel to the hard axis, that is the short side of the bars, the SF signal fades away and the NSF intensities increase.

PNR studies were also performed on a Co/CoO stripe array of about 1 µm width and with a periodicity of 15 µm exhibiting the EB effect (Temst *et al*., 2005a). Similarly Temst *et al*. studied Co/CoO bars with a length of 4 µm and a width of 1 µm placed on a square lattice with a periodicity of 10 µm. (Temst *et al*., 2005b). For the stripes Temst *et al*. present specular PNR measurements with full polarization analysis. The measurements were performed at the two different coercive fields characteristic for EB systems and with the stripes aligned either parallel or perpendicular to the neutron polarization axis (i.e., the applied magnetic field direction). Information was gained from the SF specular reflectivity. In case of the parallel orientation the authors did not observe SF specular intensity during both reversals, whereas in case of perpendicular orientation a specular SF signal was observed at one of the coercive fields. In accordance with the measurements by Radu *et al*. (2003a) on continuous and exchange-biased Co/CoO bilayers, the absence of SF specular reflectivity is explained by nucleation of domains smaller than the coherence length of the neutron beam, while enhanced SF specular reflectivity during magnetization reversal is a sign for magnetization reversal through rotation.

The magnetization state of the Co/CoO bars (Temst *et al*., 2005b) again was determined by field dependent intensity measurements at the off-specular first-order Bragg peak. Similar to the Co/CoO stripe array, for the Co/CoO rectangular bars SF scattering could not be observed when the field was applied along the long side of the bars, indicating a reversal by domain wall nucleation and motion. The polarized neutron scattering (PNS) measurements were supported by micromagnetic simulations using the object orientated micromagnetic framework (OOMMF) of the Division of the Information Technology Laboratory at the National Institute of Standards and Technology (Donahue and Porter, 1999).

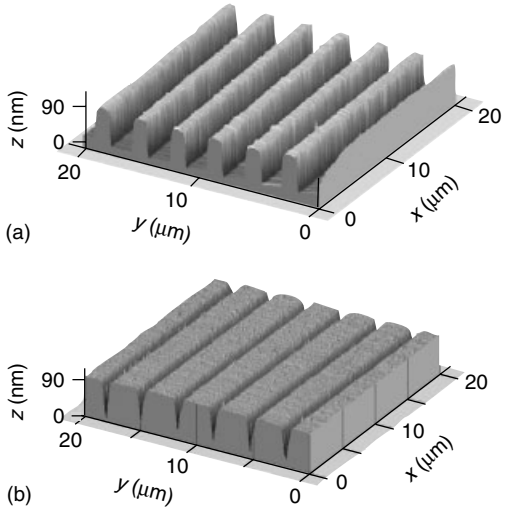

Figure 46. Surface topography of arrays of $Co_{0.7}Fe_{0.3}$ stripes obtained with an atomic force microscope shown in a 3D surface view. The displayed area is $20 \times 20\,\mu m^2$. (a) Narrow stripes with a width of 1.2 µm and (b) wide stripes with a width of 2.4 µm.

From these simulations NSF intensities were calculated and compared to the experimentally observed field dependent intensities from the Bragg peak.

Theis-Bröhl and coworkers have studied the magnetization reversal of various stripe arrays with main emphasis on the analysis of the scattering contributions from specular and off-specular intensities and from Bragg peaks (Theis-Bröhl, Schmitte, Leiner and Zabel, 2003; Theis-Bröhl *et al*., 2003; Theis-Bröhl, 2003). In (Theis-Bröhl *et al*., 2003) an array of 90-nm thick and 1.2 µm wide CoFe stripes with a periodicity of 3 µm (Figure 46a) has been analyzed. A splitting of the specular $\mathcal{R}^{++}$ and $\mathcal{R}^{--}$ reflectivity was not observed. Instead information could be gained from the intensity of the first-order Bragg peak as a function of applied magnetic field. The

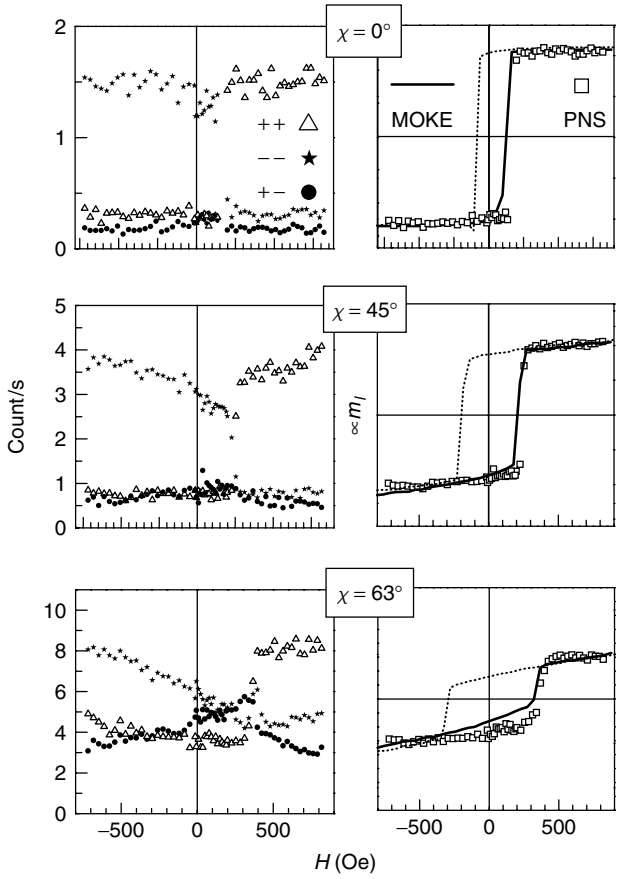

Figure 47. Magnetization reversal measurements performed at the first-order Bragg peak for three different cross sections (left column) and calculated magnetization curves from the polarized neutron measurements (right column). The neutron spin asymmetry (open square) is compared to longitudinal MOKE hysteresis loops (solid and dotted lines). The top row depicts measurements at a sample rotation of $\chi = 0^{\circ}$, the middle row measurements at a sample rotation of $\chi = 45^{\circ}$ and the bottom row measurements at a sample rotation of $\chi = 63^{\circ}$. (Reprinted figure from K. Theis-Bröhl *et al*., *Phys Rev. B.* Vol 67, 184415 (2003). © 2003 by the American Physical Society.)

Bragg intensities were converted into spin asymmetry (SA) curves and compared to longitudinal MOKE hysteresis loops as shown in Figure 47.

It should be noted here that reciprocal lattice spots from lateral stripe arrays occur along the x-axis when the stripes are oriented parallel to the y-axis (see sample geometry in Figure 48). Rotating the stripes by an angle χ causes a rotation of the reciprocal lattice points from the x-axis to the x−y plane by the same angle. Due to a poor resolution in the wave vector transfer projection q_y, as compared to a high resolution in the projection q_x, Bragg reflections still can be observed at $q_x \approx n(2\pi/d)\cos\chi$; where n is an integer and d is the lattice spacing (Toperverg *et al*., 2000; Dorner and Wildes, 2003). This fact was used in (Theis-Bröhl, Schmitte, Leiner and Zabel, 2003; Theis-Bröhl *et al*., 2003; Theis-Bröhl, 2003) for analyzing the magnetization state of stripe pattern as a function of sample rotation. The stripe array displayed in Figure 46(a) and discussed above showed a relatively simple remagnetization process dominated by a single-domain state with domain nucleation and wall movement restricted to a small field range around the coercive field. The case $\chi = 0$ is the easy axis configuration without rotation of magnetization and reversal purely takes place through domain nucleation and DW movement at the coercive field. In all other cases with $\chi \neq 0$ rotation of the magnetization within a single-domain state occurs for fields $H \neq H_c$ while the reversal through domain nucleation and DW movement is restricted to fields $H \approx H_c$. The comparison between MOKE and PNR showed a good agreement between both methods revealing that this simple qualitative method can be applied in case that a single-domain magnetic state predominates over most of the field range.

Comprehensive data analysis was performed on a pattern with CoFe stripes having a larger width of 2.4 µm (Figure 46) (Theis-Bröhl *et al*., 2005; Theis-Bröhl, McCord, Zabel and Toperverg, 2005). Between $H = 0$ and the $H = H_c$ the

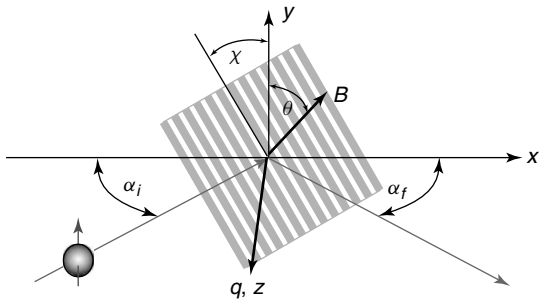

Figure 48. Sketch of the neutron scattering geometry. χ is the angle of the sample rotation with respect to the applied field (same definition as in Figure 1). The magnetic field $\vec{H}$ is applied perpendicular to the scattering plane. α_i and α_f refer to the incident and exit angles of the neutrons to the sample surface.

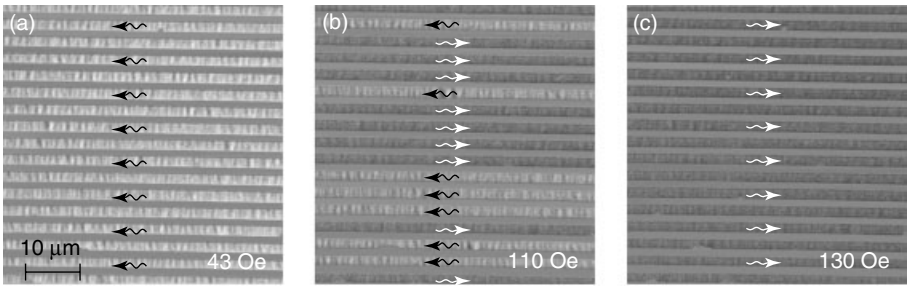

Figure 49. Kerr microscopy images taken below H_c (a), at H_c (b), and above H_c (c) with the magnetic field aligned parallel to the stripes. The plane of incidence results in a top–down magneto-optical sensitivity axis perpendicular to the stripes. The curly arrows indicate the mean magnetization direction as well as the presence of ripple domains. (Reprinted figure from K. Theis-Bröhl *et al*., *Phys Rev. B.* Vol 71, 020403 ® (2005) © 2005 by the American Physical Society.)

wide stripes decompose into a multidomain state as can be seen from Kerr microscopy measurements in Figure 49. Polarized neutron measurements without polarization analysis in the off-specular scattering range and respective simulations of the intensity maps are shown in Figure 50. The maps contain all three features described above. The specular reflectivity reveals oscillations due to the thickness of the stripes and splitting between R^+ and R^-. In the off-specular scattering range Bragg diffraction occurs and asymmetric diffuse scattering is seen indicative for a multidomain

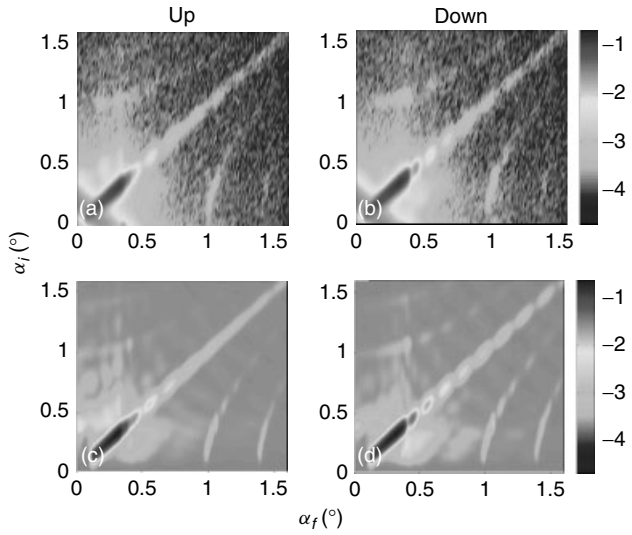

Figure 50. Experimental maps of the polarized neutron intensity on a logarithmic scale from a periodic stripe array measured at a magnetic field of 43 Oe and plotted as a function of the angles of incidence α_i, and the scattering angles α_f (a) and (b). Calculated intensity maps (c) and (d). (a) and (c) correspond to the incident neutron polarization parallel to the stripes and parallel to the external field, while in (b) and (d) the polarization and the field directions are antiparallel. (Reprinted figure from K. Theis-Bröhl *et al*., *Phys Rev. B.* Vol 71, 020403 ® (2005) © 2005 by the American Physical Society.)

state. Simulations of polarized intensity maps and specular reflectivity with full polarization analysis were performed by using a routine on the basis of DWBA. With this comprehensive study including all features occurring in the intensity maps it was shown that polarized specular and off-specular neutron scattering provide a detailed picture of the mean domain magnetization vectors in a magnetic stripe array, including longitudinal and transverse fluctuations about the mean magnetization direction and correlation effects between magnetic domains across different stripes. As a result of the quantitative analysis it was found that the domain magnetization vectors are heavily correlated not only parallel to the stripe direction, but also over a large perpendicular distance between them. This correlation creates an inherent instability of the system with respect to the formation of large domains as observed during the magnetization reversal.

Lateral magnetic structures were also measured by Lee *et al*. using time-of-flight polarized neutron reflectometry (Lee, Klose, Yin and Toperverg, 2003). The sample studied was an array of permalloy ($Ni_{80}Fe_{20}$) bars, with dimensions 10-nm thick, 2 µm wide, 10 µm long, and separated by 2 µm. As displayed in Figure 51 the authors present spin-up and spin-down intensity maps containing specular reflection, off-specular Bragg reflections and diffuse scattering. They explain the observed features qualitatively on the basis of DWBA and discuss how to obtain the F domain dispersion from polarized neutron data.

An attempt to exit into the third dimension via lateral structuring the top iron layer of an antiferromagnetically coupled Fe/Cr multilayer is illustrated by the study of Ziegenhagen *et al*. (2003). The top two-dimensional pattern consists of 15-nm-thick Fe stripes with a period of 1 µm. The array was examined by specular reflection and off-specular scattering using polarized neutrons. A schematic outline of the stripe pattern and the experimental results are shown in Figure 52. The measurements were performed with a magnetic field parallel to the Fe stripes and at a

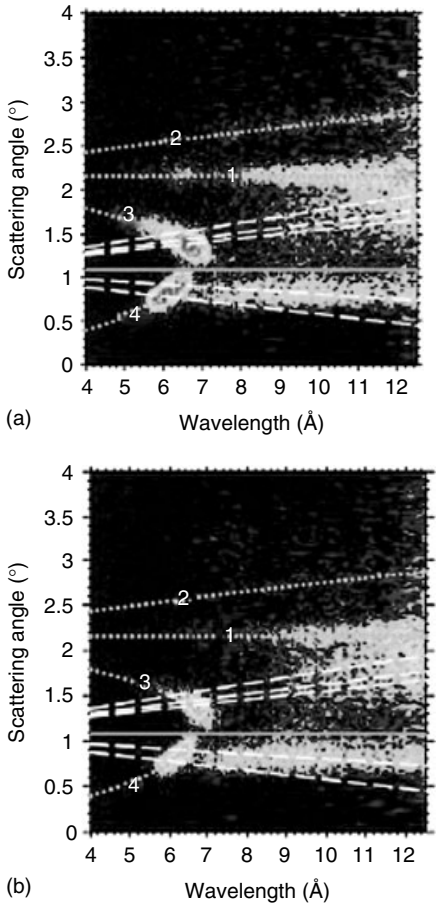

Figure 51. Log-scale intensity map for (a) spin-up and (b) spin-down incident neutrons scattered from an array of micron-sized magnetic elements on a silicon surface. The solid line at 1.08° is the horizon. The dotted lines are calculated locations of: (1) specular reflection; (2,3) off-specular reflections; and (4) diffraction. The dashed lines are the critical edges (from the horizon to higher/lower angles): the silicon edge (above the horizon only) and the permalloy edges corresponding to SLD Nb_{c+} and Nb_{c-}. (Reprodeuced from T. Lee *et al*., 2003 with permission from Elsevier. © 2003.)

level below the exchange coupling of the Fe layers in order to maintain the AF state of the Fe/Cr superlattice. The intensity maps are rather complex as they contain Bragg peaks from the chemical and magnetic perpendicular periodicity of the Fe/Cr superlattice superimposed on the intensity from the lateral stripe pattern. In detail, the maps contain specular reflectivity with half- and full-order peaks due to the perpendicular magnetic and the structural periods of the multilayer, respectively. Furthermore, intense off-specular diffuse scattering together with Bragg sheets at the half-order positions can be recognized, indicating domain formation with a strong AF correlation across the multilayer stack. Furthermore, first-order lateral Bragg diffraction peaks are visible at positions where the intensity becomes enhanced due to the AF Bragg sheet. This can be attributed to the fact that the top layer lateral magnetic structure is replicated into the inner layers.

A lateral magnetic array does not necessarily require a patterned structure by itself. Using an ion based method, such as ion bombardment induced magnetic patterning (IBMP) or focused ion-beam treatment, magnetic properties of thin magnetic films can locally be altered without changing the structural properties. Such methods are interesting with respect applications because of their high surface smoothness compared to lithographically patterned structures. Theis-Bröhl *et al*. (2006) investigated the magnetization arrangement of a smooth and continuous layer with a purely magnetic in-plane stripe pattern created by alternating EB to an AF substrate. The stripe pattern was produced by IBMP using He^+ ions, which locally changed the EB direction at the ferromagnet/antiferromagnet interface, but not the magnetic or AF properties of the $Co_{70}Fe_{30}$ and $Mn_{83}Ir_{17}$ layers, respectively. For the analysis of the magnetic domain structure evolution along the hysteresis loop a combination of experimental techniques, for example, magneto-optical Kerr effect, Kerr microscopy, polarized neutron reflectometry, and off-specular scattering of polarized neutrons with polarization analysis, was used.

For the demagnetized state antiparallel alignment of magnetization in neighboring stripes would be an ideal case. But due to the competition between EB, exchange interaction between neighboring F regions, and anisotropy, the perfect antiparallel alignment can be found only in the case that the EB dominates the others effects. For the model system studied in Theis-Bröhl *et al*. (2006) it was found that for magnetic fields parallel to the stripes and below saturation the magnetization in neighboring stripes is periodically canted with respect to the stripe axis so that the net magnetization of the F film turns almost perpendicular to the stripes. At the same time the projection of the magnetization vector onto the stripe axis has a periodically alternating sign. All this information was gained on a quantitative basis. Specular reflectivities were fitted by using an originally developed least-squares software package, which allows simultaneous evaluation of all four measured reflectivities in one cycle (Figure 53b) and simulations of intensity maps measured with full polarization analysis were performed on the basis of DWBA. The longitudinal Kerr-hysteresis loop in Figure 53(a) shows steps on both branches corresponding to the 'antiparallel' orientation of magnetization in neighboring regions. PNR measurements were performed at different fields along the hysteresis loop. Three representative cases on both branches are represented in Figure 53(b): one measured around the first coercive field $H_{c,1}$ (top row), one measured at the step of the hysteresis loop in the 'antiparallel' state (middle row) and one measured in saturation (bottom row).

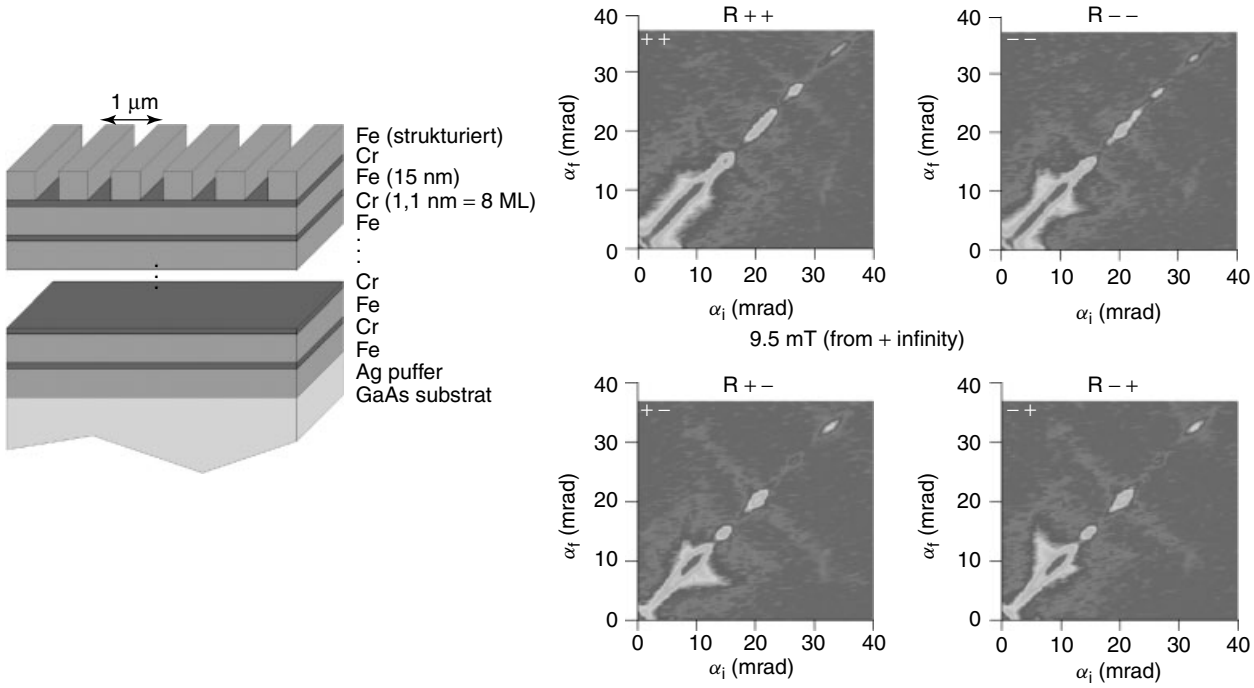

Figure 52. Specular reflection and off-specular scattering from a Fe/Cr superlattice. The top Fe layer has been lithographically structured into stripes with a 1 µm lateral period. The specular ridge contains half and full-order peaks from the perpendicular chemical and magnetic superlattice period. Patterning creates off-specular Bragg peaks and diffuse scattering forming Bragg sheets. The latter cross the specular ridge at the AF superstructure peaks on the reflectivity ridge. Diffraction signal from the lateral structure is only seen in regions of the reciprocal space where the intensity is enhanced due to the Bragg sheet scattering. (Reproduced from N. Ziegenhagen *et al*., 2003. With permission from Elsevier. © 2003.)

Telling *et al*. used IBMP for magnetic patterning of a Co/Pt multilayer and for rotating the easy axis magnetization direction in certain sample regions from out-of-plane to in-plane (Telling *et al*., 2003). The sample was irradiated through a grid stencil with a period of 13 µm assuming the sample properties do not change underneath the stencil. Specular polarized neutron reflectivity measurements performed in remanence and at saturation yield the magnetization state of the in-plane moments. Out-of-plane magnetization is not accessible to PNR. Off-specular intensity was measured as a function of q_z and the off-specular scattering angle. At remanence the authors observe Bragg diffraction peaks around the specular reflection from which the lateral long-range magnetic order in the sample can be inferred. Similar peaks cannot be observed at saturation when all domains of the sample are magnetized in-plane. Off-specular diffuse scattering was found to be small due to the smooth and uncorrelated interfaces of the sample.

In conclusion, up to now only in a few cases PNR has been applied to laterally patterned magnetic arrays. PNR and PNS was either used to qualitatively describe the remagnetization process and to discriminate between magnetization rotation on the one hand and domain nucleation and DW movement on the other hand, or for a quantitative analysis of the magnetization reversal process. Unlike PNR studies of magnetic thin films, in PNR studies of lateral patterns often no splitting between specular NSF reflectivities can be observed but qualitative information can still be gained from off-specular Bragg diffraction. Quantitative data analysis successfully can be performed within the framework of DWBA. In order to apply DWBA, the magnetization distribution within the coherence volume is decomposed into several components as discussed in Section 2.11. For lateral structures these are three components: the mean value of the magnetization, periodic perturbation of the mean magnetization due to periodic alterations of the longitudinal magnetization projection in the lateral array of magnetic elements, and random fluctuations in the magnetization due domains smaller than the coherence length. The basic features in polarized intensity maps from lateral arrays (specular NR, Bragg diffraction from the lateral period and off-specular diffuse scattering) can very well be described within this model. With this tool comprehensive PNR studies can be performed for a complete quantitative description of the magnetization state including correlations between the magnetic elements.

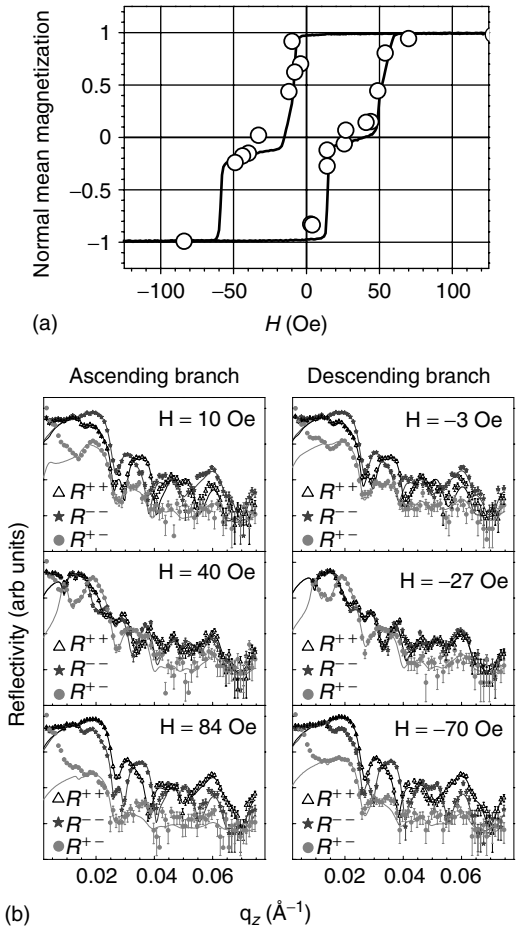

Figure 53. (a) Longitudinal MOKE hysteresis loop (line) and results of fits to the specular PNR data (symbols) of a sample magnetically patterned into stripes by ion bombardment induced magnetic patterning and measured with the field applied along the EB axis. (b) Polarized neutron reflectivity measurements performed at different applied magnetic fields. The symbols present measurements of non-spin-flip reflectivities $\mathcal{R}^{++}$ and $\mathcal{R}^{--}$ and one spin-flip reflectivity $\mathcal{R}^{+-}$. The lines represent fits to the data points. (Reprinted figure from K. Theis-Bröhl *et al.*, *Phys. Rev. B* Vol. 73, 174408 (2006) © 2006 by the American Physical Society.)

6 SUMMARY AND CONCLUSIONS

PNR is a new method in solid state physics and materials research for the analysis of magnetic thin films, magnetic heterostructures, magnetic superlattices, and lateral magnetic structures available for only some 15 years. During this time not only the magnetic systems to be studied have steadily been improved and have become more complex, also the PNR method has been appreciably developed from analyzing specular reflectivity only to a complete analysis of the specular and off-specular scattering using the distorted wave Born approximation (DWBA). Furthermore, the PNR method is now being employed at many different neutron sources using increasingly sophisticated neutron optics, neutron detectors, and sample environments. All this helps making PNR a very powerful method to meet the future challenges. Those lie in even more complex systems and smaller samples with less magnetic material. Furthermore, the time domain will likely to be explored in more detail in the future. Aside from the nano- to picosecond region investigated by time-resolved light and synchrotron experiment, there are rich physical phenomena in the subsecond to minute region which are amenable to the PNR method, such as training effects in exchange bias systems, magnetic viscosity, and spin glass relaxations.

The benefits of PNR and scattering for the investigation of magnetic nano- and heterostructures can be summarized as:

- Direct probe of atomic moments and magnetic induction;
- Cross section is known accurately;
- Both F and AF structures can be studied easily;
- Sensitivity to spin disorder and spin fluctuations;
- Magnetic correlation lengths can be probed on different length scales and in different depth below the surface.

The competition with other methods for the investigation of magnetic heterostructures is strong, in particular, with other scattering techniques such as X-ray resonant magnetic scattering (Kortright *et al.*, 2003) and diffraction MOKE (Bragg-MOKE) (Grimsditch and Vavassori, 2004; Westphalen *et al.*, 2006). The use of PNR can only be justified if the sample in question is already thoroughly characterized by other methods and if PNR can add information not available otherwise. This is indeed the case whenever the complete magnetization state including correlations between the magnetic elements need to be analyzed even in deeply buried layers.

NOTES

[1] NSF reflectivity must turn to zero along with the phase difference χ_{+-} at either $p_0 = 0$ and at $p_0 \geq p_{c+}$ just due to the fact that in the first limit $\chi_+ = \chi_- = \pi$, while in the second one $\chi_+ = \chi_- = 0$. Therefore NSF reflectivity cannot be a monotonous function of p_0 and should show at least one maximum in the range $p_{c-} \leq p_0 \leq p_{c+}$.

[2] In the following the unit matrix will be omitted and the quantities without 'hat' are be assumed to be proportional to $\hat{1}$.

[3] This consideration does not take into account that actually the identity $\mathcal{R} \equiv 1$ is achieved only in the limit $\alpha_i \to 0$. Otherwise some intensity lost from the

specular reflection channel due to off-specular scattering has to be recovered via the optical theorem (Toperverg, Schärpf and Anderson, 2000; Toperverg, 2003). This loss is, however, negligible far below the total reflection edge, where the neutron wave does not penetrate deep into the matter.

[4] To the best of our knowledge such kind of GIND was observed for the first time by Ioffe, Turkevitch and Drabkin (1981) from Ni grating with the lateral period of $a = 21\,\mu\text{m}$.

[5] Generally speaking, the coherence area is the lateral cross section of the 3D coherence volume (Sinha, Tolan and Gibaud, 1998) which also includes the uncertainty $\Delta Q_z \sim (2\pi/\lambda)\sqrt{(\Delta\alpha_i)^2 + (\Delta\alpha_f)^2}$. The latter smears out the interference of waves reflected from different interfaces. The resolution function also includes the spread $\Delta\lambda$ over the neutron wavelengths λ, which may affect the resolution in Q_y and Q_z, but is not important for the coherence volume anisotropy discussed here. In real PNR experiments the collimation in ϑ_y is quite relaxed so that an uncertainty $\Delta\vartheta_y$ is by 1–2 orders of magnitude higher than that in α_i and α_f. This is responsible for the anisotropy of the coherence volume in all three direction and also increases the anisotropy of the coherence area.

[6] Strictly speaking, the long axis of the coherence ellipsoid is usually smaller than the sample size. Therefore $\overline{Nb}$, in principle, depends on both, the y and the x coordinates. However, if the long axis crosses many structural elements then relative deviations in their number within different ellipsoids shifted along the x-axis are small and can be neglected.

[7] This result of BA is incorrect. In the more consistent DWBA approach Bragg diffraction contains both: SF and NSF contribution

[8] This linear combination serves instead of well-known equation for the scattering amplitude written as a product $T^f S(\boldsymbol{Q}) T^i$, where T^f and T^f are transmittances of incoming and scattered wave and $S(\boldsymbol{Q})$ is the scattering function. This equation is often used to describe off-specular scattering from roughness (Sinha, Sirota, Garoff and Stanley, 1988) and surface diffraction (Dosch, 1993) in the case of semi-infinite systems. However, it does not properly take into account refraction effects and ignores scattering of waves reflected from the mean potential. Both types of effects are of the crucial importance in the case of neutron scattering from patterned magnetic films and multilayers.

[9] Similar experimental maps have recently been obtained by (te Velthuis *et al*., 2006) on the Co/CoO system exhibiting EB effect (see also **Domain States Determined by Neutron Refraction and Scattering, Volume 3**).

[10] Let us to remind that the dispersion signifies fluctuations of the angle of domain magnetization rotation. In the case of a binary distribution of these angles, that is, if for instance, the domain magnetization is randomly turned for only angles $\pm\Delta\gamma$, then the dispersion equals zero.

[11] The negative SLD of the Co layer forms a potential well in front of the positive barrier of the substrate. The neutron wave passing through the well interferes with that reflected from the substrate. As a result, such a potential profile condenses the neutron wave field in the film if the corresponding wave number matches the width of the well. This brings new features (Seregin, 1977; Kentzinger, 2003; Feygenson *et al*., 2004) into the off-specular intensity distribution. However, the resonance levels are usually very narrow and quite difficult to observe with PNR.

[12] Similar maps were obtained experimentally (Radu *et al*., 2003b) for a slightly more complicated stack of layers.

[13] Features similar to those displayed in Figure 17 were recently observed experimentally (Radu *et al*., 2005a)

[14] A more complete review on the general aspects of EB systems can be found in this Handbook, and more PNR work on EB systems is covered by Felcher and Hoffmann, **Domain States Determined by Neutron Refraction and Scattering, Volume 3**.

[15] In the paper of Lee *et al*. (2002) the notation is $\gamma = \varphi$ and $\Delta = \chi^2$.

[16] In both systems the main scattering features are due to the Co layer before (Figure 25) and after (Figure 29) EB with the AF CoO layer.

[17] The aim of Figure 15 was not to reproduce exactly the experimental results in Figure 29, but rather to illustrate different contributions of the magnetic scattering from domains. In particular, off-specular SF scattering in the upper maps can easily be eliminated via suppression of the domain magnetization fluctuations in the direction parallel to net magnetization.

[18] In Figure 19 the scattering intensity maps are presented in the coordinates p^i versus p^f. Then the specular ridge runs parallel to $p^i = p^f$, which is the diagonal of the map. The Bragg sheets are perpendicular oriented and cross the specular ridge at normal angle. In the case of rocking scans the natural coordinates are $Q_x \approx \frac{1}{2}(\alpha^f - \alpha^f)Q_z$ versus $Q_z = p^i + p^f$. These coordinates are nonlinear with respect to the angles of incidence and scattering, but they are especially convenient if the Born (kinematic) approximation holds, for example, if optical effects are not important.

[19] These maps are plotted in the rectangular coordinate system with the axis $p^i + p^f = Q_z$ versus $p^i - p^f$.

This system is just turned by 45° with respect to that in Figure 19.

[20] Noncollinear magnetization arrangement was already noticed by Schreyer *et al*. (1997) as discussed above in view of the nonlinear interlayer coupling. Here the effect of magnetization canting is different in origin. It occurs only in an applied field and does not require nonlinear exchange coupling. The former conclusions of Schreyer *et al*. (1997) are based on the analysis of solely specular reflectivity assuming sublayer magnetization homogeneous over the range greater than the coherence length. This assumption holds if off-specular scattering is negligible and SF specular reflection is ascribed to the canting of mean magnetization. The same assumption was also made for other superlattices, such as in Co/Cr(001) (Zeidler *et al*., 1995) and in Fe/Cr(211) (te Velthuis *et al*., 2002) superlattices. In theses studies it was, however, suggested that the tilt angle of magnetization varies from layer to layer due to the surface spin-flop transition. With increasing field a DW formed first at the surface and then penetrated into the superlattice, thus splitting the SL into two antiphase, AF domains.

[21] In Figure 44(b) the x corresponds to the NSF y-axis.

ACKNOWLEDGMENTS

The authors would like to acknowledge fruitful discussions with Florin Radu, Andreas Schreyer, Chuck Majkrzak, and Julie Borchers. This work was supported by DFG, SFB 491 and by the BMBF under contract O3ZA6BC1.

REFERENCES

Abbe, C.L., Meersschaut, J., Sturhahn, W., *et al*. (2004). Nuclear resonant magnetometry and its application to Fe/Cr multilayers. *Physical Review Letters*, **93**, 037201.

Adenwalla, S., Felcher, G.P., Fullerton, E.E. and Bader, S.D. (1996). Polarized-neutron-reflectivity confirmation of 90° magnetic structure in fe/cr(001) superlattices. *Physical Review B*, **53**, 2474.

Ankner, J.F. and Felcher, G.P. (1999). Polarized neutron reflectometry. *Journal of Magnetism and Magnetic Materials*, **200**, 741.

Ankner, J.F., Majkrzak, C.F. and Homma, H. (1993). Magnetic dead layer in Fe/Si multilayer: Profile refinement of polarized neutron reflectivity data. *Journal of Applied Physics*, **73**, 6436.

Ankner, J.F., Majkrzak, C.F. and Satija, S.K. (1993). Neutron reflectivity and grazing angle diffraction. *Journal of Research of the National Institute of Standards and Technologys*, **98**, 47.

Ankner, J.F., Kaiser, H., Schreyer, A., *et al*. (1997). Temperature dependence of noncollinear magnetic coupling in Fe/Cr(001) superlattices. *Journal of Applied Physics*, **81**, 3765.

An up-to-date list of neutron reflectometers is available on the world wide web: http://material.fysik.uu.se/group_members/adrian/reflect.htm.

Bedanta, S., Petracic, O., Kentzinger, E., *et al*. (2005). Superferromagnetic domain state of a discontinuous metal insulator multilayer. *Physica B*, **72**, 024419.

Beesley, A.M., Thomas, M.F., Herring, A.D.F., *et al*. (2004). Magnetism of uranium/iron multilayers: I. fabrication and characterization. *Journal of Physics: Condensed Matter*, **16**, 8491.

Bergmann, A., Grabis, J., Toperverg, B.P., *et al*. (2005). Antiferromagnetic dipolar ordering in $(Co_2MnGe/V)_n$ multilayers. *Physical Review B*, **72**, 214403.

Berkowitz, A.E. and Takano, K. (1999). Exchange anisotropy – a review. *Journal of Magnetism and Magnetic Materials*, **200**, 552.

Bland, J.A.C. and Vaz, A.F. (2005). In *Polarized Neutron Reflection Studies on Thin Magnetic Films in: Ultrathin Magnetic Structures iii: Fundamentals of Nanomagnetism*, Bland, J.A.C. and Heinrich, B. (Eds.), Springer.

Blomqvist, P., Krishnana, K.M., Srinath, S. and te Velthuis, S.G.E. (2004). Magnetization processes in exchange-biased MnPd/Fe bilayers studied by polarized neutron reflectivity. *Journal of Applied Physics*, **96**, 6523.

Blundell, S.J. and Bland, J.A.C. (1992). Polarized neutron reflection as a probe of magnetic films and multilayers. *Physical Review B*, **46**, 3391.

Böni, P. (1997). Supermirror-based beam devices. *Physica B*, **234–236**, 1038.

Böni, P., Clemens, B.D., Senthil Kumar, M. and Pappas, C. (1999). Applications of remanent supermirror polarizers. *Physica B*, **267**, 320.

Borchers, J.A., Ankner, J.F., Majkrzak, C.F., *et al*. (1994). Spatial modulation of the magnetic moment in Co/Pd superlattices observed by polarized neutron reflectivity. *Journal of Applied Physics*, **75**, 6498.

Borchers, J.A., Gehring, P.M., Erwin, R.W., *et al*. (1996). Nature of the interlayer coupling in annealed $Ni_{80}Fe_{20}$/Ag multilayers *Journal of Applied Physics*, **79**, 4762.

Borchers, J.A., Gehring, P.M., Majkrzak, C.F., *et al*. (1997). Dependence of the interlayer coupling on anneal temperature in Ni–Fe/Cu evaporated multilayers. *Journal of Applied Physics*, **81**, 3771.

Borchers, J.A., Dura, J.A., Unguris, J., *et al*. (1999). Observation of antiparallel magnetic order in weakly coupled CoyCu multilayers. *Physical Review Letters*, **82**, 2796.

Born, M. and Wolf, E. (1975). *Principles of Optics*, Pergamon Press.

Bratkovsky, A.M. (1998). Assisted tunneling in ferromagnetic junctions and half-metallic oxides. *Applied Physics Letters*, **72**, 2334.

Brown, S.D., Beesley, A., Herring, A., *et al*. (2003). Resonant magnetic reflectivity from U/Fe multilayers. *Journal of Applied Physics*, **93**, 6519.

Charlton, T., Lederman, D., Yusuf, S.M. and Felcher, G.P. (1999). Anisotropy of the sublattice magnetization and magnetoresistance in Co/Re superlattices on Al_2O_3(11–20). *Journal of Applied Physics*, **85**, 4436.

Cheng, L., Altounian, Z., Ryan, D.H., *et al*. (2004). Pd polarization and interfacial moments in pd-fe multilayers. *Physical Review B*, **69**, 144403.

Choi, B.C., Samad, A., Vaz, C.A.F., *et al*. (2000). Layer selective determination of magnetization vector configurations in an epitaxial double spin valve structure: Si(001)/Cu/Co/Cu/FeNi/Cu/Co/Cu. *Applied Physics Letters*, **77**, 892.

Clemens, D., Gross, P., Keller, P., *et al*. (2000). AMOR-the versatile reflectometer at SINQ *Physica B*, **276**, 140.

Coey, J.M.D.M. and Chien, C.L. (2003). Half-metallic ferromagnetic oxides. *MRS Bulletin*, **28**, 720.

Cubitt, R. and Fragnetto, G. (2002). D17: the new reflectometer at the ill. *Applied Physics A*, **74**, S329.

Diwekar, M., Borchers, J.A., O'Donovan, J.V., *et al*. (2004). Magnetic properties of (Ga,Mn)As digital ferromagnetic heterostructures. *Journal of Applied Physics*, **95**, 6509.

Doi, M., Roldan Cuenya, B., Keune, W., *et al*. (2002). Magnetic and structural properties of epitaxial fe thin films on gaas(0 0 1) and interfaces. *Journal of Magnetism and Magnetic Materials*, **240**, 407.

Donahue, M.J. and Porter, D.G. (1999). *Interagency* Report NISTIR 6376, National Institute of Standards and Technology, Gaithersburg, MD.

Dorner, B. and Wildes, A. (2003). Some considerations on resolution and coherence length in reflectrometry. *Langmuir*, **19**, 7823.

Dosch, H. (1993). Surface-sensitive magnetic neutron bragg scattering: perspective and limits. *Physica B*, **192**, 163.

Drabkin, G.M., Okorokov, A.I. and Runov, V.V. (1972). Anisotropy of neutron beam depolarization. *JETP Letters*, **5**, 324.

Felcher, R.O., Hillecke, R.K., Crawford, J., *et al*. (1987). Polarized neutron reflectometers: A new instrument to measure magnetic depth profiles. *Review of Scientific Instruments*, **58**, 609.

Felici, R., Penfold, J., Ward, R.C., *et al*. (1988). A polarised neutron reflectometer for studying surface magnetism. *Applied Physics A*, **45**, 169.

Fermon, C. and Menelle, A. (1999). *X-ray and Neutron Reflectivity: Principles and Applications*, *Lecture Notes in Physics*, Daillant, J. and Gibaud, A. (Eds.), Springer Verlag.

Feygenson, M., Toperverg, B.P., Rücker, U., *et al*. (2004). Neutron quantum well states in Fe/Co/Fe trilayers. *Physica B*, **350**, E233.

Fitzsimmons, M.R., Yashar, P., Leighton, C., *et al*. (2000). Asymmetric magnetization reversal in exchange-biased hysteresis loops. *Physical Review Letters*, **84**, 3986.

Fitzsimmons, M.R., Leighton, C., Hoffmann, A., *et al*. (2001). Influence of interfacial disorder and temperature on magnetization reversal in exchange-coupled bilayers. *Physical Review B*, **64**, 104415.

Fitzsimmons, M.R., Leighton, C., Nogue's, A., *et al*. (2002). Influence of in-plane crystalline quality of an antiferromagnet on perpendicular exchange coupling and exchange bias. *Physical Review B*, **65**, 134436.

Fitzsimmons, M.R., Bader, S.D., Borchers, J.A., *et al*. (2004). Neutron scattering studies of nanomagnetism and artificially structured materials. *Journal of Magnetism and Magnetic Materials*, **271**, 103.

Fritzsche, H., Van Bael, M.J. and Temst, K. (2003). Off-specular polarized neutron reflectometry from periodic arrays of lithographically structured Co dots. *Langmuir*, **19**, 7789.

Fullerton, E.E., Adenwalla, S., Felcher, G.P., *et al*. (1996). Neutron diffraction and reflectivity studies of the Cr Néel transition in Fe/Cr (001) superlattices. *Physica B*, **221**, 370.

Fullerton, E.E., Bader, S.D. and Robertson, J.L. (1996). Spin-density-wave antiferromagnetism of Cr in FeyCr(001) superlattices. *Physical Review Letters*, **77**, 1382.

Fullerton, E.E., Jiang, J.S. and Bader, S.D. (1999). Hard/soft magnetic heterostructures: model exchange-spring magnets. *Journal of Magnetism and Magnetic Materials*, **200**, 392.

Fullerton, E.E., Riggs, K.T., Sowers, C.H., *et al*. (1995). Suppression of biquadratic coupling in Fe /Cr(001) superlattices below the Néel transition of Cr. *Physical Review Letters*, **75**, 330.

Geoghegan, S., McCormick, P.G. and Street, R. (1998). Anomalous magnetic viscosity in nio/ni. *Journal of Magnetism and Magnetic Materials*, **177**, 937.

Gierlings, M., Prandolini, M., Fritzsche, H., *et al*. (2002). Change and asymmetry of magnetization reversal for a co/coo exchange-bias system. *Physical Review B*, **65**, 092407.

Goodman, A.M., Laidler, H., O'Grady, K., *et al*. (2000). Magnetic viscosity effects on the pinned layer loop of spin-valve materials. *Journal of Applied Physics*, **87**, 6409.

Griffiths, R.B. (1970). Dependence of critical indices on a parameter. *Physical Review Letters*, **24**, 1479.

Grimsditch, M. and Vavassori, P. (2004). The diffracted magneto-optic kerr effect: what does it tell you? *Journal of Physics: Condensed Matter*, **16**, R275–R294.

Günther, R., Donner, W., Toperverg, B.P. and Dosch, H. (1998). Birefringent bragg diffraction of evanescent neutron states in magnetic films. *Physical Review Letters*, **81**, 116.

Hauet, T., Borchers, J.A., Mangin, P., *et al*. (2006). Training effect in an exchange bias system: the role of interfacial domainwalls. *Physical Review Letters*, **96**, 067207.

Hillebrands, B. and Felser, C. (2006). High-spin polarization of heusler alloys. *Journal of Physics D*, **39**, 765–865.

Hjörvarsson, B., Dura, J.A., Isberg, P., *et al*. (1997). Reversible tuning of the magnetic exchange coupling in FeyV (001) superlattices using hydrogen. *Physical Review Letters*, **79**, 901.

Hoffmann, A., Seo, J.W., Fitzsimmons, M.R., *et al*. (2002). Induced magnetic moments at a ferromagnet-antiferromagnet interface. *Physical Review B*, **66**, 220406.

Huiberts, J.N., Griessen, R., Rector, J.H., *et al*. (1996). Yttrium and lanthanum hydride films with switchable optical properties. *Nature*, **380**, 231.

Ioffe, A.I., Turkevitch, Yu.G. and Drabkin, G. (1981). Diffraction-grating neutron interferometer. *Journal of Experimental and Theoretical Physics Letters*, **33**, 374.

Jiang, J.S. Felcher, G.P. Inomata, A., *et al*. (2000). Exchange bias in Fe/Cr double superlattices. *Journal of Vacuum Science and Technology A*, **18**, 1264.

Kentzinger, E.R., Rücker, U., Toperverg, B.P. and Brückel, Th. (2003). Determination of the magnetic fluctuations in an Fe/Cr/Fe trilayer exhibiting a neutron resonance state. *Physica B*, **335**, 89.

Kentzinger, E., Toperverg, B.P. and Rücker, U. (2003) Simulations of off-specular scattering of polarized neutrons from laterally patterned magnetic multilayers. *Physica B*, **335**, 82.

Kepa, H., Kutner-Pielaszek, J., Twardowski, A., *et al*. (2001). Ferromagnetism of gamnas studied by polarized neutron reflectometry. *Physical Review B*, **64**, 121302(R).

Kirby, B.J., Borchers, J.A., Rhyne, J.J., *et al*. (2004). Annealing-dependent magnetic depth profile in ga1−xmnxas. *Physical Review B*, **69**, 081307.

Kiwi, M. (2001). Exchange bias theory. *Journal of Magnetism and Magnetic Materials*, **234**, 584.

Klose, F., Rehm, Ch. D. Nagengast, H., *et al*. (1997). Continuous and reversible change of the magnetic coupling in an Fe/Nb multilayer induced by hydrogen charging. *Physical Review Letters*, **78**, 1150.

Kneller, E.F. and Hawig, R. (1991). The exchange-spring magnet: a new material principle for permanent magnets. *IEEE Transactions on Magnetics*, **27**, 3588.

Kortright, J.B., Jiang, J.S., Bader, S.D., *et al*. (2003). Magnetism in heterogeneous thin film systems: resonant x-ray scattering studies. *Nuclear Instruments and Methods in Physics*, **199**, 301.

Kozlowski, A., Rasmussen, R.J., Sabol, J.E., *et al*. (1993). Electrical conduction in single-crystal fe3-ytiyo4 ($0 < y < 0.9$). *Physical Review B*, **48**, 2057.

Krist, T., Fritzsche, H. and Mezei, F. (2002). A large-angle neutron polarisation analyser. *Applied Physics A*, **74**, S221.

Krist, Th., Pappas, C., Keller, Th., *et al*. (1995). The polarizing beam splitter guide at bensc. *Physica B*, **213**, 939.

Landau, L.D. and Lifshits, E.M. (1977). *Quantum Mechanics*, Pergamon Press: Oxford.

Langridge, S., Schmalian, J., Marrows, C.H., *et al*. (2000). Quantification of magnetic domain disorder and correlations in antiferromagnetically coupled multilayers by neutron reflectometry. *Physical Review Letters*, **85**, 4964.

Lauter-Pasyuk, V., Lauter, H.J., Toperverg, B., *et al*. (2001). Magnetic neutron off-specular scattering for the direct determination of the coupling angle in exchange-coupled multilayers. *Journal of Magnetism and Magnetic Materials*, **226–230**, 1694.

Lauter-Pasyuk, V., Lauter, H.J., Toperverg, B.P., *et al*. (2002). Transverse and lateral structure of the spin-flop phase in Fe/Cr antiferromagnetic superlattices. *Physical Review Letters*, **89**, 167203.

Lee, W-T., Klose, F., Yin, H.Q. and Toperverg, B.P. (2003). Measuring lateral magnetic structures in thin films using time-of-flight polarized neutron reflectometry. *Physica B*, **335**, 77.

Lee, W-T., te Velthuis, S.G.E., Felcher, G.P., *et al*. (2002). Ferromagnetic domain distribution in thin films during magnetization reversal. *Physical Review B*, **65**, 224417.

Leighton, C., Fitzsimmons, M.R., Hoffmann, A., *et al*. (2002). Thickness-dependent coercive mechanisms in exchange-biased bilayers. *Physical Review B*, **65**, 064403.

Leighton, C., Fitzsimmons, M.R., Yashar, P., *et al*. (2001). Two-stage magnetization reversal in exchange biased bilayers. *Physical Review Letters*, **86**, 4394.

Leiner, V., Ay, M. and Zabel, H. (2004). Hydrogen and the magnetic interlayer exchange coupling: variable magnetic interlayer correlation in ho/y(00.1) superlattices. *Physical Review B*, **70**, 104429.

Leiner, V., Westerholt, K., Blixt, A.M., *et al*. (2003). Magnetic superlattices with variable interlayer exchange coupling: A new approach for the investigation of low-dimensional magnetism. *Physical Review Letters*, **91**, 037202.

Loewenhaupt, M., Hahn, W., Huang, Y.Y., *et al*. (1993). Spin structures of Fe/Gd and Fe/Cr multilayers determined by polarized neutron reflectometry. *Journal of Magnetism and Magnetic Materials*, **121**, 173.

Lohstroh, W., Leuenberge, F., Felsch, W., *et al*. (2001). Hydrogen-controlled interlayer exchange coupling in Fe/Lahx multilayers. *Journal of Magnetism and Magnetic Materials*, **237**, 77.

Lohstroh, W., Schulte, O., Felsch, W., *et al*. (2000). The fragile magnetic structures of Fe/Ceh2-d multilayers. *Journal of Magnetism and Magnetic Materials*, **210**, 357.

Majkrzak, C.F. (1989). Polarized neutron scattering methods and studies involving artificial superlattices. *Physica B*, **156–157**, 619.

Majkrzak, C.F. (1991). Polarized neutron reflectometry. *Physica B*, **173**, 75–88.

Majkrzak, C.F., Satija, S.K., Berk, N.F., *et al*. (2001). Neutron reflectometry at the NCNR. *Neutron News*, **12**, 25.

Majkrzak, C.F. (1996). Neutron scattering studies of magnetic thin films and multilayers. *Physica B*, **221**, 342.

Majkrzak, C.F., O'Donovan, K.V., and Berk, N.F., Chatterji, Tapan (Eds.), (2006). In *Neutron Scattering from Magnetic Materials*, Elsevier Science.

Major, J., Dosch, H., Felcher, G.P., *et al*. (2003). Combining of neutron spin echo and reflectivity: a new technique for probing surface and interface order. *Physica B*, **336**, 8.

Mannix, W.G., Stirling, D.G., Bucknall, P.W., *et al*. (1997). Polarised neutron reflectivity from a [UAs/Co] multilayer. *Physica B*, **234–236**, 470.

Matsukuraa, F., Ohnoa, H. and Dietl, T. (2002). Iii-v ferromagnetic semiconductors. In *Handbook of Magnetic Materials*, Buschow, K.H.J. (Eds.), Elsevier Science, pp. 1–87, Vol. 14.

Meiklejohn, W.H. (1962). Exchange anisotropy–A review. *Journal of Applied Physics*, **33**, 1328.

Meiklejohn, W.H. and Bean, C.P. (1956). New magnetic anisotropy. *Physical Review*, **102**, 1413.

Meiklejohn, W.H. and Bean, C.P. (1957). New magnetic anisotropy. *Physical Review*, **105**, 904.

Morall, P., Schedin, F., Langridge, S., *et al*. (2003). Magnetic moment in an ultrathin magnetite film. *Journal of Applied Physics*, **93**, 7960.

Mott, N.F. and Massey, H.S.W. (1965) *The Theory of Atomic Collisions. International Series of Monographs on Physics*, Oxford Press, Oxford, England.

Névot, L. and Croce, P. (1980). Caractérisation des surfaces par réflexion rasante de rayons x. application à l'étude du polissage de quelques verres silicates. *Revue De Physique Appliquee*, **15**, 761–779.

Nogués, J. and Schuller, I.K. (1999). Exchange bias. *Journal of Magnetism and Magnetic Materials*, **192**, 203.

Nickel, B., Rühm, A., Donner, W., *et al*. (2001). Spin-resolved off-specular neutron scattering maps from magnetic multilayers using a polarized 3-He gas spin filter. *Review of Scientific Instruments*, **72**, 163.

Okorokov, A.I. and Runov, V.V. (2001). Vector analysis of polarization at small-angle neutron scattering. *Physica B*, **297**, 239.

Pannetiera, M., Ott, F., Fermon, C. and Samson, Y. (2003). Surface diffraction on magnetic nanostructures in thin films using grazing incidence sans. *Physica B*, **335**, 54.

Parrat, L.G. (1954). Surface studies of solids by total reflection of X-rays. *Physical Review*, **95**, 359.

Paul, A., Kentzinger, E., Rücker, U. and Brückel, T. (2006). Symmetry and asymmetry during magnetization reversal in exchange biased multilayers and bilayers. *Physical Review B*, **73**, 092410.

Paul, A., Kentzinger, E., Rücker, U., *et al*. (2004). Sequence, symmetry, and magnetic fluctuations of the magnetization reversal in exchange-biased multilayers. *Physical Review B*, **70**, 224410.

Paul, A., Kentzinger, E., Rücker, U., *et al*. (2005). Polarized neutron scattering from polycrystalline, exchange-biased magnetic multilayers. *Physica B*, **356**, 26.

Pechan, M.J., Ankner, J.F., Majkrzak, C.F., *et al*. (1994). Magnetic profile as a function of structural disorder in Fe/Cr superlattices. *Journal of Applied Physics*, **75**, 6178.

Primus, J-L., Fritzsche, H., Malfait, M., *et al*. (2005). Magnetic anisotropy and magnetization reversal in $Ga_{1-x}Mn_xAs$ layers studied by polarized. *Journal of Applied Physics*, **97**, 123909.

Pynn, R., Fitzsimmons, M.R., Fritzsche, H., *et al*. (2003). Does beam divergence matter for neutron reflectometry. *Physica B*, **336**, 1.

Radu, F. (2005). Fundamental Aspects of Exchange Bias, Dissertation, Ruhr-University, Bochum.

Radu, F., Etzkorn, M., Leiner, V., *et al*. (2002a). Polarised neutron reflectometry study of CoO/Co exchange-biased multilayers. *Applied Physics A*, **74**, S1570.

Radu, F., Etzkorn, M., Schmitte, T., *et al*. (2002b). Asymmetric magnetization reversal on exchange biased CoO/Co bilayers. *Journal of Magnetism and Magnetic Materials*, **240**, 251.

Radu, F., Etzkorn, M., Siebrecht, R., *et al*. (2003a). Interfacial domain formation during magnetization reversal in exchange-biased coo/co bilayers. *Physical Review B*, **67**, 134409.

Radu, F. and Ignatovich, V.K. (1999). Generalized matrix method for the transmission of neutrons through multilayer magnetic systems with noncollinear magnetization. *Physica B*, **267–268**, 175.

Radu, F., Leiner, V., Westerholt, K., *et al*. (2005a). Magnetic induction and domain walls in magnetic thin films at remanence. *Journal of Physics: Condensed Matter*, **17**, 1711.

Radu, F., Leiner, V., Wolff, M., *et al*. (2005b). Quantum states of neutrons in magnetic thin films. *Physical Review B*, **71**, 214423.

Radu, F., Nefedov, A., Grabis, J., *et al*. (2006). Soft x-ray resonant magnetic scattering studies on Fe/CoO exchange bias system. *Journal of Magnetism and Magnetic Materials*, **300**, 206.

Radu, F., Vorobiev, A., Major, J., *et al*. (2003b). Spin-resolved off-specular neutron scattering from magnetic domain walls using the polarized 3he gas spin filter. *Physica B*, **335**, 63–67.

Rekveldt, M.Th. (1971). Neutron depolarisation as a method to determine the magnetization, the mean domain size and the mean square components of the inner magnetization of ferromagnets. *Journal de Physique Colloque (C1)*, **32**, 579.

Rücker, U., Bergs, W., Alefeld, B., *et al*. (2001). Polarization analysis for the 2d position-sensitive detector of the hadas reflectometer in jülich. *Physica B*, **297**, 140.

Rücker, U., Kentzinger, E., Toperverg, B., *et al*. (2002). Layer-by-layer magnetometry of polarizing supermirrors. *Applied Physics A*, **74**, S607.

Rühm, A., Toperverg, B.P. and Dosch, H. (1999). Supermatrix approach to polarized neutron reflectivity from arbitrary spin structures. *Physical Review B*, **60**, 16073.

Schmitte, T., Schreyer, A., Leiner, V., *et al*. (1999). Proximity effect in exchange-coupled Fe/Cr(001) superlattices. *Europhysics Letters*, **48**, 692.

Schreyer, A. (1994). Spin polarized neutron reflectometry and x-ray scattering on exchange coupled superlattices, Dissertation, Ruhr-University, Bochum.

Schreyer, A., Ankner, J.T., Zeidler, Th., *et al*. (1995a). Noncollinear and collinear magnetic structures in exchange coupled Fe/Cr(001) superlattices. *Physical Review B*, **52**, 16066.

Schreyer, A., Ankner, J.F., Zeidler, M.Th., *et al*. (1995b). Direct observation of non-collinear spin structures in Fe/Cr(001) superlattices by polarized neutron reflectometry. *Europhysics Letters*, **32**, 595.

Schreyer, A., Bröhl, K., Ankner, J.F., *et al*. (1993a). Oscillatory exchange coupling in Co/Cu(111) superlattices. *Physical Review B*, **47**, 15334.

Schreyer, A., Majkrzak, C.F., Zeidler, T., *et al*. (1997). Magnetic structure of Cr in exchange coupled Fe/Cr(001) superlattices. *Physical Review Letters*, **79**, 4914.

Schreyer, A., Zeidler, T., Morawe, Ch., *et al*. (1993b). Spin-polarized neutron reflectivity study of a Co/Cu(111) superlattice. *Journal of Applied Physics*, **73**, 7616.

Seregin, A.A. (1977). *Zhurnal Eksperimentalnoi I Teoreticheskoi Fiziki*, **73**, 1634.

Siebrecht, R. (2001). Untersuchung magnetischer $Fe_{1-x}Cr_x$/Cr-Übergitter mit dem Neutronenreflektometer ADAM. Dissertation, Ruhr-University, Bochum.

Siebrecht, R., Schreyer, A., Englisch, U., *et al*. (1997). The new reflectometer adam at the ill. *Physica B*, **241–243**, 169.

Siebrecht, R., Schreyer, A., Schmitte, T., *et al*. (1999). Investigation of magnetic coupling phenomena in FeCr/Cr - superlattices with spin-polarized neutrons. *Physica B*, **267–268**, 207.

Sinha, S.K., Sirota, E.B., Garoff, S. and Stanley, H.B. (1988). X-ray and neutron scattering from rough surfaces. *Physical Review B*, **38**, 2297.

Sinha, S.K., Tolan, M. and Gibaud, A. (1998). Effects of partial coherence on the scattering of x rays by matter. *Physical Review B*, **57**, 2740.

Slonczweski, J.C. (1995). Overview of interlayer exchange theory. *Journal of Magnetism and Magnetic Materials*, **150**, 13.

Solina, D.M., Liedke, M.O., Tietze, U., *et al*. (2005). Reflectivity characterisation of ion irradiated exchange bias femn–feni films. *Journal of Magnetism and Magnetic Materials*, **286**, 225.

Stamps, R.L. (2000a). Mechanisms for exchange bias. *Journal of Physics D*, **33**, R247.

Stamps, R.L. (2000b). Dynamic magnetic hysteresis and anomalous viscosity in exchange bias systems. *Physical Review B*, **61**, 12174.

Steadman, P., Ali, M., Hindmarch, A.T., *et al*. (2002). Exchange bias in spin-engineered double superlattices. *Physical Review Letters*, **89**, 077201.

Su, H-C., Peir, J-J., Lee, C-H., *et al*. (2005). The polarized neutron reflectivity and X-ray reflectivity studies of the magnetic profiles of epitaxial $Ni_{80}Fe_{20}$/Ru multilayers. *Physica B*, **357**, 80.

Syromyatnikov, V.G., Toperverg, B.P., Kentzinger, E., *et al*. (2001). Off-specular polarized neutron scattering from periodic co/ti and aperiodic Fe/Al magnetic multilayers. *Physica B*, **297**, 175.

Tasset, F. (2001). Neutron beams at the spin revolution. *Physica B*, **297**, 1.

Telling, N.D., Langridge, S., Dalgliesh, R.M., *et al*. (2003). Observation of ion beam induced magnetic patterning using off-specular polarized neutron reflectometry. *Journal of Applied Physics*, **93**, 7420.

Temst, K., Girgis, E., Portugal, R.D., *et al*. (2005a). Magnetization and polarized neutron reflectivity experiments on patterned exchange bias. *European Physical Journal B*, **45**, 261.

Temst, K., Popova, E., Van Bael, M.J., *et al*. (2005b). Magnetization reversal in patterned ferromagnetic and exchange-biased nanostructures studied by neutron reflectivity. *Journal of Applied Physics*, **97**, 10K117.

Temst, K., Van-Bael, M.J. and Fritzsche, H. (2001). Application of off-specular polarized neutron reflectometry to measurements on an array of mesoscopic ferromagnetic disks. *Applied Physics Letters*, **79**, 991.

Temst, K., Van Bael, M.J., Swerts, J., *et al*. (2003a). Polarized neutron reflectometry on lithographically patterned thin film structures. *Superlattices and Microstructures*, **34**, 87.

Temst, K., Van Bael, M.J., Swerts, J., *et al*. (2003b). In-plane vector magnetometry on rectangular Co dots using polarized neutron reflectivity. *Journal of Vacuum Science and Technology*, **21**, 2043.

te Velthuis, S.G.E., Berger, A., Felcher, G.P., *et al*. (2000). Training effects and the microscopic magnetic structure of exchange biased Co/CoO bilayers. *Journal of Applied Physics*, **87**, 5046.

te Velthuis, S.G.E., Felcher, G.P., Welp, U., *et al*. (2006). Magnetic domain configurations in the hysteresis cycle of an exchange-coupled ferromagnetic film (Co/CoO). *Physical Review B*.

te Velthuis, S.G.E., Jiang, J.S., Bader, S.D., *et al*. (2002). Spin flop transition in a finite antiferromagnetic superlattice: evolution of the magnetic structure. *Physical Review Letters*, **89**, 1272031.

te Velthuis, S.G.E., Jiang, J.S. and Felcher, G.P. (2000). Switching of the exchange bias in Fe/Cr(211) double-superlattice structures. *Applied Physics Letters*, **77**, 2222.

te Velthuis, S.G.E., Felcher, G.P., Blomquist, P. and Wäppling, R. (2001). Neutron spin rotation in magnetic mirror. *Journal of Physics: Condensed Matter*, **13**, 5577.

Theis-Bröhl, K. (2003). Magnetisation reversal of stripe arrays-comparison of MOKE with polarized neutron reflectivity. *Advances in Solid State Physics*, **43**, 801.

Theis-Bröhl, K., McCord, J., Zabel, H. and Toperverg, B.P. (2004). Quantification of the magnetization arrangement of patterned films measured by polarized neutron reflectivity. *Physica B*, **356**, 14–20.

Theis-Bröhl, K., Schmitte, T., Leiner, V., *et al*. (2003). Cofe stripes: magnetization reversal study by polarized neutron scattering and magneto-optical Kerr effect. *Physical Review B*, **67**, 184415.

Theis-Bröhl, K., Schmitte, T., Leiner, V. and Zabel, H. (2003). Magnetization reversal studies of magnetic wire arrays by polarized neutron scattering. *Phase Transitions*, **76**, 413.

Theis-Bröhl, K., Toperverg, B.P., Leiner, V., *et al*. (2005). Correlated magnetic reversal in periodic stripe patterns. *Physical Review B*, **71**, 020403R.

Theis-Bröhl, K., Toperverg, B.P., Westphalen, W.A., *et al*. (2006). Exchange-bias instability in a bilayer with an ion-beam imprinted stripe pattern of ferromagnetic/antiferromagnetic interfaces. *Physical Review B*, **73**, 174408.

Toney, M.F., Borchers, J.A. O'Donovan, K.V., *et al*. (2005). Magnetization profile in antiferromagnetically coupled recording media. *Journal of Applied Physics*, **86**, 162506.

Toperverg, B.P. (2002a). In *Polarized Neutron Scattering, Series Matter and Materials*, Brückel, Th. and Schweika, W. (Eds.), Forschungszentrum Juelich GmbH, Institut für Festkörperforschung: Germany, p. 274, Vol. 12.

Toperverg, B.P. (2002b). Off-specular polarized neutron scattering from magnetic fluctuations in thin films and multilayers. *Applied Physics A*, **74**, S1560.

Toperverg, B.P. (2003). Optical theorem, depolarization and vector tomography. *Physica B*, **335**, 174.

Toperverg, B.P., Felcher, G.P., Metlushko, V.V., *et al*. (2000). Grazing incidence neutron diffraction from large scale 2d structures. *Physica B*, **283**, 149.

Toperverg, B.P., Lauter, H.J. and Lauter-Pasyuk, V.V. (2005a). Larmor pseudo-precession of neutron polarization at reflection. *Physica B*, **356**, 1.

Toperverg, B.P., Lauter-Pasyuk, V.V. and Lauter, H.J. (2005b). Grazing incidence neutron diffraction from ferromagnetic films in multi-domain state. *Physica B*, **356**, 51.

Toperverg, B., Nikonov, O., Lauter-Passyuk, V. and Lauter, H. (2001). Towards 3d polarization analysis in neutron reflectometry. *Physica B*, **279**, 169.

Toperverg, B.P., Rühm, A., Donner, W. and Dosch, H. (1999). Polarized neutron grazing angle birefrigent diffraction from magnetic stratified media. *Physica B*, **267–268**, 198.

Toperverg, B.P., Schärpf, O. and Anderson, I.S. (2000). Optical theorem for neutron scattering from rough interfaces. *Physica B*, **276**, 954.

Toyoshima, N., Miyamoto, T., Takeda, M., *et al*. (1999). Polarized neutron reflectivity of Co/Cu multilayers with Co–Cu mixed layers at interfaces between Co and Cu layers. *Journal of Physics and Chemistry of Solids*, **60**, 1487.

Van De Kruijs, R.W.E., Ul'yanov, V.A., Rekveldt, M.Th., *et al*. (2001). Probing magnetic structures by neutron reflectometry: Off-specular scattering from interfaces and domains in FeCoV/TiZr multilayers. *Physica B*, **297**, 180.

Vaz, C.A.F., Ionescu, A., Trypiniotis, T., *et al*. (2005). Magnetic properties of Fe/Alo$_x$/gaas(001) structures. *Journal of Applied Physics*, **97**, 10J119.

Westphalen, A., Schumann, A., Remhof, A., *et al*. (2006). Magnetization reversal of equilateral fe triangles. *Physical Review B*, **74**, 104417.

Wolff, M., Radu, F., Petoukhov, A., *et al*. (2006). Scientific reviews: 3he spin filter at the institut laue-langevin: polarization analysis of diffuse scattering. *Neutron News*, **17**, 26–29.

Yi Li, C., Polaczyk, J., Kapoor, F., *et al*. (1997). Polarized neutron reflection study of Gd/W multilayers. *Physica B*, **234–236**, 492.

Yoneda, Y. (1963). Anomalous surface reflection of x-rays. *Physical Review*, **131**, 2010.

Zabel, H. and Theis-Bröhl, K. (2003). Polarized neutron reflectivity and scattering studies of magnetic heterostructures. *Journal of Physics: Condensed Matter*, **15**, S505.

Zeidler, Th., Donner, W., Metoki, N., *et al*. (1995). Antiferromagnetic coupling and magnetic anisotropy of co/cr(001) superlattices. *Journal of Magnetism and Magnetic Materials*, **148**, 211.

Zhengdong Zhang, R.A., Lukaszewa, C., Cionca, X., *et al*. (2004). Correlated structural and magnetization reversal studies on epitaxial ni films grown with molecular beam epitaxy and with sputtering. *Journal of Vacuum Science and Technology*, **A22**, 1868.

Ziegenhagen, N., Rücker, U., Lehmann, R., *et al*. (2003). Magnetic properties of laterally structured Fe/Cr multilayers. *Physica B*, **335**, 50.

Zimmer, O., Hautle, P., Heil, W., *et al*. (2000). Spin filters and supermirrors: a comparison study of two methods of high-precision neutron polarisation analysis. *Nuclear Instruments and Methods in Physics Research A*, **440**, 764.

APPENDIX

A AMPLITUDE OF NUCLEAR SCATTERING FROM A GRATING

In BA, $F_l^0(\boldsymbol{Q}) = F_l^N(\boldsymbol{Q})$ and for the case of patterned layers the function $F_l^0(Q_z, Q_x; y)$ is given by the equation

$$F_l^0(Q_z, Q_x; y) = F_l^z(Q_z, y) \sum_j \boldsymbol{e}^{i Q_x x_j} F_{lj}^L(Q_x, y) \quad \text{(A1)}$$

where $x_j = x_j(y)$ are coordinates of the lateral structure elements. The function $F_l^z(Q_z, y)$ is simply a form-factor of the l^{th} layer

$$F_l^z(Q_z, y) = \boldsymbol{e}^{i Q_z z_{l-1}} \frac{\boldsymbol{e}^{i Q_z d_l} - 1}{i Q_z} \quad \text{(A2)}$$

and $d_l = d_l(y)$ is the height of the structural element at a fixed coordinate y. As shown in the bottom panel of Figure 8, it may be happened that for some choice of y that $d(y) = 0$, while $d(y) = d$ for the other value of y. The function $F_{lj}^L(Q_x, y)$ in equation (A1),

$$F_{lj}^L(Q_x, y) = \int_0^{a_j} \mathrm{d}x\, \boldsymbol{e}^{i Q_x x} \Delta(Nb)_l^N(x, y) \quad \text{(A3)}$$

is the Fourier transform of the lateral SLD deviations profile $F_{lj}^L(x, y)$ of a single structural element j along the x-axis at fixed coordinate y. In the case of a regular pattern, $a_j = a(y)$ is the structural period in the lateral direction parallel to the x-axis. If each of the lateral periods contains n_x elements in a unit cell, then from equation (A3) it follows that $F_{lj}^L(Q_x, y) = F_l^L(Q_x, y)$, and

$$F_l^L(Q_x, y) = \sum_{m=1}^{n_x} \Delta(Nb)_l^{(m)} \boldsymbol{e}^{i Q_x x_l^{(m-1)}} \frac{\boldsymbol{e}^{i Q_x a_l^{(m)}} - 1}{i Q_x} \quad \text{(A4)}$$

where $\Delta(Nb)_l^{(m)} = (Nb)_l^{(m)} - \overline{(Nb)}_l^N$, $(Nb)_l^{(m)}$ is the nuclear SLD, while $a_l^{(m)} = x_l^{(m)} - x_l^{(m-1)}$ is the width of the m^{th} element in the l^{th} layer, and $x_l^{(0)} = 0$. Due to fact that

$$\overline{Nb}_l^N = \sum_{m=1}^{n} \frac{a_l^{(m)}}{a_l} (Nb)_l^{(m)} \quad \text{(A5)}$$

$F_l^L(Q_x, y) = 0$ at $Q_x = 0$ and does not contribute to specular reflection. For the stripe array the SLD in Figure 10 $\overline{(Nb)}^N = (a^{(1)}/a)(Nb)^N$, where $a = a^{(1)} + a^{(2)}$, and $\Delta(Nb)^{(1)} = (a^{(2)}/a)(Nb)^N$ at $0 \le x < a^{(1)}$, and $\Delta(Nb)^{(2)} = -\overline{Nb}^N$ if $a^{(1)} \le x < a$.

Synchrotron Radiation Techniques Based on X-ray Magnetic Circular Dichroism

Gisela Schütz, Eberhard Goering and Hermann Stoll

Max-Planck-Institut für Metallforschung, Stuttgart, Germany

1 INTRODUCTION

The use of X-rays in the investigation of matter started with Röntgen's discovery in 1895. The very first application was the imaging of density distributions of human bodies and solids. The observation of the element-specific absorption edges has provided an effective method to measure the density of a certain atomic species, so a new tool for material analysis was born. With the support of commercially available intense X-ray tubes and effective monochromators, it was possible to resolve details of the absorption edges (Stumm von Bordwehr, 1989). In a range of several electron volts close to the absorption edge, the observed structures in the absorption coefficient could be related to the density of the unoccupied states at the absorbing atom site. This gives a new opportunity to get insight into the electronic structure of the absorbing media. A breakthrough for the interpretation of oscillatory features, observed up to several 100 eV above the transition threshold, has been achieved by Sayers, Lytle and Stern (1970) and Sayers, Stern and Lytle (1971) by a Fourier analysis technique. This provides direct information of the short-range order close to the absorbing atom.

With the advent of synchrotron X-ray sources in the 1980s, highly intense and collimated X rays of variable well-defined polarization became available. This caused the development of new powerful techniques as well as a significant improvement of the conventional ones. In the early 1980s first anomalous reflectivity studies were reported as a means to study the structure of buried interfaces and, more generally, nontransparent samples (Bremer, Kaihola and Keski-Kuha, 1980). The development of X-ray microscopy on the basis of Fresnel optics started at HASYLAB/DESY by pioneering work led by Schmahl *et al*. (1996).

Since the first experimental proof of the existence of X-ray magnetic circular dichroism (XMCD) by Schütz *et al*. (1987) at HASYLAB a new field was opened to study the magnetic characteristic of solids by various spectroscopic X-ray methods. As initially expected, these effects occur for energies close to an inner-shell absorption edge and are intimately related to the polarization of the symmetry-selected empty density of states (DOS). The subsequent theoretical development of sum rules results in a quantitative determination of local magnetic spin and orbital moments in an element-specific manner. Owing to large magnetic contributions to the absorption and scattering cross sections – up to 50% at the transition metal $L_{2,3}$ edges and the rare-earth (RE) $M_{4,5}$ edges – a magnetic moment below $10^{-5}\,\mu_B$ can be detected. In this contribution the basis of the experimental aspects and the underlying physics are presented and discussed. Selected, X-ray-related technologies

Handbook of Magnetism and Advanced Magnetic Materials. Edited by Helmut Kronmüller and Stuart Parkin. Volume 3: *Novel Techniques for Characterizing and Preparing Samples*. ISBN: 978-0-470-02217-7.

such as magnetic extended absorption fine structures (MEXAFS), magnetic reflection, and time-resolved scanning X-ray microscopy are introduced in more detail.

2 EXPERIMENTAL ASPECTS

2.1 Synchrotron radiation

2.1.1 Circular polarized X rays from bending magnets and helical undulators

Since the discovery of X rays by Röntgen at the end of the nineteenth century, Bremsstrahlung of electrons accelerated by high voltage to several kiloelectron volts is used in X-ray tubes and later for higher energies in particle accelerators. With the advent of modern electron storage rings in the 1970s, these new powerful X-ray sources have initiated a breakthrough in the application of X rays in a wide field of science and technology. The synchrotron radiation is emitted by highly relativistic electrons with energies in the gigaelectron volt range, that is, $E/m_e c^2 > 1000$, which are radially accelerated when bended onto a circular motion. The spectrum of the emitted radiation is a very broad continuum of highly collimated X rays with extremely large intensity several orders higher compared to the best X-ray tubes. The radiation has well-defined polarization, as sketched in Figure 1, for the radiation emitted from a simple bending magnet device (Schwinger, 1949). The radiation emitted in the plane of the electron orbit is linearly polarized, while viewing from above and below the center of the beam the intensity drops significantly off, but the degree of circular polarization P_C of the radiation increases drastically. Taking into account a decrease of about a factor 5, one can achieve a large value of $P_C > 90\%$.

To overcome the intensity reduction by the inclined view methods today, insertion devices such as helical wigglers and undulators are used, where an additional oscillating motion of the electrons is induced inside the special magnet structure arrangement (Sasaki, 1994). Thus, additional synchrotron radiation is emitted in the case of undulators with coherent overlap of each motion period. The polarization is adjustable by the relative horizontal position of the upper and lower magnet structure (Figure 2) (Bahrdt *et al*., 2001). In Figure 3, the brilliance of various X-ray sources is shown as a function of energy (Thompson *et al*., 2001). Typical values for bending magnets, undulators, and wigglers (the less coherent version of an undulator) are given for 1.7 GeV (like BESSY II in Berlin) and 7 GeV (like Spring 8 in Japan) electron storage rings.

2.1.2 Quarter-wave plates for fast polarization switching

In the case of visible optics, quarter-wave plates are usually used to provide circular polarized light. Typically the light beam with linear polarized **E**-vector is oriented at 45° to the two principal axes of the single crystal which provides birefringence. The **E**-vector is then split 50:50 along two different principal axes. For the correct crystal thickness one half is delayed in phase by 90° with respect to the other half, giving perfectly circular polarized light. For hard X rays, this is realized by a dynamical scattering approach and is excellently suited to provide switchable polarizations (Giles *et al*., 1994a,b; 1995; Justen, 2000; Leitenberger, 1997; Pizzini *et al*., 1998; Richter, 1992). For the generation of circular polarized X rays, the Bragg transmission mode is typically used. Such an arrangement is shown in Figure 4(a), where the quarter-wave plate is placed in the monochromatic beam just before the sample. In a simple consideration close to a Bragg condition, the interaction of the light is enhanced due to standing waves phenomena resulting in a reduction of the phase propagation, which is different for electrical polarization directions in the scattering plane and perpendicular. If

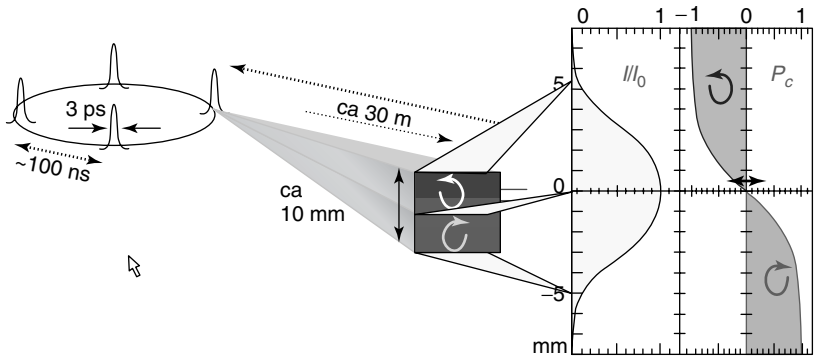

Figure 1. Synchrotron radiation emitted from a bending magnet and its polarization characteristics. Owing to the filling of the electron storage ring with electron packages this synchrotron radiation has a defined and adjustable time structure in the picosecond range.

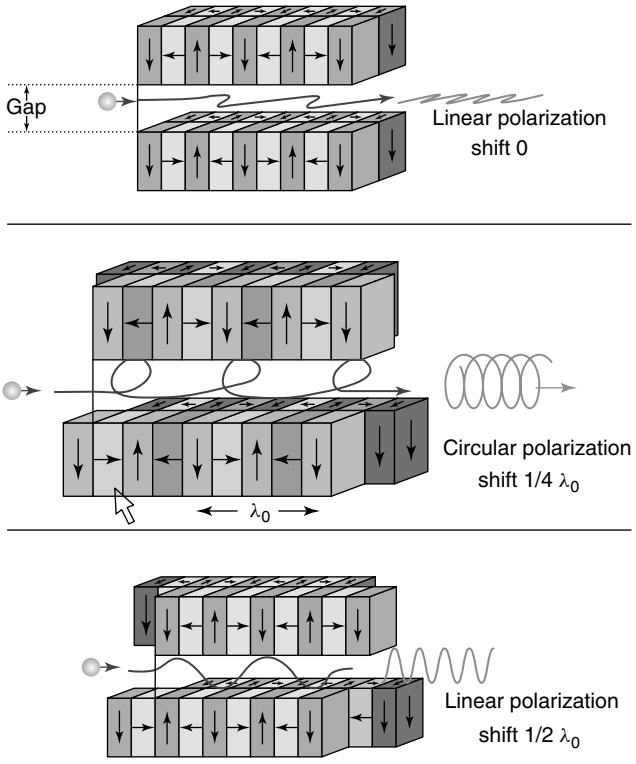

Figure 2. Magnet structure and emission characteristics of a helical undulator. The polarization can be varied by a horizontal shift of the arrangement of the permanent magnets. (Reproduced from Wende *et al*. (2004) *Reports on Progress in Physics* **67**, 2105–2181.)

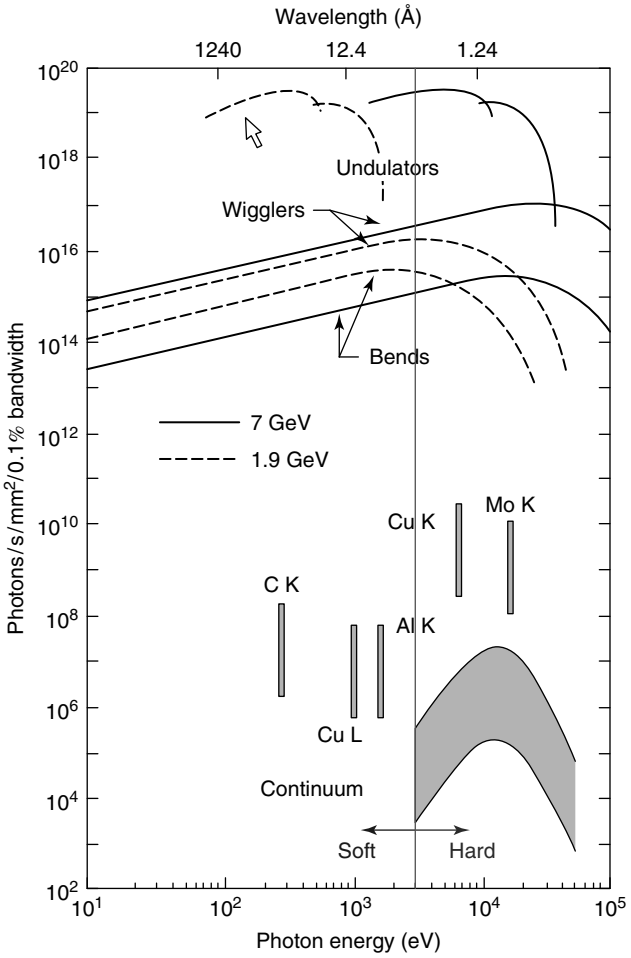

Figure 3. Brilliance in photons/s/mm^2/0.1% bandwidth for various X-ray sources in the soft X-ray range below approximately 2 keV and hard X-ray range above 2 keV. (Reproduced from Thompson *et al*. (2001) *X-ray data booklet*. LBNL.)

the scattering plane is tilted by 45° respective to the electrical field vector, a similar condition is present as for conventional quarter-wave plates as sketched in Figure 4(b). The electrical field vector is oriented parallel to the bisector between π and σ polarization [1]. The phase difference $\Delta\Phi$ between the π and σ and polarizations can be expressed analytically (Justen, 2000) by

$$\Delta\Phi(\Delta\theta) = \frac{k\chi_{\vec{h}}\chi_{-\vec{h}}\sin(2\theta)}{4} \cdot \frac{1}{\Delta\theta} \cdot \frac{\mathrm{d}}{\sin(\theta)} \qquad (1)$$

where the dielectric susceptibility

$$\chi_{\vec{h}} = \left(\frac{r_e\lambda^2}{\pi V_{EZ}}\right)^2 F_{\vec{h}} \qquad (2)$$

describes the scattering strength at a Bragg reflex $\vec{h}$ as a function of the wavelength z and $\mathrm{V}\theta_2$. $F_{\vec{h}}$ is the corresponding structure factor, normalized to the volume of the unit cell $F_{\vec{h}}$. $\Delta\theta$ is the difference angle to the corresponding Bragg condition, and d is the effective crystal thickness as shown in Figure 4(b).

As shown in Figure 4(c) $\Delta\theta$ diverges at the Bragg condition and is proportional to the thickness d. $\Delta\theta$ determines the degree of circular polarization P_C. The calculated values for equal π and σ intensities are presented in the center part of Figure 4(c). Close to the Bragg condition the circular polarization shows strong oscillations which, in reality, is smeared out due to the finite beam divergence as shown in the lower part of Figure 4(c) in combination with a measurement of the circular polarization [2]. It should be noticed that no free parameters have been used for the simulation.

To optimize the quarter-wave plate, a balance has to be found for minimal absorption realized by very thin crystal and the polarization increasing with the thickness. A careful simulation is required to determine the parameters of the set of crystals appropriate for the different energy ranges. Usually the Bragg condition will be roughly tuned by a goniometer, to the appropriate Bragg condition. The sign of $\Delta\Phi$ for off-center conditions and thus the sign of

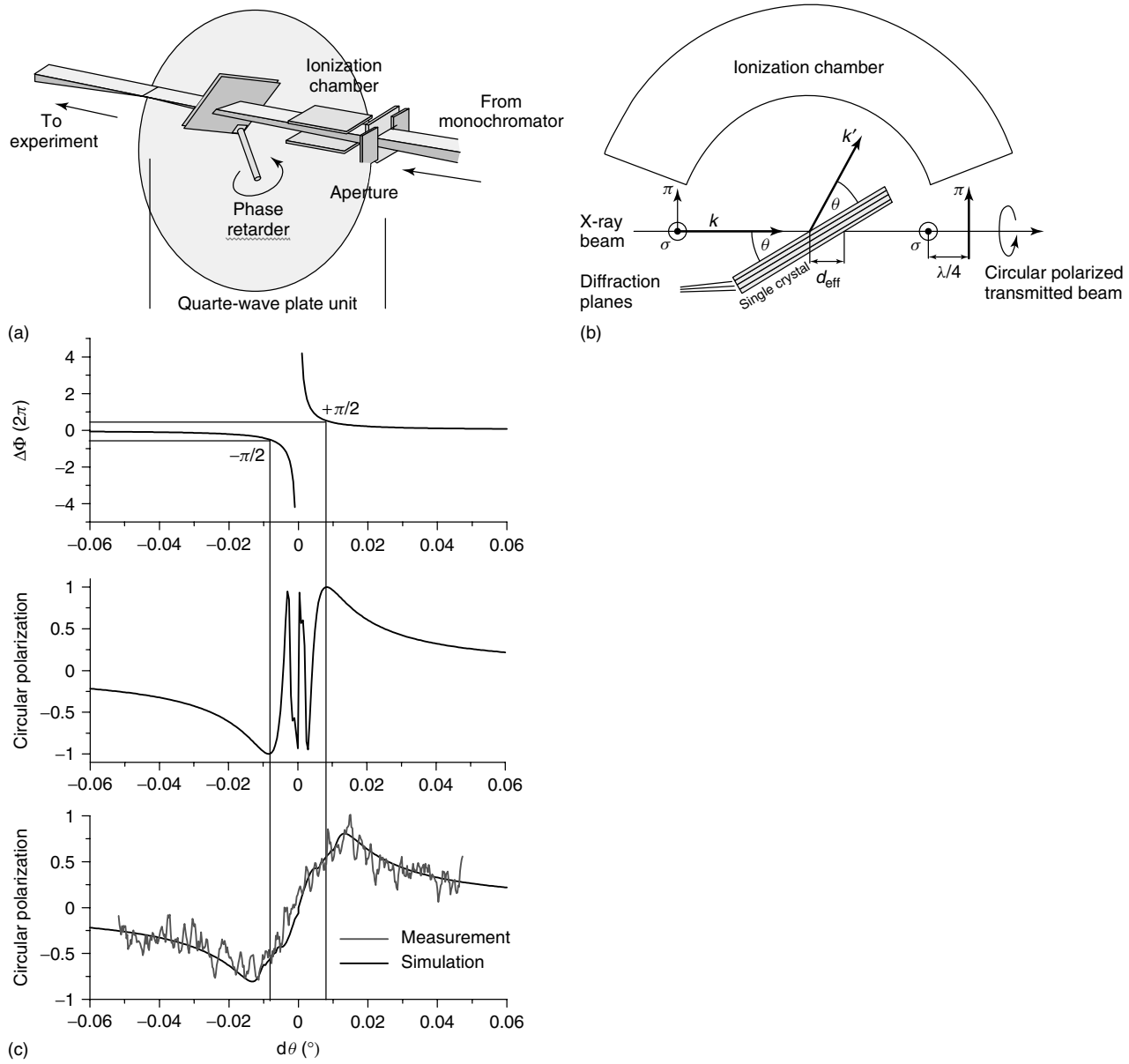

Figure 4. (a) Principle of a quarter-wave plate for the hard X-ray range. Linear polarized X rays, which are monochromatized at the Si(111)-double-crystal monochromator. The quarter-wave arrangement is positioned just before the XMCD (XRMS) experiment. (b) Principle of the function of a X-ray quarter-wave plate creating circularly polarized X-ray owing to dynamical scattering. (c) Polarization characteristics in dependence of the deviation of the Bragg angle.

the circular polarization can be changed by a fast switching piezo driver, where frequencies of 100 Hz and higher can be realized providing the opportunity to measure the XMCD effect by a lock-in technique. If the scattered Bragg intensity is also measured simultaneously [3], the exact Bragg angle could also be used to permanently retune the angle to its optimal center position. This is absolutely necessary for energy dependent measurements (Justen, 2000; Weigand, 2003) due to dynamical scattering dependent variations of the quarter-wave plate X-ray absorption (abnormal absorption (Borrmann, 1951, Borrmann, Hildebrandt and Wagner, 1955)).

2.2 XAS and XMCD: experimental aspects

2.2.1 General aspects

The interaction of photons with matter exhibits several interaction channels whose contributions vary strongly with

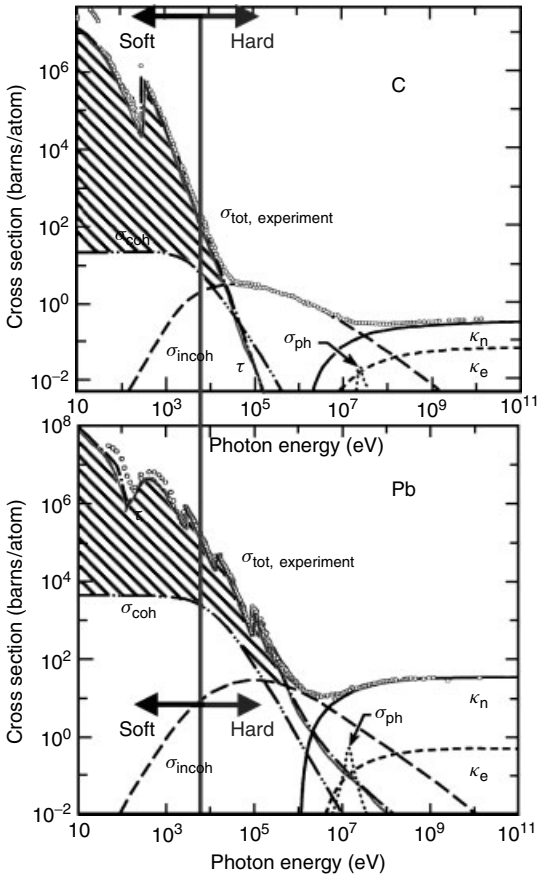

Figure 5. Carbon and lead cross section of various interaction channels of photon with matter in the energy range of 10–100 GeV. σ_{tot}: total photon cross section; τ: atomic photoeffect; κ_n: pair production (nuclear field); κ_e: pair production (electron field). (Reproduced from Thompson *et al*. (2001) *X-ray data booklet*. LBNL; Hubbell *et al*. (1980) *J. of Phys. and Chem. Ref. Data* **9**, No. 4, 1023–1047.)

energy. This is demonstrated in Figure 5, where the interaction cross sections of photons with matter from the 10 eV (VUV–range) to 100 GeV (extremely hard X rays) for the light element carbon and the heavy element lead is illustrated (Hubbell, Gimm and Overbo, 1980). For X rays in the energy range below 100 keV down to 0.1 keV, the photoeffect related absorption τ is the prominent interaction channel. In the soft X-ray range the photoeffect exceeds the Thomson scattering cross section by more than two orders of magnitude and τ drops with $E^{-7/2}$ to the credit of an increasingly inelastic scattering cross section (Bransden and Joachain, 1983).

In general, the absorption cross section σ_τ exhibits element-specific absorption edges which originate from an additional absorption possibility, if the X-ray energy reaches the element-specific binding energy of an inner atomic electron level. The off-resonant absorption edge heights are well-known tabulated values (Henke, Gullikson and Davis, 1993, 2002). The measured step feature in an absorption spectrum marks the optical density of an atomic species in a sample, and absorption spectroscopy can be used as an effective method to identify optical density of the different components of each element in a sample separately. The edges are defined as K, L, and M edges with respect to the initial atomic shell, that is, the 1s (K), 2s and 2p (L), and 3s, 3p, and 3d (M) states. In addition, the spin-orbit quantum number j is labeled, that is, $2p_{1/2}$ for the L_2 edge, $2p_{3/2}$ for the L_3 edge, $3d_{3/2}$ for the M_4 edge, and $3d_{5/2}$ for the M_5 edge. As seen in Figure 5, the photo cross section contributes only for nonrelativistic energies. Here it is set in advance to the theoretical considerations in Section 3 that in this case the dipole approximation is valid and the orbital quantum number l of final states f are changed by $l_f = l_i \pm 1$.

The formulation for the description of circular magnetic dichroism or magnetic absorption in analogy to the corresponding effects is well known for spin-dependent Compton scattering which is introduced by an additive dichroic or magnetic part of the cross section in the Klein–Nishina formula $\sigma_\tau \rightarrow \sigma_\tau \pm \Delta\sigma_\tau$. In a real experiment, the degree of circular polarization P_C is smaller than 1 and the sample magnetization $\mathbf{M}$ not fully aligned along the photon propagation direction and the experimentally determined magnetic cross section scales with the scalar product $\mathbf{P} \cdot \mathbf{M}$ resulting in $\sigma_\tau \rightarrow \sigma_\tau \pm \mathbf{P} \cdot \mathbf{M} \cdot \Delta\sigma_\tau$.

2.2.2 *Transmission method for hard X rays*

Following Lambert–Beer's law

$$I(E)/I_0(E) = e^{-\mu(E)\cdot x} \tag{3}$$

the absorption coefficient

$$\mu(E) = \sum_i \frac{N_A}{A_i} \cdot \sigma_{\mathrm{tot,i}},(E) \cdot \rho_i \tag{4}$$

which is correlated to the inverse penetration depth, can be related to the ratio between incident $I_0(E)$ and transmitted intensity $I(E)$ through a sample with thickness x as sketched in Figure 5(a). For a real target it is a summation over all elements i with atomic weight A and density ρ (g cm^{-3}), and directly correlated to the energy dependent absorption cross section as drawn in Figure 5.

Hard X rays can penetrate samples of thicknesses of typical several μm, where the mean free path strongly decreases with the atomic number by Z^5. Appropriate samples are free-standing polycrystalline foils, possibly covered with evaporated thin target films, or powder targets fixed on tapes consisting of soft matter such as Kapton or hard Si_3N_4. To take a circular dichroic spectrum, which requires in a

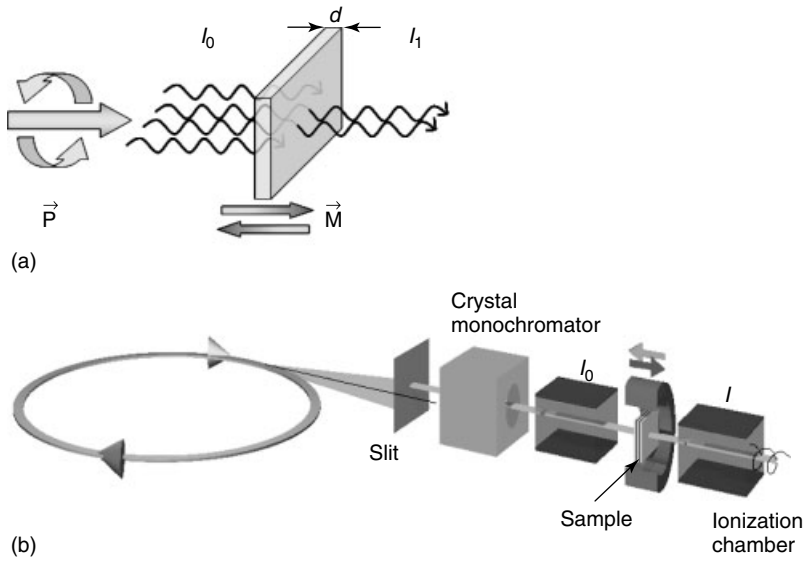

Figure 6. (a) Principle of the measurement of XMCD in the transmission mode for hard X rays. (b) Experimental realization of (a) for hard X rays emitted from a bending magnet by the inclined view method. Formed by a proper deposited slit and monochromatized by a crystal monochromator (Si111/Si311/Ge111) the incident and transmitted intensity is monitored by ionization chambers. The magnetization of the sample mounted inside an electromagnet is periodically reversed.

simplest way the reverse of the sample magnetization, the radiation is monochromatized by a crystal monochromator and the incident and transmitted intensity I is monitored by ionization chambers as a function of the photon energy. The magnetic sample can be mounted inside a solenoid, providing a reversible magnetic external field. In the case of a thin polycrystalline foil, where in general, the magnetization lies in plane, the sample has to be tilted with respect to the photon beam direction resulting in a nonvanishing projection of the magnetization along the photon beam direction. A typical arrangement is shown in Figure 6(b), where a magnetic multilayered sample has an easy direction perpendicular to the plane.

2.2.3 *Soft X rays*

In the case of soft X rays the absorption is stronger by 1 to 2 orders of magnitude and the corresponding exponential penetration depth decreases down to the nanometer range. Therefore, a conventional transmission experiment is very hard to accomplish. For this type of conventional absorption measurement it is necessary to prepare thin-film samples, quite similar to the techniques known from transmission electron microscopy. In the case of thin-film systems it is an established method to prepare samples on extreme window-like thinned substrates, typically made of SiN. Owing to this relative complex sample preparation, the absorption coefficient is usually measured indirectly by two secondary processes called *total electron yield* (*TEY*) and *total fluorescence yield* (*TFY*). In the case of TEY the basic physical process is the excitation of Auger electrons, which thermalize by creating a large number of secondary electrons by inelastic e–e scattering processes. For TFY the characteristic fluorescence light emitted by the de-excitation of the core hole is detected. These intensities are proportional to the number of absorption events per volume and therefore proportional to the absorption process itself. This proportionality is quite good in terms of TEY and less reasonable in cases of TFY. A sketch of the experimental setup is shown in Figure 7(a).

Total electron yield (TEY)

Owing to the very short escape length of the Auger electrons the secondary electrons of lower energies are the dominant fraction of the total electron current and as seen in Figure 7(b) the escape depth increases from 50 eV to lower energy (Zangwill, 1988). Only Auger electrons close to the surface (a few angstroms) have the possibility to leave the sample without being involved in an inelastic electron–electron scattering process. The scattered electrons will excite many other electrons resulting in a shower of low-energy electrons, so-called secondary electrons, where a large fraction will migrate from a region of a few nanometers to the surface. Electrons with an energy above the electron work function, that is, the energy needed to leave the surface, have the possibility to escape into the vacuum (Figure 7c). The circular polarized synchrotron radiation hits the sample and excites electrons inside the sample. The total electron drain

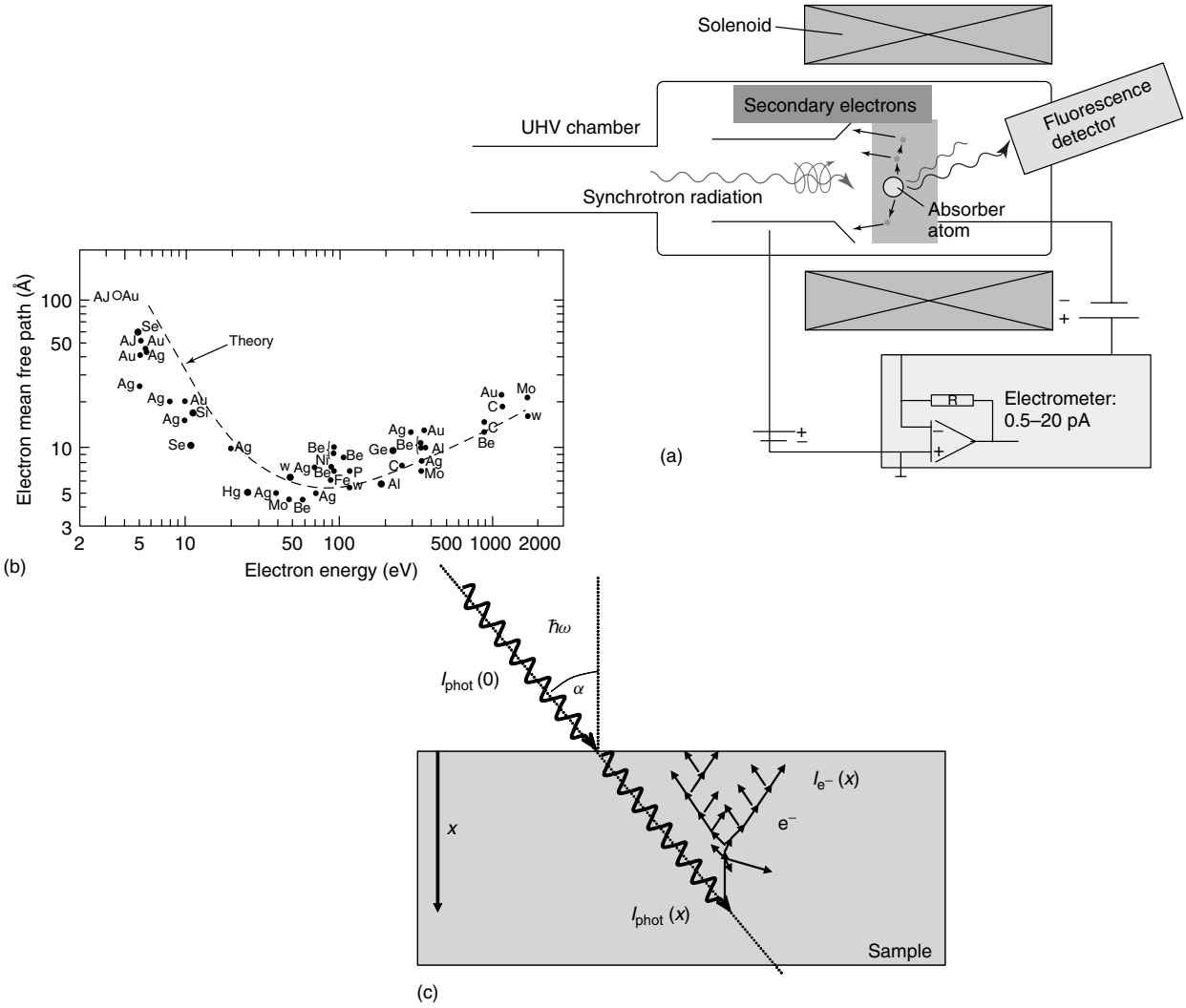

Figure 7. (a) Principle of measurement of XMCD in the soft X-ray range. The absorption coefficient can be detected via the fluorescence radiation of the sample current after emission of the secondary electrons the sample surface, (b) mean-free electron scattering length as a function of energy (Reproduced from Zangwill (1988) *Physics at surfaces*, Cambridge Univ. Press, Cambridge.), (c) important values for the estimation of the relation of the sample current and the absorption coefficient.

current (TEY signal) is measured by a very sensitive electrometer connected to the ground or by an external electron detector like channeltrons, channelplates, or similar detectors. For magnetic absorption measurements, the sample should be magnetized preferentially parallel and antiparallel along the photon beam direction by using a switchable magnet (permanent or current driven).

As quantitatively discussed in the appendix, the electron current is in good approximation proportional to the absorption coefficients

$$I_{e^-}(x) = k \cdot I_{\text{phot}}(0) \cdot \frac{\mu(E)}{\cos\alpha}\xi \qquad (5)$$

where ξ is an effective exponential decay length of the secondary electrons, α is the angle respective to the surface normal, $\mu(E)$ is the energy dependent absorption, and $I_{\text{phot}}(0)$ is the photon beam intensity at the surface. The effective exponential decay length ξ is in a first approximation an energy average over the electron scattering length curve as shown in Figure 7(b), and well known in photoemission spectroscopy.

Nevertheless, for a very short photon absorption length – compared to the electron escape length – the resonant absorption is damped by the so-called saturation or self-absorption effect. A detailed discussion is also given in the Appendix.

In reality the electrons will perform spiral-like traces in an applied magnetic field, where some of the electrons can even be redirected to the sample, reducing the total measured electron current. To reduce this effect, the sample is usually

set to a negative bias voltage by a nearly noise-free DC power supply. This reduces the backscattering probability and enhances the overall performance, especially when measuring the difference between opposite field directions to measure XMCD.

Total fluorescence yield (TFY)

In the case of TFY, the core-hole excitation is monitored by the emitted fluorescence photons. The strength of this decay channel is determined by the fluorescence yield, strongly increasing with the atomic number and is less than 1% for K edge at oxygen and L edges at 3d elements and 20% for 3d K edges and L edges. This small number of events dramatically modifies the statistical quality of the X-ray absorption spectra (XAS) (XMCD) data especially in the soft X-ray range. Therefore, it is typically necessary to probe a significant number of absorption processes using TFY, which could be realized by intensive undulator radiation from second generation synchrotron sources like ESRF and BESSY II. On the other hand, fluorescence photons have much higher decay lengths compared to the secondary electrons in the TEY, providing less surface sensitivity and more reliable bulk information. TFY is therefore more appropriate for systems with buried layers compared to the electron escape length, or systems where the main interest is related to probe the bulk properties, whereas TEY provides more surface-sensitive information on intrinsic-like surface variations or chemical or structural modifications.

Nevertheless, for a quantitative XAS and XMCD analysis TFY is quite problematic due to the strongly enhanced self-absorption processes. In principle, this could be handled numerically similar to the above described TEY self-absorption correction, but the typical systematic error is much higher. In this case the mathematical procedure needs the attenuation lengths for both photon types, the primary beam and the fluorescence. The latter could be quite problematic, especially when the energy distribution of all TFY decay channels is not simple or even known, for example, if the TFY photons have a main distribution in the X-ray region and an additional contribution in the UV region [4]. In this case, two different escape length scales are present, preventing the simple analysis.

2.3 Circular magnetic X-ray dichroism spectra

2.3.1 History

As theoretically outlined in Section 3 in the vicinity of the absorption edges the occurrence of X-ray magnetic circular dichroism is expected as a universal effect and experimentally verified. XMCD was initially measured as the difference of the absorption coefficient for circularly polarized X rays for reversed magnetization of the absorber. The circular dichroic or magnetic absorption profile $\mu_C(E)$ or $\Delta\mu(E)$ are related to the measured differences for projection of the saturation magnetization parallel (μ^+) and antiparallel (μ^-) onto propagation direction of the circularly polarized photon beam by $\mu^+(E) - \mu^-(E) = P_C \cdot \boldsymbol{M(T)/M(0)} \cdot \mu_C\ (E)$. These values are deduced from the experimental data by a rescaling of the difference, taking into account the incomplete circular polarization, the sample magnetization alignment with respect to the photon beam and the achieved degree of saturation magnetization at the finite temperature.

First evidence of the existence of XMCD or magnetic absorption was found in the hard X-ray range at the K edge of iron metal (Schütz *et al*., 1987). The effect is smaller than 1% as sketched in Figure 8 where the original data provides an experimental accuracy of 10^{-4}. This was high enough to manifest the occurrence of the effect in the near edge and the extended absorption X-ray fine structure (Schütz *et al*., 1987). Also in the hard X-ray range it has been found that at the Gd and Tb metal $L_{2,3}$ edges (Schütz *et al*., 1988, 1989) and subsequently at the corresponding absorption in 5d impurities much stronger XMCD signals up to more than 20% have been measured as shown again by the original data (see original data from Schütz *et al*. (1988, 1989) in Figure 9). One year later the corresponding experiments were performed at the $L_{2,3}$ edges in the 3d transition metals (TMs) (Chen, Sette, Ma and Modesti, 1990) as shown in Figure 10.

In the meantime, XMCD studies for a large number of elements in various systems have been performed and the method is established as an important tool to address element-specific magnetic structures and a large variety of phenomena and aspects in magnetism.

2.3.2 Systematics of XAS and XMCD at the L edges in 3d metal systems

The XMCD spectra at the $L_{2,3}$ edge of the 3d TMs are the most important phenomena studied as can be understood by the theoretical consideration in Section 3. The energy region, in which these edges occur, is located in the soft X-ray energy range between 400 and 1000 eV. To give an overview a typical 3d metal series of the $L_{2,3}$ edge XAS and XMCD spectra are shown in Figure 11. The visible XMCD effect is strong and pronounced and could achieve about 50% of the white line intensity, reflecting the strong and intensive magnetic cross sections. General trends in the 3d metal series could be observed. For the nonmagnetic XAS, the observed total linewidth is increasing for the light TMs. This is in contrast to the behavior of the lifetime broadening (Fuggle and Alvarado, 1980), but reflecting the increase in

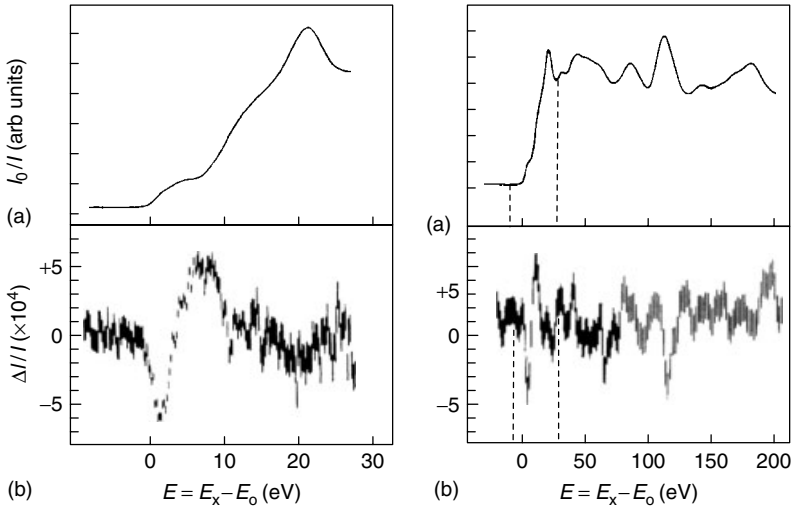

Figure 8. First experimental proof of the existence of magnetic absorption of XMCD found in the hard X-ray range at the K edge at 7111 in an iron foil corresponding to the origin of the energy scale. The transmission I_O/I (a) and the difference for opposite magnetization of the sample $\Delta I/I$ (b) was detected in a similar arrangement as sketched in Figure 4(b) but with the cold rolled Fe foil tilted with 30° with respect to the photon beam. (Reproduced from Schütz *et al*. (1987) *Physical Review Letters* **58**, 737–740.)

the number of unoccupied states. So, for the heavy TM the 3d shell is nearly filled up and only a fraction of typical e_g character is available for resonant core level excitations. For the light TM the major part of the 3d shell is empty, providing a large number of possible excitation channels and broader XAS structures, according to the broader unoccupied fraction of the DOS. General trends are also observable for the XMCD spectra. For the heavy TM the XMCD spectra reveal a simple structure, with a 'down peak' at the L_3 edge and an 'up peak' at the L_2 edge. For the light TM, the shape of the XMCD spectra becomes more complicated.

Without discussing all the details of the spectra, which are based on complicated band structure details, two predominant features could be identified. The simple 'up–down structure' is now superimposed by a peak derivative-like structure, and at the threshold of the transition another relative sharp feature appears. The first mentioned derivative-like structure has been identified by an increase in the number of unoccupied states, providing a related ground-state moment feature with peak derivative-like structures (van der Laan, 1997a,c,d), while the second feature represents the partial empty t_{2g} states.

2.3.3 XAS and XMCD in rare-earth metals

The RE elements, that is the lanthanide series, also play an important role in the field of magnetism. This is related to the unusual properties of the 4f shell electrons. Owing to the fact that the $4f^n$ state is of atomic character the 4f electrons exhibit well-known magnetic states following Hund's rules. Relatively large effects at the $L_{2,3}$ edges, found in the hard energy range between 5 and 10 keV, are shown in Figure 9. They can be observed in any RE metals system as demonstrated by a systematic study of the RE_2Co_{17}-system (Fischer, Schütz and Wiesinger, 1990). The absorption edge itself, which is energetically split by several 100 eV, is a clear step function superimposed by the so-called white line feature. In its vicinity, the XMCD signals in the order of percent are found. Especially at the low-energy side of the $L_{2,3}$ edges, except for Ce and Gd, pronounced negative contributions are visible (see Figure 12).

In contrast to the L edge of the RE metals, in which a photoelectron transition $2p \rightarrow 5d$ is involved, the $M_{4,5}$ edge absorption, located in the soft-energy range, probe the magnetic 4f state which is highly polarized. Both spin-orbit states are separated by 20–50 eV and the strong absorption lines, which exhibit a pronounced fine structure, are superimposed on a very small step function. The XMCD signal also shows sharp derivative-like features. Typical spectra of the Gd and Sm $M_{4,5}$ edges are shown in Figure 13.

3 THEORETICAL MODELS AND NEW INSIGHTS INTO MAGNETISM

3.1 XANES and its relation to local electronic structures

Following Fermi's golden rule, the one electron absorption cross section is described by Bransden and Joachain (1983)

and Cowan (1981)

$$\mu(\hbar\omega) \propto \sum_{\mathrm{f}} \left|\left\langle \psi_{\mathrm{f}} \left| \vec{p} \cdot \vec{A} \right| \psi_{\mathrm{i}} \right\rangle\right|^2 \delta(E_{\mathrm{f}} - E_{\mathrm{i}} - \hbar\omega)$$
$$= |M_{\mathrm{fi}}(E)|^2 \cdot \rho(E) \qquad (6)$$

Thus, the absorption coefficient is directly proportional to the square of the dipole transition matrix element times the density of the final states. The dipole selection rules $\Delta l = \pm 1$ allows only transitions from initial s to a final p state. Thus, the K-edge absorption near edge structure represents the density of the unoccupied p states with an energy spread of

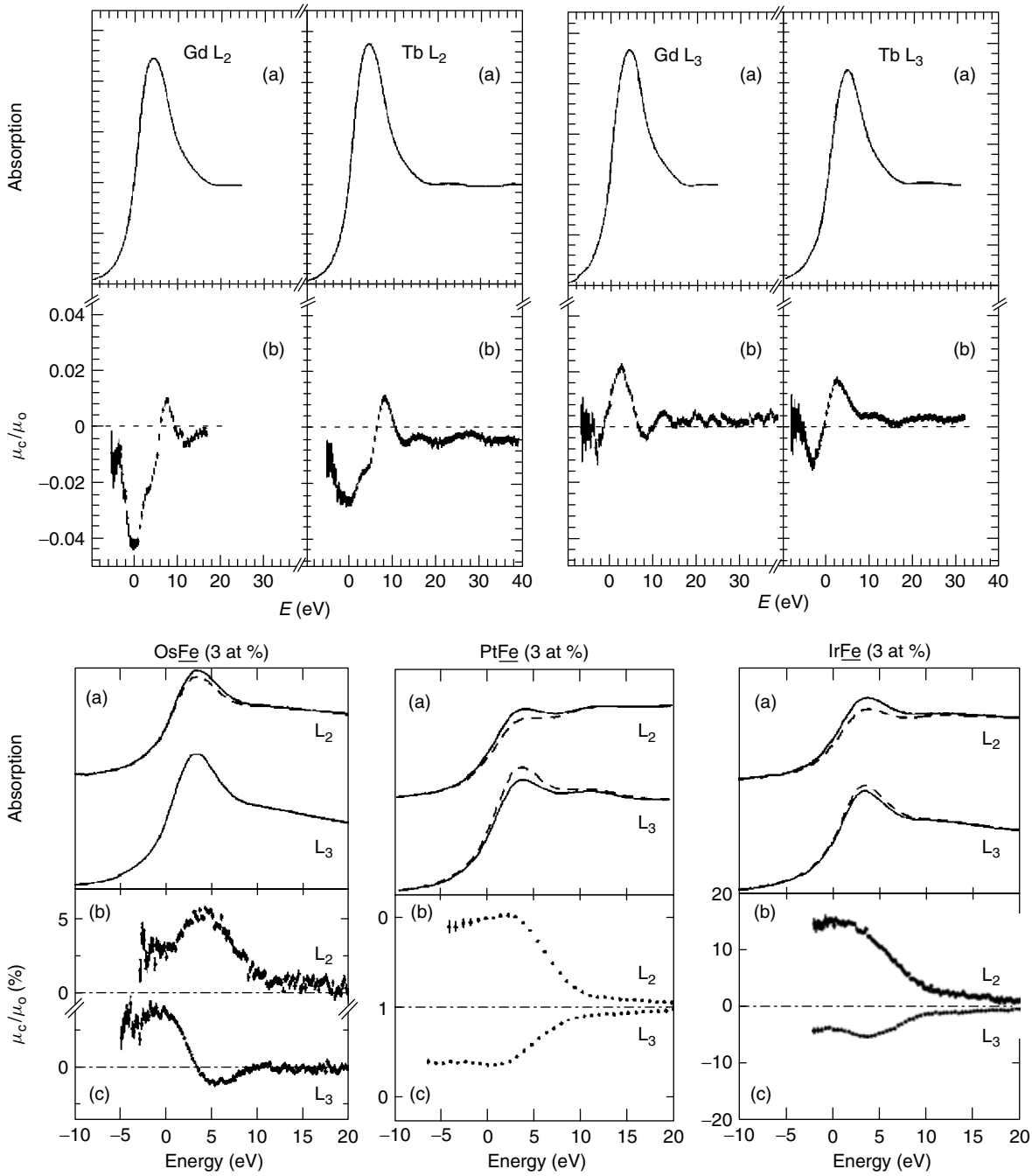

Figure 9. $L_{2,3}$ dichroic signals at Gd and Tb metal (Reproduced from Schütz *et al*. (1988) *Zeitschrift für Physik B: Condensed Matter* **73**, 67–75.) and Os, Ir, and Pt impurities in iron (Reproduced from Schütz *et al*. (1989) *Zeitschrift für Physik B: Condensed Matter* **75**, 495–500.), where the giant effects of larger than 20% have been observed. The absorption and the relative magnetic absorption coefficients $\mu_{\mathrm{C}}/\mu_{\mathrm{O}}$ have been measured in the same experimental arrangement as in Figure 6 (Schütz *et al*., 1988).

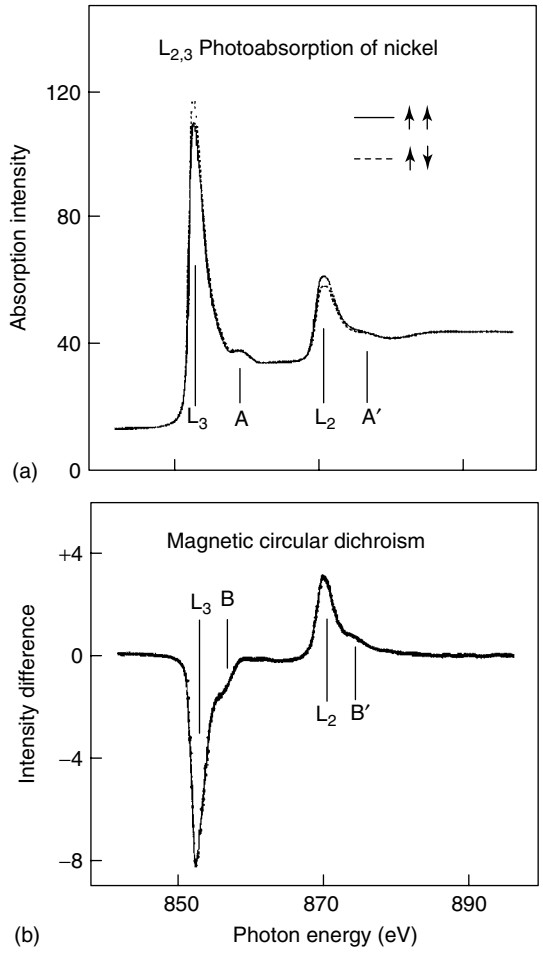

Figure 10. First evidence of soft X-ray XMCD observed at the Ni $L_{2,3}$ edge in the pure metal studied by TEY measurements using the inclined view method and the experimental setup as shown in Figure 7. (a) XAS and (b) XMCD of Ni. (Reproduced from Chen *et al*. (1990) *Physical Review B* **42**, 7262–7265.)

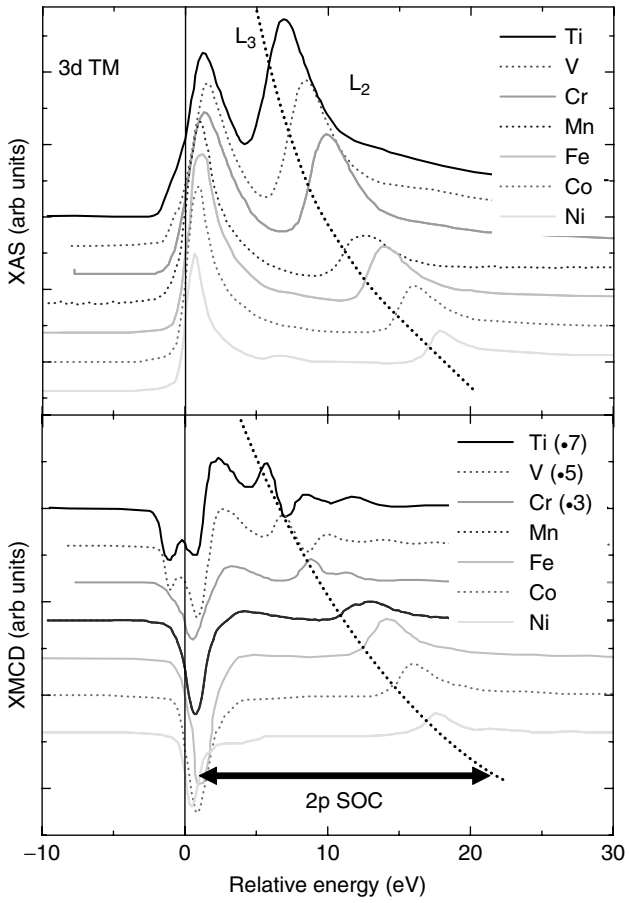

Figure 11. XAS and XMCD spectra of the whole 3d series. The splitting between the L_3 and L_2 edges increases with nuclear charge and the related 2p spin-orbit split energy (SOC), as indicated by the dotted line. All spectra have been aligned in energy at the half height of the L_3 edge. All spectra have been extracted from (Scherz, 2003), except the Mn spectra are from (O'Brien and Tonner, 1994).

several electron volts. For atoms with a large nuclear charge, the information of the fine structure is smeared out by the strong lifetime broadening effects, due to the fast decay of the core hole (Krause and Oliver, 1979). It is about 1 eV at the K edge of 3d transition elements with energies between 5 and 9 keV due to the fast decay of the created core hole. After excitation of a $2p_{1/2}$ and $2p_{3/2}$ electron, corresponding to the $L_{2,3}$ edges, final s and d states are populated, whereby the strengths of the matrix elements is, for the $p \rightarrow s$ transition, weaker by a factor 100 and often neglected [5]. At the 3d L edges of 3d transition element with energies in the soft X-ray range between 400 and 1000 eV the lifetime widths are smaller. Owing to the stronger radial overlap of the 2p level with the final more localized d states, the matrix element has a resonance-like character resulting in prominent white line features and for the 3d elements very fine details of the final state density are measured and splitting is directly observable. For 4d and 5d L edges this broadening is of the order of 5 eV. This is demonstrated in Figure 14 showing a comparison of the final p and d projected DOS to the corresponding K and L X-ray absorption near edge spectroscopy (XANES) spectra.

Owing to fast decay, via Koster–Kronig radiationless transitions, the p levels of M and N states are too broad and not suitable for XANES analysis.

The final state structure for the $M_{4,5}$ edges of the RE elements is not related to band structure-like features, due to the small Coulomb interaction of the 4f electrons and the valence band, where the 4f energy could be considered as atomically sharp. Therefore, the transition from the 3d shell to the 4f shell could be treated in an atomic multiplet calculation, where on-site 4f correlations and 3d–4f hole interactions are relevant for the shape of the spectra.

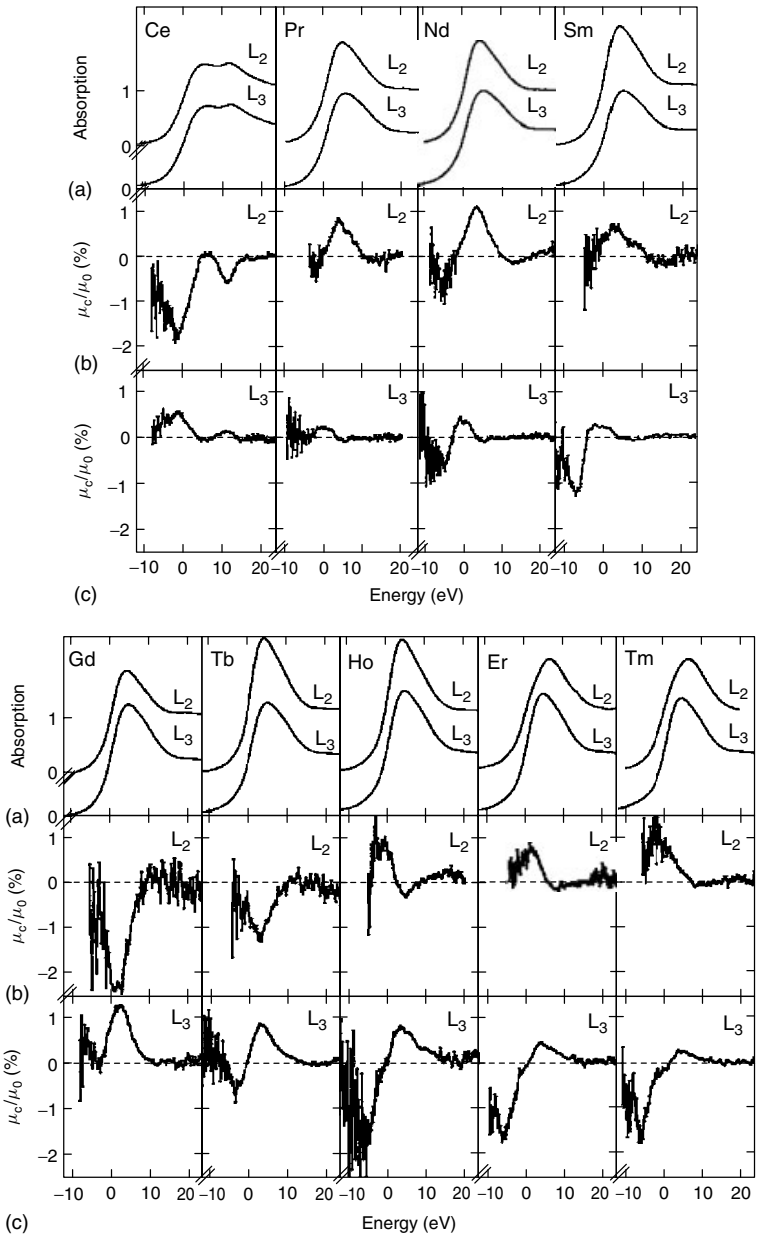

Figure 12. XAS and XMCD spectra at the $L_{2,3}$spectra of a series of rare-earth elements in the compound RE_2Co_{17}. (Reproduced from Fischer *et al*. (1990) *Solid State Communications* **76**, 772–781.)

3.2 The two-step model for XMCD

Step 1: The origin of the occurrence of XMCD as a universal effect is simply explained by basic quantum-mechanical vector coupling rules. When a circularly polarized photon beam is absorbed, an additional constrain is that the magnetic orbital quantum number has to be changed by $\Delta m = +1$ or -1 for right or left-handed photons [6]. The consequence for an absorption of a right circular polarized photon beam in an initial $p_{1/2}$ state is illustrated in Figure 15(a), where the initial level is separated for the different m components of the $j = 1/2$ and their statistical weight. Taking into account that the Clebsch–Gordon coefficients for the coupling of an initial electron state photon beam to the initial and final d state, prefer strongly the $m_i = 1$ to the $m_f = 2$ state transition to the credit of the transition $m_{il} = -1$ to the $m_{fl} = 0$. This shows that the spin character of the photoelectron in the final state is negative. The polarization of its angular momentum is, on the other hand, strongly positive since $m_l = +1$ and m final states are populated. The expectation values of the spin and orbital polarization with respect to the quantization axis z, that is, the photon **K** vector, are $\langle \sigma_z \rangle = -1/2$ and

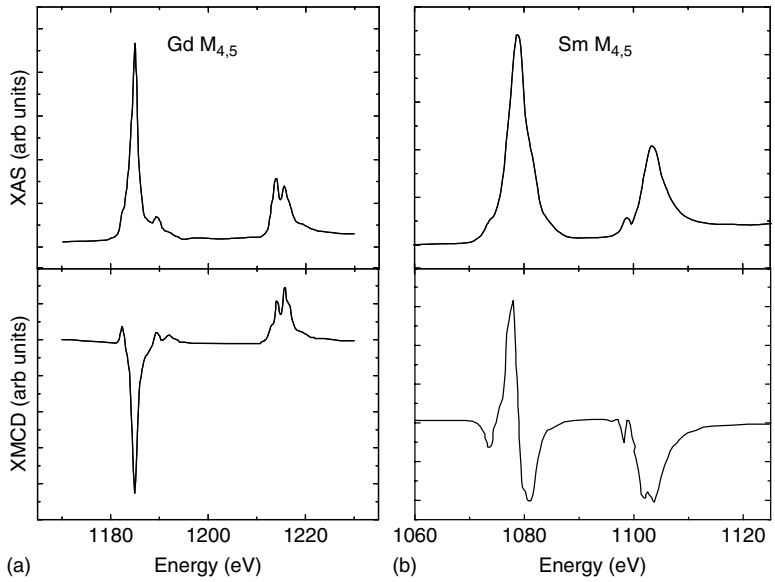

Figure 13. (a) Shows the nonmagnetic and the magnetic absorption spectra at the Gd $M_{4,5}$ edges of a GdFe thin-film system (From Peters *et al*., 2004.) and (b) shows the corresponding Sm $M_{4,5}$ spectra of a Sm_4As_3 sample. (From Suga and Imada, 1996.)

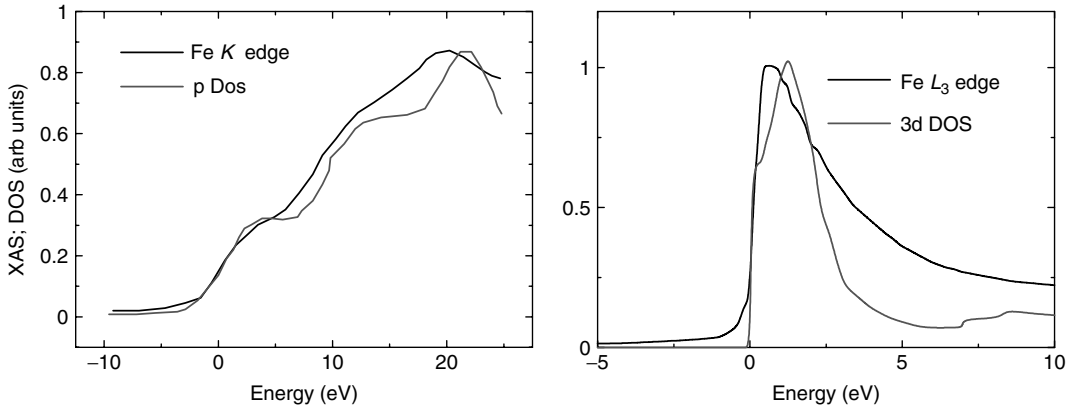

Figure 14. Relation of the Fe K- (Stähler, Schütz and Ebert, 1993)and L_3 - (Chen *et al*., 1995) absorption coefficient in Fe to the p- (Stähler, Schütz and Ebert, 1993) and d-projected density of the final unoccupied states at the Fermi level.

$\langle l_z \rangle = +3/4$. The analogous calculation for an initial $p_{3/2}$ level results in opposite spin but identical orbital polarization $\langle \sigma_z \rangle = +1/4$ and $\langle l_z \rangle = +3/4$.

In the transition $s \rightarrow p$ for a right circularly polarized photon the only transition possible is the transition $m_i = 0$ to $m_f = +1$ creating a final photoelectron with $\langle \sigma_z \rangle = 0$ and $\langle l_z \rangle = 1$. This implies that in the absorption process of a circularly polarized photon beam, only an orbital polarized photoelectron without spin polarization is created. The corresponding values can be seen in Figure 15(b).

This phenomenon of the creation of spin-polarized electrons is only a result of simple quantum-mechanical vector coupling rules where magnetic states play no role at all. On the basis of the same effect, the excitation of a selected $p_{3/2}$ occupied band state close to the Fermi level in GaAs photocathode (Pierce and Meier, 1976) to a $s_{1/2}$ vacuum level by a circular polarized 1.42 eV light is commonly used as an effective source for spin-polarized electrons.

Step 2: The magnetism in this model is introduced by the fact that, in the vicinity of an absorption edge in a magnetic material, the final state DOS is spin split in a simple band structure model. Therefore, the excitation probability of polarized excited electrons depends on the spin-polarized DOS of the final state atom, and the strength of the absorption depends on the polarization of the empty states available in the absorption process following Pauli's exclusion principle [7]. This results in a difference in the absorption coefficients for flipping the light helicity of the photon beam with respect to the sample magnetization. For spin-only systems this fact can be simply implemented into Fermi's golden rule

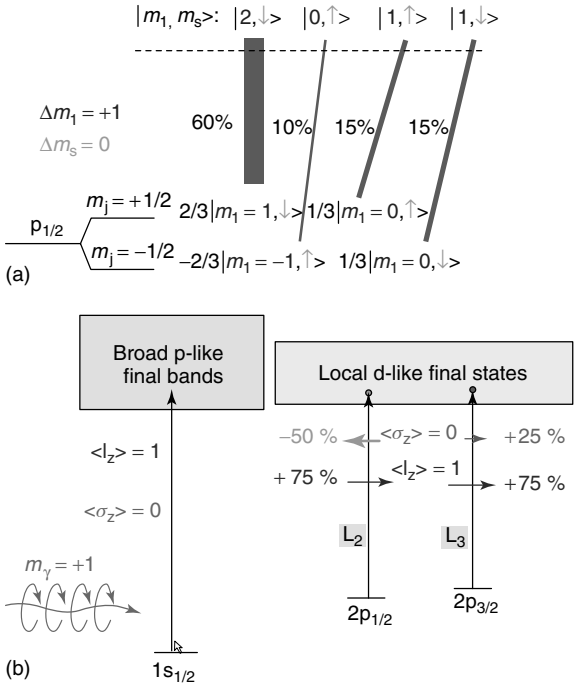

Figure 15. (a) Transition probabilities from the different $m_j = \pm 1/2$ configuration (energetically identical) of the $p_{1/2}$ spin–orbit coupled level separated into the two possible $m_l m_s$ configurations to a final d state in an L–S coupling scheme of initial and final states. The numbers before the sets indicate their statistical weights corresponding to the square of the Clebsch–Gordon coefficients. (b) Spin and orbital polarization of the photon in an initial $1s_{1/2}$, $2p_{1/2}$, and $2p_{3/2}$ atomic level corresponding to a K, L_2, and L_3 absorption.

$$\mu_{\pm}(E) = \mu_0(E) \pm \mu_C(E) \propto \sum_{|f\rangle |i\rangle} |\langle f| \mathbf{W}(E) |i\rangle|^2 \times \left(\rho_{|f\rangle}(E) \pm \langle \sigma_z \rangle \cdot \Delta\rho_{|f\rangle}(E)\right) \tag{7}$$

or simplified to

$$\frac{\mu_C(E)}{\mu_0(E)} = \langle \sigma_z \rangle \cdot \frac{\Delta\rho_{spin}(E)}{\rho(E)} \tag{8}$$

Thus, the measured signal in this simple model is directly correlated to the spin density difference of the unoccupied states.

To illustrate how the information on the spin density difference is related to the local magnetic spin moment, see Figure 16, a simple model of the formation of local magnetic d moments in the band structure picture is drawn. The magnetic d moment corresponds to the spin density difference of the occupied part $m^{occupied}(\mu_B) = \int_{-10\,eV}^{0} \Delta\rho(E)dE$ integrated from the lower band edge at about -10 eV edge to the Fermi level $E = 0$, which is nonzero due to the energy shift of the majority and minority contribution with respect to the Fermi level. It is assumed that the complete d band,

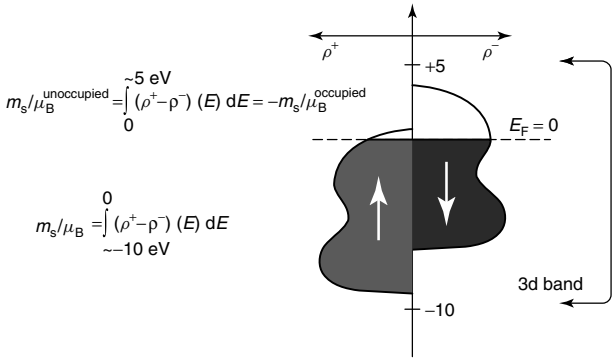

Figure 16. Correlation of the integrated density of the unoccupied state to the local moment carried by the occupied spin-split 3d states.

consisting of the occupied part and the unoccupied part, contains five up and five down electrons. An integral covering the whole d band has to vanish

$$m^{total}(\mu_B) = \int_{-10\,eV}^{+5\,eV} \Delta\rho(E)\,dE = 0 \tag{9}$$

Thus, the 'hole' moment carried by the spin density difference of the unoccupied part is given by $m^{unoccupied}(\mu_B) = \int_0^{+5\,eV} \Delta\rho(E)\,dE = -m^{occupied}(\mu_B)$. On the basis of this simple picture one can find a simple relation of the integrated XMCD signal to the local magnetic spin moment following equation (9)

$$m^{occupied}(\mu_B) = -\int_0^{+5\,eV} \Delta\rho(E)\,dE = -\langle \sigma_z \rangle \frac{\int \mu_C(E)\,dE}{\int \mu_0(E)\,dE} \cdot \int \rho(E)\,dE \tag{10}$$

where $\int \rho(E)\,dE$ is the 'number' of holes.

If an orbital polarization has to be taken into account one can show that, on the basis of the L–S coupling scheme of initial and final state, an additive contribution occurs

$$\frac{\mu_C(E)}{\mu_0(E)} = \langle \sigma_z \rangle \cdot \frac{\Delta\rho_{spin}}{\rho} + \langle l_z \rangle \cdot \frac{\Delta\rho_{orbit}}{\rho} \tag{11}$$

with $m_{spin}(\mu_B) = -\int \Delta\rho_{spin}(E)\,dE$ and $m_{orbit}(\mu_B) = -\int \Delta\rho_{orbit}(E)\,dE$.

Since the sensitivity on the spin moment has a different sign at both edges, but the sensitivity to the orbital moment is identical, a comparison of the dichroic profiles at L_2 and L_3 XMCD by a proper addition/subtraction is able to cancel either spin or orbital moment sensitivity. This is the basis of the sum rules developed in a more complex theoretical framework, which are discussed in the following chapter, but resulting in the same final formulae for cubic symmetry.

3.3 Sum rules

3.3.1 General formulation

The phenomenon of XMCD has been described by a more sophisticated theory, resulting in the 'sum rules', providing a separation of the spin and orbital contributions to the absorption difference. This has been derived by the pioneering work of Carra, Thole, Altarelli and Wang (1993) and Thole, Carra, Sette and van der Laan (1992), who investigated theoretically the transition probabilities of the core electrons depending on different ground-state properties of the sample, providing spin orbital and magnetic dipole term projections. One key issue was the elimination of the radial matrix elements using the ratio of magnetic and nonmagnetic absorption profiles. The first experimental verification of the sum rules have been done for the $L_{2,3}$ edges in the work of Chen *et al.* (1995). This was the starting point, where the number of papers using XMCD sum rules exploded during the following years. In this correct description an important new aspect in magnetism has to be taken into account: the aspheric spin contribution, described by the so-called magnetic dipole term T_z, which might occur in noncubic systems. Similar to the simple two-step model, described above, to deduce the spin and orbital momentum and the T_z term, the areas of the nonmagnetic absorption spectra (XAS) and the corresponding magnetic difference (XMCD) have to be analyzed.

Here too, the ground-state number of the unoccupied states of the final state shell has to be known.

The expressions as developed by Thole and Carra are given here:

$$\frac{-\int_{j_+ + j_-}\left(\mu^+(E)-\mu^-(E)\right)\cdot \mathrm{d}E}{\int_{j_+ + j_-}\left(\mu^+(E)+\mu^-(E)+\mu^0(E)\right)\cdot \mathrm{d}E} = a\cdot\frac{\langle \mathrm{L}_z\rangle}{n_h}$$
$$\frac{-\left(\int_{j_+}\left(\mu^+(E)-\mu^-(E)\right)\cdot \mathrm{d}E - b\cdot\int_{j_-}\left(\mu^+(E)-\mu^-(E)\right)\cdot \mathrm{d}E\right)}{\int_{j_+ + j_-}\left(\mu^+(E)+\mu^-(E)+\mu^0(E)\right)\cdot \mathrm{d}E}$$
$$= \frac{c\cdot\langle \mathrm{S}_z\rangle + \mathrm{d}\cdot\langle \mathrm{T}_z\rangle}{n_h} \qquad (12)$$

Here, $n_h = 4l_\mathrm{f} + 2 - n$ is the number of holes present in the final state shell.

l_f and l_i are the orbital angular momentum quantum numbers of the final and initial states, which are connected to each other by the dipole selection rule as $l_\mathrm{f} = l_\mathrm{i} \pm 1$. $\langle \mathrm{S}_z\rangle$, $\langle \mathrm{T}_z\rangle$, and $\langle \mathrm{L}_z\rangle$ are the expectation values of the spin, dipole term, and orbital moment projection along the z (photon beam) direction. The values for the prefactors a–d are shown in Table 1.

Table 1. Sum-rule related prefactors.

l_i	l_f	a	b	c	d
s:0	p:1	1	–	–	–
p:1	d:2	1/2	2	2/3	7/3
d:2	f:3	1/3	3/2	2/3	2

It is important to mention that for s-shell absorption ($l_\mathrm{i} = 0$) without spin-orbit splitting (SOC) in the initial state, no spin and no dipole term contributions are observable with XMCD. On the other hand, the spin moment could not be extracted without the contribution of the dipole term $\langle \mathrm{T}_z\rangle$, which will be discussed later.

Usually, the absorption is just measured for the left and right circular polarized light, and the absorption of z-polarized light is not known. This part is approximated by the average of the two circular polarized absorption coefficients. Therefore, the integral in the denominator reduces to

$$\mu^+(E) + \mu^-(E) + \mu^0(E) \approx \mu^+(E) + \mu^-(E) + \left(\mu^+(E) + \mu^-(E)\right)/2 = 3/2\left(\mu^+(E) + \mu^-(E)\right) \qquad (13)$$

This approximation is valid for systems with cubic symmetry and powder samples, but even for reduced symmetry the approximated integral is not differing significantly from the measured sum over all three different polarization vectors.

The situation for Fe metal is shown in Figure 17 illustrating the magnetic Fe $L_{2,3}$ absorption, measured in transmission mode, for parallel and antiparallel aligned sample magnetization with respect to the photon beam helicity. The energy is located at the resonant absorption profile of the Fe $2\mathrm{p} \rightarrow 3\mathrm{d}$ excitation. In all spectra, the backgrounds of the less bound electrons have been subtracted by the same straight line for both magnetization (helicity) directions. A clear and pronounced difference is observable. The difference, which is the XMCD signal, is plotted in Figure 17, where the dark shaded curve is related to the L_3-edge absorption (2p shell: $j = 3/2$) and the light shaded curve to the L_2-edge absorption (2p shell: $j = 1/2$). The magnetic effect is quite dramatic.

According to the sum rules of Thole and Carra we have to gather three different integrals, that is the XAS, dark shaded, and light shaded areas. In the case of the XAS signal (Figure 17c) a background must be subtracted, which results from an excitation into higher unoccupied d states (as 4d, 5d, etc.), which are typically nonmagnetic, less localized and broader in energy. The step height for the background approximation is 2/3 of the full edge jump at the L_3 edge and 1/3 at the L_2 edge, according to the degeneracy of the spin-orbit split 2p shell initial states (L_3: $m_j = -3/2; -1/2;$ 1/2; 3/2 and L_2: $m_j = -1/2;$ 1/2).

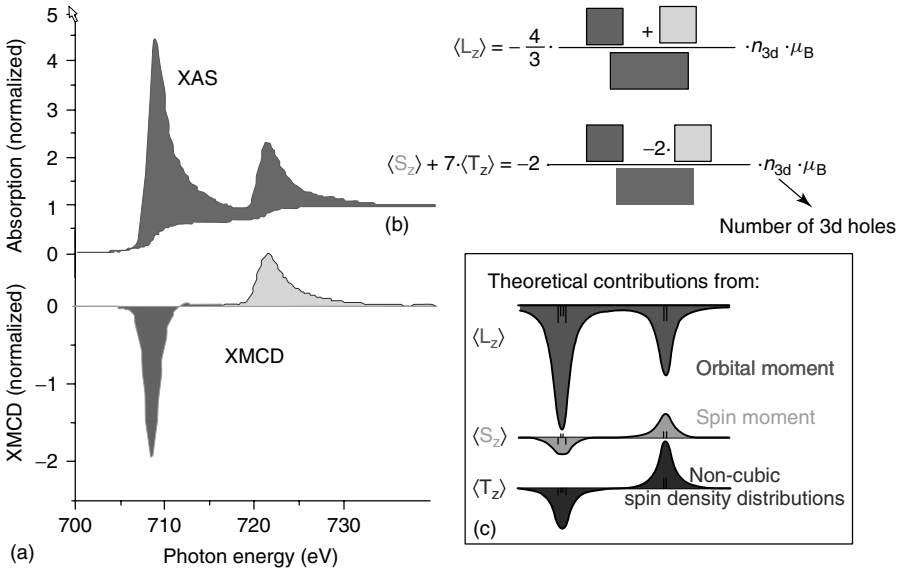

Figure 17. (a) Fe $L_{2,3}$ XAS and XMCD spectra and the (b) analysis via the sum rules on the basis of the theoretical contributions (c) to the XMCD by the orbital, spin and magnetic dipole moment.

Using the coefficients given in Table 1, we can give the corresponding sum rule expressions

$$\begin{aligned}\langle \mathrm{L}_z\rangle &= -n_h \cdot 2\frac{\int_{j_+ + j_-}\left(\mu^+(E)-\mu^-(E)\right)\cdot \mathrm{d}E}{\frac{3}{2}\cdot\int_{j_+ + j_-}\left(\mu^+(E)+\mu^-(E)\right)\cdot \mathrm{d}E}\\ &= -n_h\cdot\frac{4}{3}\cdot\frac{\text{dark gray}+\text{light gray}}{\text{XAS}}\frac{2}{3}\langle \mathrm{S}_z\rangle+\frac{7}{3}\langle \mathrm{T}_z\rangle\\ &= -2\cdot\frac{\int_{j_+}\left(\mu^+(E)-\mu^-(E)\right)\cdot \mathrm{d}E - 2\cdot\int_{j_-}\left(\mu^+(E)-\mu^-(E)\right)\cdot \mathrm{d}E}{\int_{j_+ + j_-}\left(\mu^+(E)+\mu^-(E)+\mu^0(E)\right)\cdot \mathrm{d}E}\cdot n_h\\ &= -n_h\cdot 2\cdot\frac{\text{dark gray}-2\cdot\text{light gray}}{\text{XAS}} \qquad (14)\end{aligned}$$

For the magnetic moments, one gets one Bohr magnetron for each projected orbital moment [8] and two for each spin value, due to the g factors.

As a consequence the 2p → 3d XMCD sum rule is as follows:

$$\begin{aligned}\langle m_l\rangle &= -2\frac{\int_{j_+ + j_-}\left(\mu^+(E)-\mu^-(E)\right)\cdot \mathrm{d}E}{\frac{3}{2}\cdot\int_{j_+ + j_-}\left(\mu^+(E)+\mu^-(E)\right)\cdot \mathrm{d}E}\cdot n_h\cdot\mu_\mathrm{B}\\ &= -\frac{4}{3}\cdot\frac{\text{dark gray}+\text{light gray}}{\text{XAS}}\cdot n_h\cdot\mu_\mathrm{B}\langle m_s\rangle+7\langle \mathrm{T}_z\rangle\\ &= -2\cdot\frac{\int_{j_+}\left(\mu^+(E)-\mu^-(E)\right)\cdot \mathrm{d}E - 2\cdot\int_{j_-}\left(\mu^+(E)-\mu^-(E)\right)\cdot \mathrm{d}E}{\int_{j_+ + j_-}\left(\mu^+(E)+\mu^-(E)\right)\cdot \mathrm{d}E}\cdot n_h\cdot\mu_\mathrm{B}\\ &= -2\cdot\frac{\text{dark gray}-2\cdot\text{light gray}}{\text{XAS}}\cdot n_h\cdot\mu_\mathrm{B} \qquad (15)\end{aligned}$$

The left part $\langle m_s\rangle + 7\langle \mathrm{T}_z\rangle$ is called the *effective XMCD spin*. The sign of the integrals must be carefully taken into account. Negative XMCD signals provide negative integrals and positive signals positive integrals.

One very important point is the necessity to know the number of holes in the final state shell before the excitation of the 2p electron. The nominator provides a magnetic XMCD signal and the denominator the nonmagnetic part, both are proportional to the number of 3d holes. While for the XAS part the resonant intensity is directly proportional to the number of unoccupied states, the ratio is proportional to the magnetism per 3d hole. To get the full magnetic moment, the number of 3d holes which can usually be deduced from local density band structure calculations (LDA) must be known and are usually not critical. If not known, simple chemical estimates of typical electron configurations provide a first approximation. In addition, sum rules contain only integral information. An additional insight into the magnetic character of different unoccupied parts of the 3d shell could be deduced from the fine structure present in the XMCD spectra.

Note that the two-step model, as well as the sum rules, implies some important premises for the application, given as follows:

1. The absorption into final states with reduced orbital moments, like 2p → 4s, must be negligible as compared to the absorption for increased orbital moments, as 2p → 3d.
2. The radial matrix elements should not be varying as a function of the energy of the final state. This happens if final state electrons are less bound and more delocalized

compared to final state excitations close to the absorption threshold.

3. Relativistic corrections to the radial matrix elements should be negligible. Or, in other words, the radial matrix element should not be different for the $l_i + 1/2$ and the $l_i - 1/2$ excitations.
4. The dipole approximation should be a good approximation, or higher terms in the expansion, like the quadrupolar transition, should have spectral weight less than the error bar.
5. For the effective spin sum rule the $l_i + 1/2$ and the $l_i - 1/2$ excitations, for example. The L_2 and L_3 resonances, must be separable in terms of energy. This includes spectral overlap and quantum-mechanical mixing, that is a mixture of $l_i + 1/2$ and $l_i - 1/2$ excitations of the same energy induced by an additional interaction, for example, 2p–3d Coulomb interaction.

3.3.2 *Atomic multiplet description for $M_{4,5}$ edges*

In RE metals the 4f electrons carrying large magnetic moments, which are well localized and the small Coulomb interaction of the 4f electrons with all outer electrons, can be treated in a perturbative atomic model (de Groot, Fuggle, Thole and Sawatzky, 1990). The XAS and XMCD at the $M_{4,5}$ edges can be successfully calculated in a so-called atomic multiplet approach taking into account all dipole allowed transition strengths and the variety of all possible final states. The final $4f^{n+1}$ and the $3d^9$ states consist of a large number of possible electron configurations and related symmetries. Owing to the 3d–4f Coulomb interaction, these final states usually have a different energy, which could be excited preferentially, if the corresponding photon energy is applied in the absorption process. It is beyond the scope of this chapter to explain all the theoretical details about multiplet theory, but it has been demonstrated that this many-particle approach is able to provide theoretical spectra, which are in nearly perfect agreement with available experimental data as shown for the nonmagnetic $M_{4,5}$ spectra of the whole series (Thole *et al*., 1985) and for linear and circular magnetic dichroism. As shown in Figure 19, Goedkoop *et al*. (1988a,b) have successfully described the experimental Gd $M_{4,5}$-edge spectra from Peters *et al*. (2004) and the Sm $M_{4,5}$ spectrum (Suga and Imada, 1996). The origin of the XMCD effect is also shown in Figure 18(b), where all atomic transitions from different m_j are shown, including the strength of the corresponding transition.

The excellent agreement between the experimental curves and theoretical spectra is obvious. Usually the 4f spectra are not significantly altered in different chemical environments. The determination of orbital and spin moments via sum rules is not essential, because Hund's rule values are usually a good estimate. Nevertheless, XMCD provides the unique opportunity to give sublattice magnetizations in complex systems containing many different magnetic elements, for example, in the RE–Iron–Garnets (Goering, Gold and Schütz, 2001; Knülle, Ahlers and Schütz, 1995; Rudolf *et al*., 1991, 1992).

One additional aspect in the $M_{4,5}$ edges arises for some 4f systems with mixed valent 4f states. On the other hand, it is possible to have the same valency with different 4f J states present, which are not strict Hund's rule J values. Those systems could be nicely probed by XAS and XMCD.

Figure 19 shows experimental XAS and XMCD results of ultra thin layers of α-Ce at the $M_{4,5}$ edges and the corresponding multiplet calculations for Ce^{3+} in $4f^1_{J=5/2}$ and $4f^1_{J=7/2}$ (Finazzi *et al*., 1995). Similar to the results of the $M_{4,5}$ edges shown earlier, a clear fingerprint structure for different J states of Ce is observable, which is well reproduced by a weighted superposition of the two $4f^1_{J=5/2}$ and $4f^1_{J=7/2}$ related spectra giving the ratio of the spectral weights between $J = \frac{7}{2}$ and $J = \frac{5}{2}$ of 0.12 ± 0.03 (Finazzi *et al*., 1995).

3.3.3 *The quadrupolar spin density described by the T_z term*

The magnetic dipole term T_z, which was not addressed in magnetism prior to the development of the sum rules, is a quadrupolar spin distribution resulting from lower than noncubic symmetry of the surrounding charge density. The left side of Figure 20 shows an absorber atom (light gray center) with its surrounding atoms (dark gray) in noncubic symmetry with a fourfold symmetry. If this environment is now uniaxially squeezed [9], as indicated by the vertical arrows on the left side, the charge distributions will be modified and rearranged, as schematically sketched on the right. The atoms on the left and right side will move away from the central atom. Thus the charge density is higher above and below the central atom, and reduced at the left and right side. Without symmetry breaking, the total charge distribution at the central atom is predominantly characterized by a radially dependent monopolar charge distribution. With symmetry breaking, an additional quadrupolar charge distribution is necessary to describe the whole charge distribution correctly. If the sample is fully magnetically saturated, the spin expectation value is always aligned along the external field. Owing to the fact that each electron provides a spin, a quadrupolar charge distribution directly corresponds to a quadrupolar spin distribution, which is exactly the T_z term. As shown in Figure 20, the increased charge along the z direction is exactly the part which is reduced along the x and y directions. Mathematically this could be described by

the magnetic dipole term $\mathbf{T} = \mathbf{S} - 3\hat{r} \cdot (\hat{r} \cdot \mathbf{S})$, as known for a dipole field in electrostatics. If the spin is aligned along the axis α, T_z could be expanded in terms of the mentioned quadrupolar charge tensor $Q_{\alpha\beta}$ (Stöhr and König, 1995; van der Laan, 1998b) [10].

$$T_\alpha = \sum_\beta Q_{\alpha\beta} S_\beta \tag{16}$$

Measuring with a high field aligned parallel to the photon beam direction provides full sample saturation and a constant isotropic spin related XMCD signal. Measuring along the x and y axis provides a T_z projection, which is half of the value measured along the z direction and of opposite sign, corresponding to the charge distribution. Thus, an angular averaging XMCD measurement provides the full cancellation of crystallographic T_z moment contributions formulated as the sum rule $\sum_\alpha \langle T_\alpha \rangle \approx 0$, where the 'approximate' symbol is related to the part of the T_z term induced by the spin-orbit interaction of the final state shell (Stöhr and König, 1995).

As discussed above, a uniaxial force will introduce a magnetic dipole term. If this is purely related to the crystal structure itself, the average over all three crystallographic directions will provide the pure spin moment, where all dipole term contributions are canceled. Another possible 'uniaxial force' is related to the spin moment itself, aligned along one preferred direction. In this case, the charge distribution is altered by the spin-orbit interaction in the magnetic shell, and the uniaxial symmetry breaking is oriented along the direction of the sample magnetization. The related T_z term will not cancel since it aligns along the spin moment direction. Rotating the spin along different directions will also rotate the T_z contribution, and the absolute value of the effective spin moment always includes the spin-orbit induced dipole term contribution. Stöhr and König have discussed this influence and they found only minor contributions (Stöhr and König, 1995). Nevertheless, with

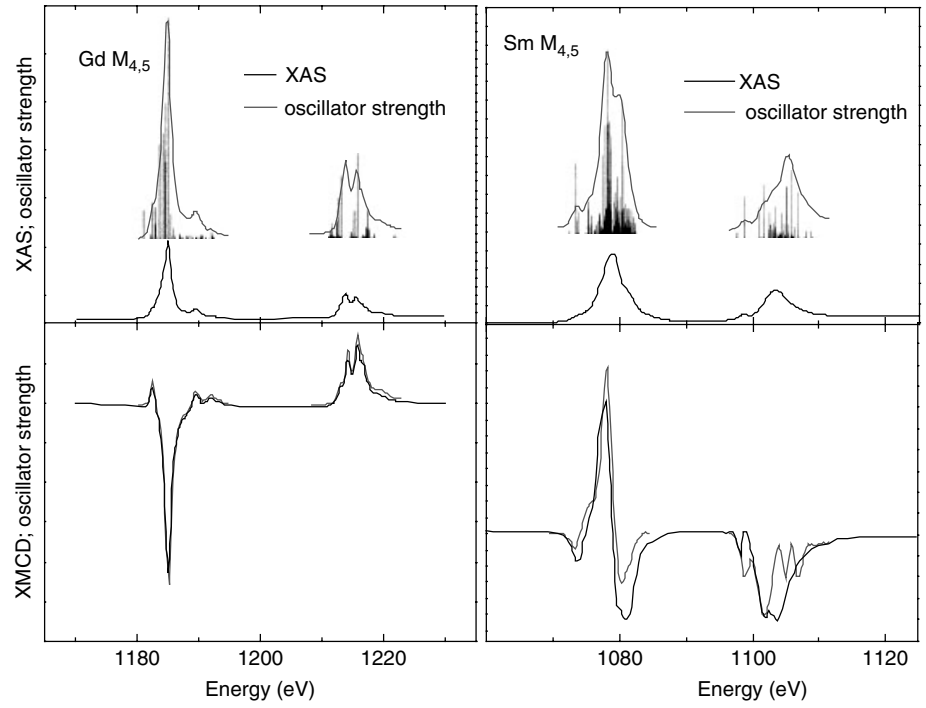

Figure 18. (a) Comparison of the Gd and Sm $M_{4,5}$ spectra, already shown in Figure 13, with the oscillator strength derived by atomic multiplet theory. The left side shows the nonmagnetic and the magnetic absorption spectra (black line) at the Gd $M_{4,5}$ edges of a GdFe thin-film system, while the gray curves are the related multiplet theory based oscillator strength reproduced from Peters *et al*. (2004). The right side shows the corresponding spectra of a Sm_4As_3 sample (from Suga and Imada, 1996) and the theoretical curves extracted from Goedkoop *et al*. (1988b) for Sm^{3+}. The upper part shows additional line intensities for Gd^{3+} and Sm^{3+} reproduced from Goedkoop *et al*. (1988b). The energy of the theoretical data has been adapted to the experimental results. To improve visibility, the experimental and theoretical spectra are shifted along the ordinate. (b) Atomic model for $3d^{10}4f^{13} \rightarrow 3d^9 4f^{14}$ transition in the rare earth element Yb^{3+}. The left (right) part shows the transition in the nonmagnetic (magnetic) case, respectively. The vertical arrows indicate the dipole allowed transitions for the various m_j states of the atom for left, linear and right polarized light. The polarization dependent relative intensities, due to the angular parts of the matrix elements, are indicated below by the small dots. (Reproduced from Goedkoop *et al*. (1988a) *Journal of Applied Physics* **64**, 5595–5597.)

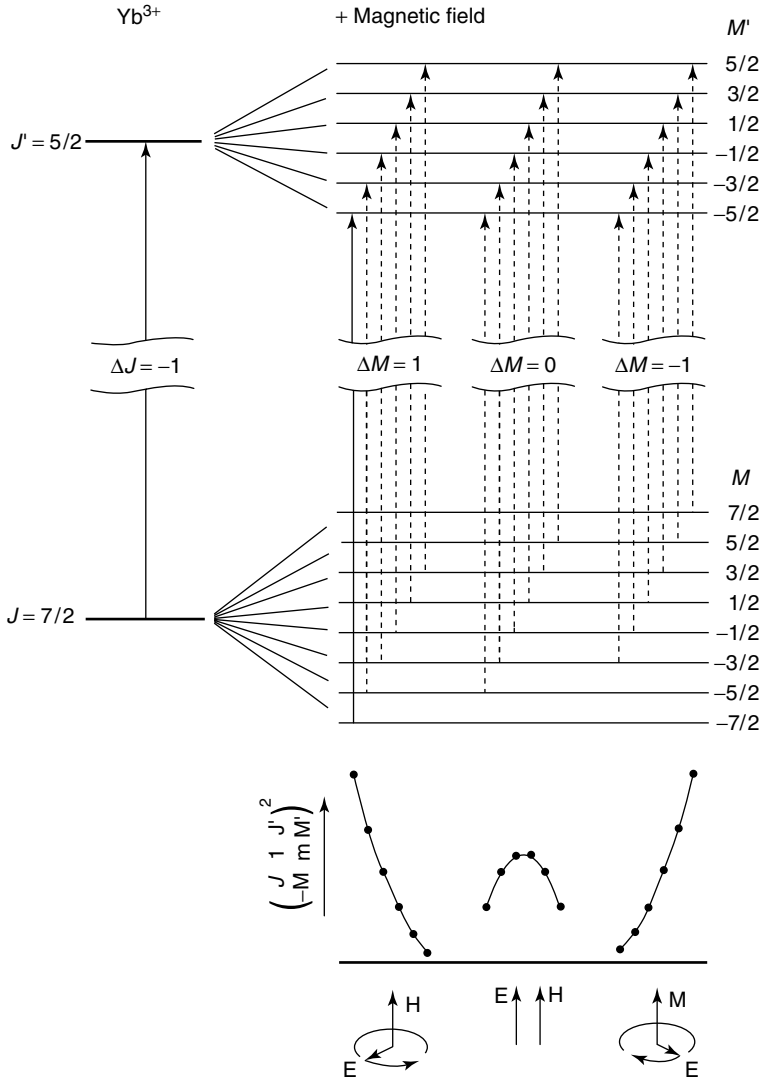

Figure 18. *Continued.*

increased spin-orbit interaction this part of the T_z term could not be separated from the spin moment consequently. Usually the absolute error in spin moment determination is in the range of 10% or slightly above, while relative errors are much smaller, for example, angular dependencies. Therefore, for 3d metal systems the spin-orbit induced T_z contribution should be in the error bar of the absolute value.

3.3.4 Moment analysis

A recent approach to go beyond the sum rules is provided by the moment analysis generally based on the findings of Gerrit van der Laan. The general shape modifications, found for the 3d TM series shown in Figure 21 could be understood by a single particle approach, which takes into account the important 2p–3d Coulomb and exchange interaction (van der Laan, 1997b,c,d, 1999a,b). The spectral XMCD shape of the heavy 3d TM as Fe, Co, and Ni consist roughly of simple down and up structures at the L_3 and L_2 edges respectively, as shown in Figure 11. This shape changes to a more peak derivative-like shape while going to light TMs. This has been explained in terms of a change in band filling, nearly empty for the light 3d TM as Ti and V, and nearly filled for the heavy ones such as Fe, Co, and Ni. Different ground-state expectation values provide different spectral shapes as shown in Figure 21. In the spectral analysis the complex XMCD profile is treated as a superposition of these spectral shapes, where the relevant intensity is proportional to various ground-state expectation values of tensor operators $\langle \underline{w}^{xyz} \rangle$. The underscore describes that the ground-state moment is related to the unoccupied part of the d shell. So, Figure 21 shows the dominating spectral shapes

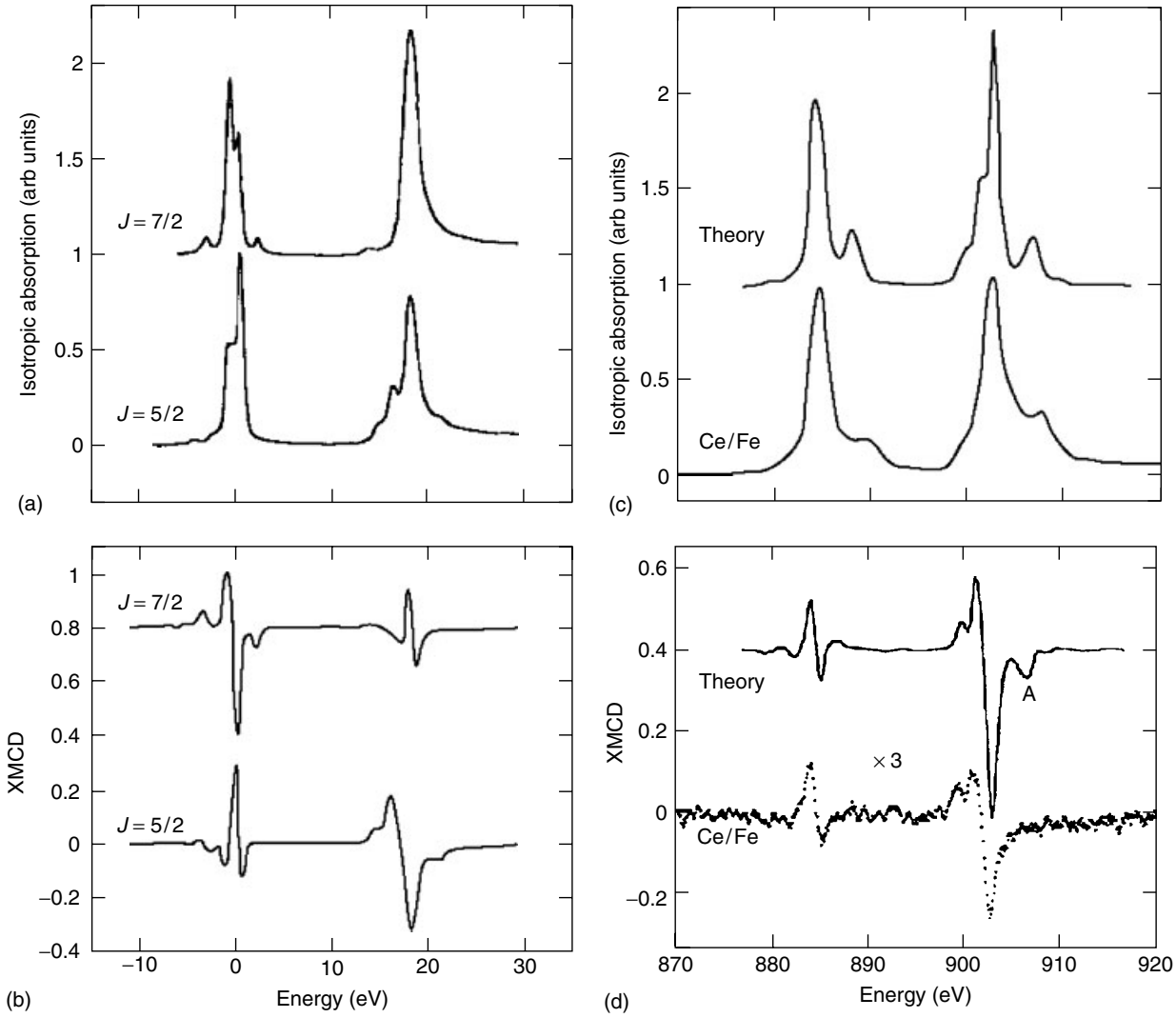

Figure 19. (a) Multiplet calculations of Ce for two different configurations $4f^1_{J=5/2}$ and $4f^1_{J=7/2}$. (b) The corresponding XMCD spectra. (c) Measured M4,5 result for the measured α-Ce and a weighted sum of the two $4f^1_{J=5/2}$ and $4f^1_{J=7/2}$ configurations shown in (a) to provide the best agreement to the experimental data. (d) Shows the XMCD comparison corresponding to (c). (Reproduced from Finazzi *et al*. (1995) *Physical Review Letters* **75**, 4654–4657.)

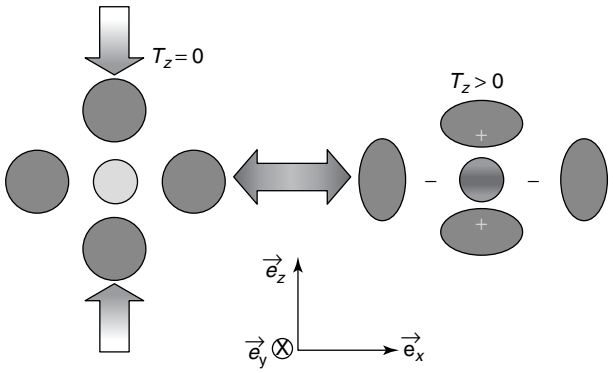

Figure 20. Schematic explanation of the charge and spin distribution, providing a nonvanishing T_z term.

present at the p → d excitation with a given (SOC) of the 2p shell. The following physical expectation values of the unoccupied part of the 3d shell are represented: $\langle \underline{w}^{000} \rangle$ is proportional to the number of holes n_h, $\langle \underline{w}^{110} \rangle$ to the spin-orbit coupling, $\langle \underline{w}^{101} \rangle$ to the orbital moment, $\langle \underline{w}^{011} \rangle$ to the spin, and $\langle \underline{w}^{211} \rangle$ to the magnetic dipole term T_z (van der Laan, 1997c,b).

The spectral shapes in Figure 21 are a sum of Lorentzian broadened line intensities, indicated as vertical lines below the spectra, originating from an energy splitting of various m_j states of the 2p core hole, related to the 2p–3d exchange energy. So, the $2j + 1$ degenerated core-hole states will split in energy into four (L_3:$2p_{3/2}$) and two (L_2:$2p_{1/2}$) channels. The energy splitting respective to the excitation center of

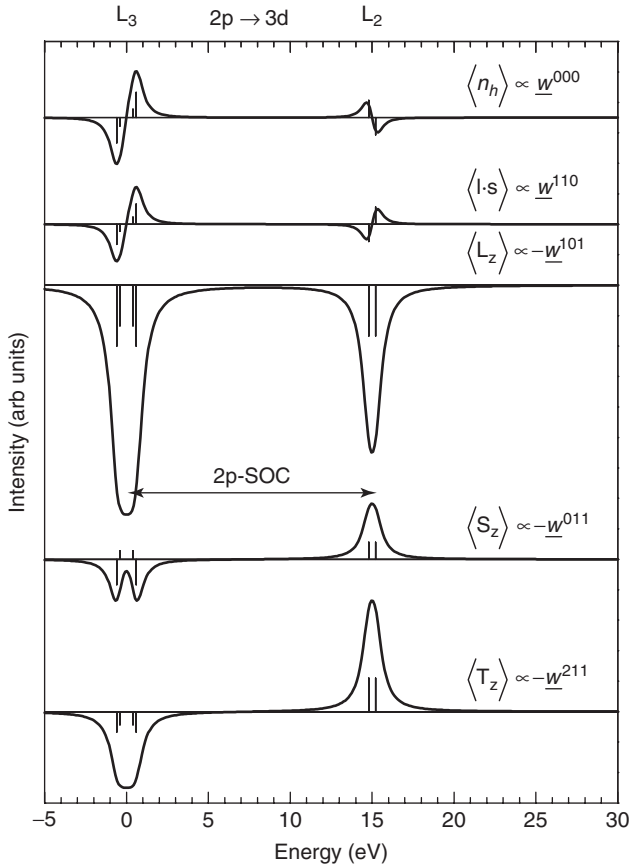

Figure 21. XMCD spectral shape of different ground-state moments $\underline{w}^{xyz}$, which are proportional to the corresponding expectation values.

gravity is

$$E_{jm} = H_s m_j \frac{j(j+1) + s(s+1) - l(l+1)}{2j(j+1)} \qquad (17)$$

where j is the total angular momentum of the p hole, m_j is the z component of j, s, and l are the spin and orbital moments of the p hole and H_s is equal to the effective pd exchange (van der Laan, 1997c,b). This expansion is a direct consequence of the Coulomb interaction between the core hole and the 3d final states and tries to take the dominating parts quantitatively into account. Different 3d final state configurations and possible different final state energies are not covered by this method. For a detailed understanding of this method, the reader is asked to refer to the literature (Goering *et al*., 1999, 2002c; Goering, Gold and Schütz, 2001; Goering, Bayer, Gold and Schütz, 2002; Goering, Gold and Bayer, 2004; van der Laan, 1997a,b,c,d; van der Laan and Thole, 1996).

Although introduced as a phenomenological model to describe complex 3d TM XMCD spectra, the validity was just checked for consistency, but it has recently been proved by theory to be also a correct description, demonstrating a more general character with extended validity (Dörfler and Fähnle, 2006).

The XMCD in Holmium iron garnets formula unit $Ho_3Fe_5O_{12}$ has been analyzed, where two different types of antiferromagnetic coupled Fe^{3+} sublattices, slightly separated in energy because of different chemical coordination, (three tetrahedral and two octahedral Fe ions) are present (Bloch, Chaisse and Pauthenet, 1967; Guillot and Pauthenet, 1967; Pauthenet, 1958). Figure 22 shows the room-temperature (RT) Fe $L_{2,3}$ XMCD spectrum of HoIG, which is much more structured compared to the pure Fe metal spectrum (see Figures 11 and 17). The most evident difference is the strong positive peak at the L_3 edge, directly suggesting an antiparallel ordered Fe sublattice magnetization. Dunaevsky *et al*. have calculated the DOS by a recursive calculation method for YIG, which has a similar 5d hybridization to

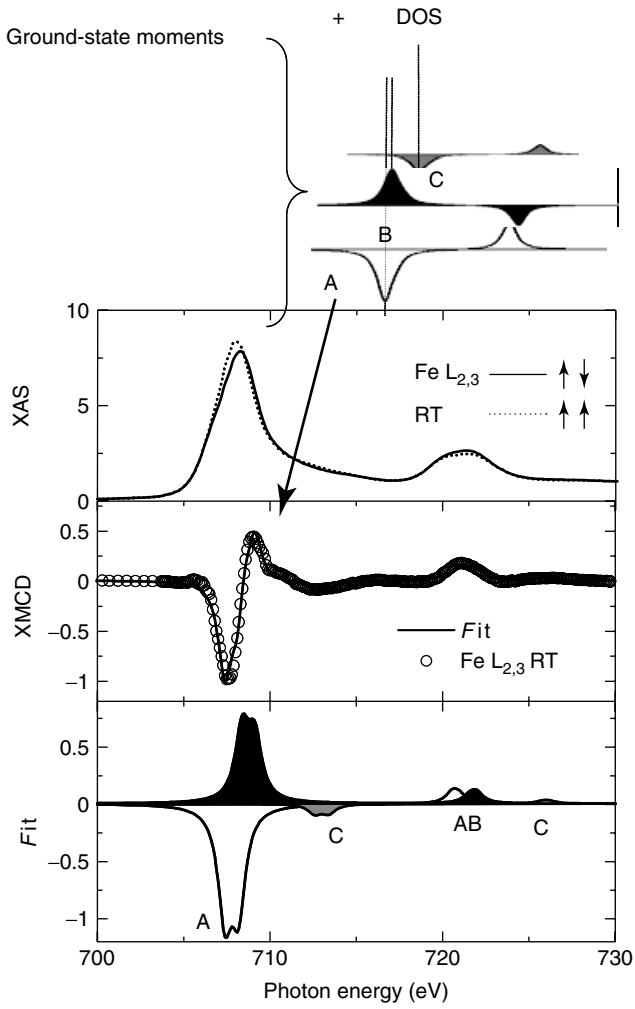

Figure 22. Moment expansion of iron garnets.

Fe 3d compared to the other rare elements like Ho. We have reproduced at the top of Figure 22 the DOS from Dunaevskii and Savel'ev (1989). The white shaded part corresponds to the octahedral (A) and the black shaded part to the tetrahedral (B) oxygen coordinated Fe ions. A clear energy shift between the two Fe sublattices is directly observable. The gray shaded part corresponds to the RE (Y) 5d DOS (C), which is important for the magnetic interaction between the RE and the Fe ions.

For the approximation of the XMCD spectrum, three sets of ground-state moments are generated and located at the three mentioned DOS related energy positions. The fit result and the room-temperature XMCD spectrum are shown in the middle part of Figure 21. The corresponding moment analysis contributions are shown below. All spectral shapes in the XMCD spectrum are nearly perfectly reproduced by the fit. As suggested above, the antiparallel coupling of the Fe sublattices is clearly observable. The extracted ratio of the spin moments A and B is 2.39, which should be 1.5 according to sublattice estimates from the literature (Geller *et al*., 1963), denoting a slightly higher magnetic moment for the Fe^{3+} at tetrahedral sites (B) compared to octahedral sites (A) which has also been predicted by theory (Dunaevskii and Savel'ev, 1989). It should be mentioned that the used linewidth to broaden the line spectra from the ground-state moments is large and dominated by the band structure.

3.4 Magnetic anisotropy and microscopic orbital moments

3.4.1 General aspects

One of the most important and technical relevant issues in magnetism of crystalline solids is the magnetocrystalline anisotropy energy (MAE). This energy provides the controllability of preferred easy axis behavior and influences magnetic switching and the coercivity. Owing to the fact that the spin itself does not interact with the electric crystal, an orbital moment must be present to couple the spin to the crystal lattice by spin-orbit field interaction. In the case of the 3d TM, the orbital moment is usually quenched and quite small compared to the spin moment and could not be addressed properly in the past by experiment [11]. Since XMCD now provides the separate determination of the spin and orbital magnetic moment projections in different crystallographic directions, understanding a new profound anisotropic behavior of 3d metal compounds in a microscopic, element specific, and quantitative way is possible especially in order to prove microscopic models. P. Bruno has formulated a perturbative approach of the MAE to reach a quantitative description for TM systems, which has the favorable effect of being intuitive: On the basis of 3d spin-orbit coupling, an enhanced orbital moment along the easy axis of a uniaxial anisotropic magnetic material is postulated. In such a system, the spin-orbit energy tries to align the spin moment along the direction with enhanced orbital projections. So the anisotropy is microscopically reflected in anisotropic magnetic moment projections (Bruno, 1989), and described quantitatively by $E_{\mathrm{S.O.}} = \frac{\xi}{4}\Delta\langle L\rangle$. This is sketched in Figure 23. While this model has been derived for systems with fully occupied majority spin band, Gerrit van der Laan extended it to include a higher term in perturbation theory of the spin-orbit energy, which includes the magnetic dipole term T_z

$$\begin{aligned}\Delta E &\approx -\frac{\xi}{4}\cdot\hat{S}\cdot\left[\left\langle L^{\downarrow}\right\rangle - \left\langle L^{\uparrow}\right\rangle\right] \\ &\quad + \frac{\xi^2}{\Delta E_{\mathrm{ex}}}\left[\frac{21}{2}\cdot\hat{S}\cdot\langle T\rangle + 2\left\langle (L_\xi S_\xi)^2\right\rangle\right] \\ &= E_{\mathrm{L}}^{\downarrow} + E_{\mathrm{L}}^{\uparrow} + E_{\mathrm{T}} + E_{\mathrm{LS}} \end{aligned} \tag{18}$$

With reduced symmetry the dipole operator term can play an important part. Owing to the fact that the absolute value of the spin moment also changes with chemical and crystallographic environments, the small orbital moment of 3d TM systems could not simply be separated quantitatively from the spin moment. Therefore, understanding their anisotropy was difficult up to now since XMCD gives the integral projected orbital moments. Regarding the formula of van der Laan shown above, the full orbital moment anisotropy could be a mixture of majority and minority orbital anisotropies with opposite signs. Thus, the total orbital anisotropy could be very small due to cancellation of large anisotropies of the minority and the majority band. Quantitative experimental verification of these models needs the presence of either a completely filled majority or an empty minority band. Completely filled or empty sub-bands do not provide an orbital moment and therefore the full anisotropy is only due to the remaining partially filled band as identified by *XMCD measurement*.

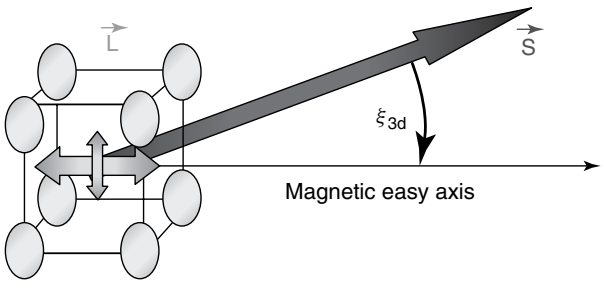

Figure 23. Bruno model of the magneto crystalline anisotropy in relation to spin and orbital moments.

Three examples will be shown which clearly demonstrate the unique possibilities of XMCD providing a deep, clear and unambiguous understanding of the anisotropy in 3d metal compounds.

3.4.2 The Au/Co/Au reorientation transition

One important phenomenon to be addressed is the transition between in-plane and out-of-plane magnetization behavior for ultra thin ferromagnetic films, like Co covered by Au. For thick films the shape anisotropy dominates the whole scenario, while for ultrathin films, just by adding some monolayers of Co, the axis direction is easily flipped from in plane to out of plane. The basic idea behind this phenomenon is the increased influence of the surface: Its symmetry breaking results in enhanced Co orbital magnetic moment projections along the surface normal, and a corresponding spin-orbit energy. The enhanced surface orbital moment interacts with the spin, trying to align the sample magnetization along the surface normal, via 3d shell spin-orbit coupling. It overcomes the shape energy and reduces with thickness; the magnetization rotates to the normal direction.

D. Weller and coworkers have investigated this transition and measured the Co orbital moment projections using XMCD at the Co $L_{2,3}$ edges, as shown in Figure 24 along the surface normal and at more grazing incidence geometry. Despite the fact that they had to face self-absorption phenomena (see above), they found clear thickness dependent orbital- and T_z moment variations at a Co wedge covered in Au. This observation clearly reflects the increased influence of the orbital moment at the surface layer, verifying the ideas of P. Bruno. As mentioned, the self-absorption problem in these studies has prevented reliable quantitative comparisons between the microscopic moment projections given by XMCD and the macroscopic magnetization behavior mediated by the Bruno model.

3.4.3 Co on Pt steps: the reduction of symmetry

An illustrative example of the potential of XMCD has been shown by the studies of Co atom chains and monolayers decorated on Pt(997) surface by Gambardella *et al*. (2003, 2004). While the spin sum rule application is hindered by the large dipole term T_z, the orbital moment can be directly deduced and is listed in Table 2 for different Co systems of reduced symmetry. The L_z values are compared with the magnetocrystalline anisotropy K_1.

The XMCD spectra shown in Figure 25, illustrates a comparison of Co nanoparticles going from the bulk to the atomic chains, monoatomic layers, and bulk Co. The increasing L_3-XMCD effect directly indicates a significant increase of an angular momentum, oriented parallel to the spin moment.

Table 2. Orbital moment projections and its correspondence to uniaxial anisotropy.

System	$\langle L_z \rangle$ (μ_B)	K_1(meV/atom)
Co metal (hcp)	0.14	0.053
Co/Pt(997) ML	0.31	0.14 ± 0.01
Co/Pt(111) ML	0.29	
Co/Pt(997) chain	0.68 ± 0.05	2.0 ± 0.2
Co/Pt(111) adatom	1.1 ± 0.1	9.3 ± 1.6

3.4.4 The magnetic anisotropy of CrO_2

CrO_2 is a classical ferromagnetic oxide, important for magnetism and of significant technological relevance. During recent years its half-metallicity with nearly 100% spin polarization at the Fermi level has attracted the interest of this chalcogenide as a candidate for injection of highly spin-polarized electrons and applications in spintronics, (Das Sarma, Fabian, Hu and Zutic, 2000; Wolf *et al*., 2001). CrO_2 crystallizes in the Rutile structure with a ratio of lattice constants of $a/c = 1.51$ (Porta, Marezio, Reimeika and Dernier, 1972; Swoboda, Arthur and Cox, 1961; Thamer, Douglass and Staritzky, 1957). Magnetometry reveals a magnetic moment of $2\,\mu_B$/fut (Kubota, 1960), which is consistent with two different theoretical approaches: The description of local magnetic moments of Cr^{4+} ions in a $3d^2$ configuration gives the same correct magnetic moment as band structure calculations on the basis of an itinerant picture (Korotin, Anisimov, Khomskii and Sawatzky, 1998; Lewis, Allen and Sasaki, 1997; Mazin, Singh and Ambrosch-Draxl, 1999; Schwarz, 1986). CrO_2 is difficult to access experimentally due to its reconfiguration into the more stable Cr_2O_3 phase. Recently a chemical-vapor-deposition technique has been established, which provides epitaxial single-phase thin films, grown on TiO_2 substrates (Li, Gupta and Xiao, 1999; Spinu *et al*., 2000, 2001) achieving spin polarization close to 100% measured by Andreev reflection (DeSisto *et al*., 2000; Ji *et al*., 2001; Ji, Strijkers, Yang and Chien, 2001; Soulen *et al*., 1998, 1999) and spin-polarized photoemission (Dedkov *et al*., 2002). Using these samples, 2p XAS and XMCD spectra for CrO_2 grown with its rutile *c* axis in plane have been studied for parallel and antiparallel aligned magnetization as shown in Figure 26(b) for $\vartheta = 7^\circ$, 40°, 86° and $\phi = 60^\circ$. The angle $\vartheta = 40^\circ$ represents an intermediate angle between *a*- and *c*-axis projection. The angle of incidence $\phi = 60^\circ$ has been chosen as a good compromise for a significant amount of in-plane sensitivity [12] and reduced self-absorption. The dichroic

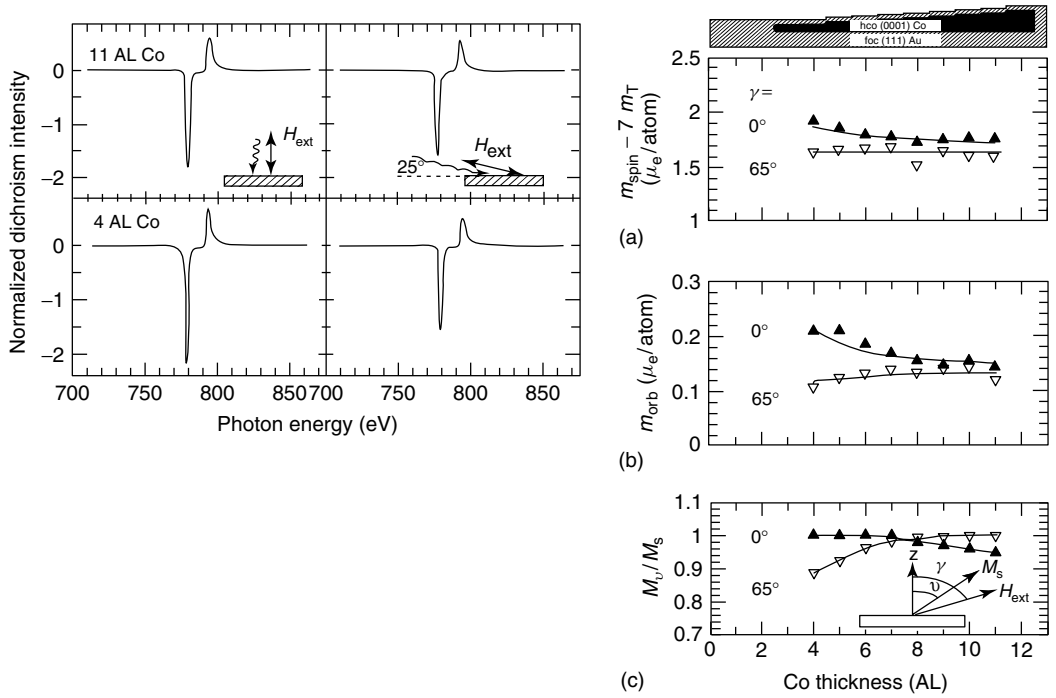

Figure 24. XMCD measurements of a Co wedge covered in Au, and the extracted magnetic moment projections. (Reproduced from Weller *et al*. (1995) *Physical Review Letters* **75**, 3752–3755.)

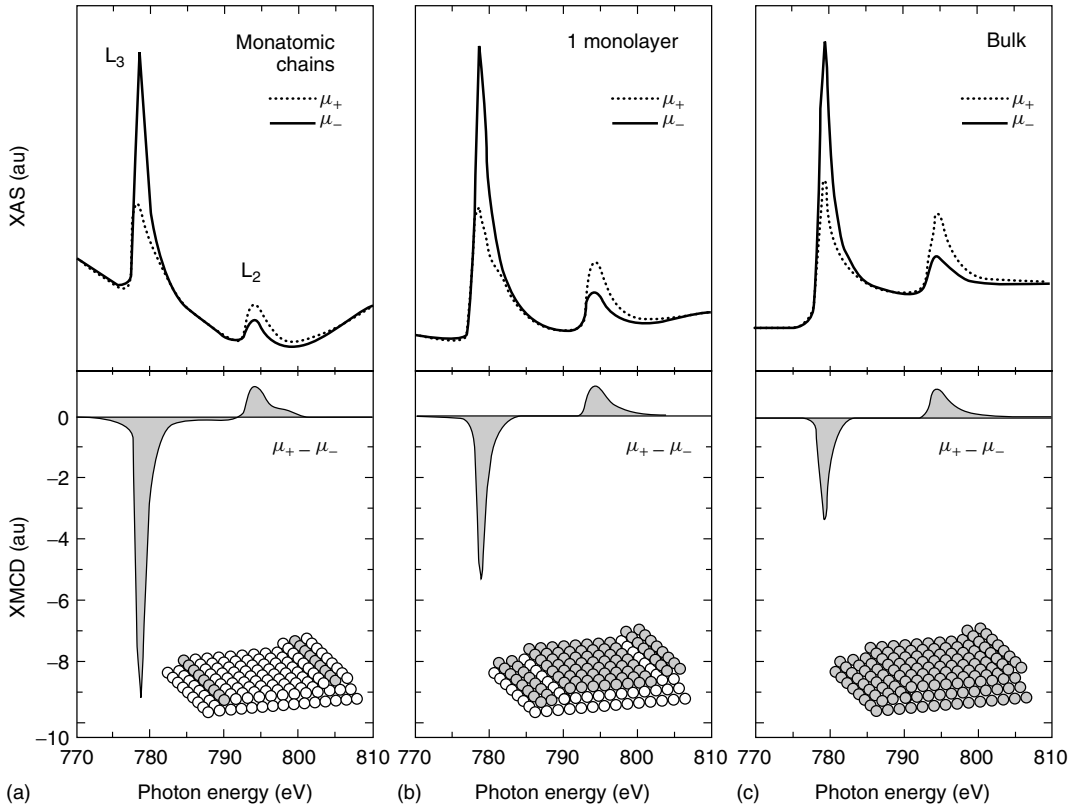

Figure 25. XMCD spectra for different Co decoration of Pt (711), from single atomic chains (a), over monolayer coverage (b) to bulk Co spectra (c). (Reproduced from Gambardella *et al*. (2002) *Nature* **416**, 301–304.)

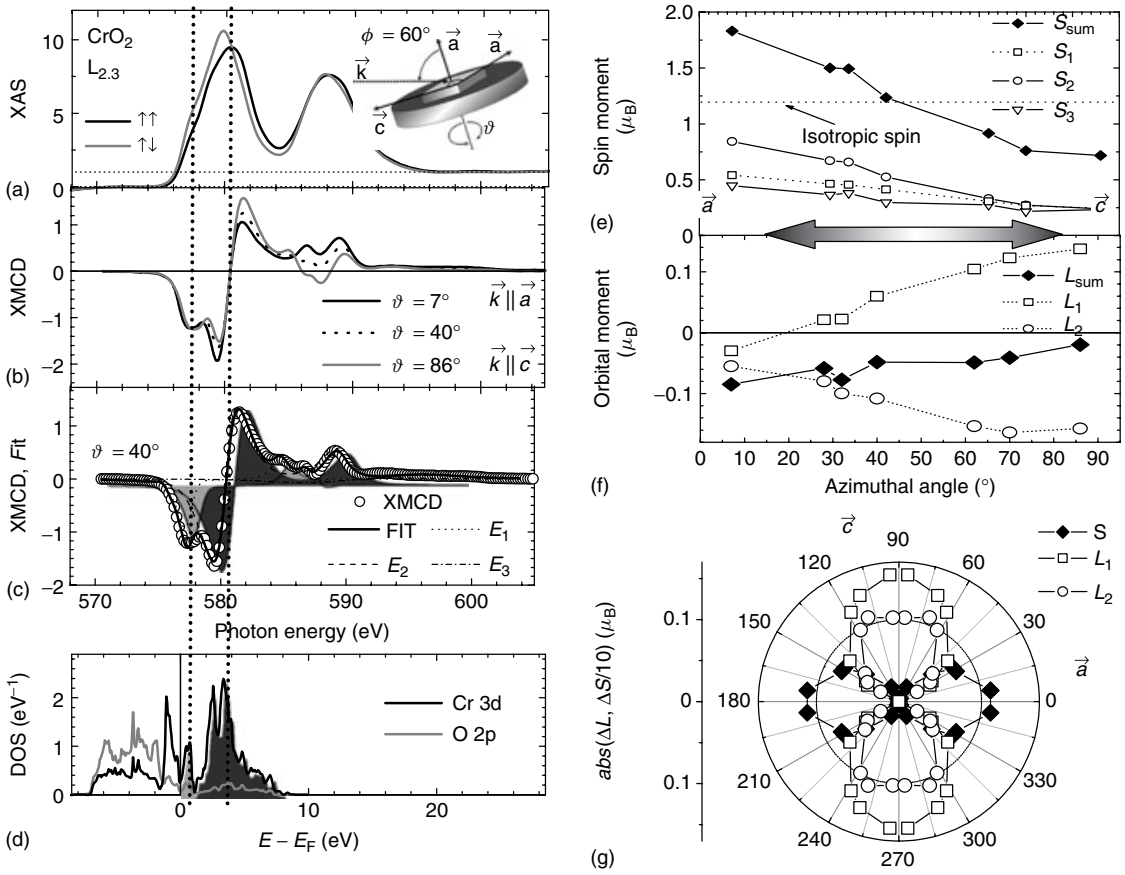

Figure 26. CrO_2 XAS (a) and XMCD (b) results, measured at the Cr $L_{2,3}$ edges at 80 K. (c) XMCD moment-analysis fit at an intermediate angle of 40° and (d) corresponding p and d projected DOS. Anisotropy of the effective spin (e) and the orbital moments (f), also shown as the difference in a polar plot (g).

spectra exhibit many structures with very strong unusual azimuthal variations. For *c*-axis enhanced projection ($\vartheta = 86^\circ$), a direct observable change of sign at 587 eV is present. This negative XMCD intensity suggests a strong increase in a projected orbital moment along the *c* axis (see Section 3.3.4 moment analysis: $\langle L_z \rangle \propto -\underline{w}^{101}$ exhibit only negative contributions) in contradiction to the nearly constant XAS. Owing to the spectral overlap of both L edges, the conventional sum rule analysis cannot be addressed to Cr 3d spin moments. A detailed analysis of the experimental data is based on the spin-up and spin-down DOS for Cr 3d and O 2p states, derived by LSDA $+U$ calculation (shown in Figure 25d (Korotin, Anisimov, Khomskii and Sawatzky, 1998)). Two prominent features are directly observable, a narrow (1-eV wide) fully spin-polarized unoccupied majority t_{2g} band at 0.5 eV and a broader mixture of e_g-majority and t_{2g}/e_g-minority states (Stagarescu *et al.*, 2000) at 3 eV. Two sets on a basis of the DOS (at E_1 and E_2) and one set according to the MEXAFS signal at E_3 (see also Section 4.1) are taken into account in the fitting procedure to separate the spectral overlap of L_3 and L_2 edges (Goering *et al.*, 2002a).

The original XMCD spectrum and the moment-analysis-fit result for an intermediate azimuthal angle are shown in Figure 25(c) ($E_1 = 577.0$ eV (dotted), $E_2 = 580.5$ eV (dashed), and $E_3 = 587.0$ eV (dot dash)). The two mentioned dominating parts E_1 and E_2 are shaded in light and dark gray. To reduce the number of free parameters, the sum over all orbital contributions has been set to the sum rule determined integral value. Peak width and broadening have been held fixed for all fitted XMCD spectra.

All spectral features could be reproduced nearly perfectly by this fitting procedure. The extracted three effective spin and two orbital [13] contributions for the areas E_1, E_2, and E_3 are shown in Figure 26(e, f, and g), indicating a very strong anisotropy. The azimuthal spin anisotropy is clearly related to the strong anisotropic T_z; that is, the quadrupolar spin distribution at the Cr site (Stöhr and König, 1995), which (van der Laan, 1998b) is extremely high compared to previously published experiments (Weller *et al.*, 1995) and theoretical predictions (Crocombette, Thole and Jollet, 1996). Applying the T_z sum rule the total isotropic spin of 1.2 μ_B has been determined and separated from the T_z

part. Figure 26(f) shows the corresponding orbital moment projections, where for E_1 a positive orbital (along the c axis) moment with a strong azimuthal variation, and for the broad part at E_2 a negative contribution with a reduced azimuthal variation are observed. The total orbital moment is negative and maximum along the a axis and a minimum along the c axis.

According to Hund's rules an antiparallel coupling of spin and orbital moments is expected (Ashcroft and Mermin, 1976; Kittel, 1976), which is consistent to the total observed orbital moment, but the total orbital moment has its maximum along the hard axis direction, which is in contradiction to the simple Bruno model. As we have shown, a large T_z term is present for CrO_2 which is included in the MAE model of van der Laan (1998a).

The microscopic moments can be used to test the anisotropy formula of van der Laan. The total orbital change by a rotation of 90° is $\Delta \langle L_z \rangle = (0.065 \pm 0.005)\,\mu_B$, a total dipole term part of $\langle 7T_z \rangle = -3$ and a spin moment of $\langle S_z \rangle = 2.4$ [14]. From the LSDA $+U$ calculation (Korotin, Anisimov, Khomskii and Sawatzky, 1998), an averaged exchange energy of 3 eV is extracted. From the *in situ* XMCD- and superconducting quantum interference device (SQUID)-derived hysteresis curves, a uniaxial anisotropy energy $K_1 = (5.8 \pm 0.5) \cdot 10^4 \mathrm{J\,m^{-3}}$ has been derived.

If we neglect the squared diagonal spin-orbit interaction and take into account the completely empty minority band, the van der Laan formula reduces to $\delta E \approx \frac{\xi}{4} \cdot \hat{S} \cdot \langle \mathbf{L}^{\uparrow} \rangle + \frac{\xi^2}{\Delta E_{ex}} \frac{21}{2} \cdot \hat{S} \cdot \langle \mathbf{T} \rangle$. With the above values the correct correspondence between the macroscopic anisotropy energy K_1 and the microscopic formula is obtained using a spin-orbit coupling energy of $\xi = 14\mathrm{meV}$ [15].

The orbital term favors an a–a plane easy axis behavior, directly observable from the enhanced orbital moment projection, while the dipole term T_z favors the c axis. Both MAE contributions nearly cancel each other, but the dipole term dominates. This is a possible explanation for the observed reorientation transition for ultra thin CrO_2 films (Li, Gupta and Xiao, 1999), which could be interpreted by lattice mismatch-induced changes in the delicate balance between orbital projections and the magnetic dipole term.

3.5 K-edge XMCD

In the K-edge absorption process the initial $1s_{1/2}$ photoelectron populates a final p-like state, which plays a minor role in magnetism in 3d elements. Following the sum rule it is expected that the XMCD effect is only sensitive to the p-projected orbital polarization, which, on the other hand, is generally rather small due to the quenching mechanism. Thus the fascinating possibilities arising from the direct application of sum rules on $L_{2,3}$-XMCD spectra of 3d-transition elements will not be touched by K-XMCD.

From an experimental point of view, the K edges of the 3d elements are energetically located in the hard X-ray range. Thus a large variety of bulk systems and related magnetic problems can be addressed, where soft XMCD studies suffer from the strong surface sensitivity. For example, important classes of materials in magnetism are 3d RE compounds, which exhibit strong surface oxide contamination and can often hardly be addressed by soft XMCD at the 3d L edges or 4f $M_{4,5}$ edges, 3d K edges. Using hard X rays for these systems parallel measurements of the 3d K edges in combination with RE $L_{2,3}$ edges can give interesting complementary information. The simple sample handling and high penetration depth in combination with the highly achievable accuracy allows, in some cases, to monitor changes in the local magnetic properties with external sample conditions such as temperature, external fields, and pressure. Thus, the K-edge XMCD signal can provide information on even small changes in the magnetic orientation of the absorbing atom.

Furthermore, although no direct relation of the K-XMCD and its strength to the local magnetic moment is easily accessible, (Stähler, Schütz and Ebert, 1993) the fine structure which often provides significantly more pronounced characteristics compared to the broad near-edge profile itself, can play the role of a fingerprint of the chemical state. As an example, studies of the Fe K-edge profile in Tb/Fe multilayers are shown in Figure 27 in comparison with the corresponding signal in the pure metal and the binary compound $TbFe_2$. The multilayer XMCD profiles can easily be explained by a mixture of both components (Attenkofer *et al*., 1993) giving interesting insight into the chemical state of the interfaces. An accuracy of 10^{-5} can be achieved and a large number of K-edge XMCD studies have been reported in a variety of 3d TM systems.

Recently, the corresponding signals at the oxygen K edge have gained considerable interest since, at the moment, no other method is able to address the problem of oxygen polarization. As observed in CrO_2 (Goering *et al*., 2002b) large dichroic oxygen K-edge contributions, with a strength up to several percent (Figure 28), are observed, where oxygen has been normally considered to be a nonmagnetic component. Although the understanding of this phenomenon and its quantitative relation to the local magnetic moment is still complicated, it is expected to serve as proof of a significant magnetic polarization at the oxygen site. Systematic comparison of the oxygen K-XMCD signal in different systems might provide some information about the existence of oxygen polarization. A unique possibility arises by studying the hysteresis loop at the oxygen site as shown in the insert of Figure 28. Often

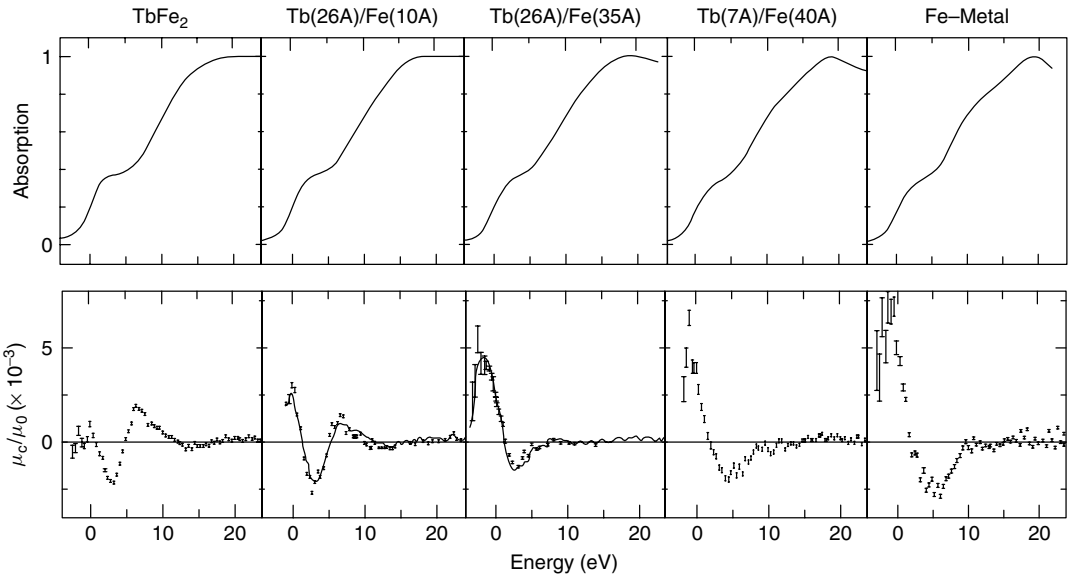

Figure 27. Normalized Fe K-edge XMCD signal of TbFe Multilayers in comparison with the XMCD profile in pure Fe and the binary compound $TbFe_2$. The solid line in lower part of the second and third panel correspond to the modeling of the K-XMCD spectra by an admixture of Fe- and TbFe2-like components in the Fe layer.

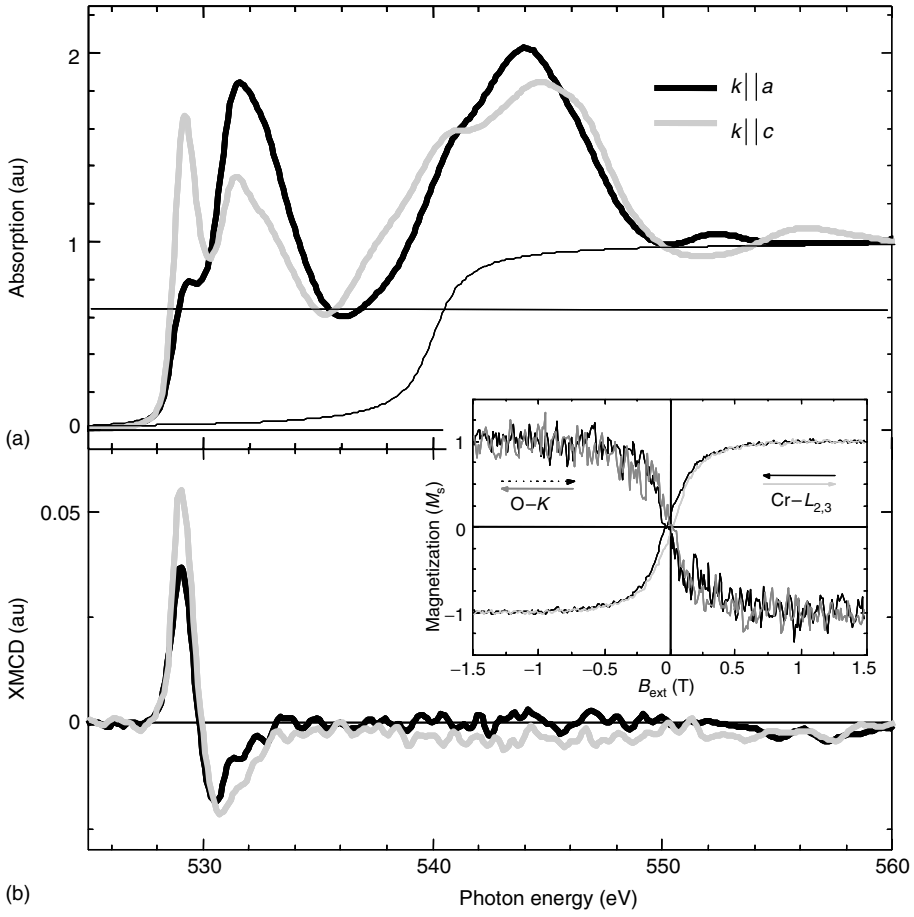

Figure 28. (a) Oxygen K-edge absorption spectra for different crystal orientations. (b) Corresponding dichroic XMCD signal. Inset shows the element specific magnetization curves.

the oxygen K-edge XMCD and the deduced orbital moments are too large compared to the theoretical expected value, a phenomenon which has not yet been understood. Very recently oxygen K-XMCD studies have been addressed to oxide interlayer (Bowen *et al*., 2006). Owing to the absence of a corresponding signal in $Co/Al_2O_3/Co$ and Fe/MgO/Fe tunnel magneto resistance systems with an upper limit of $0.05\,\mu_B$ have been deduced by comparison with the results in $La_{0.7}Sr_{0.3}MnO_3$, where a dichroic O–K edge signal of 1.6% has been associated with a calculated moment of $0.08\,\mu_B$ (Pellegrin *et al*., 1997). This finding is in striking contradiction to the predicted value ranging from 0.07 to $0.2\,\mu_B$. (Bowen *et al*., 2006) since a significant spin moment is present in systems with vanishing or nearly quenched orbital polarization as in cubic systems. In general, the integration of the oxygen XMCD in terms of local moment is doubtful.

3.6 Limits of the sum rules for $L_{2,3}$ edges in rare-earth metals

As demonstrated in Figures 9, 12, and 29 at the $L_{2,3}$ edges in RE metals significant XMCD signals can also be observed. For example in Gd metal, as drawn in Figure 29, the $L_{2,3}$-edges XMCD ratio is -0.87 and close to the value of -1 for spin-only systems, as expected from the sum rules. The deviation suggests the presence of a small orbital contribution in the 5d states, which couple antiparallel to the spin. If one compares the $L_{2,3}$ XMCD signal of Gd metal with the corresponding dichroic profile in iron metal, as shown in Figure 29(b) an opposite sign can be found for both edges. This is in striking contradiction to the experimental macroscopic measurements and theoretical expectations indicating and predicting for Gd a spin moment of $0.47\,\mu_B$ and only a small negative orbital contribution of $-0.05\,\mu_B$ (Sticht and Kübler, 1985). This manifests the 'positive' breakdown of the sum rules for the $L_{2,3}$ edges in RE metals. But on the basis of various *ab initio* theories, it is possible to provide a satisfying description of the XMCD spectra. Theoretical *ab initio* investigations are based either on linearized band structure methods (Carra *et al*., 1991) or on multiple scattering theory (Ankudinov and Rehr, 1995; Ebert, Schütz and Temmerman, 1990) and achieved a good qualitative and quantitative agreement with the experimental findings. The theoretical spectra presented here have been obtained, analogous to those in Ebert (2000b) using a spin-polarized fully relativistic implementation of the Korringa–Kohn–Rostoker Green's function method (Ebert, 2000b). Another complication arises in the case of the RE metals where the $2p \rightarrow 5d$ transition can be superimposed by quadrupolar $2p \rightarrow 4f$ transitions. In Figure 30, the experimental Tb and theoretical $L_{2,3}$-XMCD spectra are shown, proving that these $E2$ transitions can also be treated properly on a theoretical basis (Wende *et al*., 2002). Details of the calculations illuminate furthermore that the spin dependence of the radial matrix elements in these elements accounts for the failure of the sum rules. It has been demonstrated that a proper generalization of the sum rules, taking

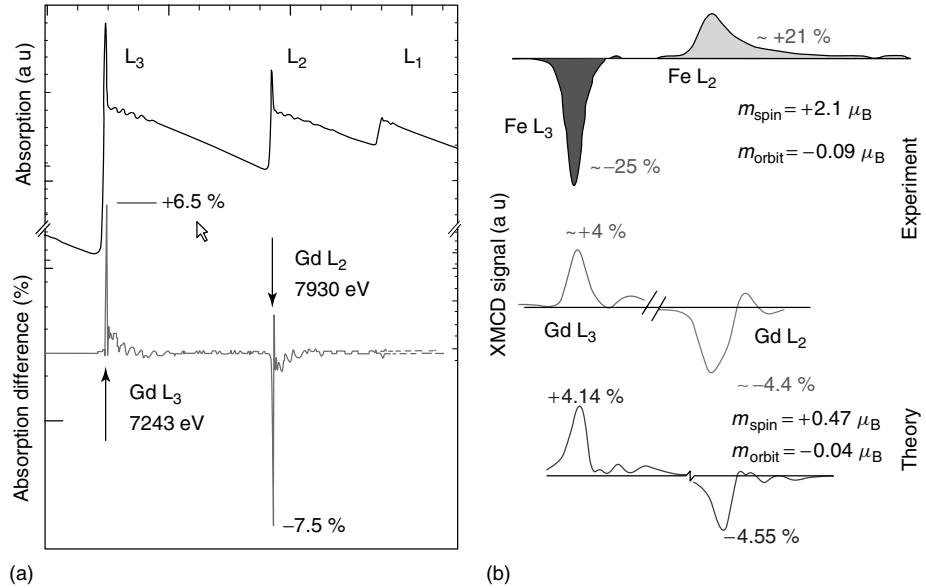

Figure 29. (a) X-ray Absorption and XMCD in an energy range of 7 to 8.5 keV covering all L edges of Gd metal. (b) Comparison of the Fe metal $L_{2,3}$ XMCD with the corresponding profiles at the Gd $L_{2,3}$-edges in comparison with the theoretical calculation of V. Popescu (2006) Private Communication.

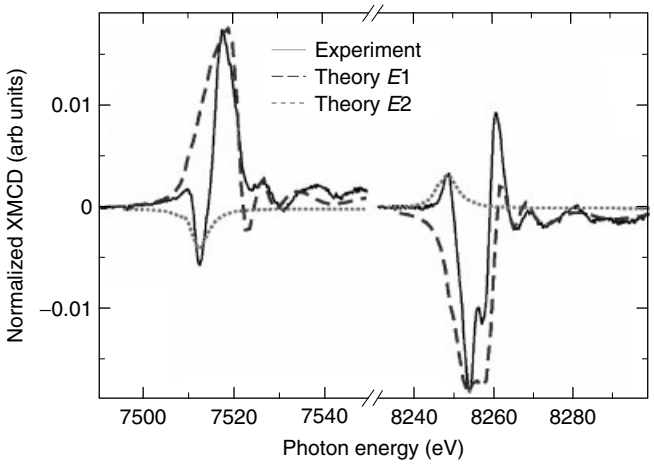

Figure 30. Experimental Tb $L_{2,3}$-XMCD spectra in comparison with theoretical profiles for $E1$ and $E2$ transitions. (Reproduced from Wende *et al.* (2004) *Reports on Progress in Physics* **67**, 2105–2181.)

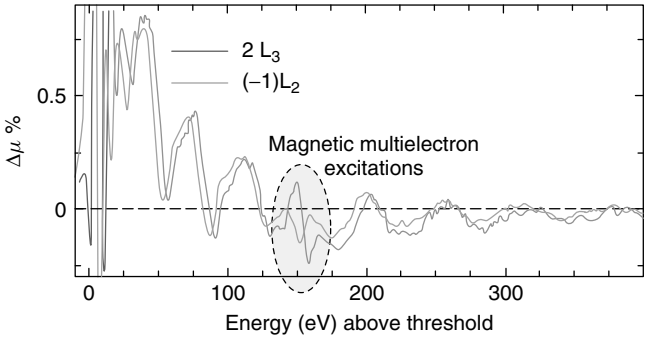

Figure 31. Magnetic EXAFS oscillations at the L_2 and L_3 edges in Gd metal as shown already in Figure 28 rescaled by a factor 2 and – 1 for the L_2- and L_3-signal, respectively.

this phenomenon into account, allows their application without a change of the sum rules in form or nature (Wende *et al.*, 2002).

4 XMCD-RELATED TECHNIQUES

4.1 Magnetic EXAFS

4.1.1 Experimental aspects

In an energy range of approximately 30 eV to 2 keV above an absorption edge in solid materials, the absorption coefficient exhibits an oscillating contribution. These oscillating structures, called *extended absorption fine structures* (*EXAFS*), show a decaying amplitude as a function of distance to the absorption edge and provide a strength of roughly 10% to the absorption jump height.

The oscillations $\chi(E) = \frac{\mu(E)-\mu_0(E)}{\Delta\mu_0}$ are extracted from the absorption $\mu(E)$ by the subtraction of the atomic-like smooth background $\mu_o(E)$ and normalization to the absorption jump $\Delta\mu_0$. This oscillating absorption is discussed here as a function of the photoelectron wave vector $k = \frac{1}{\hbar}\sqrt{2m(E-E_0)}$, where E_0 denotes the absorption threshold energy and m the electron mass. Viewing Figure 29, the energy range from about 7 to 8.5 keV covering all three Gd metal L absorption edges, it is evident that also an extended X-ray fine structure circular magnetic dichroic contribution is present. In contrast, the conventional corresponding MEXAFS can be detected directly by the circular magnetic absorption difference for reversed sample magnetization, $\chi(E) = \mu^+(E) - \mu^-(E)$ similar to the XMCD effect. In Figure 31, these magnetic oscillations are compared with Gd metal $L_{2,3}$ edges renormalized to each other by a factor 2. These structures appear to be nearly identical, except in the region of about 150 eV, that is, the range where multielectron effects are involved and significant differences from this relation are observed. These contributions result from the complex excitation from an additional 4d $\rightarrow$ 4f electron excitation channel, which is relatively weak but exhibits a large spin dependence since the fully polarized 4f-final state is involved in these magnetic multielectron excitations (MMEE) (Dartyge *et al.*, 1992).

In the meantime, it has been manifested by several MEXAFS studies that their occurrence is a universal effect, which exists even for absorbing atoms with vanishing magnetic moments. In Figure 32, the La L_3 edge in the ferromagnetic perovskite $La_{0.7}Ca_{0.3}MnO_3$ is shown (from Weigand, 2003). Here, the near-edge XMCD can be interpreted in terms of sum rules indicating the existence of a nearly vanishing spin and orbital moment of $m_S \sim +0.043\,\mu_B$ and $m_L \sim +0.003\,\mu_B$ of the La component, which is two orders smaller than the Mn moments of $3.4\,\mu_B$. Taking into account the scaling factor 2, the comparison of the corresponding MEXAFS $L_{2,3}$ edges proves that they are nearly identical within the statistical accuracy achievable today for the MEXAFS investigations in the hard X-ray range. It is evident that for the absorbing La atoms without a 4f occupation, as expected, no MMEE occurs.

As already observed in the first observation of the XMCD at the Fe K edges an extension of the magnetic effects toward the EXAFS range has also been indicated as seen in Figure 8 which is nearly of the same amplitude as the magnetic XANES. Another example for K-edge MEXAFS is given for Co metal in Figure 33 and is more than one order of magnitude smaller than the MEXAFS at $L_{2,3}$ edges. The magnetic part contributes only by less than 1% to the spin-averaged oscillation. Also, here MMEE contributions disturb the oscillating behavior in the

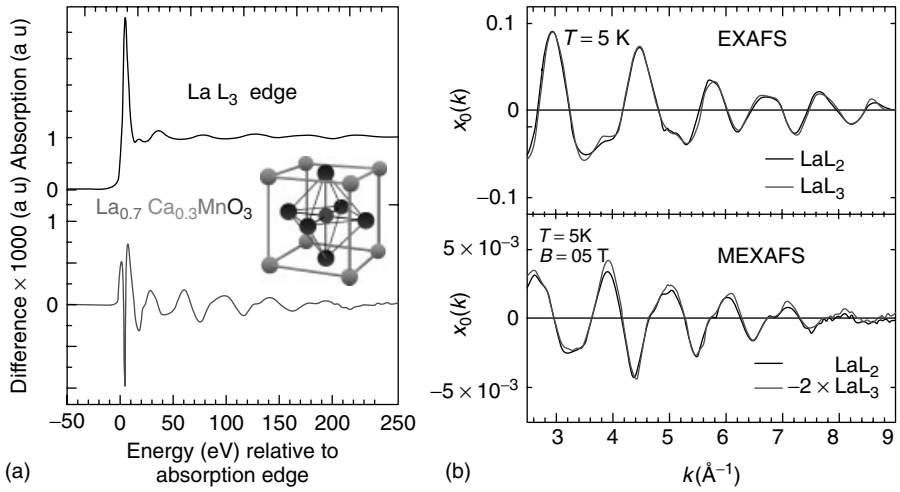

Figure 32. (a) Absorption and XMCD signal taken at the La L_3 edge in the ferromagnetic perovskite $La_{0.7}$ $Ca_{0.3}MnO_3$, (b) La L-EXAFS oscillation $\chi_0(k)$ and corresponding magnetic contributions $\chi_c(k)$ as function of the photoelectron k-number. By rescaling the L_3 MEXAFS by a factor -2 the MEXAFS at both edges are identical.

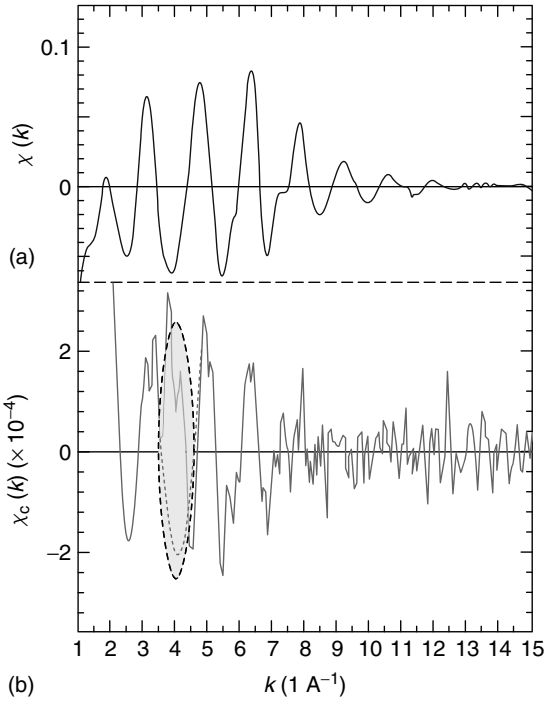

Figure 33. EXAFS (a) and MEXAFS (b) at the Co K edge in fcc Co metal. The shaded area corresponds to the expected energetical position of the 1s3p–4p3d multielectron excitations.

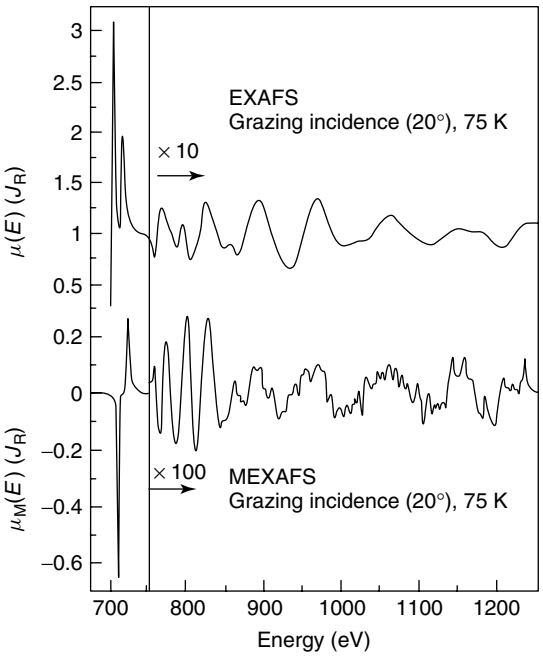

Figure 34. EXAFS and MEXAFS at the Fe metal L edges. (Reproduced from Lemke *et al*. (1998) *J. of Physics: Condensed Matter* **10**, 1917–1930.)

energy range of the 3p binding energy 60 eV, which indicates the occurrence of a strongly spin-dependent additional 3p–3d transition. As generally observed in K-edge MEXAFS a high-frequency fine structure seems to be superimposed to the broader oscillation correlated with conventional EXAFS.

Following the scenario described above one would expect much stronger MEXAFS at the $L_{2,3}$ edges of the 3d transition elements. However, serious complications result from the L_2–L_3-edge overlap of only 10–20 eV spin-orbit split edges, which is just in the order of a typical next neighbor distance-related (0.2–0.4 nm) half-wavelength. Figure 34 shows the experimental results of MEXAFS studies at the $L_{2,3}$ edges in a 30 ML Fe film on Cu(001) taken from Lemke *et al*. (1998),

where the MEXAFS oscillation can be clearly monitored with a relative amplitude of about 3% owing to a partially constructive overlap.

4.1.2 Theoretical description and data analysis

As already suggested by Kronig in 1932, who related the EXAFS to an influence of the next neighbors, and since the breakthrough by Sayers, Lytle and Stern (1970) and Sayers, Stern and Lytle (1971) the EXAFS are a powerful structural tool to study short-range order in an element-specific manner. The EXAFS have been described as an interfering sum of backscattered electron contributions from the next coordination shells j with N_j atoms at the distance r_j, which are smeared locally out by the Debye–Waller factor $\exp(2\sigma_{\mathrm{j}}(\mathrm{k})\mathrm{k}^2)$. These three parameters depend on the local structure of the system. The influence of the emitting atom itself is taken into account by the factor $S_i(k)$

$$\chi(k) = -\sum_j N_j S_i(k) F_j(k)\, \mathrm{e}^{-2\sigma_j^2(k)k^2}\, \mathrm{e}^{-2r_j/\lambda_j(k)} \times \frac{\sin\left(2kr_j + \Phi_{ij}(k)\right)}{kr_j^2} \qquad (19)$$

The electron–electron interaction is introduced by the elastic backscattering amplitude $F_{\mathrm{j}}(k)$, the inelastic mean free path $\lambda_{\mathrm{j}}(k)$ and the phase shifts Φ_{ij} acting on the electron waves.

Following the explanation of the XMCD in the XANES by the simple two-step model in the case of a right (left) circular polarized photon the outgoing photoelectron wave is spin polarized; therefore, one has to distinguish between 'singlet' and 'triplet' scattering indicated in Figure 35. A dependence of the interaction parameter on the relative spin orientation of the magnetic electrons of a neighboring atom polarized in photon beam direction can be introduced in a most simple manner by $F^{\pm}(k) = F_0(k) \pm \sigma_z F_{\mathrm{C}}(k)$ for the elastic backscattering amplitude and

$\Phi^{\pm}(k) = \Phi_0(k) \pm \sigma_z \Phi_{\mathrm{C}}(k)$for the phase shifts, while the inelastic scattering of the spin-dependent effects are of minor importance and can be neglected. Hereby – similar to the description of the spin-dependent Compton scattering – an additive spin-dependent part has been introduced which scales with the photoelectron polarization. Although this picture is very simple, it easily explains the ratio of 2 of the MEXAFS amplitude, which is observed at the L_3 and L_2 edges in magnetic systems.

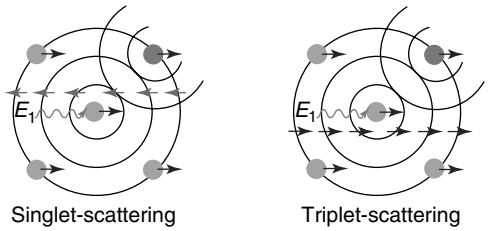

Figure 35. Two-step model of the magnetic EXAFS.

Another similar approach is the ansatz with an energy shift (Wende, 2004). More sophisticated theoretical treatments based on *ab initio* theories have been developed to describe successfully the MEXAFS (Ebert, 2000a).

Following the simple two-step model it is expected that only neighboring atoms account for the occurrence of dichroic signals in the EXAFS oscillations. This can be proved straightforwardly by an analysis of the MEXAFS by a Fourier transform (FT) of the conventional spin-averaged oscillations.

Taking the example shown in Figure 32 into consideration and following the EXAFS formula, the FT of $\chi(k)$ at the La $L_{2,3}$ edges will predominantly appear at distances given by the next neighbor coordination shell, which is slightly modified by the presence of the corresponding phase shift. The strengths of the lines are proportional to the number of atoms at these distances. As a typical result the FT($\chi(k)$) of the example given above is shown in the left panel of Figure 36 where the next neighboring oxygen, manganese, and La/Ca neighbors are clearly visible. In the FT of the corresponding $\chi_{\mathrm{C}}(k)$ spectrum only the line of the next magnetic Mn atoms appears, proving unambiguously that the spin-dependent contribution results only from backscattering

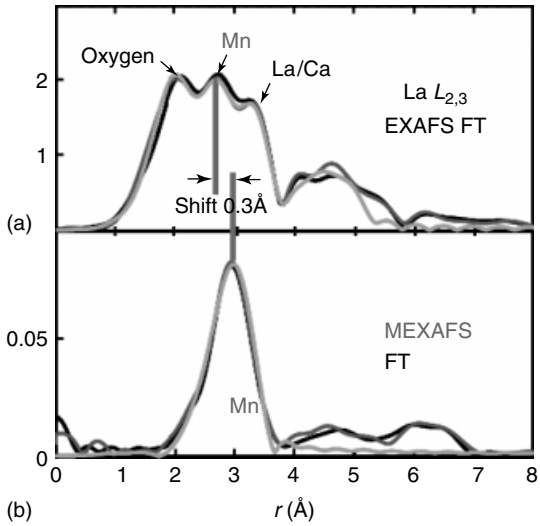

Figure 36. Fourier Transform FT(χ_0(k)) (a) and FT(χ_0(k)) of the La L_2- edges (black) and L_3-edges rescaled by a factor 2 (gray) in comparison with the theoretical spectra calculated with the FEEF8.2 program modified following the equation.

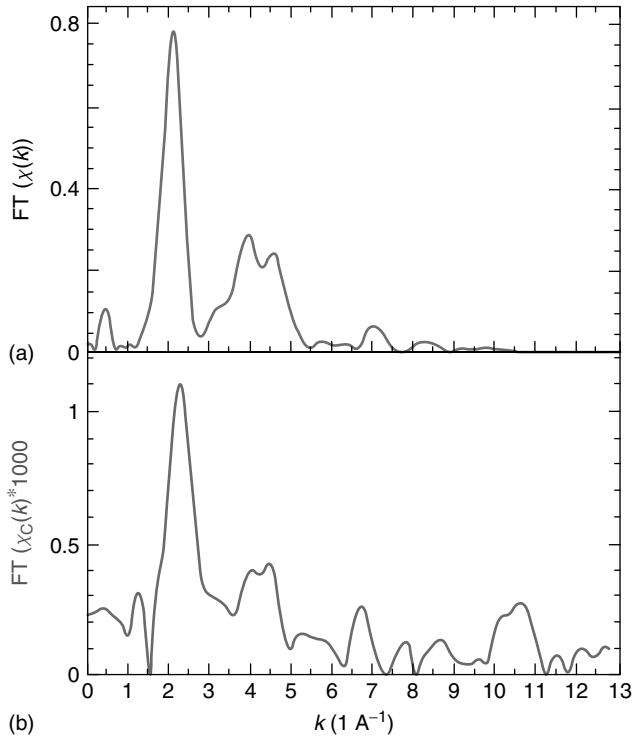

Figure 37. Fourier Transform FT($\chi_0(k)$) (a) and FT($\chi_0(k)$) of the EXAFS and MEXAFS shown in Figure 32.

from the magnetic neighbors. This proves that the MEXAFS is an appropriate method to probe the magnetic short-range order even for nonmagnetic absorbing atoms as the La component in this perovskite. It has been verified in ferrimagnetic iron garnets that the phases in the FT help to distinguish between ferro- and antiferromagnetic coupling of the corresponding sublattices.

On all the sample studies up to now, we found an interesting correlation of the relative strength of the MEXAFS: A rescaling of the ratio maxFT($\chi_C(k)$)/maxFT($\chi(k)$) by the spin polarization of the outgoing photoelectron wave and the magnetic spin moment of the next nearest neighbor in units of Bohr magnetrons seems to be a constant value, indicating a spin-dependent contribution to the backscattering amplitude of 2–3% per spin-polarized electron in the atomic shells of the next neighbors (Figure 37).

Significant effects at the K edge are observed in the MEXAFS as shown in Figure 8 and also at the Co K edge in Figure 33, as expected from the sum rules only the orbital polarization can be addressed. The FT for this pure metal provides the same local information in the spin-averaged and spin-dependent case, but a significant enhancement of the multiple scattering paths is observed. This might be correlated to an increase of the spin polarization of the outgoing photoelectron wave due to the presence of the spin-dependent elastic scattering if the electron is scattered several times.

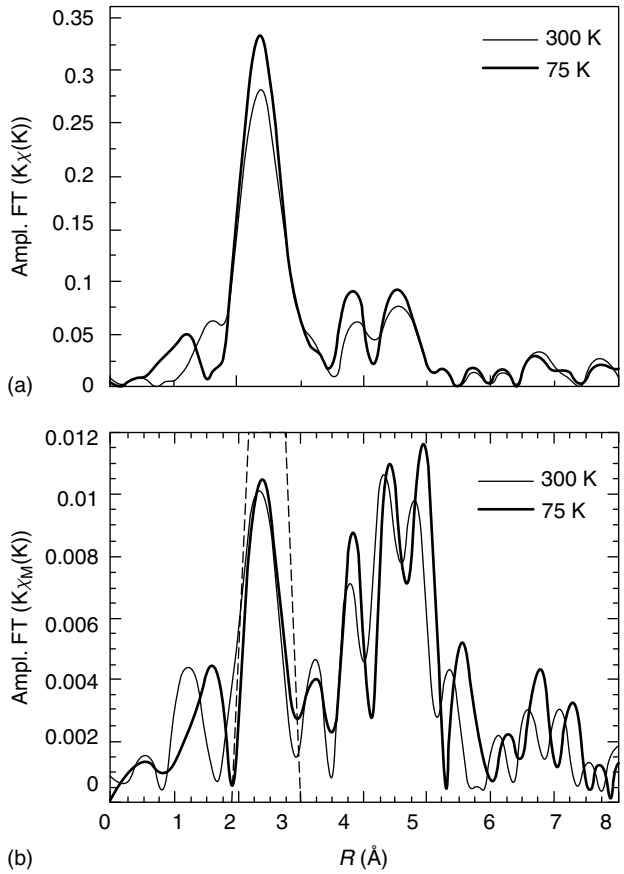

Figure 38. Fourier Transform FT($\chi_0(k)$) (a) and FT($\chi_0(k)$) of the EXAFS and MEXAFS shown in Figure 34. (Reproduced from Lemke *et al*. (1998) *J. of Physics: Condensed Matter* **10**, 1917–1930.)

This phenomenon is prominent at the K edges, where the starting spin polarization is expected to be induced by spin-orbit effects and in the order of only 1%. A more detailed systematic investigation of the MEXAFS may well provide a new direct possibility to study spin–spin interaction of hot electrons with kinetic energies up to several 100 eV. Similar behavior is indicated in the FT of the MEXAFS at the Fe $L_{2,3}$ edges of metallic Fe (Figure 38). Besides the influence of multiple scattering paths, the overlap of the L_2 and L_3 MEXAFS result in additional, obviously unphysical, line features. This demonstrates the general difficulty in analyzing 3d L-MEXAFS in terms of investigating short-range magnet orders.

4.2 Magnetic reflectometry

4.2.1 General aspects

Since the discoveries of Max von Laue and Luis Néel, the use of X-ray scattering for the structural analysis of

condensed matter is well known and highly established. Hereby the momentum transfer in the scattering process provides structural information along its direction.

One special case of structural determination is the investigation of ultrathin films in the thickness range of several monolayers of atoms at relative small momentum transfer ranges by reflectometry, providing information of film thickness and interfacial properties like roughness. For the X-ray scattering processes resulting in the presence of the cross section σ_{coh} drawn in Figure 5 the basic interaction is described by the scattering amplitude f_0 by $\sigma_{\mathrm{coh}}(E) = \int |f_0(E,\theta)|^2 \,\mathrm{d}\Omega$, where θ is the scattering angle as introduced in Figure 4(b).

In the vicinity of an absorption edge additional dispersive (f') and absorptive (f'') scattering factors occur to the elastic scattering amplitude $f(E) = f_0 + f' + f''$, which are related to each other by Kramers–Kronig relations (Hoyt, Warburton and de Fontaine, 1984; Neumann *et al.*, 1998).

$$f'(E) = \frac{2E_0}{\pi} \oint \frac{f''(E)}{E_0^2 - E^2} \mathrm{d}E \tag{20}$$

Following the optical theorem, the absorptive scattering amplitude is directly correlated to the absorption cross section by $\mu_{\mathrm{abs}}(E) = \rho_{\mathrm{a}} 2 r_0 \lambda f''(E)$. This close relationship is explained in Figure 39 where the left part illustrates the absorption process and the right part symbolizes the resonant scattering process into a single intermediate state and results in the emission of an elastically scattered photon with the same energy.

At a circular dichroic active absorption edge – in analogy to the XMCD contributions – a magnetic scattering factor has to be taken into account as expressed in the pioneering work of Hannon, Trammell, Blume and Gibbs (1988)

$$f(q,E) = \underbrace{-\left(\vec{e}_f^{\,*} \cdot \vec{e}_i\right) \cdot \left[f_0 + f'(E) + f''(E)\right]}_{\text{Nonmagnetic Colomb Part}} + \underbrace{i\left(\vec{e}_f^{\,*} \times \vec{e}_i\right) \cdot \vec{b} \cdot \left[m'(E) + i m''(E)\right]}_{\text{Magnetic Part}} + \cdots \tag{21}$$

where $\boldsymbol{q}$ is the scattering vector, $\vec{e}_i$ and $\vec{e}_f$ are the complex polarization vectors of the incident and scattered beam, $\vec{b}$ is the unit vector of the magnetization. The residual resonant scattering amplitude is separated in a charge and magnetic term with different dependencies of the polarization vectors. The complex amplitude of the magnetic term with dispersive part m' and absorptive part m'' changes its sign by reversal of the external magnetic field. The absorptive contribution to the magnetic scattering amplitude is usually derived by XMCD experiments, similar to the dispersive time-even part $f'(E)$ and time-odd part $m'(E)$ of the scattering factor, which are deduced by Kramers–Kronig relations equal to equation (20)

$$m'(E) = \frac{2E_0}{\pi} \oint \frac{m''(E)}{E_0^2 - E^2} \mathrm{d}E \tag{22}$$

To give an example of this procedure, the charge and magnetic scattering factors at the Pt L_3 edge of a $Pt_{20}Fe_{80}$

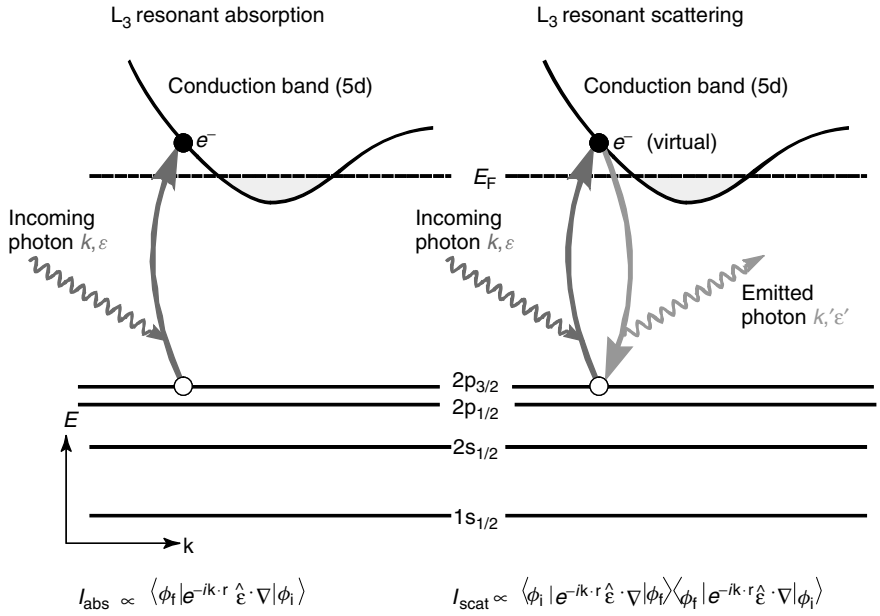

Figure 39. Physical process of the excitation of an inner shell $2p_{3/2}$ electron to a 5d unoccupied conduction band (left side) in comparison with the resonant scattering event.

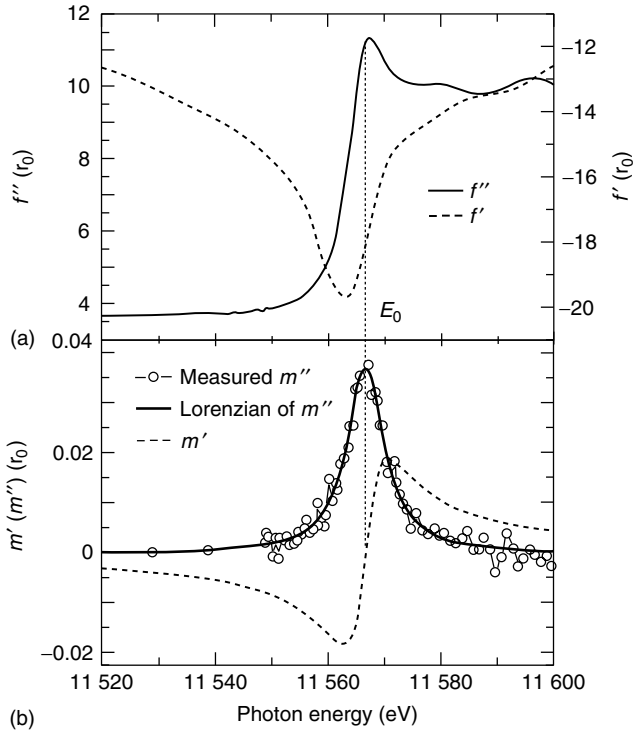

Figure 40. (a) Dispersive f' and imaginary part f'' in the vicinity of the Pt L_3 edge in a $Pt_{20}Fe_{80}$ alloy and (b) the corresponding magnetic contribution m' and m''. (Reproduced from Geissler *et al.* (2002) *Zeitschrift für Metallkunde* **93**, 946–952.)

and the Co $L_{2,3}$ edges of Co metal sample are shown in Figures 40 and 41, respectively.

4.2.2 The description by the complex index of reflection

In grazing incidence conditions the momentum transfer $q_z = 2k_0 \sin\theta$ along the surface normal is small compared to reciprocal lattice vectors and the granular atomic structure of the material can be neglected, providing a description in a continuum approach. The interaction with electromagnetic waves is handled by a complex index of refraction $n = 1 - \delta + i\beta$, where the energy dependent optical constants δ and β are related to the complex scattering amplitude f_j of each site by the well-known optical theorem (Compton and Allison, 1935)

$$n = 1 - \delta + i\beta = 1 - \frac{r_0}{2\pi}\lambda^2 \sum n_j f_j \qquad (23)$$

where n_j is the number of atoms per unit volume, r_0 is the classical electron radius and λ is the wavelength of the incoming electromagnetic wave. Concerning the imaginary contributions a simple relation between β and the absorption coefficient is found by $\beta(E) = \frac{\mu(E)}{4\pi}\lambda$. The reflectivity R_i of each single interface is calculated by the well-known Fresnel equations (Jackson, 1975) for reflection of s- and p-polarized electromagnetic plane waves. This is schematically shown in Figure 42 for a multilayer system. These angular dependent reflectivity spectra are evaluated by the well-known Parratt algorithm (Parratt, 1954), which could be handled even for structures consisting of a sequence of layered media with different indices of refraction

$$R_i = \frac{R_{\mathrm{t,i}} + R_{\mathrm{b,i}} \exp(2i\varphi)}{1 + R_{\mathrm{t,i}} R_{\mathrm{b,i}} \exp(2i\varphi)} \qquad (24)$$

Hereby $R_{\mathrm{t,\,i}}$ and $R_{\mathrm{b,\,i}}$ are the Fresnel reflection amplitudes at the top and bottom surface of the layer i. For rough interfaces, these coefficients must be modified by an exponential damping factor (Névot and Croce, 1980; Holy *et al.*, 1993; Holý, Pietsch and Baumbach, 1999; Sinha, Sirota, Garoff and Stanley, 1988),

$$R_{i\to j}^{\mathrm{rough}} = R_{i\to j}^{\mathrm{flat}} e^{-q_{z,i} q_{z,i+1} \sigma^2} \qquad (25)$$

where $R_{i\to j}$ means the Fresnel coefficient for reflection from the interface and the related transition of light from medium i to j. $q_{z,i}$ and $q_{z,i+1}$ are the components of the complex wave vectors in medium i and $i+1$ perpendicular to the interface.

The phase difference $\varphi = 2\pi / d_i n_i \lambda \sin\theta_i$ is responsible for the interference patterns in the reflectivity curves, containing the thickness d_i and the index of refraction n_i. In an angle dispersive setup, the intensity maxima appear whenever $\exp(2i\varphi) = 1$, which is analogous to the Bragg equation modified by the influence of refraction. All scattered light intensities and phase differences are taken into account, which are essential for a high qualitative and quantitative simulation of experimental data.

Surface imperfections yield to a decrease in reflectivity and an increase of diffuse scattered light. Stearns (1989) has shown that in the case of a smooth or nonabrupt change in the index of refraction, which can be described by an interface profile function $p(z)$, the resultant loss in specula reflectance can be approximated by a simple multiplication of the Fresnel coefficients by the FT $\tilde{w}(q_z)$ of the function $w(z) = \mathrm{d}p/\mathrm{d}z$. Assuming a Gaussian distribution of the atoms of two layers at the interface, corresponding to an error function as $p(z)$, the mean vertical roughness or interdiffusion or a combination of the two cases can be described by the quantity σ, the root mean square (rms) roughness.

Reflectometry at thin layered systems yields to information about layer thickness and interface roughness due to the above mentioned interference phenomena of the reflected intensity at each interface (Holy *et al.*, 1993; Sinha, Sirota, Garoff and Stanley, 1988). Hereby the maxima and minima

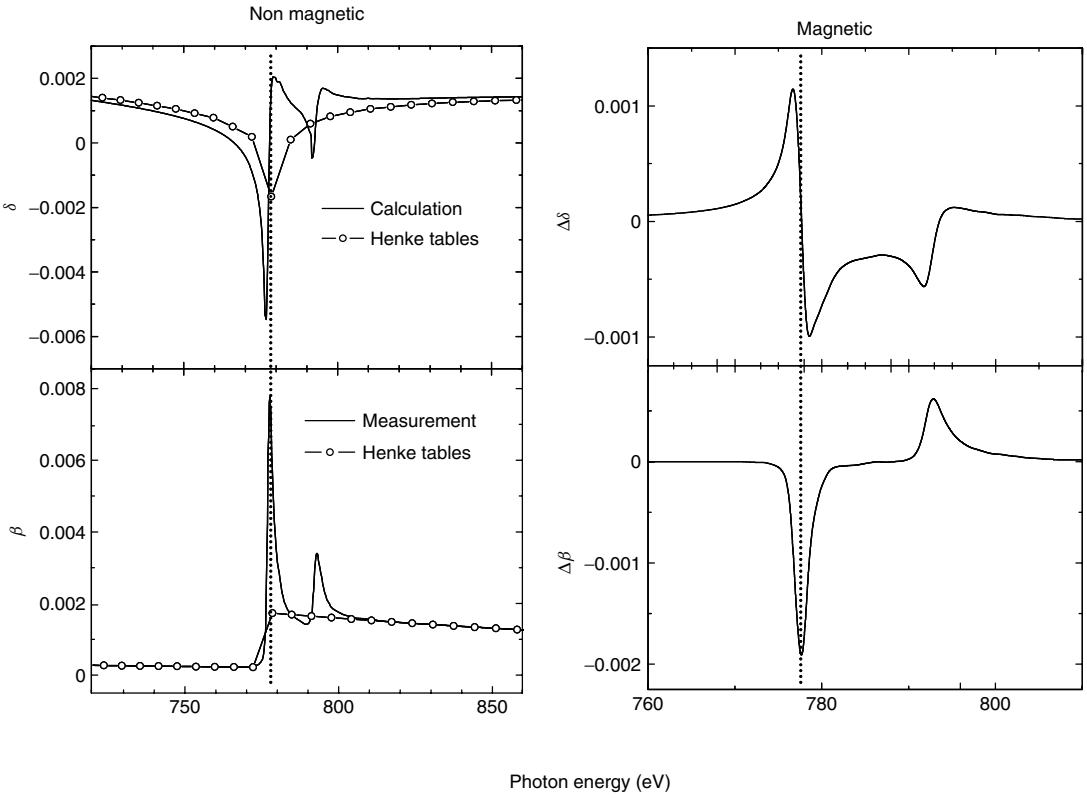

Figure 41. The nonmagnetic and magnetic energy dependent parts of the complex index of refraction. The nonmagnetic (magnetic) absorptive parts are based on corresponding XAS (XMCD) measurements, which have been scaled to nonresonant tabulated values (Henke table). The dispersive parts are calculated by Kramers–Kronig calculation, discussed in chapter.

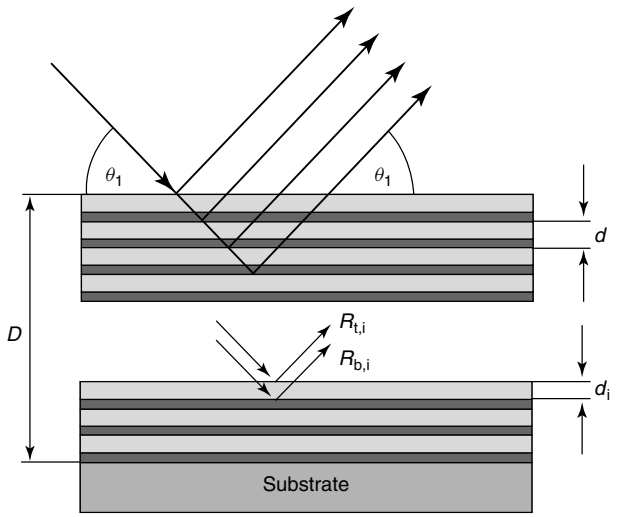

Figure 42. Schematic X-ray reflection in a multilayer structure. (Reproduced from Geissler *et al*. (2002) *Zeitschrift für Metallkunde* **93**, 946–952.)

in the reflectivity curve are caused by the interference of the waves reflected from the upper and lower interfaces of a thin film.

4.2.3 Magnetic reflectometry in multilayers

Multilayer systems provide Bragg peaks related to the superstructure of the multilayer (Ferrer *et al*., 1997) containing information of layer-averaged properties, for example, depth profiles of one component of the whole multilayer system (Jaouen *et al*., 2000; Seve *et al*., 1999; Tonnerre *et al*., 1995). Figure 43 shows the experimental nonmagnetic resonant reflectivity curves of a Ce/Fe multilayer system reproduced from Seve *et al*. (1999), in combination with the simulated reflectance for a multilayer system. The Bragg reflections of the multilayer superstructure of the multilayers are directly observable.

The magnetization induced changes in the reflectivity are measured by the weighted reflectivity difference for reversed sample magnetization

$$A = \frac{R^+ - R^-}{R^+ + R^-} \tag{26}$$

The magnetic asymmetry ratios are also plotted as a function of photon energy (Figure 44), where the scattering angle has been chosen to be at various superstructure Bragg peaks, indicated by the diffraction order. Without

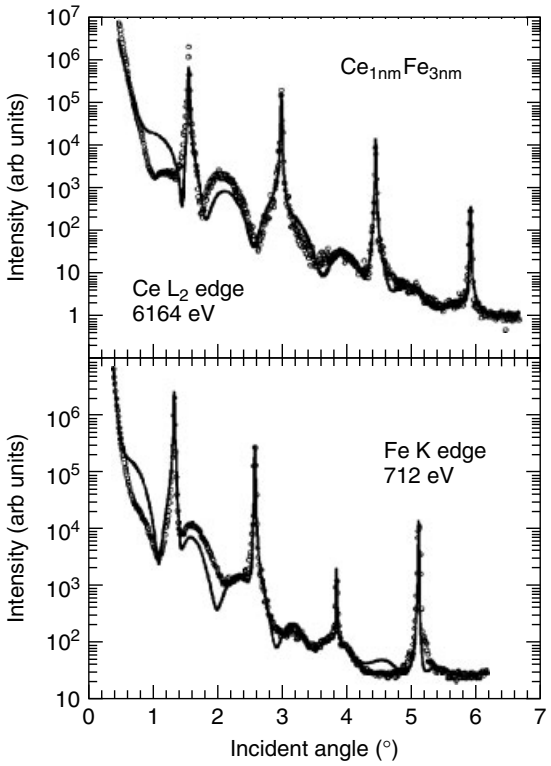

Figure 43. Resonant nonmagnetic reflection curves of a Ce–Fe multilayer system. Clear superstructure Bragg reflections are visible. The shift of the superstructure peaks reflects different the variation of the photon wavelength from the Fe K edge to the Ce L2 edge. (Reproduced from Seve *et al*. (1999) *Physical Review B* **60**, 9662–9674.)

going into details of the analysis, the chemical profile has been extracted from the nonmagnetic spectra, and magnetic counterpart from the magnetic asymmetry. Multilayer systems provide the unique opportunity to extract nonmagnetic and magnetic multilayer information in an analytical way (Seve *et al*., 1999; Tonnerre, 1997). Thus variations and their dependence on the distance of an individual layer from the substrate, important for components with large lattice mismatch, can hardly be addressed. Furthermore, diffuse X-ray resonant magnetic scattering (XRMS) in the soft X-ray region can be applied to investigate correlations between chemical and magnetic roughness in thin films and multilayers (MacKay, Teichert, Savage and Lagally, 1996; Osgood *et al*., 1999). Magnetic resonant reflectivity measurements in the soft X-ray region were performed (Kao *et al*., 1990, 1994; Sacchi and Mirone, 1998; Tonnerre *et al*., 1995, 1998) to measure the energy dependence of the reflected intensity for parallel and antiparallel alignment of the photon helicity and the direction of the magnetization.

4.2.4 Resonant magnetic reflectometry at single layers

Hard X rays

The experimental setup of the magnetic reflectivity experiment in specular geometry, where the incident and reflected intensity has been detected by ionization chambers, is shown in Figure 45. To simplify the analysis the energy of the scattering experiment has been adjusted to the Pt L_3 maximum of the absorptive part m'' where the dispersive part m' nearly vanishes, as shown in Figure 40 (marked with E_0). f'' and m$''$ were derived from the nonmagnetic and magnetic absorption profiles respectively, measured in a separate transmission experiment (Ruegg, Schütz, Fischer and Wienke, 1991). The structural profile information, that is, layer thickness and roughness, is derived by a nonresonant Cu K_α experiment by conventional Parratt simulation (Figure 45). Figure 46(a) shows the magnetic asymmetry and the result of simulations based on a technique called *multislicing* (Geissler *et al*., 2001): The reflectance of a rough interface was initially modeled by the reflectance of a sharp interface, damped by an exponential damping factor, and then approximated by a series of many virtual slices with no roughness in between, providing the same smooth distribution of the corresponding optical constants, which reflects the same optical and chemical profile. For the magnetic profile simulation the magnetic scattering part is added (subtracted) to the optical profile (determined by the chemical profile), providing two different reflectivities R^+ and R^-. Figure 46 shows the simulated magneto-optical profile and the corresponding magnetization per Pt atom. The magnetization per atom has been deduced from the normalization of the magneto-optical profile to the chemical profile, as shown in the inset of Figure 46(b) (Geissler *et al*., 2001; Geissler, Goering, Weigand and Schütz, 2002).

Since for hard X rays the typical scattering angle range is below 4°, the dipole scattering formula can be reduced by the small angle approximation to [16]

$$f_{\mathrm{res},\theta\approx 0}(E) = -r_0\left[\left(f_0 + f'(E) - if''(E)\right) + P_{\mathrm{C}}\left(m'(E) - im''(E)\right)\right] \qquad (27)$$

This provides a strongly reduced numerical effort, necessary for the reflectivity simulations. Since the magnetic effect is in the order of 4%, it does not provide a strong impact to the total reflectance. This conserves the general momentum transfer and the related interference conditions, and the magnetic asymmetry can be considered proportional to the magnetic moment.

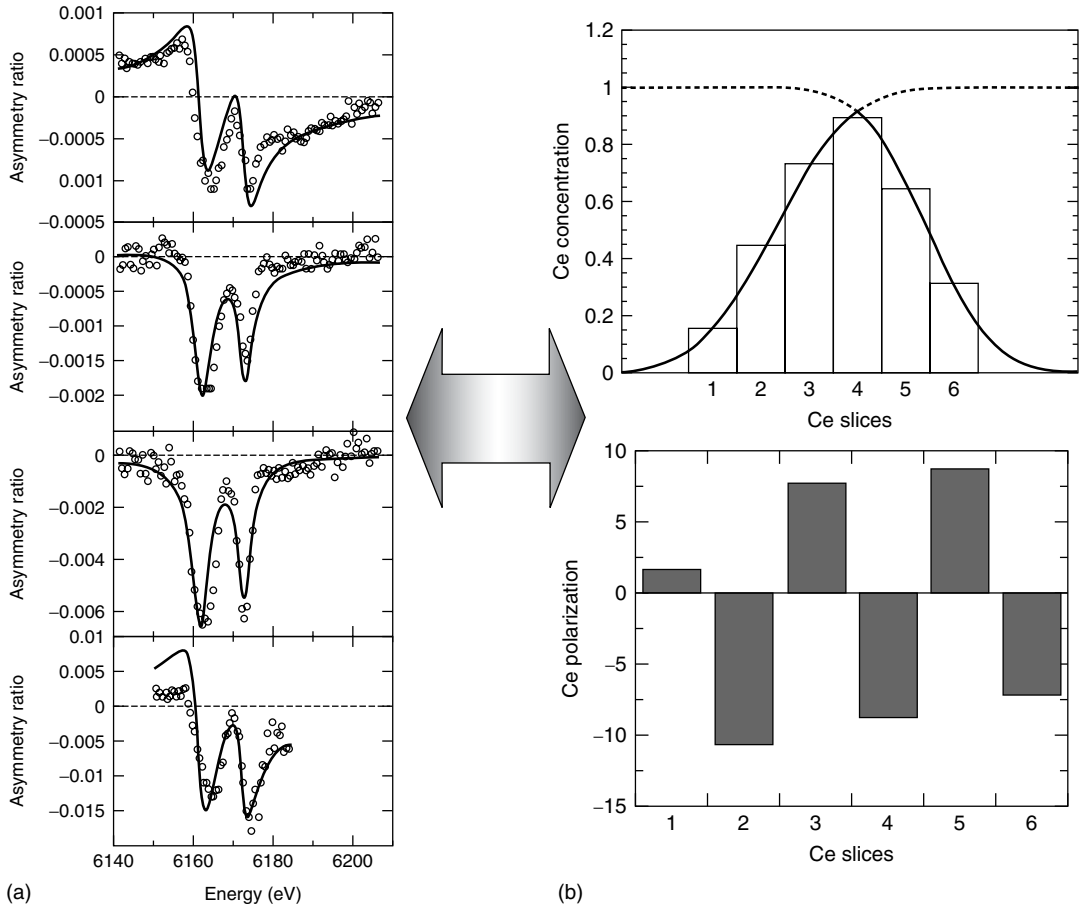

Figure 44. (a) The energy dependent asymmetry ratio measurement (circles) and simulation (line). (b) The upper curve shows the chemical profile, estimated from the nonmagnetic simulation shown in the previous figure. The lower part represents the Ce magnetic polarization, extracted from the asymmetry fit. (Reproduced from Seve *et al*. (1999) *Physical Review B* **60**, 9662–9674.)

Soft X rays

In this energy range, two major difficulties arise owing to the larger scattering range of about to 40–50° and very strong resonant nonmagnetic and magnetic absorption lines. The whole geometry of the magnetic scattering scenario, which is discussed here, is sketched in Figure 47. A typical experimental asymmetry, measured at the Co L_3 edge for the same PtCo sample, is shown in Figure 48 in comparison with the simulations, which provide a very good representation of the experimental data. The principle calculation method is quite comparable to the Pt spectra shown above, but owing to the large range of scattering angles a full treatment of the scalar and cross products of the incoming and scattered polarization vectors separated into σ and π channels is necessary

$$f_{\mathrm{E1},\sigma} = -r_0 \frac{\left(f_0 + f' - if''\right) \pm K \cdot \cos\theta \cdot M \cdot \left(m' - im''\right)}{\left(1 + K^2\right)^{1/2}} \qquad (28)$$

$$f_{\mathrm{E1},\pi} = -r_0 \frac{K \cdot \cos 2\theta \cdot \left(f_0 + f' - if''\right) \pm \cos\theta \cdot M \cdot \left(m' - im''\right)}{\left(1 + K^2\right)^{1/2}} \qquad (29)$$

The degree of circular polarization is described as $P_C = 2K/(1 + K^2)^{1/2}$, and the magnetic part of the scattering amplitude varies with the cosine of the angle of incidence. For the calculation of the asymmetry ratio the intensities of the σ and π components have been added in a kinematic approximation. This approximation breaks down at very small scattering angles owing to the enhanced influence of multiscattering processes. Nevertheless, for systems with a nonmagnetic protective top layer, the asymmetries are usually small at graving incidence conditions, where the interface of the nonmagnetic protective top layer to the vacuum dominates the reflection.

After determination of the resonant optical properties, as shown for the Co $L_{2,3}$ edges in Figure 41, the magnetic profile could be determined by the same general procedure used above, where the interface is artificially sliced into ultra

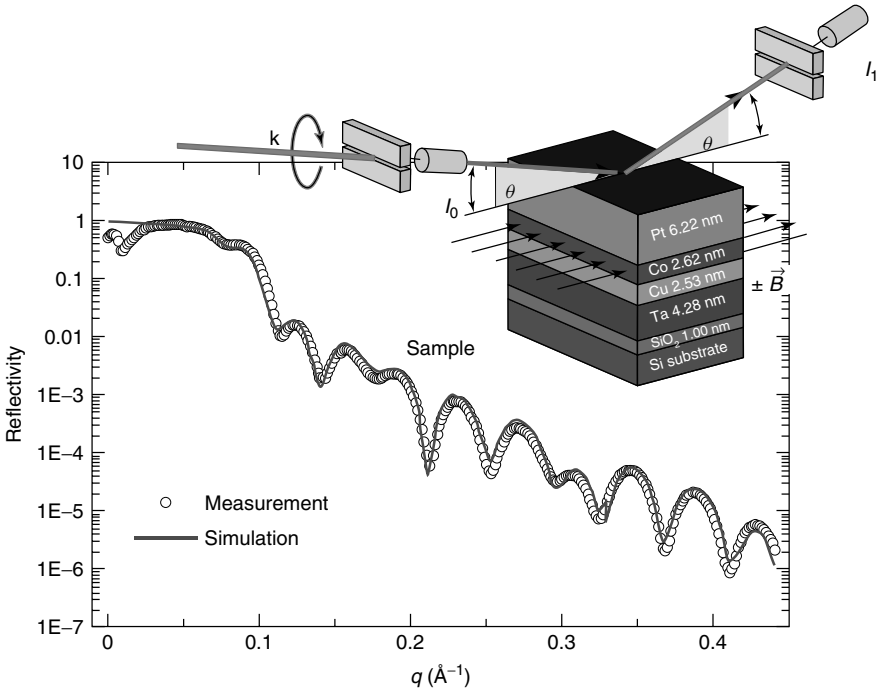

Figure 45. Experimental geometry of a reflection measurement for a Pt/Co/Cu-layered system and a nonresonant reflection curve, performed at the CuK_α energy.

thin layers. The nonmagnetic optical profile corresponds to the roughness determined chemical profile, convoluted with the optical constants as shown in Figure 49. The lighter gray part shows the resonant nonmagnetic absorption profile, clearly reflecting the increase inside the Co layer. For the magnetic simulation the darker gray part is added (as shown) and subtracted from the lighter gray curve, giving two magnetic reflectivity curves and the asymmetry. As for Pt, the element-specific Co magnetization profile could be extracted as shown in Figure 50, which compared to bulk Co is enhanced at the Pt site by a factor of 1.25 and reduced at the Cu site by a factor of 0.7. These results are in very good quantitative agreement with complementary experimental results for Co/Pt layers (Canedy, Li and Xiao, 2000; Nakajima *et al.*, 1998) and Co/Cu (Bland, Daboo, Patel and Fujimoto, 1998; Ney, Poulopoulos and Baberschke, 2001).

4.2.5 Restrictions and limits

- Since XRMS is a conventional scattering method and – in contrast to holography – the absolute phase information is lost, the result is not unambiguous. Thus, it is absolutely necessary to restrict the shape of the magnetization to intentionally reasonable and meaningful profiles.
- The determination of the optical constants and the corresponding energy calibration must be done very carefully. The best way is a simultaneous determination of the absorption coefficient at the same experimental station.
- Measurements at the energy of the maximum XMCD effect provide, in most cases, the opportunity for the magnetic dispersive part to nearly vanish (see Figure 41 for the optical Co profile). This reduces a possible error source from the determination of the dispersive part.
- The determination of the magnetic moment per atom needs the knowledge of the thickness dependent variation in the absorption which must be monitored by XAS/XMCD experiments. Auxiliary sources of information are usually theoretical investigations.
- As demonstrated for Magnetite (Goering, Gold, Lafkioti and Schuetz, 2006). Self-absorption, careful background approximation, long energy range measurements and calibration to the efficiency of the I_0 detector are all necessary to provide good estimates of the absolute resonant absorption coefficients.

4.3 Magnetic X-ray microscopy

4.3.1 General aspects

During the 1980s the availability of high-brilliance synchrotron sources and the fast development in nanotechnology

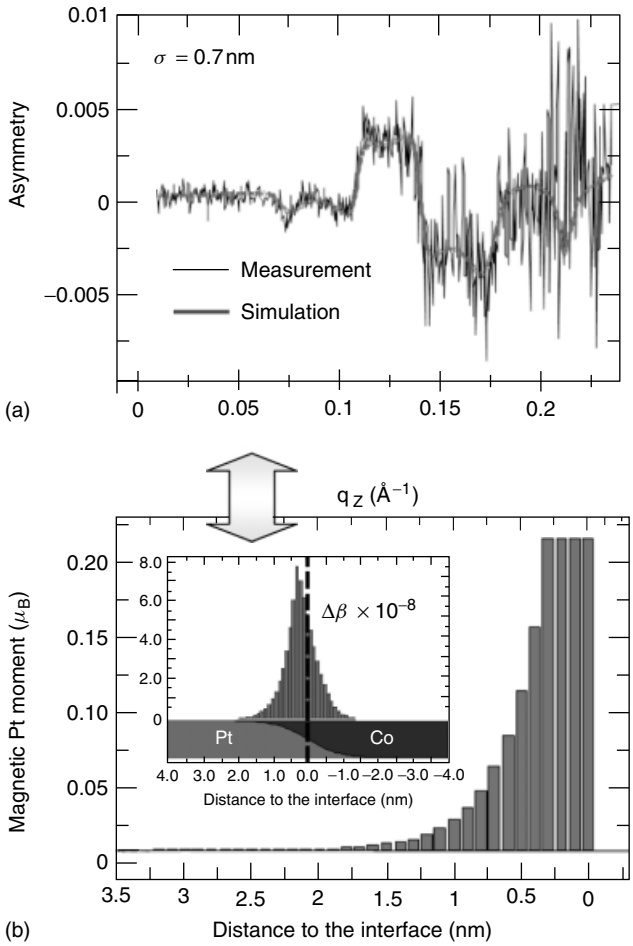

Figure 46. (a) Measured and simulated magnetic reflectivity. (b) Magnetic Pt moment per Pt atom. The inset shows the magneto-optical profile of Pt (slices). The roughness determined chemical profile is indicated by the gray and black shaded areas, shown at the bottom of the inset.

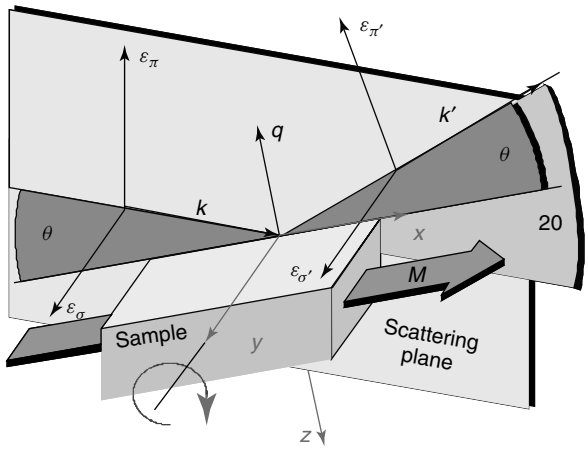

Figure 47. Scattering geometry used for the evaluation of the σ and π intensities.

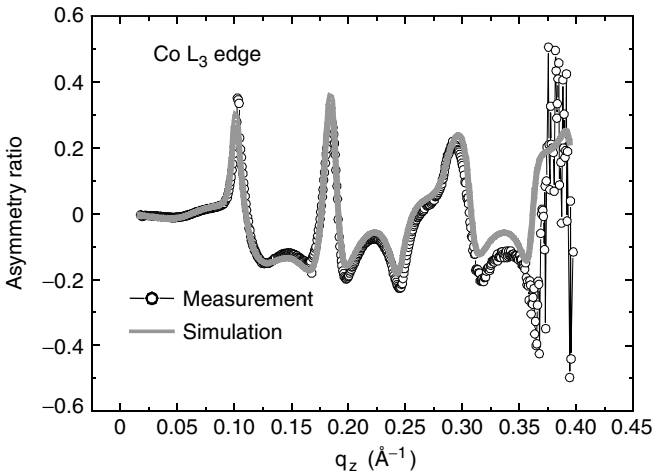

Figure 48. The asymmetry ratio measured at the Co L3 edge at the maximum XMCD effect in comparison with the best asymmetry simulation.

led to new powerful concepts using X rays for imaging of submicron structures by photoemission electron microscopy (PEEM), (Tonner and Harp, 1988) and Fresnel lens-based X-ray transmission microscopes (Attwood, 1999). More recently lensless coherent imaging techniques (Eisebitt *et al.*, 2004) were established.

The basic experimental set ups are sketched in Figure 51(a–d). Using XMCD as a magnetic contrast, all four types of methods can be used to image magnetic structures. Owing to the smaller wavelength of the X rays and the huge magnetic cross sections, especially for prominent absorption edges of the magnetically relevant elements, as shown in Section 2, these magnetic X-ray imaging techniques overcome the commonly used Kerr microscopes (Hubert and Schäfer, 1998) concerning image contrast and lateral resolution. These X-ray imaging techniques cannot provide atomic resolution in contrast to the spin-polarized scanning tunneling microscope (SP-STM) (Bode, 2003; Wachowiak *et al.*, 2002) and the magnetic force microscope (Martin and Wickramasinghe, 1987; Koblischka and Hartmann, 2003). However, the element specificity of magnetic X-ray imaging techniques and the direct correlation of the contrast to local magnetic spin and orbital moments make them unique tools for investigating magnetism of micro- and nanostructures. These systems are important subjects in solid state and material sciences as well as in data storage and sensor technologies.

The PEEM is sketched in Figure 51(a). Secondary electrons, which are commonly emitted after irradiation with monochromatic X rays from an undulator, are imaged by an electron microscope. The lateral resolution is determined by the electron optics and for magnetic applications is in

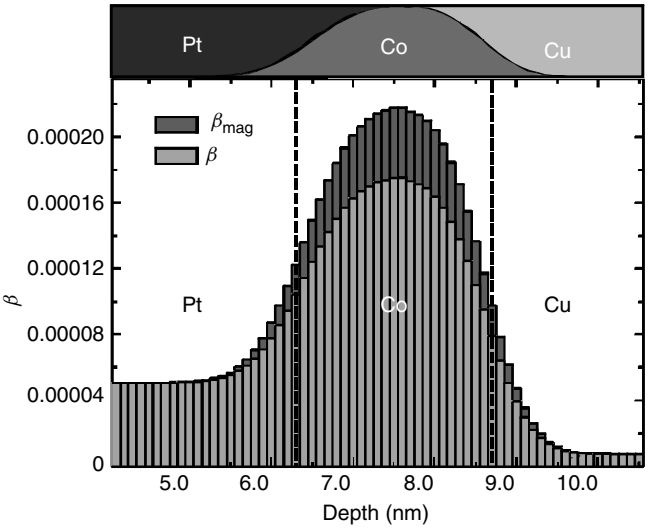

Figure 49. The determined absorptive nonmagnetic dark gray and magnetic light gray amplitudes at the CoPt interface are shown as a function of depth. The dashed lines indicate the average interface position, given by the nonmagnetic Parratt reflectivity simulation.

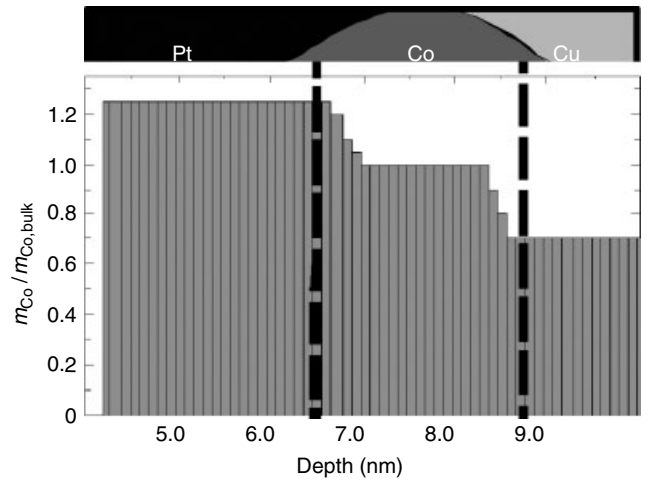

Figure 50. Determined magnetic moment per Co atom, derived from the normalization of the resonant magneto-optical profile by the chemical distribution shown above.

the order of 50–100 nm. Similar to the TEY detection mode for XMCD studies for soft X rays, described in Section 2, this method is inherently strong surface-sensitive to a few atomic layers with the advantage that nontransparent samples and very thin layers can be studied. Since low-energy electrons are involved in this photon-in/electron-out technique, the application of an external magnetic field in the XMCD/PEEM and the high voltage present at the sample, introduce experimental difficulties.

In X-ray microscopy techniques where only photons are involved, Fresnel zone plates (Attwood, 1999) are used as optical elements and the magnetic field is not modifying the image. Both types of microscopes operate in the transmission mode: a full-field X-ray microscope (Figure 51b) and a scanning transmission X-ray microscope (STXM, Figure 51c). The lateral resolution is determined by the width of the outermost ring of the zone plate and is in the order of about 25 nm (record 15 nm (Chao *et al*., 2005)) limited by current electron-beam lithography techniques. Both types of microscopes image the structures of samples with thicknesses in the order of some 100 nm deposited on transparent substrates as Si_3N_4 or on grids as used for transmission electron microscopy. Since the focal length of the Fresnel lenses is proportional to the photon energy for full-field microscopy, the first condenser lens can work as a monochromator with an energy resolution $E/\Delta E$ of 200–1000 by focusing a polychromatic beam from a bending magnet onto a sample spot with a diameter of several micrometers. The micro zone plate images the sample onto an X-ray-sensitive CCD camera. In contrast to this, the STXM uses one micro zone plate to focus the beam onto the sample mounted on a scanning stage and the transmitted intensity is monitored by a typical photomultiplier tube or an avalanche photodiode. More sophisticated detector schemes allow simultaneous imaging in four ways; bright-field and darkfield imaging, as well as differential phase contrast in the x and y direction (Kirz *et al*., 2004).

New paths are treated by lensless imaging with coherent X-ray scattering where, as sketched in Figure 51(d), the images are reconstructed in real space either by iterative phase retrieval schemes using over-sampling techniques. Miao, Charalambous, Kirz and Sayre (1999) or by FT holography. The latter technique has also been applied for imaging magnetic nanostructures (Eisebitt *et al*., 2004) where a resolution of about 50 nm was obtained.

All of these methods have been extended to explore magnetic nanostructures using the XMCD effect. Up to now soft X rays have been used for covering the L edges of 3d elements and M edges for RE elements.

4.3.2 Time-resolved imaging

As an example for third generation synchrotrons, the inherent time structure of the Advanced Light Source (ALS) at Berkeley, CA, is outlined in Figure 52, with its sub-100-ps wide X-ray flashes. This forms the basis for the implementation of stroboscopic pump and probe measurements with subnanosecond time resolution (Stoll *et al*., 2004; Choe *et al*., 2004). In addition to the standard multibunch operation of the synchrotron, a two-bunch mode is provided but this special operation mode is only available for about 10% of an annual beam time. The time structure in a two-bunch mode operation allows 328-ns time-intervals between the magnetic

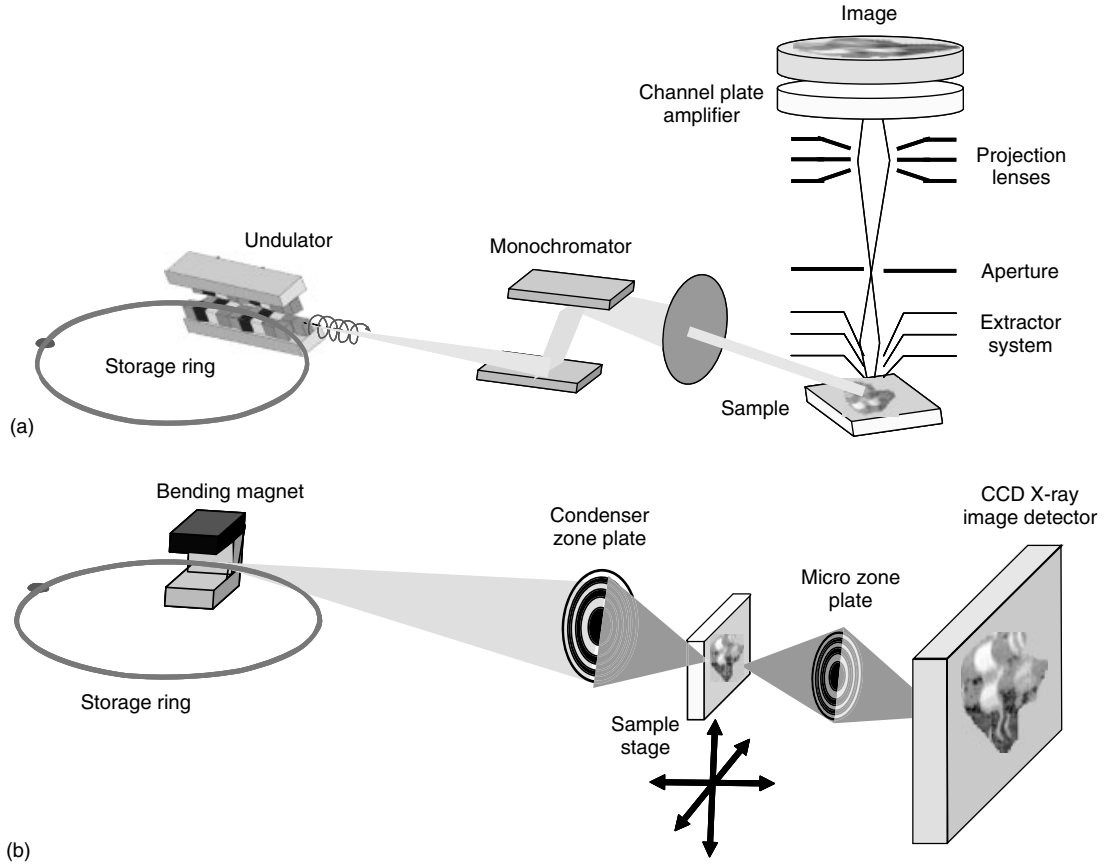

Figure 51. (a) Scheme of the X-ray photoemission electron microscope (X-PEEM). The incident X rays excite secondary electrons in an area of 1–50 µm, which are imaged by an arrangement of electrostatic and magnetic lenses onto a phosphor screen. (b) Scheme of a full-field transmission X-ray microscope. A polychromatic photon beam is focused by a condenser zone plate onto a field of the transparent sample of about 10 µm. The magnified image, generated by a micro zone plate, is thrown onto an X-ray-sensitive CCD camera. (c) Scheme of a scanning transmission X-ray microscope (STXM). A monochromatic photon beam is focused by a Fresnel micro zone plate onto the sample mounted on a piezo driven stage. The transmitted radiation is measured by an X-ray detector as a function of the sample position. (d) Set up for lensless imaging with coherent X rays. Monochromatized undulator radiation is directed to a pinhole. Coherent scattering at the sample causes a fine structure known as 'speckle' in the diffraction pattern which allows reconstruction of the real space image of the sample by an iterative phase retrieval scheme.

excitation pulses of the sample and therefore enables the sample's magnetization to relax and to reach its equilibrium state again, in contrast to the 2-ns interval between successive X-ray flashes in a multibunch mode operation, which is too frequent for most magnetic experiments. A sophisticated data acquisition scheme was built up which overcomes this drawback and allows us to perform time-resolved STXM measurements in multibunch mode with variable relaxation times. A pump pulse is followed by n successive X-ray flashes routed in separate image storage areas (for example, $n = 4$: 'pump' (magnetic excitation) pulses show up every 8 ns, and all X-ray 'probe' flashes in between are used for data acquisition). A similar set up was incorporated for the 'sine-excitation' experiments described later. In this way, by taking advantage of the higher photon flux in multibunch mode compared to the two-bunch mode operation, data acquisition for time-resolved magnetic STXM experiments is speeded up by a factor of about 10.

In order to generate the magnetic field as the pump pulse, an electric current is sent through a Cu wire as sketched in Figure 53(a), which provides a magnetic field parallel to the plane of the micrometer-sized platelet prepared directly on the Cu strip line. A magnetic pulse perpendicular to the sample can be applied by a Cu microcoil, which surrounds the sample on the Si_3N_4 membrane as shown by the scanning electron microscope (SEM) image in Figure 53(b).

For the time-dependent measurements several complementary stroboscopic techniques have been used:

1. 'Time-domain' *pump and probe excitation,* Figure 54(a) (Stoll *et al*., 2004), where current pulses through the microcoil or strip line, synchronized with the storage

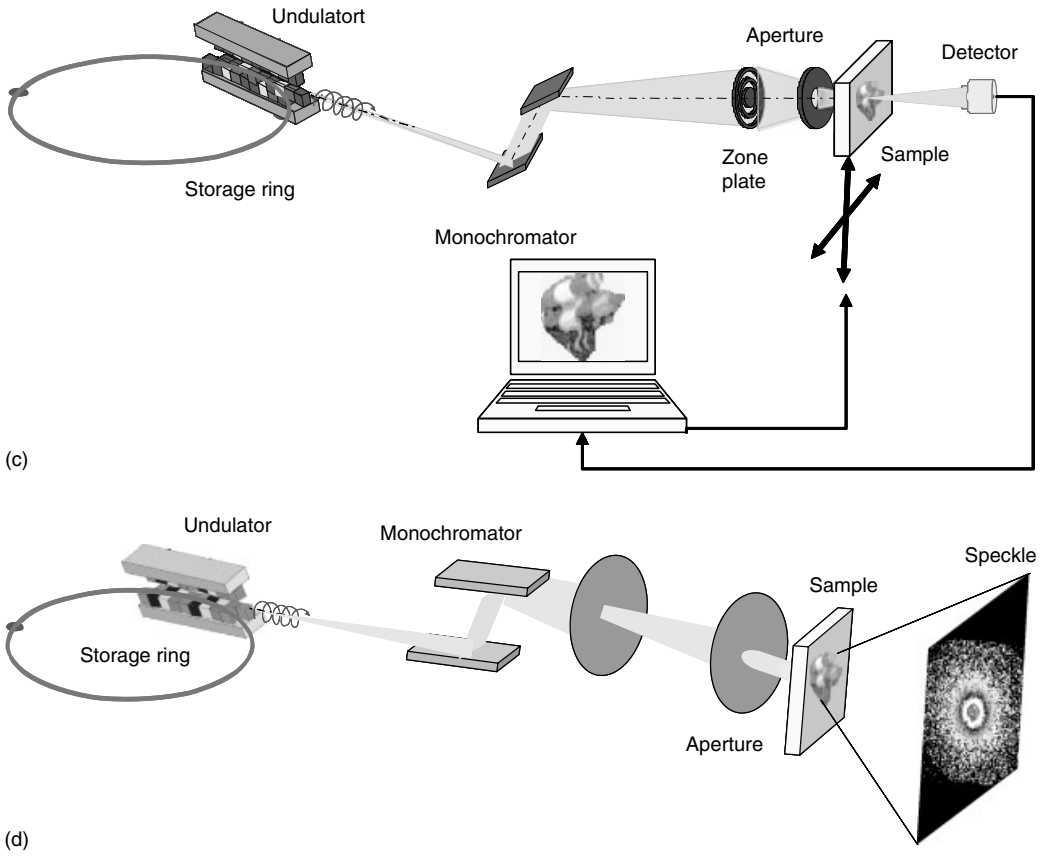

Figure 51. *Continued.*

ring, generate magnetic pulses which act as a 'pump' and the subsequent X-ray flashes, delayed properly, serve as 'probe'.

2. 'Frequency-domain' *sine excitation* or *spatially resolved ferromagnetic resonance* technique, implemented to time-resolved X-ray microscopy by Puzic *et al*. (2005) (Figure 54b), where the sample is excited by a continuous alternating field and the response of the sample's magnetization is determined dependent of the phase of the excitation. Generally speaking, pump and probe performs a broadband excitation of all magnetic modes involved, whereas the sine excitation allows excitation of distinct magnetic eigenmodes by choosing the excitation frequency close to their eigen frequencies.
3. A combination of both techniques above is called a *burst mode excitation* and is sketched in Figure 54(c). The sample is excited by one or several periods of an alternation magnetic field, and although this is a 'resonant' excitation, the sample is excited from its ground state.
4. In addition, an oscillating field with small amplitude can be superimposed to the burst excitation as shown in Figure 54(d).

4.3.3 Investigation of magnetic vortex dynamics by the STXM

It is well known that micrometer- or submicrometer-sized magnetic patterns can minimize their stray field energy by an inhomogeneous magnetization like the formation of domains separated by domain walls. In square-shaped ferromagnetic structures, the competition of the exchange interaction between nearest-neighbor spins and the long-range dipole–dipole energies can result in a vortex structure, or so-called Landau pattern (Hubert and Schäfer, 1998). Uniform magnetized domains form an in-plane flux closure around its center (Figure 55), where the magnetization goes out of the plane because of the short-range exchange interaction forming the vortex core, which is extended over about 20 nm. The direction of the out-of-plane component of the magnetization (up or down, see Figure 55) is defined as the polarization of the vortex core. The stability in an external static magnetic field (Wachowiak *et al*., 2002) has already been investigated and is well understood (Shinjo *et al*., 2000; Cowburn, Koltsov, Adeyeye and Welland, 1999; Novosad *et al*., 2002a; Guslienko *et al*., 2001; Shibata and Otani, 2004). Its dynamics have gained strong interest by magneto-optical techniques

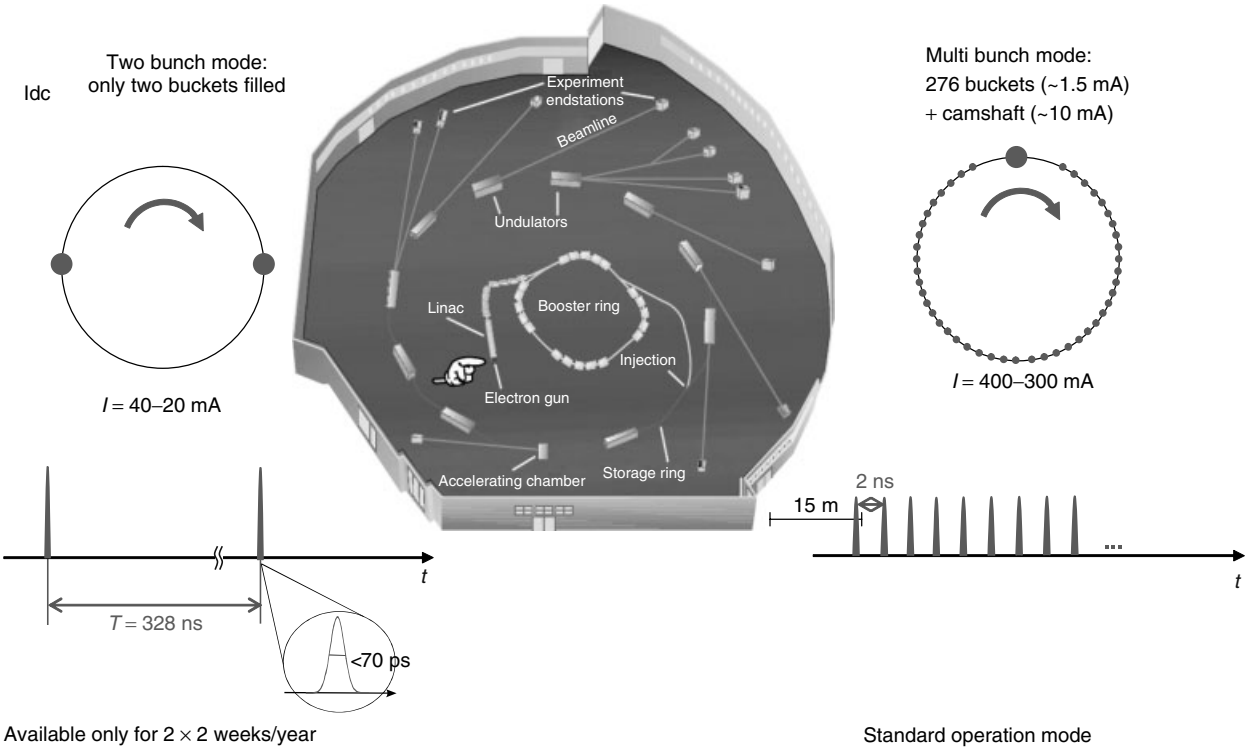

Figure 52. Operation modes at the Advanced Light Source with a sketch of the electron storage ring in the mid-panel. In the standard operation (multibunch mode, right panel) 276 buckets are filled into the storage ring. In a small fraction of the beam time period – especially for time-dependent measurements – only two bunches with a distance of 328 ns are injected into the storage ring. Hereby the current in the accelerator ring and thus the X-ray photon flux is significantly reduced by more than one order of magnitude.

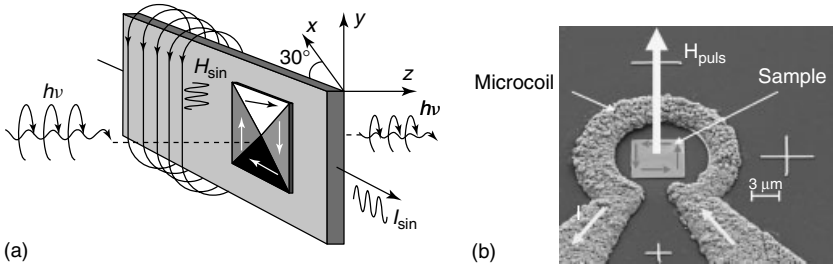

Figure 53. (a) A micrometer-sized Permalloy sample, showing a Landau pattern, is prepared on a Cu strip line. The electric ac current through this strip line generates an oscillating magnetic field parallel to the sample plane. To image the Landau structure, the whole sample arrangement is tilted by 60° with respect to the incident photon beam, creating a net component of the 'in-plane' sample magnetization onto the photon propagation direction. The sample has to be mounted perpendicular to the beam, for imaging the 'out-of-plane' magnetization perpendicular to the surface. (b) To create a magnetic field perpendicular to the sample plane, the electric current is sent through a Cu microcoil.

(Park *et al*., 2003; Cowburn, Koltsov, Adeyeye and Welland, 1999; Novosad *et al*., 2002b), a translational mode in the sub-gigahertz range corresponding to a gyrotropic motion of the vortex core around the structure center (Argyle, Terrenzio and Slonczewski, 1984) was observed. Since lateral dimensions of the vortex structure are in the submicrometer range and its timescales relevant in the subnanosecond range, it is an ideal subject to be addressed by time-dependent magnetic microscopy studies. Hereby, details in the dynamic response of a vortex structure to externally applied magnetic fields as pulsed or sine excitation were gained with time-resolved transmission X-ray microscopy (Puzic *et al*., 2005) and PEEM (Choe *et al*., 2004).

Up to now, very high external magnetic fields of about half a tesla (Okuno *et al*., 2002; Thiaville *et al*., 2003) were required to reverse the vortex core owing to the high stability typical for vortex structures. Recently, vortex-core switching with short bursts of an alternating magnetic field as low

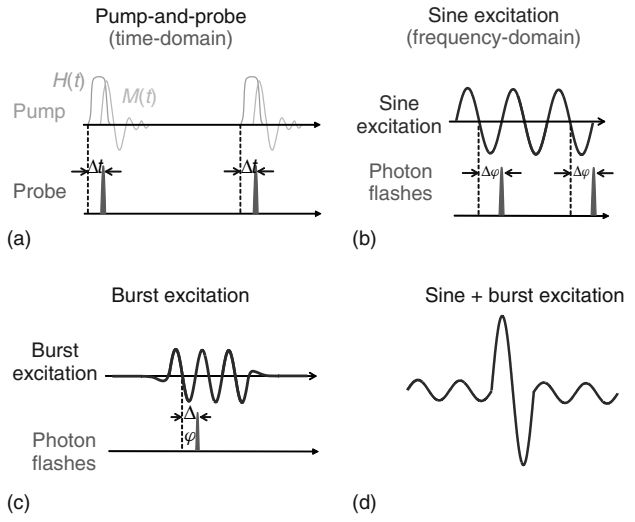

Figure 54. Stroboscopic measurement techniques: (a) 'time-domain' pump and probe technique, (b) 'frequency-domain' sine excitation (spatially resolved ferromagentic resonance), (c) burst excitation, (d) sine excitation combined with a single period burst.

as 1.5 mT was discovered by time-resolved imaging at a scanning transmission X-ray microscope (Van Waeyenberge *et al*., 2006). This dynamic low-field vortex-core reversal scheme is sketched in Figure 56. The sample was excited by a small alternating magnetic field (250 MHz, amplitude: 0.1 mT) parallel to the surface. The sense of gyration of the vortex structure could be reversed by a single period magnetic burst field (amplitude: 1.5 mT, see Figure 56). As the sense of the gyrotropic vortex motion only depends on the polarization of the vortex core (up or down), magnetic vortex-core reversal by excitation with short bursts of an alternating field (1.5 mT) was discovered this way (Van Waeyenberge *et al*., 2006). The Permalloy ($Ni_{80}Fe_{20}$) platelet, prepared on a strip line, was tilted by 60° with respect to the incoming photon beam, which resulted in a net magnetization projection onto the quantization axis (see Figure 53a).

A vortex-core switching mechanism derived from micromagnetic simulations (Van Waeyenberge *et al*., 2006), which was unknown so far, explains this reversal by low alternating fields as a result of the creation of a vortex-antivortex pair as sketched in Figure 57(a). This dynamic switching encounters is illustrated in Figure 57(b) and describes the following steps: (i – iii) excitation of the sample with an external in-plane alternating field generates an increasing out-of-plane polarization opposite to the original vortex, resulting in (iv) the creation a vortex–antivortex pair both with opposite polarization compared to the original vortex which results in (v) the annihilation of the antivortex with the original vortex and at the end (vi) a vortex with opposite polarization remains.

4.3.4 Dynamic imaging of the out-of-plane vortex core

As shown recently, owing to the high magnetic contrast at the dichroic active absorption edge, it is possible to resolve even directly a magnetic vortex core for a sample mounted with its plane perpendicular to the photon beam. Typical contrast images for reversed polarization of the X-ray beam before and after switching the vortex core by an appropriate burst are presented in Figure 58(a). A differential image of optimum statistical accuracy is taken by a proper subtraction of the dichroic images for reversed vortex-core orientation, and is plotted in a 3D image in Figure 58(b). As shown in Figure 58(c) it exhibits a slightly asymmetric shape with a maximum contrast of about 2% and a full width at half maximum (FWHM) in the order of 50 nm. The extension

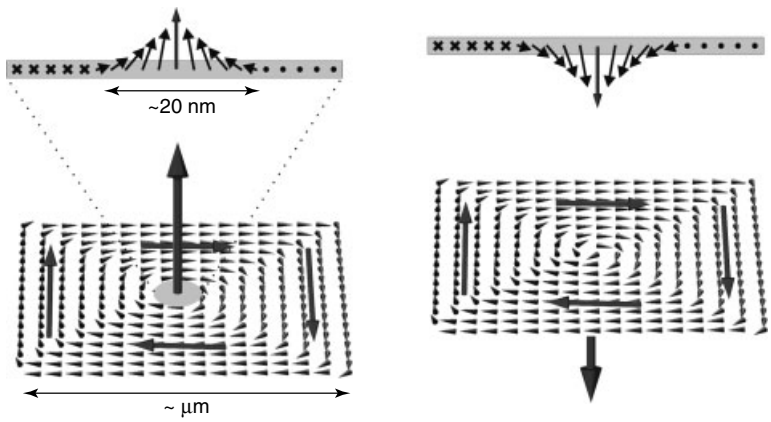

Figure 55. In a Landau pattern, the uniform magnetized domains form an in-plane flux closure around its center. In the center, because of the short-range exchange interaction, the magnetization goes out of the plane creating the vortex core. The direction of the out-of-plane component of the magnetization is defined as the polarization of the vortex core (up or down). Both states are energetically degenerate.

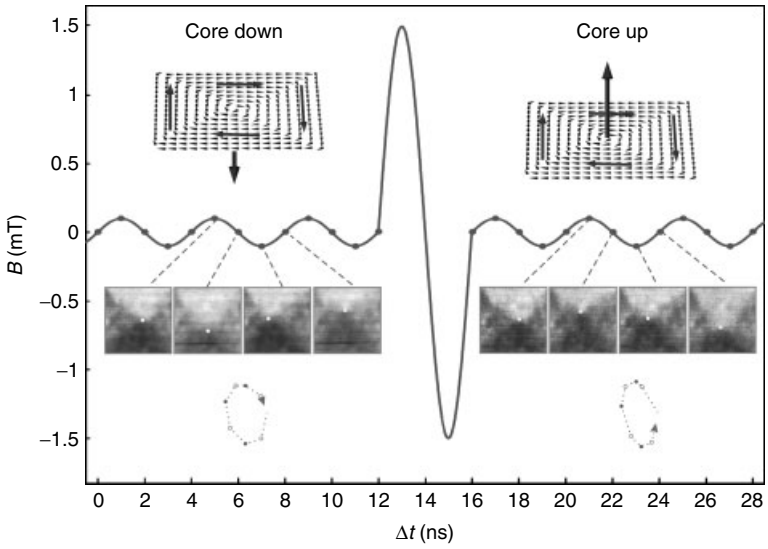

Figure 56. STXM images of the response of the Landau structure on the excitation by an alternating in-plane field (amplitude: 0.1 mT) and an additional alternating field pulse (one period with 1.5 mT amplitude). Since the sense of rotation only depends on the polarization of the vortex core, it is proven that the vortex-core polarization has been switched by the field pulse.

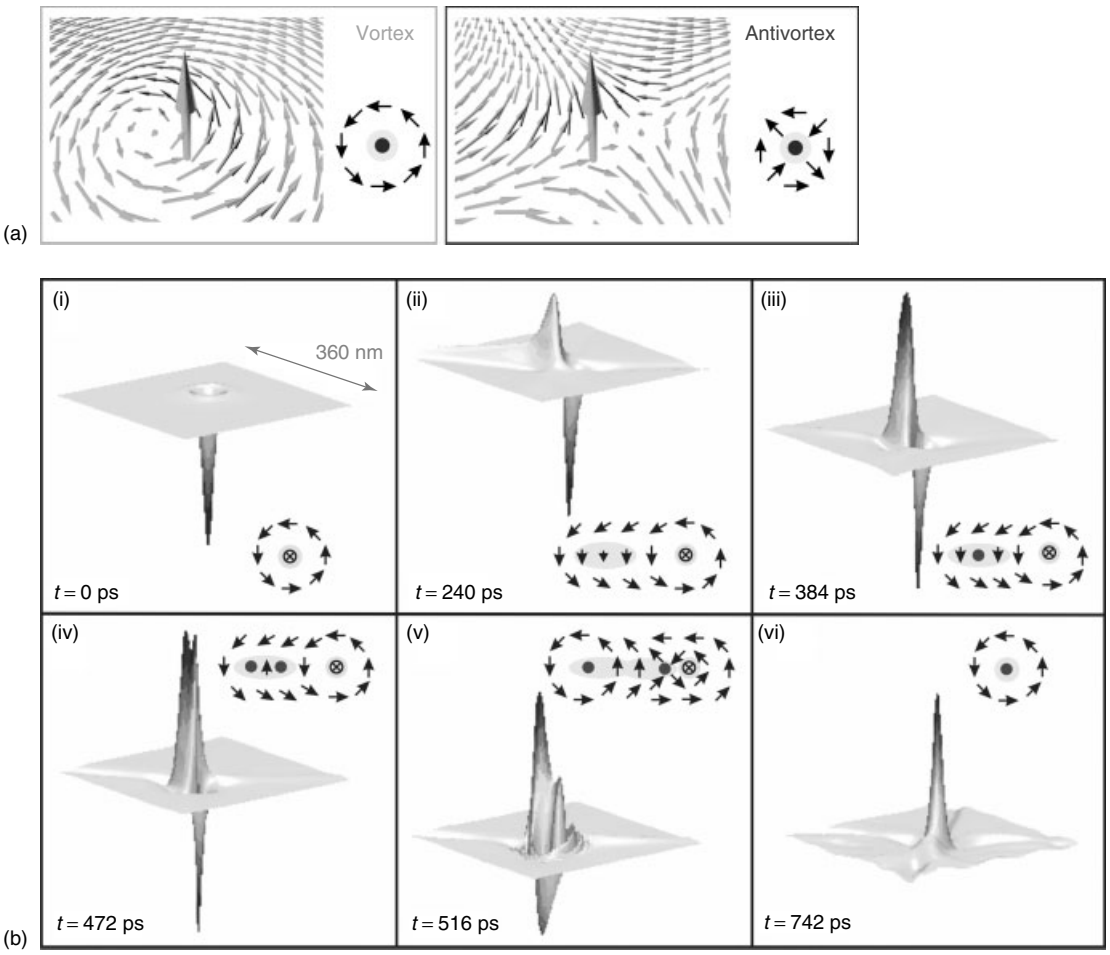

Figure 57. (a) A sketch of a vortex structure compared to an antivortex structure. (b) Details of the switching of the vortex core simulated by the OOMMF (Donahue and Porter, 1999) program showing the formation of a halo with opposite polarization splitting in a vortex and antivortex pair. Finally, the antivortex annihilates with the original vortex by emission of spin waves.

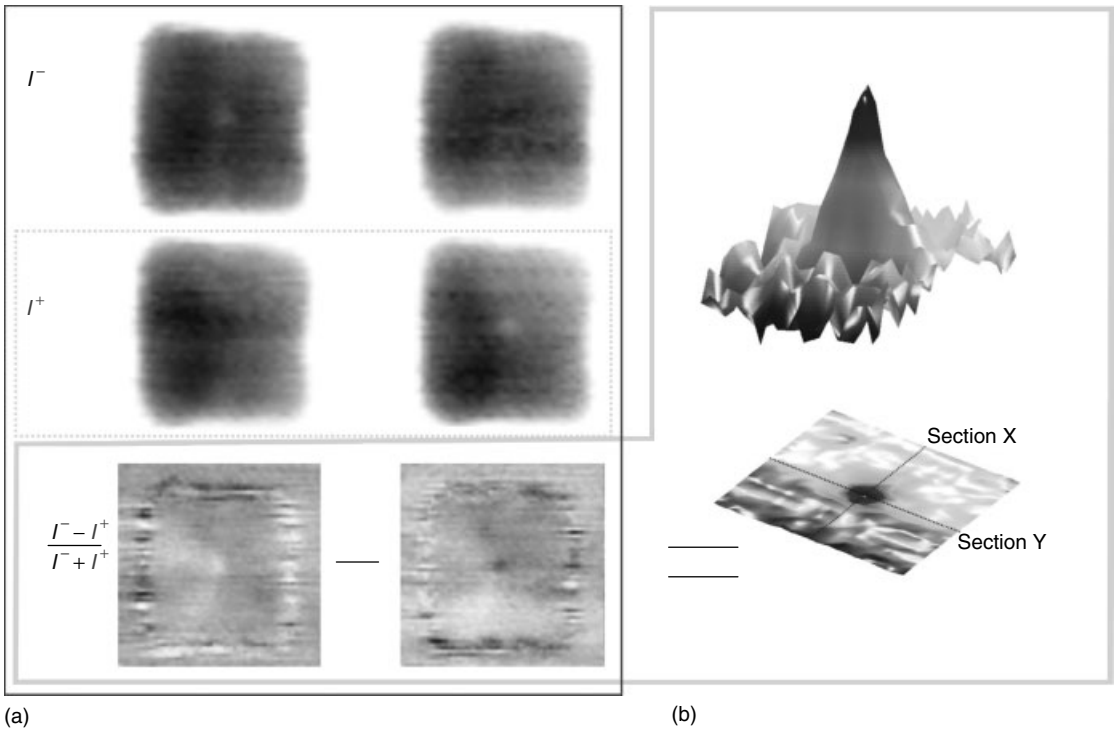

Figure 58. (a) Shows the static configuration of a vortex structure ($500 \times 500\,\mathrm{nm}^2$, 40 nm thick) with a vortex core pointing up (left column) and pointing down (right column). In the first row images were taken for negative polarization of the photons (I^-), while images with opposite polarization (I^+) are shown in the second row. The 'dichroic image' is depicted in the third row. A white or black spot can be observed, corresponding to a vortex-core pointing up or down respectively. The jitter around the vortex structure is an artifact caused by mechanical vibrations. Both 'dichroic images' were subtracted from one another and a 3d image is given in (b) ($200 \times 200\,\mathrm{nm}^2$ cut).

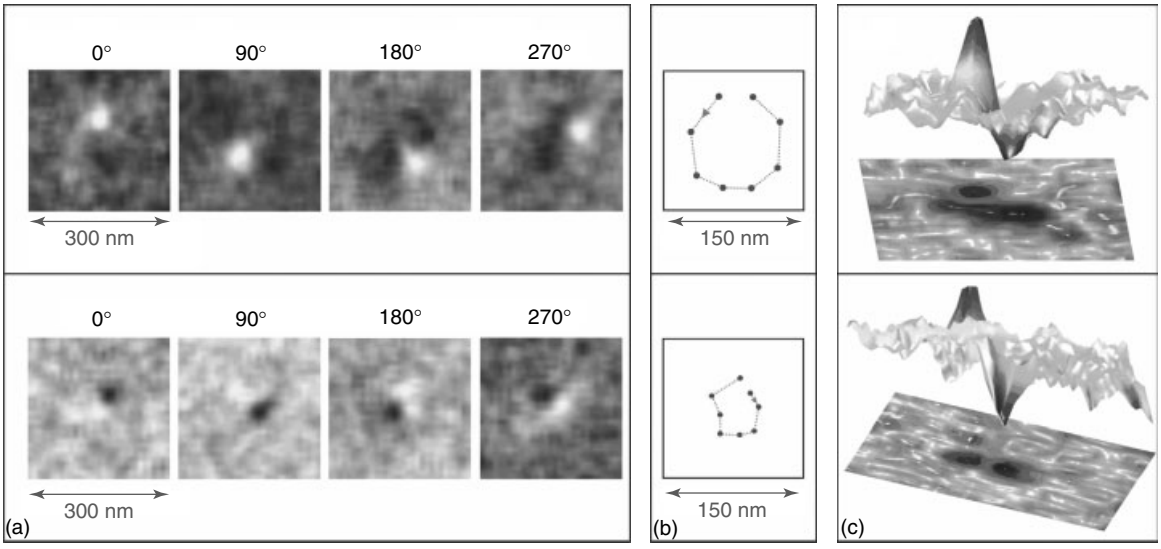

Figure 59. Dynamic response of a vortex structure (sample A: $500 \times 500\,\mathrm{nm}^2$, 40 nm thick) due to an in-plane alternating magnetic field ($f = 437.5\,\mathrm{MHz}$, $H_0 = 710\,\mathrm{A\,m^{-1}}$) with a vortex core pointing up (upper row) and down (lower row). (a) Shows the out-of-plane magnetic contrast of the Landau structure at different phases of the external field (uneven phases are not shown). The images are cuts ($300 \times 300\,\mathrm{nm}^2$) from the complete structure. The position at the different phases is depicted in (b) ($150 \times 150\,\mathrm{nm}^2$), and (c) is a 3D representation of the vortex structure ($300 \times 300\,\mathrm{nm}^2$) at phase 270° (upper row) and phase 135° (lower row).

of the vortex core (about 20 nm) and a maximum value of the XMCD effect at the Ni L_3 edge of about 26%, give exactly the expected magnetic absorption effect owing to the experimentally smeared-out perpendicular magnetization component of the vortex core.

In Figure 59(a), the gyrotropic motion of the vortex core is shown for a $500 \times 500\,\mathrm{nm}^2$ large Permalloy platelet mounted with its normal parallel to the photon beam inside the scanning X-ray microscope. This motion has been studied for the two polarization states of the vortex core, indicating a large difference in the amplitude of the gyrotropic vortex motion for the two cases (Figure 59b). This asymmetry may be attributed to local imperfections in the thin film causing nonuniform magnetization distributions over the sample which have an influence on the motion. The speed of the vortex-core motion was also deduced from the trajectories. For the vortex-core pointing up, a speed of $140\,\mathrm{m\,s}^{-1}$ was calculated, while a much smaller speed of $\approx 80\,\mathrm{m\,s}^{-1}$ was found when the vortex-core is pointing down.

The 3D representations in Figure 59(c) indicate the occurrence of a broad contribution of opposite sign at one side of the vortex core. The procedure used during the data analysis can introduce such a negative contribution as an artifact. On the other hand, it was recently discovered that a vortex core deforms with a similar halo prior to the switching of the vortex core by creation and annihilation of a vortex–antivortex pair (Novosad *et al*., 2005). Today it cannot be excluded that the dynamical vortex deformation, which could up to now not be proved experimentally, is partly responsible for the negative contributions in Figure 59(c). This has to be clarified by future experimental magnetic STXM studies with a significantly enhanced accuracy, especially a better lateral resolution.

NOTES

[1] To be more precise, the Borrmann effect has to be taken into account, which gives different absorption for the two field components. To provide the same intensity for both interfering field components, the angle of incidence must be chosen slightly different from the 45° condition to give 100% circular polarized light.

[2] This has been done by the XMCD effect. So the energy is tuned to the maximum XMCD effect of a magnetized sample. Then the absorption is measured as a function of the Bragg angle, which directly reflects the circular polarization. Other dynamical effects, like the Borrmann, 1951, Borrmann, Hildebrandt and Wagner, 1955) effect have to be cancelled by averaging over different sample magnetizations.

[3] This could be done by measuring the intensity of the scattered beam by an additional ionization chamber.

[4] This could be a problem if the sample provides a band gap, large enough to be transparent for a secondary UV channel.

[5] This is related to the much weaker radial matrix element due to the oscillating radial wave function of the higher s electrons in the radial distribution of the excited core electron.

[6] This is a direct consequence of the dipole approximation in Fermi's golden rule (Bransden and Joachain, 1983).

[7] This assumes forbidden spin flip processes!

[8] In units of $\mu_B \nabla$.

[9] This could be realized by external or internal forces.

[10] The description given here, is close to the discussion of Stöhr and König (1995).

[11] Orbital moments could also be investigated by precise g-factor measurements in ferromagnetic resonance.

[12] As explained in the previous chapters, XMCD is sensitive to the projection of the magnetization along the circular polarized photon beam **K** vector.

[13] The MEXAFS part has been approximated by pure effective spin contributions!

[14] Dipole term and spin moments have been renormalized owing to the $j_{3/2} - j_{1/2}$ mixing, present for reduced spin-orbit splitting of the 2p excitation (Goering, 2005).

[15] This value is smaller than the pure atomic values, reflecting the delocalization and the band character of the 3d electrons in CrO_2.

[16] The polarization dependent prefactors will reduce in small angle approximation for circular polarized light to $\left(\varepsilon'^{\dagger} \cdot \varepsilon\right) = \varepsilon \cdot \varepsilon = 1$ und $\left(\varepsilon'^{\dagger} \times \varepsilon\right) = i\boldsymbol{q}\,P_C$, where $\boldsymbol{q}$ is the wave vector of the photon beam and P_C is the degree of circular polarization.

REFERENCES

Ankudinov, A. and Rehr, J.J. (1995). Calculation of X-ray magnetic circular-dichroism in Gd. *Physical Review B*, **52**, 10214–10220.

Argyle, B.E., Terrenzio, E. and Slonczewski, J.C. (1984). Magnetic vortex dynamics using the optical Cotton-Mouton effect. *Physical Review Letters*, **53**(2), 190–193.

Ashcroft, N.W. and Mermin, N.D. (1976). *Solid State Physics*, Holt-Saunders Japan Ltd.: Philadelphia.

Attenkofer, K., Stähler, S., Knülle, M., *et al*. (1993). Magnetic circular x-ray dichroism studies of Fe/Tb multilayers. *Journal of Applied Physics*, **73**, 6910–6912.

Attwood, D. (1999). *Soft X-Rays and Extreme Ultraviolet Radiation: Principles and Applications*, Cambridge University Press.

Bahrdt, J., Frentrup, W., Gaupp, A., *et al*. (2001). A quasi-periodic hybrid undulator at BESSY II. *Nuclear Instruments and Methods*

in Physics Research Section A: Accelerators, Spectrometers, Detectors and Associated Equipment, **467**, 130–133.

Bland, J.A.C., Daboo, C., Patel, M. and Fujimoto, T. (1998). Interface selective vector magnetometry of FeNi/Cu/Co trilayer spin-valve structures. *Physical Review B*, **57**, 10272–10275.

Bloch, D., Chaisse, F. and Pauthenet, R. (1967). Effects of hydrostatic pressure on compensation temperatures of iron garnets. *Journal of Applied Physics*, **38**, 1029–1030.

Bode, M. (2003). Spin-polarized scanning tunnelling microscopy. *Reports on Progress in Physics*, **66**, 523–582.

Borrmann, G. (1951). Die übernormal durchdringende Röntgenstrahlung im Bragg-Fall der Interferenz. *Die Naturwissenschaften*, **38**, 330.

Borrmann, G., Hildebrandt, G. and Wagner, H. (1955). Röntgenstrahl-Fächer im Kalkspat. *Zeitschrift fur Kristallographie*, **142**, 400–414.

Bowen, M., Cros, V., Jaffres, H., *et al*. (2006). Absence of induced moment in magnetic tunnel junction barriers. *Physical Review B*, **73**, 012406.

Bransden, B.H. and Joachain, C.J. (1983). *Physics of Atoms and Molecules*, Longman Scientific & Technical: New York.

Bremer, J., Kaihola, L. and Keski-Kuha, R. (1980). X-ray reflectivity of Cobalt and Titanium in the vicinity of the $L_{2,3}$ absorption edges. *Journal of Physics C: Solid State Physics*, **13**, 2225–2230.

Bruno, P. (1989). Tight-binding approach to the orbital magnetic moment and magnetocrystalline anisotropy of transition-metal monolayers. *Physical Review B*, **39**, R865–R868.

Canedy, C.L., Li, X.W. and Xiao, G. (2000). Large magnetic moment enhancement and extraordinary Hall effect in Co/Pt superlattices. *Physical Review B*, **62**, 508–519.

Carra, P., Harmon, B.N., Thole, B.T., *et al*. (1991). Magnetic-X-ray dichroism in Gadolinium metal. *Physical Review Letters*, **66**, 2495–2498.

Carra, P., Thole, B.T., Altarelli, M. and Wang, X. (1993). X-ray circular dichroism and local magnetic fields. *Physical Review Letters*, **70**, 694–697.

Chao, W.L., Harteneck, B.D., Liddle, J.A., *et al*. (2005). Soft X-ray microscopy at a spatial resolution better than 15 nm. *Nature*, **435**, 1210–1213.

Chen, C.T., Idzerda, Y.U., Lin, H.J., *et al*. (1995). Experimental confirmation of the X-ray magnetic circular dichroism sum rules for iron and cobalt. *Physical Review Letters*, **75**, 152–155.

Chen, C.T., Sette, F., Ma, Y. and Modesti, S. (1990). Soft-x-ray magnetic circular dichroism at the L2, 3 edges of Nickel. *Physical Review B*, **42**, 7262–7265.

Choe, S-B., Acremann, Y., Scholl, A., *et al*. (2004). Vortex core-driven magnetization dynamics. *Science*, **304**, 420–422.

Compton, A.H. and Allison, K. (1935). *X-Rays in Theory and Experiment*, Van Nostrand Inc.: New York.

Cowan, R.D. (1981). *The Theory of Atomic Structure an Spectra*, University of California Press: Berkeley.

Cowburn, R.P., Koltsov, D.K., Adeyeye, A.O. and Welland, M.E. (1999). Single-domain circular nanomagnets. *Physical Review Letters*, **83**(5), 1042–1045.

Crocombette, J.P., Thole, B.T. and Jollet, F. (1996). The importance of the magnetic dipole term in magneto-circular x-ray absorption dichroism for 3d transition metal compounds. *Journal of Physics: Condensed Matter*, **8**, 4095–4105.

Dartyge, E., Fontaine, A., Giorgetti, C., *et al*. (1992). Multielectron excitations in Rare-Earth compounds revealed by magnetic circular X-ray dichroism. *Physical Review B*, **46**, 3155–3158.

Das Sarma, S., Fabian, J., Hu, X.D. and Zutic, I. (2000). Theoretical perspectives on spintronics and spin-polarized transport. *IEEE Transactions on Magnetics*, **36**, 2821–2826.

Dedkov, Yu.S., Fonine, M., König, C., *et al*. (2002). Room temperature observation of high spin polarization of epitaxial CrO2 (100) films at the Fermi energy. *Applied Physics Letters*, **80**, 4181–4183.

DeSisto, W.J., Broussard, P.R., Ambrose, T.F., *et al*. (2000). Highly spin-polarized chromium dioxide thin films prepared by chemical vapor deposition from chromyl chloride. *Applied Physics Letters*, **76**, 3789–3791.

Dörfler, F. and Fähnle, M. (2006). Theoretical justification of the ground-state-moment-analysis of magnetic dichroic X-ray absorption spectra in 3d-transition metals. *Physical Review B*, **74**, 224424.

Dunaevskii, S.M. and Savel'ev, A.P. (1989). Recursion calculation of the spin-polarized electron structure of yttrium iron garnet. *Soviet Physics Solid State*, **31**, 114–116.

Donahue, M. and Porter, D. (1999). OOMMF Users Guide, version 1.0. Interagency Report NISTIR 6376 (National Institute of Standards and Technology, Gaithersburg, Maryland).

Ebert, H. (2000a). In *Fully relativistic band structure calculations for magnetic solids - Formalism and Application*, Dreysse, H. (Ed.) *Lecture Notes in Physics*, Springer: Berlin, pp. 191, Vol. 535.

Ebert, H. (2000b). The Munich SPR-KKR Package, Version 3.6. http://olymp.cup.uni-muenchen.de/ak/ebert/SPRKKR/.

Ebert, H., Popescu, V., Ahlers, D., *et al*. (1998). Theoretical and experimental investigations on the magnetic EXAFS at the K-and L-2, L-3-edges of bcc-Fe. *Europhysics Letters*, **42**, 295–300.

Ebert, H., Schütz, G. and Temmerman, W.M. (1990). Theoretical study of the magnetic X-ray dichroism of HCP-Gd. *Solid State Communications*, **76**, 475–478.

Eisebitt, S., Luning, J., Schlotter, W.F., *et al*. (2004). Lensless imaging of magnetic nanostructures by X-ray spectro-holography. *Nature*, **432**, 885–888.

Ferrer, S., Alvarez, J., Lundgren, E., *et al*. (1997). Surface x-ray diffraction from Co/Pt(111) ultrathin films and alloys: structure and magnetism. *Physical Review B*, **56**, 9848–9857.

Finazzi, M., de Groot, F.M.F., Dias, A.M., *et al*. (1995). Direct evidence of the role of hybridization in th x-ray magnetic circular dichroism of alpha-Ce. *Physical Review Letters*, **75**, 4654–4657.

Fischer, P., Schütz, G. and Wiesinger, G. (1990). Spin-dependence of the rare earth L2, 3 absorption in (RE)2Co17. *Solid State Communications*, **76**, 772–781.

Fuggle, J.C. and Alvarado, F. (1980). Core-level lifetimes as determined by x-ray photoelectron spectroscopy measurements. *Physical Review A*, **22**, 1615–1624.

Gambardella, P., Dallmeyer, A., Maiti, K., *et al*. (2004). Oscillatory magnetic anisotropy in one-dimensional atomic wires. *Physical Review Letters*, **93**, 089903.

Gambardella, P., Rusponi, S., Veronese, M., *et al*. (2003). Giant magnetic anisotropy of single cobalt atoms and nanoparticles. *Science*, **300**, 1130–1133.

Gambardella, P., Dallmeyer, A., Maiti, K., *et al*. (2002). Ferromagnetism in one-dimensional monatomic metal chains. *Nature*, **416**, 301–304.

Geissler, J., Goering, E., Justen, M., *et al*. (2001). Pt magnetization profile in a Pt/Co bilayer studied by resonant magnetic X-ray reflectometry. *Physical Review B*, **65**, 020405(R)-1–020405(R)-4.

Geissler, J., Goering, E., Weigand, F. and Schütz, G. (2002). Interplay between chemical and magnetic roughness in a Pt/Co bilayer investigated with X-ray resonant magnetic reflectometry. *Zeitschrift für Metallkunde*, **93**, 946–952.

Geller, S., Williams, H.J., Remeika, J.P., *et al*. (1963). Magnetic study of lighter rare-earth ions in iron garnets. *Physical Review*, **131**, 1080–1082.

Giles, C., Malgrange, C., Goulon, J., *et al*. (1994a). Energy-dispersive phase plate for magnetic circular-dichroism experiments in the X-ray range. *Journal of Applied Crystallography*, **27**, 232–240.

Giles, C., Malgrange, C., Goulon, J., *et al*. (1994b). Energy and polarization-tunable X-ray quarter-wave plates for energy-dispersive absorption spectrometer. *Nuclear Instruments and Methods in Physics Research Section A: Accelerators, Spectrometers, Detectors and Associated Equipment*, **349**, 622–625.

Giles, C., Malgrange, C., Goulon, J., *et al*. (1995). Perfect crystal and mosaic crystal quarter-wave plates for circular magnetic-X-ray dichroism experiments. *The Review of Scientific Instruments*, **66**, 1549–1553.

Goedkoop, J.B., Fuggle, J.C., Thole, B.T., *et al*. (1988a). Magnetic x-ray dichroism of rare-earth materials. *Journal of Applied Physics*, **64**, 5595–5597.

Goedkoop, J.B., Thole, B.T., van der Laan, G., *et al*. (1988b). Calculations of magnetic x-ray dichroism in the 3d absorption spectra of rare-earth compounds. *Physical Review B*, **37**, 2086–2093.

Goering, E. (2005). X-ray magnetic circular dichroism sum rule correction for the light transition metals. *Philosophical Magazine*, **85**, 2895–2911.

Goering, E., Ahlers, D., Attenkofer, K., *et al*. (1999). XMCD and magnetism of the ferrimagnetic system NaV6O11. *Journal of Synchrotron Radiation*, **6**, 537–539.

Goering, E., Bayer, A., Gold, S., *et al*. (2002a). Strong anisotropy of projected 3d moments of epitaxial CrO2-Films. *Physical Review Letters*, **88**, 207203.

Goering, E., Bayer, A., Gold, S., *et al*. (2002b). Direct correlation of Cr 3d orbital polarization and O 2p X-ray magnetic circular dichroism of epitaxial CrO2-films. *Europhysics Letters*, **58**, 906–911.

Goering, E., Bayer, A., Gold, S., *et al*. (2002c). Strong anisotropy of projected 3d moments of epitaxial CrO2- films. *Physical Review Letters*, **88**, 207203-1–207203-4.

Goering, E., Bayer, A., Gold, S. and Schütz, G. (2002). Strong anisotropy of projected Cr 3d moments of epitaxial grown CrO2-films. *BESSY Highlights*, **2001**, 26–27.

Goering, E., Gold, S. and Bayer, A. (2004). Ground-state-moment-analysis: a quantitative tool for X-ray magnetic circular dichroism analysis for 3d transition metals. *Applied Physics A*, **78**, 855–865.

Goering, E., Gold, S., Lafkioti, M. and Schuetz, G. (2006). Vanishing Fe 3d orbital moments in single-crystalline magnetite. *Europhysics Letters*, **73**, 97–103.

Goering, E., Gold, S. and Schütz, G. (2001). HoFe – garnet soft XMCD measurements below and above the compensation temperature. *Journal of Synchrotron Radiation*, **8**, 422–424.

Gold, S. (2006). *Winkel-und Temperaturabhängigkeit der magnetikristallinen Anisotropieenergie un der mikroskopischen magnetischen Momente des ferromagnetischen Halbmetals CrO2*, Ph.d. Thesis, Universität Würzburg.

de Groot, F.M.F., Fuggle, J.C., Thole, B.T. and Sawatzky, G.A. (1990). 2p x-ray absorption of 3d transition-metal compounds: an atomic multiplet description including the crystal field. *Physical Review B*, **42**, 5459–5468.

Guslienko, K.Yu., Novosad, V., Otani, Y., *et al*. (2001). Magnetization reversal due to vortex nucleation, displacement, and annihilation in submicron ferromagnetic dot arrays. *Physical Review B*, **65**, 024414-1–024414-10.

Guillot, M. and Pauthenet, R. (1967). Magnetic properties of rare earth gallium garnets 5 Ga2O3.3 M2O3 in high magnetic fields. *Ceskoslovensky Casopis Pro Fysiku Sekce A*, **17**, 380.

Hannon, J.P., Trammell, G.T., Blume, M. and Gibbs, D. (1988). X-ray resonance exchange scattering. *Physical Review Letters*, **61**, 1245–1248.

Henke, B.L., Gullikson, E.M. and Davis, J.C. (1993). X-ray interactions: photoabsorption, scattering, transmission, and reflection at E=50-30000eV, Z=1-92. *Atomic Data and Nuclear Data Tables*, **54**, 181–342.

Henke, B.L., Gullikson, E.M. and Davis, J.C. (2002). *Center of X-ray Optics*, Lawrence Berkeley National Laboratory, http://www.cxro.lbl.gov/optical_constants/.

Holy, V., Kubena, J., Ohlidahl, I., *et al*. (1993). X-ray reflection from rough layered systems. *Physical Review B*, **47**, 15896–15903.

Holý, V., Pietsch, U. and Baumbach, T. (1999). In *High-Resolution X-Ray Scattering from Thin Films and Multilayers*, Managing Editor: Höhler, G. (Ed.) Springer Tracts in Modern Physics, Springer: Karlsruhe, Vol. 149. ISSN: 0081–3869.

Hoyt, J.J., Warburton, W.K. and de Fontaine, D. (1984). Determination of the anomalous scattering factors for Cu, Ni and Ti using the dispersion relation. *Journal of Applied Crystallography*, **17**, 344–351.

Hubbell, J.C., Gimm, H.A. and Overbo, I. (1980). Pair, triplet, and total atomic cross sections (and mass attenuation coefficients) for 1 MeV-100 GeV photons in elements Z = 1 to 100. *Journal of Physical and Chemical Reference Data*, **9**, 1023–1047.

Hubert, A. and Schäfer, R. (1998). *Magnetic Domains - The Analysis of Magnetic Microstructures*, Springer: Berlin.

Hunter-Dunn, J., Arvanitis, D., Martensson, N., *et al*. (1995). An angle-dependent magnetic circular x-ray dichroism study of Co/Cu(100): experiment versus theory. *Journal of Physics: Condensed Matter*, **7**, 1111–1119.

Jackson, J.D. (1975). *Classical Electrodynamics*, *Second Edition*, John Wiley & Sons: New York.

Jaouen, N., Tonnerre, J.M., Bontempi, E., *et al*. (2000). Chemical and magnetization profile study of Ce in [CeLaCe/Fe] and

[LaCeLa/Fe] multilayers by resonant X-ray reflectivity. *Physica B*, **283**, 175–179.

Ji, Y., Strijkers, G.J., Yang, F.Y., *et al*. (2001). Determination of the spin polarization of half-metallic CrO2 by point contact Andreev reflection. *Physical Review Letters*, **86**, 5585–5588.

Ji, Y., Strijkers, G.J., Yang, R.Y. and Chien, C.L. (2001). Comparison of two models for spin polarization measurements by Andreev reflection. *Physical Review B*, **6422**, art-224425.

Justen, M. (2000). *Konstruktion und Charakterisierung eins* $\lambda/4$*-Plättchens zur Erzeugung Zirkular Polarisierter Röntgenstrahlung und Magnetische Ultrakleinwinkelstreuung zur Vermessung von Domänenstrukturen*, Diplom Thesis, Universität Würzburg.

Kao, C-C., Chen, C.T., Johnson, E.D., *et al*. (1994). Dichroic interferences effects in circularly polarized soft-x-ray resonant magnetic scattering. *Physical Review B*, **50**, 9599–9602.

Kao, C-C., Hastings, J.B., Johnson, E.D., *et al*. (1990). Magnetic-resonance exchange scattering at the iron $L_{II \text{ and } LIII \text{ Edges}}$. *Physical Review Letters*, **65**, 373–376.

Kittel, C. (1976). *Introduction to Solid State Physics*, John Wiley & Sons: New York.

Kirz, J., Beetz, T., Feser, M., *et al*. (2004). *Microscopy and Microanalysis*, Cambridge University Press, pp. 120–121, Vol. 10.

Knülle, M., Ahlers, D. and Schütz, G. (1995). Spin dependent EXAFS in pure metals and garnets. *Solid State Communications*, **94**, 267–273.

Koblischka, M.R. and Hartmann, U. (2003). Recent advances in magnetic force microscopy. *Ultramicroscopy*, **97**, 103–112.

Korotin, M.A., Anisimov, V.I., Khomskii, D.I. and Sawatzky, G.A. (1998). CrO2: a self-doped double exchange ferromagnet. *Physical Review Letters*, **80**, 4305–4308.

Krause, M.O. and Oliver, J.H. (1979). Natural widths of atomic k-levels and l-levels, k-alpha X-ray-lines and several KLL auger lines. *Journal of Physical and Chemical Reference Data* , **8**, 329–338.

Kubota, B. (1960). Preparation of ferromagnetic chromium dioxide. *Journal of the Physical Society of Japan*, **15**, 1706–1706.

van der Laan, G. (1997a). Core hole polarization made easy. *Applied Physics A*, **65**, 135–140.

van der Laan, G. (1997b). Line shape of 2p magnetic-x-ray-dichroism spectra in 3d metallic systems. *Physical Review B*, **55**, 8086–8089.

van der Laan, G. (1997c). The role of the spin polarization in X-ray magnetic circular dichroism spectra of itinerant magnets. *Journal of Physics: Condensed Matter*, **9**, L259–L265.

van der Laan, G. (1997d). Theory of simple spectra. *Journal of Electron Spectroscopy and Related Phenomena*, **86**, 41–47.

van der Laan, G. (1998a). Microscopic origin of magnetocrystalline anisotropy in transition metal thin films. *Journal of Physics: Condensed Matter*, **10**, 3239–3253.

van der Laan, G. (1998b). Microscopic origin of magnetocrystalline anisotropy in transition metal thin films. *Journal of Physics: Condensed Matter*, **10**, 3229–3253.

van der Laan, G. (1999a). Sum rule practice. *Journal of Synchrotron Radiation*, **6**, 694–695.

van der Laan, G. (1999b). Sum rules and beyond. *Journal of Electron Spectroscopy and Related Phenomena*, **103**, 859–868.

van der Laan, G. and Thole, B.T. (1996). X-ray-absorption sum rules in jj-coupled operators and ground-state moments of actinide ions. *Physical Review B*, **53**, 14458–14469.

Leitenberger, W. (1997). *Polarisationserscheinungen bei der Dynamischen Röntgenbeugung*, Ph.d. Thesis, Universität Halle.

Lemke, L., Wende, H., Srivastava, P., *et al*. (1998). Magnetic extended x-ray absorption fine structure at the L-3, L-2 edges of 3d elements. *Journal of Physics: Condensed Matter*, **10**, 1917–1930.

Lewis, S.P., Allen, P.B. and Sasaki, T. (1997). Band structure and transport properties of CrO2. *Physical Review B*, **55**, 10253–10260.

Li, X.W., Gupta, A. and Xiao, G. (1999). Influence of strain on the magnetic properties of epitaxial (100) chromium dioxide (CrO2) films. *Applied Physics Letters*, **75**, 713–715.

MacKay, J.F., Teichert, C., Savage, D.E. and Lagally, M.G. (1996). Element specific magnetization of buried interfaces probed by diffuse x-ray resonant magnetic scattering. *Physical Review Letters*, **77**, 3925–3928.

Martin, Y. and Wickramasinghe, H.K. (1987). Magnetic imaging by "force microscopy" with 1000 Å resolution. *Applied Physics Letters*, **50**, 1455–1457.

Mazin, I.I., Singh, D.J. and Ambrosch-Draxl, C. (1999). Transport, optical, and electronic properties of the half-metal CrO2. *Physical Review B*, **59**, 411–418.

Miao, J., Charalambous, P., Kirz, J. and Sayre, D. (1999). Extending the methodology of X-ray crystallography to allow imaging of micrometre-sized non-crystalline specimens. *Nature*, **400**, 342–344.

Nakajima, N., Koide, T., Shidara, T., *et al*. (1998). Perpendicular magnetic anisotropy caused by interfacial hybridization via enhanced orbital moment in Co/Pt multilayers: magnetic circular x-ray dichroism study. *Physical Review Letters*, **81**, 5229–5232.

Nakajima, R., Stöhr, J. and Idzerda, Y.U. (1999). Electron-yield saturation effects in L-edge x-ray magnetic circular dichroism spectra of Fe, Co, and Ni. *Physical Review B*, **59**, 6421–6429.

Neumann, C., Rogalev, A., Goulon, J., *et al*. (1998). X-ray magnetic reflectometry using circularly polarized radiation. *Journal of Synchrotron Radiation*, **5**, 998–1000.

Névot, L. and Croce, P. (1980). Caractérisation des surfaces par réflexion rasante de rayons X. Application à l'étude du polissage de quelques verres silicates. *Revue de Physique Appliquée*, **15**, 761–779.

Ney, A., Poulopoulos, P. and Baberschke, K. (2001). Surface and interface magnetic moments of Co/Cu(001). *Europhysics Letters*, **54**, 820–825.

Novosad, V., Fradin, F.Y., Roy, P.E., *et al*. (2005). Magnetic vortex resonance in patterned ferromagnetic dots. *Physical Review B*, **72**(2), 024455-1–024455-5.

Novosad, V., Guslienko, K.Yu., Shima, H., *et al*. (2002a). Effect of interdot magnetostatic interaction on magnetization reversal in circular dot arrays. *Physical Review B*, **65**, 060402-1–060402-4.

Novosad, V., Grimsditch, M., Guslienko, K.Yu., *et al*. (2002b). Spin excitations of magnetic vortices in ferromagnetic nanodots. *Physical Review B*, **65**(2), 052407-1–052407-4.

O'Brien, W.L. and Tonner, B.P. (1994). Surface-enhanced magnetic moments and ferromagnetic ordering of Mn ultrathin films on fcc Co(001). *Physical Review B*, **50**, 2963–2969.

Okuno, T., Shigeto, K., Ono, T., *et al*. (2002). MFM study of magnetic vortex cores in circular permalloy dots: behavior in external field. *Journal of Magnetism and Magnetic Materials*, **240**, 1–6.

Osgood, R.M., Sinha, S.K., Freeland, J.W., *et al*. (1999). X-ray scattering from magnetic, rough surfaces. *Journal of Applied Physics*, **85**, 4619–4621.

Park, J.P., Eames, P., Engebretson, D.M., *et al*. (2003). Imaging of spin dynamics in closure domain and vortex structures. *Physical Review B*, **67**(2), 020403(R)-1–020403(R)-4.

Parratt, L.G. (1954). Surface studies of solids by total reflection of X-rays. *Physical Review*, **95**, 359–369.

Pauthenet, R. (1958). Spontaneous magnetization of some garnet ferrites and the aluminum substituted garnet ferrites. *Journal of Applied Physics*, **29**, 253–255.

Pellegrin, E., Tjeng, L.H., de Groot, F.M.F., *et al*. (1997). Soft X-ray magnetic circular dichroism study of the colossal magnetoresistance compound La1-xSrxMnO3. *Journal de Physique IV*, **7**, 405–408.

Peters, J.F., Miguel, J., de Vries, M.A., *et al*. (2004). Soft x-ray resonant magneto-optical constants at teh Gd M4, 5 and Fe L2, 3 edges. *Physical Review B*, **70**, 224417-1–224417-10.

Pierce, D.T. and Meier, F. (1976). Photoemission of spin-polarized electrons from GAAS. *Physical Review B*, **13**, 5484–5500.

Pizzini, S., Bonfim, M., Baudelet, F., *et al*. (1998). Quarter-wave plates and X-ray magnetic circular dichroism on ID24 at the ESRF. *Journal of Synchrotron Radiation*, **5**, 1298–1303.

Porta, P., Marezio, M., Reimeika, J.P. and Dernier, P.D. (1972). Chromium dioxide: high pressure synthesis and bond lengths. *Materials Research Bulletin*, **7**, 157–762.

Puzic, A., van Waeyenberge, B., Chou, K.W., *et al*. (2005). Spatially resolved ferromagnetic resonance: imaging of ferromagnetic eigenmodes. *Journal of Applied Physics*, **97**(10), 10E704-1–10E704-3.

Richter, D., (1992). Dynamische Theorie der Beugung. *Synchtrotronstrahlung zur Erforschung kondensierter Materie*, Vorlesungsmanuskripte des 23. IFF-Ferienkurses, Forschungszentrum Jülich GmbH: Jülich, ISBN: 3-89336-088-3.

Rudolf, P., Sette, F., Tjeng, L.H., *et al*. (1991). Element specific magnetic moments of gadolinium iron garnet probed by soft-x-ray magnetic circular dichroism. *Journal of Applied Physics*, **70**, 6338–8979/91.

Rudolf, P., Sette, F., Tjeng, L.H., *et al*. (1992). Magnetic moments in a gadolinium iron garnet studied by soft-x-ray magnetic circular dichroism. *Journal of Magnetism and Magnetic Materials*, **109**, 109–112.

Ruegg, S., Schütz, G., Fischer, P. and Wienke, R. (1991). Spin-dependent x-ray absorption in Co/Pt multilayers. *Journal of Applied Physics*, **69**, 5655–5657.

Sacchi, M. and Mirone, A. (1998). Resonant reflectivity from a Ni(110) crystal: magnetic effects at the Ni 2*p* edges using linearly and circularly polarized photons. *Physical Review B*, **57**, 8408–8415.

Sasaki, S. (1994). Analyses for a planar variably-polarizing undulator. *Nuclear Instruments and Methods in Physics Research Section A: Accelerators, Spectrometers, Detectors and Associated Equipment*, **347**, 83–86.

Sayers, D.E., Lytle, F.W. and Stern, E.A. (1970). *Advances in X-Ray Analysis*, **13**, 248–271.

Sayers, D.E., Stern, E.A. and Lytle, F.W. (1971). New technique for investigating noncrystalline structures – Fourier analysis of extended x-ray – absorption fine structure. *Physical Review Letters*, **27**, 1204–1207.

Scherz, A. (2003). *Spin-Dependent X-Ray Absorption Spectroscopy of 3d Transition Metals: Systematics and Applications*. Ph.d. Thesis, Freie Universität Berlin.

Schmahl, G., Rudolph, D., Niemann, B., *et al*. (1996). Röntgenmikroskopie. *Naturwissenschaften*, **83**, 61–70.

Schütz, G., Knülle, M., Wienke, R., *et al*. (1988). Spin-dependent photoabsorption at the L-edges of ferromagnetic Gd and Tb metal. *Zeitschrift fur Physik B: Condensed Matter*, **73**, 67–75.

Schütz, G., Wagner, W., Wilhelm, W., *et al*. (1987). Absorption of circularly polarized x-rays in iron. *Physical Review Letters*, **58**, 737–740.

Schütz, G., Wienke, R., Wilhelm, W., *et al*. (1989). Strong spin-dependent absorption at the L2, 3-edges of 5d-impurities in iron. *Zeitschrift fur Physik B: Condensed Matter*, **75**, 495–500.

Schwarz, K. (1986). CrO2 predicted as a Half-metallic ferromagnet. *Journal of Physics F: Metal Physics*, **16**, L211–L215.

Schwinger, J. (1949). On the classical radiation of accelerated electrons. *Physical Review*, **75**, 1912–1925.

Seve, L., Jaouen, N., Tonnerre, J.M., *et al*. (1999). Profile of the induced 5*d* magnetic moments in Ce/Fe and La/Fe multilayers probed by x-ray magnetic-resonant scattering. *Physical Review B*, **60**, 9662–9674.

Shibata, J. and Otani, Y. (2004). Magnetic vortex dynamics in a two-dimensional square lattice of ferromagnetic nanodisks. *Physical Review B*, **70**(1), 012404(R)-1–012404(R)-4.

Shinjo, T., Okuno, T., Hassdorf, R., *et al*. (2000). Magnetic vortex core observation in circular dots of permalloy. *Science*, **289**(5481), 930–932.

Sinha, S.K., Sirota, E.B., Garoff, S. and Stanley, H.B. (1988). X-ray and neutron scattering from rough surfaces. *Physical Review B*, **38**, 2297–2311.

Soulen, R.J., Byers, J.M., Osofsky, M.S., *et al*. (1998). Measuring the spin polarization of a metal with a superconducting point contact. *Science*, **282**, 85–88.

Soulen, R.J., Osofsky, M.S., Nadgorny, B.E., *et al*. (1999). Andreev reflection: a new means to determine the spin polarization of ferromagnetic materials. *Journal of Applied Physics*, **85**, 4589–4591.

Spinu, L., Srikanth, H., Gupta, A., *et al*. (2000). Probing magnetic anisotropy effects in epitaxial CrO2 thin films. *Physical Review B*, **62**, 8931–8934.

Spinu, L., Srikanth, H., O'Conner, C.J., *et al*. (2001). Switching behavior and its strain dependence in epitaxial CrO2 thin films. *IEEE Transactions on Magnetics*, **37**, 2596–2598.

Stagarescu, C.B., Su, X., Eastman, D.E., *et al*. (2000). Orbital character of O-2p unoccupied states near the Fermi level in CrO2. *Physical Review B*, **61**, R9233–R9236.

Stähler, S., Schütz, G. and Ebert, H. (1993). Magnetic K-edge absorption in 3d elements and its relation to local magnetic structure. *Physical Review B*, **47**, 818–826.

Stearns, D.G. (1989). The scattering of X-rays from non-ideal multilayer structures. *Journal of Applied Physics*, **65**, 491–506.

Sticht, J. and Kübler, J. (1985). Electronic-structure of ferromagnetic Gd. *Solid State Communications*, **53**, 529–532.

Stöhr, J. and König, H. (1995). Determination of spin- and orbital-moment anisotropies in transition metals by angle-dependent x-ray magnetic circular dichroism. *Physical Review Letters*, **75**, 3748–3751.

Stoll, H., Puzic, A., van Waeyenberge, B., *et al*. (2004). High-resolution imaging of fast magnetization dynamics in magnetic nanostructures. *Applied Physics Letters*, **84**, 3328–3330.

Stumm von Bordwehr, R. (1989). A history of X-ray absorption fine structure. *Annales de Physique Fr.*, **14**, 377–466.

Suga, S. and Imada, S. (1996). Magnetic circular dichroism of transition metal-and rare earth-compounds. *Journal of Electron Spectroscopy and Related Phenomena*, **78**, 231–236.

Swoboda, T.J., Arthur, P., Cox, N.L. Jr., *et al*. (1961). Oxides: synthesis and properties of ferromagnetic chromium oxide. *Journal of Applied Physics*, **32**, 5374–5375.

Thamer, B.J., Douglass, R.M. and Staritzky, E. (1957). The thermal decomposition of aqueous chromic acid and some properties of the resulting solid phases. *Journal of the American Chemical Society*, **79**, 547–550.

Thiaville, A., Garcia, J.M., Dittrich, R., *et al*. (2003). Micromagnetic study of Bloch-point-mediated vortex core reversal. *Physical Review B*, **67**, 094410-1–094410-12.

Thole, B.T., Carra, P., Sette, F. and van der Laan, G. (1992). X-ray circular dichroism as a probe of orbital magnetization. *Physical Review Letters*, **68**, 1943–1946.

Thole, B.T., van der Laan, G., Fuggle, J.C., *et al*. (1985). 3d x-ray-absorption line and the 3d94fn+1 multiplets of the lanthanides. *Physical Review B*, **32**, 5107–5118.

Thompson, A., Attwood, D., Gullikson, E.M., *et al*. (2001). *X-Ray Data Booklet*, Lawrence Berkeley National Laboratory.

Tonner, B.P. and Harp, G.R. (1988). Photoelectron microscopy with synchrotron radiation. *The Review of Scientific Instruments*, **59**(6), 853–858.

Tonnerre, J.M. (1997). *Magnetism and Synchrotron Radiation*, Beaurepaire, E., Carriére, B. and Kappler J.P. (Eds.) Les Editions de Physique: Paris, p. 245.

Tonnerre, J.M., Seve, L., Barbara-Dechelette, A., *et al*. (1998). Soft x-ray resonant magnetic reflectivity study of thin films and multilayers. *Journal of Applied Physics*, **83**, 6293–6295.

Tonnerre, J.M., Seve, L., Raoux, D., *et al*. (1995). Soft x-ray resonant magnetic scattering from a magnetically coupled AgNi multilayer. *Physical Review Letters*, **75**, 740–743.

Van Waeyenberge, B., Puzic, A., Stoll, H., *et al*. (2006). Magnetic vortex core reversal by excitation with short bursts of an alternating field. *Nature*, **444**(7118), 461–464.

Wachowiak, A., Wiebe, J., Bode, M., *et al*. (2002). Direct observation of internal spin structure of magnetic vortex cores. *Science*, **298**, 577–580.

Weber, W. (1998). *Zirkular Dichroische Untersuchungen der Uniaxialen Anisotropie an Epitaktisch Gewachsenen, Dünnen Fe-Filmen auf GaAs(001)*, Diplom Thesis, Universität Würzburg.

Weigand, F. (2003). *XANES und MEXAFS an Magnetischen Übergangsmetalloxiden; Enticklung Eines Digitalen Lock-In XMCD-Experiments mit Physenschieber*, Ph.d. Thesis, Universität Würzburg.

Weller, D., Stöhr, J., Nakajima, R., *et al*. (1995). Microscopic origin of magnetic anisotropy in Au/Co/Au probed with X-ray magnetic circular dichroism. *Physical Review Letters*, **75**, 3752–3755.

Wende, H. (2004). Recent advances in x-ray absorption spectroscopy. *Reports on Progress in Physics*, **67**, 2105–2181.

Wende, H., Li, Z., Scherz, A., *et al*. (2002). Quadrupolar and dipolar contributions to x-ray magnetic circular dichroism at the Tb L-3, L-2 edges: experiment versus theory. *Journal of Applied Physics*, **91**, 7361–7363.

Wolf, S.A., Awschalom, D.D., Buhrman, R.A., *et al*. (2001). Spintronics: a spin-based electronics vision for the future. *Science*, **294**, 1488–1495.

Zangwill, A. (1988). *Physics at Surfaces*, Cambridge University Press: Cambridge.

APPENDIX

Owing to the absorption coefficient $\mu(E)$, which is a function of the photon energy E, the intensity will be reduced as a function of the effective path length $s(x) = x/\cos\alpha$, according to the Lambert–Beer's Law

$$I_{\text{phot}}(x) = I_{\text{phot}}(0) \cdot \exp\left[-\frac{\mu(E) \cdot x}{\cos\alpha}\right] \qquad \text{(A1)}$$

The number of excited electrons per volume fraction is now proportional to the local and depth- dependent intensity of the photon beam and to the absorption coefficient itself, taking into account the local excitation probability. To quantify this we estimate the number of produced electrons, including all secondary electrons, to be proportional to the photon beam intensity. Despite the fact that the generation of the secondary electrons is different as a function of distance to the absorption site, we assume further that the exited electron density, which is able to leave the sample, is exponentially damped by secondary processes. The number of electrons exited at the depth x at photon energy E is

$$n(x, E) = k \cdot I_{\text{phot}}(0) \cdot \exp\left[-\frac{\mu(E)}{\cos\alpha}\right] \cdot \frac{\mu(E)}{\cos\alpha} \qquad \text{(A2)}$$

The 1/cos at the right side is related to the intensity per surface area present at depth x.

So the total number of electrons leaving could be now determined by a simple integration over $n(x, E)$ by a given sample of thickness d

$$I_{\text{e}^-}(x) = \int_0^d n(x, E) \cdot \mathrm{d}x = k \cdot I_{\text{phot}}(0) \cdot \frac{\mu(E)}{\cos\alpha} \times \int_0^d \exp\left[\frac{-\mu(E) \cdot x}{\cos\alpha}\right] \cdot \exp\left[\frac{-x}{\xi}\right] \cdot \mathrm{d}x \qquad \text{(A3)}$$

After integration this reduces to

$$I_{\text{e}^-}(x) = k \cdot I_{\text{phot}}(0) \cdot \frac{\frac{\mu(E)}{\cos\alpha}}{\frac{\mu(E)}{\cos\alpha} + \frac{1}{\xi}} \times \left(1 - \exp\left[-\left(\frac{\mu(E)}{\cos\alpha} + \frac{1}{\xi}\right) \cdot d\right]\right) \qquad \text{(A4)}$$

Assuming a thick sample $d >> 1/\mu(E)$ this reduces to

$$I_{\text{e}^-}(x) = k \cdot I_{\text{phot}}(0) \cdot \frac{\frac{\mu(E)}{\cos\alpha}}{\frac{\mu(E)}{\cos\alpha} + \frac{1}{\xi}} \qquad \text{(A5)}$$

If the photon absorption length is much larger compared to the effective electron escape length, or, in other words, $\mu(E)/\cos\alpha << 1/\xi$, then the description of the TEY current reduces to

$$I_{\text{e}^-}(x) = k \cdot I_{\text{phot}}(0) \cdot \frac{\mu(E)}{\cos\alpha}\xi \qquad \text{(A6)}$$

clearly demonstrating the nice proportionality between the absorption and the observed TEY current. Now we want to discuss what happens if the absorption of light is very strong or the angle of incidence is more grazing. This is mathematically reflected by the condition $\mu(E)/\cos\alpha \gg 1/\xi$. In this case the current reduces to

$$I_{\text{e}^-}(x) = k \cdot I_{\text{phot}}(0) \cdot \frac{\frac{\mu(E)}{\cos\alpha}}{\frac{\mu(E)}{\cos\alpha}} = k \cdot I_{\text{phot}}(0) \qquad \text{(A7)}$$

This shows quite a dramatic effect which could be understood in the following way. If the angle of incidence is quite grazing, all the photons will be absorbed in a very thin top layer close to the surface, because the effective way of traveling through the sample is very large. If this effective length is much longer compared to the absorption length, all photons will be absorbed at the top, no matter what exact energy dependence is given by the absorption length. Therefore, the energy dependent current signal is more or less a straight line. In the range between those two extremes the measured TEY signal exhibits damped high absorption lines, for example, as present at the 2p absorption lines for the 3d TMs.

This resonance damping or saturation effect in the TEY signal is enhanced for high absorption, as present at the 2p ($L_{2,3}$) or 3d ($M_{4,5}$) absorption resonance lines, and for large atomic density, as for pure 3d TM samples and/or at grazing incidence. In contrast a reduced number of atoms per volume, for example, as present for the minority part in alloys or in chalcogenides, give only small self-absorption effects.

Now we discuss the influence of self-absorption for films with reduced thickness d. In this case, we can expand the equation for the thickness dependent TEY signal (equation (A4)) for small thickness d.

$$\begin{aligned} I_{\text{e}^-}(x) &= k \cdot I_{\text{phot}}(0) \cdot \frac{\frac{\mu(E)}{\cos\alpha}}{\frac{\mu(E)}{\cos\alpha} + \frac{1}{\xi}} \times \left(1 - \exp\left[-\left(\frac{\mu(E)}{\cos\alpha} + \frac{1}{\xi}\right) \cdot d\right]\right) \\ &= \frac{k \cdot I_{\text{phot}}(0)}{\frac{\mu(E)}{\cos\alpha} + \frac{1}{\xi}} \cdot \frac{\mu(E)}{\cos\alpha} \times \left(1 - 1 + \left(\frac{\mu(E)}{\cos\alpha} + \frac{1}{\xi}\right) \cdot d + \cdots\right) \\ &= \frac{k \cdot I_{\text{phot}}(0)}{\cos\alpha} \cdot \mu(E) \cdot d \end{aligned} \qquad \text{(A8)}$$

This expansion is valid in the case of extreme thin layers, where $d << \xi$ and $d << \cos\alpha/\mu(E)$. It also reflects the intuitive experimental result. The number of produced electrons increases as more photons are absorbed in a thin layer close to the surface and not in the substrate below.

To correct the saturation effect of reduced resonance line absorption profiles, it is necessary to know the relevant parameters, as the effective electron escape length ξ and the energy dependent photon absorption profile $\mu(E)$. Unfortunately, both parameters are not known, especially the absorption coefficient is unknown until the correction has been performed.

An example of a corrected absorption profile, deduced from the TEY signal by adapting the current profile before and after the resonances to well-known absorption coefficients, is being shown later in Figure 50. In this case, the measured absorption profile has been used to determine the self-absorption corrected signal in an iterative way. This could be done in the case of smooth and polished samples, where the electron escape length can be determined by a self-consistent saturation correction as the function of the angle of incidence or film thickness (Goering, Gold, Lafkioti and Schuetz, 2006; Gold, 2006; Hunter-Dunn *et al.*, 1995; Nakajima, Stöhr and Idzerda, 1999; Weber, 1998).

Ultrafast Magnetodynamics with Lateral Resolution: A View by Photoemission Microscopy

Hermann A. Dürr[1] and Claus M. Schneider[2]

[1] *BESSY GmbH, Berlin, Germany*
[2] *Institut für Festkörperforschung, Jülich, Germany*

1 INTRODUCTION

The dynamic behavior of magnetic systems with a nonuniform magnetization distribution is a complex issue. Individual magnetic structures, such as domains, domain walls, vortices, and other noncollinear configurations each contribute with their specific dynamic response to the overall picture. This is particularly true in the ultrafast regime, that is, on the nanosecond timescale and below. In order to disentangle these contributions, suitable laterally resolving approaches must be employed. Time-resolved photoemission microscopy (TR-PEEM) has been developed into a versatile tool to probe the dynamic response of magnetic systems with high spatial resolution. Two complementary avenues are currently pursued, each probing specific aspects. Soft X-ray pulses are employed to address element-selective aspects of magnetization dynamics down to the picosecond timescale. Photoexcitation with ultrashort laser pulses provides access to the spin dynamics even in the subpicosecond regime. With free-electron laser (FEL) light sources coming on line in the near future, these avenues may converge into a unique approach to magnetodynamic phenomena, combining element and chemical selectivity with a high lateral (∼10 nm) and time resolution (∼100 fs).

Handbook of Magnetism and Advanced Magnetic Materials. Edited by Helmut Kronmüller and Stuart Parkin. Volume 3: *Novel Techniques for Characterizing and Preparing Samples*. ISBN: 978-0-470-02217-7.

1.1 Magnetism and photoemission microscopy

Magnetic thin films and nanostructures play a central role for many areas in information technology. First of all, they provide highly specialized functionalities in various elements of a magnetic mass storage device, such as a hard disk. These are still the first choice, if it comes to fast, high-capacity random access memory (Lodder, 1998; Wang, 2005). With the discovery of large magnetoresistive effects (Baibich *et al*., 1988; Binasch, Grünberg, Saurenbach and Zinn, 1989; Meservey and Tedrow, 1994; Moodera, Kinder, Wong and Meservey, 1995) in thin-film systems at room temperature, not only novel applications but also an entire new research field emerged – spinelectronics or spintronics (Prinz, 1998; Wolf *et al*., 2001). Spintronics operates at a crossover of electronics and magnetism by treating the charge and the spin degrees of freedom of electrons in transport processes on an

equal footing. In this way one can hope to combine the best of two worlds, such as the well-established charge control in semiconductors with the nonvolatility of magnetic bits. The first realization of such a spintronics device may be a hybrid, the so-called magnetic random access memory, which is currently in the test phase in many major microelectronics companies (Freescale, 2006).

The breathtaking development in thin film and nanomagnetism has been fostered significantly by the improvement of analytical methods and approaches. In this context, synchrotron radiation adopted a key role (see also **Synchrotron Radiation Techniques Based on X-ray Magnetic Circular Dichroism, Volume 3**). It paved the path for detailed spectroscopic studies of magnetic materials, which largely shaped our understanding of the electronic foundation of magnetism. Milestones along this way were the discoveries of X-ray magnetic dichroism with linearly (van der Laan *et al*., 1986) and circularly polarized light (Schütz *et al*., 1987) (Chen, Sette, Ma and Modesti, 1990). Magnetic x-ray linear (MXLD) and circular dichroism (MXCD) provide a unique combination of magnetic sensitivity and element selectivity, and they laid the foundation to the field of x-ray magneto-optics. Sum rules enabled a quantitative determination of spin and orbital magnetic moments on the basis of spectroscopic investigations (Thole, Carra, Sette and van der Laan, 1992; Carra, Thole, Altarelli and Wang, 1993; Thole and van der Laan, 1993) – at least within certain limits.

Moreover, the access to synchrotron radiation and the discovery of magnetic dichroism, in particular, led to the revival of a very interesting full-field imaging technique – photoelectron emission microscopy (PEEM) – unleashing its full power. Originally invented by Brüche (1933, 1934), photoemission microscopy remained for a long time a specialized technique in surface science, despite some major achievements in the electron-optical concept, such as the low-energy electron microscope and its spin-polarized version introduced by Bauer and Telieps (1988) and Altman *et al*. (1991). With the increasing availability of brilliant soft X-ray sources, however, PEEM was recognized as a technique enabling a high lateral resolution mapping of surfaces with chemical information. Imaging of magnetic domains with threshold PEEM was performed as early as 1957 (Spivak, Dombrovskaia and Sedov, 1957) exploiting the stray field emanating from a ferromagnet's surface as a contrast mechanism. Its enormous potential for magnetic studies with synchrotron radiation was demonstrated by Stöhr *et al*. (1993), Schneider *et al*. (1993), when first domain imaging experiments of magnetic surfaces and thin films were successfully performed. Since then, PEEM has matured into a valuable tool to unravel the magnetic microstructure in complex thin-film systems. Its unique features arise from the fact that the choice of the light polarization permits the study of ferro- and antiferromagnetic components of a system (Stöhr *et al*., 1999; Nolting *et al*., 2000). In this way, in-depth studies of antiferromagnetic systems and their domain structures became available for the first time (Ohldag *et al*., 2001).

1.2 Dynamical aspects of magnetism

Recently, the dynamical aspects of magnetism moved into the focus of interest. From a technical viewpoint, the main topic is the switching speed, that is, the time it takes to flip the magnetization vector from one given orientation to another. This speed issue is at the heart of magnetic data storage, spintronics, and other areas involving high-frequency modulations of a magnetic system. The faster a magnetic system switches, the faster can be the data transfer rate in a memory or the clock speed of a spintronic device. From a more fundamental point of view, however, one would like to understand the physical processes and limitations governing the magnetization reversal, the origin of the damping mechanisms, and the nature and types of the magnetic excitations appearing in a given system. For these reasons, the recent years have witnessed an increasing interest in fast and ultrafast dynamic processes in magnetic systems (Hillebrands and Ounadjela, 2001, 2003, 2006). The relevant timescales dealt with in the experimental studies range from a few nanoseconds down to less than 100 fs, depending on the type of interaction triggering the dynamic response of the magnetic system. In addition to the 'traditional' way of controlling the magnetization reversal by an external magnetic field, spin-polarized currents (Myers *et al*., 1999) or even photons (Kimel *et al*., 2005) have been successfully employed for this purpose recently.

In order to access the microscopic mechanisms and processes, which determine the magnetization dynamics, time-resolving magnetic imaging techniques are mandatory. Most of our knowledge until now was obtained from Kerr microscopy (Freeman and Hiebert, 2001), employing pulsed-laser sources as a 'clock' to provide a time resolution in the nanosecond and subnanosecond regime. Synchrotron radiation also has a well-defined intrinsic time structure due to the very way it is created (Wiedemann, 2003). The width of these light pulses is usually in the picosecond range, whereas their spacing can be adjusted to any value between 1 ns and 1 µs, depending on the storage ring operation mode and filling pattern. This provides an extremely versatile time-resolved access to magnetization dynamics, both laterally integrated and resolved, as has been demonstrated recently (Krasyuk *et al*., 2003; Vogel *et al*., 2003). They allow access to phenomena such as domain nucleation, magnetization rotation,

or precessional switching, which may be described in continuum models, for example, in the Landau–Lifshitz–Gilbert (LLG) framework.

With laser irradiation even shorter light pulses are available, providing a convenient probing of processes on the 100 fs timescale. Usually the wavelength of these light pulses lies in the near infrared region and can be easily transposed into the visible or ultraviolet regime by means of frequency doubling or tripling schemes. This already allows the study of the influence of electronic excitations on the magnetic properties as well as the interactions between spin and electron systems and the lattice, that is, to probe the transfer of energy and angular momentum (Rhie, Dürr and Eberhardt, 2003). An X-ray counterpart is expected to become available soon through new synchrotron radiation sources, the so-called free-electron lasers (DESY, 2006). The perspective for the future will thus be a combination of element selectivity with femtosecond time resolution and the high lateral resolution provided by PEEM.

This chapter addresses the new developments and achievements in magnetization and spin dynamics obtained with the method of photoemission microscopy using picosecond soft X-ray and femtosecond optical laser pulses. We are well aware of the fact that there are many other interesting imaging approaches to magnetization dynamics, such as various types of Kerr microscopy or the techniques of X-ray transmission microscopy, which became available recently (for details see **Synchrotron Radiation Techniques Based on X-ray Magnetic Circular Dichroism, Volume 3**). Other methods, such as magnetic X-ray holography (Eisebitt *et al*., 2004) are currently extended into the time regime. These techniques are addressed in other parts of this book. Here we focus onto a particular subset of experiments performed with photoemission microscopy, in order to illustrate the virtues and future potential of probing magnetization dynamics with lateral resolution down to the nanometer regime.

This contribution is organized as follows. In Section 2 we briefly review the various important timescales playing a role in magnetism. In Section 3 we give a short account of the technical details of time-resolving PEEM experiments. Sections 4 and 5 are devoted to the experimental results obtained on the picosecond and femtosecond timescales, respectively and their discussion. In Section 6 we outline the future development of the PEEM technique with respect to time-resolved studies in and outside of magnetism.

2 TIMESCALES IN MAGNETISM

In the quasistatic limit, each magnetic system assumes a spatial distribution of the magnetization, which is determined by energy minimization principles. In very small particles, that is, far below a size of 1 μm, one often finds a single domain state, where the magnetization is uniformly oriented along one direction throughout the entire particle, creating a sizable magnetic stray field outside the particle. If the particle becomes larger, the stray field increases up to the point where the total energy of the system may be reduced at the expense of exchange energy by the spontaneous formation of domains, domain walls, and noncollinear magnetization distributions (buckling, curling, etc.). The details of the magnetic microstructure depend sensitively on the shape of the magnetic particle and the material parameters, and so does the transition from a single- to a multidomain state as a function of particle size. As a result, one observes a large zoo of magnetic domain structures in the quasistatic case (Hubert and Schäfer, 1998) already. Understanding the formation of these domain structures and their dynamic response to external magnetic fields is at the heart of the technological exploitation of magnetism. The experimental visualization of magnetic structures and magnetization reversal processes provides a major key to this understanding.

It is important to note that the relevant timescales in magnetism cover an extremely wide range of more than 20 orders of magnitude (Figure 1) – determined by both applications and fundamental processes. On the one end of the scale, we find the retention time in magnetic data storage. As the stored information consists essentially of a sequence of well-defined magnetic domains, these magnetic domains have to be extremely stable against thermal fluctuations. Therefore, a value of 10–15 years (10^8 s) is usually considered desirable as retention time. On the other end of the timescale, we are confronted with ultrafast energy and angular momentum transfer processes in magnetic systems on a timescale of 10^{-14} s. These processes are related to nonequilibrium electron distributions and are held responsible for an extremely fast decay of the magnetic order, for example, in the wake of a highly energetic laser pulse. In the intermediate time regime between 10^{-3} and 10^{-12} s we find a wealth of different dynamical processes. These range from relatively slow phenomena, such as magnetization creep and aftereffects, to fast mechanisms, which determine the technological limits of magnetization reversal such as domain nucleation, domain wall propagation, and coherent rotation. It is often overlooked that the ongoing increase in storage density is accompanied by a corresponding increase in the data transfer rates, that is, the read/write speeds, slowly approaching the gigahertz regime. A similar development takes place in the field of magnetic random access memories, where a duty cycle of about 20 ns has already been demonstrated (Freescale, 2006).

The dynamic aspects of a magnetic system are often described as *magnetization dynamics* or *spin dynamics*. It

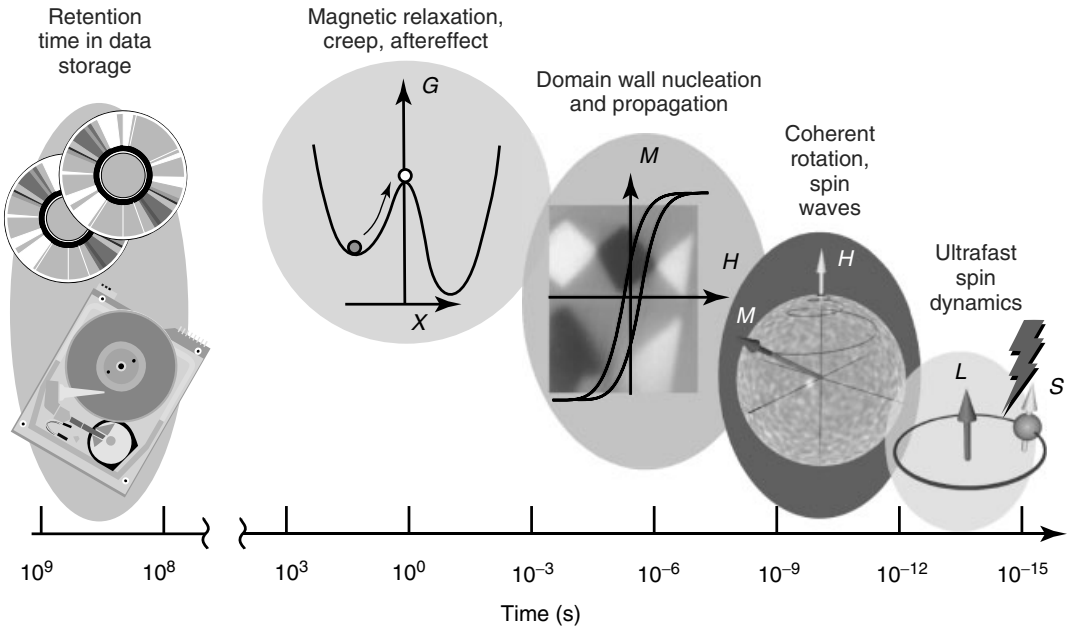

Figure 1. Timescales in magnetism and the associated microscopic processes determining the dynamic behavior of a magnetic system.

should be stated that this terminology contains more than just a semantic difference, but is unfortunately not unambiguous in use. In our view, the term magnetization dynamics refers to the response of a magnetic continuum system, that is, the spins or magnetic moments of the system are strongly coupled by the exchange interaction, to a low-energy excitation, for example, a magnetic field pulse or a spin-polarized current pulse. From a theory point of view, this situation can be rather successfully described in small particles by means of macrospin models within the LLG formalism (Miltat, Albuquerque and Thiaville, 2003). This approach works also – with increased computational efforts – for nonuniform magnetization distributions, such as domains and domain walls. One of the main restrictions of this approach is that locally only the direction of the magnetization $\vec{M}$ is changing, but not its magnitude. In other words, the absolute value of $\vec{M}$ is always preserved in this continuum theory. This continuum picture represents one limiting case and is capable of describing the response of a magnetic system down to the picosecond regime.

The other extreme situation is encountered when an excitation acts directly on the electronic system first. In fact, this can be readily achieved by strong laser pulses, which lead to electronic transitions on the electronvolt scale. The consequence is an electron distribution in strong nonequilibrium – at least on a timescale of several 10 fs. This nonequilibrium state represents a formidable problem for the theoretical treatment and strong efforts are currently devoted to its solution. The physical mechanisms in this temporal regime rather act on the individual electron and, in this way, on the individual spin for that matter. It is thus justified to describe this regime as ultrafast spin dynamics [1]. In subsequent steps, the energy and angular momentum associated with the electronic excitation is then transferred to the magnetic and lattice subsystems. Most of these processes are already terminated during the first few picoseconds. On a longer timescale, however, the system still responds by means of precessional motion of the magnetization. A first interesting attempt has been made recently to connect the processes on the electronic timescale with the magnetodynamic timescale in the 100 ps regime (Koopmans, Ruigrok, Longa and de Jonge, 2005).

In Sections 4 and 5 we discuss results obtained for both regimes.

3 PHOTOEMISSION ELECTRON MICROSCOPY

3.1 Electron-optical layout

The electron-optical system of a standard photoemission electron microscope allows a wide-field imaging of a surface with electrons emitted from this surface. Its basic concept is very similar to that of an optical immersion lens microscope (Bauer and Telieps, 1988; Schönhense, 1999; Bauer, 2001a). The PEEM consists of three main parts: (i) the objective lens, (ii) contrast aperture, and (iii) projective lens system

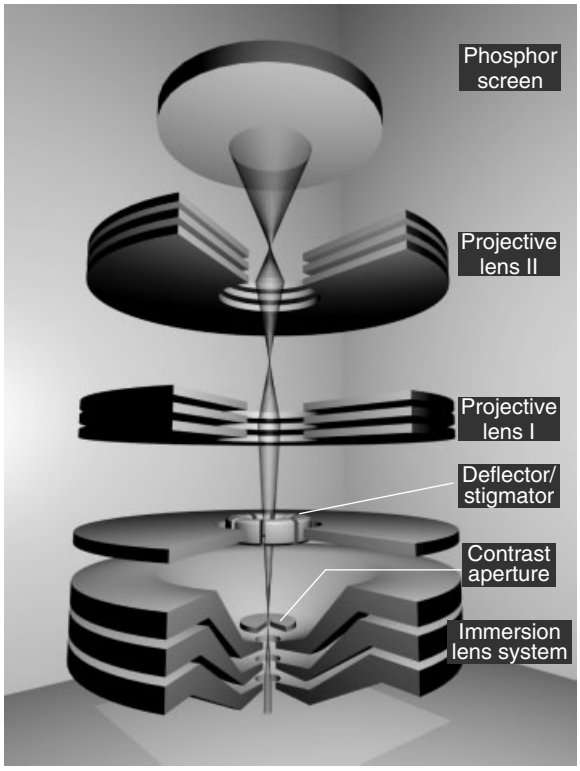

Figure 2. Electron-optical column of a an electron emission microscope.

(Figure 2). The objective lens system is designed to collect the emitted electrons up to large starting angles with respect to the surface normal. For this purpose, a large electrostatic extraction field ($\approx$10 kV mm^{-2}) of axial symmetry $\vec{E}_{\rm ex}(r, \theta, z)$ is applied between the sample and the objective lenses. This approach makes the sample an inherent part of the electron-optical system giving rise to a variety of nonmagnetic contrast mechanisms, induced by the topography, chemical or crystalline heterogeneity of a surface (Bauer *et al*., 1996). As the distance between sample and immersion lens objective is only about 2–3 mm, the light reaches the sample surface usually at a flat angle of 15–25°. A contrast aperture (size of 20–50 µm) in the backfocal plane of the objective lens serves to select the proper trajectories and thus to reduce the influence of lens aberrations. The smaller the contrast aperture, the better the contrast and the lateral resolution that can be obtained. The projective lens system is used to magnify the image onto the image detector, consisting of a multichannel plate and a phosphor screen, which converts the image, so that it can be acquired by a CCD camera. More sophisticated electron-optical configurations may also involve electromagnetic instead of electrostatic lenses, or they may include electrostatic energy filters to further select the electron trajectories and improve the image quality (Bauer, 2001b).

3.2 Magnetic contrast in PEEM

The information about the magnetic state of the sample is contained in the spin polarization *and* the intensity distributions of the electrons emitted from the sample. It can be extracted by various magnetic contrast mechanisms, which fall into two classes. The first class involves a direct analysis of the electron spin polarization vector $\vec{P}$. The second class exploits a difference in the intensity distributions ΔI – a magnetic *dichroism* – for different geometrical configurations of the spin quantization axes describing the system. The physical mechanism underlying magnetic dichroism involves the excitation of spin-polarized photoelectrons due to optical orientation (Meier and Zakharchenya, 1984) into exchange split, that is, spin-polarized final states. The magnitude of the transition matrix element thus depends on the spin character of both photoelectron and final state. As a consequence, the final state effectively serves as an *internal* spin detector, translating the magnetic information carried by the spin into an intensity signal.

The most prominent magnetic contrast mechanisms in X-ray photoemission electron microscopy (XPEEM) exploit soft X-ray magnetodichroic phenomena with circularly or linearly polarized soft X rays in the electron yield mode (Stöhr and Anders, 2000 Schneider and Schönhense, 2002). This holds for the imaging of both static and dynamic magnetization configurations. With circularly polarized light (X-ray magnetic circular dichroism, XMCD), the ferromagnetically ordered state may be probed (Schütz *et al*., 1987), whereas linearly polarized light gives access to the antiferromagnetically ordered state via magnetic linear dichroism (X-ray magnetic linear dichroism, XMLD) (van der Laan *et al*., 1986). This unique feature of XPEEM permits the investigation of composite magnetic systems, comprising ferro- and antiferromagnetic components (Nolting *et al*., 2000; Kuch *et al*., 2006).

Although X-ray magnetic dichroism is sometimes referred to as the *X-ray counterpart of the Kerr effect*, there are important differences. First, the magnetic dichroism directly results in an intensity change, whereas the polar and longitudinal Kerr effects lead to polarization changes in the reflected light. In addition, the X-ray dichroic signal may be rather large (e.g., $\sim$20% intensity change at the Fe L_3 absorption with XMCD). Thus the magnetic microstructure may give rise to a contrast comparable with topographically induced contrast levels. In order to enhance the magnetic contrast, often two images taken at opposite light helicity are subtracted, thereby eliminating the nonmagnetic contrast. The XPEEM approach allows also microspectroscopy studies and thus gives access to quantitative magnetic parameters, such as the spin and orbital magnetic moments via XMCD sum rules (Thole, Carra, Sette and van der Laan, 1992;

Carra, Thole, Altarelli and Wang, 1993; Thole and van der Laan, 1993; Goering, 2005; Goering *et al.*, 2005), or the magnetocrystalline anisotropy energy via XMLD analyses (van der Laan, 1999; Dhesi, van der Laan, Dudzik and Shick, 2001). In metallic systems the information depth is about 2–3 nm. The lateral resolution of the present instruments with respect to soft X-ray-based magnetic imaging is of the order of 50 nm and basically limited by the rather large energy spread of the photoelectrons entering the PEEM. A much more narrow energy spread can be obtained in threshold photoemission, pushing the lateral resolution down to less than 20 nm. Also for threshold photoemission conditions a magnetodichroic contrast mechanism has been reported (Marx, Elmers and Schönhense, 2000), but has not yet found widespread use.

A certain complication arises from the fact that the PEEM operates with electrons, which can easily be deflected in external magnetic fields because of the Lorentz force. On the one hand, this circumstance severely limits the application of a photoemission microscope for the investigation of magnetic structures in an applied magnetic field, as the imaging capabilities are impaired. On the other hand, the sensitivity to magnetic fields can be turned into a virtue. A careful analysis of the electron trajectory changes can yield detailed information about the magnetic field distribution around and above the sample. This can be used, for example, to quantitatively determine the stray fields at the edges of microstructured magnetic elements (Nepijko, Sedov and Schönhense, 2000). In certain cases of hard magnetic materials or permanent magnets with their large stray fields, this Lorentz force deflection can even be used to image the magnetic domain distribution of the surface (Mundschau *et al.*, 1996), although only with moderate lateral resolution. We should also recall that the Lorentz force-related contrast formed the basis for the first ever observation of magnetic domains in a photoelectron emission microscope (Spivak, Dombrovskaia and Sedov, 1957).

When the photoelectrons are excited by ultrashort pulses of a Ti:sapphire laser system operating typically at a photon energy of 1.5 or 3.1 eV, frequency multiplication schemes or multiphoton excitation processes must be involved to overcome the work function. In this case, the magnetic sensitivity is achieved by explicitly analyzing the photoelectron spin polarization $\vec{P}$. The spin polarization analysis can be implemented into a PEEM as shown schematically in Figure 3 (Dürr, Kronast and Eberhardt, 2001). In addition to imaging the lateral photoelectron distribution, the photoelectron beam can be deflected into a spin detector, where its spin polarization is quantified via spin-dependent scattering of low-energy electrons from a W(100) single crystal surface (Kirschner, 1985). The normalized intensity difference between conjugate diffraction beams (marked '1' and '2' in Figure 3) – the scattering asymmetry – is a direct measure of the magnitude of the component of $\vec{P}$ perpendicular to the plane connecting the diffracted beams. Thus, the perpendicular component and one in-plane component of the spin polarization vector with respect to the sample surface can be measured simultaneously. To retain lateral resolution in spin-resolved measurements an adjustable iris aperture mounted in the first image plane of the PEEM is used to define the width of the transmitted photoelectron beam, that is, only photoelectrons emitted from a selected sample area are transmitted into the spin detector, thereby carrying local spin polarization information.

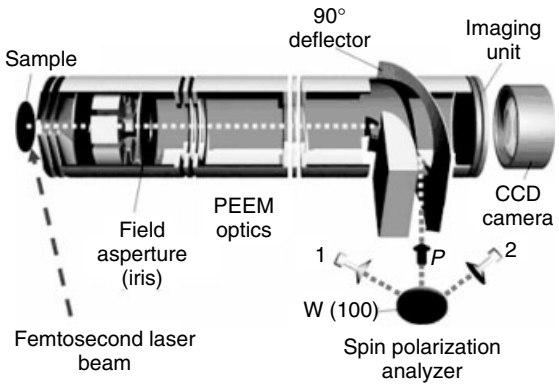

Figure 3. Schematic diagram of the spin-polarized photoemission electron microscope.

3.3 Time resolution in microscopy experiments

Time-resolved studies – or more specifically time-resolved magnetic imaging – may adopt one of the following two procedures. In the *one-shot approach* the entire image is acquired during a single pulse-wise illumination of the sample. The result represents the momentary magnetic state of the sample and is also capable of capturing nonperiodic and stochastic events, such as fluctuations in the vicinity of phase transitions, statistical switching events, or traveling spin waves. In order to be able to perform a one-shot imaging, however, one needs a very bright illumination source (photons or electrons) and a very fast and sensitive image detector. This combination is currently not yet available, and high hopes are set on the upcoming FELs and the associated instrument development.

At present, most of the time-resolved magnetic imaging experiments follow a stroboscopic imaging scheme. In this case, one repeatedly records images of the magnetic system – typically 10^6–10^8 cycles – and adds them up until a sufficient signal-to-noise ratio is achieved. It is obvious that this procedure allows one to only observe the repeatable events in the magnetization reversal process, that is, those

processes that occur during each cycle at the same location of the sample. Fluctuations and statistical switching events will be averaged out. In practice, this requires the magnetic system to be always in the same state when the data are taken. In other words, one needs to carefully control the momentary magnetic configuration of the sample of interest during the experiment by an external magnetic field or by other means. These considerations hold for experiments in the nano-, pico-, and femtosecond regimes.

A photoemission microscopy experiment dedicated to the investigation of time-resolved magnetic processes must thus include two further major ingredients: (i) a time-dependent excitation of the magnetic system and (ii) a time-resolved data acquisition scheme. The first one is usually achieved by short magnetic field pulses or laser light pulses, whereas the second one involves sophisticated synchronization schemes and/or time-resolving imaging detectors.

3.4 Short magnetic field pulses

In order to map the time evolution of the magnetization, the magnetic system is most conveniently 'excited' by an external magnetic field – sometimes called *Oersted field* – with a well-defined time structure. In most cases this time structure is either smoothly periodic (sine wave excitation) or consists of a periodic sequence of short pulses (pulse excitation) provided by a signal generator. Well up into the megahertz regime, these time-dependent magnetic fields can be generated by means of coil/yoke systems similar to the write heads used in present hard disk drives. However, the inductivity of these system limits the rise time of the magnetic field to a few 10 ns.

For faster rise times of the magnetic field pulse one has to resort to alternative approaches. An appropriate way to overcome the inductivity problem is the use of planar thin-film structures as high-frequency transfer lines. These are prepared on insulating substrates and can be appropriately designed for high-frequency applications. The structures are usually defined by optical or electron beam lithography and etching or lift-off procedures in Cu or Au films. The key to a proper control of the time dependence of the magnetic field, that is, avoiding unwanted reflections or damping of the current signal, is a proper impedance matching of the thin-film structure to the current source. Two principal geometries of these thin-film structures are most often used: microcoils and microstrip lines. The choice determines the direction of the magnetic field $\vec{H}$ with respect to the sample. If the thin-film structure and the transfer lines are properly designed taking into account geometry and material parameters, the limiting factor of the rise time of the magnetic field is the pulse generator. In many applications conventional electronic circuits are used to create short current pulses. Commercial pulse generators may provide current pulses with a minimum of about 500 ps pulse width and less than 100 ps rise time. The use of these microcoil or -strip lines requires some lithographic efforts and the structures must be adapted to the specific environment in a photoemission microscope. At present, however, this has proved to be a very successful approach, yielding many interesting results on the magnetodynamics in the nanosecond and subnanosecond regime (Schönhense, Elmers, Nepijko and Schneider, 2006).

If still faster current pulses are required, one has to resort to other means, for example, to photoconductive switches, for example, Auston switches (Keil, Gerritsen, Haverkort and Wolter, 1995) or Schottky barrier approaches (Acremann *et al*., 2001). In these cases, the excitation involves a very short laser pulse (e.g., from a Ti:sapphire laser) and enables rise times of the order of a few picoseconds. A detailed control of the pulse shape may be achieved by combining two Auston switch circuits with opposite current polarities, one of which is illuminated with a short time delay with respect to the other (Gerrits *et al*., 2001). Because of the longer recombination time of the charge carriers, the falling edges of the two current pulses are rather similar on the timescale and very closely compensate each other. In this way, even subpicosecond-width electrical pulses may be generated (Keil, Gerritsen, Haverkort and Wolter, 1995).

3.5 Pulsed light sources

In the visible range of light, lasers are the instruments of choice to generate short light pulses. Most widely employed are solid-state lasers, such as Nd-YAG systems, which deliver pulses in the 10 ps range. Also fast pulsed-laser diodes may reach into this regime. The repetition frequencies are of the order of several 10 MHz. These light sources are used in Kerr microscopy (Chumakov *et al*., 2005) or to trigger optical switches in PEEM (Raabe *et al*., 2005). Still shorter pulses of the order of 30–100 fs are obtained, if these picosecond pulses are used to pump a mode-locked Ti:sapphire oscillator. The resulting femtosecond pulses are emitted with a wavelength of about 800 nm at a repetition frequency of typically around 80 MHz. The majority of the ultrafast time-resolved experiments in the laboratory are carried out with these light sources. The ongoing development of laser sources, however, has already demonstrated the feasibility of creating pulses of several hundred attoseconds width, even at photon energies as high as $h\nu = 100$ eV (Hentschel *et al*., 2001).

For studies with chemical selectivity, the soft X-ray range ($h\nu = 50$–1500 eV) is of particular interest. In third

generation synchrotron radiation laboratories, highly brilliant beams of this light are generated by means of insertion devices, so-called undulators. Depending on the undulator type, the radiation may be linearly or elliptically polarized (Wiedemann, 2003). The emission of synchrotron radiation dissipates energy from the electrons in the storage ring. In order to compensate this energy loss the electrons are accelerated after each cycle in a microwave cavity. As a consequence, the electrons are not distributed evenly along the orbit, but are grouped into packets (bunches), with a separation determined by the microwave frequency. Since synchrotron radiation is generated only at the moment when an electron bunch passes through a bending magnet or undulator, the bunch structure results in a natural time structure of the synchrotron radiation. Depending on the operation mode of the storage ring, that is, the bunch pattern in the ring, the light pulse width ranges between $\Delta t = 1-100$ ps, at repetition frequencies from $\Delta T = 2$ ns–1 μs (Table 1).

Synchrotron radiation with an even shorter pulse width in the 100 fs range may become available soon in a novel type of facility, the FEL (DESY, 2006). The FEL comprises a linear accelerator, which feeds the relativistic electrons into a long undulator. At both ends of the undulator, optical mirrors are placed to form an optical resonator on the undulator axis. The synchrotron radiation generated in the undulator is reflected between the mirrors and can thus more efficiently interact with the electron bunches passing through the undulator. This interaction has two consequences. First, energy is directly transferred from the electrons into the electromagnetic wave field in the resonator. Second, the interaction also modulates the electron density in a bunch along its direction of motion, that is, the bunch will be segmented into short microbunches, each of which generates radiation with a pulse width in the subpicosecond regime. A more advanced concept omits the optical resonator and instead employs two undulators – a *radiator* and an *amplifier*. The light created in the radiator is fed into the amplifier to enhance the interaction between light and electrons. This approach is called *self-amplified spontaneous emission* and yields a much better control of the light pulse width. Pulses as short as 50 fs have already been generated in this mode of operation (Ayvazyan *et al*., 2006).

Table 1. Pulse train characteristics of various synchrotron and laser light sources.

Light source	Pulse width (ps)	Repetition time (ns)
BESSY multibunch	30	2
BESSY single bunch	100	805
BESSY low alpha	3	2 or 805
ESRF multibunch	20	2.8
ESRF 16 bunch	60	176
YAG laser	15	44
Ti:Sapphire	0.01–0.1	12
FEL	0.1	xx

The combination of variable photon energy and light polarization, high brilliance, and well-defined time structure renders synchrotron radiation a unique tool to study static and dynamic aspects of magnetism. It thus forms the basis of the experiments described in Section 3.

3.6 Time-resolving image detection

In the operation modes described in the preceding text, the time resolution in the PEEM is essentially determined by the width of the photon pulse. Moreover, the repetition rate in the experiment also is determined by the timing characteristics of the light source, as each light pulse will contribute to the measured signal. In order to allow for more flexible timing schemes without having to change the bunch pattern in the ring, it is advantageous to introduce some time-resolution capability in the PEEM itself. This can be achieved, for example, by using gated-detector schemes. In some cases, gating the PEEM image detector can be necessary to improve the signal-to-noise ratio and to select the proper events. In the so-called camshaft mode operation provided by several synchrotron radiation facilities, the bunch pattern consists of a multibunch sequence covering, say, about three quarters of the ring circumference. The fourth quarter which can cover a time window of up to 200 ns is empty, except for a singular highly filled bunch ('cam') placed somewhere in the center of this empty region. By ramping the operating voltage of the PEEM image converter (multichannel plate) up only in the vicinity of the cam pulse, the image detector will capture information solely related to the cam pulse, that is, the PEEM is operated in an effectively single-bunch mode (Raabe *et al*., 2005).

A complementary approach involves image detectors with intrinsic time resolution, such as, for example, a delay line detector (DLD) (Oelsner *et al*., 2001). The DLD measures the position of individual counting events in the image plane by means of a crossed-wire system with a time resolution of about 50 ps. This feature can be used to establish a particular 'interleave' operating mode of the PEEM, meaning that only every nth light pulse is used to trigger the magnetic excitation (e.g., field pulse), but a time sequence of $n-1$ images is recorded after each excitation, mapping the response of the system at regular time intervals given by the detector. In this way, the detection efficiency during the time-resolved experiments can be considerably enhanced. At present, however, the maximum counting rates of these DLD systems are still limited to a few megahertz, rendering

them appropriate only for very specialized applications. More on the implementation and use of time-resolving imaging detectors in PEEM, in particular, with respect to time-of-flight applications may be found in a recent review article (Schönhense, Elmers, Nepijko and Schneider, 2006).

3.7 Ultrafast timing configurations

The achievable temporal resolution in stroboscopic time-resolved imaging experiments is given by the duration of pump and probe pulses as well as by the temporal jitter between them. Aiming for picosecond resolution, it is possible to electronically synchronize the sources for pump and probe pulses. The resulting jitter may be of the order of a few up to 10 ps. However, when utilizing subpicosecond laser pulses down to a few femtoseconds, eliminating the jitter is imperative. This is conveniently achieved by generating both pump and probe pulses from the same source, which is then usually a femtosecond laser system. Using this approach, even experiments involving magnetic field pulses generated via an Auston switch can easily reach a temporal resolution of less than 100 fs (Gerrits *et al*., 2001).

A schematic overview of a typical full-optical pump-probe setup is displayed in Figure 4 (Link, Dürr and Eberhardt, 2001). After the first frequency conversion stage, a beam splitter generates two pulses. The reflected part, which contains 70% of the beam intensity is again frequency converted producing UV photons of around 4.5 or 6 eV and serves as the pump pulse. The transmitted part runs through an optical delay stage (retroreflector) and serves as probe pulse. Both pulses are focused onto the sample and are brought into spatial overlap. By physically moving the retroreflector, both pulses can be delayed in time with respect to each other. A retroreflector shift of 1 μm corresponds to a delay of 6.7 fs, so that precise time-resolved measurements are possible. In such a setup each pump pulse is inherently synchronized to a probe pulse. Consequently the time-resolved signal detection requires no special adjustment of the PEEM data acquisition compared to the time averaging mode.

4 MAGNETIZATION DYNAMICS INDUCED BY SHORT MAGNETIC FIELD PULSES

In the following, we will discuss some selected results from recent spatiotemporal investigations of the magnetization reversal and magnetodynamics in microstructured elements. These results illustrate that the detailed dynamic behavior of

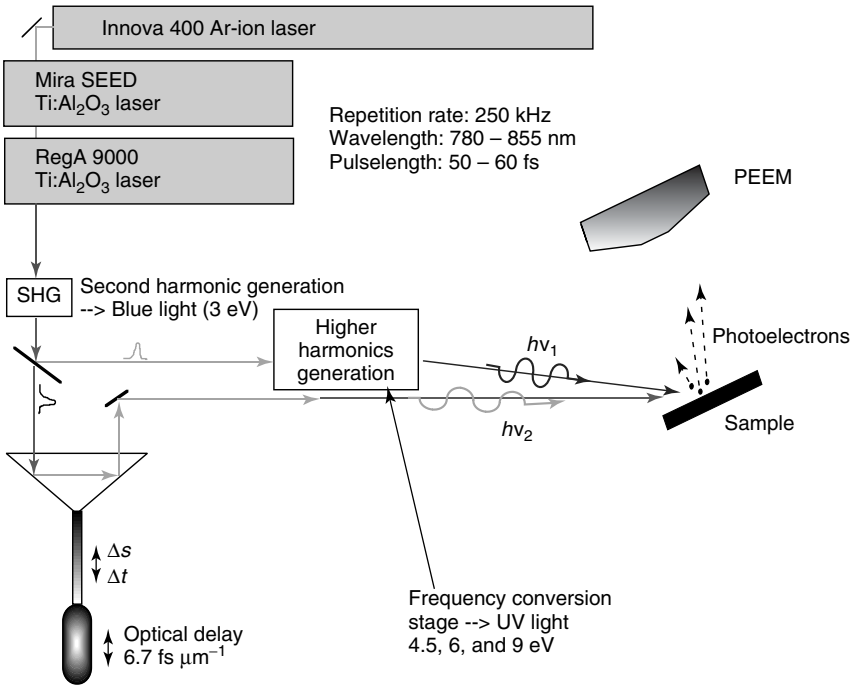

Figure 4. Schematic diagram of a femtosecond laser pump-probe setup (Link, Dürr and Eberhardt, 2001). The infrared femtosecond laser radiation is frequency doubled and split into two parts. The reflected light is again frequency converted while the other part could be delayed in time using a retroreflector. Both beams are focused onto the same spot of the sample mounted in a PEEM. (Reproduced from Link *et al*., 2001, with permission from IOP Publishing Ltd. © 2001.)

the magnetization depends in a complicated manner not only on the magnetic field conditions but also on the geometrical (shape and thickness) and intrinsic magnetic properties (anisotropy and damping) of the elements. Moreover, in the ground state these elements usually exhibit an inhomogeneous magnetization distribution, which may be described by a set of micromagnetic entities of different topology and dimensionality, such as domains, domain walls, vortices, Bloch lines, and so on. Each of these magnetic structures contributes with its individual response on a characteristic timescale to the overall magnetodynamic response. A more extensive description of these phenomena may be found in Schönhense, Elmers, Nepijko and Schneider (2006).

For educational purposes it may be useful to distinguish between small-angle excitations, which are related to spin waves and dynamic magnetization modes, and large-angle motions ($\theta > 90^\circ$) of the local magnetization vector, which are related to magnetization reversal events. By a proper choice of the experimental conditions, a certain type of excitations can be specifically prepared for studies. It should be kept in mind, however, that in a general experimental situation, both small- and large-angle excitations of the magnetization are present and will be interacting in a complex pattern.

4.1 Incoherent versus coherent magnetization rotation

In this section we deal with the most prominent configuration in a magnetodynamic XPEEM experiment. The magnetic field pulse $H_\mathrm{p}(t)$ is applied within the plane of a film with in-plane magnetization. If the field pulse is strong enough, it can initiate large-angle precessions leading to a partial or complete magnetization reversal. Of particular importance for the dynamic behavior is the initial state of the magnetic system, that is, whether the system starts from a magnetically saturated or a domain state. In the following, we will concentrate on experiments starting from an initial state with a well-defined domain configuration. This approach differs from most magneto-optic studies, in which the initial state is usually magnetically saturated (Chumakov *et al.*, 2005).

We consider a set of relatively large rectangular elements (size $20 \times 80\,\mu\mathrm{m}^2$ and $80 \times 80\,\mu\mathrm{m}^2$) of 30-nm-thick permalloy. These elements are placed on a coplanar waveguide similar to the one discussed in Section 3.4. The ground state magnetic configuration (minimal magnetic stray field) takes a characteristic Landau domain pattern (Hubert and Schäfer, 1998), consisting of a geometrical arrangement of triangular and diamond-shaped domains, which closes the magnetic flux within the structure. The domains are separated by 90° Néel walls at this film thickness. At the intersection of two domain walls in the inner part of the sample we find magnetic vortices, which will be discussed in more detail in Section 4.4. This domain pattern is also observed in the leftmost image in Figure 5), corresponding to a time $\Delta t = -1.5$ ns, that is, *before* the onset of the field pulse. The magnetic contrast in these domain images arises from MXCD at the Ni L_3 absorption edges. The arrows in the image mark the direction of the local magnetization $\vec{M}$, as reconstructed from the gray level in the domain on the basis of the angular dependence of the MXCD effect. As the geometry of the experiment is fixed, we are most sensitive to the magnetization directions pointing to the right and to the left, which result in a bright and dark contrast level, respectively.

The image sequence in Figure 5 displays time slices of the response of the magnetic system during a field pulse of 10 ns width, the time profile of which is given in the figure. The time resolution in this experiment is mainly determined by the width of light pulse, that is, $\delta t \simeq 60$ ps (see Table 1). The time slices have been recorded at intervals of $\Delta t = 125$ ps being essentially determined by the minimum increment of the delay generator. The synchronization between magnetic field pulse and synchrotron radiation pulse was achieved by means of a clock signal derived from the frequency of the microwaves used to accelerate the electrons in the storage ring. The solid line in Figure 5 maps the pulse profile at the output of a commercial pulse generator used to drive the coplanar waveguide. The second profile (circles) reflects the pulse shape directly on the waveguide and has been extracted by means of a PEEM-specific procedure making use of the fact that the current pulse on the waveguide is accompanied by an electric-field pulse $\vec{E}_\mathrm{p}(t)$ (for details, see Krasyuk *et al.*, 2003). As we can see, both the rising and the falling edge of the pulse are somewhat broadened as compared to the generator output, but the field pulse still has a well-defined plateau. It takes about 2 ns to reach this plateau value, the limiting factor basically being the capacitance of the waveguide.

Two important aspects must be considered. First, the XPEEM experiment does not involve external magnetic guiding fields, in contrast to what is customary in optical techniques (Freeman, Hiebert and Stankiewicz, 1998). This means that the initial Landau domain pattern can only be restored by the intrinsic anisotropies (dipolar and magnetocrystalline anisotropy) in the microstructure. Second, the measurements have been carried out at a repetition rate of 5.7 MHz, giving the system 176 ns time to relax in between magnetic field pulses. In this stroboscopic experiment, each image is formed by averaging over about 10^8 individual pulse events. The sharpness of the features in the image proves the Landau pattern to be a stable initial state, into which the domain structure reproducibly relaxes back after each field pulse. This reproducibility is a crucial requirement

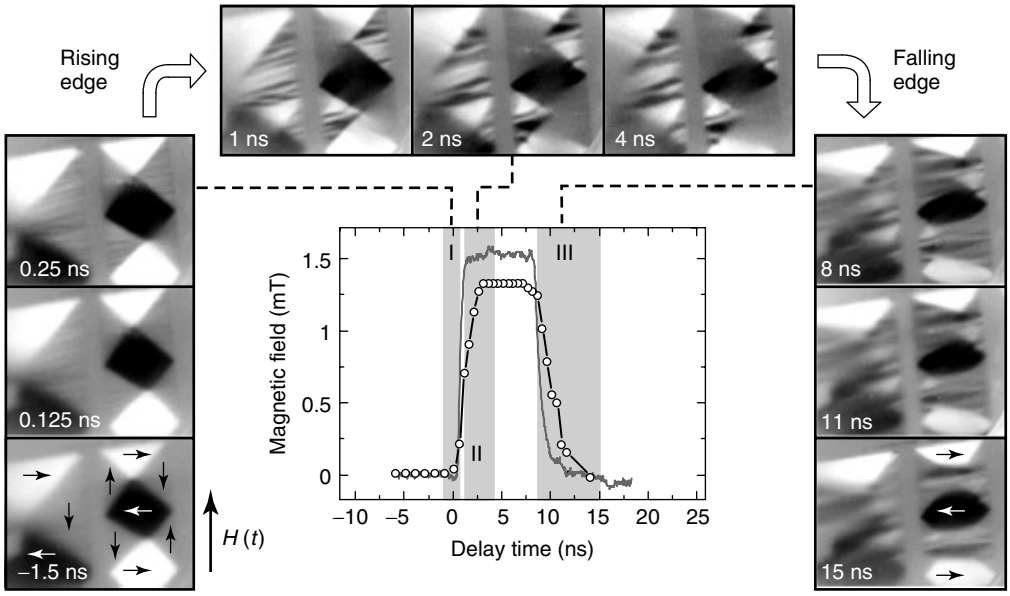

Figure 5. Time evolution of the magnetic domains in a set of rectangular permalloy microstructures (smaller one $20 \times 80\,\mu m^2$) at the rising edge (left, I), plateau region (top, II), and falling edge of a magnetic field pulse (right, III). Pulse profiles (center) measured at the pulser output (- - - -) and on the coplanar waveguide (○). The time stamps refer to the onset of the pulse and arrows give the direction of the local magnetization vector $\vec{M}$ and the pulse field $\vec{H}_p$. (Taken from Schneider *et al.*, 2006.)

in these time-resolved XPEEM experiments. Otherwise, a sampling of different magnetic configurations in subsequent pulse cycles would wash out the information in the averaged image.

During the magnetic field pulse, the transient magnetic field $\vec{H}_p(t)$ is oriented upwards in the images in Figure 5. When the pulse sets in (region I) we start to see the first changes in the magnetization distribution – the formation of a network of fine stripes in those domains, where $\vec{M}$ in the initial state is oriented opposite to the pulse field $\vec{H}_p$. Interestingly, this is a configuration in which no or little torque $\tau \sim \vec{M} \times \vec{H}_p(t)$ on the magnetization is exerted. These stripes become more pronounced with increasing $\vec{H}_p$ ($\Delta t = 0.25$ ns) up to the pulse plateau (region II). From the dark/bright contrast in the stripes we can directly conclude that they must have large components of $\vec{M}$ *perpendicular* to the field $\vec{H}_p$, which are pointing either to the left or the right. This behavior is known to be due to an *incoherent* magnetization rotation (Freeman, Hiebert and Stankiewicz, 1998; Hiebert *et al.*, 2002). This implies that the initial domain breaks up into smaller regions, each of which rotates incoherently in the external field, thereby forming this transient stripe pattern. The reason for the incoherent rotation is a limited domain wall velocity (typically several $100\,ms^{-1}$), prohibiting a response of the domain structure to the fast pulse by simple domain wall motion. It is remarkable, that these fine stripes are apparently formed always at the same location on the sample, otherwise they would not show up as sharp features in the images. This already suggests that the formation mechanism may involve a network of nucleation sites provided, for example, by magnetic inhomogeneities such as magnetization ripple. In the latter case, the local magnetization changes its direction slightly from point to point because of laterally varying magnetic anisotropies. We note that the other domains are not yet affected significantly. In particular, those domains with $\vec{M} \parallel \vec{H}_p(t)$ do not exhibit the stripe pattern.

In region II we can discern further details of the remagnetization process. The previously sharp boundaries between the triangular domains with $\vec{M} \parallel \vec{H}_p$ and $\vec{M} \perp \vec{H}_p$ appear to gradually wash out when moving from the corner of the sample toward the vortex position ($\Delta t = 1$ ns). This can be seen more clearly in Figure 6(b), which displays the upper end of the narrow rectangle in Figure 5 imaged with higher magnification. The reconstructed magnetization distribution is given in Figure 6(e–h), the arrows marking the in-plane direction of the local magnetization vector. From there we can see that the entire area that was initially magnetized opposite to the pulse field is subject to incoherent rotation processes. In particular, the vortices remain at the same positions.

The transient domain walls bounding the incoherently rotated areas resemble to some extent so-called cross-tie walls. This has been noticed in comparable Kerr effect experiments also (Neudert *et al.*, 2005). However, there is a distinct difference from the static cross-tie walls, which are well known for thin-film elements Hubert and Schäfer

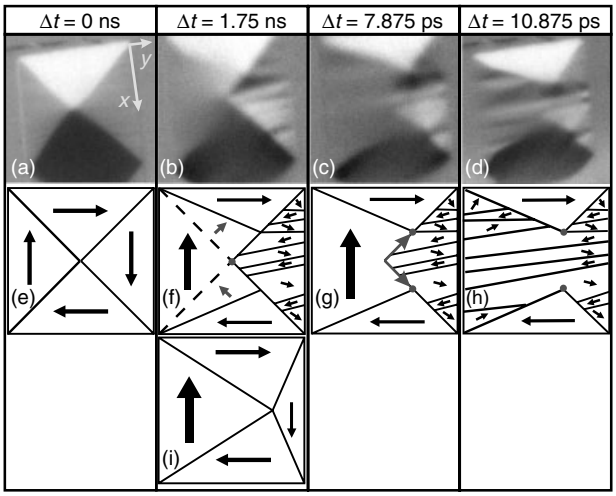

Figure 6. Time evolution of the magnetic domains at the upper end of the rectangular $20 \times 80\,\mu^2$m permalloy microstructure at $\Delta t = 0$ ns (a), $\Delta t = 1.75$ ns (b), $\Delta t = 7.875$ ns (c), and $\Delta t = 10.875$ ns (d). The panels (e–h) display the reconstructed magnetization distribution, reflecting the evolution of the triangular domain with 'up' magnetization into a 'W'-shaped structure via magnetization rotation and formation of vortices (gray circles). (Reproduced from Schneider *et al*., 2004, with permission from the American Physical Society. © 2004.)

(1998) and Kronmüller and Hertel (2000). In the static case, the 90° walls, which intersect a classic 180° Néel wall to form the cross-tie configuration extend to both sides of the 180° wall, that is, the configuration is somehow symmetric with respect to the 180° wall. In the dynamic case described in Figures 5 and 6, the situation is much more asymmetric. The two 90° Néel walls separate the coherently rotated region of the left-hand side from the incoherently rotated region on the right-hand side. Therefore, a direct comparison of these wall types in the static and dynamic cases should be made with great care.

The gradual contrast change in the transition regions between $\vec{M} \parallel \vec{H}_\mathrm{p}$ and $\vec{M} \perp \vec{H}_\mathrm{p}$ can be understood as a *coherent* rotation of $\vec{M}$. This behavior is due to the fact that for the situation $\vec{M} \perp \vec{H}_\mathrm{p}$ the torque acting on the magnetization is highest, and the system can easily respond by simply rotating $\vec{M}$ into the direction of the external field. As a consequence, the triangular domains with $\vec{M} \parallel \vec{H}_\mathrm{p}$ grow on the expense of the neighboring ones with $\vec{M} \perp \vec{H}_\mathrm{p}$ ($\Delta t = 2$ ns). Further studies show that the coherent rotation process starts with the onset of the field pulse and is thus – as expected – faster than the incoherent rotation events. As a consequence, the domain wall, which is still clearly visible, is displaced at very high speeds of up to $1000\,\mathrm{ms}^{-1}$ (Schönhense, Elmers, Nepijko and Schneider, 2006). We also note that these coherently rotated regions narrow down, if we move from the position of the central vortex to the edge of the microstructure, giving rise to a triangular shape of this region (Figure 6b). This is due to the fact that the domain wall is more strongly pinned in the corner of the microstructure. As a general feature of this multidomain state, the response is obviously determined by a competition between coherent and incoherent rotation processes, depending on the orientation of the local magnetization with respect to the pulse field $\vec{H}_\mathrm{p}$.

It is instructive to compare the experimental findings up to this point to the known response of the Landau pattern to a slowly varying field. In this case, the magnetization reversal takes place via domain wall displacement. Upon applying the field, the domain with $\vec{M} \parallel \vec{H}$ grows on the expense of the other domains (Figure 6i). In particular, the position of the vortex moves, in the given example toward the right edge of the sample. As a result the domain in which $\vec{M}$ is oriented antiparallel to the applied field shrinks. This behavior is in clear contrast to our observations and thus cannot describe the highly dynamic situation created by a fast field pulse.

The interplay between coherently and incoherently rotated regions also has another interesting consequence. As the field strength increases, the central vortex retains its position, but the locations where the domain walls meet the incoherently rotated area shift away from the central vortex ($\Delta t = 4$ ns in Figure 5), thereby creating two new vortices. In this course, the domains with $\vec{M} \parallel \vec{H}_\mathrm{p}$ take the shape of a 'W' lying on its side, with the new vortices moving along the long legs of the 'W'. Again, this is seen more clearly in the magnified image in Figure 6(c) and the corresponding graphical reconstruction (Figure 6g). The position of the vortices is marked by the grey circles in Figure 6(e–g).

The microscopic mechanisms determining the magnetization dynamics can also be sensitively influenced by static fields. XPEEM experiments to this issue are still missing. However, Kerr microscopy studies on comparable samples have demonstrated that even a small additional magnetic field – in the transverse direction in this case – may significantly modify the response of the system (Choi *et al*., 2001a,b).

4.2 Blocked relaxation

Finally, in region III of Figure 5 the pulse field drops again and the magnetic system is allowed to relax. This relaxation, however, also exhibits a peculiar behavior. First, we note that the stripe pattern almost instantaneously expands into the domains with $\vec{M} \parallel \vec{H}_\mathrm{p}$ as soon as the field drops ($\Delta t = 8$ ns). Although it may be tempting to invoke domain wall motion as the driving mechanism, this hypothesis must be dismissed because of the limited domain wall velocity. A faster mechanism must involve rotational processes and

can be understood in the following way. On the rather long plateau of the field pulse, the magnetic system has sufficient time to assume a new quasiequilibrium state, which is determined by an effective field H_{eff} including the pulse field. On the trailing edge of the pulse, H_{eff} is reduced and this change ΔH_{eff} acts onto the system like a field pulse into the opposite direction. For the 'W'-shaped area, in particular, this means ΔH_{eff} is directed *opposite* to the local magnetization direction. As a consequence, incoherent rotation events start to take place and can form a stripelike domain structure containing small- and large-angle domain walls in this region. It is thus a local magnetization rotation rather than a domain wall motion that leads to the 'expansion' of the stripe pattern.

After this fast initial change, however, the magnetization configuration remains rather stable. Only marginal changes appear in the images between $\Delta t = 8$ and 15 ns. This means that the relaxation of the 'excited' magnetic state, that is, the decay of the stripelike phase, takes place on a significantly longer timescale (>10 ns) than its buildup ($\simeq$1 ns). Even after $\Delta t = 20$ ns we did not observe a full relaxation of the system. The stability of the stripe domain phase is another consequence of the limited domain wall velocity. In this context, we would like to recall that in the absence of the pulse field, the restoring force that drives the system back to the initial state results only from the demagnetizing field and the anisotropy. Apparently, this restoring force is not strong enough to initiate rotation processes to resolve the domain walls locally. Instead, the walls are removed from the system via domain wall displacement. If there is a pulse field acting in the opposite direction, however, the incoherently rotated regions may be restored much faster. This has been observed in experiments with bipolar pulses (Schneider *et al.*, 2004).

4.3 Transient stray fields

The PEEM is also ideally suited to investigate the issue of transient magnetic stray fields. As stated above, the Landau domain pattern forming the initial state in the experiment (Figure 5) is a consequence of energy minimization. If we inspect the incoherently rotated regions close to the sample edge, we note, however, that this magnetization distribution causes many magnetic poles at the sample edge. This can be seen more clearly at the right-hand side of the structure in Figure 6(h), which displays the graphical reconstruction of the magnetization distribution at $\Delta t \approx 11$ ns after the field pulse onset. These magnetic poles should generate a sizable stray field outside the permalloy microstructure. Considering the fact that the XPEEM image is built up by low-energy electrons, a question arises as to whether this stray field has some influence on the image. Recalling our discussion of the Lorentz force-related contrast in Section 3.2, we can use similar arguments in the present case. Let us assume the sample edge to be ideally straight (Figure 7a). In the absence of a magnetic stray field, the image of the edge will also show a straight line. In the presence of a stray field, the electron trajectories starting in the vicinity of the sample edge and passing through the stray field region will be changed by the Lorentz force, and the image of a straight edge will appear rather as a 'jagged' line. In a realistic sample, this interaction will thus lead to a stray field-induced distortion in the image of the object. Knowing the imaging parameters of the microscope and the exact shape of the object, we can quantitatively determine the stray field (Nepijko, Sedov and Schönhense, 2000). As an example, we take the image recorded at $\Delta t \approx 11$ ns (Figure 7b). In order to visualize the distortion of the sample edge in the image, we have magnified the sample edge in the horizontal direction. The straight edge is imaged into the wavy line A $\longmapsto$ B. From this line we can extract a quantitative value of the trajectory deflection $S_y(x)$ (Figure 7c), which serves as an input for the calculation of the stray field component $B_x(x)$ along the sample edge. As can be seen in Figure 7(d), the stray field at the edge can easily reach values of $B_x > 100$ mT. This result confirms the expectation that the energy minimization may be violated on nanosecond timescales, because it is less important than torque arguments.

4.4 Vortex-core rotation

A particularly interesting structure that occurs in thin films is a magnetic *vortex*. A vortex is an almost singular point in the magnetization distribution. It can be most clearly observed in microstructured systems with an in-plane magnetization. The geometrical shape of the microstructure gives rise to a demagnetizing field, which forces the magnetization into a closed path around the center of the structure. In the center of this magnetization swirl or vortex, however, the magnetization vector turns out of the film plane despite the in-plane magnetic anisotropy in order to meet the constraint $|\vec{M}| = \text{const.}$ and avoid magnetic frustration. This vortex-core structure and particularly the out-of-plane magnetization $\vec{M}_z$ have been experimentally confirmed first by magnetic force microscopy studies (Shinjo *et al.*, 2000). Further details on the internal magnetic structure of the vortex region were revealed by spin-polarized scanning tunnelling microscopy (STM) (Wachowiak *et al.*, 2002). With respect to the film plane, for a given sense of rotation of the vortex, two energetically equivalent configurations are possible, with $\vec{M}_z$ pointing away from or toward the surface. These two configurations differ only by their 'handedness'. This handedness will be of importance for the dynamical behavior.

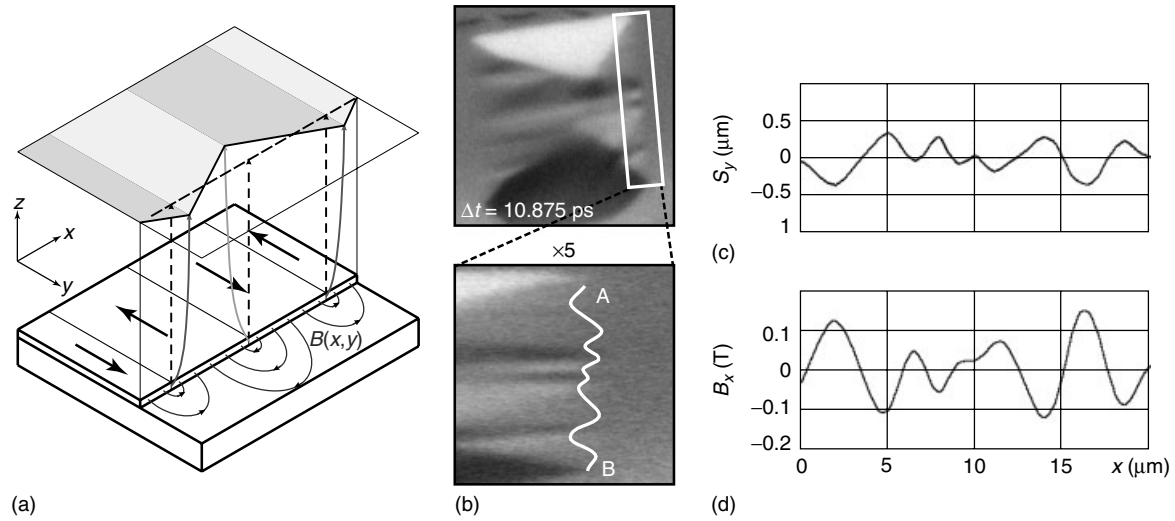

Figure 7. Image distortion due to magnetic stray fields at the sample edge. (a) Change of the electron trajectories due to the Lorentz force. (b) Magnetization configuration at $\Delta t = 10.875$ ns and horizontally magnified (×5) edge region. (c) Quantitative evaluation of the edge shift $S_y(x)$ along the path A $\longmapsto$ B. (d) and resulting magnetic stray field component $B_x(x)$. (Reproduced from Schneider *et al*., 2004, with permission from the American Physical Society. © 2004.)

The question of how such a three-dimensional magnetic object like a vortex behaves dynamically was first addressed by time-resolved Kerr effect investigations on submicrometer-size permalloy disks (Park *et al*., 2003). These experiments probed the polar Kerr effect close to the center of the disk and observed a distinct periodic variation of the polar Kerr signal, when the system was magnetically excited by a short in-plane field pulse. Since most of the polar Kerr signal should originate from the $\vec{M}_z$ component in the vortex core, the periodic signal variation was explained by a motion of the vortex core in and out of the laser spot. The entire vortex core was proposed to undergo a *gyrotropic* motion, that is, to rotate around the geometrical center of the disk. Owing to the small size of the disk, however, a direct imaging was beyond the lateral resolution of Kerr microscopy.

The issue of the gyrotropic motion of the vortex core was also addressed with the better lateral resolution provided by XPEEM (Choe *et al*., 2004). The samples consisted of microstructured elements of a CoFe alloy film of 15 nm thickness, placed on a coplanar waveguide. The current pulse was launched by means of an Auston switch and had a width of around 300 ps full width half maximum (FWHM) at a maximum amplitude of $B_{\max} \sim 15$ mT. The repetition rate of the field pulse was around 125 MHz, giving the magnetic system about 8 ns to relax into the ground state.

We first compare domain image 'snapshots' taken at two different time delays Δt after the exciting field pulse (Figure 8) for rectangles with increasing aspect ratio: (I) $1 \times 1\,\mu m^2$, (II) and (III) $1.5 \times 1\,\mu m^2$, and (IV) $2 \times 1\,\mu m^2$. All rectangles exhibit the simple Landau pattern with two diagonal 90° domain walls and a central vortex. In each image sequence, however, the position of the vortex in the center region shifts more or less strongly between the first and the second image. The most pronounced difference occurs in the rectangle with the largest aspect ratio (IV). In the image taken at $\Delta t = 3.3$ ns the vortex core is shifted from the center to the *left* by around 400 nm, whereas at $\Delta t = 7.7$ ns the core position is located at around 400 nm to the *right* of the geometrical center. Recalling the fact that the magnetic field pulse has a width of less than 1 ns, it apparently has initiated a motion of the vortex core, which continues beyond the field pulse duration.

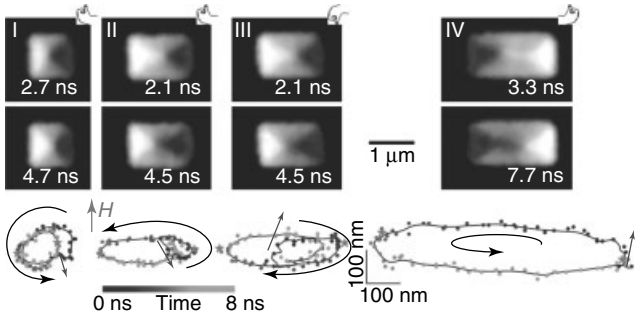

Figure 8. XPEEM domain images of various rectangular CoFe elements (XMCD signal at the Co $L_{2,3}$ edges) with increasing aspect ratio (denoted as I–IV) as a function of the specified time elapsed after the magnetic field pulse. The bottom panels map the respective trajectories of the vortex in 100 ps steps. The progression in time is indicated by the dot greyscale. Hands illustrate the vortex handedness and the direction of the out-of-plane core magnetization. (Taken from Choe *et al*., 2004.)

In order to map this behavior in more detail, the vortex-core position has been determined from subsequent images acquired in time increments of 100ps for the maximum timeline of 8ns. The resulting trajectories of the core movement (bottom part of Figure 8) can be decomposed into two phases. During the field pulse, the vortex core responds by a linear accelerated motion along the direction indicated by the gray arrows. After the field pulse it follows the curved path marked by the black line. Whereas for the quadratic structure (I) this curved trajectory closely approaches a circle, it is strongly elliptical for the $2 \times 1\,\mu m^2$ element. These curved trajectories directly reflect the gyroscopic motion of the vortex cores, which is driven by the magnetostatic field of the moving vortex. A closer inspection of the data in Figure 8, however, reveals two peculiarities. First, there seems to be no common sense of rotation (indicated by the black arrow) or direction of the linear motion. In other words, for two elements with a similar in-plane domain pattern, opposite senses of rotation can occur, for example, clockwise for element (III) and counterclockwise for element (II). As will be discussed below, this difference is related to the chirality of the vortex. Second, the initial linear motion is directed mainly *along* the axis of the pulse field, not perpendicular to it.

For reasons of simplicity, we assume an ideal vortex structure on a square (Figure 9). Together with the in-plane magnetic configuration, the out-of-plane component M_z of the vortex (arrow at the center of the squares in Figure 9a) defines a chirality of the system, being left handed (right handed) for the structure on the left (right) side of the figure. From the results discussed in Section 4.1 we know already, that a nanosecond field pulse may not simply cause a simple domain wall motion resulting in a motion of the vortex perpendicular to the applied field (Figure 6i). If the pulse field $H_p(t)$ is even shorter, the precessional motion of $\vec{M}$ becomes important. $H_p(t)$ generates a torque (indicated by the blue arrows) on those magnetization components with $M_i \perp H_p$. On the subnanosecond timescale, the initial motion is a precession of the magnetic moment around H_p, which is stronger than the damping along the field direction (Choe *et al*., 2004). If we consider the left-hand case in Figure 9(a), the magnetization in domain 3 precesses toward the core magnetization, that is, develops an out-of-plane component, whereas the core magnetization precesses toward domain 1, that is, develops an in-plane component. If we define the position of the vortex core by the maximum M_z component, this concerted precessional motion of the magnetization distribution results in an effective movement of the vortex core antiparallel to the applied field. The same arguments explain the initial movement of the right-handed vortex parallel to $H_p(t)$.

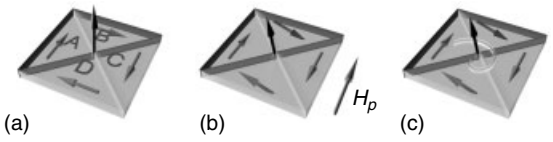

Figure 9. (a) Spin structure of a left-handed vortex structure (vortex core indicated by the vertical arrow). (b) Initial sideways motion of the vortex core due to the magnetization torque exerted by the pulse field. (c) Subsequent trajectory of the vortex core projected onto the surface (spiral line). (After Choe *et al*., 2004.)

This initial linear displacement of the vortex core by $H_p(t)$ is the key process, which starts the subsequent gyrotropic rotation of the core. The displacement is accompanied by an imbalance of the in-plane magnetization components, which in turn causes a magnetostatic field perpendicular to this displacement, trying to restore a balanced configuration. This situation sends the vortex core onto a counterclockwise (Figure 9b) or clockwise spiraling trajectory (Figure 9c). The trajectories plotted in Figure 9(b) and (c) are the result of a micromagnetic simulation, covering the first 3 ns after the field pulse. The magnetic damping in the system causes the trajectory of this gyrotropic motion to spiral inwards again, until the balance of the in-plane magnetization components is restored.

Raabe *et al*. (2005) report a similar experiment with a repetition time of the field pulse of 16 ns. In contrast to a gyrotropic motion, however, they find only a linear displacement of the vortex perpendicular to the applied field. The shorter relaxation period in the experiment of Choe *et al*. (2004) is proposed as a possible explanation for this discrepancy. According to the findings by Raabe *et al*.'s findings, the vortex is still moving with a speed of $\sim 100\,m\,s^{-1}$ by the time the next field pulse arrives in Choe *et al*. experiment. Another difference between these experiments, however, which has not been noted so far, is found in the rise times and peak values of the field pulse. According to the reported values in both publications, the field sweep rate $\delta H/\delta t$ is at least a factor of 5 higher in the approach by Choe *et al*. This difference could also have a significant impact on the dynamic response by virtue of exciting modes in a broader frequency range. These examples demonstrate that the dynamic response of a magnetic system in the subnanosecond regime depends not only on the initial state but also significantly on the details of the experimental procedure.

A vortex is a very stable structure and a high field of the order of $H \sim 0.5\,T$ is required to reverse the direction of the vortex core. In this case, the field is applied opposite to the vortex-core direction. In the fast dynamic case, the situation may be significantly different. It has been shown that a continuous excitation of the vortex by a small periodic in-plane field causes the vortex core to precess on a stable

orbit (Chou *et al*., 2006). Taking this precessional motion as a dynamic ground state of the system, a pioneering experiment by Stoll *et al*. showed a small burstlike increase of the field amplitude by a few millitesla to be sufficient to switch the vortex core (van Waeyenberge *et al*., 2006). Detailed micromagnetic simulations revealed a complex microscopic mechanism, which involves a complex sequence of vortex–antivortex creation and annihilation steps (Hertel and Schneider, 2006).

5 QUASIRESONANT EXCITATIONS

In this section, we discuss the results of an experiment involving a periodic magnetic field excitation (Krasyuk *et al*., 2005). As already demonstrated in Section 4.2, the relaxation of the transient magnetization configuration induced by a field pulse may take several nanoseconds to several tens of nanoseconds, depending on the configuration. On the other hand, it is well known from several studies that the precessional motion in permalloy involves frequencies down to the low gigahertz regime (Choi *et al*., 2001; Park *et al*., 2003; Raabe *et al*., 2005; Neudert *et al*., 2005). If we take a 10–nm-thick rectangular element of $16 \times 32\,\mu m^2$ size, micromagnetic simulation predicts a precessional mode with a frequency of 1.25 GHz (Krasyuk *et al*., 2005). The question is thus, whether the XPEEM imaging is able to pick up the response of such a particular mode.

In the respective experiment, the element was excited with a pulse train at a repetition rate of 500 MHz. As this corresponds to the regular multibunch operation of the storage ring, each field pulse is followed by a soft X-ray pulse for imaging. The sample was adjusted such that the light impinged *perpendicular* to the magnetization of the long domains with the magnetization vector pointing up and down, respectively (Figure 10). In the static image, the contrast arises thus mainly from the top and bottom closure domains of the Landau pattern. In addition, there is a line contrast from the 180° domain wall in the center of the structure. This contrast arises from the fact that in a Néel wall the magnetization vector rotates within the film plane and thus has a component along the direction of light incidence $\vec{q}$ in the center portion of the wall. This wall contrast will become important in the second part of this section.

In the chosen geometry the magnetic contrast in the vertically magnetized domains vanishes in the static case, because of $\vec{M} \perp \vec{q}$. Therefore, this arrangement is very sensitive to small changes in the magnetization direction in these domains, as any component of $\vec{M}$ along $\vec{q}$ will give rise to a change in the contrast level. This property is exploited in the dynamic experiment, where one observes a clear change

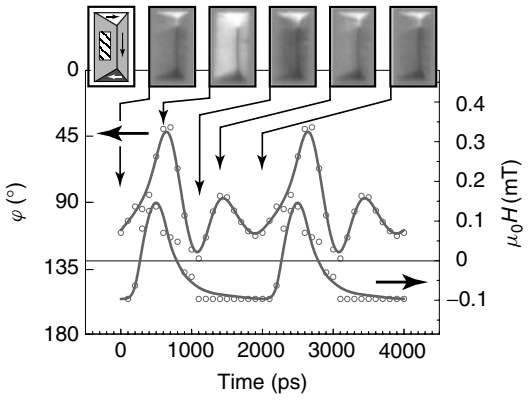

Figure 10. Response of a permalloy microelement to a periodic excitation. (Top) Selected XMCD domain images recorded at the temporal positions indicated. The leftmost sketch depicts schematically the transient domain configuration during the experiment, the shaded area marking the integration area for quantitative contrast evaluation. (Bottom) Experimentally determined field pulse shape $H(t)$ and rotation of the magnetization vector $\varphi(t)$ as calculated from the contrast change in the shaded area. (Taken from Schneider *et al*., 2006.)

of the magnetic contrast in these areas as soon as the field pulse acts on the element (Figure 10).

The pulse field in this experiment is directed in plane and perpendicular to the magnetization direction in the long domains, thus exerting the maximum torque in these domains. We note that the change in contrast is the same in both domains, although the magnetization direction in the long domains is opposite. This contrast change is due to an additional in-plane component of $\vec{M}$, which arises because of the precessional motion started by the field pulse. Initially, the torque acting on the magnetization pulls it out of the film plane in opposite directions for the left and the right domain. This motion is counteracted by the increase in demagnetizing energy and leads to a precessional trajectory with an opposite sense of rotation with a large in-plane magnetization component M_x along $\vec{q}$. The initial part of the precession is basically in phase for both domains, therefore the in-plane components M_x yield a comparable magnetic contrast. The damped precessional nature of the motion is clearly visible by the alternating magnetic contrast levels in selected images of a longer sequence.

From the XMCD signals in the image sequence, one can quantitatively determine the magnitude of M_x and thus the angle φ, by which the magnetization vector $\vec{M}$ is rotated out of the equilibrium position (bottom part of Figure 10). Comparing the results for $\varphi(t)$ to the field pulse shape reveals the damped oscillatory character of the motion of $\vec{M}$. The maximum deflection is reached slightly after the maximum of the field pulse and the period of this oscillation is about 800 ns, being in agreement with the prediction of 1.25 MHz

from the simulation. Therefore, only about two periods are visible, before the next field pulse excites the system again. The numerical values of $\varphi(t)$ prove that the motion involves in fact a large-angle precession of the magnetization within the individual domains.

A closer inspection of the domain images reproduced in Figure 10 reveals another interesting finding, namely, a distinct displacement of the domain wall away from the center of the structure, as compared to the field-free ground state. We verified that this displacement is indeed a transient effect and occurs as a response to the periodic magnetic excitation of the system. In particular, the displacement increases with increasing field pulse amplitude and thus growing precession amplitude (Figure 11). Above a certain critical amplitude, the wall is essentially driven out of the system. In passing, we note that the 180° wall seen in Figure 11 contains a Bloch line across which the sense of the in-plane rotation of the magnetization within the wall changes. Therefore, the upper part of the wall appears bright, whereas the bottom part appears dark.

The reason for the unidirectional shift Δx of the domain wall is a specific resonance phenomenon. A Fourier analysis of the magnetic field pulse sequence reveals significant contributions of higher harmonics of the fundamental frequency of 500 MHz, that is, at 1 and 1.5 GHz. The second and third harmonic components are the most important ones, as the eigenfrequency of the precessional mode is around 1.25 GHz. This means that the magnetic system is driven close to resonance. The system can absorb more energy from the excitation and increase its entropy by moving its eigenfrequency closer to the component of exciting frequency spectrum which has the higher power. In our case this is the 1 GHz component. By increasing the size of the already larger domain, its precessional frequency is lowered and thus moves a little closer to the second harmonic component. This process is counteracted by an increase of the demagnetizing energy, establishing a new quasistationary domain configuration. An increase of the precessional amplitude via the field pulse amplitude thus leads to a further increase of the domain area and shift of the wall. This situation can be modeled more quantitatively (for details, see Krasyuk *et al*., 2005), with the result for the displacement Δx as a function of the precession amplitude being shown by the line in Figure 11(e). The data points I, II, and III correspond to the experimental situation depicted by the images (b–d). The delayed onset is due to domain wall pinning. This example demonstrates that high-frequency excitations may lead to both a high-frequency and a quasistatic response in the same experiment.

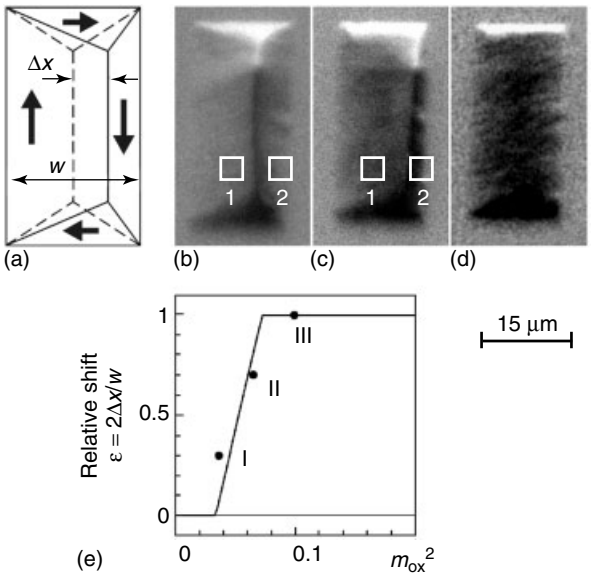

Figure 11. Quasistatic displacement of a domain wall due to resonant excitation. The images (b), (c), and (d) show the transient domain configuration at $\Delta t = 600$ ps for increasing field pulse amplitudes, (a) gives a sketch of the domain structure. (e) Relative domain wall displacement ϵ as a function of precessional amplitude (represented here by the maximum magnetization component m_x occurring during precession). (Taken from Krasyuk *et al*., 2005.)

6 ULTRAFAST EXPERIMENTS

Femtosecond pump-probe studies are of increasing importance for many new research areas such as femtochemistry (Bonn *et al*., 1999), ultrafast magnetization dynamics (Koopmans, van Kampen, Kohlhepp and de Jonge, 2000), ultrafast surface melting (Rousse *et al*., 2001), and coherent excitation of phonons (Sokolowski-Tinten *et al*., 2003), or magnons (Melnikov *et al*., 2003). In such studies the electronic system is excited by the absorption of a femtosecond laser pump pulse. The energy transfer to other degrees of freedom is then measured stroboscopically in real time by a subsequent femtosecond laser probe pulse. Pump-probe studies offer the opportunity to observe changes in the electronic system while the nuclei are practically at rest. Also the influence of other quasiparticles such as spin excitations can be separated since the timescales of these processes is usually different. In all of these cases the optical excitation represents a significant disturbance to the electronic system. For instance in pump-probe investigations of the femtosecond magnetization dynamics on average one electron–hole excitation takes place for about every 10th atom throughout the material (Koopmans, van Kampen, Kohlhepp and de Jonge, 2000; Rhie, Dürr and Eberhardt, 2003). Comparable excitation densities are expected for other applications (Bonn *et al*., 1999; Rousse *et al*., 2001; Sokolowski-Tinten *et al*., 2003; Melnikov *et al*., 2003). The evolution of electronic and magnetic excitations in this regime is a very active research field

(see also **Time-resolved Kerr-effect and Spin Dynamics in Itinerant Ferromagnets, Volume 3**) which will become even more interesting with the availability of X-ray FEL sources in the future.

In addition to femtosecond temporal resolution, probing the system on the nanometer scale is important since electronic and spin excitations typically travel only submicrometer distances on such timescales. It is well known that a dielectric medium can be used to manipulate the properties of light pulses even leading to the trapping of light inside photonic crystals (Mok and Eggleton, 2005). For metals the dielectric material's response to light is mainly determined by the plasmon resonance, that is, by collective oscillation of the electrons. This is utilized in the emerging field of plasmonics for manipulating optical radiation at subwavelength dimensions by metallic nanostructures (Ozbay, 2006). The use of pulsed-laser radiation offers the exciting prospect of tailoring the pulse structure (length, polarization intensity, etc.) by coherent control to optimize the nanoscale system response (Brixner, de Abajo, Schneider and Pfeiffer, 2005). Ultimately it should be possible to use femtosecond pump-probe spectroscopy with optimally shaped laser pulses for exciting one quantum system and observe in real time the nonlocal information transfer to another system (Brixner, de Abajo, Schneider and Pfeiffer, 2005).

In this chapter we review recent attempts to achieve nanometer spatial and femtosecond temporal resolution on magnetic nanostructures. This approach is based on the plasmonic enhancement of the photoemission yield from nanostructures.

6.1 Imaging plasmonic near fields of nanostructures

Surface plasmon enhanced optical fields at microscopically rough surfaces were employed early to explain the chemical sensitivity enhancement in various optical spectroscopies (Wokaun, Gordon and Liao, 1982). Similar plasmon enhancement effects were used in two-photon photoemission spectroscopy to specifically probe laser-induced electronic excitations in Ag nanoparticles although without any lateral resolution (Lehmann *et al*., 2000). The plasmon enhanced optical near fields at the boundaries of Ag nanostructures have been directly imaged using PEEM (Cinchetti *et al*., 2005). The spatial and temporal plasmon propagation was determined in real time using pump-probe PEEM spectromicroscopy (Kubo *et al*., 2005).

Near field enhancements occur also for transition metals which do not display strong plasmon resonances. An example is shown in the following text. Utilizing the light polarization dependent dielectric response of ferromagnetic CoPt nanodots energy is pumped into electron–hole excitations. Femtosecond pump-probe spectroscopy is then employed (see the next section) to probe the real-time energy transfer into spin excitations leading to a reduction of the ferromagnetic spin alignment in the nanodots.

The experimental setup is shown schematically in Figure 3. The sample consisted of $200 \times 200\text{-nm}^2$ wide magnetic structures separated from each other by 100-nm-wide and 100-nm-deep troughs (see Figure 12a) (Dürr, Kronast and Eberhardt, 2001). A multilayer with Pt(1.8 nm)[Co(0.5 nm) Pt(1.8 nm)]$_4$ was sputter deposited on top of a patterned Si substrate. The multilayer structure of the nanodots induces an equilibrium spin alignment along the surface normal owing to a large perpendicular magnetic anisotropy at the CoPt interfaces (Dürr, Kronast and Eberhardt, 2001).

Figure 12 shows typical PEEM images of this sample. The sample was illuminated from the left by 3.1 eV (b) and 6.2 eV photons (c) with s- and p-polarization, respectively. Although the dot structure is resolved in both images there are clear differences. The image taken with 3.1 eV photons shows much better lateral contrast due to the more

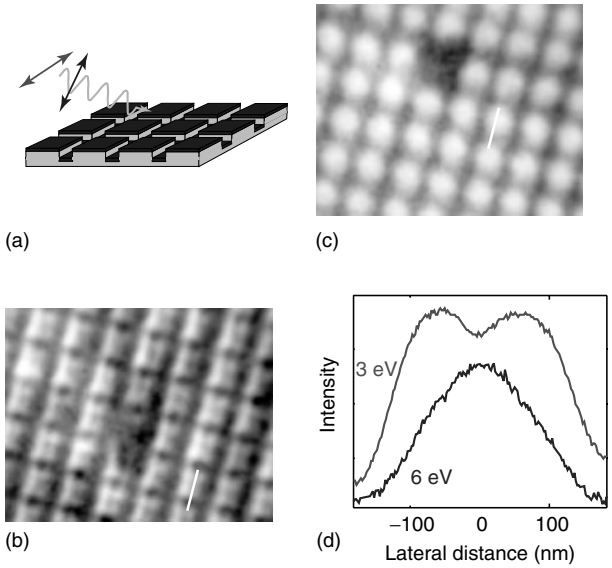

Figure 12. (a) A schematic view of the sample. In all images the light is incident from the left at an angle of 25° to the sample surface. (b) and (c) PEEM images of the same sample area taken with laser excitation at 3.1 eV photon energy for s-polarized (gray double arrows) and 6.2 eV photons for p-polarized (black double arrows) light, respectively. Note that one nanodot is missing near the center of the images. In (d) the linescans over a single nanodot (indicated by the white lines in (b) and (c) illustrate the different emission characteristics for 3.1 eV s- and 6.2 eV p-polarized light as gray and black lines, respectively. Data in (d) have been scaled to equal intensity and are offset for clarity. (Reproduced from Dürr *et al*., 2001, with permission from Springer-Verlag GmnH. © 2001.)

pronounced edges of the dots. This can also be seen in the linescans shown in Figure 12(d). For 3.1 eV photons, the photoemission intensity is concentrated at the edge of the dots while for 6.2 eV emission takes place mainly in the dot center. The images in Figure 12 were normalized to maximum/minimum contrast. In the raw data there are additional differences visible. While for 3.1 eV photons there is almost no photoemission intensity detectable coming out of the troughs, there is a significant contribution from these areas at 6.2 eV.

The photon energy dependence of the PEEM images in Figure 12 is an indication that the nanodot dielectric response modifies the laser field amplitude at the sample surface (Dürr, Kronast and Eberhardt, 2001). This process can be modeled approximating the CoPt nanodots or by ellipsoidal particles with lateral and vertical dimensions of 200 and 10 nm, respectively. Neglecting interactions between the nanodots and using bulk optical constants for Co and Pt the electric-field enhancement, $f(h\nu)$, at the tips of the long and short axis of ellipsoidal nanodots can be calculated for s- and p-polarized light (see Figure 13) (Wokaun, Gordon and Liao, 1982). The curves are dominated by a Mie-plasmon resonance broadened by interband transitions. The resonances depend on the particle shape and are red shifted for plasma oscillations along the long axis of the spheroid (excited by s-polarized light) and blue shifted for oscillations along the short axis (excited by p-polarized light).

This polarization dependence in Figure 3 implies different emission directions for photoelectrons. In photoemission the maximum intensity usually occurs when the light electric-field vector is aligned along the surface normal. This can easily be seen considering the dipole transition matrix element between initial $|i>$ and final $|f>$ states which is $<i|\nabla V|f> \cdot \mathbf{A}$, where $\mathbf{A}$ is the electric-field vector potential and ∇V is the surface potential gradient along the sample normal. Consequently mainly horizontal photoelectron trajectories starting from the nanodot edges are expected with s-polarized light. Such trajectories are indeed observed in Figure 14(a) and (b) when the contrast aperture in the objective lens backfocal plane (see Figure 2) is moved off center. The resulting PEEM images show photoemission only from the upper (lower) nanodot edges when electron trajectories starting upward (downward) are selected in Figure 12(a,b). These structures contribute to the double peaks of the linescan with s-polarized light in Figure 12(a). Their width is determined from Figure 14(a,b) to typically 60 nm (Heitkamp *et al*., 2006).

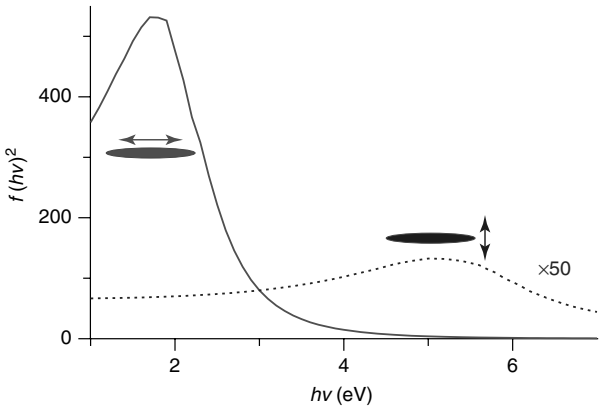

Figure 13. Calculated dielectric response of spheroidal ($10 \times 200\,\mathrm{nm}^2$) Pt particles (schematically shown as insets) as a function of photon energy. (Reproduced from Dürr *et al*., 2001, with permission from Springer-Verlag GmnH. © 2001.)

6.2 Femtosecond electron and spin dynamics of nanostructures

A microscopic description of the processes following the absorption of a femtosecond laser pulse can proceed in terms of energy relaxation between different reservoirs of quasiparticles such as electrons, spins, and phonons. Initially laser heating of the electron system creates a nonequilibrium electron distribution of the available energy levels. This exited state decays and after typical relaxation times the energy is transferred to the other quasiparticle systems such as spin excitations until it is finally dissipated via phonons to an external heat sink. Observing these processes in real time for magnetic materials is presently a very active research field. Although there is agreement on the subpicosecond timescale for energy transfer between electron and spin systems (Beaurepaire, Merle, Daunois and Bigot, 1996; Scholl, Baumgarten, Jacquemin and Eberhardt, 1997; Güdde *et al*., 1999; Koopmans, van Kampen, Kohlhepp and de Jonge, 2000) the microscopic mechanism is still under debate. It has been suggested theoretically that spin-orbit coupling alone may be too weak and that it is rather an interplay between spin-orbit forces and a strong laser field

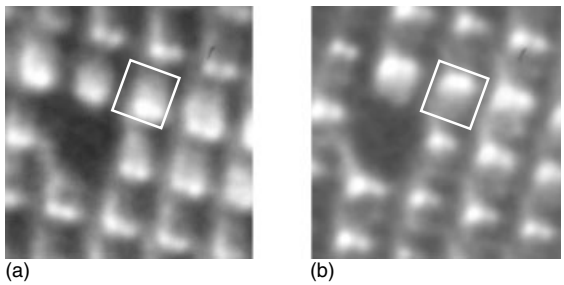

Figure 14. (a) and (b) Images with opposite off-center positions of the contrast aperture in the objective lens backfocal plane (see Figure 2). The white frame indicates the position of the same nanodot in both images.

that leads to an ultrafast sample demagnetization (Zhang and Hübner, 2000). Very recently it was suggested that laser heating might open a very efficient channel for transfer of spin angular momentum to the lattice (Koopmans, Ruigrok, Longa and de Jonge, 2005).

In the following we concentrate on showing that the locally enhanced laser field for s-polarized light described in the last section can induce a transient demagnetization of the nanodots, that is, that it is possible to probe the magnetization dynamics with subwavelength spatial resolution. To investigate the spin dynamics in a pump-probe experiment an area of 5×5 uniformly magnetized nanodots from Figure 12(a) was selected. Time resolution was achieved by splitting each laser pulse in two and introducing a variable time delay, Δt, between them. The work function of the topmost Pt layer was about 5.9 eV. Thus, two 3.1 eV photons have to be absorbed to generate one photoelectron. In a first photoabsorption process, electronic states up to 3.1 eV above the Fermi level become partially populated. A subsequent photoemission process using a second 3.1 eV photon then probes the population of states confined to an energy interval of 2.9–3.1 eV above the Fermi level. For this two-photon photoemission event the absorption of two photons has to occur almost simultaneously since the lifetime of the intermediate states is only a few femtoseconds (Aeschlimann *et al*., 1997;Knorren, Bennemann, Burgermeister and Aeschlimann, 2000).

Typical spectra are shown in Figure 15(b) and (c) where the time delay, Δt, between the two laser pulses was varied (Heitkamp *et al*., 2006). When the laser pulses overlap in time they can interfere. The alternating pattern of high and low two-photon photoemission intensity indicated by the shaded area in Figure 15(b) corresponds to constructive and destructive interference, respectively. From the width of this interference region the laser pulse length can be deduced (Lehmann *et al*., 2000) to 150 fs for the present example.

In Figure 15(c) the relative photoelectron spin polarization signal is shown as a function of Δt (Heitkamp *et al*., 2006), interference near zero time delay also leads in this case to fluctuations in the spin polarization (shaded area in Figure 15c). However, in the adjacent region the two laser pulses are in close enough temporal proximity so that each pulse probes the transient sample demagnetization generated by the other pulse. This pattern is clearly apparent in Figure 15(c) through the transient reduction of the photoelectron spin polarization nearly symmetric around time zero. The photoemission yield, N, measured in a one-color experiment is the sum of that for the indistinguishable individual laser pulses, that is, $N = N_1 + N_2$. The reduction of the spin polarization during the first laser pulse is S_1. That during the second pulse is S_2 if it arrives after the transient demagnetization of the first pulse (red curves in Figure 15a).

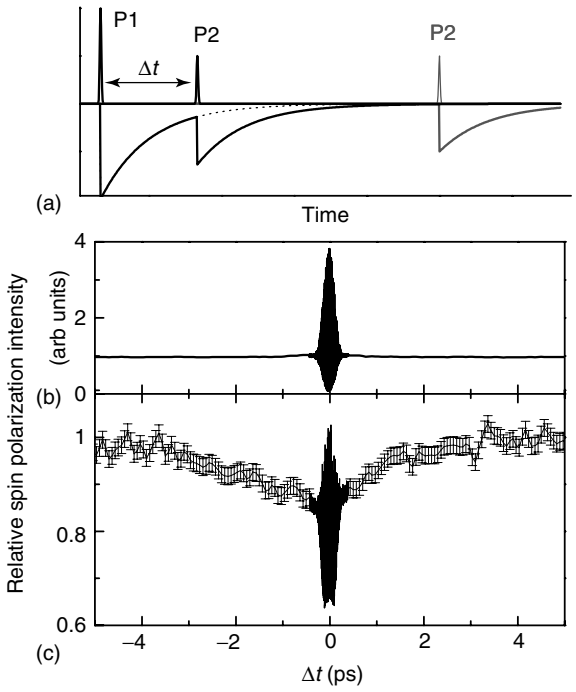

Figure 15. (a) Schematic diagram of the two-photon photoemission intensity (top panel) for two laser pulses P1 and P2 with different intensities (black lines). The gray line shows the laser pulse P2 arriving at a different time delay, Δt, after P1. The lower panel shows the transient change of photoelectron spin polarization due to sample demagnetization. (b) Measured two-photon photoemission intensity versus Δt. (c) Measured photoelectron spin polarization versus Δt.

The reduction in spin polarization during the laser pulses is then given by $S = A(N_1S_1 + N_2S_2)/N$. The scaling parameter A describes the initial sample demagnetization. If the second laser pulse (black P2 in Figure 15a) arrives within the transient demagnetization of the first pulse the spin polarization is given by $S' = [AN_1S_1 + N_2(AS_2 + S_1e^{-\Delta t/\tau})]/N$ with τ being the time constant for remagnetizing the sample. The spin polarization measured in Figure 15(c) is $\Delta S = S' - S = S_1e^{-\Delta t/\tau}N_2/N$, which depends only on the relative photoemission yield of the second and the initial reduction of the spin polarization for the first pulse as well as the exponential remagnetization term. This expression is independent of A since τ is much larger than the initial demagnetization time. The asymmetry in the spin polarization observed in Figure 15(c) for negative and positive time delays, respectively, is due to an intensity difference of 23% for the two laser pulses, that is, for negative time delay the more intense pulse arrives first. This experiment demonstrates that femtosecond laser-induced demagnetization can indeed be probed with nanometer spatial resolution.

7 CONCLUSION AND OUTLOOK

We gave an overview how dynamical magnetic phenomena that evolve on the picosecond and femtosecond timescales can be probed with nanometer spatial resolution. The emphasis of this review was on the application of photoemission microscopy, which has evolved into a state-of-the-art imaging technique. Other techniques such as optical and X-ray microscopy can give similar or complementary insight and are described in other parts of this book.

Section 4 reviewed recent experiments on the picosecond magnetization dynamics which were induced by ultrafast magnetic field pulses. Relevant devices such as magnetic sensors, magnetic random access memory, or spintronic applications demand simultaneous access to high spatial and temporal resolution. We showed for several examples that these requirements can be fulfilled by photoemission microscopy with synchrotron radiation. Parallel magnetic imaging becomes possible due to the strong magneto-optical effects in the X-ray range. This results in a large magnetic contrast for studying dynamical effects such as domain nucleation, domain wall movements, magnetization precession, and vortex-core rotation.

An even faster timescale is assessed in Section 5. The use of femtosecond laser pulses allows heating magnetic elements above their Curie temperature on a subpicosecond timescale. This is of applied interest for magneto-optical storage media where the information is erased by laser heating. The sample magnetization is probed in this regime by analyzing the photoelectron spin. In this case photoemission microscopy is used as a scanning probe technique with typically micrometer spatial resolution. We showed that spatial resolution can be dramatically enhanced by utilizing the dielectric response of nanostructures. This allows focusing optical radiation to subwavelength dimensions and is of interest for the emerging field of plasmonics.

The versatility and the wide range of different magnetic contrast mechanisms enable photoemission microscopy to exploit the full potential of complementary radiation sources such as picosecond synchrotron and femtosecond laser. The availability of FELs in the not too distant future is expected to revolutionize the field of ultrafast magnetization dynamics. When X-ray pulses of femtosecond duration as well as variable photon energy and polarization will become available, parallel magnetic imaging with nanometer resolution presently only feasible with picosecond synchrotron radiation will become possible on the femtosecond timescale. The proven versatility of photoemission microscopy is expected to play a central role also for these light sources also (BESSY, 2004).

NOTE

[1] The term spin dynamics is also often used in the context of spin waves.

ACKNOWLEDGMENTS

Claus M. Schneider would like to thank Alexander Krasyuk, Andreas Oelsner, Sergey Nepijko, Hans-Joachim Elmers, and Gerd Schönhense (all Johannes Gutenberg University, Mainz) for a very fruitful collaboration and many extensive discussions. Thanks are due to Nick Brookes and Céline de Nadaï (European Synchrotron Radiation Facility, Grenoble), Stefan Cramm (Research Center Jülich), Detlev Schmitz (Hahn-Meitner Institute, Berlin), and the staff at BESSY for their support during the beamtimes. The samples have been fabricated and supplied by Rainer Kaltofen and Ingolf Mönch (both Leibniz Institute for Solid State and Materials Research IFW, Dresden).

REFERENCES

Acremann, Y., Buess, M., Back, C.H., *et al*. (2001). Ultrafast generation of magnetic fields in a Schottky diode. *Nature*, **414**, 51.

Aeschlimann, M., Bauer, M., Pawlik, S., *et al*. (1997). Ultrafast spin-dependent electron dynamics in fcc Co. *Physical Review Letters*, **79**(25), 5158.

Altman, M.S., Pinkvos, H., Hurst, J., *et al*. (1991). Spin polarized low energy electron microscopy of surface magnetic structure. *Materials Research Society Symposium Proceedings*, **232**, 125.

Ayvazyan, V., Baboi, N., Bähr, J., *et al*. (2006). First operation of a free-electron laser generating GW power radiation at 32-nm wavelength. *European Physical Journal D*, **37**(2), 297.

Baibich, M.N., Broto, J.M., Fert, A., *et al*. (1988). Giant magnetoresistance of Fe(001)Cr(001) magnetic superlattices. *Physical Review Letters*, **61**, 2472.

Bauer, E. (2001a). Photoelectron microscopy. *Journal of Physics: Condensed Matter*, **13**, 11391.

Bauer, E. (2001b). Photoelectron spectromicroscopy: present and future. *Journal of Electron Spectroscopy and Related Phenomena*, **114–116**, 975.

Bauer, E., Franz, T., Koziol, C., *et al*. (1996). Chemical, structural, and electronic analyses of heterogeneous surfaces on a nanometer scale. In *Recent Advances in LEEM/PEEM for Structural and Chemical Analyses*, Rosei, R. (Ed.), Kluwer Academic Publishing, Dordrecht.

Bauer, E. and Telieps, W. (1988). Emission and low energy reflection electron microscopy. In *Surface and Interface Characterization by Electron Optical Methods*, Howie, A. and Valdrè, U.

(Eds.), *Volume 191 of NATO ASI Series B: Physics*, Plenum Press: New York, p. 195.

Beaurepaire, E., Merle, J.C., Daunois, A. and Bigot, J.Y. (1996). Ultrafast spin dynamics in ferromagnetic nickel. *Physical Review Letters*, **76**(22), 4250.

BESSY. (2004). *The BESSY Soft X-Ray Free Electron Laser Project*. Technical Design Report. BESSY GmbH, see, i.e., at: http://www.bessy.de.

Binasch, G., Grünberg, P., Saurenbach, F. and Zinn, W. (1989). Enhanced magnetoresistance in layered magnetic structures with antiferromagnetic interlayer exchange. *Physical Review B*, **39**(7), 4828.

Bonn, M., Funk, S., Hess, C., *et al*. (1999). Phonon-versus electron-mediated desorption and oxidation of CO on Ru(0001). *Science*, **285**, 1042.

Brixner, T., de Abajo, F.J.G., Schneider, J. and Pfeiffer, W. (2005). Nanoscopic Ultrafast Space-Time-Resolved Spectroscopy. *Physical Review Letters*, **95**(9), 093901.

Brüche, E. (1933). Elektronenmikroskopische Abbildung mit lichtelektrischen Elektronen. *Zeitschrift fur Physik*, **86**, 448.

Brüche, E. (1934). Elektronenmikroskopische Abbildung mit lichtelektrischen Elektronen. *Zeitschrift fur Naturforschung*, **11**, 287.

Carra, P., Thole, B.T., Altarelli, M. and Wang, X. (1993). X-ray circular dichroism and local magnetic fields. *Physical Review Letters*, **70**(5), 694.

Chen, C.T., Sette, F., Ma, Y. and Modesti, S. (1990). Soft-x-ray magnetic circular dichroism at the $L_{2,3}$ edges of Nickel. *Physical Review B*, **42**(11), 7262.

Choe, S-B., Acremann, Y., Scholl, A., *et al*. (2004). Vortex core-driven magnetization dynamics. *Science*, **304**, 420.

Choi, B.C., Ballentine, G.E., Belov, M., *et al*. (2001a). Picosecond time-resolved magnetization reversal dynamics in $Ni_{80}Fe_{20}$ microstructure. *Journal of Applied Physics*, **89**(11), 7171.

Choi, B.C., Belov, M., Hiebert, W.K., *et al*. (2001b). Ultrafast magnetization reversal dynamics investigated by time domain imaging. *Physical Review Letters*, **86**(4), 728.

Chou, K.W., Puzic, A., Stoll, B.H., *et al*. (2006). Vortex dynamics in coupled ferromagnetic multilayer structures. *Journal of Applied Physics*, **99**, 09F305.

Chumakov, D., McCord, J., Schäfer, R., *et al*. (2005). Nanosecond time-scale switching of permalloy thin film elements studied by wide-field time-resolved Kerr microscopy. *Physical Review B*, **71**(1), 014410.

Cinchetti, M., Gloskovskii, A., Nepjiko, S.A., *et al*. (2005). Photoemission electron microscopy as a tool for the investigation of optical near fields. *Physical Review Letters*, **95**(4), 047601.

DESY. (2006). See, for example, the websites http://www-hasylab.desy.de/facility/fel/main.htm.

Dhesi, S.S., van der Laan, G., Dudzik, E. and Shick, A.B. (2001). Anisotropic spin-orbit coupling and magnetocrystalline anisotropy in vicinal Co films. *Physical Review Letters*, **87**(6), 067201.

Dürr, H.A., Kronast, F. and Eberhardt, W. (2001). Spin-polarized photoelectron emission microscopy of magnetic nanostructures. In *Advances in Solid State Physics*, Kramer, B. (Ed.), Springer-Verlag: Berlin, p. 557, Vol. 41.

Eisebitt, S., Lüning, J., Schlotter, W.F., *et al*. (2004). Lensless imaging of magnetic nanostructures by x-ray spectro-holography. *Nature*, **432**, 885.

Freeman, M.R. and Hiebert, W.K. (2001). Stroboscopic microscopy of magnetic dynamics. In *Spin Dynamics in Confined Magnetic Structures*, Hillebrands, B. and Ounadjela, K. (Eds.), Springer-Verlag, Berlin, p. 93, Vol. 1.

Freeman, M.R., Hiebert, W.K. and Stankiewicz, A. (1998). Time-resolved scanning Kerr microscopy of ferromagnetic structures. *Journal of Applied Physics*, **83**(11), 6217.

Freescale. (2006). 256K x 16-Bit 3.3-V Asynchronous Magnetoresistive RAM. Preliminary data sheet MR2A16A Rev. 3, available through http://www.freescale.com.

Gerrits, T., Hohlfeld, J., Gielkens, O., *et al*. (2001). Magnetization dynamics in NiFe thin films induced by short in-plane magnetic field pulses. *Journal of Applied Physics*, **89**(11), 7648.

Goering, E. (2005). X-ray magnetic circular dichroism sum rule correction for the light transition metals. *Philosophical Magazine*, **85**, 2895.

Goering, E., Will, J., Geissler, J., *et al*. (2005). X-ray magnetic circular dichroism – a universal tool for magnetic investigations. *Journal of Alloys and Compounds*, **328**, 14.

Güdde, J., Conrad, U., Jähnke, V., *et al*. (1999). Magnetization dynamics of Ni and Co films on Cu(001) and of bulk nickel surfaces. *Physical Review B*, **59**(10), R6608.

Heitkamp, B., Kronast, F., Heyne, L., *et al*. (2006). Submitted.

Hentschel, M., Kienberger, R., Spielmann, C., *et al*. (2001). Attosecond metrology. *Nature*, **414**, 509.

Hertel, R. and Schneider, C.M. (2006). Exchange explosions: magnetization dynamics during vortex-antivortex annihilation. *Physical Review Letters*, **97**, 177202.

Hiebert, W.K., Ballentine, G.E., Lagae, L., *et al*. (2002). Ultrafast imaging of incoherent rotation magnetic switching with experimental and numerical micromagnetic dynamics. *Journal of Applied Physics*, **92**(1), 392.

Hillebrands, B. and Ounadjela, K. (Eds.) (2001). *Spin Dynamics in Confined Magnetic Structures*, Springer-Verlag: Berlin, Vol. 1.

Hillebrands, B. and Ounadjela, K. (Eds.) (2003). *Spin Dynamics in Confined Magnetic Structures*, Springer-Verlag: Berlin, Vol. 2.

Hillebrands, B. and Ounadjela, K. (Eds.) (2006). *Spin Dynamics in Confined Magnetic Structures*, Springer-Verlag: Berlin, Vol. 3.

Hubert, A. and Schäfer, R. (1998). *Magnetic Domains*, Springer-Verlag: Berlin.

Keil, U.D., Gerritsen, H.J., Haverkort, J.E.M. and Wolter, J.H. (1995). Generation of ultrashort electrical pulses with variable pulse widths. *Applied Physics Letters*, **66**(13), 1629.

Kimel, A.V., Kirilyuk, A., Usachev, P.A., *et al*. (2005). Ultrafast non-thermal control of magnetization by instantaneous photomagnetic pulses. *Nature*, **435**, 655.

Kirschner, J. (1985). Sources and detectors for spin polarized electrons. In *Polarized Electrons in Surface Physics*, Feder, R. (Ed.), World Scientific: Singapore.

Knorren, R., Bennemann, K.H., Burgermeister, R. and Aeschlimann, M. (2000). Dynamics of excited electrons in copper and

ferromagnetic transition metals: theory and experiment. *Physical Review B*, **61**(14), 9427.

Koopmans, B., van Kampen, M., Kohlhepp, J.T. and de Jonge, W.J.M. (2000). Ultrafast magneto-optics in nickel: magnetism or optics. *Physical Review Letters*, **85**(4), 844.

Koopmans, B., Ruigrok, J.J.M., Longa, F.D. and de Jonge, W.J.M. (2005). Unifying ultrafast magnetization dynamics. *Physical Review Letters*, **95**(26), 267207.

Krasyuk, A., Oelsner, A., Nepijko, S., *et al*. (2003). Time-resolved photoemission electron microscopy of magnetic field and magnetization changes. *Applied Physics A*, **76**(6), 836.

Krasyuk, A., Wegelin, F., Nepijko, S.A., *et al*. (2005). Self-trapping of magnetic oscillation modes in Landau flux-closure structures. *Physical Review Letters*, **95**, 207201.

Kronmüller, H. and Hertel, R. (2000). Computational micromagnetism of magnetic structures and magnetisation processes in small particles. *Journal of Magnetism and Magnetic Materials*, **215–216**, 11.

Kubo, A., Onda, K., Petek, H., *et al*. (2005). Femtosecond imaging of surface plasmon dynamics in a nanostructured silver film. *Nano Letters*, **5**(4), 1123.

Kuch, W., Chelaru, L.I., Offi, F., *et al*. (2006). Tuning the magnetic coupling across ultrathin antiferromagnetic films by controlling atomic-scale roughness. *Nature Materials*, **5**, 128.

van der Laan, G. (1999). Magnetic linear x-ray dichroism as a probe of the magnetocrystalline anisotropy. *Physical Review Letters*, **82**(3), 640.

van der Laan, G., Thole, B.T., Sawatzky, G.A., *et al*. (1986). Experimental proof of magnetic x-ray dichroism. *Physical Review B*, **34**, 6529.

Lehmann, J., Merschdorf, M., Pfeiffer, W., *et al*. (2000). Surface plasmon dynamics in silver nanoparticles studied by femtosecond time-resolved photoemission. *Physical Review Letters*, **85**(14), 2921.

Link, S., Dürr, H.A. and Eberhardt, W. (2001). Femtosecond spectroscopy. *Journal of Physics: Condensed Matter*, **13**, 7873.

Lodder, J.C. (1998). Magnetic recording hard disk thin film media. In *Handbook of Magnetic Materials*, Buschow, K.H.J. (Ed.), Elsevier B. V.: Amsterdam, Vol. 11, p. 291.

Marx, G.K.L., Elmers, H-J. and Schönhense, G. (2000). Magneto-optical linear dichroism in threshold photoemission electron microscopy of polycrystalline Fe films. *Physical Review Letters*, **84**(25), 5888.

Meier, F. and Zakharchenya, B.P. (Eds.) (1984). *Optical Orientation*, North Holland: Amsterdam.

Melnikov, A., Radu, I., Bovensiepen, U., *et al*. (2003). Coherent optical phonons and parametrically coupled magnons induced by femtosecond laser excitation of the Gd(0001) surface. *Physical Review Letters*, **91**, 227403.

Meservey, R. and Tedrow, P.M. (1994). Spin-dependent tunneling. *Physics Reports*, **238**, 173.

Miltat, J., Albuquerque, G., and Thiaville, A. (2003). An introduction to micromagnetics in the dynamic regime. In *Spin Dynamics in Confined Magnetic Structures*, Hillebrands, B. and Ounadjela, K. (Eds.), Springer-Verlag: Berlin, p. 1, Vol. 2.

Mok, J.T. and Eggleton, B.J. (2005). Photonics: expect more delays. *Nature*, **433**(7028), 811.

Moodera, J.S., Kinder, L.R., Wong, T.M. and Meservey, R. (1995). Large magnetoresistance at room temperature in ferromagnetic thin film tunnel junctions. *Physical Review Letters*, **74**(16), 3273.

Mundschau, M., Romanowicz, J., Wang, J.Y., *et al*. (1996). Imaging of ferromagnetic domains using photoelectrons: photoelectron emission microscopy of neodymium-iron-boron ($Nd_2Fe_{14}B$). *Journal of Vacuum Science and Technology B*, **14**(4), 3126.

Myers, E.B., Ralph, D.C., Katine, J.A., *et al*. (1999). Current-induced switching of domains in magnetic multilayer devices. *Science*, **285**, 867.

Nepijko, S.A., Sedov, N.N. and Schönhense, G. (2000). Measurements of magnetic fields and domain structures using a photoemission electron microscope. *Advances in Imaging and Electron Physics*, **113**, 205.

Neudert, A., McCord, J., Chumakov, D., *et al*. (2005). Small-amplitude magnetization dynamics in permalloy elements investigated by time-resolved wide-field Kerr microscopy. *Physical Review B*, **71**, 134405.

Nolting, F., Scholl, A., Stöhr, J., *et al*. (2000). Direct observation of the alignment of ferromagnetic spins by antiferromagnetic spins. *Nature*, **405**, 767.

Oelsner, A., Schmidt, O., Schicketanz, M., *et al*. (2001). Microspectroscopy and imaging using a delay line detector in time-of-flight photoemission microscopy. *The Review of Scientific Instruments*, **72**(10), 3968.

Ohldag, H., Scholl, A., Nolting, F., *et al*. (2001). Spin reorientation at the antiferromagnetic NiO(001) surface in response to an adjacent ferromagnet. *Physical Review Letters*, **86**(13), 2878.

Ozbay, E. (2006). Plasmonics: merging photonics and electronics at nanoscale dimensions. *Science*, **311**(5758), 189.

Park, J.P., Eames, P., Engebretson, D.M., *et al*. (2003). Imaging of spin dynamics in closure domain and vortex structures. *Physical Review B*, **67**(2), 020403(R).

Prinz, G.A. (1998). Magnetoelectronics. *Science*, **282**, 1660.

Raabe, J., Quitmann, C., Back, C.H., *et al*. (2005). Quantitative analysis of magnetic excitations in Landau flux-closure structures using synchrotron-radiation microscopy. *Physical Review Letters*, **94**, 217204.

Rhie, H-S., Dürr, H.A. and Eberhardt, W. (2003). Femtosecond electron and spin dynamics in Ni/W(110) films. *Physical Review Letters*, **90**, 247201.

Rousse, A., Rischel, C., Fourmaux, S., *et al*. (2001). Non-thermal melting in semiconductors measured at femtosecond resolution. *Nature*, **410**, 65.

Schneider, C.M., Holldack, K., Kinzler, M., *et al*. (1993). Magnetic spectromicroscopy from Fe(100). *Applied Physics Letters*, **63**(17), 2432.

Schneider, C.M., Krasyuk, A., Nepijko, S.A., *et al*. (2006). Accessing fast magnetization dynamics by XPEEM: status and perspectives. *Journal of Magnetism and Magnetic Materials*, **304**, 6.

Schneider, C.M., Kuksov, A., Krasyuk, A., *et al*. (2004). Incoherent magnetization rotation observed in sub-nanosecond time-resolving XPEEM studies. *Applied Physics Letters*, **85**(13), 2562.

Schneider, C.M. and Schönhense, G. (2002). Investigating surface magnetism by means of photoexcitation electron emission microscopy. *Reports on Progress in Physics*, **65**, R1785.

Scholl, A., Baumgarten, L., Jacquemin, R. and Eberhardt, W. (1997). Ultrafast spin dynamics of ferromagnetic thin films observed by fs spin-resolved two-photon photoemission. *Physical Review Letters*, **79**(25), 5146.

Schönhense, G. (1999). Imaging of magnetic structures by photoemission electron microscopy. *Journal of Physics: Condensed Matter*, **11**, 9517.

Schönhense, G., Elmers, H.J., Nepijko, S.A. and Schneider, C.M. (2006). Time-resolved photoemission electron microscopy. *Advances in Imaging and Electron Physics*, **142**, 159.

Schütz, G., Wagner, W., Wilhelm, W., *et al*. (1987). Absorption of circularly polarized x rays in iron. *Physical Review Letters*, **58**(7), 737.

Shinjo, T., Okuno, T., Hassdorf, R., *et al*. (2000). Magnetic vortex core observation in circular dots of permalloy. *Science*, **289**, 930.

Sokolowski-Tinten, K., Blome, C., Blums, J., *et al*. (2003). Femtosecond x-ray measurement of coherent lattice vibrations near the Lindemann stability limit. *Nature*, **422**, 287.

Spivak, G.V., Dombrovskaia, T.N. and Sedov, N.N. (1957). The observation of ferromagnetic domain structure by means of photoelectrons. *Soviet Physics Doklady*, **2**, 120.

Stöhr, J. and Anders, S. (2000). X-ray spectro-microscopy of complex materials and surfaces. *IBM Journal of Research and Development*, **44**(4), 535.

Stöhr, J., Scholl, A., Regan, T.J., *et al*. (1999). Images of the antiferromagnetic structure of a NiO(100) surface by means of x-ray magnetic linear dichroism spectromicroscopy. *Physical Review Letters*, **83**(9), 1862.

Stöhr, J., Wu, Y., Samant, M.G., *et al*. (1993). Element-specific magnetic microscopy with circularly polarized x-rays. *Science*, **259**, 658.

Thole, B.T., Carra, P., Sette, F. and van der Laan, G. (1992). X-ray circular dichroism as a probe of orbital magnetization. *Physical Review Letters*, **68**(12), 1943.

Thole, B.T. and van der Laan, G. (1993). Sum rules for magnetic dichroism in rare earth 4f photoemission. *Physical Review B*, **38**(4), 1943.

Vogel, J., Kuch, W., Bonfim, M., *et al*. (2003). Time-resolved magnetic domain imaging by x-ray photoemission electron microscopy. *Applied Physics Letters*, **82**, 2299.

Wachowiak, A., Wiebe, J., Bode, M., *et al*. (2002). Direct observation of internal spin structure of magnetic vortex cores. *Science*, **298**, 577.

van Waeyenberge, B., Puzic, A., Stoll, H., *et al*. (2006). Magnetic vortex core reversal by excitation with short bursts of an alternating field. *Nature*, **444**, 461–464.

Wang, J-P. (2005). Tilting for the top. *Nature Materials*, **4**, 191.

Wiedemann, H. (2003). *Synchrotron Radiation*, Advanced Texts in Physics, Springer-Verlag: Berlin.

Wokaun, A., Gordon, J.P. and Liao, P.F. (1982). Radiation damping in surface-enhanced Raman scattering. *Physical Review Letters*, **48**(14), 957.

Wolf, S.A., Awschalom, D.D., Buhrman, R.A., *et al*. (2001). Spintronics: a spin-based electronics vision for the future. *Science*, **294**, 1488.

Zhang, G.P. and Hübner, W. (2000). Laser-induced ultrafast demagnetization in ferromagnetic metals. *Physical Review Letters*, **85**(14), 3025.

FURTHER READING

Lukin, M.D. and Imamoglu, A. (2001). Controlling photons using electromagnetically induced transparency. *Nature*, **413**(6853), 273.

Lorentz Microscopy of Thin-film Systems

Josef Zweck[1] and Thomas Uhlig[2]

[1] *Universität Regensburg, Regensburg, Germany*
[2] *Argonne National Laboratory, Argonne, IL, USA*

1 INTRODUCTION

Until the availability of electron microscopes the imaging of magnetic domain structures was limited to the use of optical methods.

For the Bitter decoration technique (Hámos and Thiessen, 1931; Bitter, 1931, 1932; Hubert and Schäfer, 1998), one used fine magnetic grains, which were suspended in a solvent, to visualize areas where a high gradient of the magnetic induction was present at the specimen's surface. After application of the Bitter fluid one had to wait a short period of time until the fluid was dried up fully, leaving the magnetic grains bunched around areas where the gradient was largest. For a sufficiently large concentration of the grains, these agglomerates could be seen rather easily by a simple light-optical microscope. It is needless to say that the resolution achievable by this technique was ultimately limited by the optical resolution of the microscope, while the grains can in principle be finer than a light microscope's resolution. There have been some attempts later to embed the agglomerates into thin, electron transparent carbonaceous films which could then be transferred into an electron microscope to make use of its better resolution.

Another technique of visualization of magnetic surface structures was to employ the magneto-optical Kerr effect (Kerr, 1877), which is based on the rotation of the polarization plane of linearly polarized light when it is reflected from magnetic surfaces. The detection of this effect can be done simply by using a correctly aligned analyzer which will darken areas where due to reflection the polarization plane was rotated, leaving other areas, where no or opposite rotation occurred, relatively bright. Thus, a gray scale image can be observed, where regions of different magnetic orientation show up in different shades of gray. Obviously this technique is also limited basically by the optical resolution of the microscope used and can be as good as 0.15 µm when blue illumination is used.

However, only after the electron microscope was invented in 1934 by Ernst Ruska and his coworker Knoll (Ruska, 1934) further progress in magnetic microstructural observation was possible. From that date it lasted still another 25 years until the first reports of successful attempts to directly visualize the micromagnetic structures which can be found in magnetic materials (Hale, Fuller and Rubinstein, 1959; Boersch and Raith, 1959; Boersch, Raith and Wohlleben, 1960). Shortly thereafter, the new technique was already used to characterize and measure properties of magnetic materials (Fuller and Hale, 1960; Fuchs, 1961;

Handbook of Magnetism and Advanced Magnetic Materials. Edited by Helmut Kronmüller and Stuart Parkin. Volume 3: *Novel Techniques for Characterizing and Preparing Samples*. ISBN: 978-0-470-02217-7.

Puchalska and Spain, 1962; Cohen, 1965; Grundy and Tebble, 1968; Wade, 1968; Petrov, Spivak and Pavlyuchenko, 1972a,b). So far, the technique in use was the rather simple-to-use defocused (or Fresnel) imaging, which is highly nonlinear in contrast. Thus, the newly found technique was frequently used to qualitatively characterize micromagnetic structures, but in general lacked the ability to allow quantitative measurements, except for some favorable cases. First measurements of magnetic domain wall widths were performed by Wade (1962), based on a pure geometrical optics approach, improved wave optical calculations allowed a quantum mechanical description as given by (Boersch, Hamisch, Wohlleben and Grollmann, 1960; Boersch, Hamisch, Grohmann and Wohlleben, 1962; Reimer, 1997; Chapman, McFadyen and McVitie, 1997; Hirsch *et al*., 1965).

Electron microscopy can visualize the magnetic induction $\vec{B}$, as there is an interaction between the electrons of charge $q = -e$ and velocity $\vec{v}$ and the magnetic induction, the Lorentz force $\vec{F}_L$,

$$\vec{F}_L = q \cdot \vec{v} \times \vec{B} \tag{1}$$

Equation (1) also emphasizes, that due to the vector product there is no Lorentz force connected with components of the magnetic induction, which are parallel or antiparallel to the electron beam's direction (which coincides with the direction of $\vec{v}$). Therefore, Lorentz microscopy is not sensitive to the out-of-plane component of a specimen's induction. For most cases, this is not a severe constraint, as in thin films, which are mainly under investigation in the transmission electron microscope (TEM), the large demagnetizing fields prevent a perpendicular magnetization anyway.

The theoretical treatments which are given in the subsequent text can only give an impression of the theory involved. Although not false, they are often strongly simplified and contain only the parameters necessary for our purposes. Thus they should not be considered as complete, further interested readers may consult the literature provided in the corresponding section.

2 SPECIMENS SUITABLE FOR INVESTIGATION

2.1 Thin films

Thin magnetic films have been the first magnetic specimens looked at in the TEM by Lorentz microscopy. They are created by means of evaporation, sputtering or similar vacuum deposition techniques. The main advantage of having a thin film lies in the fact that it is already electron transparent. The only preparation step, which is generally rather simple, consists in a liftoff of the film from the substrate onto which it was deposited. This may be achieved by dissolving the substrate in various chemical etchants (which usually have also a tendency to affect the specimen itself) or by using glue or polymers to tear the film off the substrate, before they in turn are dissolved in an agent, which in general is not harmful for the specimen itself. The last step involved is then the deposition of the freely floating specimen onto a metallic grid which then allows the observation in the TEM.

The main advantage of continuous thin films is that there are no boundary or edge effects, provided that the lateral extension of the films is large compared to any micromagnetic structures involved. Thus, thin magnetic films have been extensively studied with respect to their domain configuration, remagnetization behavior, domain structure, and so on.

2.2 Patterned thin films on transparent membranes

The technical ability to decrease the dimensionality of a magnetic specimen has led to a vast field of new and exciting phenomena in the last few years. The size of the specimen has become a very important parameter having a major impact on the magnetic configurations and their switching behavior.

Various methods allow the patterning of thin film, and thus the restriction of the magnetization to a very small volume. Typical dimensions accessible for patterning are laterally from 30 nm upward, with specimen thicknesses from a few monolayers up to more than 100 nm. However, for transmission electron microscopy the substrate has to be considered carefully. As the direction of the electron beam is generally normal to the specimen's plane, it has to be chosen transparent for electrons. This restriction limits the substrate thickness to a few tens of nanometers, which in turn makes these membranes mechanically very sensitive. Widely spread is the use of silicon nitride (Si_3N_4) membranes, which will briefly be introduced in the subsequent text.

The patterning itself is mostly done by electron lithography, less frequently by optical lithography with several possibilities to use lift-off processes. However, recently focused ion beam (FIB) systems became available for the patterning process. This novel possibility, often in combination with 'conventional' techniques allows a very accurate fabrication of structures down to the 10-nm scale.

2.3 Silicon nitride membrane substrates

Membranes for TEM purposes are commercially available, so that most groups abandoned fabricating them themselves. A broad range of different types is offered in the meantime, with membranes of several mm^2 area and thickness down to 20 nm.

Basically, they are prepared by the deposition of Si_3N_4 on both faces of a silicon wafer. On one side of the wafer, the nitride is removed, usually in the shape of a square. Then the wafer is brought into a wet etchant (such as hot KOH or NaOH) which starts a preferential etching process where the etching proceeds much faster (depending on the etchant and crystal orientation) into the wafer rather than in lateral direction. Thus, while the initial square window is hardly widened, an etch pit evolves in the shape of an inverted pyramid. When the top of this pyramid touches the Si_3N_4 layer on the opposite face of the wafer, the vertical etch process is effectively stopped, since this material is removed slower by orders of magnitude. When the wafer is kept in the etchant, only a lateral etching takes place, therefore widening the pyramid's body in lateral dimension. This finally leads to the formation of a truncated pyramid hollow, which at its top is covered by the remaining Si_3N_4 membrane, typically $100 \times 100\,\mu m^2$ wide. A free-standing membrane has formed, which can be used as an electron transparent substrate for transmission electron microscopy experiments.

2.4 Electron lithography

A standard method to pattern magnetic structures on supporting membranes is electron lithography. Different variations of subsequent steps are possible, depending on the respective demands. We describe one of the easiest ways to achieve high quality patterned specimens.

Onto a silicon nitride membrane (Figure 1a) two layers of resists (i.e., polymethylmethacrylate, PMMA) with different molecular weights and thus various sensitivities are spun. The more sensitive resist is deposited first and is capped by the less sensitive resist (Figure 1b).

After that, the structures are transferred to the resist by electron lithography (Figure 1c). For this purpose, a scanning electron microscope in combination with suitable software package is used. In most cases, it is desirable to use a double layer of resist which forms a distinct 'undercut' profile (Figure 1d). This means that the lower layer of resist forms a wider mask than the upper layer. When the material is then deposited into the pattern (by any method of thin film deposition, such as – for example – evaporation or sputtering) the upper (narrower) mask defines the overall dimensions of the structure deposited. Since the underlying mask is hardly in contact with the deposited patterned material, the subsequent lift-off process of the resist is largely facilitated. As many ferromagnetic materials suffer from oxidation it is in general necessary to cap the magnetic structures with a protective layer. Commonly used elements for this purpose are Al or Ti (Figure 1e). After the lift-off process, which dissolves and thereby removes both the resist and the residual deposited material, the patterned structure, supported by the membrane is ready for investigation (Figure 1f).

A critical point in specimen preparation for TEM or scanning transmission electron microscopy (STEM) investigations are charge effects. If the specimen is not conductive, the electron beam charges the specimen during observation. This causes deflections and/or instabilities of the electron

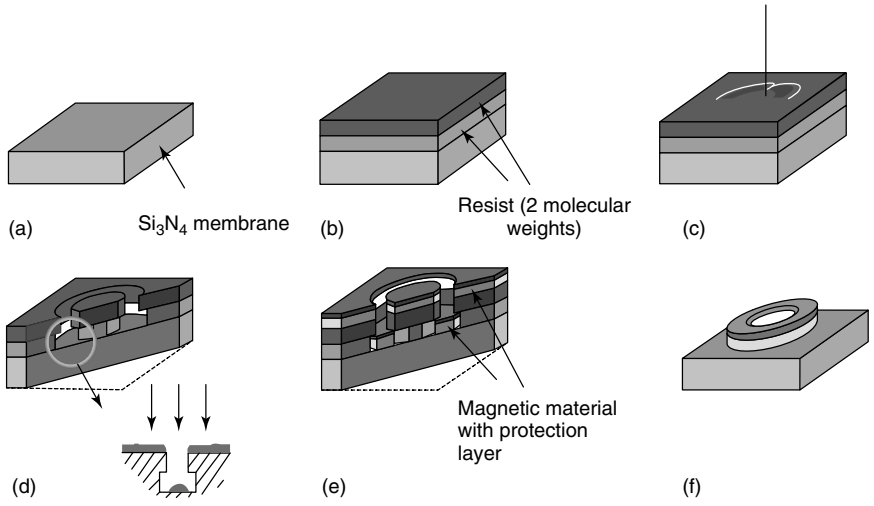

Figure 1. Procedure used to create patterned magnetic structures on electron transparent membranes by electron beam lithography. (See text for details (a–f).)

beam and can in severe cases prevent a proper investigation of the specimen.

To avoid this, it is useful to coat the entire sample, including the membrane, with a thin layer of conductive material like aluminium or carbon.

2.5 Focused ion beam (FIB)

Another technique to prepare patterned specimens of very high quality is given by the FIB technique. FIB Equipment is presently available from basically all manufacturers of electron beam related equipment or electron microscopes. Here, a finely focused beam of Ga ions is scanned across the specimen in the same way as in a scanning electron microscope. The Ga ions, however, sputter away the exposed parts of the specimen, and using a mask generator – usually driven by a computer – it is possible to safely remove unwanted parts of the specimen, leaving behind a patterned layer. Beam diameters down to 10 nm have been achieved and therefore patterning on this level is possible. However, the sputtering process tends to amorphize the vicinity of the irradiated area, and Ga may be implanted into the remaining areas. Especially in the case of very small structures one has to be aware of the creation of magnetically dead layers from the patterning process. On the other hand, the destructive action of ion beams has been shown to be useful for patterning when the material separating the structures is made non-magnetic by irradiation with an ion beam (see, for example, Bernas *et al*., 1999; Terris *et al*., 1999; Toporov, Langford and Petford-Long, 2000a). This is especially useful for Lorentz microscopy since the Fresnel diffraction effects from patterned specimens can be avoided or at least significantly reduced, since the magnetic structures are embedded into a thin film of equal thickness, however nonmagnetic material. Therefore, the electron beam does not experience differences in the electron optic refractive index which would in turn cause Fresnel diffraction, blurring the image at the particle's edges.

2.6 Bulk material, preparation problems

Nowadays it is rather uncommon to use bulk materials, which have to be thinned down to electron transparency prior to investigation, since most areas of interest deal with continuous thin films or particulate materials of very small dimensions which are already electron transparent. There are, however, various thinning techniques, which are well-established in the electron microscopy community (Schimmel and Vogell, 1981; Reimer, 1959; Williams, 1984) which can be used to prepare TEM specimens from bulk samples. In any case, two things have to be kept in mind. Firstly, care has to be taken not to change the magnetic properties by the process of thinning, and secondly it is important to consider the fact that the specimen is sometimes subjected to magnetic fields of typically 1–2 T in the objective lens in standard imaging mode. Although this is of no significance for thin film specimens, for thicker specimens the resulting forces may well lift the specimen out of the specimen holder, leaving the specimen to stick on the microscope's pole pieces.

Electron microscopy has established itself as a very powerful research tool in solid-state physics and instruments of various kinds are wide-spread. Thus, some fundamental facts about these techniques belong meanwhile to the basics of physics. Nevertheless the understanding of Lorentz microscopy, the difficulties and possibilities connected with it demands a fundamental knowledge on how transmission electron microscopy works. Prior to the description of the various techniques of Lorentz microscopy, a short introduction in electron optics and the instrument itself should be given. We restrict this description on the facts necessary to understand what follows.

Then, we introduce the magnetic specimen as a (strong) phase object, before we start to treat the main techniques of Lorentz microscopy, Fresnel and Foucault imaging, differential phase contrast (DPC) microscopy and electron holography in more detail.

3 BASIC IMAGING TECHNIQUES OF LORENTZ MICROSCOPY

3.1 Introduction to electron microscopy

In the subsequent text, a short introduction to an electron microscope is provided. Further information about practical aspects can be found in the textbook of Williams and Carter (1996), the theoretical background is comprehensively treated by Reimer (1997).

3.1.1 Conventional and scanning transmission electron microscopes (CTEM and STEM)

There are two different modes to record an image with a transmission electron microscope.

Similar to a light optical microscope, an image can be generated by illuminating the object and recording the magnified image. In a certain sense, this can be considered as 'parallel' recording and is usually termed as conventional transmission electron microscopy (CTEM).

However, it is also possible to record the image serially. To achieve this, a focused electron probe is scanned across

the specimen, the electron beam passes through the sample and for every point of the sample, the signal of a detector in the subsequent text the specimen is used to characterize the respective point. If the registered signals are plotted according to the current position of the electron probe on the specimen, an image of the sample is generated. This method is termed STEM. It is important to point out that there exists a variety of detectors which are sensitive for different electron-matter interactions. In the subsequent text, a description will be given which detector is suitable to record the local magnetic properties of the specimen and therefore to visualize and measure quantitatively magnetic properties.

It has been shown (Cowley, 1969) that CTEM and STEM have a close relationship and can considered as complementary techniques. It depends on the task to decide, which technique should be chosen.

3.1.2 Components of a TEM

The electrons are provided by an electron gun (see Figure 2). Presently, both thermal and field emission emitters are in use. In a thermal emitter, the filament consists of a tungsten or a LaB_6 crystal, which is electrically heated and accordingly emits electrons. The electrons in a field emission gun (FEG), however, are extracted from an extremely pointed cathode by an electric field. The sharp tip causes a strong electric field at its very end, as the field is inversely proportional to the radius of the tip's curvature. Therefore, electrons are emitted from a very limited area which in turn provides an excellent spatial coherence of the electron wave, a crucial requirement for electron holography.

The emitted electrons are accelerated in a multistage process to reach their final highly relativistic energy of several hundred keV, depending on the microscope. A higher acceleration voltage causes a smaller de-Broglie wavelength λ of the electrons, typically in the pm range ($\approx$1.97 pm for 300 keV electrons). The influence of the wavelength on the resolution of the TEM is not crucial, as it is limited by the lens aberrations rather than by the wavelength. The high energy, however, ensures sufficient penetration power to penetrate thin metallic films with typical thicknesses of $\approx$100 nm. A disadvantage of high energy electrons is the higher beam 'stiffness' compared to electrons of less energy. This can be seen easily from equation (12), where the Lorentz angle of deflection is directly related to the de Broglie wavelength of the electron.

Leaving the gun area, a condenser lens system consisting of at least two lenses and an aperture forms the electron beam. These lenses define the illuminated area on the specimen.

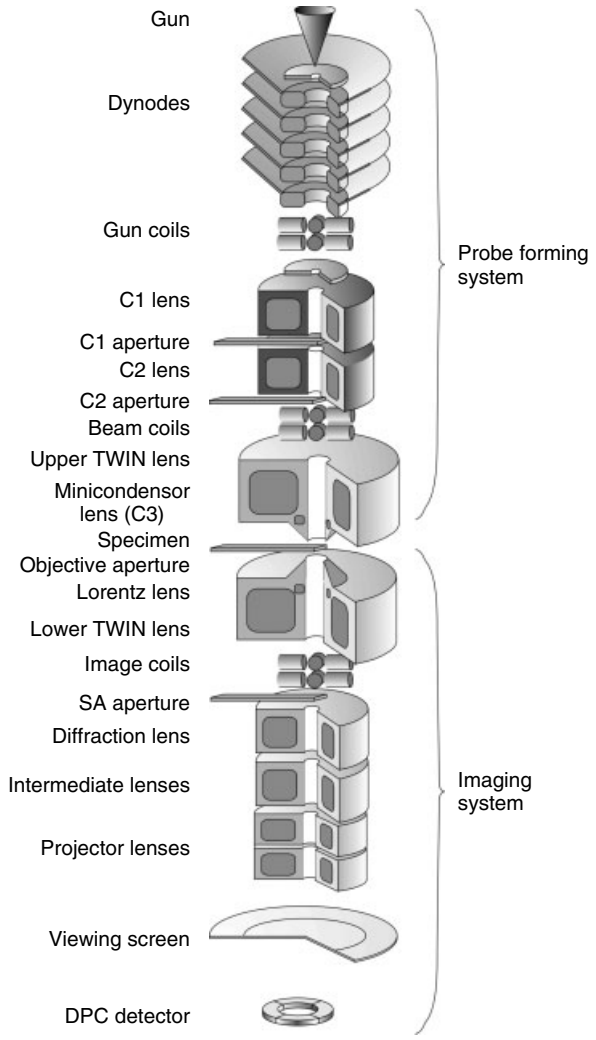

Figure 2. Typical components of a commercial TEM, equipped with a Lorentz lens and a DPC detector.

In CTEM mode, a beam as parallel as possible is of advantage to gain high coherence. In most cases, however, a compromise between high coherence (parallel illumination) and the brightness of the illuminated region (convergent illumination) has to be chosen.

In the STEM case, the condenser system provides an electron beam focused to a point-like electron probe on the specimen. Here, the condenser aperture is of crucial importance, as it defines the illuminated area on the STEM detector.

The specimen itself is inserted into the electron microscope with a specimen holder (Williams and Carter, 1996), which restricts the dimensions of the sample to approximately 2 mm.

In a modern microscope, the sample sits right inside the objective lens, which often acts as a combination of a further condenser lens and an imaging lens. The magnetic field in the

fully excited objective lens exceeds 1 T and would severely influence the micromagnetic configuration of the specimen. Therefore, the objective lens cannot be used for magnetic imaging techniques.

However, a low magnification mode is usually implemented in all microscopes, which operates with the objective lens turned off. Its action is performed by an other lens (called *intermediate* or *diffraction lens*) which is located at a larger distance from the specimen. This requires a long focal length lens, which yields only a very moderate magnification (in the order of 10^3) and at the same time causes only a negligible magnetic field at the specimen's location.

A different approach uses a special Lorentz lens (Zweck and Bormans, 1992), which serves as an objective lens. This Lorentz lens is located at a larger distance from the sample than the objective lens but still closer than the lenses usually in use.

The Lorentz lens allows investigations with virtually zero magnetic field in the sample's region, whereas the optical quality of that lens is worse than the standard objective lens, but better than what can be achieved without it. The magnification is in the 10^5 range, the resolution can reach 2 nm.

Several lenses follow, which magnify the CTEM (and Lorentz TEM) image further.

A fluorescent screen allows the direct observation of the image. It can be recorded with a conventional plate camera, although in the meantime most microscopes are equipped with a CCD camera, which allows a digital acquisition of the image for simple further processing.

A growing number of microscopes has also the ability to generate energy filtered images. This, in terms of Lorentz microscopy, has the advantage to exclude inelastically scattered electrons from the image, which in turn allows to reduce the 'background noise' and opens the opportunity to investigate thicker specimens or samples with weak magnetic inductions.

The energy filter is expected to enable the implementation of a new magnetic imaging technique as well, which is currently under investigation and based on chiral dichroitic effects (Hébért and Schattschneider, 2003; Schattschneider *et al*., 2006).

In the STEM mode the electron beam propagates after the specimen along a certain distance, the camera length, to the detector plane. As the distance between detector and specimen plane is a fixed distance, given by the geometry of the microscope, the imaging lenses are used to generate a 'virtual' camera length from the mm to the several 100 m regime.

In most cases, the STEM signal is recorded subsequently by a solid-state detector, the whose shape determines the imaging conditions, as will be shown in the subsequent text.

3.1.3 Theoretical description

In standard TEM mode the specimen is illuminated with a beam, which is ideally parallel. This ideal case shall for simplicity be treated in the following description. Therefore, the illuminating plane electron wave can be considered to have a uniform (normalized) intensity equal to 1 everywhere in the sample's plane.

In a theoretical treatment (i.e., Cowley, 1995) a specimen's transmission function $T(\vec{r})$ is described by its absorption $U(\vec{r})$ and its phase shift $\varphi(\vec{r})$, both depending on the local properties of the specimen at position $\vec{r}$,

$$T(\vec{r}) = U(\vec{r}) \cdot e^{i\varphi(\vec{r})} \tag{2}$$

The observable image is obtained by a convolution of the specimen function with the point spread function (PSF) $C(\vec{r})$, which is the Fourier transform of the so-called phase contrast transfer function (CTF) $c(\vec{k})$, given in reciprocal space as

$$c(\vec{k}) = p(\vec{k}) \cdot e^{i\chi(\vec{k})} \tag{3}$$

Here, $p(\vec{k})$ describes an aperture in the back focal plane and is in fact a pupil function ($p(\vec{k}) = 1$ for $|\vec{k}| \leqslant k_0$, $p(\vec{k}) = 0$ for $|\vec{k}| > k_0$), while $\chi(\vec{k})$ comprises the defocus term $-\pi \cdot \Delta z \cdot \lambda \cdot k^2$ with the electron wavelength λ and the defocus Δz and other terms of higher order describing spherical aberrations. For simplicity, these terms and also damping terms according to chromatic aberrations and beam convergence have been omitted. Please note that in this treatment we assumed the magnification to be equal to 1 to keep the equations as simple as possible.

The convolution with the PSF is equivalent to a multiplication of the CTF with the Fourier transform of the specimen function

$$t(\vec{k}) = FT[T(\vec{r})] \tag{4}$$

followed by a transformation back to real space. The image intensity is readily obtained from the square modulus of the resulting function

$$I(\vec{r}) = \left| FT^{-1}[t(\vec{k}) \cdot c(\vec{k})] \right|^2 \tag{5}$$

A similar approach is possible when dealing with STEM. Here, the specimen is illuminated with a convergent electron beam. Thus, the STEM image is generated serial rather than in parallel. Having that in mind, the specimen's exit wave function, that is the wave leaving the specimen after transmission, can also be described by a convolution, in this case between the shapes of the convergent probe formed by

the condenser lenses and the specimen function. Since STEM is a scanning technique, this convolution has to be performed on every spot of the specimen which is illuminated by the beam. This can conveniently be described by a laterally shifted δ function. Thus the wave $\Phi(\vec{r})$ emerging from the sample can be described by

$$\Phi(\vec{r}) = T(\vec{r}) \cdot [C(\vec{r}) \otimes \delta(\vec{r} - \vec{r}_0)] \tag{6}$$

where $\vec{r}_0$ is the position of the electron probe on the specimen and $C(\vec{r})$ is again the PSF, this time of the probe forming condenser lens (and the condenser aperture).

The propagation to the detector plane is again the mathematical equivalent of a Fourier transform, which leads to

$$\Phi_{det}(\vec{k}) = t(\vec{k}) \otimes c(\vec{k}) \cdot e^{-2\pi i \vec{k}\vec{r}_0} \tag{7}$$

where we used the Fourier theorems of multiplication and convolution which state that a convolution in real space is equal to a multiplication in Fourier space and vice versa.

The measured signal $S(\vec{r}_0)$ is then the wave intensity integrated over the detector area D and weighted with a detector function $\mathrm{d}(\vec{k})$,

$$S(\vec{r}_0) = \int_D \left|\Phi_{det}(\vec{k})\right|^2 \cdot \mathrm{d}(\vec{k}) \cdot \mathrm{d}\vec{k} \tag{8}$$

Thus, the detector function determines the measured properties in a crucial way and has to be considered carefully when dealing with DPC microscopy in the subsequent text.

For both, CTEM and STEM we would like to emphasize, that the recording media is only able to record the intensity of the incoming wave. The phase of a wave front which hits the detector can in general not be recorded, except when a holographic technique is used, where the phase can be reconstructed from an interference pattern. Unfortunately, magnetic information is phase information of the wave leaving the specimen, as will be shown in the subsequent text. Thus – with the exception of electron holography – the techniques of Lorentz microscopy which are described in the subsequent text aim on converting the phase information of the exit wave into an intensity information of the detected wave front.

3.2 The magnetic specimen as phase object

In geometrical optics it is straightforward to calculate the deflection of the electron beam caused by the Lorentz force according to equation (12) in the subsequent text. This very descriptive treatment allows a first approach to the various methods of Lorentz microscopy. However, this description is usually not sufficient to completely understand the image formation process and the interpretation of image intensities. Therefore another more theoretical formulation is necessary.

3.2.1 Magnetic phase shift

It has been shown by Aharonov and Bohm (1959), that the vector potential $\vec{A}(\vec{r})$ generated by a magnetic induction distribution $\vec{B}(\vec{r})$ manifests itself in a phase shift of a bypassing electromagnetic wave.

The phase shift φ between two different paths γ_a and γ_b which share the same starting and end point can be calculated to be

$$\varphi = \frac{e}{\hbar}\left(\int_{\gamma_b} \vec{A} \cdot \mathrm{d}\vec{s} - \int_{\gamma_a} \vec{A} \cdot \mathrm{d}\vec{s}\right) = \frac{e}{\hbar}\left(\int_{\gamma_b - \gamma_a} \vec{A} \cdot \mathrm{d}\vec{s}\right)$$
$$\overset{(*)}{=} \frac{e}{\hbar}\int_{\Omega} \nabla \times \vec{A} \cdot \mathrm{d}\vec{f} \overset{(**)}{=} \frac{e}{\hbar}\int_{\Omega} \vec{B} \cdot \mathrm{d}\vec{f} \tag{9}$$

where at $(*)$ Stokes rule is applied, leading to an integral over the area Ω limited by γ_a and γ_b. Furthermore at $(**)$ the identity

$$\vec{B} = \nabla \times \vec{A} \tag{10}$$

was used. This is illustrated in Figure 3 where the location where the two different paths enter the specimen are denoted by 'a' and 'b'.

Equation (9) connects the phase shift φ with the magnetic flux that penetrates the area Ω enclosed between the two paths. As a transmission technique measures physical values only integrated along the beam trajectory (z direction), a further modification of equation (9) makes sense,

$$\varphi = \frac{e}{\hbar}\int_{\Omega} \vec{B} \cdot \mathrm{d}\vec{f} = \frac{e}{\hbar}\iint B_{\perp} \cdot \mathrm{d}z \cdot \mathrm{d}x \tag{11}$$

where $\int B_{\perp} \cdot \mathrm{d}z$ can be attributed to the collected phase shift along the electron trajectories. This notation also emphasizes that only the component of $B_{\perp}$ perpendicular to the electron beam's trajectory contributes to φ. For a simple treatment, one can assume that the fields outside the ferromagnetic specimens are negligible, which is often the case for thin and longitudinally extended films. In a further assumption, the induction is considered to be constant over the thickness z of the specimen. Then, it is easily understood that equation (11) describes the total flux contained within a rectangular section of the specimen $\mathrm{d}x \cdot \mathrm{d}z$ which leads to the observable phase shift φ.

This redraft of equation (9) shows, that the integrated magnetic induction which is accessible in the experiment

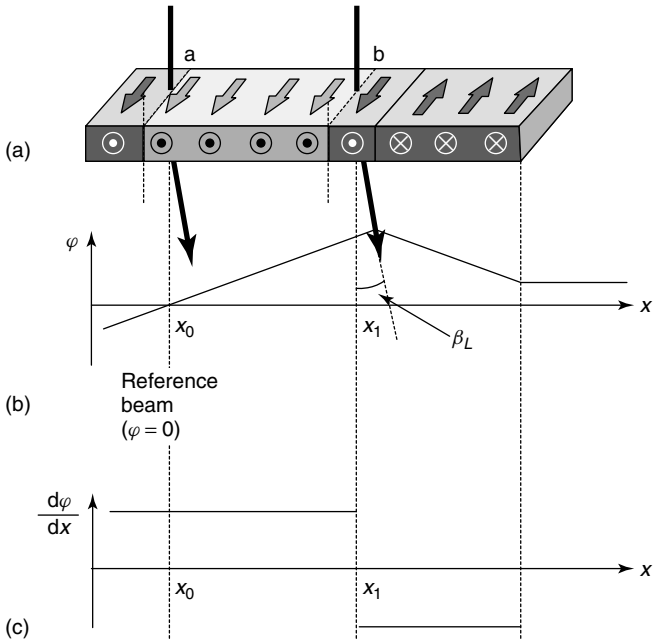

Figure 3. Demonstration of the interrelationship between beam deflections due to the Lorentz force and the corresponding phase shift. (a) Specimen with in-plane induction. (b) Phase shift of electron wave after the magnetic specimen that can also be interpreted as tilting the incoming beam by the Lorentz angle β_L. (c) Course of the signal detected by a DPC detector.

is directly connected with the spatial derivative of the phase ($\mathrm{d}\varphi/\mathrm{d}x$) rather than with the phase φ itself. A fundamental principle, which can be derived from equation (11) is also, that in electron microscopy, as in most measurements, it is the magnetic induction which is detected rather than the magnetization $\vec{M}$ itself. Even though $\vec{B} \sim \vec{M}$, if stray (and internal demagnetizing) fields are neglected for simplicity this is important to keep in mind.

Furthermore, the Lorentz angle for a magnetic induction B_0 can be derived from equation (11), if the x direction is thought to be perpendicular to the B field.

The phase shift φ is connected with a wave propagation of $\frac{\varphi}{2\pi} \cdot \lambda$ for the electron wavelength λ ($\approx 1.97\,\mathrm{pm}$ for 300 keV electrons), which leads in a geometrical optic approach to the Lorentz angle

$$\beta_L = \frac{\lambda e}{2\pi\hbar} \int B_0 \cdot \mathrm{d}z \tag{12}$$

Assuming realistic values the Lorentz angle β_L is in the microradian range, which is small compared to typical Bragg angles of 1–10 mrad for diffraction from crystalline lattice planes.

As a tilt of a parallel beam with respect to the optic axis converts in the back focal plane of a lens into a focal point not centered on the optic axis, in reciprocal space (which is equivalent to the back focal plane of a lens) the beam deflection can be expressed as a distinct point located at

$$\delta\left(\vec{k} - \frac{e}{2\pi\hbar} \int B \cdot \mathrm{d}z \cdot \hat{k}_x\right) \tag{13}$$

where $\hat{k}_x$ is the unit vector in k_x direction within the coordinate system assumed in the preceding text. For a common magnetic specimen that point is located very close to the central beam, because the deflection is usually rather small.

In the case of thin magnetic samples, the specimen's absorption is often neglected, since the effect of magnetism is a pure phase shift, as explained in the preceding text. The specimen's transmission function in equation (2) then simplifies to

$$T(\vec{r}) = e^{i\varphi(\vec{r})} \tag{14}$$

3.2.2 Electrostatic phase shift

In the previous section the phase shift of the electron wave due to magnetic induction was treated, which is the fundamental mechanism for Lorentz microscopy.

However, there exists also a phase shift due to (inner) electrostatic fields. This phase shift occurs in 'real' samples, which have a finite material thickness and thus modify the refractive index for electrons. The effect shall be briefly discussed in the subsequent text.

For Lorentz microscopy it is especially important to distinguish between magnetic and electrostatic phase shifts. Here we will describe several possibilities.

In the absence of external electric fields, the electrostatic phase shift φ_el from a specimen is given by

$$\varphi_\mathrm{el} = \frac{2\pi}{\lambda} \cdot \frac{E + E_0}{E(E + 2E_0)} \cdot \int V \cdot \mathrm{d}z \tag{15}$$

where V is the mean inner potential of the sample, E and E_0 are, respectively, the kinetic energy and the rest energy of the electrons (Reimer, 1997).

Comparing equation (15) with the magnetic phase shift (equation (11)) shows a way to separate the magnetic phase shift from the electrostatic phase shift.

The first method uses the fact that due to the vectorial character of the integration in equation (11) the phase from the magnetic signal will be inverted after a rotation of the specimen around a horizontal axis by 180°, while this is not the case for pure electrostatic phase shifts. Obviously, if two images are taken with the specimen rotated by 0° and 180°, the magnetic and the electrostatic phase shifts can be separated by addition or subtraction of the two images.

An addition of the images (possibly after an inversion and realignment of the images by means of image processing techniques) renders purely the electrostatic phase shift, while from a subtraction one obtains purely magnetic phase shifts. It is important to note for quantitative measurements that the obtained phases are multiplied by a factor of 2 since the corresponding phases add up, while the unwanted ones cancel to zero. These experiments can be performed using a special specimen holder which allows the specimen to be rotated by 180° as in Huhle, Goldberg and Lichte (2000).

Another possibility is the separation by magnetic saturation. This method was proposed by Dunin-Borkowski, McCartney and Smith (1998) and utilizes the fact that a magnetic particle saturated in two antiparallel directions reverses its magnetic contribution to the phase shift. Thus, the electric phase shift can be extracted from two images in antiparallel saturation simply by adding both phases, while the magnetic phases simply cancel out. Once the electric phase is known, it can be subtracted from images of the same particle recorded at arbitrary external field values.

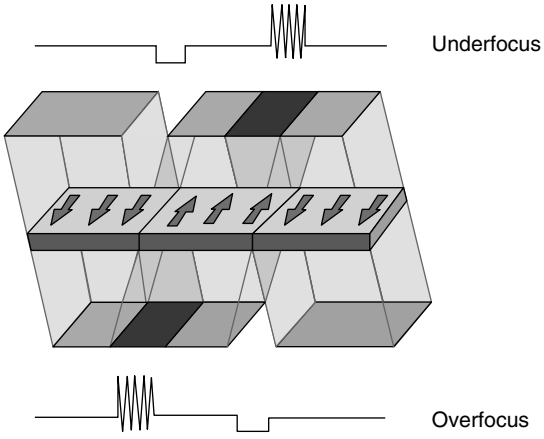

Figure 4. Schematic representation of Fresnel imaging. The electron beam, deflected by the Lorentz force leads to convergent and divergent beams below the specimen (overfocus) which lead to increased or decreased electron intensity in the corresponding areas. In converging areas, interference of the coherent partial waves can be observed, while in divergent areas only a decrease in intensity is observable. If a plane above the specimen is imaged (overfocus), the contrast changes sign.

3.3 Fresnel imaging

3.3.1 Introduction

As pure phase objects magnetic specimens do not produce an in-focus contrast which can be related to the internal magnetic structure of the sample. This can easily be seen in the case of an ideal imaging condition, where one assumes a δ-shaped PSF and also the CTF $c(\vec{k}) \equiv 1$. This yields $I(\vec{r}) = |e^{i\varphi(vecr)}|^2 = 1$ without any spatial information about the object.

The easiest way to obtain images of micromagnetic structures is to defocus the imaging lens by values of micrometers to centimeters, depending on the thickness and induction strength of the specimen, which leads to out-of-focus Fresnel images. In terms of geometric optics this is visualized in Figure 4.

Owing to the Lorentz force the electrons exit from the specimen at certain angles, depending on the direction and strength of the magnetic induction within the specimen. This leads at each domain wall to two neighboring beams, which are convergent or divergent below the sample. If now the lens is not focused on the specimen's exit surface, but on a plane slightly below, a higher (or lower) intensity is recorded owing to the converging (or diverging) beams. Thus, in Fresnel imaging it is the change of the magnetic induction which is imaged rather than the induction itself. Domain walls appear as bright or dark lines, depending on the relative alteration of the magnetization in the two adjacent domains.

This defocusing works both ways, both for the imaging of a plane below and also above the specimen, leaving the location of the visible domain walls unaltered, but changing the contrast from white walls to black walls and vice versa. This is because the deflected electron beams can be considered also to come already tilted by β_L from the area above the specimen, as can be seen in Figure 4 and for a practical example in square-shaped magnetic particles in Figure 5.

The description of the Fresnel mode in terms of wave optics shall be only briefly sketched, as a complete treatment is rather demanding. As shown in equation (13), an area with a certain constant magnetic induction B_0 can be attributed to

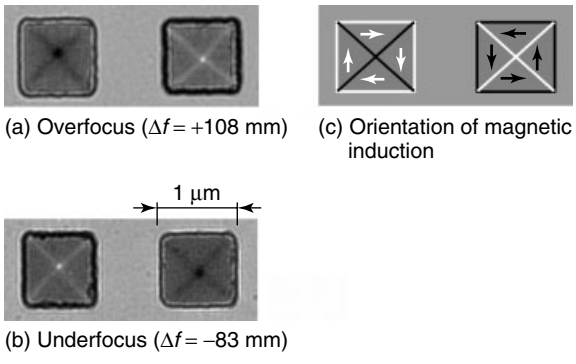

Figure 5. Experimental Fresnel images of square shaped magnetic particles ($Ni_{80}Fe_{20}$), taken in overfocus (a) and underfocus (b) condition. (c) Gives a schematic representation of the specimen's induction (arrows).

a distinct point in the Fourier space of the back focal plane. Defocusing the microscope results in a shift of the phase in the back focal plane due to the multiplication with the phase factor $e^{-i\pi\lambda\cdot\Delta z\cdot k^2}$ in equation (3). This phase factor in reciprocal space in turn causes a spatial shift of the image of the corresponding domain in real space by $\frac{e\lambda}{2\pi\hbar}\cdot\Delta z\cdot\int B_0\,\mathrm{d}z$ and thus an overlap or separation of the images of individual domains. In the region of overlap, one has higher intensity (a bright wall), in regions of separated domains due to the shift the intensity is reduced (a dark wall).

It should be noted here, however, that due to the necessary defocusing to be able to see contrast, one does unavoidable get Fresnel fringes, especially at the borders of the specimen. This is mainly due to electrostatic phase shifts, but also at any region boundary, where the refractive index, that is the phase shifting property of the specimen changes abruptly, one will observe Fresnel fringes. Thus, also black domain walls are usually lined with Fresnel fringes. The same holds for white domain walls. However, in addition to Fresnel fringes one also obtains biprism interferences due to the coherent overlap of partial electron wave fields which have been deflected toward each other below the specimen.

3.3.2 Pros and cons

Fresnel imaging is easy and cheap. On an existing TEM it is not a problem to do magnetic observation using Fresnel imaging, provided the objective lens field does not influence the sample. This can be achieved in most commercial microscopes by switching to the 'low magnification' mode, where the objective lens is usually turned off, and a long focal length intermediate or diffraction lens is used for imaging. However, the interpretation of the images in terms of magnetic induction maps is not straightforward and requires some knowledge, as only induction variations are recorded. Even for experts it is often not possible to reconstruct the magnetization of a sample because continuous rotation of the magnetization causes no detectable contrast.

Furthermore for the defocus value a compromise has to be found. A small defocus causes only small magnetic contrast in the image, while a strong defocus of the microscope – giving bright and clearly visible domain images – results in a large area covered with Fresnel fringes, blurring the details within the specimen. This is equivalent to a decrease of the maximum achievable resolution. Therefore, for structures with lateral extensions smaller than 300 nm it becomes increasingly difficult to gain useful magnetic information.

In the last few years, a new trend in Fresnel microscopy has appeared. As described in Section 5.1, Fresnel images of different defoci are used to reconstruct the exit wave function and thus allow a detailed insight into the interior magnetic structure of the specimen.

3.3.3 Example

As a typical example, Figure 5 shows Fresnel images obtained from a patterned polycrystalline $Ni_{80}Fe_{20}$ alloy. The squares hava a lateral dimension of 1 µm and 30 nm thickness and are supported by an electron transparent Si_3N_4 membrane. Figure 5(a) and (b) show the contrast reversal when changing the defocus from overfocus Figure (a) to underfocus Figure (b). Figure 5(c) schematically shows the induction distribution which is the same for images Figure 5(a) and (b). The domain wall contrast (bright or dark with respect to the specimen's average brightness) shown corresponds to an overfocus condition. It is obvious that for a given defocus it is possible to determine the direction of rotation of the specimen's induction from the wall contrast. It is also worth to note that the bright and dark perimeter of the squares in Figure 5(c) also changes with both the direction of rotation of the induction and with the defocus. In the experimental images, this contrast at the specimen's perimeter is masked by the always present contrast due to Fresnel fringes. Nevertheless, it can be recognized since the appearance of the fringe at the specimen's perimeter is different in gray shade and width for the two different cases.

3.4 Foucault imaging

3.4.1 Standard Foucault imaging

Introduction

In principle not difficult to understand, Foucault imaging needs some experimental skill to yield interpretable results and often suffers from experimental deficiencies.

As pointed out in the preceding text, every Lorentz angle (equation (12)) forms a distinct point in reciprocal space, according to equation (13). Thus, the back focal plane of the imaging lens comprises, in spatial separation, the various magnetic inductions which exist within the specimen. Therefore, if an aperture is introduced into the diffraction plane of the imaging lens, it will allow the selection of particular magnetic inductions by selecting the corresponding focal points to be transmitted through or blocked by the aperture. In this sense, it may be considered to be a 'directional induction filter' (see Figure 6).

An image which is obtained with an aperture in the back focal plane shows dark areas, if the corresponding magnetic induction is blocked by the aperture, otherwise the domains appear bright, with gradual shades in the boundary regions (see Figure 7). It should be noted here that there are bright (upper right corners) and dark (top of particles

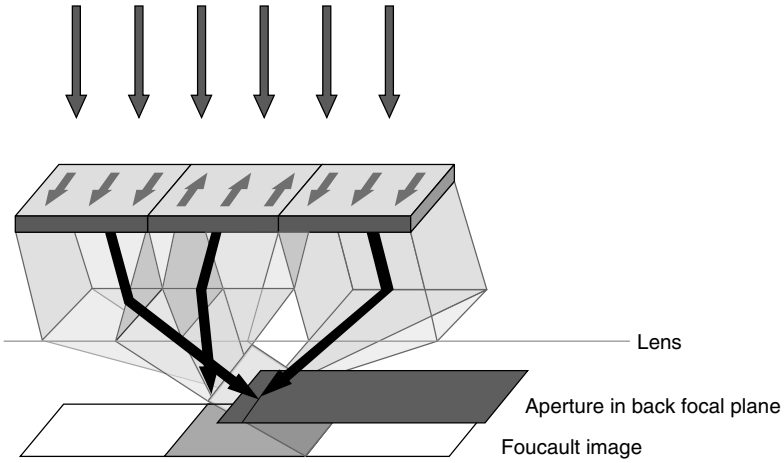

Figure 6. Contrast formation in Foucault imaging mode. The incoming parallel electron beam becomes deflected by the specimen's induction. Differently deflected beams are focused into different spots in the back focal plane of the lens. A semiinfinite aperture can be used to block certain spots to contribute to the final image, that is, certain areas of the specimen which are magnetized in the same direction become dark.

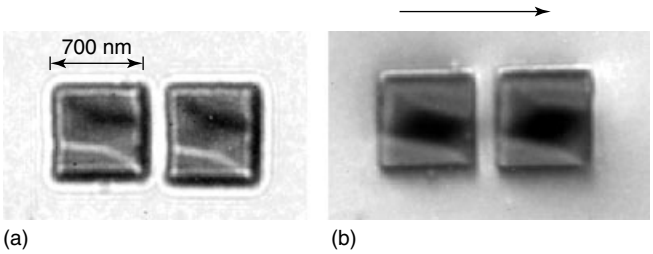

Figure 7. Comparison of (a) a Fresnel image and (b) a Foucault image taken from the same specimen. Whereas in (a) the domain walls are visible as bright and dark features, in (b) areas of sequal induction direction are shown in equal gray shades. The induction direction selected by the aperture position is indicated by an arrow. Please note that stray fields emerging from the specimen can be seen as bright and dark shades surrounding the specimen.

and right lower corner of right particle) shades outside the specimen which are effects of stray fields which emerge locally from the specimens. Although the explanation of contrast formation given in the preceding text was based strictly on geometrical optics it shall be noted that in terms of wave mechanics it is straightforward to modify the aperture function $p(\vec{k})$ in equation (3) in order to build a 'directional induction filter function'.

Pros and cons

Similar to the Fresnel technique, the Foucault mode principally does not need any special equipment, provided the specimen area is magnetic field free. In addition, it is an in-focus technique, which avoids the Fresnel fringes which tend to blur the magnetic information, especially for large defoci and small particle dimensions (i.e., smaller than approximately 300 nm). The crucial point in this case is the aperture – and at the same time the largest problem which in most cases prevents the technique to be used practically. As pointed out in Section 3.4.1, the angles between the magnetically deflected beams and the central beam are very small which in turn means that in the back focal plane of the imaging lens the central beam and the Lorentz deflected beams are very close to each other. This makes the lateral positioning of the aperture a very tedious task, especially as the apertures usually are not confined by smooth boundaries, but are in general rather jagged and rough, which makes it extremely difficult to determine which parts of the Lorentz deflected beams have been blocked by the aperture. In addition to that, the aperture usually is contaminated by more or less insulating debris, which causes intolerable phase shifts due to electrostatic charging. In total, these technical problems presently prevent the Foucault technique from being widely used.

3.4.2 Coherent Foucault imaging

Coherent Foucault imaging is also a Foucault imaging technique as in 3.4.1. In this case, the contrast is not achieved by an absorbing semi-infinite aperture placed in the diffraction plane, but rather by a phase shifting electron transparent membrane. For these operation conditions, areas of equal phase shift, that is equal magnetic flux can be made visible (Chapman *et al*., 1994; Chapman, Johnston and Heyderman, 1994). The technique requires coherent illumination, that is a field emission electron gun and suffers from contamination problems of the phase shifting membranes. Nevertheless, under optimum experimental conditions, meaningful results have been obtained in the past (Johnston and Chapman, 1995; Chapman *et al*., 1994).

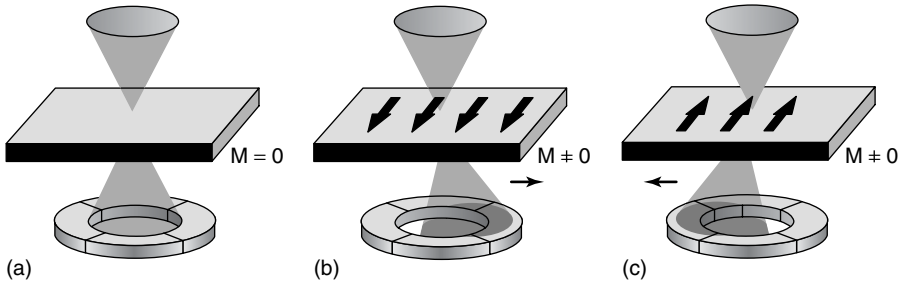

Figure 8. Schematic representation of the beam tilt and corresponding shift of the electron beam cone leaving the specimen in the detector's plane. (a) For a non-magnetic specimen, the beam is not deflected, the segmented detector does not measure any deflection. (b), (c) Owing to a nonzero induction within the specimen, the beam becomes tilted, causing different segments of the detector to record intensity. Thus, the direction of deflection indicates the direction of the induction in the probed spot. The direction and amplitude of deflection can be measured by a four-segment position sensitive device.

3.5 Differential phase contrast (DPC)

3.5.1 Introduction

One of the more advanced and also more demanding techniques of Lorentz microscopy is DPC microscopy. Unlike the previous methods, DPC utilizes a scanning transmission microscope (STEM) and needs a special detector configuration as described in the subsequent text. It should, however, be noted here that it has been shown by McCartney, Kruit, Buist and Scheinfein (1996) that it is also possible to obtain DPC in a modified TEM, when an electron biprism is mounted on a condensor aperture.

For STEM-based DPC, a focused electron beam with a certain convergence semi-angle α_{in} is scanned across the specimen (see Figure 8). The electrons leave the sample in a cone-shaped beam, which causes a disk shaped illumination on a detector located a certain distance from the sample, termed the *camera length*. The Lorentz force causes a tilt of the cone due to beam deflection from the specimen which is usually in the range of $10^{-5} - 10^{-7}$ rad. This results in a shift of the illuminating disk in the detector plane, which is – depending on the camera length used – typically in the µm to mm range. If now the detector has the ability to record the shift with respect to both direction and strength, it is possible to derive information on the magnetic induction of the area which is illuminated by the electron probe.

DPC was first proposed by Dekkers and de Lang (1974). They discovered that an asymmetric detector function in equation (8) can detect the spatial derivative of the phase shift along a particular direction.

Since in the STEM mode only a small area of the specimen around $\vec{r}_0$ is illuminated by the beam, the phase shift acting on the beam from this area can be linearly approximated by

$$\varphi(\vec{r}) \approx \varphi(\vec{r}_0) + (\vec{r} - \vec{r}_0) \cdot \nabla_{\vec{r}-\vec{r}_0}\varphi(\vec{r}_0) \tag{16}$$

This modifies the specimen function (equation (2)) to

$$T(\vec{r}) \approx e^{i\varphi(\vec{r}_0) - i\vec{r}_0 \cdot \nabla\varphi(\vec{r}_0)} \cdot e^{i\vec{r} \cdot \nabla\varphi(\vec{r}_0)} \tag{17}$$

For the action of this linearly approximated phase shift in the detector plane (which again is in reciprocal space) on the intensity distribution of the probe beam one obtains

$$\left|\Phi_{det}(\vec{k})\right|^2 \approx \left| c(\vec{k}) \otimes e^{i\varphi(\vec{r}_0) - i\vec{r}_0 \cdot \nabla\varphi(\vec{r}_0) - 2\pi i\vec{k}\vec{r}_0} \cdot \delta\left(\vec{k} - \frac{1}{2\pi}\nabla\varphi(\vec{r}_0)\right)\right|^2 = p\left(\vec{k} - \frac{1}{2\pi}\nabla\varphi(\vec{r}_0)\right) \tag{18}$$

where Φ_{det} stands for the Fourier transform of the specimen function (17) convoluted with the probe's point spread function $c(\vec{k})$. When the observable intensity $\left|\Phi_{det}(\vec{k})\right|^2$ is calculated one obtains the microscope's aperture function $p(\vec{k})$, however shifted by $-\frac{1}{2\pi}\nabla\varphi(\vec{r}_0)$. This can be interpreted as a shift of the electron beam on the detector by a distance which is proportional to the local phase gradient $\nabla\varphi(\vec{r}_0)$.

These considerations explain the name of this particular method and also show its limits. If the variation of φ occurs at a length scale comparable or smaller than the probe diameter, this simplified treatment is no longer valid. Modern microscopes, however, are capable to form probe diameters of 5–10 nm even without an excited objective lens, when equipped with a field emitter. Therefore, at present this does not impose severe limitations on the method.

3.5.2 Signal detection, four quadrant detector

Various detector configurations have been considered, such as the four quadrant detector (Rose, 1977) and the annular four quadrant detector (Chapman, McFadyen and McVitie, 1997). The latter is superior concerning both the signal to noise ratio and the separation of the magnetic phase shift from other

effects which can also modify the measured intensity, which might falsely be interpreted as an additional magnetic phase (Chapman, McFadyen and McVitie, 1997).

As these position sensitive detectors are not part of the standard detectors delivered with common electron microscopes, the usual commercial bright-/dark-field detector used in a regular STEM has to be replaced by a custom-made four quadrant detector with amplifiers.

To record a DPC image, the specimen is scanned with the electron probe and for every beam position the difference values of two opposite detector segments are recorded, as shown in Figure 9. Here, for simplicity a line scan across a 180° domain wall is chosen for demonstration (a).

The beam position on the detector is shown in (c) as a shaded area for two scanning positions r_1 and r_2. Taking the difference values of two opposite detector segments leads to two recorded values shown in (b) for the complete line scan. For real imaging, not only line scans are recorded. Instead, a two-dimensional scan is performed which leads to a set of two-dimensional arrays of image data. In general, these sets are represented in a gray or color encoded image rather than a graph. Thus, a DPC data set consists of two images representing the x and the y component of the magnetic induction in the specimen plane. A double arrow is shown in the image pairs (Figure 10) to indicate both the mapping direction and the sign and amplitude of the local induction component as indicated by the gray scale given.

In Figure 10(c) an alternative variant of illustration is used. The two measured (gray) values at each scan point (x,y) are combined to locally construct a vector, which gives the direction and amplitude of $\vec{B}(x, y)$. Doing so for every image

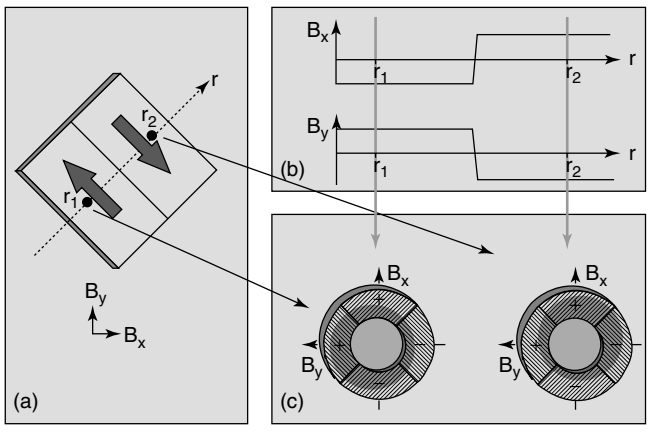

Figure 9. Interrelation of specimen's local induction, beam shift on the detector segments and measurable signal. (a) An electron probe is scanned across a magnetic specimen. The two locations indicated by r_1 and r_2 lead to the beam displacement on the detector segments shown in (c). If the signals of opposing segment are subtracted, positive and negative signals are obtained, indicating the B_x and B_y components at the probe's location.

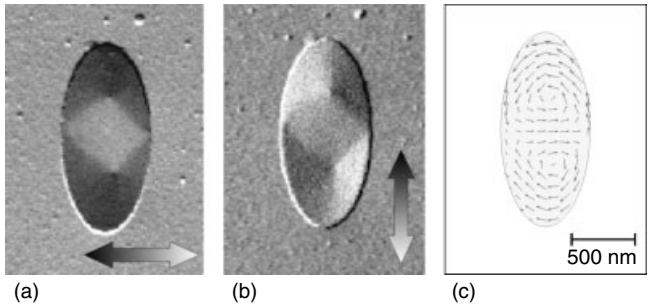

Figure 10. DPC image pair with (a) horizontal and (b) vertical induction component recorded. The double-headed arrow indicated the mapping direction and with its gray scale also the strength of the local induction in that direction. From the individual image points a local induction vector map can be reconstructed as shown in (c) for this example.

point, one is able to reconstruct a vector field, which reflects the magnetic induction. It turns out to be useful to use a threshold value to suppress noise contributions from outside the particle or from the particle's edges. This illustrates the problems of this type of representation. Even contrasts due to edge effects will lead to the creation of local 'induction vectors', which are, however, not meaningful. A misinterpretation can usually be avoided by simple comparison of contrasts in the component images with the reconstructed induction vector map.

As a DPC instrumentation is up to now commercially not available, only custom-made solutions are in use. Though analog recording systems have delivered excellent results, a fully digitized system facilitates the operation (Uhlig and Zweck, 2002). For this purpose, a fast AD/DA (analog-to-digital/digital-to analog) converter is necessary to read out the detectors. The synchronization of the scanning with the detector read out timing is of crucial importance, so it can be advantageous not to use the scan signal generated by the STEM software of the microscope. A good solution is to provide an external scan signal, which is driven by the same computer which also triggers the detector read out. This can be achieved by a corresponding software package which provides the recording functions and image processing routines for vector fields as well. It is of great use if there is also the ability to control further microscope functions with the same software.

3.5.3 Pros and cons

As in every scanning technique, the achievable spatial resolution depends mainly on the diameter of the electron probe. Although in regular STEM imaging probe diameters in the 0.1 nm regime can be achieved (Crewe, 1970), this is not possible for DPC imaging. Since the specimen region is required to be magnetic field free, the probe forming objective lens

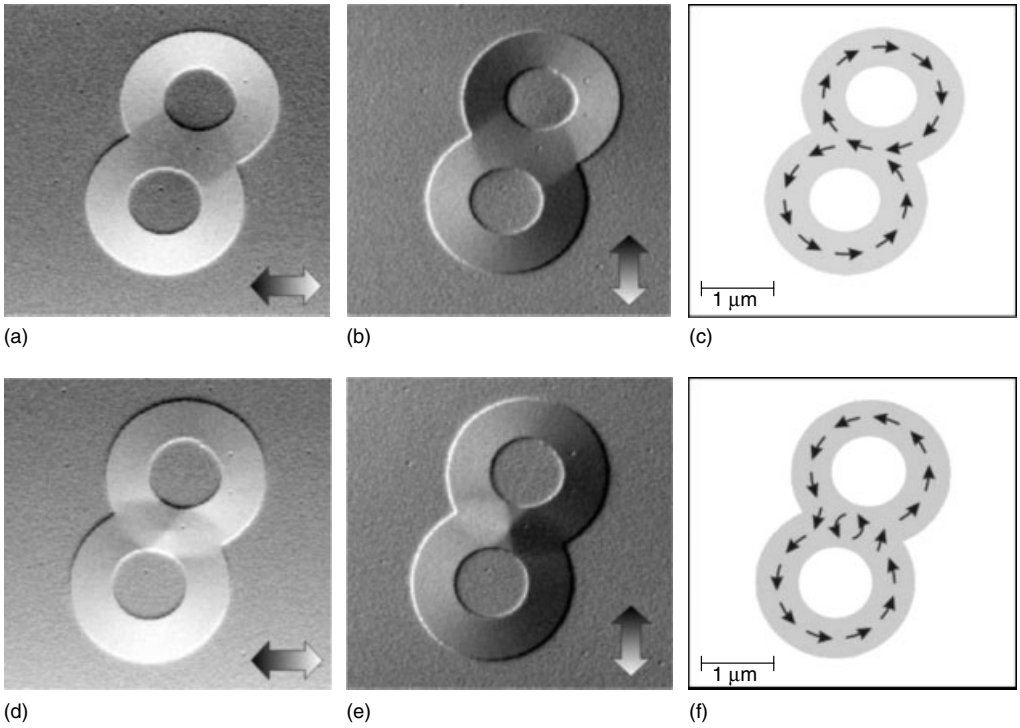

Figure 11. DPC image pairs (a), (b) and (d), (e) for double ring systems which show two different micromagnetic configurations. These configurations are shown in (c) and (f). In (c) the two rings show opposite sense of induction circulation, while in (f) the circulation is in both rings counterclockwise. Obviously, the specimen areas which are common to both rings exhibit a different micromagnetic situation. In (c) the common area is homogenous, while in (f) a vortex is formed in this region.

cannot be used like in standard STEM. A compromise can, however, be made if the probe forming condenser lenses are used in combination with a FEG to form a probe as small as possible. An achievable resolution of 5 nm has been demonstrated.

A disadvantage of DPC – at least for lithographically structured specimens as described in the preceding text – is the comparably high contamination rate of the specimen. Especially after subsequent scans over the same area considerable amounts of contamination are deposited onto the sample rendering it useless in the worst case. This effect is probably due to the impossibility of thoroughly cleaning the specimens after structuring, since the electron transparent membrane would be destroyed by standard procedures. Therefore, residual resist from the e-beam lithography process is the main source for contamination.

3.5.4 Examples

DPC microscopy is capable to image the internal magnetic structure of specimens, even if the change of the induction's direction is not as strong as necessary to create a reasonable contrast in the Fresnel mode. This is demonstrated in magnetic ring structures, as shown in Figure 11.

The double ring system presented in Figure 11 has inner diameters of 1 µm and the outer diameters are 2 µm. The two rings overlap in such a way that in the region of overlap the ring width is identical to the width of each individual ring, that is, the overlap is 100%. The material used is Permalloy ($Ni_{80}Fe_{20}$) with a thickness of 20 nm. The structure, resembling the number '8', shows two different magnetic configurations in remanence. In (a) and (b) the DPC image pair shows a state with different directions of magnetization rotation in the two rings, (c) provides a sketch of the magnetization. The continuous rotation can be seen especially in (b) by the continuous change of the gray scale along the circumference, except in the immediate vicinity of the overlap region of both rings. This intersection area is clearly bordered by a distinct contrast and is of constant color. Differently from the continuous rotation in the rest of the ring, one finds a constant magnetization direction inside that area.

In contrary, Figure (d) and (f) show the same sense of magnetization rotation in both rings. This causes a 180° change in the magnetization direction in the intersection region. Here a vortex-like structure as described in Raabe *et al*. (2000) has formed.

DPC also enables a deeper insight in the internal structure of magnetic configurations. In Figure 12, a Permalloy ring of inner/outer diameters of 2.5/3 µm, respectively

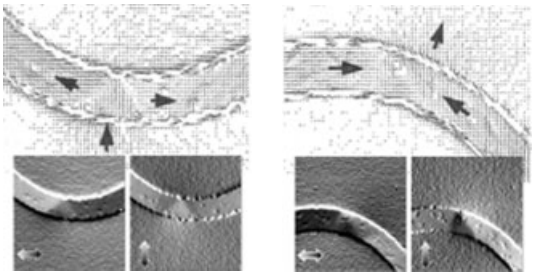

Figure 12. Detailed structure of domain walls in magnetic ring structures. (a) Induction vector map of a transverse wall which consists of two 90° walls, forming a triangular structure. (b) Induction vector map of a vortex domain wall, where a vortex mediates the change of induction between the two opposing parts of the head-to-head wall. Below the induction maps the corresponding DPC component image pairs are displayed.

and a thickness of 20 nm is shown for an external field of $7.9\,\mathrm{kA\,m^{-1}}$ applied in the vertical image direction. The so-called onion state (Rothman *et al*., 2001) which appears here comprises two 180° domain walls, which according to theory can be of two domain wall types, the transverse and the vortex domain wall (McMichael and Donahue, 1997).

In Figure 12(a) a transverse domain wall is imaged by DPC. The region of the wall is shown as a gray scale image pair (bottom) and also as a vector field reconstruction (top). Owing to limitations in hardware, the individual arrows, indicating the local induction direction are hardly distinctly visible. Larger arrows are used to indicate the averaged induction direction in different areas of the structure. The typical theoretically predicted triangular structure is visible, where inside the triangle the magnetization is perpendicular to the structure's edge and also to the magnetization outside the triangular region.

Figure 12(b) visualizes the vortex domain wall type, where the 180° change in magnetization direction is accomplished via a vortex generation.

For the vector field reconstruction threshold values have been used to omit vectors with too small or too large absolute values, which can attributed to structural properties.

3.6 Holography

3.6.1 Introduction

Another technique, capable to give information on magnetic structures, is electron holography (Bromwich *et al*., 2005; Lau and Pozzi, 1978; Tonomura, 1983; Tonomura *et al*., 1980; Dunin-Borkowski, McCartney and Smith, 1998; Lichte, 2002; Lehmann and Lichte, 2002), which was invented by Dennis Gabor in 1948 (Gabor, 1948). Holography was initially proposed as a method to reconstruct the wave field which exits from a specimen both in amplitude and phase. Since, after Aharanov and Bohm (1959), the vector potential of a magnetic specimen influences the phase of an electron wave, it is obvious that the phase shifting action of a magnetic specimen on an initially plane wave can be measured by electron holography.

To record the phase of a wave, an interference experiment has to be carried out. If the electron wave after transmission through the specimen interferes with a coherent reference wave and the corresponding interference pattern is recorded, the phase shift can be recovered by mathematical procedures.

This procedure of two interfering wave fronts, whose wave vectors form an angle $\alpha(\vec{k}_1,\vec{k}_2) \neq 0$ is termed off-axis holography. Is has the advantage that in the reconstruction process the image and its conjugate (twin image) are spatially separated, that is, a mutual influence between the two images can be excluded (Leith and Upatnieks, 1962).

In practice, the region of interest of the sample is placed in one half of the illuminating electron beam, while the second half of the beam is ideally unaffected by the specimen and therefore can act as a reference wave (Figure 13). A positively charged wire with a diameter in the sub-µm range is used as a Möllenstedt biprism (Möllenstedt and Düker, 1956) to tilt the two partial beams toward each other, producing an interference pattern in the recording plane.

In a strongly simplified mathematical model in which the influence of the microscope itself is omitted, the object wave $\Phi_{Obj}(\vec{r})$, that is the primary wave modulated by the specimen's transmission function according to equation (2) can be written as $\Phi_{Obj}(\vec{r}) = U(\vec{r}) \cdot e^{i(\vec{k}_0\vec{r}+\varphi(\vec{r}))}$, while the reference wave would be written as $\Phi_{Ref}(\vec{r}) = e^{i\vec{k}_0\vec{r}}$. If both waves are tilted toward the optic axis by $\pm\vec{k}'$, the resulting two waves can be written as

$$\begin{aligned} &\Phi_{Obj}(\vec{r}) = U(\vec{r}) \cdot e^{i((\vec{k}_0-\vec{k}')\vec{r}+\varphi(\vec{r}))} \quad \text{and} \\ &\Phi_{Ref}(\vec{r}) = e^{i((\vec{k}_0+\vec{k}')\vec{r})} \end{aligned} \tag{19}$$

Then, in the plane of observation the intensity is given by

$$\begin{aligned} I(\vec{r}) &= \left|\Phi_{Obj}(\vec{r}) + \Phi_{Ref}(\vec{r})\right|^2 = \left(U(\vec{r}) \cdot e^{i(\vec{k}_0-\vec{k}')\vec{r}+i\varphi(\vec{r})}\right. \\ &\quad \left. + e^{i(\vec{k}_0+\vec{k}')\vec{r}}\right) \cdot \left(U(\vec{r}) \cdot e^{-i(\vec{k}_0-\vec{k}')\vec{r}-i\varphi(\vec{r})} + e^{-i(\vec{k}_0+\vec{k}')\vec{r}}\right) \\ &= U^2(\vec{r}) + 1 + U(\vec{r}) \cdot \left(e^{-i(2\vec{k}'\vec{r}-\varphi(\vec{r}))} + e^{i(2\vec{k}'\vec{r}-\varphi(\vec{r}))}\right) \\ &= U^2(\vec{r}) + 1 + 2U(\vec{r})\cos(2\vec{k}'\vec{r} - \varphi(\vec{r})) \end{aligned} \tag{20}$$

As is obvious in equation (20), the phase information $\varphi(\vec{r})$ of the magnetic specimen is contained in the interference cosine term. It can, however, be extracted in Fourier space. For this purpose, first the recorded image (i.e., $I(\vec{r})$) is

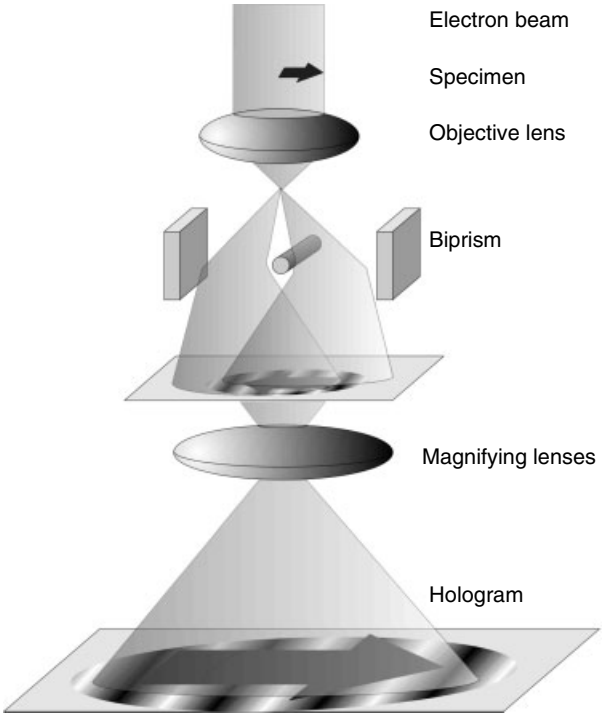

Figure 13. Typical setup for off-axis holography. The specimen is illuminated by one half of the incoming electron beam, the second half acts as the reference wave. The two partial waves are then brought to interference by the electron biprism, a positively charged wire. After further magnification, the hologram can be recorded in the image plane.

Fourier transformed, leading to

$$
\begin{aligned}
FT\left[I(\vec{r})\right] &= FT\left[U^2(\vec{r})\right] + FT\left[1\right] + \int U(\vec{r})\left(e^{-i2\vec{k}'\vec{r}+i\varphi(\vec{r})}\right. \\
&\quad \left. + e^{i2\vec{k}'\vec{r}-i\varphi(\vec{r})}\right)\cdot e^{2\pi i\vec{k}\vec{r}}\mathrm{d}\vec{r} = FT\left[U^2(\vec{r})\right] \\
&\quad + \delta(\vec{k}) + \int U(\vec{r})\left(e^{-i2\vec{k}'\vec{r}+i\varphi(\vec{r})+2\pi i\vec{k}\vec{r}}\right)\mathrm{d}\vec{r} \\
&\quad + \int U(\vec{r})\left(e^{i2\vec{k}'\vec{r}-i\varphi(\vec{r})+2\pi i\vec{k}\vec{r}}\right)\mathrm{d}\vec{r} = FT\left[U^2(\vec{r})\right] \\
&\quad + \delta(\vec{k}) + \int U(\vec{r})\left(e^{i\varphi(\vec{r})}\cdot e^{-i2\vec{k}'\vec{r}}\right)e^{2\pi i\vec{k}\vec{r}}\mathrm{d}\vec{r} \\
&\quad + \int U(\vec{r})\left(e^{-i\varphi(\vec{r})}\cdot e^{-i2\vec{k}'\vec{r}}\right)\cdot e^{2\pi i\vec{k}\vec{r}}\mathrm{d}\vec{r} \\
&= FT\left[U^2(\vec{r})\right] + \delta(\vec{k}) + FT\left[U(\vec{r})\cdot e^{i\varphi(\vec{r})}\right] \\
&\quad \otimes \int\left(e^{2\pi i\vec{k}\vec{r}-i2\vec{k}'\vec{r}}\right)\mathrm{d}\vec{r} + FT\left[U(\vec{r})\cdot e^{-i\varphi(\vec{r})}\right] \\
&\quad \otimes \int\left(e^{i2\vec{k}'\vec{r}+2\pi i\vec{k}\vec{r}}\right)\mathrm{d}\vec{r} = FT\left[U^2(\vec{r})\right] + \delta(\vec{k}) \\
&\quad + FT\left[U(\vec{r})\cdot e^{i\varphi(\vec{r})}\right]\otimes\delta\left(\vec{k}-\frac{\vec{k}'}{\pi}\right) \\
&\quad + FT\left[U(\vec{r})\cdot e^{-i\varphi(\vec{r})}\right]\otimes\delta\left(\vec{k}+\frac{\vec{k}'}{\pi}\right) \qquad (21)
\end{aligned}
$$

The first term describes the Fourier transform of the transmission function of the specimen. For all practical cases, the specimen's dimensions are larger than the resolution of the technique by at least a factor of 10, which leads to Fourier coefficients which are located very close to the center of the Fourier spectrum, compared to the extension of the complete Fourier spectrum out to its resolution limits. The second term also contributes explicitly to the center of the Fourier spectrum. The latter two terms are shifted by $\pm\frac{\vec{k}'}{\pi}$ and contain the specimen's amplitude and phase information and the corresponding complex conjugate.

Since, obviously, the terms $FT\left[U(\vec{r})\cdot e^{\pm i\varphi(\vec{r})}\right]$, which make up the so-called side bands, contain all information about the specimen, one simply has to cut out the part of the Fourier transform and undo the shift by $\pm\frac{\vec{k}'}{\pi}$ before inversely transforming the partial spectrum. This back transformation yields then both the amplitude and phase function, that is, the exit wave function of the specimen under investigation. To prevent artifacts, care has to be taken to ensure that the side band information does not overlap with the central band's information content. This can conveniently be achieved by changing $\vec{k}'$ to the desired value by tuning the biprism's voltage.

As the specimen is not the only source of phase shifts in the electron microscope, these other sources have to be eliminated to reveal the specimen's phase shift only.

For this purpose, the specimen holder is removed from the microscope without changing the imaging conditions after every acquisition and a reference hologram is recorded. This hologram now contains only the parasitic phase shifts caused by the microscope, due to lens aberrations, charging effects, and so on. After identical treatment of this reference hologram, one obtains a reference wave function and consequently the specimen's exit wave function can be calculated by simply taking the difference of the disturbed and reference wave functions (Rau, Lichte, Völkl and Weierstall, 1991; Franke, Herrmann and Lichte, 1988; Lehmann, Völkl and Lenz, 1994).

The mathematical procedures described in the preceding text are commercially available in the meantime, that is the software package HoloWorks (Völkl, Allard and Frost, 1995).

Without going into any details it seems helpful to mention here that for electron holography a highly coherent and bright illumination is essential. Sufficient brightness gives reasonably short exposure times during which typical experimental artifacts such as drift or contamination play no or only a negligible role. For the coherence required, a FEG is required. To further optimize the imaging conditions, the use of a so-called elliptical illumination is common. Detailed experimental procedures are

given in the literature (Speidel and Kurz, 1977; Düker, 1955; Lehmann and Lichte, 2002; Völkl, Allard and Joy, 1999).

4 BASIC EXPERIMENTAL TECHNIQUES

4.1 Application of magnetic fields

To observe not only the remanent state of magnetic samples but also investigate magnetization processes makes it necessary to generate a well-defined magnetic field in the specimen area. As the samples are thin films, especially magnetic in-plane fields are of interest. To generate these fields is possible in some different ways, which are described in more detail in the subsequent text.

4.1.1 Tilting method

The electromagnetic lenses in the TEM generate a vertical magnetic field in the specimen region. Usually one tries to minimize these fields by using a special low-field Lorentz lens, as explained in the preceding text. However, moderate vertical fields and a tilted specimen can be used to generate the magnetic in-plane fields needed in the specimen plane. For this method a fixed vertical field is applied and the strength of the specimen's in-plane field is regulated by the tilting angle. Although simple to use, this method suffers from some disadvantages.

The worst effect is, that in order to create an in-plane field one always has to accept the presence of an even stronger magnetic out-of-plane field. The effect of this field in experiments is difficult to estimate, but a biasing effect on switching processes is probable, especially when areas of perpendicular magnetization are present (i.e., a vortex core structure) in the sample.

A second disadvantage is that the rate of change of the magnetic field is limited by the tilt speed of the holder which means generally a few seconds for a full field sweep from +B to −B. Experiments with fast magnetic pulses are in general not possible. Another possible problem can arise from the different tilt speeds for orthogonal axes in regular double tilt holders, which have to be taken into account if during a change of field strength and direction precise control over the external field at any time rather than simply at the beginning and the end of the process is required.

4.1.2 Special specimen holder

Another solution which was pursued in the last years is to implement small electromagnetic coils on the specimen holder to generate pure magnetic in-plane fields (i.e., Uhlig, Heumann and Zweck, 2003). These coils can be controlled by an external computer device connected to a DA converter (see Figure 14).

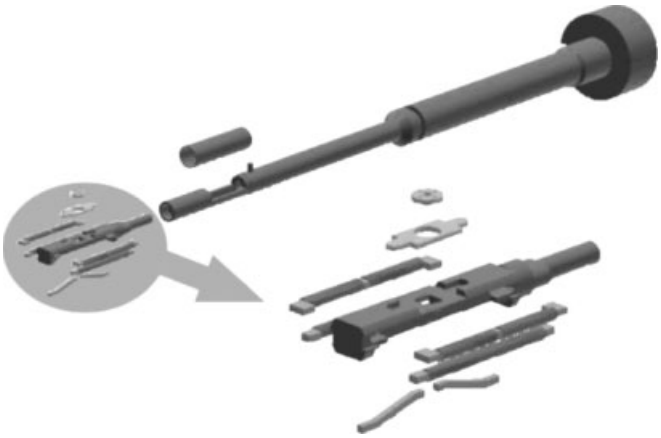

Figure 14. Explosion view of the special holder for magnetic in-plane fields. The specimen sits in the center of two orthogonal magnetic fields, generated by electromagnets. The magnets can be controlled in their strength by an external computer, which allows perfect control over the direction of the local field. The field strength, however, is very limited. (Drawing and construction by Stephan Otto, University of Regensburg.)

The solution with coils on the specimen holder suffers from different problems. Primarily, space on the specimen holder is very limited. Only small coils can be implemented which in turn limits the maximal achievable magnetic field. For example, in an FEI microscope (Tecnai F30) even with a sophisticated coil design effective fields of only about 0.02 T were achieved due to the small specimen holder size. For many magnetization experiments such a holder can only be used in a reasonable way in combination with the tilt technique, but tilting is often not possible because of space restrictions.

Instead of using electromagnetic coils, it is also possible to utilize the magnetic Biot–Savart fields which surround a current carrying wire. To get a reasonable magnetic field strength the specimen must be placed very close to the wires, resulting in another specialized specimen holder (Yi *et al.*, 2004). A big advantage of this design is the predictability of the generated magnetic fields, as the geometry is simple and no magnetic material with hysteretic properties is involved. Furthermore, it was shown, that the tilting of the electron beam due to the horizontal magnetic field is cancelled out by an opposite field of the same strength beneath the sample. However, the problem of limited field amplitudes remains. The fields are only applicable in one in-plane direction.

Both designs have in common the problem of heating of the specimen holder. If a current through the wires is applied, the coils (or wires) heat up (in most cases the devices are operated at their very limit in order to generate sufficient magnetic fields) and thus also the specimen holder itself.

Since this heating causes thermal expansion of the holder, investigations in the μm and nm range may suffer from specimen drift.

Furthermore, the combination with other ways of specimen manipulation is very limited. Cooling or defined heating experiments, tilting (in order to orient the specimen to a special crystallographic direction) or other *in situ* measurements, which require a different specimen holder are not possible with these holders.

4.2 Variation of temperature, *in situ* experiments

It shall be only briefly mentioned that with the availability of various specimen holder which allow the specimen to be at low (LHe, LN_2) temperatures or high temperatures up to 1200 °C, the experimentator has a wide range of experimental possibilities which will be useful for future investigations on magnetic materials. It is also possible to use specimen holders with integrated electrical leads which can serve to contact the specimen and to drive currents through it while under observation.

4.3 Imaging of stray fields, elimination of inner potentials

As was described in the preceding text, especially for patterned magnetic materials it is often a problem that the electron wave's phase shift due to the electrostatic inner potential is generally much stronger than the magnetically caused phase shift. Ways to separate the two effects have been described in the preceding text. In Figure 15(a), two reconstructed holograms are shown. The specimen is in a remanent magnetization state after having been saturated in the direction indicated by the arrows. For further processing, it is necessary to be sure that the remanent states represent as good as possible the state of saturation, because otherwise local deviations from the purely saturated state will lead to artifacts in the final image which can be easily misinterpreted. Equal colors represent equal phase shifts and may, for a simple interpretation, be associated with 'magnetic field lines'. However, the signal is rather noisy, and it is difficult to derive a reasonable micromagnetic pattern from these images. After image processing according to (Dunin-Borkowski, McCartney and Smith, 1998), the images in Figure 15(b) are obtained. The phase shifts caused by the inner electrostatic potential of the specimen (which is due to thickness variations, if a homogeneous composition may be safely assumed) have been removed and the pure magnetic phase shift is visible. In the same way, the pure electrostatic phase shift can be derived, as shown in Figure 15(c), left image. The gray scale variations can be regarded to represent the specimen's thickness fluctuations. The Figure 15(c) right image finally shows equal phase shift contour lines, superimposed by a shadow image of the specimens boundary. The contour lines may be interpreted to be 'magnetic field lines', which also extend outside the specimen.

4.4 Hysteresis loops

In order to determine hysteresis loops from individual particles, the experimenter has to have the ability to control the magnetic field experienced by the specimen under investigation and to measure a quantity which is proportional to the specimen's magnetization or induction. As was shown in Section 4.1, the application of magnetic fields in the microscope is possible by various methods. In the case of DPC it was shown that the signal is given by

$$I \sim \vec{\nabla}\varphi(\vec{r}) = \vec{\nabla}(B_\perp \cdot A) \tag{22}$$

where $\varphi = B_\perp \cdot A$ is the magnetic flux through a specimen cross section A. If the induction is considered to be constant over the specimen's thickness, equation (22) becomes

$$I \sim \left| \frac{\mathrm{d}}{\mathrm{d}(x,y)} (B_\perp \cdot L(x,y) \cdot t) \right| \tag{23}$$

where $L(x, y)$ is a distance along the specimen's plane and t is the specimen's thickness, giving in combination $L(x, y) \cdot t = A$. For the given situation of a position sensitive detector, one is able to decompose the signal strength into two partial signals which correspond to two orthogonal directions

$$I_x(\vec{r}) \propto \frac{\mathrm{d}}{\mathrm{d}x}(B_\perp \cdot L(x,y) \cdot t) \propto \frac{\mathrm{d}}{\mathrm{d}x}(B_\perp \cdot A) \propto \frac{\mathrm{d}}{\mathrm{d}x}(\phi(\vec{r})) \text{ and}$$
$$I_y(\vec{r}) \propto \frac{\mathrm{d}}{\mathrm{d}y}(B_\perp \cdot L(x,y) \cdot t) \propto \frac{\mathrm{d}}{\mathrm{d}y}(B_\perp \cdot A) \propto \frac{\mathrm{d}}{\mathrm{d}y}(\phi(\vec{r})) \tag{24}$$

Electron holography records the electron wave's phase shift due to the flux enclosed between two partial waves a distance $L(x, y)$ apart. Thus, using equations (22) or (24) one can simply calculate the vector components $I_x(\vec{r})$ and $I_y(\vec{r})$ which allow a direct calculation of local induction vectors. Obviously, both DPC and electron holography are techniques capable to reconstruct quantitatively induction maps of micromagnetic configurations within specimens with a lateral resolution down to presently 5 nm.

A state-of-the-art electron microscope with its ability to control the most important functions via a script language allows automatization of time consuming processes. This opens the possibility to generate hysteresis curves of single

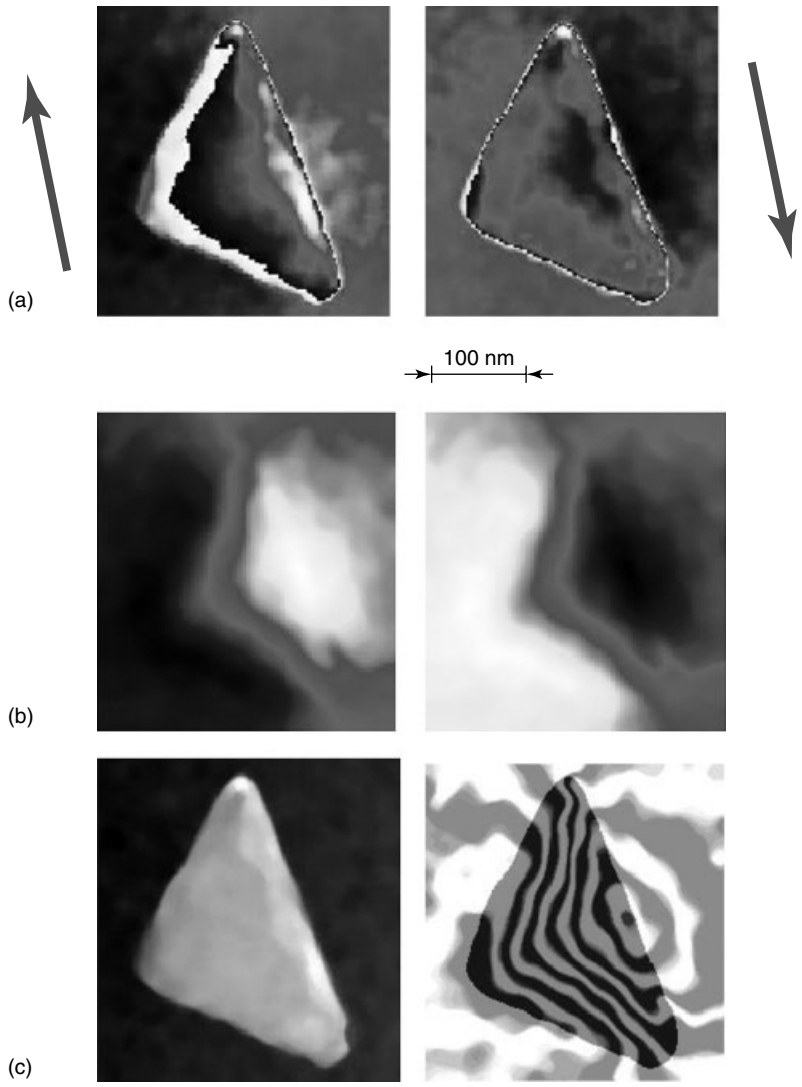

Figure 15. Separation of electrostatic and magnetic phase shifts. (a) Two reconstructed holograms taken in remanent conditions with specimens oppositely magnetized. (b) Pure magnetic phase shifts after subtraction of the electrostatic component. (c) Gray scale image of the electrostatic phase shift (= thickness contours, left image) and magnetic field lines (= lines of equal magnetic phase shift, right image), superimposed with a shade image of the specimen's contour.

particles in the μm- and sub-μm range (Uhlig and Zweck, 2004).

Only a few techniques have the ability to generate true single particle hysteresis curves. An electron microscopy based method can additionally provide the magnetic configuration within the specimen at every point of the loop, which makes it superior to other comparable techniques.

The hysteresis loop in Figure 16 of a 1.5/0.75 μm outer/inner diameter ring structure made of 20-nm thick Permalloy was recorded automatically in approximately 18 h with a fully digitized DPC device attached to a FEI Tecnai F30. The data series consists of 209 images, which were recorded with different external field values by tilting the specimen in the vertical objective lens field. Before each image was recorded, some alignment procedures were done automatically. The images were aligned with respect to each other using a cross correlation procedure. The software then calculates the average magnetic induction inside the specimen in every image and plots its value versus the external field value.

The jumps in the hysteresis loop indicate a switching process, when the initial onion state changes into a flux closure state at a field value of $6.1\,\mathrm{kA\,m^{-1}}$ and into the reversed onion state at $11.6\,\mathrm{kA\,m^{-1}}$. The magnetic field sweep in the opposite direction first provides a switching into the flux closure state at $-2.3\,\mathrm{kA\,m^{-1}}$ and back into the original onion state at $-12.6\,\mathrm{kA\,m^{-1}}$. The fact that the loop is not closed

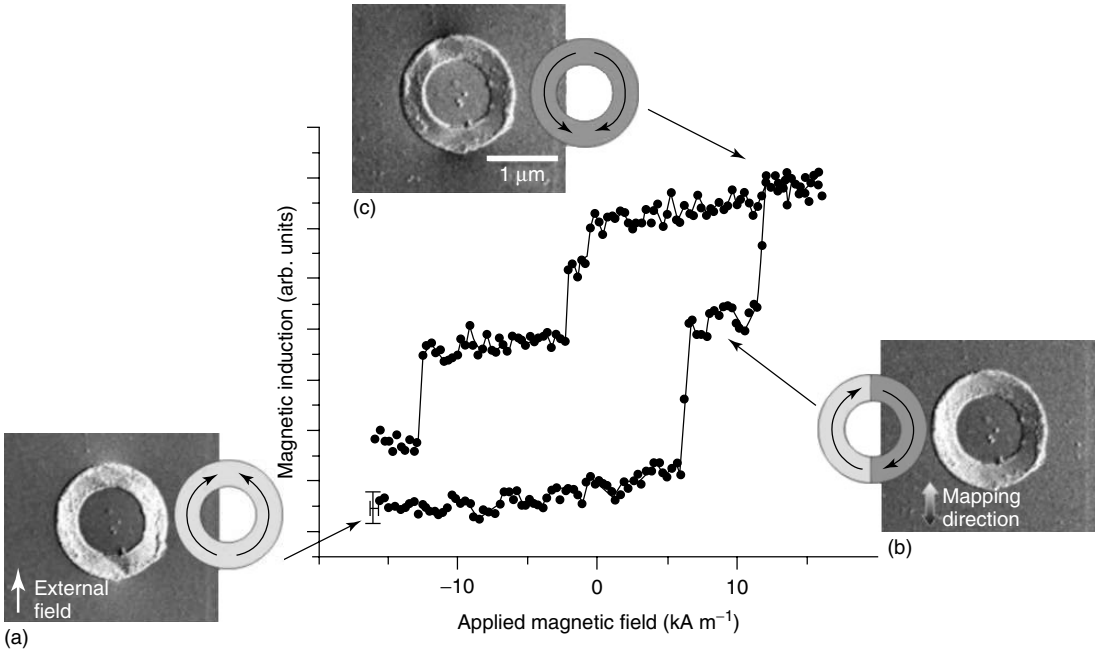

Figure 16. Hysteresis loop of a single magnetic ring. As is obvious from the DPC images, (a), (b) and (c), together with the schematic drawings besides them, the ring switches from an upwards oriented 'onion state' (a) into a 'vortex state' (b) and then into a 'reversed onion state' (c). Each change of magnetic configuration is accompanied by distinct features in the hysteresis loop. The loop is not closed completely, which is due to instrument instabilities and contamination problems during the experiment.

at the left side is due to the fact, that during the long recording time of 18 h contamination of the specimen occurs which changes the experimental conditions slightly.

In Figure 17, a complete hysteresis loop, derived from electron holograms made on a $Ni_{80}Fe_{20}$ specimen is shown. Figure 17(a) shows the geometric shape of the particle investigated, while images (b) through (l) give induction distributions for various stages of the loop. As can be seen clearly, for this specimen the remagnetization starts from a saturated state, until the specimen relaxes into a so-called vortex state (Raabe *et al*., 2000; Shinjo *et al*., 2000). With increasing, however reversed field direction, the vortex core becomes shifted toward the specimen's edge until a new, inversely magnetized saturated state is reached. If the field is now decreased again, first a so-called 'C'-state forms (Figure 17h) as an intermediate state which is then followed by the creation of a vortex with subsequent shift and saturation as before. This series illustrates nicely the tremendous advantage of micromagnetic imaging. For each stage of the hysteresis loop of *one single individual* particle the micromagnetic configuration is known precisely, the mechanisms involved in magnetization reversal become obvious.

Even more impressive is the loop shown in Figure 18 of a 6-nm thick Permalloy ellipse with short and long axis lengths of 155 and 170 nm, respectively. The data for this image were recorded with electron holography (Heumann, Uhlig and Zweck, 2005).

After differentiation of the reconstructed holograms according to equation (24), the local induction vectors can be reconstructed and the average induction of the specimen can readily be calculated for each external field value.

The particle in Figure 18 shows a single domain switching behavior. The switching occurs between 0.24 and 0.32 kA m^{-1}, and does not show any intermediate states as would be expected if there was a nucleation of domain walls or other micromagnetic configurations which might form during the magnetization reversal. The switching can also be seen from the inversion of the grayscale superimposed on the particle's images below the hysteresis loop shown. The gray scale indicates the slope of the electron wave which was generated by the specimen's vector potential acting on the initially plane wave. The induction is directed perpendicular to the gray scale's slope, pointing left or right. Lines of equal phase shift are also displayed which indicate the magnetic field lines within and outside the specimen.

5 IMAGE PROCESSING AND SIMULATIONS

5.1 Transport-of-intensity equation (TIE)

A comparably new approach is the reconstruction of the exit wave phase by using several images with

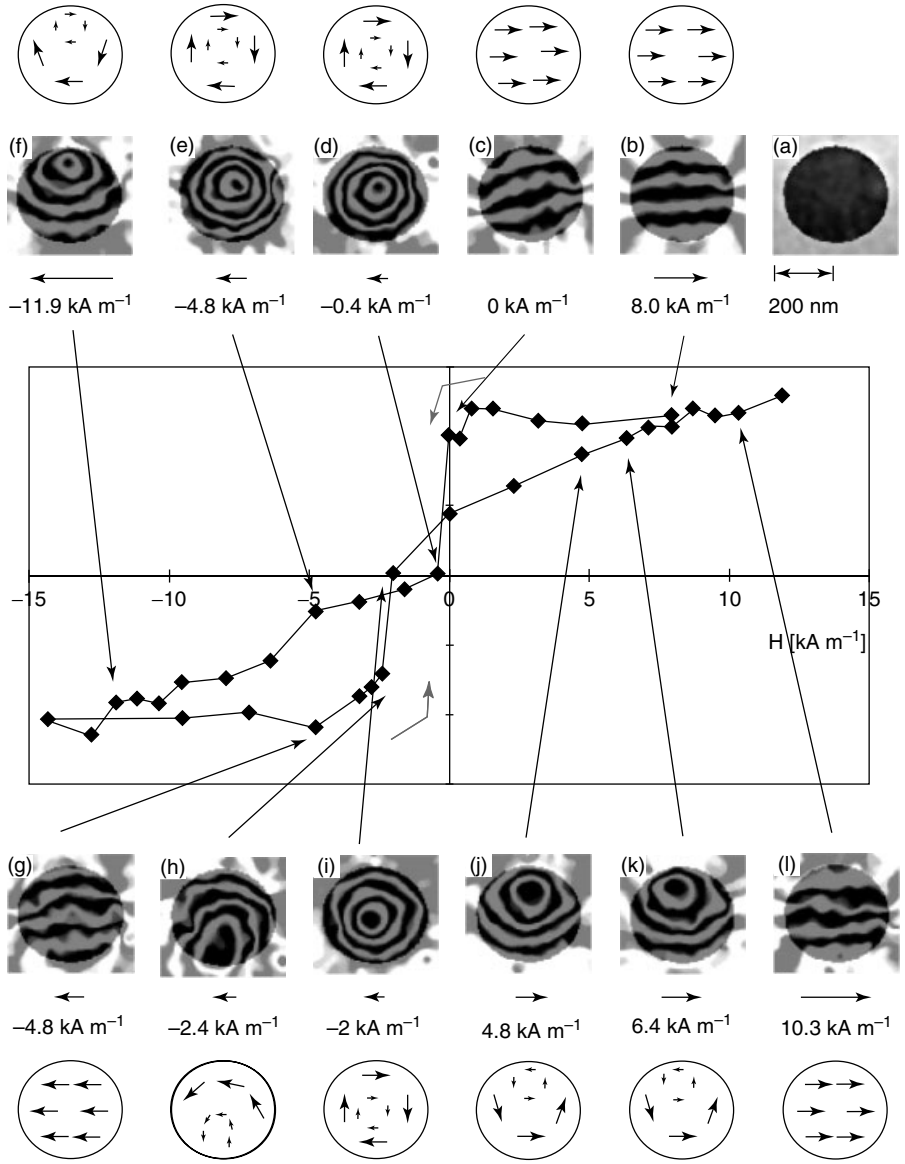

Figure 17. Complete hysteresis cycle derived from electron holograms as described in the preceding text. The experimental images represent the phase shift caused by the magnetic particle on the electron beam for each step of the hysteresis loop. Above and below the experimental images, a schematic view of the induction's course is given.

different focus conditions. Of course this technique is also applicable for magnetic imaging (Volkov and Zhu, 2004; Bajt *et al.*, 2000). To illustrate the background of this method, we follow the calculations of (Allen and Oxley, 2001).

If the wave function of the electrons is considered as a plane wave e^{ikz}, which propagates along the z direction and is perturbed by $\xi(\vec{r}_\perp, z)$,

$$\Phi(\vec{r}_\perp, z) = e^{ikz} \cdot \xi(\vec{r}_\perp, z) \tag{25}$$

where $\vec{r}_\perp$ is a vector in the x-y plane.

The Schrödinger equation for wave propagation in free space

$$(\nabla^2 + k^2)\Phi(\vec{r}) = 0 \tag{26}$$

leads with the paraxial approximation, that is when the second derivative of $\xi(\vec{r}_\perp, z)$ with respect to z is small $\left(\frac{\partial^2}{\partial z^2}\xi(\vec{r}_\perp, z) \approx 0\right)$, to

$$\left(\nabla_\perp^2 + 2ik\frac{\partial}{\partial z}\right)\xi(\vec{r}_\perp, z) \tag{27}$$

with $\nabla_\perp$ operating in the x-y plane.

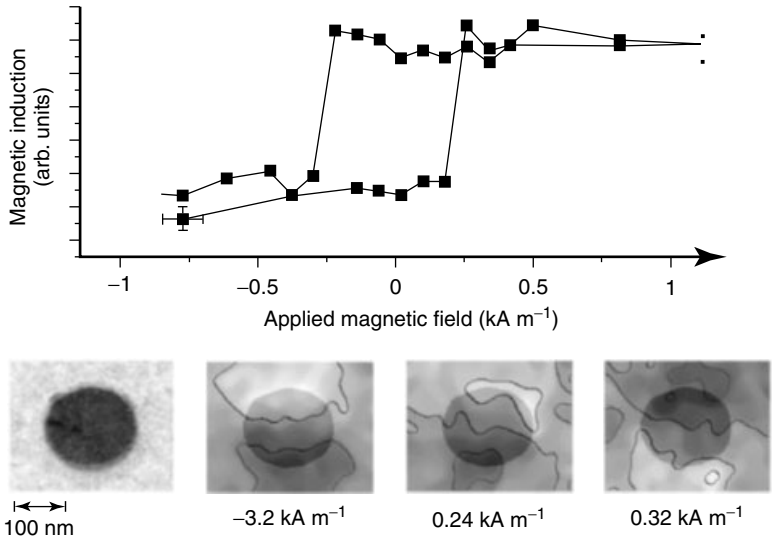

Figure 18. Hysteresis loop of a $Ni_{80}Fe_{20}$ particle with approximately 160-nm diameter. The hysteresis loop has been determined from holograms taken at various applied fields and shows single domain behavior of the specimen, that is, a switching between two magnetic states without any intermediate stages. The micrographs below the hysteresis loop show (left to right) a shadow image of the specimen used to determine the geometrical shape and holographic phase reconstructions of the induction distribution within the specimen vor the applied fields as indicated. Between 0.24 and 0.32 kA m^{-1} a switching occurs as can be seen from the inverted gray scale contrast.

If now the perturbation term is replaced by

$$\xi(\vec{r}_\perp, z) = \sqrt{I(\vec{r}_\perp, z)} \cdot e^{i\varphi(\vec{r}_\perp, z)} \tag{28}$$

which separates the intensity from the phase of the wave, it is possible to obtain the following expression which is termed the transport of intensity equation (TIE),

$$\nabla_\perp \cdot \left[I(\vec{r}_\perp, 0) \cdot \nabla_\perp \varphi(\vec{r}_\perp, z) \right] = -k \frac{\partial_{z=0}}{\partial z} I(\vec{r}_\perp, z) \tag{29}$$

As $I(\vec{r}_\perp, 0)$ is known as the *intensity of the in-focus image* and $\frac{\partial_{z=0}}{\partial z} I(\vec{r}_\perp, z)$ can be calculated from slightly defocused images, the phase can be extracted by mathematical procedures. Principally, this method measures the second spatial derivative of the phase and thus the first derivative of the magnetic induction.

Mathematical methods (Allen and Oxley, 2001) are used to extract the phase information from a series of images taken at various focus distances.

It is obvious from Figure 19 that the TIE technique is capable to generate induction maps similar to those obtained from differential phase contrast and electron holography. One obvious limitation, however, seems to be the same as for regular Fresnel imaging. For thin or weakly magnetic specimens the defocus distance Δz has to be chosen rather large in order to generate sufficient contrast. Especially for patterned materials, the large defocus will in combination with the electrostatic contribution cause strong Fresnel fringes at the perimeter of the specimen. If the specimen is small, that is in the dimension of 300 nm or below, and thin, this will deteriorate the useful signal. Also, owing to a large defocus, the PSF will blur the image and reduce lateral resolution. However, since the TIE technique is still rather new, it will be interesting to observe what new possibilities and advanced data processing techniques will be developed in the future (Belaggia, Schofield, Volkov and Zhu, 2004; de Graef and Zhu, 2001).

5.2 Image simulation from induction distributions

Fresnel images only display the magnetic induction in an indirect way since the contrast shows only the rate of change of the induction (see equations (9) and (11)). Experienced Lorentz microscopists can rather easily deduce a micromagnetic configuration which explains qualitatively the contrasts observed, but sometimes the simple models fail to explain details of the experimental images. To understand all features of an experimental image in detail, it is therefore often necessary to perform image simulations from a given micromagnetic configuration, which precisely take all imaging parameters into account. To do these simulations, a realistic model of the configuration under investigation is needed for a start. Fortunately, there are various computer programs available which are able to calculate the energetically stable arrangement of local magnetic moments, usually by solving the Landau-Lifshitz-Gilbert equation, such as MicroMagus, OOMMF, LLG or by the code written by Hertel and

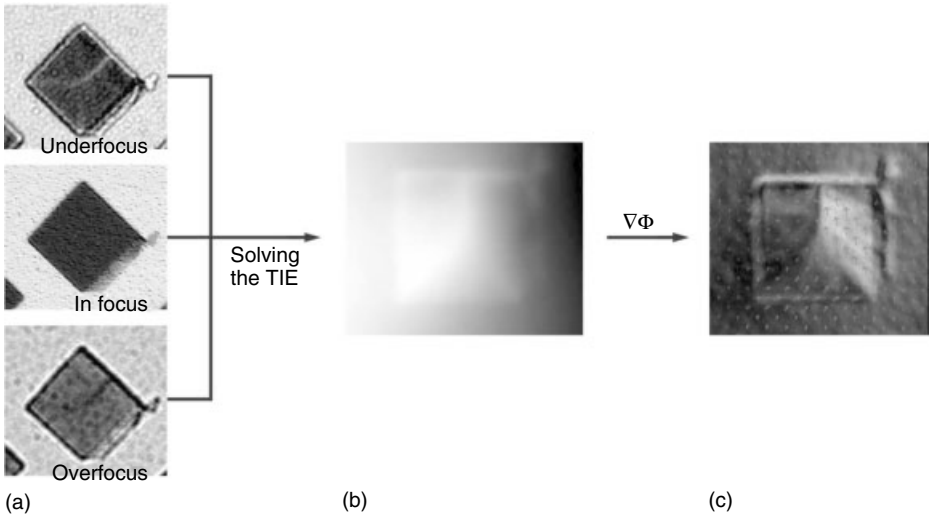

Figure 19. Induction map reconstruction from Fresnel images using the transport-of-intensity-equation (TIE) approach. Three micrographs (a), taken at different defoci, are used as input for the TIE computation and render a Phase map (b) and – after differentiation – an induction vector map. (Images courtesy of Kohn, Petford-Long and Anthony, 2005.)

Kronmüller (1999), which uses a finite element-like mesh and is less susceptible to artifacts which arise from the discretization of edges with square elements. Even for DPC images, which are by far more directly interpretable, and for reconstructed electron holograms these simulations turn out extremely useful, as from the micromagnetic simulations one can calculate not only the phase shift which the electron wave suffers from within the specimen but also due to stray fields which extend outside the specimen. This is especially important for patterned materials, where stray fields become important. The simulations also allow to take into account the stray fields above and below the specimen which are usually simply neglected because they are difficult to deal with.

Once a micromagnetic configuration is available – usually in the form of a three-dimensional matrix of induction vectors – the phase shifting action on an electron wave has to be calculated. This can be done using an algorithm proposed by Mansuripur (1991) which allows a fast calculation. The result is a so-called 'phase plate' which in detail incorporates the local variations of phase shifts which a certain micromagnetic configuration will imprint on an electron wave upon transmission. Using standard electron optical treatment, the phase distribution can then easily be converted to either Fresnel images, DPC image pairs or reconstructed holograms. This task is done by a software package (Haug, Otto, Schneider and Zweck, 2003) which also allows the specimen to be tilted with respect to the electron beam. This is an important feature, since it allows the investigation of specimens which have strong out-of-plane components. These will be observable only if the specimen is tilted to partially project the induction into the plane of observation, that is, create a sufficiently large induction $B_\perp$ which is perpendicular to the electron beam (Köhler *et al*., 2000).

Figures 20 and 21 give an example of the usefulness of these image simulations. Figure 20 shows an experimental image of a Landau structure (a, left) and a so-called

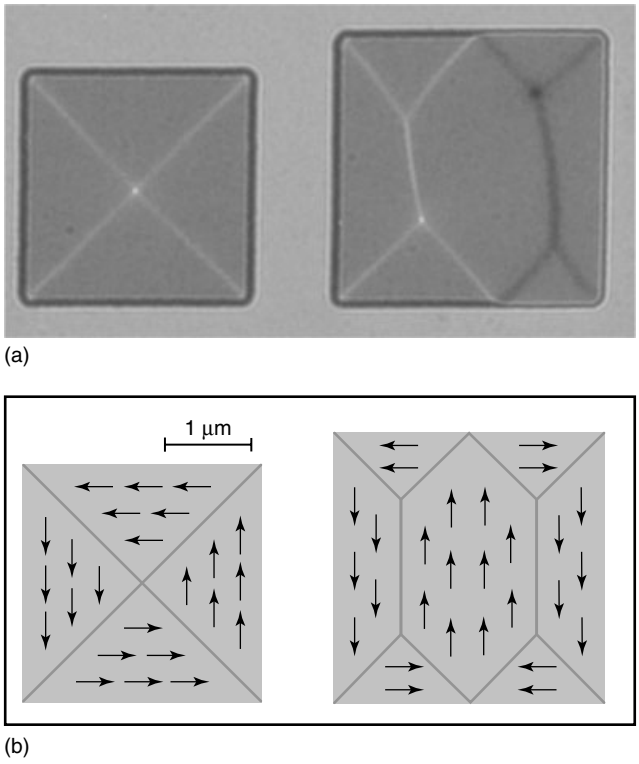

Figure 20. Comparison of experimental Fresnel images (a) with schematic representations of the internal induction distribution (b).

seven-domain structure (a, right), together with simple models (b) for the micromagnetic situation. Although on first glance the model seems to describe all features satisfactorily, on closer inspection it does not. Although the contrast of the walls (white or dark walls) would be correctly deduced from the model, another detail remains unexplained. When looking at the white walls of the 7-domain structure (a, right) only, they appear in the shape of a double fork, which is slightly tilted with respect to the specimen's outer edges. Also, the two forks are different. Whereas in the upper fork the legs join smoothly into the vertical white wall, the lower one forms a rather sharp junction with a bright spot at the center of this junction. The same is observable for the dark walls, but with reversed order. Obviously, the simple model cannot explain these differences.

A micromagnetic simulation gives a more detailed picture of the situation, as shown in Figure 21(a). The two forks show different micromagnetic properties, as on one fork a vortex structure is formed while the other, smoother side is generated by a more gradual change of the direction of the induction. Even the slight tilt with respect to the specimen's edges is reproduced. In Figure 21(b) the phase shifting action of the specimen is shown. Within the specimen, contour lines of equal phase shift are visible, which can be interpreted in terms of magnetic field lines. Outside of the specimen's boundary, white and dark shades indicate the phase shifting action of stray fields which are generated from this configuration. Please note that between subsequent transitions from black to white a phase shift of 2π is included. Figure 21(c) and (d) finally show a comparison of the simulated and the experimental Fresnel images in perfect agreement. (Please note that the two dark spots beneath the walls which appear in the experimental image only are artifacts caused by dirt particles and have no magnetic origin.)

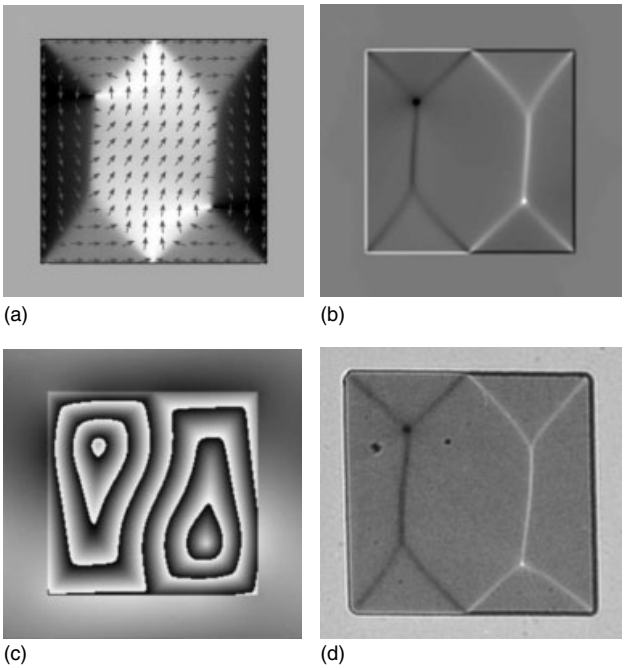

Figure 21. Comparison of an experimental Fresnel image of a so-called 7-domain structure (d) with the result of micromagnetic simulations (a). (b) The phase contour map of the structure in consideration, (c) is the simulated Fresnel image, which reflects all-important features of the true image. Note that two dark spots in (d) stem from dirt particles. Simulation parameters are: FEI Tecnai F30 characteristics, 300 kV, $C_S = 8$ m (Lorentz lens), $C_C = 41$ mm, $\theta_C = 1.6 \times 10^{-6}$ rad, size $= 2 \times 2\,\mu$m, thickness $= 20$ nm. (Images courtesy of T. Haug.)

6 APPLIED LORENTZ MICROSCOPY

In this chapter, it is intended to present an overview of recent published work, which used magnetic imaging by electron microscopy either as the main tool of investigation or as a complementary tool to cross-check results gained from other sources. As it is beyond the scope of this contribution to discuss in detail what has been found by various groups this will be hardly more than a commented list of references which may serve as a first start for a more detailed reading. The intention is to demonstrate that Lorentz microscopy has already been applied to a broad field of problems not only of model specimens but in contrary on many specimens which are of immediate interest both to basic research and industrial applications. Since domain wall movements are the most important process for magnetization reversal processes in extended specimens, it is an obvious task to study the properties of domain walls in various materials (Young and Chapman, 1993; Ploessl *et al*., 1993; McVitie and Chapman, 1990; Gong and Chapman, 1987; Chapman and Morrison, 1983; Chapman, Batson, Waddell and Ferrier, 1978; Akhter *et al*., 1998; Petford-Long, Doole and Donovan, 1993; de Graef, Kishi, Zhu and Wuttig, 2003; Zhu, Volkov and de Graef, 2001; de Graef, Willard, McHenry and Zhu, 2001; Dooley, de Graef and McHenry, 1998; Dooley and de Graef, 1997; Dooley *et al*., 1995; McVitie, 1995; Chapman, McVitie and McFadyen, 1987; Chapman *et al*., 1977; Zweck *et al*., 2001). Since the domain walls can – while moving during a remagnetization process – get pinned at so-called pinning sites, which contributes partially to the hysteretic properties, investigations of these pinning sites or 'domain wall traps' have been conducted by Brownlie, McVitie, Chapman and Wilkinson (2006), Ozkaya, Langford, Chan and Petford-Long (2002) and McVitie, Brownlie, Chapman and Wilkinson (2005). When not only slow, quasi-static magnetization processes have to be considered, the domains exhibit inertia or some sort of viscous properties (Rose *et al*., 1998;

Goodman *et al*., 2000). As domain walls contain energy which is due to increased exchange energy caused by the spatially close location of directionally varying spins within the wall, nature shows a tendency to reduce the domain wall energy by either transforming into a 'single domain state', which is preferred for small particles (Heumann, Uhlig and Zweck, 2005) or by forming a vortex state (Gillies, Chapman and Kools, 1996; Raabe *et al*., 2000; Shinjo *et al*., 2000; Schneider, Hoffmann and Zweck, 2000, 2001, 2003; Schneider *et al*., 2002, 2003; Rahm *et al*., 2001, 2003).

Patterned magnetic elements show under certain conditions properties, which differ from those of bulk material, simply due to the reduction in length scale. These changes may be dipolar interaction (Kundrotaite, Rahman, Aitchison and Chapman, 2001; Ridley *et al*., 2000; Kirk *et al*., 2000; Bromwich *et al*., 2005, 2006), or plainly the formation and behavior of magnetic domains in these patterned media (Liu, Chapman, McVitie and Wilkinson, 2004; Lim *et al*., 2003; Kirk *et al*., 1999, 2000, 2001; Kirk, McVitie, Chapman and Wilkinson, 2001; Kirk *et al*., 2001; McVitie and Chapman, 1997; Kirk, Chapman and Wilkinson, 1999; Gomez *et al*., 1999a,b; Aitchison *et al*., 1998; Gu *et al*., 1998; Kirk, Chapman and Wilkinson, 1997; McVitie, Chapman, Hefferman and Nicolson, 1988; Ross *et al*., 2006; Bromwich, Petford-Long, Castano and Ross, 2006; Petford-Long *et al*., 2006; Bromwich *et al*., 2004; Owen, Hang-Yan and Petford-Long, 2002; Ozkaya, Langford, Chan and Petford-Long, 2002; Hu, Wang, McCartney and Smith, 2005; Dunin-Borkowski *et al*., 2000, 2001; Hefferman, Chapman and McVitie, 1990; McVitie, Chapman, Hefferman and Nicolson, 1988; McVitie and Chapman, 1988). In this context, it is also important to study anisotropy effects (Gentils, Chapman, Xiong and Cowburn, 2005) and to be able to apply *in situ* magnetic fields in order to study the intermediate processes during magnetization reversal (Hefferman, Chapman and McVitie, 1991; McVitie *et al*., 2003; Yu *et al*., 2002; Yu, Petford-Long and Miyazaki, 2001; Shang, Hogwood, Petford-Long and Anthony, 2001; Yu, Petford-Long and Jakubovics, 1999; Hu, Wang, McCartney and Smith, 2005; Yi *et al*., 2004; Kirk *et al*., 2001; McVitie and Chapman, 1997; Uhlig and Zweck, 2002).

In patterned magnetic media, it was found that the edge roughness, rounding of corners of patterned particles and, in general, the geometric shape does significantly contribute to the magnetic behavior, mostly due to increased shape anisotropies or because irregularities at the perimeter of a particle act either as pinning sites or facilitate the formation of domain walls or vortices (Langridge *et al*., 2006; Yi *et al*., 2002; Crawford *et al*., 2002; Herrmann, McVitie and Chapman, 2000).

The broad interest of industry in micromagnetic properties (mostly of patterned media) stems from the possibilities, which arise for technology and production of new devices. Some of these new devices could be patterned hard disks, magnetic memory devices such as the frequently mentioned MRAM (magnetic random access memory), which would be a nonvolatile, but fast, small and energy-efficient computer memory. Other devices are already in use, either as read heads in hard disks, as so-called spin valves for sensor applications (Lim *et al*., 2002a,b, Lim *et al*., 2004; Marrows *et al*., 2001; Murdoch *et al*., 2000; King, Chapman, Kools and Gillies, 1999; King, Chapman and Kools, 1998; Chapman *et al*., 1998; Petford-Long *et al*., 1998, 1999; de Morais and Petford-Long, 2000; Portier and Petford-Long, 1999, 2000; Portier, Petford-Long, Anthony and Brug, 1998, 1999b; Portier *et al*., 1997a,b, 1998; Kasama *et al*., 2005; Ardhuin *et al*., 2000; Warot, Petford-Long and Anthony, 2003; Shang, Hogwood, Anthony and Petford-Long, 2001; Shang, Petford-Long and Anthony, 2002). These sensors always rely on one magnetic layer to be fixed ('hard magnetic') while another layer ('soft magnetic'), which acts as the sensing layer, is free to align its magnetic moment with an externally applied field. To fix the hard layer, it is usually exchange biased to an antiferromagnet underneath. During switching, local stray fields can deteriorate the fixed layer by creation of domain walls, reducing the desired effect (Rickart *et al*., 2005; Gogol, Chapman, Gillies and Vanhelmont, 2002; Fassbender *et al*., 2002; King, Chapman, Gillies and Kools, 2001; Rijks *et al*., 1997; Choi, Petford-Long and Ward, 2003; Wang, Petford-Long and Kief, 2001; Wang and Petford-Long, 2002; O'Grady *et al*., 2001; Portier *et al*., 2000). This is also relevant for magnetic tunnel junctions (Cardoso *et al*., 2006; Shang, Hogwood, Petford-Long and Anthony, 2001; Portier *et al*., 1998; Portier, Petford-Long, Anthony and Brug, 1999a).

Interesting and rather easily experimentally accessible are magnetic media, which have been patterned by ion irradiation. In this case, the ion bombardment and implantation renders the exposed areas nonmagnetic. Thus it is rather simple to obtain patterned magnetic media which during Lorentz imaging do not suffer from the effects of inner electrostatic potentials, since the magnetic and nonmagnetic areas consist of the same material (McGrouther, Nicholson, Chapman and McVitie, 2005; McGrouther and Chapman, 2005; McGrouther, Chapman and Vanhelmont, 2004; Hyndman *et al*., 2001, 2002; Fassbender *et al*., 2002; Warin *et al*., 2001; Owen and Petford-Long, 2003). For patterned magnetic materials in the μm and sub-μm regime, theoreticians perform micromagnetic calculations both for static and dynamic behavior (http://math.nist.gov/oommf/; http://llgmicro.home.mindspring.com/; Hertel and Kronmüller, 1999; http://www.micromagus.de/) which then may be compared to the behavior of real materials (Kirschner *et al*., 2003; Schrefl, Fidler, Chapman and Kirk, 2001;

Suss, Schrefl, Fidler and Chapman, 1999; Schrefl, Fidler, Kirk and Chapman, 1997a,b, 1999; de Graef *et al*., 2006; Saxena *et al*., 2004; de Graef, Nuhfer and McCartney, 1999). Comparisons have also been made between the results from magnetic force microscopy (MFM) and Lorentz imaging of patterned materials (McVitie *et al*., 2001). Patterned magnetic media considerably smaller than approximately 100 nm are expected to reach the superparamagnetic limit, where thermal excitations are sufficient to temporarily overcome the exchange energy. If this happens, the material will in temporal average appear paramagnetic. Therefore, it is important to be able to study thermal effects in magnetic materials in nanometer dimensions (Wang *et al*., 2002; Portier, Petford-Long, Anthony and Brug, 1999a).

Lots of investigations have also been devoted to multilayered thin films and their magnetic properties. Lorentz microscopy proved here also to be of immediate value, since it was possible to directly observe the magnetic configurations and processes (Chapman *et al*., 1999; Weir *et al*., 1999; Aitchison, Chapman, Jardine and Evetts, 1997; Heyderman, Chapman and Parkin, 1994; Hosomi, Petford-Long and Doole, 1999; Ormston, Petford-Long and Teer, 1999; Zimmermann, Zweck and Hoffmann, 1995a,b; Zweck, Zimmermann and Schuhrke, 1997). Lorentz microscopy is even of use when magnetic thin films with a soft magnetic axis perpendicular to the specimen's plane are of interest (Aitchison *et al*., 2001).

As has been shown in the preceding text, Foucault imaging is – just as DPC and holography – capable to image external stray fields leaking from a specimen (Daykin and Petford-Long, 1995; Doole, Petford-Long and Jakubovics, 1993; te Lintelo, Lodder, McVitie and Chapman, 1994). This has been used to characterize the magnetic configuration which one can find in MFM tips (Ruhrig *et al*., 1996; Zhou, McVitie and Chapman, 1995; te Lintelo, Lodder, McVitie and Chapman, 1994). A similar task was attempted with magnetic read/write heads used in data storage technology by DPC in combination with a tomographic 3D reconstruction of the magnetic fields emerging from the gap region (Ferrier, McVitie and Nicholson, 1990; Petri *et al*., 1996).

Electron holography has successfully been applied to study the magnetic crystals which can be found in magnetotactic bacteria (de Graef and Zhu, 2001; Dunin-Borkowski *et al*., 1998).

Extensive research was also conducted on the effect of crystallography and morphology on the magnetic properties of materials (Marrows *et al*., 1999; Thompson, Gutfleisch, Chapman and Harris, 1998, 1999; Thompson *et al*., 1998; Chapman *et al*., 1995; Wong, Chapman, McVitie and Hefferman, 1992; Youhui, Shindo and Petford-Long, 2003; Jackson *et al*., 2000; Kim *et al*., 1994; Kim, Petford-Long and Jakubovics, 1994; Petford-Long *et al*., 1993; Portier *et al*., 1999), which is also of enormous importance in the case of hard magnets (Craig *et al*., 2006)

Certainly it is not surprising that a number of publications deal with the various imaging techniques and their development and interpretation. An overview of the frequently used imaging modes is given in Chapman and Scheinfein (1999), Chapman (1984) and Chapman, Waddell, Batson and Ferrier (1979). Coherent imaging is treated in McVitie and Chapman (1995), Johnston and Chapman (1995), McVitie *et al*. (1995), Chapman, Gillies and Freitas (1996), Chapman, Johnston and Heyderman (1994) and Chapman *et al*. (1977), DPC in Chapman, Ploessl and Donnet (1992), Donnet, Chapman, van Kesteren and Zeper (1992), Zweck, Chapman, McVitie and Hoffmann (1992), Chapman, McVitie and Hefferman (1991), Chapman, McFadyen and McVitie (1990), McVitie and Chapman (1990), Chapman and Morrison (1983), McCartney, Kruit, Buist and Scheinfein (1996) and Ferrier, Morrison and Chapman (1984) .

Further developments imply STEM holography (Mankos *et al*., 1995) of magnetic materials and Fresnel STEM (Chapman, Waddell, Batson and Ferrier, 1979). A new interpretation of the micromagnetic features in terms of amperian currents was given by McVitie and White (2004).

7 FUTURE TRENDS

It is certainly difficult to predict future developments in Lorentz microscopy. Nevertheless, we will try to give an idea of what seems possible in near future in the field of magnetic imaging.

One rather obvious field of research, which already became started, deals with ferromagnetic semiconductors. These materials in general consist of a conventional semiconductor material, where a certain species of atoms has been partially replaced by atoms with a non-vanishing magnetic moment, as for example in (Ga,Mn)As. At present, the Curie temperature is still well below room temperature, and the average magnetic moment per unit volume is rather low. This calls for magnetic imaging techniques which utilize low temperature cooling holders, to go below T_C and lead to an optimum magnetic ordering, yielding a higher detectable induction.

Another possibility for future applications will be dynamic imaging of magnetic Eigen modes. Using stroboscopic illumination and/or a gateable camera will allow the experimentator to repeatedly excite the magnetic modes and then – similar as it is done in magneto-optic pump-probe experiments – record an image at a given instant of time after a defined delay. Early experiments have been done by Bostanjoglo (Bostanjoglo and Rosin, 1981a,b). The techniques developed by him have been recently extended and modernized for biological research (Meurig, 2005; Baum

and Zewail, 2006). Thus, time resolution in the regime of nanoseconds seems to be at reach for magnetic imaging.

The current development of lens correctors for high resolution electron microscopes and their commercial availability leads to the question, what magnetic imaging might profit from them. Especially for STEM imaging modes such as DPC imaging it seems reasonable to expect smaller probe sizes at even higher probe current and in turn higher resolution when a corrected condenser lens is used to focus the beam onto the specimen.

In recent publications (Hébért and Schattschneider, 2003; Schattschneider *et al*., 2004, 2006) it was shown that it is possible to detect a dichroic behavior of magnetic materials with electrons which can be considered to be the electron analog on for X-ray magnetic circular dichroism (XMCD) (Schneider, 1996; Ebert, 1996). This effect is presently investigated and may in the future lead to a new, element specific technique to image the magnetic moment distribution within a specimen. In analogy to XMCD, even a separation of orbital and spin magnetic moments seems possible, in principle.

Finally, as electron microscopic tomography has become a commercially available tool it may make sense to think about magnetic tomography in more detail, where one would be able to reconstruct the three-dimensional magnetic vector fields inside and around magnetic specimens of specific shapes. Pioneering work on this topic has been done in the past (Ferrier, Liu, Martin and Arnoldussen, 1995; Petri *et al*., 1996) and is continued nowadays (Paganin, Lade and Morgan, 2005; Stolojan, Dunin-Borkowski, Weyland and Midgley, 2001). With the availability of better and faster program code as well as much faster computers this seems to be a feasible task.

ACKNOWLEDGMENTS

We are thankful to all persons, who contributed to this publication by providing images, especially Dipl. Phys. St. Otto, Dr. M. Heumann, Dr. M. Schneider and Dr. Th. Haug. The preparation of most of the samples presented here would not been possible without the nanofabrication laboratory of Prof. Dieter Weiss. Further we would like to thank Dr. A. Kohn, whose help and corrections were necessary to present the novel technique of TIE based phase reconstruction in an appealing way.

REFERENCES

Aharonov, Y. and Bohm, D. (1959). Significance of Electromagnetic Potentials in the Quantum Theory. *Physical Review*, **115**, 485–491.

Aitchison, P.R., Chapman, J.N., Gehanno, V., *et al*. (2001). High resolution measurement and modelling of magnetic domain structures in epitaxial FePd(001) L1/sub 0/ films with perpendicular magnetisation. *Journal of Magnetism and Magnetic Materials*, **223**(2), 138–146.

Aitchison, P.R., Chapman, J.N., Jardine, D.B. and Evetts, J.E. (1997). Correlation of domain processes and magnetoresistance changes as a function of field and number of bilayers in Co/Cu multilayers. *Journal of Applied Physics*, **81**(8), 3775–3777.

Aitchison, P.R., Chapman, J.N., Kirk, K.J., *et al*. (1998). Domain structures supported by micron-sized patterned Co/Cu multilayers with AF and FM coupling. *IEEE Transactions on Magnetics*, **34**(4), 1012–1014.

Akhter, M.A., Mapps, D.J., Ma, Y.Q., *et al*. (1998). Domain walls and magnetic properties of very thin permalloy films for magnetoresistive sensors. *IEEE Transactions on Magnetics*, **34**(4), 1147–1149.

Allen, L.J. and Oxley, M.P. (2001). Phase retrieval from series of images obtained by defocus variation. *Optics Communications*, **199**, 65–75.

Ardhuin, H., Chapman, J.N., Aitchison, P.R., *et al*. (2000). Magnetization reversal of patterned spin-tunnel junction material: A transmission electron microscopy study. *Journal of Applied Physics*, **88**(5), 2760–2765.

Bajt, S., Barty, A., Nugent, K.A., *et al*. (2000). Quantitative phase-sensitive imaging in a transmission electron microscope. *Ultramicroscopy*, **83**(1–2), 67–73.

Baum, P. and Zewail, A.H. (2006). Breaking resolution limits in ultrafast electron diffraction and microscopy. *Proceedings of the National Academy of Sciences of the United States of America*, **103**(44), 16105–16110.

Belaggia, M., Schofield, M.A., Volkov, V.V. and Zhu, Y. (2004). On the transport of intensity technique for phase retrieval. *Ultramicroscopy*, **102**, 37–49.

Bernas, H., Devolder, T., Chappert, C., *et al*. (1999). Ion beam induced magnetic nanostructure patterning. *Nuclear Instruments and Methods in Physics Research Section B-Beam Interactions with Materials and Atoms*, **148**(1–4), 872–879.

Bitter, F. (1931). On Inhomogeneities in the Magnetization of Ferromagnetic Materials. *Physical Review*, **38**, 1903–1905.

Bitter, F. (1932). Experiments on the Nature of Ferromagnetism. *Physical Review*, **41**, 507–515.

Boersch, H. and Raith, H. (1959). Elektronenmikroskopische Abbildung Weißscher Bezirke in dünnen ferromagnetischen Schichten (Electron microscopic imaging of Weißdomains in thin ferromagnetic films). *Naturwissenschaften*, **46**, 574.

Boersch, H., Raith, H. and Wohlleben, D. (1960). Elektronenoptische Untersuchungen Weißscher Bezirke in dünnen Eisenschichten (Electron optical investigations of Weißdomains in thin iron films). *Zeitschrift fur Physik*, **159**, 388–396.

Boersch, H., Hamisch, H., Wohlleben, D. and Grollmann, K. (1960). Antiparallele Weißsch Bereiche als Biprisma für Elektroneninterferenzen (Antiparallel Weißdomains as biprism for electron interference). *Zeitschrift fur Physik*, **159**, 397.

Boersch, H., Hamisch, H., Grohmann, K. and Wohlleben, D. (1962). Experimenteller Nachweis der Phasenschiebung von Elektronenwellen durch das magnetische Vektorpotential (Experimental

proof of the phase shift of electron waves by the magnetic vector potential). *Zeitschrift fur Physik*, **167**, 72.

Bostanjoglo, O. and Rosin, T. (1981a). Resonance oscillations of Bloch lines in Permalloy films. *Physica Status Solidi A*, **66**(1), K5–K10.

Bostanjoglo, O. and Rosin, Th. (1981b). New reversal process of Neel walls due to nanosecond field pulses. *Physica Status Solidi A*, **65**(2), K117–K119.

Bromwich, T.J., Bucknall, D.G., Warot, B., *et al*. (2004). TEM analysis and fabrication of magnetic nanoparticles. *Electron Microscopy and Analysis 2003*. McVitie, S. and McComb, D. (eds). *Institute of Physics Electron Microscopy and Analysis Group Conference Institute of Physics Conference Series*. Vol.179. Institute of Physics Publishing Ltd: Bristol, UK, pp. 95–98.

Bromwich, T.J., Kasama, T., Chong, R.K.K., *et al*. (2006). Remanent magnetic states and interactions in nano-pillars. *Nanaotechnology*, **17**(17), 4367–4373.

Bromwich, T.J., Kohn, A., Petford-Long, A.K., *et al*. (2005). Remanent magnetization states and interactions in square arrays of 100-nm cobalt dots measured using transmission electron microscopy. *Journal of Applied Physics*, **98**(5), 53909-1–153909-8.

Bromwich, T.J., Petford-Long, A.K., Castano, F.J. and Ross, C.A. (2006). Lorentz microscopy of elliptical magnetic rings. *Journal of Applied Physics*, **99**(8), 8H304-1–8H304-3.

Brownlie, C., McVitie, S., Chapman, J.N. and Wilkinson, C.D.W. (2006). Lorentz microscopy studies of domain wall trap structures. *Journal of Applied Physics*, **100**(3), 33902-1–33902-9.

Cardoso, S., Ferreira, R., Silva, F., *et al*. (2006). Double-barrier magnetic tunnel junctions with GeSbTe thermal barriers for improved thermally assisted magnetoresistive random access memory cells. *Journal of Applied Physics*, **99**(8), 8N901-1–8N901-3.

Chapman, J.N. (1984). The investigation of magnetic domain structures in thin foils by electron microscopy. *Journal of Physics D: Applied Physics*, **17**(4), 623–647.

Chapman, J.N., Aitchison, P.R., Kirk, K.J., *et al*. (1998). Direct observation of magnetization reversal processes in micron-sized elements of spin-valve material. *Journal of Applied Physics*, **83**(10), 5321–5325.

Chapman, J.N., Batson, P.E., Waddell, E.M., *et al*. (1977). Domain wall structure investigations by scanning transmission Lorentz microscopy. *Developments in Electron Microscopy and Analysis 1977*, Misell, D.L. (Ed.), Institute of Physics, London, UK, pp. 233–236.

Chapman, J.N., Batson, P.E., Waddell, E.M. and Ferrier, R.P. (1978). The direct determination of magnetic domain wall profiles by differential phase contrast electron microscopy. *Ultramicroscopy*, **3**(2), 203–214.

Chapman, J.N., Gillies, M.F. and Freitas, P.P. (1996). Magnetization reversal process in TbCo-biased spin valves. *Journal of Applied Physics*, **79**(8), 6452–6454.

Chapman, J.N., Heyderman, L.J., Young, S., *et al*. (1995). Micromagnetic and microstructural studies of NdFeB by TEM. *Scripta Metallurgica et Materialia*, **33**(10–11), 1807–1816.

Chapman, J.N., Johnston, A.B. and Heyderman, L.J. (1994). Coherent Foucault imaging: A method for imaging magnetic domain structures in thin films. *Journal of Applied Physics*, **76**(9), 5349–5355.

Chapman, J.N., Johnston, A.B., Heyderman, L.J., *et al*. (1994). Coherent magnetic imaging by TEM. *IEEE Transactions on Magnetics*, **30**(6, Pt. 1), 4479-4–4479-84.

Chapman, J.N., McFadyen, I.R. and McVitie, S. (1990). Modified differential phase contrast lorentz microscopy for improved imaging of magnetic structures. *IEEE Transactions on Magnetics*, **26**(5), 1506–1511.

Chapman, J.N., McFadyen, I.R. and McVitie, S. (1997). Modified differential phase contrast lorentz microscopy for improved imaging of magnetic structures. *IEEE Transactions on Magnetics*, **26**(5), 1506–1511.

Chapman, J.N., McVitie, S. and Hefferman, S.J. (1991). Mapping induction distributions by transmission electron microscopy. *Journal of Applied Physics*, **69**(8), 6078–6083.

Chapman, J.N., McVitie, S. and McFadyen, I.R. (1987). Magnetic structure determination by scanning transmission electron microscopy. *Scanning Microscopy*, **1**(1), 221–228.

Chapman, J.N. and Morrison, G.R. (1983). Quantitative determination of magnetisation distributions in domains and domain walls by scanning transmission electron microscopy. *Journal of Magnetism and Magnetic Materials*, **35**(1–3), 254–260.

Chapman, J.N., Ploessl, R. and Donnet, D.M. (1992). Differential phase contrast microscopy of magnetic materials. *Ultramicroscopy*, **47**(4), 331–338.

Chapman, J.N., Rose, J., Aitchison, P.R., *et al*. (1999). Magnetization processes in Co/Cu multilayers with low magnetoresistive hysteresis. *Journal of Applied Physics*, **86**(3), 1611–1620.

Chapman, J.N. and Scheinfein, M.R. (1999). Transmission electron microscopies of magnetic microstructures. *Journal of Magnetism and Magnetic Materials*, **200**(1–3), 729–740.

Chapman, J.N., Waddell, E.M., Batson, P.E. and Ferrier, R.P. (1979). The Fresnel mode of Lorentz microscopy using a scanning transmission electron microscope. *Ultramicroscopy*, **4**(3), 283–292.

Choi, Y.S., Petford-Long, A.K. and Ward, R.C.C. (2003). Magnetic field-induced degradation of magnetic properties in molecular beam epitaxy grown FeMn/NiFe exchange-coupled bilayers. *Journal of Applied Physics*, **93**(10), 7720–7722.

Cohen, M.S. (1965). Magnetic Measurements with Lorentz Microscopy. *IEEE Transactions on Magnetics*, **1**, 156–167.

Cowley, J.M. (1969). Image contrast in a transmission scanning electron microscope. *Applied Physics Letters*, **15**(2), 58–59.

Cowley, J.M. (1995). *Diffraction Physics*, *Third Edition*, Elsevier Science Publisher .

Craig, B.R., McVitie, S., Chapman, J.N., *et al*. (2006). Transmission electron microscopy study of CoFe films with high saturation magnetization. *Journal of Applied Physics*, **100**(5), 53915-1–53915-7.

Crawford, M., Long, A.R., Wright, P.J., *et al*. (2002). Resonances in hybrid magnetic/semiconductor electron waveguides Intermag Europe 2002 Digest of Technical Papers. *2002 IEEE International Magnetics Conference Cat.No.02CH37323* , GW9.

Crewe, A.V., Wall, J. and Langmore, J. (1970). Visibility of single atoms. *Science*, **37**, 1338–1340.

Daykin, A.C. and Petford-Long, A.K. (1995). Quantitative mapping of the magnetic induction distribution using Foucault images formed in a transmission electron microscope. *Ultramicroscopy*, **58**(3–4), 365–380.

Dekkers, N.H. and de Lang, H. (1974). Differential phase contrast in a STEM. *Optik*, **41**(4), 452–456.

Donnet, D.M., Chapman, J.N., van Kesteren, H.W. and Zeper, W.B. (1992). Investigation of domain structures in Co/Pt multilayers by modified differential phase contrast microscopy. *Journal of Magnetism and Magnetic Materials*, **115**(2–3), 342–352.

Doole, R.C., Petford-Long, A.K. and Jakubovics, J.P. (1993). Improved Foucault imaging of magnetic domains with a modified 400 kV transmission electron microscope. *The Review of Scientific Instruments*, **64**(4), 1038–1043.

Dooley, J. and de Graef, M. (1997). Energy filtered Lorentz microscopy. *Ultramicroscopy*, **67**(1–4), 113–131.

Dooley, J., de Graef, M., George, E.P., *et al*. (1995). TEM study of twinning and magnetic domains in Terfenol-D. *Materials for Smart Systems Symposium*, Materials Research Society: Pittsburgh, PA, USA, pp. 189–194.

Dooley, J., de Graef, M. and McHenry, M.E. (1998). Induction mapping of magnetostrictive materials. *Journal of Applied Physics*, **83**(11), 6837–6839.

Düker, H. (1955). Lichtstarke Interferenzen mit einem Biprisma für Elektronenwellen (Bright interferences with a biprism for electron waves). *Zeitung für Naturforschung*, **10**, 255–256.

Dunin-Borkowski, R.E., Kardynal, B., Mccartney, M.R., *et al*. (2001). Electron holography of nanostructured magnetic materials. *Advances in materials problem solving with the electron microscopy*. In *Symposium Materials Research Society Symposium Proceedings*. Bentley, J., Allen, C., Dahmen, U. and Petrov, I. (Eds.), Materials Research Society: Warrendale, PA, USA, pp. 13–18, Vol.589.

Dunin-Borkowski, R.E., McCartney, M.R., Frankel, R.B., *et al*. (1998). Magnetic microstructure of magnetotactic bacteria by electron holography. *Science*, **282**(5395), 1868–1870.

Dunin-Borkowski, R.E., McCartney, M.R., Kardynal, B., *et al*. (2000). Off-axis electron holography of patterned magnetic nanostructures. *Journal of Microscopy*, **200**, 187–205.

Dunin-Borkowski, R.E., McCartney, M.R. and Smith, D.J. (1998). Towards quantitative electron holography of magnetic thin films using in situ magnetization reversal. *Ultramicroscopy*, **74**, 61–73.

Ebert, H. (1996). Circular magnetic X-ray dichroism in transition metal systems, In *Spin-orbit influenced spectroscopies of magnetic solids*, Ebert, H. and Schuetz, G. (Eds.), Springer: Berlin, Germany, pp. 159–177.

Fassbender, J., Poppe, S., Mewes, T., *et al*. (2002). Magnetization reversal of exchange bias double layers magnetically patterned by ion irradiation. *Physical Status Solidi A*, **189**(2), 439–447.

Ferrier, R.P., Liu, Y., Martin, J.L. and Arnoldussen, T.C. (1995). Electron beam tomography of magnetic recording head fields. *Journal of Magnetism and Magnetic Materials*, **149**(3), 387–397.

Ferrier, R.P., McVitie, S. and Nicholson, W.A.P. (1990). Magnetisation distributions in thin film recording heads by Type II contrast. *IEEE Transactions on Magnetics*, **26**(5), 1337–1339.

Ferrier, R.P., Morrison, G.R. and Chapman, J.N. (1984). An investigation of the maximum specimen thickness for differential phase contrast Lorentz microscopy. In *Electron beam interactions with solids for microscopy, microanalysis and microlithography*, Proceedings of the 1st Pfefferkorn Conference, Kyser, D.F., Niedrig, H., Newbury, D.E. and Shimizu, R. (Eds.), Scanning Electron Microscopy AMF: O'Hare, IL, USA, pp. 281–286.

Franke, F.J., Herrmann, K.H. and Lichte, H. (1988). Numerical reconstruction of the electron object wave from an electron hologram including the correction of aberrations. *Scanning Microscopy*, **2**(2), 59–67.

Fuchs, E. (1961). Die Ummagnetisierung dünner Nickeleisenschichten in der schweren Richtung. (The magnetization reversal of thin nickel iron films along a hard axis). *Zeitschrift fur Angewandte Physik*, **13**, 157–164.

Fuller, H.W. and Hale, M.E. (1960). Determination of Magnetization Distribution in Thin Films Using Electron Microscopy. *Journal of Applied Physics*, **31**, 38–248.

Gabor, D. (1948). A new microscopic principle. *Nature*, **161**, 777–778.

Gentils, A., Chapman, J.N., Xiong, G. and Cowburn, R.P. (2005). Variation of domain-wall structures and magnetization ripple spectra in permalloy films with controlled uniaxial anisotropy. *Journal of Applied Physics*, **98**(5), 53905-1–53905-7.

Gillies, M.F., Chapman, J.N. and Kools, J.C.S. (1996). The stabilisation of a magnetic vortex using a large vertical field. *Journal of Magnetism and Magnetic Materials*, **161**, L17–L21.

Gogol, P., Chapman, J.N., Gillies, M.F. and Vanhelmont, F.W.M. (2002). Domain processes in the magnetization reversal of exchange-biased IrMn/CoFe bilayers. *Journal of Applied Physics*, **92**(3), 1458–1465.

Gomez, R.D., Luu, T.V., Pak, A.O., *et al*. (1999a). Domain wall motion in micron-sized permalloy elements. *Journal of Applied Physics*, **85**(8), 6163–6165.

Gomez, R.D., Luu, T.V., Pak, A.O., *et al*. (1999b). Domain wall motion in micron-sized permalloy elements. *Journal of Applied Physics*, **85**(8), 4598–4600.

Gong, H. and Chapman, J.N. (1987). On the use of divergent wall images in the Fresnel mode of Lorentz microscopy for the measurement of the widths of very narrow domain walls. *Journal of Magnetism and Magnetic Materials*, **67**(1), 4–8.

Goodman, A.M., Laidler, H., O'Grady, K., *et al*. (2000). Magnetic viscosity effects on the pinned layer loop of spin-valve materials. *Journal of Applied Physics*, **87**(9), 6409–6411.

de Graef, M., Beleggia, M., Lau, J.W., *et al* (2006). Phase diagram for magnetic nano-rings. *Journal of Magnetism and Magnetic Materials*, **301**(1), 131–146.

de Graef, M., Kishi, Y., Zhu, Y. and Wuttig, M. (2003). Lorentz study of magnetic domains in Heusler-type shape memory alloys. *Journal de Physique IV-Proceedings*, **112**, 993–996.

de Graef, M., Nuhfer, N.T. and McCartney, M.R. (1999). Phase contrast of spherical magnetic particles. *Journal of Microscopy*, **194**, 84–94.

de Graef, M., Willard, M.A., McHenry, M.E. and Zhu, Y. (2001). In-situ Lorentz TEM cooling study of magnetic domain configurations in Ni/sub 2/MnGa. *IEEE Transactions on Magnetics*, **37**(4), 2663–2665.

de Graef, M. and Zhu, Y. (2001). Quantitative noninterferometric Lorentz microscopy. *Journal of Applied Physics*, **89**(11 Pt. 1–2), 7177–7179.

Grundy, P.J. and Tebble, R.S. (1968). Lorentz electron microscopy. *Advances in Physics*, **17**, 153–243.

Gu, E., Ahmad, E., Bland, J.A.C., *et al*. (1998). Micromagnetic structures and microscopic magnetization-reversal processes in epitaxial Fe/GaAs(001) elements. *Physical Review B Condensed Matter*, **57**(13), 7814–7822.

Hale, M.E., Fuller, H.W. and Rubinstein, H. (1959). Magnetic Domain Observations by Electron Microscopy. *Journal of Applied Physics*, **30**, 789–790.

Hámos, L.v. and Thiessen, P.A. (1931). über die Sichtbarmachung von Bezirken verschiedenen ferromagnetischen Zustands fester Körper (On the visualization of areas with different ferromagnetic states in solid materials). *Zeitschrift fur Physik*, **71**, 442–444.

Haug, T., Otto, S., Schneider, M. and Zweck, J. (2003). Computer simulation of Lorentz electron micrographs of thin magnetic particles. *Ultramicroscopy*, **96**, 201–206.

Hébért, C. and Schattschneider, P. (2003). A proposal for dichroic experiments in the electron microscope. *Ultramicroscopy*, **96**, 463–468.

Hefferman, S.J., Chapman, J.N. and McVitie, S. (1990). In-situ magnetising experiments on small regular particles fabricated by electron beam lithography. *Journal of Magnetism and Magnetic Materials*, **83**(1–3), 223–224.

Hefferman, S.J., Chapman, J.N. and McVitie, S. (1991). In-situ magnetising experiments on small regularly shaped permalloy particles. *Journal of Magnetism and Magnetic Materials*, **95**(1), 76–84.

Herrmann, M., McVitie, S. and Chapman, J.N. (2000). Investigation of the influence of edge structure on the micromagnetic behavior of small magnetic elements. *Journal of Applied Physics*, **87**(6), 2994–2999.

Hertel, R. and Kronmüller, H. (1999). Micromagnetic simulation of the domain structure of a flat rectangular permalloy prism. *Journal of Applied Physics*, **85**(8), 6190–6192.

Heumann, M., Uhlig, T. and Zweck, J. (2005). True single domain and configuration-assisted switching of submicron permalloy dots observed by electron holography. *Physical Review Letters*, **94**, 077202.

Heyderman, L.J., Chapman, J.N. and Parkin, S.S.P. (1994). Investigation of the magnetic structures in giant magnetoresistance multilayer films by electron microscopy. *Journal of Applied Physics*, **76**(10), 6613–6615.

Hirsch, P.B., Howie, A., Nicholson, R.B., *et al*. (1965). *Electron Microscopy of Thin Crystals*, Butterworths: London.

Hosomi, M., Petford-Long, A.K. and Doole, R.C. (1999). Lorentz microscopy observation of magnetic domain structure variation in NiFe/Au multilayer films caused by Au layer thickness. *Materials Transactions, JIM*, **40**(9), 883–886.

Hu, H., Wang, H., McCartney, M.R. and Smith, D.J. (2005). Magnetization reversal of circular nanoscale ferromagnetic elements with modified shapes. *INTERMAG Asia 2005: Digest of the IEEE International Magnetics Conference IEEE Cat. No.05CH37655*, IEEE: Piscataway, NJ, USA, pp. 915–916.

Hubert, A. and Schäfer, R. (1998). *Magnetic Domains*, Springer, ISBN: 3-540-64108-4.

Huhle, R., Goldberg, R. and Lichte, H. (2000). *Proceedings of EUREM 12 (European Congress on Electron Microscopy)*, Brno, (Cz), pp. 163–164.

Hyndman, R., Mougin, A., Repain, V., *et al*. (2002). Magnetic nanostructures patterned by focused ion beam in an ultrathin Pt/Co/Pt film. *Transactions of the Magnetics Society of Japan*, **2**(4), 175–178.

Hyndman, R., Warin, P., Gierak, J., *et al*. (2001). Modification of Co/Pt multilayers by gallium irradiation-Part 1: The effect on structural and magnetic properties. *Journal of Applied Physics*, **90**(8), 3843–3849.

Jackson, M., Mendus, T., Short, G.R., *et al*. (2000). Correlation of magnetic and microstructural properties of obliquely deposited Co/Cr thin films. *Journal of Magnetism and Magnetic Materials*, **213**(1–2), 234–244.

Johnston, A.B. and Chapman, J.N. (1995). The development of coherent Foucault imaging to investigate magnetic microstructure. *Journal of Microscopy*, **179**, 119–128.

Kasama, T., Barpanda, P., Dunin-Borkowski, R.E., *et al*. (2005). Off-axis electron holography of pseudo-spin-valve thin-film magnetic elements. *Journal of Applied Physics*, **98**(1), 13903-1–13903-7.

Kerr, J. (1877). On rotation of the plane of polarization by reflection from the pole of a magnet. *Philosophical Magazine*, **3**(5), 321–343.

Kim, Y.H., Petford-Long, A.K. and Jakubovics, J.P. (1994). The relationship between the microstructure and magnetic properties of sputtered Co/Pt multilayer films. *Journal of Applied Physics*, **76**(10), 6099.

Kim, J.D., Petford-Long, A.K., Jakubovic, J.P., *et al*. (1994). Magnetic and structural studies of sputtered Co/Cu multilayer films. *Journal of Applied Physics*, **76**(10), 6513–6515.

King, J.P., Chapman, J.N., Gillies, M.F. and Kools, J.C.S. (2001). Magnetization reversal of NiFe films exchange-biased by IrMn and FeMn. *Journal of Physics D: Applied Physics*, **34**(4), 528–538.

King, J.P., Chapman, J.N. and Kools, J.C.S. (1998). Magnetisation reversal mechanisms of FeMn-biased spin-valves as a function of interlayer coupling strength and field orientation. *Journal of Magnetism and Magnetic Materials*, **177–181**, 896–897.

King, J.P., Chapman, J.N., Kools, J.C.S. and Gillies, M.F. (1999). On the free layer reversal mechanism of FeMn-biased spin-valves with parallel anisotropy. *Journal of Physics D: Applied Physics*, **32**(10), 1087–1096.

Kirk, K.J., Chapman, J.N., McVitie, S., *et al*. (1999). Switching of nanoscale magnetic elements. *Applied Physics Letters*, **75**(23), 3683–3685.

Kirk, K.J., Chapman, J.N., McVitie, S., *et al*.(2000). Interactions and switching field distributions of nanoscale magnetic elements. *Journal of Applied Physics*, **87**(9), 5105–5107.

Kirk, K.J., Chapman, J.N. and Wilkinson, C.D.W. (1997). Switching fields and magnetostatic interactions of thin film magnetic nanoelements. *Applied Physics Letters*, **71**(4), 539–541.

Kirk, K.J., Chapman, J.N. and Wilkinson, C.D.W. (1999). Lorentz microscopy of small magnetic structures (invited). *Journal of Applied Physics*, **85**(8), 5237–5242.

Kirk, K.J., McVitie, S. and Chapman, J.N. (2001). Lorentz imaging of sub-micron patterned elements. *Magnetic Storage Systems Beyond 2000*. In *Proceedings of the NATO Advanced Study Institute*, Hadjipanayis, G.C., (Ed.), Kluwer Academic Publishers: Dordrecht, Netherlands, pp. 145–152.

Kirk, K.J., McVitie, S., Chapman, J.N. and Wilkinson, C.D.W. (2001). Imaging magnetic domain structure in sub-500 nm thin film elements. *Journal of Applied Physics*, **89**(11), 7174–7176.

Kirk, K.J., Scheinfein, M.R., Chapman, J.N., *et al*. (2001). Role of vortices in magnetization reversal of rectangular NiFe elements. *Journal of Physics D: Applied Physics*, **34**(2), 160–166.

Kirschner, M., Suess, D., Schrefl, T., *et al*. (2003). Micromagnetic calculation of bias field and coercivity of polycrystalline ferromagnetic/antiferromagnetic layers. *IEEE Transactions on Magnetics*, **39**(5), 2735–2737.

Köhler, M., Schweinböck, T., Schmidt, T., *et al*. (2000). Imaging of sub-100-nm magnetic domains in atomically stacked Fe(001)/Au(001) multilayers. *Journal of Applied Physics*, **87**(9, Pt. 1–3), 6481–6483.

Kohn, A., Petford-Long, A.K. and Anthony, T.C. (2005). Magnetic potential in patterned materials determined using energy-dependent Lorentz phase microscopy. *Physical Review B: Condensed Matter and Materials Physics*, **72**(1), 14444-1–14444-11.

Kundrotaite, A., Rahman, M., Aitchison, P.R. and Chapman, J.N. (2001). Interactions in magnetic arrays for storage and computation. *Microelectronic Engineering*, **57–58**, 975–979.

Langridge, S., Michez, L.A., Ali, M., *et al*.(2006). Controlled magnetic roughness in a multilayer that has been patterned using a nanosphere array. *Physical Review B*, **74**(1), 14417-1–14417-6.

Lau, B. and Pozzi, G. (1978). Off-axis electron micro-holography of magnetic domain walls. *Optik*, **51**(3), 287–296.

Lehmann, M. and Lichte, H. (2002). Tutorial on off-axis electron holography. *Microscopy and Microanalysis*, **8**, 447–466.

Lehmann, M., Völkl, E. and Lenz, F. (1994). Reconstruction of electron off-axis holograms: a new and fast alternative method. *Ultramicroscopy*, **54**(2–4), 335–344.

Leith, E. and Upatnieks, J. (1962). Reconstructed wavefronts and communication theory. *Journal of the Optical Society of America*, **52**, 1123.

Lichte, H. (2002). Electron interference: mystery and reality. *Philosophical Transactions of the Royal Society of London Series A: Mathematical Physical and Engineering Sciences*, **360**(1794), 897–920.

Lim, C.K., Chapman, J.N., Rahman, M., *et al*. (2002a). Asymmetric magnetization reversal of the free layer of a spin-valve. *Journal of Physics D: Applied Physics*, **35**(19), 2344–2351.

Lim, C.K., Chapman, J.N., Rahman, M., *et al*. (2002b). Lorentz microscopy investigation of the free layer reversal in CoFe and Co top spin-valves. *Journal of Magnetism and Magnetic Materials*, **328**(2–3), 301–305.

Lim, C.K., Chapman, J.N., Rahman, M., *et al*. (2004). Lorentz microscopy studies of the variation with temperature and processing conditions of free layer reversal mechanisms in spin valves. *Journal of Applied Physics*, **95**(3), 1510–1515.

Lim, C.K., Yi, G., Chapman, J.N., *et al*. (2003). TEM studies of the switching characteristics of small permalloy elements as a function of field orientation. *Journal of Physics D: Applied Physics*, **36**(24), 3099–3102.

te Lintelo, J.G.Th., Lodder, J.C., McVitie, S. and Chapman, J.N. (1994). Magnetic stray fields of Co-Cr microstrips measured by Lorentz microscopy, te Lintelo, JGTh. *Journal of Applied Physics*, **75**(6), 3002–3007.

Liu, X., Chapman, J.N., McVitie, S. and Wilkinson, C.D.W. (2004). Reversal mechanisms and metastable states in magnetic nanoelements. *Journal of Applied Physics*, **96**(9), 5173–5179.

http://llgmicro.home.mindspring.com/.

Mankos, M., de Haan, P., Kambersky, V., *et al*. (1995). STEM holography of magnetic materials. *Electron Holography*. In *Proceedings of the International Workshop on Electron Holography*, Tonomura, A., Allard, L.F., Pozzi, G., *et al*. (Eds.), Elsevier: Amsterdam, Netherlands, pp. 329–341.

Mansuripur, M. (1991). Computation of electron diffraction patterns in Lorentz electron microscopy of thin magnetic films. *Journal of Applied Physics*, **69**(4), 2455.

Marrows, C.H., Creeth, G.L., Stanley, F.E., *et al*. (2001). Micromagnetic disorder in antiparallel biased spin valves. *Applied Physics Letters*, **79**(26), 4384–4386.

Marrows, C.H., Hickey, B.J., Herrmann, M., *et al*. (1999). Effects of gas damage on coupling and anisotropy in sputtered Co/Cu multilayers. *Journal of Magnetism and Magnetic Materials*, **198–199**, 408–411.

McCartney, M.R., Kruit, P., Buist, A.H. and Scheinfein, M.R. (1996). Differential phase contrast in TEM. *Ultramicroscopy*, **65**(3–4), 179–186.

McGrouther, D. and Chapman, J.N. (2005). Nanopatterning of a thin ferromagnetic CoFe film by focused-ion-beam irradiation. *Applied Physics Letters*, **87**(2), 22507-1–22507-3.

McGrouther, D., Chapman, J.N. and Vanhelmont, F.W.M. (2004). Effect of Ga/sup +/ ion irradiation on the structural and magnetic properties of CoFe/IrMn exchange biased bilayers. *Journal of Applied Physics*, **95**(12), 7772–7778.

McGrouther, D., Nicholson, W.A.P., Chapman, J.N. and McVitie, S. (2005). Focused ion beam irradiation of ferromagnetic thin films in the presence of an applied field. *Journal of Physics D: Applied Physics*, **38**(18), 3348–3353.

McMichael, R.D. and Donahue, M.J. (1997). Head to head domain wall structures in thin magnetic strips. *IEEE Transactions on Magnetics*, **33**, 4167–4169.

McVitie, S. (1995). In-situ quantitative imaging of magnetic material. In *Electron Microscopy and Analysis 1995, Proceedings of the Institute of Physics Electron Microscopy and Analysis Group Conference*, Cherns, D. (Ed.), IOP Publishing: Bristol, UK, pp. 305–308.

McVitie, S., Brownlie, C., Chapman, J.N. and Wilkinson, C.D.W. (2005). Lorentz microscopy studies of domain wall trap structures. *INTERMAG Asia 2005: Digest of the IEEE International Magnetics Conference IEEE Cat. No.05CH37655*, IEEE: Piscataway, NJ, USA, pp. 195–196.

McVitie, S. and Chapman, J.N. (1990). Measurement of domain wall widths in Permalloy using differential phase contrast imaging in STEM. *Journal of Magnetism and Magnetic Materials*, **83**(1–3), 97–98.

McVitie, S. and Chapman, J.N. (1995). Coherent Lorentz imaging of soft, thin-film magnetic materials. *MRS Bulletin*, **20**(10), 55–58.

McVitie, S. and Chapman, J.N. (1997). Reversal mechanisms in lithographically defined magnetic thin film elements imaged by scanning transmission electron microscopy. *Microscopy and Microanalysis*, **3**(2), 146–153.

McVitie, S. and Chapman, J.N. (1988). Magnetic structure determination in small regularly shaped particle using transmission electron microscopy. *IEEE Transactions on Magnetics*, **24**(2), 1778–1780.

McVitie, S., Chapman, J.N., Hefferman, S.J. and Nicolson, W.A.P. (1988). Effect of application of fields on the domain structure in small regularly shaped magnetic particles. *Journal de Physique Colloque*, **49**(C-8), 1817–1818.

McVitie, S., Chapman, J.N., Zhou, L., *et al*. (1995). In-situ magnetising experiments using coherent magnetic imaging in TEM. *Journal of Magnetism and Magnetic Materials*, **148**(1–2), 232–236.

McVitie, S., Lim, C.K., Yi, G., *et al*. (2003). In-situ Lorentz microscopy of magnetic nanostructures. *Digest of INTERMAG 2003. International Magnetics Conference Cat. No.03CH37401*, IEEE: Piscataway, NJ, USA, p. DC-02.

McVitie, S. and White, G.S. (2004). Imaging amperian currents by Lorentz microscopy. *Journal of Physics D: Applied Physics*, **37**(2), 280–288.

McVitie, S., White, G.S., Scott, J., *et al* (2001). Quantitative imaging of magnetic domain walls in thin films using Lorentz and magnetic force microscopies. *Journal of Applied Physics*, **90**(10), 5220–5227.

Meurig, T.J. (2005). Ein Durchbruch in der Elektronenmikroskopie (A breakthrough in electron microscopy). *Angewandte Chemie*, **117**(35), 5699–5702.

http://www.micromagus.de/.

Möllenstedt, G. and Düker, H. (1956). Beobachtung und Messungen an Biprisma-Interferenzen mit Elektronenwellen (Observation and measurements on biprism interferences with electron waves). *Zeitschrift fur Physik*, **154**, 377–397.

de Morais, A. and Petford-Long, A.K. (2000). Spin valve structures with artificial antiferromagnets. *Journal of Applied Physics*, **87**(9), 6977–6979.

Murdoch, S.J.T., Chapman, J.N., Pokhil, T.G., *et al*. (2000). Transmission electron microscopy study of thermal effects on the free-layer reversal of a crossed-anisotropy spin valve. *Journal of Applied Physics*, **87**(9), 4945–4947.

O'Grady, K., Owen, N.W., Hughes, T., *et al*. (2001). Magnetisation processes in exchange-biased systems. *Journal of Magnetism and Magnetic Materials*, **226–230**, 1798–1799.

http://math.nist.gov/oommf/.

Ormston, M.W., Petford-Long, A.K. and Teer, D.G. (1999). Study of magnetic thin films deposited by closed-field unbalanced magnetron sputtering. *Journal of Applied Physics*, **85**(8), 5747–5749.

Owen, N.W., Hang-Yan, Y. and Petford-Long, A.K. (2002). Patterning magnetic antidot-type arrays by Ga/sup +/− implantation. *Intermag Europe 2002 Digest of Technical Papers. 2002 IEEE International Magnetics Conference Cat.No.02CH37323*, BC11, IEEE: Piscataway, NJ, USA.

Owen, N.W. and Petford-Long, A.K. (2003). Structural characterization and magnetization reversal of 0.1 μm scale antidot-type arrays patterned by Ga/sup +/− irradiation. *Digest of INTERMAG 2003. International Magnetics Conference Cat. No.03CH37401*, ET–02, IEEE: Piscataway, NJ, USA.

Ozkaya, L.D., Langford, R.M., Chan, W.L. and Petford-Long, A.K. (2002). Effect of Ga implantation on the magnetic properties of permalloy thin films. *Journal of Applied Physics*, **91**(12), 9937–9942.

Paganin, D., Lade, S.J. and Morgan, M.J. (2005). Electron tomography of electromagnetic fields, potentials and sources. *Optics Communications*, **253**(4–6), 392–400.

Petford-Long, A.K., Doole, R.C., Cerezo, A., *et al*. (1993). The effects of annealing on magnetic domain structure and interface profile in sputtered Fe/Cr multilayer films. *Journal of Magnetism and Magnetic Materials*, **126**(1–3), 117–120.

Petford-Long, A.K., Doole, R.C. and Donovan, P.E. (1993). The magnetic domain structure of Gd/W multilayer films observed at low temperatures by Lorentz microscopy. *Journal of Magnetism and Magnetic Materials*, **126**(1–3), 41–44.

Petford-Long, A.K., Kohn, A., Bromwich, T., *et al*. (2006). Application of TEM to the development of information storage materials. *Thin Solid Films*, **505**(1–2), 10–15.

Petford-Long, A.K., Portier, X., Bayle-Guillemaud, P., *et al*. (1998). In situ transmission electron microscopy studies of the magnetization reversal mechanism in information storage materials. *Microscopy and Microanalysis*, **4**(3), 325–333.

Petford-Long, A.K., Portier, X., Tsymbal, E.Y., *et al*. (1999). In-situ Lorentz microscopy studies of spin-valve structures. *IEEE Transactions on Magnetics*, **35**(2), 788–793.

Petri, I., Zimmermann, T., Zweck, J., *et al*. (1996). Investigations on the stray-fields of magnetic read/write heads and their structural reasons. *IEEE Transactions on Magnetics*, **32**(5, pt. 1), 4141–4143.

Petrov, V.I., Spivak, G.V. and Pavlyuchenko, O.P. (1972a). Electron microscopy of the magnetic structure of thin films. *Soviet Physics Uspekhi*, **15**(66), 88–94.

Petrov, V.I., Spivak, G.V. and Pavlyuchenko, O.P. (1972b). Electron microscopy of the magnetic structure of thin films. *Uspekhi Fizicheskikh Nauk*, **106**, 229–278.

Ploessl, R., Chapman, J.N., Thompson, A.M., *et al*. (1993). Investigation of the micromagnetic structure of cross-tie walls in Permalloy. *Journal of Applied Physics*, **73**(5), 2447–2452.

Portier, X. and Petford-Long, A.K. (1999). Electron microscopy studies of spin-valve materials. *Journal of Physics D: Applied Physics*, **32**(16), R89–R108.

Portier, X. and Petford-Long, A.K. (2000). The formation of 360 degrees domain walls in magnetic tunnel junction elements. *Applied Physics Letters*, **76**(6), 754–756.

Portier, X., Petford-Long, A.K., Anthony, T.C. and Brug, J.A. (1998). Contribution of the magnetic field induced by the current

passing through a spin-valve element. *Journal of Magnetism and Magnetic Materials*, **187**(2), 145–153.

Portier, X., Petford-Long, A.K., Anthony, T.C. and Brug, J.A. (1998). Influence of current density on the magnetization process in active spin-valve elements. *Journal of Applied Physics*, **83**(11), 6840–6842.

Portier, X., Petford-Long, A.K., Anthony, T.C. and Brug, J.A. (1999a). Temperature dependence of the reversal mechanism in spin-valve films. *Applied Physics Letters*, **75**(9), 1290–1292.

Portier, X., Petford-Long, A.K., Anthony, T.C. and Brug, J.A. (1999b). Effect of stray-field coupling on active spin-valve elements analyzed by Lorentz transmission electron microscopy. *Journal of Applied Physics*, **85**(8), 4120–4126.

Portier, X., Petford-Long, A.K., Doole, R.C., *et al*. (1997a). In-situ magnetoresistance measurements on spin valve elements combined with Lorentz transmission electron microscopy. *IEEE Transactions on Magnetics*, **33**(5), 3574–3579.

Portier, X., Petford-Long, A.K., Doole, R.C., *et al*. (1997b). Lorentz transmission electron microscopy on NiFe/Cu/Co/NiFe/MnNi active spin valve elements. *Applied Physics Letters*, **71**(14), 2032–2034.

Portier, X., Petford-Long, A.K., Mao, S., *et al*. (1999). Microstructure and magnetic domain structure of Co/NiFe/MnNi systems. *IEEE Transactions on Magnetics*, **35**(5), 3091–3093.

Portier, X., Petford-Long, A.K., de Morais, A., *et al*. (2000). Magnetization reversal processes in exchange-biased systems. *Journal of Applied Physics*, **87**(9), 6412–6414.

Portier, X., Tsymbal, E.Yu., Petford-Long, A.K., *et al*. (1998). Correlation between domain structure and magnetoresistance in an active spin-valve element. *Physical Review B*, **58**(2), R591–R594.

Puchalska, I.B. and Spain, R.J. (1962). Observation des mé chanismes de I'hysté ré sis magné tique dans les couches minces. (Observation of the magnetic hysteresis mechanisms in thin films). *Comptes Rendus de l' Academie des Sciences Paris*, **254**, 72–74.

Raabe, J., Pulwey, R., Sattler, R., *et al*. (2000). Magnetization pattern of ferromagnetic nanodisks. *Journal of Applied Physics*, **88**(7), 4437–4439.

Rahm, M., Bentner, J., Schneider, M., *et al*. (2001). Hall-magnetometry on ferromagnetic micro-rhombs. *IEEE Transactions on Magnetics*, **37**, 2085.

Rahm, M., Schneider, M., Biberger, J., *et al*. (2003). Vortex nucleation in submicrometer ferromagnetic disks. *Applied Physics Letters*, **82**, 4110.

Rau, W.D., Lichte, H., Völkl, E. and Weierstall, U. (1991). Real-time reconstruction of electron-off-axis holograms recorded with a high pixel CCD camera. *Journal of Computer Assisted Microscopy*, **3**(2), 51–63.

Reimer, L. (1959). *Elektronenmikroskopische Untersuchungs- und Präparationsmethoden*, Springer-Verlag: Berlin.

Reimer, L. (1997). *Transmission Electron Microscopy*, *Fourth Edition*, Springer: Berlin.

Rickart, M., Guedes, A., Franco, N., *et al* (2005). Exchange bias in ordered antiferromagnets by rapid thermal anneal without magnetic field. *Journal of Physics D: Applied Physics*, **38**(13), 2151–2155.

Ridley, P.H.W., Roberts, G.W., Chantrell, R.W., *et al*. (2000). Computational and experimental micromagnetics of arrays of 2-D platelets. *IEEE Transactions on Magnetics*, **36**(5), 3161–3163.

Rijks, T.G.S.M., Reneerkens, R.F.O., Coehoorn, R., *et al*. (1997). Switching field interval of the sensitive magnetic layer in exchange-biased spin valves. *Journal of Applied Physics*, **82**(7), 3442–3451.

Rose, H. (1977). Nonstandard imaging methods in electron microscopy. *Ultramicroscopy*, **49**, 4–13.

Rose, J., Chapman, J.N., Phillips, G.N., *et al*. (1998). Time-dependent effects in materials with two-stage reversal processes. *Journal of Magnetism and Magnetic Materials*, **177–181**, 223–224.

Ross, C.A., Castano, F.J., Morecroft, D., *et al*. (2006). Mesoscopic thin-film magnetic rings (invited). *Journal of Applied Physics*, **99**(8), 8S501-1–8S501-6.

Rothman, J., Kläui, M., Lopez-Dias, L., *et al*. (2001). Observation of a bi-domain state and nucleation free switching in mesoscopic ring magnets. *Physical Review Letters*, **86**, 1098–1101.

Ruhrig, M., Porthun, S., Lodder, J.C., *et al*. (1996). Electron beam fabrication and characterization of high-resolution magnetic force microscopy tips. *Journal of Applied Physics*, **79**(6), 2913–2919.

Ruska, E.R. (1934). über Fortschritte im Bau und in der Leistung des magnetischen Elektronenmikroskops (About progess in construction and performance of the magnetic electron microscope). *Zeitschrift fur Physik*, **87**, 580.

Saxena, A., Castan, T., Planes, A., *et al*. (2004). Origin of magnetic and magnetoelastic tweedlike precursor modulations in ferroic materials. *Physical Review Letters*, **92**(19), 197203-1–197203-4.

Schattschneider, P., Carlino, E., Lichte, H., *et al*. (2004). CHIRAL-TEM-circular dichroism in the TEM. *13th European Microscopy Congress, Proceedings of EMC 2004, Belgian Society for Microscopy*, IM 11.O2.

Schattschneider, P., Rubino, S., Hébért, C., *et al*. (2006). Detection of magnetic circular dichroism using a transmission electron microscope. *Nature*, **441**, 486–488.

Schimmel, G. and Vogell, W. (1981). *Methodensammlung der Elektronenmikroskopie*, Wissenschaftliche Verlagsgesellschaft: Stuttgart.

Schneider, C.M. (1996). Spin-orbit influenced spectroscopies of magnetic solids, In Proceedings *Imaging Magnetic Microstructures with Elemental Selectivity: Application of Magnetic Dichroisms*, Ebert, H. and Schuetz, G. (Eds.), Springer: Berlin, pp. 179–196.

Schneider, M., Hoffmann, H., Otto, S., *et al*. (2002). Stability of magnetic vortices in flat submicron permalloy cylinders. *Journal of Applied Physics*, **92**, 1466.

Schneider, M., Hoffmann, H. and Zweck, J. (2000). Lorentz microscopy of circular ferromagnetic permalloy nanodisks. *Applied Physics Letters*, **77**, 2909–2911.

Schneider, M., Hoffmann, H. and Zweck, J. (2001). Magnetic switching of single vortex permalloy elements. *Applied Physics Letters*, **79**(19), 3113–31151.

Schneider, M., Hoffmann, H. and Zweck, J. (2003). Magnetisation reversal of thin submicron elliptical Permalloy elements. *Journal of Magnetism and Magnetic Materials*, **257**, 1–10.

Schneider, M., Liszkowski, J., Rahm, M., *et al*. (2003). Magnetization configurations and hysteresis loops of small permalloy ellipses. *Journal of Physics D: Applied Physics*, **36**(18), 2239–2243.

Schrefl, T., Fidler, J., Chapman, J.N. and Kirk, K.J. (2001). Micromagnetic simulation of domain structures in patterned magnetic tunnel junctions. *Journal of Applied Physics*, **89**(11), 7000–7002.

Schrefl, T., Fidler, J., Kirk, K.J. and Chapman, J.N. (1997a). Domain structures and switching mechanisms in patterned magnetic elements. *Journal of Magnetism and Magnetic Materials*, **175**(1–2), 193–204.

Schrefl, T., Fidler, J., Kirk, K.J. and Chapman, J.N. (1997b). A higher order FEM-BEM method for the calculation of domain processes in magnetic nano-elements. *IEEE Transactions on Magnetics*, **33**(5), 4182–4184.

Schrefl, T., Fidler, J., Kirk, K.J. and Chapman, J.N. (1999). Simulation of magnetization reversal in polycrystalline patterned Co elements. *Journal of Applied Physics*, **85**(8), 6169–6171.

Shang, P., Hogwood, A., Anthony, T.C. and Petford-Long, A. (2001). Lorentz microscopy study of spin tunnel junction elements. In *Electron Microscopy and Analysis 2001, Proceedings*, Aindow, M. and Kiely, C.J. (Eds.), IOP Publishing: Bristol, UK, pp. 461–464.

Shang, P., Hogwood, A., Petford-Long, A.K. and Anthony, T.C. (2001). Lorentz microscopy study of magnetization reversal mechanism in magnetic tunnel junction elements. *Journal of Applied Physics*, **89**(11), 7368–7370.

Shang, P., Petford-Long, A.K. and Anthony, T.C. (2002). Effects of two in-plane fields on the magnetization reversal mechanism in magnetic tunnel junction elements. *Journal of Applied Physics*, **91**(10), 7703–7705.

Shinjo, T., Okuno, T., Hassdorf, R., *et al*. (2000). Magnetic vortex core observation in circular dots of Permalloy. *Science*, **289**, 930.

Speidel, R. and Kurz, D. (1977). Measurement of the brightness of a field emission electron gun. *Optik*, **49**, 173.

Stolojan, V., Dunin-Borkowski, R.E., Weyland, M. and Midgley, P.A. (2001). Three-dimensional magnetic fields of nanoscale elements determined by electron-holographic tomography. In *Electron Microscopy and Analysis 2001, Proceedings*, Aindow, M. and Kiely, C.J. (Eds.), IOP Publishing: Bristol, UK, pp. 243–246.

Suss, D., Schrefl, T., Fidler, J. and Chapman, J.N. (1999). Micromagnetic simulation of the long-range interaction between NiFe nano-elements using the BE-method. *Journal of Magnetism and Magnetic Materials*, **196–197**, 617–619.

Thompson, P., Gutfleisch, O., Chapman, J.N., *et al*. (1998). A magnetic and compositional study of the disproportionated stage of the solid-HDDR process in NdFeB-type materials. *Journal of Alloys and Compounds*, **281**(1), 12–16.

Thompson, P., Gutfleisch, O., Chapman, J.N. and Harris, I.R. (1998). Domain studies in thin sections of HDDR-processed Nd-Fe-B-type magnets by TEM. *Journal of Magnetism and Magnetic Materials*, **177–181**, 978–979.

Thompson, P., Gutfleisch, O., Chapman, J.N. and Harris, I.R. (1999). A comparison of the micromagnetic and microstructural properties of four NdFeB-type materials processed by the HDDR route. *Journal of Magnetism and Magnetic Materials*, **202**(1), 53–61.

Terris, B.D., Folks, L., Weller, D., *et al*. (1999). Ion-beam patterning of magnetic films using stencil masks. *Applied Physics Letters*, **75**(3), 403–405.

Tonomura, A. (1983). Observation of magnetic domain structure in thin ferromagnetic films by electron holography. *Journal of Magnetism and Magnetic Materials*, **31–34**(pt. 2), 963–969.

Tonomura, A., Matsuda, T., Endo, J., *et al*. (1980). Direct observation of fine structure of magnetic domain walls by electron holography. *Physical Review Letters*, **44**(21), 1430–1433.

Toporov, A.Yu., Langford, R.M. and Petford-Long, A.K. (2000a). Lorentz transmission electron microscopy of focused ion beam patterned magnetic antidot arrays. *Applied Physics Letters*, **77**(19), 3063–3065.

Uhlig, T., Heumann, M. and Zweck, J. (2003). Development of a specimen holder for in situ generation of pure in-plane magnetic fields in a transmission electron microscope. *Ultramicroscopy*, **94**, 193–196.

Uhlig, T.and Zweck, J. (2002). The performance of a fully digitized DPC device, S23. *Proceedings of the 15th International Congress on Electron Microscopy (ICEM XV)*, S23 Durban, 1–6 September 2002.

Uhlig, T. and Zweck, J. (2004). Recording of single-particle hysteresis loops with differential phase contrast microscopy. *Ultramicroscopy*, **99**, 137–142.

Völkl, E., Allard, L.F. and Frost, B. (1995). A software package for the processing and reconstruction of electron holograms. *Journal of microscopy*, **180**, 39–50.

Völkl, E., Allard, L.F. and Joy, C. (1999). *Introduction to Electron Holography*, Kluwer-Verlag: New York.

Volkov, V.V. and Zhu, Y. (2004). Lorentz phase microscopy of magnetic materials. *Ultramicroscopy*, **98**, 271–281.

Wade, R.H. (1962). The determination of domain wall thickness in ferromagnetic films. *Proceedings of the Physical Society of London*, **79**, 1237.

Wade, R.H. (1968). Transmission electron microscope observations of ferromagnetic domain structures. *Journal de Physique*, Colloque C2, **29**, 95–109.

Wang, Y.G. and Petford-Long, A.K. (2002). Magnetization reversal of the ferromagnetic layer in IrMn/CoFe bilayers. *Journal of Applied Physics*, **92**(11), 6699–6707.

Wang, Y.G., Petford-Long, A.K. and Kief, M.T. (2001). Lorentz electron microscopy study of magnetisation reversal mechanism in exchange-coupled bilayers. In *Electron Microscopy and Analysis 2001, Proceedings*, Aindow, M. and Kiely, C.J. (Eds.), IOP Publishing: Bristol, UK, pp. 453–456.

Wang, Y.G., Petford-Long, A.K., Laidler, H., *et al*. (2002). Thermally activated reversal in exchange-coupled structures. *IEEE Transactions on Magnetics*, **38**(5), 2773–2775.

Warin, P., Hyndman, R., Glerak, J., *et al*. (2001). Modification of Co/Pt multilayers by gallium irradiation-Part 2: The effect of patterning using a highly focused ion beam. *Journal of Applied Physics*, **90**(8), 3850–3855.

Warot, B., Petford-Long, A.K. and Anthony, T.C. (2003). Magnetic properties of patterned tunnel junctions. *Journal of Applied Physics*, **93**(10), 7287–7289.

Weir, I.S., Chapman, J.N., Molchanov, I.S., *et al*. (1999). Observation and modelling of magnetization reversal in multilayers supporting perpendicular magnetization. *Journal of Physics D: Applied Physics*, **32**(4), 395–403.

Williams, D.B. (1984). *Practical Analytical Electron Microscopy in Materials Science*, Verlag Chemie International: Deerfield Beach, ISBN/ISSN 3-527-26224-5.

Williams, D.B. and Carter, C.B. (1996). *Transmission Electron Microscopy*, Plenum Press: New York, pp. 1–4.

Wong, H.Y., Chapman, J.N., McVitie, S. and Hefferman, S.J. (1992). The influence of evaporation rate on the domain structures of Permalloy and cobalt small magnetic particles. *Journal of Magnetism and Magnetic Materials*, **104–107**, 329–330.

Yi, G., Aitchison, P.R., Doyle, W.D., *et al*. (2002). Influence of end shape, temperature, and time on the switching of small magnetic elements. *Journal of Applied Physics*, **92**(10), 6087–6093.

Yi, G., Nicholson, W.A.P., Lim, C.K., *et al*. (2004). A new design of specimen stage for in situ magnetising experiments in the transmission electron microscope. *Ultramicroscopy*, **99**, 65–72.

Youhui, Gao., Shindo, D. and Petford-Long, A.K. (2003). Nonuniform magnetic structure in Nd/sub 2/Fe/sub 14/B/Fe/sub 3/B nanocomposite materials. *Journal of Applied Physics*, **93**(10), 8119–8121.

Young, S. and Chapman, J.N. (1993). An investigation of domains and walls in two NdFeB alloys by transmission electron microscopy. *IEEE Transactions on Magnetics*, **29**(6), 2779–2781.

Yu, A.C.C., Lo, C.C.H., Petford-Long, A.K., *et al*. (2002). Lorentz transmission electron microscopy and magnetic force microscopy characterization of NiFe/Al-oxide/Co films. *Journal of Applied Physics*, **91**(2), 780–784.

Yu, C.C., Petford-Long, A.K. and Jakubovics, J.P. (1999). Direct observation of domains and magnetization switching processes in NiFe/alumina/Co trilayer junctions. *Journal of Magnetism and Magnetic Materials*, **198–199**, 503–505.

Yu, A.C.C., Petford-Long, A. and Miyazaki, T. (2001). Direct observation of domain structure and magnetization reversal of magnetic thin films using Lorentz transmission electron microscopy. *Japanese Journal of Applied Physics, Part 1 Regular Papers, Short Notes and Review Papers*, **40**(8), 4891–4896.

Zhou, L., McVitie, S. and Chapman, J.N. (1995). Magnetic imaging of magnetic force microscope tips. *Journal of Magnetism and Magnetic Materials*, **148**(1–2), 237–238.

Zhu, Y., Volkov, V.V. and de Graef, M. (2001). Understanding magnetic structures in permanent magnets via in situ Lorentz microscopy, interferometric and non-interferometric phase-reconstructions. *Journal of Electron Microscopy*, **50**(6), 447–455.

Zimmermann, T., Zweck, J. and Hoffmann, H. (1995a). Quantification of Lorentz microscopy images of Co/Cu multilayer systems. *Journal of Magnetism and Magnetic Materials*, **148**(1–2), 239–240.

Zimmermann, T., Zweck, J. and Hoffmann, H. (1995b). Magnetic coupling of Co layers through a Cu spacer layer. *Journal of Magnetism and Magnetic Materials*, **149**, 409–417.

Zweck, J. and Bormans, B. (1992). The CM 30 Lorentz Lens. *Philips Electron Optics Bulletin*, **132**, 1–8.

Zweck, J., Chapman, J.N., McVitie, S. and Hoffmann, H. (1992). Reconstruction of induction distributions in thin films from DPC images. *Journal of Magnetism and Magnetic Materials*, **104–107**, 315–316.

Zweck, J., Schneider, M., Sessner, M., *et al*. (2001). Lorentz Electron Microscopic Observation of Micromagnetic Configurations in Nanostructured Materials. In *Advances in Solid State Physics*, Kramer (Hrsg.), B. (Ed.), Vieweg Verlag, pp. 533–545, Vol. 41, ISBN: 3-540-42000-2.

Zweck, J., Zimmermann, T. and Schuhrke, T. (1997). TEM imaging and evaluation of magnetic structures in Co/Cu multilayers. *Ultramicroscopy*, **67**, 153–162.

FURTHER READING

Chapman, J.N., Ferrier, R.P., Heyderman, L.J., *et al*. (1993). Micromagnetics, microstructure and microscopy. In *Electron Microscopy and Analysis 1993*, Proceedings of the Institute of Physics Electron and Analysis Group Conference, Craven, A.J. (Ed.), IOP Publishing: Bristol UK, pp. 1–8.

Chapman, J.N., Rogers, D.J. and Bernards, J.P.C. (1988). Analysis of magnetic domain structures in CoCr sputtered films using differential phase contrast electron microscopy. *Journal de Physique Colloque*, **49**(C-8), 1965–1966.

Chapman, J.N. (1984). The investigation of magnetic domain structures in thin foils by electron microscopy. *Journal of Physics D: Applied Physics*, **17**, 623–647.

Harscher, A. and Lichte, H. (1996). Experimental study of amplitude and phase detection limits in electron holography. *Ultramicroscopy*, **64**, 57–66.

Lichte, H. (1986). Electron holography approaching atomic resolution. *Ultramicroscopy*, **20**, 293–304.

Petri, I., Zimmermann, T., Zweck, J., *et al*. (1996). Investigations on the stray-fields of magnetic read/write heads and their structural reasons. *IEEE Transactions on Magnetics*, **32**(5, pt. 1), 4141–4143.

Tonomura, A. (1998). *Electron Holography*, *2nd Edition*, Springer.

Electron Holography of Ferromagnetic Materials

Martha R. McCartney and David J. Smith
Arizona State University, Tempe, AZ, USA

1 INTRODUCTION

The transmission electron microscope (TEM) has long been considered to be an indispensable tool for characterizing microstructure. Applications of the TEM span across many scientific disciplines and many different types of material. However, information about magnetic induction cannot easily be obtained. Under normal operating conditions, the magnetic field of the objective lens used for imaging is in the order of 1.5–2.0 T, which would fully saturate most magnetic materials in the vertical direction. Studies of inherent remanent states or magnetization reversal behavior are automatically precluded. The microscopist must either remove the magnetic sample from the normal imaging plane out of the strong lens field or switch off the objective lens current and rely on an auxiliary lens for imaging purposes. The latter approach is nowadays most commonly used for TEM examination of magnetic materials.

Handbook of Magnetism and Advanced Magnetic Materials. Edited by Helmut Kronmüller and Stuart Parkin. Volume 3: *Novel Techniques for Characterizing and Preparing Samples*. ISBN: 978-0-470-02217-7.

Several TEM techniques suitable for studying magnetic materials have been developed over the years. The well-known Lorentz microscopy takes advantage of the sideways deflection of the incident electrons by the magnetic field within the sample (Chapman, 1984; McVitie and Chapman, 1997). For the in-focus imaging condition, there is no distinct magnetic contrast, but black and white lines become visible, corresponding to the positions of magnetic domain walls, when the lens is defocused. Drawbacks of Lorentz microscopy are that long-range magnetic fields are difficult to visualize, the resolution is somewhat limited except for special variants that are available with a scanning microscope, and absolute quantification of field strengths can be difficult to achieve. Nevertheless, a major attraction of Lorentz microscopy is that domain-wall nucleation, as well as motion, can be observed in real time during magnetization reversal.

Off-axis electron holography is an alternative electron microscopy technique that has proved ideal for studying the magnetic state and response of ferromagnetic materials at length scales approaching the nanometer level (Lichte, 1986, 1991; Tonomura, 1993). By measuring the phase change of the electron wave that has traveled through the sample relative to an unperturbed reference wave, a quantitative measure of the local magnetic field can be obtained. Important micromagnetic properties such as coercivity, magnetization reversal behavior, and remanent states can be extracted following hologram analysis.

There are at least 20 different forms of electron holography (Cowley, 1992), but the off-axis or sideband variant is almost invariably used because it is relatively straightforward to implement in modern TEMs. This particular technique relies on the interference between two coherent electron waves, as illustrated in Figure 1. The field emission electron gun (FEG) provides the essential beam coherence, and the electrostatic biprism, normally located in the selected-area

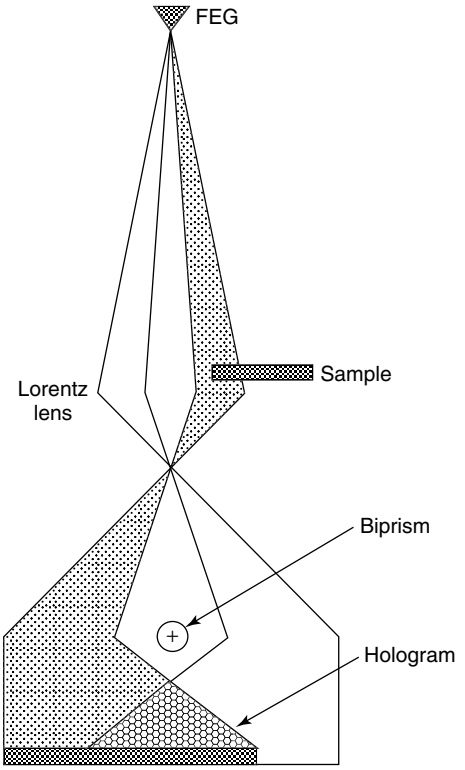

Figure 1. Schematic ray diagram illustrating experimental geometry used for off-axis electron holography in the TEM. Essential components are the field emission electron gun (FEG) used to provide coherent illumination, and the electrostatic biprism, which causes overlap of object and (vacuum) reference waves. Lorentz mini-lens enables field-free observation of specimen at moderate magnification (∼70 000×) and resolution (∼1.4 nm).

aperture plane, is used to overlap the wave scattered by the object with the reference vacuum wave. The resulting interference pattern is then processed in order to retrieve the electron phase, in turn allowing access to the desired information about the magnetic field of the sample. In the next section, the basic theory and experimental practice of off-axis electron holography are outlined. Representative examples that illustrate applications of the technique to magnetic materials, including hard magnets, thin films, and nanostructures, are then described. Finally, future prospects are briefly discussed.

2 OFF-AXIS ELECTRON HOLOGRAPHY

The technique of off-axis electron holography has attracted much recent attention because it enables magnetic materials to be studied at high spatial resolution and sensitivity. One attractive feature relative to other magnetic imaging techniques is that unwanted effects arising from local variations in sample thickness and composition are normally removed relatively easily so that much smaller regions of the sample can be analyzed. The technique can in principle achieve a spatial resolution of better than 1 nm for magnetic materials although there are practical limitations associated primarily with the signal-to-noise ratio available during hologram recording and processing (Harscher and Lichte, 1996). Moreover, the specimen thickness must be restricted to a maximum of perhaps 400 nm, and preferably considerably less, so that elastic and inelastic scattering effects do not adversely affect the hologram quality.

2.1 Basic theory

Off-axis electron holography relies on having a high-brightness electron source to emit a highly coherent beam of electrons onto the sample region of interest. The phase across the electron wave front emerging from the sample will vary according to the local composition and density (i.e., mean inner potential, MIP) in addition to the magnetic field component. Making an assumption of negligible dynamical diffraction, which would impact the phase for crystalline materials that are close to a strongly diffracting condition (Gajdardziska-Josifovska *et al*., 1993), the relative phase change of the object (or scattered) wave compared with the reference (or vacuum) wave can be expressed as

$$\phi(x) = C_E \int V(x,z)\,\mathrm{d}z - \frac{e}{\hbar}\iint B_\perp(x,z)\,\mathrm{d}x\,\mathrm{d}z \qquad (1)$$

where z represents the incident beam direction, x is a direction in the sample plane, V is the MIP, and $B_\perp$ is the magnetic induction component that is perpendicular to both x and z (Reimer, 1989). The constant C_E is given by the expression

$$C_E = \frac{2\pi}{\lambda E}\frac{E+E_0}{E+2E_0} \qquad (2)$$

where λ is the electron wavelength, and E and E_0 are the kinetic and rest mass energies, respectively, of the incident electron.

When neither V nor B vary along the beam direction within the sample thickness t, and assuming that the electric field as well as magnetic fringing fields outside the sample can be neglected, this expression for the phase can be simplified as

$$\phi(x) = C_E V(x)t(x) - \frac{e}{\hbar}\int B_\perp(x)t(x)\,\mathrm{d}x \qquad (3)$$

This latter expression means that the strength of the magnetic signal, as given by the second term, depends on both the thickness and the lateral width of the particular magnetic material(s) present.

Differentiation with respect to x then leads to

$$\frac{\mathrm{d}\phi(x)}{\mathrm{d}x} = C_E \frac{\mathrm{d}}{\mathrm{d}x}\{V(x)t(x)\} - \frac{e}{\hbar}B_{\perp}(x)t(x) \tag{4}$$

The first term in this expression will be zero in the event that the sample has uniform thickness and composition. Thus, the gradient of the phase is directly interpretable in terms of the in-plane magnetic induction. Equiphase contours are easily added to a phase image, and their relative separation provides a convenient way to 'visualize' any local variations in field strength. Indeed, the in-plane field can be quantified on an absolute basis. Extra complications will arise when the sample thickness and/or composition are not uniform: as described later, further processing is necessary before quantitative information can be reliably extracted.

When the object and reference waves are overlapped by the electrostatic biprism to produce an interference pattern or hologram, then the intensity can be written in the form

$$I(x, y) = |\Psi_1(x, y)|^2 + |\Psi_2(x, y)|^2 + |\Psi_1(x, y)|\,|\Psi_2(x, y)| \times (e^{i(\phi_1-\phi_2)} + e^{-i(\phi_1-\phi_2)}) \tag{5}$$

or it can be rewritten in the simpler form

$$I(x, y) = A_1^2 + A_2^2 + 2A_1A_2\cos(\Delta\phi) \tag{6}$$

where Ψ is the electron wave function, $\Delta\phi$ is the relative electron phase change, and the subscripts refer to the reference and object waves. This expression can be interpreted as the normal TEM image in addition to a superimposed cosine function, which represents the interference fringes of the hologram. Shifts in the positions of these interference fringes are caused by local changes in the electrostatic and/or magnetic fields of the sample.

For better comprehension of this technique, the steps involved in hologram recording and processing are illustrated in Figure 2. An electron hologram from part of a chain of magnetic nanocrystals from a magnetotactic bacterial cell, supported on a holey carbon film, is shown in Figure 2(a). Note how the spacings and directions of the fringes change as they cross the crystallites. The hologram is then Fourier transformed to produce a two-dimensional frequency map, as shown in Figure 2(b). The strong side spots correspond to the basic cosine interference, and their separation depends primarily on the biprism voltage. The variations of intensity that are visible in the vicinity of these spots originate from the phase shifts caused by the sample. These sidebands contain the desired phase information about the image wave, which cannot be obtained from the central 'autocorrelation' function. Reconstruction of the complex image wave then utilizes one of these sidebands.

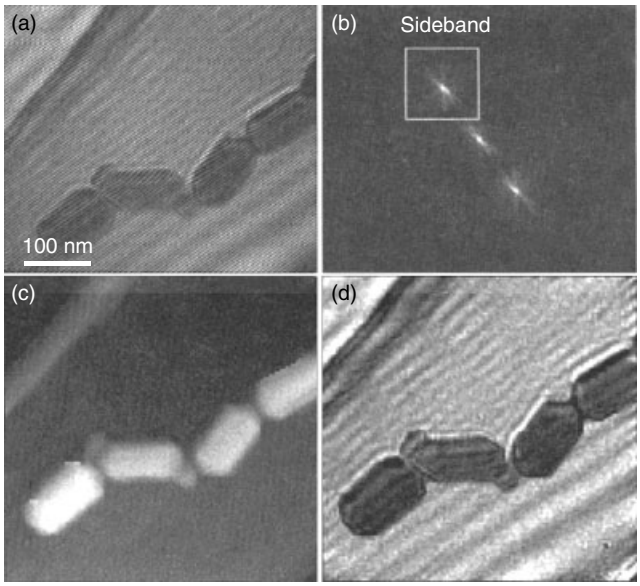

Figure 2. (a) Off-axis electron hologram showing part of a chain of magnetite nanocrystals; (b) Fourier transform of (a) indicating sideband used in phase reconstruction; (c) reconstructed phase image; (d) reconstructed amplitude image.

The actual reconstruction process involves extraction and recentering of one of the sidebands, followed by calculation of its inverse Fourier transform to retrieve the complex image wave function. The phase and amplitude of the complex image are then given by

$$\phi = \arctan(i/r)$$
$$A = \mathrm{sqrt}(r^2 + i^2) \tag{7}$$

where 'r' and 'i' refer to the real and imaginary parts of the wave function, respectively.

This reconstruction process was applied to the hologram shown in Figure 2(a) and the corresponding phase and amplitude, respectively, are shown in Figure 2(c) and (d). Note that the phase is normally calculated modulo 2π so that phase shifts which exceed this amount will cause 2π phase discontinuities at positions in the phase image that are unlikely to be related in any meaningful way to specific specimen features. Thus, the phase should be carefully unwrapped to make sure that the image features are interpreted correctly. In this regard, it is helpful when the hologram is recorded digitally, since this recording mode facilitates the subsequent reconstruction process.

2.2 Experimental geometry

The geometry for carrying out off-axis electron holography studies in the electron microscope has been illustrated

schematically in Figure 1. The FEG provides the defocused illumination onto the sample, which is located in such a way that it covers roughly half the field of view. The electrostatic biprism is used to achieve overlap between the object (scattered) wave and the vacuum (reference) wave. The biprism usually consists of a thin (<1 μm) metallic wire or quartz fiber coated with gold or platinum. Application of an electric potential from a dc power supply or battery results in formation of the interference pattern or hologram. Typical biprism voltages for the medium-resolution studies considered here are between 50 and 200 V. Higher voltages are, however, necessary in order to achieve the subangstrom fringe spacings that are required for high-resolution applications (Orchowski, Rau and Lichte, 1995). Finally, note that a rotatable biprism is highly useful in practice since the direction of the interference fringes should often be aligned preferentially with particular features of the sample.

The usual location for the biprism is in the plane of the selected-area aperture holder, often replacing one of the selected-area apertures. For this geometry, the first image plane must be shifted electron-optically to slightly below the selected-area plane by increasing the excitation of the diffraction or intermediate lens. The spacing of the interference fringes and the amount of fringe overlap will be determined by the voltage on the biprism as well as by the specific lens-specimen geometry (Smith and McCartney, 1999).

Several geometries have been used by electron microscopists to ensure that a magnetic sample is located in a field-free region for observation. By simply turning off the normal objective lens, a low-magnification image and a large field of view can be obtained. The image resolution is relatively poor although a postcolumn image filter, if available, could be used to obtain additional image magnification. Another alternative is to use a weak imaging lens below the normal objective lens. For example, the Philips CM200 FEG-TEM has a special mini-lens, which permits an overall image magnification of up to 70 000×, although the reconstructed phase image has a spatial resolution that is limited by the lens aberrations to about 1.4 nm (McCartney, Smith, Farrow and Marks, 1997). Many of the holography results described later originated from a microscope of this type. Yet another approach is to use a modified specimen holder, whereby the sample is located just outside the field of the immersion objective lens. A far-out-of-focus image is obtained, so that extra phase shifts caused by the lens defocus must be corrected (Mankos, Higgs, Scheinfein and Cowley, 1995). This geometry, unfortunately, is not available with most commercial instruments.

The attachment of a slow-scan charge-coupled-device (CCD) camera at the base of the lens column permits digital recording of electron holograms (de Ruijter, 1995), greatly expediting the reconstruction process (de Ruijter and Weiss, 1993; Smith and McCartney, 1999). The CCD camera is a sensitive electron detector, with linear output versus input over a wide dynamic range. Thus, the nonlinear optical density of the conventional photographic plate is no longer a problem. Subsequent computer processing is also facilitated by the digital hologram acquisition (de Ruijter and Weiss, 1993). Holograms recorded using a CCD camera enable phase shifts to be measured with high accuracy and sensitivity once due correction for phase distortions has been made using the reference hologram.

2.3 Practical factors

The spatial coherence of the incident electron beam is crucial for practical electron holography. It is necessary to minimize the beam convergence angle since poor interference-fringe contrast will otherwise result and weak phase detail will then be lost from the reconstructed hologram. It has become common in off-axis electron holography to use highly elliptical illumination. The condenser lens stigmator settings are adjusted to achieve high illumination aspect ratios: 100:1 is not uncommon (Smith and McCartney, 1999). Note also that the major axis of the elliptical illumination patch must be aligned so that it is perpendicular to the biprism wire direction. The beam coherence, and hence the fringe contrast, will then be maximized (Völkl and Lehmann, 1999).

The reconstruction process is impacted by several additional factors. Smaller fringe spacings are needed for small object dimensions and/or wider regions of fringe overlap, and this in turn necessitates higher biprism voltages. However, the fringe contrast usually drops when the biprism voltage is increased. Moreover, the magnification must be increased to ensure sufficient sampling of the finely spaced interference fringes. Four recording pixels per hologram fringe is commonly considered as the minimum acceptable sampling (Joy *et al.*, 1993), but even greater sampling is recommended when sensitive phase measurements are being made (Smith and McCartney, 1999). Lens aberrations do not usually limit the spatial resolution of the final reconstructed phase image for magnetic materials, which depends instead mainly on the effective size of the sideband selected during hologram reconstruction. The resolution will be limited by the available signal strength and the required phase sensitivity (i.e., the signal-to-noise ratio in the phase image). Phase sensitivities of perhaps $2\pi/100$ can be achieved routinely during holographic studies (de Ruijter and Weiss, 1993), making it possible to detect details in thin magnetic films on a scale of about 5 nm (Harscher and Lichte, 1996). The resolution of smaller features normally requires longer acquisition times or stronger magnetic induction within the sample.

It is usual practice to record reference holograms with the sample removed from the field of view so that any artifacts associated with local imperfections or irregularities of the imaging and recording system can be excluded. Otherwise, phase distortions occur that will limit the accuracy and integrity of the hologram reconstruction process. Finally, note that accurate registration of sample and reference holograms is conveniently achieved when digital recording is used, which is unlike the situation for conventional photographic recording.

2.4 Magnetization reversal and phase contributions

Under normal conditions for off-axis electron holography, the magnetic sample must be located in a field-free environment, which enables its inherent magnetization, or 'remanent state', to be determined. Knowledge of magnetization reversal mechanisms is, however, important for many practical applications. One straightforward way for these processes to be studied via electron holography is to slightly excite the current in the objective lens coil, and then in-plane magnetic fields, as determined by prior calibration, can be applied by tilting the sample by fixed amounts (Dunin-Borkowski *et al*., 2000). Thus, the magnetization reversal behavior can be fully documented over an entire hysteresis cycle by recording holograms throughout the tilting process.

An additional benefit of carrying out *in situ* magnetization reversal is that the MIP and magnetic contributions to the phase, as described in equations (3) and (4), can be conveniently separated. Thus, pairs of holograms that differ only in the magnetization direction during recording can be added to give the MIP term, while subtraction yields the magnetic term. The MIP term can then be subtracted from all of the other phase images recorded during the cycle to retrieve the magnetic signal. An alternative approach, but not really a practical option in many cases, would be to turn the sample upside down, thereby changing the sign of the magnetic contribution. This separation of phase contributions also means that the magnetic fields can then be quantified on an absolute basis. For example, phase contours can be easily added to the reconstructed phase image, where phase differences of 2π correspond to the quantity $(h/e) = 4 \times 10^{-15}$ Wb.

3 APPLICATIONS TO MAGNETIC MATERIALS

Electron holography was originally proposed by (Gabor, 1949) as a means of correcting electron microscope lens aberrations. This goal was not realized for many years due to various factors – especially the poor coherence of the electron sources available then. Using FEG electron sources, conventional microscope resolution limits were finally surpassed for electron holography with both optical reconstruction methods (Tonomura, Matsuda and Endo, 1979) and digital reconstruction (e.g., Orchowski, Rau and Lichte, 1995; Rau and Lichte, 1999). Off-axis electron holography has since been successfully used in a wide variety of applications. The examination of ferroelectric and electrostatic fields has been attracting increasing attention in recent years. However, such topics are beyond the scope of this review, and the interested reader is referred elsewhere to a recent comprehensive review for further details (Dunin-Borkowski, McCartney and Smith, 2004a).

3.1 Early studies

Historically, the early studies of magnetic materials using electron holography were limited by poor spatial resolution (considerably worse than 10 nm), caused mainly by the need to locate the sample in a region of very low magnetic field. Imaging was restricted to the diffraction/projector system of lenses below the sample with the strong objective lens switched off. The total magnification was only in the order of a few thousand times, and reconstruction of the hologram was done optically because photographic film had been used for recording the holograms. Notable results included confirmation of the Aharonov–Bohm effect in superconducting Nb at low temperature (Tonomura *et al*., 1986) and studies of quantized vortex 'lattices' in a superconducting Nb thin film (Bonevich *et al*., 1993). Another interesting example involved examination of a thin magnetized Co film, used for high-density recording media applications: in this particular study, fringing fields were clearly visualized leaking out from the edge of the thin film (Osakabe *et al*., 1983).

3.2 Hard magnets and magnetic domains

Permanent magnets with large remanence and high coercivity have many practical applications so that any information about magnetic microstructure that can be provided by electron holography should be highly useful. Ternary alloys based on Nd–Fe–B (McCartney and Zhu, 1998a; Park and Shindo, 2002) and related nanocomposite materials (Park, Shindo, Kanekiyo and Hirosawa, 2004) have received considerable recent attention. Figure 3 shows some results from a study of magnetic domain structure in sintered $Nd_2Fe_{14}B$ (McCartney and Zhu, 1998b). A pair of overfocus and underfocus Lorentz images are shown in Figure 3(a) and (b): note the contrast

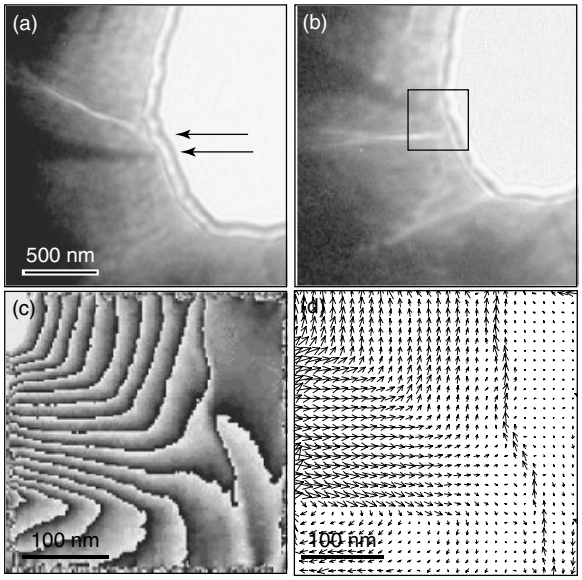

Figure 3. (a, b) Overfocus and underfocus Lorentz micrographs showing domain walls (arrows in a) in sample of $Nd_2Fe_{14}B$; (c) reconstructed phase image from region outlined in (b), contoured at 0.5π radian intervals; (d) induction map derived from phase gradients showing 90° and 180° domain walls. (Reproduced from McCartney & Zhu 1998, with permission from the American Institute of Physics. © 1998.)

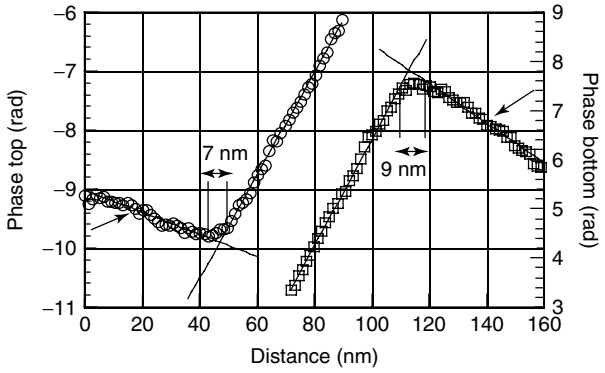

Figure 4. Profile of phase across 90° and 180° domain walls in $Nd_2Fe_{14}B$. Maximum wall widths of 6.7 and 9.2 nm, respectively. (Reproduced from McCartney & Zhu 1998, with permission from the American Institute of Physics. © 1998.)

inversion at the domain walls (arrows). The contoured phase image in Figure 3(c) was reconstructed from an off-axis electron hologram of the region indicated in Figure 3(b). Those regions with equispaced phase contours indicate uniform magnetization giving rise to a constant phase plane, whereas the ridges and valleys correspond to the domain-wall positions visible in the Lorentz images. Phase gradient maps are easily calculated, and by combining two perpendicular gradient images it is possible to produce a vector map, which is a direct image of the magnetic domain structure of the sample. The vector map, shown in Figure 3(d), is divided into $10 \times 10\,\text{nm}^2$ squares. Three distinct domains are visible, with the magnetic induction in the top and middle domains oriented at approximately 90° and oriented at roughly 180° in the middle and lower domains. Moreover, by measuring the distance over which the slope of the phase abruptly changes, estimates of the domain-wall width can be extracted. Figure 4 shows corresponding phase profiles from the 90° and 180° domain walls of Figure 3, and measurements indicate maximum wall widths of 6.7 ± 1.4 and 9.2 ± 1.4 nm, respectively. Finally, it is interesting that, based on estimates for the foil thickness derived from the mean free path for inelastic electron scattering (McCartney and Gajdardziska-Josifovska, 1994), the vector lengths can be used to calculate the corresponding magnetizations of $4\pi M_s = B = 0.8$, 1.2, and 0.5 T for the top, middle, and bottom domains, respectively. The differences may come from undetermined fringing fields immediately above and below the sample surface, or because the technique is insensitive to any out-of-plane components.

The rearrangement of magnetic domains in ferromagnetic shape memory alloys (FMSAs) is an important aspect of developing practical applications. Alloys with stoichiometry close to Ni_2MnGa are of particular interest because of the large shape deformation (~6%) induced by an applied field (Ullakko *et al*., 1996), which has been attributed to rearrangement of twin-related plates of the martensitic material. Electron holography and Lorentz microscopy have been used in recent studies of magnetic domain structure of FMSA Ni_2MnGa, both in thin-film form prepared by sputtering (Murakami *et al*., 2003, 2004), and in spherical particles prepared by spark erosion and annealed to achieve the martensitic phase (Solomon *et al*., 2005). The results shown in Figure 5 are taken from this latter study. The stripes visible in Figure 5(a) correspond to the twin-related martensitic variants, and out-of-focus Lorentz microscopy showed that the twin boundaries corresponded to the positions of the magnetic domain walls. Figure 5(b) shows the reconstructed phase image after electron holography from the area indicated in Figure 5(a), while Figure 5(c) shows the x-phase gradient which is proportional to the in-plane magnetization component. The vector map derived from the phase gradient images is shown in Figure 5(d). Careful measurement reveals that the in-plane projections of the magnetization across the domains are oriented at roughly 60°, corresponding closely to the value expected when the c axes of the twin-related variants are projected onto the sample plane. Finally, Figure 5(e) shows the line profile across the domain indicated in Figure 5(b), and the domain-wall width is measured to be about 17 nm (Solomon *et al*., 2005), consistent with theoretical estimates. These studies of magnetic domains in giant

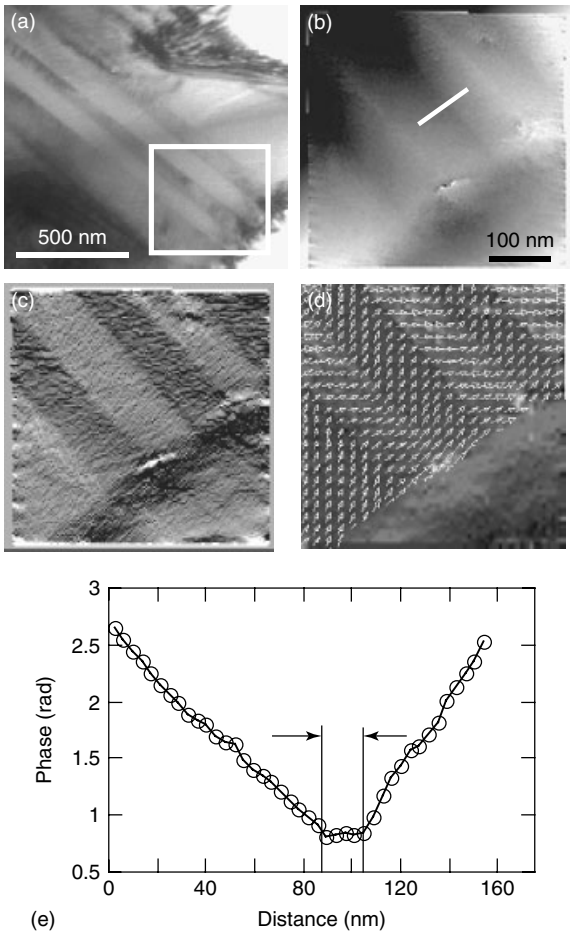

Figure 5. (a) In-focus Lorentz electron micrograph showing martensitic twin boundaries in a $Ni_{51}Mn_{29}Ga_{20}$ particle grown by spark erosion; (b) reconstructed phase image from hologram of region shown in (a); (c) x-phase gradient proportional to magnetization component; (d) vector map obtained from phase gradient images showing changes of magnetization direction across domain walls; (e) line profile across the domain wall indicated by line in (b). (Reproduced from Solomon *et al*., 2005, with permission from the American Physical Society. © 2005.)

magnetorestrictive materials indicate that electron holography should play a valuable role toward developing a better understanding of other FMSA materials in future studies.

3.3 Thin films

An important consideration with hard magnets, especially when thinned down to an electron-transparent foil from the bulk form of the material, is the likelihood that magnetic fringing fields will emerge from the top and bottom surfaces. Off-axis electron holography (and Lorentz microscopy) is not sensitive to these out-of-plane field components so that the true three-dimensional nature of the magnetic vector field in and surrounding a magnetic sample may not always be fully determined. Moreover, the magnetic properties could be altered by the actual thinning process. Such issues are obviously less troublesome for the nanostructures that are the topic of the following section. For several reasons, continuous films can be challenging materials for examination by off-axis electron holography. The presence of a hole or edge in the field of view, or at least access to a continuous uniform background, is essential for provision of the requisite vacuum or reference wave. Removal of the substrate, or at least perforation by back-side ion-milling, is likely to cause stress and/or local bending in the film, especially around the edges, which could possibly mask the intrinsic magnetic structure. Our experience is that rapid thickness variations around edges and small holes can make holograms from such areas difficult, or even impossible in some cases, to interpret reliably.

Thin films of ordered Co-Pt and Fe-Pt alloys have the $L1_0$ crystal structure, leading to potentially useful applications for magnetic recording because of the pronounced magnetocrystalline anisotropy. Depending on the substrate used for thin film deposition, the tetragonal c axis will be primarily either in plane or out of plane. Figure 6(a) shows the hologram for a cross-sectional sample of an epitaxial $Fe_{0.5}Pt_{0.5}$ ordered alloy film (thickness ~100 nm) deposited onto an MgO(110) substrate (McCartney, Smith, Farrow and Marks, 1997). The (001) easy axis of the ordered alloy is parallel to the film normal for this growth direction. Magnetic fringing fields are visible outside the material in the reconstructed phase image shown in Figure 6(b), and corresponding induction maps confirmed that adjacent domains within the Fe-Pt film had the expected opposite polarity. Note here that Lorentz imaging was not particularly useful in these studies because of the coarse Fresnel fringes that occurred at the large defocus values that were necessary to achieve appreciable magnetic contrast.

In this application of electron holography to Fe–Pt ordered alloys described in the previous paragraph, no attempt was made, nor was it felt to be necessary, to quantify the strength or extent of the fields within or emerging from the sample. Such a task is quite challenging for multilayered thin films in cross-sectional geometry because of the often rapid and unknown variations in thickness and contrast, which can easily overwhelm any changes in the magnetic signal. Careful consideration of equations (3) and (4) shows, however, that by combining phase profiles and phase gradients for holograms with reversed magnetization directions, it is possible to remove the specimen thickness and composition profiles and thus finally determine the magnetization with some reasonable level of confidence and respectable accuracy (Dunin-Borkowski, McCartney, Smith and Parkin, 1998a). Conversely, failure to properly account for thickness and

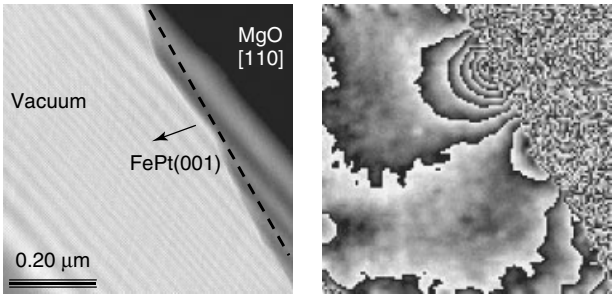

Figure 6. (a) Off-axis electron hologram obtained from epitaxial Fe-Pt/MgO with (001) easy axis parallel to film normal; (b) contoured phase image showing magnetic flux extending into vacuum. (Reproduced from McCartney *et al*., 1997, with permission from the American Institute of Physics. © 1997.)

composition variations will most likely cause erroneous interpretation when studying complex layered structures such as magnetic tunnel junctions in cross section.

3.4 Nanostructures

Interest in magnetic nanostructures is increasing in recent times both for scientific reasons and because of possible applications for magnetic recording. However, a micromagnetic structure becomes increasingly difficult if not impossible to characterize by most imaging techniques as lateral dimensions are reduced. Another concern is that shape irregularities in small magnetic elements are likely to play a more prominent role during magnetization reversal. Domain walls are obviously less likely because of energy considerations to be found in the remanent state of magnetic nanostructures. However, extensive simulations may still be required before quantitative analysis of magnetization can be achieved, especially since interactions between closely spaced adjacent particles can sometimes lead to interesting and unexpected results.

Off-axis electron holography represents a powerful method for probing the magnetic response of individual nanostructures, especially for elements having one or more dimensions on the scale of 100 nm or below. Analysis by holography does, however, become more challenging because the corresponding magnetic phase changes that are produced will decrease with the element width, which is unlike the MIP term that has no such length dependence. Close attention must be given to experimental parameters such as the total signal acquired before reconstruction to compensate for the loss of interference-fringe contrast which, as we noted earlier, decreases with smaller fringe spacing. Some local smoothing of noise fluctuations can be helpful in clarifying any significant features of the reconstructed phase images.

3.4.1 Spheres, rings, and chains

Spherical nanoparticles represent an interesting model system but they are challenging to study because of rapid variations in the projected thickness. Analytical expressions have been derived for the magnetic and electrostatic phase expected for an electron wave passing through uniformly magnetized spherical particles (de Graef, Nuhfer and McCartney, 1999). Figure 7(a) shows an electron hologram from a chain of carbon-coated Co nanospheres and the reconstructed phase image is shown in Figure 7(b). The corresponding phase profile across the center of a 33-nm-diameter particle is shown in Figure 7(c), together with a least-squares-fitted profile generated by varying the particle diameter, the saturation induction, and the MIP. The fitted values of 1.7 T and 26 V for the latter two parameters are in good agreement with expected results, thus establishing confidence that quantitative measurements can be achieved even at the nanoscale using electron holography.

Chains of spherical Fe–Ni nanoparticles have received further attention (Hÿtch *et al*., 2003; Dunin-Borkowski *et al*., 2004b). Perhaps the most interesting result emerging from this study was confirmation that magnetic vortices rather than single domains could be supported in particles above a certain critical size for vortex formation. Moreover, as shown by the examples reproduced in Figure 8, vortex axes could be either parallel or perpendicular to the chain axis. It was also found that flux channeling and vortex formation depended on the Fe–Ni alloy concentration, as well as being strongly influenced by the size and proximity of other particles in the chain. Finally, it is worth noting here that careful comparisons with the results of micromagnetic simulations were essential to a full interpretation and explanation of the experimental contours in these studies.

The flux closure associated with vortex formation is an interesting and potentially useful property for high-density information storage, and several examples will be mentioned in Section 3.4.3. A recent study showed that stable flux closure states could also be achieved at room temperature with self-assembled Co rings formed by nanoparticles with sizes in the range of 27 ± 4 nm and ring diameters of $\sim$100 nm (Tripp, Dunin-Borkowski and Wei, 2003).

3.4.2 Rods and wires

Magnetic rods and nanowires should have a unidirectional remanent state, and their well-defined geometry enables magnetostatic effects to be easily separated from thickness and electrostatic effects. Early holography studies of Co and Ni nanowires indicated that wires of small radius (20–35 nm) behaved like tiny magnetic dipoles with uniform magnetization close to the expected saturation value (Beeli, Doudin,

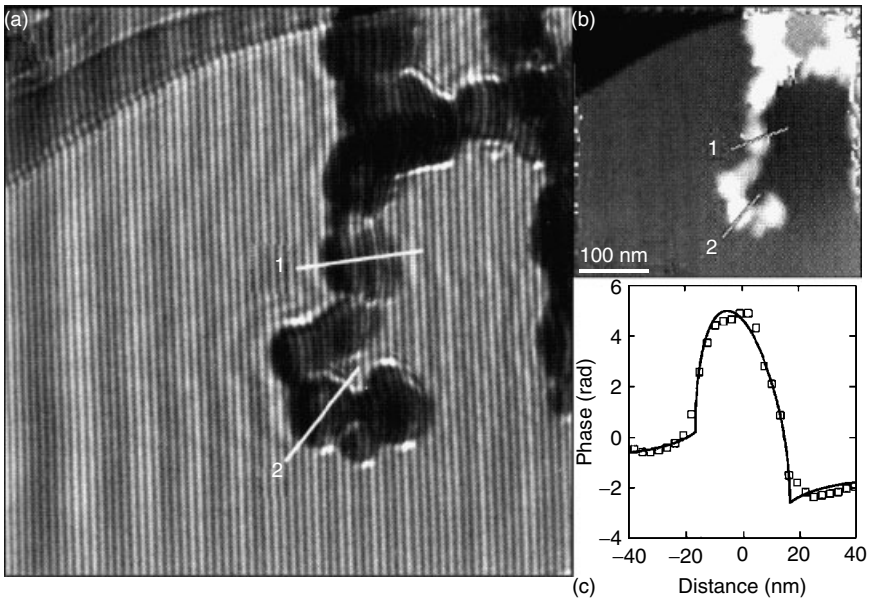

Figure 7. (a) Electron hologram showing chain of Co nanospheres supported over a hole in carbon support film; (b) reconstructed phase image after phase unwrapping; (c) experimental and fitted phase profile for linear trace across spherical Co nanoparticle (de Graef *et al*., 1999). (Reproduced from de Graef *et al*., 1999, with permission from Blackwell Publishing. © 1999.)

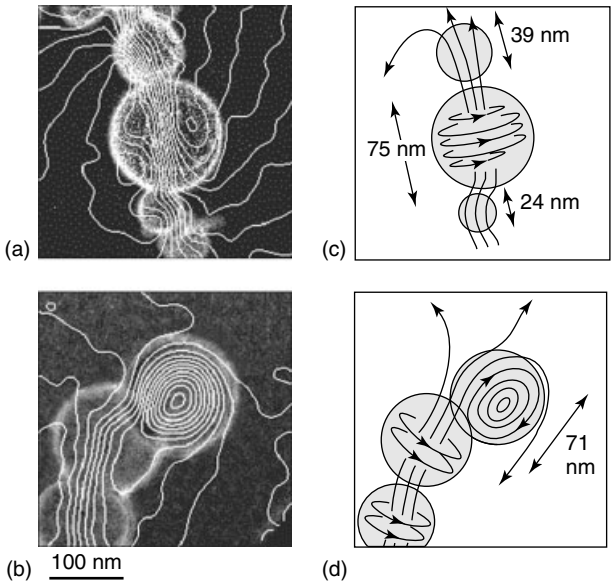

Figure 8. (a, b) Experimental magnetic phase contours for chains of $Fe_{0.56}Ni_{0.44}$ nanoparticles showing strength of local magnetic induction (integrated in beam direction); (c, d) schematic illustration showing magnetic microstructure within chains. Note magnetic vortices spinning about chain axis in (c) and (d), and vortex spinning perpendicular to axis in (d). (Reproduced from Hÿtch *et al*., 2003, with permission from the American Physical Society. © 2003.)

Ansermet and Stadelmann, 1996). In contrast, wires with larger radii showed increasing amounts of nonuniform magnetization, and multidomain wires were sometimes observed. Later studies have focused on magnetic nanowires of smaller diameter. For example, Fe-Pt nanorods with diameters of ∼26 nm were grown *in situ* by electron-beam-induced deposition and developed randomly oriented crystallites of the ordered $L1_0$ magnetic phase after annealing at 600 °C (Che *et al*., 2005). Single crystal Co nanowires, with diameters as small as 4 nm, were shown to be fully magnetized, assuming bulk values for Co MIP and magnetization (Snoeck *et al*., 2003). It was also reported in this last study that the phase contrast contours along the wire axes were not always straight, but further work is needed to fully understand this result.

3.4.3 Patterned shapes

Nanostructured shapes enable micromagnetic behavior, especially during hysteresis cycling, to be conveniently investigated in a controlled fashion, both as a function of particle geometry as well as proximity to other particles. Elements with a wide range of shapes, sizes, and separations have been prepared by electron-beam evaporation onto self-supporting 55-nm-thick silicon nitride membranes using standard electron-beam lithography and lift-off processes (Dunin-Borkowski, McCartney, Kardynal and Smith, 1998b). Figure 9 is a low-magnification bright-field image showing part of a typical array of such patterned elements. Some loss of interference-fringe contrast occurs because of the underlying silicon nitride support, but off-axis electron holography can still be successfully carried out using the

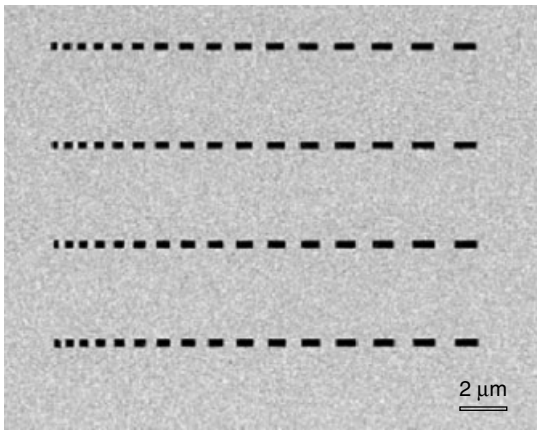

Figure 9. Low-magnification, bright-field image showing typical array of lithographically patterned magnetic elements supported on 55-nm-thick silicon nitride membrane.

Lorentz mini-lens configuration described earlier. Samples are tilted *in situ* within the microscope using the normal objective lens slightly excited to obtain the desired in-plane field. The hysteresis behavior and remanent states of individual elements can then be determined. The featureless silicon nitride regions nearby are used for acquisition of the reference holograms that are needed to remove phase distortions associated with the imaging/recording system.

Our initial studies involved rectangular 30-nm-thick Co elements (Dunin-Borkowski, McCartney, Kardynal and Smith, 1998b), where removal of the MIP phase contribution was accomplished by the aforementioned method of fully reversing the magnetization and then halving the difference between the corresponding pair of holograms. Micromagnetic simulations based on the Landau–Lifshitz–Gilbert equations were also carried out (Dunin-Borkowski *et al*., 1999). Reasonable agreement with the experimental results was obtained, but some important differences were also revealed. For example, simulations showed that the strength and direction of the applied field had a marked impact on the observed domain structure. It was also shown that the magnetization behavior of the adjacent Co elements was affected by their close proximity and interaction, with fringing fields extending between the elements when fully magnetized. This result thus emphasized the need to consider intercell coupling when designing high-density storage devices. The characteristic flux closure associated with a vortex state was invariably seen during hysteresis cycling, while other new and unexpected domain configurations were sometimes observed during investigation of remanent states from different stages of the magnetization cycle (Dunin-Borkowski *et al*., 2000).

Trilayered spin-valve (SV) structures consisting of two ferromagnetic layers separated by a thin metallic spacer layer have recently received much attention because of the large differences in resistance when the magnetization directions of the magnetic layers are aligned parallel or antiparallel – the so-called giant magnetoresistance (GMR) effect. We have studied patterned SV structures based on submicron Co (10 nm)/Au (5 nm)/Ni (10 nm) combinations shaped as rectangles, diamonds, ellipses, and bars and with lateral dimensions on the 100-nm scale (Smith *et al*., 2000; Dunin-Borkowski *et al*., 2000). Figure 10 shows some representative results from a complete hysteresis cycle for elliptical and bar-shaped elements. The arrows within each element indicate the field direction, and the in-plane component of the applied field is aligned along the long axis of each element. The occurrence of two different contour spacings within each element at different applied fields, with corresponding steps in the hysteresis loops was a significant observation of these SV studies. Micromagnetic simulations, described elsewhere (Smith *et al*., 2000), indicated that antiferromagnetic coupling between the Co and Ni layers, due to the strong demagnetization field of the closely adjacent and more magnetically massive Co layer, was the reason for this behavior. Vortex states were not observed in any of the remanent states in further studies of rectangular SV elements, unlike magnetization states sometimes observed during hysteresis cycling. This difference in behavior can presumably again be attributed to the presence of the strong coupling between the Co and Ni layers following removal of the external field. Similar coupling between layers was reported in a more recent study of Co/Cu/NiFe thin-film elements (Kasama *et al*., 2005). The observed variability in switching fields in this case was attributed to slight variations in the shape and size of the elements, as well as microstructural variability.

More recent studies of the remanent states of nanopatterned Co elements have concentrated on thinner elements (Hu, Wang, McCartney and Smith, 2005, 2006; Wang, Hu, McCartney and Smith, 2006). The remanent states of 10-nm-thick triangles, squares, pentagons, and hexagons were found to have a 'twisted' configuration, whereas those of rectangles, ellipses, and 'dumbbells' were basically linear (Wang, Hu, McCartney and Smith, 2006). In contrast, the remanent states of disk- and ring-shaped elements were primarily circular, whereas slotted disks and rings had modified circular states that were highly reproducible and had minimal fringing fields. This latter characteristic is very unlike what is observed for linear shapes such as rectangles and ellipses, which typically display considerable stray fields near their ends. Figure 11 shows some representative examples for sets of slotted disks and rings illustrating the interesting remanent states of these modified circular elements. When the applied field was parallel or nearly parallel to the slot curves, the remanent states appeared to be stable single domains (Wang, Hu, McCartney and Smith, 2006).

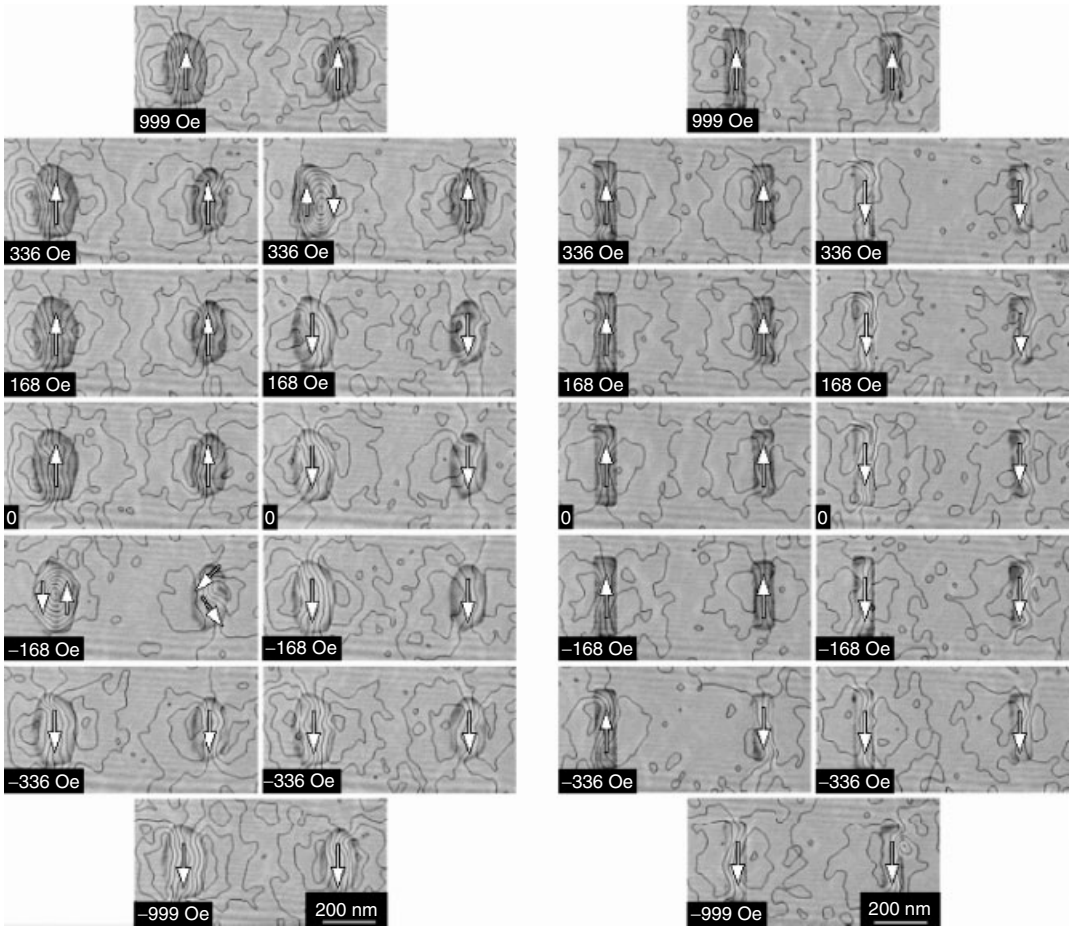

Figure 10. Magnetic contributions to phase for elliptical and bar-shaped Co (10 nm)/Au (5 nm)/Ni (10 nm) spin-valve elements over complete hysteresis cycle. Phase contours of 0.064π rad. Field applied in vertical direction. Loop should be followed counterclockwise. Average out-of-plane field of 3600 Oe directed into the page.

The circular magnetization state of disk- and ring-shaped elements clearly avoids any edge-domain problems, while the flux closure helps to minimize any interelement interactions. Two stable magnetization states have been identified in submicron magnetic ring elements: the so-called onion state with domain walls on opposite sides of the ring, and the vortex state, which has fully enclosed flux (Rothman *et al*., 2001). Electron holography has allowed us to study magnetization reversal processes for nanoscale Co rings into the deep-submicron regime (Hu, Wang, McCartney and Smith, 2005). The most important finding was that the ratio of the outer to the inner diameter of the rings played the major role in determining the actual switching process. Figure 12 shows an example of coherent rotation of domain walls for a ring of 150 nm inner diameter and 400 nm outer diameter.

Our most recent study has involved slotted disks and rings (Hu, Wang, McCartney and Smith, 2006). It was found that both of these shapes had very stable and well-defined remanent states, unlike complete disks and rings of similar dimensions. Representative examples are shown in Figure 13. In the case of slotted disks ('pacman shape'), vortex states were invariably observed during the switching process, whereas rapid switching without vortex formation was the behavior mostly shown by the slotted rings. Because of this nonvortex switching mode for slotted rings, the field at which the magnetization reversed direction was very well defined, typically to within ∼40 Oe. Thus, this modified geometry should be particularly attractive for information storage applications based on circular elements rather than linear elements (Zhu, Zheng and Prinz, 2000).

3.5 Rocks, minerals, and bacteria

Ferromagnetic materials abound in nature but the use of electron holography to study these materials is virtually unexplored. A wealth of valuable information is

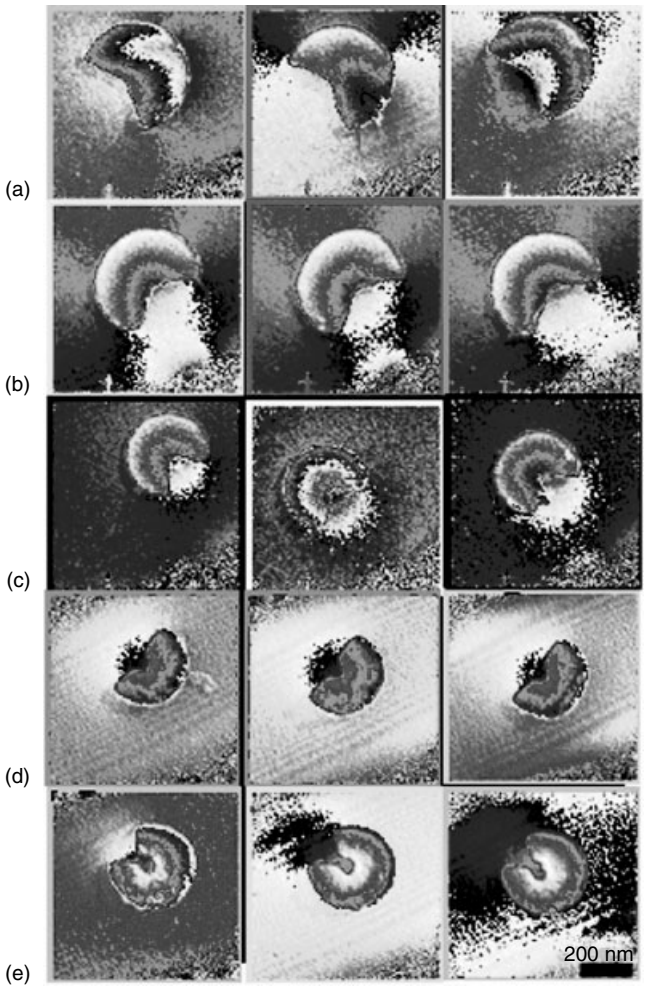

Figure 11. Reconstructed phase images showing remanent states for sets of three identical 10-nm-thick Co elements. (a) 400-nm slotted disk with 120° slot angle (curve perpendicular to magnetic field direction); (b) 400-nm slotted disk with 120° slot angle (curve parallel to magnetic field direction); (c) 300-nm slotted disk with 90° slot angle; (d) 300-nm slotted ring with 180° slot angle; (e) 300-nm slotted ring with 90° slot angle. (Reproduced from Wang *et al*., 2006, with permission from Elsevier. © 2006.)

seemingly waiting to be discovered. In the field of geology, planar arrays of magnetite nanoparticles from titanomagnetite minerals have received recent attention (Harrison, Dunin-Borkowski and Putnis, 2002; Dunin-Borkowski *et al*., 2004b). Unlike the well-controlled geometries of lithographically patterned nanostructures, the roughly equidimensional magnetite nanocrystals display considerable variability in their sizes and spacings. This feature makes for a fascinating case study of nanomagnetism. Some small, closely spaced crystals couple together to form flux closure domains much like the Co rings described earlier, whereas other larger blocks appear to form vortex states with flux closure. The

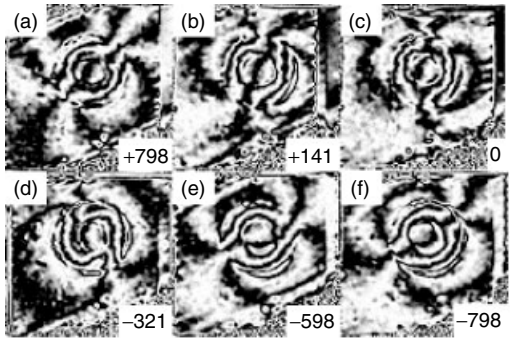

Figure 12. Amplified (8×) phase images showing reversal behavior of 400/150-nm ring during half of hysteresis cycle (in-plane fields indicated under each image: units of Oe). Note two domain walls rotating coherently around the ring. (Reproduced from Hu *et al*., 2005, with permission from the American Institute of Physics. © 2005.)

observed abundance of single-domain states, rather than vortex states prevailing in isolated cubes, was attributed to strong particle interactions based on demagnetizing fields for the local crystal environments.

Ferromagnetic nanomaterials occur naturally in many biogenic systems. Interesting examples are the magnetosomes, composed of magnetite or greigite crystals, found in magnetotactic bacteria. In these organisms, the magnetite crystals are invariably found in chains, as shown in Figure 14(a), which provide an internal navigation aide. Off-axis electron holography has been used extensively to study the individual and collective micromagnetic behavior of these magnetite nanocrystal chains (Dunin-Borkowski *et al*., 1998c; McCartney *et al*., 2001). Figure 14(b) shows the corresponding hologram taken from the area indicated in Figure 14(a). After magnetization reversal and phase addition, the electrostatic phase contribution can be extracted, and the nanocrystallites are revealed to be cubo-octahedral in shape. The magnetic phase contribution is shown in Figure 14(c), where the phase contours have been overlaid onto the MIP contribution so that the positions of the crystals and the magnetic contours can be correlated. Thus, the distribution of magnetic flux within and between the crystallites can be observed. Interestingly, the contour lines do not lie entirely on a continuous curve along the chain axis but rather display slight misalignment from nanocrystal to nanocrystal. It was also found that individual crystals were fully magnetized into single-domain states even though many were below the critical size for superparamagnetism at room temperature. Finally, note that it was possible to determine the total dipole moments of the particle chains (Dunin-Borkowski *et al*., 2001). Further studies of other bacterial strains, and more information about differences in domain structure and magnetic properties of these intriguing nanocrystal ensembles can be found elsewhere (Dunin-Borkowski *et al*., 2001; McCartney *et al*., 2001).

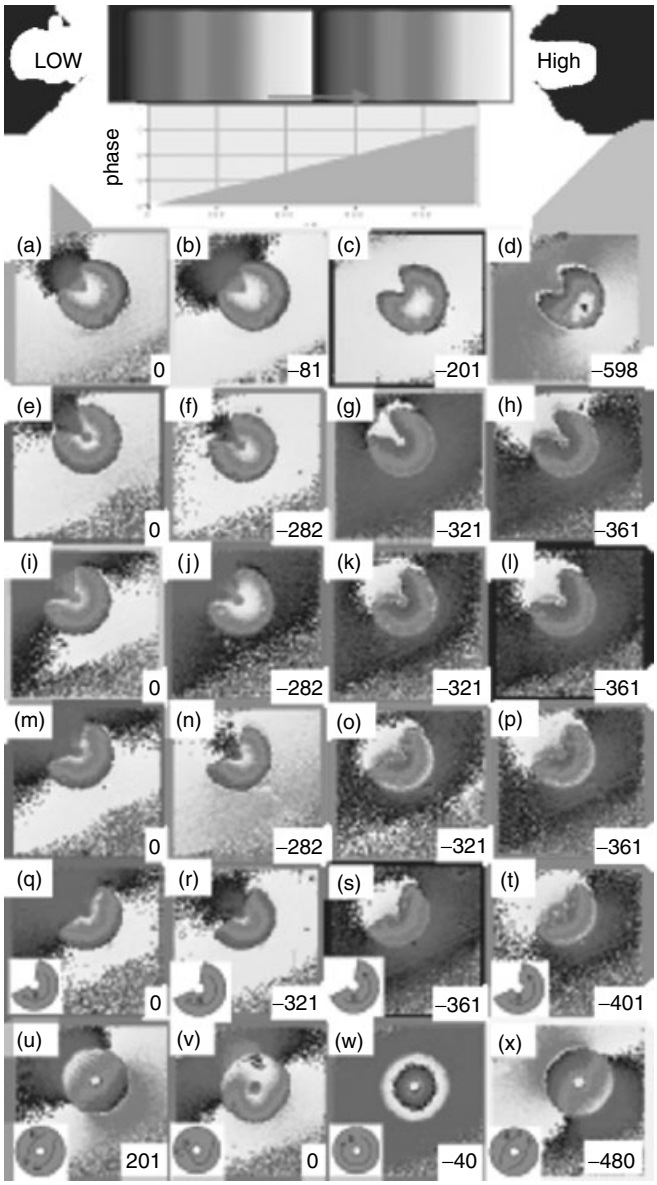

Figure 13. Phase images from 400-nm slotted disks and slotted rings during switching: (a–d) 60° slotted disk. Note the presence of a vortex state; (e–h) 60° slotted ring. Switching occurs rapidly between (f) and (g); (i–l) 90° slotted ring; (m–p) 120° slotted ring; (q–t) 150° slotted ring. Single-domain state illustrated at bottom left of each image; (u–x) vortex switching process in 400/50-nm ring. U-shaped state visible in (v), vortex state visible in (w), with onion states visible in (u) and (x). (Reproduced from Hu *et al*., 2006, with permission from the American Physical Society. © 2006.)

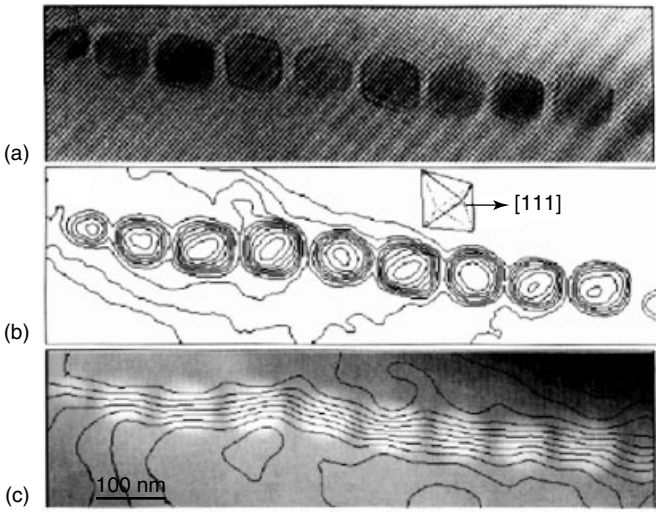

Figure 14. (a) Electron hologram for chain of magnetite crystal in magnetotactic bacterium; (b) mean inner potential contribution to phase. Thickness contours indicate cubo-octahedral shape; (c) magnetic contributions to phase.

4 FUTURE PROSPECTS

This chapter has introduced the technique of off-axis electron holography and described its development as a tool for characterizing ferromagnets at the nanometer scale. The representative examples described should have clearly demonstrated that off-axis electron holography is already playing a valuable role in understanding the response of magnetic nanostructures. And it can be expected that electron holography will become a more widely used tool for future micromagnetic characterization studies.

Despite this optimistic outlook, there are several challenges that need to be faced. A major problem is that visualization of dynamic effects caused by changes of an applied magnetic field, considered to be necessary for a complete understanding of micromagnetic behavior, is not easily implemented. In our experiments, we have changed the in-plane field component by tilting the sample *in situ* within the field of the weakly excited objective lens, but this process clearly does not allow for real-time observations. Moreover, it has been shown that the out-of-plane component of the applied field imposes switching asymmetries during hysteresis cycling (Dunin-Borkowski *et al*., 1999). The development of a specimen holder with in-built coils capable of applying a horizontal field has been reported (Yi *et al*., 2004). However, the maximum field that can so far be applied is insufficient for many important applications. An alternative approach is to change the applied field of the objective lens, but the electron trajectories through the objective lens will then be affected. This problem could be solved by provision of three sets of auxiliary coils, with one set to apply the field close to the level of the sample, and the subsequent sets to steer the beam back onto the optic axis (Bonevich, Pozzi and Tonomura, 1999). This possibility is tedious to implement in practice and is not

yet generally available. Another problem is that off-axis electron holography is not suited for real-time observations because the recorded holograms are usually processed off-line. As faster computers and better CCD cameras become available, then real-time viewing of reconstructed phase images might just become possible. A third issue relates to the three-dimensional nature of the magnetic vector field, which was not considered for many of the applications described here. This omission is not so serious for objects such as thin films and nanostructures when the fields are constrained by the sample geometry to lie primarily in the plane, although subtle changes during the reversal cycle of the nanopatterned SV shapes were attributable to some out-of-plane rotation effects (Smith *et al*., 2000). For more massive three-dimensional objects such as probes for magnetic force microscopes, the out-of-plane field components must be taken properly into account (Streblechenko, Scheinfein, Mankos and Babcock, 1996; Matteucci, Frost and Medina, 2004).

ACKNOWLEDGMENTS

Much of the electron holography described here was carried out at the John M. Cowley Center for High Resolution Electron Microscopy at Arizona State University. We are grateful to Drs R. E. Dunin-Borkowski, R. F. C. Farrow, R. B. Frankel, H. Hu, B. Kardynal, S. S. P. Parkin, M. Posfai, M. R. Scheinfein, H. Wang, and Y. Zhu for provision of samples and ongoing collaborations.

REFERENCES

Beeli, C., Doudin, B., Ansermet, J.P. and Stadelmann, P. (1996). Study of Co. Ni and Co/Cu nanowires: magnetic flux imaging by off-axis electron holography. *Journal of Magnetism and Magnetic Materials*, **164**, 77–90.

Bonevich, J., Harada, K., Matsuda, T., *et al*. (1993). Electron holography observation of vortex lattices in a superconductor. *Physical Review Letters*, **70**, 2952–2955.

Bonevich, J., Pozzi, G. and Tonomura, A. (1999). Electron holography of electromagnetic fields. In *Introduction to Electron Holography*, Völkl, E, Allard, L.F. and Joy, D.C. (Eds.), Kluwer Academic: New York, pp. 153–181.

Chapman, J.N. (1984). The investigation of magnetic domain structures in thin foils by electron microscopy. *Journal of Physics D-Applied Physics*, **17**, 623–634.

Che, R.C., Takeguchi, M., Shimojo, M., *et al*. (2005). Fabrication and electron holography characterization of FePt alloy nanorods. *Applied Physics Letters*, **87**, 223109.

Cowley, J.M. (1992). Twenty forms of electron holography. *Ultramicroscopy*, **41**, 335–348.

de Graef, M., Nuhfer, T. and McCartney, M.R. (1999). Phase contrast of spherical magnetic particles. *Journal of Microscopy*, **194**, 84–94.

de Ruijter, W.J. (1995). Imaging properties and applications of slow-scan charge-coupled-device cameras suitable for electron microscopy. *Micron*, **26**, 247–275.

de Ruijter, W.J. and Weiss, J.K. (1993). Detection limits in quantitative off-axis electron holography. *Ultramicroscopy*, **50**, 269–283.

Dunin-Borkowski, R.E., McCartney, M.R., Kardynal, B., *et al*. (1999). Switching asymmetries in closely coupled magnetic nanostructure arrays. *Applied Physics Letters*, **75**, 2641–2643.

Dunin-Borkowski, R.E., McCartney, M.R., Kardynal, B., *et al*. (2000). Off-axis electron holography of patterned magnetic nanostructures. *Journal of Microscopy*, **200**, 187–205.

Dunin-Borkowski, R.E., McCartney, M.R., Posfai, M., *et al*. (2001). Off-axis electron holography of magnetotactic bacteria: magnetic microstructure of strains MV-1 and MS-1. *European Journal of Mineralogy*, **13**, 671–684.

Dunin-Borkowski, R.E., Kasama, T., Wei, A., *et al*. (2004b). Off-axis electron holography of magnetic nanowires and chains, rings and planar arrays of magnetic nanoparticles. *Microscopy Research and Technique*, **64**, 390–402.

Dunin-Borkowski, R.E., McCartney, M.R., Smith, D.J. and Parkin, S.S.P. (1998a). Towards quantitative electron holography of magnetic thin films using *in situ* magnetization reversal. *Ultramicroscopy*, **74**, 61–73.

Dunin-Borkowski, R.E., McCartney, M.R., Kardynal, B. and Smith, D.J. (1998b). Magnetic interactions within patterned cobalt nanostructures using off-axis electron holography. *Journal of Applied Physics*, **84**, 374–378.

Dunin-Borkowski, R.E., McCartney, M.R., Frankel, R.B., *et al*. (1998c). Magnetic microstructure of magnetostatic bacteria by electron holography. *Science*, **282**, 1868–1870.

Gabor, D. (1949). Microscopy of reconstructed wave-fronts. *Proceedings of the Royal Society. of'. London Series, A*, **197**, 454.

Gajdardziska-Josifovska, M., McCartney, M.R., de Ruijter, W.J., *et al*. (1993). Accurate measurements of mean inner potential of crystal wedges using digital electron holograms. *Ultramicroscopy*, **50**, 285–299.

Harrison, R.J., Dunin-Borkowski, R.E. and Putnis, A. (2002). Direct imaging of nanoscale magnetic interactions in minerals. *Proceedings of the National Academy of Sciences*, **99**, 16556–16561.

Harscher, A. and Lichte, H. (1996). Experimental study of amplitude and phase detection limits in electron holography. *Ultramicroscopy*, **64**, 57–66.

Hu, H., Wang, H., McCartney, M.R. and Smith, D.J. (2005). Study of *in situ* magnetization reversal processes for nanoscale Co rings using off-axis electron holography. *Journal of Applied Physics*, **97**, 054305.

Hu, H., Wang, H., McCartney, M.R. and Smith, D.J. (2006). Switching mechanisms and remanent states for nanoscale slotted Co circular elements studied by electron holography. *Physical Review B*, **73**, 153401.

Hÿtch, M.J., Dunin-Borkowski, R.E., Scheinfein, M.R., *et al*. (2003). Vortex flux channeling in magnetic nanoparticle chains. *Physical Review Letters*, **91**, 257207.

Joy, D.C., Zhang, Y.S., Zhang, X., *et al*. (1993). Practical aspects of electron holography. *Ultramicroscopy*, **51**, 1–14.

Kasama, T., Barpanda, P., Dunin-Borkowski, R.E., *et al*. (2005). Off-axis electron holography of pseudo-spin-valve thin-film elements. *Journal of Applied Physics*, **98**, 013903.

Lichte, H. (1986). Electron holography approaching atomic resolution. *Ultramicroscopy*, **20**, 293–304.

Mankos, M., Higgs, A.A., Scheinfein, M.R. and Cowley, J.M. (1995). Far-out-of-focus electron holography in a dedicated FEG STEM. *Ultramicroscopy*, **58**, 87–96.

Matteucci, G., Frost, B.G. and Medina, F.F. (2004). Study of the field around magnetic force microscopy probes using electron holography. *Ultramicroscopy*, **99**, 95–102.

McCartney, M.R. and Gajdardziska-Josifovska, M. (1994). Absolute measurement of normalized thickness, t/λ_i, from off-axis electron holography. *Ultramicroscopy*, **53**, 283–289.

McCartney, M.R., Lins, U., Farina, M., *et al*. (2001). Magnetic microstructure of bacterial magnetite by electron holography. *European Journal of Mineralogy*, **13**, 685–689.

McCartney, M.R., Smith, D.J., Farrow, R.F.C. and Marks, R.F. (1997). Off-axis electron holography of epitaxial FePt films. *Journal of Applied Physics*, **82**, 2461–2465.

McCartney, M.R. and Zhu, Y. (1998a). Induction mapping of $Nd_2Fe_{14}B$ magnetic domains by electron holography. *Applied Physics Letters*, **72**, 1380–1382.

McCartney, M.R. and Zhu, Y. (1998b). Off-axis electron holographic mapping of magnetic domains in $Nd_2Fe_{14}B$. *Journal of Applied Physics*, **83**, 6414–6416.

McVitie, S. and Chapman, J.N. (1997). Reversal mechanisms in lithographically defined magnetic thin film elements imaged by scanning transmission electron microscopy. *Microscopy and Microanalysis*, **3**, 146–153.

Murakami, Y., Shindo, D., Oikawa, K., *et al*. (2004). Microstructural change near the martensitic transformation in a ferromagnetic shape memory alloy $Ni_{51}Fe_{22}Ga_{27}$ studied by electron holography. *Applied Physics Letters*, **85**, 6170–6172.

Murakami, Y., Shindo, D., Susuki, M., *et al*. (2003). Magnetic domain structure in $Ni_{53.6}Mn_{23.4}Ga_{23.0}$ shape memory films studied by electron holography and Lorentz microscopy. *Acta Materialia*, **51**, 485–494.

Orchowski, A., Rau, W.D. and Lichte, H. (1995). Electron holography surmounts resolution limit of electron microscopy. *Physical Review Letters*, **74**, 399–402.

Osakabe, N., Yoshida, K., Horiuchi, S., *et al*. (1983). Observation of recorded magnetization pattern by electron holography. *Applied Physics Letters*, **42**, 792–794.

Park, Y.G. and Shindo, D. (2002). Magnetic domain structures of overquenched Nd-Fe-B permanent magnets studied by electron holography. *Journal of Magnetism and Magnetic Materials*, **238**, 68–74.

Park, Y.G., Shindo, D., Kanekiyo, H. and Hirosawa, S. (2004). Magnetization distribution in $Nd_{4.5}Fe_{77}B_{18.5}$ nanocomposite magnets studied by electron holography. *Applied Physics Letters*, **85**, 5302–5304.

Rau, W.D. and Lichte, H. (1999). High resolution off-axis electron holography. In *Introduction to Electron Holography*, Völkl, E, Allard, L.F. and Joy, D.C. (Eds.), Kluwer Academic: New York, pp. 201–229.

Reimer, L. (1989). *Transmission Electron Microscopy*, Springer-Verlag: Berlin, p. 57.

Rothman, J., Klaui, M., Lopez-Diaz, L., *et al*. (2001). Observation of a bi-domain state and nucleation free switching in mesoscopic elements. *Physical Review Letters*, **86**, 1098–1101.

Smith, D.J., Dunin-Borkowski, R.E., McCartney, M.R., *et al*. (2000). Interlayer coupling within individual submicron magnetic elements. *Journal of Applied Physics*, **87**, 7400–7404.

Smith, D.J. and McCartney, M.R. (1999). Practical electron holography. In *Introduction to Electron Holography*, Völkl, E, Allard, L.F. and Joy, D.C. (Eds.), Kluwer Academic: New York, pp. 87–106.

Snoeck, E., Dunin-Borkowski, R.E., Dumestre, F., *et al*. (2003). Quantitative magnetization measurements on nanometer ferromagnetic cobalt wires using electron holography. *Applied Physics Letters*, **82**, 88–90.

Solomon, V.C., McCartney, M.R., Smith, D.J., *et al*. (2005). Magnetic domain configurations in spark-eroded ferromagnetic shape memory Ni-Mn-Ga particles. *Applied Physics Letters*, **86**, 192503.

Streblechenko, D.G., Scheinfein, M.R., Mankos, M. and Babcock, K. (1996). Quantitative magnetometry using electron holography: field profiles near magnetic force microscopy tips. *IEEE Transactions on Magnetics*, **32**, 4124–4129.

Tonomura, A., Matsuda, T. and Endo, J. (1979). Spherical aberration correction of an electron lens by electron holography. *Japanese Journal of Applied Physics*, **18**, 1373.

Tonomura, A., Osakabe, N., Matsuda, T., *et al*. (1986). Evidence for the Aharonov-Bohm effect with magnetic field completely shielded from electron wave. *Physical Review Letters*, **56**, 792–795.

Tripp, S.L., Dunin-Borkowski, R.E. and Wei, A. (2003). Flux closure in self-assembled nanoparticle rings. *Angewandte Chemie*, **42**, 5591–5593.

Ullakko, K., Huang, J.K., Kantner, C., *et al*. (1996). Large magnetic-field-induced strains in Ni_2MnGa single crystals. *Applied Physics Letters*, **69**, 1966–1968.

Völkl, E. and Lehmann, M. (1999). The reconstruction of off-axis electron holograms. In *Introduction to Electron Holography*, Völkl, E., Allard, L.F. and Joy, D.C. (Eds.), Kluwer Academic: New York, pp. 125–151.

Wang, H., Hu, H., McCartney, M.R. and Smith, D.J. (2006). Remanent states of nanoscale Co ferromagnets having different shapes. *Journal of Magnetism and Magnetic Materials*, **303**, 237–242.

Yi, G., Nicholson, W.A.P., Lim, C.K., *et al*. (2004). A new design of specimen stage for *in situ* magnetizing experiments in the transmission electron microscope. *Ultramicroscopy*, **99**, 65–72.

Zhu, J.G., Zheng, Y. and Prinz, G.A. (2000). Ultrahigh density vertical magnetoresistive random access memory. *Journal of Applied Physics*, **87**, 6668–6673.

Zhu, Y. and McCartney, M.R. (1998). Magnetic-domain structure of $Nd_2Fe_{14}B$ permanent magnets. *Journal of Applied Physics*, **84**, 3267–3272.

FURTHER READING

Dunin-Borkowski, R.E., McCartney, M.R. and Smith, D.J. (2004a). Electron holography of nanostructured materials. In *Encyclopedia of Nanoscience and Nanotechnology*, Nalwa, H.S. (Ed.), American Scientific: Stevenson Ranch, pp. 41–100.

Lichte, H. (1991). In *Advances in Optical and Electron Microscopy*, Mulvey, T. and Sheppard, C.J.R. (Eds.), Academic Press: New York, pp. 25–91, Vol. 12.

Smith, D.J., de Ruijter, W.J., Weiss, J.K. and McCartney, M.R. (1999). Quantitative electron holography. In *Introduction to Electron Holography*, Völkl, E, Allard, L.F. and Joy, D.C. (Eds.), Kluwer Academic: New York, pp. 107–124.

Tonomura, A. (1993). *Electron Holography*, *Springer Series in Optical Sciences*, Vol. 70 Springer: Heidelberg.

Spin-polarized Low Energy Electron Diffraction

Hans-Joachim Elmers
Johannes Gutenberg Universität, Mainz, Germany

1 INTRODUCTION

Magnetic properties of surfaces, ultrathin films, and nanostructures are of great interest. A vital precondition for their investigation is an experimental method that is sensitive enough to probe magnetic order in structures consisting of a limited number of atoms and even time-resolved investigation of magnetization dynamics in them. On the other hand, diffraction of low-energy electrons (low-energy electron diffraction, LEED) is one of the most often used versatile methods in surface science for the investigation of structural properties of nanostructures. In the usual energy range up to a few hundred electronvolts, the mean free path of electrons in a solid is of the order of atomic distances. Therefore, the information depth is of this order and the diffracted electrons provide exclusive information on the surface, in contrast, for example, to X-ray or neutron diffraction methods. With comparatively low experimental effort the crystal structure of surfaces can be determined. By providing a polarized incident electron beam and/or a polarization analysis of diffracted electrons, magnetic surface properties can be analyzed. The combination of elastic electron diffraction and polarization analysis, usually called spin-polarized low-energy electron diffraction (SPLEED), is the aim of the present review.

The first experimental approach to spin-polarized electron diffraction was attempted by Davisson and Germer (1929) soon after their pioneering discovery of electron diffraction; however, they found no effect. It took half a century until the first convincing SPLEED data were reported by Celotta *et al*. (1979). Feder (1977, 1985) undertook the first rigorous calculations in order to predict magnetically induced asymmetries for the scattering of spin-polarized electrons at magnetic surfaces. The development of efficient sources for a polarized electron beam (Kirschner, 1985a) immediately boosted the number of experiments using SPLEED. The first path breaking SPLEED experiments were reviewed by Gradmann and Alvarado (1985).

Since then, the development of computational power has stimulated extensive effort in this field. Further development of experimental techniques including a higher spin polarization of the sources (Maruyama *et al*., 1991), a free manipulation of the spin direction (Duden and Bauer, 1995), and imaging with diffracted electrons (spin-polarized low-energy electron emission microscopy, SPLEEM) (Altman *et al*., 1991; Bauer, Duden and Zdyb, 2002) allowed a wide range of applications (**Spin-polarized Low Energy Electron Microscopy, Volume 3**).

Most of the experiments using elastic SPLEED pursue three main aims. The first aim is a quantitative analysis of space-dependent spin densities from quantitative comparison of relativistic dynamical scattering calculations with SPLEED experiments. Secondly, the comparatively large magnetic SPLEED asymmetries are used to detect and analyze magnetic order in nanostructures with a small magnitude of magnetization, particularly in the vicinity of the magnetic

Handbook of Magnetism and Advanced Magnetic Materials. Edited by Helmut Kronmüller and Stuart Parkin. Volume 3: *Novel Techniques for Characterizing and Preparing Samples*. ISBN: 978-0-470-02217-7.

phase transition. The third group of experiments addresses the improvement of electron polarization detectors, that still have an efficiency far lower than optical devices.

It is the aim of the present chapter to give a review of physical principles and experimental results, emphasizing the experimental point of view. Section 2 outlines the basic principles of SPLEED, a short discussion of inelastic scattering and comments comprehensive references that are relevant for understanding the theoretical calculations. The experimental methods used for SPLEED are described in Section 3 with a focus on new developments. Section 4 describes applications of SPLEED to the experimental determination of magnetic and structural properties of surfaces and ferromagnetic monolayer (ML) structures. Valence band structure properties of ultrathin films providing a path to more efficient spin detectors are inferred from SPLEED at kinetic electron energies below 10 eV.

2 PRINCIPLES OF SPLEED

2.1 Spin polarization of an electron beam

The spin of an electron is described as an operator ($\mathbf{s} = s_x, s_y, s_z$) satisfying the permutation relation $[s_x, s_y] = -i\hbar s_z$ (and cyclic permutations). In the limit of nonrelativistic interactions, which may be assumed for low-energy electrons, the spin operator is proportional to the operator of the angular momentum:

$$\mathbf{s} = \frac{\hbar}{2}\sigma \tag{1}$$

$$\sigma_x = \begin{pmatrix} 0 & 1 \\ 1 & 0 \end{pmatrix} \quad \sigma_y = \begin{pmatrix} 0 & -i \\ i & 0 \end{pmatrix} \quad \sigma_x = \begin{pmatrix} 1 & 0 \\ 0 & -1 \end{pmatrix} \tag{2}$$

with σ_i being Pauli's spin matrices. For a pure spin state all electrons in the beam obtain the same spin function

$$\chi = a_1 \begin{pmatrix} 1 \\ 0 \end{pmatrix} + a_2 \begin{pmatrix} 0 \\ 1 \end{pmatrix} = \begin{pmatrix} a_1 \\ a_2 \end{pmatrix} \tag{3}$$

where $\begin{pmatrix} 1 \\ 0 \end{pmatrix}$ and $\begin{pmatrix} 0 \\ 1 \end{pmatrix}$ are the eigenfunctions of the operator σ_z. At a measurement of the spin component s_z one finds a value of either $+\hbar/2$ or $-\hbar/2$ with the probability $|a_1|^2$ and $|a_2|^2$. Because the components of the angular momentum operator are noncommutative, only one component of the spin of absolute value $|s| = \sqrt{3/4}\hbar$ can be measured simultaneously. The polarization P is a vector, given by the expectation value of the spin operator:

$$P = \frac{\langle \chi | \sigma | \chi \rangle}{\langle \chi | \chi \rangle} \tag{4}$$

The degree of polarization parallel to the quantization axis z is a scalar:

$$P_z = \frac{\langle \chi | \sigma_z | \chi \rangle}{\langle \chi | \chi \rangle} = \frac{|a_1|^2 - |a_2|^2}{|a_1|^2 + |a_2|^2} = \frac{N^{\uparrow} - N^{\downarrow}}{N^{\uparrow} + N^{\downarrow}} \tag{5}$$

with $-1 \leq P_z \leq 1$. $N^{\uparrow}$ ($N^{\downarrow}$) denotes the number of electrons with spin parallel (antiparallel) to the quantization axis. A mixed spin state can be described by a sum over pure spin states with appropriate coefficients. P_z can then be calculated in a similar way as for pure spin states (Kessler, 1976).

2.2 Spin-orbit coupling

For a calculation of electron scattering, one considers as a first step the scattering by a radially symmetric potential $V(r)$. In the vicinity of the atomic nucleus, electrons acquire relativistic velocities. Therefore, the relativistic Dirac equation has to be solved. As a direct consequence, the spin of the electron is always coupled to its orbital momentum. In a nonrelativistic approximation, this spin-orbit interaction can be described by an additional spin-orbit interaction potential (Kessler, 1976)

$$V_{\mathrm{so}} = \frac{1}{2m^2c^2}\frac{1}{r}\frac{\mathrm{d}V}{\mathrm{d}r}(\mathbf{s} \cdot \mathbf{l}) \tag{6}$$

with $\mathbf{s}$ being the spin and $\mathbf{l}$ the orbital moment operator. The sign of this additional spin-orbit potential depends on the path of the electron, that is, whether it passes the nucleus left-hand or right-hand wise, and on the spin direction.

A classical interpretation would be based on the fact that in the system of the electron, the positive charge of the nucleus forming the scattering potential passes by and generates a magnetic field that in turn interacts with the magnetic moment of the electron.

We consider the electron traveling along the x axis, transversally polarized parallel to the z axis and scattered in the $x - y$ plane at a scattering angle θ (thus the orbital moment is parallel to the spin). The spin-orbit interaction results in different differential scattering cross sections for spin-up and spin-down electrons $\sigma^{\uparrow}(E, \theta)$ and $\sigma^{\downarrow}(E, \theta)$. The contribution of the spin-orbit coupling to the total scattering potential is weak. Exclusively for minima of the differential cross sections, a significant difference depending on the spin can be observed. The scattering asymmetry is defined as:

$$A_{\mathrm{so}}(\theta) = \frac{\sigma^{\uparrow}(\theta) - \sigma^{\downarrow}(\theta)}{\sigma^{\uparrow}(\theta) + \sigma^{\downarrow}(\theta)} \tag{7}$$

Since the number of scattered electrons N is proportional to the scattering cross section, an unpolarized electron beam

will be polarized after the scattering according to:

$$P = A_{so}(\theta) = \frac{N^{\uparrow}(\theta) - N^{\downarrow}(\theta)}{N^{\uparrow}(\theta) + N^{\downarrow}(\theta)} \tag{8}$$

with the polarizing power P (Kessler, 1976). If the scattering potential shows a mirror symmetry with respect to the scattering plane, change of sign of the orbital momentum will be equivalent to a change of sign of the polarization: $\sigma^{\uparrow}(-\theta) = \sigma^{\downarrow}(\theta)$ and consequently $A_{so}(\theta) = -A_{so}(-\theta)$. This relation is exploited for a polarization analysis in a Mott detector, where intensities are measured at complementary scattering angles. Considering a totally polarized electron beam one will measure an asymmetry A according to:

$$A = \frac{N^{\uparrow}(\theta) - N^{\uparrow}(-\theta)}{N^{\uparrow}(\theta) + N^{\uparrow}(-\theta)} = \frac{\sigma^{\uparrow}(\theta) - \sigma^{\downarrow}(\theta)}{\sigma^{\uparrow}(\theta) + \sigma^{\downarrow}(\theta)} = P \tag{9}$$

that is, the polarization generated by the scattering of an unpolarized electron beam because of the spin-orbit interaction is identical to the scattering asymmetry generated by a totally polarized electron beam (analyzing power equals polarizing power) (Feder, 1981).

2.3 Exchange coupling

Exchange coupling is a quantum-mechanical effect without any classical analogon. Its origin is the Pauli principle demanding for a spin-1/2 particle a wave function that is antisymmetric with respect to the exchange of two particles. As a direct consequence of this principle, the differential scattering cross section depends on the relative orientation between the spin of the incoming electron and the spin of the target (e.g., a polarized atom). Note that this is not a direct spin–spin dipole interaction, which can be neglected for the energy range of interest here, but a Coulomb interaction (Kessler, 1976).

Let us consider the scattering of polarized electrons $e^{\uparrow\downarrow}$ at polarized atoms $A^{\uparrow\downarrow}$ with a neglection of spin-orbit coupling. Then we have the following scattering channels:

$$e^{\downarrow} + A^{\uparrow} \longrightarrow e^{\downarrow} + A^{\uparrow} \qquad (|f|^2) \tag{10a}$$

$$e^{\downarrow} + A^{\uparrow} \longrightarrow e^{\uparrow} + A^{\downarrow} \qquad (|g|^2) \tag{10b}$$

$$e^{\uparrow} + A^{\uparrow} \longrightarrow e^{\uparrow} + A^{\uparrow} \qquad (|f - g|^2) \tag{10c}$$

In the case of (a) the electron is directly scattered without exchange (scattering amplitude f), case (b) denotes the exchange scattering with amplitude g, and in the case of (c) the electrons cannot be distinguished and one may have exchange or direct scattering.

In a complete experiment where one knows the polarization of electron and atom before and after the scattering, the scattering cross sections can be determined directly. When unpolarized electrons are scattered at a polarized target, the scattered electrons are polarized according to:

$$A_{ex}(\theta) = \frac{|g|^2 + |f - g|^2 - |f|^2}{|f|^2 + |g|^2 + |f - g|^2} = P(\theta) \tag{11}$$

In all cases when electrons are scattered at a polarized target, the exchange scattering provides contributions to the total scattering cross section. This is true even in cases where unpolarized electrons are scattered and no polarization analysis is performed. The total cross section for scattering at a spin-up polarized atom $A^{\uparrow}$ is then given by

$$\sigma_0(\theta) = \frac{1}{2}(|f|^2 + |g|^2 + |f - g|^2) \tag{12}$$

Since the cross section depends only on the relative orientation of electron spin and target spin, one obtains the same cross section for a spin-down polarized target $A^{\downarrow}$. Therefore, a magnetization reversal does not change the intensity of the scattered electron beam along direction θ. The scattered intensity also remains constant when the polarization of an incident polarized beam on an unpolarized target is reversed.

The scattered intensity changes, however, when the incident beam and the target are polarized and the polarization of either the target or the incident beam is reversed. The cross sections for parallel and antiparallel orientations of the incident electron beam and the target is given by:

$$e^{\uparrow} \longrightarrow A^{\uparrow} \qquad \sigma_0^{\uparrow\uparrow}(\theta) = |f - g|^2 \tag{13a}$$

$$e^{\downarrow} \longrightarrow A^{\uparrow} \qquad \sigma_0^{\uparrow\downarrow}(\theta) = |f|^2 + |g|^2 \tag{13b}$$

Obviously, the exchange scattering amplitude g causes a change of the scattered intensity depending on the relative orientation of target and electron spin. One thus obtains information on the exchange scattering mechanism without analyzing the polarization of the scattered electrons. The scattering cross sections do not depend on the scattering angle. In contrast to the case of spin-orbit scattering (see Section 2.2) there is, in particular, no left–right asymmetry for the case of exchange scattering:

$$A_{ex}(\theta) = A_{ex}(-\theta) \tag{14}$$

2.4 Diffraction of spin-polarized electrons at surfaces

In the two preceding subsections, spin-orbit and exchange scattering were treated separately. However, in general both

effects are present simultaneously. An unpolarized electron beam might become polarized via the spin-orbit coupling in the vicinity of a nucleus and then responds to the exchange interaction with conduction electrons far away from the nucleus. Scattering at a solid-state surface may add multiple-scattering and inelastic processes.

Let us consider the scattering of electrons at a solid-state surface in the kinematic approximation. While the total intensity of scattered (unpolarized) electrons is determined mainly by the translational symmetry of the surface (LEED spots), the polarization of the scattered electrons depends only on the atomic scattering amplitudes (Kirschner, 1985b) and not on the lattice periodicity. This can be easily seen considering that the polarization is given by

$$P = \frac{I^{\uparrow\uparrow} - I^{\uparrow\downarrow}}{I^{\uparrow\uparrow} + I^{\uparrow\downarrow}} \tag{15}$$

and the lattice factor is a common factor for both intensities.

Within the kinematic approximation, the polarization carries no information on the crystallographic structure of the surface. As a consequence of the fact that intensity and polarization are decoupled, it should be possible to find scattering conditions with simultaneously high intensity and high polarization. This is in contrast to scattering at atoms where high polarization always occurs at intensity minima (Kessler, 1976) and might be important for the construction of polarization detectors (see Section 3.2). The polarization is also independent of the temperature because the Debye–Waller factor is a common factor for the intensities, too.

The exchange asymmetry observed for scattering at a ferromagnetic surface should depend only on the effective magnetic moment per atom, averaged over the information depth of the low-energy electrons, when only the kinematic approximation is considered.

Kirschner and Feder (1979) showed, however, that the kinematic approximation cannot be used to describe the scattering of low-energy electrons. For constant energy and constant incident angle they measured the polarization of the (00) spot after reflection at a W(100) surface as a function of the azimuthal angle. The scattering vector $(k - k')$ remains constant and therefore intensity and polarization should not vary according to the kinematic approximation. Instead, a strong variation was found for both intensity and polarization, depending on the azimuthal angle. The experimental observation could be simulated by a dynamic LEED theory considering multiple-scattering events.

Because of the inherent interconnection of spin-orbit coupling and exchange coupling, special scattering geometries have to be chosen to separate these two effects. In the longitudinal geometry the electron polarization is in the scattering plane. According to equation (6) the spin-orbit asymmetry vanishes. The scattering asymmetry is then exclusively caused by the exchange coupling and measures the magnetization component parallel to the incident spin direction. In the transversal geometry, the electron spin is perpendicular to the scattering plane. The scattering plane is adjusted to a mirror plane of the scattering surface. Then the electron spin is parallel to the normal $\vec{n}$ of the scattering plane after the scattering event, too Feder, 1981. The exchange asymmetry measures the magnetization component parallel to $\vec{n}$. In this case, the scattering can be described by four independent problems using the scalar scattering potentials:

$$V_\sigma^\mu(\vec{r}) = V_0(\vec{r}) + \sigma\mu V_{\mathrm{ex}}(\vec{r}) + V_{\mathrm{so}}(\vec{r}) \tag{16}$$

(Alvarado *et al.*, 1982) with $\sigma = +(-)$ for spin parallel (antiparallel) to $\vec{n}$ and $\mu = +(-)$ for magnetization antiparallel (parallel) to $\vec{n}$. In the experiment, one determines four scattering intensities I_σ^μ from which one calculates the scattering asymmetries:

$$A_{\mathrm{so}} = \frac{(I_+^+ + I_+^-) - (I_-^+ + I_-^-)}{(I_+^+ + I_+^-) + (I_-^+ + I_-^-)} \tag{17}$$

$$A_{\mathrm{ex}} = \frac{(I_+^+ + I_-^-) - (I_+^- + I_-^+)}{(I_+^+ + I_-^-) + (I_+^- + I_-^+)} \tag{18}$$

$$A_{\mathrm{u}} = \frac{(I_+^+ + I_-^+) - (I_+^- + I_-^-)}{(I_+^+ + I_-^+) + (I_+^- + I_-^-)} \tag{19}$$

The latter asymmetry A_{u} is obtained as the difference between the two magnetization directions after averaging over two spin directions and therefore describes the asymmetry one obtains for unpolarized electrons. It is a direct consequence of the coupling between spin-orbit and exchange interaction. A_{u} can be neglected in the case of $3d$ elements as was first shown by Tamura, Ackermann and Feder (1984) numerically using a scheme of simultaneous calculation of spin-orbit and exchange asymmetry (Ackermann and Feder, 1984; Feder, Rosicky and Ackermann, 1983). Contrarily, in the case of rare-earth elements A_{u} has to be considered (Weller *et al.*, 1985).

The magnetic information depth depends on the mean free path λ_e of the electrons (see Section 2.5) and the angle of incidence θ according to $d_e = \lambda_e \cos\theta$. At the surface of a bulk crystal or a thick film the magnetization deviates from the core of the material. Assuming that the deviation can be described by an exponential behavior with a coherence length $\xi_\perp$ perpendicular to the surface, the contribution n_{s} of the scattering asymmetry evoked by the topmost layer to the total scattering asymmetry is given by

$$n_{\mathrm{s}} = \frac{\xi_\perp}{\xi_\perp + d_e} \tag{20}$$

The temperature dependence of the coherence length $\xi_\perp$ diverges at the Curie temperature T_C according to

$$\xi_\perp(T) = \xi_\perp^0 \left(\frac{T_C}{T_C - T} \right)^\nu \tag{21}$$

Close to T_C the exchange asymmetry A_{ex} thus measures the magnetization of the topmost layer ($n_s = 1$). This fact was used to determine the critical behavior of the surface magnetization of Ni (Alvarado, Hopster and Campagna, 1982). For $T \ll T_C$ the critical lengths $\xi_\perp$ and d_e are of the same order of magnitude and therefore A_{ex} is determined only to some extent by the topmost layer. A detailed comparison of theory and experiment is needed in this case to determine the surface magnetization.

2.5 Inelastic interactions of electrons at surfaces

Inelastic processes to be considered in the low-energy regime are given by plasmon scattering, photoemission from valence states, photoemission of core level states and finally phonon and magnon scattering processes.

Scattering processes with phonons or magnons result in very small energy losses (<100 meV). Without using high resolution electron analyzers these electrons cannot be distinguished from elastically reflected electrons and therefore potentially cause erroneous intensity signals. Phonon scattering does not result in a significant amount of spin-flip processes, that is, the spin of the scattered electron is conserved. However, the momentum is changed and therefore the intensity in an off-specular direction is increased while the intensity in the specular direction is smaller than expected. Inelastic processes including excitation and annihilation of magnons are particularly interesting because they change the electron polarization. These processes have been intensively investigated by Vollmer *et al*. (2003) using spin-polarized electron energy loss spectroscopy (SPEELS). An additional scattered intensity attributed to magnon losses can only be observed for spin parallel to the magnetization of the sample at energy losses up to a few hundred millielectronvolts. The cross section for spin-wave excitation depends very strongly on the energy E_i of the incident electrons. Only below $E_i \approx 10$ eV can the spin wave be observed as a peak in the intensity spectrum for spin parallel to the magnetization. For higher incident electron energy, the contribution to elastically reflected electrons can be neglected.

Contrary to the collective spin-wave excitations, Stoner excitations that are the main contributions for higher incident energy above 25 eV (Kaemper, Abraham and Hopster, 1992) can be described in a single-particle picture: A Stoner excitation consists of an electron above the Fermi energy E_F coupled to a hole below E_F with opposite spin. They can be excited very efficiently by electron scattering, and their properties have been investigated extensively by SPEELS (Venus and Kirschner, 1988). Stoner excitations of majority-hole minority-electron character are much more likely than those of minority-hole majority-electron character with a pronounced maximum at an energy loss of 1–2 eV (Kaemper, Abraham and Hopster, 1992). By a Stoner excitation the spin of the scattered electron is apparently reversed. These spin-flip events were found to be very important in the off-specular, impact scattering regime, where they comprise up to one-third of the total electron–hole excitations and are responsible for the great majority of the observed intensity asymmetry. They are also detected under specular and near specular scattering conditions, but their relative importance decreases compared to strong dipole scattering (Venus and Kirschner, 1988).

Below 50 eV electron–hole excitations of valence electrons dominate all loss processes (Quinn, 1962). Since the momentum space for these processes becomes increasingly smaller with decreasing energy, the mean free path of electrons increases significantly at low energies. Above 50 eV electron–hole excitations are overbalanced by plasmon excitations. At higher energy the excitation of core level states becomes possible, too, although the cross section for these processes is negligibly small. The cross section for both processes, plasmon excitation and electron–hole excitations, decreases with increasing energy since the available time for a scattering process gets smaller.

The mean free path has been determined for a large number of materials (Seah and Dench, 1979; Woodruff and Delchar, 1986). Although individual values may vary by nearly an order of magnitude, the general trend following theoretical considerations (Quinn, 1962) is described by a minimum of the mean free path between 10 and 300 eV. The absolute value of the mean free path in this energy range is of the order of 1 nm. The interaction of low-energy electrons is therefore restricted to a few atomic layers at the surface, which makes electron diffraction an ideal tool for investigating the properties of surfaces and ultrathin films. Below 10 eV the mean free path increases considerably for many materials, particularly for noble metals. Surprisingly, this applies less to transition metals where the mean free path is related to the number of d-holes (Schoenhense and Siegmann, 1993).

2.6 Theory of SPLEED

Unpolarized LEED intensity calculations for various surfaces reproduce experimental data with impressive accuracy (Tong, 1994). A similar calculation concept considering the diffraction of spin-up and spin-down electrons separately has

been developed by Feder (1981, 1985). As explained below in more detail, calculation schemes for electron reflectivities may use as an input self-consistently calculated ground-state potential functions provided by separate program packages (**Density-functional Theory of Magnetism, Volume 1**).

For electron energies of several tens of electronvolts the muffin-tin (MT) approach for calculating the electron reflectivities proves very adequate. Within the core region, one may use spherically symmetric potentials, and bulk potentials generated from *ab initio* electronic-structure calculations are sufficiently accurate to describe electron scattering from atoms in the surface. At sufficiently high beam energy, the electron is scattered by the core region of the potential, and is influenced rather modestly by the details of the potential in the outer portion of the unit cell. Thus, for many materials the approach of using less time-consuming bulk calculations to approximate scattering potential at surfaces is sufficiently accurate. The crystal is divided into nonoverlapping spheres centered at each atomic site. Outside the spheres, the so-called inner potential is assumed to be constant. All inelastic processes are described by an imaginary part of the inner potential V_{i} which simulates the inelastic mean free path (IMFP). The inner potential V_{i} can be chosen in such a way that the mean free path fits the experimentally observed universal curve and is of the order of 4 eV, slightly changing with energy.

Inside the MT spheres, the portion of the ion-core potential in the electron energy range of typical LEED energies is to a large extent determined by the nuclear charge and tightly bound core-state electrons, which are not easily polarizable and retain their atomic character in the solid environment. Therefore, this portion of the potential changes only little as the atom is placed in the surface environment and is, to a good approximation, spherically symmetric. On the other hand, the outer parts of the atom, the valence and conduction electrons, are affected by the neighboring atoms and the surface. These distortions break the spherical symmetry of the ion-core potential. The distortions are important at very low energy (<30 eV) but play a minor role for electron energies >50 eV. Therefore, one may use only the spherical part of bulk potentials which in turn can be generated by *ab initio* electronic-structure calculations.

Electronic-structure calculations can be carried out on different levels of sophistication depending on the particular system and required accuracy. Ordered compounds can be calculated by means of full potential methods. A coherent potential approximation (CPA) may be used to determine the properties of doped compounds and randomly disordered alloys. The most time-consuming and most accurate calculations are given by the fully relativistic calculations.

Several calculation schemes are available and can be run on a personal computer. Self-consistent band structure calculations are useful for well ordered structures using the full potential linearized augmented plane-wave (FLAPW) method provided by Blaha, Schwarz, Sorantin and Tricky (1990) and Schwarz, Blaha and Madsen (2002) (Wien2k 04). In this method, only core states are treated relativistically. The exchange-correlation functional can be taken within the generalized gradient approximation (GGA) in the parameterization of Perdew *et al*. (1992). For comparison, calculations can also be performed using the linear muffin-tin orbital (LMTO) method provided by Savrasov (1996) (LMTART 6.5) on different levels of sophistication from simple atomic sphere approximation (ASA) to full potential plane-wave representation (FP-LMTO-PLW).

For less ordered structures, that is, random alloys, it is appropriate to carry out self-consistent band structure calculations using the Korringa–Kohn–Rostocker (KKR) method provided by Akai (1998) and Kotani and Akai (1996). The random alloys were calculated within the CPA. The program allows to use various types of the exchange-correlation functional, that are, for example, Barth and Hedin (1972), Moruzzi, Janak and Williams (1978), Vosko, Wilk and Nussair (1980) (VWN), and Vosko and Wilk (1980), or the GGA in the parameterization of Perdew and Yue (1986) and Perdew *et al*. (1992), or Engel and Vosko (1993). The program allows also to work in both approximations, MT and ASA.

The ion-core potentials are then used to calculate the various individual atomic t matrices (Feder, 1985). For SPLEED, it is convenient to assemble the atoms into layers and view the crystal as an infinite array of such layers parallel to the surface. Layer diffraction matrices $\tau_i = t_i(1 - Gt_i)^{-1}$ are then constructed that describe multiple scattering within the layer i. G is the intralayer single-particle propagator with complex self-energy. The atomic t matrix and the layer diffraction matrices are calculated usually in the angular momentum representation. The number of partial waves required for a reliable calculation depends on the number of nuclear charges of the contributing atoms. For 3d transition metals partial waves of up to $l = 4$ are sufficient while for 5d transition metals partial waves up to $l = 7$ are required (Plihal, Mills, Elmers and Gradmann, 1995).

The reflected electron intensity is then expressed by the full crystal T matrix. The exact calculation of the T matrix requires matrices too large to be handled conveniently. There are two major methods to deal with the T matrix in an appropriate way, the renormalized forward scattering (RFS) and the layer doubling method. In the RFS scheme, forward interlayer scattering events are iteratively accumulated and back interlayer events are summed sequentially. The summation over successive orders of backscattering events is stopped if numerical convergence to a desired accuracy is reached. Thus, wherever there is convergence of the power-series

expansion of backscattering matrices, the RFS method is fast and can be rapidly carried to a high degree of numerical accuracy. The layer doubling method, on the other hand, induces a larger set of scattering events than RFS. It generates the exact solutions of forward and backward-scattering matrices in the reciprocal space representation for two layers. The procedure is then repeated to scattering matrices for 2^n layers. This process converges in typically three to four iterations. The RFS method is a pertubative expansion and has therefore the virtue of being faster than both the exact T matrix calculation and the layer doubling method; however, it is less stable and diverges for small layer spacings.

3 EXPERIMENTAL METHODS

3.1 Sources

Various sources for spin-polarized electrons have been described in the literature (Kirschner, 1985a, 1985b; Maruyama *et al*., 1991). The most often used GaAs source was first introduced by Pierce and Meier (1976). The principle of the GaAs source is based on spin-polarized photoelectrons emitted from a GaAs surface, that are excited by circular polarized light. At the Γ point, the valence band which has a preferential p character is splitted by the spin-orbit coupling in fourfold degenerated $p_{3/2}$ states and twofold degenerated $p_{1/2}$ states. The conduction band possesses a preferential s character. Absorption of a photon with the gap energy (GaAs, 1.52 eV) induces an efficient dipole-allowed electron transition. For a right (left) circular polarized photon, the z component of the total angular momentum is changed by $+1(-1)$. If only electrons from the $p_{3/2}$ states are excited, right circular polarized light induces the transitions $m_j = -3/2 \rightarrow m_j = -1/2$ and $m_j = -1/2 \rightarrow m_j = +1/2$ with different transition probabilities (3:1). Therefore the expected polarization is $P = 50\%$. Using strained layers grown on substrates with slightly larger lattice constants, the degeneracy of the $p_{3/2}$ states is lifted and an even higher polarization is possible (Maruyama *et al*., 1991).

In order to extract the excited electrons from the conduction band one needs a trick. Using heavily p-doped GaAs charge redistribution in the surface region (10 nm) leads to a band bending toward lower energy. A capping of the surface with a combination of Cs and O pushes the conduction band finally below the vacuum level. Then, the electrons can escape without paying the work function energy (negative electron affinity, NEA). For NEA, the photon energy has to be adjusted to the band gap energy in order to avoid excitation of $p_{1/2}$ states. In this case, the polarization is independent of the level of the vacuum energy, which is easily changed by contamination. Alternatively, one may use photons with higher energy in the visible spectral region. In this case, the vacuum level has to be adjusted higher such that electrons excited from the $p_{1/2}$ states cannot escape (positive electron affinity, PEA).

After escaping the semiconductor surface the electrons are polarized longitudinally. Using electrostatic and/or magnetic deflectors, the polarization can be adjusted in any direction (Duden and Bauer, 1995).

Aulenbacher *et al*. (2002) investigated the limiting factors for the pulse length of electron bunches escaping a GaAs photocathode under the conditions of highly polarized beam production. For GaAs cathodes with layer thickness d that is large in comparison to the optical absorption length the photoemission time response of GaAs was explained by a diffusion model (Hartmann *et al*., 1999), typical response times being about 50–100 ps. For a highly polarized electron source, however, uniaxially strained GaAs or GaAsP cathodes are used. In these cathodes, the active layer thickness is limited to a value of $d = 125 \pm 25$ nm, which is only a fraction of the absorption length of the exciting laser radiation. In addition, the available heavy hole–light hole splitting of the valence band of the strained samples requires that the photoexcitation energy does not exceed the semiconductor band gap by more than 30–60 meV.

Using NEA-GaAs photocathodes, the pulse response of active layers with $d = 200$–1000 nm has been measured to depend quadratically on the layer thickness (Aulenbacher *et al*., 2002). For a thickness below 200 nm, the pulse length decreases to below 2 ps. The response time of a strained layer photocathode with 150 nm active layer thickness and minimized doping concentration in the active region is therefore at least a factor 25 faster than the bulk depolarization time. Therefore, the strained layer photocathodes with their inherent thickness limit of about 150 nm are relatively free from depolarization effects in the bulk of their active region. Thus, strained layer photocathodes offer ultrafast response and high spin polarization which may not only be useful in fundamental science but also for possible optospintronic devices.

3.2 Detectors

The low efficiency of spin detection is a severe experimental obstacle that impedes experimental progress. In terms of spin-detector development, a quantity of great interest is defined as the figure of merit (FOM) and is proportional to the inverse square of the statistical error in an electron counting experiment to measure the polarization of an incident beam (Kessler, 1976). The FOM can be calculated from the square of the total scattering asymmetry multiplied by the reflection coefficient. Conventional spin polarimeters (mini-Mott detectors) have a FOM below 2×10^{-4} (Pierce,

Celotta, Kelley and Unguris, 1988). Detailed investigations of the Fe(110) surface have shown that FOM of the order of 8×10^{-3} can be achieved (Fahsold, Hammond and Kirschner, 1992; Hammond, Fahsold and Kirschner, 1992). Along this direction, different surfaces have been investigated to increase the FOM, the lifetime, and the reproducibility (Hillebrecht *et al*., 2002; Jungblut, Roth, Hillebrecht and Kisker, 1992). Recently, FOM up to 6×10^{-3} have been achieved with a robust system, Fe(001)-p(1 × 1)O (Bertacco and Ciccacci, 1999; Bertacco, Merano and Ciccacci, 1998). A different approach suggested even higher FOM of up to 5×10^{-2} using high-quality ultrathin Co or Fe films on W(110) (Zdyb and Bauer, 2002a, 2002b). For Co/W(110) thin film, it has been shown that a FOM as high as 2×10^{-2} could be obtained for films grown at room temperature and that it is possible to reverse aging effects by moderate annealing (Graf *et al*., 2005).

3.3 SPLEED spectrometers

The standard setup of a SPLEED spectrometer consists of a source of spin-polarized electrons, the sample, and, in the simplest version, a Faraday cup as an electron detector. For the experiments described here (Waller and Gradmann, 1982; Elmers, 1995), the spin-polarized electrons were taken from a GaAs source, irradiated by circularly polarized light from a laser diode with a photon energy of $h\nu = 1.4\,\mathrm{eV}$ ($\lambda = 830\,\mathrm{nm}$). The electrons were electrostatically deflected by 90° resulting in a transversely polarized electron beam. Electron energies E with respect to the Fermi level of the target are given by $E = eU + h\nu$, where eU denotes the energy difference between the Fermi levels of the GaAs source and the target, respectively. The axis of electron polarization $\vec{P}_0$ is parallel to the normal $\vec{n}$ of the scattering plane, coinciding with the measured magnetization component. The magnitude of $\vec{P}_0$ can be calibrated by a comparison of scattering asymmetries obtained from a clean W(100) surface with previous studies, resulting in typical values $P_0 = 20 \pm 2\%$. A_{ex} can be determined for constant energy E as a function of the incident angle θ with respect to the target normal or, alternatively for constant angle as a function of E. The finite width of the electron beam and of the detector results in an averaging of $A(\theta)$ over a finite angle. Therefore, asymmetries are usually underestimated in sharp extrema.

Present day electron spectrometers offer energy resolutions of less than 1 meV (Ibach, 1991). Progress in instrumentation became possible through the development of efficient numerical methods to calculate electron optical properties of energy dispersive devices beyond the limitations of the classical cylindrical and spherical deflectors, and of lens systems which are not radial symmetric. The performance of spectrometers is ultimately determined by the brightness of the available electron sources.

In order to probe spin-flip events in electron energy loss spectroscopy (EELS) sources of spin-polarized electrons as described in the preceding text are used. The orientation of the spin is then longitudinal to the initial electron trajectory of the electrons. For the purpose of measuring the spin asymmetry of surface excitations, the spin should be oriented perpendicular to the scattering plane and therefore transverse to the electron trajectory at the sample position. This requires a deflection of the electron trajectory of 90° between the point of electron emission from the GaAs cathode and the sample. Unfortunately, a 90° deflection is incompatible with the standard deflecting energy dispersive elements such as the cylindrical or spherical deflector which feature 127° and 180° deflection, in the absence of fringe field corrections. Initial approaches to the problem (Kirschner, Rebensdorff and Ibach, 1984), therefore, introduced an additional deflector between the photocathode and electron monochromator on the expense of a current reduction. An optimum design for a spectrometer combines a 90° deflection in the energy dispersive elements with stigmatic imaging of the entrance slit of the first monochromator onto the exit slit of the last analyzer of the entire spectrometer. A realization of this concept was reported by Ibach *et al*. (2003) comprising a two-stage monochromator, the first stage being a 90° deflector which is followed by a 180° deflector. The combination of both deflectors provides a nearly stigmatic image of the entrance slit onto the exit slit in the presence of space charge. The overall performance of this concept was demonstrated by the determination of spin-wave dispersion curves (Vollmer *et al*., 2003).

3.4 SPLEED by SPLEEM

For a direct investigation of band structure properties, it is necessary to reflect electrons at very low energies, that is, below 20 eV. In electron spectrometers, as described above, the sample area is usually well shielded from external magnetic fields and electron diffraction can be studied at kinetic energies of a few electronvolts. An alternative approach is given by the use of a SPLEEM (Altman *et al*., 1991; Zdyb and Bauer, 2002b). In the diffraction mode the microscope allows at normal incidence the observation of the specular reflected beam. An important advantage of this instrument is the simultaneous control of the sample surface properties and the possibility to restrict the area of interest to any sample area thus avoiding an averaging over, for example, inhomogeneous film thicknesses or magnetization structures.

As demonstrated by Zdyb and Bauer (2002b) SPLEEM can be applied to SPLEED, provided that a nearly parallel beam of slow electrons with normal incidence on the sample is produced by focusing a spin-polarized 15 keV electron beam into the back focal plane of a cathode lens. In this lens, the electrons are decelerated to the desired energy at the sample, reaccelerated again after reflection, and used for imaging the surface. This high magnification is necessary in order to measure the intensity reflected from microcrystals. The electron beam was produced by a GaAs source as described in the preceding text.

4 APPLICATIONS

4.1 SPLEED at nonmagnetic surfaces

The 5d element W is not ferromagnetic and therefore one obtains $A_{ex} = 0$. Because of the large atomic number of W its surface exhibits large values of A_{so}. In a famous double scattering experiment Kirschner (1985a) showed how absolute values for A_{so} could be determined without any assumption on the polarization detector or on the electron source.

An unpolarized incident electron beam perpendicular to a W(100) surface (polarizer) generates four (2,0) spots of equal intensity. The two complementary diffracted beams in one of the two scattering planes are oppositely polarized, perpendicular to the corresponding scattering plane. The relations between counting rates $N_1^{\uparrow}$, $N_1^{\downarrow}$ of up- and down-polarized electrons and polarization P are given by

$$\left(\frac{N_1^{\uparrow}}{N_1^{\downarrow}}\right)_{(2,0)} = \frac{1-P}{1+P} \qquad \left(\frac{N_1^{\uparrow}}{N_1^{\downarrow}}\right)_{(\bar{2},0)} = \frac{1+P}{1-P} \tag{22}$$

The (2,0) spot is then diffracted at a second W(100) surface (analyzer) and generates again a (2,0) and $(\bar{2}, 0)$ spot which now have different intensities in addition to their different polarizations:

$$\begin{aligned}\left(\frac{N_2^{\uparrow}}{N_2^{\downarrow}}\right)_{(2,0)} &= \frac{(1-P)(1-A)}{(1+P)(1+A)} \\ \left(\frac{N_2^{\uparrow}}{N_2^{\downarrow}}\right)_{(\bar{2},0)} &= \frac{(1-P)(1+A)}{(1+P)(1-A)}\end{aligned} \tag{23}$$

with the asymmetry A of the second surface. From the different intensities one obtains:

$$R = \frac{I_{(2,0)} - I_{(\bar{2},0)}}{I_{(2,0)} + I_{(\bar{2},0)}} = A \cdot P \tag{24}$$

Because the scattering plane being a mirror plane of the two W(100) surfaces the asymmetries are equal, $A = P$, and the asymmetry can be determined from $P = \sqrt{R}$ (Kirschner, 1985b).

Because of the fact that W(100) can be easily cleaned in a ultrahigh vacuum by flashing and because it provides comparatively large values of P, the W(100) surface is used as a spin detector (SPLEED detector) (compare Section 3.2). Here, P depends strongly on the incident energy and the scattering energy has to be well defined for the application as a spin detector. A commercialized version using four electron counters allows simultaneous detection of two polarization components (Focus-GmbH, 2005).

The usefulness of spin-polarization analysis in LEED for the structure determination of nonmagnetic surfaces and of ordered layers adsorbed at single-crystal surfaces has been successfully demonstrated by experimental and theoretical analysis of SPLEED data (Potthoff *et al.*, 1995; Hilgers, Potthoff, Mueller and Heinzmann, 1995; Venus, 1993), where adsorbate structures and structural parameters could be determined.

Zasada (2002) proposed the interesting idea of measuring the spin-dependent diffuse LEED intensity. He considered the resulting incoherent scattering asymmetries from a single-crystal surface Pt(111) partially covered with CO molecules and calculated values for different parameters characterizing the adsorbate/substrate system. The parameters considered were geometrical parameters related to the local arrangement of molecules near chemisorption sites and order parameters related to the statistical distribution of the occupied chemisorption sites. The impressive sensitivity of the incoherent scattering asymmetries to geometry and local order examined for the CO/Pt(111) system demonstrated the practical use of the theory and implies a challenge to experimental work in this field.

4.2 Surface magnetization of bulk ferromagnets

4.2.1 Critical behavior

In the following, we concentrate on the critical behavior of the magnetization near the Curie temperature T_C. SPLEED will be a convenient experimental tool to analyze the critical behavior, if A_{ex} is proportional to the magnetization with respect to its temperature dependence. This appears reasonable near T_C, as the magnetic coherence length ξ diverges with the reduced temperature $t = (T - T_C)/T_C$ going to zero, and so ξ becomes large in comparison with the information depth of the low-energy electrons. Feder and Pleyer (1982) theoretically confirmed a similar temperature dependence of A_{ex} and magnetization. Considering the finite coherence length, an experimental analysis

using $A_{ex} \propto M$ should be restricted to $t < 0.1$, and the results should be checked by comparing $A_{ex}(T)$ for various energies.

Pioneering work was done by Palmberg, de Wames and Vredevoe (1968) on antiferromagnetic NiO surfaces, using the temperature dependence of half-order LEED spots which are caused by the antiferromagnetic order and therefore disappear at the Néel-temperature. The critical exponent for the surface magnetization was found close to 1, in contrast to $\beta \approx 1/3$ for the bulk. Note that, in this case, no spin analysis is needed and an unpolarized beam can be used, although the effect is caused by the exchange asymmetry.

An experimental study using SPLEED of the critical behavior of Ni(110) and Ni(100) surfaces was given by Alvarado, Campagna, Ciccacci and Hopster (1982) and Alvarado, Campagna and Hopster (1982). They found a critical power law $A_{ex} \propto t^{\beta}$ with a critical temperature identical with the bulk value and determined a critical exponent $\beta = 0.8 \pm 0.02$ for both Ni(100) and Ni(110) differing dramatically from the bulk value $\beta = 1/3$. The value found for the Ni surfaces is in agreement with theoretical models considering local moments and short-range interaction (Heisenberg model).

An interesting case investigated by SPLEED is the inferred existence of a remanent magnetization at the Gd(0001) surface while the bulk magnetization has vanished for temperatures above T_C. The existence of surface magnetic ordering above the bulk Curie temperature for Gd(0001) thin films grown epitaxially on W(110) was first measured by Weller *et al*. (1985) using temperature dependent SPLEED. From theoretical considerations, a pure surface transition can occur if the exchange coupling is enhanced at the surface (Binder, 1985). A spin-polarized energy-resolved photoemission study of Gd(0001) (Weller *et al*., 1985) revealed an antiferromagnetic coupling of the topmost layer to the underlying magnetic layers. The experimental result reported in (Weller *et al*., 1985) provoked a heavy debate in the scientific community because of conflicting experimental results denying a pure surface transition ((Arnold and Pappas, 2000) and references therein). Recently published articles in favor (Denecke *et al*., 2002) or disfavor (Melnikov *et al*., 2004) of an enhanced Curie temperature at the surface suggest that the topic has not been clarified, yet.

4.2.2 *Magnitude of surface magnetization at low temperatures*

The advantages of probing simultaneous A_{ex} and A_{so} in order to evaluate the magnitude of the magnetization at surfaces was first demonstrated in an investigation of the Ni(001) surface (Feder, Alvarado, Tamura and Kisker, 1983). The comparison of experimental and calculated A_{so} values confirmed the adequacy of the used exchange-correlation potential and the topmost atomic layer spacing as bulk like. Experimentally obtained A_{ex} values were compared with different model assumptions for the surface magnetization. Two independent theoretical analyses (Feder, Alvarado, Tamura and Kisker, 1983; Freeman, 1983) concluded on a slightly enhanced surface moment (+5 m%) for the Ni(001) surface.

In the following, we discuss extensively the case of the Fe(110) surface as an example for the determination of magnetization near the surface of well defined systems.

In the work of Waller and Gradmann (1982) and Waller (1986), the total scattered intensity (spin-up plus spin-down current) is measured, for the specular (00) beam and for the (11) beam. They have studied a remarkably wide range of energies. The polarization of the incident beam is parallel to the surface and perpendicular to the scattering plane defined as the plane that contains the incident beam and the normal to the surface. The magnetization of the substrate is also parallel to the surface, and to the [001] direction, which is an easy axis. The scattering plane is perpendicular to the [001] direction in the surface, so in all measurements the incident beam polarization is parallel to or antiparallel to the substrate magnetization. The geometry corresponds to the transversal geometry described in Section 2.4.

In conventional LEED analyses, in comparison between theory and experiment one does not compare the absolute intensity given by theory with the data. Indeed, it is difficult to extract the absolute intensity from the data. One typically adjusts the theoretical intensity to fit experiment at one point, and then compares the two as a function of angle at fixed energy, or energy at fixed incident angle. The exchange and spin-orbit asymmetries are intensity ratios, and the absolute values of these quantities are not affected by the difficulty of extracting a single absolute intensity from data influenced by geometric corrections, spectrometer sensitivities, and so on. Thus, a comparison between theory and experiment provides a severe test of the quality of the potentials used in the theoretical work.

Figure 1(a–c) shows a comparison between calculated and measured total intensity, spin-orbit asymmetry and exchange asymmetry for the specular beam scattered at a Fe(110) surface. The experimental data were first published in Tamura, Feder, Waller and Gradmann (1990). The calculations have been performed using the multiple-scattering theory described in Ormeci, Hall and Mills (1990, 1991). For the analysis *ab initio* self-consistent potentials calculated by Fu and Freeman (1987) for the Fe(110) surface were employed. The enhanced surface moments were simulated by simply scaling up the spin-dependent portion $\Delta V(\vec{r}) = V^{\uparrow}(\vec{r}) - V^{\downarrow}(\vec{r})$ of the self consistent potential by

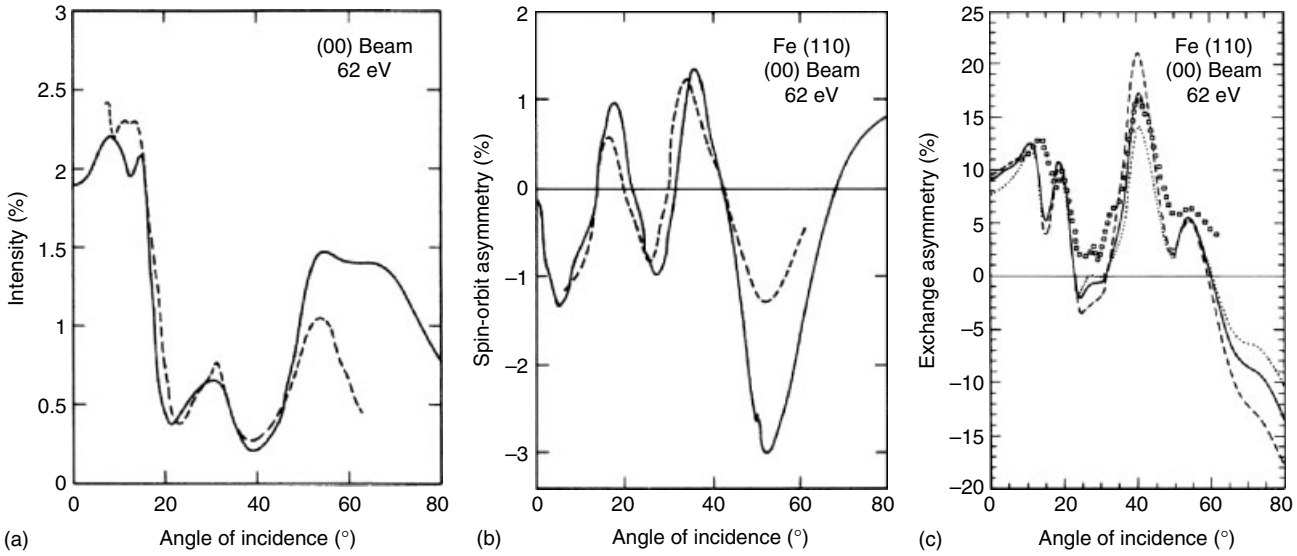

Figure 1. SPLEED from Fe(110). Comparison between theory (full lines) and experimental data (dashed lines in (a) and (b), squares in (c)) for total intensity (a), spin-orbit asymmetry (b), and exchange asymmetry (c) for the (00) spot of a Fe(110) surface at 62 eV beam energy. The measured exchange asymmetry A_{ex} (squares) is compared with theoretical results based on three different assumptions for the surface magnetic moments at the Fe(110) surface: (i) calculations based on the picture of Freeman and Fu (solid line); (ii) calculations based on the model of Tamura, Feder, Waller and Gradmann, 1990; (dashed line); (iii) calculations based on the assumption that the Fe moments assume their bulk value everywhere (dotted line). (Reproduced from A. Ormeci *et al*., 1990, with permission from American Physical Society © 1990.)

an appropriate scale factor. This is the only adjustment that was made to the potential; no adjustment was made to the overall strength of the exchange potential.

The overall agreement between theory and experiment is remarkably good. A certain discrepancy between theory and experiment remains at large angles as was pointed out in Tamura, Feder, Waller and Gradmann (1990) and Ormeci, Hall and Mills (1990). The agreement between theory and experiment for the spin-orbit asymmetry, shown in Figure 1(b), confirms the assumption for the polarization of the incident electron beam ($P = 0.3$), because it is very insensitive to the magnetic-moment profile. The features of the experimental data are reproduced nicely, though the magnitude of the negative dip in A_{so} above 40° is overestimated.

The exchange asymmetry (Figure 1c) at an incident beam energy of 62 eV comprises a considerable sensitivity to the magnitude of the near-surface moments. The solid line denotes calculations for the model of Fu and Freeman (1987), that is, 19.4% enhancement of moment in the surface layer, 6.8% in the second layer, 2.7% in the third layer, and 1.4% in the fourth. The dashed line is the prediction calculated for the model proposed in (Tamura, Feder, Waller and Gradmann, 1990), which has the surface-layer moment enhanced by 35%, and the second-layer moment diminished by 15%. All other moments assume their bulk values. The dotted line shows the exchange asymmetry calculated for a picture which takes the moments equal to their bulk value everywhere.

The prominent peak in A_{ex} near $\theta = 40^\circ$ is quite sensitive to the magnitude of the moments near the surface. The peak in the data has $A_{ex} = 0.17$, extremely close to the value provided by the model of Fu and Freeman (1987). The model of (Tamura, Feder, Waller and Gradmann, 1990) gives a maximum value of $A_{ex} = 0.21$, while the assumption of bulk moments everywhere gives $A_{ex} = 0.14$. The best overall account of the data is provided by the model of (Fu and Freeman, 1987). The finding of an enhanced surface moment at the free Fe(110) surface has been quantitatively confirmed by torsion oscillation magnetometry (TOM) (Wagner, Weber, Elmers and Gradmann, 1997).

As pointed out in Ormeci, Hall and Mills (1990), deviations between theory and experiment may occur particularly at the intensity minima. The minimum in the experimental data may be less deep than that in theory, because defects on the surface may destroy the long-range order needed for the destructive interference between scattered waves generated from various layers of the samples to produce a near zero in the total intensity. This may be a difficulty, even for samples with very high-quality surfaces. In addition, the defects produce an incoherent background of elastically scattered electrons which are collected along with those that contribute to the coherently reflected beam.

4.3 Ferromagnetic monolayer structures

4.3.1 Monolayer Fe(110) on W(110) – critical behavior

As pointed out in the preceding text, SPLEED can be used to analyze the critical behavior of ultrathin films, if A_{ex} is proportional to the magnetization with respect to its temperature dependence. SPLEED is advantageous because of its surface sensitivity, especially if the magnetization is concentrated in an ultrathin film on top of a nonmagnetic substrate (Venus and Cool, 1999). For ultrathin Fe(110)/W(110) films A_{ex} exhibits peak values of polarization up to 40 % for specific scattering conditions (Venus and Cool, 1999).

For ultrathin films, $A_{ex} \propto M$ was used for the interpretation of the data over a large range of temperatures Duerr *et al.* (1989). However, deviations from the proportionality for $t > 0.1$ ($t = (T - T_C)/T_C$) were discussed in detail for surfaces (Kirschner, 1984) and ultrathin films (Elmers and Hauschild, 1994). In (Elmers and Hauschild, 1994), strictly speaking a deviation from the proportionality has not been confirmed, because M has not been measured. But the temperature dependence of A_{ex}, at lower temperatures, deviates so strongly from everything we know about $M(T)$ that this confirms the loss of proportionality at low temperatures. $A_{ex} \propto M$ in the critical range $t < 0.1$ rests on the careful discussion in this chapter.

For a comparison of theoretical models with experiment it is crucial to prepare samples as close as possible to the structures considered by theories. The system Fe on W(110) serves as a favorable model system since it is possible to grow extended monolayers to a high degree of perfection (Przybylski, Kaufmann and Gradmann, 1989). The monolayer Fe(110)/W(110) develops a huge uniaxial magnetic anisotropy favoring an in-plane magnetic easy axis along the [1$\bar{1}$0] direction (Gradmann, Korecki and Waller, 1986; Gradmann, Przybylski, Elmers and Liu, 1989; Elmers and Gradmann, 1990; Fritzsche, Elmers and Gradmann, 1994; Elmers *et al.*, 1994; Pratzer *et al.*, 2001). According to theoretical models, one expects therefore a critical behavior close to the two-dimensional (2d)-Ising model.

2d-Ising behavior can be expected only in a narrow critical temperature region ΔT below and above T_C. As a result of the scaling theory (Pfeuty and Toulouse, 1977) $\Delta T/T_C$ is for a 3d system with anisotropy constant K of the order $K/k_bT_C \approx 10^{-3}$, which would make the critical behavior practically impossible to observe. In 2d systems, however, large regions of correlated spins occur even far from the phase transition (Demokritov, Kreines, Kudinov and Petrov, 1989), effectively broadening the critical region by a factor $J/K \approx 10^2$. For an investigation of the critical region, we therefore concentrate on the temperature region $\Delta T_C/T_C < 0.1$.

For uncovered Fe monolayers, the magnetic order $M(H, T)$ was determined via the exchange asymmetry, $A_{ex}(H, T)$, of reflected spin-polarized electrons (Elmers, 1995). The incident angle and energy of the spin-polarized electrons were chosen such that A_{ex} was maximized. In this experiment, a small field could be applied via the Oerstedt field of a current running through the substrate crystal, thus allowing to determine not only the magnetization but also the magnetic susceptibility. For fields below 2 Oe, the deflection of electrons due to the Lorentz force could be neglected. The result for the temperature dependence of the spontaneous magnetization $M_0(T) \propto A_{ex}(T)$ and of the magnetic susceptibility $\chi(T)$ is shown in Figure 2.

A careful evaluation of $A_{ex}(H, T)$ for very low fields $H \leq 2$ Oe (Elmers, Hauschild and Gradmann, 1995a, 1995b) verified that $M_0(T)$ equals the remanent magnetization $M(H = 0, T)$, which was originally determined in the experiment. Figure 2 shows a steep decrease of $M_0(T)$ near $T = 222$ K, followed by an inflection point at $T_{infl} = 222.5$ K and a final vanishing at $T^* = 223.4$ K. This typical tail is frequently observed for ultrathin films and often associated with finite size effects (Duerr *et al.*, 1989). Note, however, that the extension of the tail, in our case, is of the order of just 0.5% of T_C. We find a satisfying explanation for the tail

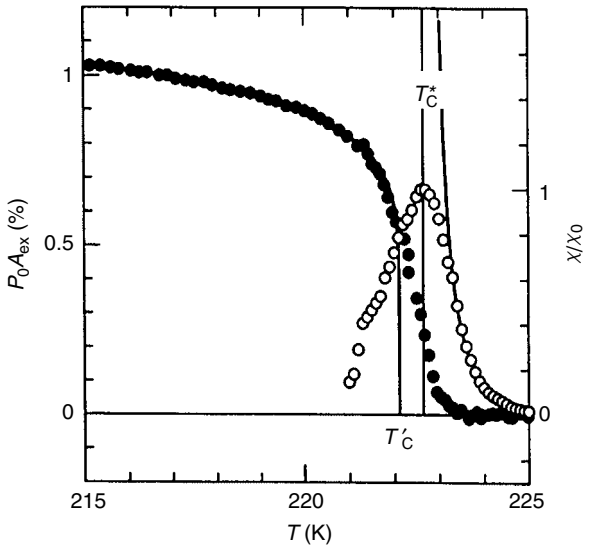

Figure 2. Exchange asymmetry P_0A_{ex} (●) in the remanent state of 0.8-ML Fe on W(110), deposited at 660 K, as a function of temperature. Susceptibility χ/χ_0 (○) versus T for the same sample. Full lines represent power laws $A_{ex} \propto (T'_C - T)^{\beta'}$ and $\chi \propto (T - T'_C)^{-\gamma'}$, with values for the critical temperature $T'_C = 222.1$ K and for exponents $\beta' = 0.124$ and $\gamma' = 3.2$. $T^*_C = 222.6$ K defines the maximum of χ. (Reproduced from H.J. Elmers *et al.*, 1995, with permission from World Scientific. © 1995.)

shown in Figure 2 assuming a small distribution of Curie temperatures in our sample. In fact, the sample consists of monolayer stripes formed adjacent to terrace steps on the substrate. The distribution of the terrace width results in a variation of the stripe widths and consequently of T_C. In this picture, every individual magnetic stripe, as formed in the step flow growth mode, shows a second-order phase transition (no tail) but with slightly different T_C. The averaging over the distribution results in the tail. Even for a single stripe of uniform width a tail has been predicted by Landau (1976) who demonstrated by MC simulations that long-range order in the 2d-Ising model on a finite sized quadratic square lattice shows similar tails above T_C. This minor effect, however, can be neglected in the experiment described here.

For a determination of the critical exponent, $A_{ex}(T)$ was fitted numerically to a power law $A_{ex}(T) \propto (T - T'_C)^{\beta'}$ in the region $0.9 < T/T_C < 0.996$, thus avoiding the temperature region affected by the tail. The fit results in a critical temperature $T'_C = 222.1(1)$ K, which can be appointed to the Curie temperature of the system, and in the critical exponent $\beta' = 0.124(1)$, which is in agreement with the theoretical value $\beta = 1/8$ of the 2d-Ising model. The accuracy of the fit can be estimated from a double logarithmic plot (Figure 3).

As was shown by a more thorough study of the critical behavior (see Elmers, Hauschild and Gradmann (1996)), the magnetization tail above T_C can be interpreted as a result of convolution of the critical power law with the monolayer stripe width distribution. Using an appropriate deconvolution

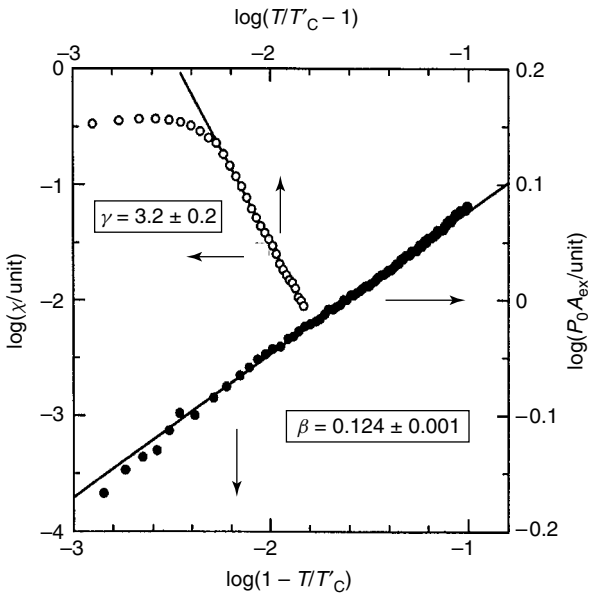

Figure 3. Double logarithmic plot of susceptibility χ (○) and exchange asymmetry A_{ex} (●) versus reduced temperatures (data from Figure 2). Exponents resulting from the slope are $\beta' = 0.124$ and $\gamma' = 3.2$. (Reproduced from H.J. Elmers *et al.*, 1995, with permission from World Scientific. © 1995.)

scheme, critical power laws could be established for both magnetization and susceptibility with critical exponents $\beta = (0.134 \pm 0.003)$ and $\gamma = (2.8 \pm 0.2)$. These values form a small but definite deviation from the 2d-Ising model. The enhanced value of γ can be explained from the fact that the anisotropy energies per atom are smaller than exchange coupling energies. The enhanced value of β is indicative of long-range interactions.

The magnetic susceptibility was determined from the initial increase of A_{ex} with increasing external fields. As shown in Figure 2, $\chi(T)$ exhibits a maximum value χ_0 at a temperature $T^*_C = 222.65$ K well above T'_C ($T^*_C = (1 + 2.5 \times 10^{-3})T'_C$). The deviation of the maximum of the susceptibility from the Curie temperature can be understood from the following argument. It is well known (Essam and Fisher, 1963) that $\chi(T)$ rises much faster when approaching T_C from $T < T_C$ than from $T > T_C$. The rise is limited at T^- (for $T < T_C$) and at T^+ (for $T > T_C$) because of the limited size of the sample (magnetic islands). Now, T^- is much closer to T_C than T^+, and consequently, the maximum will show up at some mean value in between T^- and T^+, which should be above T_C.

A rough estimate of the absolute value of χ_0, assuming bulk magnetization at $T = 0$ K and a proportionality $M \propto A_{ex}$ even for $T \ll T'_C$, results in $\chi_0 \approx 10^3$ (SI units), which is somewhat smaller than previous observations for Fe on W(110) (Back, Wuersch, Kerkmann and Pescia, 1994). As was pointed out by Farle *et al.* (1993), the maximum value of χ observable in an experiment is limited by the in-plane demagnetization factor $1/N_\parallel$, which is roughly given by $1/N_\parallel = \rho/t$ for islands of diameter ρ and thickness t. In turn, the large susceptibility we observed for the Fe(110)/W(110) monolayer, corresponds to magnetic islands with an effective diameter of $\rho = 5\,\mu$m.

At temperatures below the maximum value of the susceptibility, $\chi(T)$ can be approximated by a power law, $\chi(T) \propto (T'_C - T)^{-\gamma'}$. A double logarithmic plot (Figure 3) reveals a linear behavior, resulting in an exponent $\gamma' = 3.2(2)$, which is definitely above the 2d-Ising value $\gamma = 7/4$. Note that we used T'_C for the logarithmic plot. We find that, in contrast to the case of β', the exponent γ' strongly depends on the choice of the critical temperature (without affecting the linear behavior in the double logarithmic plot). If we took, for example, T^*_C as the Curie temperature of the system, the corresponding power-law fit would result in a critical exponent $\gamma' = 1.75(10)$, surprisingly close to the Ising value.

4.3.2 Submonolayer Fe(110) on W(110): ferromagnetic monolayer stripes

Fe grows pseudomorphically from the steps of the W substrate (step flow growth) in continuous stripes of monoatomic

height Elmers *et al*. (1994). The second layer starts only after the completion of the first layer. The width $b = \Theta w$ of the Fe stripes can be controlled by the Fe coverage Θ with w being the width of the W terrace. Certainly, the W substrate will show an arbitrary distribution of terrace widths. Employing mean values for b and w, one may reinterpret Θ in terms of an average stripe width. The mean width of the W terraces in the experiment reported here was $\overline{w} = 40\,\text{nm}$.

Figure 4 shows $P_0 A_{ex}(T) \propto M_0(T)$ for Fe films with decreasing coverage, down to a coverage of only $\Theta = 0.1$. The remarkably high signal-to-noise ratio emphasizes the sensitivity of the SPLEED probe. The magnetic phase transition, which is sharp for Θ close to the complete monolayer, smears out for decreasing Θ, that is, for decreasing stripe width. The Curie temperature $T_C(\Theta)$ was determined operationally from the point of inflection in the $M_0(T)$ curves. The increase of $T_C(\Theta)$ as a function of Θ is shown in Figure 5. It can be interpreted as an increase of $T_C(b)$ as a function of the stripe width b, as explained in the caption.

The dispersion of stripe widths can be estimated from $M(H)$ in the vicinity of T_C. Assuming a Gaussian distribution of the terrace width w with a full width at half maximum of Δw and a mean value $\overline{w} = 40\,\text{nm}$, the distribution of the stripe width then results via $T_C(b)$ (see Figure 5) in a distribution of Curie temperatures with the mean value given by $T_C(\Theta\overline{w})$. In this model, the phase transition of a single stripe follows the ideal power law; however, the averaging causes a tail in the $M_0(T)$ relation with a width ΔT roughly increasing with $\Delta w\, \mathrm{d}T_C/\mathrm{d}b$. A comparison of this simple model with the experimentally observed tails results

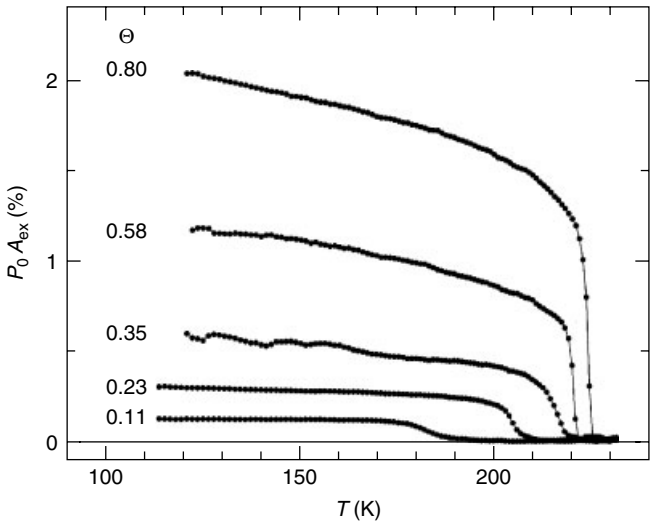

Figure 4. $P_0 A_{ex}(T) \propto M_0(T)$ versus T for electron reflection from Fe(110) films prepared at 660 K on W(110) with total coverage Θ. The spin polarization P_0 of the incident electron beam is roughly 20%. (Reproduced from H.J. Elmers *et al*., 1994, with permission from American Physical Society. © 1994.)

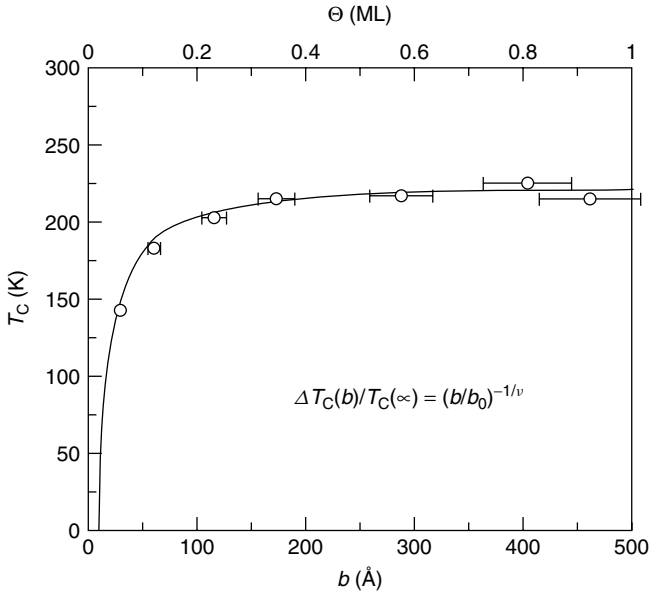

Figure 5. Curie temperature T_C versus coverage Θ for Fe(110) deposited on W(110) at 660 K (○). Stripe width from $b = w\Theta$ with $w = 40\,\text{nm}$. Error bars indicate the mean half width ($0.1b$) of the distribution of Fe stripe widths. The power-law fit as indicated in the figure (full line) results in $\nu = 0.97(14)$, $T_C(\infty) = 230\,\text{K}$, and $b_0 = 0.8\,\text{nm}$. (Reproduced from H.J Elmers *et al*., 1995, with permission from World Scientific. © 1995.)

in a value $\Delta w/\overline{w} = 0.1$, independently of the coverage. An excellent agreement of the model and the experimental data was found for all coverages $0.05 \leq \Theta(\text{ML}) \leq 0.8$.

The decreasing values of T_C for increasing $\Theta > 0.8$ are presumably related to an interaction appearing when the separated stripes are closing in. The finite size scaling for the two-dimensional stripes results in the power law, $1 - T_C(b)/T_C(\infty) = (b/b_0)^{-1/\nu_2}$, with $T_C(\infty)$ denoting the Curie temperature of the extended monolayer. A three-parameter fit to the experimental data (see Figure 5) results in $T_C(\infty) = T_C(\text{ML}) = 230\,\text{K}$, $b_0 = 0.8\,\text{nm}$ and $\nu_2 = 0.97 \pm 0.14$. The critical exponent of the two-dimensional correlation length ν_2 is close to the value $\nu_2 = 1$ predicted for the 2d-Ising model. The stripe width b_0 marks the onset of ferromagnetic order, corresponding to four atomic chains in the stripe.

4.3.3 Bilayer Fe(100) on W(100) – critical behavior of the 2d-XY model

Despite the lack of a full theoretical understanding, spontaneous magnetization was found experimentally in ultrathin films without uniaxial anisotropy (Elmers, 1995). Without uniaxial anisotropy, the spontaneous magnetization M_0 lies in the film plane. In most cases, the anisotropy was not determined explicitly, but can be deduced from the symmetry of

the film. For films of cubic symmetry in the (100) plane, the most significant contribution to the anisotropy energy will be of fourfold symmetry resulting in a biaxial anisotropy which is weak in comparison to the uniaxial anisotropy discussed in the preceding text.

The critical behavior of 2d systems where the magnetization can rotate freely in the film plane (2d-XY model) was discussed in Bramwell and Holdsworth (1993a) with the result of quasispontaneous magnetization and a critical exponent of $\beta = 1/4$. Instead of the power-law behavior regularly found in magnetic systems, the magnetic susceptibility was predicted to increase exponentially (Kosterlitz, 1974) in a 2d-XY model.

Magnetic properties were investigated (Elmers and Hauschild, 1994) for Fe layers on W(100). It was confirmed experimentally that Fe/W(100) films even up to a coverage $\Theta = 2\,\mathrm{ML}$ are thermodynamically stable (Elmers and Hauschild, 1994). Moreover, Fe grows pseudomorphically on the W(100) substrate (Elmers and Hauschild, 1994) with an expansion of 9.4% due to the lattice mismatch, thus forming a promising epitaxial system for studying 2d magnetism.

Using SPLEED, the exchange asymmetry, A_{ex}, was measured as a function of temperature and external field H for an annealed ($T_{\mathrm{a}} = 550\,\mathrm{K}$) Fe(100)/W(100) film. The thickness well below the bilayer ($\Theta = 1.6\,\mathrm{ML}$) guarantees the absence of effects evoked by triple layer islands.

Figure 6 shows the temperature dependence of the spontaneous magnetization $M_0(T)$ and the magnetic susceptibility $\chi(T)$ just in the critical regime. Imperfectnesses of the two-dimensional sample, like finite sized islands or a distribution of island sizes, cause the tail of $M_0(T)$ just above T_{C}. The tail covers only a small temperature region of $\Delta T \approx 1\,\mathrm{K}$ ($0.005\,T_{\mathrm{C}}$). This might be taken as a hint for the good quality of the sample. The power law $M_0(T) \propto (T'_{\mathrm{C}} - T)^{\beta'}$ fits the experimental data $A_{\mathrm{ex}}(T) \propto M_0(T)$, resulting in the critical temperature $T'_{\mathrm{C}} = 207.8(2)\,\mathrm{K}$ (the Curie temperature for this special film) and in an effective exponent $\beta' = 0.217(5)$. The double logarithmic plot (Figure 7) reveals the result $\beta = 0.22(1)$ of the fit. This value is consistent with the theoretical value for the 2d-XY model, $\beta = 3\pi^2/128 \approx 0.23$ (Bramwell and Holdsworth, 1993b).

Here χ was derived from the difference $\Delta M = M(H_1, T) - M(0, T)$, of the magnetization in an external field $H = 0.6\,\mathrm{Oe}$ compared with the magnetization in the remanent state. In the limited temperature interval ($0.98\ T'_{\mathrm{C}}, 1.02\ T'_{\mathrm{C}}$) around T'_{C}, $\Delta M(H)$ showed a nonlinear increase (with decreasing slope) as a function of H, thus providing only a lower limit for χ, only.

For $T < 0.98\ T'_{\mathrm{C}}$ and $T > 1.02\ T'_{\mathrm{C}}$, ΔM turned out to increase linearly with H, thus allowing for a determination of $\chi(T)$. Figure 7 shows a double logarithmic plot of $\chi(T > T'_{\mathrm{C}})$ using the critical temperature T'_{C} determined from the fit of $M_0(T)$ (Figure 6). A fit using the exponential law, $\chi \propto \exp(b/\sqrt{T/T'_{\mathrm{C}} - 1})$, agrees well with the experimental data. The fit results in a parameter $b = 1.6(1)$, which is of the order of magnitude predicted for the pure 2d-XY model with nearest-neighbor interaction, $b(2\mathrm{d} - XY) = 2.6$ (Kosterlitz, 1974).

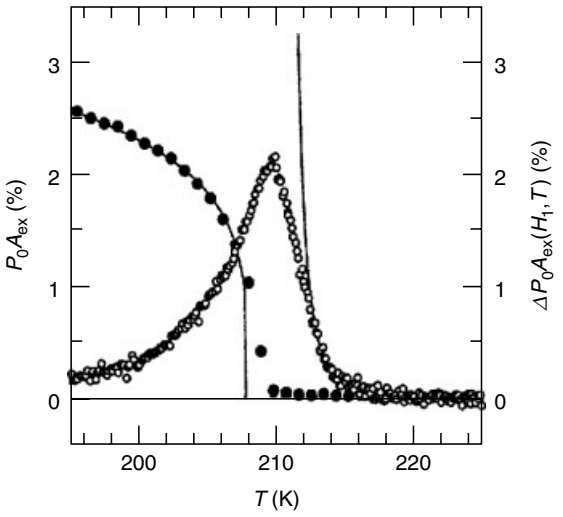

Figure 6. Exchange asymmetry P_0A_{ex} (●) in the remanent state of 1.6-ML Fe on W(100), deposited at 300 K and subsequently annealed at $T = 550\,\mathrm{K}$, as a function of temperature. Increase $\Delta P_0A_{\mathrm{ex}} = P_0[A_{\mathrm{ex}}(H_1, T) - A_{\mathrm{ex}}(0, T)]$ of exchange asymmetry with an external field $H_1 = 0.63\,\mathrm{Oe}$ as a function of temperature (○). The solid lines represent a power law $A_{\mathrm{ex}} \propto (T'_{\mathrm{C}} - T)^{\beta'}$ and an exponential law $\Delta P_0A_{\mathrm{ex}} \propto \exp(b/\sqrt{(T/T'_{\mathrm{C}} - 1)})$, respectively, with values for the critical temperature $T'_{\mathrm{C}} = 207.8\,\mathrm{K}$ and for exponents $\beta' = 0.22$ and $b = 1.6$. (Reproduced from H.J. Elmers *et al.*, 1995, with permission from World Scientific. © 1995.)

4.3.4 *Bilayer Fe(100) on W(100) – magnitude of magnetization*

In this section, an example is given about how magnetic *and* structural information can be gained by a comparison of experimental and theoretical data of SPLEED data (Plihal, Mills, Elmers and Gradmann, 1995). For this purpose, a ferromagnetic bilayer of very high quality is chosen, that is, the pseudomorphic Fe bilayer Fe(100)/W(100) (Elmers and Hauschild, 1994). Another advantage is that this bilayer has been studied theoretically by *ab initio* calculations (Wu and Freeman, 1992).

In order to obtain information on the angular variation of the specular reflectivity, the SPLEED intensities are measured at various energies. Both the spin-orbit asymmetry A_{so} and the exchange asymmetry A_{ex} is evaluated. For comparison with theoretical data, relativistic multiple-scattering theory has been applied according to the scheme outlined in Section 2.6.

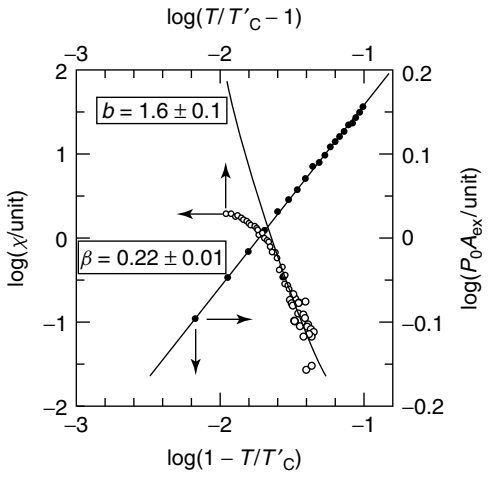

Figure 7. Double logarithmic plot of susceptibility χ (○) and exchange asymmetry A_{ex} (●) versus reduced temperatures. (Data from Figure 6.) Full lines represent fits to the power law and to the exponential law, respectively, with parameters as indicated in the figure. (Reproduced from H.J. Elmers *et al*., 1995, with permission from World Scientific. © 1995.)

The Fe bilayer was magnetized by field pulses of 2 Oe along the [001] axis in the film plane. Asymmetries A^+ and A^- for both magnetization directions were then determined in the remanent state at $T = 115$ K which is below the Curie temperature $T_C = 225$ K of this system. Spin-orbit and exchange asymmetries were separated as described in Section 2.4 neglecting a weak interference correction A_u. In this geometry, A_{ex} is sensitive to the magnetization component parallel to [001]. Plihal, Mills, Elmers and Gradmann (1995) assumed that [001] is the easy axis of this system following previous magnetic studies (Venus and Johnston, 1994; Jones and Venus, 1994; Elmers and Hauschild, 1994). Later, a magnetic easy axis along [011] as reported already in (Mulhollan, Fink, Erskine and Walters, 1991) was confirmed by Wulfhekel *et al*. (2003) using spin-polarized scanning tunneling microscopy (Wulfhekel *et al*., 2003). They observed a switch of the magnetic easy axis from [011] toward [100] with increasing thickness. Therefore, the remanent magnetization assumes in the geometry used for the SPLEED experiment only a value of 0.7.

In order to determine the geometrical structure of the film, experimental and theoretical curves were compared for the spin-orbit asymmetry. In Figure 10, the angular variation of the data (solid circles) are compared with theoretical calculations (solid lines) for various overlayer geometries. Here, a_1 is the distance between the outermost plane of the tungsten nuclei and the first layer of Fe nuclei, and a_2 is the spacing between the two Fe layers. Note that the spin-orbit asymmetries are much larger than those realized on the Fe(110) surface (Waller and Gradmann, 1982). The large values of

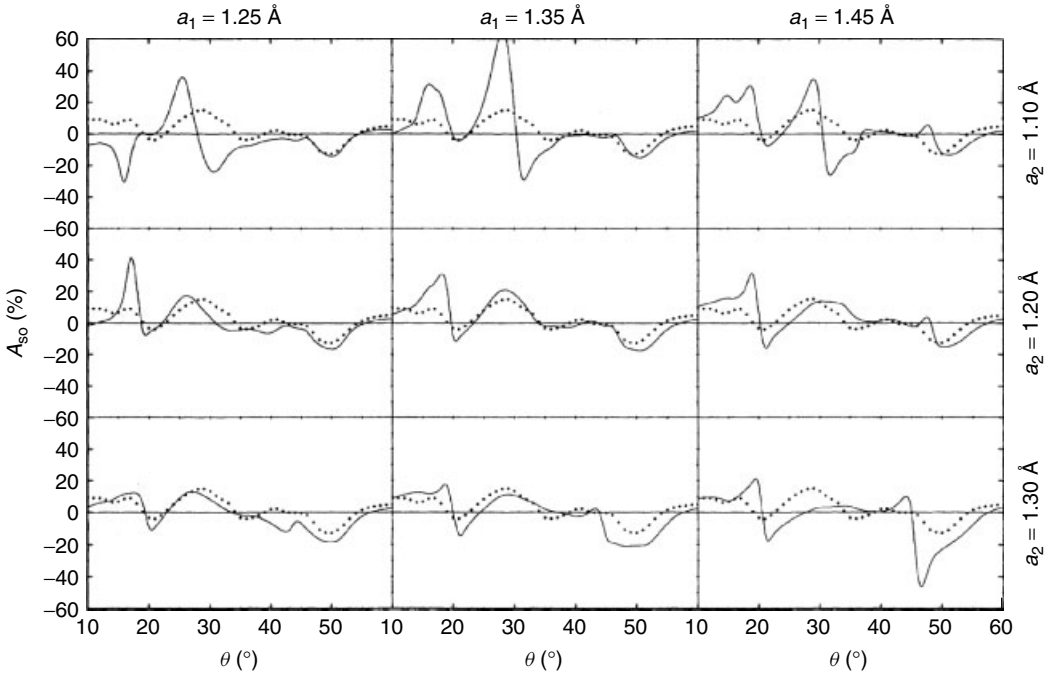

Figure 8. For various values of the layer spacings a_1 and a_2, calculated and measured values of the spin-orbit asymmetry are shown; the electron-beam energy is 90 eV, measured relative to the Fermi level. Here, a_1 is the spacing between the outer layer of W nuclei and the innermost Fe layer, while a_2 is the spacing between the outermost two Fe layers. The solid lines are theoretical results and the dotted line is experimental data. (Reproduced from M. Plihal *et al*., 1995, with permission from the American Physical Society. © 1995.)

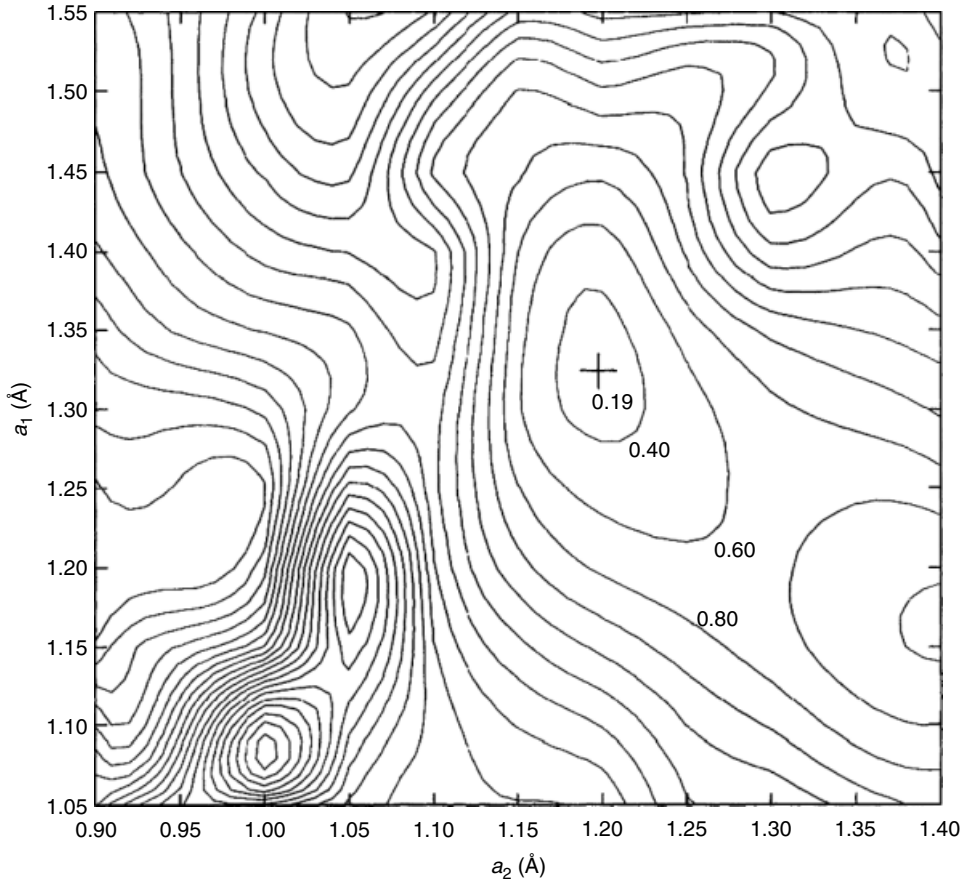

Figure 9. Contours of constant mean-square displacement, associated with the difference between the calculated and measured spin-orbit asymmetry, at 90 eV. The cross marks the absolute minimum. (Reproduced from M. Plihal *et al*., 1995, with permission from the American Physical Society. © 1995.)

A_{so} shown in Figure 10 have their origin in the penetration of the electron wave into the W substrate. The values of A_{so} are smaller than found in pure W, because the electron wave is attenuated by the Fe.

The structural sensitivity of A_{so} is apparent upon scanning the various geometries included in Figure 8. Substantial changes in the angular variations of A_{so} result from displacements of the Fe layers by ± 0.1 Å. In LEED analyses, optimum geometries usually are deduced by minimizing the R factor. Because absolute values are compared for A_{so}, it is useful to simply employ the mean-square deviation between theory and experiment as a measure of goodness of the fit here. In Figure 9, we show contour plots of the mean-square deviation, in the $a_1 - a_2$ plane. There is a clear minimum at the values $a_2 = 1.20$ Å and $a_1 = 1.32$ Å. The remaining extrema in the figure are maxima, though there is another minimum near $a_2 = 0.97$ Å and $a_1 = 1.24$ Å. From similar plots for various energies one finds the latter minimum not significant and the most likely values for the lattice distances of $a_2 = 1.20$ Å and $a_1 = 1.35$ Å. The spacing between the two outermost Fe layers a_1 is in very good agreement with theoretical values found in Wu and Freeman (1992), while for a_2 a much smaller value of 1.09 Å was found. A recent *ab initio* calculation (Qian and Huebner, 2003) considering the W-5p states correctly found a distance of $a_2 = 1.25$ Å for the first monolayer Fe on W(100), thus confirming the SPLEED analysis well.

The exchange asymmetry A_{ex} is analyzed in Figure 10 where a comparison between theory and experiment is shown. Here, μ_2 is the moment in the outermost layer and μ_1 is the moment in the innermost layer and $\mu_{Fe} = 2.2\,\mu_B$ denotes the bulk moment. The chosen moments represent the best fits out of a larger variety of calculated spectra (Plihal, Mills, Elmers and Gradmann, 1995), although the calculated spectra appear not dramatically sensitive to the choice of magnetic moments. Although the theory clearly reproduces the experimental trends, the agreement is less good than found for the spin-orbit asymmetry. Part of the problem may reside in the use of bulk Fe forms for the exchange potential. This may be a problem, particularly for the innermost Fe

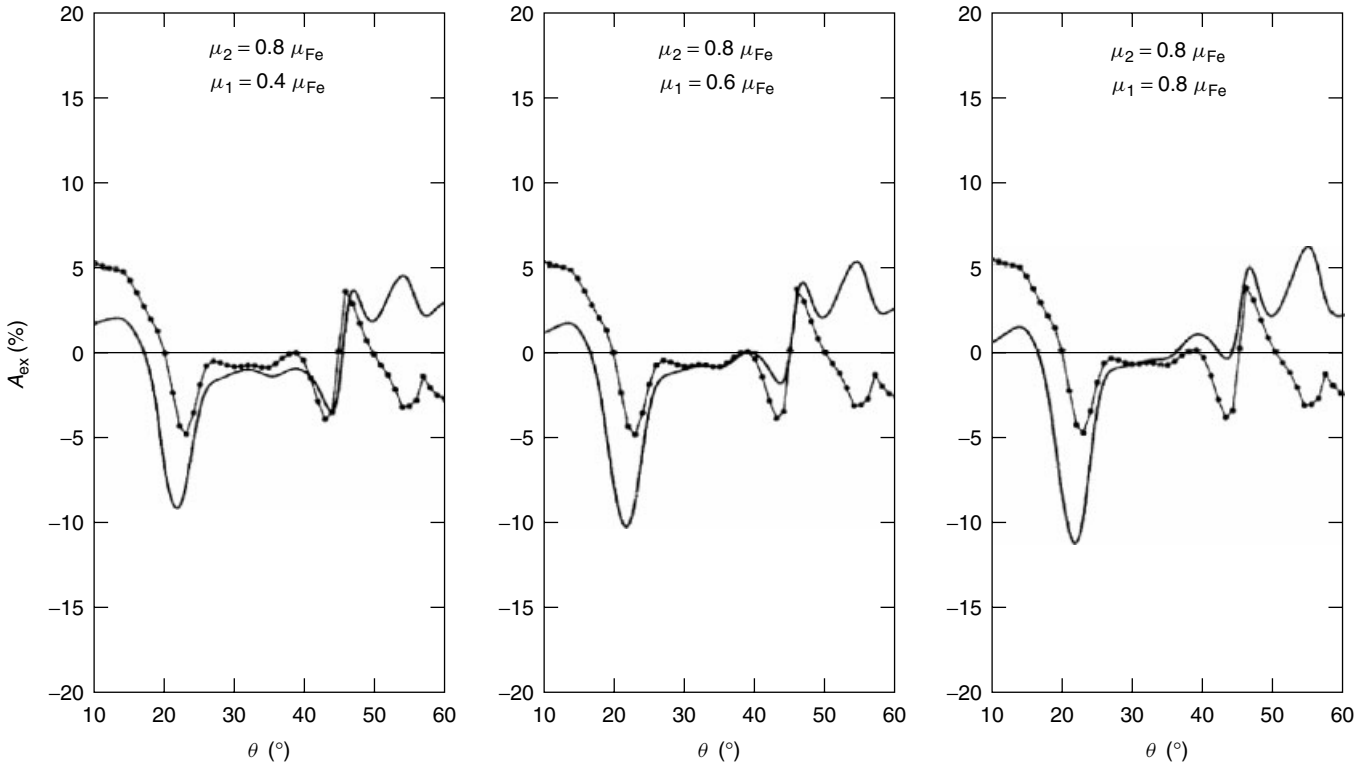

Figure 10. Sensitivity of the exchange asymmetry to the variation of surface moments. The top layer moment $\mu_2 = 0.8\,\mu_{Fe}$ is fixed. The inner Fe layer moment μ_1 is varied between 0.4 and $0.8\,\mu_{Fe}$ where μ_{Fe} is the magnetic moment of bulk Fe. The beam energy is 120 eV. The solid lines are theoretical results, and the dotted line is experimental data. (Reproduced from M. Plihal *et al.*, 1995, with permission from the American Physical Society. © 1995.)

layer, where 3d electrons will hybridize with the W 5d electrons. Indeed, Wu and Freeman (1992) found a very small moment at the outermost W layer in their calculations.

The magnetic moments of $\mu_1 = 1.3\,\mu_B$ and $\mu_2 = 1.8\,\mu_B$ (Plihal, Mills, Elmers and Gradmann, 1995) found here are smaller than magnetic moments predicted theoretically. Wu and Freeman (1992) calculated $\mu_1 = 1.68\,\mu_B$ and $\mu_2 = 2.43\,\mu_B$. Qian and Huebner (2003) found a value of $\mu_1 = 2.1\,\mu_B$ for only 1 ML Fe/W(100). Part of this discrepancy can be attributed to the fact that the experimental asymmetries were presumably measured at a remanent value of 0.7 of the saturation value. Moreover, the measurement was performed at a temperature of $0.5\,T_C$, which might reduce magnetic moments further (Elmers, 1995). Thus, the agreement between theory and experiment is acceptable. The trend of a lower moment at the W interface is correctly reproduced.

4.4 Band structure analysis – toward efficient spin detectors

The mean free path of electrons increases below ca 20 eV in many materials (Seah and Dench, 1979). Moreover, since the only remaining diffraction spot is the (00) spot, the reflected intensity increases considerably. These facts make the regime of very low kinetic energy particularly interesting for application in spin detectors (see Section 3.2) and for the investigation of buried layers. Since spurious magnetic fields easily deflect the electrons of low energy, special diffraction geometries are necessary. In most cases, an immersion lens as part of an electron emission microscope retards the electrons just before the sample surface (Altman *et al.*, 1991) as discussed in Section 3.

As an example (Graf *et al.*, 2005) Figure 11(c) and (d) show the average reflectivity for Co and Fe in a gray-scale plot versus electron energy and film thickness, respectively. The energy dependence of reflectivity for films of different thickness seems to have at least two periodic components. The authors assume (Graf *et al.*, 2005) that the energy independent component visible at low thicknesses (white arrows in Figure 11d) is due to the varying density of steps during deposition. The reflectivity minima (dark) coincide with half completed monolayers (higher surface step density) and the maxima (bright) occur with the completion of each monolayer slow surface step density. These growth oscillations are most clear at small film thickness and are

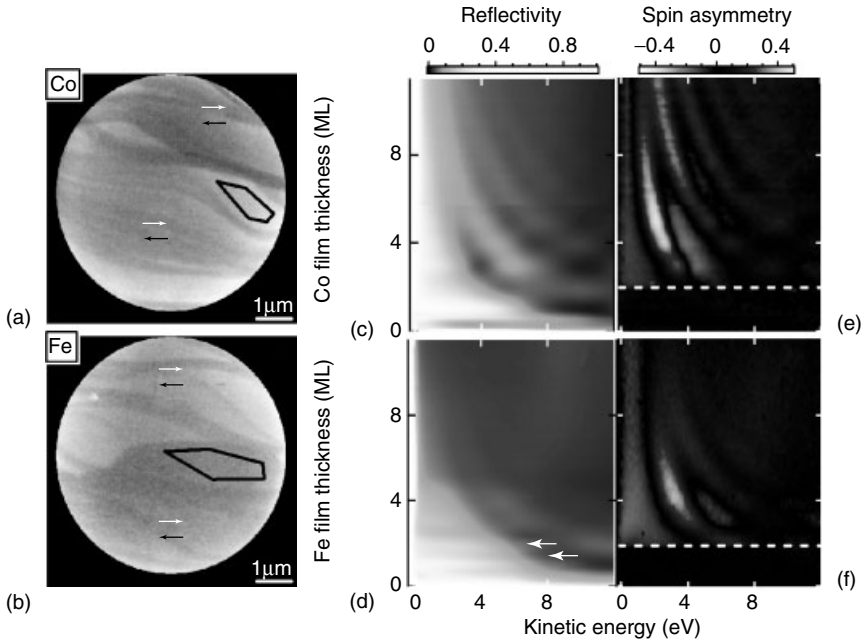

Figure 11. (a and b) Real space image of magnetic domains in Fe/W(110) and Co/W(110) films with indicated areas of uniform magnetization used for the analysis. Gray-scale (c and d) plots of the measured reflectivity as a function of the electron kinetic energy (horizontal axis) and film thickness (vertical axis) for Fe/W(110) and Co/W(110) films. (e and f) Gray-scale plots of the spin asymmetry of the reflectivity. (Reproduced from J. Graf *et al*., 2005, with permission from the American Physical Society. © 2005.)

used to calibrate the film deposition rate. The component of interest is energy dependent and looks like hyperbolic shaped maxima (bright) and minima (dark) in the reflectivity plots. This is a bulk and intrinsic effect known as the quantum size effect (QSE) (Zdyb and Bauer, 2002a, 2002b; Scheunemann *et al*., 1997). More specifically, a ferromagnetic slab acts like a resonant cavity and induces interference patterns. The QSE is more pronounced for Co/W(110) than for Fe/W(110) films. This might be attributed as suggested in Graf *et al*. (2005) to kinetic roughening during room-temperature growth of Fe/W(110) (Albrecht, Fritzsche and Gradmann, 1993).

The spin asymmetry (A_{ex}) versus kinetic energy and film thickness is shown in Figure 11(e) and (f). For the calculation of A_{ex} a polarization of $P = 0.2$ of the incident electron beam was assumed. The white dashed lines at 2 ML film thickness in Figure 11(e) and (f) clearly separate a uniform black region from a modulated red and blue region. The featureless black region indicates $A_{ex} = 0$ for both Fe and Co films. This can be explained by noting that the Curie temperature T_C of Fe/W(110) films is above room temperature only for film thicknesses greater than 2 ML (Elmers *et al*., 1995). A similar decrease of T_C was observed for thin Co films. The measurement above T_C shows a qualitatively similar hyperbolic behavior of the oscillating asymmetry. Figure 12(a) shows energy scans of the spin-dependent reflectivity for different Co film thicknesses. The reflectivity for the antiparallel spin shows a red shift with respect to the case of parallel spin. The reflectivity oscillation in the case of spin parallel are damped with respect to the antiparallel spin.

These observations suggest that two mechanisms contribute to the total spin asymmetry. The spectra for film thickness larger than 5–6 ML are mainly dominated by the damping mechanism. The damping was attributed (Graf *et al*., 2005) to different mean free paths for spin parallel or antiparallel to the majority spin. Indeed it is known that the so-called universal curve (Seah and Dench, 1979) predicts a very large value of the IMFP for transition metals at low energy. Spin-dependent values of the IMFP of the order of a few monolayers have been reported at very low energies (Pappas *et al*., 1991; Passek, Donath and Ertl, 1996; Getzlaff, Bansmann and Schoenhense, 1993). A red shift of the antiparallel spin reflectivity spectra can be clearly observed in Figure 12(b) for the spin-dependent reflectivity for a 4-ML thick Co/W(110) film. The large gradients of the reflectivity induced by the quantum well states (QWS) are slightly shifted for electrons of opposite spin owing to the exchange splitting of the band structure. The minima and the maxima of the reflectivity indicated with the light and dark arrows are shifted by 0.3 and 0.15 eV, respectively. It is the combination of this energy shift with the large gradients in the reflectivity that causes a significant enhancement or reduction of the magnetic asymmetry (Figure 12c). This seems to be the dominant mechanism at small film thickness even in

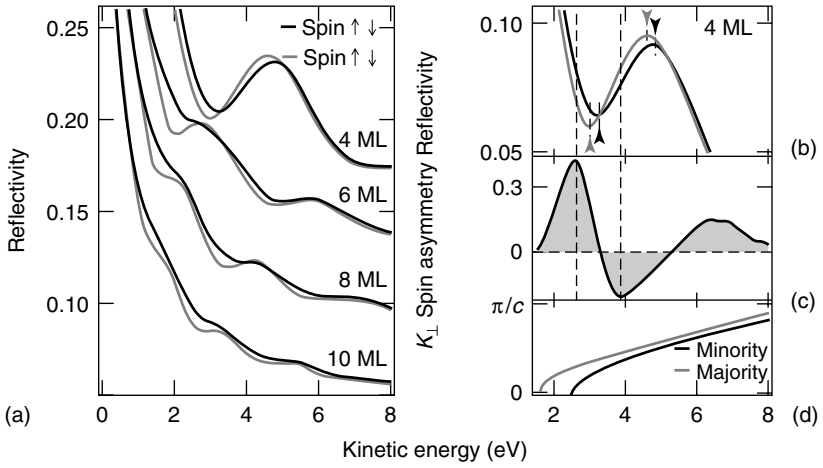

Figure 12. (a) Energy dependence of the reflectivity for spin parallel and antiparallel to the Co/W(110) film magnetization for different film thickness. The energy scans are incrementally shifted by 0.05. (b) Expanded view of the spin dependence of the reflectivity for the 4-ML thick film. (c) Spin asymmetry for a 4-ML thick Co/W(110) film obtained from Figure 11(e). (d) Band structure calculation for a 4-ML thick Co/W(110) film (Scheunemann *et al*., 1997). (Reproduced from J. Graf *et al*., 2005, with permission from the American Physical Society. © 2005.)

the presence of some inelastic damping. Figure 12(d) shows a band structure calculation along the perpendicular direction for a 4-ML Co/W(110) thin film (Scheunemann *et al*., 1997). The first maxima at 2.6 eV of the spin asymmetry may have a contribution from the exchange-split band gap. But there is no band gap at the second maxima at 4.7 eV which is caused by the finite size effects at small film thicknesses. This observation emphasizes that the interference of the electron wave function due to the reflection at both interfaces dominates and the film thus acts as an effective spin-selective interferometer (Zdyb and Bauer, 2002b; Egger, Back, Krewer and Pescia, 1999; Scheunemann *et al*., 1997).

While the example described above concerns the interference of an electron wave in the ferromagnetic film, similar spin-dependent interference patterns can also be observed in a nonmagnetic film if at least one interface is ferromagnetic. For Cu thin films grown on fcc Co/Cu(100), the electron reflectivity from the Cu thin film exhibits Fabry–Pérot type interference (Wu *et al*., 2005). When the Cu thickness increases, the energies of the interference peaks decrease (or increase) for **k** vector greater (or less) than half of the Brillouin zone (BZ) vector. This interference effect results in a spin asymmetry of the electron reflectivity from the Cu film.

Since in a nonmagnetic overlayer the electron wave function is independent of the spin, the spin-dependent reflectivity is only determined by the interfaces. If the complex reflectivities of the electron wave in Cu at the Cu/vacuum and Cu/Co interfaces are $r_B \exp(i\phi_B)$ and $r_C \exp(i\phi_C)$, respectively, where r and ϕ denote the magnitude and phase gain of the electron reflection at the corresponding interface, the total electron reflectivity is given by satisfying the continuity boundary conditions at the two Cu interfaces:

$$R = \frac{r_B^2 + r_C^2 + 2r_B r_C \cos(2kd_{Cu} + \phi_B + \phi_C)}{1 + r_B^2 + r_C^2 + 2r_B r_C \cos(2kd_{Cu} + \phi_B + \phi_C)} \qquad (25)$$

Here, d_{Cu} is the Cu overlayer thickness and k is the electron momentum vector in the Cu film. Equation 25 describes a classical Fabry–Pérot interferometer. The reflection phases for hot electrons at the upper and lower interface of the Cu film are calculated as $\phi_B = 0$ and $\phi_C = \pi - 2\arcsin\sqrt{(E - E_L)/E_U - E_L}$, where $E_U = 9.6$ eV and $E_L = 2.5$ eV are the upper and lower edges of the Co energy gap (Mankey, Willis and Himpsel, 1993; van Gelderen, Crampin and Inglesfield, 1996).

The maximum electron reflectivity takes place at the interference condition of $2kd_{Cu} + \phi_B + \phi_C = 2\pi n$, with an integer n. This is exactly the result of the phase accumulation model (Smith, Brookes, Chang and Johnson, 1994) for QWS below the vacuum level. Therefore, the phase accumulation model describes both the confined QWS below the vacuum level and the interference condition above the vacuum level. In a solid, an electron also experiences the lattice periodic potential which generates an envelope function for the electron Bloch wave (Qiu and Smith, 2002). This condition for constructive interference should be valid as well for $k < k_{BZ}/2$ (k_{BZ} is the Brillouin zone wave vector) as for $k > k_{BZ}/2$. In the latter case, the condition describes the electron envelope function arising from a beating effect between the electron wave and the periodic lattice potential at $k > k_{BZ}/2$. The different interpretation of the maximum condition leads to an opposite energy versus thickness dispersion for QWS

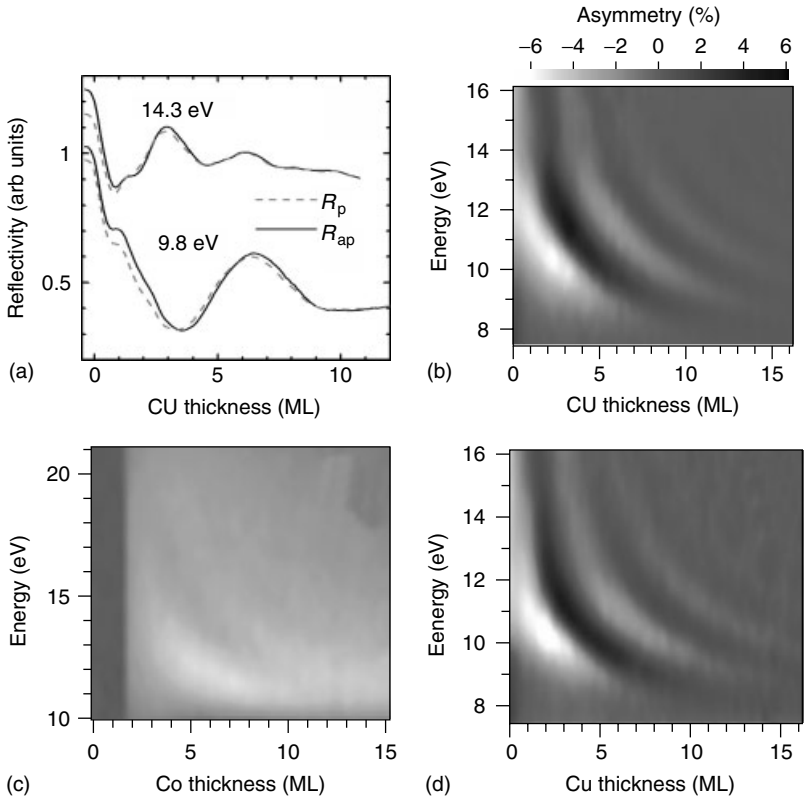

Figure 13. (a) Spin-dependent electron reflectivity from Cu/Co(5 ML)/Cu(001). Asymmetry of the spin-dependent electron reflectivity from (b) Cu/Co(5 ML)/Cu(001), (c) Co/Cu(001), and (d) Cu/Co(15 ML)/Cu(001). (Reproduced from Y.Z.Wu *et al*., 2005, with permission from the American Physical Society. © 2005.)

at $k < k_{BZ}/2$ and $k > k_{BZ}/2$ with a crossover occurring at $k = k_{BZ}/2$ (Egger, Back, Krewer and Pescia, 1999; Wu *et al*., 2005). In the energy range of 8–26 eV above E_F, there is one relevant energy band along the (001) direction (ΓX) Δ_1 symmetry, in which the energy decreases with increasing k and crosses the $k_{BZ}/2$ point at 19 eV (Mankey, Willis and Himpsel, 1993). The corresponding dispersion curves with the crossover at 19 eV were confirmed quantitatively (Wu *et al*., 2005) in the experiment.

For a polarized incident electron beam one has to consider a spin-dependent complex reflectivity (r_C^i, ϕ_C^i) at the Cu/Co interface. Figure 13(a) shows representative spin-resolved electron reflectivity measurements for a 5-ML Co film on Cu(001) capped with a thin Cu layer as a function of the Cu capping film thickness at two incident electron energies, indicating that the electron reflectivity of the Cu film is clearly spin dependent. A spin-dependent reflectivity of a nonmagnetic film was first observed in (Scheunemann *et al*., 1997) and attributed to a spin-dependent phase ϕ_C^i, which can account for the peak position, only. As emphasized in (Wu *et al*., 2005) both the positions and the magnitudes of the reflectivity peaks depend on the incident electron spin direction, indicating that the ferromagnetic Co also causes a spin dependence of r_C^i. The asymmetry of the electron reflectivity, $(R^{\uparrow\uparrow} - R^{\uparrow\downarrow})/(R^{\uparrow\uparrow} + R^{\uparrow\downarrow})$ is shown in Figure 13(b). The spin-dependent reflectivity at the Cu/Co interface results in a spin-dependent Fabry–Pérot interference from the Cu film with the asymmetry oscillating as a function of both the electron energy and the Cu film thickness. The electron reflection asymmetry in Co/Cu(001) as a function of Co film thickness and electron energy, as shown in Figure 13(c), shows a similar behavior as discussed above for Co/W(110). For Co thinner than 1.6 ML, the asymmetry is zero because the Co/Cu(001) film is paramagnetic at room temperature. For Co thicker than 1.6 ML, the reflection asymmetry exhibits a weak interference effect. The asymmetry oscillation amplitude of Cu/Co(5 ML)/Cu(001) is an order of magnitude greater than that of Co/Cu(001), thus clearly indicating that the interference shown in Figure 13(b) is dominated by the Cu film. The asymmetry does not depend significantly on the Co film (Figure 13d). The sign of the asymmetry for Cu/Co(5 ML)/Cu(001) alternates between positive and negative, while the sign of the asymmetry for Co/Cu(001) remains unchanged.

The asymmetry oscillation is damped when d_{Cu} is increased. The damping is due to the electrons retaining

their coherence only up to a finite depth because of inelastic scattering. If d_{Cu} becomes larger than this depth, interference between electrons reflected at the Cu/vacuum boundary and electrons reflected at the Cu/Co boundary is no longer possible.

The spin-dependent complex electron reflectivity at the Cu/Co interface results in a spin-dependent Fabry–Peŕot interference in the Cu film, making it possible to detect magnetic information in the Co underlayer. This observation could be quite interesting for preparing spin detectors that are insensitive to ambient conditions.

5 CONCLUSION AND OUTLOOK

A review was given on our present knowledge of SPLEED, with a main emphasis on experimental findings. We handpicked some experimental examples which are discussed in more detail to illustrate the kind of knowledge that can be gained from SPLEED.

With respect to a theoretical explanation of the observed scattering asymmetries, the calculations show that groundstate potentials generated by common numerical *ab initio* methods provide a very good account of the spin dependencies of the electron-scattering intensities from metallic surfaces, with the use of an inner potential whose real and imaginary parts are comparable with earlier LEED analyses. It turns out that spin-orbit asymmetries can be reproduced quite well by calculations. They respond sensitively to changes in the lattice structure. A comparison of theory and experiment can efficiently be used to determine lattice structures to a high degree of accuracy.

Less good agreement is achieved for the exchange asymmetry, and the extraction of quantitative data on surface magnetization still remains a challenge. The determination of magnetic moments in the surface as inferred from SPLEED rests on the sensitivity to surface moment exhibited by particular prominent regions of scattering parameter. Unfortunately, these regions are often associated with minima in the total intensity and these minima observed on scattering from solid surfaces may be sensitive to the presence of defects.

Definitely, the largest merit of SPLEED is given by its high sensitivity to magnetization in the topmost layers. In particular, close to the magnetic phase transition the critical behavior of the magnetization can be studied in great detail. Using special experimental setups it is even possible to apply small external fields. Fundamental thermodynamic theories could thus be confirmed. The high asymmetry signal can be further exploited to perform magnetic sensitive imaging using SPLEEM.

At very low energies ($<10\,eV$) the scattering probability of electrons shrinks allowing to probe buried interfaces. Because of the lower scattering rate at very low energies multiple scattering effects are less dominant and a theoretical description appears more easy. Interferometric effects similar to the physics of an optical Fabry–Pérot setup were demonstrated. These observations might provide a way to considerably improve present polarization detectors for electrons.

A very interesting future application of SPLEED is provided by the development of an electron source which is capable to produce ultrashort electron bunches of a few picoseconds (Aulenbacher *et al*., 2002). A pulsed electron beam allows a time-resolved investigation of periodic motions via stroboscopic imaging. This can be applied favorably to the investigation of magnetization dynamics at surfaces and in ultrathin films and nanostructures. Ultrafast magnetization reversal processes are presently attracting much attention. Technologically, fast magnetic recording, advanced magnetic memory elements, and spin electronics call for an in-depth understanding and control of fast magnetization reversal processes on the nano- and subnanosecond scale. More fundamental questions are associated with magnetic excitations (eigenmodes) and damping processes in confined magnetic structures. The fundamental timescales for magnetization reversal processes range down to a few femtoseconds, whereas present technologically interesting timescales are on the order of sub-nanoseconds. The time resolution in a stroboscopic experiment is limited by the pulse length of the incident electron beam. The ultrashort pulse lengths of spin-polarized electron bunches already achieved prove to be sufficient for the study of magnetization dynamics and can compete with the shortest X-ray pulses available at a synchrotron. Only optical light pulses from pulsed laser sources are shorter, however, on the expense of surface sensitivity.

The author thanks U. Gradmann and G. Schönhense for stimulating discussions and U. Gradmann for careful reading of the manuscript.

REFERENCES

Ackermann, B. and Feder, R. (1984). Relativistic scattering calculations: on the study of surface magnetism by polarized and unpolarized electrons. *Solid State Communications*, **49**, 489–492.

Akai, H. (1998). Ferromagnetism and its stability in the diluted magnetic semiconductor (In, Mn)As. *Physical Review Letters*, **81**, 3002–3005.

Albrecht, M., Fritzsche, H. and Gradmann, U. (1993). Kinetic facetting in homoepitaxy of Fe(110) on Fe(110). *Surface Science*, **294**, 1–9.

Altman, M.S., Hurst, J., Marx, G., *et al*. (1991). Spin polarized low energy electron microscopy of surface magnetic structure. In *Magnetic Materials: Microstructure and Properties*, Suzuki, T., Sugita, Y., Clemens, B.M., *et al*. (Eds.), Materials Research Society, Pittsburgh pp. 125–132, Volume 232. Materials Research Society Symposium Proceedings.

Alvarado, S.F., Campagna, M., Ciccacci, F. and Hopster, H. (1982). Experimental study of the magnetic critical behavior of the Ni(001) and Ni(110) surfaces. *Journal of Applied Physics*, **53**, 7920–7922.

Alvarado, S.F., Campagna, M. and Hopster, H. (1982). Surface magnetism of Ni(100) near the critical region by spin-polarized electron scattering. *Physical Review Letters*, **48**, 51–54.

Alvarado, S.F., Hopster, H. and Campagna, M. (1982). Surface magnetism on Ni(001) by spin-polarized electron scattering. *Surface Science*, **117**, 294–299.

Alvarado, S.F., Feder, R., Hopster, H., *et al*. (1982). Simultaneous probing of exchange and spin-orbit interaction in spin-polarized low-energy electron diffraction from magnetic surfaces. *Zeitschrift fur Physik B*, **49**, 129–132.

Arnold, C.S. and Pappas, D.P. (2000). Gd(0001): a semi-infinite three-dimensional heisenberg ferromagnet with ordinary surface transition. *Physical Review Letters*, **85**, 5202–5205.

Aulenbacher, K., Schuler, J., von Harrach, D., *et al*. (2002). Pulse response of thin III/V semiconductor photocathodes. *Journal of Applied Physics*, **92**, 7536–7543.

Back, C.H., Wuersch, C., Kerkmann, C.D. and Pescia, D. (1994). Giant magnetic-susceptibility in Fe and Co epitaxial-films. *Zeitschrift fur Physik B*, **96**, 1–3.

Barth, Uv. and Hedin, L. (1972). A local exchange-correlation potential for the spin-polarized case. *Journal of Physics C: Solid State Physics*, **5**, 1629–1642.

Bauer, E., Duden, T. and Zdyb, R. (2002). Spin-polarized low energy electron microscopy of ferromagnetic thin films. *Journal of Physics D*, **35**, 2327–2331.

Bertacco, R. and Ciccacci, F. (1999). Large spin asymmetry in electron absorption and reflection from oxidized single crystal Fe/MgO(001) films. *Surface Science*, **419**, 265–271.

Bertacco, R., Merano, M. and Ciccacci, F. (1998). Spin dependent electron absorption in Fe(001)-p(1x1)O: a new candidate for a stable and efficient electron polarization analyzer. *Applied Physics Letters*, **72**, 2050–2052.

Binder, K. (1985). Critical behavior at surfaces of ferromagnets. In *Polarized Electrons in Surface Physics*, Feder, R. (Ed.), World Scientific: Singapore, pp. 93–123, Chapter 3.

Blaha, P., Schwarz, K., Sorantin, P. and Tricky, S.B. (1990). Full-potential, linearized augmented plane wave programs for crystalline systems. *Computer Physics Communications*, **59**, 399–415.

Bramwell, S.T. and Holdsworth, P.C.W. (1993a). Magnetisation and universal sub-critical behaviour in two-dimensional xy magnets. *Journal of Physics: Condensed Matter*, **5**, L53–L59.

Bramwell, S.T. and Holdsworth, P.C.W. (1993b). Universality in two-dimensional magnetic systems. *Journal of Applied Physics*, **73**, 6096–6098.

Celotta, R.J., Pierce, D.T., Wang, G.C., *et al*. (1979). Surface magnetization of ferromagnetic Ni(110): a polarized low-energy electron diffraction experiment. *Physical Review Letters*, **43**, 728–731.

Davisson, C. and Germer, L.H. (1929). A test for polarization of electron waves by reflection. *Physical Review*, **33**, 760–772.

Demokritov, S.O., Kreines, N.M., Kudinov, V.T. and Petrov, S.V. (1989). Ferromagnetic resonance and the phase diagrams of the two-dimensional easy-plane ferromagnets (CH3NH3)2CuCl4 and K2CuF4. *Soviet Physics JETP*, **68**, 1277–1290.

Denecke, R., Morais, J., Ynzunza, R.X., *et al*. (2002). Angular and temperature dependence of the magnetic circular dichroism in 4d core-level photoemission from Gd(0001). *Physical Review B*, **65**, 245421-1–245421-16.

Duden, T. and Bauer, E. (1995). A compact electron-spin-polarization manipulator. *The Review of Scientific Instruments*, **66**, 2861–2864.

Duerr, W., Taborelli, M., Paul, O., *et al*. (1989). Magnetic phase transition in two-dimensional ultrathin Fe films on Au(100). *Physical Review Letters*, **62**, 206–209.

Egger, S., Back, C.H., Krewer, J. and Pescia, D. (1999). A spin selective electron interferometer. *Physical Review Letters*, **83**, 2833–2836.

Elmers, H.J. (1995). Ferromagnetic monolayers. *International Journal of Modern Physics B*, **9**, 3115–3180.

Elmers, H.J. and Gradmann, U. (1990). Magnetic anisotropies in Fe(110)-films on Fe(110). *Applied Physics A*, **51**, 255–263.

Elmers, H.J. and Hauschild, J. (1994). Magnetism and growth in pseudomorphic Fe films on W(100). *Surface Science*, **320**, 134–144.

Elmers, H.J., Hauschild, J. and Gradmann, U. (1995a). Coincidence of susceptibility maximum and Tc. *Journal of Magnetism and Magnetic Materials*, **140–144**, 1559–1560.

Elmers, H.J., Hauschild, J. and Gradmann, U. (1995b). SPLEED with external magnetic fields. *Journal of Magnetism and Magnetic Materials*, **140–144**, 671–672.

Elmers, H.J., Hauschild, J. and Gradmann, U. (1996). Critical behavior of the uniaxial ferromagnetic monolayer Fe(110) on W(110). *Physical Review B*, **54**, 15224–15233.

Elmers, H.J., Hauschild, J., Fritzsche, H., *et al*. (1995). Magnetic frustration in ultrathin Fe films. *Physical Review Letters*, **75**, 2031–2034.

Elmers, H.J., Hauschild, J., Hoeche, H., *et al*. (1994). Submonolayer magnetism of Fe(110) on W(110): finite width scaling of stripes and percolation between Islands. *Physical Review Letters*, **73**, 898–901.

Engel, E. and Vosko, S.H. (1993). Exact exchange-only potentials and the virial relation as microscopic criteria for generalized gradient approximations. *Physical Review B*, **47**, 13164–13174.

Essam, J.W. and Fisher, M.E. (1963). Pade approximant studies of the lattice gas and ising ferromagnet. *Journal of Chemical Physics*, **38**, 802–812.

Fahsold, G., Hammond, M.S. and Kirschner, J. (1992). Spin-dependent electron reflection from Fe(110): experiment and theory. *Solid State Communications*, **84**, 541–544.

Farle, M., Baberschke, K., Stetter, U., *et al*. (1993). Thickness-dependent Curie temperature of Gd(0001)/W(110) and its dependence on the growth conditions. *Physical Review B*, **47**, 11571–11574.

Feder, R. (1977). Spin polarization in low-energy electron diffraction from nickel. *Physical Review B*, **15**, 1751–1754.

Feder, R. (1981). Spin-polarized low-energy electron diffraction, (Review). *Journal of Physics C*, **14**, 2049–2091.

Feder, R. (1985). Spin-polarized low-energy electron diffraction. In *Polarized Electrons in Surface Physics*, Feder, R. (Ed.), World Scientific: Singapore, Chapter 4.

Feder, R., Alvarado, S.F., Tamura, E. and Kisker, E. (1983). Surface magnetic structure analysis of Ni(001) by polarized electron diffraction. *Surface Science*, **127**, 83–107.

Feder, R. and Pleyer, H. (1982). On the feasibility of studying surface magnetism by spin-polarized low-energy electron diffraction. *Surface Science*, **117**, 285–293.

Feder, R., Rosicky, F. and Ackermann, B. (1983). Relativistic multiple scattering theory of electrons by ferromagnets. *Zeitschrift fur Physik B*, **52**, 31–36.

Focus-GmbH. (2005) www.focus-gmbh.com/FOCUSPRODUCTS/SPLEED/spleed.htm.

Freeman, A.J. (1983). Electronic structure and magnetism of surfaces and interfaces. *Journal of Magnetism and Magnetic Materials*, **35**, 31–36.

Fritzsche, H., Elmers, H.J. and Gradmann, U. (1994). Magnetic anisotropies of Fe(110) interfaces. *Journal of Magnetism and Magnetic Materials*, **135**, 343–354.

Fu, C.L. and Freeman, A.J. (1987). Magnetism and the electric and magnetic hyperfine interactions at the transition metal surface: Fe(110). *Journal of Magnetism and Magnetic Materials*, **69**, L1–L4.

van Gelderen, P., Crampin, S. and Inglesfield, J.E. (1996). Quantum-well states in Cu/Co overlayers and sandwiches. *Physical Review B*, **53**, 9115–9122.

Getzlaff, M., Bansmann, J. and Schoenhense, G. (1993). Spin polarization effects for electrons passing through thin iron and cobalt films. *Solid State Communications*, **87**, 467–467.

Gradmann, U. and Alvarado, S.F. (1985). Elastic spin-polarized low-energy electron scattering from magnetic surfaces. In *Polarized Electrons in Surface Physics*, Feder, R. (Ed.), World Scientific: Singapore.

Gradmann, U., Korecki, J. and Waller, G. (1986). In-plane magnetic surface anisotropies in Fe(110). *Applied Physics A*, **39**, 101–108.

Gradmann, U., Przybylski, M., Elmers, H.J. and Liu, G. (1989). Ferromagnetism in the thermodynamically stable monolayer Fe(110) on W(110), coated by Ag. *Applied Physics A*, **49**, 563–571.

Graf, J., Jozwiak, C., Schmid, A.K., *et al*. (2005). Mapping the spin-dependent electron reflectivity of Fe and Co ferromagnetic thin films. *Physical Review B*, **71**, 144429-1–144429-5.

Hammond, M.S., Fahsold, G. and Kirschner, J. (1992). Absorption and elastic and inelastic reflection of spin-polarized low-energy electrons from Fe(110). *Physical Review B*, **45**, 6131–6141.

Hartmann, P., Bermuth, J., Harrach, Dv., *et al*. (1999). A diffusion model for picosecond electron bunches from negative electron affinity GaAs photocathodes. *Journal of Applied Physics*, **86**, 2245–2249.

Hilgers, G., Potthoff, M., Mueller, N. and Heinzmann, U. (1995). Structure investigations of Xe-adsorbate layers by spin-polarized low-energy-electron diffraction.2. (Root-3 X-Root-3)R30-degrees-Xe PD(111) and the dilute phase of Xe Pd(111). *Surface Science*, **322**, 207–220.

Hillebrecht, F.U., Jungblut, R.M., Wiebusch, L., *et al*. (2002). High-efficiency spin polarimetry by very-low-energy electron scattering from Fe(100) for spin-resolved photoemission. *The Review of Scientific Instruments*, **73**, 1229–1234.

Ibach, H. (1991). *Electron Energy Loss Spectroscopy – The Technology of High Performance*, Springer: Heidelberg.

Ibach, H., Bruchmann, D., Vollmer, R., *et al*. (2003). A novel spectrometer for spin-polarized electron energy-loss spectroscopy. *The Review of Scientific Instruments*, **74**, 4089.

Jones, T.L. and Venus, D. (1994). Structural and magnetic characterization of thin iron films on a tungsten (001) substrate. *Surface Science*, **302**, 126–140.

Jungblut, R., Roth, C., Hillebrecht, F.U. and Kisker, E. (1992). Spin-polarized electron spectroscopy as a combined chemical and magnetic probe. *Surface Science*, **269–270**, 615–621.

Kaemper, K-P., Abraham, D.L. and Hopster, H. (1992). Spin-polarized electron-energy-loss spectroscopy on epitaxial fcc Co layers on Cu(001). *Physical Review B*, **45**, 14335–14346.

Kessler, J. (1976). *Polarized Electrons*, Springer: Berlin.

Kirschner, J. (1984). Temperature effects in spin-polarized low-energy electron diffraction from ferromagnets: Fe(110). *Physical Review B*, **30**, 415–417.

Kirschner, J. (1985a). Sources and detectors for polarized electrons. In *Polarized Electrons in Surface Physics*, Feder, R. (Ed.), World Scientific: Singapore.

Kirschner, J. (1985b). *Polarized Electrons at surfaces*, *Volume 106 of Springer Tracts in Modern Physics*, Springer: Berlin.

Kirschner, J. and Feder, R. (1979). Spin polarization in double diffraction of low-energy electrons from W(001): experiment and theory. *Physical Review Letters*, **42**, 1008–1011.

Kirschner, J., Rebensdorff, D. and Ibach, H. (1984). High-resolution spin-polarized electron-energy-loss spectroscopy and the stoner excitation spectrum in nickel. *Physical Review Letters*, **53**, 698–701.

Kosterlitz, J.M. (1974). The critical properties of the two-dimensional xy model. *Journal of Physics C: Solid State Physics*, **7**, 1046–1060.

Kotani, T. and Akai, H. (1996). KRR-ASA method in exact exchange-potential band-structure calculations. *Physical Review B*, **54**, 16502–16514.

Landau, D.P. (1976). Finite-size behavior of the Ising square lattice. *Physical Review B*, **13**, 2997–3011.

Mankey, G.J., Willis, R.F. and Himpsel, F.J. (1993). Band structure of the magnetic fcc pseudomorphs: Ni(100), Co(100), and Fe(100). *Physical Review B*, **48**, 10284–10291.

Maruyama, T., Garwin, E., Prepost, R., *et al*. (1991). Observation of strain-enhanced electron-spin polarization in photoemission from InGaAs. *Physical Review Letters*, **66**, 2376–2379.

Melnikov, A., Bovensiepen, U., Radu, I., *et al*. (2004). Picosecond magnetization dynamics of the Gd(0001) surface. *Journal of Magnetism and Magnetic Materials*, **272**, 1001–1002.

Moruzzi, V.L., Janak, J.F. and Williams, A.R. (1978). *Calculated Properties of Metals*, Pergamon Press: New York.

Mulhollan, G.A., Fink, R.L., Erskine, J.L. and Walters, G.K. (1991). Local spin correlations in ultrathin Fe/W(100) films. *Physical Review B*, **43**, 13645–13648.

Ormeci, A., Hall, B.M. and Mills, D.L. (1990). Theory of spin-dependent electron diffraction from the Fe(110) surface. *Physical Review B*, **42**, 4524–4531.

Ormeci, A., Hall, B.M. and Mills, D.L. (1991). Sensitivity of spin-polarized low-energy electron-diffraction exchange asymmetries to surface magnetic moment: the case of Fe(110). *Physical Review B*, **44**, 12369–12375.

Palmberg, P.W., de Wames, R.E. and Vredevoe, L.A. (1968). Direct observation of coherent exchange scattering by low-energy electron diffraction from antiferromagnetic NiO. *Physical Review Letters*, **21**, 682–685.

Pappas, D.P., Kamper, K-P., Miller, B.P., *et al*. (1991). Spin-dependent electron attenuation by transmission through thin ferromagnetic films. *Physical Review Letters*, **66**, 504–507.

Passek, F., Donath, M. and Ertl, K. (1996). Spin-dependent electron attenuation lengths and influence on spectroscopic data. *Journal of Magnetism and Magnetic Materials*, **159**, 103–108.

Perdew, J.P. and Yue, W. (1986). Accurate and simple density functional for the electronic exchange energy: generalized gradient approximation. *Physical Review B*, **33**, 8800–8802.

Perdew, J.P., Chevary, J.A., Vosko, S.H., *et al*. (1992). Atoms, molecules, solids, and surfaces: applications of the generalized gradient approximation for exchange and correlation. *Physical Review B*, **46**, 6671–6687.

Pfeuty, P. and Toulouse, G. (1977). *Introduction to the Renormalization Group and to Critical Phenomena*, John Wiley & Sons: London.

Pierce, D.T., Celotta, R.J., Kelley, M.H. and Unguris, J. (1988). Electron spin polarization analyzers for use with synchrotron radiation. *Nuclear Instruments and Methods in Physics Research Section A*, **266**, 550–559.

Pierce, D. and Meier, F. (1976). Photoemission of spin-polarized electrons from GaAs. *Physical Review B*, **13**, 5484–5500.

Plihal, M., Mills, D.L., Elmers, H.J. and Gradmann, U. (1995). Spin-polarized-electron scattering studies of the Fe bilayer on W(100); theory and experiment. *Physical Review B*, **51**, 8193–8203.

Potthoff, M., Hilgers, G., Mueller, N., *et al*. (1995). Structure investigations of Xe-adsorbate layers by spin-polarized low-energy-electron diffraction.2. (Root-3 X-Root-3)R30-degrees-Xe PD(111) and the dilute phase of Xe Pt(111). *Surface Science*, **322**, 193–206.

Pratzer, M., Elmers, H.J., Bode, M., *et al*. (2001). Atomic-Scale magnetic domain walls in quasi-one-dimensional Fe nanostripes. *Physical Review Letters*, **87**, 127201-1–127201-4.

Przybylski, M., Kaufmann, I. and Gradmann, U. (1989). Moessbauer analysis of ultrathin ferromagnetic Fe(110) films on W(110) coated by Ag. *Physical Review B*, **40**, 8631–8640.

Qian, X. and Huebner, W. (2003). Symmetry and substrate effects on magnetic interactions from first principles: a comparison between Fe/W(100) and Fe/W(110). *Physical Review B*, **67**, 184414-1–184414-7.

Qiu, Z.Q. and Smith, N.V. (2002). Quantum well states and oscillatory magnetic interlayer coupling. *Journal of Physics: Condensed Matter*, **14**, R169–R193.

Quinn, J. (1962). Range of excited electrons in metals. *Physical Review*, **126**, 1453–1457.

Savrasov, S.Y. (1996). Linear-response theory and lattice dynamics: a muffin-tin-orbital approach. *Physical Review B*, **54**, 16470–16486.

Scheunemann, T., Feder, R., Henk, J., *et al*. (1997). Quantum well resonances in ferromagnetic Co films. *Solid State Communications*, **104**, 787–792.

Schoenhense, G. and Siegmann, H.C. (1993). Transmission of electrons through ferromagnetic material and applications. *Annals of Physics*, **2**, 465–465.

Schwarz, K., Blaha, P. and Madsen, G.K.H. (2002). Electronic structure calculations of solids using the WIEN2k package for material sciences. *Computer Physics Communications*, **147**, 71–76.

Seah, M. and Dench, W. (1979). Quantitative electron spectroscopy of surfaces: a standard data base for electron inelastic mean free path. *Surface and Interface Analysis*, **1**, 2–11.

Smith, N.V., Brookes, N.B., Chang, Y. and Johnson, P.D. (1994). Quantum-well and tight-binding analyses of spin-polarized photoemission from Ag/Fe(001) overlayers. *Physical Review B*, **49**, 332–338.

Tamura, E., Ackermann, B. and Feder, R. (1984). Relativistic diffraction theory: study of 3d and 4f surface ferromagnetism by polarised and unpolarised electrons. *Journal of Physics C*, **17**, 5455–5474.

Tamura, E., Feder, R., Waller, G. and Gradmann, U. (1990). Determination of the surface magnetization of Fe(110) by SPLEED. *Physica Status Solidi B*, **157**, 627–633.

Tong, S.Y. (1994). Electron-diffraction for surface studies - the first 30 years. *Surface Science*, **299**, 358–374.

Venus, D. (1993). Use of the spin-polarized LEED rotation curves to study disordered surfaces W(001)-(1 × 1) and W(001)-2H(1 × 1). *Surface Science*, **291**, 418–428.

Venus, D. and Cool, S. (1999). Spin-dependent scattering in magnetic films, using SPLEED. *Journal of Magnetism and Magnetic Materials*, **198–199**, 656–658.

Venus, D. and Johnston, H.L. (1994). Exchange and spin-orbit contributions to spin-polarized LEED rotation curves of magnetic films: Fe/W(001). *Physical Review B*, **50**, 15787–15795.

Venus, D. and Kirschner, J. (1988). Momentum dependence of the Stoner excitation spectrum of iron using spin-polarized electron-energy-loss spectroscopy. *Physical Review B*, **37**, 2199–2211.

Vollmer, R., Etzkorn, M., Anil Kumar, P.S., *et al*. (2003). Spin-Polarized electron energy loss spectroscopy of high energy, large wave vector spin waves in ultrathin fcc Co films on Cu(001). *Physical Review Letters*, **91**, 147201-1–147201-4.

Vosko, S.H. and Wilk, L. (1980). Influence of an improved local-spin-density correlation-energy functional on the cohesive energy of alkali metals. *Physical Review B*, **22**, 3812–3815.

Vosko, S.H., Wilk, L. and Nussair, M. (1980). Accurate spin dependent electron liquid correlation energies for local spin density calculations: a critical analysis. *Canadian Journal of Physics*, **58**, 1200–1211.

Wagner, K., Weber, N., Elmers, H.J. and Gradmann, U. (1997). Magnetization of free Fe(110) surfaces from thin film magnetometry. *Journal of Magnetism and Magnetic Materials*, **167**, 21–26.

Waller, G. (1986). *Untersuchung des Oberflaechenmagnetismus epitaktischer Fe(110)-Schichten mit elastischer Streuung spinpolarisierter Elektronen*, Ph.D Thesis, Technical University Clausthal-Zellerfeld, Germany.

Waller, G. and Gradmann, U. (1982). Spin-polarized electron scattering from ferromagnetic Fe(110) films on W(110). *Physical Review B*, **26**, 6330–6333.

Weller, D., Alvarado, S.F., Gudat, W., *et al*. (1985). Observation of surface-enhanced magnetic order and magnetic surface reconstruction on Gd(0001). *Physical Review Letters*, **54**, 1555–1558.

Woodruff, D. and Delchar, T. (1986). *Modern Techniques of Surface Science*, Cambridge University Press: Cambridge.

Wu, R. and Freeman, A.J. (1992). Magnetic properties of Fe overlayers on W(001) and the effects of oxygen adsorption. *Physical Review B*, **45**, 7532–7535.

Wu, Y.Z., Schmid, A.K., Altman, M.S., *et al*. (2005). Spin-dependent fabry-perot interference from a Cu thin film grown on fcc Co(001). *Physical Review Letters*, **94**, 02720-1–027201-4.

Wulfhekel, W., Zavaliche, F., Hertel, R., *et al*. (2003). Growth and magnetism of Fe nanostructures on W(001). *Physical Review B*, **68**, 144416-1–144416-9.

Zasada, I. (2002). On the disordered adsorption of CO on Pt(111). *Surface Science*, **498**, 293–306.

Zdyb, R. and Bauer, E. (2002a). Spin-dependent quantum size effects in the electron reflectivity of ultrathin ferromagnetic crystals. *Surface Review and Letters*, **9**, 1485–1491.

Zdyb, R. and Bauer, E. (2002b). Spin-resolved unoccupied electronic band structure from quantum size oscillations in the reflectivity of slow electrons from ultrathin ferromagnetic crystals. *Physical Review Letters*, **88**, 166403-1–166403-4.

Spin-polarized Low Energy Electron Microscopy

Ernst Bauer
Arizona State University, Tempe, AZ, USA

1 INTRODUCTION

In many applications thin ferromagnetic films are deposited on substrates that are too thick for transmission electron microscopy, so techniques such as Lorentz microscopy or holography cannot be used for imaging of the magnetic properties. Suitable imaging methods are then magnetic force microscopy (MFM), spin-polarized scanning tunneling microscopy (spin-STM), X-ray magnetic circular dichroism photo emission electron microscopy (XMCDPEEM), scanning electron microscopy with polarization analysis (SEMPA), spin-polarized low-energy electron microscopy (SPLEEM) and magneto-optical microscopies. These methods are to certain extent complementary because they give method-specific information and differ frequently in application range. This chapter tries to illustrate where SPLEEM stands among the various magnetic imaging methods. In brief, SPLEEM, SEMPA, and XMCDPEEM have in common that the electrons, which are used for imaging, are very slow. This limits the information depth from several tenths of a nanometer up to several nanometers, depending upon the material and upon the electron energy, which can range from 0 to about 20 eV. In SPLEEM and XMCDPEEM magnetic information is obtained via the spin of the incident particles, and in SEMPA via the spin of the emitted particles. Though differing strongly in the way the magnetic information is obtained, SPLEEM and XMCDPEEM are similar in that they are full-field imaging methods with parallel image acquisition while SEMPA is a scanning method with sequential image acquisition. The feature that XMCDPEEM and SEMPA have in common is that they use secondary electrons for imaging while SPLEEM uses elastically scattered electrons. SPLEEM is a laboratory method while XMCDPEEM requires a synchrotron radiation source with high brilliance. Despite the high brilliance of third-generation synchrotron radiation sources image acquisition times in XMCDPEEM are significantly longer than in SPLEEM. However, XMCDPEEM is generally applicable to surfaces that are not too rough, while SPLEEM is useful mainly for single crystals, epitaxial layers, and highly oriented films.

In order to understand the possibilities and limitations of SPLEEM it is first necessary to understand the elastic and inelastic interactions of very slow electrons with ferromagnetic and nonmagnetic materials. These will be discussed in Section 2. Aspects of the image formation are treated in the experimental part (Section 3). Applications are illustrated by a number of examples in Section 4, which is followed by a brief summary and outlook.

Handbook of Magnetism and Advanced Magnetic Materials. Edited by Helmut Kronmüller and Stuart Parkin. Volume 3: *Novel Techniques for Characterizing and Preparing Samples*. ISBN: 978-0-470-02217-7.

2 INTERACTION OF VERY SLOW ELECTRONS WITH MATTER

2.1 Elastic scattering

Two aspects of the interaction of very slow electrons with matter are important in the image formation process: the intensity and the magnetic contrast. We consider first the intensity, which determines the image acquisition time and the ability to focus. As will become clear in the experimental section (Section 3), SPLEEM uses electrons that are scattered into a narrow cone around the backward direction. The more concentrated the angular distribution is around $\theta = 180^\circ$, the higher the image intensity and the shorter the image acquisition time. Therefore, single crystalline or highly oriented surfaces are desirable because in these samples the scattered electrons are focused into diffraction beams, in particular into the specular reflected beam ((00) beam in surface crystallography nomenclature). Although the angular distribution of very slow electrons elastically scattered by free atoms has been studied extensively, little is know about the angular distribution in scattering from atoms in polycrystalline samples. Therefore, most information comes from calculations, which are not very accurate at low energies because the energy-dependent exchange and correlation contributions to the effective scattering potential are highly simplified or neglected. Results of these types of calculations indicate that at very low energies the backscattering cross sections of light atoms, for example Cu, can be higher than those of heavy atoms, for example Ag. The nonmonotonic dependence of the backscattering cross section is also true for energies in the LEED range (usually 30 eV to several hundred electronvolts) (Bauer, 1994, 1998, 2006), but at the very low energies this effect is particularly strong. In Cu, the backscattering cross section increases rapidly with decreasing energy near 0 eV and the same is true for the neighboring atoms Ni, Co, and Fe.

Reliable experimental data are available only for single crystal surfaces. As an example, Figure 1 shows the specular reflectivity of the W(110) surface at normal incidence, together with the electronic band structure along the surface normal, which gives a qualitative understanding of the reflectivity. Quantitative understanding requires taking into account the surface barrier (Herlt, Feder, Meister and Bauer, 1981). The reflectivity decreases rapidly with increasing energy as expected from the atomic backscattering cross section but the decrease is modulated by the band structure. In the energy gap between 1 and 6 eV the reflectivity is high because there are no allowed states in this energy range in the crystal. Similarly, in the energy range where the bands are steep (around 15 eV) so that the density of states is small, the reflectivity is enhanced. Fortunately,

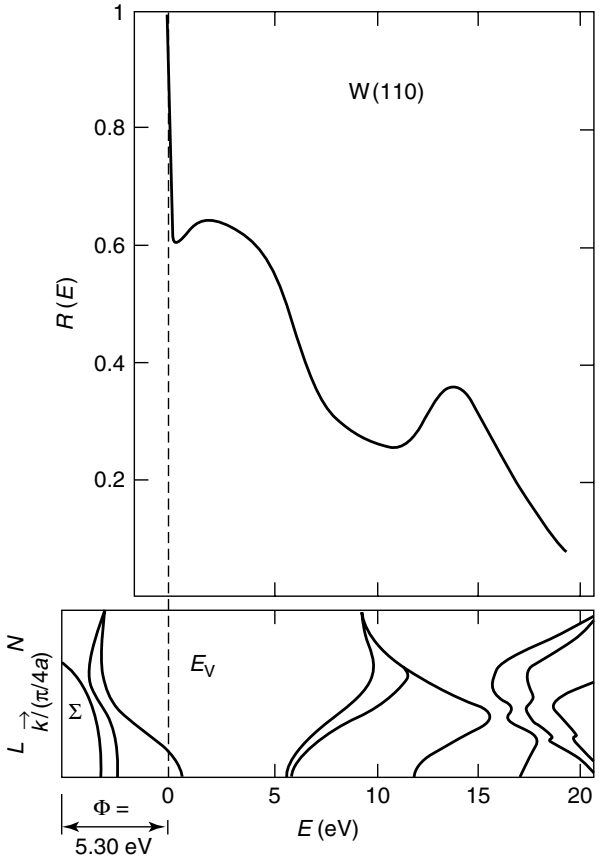

Figure 1. Specular reflectivity of a W(110) surface and comparison with the band structure along the [110] direction. (Reproduced from Herlt *et al.*, 1981, with permission from Elsevier. © 1981.)

for the interpretation of most SPLEEM images, a detailed understanding of the backscattering is not necessary. It is important only in energy regions with strong backscattering. In these regions the information depth is dominated by the elastic attenuation of the incident beam, which is determined by elastic backscattering: the incident wave is then an evanescent wave, and the sample is a reactive medium. In all other cases, the information depth in determined mainly by inelastic scattering, which will be discussed below.

The second aspect of importance for image formation is the contrast. In SPLEEM the contrast mechanisms known from LEEM are spin dependent because of the exchange interaction in which electrons with opposite spin experience a different potential. The interaction of spin-polarized electrons with matter is well described in SPLEED chapter (See also **Spin-polarized Low Energy Electron Diffraction, Volume 3**), so that only the features specific for very slow electrons need to be discussed here. First of all it has to be mentioned that in 180° scattering, which is a special case of the specular scattering described in the SPLEED chapter, only exchange scattering occurs. Because of the

Pauli principle, incident electrons with spin parallel to that of the electrons in the material experience a different potential, sometimes described by the Slater hole, than electrons with antiparallel spin. This exchange potential depends upon the density of the electrons with the same spin and is energy dependent. In crystals it manifests itself in the spin dependence of the energy-dependent band structure. In the free electron gas with electron density ρ, it is given by

$$V_{\mathrm{x}}(\eta) = -4\left[\left(\frac{3}{8\pi}\right)\rho\right]^{\frac{1}{3}} F(\eta) \tag{1}$$

where

$$F(\eta) = \frac{1}{2} + \left[\frac{(1-\eta^2)}{4\eta}\right]\ln\left[\frac{(1+\eta)}{(1-\eta)}\right] \tag{2}$$

and $\eta = k_{\mathrm{F}}/k_{\mathrm{i}} = (E_{\mathrm{F}}/E_{\mathrm{i}})^2$. Here E_{i} is the energy of the incident electron and k_{F}, E_{F} are the somewhat modified Fermi momentum and energy. Figure 2 shows the energy dependence of $F(E_{\mathrm{i}}/E_{\mathrm{F}})$. Although the 3d metals are far from being free electron–like, this dependence allows an estimate of how rapid the spin dependence caused by the exchange potential decreases with energy. With the Fermi energies of Fe, Co and Ni of 10.2, 9.5, and 8.7 eV, and the corresponding work functions of their most densely packed surfaces, the (110), (0001), and (111) surfaces, of 5.1, 5.45, and 5.45 eV, respectively, approximate $F(\eta)$ values for these metals at 1, 10, 20, and 50 eV above the vacuum level of 0.23, 0.13, 0.09, and 0.05, respectively, are obtained. Thus, the exchange potential, on which the spin selectivity of SPLEEM is based, decreases significantly with energy. This, together with the decrease of the reflectivity with increasing energy and with the decreasing spin dependence of the inelastic mean free path (IMFP) with increasing energy, is the reason for using very slow electrons in SPLEEM.

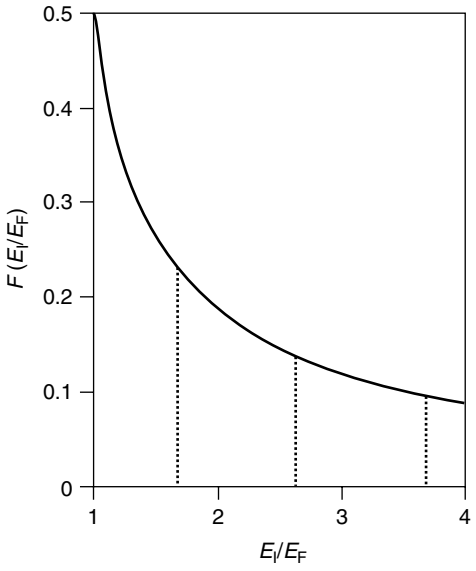

Figure 2. Energy dependence of the exchange energy of the free electron gas. The approximate values of $F(E_{\mathrm{i}}/E_{\mathrm{F}})$ of 0.23, 0.13, and 0.09 at 1, 10, and 20 eV above the vacuum level for Fe, Co, and Ni, respectively, are indicated.

2.2 Inelastic and quasi-elastic scattering

The sampling depth of SPLEEM is determined by the loss of electrons, which are elastically and quasi-elastically backscattered into a narrow cone around the direction of incidence. Both quasi-elastic scattering via phonon and magnon excitation and inelastic scattering via electron–hole pair creation cause this loss. The influence of these processes on SPLEEM intensity and magnetic contrast is determined by the momentum and energy transfer associated with them on the one hand and by the angular aperture and chromatic aberrations of the imaging system on the other. In SPLEEM only a small fraction of the momentum space around the backward direction is used for imaging and the accepted energy range below the elastic peak depends upon the dispersion of the magnetic fields used for separation of the reflected beam from the incident beam. Small energy losses such as those encountered in phonon and magnon excitation are accepted in all cases, but they can nevertheless contribute noticeably to the intensity attenuation because the small angular aperture cuts out only a small part of the momentum distribution. In addition, magnon excitation is spin selective and can influence the magnetic contrast. Little is known at present about the magnitude of these effects. Electron–hole pair creation causes larger energy losses of the order of 1 eV and higher. The resulting inelastically scattered electrons are at least partially eliminated by the chromatic aberration of the beam separation system unless it has been corrected. Hong and Mills (2000) have calculated the probability of the various electron–hole pair creation mechanisms and have found that the process shown in Figure 3a is about twice as probable as that shown in Figure 3b. In the first mechanism, the Stoner excitation, a spin-down electron excites a spin-up electron, causing an apparent spin flip of the reflected electron. In the second mechanism, the direct excitation, the spin of the reflected electron is preserved. Although the probability of Stoner excitations decreases with decreasing momentum transfer, they are still noticeable at zero momentum transfer to the crystal electron (Plihal and Mills, 1998). If the resulting inelastically scattered electrons are accepted by the SPLEEM electron optics, then they cause an increase of the reflection asymmetry due to the exchange potential mentioned above.

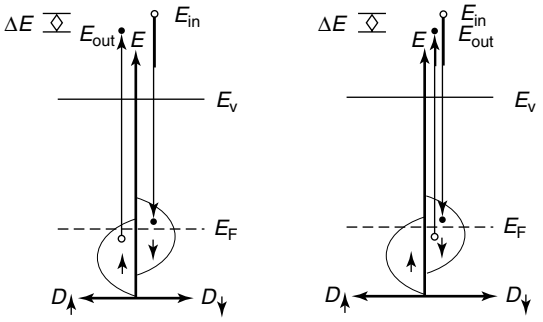

Figure 3. Schematic of electron excitations in a ferromagnet. (a) Stoner ('spin-flip') excitation, (b) direct ('nonspin-flip') excitation. Only the transition for incident spin-down electrons which are more likely than those of spin-up electrons are shown.

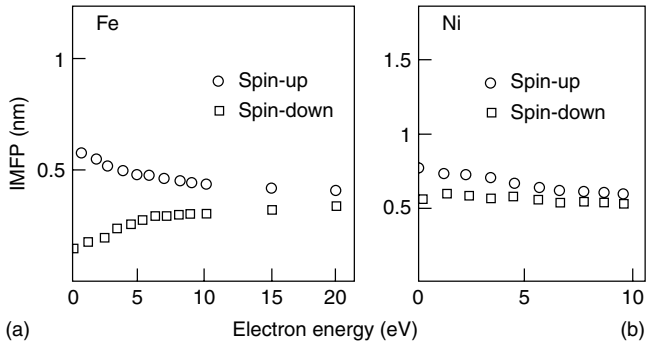

Figure 4. Inelastic mean free paths of spin-up and spin-down electrons in Fe and Ni as a function of energy obtained from explicit calculations. The zero of the energy is the vacuum level. (adapted from Hong and Mills, 2000.)

These considerations, which take into account instrumental aspects, have to be kept in mind in the discussion of the experimental and theoretical IMFPs, which ultimately determine the sampling depth of the electrons. The experimental data of the energy dependence of the spin-averaged IMFPs and their spin dependence are very limited and 'differ' considerably from author to author. A critical compilation has been given by Hopster (1999). Therefore, only theoretical data will be given here. Siegmann (1994) proposed the following relation for the spin dependence of the inelastic cross sections $\sigma_\uparrow$, $\sigma_\downarrow$ of spin-up and spin-down electrons, which determine their IMFP:

$$\sigma_{\uparrow\downarrow} = \sigma_0 + \sigma_d(5 - n_{\uparrow\downarrow}) \tag{3}$$

Here σ_d is the cross section for scattering into an unoccupied d orbital, σ_0 that for scattering into a non–d orbital, and $n_{\uparrow\downarrow}$ are the numbers of occupied majority and minority spin states, respectively. For example, for $n_\uparrow = 4$, $n_\downarrow = 2$ and $\sigma_d \gg \sigma_0$ one gets $\sigma_\uparrow/\sigma_\downarrow \approx 1/3$, so that the IMFPs of electrons with opposite spins differ by a factor of 3. Detailed accurate calculations of the energy dependence of the spin-up and spin-down IMFPs in Fe and Ni (Hong and Mills, 2000) give the results shown in Figure 4. In Fe the spin-up IMFP is larger than the spin-down IMFP by a factor of 4.3, 2.0, and 1.4 at 0, 5, and 10 eV, respectively, in Ni only by a factor of 1.4 at 0 eV and it decreases rapidly to the spin-down value. Accordingly, the magnetic contrast is significantly smaller in Ni than in Fe. Important are also the low absolute values of the IMFPs, for example, 0.2 and 0.55 nm in Fe or 0.5 and 0.7 nm in Ni at 2 eV for spin-down and spin-up IMFPs, respectively. These low values make SPLEEM an ideal tool for the study of surface magnetism.

Summarizing this section, elastic backscattering cross section, elastic exchange asymmetry, and IMFP difference between spin-up and spin-down electrons decrease rapidly with increasing energy. Therefore, optimum conditions for reflected intensity and magnetic contrast are obtained at the lowest energies. Exceptions to this rule occur around exchange-split band edges and in the presence of quantum size effects (QSEs), which will be discussed in Section 4.2.2.

3 SPLEEM INSTRUMENTATION

3.1 Overview

A SPLEEM instrument consists of the electron source, the spin manipulator, the beam separator, which separates incident and reflected electrons, the objective lens, the electron-optical systems on the illumination side and on the imaging side of the separator and finally the channel plate image intensifier–fluorescent screen from which the SPLEEM image or SPLEED pattern is recorded by a CCD camera. The electron-optical system on the illumination side has to produce a demagnified image of the source in the back focal plane of the objective lens; the electron-optical system on the imaging side has to produce a magnified SPLEEM image or SPLEED pattern on the channel plate image intensifier. These goals can be achieved with a variety of designs. Those of the presently operating SPLEEM systems are shown in Figures 5 and 6. In Figure 5 the electron source, which is at −15 kV, is seen on the far left, together with the spin-polarization manipulator, followed by the transfer optics. In the center is the beam separator, which deflects the electron beam 60° upward into the objective lens. In this lens, which includes the sample, the incident electrons are decelerated to the desired low energy and reaccelerated after reflection from the sample. The lens produces the SPLEED pattern in its back focal plane and the first SPLEEM image in the center of the separator. Both the first SPLEEM image and the SPLEED pattern are then magnified by the lens combinations in the imaging system, consisting of a transfer lens, an intermediate lens, and a

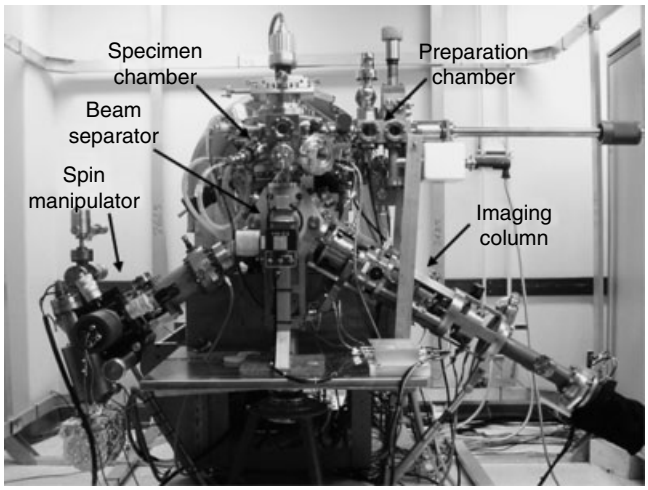

Figure 5. Spin-polarized low-energy electron microscope with 60° beam separator.

projective lens. The transfer lens transfers the first SPLEED pattern into the position of the angle-limiting aperture before the intermediate lens, the intermediate lens images either this plane or the SPLEEM image in front of the projective lens, which produces the final magnification. These lenses can be moved mechanically for rough beam alignment. Fine alignment is achieved with deflectors. An objective stigmator corrects the astigmatism of the objective lens and stigmators before and after the beam separator correct the astigmatism of the beam separator. An aperture in the illumination system limits the size of the illuminated area on the sample and also eliminates stray electrons. The sample manipulator on top allows not only three translations but also tilt so that the sample normal can be brought into coincidence with the optical axis of the objective lens. The sample is at a voltage close to that of the electron source (−15 kV). The voltage difference determines the energy of the incident electrons. The specimen chamber, which also contains the objective lens, has several ports for accessories such as evaporators, a UV light source, gas inlets, and so on, for *in situ* experiments. A small preparation chamber and airlock on the upper right side allow easy sample transfer and precleaning by sputtering, heating, and gas exposure. The whole system is pumped by sputter ion pumps and getter pumps, supported by additional pumps. The critical parts of the instrument (electron source, spin manipulator, objective lens, etc) will be discussed below in detail.

While the SPLEEM instrument shown in Figure 5 uses magnetic lenses except for the objective lens and has the specimen at high voltage, the one shown schematically in Figure 6 uses only electrostatic lenses and has the specimen near ground potential. Illumination and imaging section are parallel, which is achieved with three magnetic deflectors schematically indicated by circles. Focusing in the

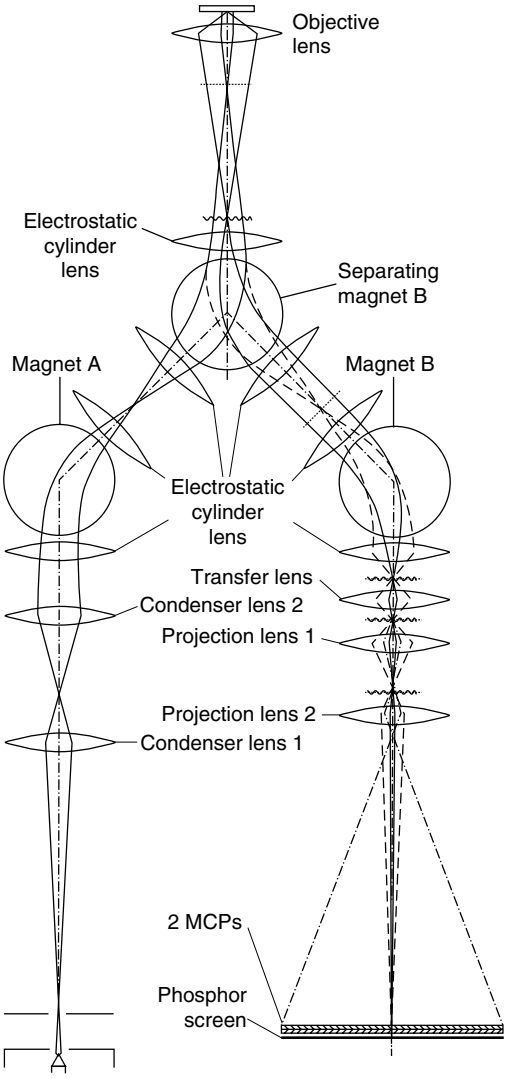

Figure 6. Schematic of a small spin-polarized low-energy electron microscope, which can be mounted on a 6′ diameter flange. The spin-polarized electron gun with spin manipulator at the left bottom is not shown. (Reused with permission from K. Grzelakowski and E. Bauer, *Review of Scientific Instruments*, **67**, 742 (1996). Copyright 1996, American Institute of Physics.)

nonfocusing plane of the magnetic deflectors is achieved by electrostatic cylinder lenses on both sides of the deflectors. The electron optics is floating at −5 kV except for the first electrode of the objective lens, which can be operated up to −15 kV. For details refer Grzelakowski and Bauer (1996).

As most SPLEEM work is done *in situ* the facilities in the sample chamber are important. Many films are grown on refractory substrates that require cleaning at high temperatures; in many SPLEEM studies the temperature must be changed during film growth or during the SPLEEM measurements. The low Curie temperatures of ultrathin films

make cooling very desirable, which has been achieved till now down to 115 K (Tober, Witte and Poppa, 2000). The study of the influence of magnetic fields on the magnetization distribution in the sample is complicated because of the deflection of the electron beam. In-plane fields can in principle be applied with window frame sample holders but to date only perpendicular fields have been used, albeit with some difficulty because the field must be aligned exactly on axis (Poppa, Tober and Schmid, 2002).

3.2 The electron source

The physical basis of photoelectron emission from negative electron affinity GaAs and related surfaces has already been described in the chapter on SPLEED (See also **Spin-polarized Low Energy Electron Diffraction, Volume 3**). There is extensive literature on this subject of which only a few overview papers can be cited (Pierce *et al*., 1980; Pierce, 1995). These give a detailed description of the cleaning of the cathode surface, of the activation procedure for obtaining a high quantum yield and high polarization, of the lifetime of the emission, and of the gun design, as well as ample references to earlier work. Here only more recent studies, in particular those which are important for the source operation in a spin-polarized electron microscope, will be discussed. As far as surface cleaning is concerned, cleaning with atomic hydrogen, long used for oxide removal from GaAs, has become popular (Maruyama *et al*., 2003) but also controversial (Baylac *et al*., 2005). It removes not only the oxide but also carbon-related contaminants, the main detrimental impurities (Petit and Houzay, 1994). Conventional cleaning by heating to about 600–620 °C has to be done very carefully in order to avoid loss of As resulting in Ga droplet formation that inactivates the surface. Atomic hydrogen cleaning, on the other hand, can be done at as low as at 300 °C but is usually done at 400–450 °C. No GaAs decomposition can occur at these temperatures. However, care has to be taken to avoid overdosing with hydrogen, which causes its incorporation into the crystal where it is believed to create yield-reducing defects and to deactivate the high p-doping used for the band bending necessary to achieve negative electron affinity.

The parameters that are important for the operation in SPLEEM are quantum efficiency, degree of spin polarization P, brightness B, and lifetime τ. Energy width ΔE is also of interest but small enough to be not resolution limiting. High polarization requires lifting of the degeneracy of the $P_{3/2}$ band at the Γ point. The band splitting into $m_j = \pm 3/2$ and $m_j = \pm 1/2$ (heavy and light hole) bands that can be achieved by strain or superlattices is usually small so that only a small photon energy range above the $P_{3/2}$ excitation threshold can be used. P values of about 85% and quantum yields of 1.7% have been reported (Maruyama *et al*., 2004). Because of the small photon energy range (<100 meV) the quantum efficiency is small and such cathodes have not been used till now in SPLEEM. Increasing the photon energy above the $P_{1/2}$ threshold causes a further decrease to the P values of 20–30% obtained also with conventional degenerate cathodes whose quantum yields are a factor of 10 or higher. Because high brightness B is needed in imaging, unstrained (nondegenerate) cathodes are, therefore, used in general. The brightness of the cathode is defined by $B = j/\pi\ \alpha^2$, where j is the emitted current density and α is the half-angle of the emission cone. For a given cathode j can be increased by focusing the photon beam into a finer spot and increasing the photon flux up to the space charge limit, α is determined by the ratio of transverse to longitudinal energy. A fine spot is needed in any case because it determines the ultimate diameter of the electron beam in the back focal plane of the objective lens. The diameter of this spot determines the divergence of the beam at the sample. The mean longitudinal and transverse energies (E_l and E_t, respectively) depend on the extraction voltage, upon the energy difference between the photon energy and the band gap, the roughness of the surface and other parameters. E_l may be as large as several 100 meV, E_t can be as small as 25 meV at room temperature (Pastuszka *et al*., 2000). This gives a lower limit of α of about 0.1. Thus, B depends upon many parameters and varies from source to source. Values as high as 1×10^5 A/cm^2-sr have been reported in a scanning electron microscope (Pierce, 1995). In the SPLEEM instruments, B has not been determined. The instrument shown in Figure 5 operates typically with 1 μA emission current at an extraction voltage of 1 kV. Imaging is still possible with several hundred nanoamperes. The lifetime τ is important not only for convenience of operation but in particular for longer experiments. It depends strongly on the pressure in the gun chamber and ranges from several hours at high pressures (10^{-10} mbar (10^{-8} Pa) range) to hundreds of hours at low pressures (10^{-12} mbar (10^{-10} Pa) range) and with continuous slow Cs supply during operation. While it is widely believed that the short lifetime in the absence of Cs supply during operation is caused by desorption of Cs, the pressure influence on the lifetime has been attributed to slow oxygen uptake. Because of the complexity of the phenomena involved, good spin-polarized electron sources are still a work of art and experience, which has to be collected for each individual case.

3.3 The polarization manipulator

In order to obtain magnetic contrast between regions with different directions of the magnetization **M** one must be able

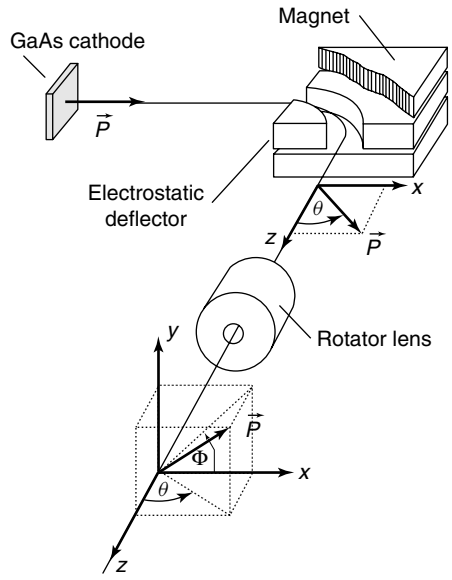

Figure 7. Principle of the spin manipulator used in the SPLEEM instruments shown in Figures 5 and 6 (Grzelakowski, Duden, Bauer *et al*., 1994). (Reprinted from *Surface Review and Letters*, **5** (1998) 12/3. Copyright 1998 with permission from World Scientific Publishing Co. Pte. Ltd, Singapore.)

to rotate the spin-polarization vector **P** of the spin-polarized electron beam, best in any direction in space. Maximum magnetic sensitivity is obtained when the spin of the incident electron is parallel or antiparallel to the spin of the electron in the sample, that is when **P** // ± **M**. In general the sensitivity is proportional to **P**·**M**. An unrestricted rotation of **P** is achieved with a spin manipulator as schematically shown in Figure 7 (Duden and Bauer, 1995; Bauer, 1997). The manipulator consists of a combined electrostatic/magnetic 90° deflector and a rotator lens. The cathode is illuminated at normal incidence through the deflector with circular polarized light from a diode laser and emits electrons with **P** parallel or antiparallel to the surface normal, depending upon the handedness of the helicity. Purely electrostatic deflection leaves **P** unchanged, purely magnetic deflection rotates **P** by 90°. By combining the two fields in the proper ratio any direction in the $x-z$ plane in Figure 7 can be reached. Out-of-plane directions are achieved by rotating **P** around the axis of the magnetic lens. While optimum magnetic contrast can be obtained by rotating **P** parallel and antiparallel to **M**, it is usual to select one or two preferred in-plane directions (magnetic easy or hard axis) and the surface normal. By vectorial addition of the three signal components the direction of **M** can be determined. In order to minimize the voltage and currents in the sector and rotator lens these components float close to the cathode potential, typically 1 kV relative to it, and the final acceleration to the full energy (15 or 5 kV, respectively, in the two instruments discussed in Section 3.1) occurs after the rotator lens.

3.4 The objective lens

The objective lens is the third crucial element of a SPLEEM instrument. In this lens the fast electrons are decelerated to the desired energy at the sample ('cathode'), which is part of the lens. For this reason the objective lens is also called a *cathode lens*. Cathode lenses, whether electrostatic, magnetic, or mixed electrostatic/magnetic, have large chromatic and spherical aberrations, which determine the limiting resolution of the instrument. The chromatic and spherical aberrations depend upon the angular aperture α as the first and third power of α, respectively, and make it necessary to limit α by a small angle-limiting ('contrast') aperture in the back focal plane (or in an image plane of it). This produces a diffraction disc of confusion whose radius is inversely proportional to sin α. The resolution can be optimized by choosing an aperture radius, which produces the smallest disc of confusion. Figure 8 shows the three contributions (b, c, d) to the resolution and the resulting overall resolution (a), together with the optimum radius (r) for the presently most frequently used cathode lenses (Chmelik, Veneklasen

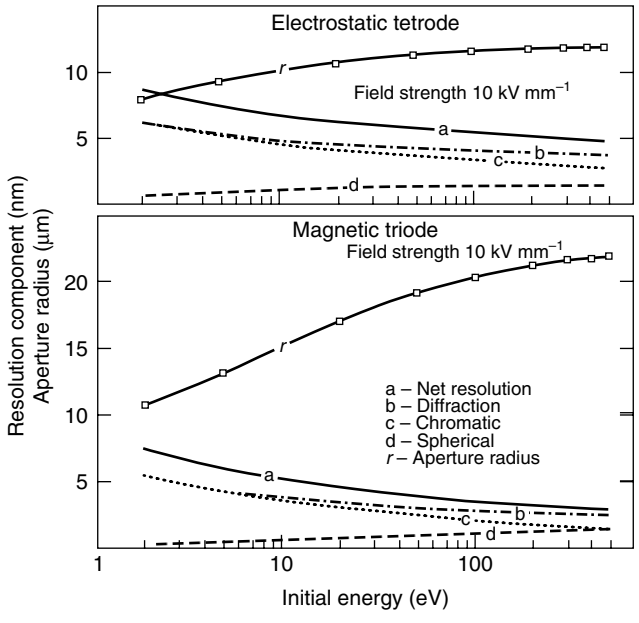

Figure 8. Radii of the resolution-limiting discs of confusion (b, c, d), resulting resolution (a) and optimal aperture radius (r) of cathode lenses. The electrostatic tetrode objective lens is used in the instruments shown in Figures 5 and 6 (Chmelik, Veneklasen and Marx, 1989). (Reprinted from OPTIK, Vol 83, 1989, Page 155, Copyright 1989 with permission from Elsevier.)

and Marx, 1989). Although the calculations are for a higher energy and larger energy width, they indicate that the limiting resolution of these instruments should be less than 10 nm between 2 and 10 eV energy at the sample. This resolution has not been achieved till now in SPLEEM for a number of reasons such as nonoptimal aperture, vibrations, voltage and current instabilities, insufficient shielding of ac fields, sample drift, increased energy width due to inelastically scattered electrons that are accepted by the aperture, and so on. Another important reason is the low signal/noise ratio because of the low **P** value. This will be discussed below. Presently a resolution of several 10 nm can be obtained routinely, under optimum conditions about 20 nm.

Ideally the image of the source in the back focal plane should be a point. Under these conditions the surface is illuminated perfectly perpendicular to the surface. In practice, the image of the source in the back focal plane has a finite extension leading to a corresponding nonperpendicular illumination of the surface. This reduces contrast and to some degree also resolution. The illumination aperture that cuts out far-off axis electrons in the illuminating beam reduces this problem.

3.5 The image acquisition/processing system

As mentioned earlier, the magnetic contribution to the backscattering caused by the exchange potential is small compared to the nonmagnetic part. As a result, the image intensity I may be written as $I = I_{st} + c\ \mathbf{P}\cdot\mathbf{M}$, where I_{st} is the structure-sensitive part seen in ordinary (nonspin-polarized) LEEM and c is a small proportionality constant. In a sample with high magnetic contrast the magnetic contribution is typically less than 10% of the total intensity; with low magnetic contrast it is 1% or less for $P \approx 25\%$. In order to eliminate the structural contrast two images with opposite **P** have to be taken (Figures 9a and 9b) and subtracted pixel by pixel (Figure 9c). Strong magnetic contrast allows image acquisition times of fractions of a second for each helicity image, which can be immediately subtracted from the opposite helicity image with present processing speeds; weak magnetic contrast as observed near the Curie temperature may require seconds per helicity image. The processing software calculates also the sum image in which the magnetic contrast is cancelled and can divide the difference image by the sum image, resulting in the so-called asymmetry image $A = (I\uparrow - I\downarrow)/(I\uparrow + I\downarrow)$. This is usually displayed. Image drifts, for example during studies of temperature-dependent phenomena, have to be corrected off-line. The asymmetry image frequently has low contrast, and is therefore contrast-enhanced, sometimes by more than a factor of 10. In such cases, the signal/noise ratio is the main resolution-limiting factor (Duden and Bauer, 1998). When the magnetic contribution to the signal is large, for example, 10%, then noise limits the resolution to about 20 nm, provided that many difference images are summed.

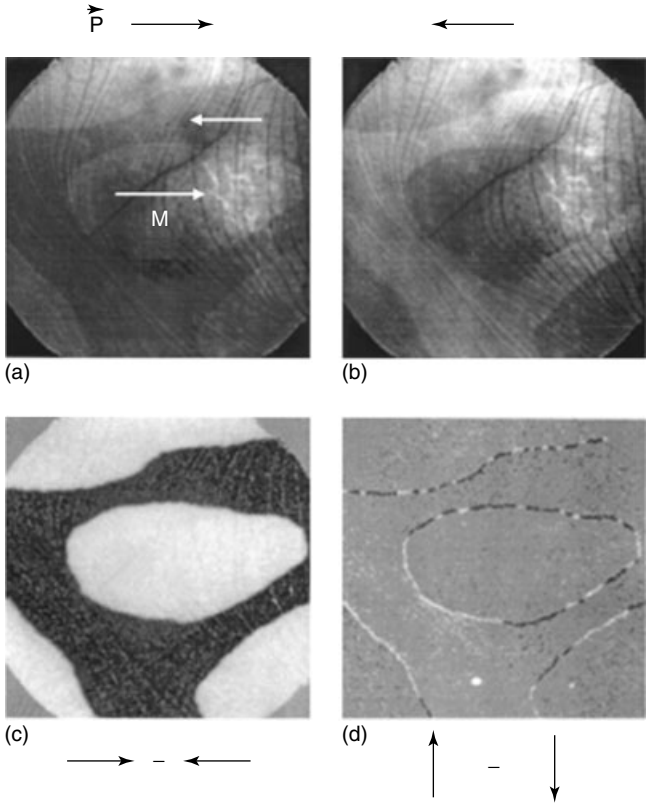

Figure 9. Magnetic contrast in a sample with strong uniaxial in-plane magnetization (6 Co ML on W(110)). (a) and (b) are images taken with **P** parallel and antiparallel to the easy axis, (c) is the contrast-enhanced difference image, and (d) the contrast-enhanced difference image of two images taken with opposite **P** perpendicular to the easy axis. Electron energy 2 eV, field of view 13 µm (Bauer, Duden, Pinkvos *et al*., 1996). (Reprinted from *Journal of Magnetism and Magnetic Materials*, Vol 156, 1991. Copyright 1991 with permission from Elsevier.)

4 APPLICATIONS

4.1 Surfaces of bulk crystals

Bulk crystals have hardly been studied because the low sampling depth of SPLEEM predestines it for the study of ultrathin films. However, SPLEEM is also suited for the study of the surface magnetism of bulk crystals. This is illustrated in Figure 10 (Altman *et al*., 1991), which

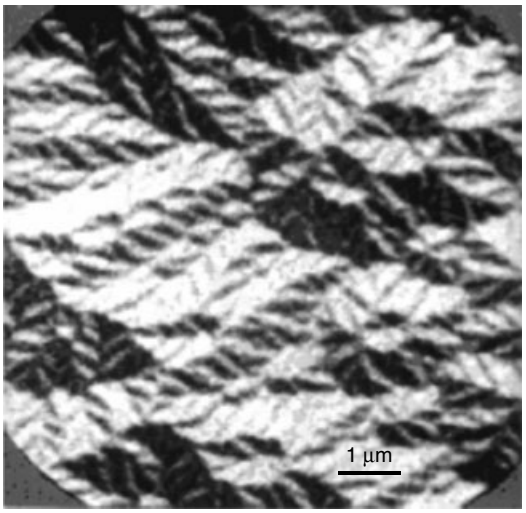

Figure 10. SPLEEM image of a Co(0001) surface. Electron energy 2 eV, field of view 12 μm (Altman, Pinkvos, Hurst *et al.*, 1991). (MRS Symposium Proceedings, 232, (1991) 125.)

shows the magnetic domain structure of a Co(0001) surface after sputter cleaning and annealing. It was taken in the early phase of SPLEEM to demonstrate the capability of this technique by comparison with SEMPA images of the Co(0001) surface in which this 'flower' domain pattern was discovered (Unguris, Scheinfein, Celotta and Pierce, 1989). It shows the sixfold symmetry of in-plane closure domains, terminating the domains in the bulk whose magnetization is perpendicular to the surface. Subsequent work concentrated on ultrathin films for reasons mentioned above.

4.2 Ultrathin films

4.2.1 Single layers, underlayers, and overlayers

Spin order in a thin film decreases rapidly with decreasing film thickness so that in monolayer films the Curie temperature T_C is in general below room temperature. In some cases, T_C is above room temperature so that the temperature dependence of the magnetization can be studied conveniently. An example is the Fe monolayer on a Au double layer on W(110). It shows weak ferromagnetic contrast at room temperature, which can be increased significantly by capping with Au. Figure 11 shows some SPLEEM images taken near T_C (Zdyb and Bauer, 2007). It is clearly seen that near the phase transition ferromagnetic (dark and white) and paramagnetic (gray) regions coexist. The local phase transition temperature decreases with decreasing step distance. In regions with large step distances, which are on large terraces, strong fluctuations of the magnetization direction occur before the transition into the paramagnetic state. These phenomena are averaged out in laterally averaging studies of the phase transition, leading to incorrect critical parameters for thin films on surfaces with varying step density.

In contrast to the Fe monolayer on a Au double layer on W(110), T_C of the Fe monolayer on a thick Au layer on W(110) is below room temperature as it is also on the (111) surface of a bulk Au crystal. The same is true for most other ferromagnetic film–nonmagnetic substrate combinations. In most of these films, the direction of the magnetization changes with thickness, a phenomenon called

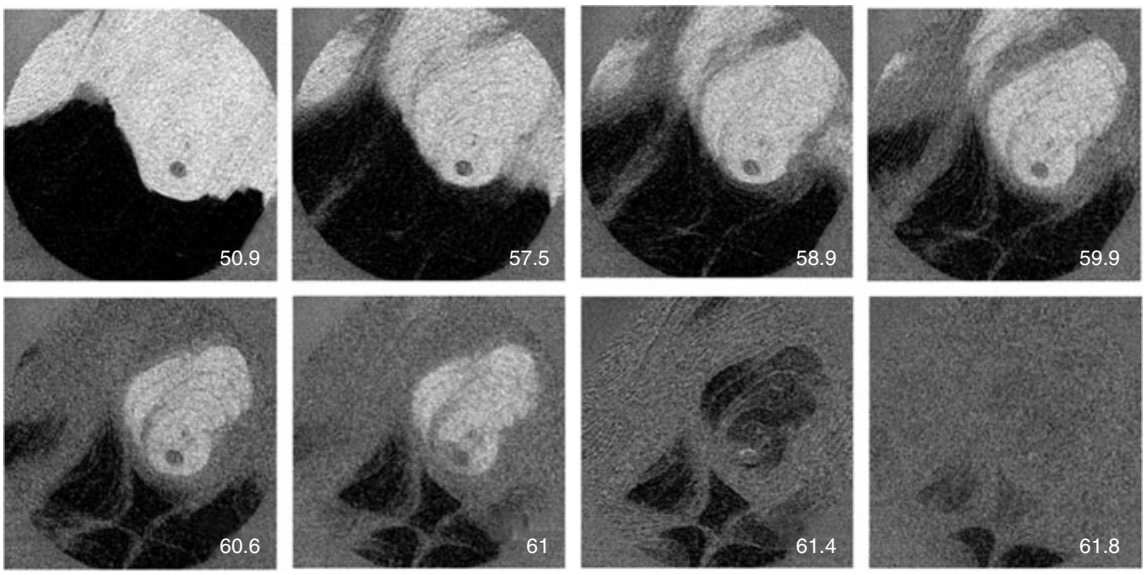

Figure 11. SPLEEM images of a Au-capped Fe monolayer on a Au double layer on W(110) at the temperatures (in °C) indicated in the images. On the large terraces the magnetization disappears at 62.0 °C. Electron energy 2 eV, field of view 14 μm (Zdyb and Bauer, 2007).

spin reorientation transition (*SRT*), which has been studied in considerable detail by SPLEEM. At the same time another phenomenon, the QSE, evolves with increasing thickness and this will be discussed before the SRT will be addressed.

Fe on W(110) and Au(111) produces strong magnetic contrast, because the surface of these films is flat. This is not the case on other substrates due to the different growth modes. For example, Co grows on the W(100) surface not with the equilibrium plane (0001) but with the (11−20) plane parallel to the substrate. The large anisotropic misfit causes growth of rectangular crystals with large aspect ratio and tilted surfaces. As a consequence, the (00) beams are reflected off-axis and there is insufficient intensity on axis at the low energies suitable for SPLEEM. The observed magnetic contrast is more or less buried in the noise (Duden, Zdyb, Altman and Bauer, 2001). On the W(111) surface the large atomic roughness supports metastable pseudomorphic Co growth at room temperature and somewhat higher temperature over a wide thickness range. At 380 K the layer becomes ferromagnetic with in-plane magnetization at 7.6 monolayers (ML). Domain structure and magnetization direction are strongly influenced by surface steps, which indicates that the in-plane anisotropy is weak (Man *et al*., 2003).

While Fe and Co and their alloys have large magnetic moments and, therefore, produce strong magnetic contrast, at least far away from the Curie temperature, Ni with its small magnetic moment is more difficult to study. Nevertheless, some results have also been obtained for Ni layers on Cu(100), for example, the domain wall width (Ramchal, Schmid, Farle and Poppa, 2004a).

Nonmagnetic underlayers are frequently used to vary the anisotropy of the substrate. The case of Au underlayers for the growth on bcc(110) surfaces that have twofold symmetry is a good example. As shown at the beginning of this section a Au double layer on W(110) induces enough uniaxial anisotropy so that an Fe monolayer is ferromagnetic at room temperature. When the Au underlayer is thicker, for example 10 ML thick, then the Fe monolayer is not ferromagnetic at room temperature and develops initially out-of-plane magnetization with a preferred domain wall orientation. The in-plane magnetization that occurs in thicker Fe films again shows uniaxial anisotropy, just like the monolayer on the Au double layer.

Another example is Co on Au on W(110). Up to 4 Au ML the magnetization of the Co layer is in plane at all thicknesses. Above an Au thickness of 4 ML the magnetization of the Co layer is perpendicular to the surface below a critical Co thickness that ranges from 3.3 ML at a Au thickness of 5 to 4.3 ML at a Au thickness of 10 ML. The domain structure changes from a striped phase with domain walls parallel to the W[001] direction to a more isotropic phase as shown in Figure 12. Above the critical Co thickness the films again have uniaxial anisotropy. The influence of underlayers has been attributed to changes in the magnetoelastic anisotropy caused by the misfit strain, but step anisotropy caused by anisotropic growth cannot be excluded, in particular as the films are grown at relative large angles of incidence.

Nonmagnetic overlayers can have a dramatic influence on the magnetization of ferromagnetic layers, as already seen above in the case of the Fe monolayer. Laterally averaging magneto-optical and magnetometric measurements frequently show a considerable enhancement of the magnetic anisotropy. Examples are Au, Ag, Cu, and Pd overlayers on Co layers, which enhance the perpendicular anisotropy strongly, with a peak at around 1 ML. This phenomenon was studied with SPLEEM, using 3−8-ML-thick epitaxial Co films on W(110) (Duden and Bauer, 1999a). As will be discussed in Section 4.2.3, in these layers, **M** is slightly tilted away from in-plane. For Au, the increase of the perpendicular anisotropy with overlayer coverage was largest (from 25 to 70°) for the thinnest film and smallest (from 10 to 25°) for the thickest film, with only a weekly pronounced maximum at 2 ML. In the case of Cu overlayers, a deposition temperature-dependent maximum was

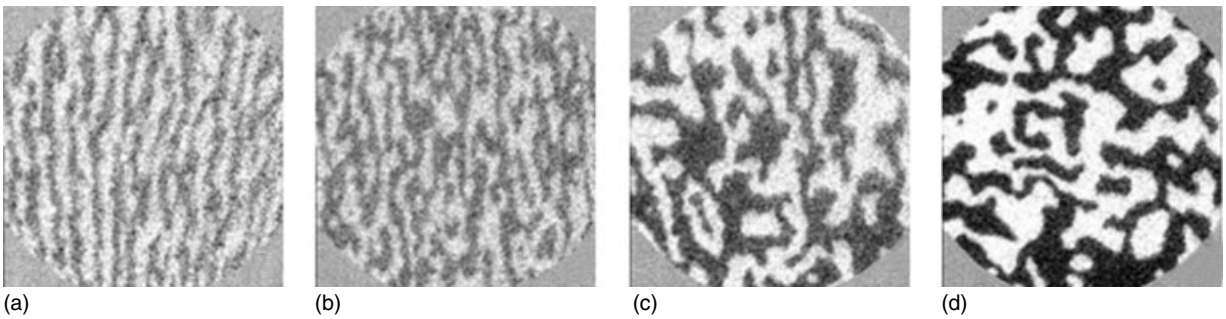

Figure 12. Out-of-plane SPLEEM images of the influence of the thickness of a Au layer on W(110) on the domain configuration of Co layers grown on top of it. Au layer thickness is 5, 6, 8, and 10 ML in a, b, c, and d, respectively. The corresponding Co thicknesses are 2.8, 3.0, 3.3, and 4.0 ML. Electron energy 1.2 eV, field of view 10 μm (from Ph.D. thesis Duden, 1996).

found, which could be connected to a structural effect using LEEM imaging: only the double layer increased the perpendicular anisotropy, which was attributed to strain effects, while the monolayer and triple layer had no noticeable effect. The temperature-dependent coexistence of monolayer and double layer regions seen in the LEEM images then causes temperature-dependent location of the maximum. This is a good example of the power of the combination of SPLEEM and LEEM imaging using difference and sum images.

4.2.2 Spin-dependent quantum size effects

A thin film bounded by parallel surfaces acts for the incident electron wave similar to the Fabry-Perót etalon in light optics: the reflectivity shows maxima and minima as a function of wavelength or film thickness due to constructive and destructive interference between the waves reflected at the two boundaries. The condition for constructive interference is $n\lambda/2 = t + \varphi$, where λ is the wavelength, t the thickness of the film, and φ represents the finite penetration depth of the wave beyond the boundaries. This is the standing wave condition and corresponds to a quantization of the electron wave, therefore the name *quantum size effect (QSE)*. In the bulk of crystals only electron states determined by the band structure E(**k**) are allowed, which in the case of ferromagnetic materials is exchange split as illustrated in Figure 13. As a consequence, at a given thickness t the QSE condition $n\lambda/2 = t + \varphi$ is fulfilled for spin-up and spin-down electrons at different energies E(**k**) because of $k = 2\pi/\lambda$ as indicated in Figure 13 for $k = 0.12$. Therefore, not only the reflectivity but also the asymmetry $A = (I_\uparrow - I_\downarrow)/(I_\uparrow + I_\downarrow)$ should change in an oscillatory manner with increasing thickness and energy. This was first observed in SPLEEM studies of Co layers on W(110) (Scheunemann *et al.*, 1997).

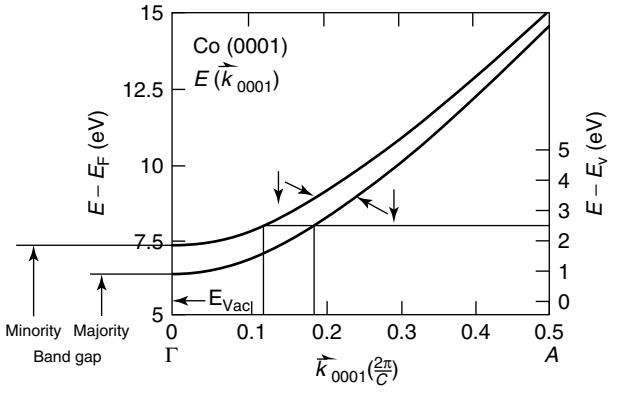

Figure 13. Band structure of Co above the vacuum level in the Γ A direction ([0001]).

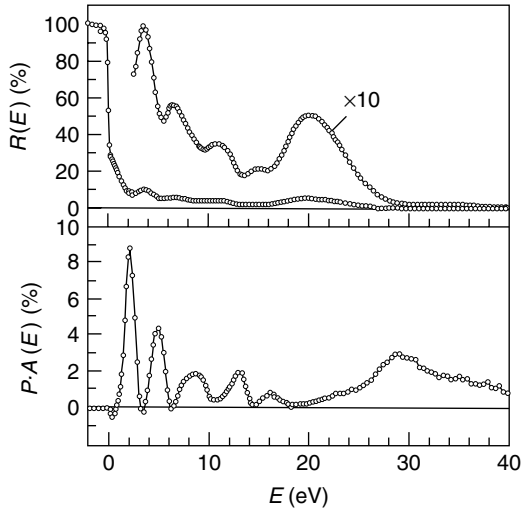

Figure 14. Reflectivity and asymmetry of the reflectivity of a 6 ML thick Co film on W(110) as a function of energy. The true asymmetry is by a factor of about 4–5 higher because of $P \approx 0.2$–0.25. (From M.S. thesis of Wurm, 1994). (Reprinted from *Journal of Magnetism and Magnetic Materials*, Vol 156, 1991. Copyright 1991 with permission from Elsevier.)

The largest asymmetry A was observed at 6 ML of Co (Figure 14).

From Figure 13 it is obvious that by measuring the reflectivity as a function of thickness and energy the exchange-split band structure above the vacuum level can be determined. Early attempts were not successful because the films consisted of small regions differing in thickness resulting in a smearing out of the thickness dependence. With proper growth conditions films with large regions with constant thickness on large substrate terraces can be prepared as illustrated in Figure 15 for Fe films on W(110) (Zdyb and Bauer, 2002a). The images in the top row show the reflectivity at several energies, while those in the lower row show the corresponding asymmetry images in which the contrast is enhanced. Large regions, 6, 7, and 8 ML thick can be seen. Such films have areas large enough for intensity measurements with good signal/noise ratio from which the band structure along the surface normal can be determined with high accuracy (Zdyb and Bauer, 2002b). This technique has been applied more recently to Co films on W(110) also (Graf *et al.*, 2005). In addition to the determination of the unoccupied band structure perpendicular to the surface the QSE has also another promising application: as a spin analyzer or polarizer. The large asymmetry values A that can be achieved when the QSE condition is fulfilled, together with the high reflected current $I = RI_0$, give a large figure of merit $Q = IA^2$ for such devices. In the first measurements on Co films consisting of regions with somewhat different thickness a Q value of about 2×10^{-2} was achieved, while

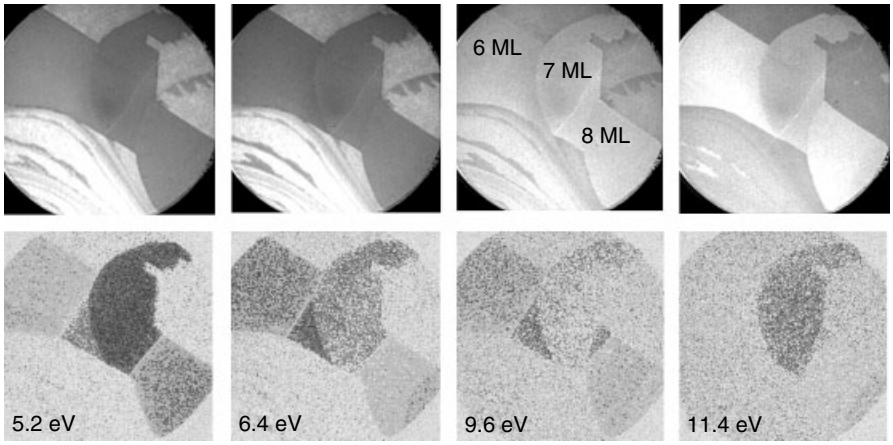

Figure 15. SPLEEM (top) and asymmetry images (bottom) of an Fe layer with large regions of constant thickness on a W(110) surface with large terraces, taken at several energies. When plotted in color, the asymmetry images show the magnitude of the asymmetry and direction of the magnetization. Electron energy 11.4 eV, field of view 9 µm (Zdyb and Bauer, 2002b).

with the constant thickness Fe layers a Q of about 5×10^{-2} (Zdyb and Bauer, 2002a) was achieved. This value can still be enhanced by Au capping, which at the same time reduces the deterioration of Q over time, which was studied in some detail in the more recent study (Graf *et al*., 2005).

Nonmagnetic overlayers have a significant influence on the spin-dependent QSE. This was actually observed before the SPLEEM QSE measurements on Co layers in a study of the influence of Cu overlayers on a Co layer on Cu(100) (Kerkmann, Pescia, Krewer and Vescovo, 1991). In a SPLEEM study (Poppa, Pinkvos, Wurm and Bauer, 1993) a strong modulation of the asymmetry was observed as a function of Cu overlayer thickness on epitaxial Co layers of fixed thickness on W(110). This effect was studied recently in more detail for Cu overlayers on fcc Co(001) on Cu(001) and attributed to the spin-dependent reflectivity of the Cu/Co interface (Wu *et al*., 2005). Overlayers also have additional effects as seen in the Au monolayer (Section 4.2.1), which will be discussed below.

4.2.3 Spin reorientation transitions

With increasing thickness the Curie temperature increases in ultrathin films according to

$$\frac{T_C(n)}{T_C(\infty)} = \frac{(n-1)}{2N_0} \tag{4}$$

where n is the number of monolayers and N_0 the range of the spin-spin coupling. Above N_0 the finite size scaling law

$$\frac{T_C(n)}{T_C(\infty)} = 1 - \left[\frac{2n}{(N_0+1)}\right]^{-1/\upsilon} \tag{5}$$

applies, where υ is the critical exponent for the correlation length for the three-dimensional system (Zhang and Willis, 2001). For Ni, for example, $N_0 \approx 5$ ML and $\upsilon \approx 1$. Thus, at small thickness T_C increases rapidly with thickness and accordingly also magnetization and, therefore, the magnetic contrast. At the same time the influence of the electronic interactions with the substrate, which determines the magnetic anisotropy of the monolayer, decreases and magnetocrystalline and shape anisotropy play an increasing role. In addition, the mismatch between film and substrate introduces magnetoelastic effects, which are particularly evident when the mismatch is anisotropic because it usually produces a well-pronounced easy and hard axis. Steps can also induce magnetic anisotropy, which changes with coverage.

Thus, with increasing thickness not only the magnitude of the magnetization but also its direction changes. This leads to a large variety of so-called SRTs. The first SPLEEM observation of a change of the direction of **M** with coverage was made on Co layers on W(110) (Duden and Bauer, 1996). **M** was not in plane in the thinnest layers as deduced previously from magnetometric measurements but tilted considerably out of plane and tilted into the plane in an apparently oscillatory manner with increasing thickness. The out-of-plane component changed its direction within the large in-plane component domains, preferentially at atomic steps, causing a 'wrinkled' magnetization in the layer.

The most-studied SRT is probably that in Co layers on Au(111) which has been the subject of several SEMPA studies with partially contradicting results. These layers have perpendicular **M** below about 4 ML and in-plane **M** above 5 ML. The SPLEEM study of this SRT, which was not made on a Au single crystal but on epitaxial Au layers of various thickness on W(110), brought additional contradictions

(Duden and Bauer, 1997). Instead of the continuous tilting of **M** into the plane (without or with breakup of the original in-plane domains) that had been deduced from the SEMPA studies, the SRT started with a broadening of the Bloch domain walls, before large in-plane domains developed. This result was later confirmed by laterally averaging magneto-optical measurements (Ding, Pütter, Oepen and Kirschner, 2001). A general theoretical analysis of the SRT (Vedmedenko, Oepen and Kirschner, 2002) finally revealed that both modes of transition, continuous tilt or coexistence of in-plane and out-of-plane regions during the transition, can occur, depending upon the relative magnitude of the various anisotropies involved. Apparently, differences in the substrate topography, in the growth process, and Au segregation to the surface of the Co layer can cause the necessary changes of the relevant anisotropies to produce different SRT modes.

While in the SRT of Co on Au(111) no major structural phase transition occurs with increasing thickness, except possibly a change between fcc and hcp stacking, that of Fe on Au(111) is accompanied by a massive change in structure from a quasi-pseudomorphic fcc layer to an initially distorted bcc (110) layer at about 3 ML (Bulou *et al*., 2004; Dekadjevi *et al*., 2005). Before this structural transition **M** has out-of-plane orientation, after it is in-plane oriented. This transition was studied in detail in $Fe_{1-x}Co_x$ alloy films with $x \leqslant 0.3$, which have bcc structure with nearly the same lattice constant as pure Fe (Zdyb and Bauer, 2003). Contrary to the Fe monolayer on the Au double layer on W(110) discussed in Section 4.2.1 these films were grown on 10 ML thick Au films on W(110) which have already relaxed considerably to the bulk structure but still transfer some of the twofold symmetry of the substrate onto the Fe film. As a consequence, the (110)-oriented bcc films have uniaxial anisotropy with an easy axis in the [001] direction. As seen in Figure 16 below the SRT the magnetization points predominantly out of plane and the domain size increases initially with increasing thickness as usual. A quantitative analysis of the out-of-plane and in-plane contrast shows that **M** is tilted about 15° against the surface normal already from the very beginning. Upon the onset of the SRT the tilt increases and the domain size decreases continuously until **M** abruptly tilts to about 60°, forming large domains when the structural phase transition occurs. With increasing thickness, **M** rotates completely into the plane. Thus, this system shows an SRT, in which the magnetization continuously rotates into the plane, but whose completion is pre-emptied by the structural phase transition. The deposition was made at a grazing angle of incidence so that the SRT occurs earlier on uphill slopes and later on downhill slopes on the terraced surface than on the flat regions. The tilted magnetization even below the onset of the SRT was subsequently also

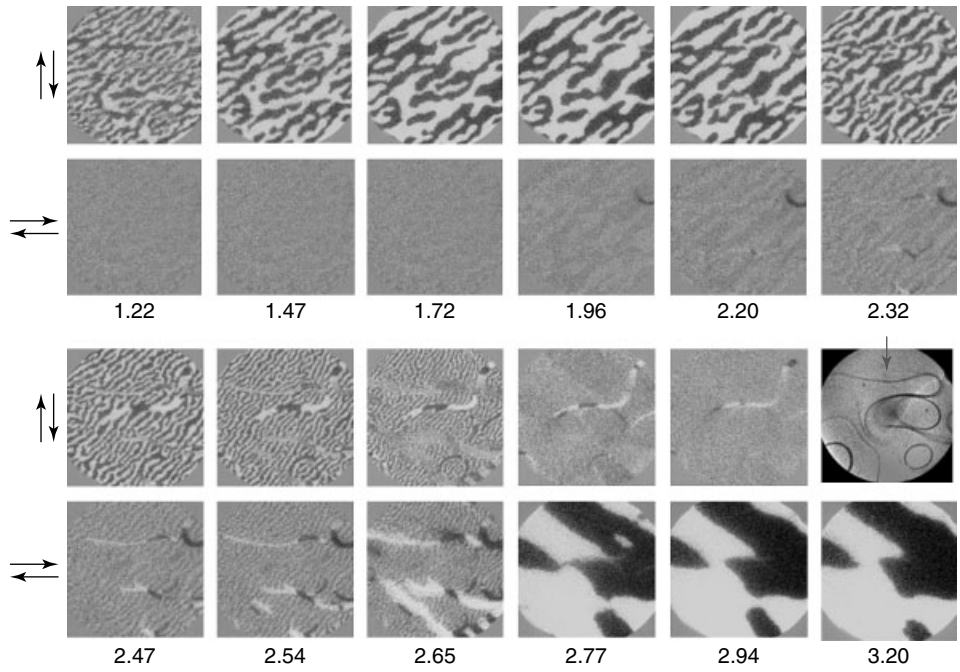

Figure 16. SPLEEM images of the spin reorientation transition (SRT) in an $Fe_{0.7}Co_{0.3}$ layer on 10 ML of Au with (111) orientation on W(110). The top row shows the out-of-plane images, the bottom row the in-plane images. The thickness is given in monolayers. The last out-of-plane image is replaced by a LEEM image to illustrate the topography of the surface. The deposition direction is indicated. Electron energy 2.5 eV, field of view 10 µm (Zdyb and Bauer, 2003).

observed in Fe films with laterally averaging magneto-optical measurements (Toulemonde, Petrov, Naid Abdi and Bucher, 2004).

Several other interesting SRTs have been studied with SPLEEM. One of them is the much studied and controversial out-of-plane to in-plane transition of Fe on Cu(100) which occurs via an apparently nonmagnetic state (Man, Altman and Poppa, 2001a; Man *et al*., 2001b). In this complicated system particular attention was paid to the connection with the film structure and the influence of H_2 on the growth, structure, and magnetic properties of the films and the study was combined with laterally averaging magneto-optical measurements. The magnetization and the domain size decreased with increasing thickness without change of the magnetization direction. This was attributed to the decrease of the Curie temperature from above room temperature at 3 ML to 285 K at about 4 ML. An attempt was made to explain the results in terms of finite size scaling but other explanations are possible too (Bauer, 2005a) in the light of more recent structural STM studies (Biedermann, Tscheliessnig, Schmid and Varga, 2001, 2004). The second part of the SRT, that is the appearance of the in-plane magnetization, was not studied.

SRTs in coupled ferromagnetic layers are of particular interest because they have frequently different anisotropies, which compete with each other. Examples are Fe layers on Ni layers on Cu(100) (Ramchal, Schmid, Farle and Poppa, 2004b). This was studied for 7.2 and 11 ML thick Ni layers, which have perpendicular and canted magnetization, respectively. Up to 2.5 Fe ML the magnetization in the Fe and Ni layers is parallel, but between 2.5 and 2.9 Fe ML the magnetization in the Fe layer rotates in a spiral-like motion into the plane with simultaneous breakup of the originally large domains into stripes with decreasing widths, similar to that seen in Figure 15, before large in-plane domains appear.

4.2.4 Multilayers

The antiferromagnetic and ferromagnetic coupling between ferromagnetic layers through nonmagnetic interlayers plays an important role in magnetoresistive devices. Early unpublished SPLEEM studies of multilayers revealed that no useful additional information could be gained by going beyond a trilayer (sandwich) because with increasing number of layers the surface becomes increasingly rougher. This decreases the intensity and sharpness of the (00) spot and accordingly the signal/noise ratio of the SPLEEM images. Therefore, later trilayers were studied, with emphasis on the influence of interface roughness and of the biquadratic exchange coupling between the layers, which is expressed by the biquadratic coupling 'constant' J_2 in the expression for the interlayer exchange energy

$$E = J_1(1 - \cos\phi) + J_2(1 - \cos^2\phi) \qquad (6)$$

where J_1 is the bilinear coupling 'constant' and ϕ the angle between the magnetization directions in the two layers. Biquadratic coupling is explained in terms of various interface roughness models. Co/Au/Co and Co/Cu/Co trilayers were chosen (Duden and Bauer, 1999b,c). In these studies the short IMFP in Co and the large IMFP in Au and Cu play an important role because the magnetic signal is dominated by the top layer, and a wide thickness range of the nonmagnetic layer can be studied. These studies revealed a complex dependence of the interlayer coupling upon the interlayer thickness as well as upon the top layer thickness.

In films grown at about 300 K, antiferromagnetic coupling occurs at 5 and 4.5 ML of Au and Cu, respectively, independent of the thickness of the top layer, however, nearly always with a strong biquadratic contribution. Bilinear coupling is dominating at 3 Cu ML, at 8 Cu ML the coupling is nearly completely bilinear. While in trilayers with a Cu spacer layer the top layer magnetization is always in-plane, in trilayers with a Au spacer layer the SRT described in Section 4.2.3 occurs in the top Co layer, with antiferromagnetic coupling at 5 Au ML. How the antiferromagnetic coupling changes with the thickness of the top layer is indicated for a few thicknesses in Figure 17; (a) and (b) show images of the Au-covered bottom Co layer which has predominantly in-plane magnetization (b), taken before the deposition of the top Co layer. Image (a) shows, however, that there is also still some out-of-plane **M** component present. (c)–(f) are images of the top Co layer. When it is 3 ML thick (c), **M** is mostly out of plane with antiferromagnetic coupling

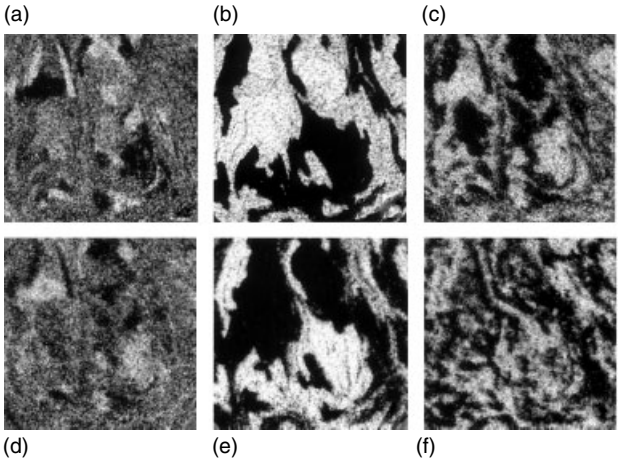

Figure 17. SPLEEM images of antiferromagnetically coupled Co/Au/Co trilayers on W(110). Electron energy 1.2 eV, field of view $6 \times 6\,\mu m^2$. For explanation see text (Duden and Bauer, 1994b).

to the out-of-plane regions in the bottom layer (a). At 4 top Co layers, out-of-plane (d) and in-plane coupling are of comparable strength and at 6 top Co layers **M** is basically only in-plane (e) with some 90° component (f). The strong 90° component in the in-plane magnetization after the SRT is seen also in the ferromagnetic coupling case in the strong domain pattern on the right side of the middle row of Figure 18 where **P** is perpendicular to the easy axis in the bottom layer. In the third row of this figure, **M** is purely out of plane and ferromagnetically coupled to the out-of-plane component in the bottom layer. A quantitative analysis of many SPLEEM images shows that the ratio of J_2/J_1 increases from 4 to 7 Au ML. On the other hand, with the Cu spacers the biquadratic coupling is strongest in the thinner Cu layers and decreases with increasing spacer thickness. These differences between Au and Cu indicate that the interface roughness, which causes biquadratic coupling, decreases in Au spacers with increasing thickness, while it decreases in Cu spacers, probably due to the different growth modes of these layers. Interface roughness is important because with increasing deposition temperature, that is increasing roughness, the correlation between the domain structure in the top and bottom layers rapidly decreases.

Noncollinear coupling, which converts into collinear coupling with increasing spacer thickness, was also observed in a completely different system: in an Fe trilayer with an antiferromagnetic NiO spacer layer (Biagioni *et al*., 2005). In this case there is no correlation between the domain size in top and bottom layers. The domains in the top layer are much smaller than those in the bottom layer and presumably depend on the size of the antiferromagnetic domains in the NiO layer. The critical thickness for the transition from noncollinear to collinear coupling seems to be preparation-dependent, a possible indication of roughness effects.

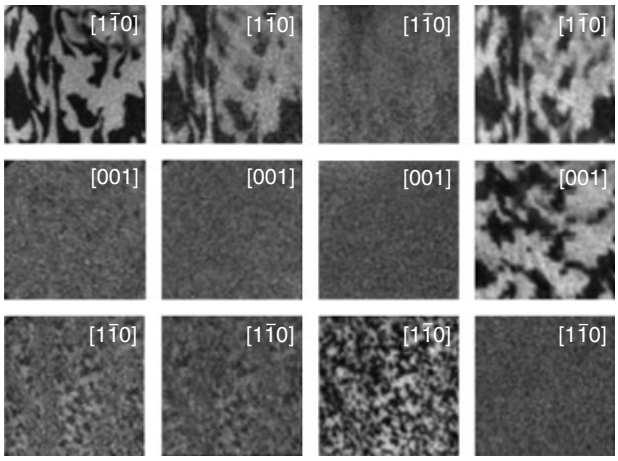

Figure 18. SPLEEM images of ferromagnetically coupled Co/Au/Co trilayers on W(110). The images in the top row are taken with **P** parallel to $\pm$**M** in the bottom layer (W[1$\bar{1}$0] direction), those in the middle row 90° with **P** rotated (W[001] direction) and those in the bottom row with **P** perpendicular to the layer (W[110] direction). The columns show from the left to the right the following layer combinations: the bottom Co layer (7 Co), the Au-covered bottom Co layer (6 Au/7 Co) and the complete sandwiches 3 Co/6 Au/7 Co and 7 Co/6 Au/7 Co, where the numbers give the number of monolayers. Electron energy 1.2 eV, field of view $6 \times 6\,\mu m^2$ (Duden and Bauer, 1994b).

4.2.5 Small particles

The samples discussed in Sections 4.2.1–4.2.4 were continuous films. SPLEEM is also suited for the study of small particles, provided that they are single crystals with the top plane parallel to the substrate. Such studies were already attempted in the early years of SPLEEM. Pinkvos, Poppa, Bauer and Kim (1993) studied small Co particles on W(110), obtained either by growth at elevated temperature or by annealing a thick film at elevated temperature. The particles grown at elevated temperature (790 K) form elongated crystals along the W[001] direction with submicron widths and were all single domain, presumably due to the shape anisotropy. The particles obtained by annealing show a pronounced memory of the original magnetization direction in the continuous film, even in the smallest particles, which are quite irregular-shaped and have a few 100-nm diameter. More recent work aimed at the understanding of the magnetic domain structure of small particles. Fe on W(110) was chosen for this purpose because growth experiments in connection with optimizing conditions for QSE experiments (Zdyb and Bauer, 2002a) had shown a wide variety of growth shapes (Zdyb, Jalochowski, Pavlovska and Bauer, 2006). They range from more or less isometric crystals to ribbons and wires as shown in Figure 19. Several energies compete in these epitaxial crystals to different degrees, depending upon the shape of the particle: stray field energy (shape anisotropy), exchange energy, surface/interface energy, magnetoelastic anisotropy energy, and magnetocrystalline energy. In the small isometric particles the first two energies are dominating, which produces multidomain states, similar to the situation in polycrystalline particles on amorphous substrates (Cherifi *et al*., 2005). In the wires (c, d) shape anisotropy is dominating, in the ribbons all energies are relevant. In the larger flat crystals in (c, d) magnetoelastic energy produces single-domain states. It should be noted that for polycrystalline particles other methods such as X-ray magnetic circular dichroism PEEM are better suited although SPLEEM can be applied to them too, albeit with much longer image acquisition times.

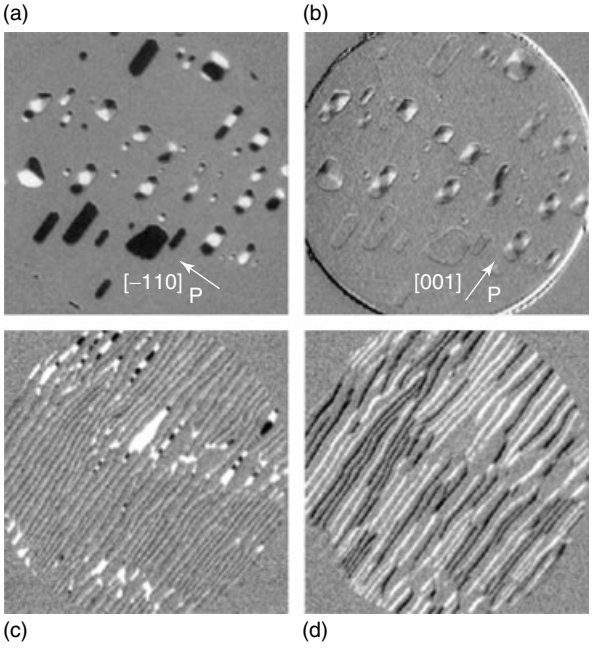

Figure 19. SPLEEM images of small epitaxial Fe crystals (a, b) and wires (c, d) obtained by annealing 5–10-ML thick films at about 700 K. The directions of the polarization and of the axes in the W(110) surface are shown in (a) and (b). Electron energy 3.5 eV, field of view 14 µm (Zdyb, Jalochowski, Pavlovska *et al*., 2006).

Finally, a study at the present resolution limits of SPLEEM should be mentioned. Micromagnetic simulations have predicted the height and thickness ranges in small hexagonal Co particles, in which single-domain and vortex domain states should (co)exist. The coexistence region ranges from about 30–40 nm width to 600–6000 nm width, depending upon thickness in the range from 1 to 10 nm. These widths are partially accessible to SPLEEM with which the thermally activated switching between the two states of Co epitaxial particles on Ru(0001) was studied (Ding *et al*., 2005).

5 SUMMARY AND OUTLOOK

In this chapter a brief overview of the field of SPLEEM was given with the goal to introduce the reader to the method and its application possibilities. Complementary, though partially overlapping, information may be found in two other recent reviews (Bauer, 2005a,b). The qualitative aspects of SPLEEM and its applications only were discussed, which does not mean that it is not possible to obtain quantitative data. Quantitative analysis of sufficiently detailed and accurate SPLEEM measurements allows extraction of many magnetic parameters that determine the direction or relative magnitude of the magnetization. Such parameters are anisotropy constants or critical exponents. It is, however, difficult to determine the absolute magnitude of the magnetization from the magnetic contrast, not only because of the complications caused by QSEs, but generally because the constant c in the magnetic contribution $c\mathbf{P}\cdot\mathbf{M}$ is not known and $|\mathbf{P}|$ is usually not known accurately either.

The strengths of SPLEEM are the high surface sensitivity and the combination of magnetic with structural information obtained in the LEEM mode via diffraction contrast, step contrast and quantum size contrast and in the LEED mode. SPLEEM of course also has its drawbacks when compared to other magnetic low-energy electron imaging methods, which do not provide the structural information. SEMPA and XMCDPEEM can be applied to amorphous and polycrystalline samples with random crystal orientation, while SPLEEM is only of limited use there. In addition, XMCDPEEM images give directly chemical information and in a SEMPA instrument this information can be obtained too if equipped with spectroscopy facilities.

The amount of information obtained till now with SPLEEM is still limited, mainly because only two home-built instruments have been available and operating until recently, partially on-off and with limited resources. The recent installation of two commercial instruments, equipped with both a spin-polarized and a high intensity LaB_6 cathode, should change this situation. The LaB_6 gun can be used for focusing so that the spin-polarized cathode does not have to have high intensity. GaAs cathodes with high polarization, but low intensity can then be used which will improve the magnetic contrast by a factor of 4–5 above the present values. This will increase the signal/noise ratio and, as a consequence, the resolution considerably, possibly to the values obtainable with the energy width-limited resolution of the cathode lens of about 5 nm. Further improvements of the resolution will require correction of the aberrations of the objective lens. While this is theoretically possible it remains to be seen whether or not it is also possible in experiment. The results from the first aberration-corrected low-energy electron microscope, the SMART (Schmidt *et al*., 2002) will have to show this in the future. Some resolution improvement has been achieved already. Another future avenue of research is time-resolved SPLEEM. This has to be done in pulsed operation of the gun, which is quite common already in high-energy physics, synchronized with pulsed changes of the magnetization. It is already used increasingly in XMCDPEEM studies. In this case the high spatial resolution alluded to above probably cannot be achieved; otherwise a too large number of pulse repetitions has to be used because of the low signal per pulse. The method is also limited to processes in which the magnetic state returns within a short time interval into the state before the pulse-induced change.

Besides these future possibilities of SPLEEM there are still many problems in the physics of ultrathin films and small

particles that can be solved with SPLEEM in its present state. Examples are (i) the influence of the lateral inhomogeneity in ultrathin films on magnetic properties, which in many cases have been studied only by laterally averaging methods. This includes the influence of steps and of the step density on SRTs and on the critical behavior; (ii) the micromagnetic aspects of the interlayer coupling; and (iii) the competition between the various anisotropies in small magnetic particles with a wide variety of shapes.

ACKNOWLEDGMENTS

The development of SPLEEM was initially supported by IBM and later by the Deutsche Forschungsgemeinschaft and by the National Science Foundation.

REFERENCES

Altman, M.S., Pinkvos, H., Hurst, J., *et al*. (1991). Spin polarized low energy electron microscopy of surface magnetic structure. *MRS Symposium Proceedings*, **232**, 125–132.

Bauer, E. (1994). Low energy electron microscopy. *Reports on Progress in Physics*, **57**, 895–938.

Bauer, E., Duden, T., Pinkvos, H., *et al*. (1996). LEEM studies of the microstructure and magnetic domain structure of ultrathin films. *Journal of Magnetism and Magnetic Materials* **156**, 1–6.

Bauer, E. (1997). Spin-polarized low energy electron microscopy. In *Handbook of Microscopy*, Amelinckx, S., Van Dyck, D., Van Landuyt J.F. and Van Tendeloo, G. (Eds.), VCH Verlagsges: Weinheim, pp. 751–759.

Bauer, E. (1998). LEEM basics. *Surface Review and Letters*, **5**, 1275–1286.

Bauer, E. (2005a). Spin-polarized low energy electron microscopy (SPLEEM). In *Modern Techniques for Characterizing Magnetic Materials*, Zhu, Y. (Ed.), Springer-Kluwer Academic Publishers: Boston, pp. 361–379.

Bauer, E. (2005b). SPLEEM. In *Magnetic Microscopy of Nanostructures*, Hopster, H. and Oepen, H.P. (Eds.), Springer: Berlin, pp. 111–136.

Bauer, E. (2006). LEEM and SPLEEM. In *Science of Microscopy*, Hawkes P. and Spence, J. (Eds.), Springer- Kluwer Academic Publishers, pp. 605–656.

Baylac, M., Adderley, P., Brittian, J., *et al*. (2005). Effects of atomic hydrogen and deuterium exposure on high polarization GaAs photocathodes. *Physical Review Special Topics - Accelerators Beams*, **8**, 123501-1–123501-11.

Biagioni, P., Brambill, A., Portalupi, M., *et al*. (2005). Magnetic properties of Fe/NiO/Fe(001) trilayers. *Journal of Magnetism and Magnetic Materials*, **290-291**, 153–156.

Biedermann, A., Tscheliessnig, R., Schmid, M. and Varga, P. (2001). Crystallographic structure of ultrathin Fe films on Cu(100). *Physical Review Letters*, **87**, 086103-1–086103-4.

Biedermann, A., Tscheliessnig, R., Schmid, M. and Varga, P. (2004). Local atomic structure of ultra-thin Fe films grown on Cu(100). *Applied Physics A*, **78**, 807–816.

Bulou, H., Scheurer, F., Ohresser, P., *et al*. (2004). Structure of self-organized Fe clusters grown on Au(111) analyzed by grazing incidence X-ray diffraction. *Physical Review B*, **69**, 155413-1–155413-6.

Cherifi, S., Hertel, R., Kirschner, J., *et al*. (2005). Virgin domain structures in mesoscopic Co patterns: comparison between simulation and experiment. *Journal of Applied Physics*, **98**, 043901-1–043901-6.

Chmelik, J., Veneklasen, L. and Marx, G. (1989). Comparing cathode lens configurations for low energy electron microscopy. *Optik*, **83**, 155–160.

Dekadjevi, D.T., Hickey, B.J., Brown, S., *et al*. (2005). Structural phase transition of Fe grown on Au(111). *Physical Review B*, **71**, 054108-1–054108-7.

Ding, H.F., Pütter, S., Oepen, H.P. and Kirschner, J. (2001). Spin-reorientation transition in thin films studied by the component-resolved Kerr effect. *Physical Review B*, **63**, 134425-1–134425-7.

Ding, H.F., Schmid, A.K., Li, D., *et al*. (2005). Magnetic bistability of Co nanodots. *Physical Review Letters*, **94**, 157202-1–157202-4.

Duden, T. and Bauer, E. (1995). A compact electron spin polarization manipulator. *Review of Scientific Instruments*, **66**, 2861–2864.

Duden, T. (1996). Ph.D. thesis, Technical University Clausthal.

Duden, T. and Bauer, E. (1996). Magnetization wrinkle in thin ferromagnetic films. *Physical Review Letters*, **77**, 2308–2311.

Duden, T. and Bauer, E. (1997). Magnetic domain structure and spin reorientation transition in the system Co/Au/W(110). *MRS Symposium Proceedings*, **475**, 283–288.

Duden, T. and Bauer, E. (1998). Spin-polarized low energy electron microscopy. *Surface Review and Letters*, **5**, 1213–1220.

Duden, T. and Bauer, E. (1999a). Influence of Au and Cu overlayers on the magnetic structure of Co films on W(110). *Physical Review B*, **59**, 468–473.

Duden, T. and Bauer, E. (1999b). Biquadratic exchange in ferromagnetic/nonferromagnetic sandwiches: a spin-polarized low-energy electron microscopy study. *Physical Review B*, **59**, 474–479.

Duden, T. and Bauer, E. (1999c). Exchange coupling in Co/Cu/Co sandwiches studied by spin-polarized low energy electron microscopy. *Journal of Magnetism and Magnetic Materials*, **191**, 301–312.

Duden, Th., Zdyb, R., Altman, M.S. and Bauer, E. (2001). Micromagnetic and microcrystalline structure of ultrathin Co layers on W single crystal surfaces. *Surface Science*, **480**, 145–152.

Graf, J., Jozwiak, C., Schmid, A.K., *et al*. (2005). Mapping the spin-dependent electron reflectivity of Fe and Co ferromagnetic films. *Physical Review B*, **71**, 144429-1–144429-5.

Grzelakowski, K., Duden, T., Bauer, E., *et al*. (1994). A new surface microscope for magnetic imaging. *IEEE Transactions on Magnetics*, **30**, 4500–4502.

Grzelakowski, K. and Bauer, E. (1996). A flange-on type low energy electron microscope. *Review of Scientific Instruments*, **67**, 742–747.

Herlt, H-J., Feder, R., Meister, G. and Bauer, E. (1981). Experiment and theory of the elastic electron reflection coefficient from tungsten. *Solid State Communications*, **38**, 973–976.

Hong, J. and Mills, D.L. (2000). Spin dependence of the inelastic mean free path in Fe and Ni: explicit calculations and implications. *Physical Review B*, **62**, 5589–5600.

Hopster, H. (1999). Spin-dependent mean free path of low-energy electrons in ferromagnetic materials. *Journal of Electron Spectroscopy and Related Phenomena*, **98-99**, 17–23.

Kerkmann, D., Pescia, D., Krewer, J.W. and Vescovo, E. (1991). Low energy electron oscillations during epitaxial growth of thin films. *Zeitschrift fur Physik B*, **85**, 311–314.

Man, K.L., Altman, M.S. and Poppa, H. (2001a). Spin-polarized low energy electron microscopy investigations of magnetic transitions in Fe/Cu(100). *Surface Science*, **480**, 163–172.

Man, K.L., Ling, W.L., Paik, S.Y., *et al*. (2001b). Modification of the initial growth and magnetism in Fe/Cu(100). *Physical Review B*, **65**, 024409-1–024409-11.

Man, K.L., Zdyb, R., Huang, S.F., *et al*. (2003). Growth morphology, structure and magnetism of ultrathin Co films on W(111). *Physical Review B*, **67**, 184402-1–184402-11.

Maruyama, T., Luh, D-A., Brachmann, A., *et al*. (2003). Atomic hydrogen cleaning of polarized GaAs photocathodes. *Applied Physics Letters*, **82**, 4184–4186.

Maruyama, T., Luh, D-A., Brachmann, A., *et al*. (2004). Systematic study of polarized electron emission from strained GaAs/GaAsP superlattice photocathodes. *Applied Physics Letters*, **85**, 2640–2642.

Pastuszka, S., Hoppe, M., Kratzmann, D., *et al*. (2000). Preparation and performance of transmission-mode GaAsphotocathodes as sources for cold dc electron beams. *Journal of Applied Physics*, **88**, 6788–6800.

Petit, E.J. and Houzay, F. (1994). Optimal surface cleaning of GaAs(001) with atomic hydrogen. *Journal of Vacuum Science and Technology B*, **12**, 547–550.

Pierce, D.T. (1995). Spin-polarized electron sources. In *Experimental Methods in the Physical Sciences*, Dunning, F.B. and Hulet, R.G. (Eds.), Academic Press: San Diego, pp. 1–38, Vol 29A.

Pierce, D.T., Celotta, R.J., Wang, G.C., *et al*. (1980). GaAs spin polarized electron source. *Review of Scientific Instruments*, **51**, 478–499.

Pinkvos, H., Poppa, H., Bauer, E. and Kim, G-M. (1993). A time-resolved SPLEEM study of magnetic microstructure in ultrathin Co films on W(110). In *Magnetism and Structure in Systems of Reduced Dimension*, Farrow, R.F.C., Dieny, B., Donath, M., *et al.* (Eds.), Plenum Press: New York, pp. 25–31.

Plihal, M. and Mills, D.L. (1998). Spin-flip exchange scattering of low-energy electrons in ferromagnetic iron. *Physical Review B*, **58**, 14407–14415.

Poppa, H., Pinkvos, H., Wurm, K. and Bauer, E. (1993). Spin Polarized Low Energy Electron Microscopy (SPLEEM) of Single and Combined Layers of Co, Cu and Pt on W(110). *MRS Symposium Proceedings*, **313**, 219–226.

Poppa, H., Tober, E.D. and Schmid, A.K. (2002). *In situ* observation of magnetic domain pattern evolution in applied fields by spin-polarized low energy electron microscopy. *Journal of Applied Physics*, **91**, 6932–6934.

Ramchal, R., Schmid, A.K., Farle, M. and Poppa, H. (2004a). Magnetic domains and domain-wall structure in Ni/Cu(001) films imaged by spin-polarized low-energy electron microscopy. *Physical Review B*, **68**, 054418-1–054418-5.

Ramchal, R., Schmid, A.K., Farle, M. and Poppa, H. (2004b). Spiral-like continuous spin-reorientation transition of Fe/Ni bilayers on Cu(100). *Physical Review B*, **69**, 214401.

Scheunemann, T., Feder, R., Henk, J., *et al*. (1997). Quantum well resonances in ferromagnetic Co films. *Solid State Communications*, **104**, 787–792.

Schmidt, Th., Groh, U., Fink, R., *et al*. (2002). XPEEM with energy-filtering: advantages and first results from the SMART project. *Surface Review and Letters*, **9**, 223–232.

Siegmann, H.C. (1994). Surface and 2D magnetism with spin polarized cascade electrons. *Surface Science*, **307-309**, 1076–1086.

Tober, E.D., Witte, G. and Poppa, H. (2000). Variable temperature and *ex situ* spin-polarized low-energy electron microscope. *Journal of Vacuum Science and Technology A*, **18**, 1845–1847.

Toulemonde, O., Petrov, V., Naid Abdi, A. and Bucher, J.P. (2004). Magnetic anisotropies of ultrathin Fe films on Au(111) as a function of iron thickness and gold capping. *Journal of Applied Physics*, **95**, 6565–6567.

Unguris, J., Scheinfein, M.R., Celotta, R.J. and Pierce, D.T. (1989). Magnetic microstructure of the (0001) surface of hcp cobalt. *Applied Physics Letters*, **55**, 2553–2555.

Vedmedenko, E.Y., Oepen, H.P. and Kirschner, J. (2002). Microstructure of the spin reorientation transition in second-order approximation of magnetic anisotropy. *Physical Review B*, **66**, 214401-1–214401-5.

Wu, Y.Z., Schmid, A.K., Altman, M.S., *et al*. (2005). Spin-dependent Fabry-Perót interference from a Cu thin film grown on fcc Co(001). *Physical Review Letters*, **94**, 027201-1–027201-4.

Wurm, K. (1994). M.S. Thesis, Technical University Clausthal.

Zdyb, R. and Bauer, E. (2002a). Spin dependent quantum size effects in the electron reflectivity of ultrathin ferromagnetic crystals. *Surface Review and Letters*, **9**, 1485–1491.

Zdyb, R. and Bauer, E. (2002b). Spin-resolved unoccupied electronic band structure from quantum size oscillations in the reflectivity of slow electrons from ultrathin ferromagnetic crystals. *Physical Review Letters*, **88**, 166403-1–166403-4.

Zdyb, R. and Bauer, E. (2003). Magnetic domain structure and spin-reorientation transition in ultrathin Fe-Co alloy films. *Physical Review B*, **67**, 134420-1–134420-8.

Zdyb, R. and Bauer, E. (2007). Coexistence of ferromagnetism and paramagnetism in a ferromagnetic monolayer, *to be published*.

Zdyb, R., Jalochowski, M., Pavlovska, A. and Bauer, E. (2006). Self-organized Fe nanostructures on W(110). *Surface Science*, **600**, 1586–1591.

Zhang, R. and Willis, R.F. (2001). Thickness-dependent curie tempetures of ultrathin magnetic films: effect of the range of spin-spin interactions. *Physical Review Letters*, **86**, 2665–2668.

Scanning Electron Microscopy with Polarization Analysis

Hans Peter Oepen and Robert Frömter
Universität Hamburg, Hamburg, Germany

1 INTRODUCTION

'Magnetism goes nano' is the slogan that describes best the activities in research on ferromagnetic systems. Those activities include basic research, as well as the research related to applications in profit oriented industrial development laboratories. As still a big business can be made with storage media, the trend goes toward higher density, that is, smaller bit structures, to compete with new storage devices like flash memories. In basic research, the dimensionality plays a fascinating role, as the size can be reduced to the limits where the collective phenomenon 'ferromagnetism' will be affected. Questions for the transition from atomic via molecular magnetism to ferromagnetism come into the reach of feasibility, promising new and highly interesting insight into collective phenomena. To perform such studies it is equally important to fabricate and to analyze such structures and devices. In this contribution, we will focus on a microscopy technique for magnetic structure analysis that bridges the scales from micrometers to nanometers, that is, spin-SEM (for scanning electron microscopy) or SEMPA (for scanning electron microscopy with polarization analysis). Besides its application in basic research, this technique has developed into a versatile tool for solving problems in development and even production of commercial devices.

With recent improvements in different components of SEMPA and in sample preparation, spin-SEM is now applicable for the investigation of all kinds of ferromagnetic systems. This ensures the technique its importance in competition with the high resolving scanning probe techniques **Scanning Probe Techniques: MFM and SP-STM, Volume 3**. The latter show an ultrahigh sensitivity for surface morphology and chemical composition on the atomic scale, which limits their applicability to systems exhibiting perfect smooth surfaces. This is commonly at variance with fabrication processes of devices. Transmission electron microscopy based techniques, like Lorentz microscopy **Lorentz Microscopy of Thin-film Systems, Volume 3** or electron holography **Electron Holography of Ferromagnetic Materials, Volume 3**, cover a similar range of scales as SEMPA. Utilizing special detector layouts (differential phase contrast technique (Chapman, Batson, Waddell and Ferrier, 1978)), scanning transmission electron microscopes can show a similar suppression of morphological structures like spin-SEM. In comparison to transmission electron microscopy techniques, however, SEMPA needs no massive

Handbook of Magnetism and Advanced Magnetic Materials. Edited by Helmut Kronmüller and Stuart Parkin. Volume 3: *Novel Techniques for Characterizing and Preparing Samples*. ISBN: 978-0-470-02217-7.

sample manipulation, like reducing the thickness to some 10 nm. Spin-SEM can be applied to investigate samples or devices in exactly the same setup they are intended for use in commercial systems. Particularly the control of industrial fabrication processes for media and devices will create an increasing demand for spin-SEM investigation in the future.

In this contribution, we will introduce the SEMPA technique with special emphasis on the scientific basics and less on the technical realization. The aim is to make a broader audience familiar with the technique, so that the nonexpert in magnetic microscopy gets information at his hand that helps decide whether the technique is suitable to solve his problems or not.

The chapter is organized as follows: In Section 2, the basics of spin-polarized secondary electron (SE) emission is presented, whereas in the succeeding section, the implications of the physical process for the instrument are discussed and principal design features and properties of SEMPA are worked out. We also discuss some drawbacks that result exclusively from the related physics. A state-of-the-art spin-SEM is presented in the following section, that is, a new generation of SEMPA that has been realized quite recently. The specifications will be given and discussed in the framework of design criteria that were realized. In Section 5, the application of spin-SEM will be demonstrated by means of the results obtained with different samples. Here, we focus on the unique features of the techniques although their limits are also shown.

2 BASICS OF SPIN-POLARIZED SECONDARY ELECTRON EMISSION

When a solid is irradiated by electrons with energies in the range of a few kiloelectron volts, electrons are reemitted showing a well-known energy distribution, which is sketched in Figure 1 (Reimer, 1998). The elastically scattered electrons create a sharp peak at the primary energy (E_0), followed by structures that are due to electrons, which have excited plasmons. On the flat background at lower energies, there are small structures that originate from Auger electrons (100–2000 eV), and finally at very low energies a pronounced intensity maximum is found. Electrons in that energy range are called *true* secondary electrons. While most of the higher-energy electrons that create structures in the distribution are used in solid state and surface physics for investigating the properties of matter, the electrons below 50 eV are used in SEM in general to visualize the morphology of surfaces. Owing to the high SE intensity, good statistics can be achieved and fast image acquisition is possible. These low-energy electrons are created in a cascade process by multiple inelastic scattering of the incident electrons and the inelastic scattering of the excited electrons that are created during preceding inelastic processes. The electrons in the low-energy tail have undergone strong interactions with electronic states around the Fermi energy during their emission process.

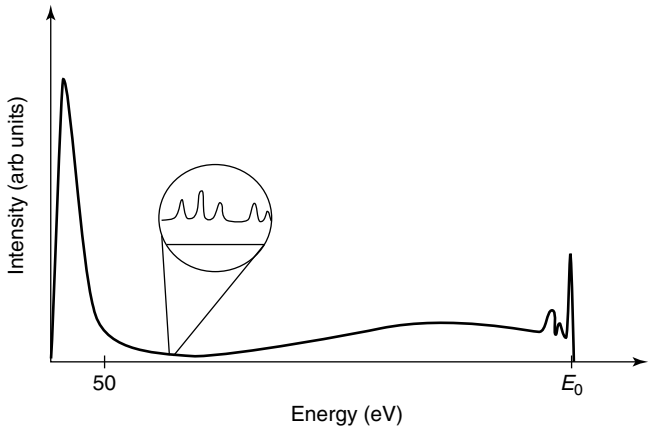

Figure 1. Intensity distribution of electrons leaving a surface, when bombarded by electrons with energy E_0. The small peak at E_0 is due to the elastically scattered electrons. As an inset, the small peaks that appear due to Auger processes are shown enlarged. Those electron energies are determined by energy levels of the atom that was excited by the primary electron. Auger electrons are used to study the chemical composition of surfaces in an energy range from 100 to 2000 eV. At very low energies, the secondary electrons generate a strong maximum. In scanning electron microscopy, the electrons below 50 eV are often called *true secondaries*.

Itinerant ferromagnets show a strong imbalance of the so-called spin-up and spin-down electrons at the Fermi level. In that nomenclature, spin-up/-down means antiparallel/parallel alignment of the electron spin with respect to the sample magnetization. Hence, owing to the aforementioned strong interaction in SE emission, one should expect some signature of this spin imbalance in the low-energy SE. Indeed, in the first investigation of spin-polarized SE emission a strong polarization of those electrons was found (Chrobok and Hofmann, 1976). Subsequent studies of the energy dependence of the spin polarization revealed a polarization enhancement for SE with energies below ∼10 eV, that is, polarization values higher than the averaged electron polarization at the Fermi energy (Figure 2). The polarization decreases with increasing SE energy. Above ∼30 eV the polarization value is that of the average polarization of the electrons at the Fermi energy P_F (Figure 2). The enhancement of the polarization scales roughly with the polarization value at E_F, which means that the polarization at low energies P_0 becomes larger in the row Ni, Co to Fe. For Fe, a polarization $P_0 \sim 48–50\%$ was found (Kisker, Gudat and Schröder, 1982; Unguris, Pierce, Galejs

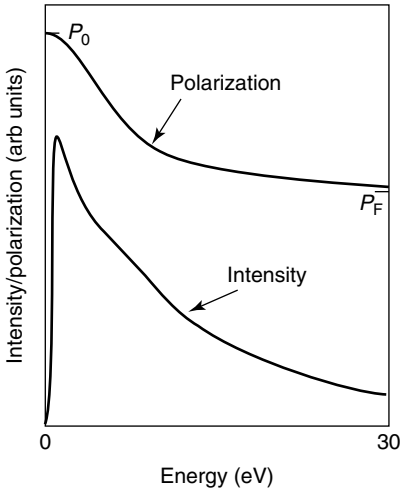

Figure 2. Intensity and polarization distribution of secondary electrons from an itinerant ferromagnet. The polarization is highest at the very low energies where the intensity also peaks. For secondary electron energies above 30 eV, the polarization value merges into the value P_F that is roughly the averaged polarization of electrons at the Fermi level. P_0 values differ for the different itinerant ferromagnets. It is highest for Fe and lowest for Ni.

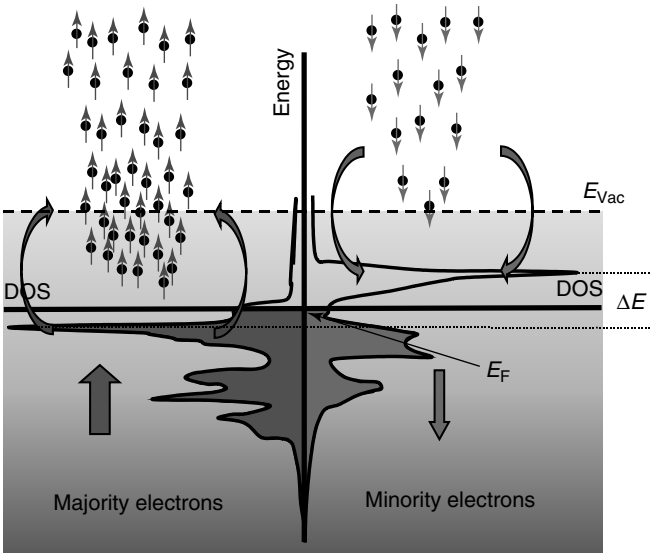

Figure 3. Spin-resolved density of states for a hypothetical itinerant ferromagnet. The electrons with minority spin have a high density of states above the Fermi level while majority spin electrons occupy states below E_F. The shaded energy range indicates the band states below the vacuum level (E_{Vac}). Electrons above E_{Vac} can leave the solid and contribute to the secondary electrons. A rough sketch of the filtering processes that cause the enhanced polarization is given. The energy loss due to Stoner excitations is on the average ΔE.

and Celotta, 1982; Hopster *et al*., 1983; Hammond, Fahsold and Kirschner, 1992; Kirschner, 1988).

The enhancement is commonly believed to originate from the cascade process of SE creation. In an itinerant ferromagnet, a filtering mechanism is effective due to the different density of states for up and down electrons. Roughly speaking, as the inelastic electron/electron scattering can only proceed via states around the Fermi level, the density of states at E_F determines the scattering probability. There are two processes involved in the inelastic scattering: on the one hand, the scattering of electrons with energies well above E_F into lower lying energy states and on the other hand, the simultaneous excitation of electrons into higher states due to energy conservation.

For minority spins, there are a great number of unoccupied states available above E_F, while almost all the majority states around E_F are occupied (see Figure 3). This means that preferably minority spin electrons are scattered into states around E_F and are filtered out of the electrons that will be emitted ($E > E_{Vac}$). For electrons with majority spin the probability for inelastic scattering is very small (Figure 3), due to a negligibly small number of states above E_F. On the other hand, if the energy difference that is available for excitation is in the range of a few electron volts, that is, when electrons with energy slightly above E_F are scattered into lower lying states, the electrons that can be excited will originate exclusively from states close to E_F. Hence, mostly electrons of majority spin character are excited, because close to the Fermi energy the occupied states are mostly majority states. In summary, with decreasing electron energy the possibility to filter out minority and excite majority electrons increases for electron energies around and below the vacuum level. Owing to the multiplication that happens within the emission process, the polarization enhancement is created.

If there is no considerable imbalance of the density of states at E_F for spin-up and spin-down electrons, the SE polarization will be very small if any is found at all. This will happen in the so-called localized ferromagnets, which have a magnetization that is originating from the occupation of inner shell states. The effect of the localized magnetic moments on the spin polarization of the conduction band electrons is generally very small. Hence, when utilizing the SE spin polarization as a tool for investigating ferromagnetism, this class of materials is out of range. This obstacle can be partially overcome when the material is covered with an ultrathin itinerant ferromagnet layer (so-called dusting, see the following text). This layer often mirrors the domain structure of the material underneath while it fulfills the requirements for SEMPA imaging.

The above-sketched process is associated with a net energy loss, as the electron that loses energy falls into states above E_F, while the excited electron comes from states

below E_F. In total, the electron exchange creates electrons with opposite spin and a mean energy loss ΔE. Roughly speaking, ΔE is, on the average, the energy difference of the maxima of the two densities of states (Figure 3). The above described interaction process in ferromagnets is called *Stoner excitation* (for an overview, see Feder, 1985).

The very existence of low-energy losses (in the range <5 eV), particularly in combination with a high scattering cross section, has a strong impact on the information depth for the electron spin polarization. It was found that the polarization is determined by the topmost layers of the ferromagnet, that is, the information depth is extremely small. For 3d ferromagnets, the latter amounts to about 5 atomic layers (Abraham and Hopster, 1987). This finding is puzzling, as it apparently contradicts the general trend, predicted for the so-called mean free path. The master or universal curve (Ibach, 1977; Seah and Dench, 1979) gives a mean free path in the range of 10 nm (30–50 atomic layers) for electrons with energies below 10 eV. As this universal curve is used in electron spectroscopy to estimate escape depths for higher-energy electrons, it only takes energy losses above 10 eV into consideration. This assumption is strongly oversimplifying the physics of electron scattering at energies a few electron volts above E_F. More recent compilations of mean free path data indicate much smaller values for certain transition metals and thus a deviation from a universal-curve behavior at low energies (Powell and Jablonski, 1999). In fact, it has been found that the d holes in 3d transition metals are responsible for strong electron–electron inelastic interaction that gives an appropriately short mean free path for low-energy electrons (Schönhense and Siegmann, 1993). Since in a ferromagnet these d holes are also spin polarized, a strongly spin-dependant mean free path can be expected (Schönhense and Siegmann, 1993; Hong and Mills, 2000). As a matter of fact the low losses and hence the small depth of information are striking when the spin polarization is taken into consideration.

As the quantization axis for the spin is given by the magnetic field **B** inside the sample, the spin polarization of the SE has a well-defined direction in real space and in general reveals the orientation of the magnetization of the ferromagnet (Unguris, Pierce, Galejs and Celotta, 1982; Kirschner and Suga, 1987). As the charge of the electrons is negative by definition, the magnetic moment of electrons is antiparallel to its angular momentum. The polarization that is defined via the angular momentum is thus antiparallel to the magnetization vector.

In conclusion, the physical processes of SE emission give a polarization enhancement at the very low energies, that is, exactly in the range where the SE intensity is high. The polarization is antiparallel to the magnetization. The polarization value is highest for Fe and decreases from Co to Ni. The low-energy losses, that is, the Stoner excitations, dominate the scattering processes and are responsible for the very small depth of information for electron polarization.

3 GENERAL CONSIDERATIONS

The physics of SE emission sets the limits and dictates the prerequisites for the microscopy of magnetic structures utilizing SE. In this paragraph, we will present the general features of a spin-SEM and will work out how the physics of SE emission implies certain solutions. In the conventional SEM, the true SEs, which have the highest intensity in the whole electron energy spectrum, are used for imaging. High intensity is superior for imaging techniques, as it makes quick measurement with high signal-to-noise ratio feasible. The fact that in SE emission from itinerant ferromagnets the highest polarization coincides with highest intensity brought about ideas and conjectures for a new imaging technique for magnetic structures (DiStefano, 1978; Celotta and Pierce, 1982; Kirschner, 1984).

The idea is to use a very narrow primary beam for SE creation and determine the SE spin polarization at the very low energies (Figure 4) to obtain a local information about the magnetization with high spatial resolution. Measuring the orientation of polarization gives the full information about the magnetization vector, as polarization and magnetization are antiparallel (according to the properties of spin-polarized SE emission). The latter proposition makes the vector analysis of the spin polarization desirable. Putting the pieces together, the basic idea is to measure the polarization orientation point

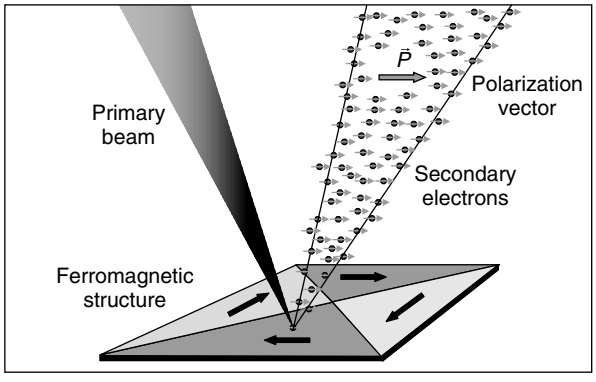

Figure 4. Principle of a spin-SEM. The primary beam creates SE at the sample surface. The SE are spin polarized. The polarization is antiparallel to the magnetization at the emission spot. Measuring the orientation of polarization reveals the magnetization orientation. Scanning the primary beam across the surface gives the lateral distribution of the magnetization orientation, that is, the domain structure.

by point using the smallest possible spot size for the impinging electron beam. The resulting polarization distribution is identical (except for the sign) to the local distribution of the magnetization orientation, that is, the micromagnetic or domain structure of the ferromagnet. From that basic consideration, it is evident that the geometry of the experiment is quite similar to that of SEM. In particular, it means that the experiment is performed in reflection and sample thickness and composition are no matters of concern.

To create the ultrafine, so-called primary, electron beam, it was conjectured to utilize a SEM column and combine a SEM and a spin-polarization analyzer. The result is a new microscope that was called *spin-SEM* or *SEMPA* (for SEM with polarization analysis). The unique feature of this type of microscope is that it gives direct access to the distribution of the magnetization orientation (as vectorial quantity), which is identical to the magnetic structure that is of interest.

The extremely low depth of information, which is synonymous with high surface sensitivity, has strong implications for the realization of a spin-SEM. First of all it means that the surface of the sample under investigation has to be absolutely clean. Therefore, any surface pollution by oxidation, contamination, or any remains of a pretreatment have to be avoided. Even contamination due to handling of samples under ambient conditions can cause the total loss of the polarization signal. In general, this means that surface preparation techniques have to be available in the microscope to produce clean ferromagnetic surfaces *in situ*. Ion milling (or sputtering) is commonly used to remove contamination layers from surfaces. Alternatively, one can deposit a ferromagnetic layer that gives a fresh clean surface. The deposited film usually adopts the magnetic structures of the underlying sample. Even when the sample surface has been perfectly prepared, the surface has to stay clean during investigation. With data acquisition times in the range of minutes, one can estimate the vacuum that is required to perform such investigations. It becomes evident that the microscope has to operate under ultrahigh vacuum (UHV) conditions and has to be equipped with sputtering and evaporation facilities.

Apparently, the high surface sensitivity seems to be a disadvantage of the technique, as it requires the very sophisticated and expensive equipment known from surface science experiments. We will demonstrate, however, in the course of this chapter that this property can be very advantageous as well, because in combination with ultrathin films it gives access to a large class of samples for investigation by SEMPA. To stress the point once more: imaging of magnetic structures utilizing spin-polarized SE emission works only with clean surfaces and experiments have to be performed under UHV conditions.

From the above considerations, the general setup can be easily imagined (Figure 5). The basic components of the instrument are the SEM column and the spin-polarization analyzer. The microscope is run under UHV conditions, which means that all equipment including the SEM column has to be UHV compatible.

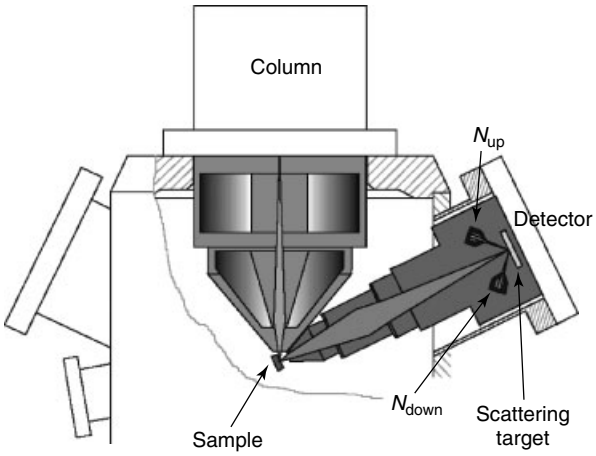

Figure 5. Sketch of a SEMPA setup. Main components are the SEM column and the spin detector, including the electron optics that focuses the SE onto the detector crystal. Two out of four counting facilities are displayed. The oppositely oriented diffracted beams give access to the polarization component perpendicular to the plane of drawing.

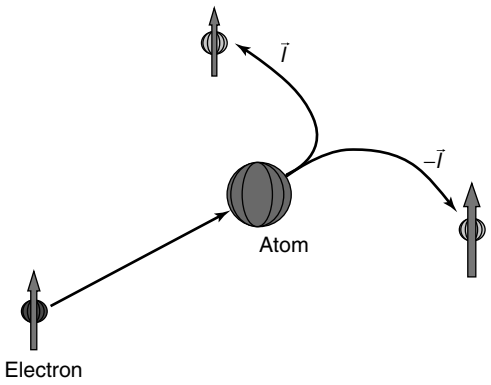

Figure 6. Sketch of the scattering of electrons at atoms. Depending on the direction in which the electrons are scattered, an angular momentum is defined. Scattering into opposite angles gives opposite angular momenta and thus opposite orbital magnetic momenta. The interaction of the electron spin with the orbital momenta is responsible for the increase/decrease of the scattering energy and thus for different cross sections. A scattering asymmetry is found.

The spin polarization of electrons is measured by means of a scattering experiment. Owing to the coupling of the electron spin and the orbital momentum (Figure 6) a right/left asymmetry can be found. It means that the scattering intensities under opposite angles are different. The asymmetry is proportional to the polarization of the incoming electrons. More

precisely, the asymmetry is proportional to the polarization component that is perpendicular to the scattering plane, spanned by the incoming and scattered electron beams. To achieve direct correlation and easy interpretation in polarization detectors, normal incidence geometry is chosen and the scattering intensities are measured under opposite angles. In Figure 5, two scattered beams and corresponding detectors are displayed (named N_{up} and N_{down}). They are used to determine the polarization component that is perpendicular to the plane of drawing, that is, the scattering plane. Additionally, a second scattering asymmetry can be determined in a direction perpendicular to the first one. The according polarization component is in the plane of drawing (parallel to the surface of the scattering target). The corresponding scattered beams point out of or into the plane of drawing.

To maximize the number of SEs that enter the detector, a specifically designed electron optics is mounted in front of the analyzer. This optics focuses the SE into the detector while enlarging the angle of acceptance of the detector. The ultimate aim is to bring all the SEs emitted into the half-space into the analyzer.

All successful realizations of spin-SEM worldwide look pretty much the same and comprise those above-mentioned basic components. For a listing, see for instance in Oepen and Hopster (2005, p. 137). The individual microscopes differ with respect to the SEM columns and the polarization detectors that are used. While the performance and features of the various commercially available SEM columns can be easily obtained from the companies selling SEM, the spin-polarization analyzers are somewhat more exotic and will be briefly discussed next.

The high-energy scattering at the cores of materials with high atomic number is used in Mott detectors for polarization analysis (typical energies 20–100 keV) (Koike and Hayakawa, 1984; Allenspach, 1994; Iwasaki, Takiguchi and Bessho, 1997; Stamm *et al*., 1998; Hopster, 1999). A gold foil is used as scattering target. The scattering angles are 120° with respect to the momentum of the incident electrons (Kessler, 1985; Barnes, Mei, Lairson and Dunning, 1999). Mott detectors are bulky for high-voltage insulation reasons.

The second type of detector is based on the low-energy electron diffraction (LEED detector) at single crystal surfaces (Kirschner and Feder, 1979; Kirschner, 1985). The scattering is performed at a W(001) surface. The (2,0) diffraction beams at 104.5 eV are taken for the polarization analysis (Frömter, Oepen and Kirschner, 2003).

A second low-energy concept is based on the diffuse scattering of electrons at polycrystalline Au films (low-energy diffuse scattering (LEDS) detector) (Scheinfein *et al*., 1989; Hembree, Unguris, Celotta and Pierce, 1987) at a scattering energy of 150 eV.

What is common for all the above-mentioned detectors is a very low efficiency for polarization analysis, that is, in the range of 10^{-4} (Scheinfein *et al*., 1990). In other words, 1 electron in 10 000 contributes to the polarization analysis. This is a disadvantage as it puts strong requirements on the specification of every instrument component and makes an optimized tuning absolutely necessary. In particular, for the SEM column this means that the primary current should be as high as possible, while the lateral resolution must be high at the same time. Some rough estimations reveal that a primary current in the range of 10^{-9} A is desirable to obtain reasonable measuring times (Oepen and Hopster, 2005). Standard thermionic emitters fail as electron source, because currents in that range are available only at the cost of spatial resolution (Reimer, 1998). The best choice under the prerequisite of good spatial resolution and high current is the field emission (FE) column (especially thermally assisted FE or Schottky guns). The number of SEs per incoming electron depends on the primary energy. Particularly at energies above 10 keV the SE yield decreases and drops by more than a factor of 3 with respect to the values at energies around 1 keV (Kirschner, 1988). Hence, it is recommendable to run the SEM column in a low voltage mode. Such working parameters are usually at variance with high spatial resolution and high primary intensities. The best compromise between resolution and SE intensity has to be experimentally found – it usually depends also on the sample under investigation. Again, FE columns can meet the requirements of high resolution, high primary current at low primary energy best.

Secondly, the electron optics and the polarization analyzer have to be optimized in the sense, that all the SE created by the primary current should be collected and focused into the analyzer. For optimization, the convolution of the SE energy distribution of polarization/intensity and the detector analyzing properties, like permissible angle and energy spread, have to be considered (Oepen and Hopster, 2005). The latest generation of a spin-SEM has been realized recently (Kohashi and Koike, 2001; Frömter, Oepen and Kirschner, 2003). We will discuss the obtained performance of our system and compare it with the idealized system in the following paragraph.

As mentioned above, the polarization detector measures the left/right asymmetry of scattered electrons. The spin-orbit coupling is the relevant effect and its contribution is small in comparison to the electrostatic (Coulomb) scattering. To separate the spin-dependent part from the much larger 'background' the normalized intensity difference between right and left scattering intensity is constructed. The scattering asymmetries

$$A_{\mathrm{vert}} = \frac{(N_{\mathrm{right}} - N_{\mathrm{left}})}{(N_{\mathrm{right}} + N_{\mathrm{left}})}, A_{\mathrm{horz}} = \frac{(N_{\mathrm{up}} - N_{\mathrm{down}})}{(N_{\mathrm{up}} + N_{\mathrm{down}})} \quad (1)$$

are proportional to the polarization, that is, the polarization component perpendicular to the respective scattering planes. The proportionality factor is the inverse of the sensitivity S (in Mott scattering called *Sherman function* (Kessler, 1985)). A 100% polarized electron beam gives an asymmetry of S. For Mott and LEED detector the sensitivity is $\sim$25% and considerably higher than S for the LEDS detector ($\sim$11%). As a general rule, one may say that the higher the sensitivity, the easier is the handling of the spin-SEM, as the system is less sensitive to slight misalignments in the detector and electron optics that cause apparatus or device asymmetries. Owing to the normalization procedure, the surface morphology is suppressed and a strong magnetic contrast can be attained.

4 REALIZATION OF A SPIN-SEM UTILIZING A LEED DETECTOR

The preceding section discussed general considerations for the implementation of spin analysis in SEM. In the following, we will exemplarily present the realization and the performance of a particular instrument. The spin-SEM, which has been realized in our laboratory, consists of a modern UHV compatible Schottky-emission SEM column and a LEED spin-polarization detector. The LEED detector has been chosen for several reasons: At first, the compact size guarantees highest flexibility with little space required for the polarization analyzer. Secondly, the angular and energy acceptance of the LEED scattering process can be well matched to the broad energy and angular spread of SE emission. This allows for comparatively high detection efficiency, since a large amount of SE contributes to the spin analysis, while the apparatus asymmetry, caused by scanning of the primary beam, can be kept low. Details will be given below. Not least, the use of the LEED detector for SEMPA has been pioneered in our lab almost 20 years ago (Oepen and Kirschner, 1989; Oepen and Kirschner, 1991). The detector discussed here represents the third generation of ongoing improvement and miniaturization processes.

4.1 Overview

The complete experimental setup consists of two vacuum chambers, one for microscopy and the other for sample preparation, including thin-film fabrication. The whole system can be baked to at least 150 °C and is operated in the low 10^{-10} mbar residual pressure regime. Under these conditions, the magnetic contrast from an iron sample has proved to be useful for several days. Samples can be quickly inserted into the microscopy chamber by means of a load lock and can be further transferred into the preparation chamber under UHV.

One design criterion has been to achieve as much flexibility as possible for applying the high resolving electron beam from the SEM column. For that purpose, several UHV ports have been orientated with straight view onto the sample. On such flanges, there are mounted the spin analyzer, a sputter gun, a hemispherical energy analyzer, and an electron beam evaporator for iron film deposition. In order to achieve high detection efficiency, it is important to keep the distance sample/detector optics small. For that reason the spin detector can be retracted, which maintains unhindered sample access for other devices. The hemispherical analyzer, which is also retractable, can be used for Auger electron spectroscopy. In combination with the SEM column, this opens up the possibility for spatially high resolution chemical analysis, that is, scanning Auger microscopy (SAM).

4.2 The SEM column

The UHV version of the Zeiss Gemini system is used in our microscope. This column was designed as primary source for SAM and SEMPA. It is equipped with a Schottky FE cathode and a combined electromagnetic/electrostatic objective lens. The electron optical properties are superior to conventional microscopes, as the column combines high current with high spatial resolution, even at relatively low primary beam energies. It thus fits very well the requirements for a SEM column to be used in spin-SEM. At a working distance of 8 mm, a resolution of 7.5 nm is specified for a beam current of 1 nA at 3 keV primary energy. This current value fits well into the range that offers good working conditions (Hopster and Oepen, 2005), while the low primary energy is superior as it allows to operate close to the energy range where the SE yield becomes maximum (Hopster and Oepen, 2005).

4.3 Geometric design considerations

As mentioned in the previous sections, the important issue for a good working spin-SEM is to maximize the angular acceptance of the polarization analyzer. For that reason, a normal takeoff geometry is chosen, as illustrated in Figure 7. Additionally, the distance between sample and detector optics is minimized. The SEs are accelerated into the optics by means of high potentials at the first elements of the optics. The first condition puts strong limitations on the geometrical arrangement. The angle between SEM column and detector optics should be much smaller than 90° to maintain an acceptable tilt angle with respect to the column axis. A too large sample tilt would cause a serious deterioration of image

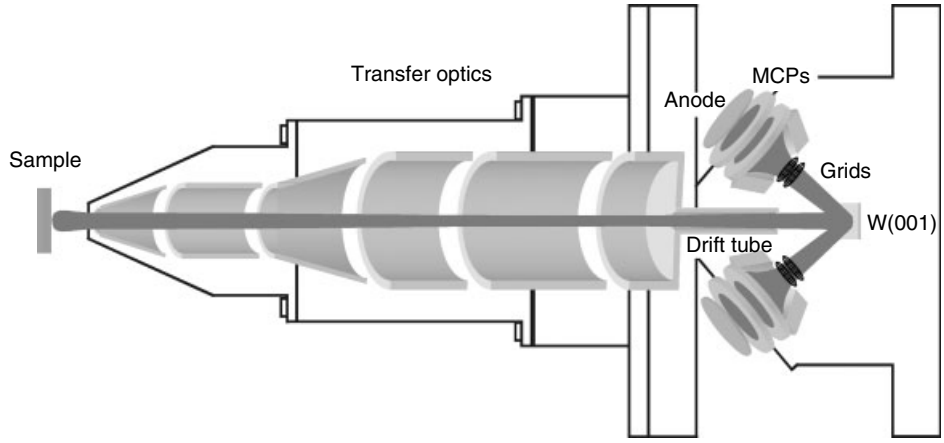

Figure 7. Schematic of the spin detector. Two of the four (2,0) LEED beams are shown in this projection, together with their associated electron counting channels. The first and fourth lenses of the transfer optics are split into quadrupole elements for beam steering.

quality in tilt direction. The small distance between sample and detector optics is a limiting condition for the smallest angle achievable and the size of the extraction optics. The final solution is as follows: straight access to the sample at a collection distance of 8 mm (to front end of detector) for a conical extractor optics with full opening angle of 49°. The sample tilt is 64° with respect to the column axis. The selected geometry is adapted to a column working distance of 8 mm. As consequence of this geometry, the column's working distance is somewhat larger than in conventional SEM applications, which causes a slight decrease in the achievable final resolution.

The objective lens is responsible for a magnetic stray field that declines with increasing working distance. A vertical field component of 2 mT has been measured at the sample position under working conditions. Owing to the fast acceleration of the electrons toward the spin detector by the first elements of the optics, no precessional rotation of the spin-polarization vector could be observed within an error margin of 1°. The electric stray field of the column at the sample surface is quite small and it is easily overcome by the potential gradient of 56 V mm^{-1} at the sample, which is generated by the electrical potentials at the first two lens elements of the transfer optics (in the range of 2–3 kV). Two elements of the electron optics are constructed as steering elements (electrostatic quadrupoles). They serve to align the electron beam with the axis of the optics and compensate for small angular deviations due to electrostatic and magnetic fields of the SEM column and sample tilt.

4.4 The spin detector

The diffraction of electrons at surfaces is a well-established technique in surface science to investigate the structure and quality of surfaces. When electrons with definite energy and low angular spread are scattered at ordered surfaces a perfect diffraction pattern is obtained. Any deficiency from one of those conditions gives a degradation of scattering probability. Surface contamination, for example, can cause superstructures or even the complete destruction of coherent scattering. In the 1980s, much attention was paid to spin effects in LEED. It was found that the scattering at nonmagnetic surfaces, like W(001), can produce diffracted beams of spin-polarized electrons owing to spin-orbit interaction in the scattering. The double scattering experiment was the realization of a self-calibrating experiment that transformed the polarization into an intensity variation (Kirschner and Feder, 1979). With this experiment, the polarization sensitivity could be measured precisely and a new spin detector was suggested and realized. The angle and energy dependence of the sensitivity was investigated for W(001), which was the prerequisite for further optimization of the LEED detector. The most important quantity to characterize the detector efficiency is twice the product of reflectivity R times the square of the polarization sensitivity S, that is, $2RS^2$ (Kirschner, 1985). This so-called Figure of Merit allows for direct comparison with other types of spin detectors, since it is derived from the uncertainty of polarization detection: the statistical error of a single polarization measurement using single electron counting technique is governed by Poisson statistics. It can be expressed as (Kessler, 1985)

$$\Delta P = \frac{1}{\sqrt{NS^2}} \tag{2}$$

For the LEED detector, $N = N(2,0) + N(\overline{2},0)$ is the total number of counts in two opposed beams for a given acquisition time. As N is proportional to R, maximizing RS^2 will minimize ΔP.

In the calibration experiments, the highest Figure of Merit has been found for the second-order diffracted beams and at a kinetic energy of 104.5 eV. With an energy spread of 1.5 eV and an angular spread of 0.5° at normal incidence, the sensitivity was determined to be $S = -0.27$, the reflectivity $R = 0.0011$, and thus the Figure of Merit was calculated to be 1.6×10^{-4} (Kirschner, 1985). In order to achieve an appropriate and reproducible analyzer performance, it is necessary to keep parameters like energy and angular spread in a certain parameter range and the surface in a well-defined condition regarding contamination and structure. Any contamination decreases the polarization sensitivity.

The new detector for the spin-SEM is displayed in Figure 7. Scattering at the W(001) surface is performed in normal incidence. For that geometry and at the chosen nominal scattering energy of 104.5 eV, the (2,0) beams appear at a fixed angle of 49.4° with respect to the normal. To preserve the initial direction of electron scattering, the complete surrounding of the crystal is held at the same potential, the scattering potential. The (2,0) beams can leave the field-free region around the W(001) crystal by traversing grids at the same potential, which separate the scattering from the counting section. A second set of grids (retarding grids) is used to separate the elastically scattered electrons from the SE generated at the W crystal as well as to suppress the inelastic background. The retarding grids act as high-energy pass filters and are set to a potential close to sample ground. An electron, which has passed both grids, is then accelerated into a dual microchannel plate (MCP) assembly for pulse amplification. Between the retarding grid and the MCP entrance, a tapered optical element is mounted. With this electrode, the electron beam is defocused before hitting the front of the first channel plate. Owing to the defocusing, the whole plate area can be illuminated by the electrons. This is important to increase the expected lifetime, that is, to increase the total number of detected events before the MCP quality degrades. In addition, the lowered area intensity reduces the dead time of the plate assembly, as subsequent electrons will not hit exactly the same microchannel. The current pulses generated in the MCP stack are collected with an anode plate and, after high-voltage decoupling, fed into counting electronics.

For cleaning the W(001) surface, the single crystal can be flash heated above 2000 K from its rear by electron bombardment. Within 30 s after flashing the detector is ready again for measuring.

As discussed in the preceding paragraphs, the SE emission is characterized by a wide energy spread with varying polarization and an emission into half-space. The above-mentioned conditions for optimized LEED analyzer spin sensitivity (small angle/energy spread) would mean that only a small portion of the total SEs could be utilized for spin polarization analysis. The limited energy spread reduces the usable number of electrons by a factor of 5 while 5 orders of magnitude are lost due to the extreme limitation of the angular acceptance. In other words, nearly all information is wasted when the detector is run at its optimized performance with respect to polarization sensitivity. The consequence is a dramatic decrease of statistics and image quality for given dwell time. As compensation, one had to increase the measuring time by orders of magnitude. Images with an appropriate number of data points could not be achieved in reasonable times. Hence, the spin polarization analyzer has to work at less favorable conditions in a spin-SEM in order to cover a large part of the SE spectrum. The goal is to find the optimum in the trade-off between degrading polarization sensitivity versus increasing count rates upon increase of the angle and energy acceptance. From general considerations about the SE emission, it was deduced that the detector with best performance (for spin-SEM application) should accept all the SE up to at least 10 eV, while the acceptance angle of the detector should be as large as possible (Oepen and Hopster, 2005). The solution for the latter requirement is to put the sample into the focal plane of the detector system. By this, a large emission angle is transformed into a quasiparallel beam configuration. This means that the majority of all the electrons that are transferred into the detector are scattered at conditions close to normal incidence. In our design (see Figure 7), there is a drift tube at the end of the optics, which is essential for adjusting the beam. The drift tube allows tuning of the electrons into a parallel beam configuration just by maximizing the observed intensities, as it permits only an angular spread of maximum ±5°.

Electrons with different energies are scattered into different angles. Hence, a LEED process gives a discrimination of energy in itself via angular selection of the scattered beams. In our setup, the diaphragms that are used as grid support act as apertures that limit the scattering angle of the diffracted beams (Figure 7). For idealized normal incidence, the apertures define an energy spread of roughly ±10 eV around the nominal scattering energy.

4.5 Performance of the spin detector

In order to quantitatively understand the key properties of the LEED detector, like the obtainable image contrast and the detection efficiency, a best-case calculation has been carried out (Frömter *et al*., subm., 2007). The most simple approach involves a convolution of the spin and intensity distributions of the SE with the calibration curves for the energy-dependent reflectivity and spin sensitivity for scattering at W(001). A more sophisticated and already a quite accurate result can be obtained if the energy and angular

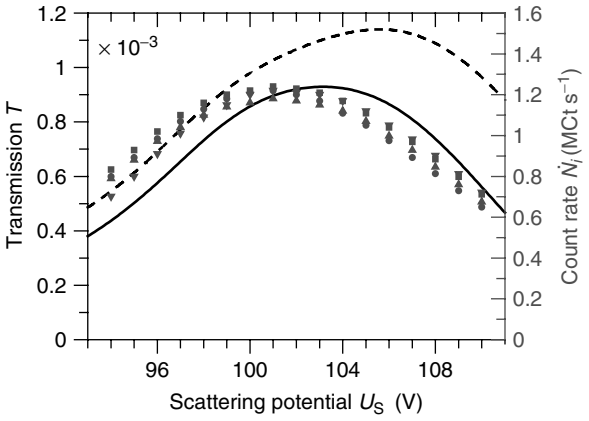

Figure 8. Model of the detector transmission. Measured count rates of all four channels (dots, right scale) from an iron sample and calculated transmission values (lines, left scale) are plotted versus the scattering potential applied to the W(001) crystal. The dashed line is calculated accepting all elastically scattered SE, regardless of their energy. The solid line gives the result for the model that accounts for energy filtering at the entrance apertures in accordance with the real geometry. The transmission in the model is normalized per incoming secondary electron. Details concerning the parameters and model are given in (Frömter *et al*., (subm. 2007)). (Reprinted from Frömter *et al*., Review of Scientific Instruments, submitted. © American Institute of Physics.)

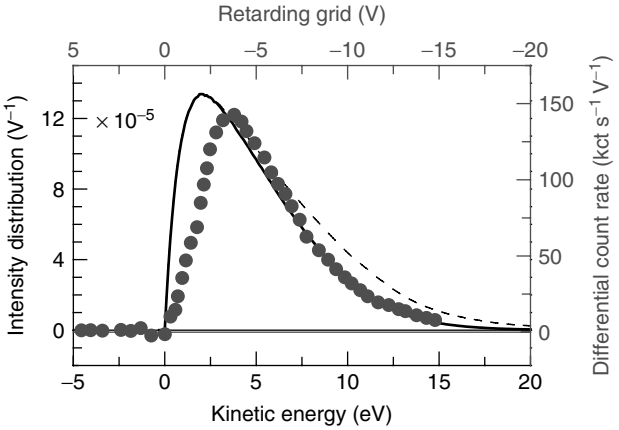

Figure 9. Energy distribution of the SE after scattering at W(001). Dots give the experimental results, when the retarding grid voltage was varied between +5 and −20 V (top axis). The data shown are differentiated with respect to energy (right axis), to obtain the distribution. From the model, we obtain the dashed line as energy distribution (left and bottom axes) if all elastically scattered SE are accepted. The energy filtering at the entrance apertures, which is included in the solid line calculation, is the reason for the gradual cutoff above 5 eV that is in perfect agreement with the measured data. At energies below 4 eV the grid transmission becomes less than unity, so the measured data falls off more rapidly.

dependent transmission properties of the apertures on the diffracted beams are included into the model.

The result for the scattered intensity is shown in Figure 8. Plotted are the calculated detector transmissions for the two conditions described in the preceding text and experimental data from an Fe whisker. The abscissa is the electrostatic potential applied to the scattering crystal with respect to sample and thus gives the variation of the kinetic energy of the scattered electrons. The influence of the energy-determining apertures is obvious from the comparison of the two theoretical curves. A gradual decrease in transmission at energies above 106 eV helps increase the overall performance, since the polarization sensitivity is reduced at these energies. The shape of the theoretical curve that includes the aperture effects (solid line) fits the experimental data quite well. A slight energy shift is found, which is probably caused by some deviation from the exact geometry.

In order to compare the absolute numbers of experiment and model, one has to estimate the number of electrons actually entering the detector. The experiment has been carried out with a primary current of 1 nA at 2 keV energy. If one assumes for these conditions a SE yield of 1, there will be roughly 6×10^9 SE per second entering the detector. Taking the optimum transmission from the theory curve, there should be 5×10^6 electrons per second detectable for each scattered beam. For the five times smaller count rate found in the experiment, several effects are responsible: roughly 20% of the counts are lost at the retarding grids owing to their reduced transmission at lowest energies (Huchital and Rigden, 1972). The magnitude of this effect has been estimated from the spectra in Figure 9. As the structure of the energy dependence is almost the same for theory and experiment, we can conjecture that the remaining effect is mostly of geometrical origin. Appointing the further reduction of count rates to the angular acceptance of the optics, one can calculate an effective full opening angle of SE acceptance. Assuming a Lambert intensity distribution, the remaining transmission of 0.25 corresponds to a full acceptance angle of 60°. This value is well above the geometrical acceptance of 49° and reflects the effectiveness of the accelerating field at the sample. Putting the exact SE yield into the calculation can vary the numbers slightly, but will not change the general result. In summary, from the comparison of the absolute numbers we may conclude that the transfer optics does not focus the SE, which are emitted at very large angles, into the detector. This is in part a consequence of the drift tube, which has been inserted in the electron path to facilitate alignment and that defines the limiting input aperture.

Nevertheless, the obtained count rate well above 1 million counts per second and per channel allows for taking quick overview images from iron samples within less than a minute, or taking high-quality images with only 1% uncertainty in the asymmetry within 5–10 min.

With the same theoretical approach the expected asymmetry can be calculated, taking the SE polarization distribution and the energy-dependent sensitivity of the scattering at W(001) into account. We assume a polycrystalline Fe surface as sample, which represents the situation when decoration with iron is performed. Although the spin polarization at zero SE energy is taken to be 48% in the model, the predicted asymmetry for the experimental setup is just 9%. For polycrystalline Fe films, asymmetries of 8.5% have been found experimentally in our SEMPA. The agreement with the theoretical prediction is perfect. Note that the calculated value is significantly smaller than the product of nominal detector sensitivity times polarization $0.27 \times 48\% = 13\%$. The latter is an ideal quantity that can only be achieved with electrons very close to zero SE energy or with a constant polarization of 48% for all SE.

The energy distribution of the SE can be measured by varying the potential of the retarding grids and differentiating the measured intensities. The obtained energy distribution and a calculation from the above model are displayed in Figure 9. Again a very good agreement is found. At higher energies the transmission of the SE is reduced by the apertures as precisely described by the model. On the low-energy side, the experimental distribution is reduced with respect to the theoretical curve, which is due to a decreased transmission of the retarding grid setup. Measuring the energy distribution of the SE has turned out to be a very useful tool for checking the operation of the LEED detector. From the results one can infer on the quality of the W(001) crystal preparation or charging of the sample.

5 FEATURES OF THE TECHNIQUE

5.1 Application of high surface sensitivity

In Sections 2 and 3, we have already discussed the surface sensitivity of spin-SEM and its implications, that is, the need for the elaborated UHV technique and necessary cleaning of the sample. These can be seen as a real disadvantage for spin-SEM applicability. On the other hand, this particular property of spin-polarized SE emission bears a big potential for SEMPA.

Obviously, the high surface sensitivity gives access to the investigation of magnetic structures in films of ultimately low thickness down to the monolayer (ML) range. Several ultrathin-film systems that exhibit epitaxial, layer-by-layer growth have been investigated *in situ* utilizing spin-SEM. For ferromagnetic films with in-plane easy axes of magnetization, those studies reveal that the films are single domain after growth, which is the state of lowest energy (Robins *et al*., 1988; Oepen *et al*., 1990). It is believed that the single domain state is created during film growth. While growing, the increasing thickness lets the film pass the phase transition from paramagnetism to ferromagnetism. At any stage of film growth, the thickness varies locally by at least ± 1 ML from the mean integer thickness. For thermodynamical reasons, the different heights appear only in larger connected clusters, statistically distributed on the substrate. These thicker parts are called *islands*. On thickness increase, the islands become ferromagnetic first and one can expect a spontaneous alignment of the moments within each island along one of its axes of easy magnetization. In the ideal case, the orientation of magnetization will equally occupy all possible easy axes. Hence, a multidomain state would be stabilized on thickness increase. As the experiment reveals the opposite, we may conclude that a different mechanism is effective: at the phase transition already small magnetic fields can determine the magnetization direction, as the magnetic susceptibility becomes infinite here (Oepen, 1991). Hence, even smallest residual fields can cause the alignment of the magnetic moments in the islands during film growth. Beyond the phase transition, ferromagnetism is stabilized and the state of aligned moments turns into the nearest lying easy axes of magnetization and is frozen in. Thus, a single domain virgin state is created.

In conclusion, the residual fields align all the moments and the easy axis that is closest to the field direction gives the magnetization direction in the ferromagnetic single domain state. It has to be mentioned that there are also stray fields created by the aligned moments of the islands, which could vary the field direction locally. This effect, however, is negligibly small because the stray field of in-plane magnetized ML islands is extremely low.

Interestingly, a stable multidomain pattern can be created in such a film by demagnetizing procedures. The local minima of the energy landscape, which are required for this behavior, are most likely created by small defects that pin extremely localized magnetic features like Bloch lines (Hubert, private communication). In such films, the domain walls have been studied (Berger and Oepen, 1992). Qualitatively, the same wall structures like in considerably thicker films (Fuchs, 1962; Feldtkeller, 1963) were found, that is, Néel walls with long-ranging tails. The domain structure is very irregular and does not reflect any symmetry (in contrast to the known behavior for bulk samples). The reason for this characteristic feature is that the aligning forces on the walls are negligibly small. The aligning forces arise from magnetic stray fields that are created by the magnetic poles, which appear when the wall orientation is such that the component of magnetization normal to the wall is noncontinuous for the two adjacent domains (pole avoidance principle). As the magnetic pole strength scales with the thickness of the film, the force is very small in

the limit of ultrathin films and hence the pole avoidance is not effective. On the contrary, the volume charges that are created due to the Néel-wall structure cause a wall interaction over large distances. This is one driving force for the observed wall bending and the irregularity.

Ferromagnetic films with an out-of-plane easy axis of magnetization behave differently: in general, multidomain structures are found in the virgin state (Allenspach, Stampanoni and Bischof, 1990; Speckmann, Oepen and Ibach, 1995). Again, this is a consequence of the growth process where local thickness variations occur. Around the phase transition, the thicker parts become ferromagnetic and create stray fields that magnetize the film oppositely in the vicinity, as soon as the thickness of those regions increases. Note that the stray fields for perpendicularly magnetized films are much larger than the fields created by in-plane magnetized films of the same thickness.

The temperature dependence of magnetization, namely, the phase transition from ferro- to paramagnetism, has also been studied in ultrathin films by observing the magnetization of oppositely magnetized domains in spin-SEM. With this technique, any influence due to applied probing fields (in hysteresis measurements) and microstructural effects could be ruled out (Kerkmann, Pescia and Allenspach, 1992).

In recent years, the perpendicular magnetic anisotropy that is caused by surface anisotropies has attracted much attention. One particular question arose with the transition from vertical to in-plane magnetization on thickness increase. It was speculated about a loss of long-range order. Spin-SEM investigations could answer that question and reveal that indeed a breakup into tiny domains appears (see Figure 10) around the thickness range where the transition takes place (Allenspach, Stampanoni and Bischof, 1990; Allenspach and Bischof, 1992; Speckmann, Oepen and Ibach, 1995). These domains caused the previously observed decrease of signal in spatially integrating methods. Moreover, it was demonstrated that from SEMPA studies, utilizing its high spatial resolution, the magnetic surface anisotropy could be determined (Speckmann, Oepen and Ibach, 1995; Oepen, Speckmann, Millev and Kirschner, 1997). What is remarkable is the fact that the first-order contribution to the surface anisotropy could be derived from the magnetic microstructure in the regime of vertical magnetization alone.

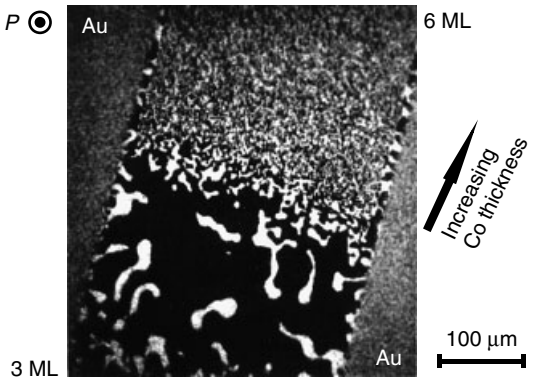

Figure 10. Spin reorientation transition in a Co wedge on Au(111). The spin-SEM image of the vertical magnetization component is shown. The Co wedge was grown *in situ* through a mask. On the left- and right-hand sides the bare Au surface is seen. The thickness increases along the diagonal (left to right) from ∼3 ML to ∼6 ML. At lower Co thickness vertically magnetized domains are found. With increasing thickness, the domains shrink and finally the magnetization reorientates into the film plane (>5 ML). Above 5 ML, the vertical polarization is zero and shows the same contrast as the bare Au surface. Owing to shadowing, the Co thickness gradually increases at the edges from zero to the nominal thickness. Along each edge a domain pattern can be observed as the thickness range with vertical magnetization orientation is contained.

Recently the high surface sensitivity of spin-SEM has been successfully employed for the investigation of the temperature behavior of the layered antiferromagnetism in $La_{1.4}Sr_{1.6}Mn_2O_7$ (Konoto *et al*., 2004), as well as the temperature dependent transitions from antiferromagnetic to ferromagnetic coupling in slightly different manganites (Konoto *et al*., 2005). In those studies, the high surface sensitivity was used to selectively probe the magnetism of the respective top layers in macrostepped surfaces of the complex material.

A very successful story of the application of SEMPA utilizing surface sensitivity was the study of exchange-coupled films (Unguris, Celotta and Pierce, 1991, 1997). A straightforward but intriguing experiment was the investigation of the domain structure that is caused by exchange coupling across a wedge shaped film. In the very first experiments, a Cr wedge was grown on an Fe whisker. On top of the wedge, a thin Fe film was grown and the magnetic structure in this layer observed via SEMPA (Unguris, Celotta and Pierce, 1991) (Figure 11). While the domain structure on the (001) surface of the whisker is very simple and stable, as was investigated before film deposition, the SEMPA investigation of the layered stack reveals a strong oscillatory contrast, which originates exclusively from the Fe film on top. The domain structure shows interlayer thickness dependent stripes that change alternatively from parallel to antiparallel alignment with respect to the whisker magnetization (Figure 11). If the Cr wedge was imaged before Fe deposition, the opposite spin polarization was observed. This is attributed mainly to the magnetization of the topmost Cr layer in the stack, thus indicating an antiparallel coupling between Cr and Fe. From those experiments, two different periods of the oscillatory exchange coupling could be identified and determined very precisely; biquadratic contributions (Pierce, Unguris, Celotta and Stiles, 1999; Tulchinsky, Unguris and Celotta, 2000) and phase slips (Unguris, Celotta and Pierce, 1991) were identified.

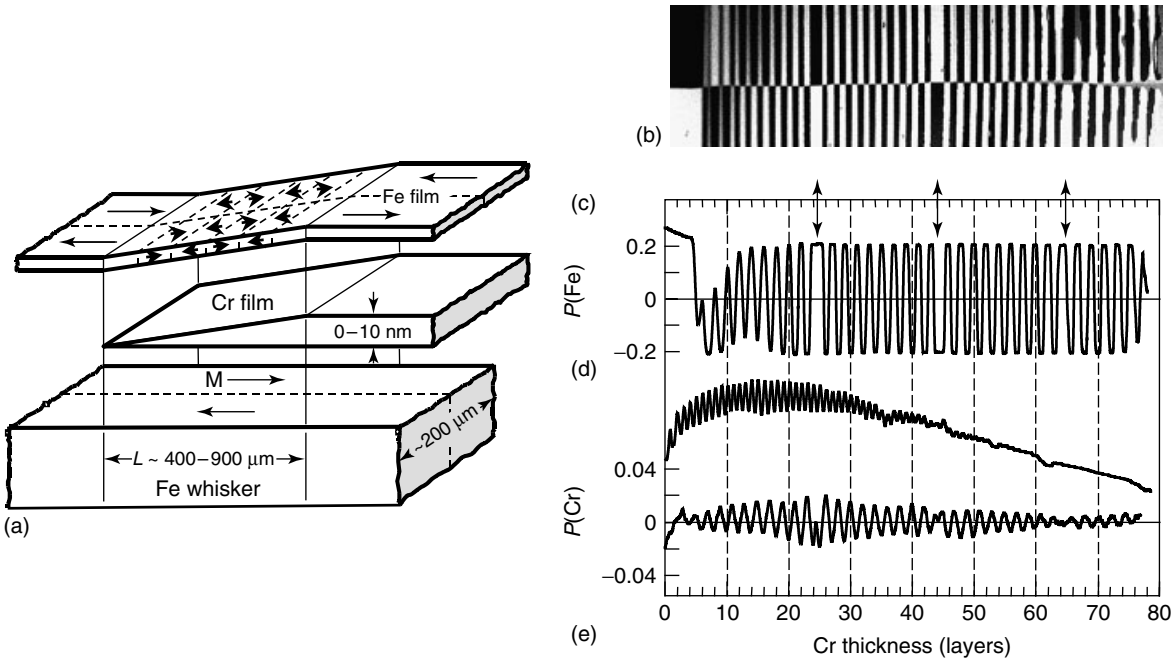

Figure 11. Oscillatory interlayer exchange coupling in Fe/Cr/Fe. (a) Schematic expanded view of Fe/Cr/Fe exchange coupling sample showing the Fe whisker substrate, the Cr wedge, and the Fe overlayer. (b) SEMPA image of the component of magnetization, M_x, in the Fe overlayer along the Fe whisker. The arrows mark the Cr spacer-layer thicknesses where phase slips in the short-period oscillations of the magnetization occur. (c) A line scan through (b) showing the measured spin-polarization profile of the overlayer. (d) Spatial reflection high-energy electron diffraction (RHEED) intensity oscillations along the Cr wedge before depositing the Fe overlayer give an accurate determination of Cr thickness. (e) The spin polarization of the Cr layer P(Cr), before depositing the Fe overlayer, after subtracting the background from the whisker. (Reprinted from *Journal of Magnetism and Magnetic Materials*, 200, Pierce, D.T., Unguris, J., Celotta, R.J. and Stiles, M.D., Effect of roughness, frustration, and antiferromagnetic order on magnetic coupling of Fe/Cr multilayers, 1999, with permission from Elsevier.)

At the very beginning of spin-SEM investigations, a new idea appeared that promised to make SEMPA a universal tool for domain structure and magnetic fine structure analysis, that is, the decoration technique (VanZandt, Browning and Landolt, 1991). It makes use of the pronounced surface sensitivity of the technique, as the main idea is to deposit a very thin layer of an itinerant ferromagnet on top of the sample to be investigated. This layer thus creates a fresh and clean ferromagnetic surface that is accessible for spin-SEM investigation and somehow mirrors the magnetic state below. In the meantime, the decoration or dusting technique has evolved into a standard procedure, whenever sample transfer is necessary at ambient conditions. It works in nearly every case. It is not only that the dusting eliminates the cleaning procedures, it also helps to increase the contrast. To make life easier, it is obvious that Fe, the material that gives the highest contrast in the spin-SEM, is mostly used for dusting. The maximum contrast is already achieved when Fe in the thickness range of a few atomic layers is deposited – independent of the ferromagnet under investigation. For every system, however, it has to be checked whether the magnetic structure is influenced (or even changed) by the dusting layer or not.

An example for magnetic imaging utilizing a dusting layer is shown in Figure 12. The sample is a thin-film Co structure on oxidized Si, fabricated by e-beam lithography. An Fe film (thickness 1 nm) was deposited *in situ* (i) to prevent charging while imaging, as large parts of the sample are insulating SiO_2 and (ii) to spare any cleaning procedure. All three images have been taken simultaneously. On the left-hand side the intensity distribution is shown, which displays the sample morphology like in conventional SEM micrographs. This image was obtained as the sum of all four scattering intensities. It shows the Co rectangle ($10 \times 20\,\mu m^2$, thickness 50 nm) with some remains of the photoresist used for structuring. On the right-hand side, two polarization images are shown, which display two components of the polarization that are perpendicular to each other, as indicated by the arrows. The polarization images show magnetic structures in the film on the bare SiO_2, as well as on top of the Co structure. Obviously, the magnetization pattern differs strongly in these two regions: the Fe film on the SiO_2 shows a uniaxial behavior, which can be seen from the black/white contrast in one component, while the second component does not show any magnetic contrast (except for the regions

of domain walls). Within the Co structure, however, the domain pattern exhibits all possible in-plane magnetization orientations, as is evident from the appearance of all the shades between black and white in both images. The expert reader directly realizes that the domain walls are cross-tie walls that are characteristic for films of soft magnetic materials in a particular thickness range. The coarse structure is a so-called Landau–Lifshitz pattern that minimizes the magnetostatic energy in magnets of limited size. Hence, the appearance of that type of micromagnetic structure and wall indicates that the Fe film indeed mirrors the magnetic structure of the Co beneath.

In the film on the bare SiO_2 the magnetic structure is much simpler; particularly the walls are straight and not as complex as cross-tie walls. The domain pattern, however, seems to be influenced by the magnetic domain structure of the ferromagnetic rectangle. This is due to stray fields leaping out of the structure. The small domains on the right-hand side of the structure obviously cannot provide a complete flux closure and stray magnetic fields are created. The property of dusting, to visualize simultaneously the magnetic pattern of a microstructure and its stray fields, is sometimes very advantageous for the complete understanding and modeling of the magnetic microstructure. If such an effect is not desirable, or if an interaction of film and magnet cannot be ruled out, the deposited film has to be thinner. In principle, the thickness can be reduced below the thickness where the ferromagnetism of an isolated iron film would set in. In that case, when films of high magnetic susceptibility and vanishing remanence are used, it will depend on the coupling if the film reflects the magnetic structure of the ferromagnet or not. A strong coupling can stabilize ferromagnetism in the part of the film where it covers the ferromagnet, whereas in the rest of the film long-range order will be missing. Hence, the film will not have any effect on the ferromagnet under investigation.

The coupling and mechanism behind the decoration technique has not yet been studied systematically. In particular, it depends on the chemical composition, thickness, and structure of the contamination layer. In the case of Figure 12, the surface composition of the microstructure was not analyzed, particularly, the thickness of the adsorbate and oxide layers is unknown.

The decoration technique makes a different class of ordered magnetic materials accessible for spin-SEM, that is, the antiferromagnetic materials. Recently, the domain structure in ferromagnetic films deposited onto antiferromagnets was imaged via SEMPA (Hopster, 1999; Matsuyama, Haginoya and Koike, 2000). The coupling between antiferromagnet and Fe adlayer, as well as the temperature behavior was in the focus of the studies. Those investigations rely upon well characterized and well prepared interfaces between antiferromagnet and film.

As further class of materials, dusting gives access to localized ferromagnets that cannot be investigated otherwise via SEMPA. This was demonstrated by Aeschlimann *et al*. (1990), who studied the bit structure in TbFe magneto-optic storage media. Owing to segregation of Fe to the surface, they obtained a kind of self-dusting layer at the surface that made the investigation feasible.

As in spin-SEM the backward-emitted SE electrons are used, there does not exist any limitation on sample thickness, like in transmission electron microscopes. Hence, SEMPA can also be applied for studying magnetic devices that are developed or produced in industrial laboratories or fabrication facilities. The advantage is that only very mild cleaning or sample manipulations are necessary (ion milling or dusting) for imaging, and surfaces have not to be perfect regarding surface morphology. Many examples of spin-SEM investigations of storage media from industrial research and production facilities have been given in a review article by Koike, recently (Koike, 2005).

In summary, we may conclude that the high surface sensitivity is a big advantage of spin-SEM. That particular property gives access to very different physical questions and systems after appropriate sample preparation. Generally speaking, mild ion milling is the adequate preparation procedure in case of thick magnetic systems, while dusting is advisable in case of thin films, multilayer systems, and nonitinerant ferromagnets. Utilizing SEMPA, however, means that some experience in surface science and the related technology are an absolute necessity for the operator in charge of microscopy.

5.2 Surface morphology

The spin polarization is proportional to the normalized intensity difference, the scattering asymmetry (equation (1)). Owing to the normalization, the sample morphology is strongly suppressed. In literature, examples have been given for strong magnetic contrast despite strong sample morphology (Matsuyama and Koike, 1990). Morphology suppression means, for instance, that surface roughness is irrelevant. This makes the cleaning of surfaces via ion milling possible, without any adverse effect on the magnetic image. The opposite is true when high spatial resolution spin-resolving scanning tunneling microscopy (spin-STM) is used for magnetic imaging. Owing to the strong sensitivity of STM for any changes of the local band structure, strong morphological contrasts, even for structures on the atomic scale (steps, impurities), are observed. High spatial resolution spin-STM requires absolutely flat and well-defined surfaces to resolve the magnetic contrast. As technical samples do not exhibit such ultimately

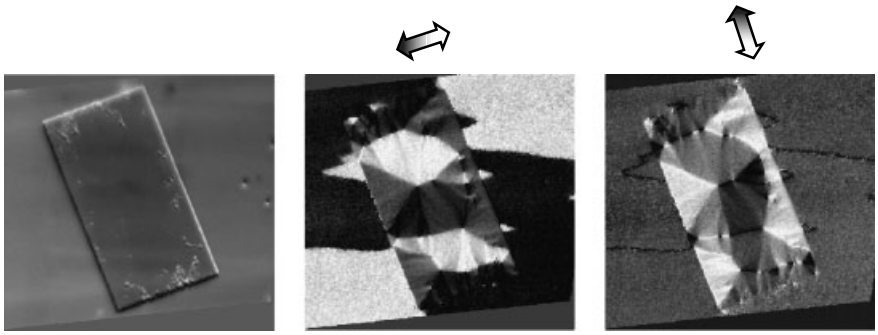

Figure 12. Morphology and domain structure of a thin-film Co structure on SiO_2. The dimensions of the Co rectangle are $10 \times 20\,\mu m^2$ and the thickness is 50 nm. To prevent charging, a 1-nm-thick Fe film was deposited prior to imaging. The picture on the left-hand side gives the topography. The pictures in the center and on the right-hand side show the magnetic structures obtained in two orthogonal in-plane polarization components, as indicated by arrows.

perfect surfaces, they are out of reach for the investigation via spin-STM. Hence, for the magnetic imaging of technical samples spin-SEM (utilizing ion milling or dusting as preparation) is superior to the scanning probe techniques, although one does not achieve the same extreme spatial resolution.

The inherent property of morphology suppression has been demonstrated many times. Nevertheless this feature of spin-SEM needs some further consideration: at first, samples that consist of mesoscopic subsurfaces, which are inclined with respect to each other, can show apparent magnetic contrast. This contrast is due to the surface orientation, which determines largely the initial emission direction of the SE. Different emission directions cause different apparatus or device asymmetries, as the electron beam that is focused into the detector hits the scatter target at a different position or changes its angle of incidence. Hence, on a mesoscopic scale a varying offset appears which is of purely experimental origin. It is like a locally changing device asymmetry. A varying offset is superimposed upon the real polarization structure and is usually difficult to eliminate. This emission cone effect is minimal in one polarization component when the surface's inclination varies only in the direction perpendicular to the scattering plane of the polarization component. The two scattered beams, which determine the scattering plane, are equally affected by the changes of the incoming beam. When calculating the polarization distribution of the component, all the changes cancel out to a large extent. Such a special geometry was chosen, when the domain structure on two macroscopic surfaces of a whisker with surfaces that enclose an angle of 90° have been imaged in one picture (Matsuyama and Koike, 1990).

Device asymmetry becomes a delicate problem in micro- and nanostructures that exhibit a significant aspect ratio of height to lateral extensions. Such structures can show emission cone effects in both polarization components and strong deviations from the true magnetic structure can result. For structures with steep side planes, the effect of varying emission angles can be observed even on the horizontal upper surface around the edges. Here it is the attractive electric field from the first detector electrode, which is no more homogenous but tends to bend the electrons outwards as it gradually follows the sample topography. The emission cone effect is pronounced in the low-energy polarization detectors while it is less important in Mott detectors.

Besides the emission cone effect, the edge effect, well known from SEM, will contribute to the polarization image. While the edge effect gives an enhancement of the edge structures in SEM micrographs owing to an apparently enhanced SE yield, the spatial resolution is not affected for conducting material in most cases (for a detailed discussion, see textbooks about electron microscopy, e.g., (Reimer, 1998)). The enhanced yield comes from the SE emission from the side planes, when the primary beam hits the top

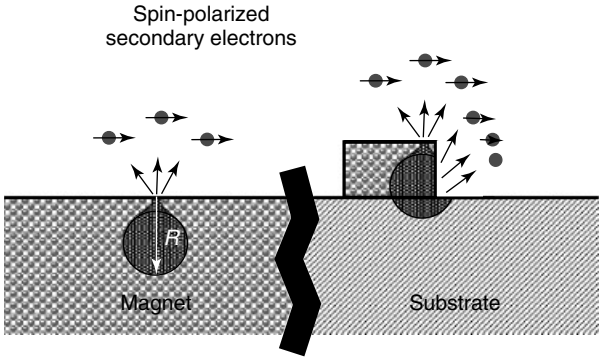

Figure 13. Sketch of the edge effect in a ferromagnetic material. When nanostructures of height that is comparable to the electron range R are analyzed, electrons from the side planes with different polarization might dominate the SE emission. Additionally SE from the bloom can be emitted from the nonmagnetic substrate. The polarization of the SE will change continuously with the distance of the primary beam from the edge. The arrows give the polarization of the SE emitted in the indicated directions.

surface and traverses the structure beneath the side plane (Figure 13). The emission from side planes might influence the polarization image and reduce the lateral resolution if the side planes give a reduced polarization due to imperfect dusting or due to surface contamination that could not be totally removed by ion milling. As the amount of SE that originate from the sidewalls depends on the distance of the primary electron beam from the edge, the polarization will change with distance to the edge and the magnetic structures seem to be washed out, that is, apparently the magnetic resolution is diminished. The edge effect depends strongly on the steepness of the side planes and the height of the nanostructure.

An estimation for the extrapolated range of high-energy electrons in iron gives, based on the phenomenological equation given in Reimer (1998), a value of $>30\,\mathrm{nm}$ for $2\,\mathrm{keV}$ primary electrons. Images from nanostructures with heights comparable to the extrapolated range will show a degradation of resolution owing to the edge effect. Additionally, resolution can be lost owing to the bloom of SEs, which is created in the substrate close to the interface (Reimer, 1998). The SE in the bloom can also create low-energy SEs when the bloom comes close to a surface. Near the edge of a nanostructure this can happen and electrons are created at the substrate surface because the bloom has a larger extent than the primary beam. The measured polarization is altered when the primary beam is approaching the edges of the structure as the number of secondaries from the substrate increases. The magnetic structure starts to fade away even before the primary beam touches the edge of the structure. In very thin nanostructures (height $\ll$ extrapolated range), however, the high-energy electrons penetrate into the substrate and SE are emitted from the topmost layers only. No image degradation is found.

The above-mentioned imperfect or inhomogeneous coverage of side planes with dusting material or contamination is mostly due to shadowing during deposition of dusting material or during sputter cleaning. The extent of the imperfection depends on the steepness and profile of the side planes, the spatial expansion of the evaporation or sputter source and the angular alignment of sample and source. Shadowing can be minimized by sample rotation during preparation. When dusting is applied to nonconducting materials, charging also might occur due to an imperfect coverage. The charging can cause a loss of resolution in the SEM image and even a loss of polarization in the SEMPA image due to the associated energy shift of the SE.

In conclusion, we may summarize that spin-SEM is very well suited for the high lateral resolution investigation of all kinds of samples, particularly technical samples, as surface roughness is not a problem. The SE-emission properties can affect magnetic images, when structures with differently oriented surfaces or steep edges are investigated. Special care has to be paid to the interpretation of the results in these cases.

5.3 Image analysis in spin-SEM

A unique feature of spin-SEM is that the polarization detection can give direct access to the orientation of the magnetization. As explained in the earlier paragraphs, two perpendicular polarization components can be detected simultaneously by one detector. The two components span a plane, which is congruent with the sample surface, if sample and scattering crystal (target) are aligned in parallel – the geometry discussed in the following. It is more complicated to derive the polarization values and finally the local magnetization from the four measured count rates in a real experiment than described so far. While scanning, the data acquisition system calculates and stores point by point a doublet of asymmetry components A_x and A_y according to equation (1). The principal axes in the so-defined asymmetry space are, by nature of the scattering process, aligned with the axes of the corresponding magnetization components M_x and M_y. This correlation is of course only true in the absence of strong magnetic fields along the path of the SE, which rotate the polarization. A well-defined polarization rotation can be used on purpose in polarization rotation devices for spin-SEM, which can give access to the three orthogonal polarization components, utilizing only one detector (Kohashi, Matsuyama and Koike, 1995).

For a qualitative understanding of the magnetization distribution in simple cases, it is sufficient to plot two grayscale images of the asymmetries $A_x(x, y)$ and $A_y(x, y)$, which have been scaled to show the whole range of occurring asymmetry values (Figure 14). The brighter areas can be attributed to a more positive polarization component and the darker to a more negative one. This simple approach is only reliable, if all representative in-plane directions occur within the selected field of view. If one direction is missing, the closest intermediate direction will be scaled to full range and thus be falsely interpreted as domain with full magnetization.

So, the question remains, why are not the exact values of the $\mathbf{A}$ vector used to determine P instead of the relative method described above? In a real spin detector there is no direct proportionality between $\mathbf{A}$ and $\mathbf{P}$, because there is always a significant vectorial offset $\mathbf{A}_0$, the apparatus or device asymmetry, which has to be corrected first:

$$\mathbf{M} \propto \mathbf{P} = S^{-1}(\mathbf{A} - \mathbf{A}_0) \tag{3}$$

The origins for the apparatus asymmetry $\mathbf{A}_0$ are different total sensitivities of the individual counterchannels, which

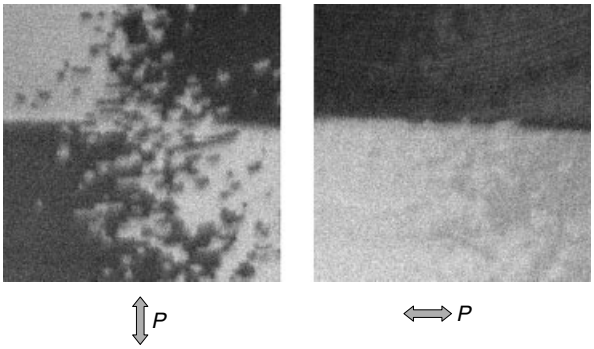

Figure 14. Domain pattern of an Fe whisker surface, obtained in two in-plane polarization-sensitive axes. Both pictures were taken simultaneously. The picture size corresponds to $5.9 \times 5.9\,\mu m^2$.

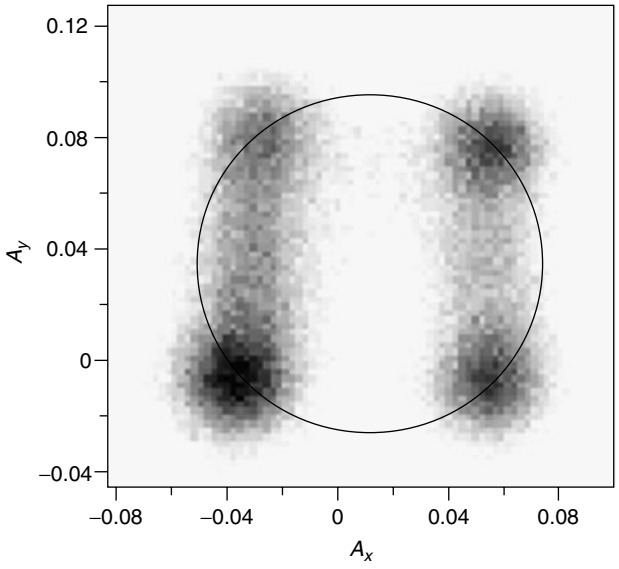

Figure 15. Two-dimensional histogram of the asymmetry corresponding to Figure 14. The number of asymmetry doublets appearing in Figure 14 are coded in gray levels in the A_x,A_y plane. Four accumulation points can be identified, which lie on a circle. This demonstrates that four orientations of domains predominate the domain pattern. The center of the circle gives the total device asymmetry $\mathbf{A}_0$ in the A_x,A_y plane. The magnetization orientation can be directly read from the plot.

are mostly determined by the beam alignment in the transfer optics and the precise sample position, different current amplifications/sensitivities of the four detector channels, or from residual magnetic fields, to name a few. The apparatus asymmetry varies from image to image and has to be determined for each measurement before any quantitative information can be extracted.

In the easiest case, for example, a magnetic nanostructure on nonmagnetic substrate, it is possible to determine the asymmetry on the nonmagnetic region inside the image. This asymmetry gives $\mathbf{A}_0$ directly and can thus be corrected straight away in the magnetic parts of the image. Even in the absence of nonmagnetic areas within the image, it is, in most cases, possible to restore and thus correct for the apparatus asymmetry. The method to employ makes use of the statistical distribution of all measured (A_x, A_y) doublets that occur in one image. In order to access this statistical distribution graphically, one can display the two-dimensional (2D) histogram of all recorded asymmetry doublets from one SEMPA measurement in one intensity graph. Such plot is the important tool to determine the device asymmetry and to cross-check the experiment. Most importantly, the 2D histogram is the prerequisite for any vectorial analysis of the magnetization. Figure 15 displays the 2D histogram of the measured asymmetry values from the image in Figure 15. The histogram exhibits four accumulation points, which indicate predominant anisotropy doublets, that is, dominant orientations of the magnetization. The maxima correspond to the magnetization of the four domains that appear in the magnetic pattern of Figure 15. Under the condition that the absolute value of the magnetization $|\mathbf{M}|$ is constant in homogeneous material, the magnetization vector is lying on the surface of a sphere and can be described by

$$\mathbf{M} = |\mathbf{M}|(\cos\varphi^* \sin\theta, \sin\varphi^* \sin\theta, \cos\theta) \qquad (4)$$

where θ, φ are the polar angles, measured with respect to symmetry adapted axes, for example, [100] and [001] in cubic systems. Depending on the surface orientation of the sample, one obtains a certain cut through that sphere. If easy directions of magnetization exist within the surface, one will find closure domains with orientation along those directions. In Fe, the easy axes of magnetization are the $<100>$ directions. Hence, in a nominal (001) surface of iron (as in the case of Figures 13 and 14) one can expect four different directions of domain magnetization. Consequently, the accumulation points found in Figure 13 have to be elements of a circle with a radius that corresponds to the value of $|\mathbf{M}|$ measured in asymmetry units. Drawing a circle through the four accumulation points, we actually find an almost perfect fit. The center of the circle, however, does not coincide with (0,0) in the asymmetry plane, although it should represent $|\mathbf{M}| = 0$. The location of the center of the circle is therefore identical to the vector of device asymmetry $\mathbf{A}_0$.

The radius of the circle, which is proportional to the value $|\mathbf{M}|$ of the magnetization, is an important quantity that gives hints on detector sensitivity. Generally speaking, the larger the radius, the better the detector works regarding polarization sensitivity. The radius of the circle is also sensitive to contamination of the sample surface.

In a system with in-plane magnetization, a deformation of the circle into an ellipse is most often caused by a tilt of the sample surface with respect to the detector target. If the latter is not the case, the ellipse will indicate some problem with detector adjustment. If out-of-plane components can exist in the system, like in ultrathin films or hard magnetic systems, the deviation of accumulation points from a circle can indicate the presence of a vertical component. The tilt of the magnetization with respect to the surface plane (or surface normal) can be calculated from the position of the accumulation point in the 2D histogram, that is, putting the distance to the center in relation to the expected circle radius. The prerequisite is that the alignment of sample and detector crystals are carefully controlled and accurately known (Frömter *et al*., (subm. 2007)).

From the 2D histogram, one can also extract information about the quality of polarization detection, particularly its statistics. The distribution of the scatter events around the maxima is determined by the uncertainty of the polarization measurement. The fact that the distribution of scattering events is rotationally symmetric (with respect to the accumulation maximum) indicates that no systematical error is influencing the polarization analysis (see Figure 15). The observed width of these accumulation maxima fits well the predicted accuracy calculated according to equation (2).

The contrast-to-noise ratio (CNR) of a micrograph can also be extracted from the 2D histogram. Magnetic structures can be resolved in the domain pattern as long as the distance between maxima is larger than the diameter of the scattering distribution, that is, the uncertainty of the polarization detection. The ratio of distance to diameter is defined as CNR (sometimes also called *contrast*). Taking the full width at half maximum of the scatter points and the distance between the centers (in Figure 13), one obtains a contrast for 180° domains of >3.7 (along the diagonal), while that for 90° is >2.7 (horizontal/vertical spacing of the scatter maxima). Currently, a CNR of 15 is obtained with the same system using a dwell time of 20 ms per pixel.

From the former discussions, it follows that the 2D histogram can be interpreted as the true angular distribution of the orientation of **M** in the sample surface. Hence, the 2D histogram can be used to combine the vector information of the two polarization components into one single domain image. For that purpose, it is useful to change from a gray scale to a color representation. In the 2D histogram, the direction of magnetization is determined as the orientation of the corresponding asymmetry doublet with respect to the circle center. In case of in-plane magnetization, a certain color can be appointed to a direction disregarding the measured polarization value. Such color representation is often used since it gives the complete survey over all magnetization orientations in one image. Owing to black/white reproduction of the book, we go without an example for the color representation.

To summarize, the magnetization vector information cannot be achieved without the investigation of the 2D histogram. The latter is used to find the device asymmetry. The device asymmetry fixes the origin of the polarization vectors, which in turn allows the association of vectors with measured asymmetry doublets.

The details of the 2D histograms are also essential to understand domain images. For instance, in Figure 15, the accumulation points in the horizontal direction are well separated, whereas in the vertical direction the polarization maxima are connected via a line of counted events with reduced frequency. Well-separated maxima appear because the corresponding domains do not have mutual boundaries. The corresponding domains are not adjacent but in opposite edges of the domain pattern. In contrast, the domains that correspond to the accumulation points on the left-/right-hand side share a boundary that is blurred. The fact that the scatter events are exactly lying on the line between the scatter maxima (and thus seem to indicate a reduced magnetization value) reveals that those asymmetry values are composed from a statistical mixture of electrons having one or the other polarization value, which belongs to the two domain orientations. As both domains have about the same A_x component, the x signal is constant, while the y signal is determined by the spread of the primary electron beam, which covers changing portions of the one or the other domain. In other words, the lateral resolution is not good enough to resolve the fine structure between the different domains that intermix at the boundary of the large domains. The same origin, an insufficient resolution, gives a sharp horizontal domain wall (in Figure 14) that shows no trace in the 2D histogram of the whole image.

The above given explanation of the domain image by means of the corresponding 2D histogram strongly supports the arrows indicated in the domain pattern, although the experienced reader with background in micromagnetics would probably insist that the given domain magnetizations were wrong. Indeed, from micromagnetic considerations alone that would be true, but secondary effects (from the magnetic point of view) dominate the magnetic structure. In fact, we find indications for misaligned surfaces and the vertical domain boundary seems to be pinned by a grain boundary that divides most likely twin grains. From the domain pattern on a larger scale (Figure 16), the complexity of the pattern is obvious, including fir tree structures, which are a direct evidence for a slight tilt of the surface out of the (001) orientation. The SEM micrograph (Figure 17) shows step bunches that bend around in the range where the domain image was taken. The different orientation of the steps supports the thesis of adjacent twin grains. Although the overall system seems to be

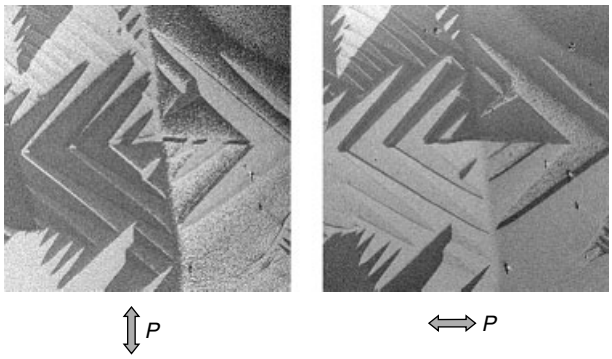

Figure 16. Overview of the domain pattern of the Fe whisker. The pattern shown in Figure 14 is a zoom into the center of this image. Image size is $200 \times 200\,\mu m^2$. The appearance of fir tree structures demonstrates that the imaged subsurfaces are vicinal to {001} surfaces.

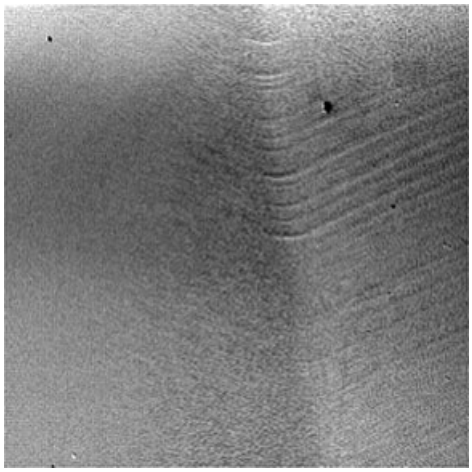

Figure 17. SEM micrograph (sum of four spin channels) of the central region of Figure 16. Image size is $100 \times 100\,\mu m^2$. The lines appearing in the image are most likely step bunches. The orientation of the lines changes going from right to left. This indicates that the whisker has two different surface orientations on the left- and right-hand side, most likely separated by a grain boundary.

very complex, we have chosen the higher resolving domain image for the sake of simplicity to demonstrate the features and strength of the 2D histogram.

Another example is depicted in Figure 18 that shows again the histogram of measured polarization components within the sample surface plane. The corresponding domain structure is shown in Figure 19. In contrast to the previous example, the 2D histogram does not show a pronounced accumulation in individual points. A ring of scattering events is found, the diameter of which is small compared to diameter of the circle drawn through the accumulation points in the previous example. There is a considerable amount of polarization doublets situated within the ring. The sample

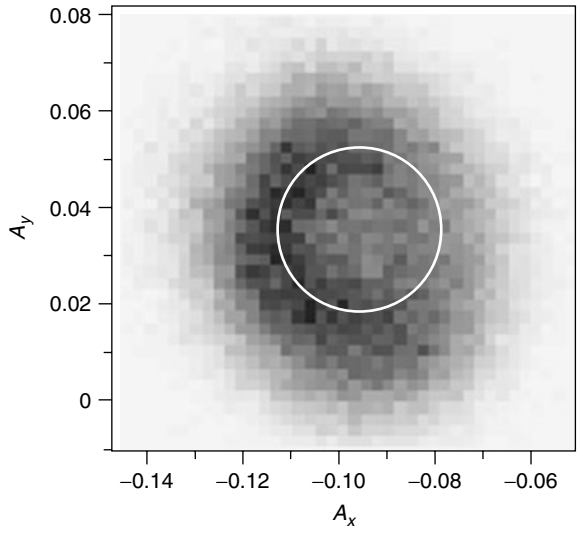

Figure 18. Two-dimensional histogram corresponding to the domain pattern shown in Figure 19. The circle marks the radius of most frequent asymmetry doublets.

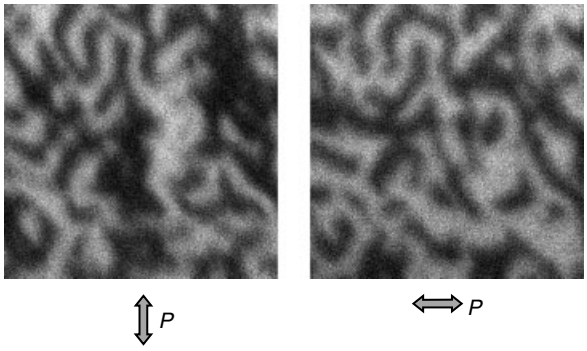

Figure 19. Domain image obtained from a $(Co/Pt)_8$ multilayer on Si wafer. Polarization components within the film plane are shown. The corresponding axes of sensitivity are indicated by the arrows. Image size is $2.35 \times 2.35\,\mu m^2$.

is a Co/Pt multilayer stack that was covered by a Pt cap layer to prevent oxidation of the thin Co layers. This sample was decorated by Fe to perform the spin-SEM investigation. From the dusting with Fe, one would expect almost the same polarization value as before, that is, a larger ring diameter.

The smaller ring diameter as well as the other listed properties can be consistently explained by magnetization canting. The shallow ring structure indicates that there exists a preferred canting angle. The radius of the ring is small, which means that the magnetization is mostly out of plane. The inhomogeneous color of the ring might indicate an anisotropy in the in-plane component, that is, a preferential orientation roughly in one direction. The uneven population can be due to an in-plane magnetic field that had been applied in-plane prior to the SEMPA investigation.

Inside the ring there are also polarization doublets found. Considering a constant value of |**M**|, this means that there are parts in the domain pattern with even less tilting of the magnetization out off the normal direction. A more quantitative examination reveals that those parts come from the transition regions between the domains.

It should be mentioned that for a disc-shaped thin-film element, made from soft magnetic material, a ring (with large ratio of radius/width) was found that did not show any magnetization components in the enclosed area. The corresponding magnetic pattern was a vortex structure in which the area covered by the vertically magnetized singularity is negligibly small (Hopster and Oepen, 2005).

In summary, to achieve a most complete set of information it is important to analyze the asymmetry histogram besides the lateral distribution of measured asymmetries. The histogram allows for the control of the experiment and detector performance. Beyond that, the careful analysis gives further insight into the magnetic behavior of the system under investigation. From the plot, the exact orientation of the local magnetization, a global preferential magnetization orientation, and a possible magnetization tilt can be quantitatively extracted.

6 SUMMARY AND OUTLOOK

In SEMPA, the spin-polarized SE emission is used for the imaging of magnetic structures. Starting from the process of SE creation, the ultimate performance and the requirements on the different components are discussed. The most restrictive property of spin-polarized SE emission is the high surface sensitivity, which demands for the application of UHV technology. The latter makes the technique sophisticated and somehow complex.

The apparently disadvantageous high surface sensitivity can be turned into an advantage, as it allows under certain preparation conditions – dusting – the applicability of SEMPA to almost all classes of materials and samples. With a resolution below the 10-nm mark, dusting makes spin-SEM most attractive for all kind of application laboratories involved in the development of new magnetic devices or storage media. Here, SEMPA can serve for the next 10 years until the lateral dimensions will finally approach the sub-nanometer range.

ACKNOWLEDGMENTS

We are grateful to J. Kirschner (Max Planck Institute of Microstructure Physics, Halle) for his steady interest, helpful discussions, and strong support. Special thanks go to C. Menk, K. Morrison, G. Steierl for their SEMPA work and W. Pfützner for technical assistance. We thank J. Kirschner for the permission to show yet unpublished spin-SEM images from our cooperation. Financial support from the BMBF (Grant No. 13N7484/5) and the Deutsche Forschungsgemeinschaft via SFB 508 and SFB 668 are gratefully acknowledged.

REFERENCES

Abraham, D.L. and Hopster, H. (1987). Magnetic probing depth in spin-polarized secondary electron spectroscopy. *Physical Review Letters*, **58**, 1352–1354.

Aeschlimann, M., Scheinfein, M., Unguris, J., *et al*. (1990). Magnetic-field-modulated written bits in TbFeCo thin films: Transmission electron microscopy Lorentz and scanning electron microscopy with polarization analysis studies. *Journal of Applied Physics*, **68**, 4710–4718.

Allenspach, R. (1994). Ultrathin films: magnetism on the microscopic scale. *Journal of Magnetism and Magnetic Materials*, **129**, 160–185.

Allenspach, R. and Bischof, A. (1992). Magnetization direction switching in Fe/Cu(100) epitaxial films: temperature and thickness dependence. *Physical Review Letters*, **69**, 3385–3388.

Allenspach, R., Stampanoni, M. and Bischof, A. (1990). Magnetic domains in thin epitaxial Co/Au(111) films. *Physical Review Letters*, **65**, 3344–3347.

Barnes, J., Mei, L., Lairson, B.M. and Dunning, F.B. (1999). Implementation of scanning electron microscopy with polarization analysis using high-efficiency retarding-potential Mott polarimeters. *Review of Scientific Instruments*, **70**, 246–247.

Berger, A. and Oepen, H.P. (1992). Magnetic domain walls in ultrathin fcc cobalt films. *Physical Review B*, **45**, 12596–12599.

Celotta, R. and Pierce, D. (1982). Possibilities for the use of electron spin polarization in scanning electron microscopy. In *Microbeam Analysis*, Heinrich, K.F.J. (Ed.), San Francisco Press: San Francisco.

Chapman, J.N., Batson, P.E., Waddell, E.M. and Ferrier, R.P. (1978). Direct determination of magnetic domain-wall profiles by differential phase-contrast electron-microscopy. *Ultramicroscopy*, **3**, 203–214.

Chrobok, G. and Hofmann, M. (1976). Electron spin polarization of secondary electrons ejected from magnetized europium oxide. *Physics Letters A*, **57**, 257–258.

DiStefano, T.H. (1978). Technology for detecting small magnetic domains and beam-addressed memory therewith. *IBM Technical Disclosure Bulletin*, **20**, 4212–4215.

Feder, R. (Ed.) (1985). *Polarized Electrons in Surface Physics*, World Scientific: Singapore.

Feldtkeller, E. (1963). Die Wandbewegungsfeldstärken in anisotropen Nickeleisenschichten. *Zeitschrift für angewandte Physik*, **15**, 206–213.

Frömter, R., Oepen, H.P. and Kirschner, J. (2003). A miniaturized detector for high-resolution SEMPA. *Applied Physics A*, **76**, 869–871.

Frömter, R., Oepen, H.P. and Kirschner, J. (subm. 2007). Design and modeling of an optimized SPLEED detector for SEMPA. *Review of Scientific Instruments*.

Fuchs, E. (1962). Magnetische Strukturen in dünnen ferromagnetischen Schichten, untersucht mit dem Elektronenmikroskop. *Zeitschrift für angewandte Physik*, **14**, 203–209.

Hammond, M.S., Fahsold, G. and Kirschner, J. (1992). Absorption and elastic and inelastic reflection of spin-polarized low-energy electrons from Fe(110). *Physical Review B*, **45**, 6131–6141.

Hembree, G.G., Unguris, J., Celotta, R.J. and Pierce, D.T. (1987). Scanning electron microscopy with polarization analysis: high resolution images of magnetic microstructure. *Scanning Microscopy International Supplement*, **1**, 229–240.

Hong, J.S. and Mills, D.L. (2000). Spin dependence of the inelastic electron mean free path in Fe and Ni: explicit calculations and implications. *Physical Review B*, **62**, 5589–5600.

Hopster, H. (1999). Magnetic domain formation in Fe films on Cr(100). *Physical Review Letters*, **83**, 1227–1230.

Hopster, H. and Oepen, H.P. (Eds.) (2005). *Magnetic Microscopy of Nanostructures*, Springer: Berlin.

Hopster, H., Raue, R., Kisker, E., *et al*. (1983). Evidence for spin-dependent electron-hole-pair excitations in spin-polarized secondary-electron emission from Ni(110). *Physical Review Letters*, **50**, 70–73.

Huchital, D.A. and Rigden, J.D. (1972). Resolution and sensitivity of the spherical-grid retarding potential analyzer. *Journal of Applied Physics*, **43**, 2291–2302.

Ibach, H. (Ed.) (1977). *Electron Spectroscopy for Surface Analysis*, Springer-Verlag: Berlin, Heidelberg, New, York, Tokyo.

Iwasaki, Y., Takiguchi, M. and Bessho, K. (1997). Spin-polarized secondary electron microscopy of soft magnetic films on antiferromagnetic substrates. *Journal of Applied Physics*, **81**, 5021–5023.

Kerkmann, D., Pescia, D. and Allenspach, R. (1992). Two-dimensional magnet at Curie temperature: epitaxial layers of Co on Cu(100). *Physical Review Letters*, **68**, 686–689.

Kessler, J. (1985). *Polarized Electrons*, *Second Edition*, Springer-Verlag: Berlin, Heidelberg, New York, Tokyo.

Kirschner, J. (1984). On the role of the electron-spin in scanning electron-microscopy. *Scanning Electron Microscopy*, **III**, 1179–1185.

Kirschner, J. (1985). *Polarized Electrons at Surfaces*, Springer-Verlag: Berlin, Heidelberg, New York, Tokyo.

Kirschner, J. (1988). Spin-polarized secondary electrons from ferromagnets. In *Surface and Interface Characterization by Electron-optical Methods*, Howie, A. and Valdré, U. (Eds.), Plenum Press: New York, pp. 267–283.

Kirschner, J. and Feder, R. (1979). Spin polarization in double diffraction of low-energy electrons from W(001): experiment and theory. *Physical Review Letters*, **42**, 1008–1011.

Kirschner, J. and Suga, S. (1987). Spin polarization vector analysis of secondary electrons from ferromagnetic Fe excited by spin-polarized primary electrons. *Solid State Communications*, **64**, 997–1000.

Kisker, E., Gudat, W. and Schröder, K. (1982). Observation of a high spin polarization of secondary electrons from single crystal Fe and Co. *Solid State Communications*, **44**, 591–595.

Kohashi, T. and Koike, K. (2001). A spin-polarized scanning electron microscope with 5-nm resolution. *Japanese Journal of Applied Physics*, **40**, L1264–L1266.

Kohashi, T., Matsuyama, H. and Koike, K. (1995). A spin rotator for detecting all three magnetization vector components by spin-polarized scanning electron microscopy. *Review of Scientific Instruments*, **66**, 5537–5543.

Koike, K. (2005). Spin-SEM of storage media. In *Magnetic Microscopy of Nanostructures*, Hopster, H. and Oepen, H.P. (Eds.), Springer: Berlin, pp. 169–180.

Koike, K. and Hayakawa, K. (1984). Scanning electron microscope observation of magnetic domains using spin-polarized secondary electrons. *Japanese Journal of Applied Physics*, **23**, L187–L188.

Konoto, M., Kohashi, T., Koike, K., *et al*. (2004). Direct imaging of temperature-dependent layered antiferromagnetism of a magnetic oxide. *Physical Review Letters*, **93**, 107201–107204.

Konoto, M., Kohashi, T., Koike, K., *et al*. (2005). Microscopy of magnetic transition in a layered manganite $La_{2-2x}Sr_{1+2x}Mn_2O_7$ ($x = 0.32$). *Physical Review B*, **71**, 184441–184445.

Matsuyama, H., Haginoya, C. and Koike, K. (2000). Microscopic imaging of Fe magnetic domains exchange coupled with those in a NiO(001) surface. *Physical Review Letters*, **85**, 646–649.

Matsuyama, H. and Koike, K. (1990). A data acquisition and display system for spin-polarized scanning electron microscopy (spin SEM). *Review of Scientific Instruments*, **62**, 970–981.

Oepen, H.P. (1991). Magnetic domain structure in ultrathin cobalt films. *Journal of Magnetism and Magnetic Materials*, **93**, 116–122.

Oepen, H.P., Benning, M., Ibach, H., *et al*. (1990). Magnetic domain structure in ultrathin cobalt films. *Journal of Magnetism and Magnetic Materials*, **86**, L137–L142.

Oepen, H.P. and Hopster, H. (2005). SEMPA studies of thin films, structures, and exchange coupled layers. In *Magnetic Microscopy of Nanostructures*, Hopster, H. and Oepen, H.P. (Eds.), Springer: Berlin, Heidelberg, New York, pp. 137–167.

Oepen, H.P. and Kirschner, J. (1989). Magnetization distribution of 180 domain walls at Fe(100) single-crystal surfaces. *Physical Review Letters*, **62**, 819–822.

Oepen, H.P. and Kirschner, J. (1991). Imaging of magnetic microstructures at surfaces: the scanning electron microscope with spin polarization analysis. *Scanning Microscopy*, **5**, 1–16.

Oepen, H.P., Speckmann, M., Millev, Y. and Kirschner, J. (1997). Unified approach to thickness-driven magnetic reorientation transitions. *Physical Review B*, **55**, 2752–2755.

Pierce, D.T., Unguris, J., Celotta, R.J. and Stiles, M.D. (1999). Effect of roughness, frustration, and antiferromagnetic order on magnetic coupling of Fe/Cr multilayers. *Journal of Magnetism and Magnetic Materials*, **200**, 290–321.

Powell, C.J. and Jablonski, A. (1999). Evaluation of calculated and measured electron inelastic mean free paths near solid surfaces. *Journal of Physical and Chemical Reference Data*, **28**, 19–62.

Reimer, L. (1998). *Scanning Electron Microscopy: Physics of Image Formation and Microanalysis*, *Second Edition*, Springer-Verlag: Berlin, Heidelberg, New York.

Robins, J.L., Celotta, R.J., Unguris, J., *et al*. (1988). Domain images of ultrathin Fe films on Ag(100). *Applied Physics Letters*, **52**, 1918–1920.

Scheinfein, M.R., Pierce, D.T., Unguris, J., *et al*. (1989). Improved low-energy diffuse scattering electron-spin polarization analyzer. *Review of Scientific Instruments*, **60**, 1–11.

Scheinfein, M.R., Unguris, J., Kelley, M.H., *et al*. (1990). Scanning electron microscopy with polarization analysis (SEMPA). *Review of Scientific Instruments*, **61**, 2501–2527.

Schönhense, G. and Siegmann, H.C. (1993). Transmission of electrons through ferromagnetic material and applications to detection of electron-spin polarization. *Annalen der Physik*, **2**, 465–474.

Seah, M.P. and Dench, W.A. (1979). Quantitative electron spectroscopy of surfaces: a standard data base for electron inelastic mean free paths in solids. *Surface and Interface Analysis*, **1**, 2–11.

Speckmann, M., Oepen, H.P. and Ibach, H. (1995). Magnetic domain structures in ultrathin Co/Au(111): on the influence of film morphology. *Physical Review Letters*, **75**, 2035.

Stamm, C., Marty, F., Vaterlaus, A., *et al*. (1998). Two-dimensional magnetic particles. *Science*, **282**, 449–451.

Tulchinsky, D., Unguris, J. and Celotta, R. (2000). Growth and magnetic oscillatory exchange coupling of Mn/Fe(001) and Fe/Mn/Fe(001). *Journal of Magnetism and Magnetic Materials*, **212**, 91–100.

Unguris, J., Celotta, R.J. and Pierce, D.T. (1991). Observation of two different oscillation periods in the exchange coupling of Fe/Cr/Fe(100). *Physical Review Letters*, **67**, 140–143.

Unguris, J., Celotta, R.J. and Pierce, D.T. (1997). Determination of the exchange coupling strengths for Fe/Au/Fe. *Physical Review Letters*, **79**, 2734–2737.

Unguris, J., Pierce, D.T., Galejs, A. and Celotta, R.J. (1982). Spin and energy analyzed secondary electron emission from a ferromagnet. *Physical Review Letters*, **49**, 72–76.

VanZandt, T., Browning, R. and Landolt, M. (1991). Iron overlayer polarization enhancement technique for spin-polarized electron microscopy. *Journal of Applied Physics*, **69**, 1564–1568.

Investigation of Domains and Dynamics of Domain Walls by the Magneto-optical Kerr-effect

Rudolf Schäfer
Leibniz Institute for Solid State and Materials Research, Dresden, Germany

1 INTRODUCTION

The magnetic microstucture, that is, the arrangement of domains and domain walls, forms the mesoscopic link between basic physical properties of a magnetic material and its macroscopic properties. Hysteresis phenomena, energy loss in inductive devises, noise in sensors, or the magnetoresistive properties of modern spintronic devices can be decisively determined by the peculiarities of the underlying magnetic microstructure, especially by irreversibilities in the magnetization process. The development and optimization of magnetic materials therefore requires the knowledge of magnetic domains and their reaction to magnetic fields, which, in most cases, can only be gained by direct imaging.

Although there has been considerable progress in magnetic imaging in recent years, the classical Kerr technique still has unbeatable advantages. The method is based on the magneto-optical Kerr effect, that is, the magnetization-dependent rotation of plane-polarized light on reflection from a nontransparent magnetic sample. By means of an analyzer, in an optical reflection polarization microscope, this rotation is converted into a (in general weak) domain contrast that can be enhanced by digital image processing. Among all observation methods, Kerr microscopy is the most versatile and flexible imaging technique. With image processing, domain contrast is seen on virtually all ferro- and ferrimagnetic samples. Often, no specific surface treatment is required and even coatings may be allowed. Magnetic fields of arbitrary strength and direction can be applied to the sample, making it possible to observe magnetization processes and to simultaneously and locally record magnetization loops. Magnetization dynamics can be studied at arbitrary frequencies, covering the whole range from slow processes (as fast as the eye can follow) to excitations beyond the gigahertz regime by employing time-resolved imaging methods. Samples may be heated and cooled in optical heating stages and cryostats respectively so that magnetic phase transitions or other thermal effects on the magnetic microstructure can be investigated. Mechanic sample deformation during domain observation is easily possible, which makes the study of stress effects on domains possible. In- and out-of-plane magnetization components can be imaged separately, and, for low-anisotropy materials, the magnetization vector field at least on the sample surface can be quantitatively evaluated. The information depth of Kerr microscopy is in the 10-nm regime for metallic materials, allowing the depth-selective observation of magnetization distributions in layered sample systems. The magnification can easily be varied by changing the microscope objective, so that overview observations in the centimeter regime down

Handbook of Magnetism and Advanced Magnetic Materials. Edited by Helmut Kronmüller and Stuart Parkin. Volume 3: *Novel Techniques for Characterizing and Preparing Samples*. ISBN: 978-0-470-02217-7.

to detailed studies of samples of micrometer size are possible. The lateral resolution of optical microscopy with visible light is limited to about 300 nm by the Rayleigh criterion. This can be a drawback for the study of sub-micrometer patterned structures or for certain micromagnetic objects like vortices or stripe domains in very thin films. In bulk samples, only the magnetization of the surface region can be seen, but this limitation also applies to most other imaging techniques.

Since the first application of Kerr microscopy (Williams, Foster and Wood 1951; Fowler and Fryer, 1952), there has been tremendous progress in methodical developments around the traditional Kerr technique. In this article, the mentioned possibilities of modern Kerr microscopy are reviewed, together with physical and technological fundamentals. A comprehensive review on magnetic domains and imaging methods with emphasis on Kerr microscopy is given in the monograph 'Magnetic Domains' (Hubert and Schäfer, 1998), where an extended bibliography can also be found.

2 MAGNETO-OPTICS

Magnetic imaging at optical frequencies employs mainly the magneto-optical Kerr and Faraday effect. Both are rotational effects, that is, plane-polarized light is rotated somewhat on transmission through an optically transparent specimen (Faraday effect) or on reflection from a nontransparent sample (Kerr effect), respectively. Both effects can also be interpreted as circular birefringence (i.e., a birefringence of circularly polarized light) and are described by the same physical laws. Another effect, mostly used for transmission observations in magnetic garnets, is the Voigt or Cotton–Mouton effect, also known as *linear magnetic birefringence* (i.e., a birefringence of linearly polarized light). This effect can also be applied in reflection, together with the magneto-optical gradient effect. All three reflection effects are helpful for domain analysis. Owing to its dominating importance, we focus on the Kerr effect in this article and mention the other effects only briefly.

2.1 Kerr effect

The rotational action of the Kerr effect (Kerr, 1877) is phenomenologically described by the dielectric law $\boldsymbol{D} = \boldsymbol{\varepsilon}\boldsymbol{E}$, in which an antisymmetric $\boldsymbol{\varepsilon}$ tensor (containing the components of the magnetization vector) connects the electrical vector $\boldsymbol{E}$ of an illuminating plane light wave with an induced displacement vector $\boldsymbol{D}$ in the regime of optical frequencies. This relation can be written in the form

$$\boldsymbol{D} = \varepsilon(\boldsymbol{E} + \mathrm{i}Q\boldsymbol{m} \times \boldsymbol{E}) \tag{1}$$

where ε is the regular dielectric constant and Q is a complex material parameter that is roughly proportional to the saturation magnetization of the sample and that describes the strength of the Kerr effect. The $\boldsymbol{D}$ vector can be interpreted as secondary light amplitude being generated by the magneto-optical interaction of $\boldsymbol{E}$ with the magnetization vector $\boldsymbol{m}$ anywhere in the sample.

The cross product in equation (1) reveals the gyroelectric nature of the Kerr effect. Its symmetry can be derived by using the concept of a Lorentz force ($\boldsymbol{m} \times \boldsymbol{E}$) on the electrons set in vibrational motion by the light wave (Figure 1a). If the Lorentz movement v_{Lor} (parallel to the second term in equation (1)) is projected onto the plane perpendicular to the propagation direction of the reflected light wave, the magneto-optic light amplitude $\boldsymbol{K}$ is obtained. This so-called Kerr amplitude is polarized perpendicularly to the regularly reflected amplitude $\boldsymbol{N}$ that is polarized in the same plane as the incident light and that is given by the Fresnel equations. By interference of $\boldsymbol{K}$ and $\boldsymbol{N}$, the polarization vector of the reflected light is rotated by the (small) angle $\Phi_{\mathrm{K}} = KN^{-1}$ (Figure 1b). Here K and N are the effective light amplitudes after the light has passed through the analyzer. For domains with opposite magnetization, the Lorentz force acts in reverse direction, that is, the Kerr amplitude changes sign. A domain contrast is produced if most of the reflected light from one domain type is blocked by the analyzer, as indicated in Figure 1(b), transferring the rotation of the polarization plane to a difference in intensities. The size of the usable signal that also determines the signal-to-noise ratio if video microscopy is applied is important for good domain visibility. The relative signal S, that is, the difference between the intensities of bright and dark domains, is derived as (Hubert and Schäfer, 1998)

$$S \cong 4\beta KN \tag{2}$$

Three properties are noted: (i) The Kerr signal is a linear function of the Kerr amplitude K and therefore of the respective magnetization components according to equation (1). (ii) The Kerr signal can be enhanced by increasing the analyzer angle β beyond Φ_{K}, allowing to increase the signal-to-noise ratio and to adjust to the sensitivity of the detector. (iii) The 'visibility' of domains is determined by the Kerr *amplitude* and not by the Kerr rotation. Although $\boldsymbol{K}$ depends on material constants, it can be enhanced in case of materials where the incoming light is not completely absorbed by magneto-optical interaction, but 'uselessly' reflected to some extent. Antireflection coatings increase the absorbed intensity (based on interference effects that reduce the regularly reflected light component while enhancing the Kerr component – see Hubert and Schäfer (1998) for a review), proportionally raising $\boldsymbol{K}$ and thus the

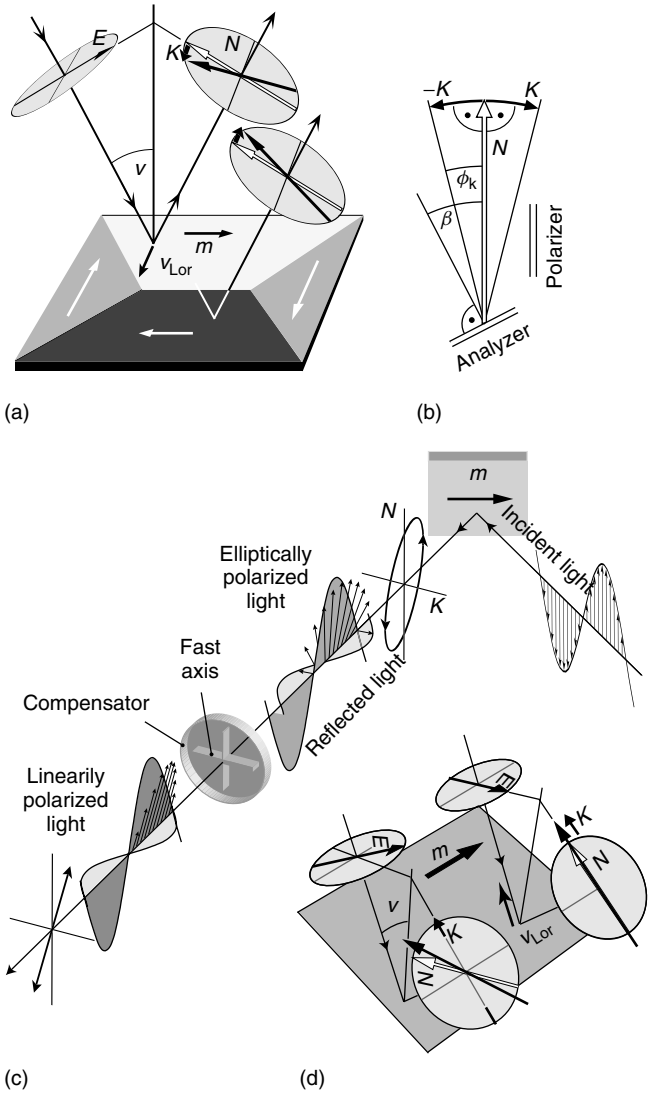

Figure 1. (a) Illustration of the elementary magneto-optical interaction for the longitudinal Kerr effect. The sample with in-plane magnetization is illuminated using light that is polarized parallel to the plane of incidence. The electric field vector $\boldsymbol{E}$ of the incident light, together with the magnetization vector $\boldsymbol{m}$, generates a Lorentz movement of the electrons ('right-hand rule'). If the resulting Lorentz speed v_{Lor} is then projected onto the plane perpendicular to the direction of propagation of the reflected light, the magneto-optical amplitude $\boldsymbol{K}$ is obtained (a similar $\boldsymbol{K}$ component would also be generated if the light would be polarized perpendicular to the plane of incidence). The interference of the normally reflected component $\boldsymbol{N}$ and the Kerr component $\boldsymbol{K}$ results in magnetization-dependent light rotation by a small angle Φ_K, which, by using an analyzer, leads to the domain contrast (b). The analyzer should actually be set at the angle $\beta > \Phi_K$ to optimize the domain visibility. The action of the compensator is illustrated in (c). It converts elliptical light into a linear wave by shifting the two constituent, orthogonal wave components. The symmetry of the transverse Kerr effect is explained in (d). Only light of parallel polarization yields an effect, so that a Kerr rotation is only possible at 45° polarization.

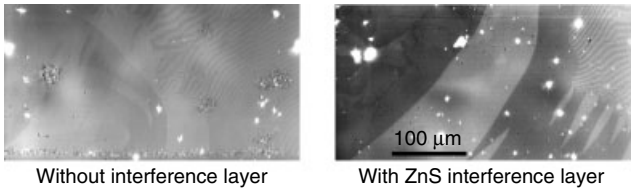

Figure 2. Effect of a dielectric antireflection coating on the Kerr contrast, demonstrated for an amorphous ribbon that is coated in the right image.

useful signal (Figure 2). Effective dielectric coatings are ZnS for metals and MgF_2 for oxides. As the Kerr effect is weak in general, this gain should not be relinquished even if digital image processing (see Section 3.1.3) is applied.

In general, the polarization plane of the reflected light is not just rotated with respect to that of the incident light, but also elliptically polarized. Ellipticity is caused by an 'intrinsic', material-dependent (Oppeneer, 2001) phase shift between the $\boldsymbol{N}$ and $\boldsymbol{K}$ components (also interference layers on top of the sample surface can add a phase shift). If a noticeable ellipticity occurs, the reflected wave is less detectable by the analyzer. This problem can be eliminated by the use of a compensator (see Figure 1c), which should be attached in front of the analyzer. A compensator is an optical device that is based on birefringent materials such as quartz or mica and that is capable of impressing a controllable retardance on a wave, that is, it changes the relative phase of the constituent orthogonal ordinary and extraordinary components of the wave in a variable way. Highest flexibility is obtained by using simple wave plates with a fixed retardance of $\lambda 4^{-1}$, for instance (rather than a regular compensator as, e.g., of the Babinet type, which requires that its optical axes are aligned along and perpendicular, respectively, to the plane of the regularly reflected light – see Figure 1c). A variable phase shift between $\boldsymbol{N}$ and $\boldsymbol{K}$ is obtained by rotating the plate, which leads to a phase shift of both components. By means of such a compensator, a beam that is reflected elliptically from the sample can be converted into a linear wave. The azimuth angle of this wave is different from that of the incident wave, however, requiring an additional analyzer rotation for extinction. In this way, it is possible to extinguish at least the light of one domain thus generating a significant Kerr contrast.

Different basic geometries are distinguished in Kerr microscopy, which can again be derived with the help of the Lorentz concept. To produce a Lorentz movement that leads to detectable Kerr rotation, an appropriate direction of light incidence and polarization has to be selected for a given magnetization direction. As a simple rule, the Kerr rotation is proportional to the magnetization component parallel to the reflected beam of light. This rule implies that

domains that are magnetized parallel to the sample surface (as shown in Figure 1a) require oblique light incidence, and that for maximum rotation the plane of incidence must be parallel to the axis of magnetization with the polarizer set either parallel or orthogonal to the incidence plane (*longitudinal* Kerr effect, $\vartheta \neq 0$). The Kerr amplitude is then proportional to the sine of the angle of incidence ϑ, and therefore disappears for perpendicular incidence. In this case, maximum rotation is exhibited by domains that are magnetized perpendicularly to the sample surface (*polar* Kerr effect, $\vartheta = 0$), while in-plane domains do not cause a Kerr amplitude. At oblique incidence, both in- and out-of-plane magnetization components generate a superimposed Kerr contrast. The separation of the two components is possible by proper difference images that are obtained at different microscope settings, as demonstrated in Figure 3. Also, the *transverse* Kerr effect, illustrated in Figure 1(d), leads to in-plane magnetization sensitivity. Here, the in-plane $\boldsymbol{m}$ vector is normal to the plane of (oblique) incidence. Light with $\boldsymbol{E}$ parallel to this plane generates a Kerr amplitude, but its polarization direction is the same as that of the normally reflected beam. The transverse Kerr effect thus causes an amplitude variation, which can be used for measuring purposes. A rotation that is detectable by an analyzer is obtained when the incident light is polarized at 45° to the plane of incidence. Then, the $\boldsymbol{E}$ component perpendicular to the incidence plane is not affected ($\boldsymbol{E} \,||\, \boldsymbol{m}$), while the parallel component is modulated in its amplitude on reflection, leading to polarization rotation by superposition, as also indicated in Figure 1(d).

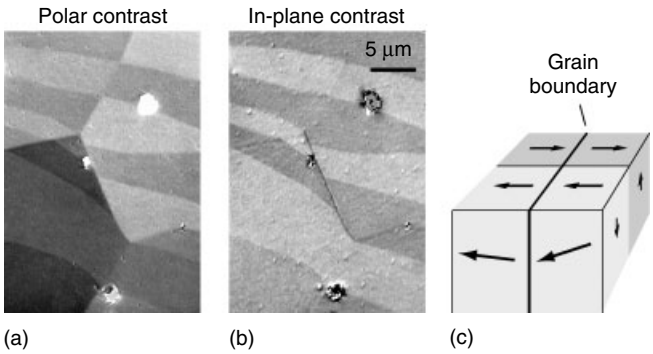

Figure 3. Domains in a coarse-grained NdFeB crystal in which the magnetization axes of the four different grains are misaligned relative to the observed surface as schematically shown in (a). The magnetization components perpendicular to the surface (polar components) can be imaged separately at perpendicular incidence (b). At oblique incidence, polar and in-plane components show up simultaneously (not shown). When the illumination direction is rotated by 180°, the polar Kerr effect does not change sign, whereas the longitudinal effect does (see Figure 13b below). By forming the image difference the polar contrast disappears, leaving just in-plane contrast (c).

2.2 Other magneto-optical effects

Three further magneto-optical effects that can be used for domain observation in a polarization microscope have to be mentioned. Related to the Kerr effect is the Faraday effect (Faraday, 1846). It follows the same symmetry rules, but is restricted to transparent samples such as magnetic garnet films and is observed in transmission experiments (Fowler and Fryer, 1956). The Faraday contrast is much stronger than the Kerr contrast and does not require electronic means for enhancement. In recent years, the Faraday effect found application in magneto-optic indicator films. These are transparent garnet films with in-plane anisotropy that are coated with a mirror layer on one side. If the mirror side is placed in contact with a magnetic specimen, the stray field of the sample induces a polar magnetization component in the active layer, which can be viewed in the polar Faraday effect at reflection. Charged domain walls, for instance, can be indirectly imaged in this way (Nikitenko *et al*., 1998).

The Voigt effect (Voigt, 1898) was mainly applied for transmission observations of in-plane domains in garnets (Dillon, 1958). It is quadratic in the magnetization components, so that only domains magnetized along different axes show a contrast. The effect is strongest at perpendicular incidence (where a Faraday or Kerr contrast of in-plane domains is not possible) and requires a compensator for adjustment. Later, the Voigt effect was also discovered in reflection experiments on metals, together with the magneto-optical gradient effect (Schäfer and Hubert, 1990) that shows up under similar experimental conditions. The gradient effect is a birefringence effect, which depends linearly on magnetization gradients. Both effects (in combination with the Kerr effect) are helpful in the analysis of domains in cubic materials such as epitaxial thin-film systems by considering their contrast laws and depth sensitivities (see Schäfer (1995) for an overview). The gradient effect can also favorably be applied to image fine transitions and domain modulations. The phenomenological differences between Kerr, Voigt, and gradient effect are compared in Figure 4, in which a typical domain pattern of an iron–silicon crystal with two orthogonal easy axes of magnetization in the surface was imaged in an optical polarization microscope under different conditions as indicated.

3 KERR MICROSCOPY

Two types of Kerr microscopes are in use: wide-field (regular) microscopes, which immediately provide an image of a certain sample area, and laser-scanning microscopes, in which a laser spot is scanned relative to the sample surface building up the image sequentially. Both have their drawbacks and advantages, as elaborated in the following

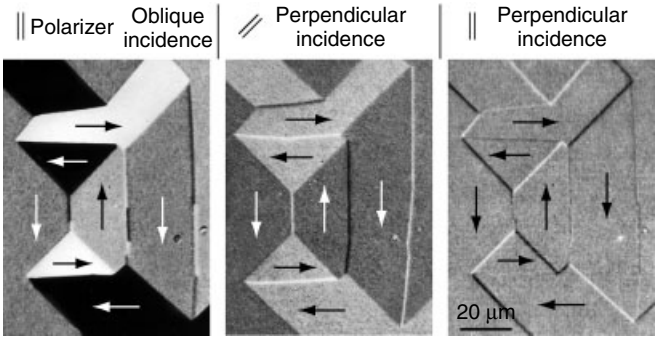

Figure 4. Domains on a (100) surface of silicon–iron (Fe 3 wt% Si, sheet thickness 0.3 mm), imaged in the magneto-optical Kerr (a), Voigt (b), and gradient effect (c). The Kerr effect is linear in the magnetization vector, so the four-domain phases in (a) show up in different colors. The same pattern imaged in the Voigt effect displays only two colors, one for each magnetization axis. This contrast is independent of the magnetization *direction* since the Voigt effect depends quadratically on the magnetization vector. The gradient effect is sensitive to changes in magnetization. Therefore, domain boundaries show up in this effect with a contrast, depending on the relative magnetization directions of the neighboring domains. Both Voigt and gradient effect are strongest at perpendicular incidence of light and require a compensator for contrast adjustment. (Reproduced from Schäfer, R. and Hubert, A. (1990). A new magnetooptic effect related to non-uniform magnetization on the surface of a ferromagnet. *Physica Status Solidi A*, **118**, 271–288 by permission of Wiley-VCH.)

sections. Emphasis is on wide-field microscopy as it is the most commonly applied and most versatile technique.

3.1 Wide-field Kerr microscopy

3.1.1 Microscope

Standard wide-field Kerr microscopes are based on commercial reflected light microscopes with strain-free optics to allow for polarization microscopy. Wide-field microscopes apply the Köhler illumination technique, which was introduced in 1893 by August Köhler from Carl Zeiss corporation, to obtain homogeneously illuminated images at maximum resolution. This technique is explained by ray diagrams in Figure 5, where the illumination and image-formation ray paths are illustrated separately for the purpose of visualization. Light emitted from the lamp is focused onto the plane of the aperture diaphragm by the lamp collector lens, passes through the opening of a variable field iris diaphragm, and is then plane polarized and deflected downward into the objective lens, for example, by a partially reflecting plane glass mirror. After reflection from the specimen, the light is captured by the objective and then passes through the half-mirror again. Modern optical microscopes are built with infinity-corrected objectives, that is, the light rays emerge from the objective in parallel bundles from every azimuth and are projected to infinity. These bundles enter the tube lens, which forms an intermediate image that is further processed toward the eyepiece or camera. In the 'infinity' space, accessories like reflector mirror, analyzer, and compensator are added with simple design and without distortion of the image. Polarizers and analyzers in today's microscopes are made of dichroic polarizing foils. Although the polarization degree (2×10^{-6}) of such sheet polarizers is sufficient for Kerr microscopy, they suffer from a high light absorption of more than 50%. Light intensity by a factor of 2–3 and better extinction can be gained by replacing sheet polarizers with Glan–Thompson prism polarizers.

The field diaphragm is imaged on the specimen and thus determines which part of the sample is illuminated. It does not affect the optical resolution or intensity of illumination. The latter is rather controlled by the *aperture* diaphragm that also determines the angles of incidence and is therefore crucial for Kerr microscopy. Closing or opening the aperture diaphragm varies the angle of the light rays reaching the specimen from all azimuths, with the largest angle of incidence being limited by the numerical aperture of the objective. A centered aperture iris (Figure 5a) results in an illumination cone that hits the sample vertically. Owing to symmetry, the Kerr amplitudes resulting from in-plane magnetization components cancel each other, so that in this case a sole sensitivity to out-of-plane magnetization is given as required for the polar Kerr effect. An off-centered aperture diaphragm (Figure 5c) leads to an obliquely incident bundle of rays (with an angle-of-incidence dispersion ranging between perpendicular and maximum) as necessary for longitudinal and transverse Kerr sensitivity. Oblique incidence is also provided by a Berek prism (Figure 5d), which is a 90° prism constructed in the form of a trapezoid, resulting in a light path where the beam is internally reflected three times before it exits the prism. A Berek prism introduces little depolarization and causes no light loss, contrary to the mentioned glass plate reflectors for which just a quarter of the illuminating light is used for image formation. However, the viewing aperture is restricted by the prism itself, leading to a reduced optical resolution in the direction transverse to the microscope plane. If light intensity poses no problem, a sheet reflector offers optimum resolution and high flexibility in the observation mode (see next paragraph). In recent years, microscope companies have largely eliminated the option of Berek prisms in their product lines. The availability of highly sensitive video cameras can partly compensate for this unfavorable circumstance.

The plane of the aperture diaphragm is conjugate to the back focal plane of the objective lens, also called *diffraction plane* or *pupil* of the objective. As the back focal plane is

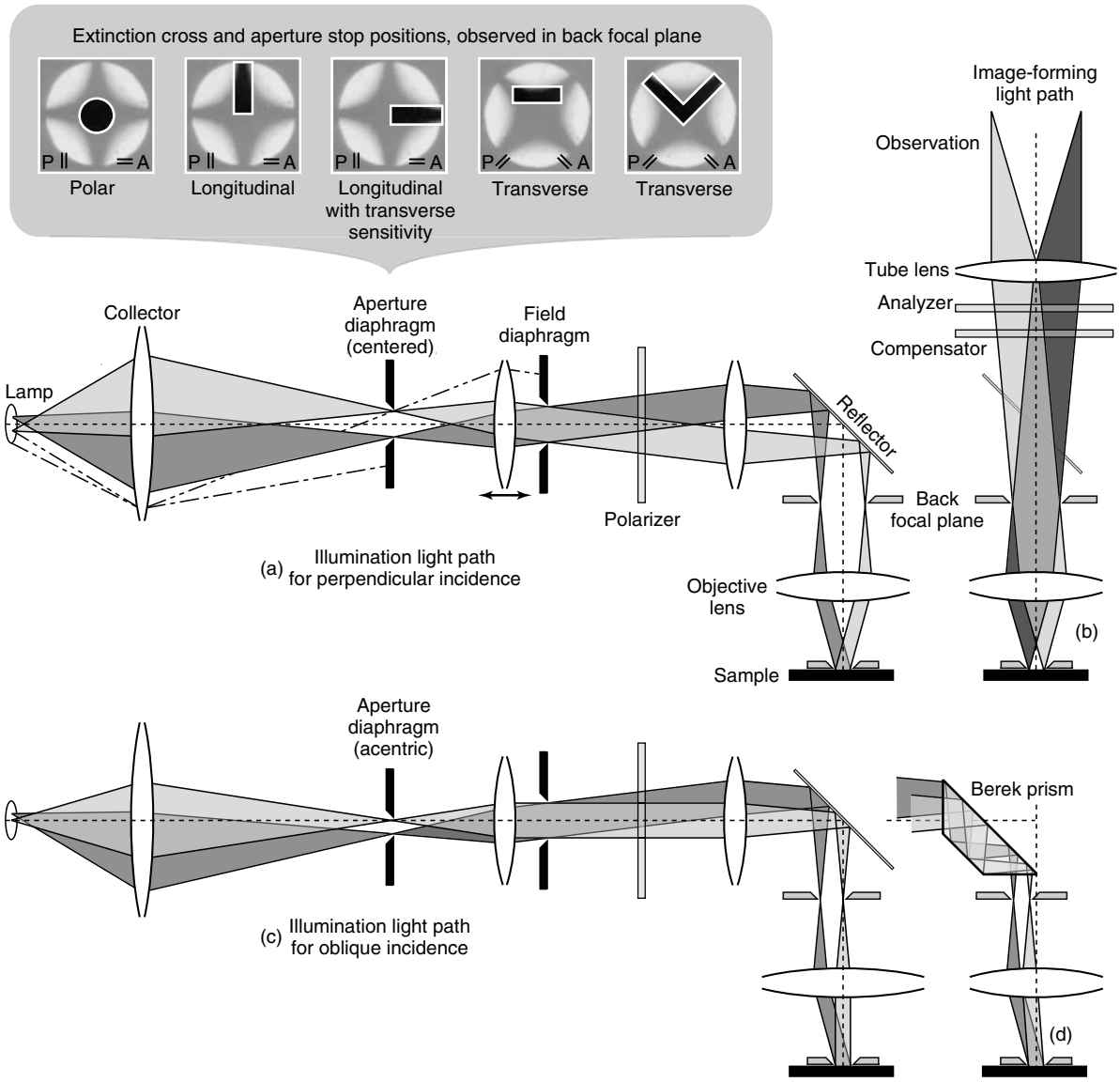

Figure 5. The essential components and ray paths of a wide-field Kerr microscope. (a) Illumination path for perpendicular light incidence, and (b) image-forming path. Oblique incidence (c) requires a displaced aperture slit and can also be obtained with a Berek prism (d). The inset shows the diffraction plane of the microscope for the case of a sheet reflector. Here, the aperture diaphragm can be viewed and adjusted to fulfill the requirements for the polar Kerr effect (centered iris diaphragm) or longitudinal and transverse effects (displaced slit diaphragm). The orientation of the extinction cross depends on the polarizer setting (indicated by P), with the analyzer (A) and eventually the compensator being adjusted for maximum extinction.

not identical for all objectives in conventional microscopes (objectives are rather constructed for identical front focal planes to guarantee identical sample positions), the relevant lens that images the aperture into the pupil has to be moved or supported by additional lenses to exactly provide this condition for all objectives – a feature that is not available in commercial microscopes. If the aperture diaphragm is not imaged exactly to the pupil, it is not effective uniformly for the whole observation field and the points on the sample are not illuminated from the same angular range. This may result in an inhomogeneous image up to a magnetic contrast inversion across the image (see Fig. 2.16 in Hubert and Schäfer (1998)). The diffraction plane can be seen in the so-called conoscopical image of the microscope by replacing the eyepiece by an auxiliary telescope or by a built-in, focusable Bertrand lens. This image is characterized by a cross-shaped extinction zone when the polarizer and analyzer are crossed for maximum extinction (Figure 5, inset), rather than being homogeneously dark as would be the ideal case. The reason for this 'Maltese' cross, which becomes more pronounced

as the numerical aperture of the objective increases, is that a convergent light bundle, rather than a parallel laser beam, is used in wide-field microscopy. All beams not lying in a central incidence plane along or perpendicular to the polarization plane cannot be extinguished by the analyzer as they are reflected in an elliptical and rotated polarization state in general. This is due to differential transmission of the p (***E*** vector parallel to plane of incidence) and s (***E*** vector perpendicular to plane of incidence) components at the steep optical interfaces of lenses. This depolarization results in four bright quadrants, separated by the Maltese cross, in the conoscopic image. For best contrast conditions, the illumination should be restricted to the area of maximum extinction in the conoscopic image by properly positioning the aperture stop, as illustrated in the inset of Figure 5 for the case of a sheet reflector (by using a Berek prism, half of the pupil would be occupied by an image of the prism itself). For the polar Kerr effect, a centered iris diaphragm is used, while the longitudinal effect is preferably adjusted by an off-centered *slit* aperture that is oriented parallel to the plane of incidence. For the transverse Kerr effect, the polarizer and consequently also the extinction cross are rotated by 45° (due to depolarization at the reflector, the use of a compensator is mandatory in this case to obtain a closed extinction cross). Here, a displaced slit perpendicular to the plane of incidence or a V-shaped slit are the best solutions. Both, longitudinal and transverse effects can be adjusted as well by using a Berek prism, while the polar effect requires a sheet reflector. If a sheet reflector is used, the 'true' transverse Kerr effect can be replaced by the longitudinal effect by placing the slit aperture on the sideward branch of the extinction cross, thus causing a transverse plane of incidence, that is, transverse sensitivity.

3.1.2 Lateral resolution

The lateral resolution in optical microscopy is determined by the numerical aperture ($NA = n \sin\alpha$) of the objective lens, where α is half the opening angle of the objective (i.e., half the angle of the cone of light from the specimen that is accepted by the objective) and n is the refractive index of the medium used between objective and object ($n = 1$ for air; $n \approx 1.5$ for immersion oil). The higher α and n, the more orders of diffracted light are collected by the objective, which increases the resolution. The smallest distance between two objects that can be resolved is given by $d_{\min} = 0.5\,\lambda N A^{-1}$ according to the Rayleigh criterion (λ is the wavelength of light, e.g., 550 nm for green light). The highest numerical aperture available is 1.4, obtained with oil-immersion objectives of 100× magnification. Using such an objective and blue light for illumination, domains as narrow as 150 nm can be resolved (Schmidt and Hubert, 1986). Smaller magnetic objects like domain walls down to a size of some 10 nm may also become visible by digital contrast enhancement, but their image is diffraction broadened. Ultraviolet (UV) light would further improve resolution; however, UV light with a wavelength of 400 nm is already absorbed to 50% by conventional lenses (at 360 nm wavelength, the absorption is 100%). UV microscopes with all-quartz optics, permitting resolutions down to about 80 nm at deep-UV wavelengths, have been developed mainly for defect inspection in semiconductors. The implementation of polarization optics in such microscopes, however, appears to be problematic (Yamasaki, 2006, Private communication).

In Figure 6, some examples of high-resolution observations, using white light and oil immersion, are collected. The surface magnetization of asymmetric Bloch walls on bulk soft magnets is well resolved, even in the case of iron–silicon with a surface wall width of just 150 nm (Figure 6a). The same is true for all kinds of domain walls in magnetic films, as shown for the examples of crosstie walls (Figure 6b) in thin films and asymmetric Bloch and Néel walls in thick films (Figure 6c). Also, small-angle magnetization modulations (ripple or patchy modulations) are easily identified. The practical limit for the observation of small particles is demonstrated in Figure 6(d) for cobalt thin-film elements. Faint contrasts are still visible on the 230-nm-wide dot. A reliable judgment on the magnetization distribution, however, requires elements larger than a micrometer (Figure 6e). The images in Figure 6(f) demonstrate an *in situ* observation of current-induced domain wall propagation (Kläui *et al*., 2005) in a NiFe stripe structure with a width close to the resolution limit.

Restrictions in the resolution of Kerr microscopy are outweighed by a highly flexible magnification. Sample areas ranging between 5 mm and 30 µm can be covered by simply changing objective lenses in standard microscopes. Often, a low-resolution overview of domain patterns on a still larger lateral scale is required, even in the research on novel, nanoscale objects such as film systems for spintronics (Schäfer, Hubert and Parkin, 1993). Custom-made Kerr setups with separated illumination and observation paths are suited for this purpose (see Fig. 2.14 in (Hubert and Schäfer, 1998)). An elegant way of realizing such microscopes is to modify an optical stereomicroscope by using one path for illumination and the other for observation. An example for multiscale imaging in shown in Figure 7, which, at the same time, is an example for the possibility of sample manipulation by stress.

3.1.3 Image processing

As the Kerr effect is weak, polarization effects from imperfect surfaces, showing up especially at nearly crossed polarizers, can strongly obscure the magnetic image. Magnetic

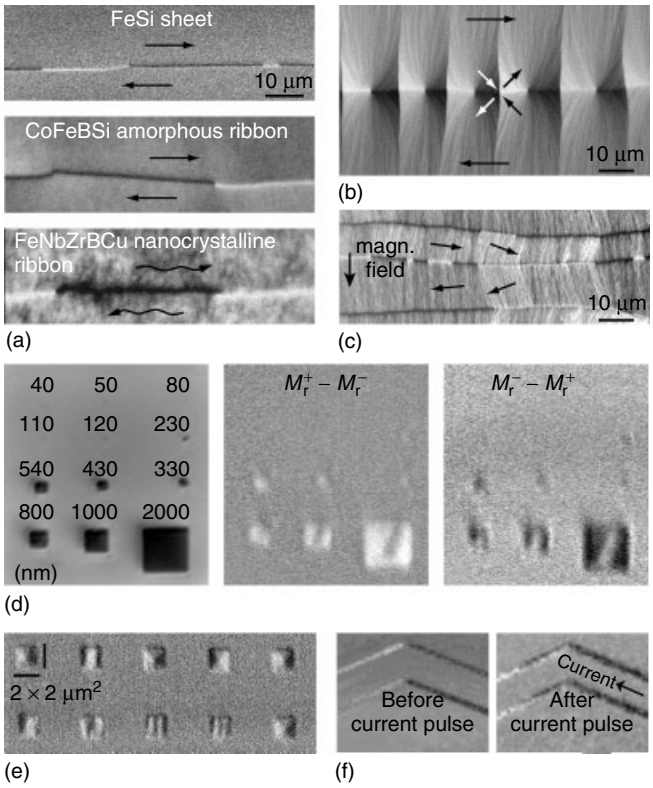

Figure 6. High-resolution Kerr observations. (a) Domain wall imaging on different bulk samples. The surface wall width for the FeSi Goss sheet (300 nm thick) with (110) surface orientation is 150 nm, for the metallic glass (25 µm thick) it is 0.9 µm, and for the nanocrystalline ribbon (20 µm thick) a surface wall width of 1.6 µm is measured, as expected due to the decreasing anisotropy in the order of materials. The black–white contrast of the wall segments is caused by the rotation sense of magnetization (see also Figure 4a). (b) Crosstie wall in a 40-nm-thick Permalloy film, and (c) coexisting asymmetric Bloch- and Néel walls in a 460-nm-thick Permalloy film, the latter being characterized by a double contrast. See (Hubert and Schäfer, 1998) for details. (d) Regular image (left) and difference images between the remanent states after positive and negative saturation (middle) and vice versa (right) on quadratic cobalt elements of various sizes. The saturation field is aligned vertically; the edge length of the elements is indicated in nanometers. (e) Domain patterns in an array of 2-µm-wide Co elements after ac demagnetization. In (f) the head-on domain walls in 500-nm-wide NiFe stripes were shifted by current pulse injection (See also **Current Induced Domain-wall Motion in Magnetic Nanowires, Volume 2**). (Sample for (d,e): courtesy *A. Carl*, Duisburg. Images (f): courtesy T. Moore, M. Kläui (University Konstanz) and J. McCord (IFW Dresden).)

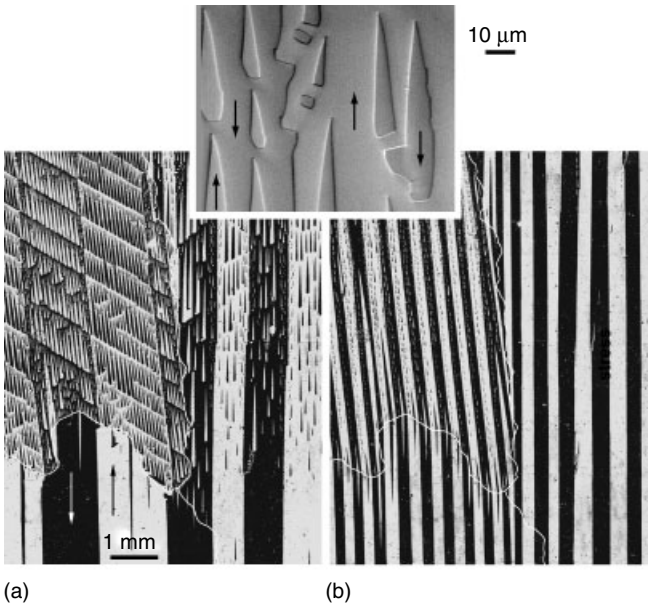

Figure 7. Demonstration of magnification range and sample manipulation abilities of Kerr microscopy. (a) Low-magnification domain overview on FeSi transformer steel sheet, showing three grains of different misorientation (characterized by the density of lancet domains (Hubert and Schäfer, 1998)) in the demagnetized state. Sixteen images, obtained with a 3.2× objective lens, were combined in this composite picture. Details of the lancet domains are presented in the inset, which was obtained with a 100× oil immersion objective at high resolution. The Kerr sensitivity was rotated by 90°, so that the domain walls are imaged rather than the domains. In (b) an external tensile, a stress of 2 kg mm^{-2} was applied to the sheet in vertical image direction, leading to domain refinement and suppression of the supplementary domains.

contrast enhancement is possible by the interference layers mentioned in Section 2. A much more powerful option, however, is the implementation of video microscopy and digital image processing (Schmidt, Rave and Hubert, 1985; Argyle, Petek and Herman, 1987). Magnetic materials are ideally suited for difference imaging because the magnetic state can be manipulated by external magnetic fields without changing the topography of the specimen. The standard procedure (Figure 8a) starts with a digitized, averaged image of the magnetically saturated state, where in an external dc magnetic field all domains are eliminated. Alternatively, an alternating field of moderate amplitude can be applied, which mixes up the domains during averaging with the advantage that forces on the sample may be smaller than in the high saturating field. This domain-free background (reference) image is then subtracted from a state containing domain information, so that in the difference image a clear micrograph of the domain pattern is obtained, which can be improved by averaging and digital contrast enhancement, free of topographic contrasts. Often, it is desirable to study domains in different aspects, for example, under longitudinal and transverse contrast conditions. This is possible by a combination experiment, as also demonstrated in Figure 8(a). After having created a regular difference image of a certain domain pattern, an image of the same pattern, but under different contrast conditions, is stored as a reference image that is

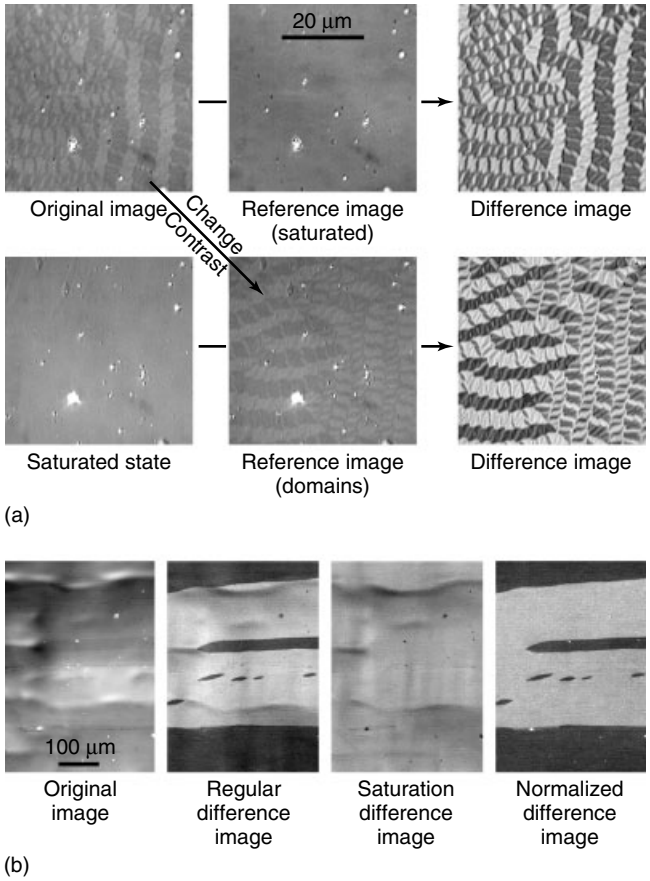

Figure 8. (a) Difference techniques for contrast enhancement, demonstrated for stress-induced domains on an iron-rich metallic glass. In a combination experiment, difference images of the same domain pattern are obtained under longitudinal (upper row) and transverse (lower row) contrast conditions. (b) Nonmagnetic contrast contributions in a 'regular' difference image can be removed by normalization by a 'saturation difference image', which is the difference image between two saturated states along opposite directions. The sample is an amorphous ribbon with a wavy surface.

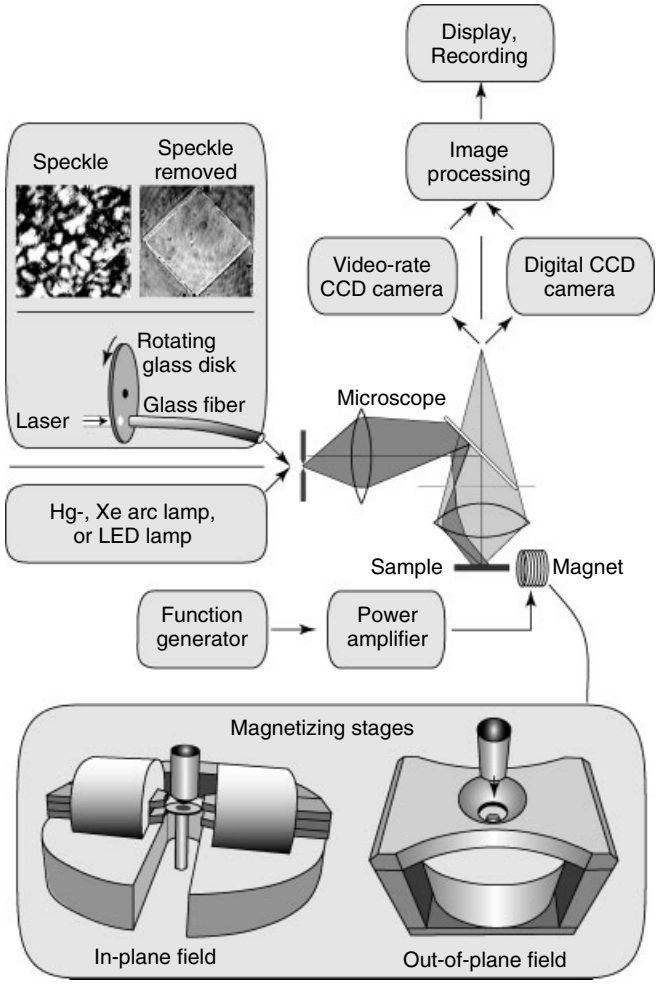

Figure 9. Experimental setup for wide-field Kerr microscopy. Options are shown for illumination, video processing, and magnetizing stages. Also shown is the presence and suppression of interference patterns by laser illumination with and without rotating glass disk respectively on a 28 by 28 μm^2 Permalloy thin-film element. (Courtesy *A. Neudert*, IFW Dresden.)

then subtracted from a saturated state obtained under the same contrast conditions. Sometimes, inhomogeneities in the illumination or nonplanar surfaces produce strong contrast in the direct image, which can remain visible as artificial contrast in a 'regular' difference image. An enhanced method (McCord and Hubert, 1999) that normalizes the standard difference image by a 'saturation difference image', thus removing these artifacts, is demonstrated in Figure 8(b). Further experimental possibilities applying difference techniques are shown in Section 4.

3.1.4 Setup

The complete experimental setup for video-enhanced, wide-field Kerr microscopy is schematically shown in Figure 9. As most of the light is thrown away in Kerr microscopy due to the small opening of the polarizer and analyzer, light sources with a high luminous density are mandatory. The best light source in most cases is a high-pressure mercury arc lamp. It offers sufficient brightness and a color spectrum that can be monochromatically used in the yellow-green as well as the blue range by suitable spectral filters. The use of monochromatic light can be useful for the imaging of certain materials, for example, ferrites. Here, the portion of linear Kerr light is largest at 400 nm so that the domains can be imaged without additional means, while at 550 nm the elliptical contribution is strongest, requiring a compensator. The disadvantage of the mercury lamp is its instability and short lifetime. Xenon-arc lamps are more stable and offer white light at a luminous density of just one-quarter of the mercury lamp. This is still sufficient if a Berek illuminator

and prism polarizers are used to avoid light loss, or if loss is compensated by a highly sensitive video camera. In any case, the infrared radiation component of these lamps has to be removed by heat-reflecting filters to protect the specimen and, possibly, sheet polarizers from damage (also video cameras may be sensitive to the near infrared).

Much higher light intensity at better stability is obtained by laser illumination (Argyle, Petek and Herman, 1987) (the luminous density of a 5-mW laser is comparable to that of a 100-W mercury lamp). The laser light is fed into the microscope by a multimode glass fiber of typically some 100 µm diameter, replacing the conventional arc lamp. The image of the fiber output is then focused to a small spot in the back focal plane of the objective by the microscope optics (alternatively, the fiber end can also be directly positioned in the back focal plane). This ensures an almost parallel illumination of the sample. As the laser spot is smaller than the arc image of a conventional lamp, the spot image can be directly placed on the extinction cross so that an aperture stop is not necessary. By moving the fiber output around in the back focal plane, the plane of incidence and the sensitivity axis is adjusted. A variety of different lasers is available that cover a wide range of wavelengths. Traditional argon ion lasers can be replaced by modern diode lasers or diode-pumped solid-state lasers such as Nd:YAG lasers with a wavelength in the infrared that can be shifted to the visible range by frequency doubling. Also, blue solid-state lasers are available. Lasers can be run in continuous wave or pulsed modes, the latter making them suitable for time-resolved imaging (see Section 4). The coherence of the laser light introduces problems in wide-field microscopy. Light scattering and diffraction patterns (speckle) develop because of interference at surfaces and dirt particles in the optics. Such mottle unsteadiness (Figure 9, inset) makes it impossible to observe magnetic responses in real time. These artifacts can be eliminated by temporally scrambling the laser light. If the interference patterns fluctuate substantially faster than the integration time of the detector (e.g., the video frame rate of the camera), the speckle and scattering artifacts disappear in the image. Several methods for despeckling have been developed (Inoué and Spring, 1997; Argyle and McCord, 2000): inserting a spinning glass wedge or a glass disk with a randomly undulated surface in the illumination, sending the light over tumbling and rotating mirrors, or mechanically vibrating the glass fiber and additionally vibrating the tip of the fiber so that its image covers a suitable area in the back focal plane. In any case, satisfactory results with laser-illuminated microscopes are only obtained in multiframe accumulated images where residual laser effects are averaged out. A promising alternative to laser illumination are high-intensity light-emitting diodes (LEDs), which are also fed into the microscope by an optical glass fiber (Kleinefeld, 2006 Private Communication). They combine high stability with the absence of speckle and interference fringes. By cooling the LED in liquid nitrogen, it tolerates higher currents, thus delivering higher intensity.

A sensitive video camera transforms the optical image into an electrical signal that is displayed on a screen, either directly or after image processing. Charge-coupled device (CCD) cameras or highly sensitive complementary metal oxide semiconductor (CMOS) cameras have replaced classical Nevicon tube cameras in recent years. A number of 'regular' integrating video-rate CCD cameras, which have been optimized for bright-field video microscopy, are available. Also, *digital* CCD cameras can be used for Kerr microscopy if their frame rate is fast enough (at least video frequency) to allow real-time imaging. The read-out speed of digital cameras can be enhanced by joining adjacent pixels together into super pixels (binning), though at the cost of resolution. An approximately 1000×1000 pixel resolution at a frame rate of 30 frames per second (fps) are reasonable numbers for standard Kerr microscopy. Owing to the low light level in Kerr imaging, high camera sensitivity is important. Image intensifiers (see Figure 22, below) can further increase sensitivity, and cooling of the CCD chip improves the signal-to-noise ratio. The option of electronic shading correction that allows to improve inhomogeneously illuminated images is advantageous. In practice, the image brightness has to be adapted properly to meet the signal requirements and optimum dynamic range of the video camera. Increasing the analyzer angle β (Figure 1b – the intensity increases with β^2) or opening the aperture stop beyond the width of the extinction cross, thus increasing the background intensity, are practical means to achieve a large signal-to-noise ratio. A possible loss in contrast is not a severe problem, as contrast can easily be enhanced electronically.

Image processing for contrast enhancement requires digital image acquisition. Digital CCD and CMOS cameras directly provide a digitized data stream, while for video-rate CCD cameras the analogous output has to be converted by an analog-to-digital converter. At least 8-bit resolution (meaning that the intensity amplitude of an image is represented by 256 discrete values) is required in the (optimized) original image to avoid visually obvious gray-level steps in the processed image (for digital cameras, this number may be higher). To create a difference image, first an averaged reference image is stored by summation of repeated images (typically 64 or 128 frames) of the same sample state. The digital frame memory, which holds the accumulated images, must have a storage capacity of at least 16 bits to also accommodate the brightest pixels of the sum of digital 8-bit images. The reference image is stored and continuously subtracted

from all following images, being displayed on the monitor at the same time. As the visual observation of domain motion is fundamental for any kind of domain analysis, it is advantageous if the subtraction process is performed in 'real time' at (at least) video frequencies without averaging. For recording and presentation purposes, noise can be reduced by adding each of the digitized images in a recursive procedure to produce a running average of the incoming images. Because noise is random and the signal is not, a running average both reduces the noise contribution and enhances the signal component of the output digital image. The result is an image of constant brightness, the noise of which is continuously reduced with increasing averaging time. Owing to the small magnitude of the Kerr contrast, the resulting difference image may contain relevant information often only in the lower bit levels. The visually meaningful 8 bits are selected and displayed. Domain images in 8-bit resolution are sufficient for pleasing visual observation as the human eye can distinguish, at most, 50 discrete shades of gray within the intensity range of a video monitor. By difference-image processing, the Kerr contrast is typically enhanced by a factor of 30; this means that contrasts below 0.1% can be visualized (the contrast sensitivity of the human eye is some percent at best). Digitized images open the way for further computer processing depending on specific demands.

The free space around the nosepiece of the microscope allows a variety of sample manipulations. The application of mechanical stress, as an example, was already documented in Figure 7. In-plane magnetic fields of arbitrary direction can be applied by rotatable coils or electromagnets. In the design of Figure 9, the specimen is mounted on a stamp that is placed between the pole pieces of an independently pivoted electromagnet. Magnetic fields $\mu_0 H$ up to some tenths of a Tesla can be achieved in such setups, reaching the Tesla regime at proper pole-tip geometry and close pole distance. Sample displacement of centimeters in the X and Y directions is possible and the entire stage unit is capable of precise up and down movement with the conventional coarse and fine focusing mechanism of the microscope. In-plane fields of arbitrary direction may alternatively be created by proper superposition of the fields of two fixed, perpendicular electromagnets. Also, perpendicular magnetic fields (i.e., parallel to the objective) can be generated in a Kerr microscope, either by regular coils or by specially designed electromagnets, as sketched in Figure 9, which provide fields up to the Tesla range. Other applications may require special designs (see Section 4.2.5 on dynamic imaging). Optical cryostats or heating stages, which fit between the pole pieces of an electromagnet, allow temperature-dependent observation of magnetization processes. As vacuum insulation is required for these devices, the sample has to be observed through a glass window. Long-distance objectives have to be used then which suffer from a reduced optical resolution of about 0.5 µm at best, as given by the numerical aperture of these objectives. A problem for the application of stronger fields is parasitical Faraday rotations in the lenses or glass windows of the optical temperature stages that may be much stronger than the Kerr effect. The Faraday contribution can be compensated by rotating the analyzer.

As extremely weak contrasts are enhanced by the difference imaging procedure, a high mechanical, thermal, and electrical stabilization of the microscope and electronics is indispensable to obtain optimal results (at least during the time where the same reference image is used). A stable light source, heat-reflection filters to avoid sample heating, and placing the microscope on a damped table to avoid vibrations are fundamental. Mechanical stabilization is most critical. Rough surfaces cause light scattering that immediately destroys the Kerr contrast in a difference image if the sample is displaced relative to the state where the reference image has been accumulated. Displacements of the order of the resolution limit of the used objective are sufficient to deteriorate a difference image. Considerable sample movement may be caused on larger samples in the gradient of the magnetizing fields. Using stiff sample holders and stiff gluing of the specimen reduces the problem (care has to be taken to avoid unwanted mechanical stress in the samples). All magnetic parts in the sample space should additionally be replaced by nonmagnetic ones as far as possible.

3.1.5 Kerr microscopy and magneto-optical magnetometry

Plotting the average image intensity in a sample area, which is defined by the objective and field diaphragm, as a function of the applied magnetic field yields a local magneto-optical hysteresis curve. At the same time, the domain images can be recorded, thus providing a visualization of the underlying magnetization process. Figure 10 shows an example of such an experiment, performed on an exchange-coupled bilayer system.

3.1.6 Quantitative Kerr microscopy

Owing to its linearity and direct sensitivity to the magnetization, the Kerr effect can be used for a quantitative determination of the magnetization direction (Rave, Schäfer and Hubert, 1987). The principle of quantitative Kerr microscopy is explained in Figure 11(a). The Kerr intensity has a sinusoidal dependence on the direction of the magnetization vector. This sensitivity function, which is used for calibration, is obtained by measuring the intensity of saturated states along different directions. Also, domain intensities can be used for calibration if their magnetization direction is known *a priori*,

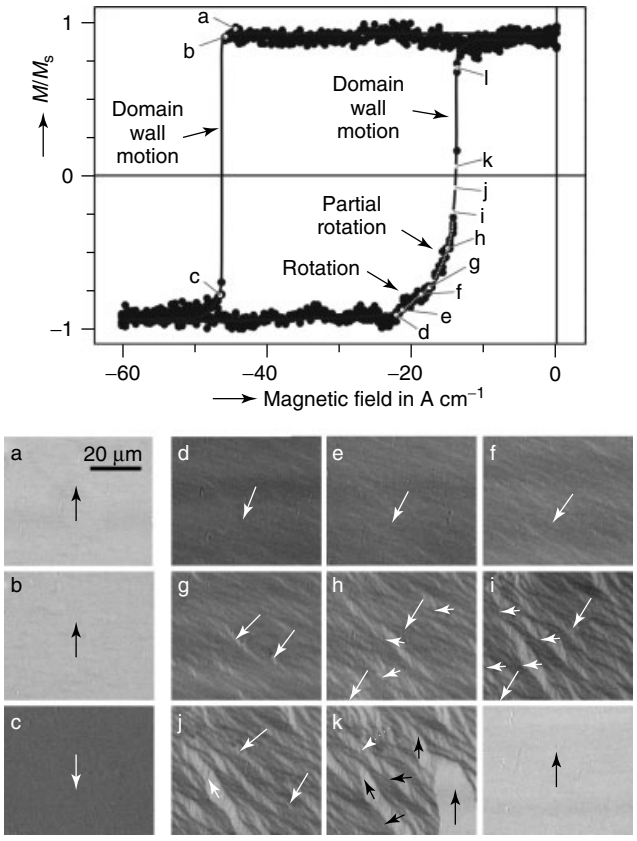

Figure 10. Magneto-optical hysteresis curve, directly measured in a wide-field Kerr microscope, together with domain images on a CoFe (20 nm)/IrMn (10 nm) bilayer film. The domains in the ferromagnetic CoFe film, which is exchange coupled to the antiferromagnetic IrMn film that is responsible for the loop shift (exchange bias effect, See also **Exchange Coupling in Magnetic Multilayers, Volume 1**) are shown. The steep forward branch of the magnetization curve is caused by domain wall motion (a–c), while inhomogeneous rotational processes (d–k) are responsible for the rounded part of the recoil branch. The wall motion along the forward branch is so fast that it cannot be recorded by static images. The magnetization M is normalized to the saturation magnetization M_s in the plot. (Reproduced from J. McCord, R. Schäfer, R. Matthesi, K.-U. Barholz: Observations by permission of American Institute of Physics.)

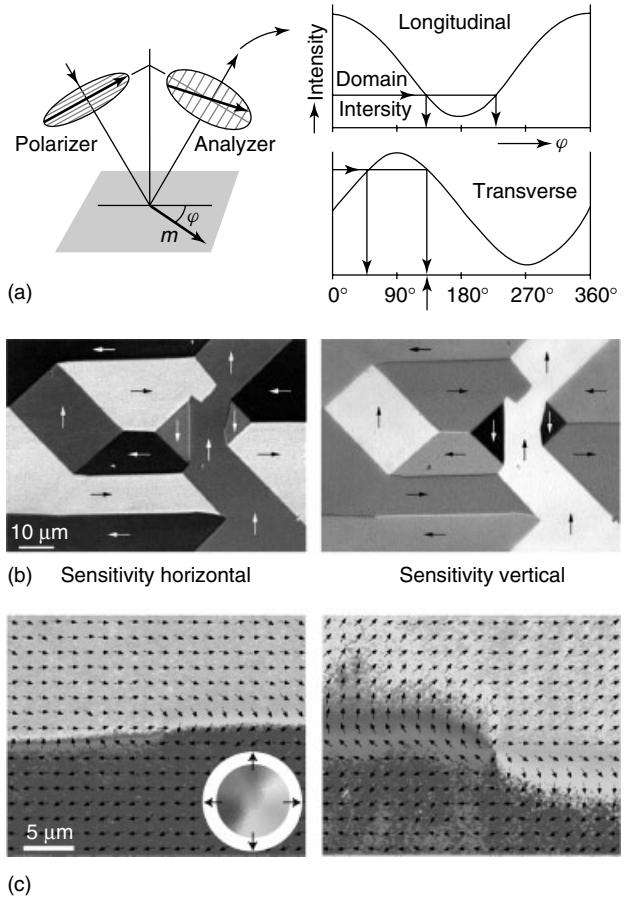

Figure 11. Principle and application of quantitative Kerr microscopy. (a) Calibration functions of the Kerr intensity at longitudinal and transverse sensitivity as a function of magnetization direction (schematically). The intensities of an unknown domain, measured under the same conditions, are compared with the calibration functions, as indicated by arrows. (b) Domain pattern on iron–silicon [100] sheet, imaged under two complementary Kerr sensitivities. (c) Quantitative images on a Co-rich amorphous ribbon. The domain wall width of the as-quenched state (left) is strongly enlarged (right) if residual anisotropies are reduced by annealing in a rotating magnetic field (Schäfer and Herzer, 2001). A vector plot and color code (here shown in black and white) can be used for presentation.

for example, due to crystal anisotropy or at sample edges. The intensity of unknown domains is then compared with the calibration function and so the angle of $\boldsymbol{m}$ in the surface can be measured. The problem is that due to the sinusoidal dependence there are two possible angles for a given domain intensity. To resolve this ambiguity, the domain pattern of interest has to be imaged twice under different sensitivity conditions that should be shifted by 90° (e.g., by choosing longitudinal and transverse Kerr effects). Figure 11(b) shows domains on an iron single crystal with [100] surface orientation that were imaged under these conditions. If the domain magnetization is transverse to the contrast sensitivity, the domain walls show up as black or white contrast, as given by their surface rotation sense. In Figure 11(c), the quantitative method was applied to domain walls in a cobalt-rich metallic glass ribbon. Originally, these images are displayed with a color code, where the in-plane magnetization directions are mapped by a color wheel. The quantitative method can reliably be applied only to soft magnetic materials for which no polar magnetization components are present at the surface, which would otherwise be difficult to calibrate or separate from in-plane contrast.

3.1.7 Depth-selective Kerr microscopy

The magnetic information depth of the Kerr effect is about 20 nm in metals. A quantification of this depth sensitivity has to consider the *phase* of the magneto-optic amplitude (Träger, Wenzel and Hubert, 1992). The total magneto-optical signal can be seen as a superposition of contributions from different depths, which are damped exponentially and which differ in phase as a function of depth according to a complex amplitude penetration function (Figure 12a).

These phase differences can be exploited in Kerr microscopy (Schäfer, 1995). Using a rotatable compensator, the phase of the Kerr amplitude, generated in a certain depth, can be adjusted relative to that of the regularly reflected light amplitude (as shown in Section 2, a detectable Kerr rotation is only possible if $\boldsymbol{K}$ and $\boldsymbol{N}$ are in phase). In this way, light from a selected depth zone may get invisible if its Kerr amplitude is adjusted out of phase with respect to the regular light. In sandwich films, (See also **Exchange Coupling in Magnetic Multilayers, Volume 1**) consisting of ferromagnetic layers that are interspaced by nonmagnetic layers, the zero of the information depth can be put somewhere into the middle of one layer so that the integral contributions of this layer just cancel, leaving only contrast from the other layer (Figure 12b). This kind of layer-selective Kerr microscopy is demonstrated in Figure 12(c) for a Co/Cu/NiFe sandwich sample. Demagnetization in an alternating field leads to a complicated mixture of wide domains in the low-coercivity bottom layer and fine, irregular domains in the high-coercivity top layer. After contrast separation, traces of these fine domains are also seen in the bottom layer, most likely induced by dipolar interaction with the magnetically charged domain walls of the top layer.

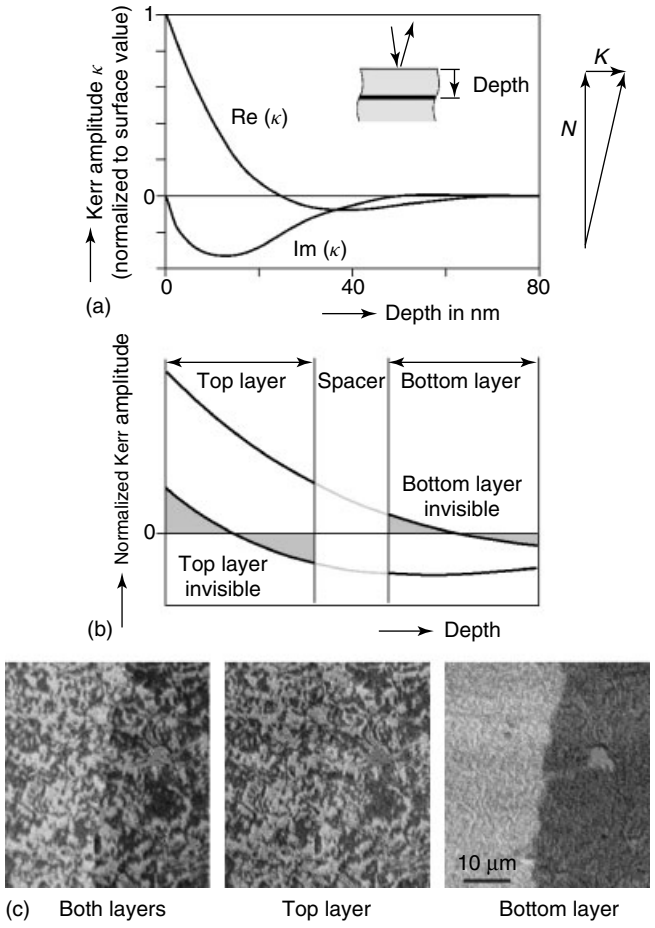

Figure 12. (a) Depth sensitivity of the normalized Kerr amplitude κ in iron. The relative phase of $\boldsymbol{K}$ and $\boldsymbol{N}$ was selected so that $\boldsymbol{N}$ is allowed to interfere with the $\boldsymbol{K}$ generated right at the surface (after Träger, Wenzel and Hubert, 1992). Proper phase selection (b) Proper phase selection (b-schematically) allows layer-selective Kerr imaging on thin-film sandwiches, as demonstrated in (c) for a sputtered Co/Cu/$Ni_{81}Fe_{19}$ (5 nm/5 nm/50 nm) trilayer. (Sample: *D. Bürgler*, FZ Jülich, imaging: *J. McCord*, IFW Dresden.)

3.2 Laser-scanning Kerr microscopy

In a laser-scanning Kerr microscope, a polarized laser beam is scanned relative to the specimen and its polarization state after reflection is analyzed by a photodetector. The early approaches of this technique were stimulated by the interest in the dynamics of magnetization processes in thin-film recording heads (see Section 4.2.1). First measurements, using a fixed laser spot and a line scan of the sample (Re, Shenton and Kryder, 1985), were soon extended to a two-dimensional scanning technique (Kasiraj, Shelby, Best and Horne, 1986). Elimination of nonmagnetic signals (due to nonideal surfaces) was achieved by synchronous detection: the magnetization was modulated by a high-frequency magnetic field. The corresponding modulation in the polarization of the Kerr light was then extracted from the optical detector with a phase-sensitive lock-in technique. Thus, a map of the high-frequency magnetization response (permeability) was obtained, in which the domain structure was revealed owing to domain wall motion. In succeeding developments, the domain information could be directly extracted by advanced detection schemes that even have the capability of vector magnetomery (Egelkamp and Reimer, 1990; Clegg, Heyes, Hill and Wright, 1991; Silva and Kos, 1997; Nagai, Sekiguchi and Ito, 2003).

The principle of such an advanced laser-scanning Kerr microscope is illustrated in Figure 13(a). A collimated and polarized laser beam is focused onto the specimen surface using an infinity-corrected objective lens. Argon lasers are widely used because of their brightness and excellent geometry. The laser spot is then moved across the specimen by

scanning probe and sample relative to each other. In commercial instruments, which have been designed mainly for biological applications, the laser spot is scanned in a TV-raster fashion (beam scanning). For Kerr microscopy, however, moving the sample itself in a rasterlike way by using a precision XY stage is more favorable. Although this stage scanning is relatively slow (the time required to produce an image is of the order of tens of seconds), it ensures that both, the angle of incidence and the polarization state of the illuminating ray bundle, are constant over the entire scan. By scanning, the image is constructed in a point-by-point manner with a lateral resolution that is basically determined by the size of the probing laser beam. Using a 100× oil immersion objective with a numerical aperture of 1.3, a laser spot size of 0.8 µm is obtained. A smaller focused spot size of 0.16 µm is achieved if the beam diameter is first increased by beam expansion to completely fill the objective aperture before it is focused on the sample (Inoué and Spring, 1997).

The reflected light, which is collected by the same objective lens, passes a rotatable quarter-wave plate to compensate ellipticity and finally enters a Thomson polarizing beam splitter. To obtain maximum sensitivity and flexibility, the splitter is set at 45° to the incident (undisturbed) polarization (Freeman and Hiebert, 2002a). Alternatively, the beam splitter can be set at 0° and the polarization plane can be rotated by 45° by using a half-wave plate before the light enters the splitter (Wright, Heyes, Clegg and Hill, 1995). The splitter provides two beams of orthogonal polarization direction (Figure 13a, inset) that hit a pair of quadrant photodiodes. Each pair of opposing quadrants is aligned along the projection of the samples x and y axes, respectively. The two beams are of equal intensity for the case of undisturbed 45° polarization, while any sample-induced polarization rotation leads to equal but opposite intensities (45° is the angle most sensitive to small polarization changes). By suitably combining the outputs of the eight photodiode quadrants, the three orthogonal components of magnetization can be simultaneously detected and separated, provided that they are sampled nearly equally, which is true for objectives with a high numerical aperture. As illustrated in Figure 13(b) (and demonstrated experimentally in Figure 3), the longitudinal Kerr contrast changes sign if excited by two beams of opposite directions of incidence, while the polar contrast remains unchanged. By adding the signals of all four diodes of one quadrant detector, the longitudinal components are cancelled, while the polar components are added. As the total intensity that reaches each detector is reduced and enhanced, respectively, by equal amounts owing to the beam splitting, the pure polar contrast can thus be separated by subtracting the two sum signals (i.e., taking the quadrant combinations $(X_1^+ + X_1^- + Y_1^+ + Y_1^-) - (X_2^+ + X_2^- + Y_2^+ + Y_2^-)$), whereas a nonmagnetic surface-contrast image

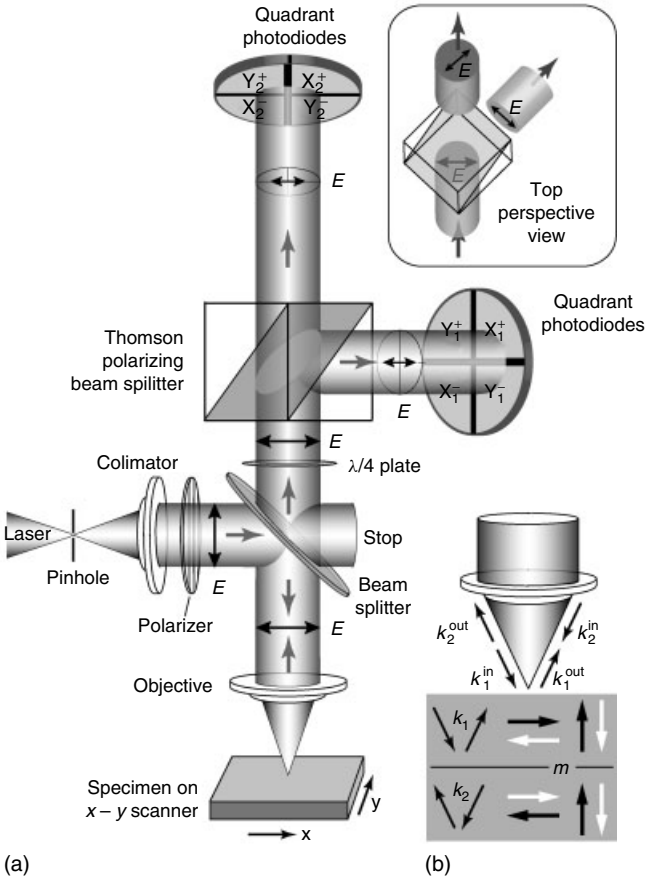

Figure 13. (a) Principle of laser-scanning Kerr microscopy (based on setups realized by Wright, Heyes, Clegg and Hill, 1995, and Freeman and Hiebert, 2002a). The polarization plane of light is indicated by the $\boldsymbol{E}$ vector. The inset shows a perspective view from top to illustrate the orthogonal polarization directions of the two beams leaving the polarizing beam splitter. (b) Contrast of in- and out-of-plane magnetization components depending on the direction of the $\boldsymbol{k}$ vector.

is generated by simply adding the signals. The longitudinal Kerr contrast of magnetization components along the x-axis is revealed by combining $(X_1^+ - X_1^-) - (X_2^+ - X_2^-)$, and that along the y-axis by $(Y_1^+ - Y_1^-) - (Y_2^+ - Y_2^-)$. Since all data are collected from the quadrants simultaneously, the three magnetization components at one sample spot are captured at the same time. This elegant method of vector magnetometry requires a highly symmetrical beam profile so that each quadrant receives the same quarter of the beam (Freeman and Hiebert, 2002a). The longitudinal contrast can be further enhanced by introducing a set of four apertures into the optical path in the back aperture of the objective lens. This restricts the range of the angles of incidence to provide a bundle of rays around an incidence angle of approximately 60°, depending on the used objective's numerical aperture (Wright, Heyes, Clegg and Hill, 1995).

Another advantage of the differential detection technique is the common mode rejection of laser noise while at the same time the signal is doubled. Further enhancement of the signal-to-noise ratio can be achieved by applying lock-in techniques: the illuminating laser beam is modulated by some photoelastic (Silva and Kos, 1997), acousto-optic (Wright, Heyes, Clegg and Hill, 1995), or electro-optic (Egelkamp and Reimer, 1990) device and the reflected light is measured by a phase-sensitive detection amplifier, thus selecting only signals that are proportional to the Kerr amplitude. By using ac detection, contrast arising from nonmagnetic surface structures is suppressed, the $1/f$ noise – inherent in the laser light source – is avoided, and polarization changes can be measured independently of intensity fluctuations in the reflected light. Signal enhancement by the lock-in technique (supported by additional subtraction of a constant background intensity in the preamplified signal) makes it possible for even the small light amplitude modulation of the transverse Kerr effect to be used for imaging purposes (Egelkamp and Reimer, 1990; Acremann *et al*., 2000). The technique, which is not easily possible in conventional Kerr imaging, has the advantage of being sensitive only to one magnetization component. By illumination from two directions, quantitative Kerr images can be obtained (Büscher and Reimer, 1993). Since the spots on the sample are illuminated sequentially in a laser-scanning microscope, interference speckle is less important and can be even completely eliminated by using an aperture (pinhole) in the detection system (Wright, Clegg, Boudjemline and Heyes, 1994). The aperture is placed conjugate to the spot being scanned so that only the light originating directly from the scanned spot is transmitted to the photodetector (such confocal systems also offer three-dimensional imaging capabilities, which is highly attractive in biological studies (Sheppard and Wilson, 1984)). The use of confocal imaging schemes has been shown to enhance the lateral resolution in non-magneto-optical microscopes by a factor of $\sqrt{2}$, which has, however, not been verified in Kerr imaging (Nutter and Wright, 1998).

A disadvantage of laser-scanning Kerr microscopy is its slow speed compared to regular imaging microscopes. The image acquisition time of some tens of seconds in stage-scanning microscopes can be lowered by beam scanning (Ping *et al*., 1995). This requires, however, special optical design to ensure a constant mean angle of incidence across the whole scan. Depolarization errors can be minimized by realizing the scanning with a vibrating single-mode optical fiber (Ping, See and Somekh, 1996). Scan rates of one frame per second can be obtained in this way, which, however, is still not fast enough for live observations of domains at video frequencies.

To conclude, scanning Kerr microscopy falls short in replacing conventional microscopy for 'routine' domain research as real-time imaging of domain motion cannot be realized. The capability to simultaneously image all three magnetization components (vector magnetometry) and to easily eliminate background contrast by lock-in techniques is advantageous. Static Kerr images of satisfactory quality, both of in- and out-of-plane domains, can therefore be obtained. Also, other quantities like permeabilities or magnetization curves can conveniently be measured on a microscopic scale, thus probing the spatial variation of magnetic properties. The biggest potential of laser-scanning microscopes, however, lies in their predestination for *stroboscopic* imaging of fast dynamic processes (see Section 4.2.4).

4 DYNAMIC KERR MICROSCOPY

Dynamic magnetization processes cover a wide range of timescales. Relaxation processes, wall creep, and aftereffect phenomena may last up to minutes and longer, eddy-current-limited processes in thick, electrically conducting specimens last microseconds, and precessional phenomena in metallic films occur in the nano- and sub-nanosecond regime (See also **Magnetization Dynamics Including Thermal Fluctuations: Basic Phenomenology, Fast Remagnetization Processes and Transitions Over High-energy Barriers, Volume 2**). Wide-field Kerr microscopy is suitable for dynamic domain studies in a frequency range from arbitrarily slow to beyond the gigahertz regime. Slow domain dynamics can be observed visually as fast as the eye can follow, either directly in the microscope or on contrast-enhanced images on the video screen if contrast enhancement by real-time image subtraction is used. As an example, domain growth by wall motion in an amorphous ribbon is presented in Figure 14(a–c) by three difference images, each obtained after stopping the field change during the (slow) magnetization cycle. However, on fast magnetization processes also, valuable information can be obtained by regular difference-image processing. In Figure 14(d), the domain state of (c) was excited by a 25-Hz sinusoidal field of small amplitude. Blurred domain boundary contrast in the averaged difference image indicates vibrational domain wall motion. Increasing the field amplitude (e) reveals immobile domains in the middle of the image and strong domain activity on the sides, as evident by the strongly blurred contrast in these areas. After switching off the alternating field (f), the domain pattern differs in details from the initial one (c), indicating irreversible processes. Reversible and irreversible wall displacements can immediately be distinguished in the experiment of Figure 14(g–i). In (g) and (h), the domain state of (f) was subtracted from averaged images of two states in which the sample was subjected to alternating fields (25 Hz) of weak and moderate amplitudes, respectively.

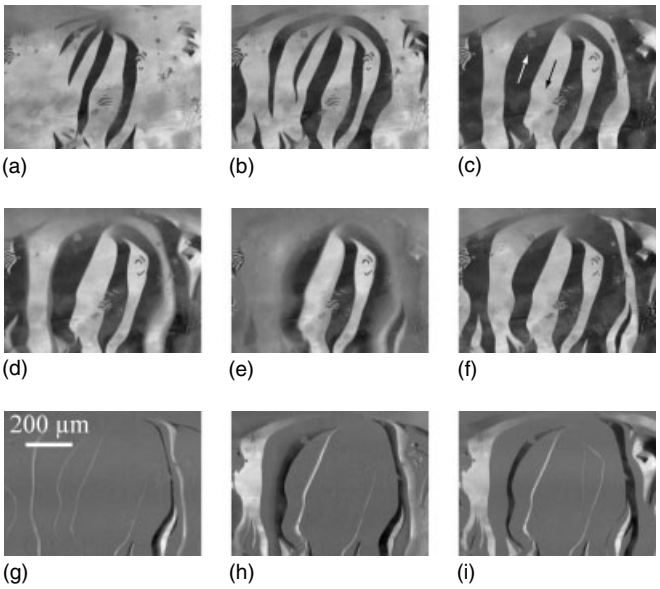

Figure 14. Studying the dynamics of a domain pattern in an amorphous ribbon ($Fe_{78}Si_9B_{13}$, thickness 20 µm) by conventional difference-image processing. The area shown is characterized by 180° domains that change their direction by about 90° at the top owing to stress-induced magnetic anisotropy. (a–c) Growth of dark domains in vertically aligned magnetic field. State (c) is excited by an alternating magnetic field of 25 Hz and increasing amplitude in (d) and (e). The moving parts of the domain pattern get blurred in the averaged difference image. In (g,h), the configuration (f) is subtracted from images with the same alternating fields applied as before. Changes in the domain pattern show up as strong black and white contrast in these dynamically averaged difference images. After switching off the ac field, some walls remain displaced irreversibly as can be seen by residual contrasts in the difference image (i).

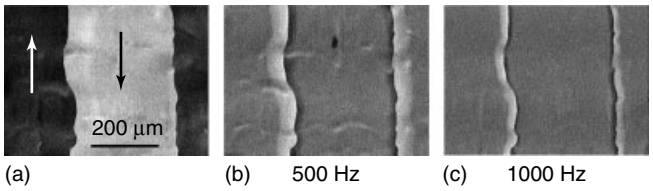

Figure 15. Imaging of periodic wall oscillation processes in a nanocrystalline ribbon ($Fe_{73}Cu_1Nb_3Si_{16}B_7$, thickness 20 µm). The domain state (a) is subtracted from images with a sinusoidal field of 500 Hz (b) and 1000 Hz (c) of same amplitude applied along the domain direction. (Courtesy *S. Flohrer*, IFW Dresden.)

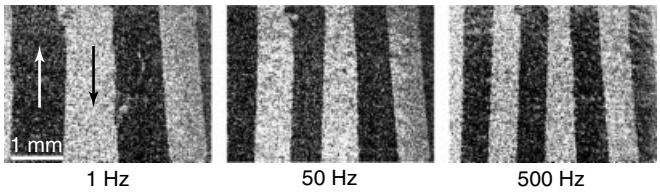

Figure 16. Eddy current–driven domain refinement in an ideally oriented grain on FeSi transformer steel. Three static domain states are shown after the sample was demagnetized with different frequencies as indicated. (Courtesy *S. Flohrer*, IFW Dresden.)

Those parts of the domain pattern that do not move stay gray in the dynamically averaged difference images, while changing parts show up as contrast. After turning down the field (i), contrast in the static difference image is left in those areas where irreversible processes took place. Such difference techniques can also be used to study periodic or quasi-periodic processes, as demonstrated in Figure 15. Here, oscillating domain walls were recorded with long exposure times at different frequencies with the static domain state subtracted. The black and white contrast gives information on the amplitude of wall motion that decreases with increasing frequency due to eddy-current damping. An asymmetry in the wall amplitude is also seen clearly. Two further examples of dynamic studies by regular image subtraction, showing domain multiplication processes as a consequence of dynamic field excitation, are presented in Figures 16 and 17.

Although dynamic effects can be studied by the aforementioned methods, such experiments do not reveal the dynamic processes by themselves because they are either smeared out by averaging procedures (as in Figure 14) or they are already over when images are taken (as in Figure 16). Time-resolved, high-speed imaging is rather required for detailed dynamic investigations. Kerr microscopy offers these possibilities both in the wide field and in the laser-scanning modes, as shown in the following sections.

4.1 Principle of high-speed microscopy

The principle of time-resolved high-speed microscopy is illustrated in Figure 18. The sample is excited by a continuously changing or pulsed periodic magnetic field. At certain time delays relative to the excitation, the magnetization is microscopically probed in a finite time window. Shifting the time delay of the probing window yields a series of time-resolved images of the magnetization process. Time resolution is either obtained by a gated high-speed video camera using a constant light source for illumination, or by a pulsed light source and continuous detection.

An ideal dynamic experiment should deliver a time-delayed series of single-shot images, as indicated in Figure 18(a), each of them representing the momentary magnetic state of the sample during the evolution of the magnetization process within the same excitation cycle. Repeating the imaging sequence in a number of following cycles would allow the study of the most general case that may also include nonreproducible and stochastic magnetization events,

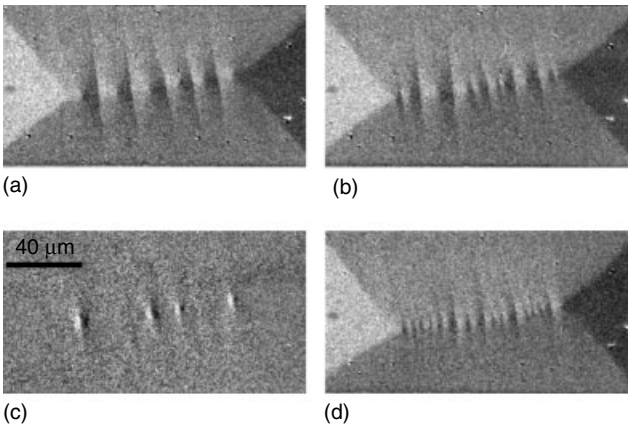

Figure 17. The dynamic multiplication of Bloch lines in a crosstie domain wall of a $Ni_{81}Fe_{19}$-film element of 50-nm thickness, again studied by conventional image processing. Image (a) shows a regular difference image in the demagnetized ground state. Image (b) was acquired after applying a single field pulse (amplitude $400\,A\,m^{-1}$, pulse length 1.2 ns, rise and fall time 120 and 170 ps, respectively) along the short axis of the element, leading to an increasing number of cross-ties, that is, the nucleation of new Bloch lines. The locations of Bloch line generation are evident in (c), where the difference of the two images before and after the field pulse is shown. In (d), a train of field pulses with a repetition rate of 23 MHz is applied. In these experiments, only the domain states before (a) and after pulse-field application (c–d) are displaced – the *mechanism* of Bloch line generation is not seen. (Courtesy *A. Neudert*, IFW Dresden. Reproduced from A. Naudert, J. McCord, R. Schäfer, R. Kaltofen, I. Mönch, H. Vinzelberg, L. Schultz: Bloch line generation in cross-tie walls by fast magnetic field pulses. *Journal of Applied Physics* (2006) by permission of American Institute of Physics.)

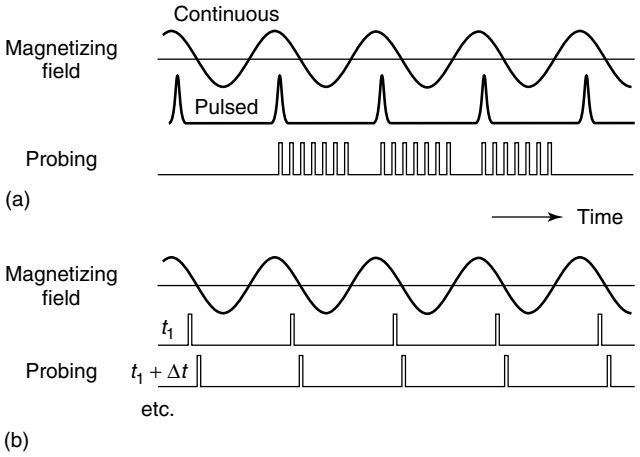

Figure 18. Principle of time-resolved imaging, (a) for an ideal single-shot experiment, and (b) in the stroboscopic mode. The sample is excited either by alternating magnetic fields or a by train of field pulses.

which may change from cycle to cycle. Single-shot imaging, however, requires a sufficient amount of photons to be accumulated in the detector during the probing time in order to obtain a sufficient signal-to-noise ratio. Very bright light sources and highly sensitive image detectors are therefore necessary. Also, the repetition rate of the experiment has to be fast enough to provide adequately short time delays for in-cycle imaging. Both conditions are increasingly difficult to meet with rising excitation frequency or if the magnetization response is too fast after pulse-field excitation.

If the repetition rate is the limiting factor (due to restrictions in the speed of light-pulse sequence, camera trigger, or delay electronics), single-shot imaging can nonetheless be applied as long as the detector sensitivity poses no limitation. By capturing images at identical time delays relative to the field excitation period (Figure 18b), but in different cycles, it is still possible to identify stochastic events. In case of repetitive processes, the full magnetization process may even be recovered by shifting the time delay of probing. If both detector sensitivity and repetition rate of the experiment are limited, time-resolved microscopy has to be performed in a different way, known as *stroboscopic imaging* (though, strictly speaking, the other methods are also of stroboscopic nature). In a strobed system, image acquisition is precisely synchronized to a periodic excitation, so that images are captured in the same time period of successive cycles (like in Figure 18b) and accumulated over many cycles (up to some 10° for fast pulse-field experiments) until a sufficient signal-to-noise ratio is achieved. The time delay is then periodically shifted to temporarily scan along the magnetization process. This accumulation technique, however, requires repetitive magnetization processes during successive cycles. If the process is different for every excitation period, a complicated mixture of contrasts (or even no contrast at all) is seen in the averaged images – in other words: only the repeatable events are seen as sharp features in the accumulated images, statistical events, and fluctuations are averaged out. A possibility to extract stochastic events ('noise') from stroboscopic images of nonrepetitive processes was described in Freeman, Steeves, Ballentine and Krichevsky (2002b).

The limitations of single-shot and stroboscopic imaging are demonstrated in Figure 19 by time-resolved (wide-field) studies on the same location of the amorphous ribbon that was already investigated in Figure 14. The pictures uncover the domain activity hidden in the blurred contrast of Figure 14(e). Time-resolved, stroboscopically obtained pictures at 25-Hz sinusoidal excitation are shown in Figure 19(a). They were recorded at three delay times as indicated, starting from an almost saturated high-field state. About 800 pictures of successive cycles, each with an illumination time of 0.4 ms, were collected and averaged for each image. Repeatable as well as nonrepetitive processes are evident in the probed area, indicated by strong and faint (or even blurred) domain contrast respectively. A strong reversibility

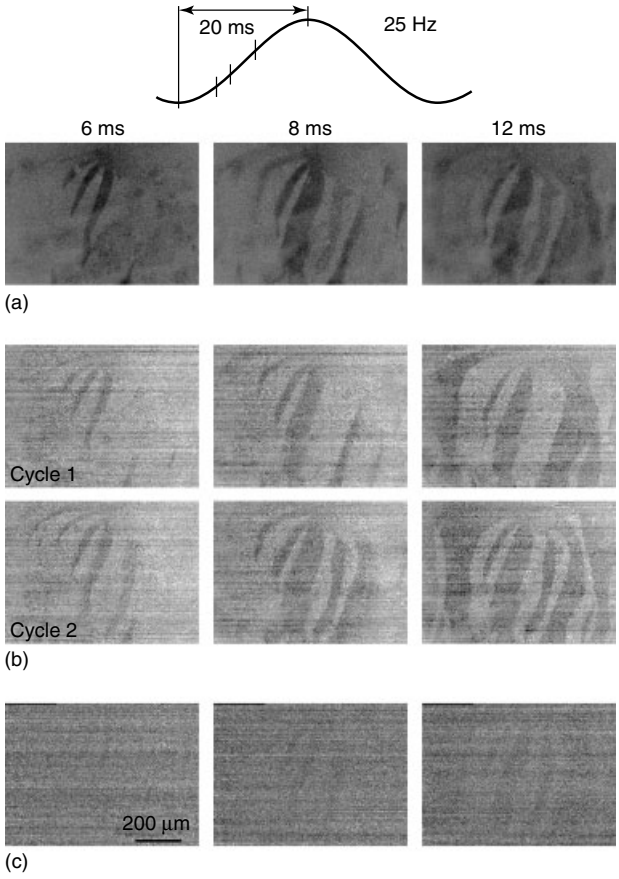

Figure 19. Dynamic studies at 25-Hz sinusoidal excitation on the same sample area as in Figure 14. (a) Stroboscopic images, obtained by a gated image intensifier and a digital CCD camera. Seven hundred and sixty-eight frames of 0.4-ms illumination time have been accumulated for each picture. The time delay relative to the maximum field is indicated. (b) Single-shot images at 2-ms illumination time, obtained by a high-speed CMOS camera with sufficiently large frame rate. The pictures in each row were taken successively within the same cycle. (c) Single-shot images at 0.4-ms illumination time. The difference images in which an averaged image of the saturated state is subtracted are shown in each case (together with *S. Flohrer* and *J. McCord*, IFW Dresden).

in the middle zone is confirmed by this experiment, which was already indicated by domain stiffening in the experiments of Figure 14. By single-shot imaging (Figure 19b) also, the irreversible processes are resolved by sharp contrasts. The two rows of images were recorded in different cycles of excitation, with the images within one row having been obtained subsequently within the same cycle at similar delay times as in Figure 19(a). A comparison of the two rows reveals similar and different domains that appear within the two cycles, indicating reversible and irreversible processes. The reversible domains add up to the strong contrast in the stroboscopic experiment of Figure 19(a). The illumination time for each image in Figure 19(b) was 2 ms, which was obviously sufficient to get a reasonable signal-to-noise ratio, but which occasionally left unsharp boundaries caused by nonnegligible wall movement within this time window. This effect should be strongly reduced if the illumination time of the single shots is reduced to 0.4 ms (Figure 19c) as for the stroboscopic image. However, strongly noisy pictures with almost vanishing domain contrast are obtained then, indicating the limits of single-shot imaging. As the conditions for serial single-shot imaging are (so far) impossible to meet for frequencies above the 50-Hz regime due to the mentioned limitations, most of the time-resolved imaging experiments at power frequencies and beyond have to follow a stroboscopic scheme.

4.2 Experimental setups for time-resolved microscopy

High-speed imaging requires the following main components: microscope (or at least objective lens in case of laser-scanning microscopy), image detection, pulsed light source or triggered video camera to obtain time resolution, power supply connected to a coil or stripe line for magnetic excitation of the sample, and some synchronous means including delay electronics to adjust and shift, respectively, the excitation and probing time. Time resolution and repetition rates of excitation and probing have to be chosen appropriately to meet the specific requirements of the sample and processes to be studied. If, for instance, the relaxation processes in a magnetic thin-film element after pulse-field excitation last 20 ns, the repetition rate of the field pulses should be less than 50 MHz to allow complete relaxation before the next pulse is applied. To provide repetitive conditions for stroboscopic imaging, it also has to be assured that the initial domain state is identically recovered between the excitation periods. For time-resolved imaging, both laser-scanning microscopy with a pulsed laser as well as wide-field microscopy can be used, the latter either based on a pulsed light source or on a triggered video camera. The three methods are compared in this chapter, following a brief historical review on the development of time-resolved Kerr microscopy.

4.2.1 Historical review

First time-resolved Kerr imaging techniques emerged in the early 1960s, based on regular wide-field microscopy and motivated by the interest of that time in the fast reversal of soft magnetic films for memory applications and in the dynamic processes and losses in electrical steel. In 1963, an optical strobing apparatus for imaging the flux reversal in NiFe films was introduced (Conger and Moore, 1963), in which light pulses of about 100-ns duration were generated

using sunlight and a mirror that was fastened to a spinning turbine. Simultaneously, Drechsel (1961) used a xenon flash-lamp to create single light pulses of 1 ms duration that were applied to single-shot imaging of iron crystals after sharply changing the magnetic field. Stroboscopic imaging on Goss sheets with several minutes averaging time at sinusoidal excitation up to 200 Hz was realized by Passon (1963) by adding a rotating disk with holes in the illumination light path of a continuously shining halogen lamp. Pictures were recorded by photographic films in these early experiments. Some years later, high-speed motion-picture cameras with frame rates up to 5000 pictures per second allowed single-shot imaging on transformer steel up to the 100-Hz regime (Houze, 1967; Haller and Kramer, 1970). The motion pictures could be examined frame by frame to analyze the character of domain wall motion. In the experiment of Houze, the high-speed camera was synchronized with a xenon flash lamp, that is, one flash per frame was recorded. In another setup of Passon (1968), time resolution was realized by a commercial television camera, equipped with a sensitive image intensifier that could be gated by trigger pulses. Stroboscopic observation of periodic processes up to 20 kHz with a gating time as low as 2 µs was possible with this system. Wall damping and wall multiplication phenomena with increasing frequency (due to eddy-current effects) were observed in these pioneering experiments. Also found was an increase in the reproducibility of magnetization processes in transformer steel with raising frequency – the precondition for stroboscopic imaging. An excellent review on these findings is given in Shilling and Houze (1974). In the meantime, laser illumination had entered the scene. A Kerr optical 'apparatus' with a Q-switched ruby laser for pulsed illumination was set up by Kryder (Kryder and Humphrey, 1969a). Time resolution of 10 ns was obtained by synchronizing the laser light pulses with the actuation of a Kerr electro-optic shutter in front of the photo camera. The intensity of the laser pulses (of some megawatts) was sufficient to provide single-shot photographs of the dynamic state during flux reversal in permalloy thin films (Kryder and Humphrey, 1969b). Many of these early dynamic Kerr experiments became possible only after contrast enhancement by optical interference layers (see Figure 2).

A decade later, the emerging bubble memories again stimulated interest in dynamic imaging. Most setups of that time (Humphrey, 1975; Kryder and Deutsch, 1976) were based on dye lasers that were triggered by pulsed nitrogen ion lasers, generating light pulses in the 10-ns-duration range at a low repetition rate of about 10 Hz. Owing to the high laser energy, caution had to be taken to avoid sample damage by overheating, for example, by defocusing the laser beam (Malozemoff, 1973). Such effects could be avoided by using continuous illumination and a gated image intensifier to obtain

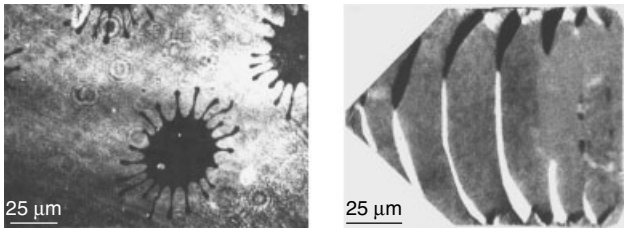

Figure 20. (a) Single-shot picture of 'exploding' magnetic bubbles in a garnet film. (b) Stroboscopic image from the yoke of a thin-film recording head, excited with a 1-MHz drive field. A difference image between two states is shown that were acquired by series of 5-ns laser pulses, where the pulses of the second series are delayed somewhat relative to the pulses of the first series. (Reproduced by permission of Springer from Hubert and Schäfer, 1998, the pictures are courtesy of *F. Humphrey* (a) and *B. Argyle* (b).)

high-speed photographs of bubble devices (Vella-Coleiro and Nelson, 1974). In Kryder's system (Kryder and Deutsch, 1976), the laser pulse frequency corresponded to the trigger rate of a TV camera so that each frame recorded had only one laser pulse for illumination. By recording on a videotape recorder, the repeatability of the magnetization process could be examined by frame-by-frame analysis of the tape. Transient bubble domain shapes during expansion and collapse in pulsed magnetic fields have been observed by high-speed photography (Gál, Zimmer and Humphrey, 1975). A snapshot of 'exploding' bubble domains, as an impressive example, is shown in Figure 20(a). Single-shot imaging in magnetic garnet films profited from strong contrasts due to the polar Faraday effect that can be favorably applied in bubble films.

Dynamic imaging in the following decade focused on the understanding of the sources of wiggle and noise in thin-film recording heads. First measurements were performed in a photometric way (Re, Shenton and Kryder, 1985): an Ar laser spot was focused on the pole tip in a regular optical polarizing microscope. The head was excited by high-frequency currents up to 50 MHz, sent through the drive coil. The reflected light, modulated by the polar Kerr effect, was then recovered with a photomultiplier and a lock-in amplifier detection scheme. By line scanning across the pole tip, the profile of the switching magnetization could be determined. This method was then extended to a two-dimensional scanning technique (Kasiraj, Shelby, Best and Horne, 1986), delivering spatially resolved images of magnetization changes with a time resolution of 50 ns. Since nonmagnetic signals were eliminated by the lock-in technique in this approach, the weak Kerr contrast of permalloy films was greatly enhanced. Different approaches, applied to the imaging of thin-film head yokes, were based on stroboscopic wide-field Kerr microscopy and background subtraction for contrast

enhancement (Petek, Trouilloud and Argyle, 1990; Liu, Schultz and Kryder, 1990; Kryder, Koeppe and Liu, 1990). A time resolution of 5–10 ns was obtained by dye laser pulses, pumped by Nd:YAG and nitrogen lasers, respectively. An example of such a stroboscopic image from the yoke of a thin-film head is presented in Figure 20(b), showing the averaged domain states at different phase positions in a difference image to emphasize wall motion.

A revival of (still ongoing) interest in high-speed imaging began in the late 1990s, owing to increasing demands for higher speeds and densities from data storage technologies, and for newer approaches such as magnetic random access memories (MRAMs) or spin electronics. The switching speeds of magnetization in metallic thin films have approached the sub-nanosecond regime where intrinsic magnetic response times due to spin-precessional effects become the limiting factor in devices, asking for an understanding and control of fast magnetization reversal processes. Motivated by these accumulated interests, dynamic behavior in micro- and nanosized particles is being actively studied in recent years by micromagnetic simulations and direct observation of the magnetization processes with simultaneous spatial and temporal resolution. The necessary breakthrough in terms of time resolution was related to the development of ps- and fs-laser systems that are most frequently applied in scanning Kerr microscopes. The first laser-scanning microscope with a time resolution of 50 ps (Freeman and Smyth, 1996) was applied for polar Kerr measurements of magnetic flux propagation in recording head pole tips. This apparatus was then extended to in-plane sensitivity (Stankiewicz *et al*., 1998) and time-resolved vector magnetometry (Ballentine, Hiebert, Stankiewicz and Freeman, 2000) (see Section 3.2) and used to study the switching behavior of patterned thin-film elements with lateral extensions of some micrometers that were deposited on coplanar transmission lines to create magnetic field pulses (see Section 4.2.5). A strongly modulated, nucleation-dominated magnetization configuration was observed during dynamic switching, which was replaced by domain wall motion if a transverse biasing field was applied, leading to a dramatic enhancement of switching speed at the same time (Choi *et al*., 2001). Excellent reviews of the outstanding work of the Freeman group are found in (Freeman and Hiebert, 2002a; Choi and Freeman, 2004; Choi, Krichevsky and Freeman, 2005b).

Laser-scanning Kerr microscopy with a temporal resolution in the 10-ps regime is now well established and used for a wide variety of time-resolved observations. (See also **Investigation of Spin Waves and Spin Dynamics by Optical Techniques, Volume 3**, **Time-resolved Kerr-effect and Spin Dynamics in Itinerant Ferromagnets, Volume 3**, and **Ultrafast Magnetodynamics with Lateral Resolution: A View by Photoemission Microscopy, Volume 3**). This includes investigations in magnetic recording heads and media (Back, Heidmann and McCord, 1999; Wakana, Nagai and Sakata, 2001; Veerdonk *et al*., 2001; Nagai, Sekiguchi and Ito, 2003), as well as in patterned soft magnetic film elements. 'Precessional switching' as reversal mechanism of small elements could be demonstrated by time-resolved imaging (Hiebert, Ballentine and Freeman, 2002; Hiebert, Lagae and Boeck, 2003b). In this method, a fast-rising field pulse is applied perpendicular to the initial direction of the magnetization, causing a large angle precession that is used to revert the magnetization if the field is stopped exactly after 180° precessional rotation. It could also be demonstrated that post-switching oscillations ('ringing') can be avoided (Krichevsky and Freeman, 2004) by properly combining easy- and hard-axis field pulses in a crossed-wire stripeline geometry (see Section 4.2.5). Other experiments using scanning Kerr microscopy focus onto the spin-wave eigenmodes of magnetization (Acremann *et al*., 2000; Park *et al*., 2002; Barman *et al*., 2004; Buess *et al*., 2004 (See also **Magnetic Modes in Circular Thin Film Elements, Experiment and Theory, Volume 2**)) and the gyrotropic motion of a central vortex in magnetic thin-film elements (Park *et al*., 2003; Park and Crowel, 2005). Though most of the research groups are using laser-scanning microscopy, there was also progress in picosecond wide-field imaging, both based on triggered video cameras (Chumakov *et al*., 2005) as well as on pulsed-laser-illuminated microscopes (Neudert *et al*., 2005).

At the moment, the interest in magnetization dynamics is shifting from field-induced to current-induced switching (Stiles and Miltat, 2006) (See also **Spin Angular Momentum Transfer in Magnetoresistive Nanojunctions, Volume 5** and **Theory of Spin-transfer Torque, Volume 2**), while at the same time the lateral dimensions of the relevant magnetic structures are getting well smaller than micrometer. Microscopy at optical frequencies will therefore meet its lateral resolution limit. Other methods with an order of magnitude higher resolution, based on X-ray dichroism (Choe *et al*., 2004; Kuksov *et al*., 2004; Stoll *et al*., 2004) or X-ray holography (Eisebitt *et al*., 2004), offer an alternative. On the basis of the latter technique, a spatial resolution of 5 nm in conjunction with a time resolution of the order of 20 fs is predicted for imaging at future X-ray free electron lasers, offering the potential for stroboscopic snapshot imaging of extremely fast magnetic switching processes of very small particles in the future.

4.2.2 Camera-based stroboscopic wide-field Kerr microscopy

In camera-based stroboscopic microscopes (Figure 21), the magnetic field excitation of the specimen is exactly synchronized with the exposure time of the video camera.

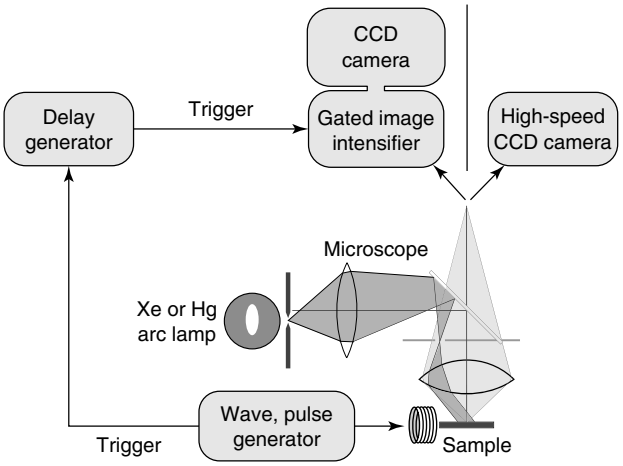

Figure 21. Block diagram for camera-based stroboscopic wide-field Kerr microscopy. Time resolution is provided by triggering a high-speed video camera or a gated image intensifier at constant illumination with precise timing relative to the field excitation.

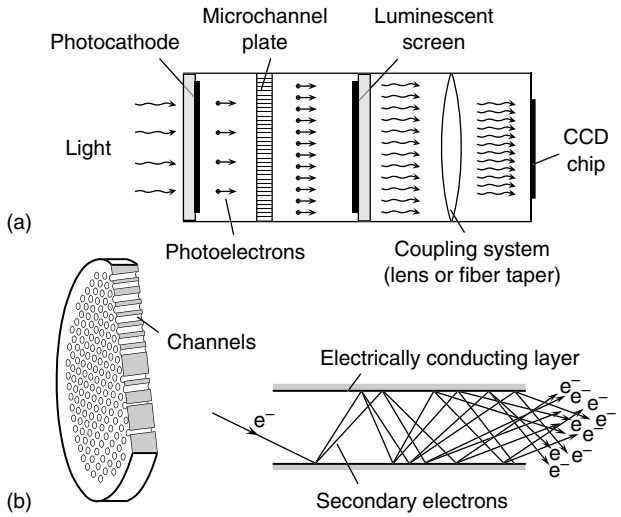

Figure 22. (a) Schematics of an image intensifier (second generation). Significant signal amplification up to four orders of magnitude is due to the microchannel plate (b). It consists of millions of very thin, electrically conducting glass capillaries with typically 10-µm diameter, which act as independent secondary electron multipliers. Their luminous gain ranges from 10 000 Lm/Lm up to 10^7 for intensifiers having two microchannel plates. Beside their gating capability, image intensifiers (combined with a CCD camera) can also be used to enhance low light level images in regular Kerr microscopy.

A function generator, which also provides the signal for the magnetic field, creates trigger pulses that are delayed in a defined way relative to the field excitation by an electric delay generator or optical delay line. These trigger pulses control the moment when the camera is exposed for a short time. The sample may be continuously illuminated in such experiments or in synchronization with a pulsed light source.

Today a variety of digital CCD and CMOS camera systems are available for time-resolved microscopy, which have replaced the traditional high-speed movie cameras of the early days of stroboscopy (see Section 4.2.1). A critical factor is the read-out time of the camera that determines the repetition rate of the experiment. Digital high-speed CCD and CMOS cameras with frame rates ranging between some hundred up to some thousand frames per second (at sufficient pixel resolution) are presently available. For comparison, the high-speed motion-picture camera used by Houze (1967) already offered rates of 5000 pictures per second (see Section 4.2.1). Frame rates up to the megahertz regime are also possible with digital cameras. Such speeds, however, are either reached by pixel binding on cost of resolution or they only allow to capture very few consecutive pictures that are stored in the (limited) memory of the camera head before being transmitted to the computer. The other important criterion is the time resolution given by the electronic or mechanic shutter of the camera, which can typically be varied from seconds down to the sub-100-ns range in present cameras. The smallest opening time in single-shot experiments depends on the sensitivity of the CCD or CMOS chip and the intensity of the light source. Single-shot imaging up to power frequencies is possible with the mentioned cameras. Higher frequencies require stroboscopic imaging and the accumulation of images at given time delays (see Figure 19a). Background subtraction for contrast enhancement is recommended just as in regular wide-field microscopy.

Much higher time resolution at increased sensitivity can be gained by using a gateable image intensifier in combination with a regular CCD camera. The intensifier primarily functions as an electronic shutter (Figure 22). A photocathode in a vacuum tube is permanently exposed to a positive potential, which prevents the emitted photoelectrons from leaving its surface. On the arrival of a trigger signal, an impulse of negative voltage is applied to the photocathode, pushing the photoelectrons into a microchannel plate (MCP) where they are accelerated and multiplied. After leaving the MCP, the multiplied electrons are further accelerated before they finally hit the phosphor layer of the output window generating photons. A regular CCD camera accumulates these photons during integration time. The gating time of the fastest image intensifiers reaches currently the 200-ps regime at a repetition rate of around 100 MHz (or less than 100 ps at kilohertz repetition rates).

Equipped with such modern, highly sensitive CCD or CMOS cameras and fast-image intensifiers, camera-based wide-field strobes have been set up in recent years for dynamic investigation of magnetic films (Chumakov *et al.*,

2005) and bulk soft magnetic materials (Moses, Williams and Hoshtanar, 2005; Flohrer *et al*., 2006). An advantage of camera-based systems is the possibility to vary the effective opening time of the camera or intensifier, respectively, between shortest and continuous exposure (as opposed to laser-based stroboscopes with usually fixed pulse frequencies – see following sections). This gives the opportunity to compare time-resolved data directly with the images acquired by static or quasistatic imaging. This comparison can be helpful in the interpretation of dynamic processes, because the peculiarities of the high-speed magnetization processes can be readily identified.

Examples for camera-based dynamic experiments have already been presented in Figure 19. The single-shot images (Figure 19b,c) were recorded with a high-speed digital CMOS camera, while time resolution in the stroboscopic pictures (Figure 19a) was achieved by a gated image intensifier. Two further examples, again obtained with image intensifiers, show the characteristic features of fast magnetization processes in bulk material (Figure 23) and thin-film elements (Figure 24). In Figure 23 (Flohrer *et al*., 2006), the outermost ribbons of nanocrystalline tape-wound cores with centimeter dimension and different uniaxial anisotropy were imaged at different frequencies of a sinusoidal magnetic field. Domain refinement (wall multiplication) was visible with increasing frequency for all three cores (Figure 23a). In the material with the weakest anisotropy, regular domains were replaced by patches at higher frequency. The partly blurred domain boundary contrast at 50 Hz resulted from domain movement during the exposure time or from slightly nonreproducible wall displacement processes. An increase in the reproducibility of the magnetization process with rising frequency and decreasing anisotropy was observed. Figure 23(b) demonstrates the high-frequency magnetization process of the low-anisotropy material that is dominated by nucleation and growth of patch domains rather than by wall motion.

The thin-film switching process in Figure 24(a) (Chumakov *et al*., 2005) was imaged at a much higher time resolution of 250 ps. A square-shaped film element was switched between two (nearly) saturated states in a sharply rising pulse-field applied along the elements diagonal and generated by a coplanar waveguide (see Section 4.2.5). A 'concertina' pattern developed, which became visible at transverse Kerr sensitivity and consisted of alternating areas of clock- and counterclockwise magnetization rotation. The magnetization was finally reverted by a mixture of rotation and domain boundary motion that lasted several nanoseconds. Two vortices were created and pushed toward the edges during this process. Quasistatic switching in a slowly changing field occured differently (Figure 24b): there was also a concertina formed when the magnetic field was decreased from saturation, which, however, broke down abruptly in the reversed field by the unpinning and fast motion of Bloch lines, leaving the element in a four-domain Landau state with a single vortex.

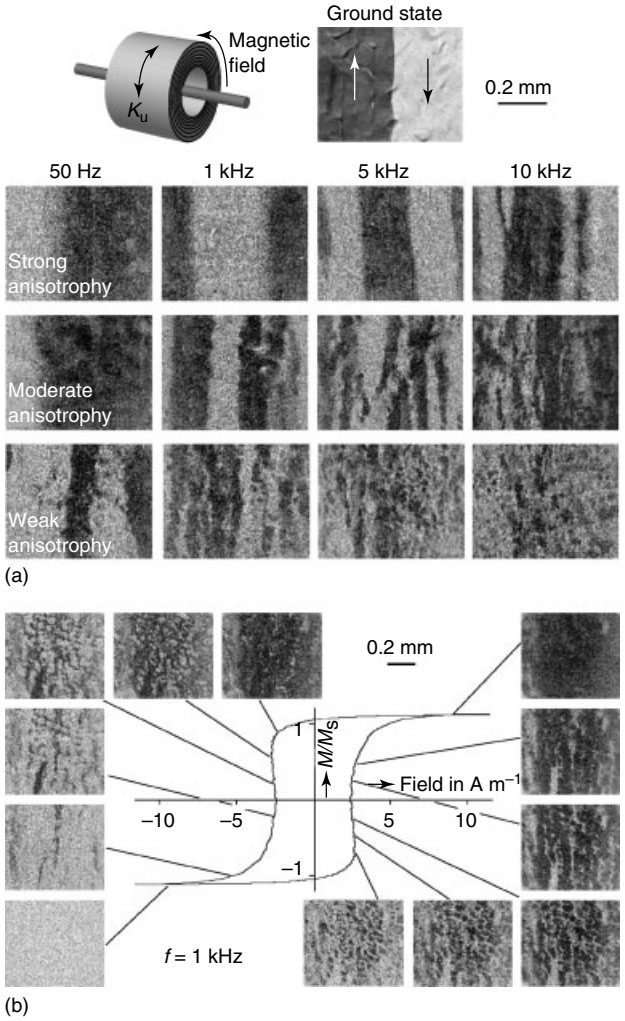

Figure 23. Time-resolved domain observations on $Fe_{73}Cu_1Nb_3Si_{16}B_7$ nanocrystalline tape-wound cores (See also **Soft Magnetic Materials – Nanocrystalline Alloys, Volume 4**) in circumferential magnetic field (core width 20 mm, outer diameter 25 mm, ribbon thickness 20 µm). A gated image intensifier with a gating time of one-hundredth of the magnetic field period was applied for time resolution; several thousand frames of independent events were accumulated for each image. (a) Stroboscopic images, taken around the point of zero induction during sinusoidal excitation with saturating peak induction at different frequencies as indicated. Three cores with different strength of induced anisotropy K_u were studied (top row: 29 J m^{-3}, middle row: 10 J m^{-3}, bottom row: 5 J m^{-3}). The domain ground state, consisting of 180° domains and obtained by static imaging, is shown for comparison. (b) Inductively measured hysteresis loop and stroboscopic images obtained at 1 kHz on the core with weak anisotropy. (Reprinted from Acta Materialia, 2006, Flohrer *et al*., 2006. Magnetization loss and domain refinement in nanocrystalline tape wound cores. *Acta Materialia*, **54** 3253–3259, with permission from Elsevier.)

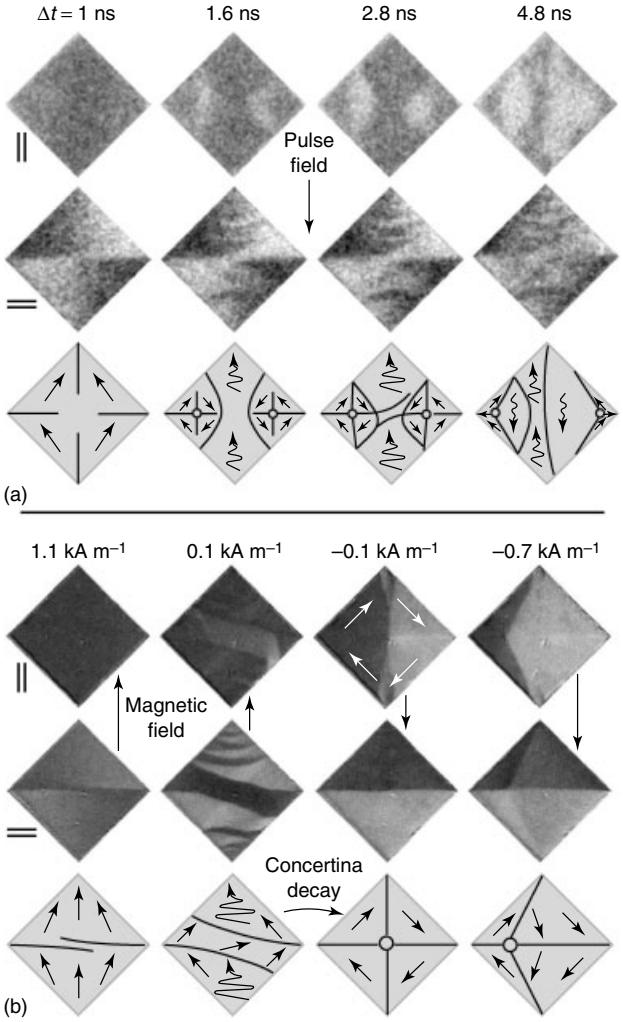

Figure 24. Comparison of magnetization processes in a Permalloy thin-film element (edge length 28 µm, thickness 50 nm) in diagonal magnetic fields. The time-resolved images in (a) were obtained after applying a pulsed magnetic field (rise time several nanoseconds, duration 1000 ns, amplitude 2 kA m^{-1}) opposite to a saturating bias field. A gated image intensifier with a gating time of 250 ps was applied for time resolution. To achieve a reasonable signal-to-noise ratio, the Kerr images of some 10^8 independent events, excited by a train of field pulses that are repeated periodically, were integrated in time. The delay time of recording after onset of the field pulses is indicated. (b) Quasistatic process in slowly changing field that is decreased from saturation and inverted. Similar states are shown at two orthogonal Kerr sensitivities as indicated by double lines. The magnetization vector fields are drawn schematically. (Reprinted with permission from D. Chumakov *et al.*, *Phys Rev. B* Vol. 71, 014410 (2005). Copyright (2005) by the American Physical Society.)

4.2.3 Light-based stroboscopic wide-field Kerr microscopy

The components of a stroboscopic wide-field microscope based on pulsed illumination are shown in Figure 25. The

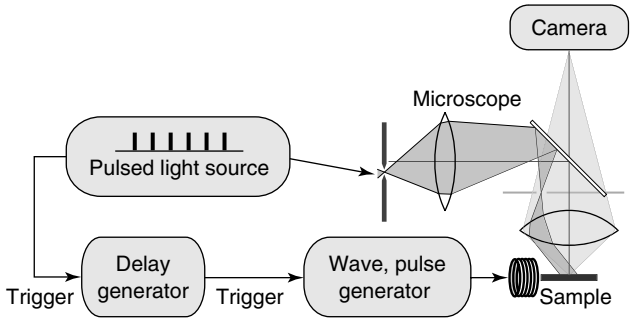

Figure 25. Block diagram for light-based stroboscopic wide-field microscopy. A pulsed light source is employed for time resolution.

wave or pulse generator is triggered by the light source with some intermediate delay electronics. The images, shot at a defined time delay, are accumulated in a regular CCD camera. For comparative (quasi) static imaging, it is advantageous to switch to a steady light source, which can be easily realized in wide-field microscopes. Like in all other wide-field techniques, contrast can be enhanced by background subtraction.

Lasers are most widely employed as a pulsed light source. The laser light is fed into the microscope by a glass fiber after employing proper means to prevent speckle patterns (see Section 3.1.4). A portion of the laser light shines on a photodiode giving the trigger pulses. Today, the traditional dye lasers (see Section 4.2.1) can be replaced by mode-locked solid-state lasers such as Nd-YVO_4 that deliver light pulses with a length in the 10-ps range at visible wavelengths after frequency doubling. The repetition rate of these lasers is fixed at some 10 MHz, and their output power has to be limited to the 100-mW range (e.g., by a rotatable half-wave plate) to match the sensitivity range of the detection CCD camera and to avoid sample damage. Externally triggerable, pulsed laser diodes can be operated in the same time regimes and are also suited for stroboscopic imaging (Wakana, Nagai and Sakata, 2001; Nagai, Sekiguchi and Ito, 2003). Still shorter pulses of 30–100 fs are achieved if the mentioned picosecond lasers are used to pump a mode-locked Ti:sapphire laser. The emitted femtosecond pulses have a wavelength around 800 nm at a repetition frequency of about 80 MHz. At present, most time-resolved experiments are carried out with the mentioned laser light sources. The ongoing progress in laser technology has already brought along sub-femtosecond lasers (Hentschel *et al.*, 2001), which so far have not been employed for imaging. A problem with laser light sources is the repetition rate that is usually fixed at a certain frequency (e.g., some 10 MHz in case of solid-state lasers), limiting the flexibility of the experiment as compared to camera-based systems. Also possible for wide-field microscopy are pulsed xenon-arc flashlamps. They provide light pulses of the typical order of

1 µs at a low repetition rate in the 100 Hz regime, but they are intense enough to allow single-shot imaging, for example, in magnetic films with perpendicular anisotropy and thus strong polar Kerr effect (Romanens *et al*., 2005). Flashlamps are an alternative to lasers if lower time resolution is sufficient. Signal-to-noise ratios like in quasistatic imaging can be obtained, however, at strongly reduced exposure times.

An example for a laser-based wide-field strobing experiment on a NiFe square element is presented in Figure 26, again in comparison with the quasistatic process. Vortex motion and wall displacement are characteristic for slowly changing magnetic fields (Figure 26a). By applying a sharp field pulse (b), fast rotational processes and spike domain nucleation are observed (c), which are slowly resolved after several nanoseconds. The development of small-angle domains with oscillatory behavior in the low-permeability closure domain is also noteworthy.

4.2.4 Stroboscopic laser-scanning Kerr microscopy

The principle components of a stroboscopic experiment based on laser-scanning microscopy are shown in Figure 27. The pulsed laser beam is split into a pump and probe beam. The probe beam is directly used for imaging, as described in Section 3.2, whereas the pump beam triggers the field excitation via an electric delay generator (or optical delay line) and pulse generator. Most of the modern scanning microscopes are based on today's standard laser, the mode-locked and frequency-doubled titanium-sapphire femtosecond laser. 'Pulse picking' may eventually be required to adapt the high repetition rate of the laser to the rates of the delay electronics (unless an optical delay line is applied). To avoid sample damage or unwanted thermal effects on the magnetization, the laser pulses may require attenuation (to an optical power of typically below 100 µW), thereby increasing the number of shots to be accumulated. The suppression of nonmagnetic contrasts and signal enhancement can be achieved by modulating the field excitation at kilohertz frequencies (as indicated in Figure 27 for a train of field pulses that is periodically interrupted) and using lock-in detection (Hicken *et al*., 2002; Buess *et al*., 2004). The time resolution achievable with laser-scanning microscopy is ultimately limited by the laser pulse width, but may practically be limited by trigger jitter from the delay electronics (Freeman and Hiebert, 2002a). A resolution of the order of some 10 ps is typically achieved in present laser-scanning microscopes.

Two stroboscopic operation modes can be employed in a laser-scanning microscope: temporal and spatiotemporal-resolving modes. In the temporal mode, (See also **Investigation of Spin Waves and Spin Dynamics by Optical Techniques, Volume 3**, **Time-resolved Kerr-effect and**

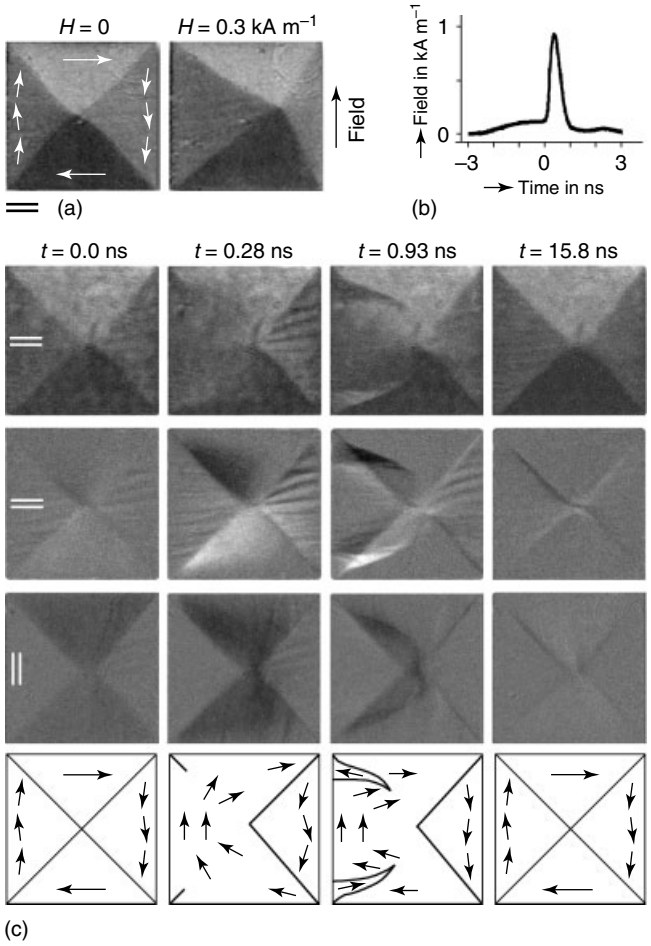

Figure 26. Excitation of a Landau ground state in a permalloy thin-film element (edge length 40 µm, thickness 50 nm) in magnetic fields parallel to the edge. (a) Quasistatic process. The dynamic process (c), excited by a sharp field pulse (b), is completely different. The difference images are shown as follows: In the upper row of (c), an image of the saturated state was subtracted, while images of the Landau ground state were subtracted in the middle and lower row at different Kerr sensitivity directions as indicated, highlighting changes in the magnetization. The time delays where the images have been captured in a stroboscopic way are indicated. The accumulation of some 10^6 single pictures, each of them obtained with a laser pulse of about 20 ps length, was necessary to obtain an image of sufficient contrast. (Reprinted with permission from A. Neudert *et al*., *Phys. Rev. B.* Vol. 71, 134405. Copyright (2005) by the American Physical Society.)

Spin Dynamics in Itinerant Ferromagnets, Volume 3, and **Ultrafast Magnetodynamics with Lateral Resolution: A View by Photoemission Microscopy, Volume 3**), the sample response is measured locally by focusing on a particular place of the sample and changing the time delay. The Kerr signal of a train of light pulses is accumulated after each time step, building up the time-dependent profile for selected magnetization components (see Park *et al*., 2003, e.g., of such

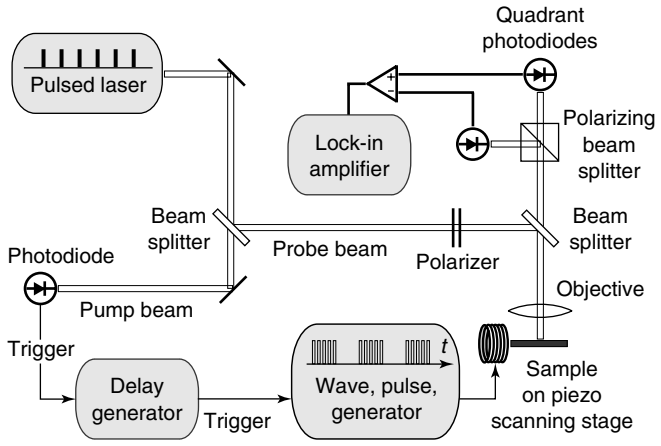

Figure 27. Block diagram of the main components of a typical stroboscopic imaging setup based on laser-scanning Kerr microscopy. Instead of the electronic delay generator, an optical delay line (not shown) may be used for the synchronization of probe beam and magnetic pulse, in which the travel path of the probe beam with respect to the pump beam is computer controlled using mirrors mounted on a slider. (After Choi and Freeman, 2004.)

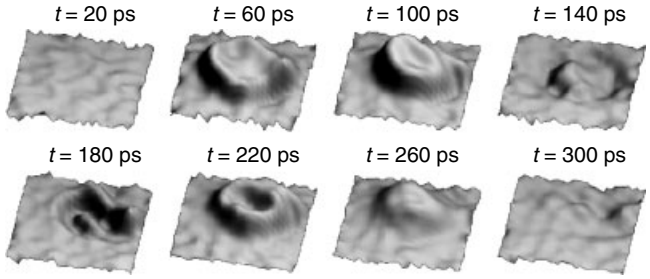

Figure 28. Stroboscopic laser-scanning Kerr microscopy of the polar magnetization component in a cobalt disk with a diameter of 6 µm and a thickness of 20 nm at increasing time delays after pulse-field excitation. Laser pulses with a width of 100 fs were used for imaging, and the magnetic field pulse was created with a photoconductive switch. (Courtesy of *Ch. Bac*k, Regensburg. See Acremann *et al*., 2000, for details.)

local magnetometry). For spatiotemporal imaging, the time-dependent profile is locally measured and then the sample is scanned at a particular fixed time delay to obtain a two-dimensional mapping of the magnetic response. Repeating the procedure at a different time delay leads to a stroboscopic image series of the dynamic process. Like in stroboscopic wide-field microscopy, only repetitive phenomena can be imaged by this technique, while single-shot imaging is not possible at all. A review of stroboscopic laser-scanning Kerr microscopy is given in Freeman and Hiebert (2002a).

An example of a spatiotemporal stroboscopic laser-scanning experiment is presented in Figure 28. A small cobalt disk was excited by sharp magnetic field pulses perpendicular to the film plane. The temporal evolution of the polar magnetization component at various time delays, revealing precessional magnetization oscillations that last several 100 ps is shown in the figure.

To conclude, laser-scanning-based stroboscopes have three main advantages: (i) The time evolution of magnetization can in a convenient and highly sensitive way be measured locally in an area of the laser beam size. (ii) The laser pulse can be used for pumping and probing by employing photoconductive switches (see Section 4.2.5). (iii) Longitudinal, transverse, and polar magnetization components can be recorded simultaneously, as described in Section 3.2. A drawback of the method is clearly related to the scanning procedure that is required to obtain full images, which makes it difficult to obtain static domain images for comparison.

4.2.5 Magnetic field generation

For time-resolved studies, the magnetic system has to be excited by an external magnetic field with a well-defined time structure (in recent years it could be shown that excitation is also possible by spin-polarized electric currents (Stiles and Miltat, 2006), by heating with femtosecond laser pulses (Koopmans, 2003) or by photomagnetic interaction (Hansteen *et al*., 2006)). In most experiments, this time structure is either harmonic (e.g., sine wave excitation) or consists of a train of periodic field pulses of variable shape and duration (pulse-field excitation) provided by a signal generator. The excitation field can be created by magnetic coils or electromagnets if large samples are to be magnetized at power frequencies. For small samples, coil/yoke systems like in magnetic recording heads can be used well up into the megahertz regime. The field rise times in these systems, however, are limited to a few nanoseconds due to inductivity. Much faster rise times are possible by overcoming the inductivity problem in coplanar waveguides (Figure 29) that are fabricated from copper or gold thin films by lithography using etching or lift-off techniques. Such approaches are of course restricted to the excitation of patterned magnetic film samples, which can be deposited onto the conductor line. The impedance of the waveguide has to be carefully matched to the current source to avoid unwanted reflections or damping of the current pulse. Magnetic fields up to the order of $10\,\mathrm{kA\,m^{-1}}$ are possible with such transmission lines. Coplanar waveguides may also be fabricated in cross-wire geometry, which allows, for example, to study precessional switching by exciting along and perpendicular to the easy axis of the deposited film elements (Hiebert *et al*., 2003a), or to control post-switching magnetization oscillations by varying the delay between two orthogonal pulses (Krichevsky and Freeman, 2004).

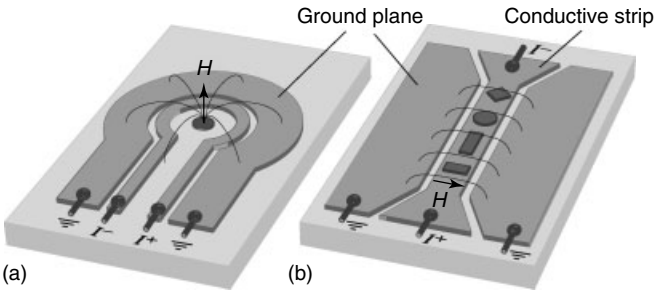

Figure 29. Coplanar waveguides, consisting of a conductor transmission line that is separated from a pair of ground lines (all on the same plane), for the generation of fast magnetic field pulses in small elements. The microcoil in (a) provides perpendicular fields, while the waveguide in (b) generates in-plane fields, as indicated. The sample elements are deposited on top of the conductor line. For wide-field Kerr microscopy, it is advisable to coat the strip by antireflection layers to prevent disturbing light effects on the sample (Chumakov *et al*., 2005). (Reprinted figure with permission from D. Chumakov *et al*., *Phys Rev. B* Vol. 71, 014410 (2005). Copyright 2005 by the American Physical Society.)

Magnetization dynamics is critically determined by the rise time of the excitation pulses (Choi, Ho, Arnup and Freeman, 2005a). Commercial electronic pulse generators may provide current pulses of down to 50-ps rise time with variable pulse width down to about 500 ps and repetition rates of several hundred megahertz. Faster rise times of a few picoseconds are possible by so-called Auston switches (Auston, 1975), which have been adapted from semiconductor physics to the fast excitation of magnetic films (Freeman, 1994). In the Auston switch, an above–band gap optical pulse from a picosecond laser strikes a biased coplanar transmission line structure, fabricated on a semi-insulating semiconductor substrate, to create a transient photoconductivity and launch a current pulse down the transmission line. The decay of the photoexcitation is determined by the recombination rate of the electron–hole pairs and is usually much slower in the nanosecond range, preventing the creation of ultrashort pulses. Laser-scanning microscopes are ideally suited for the application of photoconductive switches in stroboscopic experiments, as the probing laser can simultaneously be used for current launching after employing beam splitting and delay (Choi and Freeman, 2004). The biggest advantage of photoconductive switches is the fact that the sample can be pumped without the introduction of electronic jitter (Hicken *et al*., 2002). Examples for the application of these switches to the study of precessional excitation spectra or localized spin-wave modes in film elements may be found in Acremann *et al*. (2000); Park *et al*. (2002); Park *et al*. (2003); Gerrits *et al*. (2002); Barman *et al*. (2004); Buess *et al*. (2004).

5 OUTLOOK

The classical Kerr technique for magnetic domain observation has strongly gained in efficiency after the introduction of digital image processing in the mid-1980s. By contrast enhancement, domains get visible on virtually all relevant ferro- and ferrimagnetic materials and magnetization directions can be determined quantitatively and even selectively based on depth. The dynamic capability and the compatibility with arbitrary applied magnetic fields make Kerr microscopy ideally suited for the investigation of magnetization processes on arbitrary timescales. On bulk materials, just the surface region can be seen (like in most other domain observation techniques); therefore theoretical arguments combined with domain studies in magnetic fields are required to get a three-dimensional understanding of the magnetic microstructure. The optical resolution limit of about 200 nm limits the application of Kerr microscopy when small objects are to be studied as they are increasingly getting addressed with rising miniaturization of devices. Yet, Kerr microscopy will remain the method of choice for the visualization of moving domains in the laboratory.

ACKNOWLEDGMENTS

The careful reading of the manuscript and supply of images by Jeffrey McCord, Sybille Flohrer, and Andreas Neudert (all IFW Dresden) is highly appreciated. Thanks also to Dmitry Chumakov (IFW Dresden) and Christian Back (Regensburg) for providing images.

REFERENCES

Acremann, Y., Back, C.H., Buess, M., *et al*. (2000). Imaging precessional motion of the magnetization vector. *Science*, **290**, 492–495.

Argyle, B.E. and McCord, J. (2000). New laser illumination method for Kerr microscopy. *Journal of Applied Physics*, **87**, 6487–6489.

Argyle, B.E., Petek, B. and Herman, D. Jr. (1987). Optical imaging of magnetic domains in motion. *Journal of Applied Physics*, **61**, 4303–4306.

Auston, D.H. (1975). Picosecond optoelectronic switching and gating in silicon. *Applied Physics Letters*, **26**, 101–103.

Back, C.H., Heidmann, J. and McCord, J. (1999). Time resolved Kerr microscopy: magnetization dynamics in thin film write heads. *IEEE Transactions on Magnetics*, **35**, 637–642.

Ballentine, G.E., Hiebert, W.K., Stankiewicz, A. and Freeman, M.R. (2000). Ultrafast microscopy and numerical simulation study of magnetization reversal dynamics in permalloy. *Journal of Applied Physics*, **87**, 6830–6832.

Barman, A., Kruglyak, V.V., Hicken, R.J., *et al*. (2004). Imaging the dephasing of spin wave modes in a square thin film magnetic element. *Physical Review B*, **69**, 174426.

Buess, M., Höllinger, R., Haug, T., *et al*. (2004). Fourier transform imaging of spin vortex eigenmodes. *Physical Review Letters*, **93**, 077207.

Büscher, P. and Reimer, L. (1993). Imaging and colour coding of magnetic domains by Kerr scanning optical microscopy. *Scanning*, **15**, 123–129.

Choe, S.-B., Acremann, Y., Scholl, A., *et al*. (2004). Vortex-core driven magnetization dynamics. *Science*, **304**, 420–422.

Choi, B.C., Belov, M., Hiebert, W.K., *et al*. (2001). Ultrafast magnetization reversal dynamics investigated by time domain imaging. *Physical Review Letters*, **86**, 728–731.

Choi, B.C. and Freeman, M.R. (2004). Nonequilibrium spin dynamics in laterally defined magnetic structures. In *Ultrathin Magnetic Structure IV*, Heinrich, B. and Bland J.A.C. (Eds.), Springer: Berlin, pp. 211–232.

Choi, B.C., Ho, J., Arnup, G. and Freeman, M.R. (2005a). Nonequilibrium domain pattern formation in mesoscopic magnetic thin film elements assisted by thermally excited spin fluctuations. *Physical Review Letters*, **95**, 237211.

Choi, B.C., Krichevsky, A. and Freeman, M.R. (2005b). Magnetization dynamics using time-resolved magneto-optic microscopy. In *Modern Techniques for Characterizing Magnetic Materials*, Zhu, Y. (Ed.), Kluwer Academic Publishers: Boston, pp. 517–542.

Chumakov, D., McCord, J., Schäfer, R., *et al*. (2005). Nanosecond time-scale switching of permalloy thin film elements studied by wide-field time-resolved Kerr microscopy. *Physical Review B*, **71**, 014410.

Clegg, W.W., Heyes, N.A.E., Hill, E.W. and Wright, C.D. (1991). Development of a scanning laser microscope for magneto-optic studies of thin magnetic films. *Journal of Magnetism and Magnetic Materials*, **95**, 49–57.

Conger, R.L. and Moore, G.H. (1963). Direct observation of high-speed magnetization reversal in films. *Journal of Applied Physics*, **34**, 1213–1214.

Dillon, J.F. Jr. (1958). Observation of domains in the ferrimagnetic garnets by transmitted light. *Journal of Applied Physics*, **29**, 1286–1291.

Drechsel, W. (1961). Eine Anordnung zur photographischen Registrierung von Weißschen Bereichen bei Belichtungszeiten der Größenordnung 1 msec. *Zeitschrift fur Physik*, **164**, 324–329.

Egelkamp, S. and Reimer, L. (1990). Imaging of magnetic domains by the Kerr effect using a scanning optical microscope. *Measurement Science and Technology*, **1**, 79–83.

Eisebitt, S., Lüning, J., Schlotter, W.F., *et al*. (2004). Lensless imaging of magnetic nanostructures by X-ray spectro-holography. *Nature*, **432**, 885–888.

Faraday, M. (1846). On the magnetization of light and the illumination of magnetic lines of force. *Philosophical Transactions of the Royal Society of London*, **136**, 1–20.

Flohrer, S., Schäfer, R., McCord, J., *et al*. (2006). Magnetization loss and domain refinement in nanocrystalline tape wound cores. *Acta Materialia*, **54**, 3253–3259.

Fowler, C.A. Jr. and Fryer, E.M. (1952). Magnetic domains on silicon iron by the longitudinal Kerr effect. *Physical Review*, **86**, 426.

Fowler, C.A. Jr. and Fryer, E.M. (1956). Magnetic domains in thin films by the Faraday effect. *Physical Review*, **104**, 552–553.

Freeman, M.R. (1994). Picosecond pulsed-field probes of magnetic systems. *Journal of Applied Physics*, **75**, 6194–6198.

Freeman, M.R. and Hiebert, W.K. (2002a). Stroboscopic microscopy of magnetic dynamics. In *Spin Dynamics in Confined Magnetic Structures I*, Hillebrands, B. and Ounadjela K. (Eds.), Springer: Berlin, pp. 93–126.

Freeman, M.R. and Smyth, J.F. (1996). Picosecond time-resolved magnetization dynamics of thin-film heads. *Journal of Applied Physics*, **79**, 5898–5900.

Freeman, M.R., Steeves, G.M., Ballentine, G.E. and Krichevsky, A. (2002b). Noise imaging using magneto-optical sampling techniques. *Journal of Applied Physics*, **91**, 7326–7330.

Gál, L., Zimmer, G.J. and Humphrey, F. (1975). Transient magnetic bubble domain configurations during radial wall motion. *Physica Status Solidi A*, **30**, 561–569.

Gerrits, T., van den Berg, H.A.M., Hohlfeld, J., *et al*. (2002). Ultrafast precessional magnetization reversal by picosecond magnetic field pulse shaping. *Nature*, **418**, 509–512.

Haller, T.R. and Kramer, J.J. (1970). Observation of dynamic domain size variation in a silicon-iron alloy. *Journal of Applied Physics*, **41**, 1034–1035.

Hansteen, F., Kimel, A., Kirilyuk, A. and Rasing, T. (2006). Nonthermal ultrafast optical control of the magnetization in garnet films. *Physical Review B*, **73**, 014421.

Hentschel, M., Kienberger, R., Spielmann, Ch., *et al*. (2001). Attosecond metrology. *Nature*, **414**, 509–513.

Hicken, R.J., Hughes, N.D., Moore, J.R., *et al*. (2002). Magneto-optical studies of magnetism on pico and femtosecond time scales (invited). *Journal of Magnetism and Magnetic Materials*, **242–245**, 559–564.

Hiebert, W.K., Ballentine, G.E. and Freeman, M.R. (2002). Comparison of experimental and numerical micromagnetic dynamics in coherent precessional switching and modal oscillations. *Physical Review B*, **65**, 140404.

Hiebert, W.K., Lagae, L., Das, J., *et al*. (2003). Fully controlled precessional switching of a macrospin in a cross-wire geometry. *Journal of Applied Physics*, **93**, 6906–6908.

Hiebert, W.K., Lagae, L. and Boeck, J.D. (2003). Spatially inhomogeneous ultrafast precessional magnetization reversal. *Physical Review B*, **68**, 020402.

Houze, G.L. (1967). Domain-wall motion in grain-oriented silicon steel in cyclic magnetic fields. *Journal of Applied Physics*, **38**, 1089–1096.

Hubert, A. and Schäfer, R. (1998). *Magnetic Domains. The Analysis of Magnetic Microstructures*, Springer-Verlag: Berlin.

Humphrey, F.B. (1975). Transient bubble domain configuration in garnet materials observed using high speed photography. *IEEE Transactions on Magnetics*, **11**, 1679–1684.

Inoué, S. and Spring, K.R. (1997). *Video Microscopy: The Fundamentals*, Plenum Press: New York and London.

Kasiraj, P., Shelby, R.M., Best, J.S. and Horne, D.E. (1986). Magnetic domain imaging with a laser scanning Kerr effect microscope. *IEEE Transactions on Magnetics*, **22**, 867–839.

Kerr, J. (1877). On rotation of the plane of polarization by reflection from the pole of a magnet. *Philosophical Magazine*, **3**(5), 321–343.

Kläui, M., Jubert, P.-O., Allenspach, R., *et al*. (2005). Direct observation of domain-wall configurations transformed by spin currents. *Physical Review Letters*, **95**, 026601.

Koopmans, B. (2003). Laser-induced magnetization dynamics. In *Spin Dynamics in Confined Magnetic Structures II*, Hillebrands, B. and Ounadjela, K. (Eds.), Springer: Berlin, pp. 253–316.

Krichevsky, A. and Freeman, M.R. (2004). Precessional switching of a 3×1 micrometer elliptical element in a crossed-wire geometry. *Journal of Applied Physics*, **95**, 6601–6603.

Kryder, M.H. and Deutsch, A. (1976). A high-speed magneto-optic camera system. *SPIE High Speed Optical Techniques*, **94**, 49–57.

Kryder, M.H. and Humphrey, F.B. (1969a). A nanosecond Kerr magneto-optic camera. *The Review of Scientific Instruments*, **40**, 829–840.

Kryder, M.H. and Humphrey, F.B. (1969b). Dynamic Kerr observations of high-speed flux reversal and relaxation processes in permalloy thin films. *Journal of Applied Physics*, **40**, 2469–2474.

Kryder, M.H., Koeppe, P.V. and Liu, F.H. (1990). Kerr effect imaging of dynamic processes in magnetic recording heads. *IEEE Transactions on Magnetics*, **26**, 2995–3000.

Kuksov, A., Schneider, C.M., Oelsner, A., *et al*. (2004). Investigating magnetization dynamics in permalloy microstructures using time-resolved x-ray photoemission electron microscope. *Journal of Applied Physics*, **95**, 6530–6532.

Liu, F.H., Schultz, M.D. and Kryder, M.H. (1990). High frequency dynamic imaging of domains in thin film heads. *IEEE Transactions on Magnetics*, **26**, 1340–1342.

Malozemoff, A.P. (1973). Nanosecond camera for garnet bubble domain dynamics. *IBM Technical Disclosure Bulletine*, **15**, 2759–2757.

McCord, J. and Hubert, A. (1999). Normalized differential Kerr microscopy – an advanced method for magnetic imaging. *Physica Status Solidi A*, **171**, 555–562.

McCord, J., Schäfer, R., Mattheis, R. and Barholz, K.-U. (2003). Kerr observations of asymmetric magnetization reversal processes in CoFe/IrMn bilayers. *Journal of Applied Physics*, **93**, 5491–5497.

Moses, A.J., Williams, P.I. and Hoshtanar, A. (2005). A novel instrument for real time dynamic domain observation in bulk and micromagnetic materials. *IEEE Transactions on Magnetics*, **41**, 3736–3738.

Nagai, T., Sekiguchi, H. and Ito, A. (2003). Magnetization vector measurement with wide-band high spatial resolution Kerr microscope. *IEEE Transactions on Magnetics*, **39**, 3441–3443.

Neudert, A., McCord, J., Chumakov, D., *et al*. (2005). Small-amplitude magnetization dynamics in permalloy elements investigated by time-resolved wide-field Kerr microscopy. *Physical Review B*, **71**, 134405.

Neudert, A., McCord, J., Schäfer, R., *et al*. (2006). Bloch line generation in cross-tie walls by fast magnetic field pulses. *Journal of Applied Physics*, **99**, 08F302.

Nikitenko, V.I., Gornakov, V.S., Dedukh, L.M., *et al*. (1998). Asymmetry of domain nucleation and enhanced coercivity in exchange-biased epitaxial NiO/NiFe bilayers. *Physical Review B*, **57**, R8111–R8114.

Nutter, P.W. and Wright, C.D. (1998). Resolution issues in confocal magnetooptic scanning laser microscopy. *Japanese Journal of Applied Physics*, **37**, 2245–2254.

Oppeneer, P.M. (2001). Magneto-optical Kerr spectra. In *Handbook of Magnetic Materials*, Buschow, K.H.J. (Ed.), North-Holland: Amsterdam, pp. 229–422, Vol. 13.

Park, J.P. and Crowel, P.A. (2005). Interactions of spin waves with a magnetic vortex. *Physical Review Letters*, **95**, 167201.

Park, J.P., Eames, P., Engebretson, D.M., *et al*. (2002). Spatially resolved dynamics of localized spin-wave modes in ferromagnetic wires. *Physical Review Letters*, **89**, 277201.

Park, J.P., Eames, P., Engebretson, D.M., *et al*. (2003). Imaging of spin dynamics in closure domain and vortex structures. *Physical Review B*, **67**, 020403.

Passon, B. (1963). Eine Anwendung des Magnetooptischen Kerreffektes zur Untersuchung schnellablaufender Magnetisierungsprozesse. *Zeitschrift für Angewandte Physik*, **16**, 81–90.

Passon, B. (1968). Über die Beobachtung ferromagnetischer Bereiche bei Magnetisierung in Wechselfeldern bis zu 20 kHz. *Zeitschrift für Angewandte Physik*, **25**, 56–61.

Petek, B., Trouilloud, P.L. and Argyle, B.E. (1990). Time-resolved domain dynamics in thin-film heads. *IEEE Transactions on Magnetics*, **26**, 1328–1330.

Ping, G.L., See, C.W. and Somekh, M.G. (1996). A confocal fibre scanning microscope for magnetic domain imaging. *Journal of Microscopy*, **184**, 149–156.

Ping, G.L., See, C.W., Somekh, M.G., *et al*. (1995). A fast-scanning optical microscope for imaging magnetic domain structures. *Scanning*, **18**, 8–12.

Rave, W., Schäfer, R. and Hubert, A. (1987). Quantitative observation of magnetic domains with the magneto-optical Kerr effect. *Journal of Magnetism and Magnetic Materials*, **65**, 7–14.

Re, M., Shenton, D.N. and Kryder, M.H. (1985). Magnetic switching characteristics at the pole tips of thin film recording heads. *IEEE Transactions on Magnetics*, **21**, 1575–1577.

Romanens, F., Pizzini, S., Yokaichiya, F., *et al*. (2005). Magnetic relaxation of exchange biased Pt/Co multilayers studied by time-resolved Kerr microscopy. *Physical Review B*, **72**, 134410.

Schäfer, R. (1995). Magneto-optical domain studies in coupled magnetic multilayers. *Journal of Magnetism and Magnetic Materials*, **148**, 226–231.

Schäfer, R. and Herzer, G. (2001). Continuous magnetization patterns in amorphous ribbons. *IEEE Transactions on Magnetics*, **37**(4), 2245–2247.

Schäfer, R. and Hubert, A. (1990). A new magnetooptic effect related to non-uniform magnetization on the surface of a ferromagnet. *Physica Status Solidi A*, **118**, 271–288.

Schäfer, R., Hubert, A. and Parkin, S.S.P. (1993). Domain and domain wall observations in sputtered exchange-biased wedges. *IEEE Transactions on Magnetics*, **29**, 2738–2740.

Schmidt, F. and Hubert, A. (1986). Domain observations on CoCr layers with a digitally enhanced Kerr microscope. *Journal of Magnetism and Magnetic Materials*, **61**, 304–320.

Schmidt, F., Rave, W. and Hubert, A. (1985). Enhancement of magneto-optical domain observation by digital image processing. *IEEE Transactions on Magnetics*, **21**, 1596–1598.

Sheppard, C. and Wilson, T. (1984). *Theory and Practise of Scanning Optical Microscopy*, Academic Press: London.

Shilling, J.W. and Houze, G.L. (1974). Magnetic properties and domain structure in grain-oriented 3% Si-Fe. *IEEE Transactions on Magnetics*, **10**, 195–222.

Silva, T.J. and Kos, A.B. (1997). Nonreciprocal differential detection method for scanning Kerr-effect microscopy. *Journal of Applied Physics*, **81**, 5015–5017.

Stankiewicz, A., Hiebert, W.K., Ballentine, G.E., *et al*. (1998). Dynamics of magnetization reversal in a $20 \times 4\,\mu$m permalloy microstructure. *IEEE Transactions on Magnetics*, **34**, 1003–1005.

Stiles, M.D. and Miltat, J. (2006). Spin transfer torque and dynamics. In *Spin Dynamics in Confined Magnetic Structures III*, Hillebrands, B. and Thiaville A. (Eds.), Springer: Berlin.

Stoll, H., Puzic, A., van Waeyenberge, B., *et al*. (2004). High-resolution imaging of fast magnetization dynamics in magnetic nanostructures. *Applied Physics Letters*, **84**, 3328–3330.

Träger, G., Wenzel, L. and Hubert, A. (1992). Computer experiments on the information depth and the figure of merit in magnetooptics. *Physica Status Solidi (A)*, **131**, 201–227.

Veerdonk, R.J.M., Ju, G., Svedberg, E.B., *et al*. (2001). Real-time observation of sub-nanosecond magnetic switching in perpendicular multilayers. *Journal of Magnetism and Magnetic Materials*, **235**, 138–142.

Vella-Coleiro, G.P. and Nelson, T.J. (1974). Stroboscopic observation of magnetic bubble circuits using a gated image-intensifier tube. *Applied Physics Letters*, **24**, 397–398.

Voigt, W. (1898). Doppelbrechung von im Magnetfeld befindlichem Natriumdampf in der Richtung normal zu den Kraftlinien. *Nachrichten der Königlichen Gesellschaft der Wissenschaften Göttingen, Math.-Phys. Kl.*, **4**, 335–359.

Wakana, S.-I., Nagai, T. and Sakata, Y. (2001). Wide bandwidth scanning Kerr microscope based on optical sampling technique using externally triggerable pulse laser diode. *Journal of Magnetism and Magnetic Materials*, **235**, 213–217.

Williams, H.J., Foster, F.G. and Wood, E.A. (1951). Observation of magnetic domains by the Kerr effect. *Physical Review*, **82**, 119–120.

Wright, C.D., Clegg, W.W., Boudjemline, A. and Heyes, N.A.E. (1994). Scanning laser microscopy of magneto-optic storage media. *Japanese Journal of Applied Physics*, **33**, 2058–2065.

Wright, C.D., Heyes, N.A.E., Clegg, W.W. and Hill, E.W. (1995). Magneto-optic scanning laser microscopy. *Microscopy and Analysis*, **46**, 21–23.

Magnetization-induced Second Harmonic Generation

Andrei Kirilyuk and Theo Rasing
Radboud University Nijmegen, Nijmegen, The Netherlands

1 INTRODUCTION

The invention of lasers has radically affected the field of science and technology. Their development led to the discovery and rapid promotion of nonlinear optics (Franken, Hill, Peters and Weinreich, 1961; Akhmanov and Khokhlov, 1964; Boyd, 1965; Shen, 1984). With manifold applications, nonlinear optical phenomena play a vital role in modern optics. Compared with linear optics, nonlinear optical processes reveal novel information about the electronic structure of solids because, based on the involvement of more than a single optical field, additional experimental degrees of freedom are accessible. In the vast field of nonlinear optics second-harmonic generation (SHG), as the lowest-order nonlinear process, plays a particular role. Being a higher-order process, it brings new and complementary information in comparison with linear optics, partly due to the different selection rules for multiphoton processes and the higher-order susceptibilities involved. Another strong point of the technique is it's intrinsic surface and interface sensitivity that is derived from extremely simple yet powerful symmetry constraints. The SHG technique was therefore widely used for studies of surfaces and interfaces (Shen, 1984; Heinz, 1991; Bennemann, 1998).

The breaking of time-reversal symmetry leads to a number of well-known magneto-optical (MO) effects like Faraday rotation in transmission and Kerr rotation in reflection (Zvezdin and Kotov, 1997). For nonlinear optics, in the electric-dipole approximation, even-order effects like SHG are only allowed in media with a broken space inversion symmetry. As a consequence, even-order nonlinear MO effects can only be observed in materials in which both space-inversion and time-reversal symmetry are broken. Though the first predictions of magnetic effects in SHG were made over 40 years ago (Pershan, 1963; Adler, 1964; Lajzerowicz and Vallade, 1967) and discussed in several theoretical publications (Kielich and Zawodny, 1973; Pan, Wei and Shen, 1989; Hübner and Bennemann, 1989), the field of nonlinear magneto-optics really evolved in the past fifteen years by the observation of huge MO effects from magnetic surfaces and interfaces (Reif, Zink, Schneider and Kirschner, 1991; Reif, Rau and Matthias, 1993; Spierings *et al*., 1993). This 'revival' and recent strong development of nonlinear magneto-optics is clearly related to the enormous interest in the study and applications of magnetic multilayers and nanostructures as well as to the development of solid state mode-locked femtosecond lasers that are particularly suitable for these kinds of studies (Keller, 2003).

One of the very important fundamental achievements was the demonstration of the extreme sensitivity of magnetization-induced second-harmonic generation (MSHG)

Handbook of Magnetism and Advanced Magnetic Materials. Edited by Helmut Kronmüller and Stuart Parkin. Volume 3: *Novel Techniques for Characterizing and Preparing Samples*. ISBN: 978-0-470-02217-7.

to the slightest modifications of the spin-polarized electronic structure of transition-metal surfaces (Wierenga *et al*., 1995; Straub, Vollmer and Kirschner, 1996; Vollmer, Straub and Kirschner, 1996b; Jin, Regensburger, Vollmer and Kirschner, 1998; Veenstra *et al*., 1999; Veenstra, Petukhov, Jurdik and Rasing, 2000). Even tiny increases in the magnetization of the surface layer, caused by the presence of atoms with low coordination numbers on surfaces with atomic steps, could be detected (Jin, Regensburger, Vollmer and Kirschner, 1998). On the other hand, the possibility to distinguish the contributions from different interfaces (Kirilyuk, Rasing, Haast and Lodder, 1998) showed a way to measure the magnetization of a buried interface and therefore triggered a lot of applied interest. One of the particular intriguing problems attacked with MSHG was the spin-polarization of the interfaces between ferro- and antiferromagnets in exchange-biased structures (Sampaio *et al*., 2003, 2005; Valev, Gruyters, Kirilyuk and Rasing, 2006a,b; Valev *et al*., 2007). In addition, it has been demonstrated that, conform the original predictions, SHG can be used to study antiferromagnetic ordering and even image antiferromagnetic domains, which is very hard or even impossible to do with other techniques (Fiebig, Fröhlich, Krichevtsov and Pisarev, 1994; Fiebig, Fröhlich, Sluyterman and Pisarev, 1995).

This review is organized as follows: first, a general description of MSHG is given followed by a discussion of the theory of MSHG in Section 2. Then, the details of various experimental techniques are given in Section 2. Section 4 discusses the applications of MSHG to magnetic surfaces; Section 5 is concerned with buried magnetic interfaces, followed by a discussion of the unavoidable bulk contributions to the interface MSHG, and the consequences of the electronic quantum-well-state resonances. Further developments of the techniques are briefly outlined in Section 6.

2 THEORY OF MSHG

2.1 General idea

An incident light wave induces a polarization in a medium that serves as a source for the transmitted and reflected light. In the electric-dipole approximation, this polarization $\mathbf{P}$ can be written as an expansion in powers of the optical electric field $\mathbf{E}(\omega)$:

$$\mathbf{P}(\omega, 2\omega, \ldots) = \chi^{(1)}\mathbf{E}(\omega) + \chi^{(2)}\mathbf{E}(\omega)\mathbf{E}(\omega) + \ldots \qquad (1)$$

The tensor $\chi^{(1)}$ is the linear optical susceptibility allowed in all media. SHG is described by the second term with the corresponding nonlinear tensor $\chi^{(2)}$ allowed only in noncentrosymmetric media. The latter is easy to verify by carrying out the inversion operation that changes the sign of every *polar* vector, such as $\mathbf{P}$ or $\mathbf{E}$. Consequently, $\chi^{(2)}$ is allowed at surfaces or interfaces between centrosymmetric media, giving rise to the surface/interface sensitivity of the technique. For crystals with a spontaneous or magnetic field-induced magnetization $\mathbf{M}$, the nonlinear second-order optical polarization of a medium $\mathbf{P}^{\mathrm{nl}}(2\omega)$ can be written as:

$$\mathbf{P}^{\mathrm{nl}}(2\omega) = \chi^{\mathrm{cr}}\mathbf{E}(\omega)\mathbf{E}(\omega) + \chi^{\mathrm{magn}}\mathbf{E}(\omega)\mathbf{E}(\omega)\mathbf{M} \qquad (2)$$

where the first term describes the purely crystallographic contribution while the second one exists only in the presence of a magnetization $\mathbf{M}$ and describes MSHG. Note that $\mathbf{M}$ is an *axial* vector, so that the inversion operation does not change its sign and the surface/interface sensitivity also holds for magnetic materials. Thus these two contributions to the nonlinear polarization $\mathbf{P}^{\mathrm{nl}}(2\omega)$ are of electric-dipole character and simultaneously allowed in noncentrosymmetric media, but their properties are different. The crystallographic contribution is described by a polar tensor χ^{cr} of rank 3, whereas the magnetization-induced contribution is described by an axial tensor χ^{magn} of rank 4. In lossless media χ^{cr} is a real tensor and χ^{magn} is an imaginary tensor, therefore there is no interference between the SHG waves coming from these two sources for linearly polarized fundamental light (Pershan, 1963; Pan, Wei and Shen, 1989). The interference becomes allowed for linearly polarized fundamental light in the absorption region, because both tensors will be complex, or by using circular optical excitation. It is this interference that gives rise to new nonlinear MO effects, which have no counterparts in linear optics (Pavlov, Pisarev, Kirilyuk and Rasing, 1997; Kirilyuk, Pavlov, Pisarev and Rasing, 2000; Gridnev *et al*., 2001).

The expression (2) is general and fully describes MSHG in the electric-dipole approximation. The number of nonzero component of χ^{cr} and χ^{magn} tensors depends on the crystallographic and magnetic symmetry of the sample. For high symmetry systems (the vast majority of thin-film structures studied so far), each of these tensors consists of a few components only. Moreover, these components are not intermixing with each other, that is, the tensor

$$\chi^{(2)} = \chi^{\mathrm{cr}} + \chi^{\mathrm{magn}} \cdot \mathbf{M} \qquad (3)$$

can be written as a single third rank tensor whose components are either *even* or *odd* in $\mathbf{M}$. An important case is that of an isotropic interface (that of a quite standard polycrystalline film, for example, or a (100) surface of a cubic system). In this case, and with xz being the plane of incidence, the nonlinear MO tensor $\chi^{(2)}$ can be written as (Pan, Wei and Shen, 1989): The elements shown to depend on M_i are *odd*

$$\chi^{(2)} = \begin{pmatrix} \chi_{xxx}(M_y) & \chi_{xyy}(M_y) & \chi_{xzz}(M_y) & \chi_{xzy}(M_z) & \chi^{\mathrm{cr}}_{xzx} & \chi_{xxy}(M_x) \\ \chi_{yxx}(M_x) & \chi_{yyy}(M_x) & \chi_{xzz}(M_x) & \chi^{\mathrm{cr}}_{yzy} & \chi_{yzx}(M_z) & \chi_{yxy}(M_y) \\ \chi^{\mathrm{cr}}_{zxx} & \chi^{\mathrm{cr}}_{zyy} & \chi^{\mathrm{cr}}_{zzz} & \chi_{zzy}(M_x) & \chi_{zzx}(M_y) & \chi_{zxy}(M_z) \end{pmatrix} \tag{4}$$

in the corresponding magnetization component (roughly proportional to it–see Pustogowa, Hübner and Bennemann, 1993). Thus the nonlinear MO properties of an isotropic interface with a selected magnetization direction are characterized by up to 10 (complex) numbers.

Here $\mathbf{E}(\omega)$ and $\mathbf{P}(2\omega)$ are *local* fields and polarizations; to relate them to the amplitudes of the incoming and outgoing electromagnetic waves, appropriate Fresnel factors should be used. In fact, the $\chi^{(2)}$ tensor alone determines the geometrical symmetry properties of MSHG; for an extended treatment of these properties, both theoretical and experimental, we refer the reader to Gridnev *et al*. (2001).

The $\chi^{(2)}$ tensor of equation (4) allows one to qualitatively understand the behavior of MSHG as a function of magnetization reversal. In the transverse MO geometry, $\mathbf{M}||y$, (see Figure 1), equation (4) shows that in the case of *S*-polarized incident light (i.e., $\mathbf{E}_{\mathrm{in}} = \mathbf{E}_y$) one even ($\chi_{zyy}$) and one odd ($\chi_{xyy}(M_y)$) tensor element will produce the outgoing SH waves. Both of them lead to the same *P*-polarization of the output. Therefore, the total MSHG output can be written as

$$I^{2\omega}(\pm\mathbf{M}) \propto |E_{\mathrm{in}}|^4(\alpha\chi_{zyy} \pm \beta\chi_{xyy}(\mathbf{M}))^2 \tag{5}$$

where α and β denote the corresponding Fresnel factors (they result, for example, in the angle of incidence dependence of the MSHG signal). Thus the reversal of $\mathbf{M}$ leads to a change in the MSHG intensity.

In contrast, in the longitudinal geometry, with $\mathbf{M}||x$, the corresponding odd element ($\chi_{yyy}(M_x)$) gives rise to an *S*-polarized output. The total output polarization will thus be a vector sum of the two orthogonal vectors, one of them being reversed upon reversal of $\mathbf{M}$. The resulting MO effect is therefore a change of MSHG polarization (Reif, Rau and Matthias, 1993; Koopmans, Groot Koerkamp, Rasing and van den Berg, 1995). In both cases, the relative effects can be quite large, as the odd and even tensor elements are of similar size (see, e.g., Koopmans, Groot Koerkamp, Rasing and van den Berg, 1995). This is in strong contrast to most linear MO effects, where the odd components are generally much smaller than the even ones.

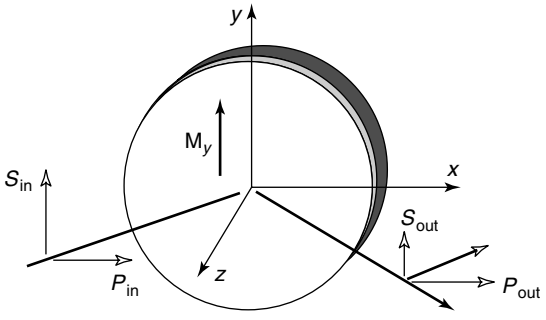

Figure 1. Schematic geometry of the experiment: xz is the plane of incidence, $\mathbf{M}$ is directed along y (transversal geometry) or along x (longitudinal geometry). Input light is either *P* polarized (E_x, E_z) or *S* polarized (E_y).

The problem of calculating the nonlinear (magneto-) optical response of a given medium contains two clearly distinct parts: (i) calculation of the nonlinear susceptibility, and (ii) with known susceptibility, calculate the outgoing MSHG intensity. Both these parts are nontrivial and require a lot of attention: part (i) involves sophisticated electronic structure calculations in a nonperiodic electronic system, while part (ii) contains nontrivial electromagnetic boundary conditions and complicated multiple-scattering processes.

2.2 Nonlinear magneto-optical susceptibility

As a first step in the calculation of the nonlinear MO susceptibility tensor $\chi^{(2)}$, a complete spin-dependent electronic band structure of the sample should be computed, including the corresponding wave functions. As by the 'sample' we mean surface or interface that is a nonperiodic structure, both the band structure and wave functions will be position dependent in the perpendicular to the surface direction.

Next, the electronic structure serves as a background for the calculation of the MO response. This approach was followed by Hübner and Bennemann (1989) and Hübner (1990) using the Heisenberg's equation-of-motion formalism in second-order perturbation theory. The screening of the driving electromagnetic field by the system's electrons were taken into account self-consistently.

The surface or interface susceptibility is then given by:

$$\chi_{ijm}(2\omega) = \frac{e^3\mathbf{q}_{||}a}{\Omega}\frac{\lambda_{s.o.}}{\hbar\omega}\sum_{\mathbf{k},l,l',l'',\sigma} M_i M_j M_m \times \left\{ \frac{\frac{f(E_{\mathbf{k}+2\mathbf{q}_{||}l''\sigma}) - f(E_{\mathbf{k}+\mathbf{q}_{||}l'\sigma})}{E_{\mathbf{k}+2\mathbf{q}_{||}l''\sigma} - E_{\mathbf{k}+\mathbf{q}_{||}l'\sigma} - \hbar\omega + i\hbar\alpha_l} - \frac{f(E_{\mathbf{k}+\mathbf{q}_{||}l'\sigma}) - f(E_{\mathbf{k}l\sigma})}{E_{\mathbf{k}+\mathbf{q}_{||}l'\sigma} - E_{\mathbf{k}l\sigma} - \hbar\omega + i\hbar\alpha_l}}{E_{\mathbf{k}+2\mathbf{q}_{||}l''\sigma} - E_{\mathbf{k}l\sigma} - 2\hbar\omega + i2\hbar\alpha_l} \right\} \tag{6}$$

Here, the symmetry of the wave functions enters through the dipole matrix elements $M_i = \langle \Psi_{k,l,\sigma} | p_i | \Psi_{k,l',\sigma} \rangle$, where p_i is the momentum operator. It is this symmetry that is responsible for the selection rules giving rise to the surface sensitivity of the response. The dependence on the electronic structure results from the eigenvalues $E_{k,l,\sigma}$, which depend on the wave vector $\mathbf{k}$, the band index l, and the spin σ. Note, the matrix elements may involve s-, or d-states, as well as quantum well states (QWS) that appear in ultrathin layers, and will depend on the corresponding wave functions. $f(E_{k,l,\sigma})$ is the Fermi function, α_l is the Lorentzian broadening of the states. Taking into account only vertical transitions, equation (6) already shows how changes of the susceptibility result from modifications in the joint density of states, which is probed by nonlinear optics. Since SHG is generated at the surface and the interface of the film, the summation over the energy eigenvalues has to be performed according to the surface and the interface electronic structure. Thus for a paramagnetic material, the band structure for both spin directions is the same and no spin dependence results. In the case of a ferromagnetic material, the nonlinear tensor $\chi_{ijm}(\mathbf{M})$ will be separated into odd and even components as discussed in the preceding text.

The only attempt to carry out the whole computational procedure in full was made by Andersen and Hübner (2002) who calculated the nonlinear MO response of a single Fe(001) monolayer on top of a 1, 2, 3, or 4 monolayer 'substrate'. The results showed indeed the expected large nonlinear MO effects. Such a sample is close to the limit of modern computation possibilities. Moreover, even in that case the calculation procedure was not entirely stable, as their own tests showed. The problem is that small errors in calculating the wave functions due to a restricted basis set (to save computation time) get amplified when three transition matrix elements are multiplied to obtain the final result.

Another approach based on the first-principles layer Korringa–Kohn–Rostocker method was employed to calculate the MSHG response from the Ni(110) surface. The preliminary results showed the contribution of the surface states to the nonlinear MO susceptibility (Calmels, Crampin, Inglesfield and Rasing, 2001), in good agreement with experimental results (Veenstra, Petukhov, Jurdik and Rasing, 2000).

2.3 Calculation of MSHG from multilayers

To calculate the MSHG response from a multilayer system one realizes that, in fact, the nonlinear susceptibility $\chi^{(2)}$ is expected to quickly decrease on both sides of the interface. As a result, the spatial distribution of $\chi^{(2)}$ can be well approximated by an infinitesimally thin nonlinear sheet between the two non-nonlinear media, see Figure 2 (Bloembergen and Pershan, 1962; Sipe, 1987; Wierenga, Prins, Abraham and Rasing, 1994; Wierenga, Prins and Rasing, 1995). This is even more true because the characteristic length to compare with is the wavelength of light, typically several hundred nanometers. Such an approximation reduces the number of parameters in the problem. A well-known concept in optics is to treat the boundary conditions at an interface, and the propagation of light through a homogeneous slab, in terms of matrices that relate the field components on both sides of the interface and the layer respectively. Describing the full multilayer is thus reduced to a simple matrix multiplication (Palik, 1985).

Owing to the very small nonlinear susceptibility values, the total problem can be split in two. In the first part, the influence of the nonlinearity on the light behavior is totally neglected. The local electric fields and polarizations induced by the incident light inside the structure are derived from the primary electric field through the linear susceptibility tensor. The tensor, in turn, may depend on the layer magnetization, thus giving rise to linear MO effects. The induced polarizations are actually quite small compared to the fundamental electric field and can be considered as a perturbation.

The second part of the problem concerns the electromagnetic waves at the second-harmonic frequency. Here, the fundamental electromagnetic field is absent and the 2ω-polarizations play the role of the only sources. If all the layers of the structure possess a center of inversion, then, within the electric-dipole approximation, there will be no volume polarization. The total second-harmonic yield can thus be related to the interfaces only, each interface being described by its own nonlinear optical tensor $\chi^{(2)}$.

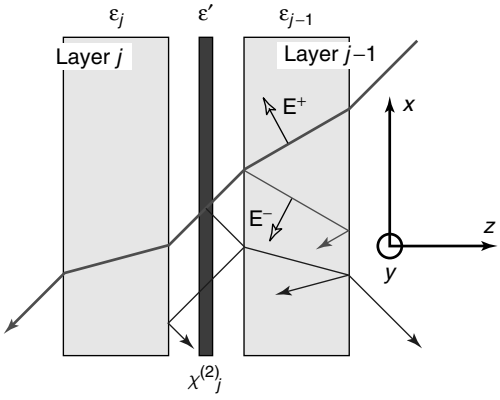

Figure 2. Infinitesimal nonlinear sheet inside an artificial vacuum sheet at an interface.

It should be noted that even in linear optics, the normal component of the electromagnetic field is discontinuous across ideal interfaces. The surface polarizations become radiation sources. The corresponding electric fields can be obtained from Maxwell's equations, which are now accompanied by the unconventional boundary conditions taking into account singular polarizations of ideal interfaces (Shen, 1984). A comprehensive treatment of problems related to a model of both linear and nonlinear MO effects in multilayers has been given by Atkinson and Kubrakov (2002). Most often, however, bulk anisotropy of layers can be neglected together with the linear MO effects that are argued to be small enough.

The parameters accessible experimentally are the MSHG intensity and polarization. In addition, also the phase of the total MSHG output can be determined quite straightforwardly (Veenstra, Petukhov, de Boer and Rasing, 1998; Leute, Lottermoser and Fröhlich, 1999). In order to determine the nonlinear susceptibilities at interfaces, the MSHG output is first measured as a function of some parameters, for example, angle of incidence, magnetization, sample thickness, azimuthal angle, and so on. Then, multiple-scattering calculations are used to fit the obtained data using the nonlinear optical tensor components as fit parameters, provided that the obtained experimental data are sufficient for an unambiguous fit. Various polarization combinations help to distinguish different tensor components by selectively exciting one or another combination of them. An example of such an analysis will be included in Section 5.

The main assumption of the discussed model is that it considers the source of the SH field in the form of an infinitely thin, coherently and homogeneously polarized sheet. Although this assumption is justifiable in many cases investigated experimentally, it is not sufficiently general. Moreover, it is based on a macroscopic-like description of the source of the SH field, which does not provide a direct physical insight into the processes involved in the SHG phenomena.

A different model was discussed recently (Hamrle, Polerecký and Ferré, 2003; see also Sampaio *et al*., 2004), where the problem of MSHG was considered from a different point of view. The SH field was considered to be generated by a point electric dipole oscillating at an angular frequency 2ω, positioned at the layer interface. This is closely related to the symmetry considerations used in the macroscopic models like that discussed in the preceding text.

This approach to the SHG has some advantages. In particular, once the electromagnetic (EM) field generated by the point dipole is known, it can be used to evaluate the SH field generated from a system with arbitrarily spatially distributed dipoles. Furthermore, as it is based on a well understood microscopic quantity (an elementary dipole), it can be more directly related to a quantum-mechanical description of MSHG.

The elegance of the developed model becomes apparent when systems with an inhomogeneous distribution of susceptibility tensors along the interfaces are considered. This is the case when the magnetization of the layers, and thus the interfaces, exhibits variations in the lateral dimension due to, for example, the presence of magnetic domains, propagating spin waves, periodic structures, magnetic nanostructures, and so on, and where the optical properties (layer thicknesses and permittivity tensors) can be assumed to be laterally homogeneous (Hamrle, Polerecký and Ferré, 2003).

2.4 Interface and bulk contributions to MSHG from a superlattice

It would be misleading to state that *all* the MSHG response from centrosymmetric media is generated at interfaces only. Strictly speaking, the surface nonlinear optical tensor χ does not even fulfill the energy conservation law, one of the basic principles of physics. Reexamined closely (Petukhov *et al*., 1998), this paradoxical result can be understood with the aid of an additional bulk contribution to the energy flow, as part of the surface response appears to be determined by the bulk parameters alone.

Having realized that, it is interesting to look more closely at the description of surface and bulk contributions to MSHG from a multilayer. The polarization $\mathbf{P}$ can be written as an expansion in powers of the optical electric field $\mathbf{E}(\omega)$:

$$\mathbf{P}(\omega, 2\omega, \ldots) = \chi^{1,d}\mathbf{E}(\omega) + \chi^{1,q}\nabla\mathbf{E}(\omega) + \chi^{2,d}\mathbf{E}(\omega)\mathbf{E}(\omega) + \chi^{2,q}\mathbf{E}(\omega)\nabla\mathbf{E}(\omega)\ldots \quad (7)$$

The tensor $\chi^{1,d}$ is the linear optical susceptibility allowed in all media. SHG is described by the third and the fourth term where the electric-dipole tensor $\chi^{2,d}$ is allowed only in noncentrosymmetric media and at surfaces and interfaces, while the quadrupole tensor $\chi^{2,q}$ is allowed everywhere. For crystals with a spontaneous or magnetic-field induced magnetization $\mathbf{M}$, expansion of the nonlinear optical polarization of a medium $\mathbf{P}^{\mathrm{nl}}(2\omega)$ can be further written (keeping only terms linear in magnetization) as:

$$\mathbf{P}^{\mathrm{nl}}(2\omega) = \chi^{\mathrm{cr}}\mathbf{E}(\omega)\mathbf{E}(\omega) + \chi^{m}\mathbf{E}(\omega)\mathbf{E}(\omega)\mathbf{M} + \chi^{q,\mathrm{cr}}\mathbf{E}(\omega)\nabla\mathbf{E}(\omega) + \chi^{q,m}\mathbf{E}(\omega)\nabla\mathbf{E}(\omega)\mathbf{M} \quad (8)$$

where the first and third term describe the purely crystallographic contributions while the second and fourth only exists in the presence of a magnetization $\mathbf{M}$.

Although smaller, the last two terms in equation (8) originate from the bulk and therefore may be comparable in magnitude to the strong dipole contribution coming from the very thin interface layer. Experimental results (see Sato *et al*., 2001, and below) confirm this assumption and substantiate the necessity to take this contribution into account in high-quality single-crystalline multilayers.

3 EXPERIMENTAL DETAILS

The strong development of nonlinear magneto-optics in the past decade is also related to the development of solid state mode-locked lasers that combine short pulse lengths with high repetition rates and allow the study of ultrathin magnetic films without destroying them. For most MSHG experiments nowadays, a Ti-sapphire laser (82 MHz × 100 fs pulses) tunable from 750–1100 nm but extendable to 400 nm–3 μm using a parametric amplifier, is used. After proper filtering the generated specular harmonic light can be analyzed.

For each polarization combination, the total MSHG response from a magnetic material can be simplified by

$$\mathbf{P}(2\omega) = (\chi_{\text{eff}}^{\text{even}} \pm \chi_{\text{eff}}^{\text{odd}}(\pm\mathbf{M}))E_{\omega}^{2} \tag{9}$$

where $\chi_{\text{eff}}^{\text{even}}$ and $\chi_{\text{eff}}^{\text{odd}}$ are effective tensor components that are even and odd in the magnetization and describe the crystallographic and magnetic contributions to the total response, respectively. As both these contributions are complex quantities, the total (MSHG) signal is thus given by

$$I^{2\omega} = |\chi_{\text{eff}}^{\text{even}}|^2 + |\chi_{\text{eff}}^{\text{odd}}|^2 \pm 2|\chi_{\text{eff}}^{\text{even}}||\chi_{\text{eff}}^{\text{odd}}|\cos\Delta\Phi \tag{10}$$

where $\Delta\Phi$ is the phase difference between the two contributions. The importance of the latter is obvious: when $\Delta\Phi = \pi/2$, the interference term is zero and changing the magnetization direction will have no effect on the total MSHG signal.

Though generally phase information is lost in intensity measurements, fortunately the phase can be measured quite easily in nonlinear optics by using interference techniques (Stolle *et al*., 1997). The latter can also be exploited in the case where there is only a purely odd response, by adding a nonmagnetic reference signal, as it is the interference between even and odd terms that gives rise to the nonlinear MO effects.

While MSHG signals give large relative MO effects, being a nonlinear optical technique the absolute intensities are rather small (10–10^4 photons/s) but easily detectable with modern photon counting or charge-coupled devices (CCD), though care should be taken to filter out the 2ω signal versus the much stronger fundamental signal at ω (see Figure 3).

Because of the simplicity of the experimental configuration, coupled with the large effects, the transverse geometry is often used for experimental studies. For that situation, one can define a magnetic contrast or asymmetry as:

$$A = \frac{I^{2\omega}(+\mathbf{M}) - I^{2\omega}(-\mathbf{M})}{I^{2\omega}(+\mathbf{M}) + I^{2\omega}(-\mathbf{M})} = \frac{2|\chi_{\text{eff}}^{\text{odd}}|/|\chi_{\text{eff}}^{\text{even}}|}{1 + |\chi_{\text{eff}}^{\text{even}}/\chi_{\text{eff}}^{\text{even}}|^2}\cos\Delta\Phi \tag{11}$$

Because A is normalized with respect to the total SHG intensity, it does not depend on the intensity or shape of the fundamental light pulses, nor on the spectral properties of optical components, such as filters, in the optical set up. Together with the already mentioned simplicity, this makes A a useful parameter for quantitative investigations. One should, however, realize that the appearance of large effects that result from the large magnetic tensor components also means that, in contrast to most linear MO effects, the nonlinear optical effects are often not simply linearly proportional to the magnetization, as directly follows from equations (10) and (11). This can for example strongly affect the shape of an MSHG loop (Pavlov *et al*., 2001; Valev, Gruyters, Kirilyuk and Rasing, 2005).

3.1 MSHG microscopy

It is interesting as well as challenging to employ the nonlinear optical effects in the imaging mode. Owing to the high sensitivity to the symmetry and order, SHG has been used to image ferroelectric domains and domain walls (Uesu, Kurimura and Yamamoto, 1995; Bozhevolnyi *et al*., 1998; Mishina *et al*., 2001), molecular surface ordering (Flörsheimer *et al*., 1997a,b), metal (Pedersen and Bozhevolnyi, 1999) and semiconductor (Erland *et al*., 2000) surface structures. In addition, owing to its high contrast, SHG microscopy could be combined with optical near-field imaging (Smolyaninov, Zayats and Davis, 1997; Bozhevolnyi, Vohnsen and Pedersen, 1998; Zayats and Smolyaninov, 2004) thus expanding the resolution possibilities.

The MSHG technique can be straightforwardly adopted to provide spatial information on the magnetization distribution at interfaces. Owing to its high MO contrast as well as some rather unusual MO effects, it can also be used as a technique complementary to the standard Magneto-optical Kerr effect (MOKE) microscopy.

The latter has been clearly demonstrated in thin films of magnetic garnets where the initial inversion symmetry of the bulk was broken by anisotropic film growth. The arising

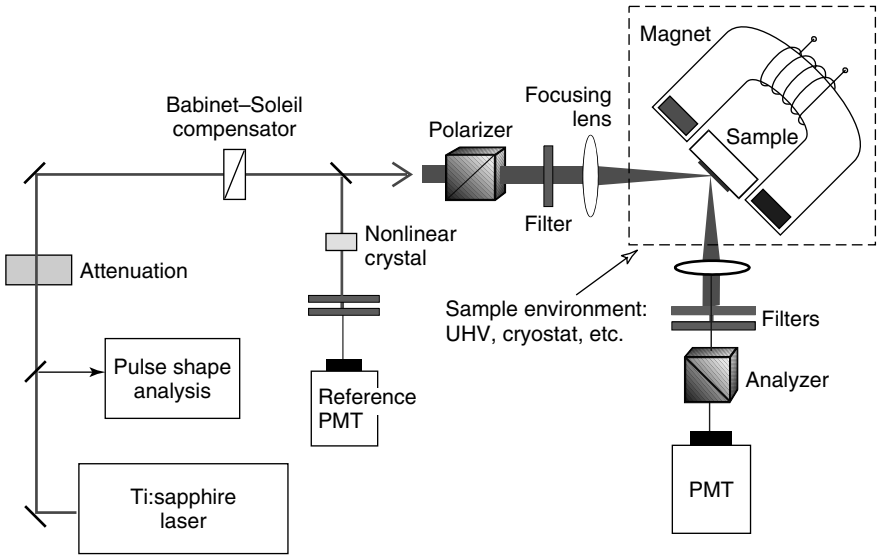

Figure 3. Typical MSHG experimental setup, with an autocorrelator for pulse shape characterization and a reference SHG channel.

strong MSHG response has different symmetry properties than the corresponding linear MO effects and was thus useful in distinguishing the complementary magnetization components, as shown in Figure 4 (Kirilyuk, Kirilyuk and Rasing, 1997).

For imaging, laser light is focused onto a sample. The generated SHG light is used, after proper filtering, for the imaging of the sample with the help of a CCD camera. Owing to the very large contrast, the images could be obtained directly and without any contrast improvement nor background subtraction, a procedure that is usually necessary to obtain the image with linear magneto-optics. The size of the MSHG image is restricted to the diameter of the focused laser beam, approximately 30 μm in this case, whereas the resolution is determined by the standard criteria for the used microscope. The size limitation for the image can be overcome by using a sample scanning procedure. Figure 5 shows a millimeter-size image of an ultrathin stepped film, where owing to electronic quantization effects (QWS) one can observe a strong contrast from monolayer-high steps (Kirilyuk, Rasing, Mégy and Beauvillain, 1996). A more elaborated procedure, demonstrated by Pavlov *et al*. (2001) (see Figure 6), involves a combination of the high-resolution imaging with scanning the sample, and a subsequent reconstruction of the total image from small parts.

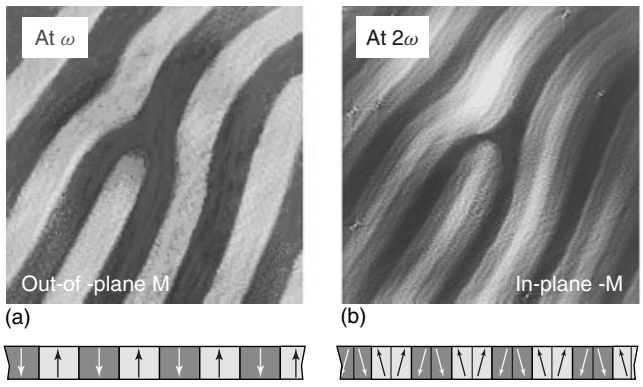

Figure 4. Images of magnetic domain structure in a thin layer of magnetic garnet: (a) linear Faraday effect, (b) MSHG in transmission. Below the images, the domain structure is shown as inferred from the pictures: Faraday effect sees the polar component of **M** only, while MSHG is able to detect also the in-plane component of the magnetization, showing that each up/down domain in the left picture is actually divided in two subdomains with tilted magnetization directions.

For the purposes of the present review, it is more interesting to consider MSHG imaging based on a pure interface response, such as for example that from CoNi/Pt interfaces (Kirilyuk, Kirilyuk and Rasing, 1999), or from Pt/Co/Pt multilayers (Pavlov *et al*., 2001). Such sputtered multilayers were found to be a promising MO material (Bijker, Donnet and Lodder, 1996) because of their low Curie temperature and strong MO effects.

Figure 7 shows the magnetization reversal process in a 9-nm thick CoNi film starting from a fully saturated sample (see Figure 7a). A magnetic field of the same value (60 Oe) was applied for the given time intervals (usually 20 s) followed each time by an image accumulation in zero field (10 min per image). In the MSHG images of Figure 7, there appear some details of the domain structure with a weaker contrast than that of the opposite domains. For example, images (d) and (e) clearly show several faint stripes extending along the diagonal of the images. All of them disappear later, in a completely saturated sample (f). Owing

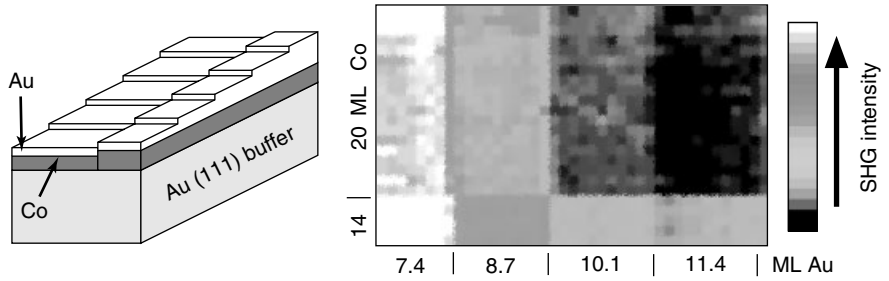

Figure 5. Large-scale image of a stepped Au/Co/Au(111) layer, showing monolayer sensitivity of SHG imaging.

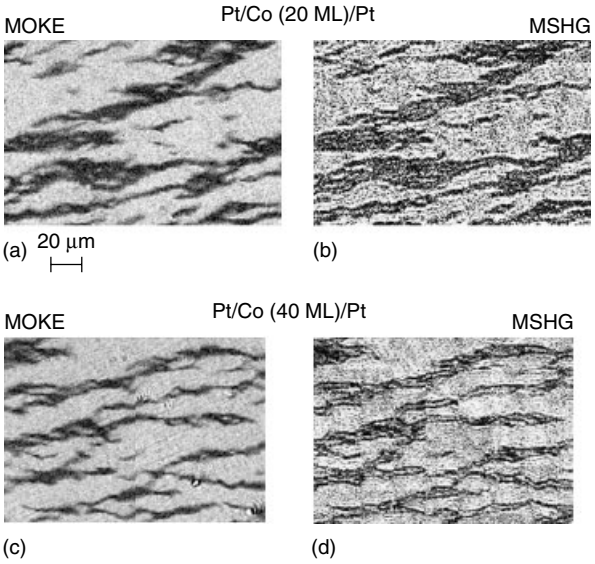

Figure 6. MOKE and MSHG images for Pt/Co(20 ML)/Pt (a and b), and for Pt/Co(40 ML)/Pt films (c and d). The field was previously applied along the easy anisotropy axis. (Reproduced from Pavlov *et al*., 2001, with permission from IOP Publishing Ltd. © 2001.)

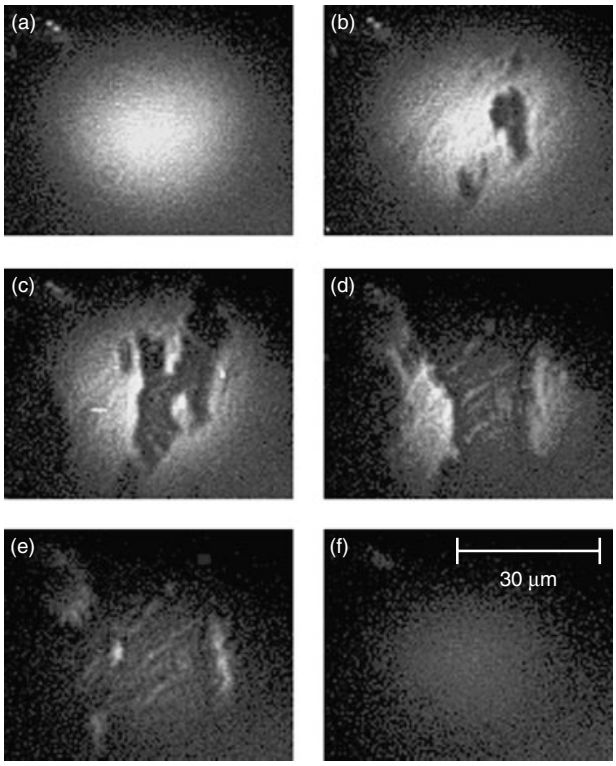

Figure 7. MSHG images of magnetization reversal in a Pt/CoNi/Pt sandwiched layer. Magnetization is saturated 'up' in image (a) and 'down' in image (f). Images (b), (c), (d), and (e) show gradual appearance and growth of opposite magnetic domains. The laser spot diameter is approximately 30 µm. No background subtraction of any kind has been used.

to the low quality of the linear MOKE images in such transversal geometry, a precise comparison of the linear and MSHG images is difficult. Therefore, it is unfortunately impossible to give an unambiguous interpretation to these structures as interface-related.

3.2 Measurements of the optical phase

In most surface, SHG experiments only the intensity of the second-harmonic light is routinely measured. The phase of SHG does, however, contain valuable information for a correct interpretation of the experimental data (Veenstra, Petukhov, de Boer and Rasing, 1998; Veenstra, Petukhov, Jurdik and Rasing, 2000). Furthermore, phase-sensitive measurements are especially useful in surface-specific SHG where the response mainly originates from a thin surface region so that the optical phase is directly related to the phase of the components of the surface nonlinear susceptibility $\chi^{(2)}$. As an example, the phase may give direct information about absolute molecular orientation on surfaces (Kemnitz *et al*., 1986) and in liquid crystals (Stolle *et al*., 1995). For MSHG, the phase between the even and odd susceptibility components is an extremely important parameter, as it determines the actual contrast in the MSHG signal (see equation (11)).

The phase of the SHG response can be determined with an interference technique described in Chang, Ducuing and

Bloembergen (1965). This method is however not compatible with, for example, UHV apparatus when femtosecond lasers are used. The reason is the dispersion of the optical windows ($\Delta n_{glass} \sim 10^{-2}$), causing a too large time delay $\tau \sim 1$ ps) between the fundamental and SHG pulses that destroys the interference. The following alternative approach overcomes this problem in an elegant way (Veenstra, Petukhov, de Boer and Rasing, 1998).

When 2ω and ω pulses propagate through air, the relative phase Φ between them gradually changes,

$$\Phi(d) = \Phi_0 + \delta\Phi = \Phi_0 + \frac{4\pi\,\Delta n_{\text{air}}}{\lambda} d \tag{12}$$

where $\Delta n_{\text{air}} = n(2\omega) - n(\omega) \sim 10^{-5}$ is the dispersion of the ambient air, d is the distance the two pulses have traveled through air, and λ is the fundamental wavelength. By using an additional SHG source (called reference) at position d in the path of the beam, interference can be observed in the detected total intensity

$$I_{2\omega,tot}(d) = I_{2\omega,s} + I_{2\omega,r} + 2\alpha\sqrt{I_{2\omega,s} I_{2\omega,r}}\cos[\delta\Phi(d) + \Phi_0] \tag{13}$$

where $I_{2\omega,s}$ and $I_{2\omega,r}$ are the SHG signals generated by the sample and the reference, respectively. The spatial coherence is described by the coherence parameter α. This interference disappears if the pulses do not overlap in time. As is shown in Figure 7(a), this may happen if the femtosecond fundamental and SH pulses have to travel through a strongly dispersive element like an optical window.

Looking at the problem more closely, in the time domain the optical field at the detector created by two pulses with a delay τ can be described by the function

$$\begin{aligned} E_{2\omega}(t) = {} & E_1 g(t)\exp(-i2\omega_0 t) \\ & + E_2 g(t-\tau)\exp(-i2\omega_0 t + i\Phi) + c.c. \end{aligned} \tag{14}$$

where $E_i g(t)$ describes a slowly varying envelope with amplitude E_i $(i = 1, 2)$. Using the so-called 'time-shifting' identity, $g(t-\tau) \Leftrightarrow G(\Omega)e^{i\Omega\tau}$, where $g(t) \Leftrightarrow G(\Omega)$ is the Fourier transformation, the measured spectrum at the detector is given by

$$\begin{aligned} & I(2\omega_0 + \Omega) \propto |G(\Omega)|^2 \\ & [E_1^2 + E_2^2 + 2\alpha E_1 E_2 \cos(2\omega_0\tau + \Omega\tau + \Phi)] \end{aligned} \tag{15}$$

where Ω denotes the deviation of the frequency from the central frequency $2\omega_0$ within the spectrum of the MSHG output. The second term in the cosine, $\Omega\tau$, leads to beatings in the spectrum of the SH light. The phase of the beatings is directly related to the phase Φ of the response from the sample. Thus the phase information can be easily recovered by using a spectrometer.

In the experimental demonstration, the phase of the MSHG response from an Rh/Co/Cu multilayer was measured. In the longitudinal geometry the *S*-polarized MSHG from this isotropic sample should be *odd* in **M** (see equation (4)) so that reversal of the magnetization must change the phase of the response by 180° (Stolle *et al.*, 1997). A 3-mm thick glass plate was used to introduce a time delay τ between the SHG response from the sample and the reference (a thin poled polymer film with high second-order nonlinearity), see Figure 8(a). The beating part of the SHG spectrum is shown in Figure 8(b) for opposite directions of **M**. The phase change introduced by the magnetization reversal is found to be $\Phi(-M) - \Phi(+M) = 176^\circ \pm 5^\circ$, in excellent agreement with the expected π shift.

In Section 4, we describe the application of this technique to the surface MSHG from Ni(110).

4 MSHG FROM MAGNETIC SURFACES

A clean magnetic surface is the benchmark object for a nonlinear MO experiment. From the theoretical point of view, it is also the simplest one. The experimental study of it, however, requires utmost care mostly devoted to the preparation of a well-defined and clean surface.

4.1 Ni(110) surface: spin-dependent spectroscopy

The spin-dependent electronic structure of ferromagnetic surfaces and interfaces forms the fundamental basis for understanding surface magnetic phenomena. The following example (taken from Veenstra, Petukhov, Jurdik and Rasing, 2000) shows how MSHG can be used to study the electronic surface states on a ferromagnetic metal surface.

Experiments were performed at room temperature on a disk-shaped Ni(110) single crystal placed in UHV conditions between the poles of an electromagnet. In a standard procedure, the sample surface was cleaned by repeated cycles of Ar^+ sputtering and annealing, until no contamination could be traced. The MSHG experiments started with the observation of the influence of the O_2 absorption. Oxygen exposure was done at approximately 3×10^{-9} mbar. Using Auger electron spectroscopy, the coverage of the sample with oxygen was found to be a nonlinear function of exposure that saturated at 45 Langmuir (L). Such saturation coverage corresponds to 1 monolayer (ML) of NiO.

Figure 9 shows the oxygen exposure dependence of the MSHG signal in the $P_{\text{in}}P_{\text{out}}$ polarization combination. It can be seen that when the clean surface is exposed the SHG

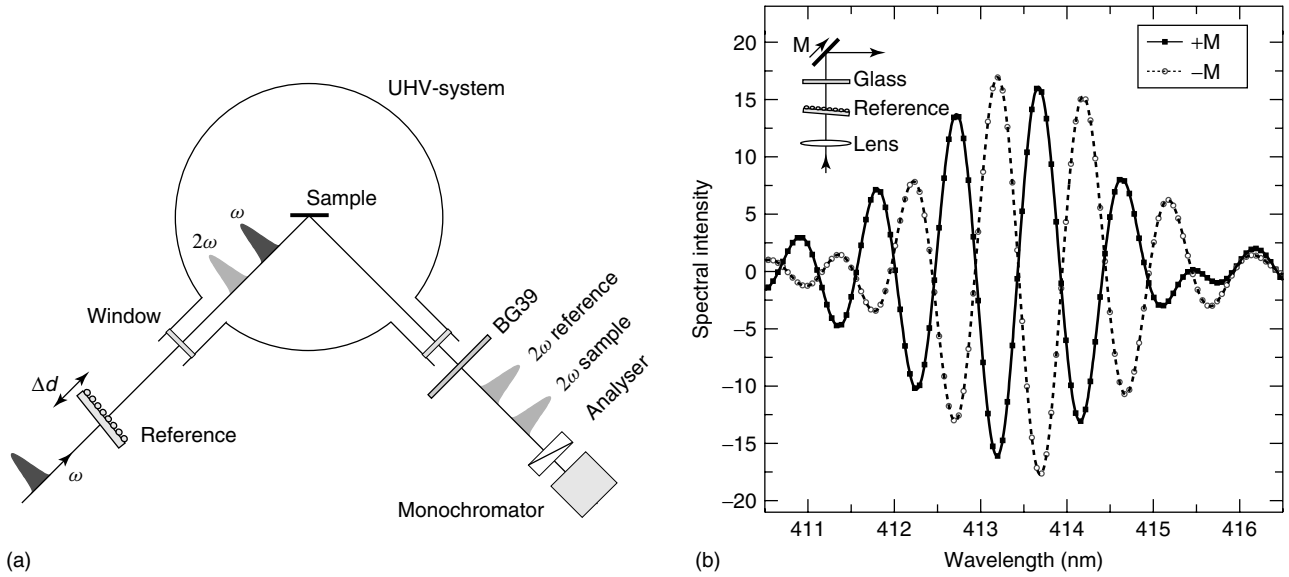

Figure 8. (a) Sketch of the experimental setup for the spectral phase measurements. The SH pulse from the reference is delayed with respect to the fundamental laser pulse due to the dispersion of the window. (b) Spectral interference from an Rh/Co/Cu multilayer for two opposite magnetization directions. (Reproduced from Veenstra *et al*., 1998, with permission from the American Physical Society. © 1998.)

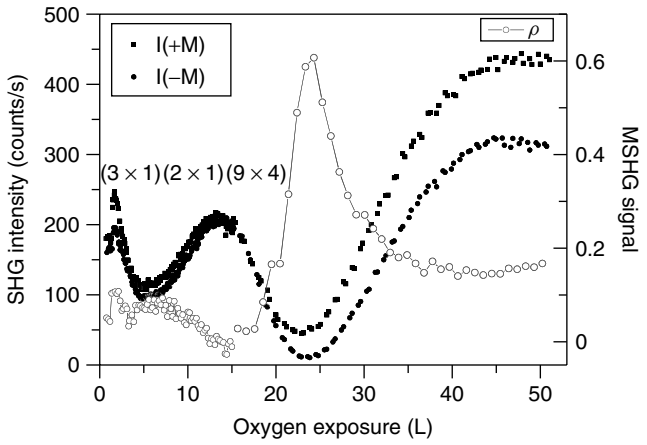

Figure 9. SHG intensity from Ni(110) surface as a function of oxygen dose for opposite directions of **M** as well as the MSHG asymmetry.

intensity increases and has a maximum at 1 L, and another maximum around 10 L. Close to 20 L, the intensity drops by more than an order of magnitude with further increase to saturate around 45 L. The observed two maxima seem to be well in line with the appearance of the $c(2 \times 1)$ and $c(3 \times 1)$ oxygen induced surface superstructures. These superstructures could be observed, at these same coverages, with low-energy electron diffraction (LEED). The magnetic asymmetry plotted in the same figure, roughly indicates the changes in the ratio $\chi^{\text{magn}}/\chi^{\text{cr}}$. Clearly, very small amounts of oxygen drastically change the asymmetry, including the change of sign. On the other hand, the observed SHG intensity maxima at 1 and 10 L do not visibly correlate with the MSHG asymmetry at all.

Spectroscopic MSHG experiments were carried out on the same surface, with the aim to obtain a better insight in the origin of the nonlinear MO response. A tunable optical parametric amplifier pumped by a Ti:sapphire regenerative amplifier was used to produce the fundamental light pulses in the wavelength range of 750–1000 nm. To normalize the measured second-harmonic intensity from the sample, the SHG intensity from a *c*-cut quartz crystal in the transmission geometry was measured with a second photomultiplier tube. The phase of the SHG was measured using the UHV compatible phase-sensitive detection technique (see preceding text in Section 3.2).

The magnetic asymmetry measured in the $P_{\text{in}}P_{\text{out}}$ polarization combination is plotted in Figure 10(a) as a function of $2\hbar\omega$ photon energy. The open circles represent the response of a clean surface while the solid squares are the response of a surface very slightly contaminated with oxygen (0.5 L). In the inset, the average SHG intensity measured on a clean surface is shown. The magnetic asymmetry has a sharp maximum at 2.7 eV and changes sign at 2.6 and 3.1 eV. This resonant feature completely disappears upon oxidation, clearly proving its surface specific nature. The relation between the effective susceptibilities and the intensity data of Figure 9 is given by

$$4|\chi_{\text{eff}}|^2 = I(+M) + I(-M) \pm 2\sqrt{I(+M)I(-M)}\cos(\Delta\varphi) \tag{16}$$

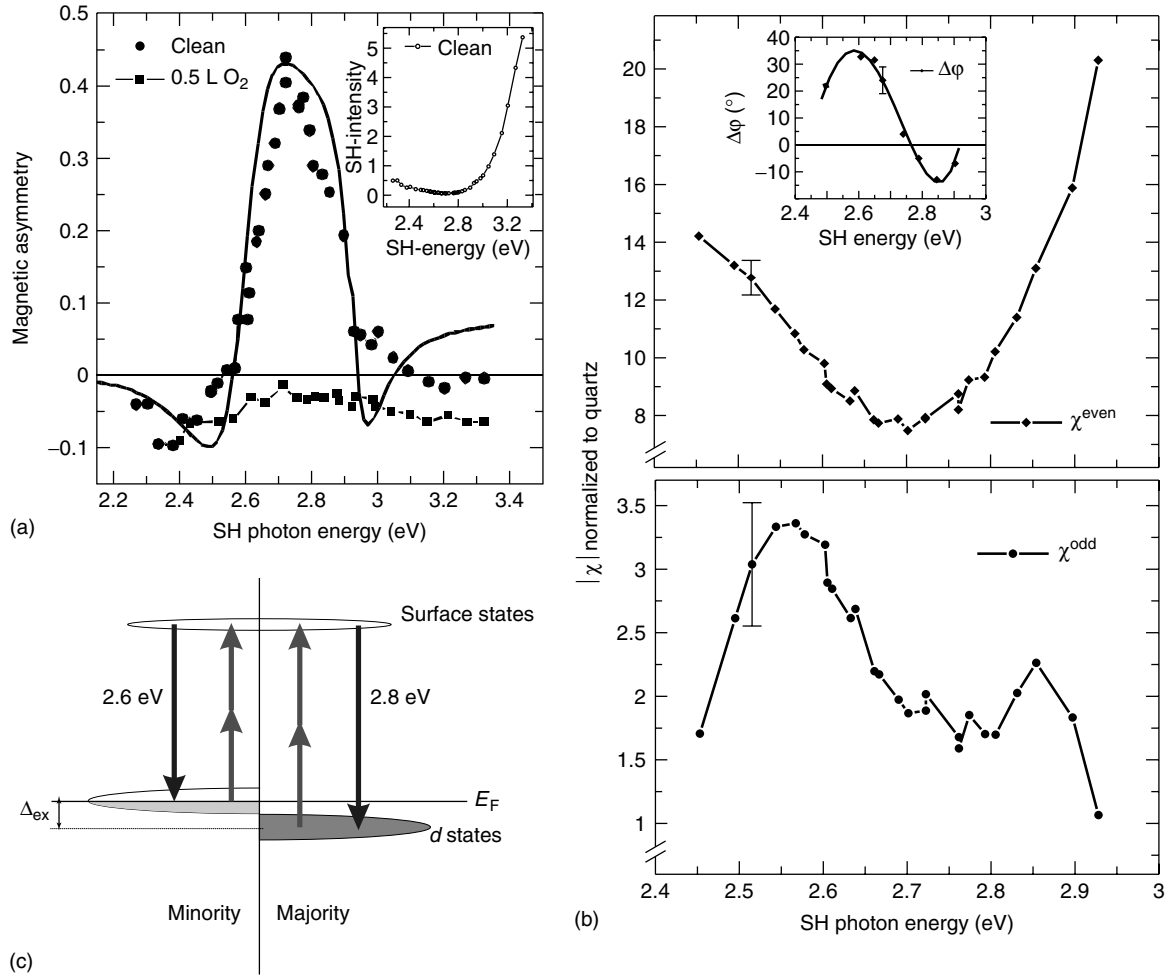

Figure 10. (a) MSHG asymmetry and total intensity (see inset) as a function of 2ω photon energy as measured on a clean and oxidized Ni(110) surface. (b) Amplitude of the effective tensor elements as derived from the measured intensity, asymmetry, and relative phase (inset). (c) Schematic picture of the exchange split density of states and empty surface states in nickel. (Reproduced from Veenstra *et al.*, 2000, with permission from the American Physical Society. © 2000.)

where $\Delta\varphi$ is the phase difference between the SH fields $E(2\omega, +\mathbf{M})$ and $E(2\omega, -\mathbf{M})$. This phase difference was measured as a function of frequency and is shown in Figure 10(b), along with the resulting effective susceptibilities $|\chi_{\text{eff}}^{\text{odd}}|$ and $|\chi_{\text{eff}}^{\text{even}}|$. Surprisingly, the sharp maximum of Figure 10(a) corresponds to the two-peak structure of $|\chi_{\text{eff}}^{\text{odd}}|$ combined with a minimum of $|\chi_{\text{eff}}^{\text{even}}|$.

The resonances as observed in the nonlinear MO spectra of Figure 10(b) can be calculated using equation (6) within a simple model shown in Figure 10(c). The model involves the spin splitting of the d bands around the Fermi energy and an empty surface state around 2.5 eV above E_{F}. The exchange splitting of the d band leads to a maximum density of states for minority spin electrons at the Fermi energy and a maximum for majority spin electrons approximately 250 meV below E_{F}. As this surface state is of nearly pure p_z character, the exchange splitting of this state is much smaller than the splitting of the d states and can be neglected. Including only these d states and a known surface state (Goldmann, Dose and Borstel, 1985) in the summation of equation (6), $|\chi_{\text{eff}}^{\text{odd}}|$ can be written as

$$\chi^{\text{odd}} = A_0 + \frac{A_1}{2\hbar\omega - E_1 + i\hbar\Gamma_1} + \frac{A_2}{2\hbar\omega - E_2 + i\hbar\Gamma_2} \quad (17)$$

where the second term describes the transitions of the minority spin electrons from filled to empty states having energy difference E_1 and the third term includes the transitions of the majority spin electrons. Because of the spin dependence of the resonant contributions to the odd tensor component, the matrix elements A_1 and A_2 should have an opposite sign and be of approximately equal amplitude. Using these relations, the model can be used to fit $|\chi_{\text{eff}}^{\text{odd}}|$ to give $E_1 = 2.58$ eV

and $E_2 = 2.85\,\text{eV}$. Using $|\chi_{\text{eff}}^{\text{even}}|$ from Figure 10(b), it is now possible to calculate the magnetic asymmetry shown in Figure 10(a) by the solid line. The typical features of the asymmetry such as the two sign changes and the maximum are described very well by the model. This proves that these features do indeed arise due to the difference in exchange splitting between the initial d states and the final surface state, which proves that MSHG spectroscopy can be a powerful tool to probe the spin-dependent electronic structure of surfaces.

4.2 Magnetic moments of Co during growth on a Cu surface

The following experiment made direct use of the enormous sensitivity of MSHG to surface magnetism as well as to structure and morphology. Jin, Regensburger, Vollmer, and Kirschner (1998) studied *in situ* the layer-by-layer growth of Co films on Cu(001). During the growth of the Co film (very slow growth with a rate of about 7 ML/h) MSHG signals were measured in the transverse MO geometry.

Figure 11(a) shows the total MSHG intensity for *S*-polarized incident light as a function of the Co film thickness d_{Co} for the two opposite magnetization directions. The MSHG yield from the uncovered Cu surface is much smaller than that from a Co film. Therefore, at the beginning of the Co deposition the MSHG intensity increases almost linearly. The onset of a difference in the $I(+M)$ and $I(-M)$ at $d_{Co} = 1.5\,\text{ML}$ indicates the onset of magnetic order. The corresponding magnetic asymmetry is shown in Figure 11(b), together with the average intensity in Figure 11(c). On top of the overall thickness dependence an oscillation with a one monolayer period is clearly visible up to $d_{Co} = 7$ to 8 ML. The slowly varying part is caused by changes in the electronic structure with increasing film thickness and the appearance of quantum size effects in the SHG.

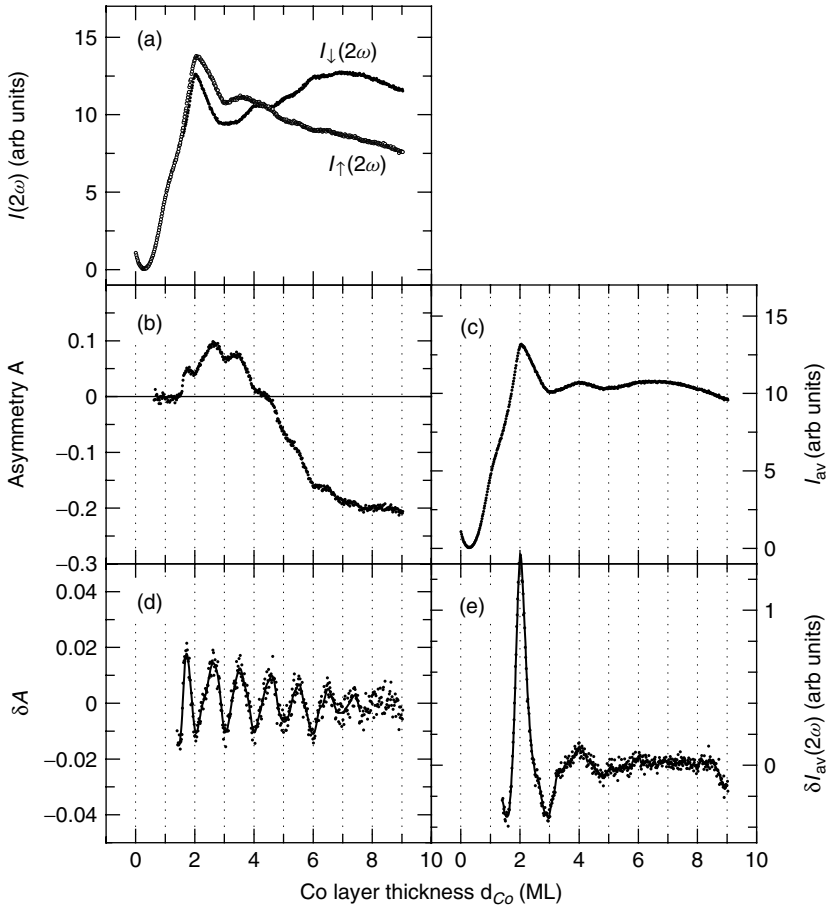

Figure 11. (a) Measured total SHG intensities as a function of the Co film thickness for *S*-polarized incident light in the transversal geometry. (b) Magnetic asymmetry and (c) average SHG intensity calculated from data of (a). In (d) the difference of the magnetic asymmetry and its running average over 50 data points is plotted. (e) Similar as (d) but for the average SHG intensity. (Reproduced from Jin *et al.*, 1998, with permission from the American Physical Society. © 1998.)

However, the one ML period oscillations must rather be related to the morphology of the surface than to the electronic structure. It is well known that SHG is quite sensitive to the surface morphology. For example, on a stepped Al surface the intensity changes by almost two orders of magnitude depending on the step density and step orientation (Janz, Bottomley, van Driel and Timsit, 1991). The enhancement of SHG from this atomic scale roughness is caused by the modified electronic structure of the flat surface. Co grows on Cu in a nearly layer-by-layer growth mode (Schmid and Kirschner, 1992). Periodically Co islands nucleate, grow in size, and coalesce (see Figure 12) causing the total length of step edges to oscillate. Therefore, the observed oscillatory component in the SH intensity may be attributed to the oscillatory varying step density.

The same periodicity is seen not only in the intensity, but in the asymmetry as well. It is very well revealed in the $S_{\text{in}}P_{\text{out}}$ polarization combination (see Figure 11), where the effect of morphology on the average SHG intensity is smaller, compared to the $P_{\text{in}}P_{\text{out}}$ one (Jin, Regensburger, Vollmer and Kirschner, 1998). For clarity, the rapidly varying component of the asymmetry is calculated as the difference of A and its smoothly varying course.

A difficult point in the data treatment was to decide, whether the increase of the measured asymmetry corresponds to the *increase* of the surface magnetization or to its *decrease*. This could be solved by a continuous increase of the film thickness up to 150 ML so that the contribution of the buried interface vanished. It was thus shown that the increase of the magnetization-induced asymmetry at half-filled layers indeed comes from the enhancement of the magnetic *surface* nonlinearity in the whole thickness range.

Though MSHG, similar to the linear MOKE, does not measure the magnetization directly, it has been shown in Pustogowa, Hübner and Bennemann (1993), that to a first approximation, the magnetic tensor elements of the second-order susceptibility depend linearly on the magnetization. Provided the amplitude of the change is small, variations of the asymmetry directly relate to the variations of the tensor elements. Therefore, the observed increase of the asymmetry at half-filled layers suggests the *increase of the magnetic moments* of the atoms at step sites as it is expected from the simple argument of reduced coordination number at these sites. It is by far not easy to estimate the absolute increase of the step magnetic moments as the probing depth of MSHG is not exactly known. Very roughly, the experimental data of Jin *et al*. fall in line with theoretical estimates of an increase in moment of a few percent at the step edges.

These measurements prove the ability of MSHG to detect changes in the magnetic moment at interfaces of the order of $\frac{1}{50}\mu_{\text{B}}$ per atom.

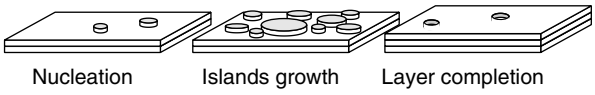

Figure 12. The layer-by-layer growth of a thin film: appearance, growth, and coalescence of islands periodically change the number of step atoms.

5 INTERFACES IN MAGNETIC MULTILAYERS

5.1 Investigation of buried interfaces of CoNi/Pt films with MSHG

This section describes the first successful attempt (from Kirilyuk, Rasing, Haast and Lodder, 1998) to derive the relative nonlinear MO susceptibilities *per interface* from the experimental MSHG data.

The samples for this study were Pt/CoNi/Pt sandwiched layers, prepared in a computer controlled sputtering system, base pressure of 5×10^{-8} mbar, with argon as a sputtering gas. The deposition rates were kept low ($1.7-2.0\,\text{Å}\,\text{s}^{-1}$ for Pt and $0.4-0.6\,\text{Å}\,\text{s}^{-1}$ for CoNi), to assure a smooth layer growth and a good control of layer thickness. A 40-nm thick Pt buffer layer was deposited on a Si(001) substrate followed by a magnetic CoNi layer (thickness varied between 3 and 12 nm) and covered by a 3-nm thick Pt cap layer. Such samples were prepared at different Ar pressures (between 4 and 36 μbar). It was found that the magnetic properties of the samples considerably depend on the growth conditions, in particular on the Ar pressure used for sputtering.

Experimentally, the asymmetry of the MSHG signal A, as defined by equation (11), was measured as a function of the angle of incidence.

In order to determine the $\chi^{(2)}$ tensor for one given interface quality, a set of samples was used with different magnetic layer thicknesses, prepared under exactly the same conditions (including of course the sputtering pressure of $p_{\text{Ar}} = 12\,\mu\text{bar}$). It was therefore assumed that the $\chi^{(2)}$'s are the same for the different samples, and only the local optical fields at the interfaces are changed, owing to absorption and multiple scattering. To fit the data, the transfer matrix technique described in Section 4.2 was employed with nonlinear susceptibilities as fitting parameters.

The results of the measurements together with the fitting curves are shown in Figure 13(a) for the $S_{\text{in}}P_{\text{out}}$ polarization combination. The number of fitting parameters is determined by the polarization used. Thus for $S_{\text{in}}P_{\text{out}}$ one can arbitrarily fix the only tensor component of the cover layer surface zyy_0 (neither the absolute intensity nor the optical phase

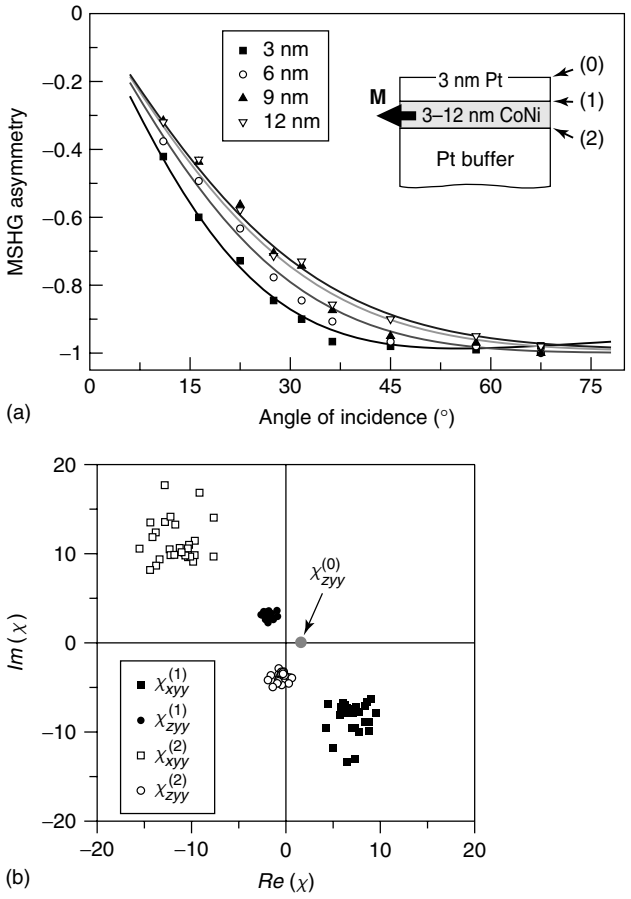

Figure 13. (a) Angle-of-incidence dependencies of the MSHG asymmetry for Pt/CoNi/Pt samples with different CoNi layer thicknesses (indicated in the figure). Lines are the theoretical fit to the experimental points using one single set of tensor elements. (b) The nonlinear tensor components derived from the fits in (a). (Reproduced from Kirilyuk *et al*., 1998, with permission from the American Physical Society. © 1998.)

of the total MSHG signal is taken into account), hence $zyy_{1,2}$ and $xyy_{1,2}$ are the only components left to be determined (inset in Figure 13(a) shows the indexing of the interfaces). This leaves eight parameters (2 interfaces $\times$ 2 complex components) to fully describe these data. The uniqueness of the fits was checked for both $S_{\rm in}P_{\rm out}$ and $P_{\rm in}P_{\rm out}$ polarization combinations by randomizing the initial choice of the fit parameters. Figure 13(b) shows the $\chi^{(2)}$ tensor components obtained from the fits of Figure 13(a). The convergence of the parameters is evident. An interesting point is that the tensor components show opposite signs for the subsequent magnetic layer interfaces (1) and (2). This is an independent experimental confirmation of a strict requirement from symmetry (It is easy to derive by using the mirror symmetry operation with respect to the center plane of the film that the second-order susceptibilities of ideal mirrored interfaces are of equal amplitude but opposite phase.) and provides a strong support for the model used in the calculations. Also, the crystallographic and magnetic contributions to $\chi^{(2)}$ appear to be of the same order of magnitude, in strong contrast to the linear case.

To determine the dependence of $\chi^{(2)}$ on the interface quality, the sample with a 3-nm thick CoNi layer was measured for different Ar sputtering pressures. The assumption was then made that *all* tensor components changed in a similar way, that is, the scaling parameters $\mathcal{M}$ and $\mathcal{C}$ could be defined as

$$\chi^{(2)}_{\rm magn}(p_{\rm Ar}) = \mathcal{M}(p_{\rm Ar}) \cdot \chi^{(2)}_{\rm magn}(p_0) \tag{18}$$

$$\chi^{(2)}_{\rm cr}(p_{\rm Ar}) = \mathcal{C}(p_{\rm Ar}) \cdot \chi^{(2)}_{\rm cr}(p_0) \tag{19}$$

with $p_0 = 12\,\mu$bar. To fit the data for any new sample only the two complex parameters $\mathcal{M}$ and $\mathcal{C}$ are used (actually this only gives three parameters in total because one phase can still be fixed). The possibility to fit the data for any Ar pressure in such a manner supports the assumption that all $\chi^{(2)}$'s are changed in a similar way.

The parameters $\mathcal{M}(p_{\rm Ar})$ and $\mathcal{C}(p_{\rm Ar})$ represent the dependence of the nonlinear MO interface properties on the interface structure (controlled via the sample preparation conditions). The value of $\mathcal{C}$ is proportional to the crystallographic contribution to the MSHG, expressed via the local symmetry breaking induced by the interface. It is incorrect to say, however, that $\mathcal{M}$ represents the purely magnetic part of MSHG. Indeed, all the 'magnetic' elements of $\chi^{(2)}$ are only nonzero in the presence of the crystallographic symmetry breaking, that is, the same factor influences both $\chi_{\rm cr}$ and $\chi_{\rm magn}$. Hence, one may write $\mathcal{M} \propto \mathcal{C} \cdot \mathbf{M}$.

To extract information on the interface magnetic properties, we take the ratio $\mathbf{m} = \frac{\mathcal{M}}{\mathcal{C}}$. In Figure 14, $\mathbf{m}$ is plotted as a function of the sputtering Ar pressure for the $S_{\rm in}P_{\rm out}$ and $P_{\rm in}P_{\rm out}$ polarizations. The precise coincidence of the $\mathbf{m}$ dependency for both polarization combinations once again supports the model used for the derivations.

Figure 14 shows that the crystallographic contribution $\chi_{\rm cr} \propto \mathcal{C}$ increases rapidly above 15 µbar, while staying almost constant below this pressure. The increase of $\chi_{\rm cr}$ indicates an increasing interfacial roughness for higher sputtering pressures. Though the crystallite size is known to stay constant in the whole pressure range, the crystallites may become slightly disoriented (Bijker, Donnet and Lodder, 1996). This increase of $\chi_{\rm cr}$ due to the increasing interface roughness can schematically be understood as being due to the increase of the effective surface area of the interface. For stronger roughness, other mechanisms may play a role (Aktsipetrov *et al*., 1990).

In contrast to the crystallographic one, the magnetic contribution $\mathbf{m}$ shows a clear maximum at pressures of 15–20 µbar.

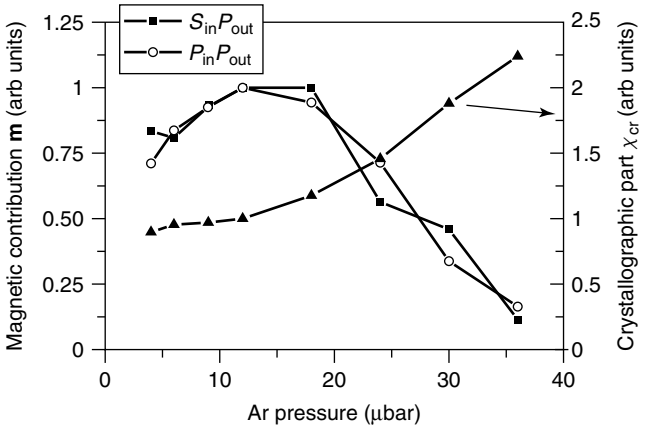

Figure 14. Crystallographic as well as magnetic contributions to the nonlinear MO tensor derived from the two different polarization combination data (indicated in the figure). (Reproduced from Kirilyuk *et al*., 1998, with permission from the American Physical Society. © 1998.)

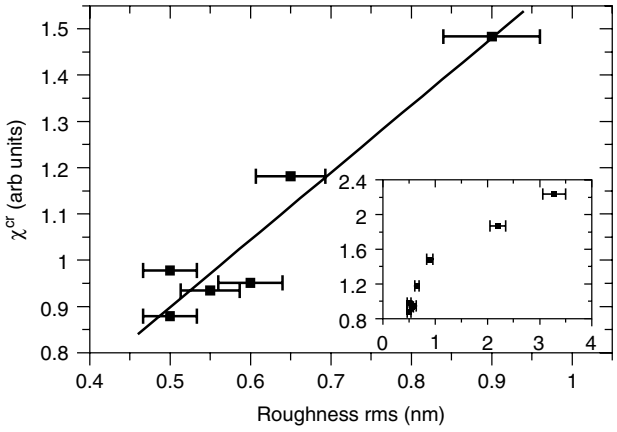

Figure 15. Crystallographic $\chi^{(2)}$ contribution as a function of interface roughness determined from AFM and X-ray scattering experiments. (Reproduced from Bal *et al*., 2001, with permission from the American Institute of Physics. © 2001.)

At very low Ar pressures the interface layers become slightly intermixed due to the high energies of sputtered atoms. This intermixing hardly affects the crystallographic part of MSHG but clearly suppresses the magnetic one. Note that the maximum in the interface magnetization does not have to coincide with the sharpest interface. Evidently, the drop of **m** for large p_{Ar} is related to a decreasing in-plane magnetic moment of the rough interface. A possible explanation here is that the increasing roughness changes the local coordination of the Co atoms, which may even lead to an out-of-plane lifting of the *local* interface magnetic moments. This explanation is supported by the observation of a specular *S*-polarized MSHG output at higher Ar pressures (Bal, van den Berg, Keen and Rasing, 2001). Such an MSHG yield can only be nonzero in the presence of a perpendicular (out-of-plane) magnetization component. In addition, polar MOKE hysteresis loops also showed a small remanence ($\leq$10% of M_s) for the sample sputtered at $P_{Ar} = 36\,\mu$bar, confirming the MSHG results.

It was also measured that up to a roughness rms value of 1.0 nm, the value of χ^{cr} is roughly proportional to the surface/interface roughness measured by other methods, such as atomic force microscopy (AFM) and grazing-incidence X-ray scattering (see Figure 15).

Summarizing, nonlinear magneto-optics is clearly able to follow the (subtle) changes in the interface structure, both crystallographic and magnetic. For the case of Pt/CoNi/Pt, an optimum sputtering pressure is found that yielded a maximum in-plane interface magnetization with only a small change in interface morphology. With further increase of the sputtering pressure, the interface roughness clearly increases while the in-plane interface magnetic moment decreases. It should be underlined that for all studied samples, no difference in the total layer magnetization was observed with either MOKE or vibrating sample magnetometry (VSM).

5.2 Interface versus bulk MSHG in Fe/Au multilayers

In this study, the MSHG technique was applied to Fe/Au superlattices with atomically controlled epitaxial layers. The superlattice with a modulation of mono-atomic layers of Fe and Au has been known to show an artificial order with an $L1_0$ structure that does not exist in nature (Takanashi *et al*., 1995). Such an artificial structure remains at interfaces between Fe and Au layers when the modulation period becomes longer than mono-atomic (Mitani *et al*., 1996). The linear MO spectra of the superlattices modulated by integer and noninteger numbers of atomic layers have been studied intensively, suggesting the formation of a peculiar band structure in such an artificial real-space structure (Sato *et al*., 1996, 1999).

Figure 16 shows the results of a rotational anisotropy measurements for all four polarization combinations in the longitudinal geometry. A sample with lattice period $x = 15$ ML was used. All curves show clear fourfold anisotropy and a clear magnetic contrast.

In Figure 17, the results of all four polarization combinations for the sample with $x = 15$ ML are plotted, for the case of the transverse geometry. Note the different vertical scales for the various data, indicating a substantial difference for the MSHG response for different polarization combinations. It is also obvious that all data involving S_{in} or S_{out} polarization, yield a much stronger anisotropy, which is a direct consequence of the in-plane xy tensor components that contribute

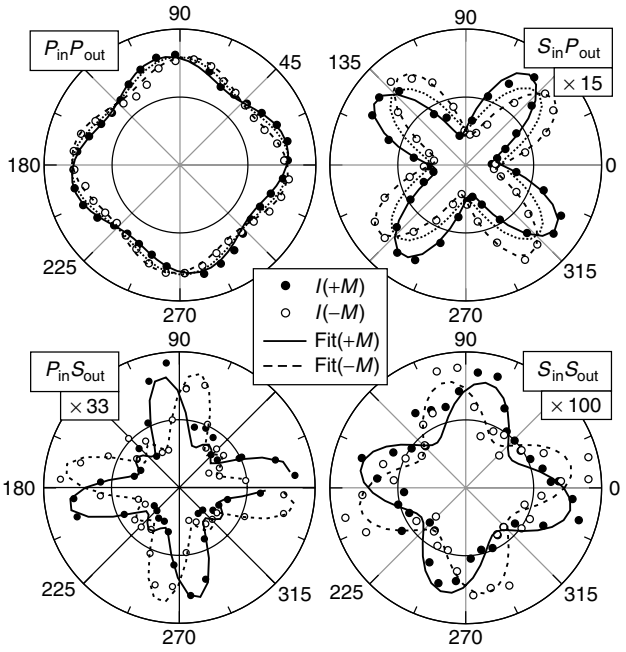

Figure 16. Rotational anisotropy curves (experimental points plus theoretical fits) for the sample with single layer thickness $x = 15$ monolayers in longitudinal geometry. Multiplication factors in three plots show the scaling of the corresponding data in order to reach the same intensity level as with the $P_{in}P_{out}$ polarization combination (this figure and the following one). (Reproduced from Sato *et al*., 2001, with permission from the American Physical Society. © 2001.)

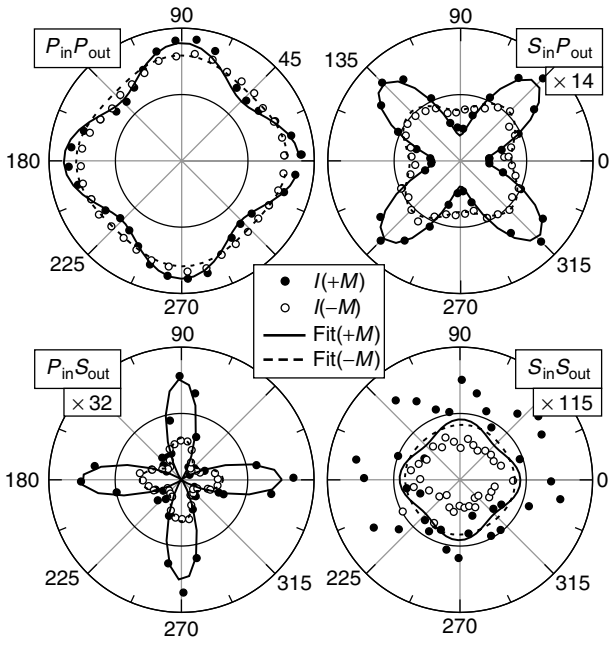

Figure 17. Rotational anisotropy curves for the sample with single layer thickness $x = 15$ monolayers in transversal geometry. (Reproduced from Sato *et al*., 2001, with permission from the American Physical Society. © 2001.)

to these signals (see subsequent text). Even the weakest $S_{in}S_{out}$−curve shows a clear fourfold symmetry pattern.

Usually, an analysis of MSHG results (Pan, Wei and Shen, 1989; Wierenga, Prins and Rasing, 1995; Hübner and Bennemann, 1989) is performed assuming that the top surface and buried interfaces are the only sources of the nonlinear MO response. Their nonlinearity is described in terms of the effective surface/interface dipole-like nonlinear susceptibility $\chi^{(2)}(\mathbf{M})$, which is a third rank tensor. Such contribution yields the azimuthal patterns described by the following formulae (Sato *et al*., 2001):

$$\begin{aligned}
E_{2\omega}^{p,p}(\phi, \pm\mathbf{M}_l) &= A^{p,p} \pm C^{p,p} \sin 4\phi, \\
E_{2\omega}^{s,p}(\phi, \pm\mathbf{M}_l) &= A^{s,p} \pm C^{s,p} \sin 4\phi, \\
E_{2\omega}^{p,s}(\phi, \pm\mathbf{M}_l) &= \pm A^{p,s} \pm B^{p,s} \cos 4\phi, \\
E_{2\omega}^{s,s}(\phi, \pm\mathbf{M}_l) &= \pm A^{s,s} \pm B^{s,s} \cos 4\phi
\end{aligned} \tag{20}$$

where the ± sign indicates those terms which change sign upon magnetization reversal, A, B and C are independent of ϕ and the direction of the longitudinal magnetization $\mathbf{M}_l$. Note that the light intensity is related to the field via $I_{2\omega}^{\alpha,\beta} = c/(2\pi)|E_{2\omega}^{\alpha,\beta}|^2$.

However, these patterns do not yield any effect of magnetization reversal for the $S_{in}S_{out}$ and $P_{in}S_{out}$ MSHG intensity, in contrast to the experimental observation shown in Figures 16 and 17. They are also unable to properly describe the patterns for the other two polarization combinations (see Figure 16, dotted lines on the plots for $P_{in}P_{out}$ and $S_{in}P_{out}$ polarization combinations; also in this case, the equations are not able to fit the magnetic contrast because of different symmetry pattern, see subsequent text). Therefore, one has to take into account additional anisotropic contributions to the second-order nonlinear response. In particular, the nonlocal (quadrupole-allowed) contribution from the bulk of cubic nonmagnetic metals (Cu, Vollmer, Straub and Kirschner, 1996a; Ag, Koos, Shanon and Richmond, 1993; and Al, Pedersen and Keller, 1989) and semiconductors (Si, Tom, Heinz and Shen, 1983) has been shown to lead to a fourfold anisotropy of SHG at their (100) surfaces. Accounting for this additional contribution modifies the rotational patterns to the following ones

$$\begin{aligned}
E_{2\omega}^{p,p}(\phi, \pm\mathbf{M}_l) &= A^{p,p} + B^{p,p} \cos 4\phi \pm C^{p,p} \sin 4\phi, \\
E_{2\omega}^{s,p}(\phi, \pm\mathbf{M}_l) &= A^{s,p} + B^{s,p} \cos 4\phi \pm C^{s,p} \sin 4\phi, \\
E_{2\omega}^{p,s}(\phi, \pm\mathbf{M}_l) &= \pm A^{p,s} \pm B^{p,s} \cos 4\phi + C^{p,s} \sin 4\phi, \\
E_{2\omega}^{s,s}(\phi, \pm\mathbf{M}_l) &= \pm A^{s,s} \pm B^{s,s} \cos 4\phi + C^{s,s} \sin 4\phi
\end{aligned} \tag{21}$$

Using these equations for the theoretical fits to the experimental data of Figures 16 and 17 showed a good agreement between experiment and theory.

Thus, we have shown that the MSHG response of Fe/Au(001) superlattices shows a strong azimuthal anisotropy in both the MSHG intensity as well as in the nonlinear MO Kerr rotation.

5.3 Quantum well states in ultrathin films

An interesting system where the interfaces play an important role are thin metal layers, where due to the electronic potential discontinuities experienced by electron states at interfaces, the perpendicular wave vector can be quantized, giving rise to resonances in the density of electronic states that are usually referred to as QWS (Ortega and Himpsel, 1992; Segivia, Michel and Ortega, 1996; Suzuki *et al*., 1992; Bruno, Suzuki and Chappert, 1996).

In MSHG experiments, QWS are mostly observed on samples consisting of a transition-metal layer with a thin (often wedge-shaped) noble metal overlayer on top. A strong influence of QWS on the second harmonic intensity as well as on the magnetic asymmetry has been observed when measuring the MSHG response as a function of this noble-metal overlayer thickness. It is nevertheless expected that the MSHG output in such systems is generated mostly at the interfaces, even in the case that QWS's are involved (Luce, Hübner and Bennemann, 1996; van Gelderen, Crampin, Rasing and Inglesfield, 1996; Luce *et al*., 1998).

It is shown that quite different experimental MSHG observations on QWS systems could be explained within the same approach (Luce *et al*., 1998). The main difference happened to come from the number of interfaces contributing to the total response: systems where both the surface and the interface are important, behave different than those with the domination of only one of them. The following two sections separately describe these two systems.

5.3.1 MSHG from Cu/Co/Cu(001) and Cu/Fe/Cu(001) layers

Cu/Co/Cu(001) was the first system showing an extremely strong dependence of the MSHG output on the copper overlayer thickness (Wierenga *et al*., 1995; Vollmer *et al*., 1995). In this study, 10 ML Co grown on Cu(001) was used as a substrate, on which a thin Cu overlayer was epitaxially grown. Figure 18 shows the very strong changes of the magnetic asymmetry as a function of the Cu layer thickness. This magnetic asymmetry oscillates between $+0.6$ and -0.6 in the range of 0–10 ML. As a reference, the dashed line on this figure shows the result of multiple-scattering calculations for

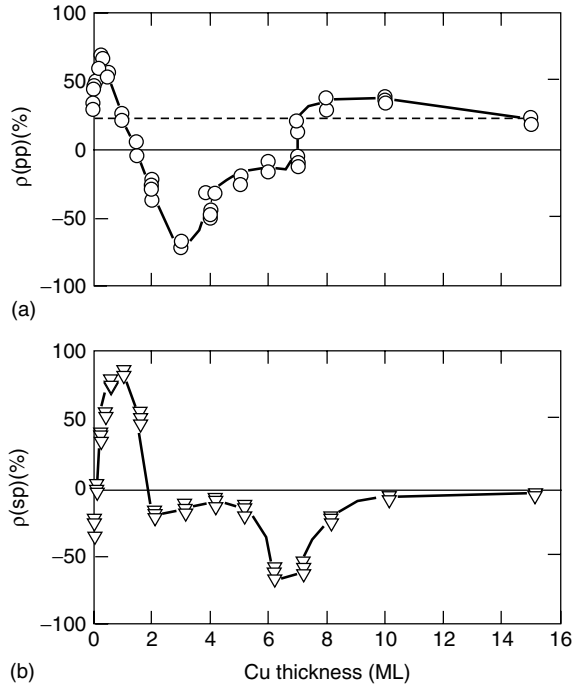

Figure 18. The MSHG asymmetry in $P_{\text{in}}P_{\text{out}}$ (a) and $S_{\text{in}}P_{\text{out}}$ (b) polarization combinations as a function of Cu overlayer thickness on top of a 10 ML Co film on Cu(001). The solid lines are guides to the eye, dashed line is the result of multiple-scattering calculations. (Reproduced from Wierenga *et al*., 1995, with permission from the American Physical Society. © 1995.)

the same system. Obviously the observed MSHG behavior is not of optical but rather electronic origin. Ortega and Himpsel have studied the same system (Ortega and Himpsel, 1992) and found an oscillating behavior of the density of states at the Fermi surface as a function of the Cu film thickness and observed an oscillation period of 5.5 ML. Oscillations of period 2.3 ML can be attributed to QWS as well.

The experimental results seem to indicate that these finite size effects of the Cu film which modulate the electronic structure at the interface can be seen by SHG, in both the magnetic and nonmagnetic parts (see Vollmer *et al*., 1995). It is, however, not clear what is the origin of the observed oscillations. There is no direct relation to the oscillation periods observed for interlayer coupling because not only electronic states close to the Fermi energy contribute but more or less all states within $\pm 2\hbar\omega$ around the Fermi energy. The situation can be described similarly to the case of the linear Kerr effect (Bruno, Suzuki and Chappert, 1996). Optical two-photon transitions from the Cu $3d$ band into the quantized Cu $4s$ band are resonantly enhanced if the energy difference between a discrete d-band state and an s-band state equals the energy of an SH photon. This is schematically illustrated in Figure 19. For films of finite thickness, k_z is no longer a good quantum number and the

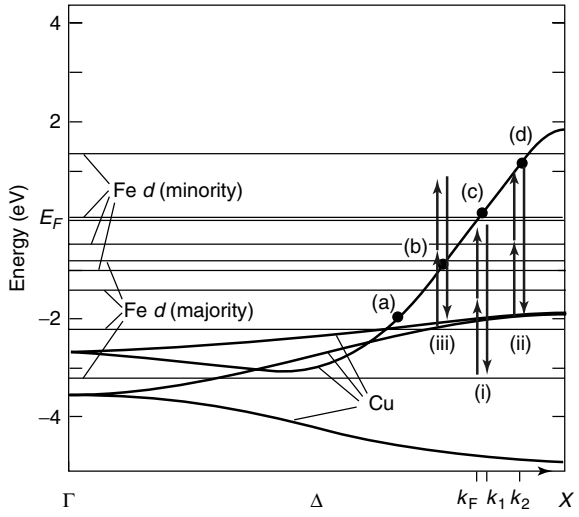

Figure 19. Illustration of the generation of SHG oscillations due to QWS. The electronic structure refers to the case of a *x* Cu/Fe/Cu(001) system. Only the rightmost QWS of a 12 ML Cu film are drawn (solid dots). (Reproduced from Luce *et al*., 1998, with permission from the American Physical Society. © 1998.)

continuous bulk bands along the k_z direction split up into a set of discrete levels, QWS, indicated by dots in the figure. The possible resonant transitions for a given wavelength are also indicated in the figure by vertical arrows. If the thickness of the film is increased, the QWS is moved more toward the X point and the optical transition becomes less resonant. Therefore, from this picture, a maximum of SHG intensity can be expected for the given film thickness D. At the thicknesses of $2D$, $3D$, and so on, there will be again a resonant optical transition into a QWS resulting in a variation of the SHG intensity with a period of D.

Another possible mechanism is related to the appearance of a new final state, due to the change in the film thickness. Each time a QWS shifts though the Fermi energy, it becomes a new possible final state. Generally speaking, this transition is nonresonant for the given wavelength but nevertheless contributes to the total signal. Because this kind of optical transition is related to the Fermi energy, a periodic SHG intensity oscillation with the same period observed for the interlayer coupling is expected.

Thus the periodicity with layer thickness in transitions of the second kind is independent of the photon energy while the period of the first kind of transitions is strongly dependent on it.

As is obvious from the figure, if only a few dominant optical transitions occur, the k selectivity of the optical response is optimal, and the SHG oscillations will be most pronounced. Of course, the strength of the absolute signal depends further on the joint density of states for optical transitions. In the case of a ferromagnetic spacer layer between the substrate and the overlayer film, resonant transitions for minority and majority electrons are possible at different overlayer thicknesses due to the spin-split d states. Thus a phase shift for the $I(+M)$ and $I(-M)$ signals occur. Consequently, one may observe an oscillatory magnetic contrast in the SHG response though a nonmagnetic overlayer is studied.

5.3.2 *Au/Co(0001)/Au(111) system: double oscillation period*

In another case of a QWS system, the interference effects play an essential role in the MSHG response, so that even the oscillatory period can be changed (Kirilyuk, Rasing, Mégy and Beauvillain, 1996). This would require that the primary contribution to $\chi^{(2)}$ comes from the overlayer itself rather than from the (magnetic) substrate. As the total response is the result of interference between the two contributions, the relative phase between the SH waves coming from two different interfaces will be important. This implies in fact that also *the parity* of the QWS wave function may influence the SHG response. Using for simplicity $|\chi^s_{ijm}(2\omega)| \approx |\chi^i_{ijm}(2\omega)|$, one gets

$$I(2\omega) \approx 2|\chi^s_{ijm}(2\omega)|^2 + 2\chi^s_{ijm}(2\omega)\chi^i_{ijm}(2\omega) \qquad (22)$$

For equally weighted contributions one gets obviously a perfect cancellation of the thickness-dependent $\chi(2\omega)$, if the resultant phase of the product of $\chi^s_{ijm}(2\omega)\chi^i_{ijm}(2\omega)$ is -1, like for inversion symmetric films. This may result from the parity of the QWS. For example, if for increasing film thickness d the first unoccupied QWS close to the Fermi energy E_F, which sets the oscillation period, has even parity and if at the interface no phase shift of π occurs, then no SHG results. Thus, in the case where the symmetry of the QWS regulates $I(2\omega, d)$, one should observe in SHG a pronounced period doubling of the oscillation period, since only the QWS with odd parity cause oscillations.

This idea was experimentally verified on step-shaped wedges of Au(111) or Cu(111) epitaxially grown on top of thin (5–20 ML) Co(0001) films on a Au(111) substrate. The copper wedge was covered by 10 ML of gold for protection. The Co films were also grown as steps, with a few different thicknesses. Because of the strong interface-induced perpendicular magnetic anisotropy in this system, it was possible to use different (polar or transversal) MO configurations, depending on the Co thickness.

Figure 20(a) shows that the generated total SH intensity exhibits a strongly oscillatory behavior as a function of the gold overlayer thickness that can be very well described by damped cosines. The slight change of the observed

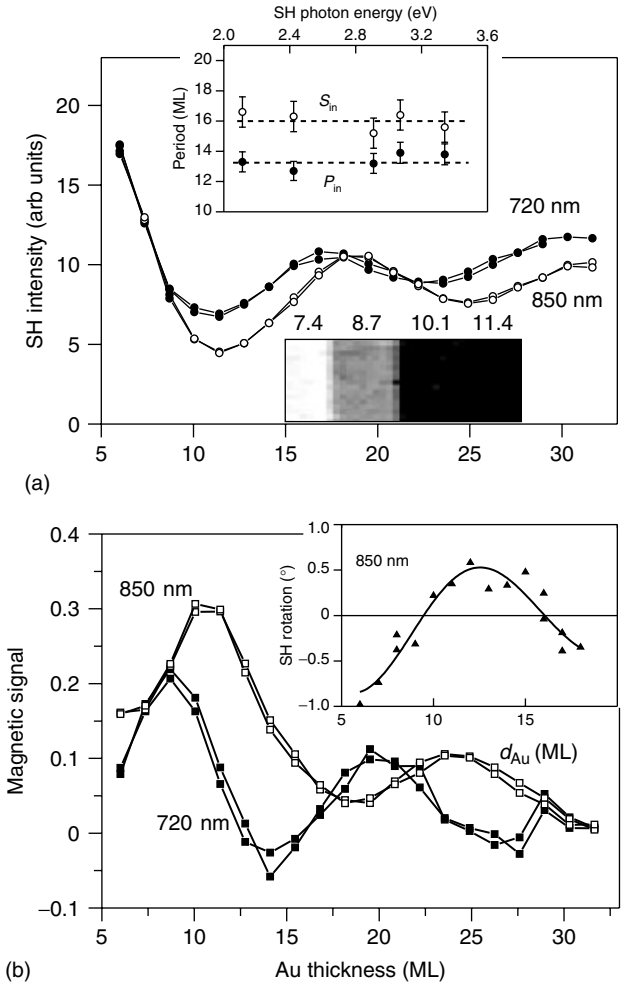

Figure 20. (a) SHG intensity ($P_{in}P_{out}$) as a function of the Au(111) overlayer thickness on a 20 ML thick Co film. Inset shows a photon energy dependence of the oscillation periods for $P_{in}P_{out}$ and $S_{in}P_{out}$ polarization combinations. (b) MSHG asymmetry as a function of the gold layer thickness. (Reproduced from Kirilyuk *et al.*, 1996, with permission from the American Physical Society. © 1996.)

periods for the curves measured with 720 and 850 nm wavelengths appeared not to be significant: in the total range of 720–1170 nm the period is constant ($\Lambda \approx 13$–14 ML) within 10–15% (see inset in Figure 20a).

The same kind of oscillatory behavior has also been found for the magnetization dependent SHG. Figure 20(b) shows the magnetic asymmetry for a 20 ML thick Co layer, while the SH polarization rotation is plotted in the inset for the perpendicularly magnetized 6 ML Co film. All the observed periods are basically the same as given above for the intensities. However, the shape of these curves is more complicated than simple damped oscillations. This is due to the fact that the magnetic signals are calculated as a ratio of different oscillatory terms (see equation (11)).

Linear MOKE studies performed on the same kind of samples (Mégy *et al.*, 1995) reported oscillations of the Kerr rotation with the much shorter period of 7.7 ML. This strong difference with MSHG might be assigned to the different wavelength region used for the MOKE experiments (540–630 nm). To fill this gap, MOKE measurements were done using the same Ti-Sapphire laser at $\lambda = 850$ nm. This resulted in a period of 7 ± 1 ML. That is, in the case of $\lambda_{MOKE} = \lambda_{SH}$, the total excitation energy was equal for the two experiments. Also the situation $2\lambda_{MOKE} = \lambda_{SH}$, was investigated, in order to study possible effects of initial and intermediate or intermediate and final states. However, again the observed MSHG period was *twice* as large as the period detected with MOKE. Hence the difference in periods cannot be explained by the different total excitation energy ($\hbar\omega$ vs $2\hbar\omega$).

It has been already discussed (see Section 5), that for a thin film the corresponding tensor elements on the opposite film interfaces are related to each other by a mirror symmetry and therefore they differ only by a phase factor of 180°. Hence the resulting total SHG signal arises from the competition between the signals from the two film interfaces that mostly cancel each other and does only depend on the difference in their local fields. In other words, the nonlinear polarization $\mathbf{P}(2\omega)$ is an *odd* function with respect to the film symmetry plane.

Within this approach, the influence of QWS on MSHG would be largely cancelled too because every QWS contributes symmetrically (via its local density of states) to the χ tensor elements of both interfaces. Even for the nonsymmetric geometry (like our case – Co/Au and Au/air interfaces) one may still argue that the corresponding electron wave functions are rather symmetric once they form a confined state.

Following these arguments, one may expect no QWS effects on the MSHG signal at all! This is contrary to the experimental observations of a total domination of QWS in the SHG response. That one does observe a (rather strong) signal is partly related to the fact that the local electromagnetic fields at the two interfaces are different (this follows from Fresnel formulae) and partly from the (a-) symmetry of the QWS wave functions. In a simple textbook picture, the confined QWS have alternating odd and even character, that is, the asymmetry of the QWS wave functions is repeated with the double period. This asymmetry can be expressed as a relative phase factor between the two QWS interface contributions (the Co/Au and the Au/air). Because the total SHG response results from a *coherent* superposition of these interface contributions, it will also display a periodic behavior with the double period, despite of the fact that the individual contributions oscillate with the single period. Because the linear MOKE experiment only probes the Co/Au

region, MOKE indeed shows the single period. It should be stressed that it is the wave function phase at a given interface which plays a crucial role and, without interference, the effect would be unobservable.

To test these ideas, the total MSHG signal was decomposed into the contributions from different interfaces, as described in Section 5.1. For this purpose, first the angle-of-incidence dependencies of the MSHG signals were measured for each gold overlayer thickness value. Next, a fit of these data was performed, using the $\chi^{(2)}$ tensor elements as fitting parameters in $S_{\text{in}}P_{\text{out}}$ polarization combination. Figure 21(a) shows the individual $\chi^{(2)}$-components of the two gold layer interfaces as a function of the film thickness, displaying an oscillatory behavior with a mean period of around 6–8 ML that is, the same period as observed by MOKE. However, the resulting SHG intensity and magnetic signal perfectly fit the experimentally observed slowly oscillating behavior with the double period (see Figure 21b). This means that while the local density of states and hence the $\chi^{(2)}$-tensor at each interface show the standard QWS period, the resulting total response includes also the phase between the corresponding elements and therefore allows a slower variation. This is possible, of course, only because the interfaces are not independent as soon as every QWS wave function is located at both interfaces simultaneously. Although it is not exactly correct to talk about 'contributions of different interfaces' in such conditions, it is still possible to formally use this model. One should mention here that the $\chi^{(2)}$-components of different interfaces may be determined accurately only relative to each other. Their absolute values, in contrary, may contain rather large systematic errors. However, the derived fast-oscillatory behavior of the $\chi^{(2)}$-tensor is obtained from the best fit of the (slowly oscillating) experimental data, and may be considered as a strong support of the model.

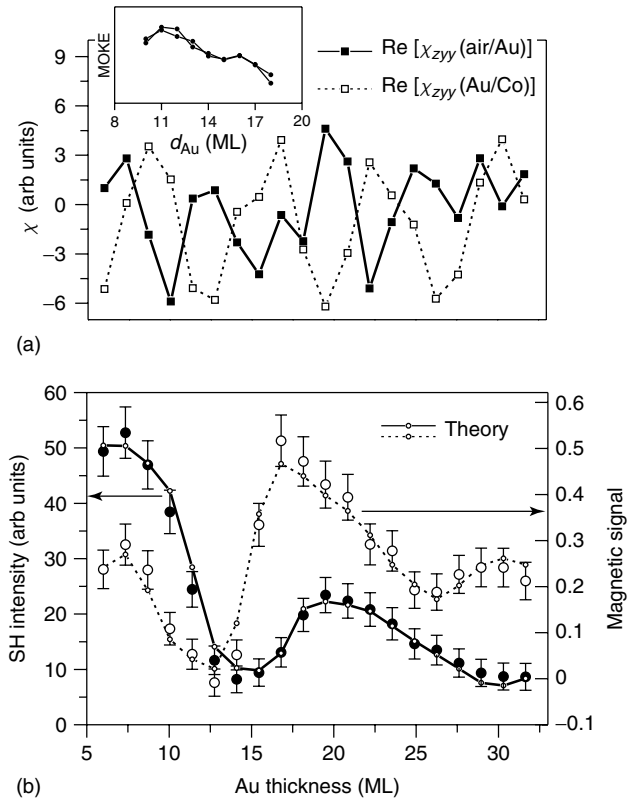

Figure 21. (a) Tensor components of different Au(111) film interfaces as a function of the film thickness. Inset shows the linear MOKE ellipticity for comparison. (b) Theoretical fit of the SHG intensity (solid dots) and MSHG asymmetry (open dots) using the parameters shown in (a). (Reproduced from Kirilyuk *et al.*, 1996, with permission from the American Physical Society. © 1996.)

As for the linear MOKE technique, although it has 'bulk' sensitivity, the oscillatory part of the signal is provided by the narrow region along the Au/Co interface, where the spin-polarization of electrons is affected the most. Therefore, it is related to the local density of states at this interface only, which oscillates with a single QWS period.

Very similar results were obtained for Cu(111) and Ag(111) overlayers, with corresponding periods of 12–14 ML. The main difference was the observed amplitude of the intensity oscillations for both of these metals which was much smaller than for Au(111). The recently detected linear MOKE oscillations on Cu(111) (Bounouh *et al.*, 1997) showed a period of 7 ML. Hence, the period doubling is confirmed also for another system. From the experimental point of view, it would be very interesting to study also a *magnetic* thin film as well as to increase the spectral region of measurements.

5.4 Magnetization reversal at the interfaces

In the discussion of thin magnetic films and multilayers, interfaces play an often dominating role determining the magnetization reversal behavior. To find out the behavior of the magnetization at the film interfaces as opposed to that in the middle of the film, MSHG can be used in combination with the linear MOKE technique. The magnetization reversal hysteresis is thus measured simultaneously, from the same spot on the sample (Zhao *et al.*, 2005). Figure 22 shows an example of such experiment on an amorphous TbFeCo layers that have recently attracted attention as possible MO hybrid-recording media (Awano *et al.*, 2000). MOKE and MSHG hysteresis loops were measured for different sample temperatures across the Curie point $T_C = 465$ K. A clear difference between the results of the two methods was observed that can only be related to the different magnetic behavior in the bulk and at the interfaces of the film. Closer

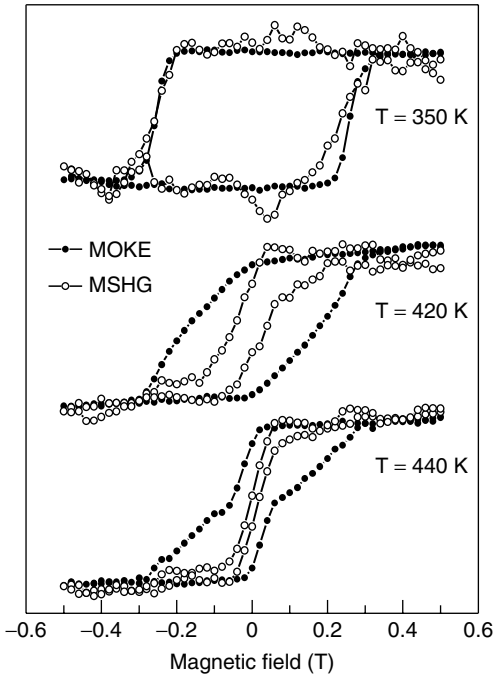

Figure 22. MOKE and MSHG hysteresis loops from a TbFeCo MO recording layer for three different sample temperatures.

inspection of the loops in Figure 22 seems to indicate that the reversal starts at the interfaces but stays somehow pinned in the bulk, thus slowing down the bulk reversal.

6 CONCLUSION

This chapter revises the recent progress and achieved milestones in the newly developed area or nonlinear magneto-optics. By no means pretending of being comprehensive, it focuses on the application of MSHG to *surface and interface* phenomena, such as enhanced magnetic moments, electronic surface states, and correlation between interface structure and magnetism. The extreme surface/interface sensitivity of the MSHG technique manifests itself in every of the considered examples.

On the other hand, various interesting developments of MSHG are not mentioned. Among them is the very extensive work on nonlinear magneto-optics in antiferromagnetic dielectrics (Fiebig *et al*., 2000, 2001; Feibig, Degenhardt and Pisarev, 2002). In addition, one should mention the attempts to study MSHG effects in complex systems such as magnetic photonic crystals (Lyubchanskii *et al*., 2003) and nanoparticles (Aktsipetrov, 2002), as well as a discussion of possible MSHG effects in vacuum (Ding and Kaplan, 1989).

Another area where the MSHG technique is used quite extensively, is for the pump-probe studies of ultrafast magnetization dynamics (Güdde *et al*., 1999; Regensburger, Vollmer and Kirschner, 2000; Silva, Pufall and Kabos, 2002; Gerrits, Hohlfeld, van den Berg and Rasing, 2002). Here, MSHG has some advantage over MOKE, because (i) owing to large *odd* components of the nonlinear optical tensor, different components of **M** can be easily separated, and (ii) it is also quite straightforward to distinguish the electron-temperature relaxation effects from those owing to the transient magnetization behavior, by analyzing the various tensor components. In addition, the MO probe of the ultrafast magnetization dynamics can only be done with femtosecond laser pulses, which makes the measurements of the MSHG response as easy as that of the MOKE. The particular direction where the MSHG probe can be especially interesting is the observation of the *magnetization dynamics at surfaces and interfaces*. The spin-orbit coupling at interfaces would become accessible with this approach.

ACKNOWLEDGMENTS

The contribution of the European TMR (Training and Mobility of Researchers) network DYNAMICS (DYNAmics in MagnetIC nanoStructures) is gratefully acknowledged. Part of this work was supported by the ‘Stichting voor Fundamenteel Onderzoek der Materie’(FOM).

REFERENCES

Adler, E. (1964). Nonlinear optical frequency polarization in a dielectric. *Physical Review*, **134**, A728–A733.

Akhmanov, S.A. and Khokhlov, R.V. (1964). *Problems of Nonlinear Optics*, VINTI: Moscow (in Russian).

Aktsipetrov, O.A. (2002). Nonlinear magneto-optics in magnetic nanoparticles. *Colloids and Surfaces*, **202**, 165–173.

Aktsipetrov, O.A., Nikulin, A.A., Panov, V.I., *et al*. (1990). Electromagnetic mechanism of surface enhanced 2nd-harmonic generation by smooth silver electrodes and scanning tunneling microscopy. *Solid State Communications*, **76**, 55–59.

Andersen, T. and Hübner, W. (2002). Substrate effects in the magneto-optical second-harmonic generation from first principles: Fe/Cu(001). *Physical Review B*, **65**, 174409.

Atkinson, R. and Kubrakov, N.F. (2002). Boundary conditions in the simplest model of linear and second harmonic magneto-optical effects. *Physical Review B*, **65**, 014432.

Awano, H., Imai, S., Sekine, M., *et al*. (2000). 20 nm domain expansion readout by magnetic amplifying MO system (MAMMOS). *IEEE Transactions on Magnetics*, **36**, 2261–2265.

Bal, K., van den Berg, H.A.M., Keen, A. and Rasing, Th. (2001). Thermal stability of the antiferromagnetically coupled Co/Cu/Co stack. *Journal of Applied Physics*, **89**, 7508–7510.

Bennemann, K.H. (Ed.) (1998) *Nonlinear Optics in Metals*, Clarendon Press: Oxford.

Bijker, M.D., Donnet, D.M. and Lodder, J.C. (1996). The effect of sputter pressure on the microstructure of CoNi/Pt multilayers. *Journal of Magnetic Society of Japan*, **20**(S1), 407–409.

Bloembergen, N. and Pershan, P.S. (1962). Light waves at the boundary of nonlinear media. *Physical Review*, **128**, 606–622.

Bounouh, A., Train, C., Beauvillain, P., *et al*. (1997). Kerr rotation and perpendicular magnetic anisotropy oscillations versus Cu(111) coverage thickness in Cu(111)/Co/Au trilayers. *Journal of Magnetism and Magnetic Materials*, **165**, 484–486.

Boyd, R.W. (1965). *Nonlinear Optics*, Benjamin: New York.

Bozhevolnyi, S.I., Hvam, J.M., Pedersen, K., *et al*. (1998). Second-harmonic imaging of ferroelectric domain walls. *Applied Physics Letters*, **73**, 1814–1816.

Bozhevolnyi, S.I., Vohnsen, B. and Pedersen, K. (1998). Near-field optical microscopy of nonlinear susceptibilities. *Optics Communications*, **150**, 49–55.

Bruno, P., Suzuki, Y. and Chappert, C. (1996). Magneto-optical Kerr effect in a paramagnetic overlayer on a ferromagnetic substrate: a spin-polarized quantum size effect. *Physical Review B*, **53**, 9214–9220.

Calmels, L., Crampin, S., Inglesfield, J.E. and Rasing, Th. (2001). Surface states and second harmonic generation at the (110) nickel surface from a first-principles calculation. *Surface Science*, **482**, 1050–1055.

Chang, R.K., Ducuing, J. and Bloembergen, N. (1965). Relative phase measurement between fundamental and second-harmonic light. *Physical Review Letters*, **15**, 6–8.

Ding, Y.J. and Kaplan, A.E. (1989). Nonlinear magneto-optics of vacuum: second-harmonic generation. *Physical Review Letters*, **63**, 2725–2728.

Erland, J., Bozhevolnyi, S.I., Pedersen, K., *et al*. (2000). Second-harmonic imaging of semiconductor quantum dots. *Applied Physics Letters*, **77**, 806–808.

Fiebig, M., Degenhardt, C. and Pisarev, R.V. (2002). Interaction of frustrated magnetic sublattices in $ErMnO_3$. *Physical Review Letters*, **88**, 027203.

Fiebig, M., Fröhlich, D., Kohn, K., *et al*. (2000). Determination of the magnetic symmetry of hexagonal manganites by second harmonic generation. *Physical Review Letters*, **84**, 5620–5623.

Fiebig, M., Fröhlich, D., Krichevtsov, B.B. and Pisarev, R.V. (1994). Second harmonic generation and magnetic-dipole-electric-dipole interference in antiferromagnetic Cr_2O_3. *Physical Review Letters*, **73**, 2127–2130.

Fiebig, M., Fröhlich, D., Lottermoser, Th., *et al*. (2001). Second harmonic generation in the centrosymmetric antiferromagnet NiO. *Physical Review Letters*, **87**, 137202.

Fiebig, M., Fröhlich, D., Sluyterman, G. and Pisarev, R.V. (1995). Domain topography of antiferromagnetic Cr_2O_3 by 2nd-harmonic generation. *Applied Physics Letters*, **66**, 2906–2908.

Flörsheimer, M., Bösch, M., Brillert, Ch., *et al*. (1997a). Surface order and symmetry determined by second-harmonic microscopy. *Supramolecular Science*, **4**, 255–263.

Flörsheimer, M., Bösch, M., Brillert, Ch., *et al*. (1997b). Second-harmonic microscopy – a quantitative probe for molecular surface order. *Advanced Materials*, **9**, 1061.

Franken, P.A., Hill, A.E., Peters, C.W. and Weinreich, G. (1961). Generation of optical harmonics. *Physical Review Letters*, **7**, 118–119.

Gerrits, Th., Hohlfeld, J., van den Berg, H.A.M. and Rasing, Th. (2002). Ultrafast precessional magnetization reversal by picosecond magnetic field pulse shaping. *Nature*, **418**, 509–512.

Goldmann, A., Dose, V. and Borstel, G. (1985). Empty electronic states at the (100), (110), and (111) surfaces of nickel, copper, and silver. *Physical Review Letters*, **32**, 1971–1980.

Gridnev, V.N., Pavlov, V.V., Pisarev, R.V., *et al*. (2001). Second harmonic generation in anisotropic magnetic films. *Physical Review B*, **63**, 184407.

Güdde, J., Conrad, U., Jähnke, V., *et al*. (1999). Magnetization dynamics of Ni and Co films on Cu(001) and of bulk nickel surfaces. *Physical Review B*, **59**, R6608–R6611.

Hamrle, J., Polerecký, L. and Ferré, J. (2003). Theory of second-harmonic generation from multilayer systems based on electric point-dipole radiation: application to magnetic multilayers. *Physical Review B*, **68**, 144401.

Heinz, T.F. (1991). Second-order nonlinear optical effects at surfaces and interfaces. In *Nonlinear Surface Electromagnetic Phenomena*, H-E. Ponath and G.I. Stegeman (Eds.), North Holland: Amsterdam.

Hübner, W. (1990). Theory of nonlinear surface magneto-optics for ferromagnetic nickel: effects of band structure and matrix elements. *Physical Review B*, **42**, 11553–11569.

Hübner, W. and Bennemann, K.H. (1989). Nonlinear magneto-optical Kerr effect on a nickel surface. *Physical Review B*, **40**, 5973–5979.

Janz, S., Bottomley, D.J., van Driel, H.M. and Timsit, R.S. (1991). Influence of steps on second-harmonic generation from vicinal metal surfaces. *Physical Review Letters*, **66**, 1201–1204.

Jin, Q.Y., Regensburger, H., Vollmer, R. and Kirschner, J. (1998). Periodic oscillations of the surface magnetization during the growth of Co films on Cu(001). *Physical Review Letters*, **80**, 4056–4059.

Keller, U. (2003). Recent developments in compact ultrafast lasers. *Nature*, **424**, 831–838.

Kemnitz, K., Bhattacharya, K., Hicks, J.M., *et al*. (1986). The phase of 2nd-harmonic light generated at an interface and its relation to absolute molecular orientation. *Chemical Physics Letters*, **131**, 285–290.

Kirilyuk, V., Kirilyuk, A. and Rasing, Th. (1997). A combined non-linear and linear magneto-optical microscopy. *Applied Physics Letters*, **70**, 2306–2308.

Kirilyuk, A., Kirilyuk, V. and Rasing, Th. (1999). Nonlinear magneto-optical imaging of interface magnetic structures. *Journal of Magnetism and Magnetic Materials*, **198–199**, 620–623.

Kirilyuk, A., Knippels, G.M.H., van der Meer, A.F.G., *et al*. (2000). Observation of strong magnetic effects in visible-infrared sum frequency generation from magnetic structures. *Physical Review B*, **62**, R783–R786.

Kirilyuk, A., Pavlov, V.V., Pisarev, R.V. and Rasing, Th. (2000). Asymmetry of second harmonic generation in magnetic thin films under circular optical excitation. *Physical Review B*, **61**, R3796–R3799.

Kirilyuk, A., Rasing, Th., Haast, M.A.M. and Lodder, J.C. (1998). Probing structure and magnetism of CoNi/Pt interfaces by nonlinear magneto-optics. *Applied Physics Letters*, **72**, 2331–2333.

Kirilyuk, A., Rasing, Th., Mégy, R. and Beauvillain, P. (1996). Nonlinear magneto-optical response from quantum well states in noble metals: double period and interface localization. *Physical Review Letters*, **77**, 4608–4611.

Kielich, S. and Zawodny, R. (1973). New nonlinear magneto-optical phenomena in crystals and liquids. *Optica Acta*, **20**, 867–877.

Koopmans, B., Groot Koerkamp, M., Rasing, Th. and van den Berg, H. (1995). Observation of large Kerr angles in the nonlinear optical response from magnetic multilayers. *Physical Review Letters*, **74**, 3692–3695.

Koos, D.A., Shanon, V.L. and Richmond, G.L. (1993). Surface-dipole and electric-quadrupole contributions to anisotropic second-harmonic generation from noble-metal surfaces. *Physical Review B*, **47**, 4730–4734.

Lajzerowicz, J. and Vallade, M. (1967). Génération du second harmonique dans les substances magnétiques ordonnées. *Comptes Rendus de l'Académie des Sciences Paris*, **264**, 1819–1824.

Leute, St., Lottermoser, Th. and Fröhlich, D. (1999). Nonlinear spatially resolved phase spectroscopy. *Optics Letters*, **24**, 1520–1522.

Luce, T.A., Hübner, W. and Bennemann, K.H. (1996). Theory for spin-polarized oscillations in nonlinear optics due to quantum well states. *Physical Review Letters*, **77**, 2810–2813.

Luce, T.A., Hübner, W., Kirilyuk, A., *et al*. (1998). Theory for the nonlinear optical response of quantum-well states in ultrathin films. *Physical Review B*, **57**, 7377–7384.

Lyubchanskii, I.L., Dadoenkova, N.N., Lyubchanskii, M.I., *et al*. (2003). Magnetic photonic crystals. *Journal of Physics D: Applied Physics*, **36**, R277–R287.

Mégy, R., Bounouh, A., Suzuki, Y., *et al*. (1995). Magneto-optical-Kerr-effect study of spin-polarized quantum-well states in a Au overlayer on a Co(0001) ultrathin film. *Physical Review B*, **51**, 5586–5589.

Mishina, E.D., Sherstyuk, N.E., Pevtsov, E.Ph., *et al*. (2001). Local probing of the polarization state in thin Pb(ZrTi)O-3 films during polarization reversal. *Applied Physics Letters*, **78**, 796–798.

Mitani, S., Takanashi, K., Nakajima, H., *et al*. (1996). Structural and magnetic properties of Fe/noble metal monatomic multilayers equivalent to L1(0) ordered alloys. *Journal of Magnetism and Magnetic Materials*, **156**, 7–10.

Ortega, J.E. and Himpsel, F.J. (1992). Quantum well states as mediators of magnetic coupling in superlattices. *Physical Review Letters*, **69**, 844–847.

Palik, E.D. (1985). *Handbook of Optical Constants of Solids*, Academic Press: Orlando.

Pan, R-P., Wei, H.D. and Shen, Y.R. (1989). Optical second-harmonic generation from magnetized surfaces. *Physical Review B*, **39**, 1229–1234.

Pavlov, V.V., Ferré, J., Meyer, P., *et al*. (2001). Linear and nonlinear magneto-optical studies of Pt/Co/Pt thin films. *Journal of Physics: Condensed Matter*, **13**, 9867–9878.

Pavlov, V.V., Pisarev, R.V., Kirilyuk, A. and Rasing, Th. (1997). Observation of a transversal nonlinear magneto-optical effect in thin magnetic garnet films. *Physical Review Letters*, **78**, 2004–2007.

Pershan, P.S. (1963). Nonlinear optical properties of solids: energy considerations. *Physical Review*, **130**, 919–929.

Pedersen, K. and Bozhevolnyi, S.I. (1999). Second-harmonic generation scanning microscopy on domains in Al surfaces. *Physica Status Solidi A*, **175**, 201–206.

Pedersen, K. and Keller, O. (1989). Experimental study of phenomenological parameters describing optical 2nd-harmonic generation in centrosymmetric materials. *Journal of the Optical Society of America B*, **6**, 2412–2419.

Petukhov, A.V., Brudny, V.L., Mochán, W.L., *et al*. (1998). Energy conservation and the Manley-Rowe relations in surface nonlinear-optical spectroscopy. *Physical Review Letters*, **81**, 566–569.

Pustogowa, U., Hübner, W. and Bennemann, K.H. (1993). Theory for the nonlinear magneto-optical Kerr effect at ferromagnetic transition-metal surfaces. *Physical Review B*, **48**, 8607–8618.

Regensburger, H., Vollmer, R. and Kirschner, J. (2000). Time-resolved magnetization-induced second-harmonic generation from the Ni(110) surface. *Physical Review B*, **61**, 14716–14722.

Reif, J., Rau, C. and Matthias, E. (1993). Influence of magnetism on second harmonic generation. *Physical Review Letters*, **71**, 1931–1934.

Reif, J., Zink, J.C., Schneider, C.M. and Kirschner, J. (1991). Effects of surface magnetism on optical second harmonic generation. *Physical Review Letters*, **67**, 2878–2881.

Sampaio, L.C., Hamrle, J., Mougin, A., *et al*. (2004). In-depth selectivity of the magnetic second-harmonic generation of light in a multilayer structure. *Physical Review B*, **70**, 104403.

Sampaio, L.C., Hamrle, J., Pavlov, V.V., *et al*. (2005). Magnetization-induced second-harmonic generation of light by exchange-coupled magnetic layers. *Journal of the Optical Society of America B*, **22**, 119–127.

Sampaio, L.C., Mougin, A., Ferré, J., *et al*. (2003). Probing interface magnetism in the FeMn/NiFe exchange bias system using magnetic second harmonic generation. *Europhysics Letters*, **63**, 819–825.

Sato, K., Abe, J., Ikekame, H., *et al*. (1996). Magneto-optical characterization of Fe-Au artificially ordered alloy. *Journal of the Magnetic Society of Japan*, **20**(Suppl. S1), 35–40.

Sato, K., Kodama, A., Miyamoto, M., *et al*. (2001). Anisotropic magnetization-induced second harmonic generation in Fe/Au superlattices. *Physical Review B*, **64**, 184427.

Sato, K., Takeda, E., Akita, M., *et al*. (1999). Magneto-optical spectra of Fe/Au artificial superlattices modulated by integer and noninteger atomic layers. *Journal of Applied Physics*, **86**, 4985–4996.

Schmid, A.K. and Kirschner, J. (1992). In-situ observation of epitaxial growth of Co thin films on Cu(001). *Ultramicroscopy*, **42–44**, 483–489.

Segivia, P., Michel, E.G. and Ortega, J.E. (1996). Quantum well states and short period oscillations of the density of states at the Fermi Level in Cu films grown on fcc Co(100). *Physical Review Letters*, **77**, 3455–3458.

Shen, Y.R. (1984). *The Principles of Nonlinear Optics*, Wiley: New York.

Silva, T.J., Pufall, M.R. and Kabos, P. (2002). Nonlinear magneto-optic measurement of flux propagation dynamics in thin permalloy films. *Journal of Applied Physics*, **91**, 1066–1073.

Sipe, J.E. (1987). New Green-function formalism for surface optics. *Journal of the Optical Society of America B – Optical Physics*, **4**, 481–489.

Smolyaninov, I.I., Zayats, A.V. and Davis, C.C. (1997). Near-field second-harmonic imaging of ferromagnetic and ferroelectric materials. *Optics Letters*, **22**, 1592–1594.

Spierings, G., Koutsos, V., Wierenga, H.A., *et al*. (1993). Optical 2nd harmonic generation study of interface magnetism. *Surface Science*, **287**, 747–749.

Stolle, R., Loddoch, M., Marowsky, G., *et al*. (1995). Studies of nematic liquid-crystal cells using 2nd-harmonic phase measurements. *Langmuir*, **11**, 3251–3254.

Stolle, R., Veenstra, K.J., Manders, F., *et al*. (1997). Breaking of time-reversal symmetry probed by optical second-harmonic generation. *Physical Review B*, **55**, R4925–R4927.

Straub, M., Vollmer, R. and Kirschner, J. (1996). Surface magnetism of ultrathin γ-Fe films investigated by nonlinear magneto-optical Kerr effect. *Physical Review Letters*, **77**, 743–746.

Suzuki, Y., Katayama, T., Yoshida, S., *et al*. (1992). New magneto-optical transition in ultrathin Fe(100) films. *Physical Review Letters*, **68**, 3355–3358.

Takanashi, K., Mitani, S., Sano, M., *et al*. (1995). Artificial fabrication of an L1[sub 0]-type ordered FeAu alloy by alternate monatomic deposition. *Applied Physics Letters*, **67**, 1016–1018.

Tom, H.W.K., Heinz, T.F. and Shen, Y.R. (1983). Second-harmonic reflection from silicon surfaces and its relation to structural symmetry. *Physical Review Letters*, **51**, 1983–1986.

Uesu, Y., Kurimura, S. and Yamamoto, Y. (1995). Optical 2nd harmonic images of 9-degrees domain-structures in BaTiO, and periodically poled inverted antiparallel domains in $LiTaO_3$. *Applied Physics Letters*, **66**, 2165–2167.

Valev, V.K., Dalla Longa, F., Kohlhepp, J.T., *et al*. (2007). Observation of periodic oscillations in magnetization-induced second harmonic generation at the Mn/Co interface. *Physical Review B*, **75**, 012401.

Valev, V.K., Gruyters, M., Kirilyuk, A. and Rasing, Th. (2005). Influence of quadratic contributions in magnetization-induced second harmonic generation studies of magnetization reversal. *Physica Status Solidi*, **242**, 3027–3030.

Valev, V.K., Gruyters, M., Kirilyuk, A. and Rasing, Th. (2006a). Direct observation of exchange bias related uncompensated spins at the CoO/Cu interface. *Physical Review Letters*, **96**, 067206.

Valev, V.K., Gruyters, M., Kirilyuk, A. and Rasing, Th. (2006b). Temperature dependence of magnetization-induced second harmonic generation at buried exchange-biased interfaces. *Physical Review B*, **73**, 233101.

van Gelderen, P., Crampin, S., Rasing, Th. and Inglesfield, J.E. (1996). Effect of interface magnetic moments and quantum-well states on magnetization-induced second-harmonic generation. *Physical Review B*, **54**, R2343–R2346.

Veenstra, K.J., Hansen, P.E., Kirilyuk, A., *et al*. (1999). Surface magnetism of Ni(110) probed by magnetic second harmonic generation. *Journal of Magnetism and Magnetic Materials*, **198–199**, 695–697.

Veenstra, K.J., Petukhov, A.V., de Boer, A.P. and Rasing, Th. (1998). Phase-sensitive detection technique for surface nonlinear optics. *Physical Review B*, **58**, R16020–R16023.

Veenstra, K.J., Petukhov, A.V., Jurdik, E. and Rasing, Th. (2000). Strong surface state effects in nonlinear magneto-optical response of Ni(110). *Physical Review Letters*, **84**, 2002–2005.

Vollmer, R., Kirilyuk, A., Schwabe, H., *et al*. (1995). Direct comparison of nonlinear and linear Kerr effect measurements on thin Co films on Cu(001). *Journal of Magnetism and Magnetic Materials*, **148**, 295–297.

Vollmer, R., Straub, M. and Kirschner, J. (1996a). Second harmonic generation from the Cu(001) surface. *Surface Science*, **352**, 684–688.

Vollmer, R., Straub, M. and Kirschner, J. (1996b). Nonlinear magneto-optical Kerr measurements on Fe(110). *Surface Science*, **352**, 937–941.

Wierenga, H.A., de Jong, W., Prins, M.W.J., *et al*. (1995). Interface magnetism and possible quantum well oscillations in ultrathin Co/Cu films observed by magnetization induced second harmonic generation. *Physical Review Letters*, **74**, 1462–1465.

Wierenga, H.A., Prins, M.W.J., Abraham, D.L. and Rasing, Th. (1994). Magnetisatization-induced optical second-harmonic generation: a probe for interface magnetism. *Physical Review B*, **50**, 1282–1285.

Wierenga, H.A., Prins, M.W.J. and Rasing, Th. (1995). Magnetisatization-induced optical second-harmonic generation from magnetic multilayers. *Physica B*, **204**, 281–286.

Zayats, A.V. and Smolyaninov, I.I. (2004). Near-field second-harmonic generation. *Philosophical Transactions of the Royal Society of London, Series A*, **362**, 843–860.

Zhao, H.B., Talbayev, D., Lüpke, G., *et al*. (2005). Interface magnetization reversal and anisotropy in Fe/AlGaAs(001). *Physical Review Letters*, **95**, 137202.

Zvezdin, A.K. and Kotov, V.A. (1997). *Modern Magnetooptics and Magnetooptical Materials*, IOP Publishing: Bristol.

Investigation of Spin Waves and Spin Dynamics by Optical Techniques

Burkard Hillebrands and Jaroslav Hamrle
Technische Universität Kaiserslautern, Kaiserslautern, Germany

1 INTRODUCTION

Dynamic properties and the eigenmode spectrum of magnetic objects have become a focus of interest in modern magnetism. The fundamentals of this area are covered in several chapters in this handbook [1].

Progress in research in this interesting field is largely determined by the availability of suitable experimental tools. A wide range of tools exists; most of them use optic and electric properties. Here we confine the discussion to optical techniques.

This chapter aims at providing an introduction into the principle of operation and the range of applicability. We discuss time-resolved Kerr effect magnetometry, Brillouin light scattering (BLS) spectroscopy, and second-harmonic generation (SHG) techniques. Emphasis is laid on the introduction and discussion of the various tools and the presentation of characteristic applications.

Optical techniques for the study of spin waves and spin dynamics can be roughly categorized into two fundamental classes. Frequency-domain techniques provide a spectroscopic approach and issues such as the dispersion of spin-wave modes can be directly obtained. The second class comprises techniques working in the time domain, where the magnetic response of a sample is probed, usually stroboscopically, as a function of a stimulating pumping signal, and, in a narrow time window, as a function of the time delay to the excitation. Some experiments have been developed, which combine both classes, such as time-resolved BLS spectroscopy.

In Section 2 the background in spin dynamics and spin−wave modes is sketched. Section 3 contains an introduction to various experimental techniques, such as BLS and its variants, time-resolved Kerr effect microscopy, and SHG techniques. The applications of these techniques to various physical problems are addressed in Section 4 with several examples. In Section 5 conclusions are given.

2 BACKGROUND IN SPIN DYNAMICS AND SPIN-WAVE MODES

The fundamentals of spin dynamics and spin waves are presented in several chapters of this handbook (see also Hillebrands, 2003; Hillebrands and Thiaville, 2006). Here we summarize this background and list the equations necessary to understand the experimental optical techniques.

Handbook of Magnetism and Advanced Magnetic Materials. Edited by Helmut Kronmüller and Stuart Parkin. Volume 3: *Novel Techniques for Characterizing and Preparing Samples*. ISBN: 978-0-470-02217-7.

In a classical picture, the magnetization precesses around the internal field, described by the Landau–Lifshitz torque equation of motion:

$$\frac{1}{|\gamma|}\frac{\partial \vec{M}}{\partial t} = -\vec{M} \times \vec{H}_{\text{eff}} \tag{1}$$

where $\gamma = \gamma_e g/2$ is the gyromagnetic ratio, $\gamma_e = -1.759 \cdot 10^7\,\text{Hz Oe}^{-1}$ is the value of γ for the free electron and g is the spectroscopic splitting factor. We neglect damping effects. The effective magnetic field acting on the magnetization, $\vec{H}_{\text{eff}}$, is given by

$$\vec{H}_{\text{eff}} = \vec{H}_0 + \frac{2A}{M_s^2}\nabla^2\vec{M} - \frac{1}{M_s}\vec{\nabla}_{\vec{\alpha}} g_{\text{vol}} + \vec{H}_d + \vec{h} \tag{2}$$

On the right-hand side, the first term is the external applied field $\vec{H}_0$. The second term accounts for the exchange interaction, where A is the exchange stiffness constant and M_s is the saturated magnetization. The third term accounts for magnetic anisotropies with the enthalpy density g_{vol} describing the volume anisotropy and the gradient operator $\vec{\nabla}_{\vec{\alpha}}$ for which the differentiation variables are the components of the unit vector $\vec{\alpha}$ pointing into the direction of the saturation magnetization $\vec{M}_s$. The fourth term describes the dipolar stray field. In the case of an in-plane magnetized infinite film, the stray field is zero, $\vec{H}_d = 0$, whereas in the case of an out-of-plane magnetized film it is $\vec{H}_d = -4\pi M_s \hat{n}$ (in CGS units), $\hat{n}$ with pointing into the normal direction of the film surface. The last term $\vec{h}$ accounts for the fluctuating field generated by the precessing moments. It has its origin in the dipolar and exchange interaction.

In a ferromagnetic system, the dipolar and exchange interactions result in the appearance of spin-wave modes. An example of the spin-wave mode is shown schematically in Figure 1. The displayed mode travels from the bottom left to the upper right corner of the square. Phase fronts, characterized by the same precession phase (dashed line in Figure 1) and the wavelength λ can easily be identified as indicated in the figure.

Inspecting equations (1) and (2) it is evident that both dipolar and exchange interactions determine the mode properties. In finite objects such as films, squares, circles, and so on, confinement and localization effects appear and modify the dispension of the spin waves. The mode properties of such confined spin waves are characterized by quantization conditions for the wave vector and by boundary conditions at the sidewalls of the object.

2.1 Exchange and dipolar modes in films

Spin waves investigated by optical techniques usually have wavelengths comparable to or larger than the wavelength of the used light. Thus interatomic distances are small compared to the wavelength, and we can apply continuum models. A good introduction is given in Hillebrands (2000). The description in such a classical picture describe most of the experimental observations. Quantum-mechanical corrections must be taken into account for films thinner than a few monolayers, but here a phenomenological correction of the demagnetizing field still allows for using a classic description (Stamps and Hillebrands, 1991).

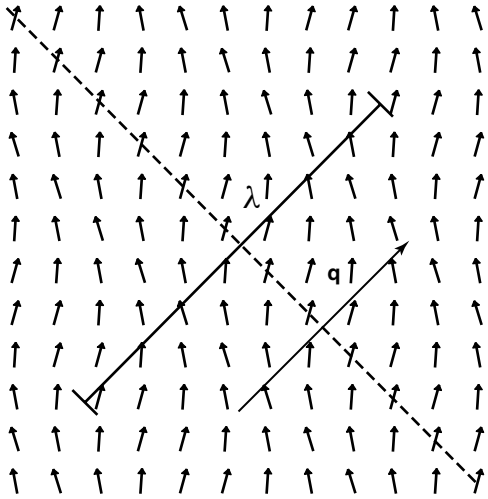

Figure 1. Sketch of a spin wave. The dashed line indicates a phase front.

We need to solve the Landau–Lifshitz torque equation of motion (equation (1)), together with the magnetostatic Maxwell equations,

$$\vec{\nabla} \times \vec{H} = 0 \tag{3}$$

$$\vec{\nabla} \cdot (\vec{H} + 4\pi\vec{M}_s) = 0 \tag{4}$$

From the equation of motion, (equation (1)), six independent partial wave solutions are obtained when exchange interaction is taken into account.

In the presence of surfaces and interfaces, boundary conditions must be fulfilled by a suitable superposition of the partial wave solutions. These are the Maxwell boundary conditions as well as a boundary condition derived from the equation of motion (equation (1)). For the surface of a film or an interface to a nonmagnetic layer this is the so-called Rado–Weertman boundary condition (Rado and Weertman, 1959; Gurevich and Melkov, 1996)

$$\vec{M} \times \left[\vec{\nabla}_{\vec{\alpha}}\sigma_{\text{inter}} - \frac{2A}{M_s}\frac{\partial \vec{M}}{\partial n}\right]\Bigg|_{\text{interface}} = 0 \tag{5}$$

Equation (5) describes the balances of torques acting on the interface where σ_{inter} is the enthalpy density describing a

magnetic interface anisotropy. It is evident that interface anisotropies provide an additional torque to the moments at the interface.

For magnetic films, a number of different spin-wave modes appear, depending on the geometry of the applied field and the wave vector of the spin wave. Both the exchange interaction and the dipolar interaction contribute to the dispersion. However, depending on the specific mode, one or the other can dominate the frequency.

If the wavelength of a spin-wave mode is very short (i.e., the wave vector is very large), exchange interaction dominates the frequency. In bulk materials, these so called modes. Their dispersion is approximately quadratic, that is, proportional to the square of the wave vector,

$$\frac{\omega(q)}{\gamma} \approx H + Dq^2 \tag{6}$$

with $D = 2A/M_s$ denoting the so-called stiffness constant. In films, perpendicular standing exchange modes, also called perpendicular standing spin waves (PSSW), are observed. Here the exchange modes propagate in a direction perpendicular to the film and form a standing wave pattern. The wave vector perpendicular to the film, $q_\perp$, is quantized due to the confinement. In case of both pinned ($\sigma_{\text{inter}} = \infty$) and unpinned ($\sigma_{\text{inter}} = 0$) boundary conditions, the perpendicular wave vector reads $q_{\perp,l} = l(\pi/d)$ where d is the film thickness and $l = 0, 1, 2 \ldots$ for unpinned boundary conditions. In case of a general boundary condition, the expression of $q_{\perp,l}$ is more complicated (Gurevich and Melkov, 1996).

Spin-wave modes investigated by optical techniques and traveling in the film plane usually have a wave vector in the range between the wavelength of the used light and many micrometers, which is much larger than interatomic distances. Thus, exchange interaction is weak and these modes are often governed by dipolar interactions. This can be easily understood by considering the oscillating dipole fields associated with the precessing moments. The local field strength increases with the wavelength as more moments locally contribute to the stray field.

The spin-wave dispersion depends on the direction of the wave vector, $\vec{q}$, and the direction of the magnetization vector, $\vec{M}$, with respect to the film orientation. Figure 2 illustrates the various modes in the so-called magnetostatic limit, where exchange interaction can be neglected. Please note that changes in geometry result in large changes in frequency as well as mode propagation characteristics.

If the magnetization and the wave vector both lie in the film plane and form an angle of $\varphi \approx 90^\circ$, then in the case of negligible anisotropy, the dispersion of the spin waves is

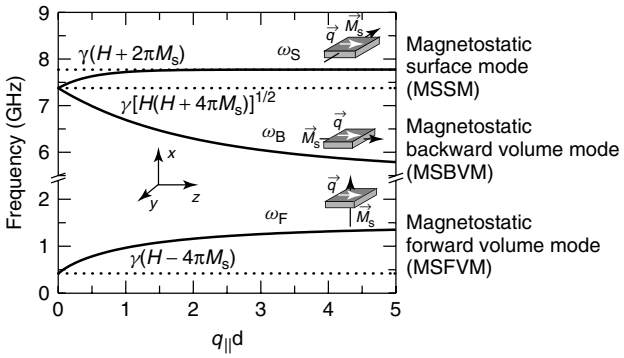

Figure 2. Typology of spin-wave modes as a function of the directions of the magnetization, $\vec{M}_s$, and the wave vector $\vec{q}$ in the dipolar limit. ω_S is the frequency of the surface spin wave when $\vec{q} \perp \vec{M}_s$ and $\vec{q}$, $\vec{M}_s$ lie in the film plane (MSSM, magnetostatic surface mode). ω_B, ω_F are the frequencies of the volume spin waves, with the wave vector parallel (MSBVM, magnetostatic backward volume mode) and perpendicular (MSFVM, magnetostatic forward volume mode) to the sample magnetization $\vec{M}_s$, respectively. Calculated for a 1000-nm-thick Yttrium iron garnet (YIG) film ($4\pi M_s = 1750\,\text{G}$, $\gamma = 17.6\,\text{MHz Oe}^{-1}$, $A = 1.6 \times 10^{-7}\,\text{erg cm}^{-1}$) at $H_0 = 1900\,\text{Oe}$ parallel to $\vec{M}_s$. (Reproduced from B. Hillebrands *et al*., 2006, with permission from Springer-Verlag. © 2006.)

given by Damon and Eshbach (1961):

$$\left(\frac{\omega_S(q)}{\gamma}\right)^2 = H_0\,(H_0 + 4\pi M_s \sin\varphi) + (2\pi M_s)^2\left(1 - e^{-2q_\parallel d}\right) \tag{7}$$

where $q_\parallel$ is the in-plane component of the wave vector, $q^2 = q_\parallel^2 + q_{\perp,l}^2$ and H_0 is the applied magnetic field. This spin-wave mode is called a *magnetostatic surface mode* (MSSM) or, sometimes, a Damon–Eshbach mode.

In the presence of in-plane anisotropy, the direction of magnetization is defined by the energy minimum of the total magnetic enthalpy density

$$g_{\text{tot}} = g_{\text{eff}} - \vec{M}_s \vec{H}_0 \tag{8}$$

which is the sum of the enthalpy density of the magnetic anisotropy and the Zeeman energy. The direction of $\vec{M}_s$ might deviate from the direction of the applied field, $\vec{H}_0$.

If the wave vector and the magnetization are collinear and both lie in the film plane, we obtain the so-called magnetostatic backward volume modes (MSBVM). The slope of the corresponding dispersion and thus the group velocity of these modes is negative, that is, the group and the phase velocity point in opposite directions, giving this mode its name (see ω_B in Figure 2). Without anisotropies and in the long wavelength limit ($q_\parallel d < 1$), the dispersion is given by Demokritov, Hillebrands and Slavin (2001), Kalinikos and

Slavin (1986), and MacDonald (1951)

$$\left(\frac{\omega_{\mathrm{B}}(q)}{\gamma}\right)^2 = H_0\left[H_0 + 4\pi M_{\mathrm{s}}\left(\frac{1-e^{-q_\parallel d}}{q_\parallel d}\right)\right] \tag{9}$$

The qualitatively different dispersions of the magnetostatic surface wave (equation (7)) and the magnetostatic backward volume wave (equation (9)) can be understood as follows: We assume that the film plane is the (y, z) plane. A spin wave propagating in the direction $\vec{q}_\parallel$ in the film plane can be written as

$$\begin{aligned}\vec{M}(\vec{r}, t) &= \begin{pmatrix} 0 \\ 0 \\ M_{\mathrm{s}} \end{pmatrix} + \begin{pmatrix} m_x \\ m_y \\ 0 \end{pmatrix} e^{\mathrm{i}(\omega t - \vec{q}_\parallel \vec{r})} \\ &= \vec{M}_{\mathrm{s}} + \vec{m} e^{\mathrm{i}(\omega t - \vec{q}_\parallel \vec{r})}\end{aligned} \tag{10}$$

with $\vec{M}_{\mathrm{s}} \perp \vec{m}$ and $\left|\vec{M}_{\mathrm{s}}\right| \gg |\vec{m}|$. The out-of-plane component m_x will create dynamic surface charges which alone lead to a reduction of energy (frequency) with decrease of wavelength (or increase of wave vector). However, there exists also an additional energy term based on the magnetic volume charges $\rho_M = -4\pi\nabla \cdot \vec{M} = 4\pi i \vec{q}_\parallel \cdot \vec{m} \exp[i(\omega t - \vec{q}_\parallel \vec{r})]$. For $\vec{q}_\parallel \parallel \vec{M}$ (magnetostatic backward volume waves) it is $\vec{q}_\parallel \cdot \vec{m} = 0$ and thus the volume charges are absent. Hence the only term remaining is the energy based on the surface charges and therefore the dispersion is negative. Contrarily, for $\vec{q}_\parallel \perp \vec{M}$ (surface waves) it is $\vec{q}_\parallel \cdot \vec{m} \neq 0$ and, therefore, this additional energy term increases in frequency with increasing wave vector, and therefore the dispersion is positive.

In most cases, the dispersion can only be calculated numerically; (Hillebrands, 2000; Hillebrands, 1990; Heinrich and Cochran, 1993). A good description of the algorithm is given in Stamps and Hillebrands (1991) for ultrathin films, that is, when the product of the wave vector and the film thickness is small compared to unity, $q_\parallel d \ll 1$. An approximate formula can be used (Stamps and Hillebrands, 1991):

$$\begin{aligned}\left(\frac{\omega(q)}{\gamma}\right)^2 = &\left(\frac{1}{M_{\mathrm{s}}}\frac{\partial^2 g_{\mathrm{eff}}}{\partial\theta^2} + H_0\cos(\varphi - \varphi_H)\right. \\ &\left. + \frac{2A}{M_{\mathrm{s}}}q^2 + 4\pi M_{\mathrm{s}} f\left(1 - \frac{1}{2}q_\parallel d\right)\right) \\ &\times\left(\frac{1}{M_{\mathrm{s}}}\frac{\partial^2 g_{\mathrm{eff}}}{\partial\varphi^2} + H_0\cos(\varphi - \varphi_H)\right. \\ &\left. + \frac{2A}{M_{\mathrm{s}}}q^2 + 2\pi M_{\mathrm{s}} f q_\parallel d\sin^2(\varphi - \varphi_q)\right) \\ &- \frac{1}{M_{\mathrm{s}}^2}\left(\frac{\partial^2 g_{\mathrm{eff}}}{\partial\theta\partial\varphi}\right)^2\end{aligned} \tag{11}$$

with θ and φ denoting the polar and azimuthal angle of the magnetization (using a conventional spherical coordinate system) the saturation magnetization M_{s}, the applied magnetic field H_0, the exchange constant A, the demagnetizing factor f (which may deviate from 1 for very thin films, see (Cochran, Heinrich and Arrott, 1986; Heinrich *et al*., 1988)), and the film thickness d. The angles φ, φ_H, φ_q indicate the directions of magnetization of the external field and of the wave vector with respect to an in-plane reference direction, which is usually chosen along a high-symmetry crystallographic axis. In equation (11) the directional derivatives of the effective anisotropy enthalpy density, g_{eff}, are written as derivatives with respect to the polar and azimuthal angles.

Equation (11) illustrates the applicability of investigating spin waves to determine magnetic anisotropies. The basic underlying equation, the Landau–Lifshitz equation, (equation (1)) is a torque equation and, correspondingly, the second derivatives of the anisotropy enthalpy, which describe torques, enter equation (11).

In the so-called magnetostatic forward volume mode (MSFVM) geometry, the magnetization is perpendicular to the film. The static internal field inside the film can be written as an applied field reduced by a static film magnetization, $H_0 - 4\pi M_{\mathrm{s}}$. Without anisotropies and in the long wavelength limit, the dispersion is given by Kalinikos and Slavin (1986) and Demokritov, Hillebrands and Slavin (2001)

$$\begin{aligned}\left(\frac{\omega_{\mathrm{F}}(q)}{\gamma}\right)^2 = &(H_0 - 4\pi M_{\mathrm{s}}) \\ &\times\left(H_0 - 4\pi M_{\mathrm{s}}\frac{1-e^{-q_\parallel d}}{q_\parallel d}\right)\end{aligned} \tag{12}$$

For the wave vector range considered here, the exchange interaction can be neglected for systems with a weak stiffness constant $D = 2A/M_{\mathrm{s}}$ such as Yttrium iron garnet (YIG). However, in the case of, for example, permalloy, the stiffness constant is about 20 times larger. Therefore, the contribution of exchange to the dispersion relation is not negligible, although it is still the dipolar interaction that governs the shape of the dispersion. This is presented in Figure 3(a), where dispersion relations of a permalloy film are calculated with and without the exchange contribution. We can see that the presence of exchange adds a contribution $\gamma D q^2$, quadratic in q, as described by equation (6). Owing to this contribution, the MSBVM ω_{B} may gain (from a certain value of $q_\parallel$) a positive slope and therefore both the phase and group velocity point in the same direction.

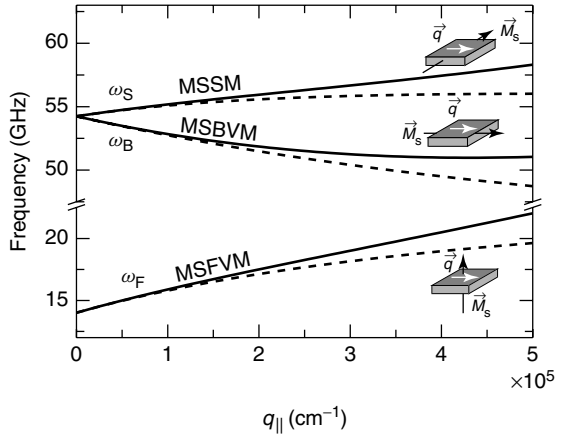

Figure 3. Full lines: The dispersions of a 30-nm thick permalloy film ($4\pi M_s = 10\,\text{kG}$, $\gamma = 17.6\,\text{MHz Oe}^{-1}$, $A = 1.3 \cdot 10^{-6}\,\text{erg cm}^{-1}$) under an applied external magnetic field $H = 15\,\text{kOe}$ parallel to $\vec{M}_s$. Both dipole–dipole and exchange interactions are taken into account. The dashed lines show the dispersions calculated for $A = 0$. ω_S, ω_B, and ω_F are different spin wave modes at different geometries as defined in Figure 2.

2.2 Quantized lateral spin-wave modes and boundary conditions

Of particular interest is the mode spectrum in confined magnetic structures, such as stripes, squares, rectangles, circles, and so on, patterned into a magnetic film. New finite size effects will appear because of the lateral boundaries of these objects. In first approximation, it is useful to address these final size effects by the simple quantization condition:

$$w = n\frac{\lambda_n}{2}; \quad q_{\parallel,n} = \frac{2\pi}{\lambda_n} = \frac{\pi}{w}n \tag{13}$$

where w is the width of the magnetic structure, n is a positive integer, and λ_n is the spin-wave wavelength. This is illustrated in Figure 4. If the magnetization lies statically in the film plane along the structure edge, no stray fields are generated for infinitely extended stripes. However, if the magnetization precesses around this direction, dynamic out-of-plane stray fields appear since the dynamic part of the magnetization has a component perpendicular to the film plane. This is properly taken into account by the Maxwell boundary conditions. In laterally confined structures, the same effect appears at the sidewalls of the objects. In zero-order approximation, we can describe quantized modes using equation (13), but the stray fields at the sidewalls are not considered. They will, however, generate surface torques, since the cross product of the stray field with the surface moments is a torque. This problem can be solved phenomenologically by including a new boundary condition, acting at the lateral edges (Guslienko, Demokritov, Hillebrands and Slavin, 2002; Guslienko and Slavin, 2005).

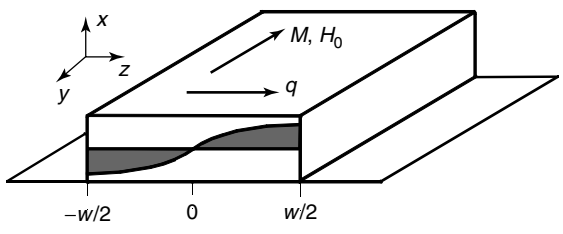

Figure 4. Sketch of a finite object with ($n = 1$) mode. Here n is the mode index and λ_n the corresponding wavelength. We can use these quantized values of the wave vector to evaluate the dispersion equation in first-order approximation.

$$\frac{\partial \vec{m}}{\partial z} + \frac{1}{\xi_D}\vec{m} = 0; \qquad \xi_D = \frac{d}{2\pi}\left(1 + 2\ln\frac{w}{d}\right) \tag{14}$$

with $\vec{m}$ denoting the dynamic part of the magnetization, and d and w the thickness and the width of the object, ($d \ll w$), respectively. Here, z is in-plane direction perpendicular to the edge of the stripe, as sketched in Figure (4). The additional surface torque of the dynamic stray fields is taken into account by the parameter ξ_D.

Finite objects are associated with dipolar stray fields. Unless the objects have an ellipsoidal shape, the internal field is inhomogeneous, and thus we need to discuss the propagation of spin waves in an intrinsically inhomogeneous system. These phenomena are discussed in Section 4.2.2.

3 EXPERIMENTAL TECHNIQUES

In this section we will discuss several optical techniques, which are applied to investigate spin wave and spin dynamic properties.

Two classes of experiments exist. The first class comprises spectroscopic techniques which allow to measure the spin-wave mode spectrum directly. For thin films and patterned structures, this is in particular the BLS spectroscopy. Here, the primary quantity of observation is the frequency of spin waves measured as a function of the wave vector. Another spectroscopic techniques are optical ferromagnetic resonance experiments. Here the fundamental precession mode, the zero wave vector ferromagnetic resonance mode, is excited, often by application of a cw microwave field. The amplitude of the forced magnetization precession is measured stroboscopically. The second class comprises techniques that work on the timescale. Most of these techniques are based on a stroboscopic approach. The sample is excited by a short perturbation, and, with defined time delay, the magnetic response is tested utilizing the magneto-optic Kerr effect

(MOKE) and SHG. For the perturbation, short field pulses or field steps, light pulses, microwave pulses, and so on, can be used. The techniques are discussed in detail in the following.

Other methods involving both spectroscopic and stroboscopic aspects exist. For instance, time-resolved BLS spectroscopy measures the intensity of spin-wave packets; however, in this case the sample is excited with microwave pulses generating spin-wave pulses, whose propagation time is then measured stroboscopically.

3.1 Brillouin light scattering spectroscopy

The fundamental principle of BLS spectroscopy is inelastic scattering of monochromatic, visible light from spin waves (Hillebrands, 2000; Hillebrands and Güntherodt, 1994; Sandercock, 1982). This is illustrated in Figure 5. In a quantum-mechanical picture, a photon of energy $\hbar\omega_L$ and momentum $\vec{q}_L$ creates or annihilates a magnon $(\omega, \vec{q})$, which is the quantum of a spin wave. Consequently, the photon frequency and wave vector are changed. Temporal and translational symmetries correspond to conservation of energy and momentum. If a magnon is created, the scattered photon has the energy $\hbar\omega_L - \hbar\omega$ and momentum $\hbar q_L - \hbar q$. If a magnon is annihilated, the energy of the scattered photon is $\hbar\omega_L + \hbar\omega$ and the momentum is $\hbar q_L + \hbar q$. For finite temperatures ($T \gg \hbar\omega/k_B \approx 5\,\mathrm{K}$) both processes have about the same probability. In a classical description the process can be understood as scattering of light from a propagating phase grating in the dielectric constant generated by the propagating spin wave via spin-orbit coupling. The laser light is Doppler shifted by the frequency of the spin wave, and the periodicity of the phase grating induces a change in the direction of the scattered light. For a detailed discussion see Hillebrands (2000) and references therein.

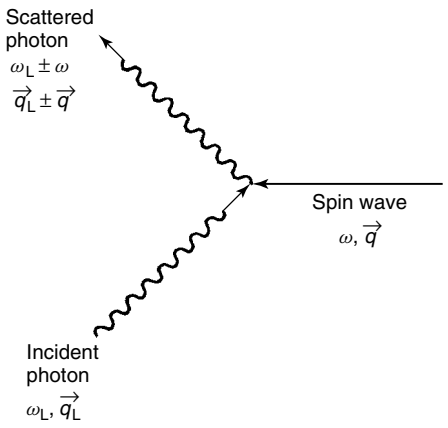

Figure 5. Scattering process of photons from spin-wave excitations (magnons).

For an infinitely extended film, translational invariance exists in the plane of the film. Correspondingly the wave vector components parallel to the film plane are conserved in the scattering process. These components can be varied in an experiment by changing the angle of light incidence. The system is time invariant, and correspondingly the frequency shift measured in the BLS experiments is equal to the frequency of the spin wave.

As BLS is an optical technique, it allows for a local measurement of spin waves with a spatial resolution defined by the diameter of the laser spot. Typically, the spot size is of the order of 40 µm. Techniques have been reported to reduce the diameter down to the optical limit (see Section 3.1.2). BLS can be applied in different environments, such as low and high temperatures, ultrahigh vacuum, and so on.

3.1.1 The Brillouin light scattering setup

A typical BLS setup is shown in Figure 6. Light from a frequency stabilized laser in single mode operation with wavelength λ is focused onto the sample. As a light source a cw laser, such as a solid-state laser or an Ar^+-laser, can be used, a typical linewidth is $\Delta\nu = 20\,\mathrm{MHz}$. From the spin waves, light is inelastically scattered. The direction under which the scattered light is analyzed determines the transferred wave vector in the scattering process and thus the wave vector of the spin wave. Often the backscattering geometry is used because of maximum momentum transfer, in particular for metallic samples, but forward scattering is also applied if spin-wave modes with large wavelengths are investigated and the sample is transparent. The scattered light containing elastic and inelastic contributions is sent through a spatial filter, consisting of two lenses and a pinhole, to suppress background noise, and then enters the monochromator. Commonly a multipass tandem Fabry–Pérot interferometer developed by Sandercock (JRS Scientific Instruments), is used. The light then passes a second spatial filter and a prism to suppress signals from common transmission orders of the two etalons outside of the measured spectrum. The light is detected by a photomultiplier or an avalanche photodiode. Single photon counting must be used, and the dark count rate should be lower than 3 counts/s. A computer or a multichannel analyzer collects the photon signals as a function of the mirror spacing and displays the data.

Optical etalons are commonly used as the frequency-selecting element. They consist of two highly flat ($\lambda/200$) glass plates enclosed with a high reflectivity coating ($R = 92$–96%). The transmission function of an etalon

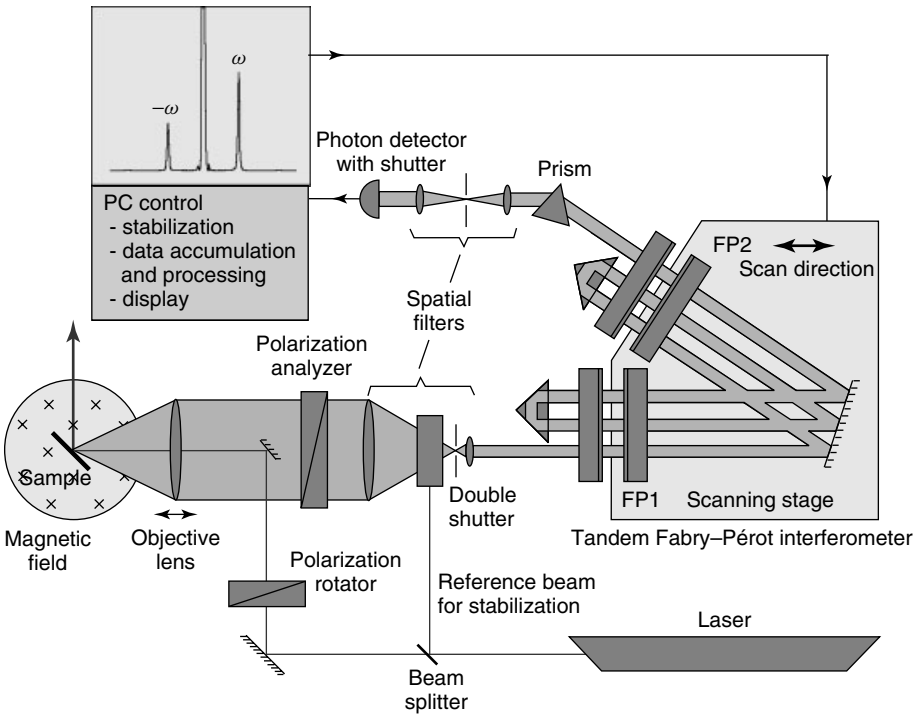

Figure 6. Schematic view of a Brillouin light scattering setup.

is the Airy function

$$I = I_0 \frac{1}{1 + F \sin^2(\Delta\phi/2)} \tag{15}$$

with I denoting the transmitted intensity as a function of the mirror spacing s, $F = 4R/(1-R)^2$ the finesse, R the mirror reflectivity, $\Delta\phi = 2\pi s/\lambda$ the phase shift for one loop (two reflections) in the etalon, and λ the wavelength. Perpendicular incidence of the light is assumed, as it is the case in the experimental setup described here. The etalon transmits all the light if the spacing between the two plates is an integer multiple of half the wavelength. In the experiment one of the two plates is scanned piezoelectrically to allow for resonance conditions for different wavelengths and corresponding frequencies.

To avoid ambiguities in the assignment of inelastic peaks to the respective transmission order, a tandem arrangement is commonly used. Its central part is shown in Figure 7. One mirror of each of the two etalons is mounted on a common translation stage. The axes of the two etalons form an angle Θ. If the translation stage is moved along the normal direction of FP_1 and if the spacing of etalon FP_1 is changed by Δ, the corresponding change in spacing of FP_2 is $\Delta \cos\Theta$.

To understand the operation let us assume that both etalons are in transmission (see Figure 7b). If the spacing of FP_1 is changed by $\lambda/2$ this etalon is again put into transmission. However, since the change in spacing of FP_2 is smaller by the factor $\cos\Theta$, FP_2 is now not in transmission. Since the light is sent through both etalons in series, transmission is only obtained in the common transmission order. Let us now assume that the light from the sample contains an inelastic contribution. The spectrum, shown in the upper left part of Figure 7, consists now of a strong line at frequency ω_L, corresponding to elastically scattered light, and two weaker side bands at $\omega_L \pm \omega$. These side bands appear in the transmission of the etalons at characteristic spacings (see Figure 7b). It is evident that only the signal from the side bands belonging to the common transmission order is transmitted through both etalons. Thus the ambiguity in the mode assignment is removed. In practice, the translation stage is piezoelectrically driven with a feedback for linearization. The frequency range between the central transmission order and the first neighboring order is called the *free spectral range*.

A frequency resolution in the subgigahertz regime and a high contrast of better than 10^{10} (Sandercock, 1982; Mock, Hillebrands and Sandercock, 1987) can be achieved, the latter by multipassing the light beam through the etalons using a system of mirrors and/or retroreflectors (see Figure 6). This sensitivity allows for the observation of spin waves down to magnetic monolayers, although the inelastic light scattering process is rather ineffective (Krams *et al*., 1992).

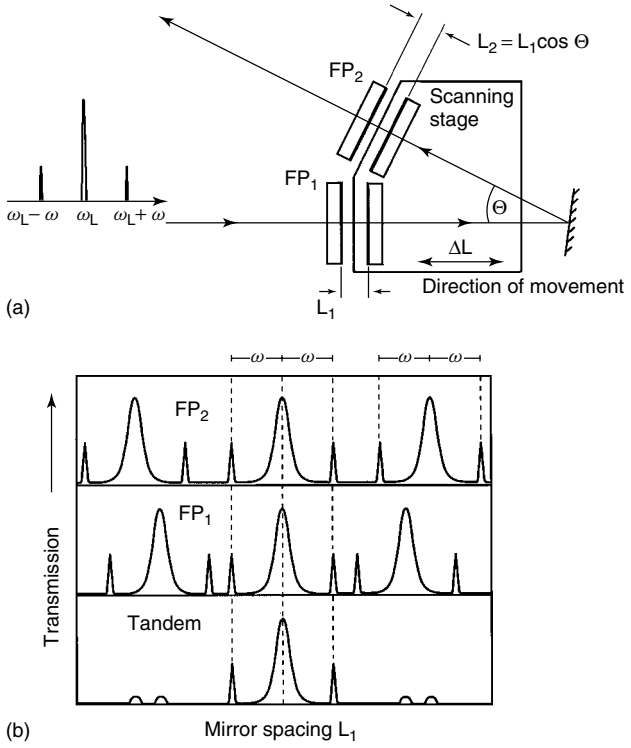

Figure 7. Schematic view of the operation of a tandem Fabry–Pérot interferometer. (a) View of the light pass. (b) Transmitted intensity of first etalon (FP_1), second etalon (FP_2), and both etalons in series. The inelastic contributions due to scattering from spin waves are indicated by ω. (Reproduced from B. Hillebrands *et al.*, 2000, with permission from Springer-Verlag. © 2000.)

To maintain stable operation, the parallelity of the mirror plates must be maintained to a very high degree (a common value is $\lambda/100$). This cannot be achieved statically, and sophisticated dynamic stabilization schemes are applied (Mock, Hillebrands and Sandercock, 1987; Sandercock, 1971; Hillebrands, 1999). Often a shutter system is used to switch between the light from the sample and reference light used for stabilization (see Figure 6). Active stabilization and the data collection can be performed by hardware as well as by software solutions, such as the TFPDAS3 package (Hillebrands, 1999).

The total accessible frequency range in a BLS experiment is in the range of 0.2 GHz–1 THz. In a typical experiment a much smaller range is used, defined by the spacing of the etalon mirror plates. The finesse, that is, the ratio of the free spectral range over the resolution is fixed and is typically of the order of 50. Thus the needed frequency resolution determines the free spectral range. Scanning over several transmission orders can be made to enhance the frequency range. Sensibility down to monolayer thickness has been shown with a good signal-to-noise ratio, for example, 2 ML of Co deposited on Cu(001) (Krams *et al.*, 1992).

3.1.2 Space-resolved Brillouin light scattering spectroscopy

The laser spot size in a standard geometry is of the order of 40 µm. Thus BLS spectroscopy can be used for imaging of spin-wave propagation and spin-wave eigenmodes in confined objects with moderate spatial resolution. A large class of experiments involves the excitation of spin waves in garnet films with wavelengths in the range of 0.1–1 mm. Here a scanning sample stage allows the realization spatial resolution by measuring the intensity of the inelastic scattered light point by point on the sample in a scanning probe fashion. Spatial resolution can be increased down into the submicrometer range using the so-called microfocus technique. Here the full numerical aperture of an objective lens is used for maximum optical resolution. Compared to standard BLS spectroscopy two major modifications are made. First, a microscope objective is used and, for maximum spatial resolution, the incoming laser light is expanded to the output aperture of the objective lens. Second, for practical reasons, an optical microscope setup is integrated to monitor the position of the laser spot on the sample. Figure 8 illustrates the light pass for both BLS spectroscopy and monitoring.

Unfortunately, a price is to be paid for the increased optical resolution, and this is the loss in wave vector resolution, in accordance with Heisenberg's principle of uncertainty. However, in small magnetic objects the excitation spectrum most often consists of quantized, dispersionless modes, so that the loss in wave vector resolution is not a real drawback.

Microfocus BLS spectroscopy has been used to measure the local mode spectra in micrometer sized objects, such as stripes, squares, rectangles, circles, and rings (see Section 4.5 for illustrations).

3.1.3 Time-resolved Brillouin light scattering spectroscopy

The BLS spectroscopy technique has been extended toward time resolution (Slavin, Demokritov and Hillebrands, 2002).

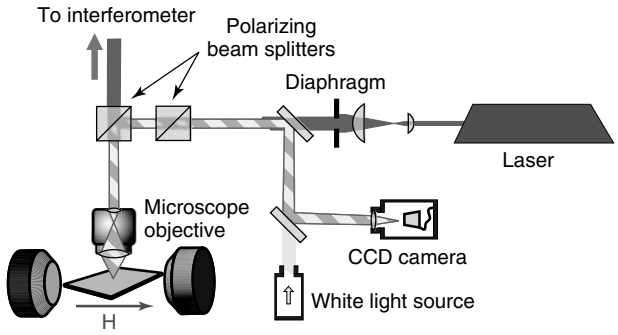

Figure 8. Schematic view of microfocus Brillouin light scattering setup.

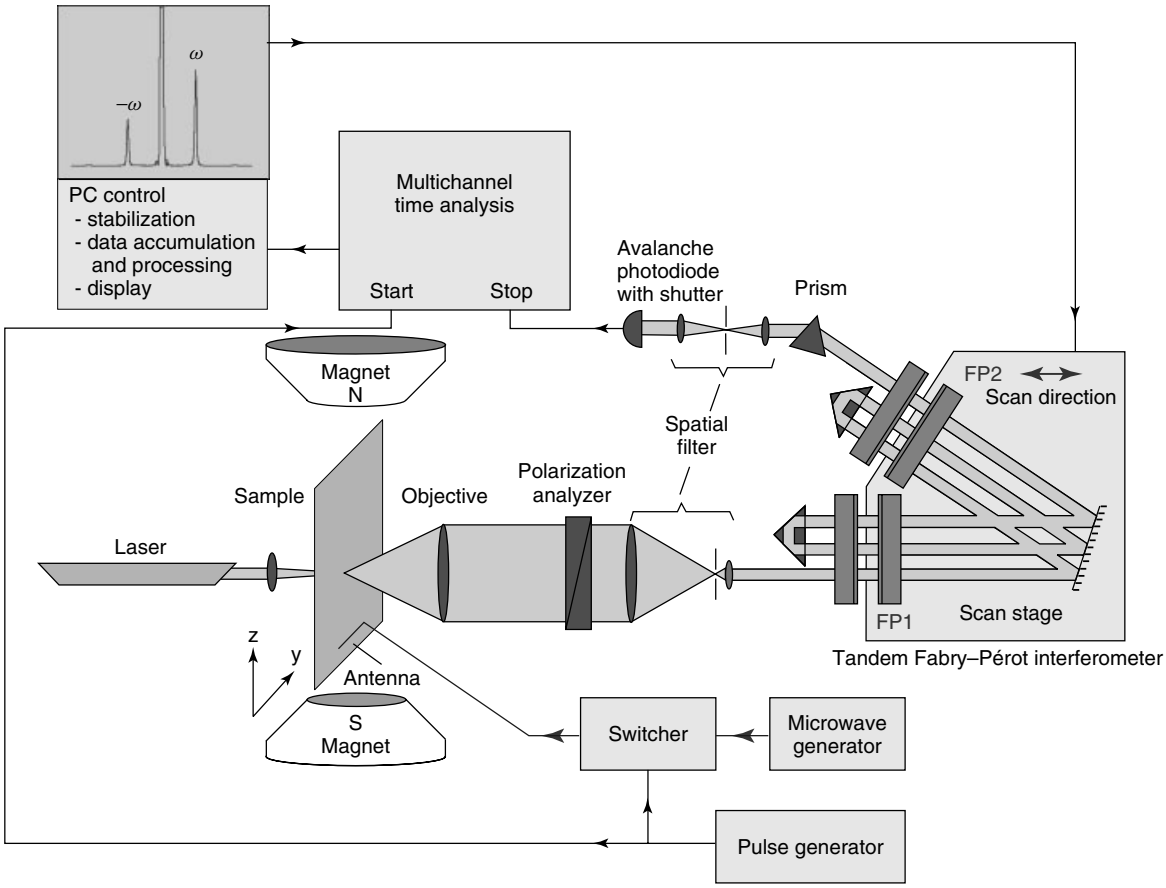

Figure 9. Schematic layout of the Brillouin light scattering apparatus with space and time resolution. For a discussion of the components see text. (Reproduced from A.N. Slavin *et al*., 2002, with permission from Springer-Verlag. © 2002.)

This allows for direct access to spin-wave propagation phenomena by monitoring the propagation of microwave excited spin-wave pulses. In a typical experiment, a spin-wave pulse is launched in a sample by application of a microwave pulse to an antenna structure. Observation of the spin-wave packet is now realized by measuring stroboscopically the time between launch and detection in the area of the laser focus. Most often this technique is combined with space-resolved BLS, enabling the full spatio-temporal observation of the packet propagation.

Figure 9 illustrates the fundamental operation. Spin-wave pulses are excited by an antenna structure connected to a microwave generator with a microwave switcher. The microwave switcher is controlled by a pulse generator, which serves as the central clock. The microwave pulses are typically 10–30 ns long and have a repetition rate upto 1 MHz. The propagating spin-wave pulse is detected in the focus of the laser light. Here, most often a transmission geometry is used because of the small wave vector of the modes to be detected. If spin-wave pulses cross the laser focus, they generate inelastically scattered photons, which are then detected by the photomultiplier. The propagation time is obtained by measuring the time between launch of the spin-wave pulse at the antenna and its detection in the laser focus (the time measurement unit is indicated in Figure 9 by 'multichannel time analysis'). For this purpose a 24-bit reference counter is used, which runs with a time base of 1.2 GHz. The counter is started by the pulse generator and stopped by the detection of an inelastic scattered photon. The content of the counter is thus a measure of the elapsed time of such an event. A memory cell is addressed by the content of the counter and its content is increased by 1. After averaging many of these events the memory contains the temporal distribution of the spin-wave signal in the laser spot. Repeating this measurement point by point by scanning the laser focus across the sample, the full spatio-temporal information of the propagating spin-wave pulse is obtained. The result is usually displayed in an animated movie format.

The time resolution is of the order of 2 ns, limited by the narrow transmission linewidth of the Fabry–Pérot interferometer. In a typical experiment, the measurement at each position on the sample takes about 1–10 s. A complete

measurement of a two-dimensional spin-wave intensity pattern in a YIG-film with a sample area of $2 \times 6\,\mathrm{mm}^2$ and a mesh size of 0.1 mm takes a little bit more than 2 h including the time caused by sample positioning.

3.2 Time-resolved magneto-optic Kerr effect magnetometry and microscopy

This class of experimental tools uses the magneto-optic Kerr effect is used to pick up information on the magnetization and its dynamics (Freeman, 2005; Rasing, van den Berg, Gerrits and Hohlfeld, 2003; Freeman and Hiebert, 2002; Choi and Freeman, 2005). The three standard Kerr effect geometries linear in the magnetization – longitudinal, transverse, and polar Kerr effect geometry – are used, although, particularly for imaging, the polar Kerr effect geometry is most often employed. In the longitudinal (transverse) geometry, the in-plane magnetization component parallel to the (perpendicular) plane of the incidence is probed. In polar geometry, the magnetization component perpendicular to the film plane is tested.

The dynamic part of the magnetization is usually perpendicular to the static part. Consequently, for an in-plane magnetized sample, both the polar Kerr effect as well as one of the two in-plane Kerr effects contribute to the signal. The polar Kerr effect is usually about a factor of 100 larger than the longitudinal or the transverse counter parts. This factor depends on many parameters, such as optical and magneto-optical parameters of the ferromagnetic layer, overlayer, and substrate as well as on the angle of incidence, light wavelength, light polarization, and so on. (Višňovský *et al*., 1995; Qiu and Bader, 1999; Hubert and Schäfer, 1998). For example, in the case of 30-nm-thick permalloy film investigated by s-polarized (p-polarized) light at an incidence angle $\varphi = 45^\circ$ and wavelength $\lambda = 680\,\mathrm{nm}$, the Kerr rotation in the case of polar magnetization is 140 mdeg, (160 mdeg), whereas in the case of longitudinal magnetization it is 6.4 mdeg (2.4 mdeg), respectively. On the other hand, in thin films there is a large ellipticity of the precession of the magnetic moments which must be taken into account. The out-of-plane dynamic component of the magnetization is typically a factor of 100 smaller than the in-plane dynamic component. Therefore, the out-of-plane and in-plane components of the dynamic magnetization contribute more or less equally to the resulting Kerr signal.

Two general classes of techniques are used: In the pump probe approach, the system is excited by a short perturbation, which can be a magnetic field pulse, heating by a light pulse, and so on. With some controlled time delay a probe light pulse is sent to the sample and the Kerr signal of the reflected light is measured. The temporary evolution of the magnetization dynamics is obtained by measuring the Kerr signal as a function of the delay time. In a second experimental approach, the system is subject to a microwave field, which excites a uniform forced precession of the magnetization. Pulsed light, which is synchronized to the microwave frequency, is sent to the sample and the Kerr signal is measured. A measurement of the Kerr amplitude as a function of the microwave frequency, applied field, and so on, yields the dynamic response of the sample. This is the so-called optical ferromagnetic resonance technique, discussed in the next subsection.

Figure 10 shows a schematic setup to measure the dynamics of all three Cartesian components of the magnetization, m_x, m_y, m_z (Freeman, 2005; Freeman and Hiebert, 2002). An electric pulse generator is used to generate current pulses, and thus the sample is stimulated by magnetic field pulses. Commonly the current pulses are sent to the sample using a strip-line geometry for reasons of high-frequency impedance matching. For the detection part, a Ti:sapphire laser system is commonly used, which typically provides 70-fs-long pulses of $\lambda = 800\,\mathrm{nm}$ wavelength and has a repetition rate of 82 MHz. The laser serves as the general clock of the system. Some part of the light and a photodiode are used to generate the electrical clock signal to trigger the electrical pulse generator. A pulse picker is used to reduce this repetition frequency of the laser down to 1 MHz, well adapted to the timing of the magnetization dynamics. Often a frequency doubler is employed to work at shorter wavelengths. Some authors also report the successful use of pulsed diode laser as a light source (Fassbender, 2003).

The laser light is sent to the sample via a beam splitter and an objective lens for focusing. The reflected light is then sent to a polarizing beam splitter and to photodiodes, which work in the geometry of an optical bridge for differential detection of the polarization rotation induced by the MOKE. When quadrant detectors are used (as shown in Figure 10), then linear combinations of signals from proper detector quadrants provide signals proportional to all three Cartesian magnetization components (Freeman, 2005; Freeman and Hiebert, 2002). Such a setup is frequency limited by the rise time of the pulse generator being about 50 ps as well as the jitter of the system. The use of coplanar strip lines and a careful matching of the impedances result in a frequency limit in the 5-GHz range.

An alternative way allowing access to a higher frequency range is to use a photoconductive switch, illuminated by a laser pulse, to generate fast transient electrical current pulses. Figure 11 shows the approach used by the Nijmegen group (Gerrits *et al*., 2001; Rasing, van den Berg, Gerrits and Hohlfeld, 2003). In such a switch the light pulse generates

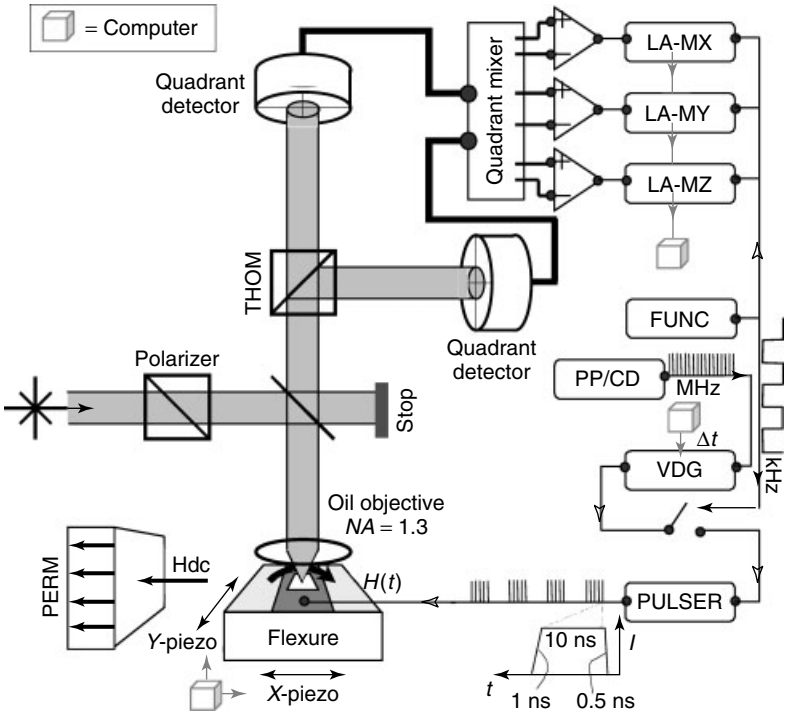

Figure 10. Scheme of the setup of the time-resolved Kerr effect experiment: A polarized pulsed-laser source is split by a beam splitter and focused onto the sample with an oil immersion objective lens (numerical aperture $NA = 1.3$). The reflected light is analyzed by a Thomson polarizing beam splitter (THOM). The light is detected by a quadrant detector that simultaneously acquires all three components of the magnetization. To reduce noise, lock-in amplifiers (LA) are employed. Temporal resolution is achieved by synchronizing the laser pulses through the output of a cavity dumper or pulse picker (PP/CD) triggering an electronic pulser (PULSER) at megahertz frequencies via a variable delay generator (VDG) with computer-controlled variable delay Δt. The pulses provided by the VDG are toggled (gated) by a fast gating switch controlled by a function generator (FUNC) at kilohertz frequency. The gated train of electrical pulses from the pulser (amplitude 50 V, length 10 ns, rise time 0.5 ns, fall time 1 ns) is launched to a coplanar transmission line, creating a transient in-plane magnetic field $\vec{H}(t)$ at the sample. The static magnetic field is generated by a permanent magnet (PERM). The spatial image is built by scanning the sample position underneath the laser spot. (Reproduced from M.R. Freedman *et al.*, 2002, with permission from Springer-Verlag. © 2002.)

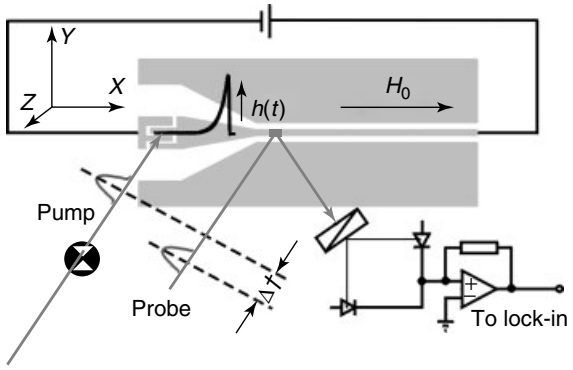

Figure 11. Scheme of the setup of the time-resolved Kerr effect experiment demonstrating the photoconductive switch. The 100-fs pump pulse excites a current pulse, which is concentrated in the taper and launched into the signal line. The response of the magnetic element to the correlated field pulse, $h(t)$, is measured by detecting the Kerr rotation of the 100-fs probe pulse as a function of the pump pulse delay Δt. (Reproduced from T. Rasing *et al.*, 2001, with permission from The Magnetics Society of Japan. © 2001.)

electron hole pairs in doped GaAs and thus increases the conductivity. Photoconductive switches show very fast current raise times (≈10 ps), but however, also slow decay times (≈600 ps). This problem can be circumvented by using two photoconductive switches which are illuminated by two laser pulses with a short delay in between. The output currents of both switches are connected in an antiparallel arrangement and thus will cancel each other in the long tail. Figure 12 demonstrates the principle.

A typical operation voltage is ±30 V and the usual peak power of the laser pulse excitation is 100 MW cm^{-2}. Well-defined magnetic pulses with a peak field strength of 100 Oe a duration of less than 50 ps, and a jitter considerably better than 1 ps can be generated. When using a single photoconductive switch, a frequency resolution of about 15–20 GHz has been achieved (Zhu *et al.*, 2005).

Experiments as described above are very well suited to measure the magnetization dynamics of small magnetic objects. Very often a high spatial resolution is needed. An

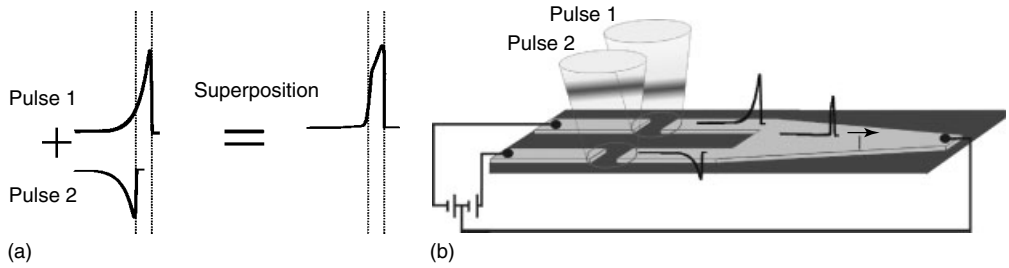

Figure 12. (a) Principle of magnetic field pulse cancellation due to the exponential character of the trailing edge. (b) Schematic drawing of the double photoconductive switch setup that allows for a control of the shape of the field pulse generated. (Reproduced from H.A.M. Gerrits *et al*., 2003, with permission from Elsevier. © 2003.)

objective lens is used to focus the light down to a minimum focus size, which is typically of the order of 1 – 10 μm. A further reduction of the focus size going to the optical limit has been studied. In Freeman and Hiebert (2002), the use of a solid immersion lens is reported and the achieved spatial resolution was 220 nm corresponding to a resolution of $\lambda/2.9$ relative to the wavelength (Rayleigh criterion). By scanning the laser focus across the sample and measuring the time-resolved magnetic response, two characteristic quantities can be obtained from the measurements: First, the dynamic response is measured point by point, as a function of the delay time. Second, images corresponding to a given delay time can be made. Such images can be presented in an animated movie format, and the experimentally determined 'wiggling' of the magnetization can be demonstrated. Furthermore, the time-resolved local magnetization response can be Fourier-transformed for each point on the surface. The Fourier components can be imaged as a function of the position. Thus, the local amplitude of individual modes with a given frequency ω can be displayed. Here the Kerr effect technique meets the microfocus-BLS technique, where the mode amplitude is directly measured locally. Section 4.3 shows a result, where both methods are compared.

A number of related stroboscopic Kerr effect techniques exist. For instance, magnetic anisotropy and an intense light pulse can be used to excite precession, which is then stroboscopically sampled with the techniques described above (van Kampen *et al*., 2002; Hansteen, Kimel, Kirilyuk and Rasing, 2005; Weber *et al*., 2005; Hicken, Barman, Kruglyak and Ladak, 2003). Here the light pulse results in a sudden local heating of the sample. In the presence of a temperature-dependent anisotropy, this may result in a change of the easy direction of magnetization, stimulating a precession of the magnetization. van Kampen *et al*. (2002); Hansteen, Kimel, Kirilyuk and Rasing (2005); Weber *et al*. (2005); and Hicken, Barman, Kruglyak and Ladak (2003) discuss this technique.

Most time-resolved Kerr microscopy setups use a scanning approach. However, for wide-field imaging a conventional Kerr microscope can be used jointly with pulse excitation. Neudert *et al*. (2005) demonstrate this approach.

3.3 Optical ferromagnetic resonance

Tamaru *et al*. (2002, 2004) have pioneered the technique of spatially resolved optical ferromagnetic resonance following early experiments by Petek, Trouilloud and Argyle (1990). They have shown that the uniform mode of a film or the eigenmode spectrum of a small magnetic object can be investigated by driving the system with an applied microwave field, for instance, in a microwave cavity or for a sample mounted on top of a coplanar strip line connected to a microwave source. This optical approach has the advantage that the full optical resolution can be used to obtain spatial information about the mode profiles. Figure 13 shows a typical setup.

A coplanar transmission line is used to apply the microwave signal to the sample, while a Ti:sapphire frequency-doubled laser system is used as a clock. The laser is controlled by a 80-MHz reference clock, which also synchronizes the microwave generator working at 8 GHz with an intervening delay generator for phase adjustment. To increase sensitivity, a lock-in technique is used. A 1-kHz signal generator modulates the microwave signal and is used as a reference signal for a lock-in amplifier used for analysis of the Kerr signal. For this type of experiment, a very precise phase synchronization between the microwave signal and the laser pulses is mandatory. The experiment is conducted in the usual ferromagnetic resonance operation: the applied field is changed and the output signal is measured as a function of the applied field point by point on the sample. In this way, the two-dimensional distribution of the mode profiles are obtained as a function of the applied field.

3.4 Second-harmonic generation techniques

As discussed in Section 3.2, the magneto-optical Kerr effect may be used to determine all three Cartesian components

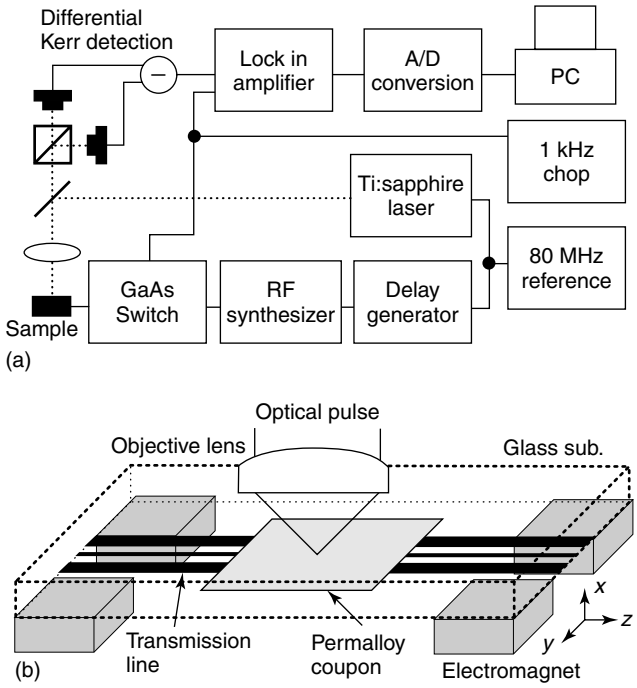

Figure 13. Schematic diagram of a Kerr effect ferromagnetic resonance setup. (a) Entire system and (b) sample with coplanar transmission line. (Reprinted with permission from S. Tamaru *et al*., 2002, © 2002, American Institute of Physics.)

of the magnetization. Therefore it is well suited to pick up the dynamic signal. However, the polar, transverse, and longitudinal Kerr effect contributions are mixed together and often there is a need to separate them (Choi and Freeman, 2005).

The employment of the SHG technique is an alternative elegant way to obtain magnetization information in all three Cartesian directions. For materials with point symmetry (such as most metals), the SHG signal originates only from the interface or surface, because here the point symmetry is broken. Using the SHG technique, the in-plane magnetic contribution can be separated by realizing different orientations of the analyzer (Gerrits *et al*., 2002a; Kabos, Kos and Silva, 2000). When the incident light is p polarized, then the s-polarized SHG yield ($p_{in} - s_{out}$) is an odd function of the longitudinal magnetization. On the other hand, the p-polarized SHG yield ($p_{in} - p_{out}$) is an odd function of transverse magnetization [2]. As the SHG signal only weakly depends on the polar magnetization, this direction was measured by means of the magneto-optical polar Kerr effect (Gerrits *et al*., 2002a; Gerrits *et al*., 2002b). The only disadvantage of this elegant approach is that it mixes surface or interface magnetic signals related to in-plane magnetic directions and the bulk magnetic signal related to the polar direction.

4 APPLICATIONS OF OPTICAL TECHNIQUES

The development of new experimental techniques, as discussed in Section 3, has enabled a large variety of new experimental results. In this section we present a few of these results. They are aimed at demonstrating the specific potentials of some of the optical techniques discussed above and are not meant as an introduction into the underlying physics. As an example of the application of space- and time-resolved BLS spectroscopy we discuss results on the spin-wave tunneling effect. BLS in the 'Fourier microscope' mode also allows to characterize the lateral extensions of confined magnetic modes. This is demonstrated in the investigation of localized modes in rectangular microelements. As a further topic, the investigation of mode patterns in squares using both time-resolved Kerr microscopy and microfocus BLS spectroscopy will be presented. Next, as an example of the optical ferromagnetic resonance technique, we demonstrate the investigation of confined modes using this approach. We finally conclude by presenting a few experiments on the investigation of propagating spin waves using time-resolved optical techniques, which complement BLS experiments.

4.1 Spin-wave tunneling

In a ferro- or ferrimagnetically ordered film spin waves may propagate, characterized by their dispersion. Spin waves can easily be excited using an antenna structure mounted on the surface of the film and connected to a microwave generator. If the antenna structure is driven by microwave pulses, spin-wave pulses are generated. Their carrier frequency is determined by the frequency of the microwave generator $\omega_{\mu W}$, and their wave vector is determined by the dispersion law $\omega(\vec{q})$. The slope in the dispersion is the group velocity of the spin-wave packets, $\vec{v}_g = \nabla_q \omega(\vec{q})$.

The method of space- and time-resolved BLS, as described in Sections 3.1.2 and 3.1.3, is used to study the propagation properties of such spin-wave packets. We demonstrate this for a specific physical problem. We assume that we have a spin-wave waveguide realized by a YIG stripe of typically 6 µm thickness, 1.5 mm width, and 10 mm length. The YIG films are grown on Ga–Gd–garnet (GGG) substrates, which are nonmagnetic. The spin waves are excited by attaching a microfabricated microwave antenna to the film, which is connected to a pulsed microwave generator.

If we inhibit propagation of such a spin wave in certain, narrow (smaller or comparable to spin-wave wavelength) areas of the spin-wave waveguide, the spin-wave tunneling effect may appear. It has been shown recently that a region of lowered magnetic field can act as a tunnel barrier for a

propagating dipolar-dominated backward volume (MSBVM) spin wave (Demokritov *et al*., 2004). In this region, the dispersion curve is shifted down on the frequency scale because of the reduced internal field, and if the dispersion does not allow any more for the propagation of a MSBVM spin wave for the given frequency $\omega_{\mu W}$ determined by the microwave generator, propagation is forbidden. If the forbidden region is small enough, tunneling of spin waves may appear. Here we demonstrate the spin-wave tunneling effect using a different scenario which is in a sample with a narrow mechanical gap cut into the YIG waveguide.

The spin-wave waveguide was fabricated by chemical etching of the YIG-film. While the mechanical gap was realized by a transverse slot of 20 µm width. The waveguide was magnetized along its longitudinal axis. Backward volume magnetostatic spin waves (BVMSW) with a carrier frequency

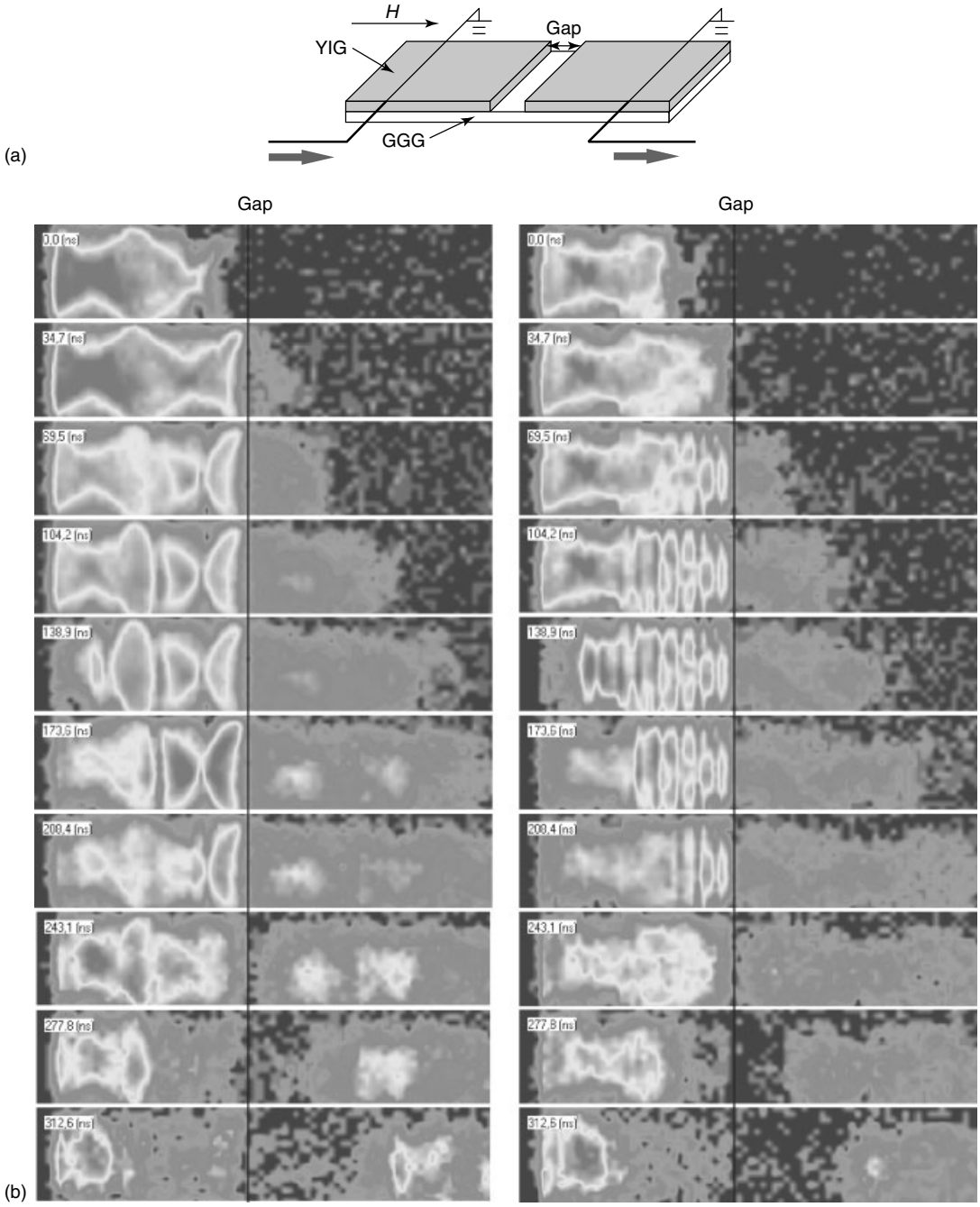

Figure 14. (a) Schema of the setup for spin-wave tunneling measurements. (b) Tunneling of a spin wave through a mechanical gap. The position of the gap is indicated by the black line. Left column: $H = 1835$ Oe, right column: $H = 1846$ Oe.

of $\omega/2\pi$ = 7.125 GHz were excited in the waveguide using a 25-μm-wide microstrip antenna.

Figure 14 shows the experimental results using space- and time-resolved BLS spectroscopy for two different values of the magnetizing field: $H = 1835$ Oe (left) and $H = 1846$ Oe (right), yielding spin waves with $q = 10$ and $4.2\,\mathrm{cm}^{-1}$, respectively. The data are normalized to the maximum value in each picture. The larger magnetic field corresponds to a smaller carrier wave number of the spin-wave packet incident on the gap.

As expected, the main part of the waves is reflected from the gap and forms a standing wave pattern together with the incoming wave. A small part of the wave energy tunnels through the gap and forms a propagating transmitted wave. One can see in Figure 14 that the amplitude of the transmitted pulse is smaller for short carrier wavelengths and larger for long carrier wavelengths.

In the experiment, frames with the spatial information are obtained for each time step, and thus an animated video can be obtained, which shows the propagation of the spin-wave pulse. Follow-up experiments have been performed to measure the wave vector dependence of the tunneling efficiency, and to investigate the trapping of spin waves in so-called spin-wave cavities, made by two gaps cut into the waveguide with a small separation.

4.2 'Fourier mode' Brillouin light scattering spectroscopy: characterization of spatial distributions of the spin-wave intensity and localization of modes

The spin dynamics in patterned magnetic structures is a very important contemporary problem, motivated, apart from basic science aspects, largely by applications in the field of data storage and sensors, where the speed of operation now reaches into the GHz regime. For this frequency regime BLS spectroscopy and time-resolved MOKE techniques are two important characterization techniques.

Let us first understand the spin-wave eigenmode properties in such small elements. The problem is nontrivial, as in many cases both dipole–dipole and exchange interactions must be taken into account simultaneously (see Section 2.1). An additional difficulty comes from the fact that many of the small magnetic elements have a inhomogeneous distribution of the internal field and the saturation magnetization, in particular, if they have a nonelliptical shape.

The complexity of spin waves inside such small magnetic elements results from several physical effects:

- Spin-wave quantization due to spatial confinement, such as in longitudinally magnetic stripes (Jorzick *et al*., 1999; Mathieu *et al*., 1998; Roussigné, Chérif, Dugautier and Moch, 2001; Wang *et al*., 2002) and in ellipsoidal magnetic elements, where the internal magnetic field is homogeneous (Mathieu *et al*., 1997; Hillebrands *et al*., 1997).
- Spin-wave quantization and localization to small regions inside the magnetic object. The inhomogeneous internal magnetic field may form so-called spin-wave wells, which may provide such a localization mechanism (Jorzick *et al*., 2002; Park *et al*., 2002; Bayer *et al*., 2004; Bayer, Demokritov, Hillebrands and Slavin, 2003; Bayer *et al*., 2005).

In Section 3.1 we have derived the fundamental properties of BLS spectroscopy. There it was stated that in the light scattering process the in-plane component of the wave vector is conserved if the film is infinitely extended. The latter is not the case anymore for finite magnetic objects. To understand the consequences we discuss Figure 15.

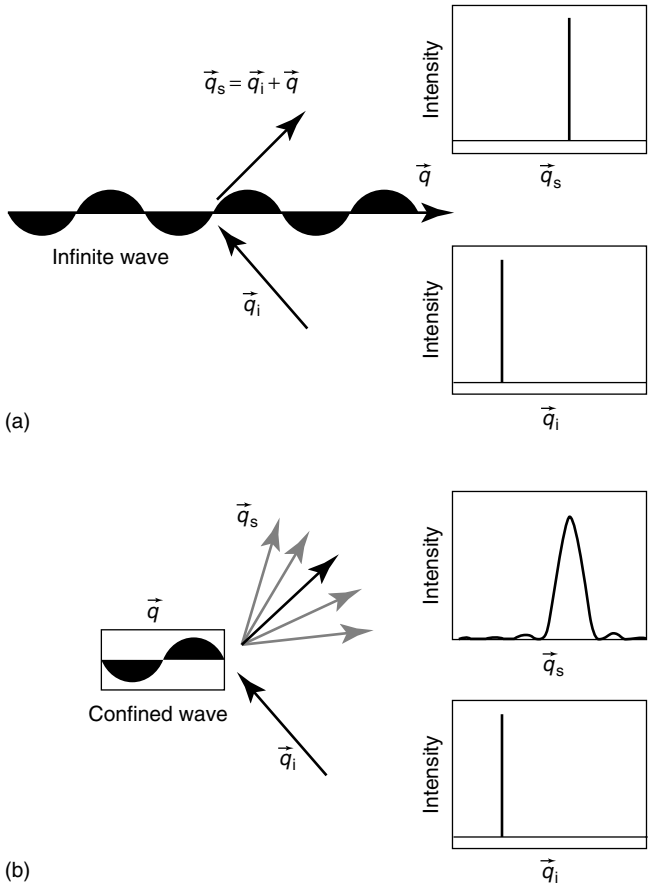

Figure 15. Schematic description of the light scattering process for (a) an infinite scattering volume (plane wave) and (b) a confined scattering volume. q_I and q_S indicate the wave vector of the incoming and scattered light, respectively.

The BLS process in an unconfined medium is illustrated in Figure 15(a): Monoenergetic photons with a frequency ω_I and wave vector $\vec{q}_I$ interact with the elementary quanta of the spin waves, which are the magnons, described by ω and $\vec{q}$. Because of the conservation laws resulting from the time and translational invariance of the system, the scattered photon has an increase or decrease in energy (ω_S and momentum $\vec{q}_S$, as described in Section 3.1). For a laterally confined structure, the in-plane translational invariance is broken. Therefore, there is a given uncertainty in the scattered wave vector $\vec{q}_S$, as is shown in Figure 15(b), where the value of the uncertainty is determined by the lateral size of the element. The intensity of the scattered light as a function of the dynamic magnetization, $m(y)$ [3] of the spin-wave mode confined to the stripe is according to Jorzick *et al.* (1999) and Mathieu *et al.* (1998) proporational to

$$I(q) \sim \left| \int_{-w/2}^{w/2} \vec{m}(y) \exp(-\mathrm{i}qy)\mathrm{d}y \right|^2 \qquad (16)$$

where w is the stripe width, q is the wave vector, and the integration is performed along the stripe width. Thus, the light scattering intensity is proportional to the squared Fourier transform of the dynamic magnetization, $|\vec{m}(y)|^2$. As the integration is performed over the interval $[-w/2, w/2]$ and the dynamic magnetization is essentially a sine function with a wave vector q, the maximum in scattering intensity will be at q and the broadening will be determined by the stripe width w. In the more complicated case of a rectangular element discussed in Section 4.2.2, a two-dimensional Fourier transform is needed.

4.2.1 Modes in longitudinal magnetized stripes

In order to understand the 'Fourier microscope' BLS technique, let us first discuss the modes in a longitudinally magnetized stripe, where the modes propagate in a direction perpendicular to the stripe axis. Since in this geometry the magnetization is parallel to the stripe axis, the magnetic field is homogeneous and equal to the applied external field (neglecting areas close to the stripe ends). These stripes are made from permalloy ($Ni_{81}Fe_{19}$) films of typically 20–40 nm thickness with a typical width in the range of 1–2 µm. Permalloy has the advantage that magnetic anisotropies are small and can be neglected. The geometry studied here supports surface waves (MSSM or Damon–Eshbach modes), which propagate in the film plane perpendicular to the stripes. When the spin wave reaches a lateral boundary of the stripe, it will be reflected and it forms a standing (confined) wave as already discussed in Section 2.2 and shown in Figure 4.

The standing wave patterns will result in quantized spin-wave frequencies. Figure 16 shows the measured results.

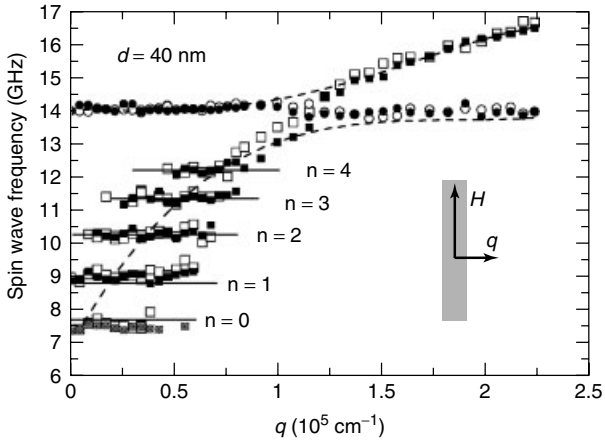

Figure 16. Obtained spin-wave dispersion curve for permalloy stripes with a thickness of 40 nm, a stripe width of $w = 1.8\,\mu m$ and a separation between the stripes of 0.7 µm (open symbols) and 2.2 µm (solid symbols). The external magnetic field along the stripe axis was 500 Oe, being perpendicular to the $\vec{q}$ vector as sketched in the Inset. The solid horizontal lines indicate the results of calculations using effective pinning (Demokritov, 2003). The dashed lines, showing the hybridization between the dispersion of the magnetostatic surface mode (MSSM) and the first perpendicular standing spin-wave mode (PSSW), were calculated numerically for a continuous film of 40 nm thickness. (Reproduced from J. Jorzick *et al.*, 1999, with permission from American Physical Society. © 1999.)

For small wave vectors, the spin-wave dispersion splits, as expected, into several modes, which are laterally standing modes due to the confinement. The mode order is characterized by the number of nodes along the propagation direction. Each mode does not show any dispersion and is observed over a finite but well-defined wave vector range. The separation between the modes decreases with increasing wave vector (increasing frequency) and, for higher order modes, this separation becomes indistinguishable. At 14 GHz, the dispersionless, perpendicular standing spin wave, determined by the exchange interaction and traveling perpendicular to the film, is observed. It intersects the regime of the MSSM modes.

We now discuss the two main properties, namely, the lack of dispersion and the finite wave vector range of observation, in more detail. The discrete nature of the mode spectrum has been already discussed in Section 2.2, so only the results are discussed here. It is important to note that, owing to the stray fields generated by the dynamic excitations outside of the stripe, an additional pinning mechanism is present, since the stray fields interact with the dynamic magnetization. This is discussed in detail in Guslienko, Demokritov, Hillebrands and Slavin (2002). As a result, the quantized values for the parallel wave vector, $q_{\parallel,n}$ are given by $q_{\parallel,n} = n(\pi/w_{\mathrm{eff},n})$, where $w_{\mathrm{eff},n} > w$ is an effective stripe width larger than the real stripe width. This is shown in Figure 17.

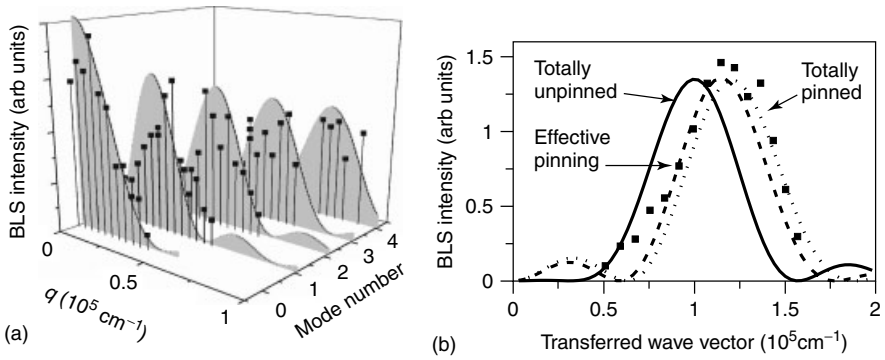

Figure 17. (a) Measured relative Brillouin light scattering intensities of the in-plane quantized spin-wave modes as a function of the wave vector $q_\parallel$ and the mode number n (black squares) compared to calculations as discussed in the text (solid lines). (b) Experimental data for the quantized $n = 3$ mode compared to calculations using three different boundary conditions. (Reproduced from S.O. Demokritov *et al.*, 2003, with permission from IOP Publishing Ltd. © 2003.)

Figure 17(a) shows the detected BLS intensities as a function of the transfer red wave vector $q_\parallel$. The mode intensities are normalized to the perpendicular standing spin-wave mode. The black squares correspond to the experimentally measured intensities, while the gray curves represent calculations based on equation (16).

Figure 17(b) shows the measured and calculated profiles for different boundary conditions. It is evident that the boundary condition determines the highest intensity of the respective mode in the Fourier space, that is, it determines value of the effective stripe width $w_{\mathrm{eff},n}$.

Measurements of intensities as a function of the wave vector, as displayed in Figure 17, provide Fourier space information. The larger the extent of the scattering regime in real space, the smaller the distribution in Fourier space, as measured with BLS. This can be used to estimate the spatial extent of such localized spin-wave modes. However, it should be noted that the BLS spectroscopy is a measurement of intensities not of amplitudes, and thus phase information is lost in this experiment. Consequently information about the lateral extent of modes can be obtained, but not the exact position of the mode amplitudes.

4.2.2 *Characterization of the spatial distribution of the spin-wave intensity and localization of modes in a rectangular element*

In the last section we have learned that information on the spatial distribution of spin waves can be obtained from the wave vector dependence of the BLS cross section of the quantized modes. Now we discuss an application where information on the lateral extent of spin-wave modes is very useful. We examine spin waves in a rectangular structure, as shown in Figure 18 (Inset).

Figure 18 displays the BLS intensity for a given mode as a function of the transferred wave vector $q_\parallel$ and perpendicular to the applied field. This system is a $Fe_{19}Ni_{81}$ rectangular of dimensions $1 \times 1.75\,\mu m^2$. For a transferred wave vector parallel to the applied magnetic field ($q_\parallel$ in Figure 18) a nearly q-independent BLS intensity is observed indicating a strong localization of the mode in real space. Investigations have shown that owing to the strongly varying internal field an additional localization mechanism operates here, which localizes the mode to regions near the two boundaries (Jorzick *et al.*, 2002; Bayer, Demokritov, Hillebrands and Slavin, 2003). Contrarily, for a transferred wave vector perpendicular to the applied field ($q_\perp$ in Figure 18) the peak in intensity shows that the mode is quantized over a much wider spatial length, consistent with the lateral dimensions of the rectangle. These experiments show very clearly that BLS microscopy in the 'Fourier microscope' mode is very useful to characterize spatial extensions of dynamic modes in such structures.

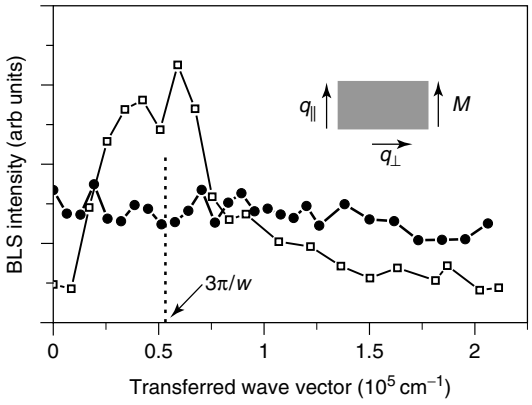

Figure 18. Brillouin light scattering study of a rectangular $Fe_{19}Ni_{81}$ element with dimensions $1 \times 1.75\,\mu m^2$. The intensity of the third localized mode as a function of the transferred in-plane wave vector parallel $q_\parallel$ (circles) and perpendicular $q_\perp$ (Squres) to the applied magnetic field. Inset: geometry of the element. (Reprinted from J. Jorzick, 2001, with permission from American Institute of Physics. © 2001.)

4.3 Spin-wave modes in a square with Landau flux-closure domain structure

In this section and discuss the spin waves inside a 16-nm-thick permalloy ($Fe_{19}Ni_{81}$) square with a lateral width $L = 4\,\mu m$ containing a Landau flux-closure domain structure. The structure was produced by e-beam evaporation on a Si-substrate and capped with a 2-nm-thick Al overlayer for corrosion protection.

The domain walls are aligned along the diagonals of the square and the magnetization directions in the four triangular domains are aligned such that the flux is closed in the square. This is indicated in Figure 19(a).

In a time-resolved Kerr microscopy experiment made at the university of Regensburg (Perzlmaier *et al*., 2005), modes were excited using a one-turn microcoil with the sample in the center. A short current pulse was applied to the microcoil generating a magnetic field pulse of duration 300 ps. The time response of the sample was measured stroboscopically with 10-ps time steps. The time response was measured stroboscopically for each point of a two-dimensional mesh across the sample in order to yield spatial information also. The spatial resolution was 300 nm. From this data mode patterns have been reconstructed by Fourier-transforming the temporal response for each point on the sample. The upper parts of the panels in Figure 19 were obtained by plotting the Fourier component values for the respective mode frequencies. As can be seen, at 0.8 GHz, intensity is observed at the positions of the domain walls indicating a domain wall resonance. With increasing frequency several spin-wave modes (indicated by the index n in Figure 19) are observed.

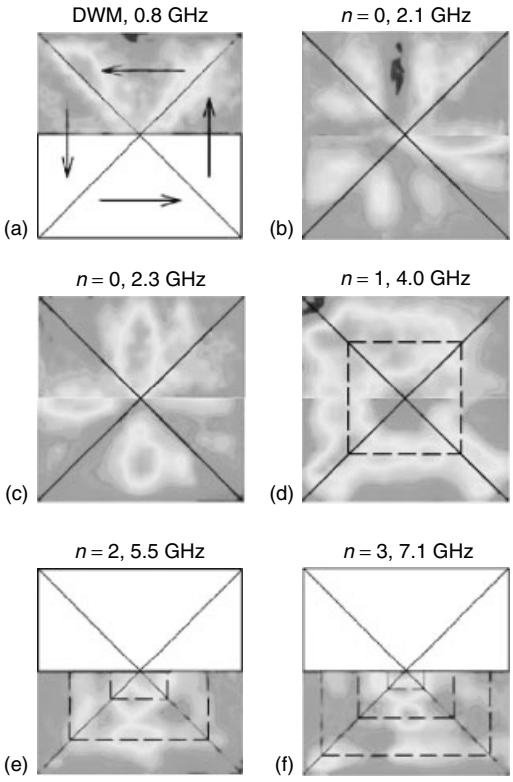

Figure 19. Spatial distribution of the amplitude of the dynamic magnetization corresponding to the eigenmodes in a $4 \times 4\,\mu m^2$ permalloy ($Fe_{19}Ni_{81}$) square. The upper and lower parts of each panel are measured using time-resolved scanning Kerr microscope and microfocus Brillouin light scattering spectroscopy, respectively. Diagonal solid lines indicate the domain walls, whereas the dashed lines indicate the mode maxima for a quantization in a transversal direction. The corresponding transversal quantization numbers n and the measurement frequencies are indicated near the distribution. Arrows in (a) indicate the direction of the static magnetization. DWM stands for domain wall mode. (Reproduced from K. Perzlmaier *et al*., 2005, with permission from American Physical Society. © 2005.)

Microfocus BLS (described in Section 3.1.2) is equally well suited to measure these dynamic modes. The lower halves of the panels in Figure 19 show the results. Here, a Fourier transform of data is not necessary, as the BLS process yields the spectral components directly. Again, using a scanning probe approach, the spectra are measured along a two-dimensional mesh of mesh size 200 nm. For frequencies, where both methods yield results, the agreement is remarkably pronounced. Modes with higher frequencies are better accessed by microfocus BLS spectroscopy, where time-resolved MOKE microscopy reaches its limit because of constraints in the pulsed field excitation. On the other hand, BLS does not access the modes with low frequencies as they are overlapped by elastically scattered light.

Figure 19 shows a clear quantization of the modes in each of the four triangular domains. Whereas a quantization

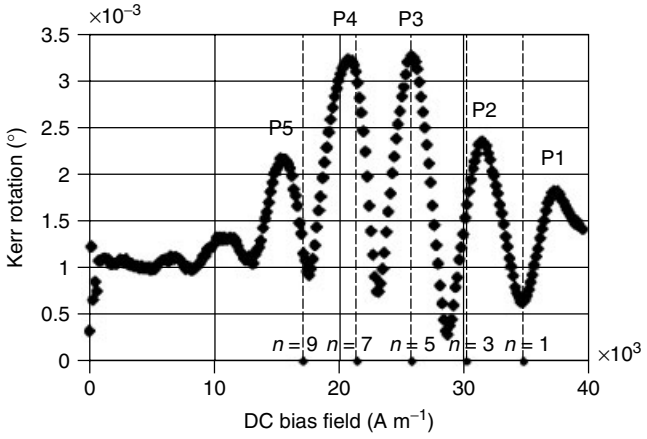

Figure 20. Magnetization response at the center of the permalloy element as a function of the dc bias field. The driving field frequency is 7.04 GHz. Broken lines mark the peak positions for the nth mode calculated by the magnetostatic surface mode model. (Reprinted with permission from S. Tamaru *et al*., 2002, © 2002, American Institute of Physics.)

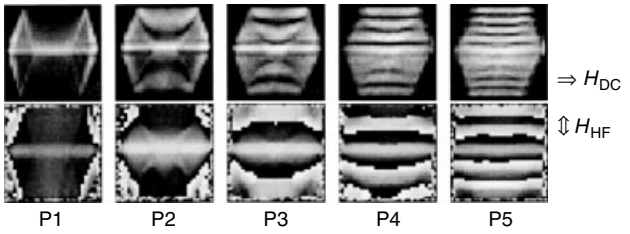

Figure 21. Spatial distribution of magnetization response at each peak. The upper and lower rows are the amplitude and phase distributions, respectively. The amplitude is normalized to the maximum value to give the largest contrast. (Reprinted with permission from S. Tamaru *et al*., 2002, © 2002, American Institute of Physics.)

along the direction of the magnetization can be observed, but not unambiguously assigned to a specific mode order; quantization in the perpendicular direction is very clearly observed. In Figure 19(b) and (c) the mode patterns show one maximum in the transverse direction, in Figure 19(d–f) the higher order modes are clearly observed.

4.4 Experiments with optical ferromagnetic resonance techniques

As shown in Section 3.3, time-resolved Kerr effect magnetometry, synchronized to a driving cw microwave field, can be used to measure spin-wave mode profiles (see Figure 12). Figure 20 shows the measured magnetization response of a 100-nm-thick permalloy film sputter deposited on a glass substrate and patterned into a $50 \times 50\,\mu m^2$ square. On top of the structure a planar transmission line of 750-nm-thick Cu with a center conductor width of 3 µm and an impedance of 50 Ω is mounted. The sample has been first saturated, and then the Kerr response has been measured as a function of the field, as shown in Figure 20. The sample is driven at 7.04 GHz. Five peaks are clearly seen. Figure 21 shows the obtained spatial distribution of the magnetization response at each peak. Standing wave patterns can easily be identified.

4.5 Propagating spin waves observed by optical techniques

The BLS spectroscopy technique is most often the method of choice to study propagating spin-wave modes. This has been demonstrated in Section 4.1, where spin-wave packets tunneling through a forbidden region have been discussed. We conclude this chapter by discussing complementary experiments using time-resolved MOKE microscopy.

Indications for the generation of spin waves have been found in a number of experiments (Silva, Kabos and Pufall,

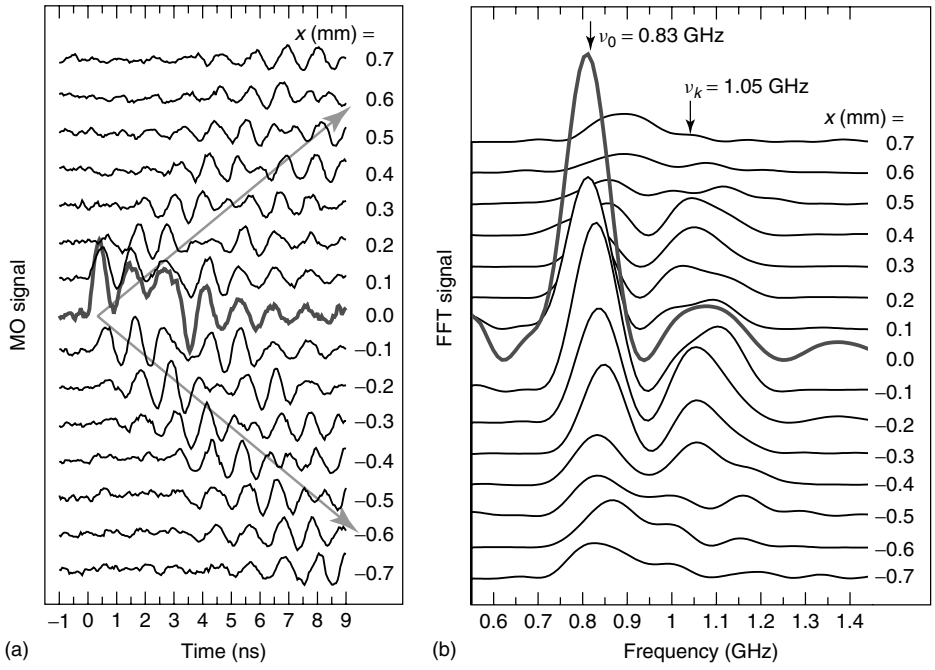

Figure 22. Response of the magneto-optic signal in time (a) and via fast Fourier transformation in frequency space (b). The distance of the investigated area from the transmission line, x, is indicated in both figures. The arrows in (a) correspond to the group velocity $6.6\,cm\,\mu s^{-1}$ as determined from change of the positions of maximum magnetization deviation after a half-precession period. The frequencies of the uniform and the propagating spin-wave mode are $\nu_0 = 0.83$ GHz and $\nu_k = 1.05$ GHz, respectively. (Reproduced from J. Fassbender *et al*., 2003, with permission from Springer-Verlag. © 2003.)

2002; Hiebert, Ballentine and Freeman, 2002; Gerrits, Silva, Nibarger and Rasing, 2004), where a reduction of the absolute value of the magnetization vector was observed. There, the excitation of high wave vector spin waves was confirmed. The direct observation of propagating spin waves using this technique has been reported by Fassbender (2003). Using a pulsed excitation of an infinitely extended film mounted on a strip line, the propagation of well-confined wave packets away from the strip line into the film was observed. Figure 22 shows some obtained results. The magneto-optic response for different distances from the transmission line as a function of time is shown in Figure 22(a), and the corresponding Fourier transforms are shown in Figure 22(b). At $x = 0$, two peaks in the frequency spectrum are observed, identified as a uniform precession mode and a propagating spin-wave mode with frequencies $\nu_0 = 0.83\,\mathrm{GHz}$ and $\nu_k = 1.05\,\mathrm{GHz}$, respectively. For the uniform precession mode the strong decrease in mode intensity in the direction perpendicular to the strip line indicates the localization of this mode to the transmission line. The intensity of the propagating wave, however, is nearly constant over a large range. For larger distances the mode is not observed for reasons of finite group velocity and damping. The propagating spin-wave mode carries energy away and reduces the energy to be dissipated in the transmission line area.

Investigations like these allow the measurement of the phase velocity v_{ph}, the wavelength λ, and the wave vector q, as demonstrated in Figure 23. Here, the magneto-optic signal, averaged along a line parallel to the transmission line, is shown as a function of the distance x from the transmission line for different delay times. The solid arrows indicate the temporal evolution of constant phases. Their slopes allow for the determination of the phase velocity, which is $v_{\mathrm{ph}} = 34 \pm 7\,\mathrm{cm\,\mu s^{-1}}$. The dashed arrow indicates the center of the spin-wave packets, which move at the smaller group velocity v_{g}. From these data a wavelength of $\lambda = 0.03\,\mathrm{cm}$ and a wave vector of $q = 210\,\mathrm{cm^{-1}}$ of the propagating spin wave are obtained. The obtained data indicates that the observed mode is an MSSM (see equation (7)).

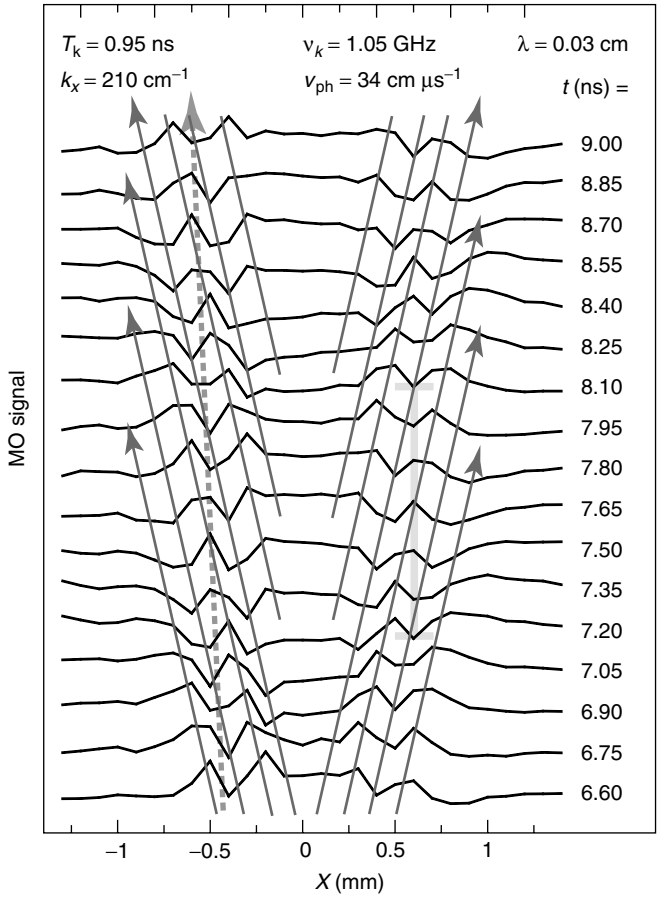

Figure 23. Data representation for determining the phase velocity v_{ph}, the wavelength λ, and the wave vector k_x. (Reproduced from J. Fassbender *et al*., 2003, with permission from Springer-Verlag. © 2003.)

5 CONCLUSIONS

This Chapter provides an introduction into the state of the art of optic techniques for investigating magnetization dynamics. Techniques on both the frequency scale and the timescale – BLS spectroscopy and the Kerr effect – have been presented. A few selected experiments have been discussed to demonstrate the specific strengths for each method.

The field of magnetization dynamics is currently advancing very fast. Progress is substantially driven by new experimental techniques. Further advancements in optical techniques will certainly help to push this very interesting field continuously forward.

NOTES

[1] See, for example, **Dissipative Magnetization Dynamics Close to the Adiabatic Regime, Volume 1**, **Nonlinear Magnetization Dynamics in Nanomagnets, Volume 2**, **Guided Spin Waves, Volume 2**, and **Magnetization Dynamics: Thermal-driven Noise in Magnetoresistive Sensors, Volume 2**.

[2] The $p_{\mathrm{in}} - p_{\mathrm{out}}$ SHG configuration also depends on the polar magnetization component (Bennemann, 1998), but this contribution is usually weak.

[3] Recall that the dynamic magnetization $\vec{m} = \vec{M} - \vec{M}_s$ is the difference between the total and the saturation magnetization.

ACKNOWLEDGMENTS

The authors are very thankful to all those who have contributed to the progress in optical techniques, in particular, to the members of the group in Kaiserslautern. They would like to thank specifically Sergej Demokritov, Jürgen Fassbender, and Alexander Serga.

REFERENCES

Bayer, C., Demokritov, S., Hillebrands, B. and Slavin, A. (2003). Spin wave wells with multiple states created in small magnetic elements. *Physical Review Letters*, **82**, 607.

Bayer, C., Jorzick, J., Demokritov, S.O., *et al*. (2006). Spin-wave excitations in finite rectangular elements. In *Spin Waves in Confined Magnetic Structures III*, Hillebrands, B. and Thiaville, A. (Eds.), Springer-Verlag: Berlin Heidelberg.

Bayer, C., Jorzick, J., Hillebrands, B., *et al*. (2005). Spin-wave excitations in finite rectangular elements of $Ni_{80}Fe_{20}$. *Physical Review B*, **72**, 064427.

Bayer, C., Park, J.P., Wang, H., *et al*. (2004). Spin waves in an inhomogeneously magnetized stripe. *Physical Review B*, **69**, 134401.

Bennemann, K.H. (Ed.) (1998). *Non-Linear Optics in Metal*, Clarendon Press.

Choi, B.C. and Freeman, M.R. (2005). Nonequilibrium spin dynamics in laterally defined magnetic structures. In *Ultrathin Magnetic Structures III: Fundamentals of Nanomagnetism*, Bland, J.A.C. and Heinrich, B. (Eds.), Springer-Verlag: New York, Berlin, Heidelberg.

Cochran, J.F., Heinrich, B. and Arrott, A.S. (1986). Ferromagnetic resonance in a system composed of a ferromagnetic substrate and an exchange-coupled thin ferromagnetic overlayer. *Physical Review B*, **34**, 7788.

Damon, R.W. and Eshbach, J.R. (1961). Magnetostatic modes of a ferromagnet slab. *Journal of Physics and Chemistry of Solids*, **19**, 308.

Demokritov, S.O. (2003). Dynamic eigen-modes in magnetic stripes and dots. *Journal of Physics: Condensed Matter*, **15**, S2575.

Demokritov, S.O. and Hillebrands, B. (2002). Spin waves in laterally confined structures. In *Spin Dynamics in Confined Magnetic Structures I*, *Volume 83 of Topics in Applied Physics*, Hillebrands, B. and Ounadjela, K. (Eds.), Springer-Verlag: Berlin, Heidelberg, New York, Tokyo, p. 65.

Demokritov, S.O., Hillebrands, B. and Slavin, A.N. (2001). Brillouin light scattering studies of confined spin waves: linear and nonlinear confinement. *Physics Reports*, **348**, 441.

Demokritov, S.O., Serga, A.A., André, A., *et al*. (2004). Tunneling of dipolar spin waves through a region of inhomogeneous magnetic field. *Physical Review Letters*, **93**, 047201.

Fassbender, J. (2003). Magnetization dynamics investigated by time-resolved Kerr effect magnetometry. In *Spin Dynamics in Confined Magnetic Structures II*, *Volume 87 of Topics in Applied Physics*, Hillebrands, B. and Ounadjela, K. (Eds.), Springer-Verlag: Berlin, Heidelberg, New York, Tokyo, p. 59.

Freeman, M.R. (2005). Magnetization dynamics using time-resolved magneto-optic microscopy. In *Modern Techniques for Characterizing Magnetic Materials*, Zhu, Y. (Ed.), Kluwer Academic Publishers.

Freeman, M.R. and Hiebert, W.K. (2002). Stroboscopic microscopy of magnetic dynamics. In *Spin Dynamics in Confined Magnetic Structures I*, *Volume 83 of Topics in Applied Physics*, Hillebrands, B. and Ounadjela, K. (Eds.), Springer-Verlag: Berlin, Heidelberg, New York, Tokyo, p. 93.

Gerrits, T., van den Berg, H.A.M., Hohlfeld, J., *et al*. (2001). Precession dynamics in NiFe thin films, induced by short magnetic in-plane field pulses generated by photoconductive switch. *Journal of the Magnetics Society of Japan*, **25**, 192.

Gerrits, T., van den Berg, H.A.M., Hohlfeld, J., *et al*. (2002a). Ultrafast precessional magnetization reversal by picosecond magnetic field pulse shaping. *Nature*, **418**, 509.

Gerrits, T., van den Berg, H.A.M., Hohlfeld, J., *et al*. (2002b). Picosecond precessional magnetization reversal by magnetic field pulse shaping. *IEEE Transactions on Magnetics*, **38**, 2484.

Gerrits, T., van den Berg, H.A.M., Hohlfeld, J., *et al*. (2002c). Picosecond control of coherent magnetisation dynamics in permalloy thin films by picosecond magnetic field pulse shaping. *Journal of Magnetism and Magnetic Materials*, **240**, 283.

Gerrits, T., Silva, T.J., Nibarger, J.P. and Rasing, T. (2004). Large-angle magnetization dynamics investigated by vector-resolved magnetization-induced optical second-harmonic generation. *Journal of Applied Physics*, **96**, 6023.

Gurevich, A.G. and Melkov, G.A. (1996). *Magnetization Oscillations and Waves*, CRC Press: Boca Raton, New York, London, Tokyo.

Guslienko, K.Y., Demokritov, S.O., Hillebrands, B. and Slavin, A.N. (2002). Effective dipolar boundary conditions for dynamic magnetization in thin magnetic stripes. *Physical Review B*, **66**, 132402.

Guslienko, K.Y. and Slavin, A.N. (2005). Boundary conditions for magnetization in magnetic nanoelements. *Physical Review B*, **72**, 014463.

Hansteen, F., Kimel, A., Kirilyuk, A. and Rasing, T. (2005). Femtosecond photomagnetic switching of spins in ferrimagnetic garnet films. *Physical Review Letters*, **95**, 047402.

Heinrich, B. and Cochran, J.F. (1993). Ultrathin metallic magnetic films. Magnetic anisotropies and exchange interactions. *Advances in Physics*, **42**, 523–639.

Heinrich, B., Purcell, S.T., Dutcher, J.R., *et al*. (1988). Structural and magnetic properties of ultrathin Ni/Fe bilayers grown epitaxially on Ag(001). *Physical Review B*, **38**, 12879.

Hicken, R.J., Barman, A., Kruglyak, V.V. and Ladak, S. (2003). Optical ferromagnetic resonance studies of thin film magnetic structures. *Journal of Physics D: Applied Physics*, **36**, 2183.

Hiebert, W.K., Ballentine, G.E. and Freeman, M.R. (2002). Comparison of experimental and numerical micromagnetic dynamics in coherent precessional switching and modal oscillations. *Physical Review B*, **65**, 140404.

Hillebrands, B. (1990). Spin-wave calculations for multilayered structures. *Physical Review B*, **41**, 530.

Hillebrands, B. (1999). Progress in multipass tandem Fabry-Pérot interferometry: I. A fully automated, easy to use, self-aligning spectrometer with increased stability and flexibility. *The Review of Scientific Instruments*, **70**, 1589.

Hillebrands, B. (2000). Brillouin light scattering from layered magnetic structures. In *Light scattering in Solids VII*, *Volume 75 of Topics in Applied Physics*, Cardona, M. and Güntherodt, G. (Eds.), Springer-Verlag: Berlin, Heidelberg, p. 174.

Hillebrands, B. (2003). Spin dynamics in confined magnetic structures. In *Spin Dynamics in Confined Magnetic Structures I and II*, Hillebrands, B. and Ounadjela, K. (Eds.), Springer-Verlag: Berlin, Heidelberg, New York.

Hillebrands, B. and Güntherodt, G. (1994). Brillouin light scattering in magnetic superlattices. In *Ultrathin Magnetic Structures II*, surHeinrich, B. and Bland, J.A.C. (Eds.), Springer-Verlag: Heidelberg, Berlin, London, New York, Tokyo.

Hillebrands, B., Mathieu, C., Hartmann, C., *et al*. (1997). Static and dynamic properties of patterned magnetic permalloy films. *Journal of Magnetism and Magnetic Materials*, **175**, 10.

Hillebrands, B. and Thiaville, A. (2006). *Spin Dynamics in Confined Magnetic Structures III*, Springer-Verlag: Berlin, Heidelberg, New York.

Hubert, A. and Schäfer, R. (1998). *Magnetic Domains: The Analysis of Magnetic Microstructures*, Springer-Verlag: Berlin.

Jorzick, J., Demokritov, S., Hillebrands, B., *et al*. (2002). Spin wave wells in nonellipsoidal micrometer size magnetic elements. *Physical Review Letters*, **88**, 047204.

Jorzick, J., Demokritov, S.O., Mathieu, C., *et al*. (1999). Brillouin light scattering from quantized spin waves in micron-size magnetic wires. *Physical Review B*, **60**, 15194.

Jorzick, J., Kramer, C., Demokritov, S., *et al*. (2001). Spin wave quantization in laterally confined magnetic structures. *Journal of Applied Physics*, **89**, 7091.

JRS Scientific Instruments, Fabrik am Weiher, 8909, Zwillikon Switzerland, http://www.jrs-si.ch.

Kabos, P., Kos, A.B. and Silva, T.J. (2000). Vectorial second-harmonic magneto-optic Kerr effect measurements. *Journal of Applied Physics*, **87**, 5980.

Kalinikos, B.A. and Slavin, A.N. (1986). Theory of dipole-exchange spin wave spectrum for ferromagnetic films with mixed exchange boundary conditions. *Journal of Physics C*, **19**, 7013.

van Kampen, M., Jozsa, C., Kohlhepp, J.T., *et al*. (2002). All-optical probe of coherent spin waves. *Physical Review Letters*, **88**, 227201.

Krams, P., Lauks, F., Stamps, R.L., *et al*. (1992). Magnetic anisotropies of ultrathin Co(001) films on Cu(001). *Physical Review Letters*, **69**, 3674.

MacDonald, J.R. (1951). Ferromagnetic resonance and the internal field in ferromagnetic materials. *Proceedings of the Physical Society, Section A*, **64**, 968.

Mathieu, C., Hartmann, C., Bauer, M., *et al*. (1997). Anisotropic magnetic coupling of permalloy micron dots forming a square lattice. *Applied Physics Letters* , **70**, 2912.

Mathieu, C., Jorzick, J., Frank, A., *et al*. (1998). Lateral quantization of spin waves in micron size magnetic wires. *Physical Review Letters*, **81**, 3968.

Mock, R., Hillebrands, B. and Sandercock, J.R. (1987). Construction and performance of a Brillouin scattering set-up using a triple-pass tandem Fabry-Pérot interferometer. *Journal of Physics E*, **20**, 656.

Neudert, A., McCord, J., Chumakov, D., *et al*. (2005). Small-amplitude magnetization dynamics in permalloy elements investigated by time-resolved wide-field Kerr microscopy. *Physical Review B*, **71**, 134405.

Park, J.P., Eames, P., Engebretson, D.M., *et al*. (2002). Spatially resolved dynamics of localized spin-wave modes in ferromagnetic wires. *Physical Review Letters*, **89**, 277201.

Perzlmaier, K., Buess, M., Back, C.H., *et al*. (2005). Spin-wave eigenmodes of permalloy squares with a closure domain structure. *Physical Review Letters*, **94**, 057202.

Petek, B., Trouilloud, P.L. and Argyle, B.E. (1990). Time-resolved domain dynamics in thin-film heads. *IEEE Transactions on Magnetics*, **26**, 1328.

Qiu, Z. and Bader, S. (1999). Surface magneto-optical Kerr effect (SMOKE). *Journal of Magnetism and Magnetic Materials*, **200**, 664.

Rado, G.T. and Weertman, J.R. (1959). Spin-wave resonance in a ferromagnetic metal. *Journal of Physics and Chemistry of Solids*, **11**, 315.

Rasing, T., van den Berg, H.A.M., Gerrits, T. and Hohlfeld, J. (2003). Ultrafast magnetization and switching dynamics. In *Spin Dynamics in Confined Magnetic Structures II*, *Volume 87 of Topics in Applied Physics*, Hillebrands, B. and Ounadjela, K. (Eds.), Springer-Verlag: Berlin, Heidelberg, New York, Tokyo, p. 213.

Roussigné, Y., Chérif, S.M., Dugautier, C. and Moch, P. (2001). Experimental and theoretical study of quantized spin-wave modes in micrometer-size permalloy wires. *Physical Review B*, **63**, 134429.

Sandercock, J.R. (1971). The design and use of a stabilised multipassed interferometer of high contrast ratio. In *Proceedings of the 2nd International Conference on Light Scattering in Solids*, Balkanski, M. (Ed.), Flammarion: Paris, p. 9.

Sandercock, J.R. (1982). Trends in Brillouin light scattering: studies of opaque materials, supported films and central modes. In *Light Scattering in Solids III*, *Volume 51 of Topics in Applied Physics*, Cardona, M. and Güntherodt, G. (Eds.), Springer-Verlag: Berlin, Heidelberg, New York, Tokyo, p. 173.

Silva, T.J., Kabos, P. and Pufall, M.R. (2002). Detection of coherent and incoherent spin dynamics during the magnetic switching process using vector-resolved nonlinear magneto-optics. *Applied Physics Letters*, **81**, 2205.

Slavin, A.N., Demokritov, S.O. and Hillebrands, B. (2002). Nonlinear spin waves in one- and two-dimensional magnetic waveguides. In *Spin Dynamics in Confined Magnetic Structures I*, *Volume 83 of Topics in Applied Physics*, Hillebrands, B. and Ounadjela, K. (Eds.), Springer-Verlag: Berlin, Heidelberg, New York, Tokyo, p. 35.

Stamps, R.L. and Hillebrands, B. (1991). Dipolar interactions and the magnetic behavior of two-dimensional ferromagnetic systems. *Physical Review B*, **44**, 12417.

Tamaru, S., Bain, J.A., van de Veerdonk, R.J.M., *et al*. (2002). Imaging of quantized magnetostatic modes using spatially resolved ferromagnetic resonance. *Journal of Applied Physics*, **91**, 8034.

Tamaru, S., Bain, J.A., van de Veerdonk, R.J.M., *et al*. (2004). Measurement of magnetostatic mode excitation and relaxation in permalloy films using scanning Kerr imaging. *Physical Review B*, **70**, 104416.

Višňovský, S., Nývlt, M., Prosser, V., *et al*. (1995). Polar magneto-optics in simple ultrathin-magnetic-film structures. *Physical Review B*, **52**, 1090.

Wang, Z.K., Kuok, M.H., Ng, S.C., *et al*. (2002). Spin-wave quantization in ferromagnetic nickel nanowires. *Physical Review Letters*, **89**, 027201.

Weber, M.C., Nembach, H., Blomeier, S., *et al*. (2005). All-optical probe of magnetization dynamics in exchange biased bilayers on the picosecond timescale. *European Physical Journal B*, **45**, 243.

Zhu, X., Liu, Z., Metlushko, V., *et al*. (2005). Broadband spin dynamics of the magnetic vortex state: effect of the pulsed field direction. *Physical Review B*, **71**, 180408(R).

Time-resolved Kerr-effect and Spin Dynamics in Itinerant Ferromagnets

Bert Koopmans
Eindhoven University of Technology, Eindhoven, The Netherlands

1 INTRODUCTION

The time-resolved optical exploration of the ultimate limits of magnetization dynamics in itinerant ferromagnets (FMs) is widely recognized as an intriguing field of research (for reviews, see Zhang, Hübner and Bigot, 2002; Koopmans, 2003; Bennemann, 2004). Clearly, it has been driven by the quest for fundamental understanding of magnetization processes in the strongly nonequilibrium regime – a particularly nontrivial issue. How to understand the magnetism of materials, when by an almost instantaneous perturbation of the material different subsystems, such as electrons and lattice, are no longer in thermal equilibrium? What are the limiting timescales at which we can manipulate the magnetic order? And what are the relevant processes that we need to understand and maybe even can control?

Apart from this fundamental interest, there are two other obvious drivers that have led to an exciting, rapidly progressing field of research. First of all there is the availability since the 1990s of commercial and easy-to-handle systems for producing femtosecond laser pulses, and the development of ultrasensitive magneto-optical (MO) pump-probe schemes with unprecedented time resolution.

Secondly, there is the intimate relation of the field with the booming area of spintronics, and related therewith all applications that require ultrafast control of magnetic materials and devices. Exemplary is the extremely rapid progress in magnetic hard disk recording, where the need for subnanosecond control over media and heads has emerged. A similar driver is provided by the development of magnetic random access memory (MRAM), for which new magnetic switching schemes are being considered. More general, the fundamental exploration of ultrafast magnetization dynamics provides generic insight in elementary spin-scattering phenomena that are of profound interest for many novel spintronic devices.

Finally, technologies that combine the interaction of laser light with magnetic materials within the application itself, such as MO recording, have to be identified as an important stimulus for laser-based studies of fast magnetic processes. Of particular interest from this viewpoint are recent activities striving for laser-based heat-assisted magnetic recording.

In general, pump-probe schemes have been most successful in search for the ultimate timescales. In such a

Handbook of Magnetism and Advanced Magnetic Materials. Edited by Helmut Kronmüller and Stuart Parkin. Volume 3: *Novel Techniques for Characterizing and Preparing Samples*. ISBN: 978-0-470-02217-7.

stroboscopic scheme, a first, pulsed perturbation is being applied to the magnetic system under investigation after which a second probe pulse, arriving at a preset delay time, is being used to probe the magnetic state. By scanning the delay time, the full temporal evolution of the magnet state after its initial perturbation can be followed. It has to be emphasized, however, that in general the probe only provides a limited access to the multidimensional character of the strongly nonequilibrium magnetic state, which makes interpretation of such experiments an art itself.

It should be stressed that any perturbation that changes the magnetic ground state will do – although the physics being probed may (and will) be strongly depending on the type of excitation chosen. Also, probing the magnetization dynamics can be achieved by different means; the choice made again affecting the view on the magnetic system being obtained. Although a number of approaches will be explained throughout this chapter, our main focus will be on all-optical approaches, in which femtosecond laser pulses are used both as the perturbation and as the probe.

By now it is generally known that pulsed-laser excitation triggers a rich spectrum of spin dynamical processes. The field started with pioneering experiments by Beaurepaire, Merle, Daunois and Bigot (1996), who addressed the truly nonequlibrium regime of itinerant FMs for the first time. It was found that laser heating of ferromagnetic thin films gives rise to a loss of magnetic order within the first picosecond. This exciting result became soon confirmed by several groups. By now, a general consensus has been achieved on a characteristic 'demagnetization' timescale of a hundred to a few hundreds of femtoseconds.

Apart from the ultrafast loss of magnetic order, the experiments provided access to spin-dependent dynamics in the population of electronic states that could be interpreted as 'artifacts' when striving for resolving the genuine magnetization dynamics, but could be seen as a highly challenging spin-dependent phenomenon on itself as well.

Moreover, in many cases it turned out possible to trigger precessional dynamics by perturbing the magnetic anisotropy on a picosecond timescale by the laser heating. On the one hand, this offered an alternative to pulsed field-induced precessional experiments, on the other hand, it provided a complementary view on the dynamics of the magnetic anisotropy itself. In this respect, a particularly interesting research topic that emerged is the ultrafast manipulation of the interlayer exchange coupling between a FM and a neighboring antiferromagnetic (AF) layer.

Despite the interest in laser-induced loss of magnetic order, from technological point of view it would be of superior interest not only to quench, but also being able to increase or even fully create ferromagnetic order at a subpicosecond timescale. Also this has been recently achieved in pioneering experiments in FeRh thin films, by driving the metamagnetic AF to FM phase transition by pulsed heating.

Today, we have reached the end of the first (extremely successful) decade of laser-induced magnetization dynamics, where the field went through a continuous discovery of new phenomena and development of novel approaches. Theoretical understanding of the processes at a microscopic level is lagging somewhat behind. However, there is a growing awareness being witnessed that these issues should be considered among the major challenges of modern condensed-matter physics. It would be welcomed if this opinion would lead to a significant increase of theoretical efforts.

The scope of this chapter is as follows. In Section 2 we start with a general overview, and introduce basic concepts. In Section 3, experimental approaches, mostly concentrating on all-optical ones, are described in detail. Particular emphasis is on the subtle and nontrivial way the targeted physical parameters are being probed. Then, a number of sections reviewing experimental progress over the past decade can be found. After a brief review of the pioneering, early days (Section 4), sections on population dynamics (Section 5), light-induced orbital momentum transfer (Section 6), demagnetization dynamics (Section 7), anisotropy dynamics induced precession (Section 8), and growth of magnetic order by triggering phase transitions (Section 9) will follow. Finally, concluding remarks will be drawn in Section 10.

2 CLASSIFICATION AND BASICS

Within this section, first the dynamics of the average magnetization vector (orientational or precessional dynamics) and the thermodynamics of spin systems (dealing with the magnitude of the magnetization) are discussed separately. Then, after some considerations regarding conservation of angular momentum, different scattering mechanisms are briefly introduced: electron–electron scattering, electron–phonon scattering, and different types of spin-flip scattering.

2.1 Precessional dynamics

The most elementary spin dynamics process is that of the precession of a single spin in an applied magnetic field H. The field introduces a splitting between spin-up and spin-down states with an energy difference equal to $\gamma\mu_0 H$, where γ is the gyromagnetic ratio. As a consequence, the dynamics of any electron that is in a superposition of the two eigenstates corresponds to a precession of the spin expectation value around the field-axis at the Larmor frequency $\omega_L = \gamma\mu_0 H/\hbar$. The same frequency is found

for an ensemble of spins, or the magnetization $\vec{M}$ of a homogeneous magnetic material. Characteristic frequencies are in the gigahertz regime, as can be estimated from $\gamma/\hbar = 176\,\mathrm{ns}^{-1}\,\mathrm{T}^{-1}$.

Including dissipation will lead to a damped precessional motion, in which a gradual decay toward the lowest energy state is accompanied by the alignment of $\vec{M}$ with the applied magnetic field. Accounting for dissipation in a phenomenological way in the spirit of Gilbert, leads to the well-known Landau–Lifshitz–Gilbert (LLG) equation of motion (Miltat, Albuquerque and Thiaville, 2002)

$$\frac{\mathrm{d}\vec{M}}{\mathrm{d}t} = \gamma\mu_0\left(\vec{M}\times\vec{H}_{\mathrm{eff}}\right) + \frac{\alpha}{M}\left(\vec{M}\times\frac{\mathrm{d}\vec{M}}{\mathrm{d}t}\right) \qquad (1)$$

where we replaced the applied (external) field $\vec{H}$ by the effective field

$$\vec{H}_{\mathrm{eff}} = \vec{H} + \vec{H}_{\mathrm{anis}} = \vec{H} - \frac{1}{\mu_0 M}\vec{\nabla}E_{\mathrm{anis}}(\vec{M}) \qquad (2)$$

Herein, the anisotropy field ($\vec{H}_{\mathrm{anis}}$, related to the gradient of the anisotropy energy E_{anis}) may include contributions from dipolar fields by the system itself (resulting in the 'shape anisotropy'), crystalline anisotropy (mediated by spin-orbit interactions), and others. Note that this effective field depends on the orientation of the magnetization vector itself, and thereby becomes explicitly time-dependent even for a constant external field. Finally, equation (1) can be generalized to a nonhomogeneous magnetization distribution $\vec{M}(\vec{r}, t)$, in which the exchange interaction between noncollinear spins has to be included as well.

It should be noted that the process of energy dissipation is much more complicated than would have been expected from the appearance of a single damping parameter in equation (1). In fact, the value of α depends on almost all details of the (micromagnetic) system; the 'constant' being far more than a materials specific parameter. Exploration of magnetic damping is an active field of research (see e.g., Urban, Woltersdorf and Heinrich, 2001; Tserkovnyak, Brataas and Bauer, 2002; Woltersdorf, Buess and Back, 2005; Buess, Haug, Scheinfein and Back, 2005; Steiauf and Fähnle, 2005).

2.2 Thermodynamics–transfer of energy

After having treated the dynamics of the average magnetization vector, we consider the thermodynamic evolution of spin fluctuations. In general, for an ordinary ferromagnetic system, the thermal equilibrium value of the magnetization (M_{eq}) displays a continuous decrease as a function of increasing temperature. Above the Curie temperature and in the absence of a magnetic field, any long-range magnetic order vanishes. Without loss of generality, one can introduce a spin temperature T_{s}, from the one-to-one relation between M_{eq} and T (Figure 1a); that is, at a spin temperature T_{s} the magnetization equals $M_{\mathrm{eq}}(T_{\mathrm{s}})$ by definition.

Let us next consider a system with interacting lattice (phonons), electronic (excluding spin) and spin degrees of freedom. Within the so-called three-temperature (3T) model (Beaurepaire, Merle, Daunois and Bigot, 1996), each of the subsystems are assumed to be internally in thermal equilibrium, and described by their own temperature (T_{p}, T_{e}, and T_{s}, respectively) and heat capacity (C_{p}, C_{e}, and C_{s}), where in general the latter can be functions of T_{p}, T_{e} and T_{s}, respectively. Given any starting set of temperatures, the evolution of the system is described by a set of three coupled differential equations:

$$C_{\mathrm{e}}\frac{\mathrm{d}T_{\mathrm{e}}}{\mathrm{d}t} = -G_{\mathrm{ep}}(T_{\mathrm{e}} - T_{\mathrm{p}}) - G_{\mathrm{es}}(T_{\mathrm{e}} - T_{\mathrm{s}}) \qquad (3)$$

$$C_{\mathrm{p}}\frac{\mathrm{d}T_{\mathrm{p}}}{\mathrm{d}t} = -G_{\mathrm{ep}}(T_{\mathrm{p}} - T_{\mathrm{e}}) - G_{\mathrm{sp}}(T_{\mathrm{p}} - T_{\mathrm{s}}) \qquad (4)$$

$$C_{\mathrm{s}}\frac{\mathrm{d}T_{\mathrm{s}}}{\mathrm{d}t} = -G_{\mathrm{es}}(T_{\mathrm{s}} - T_{\mathrm{e}}) - G_{\mathrm{sp}}(T_{\mathrm{s}} - T_{\mathrm{p}}) \qquad (5)$$

The mutual coupling constants, G_{ep}, G_{es}, and G_{sp} will strive to balance out any nonequilibrium between the subsystems by exchange of energy (Figure 1b). In laser-heating experiments (see next subsection), absorption of photons leads mostly to electronic excitations, causing a quasi-instantaneous increase of the electron temperature. The successive dynamics has been found to be phenomenologically describable by equations (3–5), as already noted in the original work by Beaurepaire, Merle, Daunois and Bigot (1996). Therefore, the model is extremely useful to parameterize transient experiments, although only limited microscopic insight is being provided.

As another limitation of this description, the three-temperature model does not properly take care of conserving the angular momentum $\vec{J}$ of the total system (Koopmans, 2003; Koopmans, van Kampen and de Jonge, 2003).

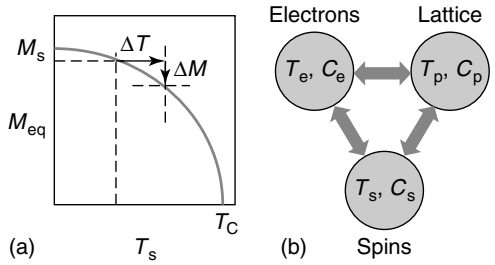

Figure 1. (a) Definition of spin temperature, and representation of a laser-induced magnetization dynamics experiment, and (b) the three interacting reservoirs in the three-temperature model.

At present, angular momentum conservation is being considered as an important ingredient of understanding the ultrafast equilibration process.

2.3 Transfer of angular momentum

At a subpicosecond timescale, it is natural to consider the interacting reservoirs being isolated from the environment. For such a closed system, not only the total energy should be conserved (discussed in Section 2.2), but also the total angular momentum $\vec{J}$. The spin ($\vec{S}_e$) and orbital ($\vec{L}_e$) moment of the electronic system are related to its magnetic moment

$$\vec{\mu} = \mu_B(\vec{L}_e + g\vec{S}_e) \tag{6}$$

where $g \approx 2$ for the materials considered here. In addition, these electronic moments are related to the total angular momentum of the system. When including possible momentum carried by the laser field (photons) and the lattice (phonons), the total angular momentum reads

$$\vec{J} = \vec{L}_e + \vec{S}_e + \vec{L}_{phonon} + \vec{L}_{photon} \tag{7}$$

Since the Hamiltonian of the entire system conserves $\vec{J}$, a change in magnetization of a closed system can only be achieved by exchange among the four contributions at the right-hand side of equation (7). This has interesting consequences not contained within the three-temperature model.

As an example, let us consider the exchange of energy between the electron and the spin reservoir, heating up the spins (lowering M) by cooling down a hot-electron gas. In the absence of interactions with the laser field and lattice this can only be achieved by an exchange of $\vec{S}_e$ and $\vec{L}_e$ as mediated by spin-orbit coupling. One has to realize that in the ground state, the magnetization of ferromagnetic transition metals is strongly dominated by the spin momentum (i.e., $\mu \approx g\mu_B S$) because of quenching of the orbital momentum (Ashcroft and Mermin, 1976). Then, for $g \approx 2$, transferring spin momentum to orbital momentum leads to a reduction of μ by a factor of 2 at most. In particular, it means that this mechanism cannot lead to a full quenching of M, whereas a complete loss of magnetic order has been experimentally observed at high enough fluences (see the discussion on the full quenching regime in Section 7).

2.4 Laser-induced electron and spin dynamics

This section addresses the different scattering processes as of relevance after laser excitation.

2.4.1 Photoabsorption and state filling

The interaction of laser pulses with matter primarily causes electronic excitations. Exploiting light sources in the (near)visible range, with typically photon energies from one to several electron volts, causes thereby excited electrons with energies a hundred times the thermal energy at room temperature. Even if the excitations conserve spin, and thereby $\vec{M}$ is conserved during the excitation, the redistribution of occupied electronic levels will change the MO response of the system (Koopmans, van Kampen and de Jonge, 2003; Oppeneer and Liebsch, 2004). In particular, excitations made by the pump pulse, will block the same transitions to be made by probe photons, a phenomenon denoted 'dichroic bleaching' (Koopmans, van Kampen, Kohlhepp and de Jonge, 2000b).

After laser excitation, the total energy of the electron system has increased. Although at this stage the system is in strong thermal nonequilibrium and thereby a temperature is not unambiguously defined, the excess energy can be used to define an electron temperature, $T_{e,E}$, according to the equilibrium relation between excess energy and electron temperature. For a free-electron system with a constant density of states (DOS) D_F one can derive $E_{ex} = \frac{1}{6}\pi^2 D_F (k_B T_{e,E})^2$, where k_B is the Boltzmann constant. In the weak perturbation limit, treating only small changes in temperature, we thus find:

$$\Delta T_{e,E} = \frac{3}{\pi^2 D_F k_B^2 T_{e,E}} \Delta E_{ex} \tag{8}$$

Alternatively, we could have defined a temperature according to the slope of the electron distribution function $f(E)$ at the Fermi energy E_F. From the analogy with a thermalized electron distribution, one can derive

$$\Delta T_{e,F} = -\left(4k_B \left.\frac{df(E)}{dE}\right|_{E_F}\right)^{-1} \tag{9}$$

Note that laser excitation causes an instantaneous increase of $T_{e,E}$, while $T_{e,F}$ displays a gradual increase in which electronic relaxation is involved.

2.4.2 Electron–electron scattering

The lifetime of 'hot' carriers is very short. Within a free-electron metal, phase space arguments can be used to derive the hot-electron lifetime (Knorren, Bennemann and Burgermeister, 2000; Bennemann, 2004)

$$\tau_{ee}(E) = \frac{1}{K_{ee}(E - E_F)^2} \tag{10}$$

where the electron–electron scattering constant K_{ee}^{-1} is typically 30 fs eV^2 for Ag and 3 fs eV^2 for nickel (Knorren, Bennemann and Burgermeister, 2000). The difference reflects the larger phase space for scattering provided by the high DOS of the Ni d-band near E_F. Note, however, that for such metals, with d-states near the Fermi level, equation (10) is not too accurately fulfilled.

After having started the cascade-like process of e–e scattering, the electron gas rapidly thermalizes (Groeneveld, Sprik and Lagendijk, 1995). Different approximations for the thermalization process lead to an expression of the form

$$\tau_T = \frac{A}{K_{ee} T_e^2} \tag{11}$$

with $A \sim 2\,\mathrm{K}^2\,\mathrm{eV}^2$ for nickel (van Kampen *et al*., 2005a). Taking $K_{ee}^{-1} = 3\,\mathrm{fs\,eV}^2$ leads to a thermalization time $\tau_T \approx 300$ fs for Ni. Significantly lower estimates ($\sim$100 fs) are obtained when correcting for deviations from equation (10), in better agreement with experimental findings (van Kampen *et al*., 2005a).

The simplest way of introducing laser excitation into the 3T-model is by inserting a source term in equation (3) (Beaurepaire, Merle, Daunois and Bigot, 1996):

$$C_e \frac{dT_e}{dt} = -G_{ep}(T_e - T_p) - G_{es}(T_e - T_s) + P(t) \tag{12}$$

where $P(t)$ denotes the power dissipated in the electron system by absorption of photons at time t. This way, however, the process of electron thermalization is not covered since in the strict 3T-model the electron system is considered to be internally in thermal equilibrium from the start ($\tau_T = 0$).

Extended models have been introduced to account for the thermalization by adding an additional bath of nonthermal electrons (Fann, Storz, Tom and Bokor, 1992; Sun *et al*., 1994). The extended 3T model (Koopmans, 2003) is sketched in Figure 2. Within such a 'E3T' model, it is essential to use $T_{e,F}$ to denote the temperature of thermalized electrons. The

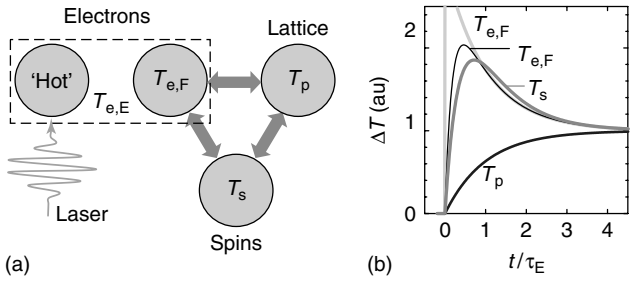

Figure 2. Extended three-temperature model: (a) The four reservoirs, including nonthermalized 'hot' electrons excited by the laser pulse. (b) Schematic transient of the four temperatures, discussed in the text, for a case where $\tau_T = 0.2\tau_E$ and $\tau_M = 0.5\tau_E$.

total energy stored in the system of nonthermal electrons is then

$$E_{\mathrm{nonthermal}} = C_e(T_{e,E} - T_{e,F}) \tag{13}$$

which vanishes after thermal equilibrium has been established, $T_{e,E} = T_{e,F}$. The temporal evolution of the Fermi temperature is often approximated by an empirical relation:

$$\Delta T_e = \Delta T_1 \left[1 - \exp\left(\frac{-t}{\tau_T}\right)\right] \tag{14}$$

where ΔT_1 is the final temperature rise, proportional to the absorbed laser power in the low-fluence limit. Note that in equation (14) we dropped the explicit subscript 'F', as we will keep on doing throughout this chapter.

2.4.3 *Electron–phonon scattering*

Equilibration of electrons with the lattice proceeds via electron–phonon (e–p) scattering (for a review, see e.g., Groeneveld, Sprik and Lagendijk, 1995). The most efficient process is the deformation potential scattering by longitudinal acoustic zone-edge phonons (with an energy of the order of the Debye energy, $\hbar\omega_D$) (van Hall, 2001). If one assumes that the heat capacities C_e and C_p are relatively constant over the temperature range covered, and neglecting the spin system for the moment ($C_s = 0$), equations (3) and (4) can be solved analytically, resulting in an exponentially converging temperature with a time constant

$$\tau_E = \frac{C_e C_p}{C_e + C_p} \frac{1}{G_{ep}} \tag{15}$$

where subscript 'E' denotes 'Energy' equilibration. Typically, $\tau_E \sim 0.5$ ps for the ferromagnetic transition metals (van Kampen *et al*., 2005a).

Incorporating the thermalization process as well, an empirical relation for the electron temperature transient can then be introduced (van Kampen *et al*., 2005a):

$$\begin{aligned}\Delta T_e = {} & \Delta T_1[1 - \exp(-t/\tau_T)]\exp(-t/\tau_E) \\ & + \Delta T_2[1 - \exp(-t/\tau_E)]\end{aligned} \tag{16}$$

where ΔT_2 is the final temperature to which T_e and T_p converge, and $\Delta T_1 \geq \Delta T_2$. It is easy to show that $\Delta T_1/\Delta T_2 = 1 + C_p/C_e$. In the limit $\tau_T \ll \tau_E$, ΔT_e approaches ΔT_1 for times $\tau_T \ll t \ll \tau_E$, and thereby a clear 'overshoot' of T_e is being witnessed.

The simplest *microscopic* approach, on equal footing with the derivation of the free-electron lifetime (10), is obtained by using a simple Einstein model with identical harmonic oscillators representing the phonon system. Matrix elements

for e–e and e–p scattering (λ_{ee} and λ_{ep}, respectively) can then be assigned to the scattering processes, represented in Figure 3. Alternatively, scattering probabilities $K_{ee} \propto \lambda_{ee}^2$ (cf. (10)) and $K_{ep} \propto \lambda_{ep}^2$ entering the Boltzmann equations describing the dynamics of the system, can be introduced. It can be derived that for T_e and T_p well above T_D the phenomenological coupling constant G_{ep} of the 3T-model is independent of temperature, and related to the microscopic parameter K_{ep} according to (Hohlfeld, 1998)

$$G_{ep} = K_{ep} E_p k_B \tag{17}$$

Using the Born–Oppenheimer approximation for the deformation potential scattering, and equations (15) and (17), yields τ_E of the order of 1 ps, in reasonable agreement with experiment (van Kampen *et al*., 2005a).

2.4.4 Spin scattering

Often, it is of relevance to assign a characteristic timescale τ_M to an experimentally obtained MO transient – independent of the microscopic interpretation. Although the full 3T-model can be used for that purpose, here we limit ourselves to a simple approximation that can be treated analytically. We use the following assumptions: (i) the spin specific heat is neglected, (ii) C_e and C_p are considered constant, which can be achieved at low enough fluence, (iii) we assume that the spin dynamics is merely controlled by T_p and $T_{e,E}$ (and *not* $T_{e,F}$), according to:

$$\frac{dT_s}{dt} = \frac{(T_{e,E} - T_s)}{\tau_{M,e}} + \frac{(T_p - T_s)}{\tau_{M,p}} \tag{18}$$

We note that the last assumption lacks a strict, physical motivation, though it is in line with the description of the energy flow in the 2T- and 3T-model. Moreover, it makes sense that the highly excited (nonthermal) electrons have a significant influence on the spin relaxation, as would not be the case if equation (18) were described in terms of $T_{e,F}$. Finally, we use the electron and phonon temperature transients: $\Delta T_{e,E}(t) = T_2 + (T_1 - T_2)\exp(-t/\tau_E)$ and $\Delta T_p(t) = T_2(1 - \exp(-t/\tau_E))$, in agreement with equation (16). Then, we find as a general solution:

$$\Delta T_s(t) = \Delta T_2 + \frac{(\tau_E \Delta T_1' - \tau_M \Delta T_2)\exp(-t/\tau_M)}{\tau_E - \tau_M} + \frac{\tau_E(\Delta T_2 - \Delta T_1')\exp(-t/\tau_E)}{\tau_E - \tau_M} \tag{19}$$

with $\tau_M^{-1} = \tau_{M,e}^{-1} + \tau_{M,p}^{-1}$, and $\Delta T_1' = \Delta T_1 \tau_M / \tau_{M,e}$. An 'overshoot' of T_s is achieved in the case that the e–s channel dominates over the s–p channel, that is $\tau_{M,e} \ll \tau_{M,p}$, unless $\tau_M \gg \tau_E$, all as expected.

The result shows that an overall τ_M (including both contributions via the s–p and s–e channel) can be fitted, without prior knowledge of which of the two channels dominates, and without needing information from transient reflection. If the latter *is* available, and thereby ΔT_1, the ratio of the fitted $\Delta T_1'/\Delta T_1$ can be used to extract $\tau_{M,e}$ and $\tau_{M,p}$ separately.

Often, in literature, an even more empirical fitting function is being used that can be described generally as:

$$\Delta T_s(t) = \left(1 - \exp\frac{-t}{\tau_M}\right)\Delta T_e(t) \tag{20}$$

It should be emphasized that although the shape of the resulting profile $T_s(t)$ can be quite similar to the one produced by (19), the extracted value of τ_M can be off by a factor two! Examples thereof are discussed in Sections 6 and 7.

As to the microscopic origin of the laser-induced demagnetization, quite a number of spin-scattering processes have to be considered. We discuss them in the context of conservation of J. First, the hot-electron lifetime can be spin dependent (Aeschlimann *et al*., 1997; Knorren, Bennemann and Burgermeister, 2000; Bennemann, 2004). Experiments using two-photon photoemission (TPPE) have indeed found significant differences between majority and minority carriers for the ferromagnetic transition metals Co, Fe, and Ni (Aeschlimann *et al*., 1997). The results have been interpreted in terms of the huge difference of phase space for scattering majority and minority carries within the spin-split DOS of these materials. Relevant timescales are in the low-femtosecond regime. It should be emphasized, however, that the spin-dependent lifetime has no relation to a change in magnetic moment of the system.

Secondly, spin scattering by redistribution of angular momentum within the electron system is considered. It has been argued that hot electrons will have high enough energy to overcome the Stoner gap (Scholl, Baumgarten, Jacquemin and Eberhardt, 1997), and thereby create Stoner excitations–changes of the local spin moment. These spin flips would be accompanied by emission (or absorption) of magnons (spin waves). However, also this process does not provide a net change of the magnetic moment of the system.

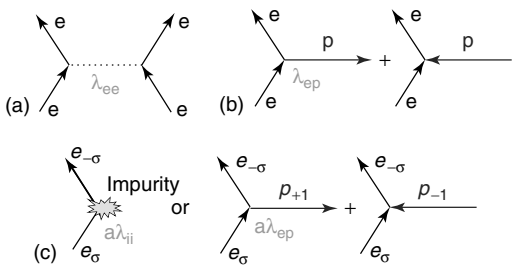

Figure 3. Feynmann diagrams for (a) e–e scattering, (b) e–p scattering, and (c) e–p scattering accompanied with spin flip.

An other purely electronic process to be considered is transfer from spin to orbital momentum as mediated by spin-orbit coupling. From the typical energy scale $\Delta_{\mathrm{exc}} \sim 0.1\,\mathrm{eV}$ fast time scales $\hbar/\Delta_{\mathrm{exc}} \sim 10\,\mathrm{fs}$ could be anticipated indeed. In Section 2.3, however, we already derived that, unlike experimental observations, this mechanism cannot account for a full quenching of M while conserving J. Moreover, the final state would be characterized by a large orbital momentum. Using arguments to be introduced in Section 3.2, this should lead to an increase rather than a decrease of MO signals upon laser heating, again contrary to experimental observations.

Thirdly, transfer of energy between the lattice and spin system can occur (Koopmans, Kicken, van Kampen and de Jonge, 2005; Koopmans, Ruigrok, Dalla Longa and de Jonge, 2005). This can be considered as ordinary spin-orbit mediated spin-lattice relaxation (Yafet, 1963). Angular momentum is being transferred from the spin to the lattice, by absorption or emission of phonons carrying orbital momentum. On a macroscopic scale, this transfer is being witnessed as a finite rotation of a magnetic bar upon changing its magnetic moment, as in the classical De Haas and Einstein experiment (Scott, 1962). For nonmagnetic metals spin-lattice scattering has been well addressed, and described by Eliot–Yafet type of scattering (Yafet, 1963). A finite probability a is assigned for an electron to flip its spin upon momentum scattering with phonons or impurities. This process is schematically represented in Figure 3(c). Although values of a have been tabulated before for some nonmagnetic metals (Beuneu and Monod, 1978), little is known about implications for ferromagnetic transition metals. In passing we not that, in principle, a similar factor a can also be related to the spin diffusion length (l_{sf}), used to describe magneto transport in, for example, current-perpendicular to the plane giant magnetoresistance (GMR) pillars (Dubois *et al*., 2006). However, a comparison between the spin-flip probability in the transport regime and the strongly nonequilibrium laser-heating case is far from trivial – and has not been discussed in literature yet. Therefore, in the present review, we will refrain from such a detailed analysis.

Finally, scenarios including the laser field itself or hybrid mechanism have been proposed, but all have their intrinsic complications. At this stage, the reader may wonder what is causing the demagnetization after all. Although a full understanding has not been achieved yet, a more quantitative discussion of the present insights is discussed in Sections 6 and 7.

3 EXPERIMENTAL APPROACHES

Over the past decade a number of techniques have been developed that give access to the dynamics of spin systems down to femtosecond timescales. Most of them rely on the use of subpicosecond laser pulses. This section provides a detailed description of the relation between magneto-optics and spin dynamics, and discusses different experimental approaches.

3.1 Excitation sources

In order to access subpicosecond magnetization dynamics, extremely short rise time or pulse-lengths should be exploited. From conceptual point of view, magnetization dynamics is triggered in the most straightforward way by short magnetic field pulses. Conventional approaches using electronic pulse generators are limited to a rise time of several tens of picoseconds at least, even when taking utmost care to feed pulses into- and guide them through microscopic strip lines (Elezzabi and Freeman, 1996; Elezzabi, Freeman and Johnson, 1996; Hiebert, Stankiewicz and Freeman, 1997). An exciting alternative has been provided by using picosecond electron bunches from a linear accelerator (Siegmann *et al*., 1995) Experiments so far (Back *et al*., 1998, 1999; Tudosa *et al*., 2004; Stamm *et al*., 2005) have been restricted to static microscopic characterization after single pulse excitation. Time-domain extrapolations of the technique could be imaginable, although stroboscopic approaches are very unlikely. In passing, we also stress the importance of spin-torque induced switching, which recently has been observed spatio-temporally resolved by ultrafast x-ray microscopy (Acremann *et al*., 2006).

Hybrid schemes, using femtosecond optical pulses to produce picosecond rise time magnetic field pulses have been demonstrated in a multitude of configurations. The standard approach employs a photoconductive switch to launch an electrical pulse into a strip line. Typically, around picosecond rise times and – when desired – tunable duration can be produced (e.g., Gerrits *et al*., 2002). An alternative, in which switch and sample are integrated, is the use of laser pulses to trigger breakthrough of a Schottky barrier that supports a thin-film FM sample (Woltersdorf, Buess and Back, 2005).

Integrating pulse generator and sample even further is established in all-optical configurations. In order to study precessional dynamics similar to the field-induced cases, a configuration can be employed in which an internal anisotropy field pulse is being generated by pulsed-laser heating of a magnetic thin-film system (van Kampen *et al*., 2002). We stress that this approach has been demonstrated to be widely applicable. However, it cannot be applied in, for example, magnetic configurations in which the applied and effective field are both along a symmetry axis of the sample. Further details will be discussed in Section 8. The next section will focus on thermodynamic processes triggered by the laser heating.

3.2 Ultrafast probes and time-resolved magneto-Optics

A number of femtosecond laser-based approaches to probe the subpicosecond magnetization dynamics have been developed. Detecting photoemitted electrons has been exploited in different schemes: spin-polarized time-resolved photoemission (SP-TRPE) (Scholl, Baumgarten, Jacquemin and Eberhardt, 1997), time-resolved photoemission (TRPE) probing the evolution of the exchange splitting (Rhie, Dürr and Eberhardt, 2003, 2005; Lisowski *et al*., 2005), or probing the spin dynamics via the image-potential states at FM surfaces (Schmidt *et al*., 2005). With the advance of new generations of synchrotrons, X-ray magnetic circular dichroism – with the unique potential of probing spin and orbital momenta separately – is expected to play an important role in the near future. Within the present chapter, though, we concentrate on all-optical approaches.

The latter are based on the MO-Kerr effect. The key link between the magnetic state of a material and the MO response is provided via the dielectric tensor. As an instructive case, for an optically isotropic material, magnetized along $\hat{z}$, the dielectric tensor reads:

$$\overleftrightarrow{\epsilon} = \begin{pmatrix} \epsilon_{xx} & \epsilon_{xy} & 0 \\ -\epsilon_{xy} & \epsilon_{xx} & 0 \\ 0 & 0 & \epsilon_{xx} \end{pmatrix} \tag{21}$$

Note that ε_{xy} transforms antisymmetrically under reversal of the magnetization, $\vec{M} \leftrightarrow -\vec{M}$, providing the 'magnetic contrast'.

Thus, polarized light experiences a rotation upon transmission (Faraday effect) or reflection (Kerr effect) from a magnetic medium. The resulting complex MO rotation is written as $\tilde{\theta} = \theta + \mathrm{i}\epsilon$, where θ and ϵ are the induced MO rotation and ellipticity, respectively. The relation between MO rotation and $\vec{M}$ can be written as (Koopmans, 2003)

$$\tilde{\theta} = \tilde{F} M \tag{22}$$

where a generalized Fresnel coefficient $\tilde{F}$ has been introduced that involves all details of the experimental configuration and sample layout. We restricted ourselves to the simplified case where $\tilde{\theta}$ depends on the magnitude (or a single component) of $\vec{M}$ only, and refer to (Koopmans, 2003) for the general case.

Measuring $\tilde{\theta}$ in a time-resolved experiment, one should be aware of the possibility that the perturbation does not only modify $\vec{M}$, but also the generalized Fresnel coefficient $\tilde{F}$. This can significantly hinder a simple interpretation solely in terms of $\vec{M}$

Another, even more subtle complication arises because MO experiments are only possible by the sake of spin-orbit coupling, through which the spatial degree of freedom (electric field) is correlated with the spin degree of freedom (magnetic ordering). In fact, it can be stated that optics is merely capable of measuring the *orbital* moments in a material, whereas a prediction about $\vec{M}$ is possible only after assuming a certain fixed ratio of spin ($\vec{S}$) to orbital ($\vec{L}$) momenta. This ratio is not *a priori* conserved upon perturbation of the material. As to the dependency on $\vec{L}$, a sum-rule has been derived that links the frequency integrated absorptive past of the off-diagonal element of the dielectric tensor to a part of the *orbital* momentum (Oppeneer, 1998). Rather than writing equation (22) in terms of $\vec{L}$, we will include those potential deviations within the explicit time dependence of $\tilde{F}$.

In the further analysis we assume the weak perturbation regime, in which changes of the Kerr rotation are relatively small. In that case, the relation $\theta(t) = F(t)M(t)$ can be linearized (Koopmans, 2003):

$$\Delta\theta(t) = M_0 \Delta F(t) + F_0 \Delta M(t) \tag{23}$$

where index '0' denotes unperturbed values (at $t < 0$) and Δ indicates pump-induced values. From equation (23) it is easily seen that, whenever $F(t) = F_0$ independent of t, the relation

$$\frac{\Delta\theta(t)}{\theta_0} = \frac{\Delta\epsilon(t)}{\epsilon_0} = \frac{\Delta M(t)}{M_0} \tag{24}$$

is fulfilled, that is, the normalized transient rotation and ellipticity should be equivalent. Therefore, any deviation from equation (24) demonstrates the presence of an explicit t-dependence of F. A similar identification of 'optical artifacts' can be based on a spectroscopic analyses. Whenever optical artifacts play a role, one may expect the normalized MO transients to depend on the probing frequency ω. If not, the relation

$$\frac{\Delta\theta(\omega_1, t)}{\theta_0(\omega_1)} = \frac{\Delta\epsilon(\omega_2, t)}{\epsilon_0(\omega_2)} = \frac{\Delta M(t)}{M_0} \tag{25}$$

holds for any set of frequencies (ω_1, ω_2).

Complementary to measuring the linear optical response, higher order optical signals can be monitored to acquire information on the magnetization dynamics. A well-known example is provided by magnetization-induced optical second-harmonic generation (MSHG) (See also **Magnetization-induced Second Harmonic Generation, Volume 3**). Also there, the aim is to extract information on those tensor elements that transform odd under reversal of $\vec{M}$. Well-known advantages of MSHG are its interface sensitivity (Pan, Wei and Shen, 1989; Hübner and Bennemann, 1989; Shen, 1989)

and the huge nonlinear Kerr angles that can be achieved (Koopmans, Groot Koerkamp, Rasing and van den Berg, 1995). Disadvantages are the small signals, down to the photon counting regime, and an even less-trivial interpretation. In principle, the analysis in terms of a generalized Fresnel factor $\tilde{F}$ can be extended to the nonlinear case, leading to similar explicit time-dependencies that affect magnetization dynamics studies in the same way as in its linear counterpart (Regensburger, Vollmer and Kirschner, 2000).

3.3 Implementations

The simplest realization of an all-optical time-resolved magneto-optical Kerr effect (TRMOKE) experiment in a *crossed-polarizer configuration* is sketched in Figure 4. Pump and probe pulses are focused to overlapping spots on the sample. The pump pulses pass a mechanical delay line to adjust the time delay. The influence of the pump beam on the polarization state of the reflected probe pulse is measured using an analyzer at an angle α_A and any type of photodetector. Either a measurement of $\tilde{\theta}(t)$ with and without pump pulses is performed, or, to enhance the sensitivity, a mechanical chopper is placed in the pump beam, and a lock-in amplifier is used to directly measure $\Delta\tilde{\theta}(t)$.

It can easily be derived that the pump-induced change in output signal is described in lowest order of $\Delta\tilde{\theta}$ and α_A by (Koopmans, 2003)

$$\Delta I(t) = 2R_0\alpha_\mathrm{A}\Delta\theta(t) + \alpha_\mathrm{A}^2\Delta R(t) \tag{26}$$

where R_0 and $\Delta R(t)$ are the reflectivity and pump-induced transient thereof. Within the basic implementation, no sensitivity on ellipticity is achieved, and care has to be taken to rule out artificial signals due to a $\Delta R(t)$ of nonmagnetic origin. Bigot *et al*. argued that part of the drawbacks of the crossed-polarizer approach are avoided by performing measurements at a multitude of analyzer angles (Bigot, Guidoni, Beaurepaire and Saeta, 2004).

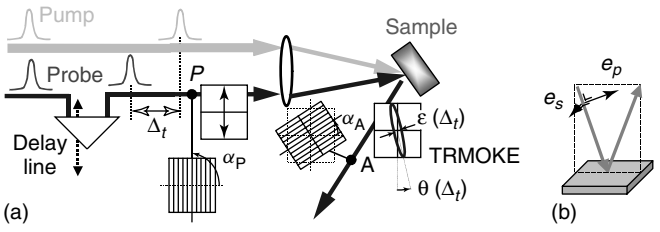

Figure 4. Schematic illustration of a TRMOKE setup. (a) In the crossed-polarizer experiment, a polarizer is inserted at 'P' and an 'analyzer' almost crossed at 'A'. (b) Definition of the polarization vectors $\vec{e}_\mathrm{s}$ and $\vec{e}_\mathrm{p}$.

A particularly attractive, alternative scheme is provided by replacing the analyzer by a polarizing beam splitter, using a pair of balanced photodiodes and generating the difference signal by a differential amplifier (Ju *et al*., 1998b). Thereby, a highly sensitive measure of the MO transient is achieved. When working exactly at the balanced configuration, a dependency on $\Delta R(t)$ can be avoided (Koopmans, 2003):

$$\Delta I(t) = 2R_0\Delta\theta(t) \tag{27}$$

When required, a sensitivity to the complementary ellipticity channel is obtained by using a quarter-wave plate, an option also available for the crossed-polarizer configuration.

A final scheme is achieved by exploiting polarization modulation using, for example, a photoelastic modulator (PEM) placed before the sample (Koopmans, van Kampen, Kohlhepp and de Jonge, 2000a). Then, the detected signal displays oscillating signals I_nf at harmonics nf of the PEM frequency f. A number of configurations has been reported, some of them solely depending on $\Delta\tilde{\theta}(t)$, others also on ΔR (Koopmans, 2003). As an example, having the main axis of the PEM parallel or perpendicular to the plane of incidence, one obtains to a fair approximation (Koopmans, van Kampen, Kohlhepp and de Jonge, 2000a; Koopmans, 2003):

$$\frac{\Delta I_\mathrm{1F}(t)}{I_{0f}} = 2J_1(A_0)\Delta\varepsilon(t) \tag{28}$$

$$\frac{\Delta I_\mathrm{2F}(t)}{I_{0f}} = 2J_2(A_0)\Delta\theta(t) \tag{29}$$

where $J_n(A_0)$ is the nth order Bessel function at the retardation A_0 of the PEM. It is obtained that the $1f$-signal is proportional to the transient ellipticity, whereas the $2f$-signal corresponds to rotation. Thus, the approach is highly applicable when identifying optical artifacts (cf. equation (24)).

Aiming at a full deconvolution of transient dielectric tensor elements of the magnetic materials, rather than just the transient (MO) reflection, a combination of experiments is required. Combining rotation and ellipticity, both in the magnetic and nonmagnetic channel, and/or combining rotation (Kerr) and transmission (Faraday) measurements, have been reported. Examples of such a transient MO ellipsometry can be found in (Guidoni, Beaurepaire and Bigot, 2002). When further striving for parallel detection of a broad spectral range, the simplest configuration, that of the crossed-polarizer, is most appropriate. Bigot introduced such a method of femtosecond spectrotemporal magneto-optics, in which spectrally broadened probe pulses (480–750 nm) were used, and the Kerr and Faraday rotation spectra where measured at a multitude of analyzer angles (Bigot, Guidoni, Beaurepaire and Saeta, 2004).

In the analysis so far, cases were treated where only the magnitude $M(t)$, or one of its vector components, $M_i(t)$, was of relevance. Vectorial schemes, to measure three components of $\vec{M}(t)$, using a high-aperture microscope objective and four-quadrant detection are widespread by now (for details, see Freeman and Hiebert, 2002). While so far being restricted to studies of magnetic field-induced dynamics, very recently, an extension to all-optical investigations down to the femtosecond regime has been reported (Vomir *et al*., 2005).

It has been discussed that dichroic bleaching can hinder a proper view on the ultrafast demagnetization process during the first hundreds of femtoseconds. Attempts to establish a full separation of $\Delta F(t)$ and $\Delta M(t)$ have been reported by van Kampen *et al*. In particular, they suggested to measure the MO transients at different ambient temperatures to establish this separation (Koopmans, van Kampen and de Jonge, 2003; van Kampen, 2003). The key approach is as follows. We start by writing the normalized $M(t)$ in terms of a spin temperature $T_s(t)$,

$$\frac{\Delta\theta(t)}{\theta_0} = \frac{\Delta F(t)}{F_0} + \frac{1}{M_0}\frac{\mathrm{d}M_0}{\mathrm{d}T_0}\Delta T_s(t) \tag{30}$$

We now consider transient experiments at two ambient temperatures ($T_{0,1}$ and $T_{0,2}$) and denote thermal differences by δ. As an important approximation, we assume that *the state-filling effects are relatively independent of temperature*, that is, $\delta\Delta F(t) \approx 0$ and $\delta F_0 \approx 0$, since broadening the Fermi-profile by a few millielectron volts hardly changes the hot-electron ($>$ eV) behavior. Then we obtain:

$$\delta\left(\frac{\Delta\theta(t)}{\theta_0}\right) = \delta\left[\frac{1}{M_0}\frac{\mathrm{d}M_0}{\mathrm{d}T_0}\right]\Delta T_s(t) + \frac{1}{M_0}\frac{\mathrm{d}M_0}{\mathrm{d}T_0}\delta\Delta T_s(t) \tag{31}$$

Note that $|M_0^{-1}\mathrm{d}M_0/\mathrm{d}T_0|$ is strongly T-dependent. In fact, it diverges while approaching T_C, providing further support for the neglect of the term $\delta(\Delta F(t)/F_0)$ in equation (30). In order to proceed, we make a second approximation: *the evolution of the spin temperature is independent of the starting temperature of the experiment*, that is, $\delta\Delta T_s(t) = 0$. Within the 3T-model, for example, this is fulfilled if C_e, C_p, and G_{ep} are T-independent, and C_s can be neglected. Then, the spin dynamics can be derived from

$$\Delta T_s(t) \approx \frac{\delta\left(\Delta\theta(t)/\theta_0\right)}{\delta\left[M_0^{-1}\left(\frac{\mathrm{d}M_0}{\mathrm{d}T_0}\right)\right]} \tag{32}$$

where the numerator is experimentally measured, and the denominator is obtained from the materials specific $M(T)$. Preliminary results of this *thermal difference scheme* have been recently reported by our group (Koopmans, van Kampen and de Jonge, 2003; van Kampen, 2003).

As a final more sophisticated approach, one might want to perform a 'thermal difference scheme' but drop the approximation of constant C_e and C_p. Such an approach has been outlined in Koopmans (2004). While potentially an interesting route for future studies, we refrain from a detailed discussion in the present review.

4 PIONEERING WORK ON LASER-INDUCED DYNAMICS

Early attempts on estimating timescales with laser-induced magnetization dynamics were by Agranat and coworkers in the mid-1980s (Agranat, Ashikov, Granovskii and Rukman, 1984, 1986). The demagnetization of transition metal thin films was studied by measuring the remnant MO contrast with a dc probing laser after pulsed-laser heating with pulses of different duration. It was concluded that the spin relaxation time in the FM lies in the interval $1\text{ns} < \tau_M < 40\text{ns}$.

First real-time experiments were performed using SP-TRPE in the beginning of the 1990's (Vaterlaus, Beutler and Meier, 1991; Vaterlaus *et al*., 1992). Detailed experiments were conducted on the rare-earth FM gadolinium (Gd), yielding $\tau_M = 100 \pm 80\,\text{ps}$, and iron. The accuracy in those experiments was limited, however, by the relatively long duration of the heating pulses ($\sim$10 ns). Nevertheless, the experimentally determined relaxation time τ_M was found to be in good agreement with theoretical estimates based on spin-lattice relaxation by Hübner and Bennemann (1996). Therefore, around 1995, it was concluded that the demagnetization upon laser heating is dominated by spin-lattice relaxation, and proceeds at a typical timescale of $\tau_M \sim 0.1$–1 ns.

In view of the previous context, a surprising result was obtained in 1996 by Beaurepaire, Merle, Daunois and Bigot (1996). They reported on a combined TRMOKE and transient reflection study. The spin temperature, as extracted from TRMOKE, was found to display a maximum around 2 ps, while the initial decay rate was a few tenths of a picosecond only, suggesting $\tau_M < 0.5$ ps (Figure 5). The complete behavior was shown to be described adequately by a 3T-model (equations (12), (4), and (5)). A complete dominance of the spin-electron coupling over the spin-lattice coupling needed to be assumed.

The experimental finding of an ultrafast ($\tau_M < 500$ fs) spin relaxation was confirmed soon thereafter by several groups. Hohlfeld *et al*. exploited time-resolved SHG (Section 3.2) to study $T_e(t)$ and $T_s(t)$ in bulk polycrystalline nickel (Hohlfeld, Matthias, Knorren and Bennemann, 1997). In contrast with the work of Beaurepaire, it was found that already after 300 fs the magnetization is governed by the electron temperature,

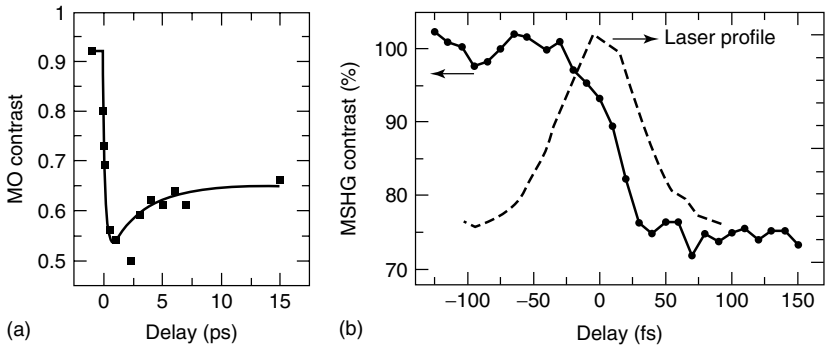

Figure 5. (a) Pioneering experiments by Beaurepaire, showing the loss of MO contrast of a nickel thin film within 1 ps after laser excitation. (Reproduced from Beaurepaire *et al*., 1996, with permission from the American Physical Society. © 1996.) (b) Similar data by Güdde and Hohlfeld, using MSHG, and showing a quasi-instantaneous demagnetization. (Reproduced from J. Güdde *et al*., 1999, with permission from the American Physical Society. © 1999.)

that is, $T_s(t) = T_e(t)$, even before electrons and *lattice* have mutually thermalized, that is, $\tau_M < \tau_E$. For even smaller delay times, $t < \tau_T$, at which the electron thermalization has not set in yet, a break down of the classical magnetization behavior was found. On the basis of this, one could conclude that $\tau_M \approx \tau_T$.

In later experiments, using shorter pulses, even a quasi-instantaneous break down of the MO contrast was found (Güdde *et al*., 1999; Hohlfeld *et al*., 1999); $\tau_M \approx 0 \ll \tau_T$. Within the experimental resolution, the loss of 'magnetic order' was described by the time integral of the absorbed pump power, that is, the absorbed energy was seen to be converted directly to the spin system. Other experiments showed a 100% quenching of M, when using high enough fluence and films with a reduced T_C (Güdde *et al*., 1999; Conrad, Güdde, Jähnke and Matthias, 1999). A similar FM→PM transition was demonstrated in more detail for $CoPt_3$ by Beaurepaire *et al*. (1998).

An alternative confirmation for an ultrafast subpicosecond loss of magnetic order in Ni thin films ($\tau_M = 300$ fs) came from TRPE by Scholl, Baumgarten, Jacquemin and Eberhardt (1997). In contrast with previous work, a second, slower transition of hundreds of picoseconds was reported. The two timescales were assigned to Stoner excitations and ordinary spin-lattice relaxation, respectively. However, such a second process has never been reproduced, despite specific search for it (Hohlfeld, 1998; Hohlfeld *et al*., 1999).

On the basis of these first experiments it was concluded that the loss of MO contrast is extremely fast, at least within a few hundred femtoseconds, that is, well before the electron and lattice system are mutually equilibrated; ($\tau_M < \tau_E$). Speculations were around on a demagnetization directly linked to electron thermalizaton ($\tau_M \approx \tau_T$), or even being quasi instantaneous ($\tau_M \ll \tau_T$), meaning that $M(t) = M_{eq}(T_{e,E}(t))$. Particularly the last claim triggered some concerns as to the simple interpretation of the data, and a potential role of 'optical artifacts'. Such optical effects will be addressed in the next two sections. After that, we will return to the genuine demagnetization process in more detail.

5 POPULATION DYNAMICS

Around the year 2000, a number of groups started to question the simple interpretation of the TRMOKE experiments that seemed to indicate an almost instantaneous demagnetization. Doubting a direct proportionality between MO signal and M is equivalent to considering a potential explicit time dependence of the effective Fresnel coefficient $\tilde{F}$ in equation (22).

First experimental evidence that this was indeed the case came from Koopmans, van Kampen, Kohlhepp and de Jonge (2000a,b), who measured the rotation and ellipticity separately in a TRMOKE experiment on (epitaxial) nickel thin films (Figure 6a). It was found that during the first hundreds of femtoseconds after laser excitation, a profound difference between the two normalized channels arose: $\Delta\varepsilon(t)/\varepsilon_0 \neq \Delta\theta(t)/\theta_0$. Those experiments provided unambiguous proof that, at least in some cases, the MO transient after pulsed-laser heating does not reflect the genuine magnetization dynamics. Effects were attributed to 'dichroic bleaching', or state blocking effects, as introduced in Section 2.4.1.

Similar conclusions were drawn from MSHG experiments on Ni(110) single crystals by Regensburger, Vollmer and Kirschner (2000). MSHG experiments can be performed in several configurations, selecting different (combinations of) second-harmonic susceptibility tensor elements. In one of the configurations, the authors observed a reversal of the MO contrast when pumping at high enough laser fluence, whereas it was carefully excluded to be related to a true magnetization reversal. It was concluded, again, that the fast initial drop of the MO signal cannot be unambiguously attributed to an ultrafast demagnetization.

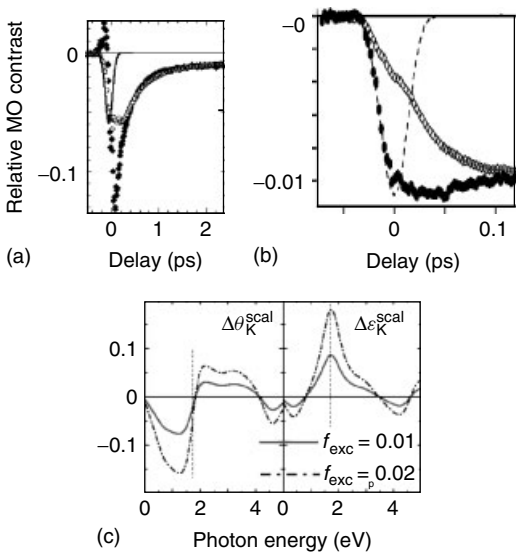

Figure 6. (a) TRMOKE ellipticity and rotation for nickel thin film. (After Koopmans, 2000b.) (b) Complementary channels for $CoPt_3$. (After Guidoni, 2000.) (c) Calculated dichroic bleaching for same excitation density as (a); the laser frequency corresponds to the vertical dashed line. (Reproduced from Oppeneer *et al*., 2004, with permission from IOP Publishing Ltd. © 2004.)

By now, a clear consensus on the explicit time dependence of $\tilde{F}$ has been achieved. However, it has been found also that the relative importance of such 'optical artifacts', as well as the timescale over which they contribute, depends strongly on sample layout and experimental settings. Comin reported results for 50-nm cobalt thin films, observing the strongest differences persisting for a few hundred femtoseconds, very similar to the original nickel work (Comin *et al*., 2004). Pronounced differences in the transients of different MSHG tensor elements of nickel and permalloy thin films were reported by Melnikov, Güdde and Matthias (2002). Beaurepaire performed detailed experiments on $CoPt_3$ (Guidoni, Beaurepaire and Bigot, 2002). It was again found that during electron thermalization ($t < \tau_T$) a difference between the real and imaginary signal exists, however, full overlap was found after thermalization was established (Figure 6b). Finally, van Kampen carefully controlled the 'chirp' (i.e., the time lag between high- and low-frequency components) of the laser pulses to investigate the optical artifacts (van Kampen, 2003; Koopmans, van Kampen and de Jonge, 2003). The MO trace depended on the chirp indeed, in a way that was fully consistent with expectations from simple models. This served as additional proof for the absence of a direct relation between $\tilde{\theta}(t)$ and $M(t)$.

Differences persisting for much longer times, up to several tens of picosecond, were observed both by van Kampen on Cu(001)/Ni (Koopmans, van Kampen, Kohlhepp and de Jonge, 2000b; van Kampen, 2003), and by Kampfrath on iron thin films (Kampfrath *et al*., 2002). In this context, it also noteworthy mentioning similar results for manganites (more specifically PCMO and LCMO) by McGill *et al*. (2004). In that case, artifacts playing a role for nanoseconds could be attributed to contrasting carrier dynamics.

In general, it has been argued that the strongest deviations would occur in cases where either of the two signals strongly dominates the static MO response, that is, cases where $\theta_0 \ll \epsilon_0$ or *vice versa*. In such a case even small changes in the minor channel (e.g., $\Delta\theta(t)$) would yield huge effects in the normalized signal ($\Delta\theta(t)/\theta_0$). In MO spectra such cases would occur near zero crossings of $\theta(\omega)$ or $\epsilon(\omega)$, with obvious divergences at the zero crossings themselves.

In cases where θ_0 and ϵ_0 are of similar magnitude, smaller differences – or even no measurable difference at all – have been reported. Identical traces have been observed, for instance, for nickel films on silicon wafers (Wilks, Hughes and Hicken, 2002) (although subtle differences were reported in Wilks *et al*., 2004), and $Si/Si_3N_4/Ni$ films (van Kampen, 2003). Moreover, Bigot used femtosecond spectroscopy with supercontinuum pulses (spectrum spreading from 480 nm to 750 nm) to demonstrate that for $CoPt_3$ films the identity $\Delta\theta(t)/\theta_0 = \Delta\epsilon(t)/\epsilon_0$) holds for the whole spectral range measured (Bigot, Guidoni, Beaurepaire and Saeta, 2004), although the temporal resolution was somewhat lower ($\geq$200 fs) in this experiment.

Altogether, lots of evidence has been gathered for optical artifacts. The few reports on long lasting effects are not fully understood yet. In contrast, dichroic bleaching during the thermalization phase of the electronic system after optical excitation has been interpreted in a quantitative way. In a naive picture, one would expect the relative change of the MO response $\Delta\theta/\theta_0$ to be of the order of the excitation density f_{exc}, defined as the number of optically excited electrons per atom. Such a behavior can easily be derived for an ensemble of two-level systems. However, effects for dichroic bleaching as reported in the original work (Koopmans, van Kampen, Kohlhepp and de Jonge, 2000b) were as high as $\Delta\theta/\theta_0 \sim 0.1$ for laser fluences corresponding to $f_{exc} = 0.01$. It was conjectured that such an effect could be understood by the fact that because of momentum conservation during optical excitations, the transitions are concentrated in specific parts of the Brillouin zone. As a result, the few states that are involved are much more effective in blocking additional transitions when using probe and pump pulses of the same photon energy (Koopmans, van Kampen, Kohlhepp and de Jonge, 2000b).

Recently, Oppeneer and Liebsch (2004) performed *ab initio* calculations of the magneto-optics for nonequilibrium electron distributions in nickel to put these hand waving arguments on more solid ground. More specifically, they

investigated the MO response right after optical excitation, treating the electronic structure and optical matrix elements within the density-functional theory. They found a quantitative agreement with the experiments, but only when properly taking the momentum conservation during optical excitation into account. At the laser frequency of 1.7 eV the calculated dichroic bleaching corresponded to $\Delta\epsilon/\epsilon_0 \approx 9 f_{\mathrm{exc}}$, in good agreement with experimental results (Figure 6c). It is fair to stress that the calculations represent a worst-case scenario in the sense that electronic relaxation of hot electrons is not included. Such a relaxation is taking place within tens of femtoseconds, most probably leading to a fast decay of the bleaching effects. Detailed calculations thereof would be of considerable interest, but require an enormous numerical effort and have not been reported to date.

Concluding this section, both experimental and theoretical results have demonstrated the nonequivalence of the MO response and the transient magnetization in the regime of the strongly excited state before thermalization has set in. By focusing on the strongest of the complementary MO signals (rotation vs ellipticity) one may hope to obtain a more direct view on the magnetization dynamics. Nevertheless, a full understanding has not yet been achieved, as also evidenced by artifacts remaining for tens of picoseconds of unknown origin that appear in some of the experiments.

6 EXPERIMENTS ON ORBITAL MOMENTUM TRANSFER

In the process of laser-induced loss (or, more generally, modification) of magnetic order, a contribution by the transfer of angular momentum between the laser field and the FM sample cannot be excluded *a priori*. As to emphasize its potential relevance, it is of interest pointing recent developments in optical control of ferromagnetic garnets. It was demonstrated by Kimel and Hansteen *et al*. that circularly-polarized light can be used to nonthermally excite and coherently control the spin dynamics via the inverse Faraday effect in, for example, $DyFeO_3$ (Kimel *et al*., 2005) and $Lu_{3-x-y}Y_xBi_yFe_{5-z}Ga_zO_{12}$ (Hansteen, Kimel, Kirilyuk and Rasing, 2005). Other related work is that on ultrafast modification of the order parameter in AF materials that has been addressed both in theory (Gomez-Abal, Ney, Satitkovitchai and Hübner, 2004) and experiment (Kimel, Pisarev, Hohlfeld and Rasing, 2002; Duong, Satoh and Fiebig, 2004). In the latter case, however, conservation of J does not play a role, since the AF ordered state carries no net M.

The feasibility of the role of the laser field to the demagnetization process in itinerant FMs could be concluded from theoretical work by Zhang and Hübner. They developed a particularly interesting model, in which an ultrafast magnetic response (within ~10 fs) is explained by the dephasing induced by a cooperative effect of spin-orbit coupling and the external laser field (Zhang and Hübner, 2000). Although not stated explicitly, either direct angular momentum transfer from/to the laser field, or laser-enhanced transfer between orbital and spin momentum should be at the basis of the described effect. It is questionable, however, whether the laser-induced mechanism plays a dominant role in the demagnetization after laser heating of the ferromagnetic transition metals, as will be discussed in the subsequent text.

The first experiments on laser-induced angular momentum transfer for itinerant FMs were reported by Ju *et al*. (1998b). They used circularly-polarized pump pulses to study ultrafast spin dynamics in $CoPt_3$. More recently, Wilks and coworkers reported on polarization dependent studies on the ultrafast MO response of nickel thin films (Wilks *et al*., 2004). Whereas linearly polarized pump pulses provided relatively conventional transient demagnetization results ($\tau_{\mathrm{M}} = 130$ fs; minor difference between rotation and ellipticity), pronounced effects showed up in the rotational channel around zero delay when using circularly-polarized pump pulses. Nevertheless, this additional signal was demonstrated to transform even under reversal of the magnetic field, while transforming odd under reversal of the handedness of the polarization. Therefore, it cannot be considered a real magnetic effect, as also becomes clear from the observation of similar features for nonmagnetic materials (Wilks and Hicken, 2004). The additional features are well described by the specular inverse Faraday effect (SIFE) and specular optical Kerr effect (SOKE) (Wilks *et al*., 2004), related to the third-order optical susceptibility tensor, $\chi^{(3)}_{xxyy}$ and $\chi^{(3)}_{xyyx}$.

More recently, Dalla Longa performed additional circularly-polarized pumping experiments on nickel thin films (Dalla Longa, 2007), fully confirming results of Wilks. In the work of Dalla Longa, however, focus was particularly on a potential influence of the handedness of the pump polarization on the demagnetization timescale τ_{M}. It was argued that when the angular momentum of the photon was parallel to the original magnetic moment of the thin film, transfer of angular momentum could never promote a fast demagnetization on itself. Results (Figure 7) showed τ_{M} to be independent of the pump polarization within experimental accuracy ($\tau_{\mathrm{M}} = 135 \pm 10$ fs when using equation (20); $\tau_{\mathrm{M}} = 74 \pm 4$ fs when using equation (19)), ruling out a significant role of the photon angular momentum in the laser-induced ultrafast demagnetization process in nickel. In passing we emphasize that these results are in line with earlier, more qualitative, conclusions on an insignificant role of circular polarization for $CoPt_3$ (Beaurepaire *et al*., 1998).

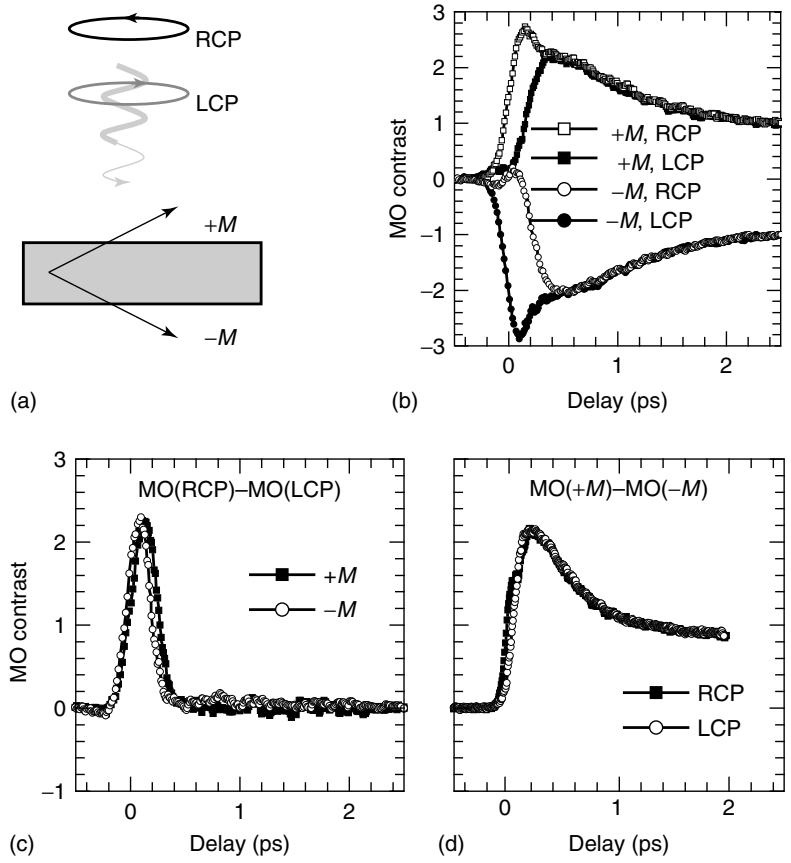

Figure 7. (a) Schematic diagram of the configuration. Applying a field perpendicular to the thin film, causes an upward ($+M$) or downward canting of the magnetization ($-M$). Photon angular momentum in a polar geometry is parallel or antiparallel for right-handed (RCP) or left-handed (LCP) polarized light, respectively. (b) TRMOKE in polar geometry on a 10-nm Ni thin film, using RCP and LCP pump light and canting magnetization upward and downward. (c) Polarization contrast (difference in contrast between RCP and LCP), and (d) magnetic contrast (difference between $+M$ and $-M$) in the same experiment. (After Dalla Longa, 2007.)

The latter conclusion cannot be considered as a complete surprise, because it agrees with earlier predictions: For example, in (Koopmans, van Kampen, Kohlhepp and de Jonge, 2000b) an excitation density $f_{\text{exc}} = 0.01$ led to a maximum demagnetization of 5%. For nickel, with an atomic magnetic moment of $0.6\,\mu_{\text{B}}$. This corresponds to a loss of $0.03\,\mu_{\text{B}}$ per Ni atom. Even if all absorbed photons would have transferred one quantum of angular momentum, the photon flux would have been a factor of 3 too small. Even more strongly, taking into account the quenching of orbital momentum in the transition ferromagnetic metals (Ashcroft and Mermin, 1976), which generally leads to a lowering of MO efficiency by one to two orders of magnitude, fully excludes a possible role of the photon-induced mechanism.

It should be emphasized that the foregoing estimate does not disqualify a photon-induced transfer between orbital and spin momenta, mediated by the laser field. However, in Section 2.3 it was argued that such a mechanism cannot lead to a full quenching of magnetization in the systems considered.

In conclusion, circularly-polarized light triggers interesting processes in the itinerant FMs, but these cannot be considered of relevance for the ultrafast demagnetization process. A simple estimate shows that the amount of photons is too small to account for the observed decrease of magnetic moment. Moreover, the experiments demonstrate that a possibly small transfer does not act as a seed for the process.

7 DEMAGNETIZATION DYNAMICS

After having read Section 5, the reader might have wondered whether TRMOKE is capable of probing the ultrafast magnetic behavior properly, and even whether a genuine demagnetization is occurring within a picosecond at all. Fortunately, the situation is far more positive. At present, it is generally

believed that – in most cases – TRMOKE closely images the genuine $M(t)$ behavior, and agrees on a characteristic timescale well below a picosecond, as based on the following arguments:

1. A loss in MO contrast within a few hundred femtoseconds is observed in almost all itinerant ferromagnetic metals (apart from Ni, e.g., Fe (Kampfrath *et al.*, 2002), NiFe (Melnikov, Güdde and Matthias, 2002), Co (Güdde *et al.*, 1999; Conrad, Güdde, Jähnke and Matthias, 1999; Comin *et al.*, 2004), $CoPt_3$ (Beaurepaire *et al.*, 1998; Guidoni, Beaurepaire and Bigot, 2002), and $Co_{25}Ni_{75}$/Pt multilayers (Wilks, Hicken, Ali and Hickey, 2005)).
2. In almost all experiments, starting with (Hohlfeld, Matthias, Knorren and Bennemann, 1997), it has been found that after approximately 300–500 fs, $\tilde{\theta}(t)$ is consistent with a spin temperature that is approaching the electron temperature, that is, $M(t) \sim M_{\rm eq}[T_{\rm e}(t)]$. From about half a picosecond, the demagnetization transient $\tilde{\theta}(t)$ reflects both the subpicosecond e–p equilibration, as well as the diffusive cooling of the thin film thereafter. Deviations from this behavior only occur in those exceptional cases where differences between $\Delta\theta(t)/\theta_0$ and $\Delta\epsilon(t)/\epsilon_0$ persist for longer times.
3. The *magnitude* of the demagnetization (as measured after a few hundred femtoseconds) displays a temperature dependence that would have been expected from a laser-heating induced change of the *equilibrium* magnetization at different ambient temperatures, that is, $\Delta\tilde{\theta} \propto ({\rm d}M_{\rm eq}(T)/{\rm d}T)\Delta T$, where ΔT is determined by the laser fluence and heat capacity (van Kampen, 2003).
4. Even in cases where differences between $\Delta\theta(t)/\theta_0$ and $\Delta\epsilon(t)/\epsilon_0$ persist for tens of picosecond, the thermal differences of the complementary channels (the real and imaginary part of ${\rm d}\tilde{\theta}/{\rm d}T$) nicely overlap (Koopmans, van Kampen and de Jonge, 2003), as shown in Figure 8.
5. If, in spite of the preceding arguments, at 1 ps the spin system would not have reached thermal equilibrium with electrons and lattice, a second (slower) transient to the final fully equilibrated state should be observed (most probably on a timescale of at most hundreds of picoseconds). Except for initial work by Scholl, Baumgarten, Jacquemin and Eberhardt (1997), in which a slower transition to the fully demagnetized state after a few hundred picosecond was claimed, such a two-step process has never been observed for the elementary itinerant FMs.
6. At large laser fluence (or reduced Curie temperature) and at a reversed bias field (i.e., H antiparallel to M) it has been shown possible to fully quench the MO contrast well within a picosecond, after which recovery is in the opposite orientation (Beaurepaire *et al.*, 1998; Hohlfeld *et al.*, 2001). It is difficult to come up with any interpretation other than a successful magnetization reversal, seeded within the first picosecond. We emphasize that the possibility to achieve full quenching in Ni thin films is not entirely uncontroversial. For example, Cheskis *et al.* claimed to see a saturation of the contrast loss at high excitation densities (Cheskis *et al.*, 2005). However, such a saturation can equally well be explained by the finite penetration depths of the pump light and the relatively thick film thickness (30 nm, i.e., twice the extinction depth) used in that work. Thereby, as a rough estimate, the laser power to heat the bottom part of the film above the Curie temperature is almost ten times higher than needed for the surface.
7. It has been demonstrated that the loss of MO contrast is accompanied by emission of a picosecond terahertz radiation pulse; which is interpreted as being due to the sudden change in magnetic moment within the first picosecond (Beaurepaire *et al.*, 2004; Hilton *et al.*, 2004).

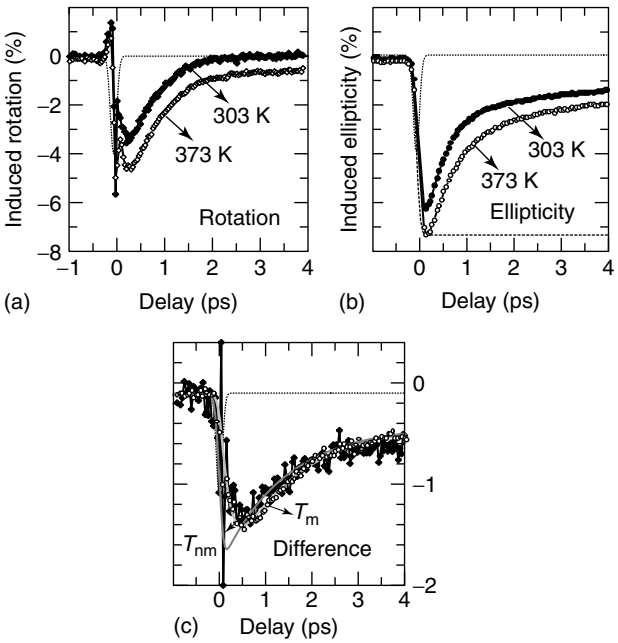

Figure 8. Transient MO response for Cu(001)/Ni/Cu at ambient temperatures of 307 K (filled) and 373 K (open). Normalized rotation (a) and ellipticity (b), respectively. (c) Thermal difference curves for rotation (filled) and ellipticity (open symbols). The line labeled T_{nm} (dark gray) indicates the fitted loss of electron plus phonon excess energy in the Ni layer (in au), the line labeled $T_{\rm M}$ (light gray) represents the fitted spin temperature (in au) (van Kampen, 2003).

8. In addition to the ultrafast demagnetization probed by TRMOKE and TRPE, it has been found from TRPE that also the exchange splitting is being reduced within approximately 300 fs (Rhie, Dürr and Eberhardt, 2003, 2005). Although also the interpretation of the photoemission data is far from trivial, it should be seen as an additional evidence for genuine magnetic effects during the first half a picosecond.
9. Despite the differences between $\Delta\theta(t)/\theta_0$ and $\Delta\epsilon(t)/\epsilon_0$ observed for some systems during the first hundreds of femtoseconds, in many other cases complementary channels do provide the same response. As an example, this has been verified in particular detail for a broad spectrum of laser frequencies in recent studies on $CoPt_3$ (Bigot, Guidoni, Beaurepaire and Saeta, 2004).
10. It has been found that the sudden reduction of magnetic moment can create an 'anisotropy field pulse' (van Kampen *et al*., 2002), its duration being estimated to be typically <2 ps for nickel thin films (cf. Section 8). Thereby, indirectly it provides additional proof of a genuine picosecond magnetic response.
11. In a special material (FeRh, cf. Section 9) a transition from an AF to FM state within 1 ps has been demonstrated unambiguously (Ju *et al*., 2004; Thiele, Buess and Back, 2004). One could well argue: if it is even possible to *generate* magnetism within 1 ps, then there is no reason to disbelieve a *lowering* of the ferromagnetic moment at a similar timescale.

Finally, we would like to stress that equally interesting results have been observed in other FM systems, such as Gd(0001) surfaces (Melnikov *et al*., 2004; Lisowski *et al*., 2005), magnetic semiconductors such as InMnAs (Wang *et al*., 2003, 2005), and several colossally magnetoresitive mangantites and other oxides (e.g., Kise *et al*., 2000; Ogasawara *et al*., 2005).

Altogether, ample of evidence for the loss of magnetic order in the elementary itinerant FMs within hundreds of femtosecond has been gathered by now. In search for the underlying mechanisms, it is of relevance agreeing on a number of relevant timescales. Here we will focus on a set of coherent experiments, both TRMOKE and transient reflection, performed for nickel thin films. Care was taken to have optically transparent films (homogeneously heating the layer), thermally well isolated from the substrate. Thereby, transport of hot electrons and thermal diffusion could be excluded, and a local description in terms of an extended 3T-model will be valid (van Kampen *et al*., 2005a). A set of characteristic data is displayed in Figure 9. It is concluded that the demagnetization time $\tau_M \approx 100$–200 fs (when using equation (20); just below 100 fs when using equation (19) (Dalla Longa, 2007)) is approximately equal or slightly longer than the thermalization time $\tau_T \approx 80$ fs, but shorter than the e−p equilibration $\tau_E \sim 0.4$ ps. Weak temperature dependencies in τ_M have been found in (van Kampen, 2003), but will not be discussed any further here.

Quite a few mechanisms have been proposed to account for such a subpicosecond demagnetization. However, as discussed in Sections 2.3 and 2.4, many of the proposed mechanisms excluding the lattice degree of freedom do not obey conservation of angular momentum. (i) Some interesting theoretical studies demonstrated femtosecond MO response, however, more in the spirit of state-filling effects than a transient $M(t)$ (Hübner and Zhang, 1998; Zhang and

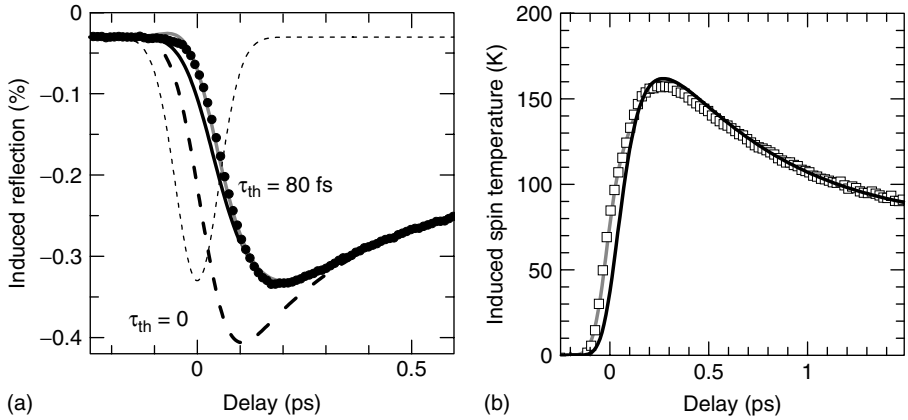

Figure 9. (a) Transient reflection on a nickel thin film, resolving τ_T and τ_E as indicated. Filled circles: measured reflection changes, thin dashed line: pump-probe autocorrelation, fat dashed line: 2T-model fit using infinitely fast thermalization ($\tau_T = 0$), fat line: fit including finite thermalization, and gray line: adding a coherent signal on top (representing weak state-filling effects). A background signal due to lattice expansion is corrected for (van Kampen *et al*., 2005a). (Reproduced from M. van Kampen *et al*., 2005, with permission from IOP Publishing Ltd. © 2005.) (b) TRMOKE data on the same film, resolving τ_M. Open circles display measured data. The black and gray lines represent 3T-model fits without- and with a coherent signal (dichroic bleaching) respectively (van Kampen, 2003).

Hübner, 1999; Vernes and Weinberger, 2005). (ii) In some explanations, the transfer of spin itself was not addressed explicitly, and it was merely stated to be occurring during electron thermalization (Hohlfeld, Matthias, Knorren and Bennemann, 1997; Guidoni, Beaurepaire and Bigot, 2002, and others). (iii) Elsewhere, a link was made with Stoner excitations (Scholl, Baumgarten, Jacquemin and Eberhardt, 1997), or a collapse of the Stoner gap (Cheskis *et al*., 2005), in both cases angular momentum conservation seems not fulfilled. (iv) Spin-orbit scattering in which spin and orbital momenta are exchanged would lead to an enhanced orbital moment upon lowering M. Thereby an increase of the MO contrast rather than a reduction would be expected (MO measuring mostly orbital effects (Oppeneer, 1998)), which has never been observed. (v) Transfer of orbital momentum during laser excitation has been demonstrated to be negligible (Section 6). (vi) Finally, emission of Tera Hertz radiation has been observed to accompany the laser-induced demagnetization (Beaurepaire *et al*., 2004; Hilton *et al*., 2004). The configuration was such, however, that it cannot explain the loss of angular momentum. At this stage, we consider it unlikely that such a scenario will provide the key answer.

Motivated by the controversy that arose, we have readdressed the possibility to include the lattice interactions in order to take care for a potential bath of angular momentum. Let us first restate two general arguments against such a scenario: (i) It is too slow, or, phrased differently, it would require an unrealistically large spin-flip probability a (see subsequent text, and Section 2.4.4). (ii) If the lattice is involved, one would expect the spin temperature to lag behind the lattice temperature that is, $\tau_M > \tau_E$.

A first numerical model including e–p induced spin-flip scattering was published in Koopmans, Kicken, van Kampen and de Jonge (2005). In search for the simplest model that just contained the essential ingredients three reservoirs were defined. A simplified electron and lattice system were defined as introduced in Section 2.4. In addition, the spin system was described as a set of identical two-level systems obeying Boltzmann statistics and with an exchange splitting Δ_{ex} that depends in a self-consistent way on the average spin moment $\overline{S}$, that is, using a mean-field (Weiss) description: $\Delta_{ex} = J\overline{S}$, where the exchange energy J is related to the Curie temperature via $k_B T_C = J/2$. A spin-flip probability a, for an e–p event to be accompanied by spin flip, was introduced. All dynamics was performed within the random-$\vec{k}$ approximation.

Numerically solving the Boltzmann equations after optical excitation of the electron system, revealed traces for T_e, T_p and T_s very similar to the ones obtained by the 3T model (Koopmans, Kicken, van Kampen and de Jonge, 2005). Some results for an arbitrary set of parameters and

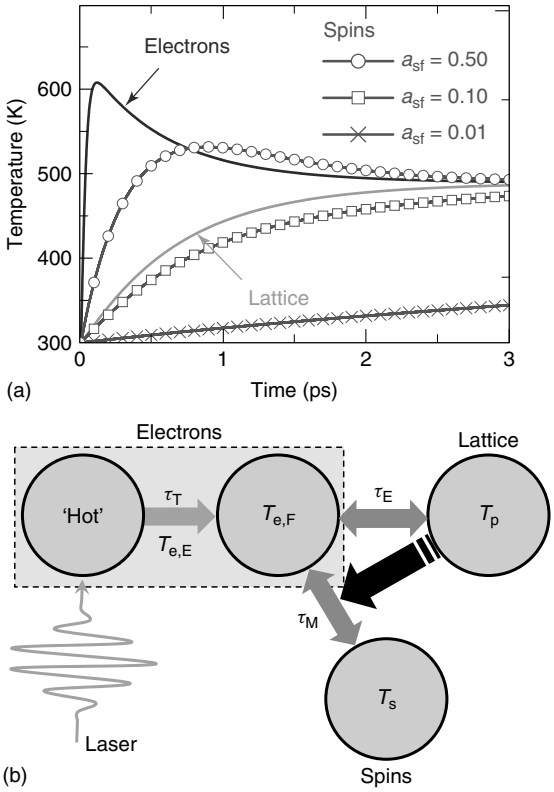

Figure 10. (a) Calculated traces of electron, lattice and spin temperature for different spin-flip probabilities a, according to the model discussed in the text. (Reproduced from B. Koopmans *et al*., 2005, with permission from Elsevier. © 2005.) (b) Schematic flow scheme of the phonon-mediated model.

as a function of spin-flip probability a are displayed in Figure 10(a). As expected, the higher a, the faster the equilibration of the spin temperature. However, as a surprising observation it can be seen that for some sets of parameters it is possible to achieve a spin response faster than the heating of the lattice (i.e) $\tau_M < \tau_E$, even though phonons are involved in the model. This clearly disproves argument (ii) against a phonon-mediated demagnetization.

These numerical efforts were later backed by an analytical approach, both including spin-flip scattering with phonons and with impurities. Equations could be derived for τ_M and τ_E in the limit of infinitely fast thermalization $\tau_T \to 0$ (Koopmans, Ruigrok, Dalla Longa and de Jonge, 2005). More specifically, for the phonon-mediated model, and for temperatures 'well-enough below T_C', a ratio

$$\frac{\tau_M}{\tau_E} = \frac{3c_0 D_s (\hbar\omega_D)^2}{\pi^2 a D_F k_B^3 T^2 T_C} \tag{33}$$

was found. For a reasonable set of parameters for Ni, it required $a \sim 0.1$ to end up with $\tau_M \sim \tau_E$. On the basis of the

band structure considerations – in particular the knowledge that band degeneracies near the Fermi level can enhance a by orders of magnitude (Fabian and Sarma, 1998) – it was concluded that phonon-mediated spin-flip scattering in the spirit of Elliot and Yafet may provide a non-negligible contribution to the subpicosecond magnetic response for realistic values of a. This significantly weakens argument (i) against a phonon-mediated demagnetization.

All of this can be understood diagrammatically as sketched in Figure 10(b): The energy flow from the electron to the spin bath, whereby T_s approaches T_e, is strongly influenced by (the temperature of) the lattice. The fact that even $a = 0.1$ is sufficient to achieve $\tau_M \sim \tau_E$ is related to the fact that it needs many e–p events ($\hbar\omega_q \sim 0.05\,\text{eV}$) to lower the kinetic energy of an optically excited electron ($<1\,\text{eV}$), whereas a single spin flip per atom is more than sufficient to quench all magnetization in nickel (with a magnetic moment of $0.6\,\mu_B$).

Finally, of even more generic interest, a potential link between the demagnetization process and Gilbert damping of precessional dynamics was derived in (Koopmans, Ruigrok, Dalla Longa and de Jonge, 2005). Therefore, the same model Hamiltonian was used to derive an analytical expression for the Gilbert parameter α. The approach followed was quite similar to the spin-flip scattering treated by Kamberský (1970), though did not include ordinary scattering between spin-dependent band levels (Kamberský, 1970; Kunes and Kamberský, 2002). Interestingly, for all mechanisms considered, that is, both the impurity- and phonon-mediated spin-flip scattering, practically the same relation between α and τ_M was found (Koopmans, Ruigrok, Dalla Longa and de Jonge, 2005):

$$\tau_M \approx c_0 \frac{\hbar}{k_B T_C} \frac{1}{\alpha} \tag{34}$$

again valid for T well-enough below T_C. The parameter c_0 is between $1/8$ and $1/4$, slightly depending on details of the models and regimes worked in. Although a strongly simplified model it sets the relevant timescale with surprising accuracy. For example, using $\alpha = 0.02$–0.03 (being the intrinsic value for nickel (Heinrich, Meredith and Cochran, 1979)), and $T_C = 630\,\text{K}$, readily predicts $\tau_M \sim 100\,\text{fs}$, within a factor of 2 of the measured value!

Thus, two major areas of contemporary research in magnetism were linked: (i) the ultrafast (subpicosecond) manipulation of magnetic matter, and (ii) the switching and precessional dynamics in multilayered and micromagnetic systems. Maybe, relating the two fields provides future answers to the origin of the femtosecond-scale magnetization processes in itinerant FMs as triggered by pulsed-laser heating. For sure, the new insight will inspire the community to come up with new and even more dedicated investigations aiming at further unraveling the secrets of ultrafast magnetization dynamics.

8 ANISOTROPY DYNAMICS AND LASER-INDUCED PRECESSION

Magnetic anisotropies arise from a subtle balance of the magnetic energy in an applied field, dipole–dipole interactions (in case of shape anisotropy) and spin-orbit interactions that give rise to coupling to the lattice (magnetocrystalline- and surface anisotropies). It has been found that sudden laser heating of a FM material can perturb the balance between the different anisotropy contributions and the applied field, launching a precessional motion of the magnetization vector. Such an approach provides access to both the precessional dynamics (frequency and damping), as well as the picosecond-dynamics of the magnetic anisotropy itself.

Ju *et al*. demonstrated the ability to use the ultrafast optical modulation of the AF/FM interaction of an exchange-biased (EB) bilayer to launch a precession of $\vec{M}$ (Ju *et al*., 1998a, 2000). In these experiments, such a modulation was obtained by heating a NiFe/NiO bilayer close to the blocking temperature T_B. A more general scheme was introduced by van Kampen *et al*. They found a similar laser-induced precession for a single magnetic layer with a canted equilibrium orientation of $\vec{M}$ (Koopmans, van Kampen, Kohlhepp and de Jonge, 2000b; van Kampen, Koopmans, Kohlhepp and de Jonge, 2001). Initially, the phenomenon was observed for specially engineered systems with a canted ground state orientation of the magnetization, such as epitaxial Cu(111)/Ni/Cu and Cu(001)/Ni/Cu at a proper (intermediate) Ni-layer thickness. Owing to the contrasting temperature dependence of the various anisotropy contributions, the canting angle Θ_c is strongly T-dependent when starting at a nontrivial angle ($\Theta_c \neq 0^\circ$ and $\Theta_c \neq 90^\circ$).

Later, it was reported that the phenomenon was even more general, and could be observed in polycrystalline films with an in-plane anisotropy as well, by pulling $\vec{M}$ to a canted orientation in an applied magnetic field (van Kampen *et al*., 2002) (Figure 11). For such a nickel polycrystalline film, the equivalence of the laser-induced precession with microwave driven magnetization oscillations was verified in a conventional 'FMR' experiment (van Kampen *et al*., 2002).

Many applications of the approach have followed. The dispersion of perpendicular standing spin waves could be resolved (van Kampen *et al*., 2002). In later experiments, discrete modes in artificial spin chains, that is, submicrometer pillars of $[NiFe/Al2O3]_n$ (n repetitions), were investigated (van Kampen *et al*., 2005b). The all-optical approach is

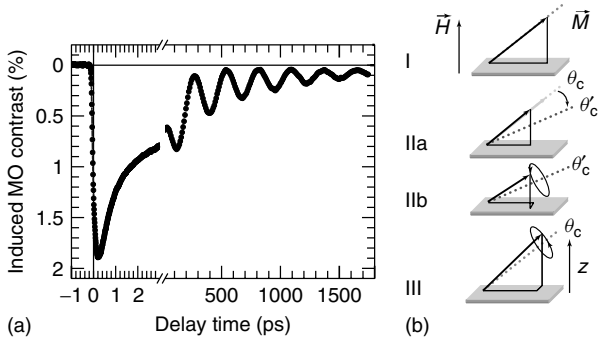

Figure 11. (a) Laser-induced precession in a polycrystalline nickel thin film, showing demagnetization (<2 ps) and successive precession, by measuring the polar component of the canted $\vec{M}$, and (b) schematic explanation: (I) In the external field, $\vec{M}$ is canted out of plane; (II) laser heating changes the equilibrium orientation, thereby triggering a precession; (III) after thermal recovery, the final precession is almost in the original anisotropy field.

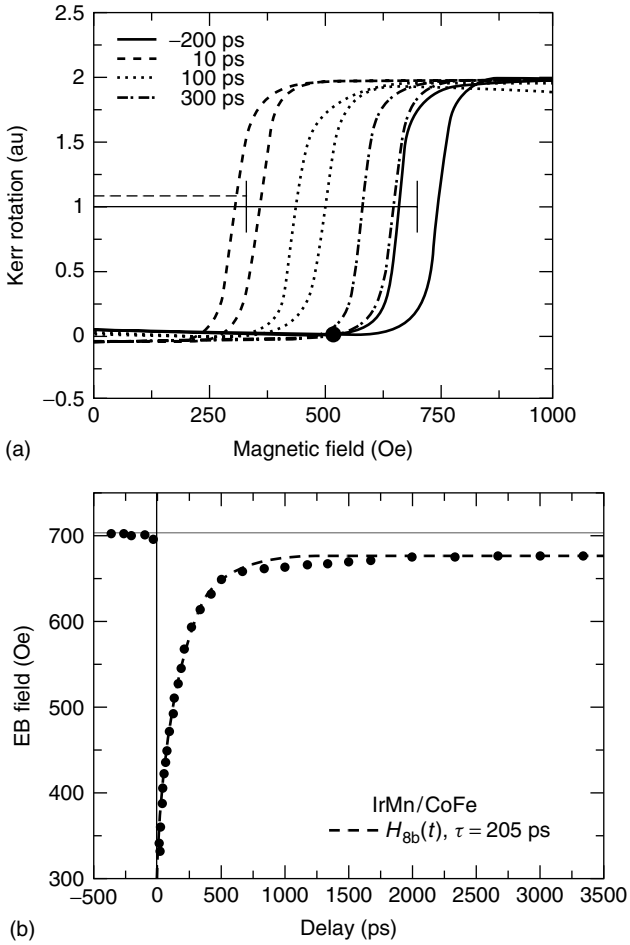

Figure 12. Exchange-bias shift field as a function of pump-probe delay measured for a IrMn/CoFe sample. (a) Easy axis transient hysteresis loops for various pump-probe delays as indicated. (b) Time evolution of H_{EB}. (Reproduced from M.C. Weber *et al.*, 2005, with permission from EDP Sciences. © 2005.)

particularly convenient for measuring dynamics on wedge-shaped samples, in which one of the film thicknesses is continuously varying over the sample area. Józsa used this configuration to explore correlations between damping and coercivity as well as damping by means of spin pumping (Józsa, 2006). Furthermore, the technique has been used to probe anisotropies, such as in the Fe/AlGaAs(001) system (Zhao *et al.*, 2005). The role of anisotropy on the ultrafast dynamics in cobalt has been addressed by Bigot, Vomir, Andrade and Beaurepaire (2005). Finally, it should be emphasized that the all-optical approach is particularly suited to measure materials with a high anisotropy (thereby a high precessional frequency) and a high damping (where a frequency domain approach is troublesome), such as hard disk recording media (Bergman *et al.*, unpublished).

Returning to the initial 'anisotropy field pulse', it has been demonstrated that the anisotropy is being modified really at the picosecond timescale. This can be concluded qualitatively from the observation of the first rotation of $\vec{M}$ already after several picoseconds. A more accurate estimate is obtained by backtracing the anisotropy field pulse from the complete precessional signal. A scheme therefore has been developed by Józsa (2006). For a nickel thin film, a characteristic timescale of at most 1–2 ps was derived this way.

Finally, a particularly interesting problem, with both scientific and technological aspects, is the quenching of the anisotropy interaction between a FM and an AFM, as originally being explored by Ju *et al.* for NiFe/NiO (Ju *et al.*, 1998a,b, 2000). More recently, Weber and coworkers reported on a collapse of the exchange-bias field H_{EB} within the first 10 ps after laser excitation, for three different EB systems (NiFe/FeMn, IrMn/CoFe and NiMn/CoFe) (Weber, Nembach and Fassbender, 2004; Weber *et al.*, 2005; Weber, Nembach, Hillebrands and Fassbender, 2005), the time scale basically determined by the relatively long pulse duration used (9 ps – see Figure 12). The fast thermal unpinning is followed by a slower heat diffusion dominated recovery of H_{EB}. Using a similar approach and identical samples, Hoffmann *et al.* found that even for 100-fs pulses the collapse of H_{EP} seemed to be just limited by the pulse duration (Hoffmann, 2006) – an observation that is not well being understood by now.

Future studies would certainly profit from the availability of well-defined, epitaxial systems. As a first attempt, Dalla Longa *et al.* started to explore the ultrafast dynamics of the EB effect in epitaxial Co/Mn films (Dalla Longa, Kohlhepp, de Jonge and Koopmans, 2006). This system displays large monolayer oscillations in both coercivity and EB field as a function of the Co thickness (Kohlhepp, Kurnosikov and de Jonge, 2005). First laser-induced precessional effects have been demonstrated for this intriguing system (Dalla Longa, Kohlhepp, de Jonge and Koopmans, 2006).

9 ULTRAFAST PHASETRANSITIONS AND GROWTH OF MAGNETISM

After having established the possibility to quench ferromagnetic order on a subpicosecond timescale, a new challenge is in generating magnetic order. Not only is this of profound fundamental interest it would also open up more serious applications of the laser-induced ultrafast magnetic manipulation.

The simplest approach is provided by cooling down a FM after laser heating above T_C (Figure 13a). Beaurepaire reported on such a laser-induced FM to PM transition within 0.5 ps in $CoPt_3$, and the successive recovery to the original FM state (Beaurepaire *et al*., 1998). Such experiments were extended to the real switching domain by Hohlfeld *et al*. (2001). The material of choice was the recording material GdFeCo, and pairs of set and reset magnetic field pulse allowed to follow the reversal process in a stroboscopic experiment (Figure 13b). However, the growth of M is basically limited by the cool-down time of the magnetic film, a slow diffusion driven process taking tens to hundreds of picoseconds.

A potentially much faster generation of magnetic order could be achieved for materials that display a magnetic phase transition (Figure 13c). A typical example is provided by FeRh. Recently, Ju *et al*. (2004) and Thiele, Buess and Back (2004) demonstrated independently the feasibility of driving therein the AF→FM phase transition within a picosecond by laser heating. When properly prepared, FeRh has the chemically ordered CsCl structure. At low temperatures, the material has an antiferromagnetic spin orientation, with iron local moments of $\pm 3\,\mu_B$ and no appreciable moment on rhodium. At a phase transition temperature of ~370 K, a first-order transition to a ferromagnetic phase takes place, with iron- and rhodium local moments of $3\,\mu_B$ and $1\,\mu_B$, respectively. The fact that the phase transition shows up slightly above room temperature makes it particular attractive for applications. The latter has been recently emphasized by Thiele, Maat and Fullerton (2003). They proposed the use of an exchange spring bilayer FePt/FeRh as a storage medium for heat-assisted recording.

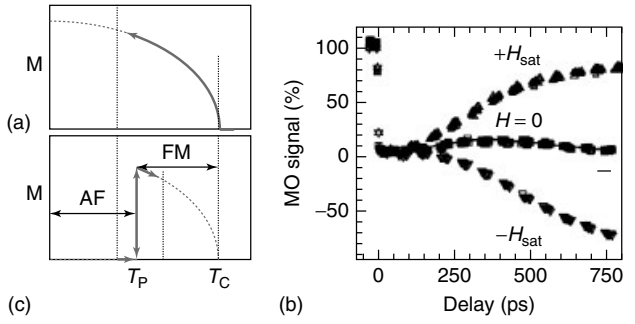

Figure 13. Schematic representation of growth of magnetic moment by cooling down below T_C (a) and by driving a AFM to FM phase transition (c). An experimental realization of the first option is displayed in (b) for a GdFeCo thin film, and applying different external fields. (Reproduced from J. Hohlfeld *et al*., 2001, with permission from the American Physical Society. © 2001.)

A typical time-resolved experiment is displayed in Figure 14(a). Using FeRh thin films, Ju *et al*. observed that about 20% of the final net MO signal establishes within the first picosecond, converging to a full signal after ~50 ps (Ju *et al*., 2004). Different fingerprints have been suggested to decide on a genuine laser-induced phase transition: (i) Appearance of a MO signal when performing the experiments in a magnetic field. (ii) The observation of a 'threshold fluence', as reported by Ju *et al*. (2004), and shown in Figure 14(b). A certain minimum laser fluence is needed to heat up the film above the transition temperature, T_P. Moreover, the higher the fluence, the longer the MO signal persists, because it takes longer to cool down below T_P – all exactly as observed in Figure 14(b). (iii) A 'two-peak feature' in the MO transient, as claimed originally by both teams (Ju *et al*., 2004; Thiele, Buess and Back, 2004). The magnetization may be expected to go twice through a maximum – that is, during heat up as well as while cooling down – since right above T_P the magnetic moment is highest. Also, at increasing laser fluence the time at which the second peak occurs should be larger. This 'two-peak argument' will next be addressed in more detail.

If the magnetic system would be in a constant equilibrium with electrons and lattice, a double pass of the state with highest M would be expected indeed. However, in the nonequilibrium experiment, the electron temperature is almost suddenly raised well above T_P. It is questionable whether in such a case the equilibration of electron and spin system is indeed accompanied by first a buildup of magnetic order, after which it is quenched again. Bergman, Ju *et al*. rephrased this consideration recently in terms of two separate timescales: τ_s to account for a process in which T_s increases monotonically, driving M through an optimum indeed, and τ_M accounting for a process in which the *magnetization* (rather than T_s) grows monotonously from zero to its final value (Bergman *et al*., 2006).

Support for the second model came from magnetic field dependent experiments, in which it was shown that the two features originally observed had to be assigned to the onset of a laser-induced precession, similar to the ones described in Section 8. This behavior was successfully accounted for by an LLG simulation in which both the magnitude and orientation of $\vec{M}$ were described (Bergman *et al*., 2006) – including heat diffusion and a gradual increase of M after passing T_P. More specifically, the effective field

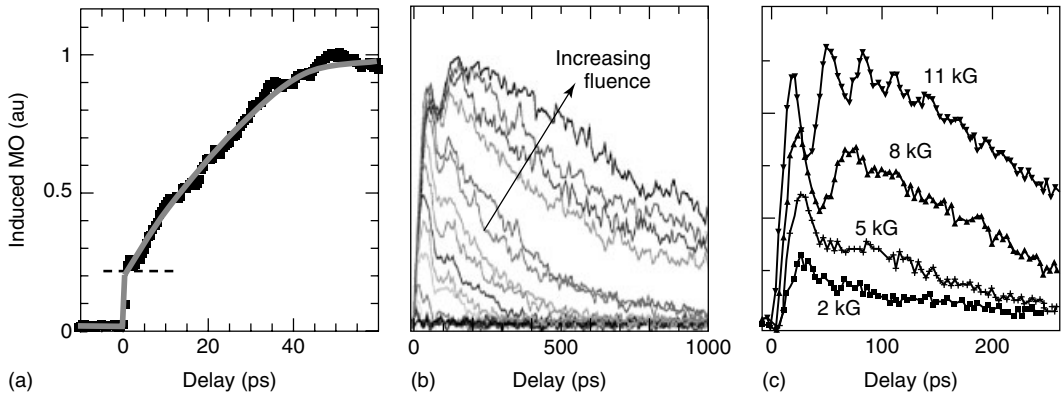

Figure 14. (a) Experimental realization of a subpicosecond growth of FM moment after pulsed-laser heating, demonstrated by TRMOKE on a thin FeRh film. (Reproduced from G. Ju *et al*., 2004, with permission from the American Physical Society. © 2004.) (b) A threshold fluence is needed to reach T_P, and the higher the fluence, the longer the system remains in the FM state. (Reproduced from B. Bergman *et al*., 2006, with permission from the American Physical Society. © 2006.) (c) At higher fields, a precession of $\vec{M}$ can be clearly observed.

($H_{\text{eff}}(t|)$) was calculated from time dependent orientation and magnitude of the magnetization vector throughout the film, $\vec{M}(z,t)|$), (z being the depth coordinate), and used in the LLG equation for the normalized magnetization: $\vec{m}(t) = \vec{M}(z,t)/M(z,t)$ requiring all spins in the system to be parallel:

$$\frac{\mathrm{d}\vec{m}}{\mathrm{d}t} = \gamma\mu_0\left(\vec{m}\times\vec{H}_{\text{eff}}\right) + \alpha\left(\vec{m}\times\frac{\mathrm{d}\vec{m}}{\mathrm{d}t}\right) \qquad (35)$$

For more details we refer to Bergman *et al*. (2006). At higher fields, a faster precession was found indeed as shown in Figure 14(c). This new interpretation shows that a two-peak feature as originally postulated is not observed upon laser heating of FeRh, asking for a description in terms of τ_M.

By observing an ultrafast, subpicosecond component in the MO response, both teams concluded to have solved the long-standing issue whether the magnetic phase transition in FeRh is driven by lattice expansion, or whether it is a purely electronic phenomenon. The observation of a growth of magnetism well before the lattice is expanded (several picoseconds) unambiguously demonstrates the latter (Ju *et al*., 2004; Thiele, Buess and Back, 2004).

The successive growth of the final MO contrast during a period of tens of picoseconds has been addressed in more detail in Bergman *et al*. (2006), exploiting a combined TRMOKE and transient reflectivity approach. It was concluded that all data are consistent with a subpicosecond nucleation of magnetic moments that grow and align during the next tens of picoseconds – driven by effective field and mutual exchange interactions.

Our understanding of the whole process on a *microscopic* scale is still limited. On the other hand, the material with its two coupled spin systems may provide a very efficient playground for acquiring more in-depth understanding of magnetic processes at the subpicosecond timescale. It is anticipated that exploring laser-induced magnetic phase transitions in general, and the FeRh case in particular, will grow toward a very rich and challenging field of research in the forthcoming years.

10 CONCLUDING REMARKS

Within a decade after the first report on femtosecond magnetization dynamics an exciting and active field of research has emerged. Hand in hand with developments in spintronics, ever new phenomena have been discovered. By now, a whole toolkit of methods for manipulating and probing FM matter on a subpicosecond time scale has become available. Main emphasis in this chapter was on all-optical approaches. It was shown that femtosecond laser pulses can demagnetize a ferromagnetic film within a few hundred femtosecond, but also drive an AF to FM phase transition and thereby generate a magnetic moment at a similar timescale. By changing the magnetic anisotropy at the subpicosecond timescale, precessional phenomena can be triggered and probed in an elegant all-optical scheme.

As will have become clear, our understanding of many of the phenomena is still at rather a phenomenological level. While the basic interactions leading to the equilibration of the electron and lattice system after pulsed-laser heating are relatively well understood, no consensus on the microscopic mechanisms underlying the femtosecond quenching and growth of magnetic order has been achieved yet. Nevertheless, the bare fact that a genuine change in magnetic order does occur within a few hundred femtoseconds is generally accepted by now. A larger number of supporting arguments were discussed, although it should be stressed that utmost care remains necessary to interpret optical data in the strong

nonequilibrium regime, where state-filling effects do mix up with the 'magnetic' signal. Within the chapter, the role of transfer of angular momentum has been emphasized, and some of the recently proposed dissipation channels were discussed. Recent approaches seem to point out a potential universal link between dissipation of precessional motion of the magnetization vector (Gilbert damping) with the relaxation time of microscopic spin fluctuations (represented by τ_M). Moreover, a possible role of phonons in the magnetic relaxation process even at picosecond timescale was estimated.

Clearly, a more comprehensive understanding of the underlying physics requires more dedicated theoretical efforts as well as novel, targeted experiments. New insight could be expected, for example, from the rapid development of synchrotron radiation sources, which may open up the possibility of performing element specific measurements of the spin dynamics at subpicosecond timescale, with the potential to discriminate between orbital and spin angular momenta. Also, rapid progress has been witnessed in the use of TRPE. Other routes, such as directly exciting and probing lower energy excitations (such as spin waves) in the system could be anticipated to provide deeper insight, but have not been explored intensively in the picosecond regime yet. Clearly, particular progress is expected from combing several of the aforementioned approaches in a clever way.

Apart from progress by improving our analytical techniques, exciting opportunities arise by engineering novel structures. Experiments on FeRh, but also spin dynamics in oxides that was not explicitly discussed in the present chapter, have shown the exciting phenomena that can be observed when moving to specific alloys and compounds. Also, a growing awareness is being witnessed that new classes of dynamics can be explored when entering the regime of exchange-coupled systems. Finally, the development of nano-structuring techniques opens up a particular challenging route for a combined spatiotemporal manipulation of the flow of energy and angular momentum in the nonequilibrium regime.

Upon completing this chapter, I'm particularly grateful to my (former) PhD and undergraduate students Maarten van Kampen, Csaba Józsa, Jeroen Rietjens, Bastiaan Bergman, Francesco Dalla Longa, Harm Kicken, and Dijon Boesten for their skillful experiments and original contributions to the research program – much of which contributed in an essential way to this chapter. Furthermore, I have profited considerably from instructive discussions and joint projects with many colleagues. Out of them, I specifically want to mention Ganping Ju and coworkers at Seagate Research, and Jaap Ruigrok at Philips Research, for our recent collaborations on FeRh (Section 9) and theory of femtosecond dynamics (Section 7), respectively. Finally, I acknowledge support by the European Communities Human Potential Programme (contract number HRPN-CT-2002-00318 ULTRASWITCH), and by the Netherlands Foundation for Fundamental Research on Matter (FOM).

REFERENCES

Acremann, Y., Strachan, J.P., Chembrolu, V., *et al*. (2006). Time-resolved imaging of spin transfer switching: beyond the macrospin concept. *Physical Review Letters*, **96**, 217202-1–217202-4.

Aeschlimann, M., Bauer, M., Pawlik, S., *et al*. (1997). Ultrafast spin-dependent electron dynamics in fcc Co. *Physical Review Letters*, **79**, 5158–5161.

Agranat, M.B., Ashikov, S.I., Granovskii, A.B. and Rukman, G.I. (1984). Interaction of picosecond laser pulses with the electron, spin and phonon subsystem of nickel. *Soviet Physics JETP*, **59**, 804–806.

Agranat, M.B., Ashikov, S.I., Granovskii, A.B. and Rukman, G.I. (1986). Interaction of picosecond laser pulses with the electron, spin, and phonon subsystems of nickel. *Zh. Eksp. Teor. Fiz.*, **86**, 1376–1379.

Ashcroft, N.W. and Mermin, N.D. (1976). *Solid State Physics*, Saunders College: Philadelphia.

Back, C.H., Allenspach, R., Weber, W., *et al*. (1999). Minimum field strength in precessional magnetization reversal. *Science*, **285**, 864.

Back, C.H., Weller, D., Heidmann, J., *et al*. (1998). Magnetization reversal in ultrashort magnetic field pulses. *Physical Review Letters*, **81**, 3251–3254.

Beaurepaire, E., Maret, M., Halté, V., *et al*. (1998). Spin dynamics in $CoPt_3$ alloy films: a magnetic phase transition in the femtosecond time scale. *Physical Review B*, **58**, 12134–12137.

Beaurepaire, E., Merle, J-C., Daunois, A. and Bigot, J-Y. (1996). Ultrafast spin dynamics in ferromagnetic nickel. *Physical Review Letters*, **76**, 4250–4253.

Beaurepaire, E., Turner, G.M., Harrel, S.M., *et al*. (2004). Coherent terahertz emission from ferromagnetic films excited by femtosecond laser pulses. *Applied Physics Letters*, **84**(18), 3465–3467.

Bennemann, K.H. (2004). Ultrafast dynamics in solids. *Journal of Physics: Condensed Matter*, **16**(30), R995–R1056.

Bergman, B., Ju, G., Hohlfeld, J., *et al*. unpublished.

Bergman, B., Ju, G., Hohlfeld, J., *et al*. (2006). Identifying growth mechanisms for laser-induced magnetization in FeRh. *Physical Review B*, **73**, R060407-1–R060407-4.

Beuneu, F. and Monod, P. (1978). The elliott relation in pure metals. *Physical Review B*, **18**, 2422.

Bigot, J.Y., Guidoni, L., Beaurepaire, E. and Saeta, P.N. (2004). Femtosecond spectrotemporal magneto-optics. *Physical Review Letters*, **93**(7), 077401-1–077401-4.

Bigot, J.Y., Vomir, M., Andrade, L.H.F. and Beaurepaire, E. (2005). Ultrafast magnetization dynamics in ferromagnetic cobalt: the role of anisotropy. *Chemical Physics*, **318**(1–2), 137–146.

Buess, M., Haug, Scheinfein, M. and Back, C.H. (2005). Micromagnetic dissipation, dispersion, and mode conversion in thin permalloy platelets. *Physical Review Letters*, **94**(12), 127205-1–127205-4.

Cheskis, D., Porat, A., Szapiro, L., *et al*. (2005). Saturation of the ultrafast laser-induced demagnetization in nickel. *Physical Review B*, **72**(1), 014437-1–014437-4.

Comin, A., Rossi, M., Mozzati, C., *et al*. (2004). Femtosecond dynamics of Co thin films on Si support. *Solid State Communications*, **129**(4), 227–231.

Conrad, U., Güdde, J., Jähnke, V. and Matthias, E. (1999). Ultrafast magnetization and electron dynamics of thin Ni and Co films on Cu(001) observed by time-resolved SHG. *Applied Physics B*, **68**, 511–517.

Dalla Longa, F., Kohlhepp, J.T., de Jonge, W.J.M. and Koopmans, B. (2006). Laser-induced ultrafast spin dynamics in epitaxial Co/Mn exchange-coupled bilayers. *Journal of Applied Physics*, **99**(8), 8F304-1.

Dalla Longa, F. (2007). *Physical Review B*, submitted.

Dubois, S., Piraux, L., George, J.M., *et al*. (2006). Evidence for a short spin diffusion length in permalloy from the giant magnetoresistance of multilayered nanowires. *Physical Review B*, **60**, 477–484.

Duong, N.P., Satoh, T. and Fiebig, M. (2004). Ultrafast manipulation of antiferromagnetism of NiO. *Physical Review Letters*, **93**(11), 117402-1–117402-4.

Elezzabi, A.Y. and Freeman, M.R. (1996). Ultrafast magneto-optic sampling of picosecond current pulses. *Applied Physics Letters*, **68**, 3546–3548.

Elezzabi, A.Y., Freeman, M.R. and Johnson, M. (1996). Direct measurement of the conduction electron spin-lattice relaxation time T_1 in gold. *Physical Review Letters*, **77**, 3220–3223.

Fabian, J. and Sarma, S.D. (1998). Spin relaxation of conduction electrons in polyvalent metals: theory and a realistic calculation. *Physical Review Letters*, **81**, 5624–5627.

Fann, W.S., Storz, R., Tom, H.W.K. and Bokor, J. (1992). Electron thermalization in gold. *Physical Review B*, **46**, 13592–13595.

Freeman, R. and Hiebert, W.K. (2002). *An Introduction to Micromagnetics in the Dynamic Regime*, *Topics in Applied Physics*, Springer: New York, pp. 93–126, Vol. 83.

Gerrits, T., van den Berg, H.A.M., Hohlfeld, J., *et al*. (2002). Ultrafast precessional magnetization reversal by picosecond magnetic field pulse shaping. *Nature*, **418**(6897), 509–512.

Gomez-Abal, R., Ney, O., Satitkovitchai, I. and Hübner, W. (2004). All-optical subpicosecond magnetic switching in NiO(001). *Physical Review Letters*, **92**(22), 227402.

Groeneveld, R., Sprik, R. and Lagendijk, A. (1995). Femtosecond spectroscopy of electron-electron and electron-phonon energy relaxation in Ag and Au. *Physical Review B*, **51**, 11433.

Güdde, J., Conrad, U., Jähnke, V., *et al*. (1999). Magnetization dynamics of Ni and Co films on Cu(001) and of bulk nickel surfaces. *Physical Review B*, **59**, R6608–R6611.

Guidoni, L., Beaurepaire, E. and Bigot, J.Y. (2002). Magneto-optics in the ultarfast regime: thermalization of spin populations in ferromagnetic films. *Physical Review Letters*, **89**(1), 017401-1–017401-4.

van Hall, P. (2001). Ultrafast processes in Ag and Au: a Monte carlo study. *Physical Review B*, **63**, 104301-1–104301-10.

Hansteen, F., Kimel, A., Kirilyuk, A. and Rasing, T. (2005). Femtosecond photomagnetic switching of spins in ferrimagnetic garnet films. *Physical Review Letters*, **95**, 047402.

Heinrich, B., Meredith, D.J. and Cochran, J.F. (1979). Wave number and temperature dependent Landau-Lifshitz damping in nickel. *Journal of Applied Physics*, **50**, 7726.

Hiebert, W.K., Stankiewicz, A. and Freeman, M.R. (1997). Direct observation of magnetic relaxation in a small permalloy disk by time-resolved scanning Kerr microscopy. *Physical Review Letters*, **79**, 1134–1137.

Hilton, D.J., Averitt, R.D., Meserole, C.A., *et al*. (2004). Terahertz emission via ultrashort-pulse excitation of magnetic metal films. *Optics Letters*, **29**(15), 1805–1807.

Hoffmann, D. (2006). Ultrafast decoupling dynamics in exchange coupled bilayers, to be published.

Hohlfeld, J. (1998). *Utrafast Electron-, Lattice- and Spin-Dynamics in Metals, Investigated by Linear and Nonlinear Optical Techniques*, Ph.D. Thesis, Freie Universität, Berlin, Germany.

Hohlfeld, J., Gerrits, T., Bilderbeek, M., *et al*. (2001). Fast magnetization reversal of GdFeCo induced by femtosecond laser pulses. *Physical Review B*, **65**, 012413-1–012413-4.

Hohlfeld, J., Güdde, J., Conrad, U., *et al*. (1999). Ultrafast magnetization dynamics of nickel. *Applied Physics B*, **68**, 505–510.

Hohlfeld, J., Matthias, E., Knorren, R. and Bennemann, K. (1997). Nonequilibrium magnetization dynamics of nickel. *Physical Review Letters*, **78**, 4861–4864.

Hübner, W. and Bennemann, K.H. (1989). Nonlinear magneto-optical Kerr effect on a nickel surface. *Physical Review B*, **40**, 5973–5979.

Hübner, W. and Bennemann, K.H. (1996). Simple theory for spin-lattice relaxation in metallic rare-earth ferromagnets. *Physical Review B*, **53**, 3422–3427.

Hübner, W. and Zhang, G.P. (1998). Ultrafast spin dynamics in nickel. *Physical Review B*, **58**, R5920.

Józsa, C. (2006). Optical Detection of Magnetization Precession, Ph.D. Thesis, Eindhoven University of Technology, Eindhoven, The Netherlands.

Ju, G., Hohlfeld, J., Bergman, B., *et al*. (2004). Ultrafast generation of ferromagnetic order via laser-induced phase transformation in FeRh thin films. *Physical Review Letters*, **93**(19), 197403.

Ju, G., Nurmikko, A.V., Farrow, R.F.C., *et al*. (1998a). Ultrafast optical modulation of an exchange biased ferromagnetic/antiferromagnetic bilayer. *Physical Review B*, **58**, R11857–R11860.

Ju, G., Vertikov, A., Nurmikko, A., *et al*. (1998b). Ultrafast nonequilibrium spin dynamics in a ferromagnetic thin film. *Physical Review B*, **57**, R700–R703.

Ju, G., Nurmikko, A.V., Farrow, R.F.C., *et al*. (2000). Coherent magnetization rotation by optical modulation in ferromagnetic/antiferromagnetic exchange-coupled bilayers. *Physical Review B*, **62**, 1171–1177.

Kamberský, V. (1970). On the landau-lifshitz relaxation in ferromagnetic metals. *Canadian Journal of Physics*, **48**, 2906.

Kampfrath, T., Ulbrich, R.G., Leuenberger, F., *et al*. (2002). Ultrafast magneto-optical response of iron thin films. *Physical Review B*, **65**, 104429-1–104429-6.

van Kampen, M. (2003). Ultrafast Spin Dynamics in Ferromagnetic Metals, Ph.D. Thesis, Eindhoven University of Technology, Eindhoven, The Netherlands.

van Kampen, M., Jozsa, C., Kohlhepp, J.T., *et al*. (2002). All-optical probe of coherent spin waves. *Physical Review Letters*, **88**, 227201.

van Kampen, M., Kohlhepp, J.T., de Jonge, W.J.M., *et al*. (2005a). Sub-picosecond electron and phonon dynamics in nickel. *Journal of Physics: Condensed Matter*, **17**(43), 6823–6834.

van Kampen, M., Soroka, I.L., Brucas, R., *et al*. (2005b). On the realization of artificial XY spin chains. *Journal of Physics: Condensed Matter*, **17**(2), L27–L33.

van Kampen, M., Koopmans, B., Kohlhepp, J.T. and de Jonge, W.J.M. (2001). Laser-induced precession in canted-spin ferromagnets. *Journal of Magnetism and Magnetic Materials*, **240**, 291–293.

Kimel, A.V., Kirilyuk, A., Usachev, P.A., *et al*. (2005). Ultrafast non-thermal control of magnetization by instantaneous photomagnetic pulses. *Nature*, **435**(7042), 655–657.

Kimel, A.V., Pisarev, R.V., Hohlfeld, J. and Rasing, T. (2002). Ultrafast quenching of the antiferromagnetic order in $FeBO_3$: direct optical probing of the phonon-magnon coupling. *Physical Review Letters*, **89**(28), 287401.

Kise, T., Ogasawara, T., Ashida, M., *et al*. (2000). Ultrafast spin dynamics and critical behavior in half-metallic ferromagnet: Sr_2FeMoO_6. *Physical Review Letters*, **85**, 1986–1989.

Knorren, R., Bennemann, K.H., Burgermeister, R. and Aeschlimann, M. (2000). Dynamics of excited electrons in copper and ferromagnetic transition metals. *Physical Review B*, **61**, 9427–9440.

Kohlhepp, J.T., Kurnosikov, O. and de Jonge, W.J.M. (2005). Oscillatory biquadratic antiferromagnet/ferromagnet interface exchange coupling. *Journal of Applied Physics*, **286**, 220.

Koopmans, B. (2003). *Laser-induced Magnetization Dynamics*, of *Topics in Applied Physics*, Springer: Berlin, pp. 253–320, Vol. 87.

Koopmans, B. (2004). Separation problems in optical spectroscopies. *Physica Scripta*, **T109**, 80–88.

Koopmans, B., Groot Koerkamp, M., Rasing, T. and van den Berg, H. (1995). Observation of large Kerr angles in the nonlinear optical response from magnetic multilayers. *Physical Review Letters*, **74**, 3692–3695.

Koopmans, B., Kicken, H.H.J.E., van Kampen, M. and de Jonge, W.J.M. (2005). Microscopic model for femtosecond magnetization dynamics. *Journal of Magnetism and Magnetic Materials*, **286**, 271–275.

Koopmans, B., Ruigrok, J.J.M., Dalla Longa, F. and de Jonge, W.J.M. (2005). Unifying ultrafast magnetization dynamics. *Physical Review Letters*, **95**, 267207.

Koopmans, B., van Kampen, M. and de Jonge, W.J.M. (2003). Experimental access to femtosecond spin dynamics. *Journal of Physics: Condensed Matter*, **15**(5), S723–S736.

Koopmans, B., van Kampen, M., Kohlhepp, J.T. and de Jonge, W.J.M. (2000a). Femtosecond spin dynamics of epitaxial Cu(111) /Ni/Cu wedges. *Journal of Applied Physics*, **87**, 5070–5072.

Koopmans, B., van Kampen, M., Kohlhepp, J.T. and de Jonge, W.J.M. (2000b). Ultrafast magneto-optics in nickel: magnetism or optics? *Physical Review Letters*, **85**, 844–847.

Kunes, J. and Kamberský, V. (2002). First-principles investigation of the damping of fast magnetization precession in ferromagnetic 3d metals. *Physical Review B*, **65**, 212411.

Lisowski, M., Loukakos, P., Melnikov, A., *et al*. (2005). Femtosecond electron and spin dynamics in Gd(0001) studied by time-resolved photemission and magneto-optics. *Physical Review Letters*, **95**(13), 137402-1–137402-4.

McGill, S.A., Miller, R.I., Torrens, O.N., *et al*. (2004). Dynamic Kerr effect and the spectral weight transfer of the manganites. *Physical Review Letter*, **93**(4), 047402-1–047402-4.

Melnikov, A., Bovensiepen, U., Radu, I., *et al*. (2004). Picosecond magnetization dynamics of the Gd(0001) surface. *Journal of Magnetism and Magnetic Materials*, **272**, 1001–1002.

Melnikov, A.V., Güdde, J. and Matthias, E. (2002). Demagnetization following optical excitation in nickel and permalloy films. *Applied Physics B*, **74**(7–8), 735–740.

Miltat, J., Albuquerque, G. and Thiaville, A. (2002). *An Introduction to Micromagnetics in the Dynamic Regime*, *Topics in Applied Physics*, Springer: New York, pp. 1–33, Vol. 83.

Ogasawara, T., Ohgushi, K., Tomioka, Y., *et al*. (2005). General features of photoinduced spin dynamics in ferromagnetic and ferrimagnetic compounds. *Physical Review Letters*, **94**(8), 087202-1–087202-4.

Oppeneer, P.M. (1998). Magneto-optical spectroscopy in the valence-band energy regime: relationship to magnetocrystalline anisotropy. *Journal of Magnetism and Magnetic Materials*, **188**, 275–285.

Oppeneer, P.M. and Liebsch, A. (2004). Ultrafast demagnetization in nickel: theory of magneto-optics for non-equilibrium electron distributions. *Journal of Physics: Condensed Matter*, **16**(30), 5519–5530.

Pan, R., Wei, H.D. and Shen, Y.R. (1989). Optical second-harmonic generation from magnetized surfaces. *Physical Review B*, **39**, 1229–1234.

Regensburger, H., Vollmer, R. and Kirschner, J. (2000). Time-resolved magnetization-induced second-harmonic generation from the Ni(110) surface. *Physical Review B*, **61**, 14716–14719.

Rhie, H.S., Dürr, H.A. and Eberhardt, W. (2003). Femtosecond electron and spin dynamics in Ni/W(110) films. *Physical Review Letters*, **90**(24), 247201-1–247201-4.

Rhie, H., Dürr, H. and Eberhardt, W. (2005). Femtosecond evolution of electronic interactions at the Ni(111) surface. *Applied Physics A*, **82**, 9–14.

Schmidt, A.B., Pickel, M., Wiemhofer, M., *et al*. (2005). Spin-dependent electron dynamics in front of a ferromagnetic surface. *Physical Review Letters*, **95**(10), 10742-1–10742-4.

Scholl, A., Baumgarten, L., Jacquemin, R. and Eberhardt, W. (1997). Ultrafast spin dynamics of ferromagnetic thin films observed by fs spin-resolved two-photon photemission. *Physical Review Letters*, **79**, 5146–5149.

Scott, G.G. (1962). Review of gyromagnetic ratio experiments. *Reviews of Modern Physics*, **34**(1), 102–109.

Shen, Y.R. (1989). Optical second harmonic generation at interfaces. *Annual Review of Physical Chemistry*, **40**, 327–350.

Siegmann, H.C., Garwin, E.L., Prescott, C.Y., *et al*. (1995). Magnetism with picosecond field pulses. *Journal of Magnetism and Magnetic Materials*, **151**, L8–L12.

Stamm, C., Tudosa, I., Siegmann, H.C., *et al*. (2005). Dissipation of spin angular momentum in magnetic switching. *Physical Review Letters*, **94**, 197603.

Steiauf, D. and Fähnle, M. (2005). Damping of spin dynamics in nanostructures: an ab initio study. *Physical Review B*, **72**(6), 64450-1–64450-13.

Sun, C.K., Vallee, F., Acioli, L.H., *et al*. (1994). Femtosecond-tunable measurement of electron thermalization in gold. *Physical Review B*, **50**, 15337.

Thiele, J.U., Buess, M. and Back, C.H. (2004). Spin dynamics of the ferromagnetic-to-antiferromagnetic phase transition in FeRh on a sub-picosecond time scale. *Applied Physics Letters*, **85**(14), 2857–2859.

Thiele, J.U., Maat, S. and Fullerton, E.E. (2003). FeRh/FePt exchange spring films for thermally assisted magnetic recording media. *Applied Physics Letters*, **82**, 2859–2861.

Tserkovnyak, Y., Brataas, A. and Bauer, G.E.W. (2002). Enhanced Gilbert damping in thin ferromagnetic films. *Applied Physics Letters*, **88**(11), 117601-1–117601-4.

Tudosa, I., Stamm, C., Kashuba, A.B., *et al*. (2004). The ultimate speed of magnetic switching in granular recording media. *Nature*, **428**, 831.

Urban, R., Woltersdorf, G. and Heinrich, B. (2001). Gilbert damping in single and multilayer ultrathin films: role of interfaces in nonlocal spin dynamics. *Physical Review Letters*, **87**(21), 217204-1–217204-4.

Vaterlaus, A., Beutler, T., Guarisco, D., *et al*. (1992). Spin-lattice relaxation in ferromagnets studied by time-resolved spin-polarized photoemission. *Physical Review B*, **46**, 5280–5286.

Vaterlaus, A., Beutler, T. and Meier, F. (1991). Spin-lattice relaxation time of ferromagnetic gadolinium determined with time-resolved spin-polarized photoemission. *Physical Review Letters*, **67**, 3314–3317.

Vernes, A. and Weinberger, P. (2005). Formally linear response theory of pump-probe experiments. *Physical Review B*, **71**(16), 165108.

Vomir, M., Andrade, L.H.F., Guidoni, L., *et al*. (2005). Real space trajectory of the ultrafast magnetziation dynamics in ferromagnetic metals. *Physical Review Letters*, **94**(23), 237601-1–237601-4.

Wang, J., Sun, C., Kono, J., *et al*. (2005). Ultrafast quenching of ferromagnetism in InMnAs induced by intense laser irradiation. *Physical Review Letters*, **95**(16), 167401-1–167401-4.

Wang, J., Khodaparast, G.A., Kono, J., *et al*. (2003). Ultrafast optical manipulation of ferromagentic order in InMnAs/GaSb. *Journal of Superconductors*, **16**(2), 373–377.

Weber, M.C., Nembach, H., Blomeier, S., *et al*. (2005). All-optical probe of magnetization dynamics in exchange biased bilayers on the picosecond timescale. *The European Physical Journal B*, **45**(2), 243–248.

Weber, M.C., Nembach, H. and Fassbender, J. (2004). Picosecond optical control of the magnetization in exchange biased NiFe/FeMn bilayers. *Journal of Applied Physics*, **95**(11), 6613–6615.

Weber, M.C., Nembach, H., Hillebrands, B. and Fassbender, J. (2005). Real-time temperature dynamics in exchange-biased bilayers upon laser excitation. *IEEE Transactions on Magnetics*, **41**(3), 1089–1092.

Wilks, R. and Hicken, R.J. (2004). Transient optical polarization response of aluminum at the interband transition. *Journal of Physics: Condensed Matter*, **16**(25), 4607–4617.

Wilks, R., Hicken, R.J., Ali, M., *et al*. (2004). Investigation of ultrafast demagnetization and cubic optical nonlibearity of Ni in the polar geometry. *Journal of Applied Physics*, **95**(11), 7441–7443.

Wilks, R., Hicken, R.J., Ali, M. and Hickey, B.J. (2005). Ultrafast demagnetization of $Co_{25}Ni_{75}$/Pt multilayers with perpendicular anisotropy at elevated temperatures. *Journal of Applied Physics*, **97**(10), 10A705.

Wilks, R., Hughes, N.D. and Hicken, R.J. (2002). Investigation of ultrafast spin dynamics in a Ni thin film. *Journal of Applied Physics*, **91**(10), 8670–8672.

Woltersdorf, G., Buess, M. and Back, B.H.C.H. (2005). Time resolved magnetization dynamics of ultrathin Fe(001) films: spin-pumping and two-magnon scattering. *Physical Review Letters*, **95**(3), 037401-1–037401-4.

Yafet, Y. (1963). *g-Factors and Spin-lattice Relaxation Times of Conduction Electrons*, *Solid State Physics*, Academic, New York, Vol. 14, pp. 1–98.

Zhang, G.P. and Hübner, W. (1999). Femtosecond spin dynamics in the time domain. *Journal of Applied Physics*, **85**, 5657–5659.

Zhang, G.P. and Hübner, W. (2000). Laser-induced ultrafast demagnetization in ferromagnetic metals. *Physical Review Letters*, **85**, 3025–3028.

Zhang, G.P., Hübner, W. and Bigot, J-Y. (2002). *Laser-induced Ultrafast Demagnetization: Ferromagnetism, A New Frontier? Topics in Applied Physics*, Springer: Berlin, pp. 245–288, Vol. 83.

Zhao, H.B., Talbayev, D., Dang, Q.G., *et al*. (2005). Ultrafast magnetization dynamics of epitaxial Fe films on AlGaAs(001). *Applied Physics Letters*, **86**(15), 152512-1–152512-3.

Investigation of Ultrathin Ferromagnetic Films by Magnetic Resonance

Klaus Baberschke
Freie Universität Berlin, Berlin-Dahlem, Germany

1 INTRODUCTION

When a magnetic dipole moment is subjected to a magnetic field $\vec{H}$, it experiences a torque motion. Its equation of motion is given by

$$\frac{\partial \vec{\mu}}{\partial t} = \gamma \left[\vec{\mu} \times \vec{H}_0\right] \quad \text{with} \quad \gamma = \frac{g\mu_B}{\hbar} = g\frac{(-e)}{2mc} \tag{1}$$

$$\frac{\partial \vec{M}}{\partial t} = -\gamma(\vec{M} \times \vec{H}_{\text{eff}}) \tag{2}$$

The motion of the angular momentum or the magnetic moment consists of a uniform precession about $\vec{H}$ with angular velocity $\vec{\omega}_L = -\gamma \vec{H}$. Without damping, the component of $\vec{\mu}$ along $\vec{H}$ remains fixed in magnitude, so that the 'Zeeman energy' $E = \vec{\mu} \cdot \vec{H}$ is a constant of the motion. Real systems have a finite damping (relaxation). The dissipation of this part of energy can be pumped into the torque motion by means of microwave radiation in resonance with $\omega_{MW} = \omega_L$, yielding a Lorentzian linewidth ΔH (Figure 1b, see Section 4). Electron paramagnetic resonance (EPR) (equation 1) and ferromagnetic resonance (FMR) (equation 2) [1] are based on the same principle – for EPR see (Abragam and Bleaney, 1966; Orton, 1968; Pake, 1962), for FMR see (Vonsovskii, 1966; Heinrich, 1994; Farle, 1998). Historically, they followed very different routes: For EPR H_0, the local and the external field are equal and known with high precision. The only unknown quantity is the g-factor or g-tensor. For FMR it is the opposite, $\vec{H}_{\text{eff}}$ of a ferromagnet is the unknown parameter. It is the vector sum of several anisotropic field contributions (dipole, spin orbit, external, and microwave).

$$\vec{H}_{\text{eff}} = \vec{H}_{\text{dipole}} + \vec{H}_K + \vec{H}_0 + \vec{h}_{\text{MW}} \tag{3}$$

Note that the exchange field in a ferromagnet is always parallel to $\vec{M}$ and does not contribute to the torque. $\vec{M}$ can be seen as the sum of the individual moments per volume $\vec{M} = \sum \vec{\mu}_i$. For ultrathin simple ferromagnetic films (e.g., Fe, Co, Ni), μ is defined per particle.

In this chapter we will give a brief overview of three aspects that are most important for the investigation of novel magnetic nanostructures by means of microwave spectroscopy: The UHV-FMR technique and its monolayer sensitivity and the static parameters of magnetism (e.g., magnetic anisotropy energy (MAE) and interlayer exchange coupling (IEC), both measured with FMR in absolute energy

Handbook of Magnetism and Advanced Magnetic Materials. Edited by Helmut Kronmüller and Stuart Parkin. Volume 3: *Novel Techniques for Characterizing and Preparing Samples*. ISBN: 978-0-470-02217-7.

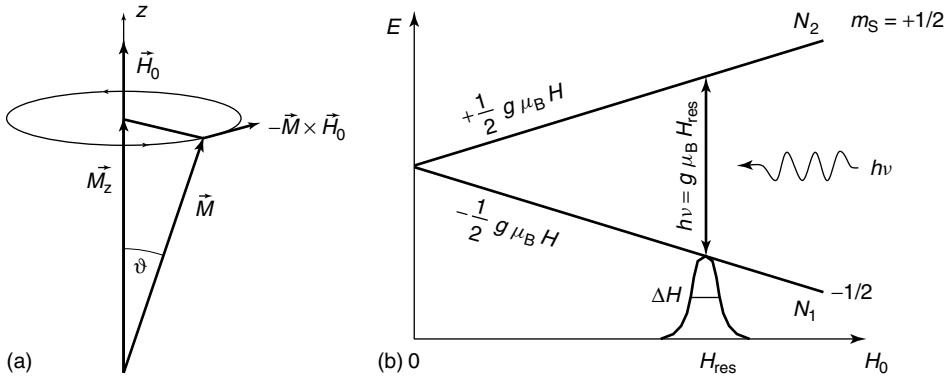

Figure 1. (a) Sketch of the uniform precession of vector $\vec{M}$ about the external field $\vec{H}_0$. (b) Zeeman levels for a spin $m_s = \pm 1/2$ system and the dipole transition for $\vec{h}_{MW}$ being perpendicular to $\vec{H}_0$.

units). Finally in Section 4 we give examples for the spin dynamics determined from the FMR linewidth.

The examples used here, mainly from our own work, will elucidate the strength of FMR and its intimate contact with *ab initio* calculations exactly adapted to FMR experiments.

2 *In situ* UHV-FMR: EXPERIMENTAL DETAILS

Magnetic resonance spectroscopy will be most instructive if external parameters can be varied. One important parameter is the temperature T. The intensity of the magnetic resonance signal (area under the resonance line) is proportional to the static susceptibility (White, 1970). Temperature variation allows us to study the EPR above the Curie temperature T_C and the FMR in the ferromagnetic phase below T_C, cf. Section 4. Other phase transitions such as those in superconductors or crystallographic phase transitions can be studied with paramagnetic impurities as a sensor by means of EPR (Baberschke, 1976; von Waldkirch *et al*., 1973). In ferromagnets, one of the most important quantities is the MAE and its temperature dependence (Heinrich, 1994; Vonsovskii, 1966; Farle, 1998). FMR measures this directly in absolute energy units, cf. Section 3 [2]. Equally important is the measurement of the angular dependence of the resonance signal. Following equation (1), it is a standard procedure in the paramagnetic regime to determine the anisotropic magnetic moment, that is, the g-tensor (Abragam and Bleaney, 1966; Orton, 1968; Pake, 1962). If these experimental requirements can be combined with UHV, the EPR/FMR will be a very powerful experimental tool to study ultrathin ferromagnetic films. The ultimate sensitivity of microwave spectroscopy is in the range of 10^{11} spins. Usually, in standard surface science and UHV technique, molecules are adsorbed with a submonolayer coverage onto a crystalline substrate, for example, a Cu(001) crystal. Equivalently, ferromagnetic monolayers (ML) of Fe, Co, and Ni are epitaxially grown on such a substrate with a surface area of a few square millimeters. This corresponds to $\sim 10^{14}$ lattice sites on the surfaces (Farle *et al*., 1985). Thus the EPR/FMR should be sensitive to submonolayer coverage. This has been demonstrated for 1/100 ML of paramagnetic molecules (Zomack and Baberschke, 1986).

2.1 *In situ* UHV-FMR

Figure 2 shows the combination of a UHV chamber and a microwave EPR/FMR spectrometer. Microwave spectrometers are commercially available (Varian, Bruker). The most popular microwave frequency is 9 GHz (X band). The corresponding microwave cavity usually has a geometric size of $\sim$4 cm $\times$ 4 cm (wavelength of the microwave $\sim$3–4 cm) with a central access hole of 0.5–1 in. diameter for inserting the sample. In this central access hole a quartz finger tip of a UHV chamber is inserted. In other words, the microwave cavity and all other parts of the spectrometer are operated in laboratory air. Only the sample itself is prepared and measured *in situ* under UHV conditions. This offers a very important variety of experiments, for example, to measure ultrathin films, first facing vacuum without protection layer. Then adding a cap layer and monitoring the effect of the capping on the magnetism of the ultrathin ferromagnet, or adding step-by-step *in situ* a second ferromagnetic film and studying IEC, and so on. Figure 2 shows the large electromagnet with external fields of 10–15 kOe and the field axis pointing horizontally in the laboratory frame. The sample itself is mounted on a vertical UHV manipulator with a rotating vertical axis. This allows full angular-dependent measurements varying the magnetic field from in plane to out of

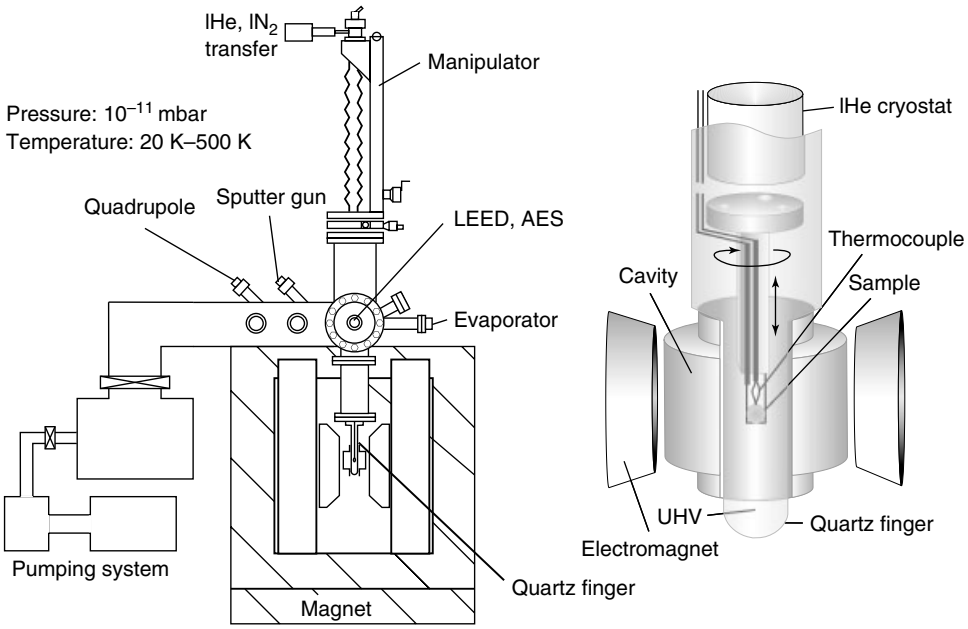

Figure 2. Sketch of the combination of a conventional EPR spectrometer with a large electromagnet and a UHV chamber equipped with all necessary installations for surface science physics (Zomack and Baberschke, 1986; Farle, 1998). The pumping station is mounted on the left-hand side, whereas the bottom part of the UHV chamber is inserted into the electromagnet and the microwave cavity. The electromagnet (being movable on a track) and the microwave cavity are taken away from the UHV chamber for a standard bakeout procedure to reach a base pressure in the 10^{-11} mbar range. For details see text.

plane. The commercial manipulator is equipped with a cooling system for ℓHe or ℓN_2. It has a very large z (vertical) travel of ∼50 cm. This specialty is necessary to move the sample above the electromagnet into the upper part of the UHV chamber for sample preparation. This upper level is equipped with standard surface science UHV instruments such as Auger, LEED, quadrupole, evaporator, sputter gun, and so on. Recording a typical FMR spectrum takes only a few minutes. Thus, a full angular dependence or temperature dependence may be measured within an hour. Afterward, the sample may be moved to the upper position for further sample preparation such as adding a cap layer or a second ferromagnet, adsorbing gas on the surface, and so on. Finally it is moved down again for a second *in situ* experiment.

Figure 3 shows the EPR/FMR of Gd/W(110) as one example. The Curie temperature of bulk Gd equals $T_{\mathrm{Cb}} \approx 292\,\mathrm{K}$, for 1.6 ML Gd/W(110) it is $T_{\mathrm{C}} < 292\,\mathrm{K}$ (open squares) due to the finite size effect. Figure 3(b) convincingly shows the high sensitivity of the FMR. At 316 K, the signal for 1.6 ML is recorded with a very good signal-to-noise ratio. The resonance signal has been monitored from 360 K to below the corresponding Curie temperature for each film (Farle and Baberschke, 1987). The steep increase of the intensity follows the temperature dependence of the susceptibility of the Gd films. The external field $\vec{H}_0$ was applied in plane along the easy axis of the Gd film. Consequently, the external resonance field shifts to lower values at lower temperature because the internal one $\vec{H}_{\mathrm{dipole}} + \vec{H}_K$ increases when the temperature is reduced.

The idea of a fingertip inserted into a microwave cavity has been used before for ^{3}He/^{4}He dilution refrigerators (Nagel *et al*., 1980; Baberschke and Tsang, 1980). The same idea of experimental setup, namely, the combination of UHV technique with magnetic measurements can be used to determine the magnetization with a SQUID (Ney *et al*., 2002) as well as the ac-susceptibility $\boldsymbol{\chi}_{\mathbf{ac}}$ (Stetter *et al*., 1992). All three techniques FMR, SQUID, and $\boldsymbol{\chi}_{\mathbf{ac}}$ combined with state-of-the-art surface physics and UHV technique offer a new insight into the understanding of the fundamentals of the magnetism of ultrathin ferromagnetic films.

2.2 Multifrequency FMR

Following equation (1), we estimate that a typical resonance condition is given for ∼10 GHz and ∼3.5 kOe. Under certain limitations the absorption of electromagnetic waves between two Zeeman levels is proportional to ω^2. Thus EPR microwave spectroscopy is more sensitive by ∼4 orders of magnitude than nuclear magnetic resonance operating in the range of 100 MHz. On the other hand, microwave spectroscopy has some limitations. It operates usually only at one fixed frequency due to microwave oscillators and the waveguide technique. Consequently, the magnetic field has

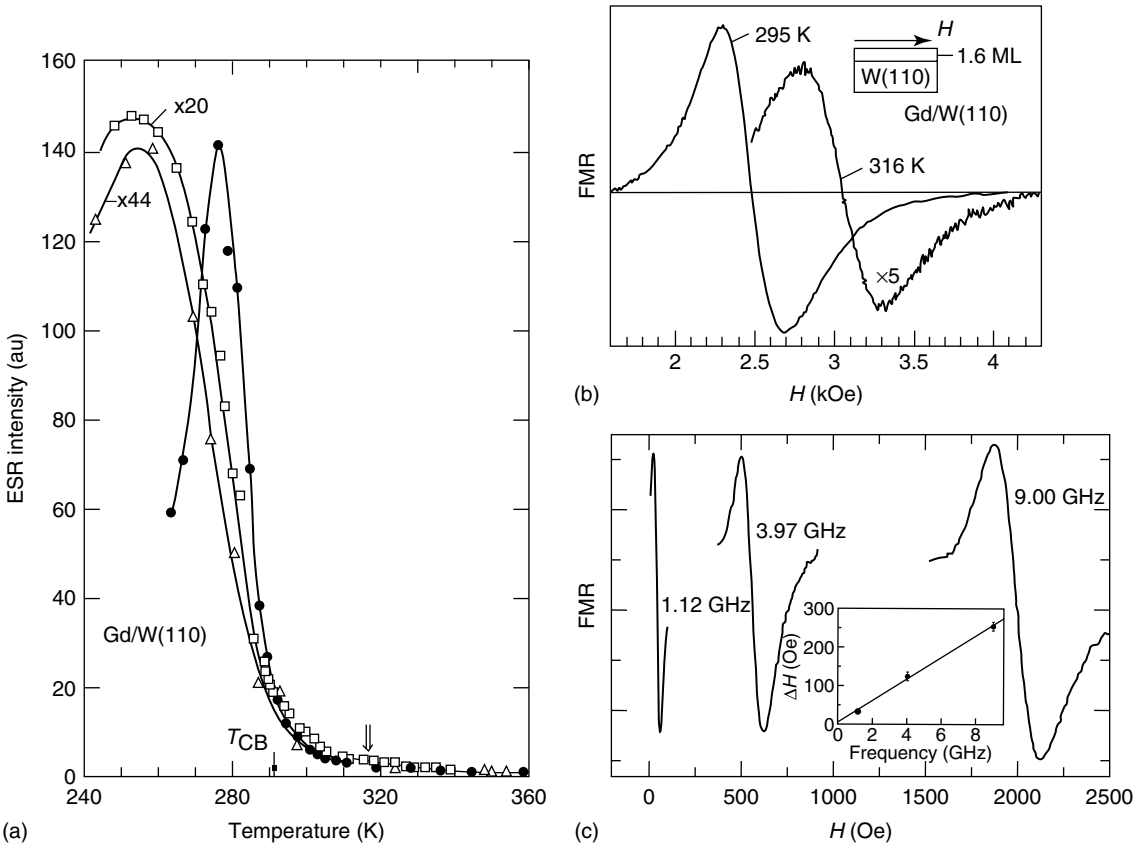

Figure 3. Typical magnetic resonance spectra of ferromagnetic monolayers (Farle and Baberschke, 1987). (a) EPR intensity for different film thickness: 80 Å (full circles), 1.6 ML (open squares), 0.8 ML (open triangles). The arrow at 316 K corresponds to the experimental spectrum given in (b). Note that the spectrum at 295 K in (b) is still above T_C. (c) FMR of 7 ML Ni/Cu(001) at 1, 4, and 9 GHz. The spectra are taken in the ferromagnetic phase. Corresponding to equations (1) and (2) also the external Zeeman field reduces if the microwave frequency is reduced. Note the narrowing of the linewidth – at 1.12 GHz the linewidth is $\Delta H = 15$ Oe only (cf. Section 4). All three spectra are taken *in situ* in UHV without protective layer for the same film, just by replacing the microwave cavities.

to be scanned (see Figure 1b). The majority of experiments are performed in dilute paramagnetic systems. These experiments focus mostly on the determination of the different components of the g-tensor (equation 1). Consequently, the larger the frequency, the better the separation of different components of the g-tensor (slopes in the Zeeman level) for a given linewidth. Field scanning in a ferromagnetic film creates some difficulties. First of all, in contrast to a paramagnet, the ferromagnet has an internal anisotropy field with an easy and a hard axis in the crystallographic frame. Thus, the applied external field and the internal field are usually not collinear. Scanning the external field through the resonance condition means, in principle, dragging the magnetization behind the field direction and, as a consequence, the Lorentzian line shape should be deformed. Fortunately, this effect is very small. More important is the analysis of the measured linewidth itself. If determined at only one frequency, it will not be so easy to interpret this value. In the past, quite frequently some inhomogeneous broadening assuming local field distribution was used for the interpretation of the width. In Figure 3(c) we show the FMR of 7 ML Ni/Cu(001) at 1, 4, and 9 GHz. Obviously, the linewidth is strongly frequency dependent and narrows down to a few oersteds only at low frequencies. This means that frequency-dependent measurements are very important to disentangle relaxation processes and other contributions to the linewidth of the FMR in ultrathin ferromagnetic films. Fortunately, microwave cavities in this lower frequency range (1, 3, 4 GHz) are available with the same geometrical size as the 9 GHz cavity and the same central access hole of 1 in. diameter. This allows us to keep the sample in UHV, only replacing the 9 GHz microwave cavity by a 1 or 4 GHz cavity, and measure the same film. In Section 4 it will be shown that FMR measurements at very high frequencies of 200 GHz and more are also of relevance to investigate the dynamics of magnetic nanostructures. For these frequencies, the wavelength reduces to below the millimeter regime. Different experimental techniques are needed (Silsbee *et al.*, 1979;

Monod and Janossy, 1977). Currently these experiments are not performed in UHV. Here, one still needs a protective cap layer to record the FMR signal.

3 *g*-TENSOR AND MAGNETIC ANISOTROPY ENERGY (MAE)

To solve the equations of motion equations (1) and (2) under the influence of a small oscillatory microwave field $\vec{h}_{\mathrm{MW}}$ with $\vec{h}\tau\perp\vec{H}_0$ and to calculate the resonance condition with ω_{MW} and a given external magnetic field H_0 we refer to standard literature, for example, (Vonsovskii, 1966; Heinrich, 1994; Farle, 1998). It is the advantage of magnetic resonance spectroscopy that the method to calculate the resonance condition and interpret, for example its angular dependence (direction of H_0 with respect to the crystallographic axis of ultrathin films), is well established for a long time. In this section we give a few examples to demonstrate the power and usefulness of FMR to gain information on the intrinsic parameters of ultrathin ferromagnetic structures. The resonance conditions are given below for the polar and azimuthal angular dependence

$$\begin{aligned}\left(\frac{\omega}{\gamma}\right)^2 = \Bigg[& H_0\cos(\theta-\theta_H) \\ & + \left(-4\pi M_{\mathrm{eff}} - \frac{2K_{2\parallel}}{M} + \frac{K_{4\perp}}{M} - \frac{K_{4\parallel}}{2M}\right)\cos 2\theta \\ & + \left(\frac{K_{4\perp}}{M} + \frac{K_{4\parallel}}{2M}\right)\cos 4\theta\Bigg] \times \Bigg[H_0\cos(\theta-\theta_H) \\ & + \left(-4\pi M_{\mathrm{eff}} - \frac{2K_{2\parallel}}{M} + \frac{K_{4\parallel}}{M}\right)\cos^2\theta \\ & + \left(\frac{2K_{4\perp}}{M} + \frac{K_{4\parallel}}{M}\right)\cos^4\theta + \frac{2K_{2\parallel}}{M} - \frac{2K_{4\parallel}}{M}\Bigg] \quad (4)\end{aligned}$$

$$4\pi M_{\mathrm{eff}} := 4\pi M - 2K_{2\perp}/M \quad (5)$$

and for $\theta = \theta_H = 90^\circ$:

$$\begin{aligned}\left(\frac{\omega}{\gamma}\right)^2 = \Bigg[& H_0\cos(\varphi-\varphi_H) + \frac{2K_{2\parallel}}{M}\cos 2(\varphi-\varphi_{\mathrm{u}}) \\ & + \frac{2K_{4\parallel}}{M}\cos 4\varphi\Bigg] \times \Bigg[H_0\cos(\varphi-\varphi_H) + 4\pi M_{\mathrm{eff}} \\ & + \frac{2K_{2\parallel}}{M}\cos^2(\varphi-\varphi_{\mathrm{u}}) + \frac{K_{4\parallel}}{2M}(3+\cos 4\varphi)\Bigg] \quad (6)\end{aligned}$$

where θ_H is the polar angle of the external magnetic field H_0 with respect to the surface normal of the thin film, θ the angle of the magnetization, and φ the azimuthal angle in plane. Only along the easy and hard axis of the magnetization, the vectors $\vec{M}$ and $\vec{H}_0$ are parallel and $\theta = \theta_H$. For all other orientations, the equilibrium angle of θ can be calculated by minimizing the free energy of the system (Smit and Beljers, 1955). Full angular-dependent measurements of the FMR of ultrathin films have shown in numerous cases the dragging of the magnetization, see for example, Figure 38 in (Farle, 1998). Equations (4)–(6) also show the various contributions of anisotropy fields K_i/M (Berghaus *et al.*, 1989). In several cases, the analysis of the experimental results was projected on two mechanisms only as given in equation (5): The dipole or shape anisotropy field $4\pi M$ and the so-called uniaxial out-of-plane anisotropy contribution $K_{2\perp}/M$, also called K_{u}/M. However, equations (4) and (6) show that full angular-dependent FMR measurements also give access to $K_{2\parallel}$. An axial in-plane symmetry is usually caused by steps at the surface or can be observed for vicinal crystal surfaces. Since many of the ultrathin ferromagnets (Fe, Co, Ni) are grown pseudomorphically on nonmagnetic single-crystal substrates like Cu or GaAs, they will not grow in their bulk crystallographic cubic structure but will be tetragonally or trigonally distorted. This can easily be detected by monitoring the $K_{4\perp}$ and $K_{4\parallel}$ contributions – K_4 is a fourth-order term but in most cases not of cubic symmetry. For details of the MAE and its notation, see Appendix B.

As stated in the introduction one focal point of FMR investigations in the past was the determination of anisotropy energies and anisotropy fields in ultrathin ferromagnets. It was often assumed that the g value is close to $g = 2$ for the free electron (Vonsovskii, 1966; Heinrich, 1994). In contrast, equations (4) and (6) offer the opportunity to determine not only anisotropy fields but also, independently, the proper g value as is common practice in standard EPR. Resolving the double parentheses product in equation (4), we see that there exists one term that depends only on the external magnetic field H_0^2. FMR experiments at different frequencies offer the possibility of determining g also from the proportionality of the parabolic behavior of $\omega^2 = f(H)$. This will be discussed in the following subsection.

3.1 *g*-tensor, μ_{L}, μ_{S}

In the past it was often assumed that the orbital magnetic moment is quenched in cubic Fe, Co, and Ni structures and magnetism was explained in terms of the spin magnetic moment only. However, giant orbital magnetic moments have been observed recently in magnetic nanostructures (Gambardella *et al.*, 2003). Even in bulk cubic materials, the survival of large orbital moments for itinerant magnets has been observed (Brewer *et al.*, 2004). Kittel (Meyer and Asch,

1961) has already shown that the departure from $g = 2$ is a measure of the ratio of orbital-to-spin magnetic moment [3].

$$\frac{\mu_L}{\mu_S} = \frac{g-2}{2} \tag{7}$$

For bulk Fe, Co, and Ni, the g value increases from 2.09 to 2.21 (Stearns, 1986). This tells us that in Ni μ_L is already 10% of the spin moment, and μ_L is parallel to μ_S in accordance with the positive sign of the spin-orbit coupling constant. In EPR, it is also well known that the light 3d elements like Cr have g values $g < 2$, the spin-orbit constant is negative and μ_L and μ_S are aligned antiparallel. EPR/FMR have the capability to measure orbital and spin magnetism. As a matter of fact, standard second-order perturbation theory (Abragam and Bleaney, 1966; Orton, 1968; Pake, 1962) shows that the MAE and the anisotropy of the orbital magnetic moment are caused by the same matrix elements mixing excited states into the magnetic ground state.

One example in thin-film magnetism is given in Figure 4. A thick Fe film and ultrathin Fe_n/V_m multilayers were measured by two techniques: FMR and X-ray magnetic circular dichroism (XMCD) (Anisimov *et al.*, 1999). For the same specimen, the ratio of the orbital-to-spin magnetic moment was measured by both techniques. In Figure 4(a), the ratio is given as function of the Fe thickness. A thick Fe film of 40 nm shows $g = 2.09$ corresponding to $\mu_L/\mu_S = 0.045$. When reducing the Fe thickness to 4 and 2 MLs only, the g value increases up to $g = 2.26$, which means an increase of μ_L by a factor of 3. In Figure 4(b), the XMCD spectra for both, the V and Fe $L_{3,2}$ edges are plotted. It is known that at an Fe/V interface a magnetic moment is induced at the V site. Following Hund's rule for V (Fe) spin and orbital moment are antiparallel (parallel) aligned. This leads to an enhancement of the effective orbital moment and a reduction of the total spin moment. FMR measures the total magnetic response of such a multilayer structure, whereas X-ray absorption spectroscopy (XAS) and XMCD (see also **Synchrotron Radiation Techniques Based on X-ray Magnetic Circular Dichroism, Volume 3** and **Magnetic Spectroscopy, Volume 1**) are element-specific methods and are, therefore, in a position to measure the magnetism at the Fe and the V site separately as shown in Figure 4(b). The apparent discrepancy between the determination of μ_L/μ_S by FMR and XMCD can therefore easily be explained. XMCD (full circles) measure only the Fe contribution. For the total response as probed by FMR we note from Figure 4(b) that the spin moment of V is antiparallel to that of Fe. The total spin moment is reduced. In contrast, the orbital moments of Fe and V are aligned parallel. Therefore, the larger value for the ratio (open circles) determined by FMR is completely understandable.

In conclusion, owing to its element-specificity, XMCD measures μ_S and μ_L at the Fe and the V site separately. FMR determines the ratio μ_L/μ_S from the g value. If a second measurement, for example by SQUID, provides the total magnetization ($\mu_L + \mu_S$), spin and orbital contributions may be separated without XMCD.

3.2 MAE in a ferromagnetic monolayer

The *in situ* FMR in ultrathin Ni/Cu(001) films of 3–25 ML has been used to study the spin reorientation transition (SRT) (Schulz and Baberschke, 1994). To analyze the experimentally determined K values properly it is important to notice that when changing the thickness of the ferromagnetic film, the Curie temperature T_C will change, too. It is therefore not advisable to plot $K(1/d)$ at a fixed thermodynamic temperature T but rather at the reduced temperature $t = T/T_C$.

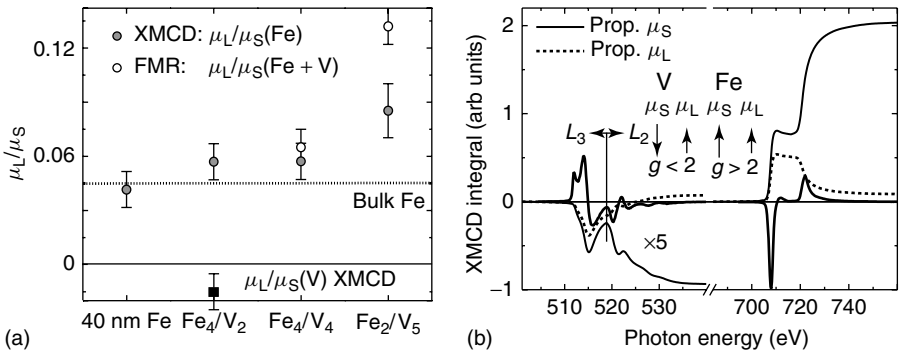

Figure 4. Orbital and spin magnetic moments, μ_L and μ_S, respectively, of Fe/V multilayers measured by FMR and XMCD (Scherz *et al.*, 2001). (a) The ratio μ_L/μ_S increases with decreasing Fe thickness. Note that XMCD measures only the Fe moments (full circles), whereas FMR measures the total (Fe and V) response (open circles). The ratio μ_L/μ_S of V in Fe_4V_2 as obtained from XMCD (full squares) is negative because μ_L and μ_S are aligned antiparallel in V. (b) XMCD spectra (thick solid line) and integrated XMCD signals as they would appear in the spin (thin solid line) and orbital (dotted line) sum rule.

Comparing experimental results only makes sense if the data are taken at the same reduced temperature. The MAE vanishes at T_C, that is, it is zero in the paramagnetic regime. In Figure 5(a) two sets of data are plotted: full circles at $t = 0.56$ and open triangles at $t = 0.74$. That this is an important point is seen in Figure 5(b) in which experimental data are plotted at a fixed temperature of $T = 300\,\mathrm{K}$ as a function of the thickness from $\sim$1 to $\sim$10 ML. At first glance, it seems that as the film becomes thinner the anisotropy K increases with a positive slope. If, however, the data of Farle *et al.* (1999) (full circles) are plotted at a fixed, reduced temperature $t = 0.21$ (Figure 5c) instead of a fixed absolute temperature $T = 300\,\mathrm{K}$, again a linear function of $1/d$ results with negative slope up to $\sim$6 ML. This is the only correct way of analyzing magnetic anisotropy of ultrathin films. Figures 5(a) and 5(c) can be interpreted in the same way: Starting from right to left, at very thin films of $\sim$3 ML we see a linear increase with negative slope of $f(1/d)$ up to a particular value of $\sim$15 ML for Ni and $\sim$6 ML for Co. In the ultrathin limit, the Ni and Co films grow pseudomorphically with tetragonal distortion for Ni(001) (trigonal for Co(111)). At the bending, the pseudomorphic growth stops and the films grow in the natural bulk structure of the specific material, for example, fcc for Ni. These linear dependences of $K(1/d)$ in Figure 5(a) and 5(c) confirm equation (A3), namely, the classical argument by Néel that the surface and interface anisotropies scale down with $1/d$. The diagrams also show the extrapolation of the linear slope to the y axis indicated as K^V. Let us assume for sake of argument that ultrathin films of Ni or Co grew with a rigid perturbed lattice structure (i.e., tetragonally distorted owing to pseudomorphic growth) up to infinite thickness, indeed an extremely large volume anisotropy of 30 or 90 μeV/atom would occur. Of course, ferromagnetic films do not do that. The growth mode collapses back to the natural bulk lattice structure of the material with much lower anisotropy per particle. We did observe that this linear function and bending in $K(1/d)$ is the most sensitive indicator for changes in the growth mode. The crystallographic structure may change only by less than 0.1 Å, which is difficult to measure by diffraction (LEED) but does have large effects on MAE and K.

FMR measures the total M_{eff} (equation (5)). After subtraction of the dipole contribution $2\pi M^2$, the K parameters (Figure 5) can be plotted as a function of $1/d$ or as a function of T (for details see Appendix B). We also see that $2\pi M^2$ has to be scaled with the reduced temperature. It is obvious that because of the small magnetic moment per Ni atom the shape anisotropy for Ni is much smaller ($\sim$10 μeV/atom) than for Co ($\sim$90 μeV/atom) with a large magnetic moment per atom. This is the simple reason why the easy axis of magnetization for ultrathin ferromagnetic films of Co is in most cases in plane. Whereas for Ni the K anisotropy caused by the spin-orbit coupling can exceed the dipole contribution and result in an SRT from in plane to out of plane at $\sim$7–9 ML (e.g., Figure 5a). For details see (Baberschke 1996, 2001; Farle, 1998). Like in bulk ferromagnets, the various K_i parameters have a different temperature dependence. For bulk, see (Stearns, 1986), for ultrathin films, see (Farle, 1998; Baberschke, 2001). In equations (4) and (6) the shift of the external resonance field H_0 as a function of the temperature or angle is measured in absolute field units, that is, Oe. For a given magnetization, this can easily be translated into energy units. Many other spectroscopies discussed in this volume measure magnetic anisotropy usually only in arbitrary units. Determining the absolute MAE is the strength of the FMR. Therefore, a new challenge is to compare FMR experiments with *ab initio* calculations from first principles.

The importance of the temperature dependence of the MAE in ferromagnetic nanoclusters recently became very evident. Various groups have investigated small ferromagnetic particles (e.g., Co) by means of MOKE and XMCD, measuring very large MAE and orbital magnetization.

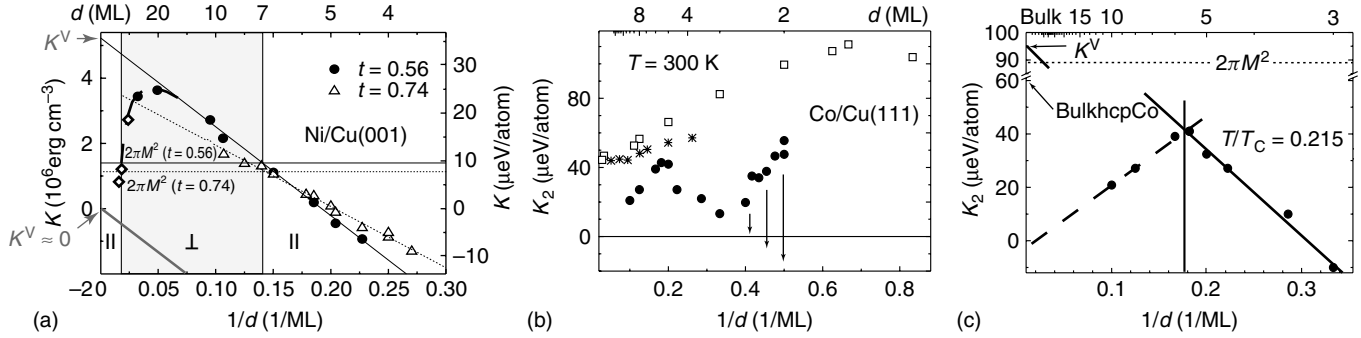

Figure 5. K_2 anisotropy as a function of $1/d$ (a) for Ni/Cu(001) at different reduced temperatures (Schulz and Baberschke, 1994), (b) and (c) for Co/Cu(111). The data in (b) are taken from (Huang *et al.*, 1994) (open squares) and (Kohlhepp *et al.*, 1993) (asterisks). Both were measured at fixed, ambient temperature. The data taken from (Farle *et al.*, 1999) (full circles) are plotted at fixed temperature in (b) and as a function of reduced temperature in (c).

Usually, one assumes a uniaxial anisotropy constant K_u. However, Antoniak *et al*. (2005) measured the temperature dependence $K(T)$ for Fe/Pt nanoparticles with FMR and observed that it changes between 50 and 300 K by one order of magnitude. This explains the whole magnetic behavior of these nanoparticles.

To demonstrate the high sensitivity of the MAE on small crystallographic lattice perturbations, we show in Figure 6(a) *ab initio* calculations for an infinite-sized single Ni crystal. It is an all electron, full relativistic calculation including orbital polarization (full symbols) and without orbital polarization (open symbols). The infinite-sized crystal was chosen to demonstrate the importance of the volume contribution K^v. K^v is defined as the difference in total energy between the hard and easy axis, for bulk Ni the [100] and [111] magnetization directions (Hjortstam *et al*., 1997). The difference in total energy was calculated for different ratios c/a, starting from an fcc lattice ($c/a = 1$), passing through a regime with tetragonal symmetry and ending in a bcc symmetry ($c/a = 1/\sqrt{2}$). For fcc and bcc, K^v almost vanishes, $K^v \ll 1\,\mu$eV/atom. In the tetragonal regime, K^v increases by orders of magnitude up to $K^v \approx 500\,\mu$eV/atom. For the FMR experiments shown in Figure 5, the pseudomorphic growth of the Ni film produces a constant ratio $c/a \approx 0.95$ (gray regime in Figure 6a). The *ab initio* calculations in Figure 6 yield an anisotropy energy of $K^v \approx 100\,\mu$eV/atom. This result is in perfect agreement with the experimental finding after extrapolating the experimental value to $K^v\,(T = 0)$. Comparing experiment and theory, one comes to the conclusion that *changes in the nearest-neighbor distance of* $\sim$*3%, that is,* $\sim$0.05 *Å, may change the MAE by orders of magnitude.*

The Weinberger group (Uiberacker *et al*., 1999) has performed similar calculations for a particular FMR experiment on a 12 ML Ni film grown on a Cu substrate and facing vacuum. Figure 6(b) shows the magnetic part of the difference in total energy per individual Ni layer. For the open triangles, a rigid, unrelaxed fcc lattice was assumed, whereas open squares and open circles are calculations for a relaxed tetragonal Ni structure adapted to the lattice of the Cu substrate. It is obvious that the topmost Ni layer facing vacuum shows a large negative contribution corresponding to the negative slope in Figure 5(a). It is also clear that the first Ni layer on the Cu substrate has a different (smaller) negative energy contribution due to hybridization with the Cu band structure. Such an effect cannot be separated in an FMR experiment – the experiment measures the sum of the two contributions. However, the center part of the 12 ML Ni film is most instructive: For a rigid cubic lattice, their energy contribution is very small. If, however, one puts the real relaxed lattice as determined from experiment into the calculation, we see that the center part of an ultrathin film also contributes to the total MAE in full agreement with the results of Figure 6(a). That is to say, *surface and interface magnetic anisotropy contributions* K^s *are certainly very large following the early argument by Néel, but they usually count only*

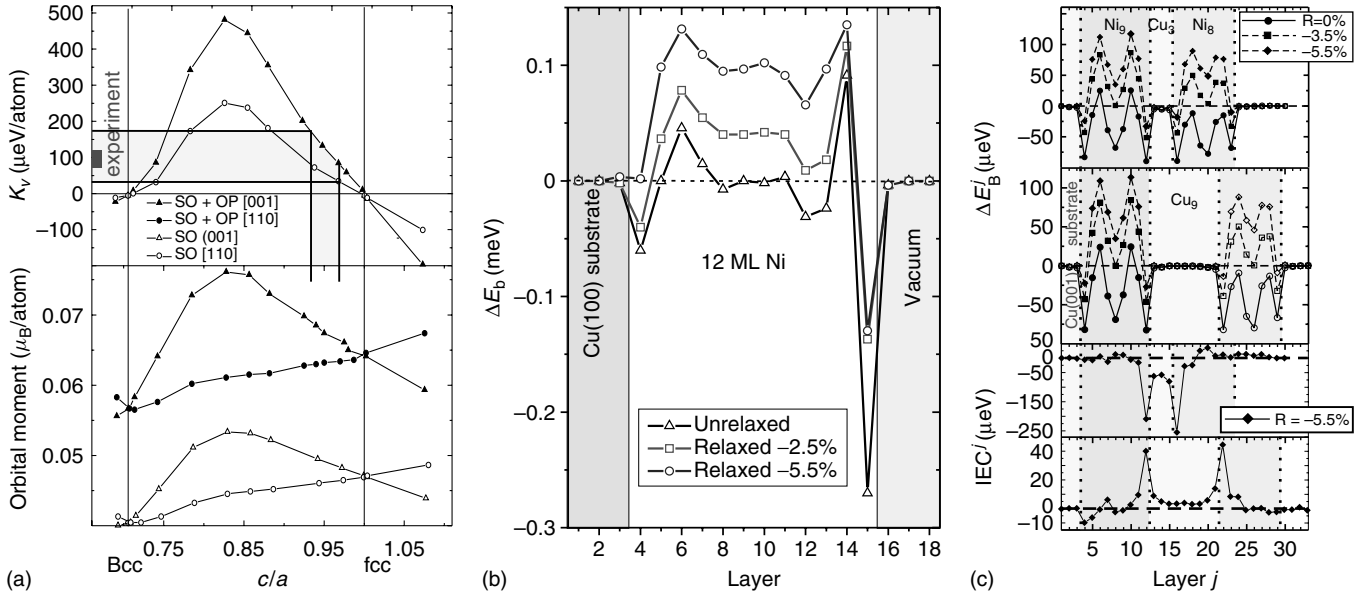

Figure 6. *Ab initio* calculations of MAE and IEC for various Ni structures. (a) The difference in total energy is calculated for an infinite-sized Ni crystal as a function of the ratio c/a. (Taken from Hjortstam *et al*., 1997.) The lower part shows the orbital moment and its anisotropy. (b) Similar *ab initio* calculations for a 12 ML Ni film, layer resolved. (Taken from Hjortstam *et al*., 1997.) (c) Similar calculations for a trilayer also showing the IEC, see Section 3.3. (Taken from Hammerling *et al*., 2003.)

for one layer each, whereas the central part of an ultrathin film counts for $n-2$ *layers.* For the particular example shown here, it is obviously clear that the K^{v} contribution to the total MAE is the dominating one. For the details of the nomenclature, see Appendix B.

3.3 UHV-FMR in a trilayer and interlayer exchange coupling (IEC)

The archetype of a magnetic multilayer structure is the so-called 'trilayer', consisting of two FM films, FM1 and FM2, weakly exchange coupled via a nonmagnetic spacer NM. Two exchange-coupled ferromagnetic films exhibit two eigenmodes of the uniform motion of the magnetizations M_1 and M_2 – like two coupled pendula. Analogous to the notion of phonon branches, they are labeled acoustic (in phase) and optic (π out of phase) modes. The FMR is the technique of choice for investigating these spin-wave dynamics (Lindner and Baberschke, 2003b). It measures both AFM and FM coupling and determines the MAE and IEC parameters. For such a case, $\vec{M}$ has to be replaced by the vector sum $\vec{M}_1 + \vec{M}_2$ in the equation of motion, equation (2). Furthermore, an additional energy contribution of the IEC energy is added to the free-energy density. Following the FMR resonance condition, equations (4–6) also have to be modified. One has to distinguish the individual anisotropy parameters of each FM film, for example, K_i^{Ni} and K_i^{Co} (for details see (Heinrich, 1994; Lindner and Baberschke, 2003a). In theoretical calculations, the IEC usually enters with an IEC constant at $T = 0$. Most of the experiments are analyzed with an effective parameter J_{inter}.

$$F_{\mathrm{ex}} = -J_{\mathrm{inter}} \frac{\vec{M}_1 \cdot \vec{M}_2}{M_1 M_2} \tag{8}$$

The scalar product $\vec{M}_1 \cdot \vec{M}_2$ takes care of the individual orientation of M_i in each film. (Note that in an FMR experiment with an external magnetic field H_0, the orientation of M changes as a function of the orientation and strength of H_0.) In Figure 7, an instructive example is given showing that in a step-by-step experiment the UHV-FMR gives detailed information on all relevant magnetic parameters for such trilayers.

Figure 7(a) and (b) show the experimental and simulated FMR spectra of a $Ni_7/Cu_9/Co_2$ trilayer at two different

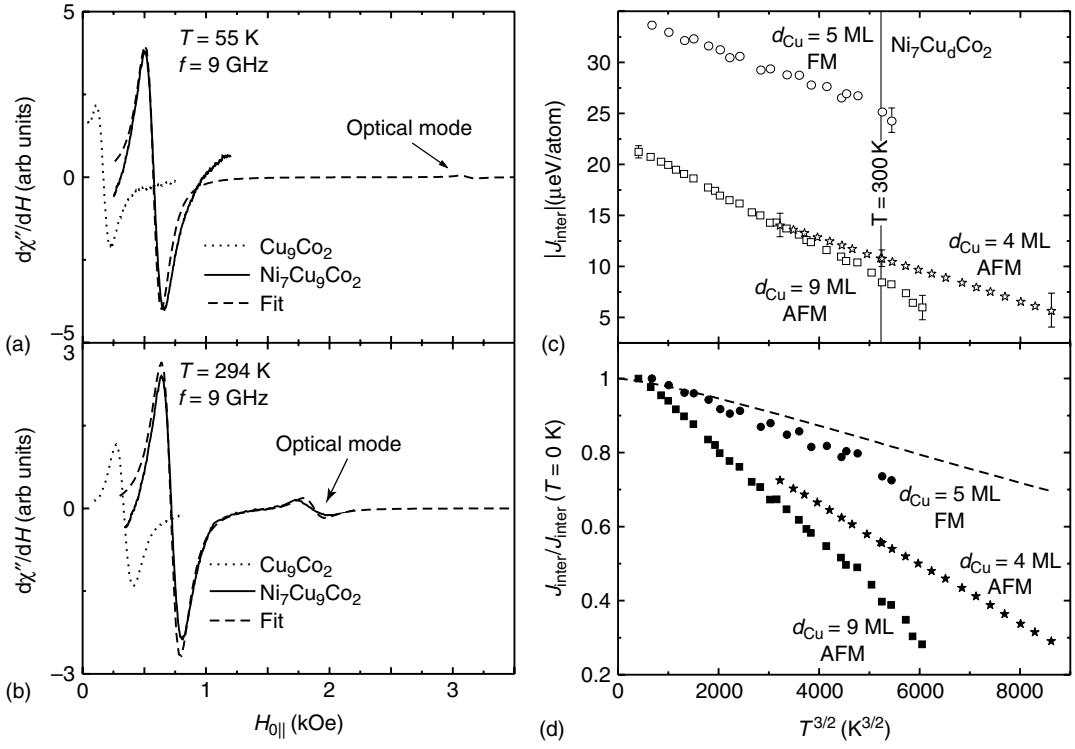

Figure 7. (a) and (b) experimental and calculated FMR spectra of a Ni/Cu/Co trilayer at different temperatures along the in-plane easy axis, taken from (Lindner *et al*., 2002). First the single Co film on Cu(001) was measured (dotted). Subsequently the top Ni film was evaporated. The same type of experiment was carried out for different spacer thicknesses d_{Cu} for AFM and FM coupling. J_{inter} determined from the FMR fitting is plotted in absolute energy units in (c) and normalized to $T = 0$ in (d) as a function of an effective $T^{3/2}$ law (Schwieger *et al*., 2007).

temperatures. First, only the Co_2 film capped with the Cu_9 spacer layer was prepared. A single resonance line (dotted) is recorded. Its intensity and position change because K_i and M are temperature dependent. In a second step, the Ni_7 film is deposited on top. At room temperature, the FMR records two resonance lines: one of the weak optical mode and a second one of the strong acoustical mode. From the intensity and position of the two lines it is immediately evident that this trilayer has an AFM coupling between the two ferromagnetic films (Heinrich, 1994; Lindner and Baberschke, 2003a). The simulation of the coupled resonance lines (dashed) is in perfect agreement with experiment. A full measurement of the dependence on the polar angle and the temperature gives access to all MAE parameters, provided $M(T)$ is known from another experiment. Taking the angular dependences of only the bottom film and the IEC trilayer, all unknown parameters influencing the resonance field of the optical and acoustical mode can be determined. The only parameter left, which determines the resonance shift, is J_{inter} itself. This straightforward way of determining the coupling demonstrates the advantage of *in situ* measurement. The coupling between FM1 and FM2 is an oscillatory function of the spacer thickness (Bruno and Chappert, 1991). For the particular system $Ni_7/Cu_d/Co_2$, this has been observed and determined by UHV-FMR for a spacer thickness in the range of $d_{\text{Cu}} = 2\text{–}9\,\text{ML}$ (Lindner and Baberschke, 2003a). Again, it is documented in textbooks (Heinrich, 1994) that FMR is equally applicable for AFM and FM coupling: for AFM coupling, the intense acoustical mode appears at a lower magnetic field than the weak optical mode; for FM coupling, this reverses such that the optical mode is at a lower magnetic field than the acoustical mode. We note that FM1 and FM2 in trilayers may also consist of the same material, for example, $Ni_8/Cu_d/Ni_9$. For Ni films of different thicknesses, the MAE values and magnetization are different, leading to different eigen resonances of the individual modes.

Another important parameter for understanding the magnetism of coupled ferromagnetic films is the *temperature dependence* of the coupling strength, that is, $J_{\text{inter}} = f(T)$. Two models were proposed in the past:

1. Thermally excited spin waves in the magnetic layers lead to a reduction of the effective IEC. In this model, the characteristic temperature is given by T_{C}. Arias and Mills calculated a $T^{3/2}$ power law (Arias and Mills, 1999, 2000):

$$\frac{J_{\text{inter}}}{J_{\text{inter},0}} = 1 - a\left(\frac{T}{T_{\text{C}}}\right)^{3/2} \tag{9}$$

   Other parameters like the thickness of the spacer layer are hidden in the prefactor a.

2. In the framework of electronic band structure, the smearing of the Fermi edge at elevated temperature makes the coupling less effective, excitations of electron–hole pairs reduce the IEC (Bruno, 1995). This temperature-dependent factor was calculated by Bruno as given in equation (10).

$$\frac{J_{\text{inter}}}{J_{\text{inter},0}} = \frac{T/T_0}{\sinh\left(\frac{T}{T_0}\right)} \tag{10}$$

The characteristic temperature T_0 is controlled by electronic band structure effects, that is, v_{Fermi} and the spacer thickness. The Curie temperature is no explicit parameter but is implicitly included via the intralayer coupling of the ferromagnets.

Lindner *et al*. (2002) have shown for various ultrathin film systems over the full temperature range from $\sim$0 K up to T_{C} that the effective temperature dependence is very close to the $T^{3/2}$ law and can be less well fitted by a $x/\sinh(x)$ function. However, Nolting and coworkers (Schwieger and Nolting, 2004; Schwieger *et al*., 2005) have reinvestigated the origin of the temperature dependence of the IEC yielding an effective functional dependence, which for given intra- and interlayer exchange parameters gets very close to an effective exponent of $\sim 3/2$ but does not follow the exact power law for spin-wave excitations with $T^{3/2}$. For the $Ni_7/Cu_d/Co_2$ trilayer system, the temperature dependence is plotted in Figure 7(c) and (d). Figure 7(c) gives the absolute values for $|J_{\text{inter}}|$. For $d_{\text{Cu}} = 5\,\text{ML}$ the coupling is FM, for $d_{\text{Cu}} = 4\,\text{ML}$ and $d_{\text{Cu}} = 9\,\text{ML}$ the coupling is AFM. In Figure 7(d) the measured values are normalized to $T = 0$, this eliminates the temperature-independent part of $|J_{\text{inter}}|$. Nonmonotonic slopes as a function of d_{Cu} are seen; that is, a nonmonotonic temperature dependence of $|J_{\text{inter}}|$. The temperature dependence for AFM coupling is larger than that for FM. This nonmonotonic behavior clearly indicates that the coupling between spin-wave modes will be more important for the *temperature dependence* of $|J_{\text{inter}}|$, than the smearing of the Fermi edge.

In conclusion, the strength of the effective $T^{3/2}$ dependence of J_{inter} depends on various parameters of the electronic band structure, electron–hole excitations, and spin-wave excitations. Further *in situ* FMR experiments with different Cu thickness and full angular- and temperature-dependent measurements will give the key information to understand the IEC. Recent quantum mechanical calculations based on an extended Heisenberg model give clear evidence that magnon excitations are responsible for about 75% of the temperature dependence of the IEC. The remaining 25% is due to temperature effects in the effective quantum well, formed by the spacer and the spacer/magnet interfaces like

reduced spin asymmetry or softening of the spacer Fermi surface (Schwieger *et al.*, 2007).

Finally, we come back to Figure 6(c) where the Weinberger group has calculated layer resolved the K anisotropy (ΔE_B) and the IEC for an $Ni_8/Cu_d/Ni_9$ trilayer. We see that the anisotropy energy depends strongly on the c/a ratio as discussed in the previous section. We also notice that for $d_{Cu} = 3$ ML and $d_{Cu} = 9$ ML the spacer does not contribute to the MAE. The layer-resolved calculated IEC demonstrates clearly that more or less only the Ni layer contributes to the exchange coupling directly at the interface but for very thin spacers (3 ML) the Cu also makes a finite contribution.

4 DYNAMICS IN THE FMR, THE LINEWIDTH ΔH

Starting from Figure 1 it is obvious that the linewidth in the EPR and FMR is a measure of the spin relaxation, scattering, and spin fluctuations. Two principal relaxation paths are discussed in standard literature: spin–lattice relaxation and spin–spin relaxation. The former is a process in which energy dissipates from the magnetic system to the thermal bath. For the latter, energy is scattered within the magnetic spin system. It depends on the concentration of magnetic moments (dilute ferromagnets) and can be discussed in the framework of spin-wave excitations, magnon–magnon scattering, Stoner excitations, and so on. For both processes, phase transitions (structural or magnetic) are of importance: diverging spin fluctuations as a function of temperature will influence the linewidth. Müller and coworkers have given a nice example for the EPR: $SrTiO_3$ undergoes a structural phase transition at $\approx$105 K. If this crystal is doped with a paramagnetic center, the EPR will show a dramatic divergence of the linewidth at this phase-transition temperature (von Waldkirch *et al.*, 1973). Similar effects were observed for the classical antiferromagnet MnF_2 at the Néel temperature of $T_N = 67$ K (Burgiel and Stranberg, 1964). In both cases, a dramatic divergence of ΔH is observed.

For bulk ferromagnets like Ni and Fe whiskers also a line broadening in the FMR occurs starting from low temperature and approaching the Curie temperature from the T_C^- side.

On the right-hand part of Figure 8, the FMR linewidth $\Delta H(T)$ is shown for bulk Ni. A very sharp peak of only 7 K width is measured at the Curie temperature of $T_C \approx 630$ K. The line broadens from below 200 Oe to more than 1.6 kOe. How can this be understood? Approaching the phase transition from the T_C^- side, one observes a breakdown of the uniform precession of the magnetization. The uniform rotation of the spin waves with infinite wavelength breaks into pieces because of thermal excitations. This increases the FMR

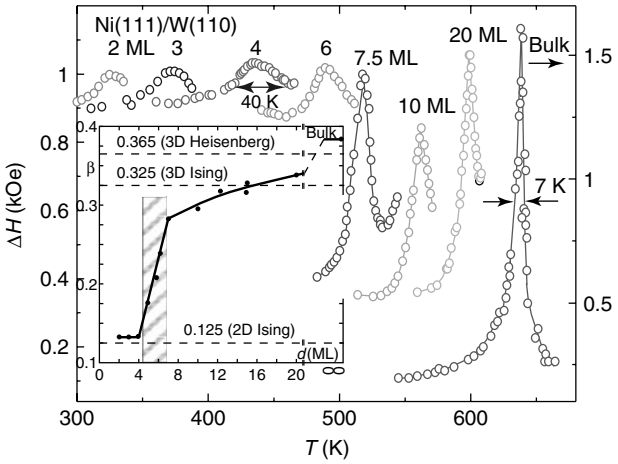

Figure 8. FMR linewidth $\Delta H(T)$ of bulk and ultrathin Ni films $d = 2$–20 ML as a function of the temperature. Note the very sharp peak for thicker films and the very broad peak for the ultrathin 2D film. The inset shows the critical exponent β and the transition 3D $\rightarrow$ 2D. For details see Li and Baberschke (1992).

linewidth. Starting from the paramagnetic side above T_C^+ also a narrow line of 250 Oe width is observed. The susceptibility and spin–spin correlation length ξ increase dramatically owing to Gaussian and critical fluctuations. The sharpness of the peak in the linewidth is surprising. It depends very much on the high perfection of the crystallographic structure of the single crystal. (Since these measurements are performed in an external magnetic field, ξ will not diverge to infinite.) Applying the UHV-FMR to Ni(111) thin films grown on W(110), we observe in the first place a shift of the diverging peak to lower temperature in full agreement with the thickness-dependent Curie temperature of ultrathin films caused by *finite size* effects (Baberschke, 1996). At a certain thickness of $d = 4$–6 ML, the Ni film undergoes a transition from 3D to 2D behavior. Immediately, we observe a broadening of the linewidth peak as indicated by $\sim$40 K in the figure. This can be easily understood because the fluctuations in less than 3D are enhanced and extended over a larger range of temperature. For details see (Li and Baberschke, 1992; Li *et al.*, 1990).

4.1 Gilbert damping and magnon–magnon scattering

In the following text we focus on the analysis of the linewidth in FMR experiments in ultrathin films deep in the ferromagnetic phase $T \ll T_C$. This is of particular importance for the investigation of magnetization dynamics and magnetization reversal in magnetic nanostructures. The commonly used ansatz is to add the so-called Gilbert

damping to the equation of motion, equation (2), that is, the second term in equation (11). This Landau–Lifshitz–Gilbert (LLG) equation has been discussed in great detail in many review articles. For FMR in bulk material see, for example (Sparks, 1964; Vonsovskii, 1966), for ultrathin films see, for example (Heinrich, 1994, 2005). The Gilbert ansatz is based on a double vector product $-\vec{M} \times (\vec{M} \times \vec{H}_{\text{eff}})$ as shown in Figure 9(b) with a resulting vector that is always pointing toward the symmetry axis of the Larmor precession. For small angles β between H_{eff} and M, this can be approximated by the time derivative $\partial \vec{M}/\partial t$.

$$\frac{\partial \vec{M}}{\partial t} = -\gamma(\vec{M} \times \vec{H}_{\text{eff}}) + \frac{G}{\gamma M_S^2}\left[\vec{M} \times \frac{\partial \vec{M}}{\partial t}\right] \quad \text{with}$$
$$\alpha = G/\gamma M \tag{11}$$

Thus it can be interpreted as a velocity-proportional viscous damping like in mechanical (Stokes) friction. The viscosity damps the Larmor precession, and the magnetization spirals into the z axis pointing to the surface of a sphere, that is, the length of $\vec{M}$ stays constant but the expectation value $\langle M_z \rangle$ increases if $\beta \to 0$. This is indicated in Figure 9(b) as relaxation path 1. A uniform motion of the magnetization plus a viscous damping leads to a dissipation of energy into the thermal bath (path 1 in Figure 9(a) – an irreversible process. Two notations are commonly used in equation (11): (i) G, the Gilbert-damping parameter, given as a relaxation rate in s^{-1}, or (ii) the dimensionless parameter α in analogy to the viscous damping. The relaxation rate per second G seems to be more instructive for easier comparison with other relaxation rates in the literature. As discussed in Section 2, standard EPR/FMR experiments use a fixed microwave frequency and scan the external Zeeman field H_0. Under these conditions, the LLG (11) leads to a linewidth ΔH_G depending linearly [4] on ω

$$\Delta H_G(\omega) \approx \frac{2}{\sqrt{3}} \frac{G}{\gamma^2 M} \frac{\omega}{\cos\beta} \tag{12}$$

One example is shown in Figure 3 in which for 1 GHz experiments the linewidth for a 10 ML Ni film is very narrow in the range of 10–20 Oe, whereas for the most commonly used 10 GHz frequency the linewidth increases up to 200–250 Oe.

A second relaxation process is discussed in standard literature and indicated in Figure 9(c): The uniform motion of the magnetization (or switching the magnetization) may scatter into excited states of the magnetic subsystem (spin waves, Stoner excitations, magnon–magnon scattering, etc.) The projection of $\vec{M}$ onto the z axis stays constant since the precessional energy is scattered into the transverse components M_x and M_y. (For details see Sparks, 1964). These processes may be reversible and are indicated in Figure 9(a) as path 2. They are in full analogy with optical spectroscopy. In the long run, these excitations will also decay into the thermal bath as indicated by path 3. One may raise the question: Is there any experimental evidence for the appearance of this second relaxation process, that is, scattering within the magnetic subsystem, in magnetic nanostructures? The theoretical background to study this question is known for a long time. One possible model is described by the Bloch–Bloembergen equation (Bloembergen, 1950; Bloch, 1946)

$$\frac{\partial \vec{M}}{\partial t} = -\gamma(\vec{M} \times \vec{H}_{\text{eff}}) - \frac{M_x}{T_2}\hat{e}_x - \frac{M_y}{T_2}\hat{e}_y - \frac{M_z - M_S}{T_1}\hat{e}_z \tag{13}$$

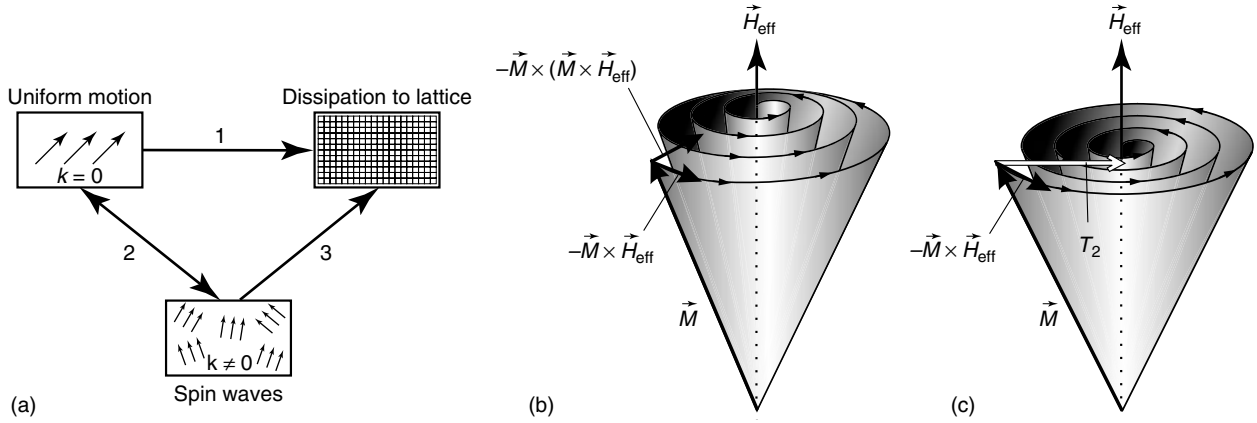

Figure 9. Schematic illustration of different relaxation processes taken from Suhl (1998); Sparks (1964): (a) The uniform motion of the magnetization with $k = 0$ in an FMR experiment may scatter with energy dissipation into the thermal bath (path 1). In path 2 it can also scatter into spin waves with $k \neq 0$ – a reversible process. In the long run, this energy also travels along path 3 into the heat sink. (b) Depicts the LLG scenario from equation (11). (c) Shows the Bloch–Bloembergen process for spin–spin relaxation.

In this case, two different relaxation rates are introduced into the equation of motion (Abragam and Bleaney, 1966): the longitudinal relaxation rate T_1, that is, the direct path into the thermal bath, and the so-called transverse rate, T_2, by which energy is scattered into the transverse magnetization components M_x and M_y. This is depicted in Figure 9(c). The projection of $\vec{M}$ on the effective field $\vec{H}_{\text{eff}}$ stays constant and energy is scattered into the transverse components M_x and M_y. This is a dephasing of the former coherent rotation of the magnetization as discussed in the previous section. This scenario of a transverse relaxation rate is known, for example, Sparks (1964); Mills and Rezende (2003); Suhl (1998). Only very recently, Arias and Mills have calculated this type of magnon–magnon scattering in a quantitative manner for standard FMR experiments in ultrathin films (Arias and Mills, 1999, 2000) (see also **Spin Waves: History and a Summary of Recent Developments, Volume 1**). The result for the FMR linewidth is given below, with Γ as a parameter

$$\Delta H_{2\text{M}}(\omega) = \Gamma \sin^{-1} \sqrt{\frac{\sqrt{\omega^2 + (\omega_0/2)^2} - \omega_0/2}{\sqrt{\omega^2 + (\omega_0/2)^2} + \omega_0/2}} \qquad (14)$$

It is obvious that the frequency dependence of the linewidth for magnon–magnon scattering is by no means linear. It saturates at very high frequency and starts with a steep slope at low frequencies (Figure 10). The first experimental evidence of a nonlinear $\Delta H(\omega)$ was reported for Fe/V nanostructure in Lindner *et al.* (2003) and for Fe/GaAs films, (Woltersdorf and Heinrich, 2004). Recently, the FMR linewidth of Fe/V multilayers has been measured and analyzed over a very large frequency range from 1 to 225 GHz as shown in Figure 10 (Lenz *et al.*, 2006). Key information can be obtained from Figure 10: (i) FMR measurements at very low frequencies (1–4 GHz) unambiguously show that the linewidth narrows dramatically, that is to say ΔH is given by relaxation processes only. A practice used in the literature for earlier experiments between 9 and 36 GHz to *assume* a linear frequency dependence (Celinski and Heinrich, 1991), extrapolating from this, an apparent residual linewidth (the tangent crossing the y axis) does not always seem to be justified. (ii) For all in-plane orientations of the external field ([001] and [110]), one observes a nonlinear frequency dependence. In contrast, for $\vec{H}$ normal to the film plane ([001], full triangles), a 100% linear frequency dependence is observed. This is in perfect agreement with the theoretical prediction in (Arias and Mills, 1999, 2000). The authors of (Lenz *et al.*, 2006) deduce a constant (independent of orientation) Gilbert damping of $\sim 0.7 \times 10^8\ \text{s}^{-1}$ for these multilayers. Fitting equation (14) to the curved frequency dependence yields a magnon–magnon scattering rate of $\gamma\Gamma \approx 10$–50 larger than the Gilbert damping. Thus, experimental evidence is given that both relaxation mechanisms (longitudinal and transverse scattering) are active in magnetic nanostructures. A combination of magnon–magnon scattering, modeled by equations (13) and (14), and a viscous Gilbert damping described by equations (11) and (12) seems to give a better insight into the spin dynamics of ultrathin films. For the particular investigated systems, Fe/V multilayers and Fe films on GaAs, the magnon–magnon scattering of $1/T_2 \approx 10^9\ \text{s}^{-1}$ seems to be about 2 orders of magnitude faster than the viscous Gilbert damping of $1/T_1 \approx 10^7\ \text{s}^{-1}$.

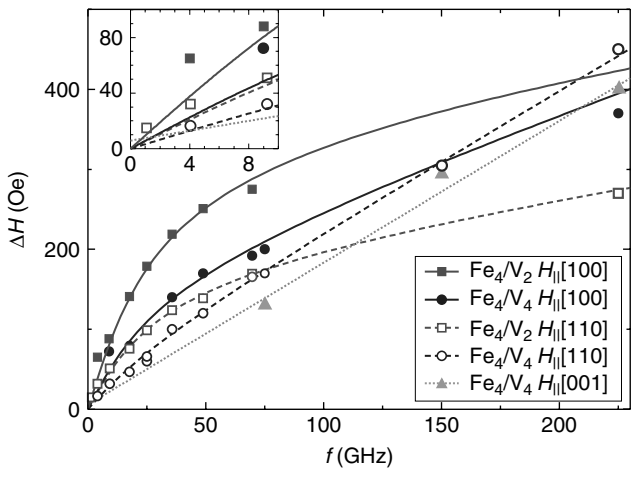

Figure 10. FMR linewidths of two Fe/V-multilayer samples for different in-plane and out-of-plane orientations of the external field as a function of the microwave frequency. The inset is a magnification of the low frequency regime. For details see Lenz *et al.* (2006).

4.2 Spin-pump effects in the FMR

Consider in Figure 11(a) that 3d magnetic moments of the FM are excited by a microwave radiation $h\nu$ and undergo a Larmor precession in an external field, equations (1) and (2). It is standard textbook reasoning that the local 3*d* moments are coupled to the sea of conduction electrons via the classical s–d exchange interaction. In turn, the conduction band of the FM is hybridized with the conduction band of the NM. This classical s–d exchange between spin waves and s electrons has been used by Janossy and coworkers (Silsbee *et al.*, 1979; Monod and Janossy, 1977) to activate and enhance the Larmor precession in the NM conduction band, the so-called conduction electron spin resonance (CESR). Angular momentum is transferred to the conduction band and then transported into the NM. These authors used highest-purity Au as NM and were able to detect the spin current of the Au conduction band through micrometer thick Au. This has been monitored at the right-hand end of Figure 11(a) either as emitted

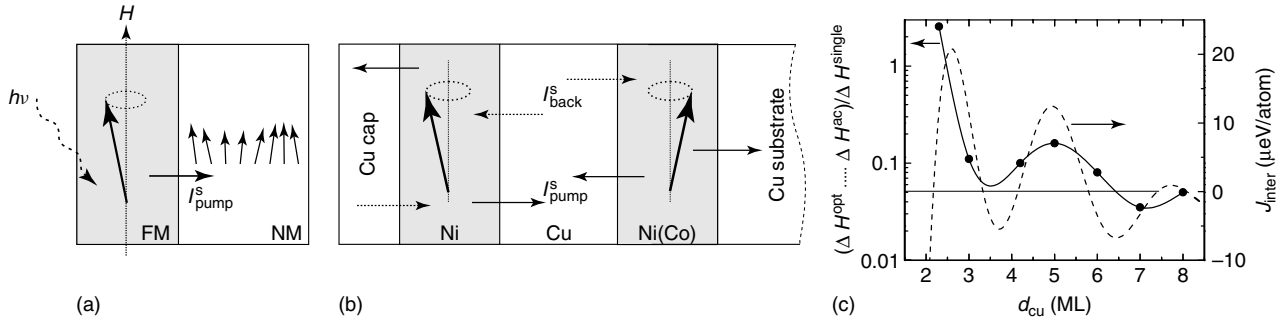

Figure 11. Schematic illustration of the spin-pump effect of (a) a single interface and (b) a trilayer consisting of two different ferromagnetic films and a nonmagnetic spacer. (c) Oscillatory behavior of the linewidth as a function of the Cu spacer. The data are taken from Lenz *et al*. (2004) for a $Ni_8/Cu_x/Ni_9$ trilayer.

microwave radiation or by exciting another magnetic system. This is the basic mechanism called *spin pumping* in our days. Thus, angular momentum and energy are lost from the ferromagnetic film and transported to the NM (metal, semiconductor). In the frame of Figure 9(a), this can be seen as a dissipation of energy like path 1 in Figure 9(a). Recently, such a mechanism became of particular interest for magnetic nanostructures consisting of two ferromagnetic films separated by an NM spacer, see Figure 11(b). Such a scenario has been investigated theoretically in Tserkovnyak *et al*. (2002) and by others. Experimental evidence was given in Heinrich *et al*. (2003) for Fe/40 ML Au/Fe (see also **Magnetic Ultrathin Films, Volume 4**). The thickness of the spacer will be of particular interest. For a larger thickness, like 40 ML Au, there is no IEC between FM1 and FM2 – see Section 3.3. Only ballistic transport is possible for the spin current depending on the perfection of the spacer and its interfaces. For ultrathin spacer films of only a few monolayers, one expects also some IEC (see Section 3.3) influencing the FMR linewidth. Constructive or destructive interference phenomena and quantum well effects should be detectable in the spin current I_{pump}. In Section 3.3 we have seen that a trilayer consisting of two different ferromagnets (Ni and Co or two Ni films with different thickness) has two different (acoustic and optic) FMR modes. In Lenz *et al*. (2004) and Heinrich *et al*. (2003) first evidence is given that indeed the FMR linewidths influence each other when both resonance conditions coincide. Figure 11(c) shows the difference between the optic and acoustic linewidth $\Delta H^{opt} - \Delta H^{ac}$ for $Ni_8/Cu_x/Ni_9$ with an ultrathin spacer thickness of $d_{Cu} = 2–8$ ML. On the left-hand side, the relative change in the linewidth normalized to the linewidth for a single film is plotted on a logarithmic scale, whereas on the right-hand side the energy scale for J_{inter} (dashed line) is shown. The broadening of the optical linewidth is the largest (more than a factor of 2) for the thinnest Cu spacer and the largest J_{inter}. A clear oscillatory behavior for both linewidth and J_{inter} is observed as a function of d_{Cu}.

5 SUMMARY, OUTLOOK

As discussed by several examples, microwave spectroscopy is a very useful technique to investigate ultrathin ferromagnetic films. It covers the ferromagnetic as well as the paramagnetic regime. It is sensitive to ferromagnetic as well as antiferromagnetic IEC in superstructures. The static resonance conditions, its angular and temperature dependence as well as the linewidth, yield reliable information on the static and dynamic parameters of ultrathin film magnetism. If the standard FMR technique is combined with state-of-the-art surface science and UHV technique, the combined UHV-FMR spectroscopy opens a new challenging research field to study the growth and crystallographic modifications, the electronic band structure, and the direct observation of the magnetism in one experiment. Such a complete set of experimental observables is the best input for a better theoretical description of the magnetism of magnetic nanostructures. Standard FMR technique might have one drawback: the spectroscopy has no spatial resolution. The wavelength of the microwave ranges from submillimeters to a few centimeters and the absorbed energy out of the microwave radiation is the macroscopic response of the whole specimen. A recent development to overcome this problem is to combine an STM or AFM tip with FMR. Several groups have developed this technique. A lateral resolution in the range of 10–100 nm was reached (Meckenstock *et al*., 2003; Meckenstock *et al*., 2004). Another interesting new development is the combination of synchrotron radiation and FMR. XMCD has the advantage of being element specific. XMCD also has access to orbital and spin magnetic moments. If this can be used to probe the change in the magnetization induced by the precession of magnetic moments, this X-ray-detected magnetic resonance (XDMR) is the analogue of the well-known optical-detected magnetic resonance (ODMR). First experimental results at the K-edge of Fe in a YIG crystal have been reported recently (Goulon *et al*., 2005). Also, the

combination of an electronic network analyzer with FMR spectroscopy offers the possibility of studying the dynamics of magnetic nanostructures in the frequency as well as in the time (pulsed) domain (Counil *et al*., 2004).

Finally we point out recent advances in the theory of the FMR in ultrathin films: The vast majority uses a classical continuum model to interpret experimental spectra, where the classical LLG equation of motion for the magnetization or an expansion of the free energy is considered. Recently a microscopic Heisenberg Hamiltonian was used to directly calculate for FMR the spin-wave resonance modes and external resonance fields as a function of the field direction and as a function of temperature (Schwieger *et al*., 2005). Future work will provide better microscopic insight into the FMR of ultrathin films.

NOTES

[1] The FMR community uses a positive γ value, whereas in EPR the negative sign of the charge is taken into account.

[2] Note that many other experimental techniques like MOKE, spin-polarized PE, and so on, measure the magnetization in arbitrary units, only. MAE and IEC, for example, measured by FMR are given in absolute energy units per particle. These numbers are of interest for comparison with theory.

[3] This equation is strictly valid only for g-values close to two.

[4] Note that this linear frequency dependence is a consequence of the field-scanning technique in conventional FMR. For other experimental techniques at fixed magnetic field and scanning the microwave frequency or for Brillouin light scattering the analysis of the measured linewidth is different, see (Mills and Rezende, 2003). Caution has to be taken when comparing different experiments.

ACKNOWLEDGMENTS

The idea of EPR and FMR in metals and its combination with UHV technique was brought to our attention by S. Hüfner (FUB) and R. Orbach (UCLA). Discussions with H. Ebert, M. Farle, K. Lenz, J. Lindner, D.L. Mills, and R.Q. Wu are acknowledged. Special thanks is given to C. Sorg, E. Kosubek, and K. Lenz for their assistance in the preparation of the manuscript. Financial support was given over decades by the Deutsche Forschungsgemeinschaft DFG under the research grants Sfb 161, Sfb 6, and Sfb 290.

REFERENCES

Abragam, A. and Bleaney, B. (1966). *Electron Paramagnetic Resonance of Transition Ions*, Clarendon Press Oxford.

Aharoni, A. (2000). *Introduction to the Theory of Ferromagnetism*, Oxford University Press.

Anisimov, A.N., Farle, M., Poulopoulos, P., *et al*. (1999). Orbital magnetism and magnetic anisotropy probed with ferromagnetic resonance. *Physical Review Letters*, **82**, 2390.

Antoniak, C., Lindner, J., Farle, M., *et al*. (2005). Magnetic anisotropy and its temperature dependence in iron-rich Fe_xPt_{1-x} nanoparticles. *Europhysics Letters*, **70**, 250.

Arias, R. and Mills, D.L. (1999). Extrinsic contributions to the ferromagnetic resonance response of ultrathin films. *Physical Review B*, **60**, 7395.

Arias, R. and Mills, D.L. (2000). Extrinsic contributions to the ferromagnetic resonance response of ultrathin films. *Journal of Applied Physics*, **87**, 5455.

Baberschke, K. (1976). Electron spin resonance in superconducting materials. *Zeitschrift fur Physik B*, **24**, 53.

Baberschke, K. (1996). The magnetism of nickel monolayers. *Applied Physics A*, **62**, 417.

Baberschke, K. (2001). *Band-Ferromagnetism*, Vol. 580, p. 27 *Lecture Notes in Physics*, Springer: Berlin.

Baberschke, K. and Tsang, E. (1980). The Kondo-effect on the paramagnetic resonance of dilute Au:Yb. *Physical Review Letters*, **45**, 1512.

Berghaus, A., Farle, M., Li, Yi., *et al*. (1989). Absolute determination of the magnetic anisotropy of ultrathin Gd and Ni/W(110). *Proceedings in Physics*, **50**, 61.

Bloch, F. (1946). Nuclear Induction. *Physical Review*, **70**, 460.

Bloembergen, N. (1950). On the ferromagnetic resonance in nickel and supermalloy. *Physical Review*, **78**, 572.

Brewer, W.D., Scherz, A., Sorg, C., *et al*. (2004). Direct observation of orbital magnetism in cubic solids. *Physical Review Letters*, **93**, 077205.

Bruno, P. (1995). Theory of interlayer magnetic coupling. *Physical Review B*, **52**, 411.

Bruno, P. and Chappert, C. (1991). Oscillatory coupling between ferromagnetic layers separated by a nonmagnetic metal spacer. *Physical Review Letters*, **67**, 1602.

Burgiel, J.C. and Stranberg, M.W.P. (1964). Antiferromagnetic resonance linewidth in MnF_2 near the transition temperature. *Journal of Applied Physics*, **35**, 852.

Celinski, Z. and Heinrich, B. (1991). Ferromagnetic resonance linewidth of Fe ultrathin films grown on a bcc Cu substrate. *Journal of Applied Physics*, **70**, 5935.

Coqblin, B. (1977). *The Electronic Structure of Rare-Earth Metals and Alloys*, Academic Press: London.

Counil, G., Kim, J-V., Shigeto, K., *et al*. (2004). Inductive measurement of the high frequency permeability of a Permalloy thin film. *Journal of Magnetism and Magnetic Materials*, **272**, 290.

Farle, M. (1998). Ferromagnetic resonance of ultrathin metallic layers. *Reports on Progress in Physics*, **61**, 755.

Farle, M. and Baberschke, K. (1987). Ferromagnetic order and the critical exponent γ for a Gd monolayer. An ESR-study. *Physical Review Letters*, **58**, 511.

Farle, M., Platow, W., Kosubek, E., *et al*. (1999). Magnetic anisotropy of Co/Cu(111) ultrathin films. *Surface Science*, **439**, 146.

Farle, M., Zomack, M., Baberschke, K., *et al*. (1985). ESR of adsorbates on single crystal metal surfaces under UHV conditions. *Surface Science*, **160**, 205.

Gambardella, P., Rusponi, S., Veronese, M., *et al*. (2003). Giant magnetic anisotropy of single cobalt atoms and nanoparticles. *Science*, **300**, 1130.

Goulon, J., Rogalev, A., Wilhelm, F., *et al*. (2005). X-ray detected magnetic resonance at the Fe K-edge in YIG: forced precession of magnetically polarized orbital components. *JETP LETTERS*, **82**(11), 696–701.

Hammerling, R., Zabloudil, J., Weinberger, P., *et al*. (2003). Interlayer exchange coupling and magnetic anisotropy in prototype trilayers: Ab initio theory versus experiment. *Physical Review B*, **68**, 092406.

Heinrich, B. (1994). *Ultrathin Magnetic Structures II*, Springer-Verlag: Berlin.

Heinrich, B. (2005). *Ultrathin Magnetic Structures III*, Springer: Berlin Heidelberg New York.

Heinrich, B., Tserkovnyak, Y., Woltersdorf, G., *et al*. (2003). Dynamic exchange coupling in magnetic bilayers. *Physical Review Letters*, **90**, 187601.

Heinrich, B., Urquhart, K.B., Arrott, A.S., *et al*. (1987). Ferromagnetic-resonance study of ultrathin bcc Fe(100) films grown epitaxially on fcc Ag(100) substrates. *Physical Review Letters*, **59**, 1756.

Hjortstam, O., Baberschke, K., Wills, J.M., *et al*. (1997). Magnetic anisotropy and magnetostriction in tetragonal and cubic Ni. *Physical Review B*, **55**, 15026.

Huang, F., Mankey, G.J., Willis, R.F., *et al*. (1994). Interfacial anisotropy and magnetic transition of cobalt films on Cu(111). *Journal of Applied Physics*, **75**, 6406.

Kohlhepp, J., Elmers, H.J., Gradmann, U., *et al*. (1993). Magnetic interface anisotropies of Co/Cu(111) and Co/Au(111) interfaces from ultrathin Co films on Cu(111). *Journal of Magnetism and Magnetic Materials*, **121**, 483.

Lenz, K., Tolinski, T., Lindner, J., *et al*. (2004). Evidence of spin-pumping effect in the ferromagnetic resonance of coupled trilayers. *Physical Review B*, **69**, 144422.

Lenz, K., Wende, H., Kuch, W., *et al*. (2006). Two-magnon scattering and viscous Gilbert damping in ultrathin ferromagnets. *Physical Review B*, **73**, 144424.

Li, Y. and Baberschke, K. (1992). Dimensional crossover in ultrathin Ni(111) films on W(110). *Physical Review Letters*, **68**, 1208.

Li, Y., Farle, M., Baberschke, K., *et al*. (1990). Critical spin fluctuations and curie temperatures of ultrathin Ni(111)/W(110): a magnetic-resonance study in ultrahigh vacuum. *Physical Review B*, **41**, 9596(R).

Lindner, J. and Baberschke, K. (2003a). Ferromagnetic resonance in coupled ultrathin films. *Journal of Physics: Condensed Matter*, **15**, S465.

Lindner, J. and Baberschke, K. (2003b). In situ ferromagnetic resonance: an ultimate tool to investigate the coupling in ultrathin magnetic films. *Journal of Physics: Condensed Matter*, **15**, R193.

Lindner, J., Lenz, K., Kosubek, E., *et al*. (2003). 'Non-Gilbert-type' damping of the magnetic relaxation in ultrathin ferromagnets: importance of magnon-magnon-scattering. *Physical Review B*, **68**, 060102(R).

Lindner, J., Rüdt, C., Kosubek, E., *et al*. (2002). $T^{3/2}$-dependence of the interlayer exchange coupling in ferromagnetic multilayers. *Physical Review Letters*, **88**, 167206.

Meckenstock, R., Rastei, M.V., Bucher, J.P., *et al*. (2004). Local magnetoresistance and ferromagnetic resonance measurements with a sliding probe contact. *Journal of Applied Physics*, **95**, 6753.

Meckenstock, R., Spoddig, D., Dietzel, D., *et al*. (2003). Scanning thermal microwave resonance microscopy of Ni nanodots. *Review of Scientific Instruments*, **74**, 789.

Meyer, A.J.P. and Asch, G. (1961). Experimental ǵ and g values of Fe, Co, Ni, and their alloys. *Journal of Applied Physics*, **32**, 330S.

Mills, D.L. and Rezende, S.M. (2003). *Spin Dynamics in Confined Magnetic Structure II*, Vol. 87, *Topics in Applied Physics*, Springer: Berlin.

Monod, P. and Janossy, A. (1977). Conduction electron spin resonance in Au. *Journal of Low Temperature Physics*, **26**, 311.

Nagel, J., Baberschke, K., Tsang, E., *et al*. (1980). ESR of Er^{3+} and Yb^{3+} in gold between 100 mK and 1 K. *Journal of Magnetism and Magnetic Materials*, **15–18**, 730.

Ney, A., Lenz, K., Poulopoulos, P., *et al*. (2002). Absolute magnetometry on ultrathin 3d-metal films by UHV-SQUID. *Journal of Magnetism and Magnetic Materials*, **240**, 343.

Orton, J.W. (1968). *Electron Paramagnetic Resonance*, Iliffe Books LTD: London.

Pake, G.E. (1962). *Paramagnetic Resonance*, W A Benjamin: New York.

Scherz, A., Wende, H., Poulopoulos, P., *et al*. (2001). Induced V and reduced Fe moment at the interface of Fe/V(001) superlattices. *Physical Review B*, **64**, 180407(R).

Schulz, B. and Baberschke, K. (1994). Crossover from in-plane to perpendicular magnetization in ultra thin Ni/Cu(001) films. *Physical Review B*, **50**, 13467.

Schwieger, S., Kienert, J., Lenz, K., *et al*. (2007). Magnetic excitations: the main source of the temperature dependence of IEC in nanostructures. *Physical Review Letters*, **98**, 057205.

Schwieger, S., Kienert, J., Nolting, W., *et al*. (2005). Temperature dependence of interlayer exchange coupling: spin waves versus spacer effects. *Physical Review B*, **71**, 174441.

Schwieger, S. and Nolting, W. (2004). Origin of the temperature dependence of interlayer exchange coupling in metallic trilayers. *Physical Review B*, **69**, 224413.

Silsbee, R.H., Janossy, A., Monod, P., *et al*. (1979). Coupling between ferromagnetic and conduction-spin-resonance modes at a ferromagnetic normal-metal interface. *Physical Review B*, **19**, 4382.

Smit, J. and Beljers, H.G. (1955). Ferromagnetic resonance absorption in $BaFe_{12}O_{19}$, a highly anisotropic crystal. *Philips Research Report*, **10**, 113.

Sparks, M.(1964). *Ferromagnetic-Relaxation Theory*, *Advanced Physics Monograph Series*, McGraw-Hill: New York.

Stearns, M. (1986). *Landolt Börnstein: Magnetic Properties of Metals*, Springer: Berlin, Vol. III/19a.

Stetter, U., Farle, M., Baberschke, K., *et al*. (1992). Critical behavior of strained epitaxial Gd films: in situ ac-susceptibility measurements in UHV. *Physical Review B*, **45**, 503.

Suhl, H. (1998). Theory of the magnetic damping constant. *IEEE Transactions on Magnetics*, **34**, 1834.

Tserkovnyak, Y., Brataas, A., Bauer, G.E.W., *et al*. (2002). Spin pumping and magnetization dynamics in metallic multilayers. *Physical Review B*, **66**, 224403.

Uiberacker, C., Zabloudil, J., Weinberger, P., *et al*. (1999). Lattice relaxation driven reorientation transition in Ni_n/Cu(100). *Physical Review Letters*, **82**, 1289.

Vonsovskii, S.V. (1966). *Ferromagnetic Resonance*, Pergamon Press: Oxford London.

Vonsovskii, S.V. (1974). *Magnetism*, Wiley: New York.

von Waldkirch,T., Müller, K.A., Berlinger, W., *et al*. (1973). Fluctuations in $SrTiO_3$ near the 105-K phase transition. *Physical Review B*, **7**, 1052.

White, R.M. (1970). *Quantum Theory of Magnetism*, McGraw-Hill Book Company.

Woltersdorf, G. and Heinrich, B. (2004). Two-magnon scattering in a self-assembled nanoscale network of misfit dislocations. *Physical Review B*, **69**, 184417.

Zomack, M. and Baberschke, K. (1986). Electron Spin Resonance study on NO_2 adsorbed on Kr/Ag(110) at 20 K. *Surface Science*, **178**, 618.

APPENDICES

A UNITS

The history of ferromagnetism and magnetic anisotropy went different routes and was uncoupled from other areas of solid-state magnetism, unfortunately. As a consequence, the classification of magnetic anisotropy contributions used an expansion different from Legendre polynomial expansion in crystal-field theory. Moreover, as a consequence various units are used in the historical part of magnetoelasticity, namely, erg cm^{-3} and erg cm^{-2}, that is to say energy per volume and area, respectively. Other parts of solid-state physics and, in particular, the theory prefers eV/atom, that is to say energy per particle (see also **Theory of Magnetocrystalline Anisotropy and Magnetoelasticity in Transition-metal Systems, Volume 1**). This newer notation started to be used in surface and thin-film magnetism and we strongly advocate it, since it facilitates communication with theory and gives an easier insight. For example, in thin-film magnetism Fe, Co, and Ni ions contribute equally strongly to the anisotropy energy, be it a surface atom or an atom in the inner part of a nanostructure, namely, $10-100\,\mu eV/atom$. In the older version it would read $1.5-15 \times 10^6\,ergcm^{-3}$ for K^v and $0.03-0.3 \times 10^6\,ergcm^{-2}$ for K^s, which is not so easy to compare. A transformation of the older into the newer notation is simply given by the atomic volume of the individual elements, for example, for fcc Ni, $10^6\,ergcm^{-3}$ corresponds to $6.83\,\mu eV/atom$ or $7.38\,\mu eV/atom$ for bcc Fe, respectively.

B NOTATION OF THE MAGNETIC ANISOTROPY ENERGY

The magnetic part of the free-energy density and its anisotropy in ultrathin ferromagnetic films has only two origins: (i) the dipole–dipole interaction, which depends on M and the shape of the specimen, (ii) all other contributions (crystalline MAE, magnetoelastic MAE, etc.) are caused by spin-orbit interaction or even better by a full relativistic treatment of the free-energy density. We recall that the exchange interaction $\vec{s}_1 \cdot \vec{s}_2$, the Heisenberg Hamiltonian, is completely isotropic, its energy levels do not depend on the direction in space in which the crystal is magnetized (Aharoni, 2000). The so-called anisotropic exchange is nothing but the anisotropy of the orbital magnetism projected to an effective spin space.

1. The dipole contribution: Mostly, a homogeneous dipole density is assumed with a dipolar field of $4\pi M$ and an energy density of $2\pi M^2$. For ultrathin films of a few monolayers only, this may not be completely appropriate. The dipolar field of a discrete lattice sum has been discussed elsewhere (Farle, 1998; Heinrich *et al*., 1987). The discrete sum of point dipoles delivers somewhat smaller values for the dipolar contribution but this may even be an underestimation because it is currently clear that for 3d or 4f ferromagnets a finite distribution of the magnetic moment density has been measured by means of neutron scattering. In conclusion, if the continuous dipole density ansatz is inadequate for magnetic monolayers or nanometer dots, the real value will be somewhat smaller but not as small as calculated from a lattice grid with point dipoles.
2. Spin-orbit effects: The experimentalist measures the total (or effective) magnetic anisotropy field or energy. Subtracting from this measured value a separately determined or calculated dipolar contribution, the remaining part is given by the spin-orbit-caused contribution and is commonly labeled with K_i. We do not advice to analyze the sum of the two contributions with K_{eff} because the temperature dependence of the dipolar contribution and the spin-orbit-caused anisotropy may be completely

different. The latter contribution, which is also called ΔE_{band} in the *ab initio* theory, is calculated from the band structure. It has anisotropic contributions in various spacial directions of the ferromagnet. To facilitate a comparison between different experimental results or comparison to theoretical *ab initio* calculations we list below different notations. Owing to the pseudomorphic growth of ultrathin Fe, Co, Ni, and Gd films on cubic substrate crystals, one hardly has cubic symmetry in the ultrathin film but rather structures of tetragonal or lower symmetry.

$$E_{\text{tetr}} = -K_2\alpha_z^2 - \frac{1}{2}K_{4\perp}\alpha_z^4 - \frac{1}{2}K_{4\parallel}\left(\alpha_x^4 + \alpha_y^4\right) + \ldots \quad \text{(A1a)}$$

$$= -K_2\cos^2\theta - \frac{1}{2}K_{4\perp}\cos^4\theta - \frac{1}{2}K_{4\parallel}\frac{1}{4}\left(3 + \cos 4\varphi\right)\sin^4\theta + \ldots \quad \text{(A1b)}$$

$$= -K_2'\sin^2\theta - K_{4\perp}\sin^4\theta + K_{4\parallel}\cos 4\varphi\sin^4\theta + \ldots \quad \text{(A1c)}$$

$$E_{\text{hex}} = K_2\sin^2\theta + \frac{1}{2}K_{2\parallel}\cos 2\varphi\sin^2\theta + K_4\sin^4\theta + K_{6\perp}\sin^6\theta + K_{6\parallel}\cos 6\varphi\sin^6\theta + \ldots \quad \text{(A2)}$$

In the preceding equations, the free-energy density is expanded in terms of trigonometric functions. Equation (A1a) used by Heinrich (1994) is identical to equation (A1b), which is given as a function of polar and azimuthal angles up to fourth order. Quite often this energy is expanded in a sine function with the same polar angle θ, given in equation (A1c). It is obviously clear that the prefactor K_2' of equation (A1c) is not identical to the one in equations (A1a) and (A1b) ($K_2' = K_2 + K_{4\perp}$). Also, the fourth-order contributions differ. Moreover, quite often the MAE is measured only in two directions: the easy and hard axes. The total energy difference is projected onto the second-order $\cos^2\theta$ term – often labeled with K_{u} for uniaxial MAE. For a proper determination of the various energy contributions, a full angular-dependent measurement is required including the field-dragging effect if the external field H_0 is not aligned parallel to the easy or hard axes. It is well established for ultrathin films that the fourth-order term $K_{4\perp}$ is by no means small. Quite often it is in the same order of magnitude as K_2. Less popular but maybe more instructive is the expansion of the free energy into spherical harmonics (Vonsovskii, 1974; Coqblin, 1977; Farle, 1998). Clearly, the terms with power $\cos^n$ are grouped differently, resulting in different prefactors and their temperature dependence. For bulk ferromagnets the trigonometric expansion has been used mostly and the K_2, K_4, and K_6 contributions as a function of temperature are listed in the literature (Stearns, 1986). This temperature dependence with the oscillatory $\pm$ values and zero crossings of the $K(T)$ parameters will change completely and look different if one expands the measured energy in terms of Legendre polynomials (Farle, 1998).

For ultrathin films of 5–10 atomic layers measured by FMR, for example, each of these K_i parameters can be decomposed into contributions of volume K_i^{v} and surface/interface K_i^{s} (Farle, 1998; Baberschke, 2001) following the reasoning by Néel.

$$K_i = K_i^{\text{v}} + 2K_i^{\text{s}}/d \quad \text{(A3)}$$

Spin-polarized Photoelectron Spectroscopy as a Probe of Magnetic Systems

Peter David Johnson[1] and Gernot Güntherodt[2]

[1] *Brookhaven National Laboratory, Upton, NY, USA*
[2] *RWTH Aachen University, Aachen, Germany*

1 INTRODUCTION

Driven by the requirements for new information storage technologies and the potential of 'spintronics' the last two decades have seen a rapid increase in research devoted to studies of low dimensional magnetic systems. New technologies such as molecular-beam epitaxy (MBE), previously developed in the semiconductor industry, are now being applied to the development of new magnetic materials with unique properties. The understanding of the properties of these two-dimensional (2D) systems has provided a number of exciting challenges for the scientific community, both experimental and theoretical.

Handbook of Magnetism and Advanced Magnetic Materials. Edited by Helmut Kronmüller and Stuart Parkin. Volume 3: *Novel Techniques for Characterizing and Preparing Samples*. ISBN: 978-0-470-02217-7.

On the experimental side, a whole range of electron spectroscopies previously developed for the study of metallic surfaces have been 'spin-sensitized' through the addition of spin polarimeters. Electron-based techniques are particularly suited to the study of surfaces and thin films because the strong Coulomb interaction between electrons results in a relatively short mean-free path and associated probing depth. In this chapter, we examine in detail the recent developments of one such technique, spin-polarized photoemission. Photoemission itself has already seen widespread application to the study of the electronic structure of a range of different materials (Kevan, 1992; Hüfner, 2003). The spin-polarized counterpart has a history spanning a period of time that is almost as long as the 'modern' era of photoemission. However, it has taken several years for the complete angle-resolved, spin-resolved photoemission experiment to be developed to the point where it provides spectra with a signal-to-noise ratio comparable to that of its non-spin-resolved counterpart. Here it should be noted that in a further contribution to the handbook by Dürr and Schneider (See also **Ultrafast Magnetodynamics with Lateral Resolution: A View by Photoemission Microscopy, Volume 3**) the time-resolved photoemission microscopy and its application to ultrafast magnetodynamics is treated in some detail.

Several reviews of spin-polarized photoelectron spectroscopy (SPPES) have already appeared in the literature (Feder, 1985; Kisker, 1987; Johnson, 1997). The present review represents an attempt to provide a perspective on the rapid developments in the last 10 years. We first examine the physics of the photoemission process itself with particular reference to the excitation of spin-polarized electrons. The experimental aspects including the different spin polarimeters

that are currently available and the unique requirements of a polarimetry measurement are discussed. We then examine a whole range of recent experiments. We discuss recent studies of magnetic surface states observed on nonmagnetic materials, spin-polarized quantum-well states that develop in nonmagnetic thin films deposited on ferromagnetic substrates, the measurement of spin-dependent self-energy effects and finally studies of a range of magnetic oxides including both ferromagnetic and antiferromagnetic materials and ferromagnet/oxide interfaces. The properties of the quantum-well states observed in thin films are particularly relevant to the discussion of the giant magnetoresistance (GMR) property observed in magnetic multilayers and studies of the oxides are relevant to the development of new capabilities in spintronics.

2 THE PHOTOEMISSION PROCESS

In studies of condensed matter systems, photoemission represents the excitation of an electron from an initial state below the Fermi level to a final state above the vacuum level. As illustrated in Figure 1, the initial state may fall within the delocalized valence bands or it may represent a more localized core level. In the absence of spin–orbit coupling, it can be shown for linearly polarized incident light that the nonrelativistic Schrödinger equation, with the momentum operator $\boldsymbol{p}$ replaced by $\boldsymbol{p}-(\mathrm{e/c})\boldsymbol{A}$, represents an adequate description of the spin-conserving transitions. Here $\boldsymbol{A} = \boldsymbol{A}_0 e^{i\omega t}$ is the vector potential of the electromagnetic field. From Fermi's Golden rule, the differential cross section $\mathrm{d}\sigma/\mathrm{d}\Omega$ for excitation from some initial state $\left|\psi_\mathrm{i}\right\rangle$ to some final state $\left|\psi_\mathrm{f}\right\rangle$ is given by

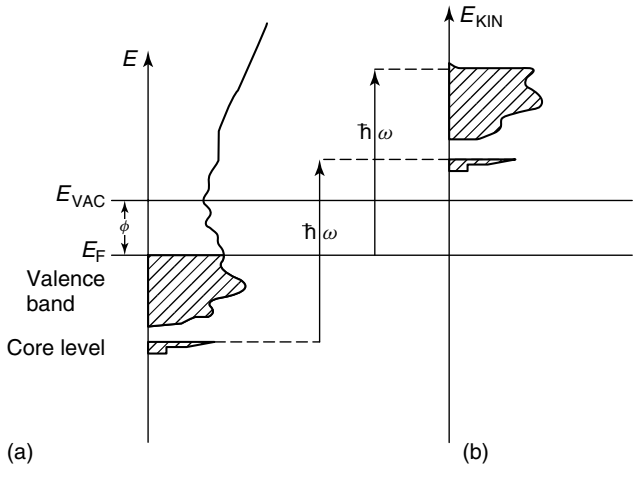

Figure 1. A schematic of the photoemission process. The incident photon with energy $\hbar\omega$ excites an electron from an initial state below the Fermi level E_F to some final state above the vacuum level E_vac. The left panel shows the electron originating either from the valence band or the more localized core level. The right panel displays the excited electron-energy distribution in the final state.

$$\frac{\mathrm{d}\sigma}{\mathrm{d}\Omega}\left(E_\mathrm{f}, \hbar\omega, k_\mathrm{f}, \boldsymbol{A}\right) \propto \sqrt{E_\mathrm{f}} \sum_\mathrm{i} \left|\left\langle\psi_\mathrm{f}\right| \left(\boldsymbol{A}\cdot\boldsymbol{p} + \boldsymbol{p}\cdot\boldsymbol{A}\right) \left|\psi_\mathrm{i}\right\rangle\right|^2 \times \delta\left(E_\mathrm{i} - E_\mathrm{f} - \hbar\omega\right) \quad (1)$$

where the δ function describes the energy conservation of the process. Measuring the kinetic energy of the electron in the final state E_f and knowing the incident photon energy, $\hbar\omega$, the experimentalist can trace back to the binding energy of the electron in the initial state E_i.

Neglecting the diamagnetic term $|\mathrm{A}|^2$ which is always small and noting that $\nabla.\mathbf{A}$ is nonzero only in the surface region, equation (1) is usually reduced to the simpler form

$$\frac{\mathrm{d}\sigma}{\mathrm{d}\Omega} \propto \sqrt{E_\mathrm{f}} \sum_\mathrm{i} \left|\left\langle\psi_\mathrm{f}\right| \left(\boldsymbol{A}\cdot\boldsymbol{p}\right) \left|\psi_\mathrm{i}\right\rangle\right|^2 \delta\left(E_\mathrm{i} - E_\mathrm{f} - \hbar\omega\right) \quad (2)$$

The matrix element introduces selection rules, which can be exploited to determine the symmetry of the initial state. In the nonrelativistic limit, excitation by linearly polarized light between one electron states of the form $|n, l, m_1\rangle$ is restricted to transitions such that $\Delta l = \pm 1$ and $\Delta m_l = 0$. In the event that the incident light is circularly polarized, the second selection rule becomes $\Delta m_l = \pm 1$ dependent on the handedness of the polarization. In the fully relativistic treatment with spin-orbit coupling included, the selection rules become $\Delta j = 0, \pm 1$ and $\Delta m_j = \pm 1$ with j and m_j now referring to the total angular momentum.

A more complete description of the photoemission process will allow for the many-body response of the system to the excitation. Here the δ function of equation (2) is replaced by the single particle spectral function of the hole state $A(\boldsymbol{k}, \omega)$ such that

$$A(\mathbf{k}, \omega) = \frac{1}{\pi} \frac{\Sigma_2(\mathbf{k}, \omega)}{\left[\omega - \varepsilon_\mathrm{k} - \Sigma_1(\mathbf{k}, \omega)\right]^2 + \left[\Sigma_2(\mathbf{k}, \omega)\right]^2} \quad (3)$$

where the real component of the self energy, $\Sigma_1\,(\mathbf{k}, \omega)$, gives a shift in energy and associated mass enhancement and the imaginary component of the self energy, $\Sigma_2\,(\mathbf{k}, \omega)$, gives the lifetime broadening. Note that ω in equation (3) represents the initial-state energy E_i and ε_k represents the bare-band dispersion in the absence of any many-body interactions. In ferromagnetic systems, because of the spin polarization of the electronic structure, we may anticipate a spin dependence in the response of the system.

Extending the technique and measuring the photoemitted current at some emission angle θ, it becomes possible to map the dispersion of the different initial-state bands. As illustrated

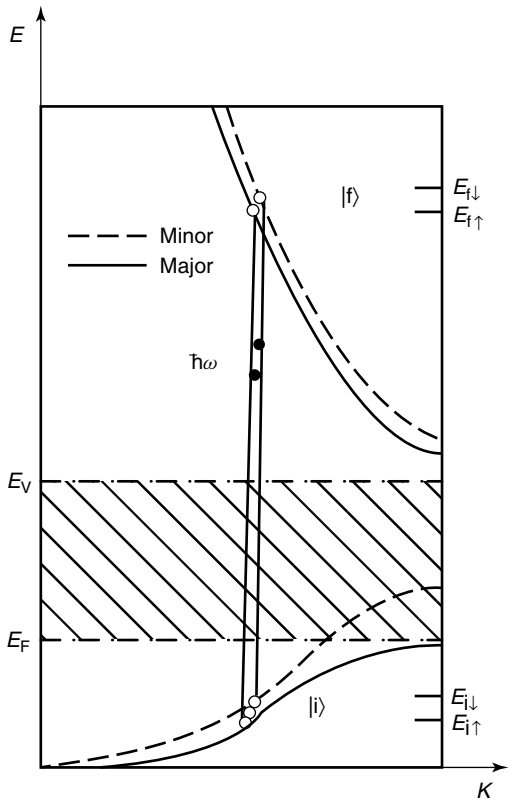

Figure 2. A schematic of the direct k-conserving transition in the photoemission process. The incident photon excites an electron from an initial state E_i below the Fermi level E_F to some final state E_f above the vacuum level E_V. Spin conservation is maintained in the transition.

in Figure 2, at a well-defined $k_{||}$, the process represents a direct transition between two bands of the same spin. In the solid-state environment, momentum conservation is maintained through the mediation of the crystal momentum giving

$$k_f = k_i + G \tag{4}$$

where k_i and k_f are the wave vectors associated with the initial and final states and G represents a suitable lattice vector. If E_{kin} represents the kinetic energy in the final state then to within a reciprocal lattice vector the parallel momentum $k_{||}$ of the photoelectron given by

$$k_{||} = \left(\frac{2m}{\hbar^2}\right)^{1/2} E_{kin}^{1/2} \sin\theta \tag{5}$$

and is conserved on crossing from the solid into the vacuum. Thus a measurement of this component in the vacuum supplies a good measure of the parallel component of the momentum in the solid. The perpendicular component is ill defined due to the breaking of translational symmetry perpendicular to the surface plane.

3 THE EXPERIMENTAL METHODOLOGY

As in any electron spectroscopy, spin-polarized photoemission requires the use of an electron spectrometer. These instruments can take many different forms although, as illustrated in Figure 3, the hemispherical analyzer represents the most commonly used instrument in SPPES at the present time. A more complete discussion of the properties of such an analyzer can be found elsewhere (e.g., Roy and Carette, 1977). Here, we note that in such an instrument the kinetic energy of the electron is measured by retarding electrostatic fields applied between the two hemispheres and the momentum is selected by defining a small angle of collection. As also illustrated in Figure 3, some form of electrostatic lens is required to couple this analyzer to whichever spin polarimeter is selected for the experiment.

An overview of the practicalities of coupling spin polarimeters to electron spectrometers has been given by Pierce, Celotta, Kelley and Unguris (1988). In particular, these authors emphasize the requirement for optimizing the experiment by matching the phase space or acceptances of the source, the electron spectrometer and finally of the spin polarimeter itself. At any point on the pathway of the electron beam the Helmholz–Lagrange law states that there will be a conservation of the product $EA\Omega$, where E is the energy, Ω the solid angle and A the cross-sectional area. In the optimum configuration this product will be matched to the acceptance phase space of the polarimeter. Pierce, Celotta, Kelley and Unguris (1988) have tabulated the latter for a number of different spin polarimeters.

3.1 Measuring the spin polarization

The two principal means of measuring spin polarization involve either the use of spin-dependent scattering via the spin-orbit interaction with a heavy atom or the use of an exchange interaction with a ferromagnetic material. We briefly examine these two different approaches. Much of the pioneering work in spin-polarized photoemission was carried out with spin polarimeters of the high-energy Mott-scattering type (Kisker, Clauberg and Gudat, 1982). Here the electrons to be analyzed are scattered off gold atoms at energies typically of the order of 100 keV. Spin-orbit coupling of the electron in the potential of the gold atom leads to an asymmetry in the scattering, left and right, dependent on the spin of the electron. Because of the high energies involved in the earlier designs, Mott polarimeters tended to be large. However, there have recently been a number of successful modifications that have allowed the polarimeter to be scaled down in size. Figure 4 shows the configuration used in one such device

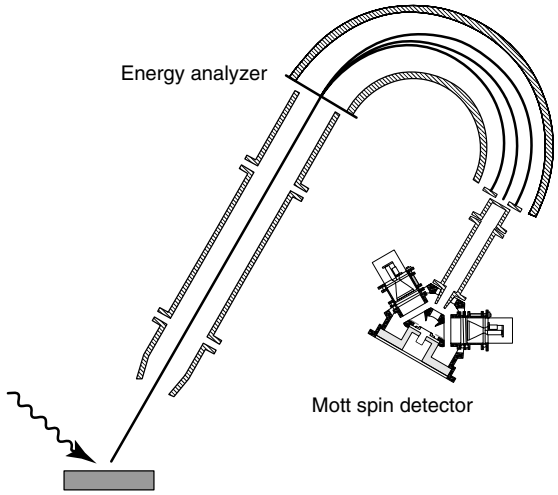

Figure 3. Overview of a spin-resolved spectrometer system. A Mott spin polarimeter is coupled to a hemispherical electron-energy analyzer via an input lens. An electron multiplier array assembly located in the exit plane of the energy analyzer is used for non-spin-resolved multichannel detection.

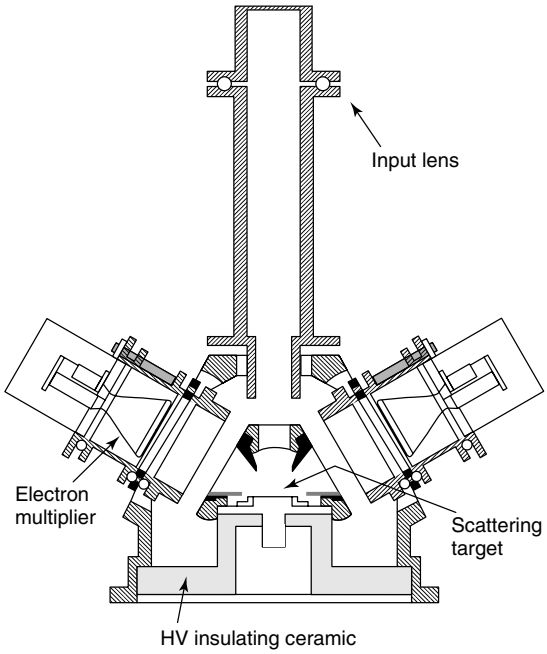

Figure 4. Cross-sectional view of the Mott spin polarimeter with enlarged conic-type collection angle. Only one pair of electron multipliers is shown; the other pair is located in the perpendicular plane.

as described by Huang *et al*. (2002a). After initially passing through a deceleration lens, the incident beam of electrons is accelerated onto the gold foil at an energy of 20 keV. As in the earlier designs (Kisker, Clauberg and Gudat, 1982), those electrons elastically scattered through 120° are detected by two symmetrically opposite channeltrons. Retarding fields in front of the latter collectors remove any electrons that have undergone inelastic losses. The spin polarization P of the incident electron beam is given by

$$P = \frac{1}{S}\frac{I_A - I_B}{I_A + I_B} \tag{6}$$

where S, the Sherman function of the device, is a measure of its ability to distinguish different spins and I_A and I_B represent the intensities measured in opposite channels. Mott polarimeters of this type are now sufficiently small that they can in principle be readily moved inside a vacuum system and, therefore, be used for angle-resolved polarization measurements. The figure of merit (FOM) used in comparing different polarimeters is defined as

$$FOM = S^2\frac{I}{I_0} \tag{7}$$

where again S is the Sherman function, I is the sum of the current collected by the two opposite detectors and I_0 is the incident beam current (Kessler, 1985). The FOM for the traditional Mott polarimeter is typically 10^{-4}; that of the compact low-energy Mott device was initially of the order of 2×10^{-5} (Tang, Zhang, Dunning and Walters, 1988). However, through the use of large area electron detectors and careful optimization of the electron optics, the FOM of the compact devices has gradually been improved. Burnett, Monroe and Dunning (1994) reported an FOM of approximately 1.6×10^{-4}. More recently (Huang *et al*., 2002a) have refined the electron optics further to achieve an FOM of $\sim 2 \times 10^{-4}$. The advantage of the Mott polarimeters, both large and small, is that they are relatively easy to operate in a reproducible fashion.

Originally designed for use in secondary electron microscopy with polarization analysis (SEMPA) studies (Unguris, Pierce and Celotta, 1986; Scheinfein *et al*., 1989), low-energy diffuse scattering from polycrystalline gold films has also proved an excellent device for energy- and angle-resolved spin-polarized photoemission studies (Johnson *et al*., 1992). Rather than the high energies, characteristic of the Mott devices, the electrons to be spin analyzed are now scattered from a polycrystalline gold surface at the much lower energy of 150 eV, an energy at which the Sherman function of gold exhibits a local maximum. The back-scattered electrons pass through retarding grids to remove low-energy secondary electrons, and are then collected by four discrete anodes allowing a measurement of two components of the polarization to be made in parallel. This type of detector has an FOM of the order of 1.0×10^{-4} (Unguris, Pierce and Celotta, 1986), that is, comparable to the traditional Mott detector.

If the scattering surface is a single crystal rather than polycrystalline it is possible to use spin-dependent diffraction to measure the polarization. The spin asymmetry in the scattering again reflects the spin-orbit interaction. Detectors of this type include a low-energy detector, which relies on spin-orbit effects in the diffraction of the electrons from a single-crystal tungsten (001) surface (Kirschner and Feder, 1979). The intensities of the symmetrically opposite (2;0) and ($\bar{2}$;0) diffracted beams are measured with the electrons incident at an energy of 100 eV. The authors report an FOM for this detector of 1.6×10^{-4}.

Spin polarimeters based on an exchange interaction fall into two categories, those employing reflection and those employing transmission. In practice, only the reflection technique has been used in working spin polarimeters to date. A detector based on low-energy reflection from a ferromagnetic film has been described by Tillman, Thiel and Kisker (1989). Here the scattering surface is a 400-Å-thick Fe(001) film grown on an Ag(001) substrate. Reflected intensities are measured when the electrons to be analyzed are incident on a magnetized iron surface at an energy of approximately 10.0 eV. The asymmetry in the scattering, A, in such a detector is given by

$$A = \frac{1}{P}\frac{I^{\uparrow\uparrow} - I^{\uparrow\downarrow}}{I^{\uparrow\uparrow} + I^{\uparrow\downarrow}} \tag{8}$$

where P is the spin polarization in the incident beam and $I^{\uparrow\uparrow}$ and $I^{\uparrow\downarrow}$ are the scattered intensities obtained when the target and primary beam magnetic moments are parallel and antiparallel, respectively. The FOM of such a device is then given by

$$FOM = A^2 \frac{I_R}{I_P} \tag{9}$$

where I_R and I_P are the reflected and primary beam currents, respectively. One difficulty with an instrument of this type is that with the reflecting or analyzing surface being effectively another 'sample', two samples have to be successfully prepared and magnetized. However, at 10.6 eV analyzing energy, the authors report a value of 0.21 for A and an FOM of 3.5×10^{-3}.

More recently the spin-dependent reflectivity of electrons from Fe single-crystal films, 2–8 monolayers (ML) thick, grown on a W(110) substrate has been studied by Zdyb and Bauer (2002). These authors analyzed their data in terms of the quantum-well structure associated with the thin films, that we discuss in detail later. The authors went on to point out the importance of considerations of the quantum-well structure in the design of future spin polarimeters. In a later study, Graf *et al*. (2005) extended these ideas to studies of both Fe and Co thin films grown on W(110). Again by measuring the spin-dependent reflectivities as a function of film thickness the authors determined that a five ML thick film of Co/W(110) represented the optimum configuration for a spin polarimeter. They further indicated that the FOM of such a device would be of the order of 0.02, some two orders of magnitude higher than that achieved in the miniature Mott detectors.

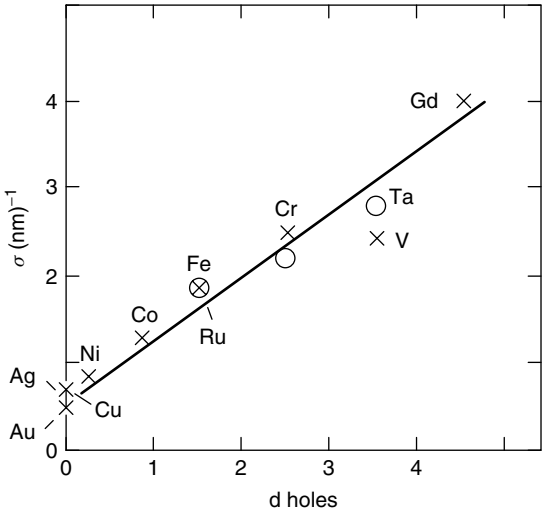

Figure 5. Total scattering cross section $\sigma = 1/\lambda$ in nm^{-1} against the number of unoccupied d orbitals for the transition metals indicated. The data are obtained by analyzing the electron spin polarization in overlayer films and are valid for electron energies within 5 eV of the vacuum level.

Turning to transmission, Schönhense and Siegmann (1993) have suggested the possibility of using the spin-dependent transmission through ferromagnetic thin films as a means of detecting spin polarization. It is evident that such a spin dependence in transmission exists in that the low-energy secondary electron cascade in all electron spectroscopies is known to display an enhanced spin polarization. The latter polarization, which is typically larger than would be expected simply on the basis of the bulk valence band polarization, reflects the spin-dependent mean-free paths of the transmitted electrons. Schönhense and Siegmann examined a number of experiments in detail. As shown in Figure 5 they find that the total scattering cross section $\sigma(E) = 1/\lambda$ is well described by the expression

$$\sigma = \sigma_0 + \sigma_d(5 - n) \tag{10}$$

where σ_d accounts for scattering into the d holes and σ_0 is a constant accounting for other inelastic scattering events. They define a transport polarization α such that an electron beam with small initial polarization P_0 will acquire a polarization after traveling a distance x such that

$$P(x) = P_0 + \alpha(x) \tag{11}$$

The transport polarization α is given by

$$\alpha = \frac{\left[\exp\left(\sigma^- - \sigma^+\right)\, x - 1\right]}{\left[\exp\left(\sigma^- - \sigma^+\right)\, x + 1\right]} \tag{12}$$

with $\sigma^{(\pm)}$ representing the spin-dependent cross sections. In their picture, the spin polarization is, therefore, dominated by the inelastic scattering involving unoccupied states above the Fermi level.

Schönhense and Siegmann note that a spin polarimeter based on the use of spin-dependent transmission will have an FOM given by $\alpha^2 I$ where $I = e^{-\sigma x}$ represents the total spin-integrated transmission through the film and σ is the spin-averaged total cross section. On the basis of their experimental observations, they show that the FOM for an iron film will peak at approximately 7×10^{-2} for film thicknesses of approximately 1.0 nm. For Co they predict an FOM of 6×10^{-2} for a film thickness of approximately 1.5 nm. These ideas have been given some support in studies of the spin-dependent transmission through a free-standing Co film (Lassailly *et al*., 1994; Van der Sluijs *et al*., 1994). The authors of the latter study found that at low energies, close to the surface vacuum level, the transmission coefficient for the minority-spin electrons was 0.7 of that found for the majority-spin electrons. The total transmitted current was of the order of 10^{-5} of the primary beam. By cesiating both sides of the film, this transmission ratio was increased to 3×10^{-4} and a Sherman function of $S = 0.4$ was measured (Van der Sluijs *et al*., 1994).

3.2 Using the spin polarimeter

Before closing our discussion of the experimental details, we offer a brief introduction to the practicalities of a spin-polarization measurement. A more detailed discussion can be found elsewhere (Kessler, 1985).

In order to measure a spin polarization, it is necessary to define a quantization direction for the spin of the electrons. In studies of ferromagnetic or ferrimagnetic systems, this is achieved by ensuring the sample is magnetically saturated. As an example, ferromagnetic thin films can be magnetized by discharging a current pulse through a small coil in close proximity to the film. As we discuss later, it is also possible to perform spin-polarization measurements on antiferromagnetic or even nonmagnetic systems when spin-orbit effects are present. In this case, the quantization direction is defined by the polarization vector of the incident light with the latter being circularly polarized.

To avoid any error being introduced into the measurement by apparatus asymmetries, it is necessary, in the case of ferromagnetic systems, to make two measurements of the spin polarization, one with the sample magnetized 'up' $\left(I_{\mathrm{L}}^+, I_{\mathrm{R}}^+\right)$ and one with the sample magnetized 'down' $\left(I_{\mathrm{L}}^-, I_{\mathrm{R}}^-\right)$. Here I_{L} and I_{R} represent the number of electrons scattered from the target into the left and right channels, respectively. Assuming that the incident beam does not move between the '+' and '−' measurements, any instrumental asymmetry derived from a misalignment of the beam incident on the scattering target can then be removed by combining the four measurements such that the true spin polarization P is given by

$$P = \frac{1}{S}\frac{\sqrt{I_{\mathrm{L}}^+ I_{\mathrm{R}}^-} - \sqrt{I_{\mathrm{L}}^- I_{\mathrm{R}}^+}}{\sqrt{I_{\mathrm{L}}^+ I_{\mathrm{R}}^-} + \sqrt{I_{\mathrm{L}}^- I_{\mathrm{R}}^+}} \tag{13}$$

where as before S represents the Sherman function of the instrument. The measured intensities combined in this manner remove, to first order, any instrumental asymmetry. The two measurements, '+' and '−', may have different count rates without affecting the measured polarization. Assuming that there is not an asymmetry that changes with the two magnetization directions, the instrumental asymmetry A is given by

$$A = \frac{\sqrt{I_{\mathrm{L}}^+ I_{\mathrm{L}}^-}}{\sqrt{I_{\mathrm{R}}^+ I_{\mathrm{R}}^-}} \tag{14}$$

The individual spin-up and spin-down spectra are obtained from the polarization P by

$$I^{\uparrow} = \langle I \rangle\,(1 + P) \quad I^{\downarrow} = \langle I \rangle\,(1 - P) \tag{15}$$

where

$$\langle I \rangle = \frac{I_{\mathrm{L}}^+ + I_{\mathrm{L}}^- + I_{\mathrm{R}}^+ + I_{\mathrm{R}}^-}{4} \tag{16}$$

In studies employing incident circularly polarized light equations (13) and (16) still apply but $(+, -)$ represent the direction of polarization of the incident light.

4 SOME RECENT APPLICATIONS OF SPPES

In the following, we highlight some recent applications of spin-polarized photoemission to problems in condensed matter physics. In particular, we highlight some of the latest developments in the study of spin-polarized surface states and quantum-well states, we examine the application of high-resolution SPPES to the study of spin-dependent

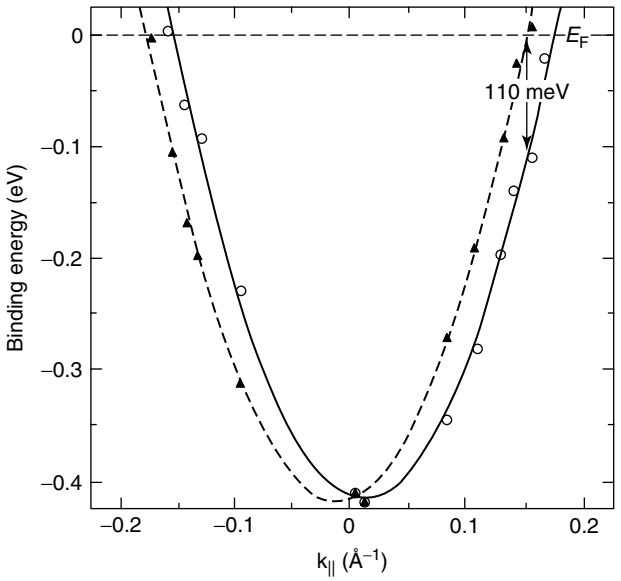

Figure 6. Experimentally determined E vs k dispersion for the surface state at the center of the zone on a Au(111) surface. The measured data points are indicated by the open circles and filled triangles; the solid and dashed lines are parabolic fits. The fit results are (eV and Å^{-1}): $E_1(\mathrm{k}) = 15.2(k - 0.0117)^2 - 0.416$, and $E_2(k) = 15.3(k + 0.0117)^2 - 0.418$. (Reproduced from La Shell *et al*., 1996, with permission from the American Physical Society. © 1996.)

self-energizing effects and finally we review some recent studies of magnetic oxide systems and ferromagnetic/oxide interfaces. The latter oxide systems present a range of exotic phenomena and are currently the subject of intense research activity with respect to spin functionality in spintronics. Primarily, we will restrict our discussion to studies of materials that display magnetic properties. However, we will also review the application of SPPES to the study of the properties of the cuprates, the basis of the high T_c superconductors.

4.1 Spin-polarized surface states

Discussed in detail elsewhere (Johnson, 1997), there have previously been a number of studies of spin-polarized surface states. In general, the spin polarization of the states investigated in those studies reflected the reduced dimensionality present at the surface or solid/vacuum interface of ferromagnetic materials. Examples include states localized on the Fe(001) (Brookes, Clarke, Johnson and Weinert, 1990) and Fe(110) surfaces (Vescovo *et al*., 1993).

It has recently been shown that electronic states at the surface of certain nonmagnetic materials can also display a measurable spin polarization. In this case, the spin polarization reflects a spin-orbit interaction. Shown in Figure 6, a state showing this property was first identified on the surface of Au(111). (LaShell, McDougall and Jensen, 1996). In a high-resolution photoemission study, these authors found that an s–p derived Shockley state displaying parabolic dispersion actually split into two bands as the state moved away from the center of the zone. The authors concluded that the splitting reflected the spin-orbit term in the Hamiltonian given by

$$H_{\mathrm{SO}} = \frac{\hbar}{4m^2c^2}\boldsymbol{\sigma} \cdot (\boldsymbol{\nabla} V x \boldsymbol{p}) \tag{17}$$

where $\boldsymbol{\sigma}$ is the Pauli spin operator and, ∇V is the local potential gradient and $\boldsymbol{p}$ is the electron momentum. The lack of inversion symmetry at the surface allows this spin-orbit interaction to lift the degeneracy between the two spin states. Similar results and hence confirmation were found in a later study of Au(111) but not Ag(111) (Nicolay, Reinert, Hufner and Blaha, 2001).

Examination of equation (17) shows that the energy of an electron depends on its spin direction and its momentum. With a given momentum the effect reverses for different spin directions and for a given spin the effect reverses either side of the zone center. Such effects were confirmed in spin-resolved studies of a surface state on the W(110) surface (Hochstrasser, Tobin, Rotenberg and Kevan, 2002) and for the Au(111) surface state (Hoesch *et al*., 2004). The results of the latter study are shown in Figure 7 where the sign convention (spin up vs spin down) is defined in a spin coordinate axis that is the counterclockwise tangent to the Fermi surface contour. The effect has also been reported in a study of the magnetic Gadolinium (0001) surface state that we discuss in detail later (Krupin *et al*., 2005). In their study, Krupin *et al*. reported the observation of the 'Rashba effect' and reported that it was enhanced upon oxidation of the surface.

As Hoesch *et al*. note, such an effect will be unobservable in the bulk of a material such as gold due to the combined restrictions of the time reversal-symmetry $E^{\uparrow}(\mathbf{k}) = E^{\downarrow}(-\mathbf{k})$ and the inversion symmetry $E^{\uparrow}(\mathbf{k}) = E^{\uparrow}(-\mathbf{k})$ leading to the Kramers degeneracy $E^{\uparrow}(\mathbf{k}) = E^{\downarrow}(\mathbf{k})$.

4.2 Thin films and magnetic multilayers

Magnetic multilayers and related thin films have been an important area of study in magnetism. This interest reflects the many potential technological applications of the GMR property observed in the multilayers. Indeed, this effect first discovered in 1987 by Fert and Grünberg, has already seen widespread use in a number of commercial applications.

GMR is observed in metallic multilayers consisting of ferromagnetic layers separated by nonmagnetic spacer layers.

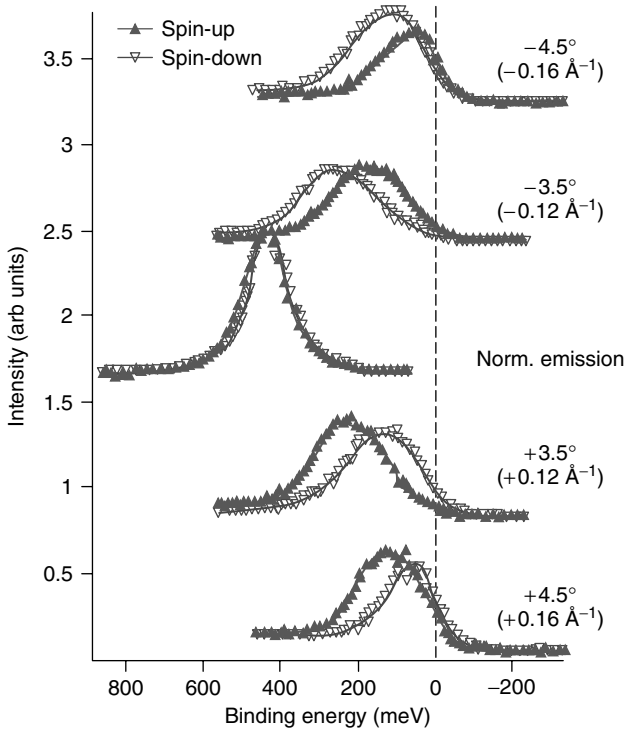

Figure 7. Spin-resolved photoemission spectra from the Au(111) surface state at various polar emission angles. The photon energy was $\hbar\omega = 21.1$ eV. The spin assignment was determined from the transverse in-plane component of the polarization vector. Spin-up and spin-down intensities are marked with filled and open triangles, respectively. (Reproduced from Hoesche *et al*., 2004, with permission from the American Physical Society. © 2004.)

Depending on the thickness of the spacer layer, the adjacent ferromagnetic layers are aligned either ferromagnetically or antiferromagnetically. In the latter configuration, a magnetic field may be applied to realign the magnetic layers and thereby modify the spin-dependent transport or resistance through the system. It is this ability to substantially modify the spin-dependent resistance in these 'GMR' materials that makes them so important.

In order to understand this phenomenon we must first understand the factors that determine the different alignments of the adjacent magnetic layers. In fact, the spacer layer thickness that results in the antiferromagnetic alignment can correspond to several atomic layers. Insight into this property comes from the recognition that the system can be treated as a series of one-dimensional quantum wells. Within these wells the electronic structure will be quantized with an energy separation that reflects the width or thickness of the spacer layer. Let us consider this quantization. In the vicinity of the interface with the adjacent magnetic layer the wave function of the electron state within the well takes the form

$$\Psi = e^{-ik_z} + r_c e^{i\phi} e^{ik_z} \tag{18}$$

where $r_c e^{i\phi_c}$ represents the complex reflectivity at the interface with the substrate and ϕ_c gives the phase change of the wave function. A stationary or bound state exists whenever the total phase change within the well is given by the Bohr–Sommerfeld quantization condition

$$2\phi_c + 2kma = 2\pi n \tag{19}$$

Here, we are considering a well bound by two adjacent magnetic layers and hence two identical interfaces. $2kma$ represents the phase change accumulated on the round trip across a well consisting of m atomic layers with interlayer spacing a. Thus we see that as the number of layers changes, the quantization condition changes and the energy of the stationary state changes to accommodate additional nodes within the wave function. Modifying equation (19) accordingly we obtain

$$\phi_c + (k + \Delta k)\,(m + 1)\,a = \pi\,(n + 1) \tag{20}$$

As we will see later, the spin-dependent scattering at the interface results in quantum-well states showing a strong spin polarization. As the thickness of the nonmagnetic layer changes, the quantum-well states move to lower energy and cross the Fermi level with a well-defined periodicity. The total energy of the system is at a maximum when an occupied quantum-well state is sitting right at the Fermi level. Because the states are spin polarized the system can achieve a lower total energy by having adjacent ferromagnetic layers realign to an antiferromagnetic configuration. By doing so the quantum-well state is allowed to 'leak' away through one interface and the total energy is reduced.

The above represents a quantum well description of the interlayer exchange coupling. In a more detailed analysis of this picture, Smith, Brookes, Chang and Johnson (1994) concluded that the appropriate quantum numbers for classifying the quantum-well states were not n, the number of nodes, or m, the number of layers, but rather $\upsilon = (m - n)$ as illustrated in Figure 8 for silver films deposited on an Fe(001) substrate. In this classification scheme, the thickness against energy relationship may be written

$$\frac{D_\upsilon(E)}{a} = \frac{\frac{\phi_c(E)}{\pi} + \upsilon}{\frac{1-k(E)}{k_{BZ}}} \tag{21}$$

where $k_{BZ} = \pi/a$ represents the zone boundary wave vector and $D = ma$. A quantum-well state crosses the Fermi level each time υ increments by one. It is clear from equation (21) that the Fermi surface will therefore be sampled every Δm layers such that

$$\Delta m = \left(\frac{1 - k_F}{k_{BZ}}\right)^{-1} \tag{22}$$

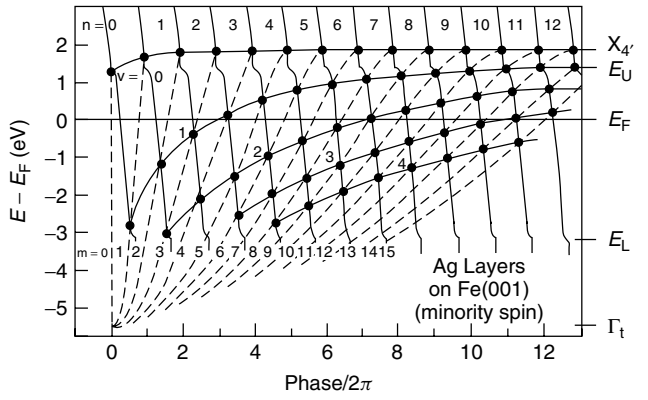

Figure 8. Graphical solutions (full circles) for the energies of quantum-well states of Ag overlayers on Fe(001) using the phase accumulation model. Full bold waves represent the phase $2\pi n - \phi_c - \phi_b$ and dashed curves represent the quantum-well phase accumulation $m2ka$. States characterized by the quantum number $v = (m - n)$ are connected by the full thin curves. (Reproduced from Smith *et al.*, 1994, with permission from the American Physical Society. © 1994.)

where k_F represents the Fermi wave vector. Recognizing that $2(k_{BZ} - k_F)$ gives the associated bulk Fermi surface spanning vectors, q, one immediately retrieves from equation (22) a period length Δma given by 2π/q identical to that obtained by Bruno and Chappert (1991) in an analytical description of the thickness dependence of the oscillatory interlayer exchange coupling in magnetic multilayers.

With a relatively short mean-free path for the escaping electrons photoemission does not lend itself to direct studies of the electronic structure of a multilayer. As such the spin-polarized photoemission studies relevant to these materials are studies that have focused on the properties of the associated overlayers or thin films. Here we refer to, for instance, silver films on Fe(001) substrates and copper films on Co(001) substrates.

The first study that identified the role of spin-dependent interfacial scattering was a study of the quantum-well states that form in silver films deposited on an Fe(001) substrate (Brookes, Chang and Johnson, 1991). In the study, the authors identified an interface state or quantum-well state characterizing a ML thick silver film. With increasing thickness this state evolves into a series of states that move up to and through the Fermi level as shown in Figure 9. The movement to lower binding energy simply reflects the fact that with each new layer the wave function describing the quantum-well state has to gain an extra half wavelength to accommodate the new atomic potential (Smith, Brookes, Chang and Johnson, 1994). We can use the same quantization condition given above for the multilayers but now the ϕ_c of one interface is replaced by the ϕ_b describing the phase shift of the wave function at the solid/vacuum interface. Thus the

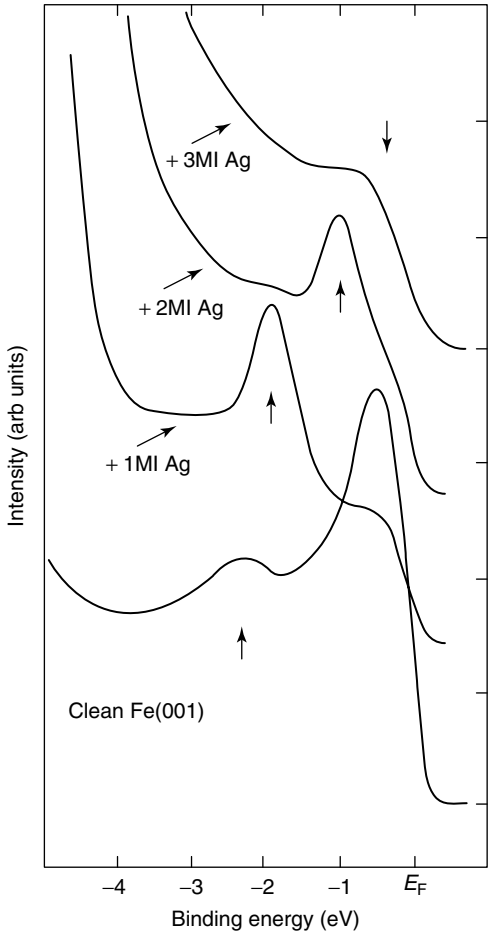

Figure 9. Spin-integrated photoemission spectra recorded from silver films deposited on an Fe(001) substrate. The different film thicknesses are indicated.

quantization condition of equation (19) now becomes

$$\phi_c + 2kma + \phi_b = 2\pi n \tag{23}$$

The spin-polarized photoemission study of Brookes, Chang, and Johnson (1991) revealed that the Ag quantum-well states are highly spin polarized, preferentially with minority spin. As discussed earlier, the observation of a strong spin polarization can be explained in terms of the spin-dependent reflectivities at the interface with the ferromagnetic substrate. If one considers the spin-dependent band structure of iron in the ΓH direction, Figure 10, one observes that in the minority-spin band structure a s–d hybridization gap exists in the vicinity of the Fermi level. At binding energies corresponding to this gap, the propagating waves will be reflected back into the silver layer. Thus, it is the gap that defines the degree of confinement of the minority-spin quantum-well state. In the majority-spin band structure, on the other hand, the hybridization gap is displaced to higher

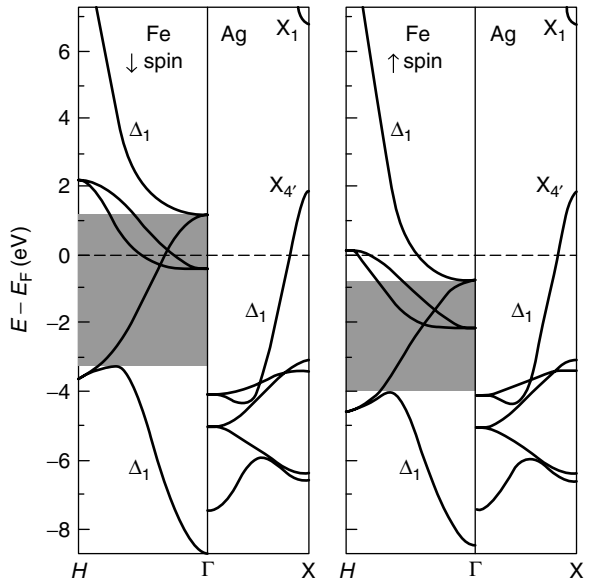

Figure 10. Energy bands of Fe and Ag along the Δ direction for both minority and majority spins. The toned areas indicate the range of the s–d hybridization gap in Fe for states of Δ_1 symmetry.

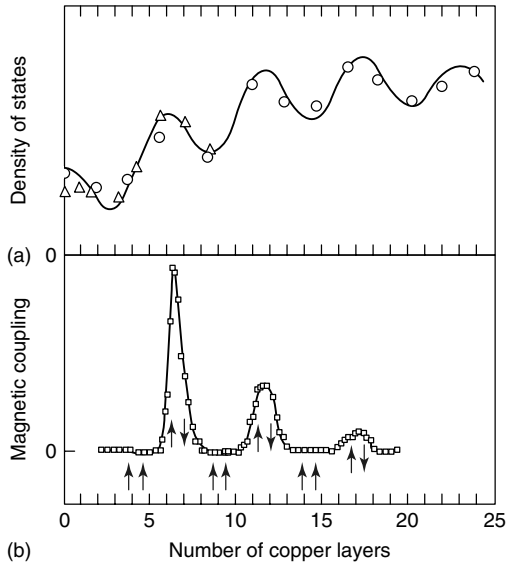

Figure 11. (a) Oscillations in the inverse photoemission intensity at E_F for copper films deposited on a fcc Co(001) substrate from the study of Ortega, Himpsel, Mankey and Willis (1993). (Reproduced from Ortega *et al.* (1993), with permission from the American Physical Society. © 1993.) (b) Results of a Kerr effect study showing the oscillatory antiferomagnetic coupling in Cu/Co(001) multilayers as a function of the copper thickness from the study of Qiu, Pearson and Bader (1992). (Reproduced from Qiu *et al.* (1992), with permission from the American Physical Society. © 1992.)

binding energies and the majority-spin states in the silver layer in the vicinity of the Fermi level will be less strongly confined. The quantum-well states that survive in the silver layer will, therefore, preferentially carry minority spin as observed experimentally.

Subsequent inverse photoemission studies of the Ag/Fe(001) system tracked the quantum-well states as they continued to evolve above the Fermi level eventually converging on the bulk X_4' critical point (Ortega and Himpsel, 1992; Ortega, Himpsel, Mankey and Willis, 1993). These studies clearly demonstrated in this and a number of other systems that the Fermi surface was sampled by the quantum-well states with a frequency identical to that observed for the oscillatory exchange coupling in the associated multilayers. This is illustrated in Figure 11 where the intensity observed at the Fermi level in inverse photoemission studies of copper films deposited on a Co(001) substrate is compared with the oscillatory coupling observed in the associated Cu/Co(001) multilayers.

An interesting question arises as to whether or not majority-spin quantum-well states exist in the spin-polarized photoemission spectra recorded from these films. Examination of Figure 10 shows that in the Fe majority-spin band structure, the top of the s–d hybridization gap falls only 0.8 eV below the Fermi level and the top of the Ag d bands falls 3.0 eV below. Thus one might anticipate seeing strong majority-spin states in the region above the silver d bands up to 0.8 eV below the Fermi level. In fact, such states are predicted in calculations using both the phase model approach of equation (23) and the tight-binding method (Smith, Brookes, Chang and Johnson, 1994) and *ab initio* calculations of the layered KKR type (Crampin, De Rossi and Ciccaci, 1996).

The spin-polarized photoemission study of Ag on Fe(001) (Brookes, Chang and Johnson, 1991) represented a study of the spin-polarization effects in very thin films. Indeed, at the ML limit it is probably more reasonable to describe the induced state as an interface state. Two studies have examined the spin-polarization characteristics of quantum-well states in thicker films. In both cases, the studies were of copper films deposited on a fcc Co(001) substrate (Garrison, Chang and Johnson, 1993; Carbone *et al.*, 1993). As in the earlier Ag/Fe (001) study, the quantum-well states shown in Figure 12 were found to be highly spin polarized with minority spin. However, now the Cu films were grown to thicknesses of the order of six atomic layers or more. In fact in a more recent study Carbone *et al.*, (1996) reported the observation of quantum-well states in copper films of the order of 50 atomic layers thick. At such thicknesses the escape depth of the photoelectrons ensures that the spin-polarization information in the spectrum clearly reflects emission from the Cu film itself rather than the cobalt substrate. In their study, Carbone *et al.* also claimed the observation of majority-spin quantum-well states with considerably less intensity than the minority-spin

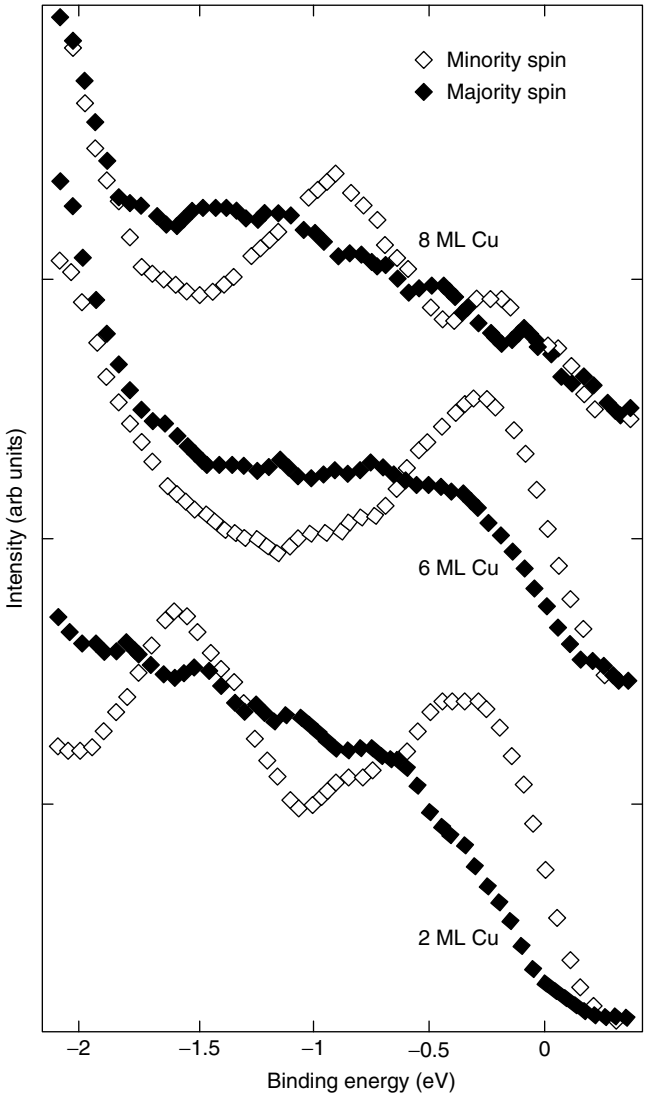

Figure 12. Spin-resolved photoemission spectra recorded from two, six, and eight monolayer thick copper films deposited on a fcc Co(001) substrate. The minority- and majority-spin spectra are represented by the open and full diamonds, respectively. The spectra are recorded for photoelectrons emitted along the surface normal.

counterparts. They determined an exchange splitting of 0.15 eV between the two spin components.

In order to obtain a better understanding of the photoemission spectra in their study Garrison, Chang and Johnson (1993) calculated the electronic structure of the different thickness copper films using a spin-dependent tight-binding scheme in a slab formulation. These tight-binding calculations were carried out using an effective Hamiltonian of the form

$$H = \sum_{\mathbf{k}} E(\mathbf{k})\, n_{\mathbf{k}} + \left(\frac{U}{N}\right) \sum_{\mathbf{k},\mathbf{k}'} n_{\mathbf{k}\uparrow} n_{\mathbf{k}'\downarrow} \qquad (24)$$

Where the first term reflects the nonmagnetic band structure and the second term represents the modification due to the on-site spin-dependent potential U. The latter was simply taken as the effective Stoner parameter. Using such an approach the authors sought a self-consistent solution such that for each layer $\Delta_{\mathrm{l}} = U_{\mathrm{l}} m_{\mathrm{l}}$ where Δ_{l} is the layer-dependent splitting introduced into the d orbitals, U_{l} the layer-dependent Stoner parameter and m_{l} the calculated moment for each layer. On the basis of their calculation Garrison *et al*. concluded that the quantum-well states have significant d as well as sp character. This interesting observation stems from the fact that, within the Cu film, as in bulk Cu, the s-, p bands will hybridize with the d bands of the same symmetry. This hybridization results in a small fraction of the d electrons being carried up to and through the Fermi level and indeed in bulk Cu, approximately 3% of the d-electron manifold is unoccupied. A similar observation has also been made in an *ab initio* layered KKR calculation of copper films deposited on Co(001) (Van Gelderen, Crampin and Inglesfield, 1996).

The observation that there is a small spin polarization in the Cu d band, and further that this band crosses the Fermi level, is a clear indication that a small magnetic moment of d character must exist on the Cu site, an observation that was confirmed in a magnetic circular dichroism (MCD) study of Cu/Co multilayers (Samant *et al*., 1994; Held *et al*., 1996). Here the authors, exploiting the dipole selection rules, studied absorption at the Cu L-edge to obtain site and spin specific information on the unoccupied d bands. The study found a small moment of d character on the copper sites and further concluded that the largest moments exist in the interface where the hybridization with the neighboring Co layers will be strongest. This observation of a localized interfacial magnetic interaction has also been confirmed in numerous other SPPES studies of the d bands in overlayer films deposited on ferromagnetic substrates. As examples, we cite the Pd(111)/Fe(110) interface (Weber, Wesner, Güntherodt and Linke, 1991; Weber, Wesner, Hartmann and Güntherodt, 1992), the Pt/Co(0001) interface (Weber *et al*., 1993), the Ag/Fe(001) interface (Brookes, Chang and Johnson, 1994) and Ru and Rh deposited on Co(0001) (Rampe *et al*., 1995). In general, these studies all identified a moment on the interfacial overlayer atoms but the induced polarization rapidly decayed away with deposition of subsequent overlayers.

More recently Qiu and coworkers have continued to investigate the properties of quantum-well systems and their relationship to the oscillatory exchange coupling (Zhang *et al*., 2000; Qiu and Smith, 2002; Wu *et al*., 2006). In particular, these authors have focused on the thickness dependence of the quantum-well electronic structure (Rotenberg *et al*., 2006) and on the properties of double quantum-well structures (Ling *et al*., 2002; Wu *et al*., 2006).

There is also the possibility of quantizing the electronic structure of d bands in a thin film. The role of this has been explored in a SPPES study of chromium films grown on an Fe(001) whisker with particular reference to the oscillatory exchange coupling in Fe/Cr multilayers (Li *et al*., 1997). In another PES study, Krajl *et al*. examined the quantization of the d bands in silver films grown on an V(001) substrate (Kralj *et al*., 2003). The authors were successfully able to explain the quantum-well structure both in terms of the phase models described in the preceding text and in terms of tight-binding calculations. It is interesting to speculate on the possible role of quantized d bands in the multilayer structures. Indeed it is known that scattering from a d resonance at energy E_d can induce a phase shift δ_l such that (Harrison, 1980)

$$\tan \delta_\mathrm{l} = \frac{\Gamma}{2(E_\mathrm{d} - E)} \tag{25}$$

Thus the scattering induces a phase shift at energy E that increases from 0 to π over the range Γ of the resonance. A phase shift of π will shift the quantum-well states from one thickness dependent branch to the next.

4.3 Collective excitations and self-energizing effects

In recent years, the energy and momentum resolution of angle-resolved photoemission have improved to a degree that allows detailed studies of self-energy effects. Thus it has become routinely possible to study the lifetime and dispersion modifications associated with a variety of collective modes including phonons, spin excitations, and charge density waves. In magnetic systems, with the added complexity of spin detection, the studies of magnetic systems have been considerably more limited. Here we review the only detailed study of spin-dependent self-energy effects, namely a recent study of gadolinium. The spin-dependent electronic structure of this material had previously been studied extensively with spin-resolved photoemission.

The ground state of gadolinium is ferromagnetic with a Curie temperature T_C of 293 K. The (0001) surface of this material has been shown both theoretically (Wu, Li, Freeman and Fu, 1991) and experimentally (Li *et al*., 1991) to support a surface state derived from the Gd 5d orbitals. The state, which is spin polarized through an exchange interaction with the localized 4f orbitals has an important history and indeed it was spin-resolved photoemission studies of the surface state that finally confirmed that the surface moments were ferromagnetically aligned with the bulk of the material (Mulhollan, Garrison and Erskine, 1992).

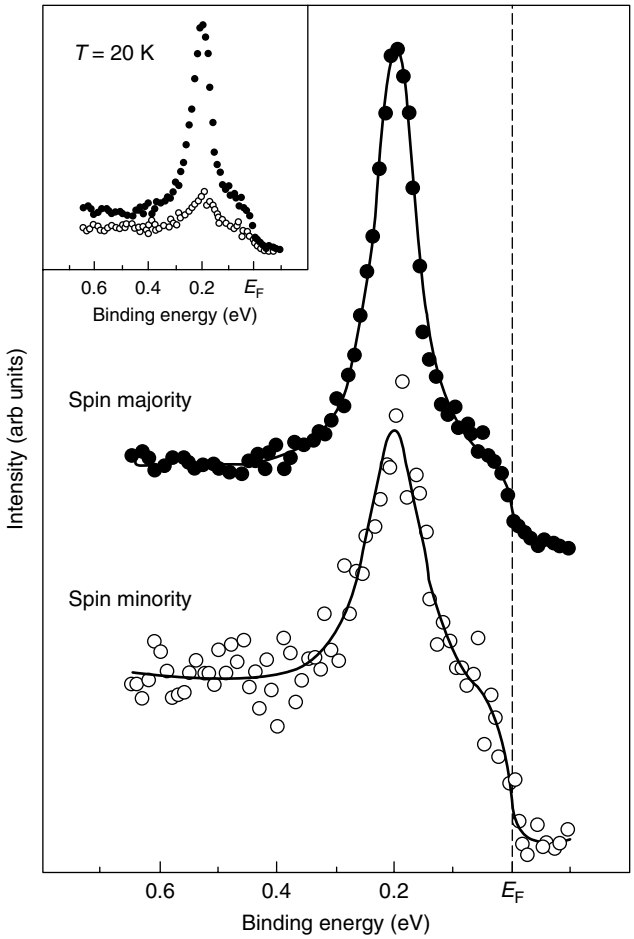

Figure 13. Spin-resolved photoemission spectra recorded from the Gd(0001) surface at 20 K. The upper and lower spectra represent the emission in the majority- and minority-spin channels, respectively. The lines indicate Lorentzian fits to the spectra superimposed on appropriate backgrounds. The inset shows the relative inteansities in the two spin channels.

The results of a more recent photoemission study of this same state held at 20 K with both high energy and spin resolution are illustrated in Figure 13 (Fedorov *et al*., 2002). As noted earlier, both experiment (Mulhollan, Garrison and Erskine, 1992; Li *et al*., 1993) and theoretical calculations (Wu, Li, Freeman and Fu, 1991) indicate that the surface state should be 100% majority spin, reflecting parallel alignment of the surface and bulk moments. The coexistence of both spin components at the same energy in Figure 13 is therefore an intrinsic property of the surface state arising from a combination of spin-orbit and spin-exchange processes. A simple model yields a polarization $P = \Delta/\sqrt{\Delta^2 + \zeta^2}$ for each quasiparticle state. With a spin-orbit parameter $\xi = 0.3$ eV and an exchange splitting $\Delta = 0.7$ eV at 0 K, we get a spin-orbit induced mixing $R = (n/n^-) = (1 - \mathrm{P})/(1 + \mathrm{P}) \sim 5\%$. This increases to 8% at $T = 150$ K as the exchange

splitting between the occupied and unoccupied surface states gets smaller (Fedorov, Starke and Kaindl, 1994; Weschke *et al*., 1996).

Fitting the spectra in Figure 13 with Lorentzian line shapes shows that the minority-spin peak has a larger width than its majority-spin counterpart, 116 meV as opposed to 86 meV. Removing the contribution from the experimental resolution, these widths become approximately 105 meV in the minority-spin channel and 70 meV in the majority channel. Possible decay modes for either spin photohole can involve electron–phonon, electron–magnon and electron–electron scattering. Each of these different mechanisms will give distinct spin-dependent contributions to the scattering rate. Electron–electron scattering by exchange processes favors the two holes in the final state being of opposite spin (Sinkovic, Shekel and Hulbert, 1995). From consideration of the total density of states in the spin channels, the authors of the spin-resolved study estimated the scattering rate from the process to be equal for a majority-spin hole and a minority-spin hole. The electron–phonon and impurity scattering rate are proportional to the density of states at the hole binding energy for the same spin while the electron–magnon rate is proportional to the density of states for the opposite spin. Since the majority-spin density of states is large while the minority-spin part is small and from consideration of the required momentum transfer, impurity and electron–phonon scattering should be more important in the majority-spin channel. The observation that the minority-spin channel is broader suggests electron–magnon scattering is the dominant decay mechanism. At $T = 0\,\mathrm{K}$, the minority-spin component of a photo-hole can scatter to the majority-spin component of a hole state higher in the surface band by emitting a spin wave (tilting the spins of the localized f electrons). The corresponding spin-flip process is not available to the majority-spin component of the photo-hole at $T = 0$ because the localized f spins have saturated magnetization and are not able to tilt upwards when the hole tilts down. At higher temperatures, inelastic scattering can occur back and forth between the two spin channels mediated by the emission or absorption of magnons, but the minority-spin component always has the higher density of final states to scatter into. An approximate treatment (Allen, 2001) using the 's–f' Hamiltonian (Zener, 1951a–c) found the result

$$\frac{\hbar}{\tau\,(\downarrow)} = \frac{\sqrt{3}}{4}\frac{P\,(\uparrow)\,m^*}{S}\left(\frac{2JSa}{\hbar}\right)^2 \tag{26}$$

for the decay of the minority ($\downarrow$) spin component due to spin-flip scattering with magnon emission. Here J is the s–f exchange parameter giving the exchange splitting $2JS = 0.65$ measured for the surface state, $m^* = 1.21$ is the effective mass measured for the surface band, and $P(\uparrow) = 0.87$ is the experimentally measured majority component of the band. With $S = 7/2$ and $a = 3.6\,\text{Å}$, $\hbar/\tau\,(\downarrow) = 0.095\,\mathrm{eV}$. Conversely, replacement of $P(\uparrow)$ by $P(\downarrow) = 1 - P(\uparrow)$ gives $\hbar/\tau(\uparrow) \approx 0.014\,\mathrm{eV}$ for the majority-spin component. Thus at low T, the majority-spin channel is dominated by electron–phonon scattering, whereas the minority-spin channel is dominated by electron–magnon scattering. On the basis of the relative spin-dependent densities of states it is possible to provide estimates of the contribution of phonon scattering in the two spin channels. These would be 46 meV in the majority-spin channel and 10 meV in the minority-spin channel, leaving approximately l0 meV in each channel due to impurity scattering. This system has also been studied by the group of Kaindl using scanning tunneling spectroscopy (Rehbein, Wegner, Kaindl and Bauer, 2003). They arrived at slightly different values for the different contributions but also concluded that the occupied majority-spin surface state preferentially decays via electron–phonon scattering. The important experimental observation in the study described in the preceding text is that the occupied minority-spin component of that state has a shorter lifetime. The only way that can occur is through the participation of magnon scattering.

4.4 Half-metallic ferromagnetic oxides

Half-metallic ferromagnets (HMF) show in the ideal case a 100% spin polarization at the Fermi level E_F. The high polarization reflects a metallic density of states for one spin direction and a band gap for the other spin direction. This class of materials was first discovered via *ab initio* calculations by de Groot, Mueller, van Engen and Buschow (1983) for Mn-based Heusler alloys, such as NiMnSb. Besides the expectation of exceptional magneto-optical properties, these materials have recently attracted considerable attention because of their potential application in the field of spintronics (Pickett and Moodera, 2001). In principle, HMFs are ideal spin injectors and detectors because under moderate voltage they can carry current of only one spin direction. A wealth of theoretical work has been devoted to the spin-dependent electronic structure of metal-based HMF (Kübler, 2003; Wurmehl *et al*., 2005) or zinc-blende chalcogenide HMF (Mavropoulos, Ležaić and Blügel, 2005). Here we focus on transition-metal oxide HMF, the existence of which, again, had all been predicted by *ab initio* electronic structure calculations. Examples include Fe_3O_4 (Yanase and Siratori, 1984; Zhang and Satpathy, 1991), CrO_2 (Schwarz, 1986; Korotin, Anisimov, Khomskii and Sawatzky, 1998), $La_{1-x}Sr_xMnO_3$ (Pickett and Singh, 1996) and Sr_2FeMoO_6 (Kobayashi *et al*., 1998). The experimental challenge ever since has been to prove the half-metallic nature of these ferromagnetic or ferrimagnetic materials. While this task would best be carried

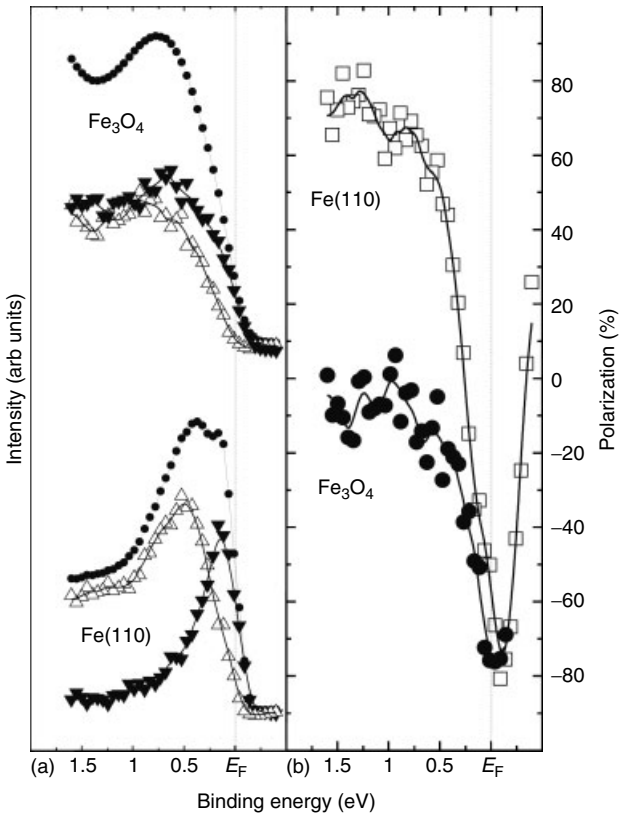

Figure 14. (a) Spin-resolved photoemission intensities (Δ spin up, ▼ spin down) measured at $h\nu = 21.2\,\text{eV}$ together with the total intensity (●) of 5-nm-thick Fe(110) (bottom) and $Fe_3O_4(111)$ (top), obtained by oxidizing Fe(110) in oxygen atmosphere at 250 °C. (b) Spin polarization of Fe(110) (●) and $Fe_3O_4(111)$ (●). (Reproduced from Dedkov *et al*., 2002a, with permission from the American Physical Society. © 2002.)

out using polycrystalline materials to yield an average over all k states of the Brillouin zone, the experimental studies have mostly been aimed at using single crystalline material or thin epitaxial films. This was necessary because the particular experimental techniques used for measuring spin polarization all show a subtle surface sensitivity. Among these are spin-polarized tunneling into superconductors, superconducting point-contact spectroscopy using Andreev reflection, magnetic tunnel junctions (MTJ) and spin-polarized photoemission. While most of the techniques depend critically on interface qualities, photoemission relies particularly on ultraclean surfaces. Another crucial point concerns the different nature of the electronic states probed by transport and by photoemission measurements. In this section, we give an account of the progress made in the field of oxidic HMF using SPPES.

1. $Fe_3O_4(111)$, (100): SPPES studies of magnetite (Fe_3O_4) began in 1975 (Alvarado *et al*., 1975). The interpretation of the valence band photoemission spectra is still a subject of controversial debate (Alvarado, Erbudak and Munz, 1976; Alvarado and Bagus, 1978; Cai, Ritter, Weiss and Bradshaw, 1998; Dedkov, Rüdiger and Güntherodt, 2002a; Dedkov *et al*., 2004; Fonin *et al*., 2005). Alvarado *et al*. performed the first SPPES measurements on cleaved $Fe_3O_4(100)$ single crystals (Alvarado *et al*., 1975; Alvarado, Erbudak and Munz, 1976; Alvarado and Bagus, 1978). The spin polarization of the photoelectrons showing a maximum value of -60% near the Fermi energy E_F was measured at 10 K using an incident photon energy of 5 eV (Alvarado, Erbudak and Munz, 1976). From a single-ion-in-a-crystal-field (SICF) model, a maximum value of $P = -66.6\%$ was obtained for the spin polarization at $T = 0\,\text{K}$ (Alvarado, Erbudak and Munz, 1976; Alvarado and Bagus, 1978). This was considered to be in agreement with the measured value of -60%. However, subsequent spin-polarization measurements on epitaxial thin films of $Fe_3O_4(111)$ and $Fe_3O_4(100)$ yielded at room temperature, values of $-(80 \pm 5)\%$ and $-(40\text{–}55)\%$ near E_F, respectively (Dedkov, Rüdiger and Güntherodt, 2002a; Morton *et al*., 2002; Huang *et al*., 2002b; Fonin *et al*., 2005). Figure 14 shows in (a) the spin-resolved photoemission intensities (▲ spin up, ▼ spin down) together with the total intensity (●) of Fe(110) (bottom) and $Fe_3O_4(111)$ (top). The spin polarization is shown in (b) for Fe(110) (■) and $Fe_3O_4(111)$ (●). In both cases, the spin polarization at E_F is accidentally -80%. For $Fe_3O_4(111)$ this provided evidence closer to the theoretically predicted half-metallic nature of magnetite (Yanase and Siratori, 1984; Zhang and Satpathy, 1991), at least for the [111] direction.

For the interface between a 25-nm-thick $Fe_3O_4(111)$ thin film and a 2-nm-thick γ-$Al_2O_3(111)$ layer a *negative* spin polarization of about -40% was found by SPPES (Bataille *et al*., 2006).

Interestingly, for the (100)-oriented epitaxial thin films of Fe_3O_4 spin-polarization values of only $-(40\text{–}55)\%$ near E_F were obtained (Morton *et al*., 2002; Huang *et al*., 2002b). These values are significantly lower than the -100% predicted by local spin density approximation (LSDA) calculations for the bulk material (Zhang and Satpathy, 1991) as well as the $-(80 \pm 5)\%$ measured at room temperature on the (111)-oriented Fe_3O_4 surface near E_F (Dedkov, Rüdiger and Güntherodt, 2002a). The low value for the (100) surface was ascribed either to surface imperfection (Morton *et al*., 2002) or to strong electron correlation effects (Huang *et al*., 2002b). Recent measurements of SPPES on epitaxial thin films of $Fe_3O_4(100)$ gave a spin polarization of $-(55 \pm 10)\%$ at E_F (Fonin *et al*., 2005). In an effort to explain this result on the basis of density-functional theory (DFT) and *ab initio* thermodynamics calculations it was discovered that the surface electronic structure of $Fe_3O_4(100)$ differs distinctly from the bulk one. A $(\sqrt{2} \times \sqrt{2})R45^0$ wavelike surface atom reconstruction due to a Jahn–Teller effect was found to lead to surface states in the majority-spin band gap, resulting

in a calculated spin polarization of -40% at E_F (Fonin *et al*., 2005). However, for all of these comparisons between experiment and theory it has to be remembered that, except for the latter reference, the electronic structure calculations have been performed for the bulk material without taking account of subtle surface reconstruction and relaxation or charge redistribution effects, particularly for (100) polar surfaces. These surface effects certainly play an important role in VUV-PES and SPPES measurements.

For correlated electron systems, such as Fe_3O_4, an atomic configuration-based approach had initially been chosen for the interpretation of the SPPES data (Alvarado, Erbudak and Munz, 1976; Alvarado and Bagus, 1978). Recent investigations (Cai, Ritter, Weiss and Bradshaw, 1998; Dedkov, Rüdiger and Güntherodt, 2002a), however, showed that band dispersions (Yanase and Siratori, 1984; Zhang and Satpathy, 1991) must be taken into account for the interpretation of photoelectron spectra of Fe_3O_4. In particular, surface symmetry-related band dispersions were identified for $Fe_3O_4(111)$. Angle-resolved PES determinations of the electronic band structure of well-ordered $Fe_3O_4(111)$ surfaces using synchrotron radiation (Dedkov *et al*., 2004) gave direct evidence for surface-Brillouin-zone (SBZ) symmetry-related contributions of the oxygen and iron sublattices. In the $\overline{\Gamma}-\overline{M}$ direction of the $Fe_3O_4(111)$ SBZ, two types of dispersing states were identified. They originate from a periodic multilayered structure of iron and oxygen ions, with Fe^{2+} and Fe^{3+} cations incorporated into the close-packed fcc oxygen sublattice. For $Fe_3O_4(100)$ a 'wavelike' atom pattern observed by STM along the [110] direction (Tarrach *et al*., 1993; Stanka, Hebenstreit, Diebold and Chambers, 2000; Fonin *et al*., 2005) gave the first hint of surface reconstruction effects, which were finally corroborated by DFT calculations (Fonin *et al*., 2005). Over a broad range of oxygen pressures, the modified B-layer bulk termination, consisting of oxygen and iron (Fe_B) in octahedral B sites and showing a pairwise 'wavelike' shift of iron atoms perpendicular to the B rows, was identified as lowest energy configuration. As a consequence of this reconstruction, surface states appear in the band gap of the majority-spin subband leading to a reduction of the spin polarization to about -40% at E_F and a loss of half-metallicity of the $Fe_3O_4(100)$ surface. These surface states are a hybridization of $d_{x^2-y^2}$ states of octahedral iron in the surface layer and p_x, p_y states of the surface oxygen without a subsurface tetrahedral iron neighbor.

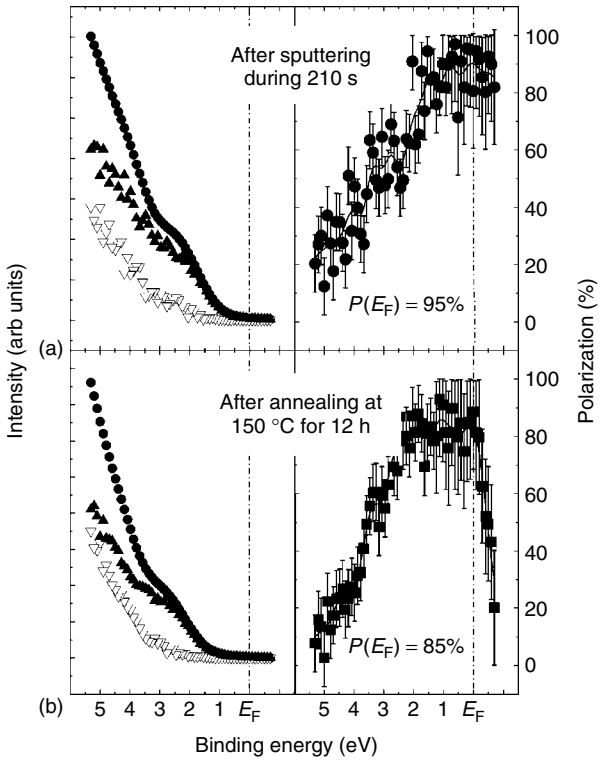

Figure 15. Right panel: spin polarization as a function of binding energy of an epitaxial CrO2(100) film (a) after Ar^+ sputtering for 210 s at 500 eV and (b) after 750 s sputtering and an additional annealing treatment at 150 °C for 12 h. Left panel: corresponding spin-polarized photoemission spectra at $h\nu = 21.2$ eV (▽ spin down, ▲ spin up) and total photoemission intensity (●). (Reproduced from Dedkov *et al*., 2002b, with permission from the American Institute of Physics. © 2002.)

2. $CrO_2(100)$: In spite of applications in magnetic tapes and potential use for magneto-optical storage, the electronic structure of CrO_2 was theoretically predicted only in 1986 using the LSDA to DFT (Schwarz, 1986). The first SPPES investigations revealed a spin polarization of up to 90% near 2 eV binding energy below E_F (Kämper *et al*., 1987). No spin analysis using a 100-kV Mott spin detector (Kisker, Clauberg and Gudat, 1982) was feasible at the time between E_F and 2 eV binding energy because of the low photoemission intensity. The low emission intensity was attributed to oxygen deficiencies. However, high quality epitaxial thin films of $CrO_2(100)$ grown on Ti(100) single-crystal substrates showed a spin polarization of up to 95% at E_F (Dedkov *et al*., 2002b). Figure 15 shows in the right panel the spin polarization as a function of binding energy of an epitaxial $CrO_2(100)$ film (a) after Ar^+ sputtering for 210 s at 500 eV and (b) after 750 s sputtering and an additional annealing treatment at 150 °C for 12 h. The left panel shows spin-polarized photoemission spectra (▼ spin down, ▲ spin up) and total photoemission intensity (●). The value of $P = 95\%$ at E_F in Figure 15(a) agrees with measurements using superconducting point-contact spectroscopy (Soulen, Byers and Osofsky, 1998; Ji *et al*., 2001). The good agreement between spin-polarization values from photoemission and transport measurements has to be attributed to the unusually strong 2p(O)-3d(Cr) hybridization found in electronic structure calculations based

on LSDA + U (Korotin, Anisimov, Khomskii and Sawatzky, 1998). A value of 90% spin polarization for unoccupied states above E_F was also found using spin-resolved O 1s X-ray absorption spectroscopy (Huang *et al*., 2003). These data give evidence that the presence of holes in the oxygen band prevents CrO_2 from being an insulator and supporting the notion that the material is a self-doped or p-type metal (Korotin, Anisimov, Khomskii and Sawatzky, 1998).

The shoulder in the photoemission intensity in Figure 15(a) and (b) which becomes most pronounced after sputtering for 750 s, has been associated with the localized Cr(3d) states. These, however, were found in LSDA + U calculations (Korotin, Anisimov, Khomskii and Sawatzky, 1998) to be near 1 eV binding energy. The photoemission intensity near 2 eV was more recently attributed to emission from the Cr_2O_3 surface layer (Chang *et al*., 2005). This conclusion was reached on the basis of MCD in resonant photoemission studies with hν tuned to the Cr 2p absorption edge. The energy positions of the Cr 3d bands in CrO_2 are then determined with no contribution from antiferromagnetic Cr_2O_3. However, this conclusion contradicts the finding of the peak at 2 eV binding energy after prolonged sputtering (750 s), removing all Cr_2O_3 (Dedkov *et al*., 2002b). Hence the peak at 2 eV is of intrinsic origin, most likely associated with the lower Hubbard band (LHB). The upper Hubbard band (UHB) may be evident in the atomic-like Cr 3d state observed in spin-resolved O 1s X-ray absorption near 0.6 eV above E_F (Huang *et al*., 2003). These observations combined give a Coulomb correlation energy U in agreement with the value $U = 3$ eV used in LSDA + U electronic structure calculations (Korotin, Anisimov, Khomskii and Sawatzky, 1998). Further, in agreement with these calculations, a more localized Cr 3d derived spectral weight near 1 eV is found by MCD in resonant photoemission (Chang *et al*., 2005). In the most recent bulk sensitive board X-ray photoelectron spectroscopy (HAX-PES) measurements using hard X-rays ($h\nu = 7942$ eV) (Suga, 2006) dispersionless Cr(3d) states were found near 1 eV binding energy. Most interesting in the HAX-PES measurements is the rather small spectral weight near E_F, similar to the previous VUV-PES data by Kämper *et al*. (1987). This is in strong contrast to a theoretical study using LSDA + DMFT (dynamic mean-field theory) and applying the iterated perturbation theory (IPT) as 'Anderson-impurity solver' to the multiorbital case (Craco, Laad and Müller-Hartmann, 2003). In this calculation, CrO_2 is found to exhibit a rather unusually high density of states at E_F. The authors stress the importance of dynamical correlation leading to a collective orbital Kondo effect and the emergence of a correlated Fermi liquid scale. However, the puzzle of the low intensity or missing Fermi edge in the earlier surface-sensitive VUV ($h\nu = 21.2$ eV) photoemission data (Kämper *et al*., 1987) has recently been attributed to a surface relaxation of CrO_2(100) deduced from LSDA-based first-principles calculations (Hong and Che, 2006). The distorted tetrahedral oxygen coordination of each surface Cr ion gives rise to an inversion of the $t_{2g} - e_g$ splitting of the Cr 3d orbitals, with E_F lying in a gap between the occupied e_g and unoccupied t_{2g} states for a local electronic structure at the surface. For future photoemission intensity calculations of CrO_2 it appears indispensable to apply computational schemes merging the local density approximation (LDA) with DMFT and using quantum Monte–Carlo simulations (QMC) to solve the effective Anderson-impurity model of DMFT.

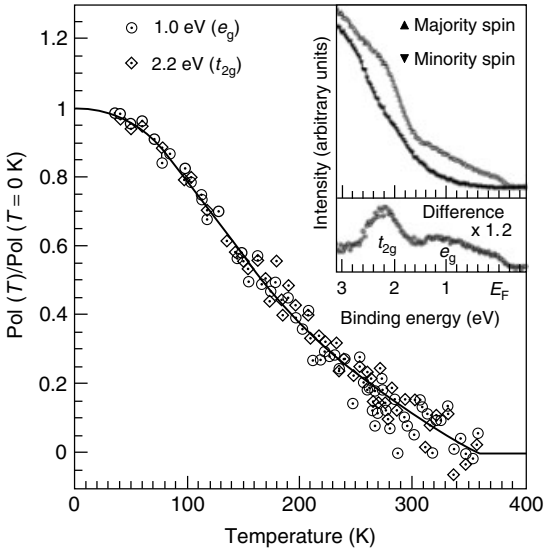

Figure 16. Temperature dependence of spin polarization of Mn 3d states, e_g at 1.0 eV binding energy and t_{2g} at 2.2 eV binding energy obtained with $h\nu = 40$ eV. The inset shows the spin-polarized photoemission spectra for the majority and minority spins and the difference at 40 K. (Reproduced from Park *et al*., 1998, with permission from the American Physical Society. © 1998.)

3. Manganites: The manganite class of materials is unusual not only because of the occurrence of the colossal magnetoresistance (CMR), but also because of its dense granular magnetoresistance, and the development of concepts like double exchange and Jahn–Teller polarons. The rich electronic phase diagrams reflect the fine balance of interactions, which determine the electronic ground state. The different competing, novel phases, including orbital order and orbiton excitations, arise from an interaction between different microscopic degrees of freedom, including charge, spin, orbitals, and lattice. The most straightforward evidence of a minority-spin gap and a concomitant 95% spin polarization near E_F was obtained in $La_{0.7}Sr_{0.3}MnO_3$ at 40 K by means of SPPES (Park *et al*., 1998a,b). This observation was consistent with first principles calculations of $La_{1-x}Ca_xMnO_3$ (Pickett and Singh, 1996). Figure 16 shows the temperature

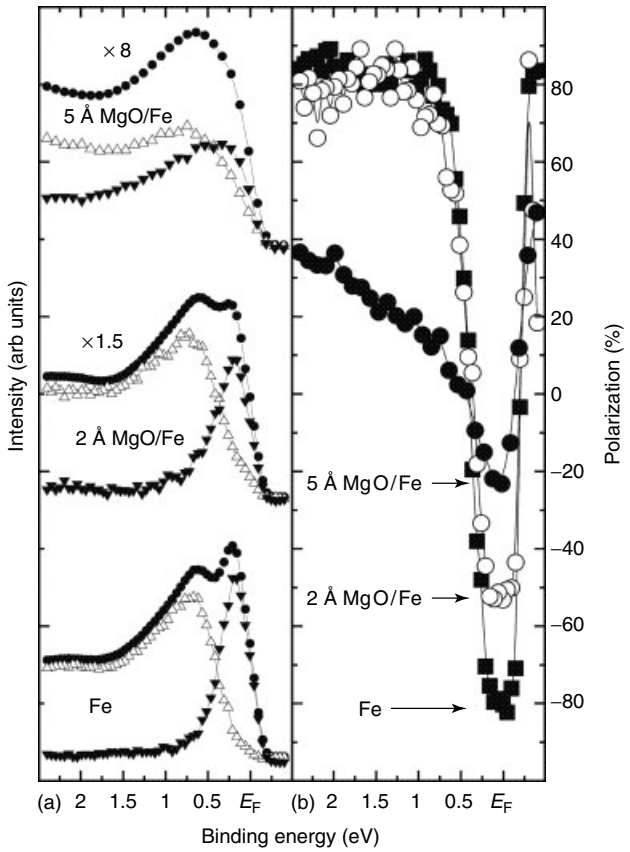

Figure 17. (a) The spin-resolved photoemission spectra (▼ spin down, △ spin up) together with the total emission intensity (●) of Fe(110), 2 Å MgO on Fe(110), and 5 Å MgO on Fe(110) (from bottom to top). (b) The spin polarization as function of binding energy of a 50-Å-thick Fe(110) film (■), 2 Å MgO on Fe(110) (○), and 5 Å MgO on Fe(110) (●). (Reproduced from Dedkov *et al*., 2006, with permission from the American Institute of Physics. © 2006.)

dependence of the spin polarization of the Mn 3d states, e_g at 1.0 eV binding energy and t_{2g} at 2.2 eV binding energy, obtained with $h\nu = 40$ eV (Park *et al*., 1998a,b). The half-metallic nature of $La_{0.7}Sr_{0.3}MnO_3$ had a crucial impact on spin-polarized tunneling into Co through a $SrTiO_3$ tunnel barrier (de Teresa *et al*., 1999).

4.5 Ferromagnet-oxide interfaces

Interfaces between electrodes of itinerant ferromagnets and insulating oxide layers play a decisive role in MTJs, giving rise to the tunnel magnetoresistance (TMR). A most prominent and successful example is Fe(100)/MgO(100)/Fe(100), which was theoretically predicted to yield a TMR of the order of about 1000% (Butler, Zhang, Schulthess and MacLaren, 2001; Mathon and Umerski, 2001). The presently highest TMR values that have currently been achieved experimentally are 220% at room temperature (300% at

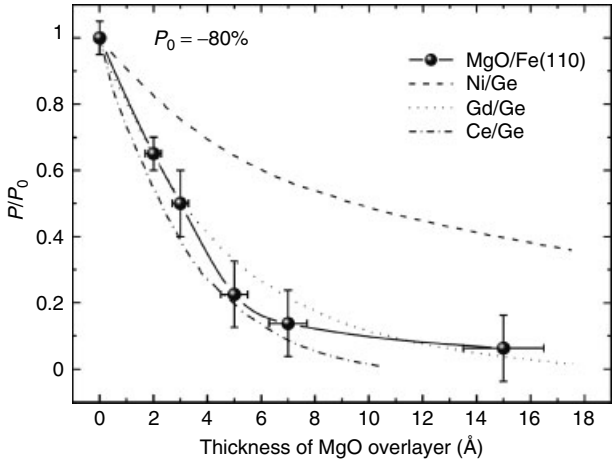

Figure 18. The change of the normalized spin polarization at E_F of the MgO/Fe(110) system with increasing MgO layer thickness. The spline fit to the experimental data is shown by a *solid line*. The reference curves for depolarization of polarized electrons ($P_0 = 23.5\%$) optically excited in germanium after traversing an evaporated overlayer of Ni (*dashed line*), Gd (*dotted line*), and Ce (*dot–dashed line*) are taken from Meier, Bona and Hüfner (1984) and Dedkov, Fonin, Rüdiger and Güntherodt (2006). (Reproduced from Dedkov *et al*., 2006, with permission from the American Institute of Physics. © 2006.)

4 K) for sputtered and textured Fe(100)/MgO(100)/Fe(100) (Parkin *et al*., 2004) and 180% at room temperature for epitaxial, MBE grown Fe(100)/MgO(100)/Fe(100) (Yuasa *et al*., 2004). Other materials combinations yielded 260% at RT (361% after annealing; 403% at 5 K) for CoFeB/MgO/CoFeB (Hayakawa *et al*., 2005; Lee *et al*., 2006) and 410% at room temperature (507% at 20 K) for bcc Co(001)/MgO(001)/Co(001) (Yuasa *et al*., 2006).

1. Fe/MgO: There also appears to be a problem with the formation of a submonolayer of FeO at the Fe/MgO interface (Meyerheim *et al*., 2001, 2002), which may be responsible for reduced TMR values (Zhang, Butler and Bandyopadhyay, 2003). The formation of FeO at the interface of MBE grown Fe(110)/MgO(111) could be identified via STM as well as by SPPES (Dedkov, Fonin, Rüdiger and Güntherodt, 2006). Figure 17 shows the spin-resolved photoemission spectra (a) as well as the spin polarization (b) for clean Fe(110) and the same with 2 Å MgO and 5 Å MgO overlayers (from bottom to top). With increasing overlayer thickness the polarization is attenuated from −80 to −50% and −20%, respectively. This attenuation of the spin polarization as a function of thickness of the MgO overlayer is represented in Figure 18.

In Figure 18, exponential fits to the experimentally observed depolarization of electrons ($P_0 = 23.5\%$) excited by circularly polarized light ($h\nu = 3.05$ eV) in germanium after traversing an evaporated overlayer of Ni (dashed line), Gd (dotted line), and Ce (dot-dashed line) are shown. All

curves show an exponential dependence of the polarization on the thickness of the overlayer possessing valence d electrons in the vicinity of E_F. The mean-free path for spin-flip scattering decreases as a function of the number of unoccupied d states in the valence band from Ni via Gd to Ce (Ni: two unoccupied d orbitals, $4s^2 3d^8$; Gd: nine unoccupied d orbitals, $6s^2 5d^1$; Ce: ten unoccupied d orbitals, $6s^2 5d^0$) (Meier, Bona and Hüfner, 1984). The reference curves for the Gd/Ge and Ce/Ge systems are very close to the experimentally observed sharp decrease of spin polarization in the MgO/Fe(110) system and can qualitatively be used as additional argument for the presence of a depolarizing FeO layer at the MgO/Fe(110) interface, that is, spin scattering into the four unoccupied d orbitals of Fe^{2+} ($3d^6$) in FeO. The comparison is only qualitative with respect to the absolute number of hole states as there may be additional spin scattering at the FeO/MgO interface. The presence of such an FeO interfacial layer and the increase of the FeO layer thickness at the MgO/Fe interface with increasing MgO layer thickness is supported by AES and STM measurements (Dedkov, Fonin, Rüdiger and Güntherodt, 2006). For these MTJs values of the TMR at RT of 32% (54% at 1.5 K) were obtained (Guerrero *et al*., 2005; Hauch *et al*., 2006).

The influence of MgO overlayers deposited on 16 ML Fe grown on GaAs(100) has been investigated for direct transitions between different symmetry Fe bulk and final states by means of SPPES (Matthes, Tong and Schneider, 2004). A spin-dependent attenuation for direct transitions related to Fe bulk initial states has been observed as a function of the MgO thickness.

2. α-Al_2O_3/Fe(110): The optimization of the oxidation process of thin Al films deposited on an Fe(110) surface was characterized in a spin-, angle-, as well as energy-resolved photoemission study (SPARPES) of the valence band (Dedkov, Fonin, Rüdiger and Güntherodt, 2002c). The spin-resolved spectra together with the total intensity and the spin polarization respectively, as a function of the binding energy for W(110), Fe(110), 7 Å Al on Fe(110) as well as α-Al_2O_3/Fe(110) are presented in Figure 19(a) and (b). For the 7 Å-Al/Fe system the spin polarization near E_F is decreased from -80% characteristic of the clean Fe(110) surface to about $-(35 \pm 5)\%$. Aluminum has no d electrons in the valence band and, therefore, the scattering of spin-polarized electrons from the valence band of Fe can be described by the spin-averaged scattering cross section (Siegmann, 1994). The spin polarization of photoelectrons for adlayer/ferromagnet systems can be calculated (Siegmann, 1994) by $P = P_0 \exp(-d \cdot \sigma)$, where $P_0 = -80\%$ is the polarization of the pure Fe(110) film, d the thickness of the adlayer (7 Å for Al and 13 Å for 1 ML of α-Al_2O_3), and σ the total

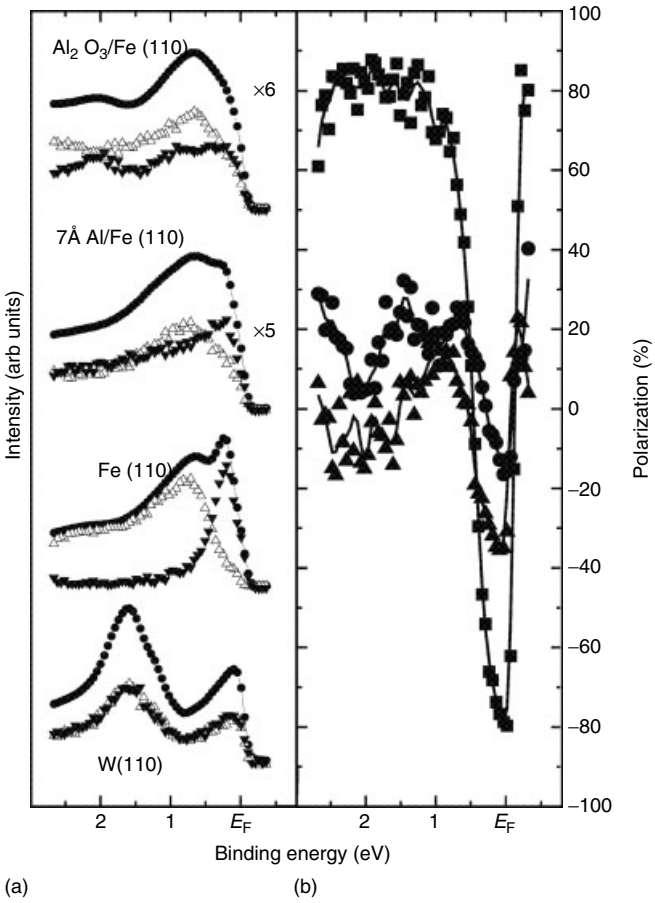

Figure 19. (a) The spin-resolved photoemission spectra (▼ spin down, △ spin up) together with the total emission intensity (●) for W(110), Fe(110), 7 Å Al on Fe(110), and approximately 1 ML Al_2O_3 on Fe(110). (b) The spin polarization as a function of binding energy of a 50-Å-thick Fe(110) film (■), 7 Å Al on Fe(110) (▲), and approximately 1 ML α-Al_2O_3 on Fe(110) (●) (Dedkov, Fonin, Rüdiger and Güntherodt, 2002c).

scattering cross section, which in our case is equal to the spin-independent part of σ, $\sigma_0 = 1/8\,\text{Å}^{-1}$ for both materials (Al and Al_2O_3) without d electrons in the valence band (Siegmann, 1994). In this case, the spin polarization would be attenuated to (-33%) which is in reasonably good agreement with the value of $-(35 \pm 5)\%$ observed experimentally.

The spin-resolved spectra following oxidation of the 7-Å-thick Al layer on Fe(110) via subsequent annealing at 250 °C are presented in Figure 19(a) (top curves). The spin polarization of the α-Al_2O_3/Fe(110) system decreases to $-(15 \pm 5)\%$ near E_F. The reason for the decrease of the spin polarization can be due to additional attenuation of the spin-polarized photoelectrons by the Al_2O_3 layer with an estimated thickness of 11 Å, close to the thickness of 1 ML of α-Al_2O_3. The estimated spin polarization of 1 ML α-Al_2O_3/Fe(110)

is -17%, which is in the range of the experimental value of $-(15 \pm 5)\%$. The spin polarization of -15% in the α-Al_2O_3/Fe(110)/W(110) system obtained by SPARPES is in contrast to the positive value determined by spin-polarized tunneling into superconductors (Meservey and Tedrow, 1994). For the photon energy of $h\nu = 21.2\,\text{eV}$, the cross section of the photoemission process from the valence band of Fe is larger for 3d electrons than for 4s electrons. Therefore, an attenuation of the negative spin polarization of Fe without change in sign, due to the coverage with α-Al_2O_3 can be described by the spin-independent part of the scattering cross section (Siegmann, 1994). In tunneling experiments, 4s electrons from the valence band of Fe have a higher tunneling probability in comparison with 3d electrons. It is the participation of the 4s electrons that explains the positive sign of the spin polarization as calculated (Tsymbal and Pettifor, 1997) and experimentally observed (Meservey and Tedrow, 1994) for tunneling from the ferromagnet into the superconductor.

4.6 The antiferromagnetic cuprates

The origin of the high T_C superconductivity observed in the cuprates presents one of the greatest challenges in condensed matter physics today. As such it is particularly important to understand the nature of the low-energy excitations in these materials. It is generally accepted that the superconductivity in the cuprates evolves from a parent insulating state by doping carriers into the two-dimensional CuO_2 planes. The ground state of the parent compound is an antiferromagnetic Mott insulator. With doping, the systems move from the antiferromagnetic state to a regime where superconductivity is possible. Cluster calculations indicate that the ground state associated with the CuO_2 planes consists of a linear combination of $3d^9$ and $3d^{10}\mathbf{L}$ states, and the photoemission final state as a combination of $3d^8$, $3d^9\mathbf{L}$ and $3d^{10}\mathbf{L}^2$ states, where $\mathbf{L}$ denotes an oxygen ligand hole orbital. Most theories predict that the $3d^8$ states close to the Fermi level are of local singlet character rather than the high spin triplet state favored by Hund's first rule (Zhang and Rice, 1998).

To investigate this possibility Tjeng and coworkers have used incident circularly polarized light and spin resolved the electrons emitted in a resonant photoemission process involving the 2p spin-orbit split core level (Tjeng *et al.*, 1997, 1999; Tjeng, Brookes and Sinkovic, 2001). The authors of these studies point out the critical importance of initially exciting from the spin-orbit split core level. In the absence of such an excitation, the measured polarization from the valence bands would be zero for an antiferromagnetic material. The results of their study of optimally doped $Bi_2Sr_2CaCu_2O_{8+\delta}$ (Brookes *et al.*, 2001) are shown in Figure 20, which shows

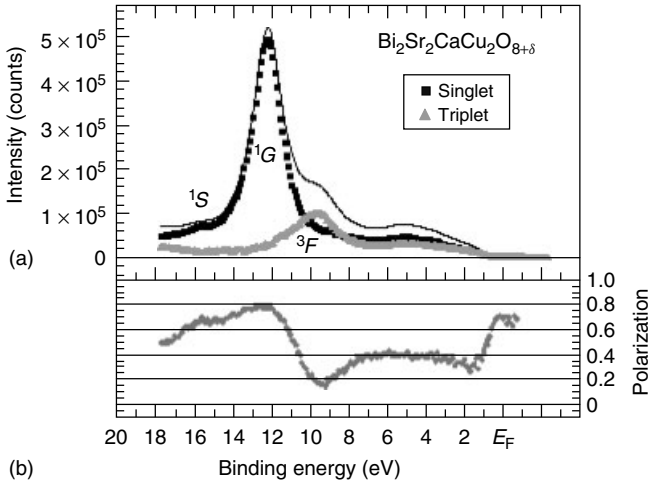

Figure 20. Spin-polarized photoemission spectra from $Bi_2Sr_2CaCu_2O_{8+\delta}$. (a) The spin-integrated resonant photoemission spectra taken at the Cu $L3$ absorption edge (full line). The symbols show the integrated spectra separated into its singlet (■) and triplet (▲) components. (b) The measured spin polarization corresponding to the spectra in panel (a).

the spin-integrated photoemission spectrum, the same spectrum resolved into triplet and singlet contributions and the measured spin polarization. The latter polarization, defined as $(\uparrow\uparrow - \uparrow\downarrow)/(\uparrow\uparrow + \uparrow\downarrow)$ where $\uparrow\uparrow$ refers to parallel alignment of the photon spin and electron spin, $\sigma^+ e^\uparrow + \sigma^- e^\downarrow$, and $\uparrow\downarrow$ refers antiparallel alignment of the same, $\sigma^+ e^\downarrow + \sigma^- e^\uparrow$, is calculated to be 5/6 or 83.3% for pure singlet states and $-1/3 * 5/6$ or -27.8% for triplet states. It is clear from the lower panel of Figure 20 that the measured polarization provides strong evidence for the presence of the so-called Zhang–Rice singlets (Zhang and Rice, 1988) in the vicinity of the Fermi level.

5 SUMMARY AND FUTURE OUTLOOK

We have seen that in the past 20 years the development and application of spin-polarized photoemission has been extensive. Because of its sensitivity to the surface region it has offered a number of new insights into the electronic structure of ferromagnetic surfaces and thin films. Studies of the latter have been particularly relevant to understand the properties of the GMR materials. Further with the increased photon fluxes now available from synchrotron radiation sources it has become possible to develop new methodologies and extend the technique to the study of nonmagnetic and antiferromagnetic materials. We may anticipate still further developments in the future particularly in the area of development of more efficient spin polarimeters. Such developments will allow experiments to be carried out with

higher energy resolution than has been achieved to date. Amongst other things this will make accessible studies of the fine details associated with magnetic anisotropies in thin films. We may also anticipate further developments in the combination of spin-polarized photoemission and microscopy. This will be particularly relevant as detailed studies of nanoscale systems are pursued, particularly with reference to materials investigated for their potential use in spintronics.

ACKNOWLEDGMENTS

Peter Johnson would like to acknowledge the many contributions of collaborators to his own work in this area including A. Clarke, N. Brookes, B. Sinkovic, K. Garrison, Y. Chang, A.V. Fedorov, S.L. Hulbert, M. Weinert, P.B. Allen, and many others. He would particularly like to thank the late Neville Smith for his continued interest and inspiration. Work at Brookhaven National Laboratory is supported by the Department of Energy under Contract No. DE-AC02-98CH10886. Gernot Güntherodt would like to thank his Ph.D. students Yu.S. Dedkov, M. Fonin, J.O. Hauch and C. König as well as his former group assistant and collaborator U. Rüdiger for the fruitful cooperation. The experimental support by P. Turban and the valuable theoretical support and inspiration by R. Pentcheva are gratefully acknowledged. He is also indebted to S. Suga and his team for a most fruitful collaboration.

REFERENCES

Allen, P.B. (2001). Electron spin-flip relaxation by one magnon processes: application to the gadolinium surface band. *Physical Review B*, **63**, 214410–214414.

Alvarado, S.F. and Bagus, P.S. (1978). Fractional spin polarization in the model of photoemission from localized shells. *Physics Letters*, **67A**, 397–398.

Alvarado, S.F., Eib, W., Meier, F., *et al*. (1975). Observation of spin-polarized electron levels in ferrites. *Physical Review Letters*, **34**, 319–322.

Alvarado, S.F., Erbudak, M. and Munz, P. (1976). Final-state effects in the 3*d* photoelectron spectrum of Fe_3O_4 and comparison with Fe_xO. *Physical Review B*, **14**, 2740–2745.

Bataille, A.M., Tagliaferri, A., Gota, S., *et al*. (2006). Negative spin polarization of the Fe_3O_4/-Al_2O_3 interface measured by spin-resolved photoemission. *Physical Review B*, **73**, 172201–172204.

Brookes, N.B., Chang, Y. and Johnson, P.D. (1991). Magnetic interface states and finite-size effects. *Physical Review Letters*, **67**, 354–357.

Brookes, N.B., Chang, Y. and Johnson, P.D. (1994). The Ag/Fe(001) interface. *Physical Review B*, **50**, 15330–15336.

Brookes, N.B., Clarke, A., Johnson, P.D. and Weinert, M. (1990). Magnetic Surface States on Fe(001). *Physical Review B*, **41**, 2643–2645.

Brookes, N.B., Ghiringhelli, G., Tjernberg, O., *et al*. (2001). Detection of Zhang-Rice singlets using spin polarized photoemission. *Physical Review Letters*, **87**, 237003–237006.

Bruno, P. and Chappert, C. (1991). Oscillatory coupling between ferromagnetic layers separated by a nonmagnetic metal spacer. *Physical Review Letters*, **67**, 1602–1605.

Burnett, G.C., Monroe, T.J. and Dunning, F.B. (1994). High-efficiency retarding-potential Mott polarization analyzer. *Review of Scientific Instruments*, **65**, 1893–1896.

Butler, W.H., Zhang, X-G., Schulthess, T.C. and MacLaren, J.M. (2001). Spin-dependent tunneling conductance of Fe|MgO|Fe sandwiches. *Physical Review B*, **63**, 054416–054427.

Cai, Y.Q., Ritter, M., Weiss, W. and Bradshaw, A.M. (1998). Valence-band structure of epitaxially grown Fe_3O_4(111) films. *Physical Review B*, **58**, 5043–5051.

Carbone, C., Vescovo, E., Klasges, R., *et al*. (1996). Magnetic quantum size effects in Cu films on Co(100). *Journal of Magnetism and Magnetic Materials*, **156**, 259–260.

Carbone, C., Vescovo, E., Rader, O., *et al*. (1993). Exchange split quantum well states of a noble metal film on a magnetic substrate. *Physical Review Letters*, **71**, 2805–2808.

Chang, C.F., Huang, D.J., Tanaka, A., *et al*. (2005). Electronic structure of CrO_2 studied by magnetic circular dichroism in resonant photoemission. *Physical Review B*, **71**, 052407–052410.

Craco, L., Laad, M.S. and Müller-Hartmann, E. (2003). Orbital Kondo effect in CrO_2: a combined local-spin-density-approximation dynamical-mean-field-theory study. *Physical Review Letters*, **90**, 237203–237206.

Crampin, S., De Rossi, S. and Ciccaci, F. (1996). Integrity of quantum-well resonances in metallic overlayers. *Physical Review B*, **53**, 13817–13823.

Dedkov, Yu.S., Rüdiger, U. and Güntherodt, G. (2002a). Evidence for the half-metallic ferromagnetic state of Fe_3O_4 by spin-resolved photoelectron spectroscopy. *Physical Review B*, **65**, 064417–064421.

Dedkov, Yu.S., Fonine, M., Konig, C., *et al*. (2002b). Room-temperature observation of high-spin polarization of epitaxial CrO_2(100) island films at the Fermi energy. *Applied Physics Letters*, **80**, 4181–4183.

Dedkov, Yu.S., Fonin, M., Rüdiger, U. and Güntherodt, G. (2002c). Growth and spin-resolved photoemission spectroscopy of the epitaxial α-Al_2O_3/Fe(110) system. *Applied Physics Letters*, **81**, 2584–2586.

Dedkov, Yu.S., Fonin, M., Rüdiger, U. and Güntherodt, G. (2006). Spin-resolved photoelectron spectroscopy of the MgO/Fe(110) system. *Applied Physics A*, **82**, 489–493.

Dedkov, Yu.S., Fonine, M., Vyalikh, D.V., *et al*. (2004). Electronic structure of the Fe_3O_4(111) surface. *Physical Review B*, **70**, 073405–073408.

Feder, R. (1985). Polarized *Electrons in Surface Physics*, World Scientific: Singapore.

Fedorov, A.V., Starke, K. and Kaindl, G. (1994). Temperature-dependent exchange splitting of unoccupied electronic states in Gd(0001). *Physical Review B*, **50**, 2739–2742.

Fedorov, A.V., Valla, T., Liu, F., *et al*. (2002). Spin-resolved photoemission study of photohole lifetimes in ferromagnetic gadolinium. *Physical Review B*, **65**, 212409.

Fonin, M., Pentcheva, R., Dedkov, Yu.S., *et al*. (2005). Surface electronic structure of the $Fe_3O_4(100)$: evidence of a half-metal to metal transition. *Physical Review B*, **72**, 104436–104443.

Garrison, K., Chang, Y. and Johnson, P.D. (1993). Spin polarization of quantum well states in copper thin films deposited on a Co(001) substrate. *Physical Review Letters*, **71**, 2801–2804.

Graf, J., Jozwiak, C., Schmid, A.K., *et al*. (2005). Mapping the spin-dependent electron reflectivity of Fe and Co ferromagnetic thin films. *Physical Review B*, **71**, 144429–144433.

de Groot, R.A., Mueller, F.M., van Engen, P.G. and Buschow, K.H.J. (1983). New class of materials: half-metallic ferromagnets. *Physical Review Letters*, **50**, 2024–2027.

Guerrero, R., Aliev, F.G., Villar, R., *et al*. (2005). Low-frequency noise and tunneling magnetoresistance in Fe(110)/MgO(111)/Fe(110) epitaxial magnetic tunnel junctions. *Applied Physics Letters*, **87**, 042501–042503.

Harrison, W.A. (1980). *Electronic Structure and the Properties of Solids*, Freeman: San Francisco.

Hauch, J.O., Fraune, M., Güntherodt, G., *et al*. (2006). Fully epitaxial Fe(110)/MgO(110) tunnel junctions: Growth and transport properties. *Applied Physics Letters*, submitted.

Hayakawa, J., Ikeda, S., Matsukura, F., *et al*. (2005). Dependence of giant tunnel magnetoresistance of sputtered CoFeB/MgO/CoFeB magnetic tunnel junctions on MgO barrier thickness and annealing temperature. *Japanese Journal of Applied Physics*, **44**, L587–L589.

Held, G.A., Samant, M.G., Stohr, J., *et al*. (1996). X-ray magnetic circular dichroism study of the induced spin polarization of Cu in Co/Cu and Fe/Cu multilayers. *Zeitschrift fur Physik: Condensed Matter B*, **100**, 335–341.

Hochstrasser, M., Tobin, J.G., Rotenberg, Eli. and Kevan, S.D. (2002). Spin-resolved photoemission of surface states of W(110)-(1×1)H. *Physical Review Letters*, **89**, 216802–216805.

Hoesch, M., Muntwiler, M., Petrov, V.N., *et al*. (2004). Spin structure of the Shockley surface state on Au(111). *Physical Review B*, **69**, 241401–241404.

Hong, F. and Che, J.G. (2006). Low photoemission intensity near E_F induced by the surface relaxed structure of $CrO_2(001)$. *Physical Review Letters*, **96**, 167206–167209.

Huang, D.J., Wu, W.P., Chen, J., *et al*. (2002a). Performance of a Mott detector for undulator-based spin-resolved spectroscopy. *Review of Scientific Instruments*, **73**, 3778–3783.

Huang, D.J., Chang, C.F., Chen, J., *et al*. (2002b). Spin-resolved photoemission studies of epitaxial $Fe_3O_4(1{\sim}0{\sim}0)$ thin films. *Journal of Magnetism and Magnetic Materials*, **239**, 261–265.

Huang, D.J., Tjeng, L.H., Chen, J., *et al*. (2003). Anomalous spin polarization and dualistic electronic nature of CrO_2. *Physical Review B*, **67**, 214419–214423.

Hüfner, S., (2003). *Photoelectron Spectroscopy*, Springer: Berlin.

Ji, Y., Strijkers, G.J., Yang, F.Y., *et al*. (2001). Determination of the spin polarization of half-metallic CrO_2 by point contact Andreev reflection. *Physical Review Letters*, **86**, 5585–5588.

Johnson, P.D. (1997). Spin-polarized photoemission. *Reports on Progress in Physics*, **60**, 1217–1304.

Johnson, P.D., Brookes, N.B., Hulbert, S.L., *et al*. (1992). Spin-polarized photoemission spectroscopy of magnetic surfaces using undulator radiation. *Review of Scientific Instruments*, **63**, 1902–1908.

Kämper, K-P., Schmitt, W., Güntherodt, G., *et al*. (1987). CrO_2–a new half-metallic ferromagnet? *Physical Review Letters*, **59**, 2788–2791.

Kessler, K. (1985). *Polarized Electrons*, Springer: Berlin.

Kevan, S.D. (1992). *Angle-resolved Photoemission*, Elsevier: Amsterdam.

Kirschner, J. and Feder, R. (1979). Spin polarization in double diffraction of low-energy electrons from W(001): experiment and theory. *Physical Review Letters*, **42**, 1008–1011.

Kisker, E. (1987). *Metallic Magnetism*, Capellmann, H. (Ed.), Springer: Berlin, p. 57.

Kisker, E., Clauberg, R. and Gudat, W. (1982). Electron spectrometer for spin-polarized angle- and energy-resolved photoemission from ferromagnets. *Review of Scientific Instruments*, **53**, 1137–1144.

Kobayashi, K-I., Kimura, T., Sawada, H., *et al*. (1998). Room-temperature magnetoresistance in an oxide material with an ordered double-perovskite structure. *Nature (London)*, **395**, 677–680.

Korotin, M.A., Anisimov, V.I., Khomskii, D.I. and Sawatzky, G.A. (1998). CrO_2: a self-doped double exchange ferromagnet. *Physical Review Letters*, **80**, 4305–4308.

Kralj, M., Pervan, P., Milun, M., *et al*. (2003). d-Band quantum well states in ultrathin silver films on V(100). *Physical Review B*, **68**, 245413–245420.

Krupin, O., Bihlmayer, G., Starke, K., *et al*. (2005). Rashba effect at magnetic metal surfaces. *Physical Review B*, **71**, 201403–201406.

Kübler, J. (2003). Curie temperatures of zinc-blende half-metallic ferromagnets. *Physical Review B*, **67**, 220403–220406.

LaShell, S., McDougall, B.A. and Jensen, E.A. (1996). Spin splitting of an Au(111) surface state band observed with angle-resolved photoelectron spectroscopy. *Physical Review Letters*, **77**, 3419–3422.

Lassailly, Y., Drouhin, H-J., Van der Sluijs, J., *et al*. (1994). Spin-dependent transmission of low-energy electrons through ultrathin magnetic layers. *Physical Review B*, **50**, 13054–13057.

Lee, Y.M., Hayakawa, J., Ikeda, S., *et al*. (2006). Giant tunnel magnetoresistance and high annealing stability in CoFeB/MgO/CoFeB magnetic tunnel junctions with synthetic pinned layer. *Applied Physics Letters*, **89**, 042506–042508.

Li, D., Hutchings, W., Dowben, P.A., *et al*. (1991). Angle-resolved photoemission evidence for a Gd(0001) surface state. *Journal of Magnetism and Magnetic Materials*, **99**, 85–90.

Li, D., Pearson, J., Bader, S.D., *et al*. (1997). *k*-Space origin of the long-period oscillation in Fe/Cr multilayers: a photoemission study of epitaxial Cr grown on an Fe(100) whisker. *Physical Review Letters*, **78**, 1154–1157.

Li, D., Zhang, J., Dowben, P.A., *et al*. (1993). Canted magnetic moments at the Gd(0001) Surface. *Materials Research Society Proceedings*, **313**, 451.

Ling, W.L., Rotenberg, Eli., Choi, H.C., *et al*. (2002). Double quantum well states in Cu/Co/Cu grown on Co(001). *Physical Review B*, **65**, 113406–115409.

Mathon, J. and Umerski, A. (2001). Theory of tunneling magnetoresistance of an epitaxial Fe/MgO/Fe(001) junction. *Physical Review B*, **63**, 220403–220406.

Matthes, F., Tong, L-N. and Schneider, C.M. (2004). Spin-polarized photoemission spectroscopy of the MgO/Fe interface on GaAs(100). *Journal of Applied Physics*, **95**, 7240–7242.

Mavropoulos, Ph., Ležaić, M. and Blügel, S. (2005). Half-metallic ferromagnets for magnetic tunnel junctions by *ab initio* calculations. *Physical Review B*, **72**, 174428–174433.

Meier, F., Bona, G.L. and Hüfner, S. (1984). Experimental determination of exchange constants by spin-polarized photoemission. *Physical Review Letters*, **52**, 1152–1155.

Meservey, R. and Tedrow, P.M. (1994). Spin-polarized electron tunneling. *Physics Reports*, **238**, 173–243.

Meyerheim, H.L., Popescu, R., Kirschner, J., *et al*. (2001). Geometrical and compositional structure at metal-oxide interfaces: MgO on Fe (001). *Physical Review Letters*, **87**, 076102–076105.

Meyerheim, H.L., Popescu, R., Jedrecy, N., *et al*. (2002). Surface x-ray diffraction analysis of the MgO/Fe(001) interface: evidence for an FeO layer. *Physical Review B*, **65**, 144433–144439.

Morton, S.A., Waddill, G.D., Kim, S., *et al*. (2002). Spin-resolved photoelectron spectroscopy of Fe_3O_4. *Surface Science*, **513**, L451–L457.

Mulhollan, G.A., Garrison, K. and Erskine, J.L. (1992). Surface magnetism of Gd(0001): evidence of ferromagnetic coupling to bulk. *Physical Review Letters*, **69**, 3240–3243.

Nicolay, G., Reinert, F., Hufner, S. and Blaha, P. (2001). Spin-orbit splitting of the L-gap surface state on Au(111) and Ag(111). *Physical Review B*, **65**, 033407–033410.

Ortega, J.E. and Himpsel, F.J. (1992). Quantum well states as mediators of magnetic coupling in superlattices. *Physical Review Letters*, **69**, 844–847.

Ortega, J.E., Himpsel, F.J., Mankey, G.J. and Willis, R.F. (1993). Quantum-well states and magnetic coupling between ferromagnets through a noble-metal layer. *Physical Review B*, **47**, 1540–1552.

Park, J-H., Vescovo, E., Kim, H-J., *et al*. (1998a). Magnetic properties at surface boundary of a half-metallic ferromagnet $La_{0.7}Sr_{0.3}MnO_3$. *Physical Review Letters*, **81**, 1953–1956.

Park, J-H., Vescovo, E., Kim, H-J., *et al*. (1998b). Direct evidence for a half-metallic ferromagnet. *Nature (London)* , **392**, 794–796.

Parkin, S.S.P., Kaiser, C., Panchula, A., *et al*. (2004). Giant tunnelling magnetoresistance at room temperature with MgO (100) tunnel barriers. *Nature Materials*, **3**, 862–867.

Pickett, W.E. and Moodera, J.S. (2001). Half metallic magnets. *Physics Today*, **54**, 39–44.

Pickett, W.E. and Singh, D.J. (1996). Electronic structure and half-metallic transport in the $La_{1-x}Ca_xMnO_3$ system. *Physical Review B*, **53**, 1146–1160.

Pierce, D.T., Celotta, R.J., Kelley, M.H. and Unguris, J. (1988). Electron spin polarization analyzers for use with synchrotron radiation. *Nuclear Instruments and Methods in Physics Research Section A: Accelerators, Spectrometers, Detectors and Associated Equipment*, **266**, 550–559.

Qiu, Z.Q., Pearson, J. and Bader, S.D. (1992). Oscillatory interlayer magnetic coupling of wedged Co/Cu/Co sandwiches grown on Cu(100) by molecular beam epitaxy. *Physical Review B*, **46**, 8659–8662.

Qiu, Z.Q. and Smith, N.V. (2002). Quantum well states and oscillatory magnetic interlayer coupling. *Journal of Physics: Condensed Matter*, **14**, R169–R193.

Rampe, A., Hartmann, D., Weber, W., *et al*. (1995). Induced spin polarization and interlayer exchange coupling of the system Rh/Co (0001) and Ru/Co (0001). *Physical Review B*, **51**, 3230–3233.

Rehbein, A., Wegner, D., Kaindl, G. and Bauer, A. (2003). Temperature dependence of lifetimes of Gd(0001) surface states. *Physical Review B*, **67**, 033403–033406.

Rotenberg, Eli., Wu, Y.Z., An, J.M., *et al*. (2006). Non-free-electron momentum- and thickness-dependent evolution of quantum well states in the Cu/Co/Cu(001) system. *Physical Review B*, **73**, 075426–075429.

Roy, D. and Carette, J.D. (1977). *Electron Spectroscopy for Surface Analysis*, Ibach, H. (Ed.), Springer: Berlin, p. 13.

Samant, M.G., Stöhr, J., Parkin, S.S.P., *et al*. (1994). Induced spin polarization in Cu spacer layers in Co/Cu multilayers. *Physical Review Letters*, **72**, 1112–1115.

Scheinfein, M.R., Pierce, D.T., Unguris, J., *et al*. (1989). Improved low-energy diffuse scattering electron-spin polarization analyzer. *Review of Scientific Instruments*, **60**, 1–11.

Schönhense, G. and Siegmann, H.C. (1993). Transmission of electrons through ferromagnetic material and applications to detection of electron-spin polarization. *Annalen der Physik, Leipzig*, **2**, 465–474.

Schwarz, K. (1986). CrO_2 predicted as a half-metallic ferromagnet. *Journal of Physics F: Metal Physics*, **16**, L211–L215.

Siegmann, H.C. (1994). Surface and 2D magnetism with spin polarized cascade electrons. *Surface Science*, **307–309**, 1076–1086.

Sinkovic, B., Shekel, E. and Hulbert, S.L. (1995). Spin-resolved Fe $L_3M_{45}M_{45}$ Auger transition on and off resonance: the effect of exchange correlation. *Physical Review B*, **52**, R15703–R15706.

Smith, N.V., Brookes, N.B., Chang, Y. and Johnson, P.D. (1994). Quantum-well and tight-binding analyzes of spin-polarized photoemission from Ag/Fe(001) overlayers. *Physical Review B*, **49**, 332–338.

Soulen Jr., R.J., Byers, J.M., Osofsky, M.S., *et al*. (1998) Measuring the spin polarization of a metal with a superconducting point contact. *Science*, **282**, 85–88.

Stanka, B., Hebenstreit, W., Diebold, U. and Chambers, S.A. (2000). Surface reconstruction of Fe_3O_4(001). *Surface Science*, **448**, 49–63.

Suga, S., *et al*. (2006), Private communicaton.

Tang, F.C., Zhang, X., Dunning, F.B. and Walters, G.K. (1988). Compact low-energy Mott polarimeter for use in energy- and

angle-resolved polarization studies. *Review of Scientific Instruments*, **59**, 504–505.

Tarrach, G., Bürgler, D., Schaub, T., *et al*. (1993). Atomic surface structure of Fe_3O_4(001) in different preparation stages studied by scanning tunneling microscopy. *Surface Science*, **285**, 1–14.

de Teresa, J.M., Barthélémy, A., Fert, A., *et al*. (1999). Inverse tunnel magnetoresistance in $Co/SrTiO_3/La_{0.7}Sr_{0.3}MnO_3$: new ideas on spin-polarized tunneling. *Physical Review Letters*, **82**, 4288–4291.

Tillman, D., Thiel, R. and Kisker, E. (1989). Very-low-energy spin-polarized electron diffraction from Fe(001) (rapid note). *Zeitschrift Physik B*, **77**, 1–2.

Tjeng, L.H., Brookes, N.B., Goedkoop, J.B., *et al*. (1999). Study of magnetic materials using spin-resolved circularly-polarized resonant photoemission. *Japanese Journal of Applied Physics*, **38**,(Suppl. 38-1), 344–347.

Tjeng, L.H., Brookes, N.B. and Sinkovic, B. (2001). Spin-resolved photoelectron spectroscopy on cuprate systems. *Journal of Electron Spectroscopy and Related Phenomena*, **117–118**, 189–201.

Tjeng, L.H., Sinkovic, B., Brookes, N.B., *et al*. (1997). *Spin*-resolved photoemission on *anti*-ferromagnets: direct observation of Zhang-Rice singlets in CuO. *Physical Review Letters*, **78**, 1126–1129.

Tsymbal, E.Yu. and Pettifor, D.G. (1997). Modelling of spin-polarized electron tunnelling from 3d ferromagnets. *Journal of Physics: Condensed Matter*, **9**, L411.

Unguris, J., Pierce, D.T. and Celotta, R.J. (1986). Low-energy diffuse scattering electron-spin polarization analyzer. *Review of Scientific Instruments*, **57**, 1314–1323.

Van der Sluijs, A., Drouhin, H-J., Lampel, G., *et al*. (1994). Spin-dependent transmission through ultra-thin magnetic layers–towards highly discriminative compact spin detectors. *Comptes Rendus De L'Academie des Sciences, Paris*, **319**, Series II, 753–759.

Van Gelderen, P., Crampin, S. and Inglesfield, J.E. (1996). Quantum-well states in Cu/Co overlayers and sandwiches. *Physical Review B*, **53**, 9115–9122.

Vescovo, E., Carbone, C., Eberhardt, W., *et al*. (1993). Spin-resolved photoemission study of the clean and oxygen-covered Fe(110) surface. *Physical Review B*, **48**, 285–288.

Weber, W., Wesner, D.A., Güntherodt, G. and Linke, U. (1991). Direct observation of spin-split electronic states of Pd at the Pd(111)/Fe(110) interface. *Physical Review Letters*, **66**, 942–945.

Weber, W., Wesner, D.A., Hartmann, D., *et al*. (1993). Electronic interface states at the Pt/Co interface. *Journal of Magnetism and Magnetic Materials*, **121**, 156–159.

Weber, W., Wesner, D.A., Hartmann, D. and Güntherodt, G. (1992). Spin-polarized interface states at the Pd(111)/Fe(110), Pd(111)/Co(0001), and Pt(111)/Co(0001) interfaces. *Physical Review B*, **46**, 6199–6206.

Weschke, E., Schussler- Langeheine, C., Meier, R., *et al*. (1996). Temperature dependence of the exchange splitting of the surface state on Gd(0001): Evidence against spin-mixing behavior. *Physical Review Letters*, **77**, 3415–3418.

Wu, R., Li, C., Freeman, A.J. and Fu, C.L. (1991). Structural, electronic, and magnetic properties of rare-earth metal surfaces: hcp Gd(0001). *Physical Review B*, **44**, 9400–9409.

Wu, Y.Z., Won, C., Rotenberg, E., *et al*. (2006). Resonant interaction between two Cu quantum wells. *Physical Review B*, **73**, 125333–125337.

Wurmehl, S., Fecher, G.H., Kandpal, H.C., *et al*. (2005). Geometric, electronic, and magnetic structure of Co_2FeSi: Curie temperature and magnetic moment measurements and calculations. *Physical Review B*, **72**, 184434–184442.

Yanase, A. and Siratori, K. (1984). Band structure in the high temperature phase of Fe_3O_4. *Journal of the Physical Society of Japan*, **53**, 312–317.

Yuasa, S., Fukushima, A., Kubota, H., *et al*. (2006). Giant tunneling magnetoresistance up to 410% at room temperature in fully epitaxial Co/MgO/Co magnetic tunnel junctions with bcc Co(001) electrodes. *Applied Physics Letters*, **89**, 042505–042507.

Yuasa, S., Nagahama, T., Fukushima, A., *et al*. (2004). Giant room-temperature magnetoresistance in single-crystal Fe/MgO/Fe magnetic tunnel junctions. *Nature Materials*, **3**, 868–871.

Zener, C. (1951a). Interaction between the *d* shells in the transition metals. *Physical Review*, **81**, 440–444.

Zener, C. (1951b). Interaction between the *d*-Shells in the transition metals. II. Ferromagnetic compounds of manganese with perovskite structure. *Physical Review*, **82**, 403–405.

Zener, C. (1951c). Interaction between the *d*-shells in the transition metals. III. Calculation of the Weiss factors in Fe, Co, and Ni. *Physical Review*, **83**, 299–301.

Zhang, Z.D., Choi, H.J., Kawakami, R.K., *et al*. (2000). Magnetic interlayer coupling between Co films across $Cu/Ni_{30}Cu_{70}$/Cu(100) double quantum wells. *Physical Review B*, **61**, 76–79.

Zhang, X-G., Butler, W.H. and Bandyopadhyay, A. (2003). Effects of the iron-oxide layer in Fe-FeO-MgO-Fe tunneling junctions. *Physical Review B*, **68**, 092402–092405.

Zhang, F.C. and Rice, T.M. (1988). Effective Hamiltonian for the superconducting Cu oxides. *Physical Review B*, **37**, 3759–3761.

Zhang, Z. and Satpathy, S. (1991). Electron states, magnetism, and the Verwey transition in magnetite. *Physical Review B*, **44**, 13319–13331.

Zdyb, R. and Bauer, E. (2002). Spin-resolved unoccupied electronic band structure from quantum size oscillations in the reflectivity of slow electrons from ultrathin ferromagnetic crystals. *Physical Review Letters*, **88**, 166403–166406.

FURTHER READING

Sinkovic, B., Tjeng, L.H., Brookes, N.B., *et al*. (1997). Local electronic and magnetic structure of Ni below and above T_c: a spin-resolved circularly polarized resonant photoemission study. *Physical Review Letters*, **79**, 3510–3513.

Steeneken, P.G., Tjeng, L.H., Elfimov, I., *et al*. (2002). Exchange splitting and charge carrier spin polarization in EuO. *Physical Review Letters*, **88**, 047201–047204.

High-energy Surface Spin Waves Studied by Spin-polarized Electron Energy Loss Spectroscopy

Markus Etzkorn[1,2], Parameswaran Sarala Anil Kumar[1,3] and Jürgen Kirschner[1]

[1] *Max-Planck-Institut für Mikrostrukturphysik, Halle, Germany*
[2] *Institut de Physique des Nanostructures, Lausanne, Switzerland*
[3] *Indian Institute of Science, Bangalore, India*

1 INTRODUCTION

In the last few decades, magnetism at surfaces and in thin films has attracted great attention. These studies are of fundamental interest and some discoveries led to important applications now used in everyday life, for example, magnetoresistance phenomena used in data storage (Jullière, 1975; Binasch, Grünberg, Saurenbach and Zinn, 1989; Baibich *et al*., 1988). Most of the studies have focused on static magnetism but recently dynamics also receives growing interest. The magnetization dynamics is governed by spin waves, which are collective excitations and can be described as quasiparticles, which carry a wave vector q, an energy E, and a magnetic moment of $1\,g\mu_B$ (where g is the gyromagnetic ratio and μ_B is a Bohr magneton), (See also **Spin Waves: History and a Summary of Recent Developments, Volume 1**). The latter places them in the class of bosons. In energy, they range from the μeV range to the 100 meV range, in momentum, from zero (the zone center) to the zone boundary (up to about $2\,\text{Å}^{-1}$). Their lifetimes range from a couple of ten femtoseconds to tens of microseconds, depending on damping. Low-energy spin waves are easily excited by phonon–magnon interaction, that is, by temperature. If a sufficient number of spin waves are excited, the global magnetic moment of a body decreases substantially. Therefore, spin waves play an important role for the magnitude of the Curie temperature, that is, the ferromagnetic versus paramagnetic transition.

The detailed description of the physical nature of these collective magnetic excitations cannot be cast into one single picture because of the many orders of magnitude of dynamic range in energy, momentum, and lifetime. In the limit of long wavelength, low energy, and long lifetime, the usual semiclassical picture of precessing (classical) spins has proved useful. In this case, each spin is only slightly tilted out of its direction along the magnetic easy axis. Thus, the reduction of the magnetic moment by $1\,g\mu_B$ occurs by the concerted action of all spins in the entire crystal. This picture relies on classical spins, because they may adapt any spin orientation continuously, as opposed to the quantum spins being quantized in direction. These 'spin waves' are damped by collisions with phonons, other spin waves, electrons, lattice deformations, and impurities, but they are usually long lived.

Spin waves have a characteristic dispersion, which links their energy to their wave vector. Depending on the wave

Handbook of Magnetism and Advanced Magnetic Materials. Edited by Helmut Kronmüller and Stuart Parkin. Volume 3: *Novel Techniques for Characterizing and Preparing Samples*. ISBN: 978-0-470-02217-7.

vector, different magnetic interactions determine the spin-wave energy. The exchange interaction is typically much stronger than other magnetic interactions. Nevertheless, owing to its relatively short range, other interactions, like the long-ranged dipole interaction, can become important at sufficiently small wave vectors. As a rule of thumb, in 3d ferromagnets this so-called dipole regime extends to wave vectors below $q < 10^{-3}\,\text{Å}^{-1}$ (Cottam and Slavin, 1994). For wave vectors above $q > 10^{-2}\,\text{Å}^{-1}$, the exchange interaction can be safely assumed to be the dominating interaction that determines the spin-wave energy (Cottam and Slavin, 1994).

For different regimes, different theoretical approaches are used to describe spin waves. As discussed in the preceding text, for the dipole or small wave-vector regime, a macroscopic continuum model description is sufficient (Mills, 1984). A large number of studies focus on the low wave-vector regime with its macroscopic description. A detailed summary can, for example, be found in Hillebrands and Ounadjela (2002), (See also **Investigation of Spin Waves and Spin Dynamics by Optical Techniques, Volume 3**, **Time-resolved Kerr-effect and Spin Dynamics in Itinerant Ferromagnets, Volume 3**, and **Investigation of Ultrathin Ferromagnetic Films by Magnetic Resonance, Volume 3**). By contrast, deep in the exchange-dominated regime, where the wavelength may become comparable in size to the interatomic distances in a crystal, a true microscopic description is needed. For such high wave vectors the strong exchange interaction leads to high spin-wave energies. These high-energy spin waves are usually short lived, because of their strong interaction with single electron–hole excitations, called *Stoner excitation*. These Stoner excitations consist of an electron excited about E_F and a hole in a filled band with opposite spins of the quasiparticles (adding up to $1\,g\mu_B$!). Electron and hole may have different wave vectors, that is, they reside at different locations in the Brillouin zone, and the wave vector of the Stoner excitation is the vectorial sum of the individual wave vectors. High-energy spin waves couple strongly with Stoner excitations because of their similarity in energy, wave vector, and spin character. This relationship is so intimate that spin wave may even be described as a coherent superposition of Stoner excitations (Majlis, 2001). It has been proved that this concept holds not only for the high-energy, short wavelength spin waves but also for the low energy, long wavelength modes (Edwards and Bechara Muniz, 1985; Bechara Muniz, Cooke and Edwards, 1985). The long lifetime of the latter is understandable because for electrons *and* holes very close to the Fermi energy (i.e., low-energy Stoner excitation) the available phase space for the de-excitation is small.

The different regimes of spin waves have been studied experimentally by various techniques, each having certain strengths and weaknesses. The regions in energy/wave vector/thickness space that are accessible by the established techniques are shown in Figure 1. Spin waves in thin ferromagnetic films have been studied by ferromagnetic resonance (FMR), Brillouin light scattering (BLS), and also by time domain methods (Hillebrands and Ounadjela, 2002). All these methods have in common that only long wavelength spin waves can be studied, having a wave vector of the order of $10^{-2}\,\text{Å}^{-1}$, at most (light gray areas in Figure 1). High wave-vector spin waves can be investigated by inelastic neutron scattering (INS) (dark gray) (Brockhouse, 1957), but the weak interaction of neutrons with matter prohibits measurements on ultrathin films or at surfaces (Schreyer *et al.*, 2000). Owing to the limitation of the established techniques, spin waves in about 99% of the Brillouin zone in ultrathin films remained unexplored experimentally (see Figure 1). This region is, however, of high interest because here the wavelength of spin waves can become comparable to the distances between the atoms in the crystal. Thus, their study allows direct access to magnetic properties at the surfaces on the atomic scale.

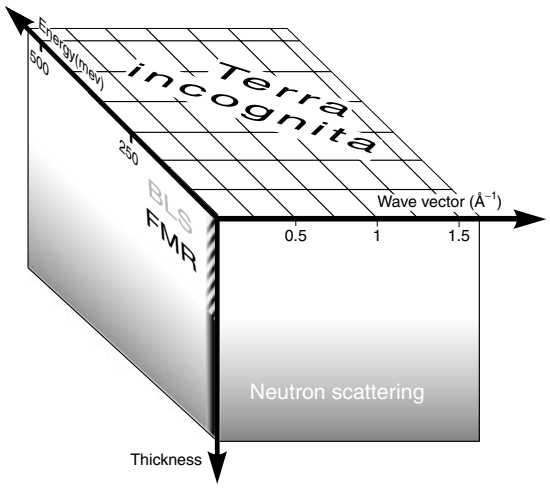

Figure 1. Scheme of the regions in wave vector/energy/thickness space in which spin waves have been studied using established experimental techniques (marked by different gray tones). None of these techniques has been able to measure high wave-vector spin waves in a single thin film or at surfaces, that is, in the 'terra incognita'.

Spin-polarized electron energy loss spectroscopy (SPEELS) is a suitable technique to access the *terra incognita* shown in Figure 1. In the experiment, a monochromatic, spin-polarized electron beam is scattered inelastically from a magnetized sample and the scattered electrons are analyzed for their wave vector and energy transfer during scattering. The use of electrons as scattering particles has certain merits. Because of the strong interaction between low-energy electrons and matter, electron scattering is highly surface sensitive. This has been used for several decades in many surface

sensitive techniques (see, e.g., Henzler and Göpel, 1994). In addition, electron scattering is known for the relatively easy realization of high-energy and high wave-vector transfers. Thus, the basic idea to study spin waves by electron scattering is evident and it has already been proposed decades ago (DeWames and Vredevoe, 1967). The history of the study of spin waves by SPEELS has been a 25 years history of trial and error until, in 1999, the proof of principle of this technique was given (Plihal, Mills and Kirschner, 1999): a spin-polarized electron with its spin antiparallel to the majority spin orientation may create a spin wave by exchanging with another electron in the surface with parallel (majority) spin, coming out with somewhat smaller energy. The energy difference equals the spin-wave energy. The interaction is of the exchange type, that is, electrostatic, no direct magnetic spin–spin interaction is involved. This is puzzling at the first glance, but it is the origin of the extraordinary sensitivity of SPEELS.

We are presently able to study spin-wave excitations with wave-vector transfers up to (and beyond) the surface Brillouin zone boundary on films as thin as 2.5 atomic layers. From the signal-to-noise ratio, one could even speculate that the sensitivity limit for the detection of spin waves by SPEELS is in the submonolayer regime. Up to now, several systems have been investigated by SPEELS (Vollmer *et al*., 2003, 2004a,b,c; Etzkorn *et al*., 2004, 2005). In this chapter, we will discuss the general method and the spectrometer used for these studies, as well as the results of studies on fcc Co on Cu(001), hcp Co on W(110), and Fe on Cu(001). We find that the magnetic excitations are confined to an extraordinarily small volume in space and time. By a Fourier analysis of the energy loss spectra and using the measured group velocity from the dispersion relation, we estimate a linear space–time range of some 10 yocto sm (yocto $\Psi = 10^{-24}$) for wave vectors about halfway to the zone boundary.

1.1 The spin-polarized electron energy loss spectrometer

In the SPEELS experiments, spin-polarized electrons are scattered from a magnetic sample. The energy and momentum transfer of the scattered electrons to the sample is analyzed to obtain information about the inelastic scattering processes. To realize the experiment, a spin-polarized, monochromatic electron beam is needed that hits the sample under controlled conditions. With the help of an analyzer, the intensity of the scattered electrons is counted in a small window in energy and wave-vector space.

The detection of spin waves demands the highest possible electron flux through the SPEEL spectrometer. To accomplish this task, a new type of high performance SPEEL spectrometer has been designed for this particular experiment (Ibach *et al*., 2003). A sketch of the spectrometer is shown in Figure 2. The spectrometer consists of three main parts. In the first part, the spin-polarized electron beam is created by a strained GaAs photocathode (Pierce and Meier, 1976; Drescher *et al*., 1996). When hitting the sample, the spin direction of the incident electrons is parallel or antiparallel to the direction of magnetization of the sample. In the following, we will talk about $I_\uparrow(I_\downarrow)$ if the spin of the incident electron is parallel to the spin of a majority (minority) electron of the sample. The second part, the monochromator, consists of a premonochromator and a main monochromator with deflection angles of 90° and 180°, respectively. The third part of the spectrometer is the analyzer, which is a standard EELS monochromator with a deflection angle of 146° (Ibach, 1993; Ibach, Balden and Lehwald, 1996) followed by a channeltron as detector. The analyzer and the detector are mounted on an arm so that they can be rotated around the sample position in the scattering plane (Figure 2). The dimensions and a detailed description of the design of this SPEEL spectrometer are given in Ibach *et al*. (2003).

In the experiment, the spectrometer was used to measure the intensity of electrons scattered from the sample under a

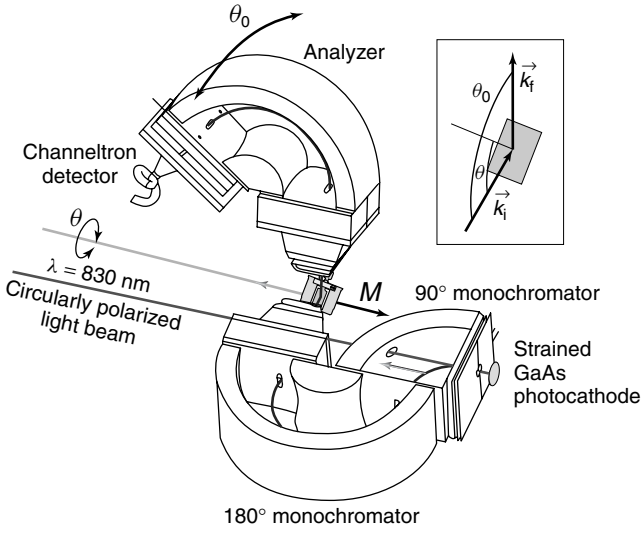

Figure 2. Sketch of the spectrometer under operation with a GaAs photocathode. The circularly polarized light excites a longitudinal spin-polarized electron beam from the cathode (the spin direction is shown by the arrow). After the electrons have traveled through the electrostatic monochromators, the beam is transversely polarized. Electrons having the proper energy then travel through the analyzer into the detector (The full path is shown as a solid line through the entire spectrometer). The inset illustrates the definition of the scattering angles θ and θ_0. (Reproduced from H. Ibach *et al*., 2003. © 2003 with permission from the American Institute of Physics.)

particular angle and with a certain energy transfer. For experimental reasons, the SPEELS measurements were performed in the 'constant wave-vector transfer mode', that is, for each scan, the wave-vector transfer is fixed by the scattering geometry and the electron intensity is measured as a function of the energy loss. The energy losses measured in the experiments are small compared to the primary kinetic energy $E^{\mathrm{i}}_{\mathrm{kin}}$ of the incoming electrons and hence $k_{\mathrm{i}} \approx k_{\mathrm{f}}$. Therefore, one can approximate the wave-vector transfer parallel to the sample surface to $\Delta K_{\parallel} \approx k_{\mathrm{i}}(\sin(\theta_0 - \theta) - \sin(\theta))$. All wave-vector transfers mentioned in the following are calculated within this approximation. Owing to the conservation of energy and momentum parallel to the surface in the scattering event, the measured intensity spectra comprise the information about the inelastic events that occurred in the scattering process.

As an example, Figure 3 illustrates the excitation of a spin wave as a scattering event. To excite a spin wave, energy, momentum, and magnetic moment have to be transferred to the sample. Both the energy and the momentum transfer are detected by the spectrometer and allow conclusions about the spin wave that was excited. Because the total magnetic moment has to be conserved in the scattering process, the excitation of spin waves is only possible if this conservation law is fulfilled. In a simple picture, the creation of a spin wave reduces the magnetization of the sample by $1\,g\mu_{\mathrm{B}}$. Therefore, the incoming electron has to be of $e_{\downarrow}$(minority) character to be able to excite a spin wave (as indicated in Figure 3b). Vice versa, the annihilation of a spin wave is only possible in the $e_{\uparrow}$ channel.

This selection rule can be used in the experiment to separate spin-wave excitations from other excitations. It is sufficient to have a spin-polarized incoming electron beam and a ferromagnetic sample with a defined magnetization direction parallel to the polarization axis. In this particular case, an energy loss caused by the excitation of spin waves is only possible for one spin direction of the incoming electrons and will appear only in $\mathrm{I}_{\downarrow}$. This

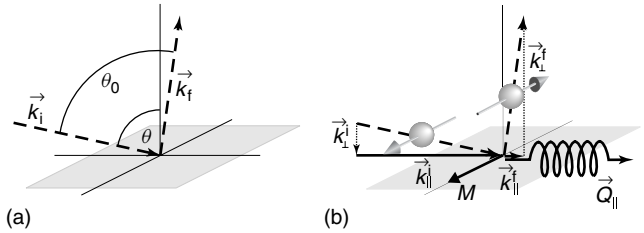

Figure 3. Schematic picture of an electron scattering process in which a spin wave is excited. θ_0 defines the angle between the incoming and outgoing electron path. θ is the angle between the surface normal and the incident beam. The wave-vector component parallel to the surface is conserved in the scattering process; the component perpendicular to it is not. (Note that, by definition, the spin and its magnetic moment point into opposite directions.)

circumvents the necessity of a 'complete' experiment with a spin analysis of the scattered electrons, which is an experimental challenge due to the notoriously inefficient detectors (Kirschner, 1985a).

1.2 Established experimental methods to study spin-wave excitations

Different experimental techniques are suited to study spin-wave excitations. In all scattering techniques (INS, BLS, and SPEELS), the approach to detect spin-wave signals is similar. A particle with known energy is scattered under defined conditions from a sample and is later analyzed with respect to its wave vector and energy transfer during scattering.

A recent example of high wave-vector and high-energy spin-wave excitations investigated by INS is shown in Figure 4 (Perring, Taylor and Squires, 1995). The experiments were performed on hcp Co using a time-of-flight technique. The peaks visible in the spectrum in Figure 4(a) are caused by energy losses due to spin-wave excitations with different wave-vector transfers in different Brillouin zones. The information measured in different Brillouin zones can be backfolded into the first Brillouin zone. The resulting dispersion relation is shown in Figure 4(b). In these measurements, the dispersion could be followed up to about $0.8\,\mathrm{\AA}^{-1}$, that is, about two-thirds of the Brillouin zone. The solid line is a fit to the data using a dispersion relation calculated from a nearest-neighbor Heisenberg model. A good agreement between the measured dispersion and this model was found (Perring, Taylor and Squires, 1995). The INS studies show a broadening of the spin-wave peaks due to itinerant effects. Nevertheless, the spin-wave losses were well defined up to the highest wave vectors investigated.

BLS and FMR are used to study spin waves with long wavelength ($Q_{\parallel} = 10^{-3}\,\mathrm{\AA}^{-1}$). Both techniques probe several similar properties of magnetic materials. They can determine the macroscopic magnetic quantities of a sample, for example, the anisotropy. In addition, in both techniques standing spin-wave modes perpendicular to the surface have been observed in films with thicknesses of several nanometers or thicker (Tannenwald and Weber, 1961; Grimsditch, Malozemoff and Brunsch, 1979). This leads to the possibility to study spin waves with higher wave vectors, up to $q_{\perp} \approx 10^{-2}\,\mathrm{\AA}^{-1}$ (Hillebrands and Ounadjela, 2002).

1.3 Spin waves within the Heisenberg description

The spin-wave dispersion relation for high wave vectors is determined by contributions of the exchange interaction. This interaction can be considered in the Heisenberg model of localized magnetic moments. This description is not expected

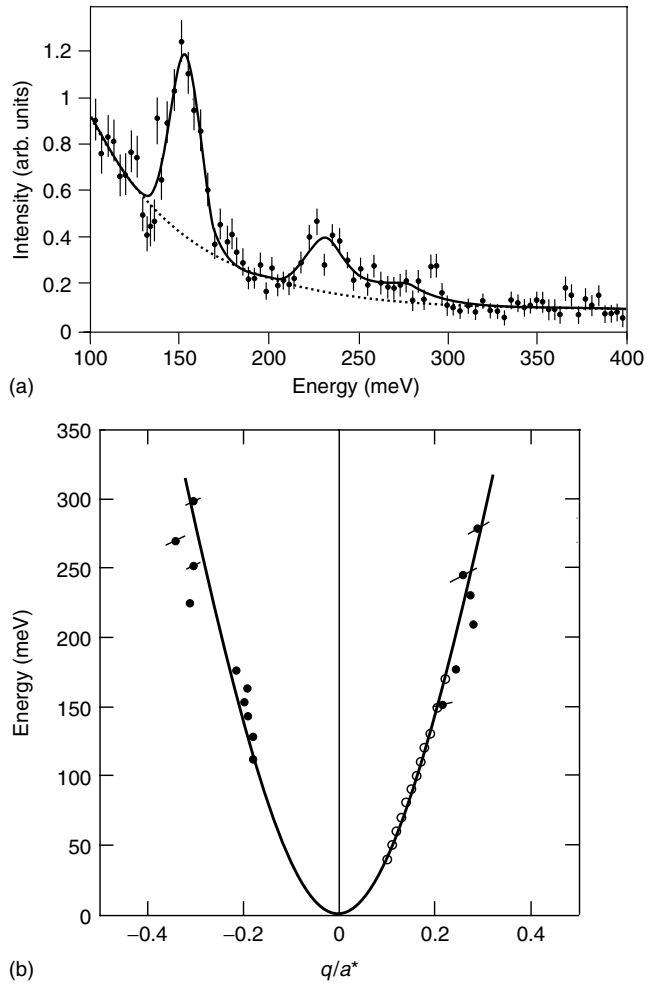

Figure 4. (a) Example of recent neutron scattering measurements of spin-wave excitations in hcp Co (Perring, Taylor and Squires, 1995). The left side shows a time-of-flight spectrum, transformed back into energy space (for details see Perring, Taylor and Squires, 1995). In (b) the resulting spin-wave dispersion is shown. The wave vector is normalized in this graph so that the Brillouin zone boundary is at $q/a^* = 0.5$. The solid line is a fit obtained by a nearest-neighbor Heisenberg model. (Reproduced from Perring *et al.*, 1995. © 1995 with permission from Elsevier.)

to be truly valid for the mobile conduction electrons, which carry the magnetic moments in 3d metals; however, it provides a simple description of the underlying physical properties.

Using the Heisenberg Hamiltonian:

$$H = -\sum_{ij} J_{ij} S_i \cdot S_j \tag{1}$$

the spin-wave dispersion can be calculated. Here, J_{ij} is the exchange-coupling constant between the magnetic moments S_i and S_j. It was found by Bloch that the Heisenberg Hamiltonian allows low-energy collective excitations of spins (Bloch, 1930, 1932). These spin waves are transverse fluctuations of the magnetic moment. As an approximation, a small angle of precession is assumed. In other words, each magnetic moment is only a little tilted out of its equilibrium position. For simplicity, we will consider only nearest-neighbor exchange interactions and a constant value of J and S (not depending on the position, i.e., equal at the surface, interface, and bulk). By considering the exchange interaction as torque acting on each magnetic moment, one obtains the equation of motion from equation (1)

$$i\hbar \frac{\mathrm{d}S_i^+}{\mathrm{d}t} = 2JS \sum_j \left[S_i^+ - S_j^+ \right] \tag{2}$$

For thin films, it is useful to consider solutions in the form of waves in the film plane,

$$S_i^+ = A_i \mathrm{e}^{i(Q_\parallel (R_i - \omega t))} \tag{3}$$

Here A_i is the amplitude of the spin wave at position R_i, $Q_\parallel$ is the wave vector parallel to the surface, and ω is the angular frequency of the spin wave. From this, we find that

$$\hbar\omega A_i = 2JS \sum_j \left[A_i - A_j e^{i(Q_\parallel (R_j - R_i))} \right] \tag{4}$$

This equation can be used as a starting point to derive the spin-wave dispersion in an arbitrary crystalline structure.

For the direction perpendicular to the surface two types of solutions are possible. One is a surface spin-wave mode that has an excitation amplitude, which decays exponentially into the bulk $A_{n+1} = A_n e^{-\alpha \frac{a_0}{2}}$. For the following it is interesting to note that the decay factor α for the surface spin-wave amplitude depends on $Q_\parallel$. The surface localization of the surface spin-wave mode increases with $Q_\parallel$ and is highest at the surface Brillouin zone boundary. The other solutions are bulk spin-wave modes, here $A_{n+1} = A_n e^{iq_\perp \frac{a_0}{2}}$ where $q_\perp$is the wave vector perpendicular to the surface.

For a semi-infinite system, one thus obtains a continuum of bulk modes and one surface mode for each given $Q_\parallel$. For example, the spin-wave dispersion for the surface mode for an face centered cubic (fcc) semi-infinite crystal with (001) surface along the (110) direction calculated from equation (4) is given by

$$\hbar\omega = 8JS \left[1 - \cos\left(Q_\parallel \frac{a_0}{\sqrt{2}} \right) \right] \tag{5}$$

In the experiments shown later, the films under investigation were only a few atomic layers thick. This can be taken into account by considering a slab of n layers with two surfaces. The introduction of a second surface leads to two

surface modes in the system, one acoustic (i.e., the spin-wave energy vanishes as q approaches 0) and one optical surface mode. In addition to the two surface modes, $n-2$ dispersion relations are obtained that belong to modes having a wave-like character perpendicular to the surface (standing waves), that is, of 'bulk' modes.

The results of the above calculations for an 8 ML fcc slab and an fcc semi-infinite crystal are shown in Figure 5(a). In Figure 5(b), the dispersions obtained from similar calculations for hexagonal closed packed (hcp) Co are presented. These systems have been chosen because both have been investigated and are discussed in the following text. The only free parameter in these calculations is the value of JS. For the two dispersions shown, we have chosen $JS = 15$ meV. The eight dispersions of the spin waves in the slab are represented by solid lines. The two surface modes of the slab calculations are the lowest energy branches of the eight modes. The acoustic mode of the surface spin wave of the 8 ML slab falls on a line with the surface spin-wave mode of the semi-infinite crystal. Noticeable differences between both of these surface modes appear only for very thin slabs, as discussed later. The above derivation of the spin-wave dispersions has been done in a classical description. Though the quantum-mechanical derivation is more appropriate, the spin-wave dispersion is one of the cases where both descriptions yield exactly the same results (Nolting, 1986).

The spin-wave energy of the acoustic branch at small wave vectors can be approximated by

$$\hbar\omega = 2JS\,a_0^2 Q_\parallel^2 = D\,Q_\parallel^2 \tag{6}$$

Here, D is the so-called spin-wave stiffness. In many experiments, the wave-vector transfer is limited to small values so that the equation (6) is valid. In these cases, the quantity published in literature is typically the spin-wave stiffness.

The Heisenberg model is valuable, especially because of its simplicity. It has already been mentioned that it is not expected to be applicable to an itinerant electron system. Nevertheless, we will see later that several of our results are described surprisingly well within this model. Other findings, however, can only be understood in an itinerant electron description. Therefore, in the following, an introduction to magnetic excitations in an itinerant electron model is given, with emphasis on the differences to the results mentioned in the preceding text.

1.4 Magnetic excitations in itinerant electron ferromagnets

In the 3d-magnetic metals, the conduction electrons that are the carriers of magnetic moments cannot be considered as localized at a particular position, but as itinerant. The discussion of magnetism in such itinerant electron systems goes back to Stoner (1936, 1938). Magnetic order results in an exchange splitting of the electron bands, which causes a higher occupation of states for electrons of one spin direction (majority electrons) compared to the other spin direction (minority electrons).

The magnetic excitations allowed in the model are the so-called Stoner excitations. The original Stoner model overestimated the Curie temperature for magnetic order substantially, because no collective spin excitations were taken into account. This led to an overestimation of the minimum energy for magnetic excitations. The consideration

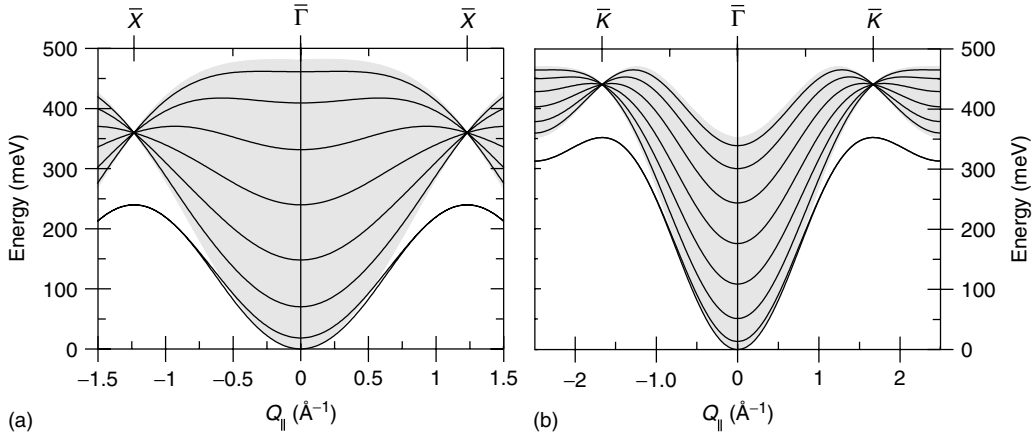

Figure 5. Spin-wave dispersions calculated within a nearest-neighbor Heisenberg model as a function of $Q_\parallel$ for an 8 ML slab (solid lines) and a semi-infinite crystal (gray area). In (a) calculations have been performed for an fcc crystal with a (001) surface and in (b) for a hcp crystal with a (0001) surface. In these calculations $JS = 15$ meV. The symbols on the top axis mark the important points in the surface Brillouin zone.

of low-energy collective excitations within the itinerant electron model is needed to describe the experimentally observed Curie temperature. Collective excitations were introduced by Slater (1937) for an itinerant electron system in which all electron spins in the system are of majority character except for one. He found that the lowest energy magnetic excitations of such a system are of collective nature. This state can be described by the superposition of single particle states and represents the correlated motion of the spin-reversed electron and the hole it left in the sea of aligned electrons (Martin, 1967). It was found that its properties are similar to the spin-wave excitations in the localized model (Slater, 1937). The extension of the model derived by Slater to more realistic itinerant metals has been performed by Herring and Kittel (1951) and Herring (1952). The general finding is that collective excitations exist in an itinerant electron system and that they have similar properties compared to the well-defined spin waves in a localized model in the limit of low wave vectors and low energies. For example, in this limit a quadratic dispersion relation of these excitations was found (Herring and Kittel, 1951), as in the Heisenberg model (see equation (6)). At high wave vectors and energies, Stoner excitations are possible in itinerant electron systems. A correlated electron–hole pair that is created in the region where Stoner excitations are possible can easily decay into such uncorrelated states. Therefore, in the region in which Stoner excitations are possible, the collective excitations are not well-defined long-living spin waves, but they are strongly damped (Herring, 1966). The general concept of magnetic excitations in itinerant ferromagnets is summarized in Figure 6.

As a simple, one-dimensional example, in Figure 6(a) one pair of exchange split bands is shown. The exchange splitting is assumed to be identical to U over the entire Brillouin zone. The majority band lies completely below E_F to represent a strong ferromagnet. The energy and wave-vector transfer needed to excite a Stoner excitation of an electron from an occupied majority state to an unoccupied minority state is shown in Figure 6(b) as a gray area. For strong ferromagnets, the minimum energy for Stoner excitations, the Stoner gap Δ, is given by the distance between the majority band and E_F. A possible acoustic spin-wave branch is also shown in Figure 6(b) as a black line. When the spin-wave branch enters the Stoner continuum it is strongly damped. This range of the dispersion is presented as a dotted line. The real physical situation is only partly described by Figure 6. For example, realistic band structures consist of more than one band, and s bands of both spin characters cross the Fermi edge so that no true overall Stoner gap exists. In our studies, we investigate spin waves at surfaces by electron scattering. In this case, additional effects have to be considered. It has been theoretically predicted that in inelastic electron scattering experiments, the creation of free electron like Stoner excitations is as probable as a creation of d-electron Stoner excitations (Penn and Apell, 1988); the calculations have been performed for Fe; however, it can be assumed that similar effects may also occur in Co. In addition, at the surface the wave vector perpendicular to the surface has not been conserved owing to the loss of translational invariance. Both considerations lead to drastic changes compared to what has been shown in Figure 6. Large parts of the Stoner excitation free area for $Q_\parallel$ are then filled owing to possible excitations having a finite $q_\perp$ (Tang, Plihal and Mills, 1998).

With the advance of theory, it became feasible to calculate the above described magnetic excitation spectrum in bulk itinerant ferromagnets on the basis of *ab initio* calculations (Savrasov, 1998). Such calculations, however, have not been made for surfaces and thin films. Other approaches are used, starting from an *ab initio* calculation of the underlying band structure. One frequently used approach is based on the adiabatic approximation, in which the electron motion is decoupled from the spin motion (see, e.g., Katsnelson and Lichtenstein, 2000; Frota-Pessôa, Muniz and Kudrnovský, 2000; Halilov, Eschrig, Perlov and Oppeneer, 1998; van Schilfgaarde and Antropov, 1999; Pajda *et al*., 2000; Grotheer, Ederer and Fähnle, 2001; Udvardi, Szunyogh, Palotás and Weinberger, 2003; and references therein). Therefore, the damping of spin waves by Stoner excitations is not taken into account. As discussed in the preceding text, this is a good approximation in itinerant electron systems only in the limit of low wave vector and low-energy spin waves. In principle, these calculations map the itinerant ferromagnetism onto a Heisenberg like description. Several publications gave values for the exchange-coupling constants derived this way (Pajda *et al*., 2000; Grotheer, Ederer and Fähnle, 2001; Razee, Staunton, Szunyogh and Györffy, 2002).

The other approach goes beyond the adiabatic approximation. This is a nontrivial extension of the model using the adiabatic approximation, because one has to take into account the full dynamics of the system (Cooke, Blackman and Morgan, 1985; Blackman, Morgan and Cooke, 1985; Trohidou, Blackman and Cooke, 1991; Bass, Blackman and Cooke, 1992; Tang, Plihal and Mills, 1998; Plihal, Mills and Kirschner, 1999; Hong and Mills, 2000a; Muniz and Mills, 2002; Muniz, Costa and Mills, 2003; Costa, Muniz and Mills, 2003, 2004a,b). This description includes the damping of spin waves caused by Stoner excitations and therefore this theory is expected to be valid throughout the Brillouin zone. So far, these calculations were only possible using an empirical tight binding description of the underlying band structure (Trohidou, Blackman and Cooke, 1991; Tang, Plihal and Mills, 1998; Hong and Mills, 2000a; Costa, Muniz and Mills, 2004a). In a recent series of publications, Mills and coworkers applied this theory to magnetic thin films of

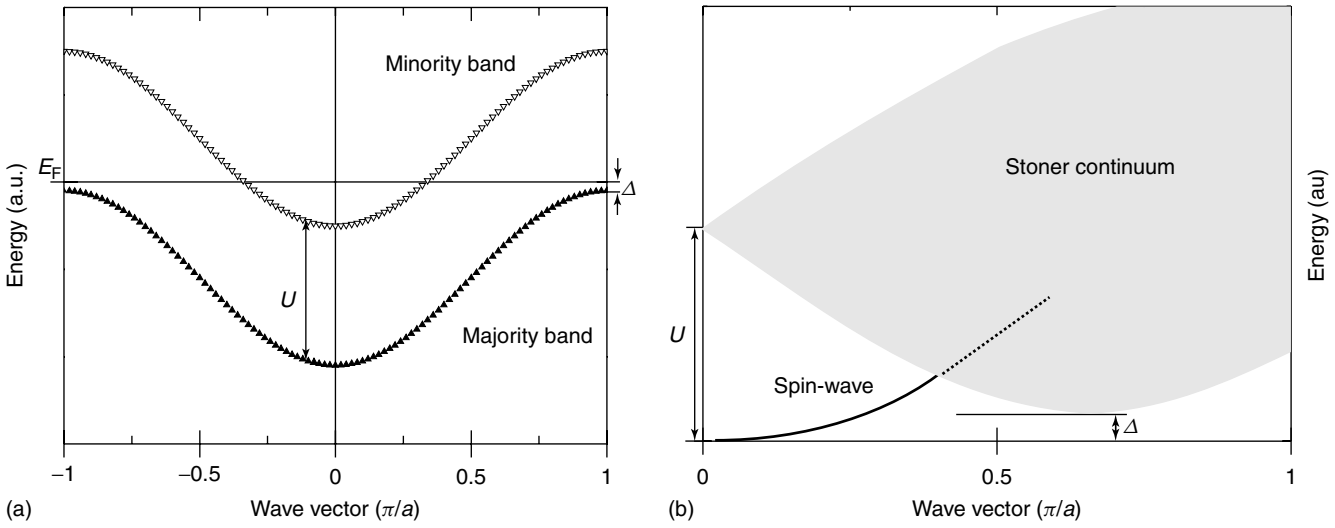

Figure 6. (a) Pair of exchange split bands with the majority band completely below the Fermi energy E_F (by the amount Δ) to represent a strong ferromagnet. The exchange splitting parameter U is assumed to be constant in the entire Brillouin zone. (b) The gray region shows the low-energy part of the Stoner spectrum calculated for the band shown in (a). At $q = 0$ the creation of a Stoner excitation costs an energy which is equal to U. The minimum energy of the Stoner excitations is equal to Δ and is located at some higher wave vector. To give a general idea, a possible spin-wave dispersion (not calculated from the bands shown in (a) is included in (b)).

Fe, Ni, and Co (Plihal and Mills, 1998; Plihal, Mills and Kirschner, 1999; Hong and Mills, 2000a; Muniz and Mills, 2002; Muniz, Costa and Mills, 2003; Costa, Muniz and Mills, 2003, 2004a,b). These calculations showed that the damping of spin waves caused by Stoner excitations is strong in these films. As shown in the last section, within the Heisenberg model one expects as many spin-wave modes at a given $Q_\parallel$ as layers are contained in the film. In the itinerant electron theory that goes beyond the adiabatic approximation, this picture changes drastically. Instead of a number of discrete modes each of zero width, the theoretical calculations show only one broad feature (Costa, Muniz and Mills, 2003, 2004a). This arises from the strong damping and smearing of the different modes. They overlap and can hardly be distinguished from each other (Costa, Muniz and Mills, 2004b).

In this section, two different theoretical concepts of magnetism have been introduced, in which high wave-vector spin waves show a different behavior. In the following, we will concentrate on spin waves in 3d metals, in which the electrons that carry the magnetic moments have itinerant character. Nevertheless, we will discuss our results to some extent in a nearest-neighbor Heisenberg model. Of course, several questions concerning the validity of such a description arise. As discussed in the preceding text, high wave-vector spin waves in this system are expected to be heavily damped. It is expected that this damping not only influences the spectral shape of the spin waves but also effects the dispersion (Costa, Muniz and Mills, 2004b). In addition, a questionable assumption is that only nearest-neighbor interactions are included in our calculations. As is shown later, it seems possible to take some of the above-mentioned criticism into account by an effective nearest-neighbor exchange-coupling constant in the Heisenberg model.

2 EXPERIMENTAL RESULTS

In this section, results of investigations of spin waves by SPEELS are presented. As model examples, the systems fcc Co on Cu(001) and hcp Co on W(110) are discussed. Some of the experimental capabilities of the SPEELS technique are demonstrated using these systems. In addition, some results obtained on tetragonal distorted Fe on Co/Cu(001) are mentioned.

2.1 SPEELS measurements of Co on Cu(001) and Co on W(110)

Figure 7 shows some representative SPEEL spectra of $I_\uparrow$ and $I_\downarrow$ measured on 8 ML fcc Co on Cu(001) (a) and on 8 ML hcp Co on W(110) (c). For the SPEELS measurements of fcc Co on Cu(001), the [110] direction of the Cu crystal was oriented parallel to the scattering plane. Thus, the measured wave-vector transfer was along the $\overline{\Gamma} - \overline{X}$ direction in the surface Brillouin zone (see inset Figure 7b). The magnetization direction of the Co film was perpendicular to the scattering plane, along $[1\overline{1}0]$, if not quoted otherwise.

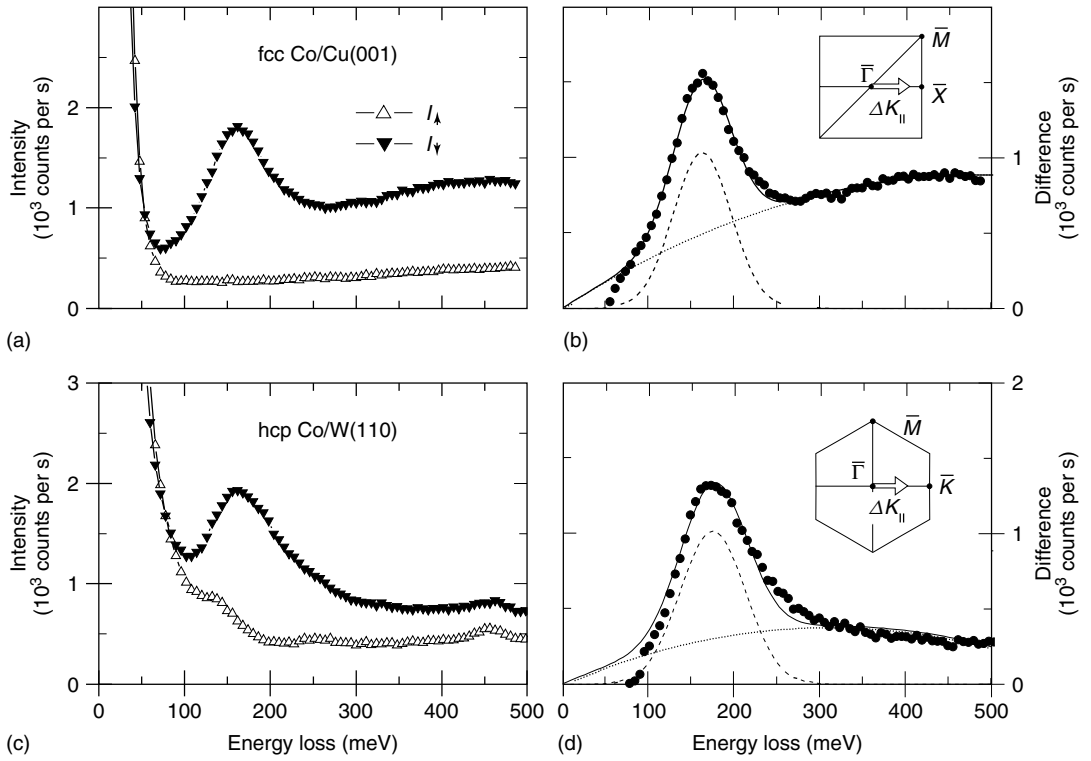

Figure 7. SPEEL spectra of $I_\uparrow$ and $I_\downarrow$ measured on 8 ML fcc Co on Cu(001) (a) and on 8 ML hcp Co on W(110) (c). The spectra have been recorded at a wave-vector transfer of $\Delta K_\parallel = 0.78\,\text{Å}^{-1}$. In Figure 7(b/d) the difference spectra of (a/c) are shown. The solid curves show fits of the difference spectra (see text for details). The insets give the reciprocal space representation of the fcc Co(001) and hcp Co(0001) surface, respectively. The arrows in the insets mark approximately the position of the wave vector at which the spectra were recorded. For the spectra in (a) $E_{\text{kin}} = 7\,\text{eV}$ and $\theta_0 = 90^\circ$ and in (c) $E_{\text{kin}} = 4\,\text{eV}$ and $\theta_0 = 80^\circ$. The energy resolution in these scans was $\Delta E \approx 40\,\text{meV}$.

For the measurements of hcp Co on W(110), the scattering plane was chosen along the Co[11$\bar{2}$0] axis, which is parallel to the W[001] axis. This corresponds to the $\overline{\Gamma} - \overline{K}$ direction in the reciprocal space (see inset Figure 7d).

All spectra plotted in Figure 7 have been recorded at a wave-vector transfer of $\Delta K_{||} = 0.78\,\text{Å}^{-1}$, which corresponds approximately to the reciprocal space position pointed out by the arrows in the insets of Figure 7(b/d). The solid and open triangle symbols mark the measured intensities of $I_\downarrow$ (incoming electron spin of minority character) and $I_\uparrow$ spectrum (incoming electron spin of majority character), respectively. The intensities of these as well as the following spectra have been corrected for the incomplete spin polarization of the incident electron beam (which has been determined in an independent scattering experiment to 0.79 ± 0.1 in this case). In the $I_\downarrow$ spectra, a prominent loss feature centered at about 170 meV is visible. This peak is caused by the excitation of spin waves by the inelastic scattering of electrons, as shown in the following text. In the spectra measured on hcp Co (Figure 7c) additional loss features show up in both spin channels. These can be attributed to the (almost) spin independent scattering processes of vibrational excitations of small amounts of adsorbates as discussed in more detail later.

As can be seen in Figure 7(a/c), the energy loss around 170 meV is only present in the $I_\downarrow$ spectra. This spin-selective excitation can be understood on the basis of the considerations given in the previous section. Since the total magnetic moment is conserved during the scattering process, the incoming electron has to transfer its spin magnetic moment to the crystal to reduce the magnetic moment of the latter. The incident electron has to have minority spin character and the outgoing electron, majority spin character to excite a spin wave and to fulfill the conservation law. Thus, this scattering event is only possible for an incoming electron of minority spin character. This spin-selective excitation process is a fingerprint of spin-wave excitations. Its unique character can be used to improve the spin-wave signal-to-background ratio by looking at the difference spectrum $(I_\downarrow - I_\uparrow)$. The difference spectra obtained from the spectra in Figure 7(a/c) are plotted in Figure 7(b/d). Assuming a spin-wave peak and a background of electron–hole pair excitations we are able to describe the difference spectra. The spin-wave peak is described well by a Gaussian peak and the

background with a second-order polynomial. The resulting fit curves of the spectra are presented in Figure 7(b/d) as solid lines. The two contributions for the spin wave and the background are indicated separately dashed and a dotted line, respectively. The energy resolution for the spectrometer in this scan was $\Delta E \approx 40$ meV full-width at half-maximum (FWHM) and the peak width of the spin-wave signal is about 75 meV (FWHM) for fcc Co and about 90 meV for hcp Co. The measured width is, therefore, not determined by the spectrometer resolution, but the loss features have an intrinsic width (Vollmer *et al*., 2003; Etzkorn *et al*., 2005).

The background is caused by the excitation of electron–hole pairs, which can be assumed to be partially Stoner excitations. Beside the spin-wave excitations, the electron–hole pair excitation processes also depend on the spin direction of the incident electron. It is known that both $I_\downarrow$ and $I_\uparrow$ contain spin flip and nonspin flip processes of electron–hole pair excitations (Hopster, Raue and Clauberg, 1984; Kirschner, Rebenstorff and Ibach, 1984; Kirschner, 1985b; Abraham and Hopster, 1989; Hopster and Abraham, 1989; Kämper, Abraham and Hopster, 1992). The intensity in the different spin channels can often be explained by the spin dependent density of occupied and unoccupied states. In the spectra, Stoner excitations appear as a broad feature with loss energies ranging from very low energies up to several electronvolts. Only little structures as a function of the loss energy have been observed. One study of Stoner excitations using a 'complete' experiment was performed on Co on Cu(001) (Kämper, Abraham and Hopster, 1992). It was found that all the four spin channels contribute strongly to the intensities at energy losses higher than 300 meV. The energy resolution in these experiments was about 300 meV so that the measurements below this loss energy are difficult to interpret. If one assumes that all spin channels contribute to the background also in the low-energy loss range, a significant amount of Stoner excitations should be possible in the energy range of spin-wave excitations. Thus, the damping of the spin waves due to the decay into these Stoner excitations provides a likely explanation for the measured spin-wave width.

Figure 7(a/c) displays the count rate in electron counts per second. The spin-wave intensity measured under these scattering conditions (for details, see figure caption) is about 1.5×10^3 counts per second using a flux of the incident electron beam of the order of 20 nA, that is, $\approx 10^{11}$ electrons per second. With this, the spin-wave intensity is of the order of a few percent of the elastically scattered electron intensity. These high intensities allow relatively short measuring times. The spectra shown in Figure 7(a/c), for example, were measured in about 30 min, only.

The spin-wave energy and shape are rather similar for both spin-wave loss features measured on the two crystalline Co phases (Figure 7), but the background of electron–hole pair excitations is different for the two. Another aspect is the varying amount of vibrational losses present in the spectra. More and stronger vibrational losses caused by small amounts of contaminations (residual gas adsorbed at the surface) are visible in the spectra measured on Co on W(110), though the vacuum conditions were similar in both studies. In the spectra shown in Figure 7(c), the vibrational loss features can be attributed to an H-metal vibration (140 meV) and probably to an H_2O vibration (450 meV). The energy values are in agreement with literature values (Ibach and Mills, 1982). The H vibration was cross-checked by additional adsorption studies. From these adsorption studies, it is also possible to estimate the amount of adsorbates. The H-loss peak in Figure 7(c) corresponds to about 10% of the saturation coverage.

To test the magnetic origin of the spin dependent excitation of the spin-wave loss feature, we use a fundamental symmetry argument. An important consequence of the spin-selective excitation of spin waves is that when the magnetization of the sample is reversed, the peak of the spin-wave loss feature should appear in the 'opposite' spin channel. This is simply because the definition of majority and minority spin reverses. The proof of the magnetic origin of the loss feature is shown in Figure 8. Here, two spectra were measured under identical conditions, except that the sample magnetization was reversed. The spectra indicated with M are measured on a Co film, which had the 'normal' direction of the magnetization. In this case also the normal notation of majority and minority spin character is used. These spectra are presented as triangles and solid circles for the difference. The star symbols in Figure 8(a) and the open circles in Figure 8(b) show the spectra measured on the reversely magnetized Co film ($-M$). For these spectra, the notation majority and minority might be confusing. Therefore, the spectra are assigned as 'the same' channel. The spin direction of the incident electrons (not with respect to the sample magnetization) was the same for the spectra with open and solid symbols in Figure 8(a). The main result of these measurements is that by reversing the magnetization of the sample, the spectra measured for the two incoming spin directions interchange almost ideally. This holds true, in particular, for the spin-wave feature. Thus, we have proved that the spin-selective excitation is of magnetic origin, as expected for a spin-wave excitation. In addition, scattering contributions to this spectra caused by spin-orbit coupling (that do not change the sign upon magnetization reversal) are seen to be negligible in this case. Since the spin-orbit contributions are small, as expected for 3d metals, they will not be considered here.

Another important characteristic of spin waves is their dispersion. Since the measured loss features are attributed

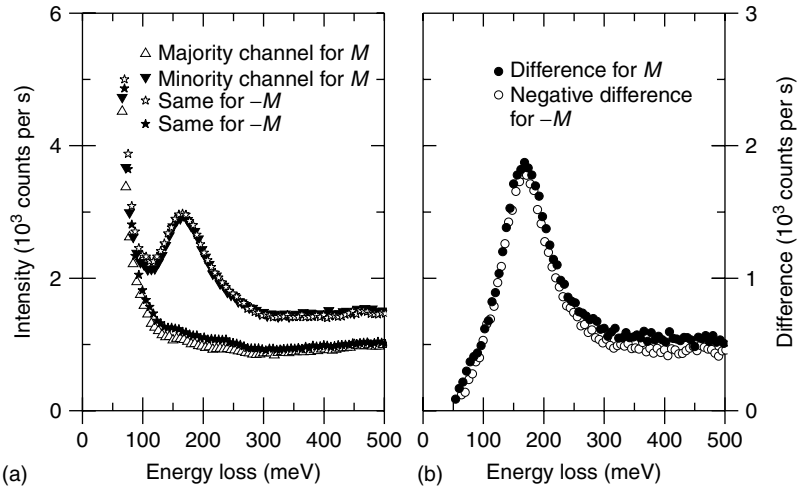

Figure 8. Comparison between SPEEL spectra and their differences measured on oppositely magnetized films. Both measurements were taken on 8 ML Co on Cu(001), with $\Delta K_{\parallel} = -0.81\,\text{Å}^{-1}$, $E_{\text{kin}} = 7\,\text{eV}$, and $\theta_0 = 90^{\circ}$. In the measurements marked with M the magnetization lies in the 'normal' direction, along $[1\bar{1}0]$ (triangles and solid dots). For the measurements labeled as $-M$, the magnetization was rotated by 180° (stars and open dots). Note that for the difference spectrum recorded with $-M$, the negative difference is shown.

to a spin wave, they should move to higher energies for higher wave-vector transfers, assuming an acoustic spin-wave branch.

In Figure 9, SPEEL spectra measured on an 8 ML Co film on Cu(001) at different wave-vector transfers are presented. Here, the measured intensity at each energy loss was divided by the intensity of the elastically scattered electrons to obtain the normalized intensity. Figure 9(a/b) show the normalized intensities for negative and Figure 9(c/d) for positive wave-vector transfers. For low absolute values of the wave-vector transfer, the spin-wave losses appear as a shoulder in the elastic peak. For higher wave-vector transfers, the spin-wave loss feature shifts to higher loss energies as a result of its dispersion.

So far, the presented results were measured on 8 ML Co. Because of the short mean free path of low-energy electrons, this can be considered as a relatively thick film for such an experiment. SPEELS measurements on thinner Co films have been made to investigate the influence of reduced dimensions on the spin waves and to test the capabilities of this method (Etzkorn *et al*., 2004). As an example, SPEEL spectra measured on 5 ML and on 2.5 ML Co films on Cu(001) are shown in Figure 10(a/b) and (c/d), respectively. It is obvious that even for 2.5 ML Co, the spin-wave loss features are clearly visible in the spectra, though the spin-wave intensities are reduced (note that the normalized intensity scales for the two film thicknesses differ by a factor of 2). From the measured signal-to-noise ratio, one may speculate that it should be possible to investigate spin-wave excitations by SPEELS in submonolayer quantities of magnetic films. Beside the spin-wave signal, other loss features are present in the spectra, especially in the spectra of 2.5 ML Co. These losses were excited for both spin directions of the incoming electrons and do not show dispersion. They can be attributed again to vibrational losses caused by traces of adsorbates on the surface. Mainly a loss feature at about 230 meV is visible, which can be assigned to CO vibrations (Ibach and Mills, 1982). We have confirmed this by additional adsorption studies, too.

In the SPEEL spectra given in Figures 9 and 10, a clear dispersion of the spin-wave peak is visible. From these spectra, one can determine the energy position of the spin waves as a function of the wave-vector transfer. The resulting dispersion curves are presented in Figure 11. Additional data have been measured at and beyond the Brillouin zone boundary ($\overline{X}$). They are also plotted in Figure 11 to confirm that the measured spin-wave dispersion obeys the periodicity of the surface Brillouin zone.

In the previous section, the spin-wave dispersion within a nearest-neighbor Heisenberg model was calculated for a semi-infinite fcc crystal along the $\overline{\Gamma} - \overline{X}$ direction. The resulting dispersion relation of the surface spin-wave mode was given in equation (5). We have fitted this dispersion relation to the measured data for 8 ML Co on Cu(001). The result is plotted as a solid line in Figure 11. A surprisingly good agreement is found between the experimental data and the calculated dispersion of the surface spin-wave mode. Note that the shape of the calculated dispersion is fully determined by the crystalline structure and geometry of the system. The only fit parameter used in this model is the product of the exchange-coupling constant and the magnetic moment (JS). It defines the amplitude of the dispersion, in

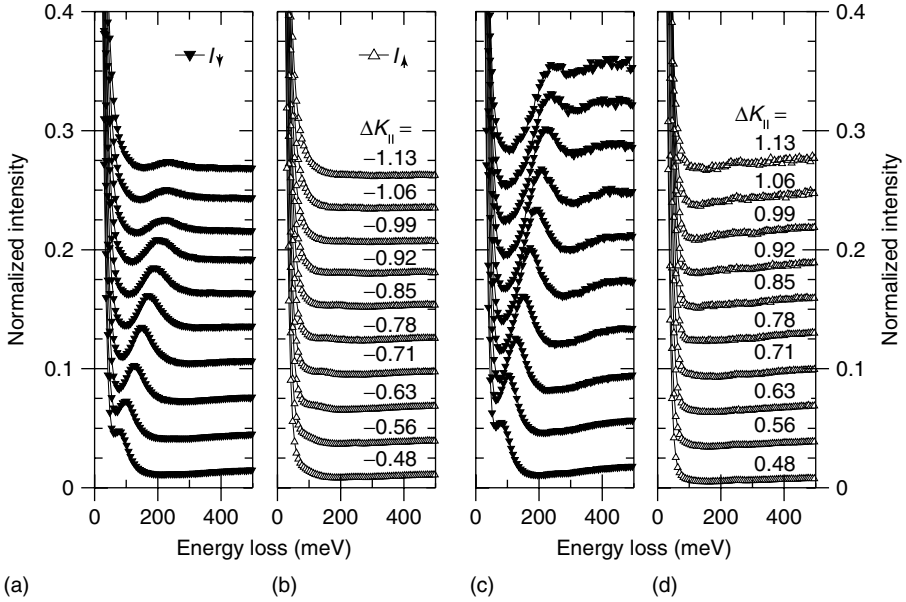

Figure 9. SPEEL spectra of 8 ML Co on Cu(001) with $E_{\text{kin}} = 6.5\,\text{eV}$ and $\theta_0 = 90^\circ$, taken at different wave-vector transfers, which are indicated by the numbers above the spectra. In (a/b) the spectra for negative and in (c/d) the spectra for positive wave-vector transfers are presented. All intensities are normalized with respect to the intensities of their elastic peaks. Each adjacent spectrum has an offset of 0.025 (one minor tick) to allow a better comparison.

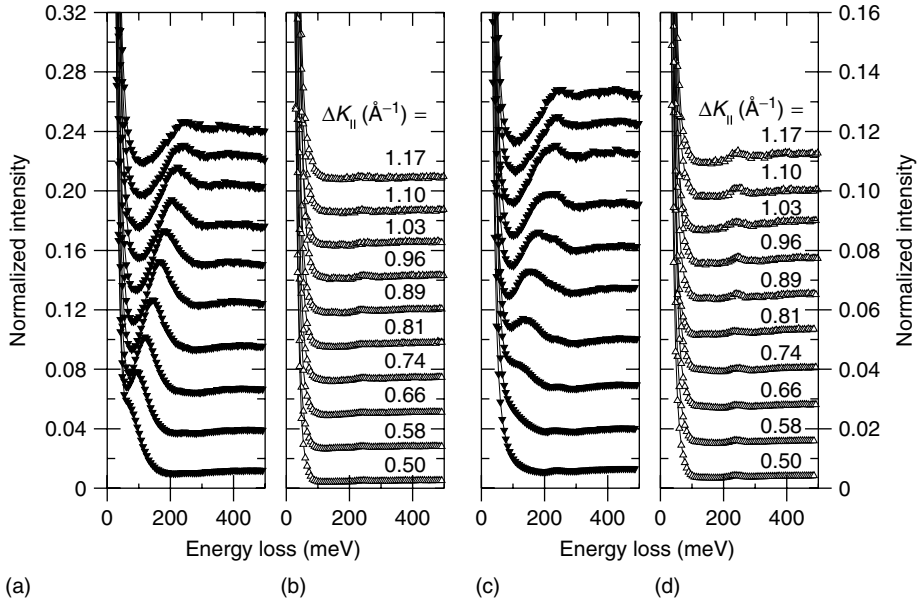

Figure 10. SPEEL spectra measured on 5 ML (a/b) and 2.5 ML (c/d) Co films on Cu(001). The numbers above the spectra indicate the different wave-vector transfers. The intensities are normalized to the intensity of the elastic peaks. Each adjacent spectrum has a vertical offset of 1/16 of the total scale (one minor tick) to allow better comparison. All spectra were taken with $E_{\text{kin}} = 7\,\text{eV}$ and $\theta_0 = 90^\circ$.

other words, the spin-wave energy at the surface Brillouin zone boundary. The value of JS resulting from the fit shown in Figure 11 is $JS = 15 \pm 1\,\text{meV}$. This value is in perfect agreement with the value of $JS = 14.7 \pm 1.5\,\text{meV}$ which was obtained by neutron scattering experiments for bulk spin waves in fcc Co (with 8% Fe to stabilize the fcc phase at room temperature) (Sinclair and Brockhouse, 1960; Pickart *et al.*, 1967).

At first glance, the dispersions of the three different film thicknesses are similar. A closer look, however, reveals

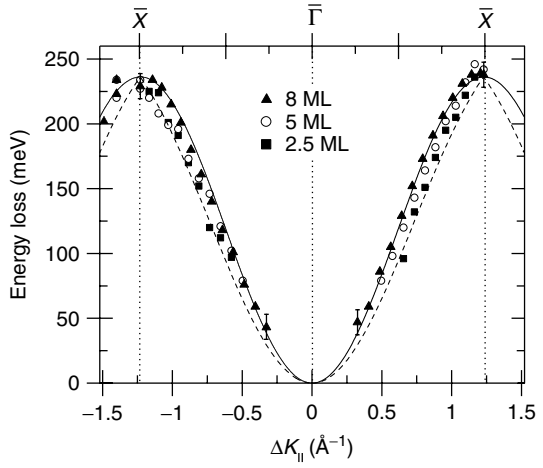

Figure 11. Spin-wave dispersion for 8, 5, and 2.5 ML Co on Cu(001) measured by SPEELS. The data points represent the energy position of the maximum of the spin-wave peaks, as determined from the data presented in Figures 9 and 10. The solid and the dashed lines are dispersions of the surface spin-wave mode calculated within a nearest-neighbor Heisenberg model with $JS = 15$ meV for a semi-infinite film and a 2 ML slab, respectively. Measurement with wave vectors at $\overline{X}$ and at $\Delta K_{\parallel} = -1.40\,\text{Å}^{-1}$ were taken with $E_{\text{kin}} = 7$ eV and $\theta_0 = 80^{\circ}$. The data point at $\Delta K_{\parallel} = -1.49\,\text{Å}^{-1}$ was taken with $E_{\text{kin}} = 8$ eV and $\theta_0 = 80^{\circ}$.

that there are small but noticeable differences between the dispersions of the different films. Although there is some scattering in the data, a clear tendency is visible that the spin-wave energies are reduced for thinner films for wave vectors not too close to the surface Brillouin zone boundary. Close to the surface Brillouin zone boundary, the spin-wave energies are independent on the thickness within the error bars. As a comparison, the calculated dispersion relation of the surface mode of a 2 ML slab is added in Figure 11 as a dashed line. For this calculation, we used a value of $JS = 15$ meV, again. For intermediate wave vectors, the calculated spin-wave energies for the 2 ML slab lie below that for an 8 ML slab (or the semi-infinite crystal). At the surface Brillouin zone boundary, however, both curves meet. This behavior describes the experimental findings very well. Although JS is the same, the calculated dispersions are different because of the surface localization of a surface spin-wave mode and the reduced thickness of the slab. The surface localization increases with increasing wave vector of the spin waves. In the nearest-neighbor Heisenberg model, the spin wave is completely localized in the surface layer at the surface Brillouin zone boundary. Since the interactions in the model are limited to the nearest neighbors, it does not make any difference for $\overline{X}$ whether the film is only 2 ML thick or semi-infinite. For lower wave vectors, the spin wave is less localized at the surface and therefore the absence of magnetic atoms below the second layer in the slab configuration reduces the spin-wave energy.

A compact representation of the main results on spin-wave excitations obtained by SPEELS measurements is a contour plot of the measured intensity of the spin waves as a function of the wave vector and energy transfer. Figure 12 shows such a contour plot of the spin-wave losses obtained from the spectra shown in Figure 9 that were measured on 8 ML fcc Co on Cu(001). The plotted intensities show the difference of the $I_{\downarrow}$ and $I_{\uparrow}$ spectra after the subtraction of the electron–hole pair background. Here, the lines connect points of equal spin-wave intensities in energy and wave-vector space. They are interpolated linearly between the measured points. The underlying grid represents the density of the measured data points.

The contour plot allows one to follow how the spin-wave excitations evolve in the spectra with increasing wave-vector transfers. For low wave vectors, the spin-wave losses start as an intense and relatively narrow feature and they end as low intensity broad humps at high wave vectors. The dispersion derived from the nearest-neighbor Heisenberg model for $JS = 15$ meV is added as a solid line in Figure 12. As already shown, this dispersion matches the measured dispersion well (compare also Figure 11). Deviations between the

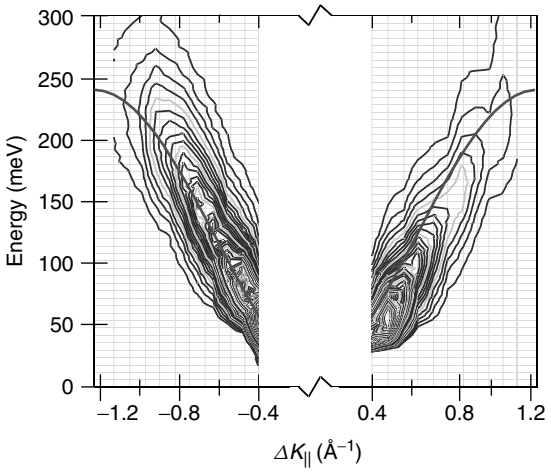

Figure 12. Contour plot of the spin-wave intensities measured by SPEELS. The graph represents the difference spectra measured on 8 ML Co on Cu(001) from which the background of electron–hole pair excitations were subtracted. The original spectra were shown in Figure 9. The contour lines connect points of the same intensity. Between the measured points, the intensity was linearly interpolated. The density of the measured data is illustrated by the underlying grid. Between adjacent dark (light) gray contour lines the intensity changes by 200(1000) counts/second. The outermost contour line marks the intensity of 200 counts per second. The thick solid line represents the surface spin-wave dispersion derived from the nearest-neighbor Heisenberg model for $JS = 15$ meV (see also Figure 11).

experimental data and the calculated dispersion occur mainly for high wave vectors on the negative wave-vector side. In this region, these deviations can be partially attributed to the underestimation of the (subtracted) background of electron–hole pair excitations by the fitting routine (see also Figure 7).

One should note that the interpretation of this graph is rather difficult. For example, the excitation mechanism of the creation of a spin wave by an electron is not fully understood. Therefore, the drop of the spin-wave intensity for higher wave vectors can be related to either a drop of the excitation probability or a drop of the spin-wave intensity itself. As discussed later in more detail, there are arguments to assume the drop to be mainly caused by the scattering process. The unknown excitation process also leads to the difficulty that spectra taken at different scattering conditions cannot be transformed into each other. Therefore, in the graph shown in Figure 12, only spectra are presented which were taken with the same E_{kin} and θ_0. Nevertheless, Figure 12 gives a good summary of the results obtained by the SPEELS measurements.

Also, in the SPEELS measurements on hcp Co on W(110), the spin-wave loss feature shows a well-defined dispersion. As visible in Figure 7, the spin-wave energies at $\Delta K_{\parallel} = 0.78\,\text{Å}^{-1}$ are similar for both the hcp and the fcc Co phase. At higher wave vectors, however, a significant difference between the two spin-wave dispersions occurs. This is illustrated in Figure 13 in which the measured spin-wave dispersions for 8 ML fcc Co and 8 ML hcp Co are plotted together with the measured spin-wave width in both systems. Owing to the different crystallographic orientations in which the spin waves are measured the dispersion relations are different in both cases. The calculated dispersion relation for the hcp crystal within the nearest-neighbor Heisenberg model for the surface mode of a semi-infinite crystal along $\overline{\Gamma} - \overline{K}$ is

$$E_{\mathrm{sw}}(Q_{||}) = \frac{16}{3} JS \left[3 - \cos(a_0 Q_{||}) - 2\cos\left(\frac{a_0 Q_{||}}{2}\right)\right] \quad (7)$$

This dispersion relation has been fitted to the measured data. The result is added as a black line in Figure 13(a). From the fit of the dispersion, we obtain a value of $JS = 14.8 \pm 1\,\text{meV}$. The agreement between the experimental data and the Heisenberg model is again fairly good. The value of JS is similar to the value obtained from the dispersion in fcc Co on Cu(001). We can conclude that the differences in the spin-wave energies in the two dispersions measured on fcc and hcp Co are due to the different crystallographic directions in which the spin-wave energies are measured, whereas the strength of the exchange coupling is similar in both crystallographic lattices. The fact that the value of JS is similar in both cases is not necessarily expected since the crystal structure is different and the nearest-neighbor distance is slightly changed (2.55 Å for fcc Co and 2.51 Å for hcp Co). The value of JS obtained from Co on W(110) is again in relatively good agreement to neutron scattering experiments performed on bulk hcp Co (Perring, Taylor and Squires, 1995) as discussed later.

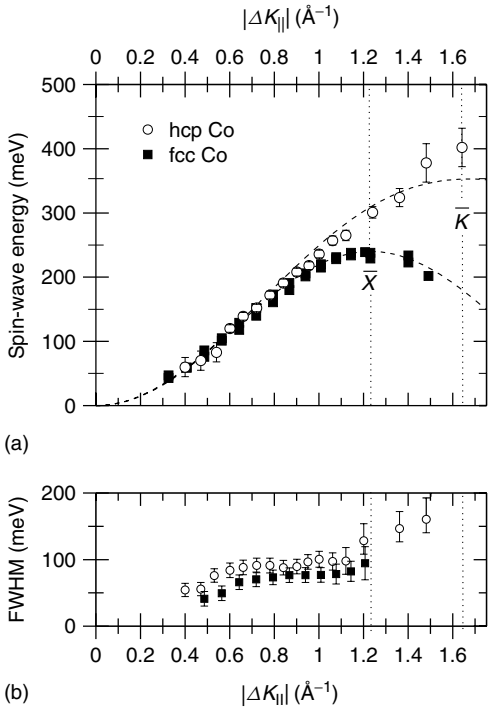

Figure 13. (a) Spin-wave dispersion of 8 ML Co on W(110) measured by SPEELS. The solid line represents a fit to the data with the dispersion of the surface mode of a semi-infinite crystal calculated within a nearest-neighbor Heisenberg model (see text for details). For comparison, data obtained for 8 ML fcc Co on Cu(001) is also plotted. The surface Brillouin zone is marked for both systems. In (b), the width of the spin-wave peak obtained from the SPEEL spectra for both fcc and hcp is given. The width has been corrected for the finite energy resolution of the spectrometer. The large error bars for the highest wave-vector transfers are caused by the low spin-wave intensities in the SPEEL spectra in this region. The low intensity is due to the combined effect of a drop of the excitation probability with both larger E_{kin} and higher wave-vector transfer as discussed later.

In addition to the spin-wave energies, the spin-wave width obtained from the measurements is plotted in Figure 13(b). The width is rather large and has a similar behavior as a function of the wave vector in both cases. The width measured for hcp Co is larger by about 15 meV compared to the width for fcc Co at each wave vector. One can speculate about possible reasons for this increased width. It may result from the different electronic structure, the crystalline quality, or the influence of the substrate. Since, for high wave vectors,

surface spin waves are largely confined in the topmost layers, the influence of the substrate should be rather small for an 8 ML thick film. In addition, we found a very similar spin-wave width for 3 (not shown) and 8 ML Co films on W(110) which suggests that the effect of the substrate may not to be the dominating contribution in this case. Instead, it could well be that the substantially larger amount of crystalline imperfections in hcp Co on W(110) causes an enlarged damping and thus a larger spin-wave width (Etzkorn *et al*., 2005).

2.2 SPEELS measurements of 3 ML Fe on 1 ML Co on Cu(001)

In addition to the studies of spin waves in the two crystallographic orientations of cobalt, we have also examined spin waves in another ferromagnet that is iron. Here, we shortly mention a study of spin waves in Fe on Cu(001). This system is of particular interest in the field of magnetism in thin films, because it has the tendency to be antiferromagnetic for ultrathin films (Li *et al*., 1994; Ellerbrock *et al*., 1995; Keavney *et al*., 1995). Fe is stabilized on Cu(001) in a strongly, rather complex tretragonal distorted lattice below thicknesses of about 12 ML (Thomassen *et al*., 1992; Müller *et al*., 1995; Biedermann, Tschelieβnig, Schmid and Varga, 2001). In the low-thickness regime, up to 3 ML, the Fe orders ferromagnetically, but above, a more complex magnetic order is observed. Above 12 ML thickness, the Fe retains a bulk like bcc phase and also the magnetic properties are bulk like (Thomassen *et al*., 1992).

Ultrathin Fe layers grown on Cu have their easy axis of magnetization perpendicular to the surface plane (Thomassen *et al*., 1992; Li *et al*., 1994). The projection of the spin of the incident electrons onto the magnetization direction for a perpendicularly magnetized sample would be zero in the SPEELS experiments. To exploit the defined spin direction of the incident electron, the easy axis of magnetization of the system must be brought into the surface plane. For that reason, we grew the Fe films on a Cu(001) substrate predeposited with 1 ML Co. This switches the easy axis of

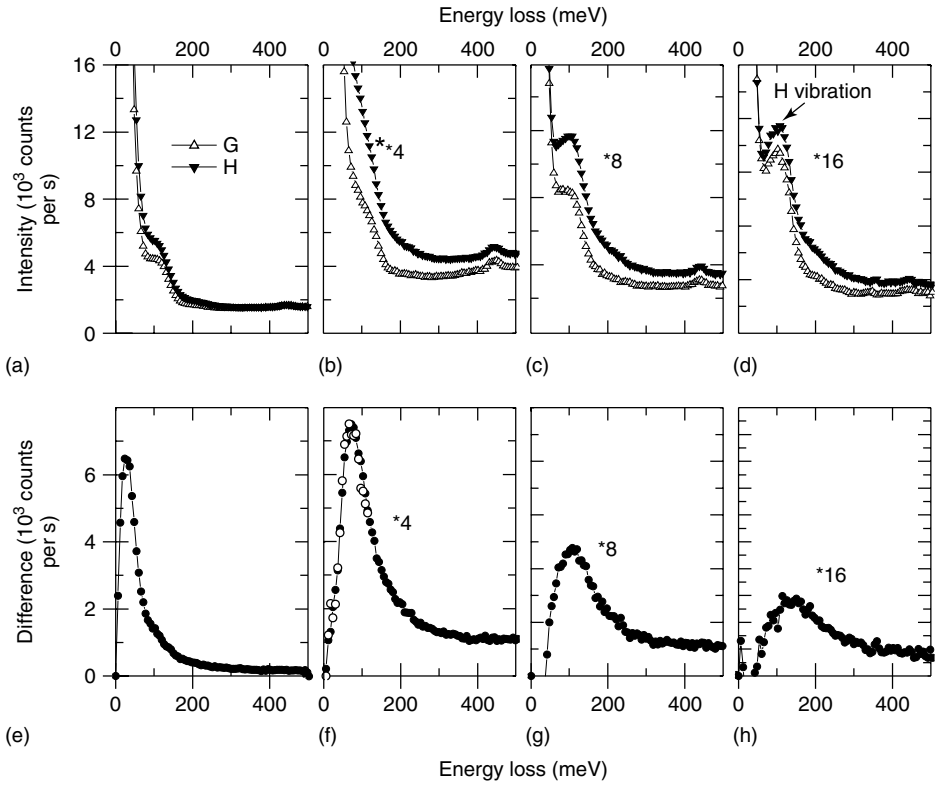

Figure 14. SPEEL intensities and difference spectra measured on 3 ML Fe on 1 ML Co on Cu(001). The wave-vector transfers were 0.5 Å^{-1} (a/e), 0.81 Å^{-1} (b/f), 1.03 Å^{-1} (c/g), and 1.17 Å^{-1} (d/h), respectively. The measured intensity has been multiplied by the number marked in each spectrum. The dominating loss feature in the intensity spectra itself is a vibrational excitation of H. In the difference spectra, however, the spin-wave loss peak is still prominently visible. The difference spectra are calculated as $I_\downarrow - \alpha I_\uparrow$, where α is a weighting factor that is chosen so that the difference vanishes at 0 meV loss energy (see text for details). Spectra have been recorded with $E_{\text{kin}} = 7$ eV, $\theta_0 = 90^\circ$, and an energy resolution of 38 meV.

magnetization of the entire film into the surface plane along a [110] direction but leaves all other properties of the film nearly unchanged (O'Brien and Tonner, 1995; Torija, Pierce and Shen, 2001).

In Figure 14(a–d), the energy loss spectra measured on 3 ML Fe on 1 ML Co on Cu(001) are shown for different wave-vector transfers. The spectra are dominated by contributions of the vibrational excitation of H at about 120 meV loss energy. By exploiting the spin-dependent excitation process of spin waves and calculating the difference of $I_\downarrow$ and $I_\uparrow$, the H contribution vanishes and one still finds a quite pronounced spin-wave feature. The spin-wave energies in this system are rather low and the low-energy side of the spin-wave loss feature might be influenced by spin dependent contributions of the elastic peak. To reduce the influence of these contributions to the difference spectra, the difference has been calculated as $I_\downarrow - \alpha I_\uparrow$. Here, α is a weighting factor which was chosen so that the difference vanished for 0 meV loss energy. For all spectra shown α is a number close to 1, since the spin dependent contributions to the elastic peak are rather weak in these spectra. To ensure that the spin-wave feature in the difference spectra are not altered by remaining contributions of the elastic peak, we have performed measurements with increased energy resolution (23 meV compared to 38 meV). The difference spectra obtained from these high-resolution measurements at 0.81 Å^{-1} are also included in Figure 14(f) as open circles. They have been scaled to match the intensity at the spin-wave maximum. It is obvious from the agreement of the two shapes that the spin-wave loss feature is well resolved at least for wave-vector transfers above 0.81 Å^{-1}.

One can also see that the spin-wave loss feature in this system is very broad and not of Gaussian peak shape. The FWHM of the spin-wave loss peaks are about the same as the spin-wave energy at each wave vector.

The spin-wave dispersion and also the width of the spin-wave loss peak measured on 3 ML Fe film on 1 ML Co on Cu(001) is shown in Figure 15. For this system, the experimental dispersion curve cannot be fitted well by the Heisenberg model using only one value of JS for the entire Fe film. If we assume, however, that the exchange-coupling constant at the surface layer (J_1) is enhanced by a factor of 2, with respect to the J in the interior of the film, the spin-wave mode of the (modified) nearest-neighbor Heisenberg model fits quite well the experimental data with a value of $JS = 5.8$ meV (thick solid line in Figure 15) (Vollmer *et al*., 2004b,c). Such an increased J_1 at the surface is generally expected from theoretical calculations for many magnetic films (Pajda *et al*., 2000; Razee, Staunton, Szunyogh and Györffy, 2002). The experimentally measured results for the Fe film on 1 ML Co on Cu(001) are compatible with theoretical expectations, while for the Co

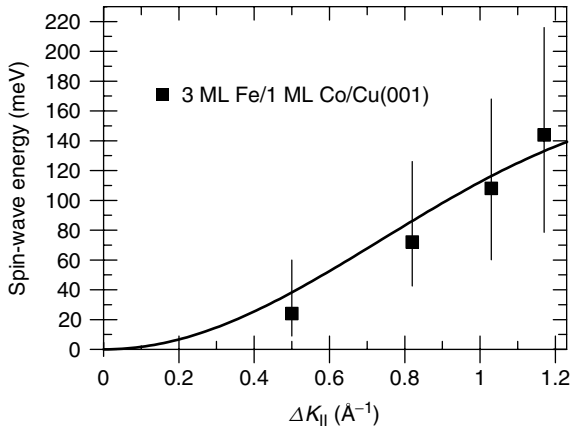

Figure 15. The spin-wave dispersion of the spin waves measured on 3 ML Fe on 1 ML Co on Cu(001). The vertical lines represent the energy range for which the spin-wave peak intensity is larger than half of its maximum intensity. The solid line is a dispersion calculated with a modified Heisenberg model (see text for details).

films, a strongly increased J_1 is in disagreement with the description of the measured dispersion using the Heisenberg model. The large width of the spin-wave excitation in the Fe indicates an extremely strong damping of this excitation, as discussed in more detail in the next section. It might well be that for such a drastic damping in this system the Heisenberg model fails to describe the properties of spin waves. Independent of the model describing the measurements the data show that the spin-wave energies are significantly reduced compared to results from bulk Fe. This reduction can be seen in the spin-wave stiffness of about $D = 150 \pm 10$ meVÅ^2 that can be estimated from our data of the tetragonally distorted Fe. This is much lower than the spin-wave stiffness of 260–280 meV Å^2 measured for bulk bcc Fe (Mook and Nicklow, 1973; Yethiraj *et al*., 1991). The reduction is much stronger than what can be estimated to result from reduced thicknesses or surface mode properties (compare Figure 11). Thus, it may be attributed to the differences in the exchange interaction of the two crystalline phases of Fe.

The spin-wave loss features measured by SPEELS have been typically measured with a low kinetic energy of the incident electrons (typically $E_{\text{kin}} < 10$ eV). At this energy, the spin-wave peaks are relatively intense in the measured spectra. The measured spin-wave intensity, however, strongly depends on the E_{kin}. This is illustrated in Figure 16 for the three systems that have been presented, fcc Co, hcp Co, and Fe on Co/Cu. The key feature in these graphs is the strong enhancement of the spin-wave intensities below $E_{\text{kin}} = 10$ eV. At these low primary energies, the intensity of the spin-wave signal is enhanced by more than an order of magnitude. This enhancement allows the clear detection

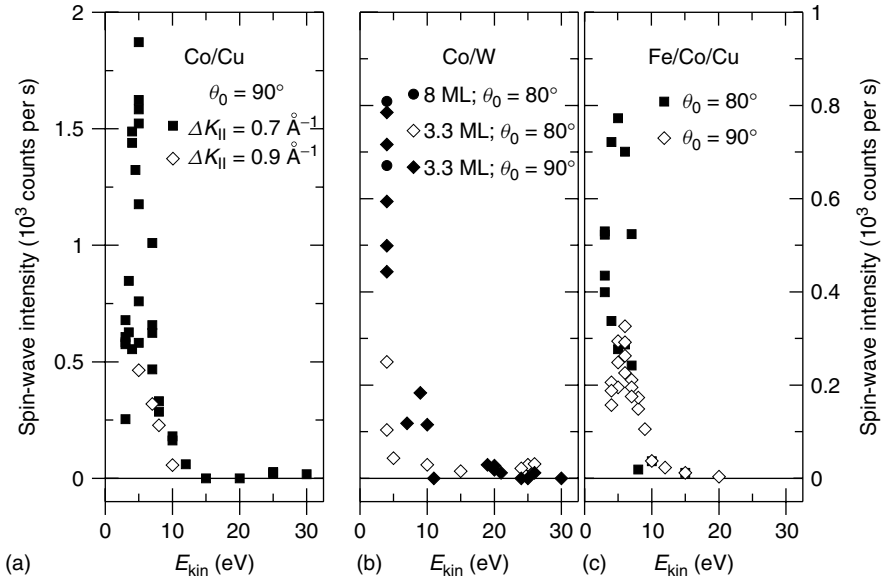

Figure 16. The spin-wave intensity in the SPEEL spectra strongly depends on the kinetic energy of the incoming electrons E_{kin}. In (a), the spin-wave intensity of 8 ML Co on Cu(001) as a function of E_{kin} is given. The solid points are for measurements with $\Delta K_{\parallel} = 0.7\,\text{Å}^{-1}$ and the open symbols for $\Delta K_{\parallel} = 0.9\,\text{Å}^{-1}$. In all measurements shown here, $\theta_0 = 90^{\circ}$. In (b), the data of 8 ML (circles) as well as of 3.3 ML Co on W(110) (diamonds) are shown. Here the measurements were carried out with $\Delta K_{\parallel} = 0.88\,\text{Å}^{-1}$ and with two different θ_0. In (c), the data for 3 ML of Fe grown on 1 ML Co on Cu(001) is given. Here the measurements were carried out with $\Delta K_{\parallel} = 0.81\,\text{Å}^{-1}$ at two different θ_0.

of the spin-wave loss features. Though this enhancement is crucial for the experimental results, its origin is not completely understood. It is, however, presumably caused by the energy dependence of the exchange scattering process. One should note that the measured spin-wave intensities shown in Figure 16 are influenced by both the cross section of the scattering event and the transmission function of the spectrometer. The latter is difficult to take into account precisely because it depends on the potentials applied to the spectrometer (about 40 different potentials) that will be optimized for each scan and thus change. The data shown in Figure 16 have a relatively large scatter, which we mainly attribute to these differences in the optimization of the potentials applied to the spectrometer.

The absolute intensity also depends on the scattering geometry, for example, on the scattering angle θ_0. The enhancement of the spin-wave intensities at low primary energies of the incoming electrons, however, is similar in all three cases shown.

3 DISCUSSION

In the following section, the results presented in the last section are discussed in more detail. We try to extract some of the fundamental magnetic properties of the materials investigated. Later, the results are compared to the experimental data obtained by other techniques and discussed in the light of recent theoretical calculations.

In the last section, we have seen that the spin-wave intensity depends strongly on E_{kin}. To discuss possible underlying reasons, we compare the results to theoretical predictions. The interaction that allows excitation of a spin wave in an electron scattering event is the exchange interaction (Feder, 1985). The probability of an exchange process is known to decrease with increasing incident electron energy (Hopster, Raue and Clauberg, 1984; Kirschner, 1985b). Mills and Hong have calculated the spin dependent inelastic mean free path in ferromagnetic metals. They have explicitly considered exchange processes that lead to the excitation of electron–hole pairs and of spin waves (Hong and Mills, 1999, 2000b). In their calculations, they found a strong increase in the probability of exchange processes for minority electrons at low incoming electron energies. The calculations predict, however, that exchange processes of electrons with energies higher than 5 eV above E_{F} (that is equivalent to $E_{\mathrm{kin}} \approx 0\,\text{eV}$ in our experiments) lead almost exclusively to Stoner excitations. In other words, in these calculations, the spin-wave excitations are probable only for primary energies lower than the work function. This energy regime is not accessible in the SPEELS experiments. Thus, the probability of exciting a spin wave by exchange processes is

underestimated in the theoretical predictions. The general finding of enhanced spin-wave intensities at low E_{kin}, however, is in agreement with the energy dependence of the exchange processes.

In many of the spectra shown, the spin-wave intensities and therefore the observed probability of an electron to scatter from a spin wave was rather large. Typically, the measured spin-wave intensities were of the order of a few hundred to a few thousands of counts per second (see Figure 7). As has been shown by the normalized intensity scale (e.g., in Figure 9), the intensity of the spin-wave signal is typically of the order of a few percent of the intensity of the elastic peak. The total background intensity can be calculated by integrating the background signal over the entire energy range up to the incident electron energy. One finds that the total background intensity is of the same order of magnitude as the intensity of the elastically scattered peak. Therefore, in each measured $I_{\downarrow}$ spectrum about one electron out of 100–1000 detected electrons was scattered from a spin wave. For the moment, we assume that a similar relation holds over the entire wave-vector range. For metals, typically a few percent of the incoming electrons are reflected from the sample. Using these assumptions, we can estimate the probability that an incoming electron of minority character is inelastically scattered by exciting a spin wave to be about 10^{-4}. This estimation should be seen as an upper limit. It will overestimate the scattering probability, because close to the specular condition, other scattering mechanisms play an important role, which will suppress the relative spin-wave intensities. The estimation is also only valid for low primary energies of the incoming electrons. As already shown, at other primary energies, we observed orders of magnitude lower excitation probabilities (see Figure 16).

Another point directly visible from the spectra or from the contour plot shown in Figure 12 is that the measured spin waves are rather broad. For high wave vectors, the ratio of the spin-wave energy to the spin-wave width is about two to three for Co and about one for Fe. This is in agreement with the behavior expected for high wave-vector spin waves in itinerant systems, especially at surfaces (Tang, Plihal and Mills, 1998; Muniz and Mills, 2002). As has been shown, for example, in Figure 7, it is possible to fit the spin-wave loss feature measured on Co by one single broad peak of Gaussian shape. If one assumes that the total width of the spin-wave loss feature is reflecting the damping of a single mode, it is straightforward to calculate, for example, the lifetime of these spin waves. Within this approximation, the behavior of the spin-wave excitations in real space and time can be calculated from the measured spectra by a two-dimensional Fourier transformation: from wave vector to real space and from energy to time. One example for spin waves with $\Delta K_{\parallel} = 0.81\,\text{Å}^{-1}$ measured on 8 ML fcc Co is shown in Figure 17. For the calculations, we assumed a Gaussian peak shape in energy and wave-vector space. The decay in time and space is inversely proportional to the width of the spin wave in energy and wave-vector space. For the example shown in Figure 17, the amplitude of the spin wave in real space drops to e^{-1} of its initial value after about ≈15 Å, only. Since the wavelength is about 8 Å, the spin wave is already damped out after a few oscillations. The lifetime of the spin wave is also short, about 30 fs. From the dispersion, the group velocity v_{G} and the phase velocity v_{P} of the excitation can be calculated by $v_{\mathrm{G}} = (\mathrm{d}E/\mathrm{d}q)$ and $v_{\mathrm{P}} = (E/q)$. For fcc Co at $\Delta K_{\parallel} = 0.81\,\text{Å}^{-1}$, one obtains the values of $v_{\mathrm{G}} \approx 40\,\mathrm{km\,s^{-1}}$ and $v_{\mathrm{P}} \approx 39\,\mathrm{km\,s^{-1}}$. Owing to the similar group and phase velocity and the short lifetime of the spin wave, the spin wave spreads only little in space. By multiplying v_{G} with the lifetime, the distance by which the center of gravity of the spin wave travels can be estimated; it is about 12 Å (Figure 17). Therefore, the high wave-vector spin waves in Co are highly confined in time and space owing to the strong damping and, thus, they are not the well-defined long-living excitations discussed in the introduction. We note in passing that the above-mentioned ratio of the spin-wave energy to the spin-wave width measured for Fe by the same arguments comes from a spin wave that is already damped out after its first oscillation. With this information on lifetime and propagation speed, we may estimate the linear phase

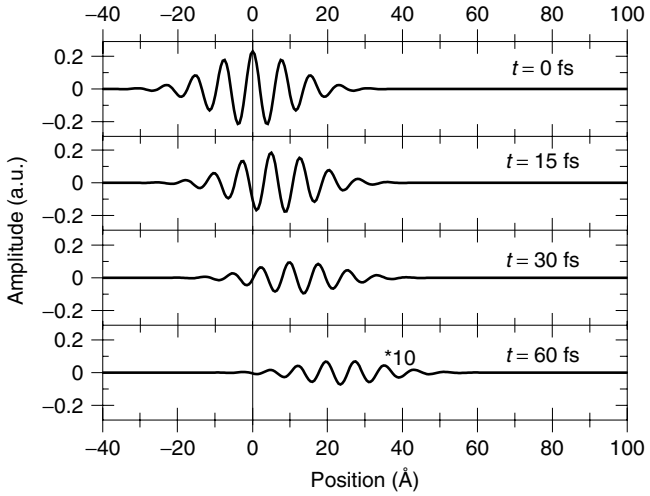

Figure 17. Classical representation of the spin-wave amplitude in real space and time obtained from a Fourier transformation of the wave vector/energy data (see text for details). The graph represents spin-wave data measured with $\Delta K_{\parallel} = 0.81\,\text{Å}^{-1}$ on fcc Co. The spin wave is created at time $t = 0$ and $x = 0$. Its decay length in space is about 15 Å. The decay time is about 30 fs. Note that the amplitude for the curve at $t = 60$ fs has been multiplied by 10.

space of these elementary excitations in terms of time–space coordinates. We find a value of roughly 10×10^{-24} sm, a remarkably small value!

This does not, of course, mean that we obtain this kind of experimental resolution in space and time with our method. It just says that we are able to study objects that are extremely confined in time and space using a method that works in wave vector and energy space. Conversely, this means, for example, for the spatial coordinate, that the high-energy spin-wave characteristics will not change significantly if we measure them on an 'infinite' thin film or on nanoscale islands with a diameter of a few nanometers. Together with the high surface sensitivity of electron scattering, SPEELS may thus be an appropriate tool to study elementary excitations in nanoscale magnets.

3.1 Comparison between the SPEELS data and other experimental results

In the following, the results of this work are compared to other experimental investigations of spin waves. Since SPEELS is a new technique to study spin waves and explores spin waves in a region, which has not been accessible by other techniques, a direct comparison is difficult. INS is the only technique, which allows the study of a similar wave-vector range as the one investigated by SPEELS. Thus, the following comparison will mainly focus on the results obtained by INS. The measurement of spin-wave excitations with high wave-vector transfers by INS is not an easy task in 3d ferromagnets, because of the high spin-wave energies in these systems. Therefore, only a few INS studies have been made.

In the case of fcc Co, which is not stable in bulk at room temperature, no INS experiments that examine very high wave-vector spin waves have been published. One way to compare the results of the low wave-vector transfer regime studied by INS with our data is to use the nearest-neighbor Heisenberg model. The value of JS derived from neutron scattering on bulk fcc Co (using crystals with 8 and 6% Fe) is $JS = 14.7 \pm 1.5$ meV (Sinclair and Brockhouse, 1960; Pickart *et al*., 1967). This is in excellent agreement with the value of $JS = 15 \pm 1$ meV obtained by SPEELS. To illustrate the results of these two experiments, Figure 18(a) shows the dispersion measured by INS (Sinclair and Brockhouse, 1960) and by SPEELS for fcc Co. One should note that strictly speaking the wave-vector axis shows a three-dimensional wave vector in the case of INS whereas it is two dimensional for the SPEELS measurements. Since the SPEELS measurements are dominated by the excitation of surface spin waves (with $q_\perp = 0$); however, both can be compared. To connect the different wave-vector transfers the solid and the dashed lines in Figure 18(a) display the dispersion calculated with the nearest-neighbor Heisenberg model for the surface and the bulk mode, respectively. The values of JS used are the ones given in the publications Sinclair and Brockhouse (1960) and Vollmer *et al*. (2003). The surface and the bulk mode have a different dispersion for similar values of JS (compare Figure 5); however, for the wave-vector range measured by INS the spin-wave energies are very similar in both cases.

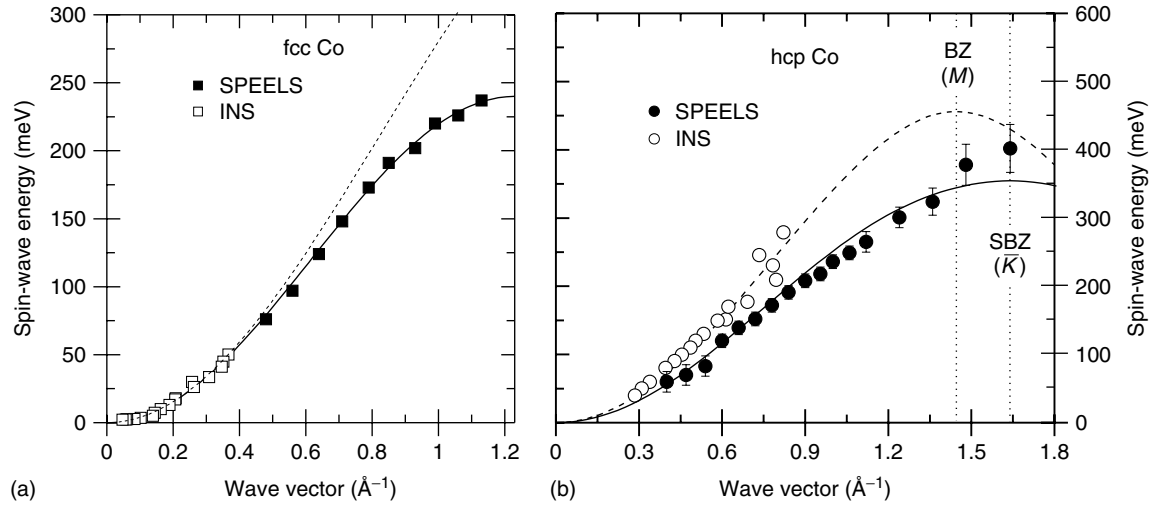

Figure 18. Comparison of the spin-wave dispersions measured with SPEELS (solid symbols) and INS (open symbols) for fcc (a) and hcp (b) Co. The solid and dashed lines are dispersions calculated with the nearest-neighbor Heisenberg model for the surface and the bulk mode of the specific crystals, respectively (for details see text). The vertical dotted lines in (b) mark the two (surface) Brillouin zone boundaries for the specific directions measured. The INS data are taken from Sinclair and Brockhouse (1960) in the case of fcc Co and from Perring, Taylor and Squires (1995) in the case of hcp Co. (Reproduced from Perring *et al*., 1995. © 1995 with permission from Elsevier.)

For bulk hcp Co, only one publication exists, to our knowledge, in which the spin-wave dispersion was measured up to the very high wave-vector transfers (Perring, Taylor and Squires, 1995) (see also Figure 4). In the neutron measurements, the dispersion of the bulk spin-wave mode was obtained along $\Gamma - M$ (Perring, Taylor and Squires, 1995) whereas in the SPEELS data the spin-wave dispersion of the surface mode is measured along $\overline{\Gamma}$-$\overline{K}$. These are the two different high symmetry directions in the basal plane. Figure 18(b) shows the results of both measurements and also indicates the different Brilluoin zone boundaries (vertical lines) of both cases. The spin-wave energies measured by INS are higher than the one measured by SPEELS. To compare the two different modes along the different directions in more detail, we use the nearest-neighbor Heisenberg model, again. A fit of the neutron data with the bulk dispersion yields a value of $JS = 19.2 \pm 0.6$ meV (Perring, Taylor and Squires, 1995) (dashed line in Figure 18b). For the SPEELS data we obtain $JS = 14.8 \pm 1$ meV (solid line) (Etzkorn *et al*., 2005). Within the Heisenberg model, it is also possible to estimate the influence of the different crystallographic directions on the spin-wave dispersion. In the case of an isotropic exchange (this seems to be a reasonable approximation, because the basal plane has a sixfold symmetry and even in fourfold symmetries the anisotropy in the exchanges are typically very small (Mook and Nicklow, 1973)), no drastic changes in the dispersion in any direction within the basal plane are expected for the wave-vector range investigated by INS. Also the bulk and surface modes are at similar energies at these wave-vector transfers. Therefore, within the Heisenberg model the differences between the two data sets are mainly caused by the differences in *JS*. One could speculate about possible reasons for this deviation, like the different properties of thin films and bulk Co. Considering the differences in the two experiments, however, in our view the agreement is rather satisfying. One should note that even within the results obtained by different INS studies on hcp Co (typically for lower wave vectors) the observed values for *JS* range from 17.3 to 20.2 meV (Perring, Taylor and Squires, 1995 and references therein).

Another point that is worth mentioning is the amount of Co used in the experiments to detect spin-wave losses. In the case of INS measurements, about 100 g of single crystalline Co was used to obtain the data shown in Figure 4. As we have seen, high wave-vector spin waves can be studied by SPEELS on a few atomic layers of Co. The electron beam used in the experiments has a lateral extension of about 1 mm^2. Therefore, the amount of material scattered from is about a factor of 10^{10} different between both experiments. For much lower wave vector and energy transfers, it is possible to reduce the amount of material needed in INS drastically. One example is the work of Schreyer *et al*. (2000). They have studied spin waves using only about 10 mg Dy. Nevertheless, this amount of material is still higher by a factor of 10^6 compared to the SPEELS experiments.

By BLS and FMR, the exchange stiffness *D* can be measured in magnetic films. Within the nearest-neighbor Heisenberg model, one can determine *JS* from *D* (see equation (6)). Liu and colleagues performed BLS measurements on about 100-nm-thick Co films of different crystalline structures (Liu *et al*., 1996). The authors found values of $JS = 17.9 \pm 0.6$ meV for fcc and $JS = 17.3 \pm 1.4$ meV for hcp Co. Therefore, in qualitative agreement with our data, no changes of *JS* were found for the different Co structures. The reported absolute values for *JS*, however, are higher than that obtained by SPEELS. Other BLS studies report values of $JS = 13.5 \pm 3$ meV (Vernon, Lindsay and Stearns, 1984) and $JS = 18.3 \pm 2.8$ meV (Grimsditch, Fullerton and Stamps, 1997). The low value reported by Vernon, Lindsay and Stearns (1984) was obtained by BLS measurements on polycrystalline films. In a FMR study also a low value of $JS = 13.5 \pm 0.7$ meV was measured on polycrystalline Co films (Tannenwald and Weber, 1961). One may speculate that these low values are related to the poor film quality. In general, the agreement between the BLS and FMR results and SPEELS data is fairly good, if one considers the difference in the order of magnitude of the investigated wave-vector range (about 2 orders of magnitude) and the uncertainty introduced by the Heisenberg model.

We emphasize again that we have compared surface spin waves to bulk spin waves and results obtained in very different wave-vector regimes. This comparison was made using the nearest-neighbor Heisenberg model. Within this model, fairly good agreement between all experimental results is observed, especially considering possible uncertainties introduced by the model. Typically, the deviations of the literature values to our experimental findings are of the same size as the deviations of literature values among themselves. Generally, the SPEELS values tend to lie slightly below the values obtained by other techniques.

3.2 Comparison to theoretical calculations

In the following, the results of the spin-wave excitations measured by SPEELS are compared to theoretical calculations. It is widely accepted that calculations using the adiabatic approximation may only give a crude estimate for high wave-vector spin waves in 3d ferromagnets (Tang, Plihal and Mills, 1998; Udvardi, Szunyogh, Palotás and Weinberger, 2003). Nevertheless, most calculations are performed within this approximation, because it is nontrivial to go further. Several recent *ab initio* calculations map itinerant magnetism on an

effective Heisenberg model to calculate the spin-wave dispersion. This allows a direct comparison between the calculated exchange-coupling constants and the experimental findings, as well as a comparison between the spin-wave dispersion relations. Because no damping is included in these theories, they must fail to predict the correct broad spectral shape of the spin waves observed experimentally. Calculations that examine spin-wave properties in thin films regularly obtain a strong enhancement of the exchange-coupling constant in the surface layer (see e.g., Pajda *et al*., 2000; Razee, Staunton, Szunyogh and Györffy, 2002; Costa, Muniz and Mills, 2004b). To the best of our knowledge, no calculations for thin hcp Co films have been published. Therefore, the discussion is limited to fcc Co. Pajda and coworkers found in their calculations an enhancement of the nearest-neighbor exchange-coupling constant for one ML Co on Cu(001) of about a factor of 2 compared to the bulk value (Pajda *et al*., 2000, 2001). In calculations by Razee, Staunton, Szunyogh and Györffy (2002), it was observed that this enhancement persists in the surface layer for Co films up to 7 ML thickness. Other exchange-coupling constants, as well as the magnetic moment, are also enhanced close to the surface (Razee, Staunton, Szunyogh and Györffy, 2002). These effects are, however, typically much smaller than a factor of 2. SPEELS seems especially suited to study such effects, because the energy of surface spin waves at high wave vectors strongly depends on the strength of the exchange coupling at the surface. As we have seen earlier, we are able to describe our measured dispersions for both fcc and hcp Co by a nearest-neighbor Heisenberg model using only one value of *JS* throughout the films and for all film thicknesses investigated. Within the description of the Heisenberg model, we therefore do not find any evidence for such an enhancement of the exchange-coupling constant at the Co surface.

As has been discussed in the last section, the spin-wave energies measured by SPEELS are typically slightly below those expected from measurements using other techniques. Following the above argument, we can bring our data in perfect agreement to other experimentally observed values of *JS* by assuming that the exchange-coupling constant is reduced at the surface. If the exchange-coupling constant at the surface is different from the bulk value, then our experimental findings on Co point in the direction of a reduction and not of an enhancement. It was also found that the spin-wave energy does not change for lower temperatures (Etzkorn *et al*., 2004). Hence, the difference between experimental values and theoretical expectations cannot be explained by temperature effects. The entire argumentation is, however, based on the nearest-neighbor Heisenberg model, which limits possible conclusions.

Since the theoretically predicted enhancement of the surface exchange is not observed in Co in the SPEELS experiments, it can be expected that the surface spin-wave energies are overestimated in the calculations that use an enhanced exchange interaction. Calculations of the spin-wave dispersions for bulk crystals do not consider the exchange coupling at surfaces. These calculated dispersions are typically in good agreement to the dispersion that we can calculate in the Heisenberg model using the values of *JS* obtained by SPEELS (Halilov, Eschrig, Perlov and Oppeneer, 1998; Pajda *et al*., 2001; Grotheer, Ederer and Fähnle, 2001).

This is illustrated in Figure 19 in which the dispersions for bulk fcc and hcp Co obtained from recent calculations using the adiabatic approximation are plotted. To compare the SPEELS results with these calculations, the bulk dispersions estimated from the nearest-neighbor Heisenberg model using a value of $JS = 15\,\text{meV}$ is shown as solid lines. Of course, the simple Heisenberg model does not allow a detailed comparison to these highly sophisticated calculations. The general agreement in the spin-wave energies is, however, very good, especially considering that the calculations were performed fully *ab initio*.

So far, the experimental results were compared to theories using the adiabatic approximation. It has already been discussed that this approximation is expected to fail for high wave-vector spin waves in the itinerant electron systems. As was pointed out by Mills and coworkers (Tang, Plihal and Mills, 1998; Costa, Muniz and Mills, 2004b; Muniz and Mills, 2002), the results from calculations within and beyond the adiabatic approximation can differ qualitatively as well as quantitatively.

In the case of Co, only a few theoretical publications are available which treat the spin-wave excitations within a nonadiabatic approach (Trohidou, Blackman and Cooke, 1991; Costa, Muniz and Mills, 2004a,b). All of them are based on an empirical tight binding description of the electronic structure, with parameters chosen by fitting to *ab initio* calculated electronic structures. One of the studies (Trohidou, Blackman and Cooke, 1991) has been performed for hcp bulk Co. The result of this study is that high wave-vector spin waves are significantly damped, as indicated by a broadening of the structures. Nevertheless, the spin-wave energies are similar to the energies which were calculated by theories using the adiabatic approximation (Halilov, Eschrig, Perlov and Oppeneer, 1998; Grotheer, Ederer and Fähnle, 2001). Two recent calculations have been performed for thin fcc Co films on Cu(001) (Costa, Muniz and Mills, 2004a,b). The calculated quantity in these publications is the layer-resolved spectral density of spin fluctuations as a function of the wave vector. The calculations by Costa, Muniz and Mills, (2004b) illustrated the changes in the spectra shape when the calculations were done within and beyond the adiabatic approximation. In the latter case, the spectral shape deviates strongly from the expectations

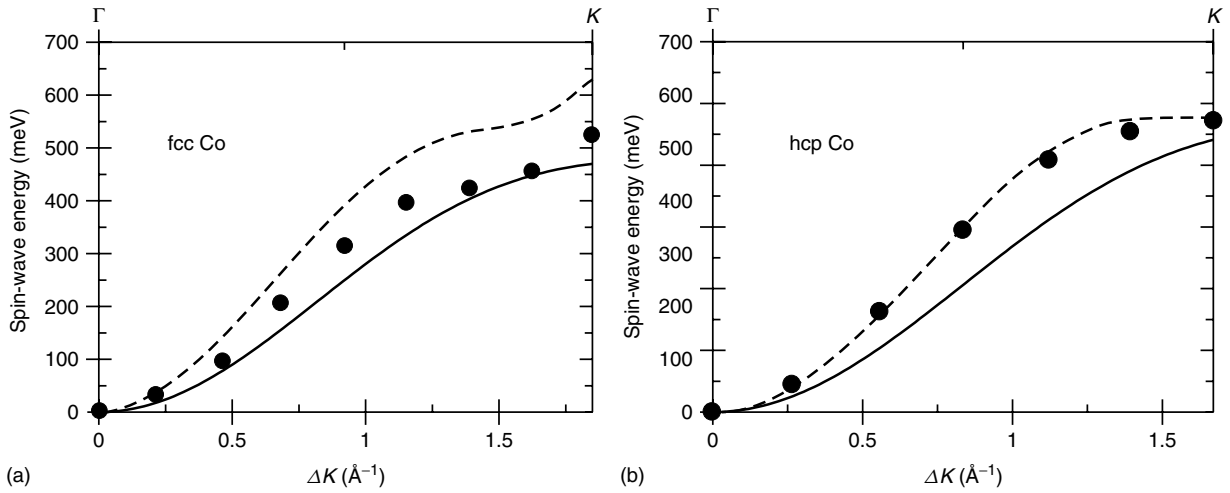

Figure 19. Comparison between the calculations of the spin-wave dispersion (dashed line and solid dots) for fcc (a) and hcp (b) Co using the adiabatic approximation and the estimated bulk dispersion from the SPEELS data using the nearest-neighbor Heisenberg model (solid line). In (a), the calculated data has been taken from Pajda *et al.* (2001) (dashed line) and Halilov, Eschrig, Perlov and Oppeneer (1998) (dots) (reproduced from Pajda *et al.*, 2001 and Halilov *et al.*, 1998, with permission from the American Physical Society. © 1998/2001) and in (b), from Grotheer, Ederer and Fähnle (2001) (dashed line) and Halilov, Eschrig, Perlov and Oppeneer (1998) (dots). (Reproduced from Grotheer *et al.*, 2001 and Halilov *et al.*, 1998, with permission from the American Physical Society. © 1998/2001.)

derived from a Heisenberg model except for very low wave vectors. For higher wave vectors, the spectral density in the nonadiabatic description consists of one single broad feature, instead of several discrete modes as expected from the Heisenberg model (see Figure 5). Only some structure in the broad feature reminds of these modes. This behavior is in qualitative agreement with the spectra measured by SPEELS and provides a quite natural explanation of the broad spin-wave loss features.

In Figure 20, the calculated spectral density in the surface layer for a wave vector of $\Delta K_{\parallel} = 0.85\,\text{Å}^{-1}$ is compared to the measured difference spectrum taken at about the same wave vector. The calculated spectral density has been shifted in the energy and scaled in the intensity axis to allow better comparison between the two shapes. These two shapes of the calculated and measured spectra are in promising agreement. One has to mention that the measured difference spectra cannot directly be related to the calculated spectral density. The calculation considers only the $e^{\downarrow\uparrow}$ spin channel. In the measured difference all spin channels contribute. This is expected to lead to differences especially concerning the background in the two cases. It is also important to mention that the calculated spectral density shown in Figure 20 is a quantity that is solely a property of the spin excitations and does not take into account the actual excitation process. This may lead to considerable effects in the calculated spectra. For example, it has been shown by Mills and coworkers (Plihal and Mills, 1998; Costa, Muniz and Mills, 2003) that the spectral weight of Stoner excitations measured by electron scattering is underestimated in the calculations. The high-energy shoulder in the calculations is slightly higher in intensity than the measured one. The effect is stronger for lower wave-vector transfers (not shown here) and may be attributed to the cross-section dependence of the spin-wave excitation. As has been mentioned by the authors, it is difficult to assign a particular spin-wave mode to a structure in the calculated spectral density (Costa, Muniz and Mills, 2004b). In these

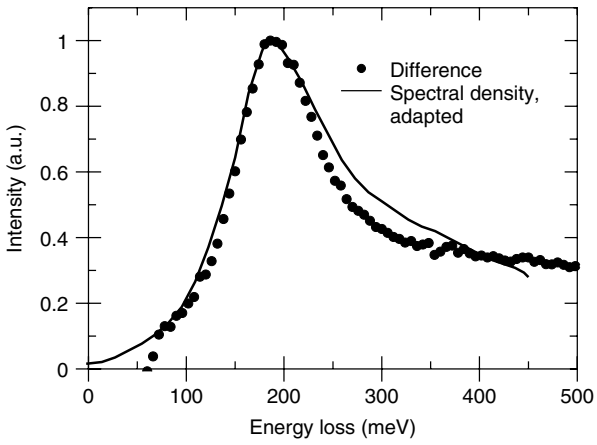

Figure 20. Comparison between the calculated spectral density in the surface layer taken from Costa, Muniz and Mills (2004b) (solid line) and the difference spectra measured by SPEELS (dots). For both, the wave vector was about $\Delta K_{\parallel} = 0.85\,\text{Å}^{-1}$. The calculated spectrum is shifted by 50 meV to lower energies and both quantities are normalized to one at their maximum. (Reproduced from Costa *et al.*, 2004b, with permission from the American Physical Society. © 2004.)

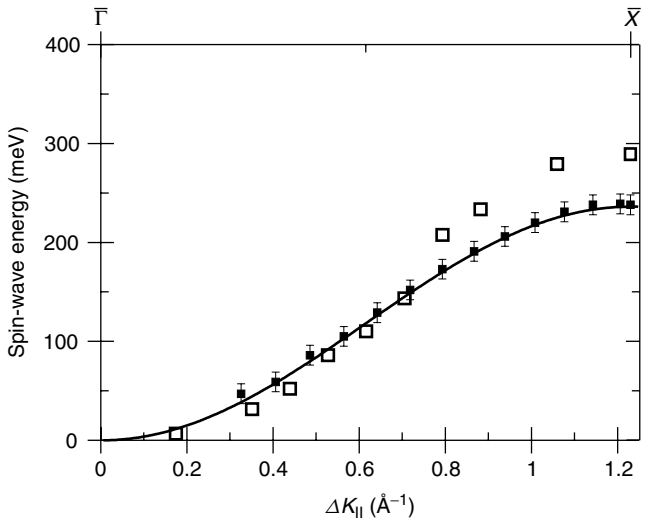

Figure 21. The dispersion obtained by the calculations of the spectral density taken from Costa, Muniz and Mills (2004b) (□) in comparison to the SPEELS data (■). Both results are for 8 ML Co on Cu(001). The open squares of the theoretically calculated dispersion mark the position of the maximum of the calculated spectral density. (Reproduced from Costa *et al*., 2004b, with permission from the American Physical Society. © 2004.)

calculations, however, the lowest energy features are always located in the surface layers. This indicates that a significant part of the low-energy spectral density within the surface layer can be attributed to what has been called a well-defined surface spin-wave mode in the Heisenberg model. Therefore, these calculations at least do not contradict the interpretation that the loss features measured by SPEELS are dominated by contributions of surface spin waves. The good agreement between the theoretical and the experimental results indicates that the effect of damping of spin waves by Stoner excitations seems to be taken into account correctly in the theory.

In addition to the spectral density, Costa, Muniz and Mills (2004b) have also calculated the dispersion of the spin waves. It was obtained by plotting the energy position of the maximum of the spectral density in the surface layer as a function of the wave vector. The resulting calculated dispersion and the dispersion measured by SPEELS are shown in Figure 21. The agreement between the two dispersions is rather satisfactory; however, as has been discussed in detail by Costa, Muniz and Mills (2004b), small changes in the choice of the tight binding parameters can change the calculated spin-wave energies by a factor of 2 (Costa, Muniz and Mills, 2004a,b). Thus, at the current stage of theory, it seems difficult to obtain precise predictions of the spin-wave energies. Here, full *ab initio* calculations going beyond the adiabatic approximation, as they have been done for the bulk (Savrasov, 1998), would be highly desirable for thin films.

4 CONCLUSIONS AND OUTLOOK

In this chapter, studies of high wave-vector spin waves in 3d-ferromagnets using inelastic spin-polarized electron scattering have been discussed. This technique allows a unique access to high-energy spin waves at surfaces. For the two investigated crystalline phases of Co (fcc and hcp) very similar spin-wave properties have been found. In both cases, the measured dispersions agree surprisingly well with the dispersion of surface spin waves calculated in a nearest-neighbor Heisenberg model. The value of the product of the exchange-coupling constant and the spin moment is similar ($JS \approx 15$ meV) in both phases. This value of JS is also in fairly good agreement with the results obtained by other experimental techniques. Although the dispersion relation agrees well with the expectations from the Heisenberg model that does not take the damping of spin waves into account, the measured energy loss features in the spectra have a large intrinsic width, which indicates a strong damping of these excitations. Indeed, recent calculations going beyond the adiabatic approximation, that is, consider the possible decay of spin waves into Stoner excitations, are in promising agreement with the measured spin-wave widths in the SPEEL spectra (Costa, Muniz and Mills, 2004b). In contrast to several theoretical predictions, no enhancement of the exchange coupling at the surface layer was measured in thin Co films.

For 3 ML Fe on 1 ML Co on Cu(001), the measured dispersion does not agree with the dispersion relation derived from the nearest-neighbor Heisenberg model, if only one value of JS for the entire Fe film was considered. The agreement can be improved considerably if an enhanced exchange coupling at the surface is taken into account. The spin-wave features in this system are, however, damped extremely strong (the ratio of spin-wave energy to spin-wave width is about 1). For such a large damping the Heisenberg model itself is expected to fail. The measured spin-wave energies in this strongly distorted Fe system are significantly smaller than that for bulk like Fe. Independent of any model description, this can only be explained by a strong reduction of the exchange interactions in the tetragonal distorted Fe phase compared to bcc Fe.

From the above-mentioned results, two other experimental approaches to study spin waves by inelastic electron scattering seem feasible. The use of a 'standard' non-spin-polarized EELS should to be possible. The higher energy resolution in such experiments may allow studying spin waves with much smaller energies. Owing to the high spin-wave intensities measured, also 'complete' experiments (in which the spin of both the incoming and the outgoing electron is determined) seem feasible. One of the interesting questions yet to be answered is whether inelastic electron scattering can also be

used to study other types of magnetic material, for example, antiferromagnets or rare-earth magnets. In addition, electrons as scattering particles to study spin excitations can be used not only by SPEELS but also, for example, by scanning tunnelling microscopy (STM). In fact, it has already been demonstrated that spin flip excitations of single atoms can be observed using STM (Heinrich, Gupta, Lutz and Eigler, 2004).

It is our hope that the results presented and discussed here stimulate further experimental and theoretical efforts in the field of elementary magnetic excitations at surfaces and in nanostructures.

ACKNOWLEDGMENTS

The authors dedicate this chapter to the memory of the late Rüdiger Vollmer, who has significantly contributed to the presented work on spin-polarized electron energy loss spectroscopy. During the short span of his scientific career, he has excelled in diverse areas of physics adding substantial knowledge to the physics of condensed matter.

We would like to thank H. Ibach for designing the SPEEL-spectrometer. In addition, we thank W. Tang and Y. Zhang for their continued help in running the experiment.

The authors would also like to acknowledge the enlightening and very helpful discussions with D.L. Mills, J. Henk, W. Wulfhekel, L. Udvardi, M. Munoz-Navia, B. Hillebrands, and B. Heinrich.

REFERENCES

Abraham, D.L. and Hopster, H. (1989). Spin-polarized electron-energy-loss spectroscopy on Ni. *Physical Review Letters*, **62**, 1157–1160.

Baibich, M.N., Broto, J.M., Fert, A., *et al*. (1988). Giant magnetoresistance of (001)Fe/(001)Cr magnetic superlattices. *Physical Review Letters*, **61**, 2472–2475.

Bass, J.M., Blackman, J.A. and Cooke, J.F. (1992). The role of the exchange matrix in the itinerant-electron theory of ferromagnetism. *Journal of Physics: Condensed Matter*, **4**, L275–L280.

Bechara Muniz, R., Cooke, J.F. and Edwards, D.M. (1985). Spin waves in ferromagnetic transition metals. II: iron and its alloys. *Journal of Physics F: Metal Physics*, **15**, 2357–2363.

Biedermann, A., Tschelieβnig, R., Schmid, M. and Varga, P. (2001). Crystallographic structure of ultrathin Fe films on Cu(100). *Physical Review Letters*, **87**, 086103-1–086103-4.

Binasch, G., Grünberg, P., Saurenbach, F. and Zinn, W. (1989). Enhanced magnetoresistance in layered magnetic structures with antiferromagnetic interlayer exchange. *Physical Review B*, **39**, 4828–4830.

Blackman, J.A., Morgan, T. and Cooke, J.F. (1985). Prediction of high-energy spin-wave excitations in iron. *Physical Review Letters*, **55**, 2814–2817.

Bloch, F. (1930). Zur theorie des ferromagnetismus. *Zeitschrift für Physik*, **61**, 206–219.

Bloch, F. (1932). Zur theorie des austauschproblems und der remanenzerscheinung der ferromagnetika. *Zeitschrift für Physik*, **74**, 295–335.

Brockhouse, B.N. (1957). Scattering of neutrons by spin waves in magnetite. *Physical Review*, **106**, 859–864.

Cooke, J.F., Blackman, J.A. and Morgan, T. (1985). New interpretation of spin-wave behavior in nickel. *Physical Review Letters*, **54**, 718–721.

Costa, A.T., Muniz, R.B. and Mills, D.L. (2003). Theory of spin excitations in Fe(110) multilayers. *Physical Review B*, **68**, 224435-1–224435-14.

Costa, A.T., Muniz, R.B. and Mills, D.L. (2004a). Theory of spin waves in ultrathin ferromagnetic films: the case of Co on Cu(100). *Physical Review B*, **69**, 064413-1–064413-5.

Costa, A.T., Muniz, R.B. and Mills, D.L. (2004b). Theory of large-wave-vector spin waves in ultrathin ferromagnetic films; sensitivity to electronic structure. *Physical Review B*, **70**, 54406-1–54406-8.

Cottam, M.G. and Slavin, A.N. (1994). Fundamentals of linear and nonlinear spin-wave processes in bulk and finite magnetic samples. In *Linerar and Nonlinear Spin Waves in Magnetic Films and Superlattices*, Cottam, M.G. (Ed.), World Scientific: Singapore, New Jersey, London, Hong Kong, Chapter 1.

DeWames, R.E. and Vredevoe, L.A. (1967). Electron-magnon scattering and polarization of the scattered beam. *Physical Review Letters*, **18**, 853–855.

Drescher, P., Andresen, H.G., Aulenbacher, K., *et al*. (1996). Photoemission of spinpolarized electrons from strained GaAsP. *Applied Physics A*, **63**, 203–206.

Edwards, D.M. and Bechara Muniz, R. (1985). Spin waves in ferromagnetic transition metals. I: general formalism and application to nickel and its alloys. *Journal of Physics F: Metal Physics*, **15**, 2339–2356.

Ellerbrock, R.D., Fuest, E., Schatz, A., *et al*. (1995). Mössbauer effect study of magnetism and structure of fcc-like Fe(001) films on Cu(001). *Physical Review Letters*, **74**, 3053–3056.

Etzkorn, M., Anil Kumar, P.S., Tang, W., *et al*. (2005). High-wave-vector spin waves in ultrathin Co films on W(110). *Physical Review B*, **72**, 184420-1–184420-6.

Etzkorn, M., Anil Kumar, P.S., Vollmer, R., *et al*. (2004). Spin waves in ultrathin Co-films measured by spin polarized electron energy loss spectroscopy. *Surface Science*, **566–568**, 241–245.

Feder, R. (1985). *Polarized Electrons in Surface Physics*, World Scientific: Singapore.

Frota-Pessôa, S., Muniz, R.B. and Kudrnovský, J. (2000). Exchange coupling in transition-metal ferromagnets. *Physical Review B*, **62**, 5293–5296.

Grimsditch, M., Fullerton, E.E. and Stamps, R.L. (1997). Exchange and anisotropy effects on spin waves in epitaxial Co films. *Physical Review B*, **56**, 2617–2622.

Grimsditch, M., Malozemoff, A. and Brunsch, A. (1979). Standing spin waves observed by Brillouin scattering in amorphous metallic Fe80B20 films. *Physical Review Letters*, **43**, 711–714.

Grotheer, O., Ederer, C. and Fähnle, M. (2001). Fast ab initio methods for the calculation of adiabatic spin wave spectra in complex systems. *Physical Review B*, **63**, 100401-1–100401-4.

Halilov, S.V., Eschrig, H., Perlov, A.Y. and Oppeneer, P.M. (1998). Adiabatic spin dynamics from spin-density-functional theory: applications to Fe, Co, and Ni. *Physical Review B*, **58**, 293–302.

Heinrich, A.J., Gupta, J.A., Lutz, C.P. and Eigler, D.M. (2004). Single-atom spin-flip spectroscopy. *Science*, **306**, 466–469.

Henzler, M. and Göpel, W. (1994). *Oberflächenphysik des Festkörpers*, Teubner Verlag: Stuttgart.

Herring, C. (1952). Energy of a bloch wall on the band picture. II. perturbation approach. *Physical Review*, **87**, 60–70.

Herring, C. (1966). In *Exchange Interactions Among Itinerant Electrons*, Volume IV of Magnetism, Rado, G.T. and Suhl, H. (Eds.), Academic Press: New York, London.

Herring, C. and Kittel, C. (1951). On the theory of spin waves in ferromagnetic media. *Physical Review*, **81**, 869–880.

Hillebrands, B. and Ounadjela, K. (2002). *Spin Dynamics in Confined Magnetic Structures*, *Topics in Applied Physics, Vol. 83*, Springer-Verlag: Berlin, Heidelberg, New York.

Hong, J. and Mills, D.L. (1999). Theory of the spin dependence of the inelastic mean free path of electrons in ferromagnetic metals: a model study. *Physical Review B*, **59**, 13840–13848.

Hong, J. and Mills, D.L. (2000a). Spin excitations in Ni: electrons and neutrons as a probe. *Physical Review B*, **61**, R858–R861.

Hong, J. and Mills, D.L. (2000b). Spin dependence of the inelastic electron mean free path in Fe and Ni: explicit calculations and implications. *Physical Review B*, **62**, 5589–5600.

Hopster, H. and Abraham, D.L. (1989). Spin-dependent inelastic electron scattering on Ni(110). *Physical Review B*, **40**, 7054–7058.

Hopster, H., Raue, R. and Clauberg, R. (1984). Spin-flip stoner excitations in a ferromagnet observed by inelastic spin-polarized electron scattering. *Physical Review Letters*, **53**, 695–697.

Ibach, H. (1993). Electron energy loss spectroscopy with resolution below 1 meV. *Journal of Electron Spectroscopy and Related Phenomena*, **64/65**, 819–823.

Ibach, H., Balden, M. and Lehwald, S. (1996). Recent advances in electron energy loss spectroscopy of surface vibrations. *Journal of the Chemical Society, Faraday Transactions*, **92**, 4771–4774.

Ibach, H. and Mills, D.L. (1982). *Electron Energy Loss Spectroscopy and Surface Vibrations*, Academic Press: New York, London, Paris.

Ibach, H., Bruchmann, D., Vollmer, R., *et al*. (2003). A novel spectrometer for spin-polarized electron energy-loss spectroscopy. *The Review of Scientific Instruments*, **74**, 4089–4095.

Jullière, M. (1975). Tunneling between ferromagnetic films. *Physics Letters*, **54A**, 225–226.

Kämper, K-P., Abraham, D.L. and Hopster, H. (1992). Spin-polarized electron-energy-loss spectroscopy on epitaxial fcc Co layers on Cu(001). *Physical Review B*, **45**, 14335–14346.

Katsnelson, M.I. and Lichtenstein, A.I. (2000). First-principles calculations of magnetic interactions in correlated systems. *Physical Review B*, **61**, 8906–8912.

Keavney, D.J., Storm, D.F., Freeland, J.W., *et al*. (1995). Site-specific mössbauer evidence of structural-induced magnetic phase transition in fcc Fe(100) thin films. *Physical Review Letters*, **74**, 4531–4534.

Kirschner, J. (1985a). Sources and detectors for polarized electrons. In *Polarized Electrons in Surface Physics*, Feder, R. (Ed.), World Scientific: Singapore.

Kirschner, J. (1985b). Direct and exchange contributions in inelastic scattering of spin-polarized electrons from iron. *Physical Review Letters*, **55**, 973–976.

Kirschner, J., Rebenstorff, D. and Ibach, H. (1984). High-resolution spin-polarized electron-energy-loss spectroscopy and the stoner excitations in nickel. *Physical Review Letters*, **53**, 698–701.

Li, D., Freitag, M., Pearson, J., *et al*. (1994). Magnetic phases of ultrathin Fe grown on Cu(100) as epitaxial wedges. *Physical Review Letters*, **72**, 3112–3115.

Liu, X., Steiner, M.M., Sooryakumar, R., *et al*. (1996). Exchange stiffness, magnetization, and spin waves in cubic and hexagonal phases of cobalt. *Physical Review B*, **53**, 12166–12172.

Majlis, N. (2001). *The Quantum Theory of Magnetism*, World Scientific: Singapore, New Jersey, London, Hong Kong, Chapter 7.

Martin, D.H. (1967). *Magnetism in Solids*, MIT Press: Cambridge.

Mills, D.L. (1984). Surface spin waves on magnetic crystals. In *Surface Excitations, Modern Problems in Condensed Matter Science*, Agranovich, M. and Loudon, R. (Eds.), Elsevier Science Publishers B.V.: North-Holland, Amsterdam, Chapter 3, Vol. 9.

Mook, H.A. and Nicklow, R.M. (1973). Neutron scattering investigation of the magnetic excitations in iron. *Physical Review B*, **7**, 336–342.

Müller, S., Bayer, P., Reischl, C., *et al*. (1995). Structural instability of ferromagnetic fcc Fe films on Cu(100). *Physical Review Letters*, **74**, 765–768.

Muniz, R.B., Costa, A.T. and Mills, D.L. (2003). Microscopic theory of spin waves in ultrathin ferromagnetic films: Fe on W(110). *Journal of Physics: Condensed Matter*, **15**, S495–S504.

Muniz, R.B. and Mills, D.L. (2002). Theory of spin excitations in Fe (110) monolayers. *Physical Review B*, **66**, 174417-1–174417-15.

Nolting, W. (1986). *Quantentheorie des Magnetismus II*, Teubner Verlag: Stuttgart.

O'Brien, W.L. and Tonner, B.P. (1995). Magnetic phases of ultrathin Fe films on fcc Co(001). *Surface Science*, **334**, 10–18.

Pajda, M., Kudrnovský, J., Turek, I., *et al*. (2000). Oscillatory Curie temperature of two-dimensional ferromagnets. *Physical Review Letters*, **85**, 5424–5427.

Pajda, M., Kudrnovský, J., Turek, I., *et al*. (2001). Ab initio calculations of exchange interactions, spin-wave stiffness constants, and Curie temperatures of Fe, Co, and Ni. *Physical Review B*, **64**, 174402-1–174402-9.

Penn, D.R. and Apell, P. (1988). Free-electron-like Stoner excitations in Fe. *Physical Review B*, **38**, 5051–5054.

Perring, T.G., Taylor, A.D. and Squires, G.L. (1995). High-energy spin waves in hexagonal cobalt. *Physica B*, **213–214**, 348–350.

Pickart, S.J., Alperin, H.A., Minkiewicz, V.J., *et al*. (1967). Spin-wave dispersion in ferromagnetic Ni and fcc Co. *Physical Review*, **156**, 623–626.

Pierce, D.T. and Meier, F. (1976). Photoemission of spin-polarized electrons from GaAs. *Physical Review B*, **13**, 5484–5500.

Plihal, M. and Mills, D.L. (1998). Spin-flip exchange scattering of low-energy electrons in ferromagnetic iron. *Physical Review B*, **58**, 14407–14415.

Plihal, M., Mills, D.L. and Kirschner, J. (1999). Spin wave signature in the spin polarized electron energy loss spectrum of ultrathin Fe films: theory and experiment. *Physical Review Letters*, **82**, 2579–2582.

Razee, S.S.A., Staunton, J.B., Szunyogh, L. and Györffy, B.L. (2002). Local moments and magnetic correlations above the Curie temperature in thin films on and embedded in nonmagnetic substrates: Fe/Cu(100), Co/Cu(100), and Fe/W(100). *Physical Review B*, **66**, 094415-01–094415-10.

Savrasov, S.Y. (1998). Linear responds calculations of spin fluctuations. *Physical Review Letters*, **81**, 2570–2573.

van Schilfgaarde, M. and Antropov, V.P. (1999). First-principles exchange interactions in Fe, Ni, and Co. *Journal of Applied Physics*, **85**, 4827–4829.

Schreyer, A., Schmitte, T., Siebrecht, R., *et al*. (2000). Neutron scattering on magnetic thin films: pushing the limits. *Journal of Applied Physics*, **87**, 5443–5448.

Sinclair, R.N. and Brockhouse, B.N. (1960). Dispersion relation for spin waves in a fcc cobalt alloy. *Physical Review*, **120**, 1638–1640.

Slater, J.C. (1937). The theory of ferromagnetism: lowest energy levels. *Physical Review*, **52**, 198–214.

Stoner, E.C. (1936). Collective electron specific hat and spin paramagnetism in metals. *Proceedings of the Royal Society of London, Series A*, **154**, 656–678.

Stoner, E.C. (1938). Collective electron ferromagnetism. *Proceedings of the Royal Society of London, Series A*, **165**, 372–414.

Tang, H., Plihal, M. and Mills, D.L. (1998). Theory of the spin dynamics of bulk Fe and ultrathin Fe(100) films. *Journal of Magnetism and Magnetic Materials*, **187**, 23–46.

Tannenwald, P.E. and Weber, R. (1961). Exchange integral in cobalt from spin-wave resonance. *Physical Review*, **121**, 715.

Thomassen, J., May, F., Feldmann, B., *et al*. (1992). Magnetic live surface layers in Fe/Cu(100). *Physical Review Letters*, **69**, 3831–3834.

Torija, M.A., Pierce, J.P. and Shen, J. (2001). Magnetic capping layer induced spin reorientation: Co on Fe/Cu(100). *Physical Review B*, **63**, 092404-1–092404-3.

Trohidou, K.N., Blackman, J.A. and Cooke, J.F. (1991). Calculation of the high-energy spin-wave spectrum in hexagonal cobalt. *Physical Review Letters*, **67**, 2561–2564.

Udvardi, L., Szunyogh, L., Palotás, K. and Weinberger, P. (2003). First-principles relativistic study of spin waves in thin magnetic films. *Physical Review B*, **68**, 104436-1–104436-11.

Vernon, S.P., Lindsay, S.M. and Stearns, M.B. (1984). Brillouin scattering from thermal magnons in a thin Co film. *Physical Review B*, **29**, 4439–4442.

Vollmer, R., Etzkorn, M., Anil Kumar, P.S., *et al*. (2003). Spin-polarized electron energy loss spectroscopy of high energy, large wave vector spin waves in ultrathin fcc Co films on Cu(001). *Physical Review Letters*, **91**, 147201-1–147201-4.

Vollmer, R., Etzkorn, M., Anil Kumar, P.S., *et al*. (2004a). Spin-polarized electron energy loss spectroscopy: a method to measure magnon energies. *Journal of Magnetism and Magnetic Materials*, **272–276**, 2126–2130.

Vollmer, R., Etzkorn, M., Anil Kumar, P.S., *et al*. (2004b). Spin-wave excitation in ultrathin Co and Fe films on Cu(001) by spin-polarized electron energy loss spectroscopy. *Journal of Applied Physics*, **95**, 7435–7440.

Vollmer, R., Etzkorn, M., Anil Kumar, P.S., *et al*. (2004c). Spin-wave excitation observed by spin-polarized electron energy loss spectroscopy: a new method for the investigation of surface- and thin-film spin waves on the atomic scale. *Thin Solid Films*, **464–465**, 42–47.

Yethiraj, M., Robinson, R.A., Sivia, D.S., *et al*. (1991). Neutron-scattering study of the magnon energies and intensities in iron. *Physical Review B*, **43**, 2565–2574.

Scanning Probe Techniques: MFM and SP-STM

Alexander Schwarz, Matthias Bode and Roland Wiesendanger
Universität Hamburg, Hamburg, Germany

1 INTRODUCTION

Soon after the invention of scanning tunneling microscopy (STM) by Binnig and Rohrer in 1982 numerous derived scanning probe methods have been developed (Binnig and Rohrer, 1982, 1987). These methods, often named SXM, where X either stands for the measured quantity or for the utilized interaction, allow the imaging of a wide variety of surface properties in real space and with high spatial resolution. Besides STM, the most frequently used SXM technique is atomic force microscopy (AFM). Whereas STM detects the quantum-mechanical tunneling current across a vacuum gap between two closely spaced conductive electrodes, that is, a sharp tip and sample surface, AFM senses the electromagnetic force between a surface and a tip, which is located at the free end of a cantilever, and is therefore not limited to conductive systems. Since magnetic properties of surfaces and small particles are of great technical relevance for the development of magnetic data storage devices it was soon considered to extend the scanning probe methods to this direction. In principle, two approaches were chosen: the detection of the rather long-range magnetostatic tip–sample force by magnetic force microscopy (MFM) (Martin and Wickramasinghe, 1987; Sáenz *et al*., 1987) or by making use of the spin-dependent conductivity between a magnetic STM tip and a magnetic sample, the so-called spin-polarized scanning tunneling microscopy (SP-STM) (Wiesendanger *et al*., 1990b).

In the following two sections we survey the basic concepts, experimental conditions, modes of operation, tip preparation, and the contrast mechanisms of MFM and SP-STM. Several examples for both methods are presented to demonstrate their capabilities. Whereas MFM requires minimum sample preparation, is easy to adopt, and can be applied to nonconducting samples as well, SP-STM is able to achieve spin sensitivity with atomic resolution. The different contrast mechanisms and the resulting resolution are particularly evident on magnetic vortices which can be observed in small magnetic structures, as discussed in Sections 2.10 and 3.4.

Handbook of Magnetism and Advanced Magnetic Materials. Edited by Helmut Kronmüller and Stuart Parkin. Volume 3: *Novel Techniques for Characterizing and Preparing Samples*. ISBN: 978-0-470-02217-7.

2 MAGNETIC FORCE MICROSCOPY

2.1 Basic concept of MFM and modes of operation

MFM detects the magnetostatic interaction between a force sensor, that is, a tip located at the free end of a cantilever, and the stray field emanating from a specimen. This technique allows the imaging of domain patterns of ferromagnetic (and ferrimagnetic) specimen with high spatial resolution down to about 10 nm (Wiesendanger and Güntherodt, 2002). In principle, MFM experiments are possible with any AFM setup. However, obviously the force sensor has to be ferromagnetic and the data acquisition has to be slightly modified. One important advantage of MFM compared to

other magnetic imaging techniques, for example, magneto-optical imaging, is the possibility to acquire high-resolution topography data simultaneously. SP-STM has the same advantage and certainly a much better spatial resolution down to the atomic scale. However, MFM is not restricted to conductive samples and, since it detects the magnetostatic interaction far above the specimen, it is quite insensitive to surface contaminations. The latter enables experiments in ambient conditions and without special surface preparation.

MFM is a noncontact technique, where the tip apex never touches the surface neither in the static nor in any dynamic mode of operation. Typical tip–sample separations range from 10 to 100 nm. Therefore, the rather long-range magnetostatic interaction can be separated from the short-range interactions, which are used in AFM to image the topography. At this point, it has to be mentioned that electrostatic forces have the same range and might still be present, thereby hampering data interpretation. Therefore, it is helpful to minimize the influence of electrostatic forces by balancing the contact potential difference with a corresponding bias voltage between tip and sample (Schönenberger, Alvarado, Lambert and Sanders, 1990; Yu, Ahner and Weller, 2004). In contrast to AFM, no z-feedback control is employed for imaging. Instead, the MFM signal is directly recorded in a constant height above the sample using either the lift mode, where the tip follows the prerecorded topography (Wadas, Moreland, Rice and Katti, 1994) or the plane-subtraction mode (Dreyer, Löhndorf, Wadas and Wiesendanger, 1998), where only the tilt between tip and sample is compensated. The former method is widely used but has one big disadvantage. While prerecording the topography, the tip is very close to the surface and the magnetostatic interaction is much stronger than during MFM data acquisition. As a result, the magnetic structure of the sample (or the tip) might be modified. In principle, the plane-subtraction mode requires only two scan lines, one in x and one in y direction, to define a plane parallel to the surface. They can be even recorded far away from the region of interest. Therefore, it should be certainly used for relatively flat samples. However, results as good as in the lift mode can be obtained on samples with large topographical features, although it is not a constant height mode in a strict sense then.

Unfortunately, the nomenclature regarding the different modes of operation of AFM, and therefore also of MFM, emerged in the context of instrumental developments and is often inconsistent and hard to understand. In general, one can distinguish between static and dynamic modes on one side and between contact, cyclic contact, and pure noncontact modes on the other side. As mentioned in the preceding text, MFM is always operated in the pure noncontact mode, that is, the tip never enters the strongly attractive or repulsive regime of short-range interactions, which are used for topography imaging. In the static mode (also known as *dc mode*), the cantilever deflection Δz due to the tip–sample interaction is monitored and can be directly converted into the tip–sample force F_z via Hook's law, that is,

$$F_z = c_z \cdot \Delta z \tag{1}$$

where c_z is the spring constant of the cantilever. In the various dynamic modes the cantilever oscillates with amplitude A, either self-excited or externally driven, at or near the resonance frequency $\omega_0 = 2\pi f_0 = \sqrt{c_z/m}$, where m_{eff} is the effective mass of the cantilever, which reflects the mass distribution along the cantilever. Two main detection schemes exist, that is, frequency modulation (FM) and amplitude modulation (AM), respectively. The former mode is used in vacuum for *true* atomic-resolution imaging and is in this context also known as *noncontact AFM* (Morita, Wiesendanger and Meyer, 2002). The cantilever is self-excited and either cantilever amplitude or excitation amplitude is kept constant (CA or CE mode, respectively). The AM mode is also named ac mode or tapping mode (TM), because of the cyclic contact during topography scans with the surface at the lower turnaround point of the oscillation. This technique is used in ambient conditions or liquids. In all dynamic modes, the MFM signal is related to the force gradient F_z' provided that A (typically between 5 and 50 nm) is much smaller than the range of the magnetostatic interaction. Owing to the stronger distance dependence, the dynamic modes are superior to the static mode, wherefore they are nowadays nearly exclusively used.

To calculate F' one can assume the spring constant of the cantilever to be effectively softened or hardened by an attractive or repulsive long-range interaction, respectively, that is, $c_{\text{eff}} = c_z - F_z'$. Thereby, the actual oscillation frequency ω deviates from the frequency of the free cantilever ω_0 by $\Delta\omega = \omega - \omega_0$. Assuming $F_z' << c_z$, the frequency shift for FM-MFM data is directly proportional to the force gradient, that is, $F_z' = -2c_z \cdot \frac{\Delta\omega}{\omega_0}$. AM-MFM uses the variation of phase ϕ or amplitude A as signal instead. Both quantities change together with frequency. This can be understood if one writes down the steady state solutions for an externally excited damped harmonic oscillator, that is,

$$A = A_0 \cdot \frac{\omega_0^2}{\sqrt{(\omega^2 - \omega_0^2)^2 + 4\gamma^2\omega^2}} \tag{2}$$

and

$$\phi = \arctan\frac{2\gamma\omega}{\omega^2 - \omega_0^2} \tag{3}$$

respectively, where γ is the damping factor, which is related to the quality factor Q of the oscillator by $Q = m_{\text{eff}}\omega_0/2\gamma$.

The resulting force gradient due to the amplitude change ΔA or phase shift $\Delta\phi$ can be calculated by $F_z' = -\Delta A \times 3^{1.5} \times c_z/2 \times Q \times A_0$ or $F_z' = -\Delta\phi \times c_z/Q$, respectively.

Like for every scanning probe method, the lateral resolution of MFM is limited by the tip–sample separation and the effective tip size. For flat samples, the separation can be below 20 nm. For rough samples, much larger distances (up to 100 nm) are necessary. The effective tip size for MFM is determined by the spreading of the emanating stray field of the tip and not by its physical size. However, the latter influences the confinement of the stray field via the shape anisotropy (cf. Section 2.3). The minimal detectable force or force gradient is limited by all sorts of external noise sources and by the sensitivity of the deflection sensor. For example, if the minimal detectable deflection is 10 pm as routinely obtained with interferometers (Rugar, Mamin and Guethner, 1989), the minimal detectable force is 1 pN for a soft cantilever with $c_z = 0.1$ typically used in the static mode. However, from a fundamental point of view the sensitivity is thermomechanically limited. In analogy with the well-known Johnson noise in a resistor a mechanical resistance Γ can be introduced. Then the minimal detectable force $F_{\min}$ for a given temperature T and measurement bandwidth B is

$$F_{\min} = \sqrt{\Gamma k_B T B} \tag{4}$$

where k_B is Boltzmann's constant. For a rectangular cantilever of length l, width w, and thickness t, Γ is given by

$$\Gamma = \frac{wt^2}{lQ}\sqrt{E\rho} \tag{5}$$

where Q, ρ, and E are the quality factor, density, and elastic modulus, respectively (Stowe *et al*., 1997). For typical soft ($c_z \approx 0.1\,\mathrm{N\,m^{-1}}$) rectangular silicon cantilevers ($E = 1.79 \times 10^{11}\,\mathrm{N\,m^{-1}}$, $\rho = 2.33\,\mathrm{kg\,m^{-3}}$, $l = 200\,\mu\mathrm{m}$, $w = 30\,\mu\mathrm{m}$, $t = 1\,\mu\mathrm{m}$) in ambient conditions ($Q = 300$) at room temperature ($T = 300\,\mathrm{K}$), the thermomechanical limit is about 0.1 pN in a bandwidth of 1 kHz. At low temperatures and in vacuum, where Q values are 1000 times larger, much higher force sensitivities are possible. With specially designed ultrasoft cantilevers, sub-attonewton force sensitivity has been achieved (Stowe *et al*., 1997; Mamin and Rugar, 2001). For the dynamic modes, the force gradient sensitivity can be formulated similarly (Albrecht, Grütter, Horne and Rugar, 1991), that is,

$$\frac{\partial F_{\min}}{\partial z} = \sqrt{\frac{4c_z k_B T B}{\omega_0 Q \langle A^2\rangle}} \tag{6}$$

where $\langle A^2\rangle$ is the mean-square amplitude of the cantilever oscillation. For typical cantilevers and parameter in ambient condition ($Q = 300$) at room temperature ($T = 300\,\mathrm{K}$) used in dynamic modes ($f_0 = 100\,\mathrm{kHz}$, $c_z = 1\,\mathrm{N\,m^{-1}}$, $A = 10\,\mathrm{nm}$), the minimal detectable force gradient is about $3 \times 10^{-5}\,\mathrm{N\,m^{-1}}$ in a bandwidth of 1 kHz. Equation (6) is valid for the FM mode. However, for the AM mode the factor 4 in the nominator has to be replaced by 2. Note that the factor $\sqrt{k_B T/Q}$ is present in equations (4) and (6), respectively. Therefore, the sensitivity can be enhanced in vacuum (higher Q values) and low temperatures (Hug *et al*., 1993; Volodin, Temst, van Haesendonck and Bruynseraede, 2000; Liebmann, Schwarz, Langkat and Wiesendanger, 2002).

2.2 Tip preparation

At the beginning of MFM, bent wires from ferromagnetic materials like iron or nickel, with electrochemically etched tips were used until de Boef (den Boef, 1990) suggested to galvanize nonmagnetic tungsten wires with a ferromagnetic material. Nowadays, standard microfabricated silicon or silicon nitride force sensors with a ferromagnetic thin film are usually employed, because their magnetic properties can be adjusted by choosing a suitable ferromagnetic material (Fe, Ni, Co, permalloy, CoCr, etc.) with an appropriate film thickness (Grütter *et al*., 1990). Coated force sensors are commercially available, but only with a limited choice. Much better results can be obtained by using a normal tip and optimizing the coating for a specific specimen. As a general rule, material and thickness should be chosen to get the largest possible MFM signal without disturbing the magnetic structure of the sample and vice versa. Another important point is the lateral resolution. In case of MFM the effective size is mainly determined by the localization of magnetic stray field emanating from the tip. The appropriate strategy is to use sharp tips with high aspect ratios.

It is possible to increase the aspect ratio of standard tips oneself, but it requires a focused ion beam instrument to tailor an existing tip (Liu, Dan, Jinjun and Wu, 2002) or a scanning electron microscope to grow a tip by electron-beam deposition (Rührig, Porthun and Lodder, 1994). Recently, carbon nanotubes have been attached to standard tips and subsequently coated with cobalt (Deng *et al*., 2004). A very convenient and effective way to reduce the spreading of the tip magnetic stray field is to coat only one side face of the pyramidal tip. The triangular shape of the side face automatically induces an easy axis toward the tip apex. Moreover, since for geometrical reasons the cantilever beam is usually not parallel to the surface, but tilted by about 15°, it is possible to prepare tips that are nearly exclusively sensitive to the z component of the sample stray field, by choosing the side face that points nearly perpendicular toward the surface (Liebmann *et al*., 2005). With such tips data interpretation is much easier, cf., equations (10) and (11) in

Section 2.3. Note that it is impossible to avoid disturbing additional in-plane sensitivities, if all side faces of a tilted pyramid are coated.

2.3 Contrast formation and image interpretation

From a physical point of view the magnetostatic tip–sample interaction energy E_{TS} can be described in two equivalent ways, that is,

$$E_{\mathrm{TS}} = -\int \vec{J}_{\mathrm{T}}\vec{H}_{\mathrm{S}}\mathrm{d}V = -\int \vec{J}_{\mathrm{S}}\vec{H}_{\mathrm{T}}\mathrm{d}V \tag{7}$$

Either the sample magnetic stray field $\vec{H}_{\mathrm{S}}$ above the surface is probed with the tip magnetic polarization $\vec{J}_{\mathrm{T}}$ or the sample magnetic polarization $\vec{J}_{\mathrm{S}}$ is probed with the magnetic stray field $\vec{H}_{\mathrm{T}}$ emanating from the tip. Since different distributions of the magnetic polarization in the sample result in the same stray field above the sample, it is generally impossible to unambiguously deduce the magnetic polarization in the sample from an MFM image. To evaluate MFM data qualitatively, it is often helpful to use a different representation of equation (7), obtained after partial integration, that is,

$$E_{\mathrm{TS}} = -\int \rho_{\mathrm{S}}\Phi_{\mathrm{T}}\mathrm{d}V - \int \sigma_{\mathrm{S}}\Phi_{\mathrm{T}}\mathrm{d}S \tag{8}$$

Here, ρ_{S} and σ_{S} are the volume and surface magnetic pole densities, respectively, and Φ_{T} is the scalar potential of the tip stray field. Both quantities are related via $\vec{H}_{\mathrm{T}} = -\vec{\nabla}\Phi_{\mathrm{T}}$. If no magnetic poles are present in the volume, that is, $\rho_{\mathrm{S}} = 0$, MFM images basically reflect the surface charge density smoothed by the finite size of the tip stray field given by the degree of localization of Φ_{T}. This simplified interpretation is valid for thin films with out-of-plane polarized magnetic domains.

As mentioned above, MFM detects either the force (static mode) or the force gradient (dynamic mode). Expressions for both quantities can be derived from equation (7). If we approximate the magnetic polarization of the tip as a simple dipole $\vec{m}$, then the force is given by

$$\vec{F} = \vec{\nabla}E_{\mathrm{TS}} = \mu_0\vec{\nabla}(\vec{m}_{\mathrm{T}}\vec{H}_{\mathrm{S}}) \tag{9}$$

Since only the vertical z component is detected, equation (9) simplifies to

$$F_z = \mu_0\frac{\partial}{\partial z}(\vec{m}_{\mathrm{T}}\vec{H}_{\mathrm{S}}) = \mu_0(m_x\frac{\partial H_x}{\partial z} + m_y\frac{\partial H_y}{\partial z} + m_z\frac{\partial H_z}{\partial z}) \tag{10}$$

Further partial differentiation leads to the force gradient,

$$\frac{\partial}{\partial z}F_z = \mu_0(m_x\frac{\partial^2 H_x}{\partial z^2} + m_y\frac{\partial^2 H_y}{\partial z^2} + m_z\frac{\partial^2 H_z}{\partial z^2}) \tag{11}$$

Note that for tips solely polarized along the z direction, that is, $m_x = m_y = 0$, force and force gradient depend only on the first or second derivative of the stray field's z component respectively.

A very helpful and successful method of interpreting MFM images qualitatively are micromagnetic simulations. The specimen is subdivided into cells, which are described by a single magnetic polarization vector. Typical cell sizes are a few cubic nanometers, so that each vector represents a large number of atomic spins. The time dependence of the magnetic polarization $\vec{J}(t)$ under the influence of an effective magnetic field $\vec{H}_{\mathrm{eff}}$ (including the external as well as the anisotropy fields) is solved for each cell until the spin orientations in all cells remain stable. This is done by means of the Landau–Lifshitz–Gilbert equation

$$\frac{\mathrm{d}\vec{J}}{\mathrm{d}t} = -\gamma\vec{J}\times\vec{H}_{\mathrm{eff}} + \frac{\alpha}{|\vec{J}|}\vec{J}\times\frac{\mathrm{d}\vec{J}}{\mathrm{d}t} \tag{12}$$

where γ is the gyromagnetic ratio and α is the damping constant of the precessing magnetic polarization vector. The calculated distribution of magnetic polarizations can be used to obtain the stray field components and its derivatives above the surface. According to equation (10) and (11) the result qualitatively corresponds to the MFM signal, if the tip is reasonably well represented by a point dipole.

Several proposals have been made to calculate magnetic properties quantitatively from MFM images by some kind of calibration procedure (Göddenhenrich *et al*., 1990; Lohau, Carl, Kirsch and Wassermann, 2001; Hug *et al*., 1998; Zhu, Lin, Shi and Luo, 1998). However, because of the principle restrictions set by equation (7), all approaches are only of limited validity. Therefore, MFM is not a well-suited tool to determine the magnitude of magnetic polarization, but to visualize magnetic structures and their correlation with topographic features with high spatial resolution and minimal sample preparation. In the following text, several examples are shown, which demonstrate the capabilities of MFM.

2.4 Magnetic data storage

From the very beginning, MFM has been applied to investigate components involved in magnetic data storage. In fact, MFM was first demonstrated on a magnetic recording head (Martin and Wickramasinghe, 1987). The quick increase of the areal density in magnetic storage devices like hard disks and tapes demanded (and still demands)

high spatial resolution techniques. From the invention of MFM in 1987 until the year 2000, the areal density on hard disks increased from about 10 Mb in.$^{-2}$ (Thompson and Best, 2000) to about 10 Gb in.$^{-2}$ with a track width of 0.9 µm and a bit length of 70 nm. Recently, more than 100 Gb in.$^{-2}$ have been reported in laboratory runs of hard disks.

The MFM image in Figure 1 shows an example of a digital tape with a longitudinal bit structure, that is, the magnetic polarization along the track direction is in plane. No specific preparation was performed for the measurement in ambient conditions. Neighboring tracks are slightly tilted against each other. Track width and bit length are about 10 and 1 µm, respectively. The areal density is considerably smaller than that on hard disks, because the magnetic coating on a tape is supported by a flexible substrate and suffers from more external disturbances than a well protected rigid disk in its stable case. However, the volume density is much higher, wherefore tapes are still used as inexpensive mass storage devices, for example, in backup applications. Whereas a read head only detects zeros and ones while reading, MFM allows to study much more details of the bit pattern. For example, the magnification in the inset shows the transition region between two tracks. This region is of particular importance, because the magnetic signals of bits in neighboring tracks interfere, whereby the readback signal is diminished. Since MFM detects basically the same quantity as the read head, that is, the magnetic stray field above the surface, it can clarify how the implementation of different materials or any other change of the design, for example, tilt angle between tracks, influence the signal quality.

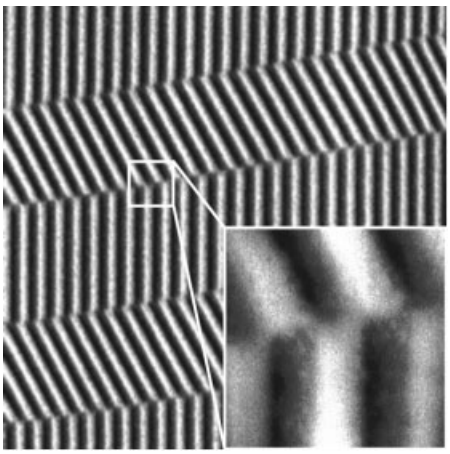

Figure 1. Lift-mode AM-MFM image ($50 \times 50\,\mu m^2$) of the bit structure of a magnetic tape for mass storage. The inset shows a magnification ($5 \times 5\,\mu m^2$) of the transition region, where two tracks meet.

2.5 Magnetization reversal

MFM can also be used in high magnetic fields, because the magnetic tip is effectively a dipole, wherefore the net force exerted on the tip is basically zero. Since the tip is typically just about 10 µm high, this is even true for quite inhomogeneous fields. In the example presented here the domain pattern evolution of an 80-nm-thick $La_{0.7}Sr_{0.3}MnO_3$ film with out-of-plane polarized domains has been recorded along its major hysteresis loop while ramping an external magnetic field $\mu_0 H = B$ from 0 mT (remanence) to 600 mT (saturation) and back again to 0 mT (Schwarz *et al*., 2004). The data have been recorded with a low-temperature force microscope (Liebmann, Schwarz, Langkat and Wiesendanger, 2002) in ultrahigh vacuum at 5.1 K. From such an image series, it was possible to reconstruct the major hysteresis loop (Liebmann *et al*., 2005). Figure 2(a) and (b) show two consecutively recorded images on the decreasing branch from saturation toward remanence. The difference image (c) = (a) − (b) reveals the individual reversal events (Barkhausen jumps) between (a) and (b). By merging (c) into the original domain pattern (a) as displayed in (d), growth events (regions, which touch an already existing domain like the event marked with G) can be distinguished from nucleation events (isolated regions like the event marked with N). By analyzing all images in this way the size distribution for nucleation (e) and growth events (f) can be studied. The Gaussian distribution for nucleation radii can be explained by the critical droplet theory. Since the energy cost for a domain wall creation scales with its surface area, and the energy gain and cost for the stray field energy and the Zeeman energy, respectively, scale with the volume, stable nucleation is only possible above a certain critical radius. Its value depends on parameters like exchange stiffness and magnetocrystalline anisotropy energy, which can vary locally and thereby result in a Gaussian distribution of radii around the mean value. The growth events are much smaller than the nucleation events (the smallest have diameters below 10 nm) and they exhibit a very different size distribution, that is, a power law with an exponential cutoff. It can be related either to self-organized criticality (Bak, Tang and Wiesenfeld, 1987), where externally driven (magnetic field) systems organize themselves in barely stable (critical) state by avalanches (Barkhausen jumps), or to domain wall propagation through a disordered medium (Alessandro, Beatrice, Bertotti and Montorsi, 1990). A similar analysis can be performed for the increasing branch (from remanence to saturation). Additionally, the correlation between domain patterns and, in particular, the position of nucleation events and with respect to topographical features, for example, due to the granular structure of the specimen, can be investigated (Liebmann, Schwarz, Langkat and Wiesendanger, 2002).

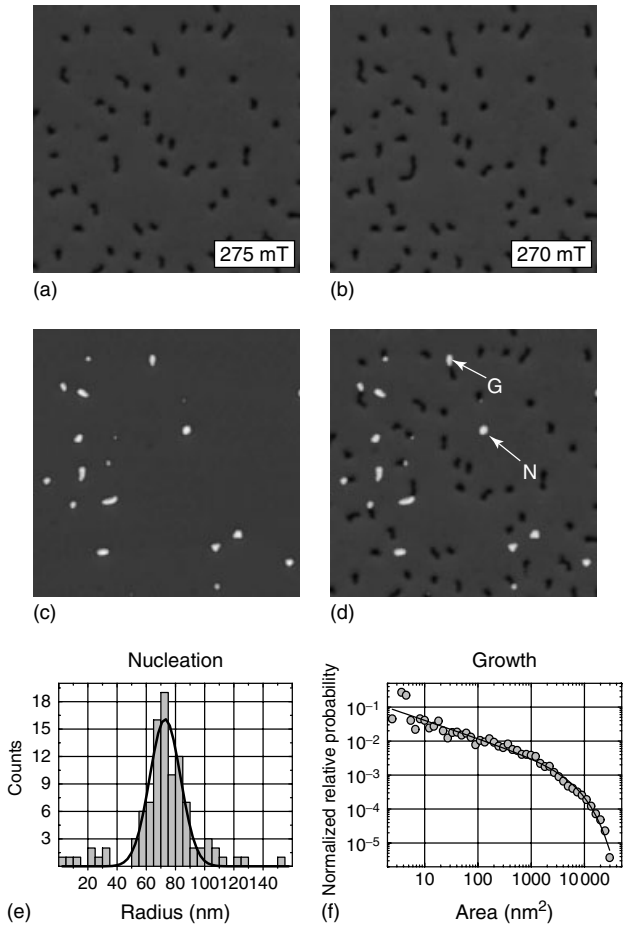

Figure 2. Real space observation of individual magnetization reversal processes in a $La_{0.7}Sr_{0.3}MnO_3$ film with out-of-plane uniaxial anisotropy. (a), (b) Two plane-subtraction mode FM-MFM images ($4 \times 4\,\mu m^2$) from a series recorded along the major hysteresis loop. They have been recorded consecutively in a slightly different external magnetic field. (c) Difference image (a) − (b). Only the magnetization reversal events, that is, the Barkhausen jumps, remain visible. After merging (c) into the original MFM image (a), nucleation (N), and growth (G) events can be distinguished in (d). (e) Gaussian distribution of nucleation radii after evaluation of the whole image series. (f) Size distribution of the growth areas. The solid line corresponds to a power law with exponential cutoff.

2.6 Reorientation transition

The energy of a ferromagnetic material is given by the magnetic anisotropy energy and the stray field energies. The former is related to the spin-orbit coupling. Symmetry changes at surfaces or those due to stress within the material can alter the bulk magnetic anisotropy significantly. The stray field energy strongly depends on the shape of the specimen. Thin films, for example, tend to be polarized in plane, whereby the density of free poles at the surface can be reduced compared to an out-of-plane polarized film. However, for very thin films (a few atomic layers), the surface anisotropy can become dominating and might force the spins in an out-of-plane direction. Consequently, a thickness-dependent reorientation transition can be observed, for example, by the magneto-optical Kerr effect (Qiu, Pearson and Bader, 1993; Baudelet *et al*., 1995), scanning electron microscopy with spin analysis (Speckmann, Oepen and Ibach, 1995) and MFM (Wadas, Dreyer, Kleiber and Wiesendanger, 1998). Figure 3 displays two images from a whole series (Dreyer, Kleiber, Wadas and Wiesendanger, 1999), where the Co thickness on a Au(111) substrate has been increased stepwise up to 7.0 monolayers (ML). The data were recorded in ultra-high vacuum with a magnetic tip that was polarized along the tip axis, which is oriented perpendicular to the surface. Below 2.0 ML no MFM signal could be verified. From 2.0 to 3.8 ML the MFM images exhibit a clear out-of-plane domain contrast, as visible in Figure 3(a). For higher thicknesses, a domain wall contrast is observed as shown for 6 ML in Figure 3(b). Since the same perpendicularly polarized tip was used, an in-plane domain structure can be inferred, indicating a thickness-dependent reorientation transition. On the same material, it was observed that the surface anisotropy energy can be strongly affected by contaminations (Dreyer, Kleiber, Wadas and Wiesendanger, 1999). For a thickness of 4.3 ML the in-plane polarization switched back to an out-of-plane polarization by adsorption of carbon onto the cobalt film from the residual gas in the vacuum chamber. Another important parameter is the temperature, which can also induce a reorientation transition due to the temperature dependence of the magnetic anisotropy energy.

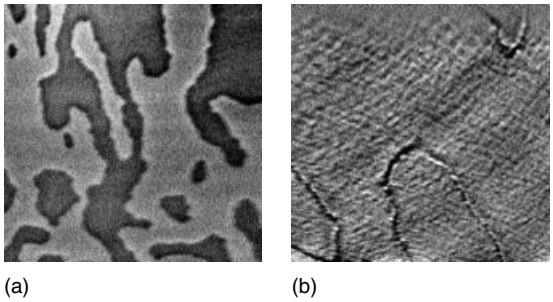

Figure 3. Thickness-dependent reorientation transition of Co on Au(111). The plane-subtraction mode FM-MFM images (a) and (b), both recorded in zero field and in an area of $5 \times 5\,\mu m^2$, have been recorded with the same out-of-plane polarized tip, but with different nominal Co thicknesses, that is, 2.0 ML and 6.0 ML, respectively. In (a) domains are visible, while (b) exhibits a domain wall contrast.

2.7 Domain wall structure

Apart from domain imaging MFM also allows the investigation of domain walls (Proksch, Foss, Dahlberg and Prinz,

1994; Schneider, Müller-Pfeiffer and Zinn, 1996; Löhndorf, Wadas, van den Berg and Wiesendanger, 1996). There are two principle ways for the magnetic polarization in neighboring antiparallel in-plane polarized magnetic domains in a film geometry to rotate by 180°. The polarization vector either rotates fully out-of-plane or remains in-plane all the time. The former case is called Bloch wall and the latter Néel wall, respectively. As a general rule, Bloch walls are observed in rather thick films, where the magnetostatic energy density due to the interaction between the free poles in the Bloch walls on opposite surfaces is negligible. For thinner films this energy contribution becomes dominant and Néel walls, where no free poles are generated at the surfaces, are energetically favorable. However, the thickness-dependent transition from a Bloch to a Néel wall is not abrupt. In an intermediate thickness range a mixture of both types is present – a so-called cross-tie wall. Figure 4 shows an MFM image of such a wall in a 50-nm-thick polycrystalline Co film on a SiO_2 substrate imaged with an out-of-plane polarized tip (Löhndorf, Wadas, van den Berg and Wiesendanger, 1996). Bright and dark areas correspond to the complex distribution of free poles at the surface (cf. equation (8)) within the domain wall as indicated in the inset. The Bloch lines in the middle of the rhombi, where the magnetic polarization points normal to the surface, exhibit the strongest contrast. Even far away from the domain wall the MFM contrast is not uniform. The textured MFM signal indicates that the magnetic polarization is not exactly in-plane everywhere, but tilts slightly out-of-plane locally (Löhndorf, Wadas and Wiesendanger, 1997). This effect results in the well-known magnetic ripple structure, which is often observed in thin films.

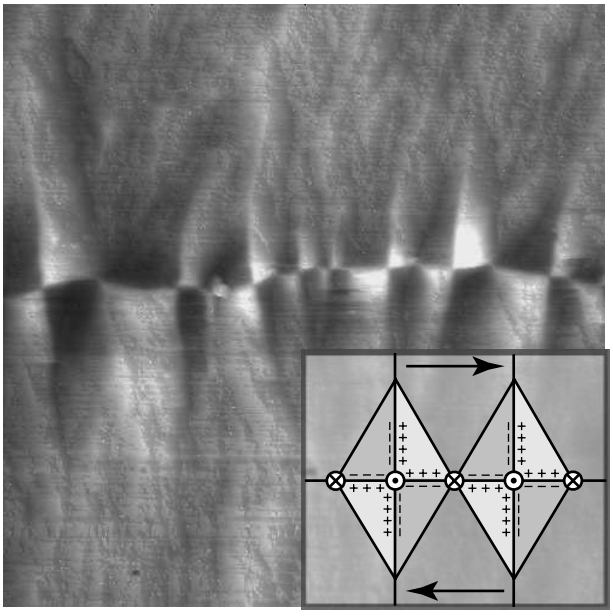

Figure 4. Static mode MFM image ($20 \times 20\,\mu m^2$) recorded in the lift mode of a cross-tie wall acquired with an out-of-plane polarized tip. Sign and distribution of magnetic poles, which are responsible for the contrast formation, are displayed in the inset.

2.8 Multidomain particles

From a technical point of view domain patterns of laterally structured thin film elements become increasingly important owing to the development of micro- and nanoscale magnetoelectronic devices. In hybrid ferromagnetic-semiconductor spintronic systems, such elements act as source for spin-polarized electrons, which is obviously influenced by local variations of the spin orientation due to the presence of differently oriented domains and domain walls between them. Since the relative portion of edges becomes larger for smaller lateral dimensions, the existence of closure domains, where the direction of the magnetic polarization runs parallel to the edges, is the most obvious feature in finite size elements. Figure 5 shows a lithographically prepared rectangular $4.0 \times 2.0\,\mu m^2$ large element. In (a) and (b) the film thicknesses are 100 nm and 70 nm, respectively (Barthelmess, Pels, Thieme and Meier, 2004). The in-plane polarized closure domain pattern remains unchanged, but the type of domain wall between the two main domains is different. In (a) a simple Bloch wall facilitates the 180° rotation, while the thinner structure in (b) exhibits a cross-tie wall, as described in the previous section (cf. Figure 4). Image (c) displays a micromagnetic simulation of (b). All features visible in the

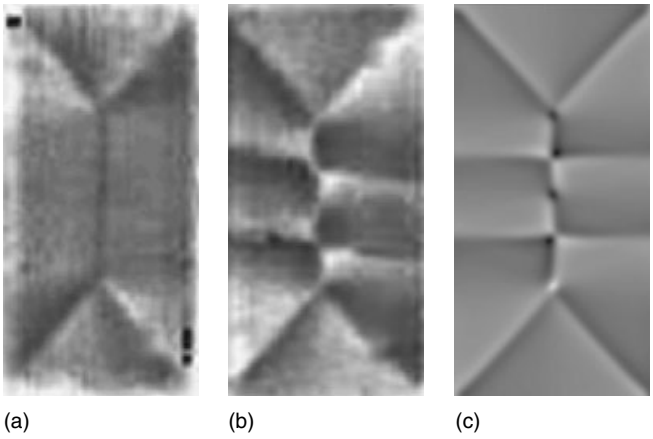

Figure 5. Lift-mode AM-MFM images of polycrystalline $Ni_{83}Fe_{15}$ (permalloy) multidomain particle ($4.0 \times 2.0\,\mu m^2$) with (a) 100 nm and (b) 70 nm thickness. The two central domains in the thicker film (a) are separated by a simple Bloch wall, while the more complex cross-tie wall evolves in the thinner film (b). In (c) a micromagnetic simulation of the experimental situation in (b) is shown, which reproduces the MFM contrast well. (Courtesy of G. Meier (Barthelmess, Pels, Thieme and Meier, 2004).)

MFM image, that is, domain pattern as well as the cross-tie wall, are very well reproduced. Note that the simulation appears sharper than the MFM image, because the real tip is not a point dipole. Furthermore, in experimental data domain walls are often somewhat distorted if the tip modifies the spin orientation locally.

2.9 Single domain particles

If the size of ferromagnetic particles is shrunk below a certain value, the energy cost by inserting a domain wall to minimize the stray field energy is too high. Since the stray field energy scales with R^3, but the domain wall energy only with R^2, a critical particle radius exists, below which the stable configuration even in remanence is the single domain state with two discrete directions of the magnetic polarization (Kittel, 1946; Frei, Shtrikman and Treves, 1957). Note that only ellipsoidal bodies can exhibit a truly uniform remanent magnetic polarization in which the magnetic polarization is parallel at all places within the particle.

Assuming a rotational ellipsoid, a critical diameter D_c can be determined by comparing the energy difference between a single- and a two-domain state (Kronmüller, Goll, Hertel and Schütz, 2004)

$$D_c = \frac{3\mu_0\gamma_{DW}}{N(1-\beta)J_S^2} \tag{13}$$

Here, γ_{DW} is the wall energy, for example, $4\sqrt{AK}$ for a Bloch wall, N is the shape-dependent demagnetization factor, and β is the factor by which the stray field energy is reduced in the two-domain configuration compared to the single domain configuration. Using typical parameters for cobalt, that is, $A_{ex} \approx 3 \times 10^{-11}\,\mathrm{Jm}^{-1}$, $K \approx 4.5 \times 10^5\,\mathrm{Jm}^{-3}$ and $J_S \approx 1.8\,\mathrm{T}$, single domain behavior can be observed for magnetic particles with diameters below $D_c \approx 34\,\mathrm{nm} \cdot (N(1-\beta))^{-1}$. Note that N, $\beta < 1$, and therefore $(N(1-\beta))^{-1} > 1$), that is, the single domain state for Co particles is observed on length scales often much larger than 34 nm.

Figure 6 shows two MFM images of a quadratic array of disks shaped particles with a periodicity of 500 nm (Kleiber *et al.*, 1998). The 17-nm-thick Co disks with a diameter of 200 nm have been produced lithographically on a GaAs substrate with 3-nm Cr adhesion layer as spacer. Owing to their shape, the easy axis of magnetic polarization is in plane. The in-plane demagnetization factor for this diameter to thickness ratio is about $N \approx 0.1$, whereby the critical length scale for the single domain state is larger than 300 nm, which is larger than the disk diameter.

Image (a) has been recorded with a standard out-of-plane polarized tip, while the tip in image (b) was polarized in plane. The inset in the lower right corner displays a simulation of the MFM contrast. In (a) the bright and dark contrast reflects the north and south pole of the magnetic dot, where the direction of the stray field is out of plane and oriented either parallel (bright) or antiparallel (dark) with the magnetic polarization of the tip. Note that the area occupied by the dark and bright contrast is somewhat larger than the particle size. For an in-plane tip the orientation of its magnetic polarization and stray field outside of the particle coincides at three positions above the particle: above the center and at two ends, where the field lines leave and reenter the particle. At the two ends the direction of the magnetic field lines are opposite to the direction of the field lines above the particle center. Therefore, image (b) exhibits a stripelike contrast. Since the sample was magnetized in plane before the measurements, all magnetic polarization vectors are in the same direction. Without magnetization they are randomly distributed as long as the interparticle distance is large enough. Otherwise, dipolar coupling results in local ordering. It is also possible to study the switching between the two states of a single domain particle by using the stray field from the tip plus an external field (Kleiber *et al.*, 1998). Specific orientations of the easy axis within the plane can be induced by preparing elliptical particles (Kleiber *et al.*, 1998).

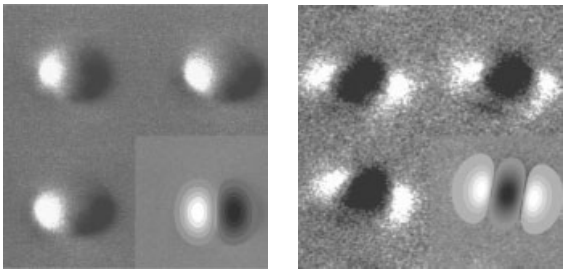

Figure 6. Two Lift-mode AM-MFM images ($1.1 \times 1.1\,\mu\mathrm{m}^2$) of the same single domain particle sample scanned with differently polarized ferromagnetic tips. The disks with a diameter of 200 nm are 17 nm thick with an in-plane easy axis and have been aligned in an external in-plane field of $\mu_0 H_{||} = B_{||} = 0.3\,\mathrm{T}$. The inset in the lower right corner shows simulations of the contrast assuming a purely out-of-plane (a) and in-plane (b) polarized tip, respectively.

The properties and behavior of single domain particles, for example, their magnetization reversal, are of particular interest for magnetic data storage. Granular thin films with typical grain diameters of about 12 nm are used in cobalt based recording media (Thompson and Best, 2000). Today, only a few hundred grains constitute one bit. One source of noise in the readback signal is the presence of domain walls. If only one bit is stored in just one grain, this problem can be overcome. However, one problem is to increase the packing

density of well-defined particle arrays. Another important issue is the so-called superparamagnetic limit. When the size is reduced even more, the direction of the magnetic polarization rotates freely due to thermal excitation and in some respects the particle behaves like a paramagnet and therefore is useless for data storage.

2.10 Magnetic vortices

In small thin square-shaped elements certain magnetic configurations exist, where the magnetic polarization is not uniform, but no real domain walls exist, for example, the so-called C-, S-, and Flower states (Goll, Schütz and Kronmüller, 2003). If the lateral dimensions of the square are large enough, the Landau flux-closure pattern develops, where the magnetic polarization is oriented parallel to the edges. Along the diagonals 90° domain walls are formed. In the center of the square, spin frustration leads to a full out-of-plane rotation of the magnetic polarization. Something similar can occur in disks. For a given disk diameter and a thickness above the critical thickness, below which the single domain state is stable, a vortex state can develop. The magnetic polarization follows the disk curvature and rotates out of plane toward the center, where it finally orients perpendicular to the disk plane. Such a vortex state can be seen in Figure 7 (Shinjo *et al*., 2000). Each permalloy ($Ni_{80}Fe_{20}$) disk is 50 nm thick. The tip was polarized along its axis. Bright and dark dots in their centers mark the positions of the vortices, where the magnetic stray field of the sample and the magnetic polarization of the tip are parallel or antiparallel, respectively. In (a) all disk diameters are 1 µm, while they vary from 100 nm to 1 µm in (b). Unlike in (a) all central dots are dark in (b), because the specimen has been magnetized prior to the MFM measurement. The resolution of MFM does not allow to investigate the fine structure of the vortex core. However, this has been achieved by SP-STM (see Section 3.4). At this point, it should be mentioned that another vortex type has been observed with MFM. Superconducting vortices (flux lines) occur in type II superconductors and consist of a normal conducting core, which is screened by circular currents from the superconducting phase. Each vortex carries one quantum flux, which can be detected by MFM via its stray field. In particular, the arrangements of vortices, for example, the glass state (Moser *et al*., 1995) or the regular Abrikosov lattice (Volodin, Temst, van Haesendonck and Bruynseraede, 1998) and the influence of defects (Pi *et al*., 2004) have been studied. Since the physics behind superconductivity is somewhat different from the magnetism treated here, it will be not discussed further.

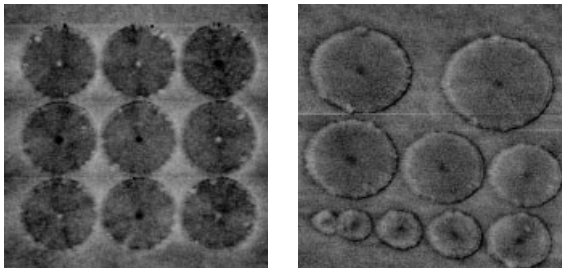

Figure 7. Lift-mode AM-MFM images ($3.6 \times 3.6\,\mu m^2$) of permalloy ($Ni_{80}Fe_{20}$) disks with a thickness of 50 nm. In (a) all disks have a diameter of 1 µm. The spot in the center indicates a vortex, where the magnetization is forced out of plane due to spin frustration. It is bright, if vortex polarity and tip magnetic polarization are parallel, or dark if vortex polarity and tip magnetic polarization are antiparallel. The diameters in (b) range from 100 nm to 1 µm. All vortices exhibit the same polarity, because they were aligned in an external magnetic field of $\mu_0 H_\perp = B_\perp = 1.5\,T$ normal to the sample surface. (Courtesy T. Shinjo (Shinjo *et al*., 2000).)

2.11 The future of MFM

MFM detects only the long-range magnetostatic tip–sample interaction. However, magnetic ordering exists due to the exchange interaction between the electron spins of neighboring atoms in a solid. Several theoretical calculations predicted the feasibility to detect the exchange force between an individual spin of a magnetically ordered sample and the spin of the foremost atom of a magnetic tip at sufficiently small tip–sample distances (Wiesendanger *et al*., 1990a; Mukasa *et al*., 1994; Foster and Shluger, 2001; Momida and Oguchi, 2005). AFM in the dynamic mode using the FM technique in vacuum has proven its capability of achieving *true* atomic resolution (FM-AFM, also known as NC-AFM, cf. Section 2.1). However, the experimental realization of *magnetic exchange force microscopy* (MExFM) is very difficult, because the exchange force is much weaker than the chemical interactions that are responsible for the atomic-scale contrast. Experiments with ferromagnetic tips have been performed on the antiferromagnetic NiO(001) surface at room temperature (Hosoi, Sueoka, Hayakawa and Mukasa, 2000) and with a considerably better signal-to-noise ratio at low temperatures (Allers, Langkat and Wiesendanger, 2001; Hoffmann *et al*., 2003). Although it was possible to achieve atomic resolution, a periodic contrast that could be attributed to the antiferromagnetically ordered spins of the nickel atoms could not be observed in those experiments. However, very recently MExFM has been successfully established by operating a low-temperature AFM in a strong external field, whereby the magnetic polarization of the tip was aligned in a favourable direction. Under these conditions the arrangement of the magnetic moments at the NiO(001) surface could clearly be resolved (Kaiser, Schwarz and Wiesendanger, 2006).

3 SPIN-POLARIZED SCANNING TUNNELING MICROSCOPY

A magnetically sensitive imaging technique which offers an even higher lateral resolution than MFM is spin-polarized scanning tunneling microscopy and spectroscopy (SP-STM/STS). It combines the atomic-resolution capability of conventional, that is, spin-averaged, STM with spin sensitivity. This is achieved by making use of the tunneling magnetoresistance effect between two magnetic electrodes which – in planar geometries and with oxidic barriers – is well studied and routinely utilized for data storage applications. Similar to conventional, that is, spin-averaged STM an atomically sharp tip is scanned at close distance ($\approx$1 nm) across the sample surface. As a bias voltage, typically in the range of several millivolts to a few volts, is applied between tip and sample; a tunneling current flows. Since this tunneling current is strongly distance dependent with a decay constant in the range of $10^{-10}\,\mathrm{m}^{-1}$ it can effectively be used for sampling contours of constant local electronic density of states (LDOS) (Tersoff and Hamann, 1983) which – in the case that the sample's LDOS does not vary too strongly – closely resembles the sample's topography. The tunneling magnetoresistance effect used in SP-STM is based on the principle that, in general, the spin of an electron is conserved during tunneling across a vacuum barrier. Since magnetic materials exhibit an intrinsic imbalance between the spin-majority and spin-minority electronic DOS this leads to a junction transmittance which depends on the relative magnetization directions of the two electrodes involved (Wiesendanger *et al*., 1990b). This review will describe three different operational modes, each with specific amenities and limitations, which allow the measurement of the sample's local magnetization direction.

3.1 Modes of operation

A simple yet powerful theoretical description of these methods was developed by Wortmann and coworkers (2001). They decomposed the tunneling current I measured at tip position $\vec{r}_\mathrm{T}$ and bias voltage U into spin-averaged and spin-dependent contributions, I_0 and I_SP, respectively:

$$I(\vec{r}_\mathrm{T}, U, \theta) = I_0(\vec{r}_\mathrm{T}, U) + I_\mathrm{SP}(\vec{r}_\mathrm{T}, U, \theta) \tag{14}$$

θ is the angle between the magnetization vectors of tip and sample, $\vec{m}_\mathrm{T}$ and $\vec{m}_\mathrm{S}$. By employing Bardeen's description of tunneling Wortmann and coworkers got

$$I(\vec{r}_\mathrm{T}, U, \theta) = \frac{4\pi^3 C^2 \hbar^3 e}{\kappa^2 m^2}\left[n_\mathrm{T}\widetilde{n}_\mathrm{S}(\vec{r}_\mathrm{T}, U) + \vec{m}_\mathrm{T}\widetilde{\vec{m}}_\mathrm{S}(\vec{r}_\mathrm{T}, U)\right] \tag{15}$$

where n_T is the non-spin-polarized LDOS at the tip apex, $\widetilde{n}_\mathrm{S}$ is the energy-integrated LDOS of the sample, and $\vec{m}_\mathrm{T}$ and $\widetilde{\vec{m}}_\mathrm{S}$ are the corresponding vectors of the (energy-integrated) spin-polarized (or magnetic) LDOS:

$$\widetilde{\vec{m}}_\mathrm{S}(\vec{r}_\mathrm{T}, U) = \int_{E=E_\mathrm{F}}^{E=eU} \vec{m}_\mathrm{S}(\vec{r}_\mathrm{T}, E)\,\mathrm{d}E \tag{16}$$

with

$$\vec{m}_\mathrm{S} = \sum \delta(E_\mu - E)\boldsymbol{\Psi}_\mu^{S\dagger}(\vec{r}_\mathrm{T})\boldsymbol{\sigma}\boldsymbol{\Psi}_\mu^{S}(\vec{r}_\mathrm{T}) \tag{17}$$

$\boldsymbol{\Psi}_\mu^S$ denotes the spinor of the sample wave function

$$\psi_\mu^S = \begin{pmatrix} \psi_{\mu\uparrow}^S \\ \psi_{\mu\downarrow}^S \end{pmatrix} \tag{18}$$

and $\boldsymbol{\sigma}$ is Pauli's spin matrix.

According to equation (15) the tunneling current is expected to depend on the relative magnetic orientation between tip and sample since – similar to Slonczewski's model (Slonczewski, 1989) for planar junctions – I_SP scales with the projection of $\widetilde{\vec{m}}_\mathrm{S}$ onto $\vec{m}_\mathrm{T}$, or, in other words, with the cosine of the angle included between the magnetization directions of the two electrodes, $\cos\theta$. Usually, an STM is operated in the constant-current mode where a feedback circuit drives the z component of the piezoelectric actuator such that the tunneling current remains constant while scanning the tip over the sample surface. Since, however, the tunneling current scales exponentially with the tip–sample distance,

$$I \propto \exp(-\kappa z) \tag{19}$$

with κ on the order of $10^{-10}\,\mathrm{m}^{-1}$, even a rather substantial variation of the total tunneling current by several 10% leads to a variation of the tip height on the order of a few tens of picometers ($1\,\mathrm{pm} = 10^{-12}\,\mathrm{m}$) only (Wiesendanger *et al*., 1990b; Kleiber, Bode, Ravlić and Wiesendanger, 2000). Such tiny effects are difficult to detect and also hard to separate from height variations of purely structural or electronic origin. Therefore, as will be demonstrated in Section 3.7, the constant-current mode of SP-STM is primarily suitable for atomic resolution studies on atomically flat surfaces.

One possibility to overcome the difficulties of separating topographic, electronic, and magnetic information is the measurement of the local differential conductance $\mathrm{d}I/\mathrm{d}U$.

Hereby, a small modulation U_{mod} is superimposed to the bias voltage U and the resulting current modulation is detected by means of lock-in technique. Assuming a featureless electronic structure of the tip, the spin-averaged measurement of the differential conductivity, $\mathrm{d}I/\mathrm{d}U_0\,(\vec{r}_{\mathrm{T}}, U) \propto n_{\mathrm{S}}$, gives access to the sample's non-spin-polarized LDOS n_{S} (Selloni, Carnevali, Tosatti and Chen, 1985; Tersoff and Hamann, 1983). If we apply magnetic tips, however, spin-polarized components also contribute and, according to Wortmann *et al*. (2001), the differential conductance can be written as:

$$\begin{aligned}\frac{\mathrm{d}I}{\mathrm{d}U}(\vec{r}_{\mathrm{T}}, U) &= \frac{\mathrm{d}I}{\mathrm{d}U}(\vec{r}_{\mathrm{T}}, U)_0 + \frac{\mathrm{d}I}{\mathrm{d}U}(\vec{r}_{\mathrm{T}}, U)_{\mathrm{SP}} \\ &\propto n_{\mathrm{T}} n_{\mathrm{S}}(\vec{r}_{\mathrm{T}}, E_{\mathrm{F}} + eU) + \vec{m}_{\mathrm{T}}\vec{m}_{\mathrm{S}}(\vec{r}_{\mathrm{T}}, E_{\mathrm{F}} + eU)\end{aligned} \tag{20}$$

This so-called local differential conductance or $\mathrm{d}I/\mathrm{d}U$ mode is sensitive to the spin polarization within a narrow energy interval ΔE around $E_{\mathrm{F}} + eU$. Therefore, it can nicely be applied to spin-polarized surface states (Bode, Getzlaff and Wiesendanger, 1998; Kleiber, Bode, Ravlić and Wiesendanger, 2000) which often provide a large conductance and a high polarization. Even more important, the $\mathrm{d}I/\mathrm{d}U$ signal can be measured simultaneously with the topographic information, thereby allowing an efficient means of separating topographic from electronic and magnetic information. It is important to note, however, that the spin polarization of the magnetic LDOS $\vec{m}_{\mathrm{S}}$ not only changes in size but may also change its sign if different energy intervals ΔE are compared. For example, the surface (and also the tip) may exhibit a positive spin polarization in one energy interval but a negative spin polarization in another (Bode, Getzlaff and Wiesendanger, 1998; Wiesendanger, Bode and Getzlaff, 1999). Consequently, a high $\mathrm{d}I/\mathrm{d}U$ signal does not imply that the magnetization directions of both electrodes are parallel, but rather that the magnetic LDOS in both electrodes have the same sign.

As long as surfaces with homogeneous (spin-averaged) electronic properties are investigated, the differential conductance mode offers a convenient way of imaging magnetic domains at high spatial resolution. For surfaces with an inhomogeneous structure a separation of spin-averaged electronic from magnetic effects can be accomplished by first recording a $\mathrm{d}I/\mathrm{d}U$ image with a bias voltage for which the spin asymmetry defined by

$$A = \frac{\mathrm{d}I/\mathrm{d}U_{\uparrow\downarrow} - \mathrm{d}I/\mathrm{d}U_{\uparrow\uparrow}}{\mathrm{d}I/\mathrm{d}U_{\uparrow\downarrow} + \mathrm{d}I/\mathrm{d}U_{\uparrow\uparrow}} \tag{21}$$

becomes zero (electronic contrast image) and simultaneously recording a second $\mathrm{d}I/\mathrm{d}U$ image with a bias voltage for which the spin asymmetry is maximum (magnetic contrast image) (Pietzsch, Kubetzka, Bode and Wiesendanger, 2004). An alternative means of separating the magnetic contributions which is based an a similar approach by Johnson and Clarke (1990) was developed by Wulfhekel and Kirschner (1999). In analogy to experiments performed on planar tunnel junctions they used a tiny coil for periodically switching the tip magnetization $\vec{m}_{\mathrm{T}}$ back and forth. If the modulation frequency exceeds the cutoff frequency of the feedback loop the measured signal of this so-called local tunneling magnetoresistance mode becomes proportional to the local magnetization of the sample (Wortmann *et al*., 2001):

$$\frac{\mathrm{d}I}{\mathrm{d}\vec{m}_{\mathrm{T}}}(\vec{r}_{\mathrm{T}}) \propto \vec{m}_{\mathrm{S}}(U) \tag{22}$$

Although this mode of operation can effectively separate structural and spin-averaged electronic contributions from magnetic effects, it is important to note that the spin polarization of the magnetic LDOS $\widetilde{\vec{m}}_{\mathrm{S}}$ is not constant, but that its size and sign depends on the respective energy range under study. It may occur, for instance, that contributions with positive and negative spin polarization cancel each other. In this case, the spin polarization of the total tunneling current and thereby the $\mathrm{d}I/\mathrm{d}\vec{m}_{\mathrm{T}}$ signal vanishes in spite of the fact that a local magnetization exists. Another limitation of this technique is that ferromagnetic probe tips have to be used and that their stray field may affect the local magnetization distribution of the sample under investigation.

3.2 Tip preparation

The most delicate part when operating an SP-STM is the preparation of suitable probe tips. So far, two concepts were successfully used, that is, thin-film tips prepared by evaporation of magnetic material onto the tip apex for the constant-current mode and the differential conductance mode as well as amorphous bulk tips for the local magnetoresistance mode.

Thin-film tips are usually prepared by deposition of magnetic material onto an electrochemically etched W tip. Upon etching, the tip is introduced into the vacuum system via a load lock. Early experiments indicated that films evaporated onto untreated tips are mechanically unstable and can easily be lost when approaching toward the sample surface or while scanning. It was found that the film stability can be improved significantly by briefly heating the tip by electron bombardment prior to deposition to about 2200 K. Probably, this high-temperature flash melts the tip apex and removes contaminations which weaken the interfacial sticking. As evidenced by the scanning electron microscopy images shown in Figure 8, however, it also results in blunt tips with a typical diameter of about 1 µm (Bode, Pietzsch, Kubetzka and Wiesendanger, 2001). If such a tip

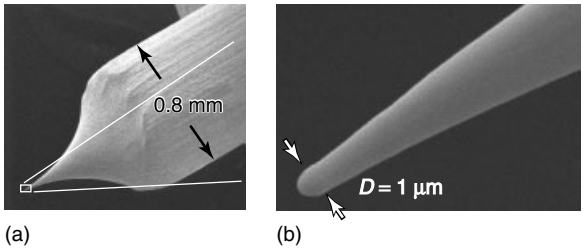

Figure 8. Scanning electron microscopy images of a flashed W tip at (a) medium and (b) higher magnification revealing a tip diameter of about 1 µm.

is coated with 5–10 AL Gd, a GdFe alloy, or a rather thin Cr film (50 AL), out-of-plane sensitivity is obtained. However, the easy magnetization axis of such tips is not always along the tip axis; for example, tips coated with 5–10 AL Fe or more than 100 AL Cr were found to be in-plane sensitive (Bode *et al.*, 2001). Obviously, material-specific surface and interface anisotropies seem to be more important than the shape anisotropy for determining the tip's magnetization direction.

The local magnetoresistance mode, where bulk magnetic material is periodically switched by an external coil, requires a careful choice of the tip material as the tip's magnetization reversal may mechanically couple into the tunnel junction by magnetoelastic coupling (Wulfhekel and Kirschner, 1999). Furthermore, the stray field may cause unwanted changes of the sample's domain structure. In order to minimize these problems, the amorphous ferromagnet CoFeSiB is a suitable material as it combines a low magnetoelastic coupling constant with a low saturation magnetization. By choosing appropriate tip geometries it was possible to tune the sensitivity between out of plane or in plane. As mentioned in the preceding text, the magnetic contrast scales with the angle between the magnetization directions of tip and sample. Out-of-plane sensitivity is easily achieved as a pointed object like an STM tip usually prefers a magnetization direction along the tip axis since this reduces its magnetostatic energy. Figure 9(a) schematically shows an out-of-plane sensitive tip together with the coil which drives the periodic magnetization reversal. Owing to the intrinsic geometry of the STM it is much more difficult to obtain in-plane magnetic contrast. This could be achieved by using tiny ring-shaped tips (Schlickum, Wulfhekel and Kirschner, 2003) as schematically illustrated in Figure 9(b).

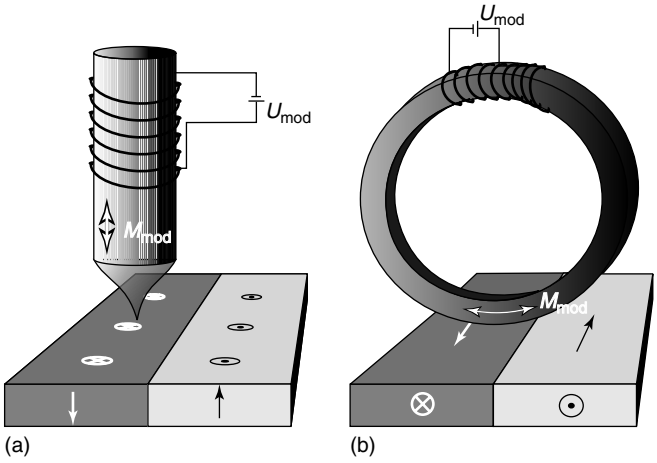

Figure 9. Schematic experimental setup for local magnetoresistance measurements with the STM using (a) an out-of-plane pointed tip and (b) an in-plane-sensitive ring-shaped probe.

3.3 Domain wall structure

In order to prove the high spatial resolution capability of SP-STM a suitable and well-defined test sample is required. The surface spin structure of in-plane magnetized Fe(001) whiskers has been intensively studied by scanning electron microscopy with polarization analysis (SEMPA) in the past (Scheinfein, Unguris, Celotta and Pierce, 1989; Oepen and Kirschner, 1989). In contrast to bulk domain walls, which exhibit a Bloch-like profile, a so-called Néel cap was found on the surface, that is, the magnetization rotates within the plane in order to reduce the magnetostatic energy.

Figure 10(a) and (b) show the topography and the simultaneously measured local magnetoresistance $\mathrm{d}I/\mathrm{d}\vec{m}$ of the

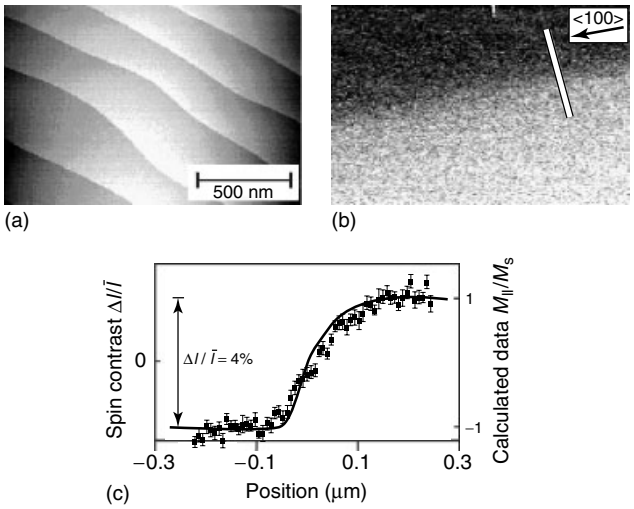

Figure 10. (a) Topography (left column) and (b) the simultaneously measured local tunneling magnetoresistance signal in the central region of an Fe(001) whisker. A domain wall running along a ⟨100⟩ direction can be recognized. A line profile measured along the line in (b) together with a simulated profile is plotted in (c). (Data with courtesy of W. Wulfhekel (Schlickum, Wulfhekel and Kirschner, 2003).)

central region of an Fe(001) whisker, respectively. The topography exhibits six monatomic step edges which separate atomically flat terraces. As visible in the $\mathrm{d}I/\mathrm{d}\vec{m}$ signal in Figure 10(b) a domain wall separates two domains being visible in the upper and the lower part of the magnetic image. The averaged line profile of Figure 10(c) which was taken along the line in (b) reveals a contrast $\Delta I/\overline{I}$ of 4% and a domain wall width of about 100 nm. Comparison with a simulated line profile (black line) shows fair agreement between experiment and micromagnetic calculations (Scheinfein *et al*., 1991).

Much more narrow domain walls were found in Fe nanowires on stepped W(110) (Kubetzka, Pietzsch, Bode and Wiesendanger, 2003). The upper left panel of Figure 11(a) shows a spin-resolved $\mathrm{d}I/\mathrm{d}U$ map of 1.8 AL Fe on W(110) as measured with an in-plane-sensitive tip at zero field (0 mT). Since the total coverage is below two atomic layers the second layer is not closed. Instead, it forms nanowires (DL) along the substrate's step edges which are separated by narrow regions of monolayer coverage. Within the DL nanowires white and black lines can be recognized. They originate from 180° walls which are parallel or antiparallel with respect to the tip magnetization direction, respectively. The wall width amounts to $w \approx 7$ nm. The intermediate $\mathrm{d}I/\mathrm{d}U$ signal (gray) corresponds to a perpendicular magnetization oriented either up or down, two cases which cannot be distinguished with a tip exhibiting pure in-plane sensitivity. The other panels of Figure 11(a) show the same sample area exposed to an increasing perpendicular magnetic field of up to 800 mT. Owing to the Zeeman energy, areas which are magnetized parallel to the field direction grow at the expense of antiparallel ones. Pairs of 180° walls which enclose an antiparallel domain (with respect to the external field) are forced together. Thereby, 360° domain walls are formed.

The internal structure of the 360° walls has been analyzed in detail by Kubetzka *et al*. (2003). Figure 11(b) shows experimental line sections (gray circles) of two adjacent domain walls. The wall profiles can be described by the sum of two 180° walls at the positions $\pm c$:

$$\varphi_{360}(x) = \sum_{+,-} \arcsin\left(\tanh\left(\frac{x \pm c}{w/2}\right)\right) \qquad (23)$$

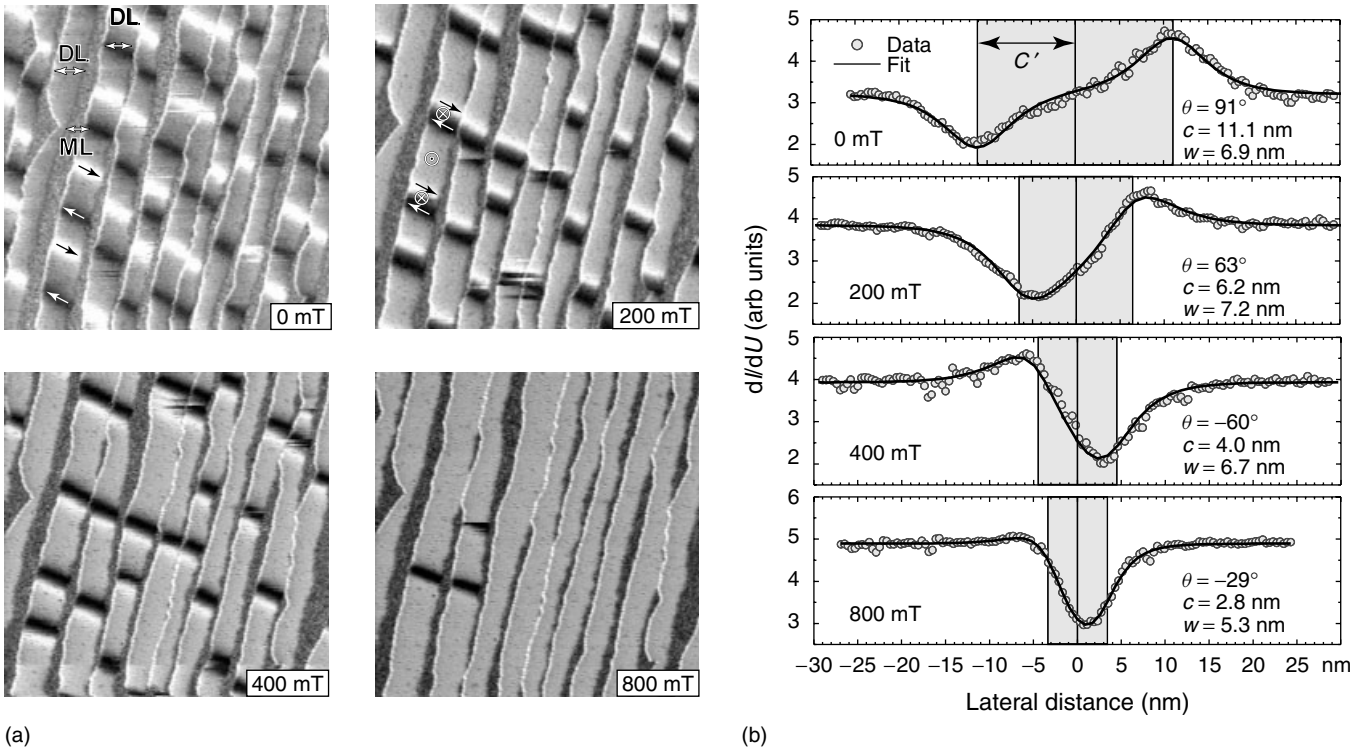

Figure 11. (a) Spin-resolved $\mathrm{d}I/\mathrm{d}U$ maps (scan range: $200 \times 200\,\mathrm{nm}^2$) of perpendicularly magnetized Fe double-layer (DL) nanowires separated by monolayer segments measured at different external fields. At zero field (upper left) black and white lines can be recognized which are approximately equidistant. These lines correspond to differently oriented domain walls (arrows) indicating that the tip is in-plane sensitive. As the external field is enhanced domain wall pairs are formed. Thereby, the domain which is antiparallel to the external field (⊗) is clamped between two domain walls. (b) Experimental line sections (○) of the spin-resolved $\mathrm{d}I/\mathrm{d}U$ signal taken across two domain walls and fits with two 180° domain wall profiles (black line).

The values of c and w can then be extracted from the data if the varying tip magnetization is taken into account. Using the function

$$y(x) = y_0 + a \cdot \cos(\varphi_{360}(x) + \theta) \tag{24}$$

one obtains the fitted curves which are shown as black lines in Figure 11(b). The resulting fit parameters θ, c, and w are displayed within the figure. Owing to the impact of the external field on the ferromagnetic tip θ decreases from 90° to about 30°. The extension of the inner 180° rotation between the two opposite in-plane orientations, which is approximately $2c$, has been marked by a shaded area.

3.4 Magnetic vortices

As described in the previous section (Section 2.10) the existence of perpendicularly magnetized magnetic vortex cores was proven by MFM (Raabe *et al*., 2000; Shinjo *et al*., 2000). However, MFM cannot elucidate the internal spin structure of vortex cores because: (i) the lateral resolution is typically limited to $\approx$20–50 nm, that is, larger than the vortex core, (ii) the magnetic stray field of the MFM tip easily interferes with the vortex, and (iii) the sensitivity is restricted to the out-of-plane component of the stray field gradient. All three problems are avoided by SP-STM using antiferromagnetic probe tips (Kubetzka, Bode, Pietzsch and Wiesendanger, 2002; Wachowiak *et al*., 2002).

Before focusing on the high spatial resolution capabilities of SP-STM we want to demonstrate that magnetic thin-film tips in the differential conductance mode can also be used to study the magnetic domain structure of soft magnetic particles on a nanometer scale. Micromagnetic calculations by Hertel (2002) showed that the lowest-energy domain configuration also depends on the thickness. With increasing thickness a transition from the so-called C-state via the Landau-type or vortex configuration into a diamond state (double-vortex) was found. This behavior is caused by the thickness-dependent contribution of the magnetostatic energy which has to be paid wherever the magnetization is perpendicular to the element's rim. At a certain critical thickness it is energetically favorable to avoid the stray field by magnetizing the element along the edges throughout the entire particle, leading to a so-called flux-closure arrangement.

This transition can be studied by SP-STM. The left column of Figure 12 shows the topography of Fe islands which were epitaxially grown on W(110). The mean island height h varies between 3.5 nm (Figure 12a) and 8.5 nm (Figure 12c). Note that the lateral dimensions of the islands – irrespective of their height – are almost equal, that is, about $250 \times 500\,\mathrm{nm}^2$ along the $[1\bar{1}0]$ and the [001] direction, respectively. In the right column of Figure 12 $\mathrm{d}I/\mathrm{d}U$ maps measured with in-plane-sensitive Cr-coated tips are shown. Since Cr is an antiferromagnetic material these tips possess no stray field and cannot interact with the sample's domain structure via magnetostatic interactions (Kubetzka, Bode, Pietzsch and Wiesendanger, 2002). Since the Fe islands exhibit either a low (dark) or a high (bright) $\mathrm{d}I/\mathrm{d}U$ signal without any significant variation on each particular island, we conclude that the Fe islands shown in Figure 12(a) are in the single domain state. Evidently, there exists a close correlation between the magnetization direction of individual Fe islands and the surrounding Fe ML: dark (bright) Fe islands are always surrounded by a dark (bright) ML. magnetized along $[1\bar{1}0]$. The island in Figure 12(b) exhibits a height $h = 7.5$ nm. The corresponding spin-resolved $\mathrm{d}I/\mathrm{d}U$ map shows the typical pattern of a single vortex state (Wachowiak *et al*., 2002). A diamond state is found on the even higher island shown in Figure 12(c) ($h = 8.5$ nm) (Bode *et al*., 2004).

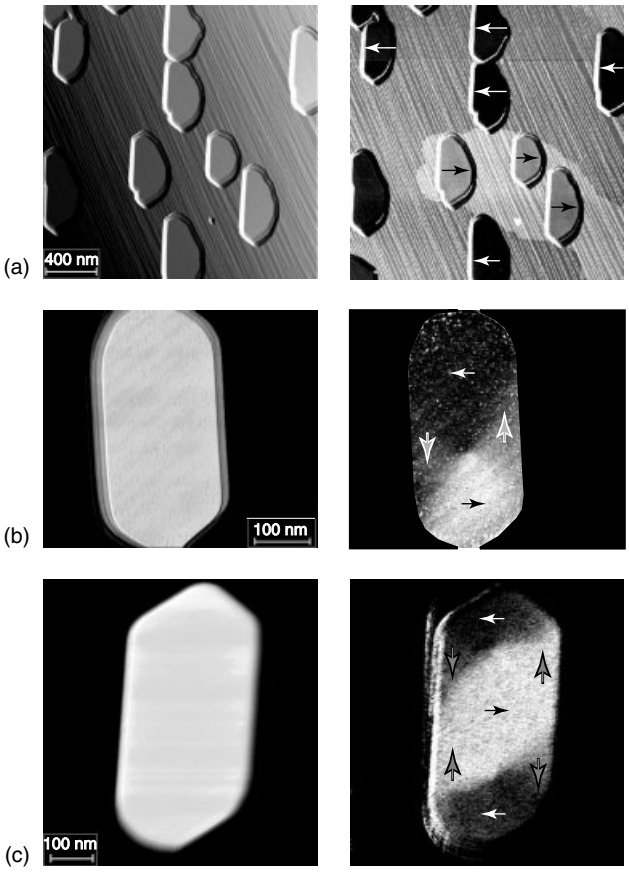

Figure 12. Topography (left column) and spin-resolved $\mathrm{d}I/\mathrm{d}U$ maps (right) of Fe islands on W(110). The mean island height is (a) 3.5 nm, (b) 7.5 nm, and (c) 8.5 nm. With increasing island thickness the magnetic ground state develops from single domain to the vortex configuration and finally to the diamond state.

According to equation (15), the magnetic contrast of SP-STM data scales with the projection of the vector representing the sample magnetization onto the tip magnetization. Consequently, we expect a cosine-like dependence of the magnetic signal if the sample magnetization rotates continuously. This condition is fulfilled in the vortex configuration as observed in Figure 12(b). Here, the magnetization tangentially curls around the particle's center, where a discontinuity of the magnetization is avoided by the formation of an out-of-plane magnetized vortex core, which – depending on the actual material used – is about 10–50 nm in diameter.

Figure 13(a) shows a schematic representation of the expected SP-STS contrast in the vicinity of a vortex core. The actual tip magnetization direction is indicated by an arrow at the left. If bias-dependent effects are not considered, we expect a high (low) signal, if tip and sample are magnetized (anti)parallel and an intermediate contrast, if they are perpendicular. This is indicated by different gray values in the background of Figure 13(a).

In order to illustrate the contrast mechanism of the differential conductance or $\mathrm{d}I/\mathrm{d}U$ mode in more detail, Figure 13(b) shows tunneling $\mathrm{d}I/\mathrm{d}U$ spectra which were measured with an in-plane-sensitive Cr-coated probe tip on top of an about 8 nm high island showing a vortex configuration (Wachowiak *et al.*, 2002). Although the spin-averaged electronic structure of the Fe(110) surface is homogeneous, the STS data reveal a strong spatial variation of the spectral intensity over a wide sample bias range. This variation is due to spin-polarized vacuum tunneling between the STM tip and the magnetic sample surface. With this particular tip only a small spin-dependent $\mathrm{d}I/\mathrm{d}U$ contrast is found at positive bias voltages $U > 0.5\,\mathrm{eV}$. At $U = +0.56\,\mathrm{V}$ all spectra cross and the corresponding spin-dependent $\mathrm{d}I/\mathrm{d}U$ map (inset) shows no systematic contrast. At $0.43\,\mathrm{V} < U < +0.56\,\mathrm{V}$ the spin-resolved $\mathrm{d}I/\mathrm{d}U$ signal in the lower right corner is higher than in the upper left corner of the $\mathrm{d}I/\mathrm{d}U$ map. The highest spin asymmetry of about 0.5 is obtained at $U = -0.18\,\mathrm{V}$. The $\mathrm{d}I/\mathrm{d}U$ peaks are probably caused by a spin-minority d-like surface resonance, which is well known from spin-resolved photoelectron emission experiments (Kim, Vescovo, Heinze and Blügel, 2001). At $U = -0.43\,\mathrm{V}$ the spin-dependent $\mathrm{d}I/\mathrm{d}U$ contrast vanishes and inverts at even lower bias voltage. At $U = 0.70\,\mathrm{V}$ the $\mathrm{d}I/\mathrm{d}U$ spectrum measured in the lower left corner of the spin-dependent $\mathrm{d}I/\mathrm{d}U$ map exhibits a local minimum, while the spectrum in the opposite corner exhibits a shoulder. This results in a very high spin asymmetry of about 70% (see bottom panel).

The data of Figure 13(b) nicely demonstrate that a high spin-resolved $\mathrm{d}I/\mathrm{d}U$ signal not necessarily implies that sample and tip are magnetized parallel. Without an external field available, the sample's magnetization direction can only be determined absolutely if the tip magnetization and the spin character (minority vs. majority) of the concerned electronic states are known. The spin-resolved $\mathrm{d}I/\mathrm{d}U$ spectra and maps of Figure 13(b) were acquired by measuring a full spectrum at every pixel which is very time consuming. If just the domain configuration has to be imaged it is sufficient to perform the measurement at one particular bias voltage with a large spin asymmetry.

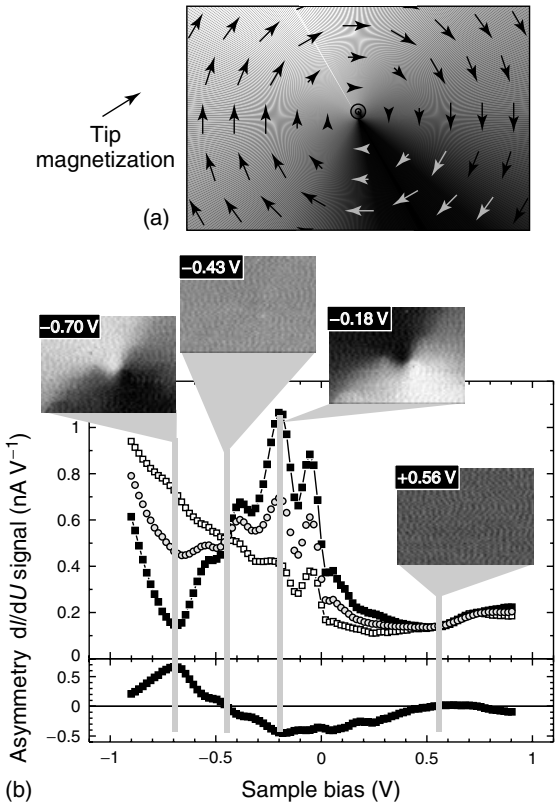

Figure 13. (a) Schematic arrow representation of the tip magnetization (left) and the magnetic structure in the vicinity of a vortex core (right). The contrast in SP-STS images, which is expected to scale with the cosine of the angle included by the tip and local sample magnetization, is shown in gray scale. White, black, and intermediate contrast represents high, low, and medium conductance due to parallel, antiparallel, and orthogonal tip and sample magnetization directions. (b) Tunneling spectra and corresponding spin-resolved $\mathrm{d}I/\mathrm{d}U$ maps (inset) measured with a magnetic tip in the vicinity of a vortex core. The lower panel shows the spin asymmetry between the $\mathrm{d}I/\mathrm{d}U$ spectra measured on the white and black domain.

We have zoomed into the central region of an Fe island where the rotation of the magnetization into the surface normal is expected. Figure 14 shows maps of the spin-resolved $\mathrm{d}I/\mathrm{d}U$ signal measured with Cr-coated tips that are sensitive to the in-plane and out-of-plane components of $\vec{M}_\mathrm{S}$ depending on the thickness of the Cr coating. While the in-plane-sensitive $\mathrm{d}I/\mathrm{d}U$ signal (left column) exhibits the

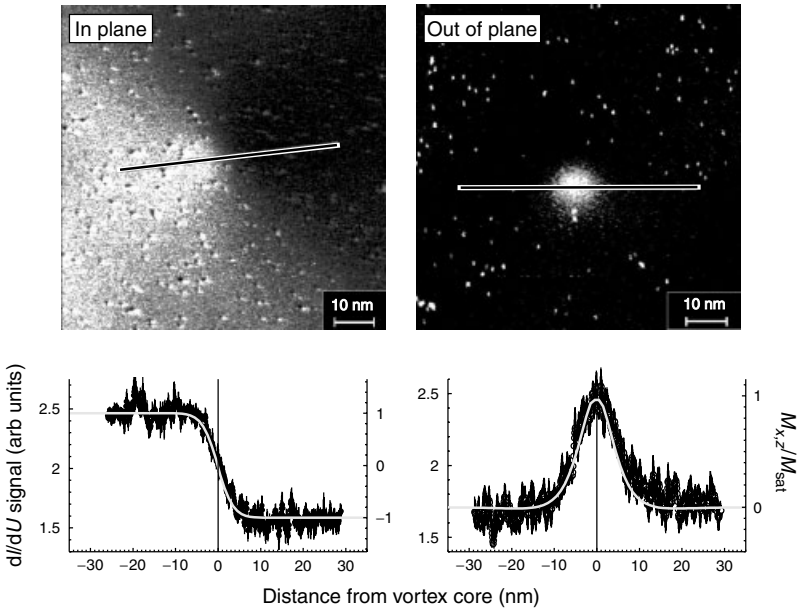

Figure 14. High-resolution spin-resolved $\mathrm{d}I/\mathrm{d}U$ maps taken with in-plane (left) and out-of-plane sensitive Cr-coated tips (right). Experimental line sections taken along the black lines are compared to micromagnetic simulations (gray lines) http://math.nist.gov/oommf/ in the lower panel.

typical Landau pattern the out-of-plane image (right column) shows a homogeneous $\mathrm{d}I/\mathrm{d}U$ signal for the entire island except for a small bright spot approximately located at the island center. This spot is caused by the perpendicular orientation of the magnetization in the vortex core. Line sections drawn along the indicated lines in the experimental $\mathrm{d}I/\mathrm{d}U$ maps (black lines) are plotted in the lower panel. It was predicted theoretically (Feldtkeller and Thomas, 1965; Hubert and Schäfer, 1998) that the shape of a vortex core is determined by the minimum of the total energy, which is dominated by the exchange and the magnetostatic or demagnetization energy. Compared to the latter the magnetocrystalline anisotropy energy, which is relevant for the width of bulk Bloch walls, and the surface anisotropy are negligible, as long as thin films made of soft magnetic materials like Fe are used. For the thin-film limit, that is, $D = 0$, it has been shown (Feldtkeller and Thomas, 1965; Hubert and Schäfer, 1998) that the vortex width as defined by the slope of the in-plane magnetization component in the vortex center is $w_{D=0} = 2\sqrt{A/K_\mathrm{d}} \approx 6.4\,\mathrm{nm}$, where A is the exchange stiffness and $K_\mathrm{d} = \mu_0 {M_\mathrm{sat}}^2/2$ is the magnetostatic energy density with M_sat being the saturation magnetization. This value is in reasonable agreement with the experimental result $w_\mathrm{exp} = 9 \pm 1\,\mathrm{nm}$. For comparison we have also performed micromagnetic calculations employing the widely used OOMMF software http://math.nist.gov/oommf/. In short, the islands were divided into cuboids with lateral dimensions of $1 \times 1\,\mathrm{nm}^2$ and a height of 8 nm. The simulation was started in a perfect vortex state, that is, without any perpendicular component even in the vortex core. Upon relaxation, the simulated profiles (gray lines) are in excellent agreement with the experimental data.

3.5 Exchange-coupled nanoparticles

The ultimate spatial resolution of SP-STM/STS makes it a unique technique for imaging single magnetic particles with dimensions on the single-digit nanometer scale, which can nicely be prepared by epitaxial growth on low-index surfaces of single crystals. For example, Figure 15 shows (a) the topography and (b) the magnetic $\mathrm{d}I/\mathrm{d}U$ signal of a 1.28 ML film as grown on a W(110) substrate held at room temperature. This preparation leads to a closed and thermodynamically stable monolayer of iron and double-layer (DL) iron islands, where the local coverage is $\theta_\mathrm{loc} = 2$ atomic layers (AL) (Gradmann, Liu, Elmers and Przybylski, 1990; Weber *et al*., 1997). As can be recognized in Figure 15(a) the Fe DL islands are about 10 nm wide and elongated along the [001] direction leading to a length of approximately 30 nm on average. This sample system has previously been investigated by Kerr effect measurements (Weber *et al*., 1997) which have been interpreted in terms of a thickness-dependent anisotropy: while the monolayer preferentially keeps the magnetization within the film plane, the DL islands exhibit a perpendicular anisotropy. Consequently, a Gd tip with out-of-plane magnetization is expected to image the domain structure of the DL islands. Indeed, as

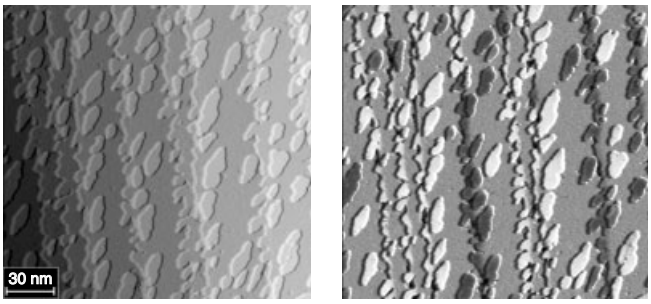

Figure 15. Overview images showing 1.3 AL Fe/W(110): (a) topography and (b) spin-resolved dI/dU map. The perpendicularly magnetized double-layer islands can reduce their magnetostatic energy by changing the magnetization direction of adjacent Fe islands between up and down.

can be recognized in Figure 15(b) two different values of the dI/dU signal are observed representing islands which are magnetized parallel or antiparallel with respect to the tip magnetization. Approximately an equal number of black and white DL islands can be found. By changing the magnetization direction of adjacent Fe islands between up and down on a nanometer scale, the stray field above the sample surface can be reduced. A similar behavior has also been found for narrow Fe DL nanowires where adjacent stripes couple antiparallel (Hauschild, Gradmann and Elmers, 1998; Elmers, Hauschild and Gradmann, 1999; Elmers, 1998; Pietzsch, Kubetzka, Bode and Wiesendanger, 2000).

Images with an even higher magnification (Figure 16) show, however, that the magnetic structure of the Fe DL islands is more complex than a simple demagnetized, noncontinuous out-of-plane medium. Instead, the topography and the corresponding magnetic dI/dU map of Figure 16(a) and (b), respectively, reveal that some islands exhibit an intermediate contrast level. While the dI/dU signal of island A and C is high and low, respectively, island B appears gray, that is, the dI/dU signal measured on this island has an intermediate value. This analysis is also supported by a histogram of the dI/dU signal strength measured above the three DL islands shown Figure 16(c). The experimental observation of Figure 16 can only be explained if island B is either nonmagnetic or in-plane ferromagnetic. As analytically described by a one-dimensional model by Kubetzka *et al.* (2001) – which is based on the model of spatially switching anisotropies introduced by Elmers (1998) – the magnetic behavior of the Fe double-layer islands is governed by the close proximity of regions with different anisotropies: while the closed ML exhibits an in-plane easy axis it is perpendicular for the DL. As long as the DL island is sufficiently large the

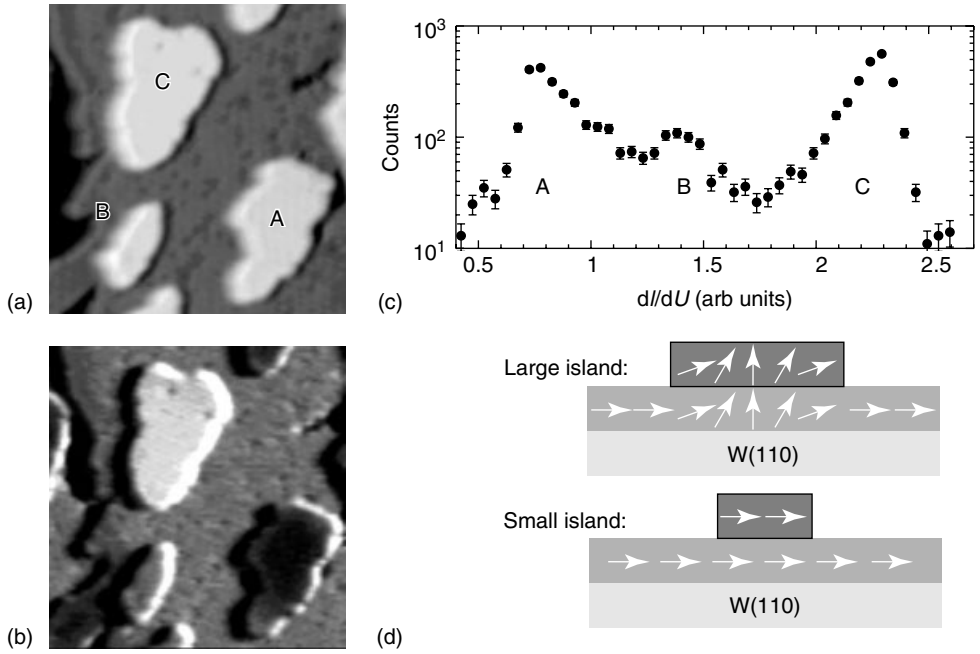

Figure 16. (a) Topography and (b) spin-resolved dI/dU map (scan range: $20 \times 22\,\mathrm{nm}^2$) showing three double-layer islands marked A–C. (c) Histogram of the spin-resolved dI/dU signal measured on the islands' surfaces. Obviously, island B exhibits an intermediate spin-resolved dI/dU signal. (d) In large Fe DL islands, the magnetization rotates out of the easy plane of the monolayer (ML) into the perpendicular easy axis of the double layer (DL) thereby forming a 90° domain wall. As the Fe DL islands become too small it is energetically favorable to keep the magnetization in plane as the domain wall costs too much energy. As a result of the exchange coupling between the DL islands and the in-plane magnetized ML the magnetization of small islands remains within the surface plane.

local magnetization rotates by 90° from in plane to out of plane at the boundary between the closed Fe ML and the DL islands. As the DL islands become smaller and smaller the energy which is gained by turning the magnetization into the easy magnetization direction of the DL decreases, until it is smaller than the energy that has to be paid for the 90° domain wall that surrounds the DL island. Then it is energetically favorable to keep the magnetization of the DL in plane, in spite of the fact that the local anisotropy suggests a perpendicular magnetization direction. This example shows that the high spatial resolution of spin-polarized STM leads to a better understanding of the magnetic properties, especially, if the material is inhomogeneous on the nanoscale.

3.6 Dynamic processes

Microscopy techniques, which acquire the data sequentially by scanning the sample point by point and line by line, offer usually a very limited time resolution which is restricted to the image sampling rate. This is also valid for STM and its spin-sensitive form, that is, SP-STM. Nevertheless, it is possible to observe dynamic processes like the thermal switching behavior of sufficiently small magnetic particles, if the switching time is sufficiently slow.

Epitaxial superparamagnetic particles can be prepared by the evaporation of about 0.1–0.3 AL Fe on Mo(110). For example, the topography of 0.25 AL Fe on Mo(110) is shown in Figure 17(a). Mo is nonmagnetic and therefore cannot couple adjacent islands by direct exchange. As can be seen in Figure 17(b) which was measured with an out-of-plane sensitive Cr tip at $T = 13 \pm 1$ K, most of the Fe islands are too large (area $a > 40\,\mathrm{nm}^2$) and therefore magnetically stable on the timescale of imaging, that is, several seconds. These islands exhibit either a high or a low spin-resolved $\mathrm{d}I/\mathrm{d}U$ signal representing islands being magnetized (anti)parallel with respect to the tip. The spin-dependent $\mathrm{d}I/\mathrm{d}U$ signal of some islands, however, is not constant but changes either between two subsequent lines within one particular image (black arrows in Figure 17(b) and (c)) or between subsequent images (white arrows) indicating that they are magnetically unstable.

As mentioned in the preceding text, the scanning process of SP-STM strongly limits the achievable time resolution. This restriction can be bypassed by giving up one or even both scanning directions and operating the STM in the so-called line or point mode, respectively. In this case, the time resolution is not limited by the image repetition rate but by the line frequency or by the increment between two successive points within one particular scan line. An example of a measurement performed in the line mode is presented in Figure 18. In the lower part of the topographic image of Figure 18(a) a line marks four islands, the section of which is shown in Figure 18(b). These islands are labeled A–D from left to right. By repeatedly scanning along the same line for about 40 min, thereby crossing islands A–D at a rate of 1 Hz, one obtains spin-resolved $\mathrm{d}I/\mathrm{d}U$ maps as shown in Figure 18(c). Since the position of the slow scanning direction is spatially fixed, this direction represents the time rather than a lateral scale. The spin-resolved $\mathrm{d}I/\mathrm{d}U$ maps of Figure 18(c) have been recorded at the same site of the sample at $T = 13$ K (bottom panel) and $T = 19$ K (top panel). At $T = 13$ K islands A and D exhibit a low and island C a high $\mathrm{d}I/\mathrm{d}U$ signal. Since these islands are rather large no switching processes were observed on the timescale of the experiment. Only island B, which is much smaller, switches about 50 times. As the temperature is raised to $T = 19$ K, however, larger islands become magnetically unstable, too. Now even the largest island, D, switched once.

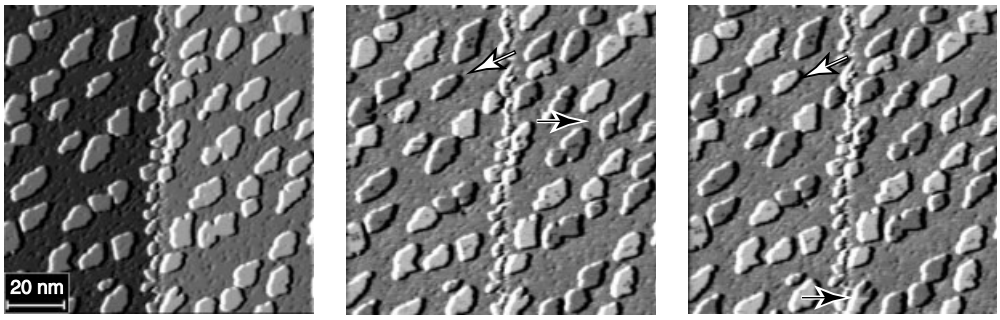

Figure 17. (a) Topography and (b) the simultaneously recorded spin-resolved $\mathrm{d}I/\mathrm{d}U$ map of 0.25 AL Fe/Mo(110). The islands are perpendicularly magnetized up or down. The use of an out-of-plane sensitive Cr-coated probe tip results in a spin-polarized contribution which appears as two distinct $\mathrm{d}I/\mathrm{d}U$ contrast levels. The black arrows indicate Fe islands which switch between two subsequent scan lines of the same image. Obviously, these islands are magnetically unstable at the measurement temperature $T = 13$ K. (c) Another island (white arrow) magnetically switches in the time interval of two successive $\mathrm{d}I/\mathrm{d}U$ maps.

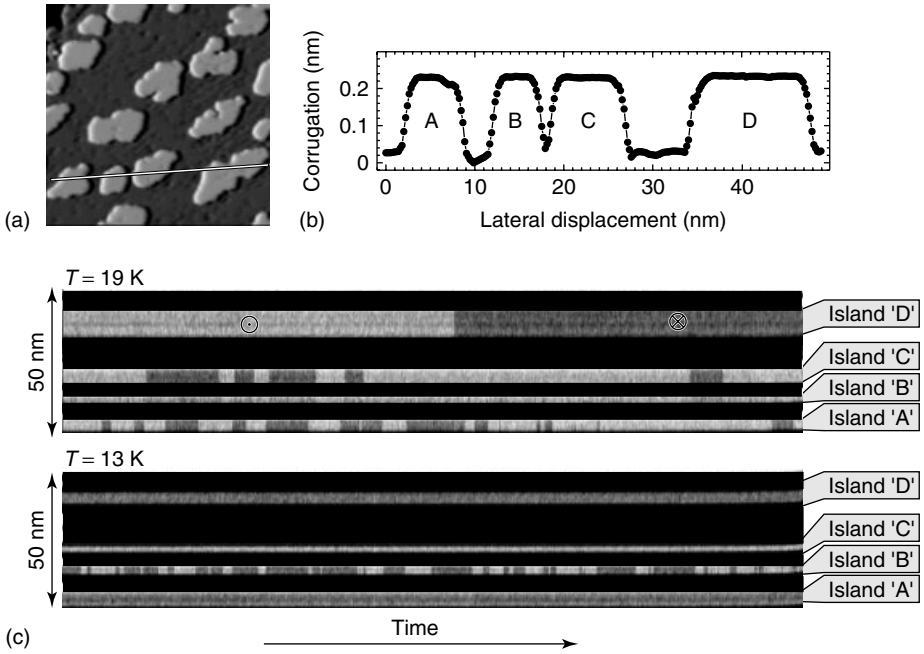

Figure 18. (a) Topography of Fe monolayer islands on Mo(110). The scan range amounts to $40 \times 40\,\mathrm{nm}^2$. (b) Line section showing the profile of four individual islands labeled A–D. (c) Spin-resolved $\mathrm{d}I/\mathrm{d}U$ maps of the islands A–D shown in (b) as measured in the line mode at $T = 13\,\mathrm{K}$ (bottom panel) and $T = 19\,\mathrm{K}$ (top panel).

3.7 Atomic resolution

The special strength of STM is its unique spatial resolution down to the atomic scale. After showing that the SP-STM can also be utilized to obtain information about magnetic properties like the surface domain structure or the spin-dependent LDOS, it is quite straightforward to ask whether atomic spin resolution can also be achieved. Obviously, this task requires an appropriate test sample. The smallest possible magnetic structure is a magnetically ordered surface where the magnetic moment alternates between adjacent atomic sites, that is, an antiferromagnet.

Many materials, which are known to be antiferromagnets in the bulk, are either alloys with a complex stoichiometry that cannot be stabilized at the surface or exhibit a surface magnetic ordering which differs from the bulk (Hänke *et al*., 2005). Therefore, we decided to search for a thin-film antiferromagnet, which can be grown epitaxially on a refractory metal. One potential candidate is the Fe monolayer on W(001). Early density-functional calculations (Wu and Freeman, 1992) surprisingly predicted an antiferromagnetic ground state that has been confirmed recently (Kubetzka *et al*., 2005). Figure 19(a) shows the topography of 1.1 AL Fe/W(001). Several double-layer islands with lateral dimensions of less than 10 nm can be recognized.

With an out-of-plane sensitive Cr-coated probe tip we have zoomed into the monolayer region approximately in the center of Figure 19(a) (see box). Figure 19(b) and (c) show the simultaneously measured spin-resolved constant-current image and $\mathrm{d}I/\mathrm{d}U$ map, respectively. Besides two adsorbates which appear as protrusions, the constant-current image shows a two-dimensional lattice which represents the antiferromagnetic (2×2) superlattice: owing to the spin-polarized contribution to the tunneling current the tip is retracted from (approached toward) the sample surface wherever the tip's magnetic LDOS is (anti)parallel with respect to the sample. As can be seen in the top panel of Figure 19(d) the corrugation amounts to 2 pm only with a periodicity of about 0.5 nm which is in good agreement with the expected 0.45 nm. In the spin-resolved $\mathrm{d}I/\mathrm{d}U$ map of Figure 19(c) the same superstructure is visible.

In order to unambiguously prove the magnetic origin of the superstructure, we have performed field-dependent experiments employing ferromagnetic tips. Since the exchange coupling within the Fe monolayer is much stronger than the Zeeman energy, the external field leaves the sample's magnetic structure unaffected but only changes the vertical component of the tip magnetization. Figure 20 shows images taken within the same $4 \times 4\,\mathrm{nm}^2$ large region around an adsorbate. Between the measurements we have changed the field direction from $+2.5\,\mathrm{T}$ to $-2.5\,\mathrm{T}$. This field strength is sufficient to force the magnetization of Fe-coated tips out of their native in-plane direction to out of plane. If the observed superstructure is indeed of magnetic origin the

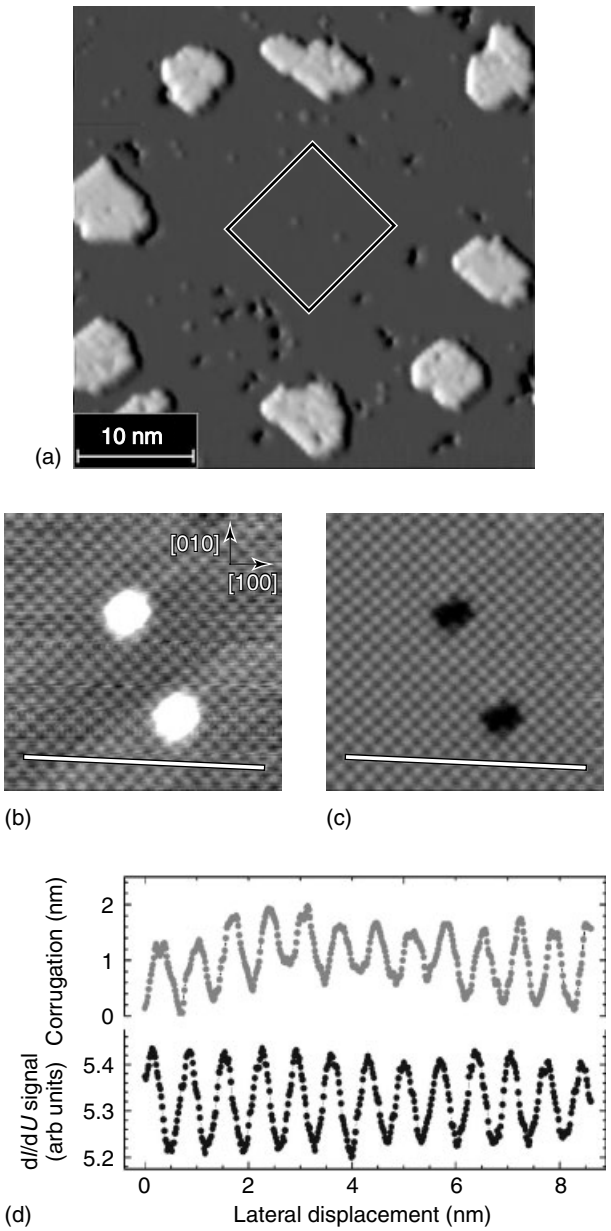

Figure 19. (a) Topography of 1.1 AL Fe on W(001). Within the region marked by the box we have simultaneously measured (b) a spin-resolved constant-current image and (c) a spin-resolved $\mathrm{d}I/\mathrm{d}U$ map. Note that the two adsorbates appear as protrusions in the topography but exhibit a lower $\mathrm{d}I/\mathrm{d}U$ signal strength. (d) Line sections taken along the lines in (b) and (c).

pattern must invert. In contrast, the superstructure would remain unchanged if it were caused by structural effects. The top and bottom images of Figure 20 display the sum and the difference of the two images, respectively. Indeed, the contrast vanishes in the sum and is enhanced in the difference image. Interestingly, the magnetic superstructure is visible even at the position of the adsorbate. This observation

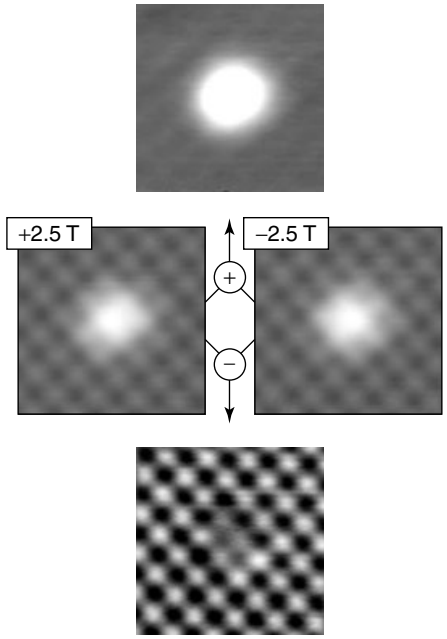

Figure 20. Constant-current images of a $4 \times 4\,\mathrm{nm}^2$ region of an Fe monolayer on W(001) around a native adsorbate measured with an Fe-coated tip at different external fields ($I = 30\,\mathrm{nA}$, $U = -40\,\mathrm{mV}$). Since the exchange coupling within the Fe monolayer is much stronger than the Zeeman energy, the external field leaves the sample's magnetic structure unaffected but only changes the vertical component of the tip magnetization. Thereby, any magnetic contrast is inverted but topographic and spin-averaged electronic contributions remain unchanged (middle row). Consequently, the sum (top row) and the difference (bottom row) of two images recorded with opposite tip magnetization directions allow the separation of nonmagnetic from magnetic contributions, respectively.

indicates that the Fe antiferromagnetic state is largely unaffected by the adsorbate.

SUMMARY

The results shown in this chapter demonstrate that both methods, MFM as well as SP-STM, have been developed into powerful tools for high-resolution studies of the domain structure of nanoscale samples. While MFM is easily applicable even under ambient conditions but offers a rather limited resolution of about 20 nm, SP-STM achieves atomic spin resolution with the drawback that it can only be applied under ultrahigh vacuum UHV conditions so far. Future developments may enable to overcome these limitations; for example, the spatial resolution of MFM can be improved by a further reduction of the tip–sample distance until the magnetic exchange force can be detected (Kaiser, Schwarz and Wiesendanger, 2006). In order to apply SP-STM under ambient conditions one may passivate the sample with an appropriate adsorbate layer (Berbil-Bautista *et al*., 2006).

REFERENCES

Albrecht, T.R., Grütter, P., Horne, D. and Rugar, D. (1991). Frequency modulation detection using high-Q cantilevers for enhanced force microscope sensitivity. *Journal of Applied Physics*, **69**, 668–673.

Alessandro, B., Beatrice, C., Bertotti, G. and Montorsi, A. (1990). Domain-wall dynamics and Barkhausen effect in metallic ferromagnetic materials. I. Theory. *Journal of Applied Physics*, **68**, 2901–2907.

Allers, W., Langkat, S. and Wiesendanger, R. (2001). Dynamic low-temperature scanning force microscopy on nickel oxide (001). *Applied Physics A*, **72**, S27–S30.

Bak, P., Tang, C. and Wiesenfeld, K. (1987). Self-organized criticality: an explanation of the 1/f noise. *Physical Review Letters*, **59**, 381–384.

Barthelmess, M., Pels, C., Thieme, A. and Meier, G. (2004). Stray fields of domains in permalloy microstructures – measurements and simulations. *Journal of Applied Physics*, **95**, 5641–5645.

Baudelet, F., Lin, M-T., Kuch, W., *et al*. (1995). Perpendicular anisotropy and spin reorientation in epitaxial Fe/Cu_3 Au(100) thin films. *Physical Review B*, **51**, 12563–12578.

Berbil-Bautista, L., Krause, S., Hänke, T., *et al*. (2006). Spin-polarized scanning tunneling microscopy through an adsorbate layer: sulfur-covered Fe/W(110). *Surface Science Letters*, **600**, L20–L24.

Binnig, G. and Rohrer, H. (1982). Scanning tunneling microscopy. *Helvetica Physica Acta*, **55**, 726–735.

Binnig, G. and Rohrer, H. (1987). Scanning tunneling microscopy – from birth to adolescence. *Reviews of Modern Physics*, **59**, 615–625.

Bode, M., Getzlaff, M. and Wiesendanger, R. (1998). Spin-polarized vacuum tunneling into the exchange-split surface state of Gd(0001). *Physical Review Letters*, **81**, 4256–4259.

Bode, M., Pietzsch, O., Kubetzka, A. and Wiesendanger, R. (2001). Imaging magnetic nanostructures by spin-polarized scanning tunneling spectroscopy. *Journal of Electron Spectroscopy and Related Phenomena*, **114–116**, 1055–1062.

Bode, M., Pietzsch, O., Kubetzka, A., *et al*. (2001). Experimental evidence for intra-atomic non-collinear magnetism at thin film probe tips. *Physical Review Letters*, **86**, 2142–2145.

Bode, M., Wachowiak, A., Wiebe, J., *et al*. (2004). Thickness dependent magnetization states of Fe islands on W(110): from single domain to vortex and diamond patterns. *Applied Physics Letters*, **84**, 948–950.

den Boef, A.J. (1990). Preparation of magnetic tips for a scanning force microscope. *Applied Physics Letters*, **56**, 2045–2047.

Deng, Z., Yenilmez, E., Leu, J., *et al*. (2004). Metal-coated carbon nanotube tips for magnetic force microscopy. *Applied Physics Letters*, **85**, 6263–6265.

Dreyer, M., Kleiber, M., Wadas, A. and Wiesendanger, R. (1999). Composition-driven change of the magnetic anisotropy of ultrathin Co/Au(111) films studied by means of magnetic-force microscopy in ultrahigh vacuum. *Physical Review B*, **59**, 4273–4278.

Dreyer, M., Löhndorf, M., Wadas, A. and Wiesendanger, R. (1998). Ultra-high-vacuum magnetic force microscopy of the domain structure of ultra-thin Co films. *Applied Physics A*, **66**, 1209–1212.

Elmers, H.J. (1998). Magnetization states in ultrathin films with laterally modulated anisotropies. *Journal of Magnetism and Magnetic Materials*, **185**, 274–282.

Elmers, H.J., Hauschild, J. and Gradmann, U. (1999). Onset of perpendicular magnetization in nanostripe arrays of Fe on stepped W(110). *Physical Review B*, **59**, 3688–3695.

Feldtkeller, E. and Thomas, H. (1965). Struktur und Energie von Blochlinien in duennen ferromagnetischen Schichten. *Physik der Kondensiterten Materie*, **4**, 8–14.

Foster, A.S. and Shluger, A.L. (2001). Spin contrast in non-contact SFM on oxide surfaces: theoretical modelling of NiO(001) surface. *Surface Science*, **490**, 211–219.

Frei, E.H., Shtrikman, S. and Treves, D. (1957). Critical size and nucleation field of ideal ferromagnetic particles. *Physical Review*, **106**, 446–455.

Göddenhenrich, T., Lemke, H., Mück, M., *et al*. (1990). Probe calibration in magnetic force microscopy. *Applied Physics Letters*, **57**, 2612–2614.

Goll, D., Schütz, G. and Kronmüller, H. (2003). Critical thickness for high-remanent single-domain configurations in square ferromagnetic thin platelets. *Physical Review B*, **67**, 094414.

Gradmann, U., Liu, G., Elmers, H.J. and Przybylski, M. (1990). The ferromagnetic monolayer Fe(110) on W(110). *Hyperfine Interactions*, **57**, 1845–1858.

Grütter, P., Rugar, D., Mamin, H.J., *et al*. (1990). Batch fabricated sensors for magnetic force microscopy. *Applied Physics Letters*, **57**, 1820–1822.

Hänke, T., Krause, S., Berbil-Bautista, L., *et al*. (2005). Absence of spin-flip transition at the Cr(001) surface: a combined spin-polarized scanning tunneling microscopy and neutron scattering study. *Physical Review B*, **71**, 184407.

Hauschild, J., Gradmann, U. and Elmers, H.J. (1998). Perpendicular magnetization and dipolar antiferromagnetism in double layer nanostripe arrays of Fe/W(110). *Applied Physics Letters*, **72**, 3211–3213.

Hertel, R. (2002). Thickness dependences of the magnetization structures of thin permalloy rectangles. *Zeitschrift fur Metallkunde*, **93**, 957–962.

Hoffmann, R., Lantz, M.A., Hug, H.J., *et al*. (2003). Atomic resolution imaging and frequency versus distance measurements on NiO(001)using low-temperature scanning force microscopy. *Physical Review B*, **67**, 085402.

Hosoi, H., Sueoka, K., Hayakawa, K. and Mukasa, K. (2000). Atomic resolved imaging of cleaved NiO(100) surfaces by NC-AFM. *Applied Surface Science*, **157**, 218–221.

Hubert, A. and Schäfer, R. (1998). *Magnetic Domains*, Springer.

Hug, H.J., Moser, A., Jung, T., *et al*. (1993). Low temperature magnetic force microscopy. *The Review of Scientific Instruments*, **64**, 2920–2925.

Hug, H.J., Stiefel, B., van Schendel, P.J.A., *et al*. (1998). Quantitative magnetic force microscopy on perpendicularly magnetized samples. *Journal of Applied Physics*, **83**, 5609–5620.

Johnson, M. and Clarke, J. (1990). Spin-polarized scanning tunneling microscope: concept, design, and preliminary results from a prototype operated in air. *Journal of Applied Physics*, **67**, 6141–6152.

Kaiser, U., Schwarz, A. and Wiesendanger, R. (2007). Magnetic exchange force microscopy with atomic resolution. *Nature*, **446**, 522–525.

Kim, H-J., Vescovo, E., Heinze, S. and Blügel, S. (2001). Surface electronic structure of Fe(110): the importance of surface resonances. *Surface Science*, **478**, 193–202.

Kittel, C. (1946). Theory of the structure of ferromagnetic domains in films and small particles. *Physical Review*, **70**, 965–971.

Kleiber, M., Bode, M., Ravlić, R. and Wiesendanger, R. (2000). Topology-induced spin frustrations at the Cr(001) surface studied by spin-polarized scanning tunneling spectroscopy. *Physical Review Letters*, **85**, 4606–4609.

Kleiber, M., Kümmerlen, F., Löhndorf, M., *et al*. (1998). Magnetization switching of submicrometer Co dots induced by a magnetic force microscope tip. *Physical Review B*, **58**, 5563–5567.

Kronmüller, H., Goll, D., Hertel, R. and Schütz, G. (2004). Critical thickness of domain formation in cubic particles and thin film. *Physica B*, **343**, 229–235.

Kubetzka, A., Bode, M., Pietzsch, O. and Wiesendanger, R. (2002). Spin-polarized scanning tunneling microscopy with antiferromagnetic probe tips. *Physical Review Letters*, **88**, 057201.

Kubetzka, A., Pietzsch, O., Bode, M. and Wiesendanger, R. (2001). Magnetism of nanoscale Fe islands studied by spin-polarized scanning tunneling spectroscopy. *Physical Review B*, **63**, 140407.

Kubetzka, A., Pietzsch, O., Bode, M. and Wiesendanger, R. (2003). Spin-polarized scanning tunneling microscopy study of 360° walls in an external magnetic field. *Physical Review B*, **67**, 020401.

Kubetzka, A., Ferriani, P., Bode, M., *et al*. (2005). Revealing antiferromagnetic order of the Fe monolayer on W(001): spin-polarized scanning tunneling microscopy and first-principles calculations. *Physical Review Letters*, **94**, 087204.

Liebmann, M., Schwarz, A., Langkat, S.M. and Wiesendanger, R. (2002). A low-temperature ultrahigh vacuum scanning force microscope with a split-coil magnet. *The Review of Scientific Instruments*, **73**, 3508–3514.

Liebmann, M., Schwarz, A., Kaiser, U., *et al*. (2005). Magnetization reversal of a structurally disordered manganite thin film with perpendicular anisotropy. *Physical Review B*, **71**, 104431.

Liu, Z., Dan, Y., Jinjun, Q. and Wu, Y. (2002). Magnetic force microscopy using focused ion beam sharpened tip with deposited antiferro-ferromagnetic multiple layers. *Journal of Applied Physics*, **91**, 8843–8845.

Lohau, J., Carl, A., Kirsch, S. and Wassermann, E.F. (2001). Magnetization reversal and coercivity of a single-domain Co/Pt dot measured with a calibrated magnetic force microscope tip. *Applied Physics Letters*, **78**, 2020–2022.

Löhndorf, M., Wadas, A., van den Berg, H.A.M. and Wiesendanger, R. (1996). Structure of cross-tie wall in thin Co films resolved by magnetic force microscopy. *Applied Physics Letters*, **68**, 3635–3637.

Löhndorf, M., Wadas, A. and Wiesendanger, R. (1997). Investigation of ripple structures of thin polycrystalline Co films by magnetic force microscopy. *Applied Physics A*, **65**, 511–515.

Mamin, H.J. and Rugar, D. (2001). Sub-attonewton force detection at millikelvin temperatures. *Applied Physics Letters*, **79**, 3358–3360.

Martin, Y. and Wickramasinghe, H.K. (1987). Magnetic imaging by "force microscopy" with 1000 Å resolution. *Applied Physics Letters*, **50**, 1455–1457.

Momida, H. and Oguchi, T. (2005). First principles study on exchange force image of NiO(001) using a ferromagnetic Fe probe. *Surface Science*, **590**, 42–50.

Morita, S., Wiesendanger, R. and Meyer, E. (Eds.) (2002). *Noncontact Atomic Force Microscopy*, Springer.

Moser, A., Hug, H.J., Parashikov, I., *et al*. (1995). Observation of single vortices condensed into a vortex-glass phase by magnetic force microscopy. *Physical Review Letters*, **74**, 1847–1850.

Mukasa, K., Hasegawa, H., Tazuke, Y., *et al*. (1994). Exchange interaction between magnetic moments of ferromagnetic sample and tip: possibility of atomic resolution images of exchange interactions using exchange force microscopy. *Japanese Journal of Applied Physics*, **33**, 6575–6579.

Oepen, H.P. and Kirschner, J. (1989). Magnetization distribution of 180° domain walls at Fe(100) single-crystal surfaces. *Physical Review Letters*, **62**, 819–822.

Donahue, M. and Porter D. (2000). We used the OOMMF program, release 1.2 alpha 2 (http://math.nist.gov/oommf/).

Pi, U.H., Khim, Z.G., Kim, D.H., *et al*. (2004). Direct observation of vortices trapped at stacking fault dislocations in $Bi_2Sr_2CaCu_2O_8$ by a low-temperature magnetic force microscope. *Physical Review B*, **69**, 094518.

Pietzsch, O., Kubetzka, A., Bode, M. and Wiesendanger, R. (2000). Real-space observation of dipolar antiferromagnetism in magnetic nanowires by SP-STS. *Physical Review Letters*, **84**, 5212–5215.

Pietzsch, O., Kubetzka, A., Bode, M. and Wiesendanger, R. (2004). Spin-polarized scanning tunneling spectroscopy of nanoscale cobalt Islands on Cu(111). *Physical Review Letters*, **92**, 057202. http://link.aps.org/abstract/PRL/v92/e057202.

Proksch, R., Foss, S., Dahlberg, E.D. and Prinz, G. (1994). Magnetic fine structure of domain walls in iron films observed with a magnetic force microscope. *Journal of Applied Physics*, **75**, 5776–5778.

Qiu, Z.Q., Pearson, J. and Bader, S.D. (1993). Asymmetry of the spin reorientation transition in ultrathin Fe films and wedges grown on Ag(100). *Physical Review Letters*, **70**, 1006–1009.

Raabe, J., Pulwey, R., Sattler, R., *et al*. (2000). Magnetization pattern of ferromagnetic nanodisks. *Journal of Applied Physics*, **88**, 4437–4439.

Rugar, D., Mamin, H.J. and Guethner, P. (1989). Improved fiber-optic interferometer for atomic force microscopy. *Applied Physics Letters*, **55**, 2588–2590.

Rührig, M., Porthun, S. and Lodder, J.C. (1994). Magnetic force microscopy using electron-beam fabricated tips. *The Review of Scientific Instruments*, **65**, 3224–3228.

Sáenz, J.J., García, N., Grütter, P., *et al*. (1987). Observation of magnetic forces by the atomic force microscope. *Journal of Applied Physics*, **62**, 4293–4295.

Schneider, M., Müller-Pfeiffer, S. and Zinn, W. (1996). Magnetic force microscopy of domain wall fine structures in iron films. *Journal of Applied Physics*, **79**, 8578–8583.

Scheinfein, M.R., Unguris, J., Celotta, R.J. and Pierce, D.T. (1989). Influence of the surface on magnetic domain-wall microstructure. *Physical Review Letters*, **63**, 668–671.

Scheinfein, M.R., Unguris, J., Blue, J.L., *et al*. (1991). Micromagnetics of domain walls at surfaces. *Physical Review B*, **43**, 3395–3422.

Schlickum, U., Wulfhekel, W. and Kirschner, J. (2003). Spin-polarized scanning tunneling microscope for imaging the in-plane magnetization. *Applied Physics Letters*, **83**, 2016–2018.

Schönenberger, C., Alvarado, S.F., Lambert, S.E. and Sanders, I.L. (1990). Separation of magnetic and topographic effects in force microscopy. *Journal of Applied Physics*, **67**, 7278–7280.

Schwarz, A., Liebmann, M., Kaiser, U., *et al*. (2004). Visualization of the Barkhausen effect by magnetic force microscopy. *Physical Review Letters*, **92**, 077206.

Selloni, A., Carnevali, P., Tosatti, E. and Chen, C.D. (1985). Voltage-dependent scanning-tunneling microscopy of a crystal surface: graphite. *Physical Review B*, **31**, 2602–2605.

Shinjo, T., Okuno, T., Hassdorf, R., *et al*. (2000). Magnetic vortex core observation in circular dots of permalloy. *Science*, **289**, 930–932.

Slonczewski, J.C. (1989). Conductance and exchange coupling of two ferromagnets separated by a tunneling barrier. *Physical Review B*, **39**, 6995–7002.

Speckmann, M., Oepen, H.P. and Ibach, H. (1995). Magnetic domain structures in ultrathin Co/Au(111): on the influence of film morphology. *Physical Review Letters*, **75**, 2035–2038.

Stowe, T.D., Yasumura, K., Kenny, T.W., *et al*. (1997). Attonewton force detection using ultrathin silicon cantilevers. *Applied Physics Letters*, **71**, 288–290.

Tersoff, J. and Hamann, D.R. (1983). Theory and application for the scanning tunneling microscope. *Physical Review Letters*, **50**, 1998–2001.

Thompson, D.A. and Best, J.S. (2000). The future of magnetic data storage technology. *IBM Journal of Research and Development*, **44**, 311–322.

Volodin, A., Temst, K., van Haesendonck, C. and Bruynseraede, Y. (1998). Observation of the Abrikosov vortex lattice in $NbSe_2$ with magnetic force microscopy. *Applied Physics Letters*, **73**, 1134–1136.

Volodin, A., Temst, K., van Haesendonck, C. and Bruynseraede, Y. (2000). Low temperature magnetic force microscopy with enhanced sensitivity based on piezoresistive detection. *The Review of Scientific Instruments*, **71**, 4468–4473.

Wachowiak, A., Wiebe, J., Bode, M., *et al*. (2002). Direct observation of internal spin structure of magnetic vortex cores. *Science*, **298**, 577–580.

Wadas, A., Dreyer, M., Kleiber, M. and Wiesendanger, R. (1998). Thickness-dependent magnetic domain structures of ultrathin Co/Au(111) films studied by means of magnetic force microscopy in ultrahigh vacuum. *Applied Physics A*, **66**, 465–467.

Wadas, A., Moreland, J., Rice, P. and Katti, R.R. (1994). Magnetic force microscopy images of magnetic garnet with thin-film magnetic tip. *Applied Physics Letters*, **64**, 1156–1158.

Weber, N., Wagner, K., Elmers, H.J., *et al*. (1997). Nanoscale spatial switching of magnetic anisotropy in pseudomorphic Fe(110) on W(110). *Physical Review B*, **55**, 14121–14124.

Wiesendanger, R., Bode, M. and Getzlaff, M. (1999). Vacuum-tunneling magnetoresistance: the role of spin-polarized surface states. *Applied Physics Letters*, **75**, 124126.

Wiesendanger, R., Bürgler, D., Tarrach, G., *et al*. (1990a). Vacuum tunneling of spin-polarized electrons detected by scanning tunnelling microscopy. *Journal of Vascular Science Technol B*, **9**, 519–524.

Wiesendanger, R. and Güntherodt, H.J. (Eds.) (2002). *Scanning Tunneling Microscopy II*, Springer.

Wiesendanger, R., Güntherodt, H.J., Güntherodt, G., *et al*. (1990b). Observation of vacuum tunneling of spin-polarized electrons with the STM. *Physical Review Letters*, **65**, 247–250.

Wortmann, D., Heinze, S., Kurz, P., *et al*. (2001). Resolving complex atomic-scale spin structures by spin-polarized scanning tunneling microscopy. *Physical Review Letters*, **86**, 4132–4135.

Wu, R. and Freeman, A.J. (1992). Magnetic properties of Fe overlayers on W(001) and the effects of oxygen adsorption. *Physical Review B*, **45**, 7532–7535.

Wulfhekel, W. and Kirschner, J. (1999). Spin-polarized scanning tunneling microscopy on ferromagnets. *Applied Physics Letters*, **75**, 1944–1946.

Yu, J., Ahner, J. and Weller, D. (2004). Magnetic force microscopy with work function compensation. *Journal of Applied Physics*, **96**, 494–497.

Zhu, J-G., Lin, X., Shi, R.C. and Luo, Y. (1998). Magnetic force microscopy image restoration technique for removing tip dependence. *Journal of Applied Physics*, **83**, 6223–6225.

Alternative Patterning Techniques: Magnetic Interactions in Nanomagnet Arrays

Jacques Ferré and Jean Pierre Jamet
UMR CNRS, Université Paris-Sud, Orsay, France

1 INTRODUCTION

There is presently an increasing challenge to prepare and study 2D assemblies of identical nanoparticles or magnetic nanoelements (nanomagnets) by sophisticated techniques. This approach is complementary to the investigation of isolated, well-characterized nanomagnets (see also **Magnetization Configurations and Reversal in Small Magnetic Elements, Volume 2** and **Superparamagnetic Particles, Volume 4**). In arrays, the interactions with the surrounding elements cannot be generally neglected. Many techniques (Martin *et al*., 2003; Carl and Wassermann, 2002) are used to prepare arrays of nanomagnets, based on bottom-up (see also **Chemical Synthesis of Monodisperse Magnetic Nanoparticles, Volume 3**, **Template-based Synthesis and Characterization of High-density Ferromagnetic Nanowire Arrays, Volume 4** and **Novel Nanoparticulate Magnetic Materials and Structures, Volume 4**) or top-down approaches (see also **Nanoimprint Technology for Patterned Magnetic Nanostructures, Volume 3**), these last methods being applied to ultrathin film structures.

A combination of lithography and ion milling processes is the most common top-down technique used for patterning ultrathin films to create arrays of magnetic nanoelements (see also **Nanoimprint Technology for Patterned Magnetic Nanostructures, Volume 3**). The ultimate resolution is presently obtained by electron-beam lithography, but this method is limited to the fabrication of small size arrays. In counterpart, optical lithography allows one to realize arrays of nanomagnets with a rather small period (80 nm) over large areas, but without perfect identicae shape. Thus, new nonconventional ways of top-down high-resolution patterning over relatively large areas are highly desirable, especially to design new types of discrete high-density magnetic recording media or arrays of memory cells.

While always focusing on the issues of Volume 3 of the Handbook, this chapter will begin in earnest in Section 2 by dealing with alternative top-down patterning methods used for designing arrays of magnetic clusters or ultrathin film nanoelements. This review will be concerned only with simple 2D-metallic patterned nanostructures. Note that only limited data are available so far on magnetic semiconductor (Heimbrodt and Klar, 2002) or insulating film nano structures. In this chapter, particular emphasis is devoted to patterning by ion irradiation, either through masks or by focused ion beam (FIB). Following a survey of magnetic properties in arrays of nanoelements in Section 3, the specific behavior

Handbook of Magnetism and Advanced Magnetic Materials. Edited by Helmut Kronmüller and Stuart Parkin. Volume 3: *Novel Techniques for Characterizing and Preparing Samples*. ISBN: 978-0-470-02217-7.

of selected nanostructures will be examined in Section 4. Periodic arrays of nanomagnets are good candidate to understand the role played by competitive interdot exchange and magnetostatic interactions. We will investigate the evolution of magnetic properties from isolated to strongly interacting and correlated nanoelements especially in the simple case of Pt/Co/Pt out-of-plane magnetized nanostructures.

All along the review, the applicability to ultrahigh density magnetic recording will be emphasized. Arrays of identical nanomagnets, also called *quantum magnetic dots* (Chou, Wei, Krauss and Fischer, 1994), are promising media for ultrahigh density recording (Ferré, 2001; Lodder, Haast and Abelmann, 2001; Lodder, 2004; Carl and Wassermann, 2002). In this spirit, nanodot arrays deposited by sputtering on preetched wafers will be examined. The case of electrodeposited magnetic wires deposited inside periodic holes in membranes or alumite templates will be treated in another contribution (see also **Template-based Synthesis and Characterization of High-density Ferromagnetic Nanowire Arrays, Volume 4**). The case of patterned nanodot arrays for magnetic recording fabricated by interference optical lithography (Lodder, 2004) will not be treated here.

2 FABRICATION METHODS

In this chapter, we will restrict ourselves to top-down fabrication techniques, excluding lithography as a single step process. Lithography techniques have been previously reviewed (Martin *et al*., 2003; Carl and Wassermann, 2002), but they do not address to new alternative techniques such as films deposited on preetched templates or patterned by ion irradiation patterning.

2.1 Deposition on prepatterned templates

2.1.1 Preetched substrates prepared by lithography

This method was first proposed by Gadetsky, Erwin, Mansuripur and Suzuki (1996) to prepare perpendicular magnetic recording media. Photolithography was used first to pattern square arrays of dots on glass or plastic substrates, on which a thin SiN (10 nm)/Tb-rich TbFeCo (25 nm) magnetic film structure was subsequently deposited. The etching depth, dot size, and periodicity were 10, 250, and 500 nm, respectively.

More recently, Landis, Rodmacq and Dieny (2000) have patterned Si wafer templates in the form of square nanopillars by conventional lithography and reactive etching techniques. The last step of the preparation consists of sputter depositing a Co/Pt multilayer at low Ar pressure onto the entire preetched substrate. The lateral size of the Si nanopillars was first reduced down to 80 nm, with spacing as small as 100 nm (Moritz *et al*., 2002) (Figure 1). But, by reactive ion etching and nanoimprinting, arrays of 30nm dots with 60nm periodicity were finally fabricated. A relatively weak surface roughness of 0.8 nm was measured on the top of 47 or 200-nm-high nanopillars. Large pattern sizes, up to 3 mm × 3 mm were realized. Sputtering of Co at normal incidence and of Pt at a small incidence angle allowed one to deposit a Pt-rich PtCo ultrathin film alloy (i.e., a nonmagnetic material) on one sidewall of the nanopillars and CoO on the opposite sidewall. As a result, ferromagnetic coupling between the CoPt nanodots deposited on the top of nanopillars and the PtCo layer located in between was eliminated.

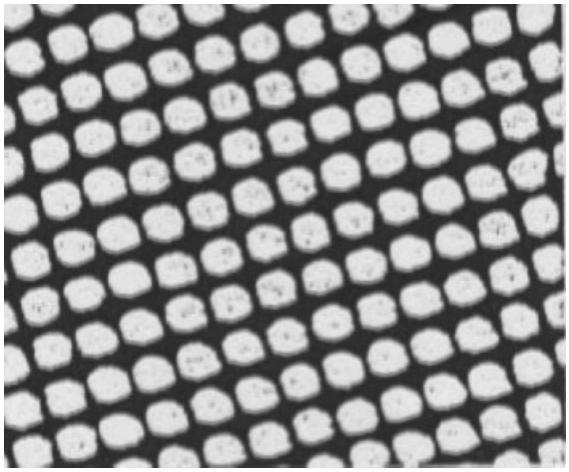

Figure 1. Atomic force microscopy (AFM) image of a square array of dots with a diameter of 80 nm, the edge to edge spacing being equal to 100 nm, prepared by ion sputtering on a preetched Si wafer. (Moritz *et al*., *IEEE Trans. Magn* **38**, 1731–36 (2002), (© 2002 IEEE).)

2.1.2 Functionalized templates prepared by focused ion beam (FIB)

A FIB or laser beam can locally modify the properties of the substrate before depositing nanostructures. The irradiated small regions serve as seeded sites that attract incident magnetic ions to form aggregates at preselected places. Square arrays of ferromagnetic CoPt aggregates were grown after functionalizing a convenient substrate at the apex of a square array of defects created by Ga FIB (Perez *et al*., 2002; Hannour *et al*., 2005). In spite of their small size, the shape of aggregates remains, up to now, highly ramified.

Another emergent technique to design periodic arrays of nanoparticles is to use a chemical FIB-assisted method (Kageyama and Suzuki, 2004). Co particles were produced at selected places on a template by decomposing its octacarbonyl precursor under a scanning FIB. This method has been

recently extended to produce periodic assemblies of FePt and CoPt magnetic particles (Xu, Kageyama and Suzuki, 2005).

2.2 Ion irradiation through a mask

Argon ions are currently used for milling material, for example, for designing patterns through a resist mask. The removal of a large amount of matter is then required and the surfacic ion dose must be rather high. In counterpart, it has been shown recently (Chappert *et al*., 1998; Vieu *et al*., 2002; Rettner *et al*., 2002a) that the magnetic properties of ultrathin film structures are often strongly modified by irradiation under low ion dose without etching and creating any additional surface roughness. Thus, before discussing ion beam patterning methods, a general survey on irradiation process in ultrathin film structures is proposed. Some aspects of this topic have been reviewed recently by Fassbender, Ravelosona and Samson (2004).

Nanopatterning can be realized by uniform ion irradiation through a contact mask deposited directly on the film, or through a removable stencil mask. All types of ions may be used. Another solution that avoids the preparation of a mask is to pattern directly the film by scanning a nanosize gallium FIB. The principles of these three techniques are schematically depicted on Figure 2.

2.2.1 Uniform ion irradiation at low dose

Before investigating the modifications of magnetic properties under irradiation, we will discuss the change of morphological, structural, and physicochemical properties of ultrathin film structures versus the type of ion, its energy, and dose.

Their radiation damage, etching depth, and intermixing of ions at interfaces under low irradiation dose can be estimated from the Transport of ions in matter (TRIM) calculations for various ion energies (Ziegler, 1992). The used ion energy ranges currently between 10 and 100 keV. For a given dose and ion energy, damage increases with the mass of the incident ions. At the same time, the mean implantation depth of incoming ions is reduced. An increase of the ion energy provides straighter trajectories, which allows one to minimize the lateral ion straggling inside the media. More damage is obviously created at higher energy, as when increasing the dose.

The structural modifications induced by irradiation depend much on the material. For example, in the Pd/FePd/Pd thin-film structure, chemical ordering can be reinforced under He irradiation since it favors the formation of the $L1_0$ stable phase (Bernas *et al*., 2003). This elegant procedure allowed significant increase of the anisotropy in this promising perpendicular recording media. In some other cases, a chemical disordering is induced under irradiation (Fassbender, Ravelosona and Samson, 2004). For the archetypal Co/Pt ultrathin layered structure, ion irradiation induces intermixing at interfaces that is found to reduce its perpendicular magnetic anisotropy (Chappert *et al*., 1998).

Now, let us focus on the widely studied case of irradiation effects by light He ions at 30 keV on a room-temperature sputter-grown Pt/Co/Pt ultrathin film structure. In that case, He ions do not themselves perturb the structure since they become deeply implanted far away from the film inside the substrate (>100 nm). But He ion irradiation produces a controlled *ion beam mixing* of the Co–Pt interfaces. This effect brings into play the purely ballistic collisional mixing and the chemical heat of mixing. At low dose, the mixing rate is linear with He dose. As a result of a large negative heat of mixing, a Co atom displaced from the interface into the Pt layer stabilizes in a collision-induced site without further relaxation. When reorganizing around a vacancy induced by irradiation, atoms have a high probability to find a higher thermodynamic configuration that minimizes energy. Since Co and Pt elements are miscible in any proportion, irradiation induce stable intermixing between Co and Pt around interfaces. One important point is that for irradiation with He ions at low dose, no etching of the film surface is observed, so that the initial sample roughness is conserved. A planar method for patterning magnetic recording media

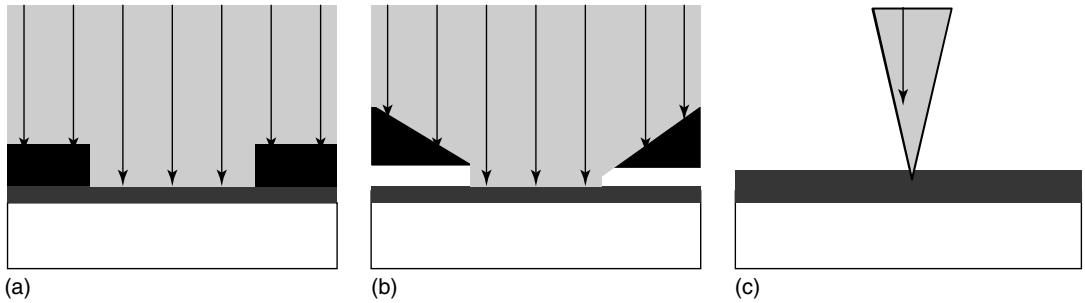

Figure 2. Local irradiation: (a) by He ions through a contact mask, (b) by irradiation through a removable stencil mask, and (c) by a focused Ga ion beam (FIB).

was proposed (Chappert *et al*., 1998); in magnetic recording, planarization ensures a higher stability of heads flying very close above the disk. It is also interesting to note that the optical indices of the Co/Pt structure are not significantly modified under irradiation by He light ions with a typical energy of 30 keV. All these features are conducive to magnetic investigations by near field techniques.

As-grown Pt/Co/Pt films are ferromagnetic at room temperature. For a Co thickness below 2 nm, the easy magnetization axis aligns perpendicular to the film plane as the result of a large positive interface anisotropy. Using a simple model, the observed magnetic changes can be related to the irradiation-induced intermixing (Bernas *et al*., 1999). This intermixing lowers the interfacial anisotropy, the coercive field, and the Curie temperature (Ferré *et al*., 1999). The magnetic properties of Co_{1-x} Pt_x alloys are well known (Sanchez, Moran-lopez, Leroux and Cadeville, 1988): for $x < 75\%$, the alloy becomes ferromagnetic at room temperature and the magnetic moment decreases monotonously from $1.7\,\mu_B$ for $x = 0$ to $0.75\,\mu_B$ for $x = 0.75$. The variation of the Co–Pt concentration within the ultrathin Co layer structure with the He dose can account for the observed Curie temperature decrease. At room temperature, the perpendicular coercive field decreases monotonously when increasing the He ion dose (Figure 3), and finally a transition to a paramagnetic state takes place for a $D = 2.5 \times 10^{16}$ ions/cm^2 dose. When changing the ion dose and temperature, paramagnetic and ferromagnetic phases with in-plane, oblique, and perpendicular anisotropy can be identified. The 'temperature versus He ion dose' phase diagram has been determined for a Pt/Co(0.5 nm)/Pt sample (Figure 4)

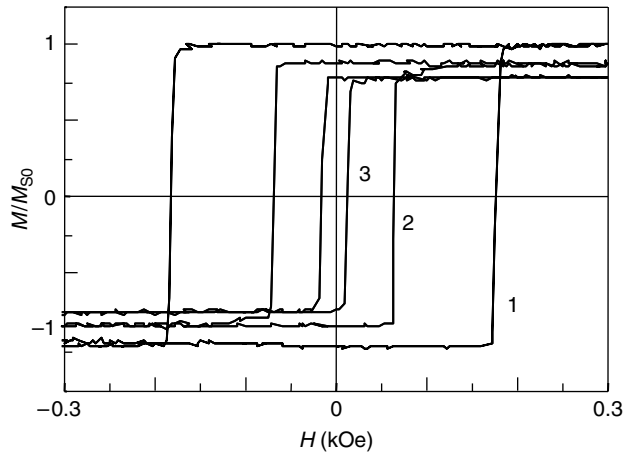

Figure 3. Polar MOKE (PMOKE) hysteresis loops of a Pt/Co(0.5 nm)/Pt film versus the He irradiation dose at 30 keV. (1) As-grown sample, (2) $D = 3 \times 10^{15}$ ions/cm^2, and (3) $D = 10^{16}$ ions/cm^2. Magnetization of all loops is normalized to the saturation magnetization M_{SO} of the as-grown sample. (Chappert, C. *et al*. (1998). *Science*, **280**, 1919.)

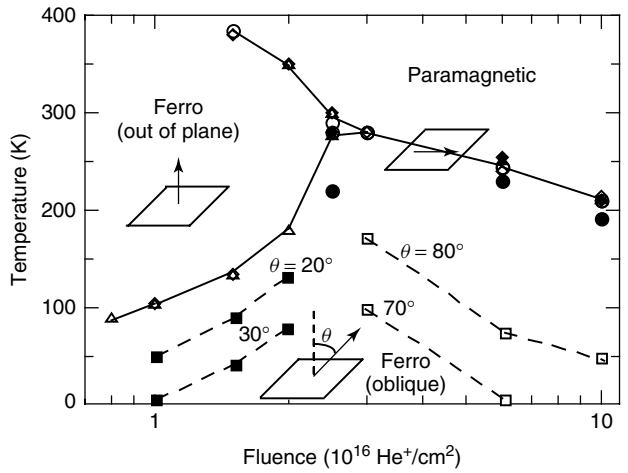

Figure 4. Temperature–dose magnetic phase diagram of an He-irradiated Pt/Co(0.5 nm)/Pt ultrathin film at 30 keV. Several isodeviation lines are indicated for the oblique phase. (J. Ferré *et al*., *J. Phys. D: Appl. Phys.* **36**, 3103 (2003).)

(Ferré *et al*., 2003). When the Co thickness exceeds 1.4 nm, another perpendicular-to-oblique reorientation transition is evidenced first when increasing the He ion dose at room temperature.

Helium irradiation effects are even more efficient in Co/Pt multilayers. Two transitions may be successively identified, first from a perpendicular to an in-plane magnetized state (Figure 5), and finally to a superparamagnetic phase (not shown in Figure 5). As proved from the pure critical behavior

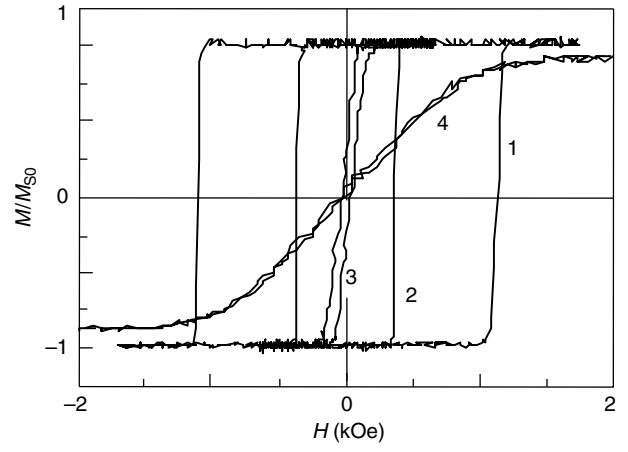

Figure 5. Room-temperature PMOKE hysteresis loop of an He-irradiated Pt/[Pt(1.4 nm)/Co(0.3 nm)]$_6$/Pt multilayer with He ions at 30 keV. (1) as-grown sample, (2) $D = 2 \times 10^{15}$ ions/cm^2, (3) $D = 6 \times 10^{15}$ ions/cm^2, and (4) $D = 10^{16}$ ions/cm^2. Magnetization, M, of all loops has been normalized to the saturation magnetization M_{SO} of the as-grown sample. (Chappert, C. *et al*. (1998). *Science*, **280**, 1919.)

of the magnetization in the vicinity of the Curie temperature, intermixing is highly uniform over the full sample area.

Since the ion intermixing at interfaces is induced by ballistic effects, the atomic displacement efficiency and damage are more significant when using ions which are heavier than He, like Ga. The Co–Pt in-depth intermixing profile produced by Ga ions inside the Pt/Co/Pt film structure has been calculated by TRIM simulations (Ziegler, 1992) (Figure 6). Qualitatively, similar magnetic changes are expected to occur in Pt/Co/Pt films irradiated either by Ga or He ions, but at a much lower dose for the heavier Ga ions (compare the dependence of the coercive field with the dose for He (Figure 3)

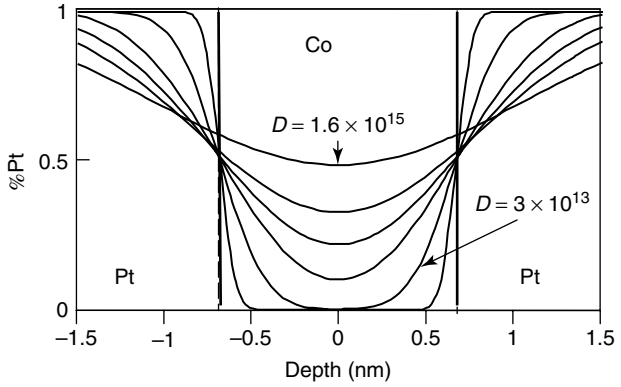

Figure 6. Co–Pt intermixing at the interfaces in a Pt/Co(1.4 nm)/Pt film calculated by TRIM simulations for different values of the Ga ion dose D increasing from 10^{13} ions/cm^2 to 1.6×10^{15} ions/cm^2. The origin of the depth is located at the center of the Co layer. (From Hyndman, unpublished.)

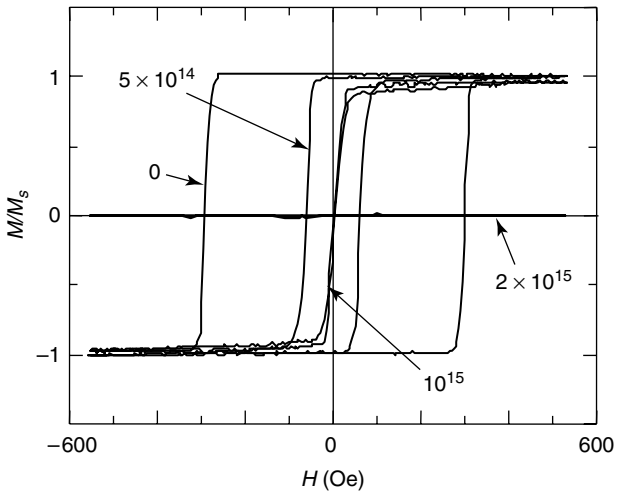

Figure 7. Normalized PMOKE hysteresis loops of the as-grown and irradiated Pt/Co(1.4 nm)/Pt film. The values of the dose D indicated in the figure are in Ga ions/cm^2 units. Note that the sample becomes paramagnetic for $D = 2 \times 10^{15}$ ions/cm^2. (Vieu *et al*., *Journal of Applied Physics.* **91**, 3103 (2002).)

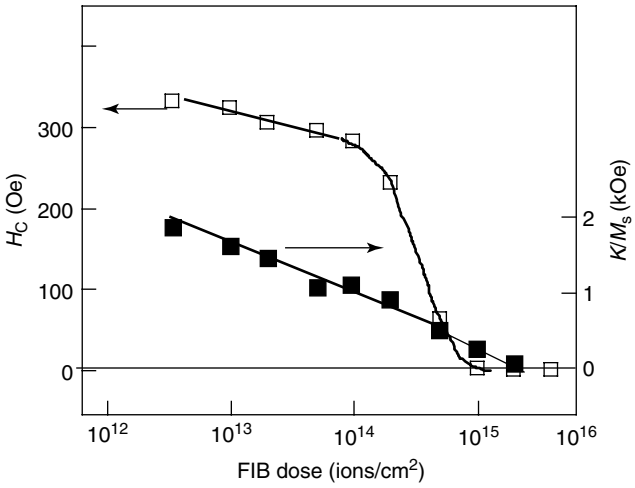

Figure 8. Semilogarithmic variation of the coercive field (open squares) and of the anisotropy (black squares) of the Pt/Co(1.4 nm)/Pt film with the Ga ion dose. (Vieu *et al*., *Journal of Applied Physics.* **91**, 3103 (2002).)

and Ga (Figures 7 and 8)). The irradiation efficiency on coercivity in a Co/Pt multilayer has been determined by Rettner *et al*. (2002a) for different types of ions with energy in the 20–30 keV range (Figure 9). Similar behavior has also been evidenced for ions with far higher energy, that is, in the megaelectron volt MeV range (Figure 9) (Rettner *et al*., 2002a; Kim *et al*., 2002). A main point is that lateral ion straggling inside the film and morphological and structural damages are relatively much more significant for heavier ions.

As an example, the results of TRIM calculations (Ziegler, 1992) in an ultrathin Pt(6.5 nm)/Co(1 nm)/Pt(3.4 nm) film,

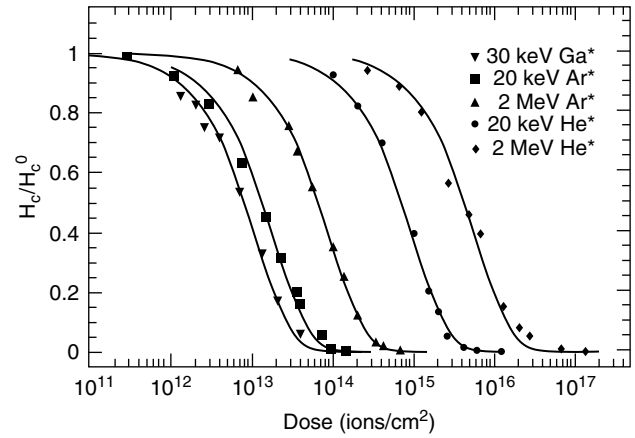

Figure 9. Semilogarithmic plot of the reduced coercive field as a function of the He, Ar, and Ga ion irradiation dose. He and Ar irradiations were performed at 20 keV, 30 keV, and 2 MeV energy. (Rettner *et al*., APL 80, 279–281 (2002).)

show the following trends:

- Sixty-five percent of the Ga ions are implanted in the Pt/Co/Pt film structure (vs no implantation with He).
- Multiple collisions for Ga (vs pure ballistic collisions for He) and creation of 80 lacuna per Ga ion (vs 0.5 for He).
- The sputtering efficiency is six atomic planes for Ga (vs 0.15 for He). The calculated etched depth has been experimentally confirmed on Co/Pt structures for different Ga ion doses (Hyndman *et al*., 2001a). Ga ions generate a rougher surface than He irradiation. Moreover, Ga irradiation favors expansion of the Pt crystallite sizes along the (111) direction.
- In terms of magnetization and magnetic anisotropy, 10^{16} He ion/cm^2 or 10^{15} Ga ion/cm^2 irradiation doses give comparable magnetic changes in this Pt/Co/Pt film.

The above trends confirm that light ions, such as He, produce far less structural and morphological damage than heavier ions, like Ar and Ga when restricting to doses that give comparable changes in magnetism.

Several authors investigated the irradiation-induced changes in the magnetic properties of permalloy films with in-plane easy anisotropy (Kaminsky *et al*., 2001). As expected, since magnetic interface effects are far less efficient in determining anisotropy in in-plane films than those with perpendicular anisotropy, rather large ion doses are necessary to modify their magnetism by implantation of Ga into the Co ferromagnetic layer. A transition from antiferromagnetic to ferromagnetic coupling between the two Fe layers in the Fe/Cr/Fe structure can be induced by Ga irradiation, allowing to design a new type of magnetic patterning (Blomeier *et al*., 2005). Magnetic micropatterning of FeNi/FeMn exchange bias layers by ion irradiation through a mask has also been demonstrated (Mougin *et al*., 2001). This method allows to modify and control the exchange bias field value locally.

2.2.2 *Patterning through a contact mask*

Starting again from a Pt/Co/Pt film structure, a thick enough resist or insulating layer (SiO_2, SiN) is deposited first on the film. Then, circular or square nanoholes are opened through the contact mask by electron lithography and ion etching. Finally, arrays of soft magnetic nanoelements in a harder medium may be designed by uniform He ion beam irradiation through this shadow mask. The contact mask may also be made of an array of nanopillars (Krauss, Fischer and Chou, 1994). In that case, by uniform ion irradiation, an array of ferromagnetic nanodots can be designed below these nanopillars, while the nonprotected irradiated surrounding area can become paramagnetic or weakly magnetized. Arrays of $Co_{25}Pt_{75}$ nanodots with perpendicular anisotropy surrounded by a weakly magnetic matrix have been fabricated through such a mask by He irradiation (Devolder *et al*., 2003).

For a first demonstration, arrays of parallel ferromagnetic stripes have been prepared by He irradiation through a resist mask (Figure 10) (Chappert *et al*., 1998). To design ultranarrow elements with highly contrasted borders, it is more appropriate to deposit first a silica mask (about 400 nm thick), which is subsequently patterned by electron lithography and reactive ion etching. Silica masks with parallel ultrathin 30-nm-wide walls have been also prepared successfully (Figure 11). Using a similar mask with 60-nm-wide walls, an array of ultranarrow ferromagnetic Pt/Co/Pt stripes, separated by micrometer wide irradiated paramagnetic regions, have been prepared (Figure 12) (Devolder *et al*., 1999, 2000).

The collisional lateral straggling inside the film, the collateral damage at mask borders, and the resolution of the mask patterning technology, limit the sharpness of magnetic nanostructures (Bernas *et al*., 1999). The lateral straggling, which characterizes He ion-stopping profile is only about

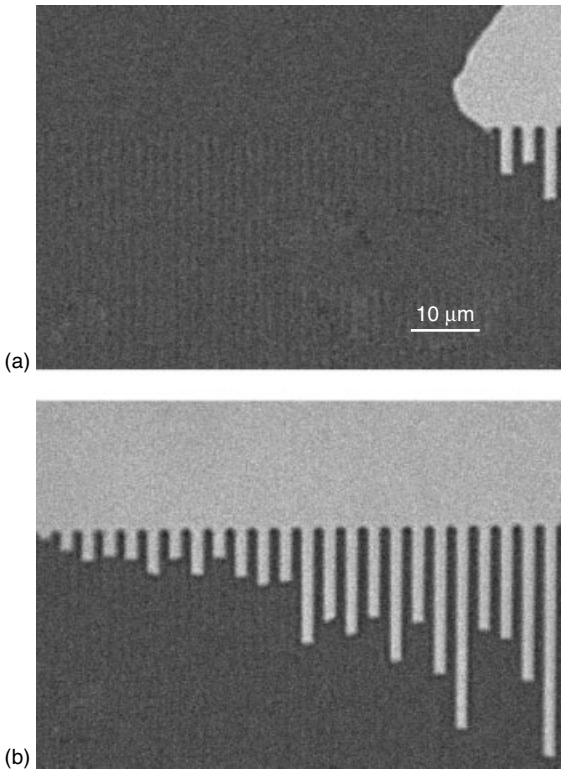

Figure 10. PMOKE images of an array of 1-μm-wide ferromagnetic stripes connected to a reservoir, separated by 1-μm-wide irradiated paramagnetic regions. Magnetic patterning, in the Pt/Co(0.5 nm)/Pt film, has been performed by He irradiation ($D = 10^{16}$ ions/cm^2, 30 keV) through a PMMA resist contact mask. Images (a) and (b) are both differences from a magnetically saturated image, and the reversed domains appear in gray. A magnetic field pulse of amplitude 82 Oe and duration 2 s was applied between snapshots A and B. (Chappert, C *et al*. (1998). *Science*, **280**, 1919.)

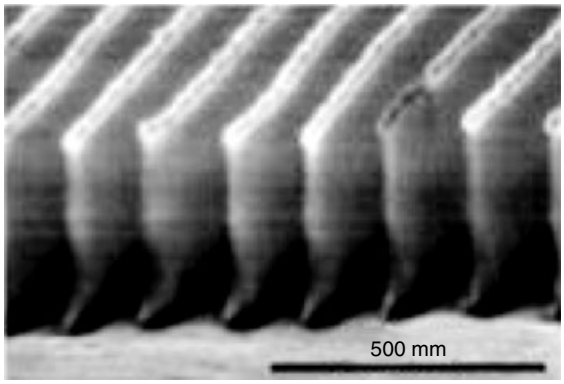

Figure 11. Scanning electron microscopy image of a SiO_2 mask. The walls are 450 nm high, 30 nm thick and are separated here by 150 nm. (Devolder *et al*., APL 74, 3383–3385 (1999).)

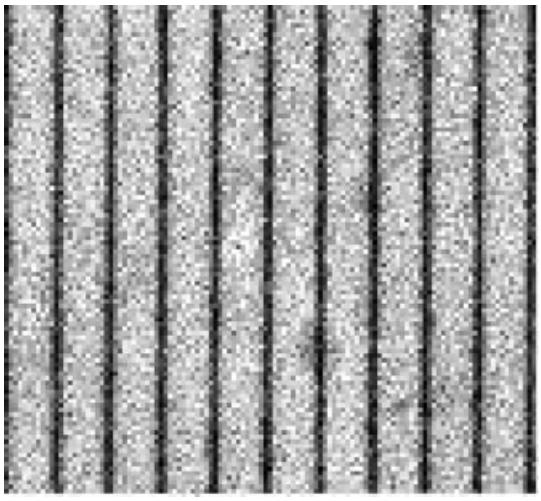

Figure 12. PMOKE image ($33 \times 29\,\mu m^2$) of the magnetic state of an array of 60-nm-wide Co/Pt tracks, separated by 2.5 µm, obtained after saturating the sample in a negative field (black) and applying a positive field of 348 Oe during 10 s. This field was large enough to reverse the magnetization in weakly ferromagnetic irradiated areas (gray) between tracks (black). (Devolder *et al*., APL 74, 3383–3385 (1999).)

2 nm in ultrathin layers. Therefore, the resolution is in fact limited by collateral damage due to ion beam divergence below the silica mask, estimated to be 14 nm in the present case (Devolder, Chappert and Bernas, 2002; Devolder *et al*., 2001). This effect limits the sharpness of the designed nanoelements. Moreover, imperfections of the mask's edges generate roughness at the border of the magnetic nanoelements. When combining state-of-the-art lithographic techniques, an ultimate nanometer-scale patterning of magnetic properties can be reached using He irradiation while preserving the smoothness of the surface, a required condition for ultrahigh density information storage technology.

2.2.3 Patterning through a stencil mask

Ion beam patterning can also be realized through a removable stencil mask placed just above the film (Figure 2). This method is also called *proximity ion beam lithography*. Wolfe *et al*. (1996) discussed about the limitations of this technique for realizing arrays of small (20–50 nm) nanostructures. Devolder, Chappert and Bernas (2002) reported on the ultimate resolution that can be reached by stencil masks using He irradiation. The pertinent parameters are the gap G separating the magnetic film from the mask, and the aspect ratio (AR), that is, the ratio between thickness and size of the mask openings. It appears that the gap must be chosen in the $0.1 \ll G \ll 25\,\mu m$ range, and the replication quality is the best if $AR > 3$. For a 200-nm-diameter hole, drilled into a 340-nm-thick SiC membrane, the collateral damage can extend over 50 nm for $G = 100$ nm. It is highly reduced (to about 10 nm) if a thicker 600-nm membrane is used.

Realistic mass production of discrete magnetic media requires removable masks that replicate a given large pattern many times. Stencil masks are potentially good candidates for such an application. They have been used to design periodically organized soft magnetic dots in Co/Pt and FePt chemically ordered superlattice films by ion irradiation (Terris *et al*., 2000). However, the quality of the stencil masks was not good enough at that time to reach the optimum resolution.

We will not discuss patterning using heavy ions at high energy since they produce too much damage that is difficult to control. Both etching and thermal effects have then to be considered (Xiao *et al*., 1994; Cai *et al*., 1997).

2.2.4 Ion projection lithography

Patterned magnetic media can be produced by highly stable ion projection lithography (Bruenger *et al*., 2002). A uniform ion beam passes through an array of nanoholes drilled into a stencil mask that is previously fabricated by lithography. An electronic lens gives a demagnified image of this hole array on the sample. Starting from a 3-µm-thick Si stencil mask with 500-nm-wide holes, separated by 2 µm, arrays of 60-nm-diameter magnetic dots have been realized using a uniform Ar beam irradiation and an eight times demagnification. This method does not require the use of a resist mask, so it can be applied to pattern recording media (Dietzel *et al*., 2002; Bruenger *et al*., 2002).

2.3 Direct writing techniques

2.3.1 Focused electron-beam writing

It has been demonstrated that magnetic properties of ultrathin magnetic film structures can also be affected by a focused

electron beam (Allenspach, Bischof, Düring and Grütter, 1998). To obtain a high electron-ion ballistic collisional efficiency, electrons must have very high energy. In most cases, the produced ion intermixing at interfaces is rather low, so only weak magnetic changes are observed. Electron-beam-assisted magnetic ion deposition can be more efficient for designing nanostructures, but nearly no example is reported so far in the literature.

2.3.2 Focused Ga ion beam (FIB) writing

This is certainly one of the most promising techniques to pattern thin films with an ultimate nanometer resolution. Since Ga ions are focused over a very small film area, damage can be controlled over an extended range of doses. At relatively high Ga doses ($D > 10^{16}$ ions/cm^2), FIB sputtering causes the film to be etched away to depths larger than 10 nm. At low doses ($D < 10^{14}$ ions/cm^2), the etching effect has a very low efficiency, but the magnetic properties of ultrathin film structures can still be locally modified. Ultrathin film FIB patterning is usually performed with a weak probe current ($\approx$10 pA) at 30 keV energy. Irradiated lines separating nanomagnetic regions are designed by scanning the FIB spot in fast successive steps with a great precision, over a distance typically equal to the FIB spot diameter in order to ascertain overlap of irradiated areas along a given direction. The ultimate FIB spatial resolution is presently 5 nm (Gierak *et al*., 2005), giving an irradiated linewidth in the film of about 10 nm at low dose. The dose deposited in lines is controlled by the exposure time of the spot varying from 0.1 to 100 ns. This allows the design of irradiated lines with an equivalent surfacic dose from 3×10^{12} to 3×10^{15} ions/cm^2. At low dose ($<10^{14}$ Ga ions/cm^2) (Figure 13a), irradiated lines become weakly ferromagnetic without creating new surface roughness on the virgin film. At mean dose (Figure 13b), the central part of irradiated lines is rendered paramagnetic, while their edges are weakly ferromagnetic. Thus, arrays of tracks or dots may be designed by scanning the FIB along one direction or two orthogonal directions, respectively (Aign *et al*., 1998; Hyndman *et al*., 2001b; Toporov, Langford and Petford-Long, 2000). Periodic arrays of drilled holes, called *antidots*, have also been fabricated (Toporov, Langford and Petford-Long, 2000). In order to realize complex structures or to isolate magnetically a single magnetic nanoelement, the FIB spot size can be adjusted between 10 and 50 nm, and even scanned over a large sample area to sputter material. This technique has been successfully used to fabricate single high-quality in-plane magnetized permalloy nanoelements (Xiong, Allwood, Cooke and Cowburn, 2001).

In most materials, the removal rate with 30 keV Ga ions is around 1–10 atoms per incident Ga ion. For each incident Ga ion on a Co/Pt film structure, approximately 500/Pt and 500 Co ion displacements are generated. This rapidly induces a large density of defects. For Pt/Co/Pt films, one estimates that 300 ion impacts over a 10mn FIB spot diameter (equivalent to $D = 4 \times 10^{14}$ ions/cm^2) give rise to a 1-nm-height surface film blister, which spreads over about 100 nm. This swelling is due not only to Ga implantation (Basnar *et al*., 2003) but also to a damage which modifies the crystal structure. Voids and interstitial atoms are created, leading to a volume enhancement associated to an amorphization process. When increasing the FIB spot dose, etching effects (drilled depth of 1.3 nm by 750 Ga ions per spot, i.e., for 10^{15} Ga ions/cm^2) tend to form a cross-section volcano-type profile. For 2250 ions, the depth of the drilled central hole is already 3 nm. This phenomenon can be evidenced from small local changes in light reflectivity, as already observed for an array of Ga ion irradiated lines in a Pt/Co(1.4 nm)/Pt film used for producing a square nanodot array (Figure 14). So, the FIB writing technique can be inappropriate for designing nanostructures in some cases, in particular, when it already modifies too much the surface topology at low dose.

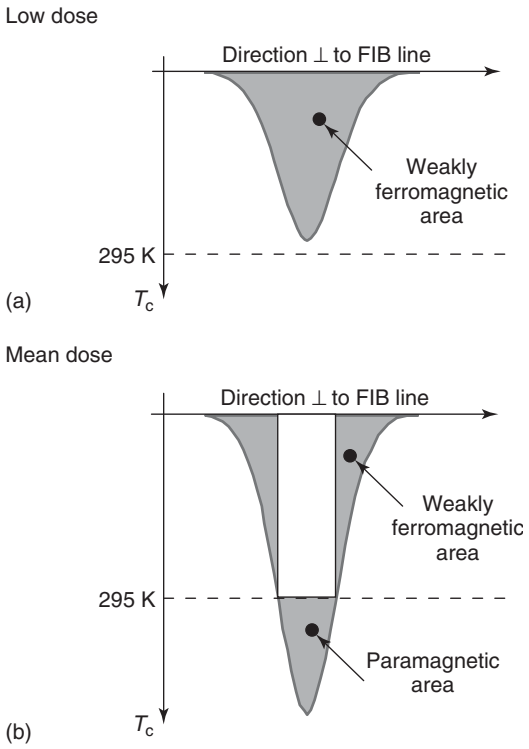

Figure 13. Schematic cross-section view of the lateral variation of the Curie temperature through a line irradiated by a scanned FIB having a Gaussian dose profile. (a) At low dose, the irradiated line is still weakly ferromagnetic at its center. (b) At higher dose, the central part of the line becomes paramagnetic while its edges are weakly ferromagnetic. This explains why nanodot borders act as a nucleation reservoir for further domain wall motion inside the dot.

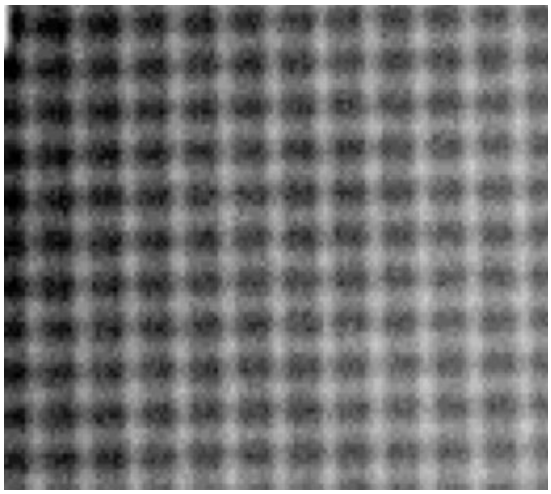

Figure 14. Optical image of a Pt/Co(1.4 nm)/Pt film patterned as a square ($1 \times 1\,\mu m^2$) nanodot array by two orthogonal sets of Ga irradiated lines, here revealed in light gray. The width of the irradiated lines is overestimated because of the convolution with the limited resolution (0.4 µm) of the optical microscope. The used lineic Ga dose was $3\,nC\,cm^{-1}$. (From Aign *et al*., 1998.)

2.4 Comparison between patterning techniques

At this stage, it is interesting to compare the performances of different top-down techniques for realizing arrays of magnetic nanoelements (Table 1).

Among the usual top-down patterning methods, only electron-beam lithography is competitive with FIB for creating so narrow nanostructures. FIB and electron lithography are both slow fabrication procedures, but FIB stands as a direct writing method while electron lithography needs first the mask fabrication and the use of a lift-off process. Another advantage of the FIB technique is that magnetic patterning in film structures can be often realized under a low dose that avoids material etching and reduces considerably the duration of the patterning process.

One possible drawback of the FIB patterning is due to the Gaussian profile of the beam, and straggling effects that lead to gradients in the magnetic properties at the edges of the patterned nanoelements. Note that the width of these regions can be limited, in the best cases, to only 10 nm. Since irradiation often reduces coercivity, a field-induced domain nucleation at dot edges can favor a better control of the magnetic switching behavior (Aign *et al*., 1998). FIB can be used to delimit the edges of a single track. Jamet *et al*. (2001a) have shown that domain walls move much more rapidly in such designed tracks than in wires patterned by engraving techniques. This can be interpreted as a magnetic wetting effect along the edges of the stripe. In other words, FIB can partly suppress pinning effects for wall motion by smoothing the track edges magnetically.

3 MAGNETISM IN NANOMAGNET ARRAYS

3.1 Definitions and characteristic lengths

Nanomagnet is used to name all types of nanometer size magnetic entities. When designed by a top-down patterning technique they will be called *magnetic nanoelements*. Nanoelements having a shape symmetry will be named *dots* when their thickness t does not exceed 50 nm, or *pillars* when t becomes comparable or thicker than their lateral size a (Krauss, Fischer and Chou, 1994). *Tracks* or *stripes* are long nanoelements with rectangular cross section (width: w, thickness: t). From this definition, they differ from wires that are generally grown by bottom-up methods in drilled templates (see also **Advanced Magnetic Microwires, Volume 4** and **Template-based Synthesis and Characterization of High-density Ferromagnetic Nanowire Arrays, Volume 4**). In the investigated periodic arrays, nanomagnets will be positioned at nodes of a square lattice with in-plane periodicity P. The separation $S = (P - a)$ represents the distance between the edges of two neighboring nanoelements.

As well known (see also **Magnetization Configurations and Reversal in Small Magnetic Elements, Volume 2**), several characteristic lengths control the magnetic behavior of magnetic nanoelements:

- The exchange length, $l_{ex} = \pi(2A/\mu_0 M_S)^{1/2}$, over which the spin orientations are highly correlated. Here A stands

Table 1. Ultimate performances of lithography and nonconventional techniques for patterning arrays of nanomagnets.

Techniques	Electron lithography	Optical lithography	Irradiation[a] through a mask	Ion projection	FIB
Complexity	Yes	No	Yes	Yes	No
Replication	No	Yes	Yes[b]/no	Yes	No
Resolution	>10 nm	>40 nm[c]	>15 nm	>20 nm	>5 nm
Size of the array	50 µm	>1 cm	100 µm	>1 mm	50 µm

[a]With light ions.
[b]Stencil mask.
[c]Conical shape of the nanoelement.

for the exchange stiffness, μ_0 the Bohr magneton, and M_S the magnetization at saturation. A typical value of l_{ex} for Fe or Co is 10 nm.

- The dipolar length, D_0 expressed as the ratio of the domain wall over the dipolar energy density, $D_0 = 2(AK)^{1/2}/\mu_0 M_S^2$. This quantity controls the stability condition for magnetic bubble formation, the vortex core size in circular magnetized nanoelements, and it allows to predict large domain size in ultrathin films with perpendicular anisotropy (Kaplan and Gehring, 1993).
- The domain wall width, $\Delta = \pi(A/K)^{1/2}$, where K is the magnetic anisotropy. Δ is about 3–10 nm for films with large out-of-plane anisotropy, and is much larger (30–100 nm) for usual films with in-plane anisotropy.

3.2 Noninteracting arrays of nanomagnets

One of the major challenges is to determine the statics and the dynamics of the magnetization reversal of well-defined magnetic nanoelements when their sizes become comparable or smaller than the characteristic exchange or dipolar length and domain wall width. For narrow tracks, the pertinent parameters are obviously the width w and thickness t. Then, the data must be compared to refined analytical calculations but more generally to micromagnetic simulations (Handbook of magnetism, Vol. 2). The size, shape, and magnetic anisotropy of these nanomagnets play a crucial role in the magnetization reversal process (Cowburn, 2000), and for determining equilibrium and field-induced metastable states. Obviously, the best solution is to select only one magnetically isolated nanoelement. Unfortunately, even sophisticated methods are, most of the time, not sensitive enough to measure such a weak magnetic moment. Up to now, only two techniques have succeeded to check the magnetic behavior of nanomagnets at a scale smaller than characteristic magnetic lengths: (i) Micro-SQUID magnetometry was used to investigate the magnetization reversal of a single Co particle as small as 3 nm in diameter (Jamet *et al*., 2001b), and therefore to test unambiguously the Néel's prediction of a coherent spin reversal process. (ii) Spin-polarized scanning tunneling microscopy (SP-STM) allowed measurements of the field-induced magnetization reversal in small nanocrystals (Bode, Pietzch, Kubetzka and Wiesendanger, 2004). Nevertheless, such sophisticated methods can only be used in a very limited number of cases. For nanoelements with sizes of a few tens of nanometers, transmission electron microscopy (TEM) in Lorentz mode or electron holography can yield useful local magnetic information (Hubert and Schäfer, 1998). However, no technique is presently able to investigate fast and ultrafast magnetization reversal dynamics on a single nanomagnet.

Consequently, it is highly desirable to deduce the magnetic behavior of individual nanoelements from that of dot assemblies. This can be only realized if nanoelements are structurally and magnetically identical, that is, with monodisperse properties and without interdot coupling. This last condition can be only fulfilled if the magnetostatic interaction can be neglected, that is, when the separation between nanoelements is at least five times larger than their thickness. This is a difficult challenge since most nanomagnet assemblies exhibit switching field distributions. Distributions are expected in many cases: of the size and shape of the nanoelements, of the magnitude and/or of the direction of their magnetic anisotropy, the statistics of nucleation, and so on. The most prejudicial effects for fundamental studies and applications come from nucleation field distributions. For example, in the case of Au/Co/Au films, with perpendicular magnetic anisotropy, an increase of the nanodot density gives rise to a huge enhancement of the mean coercive field, while the first dot is switching exactly at the field found for magnetization reversal in the virgin film (Jamet *et al*., 1998). This means that dot switching is related to the distribution of nucleation fields inside the virgin layer. All possible distributions obviously mask the predicted specific magnetization reversal process of single nanoelement. Unfortunately, the detail of distributions is generally unknown so that individual processes cannot be, *a priori*, rigorously evaluated. As discussed in the following text, these limitations can be overcome for FIB-patterned arrays of magnetic nanoelements. We will show how a very narrow distribution of magnetic dot properties can be obtained in that case.

3.3 Dipolar and exchange interactions in magnetic dot arrays

Only single spherical or elliptical nanoelements exhibit a uniform internal self-demagnetizing field. In counterpart, the self-demagnetizing field of nonspherical nano elements becomes inhomogeneous near the edges for both in-plane and out-of-plane magnetized samples. Inside ultrathin nanoelements, the demagnetizing field shape factor tends toward 0 or 2π for layers with in-plane or perpendicular magnetic anisotropy, respectively. For example, as checked by micromagnetic calculations, the self-demagnetizing field of out-of-plane magnetized nanoelements is non-homogeneous at their edges over a distance that can be up to five times the layer thickness. So, the reduction of the self-demagnetizing field favors field-induced nucleation and reversal of domains at nanoelement's edges. A clear consequence of self-demagnetizing effects is the generation of a large variety of domain configurations in thick nanodots with

perpendicular magnetic anisotropy (Hehn *et al*., 1996). When the separation S between nanoelements is smaller than their own thickness, the interelement magnetostatic interaction has to be considered.

In practice, nearly no array of nanoelements with in-plane anisotropy have been produced so far by the preparation techniques concerned in this review. Consequently, we will not report much on interelement magnetostatic effects in these in-plane magnetized nanodot arrays. They have been discussed by Fruchart *et al*. (1998). In that case, the dipole–dipole interaction between ultrathin nanoelements is short range, and decreases rapidly with their separation S. Contrarily to the 3D case, where dipole–dipole interactions are long range, a magnetic material confined in a 2D space shows a smaller associated magnetostatic energy.

The effect of interdot interaction on magnetization reversal in circular or square dot arrays with in-plane anisotropy have been studied theoretically by Guslienko *et al*. (2001). The magnetostatic interaction influences the nucleation and annihilation of magnetic vortices. This has been checked experimentally in permalloy dots by varying the dot separation (Novosad *et al*., 2003). The chirality of vortices is also controlled by magnetostatic interactions (Natali *et al*., 2002). Magnetostatic interactions in 1D-coupled dots have been investigated in simple systems with planar anisotropy. Novosad *et al*. (2003) have shown that the shape of the nanoelements influences the magnetization reversal process in chains. For in-plane magnetized nanomagnets arranged on a rectangular lattice, a transition from a magnetic disordered state to an ordered state, similar to a paramagnetic–ferromagnetic transition, has been evidenced when reducing the periodicity in one direction (Cowburn, 2000).

Let us now concentrate on dot arrays with out-of-plane magnetic anisotropy. The perpendicular (z) stray field component H^z_{dip}, created outside an ultrathin magnetic nanoelement decreases rapidly with the lateral distance x from its edge. An approached analytical expression of H^z_{dip} with x can be derived. If x is greater than the thickness t of the element, but smaller than the dot diameter, the nanomagnet can be considered as an electric wire, which surrounds the element, carrying a current $\mu_0 M_S t$. According to the Ampere's law, this current creates a dipolar stray field component H^z_{dip} proportional to $M_S t/x$. When x is larger than the element size, that is, in a macrospin approximation, H^z_{dip} vanishes more rapidly being proportional to $1/x^3$.

Now, let us try to estimate the dipolar stray field experienced by a central dot from the other dots positioned around it on a square lattice. An analytical expression has been deduced in the macrospin approximation, for nanoelements of volume V with perpendicular magnetic moments confined at nodes of a square lattice with period P. So, the dipolar stray field H^z_{dip} is written as (Haginoya *et al*., 1999):

$$H^z_{\mathrm{dip}} = [(0.716V)/P^3 + N](M_S/\mu_0) \qquad (1)$$

The self-demagnetizing field shape factor of a nanoelement, N, is supposed to be constant. The first term in the brackets represents the demagnetizing field factor due to all surrounding macrospins. As quoted by several authors (Haginoya *et al*., 1999; Haast *et al*., 1998), N is smaller for nanoelements than for the virgin continuous film, so that the equivalent demagnetizing field factor in the brackets of expression (1) is reduced as well. As a consequence, the remanent ratio, M_R/M_S, and hence the loop squareness, can be significantly improved, for example, from 0.2 for the virgin film to 1 for the patterned medium (Haginoya *et al*., 1999).

Numerical calculations are required if one wishes to account for the shape of the nanoelements. Nonhomogeneous stray fields are generated by a nanoelement on itself and by the surrounding nanoelements. For example, the case of an array of square ultrathin flat ($t \ll a$) magnetic nanoelements which are fully magnetized perpendicularly to their surface, has been treated. The mapping of the z component of the demagnetizing field in a central dot is depicted on Figure 15 (Jamet *et al*., 1999) for 1-μm wide ultrathin Co($t = 1.4$ nm) magnetic square dots separated by $S = 50$ nm. As expected, the dipolar stray field is highly non-homogeneous at dot edges and especially at corners. For arrays of thicker nanoelements, that is, pillars, stronger demagnetizing field effects are expected because of a higher magnetic moment per element.

When the magnetic ultrathin nanoelements come close to each other ($S \sim 1$–2 nm), interexchange interaction can also play a role through the nonmagnetic metal substrate

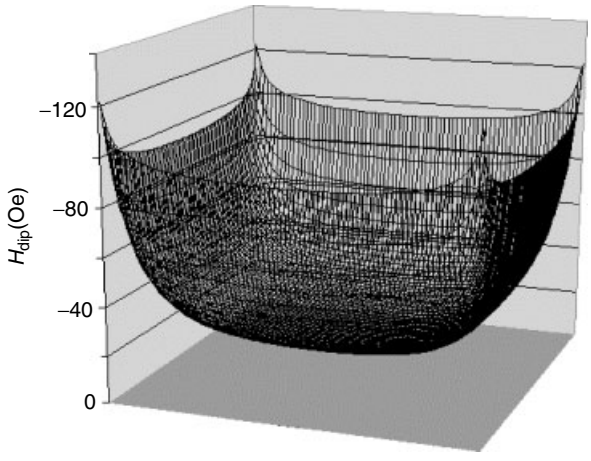

Figure 15. In-plane dipolar field mapping inside a ($1 \times 1\,\mu m^2$) Pt/Co(1.4 nm)/Pt square dot due to the field radiated by all other dots supposed to be in the same initial magnetic state. (J.P. Jamet *et al*., *J. Magn. Soc. Jpn.*, **23**, suppl No S1 (1999).)

or lateral insulating tunnel barriers (Kondratyev and Lutz, 1998). Magnetic ordering then occurs through an oscillating exchange coupling between the nanoelements that modifies the electronic state density. It results in either a net local ferromagnetic or antiferromagnetic interelement coupling depending upon the nature and size of the separation between nanoelements.

3.4 Experimental determination of interelements interactions

No direct method is able to determine the magnitude of interactions between magnetic nanoelements when the lattice period becomes smaller than the size of the magnetic probe. This happens when the distance between nanomagnets is typically shorter than 50 nm. As discussed in the preceding text, interactions can be intrinsic when they are due to the dipolar coupling or the exchange interaction mediated by the substrate, but sometimes nanoparticles can also touch each other as a consequence of an imperfect patterning process. To check magnetic interactions in dot arrays, the so-called ΔM method, related to the Henkel plot procedure, has been first proposed by Kelly, O'Grady, Mayo and Chantrell (1989). It is now widely used to probe the sign of magnetic interactions in several types of recording media, but also for studies of new chemically synthesized self-organized lattices of small quasi-monodisperse nanoparticles ($a \approx 6$ nm) which are separated by only a few nanometers (Sun *et al*., 2000). This ΔM method has been applied successfully to determine interactions in nanometer size particle assemblies designed for future magnetic recording media (Wu, van de Veerdonk, Chantrell and Weller, 2003; Zeng *et al*., 2002). It will be justified later in Section 4.3.2 for coupled Pt/Co/Pt dot arrays.

The ΔM method has been recently amended to introduce switching field distributions of nanoelements (Wu, van de Veerdonk, Chantrell and Weller, 2003). The variation of ΔM with the applied field, H, that is, the $\Delta M(H)$ curve can be extracted from the knowledge of the dc demagnetization (DCD) and of the isothermal remanent magnetization (IRM) curves. In DCD, the sample state is initially saturated in a negative field, while an ac-demagnetized initial state is considered for IRM. In both cases, the remanent magnetization $M_{\mathrm{DCD}}(H)$ or $M_{\mathrm{IRM}}(H)$ are measured for increasing H values after switching H to zero. From the $M_{\mathrm{DCD}}(H)$ and $M_{\mathrm{IRM}}(H)$ plots, the pertinent quantity, $\Delta M(H) = M_{\mathrm{DCD}}(H) - [1 - 2\ M_{\mathrm{IRM}}(H)]$ is deduced. $\Delta M(H)$ is related to deviations from the case of noninteracting elements. The integrated area between the $\Delta M(H)$ curve and the field axis is found to be positive for interparticle coupling dominated by exchange interaction, and positive when it is dipolar in origin.

3.5 Arrays of interacting nanomagnets

This topic was partly treated by Martin *et al*. (2003) in their review. In the case of a 2D array of single magnetic layer nanoelements, in-plane magnetic interactions play a major role on the magnetic switching behavior. However, for nanoelements built from a magnetic multilayer structure, interlayer interactions within a dot have also to be considered. The second case is of vivid interest for new generations of memories, such as magnetic random access memories (MRAMs). At first, we will limit ourselves to the simple case of single magnetic layer nanoelements.

Nanomagnets can be laterally coupled by exchange (Kondratyev and Lutz, 1998) or magnetostatic interactions. Exchange interactions through buffer or top layers are only efficient for very closely spaced ($S \sim 1$–2 nm) nanoelements. Only a few predictions on exchange-coupled particles or nanomagnets have been reported so far in the literature (Scheinfein, Schmidt, Heim and Hembree, 1996; Chen *et al*., 2002; Navarro *et al*., 2004). This is due to the intrinsic difficulty in designing regular assemblies of particles with controlled nanometer size separations. The study of the magnetism of model systems made up by assemblies of nanomagnets with competitive exchange and dipolar interactions is of fundamental interest since they can mimic real magnetic films for recording application (Zhu and Neal Bertram, 1989).

Most of the investigations have been limited to pure magnetostatic interactions. From the macroscopic side, a very instructive study of a lattice of in-plane dipolar-coupled compass needles has been reported by Olive and Molho (1998). They deduced the system's thermodynamic properties under a random applied field that is supposed to mimic thermal fluctuations. A phase transition between an ordered and a disordered state has been evidenced and successfully interpreted by numerical simulations.

As discussed in the preceding text for noninteracting nanomagnets in real systems (Section 3.2), we are also faced with unknown distributions of their magnetic properties. So, assuming an assembly of identical macrospins (single magnetic domain state nanoelements), simple theoretical models can only predict general trends. Nevertheless, in the best experimental cases, with nanomagnets showing quasi-monodisperse magnetic properties, several basic problems have already been solved:

1. The thermodynamics of simple 2D-Ising or XY-coupled systems, in particular, the transition between ordered and disordered macrospin states (0D (isolated element) to 1D (chains of elements), 1D to 2D (in-plane distributed elements), and 2D to 3D (elements in space) arrangements of nanomagnets (Cowburn, 2000)).

2. The switching field statistics of a nanomagnet interacting with neighbors, and their related consequences on the magnetization reversal of the array as a whole (Fruchart *et al*., 1998; Repain *et al*., 2004).
3. The dynamics of dipolar-coupled Ising nanomagnets distributed on a regular lattice and modeled using a macrospin approximation (Sampaio *et al*., 2001).

Many theoretical treatments have been proposed to evaluate magnetic properties of arrays of nanomagnets and the role of interactions including several types of distributions. A neural network approach, composed of a self-organized array of short- and long-range interacting magnetic dots, has also been proposed (Horvath, Gmitra and Vavra, 2001; Horvath and Gmitra, 2003; Gmitra and Horvath, 2003). Many theoretical treatments in statistical physics are devoted to dynamics, and some of them concern 2D interacting systems. However, most of the models predict slow dynamics only; for example, a logarithmic relaxation is expected in hierarchically constrained systems (Bray and Prados, 2001). A 2D lattice of interacting magnetic dipoles gives rise to quasilogarithmic or stretched exponential time decay (Sun and Weili, 1997; Lottis, White and Dahlberg, 1991). Experimental studies of magnetic relaxation (also called *magnetic aftereffect*) have been performed either on simple clusters of nanomagnets (Luis *et al*., 2002) or on a large array of quasi-identical nanoelements (Sampaio *et al*., 2001); the relaxation phenomenon always becomes slower when increasing the complexity of interactions and the size of the array.

With reference to applications, the performances of a so-called continuous magnetic recording medium are highly dependent on its nanoscale heterogeneity and on the magnetostatic and exchange interactions between crystallites. This is also true for discrete media made up of interacting single-domain nanomagnets. Experiments and modeling are essential to determine the stability, integrity, and compactness of data storage and processing devices.

In that context, we wish to first recall predictions or results in granular films formed by crystallites interacting through grain boundaries; some models include distributions of particle properties. The exchange coupling depends on the intercrystallite spacing, but long-range magnetostatic interactions are always efficient. Computer simulations in CoCr recording granular thin-film media with perpendicular anisotropy have been reported several years ago by Zhu and Neal Bertram (1989). They used a model consisting of a periodic nanocolumnar magnetic structure with both intergranular exchange and dipolar interactions between columns. Columns were supposed to be single crystalline with identical properties and uniformly magnetized (macrospin approximation) during magnetization reversal. In a more recent publication, also devoted to magnetic recording media with perpendicular anisotropy, Victora, Willoughby, MacLaren and Xue (2003) developped an electronic structure theory with a local spin density approximation and coupled it to micromagnetic simulations. Monte Carlo simulations with exchange and dipolar interactions between nanoparticles have also been proposed by El-Hilo, Chantrell and O'Grady (1998) to deduce the temperature and time dependence of magnetic properties. The magnetic behavior depends drastically on the strength and nature of the interactions. The main trends issued from these calculations are as follows:

- Magnetostatic effects give rounded hysteresis loops without modifying the coercivity much (Zhu and Neal Bertram, 1989). The remanent magnetization is modified accordingly.
- Domain patterns following an ac demagnetization are very sensitive to the intergranular exchange strength J (Figure 16).
- Spatial disorder or distribution of the interactions tend to round the hysteresis loop shape (Ribeiro, 1991; Victora, Willoughby, MacLaren and Xue, 2003).
- As shown on Figure 17, the value of the intergranular exchange coupling has direct consequences on the hysteresis loop squareness and coercivity.
- For a film with distributed small intergranular J values, the field-induced magnetic domain structure tends to mimic the discreteness of the film morphology (Victora, Willoughby, MacLaren and Xue, 2003; Zhu and Neal Bertram, 1989). For increasing J, the magnetization in neighboring crystallites tends more to align with each

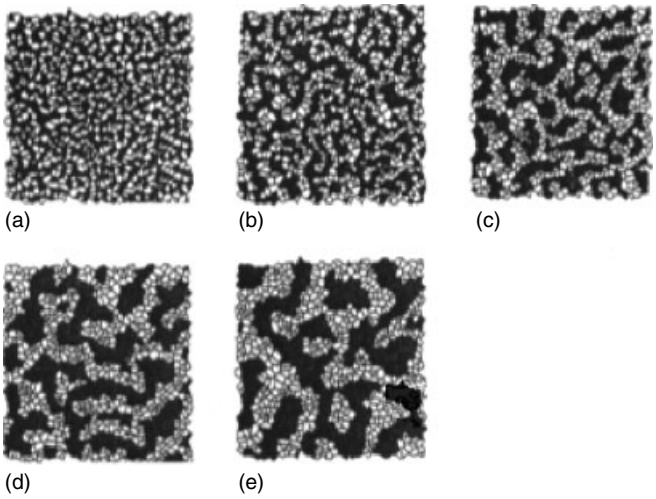

Figure 16. Simulated magnetic domain patterns for 2d ac-demagnetized granular films with perpendicular anisotropy for various intergranular exchange constants: (a) $J = 0$, (b) $J = 0.25$, (c) $J = 0.5$, (d) $J = 0.75$, and (e) $J = 1$. (Victora *et al*., *IEEE Trans. Magn.* **39**, 710–715 (2003) (© 2003 IEEE).)

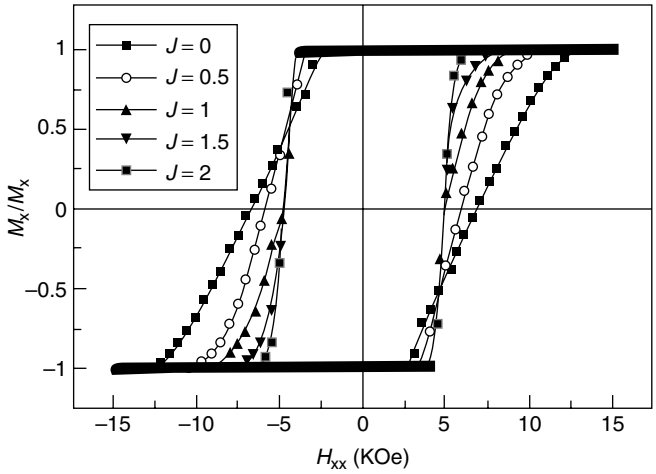

Figure 17. Hysteresis loops in a perpendicular granular medium simulated for different values of the exchange integral J, taking an anisotropy constant $K = 1.8 \times 10^6$ ergs cm^{-3}. (Victora *et al.*, *IEEE Trans. Magn.* **39**, 710–715 (2003) (© 2003 IEEE).)

other and the characteristic ac (Figure 16) or field-induced magnetic domain size grows significantly.

- As expected, the shape of the magnetic relaxation curves depend strongly on the exchange coupling, consistent with nucleation (large dipolar coupling)- or wall propagation (large exchange coupling)-dominated effects.

Kerr microscopy observations in a granular Co–Cr film (Schmidt and Hubert, 1986) allowed to verify some of the above predictions.

4 FROM MAGNETICALLY ISOLATED TO COUPLED DOT ARRAYS

4.1 Arrays of dots on prepatterned templates

In Section 2.1.1, we described the preparation method of magnetic nanodots deposited on the top of Si nanopillars (Landis, Rodmacq and Dieny, 2000). These nanodots are shown to be ferromagnetically decoupled. Owing to an easy wall motion, the final stable states in square nanodots are magnetically saturated. So, configurations with only up- or down-magnetized dots are observed in the remanent state. The distribution of switching fields depends on nucleation pinning energy at sidewalls; it is mainly related to the precise shape of the dots. Regular arrays of [Pt(20 nm)/Co(0.5 nm)/Pt(1.8 nm)]$_4$ magnetic nanodots ($a = 80$ nm, $P = 180$ nm) were deposited on 220-nm-high Si-etched pillars (Moritz *et al.*, 2002). The manipulation of the magnetization state in single nanodots can be done by local heating using an atomic force microscopy (AFM) tip (Figure 18), as well as using conventional write heads for disk drives. Good writing and reading performances have been established in Co/Pt multilayer (100×200 nm^2) nanoelement arrays (Moritz *et al.*, 2004). Compared with a continuous film, the value of the signal-to-noise ratio is high, due to a reduction of the bit transition noise. Using prepatterned Si templates, Baltz *et al.* (2005a) succeeded to prepare arrays of exchange bias ferromagnetic–antiferromagnetic nanoelements with a lateral size smaller than 100 nm.

4.2 Nanoelement arrays prepared by ion-induced magnetic patterning through masks

4.2.1 Magnetism in track arrays prepared by He ion irradiation through contact masks

High-resolution magnetic patterning by He ion irradiation through a contact mask was first demonstrated on Pt/Co(0.5 nm)/Pt films (Chappert *et al.*, 1998). The 850-nm-thick Polymethyl metacrylate (PMMA) resist layer mask was deposited directly on the film and patterned by electron-beam lithography. The irradiation dose was large enough to render the Co layer paramagnetic in nonprotected areas, as revealed by Polar magneto optical kerr microscopy (PMOKE) microscopy on a stripe array connected to a reservoir (Figure 10).

In order to check the ultimate resolution of patterning, arrays of ultranarrow tracks, with width as narrow as $w = 50$ nm, were designed in a [Pt(0.6 nm)/Co(0.3 nm)]$_6$ multilayer (Devolder *et al.*, 1999, 2001). For this purpose, a 450-nm-thick SiO_2 layer was deposited on the film, in order to stop 30 keV He ions, and patterned to form a high-resolution mask (30-nm-wide trenches) by electron-beam lithography and dry etching (Figure 11). Finally, the Co/Pt multilayer was irradiated under uniform He beam at low dose ($D = 2 \times 10^{15}$ He ions/cm^2). Under the mask-protected areas, an array of ultranarrow ferromagnetic tracks was preserved and the track magnetization state imaged by magneto-optical microscopy after the application of a small field (Figure 12), which was larger than the coercivity of the irradiated areas. The continuity of the structure and magnetism along the tracks, down to $w = 30$ nm, was then demonstrated. PMOKE microscopy is thus able to detect a large-enough magnetic contrast coming from spaced ultranarrow wires. This is possible in spite of the rather large value of the optical wavelength, $\lambda = 535$ nm, or of the optical resolution (400 nm), while the contrast is theoretically reduced by the $(w/\lambda)^2$ factor. The coercive field in tracks was found slightly lower (20%) than in the virgin film, evidencing ion straggling effects (Section 2.2.2).

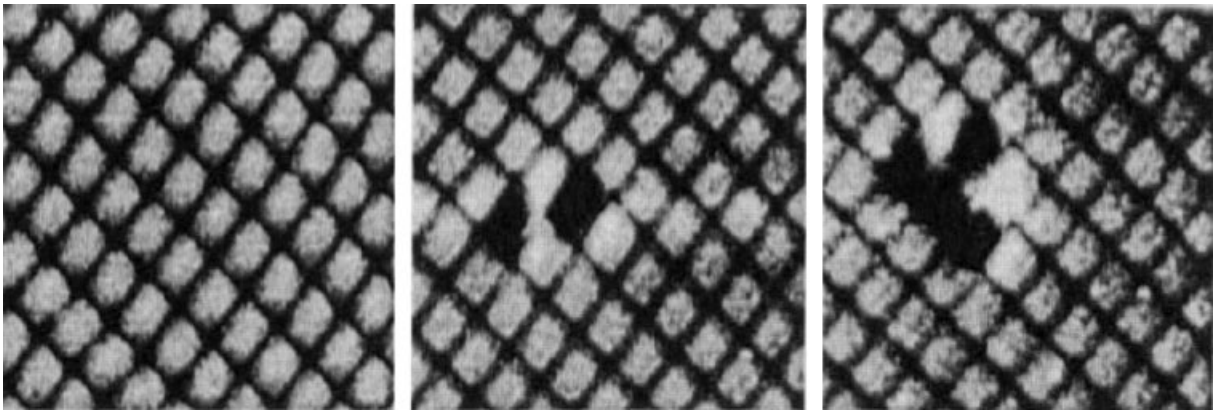

Figure 18. Magnetic force microscopy (MFM) image of an array of etched Si dots covered by a Pt(20 nm)/[Co(0.5 nm)/Pt(1.8 nm)]$_4$ multilayer before (left image) and after thermomagnetic switching of dots induced by an AFM tip. The dots have a lateral size of 400 nm, with an edge-to-edge spacing of 100 nm. The controlled thermomagnetic switching of individual dots has been achieved by flowing pulse of current from the metallic AFM tip to the dot and simultaneously applying a uniform field of about 200 Oe over the whole sample. (Moritz *et al*., *IEEE Trans. Magn* **38**, 1731–36 (2002), (© 2002 IEEE).)

Arrays of $Co_{25}Fe_{75}$ perpendicularly magnetized ferromagnetic dots have also been designed by He irradiation through a pillar-type mask (Devolder *et al*., 2003) (see Section 2.2.2). This structure is especially interesting for magnetic recording since magnetization reversal is nucleation free and proceeds by domain wall injection from the surrounding magnetically soft matrix. This guarantees a narrow coercivity dispersion.

4.2.2 Magnetism in track arrays prepared by He ion irradiation through a stencil mask

As described in Section 2.2.3, a noncontact stencil mask is fabricated by drilling holes in a membrane. This membrane is suspended above the film surface. Magnetic patterning of the film is realized by uniform ion irradiation through the stencil mask. Dense CoCrPt dot arrays with perpendicular anisotropy have been prepared using stencil masks (Terris *et al*., 2000).

More recently, Abes *et al*. (2005) demonstrated that irradiation by 40 keV He ions ($D = 6 \times 10^{16}$ ions/cm^2) transforms $L1_0$–$Co_{50}Pt_{50}$ magnetic hard films with perpendicular anisotropy into an in-plane soft magnetic alloy. So, through a stencil mask with $1 \times 1\,\mu m^2$ square apertures, they were able to pattern an array of soft in-plane magnetized dots inside a hard out-of-plane magnetized material.

4.2.3 Magnetism in nanoelement arrays with easy in-plane anisotropy fabricated by ion irradiation through a mask

Up to now there exists only a limited number of investigations devoted to estimate magnetic changes due to ion irradiation in in-plane magnetized films. Permalloy layers have been patterned under Ar ion irradiation (dose range: 10^{13}–10^{16} Ar ions/cm^2) at 200 keV, in the presence of an applied field (Woods *et al*., 2002). This field reorients the easy anisotropy axis in irradiated areas. So in-plane magnetic anisotropy patterning can be realized by irradiation through a mask. The same phenomenon has been evidenced in amorphous soft magnetic FeCoSiB films (McCord *et al*., 2005) but using He ions. Magnetic domain imaging allowed the authors to follow the rotation of the field-dependent anisotropy axis orientation. Anisotropy patterned structures have also been designed by irradiation through masks that were previously prepared by photolithography.

4.3 Magnetic nanoelement arrays prepared by focused Ga ion beam (FIB)

4.3.1 Arrays of magnetic nanodots patterned by Ga FIB

We will essentially limit ourselves to FIB patterning under low Ga ion dose for changing locally magnetic properties of ultrathin film structures at nanometer scale. Patterns are then produced by scanning a FIB over the film surface to magnetically separate the nanoelements by irradiated lines (Gierak *et al*., 2005). The first attempt to realize large ($50 \times 50\,\mu m^2$) arrays of quasi-identical ultrathin film magnetic square dots by using a FIB has been reported by Aign *et al*. (1998). In this first case, the dose was large enough to etch lines separating Pt/Co(1.4 nm)/Pt dots with a width estimated to be 50 nm.

So, under moderate Ga ion dose ($>3 \times 10^{15}$ ions/cm^2), arrays of discrete magnetic nanoelements can be efficiently

patterned (Rettner *et al*., 2002b; Aign *et al*., 1998). Fortunately, as for He ions, Ga ion irradiation at relatively low dose is able to act directly on the magnetism of Co/Pt ultrathin film structures without etching the sample too much (Sections 2.1.1 and 2.3.2). This was realized in Pt/Co/Pt films and Co/Pt multilayers with doses as low as 10^{12}–10^{14} Ga ions/cm^2 (Vieu *et al*., 2002; Hyndman *et al*., 2001a). Thus, by favoring intermixing at interfaces, irradiation strongly modifies both the interface anisotropy and the exchange interaction. For example, as seen in Section 2.1.1, a ferromagnetic Pt/Co(1.4 nm)/Pt film becomes paramagnetic at room temperature under irradiation for a dose of 2×10^{15} Ga ions/cm^2 (Ferré *et al*., 1999), while the perpendicular anisotropy orientation is maintained at smaller dose. The effect of irradiation is even more drastic in Co/Pt multilayers (Hyndman *et al*., 2001a); two successive transitions occur from a perpendicular to an in-plane anisotropy state for 10^{13} Ga ions/cm^2, and then to a paramagnetic state for 10^{15} Ga ions/cm^2. In spite of these strong changes in magnetism, the etching process is quite inefficient at low doses (1 ML for 1.5×10^{14} Ga ions/cm^2).

As we shall see later, when increasing the dose within the irradiated lines separating nanoelements, the exchange interaction is first reduced in a sharp zone (<10 nm) separating Pt/Co/Pt tracks or dots. These sharp lines become weakly ferromagnetic with either perpendicular or in-plane anisotropy (Figure 13a). Under a little higher dose, the central part of the lines becomes paramagnetic (Figure 13b). At higher doses, etching cuts the magnetic layer, and so separates physically the nanoelements.

4.3.2 *Pt/Co/Pt dot arrays with out-of-plane anisotropy: a model system for studying magnetization reversal in the presence of interdot exchange and dipolar interactions*

The magnetic properties of Ising-like Pt/Co(1.4 nm)/Pt(3.5 nm) square dot or track arrays, having perpendicular magnetic anisotropy and patterned by FIB, have been extensively studied (Aign *et al*., 1998; Jamet *et al*., 1999; Sampaio *et al*., 2001; Hyndman *et al*., 2002a,b; Repain *et al*., 2004; Gierak *et al*., 2005). Here, patterning is realized by scanning a sharp (5–30 nm diameter) FIB spot over the film (Figure 13). TRIM calculations (Ziegler, 1992) allow one to determine the density of collision events in irradiated lines (Figure 19). The interaction between Pt/Co(1.4 nm)/Pt tracks or dots can then be monitored by choosing the

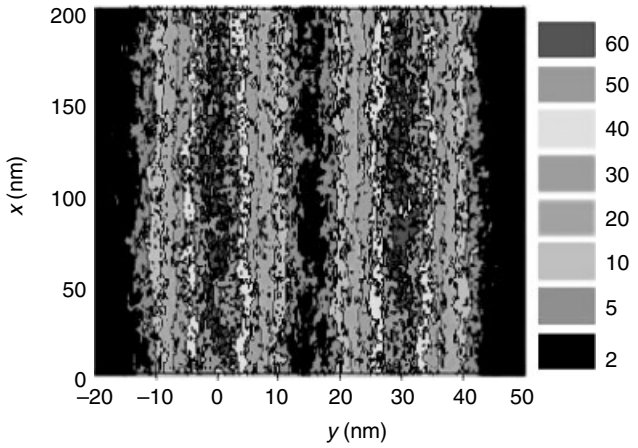

Figure 19. TRIM simulation of the density of collision events for two parallel FIB lines centered at $y = 0$ and 30 nm, and patterned on a Pt(3 nm)/Co(1.4 nm)/Pt(5.6 nm) film. The FIB spot diameter was set to 10 nm. Along x, the lines were built by a succession of overlapping FIB spot irradiations separated by 10 nm. The number of collision events is indicated on the right side of the image in 10^{16} ions/cm^2 units. (From Hyndman, unpublished.)

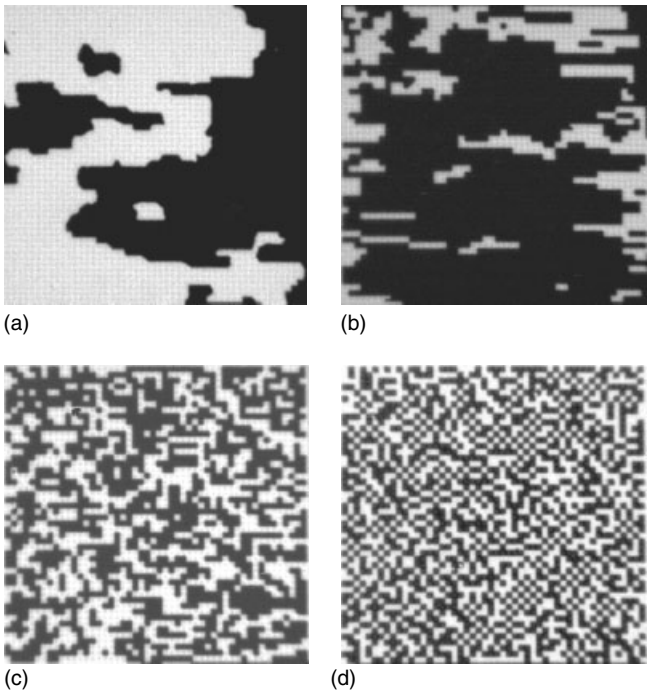

Figure 20. PMOKE images of ac-demagnetized states of ($1 \times 1\,\mu m^2$) Pt/Co(1.4 nm)/Pt dot arrays patterned with lineic Ga ion doses of: (a) 0.05 nC cm^{-1}, (b) 0.1 nC cm^{-1}, (c) 0.2 nC cm^{-1}, and (d) 0.5 nC cm^{-1}, and a spot diameter of 10 nm. (V. Repain *et al*., *Journal of Applied Physics.* **91**, 3103 (2002).)

irradiation dose (Hyndman *et al*., 2001b, 2002a; Repain *et al*., 2004) (Figure 20). At high Ga ion dose ($D > 4 \times 10^{15}$ Ga ions/cm^2), the Co layer is entirely etched away

so that the tracks and dots are surely exchange decoupled; in that case, only the interdot magnetostatic interaction remains efficient. Owing to the magnetostatic coupling in a thick-enough ferromagnetic layer, the ac-demagnetized state of a Pt/Co($t = 1.4$ nm)/Pt film shows a rather high degree of checkerboard arrangements of the magnetization in dot arrays (Figure 21e). In counterpart, no correlation is found between the magnetic state of thin enough Co dots, as for $t = 0.5$ nm (Figure 21d). At a lower dose (1.5×10^{14} Ga ions/cm^2 $< D < 3 \times 10^{15}$ Ga ions/cm^2), the Pt overlayer is partly etched, but not the Co layer. Nevertheless, the magnetism of the Co layer is affected by irradiation: the Co layer becomes paramagnetic at room temperature for a dose $D > 2 \times 10^{15}$ Ga ions/cm^2. It has been shown (Ferré *et al.*, 1999) that for a smaller dose the perpendicular anisotropy and the Curie temperature are reduced when increasing the dose. In other words, the exchange interaction between tracks or dots can be accurately modified and controlled over a short distance ($\approx$2–10 nm) on the central part of the irradiated lines. Thus, the magnetic behavior of arrays of tracks or dots can be subsequently investigated when changing the relative strength between exchange and dipolar couplings (Hyndman *et al.*, 2001a; Repain *et al.*, 2004) (Figure 20).

Let us first focus on the magnetic behavior of arrays of purely dipolar-coupled arrays of perpendicularly magnetized

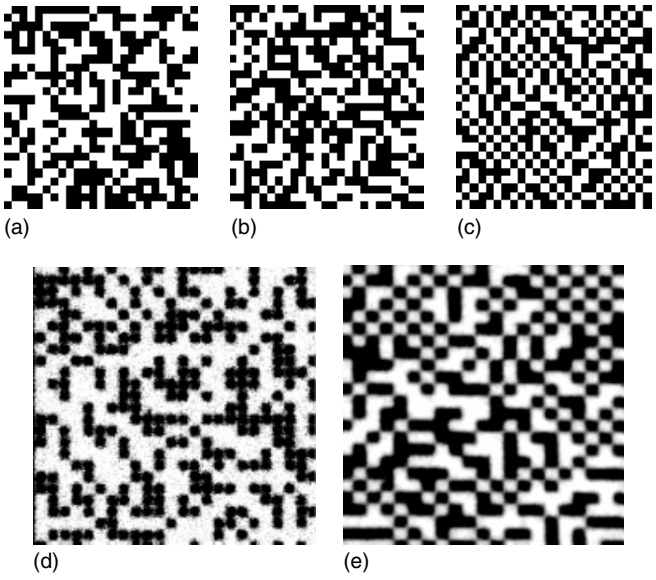

Figure 21. First row: results of the simulation of the demagnetized states of ($1 \times 1\,\mu$m^2) Pt/Co(1.4 nm)/Pt dot arrays for an increasing strength of the dipolar interaction: (a) $R = 0$, (b) $R = 0.44$, and (c) $R = 4.4$. Second row: PMOKE images of ac-demagnetized domain structures for ($1 \times 1\,\mu$m^2) dot arrays patterned on (d) Pt/Co(0.5 nm)/Pt, or (e) Pt/Co(1.4 nm)/Pt films. (Reprinted figure with permission from V. Aign *et al.*, PRL 81, 5656 (1998). Copyright 1998 by the American Physical Society.)

tracks or dots. It is not straightforward to predict the equilibrium state of a large assembly of elements coupled by long-range dipolar interactions. One way is to use Monte Carlo simulations assuming a well-defined switching field for each track or dot in the array; this treatment neglects self-magnetostatic interactions within the nanoelements. In order to model real systems, a distribution of nanoelement switching fields has to be introduced. Such calculations have been done to describe the demagnetized state of a 1.3-μm periodic array of square Pt(4.5 nm)/Co(1.4 nm)/Pt(3.5 nm) dots separated by nonmagnetic 60-nm-wide irradiated lines for several values of the parameter $R = (\Delta H_{SW}/H_{dip})$ (Figure 21a–c). R is the ratio between the width (ΔH_{SW}) of the switching field distribution and the interdot dipolar field (H_{dip}). When $H_{dip} > \Delta H_{SW}$, each dot tends to be surrounded by dots having opposite magnetization; a checkerboard configuration is then favored. However, since the magnetization reversal can be initiated by the switching of different dots at the same time, several checkerboards develop simultaneously around these centers and merge together by generating magnetically frustrated areas. Such demagnetized patterns were also found in arrays of long wires or pillars (Ross *et al.*, 2001). At a larger scale, this situation mimics a complex antiferromagnetic state with antiphase boundaries. Each antiferromagnetically coupled spin is replaced here by a dipolarly interacting macrospin. The observed magnetic pattern of a Pt/Co(1.4 nm)/Pt ac-demagnetized array (Figure 21e) is comparable to that calculated for $R = 4.4$ (c). This result agrees with independently determined experimental values of $\Delta H_{SW} \approx 20$ Oe and $H_{dip} = 81$ Oe (Aign *et al.*, 1998). FIB patterning is especially convenient to avoid distributions of switching fields in Co/Pt dots. In usual systems, a highly distributed nucleation mechanism determines local switching fields. Using a FIB patterning procedure with a Gaussian beam profile, dot borders are weakly irradiated (Figure 13); consequently, the edges become magnetically softer than the inside of the dots. Moreover, self- and interdot magnetostatic interactions also favor nucleation at dot edges. So, for these two reasons, the magnetization reverses first at dot edges in small field. This creates a reservoir of nucleation from which magnetization can subsequently switch by fast domain wall motion, as soon as H reaches H_{SW}. Thus, the distribution of switching fields here is nothing else than that of the propagation field, which is particularly narrow for high-quality films, as proved by the squareness of the hysteresis loop (Figure 3). Fast reversal has the direct consequence that all dots appear either in a single up- or down-magnetized state.

The mean dipolar field value can be calculated (Aign *et al.*, 1998; Repain *et al.*, 2004) or evaluated from the following local picture of the magnetization reversal. As expected, it was experimentally verified by PMOKE imaging that the reversal of a dot depends on the magnetic configuration of the

surrounding dots. Starting from a saturated magnetized state of the array, and applying a field in the opposite direction, the first and last dots are supposed to reverse at fields $H_S^{min} = H_{SW} - H_{dip}$ and $H_S^{max} = H_{SW} + H_{dip}$, respectively, neglecting the small H_{SW} distribution. From high-resolution PMOKE microscopy snapshots, the hysteresis loops of a single central dot have been deduced for magnetization reversal in the two extreme configurations (nearest-neighbor dots magnetized in the same direction or oppositely to the central dot) of the surrounding dots (Figure 22). This allowed the authors to estimate the strength of the dipolar field, $H_{dip} \approx (H_S^{max} - H_S^{min})/2$. In the central part of the dots, the magnetization has been found to switch abruptly, consistently with a fast wall motion-assisted reversal initiated from a low field nucleated state at dot edges.

The effects of magnetostatics on the magnetization reversal have been investigated on patterned dots, open tracks, and compared to those happening in the virgin film (Figure 23). The reversal process has been imaged for different field values, and the hysteresis loop reconstructed from the analysis of multiple snapshots similar to those presented in Figure 23. An abrupt magnetization reversal takes place in the virgin part as well as in the track array. Nevertheless, as a consequence of the dipolar interaction between tracks, intermediate states with alternate magnetized tracks are favored (Figure 23c). Some dots begin to switch before the onset of the reversal of the virgin film; this behavior is expected, as already shown when investigating the reversal of the first dot (Figure 22). As calculated, the tilted loop shape for the dot array is still a consequence of the interdot magnetostatic interaction (Figure 23).

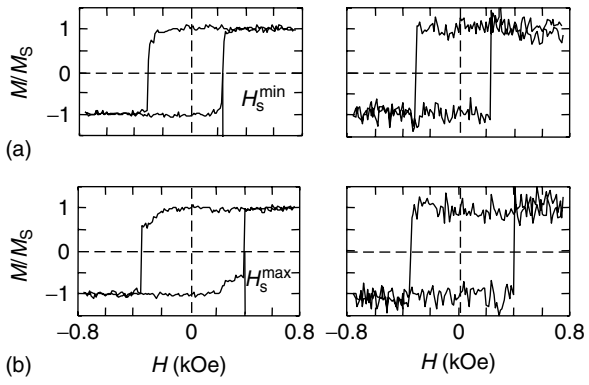

Figure 22. Magnetic hysteresis loops measured on a single Pt/Co(1.4 nm)/Pt $1 \times 1\,\mu m^2$ square dot in the FIB-patterned array. (a) Reversal of the first dot, initially surrounded by dots magnetically oriented in the same direction, (b) reversal of the last dot initially surrounded by dots magnetically oriented in the opposite direction. The loops at the left side are measured over the full area of a dot, while the loops at the right side are probing only the central part of the dot ($0.33 \times 0.45\,\mu m^2$). (Reprinted figure with permission from T. Aign *et al.*, *Phys. Rev. Lett.* Vol. 81, 5656 (1998). Copyright 1998 by the American Physical Society.)

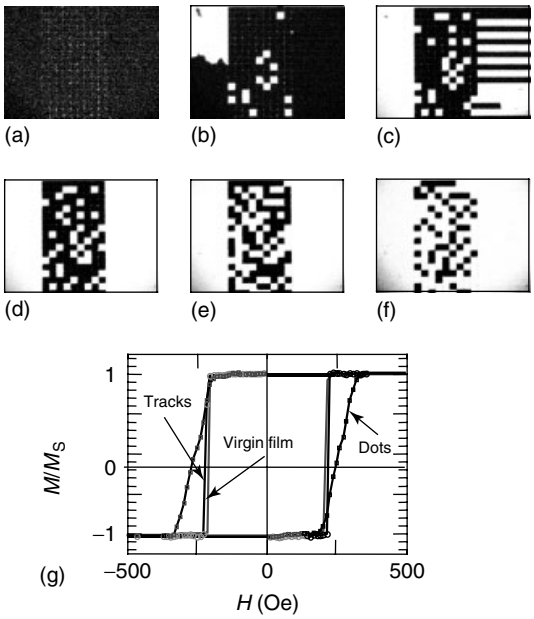

Figure 23. Pt/Co(1.4 nm)/Pt film (a–f) PMOKE snapshots of the field-induced magnetization reversal of several areas existing on the sample: (left part) virgin film, (middle part) dot array, and (right part) track array, connected to the virgin film at its right side. After saturating the film in a negative field (black state), a positive field is applied with successive values: (a) 160 Oe, (b) 211 Oe, (c) 219 Oe, (d) 230 Oe, (e) 257 Oe, and (f) 279 Oe. The patterning has been done by FIB ($D = 5 \times 10^{15}$ ions/cm^2). The image size is $30 \times 20\,\mu m^2$. (g) Remanent hysteresis loops in the virgin part of the sample, and in the dot and track patterned parts deduced from the analysis of snapshots recorded for many field values. Magnetostatic effects give an increase of coercivity in patterned areas. (Reprinted from *Journal of Magnetism and Magnetic Materials*, Vol 240, Hyndman *et al.*, Magnetization reversal in weakly coupled magnetic patterns, Pages 34–36, 2002, with permission from Elsevier.)

Starting from such a 2D-Ising model system, it is possible to investigate by PMOKE microscopy the magnetization reversal dynamics in a regular array of dipolar or exchange-coupled dots (Hyndman *et al.*, 2001b; Sampaio *et al.*, 2001). The magnetization reversal in this system exhibits slow dynamics because of the presence of many equivalent quasi-degenerate ground states. After saturating first the dot array in a positive field and reversing it to a value smaller than the coercivity, the observed slow relaxation of the magnetization M (magnetic aftereffect) can be fitted by a power law: $M = At^{-\alpha}$ (Sampaio *et al.*, 2001). The exponent α is shown to increase with the applied field. This time dependence is consistent with a many-body type of relaxation. Monte Carlo simulations also support this form for the expression of the relaxation law and the field dependence of α. A power law has also been determined by

Monte Carlo simulations for a 1D model of aligned small particles coupled by dipolar interactions (Ribas and Labarta, 1996).

For lines irradiated under a relatively large lineic dose ($0.5\,\mathrm{nC\,cm^{-1}}$), the discreteness of the magnetic dot array is clearly evidenced from the image of the ac-demagnetized state (Figure 20d). At low lineic irradiation dose ($D < 0.05\,\mathrm{nC\,cm^{-1}}$) (Figure 20a), the ac-demagnetized state is formed by large up- or down-magnetized domains whose walls are pinned on the reminiscent underlying FIB line pattern. In another case of large dipolar effects in granular Co–Cr films, the effect of textural discreteness has been already evidenced by magneto-optical microscopy (Schmidt and Hubert, 1986). When comparing granular and FIB-patterned films, crystallite boundaries and irradiated lines are supposed to play a similar role. In a narrow dose range, around $D \approx 0.2\,\mathrm{nC\,cm^{-1}}$ (Figure 20c), competitive interdot dipolar and exchange interactions take place; this mimics a kind of spin-glass state. The experimentally found demagnetized patterns, when increasing the dose in irradiated lines, can be well understood from simulations in random granular media. In that case, both magnetostatic interactions and reduction of the exchange interaction at grain boundaries are considered (Figure 16) (Victora, Willoughby, MacLaren and Xue, 2003). In the Pt/Co/Pt model system, the ratio between interdot exchange and dipolar energy can be precisely adjusted with the ion dose in irradiated lines. Thus, ideal granular media, that is, without distributions of grain sizes and interactions, can be compared to patterned Pt/Co/Pt dot arrays (Repain *et al.*, 2004) and modeled by simulations (Zhu and Neal Bertram, 1989).

As reported in the preceding text (Section 3.4), the ΔM method remains a powerful tool to characterize the sign of the resulting interdot interaction in discrete recording media. The trends of this method appeared quite empirical at first glance. With a 2D-Ising model system of quasi-identical interacting dots located at the nodes of a square lattice, it was possible to check the validity of this ΔM method (Repain *et al.*, 2004). The $\Delta M(H)$ curves have been deduced for Pt/Co(1.4 nm)/Pt dot arrays when varying the exchange to dipolar coupling ratio with the ion dose in FIB irradiated lines. Experimental data are in good qualitative agreement with predictions: ΔM is positive for exchange-dominated interdot interaction and negative for favored dipolar coupling (Figure 24). The origin of ΔM can be understood from the examination of PMOKE snapshots. Interactions can be better quantified by looking at the field dependence of the magnetic pattern at different scales. ΔM is clearly related to the two-macrospin correlation functions of neighboring dots (Figure 25).

What are the consequences of a reduction of periodicity P and lateral dot size a at nanometer scales, when preserving the irradiation dose in irradiated FIB lines? This was studied for etched lines using a 5×10^{15} Ga ions/cm^2 irradiation dose in a Pt(4.5 nm)/Co(1.4 nm)/Pt(3.5 nm) film (Hyndman *et al.*, 2002a). The width of the etched central part of the lines

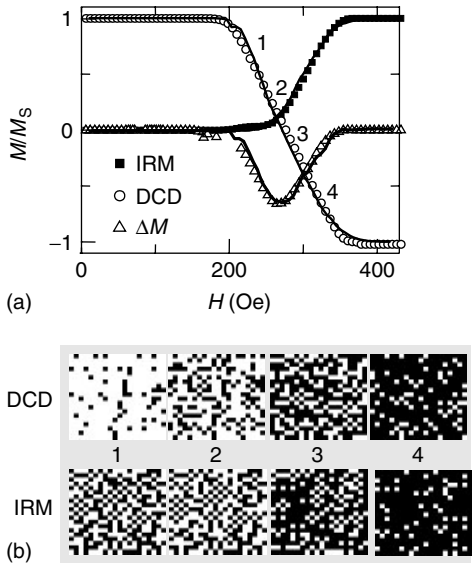

Figure 24. (a) Renormalized magnetization (DCD(H) or IRM(H)) and $\Delta M(H)$ curves for a Pt/Co(1.4 nm)/Pt dot array patterned with a lineic Ga ion dose of $0.5\,\mathrm{nC\,cm^{-1}}$. Data points are visualized on the graph by symbols. Continuous lines are simulation results considering a Gaussian switching field distribution centered at 272 Oe, with a small standard deviation of 15 Oe. (b) PMOKE snapshots of the DCD(H) and IRM(H) remanent magnetic states over the central part of the array for different values of the applied field H (indicated by 1–4 on the graph). The switched magnetic dots are in black. (V. Repain *et al.*, *Journal of Applied Physics.* **91**, 3103 (2002).)

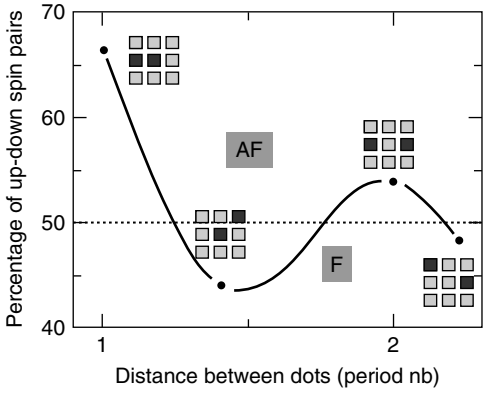

Figure 25. Macrospin pair correlation function versus the distance between Pt/Co(1.4 nm)/Pt dots in arrays patterned with a lineic Ga ion dose of $0.5\,\mathrm{nC\,cm^{-1}}$. Data points correspond to first-, second-, or third-neighbor dots, as shown in the figure. The line is a fit for the eyes. The observed oscillation does not exist and the macrospin correlation values are close to 50% for exchange-coupled dots, that is, for a dose $D = 0.2\,\mathrm{nC\,cm^{-1}}$. (From Repain *et al.*, 2004.)

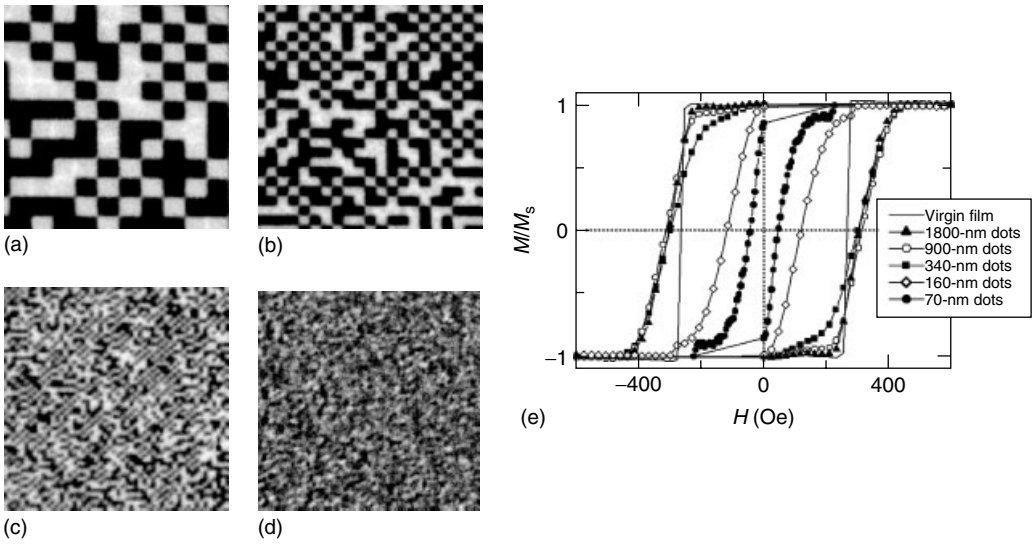

Figure 26. PMOKE images ($18 \times 18\,\mu m^2$) of the central part of each of four demagnetized dot arrays with dot sizes: (a) 1800 nm, (b) 900 nm, (c) 340 nm, and (d) 70 nm. Normalized remanent hysteresis loops are shown in (e). (R. Hyndman *et al*., *Trans. Magn. Soc. Jpn*, **2**, 175 (2002).)

was estimated to be about 20 nm in that case. PMOKE images of the demagnetized states of square dot arrays are shown in Figure 26(a–d) (four values of the lattice periodicity) ($1800 < P < 70$ nm). The limited resolution of the PMOKE microscope does not allow one to resolve separate magnetized dots when $P < 300$ nm (Figure 26d). As can be seen in Figure 26(e), the remanent magnetization and the coercive field are fortunately still finite at room temperature even for reduced dot sizes ($a = 50$ nm). This means that, in spite of a small reduction of the dot anisotropy by ion straggling effects at their edges, the superparamagnetic limit is not yet reached in that case. Starting from the usual criterium $KV = 40\,kT$ for the superparamagnetic limit, and since $V = 3500\,nm^3$, the anisotropy constant K must be higher than $0.5 \times 10^6\,erg\,cm^{-3}$ to keep ferromagnetism in these nanodots at room temperature. This is reasonable since the anisotropy constant is higher ($K = 1.4 \times 10^6\,erg\,cm^{-3}$) for the virgin 1.4 nm Co film and inside patterned dots.

As reported in the preceding text (Section 2.1.1), the change in magnetism by ion irradiation is much more efficient in Co/Pt multilayers than in Pt/Co/Pt films; the reason is that the main physical process is linked to the presence of interfaces. While a virgin Pt(6.5 nm)/[Co(0.3 nm)/Pt(0.6 nm)]$_6$/Pt(2.8 nm) multilayer exhibits perpendicular anisotropy it becomes in-plane magnetized after a uniform Ga irradiation with $D = 10^{14}$ Ga ions/cm^2 (Fig. 5). An array of 1-μm square dots has been patterned by FIB with this dose, and its magnetic state studied by PMOKE microscopy and Differential phase contrast Transmission electron microscopy (DPC-TEM) in Lorentz mode (Warin *et al*., 2001). The remanent state consists of opposite out-of-plane magnetized dots (Figure 27) separated by narrow (50 nm wide) in-plane magnetized FIB lines (Figure 28). Head-to-head domain walls were evidenced by TEM inside the irradiated lines. The direction of the magnetization may be reversed independently in the dots or in the irradiated lines under a magnetic field applied either out-of-plane or in plane. Thus, FIB appears here as a convenient technique here to produce patterning by anisotropy modulation.

Figure 27. PMOKE image ($45 \times 35\,\mu m^2$) of an ac-demagnetized state of the virgin [Pt(0.6 nm)/Co(0.3 nm)]$_6$ multilayer film (top part of the image), and of the FIB ($D = 10^{14}$ Ga ions/cm^2) patterned part (bottom of the image). (P. Warin *et al*., *Journal of Applied Physics*, **90**, 3850 (2001).)

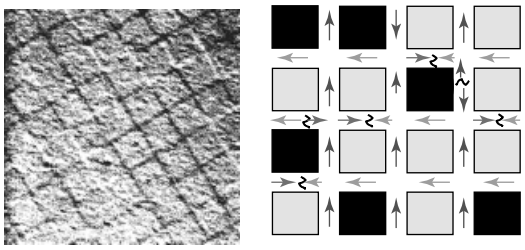

Figure 28. (a) DPC-TEM image ($7 \times 7\,\mu m^2$) of part of the ac-demagnetized multilayer array considered in Figure 27, for an untilted specimen. In this configuration in-plane magnetization is only probed. (b) Schematic view of the magnetization distribution within an area inserted in (a). Gray and black dots are oppositely perpendicularly magnetized. The arrows indicate the orientation of the magnetization inside the irradiated lines ($D = 10^{14}$ Ga ions/cm^2). (P. Warin *et al*., *Journal of Applied Physics*, **90**, 3850 (2001).)

4.3.3 Arrays of tracks with out-of-plane anisotropy

The dipolar interaction between tracks separated by non-magnetic irradiated narrow lines is clearly revealed by the magnetic configuration of the array. As expected, the PMOKE image of an ac-demagnetized periodic array of Pt/Co(1.4 nm)/Pt tracks shows that they are preferentially alternatively up and down magnetized (Figure 29) (Hyndman *et al*., 2002a). As expected, remanent magnetization remains finite for 70-nm-wide tracks. The same type of antiferromagnetic arrangement has also been found for dipolar-coupled in-plane magnetized single-domain rectangular nanoelements (Kirk, Chapman and Wilkinson, 1997) (Figure 30). Such type of configuration was also evidenced in the case of in-plane magnetized single-domain circular nanoelements which form chains and interact through dipolar fields (Cowburn, 2002). The alternate magnetized state can be interrupted after a few periods giving rise to ferromagnetically oriented nearest-neighbor nanoelements (Fig. 29b). Several equivalent demagnetized states with nearly the same probability of occurrence can be generated, depending upon slightly different initial conditions.

4.3.4 Magnetic dot arrays with out-of-plane anisotropy: Application to ultrahigh density perpendicular recording

The advantages of magnetic recording media with discrete nanodots, also called *quantum magnetic storage media*, especially with perpendicular anisotropy, have been often pointed out (Chou, Wei, Krauss and Fischer, 1994; Ferré, 2001; Lodder, Haast and Abelmann, 2001; Lodder, 2004; Khizroev and Litvinov, 2004). Importantly, the signal-to-noise ratio can be significantly improved in discrete media as compared to continuous ones. Just after the first demonstration that patterning of discrete dots could be realized efficiently by Ga FIB (Aign *et al*., 1998), IBM – Hitachi produced 140 Gbit in.$^{-2}$ CoCrPt dot arrays with perpendicular magnetic anisotropy (Rettner, Best and Terris, 2001). A that time, the quality of the patterning was not sufficiently high enough due to instabilities of the particular FIB machine when used at such a small scale. They improved the process rapidly and obtained promising ultrahigh density magnetic storage up to 200 Gbit in.$^{-2}$ using arrays of 20-nm-thick $Co_{70}Cr_{18}Pt_{12}$ square ($a = 67$ nm) dots overcoated by a 5-nm-thick C layer (Lohau *et al*., 2001; Albrecht *et al*., 2002; Albrecht *et al*., 2003) (Figure 31). The

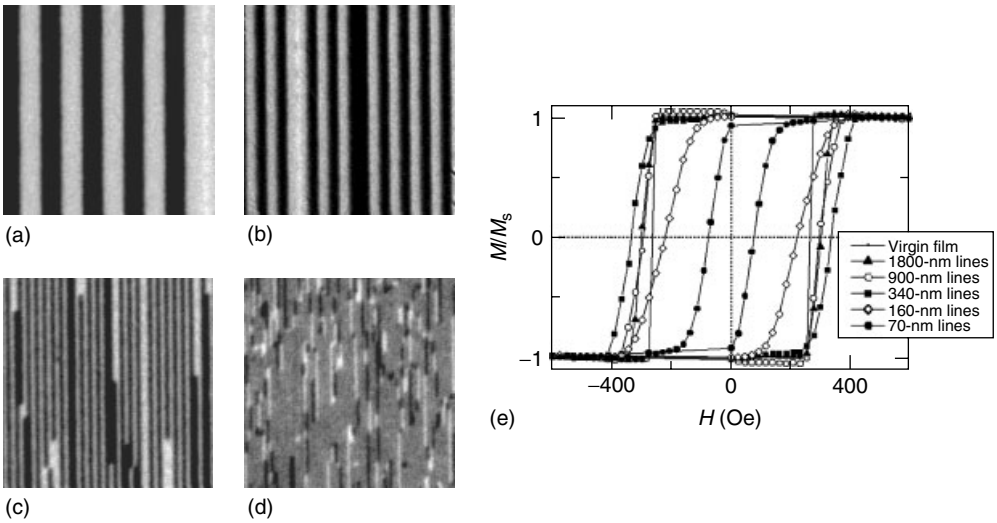

Figure 29. PMOKE images ($18 \times 18\,\mu m^2$) of the central part of four demagnetized stripe arrays. The width of the stripes are respectively: (a) 1800 nm, (b) 900 nm, (c) 340 nm, and (d) 160 nm. Together with data for 70-nm-wide stripes, normalized remanent PMOKE hysteresis loops are shown in (e). (R. Hyndman *et al*., *Trans. Magn. Soc. Jpn.*, **2**, 175 (2002).)

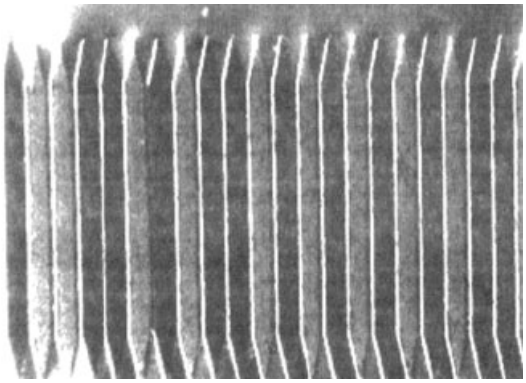

Figure 30. TEM Foucault image of NiFe elements with two pointed ends in an array with 250-nm center-to-center spacing. The component of the induction is mapped in the vertical direction. (Kirk *et al*., APL 71, 539–541 (1997).)

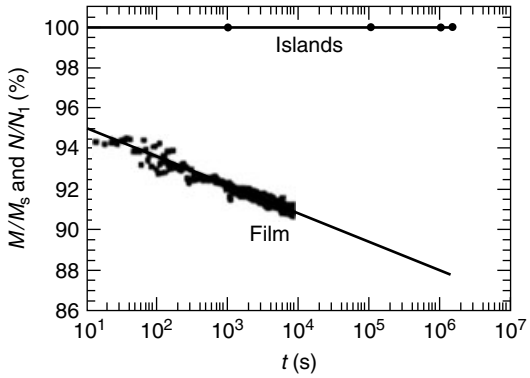

Figure 32. Thermal decay of single-domain 80-nm nanodots from MFM data and full decay as measured by Vibrating sample magnetometer VSM. The decay rates were measured at room temperature in the absence of an applied magnetic field. (Rettner *et al*., *IEEE Trans. Magn.* **38**, 1725–1730 (2002) (© 2002 IEEE).)

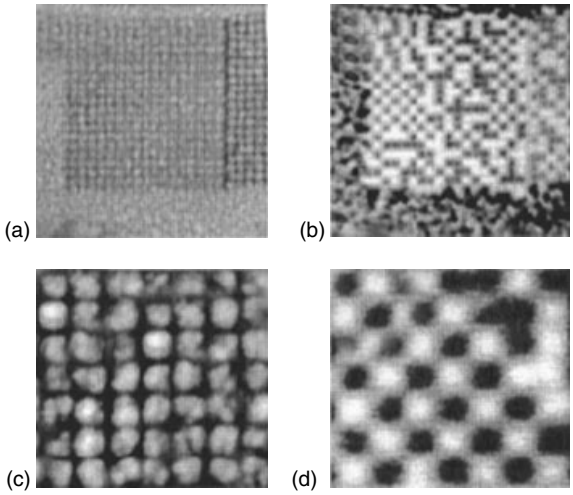

Figure 31. AFM and MFM images of a $2 \times 2\,\mu m^2$ patterned region in a CoCrPt film are shown in (a) and (b), respectively, along with higher magnification images of small regions in (c) and (d), respectively. The pattern period is ~100 nm. (Rettner *et al*., *IEEE Trans. Magn.* **38**, 1725–1730 (2002) (© 2002 IEEE).)

nonmagnetic separation of the dots by FIB trenches was estimated to be 30 nm. They found that 5-nm-deep trenches ($D = 0.04\,nC\,cm^{-1}$) were sufficient to isolate the nanodots magnetically. They suggested that the carbon overcoat was implanted into the trenches along with Ga. Thus, the magnetic isolation was achieved by a physicochemical mechanism involving a combination of Ga and C poisoning, and by damage of the Co ions, but not only from sputtering of $Co_{70}Cr_{18}Pt_{12}$. The irradiated region has certainly not a large enough anisotropy to support domain walls or remanent magnetization, so that magnetic domains could not extend beyond the nanodot edges.

As already found in other systems, due to the variation of the shape anisotropy, a transition from in-plane to out-of-plane magnetized nanodots occurs when decreasing their lateral size a (Fernandez *et al*., 1996). As proved by AFM, this reorientation transition also takes place for $Co_{70}Cr_{18}Pt_{12}$ nanodots when a <150 nm. As for Pt/Co/Pt, the magnetization at the dot edges reverses first. However, contrary to Pt/Co/Pt nanodots, a multidomain structure appears during magnetization reversal in $Co_{70}Cr_{18}Pt_{12}$ nanodots because of large self-demagnetizing effects.

An important point concerns the magnetic stability in nanodots. A very clear proof of the stabilization of the magnetization state in nanodot arrays as compared to virgin films has been demonstrated for $Co_{70}Cr_{18}Pt_{12}$ by Rettner *et al*. (2002b). Magnetic relaxation (or magnetic aftereffect) measurements show a larger decay rate for the virgin continuous film than for the nanodot array (Fig. 32). The stability is enhanced over that of the unpatterned film, even though the coercivity and anisotropy are reduced. The self-demagnetizing field is also reduced for nanodots (Section 3.3), which consequently slows down the relaxation.

As previously mentioned (Section 4.3.2), the dipolar coupling acting on single-domain nanodots gives rise to a checkerboard magnetized dot structure in an ac-demagnetized state (Figure 31). Nevertheless, Rettner *et al*. (2002b) claim that $Co_{70}Cr_{18}Pt_{12}$ dot arrays are favorable for recording since the interdot dipolar interaction does not exceed the coercivity. Moreover, these nanodots show a narrow switching field distribution and an enhanced thermal stability. Using a quasistatic write–read tester, feasibility of writing and reading information has been demonstrated at the competitive ultrahigh density of 200 Gbit in.$^{-2}$. Patterning has been shown to drastically reduce the jitter and to improve the

signal-to-noise ratio and the addressing performance. Perpendicular recording with bit widths of less than 65 nm has also been demonstrated independently by Seagate (Khizroev *et al*., 2002). Additionally, the FIB technique has also been tested satisfactorily for structuring 20-nm-thick Co longitudinal recording media (Albrecht *et al*., 2003).

The fabrication of arrays of nanosensors can be also realized by FIB (Fassbender, Ravelosona and Samson, 2004). Khizroev and Litvinov (2004) have proposed to design MRAMs and Microelectro mechanical systems (MEMS) by this FIB technique.

5 CONCLUSION

New patterning techniques for fabricating dense arrays of nanoelements with similar properties are still emerging. In the present contribution we have shown how the mastered technique of depositing films on prepatterned wafers allows one to prepare high-density recording media and MRAM cells. Multilevel recording on multiple storage layers was proposed recently (Albrecht *et al*., 2005; Baltz, Landis, Rodmacq and Dieny, 2005b).

Light He ion irradiation through a mask is a very promising planar technique to pattern ultrathin film media with an ultimate resolution. New developments are expected soon with this technique. Fassbender *et al*. (2002) have demonstrated that irradiation of NiFe/FeMn by He ions allows one to modify and control the magnitude of the exchange bias field on a submicron scale without affecting the surface roughness.

The effect of both interdot exchange and magnetostatic interaction has been considered from static and dynamic point of view, with a particular application to the Pt/Co/Pt simple case exhibiting out-of-plane anisotropy. The present storage density record in perpendicular magnetic recording media has been obtained for a thin CoPtCr film patterned by a Ga FIB. The advantage of the nucleation free magnetization reversal was underlined in some particular cases.

The most promising methods for patterning magnetic films will be certainly obtained by combining bottom-up and top-down techniques. For example, arrays of quasi-monodisperse short nanopillars ($t = 50–250$ nm) of iron with small diameter ($a = 10–14$ nm) have been prepared by combining chemical vapor deposition and scanning tunneling microscopy (Wirth, von Molnar, Field and Awschalom, 1999; Wirth, Anane and von Molnar, 2000). Nanopillars are perpendicularly magnetized, thanks to the shape anisotropy. This is a model system to study thermally activated magnetization reversal in ultrasmall entities.

Fundamental studies on fast magnetization reversal dynamics in isolated or coupled nanomagnetic systems are still needed for a better understanding of the properties of isolated or coupled nanoelements. Nanomagnetism and spinelectronics are exciting topics that will surely lead to sounding applications. For that purpose, combined patterning techniques are required for targeting ultimate spatial resolution and imagine ingenious designs.

ACKNOWLEDGMENTS

The authors wish to thank T. Aign, V. Repam R. Hyndman and A. Mougin for their active contributions on the subject, H. Bernas and J. Gierak for enlightening discussions on the physics of irradiation, and P. Metaxas for his critical reading of the manuscript. This work has been partly supported by the *Nanodynamag* project sponsored by the French Minister for Research.

REFERENCES

Abes, M., Venuat, J., Carvalho, A., *et al*. (2005). Magnetic nanopatterning of CoPt thin layers. *Journal of Magnetism and Magnetic Materials*, **286**, 297–300.

Aign, T., Meyer, P., Lemerle, S., *et al*. (1998). Magnetization reversal in arrays of perpendicularly magnetized ultrathin dots coupled by dipolar interaction. *Physical Review Letters*, **81**, 5656–5659.

Albrecht, M., Ganesan, S., Rettner, C.T., *et al*. (2003). Patterned perpendicular and longitudinal media: a magnetic recording study. *IEEE Transactions on Magnetics*, **39**, 2323–2325.

Albrecht, M., Hu, G., Moser, A., *et al*. (2005). Magnetic dot arrays with multiple storage layers. *Journal of Applied Physics*, **97**, 103910.

Albrecht, M., Rettner, C.T., Moser, A., *et al*. (2002). Recording performance of high-density patterned perpendicular magnetic media. *Applied Physics Letters*, **81**, 2875–2877.

Allenspach, R., Bischof, A., Düring, U. and Grütter, P. (1998). Local modification of magnetic properties by an electron beam. *Applied Physics Letters*, **73**, 3598–3600.

Baltz, V., Landis, S., Rodmacq, B. and Dieny, B. (2005b). Multilevel magnetic media in continuous and patterned films with out-of-plane magnetization. *Journal of Magnetism and Magnetic Materials*, **290–290**, 1286–1289.

Baltz, V., Sort, J., Landis, S., *et al*. (2005a). Tailoring size effects on the exchange bias in ferromagnetic-antiferromagnetic <100 nm nanostructures. *Physical Review Letters*, **94**, 117201.

Basnar, B., Lugstein, A., Wanzenboeck, H., *et al*. (2003). Focused ion beam induced surface amorphization and sputter processes. *Journal of Vacuum Science and Technology B*, **21**, 927–930.

Bernas, H., Devolder, T., Chappert, C., *et al*. (1999). Ion irradiation induced magnetic nanostructure patterning. *Nuclear Instruments and Methods in Physical Research B*, **148**, 872–879.

Bernas, H., Halley, D., Heinig, D., *et al*. (2003). Ordering intermetallic alloys by ion irradiation: a way to tailor magnetic media. *Physical Review Letters*, **91**, 077203.

Blomeier, S., Hillebrands, B., Demidov, V.E., *et al*. (2005). Magnetic patterning of Fe/Cr/Fe(001) trilayers by Ga ion irradiation. *Journal of Applied Physics*, **98**, 093503.

Bode, M., Pietzch, O., Kubetzka, A. and Wiesendanger, R. (2004). Shape-dependent thermal switching behavior of superparamagnetic nanoislands. *Physical Review Letters*, **92**, 067201.

Bray, J.J. and Prados, A. (2001). Slow dynamic relaxation in models with hierarchically constrained dynamics. *Physical Review E*, **63**, 021108.

Bruenger, W.H., Dzionk, C., Berger, R., *et al*. (2002). Evaluation of ion projection using heavy ions suitable for resistless patterning of thin magnetic films. *Microelectron. Eng.*, **61–62**, 295–300.

Cai, M., Veres, T., Roorda, S., *et al*. (1997). MeV ion irradiation in Co/Cu multilayers. *Journal of Applied Physics*, **81**, 5200–52002.

Carl, A. and Wassermann, E.F. (2002). Magnetic nanostructures for future magnetic data storage: fabrication and quantitative characterization by magnetic force microscopy. In *"Magnetic Nanostructures"*, Nalwa, H.S. (Ed.), American Scientific Publishers, pp. 59–92.

Chappert, C., Bernas, H., Ferré, J., *et al*. (1998). Planar patterned magnetic media obtained by ion irradiation. *Science*, **280**, 1919–1922.

Chen, X., Sichelschmidt, O., Kleemenn, W., *et al*. (2002). Domain wall relaxation, creep, sliding, and switching in superferromagnetic discontinuous $Co_{80}Fe_{20}/Al_2O_3$ multilayers. *Physical Review Letters*, **89**, 137203.

Chou, S.Y., Wei, M.S., Krauss, P.R. and Fischer, P.B. (1994). Single-domain magnetic pillar array of 35 nm diameter and 65 Gbits/in^2 density for ultrahigh quantum magnetic storage. *Journal of Applied Physics*, **76**, 6673–6675.

Cowburn, R.P. (2000). Property variation with shape in magnetic nanoelements. *Journal of Physics D: Applied Physics*, **33**, R1–R16.

Cowburn, R.P. (2002). Probing antiferromagnetic coupling between nanomagnets. *Physical Review B*, **65**, 092409.

Devolder, T., Belmeguenai, M., Chappert, C., *et al*. (2003). Magnetization dynamics of irradiation-fabricated perpendicularly magnetized dots inside a softer magnetic matrix. *Materials Research Society Symposium Proceedings*, **777**, T.6.4.1–T.6.4.11.

Devolder, T., Chappert, C. and Bernas, H. (2002). Theoretical study of magnetic pattern replication by He ion irradiation through stencil masks. *Journal of Magnetism and Magnetic Materials*, **249**, 452–457.

Devolder, T., Chappert, C., Chen, Y., *et al*. (1999). Sub-50 nm planar magnetic nanostructures fabricated by ion irradiation. *Applied Physics Letters*, **74**, 3383–3385.

Devolder, T., Chappert, C., Mathet, V., *et al*. (2000). Magnetization reversal in irradiation-fabricated nanostructures. *Journal of Applied Physics*, **87**, 8671–8681.

Devolder, T., Pizzini, S., Vogel, J., *et al*. (2001). X-ray absorption analysis of sputter-grown Co/Pt stackings before and after helium irradiation. *European Physical Journal B*, **22**, 193–201.

Dietzel, A., Berger, R., Grimm, H., *et al*. (2002). Ion projection direct structuring for patterning of magnetic media. *IEEE Transactions on Magnetics*, **38**, 1952–1954.

El-Hilo, M., Chantrell, R.W. and O'Grady, K. (1998). A model of interaction effects in granular magnetic solids. *Journal of Applied Physics*, **84**, 5114–5122.

Fassbender, J., Poppe, S., Mewes, T., *et al*. (2002). Magnetization reversal of exchange bias double layers magnetically patterned by ion irradiation. *Physical Status Solidi A*, **189**, 439–447.

Fassbender, J., Ravelosona, D. and Samson, Y. (2004). Tailoring magnetism by light-ion irradiation. *Journal of Physics D: Applied Physics*, **37**, R179–R196.

Fernandez, A., Bedrossian, P.J., Baker, S.L., *et al*. (1996). Magnetic force microscopy of single domain cobalt dots patterned using interference lithography. *IEEE Transactions on Magnetics*, **32**, 4472–4474.

Ferré, J. (2001). New magneto-optical recording media. In *"Magnetic Storage Systems Beyond 2000"*, *NATO Science Series, II. Mathematics, Physics and Chemistry*, Hadjipanayis, G.C. (Ed.), Kluwer Academic Publishers, pp. 181–200, Vol. 41.

Ferré, J., Chappert, C., Bernas, H., *et al*. (1999). Irradiation induced effects on magnetic properties of Pt/Co/Pt ultrathin films. *Journal of Magnetism and Magnetic Materials*, **198–199**, 191–193.

Ferré, J., Devolder, T., Bernas, H., *et al*. (2003). Magnetic phase diagrams of He ion-irradiated Pt/Co/Pt ultrathin films. *Journal of Physics D: Applied Physics*, **36**, 3103–3108.

Fruchart, O., Nozières, J-P., Kevorkian, B., *et al*. (1998). High coercivity in ultrathin epitaxial micrometer-sized particles with in-plane magnetization: Experiment and numerical simulation. *Physical Review B*, **57**, 2596–2606.

Gadetsky, S., Erwin, J.K., Mansuripur, M. and Suzuki, T. (1996). Magneto-optical recording on patterned substrates. *Journal of Applied Physics*, **79**, 5687–5692.

Gierak, J., Bourhis, E., Mérat Combes, M.N., *et al*. (2005). Exploration of the ultimate potential achievable with focused ion beams. *Microelectronic Engineering*, **78–79**, 266–278.

Gmitra, M. and Horvath, D. (2003). The magnetic reversal in dot arrays recognized by the self-organized adaptative neural network. *Journal of Magnetism and Magnetic Materials*, **265**, 69–82.

Guslienko, K.Y., Novosad, V., Otani, Y., *et al*. (2001). Magnetization reversal due to vortex nucleation, displacement, and annihilation in submicron ferromagnetic dot arrays. *Physical Review B*, **65**, 024414.

Haast, M.A.M., Schuurhuis, J.R., Abelmann, L., *et al*. (1998). Reversal mechanism of submicron patterned CoNi/Pt multilayers. *IEEE Transactions on Magnetics*, **34**, 1006–1008.

Haginoya, C., Heike, S., Ishibashi, M., *et al*. (1999). Magnetic nanoparticle array with perpendicular crystal magnetic anisotropy. *Journal of Applied Physics*, **85**, 8327–8331.

Hannour, A., Bertotti, L., Prével, B., *et al*. (2005). 2D arrays of CoPt nanocluster assemblies. *Surface Science*, **594**, 1–11.

Hehn, M., Ounadjela, K., Bucher, J-P., *et al*. (1996). Nanoscale magnetic domains in mesoscopic magnets. *Science*, **272**, 1782–1785.

Heimbrodt, W. and Klar, P.J. (2002). Magnetic semiconductor nanostructures. In *"Magnetic Nanostructures"*, Nalwa, H.S. (Ed.), American Scientific Press, pp. 1–58.

Horvath, D. and Gmitra, M. (2003). The neural network two-scale model of the magnetic dot array. *Journal of Magnetism and Magnetic Materials*, **256**, 195–213.

Horvath, D., Gmitra, M. and Vavra, I. (2001). Neural network approach to magnetic dot arrays modeling. *Journal of Magnetism and Magnetic Materials*, **231**, 273–286.

Hubert, A. and Schäfer, R. (1998). In *"Magnetic Domains"*, Springer Verlag, pp. 53–65.

Hyndman, R., Warin, P., Gierak, J., *et al*. (2001a). Modification of Co/Pt multilayers by gallium irradiation – Part 1: the effect on structural and magnetic properties. *Journal of Applied Physics*, **90**, 3843–3848.

Hyndman, R., Meyer, P., Ferré, J., *et al*. (2001b). Magnetization reversal in a network of dipolar coupled dots. *Journal of the Magnetics Society of Japan*, **25**, 198–201.

Hyndman, R., Mougin, A., Repain, V., *et al*. (2002a). Magnetic nanostructures patterned by focused ion beam in an ultrathin Pt/Co/Pt film. *Transactions of the Magnetics Society of Japan*, **2**, 175–178.

Hyndman, R., Mougin, A., Sampaio, L.C., *et al*. (2002b). Magnetization reversal in weakly coupled magnetic patterns. *Journal of Magnetism and Magnetic Materials*, **240**, 34–36.

Jamet, J-P., Aign, T., Meyer, P., *et al*. (1999). Irradiation effects and magnetization reversal in nanostructures with perpendicular anisotropy – effect of the dipolar coupling. *Journal of the Magnetics Society of Japan*, **23**(S1), 71–76.

Jamet, J-P., Ferré, J., Meyer, P., *et al*. (2001a). Giant enhancement of the domain wall velocity in patterned ultrathin magnetic nanowires. *IEEE Transactions on Magnetics*, **37**, 2120–2122.

Jamet, M., Wernsdorfer, W., Thirion, C., *et al*. (2001b). Magnetic anisotropy of a single cobalt nanocluster. *Physical Review Letters*, **86**, 4676–4679.

Jamet, J.P., Lemerle, S., Meyer, P., *et al*. (1998). Dynamics of the magnetization reversal in Au/Co/Au micron size dot arrays. *Physical Review B*, **57**, 14320–14331.

Kageyama, Y. and Suzuki, T. (2004). Large area fabrication of Co particles by ion-beam-induced chemical vapor deposition. *Transactions of the Magnetics Society of Japan*, **4**, 21–23.

Kaminsky, W.H., Jones, G.A.C., Patel, N.K., *et al*. (2001). Patterning ferromagnetism in $Ni_{80}Fe_{20}$ films via Ga ion irradiation. *Applied Physics Letters*, **78**, 1589–1591.

Kaplan, B. and Gehring, G.A. (1993). The domain structure in ultrathin magnetic films. *Journal of Magnetism and Magnetic Materials*, **128**, 111–116.

Kelly, P.A.E., O'Grady, K., Mayo, P.I. and Chantrell, R.W. (1989). Switching mechanisms in cobalt-phosphorous thin films. *IEEE Transactions on Magnetics*, **25**, 3881–3883.

Khizroev, S. and Litvinov, D. (2004). *Perpendicular Magnetic Recording*, Kluwer Academic Publishers: Dordrecht, The Netherlands.

Khizroev, S., Thompson, D.A., Kryder, M.H., *et al*. (2002). Direct observation of magnetization switching in focused-ion-beam fabricated magnetic nanotubes. *Applied Physics Letters*, **81**, 2256–2257.

Kim, T.G., Shin, Y.H., Song, J.H., *et al*. (2002). Effects of ion irradiation on epitaxial Cu/Ni/Cu(001) with perpendicular magnetic anisotropy. *Applied Physics Letters*, **81**, 4017–4019.

Kirk, K.J., Chapman, J.N. and Wilkinson, C.D.W. (1997). Switching fields and magnetostatic interactions of thin film magnetic nanoelements. *Applied Physics Letters*, **71**, 539–541.

Kondratyev, V.N. and Lutz, H.O. (1998). Shell effect in exchange coupling of transition metal dots and their arrays. *Physical Review Letters*, **81**, 4508–45111.

Krauss, P.R., Fischer, P.B. and Chou, S. (1994). Fabrication of single-domain magnetic pillar array of 35 nm diameter and 65 Gbits/in^2 density. *Journal of Vacuum Science and Technology B*, **12**, 3639–3642.

Landis, S., Rodmacq, B. and Dieny, B. (2000). Magnetic properties of Co/Pt multilayers deposited on silicon dot arrays. *Physical Review B*, **62**, 12271–12281.

Lodder, J.C. (2004). Methods for preparing patterned media for high-density recording. *Journal of Magnetism and Magnetic Materials*, **272–276**, 1692–1697.

Lodder, J.C., Haast, M.A.M. and Abelmann, L. (2001). Patterned magnetic thin films for ultra high density recording. In *"Magnetic Storage Systems Beyond 2000"*, *NATO Science Series, II. Mathematics, Physics and Chemistry*, Hadjipanayis, G.C. (Ed.), Kluwer Academic Publishers, pp. 117–143, Vol. 41.

Lohau, J., Moser, A., Rettner, C.T., *et al*. (2001). Writing and reading perpendicular magnetic recording media patterned by a focused ion beam. *Applied Physics Letters*, **78**, 990–992.

Lottis, D.K., White, R.M. and Dahlberg, E.D. (1991). Model system for slow dynamics. *Physical Review Letters*, **67**, 362–365.

Luis, F., Petroff, F., Torres, J.M., *et al*. (2002). Magnetic relaxation of interacting Co clusters: crossover from two- to three-dimensional lattices. *Physical Review Letters*, **88**, 217205.

Martin, J.I., Nogués, J., Liu, K., *et al*. (2003). Ordered magnetic nanostructures: fabrication and properties. *Journal of Magnetism and Magnetic Materials*, **256**, 119–451.

McCord, J., Gemming, T., Schultz, L., *et al*. (2005). Magnetic anisotropy and domain patterning of amorphous films by He-ion irradiation. *Applied Physics Letters*, **86**, 162502.

Moritz, J., Buda, L., Dieny, B., *et al*. (2004). Writing and reading bits on pre-patterned media. *Applied Physics Letters*, **84**, 1519–1521.

Moritz, J., Landis, S., Toussaint, J.C., *et al*. (2002). Patterned media made from pre-etched wafers: a promising route towards ultra-high density magnetic recording. *IEEE Transactions on Magnetics*, **38**, 1731–1736.

Mougin, A., Poppe, S., Fassbender, J., *et al*. (2001). Magnetic micropatterning of FeNi/FeMn exchange bias bilayers by ion irradiation. *Journal of Applied Physics*, **89**, 6606–6608.

Natali, M., Prejbeanu, I.L., Lebib, A., *et al*. (2002). Correlated magnetic vortex chains in mesoscopic cobalt dot arrays. *Physical Review Letters*, **88**, 157203.

Navarro, E., Huttel, Y., Clavero, C., *et al*. (2004). Magnetic coupling between nanoislands induced by capping-layer magnetic polarization. *Physical Review B*, **69**, 224419.

Novosad, V., Grimsditch, M., Darrouzet, J., *et al*. (2003). Shape effect on magnetization reversal in chains of interacting ferromagnetic elements. *Applied Physics Letters*, **82**, 3716–3718.

Olive, E. and Molho, P. (1998). Thermodynamic study of a lattice of compass needles in dipolar interaction. *Physical Review B*, **58**, 9238–9247.

Perez, A., Bardotti, L., Prevel, B., *et al*. (2002). Quantum-dot systems prepared by 2D organization of nanoclusters preformed in the gas phase on functionalized substrates. *New Journal of Physics*, **4**, 76.1–76.12.

Repain, V., Jamet, J-P., Vernier, N., *et al*. (2004). Magnetic interactions in dot arrays with perpendicular anisotropy. *Journal of Applied Physics*, **95**, 2614–2618.

Rettner, C.T., Anders, S., Baglin, J.E.E., *et al*. (2002a). Characterization of the magnetic modification of Co/Pt multilayer films by He, Ar, and Ga ion irradiation. *Applied Physics Letters*, **80**, 279–281.

Rettner, C.T., Anders, S., Thomson, T., *et al*. (2002b). Magnetic characterization and recording properties of patterned $Co_{70}Cr_{18}Pt_{12}$ perpendicular media. *IEEE Transactions on Magnetics*, **38**, 1725–1730.

Rettner, C.T., Best, M.E. and Terris, B.D. (2001). Effect of ion beam patterning on the write and read performance of perpendicular granular recording media. *IEEE Transactions on Magnetics*, **37**, 1652–1656.

Ribas, R. and Labarta, A. (1996). Magnetic relaxation of a one-dimensional model for small particle systems with dipolar interaction: Monte Carlo simulation. *Journal of Applied Physics*, **80**, 5192–5199.

Ribeiro, A.L. (1991). Magnetic hysteresis model for magnetic recording including spatial fluctuations of interaction fields. *Journal of Applied Physics*, **69**, 4841–4843.

Ross, C.A., Farhoud, M., Hwaug, M., *et al*. (2001). Micromagnetic behavior of conical ferromagnetic particles. *Journal of Applied Physics*, **89**, 1310–1319.

Sampaio, L.C., Hyndman, R., de Menezes, F.S., *et al*. (2001). Power-law relaxation decay in two-dimensional arrays of magnetic dots interacting by long-range dipole-dipole interactions. *Physical Review B*, **64**, 184440.

Sanchez, J.M., Moran-lopez, J.L., Leroux, C. and Cadeville, M.C. (1988). Magnetic properties and chemical ordering in Co-Pt. *Journal of Physics C: Solid State Physics*, **21**, L1091–L1096.

Scheinfein, M.R., Schmidt, K.E., Heim, K.R. and Hembree, G.G. (1996). Magnetic order in two-dimensional arrays of nanometer-sized superparamagnets. *Physical Review Letters*, **76**, 1541–1544.

Schmidt, F. and Hubert, A. (1986). Domain observations on CoCr-layers with a digitally enhanced Kerr-microscope. *Journal of Magnetism and Magnetic Materials*, **61**, 307–320.

Sun, S., Murray, C.B., Weller, D., *et al*. (2000). Monodisperse FePt nanoparticles and ferromagnetic FePt nanocrystal superlattices. *Science*, **287**, 1989–1992.

Sun, J.M. and Weili, L. (1997). Dynamics of low-dimensional dipolar systems. *Physical Review E*, **56**, 3986–3992.

Terris, B.D., Weller, D., Folks, L., *et al*. (2000). Patterning magnetic films by ion beam irradiation. *Journal of Applied Physics*, **87**, 7004–7006.

Toporov, A.Y., Langford, R.M. and Petford-Long, A.K. (2000). Lorenz transmission electron microscopy of focused ion beam patterned magnetic antidot arrays. *Applied Physics Letters*, **77**, 3063–3065.

Victora, R.H., Willoughby, S.D., MacLaren, J.M. and Xue, J. (2003). Effects of grain boundaries on magnetic properties of recording media. *IEEE Transactions on Magnetics*, **39**, 710–715.

Vieu, C., Gierak, J., Launois, H., *et al*. (2002). Modifications of magnetic properties of Pt/Co/Pt thin layers by focused gallium ion beam irradiation. *Journal of Applied Physics*, **91**, 3103–3110.

Warin, P., Hyndman, R., Gierak, J., *et al*. (2001). Modification of Co/Pt multilayers by gallium irradiation–Part 2: the effect of patterning using a highly focused ion beam. *Journal of Applied Physics*, **90**, 3850–3855.

Wirth, M., Anane, A. and von Molnar, S. (2000). Thermally activated magnetization reversal in nanometer-size iron particles. *Physical Review B*, **63**, 012402.

Wirth, S., von Molnar, S., Field, M. and Awschalom, D.D. (1999). Magnetism of nanometer-scale iron particles arrays. *Journal of Applied Physics*, **85**, 5249–5254.

Wolfe, J.C., Pendharkar, S.V., Ruchhoeft, P., *et al*. (1996). A proximity ion beam lithography process for high density nanostructures. *Journal of Vacuum Science and Technology B*, **B14**, 3896–3899.

Woods, S.I., Ingvarsson, S., Kirtley, J.R., *et al*. (2002). Local magnetic anisotropy control in NiFe thin films via ion irradiation. *Applied Physics Letters*, **81**, 1267–1269.

Wu, X.W., van de Veerdonk, R.J.M., Chantrell, R.W. and Weller, D. (2003). ΔM study of perpendicular recording media. *Journal of Applied Physics*, **93**, 6760–6762.

Xiao, J.Q., Liu, K., Chien, C.L., *et al*. (1994). Effects of Ar-ion implantation and annealing in structural and magnetic properties of Co/Pd multilayers. *Journal of Applied Physics*, **76**, 6081–6083.

Xiong, G., Allwood, D.A., Cooke, M.D. and Cowburn, R.P. (2001). Magnetic nanoelements for magnetoelectronics made by focused-ion-beam milling. *Applied Physics Letters*, **79**, 3461–3463.

Xu, Q.Y., Kageyama, Y. and Suzuki, T. (2005). Ion-beam-induced chemical-vapor deposition of FePt and CoPt particles. *Journal of Applied Physics*, **97**, 10K308.

Zeng, H., Li, J., Zhong, L., *et al*. (2002). Interparticule interactions in annealed FePt nanoparticules assemblies. *IEEE Transactions on Magnetics*, **38**, 2598–2600.

Zhu, J-G. and Neal Bertram, H. (1989). Magnetization reversal in CoCr perpendicular thin films. *Journal of Applied Physics*, **66**, 1291–1307.

Ziegler, J.F. (1992). *"Handbook of Ion Implantation Technology"*, North Holland: Amsterdam.

FURTHER READING

Hitachi. (2005). Hitachi global storage technology. *See the web site:* http://hitachigst.com/hdd/research/recording_head/pr/index.html.

Chemical Synthesis of Monodisperse Magnetic Nanoparticles

Chao Wang and Shouheng Sun
Brown University, Providence, RI, USA

1 INTRODUCTION

Nanometer size particles display many properties, which are both quantitatively and qualitatively different from their respective bulk materials and from the discrete atomic or molecular species from which they are derived. Novel properties arise from the large fraction of atoms that reside on the surface of the particles and from the finite number of atoms within each particle. Recently the study of finite size effects of metal nanoparticles has intensified with the promise of uncovering the evolution of material properties with particle size and harnessing novel properties in new materials and devices. Magnetic storage technology is advancing rapidly toward its scaling limits. Thin granular films of ferromagnetic nanoparticles formed by sputter deposition are already the basis of conventional rigid magnetic storage media hard drives. Progress in magnetic recording density are due, in part, to the development of media with finer and finer grain magnetic films (Weller, 2000). The study of nanoscale magnetic domains are of both fundamental and pressing technical interest as the grain size of advanced recording media is rapidly shrinking to dimensions where magnetic properties depend strongly on nanoparticle grain size.

A magnetic nanoparticle with size below 20 nm is usually in a 'single magnetic domain', within which all the spins align in one direction and magnetization reversal occurs in the case of free particles through rotation. An energy barrier, ΔE, between two orientations of the magnetization determines the relaxation in each orientation, and is proportional to the particle volume, V, and the particle's anisotropy constant, K (Morrish, 1965; Unruh and Chien, 1996). As the particle size decreases to a level that the ΔE becomes comparable to thermal energy (k_BT), the orientation of magnetic polarization in each particle begins to fluctuate randomly. The particle becomes superparamagnetic. Such size dependent nanomagnetism has stimulated tremendous interest recently with the hope to map the scaling limits of magnetic storage technology and understand spin-dependent transport phenomena in nanoscale devices.

Numerous physical and chemical methods have been employed to produce magnetic nanoparticles. These include sputtering, metal evaporation, ball milling, electrodeposition,

Handbook of Magnetism and Advanced Magnetic Materials. Edited by Helmut Kronmüller and Stuart Parkin. Volume 3: *Novel Techniques for Characterizing and Preparing Samples*. ISBN: 978-0-470-02217-7.

and solution phase chemistry synthesis, among which the solution phase synthesis has been seen as the most promising approach for preparing monodisperse magnetic nanoparticles. It is known that solution phase chemistry can offer an important homogenous nucleation step and facilitates the controlled growth of the nuclei suspended in the solution. As a result, magnetic nanoparticles with various monodisperse sizes and shapes have been prepared. Furthermore, magnetic nanoparticles prepared in this solution phase chemistry can be readily stabilized against particle aggregation or oxidation with a layer of robust organic or inorganic coating. The stabilized nanoparticle dispersion can be deposited on a solid substrate and the solvent is allowed to evaporate. By controlling the concentration of the particle dispersion and the solvent evaporation rate, 2D or 3D self-assembled magnetic nanoparticle superlattices can be formed. The magnetic properties of these nanoparticles can be tuned from superparamagnetic to ferromagnetic and the well-controlled magnetic nanoparticle arrays have shown spin-dependent tunneling (Black, Murray, Sandstrom and Sun, 2000) and can support high-density magnetization reversal transitions (Sun *et al*., 2000). Previous synthesis, characterization, and potential applications of the monodisperse magnetic nanoparticles have been well documented in several reviews (Green, 2005; Willard *et al*., 2004; Cushing, Kolesnichenko and O'Connor, 2004; Park *et al*., 2005; Huber, 2005). In this chapter, we focus on the most recent progress in the synthesis of magnetic nanoparticles, especially the synthetic work from our group, with controlled size, shape, composition, and magnetic properties. The control on nanoparticle shapes allows achieving texture and magnetic alignment of each particle in a self-organized nanoparticle assembly for ultrahigh density magnetic recording (DMR) and high-performance permanent magnetic applications.

2 SYNTHESIS OF Co AND Fe NANOPARTICLES

These two kinds of metallic nanoparticles are often synthesized by thermal decomposition of metal–organic complexes in the presence of stabilizing surfactants. Metal–organic complexes, especially metal carbonyl and metal alkene complexes are thermally unstable. Upon heating, they can decompose to give metal atoms and release small ligand, CO, or alkene. The metal atoms can aggregate to form nuclei. With the deposition of more metal atoms over the existing nuclei, metal nanoparticles are formed. Such decomposition chemistry has become a reliable approach for the production of monodisperse Co and Fe nanoparticles owing to the fast decomposition of the precursors and formation of magnetic nuclei.

Cobalt nanoparticles are prepared by thermal decomposing $Co_2(CO)_8$ in the presence of lipid-type surfactants. Fast nucleation is achieved by injection of $Co_2(CO)_8$ into hot ($\sim$200 °C) solution containing oleic acid/trialkylphosphine (R_3P) (Sun and Murray, 1999), oleic acid/trialkylphosphine oxide (R_3PO) (Puntes, Krishnan and Alivisatos, 2001; Bao, Beerman, Pakhomov and Krishnan, 2005). The surfactant combination in, for example, trialkylphosphine and oleic acid, is employed to control particle growth, stabilize the particles, and prevent Co oxidation. Trialkylphosphine reversibly coordinates neutral Co surface sites, slowing but not stopping particle's growth, that is it cannot prevent the particles from eventually growing to undispersable aggregates at high temperature when used alone. Oleic acid, when employed alone, is an excellent stabilizing agent due to the formation of cobalt oleate on the particle surface, but this strong binding to the particle surface during the synthesis prevents the particle from controlled growth. The combination of trialkylphosphine/oleic acid produces a tight ligand shell, which allows the particles to grow steadily while protecting them from aggregation and oxidation. $Co(\eta^3\text{-}C_8H_{13})(\eta^4\text{-}C_8H_{12})$ is another precursor that is commonly used to make Co nanoparticles. Under 3 bar dihydrogen atmosphere, its decomposition in anisole at 150 °C in the presence of a mixture of oleic acid and oleylamine leads to monodisperse Co nanoparticles (Dumestre *et al*., 2003).

Fe nanoparticles have been synthesized by thermal decomposition of iron pentacarbonyl (Green, 2005). Oleic acid is used for nanoparticle stabilization owing to the formation of iron oleate on the nanoparticle surface. Monodisperse Fe nanoparticles obtained from this process, however, do not have good crystallinity due to the complexity of the decomposition of $Fe(CO)_5$ under these synthetic conditions. Nonetheless, reductive decomposition of $Fe[N(SiMe_3)_2]_2$ at 150 °C under H_2 in the presence of hexadecylamine and oleic acid leads to the formation of monodisperse Fe nanoparticles with good crystallinity (Dumestre *et al*., 2004). The Fe nanoparticles synthesized under these conditions are very air sensitive and are difficult to characterize under normal conditions. A recent report shows that monodisperse Fe nanoparticles can be made and stabilized in both organic and phosphate buffered saline. The synthesis is outlined in Figure 1(a). The synthesis uses thermal decomposition of $Fe(CO)_5$ in octadecene (ODE) at 180 °C in the presence of oleylamine (Peng, Wang, Xie and Sun, 2006). Figure 1(b) shows the transmission electron microscopic (TEM) image of 13-nm Fe nanoparticles. Structural characterization of the nanoparticles shows that amorphous Fe_3O_4 produced by natural oxidation of Fe nanoparticles cannot protect the metallic Fe core from deep oxidation. But the desired stabilization is achieved by controlled oxidation of the as-synthesized nanoparticles using an oxygen transferring agent

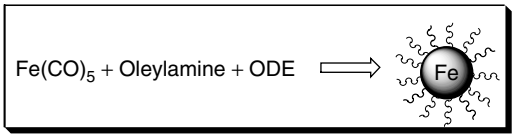

(a)

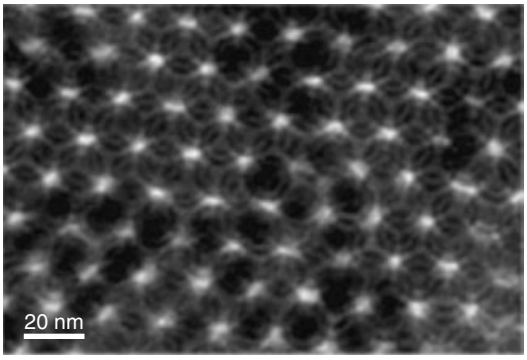

(b)

Figure 1. (a) Schematic illustration of the synthesis of Fe nanoparticles, and (b) TEM image of the 13-nm Fe nanoparticles. (Adapted from Peng, Wang, Xie and Sun, 2006.)

$(CH_3)_3NO$. This controlled oxidation gives core/shell structured Fe/Fe_3O_4 in which crystalline Fe_3O_4 has inverse spinel structure while Fe is amorphous. The thickness of the shell is tuned by controlling the amount of $(CH_3)_3NO$ added into the reaction mixture. Magnetic measurements of the 2.5-nm/5-nm Fe/Fe_3O_4 nanoparticles show that they are superparamagnetic with magnetic moment reaching 61.6 emu g^{-1} particles (90.6 emu g^{-1} [Fe]) and is stabilized at 56.2 emu g^{-1} after the dispersion is exposed to air for over 8 h. In contrast, the as-synthesized nanoparticles start to aggregate only after 2 h and completely oxidized within 8 h.

3 SYNTHESIS OF MAGNETIC IRON OXIDE NANOPARTICLES

Magnetic iron oxide included in this review are mainly cubic spinel structured MFe_2O_4. This oxide represents a well-known and important class of iron oxide materials where oxygen forms an fcc close packing, and M^{2+} and Fe^{3+} occupy either tetrahedral or octahedral interstitial sites. By adjusting the chemical identity of M^{2+}, the magnetic configurations of MFe_2O_4 can be molecularly engineered to provide a wide range of magnetic properties. Owing to this structural versatility, nanometer-scale MFe_2O_4 materials have been among the most frequently chosen systems for studies of nanomagnetism and have shown great potential for many important technological applications, ranging from information storage and electronic devices to medical diagnostics and drug delivery.

Iron oxide nanoparticles are commonly prepared by co-precipitation of M^{2+} and Fe^{3+} ions by a base, usually NaOH, or $NH_3{\cdot}H_2O$ (Kang, Risbud, Rabolt and Stroeve, 1996; Fried, Shemer and Markovich, 2001). This precipitation method is suitable for mass production of magnetic MFe_2O_4 ferrofluids, but it requires careful adjustment of the pH value of the solution for particle formation and stabilization, and it is difficult to control sizes and size distributions, particularly for particles smaller than 20 nm. An alternative approach to monodisperse iron oxide nanoparticles is via high-temperature organic-phase decomposition of an iron precursor, for example, decomposition of $FeCup_3$ (Cup: *N*-nitrosophenylhydroxylamine, $C_6H_5N(NO)O^-$), (Rockenberger, Scher and Alivisatos, 1999) or decomposition of $Fe(CO)_5$ followed by oxidation to Fe_2O_3 (Hyeon *et al*., 2001; Guo, Teng, Rahman and Yang, 2003; Redl, Cho, Murray and O'Brien, 2003). The latter process has recently been extended to the synthesis of monodisperse cobalt ferrite ($CoFe_2O_4$) nanoparticles (Hyeon *et al*., 2002).

An improved synthesis of MFe_2O_4 nanoparticles involves high-temperature (up to 300 °C) reaction between metal acetylacetonate and a 1,2-alkanediol in the presence of oleic acid and oleylamine. When pure iron acetylacetonate, for example, Fe(acac)3, is used for the reaction, monodisperse magnetite Fe_3O_4 nanoparticles are prepared (Sun and Zeng, 2002; Sun *et al*., 2004). If a different metal acetylacetonate precursor $M(acac)_2$ is added to the mixture of $Fe(acac)_3$ and 1,2-alkanediol, MFe_2O_4 nanoparticles (with M = Co, Mn) are obtained (Sun *et al*., 2004). The size of the oxide nanoparticles is controlled by varying the reaction temperature or changing reactant concentration (Xie *et al*., 2006). Alternatively, with the smaller nanoparticles as seeds, larger monodisperse nanoparticles up to 20 nm in diameter can be synthesized by seed-mediated growth (Sun and Zeng, 2002; Sun *et al*., 2004). Figure 2 shows the TEM images of 16-nm Fe_3O_4 nanoparticles made from the seed-mediated growth (Sun and Zeng, 2002).

Magnetic measurements of the Fe_3O_4 nanoparticles indicate that the particles are superparamagnetic at room temperature. Figure 3 shows the hysteresis loops of 16-nm Fe_3O_4 nanoparticles measured at both 10 K and at room temperature. It can be seen that the particles are ferromagnetic at 10 K with a coercivity of 450 Oe (Figure 3a). At room temperature there is no hysteresis (Figure 3b). The saturation magnetization, σ_s, is dependent on the size of the particles. For example, σ_s for 16-nm Fe_3O_4 nanoparticles is 83 emu g^{-1}, close to the value of 84.5 emu g^{-1} measured from the commercial magnetite fine powder. For particles smaller than 10 nm, however, σ_s is smaller under same field strength.

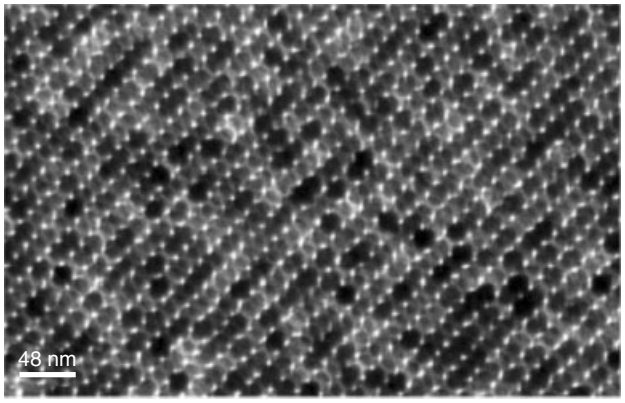

Figure 2. TEM bright field image of a self-assembled array of the 16-nm Fe_3O_4 nanoparticles. (Adapted from Sun and Zeng, 2002.)

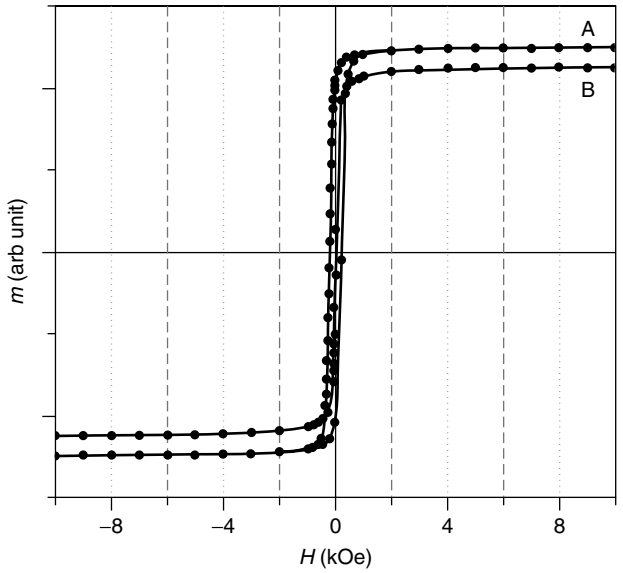

Figure 3. Hysteresis loops of the 16-nm Fe_3O_4 nanoparticle assembly measured at (A) 10 K and (B) 300 K. (Adapted from Sun *et al*., 2004.)

This is likely due to the thermal fluctuation and surface spin canting of the small nanoparticles (Morales *et al*., 1999).

The magnetic properties of the MFe_2O_4 nanoparticles can be tuned by M in the structure. Figure 4 shows the hysteresis loops of 16-nm $CoFe_2O_4$ nanoparticles measured at both 10 K and 300 K. The coercivity of the assembly is about 500 Oe at 300 K, but reaches 20 kOe at 10 K, much larger than that of the 16-nm Fe_3O_4 nanoparticles (450 Oe at 10 K), indicating that the incorporation of the Co cation in the Fe–O matrix greatly increases the magnetic anisotropy of the materials. Such anisotropy enhancement of $CoFe_2O_4$ versus Fe_3O_4 has also been observed in films deposited from aqueous solution (Kim *et al*., 2003). In contrast, the incorporation of Mn cation in the Fe–O matrix reduces the

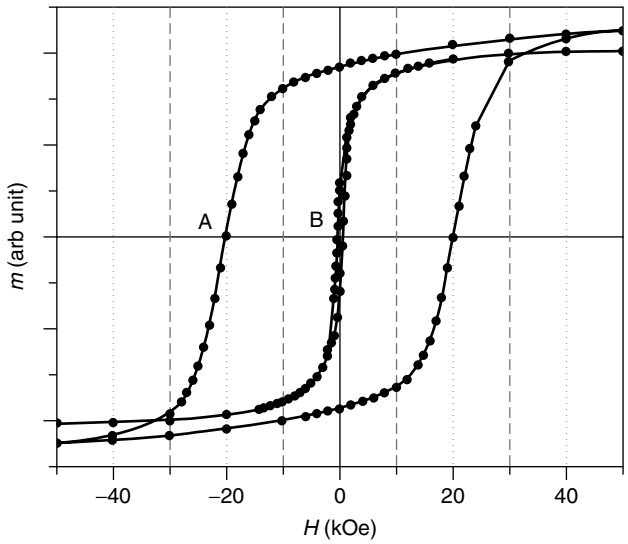

Figure 4. Hysteresis loops of the 16-nm $CoFe_2O_4$ nanoparticle assembly measured at (A) 10 K and (B) 300 K. (Adapted from Sun *et al*., 2004.)

magnetic anisotropy of the materials as the 14-nm $MnFe_2O_4$ nanoparticles shows an Hc of only 140 Oe at 10 K.

4 SYNTHESIS OF ALLOY NANOPARTICLES

Chemically prepared FePt nanoparticles have generated great interest recently because of their ease of synthesis, chemical stability, and potential applications in high-density data storage (Sun *et al*., 2000) and high-performance permanent magnets (Zeng *et al*., 2002). The particles are commonly synthesized via simultaneous decomposition of iron pentacarbonyl, $Fe(CO)_5$, and reduction of platinum acetylacetonate, $Pt(acac)_2$ (Sun *et al*., 2000; Sun, 2006). Oleic acid and oleyl amine are proven to be a good ligand combination for FePt particle stabilization. The composition of the FePt nanoparticles is tuned by varying the molar ratio of $Fe(CO)_5$ and $Pt(acac)_2$. Note that not all the $Fe(CO)_5$ contributes to the FePt formation during the synthesis. $Fe(CO)_5$ has a low boiling point (103 °C). At reaction temperature of 298 °C, $Fe(CO)_5$ is actually in the vapor phase. The formation of this vapor phase results in the slow decomposition of $Fe(CO)_5$ at a rate that matches with the reduction rate of $Pt(acac)_2$. The FePt nanoparticles are formed in a shorter period of time. Therefore, the consumption of $Fe(CO)_5$ can not be completed on this synthetic time scale. As a result, 0.5 mmol of $Fe(CO)_5$ and 0.5 mmol of $Pt(acac)_2$ yield $Fe_{38}Pt_{62}$, while 1.1 mmol of $Fe(CO)_5$ and 0.5 mmol of $Pt(acac)_2$ lead to $Fe_{56}Pt_{44}$ nanoparticle materials. The FePt particle size can be tuned

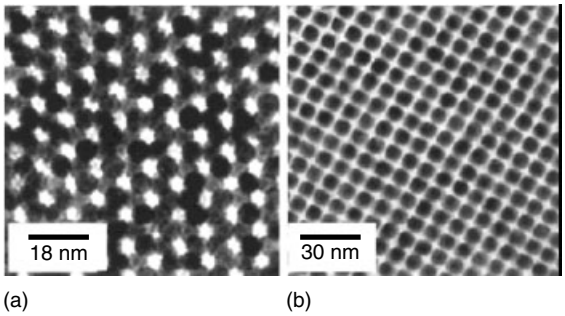

Figure 5. TEM micrographs of (a) a 3D assembly of 6-nm as-synthesized $Fe_{50}Pt_{50}$ particles and (b) a 3D assembly of 6-nm $Fe_{50}Pt_{50}$ sample after replacing oleic acid/oleyl amine with hexanoic acid/hexylamine (Sun *et al*., 2000).

from 3 to 10 nm by first growing 3-nm monodisperse seed particles *in situ* and then adding more reagents to enlarge the existing seeds to the desired size (Sun *et al*., 2000). Figure 5 gives TEM images of the 6-nm FePt nanoparticles prepared from the seed-mediated growth of 4-nm FePt nanoparticles.

The one-step decomposition/reduction method described above can yield high quality FePt nanoparticles with controlled composition but fail to produce particles larger than 4 nm unless the seed-mediated growth method is used, which gives larger FePt particles but without accurate control on Fe, Pt composition at different sizes. To overcome this synthetic problem, a diol-less one-step synthesis is developed (Chen, Liu and Sun, 2004). The lack of the diol from the reaction mixture slows down the nucleation rate, allowing more metal precursor to deposit around the nuclei formed in the solution and leading to the formation of larger particles. The size of the particles is tuned by controlling the molar ratio of stabilizers to $Pt(acac)_2$ and heating conditions. A ratio of at least 8 is needed to make FePt nanoparticles larger than 6 nm in this one-pot reaction. It is also found that, at the fixed stabilizers:$Pt(acac)_2$ ratio of 8, both heating rate and interim heating temperature are important in making FePt particles with tunable sizes. Heating rate of $\sim$15 °C/min. and interim heating temperature of 240 °C yields 6-nm FePt, while the rate of $\sim$5 °C/min. and heating temperature of 225 °C leads to 9-nm FePt. The composition of the particles is controlled by varying the molar ratio of $Fe(CO)_5$ and $Pt(acac)_2$. Under the reported reaction conditions, $Fe(CO)_5/Pt(acac)_2$ ratio of 2 gives 6-nm $Fe_{53}Pt_{47}$ and 9-nm $Fe_{44}Pt_{56}$ nanoparticles. Thermal annealing and magnetic studies show that an assembly of large (6 nm or above) FePt nanoparticles can withstand higher temperature (650 °C) annealing without noticeable particle sintering. Room-temperature coercivity of an assembly containing discrete FePt dots can reach as high as 1.3 T, a value that is suitable for hard magnetic applications.

The mechanism for the formation of FePt nanoparticles in this one-pot, diol-less reaction is given in Figure 6 (Chen, Liu and Sun, 2004). The Pt-rich nuclei (a) are formed from the reduction of $Pt(acac)_2$ either at temperature >200 °C or by Fe atoms from the decomposed $Fe(CO)_5$, or by both. More Fe atoms coat over the existing Pt-rich nuclei, forming larger clusters (b). Exposing these clusters to air leads to formation of Pt-rich $FePt/Fe_3O_4$. Heating the clusters (b) to refluxing at 300 °C results in atomic diffusion and formation of fcc structured FePt nanoparticles (c). In the presence of the excess of $Fe(CO)_5$, the extra Fe continues to coat over (c), giving core/shell structured FePt/Fe that is further oxidized to $FePt/Fe_3O_4$ (d). The intermediate and product structures proposed in Figure 6 have been separated and characterized (Chen, Liu and Sun, 2004).

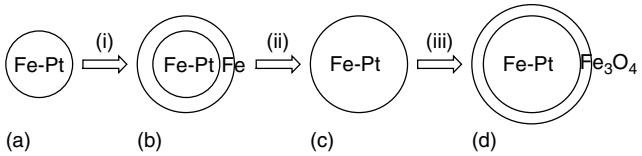

Figure 6. Schematic illustration of the mechanism for the formation of FePt nanoparticles via Fe, Pt diffusion. (i) Fe coating; (ii) Fe, Pt interface diffusion; (iii) Fe coating, then oxidation. (Adapted from Chen, Liu and Sun, 2004.)

Stable CoFe nanoparticles are important for high magnetic moment applications. Such particles can be synthesized by co-decomposition of $Fe(CO)_5$, and $Co(\eta^3\text{-}C_8H_{13})(\eta^4\text{-}C_8H_{12})$ or $Co[N(SiMe_3)_2]_2$ (Desvaux *et al*., 2005). The precursors are reacted under 3 bar H_2 pressure in toluene at 150 °C in the presence of 1 equivalent of hexadecylamine and 1 equivalent oleic acid. The solid product separated from the reaction mixture contains monodisperse CoFe nanoparticles, as shown in the scanning electron microscopy (SEM) image (Figure 7). superconducting quantum interference devices (SQUID) measurements show a ferromagnetic behavior at room temperature with a saturation magnetization (Ms)

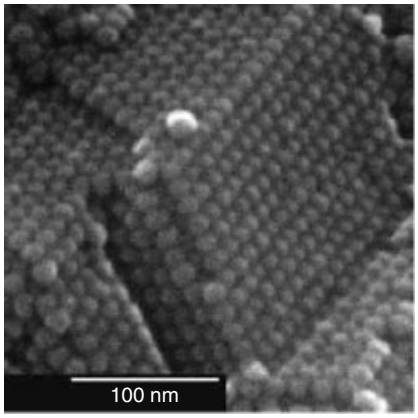

Figure 7. SEM image of the cross-section view of a CoFe nanoparticle assembly. (Reproduced from Desvaux *et al*., 2005, with permission from Nature. © 2005.)

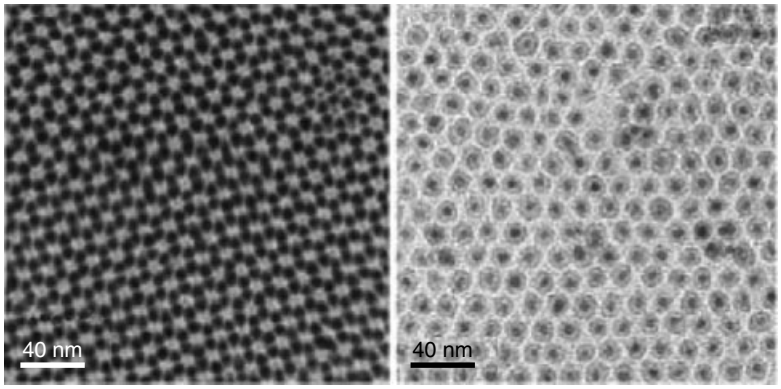

Figure 8. TEM bright field images of core/shell $Fe_{58}Pt_{42}/Fe_3O_4$ nanoparticles with core/shell being (a) 4-nm/0.5-nm and (b) 4-nm/2-nm (Zeng *et al*., 2004).

reaching as high as $183\,Am^2\,kg^{-1}$(CoFe). To improve the air-stability of the nanoparticles, the array is annealed under argon at 500 °C for 30 min. After annealing, the particles adopt the body centered-cubic structure. Furthermore, the annealing results in the formation of a carbon shell around the surface of the particles, protecting the particles from fast oxidation (no noticeable change in the magnetic properties after two weeks of exposure to air). Magnetic measurements of the annealed assembly show an improved magnetization values, $Ms = 220\,Am^2\,kg^{-1}$(CoFe), close to the bulk CoFe values, $Ms = 245\,Am^2\,kg^{-1}$(CoFe).

5 SYNTHESIS OF BIMAGNETIC CORE/SHELL STRUCTURED NANOPARTICLES

Magnetic core/shell nanoparticles can be categorized as those with magnetic core coated with a layer of a nonmagnetic, antiferromagnetic, or ferro/ferri-magnetic shell. A nonmagnetic coating is used routinely for magnetic core stabilization and surface functionalization for biomedical applications. An antiferromagnetic coating over a ferromagnetic core leads to exchange bias (a shift of the hysteresis loop along the field axis) and improvements in the thermal stability of the core (Skumryev *et al*., 2003). Compared with these two different types of core/shell systems, a bimagnetic core/shell one, where both core and shell are strongly magnetic (ferro- or ferri-magnetic) is magnetically more interesting owing to their potential in electromagnetic and permanent magnetic applications (Zeng *et al*., 2002; Carpenter, Calvin, Stroud and Harris, 2003). In such a system, the intimate contact between the core and shell leads to effective exchange coupling and therefore cooperative magnetic switching, facilitating the fabrication of nanostructured magnetic materials with tunable properties.

$FePt/Fe_3O_4$ nanoparticles represent a good example of bimagnetic core/shell structures (Zeng *et al*., 2004). They are prepared by coating the existing FePt nanoparticles with Fe_3O_4 shell in a condition similar to the synthesis of Fe_3O_4 nanoparticles. For example, the 4-nm $Fe_{58}Pt_{42}$ nanoparticles are made by the combination of reduction of $Pt(acac)_2$ and decomposition of $Fe(CO)_5$ in octyl ether solvent (Sun *et al*., 2000). These 4-nm FePt nanoparticles are then used as seeds and mixed with $Fe(acac)_3$ and 1,2-hexadecanediol, oleicacid, and oleylamine in phenyl ether solvent. Fe_3O_4 coating is achieved by heating the mixture (Zeng *et al*., 2004). By controlling the material ratio of $Fe(acac)_3$ to FePt nanoparticle seeds, the Fe_3O_4 shell thickness can be readily tuned. Figure 8(a) and (b) shows two TEM images of the core/shell structured $Fe_{58}Pt_{42}/Fe_3O_4$ nanoparticles with the darker region in the center being 4-nm $Fe_{58}Pt_{42}$ and the lighter ring being 0.5 nm (Figure 8a) and 2-nm Fe_3O_4 (Figure 8b).

The $Fe_{58}Pt_{42}/Fe_3O_4$ core/shell nanoparticles are ferromagnetic at low temperatures but superparamagnetic at room temperature (Zeng *et al*., 2004). The particles with 0.5-nm Fe_3O_4 shell have an H_c of 5 kOe, while those with 3-nm shell have an H_c value of only 1.4 kOe. The large H_c value of the core/shell nanoparticles originates from low-temperature hard magnetic properties of the $Fe_{58}Pt_{42}$ core –the coercivity of the as-synthesized 4-nm $Fe_{58}Pt_{42}$ nanoparticles is 5.5 kOe at 10 K. Fe_3O_4 is magnetically a much softer material, with 10 K H_c ranging from 200 Oe for 4 nm to 450 Oe for 16 nm nanoparticles. However, in the $Fe_{58}Pt_{42}/Fe_3O_4$ system, the magnetic behaviors of $Fe_{58}Pt_{42}$ and Fe_3O_4 are not distinguishable, and the hysteresis loops measured at 10 K show smooth change of magnetization with applied field,

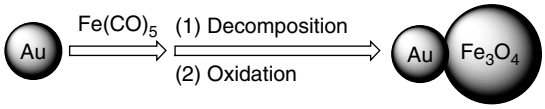

Figure 9. Schematic illustration of the synthesis of dumbbell-like Au–Fe_3O_4 nanoparticles. (Adapted from Yu *et al*., 2005.)

suggesting that the $Fe_{58}Pt_{42}$ core and the Fe_3O_4 shell are in intimate contact and are exchange coupled. Therefore, the magnetization directions of both core and shell switch coherently under an external magnetic field. The exchange-coupled FePt/Fe_3O_4 nanoparticles can be used as building blocks to form hard magnetic nanocomposites with enhanced magnetic properties (Zeng *et al*., 2004).

6 SYNTHESIS OF DUMBBELL-LIKE NANOPARTICLES

Dumbbell-like magnetic nanoparticles have two nanoparticles in intimate contact with one being magnetic. Owing to the epitaxial connection between these two units, the dumbbell structure can be considered as a nanoscale junction. In such a system, the electronic structures of both metal and metal oxide are modified by electron transfer across the interface, leading to the enhancement in chemical and physical properties at the nanoscale interface. The dumbbell-like Au–Fe_3O_4 nanoparticles with both Au and Fe_3O_4 in nanometer sizes are prepared via the decomposition of $Fe(CO)_5$ over the surface of the Au nanoparticles, as illustrated in Figure 9 (Yu *et al*., 2005). The Au nanoparticles are either synthesized *in situ* by injecting $HAuCl_4$ solution into the reaction mixture or pre-made using a modified synthetic procedure. Mixing Au nanoparticles with $Fe(CO)_5$ in 1-octadecene solvent in the presence of oleic acid and oleylamine and heating the mixture to reflux ($\sim$300 °C) followed by room temperature oxidation leads to dumbbell-like Au–Fe_3O_4 nanoparticles. The size of the Au particles is tuned by controlling the temperature at which the $HAuCl_4$ is injected, or by controlling the $HAuCl_4$/oleylamine ratio. The size of the Fe_3O_4 particles is controlled by adjusting the ratio between $Fe(CO)_5$ and Au. More $Fe(CO)_5$ leads to larger Fe_3O_4 nanoparticles. Au–Fe_3O_4 particles with Au up to 8 nm and Fe_3O_4 up to 20 nm have been synthesized.

Figure 10(a) and (b) shows two TEM images of the dumbbell-like Au–Fe_3O_4 nanoparticles with Fe_3O_4 at around 14 nm and Au at 3 and 8 nm, respectively. Figure 10(c) is the high angle annular dark field scanning transmission electron microscopy (HAADF-STEM) image of several dumbbell nanoparticles. In Figure 10(c), the Au particles are

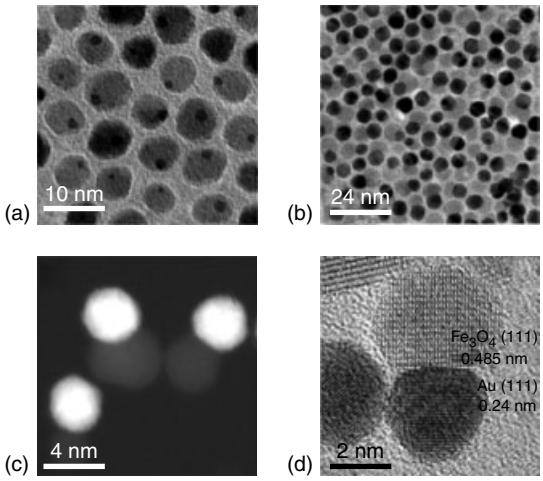

Figure 10. TEM and STEM images of the dumbbell-like Au–Fe_3O_4 nanoparticles: (a) TEM image of the 3–14-nm Au–Fe_3O_4 particles; (b) TEM image of 8–14-nm Au–Fe_3O_4 particles; (c) HAADF-STEM image of 8–9-nm Au–Fe_3O_4 particles; and (d) HRTEM image of one 8–12-nm Au–Fe_3O_4 particle (Yu *et al*., 2005).

imaged as brighter dots. Figure 10(d) is a typical high resolution TEM (high resolution transmission electron microscopy (HRTEM)) image of a dumbbell particle with Fe_3O_4 at 12 nm and Au at 8 nm. The lattice fringes in each of the particles correspond to atomic planes within the particle, indicating that both particles are single crystals. The distance between two adjacent planes in Fe_3O_4 is measured to be 0.485 nm, corresponding to (111) planes in the inverse spinel structured Fe_3O_4 and that in Au is 0.24 nm, resulting from a group of (111) planes in fcc structured Au.

The interface communication between the nanoscale Au and Fe_3O_4 leads to the change of magnetization behaviors of the Fe_3O_4 nanoparticles, especially for those smaller than 8 nm (Yu *et al*., 2005). Figure 11 shows the hysteresis loops measured at room temperature for Au–Fe_3O_4 particles with Au being 3 nm and Fe_3O_4 14 nm (Figure 11a) and 6 nm (Figure 11b), respectively. Like Fe_3O_4 nanoparticles, the dumbbell particles are superparamagnetic at room temperature. The 3–14-nm dumbbell particles show loops similar to the 14-nm Fe_3O_4 nanoparticles with saturation moment reaching 80 emu g^{-1} (Figure 11a), a value that is close to the related Fe_3O_4nanoparticles due to the negligible weight percentage of 3-nm Au in the composite. The 3–6-nm dumbbell particles, however, show a loop of slow increase in moment with the field up to 5 T (Figure 11b), while the pure 6-nm Fe_3O_4 nanoparticles are magnetically saturated within 1 T. It seems that interfacial interactions between Au and Fe_3O_4 make the small magnetic nanoparticles difficult to achieve saturation.

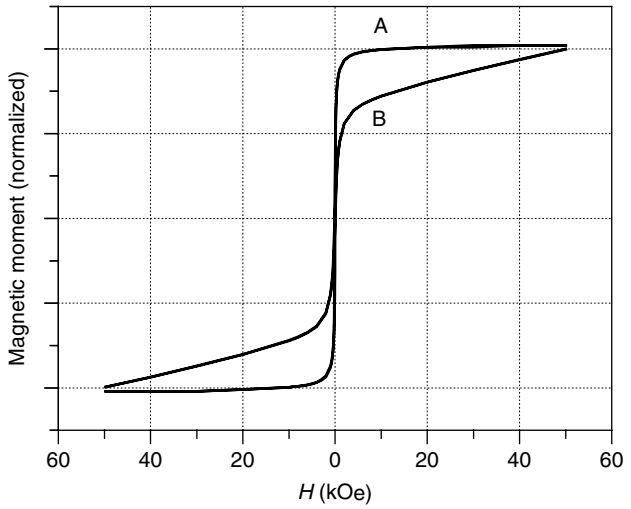

Figure 11. Hysteresis loops of $Au-Fe_3O_4$ particles measured at room temperature: (A) 3–14-nm $Au-Fe_3O_4$ and (B) 3–6-nm $Au-Fe_3O_4$ particles (Yu *et al*., 2005).

7 SHAPE-CONTROLLED SYNTHESIS OF MAGNETIC NANOPARTICLES

The shape is one of the most important factors in determining the structural, physical, and chemical properties of a nanoparticle and an assembled array of the particles. Shape-controlled synthesis of nanoparticles has become a recent focus, as different shapes of the particles can introduce electronic, optical, and magnetic properties that are different from those observed in their spherical counterparts (Burda, Chen, Narayanan and El-Sayed, 2005; Jun, Choi and Cheon, 2006). Shape-controlled synthesis and assembly of magnetic nanoparticles can induce crystal orientation and further magnetic alignment of each nanoparticle in an assembly –a key requirement for various magnetic applications.

Solution phase synthesis has shown great success in controlling the monodispersity of the nanoparticle shapes. Nearly monodisperse cobalt nanorods are synthesized by thermal decomposition of $[Co(\eta^3\text{-}C_8H_{13})(\eta^4\text{-}C_8H_{12})]$ in the presence of a mixture of hexadecylamine (HDA) and aliphatic acid (Dumestre *et al*., 2003). Using octanoic acid (C8) results in the formation of shorter and wider rods (Figure 12a). The lauric acid (dodecanoic acid, C12) leads to cobalt nanorods with an approximate size of 5:85 nm (Figure 12b). With stearic acid (octadecanoic acid), the longer nanorods are obtained.

The shape of the $MnFe_2O_4$ nanoparticles is controlled by the amount of stabilizers added to the reaction mixture during the synthesis of $MnFe_2O_4$ nanoparticles (Sun *et al*., 2004; Zeng, Rice, Wang and Sun, 2004). A reaction of 2 mmol of $Fe(acac)_3$ and 1 mmol of $Mn(acac)_2$, with 10 mmol of

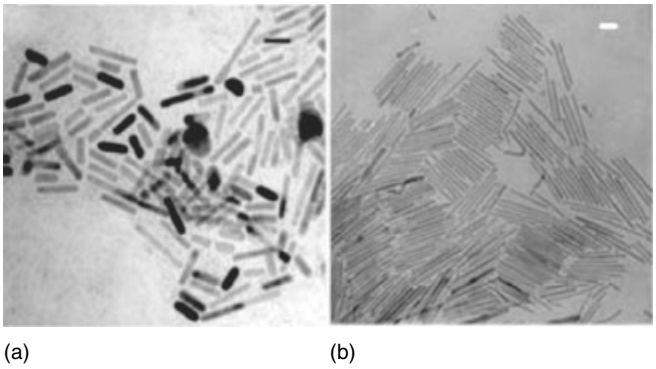

Figure 12. TEM micrographs of nanorods synthesized using hexadecylamine and (a) octanoic acid and (b) lauric acid (Dumestre *et al*., 2003).

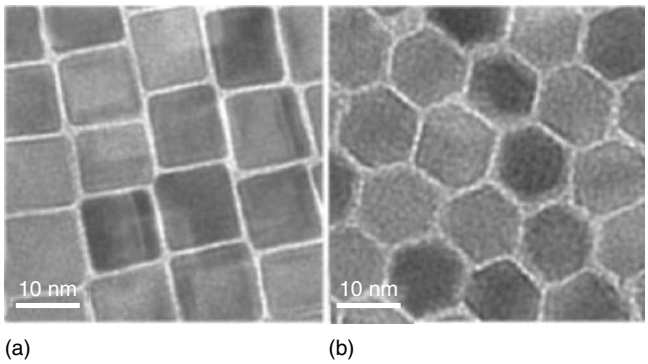

Figure 13. TEM images of the as-synthesized (a) 12-nm cube-like and (b) 12-nm polyhedron-shaped $MnFe_2O_4$ nanoparticles (Zeng, Rice, Wang and Sun, 2004).

1,2-hexadecandiol in the presence of 6 mmol of oleic acid, 6 mmol of oleyl amine and 20 ml of benzyl ether gives 12-nm $MnFe_2O_4$, while similar reaction in 22 ml or 25 ml of benzyl ether yields 10 nm or 8 nm particles, respectively (Zeng, Rice, Wang and Sun, 2004). When the surfactant/$Fe(acac)_3$ ratio is smaller than 3:1, the particles are nearly spherical with no well-defined facets. Increasing the ratio to 3:1 yields cube-like particles. If the particles are prepared using the seed-mediated growth as in the synthesis of Fe_3O_4 nanoparticles (Sun and Zeng, 2002), polyhedron-shaped particles are obtained. Figure 13 shows the representative TEM images of the $MnFe_2O_4$ nanoparticles with different morphologies, with (a) being cube-like and (b) polyhedron-shaped particles.

Self-assembly of these shaped particles can lead to crystal orientation of each particle in a self-assembled superlattice (Zeng, Rice, Wang and Sun, 2004). Controlled evaporation of the carrier solvent from the hexane dispersion ($\sim 2\,mg\,mL^{-1}$) of the particles shown in Figure 13 lead to $MnFe_2O_4$ nanoparticle superlattices. Figure 14(a) shows the superlattice assembly from the cube-like particles, whereas

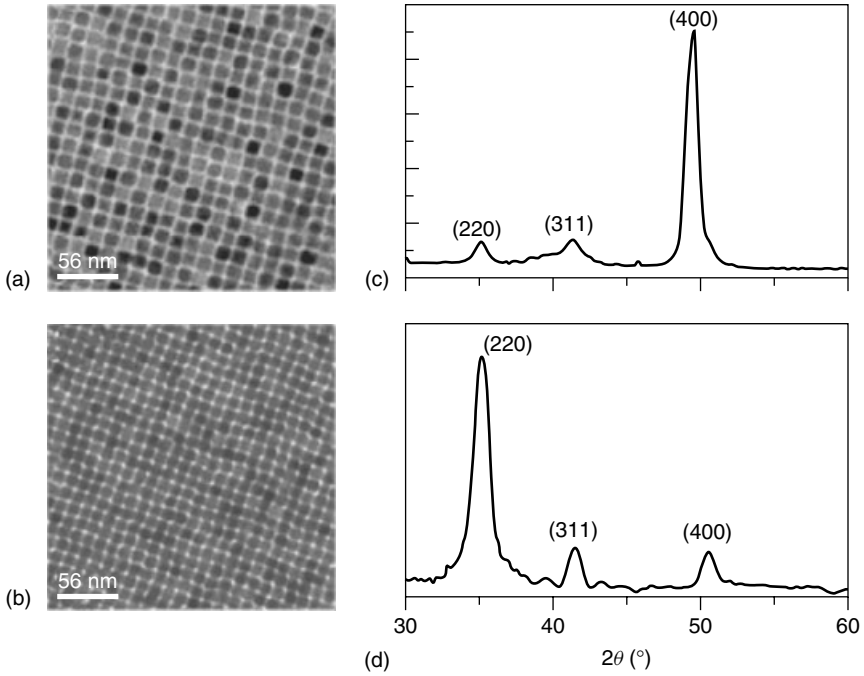

Figure 14. TEM images of 12-nm $MnFe_2O_4$ nanoparticle superlattices of (a) cubelike and (b) polyhedron-shaped nanoparticles. XRD (Co K$a\lambda = 1.788965$ Å) of (c) cubelike and (d) polyhedron-shaped nanoparticle superlattice on Si(100) substrates (Zeng, Rice, Wang and Sun, 2004).

Figure 14(b) is the assembly from the polyhedron-shaped particles. Both assemblies have the cubic packing. But the different shapes possessed by each group of the particles affect the crystal orientation of individual particles within the superlattices. X-ray diffraction (XRD) pattern of the self-assembled cube-like particles shows an intensified (400) peak (Figure 14c) while the XRD of the polyhedron-shaped particle assembly reveals a strong reflection of (220) (Figure 14d). These are markedly different from that of a 3D randomly oriented spinel structured $MnFe_2O_4$ nanoparticle assembly, which shows a strong (311) peak. These indicate that each of the cube-like particles in the cubic assembly has preferred crystal orientation with {100} planes parallel to the Si substrate while for the polyhedron-shaped particle assembly, the {110} planes are parallel to the substrate.

Nearly monodisperse FePt nanocubes are synthesized by controlled mixing of reactants and heating. (Chen *et al.*, 2006) The cubic nanoparticles are produced by first mixing olecid acid and $Fe(CO)_5$ with benzyl ether/octadecene solution of $Pt(acac)_2$ and heating the mixture to 120 °C for about 5 min. before oleylamine is added and the mixture is heated at 205 °C for 2 h (Chen *et al.*, 2006). It is believed that the nanocubes are formed from the growth of the cubic Pt-rich nuclei generated during the initial stage of the reaction, as the -COOH does not have a strong tendency to bind to Pt as the surface energy of crystallographic planes of a fcc Pt crystal generally follow the trend of $(111) < (100)$. In a kinetic growth process, the Fe-rich species prefer to deposit on the (100) plane, leading to the formation of cubes. If oleylamine is added first, sphere-like FePt nanoparticles are separated. This indicates that the amine reacts with Pt, forming stable $Pt{-}NH_2$- complex and hindering the nucleation process. The uniform FePt nanocubes must be derived from atomic diffusion between Pt-rich core and Fe-rich shell in a process that is similar to what is described in Figure 6 (Chen, Liu and Sun, 2004).

Controlled evaporation of the carrier solvent from the hexane dispersion ($\sim$2 mg mL^{-1}) of the nanocubes yields a $Fe_{50}Pt_{50}$ nanocube superlattice array, as shown in Figure 15(a) (Chen *et al.*, 2006). This assembly pattern is energetically favored as it gives the maximum van der Waals interaction energy arising from face–face interactions in short distance of the cube assembly (Korgel, Fullam, Connolly and Fitzmaurice, 1998). The interparticle distance is around 4–5 nm, close the simple thickness addition of the cube coating layer (2–2.5 nm, the length of oleate or oleylamine). Selected area electron diffraction (SAED) of the assembly in Figure 15(a) exhibits four bright (200) spots that are linked by a four-fold symmetry, as shown in Figure 15(b). The (111) diffraction ring is very weak in this diffraction pattern. These indicate that the assembly in Figure 15(a) is (100) textured. The textured cubic assembly is further revealed by a small angle diffraction of the assembly (Figure 15c). This is markedly different from that of a 3D

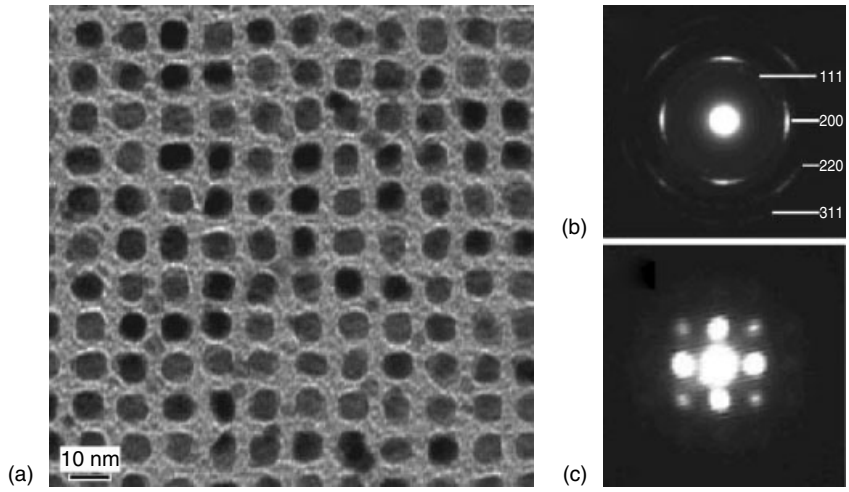

Figure 15. (a) TEM image of a multilayer assembly of 6.9-nm $Fe_{50}Pt_{50}$ nanocubes; and (b) SAED of the assembly in (a), and (c) small angle diffraction of the assembly in (a) (Chen *et al*., 2006).

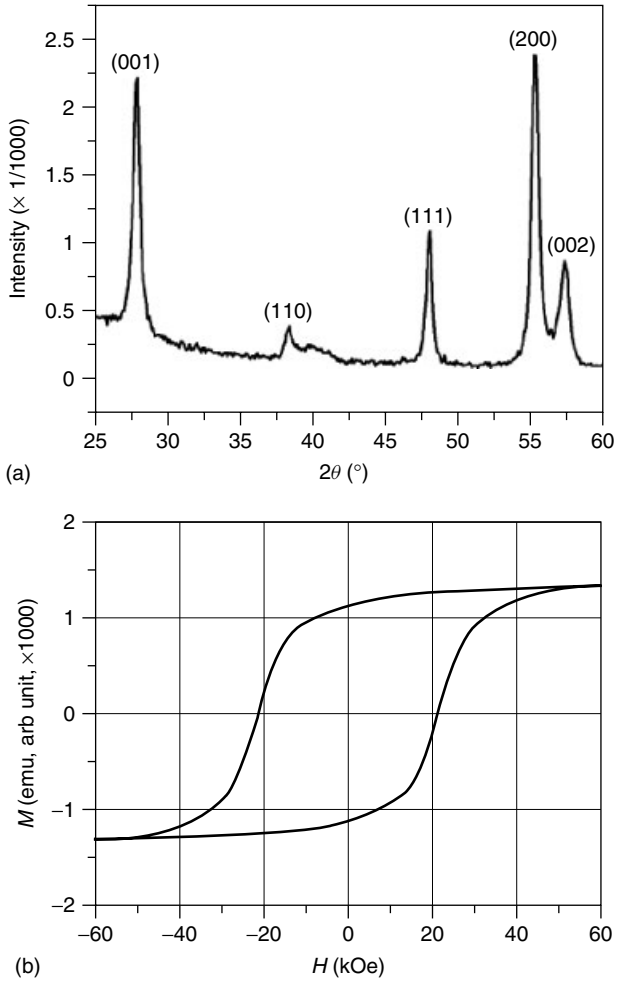

Figure 16. (a) XRD of thermally annealed FePt nanocube assembly on a Si surface, and (b) room temperature in-plane hysteresis loop of the FePt nanocube assembly in (a) (Chen *et al*., 2006).

randomly oriented FePt nanoparticle assembly with a strong (111) peak, indicating that each nanocube in the assembly has a preferred crystal orientation with {100} planes parallel to the substrate. Thermal annealing of the FePt nanocube superlattice induces FePt structure transformation from fcc to fct (Chen *et al*., 2006). The XRD pattern of the annealed assembly (675 °C under Ar for 1 h) has two strong (001) and (200) peaks, as shown in Figure 16(a). The narrowed peaks indicate the particle growth during the annealing process. However, the peak intensity is different from that of the spherical FePt nanoparticle assembly, which shows only one strong (111) peak (Sun *et al*., 2000). This indicates that (001) planes in the thermally annealed FePt nanocube array distribute equally in parallel and perpendicular directions to the substrate. Figure 16(b) is the room-temperature hysteresis loop of the annealed FePt nanocube assembly with coercivity at 22 kOe. The loop is exact the same in both parallel and perpendicular direction of the assembly, confirming what is concluded from the XRD analysis in Figure 16(b).

8 CONCLUSIONS

It is now well accepted that fabrication of ordered nanomagnet arrays with controlled magnetic alignment is an important goal in achieving high-density information storage and high-performance permanent magnets. Many experimental results have shown that solution phase chemistry is a versatile method for preparing monodisperse magnetic nanoparticles and nanoparticle superlattice array with controlled magnetic properties. With the shape-induced texture in the assembly, it is possible to align magnetic easy axis of each nanoparticle in a self-assembled superlattice structure. When this is

achieved, solution phase chemical synthesis will evolve as a new alternative for the fabrication of the advanced magnetic nanostructures for ultrahigh DMR and magnetic energy storage applications.

ACKNOWLEDGMENTS

The work was supported by DARPA/ARO, DARPA/ONR, ONR/MURI, NSF/DMR, INSIC, and Brown University.

REFERENCES

Bao, Y., Beerman, M., Pakhomov, A.B. and Krishnan, K.M. (2005). Controlled crystalline structure and surface stability of cobalt nanocrystals. *Journal of Physical Chemistry B*, **109**, 7220–7222.

Black, C.T., Murray, C.B., Sandstrom, R.L. and Sun, S. (2000). Spin-dependent tunneling in self-assembled cobalt nanocrystal superlattices. *Science*, **290**, 1131–1134.

Burda, C., Chen, X., Narayanan, R. and El-Sayed, M.A. (2005). Chemistry and properties of nanocrystals of different shapes. *Chemical Reviews*, **105**, 1025–1102.

Carpenter, E.E., Calvin, S., Stroud, R.M. and Harris, V.G. (2003). Passivated iron as core-shell nanoparticles. *Chemistry of Materials*, **15**, 3245–3246.

Chen, M., Kim, J., Liu, J.P., *et al*. (2006). Synthesis of FePt nanocubes and their oriented self-assembly. *Journal of the American Chemical Society*, **128**, 7132–7133.

Chen, M., Liu, J.P. and Sun, S. (2004). One-step synthesis of FePt nanoparticles with tunable size. *Journal of the American Chemical Society*, **126**, 8394–8395.

Cushing, B.L., Kolesnichenko, V.L. and O'Connor, C.J. (2004). Recent advances in the liquid-phase syntheses of inorganic nanoparticles. *Chemical Reviews*, **104**, 3893–3946.

Desvaux, C., Amiens, C., Pejes, P., *et al*. (2005). Multimillimetre-large superlattices of air-stable iron–cobalt nanoparticles. *Nature Materials*, **4**, 750–753.

Dumestre, F., Chaudret, B., Amiens, C., *et al*. (2003). Unprecedented crystalline super-lattices of monodisperse cobalt nanorods. *Angewandte Chemie International Edition*, **42**, 5213–5216.

Dumestre, F., Chaudret, B., Amiens, C., *et al*. (2004). Superlattices of iron nanocubes synthesized from $Fe[N(SiMe_3)_2]_2$. *Science*, **303**, 821–823.

Fried, T., Shemer, G. and Markovich, G. (2001). Ordered two-dimensional arrays of ferrite nanoparticles. *Advanced Materials*, **13**, 1158–1161.

Green, M. (2005). Organometallic based strategies for metal nanocrystal synthesis. *Chemical Communications*, 3002–3011.

Guo, Q., Teng, X., Rahman, S. and Yang, H. (2003). Patterned langmuir-blodgett films of monodisperse nanoparticles of iron oxide using soft lithography. *Journal of the American Chemical Society*, **125**, 630–631.

Huber, D.L. (2005). Synthesis, properties, and applications of iron nanoparticles. *Small*, **1**, 482–501.

Hyeon, T., Chung, Y., Park, J., *et al*. (2002). Synthesis of highly crystalline and monodisperse cobalt ferrite nanocrystals. *Journal of Physical Chemistry B*, **106**, 6831–6833.

Hyeon, T., Lee, S.S., Park, J., *et al*. (2001). Synthesis of highly crystalline and monodisperse maghemite nanocrystallites without a size-selection process. *Journal of the American Chemical Society*, **123**, 12798–12801.

Jun, Y-W., Choi, J-S. and Cheon, J. (2006). Shape control of semiconductor and metal oxide nanocrystals through nonhydrolytic colloidal routes. *Angewandte Chemie International Edition*, **45**, 3414–3439.

Kang, Y.S., Risbud, S., Rabolt, J.F. and Stroeve, P. (1996). Synthesis and characterization of nanometer-size Fe_3O_4 and γ-Fe_2O_3 particles. *Chemistry of Materials*, **8**, 2209–2211.

Kim, T.Y., Lee, M.S., Kim, Y.I., *et al*. (2003). The enhanced anisotropic properties of the $Fe_{3-x}M_xO_4$ (M = Fe, Co, Mn) films deposited on glass surface from aqueous solutions at low temperature. *Journal of Physics D: Applied Physics*, **36**, 1451–1457.

Korgel, B.A., Fullam, S., Connolly, S. and Fitzmaurice, D. (1998). Assembly and self organization of silver nanocrystal superlattices: ordered "soft spheres. *Journal of Physical Chemistry B*, **102**, 8379–8388.

Morales, M.P., Veintemillas-Verdaguer, S., Montero, M.I., *et al*. (1999). Surface and internal spin canting in γ-Fe_2O_3 nanoparticles. *Chemistry of Materials*, **11**, 3058–3064.

Morrish, A.H. (1965). *The Physical Principles of Magnetism*, John Wiley & Sons: New York.

Park, J., Lee, E., Hwang, N-M., *et al*. (2005). One-nanometer-scale size-controlled synthesis of monodisperse magnetic iron oxide nanoparticles. *Angewandte Chemie International Edition*, **44**, 2872–2877.

Peng, S., Wang, C., Xie, J. and Sun, S. (2006). Synthesis and stabilization of monodisperse Fe nanoparticles. *Journal of the American Chemical Society*, **128**, 10676–10677.

Puntes, V.F., Krishnan, K.M. and Alivisatos, A.P. (2001). Colloidal nanocrystal shape and size control: the case of cobalt. *Science*, **291**, 2115–2117.

Redl, F.X., Cho, K-S., Murray, C.B. and O'Brien, S. (2003). Three-dimensional binary superlattices of magnetic nanocrystals and semiconductor quantum dots. *Nature*, **423**, 968–971.

Rockenberger, J., Scher, E.C. and Alivisatos, P.A. (1999). A new nonhydrolytic single-precursor approach to surfactant-capped nanocrystals of transition metal oxides. *Journal of the American Chemical Society*, **121**, 11595–11596.

Skumryev, V., Stoyanov, S., Zhang, Y., *et al*. (2003). Beating the superparamagnetic limit with exchange bias. *Nature*, **423**, 850–853.

Sun, S. (2006). Recent advance in chemical synthesis, assembly and applications of FePt nanoparticles. *Advanced Materials*, **18**, 393–403.

Sun, S. and Murray, C.B. (1999). Synthesis of monodisperse cobalt nanocrystals and their assembly into magnetic superlattices. *Journal of Applied Physics*, **85**, 4325–4330.

Sun, S., Murray, C.B., Weller, D., *et al*. (2000). Monodisperse FePt nanoparticles and ferromagnetic FePt nanocrystal superlattices. *Science*, **287**, 1989–1992.

Sun, S. and Zeng, H. (2002). Size-controlled synthesis of magnetite nanoparticles. *Journal of the American Chemical Society*, **124**, 8204–8205.

Sun, S., Zeng, H., Robinson, D.B., *et al*. (2004). Monodisperse MFe_2O_4 (M = Fe, Co, Mn) nanoparticles. *Journal of the American Chemical Society*, **126**, 273–279.

Unruh, K.M. and Chien, C.L. (1996). In *Nanomaterials: Synthesis, Properties and Applications*, Edelstein, A.S. and Cammarata, R.C. (Eds.), Institute of Physics Publishing: Chap. 14.

Weller, D. (2000). Extremely high-density longitudinal magnetic recording media. *Annual Review of Materials Science*, **30**, 611–644.

Willard, M.A., Kurihara, L.K., Carpenter, E.E., *et al*. (2004). Chemically prepared magnetic nanoparticles. *International Materials Reviews*, **49**, 125–170.

Xie, J., Peng, S., Brower, N., *et al*. (2006). One-pot synthesis of monodisperse iron oxide nanoparticles for potential biomedical applications. *Pure and Applied Chemistry*, **78**, 1003–1014.

Yu, H., Chen, M., Rice, P.M., *et al*. (2005). Dumbbell-like bifunctional Au-Fe_3O_4 nanoparticles. *Nano Letters*, **5**, 379–382.

Zeng, H., Li, J., Liu, J.P., *et al*. (2002). Exchanged-coupled nanocomposite magnets via nanoparticle self-assembly. *Nature*, **420**, 395–398.

Zeng, H., Li, J., Wang, Z.L., *et al*. (2004). Bi-magnetic core/shell $FePt/Fe_3O_4$ nanoparticles. *Nano Letters*, **4**, 187–190.

Zeng, H., Rice, P.M., Wang, S.X. and Sun, S. (2004). Shape-controlled synthesis and shape-induced texture of $MnFe_2O_4$ nanoparticles. *Journal of the American Chemical Society*, **126**, 11458–11459.

FURTHER READING

Yamamuro, S. and Sumiyama, K. (2006). Why do cubic nanoparticles favor a square array? Mechanism of shape-dependent arrangement in nanocube self-assemblies. *Chemical Physics Letters*, **418**, 166–169.

Nanoimprint Technology for Patterned Magnetic Nanostructures

Stephen Y. Chou
Princeton University, Princeton, NJ, USA

1 INTRODUCTION

Patterned magnetic nanostructures (PMNs) open up great opportunities for building a broad spectrum of revolutionary magnetic devices, such as magnetic random accessible memories, quantized magnetic disks ('bit-patterned media'), new sensors, new actuators, and drug delivery, to name a few; for understanding the fundamentals of micro-/nanomagnetics; and for revolutionizing the magnetic data storage industry. The properties of a magnetic material depend upon the size, shape, spacing, orientation, and composition of the grains inside the material, as well as the material components between the grains. By patterning a magnetic material, we introduce a new, unique, and powerful way to control each of these parameters, thus creating new magnetic properties, including properties unachievable by conventional fabrication approaches (e.g., thin-film deposition).

Obviously, the realization of the PMNs' potential critically hinges upon our ability in patterning, particularly the patterning resolution, pattern-shape variety, critical dimension control, patterning area, and alignment of patterning. Furthermore, it also critically depends on the patterning throughput and cost, which dictate the commercialization potential of a PMN device and the R&D cycle time.

Among available patterning methods, nanoimprint lithography (NIL) has, in the author's view, the unique combination of ultrahigh pattern resolution ($\sim$2 nm), broad pattern variety (2D and 3D), large printing area ($>10\,\mathrm{cm}^2$), and high throughput and low cost (Chou, Krauss and Renstrom, 1995; Chou, Krauss and Kong, 1996; Chou *et al*., 1997; Guo, Krauss and Chou, 1997; Krauss and Chou, 1997; Sun, Zhuang, Zhang and Chou, 1998; Tan, Gilbertson and Chou, 1998; Wu *et al*., 1998; Heidari, Maximov, Sarwe and Montelius, 1999; Lebib *et al*., 1999; Wang, Sun, Chen and Chou, 1999; Bailey *et al*., 2000; Li, Chen and Chou, 2001; Haisma, Verheijen, vandenHeuvel and vandenBerg, 1996). Hence, NIL is playing a key role in today's development and commercialization of PMNs. For example, large-area photolithography has a resolution of $\sim$1 μm. The state-of-the-art lithography tools for semiconductor industry have a 60-nm resolution (half-pitch size), 1 in.^{2} single exposure area, and a price tag of over $40 M per tool. Electron- and ion-beam lithography and scanning probe lithography have excellent patterning resolution ($\sim$10 nm), but are low in throughput and high in cost, and therefore are more suitable for direct

Handbook of Magnetism and Advanced Magnetic Materials. Edited by Helmut Kronmüller and Stuart Parkin. Volume 3: *Novel Techniques for Characterizing and Preparing Samples*. ISBN: 978-0-470-02217-7.

writing of small areas (e.g., a few square millimeters) and for making of NIL masks. Interference lithography (IL) can produce nanostructures over a large area (Anderson, Horwitz and Smith, 1983; Yen *et al*., 1992), but it cannot compete with NIL in terms of feature size, yield, and throughput. Self-assembly is low cost and is potentially high throughput (some methods have long pattern formation times), but have very limited pattern variety, small domain size (no long-range order), and random pattern location. Guided self-assembly can alleviate some of the shortcomings of self-assembly, but is still limited (Chou and Zhuang, 1999; Chou, Zhuang and Guo, 1999).

The invention and development of nanoimprint have intertwined with that of PMNs and quantized magnetic disks (QMDs). One of the key motivations in developing nanoimprint is to find an economical viable manufacturing method for PMNs and QMDs.

As to PMN development, the idea of use of lithography to separate magnetic disk tracks (so-called discrete track or patterned media) was proposed in 1963 (Shew, 1963) and that to separate bits in 1987 (Lambert, Sanders, Patlach and Krounbi, 1987; Lambert *et al*., 1989). However, these concepts have nothing to do with the utilization of single magnetic domain (hence their unique properties), which is the key foundation of QMD that was proposed in 1993 (Chou, Wei, Krauss and Fischer, 1994). (Note: today's terminology of 'patterned media' refers to 'patterned media with single-domain bits'.)

Experimentally, the study of the patterned magnetic structures by lithography can be traced back to 1985, when the effects of patterning on the multidomain formation in magnetic structures with lateral dimension of several tens of micrometers were studied, followed by a number of other investigations on the similar structures (Ruhrig, Bartsch, Vieth and Hubert, 1990; Cosimini *et al*., 1988; Lo *et al*., 1985; Corb, 1988). But, only multidomain structures were observed. In 1988, magnetic structures with sub-250-nm feature size patterned by electron beam lithography (EBL) were reported by two groups (Ozimek, 1985; Smyth *et al*., 1991; Gibson, Smyth, Schultz and Kern, 1991). In 1993, the observation of single-domain formation in the patterned bars using magnetic force microscopy (MFM), switching of the bars using an MFM tip, and angle dependence of switching field were reported (Lederman, Gibson and Schultz, 1993; Gibson and Schultz, 1993). The patterned Co and Fe rectangles were studied (New, Pease and White, 1994, 1995a,b). In 1993, QMDs based on lithographically patterned magnetic nanostructures were proposed (Chou, Wei and Fischer, 1994; Chou, Wei, Krauss and Fischer, 1994), the fabrication and study of a QMD with a density of 65 Gbit in.$^{-2}$ using EBL were reported in 1994 (Krauss, Fischer and Chou, 1994). Yet, the QMD was regarded as being of only academic interest, because there was no viable manufacturing in 1993. To solve manufacturing problem for QMDs and other PMNs, NIL – a low-cost, high-throughput nanofabrication technology – was proposed and demonstrated in 1994 (Chou, Krauss and Renstrom, 1995, 1996).

After 1995, PMN research began to spread rapidly because of (i) application of nanofabrication technology to magnetics; (ii) availability of scanning MFM, allowing us for the first time to image and manipulate the magnetic domain structures with great precision; and (iii) invention of NIL, a sub-10-nm resolution, high-throughput, low-cost, manufacturing technology that makes commercialization of PMN-based memories and sensors economically viable. Examples of later work in different methods of fabricating patterned media include ion beam irradiation (Chappert *et al*., 1998; Terris *et al*., 1999; Albrecht, Rettner, Best and Terris, 2003), IL (Farhoud *et al*., 1999; Ross *et al*., 2001), self-assembly (Zhukov *et al*., 2003) and diblock copolymers (Thurn-Albrecht *et al*., 2000; Park, Chaikin, Register and Adamson, 2001; Asakawa *et al*., 2002; Naito *et al*., 2002; Abes, Cohen and Ross, 2003), and porous alumina (Nielsch *et al*., 2002; Yasui, Imada and Den, 2003; Castano *et al*., 2004). Nanoimprint has been used to fabricate discrete track disks (Wachenschwanz *et al*., 2005) and QMDs (Chou, 1997).

Today, QMDs (bit-patterned media) have been placed on the magnetic disks road map as one of the possible approaches to high density, and on the same roadmap, NIL is the manufacturing method.

2 PRINCIPLE AND CAPABILITY OF NANOIMPRINT LITHOGRAPHY

2.1 Principle

NIL patterns nanostructures by physical deformation of a deformable material using a mold, creating a thickness contrast in the material; rather than by changing the local chemical properties of the material using radiation (Figure 1) (Chou, Krauss and Renstrom, 1995, 1996). After imprinting, which involves material flow, a residual material layer often exists, which may need, depending on applications, to be removed by anisotropic etching (e.g., reactive ion etching, RIE), that etches vertically much faster than it does laterally. The imprinted material can serve as a resist for subsequent processing which will be removed after processing, or as a functional structure of a device that will stay as a part of the device. For simplicity, we call the imprinted materials in either case 'resists'.

An imprint process starts at the design and fabrication of a nanoimprint mold (mask), followed by the use of the mask to imprint patterns into a material (resist) on a substrate.

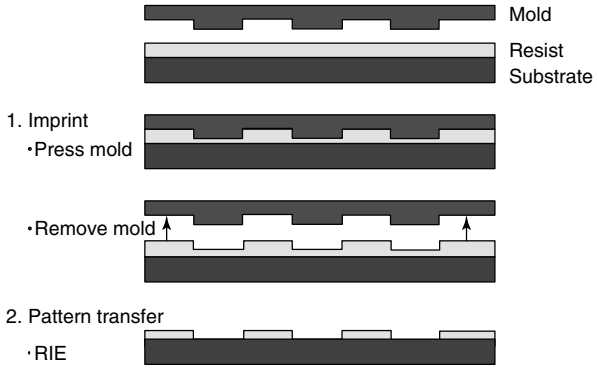

Figure 1. Schematic of nanoimprint lithography process. (1) Imprinting using a mold to create a thickness contrast in a resist; and (2) pattern transfer using anisotropic etching to remove residue resist in the compressed areas (Chou, Krauss and Renstrom, 1995, 1996).

2.2 NIL capabilities

Because it is based on a different fundamental principle, NIL has many advantages over conventional lithography, particularly in resolution, high pattern-transfer fidelity, 3D patterning, lager area (full wafer if needed), high throughput, and low cost.

2.2.1 Resolution

Since NIL is not based on the modification of the chemical structure of a resist by radiation, its resolution is not limited by the factors that limit the resolution of conventional lithography: wave diffraction, scattering and interference in a resist, backscattering from a substrate, and the chemistry of resist and developer. In fact, photocurable NIL has demonstrated 6-nm half-pitch grating with nearly atomic smooth edges imprinted into a resist (Figure 2) (Austin *et al*., 2004, 2005) and thermal NIL has demonstrated arrays of 10-nm-diameter dots separated by 40 nm (400 dots/in.^{2}) (Figure 3) (Chou *et al*., 1997). Yet, these features are not the limits of NIL, but the limits of our ability in making the features on the molds; NIL can achieve even smaller features if a mold can be made, as pointed out in the original NIL papers (Chou, Krauss, and Renstrom, 1995, 1996). Recently, imprinting of 2-nm-wide lines using carbon nanotubes as a mold was reported (Hua *et al*., 2006).

2.2.2 High pattern transfer fidelity

NIL has been demonstrated to have high fidelity in pattern transfer, accurately reproducing original mold patterns and maintaining smooth vertical sidewalls in the imprint resist. For example, repeated imprinting of static random access memory (SRAM) patterns (metal layer) of 20-nm half-pitch showed a standard deviation of 1.3 nm in the variation

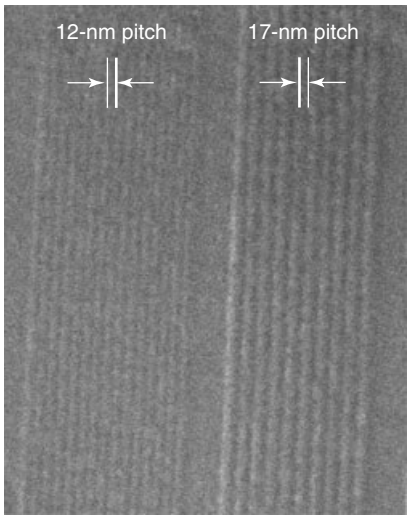

Figure 2. SEM micrograph of imprinted resist grating with a minimum 6-nm half-pitch. (Reproduced from Austin *et al*., 2004, with permission from the American Physical Society. © 2004.)

of the imprinted feature width (Figure 4) (Austin *et al*., 2005). High-aspect-ratio patterns with smooth sidewalls on the mold are transferred to the resist faithfully (Figure 5), unlike in conventional lithography, which can produce sloped sidewalls and line edge roughness, because of a Gaussian shape of the light profile, light scattering, and other noise.

2.2.3 3D patterning

The third unique feature of NIL is 3D patterning, rather than the 2D patterning as in conventional lithography. 3D features are very desirable for certain applications such as microwave circuits and microelectromechanical systems (MEMS). For example, the T-gate for microwave transistors has a narrow footprint for high-frequency operation, but a wide top for lower resistance. Fabrication of a T-gate often requires two EBL steps: one for the footprint and one for the wide top. Each electron beam exposure could take over 2 hours to pattern a single 4-in. wafer. With NIL, the entire 4-in. wafer can be patterned in one step in less than 10 s. Figure 6 shows a 40-nm T-gate fabricated by a single NIL step and lift-off of metal (Li, Chen and Chou, 2001).

2.2.4 Large patterning area

The NIL exposure area (area patterned in a single step) can be much larger that the exposure field of a conventional photolithography stepper ($\sim$1 in.^{2}) because NIL does not require high precision optics or a well conditioned monochromatic light source. Today, full 4 or 8 in. wafers are routinely imprinted at once over a full wafer. When Air Cushion Press^{TM} is used (discussed in Section 3), excellent imprint uniformity has been achieved (Figure 7) (Gao *et al*., 2006).

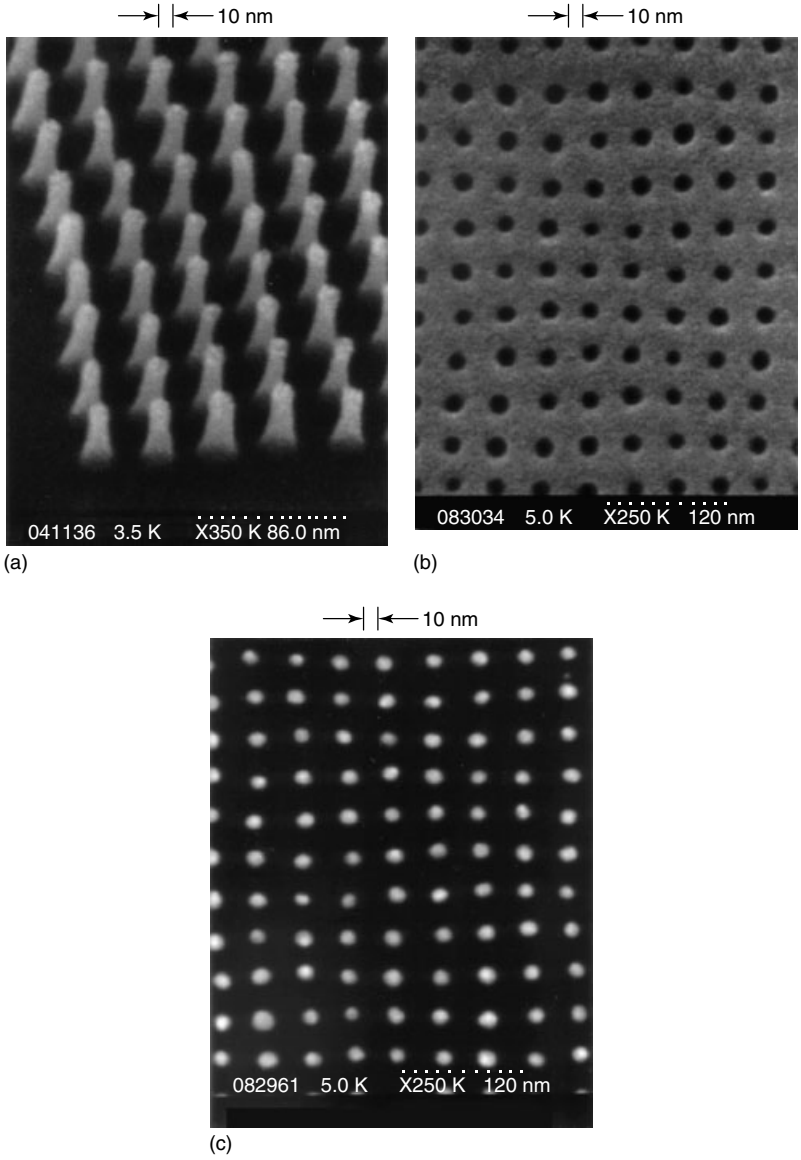

Figure 3. SEM micrographs of a dot array of 10 nm diameter and 40-nm period and hence 400G dots/in.^{2} by nanoimprint lithography and lift-off of metals. (a) A SiO_2 mold with 10-nm minimum diameter pillars with a 40-nm period which are 60 nm tall, after being used 12 times; (b) a top view of 60-nm-deep holes imprinted into PMMA which have a 10-nm minimum diameter and a period of 40 nm; and (c) a top view of 10-nm minimum diameter metal dots with a period of 40 nm, formed by imprinting into PMMA and a lift-off process. (Reproduced from Chou *et al*., 1997, with permission from IEEE. © 1997.)

2.2.5 High throughput and low cost

NIL is high throughput and low cost, because of its ability to do full-wafer-scale parallel fabrication without complicated and expensive optics systems and laser sources (Wu *et al*., 1998; Yu, Wu, Chen and Chou, 2001; Li, *et al*., 2003; Yu *et al*., 2003).

2.2.6 Self-cleaning

It has been observed, since the day one of nanoimprint development, that NIL is a self-cleaning process (Wu *et al*., 1998). That is, the dust on the mold is being cleaned every time the mold imprints a wafer. The mold release agent on the mold makes dust weakly bound to the mold, while the resist acts like a glue to the dust, taking it away from the mold. A 'dirty' mold will become completely clean after just a few imprints.

2.3 Various forms of nanoimprint

The principle of NIL can be implemented through a variety of approaches. *Thermal NIL* uses a resist material that

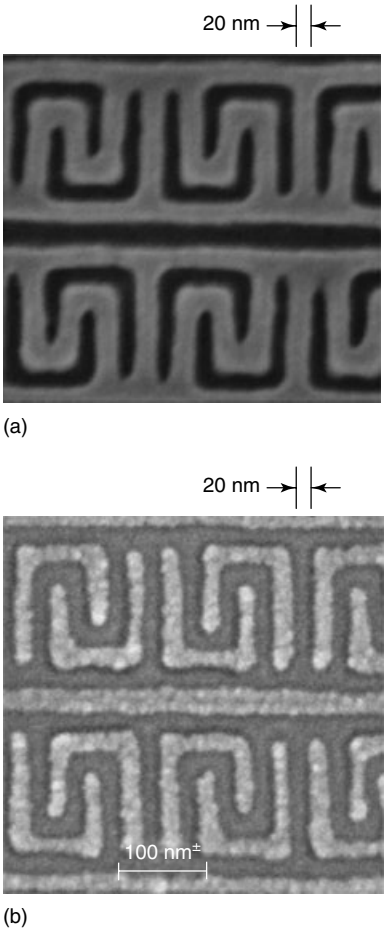

Figure 4. SEM image of 20-nm half-pitch resist pattern for SRAM metal contacts fabricated by NIL. (Reproduced from Austin *et al*., 2004, with permission from the American Physical Society. © 2004.)

is either thermoplastic or thermal curable (Chou, Krauss and Renstrom, 1995; Chou, 1998b, 2001). During a thermal imprint process, a thermoplastic material starts as a solid film, becomes a viscous liquid when its temperature is raised higher, than its glass transition temperature (T_g), and returns to a solid when its temperature is brought below T_g. This solid-liquid-solid process is reversible and repeatable for an infinite number of cycles. The imprint is performed when a resist is in its liquid state. A thermoset material is originally in a liquid form and becomes solid (cured) when heated to a certain temperature for a certain duration. This curing process is irreversible. *Photo* (*or UV*)*-NIL* uses a photocurable material as resist (Haisma, Verheijen, vandenHeuvel and vandenBerg, 1996; Chou, 2001). Like a thermal-curable material, a photo-curable material is initially in liquid form, but it is cured photochemically by photons (light) rather than heat, which is also an irreversible process. *Step-and-flash imprint lithograph* (*SFIL*) is a photo-NIL process in which drops of a resist liquid are dispensed and imprinted on one single die area at a time. This process is repeated as the imprint mold is 'stepped' from die to die across the wafer, repeating the resist drop and imprint cycle (Bailey *et al*., 2000).

Thermal NIL needs to heat an imprinted area to a temperature higher than the initial temperature for a period of time (can be as short as 100 ns). In principle, UV-NIL is carried out without a change in temperature; in reality photocuring in UV-NIL can cause local heating. Each of the methods has its own advantages and shortcomings and has its own well-suited applications. In the following text, we will discuss some commonly shared properties and then compare the pros and cons.

2.4 Pros and cons of different forms of NIL

The biggest advantage of thermal NIL is that it allows both mold and substrate to be opaque, necessary in some processes and materials systems. Thermoplastic NIL also allows the use many off-the-shelf materials as imprinting resists, making it easier to implement when sophisticated NIL resists are unavailable. In fact, thermoplastic NIL was the first form of nanoimprint to be introduced. The major disadvantage of thermal NIL is that the temperature change during the imprint process makes precision alignment difficult. The temperature change also can make demolding (i.e., the separation of the mold from the substrate) difficult because of the stress created by the differences in the thermal expansion coefficients of the mold, substrate, and resist. An opaque mold and substrate can make the viewing of alignment marks during overlay more difficult, although thermal NIL can use transparent molds or opaque mold with transparent alignment windows.

In comparison, the primary advantage of Photocurable NIL is the constant temperature during imprint, provided that heating from the photoradiation can be removed. A photocurable NIL needs either a transparent mold or substrate.

In all curable NIL (either photo or thermal), where a resist is initially in liquid form, the viscosity of the resist can be formulated in order of that of wafer (a few centipoise). A low viscosity allows excellent flow of the resist during the imprint, which is important when the pattern density varies significantly over the areas or the patterns are large and deep (e.g., 50 μm diameter features and 60 μm deep). In contrast, a thermoplastic resist often has a high viscosity ($\sim$300–3000 cP) even at temperatures significantly higher the resist's glass transition temperature. The reasons are that a curable NIL resist consists of oligomers and monomers, while a thermoplastic NIL resist is composed of long-chain polymers (high temperature allows them to slip by each other to deform). In some curable resist materials, additives (e.g., small particles) can drastically increase the viscosity.

Another form of nanoimprint, which may be in some sense more powerful, is to directly imprint a functional

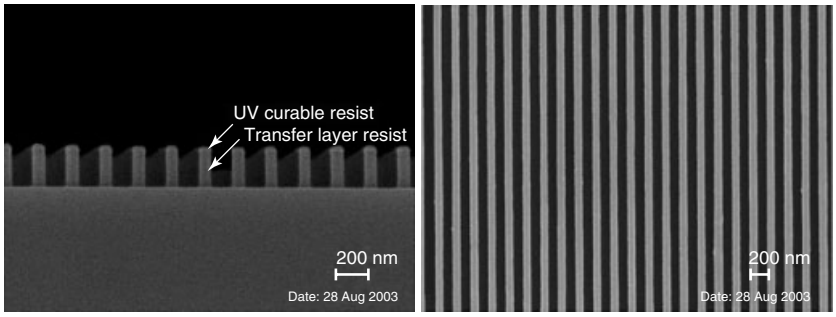

Figure 5. Resist profile by nanoimprint showing smooth vertical sidewalls. (Reproduced from Li *et al*., 2003, with permission from IOP Publishing Ltd. © 2003.)

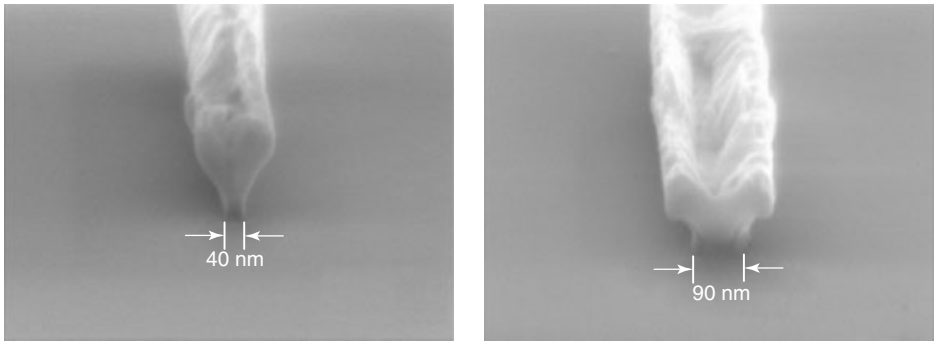

Figure 6. 3D patterning. SEM micrograph of two T gates of 40-nm and 90-nm footprint, respectively, fabricated by a single NIL and a lift-off of metal (Li, Chen and Chou, 2001; Li, Chen, Zhang and Chou, 2003).

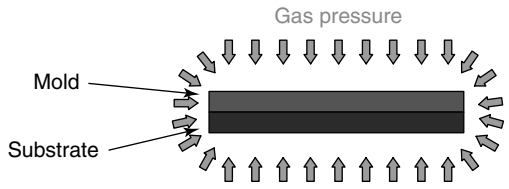

Figure 7. Schematic of Air Cushion Press™ (ACP) nanoimprint principle (Gao *et al*., 2006; Chou, 2002).

material. The functional material could be a curable material or thermoplastic, or hard solid materials such as silicon, which melt into liquid during an imprinting (Li, Chen and Chou, 2001; Chou, 2002). Sub-10-nm resolution is also demonstrated in the direct imprint (Chou, 2002).

3 KEY ISSUES IN NIL

Regardless of which particular form of nanoimprint is being used, the following issues are fundamentally important for achieving good nanoimprinting: mold, material system, pressing methods, imprint pressure uniformity, resist materials dispensing methods, vacuum, demolding, and alignment. These issues (except alignment) are discussed in the following text.

3.1 NIL masks (molds), materials, and fabrication

In principle, any material harder than the imprint resist can serve as a mold material. However, in practice, a mold material is determined by the requirements of the imprint method used, the mold material strength and durability, the ease of mold fabrication, and users' own understanding and preference of mold materials. In many cases, multiple layers of materials are used to gain more advantages.

3.1.1 Transparency to UV

In UV-NIL, unless the substrate is transparent, the mold material(s) must be transparent to UV light in order to cure the imprint resist. In thermal NIL, either transparent or opaque mold materials can be used, and a transparent mold or substrate are needed when direct heating of the resist by a lamp or laser is used. A laser can be used for ultrafast thermal imprinting (<200 ns) without much heating of the mold (Xia *et al*., 2003). A common transparent mold material used in NIL molds is fused quartz.

3.1.2 Material strength and durability

The second issue to consider in mold materials is the material's strength and durability in withstanding repeated

imprints. Quartz is hard and brittle, so to improve a quartz mold for imprinting, a thin layer of SiNx (Li, Chen, Zhang and Chou, 2003), which is known to be stronger and more durable, can be added to the surface of the mold. Other choices for good mold surfaces are SiC and diamond-like carbon films.

3.1.3 Mold fabrication

The most common way to fabricate a mold is to select a mold substrate deposited with a suitable mold surface, then use EBL to pattern a resist, followed by etching to transfer the patterns in the resist into the mold (Chou *et al*., 1997; Krauss and Chou, 1997). Sometimes a lift-off process is used to pattern a harder etching mask material (e.g., chromium) after EBL exposure to improve the etching mask durability.

Currently the feature size of EBL patterns are limited to $\sim$10 nm, the pitch to $\sim$35 nm, and the area for such size and pitch to several square millimeters. The size and pitch limitations are due to electron scattering in the EBL resist and mold substrate. The area limitation is due to the resist exposure dose requirement, which makes the writing of several square millimeters take several hours, and the writing of a much larger area becomes impractical technically and economically. Furthermore, most EBL tools write one $\sim$100 by 100 μm^2 field at a time and stitch different fields together. The stitching has an error in 10–30-nm range, depending on EBL tool. Therefore, the patterns in different fields might not be coherent. To solve the stitching error, a new approach is to move the stage while keep the electron beam fixed during writing, however, this introduces other errors.

To overcome the drawback of EBL in large-area periodic patterns, IL (Flanders, Shaver and Smith, 1978) has been extensively used to make NIL molds (Wu *et al*., 1998; Yu, Wu, Chen and Chou, 2001; Yu and Chou, 2004). The advantage of IL is the capability of fabricating periodic patterns (e.g., gratings and grids) over a large area (e.g., 6 in. wafer) in a parallel fashion, giving high throughput at relatively low cost. The pitch of the grating by IL is given by $\lambda/(2\sin\theta)$. When the interference half angle of the beams, θ, is near 90°, the pitch is near half of the wavelength, λ. However, at such small pitch, the process latitude is very small and the yield is very low, increasing the cost significantly. A high-yield and low-cost approach is to use IL to make a master mold and use NIL to make replicas (daughter molds) and manufacturing. For examples, the uniform gratings in Figure 6 were imprinted using a mold fabricated by IL.

3.1.4 Mold fabrication compatibility

Another important consideration in mold fabrication is to use materials that can be fabricated rather easily. For example, metal is more ductile than hard dielectric materials, but it is very hard to etch metal into patterns of high aspect ratio and vertical sidewalls. In practice, good molds with high-aspect-ratio intrusions and vertical sidewalls are made in dielectric materials such as SiO_2 or fused quartz.

3.1.5 Mold release agents

To separate a mold from an imprinted structure without damage and without much force, mold release agents are needed. The mold release agent can be applied by directly coating the mold or by mixing it into the imprint resist. Often both methods are used in parallel, since good commercial NIL resist always have certain mold release agents. All the mold release agents have fluorine side chains, which significantly reduce the intermolecular interaction between the mold and the imprinted resist. Mold release agents that are directly coated on the mold often have a linking group at the end of the molecular chain which attaches the molecule to the mold, as in a self-assembled monolayer. The mold release agents are often perfluorinated surfactants.

3.2 NIL materials (resists)

The materials used for NIL can be classified into three groups according to their processing properties: thermoplastic, thermocurable, and photocurable. In general, each class of material consists of five components: (i) backbone materials (e.g., polymers, oligomers, monomers); (ii) solvents (including monomers); (iii) plasticizers (for thermoplastic) and initiators (curable); (iv) mold release agents; (v) others (compatibilizers, lubricants, and other stabilizers). Clearly, there are tremendous possibilities in formulating these NIL resists, and commercial resist companies guard their formulas like the 'CocaCola recipe'. An enormous amount of research and testing is required to find a good resist formulation.

3.2.1 Thermoplastic materials (resists)

Thermoplastic materials have a characteristic glass transition temperature, T_g, below which the material is solid and above it, a viscous liquid. The backbone materials in thermoplastic materials are a mixture of linear chain polymers, with no cross-links between different chains. As the temperature is raised above the glass transition temperature, the polymer chains can slip by each other to flow, becoming a viscous liquid. The viscosity lowers as the temperature becomes higher, but does not become as low as that of a monomer-based resist. Many solvents can be used, including certain

monomers. Plasticizers are used to lower the T_g of the resist. The mold release agents in thermoplastic materials, similar to those used in curable materials, are often polysiloxane and perfluorinated surfactants.

3.2.2 Photo (UV)-curable and thermocurable materials

These materials are initially in a liquid state and become solid when irradiated with the proper dose of photons (so-called photocuring) or when heated to a certain temperature for a certain duration (so-called thermocuring). The backbones of curable materials consist of a mixture of monomers and oligomers. Again the solvents include monomers. Examples of UV and other radiation initiators for cross-linking are benzophenone, 2-hydroxy-2-methyl-1-phenyl-1-propanone, and 1-hydroxydhexyl phenyl ketone. Examples of thermal initiators are benzyl peroxide (BPO) and azobisisobutyronitrile (AIBN). Sometimes, additional additives are used to facilitate the lubrication between the mold and the substrate, so that the mold can be moved during alignment without excessive friction.

3.3 Imprinting pressure and uniformity

To deform a resist on a substrate by a mold, the mold and the substrate must be pressed toward each other to have contact. To achieve good imprint uniformity, the pressure should be not only uniform everywhere across the imprint area but also sufficiently high to create the necessary deformation in either the mold, the substrate, or both to make their surfaces conform. The latter requirement is due to the fact that a mold or a substrate initially might not be flat, but warped. In order to make the mold and substrate conform, the imprint pressure in many applications is much higher than that needed for pressing a mold into a resist.

There are several methods used for pressing the mold into the substrate, including solid parallel-plate press (SPP), Air Cushion Press^{TM} (ACP), one-sided air cushion press, and electrical force-assisted NIL (EFAN) (Liang *et al*., 2005). Clearly, for high yield – key to viable manufacturing – ACP is the key.

3.3.1 Solid parallel-plate press (SPP)

One commonly used pressing method for imprint is SPP (Figure 8). SPP, which is simple to construct, is often used in home-built NIL tools as well as many commercial NIL machines. However, SPP suffers several drawbacks: (i) Any roughness, nonflatness, or dust on the surface of a press plate (Figure 8b) and/or the backside surface of the wafer and the

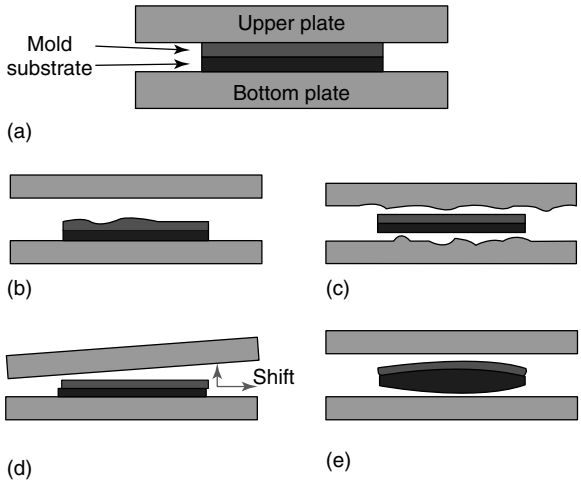

Figure 8. Schematics of solid parallel-plate press (SPP) nanoimprint process and drawbacks: (a) ideal SPP; (b) nonparallelism between plates; (c) imperfect plate surfaces; (d) uneven mold/substrate backside; and (e) curved sample surfaces (Gao *et al*., 2006).

mold (Figure 8c) will cause nonuniform pressure distribution that results in imprint nonuniformity and local high pressure points that will damage the mold and/or substrate. (ii) The two press plates may not be perfectly parallel with each other (Figure 8d), and hence assert shear and/or torque forces, causing relative shift and/or rotation between the mold and substrate. (iii) If either the mold and/or substrate has curved surfaces, SPP could not bring all mold and substrate surfaces into contact, leaving a large fraction of the wafer area unimprinted (Figure 8e). (iv) In SPP, because a constant force is applied between the two plates to provide the desired pressure, if the mold and substrate surfaces are in contact only at a point or in a small area, an enormous pressure can be generated at this contact point or area, causing damages to the mold or substrate. (v) The parallel plates of SPP have large thermal mass, making isothermal NIL take long processing time.

3.3.2 Air cushion press (ACP)

To improve pressure uniformity, yield, and thermal imprint speed, and to overcome the aforementioned issues, a new technique, air cushion press (ACP) (Figure 9) has been developed (Chou, 2002; Gao *et al*., 2006). ACP utilizes a gas (or fluid) to press the mold and substrate against each other in a chamber. ACP has a number of advantages over SPP: (i) ACP uses conformable gas (or fluid) layers to eliminate any direct contacts between the solid plates and samples (mold and/or substrate), hence removes any effects related to the imperfection of the solid plates. (ii) Because the pressurized gas is conformal to the mold and substrate,

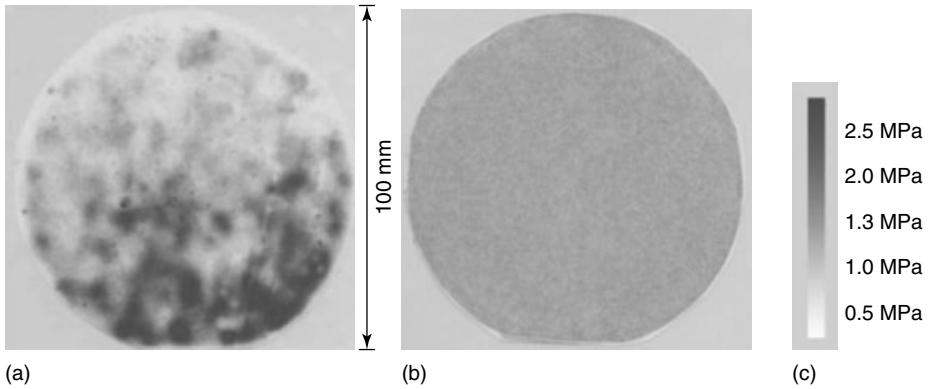

Figure 9. (a) and (b) Pressure distribution across a 100-mm-diameter imprint field when a 1.38 MPa nominal pressure is applied using SPP and ACP, respectively. (c) Pressure versus color intensity calibration chart (Gao *et al*., 2006).

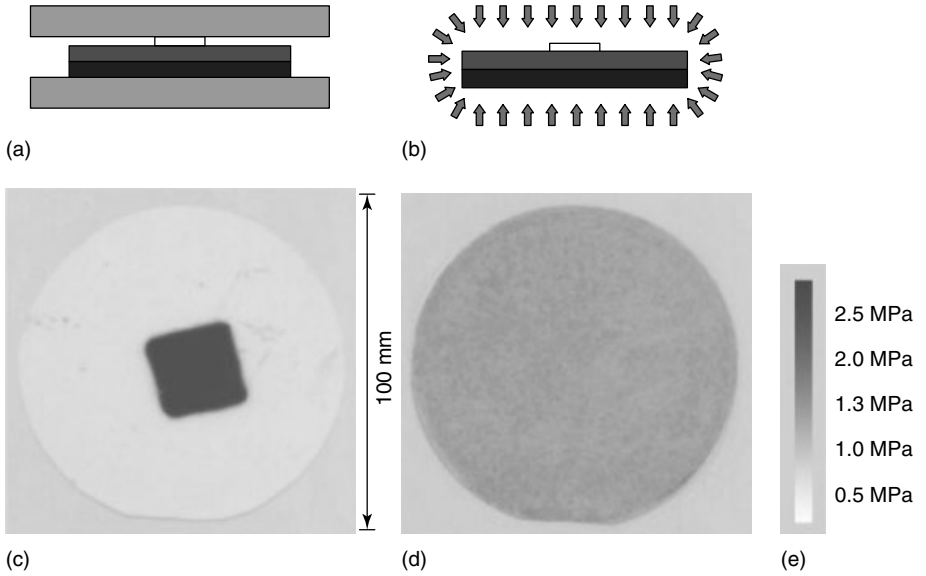

Figure 10. (a) and (b) Schematics of experimental setups for studying the effects of backside dust/topology in SPP and ACP, respectively. (c) and (d) Pressure distributions across a 100-mm-diameter imprint field with 0.1-mm-high paper piece inserted, when a 1.38 MPa nominal pressure is applied using SPP and ACP, respectively. (e) Pressure versus color intensity calibration chart (Gao *et al*., 2006).

regardless of their backside shapes or any dust particles on the backside, the pressure will be uniform everywhere over the entire imprint area. (iii) Isotropically applied gas pressure eliminates lateral shift or rotation between the mold and substrate, reducing damage to the mold and prolonging mold lifetime. (iv) Because a pressurized gas has much smaller thermal mass than a solid plate, it speeds up the heating and cooling of samples and shortens the thermal imprint time by orders of magnitude (e.g., ACP can complete the nanoimprint process in seconds rather than in tens of minutes as in SPP).

The pressure distribution of SPP and ACP over an imprint field of 100 mm diameter was investigated by placing a pressure-sensitive film between a mold and a substrate, both of which are 100-mm-diameter prime silicon wafers of 0.5 mm thickness, with flat featureless front surfaces and unpolished backsides (Gao *et al*., 2006). The pressure-sensitive film consists of a layer of microencapsulated color-forming material and a layer of color-developing material. A pressure applied to the film will break the microcapsules. As a result, the local density of broken microcapsules is determined by the local pressure, and different broken microcapsule densities will, in turn, yield different color intensities on the film. A higher pressure causes a higher density of broken microcapsules, and thus a stronger color. SPP is carried out with a solid parallel-plate nanoimprinter, and ACP is performed using a Nanonex NX-1000 nanoimprinter.

Figure 10 shows the imprint pressure distributions over 100 mm-diameter mold and wafer in both SPP and ACP, measured by pressure-sensitive films when a nominal

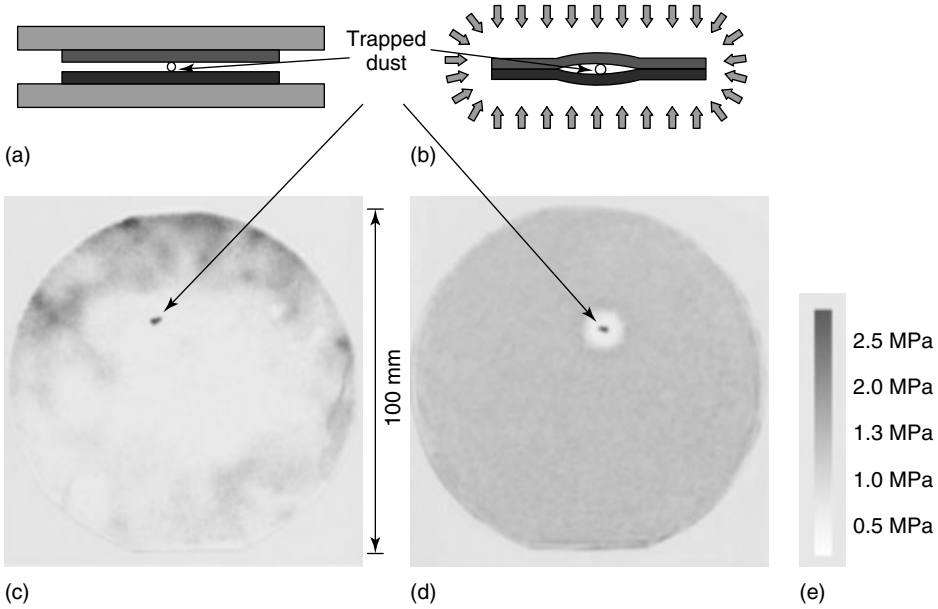

Figure 11. (a) and (b) Schematics of experimental setups for studying the effects of trapped dust in SPP and ACP, respectively. (c) and (d) Pressure distributions across a 100-mm-diameter imprint field with 0.1-mm-high paper dust trapped, when a 1.38 MPa nominal pressure is applied using SPP and ACP, respectively. (e) Pressure versus color intensity calibration chart (Gao *et al*., 2006).

pressure of 1.38 MPa (or 200 psi) is applied. In the imprint by SPP (Figure 10a), the pressure is generated by applying a constant force of 1.13×10^4 N, which corresponds to a nominal average pressure of 1.38 MPa (200 psi) over the 100-mm-diameter mold and substrate. However, the pressure-sensitive film measurement shows that the actual pressure in SPP varies tremendously across the wafers, from below 0.5 MPa (areas of lightest color) to above 2.5 MPa (areas of strongest color), showing a pressure variation over a factor of 5 across the 100-mm-diameter nanoimprint field. Furthermore, Figure 10(a) shows that the lower half of the film has a much higher average pressure than the upper half. This is due to the nonparallelism between the two pressing plates. The film also exhibits isolated local domains with strong colors with light colors over their surroundings, caused by the surface imperfections of pressing plates and wafers.

In contrast, in ACP, when the same nominal pressure of 1.38 MPa (200 psi) is supplied by a gas, the pressure-sensitive film exhibits a uniform color across the entire nanoimprint field (Figure 10b), indicating a uniform imprint pressure and complete immunity to the problems suffered by SPP.

To further study the effects of dust or topology on the backside of the mold or substrate on imprint pressure uniformity, we place a piece of 'large artificial dust', made of paper of $2.6 \times 2.6\,\text{cm}^2$ area and 0.1 mm thickness, on the backside of the mold. We then apply a 1.38 MPa nominal pressure using both SPP and ACP methods (Figure 11a and b). Clearly, in SPP (Figure 11c) under the backside-dust conditions, all the applied force is concentrated under the 'large artificial dust', with a pressure reading well above 2.5 MPa (the upper bound of the measurement range of the pressure-sensitive film), while the area surrounding the dust area has almost no imprint pressure (the pressure is below the 0.5 MPa lower bound of the pressure-sensitive film). In contrast, in ACP (Figure 11d) under the same condition, the 'large artificial dust' has no effects on the imprint pressure, which remains uniform across the entire 100-mm-diameter imprint field.

To study the effects of the dust trapped between the mold and the substrate on pressure distribution in both SPP and ACP, we place a 'small artificial dust particle', which is a triangular shaped paper piece with an in-plane dimension of 1 mm and height of 0.1 mm, between the mold and the pressure-sensitive film. Again, the same nominal pressure of 1.38 MPa is applied in the two different pressing methods (Figure 12a and b). In Figure 12(c), in SPP under this trapped-dust condition, the dust has a global effect on the pressure distribution across the entire 100-mm-diameter imprint field, causing distinct variations in pressure and contact. More than 60% of the imprint field around the dust site shows poor contact and a pressure below 0.5 MPa, while an extremely high pressure is applied on the dust site. On the other hand, in ACP under the same condition, the effects of dust on the pressure distribution are localized to a small area (Figure 12d). The affected area is limited to a circle 6 mm in radius, because of local wafer deformation. The pressure distribution outside this circle remains uniform.

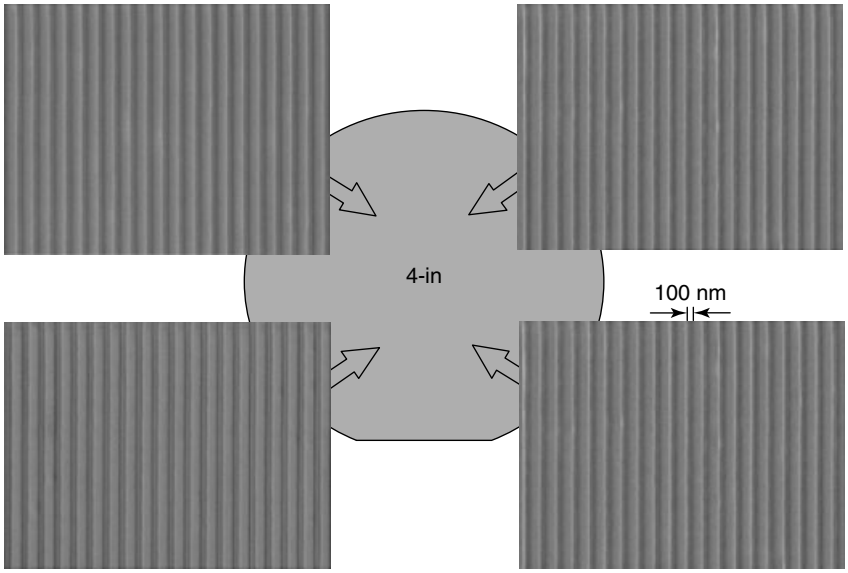

Figure 12. SEM image of uniform grating over an entire 4-in. wafer imprinted by ACP (Gao *et al*., 2006).

3.4 NIL resist dispensing methods and vacuum environment

There are two major ways of dispensing a resist on a substrate: a thin-film deposition by spinning (or spray) or droplet dispensing. For thin-film deposition, during imprint the mold needs to displace the resist from the protrusions of the molds to the valley of the mold, and from areas of high pattern density to areas of low pattern density.

For droplet dispensing, during an imprint a mold presses the droplet into a thin film while filling up the trenches in the mold. The flow of the resist liquid can remove some of the air between the mold and the substrate. If the volume of the remaining air is not too large, it can be completely absorbed into the resist (Liang, Tan, Fu and Chou, 2006). In this way, the imprint can be done without a vacuum chamber without air bubbles formed in the resist. However, as our study has indicated (Liang, Tan, Fu and Chou, 2006), complete absorption of air bubbles takes such a long time that for practical imprint conditions air bubbles exist and the throughput will be also very low. Hence, a vacuum environment is in general needed for both types of resist dispensing methods.

3.5 Mold separation

To have a good separation of the mold from an imprinted pattern, in addition to having good mold release agents, which reduce the bonding of the mold and the resist, one needs to reduce the stresses between the mold and the resist. Furthermore, the demolding can be much easier (i.e., demolding force is much smaller) if the demolding starts from a small area and propagates gradually into other areas.

4 CONTROL OF MAGNETIC NANOSTRUCTURE PROPERTY BY PATTERNING

In the demagnetized state, a thin-film or a bulk magnetic material is magnetically divided into many small regions called *domains*. Each magnetic domain, typically containing a number of polycrystalline grains, is spontaneously magnetized, but with a random magnetization direction, so that the material as whole has no net magnetization and the total energy (which is the sum of magnetostatic energy, exchange energy, crystalline anisotropy energy, magnetorestriction energy, and Zeeman energy) is minimized (Cullity, 1972). Since there are many local energy minima, each of them corresponding to a number of magnetic configurations, the exact magnetic domain configuration in a thin film or bulk material is rather unpredictable.

However, the situation is drastically different when a magnetic material is patterned into a size smaller than or comparable to a single-domain size (Cullity, 1972). In this case, each PMN contains only one or a few magnetic domains; the size, shape, and orientation of each domain become *well defined and predetermined by the pattern shape and materials*. The unique features of a PMN are attributed to new interplay among different energy terms, in particular between the magnetostatic energy and exchange energy, for minimizing the total free energy.

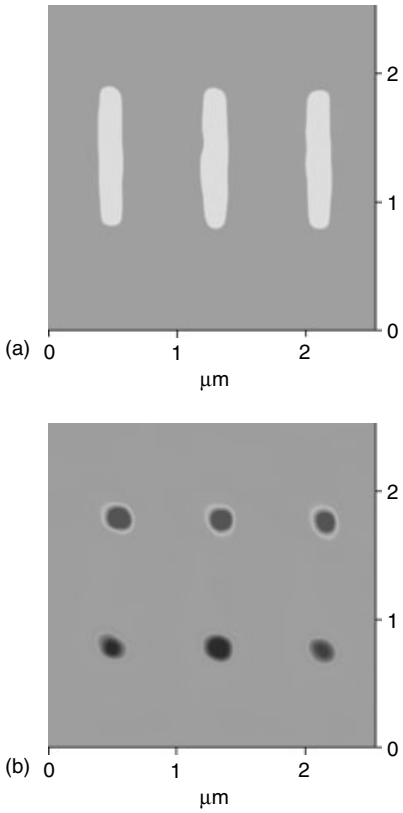

Figure 13. The atomic force microscopy (a) and magnetic force microscopy (b) of three single-domain nickel bars that are 100 nm wide, 1 μm long, and 35 nm thick. The grey dots represents attractive force between tip and sample and the black dots repulsive force.

4.1 Spontaneous formation of single domain

The first important property of a PMN is that a single domain can be formed spontaneously without an applied magnetic field, meaning the structure becomes a magnetic dipole on its own as soon as it is fabricated. This is a consequence of interplay between the magnetostatic energy and exchange energy. When the width of a patterned magnetic structure is less than the domain-wall size, the formation of multiple domains within that width requires very high energy, as it is required that the magnetization rotates to the opposite direction over a shorter distance than in the normal case. On the other hand, if all magnetic domains are aligned in the same direction (i.e., ferromagnetism) forming a single domain, there will be net magnetic poles, giving magnetostatic energy. The only way to reduce the magnetostatic energy is to break the material into multiple domains to cancel out magnetic poles. But, as indicated earlier, because of the small width of the patterned structure, formation of such multiple domains requires much higher energy. Hence the energy minimum is a single magnetic domain.

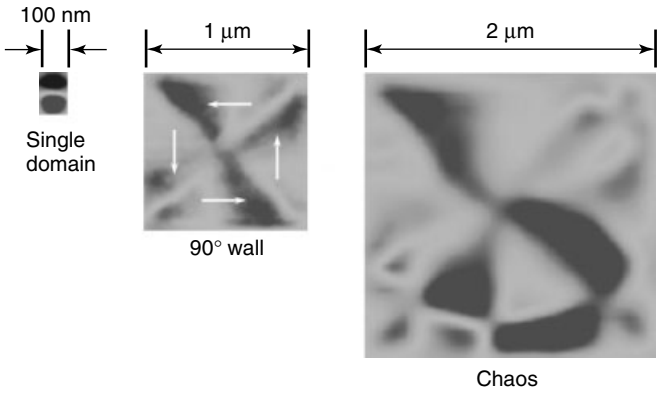

Figure 14. MFM images of magnetic domains in cobalt squares (35 nm thick) as their sizes are reduced from 2 μm to 100 nm. The gray represents attractive force between tip and sample and the black repulsive force. As the size reduces, the multidomain structure becomes single domain as shown on the left (100 nm bar) that has a south pole and a north pole.

Consider a patterned magnetic cube of a size of L. The magnetostatic energy for a single-domain cube of a side of L is proportional to its volume (L^3), and the domain-wall energy is proportional to area (L^2). Hence, the total energy of a multiple-domain cube (sum of the magnetostatic and exchange energy) is approximately proportional to $L^{2.5}$ (Cullity, 1972). Therefore, there is a critical size below which the single-domain state has the lowest energy, but above which the multiple-domain state has the lowest energy. This critical size, determined by the magnetization and exchange constant of a material, is about 100–300 nm in a thin film.

4.2 Control of domain configurations using shape

The magnetization direction in a single domain and in a multidomain PMN can be controlled well by the shape of the structure. In a single domain, the stable magnetization is always along the long axis of the structure, to reduce the demagnetization field and lower the total energy. Figure 13 shows both atomic force microscopy (AFM) and MFM images of Ni bars which are 1 μm long, 100 nm wide, and 35 nm thick. The MFM image exhibits only two opposite magnetic poles at the two ends of the bars – characteristic of a single magnetic domain.

In a multidomain PMN, the magnetization at the edges tends to be parallel to the edge to avoid free magnetic poles for lowering the magnetostatic energy (the surface pole density is equal to the discontinuity of the magnetization normal to the surface). Figure 14 shows MFM images of magnetic domains in cobalt squares (35 nm thick) as their sizes are reduced from 2 to 100 μm. At 2 μm, the domain configuration is chaos. At 1 μm, it has four well-defined closure domains.

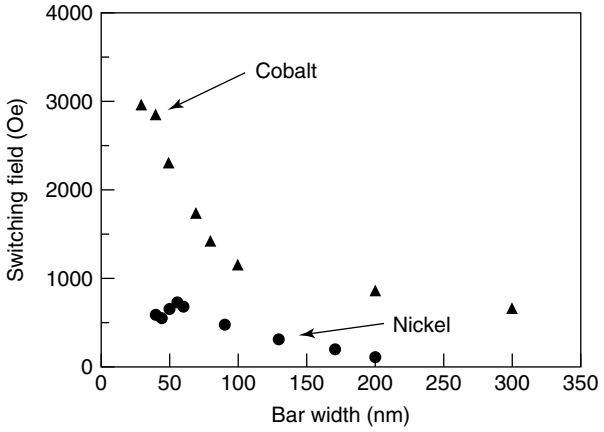

Figure 15. Experimental switching field of isolated Ni and Co bars versus bar width. The bar width was measured using SEM. The bars are 1 μm long and 35 nm thick.

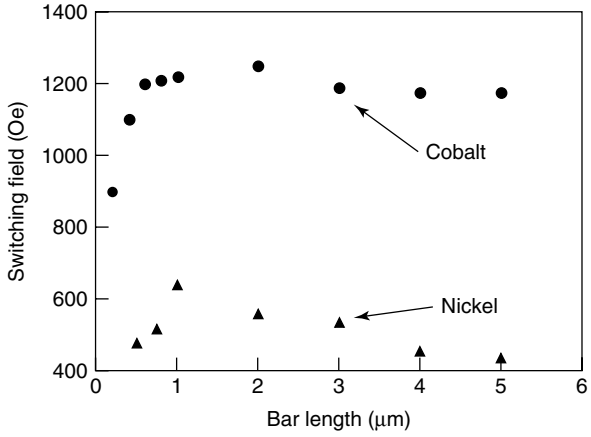

Figure 16. Experimental switching field of isolated Ni and Co bars versus bar length. The bars are 100 nm wide and 35 nm thick.

4.3 Effects of bar width on magnetic domain switching field

Another key property of PMN is that the coercivity – the magnetic field needed to switch the magnetization direction – can be controlled by changing the structure's size and shape anisotropy. This is again a consequence of the interplay between the magnetostatic energy and the exchange energy.

To investigate this property in PMN, we fabricated nickel and cobalt bars of 35 nm thickness and different width and shape anisotropies using EBL, thermal evaporation, and lift-off. Thermal evaporation, instead of sputtering, eliminates crystalline anisotropy in the materials that could mask the shape anisotropy effect. Vibrating sample magnetometer measurements show that the unpatterned thin-film samples fabricated with the bar samples have a coercivity of 50 Oe for Co and 25 Oe for Ni, and have near-zero crystalline anisotropy.

The switching fields of isolated Co and Ni bars with a 1 μm length and 35 nm thickness as a function of the bar width were measured by using an external field and MFM and are shown in Figure 15 (Chou, Wei, Krauss and Fischer, 1994; Kong and Chou, 1996). For Co bars, the switching field increases monotonically with reduction of the bar width, reaching 3000 Oe at 30 nm width. The switching field is 60 times higher that of the unpatterned thin film. For the Ni bars, the switching field first increases with decreasing bar width, reaches a maximum switching field of 740 Oe (30 times higher than that of the thin film) at a bar width of 55 nm, then decreases slightly with further reduction of the bar width. The decrease is likely due to the fact that thermal energy becomes comparable to magnetization switching energy (Cullity, 1972). The Ni bar-width dependence is similar to that of Permalloy bars studied elsewhere (Smyth *et al.*, 1991). Furthermore, the MFM shows that for 1-μm bar length and 35 nm thickness, the critical width to form single domains is 300 nm for Co and 150 nm for Ni, respectively.

4.4 Effects of bar length on magnetic domain switching field

The effects of bar length on Co and Ni bars with a fixed bar width and thickness (100 and 35 nm, respectively) were also investigated. Unlike the bar-width dependence, the switching field of the single-domain bars was found to first increase with the bar length, then decrease after reaching a peak (Figure 16). The peak switching field and the corresponding bar length are 640 Oe and 1 μm for Ni, and 1250 Oe and 2 μm for Co, respectively. Furthermore, the switching field of Ni bars decreases with the increase of the bar width much faster than that in Co bars. The length dependence observed here does not fit the Stoner–Wohlfarth model, which predicts a *coherent* switching, meaning the switching field of a bar should monotonically increase with the shape anisotropy (therefore with the bar length) (Stoner and Wohlfarth, 1948).

The nonmonotonic length dependence suggests that different bar lengths have different switching mechanisms. For short bars (<1 μm) in which the bar length is comparable to domain-wall size, all spins would rotate more or less in a same fashion, leading to a quasicoherent switching. For long bars in which the bar length is significantly longer than the domain wall, the exchange force is not strong enough to keep all spins rotating in the same direction. In this case, the domain reversal occurs at the ends of the bar where demagnetization field is the strongest, and the reversal propagates through the entire bar, leading to an incoherent switching. As Co has a much stronger exchange force than that in Ni,

Co bars should have a longer crossover length than that in Ni, consistent with experimental results.

Although the switching speed of PMN has not yet been measured, it is expected that coherent switching has time scale of 1 ns and incoherent switching should be the bar length divided by the domain propagation speed.

5 QUANTIZED MAGNETIC DISKS (PATTERNED MEDIA) AND NANOIMPRINT MANUFACTURING

QMDs (patterned media), based on fundamentally different principles of data storage than current methods, have many distinguished advantages to achieve high storage density (Chou, Wei, Krauss and Fischer, 1994). This approach is regarded as one of two recent candidates to replace the current method (vertical media) of magnetic data storage (the other one is thermal-assisted storage). QMDs are intended for a data storage density of 300 Gbit in.$^{-2}$ or higher. However, the issue of manufacturability has been raised since the conception of QMD. In fact, the drive to manufacture QMD was one of the reasons to develop NIL (Chou, Krauss and Renstrom, 1995; Chou, Krauss and Kong, 1996). Today, it has been widely accepted that NIL is the best technology for the manufacture of QMD. Here we discuss the advantages of QMD and NIL manufacturing.

The ultimate storage density of a magnetic disk is related to the magnetic recording media, write head, read head, positioning and servo, and signal processing. Although they are intricately related, the most important of all is the recording media, which dictates the requirements of all others. A good media will relax the requirements. The following discussion focuses on a new medium.

5.1 Factors limiting storage density in conventional magnetic media

The present magnetic media is a continuous, thin, magnetic film supported by a rigid, nonmagnetic disk. The film consists of many tiny, polycrystalline grains with a rather broad distribution in size and shape and a random distribution of crystallization direction. The magnetization orientation of these grains is also random until a magnetic field created by a write head aligns the magnetization of a tiny patch of these grains. The data is represented by the magnetic moment, area, size, and location of this patch.

Four factors limit the storage density capacity in a thin-film media. The first is the 'superparamagnetic limit'. Because of the statistical nature in the size and easy-magnetization axis

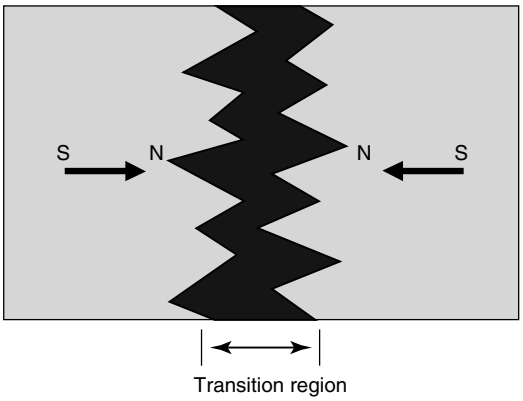

Figure 17. Schematic of transition region between two bits for the conventional magnetic recording media.

of polycrystalline grains in a magnetic media, the intrinsic signal-to-noise ratio (SNR) of a magnetic signal roughly equals the number of grains in each bit. To reduce bit size while keeping the same SNR requires a reduction of the grain size. But, when each grain becomes too small and weakly coupled to its neighboring grains by the exchange force, the energy to switch the magnetization of a grain can become less than the thermal energy. Should that happen, thermal energy will wipe out the written data. For an isolated sphere, the superparamagnetic limit will be reached when the diameter is below 9 nm. To maintain an acceptable SNR, namely 1000 grains, the superparamagnetic limit for longitudinal recording gives a maximum data density of $\sim$150 Gbit in.$^{-2}$, insufficient to meet our needs.

The second limiting factor is the transition width between two neighboring bits of opposite magnetization. The nature of ferromagnetism, that is, the positive exchange integral, (which occurs only in a few elements such as Co, Ni, and Fe) favors the case of all magnetization aligned in the same direction. When one bit is placed next to another bit with an opposite magnetization, a transition region, called a *domain wall*, must be formed to keep exchange energy reasonable. Certainly the spacing between two bits cannot be smaller than the domain-wall size. Furthermore, to lower the total energy, the interplay between the magnetostatic force and the exchange force makes the transition region between two bits have a random zig-zag shape (so-called Neel spikes), as shown in Figure 17. The zig-zag pattern not only increases the effective width of a transition region, but also creates noise in the reading signal (since the reading head, having a straight-line shape, averages the positive and negative magnetic charges in the zig-zags). The effective transition region for today's conventional medium is 10–30 nm.

The third factor is the 'side tracks'. The magnetic field distribution of a write head is not perfectly uniform and the magnetic media has quasilinear response to the magnetic

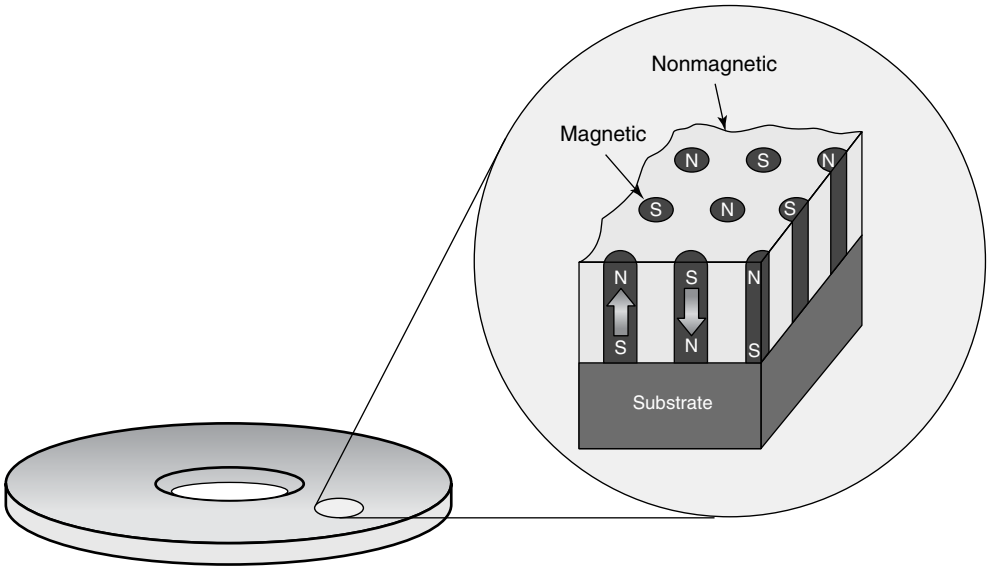

Figure 18. Schematic of a quantum magnetic disk which consists of patterned, single-domain, magnetic structures uniformly embedded in a nonmagnetic disk.

field; the fringing field at the sides of a tip pole in a write head writes two parallel tracks of useless noise next to the data (called *sidetracks*). The hysteresis loop of a conventional magnetic media has a finite slope. Since the sidetracks could erase previously written data, extra space between two data tracks must be reserved for the sidetracks, limiting data packing density.

The fourth factor is the 'tracking'. Conventional magnetic media does not automatically provide a tracking signal since a physical boundary does not always exist between two neighboring bits (it exists only between two bits of opposite magnetization). Hence, writing or reading a bit is a 'blind' process. The head first locates special codes (tacking marks) written at the beginning part of each data section, then calculates the movement between the head and disk to get the nominal bit location. Therefore, the accuracy of the disk rotation and servo will impose another limit on data density. Furthermore, much real estate area and time are wasted in writing the tracking marks, which currently use about 20% of the total disk area and are expected to be more for higher data density where tracking is more crucial.

5.2 Concept of quantized magnetic disks

All of the limitations listed in the last section can be removed or alleviated if the continuous, thin-film media is abandoned and replaced by a new media, QMDs. QMDs have prefabricated, discrete, single-domain magnetic elements uniformly embedded in a nonmagnetic disk (Figure 18) (Chou, Wei, Krauss and Fischer, 1994). Each single-domain element has a uniform, well-defined shape, a prespecified location, and most importantly, a discrete magnetization that is magnetized without an applied magnetic field and has only two possible stable states: equal in magnitude but opposite in direction. The spontaneous formation of a single domain is due to the small size and the shape anisotropy (as discussed in Section 4.2). Each magnetization direction of a single-domain element represents a single bit of binary information. A QMD of a vertical magnetization uses pillars and a longitudinal magnetization uses bars. The magnetic field needed to switch the magnetization direction can be controlled by engineering the element's size and shape anisotropy (discussed in Section 4) (Chou, Wei, Krauss and Fischer, 1994).

QMDs have many advantages over conventional disks, such as spontaneous self-quantization of each bit's magnetization and a quantized writing process to reduce requirements of write head and position accuracy; small, smooth, isolated transition region allowing high data packing density and near-zero transition noise; built-in tracking, which makes for precision tracking and positioning of write/read heads and overcomes the superparamagnetic limit.

The idea of storing one bit of information in a tiny single-domain magnetic particle could have been conceived when single-domain structure was observed (Kittel, Galt and Campbell, 1950) or when single-domain particles were used in making recording tapes. The theory of coherent switching of a single-domain particle has been discussed in the celebrated paper by Stoner and Wohlfarth (note that switching the patterned single-domain element is usually incoherent). Many other behaviors of single-domain structures were

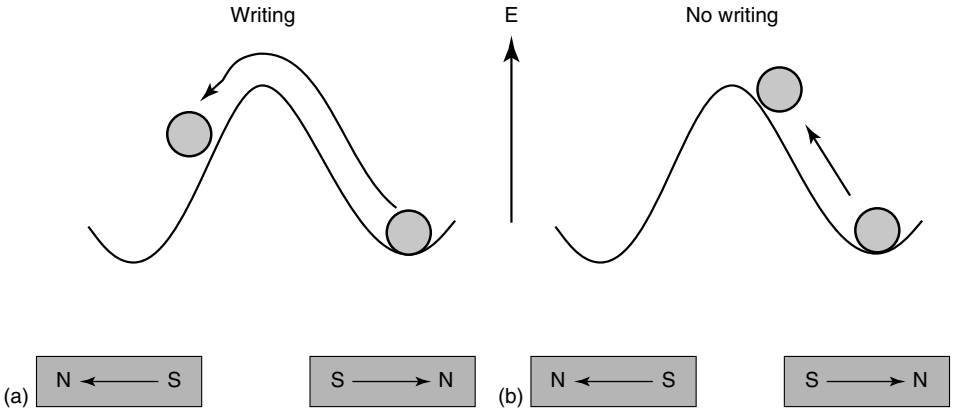

Figure 19. Schematic illustrating that the quantized switching process of a single-domain structure is like moving a ball over a hill. (a) The ball, once over a hill, will roll to another state by itself; and (b) once the drive force is removed, the ball, before reaching the top of the hill, will roll back to the original state.

theoretically investigated by Aharoni (1986, 1990, 1991). However, a number of unique properties of single-domain elements as a storage element in QMDs were not explored until 1992 when two advanced technologies became available. One is the nanofabrication technology that enables us to precisely engineer the shape, size, location, orientation, and composition of a single-domain magnetic particle (Chou, Wei and Fischer, 1994; Chou, Wei, Krauss and Fischer, 1994; Fischer, Wei and Chou, 1993). The other is magnetic force microscopy that allows us to image and manipulate the magnetic properties of each individual single-domain particle. Recently, the advent of imprint lithography has brightened the commercial potential of QMDs.

5.2.1 Overcome superparamagnetic limits

In a conventional disk, one bit is represented by approximately 1000 weakly coupled polycrystalline grains. In a QMD, each bit is stored in one discrete element that is isolated from other elements, but inside the element polycrystalline grains are strongly coupled by the exchange force behaving more like a large single magnetic grain. Therefore, the volume and switching energy for the QMD elements are much greater than that of a single grain in a conventional disk, allowing significant reduction of bit size without reaching the superparamagnetic limit. Finally, for a given material volume, a larger shape anisotropy in the QMD elements can lead to a larger switching field, allowing further increase in data density (Cullity, 1972).

5.2.2 Discrete magnetization and quantized writing process

Since each bit in a QMD spontaneously magnetizes itself without an applied field and has only two opposite stable magnetization states, the write process in a QMD is quantized with three unique features. First, in contrast to conventional disks where the magnetic moments, area, and location of each bit must be precisely defined by a write head, in QMDs these are already defined when the disk is fabricated. Thus, the writing process in a QMD is a simple flip of the magnetic direction of a discrete singledomain bit. A write head either writes the entire bit perfectly or it does not write the bit at all. Second, each bit in a QMD can be written perfectly with a write field smaller than the size of the bit (Suriono and Chou, 1996a,b). Third, a minor overlap of the writing field with a nearby bit perturbs the magnetic moment of the bit. Once the overlapping writing field is removed, the bit returns to its original magnetic state. Clearly, the quantized writing in a QMD greatly relaxes the requirements on write head design and position accuracy, and significantly avoids the writing errors and sidetracks (all of these advantages lead to a higher data storage density).

The quantized writing process in a QMD is analogous to moving a ball between two valleys separated by a mountain (each valley represents one of the two energy minima) (Figure 19). Once the ball is pushed from one valley over the top of the mountain, it will roll down to the other valley on its own (perfect writing). But, if the ball is released before being pushed over the top, it will go back its original valley (no writing).

The quantized writing property of QMDs has been demonstrated experimentally using a magnetic force microscope tip (MFM) (Chou, 1997; Kong, Shi, Krauss and Chou, 1997; Kong, Zhuang and Chou, 1997; Kong *et al.*, 1998) and theoretically using micromagnetic simulation (Suriono and Chou, 1996a,b). The magnetic field of an MFM tip splits, at the tip point, into two halves: one pointing in one direction and another in opposite direction. As the tip moves from one end of a single-domain bar to the other end, the overlap between

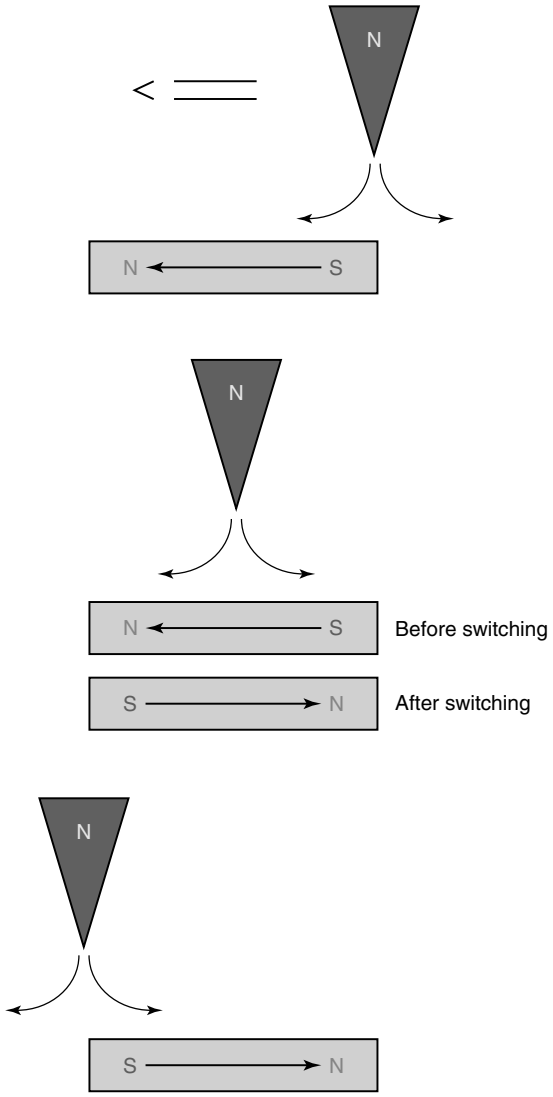

Figure 20. Schematic of the QMD writing process using an MFM tip.

the bar and the field in one moving direction decreases and the overlap between the bar and in the opposite direction increases (Figure 20). If the bar can be switched with a magnetic field of a size smaller than that of the bar, then the magnetization direction of the single-domain bar will be changed before the MFM tip reaches the other end of the bar. In this case, the magnetic images of the bar will display two poles with identical magnetizations. This is because for a single-domain bar, no magnetic charge can be seen anywhere except at the two ends of the bar. At the end where scanning starts, the MFM sees one pole before the bar is switched and at the finishing end, the MFM sees another pole after being switched. Since the magnetization switches much faster than the MFM scanning speed, the MFM image cannot tell the occurrence of the switch until the tip reaches the other end.

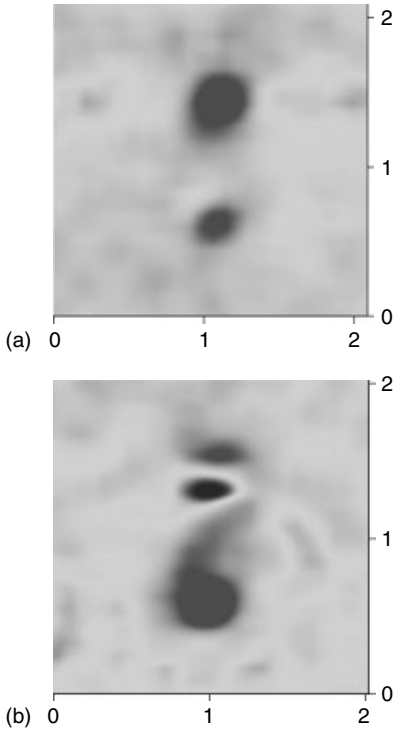

Figure 21. (a) MFM image in which the poles at the two ends of the bar have identical polarization, confirming that the magnetization of the single-domain bar is switched by the MFM tip having a field of a size smaller than that of the bar. (b) MFM image in which the switching occurs when an MFM tip is near the end of the scan, the MFM image has a perfect north pole at the starting end of the bar, but, at the finishing end, only half of a south pole (before the switching) and half of a north pole (after the switching). (Reproduced from Chou *et al*., 1997, with permission from IEEE. © 1997.)

The magnetic MFM image of a single-domain bar in Figure 21(a) shows that the poles at the two ends of the bar indeed have the identical polarization, confirming that the magnetization of the single-domain bar is switched by the MFM tip with a field size smaller than that of the bar.

When using a weaker switching field, a larger overlap between the switching field and the bar is required. Figure 21(b) shows that switching occurs when an MFM tip is near the end of a scan, therefore the MFM image has a perfect north pole at the starting end of the bar, but, at the finishing end it has only half of a south pole (before the switching) and half of a north pole (after the switching). The weaker switching field can be achieved by either reducing the amount of magnetic material on an MFM tip during the tip fabrication or increasing the space between the MFM tip and the bar.

Writing of a 20 Gbit in.$^{-2}$ longitudinal QMD using a MFM tip is shown in Figure 22(a) and (b) (Kong, Zhuang and Chou, 1997). Clearly, the writing process is quantized and

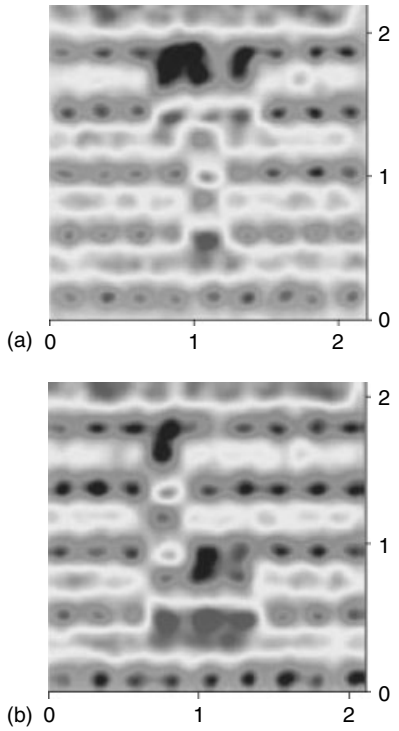

Figure 22. Writing of a 20-Gbit in.$^{-2}$ longitudinal QMD using a MFM tip. The light gray represents attractive force between the tip and the sample and the dark gray repulsive force (Kong *et al*., 1998).

perfect. The write experiments were done using two MFM tips: the writing tip with a large magnetic moment and the reading tip with very small magnetic moment (so that it would not flip the magnetization of the bar). Before writing, the magnetization of all the bars was aligned in the same direction. During the writing process, the writing tip was lifted up and then was moved to one end of a bar. The end of the bar initially had a magnetic pole opposite to that of the MFM writing tip. The actual writing process was simply to lower the writing tip, making the tip closer to the bar. It was found that when the separation between the tip and bar was less than 5 nm, the writing tip could perfectly flip the magnetization direction of the bar *without* flipping the neighboring bars, at a data density of 20 Gbit in.$^{-2}$ for longitudinal QMDs (equivalent to 80 Gbit in.$^{-2}$ for vertical QMDs). After writing one bar, the MFM writing tip was raised up and moved to write other bars. This process was continued until all the desired bars were written. After writing, the reading tip was used to nondestructively image the written pattern.

It should be pointed out that the MFM tip does not have a well-defined field distribution, and that the MFM does not have any feedback to track the exact tip movement leading to a poor positioning accuracy of MFM (about 1% of the scanning window size). Also, the switching field of

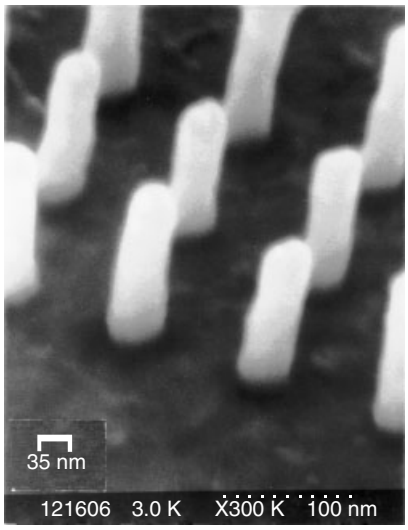

Figure 23. SEM image of Ni pillar array of 35 nm diameter, 120 nm height, and 100 nm spacing. The density is 65 Gbit in.$^{-2}$ and the aspect ratio is 3.4 (Chou, Wei, Krauss and Fischer, 1994).

each bar is not exactly the same due to the fabrication imperfection and magnetostatic interaction between the bars. However, even under these circumstances, the 7.5 Gbit in.$^{-2}$ longitudinal QMD can be written perfectly. This clearly demonstrates the advantage of quantized writing process of QMD in ultrahigh density recording. In other words, this property of the QMDs relaxes the requirement of the writing field and can increase tolerance toward the errors due to head positioning and fringing field.

5.2.3 Cut-off interbit exchange force, small and smooth transition, less noise

Since the exchange force has an effective range less than 10 nm, a thin layer of nonmagnetic material between two neighboring bits in a QMD can completely cut off the exchange force between the bits, leading to a 'transition region' that is much smaller than the transition region in a thin-film magnetic media where each grain is more or less coupled by exchange force. Furthermore, the nonmagnetic materials, patterned by a nanofabrication technique, can have very smooth and straight edges (Figure 23), giving a much quieter reading signal than that in a thin-film media where the transition regions have a zig-zag shape.

5.2.4 Built-in tracking marks, precise tracking

In a QMD, since each discrete bit is a single domain isolated by nonmagnetic materials and is spontaneously magnetized, a variation in the magnetic field always exists between neighboring bits regardless of the polarization of each bit

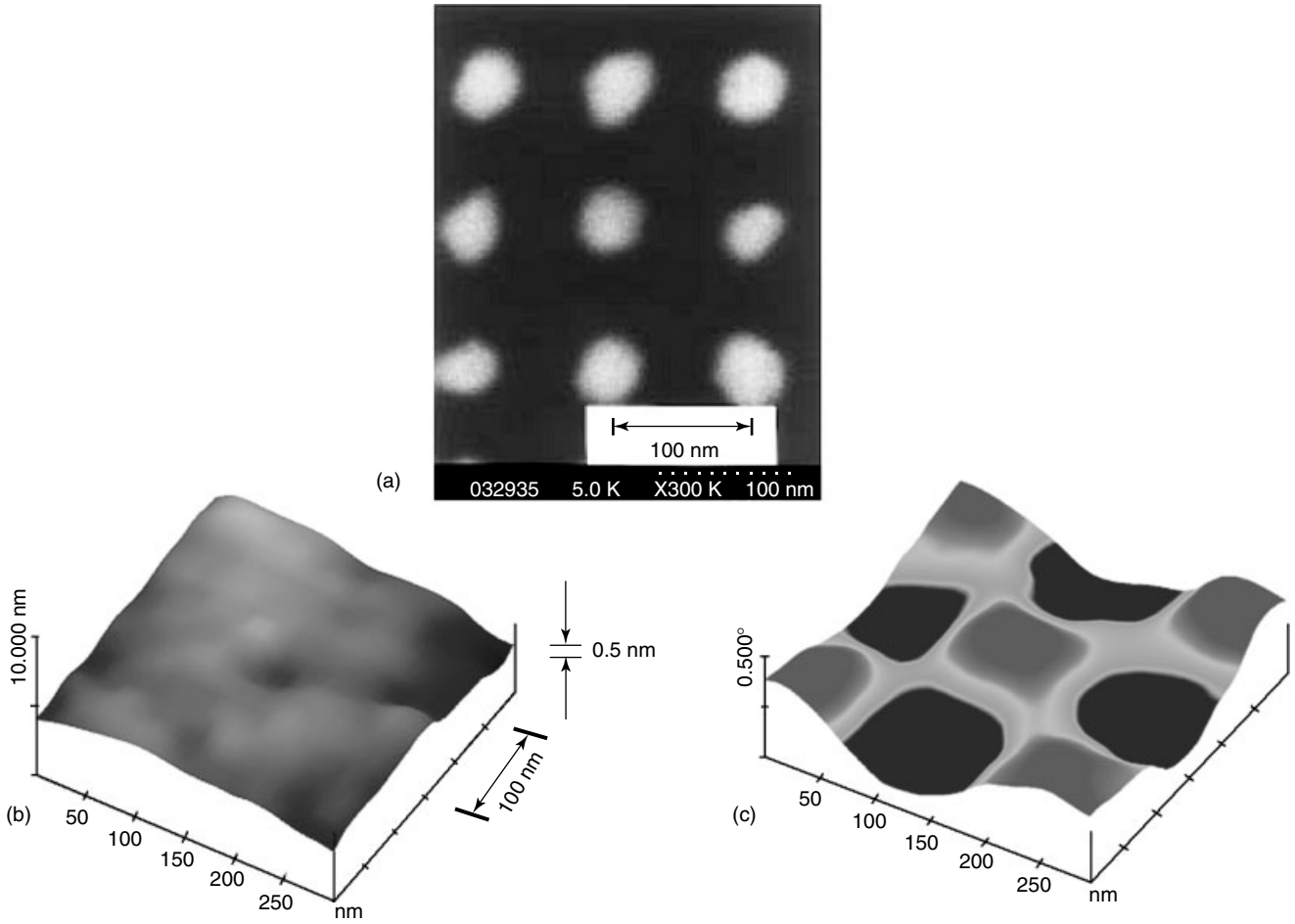

Figure 24. (a) SEM image, (b) tapping mode atomic force microscopy image (TMAFM) image, and (c) MFM image of 3×3 bits of a QMD with 65-Gbit in.$^{-2}$ density. The grey patches represents attractive force between tip and sample and the black patches repulsive force in (c). Each bit consists of a nickel pillar uniformly embedded in 200-nm SiO_2 with 50 nm diameter (aspect ratio of 4) and 100 nm period. The TMAFM image shows a very smooth surface with a roughness of 0.5-nm rms. The MFM image shows an alternating pattern of magnetization directions for each bit (Chou, Wei, Krauss and Fischer, 1994).

(Figure 24). This provides a signal for tracking each bit. In other words, in a QMD drive, discrete single-domain elements automatically provide a 'landmark'; each bit can be physically 'seen' prior to writing or reading, allowing much more precise tracking than the 'blind tracking' in a conventional disk and therefore higher data density.

5.3 Nanoimprint manufacturing of quantized magnetic disks (bit-patterned media)

A variety of structures for the implementation of QMDs have been proposed (Chou, 1997; Chou, Shi and Kong, 1997). These structures can be classified as flat surface and grooved surface. The grooved surface QMDs have grooves for the isolation of different bits unfilled on the surface. But the grooved surface QMDs have a dimension much smaller than a flying head and hence will not affect the flying. In either structure, nanoimprint will be most likely used to pattern a dielectric material and the magnetic layers will be subsequently deposited into the patterned dielectrics, since etching of metal nanostructures is well known to be very difficult. After the magnetic material deposition, for flat surface QMDs, a polishing method will be used to planarize the surface, while for grooved surface QMDs, no polishing is needed, since the groove is sufficient to break a film into discrete single magnetic domains (Chou, Shi and Kong, 1997; Chou, 1998a; Chou, 1999).

In patterning a dielectric structure for QMDs, there are again two choices: indirect or direct patterning. In indirect patterning, first nanoimprint is used to pattern a resist layer and then the resist layer is transferred into a dielectric material underneath. For direct patterning, a nanoimprint technique can directly pattern a curable dielectric material.

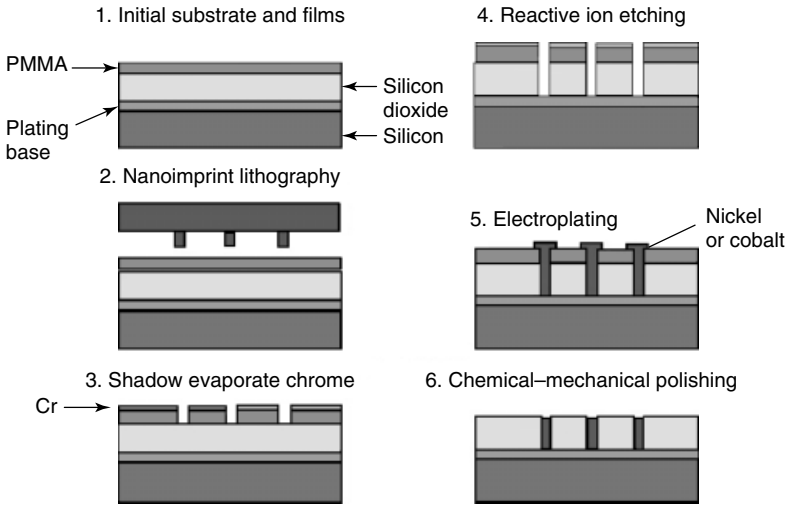

Figure 25. Schematic of the QMD fabrication process. (Reproduced from Wu *et al*., 1998, with permission from the American Institute of Physics. © 1998.)

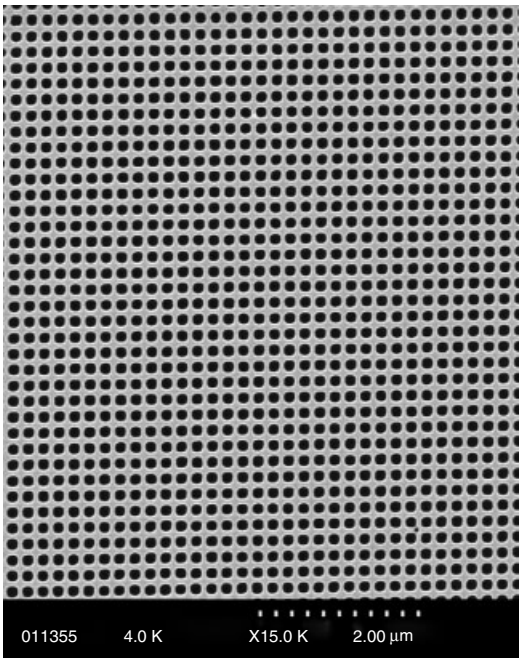

Figure 26. SEM picture of a 190-nm-period square via array on PMMA fabricated by single NIL using a pillar daughter mold. (Reproduced from Wu *et al*., 1998, with permission from the American Institute of Physics. © 1998.)

As an example, Figure 25 shows a QMD fabrication process (Wu *et al*., 1998). First, a thin metal plating base was deposited on a silicon wafer, then a SiO_2 film, followed by a 200-nm-thick NIL resist film (e.g., polymethylmethacrylate, PMMA). The SiO_2 layer is the nonmagnetic layer; its thickness determines the final height of the nickel pillars. The PMMA serves as the NIL resist. Second, pillar NIL mold was used to pattern a via array in the PMMA film using NIL. Then O_2 RIE was used in the NIL for pattern transfer, which anisotropically etched the via array into the entire PMMA thickness. Third, a 20-nm Cr layer was evaporated at a glancing angle on the top of the PMMA to provide an additional mask for etching the SiO_2. Fourth, CHF3 RIE etched the via array into the SiO_2 and stopped at the plating base. The etching had a pressure of 2 mTorr, a power of 150 W, and a CHF3 gas flow of 15 sccm. During the final several seconds of the etching, O_2 was added into the plasma to remove the passivating layer produced in the etching process on the bottom and sidewall of the SiO_2 vias, which can affect the uniformity of the subsequent electroplating. Fifth, nickel was electroplated through the holes. Finally, chemical–mechanical polishing (CMP) was used to remove the excess nickel from the top of the SiO_2 layer to achieve a smooth surface.

Figure 26 shows a 190-nm-period hole array patterned in PMMA using NIL by a daughter QMD mold. Figure 27(a), the electroplating is uniform. To examine the sidewall of the nickel pillars, SiO_2 was removed (Figure 27b). The nickel sidewall seems to conform to the SiO_2 template and no voids were found. For a uniform area of $4 \times 4\,cm^2$ and a density of $18\,Gbit\,in.^{-2}$, the total number of bits of a QMD is 45 Gbit. To make a smooth top surface, extra nickel above the SiO_2 surface was polished away using CMP. After CMP, the QMD's nonflat top surface became nearly flat. An AFM image indicates that the roughness is about 4 nm (Figure 28b). The roughness can be reduced by using an improved CMP process.

Longitudinal QMDs with densities up to $30\,Gbit\,in.^{-2}$ using NIL. The fabrication involves NIL in a 140-nm-thick PMMA layer on a silicon substrate and a lift-off of 1.5-nm Cr and 32-nm Co films evaporated thermally. As shown in

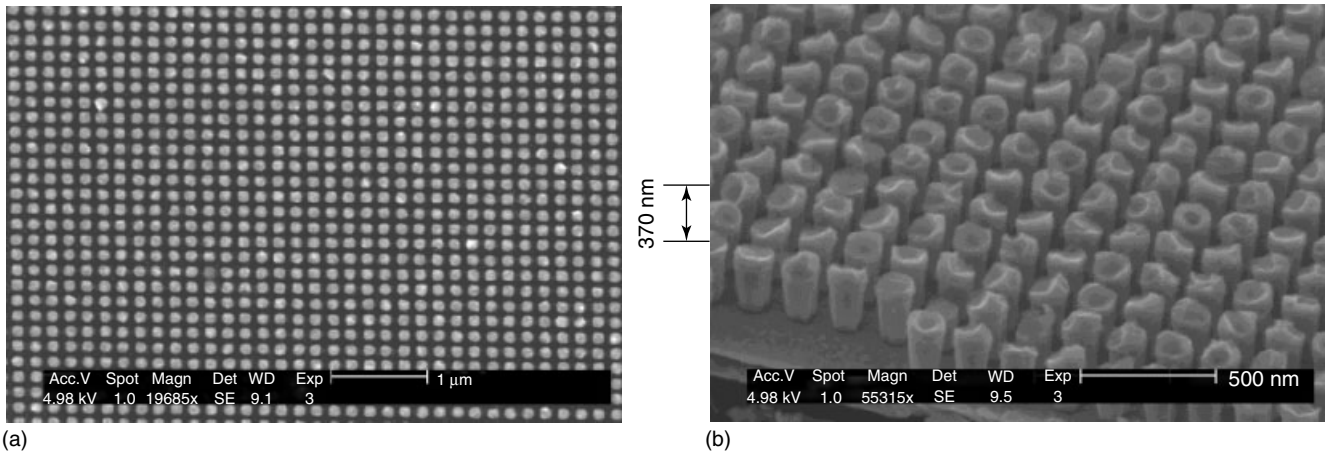

Figure 27. SEM pictures of an 18 Gbit in.$^{-2}$ large area perpendicular QMD fabricated using NIL. Each bit is an electroplated pillar. (a) Top view. (b) The SiO_2 was stripped off in order for the Ni pillars to be seen more clearly.

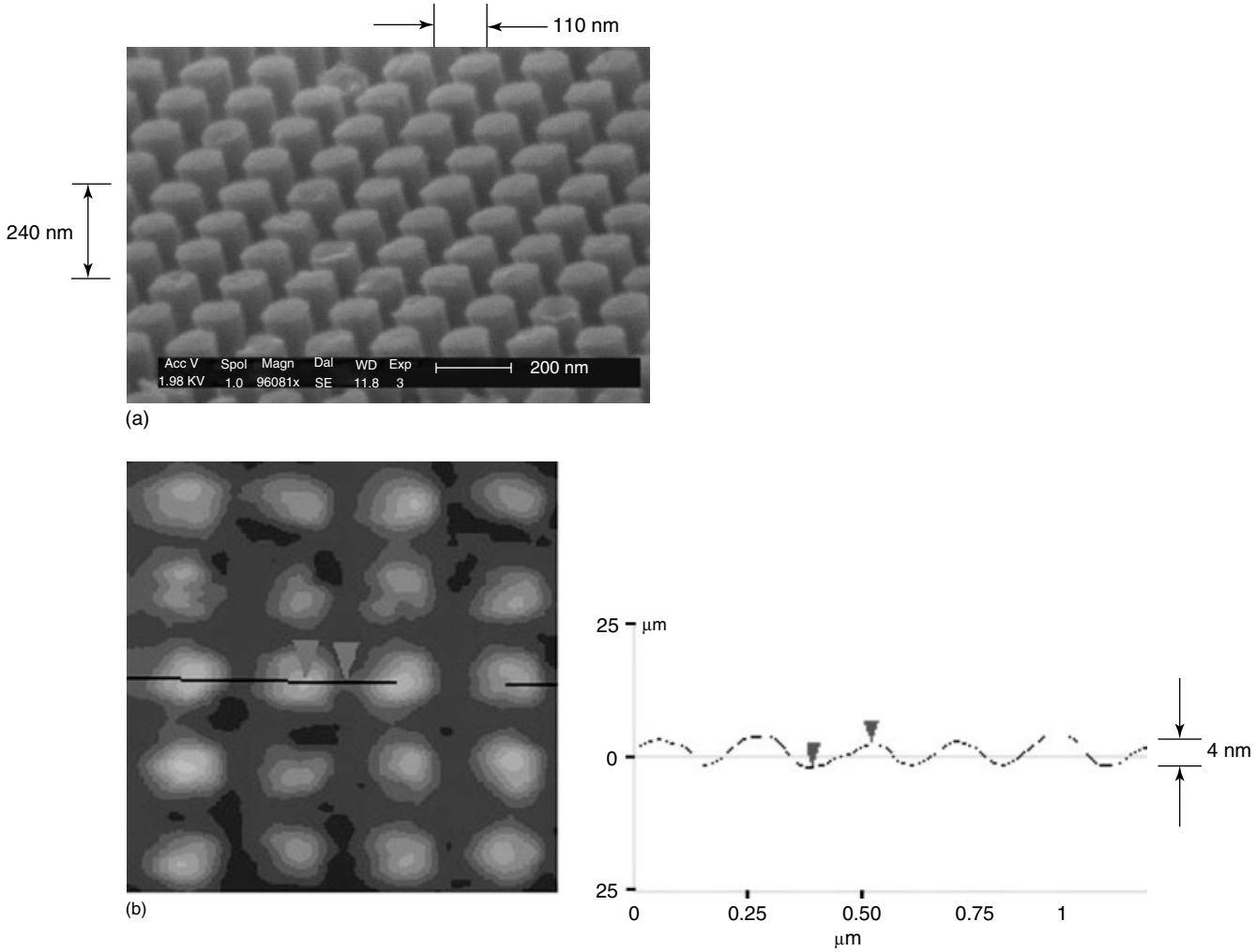

Figure 28. (a) SEM picture of an 18 Gbit in.$^{-2}$ large area perpendicular QMD fabricated using NIL. Each bit is an electroplated pillar. The SiO_2 was stripped off in order for the Ni pillars to be seen more clearly. (b) AFM image of the 18 Gbit in.$^{-2}$ large area perpendicular QMD. The image shows a surface roughness of 4 nm. (Reproduced from Wu *et al*., 1998, with permission from the American Institute of Physics. © 1998.)

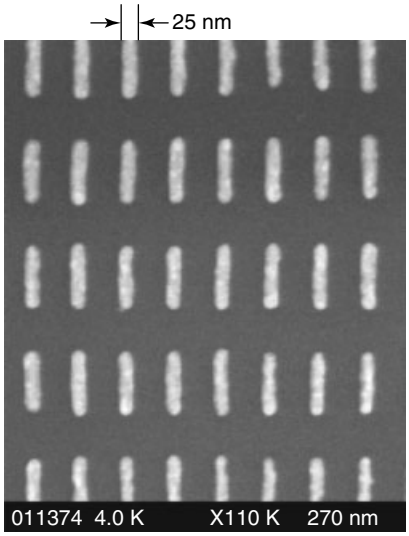

Figure 29. SEM picture of a 30 Gbit in.$^{-2}$ large area longitudinal QMD fabricated using NIL.

Figure 29, each bit is a bar 25 nm wide, 140 nm long, and 75 nm apart. MFM observations indicated that all the Co bars in the QMDs were single domains. Each bar clearly shows two opposite magnetic poles: one dark pole representing the attractive tip–bar interaction and one bright pole representing the repulsive interaction (Figures 13 and 22).

Clearly, the QMDs' density in the examples provided earlier are limited by our mold-making ability. In fact, the use of NIL to make 400G dots/in.^{2} of metal dots (Figure 3c) has been in demonstrated in 1996.

5.4 Future development of QMDs

From the discussions in the preceding text, it becomes clear that the future of QMD hinges upon our ability to make the NIL molds that not only have sub-40-nm pitch dots over a large area (at least 0.5 in. in diameter) but are also in concentric form. The rest of the NIL process has been clearly demonstrated. A promising approach to fabricate the NIL molds of QMDs is a guided self-assembly.

6 SUMMARY

We believe that nanoimprint technology is an enabling platform manufacturing technology that will impact a broad spectrum of fields. Patterned magnetic structures offer great opportunities for revolutionary magnetic materials and devices in data storage, sensors, and actuators. Nanoimprint technology is essential to the manufacturing and thus commercialization of QMD (patterned media) and other pattern magnetic structures. To accelerate the process of reaching such potential, we need to solve one of the key technological challenges in nanoimprint manufacturing of pattern media, namely, the making of the nanoimprint molds. We believe the solution comes from the combination of several innovative nanopatterning technologies. The next 5 years will be a very exciting period in both nanoimprint technology and PMNs.

ACKNOWLEDGMENTS

I thank many of my former students and postdocs who have made contributions to the work presented here, in particular, Paul Fischer, Peter Klaus, Linshu Kong, Mike Austin, Wei Wu, Bo Cui, Hua Tan, Wei Zhang, and He Gao. I also thank Patrick Murphy and Michelle Ward for grammatical editing, Linshu Kong, and Xiao-gan Liang for preparing the figures. I acknowledge ONR (Larry Cooper) and DARPA (Jan Alexande, Gernot Pomrenke, Fabian W.R. Pease, Christie Marrian, and Dave Patterson) for their partial support to the work presented here.

REFERENCES

Abes, J.I., Cohen, R.E. and Ross, C.A. (2003). Block-copolymer-templated synthesis of iron, iron-cobalt, and cobalt-nickel alloy nanoparticles. *Materials Science and Engineering C-Biomimetic and Supramolecular Systems*, **23**, 641–650.

Aharoni, A. (1986). Perfect and imperfect particles. *IEEE Transactions on Magnetics*, **22**, 478–483.

Aharoni, A. (1990). Upper bound to a single-domain behavior of a ferromagnetic cylinder. *Journal of Applied Physics*, **68**, 2892–2900.

Aharoni, A. (1991). The concept of a single-domain particle. *IEEE Transactions on Magnetics*, **27**, 4775–4777.

Albrecht, M., Rettner, C.T., Best, M.E. and Terris, B.D. (2003). Magnetic coercivity patterns for magnetic recording on patterned media. *Applied Physics Letters*, **83**, 4363–4365.

Anderson, E.H., Horwitz, C.M. and Smith, H.I. (1983). Holographic lithography with thick photoresist. *Applied Physics Letters*, **43**, 874–875.

Asakawa, K., Hiraoka, T., Hieda, H., *et al*. (2002). Nano-patterning for patterned media using block-copolymer. *Journal of Photopolymer Science and Technology*, **15**, 465–470.

Austin, M.D., Ge, H.X., Wu, W., *et al*. (2004). Fabrication of 5 nm linewidth and 14 nm pitch features by nanoimprint lithography. *Applied Physics Letters*, **84**, 5299–5301.

Austin, M.D., Zhang, W., Ge, H.X., *et al*. (2005). 6 nm half-pitch lines and 0.04 mu m(2) static random access memory patterns by nanoimprint lithography. *Nanotechnology*, **16**, 1058–1061.

Bailey, T., Choi, B.J., Colburn, M., *et al*. (2000). Step and flash imprint lithography: template surface treatment and defect

analysis. *Journal of Vacuum Science and Technology B*, **18**, 3572–3577.

Castano, F.J., Nielsch, K., Ross, C.A., *et al*. (2004). Anisotropy and magnetotransport in ordered magnetic antidot arrays. *Applied Physics Letters*, **85**, 2872–2874.

Chappert, C., Bernas, H., Ferre, J., *et al*. (1998). Planar patterned magnetic media obtained by ion irradiation. *Science*, **280**, 1919–1922.

Chou, S.Y. (1997). Patterned magnetic nanostructures and quantized magnetic disks. *Proceedings of the IEEE*, **85**, 652–671.

Chou, S.Y. (1998a). *Method for Making Magnetic Storage Having Discrete Elements Quantized Magnetic Moments*. US 5,820,769.

Chou, S.Y. (1998b). *Nanoimprint Lithography*.US Patent 5,772,905.

Chou, S.Y. (1999). *Magnetic Storage Having Discrete Elements With Quantized Magnetic*. US Patent 5,956,216.

Chou, S.Y. (2001). *Release Surfaces, Particularly for use in Nanoimprint Lithography*. US Patent 6,309,580.

Chou, S.Y. (2002). *Fluid Pressure Imprint Lithography*. US Patent 6,482,742.

Chou, S.Y., Keimel, C. and Gu, J. (2002). Ultrafast and direct imprint of nanostructures in silicon. *Nature*, **417**, 835–837.

Chou, S.Y., Krauss, P.R. and Kong, L.S. (1996). Nanolithographically defined magnetic structures and quantum magnetic disk. *Journal of Applied Physics*, **79**, 6101–6106.

Chou, S.Y., Krauss, P.R. and Renstrom, P.J. (1995). Imprint of sub-25 nm vias and trenches in polymers. *Applied Physics Letters*, **67**, 3114–3116.

Chou, S.Y., Krauss, P.R. and Renstrom, P.J. (1996). Imprint lithography with 25-nanometer resolution. *Science*, **272**, 85–87.

Chou, S.Y., Krauss, P.R., Zhang, W., *et al*. (1997). Sub-10 nm imprint lithography and applications. *Journal of Vacuum Science and Technology B*, **15**, 2897–2904.

Chou, S.Y., Shi, R.C. and Kong, L.S. (1997). Effects of nanoscale trenches and mesas patterned in a substrate on domain structures of magnetic films and ion applications in magnetic disk tracking (abstract). *Journal of Applied Physics*, **81**, 4673–4673.

Chou, S.Y., Wei, M.S. and Fischer, P.B. (1994). An ultra-high-resolution single-domain magnetic force microscope tip fabricated using nanolithography. *IEEE Transactions on Magnetics*, **30**, 4485–4487.

Chou, S.Y., Wei, M., Krauss, P.R. and Fischer, P.B. (1994). Study of nanoscale magnetic-structures fabricated using electron-beam lithography and quantum magnetic disk. *Journal of Vacuum Science and Technology B*, **12**, 3695–3698.

Chou, S.Y., Wei, M.S., Krauss, P.R. and Fischer, P.B. (1994). Single-domain magnetic pillar array of 35-nm diameter and 65-Gbits/in(2) density for ultrahigh density quantum magnetic storage. *Journal of Applied Physics*, **76**, 6673–6675.

Chou, S.Y. and Zhuang, L. (1999). Lithographically induced self-assembly of periodic polymer micropillar arrays. *Journal of Vacuum Science and Technology B*, **17**, 3197–3202.

Chou, S.Y., Zhuang, L. and Guo, L.J. (1999). Lithographically induced self-construction of polymer microstructures for resistless patterning. *Applied Physics Letters*, **75**, 1004–1006.

Corb, B.W. (1988). Charging on the metastable domain states of small NiFe rectangles. *IEEE Transactions on Magnetics*, **24**, 2386–2388.

Cosimini, G.J., Lo, D.S., Zierhut, L.G., *et al*. (1988). Improved Y-domain magnetic-film memory elements. *IEEE Transactions on Magnetics*, **24**, 2060–2067.

Cullity, B.D. (1972). *Introduction to Magnetic Materials*, Addison-Wesley: Reading, MA.

Farhoud, M., Ferrera, J., Lochtefeld, A.J., *et al*. (1999). Fabrication of 200 nm period nanomagnet arrays using interference lithography and a negative resist. *Journal of Vacuum Science and Technology B*, **17**, 3182–3185.

Fischer, P.B., Wei, M.S. and Chou, S.Y. (1993). Ultrahigh-resolution magnetic force microscope tip fabricated using electron-beam lithography. *Journal of Vacuum Science and Technology B*, **11**, 2570–2573.

Flanders, D.C., Shaver, D.C. and Smith, H.I. (1978). Alignment of liquid-crystals using submicrometer periodicity gratings. *Applied Physics Letters*, **32**, 597–598.

Gao, H., Tan, H., Zhang, W., *et al*. (2006). Air cushion press for excellent uniformity, high-yield, fast nanoimprint across 100 mm field. *Nano Letters*, **6**, 2438–2441.

Gibson, G.A. and Schultz, S. (1993). Magnetic force microscope study of the micromagnetics of submicrometer magnetic particles. *Journal of Applied Physics*, **73**, 4516–4521.

Gibson, G.A., Smyth, J.F., Schultz, S. and Kern, D.P. (1991). Observation of the switching fields of individual permalloy particles in nanolithographic arrays via magnetic force microscopy. *IEEE Transactions on Magnetics*, **27**, 5187–5189.

Guo, L.J., Krauss, P.R. and Chou, S.Y. (1997). Nanoscale silicon field effect transistors fabricated using imprint lithography. *Applied Physics Letters*, **71**, 1881–1883.

Haisma, J., Verheijen, M., vandenHeuvel, K. and vandenBerg, J. (1996). Mold-assisted nanolithography: a process for reliable pattern replication. *Journal of Vacuum Science and Technology B*, **14**, 4124–4128.

Heidari, B., Maximov, I., Sarwe, E.L. and Montelius, L. (1999). Large scale nanolithography using nanoimprint lithography. *Journal of Vacuum Science and Technology B*, **17**, 2961–2964.

Hua, F., Gaur, A., Sun, Y.G., *et al*. (2006). Processing dependent behavior of soft imprint lithography on the 1–10-nm scale. *IEEE Transactions on Nanotechnology*, **5**, 301–308.

Kittel, C., Galt, J.K. and Campbell, W.E. (1950). Crucial experiment demonstrating single domain property of fine ferromagnetic powders. *Physical Review*, **77**, 725.

Kong, L.S. and Chou, S.Y. (1996). Effects of bar length on switching field of nanoscale nickel and cobalt bars fabricated using lithography. *Journal of Applied Physics*, **80**, 5205–5208.

Kong, L.S., Shi, R.C., Krauss, P.R. and Chou, S.Y. (1997). Writing bits of longitudinal quantized magnetic disk using magnetic force microscope tip. *Japanese Journal of Applied Physics Part 1-Regular Papers Short Notes and Review Papers*, **36**, 5109–5111.

Kong, L.S., Zhuang, L. and Chou, S.Y. (1997). Writing and reading 7.5 Gbits/in(2) longitudinal quantized magnetic disk using magnetic force microscope tips. *IEEE Transactions on Magnetics*, **33**, 3019–3021.

Kong, L.S., Zhuang, L., Li, M.T., *et al*. (1998). Fabrication, writing, and reading of 10 Gbits/in(2) longitudinal quantized magnetic disks with a switching field over 1000 Oe. *Japanese Journal of Applied Physics Part 1-Regular Papers Short Notes and Review Papers*, **37**, 5973–5975.

Krauss, P.R. and Chou, S.Y. (1997). Nano-compact disks with 400 Gbit/in(2) storage density fabricated using nanoimprint lithography and read with proximal probe. *Applied Physics Letters*, **71**, 3174–3176.

Krauss, P.R., Fischer, P.B. and Chou, S.Y. (1994). Fabrication of single-domain magnetic pillar array of 35 nm diameter and 65 Gbits/in(2) density. *Journal of Vacuum Science and Technology B*, **12**, 3639–3642.

Lambert, S.E., Sanders, I.L., Howell, T.D., *et al*. (1989). Reduction of edge noise in thin-film metal media using discrete tracks. *IEEE Transactions on Magnetics*, **25**, 3381–3383.

Lambert, S.E., Sanders, I.L., Patlach, A.M. and Krounbi, M.T. (1987). Recording characteristics of sub-micron discrete magnetic tracks. *IEEE Transactions on Magnetics*, **23**, 3690–3692.

Lebib, A., Chen, Y., Bourneix, J., *et al*. (1999). Nanoimprint lithography for a large area pattern replication. *Microelectronic Engineering*, **46**, 319–322.

Lederman, M., Gibson, G.A. and Schultz, S. (1993). Observation of thermal switching of a single ferromagnetic particle. *Journal of Applied Physics*, **73**, 6961–6963.

Li, M.T., Chen, L. and Chou, S.Y. (2001). Direct three-dimensional patterning using nanoimprint lithography. *Applied Physics Letters*, **78**, 3322–3324.

Li, M.T., Chen, L., Zhang, W. and Chou, S.Y. (2003). Pattern transfer fidelity of nanoimprint lithography on six-inch wafers. *Nanotechnology*, **14**, 33–36.

Li, M.T., Tan, H., Chen, L., *et al*. (2003). Large area direct nanoimprinting of SiO_2-TiO_2 gel gratings for optical applications. *Journal of Vacuum Science and Technology B*, **21**, 660–663.

Liang, X., Tan, H., Fu, Z. and Chou, S.Y. (2006). Air bubble formation and dissolution in dispensing nanoimprint lithography. *Nanotechnology*, **18**(2), 025303.

Liang, X.G., Zhang, W., Li, M.T., *et al*. (2005). Electrostatic force-assisted nanoimprint lithography (EFAN). *Nano Letters*, **5**, 527–530.

Lo, D.S., Cosimini, G.J., Zierhut, L.G., *et al*. (1985). A Y-domain magnetic thin-film memory-element. *IEEE Transactions on Magnetics*, **21**, 1776–1778.

Naito, K., Hieda, H., Sakurai, M., *et al*. (2002). 2.5-inch disk patterned media prepared by an artificially assisted self-assembling method. *IEEE Transactions on Magnetics*, **38**, 1949–1951.

New, R.M.H., Pease, R.F.W. and White, R.L. (1994). Submicron patterning of thin cobalt films for magnetic storage. *Journal of Vacuum Science and Technology B*, **12**, 3196–3201.

New, R.M.H., Pease, R.F.W. and White, R.L. (1995a). Effect of magnetocrystalline anisotropy in single-domain polycrystalline cobalt islands. *IEEE Transactions on Magnetics*, **31**, 3805–3807.

New, R.M.H., Pease, R.F.W. and White, R.L. (1995b). Physical and magnetic-properties of submicron lithographically patterned magnetic islands. *Journal of Vacuum Science and Technology B*, **13**, 1089–1094.

Nielsch, K., Hertel, R., Wehrspohn, R.B., *et al*. (2002). Switching behavior of single nanowires inside dense nickel nanowire arrays. *IEEE Transactions on Magnetics*, **38**, 2571–2573.

Ozimek, E.J. (1985). Characteristic length of domain-structures and its effect on the coercive force of ferromagnetic materials. *Journal of Applied Physics*, **57**, 5406–5408.

Park, M., Chaikin, P.M., Register, R.A. and Adamson, D.H. (2001). Large area dense nanoscale patterning of arbitrary surfaces. *Applied Physics Letters*, **79**, 257–259.

Ross, C.A., Farhoud, M., Hwang, M., *et al*. (2001). Micromagnetic behavior of conical ferromagnetic particles. *Journal of Applied Physics*, **89**, 1310–1319.

Ruhrig, M., Bartsch, W., Vieth, M. and Hubert, A. (1990). Elementary magnetization processes in a low-anisotropy circular thin-film disk. *IEEE Transactions on Magnetics*, **26**, 2807–2809.

Shew, L. (1963). Discrete tracks for saturation magnetic recording. *IEEE Trans Broadcast Tel*, **9**, 56.

Smyth, J.F., Schultz, S., Fredkin, D.R., *et al*. (1991). Hysteresis in lithographic arrays of permalloy particles–experiment and theory. *Journal of Applied Physics*, **69**, 5262–5266.

Stoner, E.C. and Wohlfarth, E.P. (1948). A mechanism of magnetic hysteresis in heterogeneous alloys. *Philosophical Transactions of the Royal Society of London Series A-Mathematical and Physical Sciences*, **240**, 599–642.

Sun, X.Y., Zhuang, L., Zhang, W. and Chou, S.Y. (1998). Multilayer resist methods for nanoimprint lithography on nonflat surfaces. *Journal of Vacuum Science and Technology B*, **16**, 3922–3925.

Suriono, U. and Chou, S.Y. (1996a). Quantized writing processes in quantum magnetic disks. *Journal of Applied Physics*, **79**, 5066.

Suriono, U. and Chou, S.Y. (1996b). Quantized writing processes in quantum magnetic disks. Unpublished.

Tan, H., Gilbertson, A. and Chou, S.Y. (1998). Roller nanoimprint lithography. *Journal of Vacuum Science and Technology B*, **16**, 3926–3928.

Terris, B.D., Folks, L., Weller, D., *et al*. (1999). Ion-beam patterning of magnetic films using stencil masks. *Applied Physics Letters*, **75**, 403–405.

Thurn-Albrecht, T., Schotter, J., Kastle, C.A., *et al*. (2000). Ultrahigh-density nanowire arrays grown in self-assembled diblock copolymer templates. *Science*, **290**, 2126–2129.

Wachenschwanz, D., Jiang, W., Roddick, E., *et al*. (2005). Design of a manufacturable discrete track recording medium. *IEEE Transactions on Magnetics*, **41**, 670–675.

Wang, J., Sun, X.Y., Chen, L. and Chou, S.Y. (1999). Direct nanoimprint of submicron organic light-emitting structures. *Applied Physics Letters*, **75**, 2767–2769.

Wu, W., Cui, B., Sun, X.Y., *et al*. (1998). Large area high density quantized magnetic disks fabricated using nanoimprint lithography. *Journal of Vacuum Science and Technology B*, **16**, 3825–3829.

Xia, Q.F., Keimel, C., Ge, H.X., *et al*. (2003). Ultrafast patterning of nanostructures in polymers using laser assisted nanoimprint lithography. *Applied Physics Letters*, **83**, 4417–4419.

Yasui, N., Imada, A. and Den, T. (2003). Electrodeposition of (001) oriented CoPt L1(0) columns into anodic alumina films. *Applied Physics Letters*, **83**, 3347–3349.

Yen, A., Anderson, E.H., Ghanbari, R.A., *et al*. (1992). Achromatic holographic configuration for 100-Nm-period lithography. *Applied Optics*, **31**, 4540–4545.

Yu, Z.N. and Chou, S.Y. (2004). Triangular profile imprint molds in nanograting fabrication. *Nano Letters*, **4**, 341–344.

Yu, Z.N., Gao, H., Wu, W., *et al*. (2003). Fabrication of large area subwavelength antireflection structures on Si using trilayer resist nanoimprint lithography and liftoff. *Journal of Vacuum Science and Technology B*, **21**, 2874–2877.

Yu, Z.N., Wu, W., Chen, L. and Chou, S.Y. (2001). Fabrication of large area 100 nm pitch grating by spatial frequency doubling and nanoimprint lithography for subwavelength optical applications. *Journal of Vacuum Science and Technology B*, **19**, 2816–2819.

Zhukov, A.A., Goncharov, A.V., de Groot, P.A.J., *et al*. (2003). Magnetic antidot arrays from self-assembly template methods. *Journal of Applied Physics*, **93**, 7322–7324.

Growth of Magnetic Materials using Molecular Beam Epitaxy

James N. Eckstein
University of Illinois, Urbana, IL, USA

1 INTRODUCTION

Even though metals, semiconductors, and complex oxides are very different materials, molecular-beam epitaxy (MBE) has been adapted to grow films of them all (Cho and Arthur, 1975; Ploog, 1982; Eckstein and Bozovic, 1995).[2] The hallmark of MBE is the very accurate control of the synthesis process, and in practice this means control at the atomic layer level. Also, as the word 'epitaxy' implies, the growth of one layer should be in registration somehow with the layer below. Often growth occurs under ultrahigh vacuum (UHV) conditions, although sometimes carrier gases or a large overpressure of a volatile component is used. Sometimes, atomic beams are used, while in other cases, molecular beams are employed and only a part of the incident flux is destined to be incorporated in the growing layer. In many cases, accurate atomistic assembly is used for putting together devices, which depend critically on thicknesses of layers. In other cases, new aggregate phenomena can be found in samples containing interfaces that mediate charge, spin, strain, and other important factors that control electronic and magnetic properties.

The kinds of materials grown by MBE also span a wide range of structural and molecular complexity. Single component metallic films are structurally the simplest, since the total dose of atoms per unit area just determines the thickness of the layer grown, although faceting and roughening are interesting complications that often control the properties exhibited by such layers. The growth of soluble alloys is similar to the growth of single component films, but the details of how this works depend on the properties of the components, such as their vapor pressure, as well as the chemical factors that *lead to* the equilibrium phase diagram. MBE growth, however, is carried out far from thermal equilibrium. The most complex materials grown by MBE are those containing many atomic constituents and distinct atomic sites within the unit cell. Complex oxides are the most studied of such complex materials grown by MBE, and each unit cell may contain more than four different metal atom constituents located in distinct sites along with corresponding oxygen ions. Even with this diversity of materials, there are common features of the use of MBE to

Handbook of Magnetism and Advanced Magnetic Materials. Edited by Helmut Kronmüller and Stuart Parkin. Volume 3: *Novel Techniques for Characterizing and Preparing Samples*. ISBN: 978-0-470-02217-7.

grow magnetic materials of these types. This chapter covers these materials classes, summarizing the development of the growth processes and the results obtained.

2 MAGNETIC FILMS

Growth of films of magnetic metals using MBE began in the early 1980s. Load locked chambers with UHV base pressures, equipped with substrate heaters and *in situ* diagnostics such as reflection high energy electron diffraction (RHEED) were employed to grow transition-metal and rare-earth magnetic films. A number of different substrates and buffer layers were used in this work. The magnetic metals studied include rare-earth magnets, transition-metal magnets, and multilayer and device structures involving them. In this section, we describe representative results showing the most important advances in creating and understanding novel magnetism in artificial metallic structures. We begin with a description of MBE of rare-earth superlattices, and then discuss superlattices involving 3d transition metals that give rise to giant magnetoresistivity (GMR). Then we discuss the use of ferromagnetic materials as injectors of spin-polarized charge into semiconducting devices. This includes a variety of magnetic materials that are compatible with semiconductor film growth. We finish with a discussion of magnetic oxides, including the famous colossal magnetoresistive manganites. These materials have very large values of spin polarization, and magnetic tunnel junctions made with them have given the largest values of tunneling magnetoresistance observed so far.

3 MOLECULAR-BEAM EPITAXY OF METALLIC MAGNETIC FILMS

Because metal surfaces are reactive, MBE of metal films is done in UHV systems to avoid contamination. A schematic diagram of such a system is shown in Figure 1. Typical values of base pressure reported for the growth of metal films are less than 5e–10 Torr, with many groups reporting measured base pressures less than 1e–10 Torr. This requires a chamber having metal sealed valves and flanges that can be baked (typically to $>150\,^{\circ}\mathrm{C}$), a carefully designed load locked system with external substrate outgassing and adequate pumping to maintain the vacuum, including cryopanels for use during growth. Such systems are usually equipped with ion pumps, cryopumps, and titanium sublimation pumps, and the pumping speed seen by the chamber is in the range of $1000\,\mathrm{l\,s^{-1}}$.

The sources used in metal film MBE are either thermal effusion cells, capable of operating at temperatures as high as $1800\,^{\circ}\mathrm{C}$ (depending on the details of the cell), or electron beam evaporators that are used for elements that have to operate at higher temperatures. For magnetic films, elements such as manganese, copper, and most of the rare-earth atoms can be evaporated from conventional sources. Elements such as chromium, iron, cobalt, nickel, yttrium, and lanthanum require a higher temperature and often are evaporated from special 'high-temperature' cells. More refractory elements, such as the 4d and 5d transition-metal elements require evaporation from electron beam evaporators. Careful outgassing of sources prior to and during the baking of a system is important to obtaining the best vacuum possible.

Samples on which films are grown are held on a manipulator that incorporates the possibility of heating or cooling the sample and may also incorporate substrate rotation, which is used to obtain more uniform growth. Surface diagnostic tools are also usually incorporated for the measurement of structural, chemical, and even magnetic properties. The most common of these techniques is RHEED (Braun, 1999). It is well suited for MBE because it is surface sensitive and does not block the atomic or molecular beams used for growth. A RHEED system consists of a monoenergetic, focused electron beam with energy typically between 5 and 50 keV that is directed at a glancing angle toward the substrate; the electron beam diffracts from the growing surface and the diffraction pattern is characteristic of the surface lattice. On the opposite side of the chamber a phosphor screen displays the diffraction pattern, and this is often recorded in real time as growth occurs. The crystalline state of the surface can be monitored in this way. It provides a quantitative measure of surface flatness, the density, and structure of three-dimensional nanograins that sometimes emerge at heterointerfaces, and the gradual relaxation of lattice strain. Some systems incorporate tools for *in situ* chemical analysis, such as X-ray photoelectron spectroscopy (XPS) or Auger electron spectroscopy. Also, Magnetic properties of surface layers can be monitored if secondary electron microscopy with polarization analysis (SEMPA) is used (Scheinfein *et al*., 1990).

For metal films, the choice of substrate can be a complicating factor. In semiconductor MBE, the substrate is usually the same material or very similar to the film. In metal epitaxy, this is usually not the case. It is necessary to find a substrate, that is, chemically and structurally compatible with the metal film being grown. Sometimes the substrate must be an insulator, and in other cases metallic films are grown on semiconductor films that already incorporate an epitaxial device layer structure that, together with the metal film, forms the basis for an electronic or spintronic device. For devices, the most commonly used substrates for metal epitaxy have been the insulators, sapphire and magnesium oxide, as well as the semiconductors, silicon and gallium arsenide. Significant issues of chemical compatibility arise when some

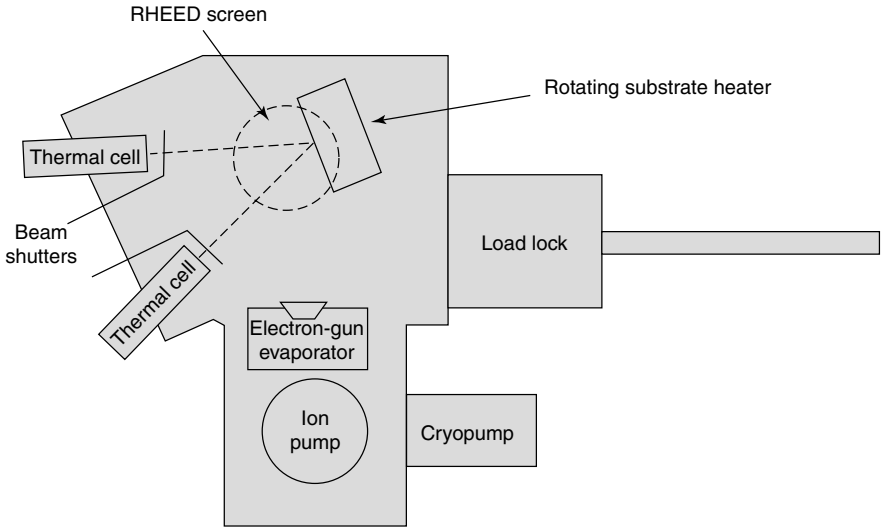

Figure 1. Schematic diagram of a typical MBE system for the growth of metallic films.

metal films are grown on sapphire. In particular, rare-earth atoms react with sapphire, removing oxygen and introducing a layer of partially oxidized rare-earth hexa-aluminate. This can be avoided by using a 'buffer layer' which is relatively stable in contact with both the sapphire as well as rare-earth atoms. Kwo and coworkers (1985b) reported that niobium provides such a buffer. It does not chemically react very rapidly with sapphire at temperatures below about 1300 °C. It grows on $(11\bar{2}0)$ sapphire with the in-plane orientation shown in Figure 2. The niobium film is oriented in the (110) direction. Niobium films grown by MBE at moderate temperatures (800–900 °C) are very flat. By annealing in UHV at somewhat higher temperatures (1300 °C) even smoother surfaces are obtained at the expense of reducing the sapphire at the interface. Figure 3(a) shows a niobium surface grown at 850 °C. The surface is covered with unit-cell-high terraces, but the direction of the terraces is not uniform. By annealing the film at 1300 °C for 20 min this changes. Figure 3(b) shows the surface that results, exhibiting fewer and more uniformly spaced terraces. Such surfaces provide a good substrate for the growth of rare-earth films.

The question of what growth conditions lead to the best metallic films and superlattices was addressed by Flynn (1988). He recognized that in many metal systems experience showed that the best growth happened over a rather narrow range of temperature. He observed that the activation energies for bulk diffusion and for surface diffusion are often proportional to the melting temperature for many elements. For a wide range of metals, the activation energy of bulk diffusion is found to be about $16\,kT_M$, while the activation energy of surface diffusion is found to be $3.5\,kT_M$, where T_M is the melting temperature and k is Boltzmann's constant. In order to quench bulk diffusion

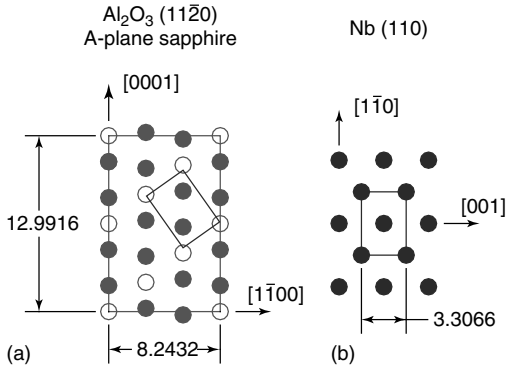

Figure 2. The orientation of Nb grown on a-plane sapphire is illustrated. (a) The position of the aluminum sites on an a-plane surface is shown. The solid circles are occupied and the open circles are vacant. The orientation of Nb atoms in a 110 plane is shown in (b), with a surface net unit cell shown outlined in the rectangle. This rectangle orients on the sapphire surface as shown in (a).

at an interface, over the time a film is grown but enable surface diffusion to adequately transport adatoms to adjacent step edges, only a limited range of temperatures may satisfy these criteria. Since a typical terrace size is about 100 unit cells wide, the required rate of surface diffusion, active only during the time an atom is on the surface and not yet buried, can be determined. By comparing these two rates, Flynn found that growth temperature should be about 3/8 times the melting temperature. In particular, this means that it should be very difficult to make structures, like superlattices, with components having very different melting temperatures. This model works well for elemental metals, but not so well for complex compounds, such as oxides. The reasons for this are numerous. For one, the phase diagrams of multicomponent systems can change with temperature. In addition, the

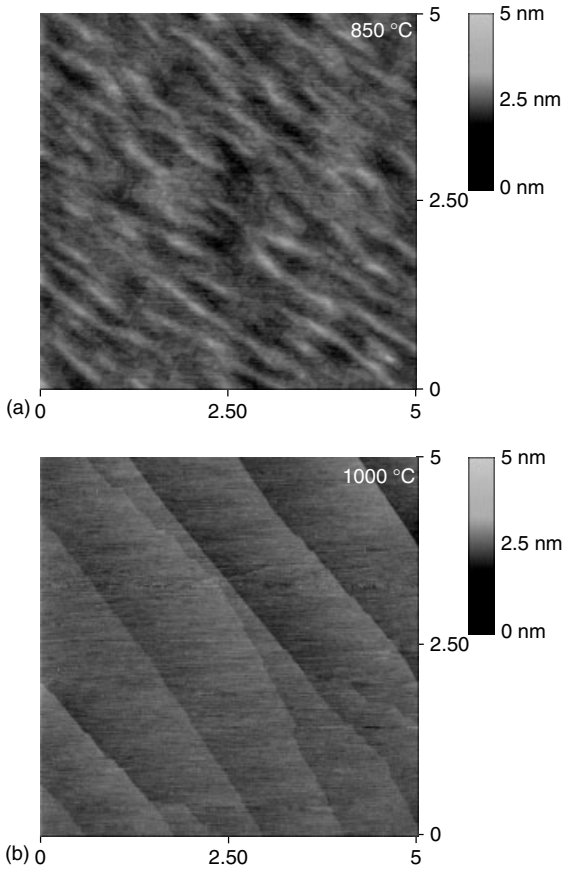

Figure 3. Surface morphology of Nb films grown by MBE. (a) An atomic force micrograph of a Nb film grown at 850 °C and removed from the growth chamber. (b) A micrograph of a similar film grown at the same temperature, but then annealed at 1300 °C.

mobility of different atoms, ions or submolecular species that diffuse on a surface during the growth of a complex material can be very different, and no simple relationship exists between the melting point of a compound and the activation energy for diffusion rates of all surface species present during growth. On the other hand, the underlying idea that a competition between bulk and surface diffusion governs the range of temperature that is optimum is still the case, even though the complexity of both bulk and surface diffusion makes it more difficult to extract a single optimum growth temperature for more complex materials.

4 MOLECULAR-BEAM EPITAXY OF RARE-EARTH MAGNETIC MULTILAYERS

Rare-earth metals exhibit phase diagrams with interesting magnetic structures in bulk samples. They crystallize into close-packed phases, either hcp or fcc (excepting samarium), and the conduction band in most of them is due to delocalization of two 6s and one 5d electrons. The 4f electrons are localized on the resulting 3^+ ions, and both their spin and their orbital angular momenta contribute to the ionic magnetic moment since the 4f orbital motion is not strongly coupled to the crystal field as the d electrons are in transition metals. The number of 4f electrons increases from zero in lanthanum (and yttrium and scandium which are electronically similar to lanthanum) to the filled 4f shell containing 14 electrons in lutetium. The 4f electrons interact with the delocalized s−d bands and this leads to an indirect coupling of the 4f angular momenta via indirect exchange. This coupling, also known as RKKY for Ruderman, Kittel, Kasuya, and Yoshida, is strongly dependent on Fermi surface properties, such as the Fermi wave vector in different directions (Kittel, 1987). It is weaker than direct exchange, which leads to magnetism in transition metals such as iron, and because it is weaker, the magnetic ordering temperatures of the rare-earth elements that do order tend to be lower. The elements gadolinium through thulium, all of which are hcp, have a low-temperature ferromagnetic phase. For terbium through thulium there is a higher-temperature antiferromagnetic phase that consists of close-packed planes with in-plane ferromagnetic alignment, and a temperature-dependent twist angle that rotates the direction of magnetic moment orientation in a spiral fashion around the *c* axis as one moves in the *c*-axis (0001) direction. Gadolinium has the highest Curie temperature, 289 K, and does not exhibit a higher-temperature spiral antiferromagnetic order, while dysprosium has a Neel temperature of 179 K below which the spiral order appears, and a Curie temperature of 89 K at which temperature a first-order transition to ferromagnetic order occurs. Two excellent reviews of the properties and discoveries found in rare-earth magnetic superlattices have been written by Majkrzak and collaborators (1991) and by Rhyne and Erwin (1995).

An early demonstration of the ability of MBE to make magnetic metallic films with new properties emerging because of layer-by-layer control of the composition was the work done studying superlattices containing layers of magnetic rare-earth atoms separated by nonmagnetic yttrium atoms. The atomic size of yttrium is close to that of gadolinium and dysprosium, and superlattices containing these atoms can be assembled with only moderate strain and with atomic plane accuracy. The superlattice results summarized subsequently were made possible by the discovery that sapphire could be used as a substrate, as long as an intervening layer of niobium was grown to chemically isolate the rare-earth atoms from the substrate Al_2O_3 (Kwo *et al.*, 1985b). Previously, Greene and coworkers found that rare-earth atoms underwent a chemical reaction with sapphire at temperatures required

for epitaxial growth (Greene *et al*., 1985). At around the same time, Durbin and coworkers showed that smooth (110)-oriented niobium films and niobium–tantalum superlattices could be grown epitaxially on a-plane sapphire substrates (Durbin *et al*., 1981). Since niobium does not react significantly with either Al_2O_3 or rare-earth atoms at the temperature ranges used for epitaxial growth, it provides chemical isolation between the rare-earth superlattice and the sapphire substrate. The niobium 110 surface can be viewed as having a distorted triangular structure on which the hexagonal close-packed rare-earth lattice orients.

The first rare-earth superlattice system studied was the Gd–Y system by Kwo and coworkers (1985a, 1987). The growth was carried out in a MBE system having a nominal base pressure of 3×10^{-11} Torr. The substrate was heated to improve the epitaxy, but the growth of the superlattice was carried out at 220 °C in order to avoid vertical diffusion. A thick Y layer was grown on top of (110) niobium to isolate the superlattice from the niobium lattice. On top of this, superlattices were grown of different numbers of Gd and Y atomic planes per supercell. Gadolinium was chosen for this work since it has the simplest magnetic phase diagram of the ferromagnetic rare-earth elements. The most important finding is illustrated in Figure 4 taken from Kwo *et al*. (1987). The supercell consists of a Y slab and a Gd slab. The Y slab had a variable number of Y planes and the Gd slab had either 4 or 10 Gd planes per slab. They observed an oscillatory dependence of the magnetic order that emerged below the Gd Curie temperature depending on the number of Y planes in each supercell. The oscillation appeared to be independent of the number of Gd planes per slab. The Gd slabs from supercell to supercell aligned either antiferromagnetically or ferromagnetically with respect to each other depending on the Y slab thickness. This result was explained in terms of RKKY coupling of the Gd spins through the nonmagnetic Y slabs. In fact, the separation leading to the first maximum of remnant magnetization was about seven Y layers, and this is in quantitative agreement with simple model of RKKY coupling through the Y slab as shown in Figure 4(c). The coupling is predicted to be antiferromagnetic for three Y layers and ferromagnetic for seven.

Superlattices of Dy and Y were grown and studied by Flynn, Salamon, and coworkers (Borchers *et al*., 1987). This system is more complicated than Gd–Y, because of the spiral magnetic order that exists in Dy between 89 and 179 K (Majkrzak *et al*., 1991). In addition, the basal plane strain is large enough to be important in this system. Since the superlattices were grown on Y films (on top of (110) niobium) that were thick enough to be relaxed, the Dy slabs were in a tensile strain of 1.6% due to the lattice mismatch between Y and Dy. If the superlattices are sufficiently perfect,

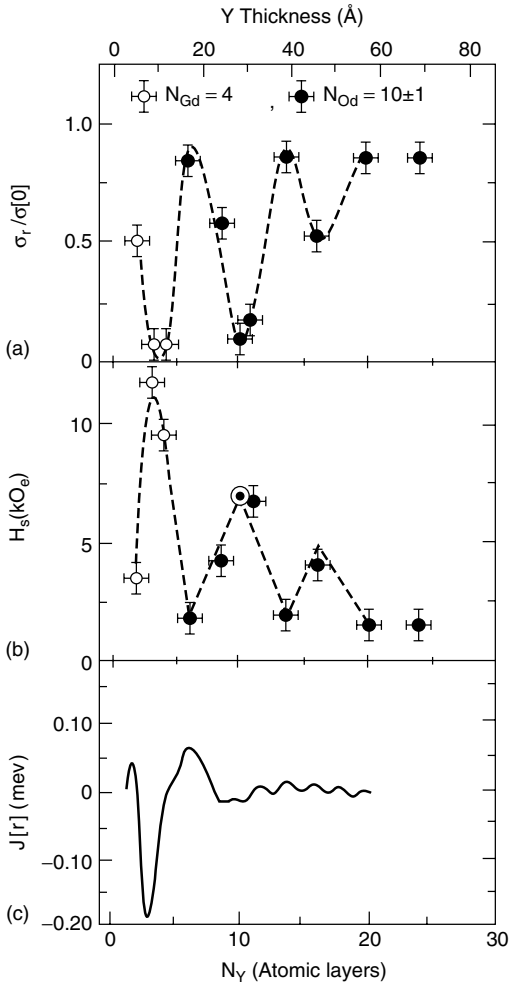

Figure 4. Magnetic characterization of Gd:Y superlattices from Kwo *et al*. (1987). Superlattices were grown in two series, with either 4 or 10 Gd layers/supercell. In each series, films with different Y layer thicknesses were grown. (a) The ratio of the magnetic remanence to the magnetization extrapolated from high field back to zero field. The authors point out that this normalizes the sample volume and makes film-to-film comparisons quantitatively possible. (b) The saturation field which behaves oppositely to the normalized magnetic remanence. (c) A calculated exchange interaction between two Gd planes separated by a Y slab of variable thickness. The sign of the exchange interaction suggests that the low remanence observed at the first minimum in (a) is due to an antiferromagnetic coupling at that Y thickness. (Reproduced from Kwo *et al*., 1987, with permission from the American Physical Society. © 1987.)

the layer architecture engineered into the film may influence the magnetic structure that naturally emerges, due to both exchange and magnetoelastic effects. The question is how the pitch of the superlattice interferes with the pitch of the magnetic spiral. The spiral magnet order exists naturally in single-phase Dy samples, and does not exist at all in single-phase Y samples. Whether the pitch of the superlattice somehow 'stabilizes' the spiral phase and prevents the

formation of the uniformly magnetized ferromagnetic phase is also complicated by the strain the Dy slab is under.

Superlattices with different layer thicknesses were grown and studied by measuring their magnetic moment as well as by neutron scattering (Salamon *et al*., 1986). In each supercell, the Dy slabs were around 15 atomic layers thick and the Y slabs ranged from 5 to about 40 in different samples. The most obvious difference between bulk Dy and these superlattices was the absence of the first-order transition to the ferromagnetic structure in the superlattices at low temperatures. Starting from the spiral ordering temperature around 180 K and extending to 10 K a spiral magnetic structure was also observed in the superlattice films. This was studied with neutron diffraction, which can distinguish magnetic order from atomic order. The length scale of magnetic order sets a minimum linewidth to magnetic superlattice reflections that are caused by the spiral order. Surprisingly, the spiral structure extended from one Dy slab to neighboring Dy slabs, even though the material connecting the Dy slab was nonmagnetic Y. Figure 5 shows magnetic superlattice reflections surrounding the 0002 structure peak. It is clear that the spiral order persists down to 10 K and that the linewidth of the magnetic peaks decreases as the temperature is reduced. On the basis of these data, it is possible to infer that the length scale of magnetic structure correlation extends through more than five superlattice periods. This means that the spiral magnetic order extended from the magnetic Dy layer into and through the nonmagnetic Y layers, although the degree of coupling through nonmagnetic Y layers was reduced for thicker Y layers. The spiral angle shift per plane was found to be constant at about 50° in the Y slabs, and Rhyne and Erwin and coworkers suggested that a spiral spin density wave was *induced* in the Y slab by proximity to the Dy layers (Erwin *et al*., 1987). This wave would then carry the spin order information between the Dy slabs. The pitch of the proximity induced spiral magnetization in the Y layer provided evidence that Y has an incipient conduction electron SDW. Alternatively, Majkrzak has suggested that introducing a finite thickness spiral order in the Dy slabs may naturally introduce spiral coupling via asymmetric strain and the RKKY interaction (Majkrzak *et al*., 1991).

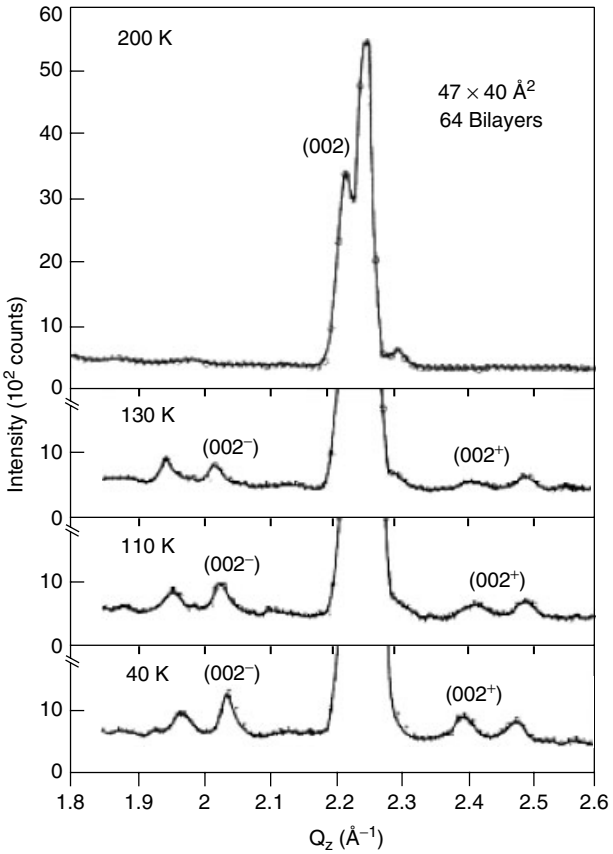

Figure 5. Magnetic reflections obtained in neutron scattering from Dy:Y superlattice from Borchers *et al*. (1987). In each supercell, the Dy layer is nominally 4.7 nm thick and the Y layer is 4.0 nm thick. The principle magnetic satellites are labeled 002− and 002+ and they emerge below the magnetic ordering temperature. Similar reflections are obtained from a single-phase Dy film in the helimagnetic phase. (Reproduced from Borchers *et al*., 1987, with permission from the American Institute of Physics.)

5 TRANSITION-METAL MULTILAYERS AND SUPERLATTICES: GIANT MAGNETORESISTANCE

Superlattices containing different magnetic transition metals have also been made by MBE. The motivation for this work has largely been to study and optimize the phenomena of 'giant magnetoresistance', in which electronic transport is strongly affected by the relative magnetic orientation of different ferromagnetic layers.[21] The underlying physics is that differences in spin-polarized density of states in two parts of a sample, magnetized in different directions, leads carrier scattering and thus resistance. If an applied magnetic field reorients the magnetization of one of the two parts, so that they become pointed in the same direction, then the magnetic scattering is eliminated and the resistance is reduced. This shows up as a negative magnetoresistance. This effect has been studied in polycrystalline as well as single crystal material, in samples with very smooth interfaces as well as in samples with rough interfaces between different layers. MBE-grown samples with controllable interface roughness have allowed a systematic investigation of the role of interface characteristics. In practical terms, the phenomena of GMR and the related tunneling magnetoresistance involving

samples made with transition metals are so robust that exquisite sample perfection is not required (Parkin, Bhadra and Roche, 1991). Excellent devices can be made with polycrystalline samples. This section reviews work done growing and studying transition-metal multilayers by MBE. For more information the reader is referred to excellent reviews by Farrow (1998) and Etienne and Massies (1993).

The 3d transition metals exhibit a wide range of magnetic properties, ranging from strong, high-temperature ferromagnetism in Co, Fe, and Ni, to antiferromagnetism in Cr and Mn, to paramagnetism in Ti, V, Cu, and Zn. The Fermi surface of ferromagnetic transition metals and alloys is significantly polarized, between 35 and 46% (Soulen *et al*., 1998). Since transport is controlled by the properties of the Fermi surface, the degree of Fermi surface spin polarization determines the amount of spin scattering that occurs in a GMR device.

In a typical GMR device, two ferromagnetic films are separated by a paramagnetic or antiferromagnetic film. Typical ferromagnets used have been Co, Fe, Ni, and permalloy (an alloy of Ni and Fe). The paramagnetic film has been Cu, V, or Au, and Cr has been used as an antiferromagnetic spacer layer. Because of the way in which RKKY changes the sign of exchange energy as a function of how far two spins are from each other, the spacing between two ferromagnetic layers and the relative direction of the spins in the two FM layers in a ferromagnet–paramagnet–ferromagnet trilayer together determine whether carriers that propagate from one interface to the other will be strongly scattered.

The earliest demonstration of GMR was reported by Baibich *et al*. (1988) who found that very large magnetoresistance could be obtained in (001)-oriented Fe/Cr superlattices if the thickness of the Cr layers was chosen correctly. The growth of the superlattice on top of (001) GaAs was monitored using RHEED. This showed that a critical thickness of Fe was required for the subsequent superlattice to grow crystallographically ordered. The growth conditions were UHV (background pressure of 5e–11 Torr) and the substrate temperature was kept near room temperature. The growth rates employed were typical of MBE, around 0.5 to 1 A s^{-1}.

The magnetization of the Fe slabs earlier had been found to be antiferromagnetically ordered for thin enough Cr layers (Grunberg *et al*., 1986). The magnetization was in plane, but oppositely directed in adjacent iron slabs. Evidence for this is shown in Figure 6, where M versus H curves of samples with different Cr thicknesses are compared. The important thing to note is the difference in the shape of the $M(H)$ curves for samples in which the Cr layer is thin, for example, see the curve for the sample with 9-Å-thick Cr slabs. For thicker Cr layers, the $M(H)$ curves show ferromagnetic behavior. The data for the larger Cr slabs, show that the magnetization shifts direction when a relatively small coercive field is applied. For thinner Cr layer thicknesses, this is not the case. Instead, a very large applied field is required to align all of the Fe magnetic moments. This was interpreted as being due to a zero-field antiparallel alignment (antiferromagnetic) of neighboring Fe slab magnetic moments for the 9-Å samples. In order to pin this down, spin flip neutron scattering was done on a sample with a thin Cr layer. For an antiferromagnet spin alignment, a 'half-order' magnetic reflection should be seen due to the doubling of the magnetic periodicity compared to the structural periodicity in the growth direction. In fact, that is what was observed, as shown in Figure 7. This reflection is sensitive to applied magnetic field; it can be eliminated

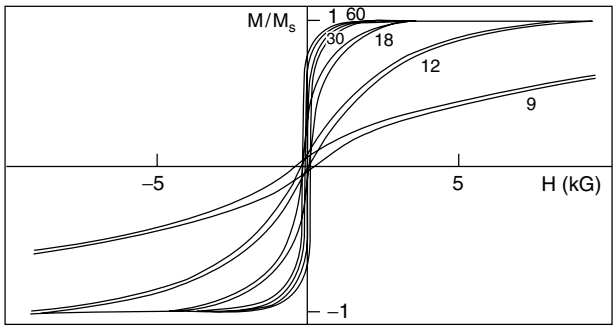

Figure 6. Magnetization curves at 4.2 K for different iron chromium superlattices. The number next to each curve indicates the thickness of the chromium layer in angstroms, while the thickness of the iron layer is 30 Å for each superlattice. For the curve labeled 60, the thickness of the iron layer was 60 Å. (From Baibich *et al*., 1988.)

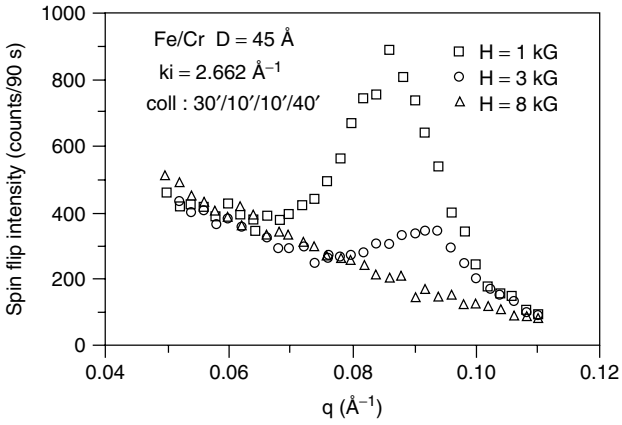

Figure 7. Neutron scattering from iron chromium superlattice with 30 Å iron layer and 15 Å chromium layer/supercell at 1.6 K. The film had 20 supercells. The magnetic reflection with periodicity equal to twice the structural periodicity is sensitive to applied field, indicating a spin flip transition leading to ferromagnetic slab alignment occurs for less than 1 T applied field. (Reproduced from Barthélémy *et al*., 1990, with permission from the American Physical Society. © 1990.)

by applying a large enough field to make all the Fe spins point in the same direction (Barthélémy *et al*., 1990). As shown in the figure, this observation was taken as evidence for ferromagnetic ordering of the superlattice by flipping the spins with a large enough applied field. At zero field, these spins had been slabwise antiferromagnetically aligned because of the slab-to-slab RKKY exchange interaction.

For samples with antiferromagnetically aligned Fe slab spins, the resistance depended strongly on magnetic field. This is shown in Figure 8, where the resistance is shown as a function of applied magnetic field for three different superlattices. Each of these samples had supercells containing the same Fe slab thickness, namely, 30 Å. They differed in Cr slab thickness. The largest effect was observed for the sample with 9-Å Cr slab thickness. Here, the resistance changed by almost a factor of two when a magnetic field large enough to align all of the Fe spins was applied. This was the discovery of GMR.

Following this work, GMR was investigated in samples with improved interfacial flatness. The results indicate substantial subtlety in the factors that influence GMR. For example, if (001) Fe/Cr superlattices with very flat interfaces are studied, a different phenomenology emerges. The underlying antiferromagnetism in the Cr slab apparently gives rise to a surface magnetization and net exchange coupling between Fe slabs that shifts for every Cr layer grown. This was discovered by Unguris, Celotta, and Pierce (1991) who used SEMPA to probe the surface of a Cr wedge grown on a flat Fe surface. In bulk Cr, which is bcc, it is *approximately true* that the magnetization of the body-centered atom

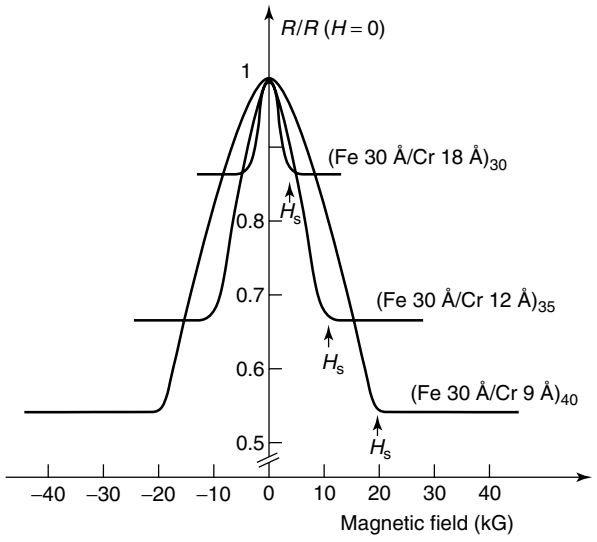

Figure 8. Dependence of in-plane resistance of superlattice on applied in-plane magnetic field. The sensitivity is largest for the thinnest chromium layer, which has quiescent antiparallel spin alignment of adjacent iron slabs. (From Soulen *et al*., 1998.)

is opposite to the magnetization of the corners. In fact, this picture is modulated by a spin density wave that has a periodicity of about 21 unit cells (Fawcett, 1988; Zabel, 1999). Unguris, Celotta, and Pierce (1991) observed an oscillation in the direction of the coupling between the Fe slabs that had a period of approximately one Cr unit cell. This was interrupted by an oscillation phase slip at relatively thick intervals, typically 20, 40, and 60 monolayers of Cr, similar to the periodicity of the bulk Cr spin density wave. This short period effect was not seen in samples having interfaces with several monolayer roughness, as evidenced by streakier RHEED patterns. (For a discussion of the use of RHEED in measuring surface roughness see Section 8 below.) Clearly, the phenomenon of GMR depends in detail on how the magnetic influence occurs at the interface to the Cr layer. The short period oscillation was attributed to the rotation of the interface magnetization direction caused by the antiferromagnetism and spin density wave present in the (001) Cr film. Observing the short period oscillations requires samples with the flatness that so far only MBE has made possible.

6 SPIN INJECTION FROM METALLIC FERROMAGNETS INTO SEMICONDUCTORS

Another area of research in which magnetic materials grown by MBE have made significant contribution is the injection of spin-polarized current into semiconductor structures. Spin injection and control of spin currents is a central component of the larger topic of spintronics. This is a wide-ranging field and includes the study of devices that sense magnetic fields by measuring spin-polarized currents, such as in magnetic tunnel junctions, as well as devices that use the spin degree of freedom to perform quantum information manipulation. In such quantum devices, spins or spin systems should be prepared in a coherent initial state, undergo time evolution in a controlled environment interacting with other quantum degrees of freedom, and then be interrogated by projecting out a final state quantum number. An important component of this is the ability to deliver a single electron with a specified spin state, at the right moment into a circuit embedded in a semiconductor heterostructure. So, highly precise injection of spins into semiconductors is required. In this section, we describe experiments working toward this goal.

Early work aimed to obtain as transparent a contact as possible between a semiconductor conduction channel and a permalloy ferromagnetic injector, $Ni_{0.8}Fe_{0.2}$ (Hammar, Bennett, Yang and Johnson, 1999; Lee *et al*., 1999). This was done in Hammar, Bennett, Yang, and Johnson (1999) by choosing the semiconductor InAs, which is known to not

have a Schottky barrier. In Fawcett (1988) and Zabel (1999) a small barrier between the permalloy and InAs channel was preserved by the processing, but the contact was very transmissive and nonrectifying. In both cases, a good connection between the carriers in the two different materials was obtained. The device geometry consisted of two magnetic films connected by a two-dimensional electron gas in the semiconductor. The spin injection in both experiments was small, and the change in interface resistance between the magnetic layer and the semiconductor was of order 1%. The reason for this small response was identified by Schmidt and coworkers who pointed out that for transmissive contact metallurgy between a ferromagnetic metal and a diffusive semiconductor, the degree of spin polarization injected into the semiconductor is less than the polarization of the ferromagnet by a factor equal to the ratio of the semiconductor conductivity to the ferromagnet conductivity (Schmidt *et al*., 2000). Since a metallic ferromagnet has many times the carrier density of a semiconductor, this factor is very small and accounts for the small injection efficiency observed in these two experiments. A solution to this problem was proposed by Rashba (2000) who considered a spin injection system in which the transport from the ferromagnetic metal into the semiconductor was due to weak tunneling. In this case, the small contact conductance effectively substitutes for the ferromagnet's large conductivity and results in much more efficient spin-polarized current injection. In practice, that barrier can be obtained from an epitaxial insulator or from an intrinsic Schottky contact.

The growth and properties of Fe films on GaAs substrates has been recently reviewed by Wastlbauer and Bland (2005). They discuss the formation of the interface between Fe and GaAs studied in experiments that systematically examine the role of temperature, substrate reconstruction, and surface stoichiometry on diffusion and interface compound formation. Since the chemistry of Fe–Ga bonding is different from Fe–As bonding, it is no surprise that the overall nature of the crystalline growth of the Fe to GaAs interface is different when the surface is predominantly terminated in Ga or As. The formation of Fe–As bonds is energetically more favorable than Fe–Ga bonds (Thibado *et al*., 1996). This leads to two-dimensional formation of the Fe film on the As-terminated GaAs surface. STM studies have shown that growth of submonolayer Fe on As-rich surfaces happens via two-dimensional nucleation and growth, followed by layer-by-layer growth of Fe on the resulting surface (Kneedler *et al*., 1997). Quite a different scenario occurs on Ga-terminated surfaces. There, the relative energetic cost of Fe–Ga bonds leads to the formation of three-dimensional grains, which coalesce when the Fe coverage exceeds five monolayers (Chambers *et al*., 1986; Xu *et al*., 1999; Monchesky, Heinrich, Urban and Myrtle, 1999; Moosbühler, Bensch, Dumm and Bayreuther, 2002). For thicker films, the surface shows a persistent As composition as seen by XPS during growth (Kneedler *et al*., 1997). A subsequent detailed investigation of the role of temperature on As and Ga surface segregation using Auger electron spectroscopy discovered diffusion and segregation of both atoms, with the diffusion of As occurring at much lower temperatures (Sano and Miyagawa, 1991). At the interface, a chemical reaction occurs between the Fe and GaAs. Studies by (Filipe, Schuhl and Galtier, 1997) suggest that a compound with composition $Fe_3Ga_{2-x}As_x$ forms at the interface.[43] This was correlated with a careful examination of the Fe–Ga–As chemical phase diagram, and interfaces annealed to high temperatures showed the growth of this phase occurring. The magnetic properties of this material are reduced compared with metallic Fe, so formation of such reacted interfacial layers can be expected to reduce the performance of spin injection. Other studies showed that growth at reduced temperatures leads to a reduced thickness of reacted interface material, but growth as low as – 15 °C still shows several monolayers of such material forms, presumably limited by bulk diffusion (Schultz *et al*., 2002).

With Fe layers grown on AlGaAs, spin injection has been obtained using both Schottky contacts as well as Al_2O_3 tunnel barriers. The first report of large spin injection from Fe into GaAs used a naturally occurring Schottky barrier and was monitored via the degree of circular polarization in the electroluminescent light. Zhu and coworkers grew Fe on top of GaAs and obtained about 2% circular polarization of the resulting electroluminescence at room temperature (Zhu *et al*., 2001). They studied the effects of different termination of the GaAs surface and found that similar luminescence polarization was obtained in all cases they studied, As and Ga stabilized surfaces. van 't Erve and coworkers (2004) compared the spin injection efficiency using intrinsic Schottky barrier with amorphous Al_2O_3 barrier. They also measured the spin injection by analyzing the circular polarization state of the electroluminescence signal. They found that spin injection occurred for both devices, but the electroluminescence signal was more than 10 times as large for the Schottky device. The luminescence signal is observed from polarized electron and unpolarized hole recombination. They suggested that the reduced emission efficiency with the grown oxide barrier was due to an enhanced rate of electron–hole recombination caused by localized states at the Al_2O_3 to AlGaAs interface. Another study looking at factors that increase the magnitude of luminescence found that either growing the Fe layer at low temperatures or introducing a very thin intervening Al layer on top of the GaAs leads to increased electroluminescence intensity (Chye, Huard, White and Petroff, 2002). They interpreted this as being due to a

reduced degree of interface compound formation. The degree of magnetic order on an atomic scale controls the magnetization of the injected current, and growth procedures that lead to a cleaner, more magnetically distinct interface appear to improve the degree of spin polarization injected across a barrier.

Other interesting candidates for ferromagnetic injectors are materials that should have completely spin-polarized bands, half-metals. In metallic systems, Heusler alloys are thought to be half-metallic, and several groups have investigated the growth of different Heusler alloys on GaAs and performed spin-injection experiments with their samples. Several groups have grown such samples on different III–V compounds and alloys. The earliest work was reported by Dong *et al*. (1999) who grew single crystal Ni_2MnGa on GaAs. They used a very thin interfacial buffer layer consisting of Sc0.3Er0.7As on top of which the magnetic alloy was grown. They obtained a somewhat reduced Curie temperature, 320 K instead of the bulk value of 376 K, but this could have been due to the film thickness – it may have been thin enough to reduce the magnetic order. Another Heusler alloy, Co_2MnGe was grown on GaAs by Ambrose, Krebs, and Prinz (2000). They grew the compound on annealed GaAs, using individual flux monitors to control stoichiometry, at a moderately low temperature, ∼175 °C, and obtained films with room-temperature ferromagnetism but unusual magnetic anisotropy that was attributed to substrate strain. Later, Dong and coworkers (2005) obtained a measure of spin injection on a sample using Co_2MnGe as the spin current injector. They obtained about 13% circular polarization of electroluminescent emission at 2 K, which corresponds to a spin polarization of 0.27. This is shown in Figure 9 along with a TEM image of the interface. At room temperature the polarization disappeared. Since the Curie temperature of this material is 905 K, the bulk is strongly magnetic at room temperature. It was suggested that some interface chemistry leads to degraded spin polarization at the junction and this becomes more noticeable as the temperature rises. In addition, control of the composition is required for this compound to form. There is a rather wide range of solubility of vacancies and antisite substitutions, so that single crystal films can be grown even without sub 1% relative composition control. But the effect of composition on resulting magnetic properties and the stability of the interface to GaAs are currently being investigated. A simpler Heusler alloy with good structural stability at the GaAs interface was investigated by Kawaharazuka *et al*. (2004). They used Fe_3Si, which is considered to be a Heusler alloy, but which is not completely characterized as a half-metal at this point in time, although as a Heusler alloy it is expected to be half-metallic. They found observable spin injection even at room temperature in electroluminescence.

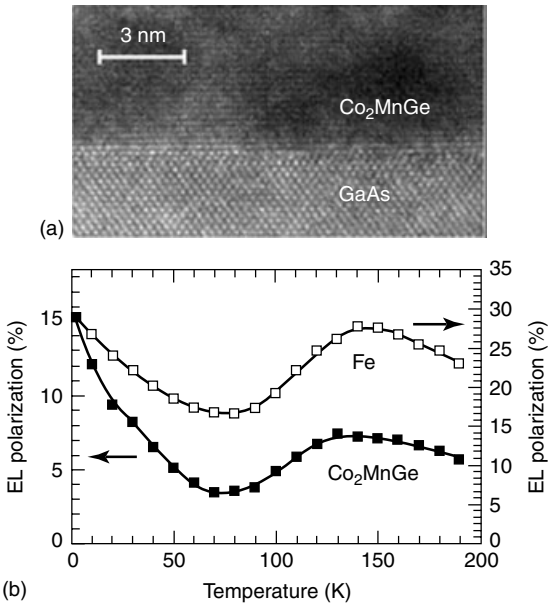

Figure 9. (a) A micrograph of a junction between the Heusler alloy, Co_2MnGe, and GaAs. (b) The temperature dependence of the electroluminescence net circular polarization. (Reproduced from Chye *et al*., 2002, with permission from the American Institute of Physics.)

7 MBE GROWTH OF DILUTE MAGNETIC SEMICONDUCTORS

Dilute magnetic semiconductors (DMS) are nominally insulating phases when undoped, into which magnetic impurities are alloyed at concentrations relatively high compared with typical 'dopant' densities. The most studied systems are based on II–VI and III–V parent phases. Magnetic impurities from the 3d transition metals have most commonly been used. The dopant atoms can do three things depending on the semiconductor. First, they introduce a local magnetic moment because the d electrons remain localized on the dopant site. Secondly, they can introduce band carrier doping if the valence of the impurity differs from the nominal valence of the site on which it sits. Finally, at a sufficiently high density, the impurity atoms give rise to an impurity band in which the Fermi energy can lie and which can mediate conduction.

In II–VI systems, zinc and cadmium telurides and selenides, as well as zinc oxide have been doped with Cr, Mn, and Co (Hou *et al*., 2006; Slobodskyy *et al*., 2004; Mofor *et al*., 2005; Buyanova *et al*., 2006; Nielsen *et al*., 2006; Saeki, Matsui, Kawai and Tabata, 2004). The nominal valence of the transition metal in these systems is 2+, so that no carrier doping occurs. For example, in the case of Co-doped ZnO, ionic absorption bands indicate a fingerprint for +2 valence (Pacuski *et al*., 2006). Since the impurity valence

is the same as the valence of the site on which it substitutes, the 'dopant' density can be very large, ∼50%. With such a large density, the Curie temperature is expected to be large. Indeed, in such systems, a $T_C >$ room temperature is found (Hou *et al*., 2006; Mofor *et al*., 2005; Nielsen *et al*., 2006; Saeki, Matsui, Kawai and Tabata, 2004).

In III–V systems, the transition-metal 3d dopant atom tends to reside on the group-III site and ionizes to a valence of 2+. This means that it introduces hole carriers as well as a magnetic moment. The fact that it has a different charge transfer means that it introduces a large energy cost and this limits the density at which it can be incorporated in equilibrium to a relatively small value. The earliest work used InAs doped with Mn (Munekata *et al*., 1989; Ohno *et al*., 1992). Later, GaAs was doped with Mn (Ohno *et al*., 1996; Hayashi *et al*., 1997) and by introducing a post-growth anneal, a Curie temperature as high as 174 K has been obtained (Ku *et al*., 2003). An excellent review of the work on III–V-based DMS by a large number of researchers is provided by Jungwirth *et al*. (2006).

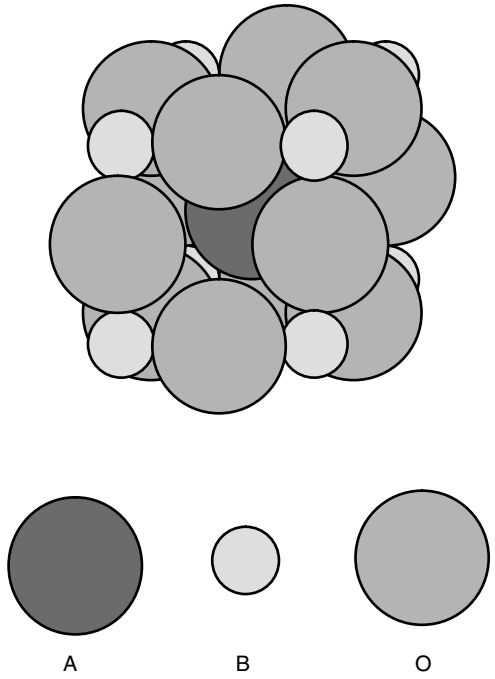

Figure 10. A ball and stick model of the atomic positions in a single unit cell of a simple cubic perovskite ABO_3. The B atom is a transition metal and is sixfold coordinated with oxygen atoms. The B-atom d orbitals hybridize with the oxygen 2p orbitals to give the states near the Fermi energy. The B-atom coordination is octahedral. In this picture to complete an octahedra around the lower right-hand B atom, three oxygen atoms should be added, one below, one to the right, and one out in front. The octahedra are corner-sharing. In real phases, such as manganites, other factors such as Jahn–Teller level splitting and charge localization in Mott–Hubbard split bands can lead to substantial distortions of the cubic structure shown.

8 MBE GROWTH AND PROPERTIES OF PEROVSKITE MAGNETIC OXIDE FILMS AND DEVICES

Perovskite manganites exhibit a rich set of potentially useful physical properties, controlled by composition, magnetic field, temperature, and other factors. These properties, along with their interesting underlying collective physics, have motivated considerable work. The basic perovskite composition can be represented as ABO_3, where A and B are different metal atom sites, and often the A site is an alloyed mixture of two different species. A ball and stick model of the undistorted perovskite structure is shown in Figure 10. The B atom is bonded covalently to six oxygen atoms in octahedral coordination, forming BO_3 molecular orbitals. Solid lines show one such octahedron. Adjacent octahedra are connected by corner-sharing each of the oxygen atoms, and the A atom fits in the space between the octahedra. The cube size is mainly determined by the size of the oxygen orbitals, although the size and valence of the A and B atoms also influence lattice size to a lesser degree. Typically, the cube size is between 3.8 and 4.0 Å. Many different kinds of materials have this structure, ranging from simple insulators, to insulators with very high dielectric constants, to superconductors and the colossal magnetoresistive manganites. In real materials the high symmetry shown in the figure is broken by various (collective) distortions, including Jahn–Teller bond length distortions of the BO_3 unit and cell-to-cell rotation of the octahedra, and these distortions play important roles in determining the electronic and magnetic properties.

The electronic structure of a perovskite phase is mainly derived from the BO_3 molecular orbital. The A site atoms ionize and transfer charge to the BO_3 bands. The valence band is mainly oxygen in character and the conduction band has B-atom character. Insulators like $SrTiO_3$ have a filled valence band and an empty conduction band. The oxygen ions are each charged 2−, the Sr ion is 2+ and the Ti ion is 4+. In conducting perovskites, the Fermi energy lies in the BO_3 band. The most studied manganite is the alloy $La_{1-x}A_xMnO_3$, where A is an alkaline earth, Sr or Ca. When A is Sr, the alloy is often referred to as LSMO, while if A is Ca the alloy is referred to as LCMO. The occupancy of the conduction band per Mn ion is equal to $4 - x$. When the Sr content is zero there are four d electrons, while for $SrMnO_3$ there are three d electrons. Figure 11(a) shows a schematic representation of the energy structure of the molecular orbitals and the occupancy for $LaMnO_3$. Because of the crystal field, the e_g orbitals have a higher energy than

the t_{2g} orbitals. The core t_{2g} spins are strongly coupled by the on-site exchange interaction. These spins align and form an essentially classical core spin. The core electrons are not strongly coupled to neighboring sites. On the other hand, the e_g states are more strongly coupled and they are itinerant in the ferromagnetic phase.

Manganites have a rich assortment of magnetic states, as Figure 11(b) shows (Chmaissem *et al*., 2003). The superexchange interaction between Mn ions occurs through an intermediate oxygen atom and is antiferromagnetic. The ferromagnetic exchange interaction between sites is due to 'double exchange', where the itinerant bandwidth is maximized for ferromagnetic spin alignment – it is more likely and therefore on average easier for an electron to hop to neighboring sites when the core spins are pointed in the same direction. Ferromagnetic exchange is quenched if the e_g electrons are immobilized. For randomly oriented core spins, magnetic scattering dramatically reduces the conductivity. Thus a metal–insulator transition (MIT) should also occur at the magnetic phase transition. However, this is not the complete picture of the MIT, as first pointed out by Millis, Littlewood, and Shraiman (1995). Strong charge-to-lattice coupling is also involved, and this amplifies the change in resistance that occurs when the material becomes magnetic. For $x = 0.35$ the Curie temperature is the largest and the material should become a half-metal, that is, have only one spin band present. This is because both the e_g and t_{2g} states for the minority spin electrons are shifted up in energy by the strong on-site exchange energy. Ideally this would lead to a completely spin-polarized MnO_3 band in the absence of parasitic effects, and this has been a strong motivation for using these manganite phases for various 'spintronic' devices.

To see how the transport and magnetization are tied together, Figure 12 shows the resistance versus temperature for a thin film of $x = 0.3$ LSMO grown by MBE on a (100) $SrTiO_3$ substrate. The MIT occurs at 350 K where the magnetization rises from zero as the temperature is lowered. The resistance drops by about two orders of magnitude and becomes as low as 40 μΩ-cm. This is one of the lowest residual resistivity values obtained for manganite phases (O'Donnell *et al*., 2000a; Coey, Viret and von Molnár, 1999).

Several groups have used MBE techniques to grow manganite films and devices. Figure 13 shows a schematic and a photograph of one such system. Samples are grown on heated substrates in a system with a base pressure of 1×10^{-9} Torr. Typical growth temperatures range from 650 to 720 °C. RHEED is used to monitor the surface during growth. The system employs thermal effusion cells for all elements used, including the transition metals Mn, Cr, Ti, Cu, Zn, Au, and Al. It also has trivalent cations La, Dy, and Bi, divalent cations Ba, Sr, and Ca and it is equipped with an ozone beam for oxidation (Johnson *et al*., 1990). In order to handle the gas flow, the system is pumped by approximately $1000\,l\,s^{-1}$ capacity turbomolecular pumping. Ozone is generated by a

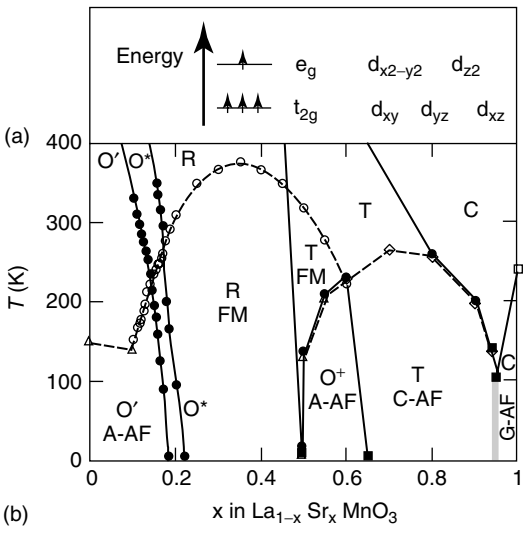

Figure 11. Electronic and magnetic structure of manganite alloys is controlled by filling the MnO_3 states. (a) A schematic representation of the energy levels. (b) Structural and magnetic phase diagram of $La_{1-x}Sr_xMnO_3$. The magnetic phases are antiferromagnetic (AF) or ferromagnetic (FM), and the AF phases are A, C, or G type, which describes the arrangement of core spins. A type has (100) FM sheets with the magnetization of alternating layers oppositely directed. G-type AF has every Mn–O–Mn bond AF, while the C-type AF structure has a more complicated spatial arrangement of spins. O+ and O′ denote orthorhombic phases in which Jahn–Teller distortions are incoherent and coherent, respectively. C, T, and R denote cubic, tetragonal, and rhombohedral phases. (Reproduced from Ambrose *et al*., 2000, with permission from the American Institute of Physics. © 2000.)

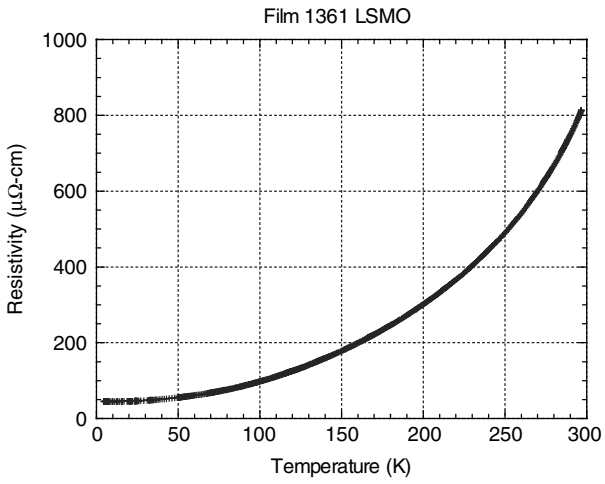

Figure 12. Resistance versus temperature for a film of LSMO, $x = 0.3$, grown by MBE. (Reproduced from Karraharusuka *et al*., 2004, with permission from the American Institute of Physics. © 2004.)

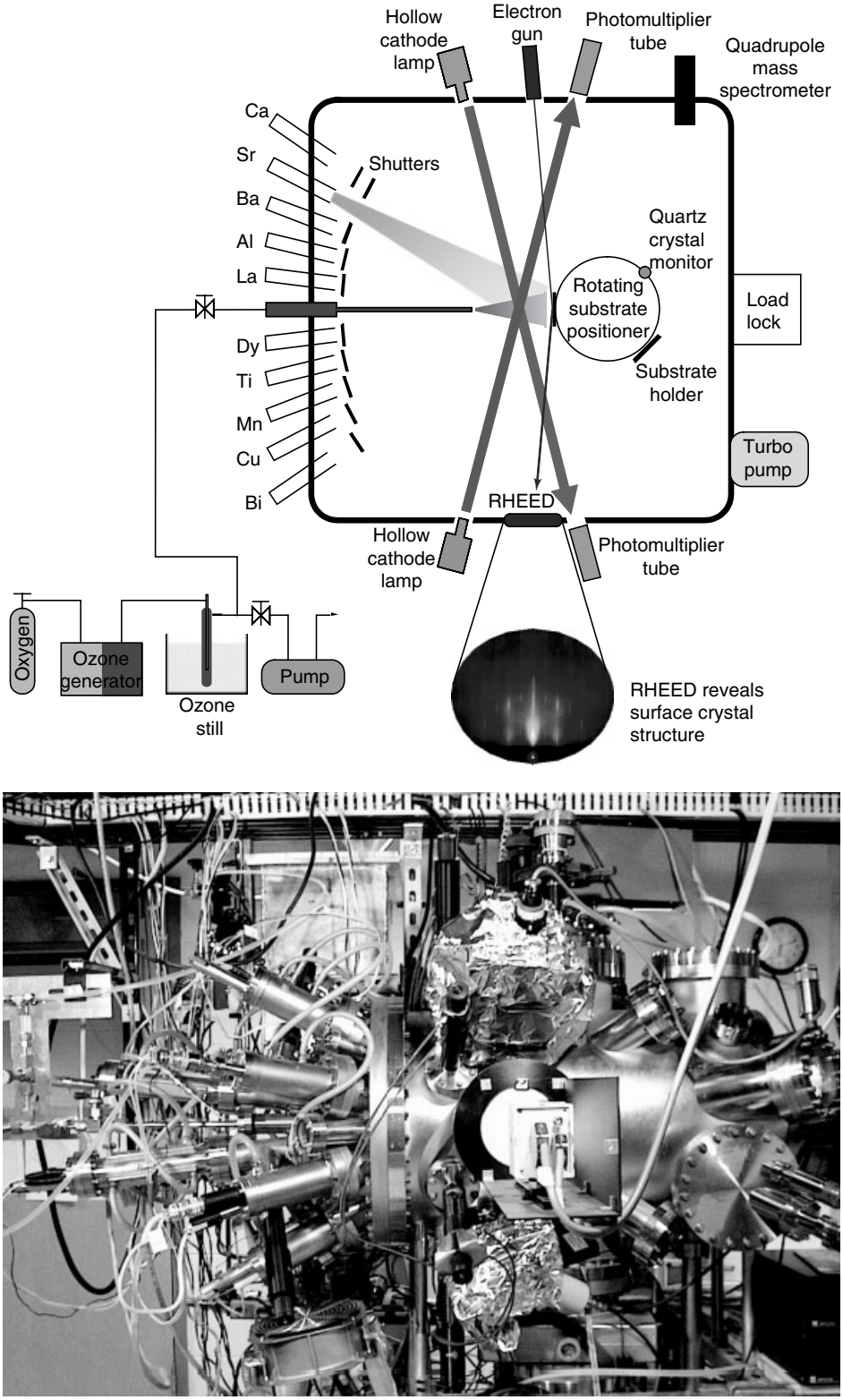

Figure 13. Schematic diagram and photograph of oxide MBE system capable of atomic layer-by-layer growth of complex oxides. The system has 13 metal atom effusion cells, an ozone beam, turbomolecular pumping, load lock and preparation chambers, and RHEED to monitor the film growth.

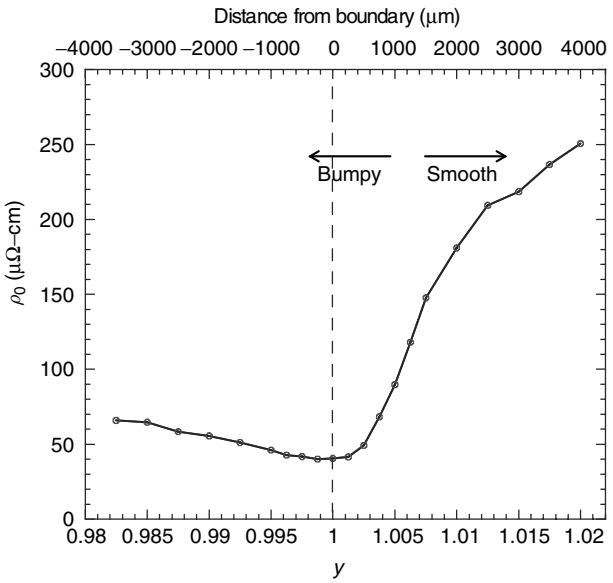

Figure 14. Residual resistivity of $(La_{1-x}Sr_x)_yMnO_3$ samples. The parameter y describes the A site to B site composition ratio. For stoichiometric LSMO $y = 1$, but single-phase material grows by MBE over a wide range of y. For Mn excess, $y < 1$ and the residual resitivity is only weakly dependent on y. For Mn deficiency, the residual resistivity is strongly dependent on y.

silent discharge using a commercial unit capable of producing 3% ozone in oxygen. The ozone is distilled on cold silica gel in a glass still. An hour of accumulation provides enough ozone for more than 10 h of growth. After accumulation, the vapor over the silica gel is pumped with a mechanical pump to a pressure of 100 mTorr, and the ozone used in the growth is drawn from the vapor flowing to the pump. The flow into the growth chamber is controlled by a manually operated needle valve, and reproducible ozone flow is obtained by monitoring the MBE system pressure. Ozone is injected from a tube about 5 in. from the substrate position. The beam expands with an angle of about 10°. Ozone is much more effective at oxidizing metals than molecular oxygen. While the ozone system is relatively simple to build, care must be taken in operation due to the danger of explosion. Too much ozone accumulation and too high a pumping manifold pressure are conditions that may lead to explosion, and consultation with an expert is advised before using such a system. Other groups use atomic oxygen beams generated by microwave discharge (Locquet and Machler, 1992).

Composition control is a very important aspect of manganite film growth. During growth using codeposition, molecular beams provide the dose of atoms to grow each monolayer. We denote the ratio of La + Sr surface composition to Mn surface composition y. This strongly controls the electronic properties of a film of LSMO as shown in Figure 14 where residual resistivity is plotted versus y. Residual resistivity is a measure of carrier scattering. The data show that excess Mn does not lead to much increase in residual resistivity, however, excess La + Sr does. This is also the case for LCMO. Furthermore, the growth dynamics are very different in these two cases. For films slightly rich in La, a smooth surface is obtained, but if the film is rich in Mn, a dramatic proliferation of step edges results. This is shown in the two AFM images in Figure 15. A change in composition of only 1 part in 1000 is enough to change between the surface structures shown. In order to obtain both a smooth surface as well as the lowest residual resistivity, the composition must be precisely controlled. Fortunately, RHEED provides a clear indication of these two regimes, and composition control at the 1/1000 level is possible using this as a diagnostic of surface composition. Figure 16 shows the RHEED patterns observed from these two kinds of surfaces. Figure 16(b) is from a smooth surface, such as shown in the Figure 15(a). Figure 16(a) shows the diffraction pattern obtained from a bumpy surface. Both of these images are obtained with the electron beam in the ⟨100⟩ direction, along the Mn−O bond direction. Figure 16(a) shows the emergence of elevated half-order streaks, which also show up in the diffraction pattern observed along the 110 azimuth. This implies a surface having k-space rods as shown in the inset to Figure 16(d).

Since the electrical and morphological properties of the surface are so sensitive to composition, it is important to control this very accurately. RHEED can provide notice that the bumpy smooth boundary has been crossed, and small corrections can be made to correct for this, but such control is possible only as a refinement to a control scheme that is accurate to the 1% level. RHEED can provide an accuracy increase to 0.1% or better, but it is not able to obtain 0.1% accuracy on its own. In order to get this, it is necessary to use *in situ* flux monitors. Quartz crystal microbalance growth rate monitors are useful if independent measurements of different sources can be made. Atomic absorption spectroscopy is also capable of providing accurate flux monitoring (Klausmeier-Brown, Eckstein, Bozovic and Virshup, 1992). However, to regularly obtain the required accuracy it is necessary to regularly calibrate the *in situ* flux monitors in some way. A convenient method for doing this is to grow a measurement film on a substrate containing only low-mass elements such as BeO, MgO, Si, and so on. If the film is thin enough, it can be analyzed in a particularly simple way by Rutherford backscattering (RBS) analysis (Chu, Mayer and Nicolet, 1978). For sufficiently thin films, each element in the film gives rise to an isolated peak, and the integral of the peak is proportional to surface density time the scattering cross section, which is element specific but available in tables. This is shown in Figure 17. The substrate signal is at lower energy and provides a reliable measure of

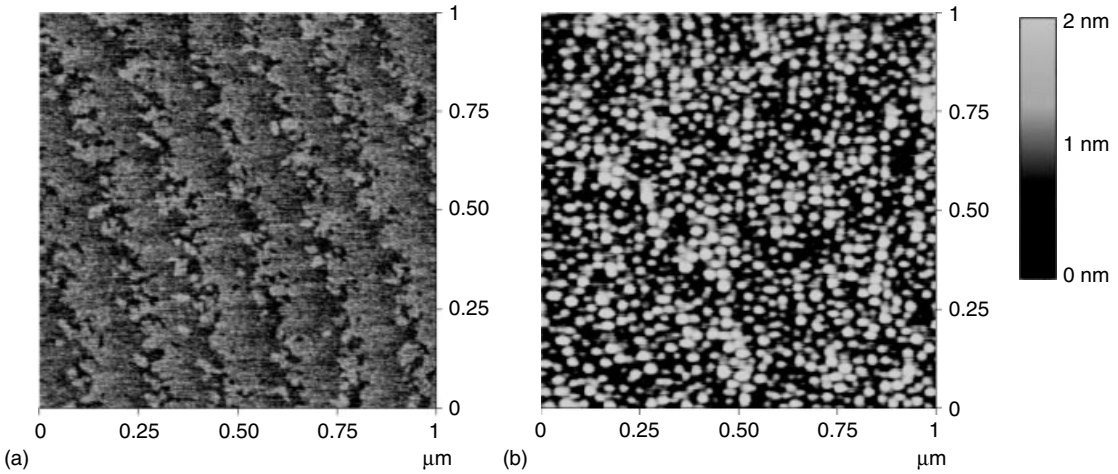

Figure 15. Besides the residual resistivity, the metal atom ratio, $y = ([La] + [Sr])/[Mn]$, also controls the surface morphology. The left panel shows an AFM image of an atomically flat film, exhibiting terracing that has y slightly greater than 1. The second image showing a very bumpy surface is for a film with $y = 0.99$. A small excess of Mn causes step-edge proliferation, leading to growth of a bumpy surface. This is also visible in RHEED, where the smooth surface shows a small reflection spot, while the bumpy surface exhibits streaks and extra reflections indicating a composition-driven surface reconstruction.

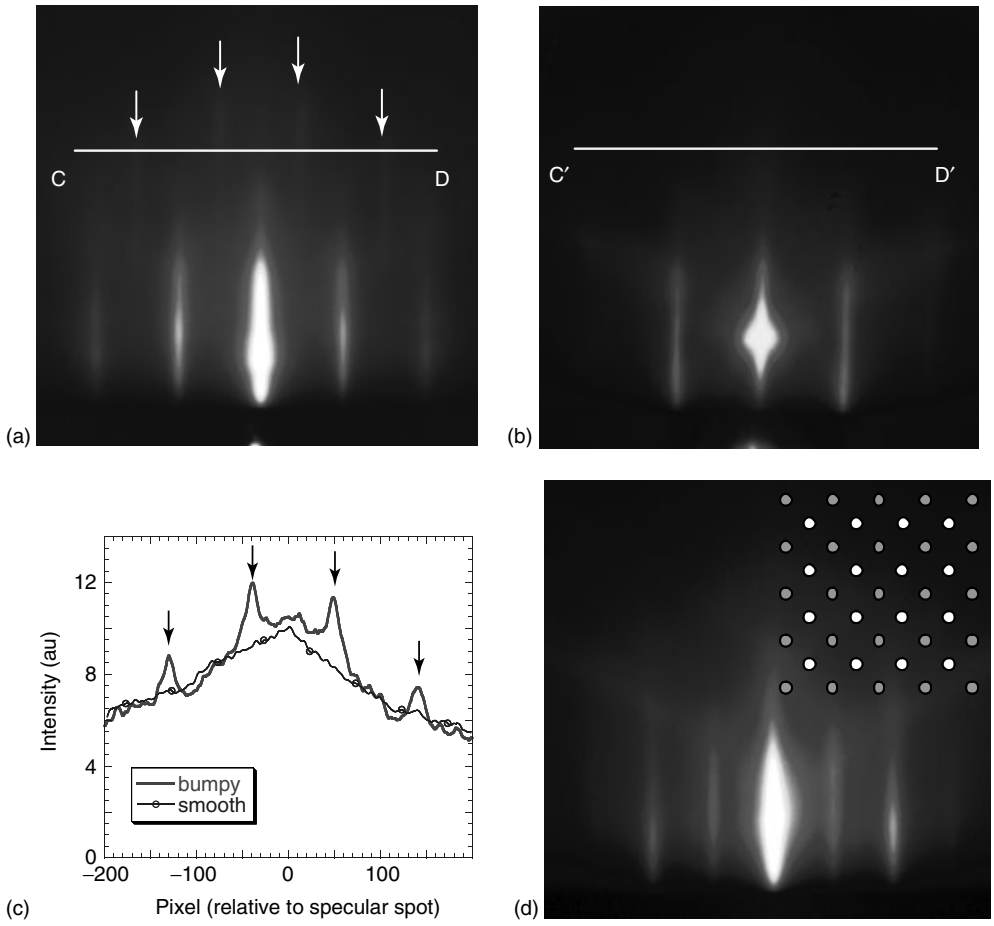

Figure 16. RHEED patterns from the *bumpy* and *smooth* regions from an LSMO sample grown on STO. (a) Bumpy region; ⟨100⟩ direction. (b) Smooth region; ⟨100⟩ direction. (c) Intensity profiles across lines CD and C′D′. Arrows indicate position of the elevated half-order streaks. (d) Bumpy region; ⟨100⟩ direction. Inset shows schematic of k-space rods because of surface reconstruction.

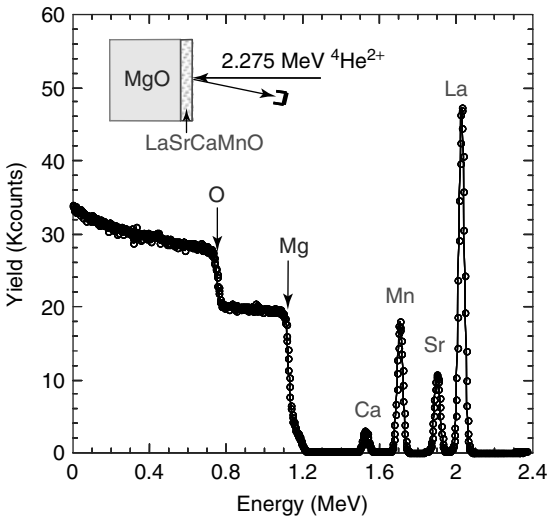

Figure 17. RBS spectrum of a thin film of La–Sr–Ca–Mn–O grown on top of MgO. Since all of the film constituent atoms are heavier than Mg and the film is thin enough, they show up as isolated peaks on a zero background.

the time-integrated beam current. With that knowledge, it is possible to reproducibly calibrate the real-time flux monitor sensors and obtain absolute composition control at the 1% level.

The ground state of the manganite oxides ($La_{0.67}A_{0.33}MnO_3$ where A = divalent dopant) is ferromagnetic and very nearly half-metallic. That is, the conduction electrons are nearly 100% spin polarized. Experiments indicate that the spin polarization, $P = (n_\uparrow - n_\downarrow)/(n_\uparrow + n_\downarrow)$ (where $n_\uparrow, n_\downarrow$ are the density of states for spin $+1/2$ and spin $-1/2$ electrons respectively), is at least 0.83, compared with 0.42 for the canonical ferromagnet, iron (Viret *et al.*, 1997; Soulen *et al.*, 1998; O'Donnell *et al.*, 2000b). These materials thus offer an interesting tool for scientists – a solid-state source of highly (possibly 100%) spin-polarized electrons in a system which is structurally, chemically, and epitaxially compatible with many other interesting perovskite oxide materials. Applications include spin-valve type magnetic tunnel junctions for disk drive read heads, spin-injection devices, and spin-polarized electron tunneling spectroscopy of high T_C superconductors (Viret *et al.*, 1997; O'Donnell *et al.*, 2000b; Sun, Abraham, Roche and Parkin 1998; Obata, Manako, Shimakawa and Kubo, 1999; Kwon *et al.*, 1998; Koller *et al.*, 1998; Stroud *et al.*, 1998). Many applications of these materials involve heteroepitaxy between manganite phases and other perovskite oxide compounds. Here, we discuss fundamental questions regarding manganite growth as it relates to heterostructure applications and describe the growth of films for 'colossal magnetoresistance' spin-valve sensors. The observations and conclusions also apply to other manganite heteroepitaxy problems as well.

The epitaxial growth architecture of a typical spin-valve device consists of a base layer of LSMO, $x = 0.35$, 100 nm thick. On top of this a thin layer of four or five unit cells of $SrTiO_3$or $CaTiO_3$ is grown. This is followed by the growth of a top LSMO film 50 nm thick. The growth of the insulating barrier, especially the interfacial layers, is just as critical as the growth of the manganite electrodes. Indeed, most speculation regarding the rapid loss of magnetoresistance in colossal magnetoresistance magnetic tunnel junctions with increasing temperature has focused on barrier and interfacial disorder (structural, magnetic, and/or compositional). By comparing RHEED oscillations before and after the growth of the insulating barrier one can see that even starting from an atomically flat base electrode, disorder can nucleate in the barrier heteroepitaxy and propagate into the top electrode. The result is a decrease in both the magnitude of the tunneling magnetoresistance, and the temperature at which the magnetoresistance vanishes. A zero bias anomaly in the tunneling conductance at low temperatures of the form predicted by Altshuler, Aronov and Lee (1980) for electron–electron interaction induced renormalization of the density of states in a disordered metal has been observed (O'Donnell *et al.*, 2000b). $SrTiO_3$, $CaTiO_3$, and $LaAlO_3$ barriers were investigated. Of the three, $CaTiO_3$ grows the best as judged by the RHEED image of the barrier surface and RHEED oscillations during barrier growth. For the growth of the insulating barrier, the substrate temperature was decreased by 90 °C in constant ozone pressure for the first two interfacial layers to quench interdiffusion, then increased by 90 °C for the remainder of the barrier growth, then decreased again by 90 °C for the initial layers of the manganite counter electrode. Five unit cell barriers give a typical tunneling conductance of $5 \times 10^{-7}\Omega^{-1}\,\mu m^{-2}$ in tunnel junctions with an area of $200\,\mu m^2$. The tunneling conductance varies exponentially with barrier thickness with each unit cell decreasing the conductance by roughly a factor of 12. The interfacial $La_{1-x}Sr_xO/CaO$ layer between the terminating MnO_2 plane of the manganite and the TiO_2 plane of the $CaTiO_3$ barrier is deposited in a layer-by-layer mode with composition 1/2 ($La_{1-x}Sr_xO$) +1/2 (CaO). The interfacial plane donates electrons to the adjacent MnO_2 plane. In a simple ionic picture, growing this mixed composition at the interface maintains a constant Mn^{4+}/Mn^{3+} ratio of x:$(1-x)$. If the interfacial layer is not doped in this way at the atomic layer level, the Mn^{4+}/Mn^{3+} ratio of the interfacial MnO_2 plane will be increased, effectively increasing the local doping level.

The films were processed into trilayer spin valves using a device geometry that eliminates the effect of resistive voltage drop from transport in the manganite layer. The device architecture is shown in Figure 18(a) and (b). Current

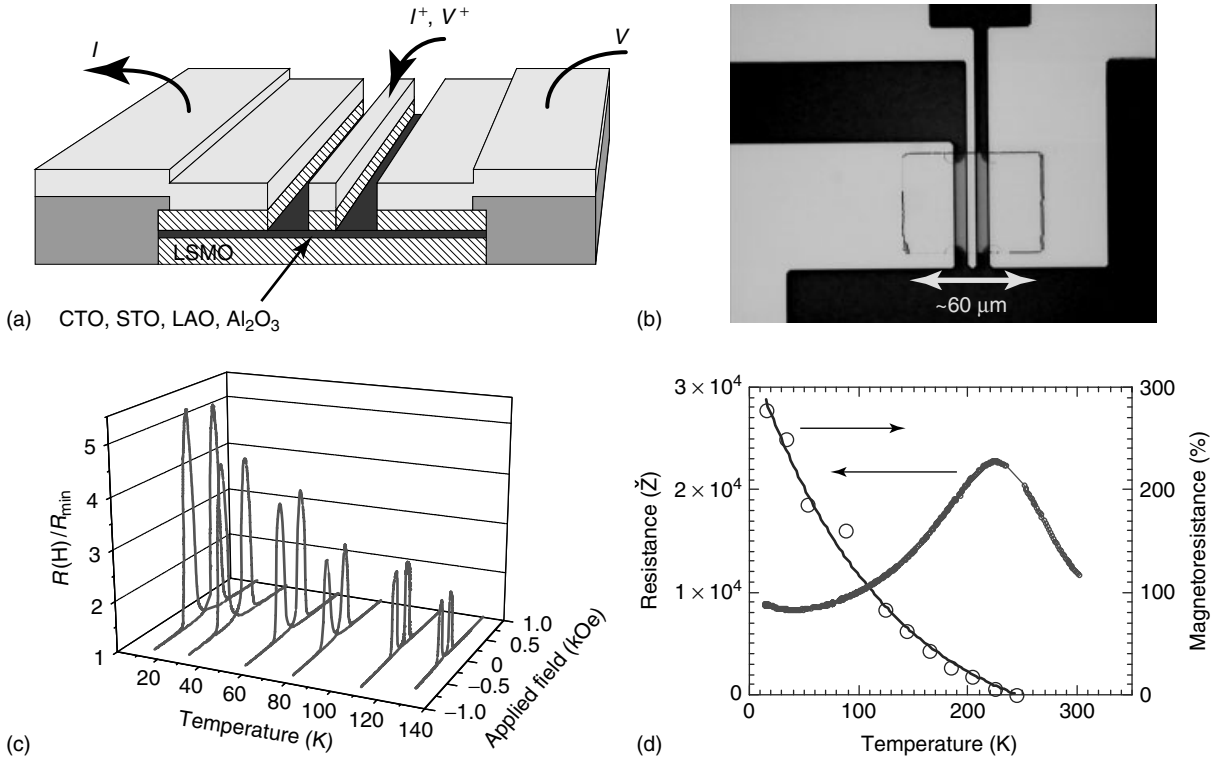

Figure 18. (a) and (b) Schematic view of a spin-valve device. An LSMO injector electrode on top provides spin-polarized carriers to tunnel into a similar LSMO base electrode. The measured tunneling magnetoresistance is shown in (c) as a function of applied field for different temperatures. The maximum measured in this experiment was 450% at 15 K. (d) Dependence of TMR on temperature. How the TMR depends on temperature. It falls faster than the bulk magnetization predicts, indicating nanoscale quenching of the magnetic order above 100 K.

is injected from the top electrode and extracted from the left electrode. A third electrode 'upstream' of the injector measures the base film voltage. The current transfer length, η is many micrometers long. It is equal to $\eta = \sqrt{R_C/R_S}$, where R_C is the specific tunneling resistance (units $\Omega\,\mathrm{cm}^2$) and R_S is the base layer two-dimensional sheet resistance (units Ω/square). This design serves two purposes. First, the use of a third electrode provides a measurement of the voltage across the barrier, without introducing any significant voltage drop from current flowing in the plane. The resistance of the junction is high, so that the series film resistance is a small correction, and this design allows a direct measurement of the tunneling voltage without the need for fine lithography. The second advantage is the large shape anisotropy introduced for one of the two electrodes, namely, the top one. This provides a different coercive field for the two electrodes and leads to a wider range of applied field in which the antialigned configuration occurs. The tunneling magnetoresistance is shown in the lower two panels of Figure 18. In the lower left panel, curves are shown for different temperature that trace out the hysteretic junction resistance as a function of applied field. Defining $\mathrm{TMR} = R_{\mathrm{ANTI}}/R_{\mathrm{ALIGN}}$ the maximum TMR was 4.5. The TMR decreased with temperature more rapidly than the temperature dependence of the bulk magnetization would predict. This was attributed to a reduced magnetization just at the interface, due to the scattering introduced by the barrier.

This hypothesis was investigated by Kavich and coworkers using resonant X-ray magnetocircular dichroism (Kavich *et al*., 2005; Freeland *et al*., 2006). This followed a study by Park *et al*. (1998) using spin resolved photoemission to measure the top layer spin polarization. Samples with two unit cells of $SrTiO_3$, grown on top of a manganite film were studied. The X rays were tuned across the Mn L edge and the dependence of magnetic scattering on energy and temperature was measured also as a function of incident angle. The results from several angles allowed the extraction of a magnetization profile as a function of depth. A second sample was also analyzed which had an interfacial layer of $LaMnO_3$. The use of such an interfacial layer to 'protect' the surface magnetization had been suggested by Yamada and coworkers and studied using optical harmonic generation, sensitive to the abruptness of the magnetic profile (Yamada *et al*., 2004). Figure 19 shows the magnetization profile inferred from the XMCD measurements, showing a substantial drop in surface magnetization as a function of temperature.

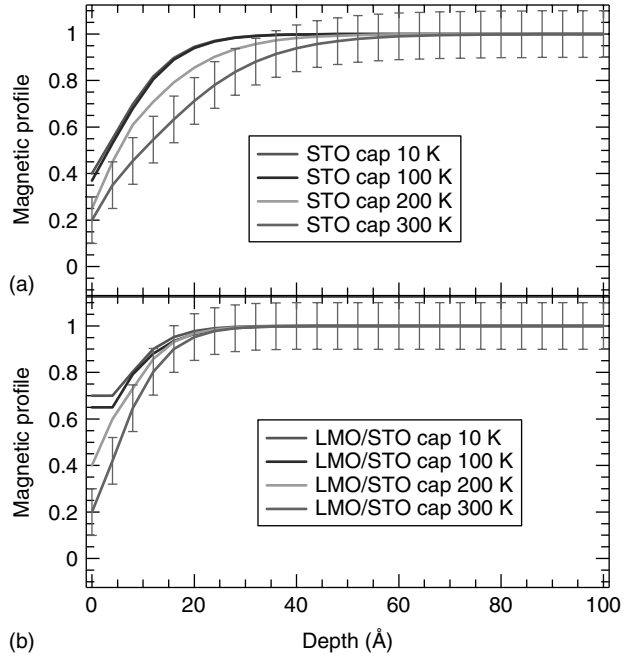

Figure 19. Magnetization profile as a function of depth for different temperatures as shown in the legends. (a) Magnetization profile for a film of LSMO, $x = 0.35$, capped with two unit cells of $SrTiO_3$ (STO). (b) Magnetization profile for a sample with two unit cells of $LaMnO_3$ between the LSMO and the STO cap. Both samples show a significant drop-off in the interface magnetization as the temperature rises. The low-temperature behavior of the LMO/STO cap sample indicates a better surface polarization.

MBE also provides a method to assemble samples with a fixed average composition, but with nanoscale organization of the atomic constituents. Early work aimed at making superlattices, having the same average composition as the highest T_C alloy ($x \sim 0.33$), but with each plane either $LaMnO_3$ or $SrMnO_3$ was carried out by Salvador *et al.* (1999). They were able to use laser-based MBE to construct superlattices consisting of alternating layers of LMO and SMO, keeping the average $x = 0.26$. They observed a systematic reduction of T_C with increasing slab thickness. They attributed this to increasing charge localization in the constituent slabs as the slab thicknesses became larger. Bhattacharya and coworkers have extended this work using MBE. Digital superlattices maintaining an average composition of $x = 0.33$ were grown, starting with samples with one unit cell of SMO and two unit cells of LMO. Resistive transitions spanning the range of superlattice pitches from 1:2 to 5:10 were grown and their properties measured. Figure 20 shows resistance versus temperature for an alloy with composition $x = 0.33$ as well as digital superlattices in this range. For the thinnest slabs, the digital superlattice reduces doping disorder and a lower residual resistivity is observed. Comparable $R(T)$ is also observed for the 2:4 sample, although a reduced

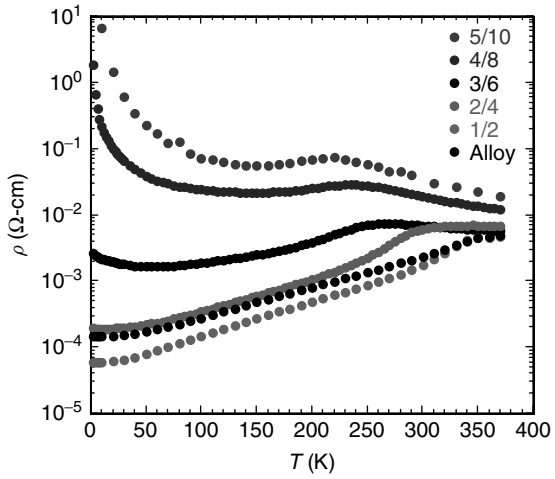

Figure 20. Resistance versus temperature for five digital superlattices, showing the emergence of charge localization as the layer thicknesses are made larger. The 1/2 digital superlattice has a lower resistivity than the random alloy of the same composition.

T_C was observed. When the slab thickness increased to 3:6 and higher, the T_C continued to drop and the low-temperature resistivity developed a strong upturn, indicating localization. These results indicate that new phase behavior can be tuned by accurate atomic-scale synthesis.

Complex oxides provide a rich set of materials with wide-ranging properties that have been observed in bulk samples. These phases provide the starting point for efforts to obtain new materials properties resulting from interaction between different materials at carefully prepared interfaces. The length scales of interactions between complex oxides at such interfaces in likely to be small, typically several unit cells at most. This places a high premium on careful atomistic growth. MBE provides this kind of control and the potential for new phenomena to emerge in cleverly engineered samples.

REFERENCES

Altshuler, B.L. and Aronov, A.G., Lee, P.A. (1980). Interaction effects in disordered Fermi systems in two dimensions. *Physical Review Letters*, **44**(19), 1288–1291.

Ambrose, T., Krebs, J.J. and Prinz, G.A. (2000). Epitaxial growth and magnetic properties of single-crystal Co_2MnGe Heusler alloy films on GaAs (001). *Applied Physics Letters*, **76**(22), 3280–3282.

Baibich, M.N., Broto, J.M., Fert, A., *et al.* (1988). Giant magnetoresistance of (001)Fe/(001)Cr magnetic superlattices. *Physical Review Letters*, **61**(21), 2472–2475.

Barthélémy, A., Fert, A., Baibich, M.N., *et al.* (1990). Magnetic and transport propoerties of Fe/Cr superlattices (invited). *Journal of Applied Physics*, **67**(9), 5908–5913.

Borchers, J., Sinha, S., Salamon, M.B., *et al*. (1987). Magnetic and structural characterization of Dy-Y superlattices. *Journal of Applied Physics*, **61**(8), 4049–4051.

Braun, W. (1999). *Applied RHEED: Reflection High Energy Electron Diffraction during Crystal Growth*, (Springer Tracts in Modern Physics). Spring-Verlag: Berlin and Heidelberg BMBH & Co. K, 1–223.

Buyanova, I.A., Chen, W.M., Ivill, M.P., *et al*. (2006). Optical characterization of ZnMno-based dilute magnetic semiconductor strutures. *Journal of Vacuum Science and Technology B*, **24**(1), 259–262.

Chambers, S.A., Xu, F., Chen, H.W., *et al*. (1986). Simultaneous epitaxy and substrate out-diffusion at a metal-semiconductor interface: FE/GaAs(001)-c(8×2). *Physical Review B*, **34**(10), 6605–6611.

Chmaissem, O., Dabrowski, B., Kolesnik, S., *et al*. (2003). Structural and magnetic phase diagrams of $La_{1-x}Sr_xMnO_3$ and $Pr_{1-y}Sr_yMnO_3$. *Physical Review B*, **67**(9), 094431-1–094431-13.

Cho, A.Y. and Arthur, J.R. (1975). *Molecular Beam Epitaxy. In: Progress in Solid State Chemistry*, McCaldin, J.O., Somorjai, G. (Ed.), Pergamon Press: New York, Vol. 110, 157–191.

Chye, Y., Huard, V., White, M.E. and Petroff, P.M. (2002). Properties of a Fe/GaAs(001) hybrid structure grown by molecular-beam epitaxy. *Applied Physics Letters*, **80**(3), 449–551.

Chu, W-K., Mayer, J.W. and Nicolet, M-A. (1978). *Backscattering Spectrometry*. Academic Press: New York, p. 384.

Coey, J.M.D. and Viret, M., von Molnár, S. (1999). Mixed-valence manganites. *Advances in Physics*, **48**(2), 167–293.

Dong, X.Y., Adelmann, C., Xie, J.W., *et al*. (2005). Spin injection from the Heusler alloy Co_2MnGe into $Al_{0.1}Ga_{0.9}As$/FaAs heterostructures. *Applied Physics Letters*, **86**, 102107-1–102107-3.

Dong, J.W., Chen, L.C., Palmstrom, C.J., *et al*. (1999). Molecular beam epitaxy growth of ferromagnetic single crystal (001) Ni_2MnGa on (001) GaAs. *Applied Physics Letters*, **75**(10), 1443–1445.

Durbin, S.M., Cunningham, J.E., Mochel, M.E. and Flynn, C.P. (1981). Nb-Ta metal superlattices. *Journal of Physics F: Metal Physics*. **11**, L223–L226.

Eckstein, J.N. and Bozovic, I. (1995). High-temperature superconducting multilayers and heterostructures grown by atomic layer-by-layer molecular beam epitaxy. *Annual Review of Materials Science*, **25**, 679–709.

Erwin, R.W., Rhyne, J.J., Salamon, M.B., *et al*. (1987). Magnetic structure of Dy-Y superlattices. *Physical Review B*, **35**(13), 6808–6825.

Etienne, P. and Massies, J. (1993). Basic considerations on the growth of metallic layers by molecular beam epitaxy: application to Cr/Fe, Ag/Fe and Cu/Co multilayers. *Journal de Physique*, **3**(8), 1581–1588.

Farrow, R.F.C. (1998). The role of molecular beam epitaxy in research on giant magnetoresistance and interlayer exchange coupling. *IBM Journal of Research and Development*, **42**(1), 43–52.

Fawcett, E. (1988). Spin-density-wave antiferromagnetism in chromium. *Reviews of Modern Physics*, **60**(1), 209–283.

Filipe, A., Schuhl, A. and Galtier, P. (1997). Structure and magnetism of the Fe/GaAs interface. *Applied Physics Letters* **70**(1), 129–131.

Flynn, C.P. (1988). Constraints on the growth of metallic superlattices.. *Journal of Physics F: Metal Physics*, **18**, L195–L200.

Freeland, J.W., Kavich, J.J., Gray, K.E., *et al*. (2006). Suppressed magnetization at the surfaces and interfaces of ferromagnetic metallic manganites. condmat/0611112-1-15.

Greene, L.H., Feldman, W.L., Rowell, J.M., *et al*. (1985). Structural, magnetic and superconducting properties of rare-earth/superconductor multilayer films. *Superlattices and Microstructures*, **1**, 407–415.

Grunberg, P., Schreiber, R., Pang, Y., *et al*. (1986). Layered magnetic structures: Evidence for antiferromagnetic coupling of Fe layers across Cr interlayers. *Physical Review Letters*, **57**(19), 2442–2445.

Hammar, P.R., Bennett, B.R., Yang, M.J. and Johnson, M. (1999). Observation of spin injection at a ferromagnet-semiconductor interface. *Physical Review Letters*, **83**(1), 203–206.

Hayashi, T., Tanaka, M., Nishinaga, T., *et al*. (1997). (GaMn)As: GaAs-based III-V diluted magnetic semiconductors grown by molecular beam epitaxy. *Journal of Crystal Growth: Molecular Beam Epitaxy*, **175/176**(2), 1063–1068.

Hou, X.J., Teo, K.L., Sreenivasan, M.G., *et al*. (2006). MBE growth and properties of Cr-doped ZnTe on GaAs(001). *Thin Solid Films*, **505**(1–2), 126–128.

Johnson, B.R., Beauchamp, K.M., Wang, T., *et al*. (1990). In situ growth of $DyBa_2Cu_3O_{7-x}$ thin films by molecular beam epitaxy. *Applied Physics Letters*, **56**(19), 1911–1913.

Jungwirth, T., Sinova, J., Mašek, J., *et al*. (2006). Theory of ferromagnetic (III,Mn)V semiconductors. *Reviews of Modern Physics*, **78**, 809–864.

Kavich, J.J., Warusawithana, M.P., Freeland, J.W., *et al*. (2005). Nanoscale suppression of magnetization at atomically assembled manganite interfaces. cond-mat/0512158-1-9.

Kawaharazuka, A., Ramsteiner, M., Herfort, J., *et al*. (2004). Spin injection from Fe_3Si into GaAs. *Applied Physics Letters*, **85**(16), 3492–3494.

Klausmeier-Brown, M.E., Eckstein, J.N., Bozovic, I. and Virshup, G.F. (1992). Accurate measurement of atomic beam flux by pseudo-double-beam atomic absorption spectroscopy for growth of thin-film oxide superconductors. *Applied Physics Letters*, **60**(5), 657–659.

Kneedler, E.M., Jonker, B.T., Thibado, P.M., *et al*. (1997). Influence of substrate surface reconstruction on the growth and magnetic properties of Fe on GaAs(001). *Physical Review B*, **56**(13), 8163–8168.

Koller, D., Osofsky, M.S., Chrisey, D.B., *et al*. (1998). Suppression of superconductivity by injection of spin-polarized current. *Applied Physics Letters*, **83**(11), 6774–6776.

Ku, K.C., Potashnik, S.J., Wang, R.F., *et al*. (2003). Highly enhanced Curie temperature in low-temperature annealed [Ga, Mn]As epilayers. *Applied Physics Letters*, **82**(14), 2302–2304.

Kittel, C. (1987). *Quantum Theory of Solids*, 2nd Revised Printing, John Wiley & Sons: New York, p. 360.

Kwo, J., Gyorgy, E.M., McWhan, D.B., *et al*. (1985a). Magnetic and structural properties of single-crystal rare-earth Gd-Y superlattices. *Physical Review Letters*, **55**, 1402–1405.

Kwo, J., Hong, M., DiSalvo, F.J., *et al*. (1987). Modulated magnetic properties in synthetic rare-earth Gd-Y superlattices. *Physical Review B*, **35**, 7295–7298.

Kwo, J., McWhan, D.B., Hong, M., *et al*. (1985b). In Structural properties of single crystal rare-earth thin films Y and Gd grown by molecular beam epitaxy. *Layered Structures, Epitaxy and Interfaces*, *Materials Research Society Symposia Proceedings*, Gibson, J.H. and Dawson, L.R. (Eds.), Materials Research Society: Pittsburgh, p. 509, Vol. 37.

Kwon, C., Jia, Q.X., Fan, Y., *et al*. (1998). Large magnetoresistance in $La_{0.7}Sr_{0.3}MnO_3/SrTiO_3/La_{0.7}Sr_{0.3}MnO_3$ ramp-edge junctions. *Applied Physics Letters*, **72**(4), 486–488.

Lee, W.Y., Gardelis, S., Choi, B-C., *et al*. (1999). Magnetization reversal and magnetoresistance in a lateral spin-injection device. *Journal Applied Physics*, **85**(9), 6682–6685.

Locquet, J-P. and Machler, E. (1992). Characterization or a radio frequency plasma source for molecular beam epitaxial growth of high-T_c superconductor films. *Journal of Vacuum Science and Technology A, Surfaces and Films*, **10**(5), 3100–3103.

Majkrzak, C.F., Kwo, J., Hong, M., *et al*. (1991). Magnetic rare earth superlattices. *Advances in Physics*, **40**(2), 99–189.

Millis, A.J., Littlewood, P.B. and Shraiman, B.I. (1995). Double Exchange Alone Does Not Explain the Resistivity of $La_{1-x}Sr_xMnO_3$. *Physical Review Letters*, **74**(25), 5144–5147.

Mofor, A.C., El-Shaer, A., Bakin, A., *et al*. (2005). Magnetic property investigations on Mn-doped ZnO layers on sapphire. *Applied Physics Letters*, **87**, 062501-1–062501-3.

Monchesky, T.L., Heinrich, B., Urban, R. and Myrtle, K. (1999). Magnetoresistance and magnetic properties of Fe/Cu/Fe/GaAs(100). *Physical Review B*, **60**(14), 10242–10251.

Moosbühler, R., Bensch, F., Dumm, M. and Bayreuther, G. (2002). Does the substrate surface reconstruction affect the uniaxial magnetic anisotropy?. *Journal of Applied Physics*, **91**(10), 8757–8759.

Munekata, H., Ohno, H., von Molnar, S., *et al*. (1989). Diluted magnetic III-V semiconductors. *Physical Review Letters*, **63**(17), 1849–1852.

Nielsen, K., Bauer, S., Lübbe, M., *et al*. (2006). Ferromagnetism in epitaxial $Zn_{0.95}Co_{0.05}O$ films grown on ZnO and Al_2O_3. *Physical Status Solidi A*, **203**(14), 3581–3596.

Obata, T., Manako, T., Shimakawa, Y. and Kubo, Y. (1999). Tunneling magnetoresistance at up to 270 K in $La_{0.8}Sr_{0.2}MnO_3/SrTiO_3/La_{0.8}Sr_{0.2}MnO_3$ junctions with 1.6-nm-thick barriers *Applied Physics Letters*, **74**(2), 290–292.

O'Donnell, J., Andrus, A.E., Oh, S., *et al*. (2000a). Growth of "colossal" magnetoresistance heterostructures by molecular beam epitaxy. *Proceedings of the 1999 Magnetoresistive Oxides and Related Materials Symposium*, Materials Research Society: Warrendale, PA, pp. 9–14, Vol. 602.

O'Donnell, J., Andrus, A.E., Oh, S., *et al*. (2000b). Colossal magnetoresistance magnetic tunnel junctions grown by molecular-beam epitaxy. *Applied Physics Letters*, **76**(14), 1914–1916.

Ohno, H., Munekata, H., Penney, T., *et al*. (1992). Magnetotransport properties of *p*-type (In, Mn)As diluted magnetic III-V semiconductors. *Physical Review Letters*, **68**(17), 2664–2667.

Ohno, H., Shen, A., Matsukara, F., *et al*. (1996). (Ga,Mn)As: A new diluted magnetic semiconductor based on GaAs. *Applied Physics Letters*, **69**(3), 363–365.

Pacuski, W., Ferrand, D., Cibert, J., *et al*. (2006). Effect of the *s,p-d* exchange interaction on the excitons in $Zn_{1-x}Co_xO$ epilayers. *Physical Review B*, **73**, 035214-1–035214-13.

Park, J-H., Vescovo, E., Kim, H-J., *et al*. (1998). Magnetic Properties at Surface Boundary of a Half-metallic Ferromagnet $La_{0.7}Sr_{0.3}MnO_3$ *Physical Review Letters*, **81**(9), 1953–1956.

Parkin, S.S.P., Bhadra, R. and Roche, K.P. (1991). Oscillatory magnetic exchange coupling through thin copper layers. *Physical Review Letters*, **66**(16), 2152–2155.

Ploog, K. (1982). Molecular beam epitaxy of III-V compounds: Application of MBE-Grown films. *Annual Review of Materials Science*, **12**, 123–148.

Rashba, E.I. (2000). Theory of electrical spin injection: Tunnel contacts as a solution of the conductivity mismatch problem. *Physical Review B*, **62**(24), R16267–R16270.

Rhyne, J.J. and Erwin, R.W. (1995). *Magnetism in Artificial Metallic Superlattices of Rare Earth Metals. Chapt. 1. Handbook of Magnetic Materials*, Buschow, K.H.J. (Ed.), North Holland Science Publishers: Amsterdam, Vol. 8. 1–56.

Saeki, H., Matsui, H., Kawai, T. and Tabata, H. (2004). Transparent magnetic semiconductors based on ZnO. *Journal of Physics: Condensed Matter*, **16**(48), S5533–S5540.

Salamon, M.B., Sinha, S., Rhyne, J.J., *et al*. (1986). Long-range incommensurate magnetic order in a Dy-Y multilayer *Physical Review Letters*, **56**(3), 259–262.

Salvador, P.A., Haghiri-Gosnet, A-M., Mercey, B., *et al*. (1999). Growth and magnetoresistive properties of $(LaMnO_3)_m(SrMnO_3)_n$ superlattices. *Applied Physics Letters*, **75**(17), 2638–2640.

Sano, K-I. and Miyagawa, T. (1991). Surface segregations during epitaxial growth of Fe/Au multilayers on GaAs(001). *Japanese Journal of Applied Physics*, **30**(7), 1434–1441.

Scheinfein, M.R., Unguris, J., Kelley, M.H., *et al*. (1990). Scanning electron microscopy with polarization analysis (SEMPA). *Review of Scientific Instruments*, **61**(10), 2501–2527.

Schmidt, G., Ferrand, D., Molenkamp, L.W., *et al*. (2000). Fundamental obstacle for electrical spin injection from a ferromagnetic metal into a diffusive semiconductor. *Physical Review B*, **62**(8), R4790–R4793.

Schultz, B.D., Farrell, H.H., Evans, M.M.R., *et al*. (2002). ErAs interlayers for limiting interfacial reactions in Fe/FaAs(100) heterostructures. *Journal of Vacuum Science and Technology B: Microelectronics and Nanometer Structures*, **20**(4), 1600–1608.

Slobodskyy, T., Rüster, C., Fiederling, R., *et al*. (2004). Molecular-beam epitaxy of (Zn,Mn)Se on Si(100). *Applied Physics Letters*, **85**(25), 6215–6217.

Soulen Jr., R.J., Byers, J.M., Osofsky, M.S., *et al*. (1998). Measuring the spin polarization of a metal with a superconducting point contact. *Science*, **282**(5386), 85–88.

Stroud, R.M., Kim, J., Eddy, C.R., *et al*. (1998). Fabrication of $YBa_2Cu_3O_{7-\delta}/SrTiO_3/La_{0.7}Sr_{0.3}MnO_{3-\delta\delta}$ junctions for the control of supercurrent by spin-polarized quasiparticle current injection. *Applied Physics Letters*, **83**(11), 7189–7191.

Sun, J.Z., Abraham, D.W. Roche, K. and Parkin, S.S.P. (1998). Temperature and bias dependence of magnetoresistance in doped manganite thin film trilayer junctions. *Applied Physics Letters*, **73**(7), 1008–1010.

Thibado, P.M., Kneedler, E., Jonker, B.T., *et al*. (1996). Nucleation and growth of Fe on GaAs(001)-(2×4) studied by scanning tunneling micorscopy. *Physical Review B*, **53**(16), R10481–R10484.

Unguris, J., Celotta, R.J. and Pierce, D.T. (1991). Observation of two different oscillation periods in the exchange coupling of Fe/Cr/Fe(100). *Physical Review Letters*, **67**(1), 140–143.

van't Erve, O.M.J., Kioseoglou, G., Hanbicki, A.T., *et al*. (2004). Comparison of Fe/Schottky and Fe/Al_2O_S tunnel barrier contacts for electrical spin injection into GaAs. *Applied Physics Letters*, **84**(21), 4334–4336.

Viret, M., Drouet, M., Nassar, J., *et al*. (1997). Low-field colossal magnetoresistance in manganite tunnel spin valves. *Europhysics Letters*, **39**(5), 545–549.

Wastlbauer, G. and Bland, J.A.C. (2005). Structural and magnetic properties of ultrathin epitaxial Fe films on GaAs(001) and related semiconductor substrates. *Advances in Physics*, **54**(2), 137–219.

Xu, Y.B., Kernohan, E.T.M., Freeland, D.F., *et al*. (1999). Structure and magnetic properties of epitaxial Fe films on GaAs(100) and InAs(100). *Journal of Magnetism and Magnetic Materials*, **198–199**, 703–706.

Yamada, H., Ogawa, Y., Isshii, Y., *et al*. (2004). Engineered interface of magnetic oxides. *Science*, **305**(5684), 646–648.

Zabel, H. (1999). Magnetism of chromium at surfaces, at interfaces and in thin films. *Journal of Physics: Condensed Matter*, **11**(48), 9303–9346.

Zhu, H.J., Ramsteiner, M., Kostial, H., *et al*. (2001). Room-temperature spin injection from Fe into GaAs. *Physical Review Letters*, **87**(1), 016601-1–016601-4.

Epitaxial Heusler Alloys on III–V Semiconductors

Thorsten Hesjedal[1,2] and Klaus H. Ploog[1]

[1] *Paul–Drude–Institut für Festkörperelektronik, Berlin, Germany*
[2] *University of Waterloo, Waterloo, Ontario, Canada*

1 INTRODUCTION

The relatively new field of spin electronics (or spintronics) deals with physical systems where the device functionality is not only determined by the charge of electrons (holes) but also by the spin of the carriers (for a review see Prinz, 1998). Whereas the charge has been exploited in electronic devices for more than a century, it was not until 1988 when the door to the technical application of the spin was opened–although already in 1936 Mott realized that up and down spins in a metallic ferromagnet have different mobilities (Mott, 1936). The giant magnetoresistance (GMR) effect, which was discovered by the groups of Grünberg (Binasch, Grünberg, Saurenbach and Zinn, 1989) and Fert (Baibich *et al*., 1988), refers to the observation that the resistance of a ferromagnet–nonferromagnet–ferromagnet multilayer system is much larger when the ferromagnetic layers are magnetized in opposite directions. Three years later, the group of Parkin (Dieny *et al*., 1991) presented magnetic read-heads incorporating spin valves which are based on the GMR effect. Since then, besides a continuous improvement of magnetic sensors, magnetic memory devices were also proposed and demonstrated, like the magnetic random access memory (MRAM) cell.

On the basis of the pioneering proposal of (Datta and Das, 1990) to replace the emitter and collector in a field effect transistor (FET) by ferromagnetic electrodes, a number of concepts have been presented since then (for a review see Prinz, 1998). A first bipolar spin transistor involving ferromagnetic emitter and collector, sandwiched between a nonmagnetic area in a trilayer geometry, was proposed and demonstrated by Johnson (1993, 1995). In a planar geometry, the injection of a spin-polarized current into a semiconductor is a key issue (Ohno *et al*., 1999), followed by the preserving of the spin state and its manipulation (Awschalom and Kikkawa, 1999).

At the basis of most spintronics devices are the ferromagnetic contacts or layers which act as polarizers (or analyzers) for the carriers. Getting beyond the typical spin polarization of about 50% – that can be reached using alloys of Fe, Co, and Ni (Monsma and Parkin, 2000) – will dramatically enhance the performance of memory devices and will be crucial for spin transistors. Consequently, it is highly desirable to obtain a large degree of polarization at the Fermi level. The ideal case of 100% spin polarization is a property of a special class of materials, the so-called half-metallic ferromagnets (HMFs). They are characterized by a metallic behavior of the majority-spin electrons and a semiconducting behavior of the minority-spin

Handbook of Magnetism and Advanced Magnetic Materials. Edited by Helmut Kronmüller and Stuart Parkin. Volume 3: *Novel Techniques for Characterizing and Preparing Samples*. ISBN: 978-0-470-02217-7.

electrons (de Groot, Mueller, van Engen and Buschow, 1983); for a review see Pickett and Moodera (Pickett and Moodera, 2001). A number of compounds were found to be half metallic through band-structure calculations, such as CrO_2 (Schwarz, 1986), Mn_2VAl (Weht and Pickett, 1999), the Mn-containing perovskite $La_{1-x}Sr_xMnO_3$, where the spin polarization was determined via spin-resolved photoemission measurements (Park *et al*., 1998) and scanning tunneling spectroscopy (Wei, Yeh, Vasquez and Gupta, 1998), and many more.

A special class of materials, the so-called Heusler alloys (HAs) (Heusler, Starck and Haupt, 1903), came into focus when de Groot *et al*. showed *theoretically* that a number of Mn-based HAs are half-metals (de Groot, Mueller, van Engen and Buschow, 1983). On the basis of the theoretical results, the unusual magneto-optical properties of PtMnSb were explained by the extreme asymmetry of the electronic properties of spin-up and spin-down electrons (de Groot, Mueller, van Engen and Buschow, 1984). HAs, which are named after Heusler, are primarily defined by their crystal structure. The half-HAs XYZ and the full-HAs X_2YZ have a $C1_b$ and $L2_1$ crystal structure, respectively, where X and Y are transition metals and Z out of the group III, IV, or V elements. The alloys crystal structure consists of four interpenetrating lattices with lattice parameters that are within the realm of common compound semiconductors. Hence, the fact that they are lattice-matched to many compound semiconductors, have a compatible crystal structure (face-centered cubic), and show high Curie temperatures (Oxely, Tebble and Williams, 1963), makes them especially promising candidates for spintronics devices.

Epitaxial layers of stoichiometric HAs have been grown on various semiconductor surfaces using d.c. (Kelekar and Clemens, 2004) and r.f. (Caballero *et al*., 1997) sputtering, pulsed-laser deposition (PLD) (Wang *et al*., 2005b) from bulk HA targets, as well as molecular-beam epitaxy (MBE) (Dong *et al*., 2001). Besides the crystallinity, stoichiometry, and smoothness of the layers, also the local ordering of the constituents has to be achieved for the HAs to be half metallic. There are several ways to determine disorder, such as X-ray diffraction (XRD), the measurement of the magnetic moments, as well as the electrical resistance. The most critical issue for the efficient injection of spin-polarized carriers into a semiconductor is the control of the atomic arrangement at the interface with the HA. For instance, for many years the formation of a magnetically dead layer at the Fe/GaAs interface has prevented spin injection. The key advantage of MBE over alternative preparation techniques such as sputter deposition, chemical vapor deposition, or PLD is the ability to monitor *in situ* the growth and determine the structure of the material. A classical example for the need for MBE in magnetism is the field of GMR systems and interlayer exchange coupling in magnetic multilayers (Farrow, 1998). Thus, MBE is the method of choice for the precise control of the growth of epitaxial single-crystal magnetic material/semiconductor heterostructures.

2 HEUSLER ALLOYS – AN OVERVIEW

HAs are intermetallic phases with a particular composition and crystal structure. They are named after Friedrich Heusler, who found that compounds containing two parts of copper, one part of manganese, and one part of aluminum are ferromagnetic, although their atomic constituents are not ferromagnetic (Heusler, Starck and Haupt, 1903; Heusler and Richarz, 1908). As will be explained in the subsequent text, it is not only the half-metallic properties of some HAs that sparked interest in these compounds but also more importantly their ability to be grown epitaxially on compound semiconductors, since interfaces are determining to a great deal the capability to inject a spin-polarized current into a semiconductor.

2.1 Structural properties

HAs consist of four interpenetrating face-centered cubic sublattices, where the atoms of the species X_1, X_2, Y, and Z, are at the positions (0,0,0), ($\frac{1}{2},\frac{1}{2},\frac{1}{2}$), ($\frac{1}{4},\frac{1}{4},\frac{1}{4}$), and ($\frac{3}{4},\frac{3}{4},\frac{3}{4}$), respectively (Persson, 1929). Thus, type Y and Z atoms are surrounded by eight X atoms. In case of the full-HAs X_2YZ with the $L2_1$ crystal structure, all positions are filled, whereas in the half-HAs XYZ with $C1_b$ crystal structure, the X_1 sublattice is empty. This empty sublattice makes the half-HAs prone to disorder due to exchanges with the filled sublattice. The crystal structures are illustrated in Figure 1. The atoms of the species X are transition metals such as Ni, Co, Fe, Pd, Pt, Cu, Mn, Rh, Ru; the Y atoms another transition metal like Mn, Ni, Fe, Co, Ti, V, Cr; and Z a group III, IV, or V element such as Al, Ga, In, Si, Ge, Sn, As, or Sb. It should be noted that if both X_2 and Y are empty, the zincblende structure of III–V compound semiconductors is formed, which is advantageous for epitaxial growth on semiconductor surfaces.

Ziebeck and Webster (1974), Webster (1971) were the first to synthesize full-HAs containing Co. Ishida and collaborators (Ishida, Akazawa, Kubo and Ishida, 1982; Ishida, Fujii, Kashiwagi and Asano, 1995; Fujii, Sugimura, Ishida and Asano, 1990) proposed that compounds of the type Co_2MnZ, where Z stands for Si or Ge, are also half-metallic ferromagnets–a new class of materials that will be explained in Section 3. Also HAs of the type Fe_2MnZ were found

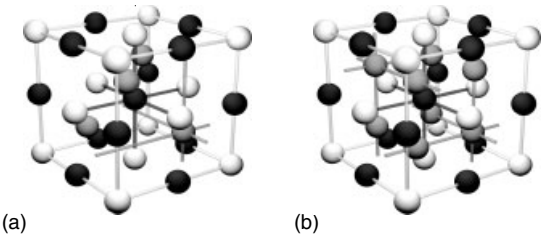

Figure 1. Crystal structures of half XYZ (a) and full X_2YZ (b) Heusler alloys. The X atoms are dark-gray, the Y atoms black and the Z atoms light-gray.

numerically to be half-magnetic metals (Fujii, Ishida and Asano, 1995). Contrary hereto, Brown *et al*. (Brown, Neumann, Webster and Ziebeck, 2000) have shown that there is a finite very small spin-down density of states at the Fermi level instead of an absolute gap by using polarized neutron diffraction. This is in agreement with the *ab initio* calculations of Kübler *et al*. for Co_2MnAl and Co_2MnSn compounds (Kübler, Williams and Sommers, 1983).

2.2 Magnetic properties

The magnetic coupling in HAs is complicated and far from being completely understood. Thus, we will restrict ourselves to a very brief summary of the most important results. The ternary alloys of the form X_2YZ and XYZ are typical local moment systems with Y the local moment material. It has been suggested that the coupling of the local moments in HAs originates from the indirect Ruderman–Kittel–Kasuya–Yosida (RKKY) type interaction; however, also other models are successfully applied (Picozzi, Continenza and Freeman, 2002). Moreover, the sole exchange via itinerant electrons is unrealistic due to the localization of the magnetic moments to the Mn atomic sites (Kübler, Williams and Sommers, 1983). It is rather believed that, due to the presence of two of the transition metals, at least some band-like contribution is also involved. Nevertheless, the resulting saturation magnetization in dependence of the constituent atoms is well understood. On the basis of *ab initio* calculations, Galanikis *et al*. showed that the total spin magnetic moment M (per formula unit in μ_B) of a Heusler alloy scales linearly with the number of the valence electrons Z, such that $M = Z - 24$ for the full-HAs and $M = Z - 18$ for the half-HAs (Galanakis, Dederichs and Papanikolaou, 2002b). For example, a half-Heusler system with 18 valence electrons per formula unit is nonmagnetic. On the basis of this well-known Slater–Pauling behavior (Kübler, 1984) it can be further deduced that the maximum magnetic moment of a half Heusler is $5\,\mu_B$, and that of a full-Heusler alloy $7\,\mu_B$.

The situation in half-HAs is illustrated by taking NiMnSb as an example (Otto *et al*., 1989a,b). It was found experimentally that the magnetic moments are present on the Mn atoms. As the distance between the local moments is too large for the direct exchange interaction to be efficient, some authors propose that the coupling occurs via itinerant holes in the Sb-5p valence band (Otto *et al*., 1987). In full-HAs, the X atoms primarily determine the lattice constant, whereas the Z atoms (group III, IV or V atoms) mediate the interaction between the d states of the local moment atoms Y (Kübler, Williams and Sommers, 1983; Reitz and Stearns, 1979). The local moment atoms do not interact directly; however, an interaction with the d states of the X atoms delocalizes their occupied d states, resulting in delocalized electrons moving in a common d band. Nevertheless, the magnetization is localized to the Y atom in case of Mn, as the minority-spin electrons (as defined locally) are excluded from the Mn 3d shell. According to Kübler *et al*. the magnetic order is sensitive depending on the occupation of the mediating p–d hybrid states–a fact that accounts well for experiments by Webster (1971) in which this occupation was varied by alloying. Depending on the coupling, the magnetic properties range from weakly antiferromagnetic in case of Pd_2MnIn to strongly ferromagnetic in case of Co_2MnSn.

The lattice constants and magnetic properties of some common HAs (bulk crystals) are listed in Table 1 (for reference see also Webster and Ziebeck, 1988).

3 HALF-METALLIC FERROMAGNETS

On the basis of band-structure calculations on the half-HAs NiMnSb and PtMnSb, de Groot and coworkers (de Groot, Mueller, van Engen and Buschow, 1983) claimed to have found a new class of materials. The so-called HMFs are characterized by one spin subband being metallic, whereas the Fermi level falls into a gap of the other subband–that is, the current-carrying electrons at the Fermi level are 100% spin polarized. This unusual behavior attracted a lot of attention since then, as HMFs are ideally suited for spintronics. Owing to various problems that will be discussed in the subsequent text, it was not until 1998 that the half-metallic character of a film was directly measured (Park *et al*., 1998).

3.1 Properties

After de Groot's discovery of a spin-splitted band structure in two Mn-based half-HAs, a number of theoretical papers followed proposing half-metallic behavior for Fe_3O_4 (magnetite) (Yanase and Shiratori, 1984), rutile-type CrO_2

Table 1. Table of properties of selected Heusler alloys with relevance to epitaxial growth. Reference, unless otherwise noted, (Webster and Ziebeck, 1988).

Class	X atom	Structure $L2_1$ B2	a(Å)	$m_{fu}(\mu_B)$	T_C or T_N(K)	Reference
X_2MnAl	Co	$B2/L2_1$	5.756	4.01	693, FM	
	Fe	$L2_1$	5.816	1.58		
	Ni	$B2/L2_1$	5.822		300, AFM	
	Cu	$L2_1$	5.949	4.12	603, FM	
	Rh	B2	6.005	>0.7	~95, FM	
	Pd	B2	6.165	4.4	240, AFM	
	Pt	$L2_1$	6.240		190, AFM	
	Au	$L2_1$	6.360	4.2	233, FM	
X_2MnGa	Co	$L2_1$	5.770	4.05	694, FM	
	Ni	$L2_1$	5.825	4.17	374, FM	
	Rh	B2	6.054	>1.2	~80, FM	
	Pt	$L2_1$	6.160		75, AFM	
X_2MnGe	Co	$L2_1$	5.743	5.11	905, FM	
	Ni	$L2_1$	5.690		>300, FM	Cherkashin, Gladyshevskiy, Kripyakevich and Kuz'ma (1958)
	Cu		b.c. tetrag.	2.84	300, FM	Oxely, Tebble and Williams (1963)
	Rh	$L2_1$	5.993	4.3	450, FM	
	Pd	$L2_1$			260, FM	Natera, Murthy, Begum and Murthy (1970)
X_2MnSi	Co	$L2_1$	5.654	5.07	985, FM	
	Fe	$L2_1$	5.663	1.76	214, FM	
X_2MnSn	Co	$L2_1$	6.000	5.08	829, FM	
	Ni	$L2_1$	6.053	4.22	360, FM	
	Cu	$L2_1$	6.173	4.11	503, FM	
	Rh	$L2_1$	6.252	3.1	412, FM	
	Pd	$L2_1$	6.380	4.23	189, FM	
X_2MnSb	$Co_{1.5}$	$L2_1$–$C1_b$	5.929	4.90	600, FM	
	Ni	$L2_1$	6.004	3.52	365, FM	
	Cu		6.096		38, AFM	Oxely, Tebble and Williams (1963)
	Rh		tetragon.		335, FM	
	Pd	$L2_1$	6.419	4.40	247, FM	
X_2MnIn	Co				>300, FM	Holmes and Pepper (2003)
	Ni	$L2_1$	6.069	4.43	314, FM	
	Cu	$L2_1$	6.206	3.95	500, FM	
	Rh	B2	6.287	>2.3	~105, FM	
	Pd	$L2_1$–B2	6.373	4.3		
	Au	$L2_1$	6.550		140, FM	Elfazani *et al*. (1981)
X_2CoGa	Fe	$L2_1$	5.767	5.09		
X_2FeSi	Co	$L2_1$	5.658	5.9	>980, FM	
	Fe	$D0_3$	5.653	2.21	823, FM	
X_2FeGa	Co	$L2_1$	5.737	5.15	>1100, FM	Brown, Neumann, Webster and Ziebeck (2000)
	Ni	$L2_1$	5.741		430, FM	Liu *et al*. (2003)
X_2FeAl	Co	$L2_1$	5.730	4.8	> RT, FM	Hirohata *et al*. (2005b)
	Fe	$D0_3$	5.792	2.59	713, FM	
	Cu	$L2_1$	5.905	1.94	870, FM	Zhang *et al*. (2004b)
XMnSn	Ni	$C1_b$	~6.03	2.0	406, FM	de Groot, van Engen, van Engelen and Buschow (1990)
	Pt	$C1_b$	6.263	3.54	330, FM	Hames and Crangle (1971)
	Au	$C1_b$	6.341	3.62	600, FM	Offernes *et al*. (1999)
XMnSb	Co	$C1_b$	5.853	4.0	490, FM	
	Fe	$C1_b$	$2 \cdot 5.875$	2.0	350, FM	de Groot, van der Kraan, and Buschow (1986)
	Ni	$C1_b$	5.927	4.2	728, FM	Otto *et al*. (1987)
	Cu	$C1_b$	6.095		AFM	Jeong, Weht and Pickett (2005)
	Rh	$C1_b$	6.152	3.63	320, FM	
	Pd	$C1_b$	6.246	3.95	500, FM	
	Pt	$C1_b$	6.201	4.14	582, FM	
	Au	$C1_b$	6.377	2.21	72, FM	

a: lattice spacing (Å); m_{fu}: magnetic moment per fu (formula unit); T_C and T_N: Curie (FM = ferromagnet) and Néel (AFM = antiferromagnet) temperature in K, respectively.

(Schwarz, 1986), full-HAs (Ishida, Fujii, Kashiwagi and Asano, 1995), perovskite manganites (Pickett and Singh, 1996), double perovskites (Kobayashi *et al*., 1998), diluted magnetic semiconductors (DMS) (Ogawa, Shirai, Suzuki and Kitagawa, 1999), and others.

The degree of spin polarization P at the Fermi level is usually defined by

$$P = \frac{N_\uparrow - N_\downarrow}{N_\uparrow + N_\downarrow} \tag{1}$$

where N_σ are the density of states at the Fermi level for the respective spin-σ band. The band structure of a HMF, illustrated in Figure 2(c), shows a spin polarization at E_F of 100%. For comparison, the band structures for a normal (a) and a ferromagnetic (b) metal are also shown.

What characterizes a half-metal? First and foremost, the definition of a half-metal as a system that is metallic for one spin and semiconducting for the other, leads to a complete spin polarization at the Fermi level. Also, there exists a gap for spin-flip (Stoner continuum) excitations due to the structure of the minority band (Irkhin and Katsnel'son, 1994). Further, an integer value of the spin moment is usually central for half-metallicity, as is the unusual combination of metallic conductivity and vanishing high-field susceptibility (Eschrig and Pickett, 2001). For example, the magnetization per functional unit of NiMnSb is $4\,\mu_B$ consisting of $3.8\,\mu_B$ for Mn and $0.2\,\mu_B$ for Ni. The reasoning behind the integer-spin criterion is that, as consequence of the gap in one of the spin bands and as the sum of electrons in the two spin states is an integer, the number of spin-up or spin-down electrons is an integer too. Their difference has an integer value, corresponding to the spin moment in units of μ_B. The integer-spin criterion is a necessary, yet not sufficient requirement for half-metals.

A more advanced classification of half-metals was introduced by Coey and Venkatesan according to their electronic and magnetic properties (Coey and Venkatesan, 2002). Five classes of half-metallic materials (HMM) are distinguished: half-metals that have metallic (I) or nonmetallic (II) conductivity, metals (III), semimetals (IV), and semiconductors (V). The subgroups X_A and X_B further denote the character of the spin-up electrons at the Fermi level, that is, A for itinerant (localized in case of nonmetallic half-metals) and B for the respective case in the spin-down band. A good indication for a type (I) HMM is metallic conductivity together with the integer-spin rule. Examples for the different types of HMM are: (II) Fe_3O_4 (magnetite); (III) $La_{0.7}Sr_{0.3}MnO_3$; (IV) $Tl_2Mn_2O_7$ (Singh, 1997); and (Ga,Mn)As (V). Type (III) $La_{0.7}Sr_{0.3}MnO_3$ is considered a transport half-metal that actually shows a finite density of states in both spin channels, however, concerning conduction only one type of spin channel is involved (Nadgorny *et al*., 2001). The half-metallic HAs belong to the type (I) HMM, and can be of subgroup A (e.g., NiMnSb) or B (e.g., Mn_2VAl).

3.2 Origin of the band gap in half-metals

Let us start by having a look at ordinary ferromagnets, which are in general not half-metals. Co, for instance, has fully spin-polarized d-bands with a filled spin-up $3d$ band and only spin-down electrons at the Fermi level. However, the Fermi level also crosses the unpolarized $4s$ band, resulting in both spin-up and spin-down electrons at the Fermi level. In order to reach full spin polarization at the Fermi level, it is necessary to reorder the $3d$ and $4s$ bands by hybridization, pushing the bottom of the $4s$ band above E_F or depressing the Fermi level in the d band below the bottom of the $4s$ band. Consequently, all half-metals contain more than one element.

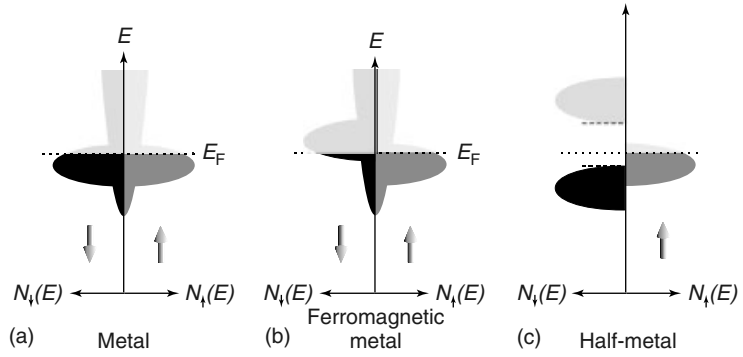

Figure 2. Spin-dependent density of states $N(E)$ of a normal metal (a), a ferromagnetic metal (b) and a half-metallic material (c) [type (I_B)]; E_F is the Fermi level. The normal metal (a) shows an equal number of electrons of spin up and spin down at E_F (at 0 K). A ferromagnetic metal (b) shows a spin polarization of the carriers at E_F. In contrast, half-metallic ferromagnets show a gap in one of the spin channels (at 0 K), that is, 100% spin-polarized carriers.

In the case of the half-HAs, the gap basically arises from the covalent hybridization between the lower-energy d states of the high-valent transition-metal-atom like Ni or Co and the higher-energy d states of the lower-valent TM atom, leading to the formation of bonding and antibonding bands with a gap in between. The bonding hybrids are localized mainly at the high-valent TM atom site while the unoccupied antibonding states are localized mainly at the lower-valent TM atom site (Galanakis, Dederichs and Papanikolaou, 2002a).

In the case of the full-HAs, each Y atom has eight X atoms as first neighbors instead of four as in the half Heuslers. Thus, the hybridization between X and Y spin-down electrons, that decreases the Y-spin moment in XYZ Heuslers, becomes even more pronounced. The X atoms are ferromagnetically coupled to the Y-spin moments and they possess a spin moment significantly smaller than that of the Y atom. The sp atom Z has a very small negative moment which is one order of magnitude smaller than the X moment. The negative sign of the induced sp moment characterizes most of the studied full- and half-HAs with very few exceptions. Both half- and full-Heusler compounds follow the Slater–Pauling curve. For an in-depth discussion of the band gap formation due to hybridization the reader is referred to Galanakis, Dederichs and Papanikolaou (2002b).

Theoretical investigations suggest that, although the half-HAs have more likely a high degree of disorder, the consequences of this disorder on the spin polarization at the Fermi level are not that drastic, since the half-HAs exhibit a larger gap with respect to the full ones (Galanakis, Dederichs and Papanikolaou, 2002b). Also, as is the case for NiMnSb, a few percent of disorder induces states in the gap that do not necessarily destroy the half-metallicity (Orgassa, Fujiwara, Schulthess and Butler, 2000).

3.3 Measurement of the spin polarization

We will briefly review the methods for measuring the spin polarization of a half-metal: point-contact Andreev reflection (PCAR) (Soulen *et al*., 1998; Upadhyay, Palanisami, Louie and Buhrman, 1998), magnetic tunnel junctions (MTJs) (Jullière, 1975), spin-resolved photoemission (Park *et al*., 1998), point-contact tunneling into a ferromagnet (Garcia, Munoz and Zhao, 1999), and tunneling into a superconducting film (Meservey and Tedrow, 1994). For further reading, please refer to Coey and Chien (2003). Interestingly, it was not until 1998 that the half-metallic property of a thin film was experimentally confirmed when Park *et al*. were measuring the band gap in the spin-down band of manganese perovskite by a surface sensitive technique. In fact, it is a real challenging task to determine the difference between spin-up and spin-down carriers in thin films. In many cases, this is due to interface and surface problems (Galanakis, Ležaić, Bihlmayer and Blügel, 2005), such as Sb segregation in case of NiMnSb (Wojcik *et al*., 2002), where the half-metallic properties were already confirmed in 1990 by spin-polarized positron annihilation that has an information depth of 40 μm (Hanssen and Mijnarends, 1986), that is, not for thin films. It has to be noted that different values for the spin polarization for a particular system are not only the result of experimental shortcomings, but may also be due to the probing of different electron states, for example, comparing photoemission and tunneling measurements.

3.3.1 *Magnetic tunnel junctions – MTJs (Jullière, 1975)*

As the tunneling probability between two ferromagnetic contacts depends on the relative magnetization of the contacts, a tunnel-junction geometry can be used to extract information about the spin polarization. However, the experimentally accessible property is the magnetoresistance (*MR*), that is, the relative difference between the resistivities of the parallel and the antiparallel magnetization configuration, which is critically depending on the interface states and barrier properties. Thus, the commonly extracted spin polarization P using Jullière's simple relationship $MR = 2P^2/(1 + P^2)$ is rather a measure of a specific device than an intrinsic material property. An in-depth discussion of spin-dependent tunneling in MTJs can be found in Tsymbal, Mryasov and LeClair (2003).

3.3.2 *Point-contact tunneling into a ferromagnet (Garcia, Munoz and Zhao, 1999)*

As in case of MTJs, the tunneling between two ferromagnetic leads in a point-contact geometry, that is, either between two tips, a tip and a surface or in a lateral point-contact structure involving a nanoconstriction, allows for the measurement of the *MR*; and the extraction of a value for the spin polarization P. Although the contacts may be difficult to control, the method is very straightforward and permits for the measurement of P as a function of temperature. The temperature dependence of P, especially the commonly observed fast decay with temperature, gives a valuable insight into the imperfections of the material system. The limitations of the method lie foremost in the preparation and reproducibility of the experiment.

3.3.3 *Tunneling into a superconducting film (Meservey and Tedrow, 1994)*

As in MTJs, a thin-film structure has to be fabricated, however, now a superconducting film is replacing one of the ferromagnetic films. Owing to the high critical field and

the well-controlled oxide in the metal–metal oxide system, the material of choice for the electrode is Al. However, this requires a working temperature below 2.5 K. A magnetic field is applied to the junction to spin split the quasi particles in the superconductor and to saturate the magnetization of the ferromagnet. The tunneling probability is proportional to the convolution of the densities of states of the superconductor and the ferromagnet, resulting in four conductance peaks. From the four conductances, the spin polarization P can be deduced.

The PCAR technique makes use of the fact that for an electron to tunnel into a superconductor, a pairing electron is required to form a Cooper pair. The process is only possible for an electron approaching the interface from the metal side, when a hole is reflected back in the opposite spin band of the metal. In case of a non-ferromagnetic electrode ($P = 0$), the conductance is doubled in the energy range of the superconducting gap, as all tunneling electrons can find partners of opposite spin to form a Cooper pair. In case of a half-metallic electrode with $P = 1$, no electrons are available for forming a Cooper pair and the tunneling current is completely suppressed. The analysis is based on the Blonder–Tinkham–Klapwijk model of Andreev reflections (Blonder, Tinkham and Klapwijk, 1982). By using the procedure described in Soulen *et al*. (1998) and Mazin (1999), the spin polarization P can be extracted from the measured conductance–voltage characteristics using $G(0)/G_n = 2(1 - P)$, with $G(0)$ and G_n the conductance at zero and high bias voltage, respectively. When interface or surface states are present, the entire conductance curve has to be modeled in order to extract P. In general, PCAR can be applied to a variety of samples and sample configurations (foils, thin films, bulk crystals). The limitations of PCAR for the determination of the spin polarization stem from the complexity of the system. Besides the influence of the type of transport regime–ballistic or diffusive–on P, also a dependence on the effective potential barrier at the interface Z has to be taken into account (Woods *et al*., 2004).

3.3.4 Spin-resolved photoemission (Park et al., 1998)

By using a spin-resolving detector for photo-excited electrons, the spin asymmetry of the emitted electrons is a direct measure of the spin polarization P. The information depth is only 5–10 Å which makes the method prone to surface contamination. The energy resolution is comparably low. The complete band structure can be probed by performing angle-resolved measurements for different wave vectors.

It has to be noted that, in principle, the thermally activated mixing of spin-up and spin-down spins limits half-metallic ferromagnetism to zero temperature (Dowben and Skomski, 2004). At finite temperatures, the spin-down density of states is no longer vanishing. Other sources of reduced spin polarization for bulk half-metals are, besides experimental deficiencies, crystal defects, interfaces, and surfaces. For example, whereas the MnSb-terminated surface of NiMnSb has a very high spin polarization similar to the half-metallic bulk crystal, the Ni-terminated surface exhibits a vanishing spin polarization (Galanakis, 2004).

3.4 Candidate materials

Half-metallic characteristics have been studied primarily in ternary compounds, such as spinels and HAs; however, also a simple oxidelike CrO_2 is a half magnet. We restrict the following discussion to HAs for two reasons. First, they hold the promise for epitaxial growth on compound semiconductor surfaces, and second, they have a large energy gap within the spin-down band structure. The calculated value for Co_2MnSi, for instance, is about 0.4 eV (Ishida, Masaki, Fujii, and Asano, 1998), which would be sufficient for providing 100% spin polarization at room temperature ($k_BT \sim 25$ meV). Other half-metals, such as CrO_2 or $La_{0.7}Sr_{0.3}MnO_3$, exhibit a high degree of spin polarization at low temperatures, but suffer from low Curie temperatures (<500 K) and thus low magnetization at room temperature. HAs, for which half-metallic behavior is predicted for a significant number of half (Galanakis, Dederichs and Papanikolaou, 2002a) and full (Galanakis, Dederichs and Papanikolaou, 2002b) systems, are very promising candidates for realizing 100% spin polarization at room temperature. Indeed, half-metallic behavior could be confirmed experimentally for many *bulk crystals*. Here, non-HAs will only be listed for reference and only materials will be discussed that are potentially interesting for forming heterostructures with semiconductors.

Table 2 gives an overview of the theoretically predicted half-metallic compounds for which experimental spin-polarization data exist. So far, CrO_2 has been among the highest degree of spin polarizations measured. It is a ferromagnetic metal with a $T_C = 387$ K, but despite the fact that this compound is commonly used in videotapes and cassettes, it is metastable (Ji *et al*., 2001). Moreover, the problem with most of the half-metallic oxides is their low Curie temperature ($T_C < 500$ K). Thus, the spin polarization measured from MR in a point contact is strongly temperature dependent, and it becomes negligible at room temperature.

3.5 Applications of half-metals

Half-metals with their inherent spin polarization of ideally 100% can be potentially used for a large variety of

Table 2. Spin polarization data of selected half-metallic compounds (theoretical predictions) and dilute magnetic semiconductors (DMS). References refer to spin polarization values. Other data are taken from references cited in Tables 1 and 3.

Material class	Compound	Magnetic state	Curie/Néel temperature (K)	M_s/fu (μ_B)	Exp. spin polarization (average)	Reference
Oxides	CrO_2	FM	387	2.0	90%, PCAR	Soulen *et al*. (1998)
					96%, PCAR	Ji *et al*. (2001)
	Fe_3O_4	FI	860	4.0	−72%, PC	Coey and Chien (2003)
					−80%, PE	Dedkov, Rüdiger and Güntherodt (2002)
					−39%, MTJ	Hu and Suzuki (2002)
Half Heusler	NiMnSb	FM	730	3.9	58%, PCAR	Soulen *et al*. (1998)
					50%, PE	de Groot, Mueller, van Engen and Buschow (1983)
					∼50%, PE	Bona *et al*. (1985)
					40%, PE	Zhu *et al*. (2001)
					45%, PCAR	Ritchie *et al*. (2003)
					<48%, PCAR	Miyoshi *et al*. (2006)
	NiFeSb	FM		2.4	100%[a], inverse PE	Ristoiu *et al*. (2000a)
					52%, PCAR	Zhang *et al*. (2003)
Full Heusler	Co_2MnSi	FM	1030	5.0	∼53%, PCAR	Cheng *et al*. (2001)
					56%, PCAR	Ritchie *et al*. (2003)
					54%, PCAR	Singh *et al*. (2004)
					<58%, PCAR	Miyoshi *et al*. (2006)
	Co_2MnGe	FM	905	5.0	∼57%, PCAR	Cheng *et al*. (2001)
	$Co_{2.4}Mn_{1.6}Ga$	FM			50%, PCAR	Hickey *et al*. (2005)
	$Co_2Cr_{0.6}Fe_{0.4}Al$	FM	665	3.7	81%, PCAR	Clifford, Venkatesan, Gunning and Coey (2004)
	Co_2FeGa	FM	>1100	5.2	59%, PCAR	Zhang *et al*. (2004a)
	Ni_2MnIn	FM	318		54%, PCAR	von Oehsen *et al*. (2005)
	Fe_3Si	FM		1.1	45%, PCAR	Ionescu *et al*. (2005)
Perovskites	$(La_{1-x}Sr_x)MnO_3$	FM	280–380		99%, MTJ	Bowen *et al*. (2005)
	Sr_2FeMoO_6	FI	420		−85%, MTJ	Bibes *et al*. (2003)
DMS	CdMnTe ZnBeMnSe	FM			50–100%, PE	Oestreich *et al*. (1999)
		FM			90%, LED	Schmidt and Molenkamp (2001)

FM: ferromagnet; AFM: antiferromagnet; FI: ferrimagnet; M_s: saturation magnetization; fu: formula unit; PCAR: point-contact Andreev reflection; PE: spin-polarized photoemission; MTJ: magnetic tunnel junction; PC: point-contact tunneling into a ferromagnet; LED: spin light-emitting photo diode configuration.
[a]100% above background, 67% at the Fermi level.

applications. As the current tunneling out of a ferromagnetic material is spin polarized, the largest polarization is obtained with half-metals. This way they can, for example, act as the polarized current source as well as the analyzing filter in spin transistors (Johnson, 1995) or scanning tunneling microscopes (STMs) for the imaging of magnetic domains. Ferrimagnetic half-metallic STM tips may even solve the problem of the perturbation of the sample magnetization due to the tip's stray field (van Leuken and de Groot, 1995).

However, the potential applications of half-metals are not limited to spin-polarized contacts. For PtMnSb, an unusually large Kerr rotation of 2.5° at 720 nm was observed which may be useful for new optical applications (van Engen, Buschow, Jongebreur and Erman, 1983). The half-metallic properties also lead to a small plasma frequency, which enhances the Kerr effect (Antonov *et al*., 1997). Moreover, half-metals will be useful in multilayer spin-valve systems, as the very large difference in the density of states for the two spin directions leads to very high differences in the low and high resistance path. For a band gap of 1 eV, one can expect MR ratios exceeding 80% (Johnson *et al*., 1996). Also for magnetic tunneling junctions that are at the heart of the MRAM cell, where higher tunneling magnetoresistance (TMR) ratios are desired, half-metals are predicted to outperform the competing materials based on theory (Lu *et al*., 1996; Viret *et al*., 1997; Mukhopadhyay and Das, 2006).

4 EPITAXIAL GROWTH OF HEUSLER ALLOYS

The magnetic properties of ferromagnetic contacts, such as the magnetic anisotropy or the degree of spin polarization, are largely influenced by the crystal structure and orientation of the films. Although polycrystalline films can be used for a number of applications, especially also for small electronic structures, they are not the first choice for spintronics applications. The epitaxy of metals on semiconductors, that is, the growth of single-crystalline metal films with a defined crystalline relationship to the substrate, has been an intensive area of research for quite some time and it is well documented in the literature (Sands *et al*., 1990). Although perfect layers of epitaxial, elemental ferromagnets can be grown on semiconductors, these contacts suffer from a small spin polarization, which is on the order of 50% at best. The first half-metal that was theoretically (de Groot, Mueller, van Engen and Buschow, 1983) and experimentally (Hanssen, Mijnarends, Rabou and Buschow, 1990) investigated was the half-Heusler alloy NiMnSb. Epitaxial growth was achieved on GaAs (van Roy, de Boeck, Brijs and Borghs, 2000), as the crystal structure is very closely related to the zincblende structure of GaAs, and NiMnSb shows a lattice mismatch of 4.4% with GaAs. In the following, we will briefly discuss the growth techniques relevant for the epitaxial growth of HAs, followed by a review of epitaxial HA-semiconductor hybrid systems (for a review, see also Palmstrøm, 2003).

4.1 Growth techniques

4.1.1 Sputter deposition

The sputter deposition of magnetic films is quite common in the magnetic device industry, as it offers the advantages of high deposition rates and large sample throughput, low cost, and stoichiometric equality of sputter target and grown layer. The most common sputter gas is Ar, which is kept at pressure in the range from 10^{-3} to 10^{-1} Torr during growth. The background pressure in the growth chamber prior to growth is commonly not better than 10^{-8} Torr, although ultrahigh vacuum (UHV) sputter systems are employed too. The substrates are commonly degreased and subsequently outgassed in vacuum. The films are then sputtered from bulk HA targets at typical r.f. sputter powers between 10 and 100 W or d.c. powers of 30 W, while the substrate is kept at temperatures between room temperature and 500 °C.

So far, mostly polycrystalline HAs were grown and structurally and magnetically characterized. Some of the high quality HA films grown on semiconductors are:

Full-HAs, Co_2MnGe on MgO(100) (Yamamoto *et al*., 2006) and Al_2O_3 *a* plane with suitable metal seed layers (Geiersbach, Bergmann and Westerholt, 2002); Co_2MnSi on GaAs (Singh *et al*., 2006); on glass (Raphael *et al*., 2001); on MgO(100) and Al_2O_3 *a* plane with suitable metal seed layers (Geiersbach, Bergmann and Westerholt, 2002; Singh *et al*., 2004); on thermally oxidized Si (Kim, Kwon and Kim, 2004); on MgO(100), $SrTiO_3$(100), Si(100), Si(111), and SiO_2 with a V seed layer (Kämmerer *et al*., 2003), $Co_2MnSi/AlO_x/Co_{75}Fe_{25}$ MTJs (Sakuraba *et al*., 2005a); Co_2MnSn on MgO(100) and Al_2O_3 *a* plane with suitable metal seed layers (Geiersbach, Bergmann and Westerholt, 2002); $Co_2(Cr,Fe)Al$ on GaAs(001) (Hirohata *et al*., 2005b), thermally oxidized Si (Inomata, Okamura, Goto and Tezuka, 2003), MgO(001) (Kelekar and Clemens, 2004; Marukame *et al*., 2005; Matsuda *et al*., 2006), AlO_x (Inomata, Okamura and Tezuka, 2004; Conca *et al*., 2005), and on *a*-plane Al_2O_3 (Jakob *et al*., 2005); Co_2MnAl on Cr-buffered MgO(001) (Sakuraba *et al*., 2005b), thermally oxidized Si (Kim, Kwon and Kim, 2004); Cu_2MnAl on MgO(100) (Geiersbach, Bergmann and Westerholt, 2002); (Bach, Westerholt and Geiersbach, 2002), thermally oxidized Si (Kim, Kwon and Kim, 2004); Ni_2MnIn on InAs (von Oehsen *et al*., 2005).

Half-HAs: NiMnSb on glass (Caballero *et al*., 1997), Cu and NiFe for multilayers (Caballero *et al*., 1998), Al_2O_3(0001) (Bobo *et al*., 1997), MgO with Mo buffer layer (Ristoiu *et al*., 2000a; Ristoiu, Nozieres and Ranno, 2000b), GaAs (Debernardi, Peressi and Baldereschi, 2003; Debernardi, Peressi and Baldereschi, 2005); NiMnSb/PtMnSb superlattices (Mancoff *et al*., 1999); NiMnGa on silicon cantilevers (Wuttig, Craciunescu and Li, 2000); and PtMnSb on MgO(001) and W(001) (Kautzky and Clemens, 1995); on Al_2O_3(0001) (Kautzky and Clemens, 1995; Bobo *et al*., 1997); and PtMnSb/CuMnSb multilayers (Watanabe, Takanashi and Fujimori, 1991).

4.1.2 Pulsed laser deposition (PLD)

The PLD method involves the evaporation of a solid target in a (ultra) high-vacuum chamber by means of high-energy laser pulses. The strong absorption of the laser radiation by the target surface leads to its rapid evaporation. The evaporated material is highly exited and ionized, forming a plasma plume of high energetic species (10–100 eV/ion). The ablated material is then deposited onto the heated substrate surface to allow for surface diffusion. Typically, excimer lasers are used as the emitted wavelengths are absorbed by a number of target materials. Other commonly employed laser types are CO_2 lasers, Q-switched Nd:YAG lasers, and also femtosecond lasers. The PLD targets are much smaller than sputtering targets. In order to avoid memory effects,

the laser is scanned over the target surface. One important feature of the PLD technique is that the stoichiometry of the target is transferred to the growing film–a result of the extremely fast heating rate of the target due to the pulsed-laser irradiation. Also, as the evaporated species have a high energy, the growth temperatures can be kept lower compared to other methods, allowing for overgrowth of sensitive device structures. Furthermore, by controlling the number of pulses, the film growth can be controlled down to the atomic level. Contrary to sputter deposition, the background pressure during growth can be kept in a range where *in situ* electron probes, like (differentially pumped) reflection high-energy electron diffraction RHEED, can be employed.

For the growth of HAs, the only requirement is that a large enough bulk target can be synthesized. So far, the following HAs have been deposited onto semiconductor surfaces: Co_2MnX (X = Si, Ga, Ge, Sn, SbSn) on Si, GaAs, and InAs (Valerio *et al*., 2005; Grigorescu *et al*., 2005); Co_2MnSi on GaAs (Autric, Valerio and Grigorescu, 2005), Al_2O_3 (*a* plane) (Stadler *et al*., 2005), GaAs (001) (Wang *et al*., 2005a,b; Stadler *et al*., 2005) and Si_3N_4 (Stadler *et al*., 2005); NiMnSb on Si and InAs (Giapintzakis *et al*., 2002a,b), Si(100) (Zhu, Lu, Lai and Ding, 2005) and InSb (Gardelis *et al*., 2004; Autric *et al*., 2004).

4.1.3 Molecular beam epitaxy (MBE)

MBE has proven its strengths in many fields of research and development of (opto-)electronic structures and devices over the past decades. Materials systems for spintronics will be no exception, as the requirement of perfect interfaces is even tighter than in case of conventional electronics (Prinz and Krebs, 1981). In solid-source MBE, ultrapure elemental materials are evaporated from effusion cells in an UHV chamber onto a heated substrate where they react. Cell shutters in combination with rather low growth rates, as well as *in situ* growth monitoring by RHEED, allows for ultimate precision in materials growth. One big advantage over the other methods is that reactive semiconductor surfaces can be properly prepared under UHV conditions, rendering them smooth and free of oxides prior to the HA growth. Furthermore, the homoepitaxial growth of a buffer layer in the III–V chamber guarantees ideal starting conditions, before the sample can be transferred to a separate metal MBE chamber in order to avoid cross-contamination.

The following HAs have been grown on semiconductor surfaces (for a review see Palmstrøm, 2003). Full-HAs: Ni_2MnGa on GaAs(001) (Dong *et al*., 2000, 2001; Lund *et al*., 2002); Ni_2MnGe on GaAs(001) (Dong *et al*., 2001; Lund *et al*., 2002; Lu *et al*., 2003); Ni_2MnAl on GaAs(001) (Lund *et al*., 2002; Dong *et al*., 2003); Ni_2MnIn on InAs(001) (Dong *et al*., 2001; Xie *et al*., 2001, 2005); Co_2MnGe on AlGaAs/GaAs (Dong *et al*., 2005); Co_2MnGe on GaAs(001) (Ambrose, Krebs and Prinz, 2000a,b, 2001) and Ge(111) (Tsui *et al*., 2006); Co_2MnAl on GaAs (Chen, Basiaga, O'Brien and Heiman, 2004; Heiman *et al*., 2005); Co_2MnGa on GaAs (Heiman *et al*., 2005; Hickey *et al*., 2005; Holmes and Pepper, 2002); Co_2FeSi on GaAs(001) (Hashimoto, Herfort, Schönherr and Ploog, 2005a,b); $Co_2(Cr_{1-x}Fe_x)Al$ on GaAs (Hirohata *et al*., 2005a,b); Fe_2AlSi on GaAs(001) (Hong *et al*., 1991); and Fe_3Si on GaAs(001) (Liou *et al*., 1993) and GaAs(113)A (Herfort, Schönherr and Ploog, 2003; Herfort, Schönherr, Friedland and Ploog, 2004; Muduli, Herfort, Schönherr and Ploog, 2005a; Muduli *et al*., 2005b,c).

Half-*HAs:* NiMnAl on MgO(001) (Hassdorf *et al*., 2003); and NiMnSb on (In,Ga)As/InP (Bach *et al*., 2003a,b; Heinrich *et al*., 2004; Koveshnikov *et al*., 2005), GaAs(001) (van Roy, de Boeck, Brijs and Borghs, 2000) and GaAs(111)A and B (van Roy *et al*., 2003).

4.2 Epitaxial growth on semiconductor surfaces

Epitaxial growth has many advantages: control and monitoring of growth, defined surfaces, perfect interfaces, correct stoichiometry. This way, in the early days of ferromagnetic-semiconductor hybrid systems (Prinz, 1990), metastable bcc (body-centered cubic) Co was synthesized on GaAs(110) (Prinz, 1985). Molecular-beam epitaxy methods, and to a limited extend also sputter deposition and PLD, have been used to grow good quality magnetic single-crystal HA films on GaAs and Si substrates. The structural properties of the films are commonly characterized by RHEED, XRD, transmission electron microscopy (TEM), and anti ferro magnet (AFM).

One prerequisite for epitaxial growth of thin films on a substrate is, besides a similar crystal structure, that both lattice constants are closely matched. In a few cases or in case of certain large misfit-systems, a coincidence lattice can be formed (Trampert and Ploog, 2000). For Co_2FeSi/GaAs, the lattice constants of bulk Co_2FeSi (5.658 Å) and GaAs (5.653 Å) differ by 0.08%, which can be considered as a small lattice mismatch allowing for epitaxial growth. Figure 3 shows the lattice parameters for selected HAs and semiconductor substrates.

Typically, the MBE growth of HAs starts with preparing a defined GaAs template in a separate III–V growth chamber using standard GaAs growth techniques. For the HA growth, the substrate is transferred in UHV into the metal deposition chamber. As arsenic can act as a contaminant for HAs, this chamber is kept As free. The metallic constituents are then codeposited from high-temperature effusion cells, where the evaporation rates can be controlled via the cell temperatures and are adjusted by measuring the beam-equivalent pressure

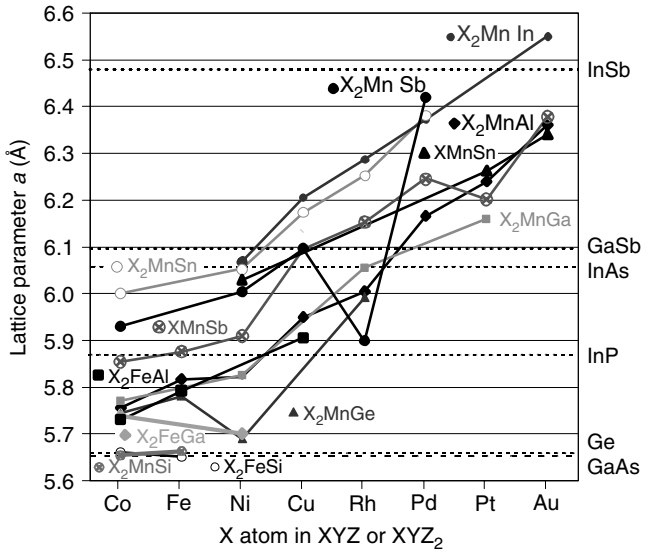

Figure 3. Full- and half-Heusler alloy (XYZ and X_2YZ) lattice parameters as a function of the atom species X, along with the lattice constants of semiconductors (horizontal lines).

using a Bayard–Alpert ionization gauge. *In situ* RHEED, together with *ex situ* XRD and AFM, are used to determine the growth mode, epitaxial relationship, lattice constants, strain, stoichiometry, and smoothness of the films. The structural properties of the heterostructure, and especially the interface quality, can further be studied by high-resolution transmission electron microscopy (HRTEM).

The material system that is best investigated in terms of growth is the half-Heusler alloy NiMnSb (see reference Turban *et al*., 2002a,b,c and references therein). A common observation is that the number of defects is lower for higher growth temperatures. This observation is generally true for inert surfaces, like MgO, however, fatal for III–V semiconductors, as interface reactions will play a critical role. As a consequence, a trade-off has to be made between interface and crystal film quality. Different from the growth of III–V materials where the stoichiometry is as result of the sticking coefficient of the group III species (within limits), HAs have a wide compositional phase field. Hence, the growth is not self-regulating and the individual fluxes have to be adjusted very precisely (Palmstrøm, 2003). Table 3 gives an overview of epitaxially grown HAs on semiconductor surfaces, listing growth temperatures, orientations, seed layers, structural, as well as magnetic properties, if available. No information about atomic disorder is given in the Table. As mentioned in the preceding text, epitaxial growth is a necessary ingredient for perfect interfaces; however, atomic disorder still remains a problem in HAs with consequences for their potential application as half-metallic contacts.

4.3 Characterization of an epitaxially grown Heusler alloy: Co_2FeSi/GaAs

We are now going to discuss some details of the epitaxial growth of a full-Heusler alloy system on GaAs by MBE (Hashimoto, Herfort, Schönherr and Ploog, 2005a). Co_2FeSi has the cubic $L2_1$ crystal structure and the lattice constant of the bulk is 5.658 Å, which is closely lattice-matched to GaAs (5.653 Å), yielding a lattice mismatch as small as 0.08%. $Fe_{3-x}Co_xSi$ shows a high stability of the cubic fcc phase over a wide compositional range ($0 < x < 2.15$), which can be used to control the magnetic properties, for example, magnetic anisotropy and magnetic moment.

According to the Slater–Pauling rule ($m = N_V - 24$, with N_V the number of valence electrons), a magnetic moment of $6\,\mu_B$ per f.u. (formula unit) and a Curie temperature of over 1000 K can be expected based on the number of valence electrons (see preceding text). Indeed, Wurmehl *et al*. confirmed the magnetic moment and measured a Curie temperature of 1100 K, making Co_2FeSi the half-metallic ferromagnet exhibiting the highest Curie temperature, and with the largest magnetic moment reported for full-HAs (Wurmehl *et al*., 2006). Recent calculations of the surface band structure of Co_2MnSi predict a stable, half-metallic Mn-terminated surface (Hashemifar, Kratzer and Scheffler, 2005). If applicable this would make Co_2FeSi indeed an excellent candidate for spintronics.

Prior to the metal growth, perfect GaAs surfaces were prepared by depositing a 100 nm-thick GaAs buffer layer in a separate III–V growth chamber. The growth conditions were chosen to obtain the As-terminated $c(4 \times 4)$ reconstruction of GaAs(001). By cooling the samples down to 420 °C under As_4 pressure, the formation of macroscopic defects on the surface during subsequent metal deposition can be prevented (Schönherr, Nötzel, Ma and Ploog, 2001). The transfer of the samples into the As-free metal chamber occurs under UHV conditions at a base pressure of $5 \cdot 10^{-10}$ Torr.

The first step for growing stoichiometric Co_2FeSi was to optimize the growth conditions for the binary alloy $Co_{0.66}Fe_{0.34}$ (bcc structure). The atomic composition of the $Co_{0.66}Fe_{0.34}$ layers was determined by measuring the film's lattice constant by XRD, and by determining the deviations from the data documented in the literature. In the next step, for obtaining the ternary alloy Co_2FeSi, Si was codeposited keeping the Fe and Co fluxes constant at the optimized values for $Co_{0.66}Fe_{0.34}$. For finding the optimum growth conditions, the growth temperature was varied from 100 to 400 °C. As the growth temperatures are comparably low, a small growth rate of about 0.1 nm min^{-1} was chosen not to compromise the crystal quality. As a free parameter, the temperature of the silicon cell (T_{Si}) was varied from 1280 to 1335 °C to obtain stoichiometric Co_2FeSi. The atomic composition of

Table 3. Epitaxially grown Heusler alloy films on semiconductor and selected insulating surfaces.

Heusler alloy	Method	Substrate	Inter-layer	Film orient.	Growth temperature (°C)	Structural properties			Magnetic properties			Reference
						(004) or (220) rocking curve width (°)	Lattice param. c (Å)	HRTEM/ interface	T_C film (K)	Magnetization (emu cm^{-3}) or (moment/fu)	Spin polarization or magneto-resistance (MR)	
Cu_2MnAl	sputter	MgO(100)		(100)	470	0.16				98/g		Geiersbach, Bergmann and Westerholt (2002)
	sputter	$Al_2O_3(11\underline{2}0)$		(110)	470	1	5.905			40/g		Geiersbach, Bergmann and Westerholt (2002)
Co_2MnAl	MBE	GaAs			200	X	5.70		800–1000	3.4 μ_B		Chen, Basiaga, O'Brien and Heiman (2004)
	sputter	MgO(001)	Cr(001)	(001)	RT–500	0.25		X		800	59% @2K	Oogane *et al.* (2006)
Co_2MnSi	PLD	GaAs(001)			177					950	12% @RT	Wang *et al.* (2005a,b,c)
	sputter	$Al_2O_3(11\underline{2}0)$	V	(110)		3	5.688			97/g		Geiersbach, Bergmann and Westerholt (2002)
	sputter	MgO(001)	Cr(001)		RT–500	X				800	89% @2K	Oogane *et al.* (2006)
	sputter	GaAs(001)			347–416	X	5.638	X		928	55% @LT	Singh *et al.* (2006)
Co_2MnGa	MBE	GaAs(001)	AlGaAs		200						13% @5K	Hickey *et al.* (2005)
Co_2MnGe	MBE	GaAs(001)	AlGaAs		175			X			27% @2K	Dong *et al.* (2005)
	MBE	GaAs(001)			175		5.77			1006		Ambrose, Krebs and Prinz (2000a)
	MBE	Ge(111)			Variat.	X			X	X		Tsui *et al.* (2006)
	sputter	$Al_2O_3(11\underline{2}0)$	Cr	(110)	470	4	5.766			103/g		Geiersbach, Bergmann and Westerholt (2002)
	sputter	MgO(001)		(001)	400–600					800		Yamamoto *et al.* (2006)
	MBE sputter	GaAs(001)		(001)		0.24	5.743					Yang *et al.* (2002)
Co_2MnSn		$Al_2O_3(11\underline{2}0)$	Au	(110)	470	3	6.003			87/g		Geiersbach, Bergmann and Westerholt (2002)
Ni_2MnGa	MBE	GaAs(001)	$Sc_{0.3}Er_{0.7}As$		300	X	6.12	X	320	200		Dong *et al.* (1999)
	MBE	GaAs(001)	NiGa		300	X	6.07	X	350	200		Dong *et al.* (2000)
	MBE	GaAs(001)	$Sc_{0.3}Er_{0.7}As$		300	X	6.18	X	340	200		Dong *et al.* (2001)
Ni_2MnGe	MBE	GaAs(001)			300	X	5.896	X	320	400		Dong *et al.* (2001)
	MBE	GaAs(001)			160	X	5.65	X	320	450		Lu *et al.* (2003)
Ni_2MnAl	MBE	GaAs(001)	$Sc_{0.3}Er_{0.7}As$		400	X	6.121		350	180		Dong *et al.* (2003)
	MBE	InAs(001)			80	X	6.15	X	290	450		Dong *et al.* (2001)
Ni_2MnIn	MBE	InAs(001)			80	X	3.065	X	170	420		Xie *et al.* (2001)
	MBE	InAs(001)		(001) B2	120	X		X	170	~370		Xie *et al.* (2005)
				$L2_1$	+200[a]	X		X	330			annealed at 200 °C

(*continued overleaf*)

Table 3. (*Continued*).

Heusler alloy	Method	Substrate	Inter-layer	Film orient.	Growth temperature (°C)	Structural properties			Magnetic properties			Reference
						(004) or (220) rocking curve width (°)	Lattice param. c (Å)	HRTEM/ interface	T_C film (K)	Magnetization (emu cm^{-3}) or (moment/fu)	Spin polarization or magneto-resistance (MR)	
Co_2FeSi	MBE	GaAs(001)			100–250	X				1250		Hashimoto, Herfort, Schönherr and Ploog (2005a,b)
Co_2FeAl	MBE	GaAs(001)		(001)	400	X			665–750	470	9% @RT	Hirohata *et al.* (2005a,b)
$Co_2CrFeAl$	sputter	MgO(001)	Cr(001)	(001)	250–350	X	2.87			2.7–3.1 μ_B	MR6.8% @RT	Kelekar and Clemens (2004, 2005)
	sputter	MgO(001)			400–600	X		X		606		Yamamoto *et al.* (2006)
	sputter	MgO(001)			?	X				512		Matsuda *et al.* (2006)
	sputter	$Al_2O_3(11\underline{2}0)$		(110)	>600	0.5	5.76			1.5–2.5 μ_B		Jakob *et al.* (2005); Auth, Jakob, Blockand Felser (2003)
Fe_2FeSi	MBE	GaAs(001)			250–500			X		140/g		Liou *et al.* (1993)
	MBE	GaAs(001)			150–250	0.14				1050		Herfort, Schönherr and Ploog (2003)
	MBE	GaAs(001)	(001)		200					~750		Herfort, Schönherr, Friedland and Ploog (2004)
	MBE	GaAs(113)A	(113)		250	0.14				1300	10% @25K	Muduli *et al.* (2005b)
	MBE	InGaAs			200						45% @4.2K	Kawaharazuka *et al.* (2004)
	MBE	GaAs(001)			300	0.17				1.107 μ_B		Ionescu *et al.* (2005)
NiMnSb	MBE	InP(001)	InGaAs		300	20 arc-sec	5.91	X	>400	3.6 μ_B		Bach *et al.* (2003a,b); Koveshnikov *et al.*(2005)
	sputter	MgO(110)	Mo(100)	(100)	250–550	X				3.9 μ_B/Mn		Ristoiu, *et al.* (2000b)
	MBE	GaAs(001)		(001)	300	X	5.924			650		van Roy, Borghs and de Boeck (2001)
	MBE	MgO(001)	V(001)	(001)	327			X		3.9 μ_B		Turban *et al.* (2002c)
PtMnSb	sputter	MgO(001)	W(001)	(001)		0.89			582	4.14 μ_B		Kautzky and Clemens (1995)
	sputter	$Al_2O_3(0001)$		(111)	500	X						Johnson *et al.* (1996)

Structural properties: rocking curve width refers to either the (004) or (220) reflection. 'X' denotes that high-resolution X-ray data are available, however, no numbers for the width of certain reflections are given. lattice param.: lattice parameter; HRTEM: high-resolution transmission electron microscopy study of the interface quality. Magnetic properties: magnetization values are given in emu cm^{-3}, emu g^{-1} or magnetic moment per formula unit (fu). The spin-polarization values, obtained at a certain temperature, or at an unspecified low temperature (LT), are given in the last column. For comparison, also a magnetoresistance (MR) value is listed for $Co_2CrFeAl$.
MBE: molecular-beam epitaxy; PLD: pulsed-laser deposition; sputter: sputter deposition; film orient.: film orientation; growth temp.: growth temperature.

Co_2FeSi was determined by high-resolution X-ray diffraction (HRXRD), monitoring the perpendicular lattice mismatch ($\Delta a/a$) of the films using the $Co_2FeSi(004)$ reflection.

4.3.1 Structural properties of epitaxial films (Hashimoto, Herfort, Schönherr and Ploog, 2005a)

The growth was monitored *in situ* using RHEED. The RHEED pattern observed during the growth of Co_2FeSi is rather spotty at growth temperatures below 100 °C. With increasing growth temperatures, the RHEED pattern gradually transforms into sharp streaks with Kikuchi lines and a Laue circle, indicating the required two-dimensional growth mode and a well-ordered single-crystal surface.

The structural properties of the films were examined *ex situ* by HRXRD using Cu K_α radiation with a Ge(220) monochrometer and a triple-bounce analyzer crystal. Figure 4 shows ω-2θ XRD curves of the $Co_2FeSi(004)$ reflection

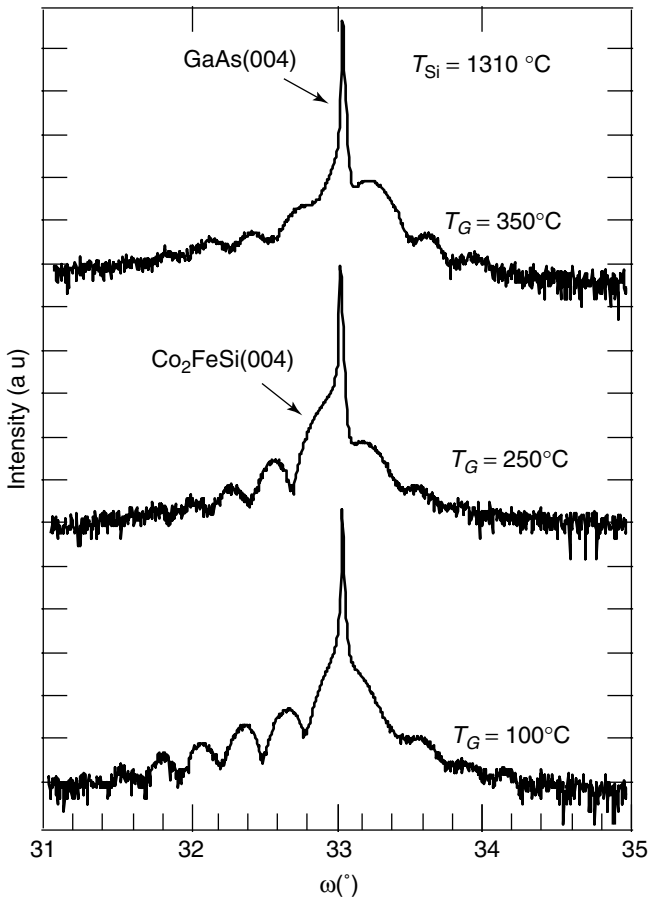

Figure 4. High-resolution X-ray diffraction ω-2θ scans for stoichiometric Co_2Fe_2Si/GaAs(001) films around the $Co_2FeSi(004)$ reflection for three growth temperatures from 100 to 350 °C. The metal effusion cell temperatures were the same for all three films.

of stoichiometric Co_2FeSi films grown at different growth temperatures (100, 250 and 350 °C). For low growth temperatures, higher order interference fringes are found (up to fifth order) – a fingerprint of high crystal quality, interface perfection, as well as smooth surfaces. At a growth temperature of 250 °C, the number of interference fringes decreases – a sign of a beginning crystal or interface degradation. At the high growth temperature, the main diffraction peak is broadened and also shifted to a larger reflection angle – most likely a sign of an interfacial reaction. This speculation was confirmed by a wide-range ω-2θ scans, showing an additional peak at around $\omega = 17.3^\circ$, which can be ascribed to the $(Co,Fe)_2As(110)$ reflection. It is worth noting that the growth temperature at which an interfacial compound is formed is much higher than that of Fe, Co or FeCo on GaAs, which makes Co_2FeSi much more suitable for device applications than these ferromagnetic metals.

The atomic ordering of the film can be studied by analyzing additional X-ray deflections, namely the (002) and (113) reflections. For the $L2_1$ structure, three types of reflections are allowed (Webster and Ziebeck, 1988): (i) h, k, l are all odd (e.g., (113) reflection); (ii) h, k, l are all even and $h + k + l = 4n + 2$ (e.g., (002) reflection); and (iii) h, k, l are all even and $h + k + l = 4n$ (e.g., (004) reflection), where n is an integer and h, k, l are the Miller indices of the diffracting plane. Type (iii) are the fundamental reflections which are not influenced by disorder and the other two are the order-dependent superlattice reflections. Type (i) reflections are reduced to zero in the limit of complete disorder between Si and Fe sublattices, which lead to the reduction of the crystal symmetry to the B2 (CsCl) structure. Type (ii) reflections, on the other hand, are reduced to zero in the limit of complete disorder between all three sublattices resulting in a further reduction of the crystal symmetry to the A2 (bcc) structure.

From the ω-2θ curve around the $Co_2FeSi(002)$ reflection and the reciprocal space map around the $Co_2FeSi(113)$ reflection of a stoichiometric Co_2FeSi film (thickness: 18.5 nm, grown at 100 °C), it was found that the two superlattice reflections of the $L2_1$ structure show interference fringes. This is an indication of long-range atomic order in the structure even for low growth temperatures. These reflections are also observed for Co_2FeSi films grown at different Si cell temperatures, that is, different Si compositions, and different growth temperatures. To precisely determine the ordering parameter, further HRXRD measurements and analysis are necessary, accompanied by electrical resistance measurements, which largely depend on the concentration of defects and impurities in the film. Further, the perfectly oriented vertical fringes indicate that the epitaxially grown Co_2FeSi layers are fully strained.

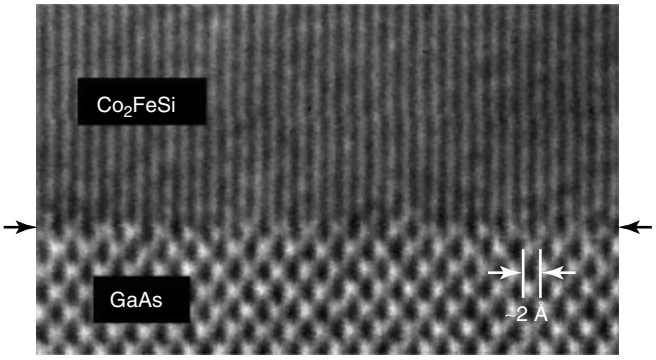

Figure 5. High-resolution cross-sectional transmission electron microscopy image of a perfect Co_2FeSi/GaAs interface. The growth temperature was 100 °C. The GaAs $d\{220\}$ lattice spacing of 2 Å is indicated below.

HRTEM is a powerful tool for studying the structural properties of the interface in great detail. Figure 5 shows a HRTEM (phase contrast) image of the Co_2FeSi/GaAs interface (Hashimoto *et al*., 2006). The abrupt interface of the Co_2FeSi layer grown at 100 °C and the GaAs substrate is indicated by arrows. A perfect matching of the Co_2FeSi(220) and GaAs(220) atomic planes across the interface is observed, that is, the Co_2FeSi layer is coherently strained. For films grown at higher temperatures, sharp interfaces are no longer observed. Already at a growth temperature of 200 °C, a 1–2 monolayer thick interlayer is found resulting from interfacial reactions.

4.3.2 Magnetic properties of epitaxial films

The magnetic properties of Co_2FeSi/GaAs heterostructures were investigated using a superconducting quantum interference device (SQUID) magnetometer. The in-plane magnetic anisotropy was determined at room temperature by applying an external magnetic field along the [110], [1$\bar{1}$0] and [100] directions.

Films grown at temperatures below 200 °C exhibit an easy axis along the [110] direction, a hard axis along [1$\bar{1}$0] and an intermediate hard axis along [100]. Along [110], square-like hysteresis loops with a small coercive field of 4.5 Oe are found. The saturation magnetization M_s of stoichiometric films is $1250 \pm 120\,\mathrm{emu\,cm^{-3}}$, which is indeed very close to the bulk value of Co_2FeSi ($1124\,\mathrm{emu\,cm^{-3}}$ at 295 K). This observation is another hint that the stoichiometric composition determined from the lattice constant is correct. The saturation magnetization decreases with increasing growth temperature, which is consistent with the proposed alteration of the interface due to chemical reactions. For the samples grown at 350 °C, the magnetization curves become more rounded and the angular-dependent difference becomes less pronounced. The previously observed uniaxial anisotropy almost disappears and the underlying cubic magnetocrystalline anisotropy dominates, turning the ⟨100⟩ direction into the easy direction.

Further, by fitting the magnetization curves along the [1$\bar{1}$0] direction with the following expression for the magnetic field as a function of magnetization (Dumm *et al*., 2000):

$$H(m) = 2K_1^{\mathrm{eff}}\frac{(2m^3 - m)}{M_s} + 2K_u^{\mathrm{eff}}\frac{m}{M_s} \qquad (2)$$

values for the cubic magnetocrystalline anisotropy term K_1^{eff} and the uniaxial anisotropy term K_u^{eff} were obtained; m is the normalized magnetization component. It was found that K_u^{eff}reaches a maximum for films grown at 200 °C, and has smaller values for growth below and above that temperature.

To study the influence of the surface and bulk part of the film on the magnetic properties, the effective anisotropy constants can be decomposed into volume $K_{u,1}^{\mathrm{vol}}$ and interface $K_{u,1}^{\mathrm{int}}$ contributions in the following way:

$$K_{u,1}^{\mathrm{eff}} = K_{u,1}^{\mathrm{vol}} + \frac{K_{u,1}^{\mathrm{int}}}{d} \qquad (3)$$

where d is the thickness of the film (Dumm *et al*., 2000). For Co_2FeSi films grown at 100 °C, K_1^{eff} is independent of d, indicating that K_1^{eff} is a volume related term, whereas K_u^{eff} is linearly dependent on 1/d. From curve fitting, K_u^{vol} is found to be almost zero and $K_u^{\mathrm{int}} = (7.3 \pm 0.9) \times 10^{-2}\,\mathrm{erg\,cm^{-2}}$, demonstrating that K_u^{eff} is a purely interface-related term as is observed in other FM/SC systems too. The value of K_u^{int} is in between those of Fe (Brockmann *et al*., 2000) and $Fe_{0.34}Co_{0.66}$ (Dumm *et al*., 2000) on GaAs: 1.2×10^{-1} and $2.6 \times 10^{-2}\,\mathrm{erg\,cm^{-2}}$, respectively. Furthermore, K_u^{int} can be expected to be larger for higher growth temperatures. In general, the uniaxial in-plane magnetic anisotropy observed in FM/SC systems is anticipated to have its origin in an anisotropic bonding at the interface (Sjöstedt, Nordström, Gustavsson and Eriksson, 2002). The quality of the interface is improved up to a growth temperature of slights below 200 °C above which interfacial reactions become limiting. Thus, it can be concluded from the analysis of the in-plane magnetic anisotropy that the optimum growth temperature for obtaining a perfect interface is below 200 °C.

5 SPIN INJECTION FROM HEUSLER ALLOYS INTO SEMICONDUCTOR HETEROSTRUCTURES

As discussed in the preceding text, spin injection into a semiconductor is key to many spintronics device ideas (de Boeck *et al*., 2002). Semiconductor-based spintronics will

potentially offer greater functionality than metal spintronics, as the electronic properties of the systems can be easily tuned in contrast to metals, and the integration with the traditional semiconductor electronics seems feasible. For instance, it was demonstrated that spin-relaxation times in GaAs can be controlled by an electric field (Sandhu, Heberle, Baumberg and Cleaver, 2001). However, the electronic excitation of spin-polarized carriers in semiconductors like GaAs or Si is still a great challenge, whereas efficient room-temperature electric spin injection in metals has been a reality for quite some time. It is even commercially employed in all-metal magnetic read-heads, making use of the GMR effect (Baibich *et al*., 1988; Binasch, Grünberg, Saurenbach and Zinn, 1989). It was not until 1999 when highly efficient spin injection into nonmagnetic GaAs was demonstrated using magnetic semiconductors as spin aligners (Fiederling *et al*., 1999; Ohno *et al*., 1999). Moreover, it was found that the spin-relaxation times in semiconductors can be orders of magnitude larger than momentum or energy relaxation times of the electron (Kikkawa and Awschalom, 1998). Another ingredient for semiconductor spintronics, the controlled manipulation and preservation of the spin over lateral distances of 100 µm and more, was reported the same year in bulk GaAs (Awschalom and Kikkawa, 1999). Recently, using simple, undoped GaAs quantum wells in connection with dynamic quantum dots, coherent spin-transport lengths approaching 1 mm seem possible (Stotz, Hey, Santos and Ploog, 2005).

5.1 Spin injection into semiconductors – an overview

The concept of a semiconductor-based spintronics device, involving spin injection, manipulation by an electrostatic gate via spin-orbit coupling, and spin detection, was introduced by Datta and Das (1990). The initial step is the efficient, electrical injection of spins into the semiconductor. Although spin injection has already been reported by Aronov and Pikus (1976), no convincing results on realizing a Datta- and Das-type device by using metal or metal alloy Ohmic contacts (e.g., NiFe) on semiconductors (e.g., InAs) have been presented (Monzon and Roukes, 1999; Gardelis *et al*., 1999; Filip, Hoving, Jedema and van Wees, 2000). Initially, it was believed that the spin-polarized electrons in the ferromagnetic metals are preserving their spin upon entering the semiconductor via an Ohmic contact. Schmidt and coworkers later realized that the conductivity mismatch in the Ohmic contact between the metal and the semiconductor might present a fundamental obstacle for spin injection (Schmidt *et al*., 2000). For a review of this topic, see also Schmidt (2005).

One way around the conductivity mismatch problem is to replace the Ohmic metal injector by a magnetic semiconductor, such as BeMnZnSe, GaMnAs, or ZnMnSe (Fiederling *et al*., 1999; Ohno *et al*., 1999; Jonker *et al*., 2001). This way, the relative resistance difference of the spin channels is larger as compared to metal injectors, and it can be further increased by a spin polarization close to 100%. In this case, the resistance of the materials plays no longer a role, as the spin-injection efficiency is always unity (Schmidt, 2005), and very large spin polarizations – up to 83% – have been reported (Jonker *et al*., 2001). It should be noted that, despite the success, the practical applicability of dilute magnetic semiconductor contacts is limited to low temperatures (still well below room temperature) and/or high magnetic fields.

A second approach to the conductivity mismatch problem is to use tunnel contacts for spin injection (Rashba, 2000), since the tunneling process is spin dependent and the tunnel contact can have a high impedance. This way, ferromagnetic metallic contacts with their advantages of simple fabrication and superior magnetic properties entered the arena again. Spin polarizations P of around 30–40% were reached in the following Schottky tunnel contact systems: Fe/GaAs, $P = 2\%$ observed between 25 and 300 K (Zhu *et al*., 2001); Fe/AlGaAs, $P = 32$ and 30% at 90 and 240 K, respectively (Hanbicki *et al*., 2002, 2003); Fe/AlGaAs, $P = 30\%$ at 2 K (Adelmann *et al*., 2005); epitxaxial MnAs/GaAs, $P = 6\%$ at 80 K (Ramsteiner *et al*., 2002); Fe/InAs, $P = 12\%$ at 6.5 K and an external magnetic field of 10 T (Ohno *et al*., 2003); and Fe_3Si/GaAs, $P = 10\%$ at 25 K (Kawaharazuka *et al*., 2004). The last system is of great importance as Fe_2FeSi marks a step into the direction of epitaxial-HAs (almost lattice-matched to GaAs).

One alternative to Schottky barriers is the use of Al_2O_3 as an insulating tunneling barrier: (Co, Fe, and NiFe)/Al_2O_3/AlGaAs, $P = 0.8\%$ for Co, 0.5% for Fe, and 0.2% for NiFe at room temperature (Manago and Akinaga, 2002); Fe/Al_2O_3/AlGaAs, $P = 40\%$ at 5 K (best case, 30% typical) (van't Erve *et al*., 2004); NiMnSb/Al_2O_3/Al, $P = 28\%$ (Tanaka, Nowak and Moodera, 1999); and CoFe/AlO_x/AlGaAs, $P = 24\%$ at 80 K and 12% at room temperature (van Dorpe *et al*., 2003). However, it will be extremely difficult to increase the spin polarization of these systems due to the preparation-related issues and the electronic properties of the Al_2O_3-metal interface.

Crystalline MgO, on the other hand, holds great promises as a barrier material since in CoFe/MgO(001), the majority electron states decay slowly in the MgO barrier as evanescent states, whereas the minority electron states decay rapidly (Zhang and Butler, 2004). The resulting high-tunneling spin polarization was experimentally verified to be 85% using superconducting tunneling spectroscopy (Parkin *et al*., 2004).

Recently, the group of Parkin reported spin-polarization values of 57% at 100 K and 47% at room temperature in FeCo/MgO(001)/GaAs (Jiang *et al*., 2005; Jiang, Wang, Shelby and Parkin, 2006). By further analyzing their data in combination with time-resolved Kerr rotation and differential reflectivity measurements, an even higher injection efficiency of 70% for temperatures from 10 K up to room temperature was claimed (Salis *et al*., 2005).

However, it has to be noted that tunneling junctions can only be used for spin injection in reverse bias. In a standard planar Datta–Das–type device geometry where the tunnel junctions are in series, it is not feasible to both inject and detect the spins this way (Schmidt, 2005).

Figure 6 illustrates the different schemes for spin injection into a semiconductor. In the general case of an Ohmic, ferromagnetic metal electrode (a), the spin-injection efficiency is very limited due to conductance mismatch. The situation is improved, if a half-metallic electrode is used (b); however, interface effects may drastically reduce the efficiency. A solution for the conductance mismatch problem is tunneling barrier, separating the half-metallic or ferromagnetic electrode and the semiconductor (c).

5.2 Detection of spin polarization by light-emitting diodes

A common approach for detecting (small) spin polarizations in direct band gap semiconductors, such as GaAs, are quantum well based light-emitting diodes (LEDs) (Fiederling *et al*., 1999; Ohno *et al*., 1999; Jonker *et al*., 2001). Spin-LEDs have been used for obtaining most of the spin-injection data presented in the previous section. Owing to the optical selection rules for radiative recombination, the spin polarization of the electrons can be extracted by analyzing the polarization of the emitted electroluminescence (EL). In the quantum well, two types of holes exist, heavy holes (HH) and light holes (LH), which both may recombine with electrons and emit photons with positive and negative helicity. In the general case, the EL spectra do not yield the spin polarization in a straightforward way. However, in the special case of quantum wells, the heavy- and light-hole states are no longer degenerated because of confinement and/or strain effects. If the heavy- and light-hole bands are separated by an energy at least several times the thermal energy, it becomes possible to spectrally resolve the heavy-hole emission. In the so-called Faraday geometry, where the spin orientation and light propagation direction are both perpendicular to the plane of the LED's quantum well, the selection rules are very simple. As a consequence of the fact that the spin carried away by the photon is ± 1, a spin-up electron can only recombine with a $+3/2$ HH (σ_+ emission) and a spin-down electron only with a spin $-3/2$ HH (σ_- emission), respectively. The circular polarization of the emitted light, P_{circ}, is now simply given by $(I_+ - I_-)/(I_+ + I_-)$, where I_+ and I_- are the peak intensities of the σ_+ and σ_- components, respectively (Jonker *et al*., 2001). P_{circ}, and the spin polarization of the electrically injected carriers, $P_{\mathrm{spin}} = (n_\uparrow - n_\downarrow)/(n_\uparrow + n_\downarrow)$, are equal in case of free exciton emission from an AlGaAs/GaAs/AlGaAs quantum well structure ($n_\downarrow$ and $n_\uparrow$ are the number of electrons of the respective spin orientation) (Jonker *et al*., 2000). As the injected electrons spend a certain amount of time in the semiconductor heterostructure before they recombine in the quantum well, the measured spin polarization is only a lower bound of the real spin polarization in the semiconductor. Thus, for a correct interpretation of the EL measurements, spin-relaxation processes have to be taken into account (Malinowski *et al*., 2000). The EL measurements are usually carried out in a temperature-controlled cryostat that is placed in a superconducting magnet. Details about a typical spin-LED setup can be found in (Ramsteiner, 2003).

5.3 Spin injection from Heusler alloys into semiconductors

To achieve the goal of efficient spin injection at room temperature, ideal half-metallic contacts with high Curie temperatures are the material system of choice, as conductivity

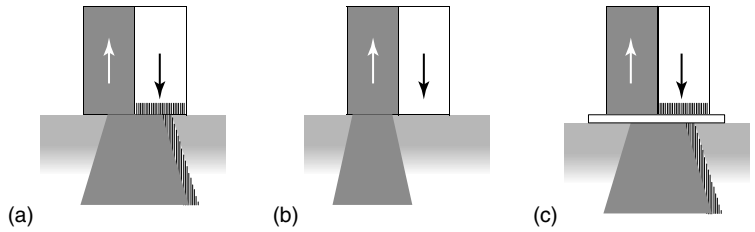

Figure 6. Schemes of spin injection into a semiconductor: (a) Ohmic (diffusive) contact between ferromagnetic metal and semiconductor. The spin-injection efficiency is very limited; (b) (Ohmic) contact between half-metal and semiconductor. Although the half-metallic film is fully spin polarized, the spin polarization at the interface may be significantly lower; (c) Tunnel barrier (Schottky barrier, insulating oxide barrier) between ferromagnetic metal and semiconductor shows an enhanced spin-injection efficiency.

mismatch for 100% spin-polarized systems may not be an issue. So far, only a few spin-LED systems involving HAs have been fabricated and characterized.

The full-HA Co_2MnGa has been deposited by MBE onto the GaAs spin-LED structure (Hickey *et al*., 2005). The InGaAs quantum well was located 300 nm below the surface and the HA was in contact with an AlGaAs layer, forming a Schottky barrier. The growth of the III–V material and metal film was carried out in two separate chambers, requiring that the GaAs device was capped with As prior to the transfer into the metal chamber. Note that instead of a film with the ideal Heusler alloy stoichiometry Co_2MnGa, a film with the composition $Co_{2.4}Mn_{1.6}Ga$ was grown. The spin polarization of the injected electrons was determined to $P = 13\%$ at 5 K; and P disappears already at 20 K. The spin polarization, determined at 6 K by the PCAR technique employing a Nb tip, yielded a transport spin polarization of about 50%. The authors attribute the discrepancy between the measured transport spin polarization and the spin injection to interfacial disorder.

Another full-Heusler system, Co_2MnGe, was also grown by MBE on a AlGaAs spin LED involving a GaAs quantum well (Dong *et al*., 2005). The spacing and intensities of the RHEED streaks suggest that Co_2MnGe grows in the (001) orientation and an $L2_1$-like crystal structure (Dong *et al*., 2003). The maximum steady-state spin polarization measured at 2 K was 13%, while the injected spin polarization was calculated to be 27% based on a calibration of the spin detector using Hanle effect measurements. In both experiments, an otherwise identical Fe electrode control structure was grown (spin polarization 40% at 2 K). Compared to this structure, the spin polarization injected from Co_2MnGe decays more rapidly with increasing temperature and despite the Curie temperature of 905 K, Co_2MnGe structures show no spin polarization at room temperature (compared to 15% at room temperature for Fe structures). Due to the small gap for minority spins in the calculated band structure of Co_2MnGe and the slight disorder observed in TEM, the lack of half-metallic behavior is not too surprising. Consequently, HAs with a larger minority-spin gap, such as Co_2MnSi, may be more effective injectors.

5.4 What next? Necessary experiments and device concepts

First of all, magnetic materials with a close to 100% spin polarization will definitely be crucial for future spintronic devices. This does not necessarily mean that spin polarizations of 100% are absolutely required, although they are intriguing. So far, the race for the best spin injection material is still too close to call. The future success of HAs largely depends on the ability to control disorder and on a theoretical treatment of the complex problem of disordered interfaces at nonzero temperature that is absolutely necessary.

However, once the problem of spin injection is solved, there is a multitude of new device concepts on the horizon (Zutic, Fabian and Das Sarma, 2004). Especially the spin transport in inhomogeneous semiconductors, like p-n junctions, holds great promises (Das Sarma, Fabian, Hu and Zutic, 2001). In a recent study of p-n junctions in which nonequilibrium spins are introduced into one (or both) regions (p and n), it was shown that the spin be transported (under an external bias) through the space-charge region separating the p and n regions. Moreover, the spin gets amplified when crossing the space-charge region. Other phenomena that have been demonstrated are the increase of an effective spin diffusion range in the p–n junction, the possibility of generating spin current in a spin-polarized solar cell, and an all-electronic control of spin (spin capacitance effect) (Zutic, Fabian and Erwin, 2006).

6 CONCLUSIONS

The future of advanced spintronic devices, like the spin transistor, relies on the efficient spin injection from a ferromagnet into a semiconductor, the scattering-free transport, manipulation, and detection of the spin-polarized current. These tough requirements make it necessary to use a growth method for the epitaxial single-crystalline magnetic film/semiconductor heterostructures that allows for extremely precise control of the growth process. In general, MBE has proven to be the method of choice when perfect interfaces and access to the structural properties of the growing film are required. HAs on III–V compound semiconductor surfaces are very promising combinations of ferromagnetic and semiconducting materials. They combine the ability to be grown epitaxially and to yield Curie temperatures well above room temperature. Moreover, some of them are most likely half-metallic ferromagnets with a degree of spin polarization of, or at least close to 100%. One caveat, however, is the inevitable problem of atomic disorder in these ternary material systems, as they exhibit a structural instability due to the fairly broad free-energy minimum. Thus, before spin transistors will become a reality, a number of problems have to be addressed in a joint effort of materials science, physics, and device engineering. The most prominent being the need to understand in detail, and consequently improve, the spin-injection probability from the ferromagnet into the unpolarized semiconductor.

ACKNOWLEDGMENTS

The authors gratefully acknowledge the numerous contributions of J. Herfort, H.-P. Schönherr, A. Trampert and the other colleagues mentioned in the references to the experimental work summarized here. This work was in part sponsored by the Bundesministerium für Bildung und Forschung of the Federal Republic of Germany.

REFERENCES

Adelmann, C., Lou, X., Strand, J., *et al*. (2005). Spin injection and relaxation in ferromagnet-semiconductor heterostructures. *Physical Review B*, **71**, 121301-1–121301-9.

Ambrose, T., Krebs, J.J. and Prinz, G.A. (2000a). Epitaxial growth and magnetic properties of single-crystal Co_2MnGe Heusler alloy films on GaAs (001). *Applied Physics Letters*, **76**, 3280–3282.

Ambrose, T., Krebs, J.J. and Prinz, G.A. (2000b). Magnetic properties of single crystal Co_2MnGe Heusler alloy films. *Journal of Applied Physics*, **87**, 5463–5465.

Ambrose, T., Krebs, J.J. and Prinz, G.A. (2001). Magnetotransport properties of single crystal Co_2MnGe/NM/Co_2MnGe trilayers epitaxially grown on GaAs (001). *Journal of Applied Physics*, **89**, 7522–7524.

Antonov, V.N., Oppeneer, P.M., Yaresko, A.N., *et al*. (1997). Computationally based explanation of the peculiar magneto-optical properties of PtMnSb and related ternary compounds. *Physical Review B*, **56**, 13012–13025.

Aronov, A.G. and Pikus, G.E. (1976). Spin injection into semiconductors. *Soviet Physics Semiconductors*, **10**, 698–700.

Auth, N., Jakob, G., Block, T. and Felser, C. (2003). Spin polarization of magnetoresistive materials by point contact spectroscopy. *Physical Review B*, **68**, 24403-1–24403-6.

Autric, M., Valerio, E., Caminat, P., *et al*. (2004). Single- and double-beam pulsed laser deposition of ferromagnetic half-heusler NiMnSb and MnSb/NiMnSb/InSb alloys. Applications to spintronics. *Proceedings of SPIE*, **5448**, 805–811.

Autric, M., Valerio, E. and Grigorescu, C. (2005). Co_2MnSi growth on semiconductor substrate by double-beams pulsed laser deposition. *Proceedings SPIE*, **5958**, 1–7.

Awschalom, D.D. and Kikkawa, J.M. (1999). Electron spin and optical coherence in semiconductors. *Physics Today*, **52**, 33–38.

Bach, P., Ruster, C., Gould, C., *et al*. (2003a). Growth of the half-Heusler alloy NiMnSb on (In,Ga)As/InP by molecular beam epitaxy. *Journal of Crystal Growth*, **251**, 323–326.

Bach, P., Bader, A.S., Ruster, C., *et al*. (2003b). Molecular-beam epitaxy of the half-Heusler alloy NiMnSb on (In,Ga)As/InP (001). *Applied Physics Letters*, **83**, 521–523.

Bach, H., Westerholt, K. and Geiersbach, U. (2002). Thin-film epitaxial growth of the Heusler alloy Cu_2AlMn. *Journal of Crystal Growth*, **237–239**, 2046–2049.

Baibich, M.N., Broto, J.M., Fert, A., *et al*. (1988). Giant magnetoresistance of (001)Fe/(001)Cr magnetic superlattices. *Physical Review Letters*, **61**, 2472–2475.

Bibes, M., Bouzehouane, K., Barthélémy, A., *et al*. (2003). Tunnel magnetoresistance in nanojunctions based on Sr_2FeMoO_6. *Applied Physics Letters*, **13**, 2629–2631.

Binasch, G., Grünberg, P., Saurenbach, F. and Zinn, W. (1989). Enhanced magnetoresistance in layered magnetic structures with antiferromagnetic interlayer exchange. *Physical Review B*, **39**, 4828–4830.

Blonder, G.E., Tinkham, M. and Klapwijk, T.M. (1982). Transition from metallic to tunneling regimes in superconducting microconstrictions - excess current, charge imbalance, and supercurrent conversion. *Physical Review B*, **25**, 4515–4532.

Bobo, J.F., Johnson, P.R., Kautzky, M., *et al*. (1997). Optical spectroscopy investigations of half metallic ferromagnetic Heusler alloy thin films: PtMnSb, NiMnSb, and CuMnSb. *Journal of Applied Physics*, **81**, 4164–4166.

de Boeck, J., van Roy, W., Das, J., *et al*. (2002). Technology and materials issues in semiconductor-based magnetoelectronics. *Semiconductor Science and Technology*, **17**, 342–354.

Bona, G.L., Meier, F., Taborelli, M., *et al*. (1985). Spin polarized photoemission from NiMnSb. *Solid State Communications*, **56**, 391–394.

Bowen, M., Barthélémy, A., Bibes, M., *et al*. (2005). Half-metallicity proven using fully spin-polarized tunnelling. *Journal of Physics-Condensed Matter*, **17**, L407–L409.

Brockmann, M., Zölfl, M., Miethaner, S. and Bayreuther, G. (2000). In-plane volume and interface anisotropies in epitaxial Fe films on GaAs(001). *Journal of Magnetism and Magnetic Materials*, **198–199**, 384–386.

Brown, P.J., Neumann, K-U., Webster, P.J. and Ziebeck, K.R.A. (2000). The magnetization distributions in some Heusler alloys proposed as half-metallic ferromagnets. *Journal of Physics-Condensed Matter*, **12**, 1827–1835.

Caballero, J.A., Park, P.D., Cabbibo, A., *et al*. (1997). Deposition of high-quality NiMnSb magnetic thin films at moderate temperatures. *Journal of Applied Physics*, **81**, 2740–2744.

Caballero, J.A., Park, Y.D., Childress, J.R., *et al*. (1998). Magnetoresistance of NiMnSb-based multilayers and spin valves. *Journal of Vacuum Science and Technology A*, **16**, 1801–1805.

Chen, Y.J., Basiaga, D., O'Brien, J.R. and Heiman, D. (2004). Anomalous magnetic properties and hall effect in ferromagnetic Co_2MnAl epilayers. *Applied Physics Letters*, **84**, 4301–4303.

Cheng, S.F., Nadgorny, B., Bussmann, K., *et al*. (2001). Growth and magnetic properties of single crystal Co_2MnX (X = Si,Ge) Heusler alloys. *IEEE Transactions on Magnetics*, **37**, 2176–2178.

Cherkashin, Y.Y., Gladyshevskiy, Y.I., Kripyakevich, P.I. and Kuz'ma, Y.B. (1958). Rentgenostrukturnoe issledovanie nekotorykh sistem perekhodnykh metallov. *Journal of Inorganic Chemistry USSR*, **3**, 650–653.

Clifford, E., Venkatesan, M., Gunning, R. and Coey, J.M.D. (2004). Magnetoresistance in point contacts of the Heusler alloy $Co_2Cr_{0.6}Fe_{0.4}Al$. *Solid State Communications*, **131**, 61–64.

Coey, J.M.D. and Chien, C.L. (2003). Half-metallic ferromagnetic oxides. *MRS Bulletin*, **28**(10), 720–724.

Coey, J.M.D. and Venkatesan, M. (2002). Half-metallic ferromagnetism: examples of CrO_2. *Journal of Applied Physics*, **91**, 8345–8350.

Conca, A., Falk, S., Jakob, G., *et al*. (2005). Magnetic tunneling junctions with the Heusler compound $Co_2Cr_{0.6}Fe_{0.4}Al$. *Journal of Magnetism and Magnetic Materials*, **290–291**, 1127–1130.

Das Sarma, S., Fabian, J., Hu, X.D. and Zutic, I. (2001). Spin electronics and spin computation. *Solid State Communications*, **119**, 207–215.

Datta, S. and Das, B. (1990). Electronic analog of the electro-optic modulator. *Applied Physics Letters*, **56**, 665–667.

Debernardi, A., Peressi, M. and Baldereschi, A. (2003). Structural and electronic properties of NiMnSb Heusler compound and its interface with GaAs. *Materials Science and Engineering C*, **23**, 743–746.

Debernardi, A., Peressi, M. and Baldereschi, A. (2005). Spin polarization and band alignments at NiMnSb/GaAs interface. *Computational Materials Science*, **33**, 263–268.

Dedkov, Y.S., Rüdiger, U. and Güntherodt, G. (2002). Evidence for the half-metallic ferromagnetic state of Fe_3O_4 by spin-resolved photoelectron spectroscopy. *Physical Review B*, **65**, 064417-1–064417-5.

Dieny, B., Speriosu, V.S., Parkin, S.S.P., *et al*. (1991). Giant magnetoresistance in soft ferromagnetic multilayers. *Physical Review B*, **43**, 1297–1300.

Dong, J.W., Chen, L.C., Palmstrom, C.J., *et al*. (1999). Molecular beam epitaxy growth of ferromagnetic single crystal (001) Ni_2MnGa on (001) GaAs. *Applied Physics Letters*, **75**, 1443–1445.

Dong, J.W., Chen, L.C., Xie, J.Q., *et al*. (2000). Epitaxial growth of ferromagnetic Ni_2MnGa on GaAs(001) using NiGa interlayers. *Journal of Applied Physics*, **88**, 7357–7359.

Dong, X.Y., Adelmann, C., Xie, J.Q., *et al*. (2005). Spin injection from the Heusler alloy Co_2MnGe into $Al_{0.1}Ga_{0.9}As$/GaAs heterostructures. *Applied Physics Letters*, **86**, 102107-1–102107-3.

Dong, X.Y., Dong, J.W., Xie, J.Q., *et al*. (2003). Growth temperature controlled magnetism in molecular beam epitaxially grown Ni_2MnAl Heusler alloy. *Journal of Crystal Growth*, **254**, 384–389.

Dong, J.W., Lu, J., Xie, J.Q., *et al*. (2001). MBE growth of ferromagnetic single crystal Heusler alloys on (001)$Ga_{1-x}In_xAs$. *Physica E*, **10**, 428–432.

van Dorpe, P., Motsnyi, V.F., Nijboer, M., *et al*. (2003). Highly efficient room temperature spin injection in a metal–insulator–semiconductor light emitting diode. *Japanese Journal of Applied Physics, Part 2 (Letters)*, **42**, L502–L504.

Dowben, P.A. and Skomski, R. (2004). Are half-metallic ferromagnets half metals? *Journal of Applied Physics*, **95**, 7453–7458.

Dumm, M., Zölfl, M., Moosbühler, R., *et al*. (2000). Magnetism of ultrathin FeCo (001) films on GaAs(001). *Journal of Applied Physics*, **87**, 5457–5459.

Elfazani, M., Demarco, M., Jha, S., *et al*. (1981). Hyperfine magnetic field at cadmium impurity in Heusler alloys Ni_2MnGa, Ni_2MnIn, Cu_2MnIn, and Au_2MnIn. *Journal of Applied Physics*, **52**, 2043–2045.

van Engen, P.G., Buschow, K.H.J., Jongebreur, R. and Erman, M. (1983). PtMnSb, a material with very high magneto-optical Kerr effect. *Applied Physics Letters*, **42**, 202–204.

van't Erve, O.M.J., Kioseoglou, G., Hanbicki, A.T., *et al*. (2004). Comparison of Fe/Schottky and Fe/Al_2O_3 tunnel barrier contacts for electrical spin injection into GaAs. *Applied Physics Letters*, **84**, 4334–4336.

Eschrig, H. and Pickett, W.E. (2001). Density functional theory of magnetic systems revisited. *Solid State Communications*, **118**, 123–127.

Farrow, R.C. (1998). The role of molecular beam epitaxy in research on giant magnetoresistance and interlayer exchange coupling. *IBM Journal of Research and Development*, **42**, 43–52.

Fiederling, R., Keim, M., Reuscher, G., *et al*. (1999). Injection and detection of a spin-polarized current in a light-emitting diode. *Nature*, **402**, 787–790.

Filip, A.T., Hoving, B.H., Jedema, F.J. and van Wees, B.J. (2000). Experimental search for the electrical spin injection in a semiconductor. *Physical Review B*, **62**, 9996–9999.

Fujii, S., Ishida, S. and Asano, S. (1995). A half-metallic band structure and Fe_2MnZ (Z=Al, Si, P). *Journal of the Physical Society of Japan*, **64**, 185–191.

Fujii, S., Sugimura, S., Ishida, S. and Asano, S. (1990). Hyperfine fields and electronic-structures of the Heusler alloys Co_2MnAl, Co_2MnGa, Co_2MnSi, Co_2MnGe, Co_2MnSn. *Journal of Physics-Condensed Matter*, **2**, 8583–8589.

Galanakis, I. (2004). Surface properties of the half- and full-Heusler alloys. *Journal of Physics-Condensed Matter*, **14**, 6329–6340.

Galanakis, I., Dederichs, P.H. and Papanikolaou, N. (2002a). Origin and properties of the gap in the half-ferromagnetic Heusler alloys. *Physical Review B*, **66**, 134428-1–13442810.

Galanakis, I., Dederichs, P.H. and Papanikolaou, N. (2002b). Slater-pauling behavior and origin of the half-metallicity of the full-Heusler alloys. *Physical Review B*, **66**, 174429-1–174429-9.

Galanakis, I., Ležaić, M., Bihlmayer, G. and Blügel, S. (2005). Interface properties of NiMnSb/InP and NiMnSb/GaAs contacts. *Physical Review B*, **71**, 214431-1–21443110.

Garcia, N., Munoz, M. and Zhao, Y.W. (1999). Magnetoresistance in excess of 200% in ballistic Ni nanocontacts at room temperature and 100 Oe. *Physical Review Letters*, **82**, 2923–2926.

Gardelis, S., Androulakis, J., Giapintzakis, J., *et al*. (2004). Structural, magnetic, and electrical properties of NiMnSb thin films grown on InSb by pulsed-laser deposition. *Applied Physics Letters*, **85**, 3178–3180.

Gardelis, S., Androulakis, J., Monnereau, O., *et al*. (2005). Possible use of the half-Heusler alloy NiMnSb in spintronics: synthesis and physical properties of arc melted NiMnSb and of NiMnSb thin films grown on InSb by pulsed laser deposition. *Journal of Physics: Conference Series*, **10**, 167–170.

Gardelis, S., Smith, C.G., Barnes, C.H.W., *et al*. (1999). Spin-valve effects in a semiconductor field-effect transistor: a spintronic device. *Physical Review B*, **60**, 7764–7767.

Geiersbach, U., Bergmann, A. and Westerholt, K. (2002). Structural, magnetic and magnetotransport properties of thin films of the Heusler alloys Cu_2MnAl, Co_2MnSi, Co_2MnGe and Co_2MnSn. *Journal of Magnetism and Magnetic Materials*, **240**, 546–549.

Geiersbach, U., Bergmann, A. and Westerholt, K. (2003). Preparation and structural properties of thin films and multilayers of the Heusler compounds Cu_2MnAl, Co_2MnSn, Co_2MnSi and Co_2MnGe. *Thin Solid Films*, **425**, 225–232.

Giapintzakis, J., Grigorescu, C., Klini, A., *et al*. (2002a). Pulsed-laser deposition of NiMnSb thin films at moderate temperatures. *Applied Surface Science*, **197–198**, 421–425.

Giapintzakis, J., Grigorescu, C., Klini, A., *et al*. (2002b). Low-temperature growth of NiMnSb thin films by pulsed-laser deposition. *Applied Physics Letters*, **80**, 2716–2718.

Grigorescu, C., Valerio, E., Tortet, L., *et al*. (2005). Co_2MnX (X=Si, Ge, Sn, SbSn) thin films grown by pulsed-laser deposition. *Journal of Crystal Growth*, **275**, e1183–e1188.

de Groot, R.A., van Engen, P.G., van Engelen, P.P.J. and Buschow, K.H.J. (1990). Magnetic and magneto-optical properties of $NiMnSb_{1-x}Sn_x$ compounds in relation to their electronic band structure. *Journal of Magnetism and Magnetic Materials*, **86**, 326–332.

de Groot, R.A., van der Kraan, A.M. and Buschow, K.H.J. (1986). FeMnSb: a half-metallic ferrimagnet. *Journal of Magnetism and Magnetic Materials*, **61**, 330–336.

de Groot, R.A., Mueller, F.M., van Engen, P.G. and Buschow, K.H.J. (1983). New class of materials: half-metallic ferromagnets. *Physical Review Letters*, **50**, 2024–2027.

de Groot, R.A., Mueller, F.M., van Engen, P.G. and Buschow, K.H.J. (1984). Half-metallic ferromagnets and their magneto-optical properties. *Journal of Applied Physics*, **55**, 2151–2154.

Hames, E.A. and Crangle, J. (1971). Ferromagnetism in Heusler-type alloys based on platinum-group or palladium-group metals. *Journal of Applied Physics*, **42**, 1336–1337.

Hanbicki, A.T., van't Erve, O.M.J., Magno, R., *et al*. (2003). Analysis of the transport process providing spin injection through an Fe/AlGaAs Schottky barrier. *Applied Physics Letters*, **82**, 4092–4094.

Hanbicki, A.T., Jonker, B.T., Itskos, G., *et al*. (2002). Efficient electrical spin injection from a magnetic metal/tunnel barrier contact into a semiconductor. *Applied Physics Letters*, **80**, 1240–1242.

Hanssen, K.E.H.M. and Mijnarends, P.E. (1986). Positron-annihilation study of the half-metallic ferromagnet NiMnSb: theory. *Physical Review B*, **34**, 5009–5016.

Hanssen, K.E.H.M., Mijnarends, P.E., Rabou, L.P.L.M. and Buschow, K.H.J. (1990). Positron-annihilation study of the half-metallic ferromagnet NiMnSb: experiment. *Physical Review B*, **42**, 1533–1540.

Hashemifar, S.J., Kratzer, P. and Scheffler, M. (2005). Preserving the half-metallicity at the Heusler alloy Co_2MnSi(001) surface: a density functional theory study. *Physical Review Letters*, **94**, 096402-1–096402-4.

Hashimoto, M., Herfort, J., Schönherr, H-P. and Ploog, K.H. (2005a). Epitaxial Heusler alloy Co_2FeSi/GaAs(001) hybrid structures. *Applied Physics Letters*, **87**, 102506–102508.

Hashimoto, M., Herfort, J., Schönherr, H.P. and Ploog, K.H. (2005b). Thermal stability and atomic ordering of epitaxial Heusler alloy Co_2FeSi films grown on GaAs(001). *Journal of Applied Physics*, **98**, 104902-1–104902-6.

Hashimoto, M., Herfort, J., Trampert, A., *et al*. (2006). Growth temperature dependent evolution of the interface structure in Co_2FeSi/GaAs(001) hybrid structures. *Journal of Vacuum Science and Technology B*, **24**, 2004–2008.

Hassdorf, R., Feydt, J., Thienhaus, S., *et al*. (2003). Combinatorial thin film synthesis of NiMnAl magnetic shape memory alloys using MBE technique *Materials and Devices for Smart Systems Symposium*, 1-5 Dec. Boston, p.57–64.

Heiman, D., Chen, Y.J., Basiaga, D., *et al*. (2005). Heusler half-metals on GaAs for spin injection. *Compound Semiconductors 2004, Proceeding, Institute of Physics Conference Series*, **184**, 153–160.

Heinrich, B., Woltersdorf, G., Urban, R., *et al*. (2004). Magnetic properties of NiMnSb(001) films grown on InGaAs/InP(001). *Journal of Applied Physics*, **95**, 7462–7464.

Herfort, J., Schönherr, H-P., Friedland, K-J. and Ploog, K.H. (2004). Structural and magnetic properties of epitaxial Fe_3Si/GaAs(001) hybrid structures. *Journal of Vacuum Science and Technology B*, **22**, 2073–2078.

Herfort, J., Schönherr, H.P., Kawaharazuka, A., *et al*. (2005). Epitaxial growth of Fe_3Si/GaAs(001) hybrid structures for spintronic application. *Journal of Crystal Growth*, **278**, 666–670.

Herfort, J., Schönherr, H-P. and Ploog, K.H. (2003). Epitaxial growth of Fe_3Si/GaAs(001) hybrid structures. *Applied Physics Letters*, **83**, 3912–3914.

Heusler, Fr. and Richarz, F. (1908). Studien über magnetisierbare manganlegierungen. *Zeitschrift Für Anorganische Chemie*, **61**, 265–279.

Heusler, Fr., Starck, W. and Haupt, E. (1903). Über die ferromagnetischen eigenschaften von legierungen unmagnetischer metalle. *Verhandlungen der Deutschen Physikalischen Gesellschaft*, **5**, 220–223.

Hickey, M.C., Damsgaard, C.D., Farrer, I., *et al*. (2005). Spin injection between epitaxial $Co_{2.4}Mn_{1.6}Ga$ and an InGaAs quantum well. *Applied Physics Letters*, **86**, 252106-1–252106-3.

Hirohata, A., Kurebayashi, H., Okamura, S., *et al*. (2005a). Magnetic properties of epitaxial $Co_2Cr_{1-x}Fe_xAl$ full Heusler alloy thin films with the $L2_1$ structure. *Ieee Transactions on Magnetics*, **41**, 2802–2804.

Hirohata, A., Kurebayashi, H., Okamura, S., *et al*. (2005b). Structural and magnetic properties of epitaxial $L2_1$-structured Co_2(Cr,Fe)Al films grown on GaAs(001) substrates. *Journal of Applied Physics*, **97**, 103714-1–103714-8.

Holmes, S.N. and Pepper, M. (2002). Magnetic and electrical properties of Co_2MnGa grown on GaAs (001). *Applied Physics Letters*, **81**, 1651–1653.

Holmes, S.N. and Pepper, M. (2003). Cobalt-based Heusler alloys for spin-injection devices. *Journal of Superconductivity*, **16**, 191–194.

Hong, M., Chen, H.S., Kwo, J., *et al*. (1991). MBE growth and properties of Fe_3(Al,Si) on GaAs(100). *Journal of Crystal Growth*, **111**, 984–988.

Hu, G. and Suzuki, Y. (2002). Negative spin polarization of Fe_3O_4 in magnetite/manganite-based junctions. *Physical Review Letters*, **89**, 276601-1–276601-4.

Inomata, K., Okamura, S., Goto, R. and Tezuka, N. (2003). Large tunneling magnetoresistance at room temperature using a Heusler alloy with the B2 structure. *Japanese Journal of Applied Physics, Part 2 (Letters)*, **42**, L419–L422.

Inomata, K., Okamura, S. and Tezuka, N. (2004). Tunnel magnetoresistance using full-Heusler alloys. *Journal of Magnetism and Magnetic Materials*, **282**, 269–274.

Ionescu, A., Vaz, C.A.F., Trypiniotis, T., *et al*. (2005). Structural, magnetic, electronic, and spin transport properties of epitaxial Fe_3Si/GaAs(001). *Physical Review B*, **71**, 094401-1–094401-9.

Irkhin, V.Y. and Katsnel'son, M.I. (1994). Half-metallic ferromagnets. *Physics Uspekhi*, **37**, 659–677.

Ishida, S., Akazawa, S., Kubo, Y. and Ishida, J. (1982). Band theory of Co_2MnSn, Co_2TiSn and Co_2TiAl. *Journal of Physics F-Metal Physics*, **12**, 1111–1122.

Ishida, S., Fujii, S., Kashiwagi, S. and Asano, S. (1995). Search for half-metallic compounds in Co_2MnZ (Z=IIIb, IVb, Vb element). *Journal of the Physical Society of Japan*, **64**, 2152–2157.

Ishida, S., Masaki, T., Fujii, S., Asano, S. (1998). Theoretical search for half-metallic films of Co_2MnZ (Z = Si, Ge). *Physica B – Condensed Matter*, **245**, 1–8.

Jakob, G., Casper, F., Beaumont, V., *et al*. (2005). Thin epitaxial films of the Heusler compound $Co_2Cr_{0.6}Fe_{0.4}Al$. *Journal of Magnetism and Magnetic Materials*, **290–291**, 1104–1107.

Jeong, T., Weht, R. and Pickett, W.E. (2005). Semimetallic antiferromagnetism in the half-Heusler compound CuMnSb. *Physical Review B*, **71**, 184103-1–184103-7.

Ji, Y., Strijkers, G.J., Yang, F.Y., e*t al*. (2001). Determination of the spin polarization of half-metallic CrO_2 by point contact Andreev reflection. *Physical Review Letters*, **86**, 5585–5588.

Jiang, X., Wang, R., Shelby, R.M., *et al*. (2005). Highly spin-polarized room-temperature tunnel injector for semiconductor spintronics using MgO(100). *Physical Review Letters*, **94**, 056601-1–056601-4.

Jiang, X., Wang, R., Shelby, R.M. and Parkin, S.S.P. (2006). Highly efficient room-temperature tunnel spin injector using CoFe/MgO(001). *IBM Journal of Research and Development*, **50**, 111–120.

Johnson, M. (1993). Bipolar spin switch. *Science*, **260**, 320–323.

Johnson, M. (1995). Bipolar spin transistor. *Journal of Magnetism and Magnetic Materials*, **140–144**, 21–24.

Johnson, P.R., Kautzky, M.C., Mancoff, F.B., *et al*. (1996). Observation of giant magnetoresistance in a Heusler alloy spin valve. *Ieee Transactions on Magnetics*, **32**, 4615–4617.

Jonker, B.T., Hanbicki, A.T., Park, Y.D., *et al*. (2001). Quantifying electrical spin injection: component-resolved electroluminescence from spin-polarized light-emitting diodes. *Applied Physics Letters*, **79**, 3098–3100.

Jonker, B.T., Park, Y.D., Bennett, B.R., *et al*. (2000). Robust electrical spin injection into a semiconductor heterostructure. *Physical Review B*, **62**, 8180–8183.

Jullière, M. (1975). Tunneling between ferromagnetic-films. *Physics Letters A*, **54**, 225–226.

Kämmerer, S., Heitmann, S., Meyners, D., *et al*. (2003). Room-temperature preparation and magnetic behavior of Co_2MnSi thin films. *Journal of Applied Physics*, **93**, 7945–7947.

Kautzky, M.C. and Clemens, B.M. (1995). *Epitaxial growth of (001)- and (111)-oriented PtMnSb films and multilayers. Magnetic Ultrathin Films, Multilayers and Surfaces. Symposium*, 17-20 April 1995, San Francisco, p.109–114.

Kawaharazuka, A., Ramsteiner, M., Herfort, J., *et al*. (2004). Spin injection from Fe_3Si into GaAs. *Applied Physics Letters*, **85**, 3492–3494.

Kelekar, R. and Clemens, B.M. (2004). Epitaxial growth of the Heusler alloy $Co_2Cr_{1-x}Fe_xAl$. *Journal of Applied Physics*, **96**, 540–543.

Kelekar, R. and Clemens, B.M. (2005). Properties of Heusler alloy $Co_2Cr_{1-x}Fe_xAl$ superlattices and spin valves. *Applied Physics Letters*, **86**, 232501-1–232501-3.

Kikkawa, J.M. and Awschalom, D.D. (1998). Resonant spin amplification in n-type GaAs,. *Physical Review Letters*, **80**, 4313–4316.

Kim, K., Kwon, S-J. and Kim, T-W. (2004). Characterization of Heusler alloy thin film, Cu_2MnAl and Co_2MnSi, deposited by co-sputtering method. *Physica Status Solidi B*, **241**, 557–560.

Kobayashi, K.I., Kimura, T., Sawada, H., *et al*. (1998). Room-temperature magnetoresistance in an oxide material with an ordered double-perovskite structure. *Nature*, **395**, 677–680.

Koveshnikov, A., Woltersdorf, G., Liu, J.Q., *et al*. (2005). Structural and magnetic properties of NiMnSb/InGaAs/InP(001). *Journal of Applied Physics*, **97**, 73906-1–73906-8.

Kübler, J. (1984). First principle theory of metallic magnetism. *Physica B and C*, **127**, 257–263.

Kübler, J., Williams, A.R. and Sommers, C.B. (1983). Formation and coupling of magnetic moments in Heusler alloys. *Physical Review B*, **28**, 1745–1755.

van Leuken, H. and de Groot, R.A. (1995). Half-metallic antiferromagnets. *Physical Review Letters*, **74**, 1171–1173.

Liou, S.H., Malhotra, S.S., Shen, J.X., *et al*. (1993). Magnetic-properties of epitaxial single-crystal ultrathin Fe_3Si films on GaAs (001). *Journal of Applied Physics*, **73**, 6766–6768.

Liu, Z.H., Zhang, M., Cui, Y.T., *et al*. (2003). Martensitic transformation and shape memory effect in ferromagnetic Heusler alloy Ni_2FeGa. *Applied Physics Letters*, **82**, 424–426.

Lu, J., Dong, J.W., Xie, J.Q., *et al*. (2003). Molecular-beam-epitaxy growth of ferromagnetic Ni_2MnGe on GaAs(001). *Applied Physics Letters*, **83**, 2393–2395.

Lu, Y., Li, X.W., Gong, G.Q., *et al*. (1996). Large magnetotunneling effect at low magnetic fields in micrometer-scale epitaxial $La_{0.67}Sr_{0.33}MnO_3$ tunnel junctions. *Physical Review B*, **54**, R8357–R8360.

Lund, M.S., Dong, J.W., Lu, J., *et al*. (2002). Anomalous magnetotransport properties of epitaxial full Heusler alloys. *Applied Physics Letters*, **80**, 4798–4800.

Malinowski, A., Britton, R.S., Grevatt, T., *et al*. (2000). Spin relaxation in $GaAs/Al_xGa_{1-x}As$ quantum wells. *Physical Review B*, **62**, 13034–13039.

Manago, T. and Akinaga, H. (2002). Spin-polarized light emitting diode using metal/insulator/semiconductor structures. *Applied Physics Letters*, **81**, 694–696.

Mancoff, F.B., Bobo, J.F., Richter, O.E., *et al*. (1999). Growth and characterization of epitaxial NiMnSb/PtMnSb $C1_b$ Heusler alloy superlattices. *Journal of Materials Research*, **14**, 1560–1569.

Marukame, T., Kasahara, T., Matsuda, K., *et al*. (2005). Fabrication of fully epitaxial magnetic tunnel junctions using full-Heusler alloy $Co_2Cr_{0.6}Fe_{0.4}Al$ thin film and MgO tunnel barrier. *Japanese Journal of Applied Physics, Part. 2 (Letters)*, **44**, L521–L524.

Matsuda, K., Kasahara, T., Marukame, T., *et al*. (2006). Epitaxial growth of $Co_2Cr_{0.6}Fe_{0.4}Al$ Heusler alloy thin films on MgO (001)

substrates by magnetron sputtering. *Journal of Crystal Growth*, **286**, 389–393.

Mazin, I.I. (1999). How to define and calculate the degree of spin polarization in ferromagnets. *Physical Review Letters*, **83**, 1427–1430.

Meservey, R. and Tedrow, P.M. (1994). Spin-polarized electron tunneling. *Physics Reports*, **238**, 173–243.

Miyoshi, Y., Bugoslavsky, Y., Syed, M.H., *et al*. (2006). Comparison of free surface polarization of NiMnSb and Co_2MnSi. *Applied Physics Letters*, **88**, 142512-1–142512-3.

Monsma, D.J. and Parkin, S.S.P. (2000). Spin polarization of tunneling current from ferromagnet/Al_2O_3 interfaces using copper-doped aluminum superconducting films. *Applied Physics Letters*, **77**, 720–722.

Monzon, F.G. and Roukes, M.L. (1999). Spin injection and the local hall effect in InAs quantum wells, *J. Magn. Magn. Mater.*, **199**, 632–635.

Mott, N.F. (1936). Electrical conductivity of transition metals. *Proceedings of the Royal Society of London*, **153A**, 699–717.

Muduli, P.K., Herfort, J., Schönherr, H.P. and Ploog, K.H. (2005a). Epitaxial Fe_3Si films stabilized on GaAs(113)A substrates. *Journal of Crystal Growth*, **285**, 514–520.

Muduli, P.K., Friedland, K-J., Herfort, J., *et al*. (2005b). Antisymmetric contribution to the planar Hall effect of Fe_3Si films grown on GaAs(113)A substrates. *Physical Review B*, **72**, 104430–104438.

Muduli, P.K., Herfort, J., Schönherr, H-P. and Ploog, K.H. (2005c). Evolution of magnetic anisotropy and spin-reorientation transition in Fe films grown on GaAs(113)A substrates by molecular-beam epitaxy. *Journal of Applied Physics*, **97**, 123904–123910.

Mukhopadhyay, S. and Das, I. (2006). Giant enhancement of room-temperature magnetoresistance in $La_{0.67}Sr_{0.33}MnO_3/Nd_{0.67}Sr_{0.33}MnO_3$ multilayers. *Applied Physics Letters*, **88**, 032506-1–032506-3.

Nadgorny, B., Mazin, I.I., Osofsky, M., *et al*. (2001). Origin of high transport spin polarization in $La_{0.7}Sr_{0.3}MnO_3$: direct evidence for minority spin states. *Physical Review B*, **63**, 184433-1–184433-5.

Natera, M.G., Murthy, M.R.L.N., Begum, R.J. and Murthy, N.S.S. (1970). Atomic and magnetic structure of the Heusler alloys Pd_2MnGe, Pd_2MnSn, Cu_2MnIn, and CoMnSb. *Physica Status Solidi A*, **3**, 959–964.

von Oehsen, S., Scholtyssek, J.M., Pels, C., *et al*. (2005). Electronic properties of thin Ni_2MnIn Heusler films. *Journal of Magnetism and Magnetic Materials*, **290–291**, 1371–1374.

Oestreich, M., Hübner, J., Hägele, D., *et al*. (1999). Spin injection into semiconductors. *Applied Physics Letters*, **74**, 1251–1253.

Offernes, L., Torgersen, A.N., Brinks, H.W., *et al*. (1999). On the ferromagnetism of AuMnSn. *Journal of Alloys and Compounds*, **288**, 117–119.

Ogawa, T., Shirai, M., Suzuki, N. and Kitagawa, I. (1999). First-principles calculations of electronic structures of diluted magnetic semiconductors (Ga,Mn)As. *Journal of Magnetism and Magnetic Materials*, **196/197**, 428–429.

Ohno, H., Yoh, K., Sueoka, K., *et al*. (2003). Spin-polarized electron injection through an Fe/InAs junction. *Japanese Journal of Applied Physics Part 2 (Letters)*, **42**, L87–L89.

Ohno, Y., Young, D.K., Beschoten, B., *et al*. (1999). Electrical spin injection in a ferromagnetic semiconductor heterostructure. *Nature*, **402**, 790–792.

Oogane, M., Sakuraba, Y., Nakata, J., *et al*. (2006). Large tunnel magnetoresistance in magnetic tunnel junctions using Co_2MnX (X = Al,Si) Heusler alloys. *Journal of Physics D-Applied Physics*, **39**, 834–841.

Orgassa, D., Fujiwara, H., Schulthess, T.C. and Butler, W.H. (2000). Disorder dependence of the magnetic moment of the half-metallic ferromagnet NiMnSb from first principles. *Journal of Applied Physics*, **87**, 5870–5871.

Otto, M.J., Feil, H., Van Woerden, R.A.M., *et al*. (1987). Electronic structure and magnetic, electrical and optical properties of ferromagnetic Heusler alloys. *Journal of Magnetism and Magnetic Materials*, **70**, 33–38.

Otto, M.J., van Woerden, R.A.M., van der Valk, P.J., *et al*. (1989a). Half-metallic ferromagnets. 1. Structure and magnetic-properties of NiMnSb and related inter-metallic compounds. *Journal of Physics-Condensed Matter*, **1**, 2341–2350.

Otto, M.J., van Woerden, R.A.M., van der Valk, P.J., *et al*. (1989b).Half-metallic ferromagnets. 2. Transport-properties of NiMnSb and related inter-metallic compounds. *Journal of Physics-Condensed Matter*, **1**, 2351–2360.

Oxely, D.P., Tebble, R.S. and Williams, K.C. (1963). Heusler alloys. *Journal of Applied Physics*, **34**, 1362–1364.

Palmstrøm, C. (2003). Epitaxial Heusler alloys: New materials for semiconductor spintronics. *MRS Bulletin*, **28**, 725–728.

Park, J.H., Vescovo, E., Kim, H.J., *et al*. (1998). Direct evidence for a half-metallic ferromagnet. *Nature*, **392**, 794–796.

Parkin, S.S.P., Kaiser, C., Panchula, A., *et al*. (2004). Giant tunnelling magnetoresistance at room temperature with MgO (100) tunnel barriers. *Nature Materials*, **12**, 862–867.

Persson, E. (1929). Über den Bau der heuslerschen legierungen. *Zeitschrift Für Physik*, **57**, 115–133.

Pickett, W.E. and Moodera, J.S. (2001). Halfmetallic magnets. *Physics Today*, **54**, 39–44.

Pickett, W.E. and Singh, D.J. (1996). Electronic structure and half-metallic transport in the $La_{1-x}Ca_xMnO_3$ system. *Physical Review B*, **53**, 1146–1160.

Picozzi, S., Continenza, A. and Freeman, A.J. (2002). Co_2MnX (X=Si, Ge, Sn) Heusler compounds: an ab initio study of their structural, electronic, and magnetic properties at zero and elevated pressure. *Physical Review B*, **66**, 094421-1–094421-9.

Prinz, G.A. (1985). Stabilization of BCC Co via epitaxial growth on GaAs. *Physical Review Letters*, **54**, 1051–1054.

Prinz, G.A. (1990). Hybrid ferromagnetic-semiconductor structures. *Science*, **250**, 1092–1097.

Prinz, G.A. (1998). Magnetoelectronics. *Science*, **282**, 1660–1663.

Prinz, G.A. and Krebs, J.J. (1981). Molecular beam epitaxial growth of single-crystal Fe films on GaAs. *Applied Physics Letters*, **39**, 397–399.

Ramsteiner, M. (2003). Electrical spin injection from ferromagnetic metals into GaAs. *Journal of Superconductivity*, **16**, 661–669.

Ramsteiner, M., Hao, H.Y., Kawaharazuka, A., *et al*. (2002). Electrical spin injection from ferromagnetic MnAs metal layers into GaAs. *Physical Review B*, **66**, 081304-1–081304-4.

Raphael, M.P., Ravel, B., Willard, M.A., *et al*. (2001). Magnetic, structural, and transport properties of thin film and single crystal Co_2MnSi. *Applied Physics Letters*, **79**, 4396–4398.

Rashba, E.I. (2000). Theory of electrical spin injection: tunnel contacts as a solution of the conductivity mismatch problem. *Physical Review B*, **62**, R16267–R16270.

Reitz, J.R. and Stearns, M.B. (1979). Theory of spin wave spectra in Heusler alloys. *Journal of Applied Physics*, **50**, 2066–2068.

Ristoiu, D., Nozieres, J.P., Borca, C.N., *et al*. (2000a). The surface composition and spin polarization of NiMnSb epitaxial thin films. *Europhysics Letters*, **49**, 624–630.

Ristoiu, D., Nozieres, J.P. and Ranno, L. (2000b). Epitaxial NiMnSb thin films prepared by facing targets sputtering. *Journal of Magnetism and Magnetic Materials*, **219**, 97–103.

Ritchie, L., Xiao, G., Ji, Y., *et al*. (2003). Magnetic, structural, and transport properties of the Heusler alloys Co_2MnSi and NiMnSb. *Physical Review B*, **68**, 104430-1–104430-6.

van Roy, W., de Boeck, J., Brijs, B. and Borghs, G. (2000). Epitaxial NiMnSb films on GaAs(001). *Applied Physics Letters*, **77**, 4190–4192.

van Roy, W., Borghs, G. and de Boeck, J. (2001). Epitaxial growth of the half-metallic ferromagnet NiMnSb on GaAs(001). *Journal of Crystal Growth*, **227-228**, 862–866.

van Roy, W., Wojcik, M., Jedryka, E., *et al*. (2003). Very low chemical disorder in epitaxial NiMnSb films on GaAs(111)B. *Applied Physics Letters*, **83**, 4214–4216.

Sakuraba, Y., Nakata, J., Oogane, M., *et al*. (2005a). Huge spin-polarization of $L2_1$-ordered Co_2MnSi epitaxial Heusler alloy film. *Japanese Journal of Applied Physics Part 2 (Letters)*, **44**, L1100–L1102.

Sakuraba, Y., Nakata, J., Oogane, M., *et al*. (2005b). Fabrication of Co_2MnAl Heusler alloy epitaxial film using Cr buffer layer. *Japanese Journal of Applied Physics Part 1*, **44**, 6535–6537.

Sakuraba, Y., Nakata, J., Oogane, M., *et al*. (2006). Magnetic tunnel junctions using *B*2-ordered Co_2MnAl Heusler alloy epitaxial electrode. *Applied Physics Letters*, **88**, 022503-1–022503-3.

Salis, G., Wang, R., Jiang, X., *et al*. (2005). Temperature independence of the spin-injection efficiency of a MgO-based tunnel spin injector. *Applied Physics Letters*, **87**, 262503-1–262503-3.

Sandhu, J.S., Heberle, A.P., Baumberg, J.J. and Cleaver, J.R.A. (2001). Gateable suppression of spin relaxation in semiconductors. *Physical Review Letters*, **86**, 2150–2153.

Sands, T., Palmstrøm, C.J., Harbison, J.P., *et al*. (1990). Stable and epitaxial metal/III-V semiconductor heterostructures. *Materials Science Reports*, **5**, 98–170.

Schmidt, G. (2005). Concepts for spin injection into semiconductors – a review. *Journal of Physics D: Applied Physics*, **38**, R107–R122.

Schmidt, G., Ferrand, D., Molenkamp, L.W., *et al*. (2000). Fundamental obstacle for electrical spin injection from a ferromagnetic metal into a diffusive semiconductor. *Physical Review B*, **62**, R4790–R4793.

Schmidt, G. and Molenkamp, L.W. (2001). Electrical spin injection using dilute magnetic semiconductors. *Physica E*, **10**, 484–488.

Schönherr, H.P., Nötzel, R., Ma, W.Q. and Ploog, K.H. (2001). Evolution of the surface morphology of Fe grown on GaAs (100), (311)A, and (331)A substrates by molecular beam epitaxy. *Journal of Applied Physics*, **89**, 169–173.

Schwarz, K. (1986). CrO_2 predicted as a half-metallic ferromagnet. *Journal of Physics F*, **16**, L211–L215.

Singh, D.J. (1997). Magnetoelectronic effects in pyrochlore $Tl_2Mn_2O_7$: role of Tl-O covalency. *Physical Review B*, **55**, 313–316.

Singh, L.J., Barber, Z.H., Kohn, A., *et al*. (2006). Interface effects in highly oriented films of the Heusler alloy Co_2MnSi on GaAs(001). *Journal of Applied Physics*, **99**, 013904-1–013904-4.

Singh, L.J., Barber, Z.H., Miyoshi, Y., *et al*. (2004). Structural, magnetic, and transport properties of thin films of the Heusler alloy Co_2MnSi. *Applied Physics Letters*, **84**, 2367–2369.

Sjöstedt, E., Nordström, L., Gustavsson, F. and Eriksson, O. (2002). Uniaxial magnetocrystalline anisotropy of metal/semiconductor interfaces: Fe/ZnSe(001). *Physical Review Letters*, **89**, 267203-1–267203-4.

Soulen, R.J., Byers, J.M., Osofsky, M.S., *et al*. (1998). Measuring the spin polarization of a metal with a superconducting point contact. *Science*, **282**, 85–88.

Stadler, S., Minott, D.H., Harley, D., *et al*. (2005). Element-specific magnetic properties of Co_2MnSi thin films. *Journal of Applied Physics*, **97**, 10C302-1–10C302-3.

Stotz, J.A.H., Hey, R., Santos, P.V. and Ploog, K.H. (2005). Coherent spin transport through dynamic quantum dots. *Nature Materials*, **4**, 585–588.

Tanaka, C.T., Nowak, J. and Moodera, J.S. (1999). Spin-polarized tunneling in a half-metallic ferromagnet. *Journal of Applied Physics*, **86**, 6239–6242.

Trampert, A. and Ploog, K.H. (2000). Heteroepitaxy of large-misfit systems: role of coincidence lattice. *Crystal Research and Technology*, **35**, 793–806.

Tsui, F., He, L., Lorang, D., *et al*. (2006). Structure and magnetism of $Co_{a(1-x)}MnaxGe_bMn_{ax}$ epitaxial films. *Applied Surface Science*, **252**, 2512–2517.

Tsymbal, E.Y., Mryasov, O.N. and LeClair, P.R. (2003). Spin-dependent tunnelling in magnetic tunnel junctions. *Journal of Physics-Condensed Matter*, **15**, R109–R142.

Turban, P., Andrieu, S., Snoeck, E., *et al*. (2002a). NiMnSb/MgO/NiMnSb heterostructures grown by MBE. *Journal of Magnetism and Magnetic Materials*, **240**, 427–429.

Turban, P., Andrieu, S., Tagliaferri, A., *et al*. (2002b). The use of NiMnSb Heusler alloy in MBE grown tunnel junction. *Materials Research Society Symposium - Proceedings*, **690**, 91–96.

Turban, P., Andrieu, S., Kierren, B., *et al*. (2002c). Growth and characterization of single crystalline NiMnSb thin films and epitaxial NiMnSb/MgO/NiMnSb(001) trilayers. *Physical Review B*, **65**, 134417-1–13441713.

Upadhyay, S.K., Palanisami, A., Louie, R.N. and Buhrman, R.A. (1998). Probing ferromagnets with Andreev reflection. *Physical Review Letters*, **81**, 3247–3250.

Valerio, E., Grigorescu, C., Manea, S.A., *et al*. (2005). Pulsed laser deposition of thin films of various full Heusler alloys Co_2MnX (X = Si, Ga, Ge, Sn, SbSn) at moderate temperature. *Applied Surface Science*, **247**, 151–156.

Viret, M., Drouet, M., Nassar, J., *et al*. (1997). Low-field colossal magnetoresistance in manganite tunnel spin valves. *Europhysics Letters*, **39**, 545–549.

Wang, W.H., Ren, X.B., Wu, G.H., *et al*. (2005a). Magnetic and transport properties of epitaxial Co_2MnSi films. *Ieee Transactions on Magnetics*, **41**, 2805–2807.

Wang, W.H., Przybylski, M., Kuch, W., *et al*. (2005b). Spin polarization of single-crystalline Co_2MnSi films grown by PLD on GaAs(001). *Journal of Magnetism and Magnetic Materials*, **286**, 336–339.

Wang, W.H., Przybylski, M., Kuch, W., *et al*. (2005c). Magnetic properties and spin polarization of Co_2MnSi Heusler alloy thin films epitaxially grown on GaAs(001). *Physical Review B*, **71**, 144416-1–14441614.

Watanabe, M., Takanashi, K. and Fujimori, H. (1991). Anomalous behavior of magnetization and perpendicular magnetic anisotropy for Heusler compound type multilayer films, PtMnSb/CuMnSb. *IEEE Translation Journal on Magnetics in Japan*, **6**, 375–381.

Webster, P.J. (1971). Magnetic and chemical order in Heusler alloys containing cobalt and manganese. *Journal of Physical Chemistry*, **32**, 1221–1231.

Webster, P.J. and Ziebeck, K.R.A. (1988). Alloys and compounds of d-elements with main group elements Part 2.. In *Series: Landolt-Börnstein: Numerical Data and Functional Relationships in Science and Technology - New Series, Group 3: Condensed Matter, Vol. 19: Magnetic Properties of Metals, Subvolume c*, Martienssen, W. (Ed.), Springer Verlag: Berlin, pp. 75–184.

Weht, R. and Pickett, W.E. (1999). Half metallic ferrimagnetism in Mn_2VAl. *Physical Review B*, **60**, 13006–13010.

Wei, J.Y.T., Yeh, N.C., Vasquez, R.P. and Gupta, A. (1998). Tunneling evidence of half-metallicity in epitaxial films of ferromagnetic perovskite manganites and ferrimagnetic magnetite. *Journal of Applied Physics*, **83**, 7366–7368.

Wojcik, M., van Roy, W., Jedryka, E., *et al*. (2002). NMR evidence for MnSb environments within epitaxial NiMnSb films grown on GaAs(001). *Journal of Magnetism and Magnetic Materials*, **240**, 414–416.

Woods, G.T., Soulen, R.J., Mazin, I., *et al*. (2004). Analysis of point-contact Andreev reflection spectra in spin polarization measurements. *Physical Review B*, **70**, 054416.

Wurmehl, S., Fecher, G.H., Kandpal, H.C., *et al*. (2006). Investigation of Co_2FeSi: the Heusler compound with highest Curie temperature and magnetic moment. *Applied Physics Letters*, **88**, 32503-1–32503-3.

Wuttig, M., Craciunescu, C. and Li, J. (2000). Phase transformations in ferromagnetic NiMnGa shape memory films. *Materials Transactions*, **41**, 933–937.

Xie, J.Q., Dong, J.W., Lu, J., *et al*. (2001). Epitaxial growth of ferromagnetic Ni_2MnIn on (001) InAs. *Applied Physics Letters*, **79**, 1003–1005.

Xie, J.Q., Lu, J., Dong, J.W., *et al*. (2005). Effects of growth temperature on the structural and magnetic properties of epitaxial Ni_2MnIn thin films on InAs (001). *Journal of Applied Physics*, **97**, 1–7.

Yamamoto, M., Marukame, T., Ishikawa, T., *et al*. (2006). Fabrication of fully epitaxial magnetic tunnel junctions using cobalt-based full-Heusler alloy thin film and their tunnel magnetoresistance characteristics. *Journal of Physics D-Applied Physics*, **39**, 824–833.

Yanase, A. and Shiratori, K. (1984). Band structure in the high temperature phase of Fe_3O_4. *Journal of the Physical Society of Japan*, **53**, 312–317.

Yang, F.Y., Shang, C.H., Chien, C.L., *et al*. (2002). Multistep magnetic switching in single-crystal (001)Co_2MnGe films. *Physical Review B*, **65**, 174410.

Zhang, M., Liu, Z.H., Hu, H.N., *et al*. (2003). A new semi-Heusler ferromagnet NiFeSb: electronic structure, magnetism and transport properties. *Solid State Communications*, **128**, 107–111.

Zhang, X-G. and Butler, W.H. (2004). Large magnetoresistance in bcc Co/MgO/Co and FeCo/MgO/FeCo tunneling junctions. *Physical Review B*, **70**, 172407-1–172407-4.

Zhang, M., Brück, E., de Boer, F.R., *et al*. (2004a). The magnetic and transport properties of the Co_2FeGa Heusler alloy. *Journal of Physics D: Applied Physics*, **37**, 2049–2043.

Zhang, M., Cui, Y., Liu, Z., *et al*. (2004b). A new Heusler compound Cu_2FeAl: electronic structure, magnetism and transport properties. *Physica Status Solidi A*, **201**, 1570–1577.

Zhu, T.J., Lu, L., Lai, M.O. and Ding, J. (2005). Growth and magnetic properties of NiMnGa thin films prepared by pulsed laser ablation. *Smart Materials and Structures*, **14**, S293–S296.

Zhu, H.J., Ramsteiner, M., Kostial, H., *et al*. (2001). Room-temperature spin injection from Fe into GaAs. *Physical Review Letters*, **87**, 016601-1–016601-4.

Ziebeck, K.R.A. and Webster, P.J. (1974). A neutron diffraction and magnetization study of Heusler alloys containing Co and Zr, Hf, V or Nb. *Journal of Physics and Chemistry of Solids*, **35**, 1–7.

Zutic, I., Fabian, J. and Das Sarma, S. (2004). Spintronics: fundamentals and applications. *Reviews of Modern Physics*, **76**, 323–410.

Zutic, I., Fabian, J. and Erwin, S.C. (2006). Bipolar spintronics: fundamentals and applications. *IBM Journal of Research and Development*, **50**, 121–139.

Crystal Growth of Magnetic Materials

Günter Behr and Wolfgang Löser
Leibniz Institute for Solid State and Materials Research, Dresden, Germany

1 INTRODUCTION

Magnetic materials cover a very wide range of substances starting from pure elements to intermetallic compounds and oxides up to molecular magnets. Magnetic materials are usually applied as polycrystalline (often textured) bulk solids or as thin films. The main purpose for studying single crystals is to provide unique physical data for understanding the bulk properties of magnetic materials or selected constituent phases as a function of their crystallographic orientation and composition. This is of outmost importance for optimization of production routes of textured transformer sheets, anisotropic hard magnets, or textured thin films, because the relevant parameters can only be derived from the single-crystalline specimens. Another important aspect is the study of magnetization processes, which depend sensitively on the stoichiometry, impurity content, and density of structural defects (apart from grain boundaries) and require well-prepared single crystals. Complex crystallographic structures or magnetic ordering of compounds, which are constituents of the magnetic materials, are preferably studied on single-crystalline specimens of various sizes. In polycrystalline or multiphase samples, many of these features inferred from X-ray or neutron diffraction patterns are often hidden because of disturbing reflections from accompanying phases. Single crystals with an optimum orientation are suitable only for special commercial purposes such as magnetostrictive materials for high-performance devices.

Generally, despite the numerous publications on properties of single-crystal specimens of magnetic metals, alloys and compounds, information about crystal growth methods and the appropriate process parameters is often scarce. Therefore, in this chapter, special emphasis is devoted to the various methods for single-crystal preparation of magnetic materials and the appropriate process parameters. One particular concern is the tight correlation between the growth method applied and the alloy phase diagram, which provides decisive information for the choice of operating temperature, feed rod composition, and other growth conditions. Some fundamental aspects and more details about the growth methods themselves can be found in the excellent handbooks (Wilke and Bohm, 1988; Hurle, 1994). Owing to the wide spectrum of existing magnetic materials and the abundance of previous measurements, we can only refer to some particularly important examples of properties determined from single crystals. We refer to the other chapters of this comprehensive handbook and previous textbooks (e.g., Kneller, 1962) for more details on measured magnetic quantities.

Handbook of Magnetism and Advanced Magnetic Materials. Edited by Helmut Kronmüller and Stuart Parkin. Volume 3: *Novel Techniques for Characterizing and Preparing Samples*. © 2007 John Wiley & Sons, Ltd. ISBN: 978-0-470-02217-7.

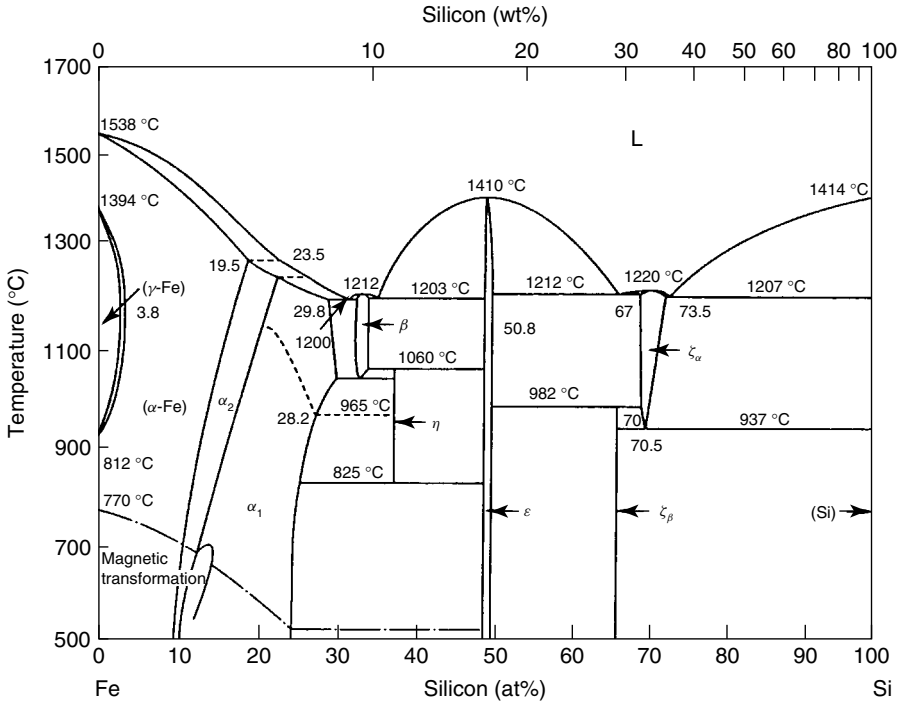

Figure 1. Phase diagram Fe–Si. (Reprinted with permission of ASM International®. All rights reserved. www.asminternational.org.)

2 PHASE DIAGRAMS AND CHOICE OF GROWTH METHODS

The growth methods, applicable to a specific magnetic material are determined by the desired size and degree of perfection of the single crystal and also by the phase diagram of the alloy system or in the case of flux growth, even by multicomponent phase diagrams, which involve possible solvents.

Among the various magnetic materials we can differentiate between pure elements (iron, rare earths), alloys (Fe–Si, Fe–Ni), binary (FePt, $TbFe_2$, Y_2Fe_{17}) or quasibinary solid solution compounds ($Dy_{1-x}Tb_xFe_2$), and multicomponent compounds ($Nd_2Fe_{14}B$) or oxides (RMn_2O_5). As different as the materials themselves, are the phase diagrams of the alloys. Within this section, we therefore can only show a few typical examples of phase diagrams important for magnetic materials and discuss their consequences for crystal growth with special emphasis on growth from the melt.

Figure 1 displays the phase diagram of the Fe–Si system. It not only contains an element with a solid-state transformation Fe (other examples are Dy, Gd) but also shows Fe–Si solid solutions (for transformer sheets) and ordered intermetallic compounds such as the congruent melting binary compound FeSi.

Pure iron crystallizes on cooling the liquid at 1538 °C as the bcc δ phase. At 1394 °C it transforms into the fcc γ phase and subsequently at 912 °C into the bcc α phase, which has same crystal structure as the δ phase. Finally, a ferromagnetic ordering transition takes place at 770 °C. This sequence of phase transitions doesn't allow the growth of perfect single crystals (growth from the melt results in a well-pronounced substructure). Therefore, for single-crystal growth of pure Fe a method has to be used which operates below the lower transition temperature (912 °C). In contrast, the Fe–Si solid solutions at concentrations >3.8 at% Si undergoes no phase transformation and therefore can be grown directly from the melt by different methods like Bridgman growth, zone melting in a crucible, floating zone (FZ) melting, and Czochralski (CZ) growth. The same statement holds for the intermetallic compound FeSi. In those cases, only the desired dimensions, purity, and physical perfection of the crystals decide about the preferred method for crystal growth.

The phase diagram Fe–Pt (Figure 2) exhibits complete solid solubility of the fcc γ-(Fe,Pt) phase at elevated temperatures apart from the small Fe-rich region (<5 at% Pt). The crystal growth from the melt of the γ-(Fe,Pt) phase can be accomplished by various growth methods (Bridgman growth, CZ, FZ). However, depending on the composition the γ-(Fe,Pt) crystal can undergo different ordering transitions. For example, around 50 at% Pt the tetragonal γ_2-FePt phase forms below 1300 °C via a solid-state ordering process from the disordered γ-(Fe,Pt) crystal. A growth directly from the melt of the ordered γ_2-FePt

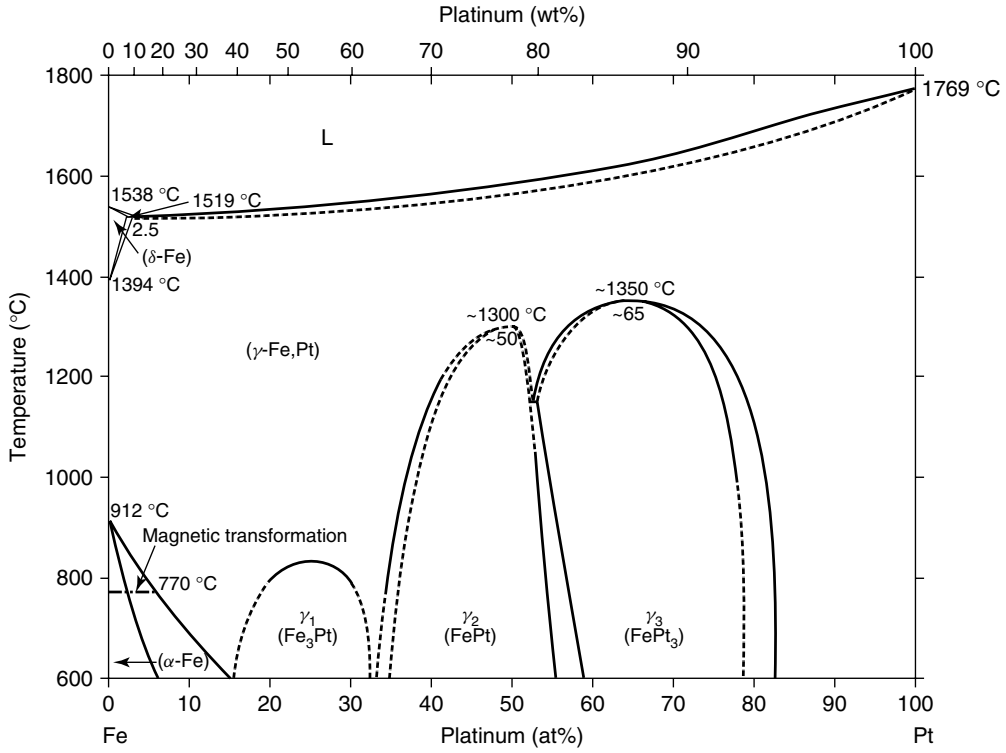

Figure 2. Phase diagram Fe–Pt. (Reprinted with permission of ASM International®. All rights reserved. www.asminternational.org.)

phase, which is interesting for magnetic recording media, is not possible. Single crystals of γ_2-FePt can be prepared by a strain-anneal treatment below the ordering temperature as described in Section 4.2.1.

In the Fe–Tb system (Figure 3) all binary phases melt incongruently, that is, by formation of a new solid phase and a melt of different composition. For example, heating the $Fe_{17}Tb_2$ phase to 1312 °C the reaction $Fe_{17}Tb_2 = \gamma\text{-Fe} + L$ takes place. This means that the phase $Fe_{17}Tb_2$ cannot coexist with a stoichiometric melt of the same composition. Direct growth of $Fe_{17}Tb_2$ is possible from a melt of a composition within the so-called primary crystallization field ranging from 17 to 21 at% Tb. The use of a FZ method is favorable with a liquid zone composition in this range. Because Tb in this case acts as a solvent, the method is known as *traveling solvent floating zone* (TSFZ) method.

Similar relations can be found in the phase diagram of Nd–Fe–B. This system is interesting because of the anisotropic magnetic phase $Nd_2Fe_{14}B$ (Φ), which has outstanding importance in permanent magnetic materials. A binary section at a Nd:B ratio of 2:1 is shown in (Figure 4). Crystal growth by TSFZ appears to be preferable due to the high sensitivity of the neodymium to oxidization and reactions with crucible materials. A detailed description is given in Section 4.2.2.

3 METHODS OF CRYSTAL GROWTH

The phase diagrams of the alloy systems of magnetic materials can show different types of phase formation (see Section 2): congruent melting compounds, peritectically melting compounds, and phases, which are not in equilibrium with the melt. As a result, quite different techniques must be used for single-crystal growth. Each method provides crystals of a characteristic size and morphology, chemical purity, and crystalline perfection.

Two main approaches can be used for the growth of magnetic single crystals, namely, the growth from a solid or a liquid phase. A growth from the gaseous phase was also used for selected materials but does not play an important role. The smallest samples, often used for a crystal-structure analysis, are simply obtained from arc melted alloy ingots. Their size may be only a few tens of micrometers, but can even reach nearly 1 mm. In order to perform magnetic, electrical, or other physical measurements single crystals with dimensions of several millimeters are needed. Still higher requirements on dimensions are valid for crystals with commercial applications (cf. Section 4.3.2). For preparation of such 'big' single-crystalline samples specific crystal growth techniques are employed. A short description of growth methods along with some details

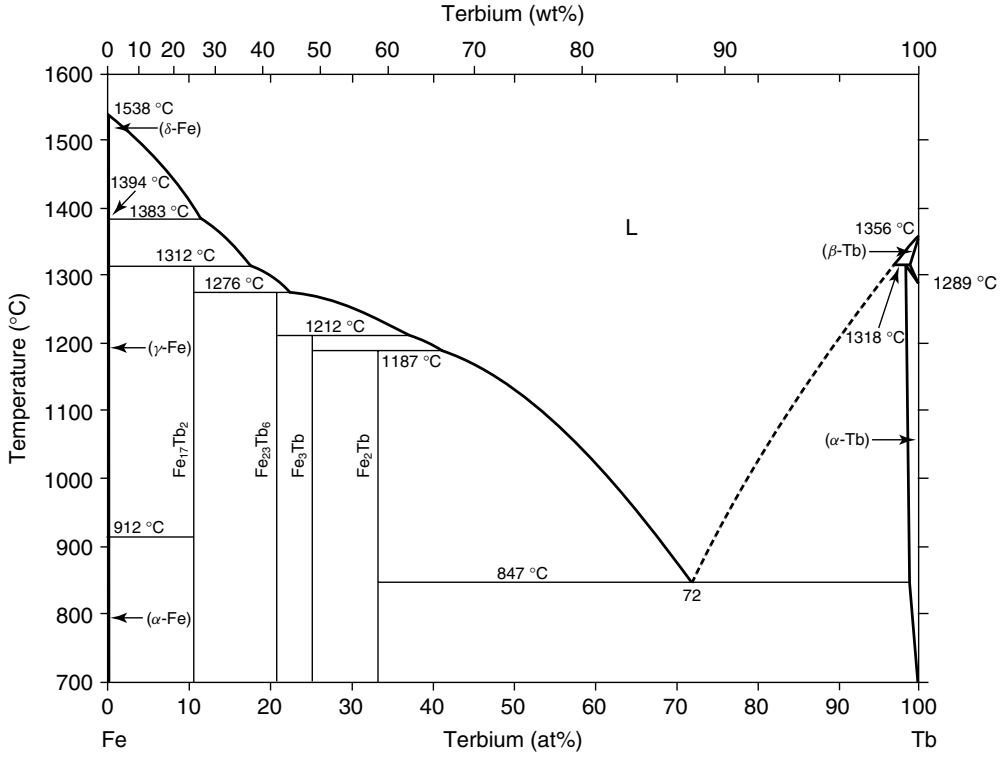

Figure 3. Phase diagram Fe–Tb. (Reprinted with permission of ASM International®. All rights reserved. www.asminternational.org.)

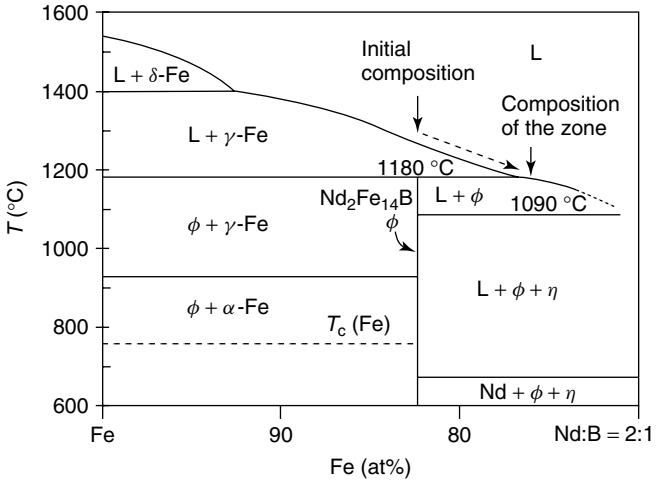

Figure 4. Binary section of the Fe–Nd–B phase diagram at a Nd:B ratio of 2:1. The pathway of melt composition during FZ crystal growth of $Nd_2Fe_{14}B$ from a stoichiometric feed rod is shown schematically (cf. Section 4.2.2). (Reproduced from G. Schneider *et al.*, 1986, with permission from Carl Hanser Verlag GmbH & Co. © 1986.)

related to the crystal growth of magnetic materials is given in the following text. The fundamentals of crystal growth and detailed information about the methods can be found in the excellent handbooks (Wilke and Bohm, 1988; Hurle, 1994).

3.1 Crystal growth from the solid phase

One possible method to grow relatively large and very pure single crystals of phases which do not coexist with the melt, for example, α-Fe, α-Gd, and α-Dy (cf. phase diagram Figure 1 for Fe), is the growth from a solid phase by a recrystallization technique. Annealing of a polycrystalline sample at elevated temperature below the phase transition leads to coarsening of crystallites by grain growth. In order to enhance the grain growth process, which is driven by the reduction of grain boundary energy, internal stress, and entropy of disorder, a controlled deformation of the sample prior to annealing can be carried out which increases the density of defects (strain-anneal technique). This process was first described for aluminum by Sauveur (1912). Furthermore, annealing in a temperature gradient improves the formation of large and perfect grains. The purity of the material plays a crucial role in this process. At elevated temperatures, impurities can segregate to grain boundaries and therefore lower their mobility. Details about the crystal growth of iron and some rare-earth metals will be given in Section 4.1.1.

3.2 Flux growth

The flux growth method is crystal growth from a melt in which the constituents of the material to be grown are dissolved. The most important advantage of using a flux is that the process temperature can be below the melting point of the desired single crystal. As a result, appropriate crucible materials can by easily found and, as for chemical vapor transport, high-temperature phase transitions, or incongruent melting can be circumvented. Therefore, the technological effort can be reduced compared with the plain melt growth methods. The main shortcomings of the method are the degraded purity of the grown crystals (due to incorporation of the flux material) and their small size. The principal problem to be solved in this method is the choice of the solvent. The properties desirable for the solvent are:

1. The compound to be grown is the only stable solid phase in the flux under growth conditions.
2. The solubility of the components of the crystal to be grown should not be too low and should decrease with falling temperature.
3. The melting point of the flux material must be much lower than the stability limit of the crystal to be grown.
4. A very low solubility of the solvent elements in the grown crystal is desirable (at least incorporated elements should not affect the measured properties).
5. A crucible material must exist, which does not react with and is not wetted by the melt solution.
6. The viscosity of the solution should be low, preferably in the range $10^{-3}-10^{-2}$ Pa s.
7. The solidified residual melt should be easy to separate from the grown crystals.

Single crystals of multiferroic compounds, for example, $RMn_{2-x}Fe_xO_5$ and $RMn_{2-x}Co_xO_5$ oxides (R = Y, Tb, Ho) have been grown from a PbO/PbF_2 flux. The solubility of the different components in the flux can be roughly estimated from binary phase diagrams. Unfortunately, the multicomponent phase diagrams in most cases have not been studied yet. Platinum is a good candidate as the crucible material for PbO/PbF_2 fluxes.

The growth process must be performed in a well-defined atmosphere (oxygen partial pressure) in a furnace with a good thermal stability and well controlled temperature. Chamber furnaces with a controllable atmosphere usually meet the requirements. The weight ratio between solvent and growing material varies in a wide range depending on the multinary phase diagram of the complex systems. The crystal growth takes place with slow cooling of the furnace. After heating to a maximum temperature and waiting for equilibrium the temperature is slowly decreased with a rate of a few degrees per hour. Spontaneous nucleation occurs first and one has to control the number of nuclei in order to obtain only a few large single crystals during subsequent growth. In order to minimize the number of growing nuclei, a temperature oscillation technique during the starting phase of the cooling can be used (Scheel and Elwell, 1972). A typical programmable temperature–time regime for the flux growth is shown in Figure 5. Depending on the crystal/solvent system, either variable cooling rates with a constant linear growth rate or a constant cooling rate or a maximum stable growth rate can be applied during crystallization. A detailed description is given by Scheel and Elwell (1972). The residual solvent can be removed from the crystals by treating samples in different etching solutions, which do not dissolve the crystals, or by crucible rotation in the hot stage to remove the solvent from the crystals grown at the bottom or at the walls of the crucible. Another variant called *flux creep method* applied for the growth of Sm–Fe crystals will be described in Section 4.2.3.

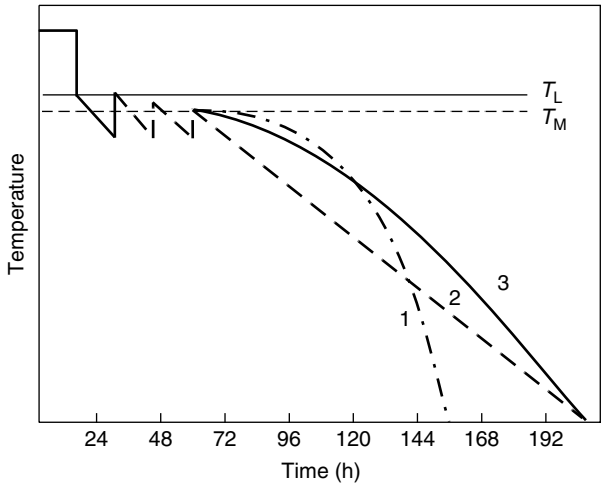

Figure 5. Typical temperature program for flux growth with a temperature oscillation in the metastable region below the liquidus temperature T_L around the melting point T_M: 1–constant linear growth, 2–constant cooling rate, 3–maximum stable growth rate. (Reproduced from Scheel *et al*., 1972, with permission from Elsevier. © 1972.)

A second method to produce single crystals from a melt solution of the components is the traveling solvent method. An alloy consisting of the components of the compound to be grown and the solvent forms the liquid zone, which is moved through the material at a very low rate. The use of a seed for growing oriented crystals is possible. Other details related to the crystal growth of refractory compounds from the flux can be found in the comprehensive review of Gurin and Korsukova (1983) who analyzed the complete process. The crucible-less TSFZ method is described together with the FZ method due to the similarity of the methods.

3.3 Crystal growth from the melt

Samples needed for crystal-structure investigations can be usually very small with a size of a few tens of micrometers. Such small single-crystal fragments of about $40 \times 45 \times 15\,\mu m^3$ can be extracted from polycrystalline arc melted and heat treated samples if the phase diagram allows this synthesis of the compound. The elements are melted in a water-cooled copper heart in purified argon at a pressure of about 0.6 bars. The melting procedure must be repeated several times in order to improve the alloy homogeneity. For further homogenization and grain coarsening the samples can be subjected to an annealing treatment with an annealing temperature as close as possible to the stability limit of the phase. Finally, single-crystalline specimens can be cut out of large grains of the button.

A growth from the melt of elemental components is the most common approach to prepare big single crystals of intermetallic magnetic compounds. In order to decide which particular method can be used, an exact knowledge of the phase diagram, the partial pressures of the components at the melting temperature, and the reactivity of the melt with the crucible material and the environmental atmosphere is necessary. The following methods for crystal growth of magnetic materials from the melt are used depending on their phase stability and melting temperature: FZ melting, horizontal FZ melting with levitation in a cold crucible, vertical container zone melting, CZ method, Bridgman–Stockbarger, and Tamann–Stöber method. The main advantage of the growth from the melt is an opportunity to obtain large single crystals (up to several cubic centimeters), which can be analyzed by various techniques including magnetic and electrical transport measurements for particular crystallographic directions. In principle, crystals can be grown from the melt of all compounds which are stable up to the melting point and which melt congruently or even incongruently with a melt composition not too far from the compound stoichiometry. The basic concept to be considered in all methods of directional solidification from a melt is the morphological stability of the solid–liquid phase boundary connected with constitutional supercooling (Rutter and Chalmers, 1953).

A possible instability of the moving solid/liquid interface is caused by the formation of a steady state boundary layer with alloy component enrichment near the interface due to deviations of the crystal stoichiometry from the melt composition described by the distribution coefficient $k = c_S/c_L < 1$ (or $k < 1$) determined from the solidus (c_S) and the liquidus (c_L) concentration of the equilibrium phase diagram (cf. Section 2). Constitutional supercooling occurs if $G_L < m{\cdot}G_C$, where G_L is the temperature gradient in the liquid near the solid/liquid interface, G_C is the solute concentration gradient in the steady state diffusion boundary layer of the liquid phase, and m is the liquidus slope in the equilibrium phase diagram. In the steady state conditions of unidirectional solidification, with a planar solid/liquid interface, this gradient is (Tiller, Jackson, Rutter and Chalmers, 1953):

$$G_C = \frac{(1-k)}{k}\cdot N_\infty \cdot \frac{V}{D} \tag{1}$$

where N_∞ is the solute concentration in the melt far from the solid/liquid interface, V is the growth rate, and D is the solute diffusion coefficient in the melt. Because of the lack of exact experimental data for melts of the various magnetic materials the simple approach of equation (1) seems to be appropriate to describe the phenomenon. Any unstable solid/liquid interface leads to a cellular growth with undesired second phase formation. While k and D are fixed by the alloy system a high-temperature gradient G_L must be realized by the design of the crystal growth facility. Moreover, the pulling rate V must be chosen to be as low as necessary to guarantee a stable growth. The various demands discussed, can be fulfilled using one of the wide variety of growth methods.

The Tamann–Stöber method is characterized by melting the material in a vertical crucible. The crucible is located in a temperature zone with a gradient so that on slow cooling the melt at the bottom of crucible crystallizes first. For a convenient seed selection the bottom of the crucible usually ends in a rounded tip with a small radius of curvature. This method is also referred to as vertical gradient freezing (VGF) method. The Bridgman technique uses a relative translation of the crucible containing a completely molten material to an axial temperature gradient in a furnace. In the crystal growth of magnetic materials, mainly vertical configurations shown in Figure 6 are used. The temperature gradient near the solid/liquid interface can be made more stable and steeper applying the vertical Stockbarger configuration consisting of two furnaces with different temperature levels divided by an adiabatic loss zone as illustrated in Figure 7. The crucible is moved into the temperature gradient zone with a velocity, which must be controlled very well.

A problem of general interest in all crucible methods is the choice of the crucible material. It must be chemically inert with respect to the melt, should not be wetted by the melt, and should have a thermal expansion coefficient less than the crystal itself. Depending on the material to be grown graphite, graphite covered with boron nitride, alumina, boron nitride, quartz, and Al_2O_3-supported silica as well as open or welded molybdenum and tantalum crucibles are used. Melts of metallic magnetic materials usually react with oxygen, and oxides contaminate the crystal and disturb the grain selection and growth process. Therefore, an inert atmosphere

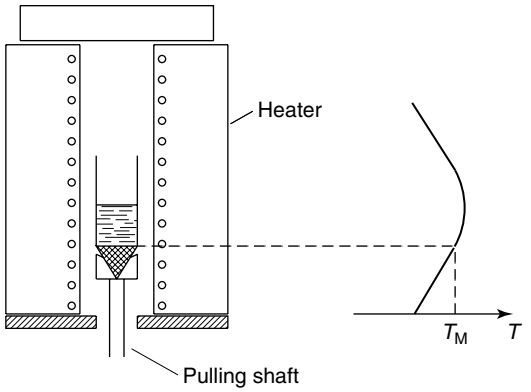

Figure 6. Vertical Bridgman method and related temperature profile. (Reproduced from G. Behr *et al*., 2000, with permission from Springer-Verlah GmbH. © 2000.)

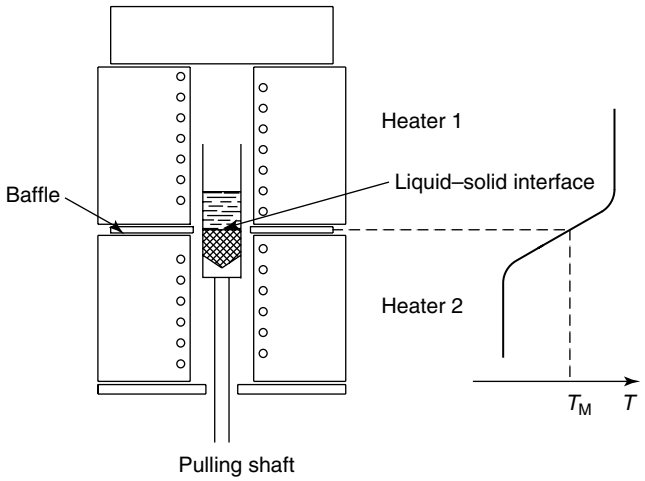

Figure 7. Vertical Stockbarger configuration and related temperature profile. (Reproduced from G. Behr *et al*., 2000, with permission from Springer-Verlah GmbH. © 2000.)

of purified argon or helium and in some cases high vacuum conditions must be realized in the growth chamber.

CZ growth by crystal pulling from a melt contained in a crucible is a widely used method in research and industry. It is schematically illustrated in Figure 8. The apparatus consists of the following components: (i) a crucible, which can be rotated, (ii) the upper pulling shaft, which enables a rotation and has a stable velocity, (iii) the heater, and (iv) a vacuum containment. Seed crystals are used if available. The choices of the crucible material and the atmosphere have to meet the same requirements as discussed for the Bridgman method. To avoid contamination from crucible material CZ growth of magnetic materials is often carried out using a tri-arc or tetra-arc configuration with a water-cooled copper hearth in an atmosphere of argon. It can also be applied in a scull-like configuration, where a

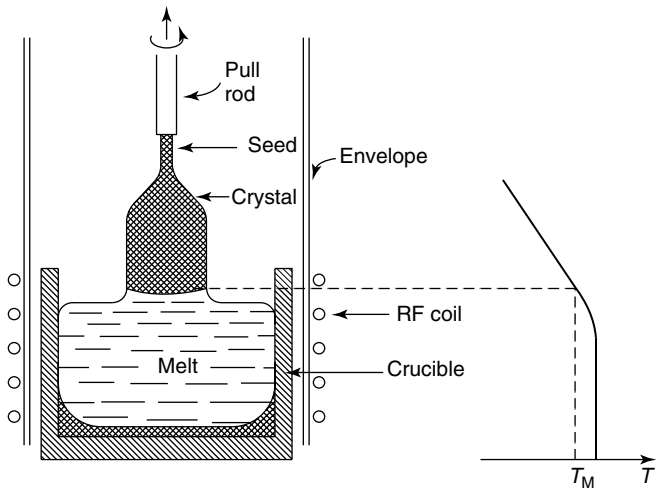

Figure 8. Czochralski method of the crystal growth and related temperature profile. (Reproduced from G. Behr *et al*., 2000, with permission from Springer-Verlah GmbH. © 2000.)

skull of unmelted material remains between the cold-copper hearth and the melt. To avoid any contact with the crucible for refractory and highly reactive materials like rare earths and rare-earth-containing compounds, radiofrequency (RF) inductive heating in a Hukin-type copper cold crucible is also utilized.

A common procedure to allow the growth of only one crystallite in all pulling methods is the bottleneck technique. Starting from a polycrystalline seed, the diameter of the growing crystal is reduced to a minimum followed by enlarging the diameter to the normal rod size. In the narrow part of the crystal only a few or sometimes one single crystallite can propagate. Otherwise, a growth process without seed can be performed starting with the polycrystalline material, which provides many small seeds for further growth.

Zone melting originally described by Pfann (1952) for purification of metals has been widely developed and used as a commercial growth technology in the past 50 years. In this method, only a relatively narrow zone of a cylindrical rod is molten and the zone travels from one end of the rod to the other one. It can be realized as a horizontal or vertical arrangement in containers or as crucible-free zone melting (FZ). The FZ method is normally preferred for refractory and highly reactive materials for which no crucible material is available.

A variety of zone melting techniques evolved with horizontal and vertical configurations, single and multiple heating zones (Pfann, 1988). The most common technique is to use a long horizontal crucible or boat to contain the material. A seed crystal is placed at one end and a molten zone is produced so that the end of the seed is just melted. The zone is then traversed away from the seed along the

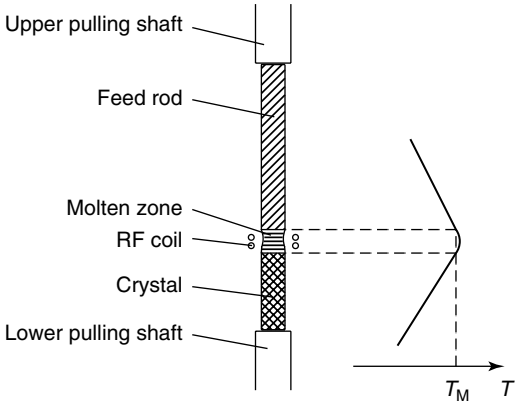

Figure 9. Floating zone (FZ) method and related temperature profile. (Reproduced from G. Behr *et al*., 2000, with permission from Springer-Verlah GmbH. © 2000.)

length of the boat. This method can lead to contamination from the boat and thus the system has been turned through 90° to give a vertical FZ. In this case, the molten material is prevented from falling down by surface tension. The molten zone is traversed up or down along the rod. In this form, it is a crucible-less technique of crystal growth and is called *floating zone technique* schematically shown in Figure 9.

There are different possibilities to heat the zone. In the past, the heat was often supplied to the molten zone using specially shaped RF coils. Apart from RF heating, halogen lamps, arc discharge, electron beam, and laser heating have been used in FZ techniques (Feigelson, 1985). In the case of RF heating, the coils are usually a single or double turn and the electromagnetic field couples directly to the material. This makes it easy to design different coil forms to obtain the correct shape of the growing interface so that a proper crystal is obtained. The main limitation of the RF heating is the necessity of electrical conductivity of the melts. For some materials with insufficient electrical conductivity at low temperatures a preheater is often used.

The use of arc discharge or halogen lamps has been very successful in growing plenty of different materials. Either an elliptical horizontal or vertical optical mirror configuration can be used, where the arc or halogen lamp is at one focus of the mirror and the FZ is at the other one. The growth usually proceeds inside a transparent holder so that gas supplies can be used to operate under inert, oxidizing, or reducing atmosphere. Thus, this method can be summarized as a moving melt zone method in which the crystal rotation is optional. It is distinguished by a small melt volume and usually relatively large temperature gradients.

Commercial systems with optical (radiation) heating specially designed for FZ growth are available only from the following companies: NEC (single- and double-ellipsoid mirror furnaces), Crystal Systems, Inc. (four-mirror furnace) in Japan, MPEI (open vertical ellipsoid configuration with aperture) in Russia, GERO in Germany and Cyberstar in France (single- and double-ellipsoid mirror furnaces). Mainly elliptical mirrors are used to focus the light from one or several lamps onto the sample. The light sources mostly used are either tungsten halogen lamps of 0.3–1.5 kW maximum power or xenon arc discharge lamps up to 10 kW for high power requirements. In all cases, lamp bulbs made of fused quartz are employed.

A disadvantage of mirror furnaces is the fact that temperature measurements during growth are quite difficult. A noncontact measurement of the sample temperature by pyrometer is virtually impossible due to the much higher level of light reflected versus radiation emitted from the sample. Feedback control of image furnaces is quite uncommon; in the case of FZ growth, the zone is usually controlled by visual observation of the sample and manual regulation of the power.

Three typical apparatuses for FZ growth are shown in Figure 10. The shape and stability of the molten zone play an important role in FZ melting. The molten zone is hanging free, between the two rods, and its length is limited to approximately the rod diameter for diameters up to 10 mm used for crystal growth of most magnetic materials. To maintain a convex solid/melt interface, which is necessary for proper grain selection (especially for the growth of peritectic melting compounds with small growth velocities, see also Section 4.7), the optical systems are preferable to RF heating due to the strong energy absorption at the surface. The RF power, by contrast, penetrates into the material depending on its electrical resistivity and the frequency of the RF generator applied.

In case of intermetallic compounds special attention has to be paid to the gas purity in the growth chamber. A common way is the use of purifying systems with heated titanium, zirconium, or alloys of these elements. The gas purity can be controlled by measuring cells with ZrO_2 as sensor material.

Two special features connected with the crystal growth of magnetic materials, especially with rare-earth-containing compounds, silicides and borides, should be mentioned.

First, the purity of the constituent components plays a key role in the growth process especially of intermetallic compounds because oxide particles hinder the grain selection very severely. The metals used for preparation of magnetic materials often do not compete with the high purity of semiconductors. Special attention has to be paid for the purity of rare-earth elements. In some commercially available materials undefined oxygen contents are present and sometimes up to about 1% tantalum is present as a relic of the preparation process. The choice of the appropriate supplier is of principal significance. In some cases purification

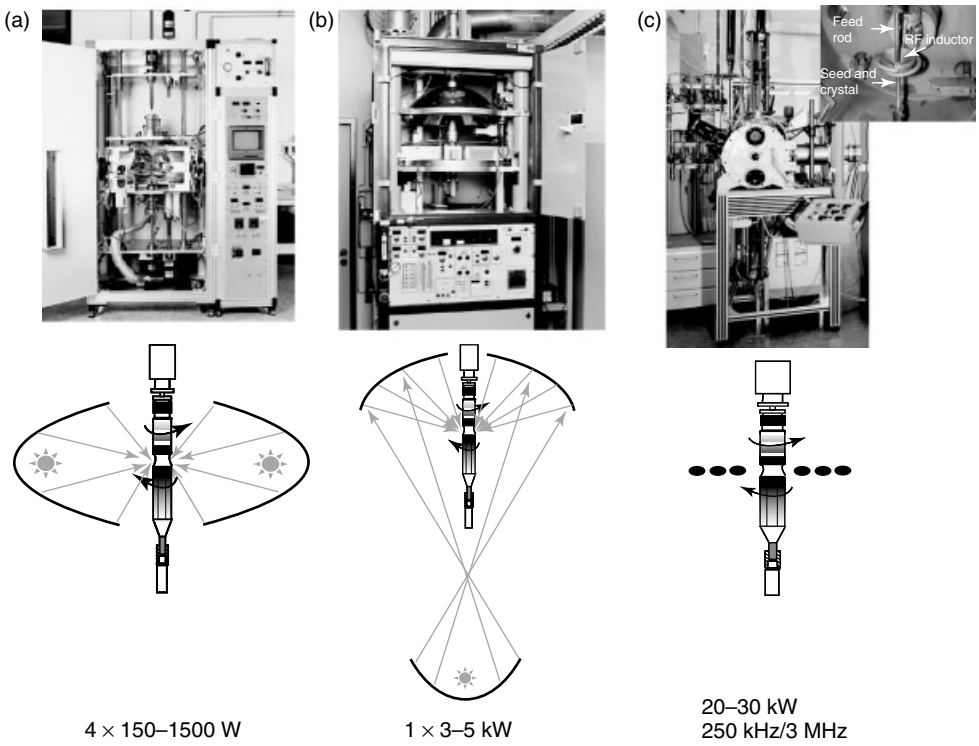

Figure 10. FZ crystal growth equipment with the quadro-mirror horizontal optical heating (CSI Japan) (a), double mirror vertical optical heating (MPEI Moscow) (b), and horizontal RF heating (IFW Dresden) (c).

by distillation or electromigration is possible and should be applied. The best results in growing of special rare-earth-containing intermetallic compounds were achieved using rare earths from the noncommercial supplier Ames Laboratories.

Secondly, silicothermic or borothermic reactions of oxygen traces with silicon or boron can arise. The reactions have the desired effect of melt refining but also shift the composition and therefore must be taken into account during preparation. The consideration of the oxygen content in materials is described, for example, in Behr *et al*. (1985).

The silicothermic and borothermic reactions of all oxide traces in the materials follow the scheme

$$\mathrm{MeO}_x + (2 + x/2)\mathrm{Si} = \mathrm{MeSi}_2 + x/2\mathrm{SiO}_2 \quad \text{or}$$

$$\mathrm{MeO}_x + (2 + 2x/3)\mathrm{B} = \mathrm{MeB}_2 + x/3\mathrm{B}_2\mathrm{O}_3 \qquad (2)$$

$$\mathrm{SiO}_2 + \mathrm{Si} = 2\mathrm{SiO} \quad \text{and} \quad \mathrm{B}_2\mathrm{O}_3 + \mathrm{B} = 3\mathrm{BO} \qquad (3)$$

Complete evaporation of SiO takes place in vacuum at temperatures above 1000 °C and for BO above 1500 °C. During growth in an argon atmosphere these temperatures change to 1400 °C and about 1600 °C.

One typical preparation route of starting materials and of feed rods for FZ melting and the TSFZ method is the follows:

First, special attention has to be paid to obtain suitable starting materials. This includes an overall purity not less than 3N and especially a low content of oxygen (often not specified by manufacturers). To reduce the oxygen contamination for rare-earth elements bulk material is favorable.

Second, the materials must be stored and handled under clean conditions mainly in glove boxes operating with purified argon, and all melting processes should proceed under purified argon or helium gas.

The alloying of compounds is possible in arc-melting facilities. Compounds with less reactive components can be melted in crucibles, too. For crystal growth by FZ or by TSFZ techniques feed rods of good homogeneity are necessary. The most effective method to obtain such rods is the use of a Hukin-type cold crucible equipped with a casting mould (see Figure 11). In this case the elements and the hot melt do not contact the crucible but levitate inside the water-cooled crucible. The melt is very effectively stirred by the electromagnetic force generated from the coil connected with HF generator (in the shown case 100 kHz, 50 kW, Hüttinger, Germany). After alloying the melt is cast into a water-cooled copper mould with 6 or 8 mm diameter. As long as the melt crystallizes radially, no macrosegregation is observed and the feed rods exhibit excellent homogeneity along the axis.

Figure 11. Hukin-type cold crucible equipped with a casting mould.

4 CRYSTAL GROWTH OF SELECTED MAGNETIC MATERIALS

4.1 Crystal growth of soft magnetic alloys

The free energy of a ferromagnetic crystal depends on the orientation of the spontaneous magnetization relative to the crystal axis. This phenomenon is known as the *magnetocrystalline anisotropy* and is displayed in the orientation dependence of the magnetization. Therefore, single crystals of magnetic materials are necessary to investigate this dependence in detail.

4.1.1 Pure metals

The 3d metals Co, Ni, Fe, and 4f metals Gd, Tb, Dy, and Ho (highest magnetic moment) are typical representatives of soft magnetic metals.

Both pure cobalt and nickel melt below 1500 °C and do not exhibit crystallographic phase transformations above 450 °C. So crystal growth can be realized directly from the melts in crucibles by Bridgman technique, CZ growth, and by zone melting in crucibles or as FZ melting.

Nickel and cobalt had been grown using Bridgman–Stockbarger technique by da Andrade and Henderson (1951) and by Šestak (1957). Alumina crucibles were used and the growth process was carried out in a hydrogen-containing atmosphere.

Better crystal perfection can be achieved by using methods with a free growing surface. Cobalt and cobalt-rich Co–Fe alloy crystals were grown by Bachmann and Wakiyama (1975) using CZ growth under argon atmosphere. The crucible consisted of alumina and was surrounded by a RF heated carbon susceptor isolated by an alumina shield. The equipment was installed in a quartz tube with flowing argon atmosphere ($1.5\,\mathrm{l\,min^{-1}}$) purified by a Ti getter. A ⟨0001⟩ oriented seed was used for pulling Co single crystals with a rate of $2.5\,\mathrm{cm\,h^{-1}}$ using the bottle-neck technique. The grown crystals were several centimeters long and up to 1 cm in diameter. To maintain the hcp cobalt structure a fast cooling rate of about $20\,\mathrm{K\,min^{-1}}$ in the vicinity of the martensitic transformation M_s (420 °C) was applied. From the same author (Bachmann, 1973) an apparatus was designed for electron beam FZ growth in a vacuum of 2×10^{-8} mbar. The apparatus can be used at a Bridgman or CZ mode, too.

Hayashi, Ono and Komatsu (1978) reported the growth of cobalt single crystals from 4N cobalt material by an electron beam FZ method using pulling rates of $0.4–0.7\,\mathrm{mm\,min^{-1}}$. About 70% of the samples were striation free single crystals the rest had one or two grain boundaries along the growth axis. By spontaneous nucleation and grain selection two preferential directions of crystallization were observed, along the ⟨0001⟩ axis and another about 60° inclined to the ⟨0001⟩ axis. As reported, striation free crystals could be grown at slow growth rates $<1\,\mathrm{mm\,min^{-1}}$ only. The same authors reported the growth of nickel single crystals by the FZ method (Hayashi and Komatsu, 1979). They used 4N nickel rods with a diameter of 5 mm as starting material for FZ growth with RF heating under flowing argon atmosphere and in vacuum with electron beam heating. The pulling rates were chosen to 0.2 and $1\,\mathrm{mm\,min^{-1}}$. With both heating methods two preferred orientations of the crystals near ⟨100⟩ and near ⟨111⟩ were found. The deviation from these orientations is slightly more severe in using the electron beam FZ method.

As concluded from the Fe–Si phase diagram (Figure 1) after crystallization from the melt pure iron exhibits two phase transitions that renders it impracticable to produce high-quality single crystals directly from the melt. But, iron is one of the very well investigated examples for preparation of highly perfect single crystals by a strain-annealing technique. For the growth high-purity iron is required, which can be achieved by the following tedious procedure:

Vapor-deposited high-purity iron was prepared in several steps with special care to avoid all electrically active elements. At first, commercial iron powder was dissolved in hydrochloric acid to prepare ferrous chloride. Next, the solution was evaporated and $FeCl_2 \cdot 4\ H_2O$ crystals were formed, which were subsequently dehydrated at 773 K to $FeCl_2$. The impurity content of nickel is high and the product has a low bulk density. The next step is vacuum distillation over lumpy sponge iron to separate the nickel from the ferrous chloride. The evaporation temperature of $FeCl_2$ is 973 K, the reduction temperature of sponge iron is 1023 K and the condensation temperature is 673–773 K. The separation of nickel on the sponge iron is due to the more negative free reaction enthalpy of $FeCl_2$ compared to $NiCl_2$, and results in Ni contents <1 wt ppm. Vacuum was used to increase the evaporation rate of $FeCl_2$ and to ensure a clean atmosphere. This process step, combining distillation with a heterogeneous chemical reaction, is referred to as *exchange distillation*. It leads to condensed $FeCl_2$ with a high density and permits a larger amount of material to be used and a more constant evaporation rate in the subsequent reaction to be achieved.

Ferrous chloride is proportioned by sublimation within a temperature range of 873–950 K from a container made of pure iron. The extrapolation of the vapor pressure of the compound, which is known between 950 K (melting point) and 1285 K (boiling point), gives vapor pressures of about 100–1500 Pa within the temperature range of 873–950 K. To ensure practical deposition rates of pure iron of 28–280 nm s^{-1}, a higher amount of ferrous chloride can be offered by increased evaporation temperatures or by increasing the evaporation rate. The reduction of the ferrous chloride was performed with hydrogen in a quartz tube of 80 mm diameter. The iron produced during the reduction process was deposited on a resistance-heated pure iron wire of 1 mm diameter.

The typical experimental conditions were described in Weise and Owsian (1976). The rods of up to 15 mm diameter and up to 300 mm length are compact. The measured density was 7875.5 kg m^{-3}, which is very close to the theoretical value. The optimum conditions are achieved for deposition rates greater than 0.14 µm s^{-1} and deposition temperatures above 1273 K. The residual resistivity ratio $r_{293\,K}/r_{4.2\,K}$ is about 3000. More details about the morphology and the defect structure as well as the properties like density, coercivity, and the residual resistivity ratio have been given by Weise and Owsian (1976). The impurity content of the prepared highly pure Fe was measured by spark source mass spectrography, gas hot extraction, and carrier gas fusion methods. The main impurity elements (with contents in wt ppm) were: Ta (13), Cu (5), Ni (2), Mo (<2), Ga (1), Zr (1), C (10), O (9), N (6), H (<6), and Cl (2). All other trace elements were below 1 wt ppm.

The crystal growth of ultrahigh-purity and doped iron by the strain-anneal technique contains the following process steps:

1. The deposited rods of high-purity (or doped) iron were subjected to a FZ process.
2. The zone floated material 13 mm in diameter contains large elongated grains which don't allow homogeneous deformation. Therefore, the material was annealed around the $\alpha-\gamma$ transformation temperature to destroy this microstructure. By radius hammering with one intermediate annealing procedure (840 °C for 2 h followed by quenching in water) it was formed to 4-mm-diameter rods with a degree of plastic deformation of about 70%.
3. The rods were annealed for recrystallization to a fine grained microstructure in a horizontal quartz furnace at 800 °C under purified hydrogen atmosphere.
4. The optimum critical deformation, about 1.5% for pure iron up to 3% for Ni-doped iron (enhancement of deformation energy in the grains), was realized by stretching at room temperature with a constant strain rate of about 10 µm s^{-1}.
5. The last step is the crystal growth in a temperature gradient, which is realized in a vertical tube furnace with a hermetic outer quartz tube and flowing argon or purified hydrogen atmosphere. The prepared 4-mm-diameter iron rod is placed inside the heated copper tube and heated to maximal 890 °C. The feed is pulled town through the temperature gradient of maximal 50 K cm^{-1} with a pulling rate of about 10 mm h^{-1}.

With this technique it is possible to grow single crystals from pure iron with a length of 100 mm and a diameter of 4–6 mm. However in many cases the rod contains–two to six crystals in a bamboo like morphology. By adding 10–20 ppm of nickel the growth becomes less perfect, but 200–500 ppm Ni stabilize the growth. The effect of different types of substitutional and interstitial impurities on the deformation created microstructure as well as the mobility of grain boundaries is different. The different behavior during grain growth is much more dependent on the microscopic dislocation substructure than on the macroscopic microstructure. In all cases a different amount of misoriented parasitic grains is observed, the origin of which is mainly the rod surface. The lowest density of parasitic grains was found in carburized nickel doped iron crystals.

Shimizu *et al*. (2001) discovered superconductivity in ε-iron transformed from α-iron under a pressure of 16–30 GPa. In their study they could not find a superconducting transition to zero values in 'normal' iron. Only after using pure iron like in the above described single-crystal growth experiments the superconducting transition to zero resistivity at about 2 K

could be demonstrated as described by Jaccard *et al*. (2002) and Holmes *et al*. (2004).

Crystals of most of the transition-metal elements were grown by chemical vapor transport, too. Due to their small dimensions these crystals are of value only for special purposes and a detailed description will not be given.

Single crystals of rare-earth elements with high purity and perfection are difficult to grow due to two main reasons:

1. The rare-earth elements react with oxygen and with practically with all crucible materials.
2. The magnetic rare-earth elements dysprosium, gadolinium, and terbium exhibit a phase transformation from a high-temperature phase with cubic bcc crystal structure to a low-temperature phase with hexagonal hcp structure. Because this transition takes place at temperatures less than 100 K below the melting point this transformation cannot be avoided by rapid quenching.

In the past there were many attempts to grow pure single crystals of rare earths. So Behrendt in 1958 reported the growth of Dy crystals (Behrendt, Legvold and Spedding, 1958), by a Bridgman technique under vacuum atmosphere in a tantalum crucible. The problem is the large amount of tantalum from the crucible material incorporated in the crystal. The Dy–Ta phase diagram (see Massalski, Okamoto, Subramarian and Kacprzak, 1990) displays a significant solubility of Ta in the rare-earth melt. All grown crystals exhibit many grains, what could be attributed to the fcc to hcp phase transition at high temperature. Nevertheless, samples cut from individual grains could be used for measurements of anisotropic magnetic properties.

Really large single-crystalline grains were obtained by Nigh (1963) using the following strain-anneal method. The sample was melted under argon in an arc furnace. The resulting 8-mm-thick and 30-mm-diameter buttons had a high degree of crystal orientation. Grain growth was accomplished by annealing the button at temperatures somewhat below the melting point of the respective rare earths. The annealing took place in a vacuum furnace hanging at a thin tungsten wire. It was possible to anneal Gd and Tb in vacuum, but an argon atmosphere was required for Dy and Ho to reduce distillation. To illustrate this procedure we report here results on Gd. The largest crystals were obtained by annealing at 1050 °C for 12 h followed by an increase of temperature by 50 K increments every 12 h up to a maximum of 1200–1225 °C (the fcc/hcp phase transition temperature of Gd is 1235 °C). The best results were obtained with the specimen near the top of the heater in a temperature gradient of approximately 25 K cm^{-1}. A similar technique has applied in growing Dy crystals. For Dy and Ho annealing in a temperature gradient for one single temperature level was applied.

Sousa *et al*. (1985) reported measurements on zone refined crystals with dimension of $10 \times 1 \times 1$ mm^3 and with a resistivity ratio of 15. The crystals were obtained by a FZ process followed by a zone annealing process at a temperature below the solid-state phase transition by Fort (1991a). The author describes the FZ growth in an ultrahigh vacuum (UHV)-rated RF induction heating FZ facility reconstructed from a commercially available high vacuum RF FZ apparatus (Metals Research Ltd., Royston). The starting materials are obtained from Rare Earth Products Ltd. (REP), Widnes, UK, or the Materials Preparation Center, Ames Laboratories, Iowa State University, USA. The rods for float zoning were cast in a cold boat system using RF heating, which is capable of melting metals under UHV conditions (Fort, Jones, Beaudry and Gschneidner, 1981). The FZ growth was carried out under an argon atmosphere purified to better than 1 ppm of all impurity gases. The sample was also degassed in vacuum under UHV conditions by running a hot (not molten) zone along the rod. The growth of Dy crystals from REP starting metal, which was further purified by resublimation under UHV conditions, was carried out under 0.7 bar argon with a growth rate of 42 mm h^{-1} followed by an annealing pass (with reduced power) at approximately 1470 K. Overall, however, any strain induced by cooling through the bcc–hcp transformation at 1653 K did not significantly impair the crystal quality. Crystals obtained from attempts using metal as received from REP were less successful as they are smaller and generally showed considerable substructure on X-ray examination. By the same procedure Ho crystals were grown without subsequent annealing pass.

Fort (1991b) reported crystal growth attempts by solid-state recrystallization on rare-earth metal elements and rare-earth alloys, which adopt the hexagonal close-packed crystal structure. The procedure involved annealing ingots, which had been strained by fast cooling from the melt. A heat treatment recipe of annealing for at least 40–60 h at a temperature equivalent to 85% of the absolute melting temperature or 95% of any hcp–bcc transformation temperature (whichever was the lower one) was deduced to lead to the most extensive grain growth. The potential advantages of solid-state crystal growth over melt growth for these materials are: the experimental simplicity, the improved quality of crystals prepared, and the lower volatilization losses for materials with high vapor pressure.

4.1.2 Fe-based alloys

One of the most important magnetic materials is the widely used electrical steel or silicon electrical steel. It is an iron-based steel containing from 3- to 4.5-wt% silicon. It is usually used in the form of cold-rolled strips less than 2 mm thick, which are called *laminations* when packed together.

The assembled laminate cores are used in transformers and stators and rotors of electric motors. To improve the magnetic properties grain-oriented electrical steel is used. Therefore, it is of interest to study the electrical and magnetic properties of the corresponding single crystals.

As far as the silicon concentration in this alloy is >1.9 wt% Si the δ to γ to α transformations of the pure iron disappear and a direct crystallization from the melt becomes possible (see Fe–Si phase diagram Figure 1). Therefore, all methods of crystal growth from the melt can be used to obtain single crystals.

Ringpfeil, Wiesinger and Fischer (1962) reported the growth of Fe-(2.5–4)wt%Si crystals by the Bridgman technique in alumina crucibles under flowing hydrogen (ca. 3 mbar pressure) with growth rates from 10 to 60 mm h^{-1}.

Vaněk and Kadečková (1979) reported the RF (360 kHz) FZ growth of Fe-3wt%Si crystals 13 mm in diameter in a hydrogen atmosphere. The molten zone was moved downwards at rates of 7–120 mm h^{-1} with (30 rpm) and without rotation of the lower part. Striations from inhomogeneities in the silicon concentration start to form at rates >21 mm h^{-1} and are well developed at high growth rates. The formation of striations does not depend on rotation of the feed rod. Vaněk, Kadečková, Jurisch and Löser (1983) achieved Fe-3wt%Si crystals 7 mm in diameter by FZ melting with both electron beam and RF heating with growth rates of 60 and 120 mm h^{-1}.

Ringpfeil, Wiesinger and Fischer (1962) reported the growth of Fe–Ni and other soft magnetic alloys. Since the Fe–Ni phase diagram displays a solid solution of the γ-Fe(Ni) phase above about 7 up to 100 mol% Ni (see Massalski, Okamoto, Subramarian and Kacprzak, 1990) this phase can easily be grown from the melt by a Bridgman technique using alumina crucibles.

More detailed orientation dependent magnetic measurements are shown in standard textbooks (Kneller, 1962).

4.2 Crystal growth of hard magnetic alloys

4.2.1 FePt, CoPt, and FePd compounds with large magnetocrystalline anisotropy

Ferromagnetic ordered alloys with the $L1_0$ crystal structure, FePd, FePt, and CoPt, have drawn much attention as promising materials for ultrahigh dense magnetic storage media due to their large magnetocrystalline anisotropy (Maykov *et al*., 1989). The anisotropic crystal field in single crystals causes a large magnetocrystalline anisotropy constant K_u as well as anisotropic magnetostriction. Since K_u is a measure for the achievable recording data density its precise determination is practically important. Multivariants, twin boundaries, and residual stress, surface and interface anisotropies cause barriers to evaluate the precise K_u for $L1_0$-type Fe–Pt thin films and nanoparticles. Therefore, $L1_0$-type bulk single crystals in a single-variant state are necessary for the accurate evaluation of K_u of these ordered alloys. Furthermore, the investigation of the temperature dependence of the magnetocrystalline anisotropy is meaningful for heat-assisted magnetic recording techniques, because the switching field governed by K_u can be reduced by heating during writing processes.

In order to investigate the magnetic properties associated with crystallographic orientations, single crystals of FePd and CoPt have been grown by the Bridgman technique (Maykov *et al*., 1989; Tanaka, Ichitsubo and Koiwa, 2001) and the FZ method under a purified He atmosphere (Shima *et al*., 2004a,b, 2005). Single crystals of $Fe_{60}Pt_{40}$ have been grown with the FZ method as well (Inoue *et al*., 2006). The equiatomic phases undergo a transition from a disordered fcc to an ordered tetragonal $L1_0$ phase. Since the symmetry of the ordered phase is lower than that of the disordered one, there are three variants of the ordered phase. In the absence of any external field, all three variants are formed with an equal probability, resulting in a twinned structure. The application of external stress or a magnetic field during the ordering processes leads to the preferential formation of a favorably oriented variant (Tanaka, Ichitsubo and Koiwa, 2001; Yermakov and Maykov, 1989).

Accordingly, single-variant $Fe_{48}Pd_{52}$ single crystals were prepared by a compressive stress method (Shima *et al*., 2004a). Single-crystalline samples with disordered fcc structure were received after homogenization of FZ grown crystals at 1473 K for 24 h in an evacuated quartz tube and quenching into ice water. The crystalline orientation was determined by the electron backscattering pattern method and the back reflection Laue method. The disordered fcc $Fe_{48}Pd_{52}$ single crystal was cut into a cube with six crystallographic equivalent {001} planes. The heat treatment for ordering under the compressive stress along the [100] direction was carried out using a Mo implement. The specimen was fixed between Mo plates and the temperature was increased up to 973 K followed by a slow cooling with the rate of 3 K min^{-1}. The difference in the thermal expansion coefficients between the Mo plate and the specimen causes the compressive stress. The back reflection Laue patterns for the ordered $L1_0$ $Fe_{48}Pd_{52}$ exhibited clear spots indicating that the *c* axis is selectively aligned.

Figure 12 shows the magnetization curves along the *c* and *a* axis in the ordered $L1_0$ $Fe_{48}Pd_{52}$ at 4.2 K (Shima *et al*., 2004a). The easy axis of magnetization is the *c* axis. On the contrary, there is no difference in the magnetization curves along the [100] and the [010] directions of the disordered fcc $Fe_{48}Pd_{52}$. The uniaxial magnetocrystalline anisotropy

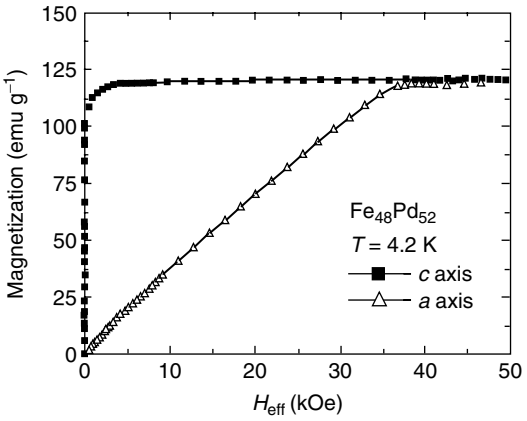

Figure 12. The magnetization curves of $L1_0$ $Fe_{48}Pd_{52}$ showing the difference between the *c* and the *a* axis. (Reproduced from Shima *et al*., 2004, with permission from Elsevier. © 2004.)

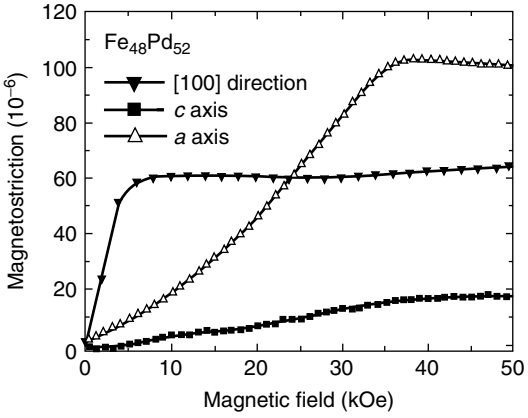

Figure 13. The longitudinal magnetostriction curves along the *c* and the *a* axis in the $L1_0$ $Fe_{48}Pd_{52}$ and the [001] direction in fcc $Fe_{48}Pd_{52}$. (Reproduced from Shima *et al*., 2004, with permission from Elsevier. © 2004.)

constant at 4.2 K becomes $K_u = 2.5 \times 10^6\,\mathrm{J\,m^{-3}}$, but there is some variance in the values of various authors (cf. Yermakov and Maykov, 1989; Shima *et al*., 2004a). The uniaxial magnetocrystalline anisotropy becomes weaker at higher Pd concentrations. As shown in Figure 13 the longitudinal magnetostriction increases with external magnetic field in analogy with the magnetization curves (Shima *et al*., 2004a).

The value of the magnetostriction constant λ_{100} in the disordered fcc $Fe_{48}Pd_{52}$ is 60×10^{-6}. In the ordered $L1_0Fe_{48}Pd_{52}$ sample the value $\lambda_a = 100 \times 10^{-6}$ along the *a* axis is larger, whereas the value of $\lambda_c = 20 \times 10^{-6}$ along the *c* axis is smaller than λ_{100}.

Single crystals of $Co_{100-x}Pt_x$ ($x = 45$, 50, and 55) were similarly prepared by the FZ method (Shima *et al*., 2005). The heat treatment for homogenization was carried out at 1473 K for 48 h. The $L1_0$-type $Co_{100-x}Pt_x$ in a single-variant state was obtained by a heat treatment under uniaxial compressive stress. A compressive stress of 20–25 MPa was applied along one of the ⟨001⟩ directions in the fcc-type $Co_{100-x}Pt_x$. The *c* axis, which becomes the easy magnetic axis, aligns parallel to the compressive stress direction. Both the *a* and *c* axes elongate with increasing Pt concentration, whereas the axial ratio *c*/*a* has a minimum value of 0.976 at $x = 50$, resulting in the largest tetragonal distortion (Shima *et al*., 2005). The magnetization curve along the *c* axis is immediately saturated under an effective magnetic field of less than $80\,\mathrm{kA\,m^{-1}}$ (1 kOe). In contrast, a very high magnetic field of 1.11×10^5 kA m^{-1} (140 kOe) is necessary for saturation along the *a* axis. The coercive force H_c observed in the magnetization curves along the *c* and *a*-axes are, respectively, about $32\,\mathrm{kA\,m^{-1}}$ (0.4 kOe) and $64\,\mathrm{kA\,m^{-1}}$ (0.8 kOe), and much smaller than that in the multivariant $L1_0$-type Co–Pt alloys. The uniaxial magnetocrystalline anisotropy constant K_u at 298 K exhibits the largest value of $4.5 \times 10^6\,\mathrm{J\,m^{-3}}$ for $x = 50$.

$L1_0$-type $Fe_{60}Pt_{40}$ single crystals in the single-variant state have been prepared in a similar way (Inoue *et al*., 2006). It should be noted that $Fe_{50}Pt_{50}$ bulk single crystals in a single-variant state are difficult to obtain because $Fe_{50}Pt_{50}$, probably the most desirable substance for recording media, has a high ordering temperature, and hence preparation at high temperature is necessary, which induces recovery and recrystallization.

Large magnetocrystalline anisotropy between the magnetization curves along the *c* and *a* axes is observed in the single-variant $Fe_{60}Pt_{40}$ single crystals. The magnetization curve along the *c* axis is easily saturated below $398\,\mathrm{kA\,m^{-1}}$ (5 kOe), while the saturation along the *a* axis is achieved above the high magnetic field of about 8.75×10^3 kA m^{-1} (110 kOe). The values of the coercivity H_c along the *c* and *a* axes are about $36\,\mathrm{kA\,m^{-1}}$ (0.45 kOe) and $28\,\mathrm{kA\,m^{-1}}$ (0.35 kOe), respectively. The value of H_c along the *c* axis is much smaller than that of $L1_0$-type Fe–Pt bulk alloy in the multivariant state, and also than in thin films and the nanoparticles. The values of anisotropy constants, at 5 K are evaluated to be $K_1 = 7.4 \times 10^6\,\mathrm{J\,m^{-3}}$, $K_2 = 0.13 \times 10^6\,\mathrm{J\,m^{-3}}$, and $K_u = 6.9 \times 10^6\,\mathrm{J\,m^{-3}}$, respectively (Inoue *et al*., 2006). The present values of $K_1 + K_2$ and K_u are larger than those of $L1_0$-type FePd (Shima *et al*., 2004b) and CoPt (Shima *et al*., 2005) single crystals in the single-variant state. That is, the $L1_0$-type $Fe_{60}Pt_{40}$ alloy has large magnetocrystalline anisotropy constants despite the deviation from the equiatomic composition. The second-order magnetocrystalline anisotropy constant K_1 and the uniaxial magnetocrystalline anisotropy constant K_u monotonically decrease with increasing temperature, while K_2 is almost independent of T. However, both K_1 and K_u keep a large value up to 298 K, being $6 \times 10^6\,\mathrm{J\,m^{-3}}$ and $5.5 \times 10^6\,\mathrm{J\,m^{-3}}$, respectively.

Finally, we remark that apart from these compounds with large magnetocrystalline anisotropy prospective for magnetic storage media, single crystals of invar alloys $Fe_{75}Pt_{25}$, $Fe_{72}Pt_{28}$, and $Fe_{72}Ni_3Pt_{25}$ have also been grown by the Bridgman–Stockbarger technique. Elastic constants of the compounds in the presence of an external magnetic field have been determined for single-crystalline samples with the ultrasonic pulse echo technique (Kawald *et al*., 1989).

4.2.2 *Crystal growth of $R_2Fe_{14}B$ compounds for high-performance permanent magnets*

Compounds of $R_2Fe_{14}B$, where R stands for rare earths including Y, have attracted much attention after discovering the outstanding permanent magnetic properties in ternary Nd–Fe–B alloys, which are based on the formation of a new phase $Nd_2Fe_{14}B$ (Sagawa *et al*., 1984). A brief overview on crystal growth activities of $R_2Fe_{14}B$ compounds and their intrinsic properties determined is given by Franse and Radwanski (1996).

Small single-crystalline samples of $Nd_2Fe_{14}B$ were simply obtained by Hukin-type cold-crucible induction melting of alloys from high-purity elements (Nd: 99.9%, Fe: 99.99%, B: 99.99%). Crystals (0.3 mm in diameter) were observed to grow in shrinkage cavities obtained after slow cooling of the melt under vacuum (Givord, Li and Moreau, 1984). From the intensities of Laue photographs of these single-crystalline samples the tetragonal structure of the $Nd_2Fe_{14}B$ phase was revealed. In this structure, Nd atoms are distributed on two crystallographic sites of low symmetry, whereas Fe atoms occupy six different sites. Large single crystals for studies of fundamental magnetic properties are difficult to grow for the following reasons: (i) the compound does not melt congruently (cf. Figure 4 in Section 2), (ii) the rare earths have a high affinity to oxygen and their melts are quickly covered by an oxide film, and (iii) the melt reacts with most crucible materials. In the cold-crucible method the melt is levitated by inductive forces within the split water-cooled Cu-crucible and melt-crucible contact is effectively avoided. Indeed, Givord, Li and Delabathie (1984) succeeded in growing 3-cm-long $Nd_2Fe_{14}B$ and $Y_2Fe_{14}B$ bars of 1 cm^2 cross section by a CZ method from a Nd-rich $Nd_{15}Fe_{77}B_8$ melt in a Hukin-type cold-crucible facility (cf. Section 3.3). The values of the magnetic ordering temperatures, 573 K for $Y_2Fe_{14}B$ and 595 K for $Nd_2Fe_{14}B$, are similar. From the $Nd_2Fe_{14}B$ crystal a cube of $4.5 \times 4.5 \times 4.3$ mm^3 was cut for magnetization measurements. As shown in Figure 13 the large uniaxial anisotropy observed in $Nd_2Fe_{14}B$ at 300 K favors the *c* axis (Givord, Li and Delabathie, 1984). However, below 135 K, an easy direction is stabilized, which is at an angle θ with respect to the *c* axis (inset to Figure 14). At higher temperatures, the reorientation of the magnetization toward the *c* axis results from the relative decrease of crystal-field interactions with respect to exchange interactions, which favor a collinear arrangement of Nd and Fe moments.

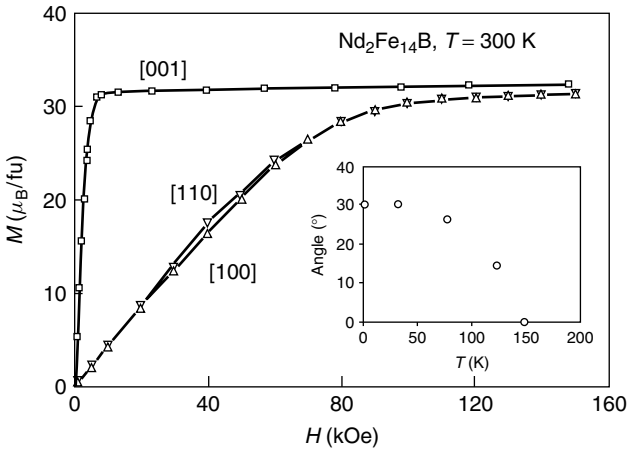

Figure 14. Field dependence of the magnetization at 300 K in $Nd_2Fe_{14}B$. Inset: temperature dependence of the angle Θ between the easy magnetization direction and the *c* axis. (Reproduced from Givord *et al*., 1984, with permission from Elsevier. © 1984.)

More details about the growth of $Nd_2Fe_{14}B$ single crystals between 5 and 10 mm diameter and >1 cm length by the cold-crucible CZ method are provided by Swets (1986). Special care was devoted to avoiding oxygen. The crucible was contained in a quartz walled chamber flushed with high-purity Ar, which was further purified by passing over Ti at 800 °C and through a Ga–In–Al bubbler at room temperature. Even under these circumstances an oxide layer was initially formed on the melt surface. It was 'skimmed off' with a quartz rod from the top of the growth chamber. Because of the peritectic formation of $Nd_2Fe_{14}B$, Nd-rich melts and slow growth velocities are favorable. Beyond a pulling rate of >5 mm h^{-1} Nd-rich phases were precipitated. The preferred growth direction for polycrystalline seeds is either along the *a* axis or the [110] direction, whereas a *c* axis oriented crystals can be grown with a single-crystalline seed with the respective the *c* axis orientation. The cold-crucible CZ technique was also used by Koon *et al*. for the growth of $R_2Fe_{14}B$ (R = Y, Nd, Tb) with 5 mm h^{-1} (Koon, Das, Rubinstein and Tyson, 1985).

$Nd_2Fe_{14}B$, $Y_2Fe_{14}B$ as well as R_2Fe_{17} crystals were grown with the tri-arc CZ method (Sinnema, Verhoef, Menovsky and Franse, 1987). In the method the skull of the material prevents the contact of the melt with the water-cooled Cu crucible. A Ti getter has been used to purify the Ar atmosphere; a titanium button was melted by a tetra arc that burns continuously during the growth process. Pulling rates of 3 mm h^{-1} similar as in FZ melting (cf. Hirosawa *et al*., 1986) were applied. In case of $Nd_2Fe_{14}B$ the crystal was

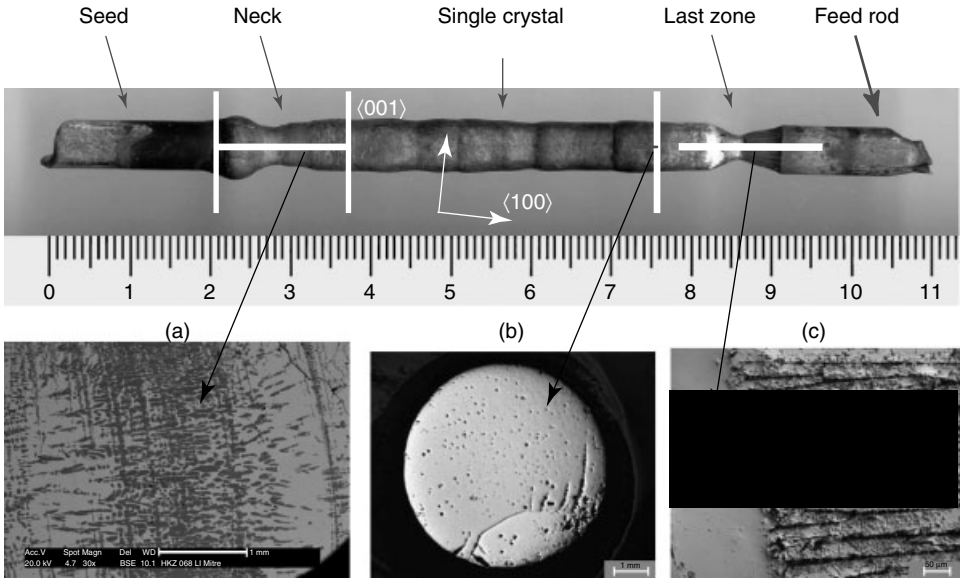

Figure 15. $Nd_2Fe_{14}B$ single-crystal FZ grown from a stoichiometric feed rod (top). Crystal orientations with respect to the rod axis are indicated. Longitudinal sections of initial part of the crystal: $Nd_2Fe_{14}B + Fe$ (dark) (a), cross section of the $Nd_2Fe_{14}B$ crystal (b), and last part with frozen zone: $Nd_2Fe_{14}B$ + Nd-rich phases (dark) (c). (Reproduced from I. Mazilu, PhD Thesis, 2006.)

grown with a stoichiometric seed from the $Nd_{15}Fe_{77}B_8$ melt, whereas a tungsten tip was utilized as seed for the $Y_2Fe_{14}B$. Laue photographs taken from different places proved that the mosaic structure in the $Nd_2Fe_{14}B$ crystal is $<1^\circ$. The bars contained a few large single-crystalline grains with a maximum size of $1\,cm^3$.

Single crystals of a series of $R_2Fe_{14}B$ (R = rare earth except of Sm) were grown by the FZ method with an infrared imaging furnace under purified Ar atmosphere (Hirosawa *et al*., 1986). This technique turned out to be very effective for $R_2Fe_{14}B$ crystal growth but also for related $R_2Co_{14}B$ compounds (Hiroyoshi *et al*., 1987). The typical dimensions of single crystals grown by this technique are several millimeters in diameter. Because $Nd_2Fe_{14}B$ (as well as related compounds) forms by a peritectic reaction, the TSFZ technique (cf. Section 3.3) is appropriate where the feed rod and the seed are of stoichiometric composition, whereas the FZ is off-stoichiometric. It can be generated by placing a small disk of (Nd,B)-rich composition between seed and feed rod and melting it together with its adjacent parts.

Alternatively, an off-stoichiometric zone can be established by progressive growth from a stoichiometric feed rod. This is shown for a FZ growth experiment with optical heating. In the initial stage of the growth process primary, γ-Fe dendrites along with the peritectic $Nd_2Fe_{14}B$ phase (Figure 15a) grow from the melt in agreement with the phase diagram. In this way, the melt composition in the zone is continuously enriched in Nd and B until it encountered the primary solidification range where the single $Nd_2Fe_{14}B$ phase grows (Figure 15b). The composition difference between the stoichiometric crystal and the frozen zone, which also contains Nd-rich phases, is illustrated in Figure 15(c).

For the whole series of FZ grown $R_2Fe_{14}B$ single crystals the temperature dependence of the saturation magnetization from 4.2 K to magnetic ordering temperatures, the magnetocrystalline anisotropy field H_A (Hirosawa *et al*., 1986; Hiroyoshi *et al*., 1986) and the anisotropy constants K_{u1}(Hirosawa *et al*., 1985) have been measured. Spin-reorientation processes similar to $Nd_2Fe_{14}B$ have been detected and the angle of easy axis of magnetization direction from the c axis has been measured for $Ho_2Fe_{14}B$, $Er_2Fe_{14}B$, $Tm_2Fe_{14}B$ compounds (Hirosawa *et al*., 1986). The coupling scheme of the $R_2Fe_{14}B$ compounds leads to ferromagnetism for light rare earths (Y, Ce, Nd, Pr, Sm) but ferrimagnetism for heavy rare earths (Er, Tb, Gd, Ho, Dy, Tm) with obvious differences in the magnetic behavior. For heavy rare-earth-containing compounds, the partial compensation between Fe and R sublattice magnetization leads to a positive thermal coefficient of the saturation magnetization in some restricted temperature range. As shown by Hirosawa *et al*. (1986) (Figure 16) the value of magnetocrystalline anisotropy field H_A of $Nd_2Fe_{14}B$ is not the largest among the $R_2Fe_{14}B$ compounds at room temperature and may be enhanced by alloying with other rare earths such as Tb or Dy. In fact Dy is utilized for improving permanent magnetic properties of $Nd_2Fe_{14}B$-based materials.

Mechanical properties were studied in uniaxial compression tests with $2 \times 2 \times 5\,mm^3$ samples from big CZ grown crystals crystallographically oriented with the (001) plane at an angle of 45° to the cuboid axis (Kuhrt *et al*., 1991). The

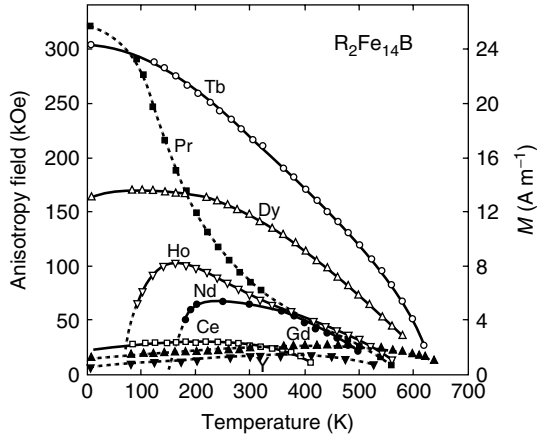

Figure 16. Temperature dependence of magnetocrystalline anisotropy field H_A of $R_2Fe_{14}B$ for R = Y, Ce, Pr, Nd, Gd, Tb, Dy, and Ho measured at applied fields up to 1.5 T. (Reproduced from S. Hirosawa *et al*., 1986, with permission from the American Institute of Physics. © 1986.)

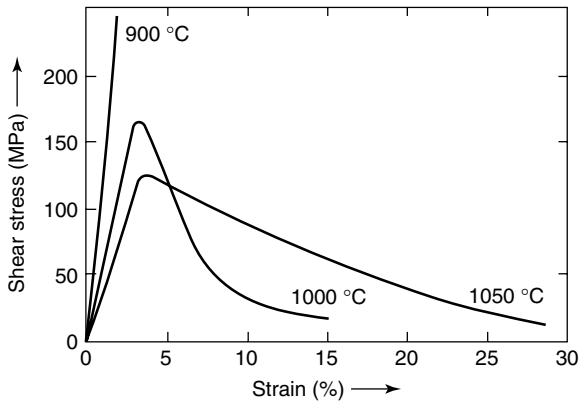

Figure 17. Compressive shear stress–strain curves of $Nd_2Fe_{14}B$ single crystals at 900, 1000, and 1050 °C, at strain rates of 5×10^{-5} s^{-1}. (Reproduced from Kuhrt *et al*., 1991, with permission from the American Inst.)

stress–strain curves at elevated temperatures 900–1050 °C of single-crystalline samples are shown in Figure 17. Substantial ductility of $Nd_2Fe_{14}B$ crystals occurs only at appreciably higher temperatures and lower strain rates than those generally used in the die-upsetting process (typically 700–800 °C) (Lee, 1985). The results support the assumption that it is not the plasticity of the $Nd_2Fe_{14}B$ phase, but other mechanisms such as grain boundary sliding combined with anisotropic grain growth that allow the microcrystalline Nd–Fe–B alloys to be so easily deformed and crystallographically textured.

The detailed oxidation and corrosion mechanisms of commercial rare-earth hard magnets are still a current research topic. Studying single crystals the different behavior of commercial polycrystalline materials and the $Nd_2Fe_{14}B$

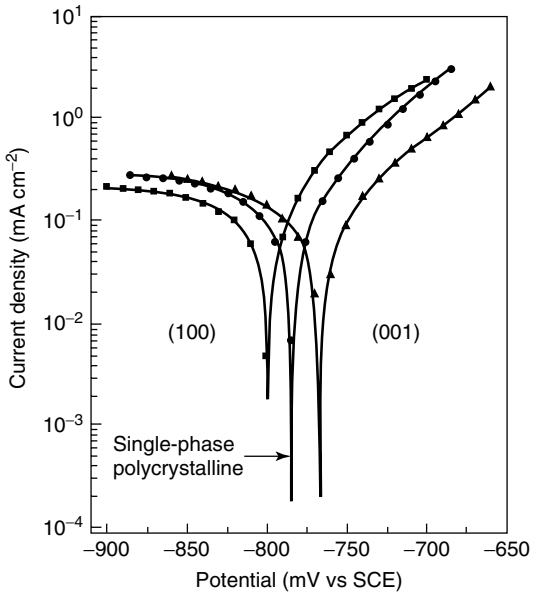

Figure 18. Potentiodynamic polarization curves recorded close to the corrosion potential U_{corr} in 0.1 M sodium sulphate solution (ph = 5) at 730 rpm at the surfaces of a $Nd_2Fe_{14}B$ single crystal which are in plane with the crystallographic (100) plane or with the (001) plane; comparative curve for polycrystalline $Nd_2Fe_{14}B$ with random grain orientation. (Reproduced from Rada *et al*., 2006, with permission from Elsevier. © 2006.)

phase itself can be distinguished. An anisotropic corrosion behavior on the two surface planes of a $Nd_2Fe_{14}B$ single crystal, namely, (100): a plane parallel to the *c* axis and (001): a plane perpendicular to the *c* axis was recently reported (Figure 18), which corresponds to the behavior of highly textured sintered Nd–Fe–B magnets (Rada *et al*., 2006). It is interesting to note that the (100) plane displaying the most active dissolution tendency in aqueous environment is identical with the (100) plane (perpendicular in *a* axis [100] direction) of preferred growth of the single crystal.

By means of calibrated dynamic secondary ion mass spectrometry (SIMS) using Cs^+ primary ions an upper limit for the oxygen content $c_O = 0.006 \pm 0.002$ at% in the single-crystalline $Nd_2Fe_{14}B$ matrix was determined, which is at least 1 order of magnitude lower than in polycrystalline samples. Another striking difference is the oxygen uptake, which depends on processing and sample handling in cast polycrystalline samples, whereas $Nd_2Fe_{14}B$ single crystals are much less sensitive (Oswald *et al*., 2005).

4.2.3 Crystal growth of other rare earth–transition metal compounds

In this section crystal growth attempts and selected magnetic properties of other classes of rare earth–transition metal intermetallic compounds prospective for the development of

permanent materials are briefly reported, which were studied in the past years but did not attract such an outstanding commercial interest like $Nd_2Fe_{14}B$.

R_2T_{17} (T = Fe, Co) compounds are distinguished by the combination of their large values of magnetic moments, high Curie temperatures, large anisotropy, and a strong coupling of magnetic moments of rare earths and transition metals. Moreover, exiting phenomena like a first order magnetic transition have been reported (Sinnema, Franse, Menovsky and Radwanski, 1986; Garcia-Landa *et al*., 1995; Garcia-Landa, Algarabel and Ibarra, 1997). For the crystal growth of R_2Fe_{17} and R_2Co_{17} compounds the same methods as for $Nd_2Fe_{14}B$ can be applied (Sinnema, Verhoef, Menovsky and Franse, 1987). Sinnema *et al*. reported the growth of R_2Fe_{17} (R = Y, Dy, Er, Ho), R_2Co_{17} (R = Y, Dy, Er, Nd, Pr, Gd, Tb), and also substitutional compounds such as $Ho_2Co_{14}Fe_3$ by the modified tri-arc CZ method (Sinnema, Verhoef, Menovsky and Franse, 1987) described in Section 4.2.2. Different from ternary systems, most binary R–T phase diagrams are known (Massalski, Okamoto, Subramarian and Kacprzak, 1990). Many R_2T_{17} compounds melt congruently or almost congruently. Compounds such as Tb_2Fe_{17} (cf. Figure 3 in Section 2), Sm_2Fe_{17} and Nd_2Fe_{17} are formed peritectically (Massalski, Okamoto, Subramarian and Kacprzak, 1990), and the composition difference between the compound and the peritectic melt increases in this sequence, which aggravates the crystal preparation. The crystals congruent melting R_2T_{17} compounds can easily be grown with relatively high pulling rates of $30\,mm\,h^{-1}$ (Sinnema, Verhoef, Menovsky and Franse, 1987). This is about 1 order of magnitude faster than for $Nd_2Fe_{14}B$ crystal growth. As-cast materials of the same alloy or W tips were used as seeds and rotated with 33 rpm during the growth. The compounds display either the hexagonal Th_2Ni_{17}-type structure (Y_2Fe_{17}, Dy_2Fe_{17}, Er_2Fe_{17}, and Tb_2Co_{17}) or the rhombohedral Th_2Zn_{17}-type structure (Nd_2Co_{17}, Gd_2Co_{17}, and Pr_2Co_{17}). The preferred growth direction was often close to the *c* axis with typical orientation deviations of the order of 10°. The crystals grown by the tri-arc method were of high quality and the magnetic transitions are very sharp (Sinnema, Verhoef, Menovsky and Franse, 1987). Crystal growth with volatile elements like Sm_2Fe_{17} or Yb_2Fe_{17} was not possible by this method. From the single crystals the crystallographic structure, the lattice constants of various R_2Fe_{17} and R_2Co_{17} compounds (Sinnema, Verhoef, Menovsky and Franse, 1987) and their fundamental magnetic properties (Garcia-Landa, Algarabel and Ibarra, 1997; Thang *et al*., 1998) were determined. As shown in Figure 19 for Er_2Fe_{17} (Sinnema, Verhoef, Menovsky and Franse, 1987) the magnetic easy direction is in the basal plane of the hexagonal unit cell, different from the uniaxial magnetic behavior of $Nd_2Fe_{14}B$. Substituted $Tb_2Fe_{17-x}Si_x$

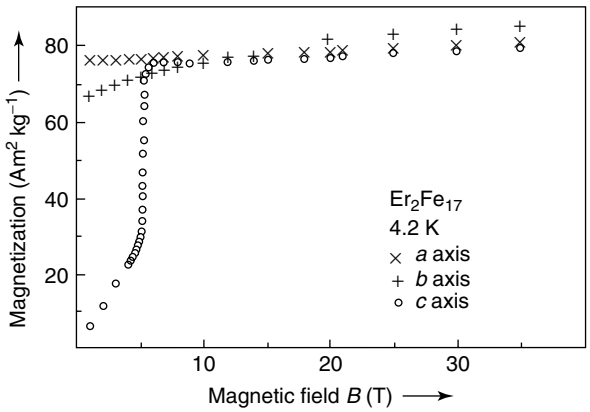

Figure 19. Magnetization curves of Er_2Fe_{17} measured in magnetic fields up to 35 T. The very sharp magnetic transition in the *c* axis illustrates the high quality of the single crystal. (Reproduced from Sinnema *et al*., 1987, with permission from Elsevier. © 1987.)

($x = 0–3.3$) single crystals were grown by a CZ method, too (Du *et al*., 1998). Oriented Er_2Fe_{17} seeds with rotation rates 30 rpm and relatively high growth velocities of $12–15\,mm\,h^{-1}$ were utilized. The substitution of Si for Fe leads to the reduction of lattice parameters and a significant increase of the Curie temperature from 413 to 526 K.

Alternatively, Dy_2Fe_{17} (Coelho, Mohan, Gama and Kronmüller, 1996) and substituted $Sm_2(Fe_{1-x}Al_x)_{17}$ (Kato *et al*., 1995) compounds were also grown with the Bridgman method. High pressures (1 MPa) of Ar and BN coated alumina crucibles were utilized for the growth of substituted $Sm_2(Fe_{1-x}Al_x)_{17}$ single crystals (Kato *et al*., 1995). Some amounts of A1 were found to be transferred from the crucible to the sample, due to an appreciable reaction between Al_2O_3 and Sm. The angle between the magnetization direction and the *b* axis increases linearly with increasing Al fraction *x* (Ono *et al*., 1998).

RCo_5 and related R–Co compounds

Among the intermediate phases which cobalt forms with rare earth the $SmCo_5$ and Sm_2Co_{17} are of importance for permanent magnetic materials (Strnat *et al*., 1967). The series of intermetallic compounds RCo_5 crystallizes in the $CaCu_5$-type hexagonal structure. The Curie temperatures and the magnetocrystalline anisotropy of these compounds are rather high and can reach 747 °C and $1 \times 10^7\,J\,m^{-3}$, respectively, for $SmCo_5$ (Strnat *et al*., 1967; Alameda, Givord, Lemaire and Lu, 1981). Because of the volatile character of Sm single crystals are difficult to achieve. Single crystals of Y_2Co_{17} and YCo_5 were grown by a FZ method (Hoffer and Strnat, 1967). The magnetization curves in the principal crystallographic directions were measured in the temperature range 20–300 K (Hoffer and Strnat, 1967) and down to

4.2 K (Alameda, Givord, Lemaire and Lu, 1981). Different from the Y_2Co_{17}, which exhibits an easy plane, YCo_5 is a uniaxial ferromagnet where the *c* axis is the easy magnetic axis and displays no detectable basal plane anisotropy. At 4.2 K the anisotropy constant can reach $K_1 = 7.38 \times 10^6\,\mathrm{J\,m^{-3}}$ and shows weak temperature dependence because of the high Curie temperature 704 °C of YCo_5 (Alameda, Givord, Lemaire and Lu, 1981). Single crystals of the ferrimagnet $DyCo_5$ were grown by the Bridgman method using the BN coated crucible technique (Ohkoshi *et al*., 1977). A magnetic study revealed the rotational-type spin-reorientation phenomenon that occurs in single crystals of $DyCo_5$.

Single crystals of other RCo_2 (R = Gd, Ho) and $HoNi_2$ Laves phases were achieved by slow cooling ($20\,\mathrm{K\,h^{-1}}$) of the melt and by the Bridgman method (Gignoux, Givord and Lemaire, 1975). Crystal-field parameters have been determined from the magnetization variation in intense magnetic fields up to $1.03 \times 10^4\,\mathrm{kA\,m^{-1}}$ (130 kOe).

RT_{12}-type compounds

Fe-rich rare-earth compounds crystallizing in the tetragonal $ThMn_{12}$ (*I*4/*mmm*) structure type are of interest as potential permanent magnet materials (Buschow, 1991). The pure RFe_{12} compound does not exist for any of the rare earth, however, the $ThMn_{12}$ structure can be stabilized in pseudobinary compounds $RFe_{12-x}M_x$ with M = Ti, V, Cr, Mo, W, or Si for values of $x \sim 1.0$. Single crystals of Er(Fe_{11}Ti), Lu(Fe_{11}Ti) (Andreev *et al*., 1988), and Dy(Fe_{11}Ti) (Hu, Li, Coey and Gavigan, 1990) have been prepared. The large Dy(Fe_{11}Ti) crystals, 40 mm long and 5 mm in diameter, have been grown by the tri-arc CZ method. The magnetic structure and the corresponding easy magnetic moment direction in the $RFe_{12-x}M_x$ compounds is governed by the Fe sublattice anisotropy and the R sublattice anisotropy. The Fe sublattice anisotropy favors an easy magnetization direction parallel to the *c* axis and the corresponding K_1 value has about the same magnitude as in $R_2Fe_{14}B$ and $R_2Fe_{14}C$ compounds. However, the crystal field induced by the rare-earth sublattice in $RFe_{12}M$ differs drastically from that found in $RFe_{14}B$ and $R_2Fe_{14}C$, both in sign and magnitude. This may be seen, for instance, by comparing the magnetic structures of $Dy_2Fe_{14}B$ and $DyFe_{11}Ti$. The former compound is a normal ferrimagnet with the magnetic moments oriented along the *c* direction at all temperatures $T < T_C$. By contrast, $DyFe_{11}Ti$ is a ferrimagnet with $M||c$ only in the limited temperature range $200\,\mathrm{K} \leq T \leq T_C = 534\,\mathrm{K}$. Below 200 K two spin reorientations occur, as can be derived from the results of magnetic measurements of Hu, Li, Coey and Gavigan (1990) shown in Figure 20. The magnetic moment is parallel to the [100] direction below 58 K and parallel to the *c* axis above 200 K.

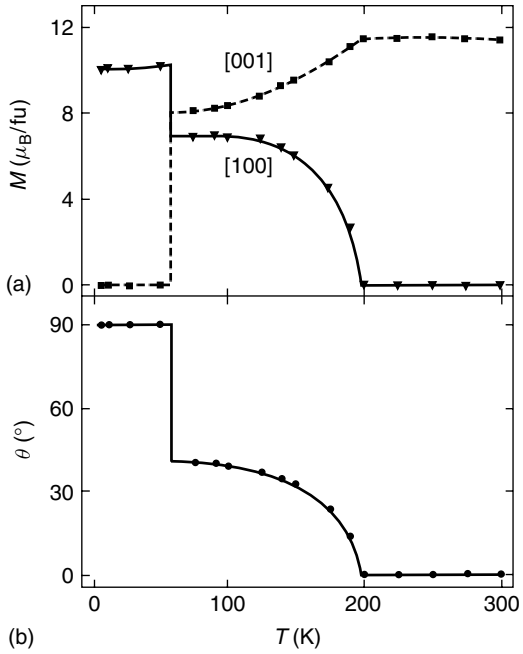

Figure 20. Temperature dependence of the magnitude and the orientation of the spontaneous magnetization M_s obtained from a $DyFe_{11}Ti$. (a) Components of M_s along [100] and [001]. (b) Angle between M_s and the *c* axis. (Reproduced from B.P. Hu *et al*., 1990, with permission from the American Physical Society.)

At temperatures between the two spin-reorientation transitions (first order at 58 K and second order at 200 K) the spin structure is canted. A slight variance between results of magnetic measurements on single crystals by various authors may be due to different concentrations (Wu *et al*., 1998). Indeed, in single crystals of $Tb(Fe,Ti)_{12}$ grown by the cold-crucible CZ technique a segregation of titanium along the crystal axis was quantified by chemical analysis (Wu *et al*., 1998). An effective macrosegregation coefficient of titanium $k_{\mathrm{eff}} = 0.92$ was derived by fitting the experimental data of crystals grown at $5\,\mathrm{mm\,h^{-1}}$ from a melt with $Tb_{1.2}Fe_{10.61}Ti_{1.39}$ starting composition shown in Figure 21. From their experimental results Wu *et al*. have defined the pseudobinary phase diagram around the $Tb(Fe,Ti)_{12}$ phase as peritectic. This peritectic reaction causes a complex of α-Fe and $TiFe_2$ as a nonhost phase with a high titanium fraction of 25 at%. To avoid this, the optimum Tb-rich melt composition $Tb_{1+\delta}Fe_{12-x}Ti_x$ with $\delta = 0.20$ was experimentally determined. Using high-quality single-crystalline samples with no nonhost phase impurities the reliable spin-reorientation transition temperature $T_{SR} = 290 \pm 3\,\mathrm{K}$ for $TbFe_{11}Ti$ in three main crystallographic directions was confirmed. From a series of $Tb(Fe,Ti)_{12}$ compounds it has been revealed that T_{SR} is strongly reduced with increasing Ti fraction in the samples.

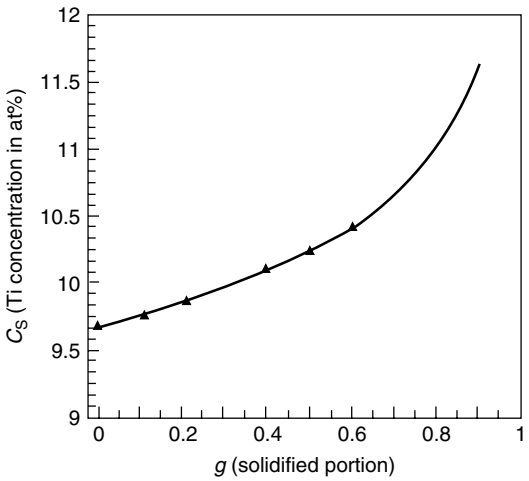

Figure 21. Titanium concentration (symbols) determined at different positions of the single crystal grown from the starting material of $Tb_{1.2}Fe_{10.61}Ti_{1.39}$ and theoretically fitting result (solid line) by $k_{\text{eff}} = 0.92\,g$ defined as in text. (Reproduced from G.H. Wu *et al.*, 1998, with permission from Elsevier. © 1998.)

R_3T_{29}-type compounds

Other novel classes of iron-based metastable intermetallic compounds, $R_3(Fe,M)_{29}$ and their nitrides $R_3(Fe,M)_{29}N_y$ (M = Ti, V, Cr, and Mo), were extensively investigated for potential application as permanent magnets (Cadogan *et al.*, 1994). The new family of $R_3(Fe,M)_{29}$ possesses the monoclinic $Nd_3(Fe,Ti)_{29}$-type structure and can be considered as an intermediate structure consisting of the 1:12 structure and the 2:17 structure at the ratio of 1:1. Like the iron-based intermetallic compounds of 2:17 and 1:12, a marvelous improvement in the Curie temperature, for example, from $T_C = 486\,K$ for $Sm_3(Fe,Ti)_{29}$ to $T_C = 750\,K$ $Sm_3(Fe,Ti)_{29}N_y$, and a drastic modification in anisotropy take place upon the introduction of interstitial atoms of C, and especially N, in 3:29 compounds. This is connected with a considerable lattice expansion (Cadogan *et al.*, 1994). Accurate determination of the crystallographic structure as well as the anisotropic magnetic properties of the $R_3(Fe,M)_{29}$ compounds require the preparation of single crystals (Courtois *et al.*, 1998a,b). The $Nd_3(Fe,Ti)_{29}$ phase is metastable. A solid-state heat treatment at temperatures typically around 1000 °C, followed by water quenching, is required to obtain compounds, which possess the 3:29 structure at room temperature. However, it is known that in the case of heavy rare-earth compounds a crucial shift in composition is needed to stabilize the binary R_2Fe_{17} compounds. Therefore it is possible to prepare $R_3(Fe,M)_{29}$ single crystals by a solid-state transformation of a $R_2(Fe,M)_{17}$ single crystal whose actual chemical composition is $R_3(Fe,M)_{29}$.

Following this route a $Y_2(Fe,V)_{17}$ single crystal (hexagonal Th_2Ni_{17}-type structure) with a chemical composition close to $Y_3(Fe,V)_{29}$ was grown under an argon atmosphere using the cold-crucible CZ method (Courtois *et al.*, 1998a). A cylindrical seed 0.5 mm in diameter with a length side parallel to the *c* axis of the 2:17 hexagonal structure was placed at the end of a head rotating with 5 rpm. The pulling rate was $22\,mm\,h^{-1}$. The $Y_2(Fe,V)_{17}$ single crystal obtained was subsequently sealed in a quartz tube under an argon atmosphere and annealed at 1015 °C for three days, followed by water quenching.

Powder X-ray diffraction showed the expected monoclinic cell, but single crystal X-ray data exhibited hexagonal symmetry. This discrepancy has been resolved by performing magnetization measurements on the crystal, which showed hexagonal symmetry with significant in-plane anisotropy. These observations have been quantitatively analyzed by considering that the crystal is, in fact, twinned. The magnetization was measured in applied fields up to $\mu_0 H = 7\,T$ in the temperature range $5\,K < T < 300\,K$. Over the whole temperature range investigated, the [001] axis of the $CaCu_5$ cell (which corresponds to the [102] axis of the $Nd_3(Fe,Ti)_{29}$ monoclinic cell) is the hardest magnetization direction and the spontaneous magnetization lies in the plane perpendicular to this axis (Courtois *et al.*, 1998a,b).

In a similar way, a novel $Y_3(Fe,Cr)_{29}$ single crystal with the $Nd_3(Fe,Ti)_{29}$-type structure has been successfully prepared (Yang *et al.*, 1999). $Y_2Fe_{15}Cr_2$ single crystals with a Th_2Ni_{17}-type structure were grown with growth rates of $15–25\,mm\,h^{-1}$ and a rotation rate of 30 rpm using the CZ method. Crystals were subjected to a heat treatment at 1000 °C for four days followed by quenching in water, which resulted in a 3:29 structure. The lattice parameters of the crystal are $a = 1.0645\,nm$, $b = 0.8455\,nm$, $c = 0.9678\,nm$, and $\beta = 97.462°$, respectively. The Curie temperature 410 K is similar to $T_C = 439\,K$ of the $Y_3(Fe,V)_{29}$ single crystal (Courtois *et al.*, 1998a). From the magnetization curves measured along the easy and hard direction it was concluded that the hard magnetic direction is [102] and that the crystal keeps a planar anisotropy from 1.5 to 293 K. The magnetocrystalline anisotropy constants at 1.5 K are $K_1 = -0.87 \times 10^6\,J\,m^{-3}$ and $K_2 = 0.19 \times 10^6\,J\,m^{-3}$.

Sm_xFe_y and miscellaneous compounds

In this section, we briefly review a few other attempts of crystal growth of hard magnetic materials. As mentioned earlier crystal growth of several compounds containing volatile elements is difficult or impossible. In some cases the so-called flux method can be applied to reduce the operating temperatures (as discussed in Section 3.2).

In the case of Fe–Sm compounds a Sm self-flux was successfully applied to grow crystals, which cannot be prepared otherwise (Samata *et al.*, 1998; Samata, Sakamoto, Yashiro and Nagata, 2001). After arc melting an appropriate amount of rare earth (Sm) and iron the button (∼30 g) was

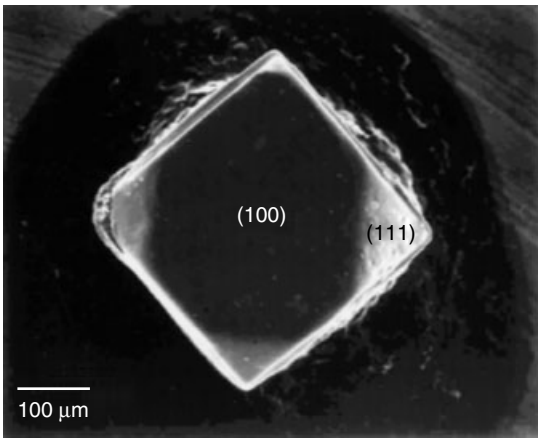

Figure 22. A SEM image of an as-grown Sm_6Fe_{23} crystal. The large square plane and the small triangular planes are the (100) and (111) planes, respectively. (Reproduced from Samata *et al*., 2001, with permission from Elsevier. © 2001.)

placed in a BN coated alumina or yttria crucible. The crucible was further sealed in a quartz ampoule with Ar gas after evacuation to 6.7×10^{-2} Pa (5×10^{-5} Torr). The mixture was heated over the dissolution temperature (900–1050 °C) using an electric furnace. After being held at that temperature for 0.5–6 h, it was cooled with 0.1–4 K h^{-1} to 700–850 °C, and then the quartz ampoule was cooled to room temperature by turning off the electric furnace. One special feature of this flux-creep-up method is that the flux creeps up the inner wall of the crucible during the crystal growth (Samata, Sakamoto, Yashiro and Nagata, 2001). Since the Sm flux around the crystal was easily oxidized into oxide powder in a few days, crystals could be removed easily from the bottom of the crucible without applying any mechanical strain. The crystallization of various intermetallic compounds is possible by adjusting the growth condition. Crystals of $SmFe_2$, $SmFe_3$ (Samata, Sakamoto, Yashiro and Nagata, 2001), Sm_6Fe_{23} (Samata, Sakamoto, Yashiro and Nagata, 2001; Samata *et al*., 2001), and $Nd_6Fe_{13-x}Al_{1+x}$ (Samata *et al*., 2001) were grown using this technique. In the latter case a Nd(Al)-rich flux was utilized. A scanning electron microscopy (SEM) image of a flux-grown Sm_6Fe_{23} crystal is shown in Figure 22.

Since the chemical composition of the mixture in the crucible changes in accordance with the creep-up of the flux, this method may be promising for both, the search for new phases and the crystal growth of known materials. In particular, $SmFe_7$ is a new phase (Samata *et al*., 1998; Samata, Sakamoto, Yashiro and Nagata, 2001) crystallizing in the tetragonal structure (space group $P4_2/mmm$) with a significantly large spontaneous magnetization 136 emu g^{-1} at 293 K, high $T_C = 608$ K, and huge magnetocrystalline anisotropy constants $K_1 + K_2 = -6.9 \times 10^6$ J m^{-3} at 293 K (Samata *et al*., 1998), which are comparable with those of $Nd_2Fe_{14}B$.

With this promising method also crystals of Al-substituted compounds $Sm(Fe_{1-x}Al_x)_2$, $Sm(Fe_{1-x}Al_x)_3$, $Sm_6(Fe_{1-x}Al_x)_{23}$, and $Sm(Fe_{1-x}Al_x)_7$ were grown and their magnetic properties were investigated (Samata, Kasai, Taniguchi and Nagata, 2003). The saturation magnetization of all compounds decreases by Al substitution. In the $Sm(Fe_{1-x}Al_x)_3$ and $Sm(Fe_{1-x}Al_x)_7$ systems, the anisotropy field is decreased with the Al substitution, while, in the cubic $Sm(Fe_{1-x}Al_x)_2$ and $Sm_6(Fe_{1-x}Al_x)_{23}$ systems, it is increased significantly. The Curie temperature of these compounds seems to be dependent on the average distance between the Fe nearest-neighbor atoms.

Flux methods have been utilized for crystal growth of various other magnetic compounds, too, which cannot be mentioned in this report.

4.3 Crystal growth of high-magnetostrictive compounds

4.3.1 Binary RFe_2 compounds

Heavy rare-earth elements, R = Tb and Dy, display the largest known magnetostrictions (∼1%), however, only at cryogenic temperatures (Clark, 1980). Among the various magnetostrictive materials RFe_2 Laves phase compounds exhibit huge (up to 10^{-3}) magnetostrictive strain at room temperature, which is important for technological reasons (Clark, Tamagawa and Belson, 1972). Among the RFe_2 compounds single crystals of $TbFe_2$, $ErFe_2$, and $TmFe_2$ exhibit [111] as the easy magnetization direction, whereas for $DyFe_2$ and $HoFe_2$ the easy magnetization direction is [100]. The room-temperature magnetostriction constants λ_{111}, for $TbFe_2$, $ErFe_2$, and $TmFe_2$ single crystals, and λ_{100} for $DyFe_2$, $HoFe_2$ single crystals as function of a magnetic field in the easy magnetization direction are shown in Figure 23 (Clark, 1980). The highly anisotropic magnetostriction reveals the importance of grain orientation in achieving high magnetostriction with two beneficial effects (i) the increase of the magnetostriction constant ($\lambda_s \approx 0.6\ \lambda_{111}$ in an isotropic polycrystal) and (ii) the lower internal losses at grain boundaries.

Various attempts of single-crystal growth of RFe_2 compounds are described by McMasters, Holland and Gschneider (1978). Small single crystals of $TbFe_2$, $DyFe_2$, and $ErFe_2$ have been prepared by the Bridgman technique using tungsten crucibles. However, the crucible-sample interface contained dendrites of the contamination product, which seriously limited the size of the crystals. Other crucible materials led to even more crucible contamination.

Single crystals of $HoFe_2$ and $Ho_{1-x}Tb_xFe_2$ compounds have been prepared by a tri-arc CZ technique described in

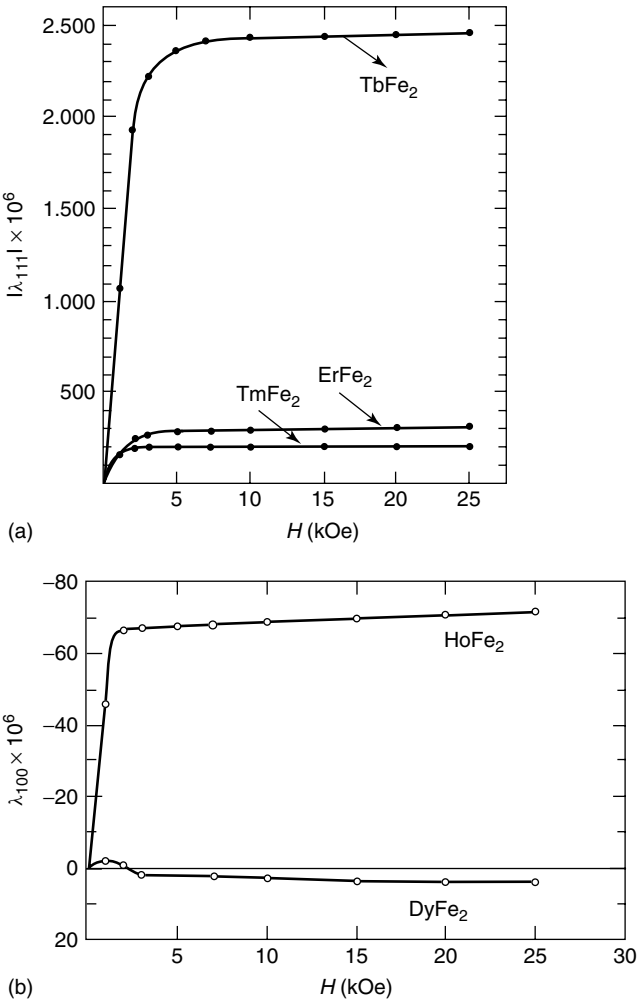

Figure 23. Room-temperature magnetostriction $|\lambda_{111}|$ for $TbFe_2$, $ErFe_2$ and $TmFe_2$ single crystals (a). For $TbFe_2$, $\lambda_{111} > 0$; for $ErFe_2$, and $TmFe_2$, $\lambda_{111} < 0$ is valid. Room-temperature magnetostriction λ_{100} for $DyFe_2$, $HoFe_2$ single crystals (b). (Reproduced from Clark, 1980, with permission from Elsevier. © 1980.)

Section 3.3 (Milstein, Koon, Johnson and Williams, 1974). Master alloy compositions 1% rich in rare earths were utilized in order to suppress Fe-rich phases. Preferable results were obtained with single-crystalline seeds rotated with 40–80 rpm at a pull rate 5 mm h^{-1}. However, suppression of spontaneous nucleation of second grains and beneficial effects on crystal quality were achieved by counterrotation of hearth of the tri-arc facility with 50–75 rpm. The growth atmosphere employed was Ar gas purified by gettering over a Ti sponge at red heat, which passed through a molecular sieve held at −78 °C. High-quality crystals of up to 1 cm in diameter and some centimeter in length have been grown. Electron probe and physical measurements, in particular, anisotropy data measured on spheres ground from different portions of the boules proved the uniform composition over some centimeters length, the absence of second phase and second grains, and the small strains in the samples.

However, this technique leads only to favorable results for congruent or nearly congruent melting compounds with moderate or low vapor pressures at their melting temperatures. More recently, a cold-crucible CZ technique was applied for the crystal growth of $NbFe_2$, $HoFe_2$, $Tb_{0.27}Dy_{0.73}Fe_x$ ($x = 1.9$, 1.95) (Terfenol-D) (Bi, Abell and Ford, 1996). In contrast to the tri-arc method, melting is accomplished by RF (350 kHz) induction heating in a Hukin-type vertical cold crucible (cf. Section 3.3). The contact between the crucible and the melt of ∼50-g mass is eliminated by levitation in an electromagnetic field. The process proceeds under a 0.2 MPa Ar atmosphere. A tungsten rod is used as a seed rotating with 5 rpm for crystal growth of $HoFe_2$, and Terfenol-D with 28 mm h^{-1} pull rate. The crystal boules 10 mm in diameter and ≥20 mm in length consist of a couple of large grains and the perfection of Terfenol-D crystals suffers from twin boundaries and needle-shaped Widmannstaetten precipitates of $(Tb/Dy)Fe_3$.

A horizontal levitation zone melting technique was developed by McMasters, Holland and Gschneider (1978) at Ames Laboratory, which circumvents crucible reactions of the reactive melt. Principal problems which had to be solved for a successful crystal were (i) reduction of the ripples of the output signal of the 25 kW RF generator (200–550 kHz), which are detrimental for the control of the molten zone in crystal growth (ii) the appropriate arrangement of the copper tube for best levitation in this open boat configuration (iii) designing of the pancake shaped work coil in order to achieve a narrow molten zone and steep temperature gradients, and (iv) proper adjustment of the conditions for levitating the zone, which are different for each material. The growth proceeds in a quartz tube evacuated and backfilled with a protective He/Ar gas mixture, which could vary from 0.13 MPa to 0.5 MPa.

The single-crystal growth of $TbFe_2$ is described here as an example since it encompasses most problems associated with other substances of this family (McMasters, Holland and Gschneider, 1978). The compound $TbFe_2$ is formed by a peritectic reaction $L + TbFe_3 \leftrightarrow TbFe_2$ at 1187 °C and the peritectic horizontal extends from 75 at% ($TbFe_3$) to 55 at% Fe (cf. Tb–Fe phase diagram Figure 3 in Section 2). At the Tb-rich side a eutectic reaction between $TbFe_2$ and Tb occurs at 847 °C and 27 at% Fe. $TbFe_{1.98}$ feed rods 9 mm in diameter and 75 mm in length were prepared by arc melting from high-purity elements. At about 10-mm distance from the end the feed rod was cut and a 3-mm-thick disk with composition $Tb_{45}Fe_{55}$ was placed between the two pieces. Finally the three pieces were welded together. The $Tb_{45}Fe_{55}$ section is melted and the molten zone passed along the rod at a rate of 0.8 mm h^{-1}. The slow rate of this TSFZ growth process is necessary since it proceeds below the peritectic temperature

and involves diffusion of the stoichiometric composition $TbFe_2$ across the molten zone. The success of the crystal growth process, which takes place under a gettered 0.4 MPa Ar atmosphere to minimize evaporation, depends on the stability of the molten zone and the solid-liquid interface shape. Zoned samples contained single-crystalline sections of about 15 mm length ($\sim$1 cm^3). At the bottom because of incomplete levitation a thin polycrystalline layer occurred, which is removed from the crystal like other polycrystalline parts. The method was also successfully utilized for the growth of smaller crystals of $TmFe_2$ (Abbundi and Clark, 1978), $DyFe_2$, and $Tb_{0.27}Dy_{0.73}Fe_2$ and also 1–2 cm^3 large crystals of Nd, Pr, and γ-Ce (McMasters, Holland and Gschneider, 1978). The latter rare-earth crystals were grown with considerable higher rates of 3–6 mm h^{-1} in conjunction with a strain-anneal technique (cf. Section 4.1.1).

4.3.2 *Quasibinary $Dy_{1-x}Tb_xFe_2$ compounds (Terfenol)*

The RFe_2 compounds possess unusually large magnetostriction strains and also a high magnetic anisotropy. For certain magnetostrictive applications high strains at low fields are necessary. In these cases, a low magnetic anisotropy is important in order to maximize domain wall mobility and easy domain rotation at low fields. RFe_2 compounds with different rare earths can display room-temperature anisotropy constants of opposite sign (cf. Table 7 in Clark (1980)). This makes it possible to tailor compounds with optimum magnetostriction and low anisotropy. Studies by Clark (1980) have demonstrated that the pseudobinary compound $Tb_{1-x}Dy_xFe_2$, known as *Terfenol-D*, has a significantly reduced magnetic anisotropy. The room-temperature magnetostriction constant $\lambda_{111} \approx 1600 \times 10^{-6}$ of single crystals at the compensation region $x \approx 0.73$ is still high in comparison with $\lambda_{111} \approx 2450 \times 10^{-6}$ of the binary $TbFe_2$. Because of its high magnetostriction in low external magnetic fields the $Tb_{0.27-0.30}Dy_{0.73-0.70}Fe_2$ compounds in the last years became outstanding candidates for applications such as sonar devices (Abbundi and Clark, 1978). Accordingly, preparation, microstructure, and physical properties of this particular compound have been widely investigated. The Laves phase $(Tb,Dy)Fe_2$ compound has a $MgCu_2$ structure type, its magnetic easy axis is the $\langle 111 \rangle$ direction and the magnetostrictive strain along this direction is 16.6 times larger than that along the $\langle 100 \rangle$ direction. Considering this huge magnetostrictive anisotropy and the hindrance to magnetic domain processes of inhomogeneity, boundaries, impurities, and so on, Tb–Dy–Fe single crystals with a minimum amount of defect structure and impurity content which are oriented along the $\langle 111 \rangle$ crystal axis are desirable not only as subjects of fundamental research but as material with optimum magnetostriction characteristics for the applications itself.

As already discussed in the foregoing section, there are three common crystal growth techniques, which one might consider for producing aligned grains and possibly single crystals of Terfenol-D, (i) Bridgman growth, (ii) CZ growth, and (iii) FZ solidification. Methods (i) and (ii) both require the alloy to be held in a container material which could lead to contamination, whereas no container is required in method (iii). FZ solidification also has another advantage as a steady state process in which the composition of the solid freezing from the zone must equal the composition of the solid being fed into the zone. In the FZ method RF induction heating (McMasters, Verhoeven and Gibson, 1986; Verhoeven, Gibson, McMasters and Baker, 1987) as well as optical heating (Mei, Okane, Umeda and Zhou, 1997; Mei, Yoshizumi, Okane and Umeda, 1997) was applied. Maximum 8 mm rod diameters can be achieved because the surface tension limits the size of the zone with a typical length of 8–10 mm. In the case of the induction furnace an electromagnetic force also contributes to zone stability.

Indeed, Terfenol-D crystals have been grown by the vertical FZ method with a pancake RF induction coil (450 kHz) from $Tb_{0.27}Dy_{0.73}Fe_x$ $(1.9 < x < 1.975)$ (McMasters, Verhoeven and Gibson, 1986), and $Tb_{0.3}Dy_{0.7}Fe_x$ (Verhoeven, Gibson, McMasters and Baker, 1987) feed rods typically 10 mm in diameter and 200 mm in length prepared by arc melting from >99.97 wt% pure elements. The binary Dy–Fe and Tb–Fe phase diagrams (Massalski, Okamoto, Subramarian and Kacprzak, 1990) are quite similar and in both systems the RFe_2 compound melts peritectically. It is reasonable to assume that the isopleth of interest in the ternary Dy–Tb–Fe system would be a quasibinary diagram, which would appear nearly identical to the Dy–Fe diagram. A schematic ternary Dy–Tb–Fe phase diagram along with the resulting composition profile of growing cells is given by Mei, Okane, Umeda and Zhou (1997).

For a steady state at the growth front one would require a rare-earth concentration beyond the liquidus composition at the RFe_2 peritectic temperature in order to grow pure RFe_2 without formation of a primary RFe_3 phase. The $TbFe_3$ phase was detected in the center of the $TbFe_2$ dendrites. FZ experiments with $Tb_{0.27}Dy_{0.73}Fe_2$ alloys have shown that for growth rates in excess of 125 mm h^{-1}, the Terfenol-D compound grows directly from the melt as a primary phase. Considering that for both Dy–Fe and Tb–Fe binary alloys the RFe_2 compound melts incongruently it is likely to assume that the Terfenol-D compound also melts incongruently, but it is stabilized kinetically and grows above the peritectic temperature by a metastable congruent reaction (McMasters, Verhoeven and Gibson, 1986). In all cases, the microstructures contained a second, darkly etching phase as

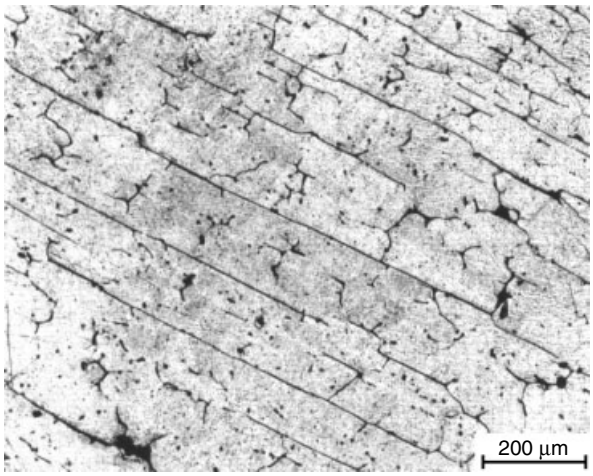

Figure 24. Cellular microstructure of Terfenol-D single crystals. (Reproduced from Mei *et al*., 1997, with permission from Elsevier. © 1997.)

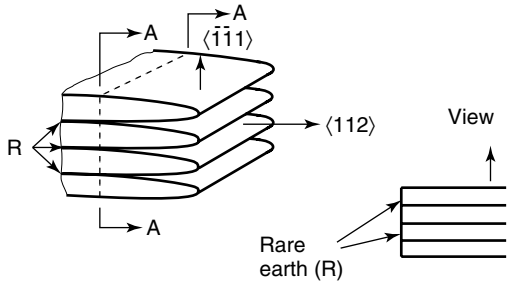

Figure 25. Schematic view of a dendrite growth front. (a) Three-dimensional view. (b) Transversal view along A–A. (Reprinted with permission of ASM International®. All rights reserved. www.asminternational.org.)

shown in (Figure 24). The dark phase was examined by scanning electron microscopy, scanning Auger microscopy and optical microscopy, and it was shown to be pure rare-earth metal. These results demonstrate that in this alloy system the eutectic reaction at the base of the cells or dendrites occurs by a divorced eutectic reaction mode for the rate of solidification 125–500 mm h^{-1} employed in FZ melting. The pure RFe_2 compound is extremely brittle but structures of RFe_2 + eutectic, while still brittle, are much less subject to breakage upon handling. Therefore crystals often are prepared from Fe-depleted RFe_x feed rods ($x < 2$). The ductile second phase consisting of pure rare-earth metal forms as an interconnected skeleton network, which probably accounts for the reduction of brittleness found for alloys of $x = 1.9$ versus alloys of $x \approx 2$. It has been demonstrated that FZ solidification with induction heating (450 kHz) in alloys of $Tb_{0.27}Dy_{0.73}Fe_x$ ($x = 1.9 - 1.975$) produces samples with essentially no macrosegregation along the axis in crystals over 18 cm length. The term *single crystal* for Terfenol-D is often used for aligned multigrain structures consisting of primary dendrites or cells of the RFe_2 compound with rare-earth metal in the intercellular/interdendritic regions (cf. Figure 23). However, it was reported that the desired ⟨111⟩ crystal was not obtained even using a seed technique. On the other hand, ⟨112⟩ and ⟨110⟩ oriented twinned crystals (Figure 25) were easily produced due to the preferred growth of the Tb–Dy–Fe alloy (Verhoeven, Gibson, McMasters and Baker, 1987). The ⟨112⟩ orientation is 19.5° tilted with respect to the desired ⟨111⟩ direction and $\lambda_{112} = 94\%\ \lambda_{111}$. The twinning in the crystals is harmful to their magnetostrictive properties because of its hindrance to magnetization process.

In the induction furnace it is difficult to obtain ⟨111⟩ oriented crystals even with seed crystals, because the liquid interface is a little concave to the melt. The direct driving force of twinning seems to be the growth rate. The rate dependence of the twinning was studied and ⟨111⟩ oriented Tb–Dy–Fe single crystals (6 mm diameter; 100 mm length) were successfully grown in an optical image zone melting furnace from a master alloy $Tb_{0.3}Dy_{0.7}Fe_{1.90}$ (Mei, Yoshizumi, Okane and Umeda, 1997). An ideal seed is an oriented Tb–Dy–Fe single crystal, which is usually obtained by cutting from a twinless crystal. Another simple method was found to grow the ⟨111⟩ twinless crystals directly from the twinned seed crystals (Mei, Yoshizumi, Okane and Umeda, 1997). One seed crystal was cut from the ⟨112⟩ oriented twinned 'single' crystal with the originally lateral (111) planes as its upper face. The perpendicular ⟨111⟩ direction was easily determined owing to the sheetlike morphology of the twinned crystals. Along this direction, both of the twinned parts and parent parts exhibited the same {111} planes, and the obtained ⟨111⟩ twinned seed had its original twin planes perpendicular to the following growth direction. From the ⟨111⟩ oriented seed crystals, ⟨111⟩ oriented twinless $Tb_{0.3}Dy_{0.7}Fe_{1.90-1.95}$ single crystals were successfully grown at rates of 3–15 mm h^{-1} in the image furnace. These rates are considerably constrained compared to the growth of the twinned crystals with ⟨112⟩ orientation cited above.

Recently, the growth of ⟨113⟩ orientated crystals (10 mm diameter; 50 mm length) with a horizontal crystal growth furnace with induction heating was accomplished with a ⟨113⟩ oriented seed crystal by carefully controlling the temperature gradients and the growth rates between 30 and 240 mm h^{-1}, which are well beyond that for growth of ⟨111⟩ oriented crystals (Zhang, Gao, Zhou and Shi, 2004). The magnetostrictive properties are superior to the specimens with ⟨112⟩ oriented twinned 'single' crystals.

Alternatively, Terfenol-D crystal growth was carried out in Bridgman furnaces. Arc-cast fingers were placed in quartz crucibles with 2–2.5 cm diameter and directional solidified from bottom to top (Verhoeven, Gibson, McMasters and Baker, 1987). The heat was supplied by an induction coil (450 kHz) and the temperature gradient was produced by placing the round bottom of the crucible on a water-cooled pedestal. Growth rates of 200–250 mm h^{-1} were employed. The solidification front was dendritic with planar-sheet morphology. The sheet faces are parallel to {111} planes, the primary growth direction lies along the ⟨112⟩ direction and grains are aligned within 5–10° of the growth axis. Similar to the FZ crystals a rare-earth phase (Tb + Dy) is placed between the sheets, but the alignment of the sheet dendrites into parallel arrays is not always obtained for the Bridgman crystals. Crystals were also grown from induction cast $Tb_{0.3}Dy_{0.7}Fe_{1.9}$ alloy rods in a Bridgman furnace with $A1_2O_3$ crucibles at 30–3600 mm h^{-1} pulling rates (Mei, Yoshizumi, Okane and Umeda, 1997). Contamination from Al_2O_3 crucible material and atmosphere was severe. A significant rare-earth loss along the axial direction was observed even at high growth rates of 600 mm h^{-1}. A change of the preferred growth direction from ⟨112⟩ to ⟨110⟩ was observed for lower growth rates (<60 mm h^{-1}) (Mei, Okane, Umeda and Zhou, 1997; Mei, Yoshizumi, Okane and Umeda, 1997).

Owing to very low growth rates of single crystals, both the FZ and the modified Bridgman method are not economical for volume production. Therefore, a crystal growth technique for the production of large diameter drivers and for mass production of smaller diameter elements within one heat was developed by ETREMA Products, Inc., Ames (Iowa). It is based on a modified Bridgman technique (Snodgrass and McMasters, 1997). Terfenol-D alloy is melted in a ceramic crucible, and then poured via a hole in the bottom of the crucible into preheated molds. The molds are withdrawn from secondary furnace sections in a standard Bridgman manner. As the material is solidified, the rate of withdrawal and the direction of heat flow are controlled to produce crystallographically aligned drivers of Terfenol-D. This method is capable of producing drivers as large as 65 mm in diameter and lengths as great as 175 mm. For rods <50 mm, the system can produce aligned drivers of 250 mm in length. The system is also capable of producing several smaller rods (<28 mm diameter) simultaneously.

4.3.3 *Ni_2MnGa-based ferromagnetic shape memory alloys*

Ferromagnetic shape memory alloys (FSMAs) moved from a hypothetical new class of active materials, to join piezoelectric and magnetostrictive materials, upon observation of a 0.2% magnetic-field-induced strain at 265 K in a single crystal of Ni_2MnGa by Ullakko *et al*. (1996). By comparison, piezoelectric materials show strains of the order 0.1% (Haertling, 1999) and the leading magnetostrictive material, Terfenol-D, shows a field-induced strain of about 0.24% (Cullen, Clark and Hathaway, 1990). The magnetic alloy exhibiting a martensitic phase transformation allows control of large displacements by application of a magnetic field at constant temperature. Ni_2MnGa is a Heusler alloy, $L2_1$, having a cubic lattice with $a = 5.822$ Å in the high-temperature phase. The martensitic transformation temperature is near 276 K. The low-temperature phase evolves from the parent phase by a diffusionless, displacive transformation that gives a tetragonal structure, $a = b = 5.90$ Å, $c = 5.44$ Å. The properties of Ni–Mn–Ga samples sensitively depend on the alloy composition (Chernenko, Cesari, Kokorin and Vitenko, 1995). Compositions slightly off the Heusler stoichiometry are chosen in order to render alloys having Curie temperatures greater than the martensite transformation temperature, which in turn was to be greater than room temperature.

Crystals were grown by the Bridgman technique (Ullakko *et al*., 1996; Chernenko, Cesari, Kokorin and Vitenko, 1995; Murray *et al*., 2000; Sozinov, Likhachev, Lanska and Ullakko, 2002) as described in by Murray *et al*. (2000). Master alloys from high-purity nickel, manganese, and gallium were arc melted into buttons and then drop cast into a chilled copper mold. The as-cast ingots were placed in alumina crucibles and heated to 1350 °C for 1 h to allow homogenization before withdrawing the sample from the heat zone at a rate of 5 mm h^{-1}. In order to minimize evaporation of the Mn during crystal growth, the furnace was backfilled to a positive pressure of 6.83×10^5 Pa with purified argon after the chamber and sample had been degassed at 1350 °C under vacuum. A typical single-crystal boule measured 1 cm in diameter and 5 cm in length. After Laue orientation, several samples were cut from the crystal boule by electric spark erosion.

Usually, after a martensitic phase transition multiple variants of martensite form within a single crystal of the parent high-temperature phase. Afterwards, that multivariant state can be transformed into a nearly single variant of martensitic phase by an appropriate mechanical treatment. In this way nearly single-variant martensitic samples were prepared where the full field-induced strain can be exploited. Strains of 6% associated with the crystallographic distortion by application of a field of 320 kA m^{-1} (4 kOe) to a single-variant sample from an off-stoichiometric $Ni_{47.4}Mn_{32.1}Ga_{20.5}$ crystal were reported (Murray *et al*., 2000). Electron probe microanalysis of this crystal showed the composition to vary along the boule axis with Mn content increasing and Ga content decreasing in the growth direction. A very large 10% strain was achieved for a $Ni_{48.8}Mn_{29.7}Ga_{21.5}$ single crystal grown with 30 mm h^{-1}, after homogenization at 1253 K and aging

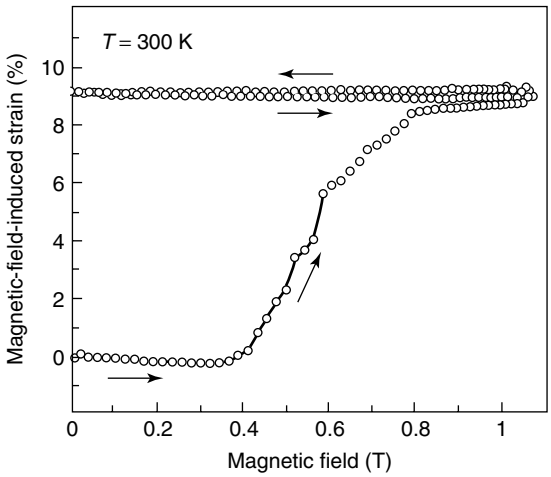

Figure 26. Field-induced strain of a single-variant sample of orthorhombic seven-layer phase in the $Ni_{48.8}Mn_{29.7}Ga_{21.5}$ alloy at 300 K measured perpendicular to the magnetic field applied along the [100] direction. (Reproduced from A. Sozinov *et al*., 2002, with permission from the American Institute of Physics. © 2002.)

at 1073 K (Sozinov, Likhachev, Lanska and Ullakko, 2002). The Curie temperature is about $T_C = 368$ K. The martensitic transformation starts at 337 K (M_s) and is completed at 333 K (M_f) during cooling. At lower temperatures, starting at 245 K, the magnetic susceptibility increased, indicating the intermartensitic transformation. By X-ray studies it was found that the crystal structure of the first high-temperature martensitic phase is nearly orthorhombic and has lattice parameters of $a = 0.619$ nm, $b = 0.580$ nm, and $c = 0.553$ nm at ambient temperature. Seven-layer modulation along the $(110)[1\bar{1}0]_p$ system was observed. The crystal structure of the second martensite is tetragonal with lattice parameters of $a = b = 0.547$ nm, and $c = 0.660$ nm ($c/a = 1.207$) at 200 K and $a = b = 0.551$ nm and $c = 0.654$ nm ($c/a = 1.187$) at ambient temperature. Figure 26 shows the results of the field-induced strain measurements of the alloy at ambient temperature. The magnetic field was applied parallel to the a axis. The maximum strain achieved in the first cycle at the field of 1.05 T is $\varepsilon_{MSM} = 9.5\%$. This value is lower than the crystallographic limit $e_0 = (1-c/a) = 10.66\%$ expected for complete transformation between two single variants.

4.4 Crystal growth of magnetocaloric materials

The magnetocaloric effect is a change in the temperature of a magnetic solid in response to a changing magnetic field. The magnetocaloric effect is intrinsic to all magnetic materials and is due to the coupling of the magnetic sublattice with the magnetic field, which changes the magnetic part of the entropy of a solid (Pecharsky and Gschneidner, 1999). This process has been used for about 70 years to achieve very/ultra low temperatures in small volumes by a process known as *adiabatic demagnetization refrigeration* (Gschneidner and Pecharsky, 1999). The magnetocaloric effect can be measured directly or it can be calculated indirectly from the measured magnetization or field dependence of the heat capacity. The range of operating temperatures of various classes of substances such as $PrNi_5$, pure rare earths (Pr, Nd, Er, Tm, Dy), rare-earth-containing intermetallic compounds (RAl_2, GdPd, RNi_2) depends on the magnetic phenomena utilized for the magnetocaloric effect. Gd, Gd_5Si_4, and Ge-substituted compounds $Gd_5(Si_xGe_{1-x})_4$ operate near room temperature. The giant magnetocaloric effect of the latter compound results from a simultaneous first order magnetostructural transformation and a structural transition from a paramagnetic monoclinic high-temperature phase into a ferromagnetic orthorhombic phase (Pecharsky and Gschneidner, 1999). Single crystals of magnetocaloric substances are exploited for details of crystallographic structures, the magnetic order, and anisotropic material properties.

The single crystals of Gd (Tishin, Gschneidner and Pecharsky, 1999) and Dy (Chernyshov *et al*., 2005), which were prepared from high-purity polycrystalline metals via a strain-anneal process (cf. Section 4.1.1), were studied over broad temperature (T) and magnetic field (H) intervals and have revealed peculiarities of magnetothermal properties especially in the vicinities of the magnetic ordering temperatures. When the magnetic field vector is parallel to the a axis of a crystal, the refined H–T phase diagram of Dy is more complicated than previously thought, and it contains several new phases (Chernyshov *et al*., 2005).

The crystal growth of $Gd_5(Si_xGe_{1-x})_4$, which is of considerable interest for practical application, is hampered by the high melting point of the compounds (>2073 K) and the reactivity of both the rare-earth metal and silicon at these temperatures. Moreover, the phase diagram near the $Gd_5(Si_xGe_{1-x})_4$ region at high temperatures is not well known. Single crystals of the monoclinic $Gd_5(Si_xGe_{1-x})_4$ compound were synthesized only recently by the Bridgman method in a conical tipped tungsten crucible (Lograsso, Schlagel and Pecharsky, 2005). The as-cast $Gd_5(Si_xGe_{1-x})_4$ ingot was electron beam welded under vacuum into the crucible for crystal growth. The ingot was heated in a tungsten-mesh resistance furnace under a pressure of 8.8×10^{-5} Pa up to 1273 K and held at this temperature for 1 h to degas the crucible and furnace chamber. The chamber was then backfilled to a pressure of 3.4×10^4 Pa with high-purity argon. The ingot was then heated to 2273 K and held at this temperature for 1 h to allow thorough mixing before withdrawing the sample from the heat zone at 4 mm h^{-1}. Tungsten crucibles

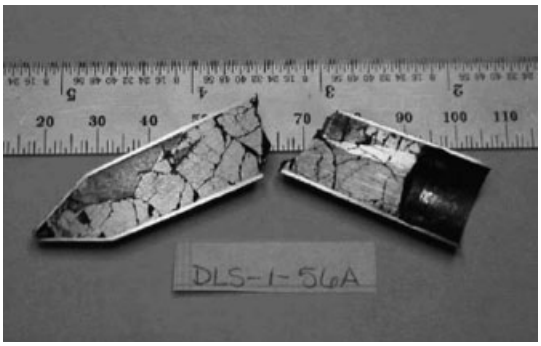

Figure 27. Longitudinal section of a typical as-grown $Gd_5Si_2Ge_2$ ingot. The ingot is comprised of three to four single crystals and is severely cracked along the entire length. (Reproduced from Lograsso *et al*., 2005, with permission from Elsevier. © 2005.)

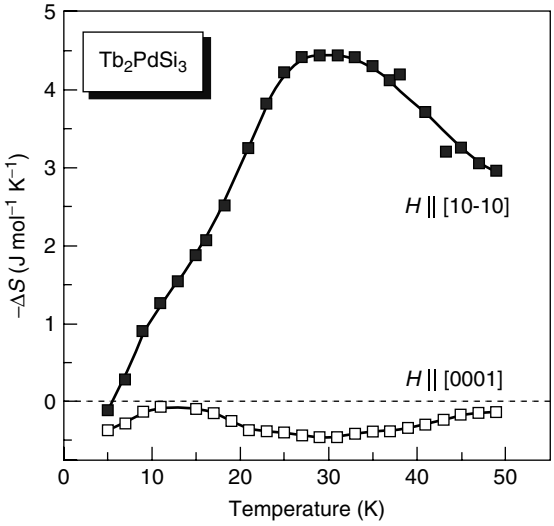

Figure 28. Entropy change by increasing the applied magnetic field from 0 to 4×10^3 kA m^{-1} (50 kOe), as derived from magnetization data as a function of temperature for Tb_2PdSi_3. (Reproduced from S. Majumdar *et al*., 2000, with permission from the American Physical Society. © 2000.)

were found to be inert, that is, no formation of tungsten silicides or germanides were observed, but slight solubility of W in molten $Gd_5(Si_xGe_{1-x})_4$ resulted in the precipitation of pure W dendrites in the bulk alloy and along the crucible wall, leading to mechanical bonding between crucible and ingot. Upon cooling the $Gd_5Si_2Ge_2$ ingot was severely cracked (Figure 27) due to the mismatch of thermal expansion between specimen and crucible (Lograsso, Schlagel and Pecharsky, 2005). Overall, the bulk crystal solidified in the monoclinic phase with a slight increase in lattice parameters reflecting the slight increase in Si:Ge ratio along the ingot. The temperature $T_C = 261$ K of the magnetostructural transformation increased by approximately 10 K. The large values of the magnetocaloric effect in specimens taken from the start of crystal growth slightly decreased over the length. No evidence was found for the solidification of second phases. Magnetization measurements using a $Gd_5(Si_{1.95}Ge_{2.05})$ single crystal with the magnetic field applied along three crystallographic directions [001], [010], and [100] were carried out. The giant magnetocaloric effect is maximum in the vicinity of T_C. The H–T phase diagrams were constructed for the $Gd_5(Si_{1.95}Ge_{2.05})$ single crystal with field along the three directions and a small anisotropy was observed, which is correlated with the nature of the crystalline anisotropy (Tang *et al*., 2003).

On the other hand, significant anisotropy of the magnetocaloric effect was derived from magnetization measurements in Tb_2PdSi_3 single crystals grown by the FZ method (Majumdar *et al*., 2000). The Tb_2PdSi_3 compound exhibits a hexagonal AlB_2-type structure and undergoes a paramagnetic–antiferromagnetic transition at $T_N = 23$ K. From the entropy change $-\Delta S$ shown in Figure 28 a large anisotropy is emphasized in the sense that the observed magnetocaloric effect over a wide T range in the vicinity of T_N is large for a [10-10] direction, in sharp contrast to relatively smaller values for [0001] direction. This implies that, if the present material could be used for magnetic refrigeration at low temperatures, one may have a relatively better cooling power if the magnetic field H is applied along a [10-10] direction of the crystal (in the basal plane of the hexagonal unit cell) instead of [0001] the perpendicular c axis. Another noteworthy point is that the sign of $-\Delta S$ is essentially positive for the former direction, whereas it is negative for the latter.

The utilization of anisotropic materials was subject of a recent theoretical study, too (Lima, Gschneidner and Pecharsky, 2004). The results indicated that using single domain magnetic materials it is theoretically possible to increase the efficiency of magnetic refrigeration up to 65% for a device operating at low temperature and utilizing $TbAl_2$.

4.5 Selected intermetallic compounds for spintronics

Spin-polarized transport in magnetic materials is beginning to play an important role in the development of magnetoelectronic devices. Half-metallic (HM) ferromagnetic materials have recently drawn intense interest due to their potential use in this field (see contributions in Vol. 5 of this Handbook).

Investigation of single crystals are usually used to verify theoretically predicted magnetic effects and properties since it is believed that they represent the least disturbed structure of a compound and its intrinsic properties. There are only a few publications about the growth of single crystals in this group of materials. The ferromagnetic shape memory compound Ni_2MnGa plays an important role (Schlagel, Wu,

Hang and Lograsso, 2000) (cf. Section 4.3.3) as do the compounds Co_2MnX (X = Si, Ge) (Cheng *et al*., 2001) due to their high Curie temperatures and the predicted high spin polarization.

Cheng *et al*. (2001) reported the growth of both Co_2MnSi and Co_2MnGe high-quality crystals. The magnetic moment per formula unit of 5.1 μ_B well agrees with the known predictions and confirmes the semimetallic nature of these materials. Cheng started from the pure elements (better 3N purity), which were melted together by arc melting under argon atmosphere. The compound was homogenized by turning and remelting the boule. The crystal growth proceeded using the tri-arc Czochalski method. Using small seed crystals from a previous experiment, single crystals about 6 mm in diameter and 30–40 mm in length were grown at 7 mm h^{-1} with a seed rotation of 15 rpm opposite to the rotation of the hearth of the tri-arc facility. The temperature of the melt, measured by optical pyrometry, was raised to about 1523 K before immersing the starting seed. Slices of both crystals were annealed at 1073 K for nine days followed by water quenching. The crystals are single phase and single crystalline with an orientation near [100].

Single crystals of the full-Heusler compound $Co_2Cr_{0.6}Fe_{0.4}Al$ were grown by the FZ technique by the authors. Firstly, starting materials (purity better than 3N) are mechanically or chemically treated, to remove oxide films often present on metal pieces in spite of highly pure conditions of storage. Then all the materials are initially melted in an arc-melting furnace on a water-cooled Cu plate under purified argon atmosphere. The resulting master alloy is remelted in a Hukin-type cold crucible with RF induction heating and cast into a copper mould with a cylindrical cavity. The cylindrical rod produced, typically 6 mm in diameter and 60–80 mm in length, is used for FZ crystal growth as a feed rod.

The single-crystal growth was accomplished by vertical FZ techniques with optical heating (see Figure 10) at a growth rate of 12 mm h^{-1}. Axially symmetric counterrotation of crystal (30 rpm) and feed rod (10 rpm) was employed. The crystals shown in Figure 29 were single crystalline over the whole diameter for the last 20 mm. They were oriented by Laue technique and cut for magnetic measurements.

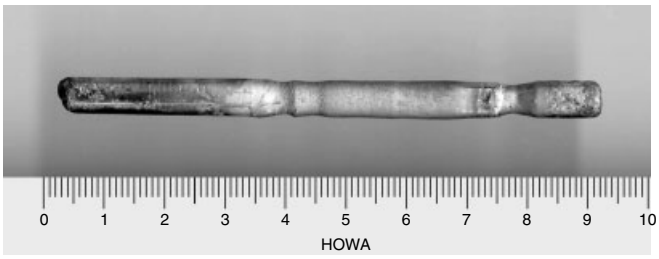

Figure 29. $Co_2Cr_{0.6}Fe_{0.4}Al$ single crystal grown by FZ method. (Courtsey of G. Behr, IFW Dresden, 2005.)

4.6 Crystal growth of multiferroic materials

Multiferroics, sometimes called *magnetoelectrics*, possess two or more switchable properties (order parameters) such as electrical polarization, magnetization, or strain (Smolenski and Chupis, 1982; Schmid, 1994a,b). Although a number of materials exhibit both ferroelectricity and (anti)ferromagnetism, there is not always a substantial coupling between them. In contrast, in most cases ferroelectricity and magnetic ordering exclude each other (Khomskii, 2006). Of practical interest is the potential to control (i) the spontaneous electric polarization by a magnetic field or (ii) the magnetization by an electric field through magnetoelectric coupling. These materials may have a perspective for future device applications such as electrically recorded magnetic media.

Magnetoelectric effects have been studied in some multiferroics since the late 1960s. In general, the applied magnetic field results in a small modulation of the spontaneous polarization. Why and under which circumstances a large coupling should come about is a major open question, but this problem has proved difficult to tackle owing to the lack of materials that show such strong coupling (Hur *et al*., 2004a). Recently, some compounds with huge magnetoelectric effects have been found among Mn oxides: in $HoMnO_3$, ferromagnetic ordering can be switched on and off by an electrical voltage (Lottermoser *et al*., 2004), and $TbMn_2O_5$ exhibits a practical value for magnetically controlling a ferroelectric polarization, which can be continuously tuned by a magnetic field between two states with opposite direction (Hur *et al*., 2004a).

4.6.1 Magnetic and ferroelectric phases of the family of RMn_2O_5 compounds

In comparison to the family of the hexagonal manganites $RMnO_3$ (R = Ho-Lu), the number of investigations on RMn_2O_5 single crystals (R = Y, Bi, or a rare-earth element) is scarce. In spite of the detailed studies of selected RMn_2O_5 compounds, little is actually known about the detailed interplay of ferroelectricity and magnetism in RMn_2O_5, primarily owing to its chemical and structural complexity (Saito and Kohn, 1995; Golovenchits, Morozov, Sanina and Sapozhnikova, 1992). According to the authors (Chapon *et al*., 2004) the emergence of ferroelectricity is a consequence of magnetic frustration between nearest and next-nearest Mn^{4+} neighbors in an antiferromagnetic square lattice.

RMn_2O_5 belongs to the orthorhombic space group *Pbam* at room temperature. Upon cooling below 50 K it displays a sequence of magnetic and electric phase transitions the nature of which is a result of the interplay of magnetic exchange interactions among Mn^{3+}, Mn^{4+}, and R^{3+} spins (if the R^{3+} ion is magnetic) and the lattice polarization (Sanina, Sapozhnikova, Golovenchits and Morozov, 1988; Kagomiya and Kohn, 1998). Mn spins order at the antiferromagnetic Neel temperature T_{N1} of about 40 K. According to earlier neutron diffraction studies, magnetic moments of Mn^{3+} and Mn^{4+} ions form a helical magnetic structure below $T_{N1} = 39 - 45$ K (Wilkinson *et al*., 1981; Kagomiya, Kimura, Noda and Kohn, 2001; Hur *et al*., 2004a).

The technological potential of most of the known magnetoelectric compounds is limited by (i) the small magnitude of the observed effects and (ii) by the low operating temperatures (<100 K). The rather low values of the ferroelectric Curie temperature T_C and the spontaneous polarization with respect to typical ferroelectrics seem to indicate a weak nature of the ferroelectricity of RMn_2O_5, which is induced by an ordering process differing from that of typical ferroelectrics (Kato, Kohn and Ishikawa, 1997).

However, operating temperatures might be increased by an appropriate substitution of Mn by other transition metals T = Fe, Co, as was shown by Shim *et al*. (2004). The small magnitude of magnetoelectric effects observed so far has been overcome in some recently investigated compounds of RMn_2O_5 (Fiebig, 2005). A significant magnetodielectric effect, that is, a change of the dielectric constant ε in an applied magnetic field, was reported near a unique commensurate–incommensurate magnetic transition in (Tb, Dy, Ho)Mn_2O_5, which is intricately coupled with a dielectric transition. In particular, the magnetodielectric effect for $DyMn_2O_5$ is more than 100% (along the crystallographic *b* axis) in a broad temperature range below T'_N if the magnetic field is applied along the *a* axis of the crystal (Hur *et al*., 2004b). This 'colossal magnetodielectric' (CMD) effect demonstrates a new kind of an intriguing interplay between spin and lattice degrees of freedom being active in RMn_2O_5. It provides an important means to tune dielectric properties with external magnetic fields (Hur *et al*., 2004a).

In $TbMn_2O_5$, a reversal of the electric polarization in a magnetic field of the order of 1 T has been observed below the antiferromagnetic ordering at $T_{N1} = 38$ K, including a memory effect with remnant states (Hur *et al*., 2004a). The behavior is reproducible throughout many cycles. This effect can be used to set the polarization in a controlled way with a magnetic field. In ferroelectric YMn_2O_5 crystals, a strong enhancement of the electrical polarization can be achieved by application of large magnetic fields of about 20 T (Kadomtseva *et al*., 2003).

The unit cell parameters of the RMn_2O_5 phase differ significantly from those in the adjacent regions of the bivariant equilibrium in the corresponding thermodynamic phase diagrams (Fedorova, Titova, Golikov and Balakirev, 2003). The fact that the unit cell can be varied with the chemical composition of the initial components indicates the existence of a sizable region of homogeneity of this substance both with respect to metal components and oxygen. No further studies in this direction have been reported, although a possible strong effect of the crystal composition and corresponding point defect structure on physical properties can take place similar to those of superconducting cuprates (Liang and Lin, 2002; Gorina *et al*., 1998).

4.6.2 Thermodynamics and crystal growth of RMn_2O_5 compounds

The study of the phase diagrams of R–Mn–O (R = Y, Tb, and Ho) systems as function of temperature, composition, and the oxygen partial pressure p_{O_2} is of great importance for controllable single-crystal growth of RMn_2O_5. The previous studies were mainly focused on subsolidus phase diagrams at low oxygen pressures ($p_{O_2} = 0.02 - 0.1$ MPa) (Balakirev and Golikov, 2003; Munoz, Alonso, Martinez-Lope and Martinez, 2004; Kitayama *et al*., 2002; Fu, Huebner, Trubelja and Stubican, 1994). Systematic studies at elevated oxygen pressures are missing, but are extremely important for RMn_2O_5 phase formation, since at lower p_{O_2} the decomposition reaction proceeds at high temperatures:

$$RMn_2O_5 \Longleftrightarrow RMnO_3 + \frac{1}{3}Mn_3O_4 + \frac{1}{3}O_2 \qquad (4)$$

An increase of the decomposition temperature of RMn_2O_5 with increasing p_{O_2} is expected and has been confirmed by Fu, Huebner, Trubelja and Stubican (1994). This behavior of RMn_2O_5 is evident since the high oxygen pressure favors the stabilization of the high oxidation states of manganese, Mn^{4+} and Mn^{3+}. Oxygen pressures of more than 20 MPa seem to be overstated for the synthesis of RMn_2O_5 compounds, since heat treatment of $LaMn_2O_5$ and $SmMn_2O_7$, which can not be synthesized at 0.02 MPa, at these pressures show higher Mn mean oxidation states of 3.56+ and 3.63+, respectively. That corresponds to an increased oxygen concentration with respect to the stoichiometry (Munoz *et al*., 2004).

The polycrystalline materials of RMn_2O_5 (R = Y, Tb, Ho) can be synthesized by conventional solid-state reactions at around 1100 °C in air for 48–72 h. La and Nd systems require higher pressures p_{O_2} at these temperatures (Kitayama *et al*., 2002). But, since RMn_2O_5 materials show strongly anisotropic properties (Hur *et al*., 2004a; Fiebig, 2005) the studies are preferably carried out on single-crystalline samples oriented in an appropriate way. In this case, the

effects of minor phases, grain size and grain boundaries are excluded and the intrinsic behavior of the crystal lattice can be studied. Therefore, availability of single crystals of several tens of cubic millimeter size, high purity, and structural perfection is of great importance.

Single crystals of RMn_2O_5 compounds have been grown by a flux technique (cf. Section 3.2) at various solvent compositions (Wanklyn, 1972; Sanina, Sapozhnikova, Golovenchits and Morozov, 1988; Golovenchits, Morozov, Sanina and Sapozhnikova, 1992).

Rare-earth manganites have been grown firstly from Bi_2O_3 and from PbO/Bi_2O_3 solvents (Tamura, Sawaguch and Kikuchi, 1965). These fluxes attack Pt crucibles severely, and since Bi^{3+} is similar in size and charge to R^{3+}, it tends to replace R^{3+} in the crystal lattice up to several at% (Wanklyn, 1972; Sanina, Sapozhnikova, Golovenchits and Morozov, 1988). Better RMn_2O_5 crystals of higher purity have been grown from PbO/PbF_2 flux, which is less corrosive and does not show a noticeable solubility of the solvent elements in the RMn_2O_5 phase (Wanklyn, 1972). Single crystals of RMn_2O_5 of several cubic millimeters in size grown from $PbO/PbF_2/B_2O_3$ flux in a Pt crucible have been reported by Wanklyn (1972). Afterwards the same technology was repeated by almost all other groups for preparing single crystals of RMn_2O_5 compounds (Kagomiya *et al*., 2003; Inomata and Kohn, 1996; Gardner, Wilkinson, Forsyth and Wanklyn, 1988; Kobayashi *et al*., 2004a,b; Doi and Kohn, 1992; Kagomiya and Kohn, 1998; Kato, Kohn and Ishikawa, 1997; Koyata and Kohn, 1997; Koyata *et al*., 1996) and with small variations in the growth parameters (Golovenchits, Morozov, Sanina and Sapozhnikova, 1992; Sanina, Sapozhnikova, Golovenchits and Morozov, 1988). The flux was usually held at 1280–1300 °C for 10–15 h at ambient oxygen pressure and then slowly cooled down to 950–1000 °C. Crystals grow in the form of black pellets or cubes with a typical size of 0.5–5 mm (Hur *et al*., 2004a). No characterization of the crystal perfection, inclusions of other phases and crystal purity were reported so far.

There are only a few reports about doping of $RMn_{2-x}T_xO_5$ polycrystalline materials (Shim *et al*., 2004; Munoz *et al*., 2002) and to our knowledge nothing about doping of the single crystals.

4.7 Crystal growth activities of less-common magnetic alloys

Numerous multicomponent intermetallic rare earth–transition metal compounds with interesting magnetic properties have only minor practical interest and therefore we can cite only a few recent examples of crystal growth activities.

In 1994 intermetallic R–T borocarbides, RT_2B_2C (R = rare-earth elements, Sc, Y, or La; T = Ni, Pd) were discovered (Nagarajan *et al*., 1994). Depending on the rare-earth component the compounds with the tetragonal body-centered $ThCr_2Si_2$-type crystallographic structure can exhibit magnetic ordering, superconductivity, or an interesting interplay of both phenomena. Because of the high melting temperatures (>1500 °C) and the extreme reactivity of the melts with oxygen and practically all known crucible materials the crystal growth of these compounds is rather challenging. So far two methods of crystal growth were successfully applied. Crystals grown by the Ni_2B-flux method provide a basis for the determination of several anisotropic physical properties of quaternary RNi_2B_2C but suffer from the relatively small size and imperfections arising from the flux (Cho *et al*., 1995; Rathnayaha *et al*., 1997). For some of the compounds the FZ methods were applied for the growth of bulk crystals typically 6 mm in diameter and up to 40 mm in length (Takeya, Hirano and Kadowaki, 1996; Takeya, Kadowaki, Mirata and Mirano, 1996; Behr *et al*., 1999; Souptel *et al*., 2005; Behr and Löser, 2005). The $TbNi_2B_2C$ compound displays antiferromagnetic ordering below $T_N = 14$ K. The relevant pseudobinary section TbB_2C_2–$TbNi_2B_2C$–$TbNi_4B$ of the quaternary phase diagram with a peritectic temperature of $T_p = 1518$ °C is shown in Figure 30 (Behr *et al*., 1999). The incongruent melting of the RNi_2B_2C compound implies that the phase is only formed from the off-stoichiometric FZ composition. This corresponds to a TSFZ method in a stable growth process and limits the pulling velocities to $<2\,mm\,h^{-1}$. If stoichiometric feed rods are used, the initial part of the crystal contains inclusions of the TbB_2C_2 primary phase before the composition of the FZ gradually approaches the composition in the primary solidification range of $TbNi_2B_2C$ (Figure 31).

Single crystals of ternary R_2PdSi_3 (R = Ce, Gd, Tb, Dy, Ho, Er, Tm) compounds, which display hexagonal AlB_2-type structures, where successfully prepared both by the tri-arc CZ method (Saha *et al*., 1999, 2000) as well as by FZ methods in Ar atmosphere (Graw *et al*., 2000; Mazilu *et al*., 2005). The challenges for crystal growth are similar to the above-mentioned RNi_2B_2C compounds; however, the compounds are congruent melting and therefore enable higher growth velocities of $5–10\,mm\,h^{-1}$ (Graw *et al*., 2000; Mazilu *et al*., 2005). The compounds exhibit various types of incommensurate magnetic orderings, metamagnetic transitions, and a giant negative magnetoresistance if the critical temperatures are approached (Saha *et al*., 1999, 2000; Majumdar *et al*., 2000).

The availability of high-quality single crystals of R_2PdSi_3 compounds (R = Ce, Gd, Tb, Dy, Ho, Er, Tm) made it possible to study in more detail the magnetic properties of compounds of the same crystallographic structure but for

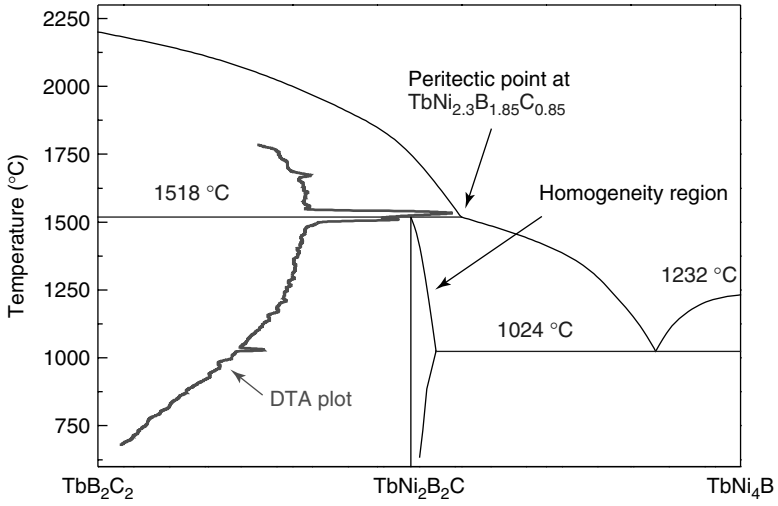

Figure 30. Tb–Ni–B–C phase diagram section TbB_2C_2–$TbNi_2B_2C$–$TbNi_4B$ relevant for $TbNi_2B_2C$ crystallization processes. Superposed is a differential thermal analysis (DTA) heating plot. (Courtesey of H. Bitterlich IFW, Dresden, 2000.)

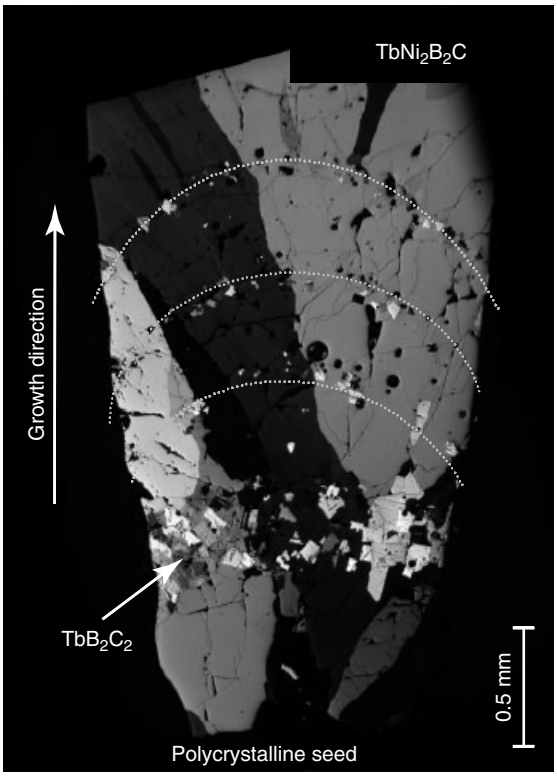

Figure 31. Metallographic image of a longitudinal section of a $TbNi_2B_2C$ crystal growth experiment with inclusions of the TbB_2C_2 primary phase. (Reproduced from Souptel *et al*., 2005, with permission from Elsevier. © 2005.)

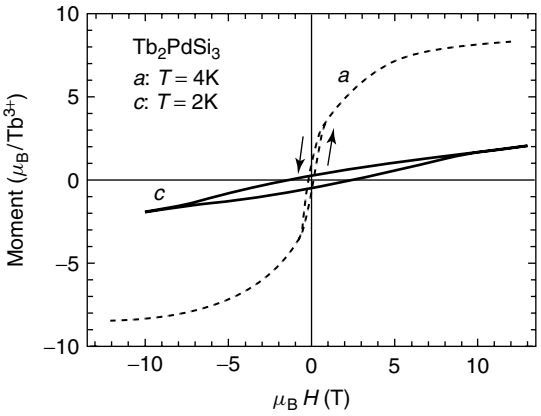

Figure 32. Tb_2PdSi_3 single-crystal magnetization data at $T = 2\,K$ for the c direction and at 4 K for the a direction well below the ordering temperature ($T_N = 23.6\,K$). (Reproduced from Frontzek *et al*., 2006, with permission from Elsevier. © 2006.)

rare-earth elements with different shapes of the 4f orbital (Frontzek *et al*., 2006). Investigations on these single crystals yielded anisotropic magnetic behavior in all substances, surprisingly even for the Gd compound, which is an S-state ion. In the high-temperature regime the magnetocrystalline anisotropy is dominated by the lowest order crystal electric field (CEF) term B_{02}. At lower temperatures CEF terms of higher order induce deviations from the Curie-Weiss law. Still, the B_{02} term dominates the CEF for Tb_2PdSi_3 and Er_2PdSi_3 and determines the magnetic easy direction in the ordered state, too (Figures 32 and 33). In contrast, the magnetic easy and magnetic hard directions in the ordered state are determined by higher order terms for Dy_2PdSi_3 and Ho_2PdSi_3. This leads to the crossing of the magnetic easy and hard direction in the paramagnetic state far above the Neél temperature in both compounds. The low ordering temperatures also indicate a delicate balance of magnetic exchange interaction and CEF.

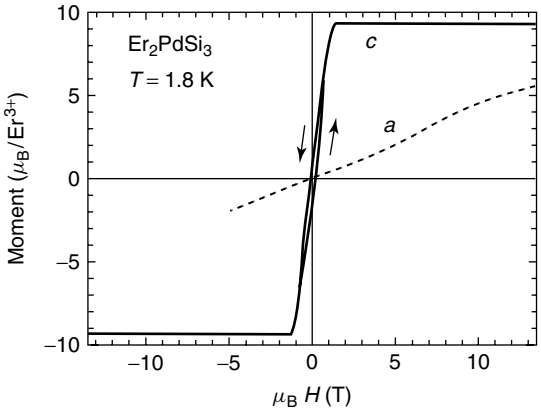

Figure 33. Er_2PdSi_3 single-crystal magnetization data at $T = 1.8$ K well below the ordering temperature ($T_N = 7$ K). (Reproduced from Frontzek *et al*., 2006, with permission from Elsevier. © 2006.)

5 CONCLUSIONS

In this chapter, we have summarized the crystal growth methods, single-crystal growth attempts, and some characteristic measurements of magnetic properties of various classes of magnetic materials: soft magnetic pure metals and alloys, highly anisotropic compounds for high-density magnetic recording media, rare earth–transition metal compounds for high-performance permanent magnets, highly magnetostrictive intermetallic compounds and FSMAs for magnetomechanical applications, magnetocaloric materials, selected intermetallic compounds for spintronics, multiferroic materials, and some other less-common magnetic compounds. The main purpose of single-crystalline specimens is to carry out measurements of intrinsic properties of magnetic materials or their constituent phases as a function of the crystallographic orientation and composition, but complex crystallographic structures or magnetic ordering of compounds and magnetization processes can also be revealed. Single crystals with optimum orientation of magnetostrictive materials and FSMAs are even prospective for commercial applications in high-performance devices.

It was shown in various examples for crystal growth of magnetic materials how phase diagram features of the alloy system, the required size of the single-crystalline specimen and its physical and chemical perfection determine the choice of the appropriate growth method and appropriate process parameters. For example, if a compound is formed by a peritectic reaction, slower growth rates are applied for crystal growth than for congruent melting compounds. In case of solid-state transformations below the melting temperature, high-quality crystals cannot be prepared directly from the melt, but strain-anneal techniques of the as-grown samples are required. Other important issues are the melt reactivity with crucible materials and the environmental gas, and volatile elements. Here container-less growth techniques (FZ melting) and special flux techniques, which operate at reduced temperature, can be useful. However, there are still a number of magnetic systems from which 'highly desirable' single crystals cannot be prepared or only with insufficient quality. In this case, single crystals with substituted elements of the same class of compounds (with the same crystallographic structure) turned out to be helpful to reveal important anisotropic magnetic features. Novel techniques, phase diagram studies as well as new ideas on growth processes are necessary for further progress in single-crystal preparation of some well-known and prospected new magnetic materials.

ACKNOWLEDGMENTS

The authors would like to express their gratitude to H. Bitterlich, M. Frontzek, A. Gebert, G. Graw, W. Gruner, I. Mazilu, S. Oswald, M. Rada, R. Scharfenberg, D. Souptel, and A. Teresiak for providing experimental data, text contributions, and helpful discussions. We thank S. Müller-Litvanyi, R. Müller, and S. Pichl for their engaged work in crystal characterization, J. Werner and J. Stöhr for technical assistance during the preparation of the manuscript, and T. Woodcock for carefully reading the text. The financial support of the Deutsche Forschungsgemeinschaft within the SFB 463 'Rare-Earth Intermetallics: Structure, Magnetism, and Transport' is grateful acknowledged.

REFERENCES

Abbundi, R. and Clark, A.E. (1978). Low-temperature magnetization and magnetostriction of single-crystal $TmFe_2$. *Journal of Applied Physics*, **49**, 1969–1971.

Alameda, J.M., Givord, D., Lemaire, R. and Lu, Q. (1981). Co energy and magnetization anisotropies in RCo_5 intermetallics between 4.2 K and 300 K. *Journal of Applied Physics*, **52**, 2079–2087.

da Andrade, E.N.C. and Henderson, C. (1951). The mechanical behaviour of single crystals of certain face centered cubic metals. *Philosophical Transactions of the Royal Society*, **A 244**, 177–202.

Andreev, A.V., Sechovsky, V., Kudrevatykh, N.V., *et al*. (1988). Magnetic properties of single crystals of $ErFe_{11}Ti$ and $LuFe_{11}Ti$. *Journal of the Less-Common Metals*, **144**, L21–L24.

Bachmann, K.J. (1973). A new apparatus for crystal growth from the melt under very high vacuum conditions. *Journal of Crystal Growth*, **18**, 13–19.

Bachmann, K.J. and Wakiyama, T. (1975). Czochralski pulling of cobalt and cobalt-rich cobalt/iron alloy crystals. *Journal of Crystal Growth*, **30**, 327–334.

Balakirev, V.F. and Golikov, Y.V. (2003). Heterogeneous phase equilibria in rare earth-Mn-O systems in air. *Inorganic Materials*, **39**, S1–S10.

Behr, G. (2000). Crystal growth. In *Semiconducting Silicides*, *Springer Series in Materials Science, Vol. 39*, Borisenko, V.E. (Ed.), Springer-Verlag: Berlin, pp. 137–179.

Behr, G., Bartsch, K., Jurisch, M., *et al*. (1985). Preparation of high-purity V_3Si single-crystals using a silicothermic reaction. *Crystal Research and Technology*, **20**, K93–K95.

Behr, G. and Löser, W. (2005). Floating zone crystal growth of multi-component rare earth-transition metal intermetallic compounds. In *Recent Research Developments in Crystal Growth* Pandalai, S.G. (Ed.), Transworld Research Network: Trivandrum, pp. 129–165, Vol. 4.

Behr, G., Löser, W., Graw, G., *et al*. (1999). Growth of RNi_2B_2C single crystals by r.f.–zone melting. *Journal of Crystal Growth*, **198/99**, 642–648.

Behrendt, D.R., Legvold, S. and Spedding, H. (1958). Magnetic properties of dysprosium single crystals. *Physical Review*, **109**, 1544–1547.

Bi, Y.J., Abell, J.S. and Ford, D. (1996). Crystal growth of iron-based compounds by the cold-crucible Czochralski technique. *Journal of Crystal Growth*, **166**, 298–302.

Buschow, K.H.J. (1991). New developments in hard magnetic materials. *Reports on Progress in Physics*, **54**, 1123–1213.

Cadogan, J.M., Li, H.S., Margarian, A., *et al*. (1994). New rare-earth intermetallic phases $R_3(Fe,M)_{29}X_N$ - (R = Ce, Pr, Nd, Sm, Gd, M = Ti, V, Cr, Mn, and X = H, N, C). *Journal of Applied Physics*, **76**, 6138–6143.

Chapon, L.C., Blake, G.R., Gutmann, M.J., *et al*. (2004). Structural anomalies and multiferroic behavior in magnetically frustrated $TbMn_2O_5$. *Physical Review Letters*, **93**, 177402/1–177402/4.

Cheng, S.F., Nadgorny, B., Bussmann, K., *et al*. (2001). Growth and magnetic properties of single crystal Co_2MnX (X = Si, Ge) Heusler alloys. *IEEE Transactions on Magnetics*, **37**, 2176–2178.

Chernenko, V.A., Cesari, E., Kokorin, V.V. and Vitenko, I.N. (1995). The development of new ferromagnetic shape-memory alloys in Ni-Mn-Ga system. *Scripta Metallurgica et Materialia*, **33**, 1239–1244.

Chernyshov, A.S., Tsokol, A.O., Tishin, A.M., *et al*. (2005). Magnetic and magnetocaloric properties and the magnetic phase diagram of single-crystal dysprosium. *Physical Review B*, **71**, 184410/1–184410/17.

Cho, B.K., Canfield, P.C., Miller, L.L., *et al*. (1995). Magnetism and superconductivity in single-crystal $ErNi_2B_2C$. *Physical Review B*, **52**, 3684–3695.

Clark, A.E. (1980). Magnetostrictive rare earth-Fe_2 compounds. In *Ferromagnetic Materials*, Wohlfarth, E.P. (Ed.), North-Holland: Amsterdam, pp. 531–589, Vol. 1.

Clark, A.E., Tamagawa, N. and Belson, H.S. (1972). Huge magnetocrystalline anisotropy in cubic rare earth Fe_2 compounds. *Physics Letters A*, **A 42**, 160–161.

Coelho, A.A., Mohan, C.V., Gama, S. and Kronmüller, H. (1996). The magnetic phase transition in $Fe_{17}Dy_2$ and $Fe_{23}Er_6$ single crystals. *Journal of Magnetism and Magnetic Materials*, **163**, 87–95.

Courtois, D., Amako, Y., Givord, D., *et al*. (1998a). Magnetic properties of single crystal $Y_3(Fe_{0.93}V_{0.07})_{29}$. *Journal of Magnetism and Magnetic Materials*, **177**, 995–996.

Courtois, D., Givord, D., Lambert-Andron, B., *et al*. (1998b). X-ray and magnetic single-crystal analysis of the crystallographic structure of the $Y_3(Fe_{0.933}V_{0.067})_{29}$ compound. *Journal of Magnetism and Magnetic Materials*, **189**, 173–182.

Cullen, J.R., Clark, A.R. and Hathaway, K.B. (1990). Magnetostrictive materials. In *Materials Science and Technology*, Cahn, R.W., Haasen, P. and Kramer, E.J. (Eds.), *Vol. 3, Electronic and Magnetic Properties of Metals and Ceramics*, Buschow, K.H.J. (Ed.), VCH: Weinheim, New York, Basel, Cambridge, pp. 529–565.

Doi, T. and Kohn, K. (1992). Magnetoelectric effect and simultaneous electric and magnetic transition in $EuMn_2O_5$. *Phase Transitions*, **38**, 273–284.

Du, J., Wu, G.H., Tang, C.C., *et al*. (1998). Effect of silicon substitution on the magnetic properties of Tb_2Fe_{17} single crystals. *Journal of Applied Physics*, **84**, 3305–3310.

Fedorova, O.M., Titova, S.G., Golikov, Y.V. and Balakirev, V.F. (2003). Heterogeneous equilibriums in the Ho-Mn-O and Er-Mn-O systems in air. *Russian Journal of Physical Chemistry*, **77**, 1886–1888.

Feigelson, R.S. (1985). Growth of fiber crystals. In *Crystal Growth of Electronic Materials*, Kaldis, E. (Ed.), North-Holland: Amsterdam, pp. 127–144.

Fiebig, M. (2005). Revival of the magnetoelectric effect. *Journal of Physics D: Applied Physics*, **38**, R123–R152.

Fort, D. (1991a). Crystal growth of rare earth metals using the floating zone method. *Journal of Crystal Growth*, **94**, 85–96.

Fort, D. (1991b). Solid-state-growth of rare earth metals and alloys adopting the hcp crystal-structure. *Journal of Alloys and Compounds*, **177**, 31–47.

Fort, D., Jones, D.W., Beaudry, B.J. and Gschneidner, K.A. Jr. (1981). Zone-refining of rare-earth-metals–lanthanum, cerium and gadolinium. *Journal of the Less-Common Metals*, **81**, 273–292.

Franse, J.J.M. and Radwanski, R.J. (1996). Intrinsic magnetic properties. In *Rare-Earth Iron Permanent Magnets*, Coey, J.M.D. (Ed.), Clarendon Press: Oxford, pp. 58–158.

Frontzek, M., Kreyssig, A., Doerr, M., *et al*. (2006). Magneto-crystalline anisotropy in R_2PdSi_3 (R = Tb, Dy, Ho, Er, Tm) single crystals. *Journal of Magnetism and Magnetic Materials*, **301**, 398–406.

Fu, B., Huebner, W., Trubelja, M.F. and Stubican, V.S. (1994). Synthesis and properties of strontium-doped yttrium manganite. *Journal of Materials Research*, **9**, 2645–2653.

Garcia-Landa, B., Algarabel, P.A. and Ibarra, M.R. (1997). Analysis of the intrinsic magnetic properties of R_2Fe_{17} single crystals (R = Y, Dy, Ho, Er). *Physical Review B*, **55**, 8313–8323.

Garcia-Landa, B., Algarabel, P.A., Ibarra, M.R., *et al*. (1995). Magnetization measurements on RE_2Fe_{17} single crystals. *Journal of Magnetism and Magnetic Materials*, **140–144**, 1085–1086.

Gardner, P.P., Wilkinson, C., Forsyth, J.B. and Wanklyn, B.M. (1988). The magnetic structures of the rare-earth manganates $ErMn_2O_5$ and $TbMn_2O_5$. *Journal of Physics C: Solid State Physics*, **21**, 5653–5661.

Gignoux, D., Givord, F. and Lemaire, R. (1975). Magnetic properties of single crystals of $GdCo_2$, $HoNi_2$, and $HoCo_2$. *Physical Review B*, **12**, 3878–3884.

Givord, D., Li, H.S. and Delabathie, R.P. (1984). Magnetic properties of $Y_2Fe_{14}B$ and $Nd_2Fe_{14}B$ single crystals. *Solid State Communications*, **51**, 857–860.

Givord, D., Li, H.S. and Moreau, J.M. (1984). Magnetic properties and crystal structure of $Nd_2Fe_{14}B$. *Solid State Communications*, **50**, 497–499.

Golovenchits, E.I., Morozov, N.V., Sanina, V.A. and Sapozhnikova, L.V. (1992). Correlation between the magnetic and dielectric properties of $EuMn_2O_5$ single crystals. *Fizika Tverdogo Tela*, **34**, 108–114.

Gorina, J.I., Kaljushnaia, G.A., Martovitsky, V.P., *et al*. (1998). Comparative study of Bi2201 single crystals grown from solution melt and in cavities formed in KCl. *Solid State Communications*, **108**, 275–278.

Graw, G., Bitterlich, H., Löser, W., *et al*. (2000). Constitution and crystal growth of RE_2TMSi_3 intermetallic compounds. *Journal of Alloys and Compounds*, **308**, 193–199.

Gschneidner, K.A. Jr. and Pecharsky, V.K. (1999). Magnetic refrigeration materials. *Journal of Applied Physics*, **85**, 5365–5368.

Gurin, V.N. and Korsukova, M.M. (1983). Crystal growth of refractory compounds from solutions in metallic melts. *Progress in Crystal Growth and Characterization of Materials*, **6**, 59–101.

Haertling, G.H. (1999). Ferroelectric ceramics: history and technology. *Journal of the American Ceramic Society*, **82**, 797–818.

Hayashi, S. and Komatsu, H. (1979). Preferred growth direction of Ni single crystals by floating-zone method. *Kristall Und Technik*, **14**, 761–764.

Hayashi, S., Ono, S. and Komatsu, H. (1978). Growth of cobalt single crystals by electron beam floating-zone method. *Kristall Und Technik*, **13**, 263–267.

Hirosawa, S., Matsuura, Y., Yamamoto, H., *et al*. (1985). Single-crystal measurements of anisotropy constants of $R_2Fe_{14}B$ (R=Y, Ce, Pr, Nd, Gd, Tb, Dy and Ho). *Japanese Journal of Applied Physics Part 2-Letters*, **24**, L803–L805.

Hirosawa, S., Matsuura, Y., Yamamoto, H., *et al*. (1986). Magnetization and magnetic anisotropy of $R_2Fe_{14}B$ measured on single crystals. *Journal of Applied Physics*, **59**, 873–879.

Hiroyoshi, H., Saito, N., Kido, G., *et al*. (1986). High-field magnetization of $R_2Fe_{14}B$ single crystals. *Journal of Magnetism and Magnetic Materials*, **54–57**, 583–584.

Hiroyoshi, H., Yamada, M., Saito, N., *et al*. (1987). High-field magnetization and crystalline field of $R_2Fe_{14}B$ and $R_2Co_{14}B$. *Journal of Magnetism and Magnetic Materials*, **70**, 337–339.

Hoffer, G. and Strnat, K. (1967). Magnetocrystalline anisotropy of 2 yttrium-cobalt compounds. *Journal of Applied Physics*, **38**, 1377–1378.

Holmes, A.T., Jaccard, D., Behr, G., *et al*. (2004). Unconventional superconductivity and non-Fermi liquid behaviour of ε -iron at high pressure. *Journal of Physics: Condensed Matter*, **16**, S1121–S1127.

Hu, B.P., Li, H.S., Coey, J.M.D. and Gavigan, J.P. (1990). Magnetization of a $Dy(Fe_{11}Ti)$ single-crystal. *Physical Review B*, **41**, 2221–2228.

Hur, N., Park, S., Sharma, P.A., *et al*. (2004a). Electric polarization reversal and memory in a multiferroic material induced by magnetic fields. *Nature*, **429**, 392–395.

Hur, N., Park, S., Sharma, P.A., *et al*. (2004b). Colossal magnetodielectric effects in $DyMn_2O_5$. *Physical Review Letters*, **93**, 107207/1–107207/4.

Hurle, D.T.J. (Ed.) (1994). *Handbook of Crystal Growth*, North-Holland: Amsterdam.

Inomata, A. and Kohn, K. (1996). Pyroelectric effect and possible ferroelectric transition of helimagnetic $GdMn_2O_5$, $TbMn_2O_5$ and YMn_2O_5. *Journal of Physics: Condensed Matter*, **8**, 2673–2678.

Inoue, K., Shima, H., Fujita, A., *et al*. (2006). Temperature dependence of magnetocrystalline anisotropy constants in the single variant state of $L1_0$-type FePt bulk single crystal. *Applied Physics Letters*, **88**, 102503/1–102503/3.

Jaccard, D., Holmes, A.T., Behr, G., *et al*. (2002). Superconductivity of ε-iron: complete resistivity transition. *Physics Letters A*, **299**, 282–286.

Kadomtseva, A.M., Popov, Y.F., Vorob'ev, G.P., *et al*. (2003). Induced by magnetic field spin reorientation in YMn_2O_5. *Physica B: Condensed Matter*, **329**, 856–857.

Kagomiya, I., Kimura, H., Noda, Y. and Kohn, K. (2001). Incommensurate antiferromagnetic ordering of ferroelectric YMn_2O_5. *Japanese Journal of Applied Physics*, **70**(Suppl. A), 145–147.

Kagomiya, I. and Kohn, K. (1998). Ferroelectric transitions of $LuMn_2O_5$. *Ferroelectrics*, **219**, 805–812.

Kagomiya, I., Matsumoto, S., Kohn, K., *et al*. (2003). Lattice distortion at ferroelectric transition of YMn_2O_5. *Ferroelectrics*, **286**, 889–896.

Kato, S., Kohn, K. and Ishikawa, M. (1997). Ferroelectricity of holmium manganese oxide $HoMn_2O_5$ with helical spin ordering. *Ferroelectrics*, **203**, 323–334.

Kato, H., Shiomi, J., Koide, T., *et al*. (1995). High-field magnetization and spin reorientation in $Sm_2(Fe_{1-x}Al_x)_{17}$ single-crystals. *Journal of Alloys and Compounds*, **222**, 62–66.

Kawald, U., Zemke, W., Bach, H., *et al*. (1989). Elastic constants and martensitic phase transitions in FePt and FeNiPt invar alloys. *Physica B*, **161**, 72–74.

Khomskii, D.I. (2006). Multiferroics: different ways to combine magnetism and ferroelectricity. *Journal of Magnetism and Magnetic Materials*, **306**, 1–8.

Kitayama, K., Ohno, H., Ide, Y., *et al*. (2002). Phase equilibrium in the system Ln-M-O - III. Ln = Gd at 1100 C. *Journal of Solid State Chemistry*, **166**, 285–291.

Kneller, E. (1962). *Ferromagnetismus*, Springer-Verlag: Berlin.

Kobayashi, S., Osawa, T., Kimura, H., *et al*. (2004a). 2D-to-1D modulated-to-lock in successive magnetic phase transitions associated with ferroelectricity in $ErMn_2O_5$. *Journal of the Physical Society of Japan*, **73**, 1031–1035.

Kobayashi, S., Osawa, T., Kimura, H., *et al*. (2004b). Neutron diffraction study of successive magnetic phase transitions in ferroelectric $TbMn_2O_5$. *Journal of the Physical Society of Japan*, **73**, 3439–3443.

Koon, N.C., Das, B.N., Rubinstein, M. and Tyson, J. (1985). Magnetic properties of $R_2Fe_{14}B$ single crystals. *Journal of Applied Physics*, **57**, 4091–4093.

Koyata, Y. and Kohn, K. (1997). Low-temperature phase transition in $ErMn_2O_5$. *Ferroelectrics*, **204**, 115–124.

Koyata, Y., Nakamura, H., Iwata, N., *et al*. (1996). Electric and magnetic low-temperature phase transitions of $YbMn_2O_5$. *Journal of the Physical Society of Japan*, **65**, 1383–1386.

Kuhrt, C., Schultz, L., Schnitzke, K., *et al*. (1991). High-temperature compressive plastic deformation of $Nd_2Fe_{14}B$ single crystals. *Applied Physics Letters*, **59**, 1418–1420.

Lee, R.W. (1985). Hot-pressed neodymium-iron-boron magnets. *Applied Physics Letters*, **46**, 790–791.

Liang, B. and Lin, C.T. (2002). On the growth of underdoped $Bi_2Sr_2CaCu_2O_{8+\delta}$ single crystals by TSFZ method. *Journal of Crystal Growth*, **237**, 756–761.

Lima, A.L., Gschneidner, K.A. Jr. and Pecharsky, V.K. (2004). Anisotropic materials: a way to increase the efficiency of magnetic refrigeration. *Journal of Applied Physics*, **96**, 2164–2168.

Lograsso, T.A., Schlagel, D.L. and Pecharsky, A.O. (2005). Synthesis and characterization of single crystalline $Gd_5(Si_xGe_{1-x})_4$ by the Bridgman method. *Journal of Alloys and Compounds*, **393**, 141–146.

Lottermoser, T., Lonkai, T., Amann, U., *et al*. (2004). Magnetic phase control by an electric field. *Nature*, **430**, 541–544.

Majumdar, S., Sampathkumaran, E.V., Paulose, P.L., *et al*. (2000). Anisotropic giant magnetoresistance, magnetocaloric effect and magnetic anomalies in single crystalline Tb_2PdSi_3. *Physical Review B*, **62**, 14207–14211.

Massalski, T.B., Okamoto, H., Subramarian, P.R. and Kacprzak, L. (Eds.) (1990). *Binary Alloy Phase Diagrams*, Second Edition, American Society for Metals: Metals Park, Vols. 1–2.

Maykov, V.V., Yermakov, A.Y., Ivanova, G.V., *et al*. (1989). Influence of long range order degree on magnetic properties of CoPt and FePd single crystals. *Fizika Metallov i Metallovedenie*, **67**, 79–84.

Mazilu, I., Frontzek, M., Löser, W., *et al*. (2005). Single crystal growth of the Er_2PdSi_3 intermetallic compound. *Journal of Crystal Growth*, **275**, e103–e107.

McMasters, O.D., Holland, G.E. and Gschneider, K.A. Jr. (1978). Single crystal growth by horizontal levitation zone melting method. *Journal of Crystal Growth*, **43**, 577–583.

McMasters, O.D., Verhoeven, J.D. and Gibson, E.D. (1986). Preparation of Terfenol-D by float zone solidification. *Journal of Magnetism and Magnetic Materials*, **54–57**, 849–850.

Mei, W., Okane, T., Umeda, T. and Zhou, S.Z. (1997). Directional solidification of Tb-Dy-Fe magnetostrictive alloy. *Journal of Alloys and Compounds*, **248**, 151–158.

Mei, W., Yoshizumi, M., Okane, T. and Umeda, T. (1997). Crystal growth of giant magnetostrictive Tb-Dy-Fe alloy. *Journal of Alloys and Compounds*, **258**, 34–38.

Milstein, J.B., Koon, N.C., Johnson, L.R. and Williams, C.M. (1974). Growth of single crystals of cubic laves phase compounds in Ho-Tb-Fe system. *Materials Research Bulletin*, **9**, 1617–1622.

Munoz, A., Alonso, J.A., Casais, M.T., *et al*. (2002). Magnetic structure and properties of $BiMn_2O_5$ oxide: a neutron diffraction study. *Physical Review B*, **65**, 144424/1–144424/8.

Munoz, A., Alonso, J.A., Martinez-Lope, M.J. and Martinez, J.L. (2004). Synthesis, structural, and magnetic characterization of a new ferrimagnetic oxide: $YFeMnO_5$. *Chemistry of Materials*, **16**, 4087–4094.

Murray, S.J., Marioni, M., Allen, S.M., *et al*. (2000). 6% magnetic-field-induced strain by twin-boundary motion in ferromagnetic Ni-Mn-Ga. *Applied Physics Letters*, **77**, 886–888.

Nagarajan, G., Mazumdar, G., Hossain, Z., *et al*. (1994). Bulk superconductivity at an elevated temperature ($T_c \approx 12$ K) in a nickel containing alloy system Y-Ni-B-C. *Physical Review Letters*, **72**, 274–277.

Nigh, H.E. (1963). A method for growing rare-earths single crystals. *Journal of Applied Physics*, **34**, 3323–3324.

Ohkoshi, M., Kobayashi, H., Katayama, T., *et al*. (1977). Spin reorientation in $DyCo_5$. *Physica B & C*, **86**, 195–196.

Ono, Y., Shiomi, J., Kato, H., *et al*. (1998). X-ray diffraction study of $Sm_2(Fe_{1-x}Al_x)_{17}$ single crystals with x = 0.058, 0.081. *Journal of Magnetism and Magnetic Materials*, **187**, 113–116.

Oswald, S., Mazilu, I., Fähler, S., *et al*. (2005). SIMS measurements of oxygen content in the $Nd_2Fe_{14}B$ phase. *Journal of Magnetism and Magnetic Materials*, **290**, 1240–1242.

Pecharsky, V.K. and Gschneidner, K.A. Jr. (1999). Magnetocaloric effect and magnetic refrigeration. *Journal of Magnetism and Magnetic Materials*, **200**, 44–56.

Pfann, W.G. (1952). Principles of zone-melting. *Journal of Metals*, **4**, 747–753.

Pfann, W.G. (1988). Zone melting. In *Techniques of Melt Crystallization*, Sloan, G.J. and McGhie, A.R. (Eds.), Second Edition, John Wiley & Sons: New York.

Rada, M., Gebert, A., Mazilu, I., *et al*. (2006). Corrosion studies on highly textured Nd-Fe-B sintered magnets. *Journal of Alloys and Compounds*, **415**, 111–120.

Rathnayaha, K.D.D., Bhatnagar, A.K., Parasiris, A., *et al*. (1997). Transport and superconducting properties of RNi_2B_2C (R = Y, Lu) single crystals. *Physical Review B*, **55**, 8506–8519.

Ringpfeil, H., Wiesinger, D. and Fischer, K. (1962). Herstellung von Einkristallen vorwiegend magnetischer und hochschmelzender Metalle und Legierungen. *Abhandlungen der Deutschen Akademic der Wissenschaften zu Berlin, Klasse für Mathematik, Physik and Technik*, **6**, 25–30.

Rutter, J.W. and Chalmers, B. (1953). A prismatic substructure formed during solidification of metals. *Canadian Journal of Physics*, **31**, 15–39.

Sagawa, M., Fujimura, S., Togawa, N., *et al*. (1984). New material for permanent magnets on a base of Nd and Fe. *Journal of Applied Physics*, **55**, 2083–2087.

Saha, S.R., Sugawara, H., Matsuda, T.D., *et al*. (1999). Magnetic anisotropy, first-order-like metamagnetic transitions, and large negative magnetoresistance in single-crystal Gd_2PdSi_3. *Physical Review B*, **60**, 12162–12165.

Saha, S.R., Sugawara, H., Matsuda, T.D., *et al*. (2000). Magnetic, thermal, and transport properties of single crystals of antiferromagnetic Kondo-lattice Ce_2PdSi_3. *Physical Review B*, **62**, 425–429.

Saito, K. and Kohn, K. (1995). Magnetoelectric effect and low-temperature phase transitions of $TbMn_2O_5$. *Journal of Physics: Condensed Matter*, **7**, 2855–2863.

Samata, H., Fujiwara, N., Nagata, Y., *et al*. (1998). Magnetic anisotropy of new intermetallic compound $SmFe_7$. *Japanese Journal of Applied Physics Part 1-Regular Papers Short Notes and Review Papers*, **37**, 3290–3294.

Samata, H., Kasai, R., Taniguchi, T. and Nagata, Y. (2003). Al substitution effects to the magnetic properties of the compounds in the Sm-Fe system. *Journal of Solid State Chemistry*, **171**, 339–344.

Samata, H., Sakamoto, K., Yashiro, S. and Nagata, Y. (2001). Crystal growth of rare earth-iron intermetallic compounds by the flux-creep-up method. *Journal of Crystal Growth*, **229**, 482–486.

Samata, H., Uchida, T., Shimizu, Y., *et al*. (2001). Magnetic properties of Sm_6Fe_{23} crystal. *Journal of Alloys and Compounds*, **322**, 37–41.

Sanina, V.A., Sapozhnikova, L.M., Golovenchits, E.I. and Morozov, N.V. (1988). Series of phase-transitions in $EuMn_2O_5$. *Fizika Tverdogo Tela*, **30**, 3015–3023.

Sauveur, A. (1912). Note on the crystalline growth of ferrite below its thermal critical range. *Proceedings of the International Association for Testing Materials London*, **2**(II.6), 11.

Scheel, H.J. and Elwell, D. (1972). Stable growth rates and temperature programming in flux growth. *Journal of Crystal Growth*, **12**, 153–161.

Schlagel, D.L., Wu, Y.L., Hang, W. and Lograsso, T.A. (2000). Chemical segregation during bulk single crystal preparation of Ni–Mn–Ga ferromagnetic shape memory alloys. *Journal of Alloys and Compounds*, **312**, 77–85.

Schmid, H. (1994a). Magnetic ferroelectric materials. *Bulletin of Materials Science*, **17**, 1411–1414.

Schmid, H. (1994b). Multi-ferroic magnetoelectrics. *Ferroelectrics*, **162**, 317–338.

Schneider, G., Henig, E.Th., Petzow, G. and Stadelmaier, H.H. (1986). Phase relations in the system Nd-Fe-B. *Zeitschrift fur Metailkunde*, **77**, 755–761.

Šestak, B. (1957). Facility for producing single crystals of metals (in Czech). *Ceskoslovensko Casopis Fysiku*, **7**, 234–241.

Shim, I.B., Yeom, J.H., Choi, K.R., *et al*. (2004). Magnetic properties of helimagnetic $YMn_{2-x}(Fe,Co)_xO_{5-\delta}$ ($0.0 < x < 1.0$) for the room temperature ferroism. *Journal of Applied Physics*, **95**, 7070–7072.

Shima, H., Oikawa, K., Fujita, A., *et al*. (2004a). Magnetic anisotropy and mangnetostriction in $L1_0$ FePd alloy. *Journal of Magnetism and Magnetic Materials*, **272–76**, 2173–2174.

Shima, H., Oikawa, K., Fujita, A., *et al*. (2004b). Lattice axial ratio and large uniaxial magnetocrystalline anisotropy in $L1_0$-type FePd single crystals prepared under compressive stress. *Physical Review B*, **70**, 224408/1–224408/7.

Shima, H., Oikawa, K., Fujita, A., *et al*. (2005). Large magnetocrystalline anisotropy energy of $L1_0$-type $Co_{100-x}Pt_x$ bulk single crystals prepared under compressive stress. *Applied Physics Letters*, **86**, 112515/1–112515/3.

Shimizu, K., Furomoto, T., Takeda, S., *et al*. (2001). Superconductivity in the non-magnetic state of iron under pressure. *Nature*, **416**, 316–318.

Sinnema, S., Franse, J.J.M., Menovsky, A. and Radwanski, R.J. (1986). High-field magnetization studies on single crystalline Dy_2Co_{17}. *Journal of Magnetism and Magnetic Materials*, **54–57**, 1639–1640.

Sinnema, S., Verhoef, R., Menovsky, A.A. and Franse, J.J.M. (1987). Crystal growth of R_2T_{17} and $R_2Fe_{14}B$ intermetallics (R = Rare Earth, T = Co, Fe). *Journal of Crystal Growth*, **85**, 248–251.

Smolenski, G.A. and Chupis, I.E. (1982). Segnetomagnetics. *Uspekhi Fizicheskikh Nauk*, **137**, 415–448.

Snodgrass, J.D. and McMasters, O.D. (1997). Optimized TERFENOL-D manufacturing processes. *Journal of Alloys and Compounds*, **258**, 24–29.

Souptel, D., Behr, G., Kreyssig, A. and Löser, W. (2005). Growth features of $RENi_2B_2C$ (RE = Y, Ho, Tb) single crystals. *Journal of Crystal Growth*, **276**, 652–662.

Souptel, D., Behr, G., Löser, W., *et al*. (2005). Crystal growth and perfection of $RENi_2B_2C$ (RE = Ho, Tb, Y). *Journal of Crystal Growth*, **275**, e91–e95.

Sousa, J.B., Moreira, J.M., Braga, M.E., *et al*. (1985). Search of commensurate locking effect in the helical magnetic structures of Tb and Dy single crystals. *Journal of Magnetism and Magnetic Materials*, **49**, 219–224.

Sozinov, A., Likhachev, A.A., Lanska, N. and Ullakko, K. (2002). Giant magnetic-field-induced strain in NiMnGa seven-layered martensitic phase. *Applied Physics Letters*, **80**, 1746–1748.

Strnat, K., Hoffer, G., Olson, J., *et al*. (1967). A family of new cobalt-base permanent magnet materials. *Journal of Applied Physics*, **38**, 1001–1002.

Swets, D.E. (1986). Growth of single crystals of $Nd_2Fe_{14}B$. *Journal of Crystal Growth*, **75**, 277–280.

Takeya, H., Hirano, T. and Kadowaki, K. (1996). Single crystal growth of quaternary superconductor YNi_2B_2C by floating zone method. *Physica C*, **256**, 220–226.

Takeya, H., Kadowaki, K., Mirata, K. and Mirano, T. (1996). Single crystal growth and physical properties of YNi_2B_2C and $HoYNi_2B_2C$. *Journal of Alloys and Compounds*, **245**, 94–99.

Tamura, H., Sawaguch, E. and Kikuchi, A. (1965). Ferroelectric hysteresis character of $YMnO_3$. *Japanese Journal of Applied Physics*, **4**, 666–671.

Tanaka, K., Ichitsubo, T. and Koiwa, M. (2001). Effect of external fields on ordering of FePd. *Materials Science and Engineering A-Structural Materials Properties Microstructure and Processing*, **312**, 118–127.

Tang, H., Pecharsky, A.O., Schlagel, D.L., *et al*. (2003). Magnetic field induced phase transitions in $Gd_5(Si_{1.95}Ge_{2.05})$ single crystal and the anisotropic magnetocaloric effect. *Journal of Applied Physics*, **93**, 8298–8300.

Thang, P.D., Thuy, N.P., Khuong, L.V.D., *et al*. (1998). The temperature dependence of the magnetization in the basal plane of R-T single crystals. *Journal of Magnetism and Magnetic Materials*, **177**, 1099–1100.

Tiller, W.A., Jackson, K.A., Rutter, J.W. and Chalmers, B. (1953). The redistribution of solute atoms during the solidification of metals. *Acta Metallurgica*, **1**, 428–437.

Tishin, A.M., Gschneidner, K.A. Jr. and Pecharsky, V.K. (1999). Magnetocaloric effect and heat capacity in the phase transition region. *Physical Review B*, **59**, 503–511.

Ullakko, K., Huang, J.K., Kantner, C., *et al*. (1996). Large magnetic-field-induced strains in Ni_2MnGa single crystals. *Applied Physics Letters*, **69**, 1966–1968.

Vaněk, P. and Kadečková, S. (1979). Growth striations in Fe-3at%Si single crystals grown by floating zone melting at various growth rates. *Journal of Crystal Growth*, **47**, 458–462.

Vaněk, P., Kadečková, S., Jurisch, M. and Löser, W. (1983). Melt convection driven by electrodynamic forces from induction heating. *Journal of Crystal Growth*, **63**, 191–196.

Verhoeven, J.D., Gibson, E.D., McMasters, O.D. and Baker, H.H. (1987). The growth of single-crystal Terfenol-D crystals. *Metallurgical Transactions A-Physical Metallurgy and Materials Science*, **18**, 223–231.

Wanklyn, B.M. (1972). Flux growth of some complex oxide materials. *Journal of Materials Science*, **7**, 813–821.

Weise, G. and Owsian, G. (1976). Preparation of highly pure iron by vapor deposition. *Kristall Und Technik*, **11**, 729–737.

Wilke, K-T. and Bohm, J. (1988). *Kristallzüchtung*, VEB Deutscher Verlag der Wissenschaften: Berlin.

Wilkinson, C., Sinclair, F., Gardner, P., *et al*. (1981). The antiferromagnetic structure of $DyMn_2O_5$ at 4.2 K. *Journal of Physics C: Solid State Physics*, **14**, 1671–1683.

Wu, G.H., Hu, B.P., Gao, S.X., *et al*. (1998). Growth and spin reorientation transition of $Tb(Fe,Ti)_{12}$ single crystal. *Journal of Crystal Growth*, **192**, 417–422.

Yang, C.P., Wang, Y.Z., Wu, G.H., *et al*. (1999). Magnetic properties of the novel $Y_3(Fe,Cr)_{29}$ single crystal. *Journal of Physics: Condensed Matter*, **11**, 6843–6849.

Yermakov, A.Y. and Maykov, V.V. (1989). Temperature dependence of magnetocrystalline anisotropy and spontaneous magnetization CoPt and FePd single-crystals. *Fizika Metallov i Metallovedenie*, **67**, 79–84.

Zhang, M.C., Gao, X.X., Zhou, S.Z. and Shi, Z.H. (2004). Magnetostrictive properties and microstructure of Tb-Dy-Fe alloy with ⟨113⟩ crystal orientation. *Journal of Alloys and Compounds*, **385**, 309–311.

FURTHER READING

Alonso, J.A., Casais, M.T., Martinez Lope, M.J. and Rasines, I. (1997). High oxygen pressure preparation, structural refinement, and thermal behavior of RMn_2O_5 (R = La, Pr, Nd, Sm, Eu). *Journal of Solid State Chemistry*, **129**, 105–112.

Behr, G., Werner, J., Weise, G., *et al*. (1997). Preparation and properties of high-purity β-$FeSi_2$ single crystals. *Physica Status Solidi A: Applied Research*, **160**, 549–556.

Clark, A.E. and Savage, H.T. (1975). Giant magnetically induced changes in elastic-moduli in $Tb_3Dy_7Fe_2$. *IEEE Transactions on Sonics and Ultrasonics*, **22**, 50–52.

Polyakov, V., Plakhty, V., Bonnet, M., *et al*. (2001). Coupled magnetic and structural transitions in $EuMn_2O_5$ as studied by neutron diffraction and three-dimensional polarization analysis. *Physica B*, **297**, 208–212.

Souptel, D., Behr, G., Ivanenko, L., *et al*. (2002). Floating zone growth and characterization of semiconducting Ru_2Si_3 single crystals. *Journal of Crystal Growth*, **244**, 296–304.

Souptel, D., Behr, G., Löser, W., *et al*. (2004). $CeSi_{2-\delta}$ single crystals: growth features and properties. *Journal of Crystal Growth*, **269**, 606–616.

Tabata, H. and Hirano, T. (1988). Growth of $MoSi_2$ single crystals by the floating zone method. *Journal of the Japan Institute of Metals*, **52**, 1154–1158.

Wanklyn, B.M. (1969). The flux growth of single crystals of rare earth perovskites (orthoferrites, orthochromites and aluminates). *Journal of Crystal Growth*, **5**, 323–328.

Amorphous Alloys

Hywel A. Davies and Michael R.J. Gibbs
University of Sheffield, Sheffield, UK

1 INTRODUCTION AND BACKGROUND

Amorphous alloys, also frequently referred to as *metallic glasses*, *noncrystalline alloys*, or *glassy alloys*, are metallic materials that are devoid of long-range atomic order. They can be produced by several different techniques, most of which involve rapid solidification from the liquid or gaseous state. However, other, very different routes, including (i) mechanical alloying of crystalline precursor materials, either elemental or partly prealloyed; (ii) mechanical milling of prealloyed crystalline precursors; (iii) high energy ion or neutron bombardment of crystalline alloys; (iv) electroless deposition from solution; or (v) electrodeposition from solution, have been successfully employed to produce amorphous alloys.

Handbook of Magnetism and Advanced Magnetic Materials. Edited by Helmut Kronmüller and Stuart Parkin. Volume 4: *Novel Materials*. ISBN: 978-0-470-02217-7.

This overview is concerned specifically with soft ferromagnetic amorphous alloys. It is restricted very largely to material produced in ribbon forms by rapid solidification from the liquid state, except for, where necessary for the purposes of comparison, brief mention of materials produced by other routes. These soft ferromagnetic glassy alloy ribbon materials, often described by their trade names 'METGLAS®' or 'VITROVAC®', together with the nanocomposite ultrasoft magnetic 'FINEMET®' and 'VITROPERM®' alloys and the nanocrystalline melt spun rare earth (RE)–iron–boron-based hard magnetic alloys, having the trade name 'MQP®', are among the most successful examples of the commercial exploitation of rapid solidification technology in the production of advanced alloys.

The first explicit report of a ferromagnetic amorphous alloy was for sputter-deposited thin-film Co–Au by Mader and Nowick (1965), following the earlier theoretical prediction of amorphous ferromagnetism (Gubanov, 1960). The first reported ferromagnetic melt-quenched glassy alloys were $Pd_{12}Co_{68}Si_{20}$ (Tsuei and Duwez, 1966) and $Fe_{83}P_{10}C_7$ (Duwez and Lin, 1967), produced by a piston and anvil splat-quenching technique. The discovery of other, more favorable, ferrous alloy glass-forming compositions, particularly those based on (Fe, Co, Ni)SiB, and the demonstration of the excellent soft magnetic properties of alloy glasses after annealing to remove the quenched-in stresses (Luborsky *et al*., 1975) stimulated rapid growth of scientific and technological interest in the materials. With the utilization of the single-roll melt-spinning technique for producing thin ribbon in extended lengths (Liebermann and Graham, 1976; Kavesh, 1978), the pace of development accelerated greatly in the late 1970s and 1980s. A key step in the commercial exploitation of metallic glasses, pioneered by Allied Chemical in the United States, was the development of the planar flow casting (PFC) process (Narasimhan, 1979), which

facilitated the continuous casting of glassy alloy ribbon in uniform widths up to 300 mm and with good thickness tolerance down to as low as 15 μm but, more typically, 25–30 μm. This led to the use of FeSiB-based glassy alloys for the cores of toroidally wound distribution transformers, typically of capacity 25 kVA, on the basis of significantly lower core losses and exciting currents than for the long entrenched Fe-3wt%Si crystalline materials (Smith, 1993; Hasegawa, 2004). Similarly, very low magnetostriction CoFeSiB-based alloy glass ribbons have been widely exploited, where very high permeabilities μ and low coercivities H_c are required, as in small high-frequency transformers, inductors, and chokes, in competition with the commercially established Fe–80Ni crystalline permalloys. Another major application of the alloy glass ribbons has been for security tags in stores and libraries. These aspects of the magnetic properties and applications are discussed in Sections 7 and 8.

Amorphous FeSiB- and FeZrB-based alloys with, in the former case, small additions of Cu and Nb are also used in ribbon forms as precursors for the evolution by heat treatment of exceptionally low H_c and high μ nanocomposite structures (Yoshizawa, Oguma and Yamauchi, 1988; Suzuki *et al*., 1990). These are based on a 70/30 vol% mix of Fe–Si or Fe nanocrystallites in an untransformed residual amorphous matrix. This class of alloys is reviewed by Herzer in **Soft Magnetic Materials – Nanocrystalline Alloys, Volume 4**.

In the early 1980s, a variant of melt spinning, involving the casting of a fine stream (typically ~100 μm diameter) of glass-forming alloy melt into a rotating bath of water, was adopted in the production of amorphous ferromagnetic round section wire (Ohnaka, Fukusako and Ohmichi, 1982). These wires, because of their particular cylindrical geometry and magnetic domain structure, can have magnetic hysteresis characteristics substantially different from those of amorphous alloy ribbons of the same compositions. Even finer glassy alloy filaments, with diameters down to below 5 μm and known as *microwires*, can be produced by a variant of the Taylor wire process (Taylor, 1924). Here, the molten alloy, encased within a viscous molten silicate glass jacket, is drawn down by a continuous process and vitrified by water quenching. The stress induced by the differential thermal contraction of the alloy core and silicate sheath during solidification also imparts unique magnetic characteristics. These amorphous wires and microwires can be exploited for practical devices such as magnetic field or stress sensors. The processing and magnetic properties of such wires are reviewed by Vazquez in **Advanced Magnetic Microwires, Volume 4**.

Recently, several multicomponent ferromagnetic alloys have been shown to be glass forming at low rates of cooling such that they can be vitrified in thicknesses >1 mm (Inoue, 1997, 2000). This class of alloys, which offers the possibility of producing soft magnetic cores in a wide range of shapes by direct casting from the melt, is reviewed by Inoue *et al*. in **Soft Magnetic Bulk Glassy and Bulk Nanocrystalline Alloys, Volume 4**.

2 FORMATION AND GENERAL CHARACTERISTICS OF GLASSY ALLOYS

2.1 Glass-forming criteria and structure

A noncrystalline solid formed by continuous cooling from the equilibrium liquid state is known as a *glass* in the classical sense of the word. Such vitrification necessitates cooling to below the glass transition temperature T_g at a rate that is sufficiently high to avoid the development of the long-range order that characterizes the crystalline state. It is unlikely that a *pure* metal could be vitrified to a stable glass from the liquid state, and additions of one or more solute elements are required in order to render the glass resistant to crystallization at room temperature and above. The structure, after vitrification, can be described (Polk, 1972) as a dense random packing of hard spheres. However, it is not entirely random and retains a significant degree of *short-range* order (SRO), both topological and chemical, from the equilibrium liquid state. The chemical SRO was first explicitly demonstrated experimentally by Sadoc and Dixmier (1976) for a CoP alloy, on the basis of atomic pair correlation functions, derived from Fourier transforms of neutron and X-ray diffraction data; the results clearly showed the absence of P–P pairs at the distance expected from the P atom diameter. The SRO can be enhanced or modified by elevated temperature annealing of the glassy structure, as is evident from the fact that this causes mechanical embrittlement in certain compositions, particularly Fe-based alloys (Davis, 1976). This evidently results from reduction in quenched-in 'free volume' through short-range diffusive displacements, particularly of the small metalloid atoms. The effects of annealing on magnetic properties, especially including field and stress annealing, provide further evidence of changes in the local order (Luborsky and Walter, 1977a,b); in fact, such field and stress annealing evidently result in *directional* chemical ordering of the metal–metalloid bonds.

In addition to thermally stabilizing the glassy state, the additions of suitable solute elements in appropriate concentrations to a base metal are a prerequisite for increasing the glass-forming ability (GFA) such that the glassy phase can be produced in tractable and useful section thicknesses. Thus, the GFA can be expressed either as the critical cooling rate for glass formation R_c or the minimum thickness of fully

glassy phase x_c that can be formed by a particular quenching process (Davies, 1978, 1983). The aim in rendering an alloy readily glass forming (RGF) is to depress the liquidus temperature T_l to a level well below the weighted mean melting temperature for the pure component elements or of the pure base metal and any intermediate high-melting-point compound phase. Here, we define an RGF composition as one having an $R_c \leq 10^6\,\mathrm{K\,s^{-1}}$, which corresponds to a fully glassy phase having a section thickness formed by chill block melt spinning of $>15-20\,\mu\mathrm{m}$. Hence, compositions at or near deep eutectics, such as those that commonly occur in late transition metal–metalloid (LTM–Met) systems, are generally RGF. Examples of deep eutectics in ferromagnetic binary alloy systems include (Fe, Co, or Ni)–(P or B), with eutectic compositions at approximately 20 wt% Met, and these are all RGF. The NiP and NiB alloy glasses are essentially nonmagnetic at room temperature because their Curie temperatures T_C are close to, or below, ambient. Examples of RGF binary ferromagnetic LTM–Met alloys with T_C well above room temperature are Fe-(15–25)at%B and Co-(16–25)at%P.

Addition of a second LTM and/or of a second or more metalloid element tends to enhance the GFA by further depressing the liquidus temperature and preferably also by increasing T_g. A corollary of this is that the composition range for RGF tends to be widened. Examples of such multicomponent ferromagnetic alloy glasses are $Fe_{40}Ni_{40}B_{20}$, $Fe_{78}Si_9B_{13}$, and $Co_{75}Fe_4Si_5B_{16}$. An example of the influence on GFA of Si additions to FeB alloys is given in Figure 1, where some isometrics for various values of critical ribbon thickness of glassy phase x_c, accurately determined from magnetic coercivity measurements, are plotted for the FeBSi ternary system (Luborsky, Reeve, Davies and Liebermann, 1982). This clearly shows how the composition range for RGF of ~14–22 at%B for the binary Fe–B alloys, centered approximately about the eutectic at ~17 at%B, is substantially widened on substitution of Si. The maximum GFA corresponds to a ternary eutectic at $Fe_{75}Si_{10}B_{17}$ with x_c being about 42 μm for ribbon spun on a Cu roll and ~60 μm when spun on a steel roll, for which the thermal contact with the melt is better because of a higher surface temperature.

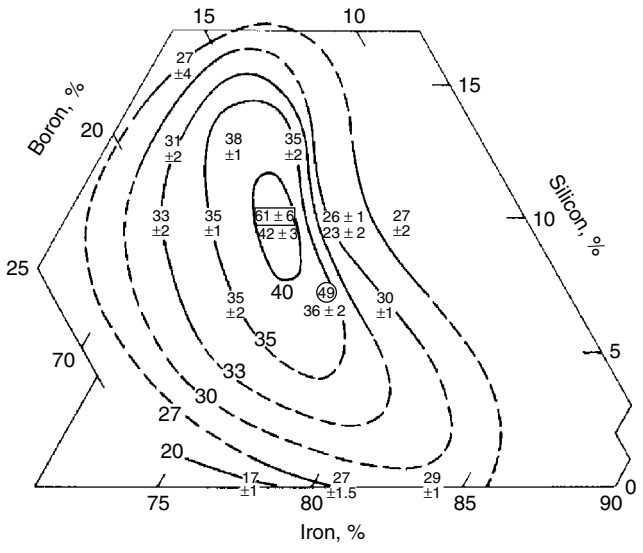

Figure 1. Critical mean thickness determined for various amorphous Fe–B–Si alloys all cast onto a 250-mm-diameter OFHC copper wheel except: cast onto a 300-mm-diameter tool steel roll; ○ cast onto a 76-mm-diameter OFHC copper roll. (Reproduced from Luborsky *et al*., 1982, with permission from IEEE. © 1982.)

Binary alloy systems of the LTM metals Fe, Co, and Ni with the early transition metals (ETMs) Zr, Hf, and Nb from periods 5 and 6 also manifest deep eutectics, generally in the range 8–15 at% ETM; and thus they are RGF. A metalloid element such as B can be added to further enhance the GFA. Examples are $Co_{90}Zr_{10}$ (Nose and Masumoto, 1980) and $Co_{82}Nb_{12}B_6$ (Inoue, Kobayashi, Nose and Masumoto, 1980), which, as for many of the LTM–Met alloys, are soft ferromagnetic at room temperature.

Many of the binary alloys systems of RE metals and of yttrium with LTMs show deep eutectics on the RE-rich side of the system in each case and several have been shown to be RGF by melt spinning, centered approximately about the eutectic composition. Examples of ferromagnetic melt-quenched glassy alloys of the RE–LTM type are Gd-(33–55)at%Co and Gd-(32–50)at%Fe (Fukamichi, Kikuchi, Masumoto and Matsuura, 1979; Buschow, 1979). These are magnetically harder than the LTM–Met and LTM–ETM alloys because of the local anisotropy induced by the RE metals (Coey, 1978). The coercivity level can be manipulated by adjusting the alloy composition. Amorphous RE–TM alloys of interest for magneto-optic recording applications tend, however, to cover different ranges of composition such that they need to be produced by sputter deposition (Grundy, 1980). Because of the absence of the long-range order characteristic of the crystalline state, amorphous alloys do not manifest magnetocrystalline anisotropy and the LTM–Met type can have very high μ and low H_c. Nevertheless, the directionally random chemical order that exists in alloy glasses in the as-quenched state leads to random anisotropy (Alben, Becker and Chi, 1978) . Marked magnetic anisotropy can be induced by the application of a uniaxial stress or a magnetic field during elevated temperature annealing, where significant local atomic diffusion can occur. The degree of strain-induced anisotropy is influenced by the magnitude of the saturation magnetostriction λ_s. These aspects of induced anisotropy are discussed in greater detail in a later section of this chapter. As for all magnetic materials, shape anisotropy also has an influence on the magnetic properties.

The absence of a microstructure in a metallurgical sense, that is, no crystal boundaries that normally act to pin domain walls, also promotes magnetic softness. Moreover, the noncrystalline structure results in high electrical resistivity, typically in the range 100–200 μΩcm, compared, for instance, to values in the range 30–50 μΩcm for crystalline Fe–Si and Fe–Ni permalloys, which favors their application for mains and high-frequency transformers and other devices.

2.2 Strength, deformation, and embrittlement

As a consequence of the absence of crystalline order in the structure, lattice dislocations, which are present in all crystalline metals, are no longer a consideration. Such mobile dislocations in crystalline metallic materials result in yield strengths or elastic limits that are only a fraction of the theoretical values, which correspond to the stresses required to break the interatomic bonds. The yield strengths of metallic glasses typically range between $\sim E/30$ and $\sim E/50$, where E is the Young's modulus (Davis, 1976; Kimura and Masumoto, 1983); thus, they approximate in each case the corresponding theoretical cohesive strength. Fracture strengths of Fe–Met alloy glasses range between ~2.2 and ~4 GPa (the value for $Fe_{78}B_{10}Si_{12}$, for instance, is 3.4 GPa) (Kimura and Masumoto, 1983), but a compressive strength in excess of 5000 MPa was recently recorded for a $Co_{43}Fe_{20}Ta_{5.5}B_{31.5}$ bulk glass (Inoue *et al.*, 2003). It should be borne in mind that values of E for alloy glasses are lower than those of equivalent crystalline alloys, typically by ~20–40% for Fe-based alloys, for example; this reflects the slightly larger mean interatomic distances in the glass than in the crystal, consistent with a lower atomic packing density. The ultrahigh strengths of metallic glasses are also reflected in very high microhardness, for instance, typically ~900–1000 H_v for Fe–Met and Co–Met-type ferromagnetic alloy ribbons but somewhat lower for corresponding Ni–Met-based glasses.

At temperatures well below T_g and at high values of stress τ, where $\tau > \mu/50$ (μ is the shear modulus), metallic glasses deform heterogeneously by a highly localized shear mechanism. The shear bands are thought to be extremely narrow –a few nanometers wide (Donovan and Stobbs, 1981). The fact that they can be revealed by metallographic etching of a deformed cross section indicates that the chemical SRO is locally modified by the shearing process. When deformed in pure tension, most Fe-, Co-, and Ni-based alloy glasses in their as-cast state fail by a single shear displacement at the yield stress, which is usually slightly above the limit of proportionality, on a plane ~55° to the applied stress (Kimura and Masumoto, 1983). In bending, which is a mixture of tensile and compressive straining, the compressive component stabilizes the material against tensile failure, and Fe-, Co-, and Ni–Met-type alloy glass ribbons in their as-cast state (unless the total metalloid element concentration is high) can generally be bent back on themselves to a true tensile strain of unity on the outer surface, through the occurrence of multiple shearing. Thus, in such cases, the toughness of the material can be described as high. However, on annealing at elevated temperatures, for instance, to relieve the quenching stresses and thus optimize the soft magnetic properties, Fe–Met-based glasses undergo irreversible embrittlement, prior to crystallization (Davis, 1976; Luborsky and Walter, 1976). The particularly detrimental role of P in promoting embrittlement was demonstrated by Luborsky and Walter (1976). It is interesting that Ni-based LTM–Met glasses, in contrast, tend not to embrittle in the glassy state prior to crystallization, particularly if the metalloid concentration is <20 at% (Lewis, Ward and Davies, 1979) and P is avoided as an alloying element. Progressive substitution of Ni by Fe results in a transformation from a nonembrittling to an embrittling regime, depending on the metalloid species and concentration (Ward, Hunger, Lewis and Davies, 1979).

The embrittlement phenomenon in metallic glasses is not clearly understood. It results from subtle changes in the chemical SRO associated with structural relaxation, that is, the removal by annealing of excess free volume quenched during the vitrification. All Fe-based LTM-Met metallic glasses are characterized by ductile–brittle transitions at a temperature T_{db}, by analogy with crystalline Fe and other bcc metals. In the as-cast state, T_{db}, for technologically important Fe–Met alloys glasses, for instance, $Fe_{78}Si_9B_{13}$, is below ambient temperature, whereas on annealing at elevated temperature, T_{db} increases, largely irreversibly, to above ambient temperature.

At low stresses, or as the temperature approaches T_g, metallic glasses deform by homogeneous flow or creep and, at sufficiently low stresses, the flow is Newtonian viscous, that is, the strain rate is proportional to stress (Spaepen and Taub, 1983). This is a common feature of many noncrystalline materials, pitch being a classical example.

3 FUNDAMENTAL MAGNETIC PROPERTIES

3.1 Magnetic moment

The dependence of saturation moment per TM atom, determined at 4.2 K, on the TM content for $LTM_{80}B_{20}$ and

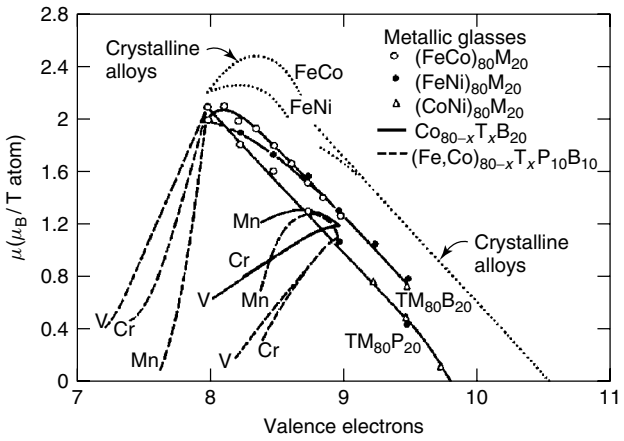

Figure 2. Variation of magnetic moment per transition-metal atom in crystalline and amorphous alloys as a function of number of valence electrons n_v. The values $n_v = 8$, 9, and 10 correspond to Fe, Co (or $Fe_{0.5}Ni_{0.5}$), and Ni respectively. (Reproduced from R.C. O'Handley, 2000. © 2000 John Wiley & Sons Inc.)

$LTM_{80}P_{20}$ glassy alloys (O'Handley, 2000) is given in Figure 2 (LTM in this case indicates Fe, Co, and/or Ni). The corresponding variations of moments for crystalline alloys are included as dotted lines. The displacement of the data for the glassy $LTM_{80}B_{20}$ alloys, relative to the Slater–Pauling curve, is consistent with data for crystalline (LTM)B and $(LTM)_2B$ compounds and alloys (O'Handley, 2000). Relatively large magnetic moments are achieved in a wide range of glassy alloys based on Fe, Co, Ni. The lower moments than for the corresponding crystalline alloys are not only consistent with the concentration(s) of the nonmagnetic metalloid atom(s), B and/or P in the present case, but also commonly including Si, which are added to promote vitrification by rapid quenching. Hence, the influence of the absence of a long-range order in the glassy alloys on the magnetic moment per LTM atom is considered to be negligible (O'Handley, 2000). The effects of the ETM solute substitutions, exemplified in Figure 2 by Cr, Mn, and V, can be rationalized on the basis of the virtual-bound-state model (O'Handley, 2000).

The saturation moment per TM atom increases with increasing TM:Met ratio for both Fe-based (FeB and FeP) and Co-based (CoB, CoB, CoZr) alloy glasses and extrapolates to values only slightly lower than those for bcc Fe and hcp Co, respectively (O'Handley, 2000).

3.2 Curie temperature

The dependence of the Curie temperature T_C on the LTM content for glassy $(FeNi)_{80}B_{20}$, $(FeCo)_{80}B_{20}$ alloys and for various other amorphous alloy systems is shown in Figure 3 (O'Handley, 2000). The T_C data for FeNi and FeCo crystalline alloys are summarized by the dotted lines. The compositional dependence of T_C for the glassy alloys is not as amenable to theoretical analysis as is the case for that of the magnetic moment. Although the shape of the dependences for the amorphous FeNi-based alloy systems is broadly similar to that for the crystalline FeNi system, the maxima in the glassy alloy curves are displaced to lower valence electron to atom ratios.

The influence on T_C of a wide range of TM and platinum group metal solute substitutions for Fe in $FeSi_{10}B_{12}$ metallic glasses, up to concentrations x of ∼10 at%, were investigated by Donald, Kemeny, and Davies (1981). The dependence of T_C on x was generally linear or nearly linear and the values of dT_C/dx are plotted against the group number of the solute in Figure 4.

It is interesting to note that the shapes and positions of the curves bear a much closer resemblance to that for $Ni_{100-x}M_x$ binary crystalline alloys than to that for $Fe_{100-x}M_x$ alloys (see Donald, Kemeny and Davies, 1981). This suggests that the majority subband in Fe-based glasses is full, due to the hybridization of the s–p states of the metalloid with the d orbitals of the TMs, as is the case for crystalline Ni. Also, the approximately 12-fold atomic coordination in the glassy state for the Fe-based glass bears a much closer resemblance to that in crystalline fcc Ni than to that in bcc Fe.

The magnitude of T_C for LTM–Met glasses is also strongly influenced by the metalloid element concentration and, especially in Co-based alloys, by the metalloid species. In FeB glassy alloys, T_C increases from ∼510 °C at 12 at%B to ∼750 °C at 28 at%B (Hasegawa and Ray, 1978). In contrast, for Co–Met binary alloy glasses, T_C decreases with increasing metalloid content at a rate of approximately 50 °C per at% metalloid, though CoP alloys have substantially lower T_C values than CoB alloys at any given metalloid concentration, clearly indicating the strong influence of the local atomic environment on this parameter (O'Handley, 1983). However, the concentration ranges over which measurements are possible for these Co-based binary alloy glasses, and indeed for most other Co-based glassy alloys, is limited because T_C is higher than the crystallization temperature T_x.

It should be borne in mind that T_C for a glassy alloy is not absolutely fixed and depends on the structural state of the glass. Generally, T_C increases by typically ∼10 K, when the as-cast glassy structure is relaxed, evidently because of subtle changes in, topological and chemical, short-range atomic order (Chen, Sherwood, Leamy and Gyorgy, 1976).

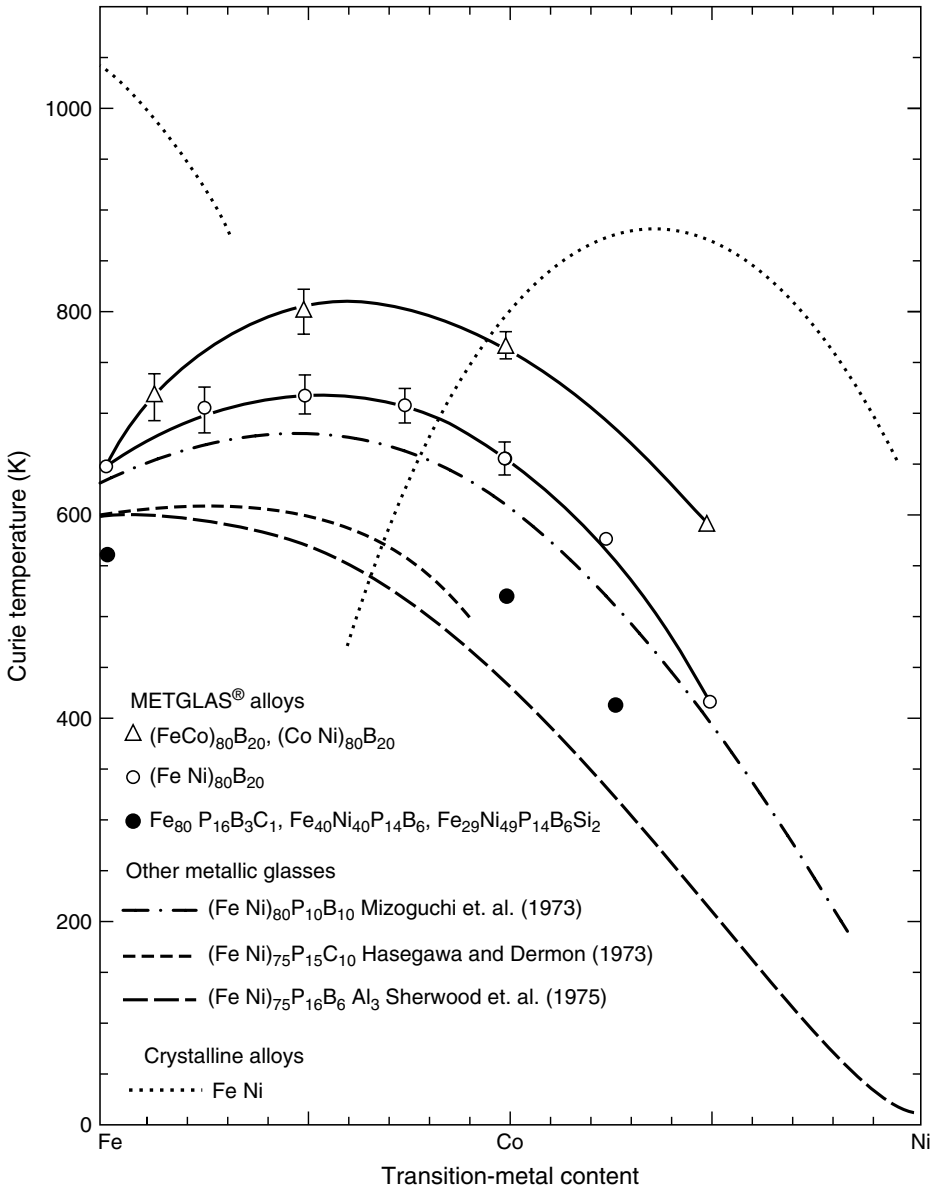

Figure 3. Variation of Curie temperatures of TM–B alloys with transition-metal content. Solid line over (FeNi)B data is a mean-field fit. Dotted lines show trends for crystalline FeNi alloys. (Reproduced from R.C. O'Handley, 2000. © 2000 John Wiley & Sons Inc.)

The influence of composition on the saturation magnetostriction of Fe-, Ni-, and Co-based alloy glasses is discussed in Section 6.

4 PROCESSING OF METALLIC GLASSES

4.1 Requirements for metallic glass formation

The alloy compositional factors that favor glass formation in metallic systems have been outlined in the previous section, in the context of ferromagnetic alloys. As indicated, alloys with compositions at, or close to, eutectics are RGF. A useful empirical parameter for predicting whether or not an alloy is RGF, which we assume rather arbitrarily, though for sound practical reasons, to be a composition which can be completely vitrified at a cooling rate $\dot{T} \leq 10^6\,\mathrm{K\,s^{-1}}$, is ΔT^* (Donald and Davies, 1978), which is given by

$$\Delta T^* = \frac{T_\mathrm{l}^\mathrm{mix} - T_\mathrm{l}}{T_\mathrm{l}^\mathrm{mix}} \tag{1}$$

Equation 1 represents the fractional departure of the liquidus temperature T_l from the simple rule of mixtures melting

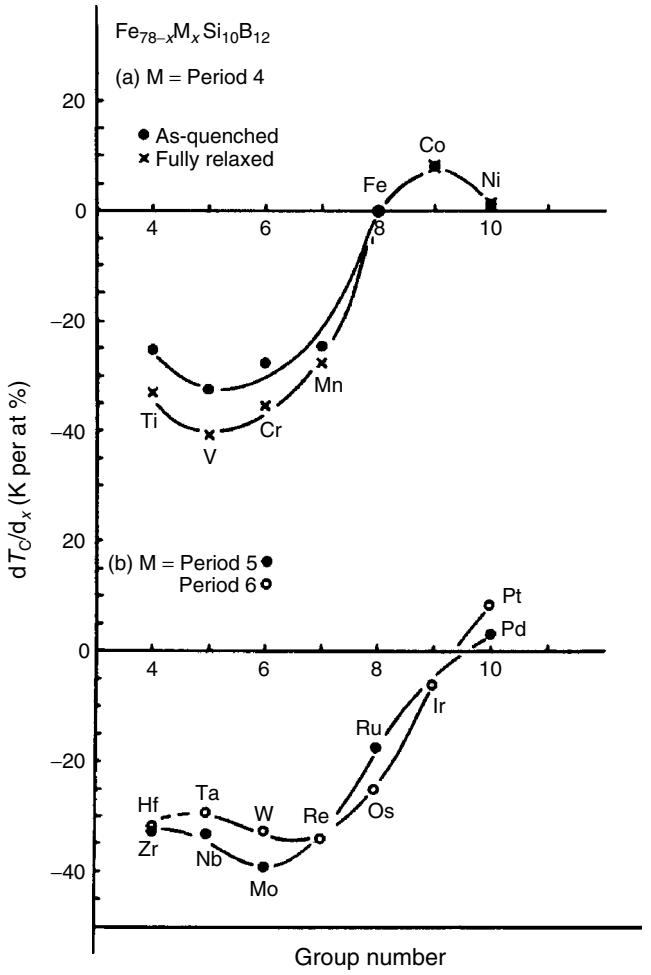

Figure 4. Variation of dT_C/dx (where x is the concentration of solute metal M) with group number (i.e. the number of outer d + s electrons) of M for dilute additions of (a) period 4 solutes (shown also are values of dT_C/dx for samples which have been relaxed fully), and (b) periods 5 and 6 solutes, to glassy $FeSi_{10}B_{12}$-based alloys. (Reproduced from Donald *et al*., 1981. © 1981, with permission from IOP Publishing Ltd.)

temperature T_l^{mix} where $T_l^{mix} = \Sigma x_i T_m^i \cdot x_i$ and T_m^i are the mole fraction and melting point, respectively, of the ith component of an alloy of n component elements. Some adjustment is required for systems where intermediate phases with exceptionally high congruent melting points occur. It was shown in a survey of numerous binary and ternary alloys that, with a few exceptions, compositions that were RGF had values of $\Delta T^* > 0.2$ (Donald and Davies, 1978). This was subsequently used to identify RGF compositions in several systems (Holt, Ankeny and Cline, 1980).

Another useful empirical approach for predicting RGF in metallic systems, first proposed by Giessen (1982) for binary alloys, is based on two parameters: the excess negative enthalpy of mixing ΔH_m and the component atomic radius ratio r_A/r_B, where A and B represent the smaller and larger atomic species, respectively. Two-dimensional maps for two series of binary alloy systems, based on Ni and on Zr, with ΔH_m and r_A/r_B axes, gave satisfactory delineation between RGF and non-RGF systems, with the former group being concentrated in the regime having coordinates of high ΔH_m and low r_A/r_B. This principle has been incorporated by Inoue and coworkers to formulate a set of rules for bulk metallic glass formation (having critical cast rod diameters >0.5 mm) with the additional requirement that the alloys should have at least three components (Inoue, 1997).

Numerous Fe-, Co-, and Ni-based bulk glass-forming alloys, generally with several solute metal additions to minimize the melting temperature, have now been demonstrated (Inoue, 2000; also, see **Soft Magnetic Bulk Glassy and Bulk Nanocrystalline Alloys, Volume 4**.)

The process of rapid quenching for vitrification is illustrated in Figure 5 by the time–temperature–transformation (T–T–T) curves for three extreme examples, pure Ni and two easy glass-forming alloys, $Pd_{82}Si_{18}$ and $Pd_{77.5}Si_{16.5}Cu_6$. The T–T–T curves indicate, in each case, the time required effectively for the start of crystallization as a function of temperature. Glass formation occurs when the cooling rate exceeds a critical value R_c, such that it bypasses the nose of the T–T–T curve, as shown. In the general case, the lower the T_l relative to T_g, the narrower the gap between T_l and T_g, the more rapid the increase in melt viscosity with increasing undercooling below T_l and, consequently, the nose of

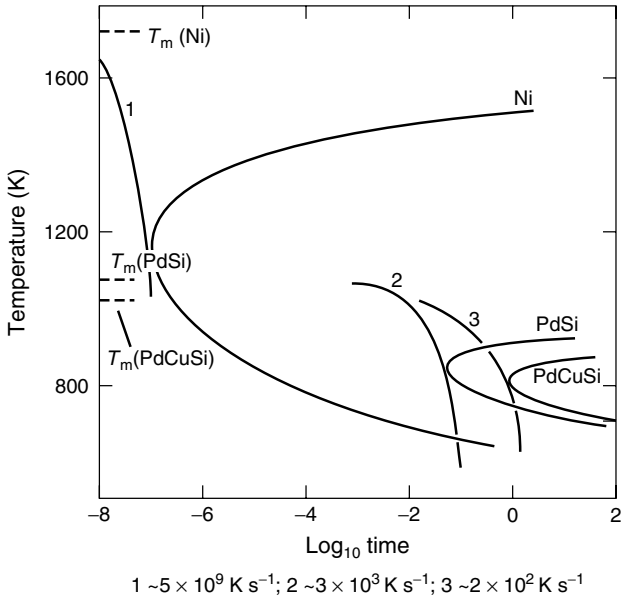

Figure 5. Computed T–T–T curves corresponding to a fraction crystal of 10^{-6} for Ni, $Pd_{82}Si_{18}$, and $Pd_{77.5}Cu_6Si_{16.5}$. Also indicated are the critical cooling curves required to effectively avoid crystallization.

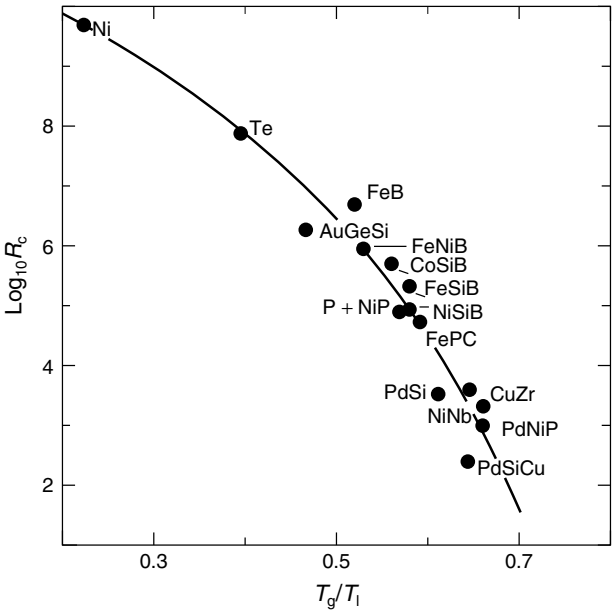

Figure 6. Theoretically predicted values of the critical cooling rate for glass formation (R_c) as a function of the reduced glass temperature T_g/T_l (actual compositions of the alloys are $Fe_{83}B_{17}$, $Au_{77.8}Ge_{13.8}Si_{8.4}$, $Fe_{41.5}B_{17}$, $Co_{75}Si_{15}B_{10}$, $Fe_{79}Si_{10}B_{11}$, $Ni_{75}Si_8B_{17}$, $Pt_{60}Ni_{15}P_{25}$, $Fe_{80}P_{13}C_7$, $Cu_{60}Zr_{40}$, $Ni_{62.4}Nb_{37.6}$, $Pd_{40}Ni_{40}P_{20}$, $Pd_{77.5}Si_{16.5}Cu_6$, $Pd_{82}Si_{18}$).

the T–T–T curve is moved to progressively longer times. Thus, R_c decreases with increasing T_g/T_l (Turnbull, 1969; Davies and Lewis, 1975). Predicted values of R_c, based on theories of crystal nucleation and growth and of transformation kinetics and involving several simplifying assumptions (Uhlmann, 1972; Davies, 1976), are plotted against T_g/T_l in Figure 6 for several glass-forming alloys, including ferromagnetic LTM–Met alloys based on Fe, Co, and Ni–Fe, as examples. The predicted values of R_c for the latter are in the range 10^5–10^6 K s^{-1}, in good agreement with corresponding experimentally estimated values. Correlation between R_c and T_g/T_l for bulk alloy glass formers is less satisfactory, partly because of high melt viscosities above T_l for these very low T_l alloys (Davies, 1995) and the greater influence of heterogeneous nucleants (Lewis and Davies, 1977).

4.2 Thermal stability of metallic glasses

The thermal stability of a glassy alloy, measured by its T_g, or in cases where the glass transition is masked by the devitrification event, the crystallization temperature T_x, is of particular interest and relevance for soft magnetic alloys, since they must generally be annealed at elevated temperature to remove quenched-in stresses, in order to optimize the magnetic properties, and, in some cases, to develop a specific anisotropy. Globally, T_g (or T_x) has been shown to scale satisfactorily with the cohesive energy, measured, for instance, by the molar heat of sublimation ΔH_s for a wide range of glass-forming alloys (Donald and Davies, 1978); the larger the ΔH_s, the higher the T_g, as would be expected for a phenomenon related to atomic diffusivity. Accordingly, ferromagnetic alloy glasses based on Fe, Ni, and Co generally have values of T_g or T_x that are intermediate between those of the glasses based on or containing large concentrations of refractory metals, such as CoTa and those based on the noble metals, such as AuSi.

A more detailed investigation of the influence of composition on the T_x of Fe-, Ni-, and Co-based metallic glasses was undertaken by Donald and Davies (1980). The measured T_x values for a broad series of glassy alloys based on Fe, Ni, and Co, with a constant metalloid content of 10 at% Si + 12 at% B and with substitutions of other metals from period 4, including Cr, Mn, Ti, V, and the noble metal Cu, and also including binary intermixtures of Fe, Ni, and Co, are plotted against valence (s + d) electron to atom ratio in Figure 7. There is a remarkably smooth correlation for the alloys containing Fe, Ni, and Cr, which are characterized by having very similar hard sphere atomic diameters. Additionally, size effect contributions to the thermal stability are associated with the Mn, Ti, and V substitutions, whose atomic diameters are significantly different from the Fe and Ni, while Cu rapidly destabilizes both the Fe- and Ni-based glasses. However, for the Ni–Co-based alloys and the Co–Fe-based alloys containing up to 15 at% Fe, T_x follows a separate half loop, the reason for which has not yet been established. The effects of other metals from periods 5 and 6 were also studied (but are not included here) and these showed a clear correlation with the atomic size difference from those of Fe and Ni. The additional increment in T_x over and above that due to conduction electron density is approximately proportional to the second power of the fractional difference in diameter between solvent and solute metal atoms.

These data provide guidelines for predicting the safe maximum temperatures for annealing of ferromagnetic glassy alloy of various compositions.

4.3 Thermal requirements for rapid solidification

The aim for all rapid solidification processes is to bring the melt into intimate thermal contact with a cool and thermally conducting heat sink, generally at a high relative velocity, in order to promote efficient and uniform melt spreading to a thin section or subdivision into small droplets. The higher the R_c for an alloy, the smaller the section thickness or the droplet diameter must be, that is, the smaller the length of the heat path should be.

The cooling rate in the melt is also dependent on the efficiency of heat transfer h across the interface with the

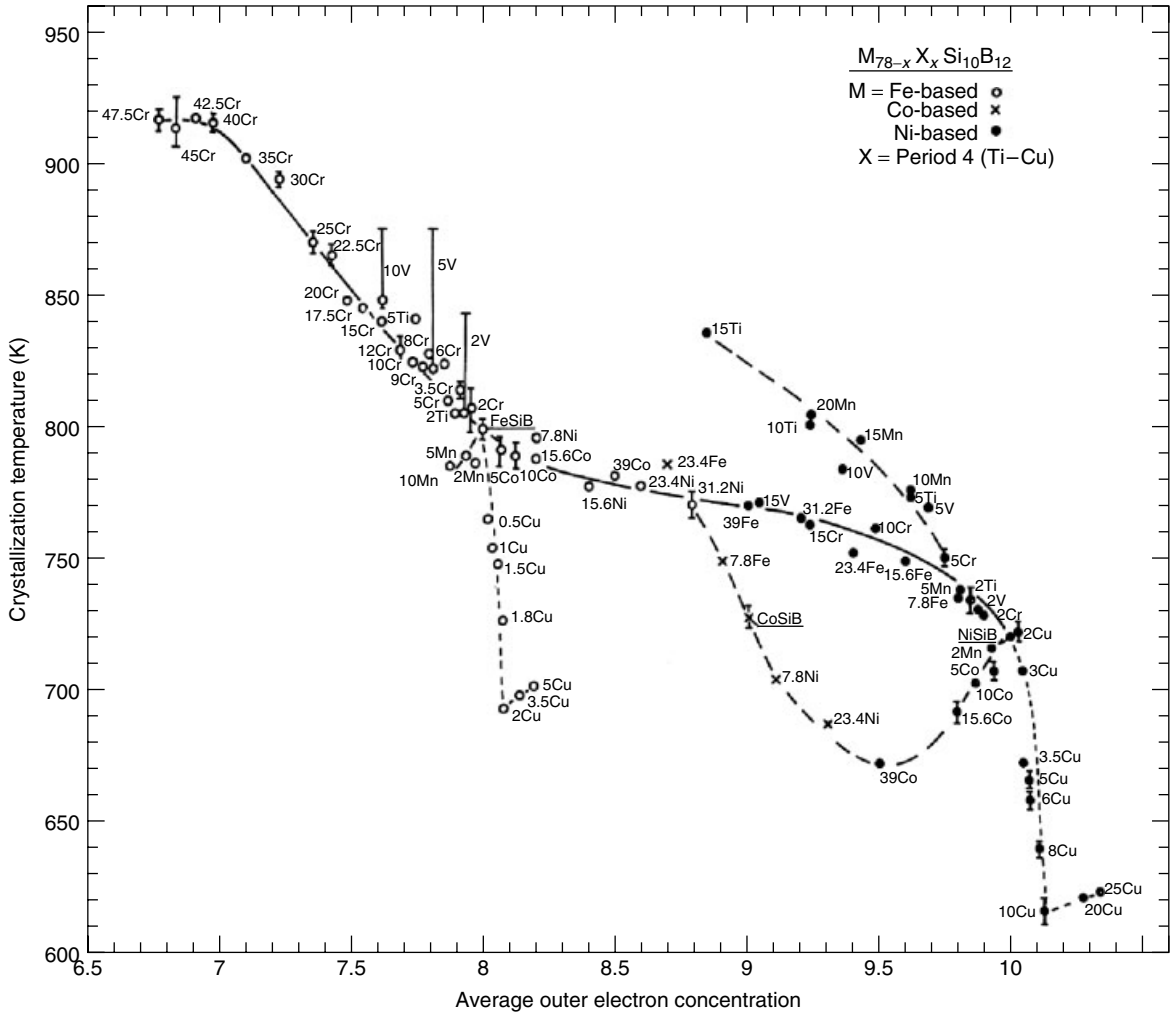

Figure 7. Variation of crystallization temperature with outer (d and s) electron concentration *e/a*, of the constituent transition elements for Fe- and Ni-based glassy alloys containing period 4 alloying additions (Donald and Davies, 1980).

heat sink. In the absence of interfacial resistance to heat flow and for a highly conducting heat sink, that is, ideal cooling conditions, $\dot{T}$ is determined by the thickness x and the thermal conductivity of the melt section, with $\dot{T}$ being proportional to x^{-2}. For melt spinning of ribbon, for instance, h has been estimated experimentally to be $\sim 10^5\,\mathrm{Wm^{-2}\,K^{-1}}$ (Warrington, Davies and Shohoji, 1982), with a spread of $\sim \pm 5\,\mathrm{Wm^{-2}\,K^{-1}}$ between alloys. This is a very high value for a metal-casting process, principally because a new clean melt surface is continually being created at the interface with the roll and intimate physical contact is being maintained. Figure 8 shows the computed variation of $\dot{T}$ with x for $h = 10^5\,\mathrm{Wm^{-2}\,K^{-1}}$, for the ideal cooling limit, computed for an RGF alloy $Fe_{40}Ni_{40}P_{14}B_6$ (Davies, 1978, 1983). For $x < \sim 10\,\mu\mathrm{m}$, $\dot{T} \propto x^{-2}$, that is, Newtonian (interface control) conditions prevail, but, as x increases, the cooling regime progressively approaches ideal, since the heat transfer is increasingly controlled by the thermal resistance of the liquid medium. Thus, for example, a ribbon of thickness $10\,\mu\mathrm{m}$ is predicted to cool at $\sim 2 \times 10^6\,\mathrm{K\,s^{-1}}$ and a 100-μm-thick ribbon at $10^5\,\mathrm{K\,s^{-1}}$. The data in Figure 8 can be combined with those given in Figure 6 to yield a plot of approximate maximum thickness of glassy phase that can be melt spun to ribbon x_c versus T_g/T_l (Figure 9).

5 LIQUID STATE PROCESSING OF METALLIC GLASSES

5.1 Ribbon casting

5.1.1 Chill block melt spinning (free jet)

A jet of molten alloy is ejected under pressure through a circular orifice at the base of a crucible and impinges onto

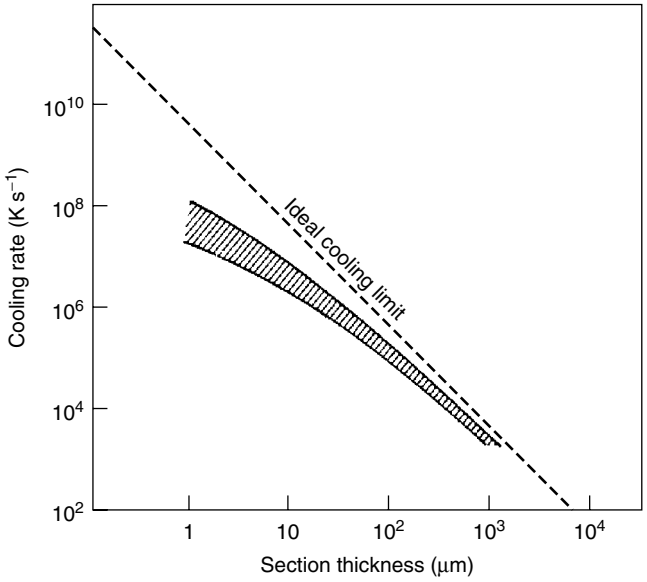

Figure 8. Cooling rate $\dot{T}$ as a function of section thickness x, computed for the glass-forming alloy $Fe_{40}Ni_{40}P_{14}B_6$ and based on experimentally derived values of heat transfer coefficient (cross hatched area) and on ideal cooling, that is, no interface resistance (dashed line), for chill block melt spinning. Unidirectional cooling of a rectangular section to one heat sink is assumed.

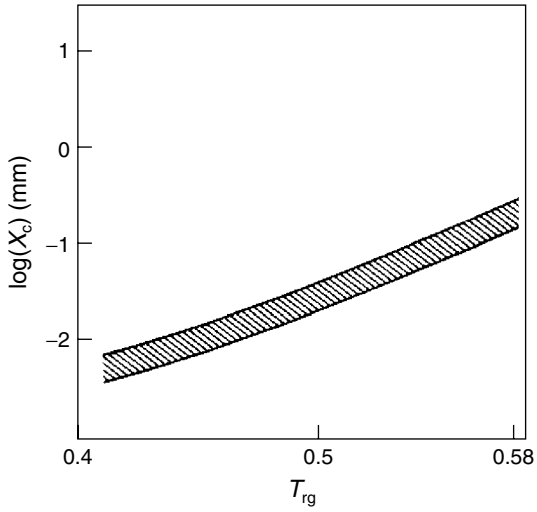

Figure 9. Predicted range of maximum section thickness of glassy alloy phase versus the reduced glass temperature $T_{rg} = T_g/T_l$.

the circumferential surface of a rapidly rotating roll (typical linear velocity: 20 m s^{-1}; Liebermann and Graham, 1976). The roll is generally fabricated from Cu or, preferably, a highly conducting Cu alloy such as Cu-1wt%Cr, which is harder and more wear resistant than pure Cu. An elongated puddle is established at the point of impingement, from which a thin ribbon is continuously extracted and solidified

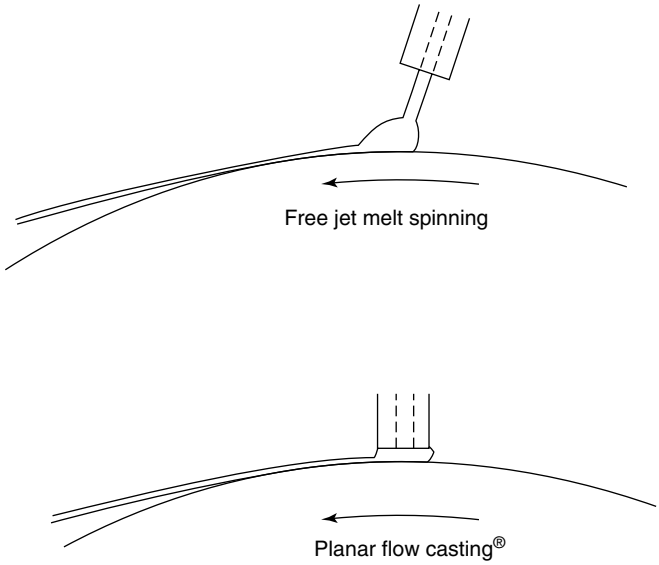

Figure 10. Nozzle configuration for free jet melt spinning and planar flow casting.

(Figure 10). This then parts from the roll surface well downstream of the puddle. The higher the roll speed V_r, the shorter the puddle and the smaller the ribbon thickness x. In this process, the puddle is also able to spread laterally since it is unconstrained. Thus, the ribbon width w is also a function of V_r.

It has been shown (Kavesh, 1978) that:

$$x \propto \frac{Q^m}{V_r^n} \tag{2}$$

where Q is the flow rate of melt and m and n are constants which depend on melt composition and roll material. Ideally, $n = 0.75$ and $m = 1 - n$ but, in practice, n varies between ~0.65 and ~0.85 (Vincent and Davies, 1982). Similarly (Kavesh, 1978),

$$w \propto \frac{Q^m}{V_r^n} \tag{3}$$

Thus, V_r principally influences x while Q has a greater influence on w.

In practice, w is limited to 4–5 mm by instability of the puddle, while the limit on x tends, in practice, to be ~80 μm, beyond which it becomes nonuniform. However, the maximum thickness of amorphous phase equates to x_c, which is governed by R_c and the interfacial heat transfer coefficient h.

5.1.2 Planar flow casting (PFC)

In this process, the nozzle tip is in close proximity to the roll surface (the typical gap size is 0.3–0.5 mm) and the

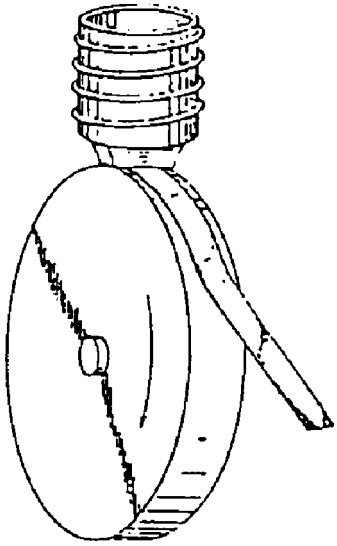

Figure 11. Schematic of the planar flow casting process.

melt is streamed through a rectangle-shaped slot nozzle (Narasimhan, 1979). Since the puddle is now constrained between the nozzle tip and the roll (Figure 10), convergence of the stream through capillary forces is prevented and a ribbon of width equal to the slot length can be cast (Figure 11). Thus, in principle, there is no limit to the width of the strip that can be cast, although, in practice, there are engineering limitations related to the uniformity of gap that can be achieved for a long slot. The melt flow rate is given by $Q = wV_r x$ (ignoring thermal contraction). Since w is now constant, then, for constant Q, x is proportional to V_r^{-1}. Because the puddle is constrained, in addition to facilitating the production of ribbon of width >4 mm, the process also gives a more uniform ribbon thickness than the free jet variant, since oscillations or vibrations of the puddle are reduced in amplitude.

On the basis of Bernoulli's equation, the ribbon thickness x can be shown to be given (Fiedler, Mühlbach and Stephani, 1984) by

$$x = \left(\frac{g}{b}\right)^c \frac{b}{v}\left(\frac{2p}{\rho}\right)^{1/2} \tag{4}$$

where b is the slot breadth, p is the pressure at the slot, ρ is the density of the liquid, g is the nozzle tip/roll gap, and c is a constant ≈1/3. An analysis of casting conditions for glassy alloy strip ($Fe_{40}Ni_{40}B_{20}$) was also made by Takayama and Oi (1979).

A significant problem with both free jet and PFC ribbon are the gas pockets (air pockets, if casting is in air) that are entrapped between the melt and the roll surface during casting. These cause roughness on the roll contact surface of the ribbon and thus reduce the packing fraction in a wound core and can adversely influence H_c (Kronmüller, 1981). They can also act as centers where localized crystallization may occur during casting or where premature crystallization may occur during subsequent annealing. The gas pockets can be eliminated by casting in reduced pressures, particularly in a helium atmosphere (Todd *et al*., 1999), though this is not economically viable for commercial production. Clearly, for extended operations, the roll must be internally water cooled to avoid overheating of the substrate; however, for laboratory-scale samples of ribbon, this is not generally necessary. PFC is now used for all commercial production of soft magnetic glassy alloys, and ribbon widths up to 300 mm are routinely produced.

5.1.3 Stacking of ribbons

The severe embrittlement of Fe-based LTM–Met metallic glasses at the temperatures required for effective annealing out of quenched-in stresses, in addition to the small thickness of the cast ribbon (~25 μm for METGLAS® 2605SC, for instance), results in difficulties in handling, punching, and stacking of individual laminations for the construction of a conventional transformer yoke. Thus, the ribbon is toroidally wound, prior to annealing, in commercial distribution transformers, which typically have a capacity of ~25 kVA for 110/120 V output voltage systems (Smith, 1993). However, for large power transformers, toroidally wound cores are less practicable than a stacked configuration. In an attempt to overcome this limitation and also to improve the packing density, the hot rolling of stacks of 5–10 ribbons was investigated. Although this material, known as Powercore®, improved the stacking density and had good magnetic properties without additional annealing (Smith, 1993), it has proved, as for annealed ribbon, to be very brittle and difficult to cut (Hasegawa, 2003). Nevertheless, stacked cores have been fabricated by cutting segments of large METGLAS® wound cores and used as the pole piece magnets for magnetic resonance imaging equipment (Hasegawa, 2003).

5.2 Production of metallic glass powder

5.2.1 Pulverization of melt spun ribbon

The most efficient and widely applicable method of producing ferromagnetic LTM–Met amorphous alloy powders for consolidation into magnetic cores is the fragmentation of melt spun glassy alloy ribbon into a flaky powder having platelet-shaped particles, using, for example, a ball mill or a hammer mill. This has the advantage that a much wider range of compositions can be efficiently fully vitrified in

bulk quantities by melt spinning onto a solid heat sink than is possible by atomization processes. It is advantageous for pulverization, though not a prerequisite, if the ribbon is either intrinsically brittle in the as-cast state or can be embrittled by annealing at temperatures well below T_g or T_x. The size of the platelets, which has an influence on the magnetic properties of the pressed cores (Hasegawa, Hathaway and Chang, 1985; Raybould and Tan, 1985), is controlled by the milling parameters and time.

Various consolidation techniques have been investigated for amorphous ferromagnetic alloy powders, including explosive compaction (Cline and Hopper, 1977; Hasegawa and Cline 1985), gas-gun compaction (Morris, 1982), isostatic pressing (Hasegawa, Hathaway and Chang, 1985), vacuum hot pressing or cold pressing (Raybould and Tan, 1985), and warm extrusion (Kawamura, Takagi and Akai, 1988). In some cases, an insulating ceramic binder was employed to reduce AC losses and to increase the roll-off frequency. Annealing of compacts to reduce any residual stresses that are present is important, particularly for cold consolidated materials. Surprisingly, it was reported (Raybould and Tan, 1985) that variations in consolidate density between 80 and 90% of the theoretical density had no significant effect on the magnetic properties; in particular, consolidation to intermediate densities was found to be amenable to mass production techniques.

5.2.2 *Fluid atomization*

These processes involve the breakup of a molten alloy stream into small droplets by a high-velocity fluid, either liquid or gas, or, in some cases, a combination of liquid and gas (see review by Miller, 1983). The higher the velocity of the quenchant, the smaller the mean droplet diameter d_p, and thus the higher the mean $\dot{T}$. Gas atomization generally employs N_2 or Ar, though He gives higher $\dot{T}$ because of its higher thermal conductivity. Liquid atomization usually employs water, which is a more efficient atomizer and coolant than a gas. Water-atomized powder generally consists largely of irregular shaped particles, which enhances the strength of a compacted core. $\dot{T}$ for gas atomization is usually $<10^4\,\mathrm{K\,s^{-1}}$, even for the finest particles, though ultrasonic gas nozzles can increase $\dot{T}$ up to $10^5\,\mathrm{K\,s^{-1}}$ for 20-μm particles (Miller, 1983). $\dot{T}$ for water-atomized powder particles is frequently in the range 10^5–$10^6\,\mathrm{K\,s^{-1}}$ and up to 80% of glassy phase has been reported for sub–20-μm powder particles of $Fe_{69}Si_{17}B_{14}$ and $Fe_{74}Si_{15}B_{11}$ alloys (Yamaguchi and Narita, 1978). Gas–liquid atomization, typically using argon and water, has been reported as yielding fully amorphous sub-20-μm particles for $Fe_{75}Si_{10}B_{15}$ and $Fe_{81.5}Si_{14.5}B_4$, alloys (Miller, 1983).

5.2.3 *Centrifugal atomization*

In the variant of this process developed by Pratt and Whitney (Miller, 1983), the melt stream impinges on a concave-shaped disc rotating at extremely high velocity (typically 150 000 rpm). This accelerates the melt to close to the rim speed and atomizes it directly to very fine droplets at the disc edge. These are quenched by helium gas jets. The process was reported as having been used to produce amorphous powder for several ferromagnetic FeSiB alloys. The powder has a narrow particle size distribution, though the particles are spherical and thus not well suited to compaction to solid bodies.

5.2.4 *Other atomization techniques*

Spark erosion, which is essentially the electrical discharge machining process, has been successfully employed to produce a wide range of ferromagnetic alloy powders (Berkowitz, Walter and Wall, 1981). The powder is formed during the discharge when local melting or vaporization of the electrodes occurs, which then condenses and solidifies in the dielectric fluid; $\dot{T}$ is reported as being up to $10^6\,\mathrm{K\,s^{-1}}$ for 20-μm particles. Particles are spherical and range in size from a few submicrometers up to 50 μm.

Electrohydrodynamic atomization (Perel, Mahoney, Duwez and Kalensher, 1980) involves the use of a very high electric-field gradient generated at the tip of a heated capillary nozzle containing molten alloy. A gradient of the order of 1 MV $\mathrm{cm^{-1}}$ is produced by applying a potential of typically 10 kV between the melt and electrode in close proximity with the nozzle. When the electrostatic forces overcome the surface tension of the melt, an extremely fine droplet is omitted and solidified as a spherical particle. Particle diameters are typically ~0.1 μm and amorphous $Fe_{40}Ni_{40}P_{14}B_6$ powder has been successfully produced.

The disadvantage of both these techniques is that production rates are only of the order of grams per hour.

6 INDUCED MAGNETIC ANISOTROPY AND MAGNETOSTRICTION

The absence of macroscopic magnetocrystalline anisotropy in amorphous ferromagnetic alloys means that other sources of anisotropy may dominate in these materials. In general, induced magnetic anisotropies in amorphous ferromagnets have energy densities of the order of 10^2–$10^3\,\mathrm{J\,m^{-3}}$ and can have their absolute magnitude and direction controlled by postproduction thermomechanical treatment. These treatments include annealing in the presence of a magnetic field, annealing under load or the introduction by annealing of

a surface layer of devitrified material (Thomas and Gibbs, 1992).

Figure 12(a) emphasizes, in a schematic representation, that in zero applied field, neighboring magnetic moments align parallel to one another because of the quantum-mechanical exchange interaction and also, in general, make some angle θ_0 with the nearest-neighbor bond direction. The angle θ_0 is defined from the *local* anisotropy symmetry in an amorphous ferromagnet. It has remained unclear as to whether this local symmetry has the same or similar form to crystalline materials that may appear on devitrification, such as bcc iron. The case where all moments are perfectly collinear in the induced easy axis direction in the demagnetized state is an ideal one in amorphous ferromagnets. There is strong evidence (Kronmüller, 1979; Pankhurst, Betteridge, Jiang and Gibbs, 1994; Wildes *et al*., 2004) of moment noncollinearity (θ_0 varying spatially about some mean value, usually related to a dominant anisotropy direction) in the ferromagnetic ground state. The degree of noncollinearity may vary with imposed thermal history, but is never absent. It is surprising that this is equally the case in alloys containing RE or TM atoms, the former being intuitively more likely to show such an effect due to the more localized moment on such atoms.

In these amorphous structures, where *a priori* no two atomic environments are topologically or chemically equivalent, there can be a distribution in magnitude and direction of the local anisotropy and exchange interactions. Where the exchange is weak, the moments follow the local anisotropy vector, and where the exchange is strong the local anisotropy can be spatially averaged out. This noncollinearity can directly impact on technical applications. We consider later in this chapter sensors that rely on magnetization by pure and coherent rotation of the moments for maximum response. The noncollinearity affects the response, especially at low fields.

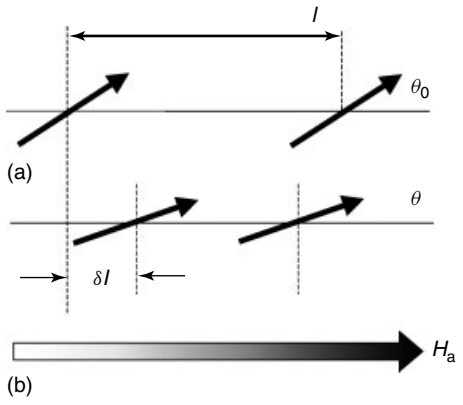

Figure 12. A schematic illustration of the effect of a magnetic field on two neighboring dipole moments in an amorphous ferromagnet (a) in zero applied field and (b) in a field applied as indicated, with rotation of the dipoles toward the field direction and a concomitant change in bond length from the magnetostriction.

Figure 12(b) represents schematically the effect of changes in bond length when the magnetization direction rotates on the application of an external magnetic field. The *total* magnetic contribution to the free energy includes contributions from exchange, anisotropy, and magnetoelastic effects. The exchange contribution to the magnetic part of the free energy causes the moments to remain parallel, and the Zeeman term promotes rotation toward the applied field direction. The moment rotation depicted can therefore in general result in a change in bond length, δl, as the magnetization rotates. Such a field-induced strain is known as *Joule magnetostriction*, and the inverse (Villari) effect is that a mechanical strain in the material (intrinsic or extrinsic) can change the ease with which the magnetization may rotate in a given field. This field-induced strain introduces the magnetoelastic contribution to the free energy.

The measurement of anisotropy and magnetoelastic properties in amorphous ferromagnets presents challenges from the point of view of the extreme magnetic softness of the alloys, and also their standard thin-ribbon geometry. This whole area has been comprehensively reviewed (Squire, 1994). Bonding to other materials must be avoided as this can lead to stress-induced anisotropy as the bond cures. The thin section (typically 25 μm) and nonuniform cross section (a legacy of the rapid solidification processing) lead to further practical difficulties. The dilatometric method has proved to be the most robust and insightful technique (Squire, 1994).

6.1 Induced magnetic anisotropy

We consider this topic within the context of samples from which the stresses arising from the casting process have been removed by a simple thermal treatment (typically 30 min at $T_x - 50\,^{\circ}\mathrm{C}$, where T_x is the temperature of the onset of crystallization as determined in slow-scan-rate differential scanning calorimetry, for example). It can further be assumed that for all the data discussed the samples have remained fully amorphous as determined by X-ray diffraction and the maintenance of magnetic softness. The latter may be a more sensitive guide than the former in amorphous ferromagnets.

The first method of introducing a uniaxial magnetic anisotropy of controlled magnitude and direction is to perform an isothermal anneal in the presence of a saturating magnetic field at a temperature below the ferromagnetic Curie temperature of the alloy. Alternatively, the sample may be cooled slowly (say $10\,\mathrm{K\,min^{-1}}$) down through the Curie temperature to ambient. Field annealing drives a rearrangement of the topological and chemical short-range structure

of the amorphous alloy to produce a material with directionally ordered metal–metal and metal–metalloid pairs. The resulting anisotropy constant for this uniaxial anisotropy, K_u, depends on both annealing time and temperature. An easy axis is induced in the direction of the annealing field, which is retained when the material is cooled to ambient temperature in the presence of the field. The kinetics of the development of the easy axis has been shown to obey a two-level model (Gibbs, Evetts and Leake, 1983; Kronmüller *et al*., 1985; Kronmüller, 1983) where, for a field anneal at a given temperature, the anisotropy constant of a material approaches a maximum value. This value is annealing temperature dependent when the anisotropy is induced owing to two-ion interactions, and temperature independent when it is induced owing to single-ion anisotropy (Callen and Callen, 1963, 1965). Thus, K_u is temperature independent in single-TM alloys (e.g., Fe-based alloys) and temperature dependent in two- or three-TM alloys (e.g., Fe–Ni or Fe–Co alloys). Figure 13(a) and (b) illustrates such data (Thomas and Gibbs, 1992).

It is important to note that the introduction of anisotropy from an applied field can take place at any temperature below the Curie temperature (it is driven by thermal activation), and effects can take place at temperatures that are a little removed from ambient. In the region of a domain wall, the magnetization distribution can act on the local topology and chemical order to produce a profile to the local easy axis, which matches the magnetization profile in the domain wall. This pins the domain wall and reduces the initial permeability, an effect known as *disaccommodation*. This possibility must be taken into account in lifetime predictions of properties in these materials, but, because it is a thermally activated process, equilibrium is reached even if there is an initial transient response in the permeability.

Annealing under a tensile load has been studied in Co-rich (low magnetostriction $-\lambda_s \approx 10^{-8}$) amorphous alloys. The induced anisotropy has two components, K_{an} arising from an anelastic response of the materials and K_{pl} arising from the plastic response (Nielsen, 1985). It is significant that both components are nonzero at the composition for which the magnetostriction (and hence the basic strain magnetostriction coupling) is zero. The anelastic component can be recovered by a second zero-applied-stress anneal. At low anneal temperatures, the easy direction is parallel to the applied stress, turning orthogonal to the applied stress at higher temperatures. This is viewed as arising from the competition between the anelastic and plastic components of the strain. At high annealing temperatures, $|K_i|_{max}$ can reach $800\,J\,m^{-3}$ (Gibbs, 1990).

There have been studies (Vázquez, Ascasibar, Hernando and Nielsen, 1987) on the simultaneous application of a tensile stress and a transverse magnetic field on ribbon

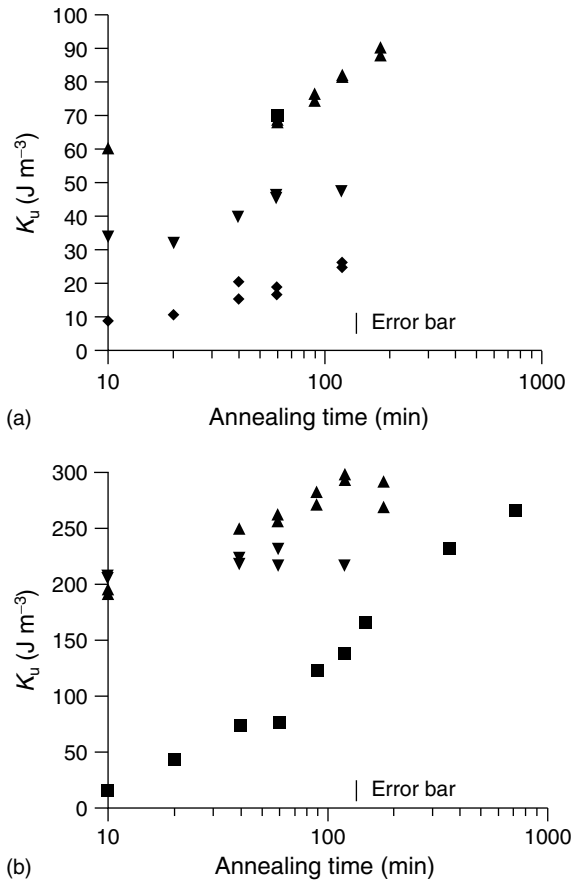

Figure 13. (a) Anisotropy constant, K_u, versus anneal time for METGLAS®2605S2 for different annealing temperatures (squares 420 °C, triangles 400 °C, inverted triangles 350 °C, diamonds 250 °C). (b) Anisotropy constant, K_u, versus anneal time for VAC®0040 for different annealing temperatures (squares 250 °C, triangles 300 °C, inverted triangles 350 °C, diamonds 370 °C).

samples; in this case, $|K_i|_{max} = 1100\,J\,m^{-3}$. It was proposed that the applied stress enhanced the field annealing effect as the sum of a tensile stress anneal and a transverse field anneal was less than that of the combined stress-field anneal.

A third method of introducing a uniaxial anisotropy in amorphous alloys is to precipitate surface crystallinity in Fe-based magnetostrictive ($\lambda_s \approx 10^{-6}$) alloys (Hang Nam and Morrish, 1981). The easy direction is perpendicular to the ribbon plane and $|K_i|_{max}$ can reach $6000\,J\,m^{-3}$ as the thickness of the surface crystalline layer increases (Herzer and Hilzinger, 1986). The mechanism proposed is that the crystalline surface layer, which is of higher density than the amorphous underlayer, will place the underlayer in biaxial compression. In a material of positive magnetostriction, this will bring the easy axis in the amorphous material to lie perpendicular to the ribbon plane, dominating the shape anisotropy in this direction.

6.2 Magnetostriction

Fe-based amorphous alloys have saturation magnetostriction constants, λ_s, in the range $20 - 30 \times 10^{-6}$. If Fe and Ni are present in equal proportions, the value of λ_s is reduced to around 10×10^{-6}. The basic mechanisms of magnetostriction in amorphous alloys have been extensively discussed (O'Handley, 1987). Figure 14 summarizes the composition dependence of λ_s in the (Fe, Co, Ni)B alloy system (O'Handley, 1978). The ability to smoothly vary the saturation magnetostriction by compositional control makes amorphous ferromagnetic alloys very attractive in device development.

Magnetostrictive strain, λ_i in a direction i in a material can be defined by

$$\lambda_i = \frac{1}{c_{ij}} \frac{\partial E_K}{\partial \varepsilon_i} \tag{5}$$

where ε_i is the strain in the direction i, c_{ij} is the appropriate elastic constant, and E_K is the anisotropy energy density. The topological disorder prevents simple macroscopic summation of the microscopic λ_i. Amorphous alloys, which may be taken as topologically isotropic to first order, have nonzero λ_i. This summation problem has been addressed (Furthmüller, Fähnle and Herzer, 1987), with each 'structural unit' characterized by a unique uniaxial anisotropy, and the magnetostrictive strain can be calculated using equation 5. The units are mechanically coupled (the solid is dense and contiguous) and the macroscopic strain manifests itself by elastic strain transfer from unit to unit. The summation is nonzero due to the anisotropic elastic properties of the 'structural units'.

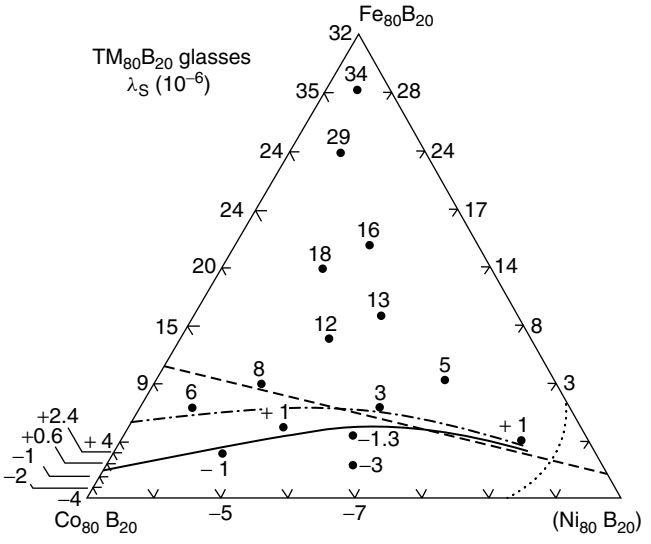

Figure 14. Saturation magnetostriction at room temperature for amorphous $(FeCoNi)_{80}B_{20}$ alloys. Solid line shows course of zero magnetostriction compositions and dashed line shows predictions based on the split band model. (Reproduced from R.C. O'Handley, 2000. © 2000 John Wiley & Sons Inc.)

The engineering magnetostriction, λ_e, is defined as the difference in magnetostrictive strain in a given direction in a sample before and after the application of a magnetic field (Bucholtz, Koo, Dandridge and Sigel, 1986). For amorphous alloys, λ_s is assumed to be isotropic, and therefore λ_e can be written as

$$\lambda_e = \frac{3}{2}\lambda_s \sin^2\theta \tag{6}$$

where θ is the angle through which the magnetization has rotated away from the easy axis direction in which it lay in zero applied field.

The basic model for magnetization by coherent moment rotation in amorphous alloys (Livingston, 1982) can be developed to deduce a number of important parameters related to the magnetostriction. If a magnetic field H rotates the magnetization through an angle θ, the magnetization M in the direction of the field is given by

$$M = M_s \cos\theta = M_s \frac{H}{H_a} \quad (H \leq H_a) \tag{7}$$

where M_s is the saturation magnetization and H_a the anisotropy field. In terms of the anisotropy constant

$$H_a = \frac{2K_u}{\mu_0 M_s} \tag{8}$$

Considering equations (6) and (7), the strain λ_e in the field direction is given by

$$\lambda_e = \frac{3\lambda_s}{2}\left(\cos^2\theta - \frac{1}{3}\right) = \frac{3\lambda_s}{2}\left(\frac{H^2}{H_a^2} - \frac{1}{3}\right) \tag{9}$$

The magnetomechanical coupling constant, d, is defined by

$$d = \frac{d\varepsilon}{dH} = \frac{3\lambda_s H}{H_a^2} \qquad d_{max} = \frac{3\lambda_s M_s}{2K_u} \tag{10}$$

If a longitudinal stress, σ, is applied to an amorphous ferromagnet of nonzero magnetostriction, then there is a magnetoelastic contribution to the free energy given by

$$E_{me} = -\frac{3}{2}\lambda_s \sigma \cos^2\theta \tag{11}$$

The anisotropy field is reduced to

$$H_{a\sigma} = \frac{2K_u - 3\lambda_s\sigma}{\mu_0 M_s} \tag{12}$$

The total strain in the field direction, ε, is the sum of elastic and magnetostrictive terms, hence

$$\varepsilon = \frac{\sigma}{E_s} + \frac{3\lambda_s}{2}\left(\frac{H^2}{H_{a\sigma}^2} - \frac{1}{3}\right) \tag{13}$$

where E_s is the Young's modulus in a saturating magnetic field. Equation (9) states that the effective Young's modulus is magnetic field dependent – the so-called ΔE effect.

$$\frac{\Delta E}{E_s} = \frac{9\lambda_s^2 E H^2}{M_s H_{a\sigma}^3} \tag{14}$$

The magnetomechanical coupling factor, k, related to the fractional energy transfer between magnetic and mechanical energy, important in transducer applications, is given by

$$k = d\left(\frac{EM_s}{H_{a\sigma}}\right)^{\frac{1}{2}} = \left[1 + \frac{M_s H_{a\sigma}^3}{9\lambda_s^2 E_s H^2}\right]^{-\frac{1}{2}} \leq 1 \tag{15}$$

For certain Fe-rich amorphous alloys (e.g., METGLAS® 2605SC), $k = 0.98$ and $(\Delta E/E_s) \geq 10$ have been achieved, which implies that outstanding sensor and actuator properties should be available from these materials (Squire and Gibbs, 1989).

Figure 15 shows the engineering magnetostriction data corresponding with the anisotropy data shown in Figure 13. It is important to note that the engineering magnetostriction reaches a saturation value at a given time and temperature before the anisotropy has saturated. Saturation of the engineering magnetostriction comes about from rotational reorientation of the local 'structural units', whereas the appropriate directional order has to reach saturation (requiring long-range diffusional processes) before the anisotropy can saturate (Thomas and Gibbs, 1992).

Figure 16 shows the ΔE effect in METGLAS®2605SC as a function of the field annealing angle (Squire and Gibbs, 1989). E/E_s is not unity at zero field, reflecting the moment noncollinearity discussed earlier. The maximum reduction in modulus (~80%) occurs in fields that are only five times the ambient field of the earth, demonstrating the extreme magnetic softness and outstanding magnetomechanical properties of appropriately treated material.

The basics (Livingston, 1982), and a more advanced treatment (du Trémolet de Lacheisserie, 1982), of magnetoelasticity in amorphous ferromagnetic alloys have been reviewed in the literature. A comprehensive phenomenological model for magnetization, magnetostriction, and ΔE effect has also been published (Squire, 1990). This model takes explicit account of the moment noncollinearity discussed earlier in the chapter.

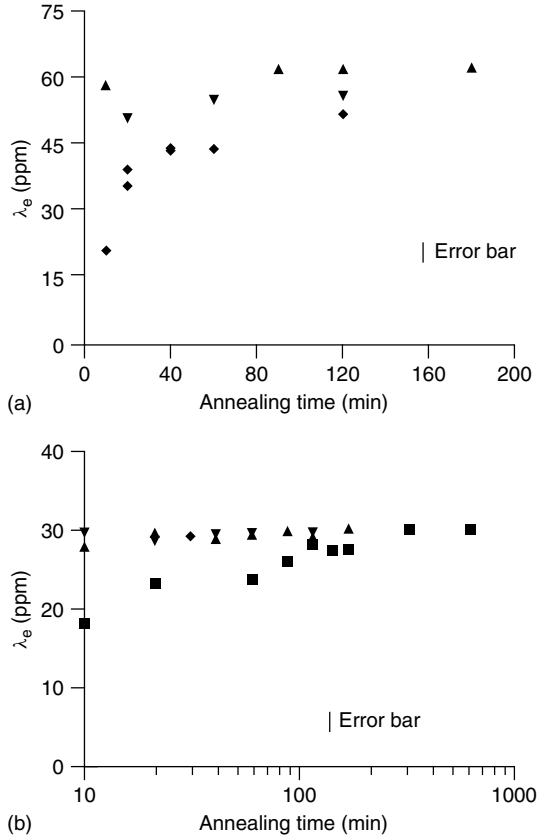

Figure 15. (a) Engineering magnetostriction, λ_e, versus anneal time for METGLAS®2605S2 for different annealing temperatures (squares 420 °C, triangles 400 °C, inverted triangles 350 °C, diamonds 250 °C). (b) Engineering magnetostriction, λ_e, versus anneal time for VAC®0040 for different annealing temperatures (squares 250 °C, triangles 300 °C, inverted triangles 350 °C, diamonds 370 °C).

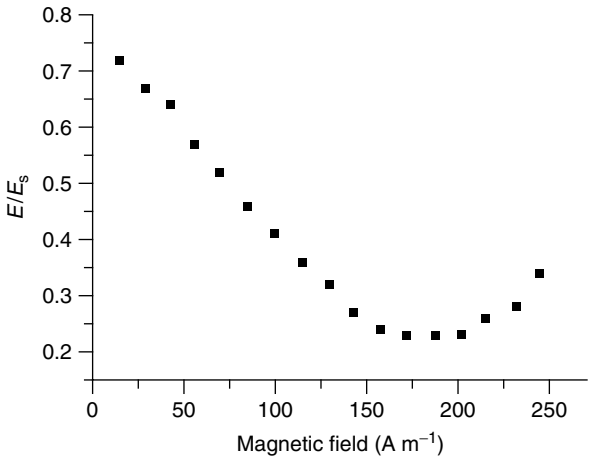

Figure 16. Ratio of Young's modulus to that at magnetic saturation as a function of magnetic field for METGLAS®2605SC.

7 PERMEABILITY, MAGNETIC LOSSES, AND TRANSFORMER APPLICATIONS

The combination of zero magnetocrystalline anisotropy and low induced anisotropies in amorphous ferromagnetic alloys, with the absence of features (e.g., grain boundaries) for domain wall pinning produces materials with relative permeabilities of up to 10^5 after optimized heat treatment. The structural disorder of the alloys also gives rise to electrical resistivities around three times larger than in comparable crystalline magnetic materials.

If as-cast material is taken, accepting some loss of permeability from the effect of cast-in stress, with its excellent mechanical properties, then high-grade, flexible magnetic shielding can be provided (Smith, 1982). The magnetic and mechanical advantages over crystalline Ni–Fe-based shielding products can be considerable.

At power frequencies (50–400 Hz), the drive for greener energy supply has worked in favor of amorphous alloys. The lower saturation magnetization caused by the greater solute content than for Si steel can be tolerated as cores are now designed not to be driven to such high levels of magnetization. The frequency dependence of eddy current loss is usually taken as $\propto f^n$ with $n = 2$ for common crystalline materials such as Si–Fe, but $n = 1.5$ in amorphous ferromagnetic materials. It should be borne in mind, however, that, to a significant degree, the smaller losses for the Fe-based amorphous alloys are due to smaller strip thickness than for the silicon steel, which results in significantly smaller eddy current losses. It has been shown that Hi–B silicon steel strip of thickness 100 µm, manifests lower AC losses that are only slightly larger than 25-µm-thick amorphous alloy. It is implicit that, at the 25-µm thickness level, the Fe–Si alloy would have significantly lower losses than the amorphous alloy due to its much smaller λ_s. The level of harmonic distortion caused by loads on transformer cores significantly affects the total loss. The lower core loss in amorphous alloys offers much reduced higher harmonics, and therefore lower overall losses (Hasegawa, 2004). As frequency rises to the airborne transformer range (400 Hz), the losses in amorphous alloy cores are one-fifth of those in grain-oriented silicon steel. For design purposes, ample data on permeability and loss as a function of frequency may be found on the manufacturers' websites (METGLAS® Products, www.metglas.com; Vacuumschmelze, www.vacuumschmelze.de).

While the resistivity of amorphous alloys is much higher than that of their crystalline counterparts, further improvement may be obtained by producing powder cores. Powderform amorphous material may be produced directly by powder atomization or by grinding up of ribbon material. The increased brittleness of annealed ribbon can aid in this process. In the kilohertz operating range, losses can be comparable with N–Zn ferrites (Hasegawa, Hathaway and Chang, 1985). The highest densities after dynamic compaction are around 90% (Hasegawa, Hathaway and Chang, 1985); however, increased stress on the core material lowers the permeability (Hasegawa, 2003).

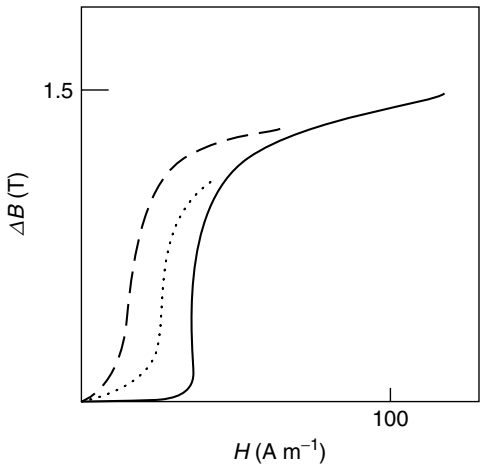

Figure 17. The pulse reversal curve of three toroids of VAC®6030 (solid line) in as-received state, (dotted line) slow cooled ($2^\circ\,s^{-1}$) from above the Curie point to ambient, and (dashed line) fast cooled ($100^\circ\,s^{-1}$) from above the Curie point to ambient. The pulse was at a rate of 300 T $(ms)^{-1}$.

Switched-mode power supplies (SMPS), operating at 10–200 kHz, require low loss and high-saturation induction, and for high-power SMPS there is an advantage from the low losses and high-saturation induction of amorphous alloys. Ferrite cores that are electrically insulating, but have low saturation induction have been used. The amorphous ferromagnets have much higher induction, and sufficient resistivity to offer better overall performance.

Magnetic switching using a saturable inductor has been known for over 50 years, but interest was rekindled with the advent of amorphous alloy cores (Smith, 1982). Pulse characteristics have been studied (Jones, 1982, 1983). The pulse response for a core of Co-based (low magnetostriction) alloy is shown in Figure 17.

Careful postprocessing of the core can give a pulse response close to ideal (Sheard, Gibbs and Avery, 1989).

8 SENSORS

It is the combination of magnetic softness and high magnetomechanical coupling that has led to numerous suggestions for sensors based on amorphous alloys. The application of amorphous alloy ribbons (Hernando, Vázquez and

Barandiaran, 1988; Hasegawa, 2004) for sensors has been comprehensively reviewed.

In terms of market penetration, the leader is electronic article surveillance of consumer products (Herzer, 2003). In this application, a length of amorphous alloy is packaged together with a piece of semihard magnet strip. The latter is incorporated for activation and deactivation. Sensing is by harmonic or acoustomechanical means. The very square loop possible with carefully treated amorphous ferromagnets, coupled with high yield strength and electrical resistivity, makes them the material of choice for the harmonic system. It is usually a Co-based low magnetostriction material that is used. The acoustomechanical system relies on mechanical resonance in the sensing layer and on the ΔE *effect*. Fe-based, high-magnetostriction amorphous alloys are used in this case. The unit cost in both cases is low, and the market penetration is high.

A range of magnetometry devices has been proposed on the basis of modulation of fibre-optic interferometers (Dandridge *et al*., 1980; Bucholtz *et al*., 1987) and shear wave propagation (Squire and Gibbs, 1988; Kilby, Squire and Willcock, 1993). The fiber-optic route using ribbon-form amorphous alloy was shown to have problems both with frequency response (Brugel, Gibbs and Squire, 1988a) and high sensitivity to bonding (Brugel, Gibbs and Squire, 1988b). The shear wave option has generated a sensitivity of 0.1 nT/$\sqrt{\text{Hz}}$. This is in the range where there are application windows, and several devices are close to commercialization.

Stress or strain sensing via changes in susceptibility has been demonstrated. There are significant advantages in using negative magnetostriction amorphous alloy ribbons, and a figure of merit (FOM) of 10^4 can be achieved (Barandiaran and Gutierrez, 1997). The degradation caused by bonding has been addressed (Wun-Fogle *et al*., 1987), and with a viscous bond, limiting application to AC strain detection, an FOM of $>2 \times 10^5$ was achieved. A semiconductor strain gauge has an FOM of $\sim$250 by comparison.

If the constraint of bulk magnetic material (in this case ribbon) can be relaxed, then thin-film deposition may be used to advantage. Amorphous ferromagnetic films derived from commercial METGLAS® alloy targets have been used in conjunction with microbridges and membranes to produce pressure sensors with FOM up to 2×10^5 (Gibbs *et al*., 1996; Karl *et al*., 2000). The potential for further application and integration within the microelectromechanical systems (MEMS) has been discussed (Gibbs, Hill and Wright, 2004). Thin-film technology overcomes many of the drawbacks of bonding, and a microstrain sensor using amorphous $(Fe_{90}Co_{10})_{78}Si_{12}B_{10}$ sputtered on to a soft glass substrate, demonstrated an FOM of 1.2×10^5 (Shin, Inoue and Arai, 1999).

The high magnetomechanical coupling also implies that there could be highly efficient transfer of sound waves into electrical signals (hydrophonics) using amorphous alloy cores. Scrolls of METGLAS®2605SC have been shown to demonstrate an optimum effective magnetomechanical coupling coefficient of 0.75 (maximum is 1). Very low bias fields were required (Rees, Gibbs and Pace, 1989; Rees *et al*., 1992).

REFERENCES

Alben, R., Becker, J.J. and Chi, M.C. (1978). Random anisotropy in amorphous ferromagnets. *Journal of Applied Physics*, **49**, 1653–1658.

Barandiaran, J.M. and Gutierrez, J. (1997). Magnetoelastic sensors based on soft amorphous magnetic alloys. *Sensors and Actuators, A*, **59**, 38–42.

Berkowitz, A.E., Walter, J.L. and Wall, K.F. (1981). Magnetic properties of amorphous particles produced by spark erosion. *Physical Review Letters*, **46**, 1484–1487.

Brugel, D., Gibbs, M.R.J. and Squire, P.T. (1988a). Particulate metallic glass composite magnetostrictors for interferometric magnetometry. *Journal of Applied Physics*, **63**, 4249–4251.

Brugel, D., Gibbs, M.R.J. and Squire, P.T. (1988b). On the choice of a magnetostrictive transducer for interferometric magnetometry. *Journal of Applied Physics*, **64**, 3149–3152.

Bucholtz, F., Koo, K.P., Dandridge, A. and Sigel, G.H. (1986). Easy axis distributions in transversely annealed METGLAS®2605S2. *Journal of Magnetism and Magnetic Materials*, **54–57**, 1607–1608.

Bucholtz, F., Koo, K.P., Yurek, A.M., *et al*. (1987). Preparation of amorphous metallic-glass transducers for use in fiber optic magnetic sensors. *Journal of Applied Physics*, **61**, 3790–3792.

Buschow, K.H.J. (1979). Crystallization and magnetic properties of amorphous Gd-Fe and Er-Fe alloys. *Journal of the Less-Common Metals*, **66**, 89–97.

Callen, E.R. and Callen, H.B. (1963). Static magnetoelastic coupling in cubic crystals. *Physical Review*, **129**, 578–593.

Callen, E. and Callen, H.B. (1965). Magnetostriction, forced magnetostriction, and anomalous thermal expansion in ferromagnets. *Physical Review*, **139**, A455–A471.

Chen, H.S., Sherwood, R.C., Leamy, H.J. and Gyorgy, E.M. (1976). The effect of structural relaxation on the Curie temperature of Fe based metallic glasses. *IEEE Transactions on Magnetics*, **MAG-12**, 933–935.

Cline, C.F. and Hopper, R.W. (1977). Explosive fabrication of rapidly quenched materials. *Scripta Metallurgica*, **11**, 1137–1138.

Coey, J.M.D. (1978). Amorphous magnetic order. *Journal of Applied Physics*, **49**, 1646–1652.

Dandridge, A., Tveten, A.B., Sigel, G.H. Jr., *et al*. (1980). Optical fibre magnetic-field sensors. *Electronics Letters*, **16**, 408–409.

Davies, H.A. (1976). The formation of metallic glasses. *Physics and Chemistry of Glasses*, **17**, 159–173.

Davies, H.A. (1978). Rapid quenching techniques and formation of metallic glasses. In *Rapidly Quenched Metals III*, Cantor, B. (Ed.), The Metals Society: London, pp. 1–21.

Davies, H.A. (1983). Metallic glass formation. In *Amorphous Metallic Alloys*, Luborsky, F.E. (Ed.), Butterworths: London, pp. 8–25.

Davies, H.A. (1995). Metallic glass formation re-visited. In *Nanostructured and Non-Crystalline Materials*, Vazquez, M. and Hernando, A. (Eds.), World Scientific: Singapore, pp. 3–14.

Davies, H.A. and Lewis, B.G. (1975). A generalised kinetic approach to metallic glass formation. *Scripta Metallurgica*, **9**, 1107–1112.

Davis, L.A. (1976). Mechanics of metallic glasses. In *Rapidly Quenched Metals: Proceedings of the 2nd International Conference on Rapidly Quenched Metals*, Grant, N.J. and Giessen, B.C. (Eds.), M.I.T. Press: Cambridge, pp. 369–391.

Davis, L.A., Ray, R., Chou, C-P. and O'Handley, R.C. (1976). Mechanical and thermal properties of $Fe_{80}B_{20}$ glass. *Scripta Metallurgica*, **10**, 541–546.

Donald, I.W. and Davies, H.A. (1978). Prediction of glass-forming ability for metallic systems. *Journal of Non-Crystalline Solids*, **30**, 77–85.

Donald, I.W. and Davies, H.A. (1980). Influence of transition metal substitutions on the formation, stability and hardness of some Fe- and Ni-based metallic glasses. *Philosophical Magazine*, **42**, 277–293.

Donald, I.W., Kemeny, T. and Davies, H.A. (1981). The influence of transition metal substitutions on the Curie temperature of as-quenched $FeSi_{10}B_{12}$-based metallic glasses. *Journal of Physics F: Metal Physics*, **11**, L131–L136.

Donovan, P.E. and Stobbs, W.M. (1981). The structure of shear bands in metallic glasses. *Acta Metallurgica*, **29**, 1419–1436.

Duwez, P. and Lin, S.C.H. (1967). Amorphous ferromagnetic phase in Iron-Phosphorous-Carbon alloys. *Journal of Applied Physics*, **38**, 4096–4097.

Fiedler, H., Mühlbach, H. and Stephani, G. (1984). The effect of main processing parameters on the geometry of amorphous ribbons during planar flow casting (PFC). *Journal of Materials Science*, **19**, 3229–3235.

Fukamichi, K., Kikuchi, M., Masumoto, T. and Matsuura, M. (1979). Magnetic properties and invar effects of amorphous Gd-Co ribbons. *Physics Letters*, **73A**, 436–438.

Furthmüller, J., Fähnle, M. and Herzer, G. (1987). Theory of magnetostriction in amorphous and polycrystalline ferromagnets. 1. Description of the formalism. *Journal of Magnetism and Magnetic Materials*, **69**, 79–88.

Gibbs, M.R.J. (1990). Anisotropy and magnetostriction in amorphous alloys. *Journal of Magnetism and Magnetic Materials*, **83**, 329–333.

Gibbs, M.R.J., Evetts, J.E. and Leake, J.A. (1983). Activation energy spectra and relaxation in amorphous materials. *Journal of Materials Science*, **18**, 278–288.

Gibbs, M.R.J., Hill, E.W. and Wright, P.J. (2004). Magnetic materials for MEMS applications. *Journal of Physics D: Applied Physics*, **37**, R237–R244.

Gibbs, M.R.J., Shearwood, C., Dancaster, J.L., *et al*. (1996). Piezomagnetic tuning of a micromachined resonator. *IEEE Transactions on Magnetics*, **32**, 4950–4952.

Giessen, B.C. (1982). Glass formation diagrams: a two-parameter representation of readily glass forming systems. In *Proceedings of the 4th International Conference on Rapidly Quenched Metals*, Masumoto, T. and Suzuki, K. (Eds.), Japan Institute of Metals: Sendai, pp. 213–216.

Grundy, P.J. (1980). The structure and magnetic properties of amorphous magnetic thin films. *Journal of Magnetism and Magnetic Materials*, **21**, 1–23.

Gubanov, A.I. (1960). Quasi-classical theory of amorphous ferromagnetics. *Soviet Physics-Solid State*, **2**, 468–471.

Hang Nam, OK and Morrish, A.H. (1981). Surface crystallisation and magnetic anisotropy in amorphous $Fe_{40}Ni_{38}Mo_4B_{18}$ ribbons. *Journal of Applied Physics*, **52**, 1835–1837.

Hasegawa, R. (2003). Design and fabrication of new soft magnetic materials. *Journal of Non-Crystalline Solids*, **329**, 1–7.

Hasegawa, R. (2004). Applications of amorphous magnetic alloys. *Materials Science and Engineering A*, **375–377**, 90–97.

Hasegawa, R. and Cline, C.F. (1985). Magnetic properties of dynamically compacted glassy metal cores. In *Rapidly Quenched Metals*, Steeb, S. and Warlimont, H. (Eds.), Elsevier Science: Amsterdam, pp. 1667–1669.

Hasegawa, R., Hathaway, R.E. and Chang, C.F. (1985). Magnetic properties of consolidated glassy metal-powder cores. *Journal of Applied Physics*, **57**, 3566–3568.

Hasegawa, R. and Ray, R. (1978). Iron-boron metallic glasses. *Journal of Applied Physics*, **49**, 4174–4179.

Hernando, A., Vázquez, M. and Barandiaran, J.M. (1988). Metallic glasses and sensing applications. *Journal of Physics E: Scientific Instruments*, **21**, 1129–1139.

Herzer, G. (2003). Magnetic materials for electronic article surveillance. *Journal of Magnetism and Magnetic Materials*, **254–255**, 598–602.

Herzer, G. and Hilzinger, H.R. (1986). Surface crystallisation and magnetic properties in amorphous iron rich alloys. *Journal of Magnetism and Magnetic Materials*, **62**, 143–151.

Holt, J.B., Ankeny, D.C. and Cline, C.F. (1980). Beryllium-containing high specific strength amorphous alloys. *Scripta Metallurgica*, **14**, 959–962.

Inoue, A. (1997). Bulk amorphous alloys with soft and hard magnetic properties. *Materials Science and Engineering*, **A226–A228**, 357–363.

Inoue, A. (2000). Ferromagnetic bulk glassy alloys. *Journal of Magnetism and Magnetic Materials*, **215–216**, 246–252.

Inoue, A., Kobayashi, K., Nose, M. and Masumoto, T. (1980). Mechanical properties of (Fe, Co, Ni)-M-B (M = Ti, Zr, Hf, V, Nb, Ta and Mo) amorphous alloys with low boron concentration. *Journal de physique, Colloques*, **41**(Suppl. 8), C8-831–C8-834.

Inoue, A., Shen, B., Koshiba, H., *et al*. (2003). Cobalt-based bulk glassy alloy with ultra-high strength and soft magnetic properties. *Nature Materials*, **2**, 661–663.

Jones, R.M. (1982). Step dB/dt magnetization losses in toroidal amorphous ribbon and polycrystalline cores. *IEEE Transactions on Magnetics*, **MAG-18**, 1559–1561.

Jones, R.M. (1983). Step dB/dt switching characteristics of square loop, strip wound Ni-Fe toroids. *IEEE Transactions on Magnetics*, **MAG-19**, 2024–2026.

Karl, W.J., Powell, A.L., Watts, R., *et al*. (2000). A micromachined magnetostrictive pressure sensor using magneto-optical interrogation. *Sensors and Actuators, A*, **81**, 137–141.

Kavesh, S. (1978). Metallic glasses – the technology of rapid solidification processing. In *Rapid Solidification Processing-Principles and Technologies*, Mehrabian, R., Kear, B.H. and Cohen, M. (Eds.), Claitor's Publishing Division: Baton Rouge, pp. 165–187.

Kawamura, Y., Takagi, M. and Akai, M. (1988). A newly developed warm extrusion technique for compacting amorphous alloy powders. *Materials Science and Engineering*, **98**, 449–452.

Kilby, C.F., Squire, P.T. and Willcock, S.N.M. (1993). Analysis and performance of a shear-wave magnetometer. *Sensors and Actuators, A*, **37–38**, 453–457.

Kimura, H. and Masumoto, T. (1983). Strength, ductility and toughness – a study in model mechanics. In *Amorphous Metallic Alloys*, Luborsky, F.E. (Ed.), Butterworths: London, pp. 187–230.

Kronmüller, H. (1979). Micromagnetism in amorphous alloys. *IEEE Transactions on Magnetics*, **15**, 1218–1225.

Kronmüller, H. (1981). Theory of the coercive field in amorphous ferromagnetic alloys. *Journal of Magnetism and Magnetic Materials*, **24**, 159–167.

Kronmüller, H. (1983). Theory of magnetic after-effects in ferromagnetic amorphous alloys. *Philosophical Magazine*, **B 48**, 127–150.

Kronmüller, H. (1985). The role of two-level systems in amorphous metallic alloys. *Physica Status Solidi, B*, **127**, 531–541.

Kronmüller, H., Guo, H-Q., Fernengel, W., *et al*. (1985). Activation energy spectra of induced anisotropy and coercive field in amorphous ferromagnetic $Co_{58}Ni_{10}Fe_5Si_{11}B_{16}$. *Crystal Lattice Defects and Amorphous Materials*, **11**, 135–150.

Lewis, B.G. and Davies, H.A. (1977). The formation of amorphous metallic phases by continuous cooling from the melt. In *Liquid Metals*, Evans, R. and Greenwood, D.A. (Eds.), Institute of Physics: London, pp. 274–282.

Lewis, B.G., Ward, K.D. and Davies, H.A. (1979). The crystallisation and associated changes in ductility of some Fe-Ni-B amorphous alloys. *Scripta Metallurgica*, **13**, 313–317.

Liebermann, H.H. and Graham, C.D. (1976). Production of amorphous alloy ribbons and effects of apparatus parameters on ribbon dimensions. *IEEE Transactions on Magnetics*, **MAG-12**, 921–923.

Livingston, J.D. (1982). Magnetomechanical properties of amorphous metals. *Physical Status Solidi A* , **70**, 591–596.

Luborskty, F.E., Becker, J.J. and McCary, R.O. (1975). Magnetic annealing of amorphous alloys. *IEEE Transactions on Magnetics*, **MAG-11**, 1644–1649.

Luborsky, F.E., Reeve, J., Davies, H.A. and Liebermann, H.H. (1982). Effect of Fe-B-Si composition on maximum thickness for casting amorphous metals. *IEEE Transactions on Magnetics*, **MAG-18**, 1385–1388.

Luborsky, F.E. and Walter, J.L. (1976). Stability of amorphous metallic alloys. *Journal of Applied Physics*, **47**, 3648–3650.

Luborsky, F.E. and Walter, J.L. (1977a). Magnetic anneal anisotropy in amorphous alloys. *IEEE Transactions on Magnetics*, **MAG-13**, 953–956.

Luborsky, F.E. and Walter, J.L. (1977b). Magnetically induced anisotropy in amorphous alloys of Fe-Ni-P-B. *IEEE Transactions on Magnetics*, **MAG-13**, 1635–1638.

Mader, S. and Nowick, A.S. (1965). Metastable Co-Au alloys: an example of an amorphous ferromagnet. *Applied Physics Letters*, **7**, 57–59.

METGLAS® Products, (2006). www.metglas.com.

Miller, S.A. (1983). Amorphous metal powder: production and consolidation. In *Amorphous Metallic Alloys*, Luborsky, F.E. (Ed.), Butterworths: London, pp. 506–521.

Morris, D.G. (1982). Dynamic compaction of rapidly quenched materials. In *Proceedings of the 4th International Conference on Rapidly Quenched Metals*, Masumoto, T. and Suzuki, K. (Eds.), Japan Institute Metals: Sendai, pp. 145–148.

Narasimhan, M.C. (1979). *Continuous Casting Method for Metallic Strips*. U.S. Patent 4 142 571.

Nielsen, O.V. (1985). Effects of longitudinal and torsional stress annealing on the magnetic anisotropy in amorphous ribbon materials. *IEEE Transactions on Magnetics*, **MAG-21**, 2008–2013.

Nose, M. and Masumoto, T. (1980). Amorphous phase formation in the zirconium-poor corner of (Fe, Co, Ni)-Zr systems. *Science Reports of the Research Institutes, Tohoku University*, **28**, 232–241.

O'Handley, R.C. (1978). Magnetostriction of transition-metal-metalloid glasses: temperature dependence. *Physical Review B*, **18**, 930–938.

O'Handley, R.C. (1983). Fundamental magnetic properties. In *Amorphous Metallic Alloys*, Luborsky, F.E. (Ed.), Butterworths: London, pp. 257–282.

O'Handley, R.C. (1987). Physics of ferromagnetic amorphous alloys. *Journal of Applied Physics*, **62**, R15–R49.

O'Handley, R.C. (2000). *Modern Magnetic Materials-Principles and Applications*, John Wiley & Sons: New York, pp. 395–401.

Ohnaka, I., Fukusako, T. and Ohmichi, T. (1982). Production of amorphous filament by in-rotating liquid spinning method. In *Proceedings of the 4th International Conference on Rapidly Quenched Metals*, Masumoto, T. and Suzuki, K. (Eds.), Japan Institute Metals: Sendai, pp. 31–34.

Pankhurst, Q.A., Betteridge, S., Jiang, J. and Gibbs, M.R.J. (1994). In-plane moment canting in amorphous $Fe_{78}B_{13}Si_9$ in applied fields measured using polarized Mössbauer spectroscopy. *IEEE Transactions on Magnetics*, **30**, 4809–4811.

Perel, J., Mahoney, J.F., Duwez, P. and Kalensher, B.E. (1980). Application of electrohydrodynamics to rapid solidification of fine droplets and splats. In *Rapid Solidification Processing-Principles and Technologies*, Mehrabian, R., Kear, B.H. and Cohen, M. (Eds.), Claitor's Publishing Division: Baton Rouge, pp. 287–293.

Polk, D.E. (1972). Structure of glassy metallic alloys. *Acta Metallurgica*, **20**, 485–491.

Raybould, D. and Tan, K.S. (1985). Factors affecting the magnetic properties of consolidated amorphous powder cores. *Journal of Materials Science*, **20**, 2776–2785.

Rees, D.W., Gibbs, M.R.J. and Pace, N.G. (1989). The use of a metallic glass scroll as an acoustic transducer element. *IEEE Transactions on Ultrasonics, Ferroelectrics, and Frequency Control*, **36**, 332–336.

Rees, D.W., Gibbs, M.R.J. and Pace, N.G. (1992). Metallic glasses as acoustic transducers. *IEEE Transactions on Magnetics*, **28**, 3006–3008.

Sadoc, J.F. and Dixmier, J. (1976). Structural investigation of amorphous CoP and NiP by combined x-ray and neutron diffraction. *Materials Science and Engineering*, **23**, 187–192.

Sheard, S.M., Gibbs, M.R.J. and Avery, R.K. (1989). Characterisation of Co-based metallic glasses for saturable inductor cores. *Journal of Magnetism and Magnetic Materials*, **75**, 397–406.

Shin, K-H., Inoue, M. and Arai, K-I. (1999). Strain sensitivity of highly magnetostrictive amorphous films for use in microstrain sensors. *Journal of Applied Physics*, **85**, 5465–5467.

Smith, C.H. (1982). Magnetic pulse compression by metallic glasses. *Journal of Applied Physics*, **64**, 6032–6034.

Smith, C.H. (1993). Applications of rapidly solidified soft magnetic alloys. In *Rapidly Solidified Alloys*, Liebermann, H.H. (Ed.), Marcel Dekker, pp. 617–663.

Spaepen, F. and Taub, A.I. (1983). Flow and fracture. In *Amorphous Metallic Alloys*, Luborsky, F.E. (Ed.), Butterworths: London, pp. 231–256.

Squire, P.T. (1990). Phenomenological model for magnetization, magnetostriction and ΔE effect in field-annealed amorphous ribbons. *Journal of Magnetism and Magnetic Materials*, **87**, 299–310.

Squire, P.T. (1994). Magnetomechanical measurements of magnetically soft amorphous materials. *Measurement Science and Technology*, **5**, 67–81.

Squire, P.T. and Gibbs, M.R.J. (1988). Shear-wave magnetometry. *IEEE Transactions on Magnetics*, **24**, 1755–1757.

Squire, P.T. and Gibbs, M.R.J. (1989). ΔE effect in obliquely field annealed METGLAS®2605SC. *IEEE Transactions on Magnetics*, **25**, 3614–3616.

Suzuki, K., Kataoka, N., Inoue, A., *et al*. (1990). High saturation magnetization and soft magnetic properties of bcc Fe-Zr-B-Cu alloys with ultrafine grain structure. *Materials Transactions, JIM*, **31**, 743–746.

Takayama, S. and Oi, T. (1979). The analysis of casting conditions of amorphous alloys. *Journal of Applied Physics*, **50**, 4962–4965.

Taylor, G.F. (1924). A method of drawing metallic filaments and a discussion of their properties and uses. *Physical Review*, **23**, 655–660.

Thomas, A.P. and Gibbs, M.R.J. (1992). Anisotropy and magnetostriction in metallic glasses. *Journal of Magnetism and Magnetic Materials*, **103**, 97–110.

Todd, I., Davies, H.A., Gibbs, M.R.J., *et al*. (1999). The effect of ambient gases on surface quality and related properties of nanocrystalline soft magnetic ribbons produced by melt spinning. *Journal of Magnetism and Magnetic Materials*, **196–197**, 196–198.

du Trémolet de Lacheisserie, E. (1982). Magnetoelastic properties of amorphous alloys. *Journal of Magnetism and Magnetic Materials*, **25**, 251–270.

Tsuei, C.C. and Duwez, P. (1966). Metastable amorphous ferromagnetic phases in palladium-base alloys. *Journal of Applied Physics*, **37**, 435.

Turnbull, D. (1969). Under what conditions can a glass be formed? *Contemporary Physics*, **10**, 473–488.

Uhlmann, D.R. (1972). A kinetic treatment of glass formation. *Journal of Non-Crystalline Solids*, **7**, 337–348.

Vacuumschmelze, (2006). www.vacuumschmelze.de.

Vázquez, M., Ascasibar, E., Hernando, A. and Nielsen, O.V. (1987). Co-Si-B and Fe-Co-B amorphous alloys: induced anisotropy and various magnetic properties. *Journal of Magnetism and Magnetic Materials*, **66**, 37–44.

Vincent, J.H. and Davies, H.A. (1982). High speed continuous casting of alloy strip by chill block melt spinning, *Solidification Technology in the Foundry and Casthouse*, The Metals Society: London, pp. 153–158.

Ward, K.D., Hunger, G., Lewis, B.G. and Davies, H.A. (1979). The embrittlement and crystallisation of some glassy alloys. *Phase Transformations Spring Residential Conference*, Series 3, No. 11, Institute of Metallurgists: London, pp. III-33–III-35, Vol. 2.

Warrington, D.H., Davies, H.A. and Shohoji, N. (1982). Estimation of cooling rate during rapid solidification processing of Ni-based superalloys using photography. In *Proceedings of the 4th International Conference on Rapidly Quenched Metals*, Masumoto, T. and Suzuki, K. (Eds.), Japan Institute Metals: Sendai, pp. 69–72.

Wildes, A.R., Cowlam, N., Pankhurst, Q.A., *et al*. (2004). The magnetic structure of $Fe_{78}Si_9B_{13}$. *Europhysics Letters*, **68**, 582–588.

Wun-Fogle, M., Savage, H.T., Clarke, A.E. (1987). Sensitive, wide frequency range magnetostrictive strain gage. *Sensors and Actuators*, **12**, 323–331.

Yamaguchi, T. and Narita, K. (1978). Preparation of amorphous magnetic powder by atomization technique. *Applied Physics Letters*, **33**, 468–470.

Yoshizawa, Y., Oguma, S. and Yamauchi, K. (1988). New Fe-based soft magnetic alloys composed of ultrafine grain structure. *Journal of Applied Physics*, **64**, 6044–6046.

FURTHER READING

FINEMET®, (2006). www.hitachi-metals.co.jp.

Kojima, A., Horikiri, H., Makino, A., *et al*. (1995). Soft magnetic properties of nanocrystalline bcc Fe-(Nb,Zr)-B bulk alloys consolidated by warm extrusion. *Materials Transactions, JIM*, **36**, 945–951.

Koo, K.P., Bucholtz, F., Dagenais, D.M. and Dandridge, A. (1989). A compact fibre optic magnetometer employing an amorphous metal wire transducer. *IEEE Photonics Technology Letters*, **1**, 464–466.

Kronmüller, H. (1984). Magnetic after-effects, induced anisotropies, and the role of two-level systems in amorphous alloys. *Journal of Magnetism and Magnetic Materials*, **41**, 366–375.

MQP®, (2006). www.magnequench.com.

Nuetzel, D., Rieger, G., Wecker, J., *et al*. (1999). Nanocrystalline soft magnetic composite cores with idea orientation of the powder flakes. *Journal of Magnetism and Magnetic Materials*, **196–197**, 327–329.

VITROPERM®, (2006). www.vacuumschmelze.de.

VITROVAC®, (2006). www.vacuumschmelze.de.

Soft Magnetic Materials – Nanocrystalline Alloys

Giselher Herzer
Vacuumschmelze GmbH & Co. KG, Hanau, Germany

1 INTRODUCTION

It is well known that the microstructure, noticeably the grain size, essentially determines the hysteresis loop of a ferromagnetic material. Figure 1 gives an example for the variation of the coercivity H_c over the whole range of structural correlation lengths starting from atomic distances in amorphous alloys over grain sizes, D, in the nanometer regime up to macroscopic grain sizes. The permeability shows an analogous behavior being essentially inversely proportional to H_c. The $1/D$ dependence of coercivity for large grain sizes (cf. Pfeifer and Radeloff, 1980) reflects the conventional rule that good soft magnetic properties require very large grains ($D > 100\,\mu m$). Thus, the reduction of particle size to the regime of the domain wall width increases the coercivity H_c toward a maximum, controlled by the anisotropies present. Accordingly, fine particle systems have been mostly discussed as hard magnetic materials (cf. Luborsky, 1961). Lowest coercivities, however, are again found for smallest structural correlation lengths like in amorphous alloys ('grain size' of the order of atomic distances) and in nanocrystalline alloys for grain sizes $D < 20\,nm$. The extraordinary D^6 dependence of coercivity at small grain size moreover demonstrates how closely soft and hard magnetic behavior actually can be neighbored. Indeed, the soft magnetic alloys are only one manifestation of the novel and extraordinary magnetic properties that can be realized by establishing structural features on the nanometer scale. Thus, nanocrystalline microstructures are also of high interest in order to enhance the properties of rare-earth hard magnets (cf. Buschow, 1997).

The decrease of coercivity in nanocrystalline soft magnetic materials has to be well distinguished from superparamagnetic phenomena, that is, the well-known decrease of coercivity in small, isolated, or weakly coupled particles due to thermal excitation (Kneller, 1969; Luborsky, 1961). In the present case, we consider small ferromagnetic crystallites well coupled by exchange interaction that results in low coercivity and, unlike superparamagnetic particles, in a simultaneously high permeability.

The most prominent example of soft magnetic nanocrystalline materials are devitrified glassy Fe–Cu–Nb–Si–B alloys introduced by Yoshizawa, Oguma and Yamauchi (1988). The material reveals an ultrafine microstructure of bcc Fe–Si with grain sizes of 10–15 nm embedded in an amorphous minority matrix. This particular microstructure enables a unique combination of the low losses, high permeability, and low magnetostriction achieved by permalloys and Co-based amorphous alloys, but with a saturation magnetization up to 1.3 T–much higher than either of these materials can conventionally offer. The material was produced by crystallization of an amorphous Fe–Si–B alloy with small additions of Cu and Nb, a hitherto somewhat unusual combination which proved to be the key for the

Handbook of Magnetism and Advanced Magnetic Materials. Edited by Helmut Kronmüller and Stuart Parkin. Volume 4: *Novel Materials*. ISBN: 978-0-470-02217-7.

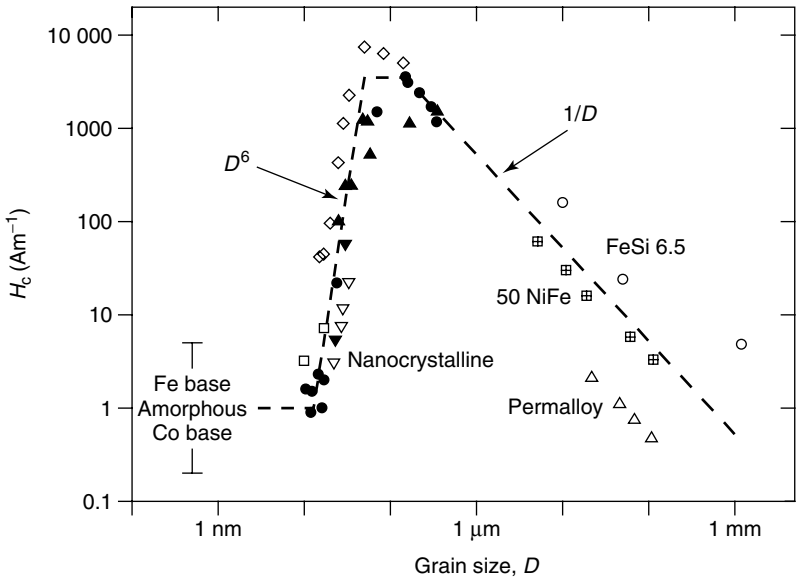

Figure 1. Coercivity, H_c, versus grain size, D, for various soft magnetic metallic alloys: Fe–Nb–Si–B (solid up triangles, Herzer, 1990), Fe–Cu–Nb–Si–B (solid circles, Herzer, 1990–1995), Fe–Cu–V–Si–B (solid down triangles, Herzer, 1997 and open down triangles, Sawa and Takahashi, 1990), Fe–Zr–B (open squares, Suzuki *et al*., 1991a,b), Fe–Co–Zr (open diamonds, Guo *et al*., 1991), NiFe alloys (+ center squares and open up triangles, Pfeifer and Radeloff, 1980), and FeSi 6.5 wt% (open circles, Arai, Tsutsumitakae and Ohmori, 1984). (Reprinted from *J. Magn. Magn. Mat.*, **112**, Herzer, Nanocrystalline Soft Magnetic Materials, 258–262, 1992, with permission from Elsevier.)

particular ultrafine grain structure and the associated soft magnetic properties.

The work of Yoshizawa *et al*. stimulated an intensive research for alternative alloy compositions. Thus, low-magnetostrictive nanocrystalline Fe–(Cu)–Zr–B alloys (Suzuki *et al*., 1990, 1991a,b) or Fe–Hf–C thin films (Hasegawa and Saito, 1991) have been established which exhibit a still higher saturation magnetization up to 1.7 T due to the higher Fe content in the alloy. Still, the outstanding soft magnetic properties of the original alloy system could not be reached. Interestingly, as a kind of precursor, the first example for soft magnetic behavior in the nanocrystalline state was given by O'Handley *et al*. (1985) for a devitrified glassy *cobalt*-based alloy. However, the soft magnetic properties were inferior to the amorphous state and, thus, not very attractive, which at present seems to be typical for cobalt-based nanocrystalline materials. Indeed, the most promising properties so far have been found in *iron*-based alloys on which we will focus this article. Table 1 summarizes some examples and their magnetic properties in comparison with conventional soft magnetic alloys.

We continue in Section 2 with a review of the *random anisotropy model* which provides the theoretical background for the soft magnetic properties observed in nanocrystalline and amorphous materials. This is followed in Section 3 by an overview of the most important alloy systems and their basic characteristics. Section 4 provides the experimental complement of Section 2 and discusses the various magnetic anisotropy contributions ultimately relevant for the soft magnetic properties in optimized nanocrystalline alloys. Concluding remarks are found in Section 5.

2 RANDOM ANISOTROPY MODEL

The basic conditions for good soft magnetic properties generally are a low or vanishing magnetic anisotropy constant K, which is a measure for the energy density needed to rotate the magnetization vector out of its energetically preferred orientation (magnetic easy axis). The most important contribution, the *magnetocrystalline* anisotropy, is related to the symmetry of the local atomic structure. For bcc-FeSi 20 at%, the constituent phase in nanocrystalline $Fe_{73.5}Cu_1Nb_3Si_{13.5}B_9$, the magnetocrystalline anisotropy constant is about $K_1 = 8.2\,\mathrm{kJ\,m^{-3}}$ (Gengnagel and Wagner, 1961), which is orders of magnitude too large in order to explain by itself the low coercivity ($H_c < 1\,\mathrm{A\,m^{-1}}$) and high permeability ($\mu_i \approx 10^5$) observed in the nanocrystalline material.

The key to understanding the soft magnetic properties in nanocrystalline materials is to recognize that the microstructure leads to a distribution of magnetic anisotropy axes randomly varying their orientation on a scale smaller than the domain wall width. The smoothing action of ferromagnetic exchange interaction, thus, impedes the magnetization

Table 1. Typical values of grain size D, saturation magnetization J_s, saturation magnetostriction λ_s, coercivity H_c, initial permeability μ_i, electrical resistivity ρ, core losses P_{Fe} at 0.2 T, 100 kHz, and ribbon thickness t for nanocrystalline, amorphous, and crystalline soft magnetic ribbons. (Reprinted from *Handbook of Magnetic Materials*, Vol 10, Buschow, K.H.J, Nanocrystalline Soft Magnetic Alloys, Elsevier Science B.V., pp 415–462, 1997, with permission from Elsevier.)

Alloy	D (nm)	J_s (T)	λ_s (10^{-6})	H_c (A m^{-1})	μ_i (1 kHz)	ρ (μΩcm)	P_{Fe} (W kg^{-1})	t (μm)	References
$Fe_{73.5}Cu_1Nb_3Si_{13.5}B_9$	13	1.24	2.1	0.5	100 000	118	38	18	Yoshizawa *et al.* (1988)
$Fe_{73.5}Cu_1Nb_3Si_{15.5}B_7$	14	1.23	∼0	0.4	110 000	115	35	21	Vacuumschmelze (1990, 1993)[a]
$Fe_{84}Nb_7B_9$	9	1.49	0.1	8	22 000	58	76	22	Suzuki *et al.* (1991, 1993)
$Fe_{86}Cu_1Zr_7B_6$	10	1.52	∼0	3.2	48 000	56	116	20	Suzuki *et al.* (1991, 1993)
$Fe_{91}Zr_7B_3$	17	1.63	−1.1	5.6	22 000	44	80	18	Suzuki *et al.* (1991, 1993)
$Co_{68}Fe_4(MoSiB)_{28}$	am.	0.55	∼0	0.3	150 000	135	35	23	Vacuumschmelze (1990, 1993)[a]
$Co_{72}(FeMn)_5(MoSiB)_{23}$	am.	0.8	∼0	0.5	3000	130	40	23	Vacuumschmelze (1990, 1993)[a]
$Fe_{76}(SiB)_{24}$	am.	1.45	32	3	8000	135	50	23	Vacuumschmelze (1990, 1993)[a]
80%Ni–Fe (permalloys)	$\sim 10^5$	0.75	<1	0.5	100 000[b]	55	>90[c]	50	Vacuumschmelze (1990, 1993)[a]
50–60%Ni–Fe	$\sim 10^5$	1.55	25	5	40 000[b]	45	>200[c]	70	Vacuumschmelze (1990, 1993)[a]

[a]Typical commercial grades for low remanence hysteresis loops.
[b]50 Hz values
[c]Lower bounds due to eddy currents

to follow the easy axes of the individual grains. The effective anisotropy constant for the magnetization process will therefore be an average over several grains and, hence, be reduced in magnitude. This makes the essential difference to large grained materials where the magnetization follows the randomly oriented easy axis of each grain and, accordingly, the magnetization process is controlled by the full local magnetocrystalline anisotropy.

The degree to which the local magnetocrystalline anisotropies are finally averaged out has been successfully addressed in terms of the so-called random anisotropy model (Herzer, 1989, 1990) which was originally developed in order to explain the soft magnetic properties of amorphous ferromagnets by Alben, Becker and Chi (1978). We review in this section the basic concepts of this model as well as its extensions (Herzer, 1995, 2005a; Suzuki, Herzer and Cadogan, 1998b) to multiphase systems with mixed random and uniform anisotropies.

2.1 Basic concepts

The random anisotropy model starts from a microstructure characterized by a distribution of magnetic anisotropy axes randomly varying their orientation over the scale of the grain size, D. The interplay between exchange and anisotropy energy is basically described by the following free energy density

$$\phi = A \sum_{i=x,y,z} (\nabla m_i)^2 + K_1 \, f_K(\underline{m} \cdot \underline{u}) + \ldots \qquad (1)$$

where A is the exchange stiffness, $\underline{m}$ is the direction of the magnetization vector, K_1 is the local magnetocrystalline anisotropy constant, and f_K is a dimensionless function describing the angular variation of the anisotropy energy density with respect to a local symmetry axis denoted by $\underline{u}$.

It is evident from equation (1) that the exchange energy density scales as A/L^2 if the magnetization changes its orientation on a length scale L, for example, by following the easy axes of the local magnetic anisotropies. Consequently, the exchange energy would exceed the local anisotropy energy (i.e., $A/L^2 > K_1$) if the magnetization followed the local anisotropy variations on a scale smaller than

$$L_0 = \varphi_0 \sqrt{A/K_1} \qquad (2)$$

where φ_0 is a dimensionless parameter in the order of 1. This *basic* ferromagnetic correlation length represents the characteristic minimum scale below which the direction of the magnetization cannot vary appreciably. It, for example, determines the order of the domain wall width for grains larger than L_0. Typical values are $L_0 \approx 5$–10 nm for Co-based and $L_0 \approx 20$–40 nm for Fe-based alloys. Accordingly, both amorphous ($D \approx$ atomic scale) and nanocrystalline alloys ($D \approx 5$–20 nm) fall into the regime where the structural correlation length D is smaller than L_0 and where the local randomly oriented anisotropies are, hence, averaged by the smoothing effect of exchange interaction.

The magnetic anisotropy relevant to the magnetization process for $D < L_0$ is given by the average of the anisotropy energy density over the volume $V_{ex} = L_{ex}^3$ defined by a correlation length L_{ex}, where the magnetization direction

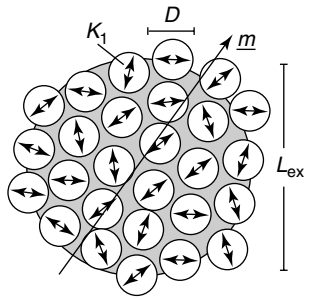

Figure 2. Schematic representation of the random anisotropy model for grains embedded in an ideally soft ferromagnetic matrix. The double arrows indicate the randomly fluctuating anisotropy axis, the hatched area represents the ferromagnetic correlation volume determined by the exchange length L_{ex} within which the orientation $\underline{m}$ of the magnetization is constant.

is kept constant by exchange interaction. The situation is schematically sketched in Figure 2. The average over the randomly oriented anisotropies of the $N = (L_{ex}/D)^3$ grains in the exchange-coupled volume is determined by statistical fluctuations. The average anisotropy constant $\langle K_1 \rangle$, hence, scales down as (cf. Appendix)

$$\langle K_1 \rangle = \frac{K_1}{\sqrt{N}} = K_1 \cdot (D/L_{ex})^{3/2} \tag{3}$$

The resulting easiest magnetic axis of the N grains is randomly oriented from one region of exchange-coupled grains to the other. The magnetization will follow these easy axes and the exchange energy consequently scales as $A/{L_{ex}}^2$. Accordingly, the average total free energy density with respect to the homogeneously magnetized state becomes

$$\langle \phi \rangle \approx A \cdot (\alpha/L_{ex})^2 - \tfrac{1}{2}\beta\,|K_1| \cdot (D/L_{ex})^{3/2} \tag{4}$$

where the dimensionless parameters α and β are basically related to the effective average angle between the easiest axes of the exchange-coupled regions and to the symmetry of the random anisotropy axis, respectively (cf. Herzer, 2005a).

The minimum of $\langle \phi \rangle$ with respect to L_{ex} is given for

$$L_{ex} = \varphi_0 \sqrt{A/\langle K_1 \rangle} \tag{5}$$

with $\varphi_0 = \alpha\sqrt{8/(3\beta)}$. The resulting exchange length L_{ex}, thus, follows from the *basic* exchange length L_0 as defined in equation (2) by self-consistently substituting the average anisotropy constant $\langle K_1 \rangle$ for the local anisotropy constant K_1. This renormalization accounts for the fact that the scale on which the exchange interaction dominates expands at the same time as the anisotropy is averaged out and, hence, the local anisotropies are averaged out even more efficiently. Combining equations (3) and (5) finally yields

$$\langle K_1 \rangle = K_1 \cdot (D/L_0)^6 \tag{6}$$

This final result is essentially based on statistical and scaling arguments and, therefore, is not limited to uniaxial anisotropies (as may be anticipated from Figure 2 or from the original work of Alben *et al.*) but also applies for cubic or other symmetries. The prefactors α, β, and φ_0 remain open parameters within this scaling analysis. Their theoretical determination would require a by far more complex micromagnetic analysis of the problem. Yet, all these parameters can be ultimately combined in a single material constant, which is given by the basic exchange length L_0, that is, the critical scale below which the averaging mechanism becomes effective. It is therefore more appropriate to write down the final result in the rationalized form of equation (6) involving the ratio D/L_0 rather than in the explicit form found in the original literature (cf. Alben, Becker and Chi, 1978; Herzer, 1990) involving all the individual material parameters and, in particular, more or less arbitrary prefactors.

The most significant feature predicted by the random anisotropy model is the strong variation of $\langle K_1 \rangle$ with the sixth power of the grain size. In typical nanocrystalline Fe-based alloys with grain sizes in the order of 10–15 nm, that is, $D \approx L_0/3$, the local magnetocrystalline anisotropy of $K_1 \approx 10^5\,\mathrm{J\,m^{-3}}$ is thus reduced by 3 orders of magnitude toward a few joules per cubic meter, which is small enough to enable superior soft magnetic behavior. Correspondingly the renormalized exchange length, L_{ex}, expands into the micrometer regime and is almost 2 orders of magnitude larger than the basic exchange length L_0 ($\approx$40 nm). High-resolution Kerr effect studies of nanocrystalline $Fe_{73.5}Cu_1Nb_3Si_{13.5}B_9$ indeed reveal very wide domain walls of about 2 µm in thickness, indicative of the low effective anisotropy of the material (Schäfer, Hubert and Herzer, 1991).

2.2 Multiphase systems and mixed anisotropies

The preceding arguments were based on a single phase system. In real materials, however, we deal with various structural phases. In typical soft magnetic nanocrystalline materials, the randomly oriented crystallites of about 10 nm in size are embedded in an amorphous matrix. The latter is made up again of structural units with magnetic easy axes randomly fluctuating on the much smaller scale of atomic distances. Moreover, real materials reveal additional anisotropies, such as magnetoelastic- and field-induced anisotropies, which are uniform on a scale much larger than the exchange length. Such long-range anisotropies ultimately determine the soft magnetic properties of optimized nanocrystalline alloys where the contribution of the random anisotropies tends to become negligible. The original model

has been extended correspondingly (Herzer, 1995, 2005a; Suzuki, Herzer and Cadogan, 1998b).

2.2.1 *Average anisotropy*

The average anisotropy constant $\langle K \rangle$ of a *coupled* multiphase system with anisotropies randomly oriented on a scale smaller than a magnetic correlation length L_{ex} can be described by (Herzer, 2005a)

$$\langle K \rangle = \sqrt{K_u^2 + \sum_\nu x_\nu \beta_\nu^2 K_{1,\nu}^2 \cdot (D_\nu / L_{ex})^3} \qquad (7)$$

where K_u denotes a uniaxial anisotropy, which is *uniform* on a scale much larger than L_{ex}. The random contributions are represented by the local anisotropy constants $K_{1,\nu}$, the grain sizes D_ν, and the volume fractions x_ν of the individual structural phases labeled by the index ν. The result includes a grain size distribution if the term *structural phase* is used in a more general sense for all grains with the same $K_{1,\nu}$ and the same grain size D_ν. The parameters β_ν mainly involve conventions used for defining the anisotropy constants for different symmetries but also include some statistical corrections in the order of 10–20%. Numerical simulations for single phase systems result in $\beta \approx 1$ for uniaxial and $\beta \approx 0.4$ for cubic symmetry. The rather distinct value of β for the *cubic* case is largely a consequence of common conventions for the anisotropy energy. The latter result in $\Delta\phi_K = |K_1|/3$ for cubic and $\Delta\phi_K = |K_1|$ for uniaxial anisotropies, where $\Delta\phi_K = \phi_K^{max} - \phi_K^{min}$ is the difference of the anisotropy energy density between the hardest and easiest axis. The average anisotropy constant $\langle K \rangle$ in equation (7) is defined as the difference between the maximum and minimum of the average anisotropy energy density. For a single phase system with $K_u = 0$, it is related to $\langle K_1 \rangle$ as introduced in equation (3) by $\langle K \rangle = \beta \langle K_1 \rangle$.

The above result is valid as long as the average number of *coupled* grains $N_\nu = x_\nu (L_{ex}/D_\nu)^3$ is larger than one for each individual phase. For the derivation it is only necessary to assume that the magnetization is parallel within a volume defined by a correlation length L_{ex}, without specifying the precise coupling mechanism. This reduces the problem to adding up random anisotropies which can be done analytically using statistical concepts and/or by straightforward micromagnetic simulations (cf. Herzer, 2005a).

If the coupling mechanism is dominated by *exchange interaction*, the correlation length L_{ex} is self-consistently related to the total average anisotropy constant $\langle K \rangle$ by

$$L_{ex} = \varphi \sqrt{A / \langle K \rangle} \qquad (8)$$

where φ is a prefactor in the order of unity.

In the general case, the average anisotropy $\langle K \rangle$ has to be determined from equations (7) and (8) by numerical iteration. Explicit solutions can be obtained in the limiting cases of a vanishing or dominating macroscopic anisotropy K_u. The results are

$$\langle K \rangle = \left(\sum_\nu x_\nu \sqrt{\beta_\nu \left| K_{1,\nu} \right|} \left(D_\nu / L_{0,\nu} \right)^3 \right)^2 \qquad (9)$$

for $K_u = 0$, and

$$\langle K \rangle \approx K_u + \tfrac{1}{2} \textstyle\sum_\nu x_\nu \sqrt{\beta_\nu \left| K_{1,\nu} \right| K_u} \left(D_\nu / L_{0,\nu} \right)^3 \qquad (10)$$

if the uniform anisotropy is dominating over the random contributions. The latter is accompanied by a change of the scaling behavior of the random anisotropy contribution from D^6 to D^3. In the above relations

$$L_{0,\nu} := \varphi_{0,\nu} \sqrt{A / K_{1,\nu}} \quad \text{with} \quad \varphi_{0,\nu} := \varphi / \sqrt{\beta_\nu} \qquad (11)$$

define the *basic* exchange lengths related to the *local* anisotropies of the individual structural phases (cf. equation (2)). These length scales should not be confused with the *renormalized* exchange length L_{ex} of equation (8), which is self-consistently related to the *average* anisotropy $\langle K \rangle$. The corresponding prefactors have been estimated to be about $\varphi_0 \approx 1.5$ for cubic and $\varphi_0 \approx 1.7$ for uniaxial symmetry, respectively.

Figure 3 illustrates the competition of a uniform uniaxial anisotropy K_u and the average random anisotropy $\langle K_1 \rangle$ as obtained by numerical simulations (Herzer, 2005a). For small K_u the easiest magnetic axis is dominated by the random anisotropy. Accordingly, the easiest axes reveal a large angular dispersion from one region of exchange-coupled grains to the other. However, as K_u approaches and finally exceeds the average random anisotropy contribution $\langle K_1 \rangle$, the easiest magnetic axis is rotated toward the macroscopic anisotropy axis and the angular dispersion of the easiest axis disappears more and more.

Figure 4 illustrates the expected grain-size dependence of the average random anisotropy for the material parameters of optimized nanocrystalline Fe–Si–B–Nb–Cu alloys (Herzer, 2005b). We have included the contribution of the random atomic scale anisotropy of the amorphous matrix as well as the case of a small uniform anisotropy K_u here.

In the absence of long-range anisotropies, the average anisotropy $\langle K \rangle$ scales with D^6 down to grain sizes of about 5 nm. Although the atomic scale anisotropy of the amorphous phase in this simulation is almost 2 orders of magnitude higher than that of the bcc crystallites, its average contribution is virtually negligible for $D > 5$ nm since the structural anisotropies are fluctuating on the much shorter

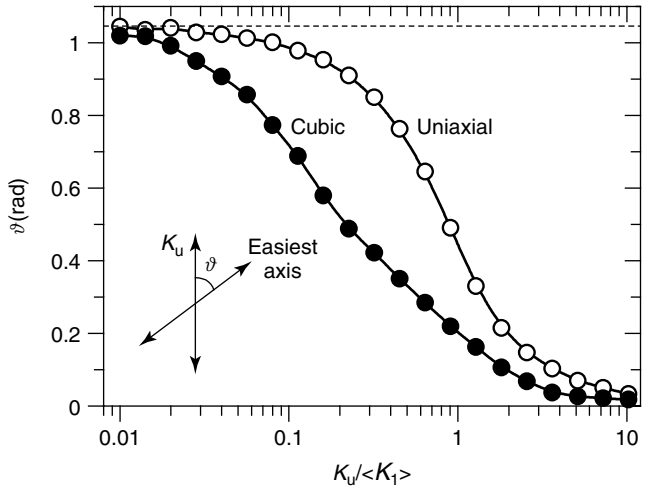

Figure 3. Average orientation of the easiest magnetic axis for a system of randomly oriented particles with average anisotropy constant $\langle K_1 \rangle = K_1/N^{1/2}$ and a superimposed, uniform uniaxial anisotropy K_u (full symbols: randomly oriented cubic grains; open symbols: uniaxial grains, dashed line: limit for $K_u = 0$).) (With permission from *Properties and Applications of Nanocrystalline Alloys from Amorphous Precursors*, Idzikowski, B. Svec, P. and Miglierini, M. (Eds), The Random Anisotropy Model, pp 15–34, 2005.)

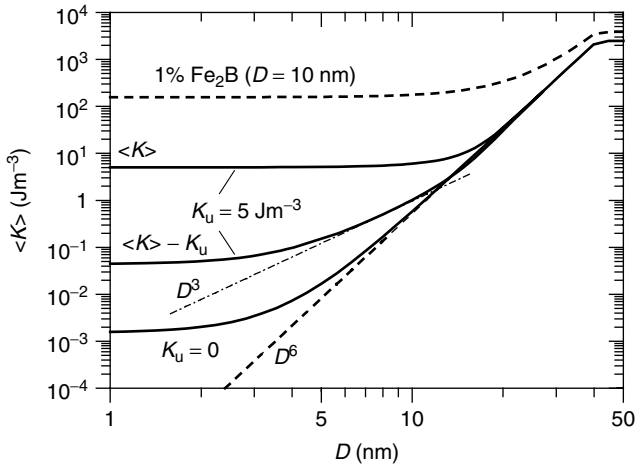

Figure 4. Theoretical estimate of the average anisotropy $\langle K \rangle$ for a system of randomly oriented crystallites of bcc $Fe_{80}Si_{20}$ ($K_1 = 8.2\,\mathrm{kJ\,m^{-3}}$) with grain size D and embedded in an amorphous matrix with a volume fraction $x = 0.75$. The atomic scale anisotropy constant of the amorphous phase was assumed as $K_1 = 430\,\mathrm{kJ\,m^{-3}}$ which is the value for Fe_2B and which can be looked upon as an upper bound. The exchange stiffness constant was assumed as $A = 6 \times 10^{-12}\,\mathrm{J\,m^{-1}}$ which is the experimental value for nanocrystalline $Fe_{73.5}Cu_1Nb_3Si_{13.5}B_9$. (Reprinted from *J. Magn. Magn. Mat.* **294**, G. Herzer, Anisotropies in Soft Magnetic Nanocrystalline Alloys, pp 99–106, 2005, with permission from Elsevier.)

scale of atomic distances ($D_{\mathrm{am.}} \approx 0.5\,\mathrm{nm}$). In this regime where the contribution of the bcc crystallites is dominating, equation (7) simplifies drastically and $\langle K \rangle$ becomes

$$\langle K \rangle := \beta \langle K_1 \rangle = \beta K_1 \cdot x_{\mathrm{cr}}^2 (D/L_0)^6 \qquad (12)$$

This result corresponds to exchange-coupled crystallites diluted in an ideally soft magnetic matrix. The only modification made over the original single phase model is the inclusion of the crystalline volume fraction x_{cr}. The statistical precondition for the averaging mechanism, that is, $N > 1$, then becomes $D < L_0/x_{\mathrm{cr}}^{1/6}$. This means that the critical grain size below which exchange interaction starts to suppress the local anisotropies is somewhat enhanced owing to the dilution effect.

The random anisotropy of the amorphous matrix becomes only visible for very small grain sizes below about 5 nm, resulting in a grain size independent anisotropy. However, this theoretical minimum value of $\langle K \rangle$ and the related coercivity ($H_c \sim 0.001\,\mathrm{A\,m^{-1}}$) are so small that the situation shown for smallest grain sizes in Figure 4 remains academic.

In real materials, whether amorphous or nanocrystalline, the minimum anisotropy is ultimately determined by more long-range anisotropies. To illustrate this more realistic situation, we have assumed the presence of a small uniform anisotropy $K_u = 5\,\mathrm{J\,m^{-3}}$. As can be seen from Figure 4, the average anisotropy constant $\langle K \rangle$ is almost totally determined by K_u for grain sizes below about 10–15 nm. The grain-size dependence of the random contribution, that is, $\delta K = \langle K \rangle - K_u$, changes from a D^6 dependence to a D^3 dependence, and finally, gets grain size independent due to the random anisotropy of the amorphous phase. The latter is larger than that for the case $K_u = 0$, because the maximum value for the renormalized exchange length is limited by $L_{\mathrm{ex}} = \varphi(A/K_u)^{1/2}$. As a consequence, the random anisotropies of the amorphous phase are less effectively averaged out.

A very small volume fraction of an additional crystalline phase with significantly higher anisotropy can finally change the picture totally. This is illustrated in Figure 4 assuming a 1% fraction of Fe_2B precipitates ($K_1 = 430\,\mathrm{kJ\,m^{-3}}$) with 10 nm grain size. The example explains at least qualitatively the finding in experiment that Fe_2B precipitates can significantly degrade the soft magnetic properties even though the grain size of the bcc crystallites remains unchanged.

2.2.2 *Grain coupling*

Adding up anisotropies is only one aspect of extending the random anisotropy model to multiphase systems. Another most challenging problem is how to relate the effective

exchange stiffness constant A to the local material parameters. It is intuitively clear that A has to be ultimately understood as an effective average value on the scale of the exchange length. However, as demonstrated by experiment (cf. Section 4.1.2), it is not a simple volume average. It is rather determined by the 'weakest link' in the exchange chain, which, for example, is the amorphous intergranular phase in typical nanocrystallized materials (Herzer, 1989). Hence, A should result from some kind of 'inverse averaging' of the local exchange constants. The most promising approach to the problem so far has been proposed by Suzuki and Cadogan (1998a). They consider the situation where the magnetization changes its orientation over the scale of the exchange length $L_{ex} \propto (A/\langle K\rangle)^{1/2}$. Like in a domain wall, the average tilting between neighboring spins is then approximately inversely proportional to L_{ex}, that is, proportional to $1/A^{1/2}$. The key argument of Suzuki *et al.* is that the local tilting angle should increase if the local exchange interaction becomes weaker and vice versa. Accordingly they assume the local tilting angle to be proportional to $1/A_{loc}^{1/2}$, where A_{loc} is the local exchange stiffness. The effective exchange stiffness, hence, can be calculated by averaging the local tilting angles. The result is

$$\frac{D+\delta}{\sqrt{A}} = \frac{D}{\sqrt{A_{cr}}} + \frac{\delta}{\sqrt{A_{am}}} \tag{13}$$

where D is the grain size, δ is the intergranular spacing, and A_{am} and A_{cr} denote the exchange stiffness constants of the amorphous matrix and the crystallites, respectively. Although physically very reasonable, this model is a rather phenomenological approach limited to the typical two-phase structure of nanocrystallized materials where the crystalline phase is completely surrounded by the amorphous phase. A more rigorous micromagnetic treatment including extensions to multiple phases or to situations like incomplete wetting of the crystallites by the amorphous matrix still provides a most challenging theoretical task.

For the derivation of equation (7), it is only necessary to assume that the magnetization is parallel within a volume defined by a correlation length L_{ex} without specifying the precise coupling mechanism. The coupling mechanism hereby has not necessarily to be exchange interaction but could also be dipolar interaction. In the latter case, 'L_{ex}' should be understood as *magnetic correlation length*, which is not necessarily proportional to $1/\langle K\rangle^{1/2}$ like it is for exchange interaction. Dipolar interactions, without any doubt, become increasingly important when the exchange interaction between the crystallites is largely interrupted, for example, when the amorphous intergranular phase becomes paramagnetic at elevated temperatures (cf. Section 4.1.2). The proper incorporation of dipolar interactions into the concepts of the random anisotropy model still provides another basic theoretical challenge for future investigations.

2.3 Coercivity and permeability

For pure random anisotropies averaged out by exchange interaction, coercivity H_c and initial permeability μ_i are directly related to the average anisotropy constant $\langle K\rangle$ by

$$H_c = p_c \frac{\langle K\rangle}{J_s}; \quad \mu_i = p_\mu \frac{J_s^2}{\mu_0 \langle K\rangle} \tag{14}$$

where J_s is the average saturation magnetization of the material and p_c and p_μ are dimensionless prefactors in the order of unity. These relations have been originally derived for coherent magnetization rotation in conventional fine particle systems (cf. Bozorth, 1951). In the regime $D < L_{ex}$, however, they also apply for domain wall displacements (Herzer, 1990). Accordingly, coercivity and permeability are expected to vary with grain size as $H_c \propto D^6$ and $\mu \propto 1/D^6$.

However, if the magnetization process is controlled by more long-range anisotropies, the theoretical description of H_c and μ_i gets more complex, similar to the case in conventional soft magnetic materials. For domain wall displacements, the coercivity is then determined by anisotropy fluctuations δK according to

$$H_c \approx \frac{1}{2J_s}\left|\overline{\frac{\partial \gamma_W}{\partial x}}\right|_{max} \approx \frac{\delta K}{J_s}\frac{L_{ex}}{\lambda} \tag{15}$$

where $\gamma_W = 4(A\langle K\rangle)^{1/2}$ is the domain wall energy, L_{ex} is the exchange length as introduced in equation (8), and λ is the fluctuation length of the effective anisotropy.

For large grains, $D > L_{ex}$, we have $\lambda \approx D$ and $\delta K \approx K_1$, such that equation (15) yields $H_c \propto K_1^{1/2}/D$, that is, the well-known $1/D$ dependence of coercivity in conventional soft magnetic materials.

In the regime $D < L_{ex}$, the effective contribution of the random magnetocrystalline anisotropies to the magnetization process is an average over the volume of the exchange length L_{ex}. Accordingly, the wavelength of the effective anisotropy fluctuations is given by the exchange length itself, that is, $\lambda \approx L_{ex}$, and the fluctuation amplitude is $\delta K = \langle K\rangle - K_u$. The coercivity, thus, is $H_c \sim (\langle K\rangle - K_u)/J_s$ and we expect for H_c the grain-size dependence shown in Figure 4 for $\langle K\rangle - K_u$. The most significant feature hereby is the transition from a D^6 to a D^3 law as K_u starts to dominate.

The preceding discussion assumed that the superimposed uniaxial anisotropy is perfectly uniform. This is rather the exception than the rule in reality, mostly due to internal

mechanical stresses and/or surface defects. The typical fluctuation wavelengths λ are much larger than L_{ex} and range from a few to about 100 µm. Such K_u fluctuations ultimately provide the limiting factor for the soft magnetic properties in amorphous and optimized nanocrystalline alloys. The result is a grain size independent contribution, $H_c \propto K_u^{1/2}/\lambda$, which finally dominates over the random microstructural anisotropies. This is the case in amorphous alloys and in optimized nanocrystalline Fe–Cu–Nb–Si–B alloys for grain sizes below about 15–20 nm.

Permeability μ behaves even more complex if we deal with a dominating long-range anisotropy K_u. In particular, it depends sensitively on the angle between applied magnetic field and macroscopic anisotropy direction. If the sample is magnetized perpendicular to the K_u axis, μ is determined by magnetization rotation and, hence, is inversely proportional to the total anisotropy, that is, $\mu \propto 1/\langle K \rangle$. It is, thus, grain size independent although coercivity may simultaneously vary proportional to D^3. If magnetized parallel to the uniform anisotropy axis μ is determined by domain wall pinning and we expect permeability to vary inversely proportional to H_c again, that is, $\mu \propto 1/\delta K$.

3 ALLOY SYSTEMS AND BASIC CHARACTERISTICS

The most suitable method to synthesize nanocrystalline alloys with attractive soft magnetic properties is controlled crystallization from the amorphous state. The amorphous precursor material is prepared either as a thin film by sputtering techniques or, more typically, as a ribbon by rapid solidification from the melt. A typical nanocrystalline structure with good soft magnetic properties occurs if the amorphous state is crystallized by the primary crystallization of bcc Fe, before intermetallic phases like Fe–B compounds may be formed. Both an extremely high nucleation rate and a slow growth of the crystalline precipitates are needed in order to obtain the nanoscaled microstructure. However, such a crystallization characteristics is rather the exception than the rule and needs an appropriate alloy design which promotes the nucleation of bcc Fe, retards the grain growth, and simultaneously inhibits the formation of intermetallic phases. The requirement of a good glass-forming ability puts further constraints on the accessible alloy compositions.

3.1 Fe–Cu–Nb–Si–B alloys

The most attractive soft magnetic properties in the nanocrystalline state are found for compositions like $Fe_{bal.}Cu_{0.5-1}Nb_{2-3}Si_{12-16}B_{6-9}$. The basic alloy design corresponds to that of a typical Fe–Si–B metallic glass. The alloys have a good glass-forming ability and are easily accessible by rapid solidification as originally amorphous ribbons, typically 20 µm thick. The nanocrystalline state is achieved by a subsequent heat treatment above the crystallization temperature. The desired crystallization characteristics is provided by the combined addition of Cu and Nb.

Figure 5 shows a typical example for the evolution of the microstructure and the soft magnetic properties with the annealing temperature. Accordingly, annealing of $Fe_{73.5}Cu_1Nb_3Si_{13.5}B_9$ at temperatures between about 500 and 600 °C leads to the primary crystallization of ultrafine bcc $Fe_{\sim 80}Si_{\sim 20}$ grains with typical grain sizes of 10–15 nm. The bcc grains are randomly oriented and embedded in a residual amorphous matrix which occupies about 20–30% of the volume and separates the crystallites at a distance of about 1–2 nm. This nanocrystalline structure is the basis

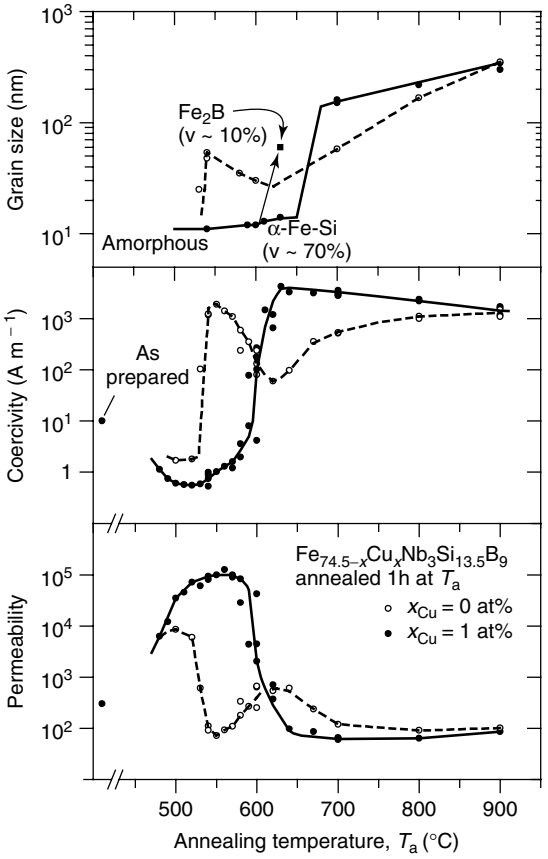

Figure 5. Average grain size, coercivity, and initial permeability of $Fe_{74.5-x}Cu_xNb_3Si_{13.5}B_9$ ($x = 0, 1$ at%) as a function of the annealing temperature. (Reprinted from *Handbook of Magnetic Materials*, Vol 10, Buschow, K.H.J, Nanocrystalline Soft Magnetic Alloys, Elsevier Science B.V., pp 415–462, 1997, with permission from Elsevier.)

for the excellent soft magnetic properties indicated by the high values of the initial permeability of about 10^5 and correspondingly low coercivities of less than $1\,A\,m^{-1}$. The magnetic properties and the underlying microstructure are relatively insensitive to the precise annealing conditions within a wide range of annealing temperatures, T_a, of about $\Delta T_a \approx 50-100\,^{\circ}C$. They develop in a relatively short period of time (about 10–15 min) and do not much alter even after prolonged heat treatment of several hours (cf. Yoshizawa and Yamauchi, 1991a). Only annealing at more elevated temperatures above about 600 °C leads to the precipitation of small fractions of boride compounds like Fe_2B or Fe_3B with typical dimensions of 50–100 nm, while the ultrafine grain structure of bcc Fe–Si still persists. Further increase of the annealing temperature above about 700 °C finally yields grain coarsening. Both the formation of Fe borides and grain coarsening deteriorates the soft magnetic properties significantly.

For comparison, Figure 5 includes the data for a $Fe_{74.5}Nb_3Si_{13.5}B_9$ alloy. The crystallization behavior of this Cu-free alloy is quite different and leads to a severe degradation of the soft magnetic properties as typically observed for conventional amorphous alloys. The average grain size is relatively large and shows a distinct variation with the annealing temperature. The crystallization of the Cu-free alloy is furthermore characterized by the almost simultaneous formation of bcc Fe–Si and Fe–B compounds, while the addition of already a few tenth at% of Cu leads to two clearly separated crystallization stages (Kataoka *et al*., 1989a; Herzer and Warlimont, 1992).

The formation of the particular nanocrystalline structure is essentially related to the combined addition of Cu and Nb (or other group IV to VI elements) and their low solubility in bcc Fe–Si: copper enhances the nucleation of the bcc grains while niobium impedes coarsening and, at the same time, inhibits the formation of boride compounds. The microstructure evolution is schematically illustrated in Figure 6 and can be described as follows:

In the early stage of annealing, prior to the primary crystallization of bcc Fe–Si, the phase separation tendency between Cu and Fe leads to the formation of Cu-rich clusters with a diameter of a few nanometer (Hono *et al*., 1992). These Cu clusters directly serve as heterogeneous nucleation sites for the Fe–Si primary crystals (Hono, Ping, Ohnuma and Onodera, 1999). The consequence is an extremely fine nucleation of bcc Fe–Si crystallites at a high rate which subsequently grow in a diffusion controlled process as the annealing proceeds further. As the bcc Fe–Si phase forms, Nb and B are excluded from the crystallites because of their low solubility in bcc Fe–Si and, hence, are enriched in the residual amorphous matrix. At the same time, effectively all Si tends to be partitioned into the bcc Fe–Si phase (Herzer, 1991; Hono *et al*., 1992). The enrichment with B

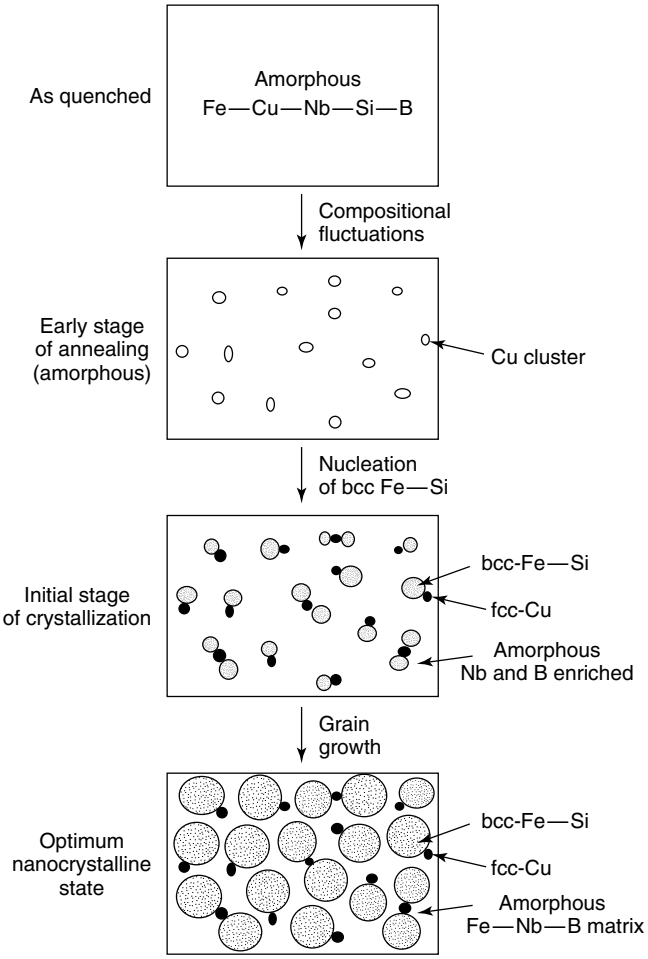

Figure 6. Schematic illustration of the formation of the nanocrystalline structure in Fe–Cu–Nb–Si–B alloys based on atom probe analysis results and transmission electron microscopy observations by Hono *et al*. (1992, 2000), Hono, Ping, Ohnuma and Onodera (1999).

and, in particular, with Nb increasingly stabilizes the residual amorphous matrix and, thus, hinders coarsening of the bcc grains. The presence of Nb also inhibits the formation of Fe boride compounds. The transformation finally ceases in a metastable two-phase microstructure of bcc Fe–Si embedded in an amorphous Fe–Nb–B matrix.

Figures 7 and 8 show the Curie temperatures T_C and the room-temperature magnetization J_s of Fe–Cu–Nb–Si–B alloys in the amorphous and in the nanocrystalline state. The precipitation of the bcc Fe–Si phase is clearly manifested in a significant increase of the Curie temperature T_C from 250 to 320 °C in the original amorphous state to about 600–740 °C after nanocrystallization. The residual amorphous matrix is ferromagnetic. Its Curie temperature and saturation magnetization, however, are clearly different from that of the amorphous precursor which reflects the discussed change in composition.

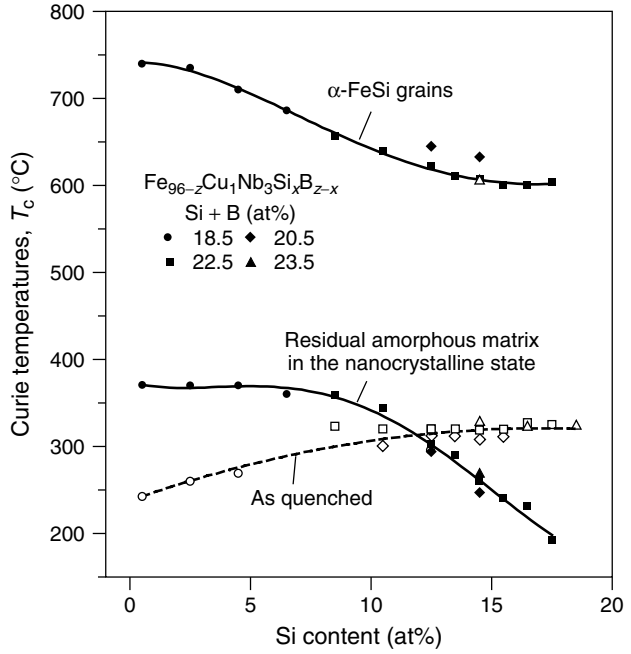

Figure 7. Curie temperatures of the bcc-FeSi grains and the residual amorphous matrix in nanocrystalline $Fe_{96-z}Cu_1Nb_3Si_xB_{z-x}$ alloys after annealing 1 h at 540 °C (solid symbols). The open symbols show the Curie temperature in the as quenched amorphous state. (Reprinted from *Handbook of Magnetic Materials*, Vol 10, Buschow, K.H.J, Nanocrystalline Soft Magnetic Alloys, Elsevier Science B.V., pp 415–462, 1997, with permission from Elsevier.)

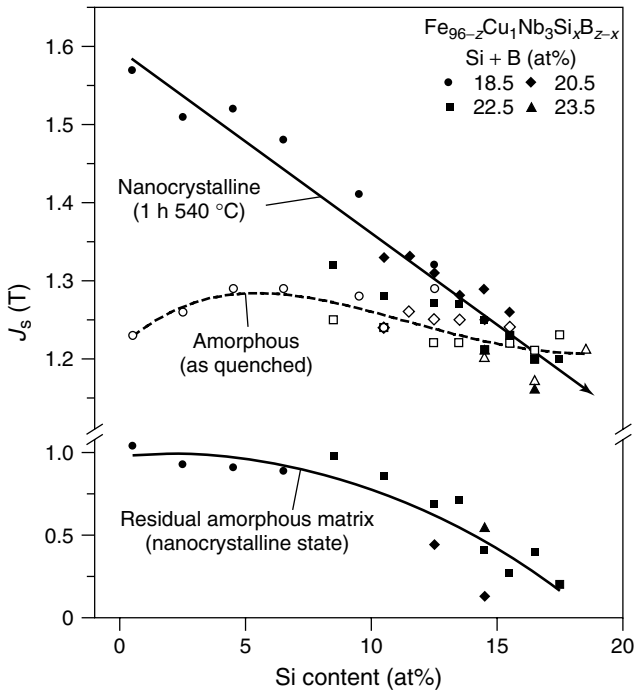

Figure 8. Room-temperature saturation magnetization, J_s, of $Fe_{96-z}Cu_1Nb_3Si_xB_{z-x}$ in the as quenched amorphous (open symbols) and nanocrystalline state after annealing 1 h at 540 °C (solid symbols, upper part). The lower part of the figure shows the local magnetization of the residual amorphous matrix in the nanocrystalline state (note the change in the axis scale). (Reprinted from *Handbook of Magnetic Materials*, Vol 10, Buschow, K.H.J, Nanocrystalline Soft Magnetic Alloys, Elsevier Science B.V., pp 415–462, 1997, with permission from Elsevier.)

Figures 9 and 10 show the crystalline fraction and the Si content of the crystallites as evaluated from thermomagnetic investigations by comparison with literature data for α-Fe–Si (Herzer, 1989, 1991). X-ray investigations of Ueda, Ikeda and Minami (1994) give comparable results. The crystalline fraction is mainly determined by the boron content and independent of the Si content. Both the crystalline fraction and the average grain size decreases with increasing boron content. This indicates that the boron plays a similar role as Nb in retarding the grain growth. The local Si content in the bcc grains is considerably larger than the average Si content of the alloy. For the high Si-content alloys the composition of the bcc grains is close to stoichiometric Fe_3Si which results in a DO_3 superlattice structure (Müller, Mattern and Illgen, 1991).

The transformation to the nanocrystalline state can be approximately described by the reaction

$$\text{Fe–Cu–Nb–Si–B} \longrightarrow x_{\text{cr}}\alpha - \text{Fe}_{1-y}\text{Si}_y + (1 - x_{\text{cr}})(\text{Fe}_{1-a}\text{Nb}_a)_n\text{B} \qquad (16)$$

which allows to estimate the crystalline fraction x_{cr} and the local atomic compositions by balance of atomic concentrations. A reasonable fit of the experimental data is obtained with $n \approx 2.2$, indicating that the nucleation and growth of the bcc grains proceeds until the residual amorphous matrix is enriched with boron such that its composition is close to stoichiometric $(Fe_{1-a}Nb_a)_2B$. In nanocrystalline $Fe_{73.5}Cu_1Nb_3Si_{13.5}B_9$, for example, the crystalline volume fraction is about 70% and the local compositions are close to $Fe_{\sim 80}Si_{\sim 20}$ in the bcc crystallites and $Fe_{\sim 60}Nb_{\sim 10}B_{\sim 30}$ in the residual amorphous matrix, respectively.

The effect of copper in enhancing the nucleation density, in a way, is unique. Gold is the only element which has been verified to have a comparable effect on the crystallization behavior (Kataoka, Matsunaga, Inoue and Masumoto, 1989b). Niobium can be substituted by other group V or VI refractory elements, like Cr, V, Mo, W, or Ta which act similarly on the crystallization process and on the magnetic properties (Yoshizawa and Yamauchi, 1991b). Like for Nb, the atomic volumes of these refractory elements are larger than that of Fe which reduces the diffusion coefficients and, thus, stabilizes the amorphous matrix and slows down the kinetics of grain coarsening (Müller and Mattern, 1994). Accordingly the efficiency of these elements for grain-size

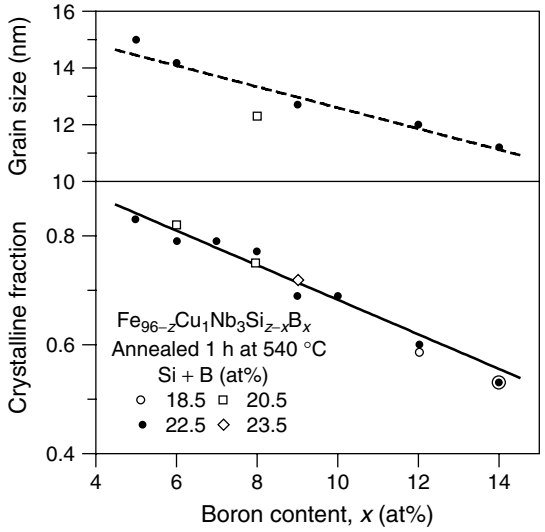

Figure 9. Average grain size and crystalline fraction in nanocrystalline $Fe_{96-z}Cu_1Nb_3Si_xB_{z-x}$ alloys versus the boron content. The solid line is the crystalline fraction calculated from the balance of atomic concentrations according to the reaction given by equation (16) with $n = 2.2$. (Reprinted from *Handbook of Magnetic Materials*, Vol 10, Buschow, K.H.J., Nanocrystalline Soft Magnetic Alloys, Elsevier Science B.V., pp 415–462, 1997, with permission from Elsevier.)

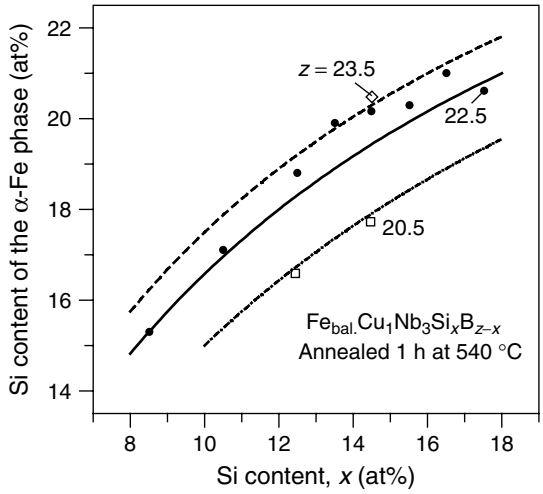

Figure 10. Local Si content in the bcc grains of nanocrystalline $Fe_{96-z}Cu_1Nb_3Si_xB_{z-x}$ alloys versus the Si content. The lines correspond to the theoretical result from the balance of atomic concentrations according to the reaction given by equation (16) with $n = 2.2$. (Reprinted from *Handbook of Magnetic Materials*, Vol 10, Buschow, K.H.J., Nanocrystalline Soft Magnetic Alloys, Elsevier Science B.V., pp 415–462, 1997, with permission from Elsevier.)

refinement increases in the order of their atomic volumes, that is, Cr < V < Mo ≈ W < Nb ≈ Ta. Finest grain structures and superior magnetic properties require a certain minimum amount (typically 2–3 at%) of the elements Nb or Ta. More recent investigations by Ohnuma *et al*. (2000) indicate that the grain-size refinement and, hence, the soft magnetic properties can be optimized further by mutually adjusting the Cu and Nb content such that the Cu clustering occurs just before the onset of primary crystallization.

Another aspect of alloy design is that good soft magnetic properties require not only a small grain size but at the same time the absence of boron compounds. The required separation between the primary crystallization of bcc Fe and the precipitation of Fe–B compounds not only is determined by Cu and Nb but also needs a low or moderate boron content in order to minimize the driving force for the formation of boride compounds. On the other hand, Fe–Si–B metallic glasses require a certain minimum amount of B as well as minimum content of (Si + B), for the sake of glass-forming ability. This is one of the reasons that superior soft magnetic properties are only found for relatively low boron contents in the range 5–10 at% and correspondingly high Si contents of about 12–16 at% (cf. Figure 11).

Further aspects of alloy design and microstructure of the Fe–Cu–Nb–Si–B system can be found, for example, in the reviews of Herzer (1997), Yoshizawa (1999) and Hono and Ohnuma (2002).

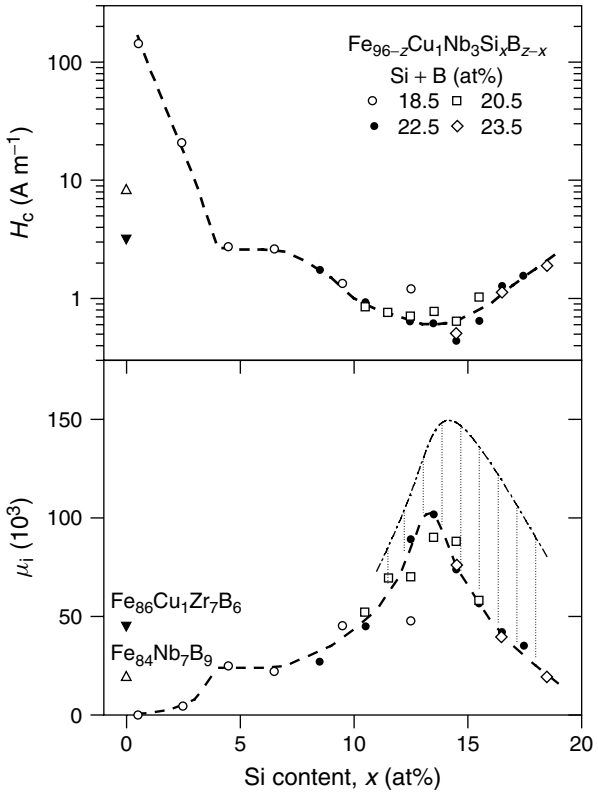

Figure 11. Coercivity, H_c, and initial permeability, μ_i, of nanocrystalline $Fe_{96-z}Cu_1Nb_3Si_xB_{z-x}$ annealed 1 h at 540 °C versus the Si content. The shaded area in the permeability plot represents the technological progress made since the introduction of the material around 1990.

3.2 Further alloy compositions

A major driving force in the search for further alloy compositions was to increase the saturation magnetization which, in the optimized compositions around $Fe_{73.5}Cu_1Nb_3Si_{13.5}B_9$, is limited to about $J_s \approx 1.2-1.3$ T due to the high Si content in the bcc grains. An appreciable increase of J_s, thus, requires a nanocrystalline structure which essentially consists of pure α iron. The major problem hereby is to find appropriate amorphous precursor compositions with both sufficient glass-forming ability and the necessary crystallization characteristics.

As, for example, shown in Figure 8, the saturation magnetization in the $Fe-Cu_1Nb_3Si_xB_{z-x}$ system increases up to about 1.6 T if the Si content is reduced by replacing it with boron. However this benefit is finally accompanied by a severe degradation of the soft magnetic properties (cf. Figure 11) since the higher boron content favors the formation of boron compounds. In order to obtain a homogeneous nanocrystalline bcc structure with good soft magnetic properties, it is ultimately necessary to keep the boron content at a moderate level below about 10 at%. However, a corresponding reduction of the boron content at low Si contents, for the sake of glass-forming ability, is only possible if other good glass-forming elements are added simultaneously. Such elements which extend the glass-forming range at low Si and B contents are group IVa to VIa transition metals. The glass-forming range is the widest for Hf containing alloys and decreases in the order of Zr > Nb ≈ Ta > Mo ≈ W > V > Cr. The most stable amorphous phase is, thus, obtained in alloys containing refractory metals with large atoms and low d-electron concentrations, that is, particularly Zr, Hf, Nb, and Ta. These elements at the same time are very effective in suppressing the formation of the undesired boride compounds.

Accordingly, high iron content $Fe-(Cu_1)-M_{\sim 7}B_{2-9}$ alloys with M = Hf, Zr, Nb, and/or Ta have been found to exhibit both a more or less sufficient glass-forming ability and the necessary crystallization characteristics in order to give a nanocrystalline structure with good soft magnetic properties, low magnetostriction, and a high saturation induction up to 1.7 T (Suzuki *et al*., 1990, 1991a,b, 1993). Yet glass-forming ability and castability still remain a major problem with these alloys. Thus, the Nb containing alloys which yield reasonable properties, like, for example, $Fe_{84}Nb_7B_9$, are located at the border of the glass-forming range (Suzuki, Makino, Inoue and Masumoto, 1994) which makes them most difficult to produce, in particular, on larger scale. The glass-forming ability is considerably improved with the addition of Zr or Hf. However, the strong oxygen reactivity of either of the two elements is a severe problem and requires a good protecting casting atmosphere. Moreover, the compositions with the highest saturation magnetization of $J_s = 1.6-1.7$ T, like $Fe_{91}Zr_7B_2$ are again located at the border of the glass-forming range. The preparation of Fe–M–B thin ribbons by rapid solidification, thus, requires substantially more effort than necessary for the more conventional Fe–(Cu,Nb)–Si–B compositions and, therefore, is presently still limited to smaller quantities.

In the Fe–M–B alloy system, the addition of copper is not necessarily required in order to yield a nanocrystalline structure with reasonable magnetic properties. Quenched-in compositional fluctuations in the amorphous state due to a relatively low glass-forming ability and the enhanced concentration of refractory elements insoluble in α-Fe are considered as a possible explanation (Suzuki, Makino, Inoue and Masumoto, 1994). Still, the addition of Cu again promotes the primary nucleation of the bcc Fe and enhances the soft magnetic properties significantly.

It should be finally mentioned that the spectrum of accessible nanocrystalline systems can still be considerably expanded by thin-film sputtering techniques. One example are Hf carbide dispersed nanocrystalline Fe–Hf–C films crystallized from the amorphous state (Hasegawa and Saito, 1991; Hasegawa, Kataoka and Fujimori, 1992). They combine good thermal stability, good high-frequency properties in the megahertz range with low magnetostriction, and high saturation induction of $J_s = 1.7$ T which can be even increased up to 2.0 T by multilayering these films with Fe. Another example are (Fe,Co,Ni)–(Si,B)–(F,O,N) granular alloy films (cf. Fujimori, 1995) which, at a saturation induction of about 1 T, possess a uniquely high electrical resistivity of 10^3-10^4 μΩcm which makes them a possible candidate for future high-frequency devices.

4 ANISOTROPIES AND SOFT MAGNETIC PROPERTIES

Figure 11 summarizes the soft magnetic properties of typical nanocrystalline Fe-based alloys. Lowest coercivities ($H_c \approx 0.5-1$ A m^{-1}) and highest permeabilities ($\mu \approx 10^5$) are found around the originally proposed compositions, that is, $Fe_{\sim 74}Cu_1Nb_3Si_{13-16}B_{6-9}$. Figure 12 compares the properties with other near-zero magnetostrictive alloys. Accordingly, nanocrystalline materials offer a unique combination of a high saturation induction and a high permeability.

The soft magnetic properties found in the optimized compositions can be only partially understood by the grain-size effect. They are ultimately determined by the competition of magnetocrystalline, magnetoelastic, and annealing-induced anisotropies as well as by the ribbon quality (i.e., impurities, surface roughness, oxide layers, etc.). Thus, the degradation of the soft magnetic properties shown in Figure 11

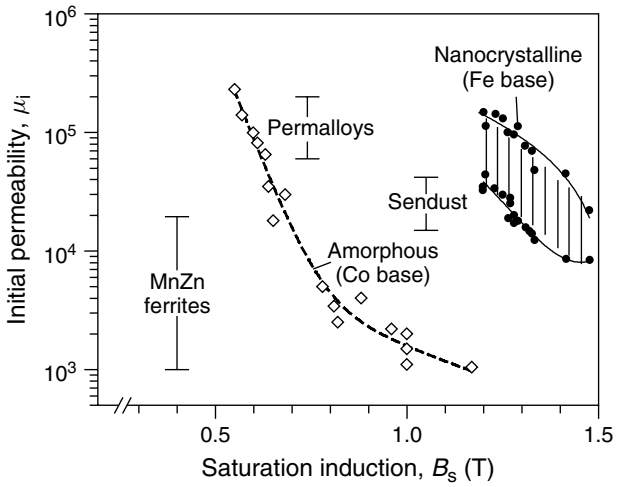

Figure 12. Initial permeability versus saturation induction for low-magnetostrictive, soft magnetic materials. (Reprinted from *Handbook of Magnetic Materials*, Vol 10, Buschow, K.H.J., Nanocrystalline Soft Magnetic Alloys, Elsevier Science B.V., pp 415–462, 1997, with permission from Elsevier.)

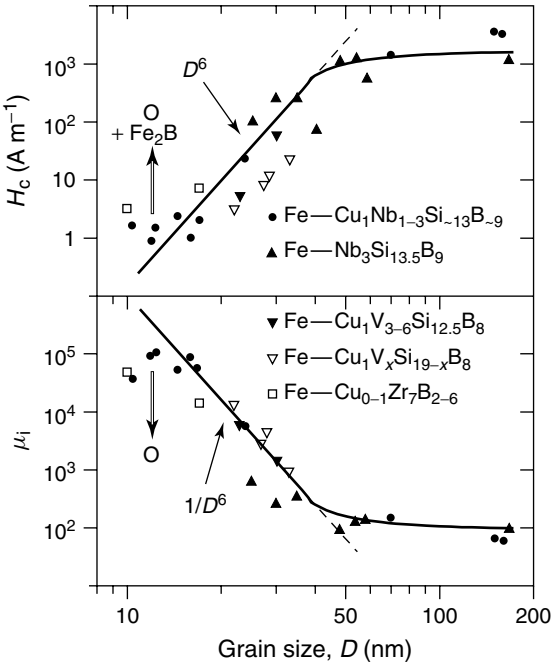

Figure 13. Coercivity, H_c and initial permeability, μ_i of nanocrystalline iron base alloys versus the average grain size. The open circle corresponds to an 'overannealed' $Fe_{73.5}Cu_1Nb_3Si_{13.5}B_9$ alloy with a small fraction (less than 10%) of Fe_2B precipitates. References to the symbols are given in Figure 1. (Reprinted from *J. Magn. Magn. Mat.*, **157/158**, G. Herzer, Nanocrystalline Soft Magnetic Materials, 133–136, 1996, with permission from Elsevier.)

for decreasing Si contents is a consequence of the simultaneously increasing magnitudes of the saturation magnetostriction, the field-induced anisotropy, and the local magnetocrystalline anisotropy constant. At very low Si contents, the simultaneously enhanced boron content additionally promotes the precipitation of boride compounds even after optimized annealing. The degradation toward high Si contents results from an increasing grain size due to the simultaneously decreasing boron content and from the enhanced tendency for the formation of silicon oxide layers. At very high Si contents, finally, the correspondingly low boron content reduces the glass-forming ability which additionally promotes coarse-grained crystalline precipitations already in the as-cast state. On the basis of the theoretical background given in Section 2, we will now discuss in more detail the various magnetic anisotropy contributions relevant for the soft magnetic properties.

4.1 Magnetocrystalline anisotropy

4.1.1 Grain-size effect

Figure 13 shows the coercivity H_c and the initial permeability μ_i of various nanocrystallized alloys as a function of the grain size D. The relatively broad scatter of the data is mainly related to the circumstance that the experimental variation of the grain size cannot be performed in a straightforward manner. It inevitably requires variations of the alloy composition and/or the annealing conditions which changes both the volume fraction and composition of the precipitated crystallites and the residual matrix. As a consequence, the local magnetocrystalline anisotropy constant, K_1, and the exchange interaction, A, between the grains change simultaneously. Nonetheless, the D^6 dependence predicted by the random anisotropy model seems to provide a good guiding principle through most of the coercivity and permeability data for grains smaller than $L_0 \approx 40$ nm.

However, there are also systematic deviations from the simple D^6 law. The major reasons are (i) precipitates of highly anisotropic compounds like Fe_2B and/or (ii) more long-range anisotropy contributions which are uniform on a scale much larger than the exchange length.

The formation of Fe_2B compounds can indeed drastically deteriorate the soft magnetic properties while the grain size of the bcc crystallites may remain unchanged (cf. Figures 5 and 13). The effective hardening caused by the Fe_2B precipitates already at smallest volume fractions is related to their relatively large size of 50–100 nm and, in particular, to their large magnetocrystalline anisotropy constant, K_1, of about 430 kJ m^{-3} which is orders of magnitude higher than that of the bcc crystallites. As demonstrated in Figure 14, the good soft magnetic properties of the nanocrystalline bcc structure are largely recovered when $K_1(Fe_2B)$ passes through zero

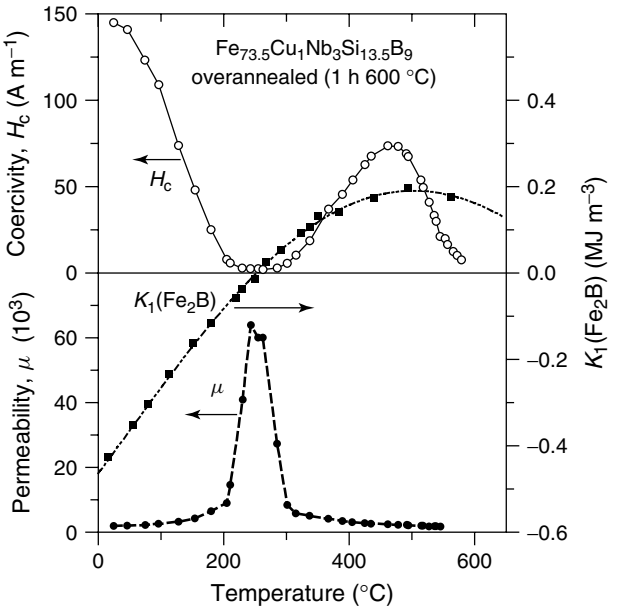

Figure 14. Temperature dependence of coercivity, H_c, and initial permeability, μ_i, of overannealed nanocrystalline $Fe_{73.5}Cu_1Nb_3Si_{13.5}B_9$ with slight traces of Fe_2B, whose magnetocrystalline anisotropy constant K_1 (cf. Iga, Tawara and Yanase, 1966) is included in the figure. (Reprinted from *Handbook of Magnetic Materials*, Vol 10, Buschow, K.H.J., Nanocrystalline Soft Magnetic Alloys, Elsevier Science B.V., pp 415–462, 1997, with permission from Elsevier.)

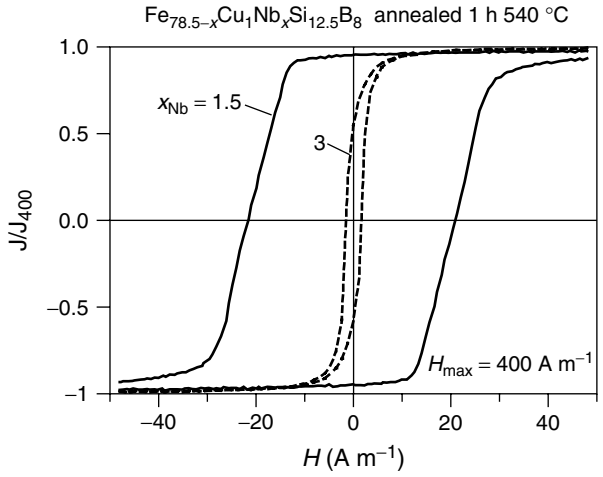

Figure 15. Characteristic hysteresis loops in the nanocrystalline state. The average grain sizes for the examples shown are about 25 nm for $x_{Nb} = 1.5$ at% and 12 nm for $x_{Nb} = 3$ at%, respectively. (Reprinted from *J. Magn. Magn. Mat.*, **157/158**, G. Herzer, Nanocrystalline Soft Magnetic Materials, 133–136, 1996, with permission from Elsevier.)

at 250 °C. This particular temperature dependence allows to detect even smallest amounts of borides, hardly visible by more direct structural investigations, and thus provides a most sensitive tool in order to separate whether an eventual degradation of the soft magnetic properties arises from too large bcc grains or from hard precipitates.

Long-range anisotropies lead to modified or vanishing grain-size dependence for small grain sizes. Relevant to this are magnetoelastic anisotropies, creep- or field-induced anisotropies and/or shape anisotropies which control the magnetization process when the random magnetocrystalline anisotropy is sufficiently averaged out. Thus, it is evident from Figure 13 that the soft magnetic properties of nanocrystalline Fe–Cu–Nb–Si–B alloys become basically grain size independent for grain sizes below 15–20 nm. Suzuki, Herzer and Cadogan (1998b) confirm this behavior for the coercivity of Fe–Cu–M–Si–B (M = IVa to VIa metal) alloys while they find a $H_c \propto D^3$ law, for example, for nanocrystalline $Fe_{91}Zr_7B_2$ with grain sizes $D \approx 12$–18 nm.

Figure 15 shows some typical hysteresis loops for $D < L_0$. In the regime of the D^6 law, the hysteresis loops reveal a high remanence to saturation ratio J_r/J_s. An example with $J_r/J_s \approx 0.95$ is given in Figure 15 by the sample with $D \approx 25$ nm. Such an isotropic remanence enhancement toward $J_r/J_s = 1$ is another characteristic feature when exchange interaction starts to dominate over anisotropy. The phenomenon is of particular interest for tailoring isotropic, nanoscaled hard magnets (cf. Buschow, 1997). However, the effect disappears at smaller grain sizes where more long-range anisotropies dominate over the averaged random anisotropies. Figure 15 includes a typical example (sample with $D = 12$ nm) with a remanence ratio around 0.5. The latter clearly indicates that the magnetization process is dominated by a distribution of uniaxial anisotropies which are uniform on a scale much larger than the exchange length.

Figure 16 shows typical domain patterns found for small grain sizes below 15 nm. The wide regular domains as well as typical stress patterns provide further evidence for the dominance of more uniform anisotropies in such optimized samples. Only high-resolution optical Kerr microscopy still reveals irregular magnetization patches within the wide domains (Flohrer, Schäfer, Polak and Herzer, 2005). A corresponding example is given in Figure 16(c). These magnetization patches are fluctuating on a scale of a few micrometers which is in the order of the renormalized exchange length L_{ex}. They arise from the residual contribution of the random magnetocrystalline anisotropies and reflect the angular dispersion of the easiest magnetic axis from one region of exchange-coupled grains to the other. Accordingly, these patches are found to be more pronounced, the more the random anisotropies contribute to the total magnetic anisotropy and, vice versa, they tend to disappear, the more long-range anisotropies dominate. Comparable magnetization patches are virtually invisible in soft magnetic amorphous alloys due

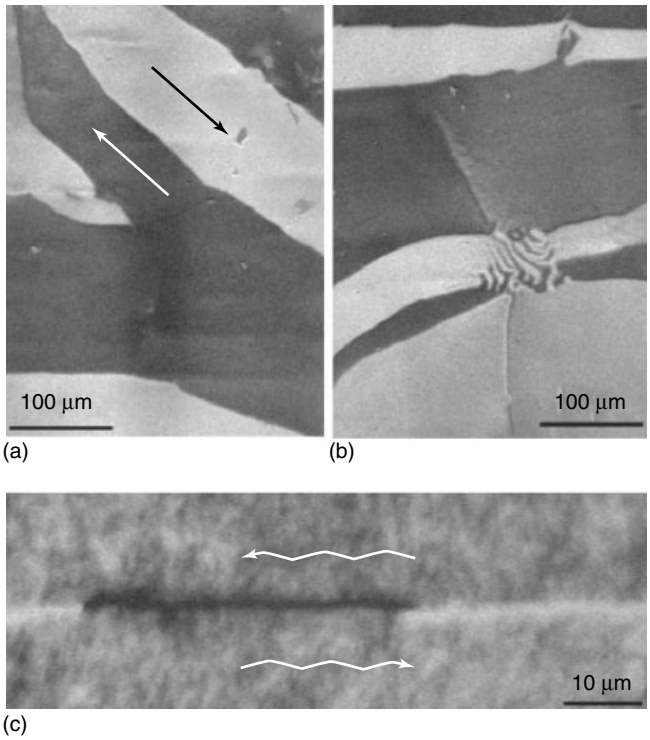

Figure 16. Magnetic domains observed in nanocrystalline $Fe_{73.5}Cu_1Nb_3Si_{16}B_7$ (annealed 1 h 540 °C). Examples for regular wide domains (a), rare zones with stress patterns (b) and a high-resolution image of a domain wall (c) are shown. The high-resolution image (c) also exemplifies the patchy magnetization fluctuations typically observed within the wide domains. (By courtesy of R. Schäfer, IFW Dresden.)

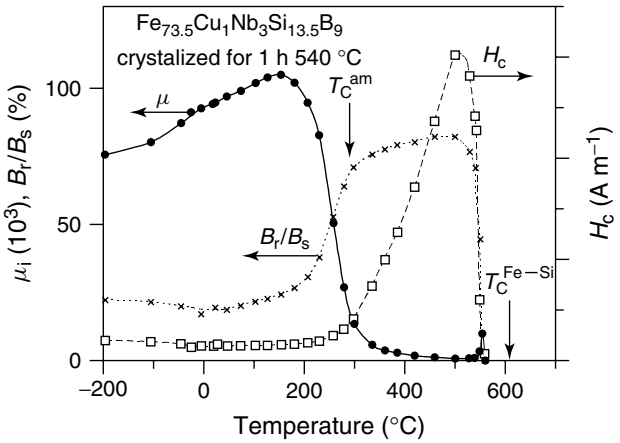

Figure 17. Initial permeability, μ_i, coercivity, H_c, and remanence to saturation ratio, B_r/B_s, of nanocrystalline $Fe_{73.5}Cu_1Nb_3Si_{13.5}B_9$ (annealed 1 h at 540 °C + 4 h at 350 °C in a transverse magnetic field) versus the measuring temperature (measuring frequency f = 50 Hz). The arrows indicate the Curie temperatures of the residual amorphous matrix (T_C^{am} = 291 °C) and the bcc grains (T_C^{FeSi} = 607 °C), respectively. (Reprinted from *Scr. Metall. Mater.*, **33**, G. Herzer, Soft Magnetic Nanocrystalline Materials, 1741–1756, 1995, with permission from Elsevier.)

to the extremely small contribution of the averaged random anisotropies.

In summary, it appears that, like in amorphous metals, the average random anisotropy of optimized nanocrystalline alloys like $Fe_{bal.}Cu_{0.5-1}Nb_{2-3}Si_{12-16}B_{6-9}$ is negligibly small and that the soft magnetic properties are predominantly controlled by more long-range uniaxial anisotropies like magnetoelastic and annealing-induced anisotropies. Yet, unlike soft magnetic amorphous metals, there are still situations where the random magnetocrystalline anisotropy becomes significant even for smallest grain sizes. The most prominent example is the temperature dependence of the soft magnetic properties which will be discussed in the following.

4.1.2 Grain coupling

The suppression of magnetocrystalline anisotropy requires that the randomly oriented grains are ferromagnetically coupled by exchange interaction. Consequently, if the exchange interaction is reduced, the local anisotropies will be less effectively averaged out and the soft magnetic properties will degrade.

The crucial role of the exchange interaction becomes most evident from the temperature dependence of the magnetic properties (Herzer, 1989) which is shown in Figure 17. The exchange coupling between the bcc grains mainly occurs via the intergranular amorphous matrix. The latter has a much lower Curie temperature than the bcc grains (cf. Figure 7). As a consequence, the intergranular coupling is largely reduced as the measuring temperature approaches the Curie temperature T_C^{am} of the amorphous matrix and the soft magnetic properties degrade correspondingly. Simultaneously, as shown in Figure 18, the domain structure simultaneously changes from wide domains to a pattern of small, irregular domains (Schäfer, Hubert, and Herzer, 1991; Flohrer, Schäfer, Polak and Herzer, 2005). These features are basically reversible and, thus, are not connected with irreversible, microstructural changes during the measurement.

The particular example shown in Figure 17 reveals a small uniaxial anisotropy ($K_u \approx 6\,J\,m^{-3}$) transverse to the ribbon axis induced by magnetic field annealing. In the low temperature regime, this induced anisotropy dominates over the averaged magnetocrystalline anisotropy, as indicated by the small remanence to saturation ratio B_r/B_s. However, when approaching T_C^{am}, the random anisotropies rapidly increase due to the reduced grain coupling and take over the control of the hysteresis loop. As a consequence, the remanence to saturation ratio steeply increases around 250 °C. From the theoretical analysis of the interplay between random and uniform anisotropies (cf. Figure 3) we expect this transition to

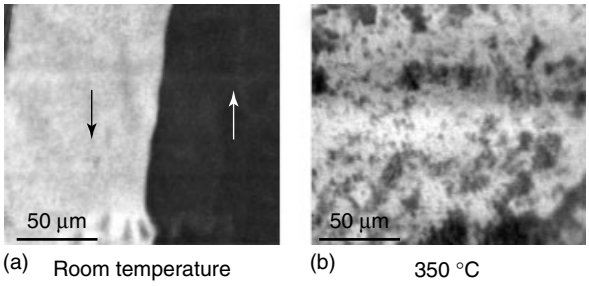

Figure 18. Transition from wide domains at room temperature to a patchy domain pattern at 350 °C for nanocrystalline $Fe_{73}Cu_1Nb_3Si_{16}B_7$ with a small field-induced anisotropy $K_u \approx 3\,J\,m^{-3}$. (Reprinted from *Acta mater.*, **53**, Flohrer, S., Schäfer, R., Polak, Ch. and Herzer. G., Interplay of Uniform and Random Anisotropy in Nanocrystalline Soft Magnetic Alloys, pp 2937–2942, 2005, with permission from Elsevier.)

occur at $K_u \approx 0.5\langle K_1\rangle$ for cubic crystallites. Accordingly, the increase of B_r/B_s is shifted toward higher temperatures with increasing magnitude of the induced anisotropy. Thus, for a sample with $K_u \approx 30\,J\,m^{-3}$, the remanence starts to increase significantly only at about 450 °C and wide domains can be still observed beyond temperatures of 500 °C (Flohrer, Schäfer, Polak and Herzer, 2005). Yet, the temperature dependence of H_c, being mainly determined by the random anisotropies, remains essentially comparable to that of a low K_u sample.

Above T_C^{am} the coercivity reaches a maximum with increasing measuring temperature and, finally, decreases toward zero together with the remanent magnetization. Interestingly, the latter occurs at a temperature (560 °C) below the Curie temperature (607 °C), of the bcc grains. This indicates the transition to superparamagnetic behavior which has been confirmed by a more detailed analysis of Lachowicz and Slawska-Waniewska (1994). Hernando and Kulik (1994) showed that the maximum of H_c shifts toward T_C^{am}, and that, H_c increases by one order of magnitude as the intergranular distance is increased from $\delta \approx 1$–2 nm to $\delta \approx 5$ nm. Simultaneously the onset temperature for superparamagnetic behavior decreases and approximately coincides with T_C^{am} for $\delta \approx 13$ nm.

The whole results for the magnetic behavior above the Curie point, T_C^{am}, of the amorphous matrix indicate that the grain coupling is largely, but not completely, interrupted above T_C^{am} and still persists to higher temperatures. Yet, the precise coupling mechanism for $T > T_C^{am}$ is still under discussion. Both exchange penetration through the thin, paramagnetic intergranular layer (Hernando and Kulik, 1994) and dipolar interactions (Herzer, 1995) provide reasonable explanations in order to interpret the experimental findings. In any case, the strength of the coupling decreases with increasing temperature due to the simultaneous decrease of the magnetization in the bcc grains. Consequently, the soft magnetic properties keep on degrading even above T_C^{am} until thermal energy dominates and the system gets superparamagnetic.

The temperature dependence of the magnetic properties demonstrates that it is important to maintain an efficient exchange coupling between the grains by appropriate alloy design such that the Curie temperature of the residual amorphous matrix is clearly higher than application temperatures. Thus, for example, too high additions of Nb (or comparable elements), although favorable for grain refinement, can be disadvantageous because they decrease the Curie temperature of the matrix considerably (Yoshizawa and Yamauchi, 1991a). Similarly, reduced grain coupling due to a low Curie temperature of the intergranular phase also provides one of the explanations for the minor soft magnetic properties in nanocrystalline Fe–Zr–B alloys (cf. Slawska-Waniewska *et al.*, 1994) or Fe–Hf–C thin films (Hasegawa, Kataoka and Fujimori, 1992).

Figure 19 finally shows the temperature dependence of the permeability in comparison with other soft magnetic materials. In highly permeable crystalline alloys, like permalloy (80% NiFe), the magnetocrystalline anisotropy constant K_1 is adjusted to zero by alloying and annealing which, however, is effective only for a certain temperature. Thus, the temperature dependence of K_1 yields a pronounced variation of the soft magnetic properties around the temperature where K_1 is zero (cf. Pfeifer, 1992). In particular, the drop of permeability toward lower temperatures (because of $K_1 > 0$) can be a problem for certain applications like, for example, magnetic cores for ground fault interrupters. In

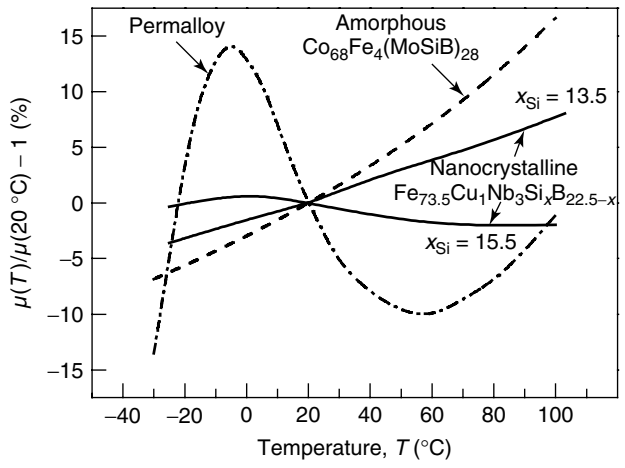

Figure 19. Relative change of the initial permeability normalized to its room-temperature value versus the typical range of application temperatures for highly permeable soft magnetic materials. All examples have been transverse field annealed and reveal an initial permeability in the range $\mu_i \approx 70 \times 10^3 - 90 \times 10^3$.

comparison, in nanocrystalline and amorphous materials, the magnetocrystalline anisotropy is averaged out by exchange interaction which is effective over a large temperature range. Accordingly the magnetic properties vary smoothly in both materials. In amorphous alloys, the behavior is mainly determined by induced anisotropies whose magnitude decreases and, thus, the permeability typically increases with increasing temperature. This mechanism also applies to nanocrystalline materials but is opposed by the reduction of the intergranular coupling at higher temperatures. Accordingly, the permeability runs through a maximum at an intermediate temperature, T_{max}. The latter depends on the details of the annealing conditions as well as on the alloy composition–though the physical mechanisms are still under investigation. Depending on T_{max}, the permeability may thus be found to increase, to decrease, or to be even largely temperature independent over the range of application temperatures.

4.2 Saturation magnetostriction

Apart from a low or vanishing magnetocrystalline anisotropy, another basic requirement for excellent soft magnetic properties is the absence of magnetostriction in order to minimize magnetoelastic anisotropies

$$K_\sigma = -\tfrac{3}{2}\lambda_s\sigma \tag{17}$$

arising from internal or external mechanical stress, σ. For example, even stress-relieved toroidal wound cores may still reveal internal stresses of a few MPa. In the amorphous state the material reveals a high positive saturation magnetostriction of $\lambda_s \approx +23 \times 10^{-6}$, typical for Fe-based amorphous alloys. The associated magnetoelastic anisotropy of about $K_\sigma \approx 50\,\mathrm{J\,m^{-3}}$, thus, limits the achievable initial permeability to typically $\mu_i \approx 10^4$.

It is the actual highlight of nanocrystalline Fe-based alloys that the phases formed on crystallization can lead to low or vanishing saturation magnetostriction, λ_s. Figure 20 summarizes the situation in the Fe–Cu–Nb–Si–B system. The decrease of λ_s is ultimately responsible for the simultaneous increase of the initial permeability upon the formation of the nanocrystalline state (cf. Figure 5).

While λ_s is fairly independent of the composition in the amorphous state (cf. Herzer, 1991), it depends sensitively on the Si content in the nanocrystalline state, passing through zero at low and at high Si concentrations around 16 at%. Still, the maximum permeability is not necessarily found for the $\lambda_s \approx 0$ compositions, but for Si contents around 13 at% (cf. Figure 11) due to the impact of the other anisotropy contributions.

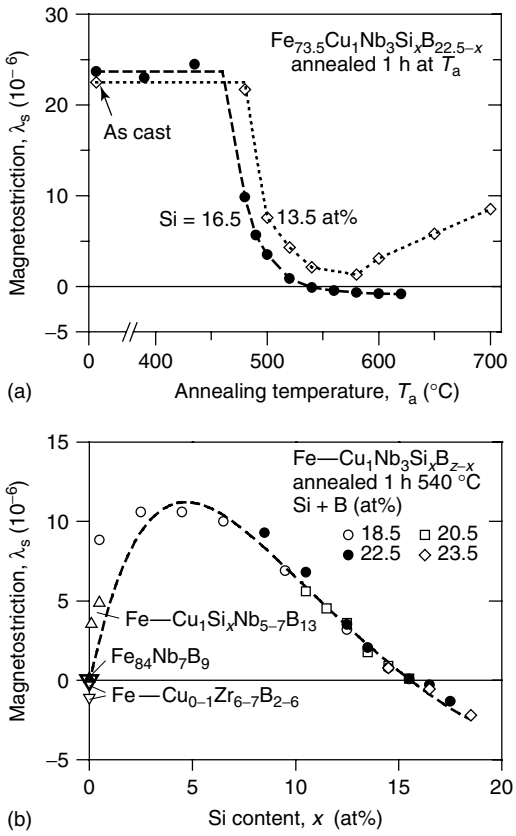

Figure 20. The saturation magnetostriction, λ_s, of Fe–Cu–Nb–Si–B alloys: (a) Influence of the annealing temperature, T_a and (b) influence of the Si content in the nanocrystalline state. The figure includes the data for Fe–Nb–B (solid up triangle) and Fe–(Cu)–Zr–B alloys (open down triangles) from Suzuki *et al.* 1991, 1993. (Reprinted from *Handbook of Magnetic Materials*, Vol 10, Buschow, K.H.J., Nanocrystalline Soft Magnetic Alloys, Elsevier Science B.V., pp 415–462, 1997, with permission from Elsevier.)

The detailed behavior of λ_s can be understood from the balance of magnetostriction among the structural phases present in the nanocrystalline state, that is, (Herzer, 1991)

$$\lambda_s \approx x_{cr} \cdot \lambda_s^{FeSi} + (1 - x_{cr}) \cdot \lambda_s^{am} \tag{18}$$

where x_{cr} is the crystalline volume fraction, and λ_s^{FeSi} and λ_s^{am} denote the local magnetostriction constants of the α-Fe–Si grains and the residual amorphous matrix, respectively. The composition dependence essentially reflects the compositional variation of λ_s found for polycrystalline α-$Fe_{100-x}Si_x$ (cf. Yamamoto, 1980). Thus, near-zero magnetostriction in nanocrystalline Fe-based alloys requires a large crystalline volume fraction with negative magnetostriction in order to compensate the high positive value of the amorphous Fe-based matrix. This is achieved either by a high Si content in the bcc grains ($\lambda_s^{FeSi} \approx -6 \times 10^{-6}$ for α-$Fe_{80}Si_{20}$), like in

the Fe–Cu–Nb–Si–B system, or if the grains consist of pure α-Fe ($\lambda_s^{Fe} \approx -4 \times 10^{-6}$) like in Fe–Zr–B alloys (Suzuki *et al*., 1991a,b) or Fe–(Si)–Hf–C thin films (Hasegawa, Kataoka and Fujimori, 1992). For the low Si-content alloys it is further important to have a low boron concentration in order to obtain a large crystalline fraction and to suppress the formation of boride compounds which yield a positive contribution to λ_s (cf. the increase of λ_s in Figure 20a at elevated annealing temperatures where such boride compounds are formed).

An important point to stress is that the superposition of the local magnetostriction constants to zero really results in stress insensitivity of the magnetic properties like in amorphous Co(Fe)-based alloys. This is again a consequence of the smoothing effect of exchange interaction for structural correlation lengths much smaller than the domain wall width. Thus, the nanoscale fluctuations in magnetoelastic anisotropy associated with the locally varying magnetostrictions are randomly averaged out which results in a single isotropic magnetostriction coefficient. The situation contrasts with that for large grained crystalline systems, where an average zero saturation magnetostriction does not generally imply stress insensitivity of the hysteresis loop. Thus, the small grain size is also a decisive factor for the magnetostriction: although it does not directly influence the value of λ_s, it opens a new way in order to achieve isotropically low magnetostriction by combining the properties of different structural phases with the help of exchange interaction.

4.3 Annealing-induced anisotropies

So far magnetic anisotropies have been discussed as a rather disturbative factor for the soft magnetic properties. However, if properly controlled, they also can be a powerful tool in order to tailor the shape of the hysteresis loop according to the demands of various applications. Like, for example, in amorphous materials, this can be realized in nanocrystalline materials by either magnetic field annealing or tensile stress annealing which both yields a uniform uniaxial anisotropy.

4.3.1 Magnetic field–induced anisotropies

Magnetic field annealing induces a uniaxial anisotropy with an easy axis parallel to the direction of the magnetic field applied during the heat treatment. The anisotropy formation is related to directional atomic ordering along the direction of the local magnetization in order to minimize spin-orbit coupling energy (cf. Néel, 1954; Fujimori, 1983). Figure 21 shows some typical examples for the hysteresis loops and the corresponding impedance permeability as obtained after characteristic heat treatments.

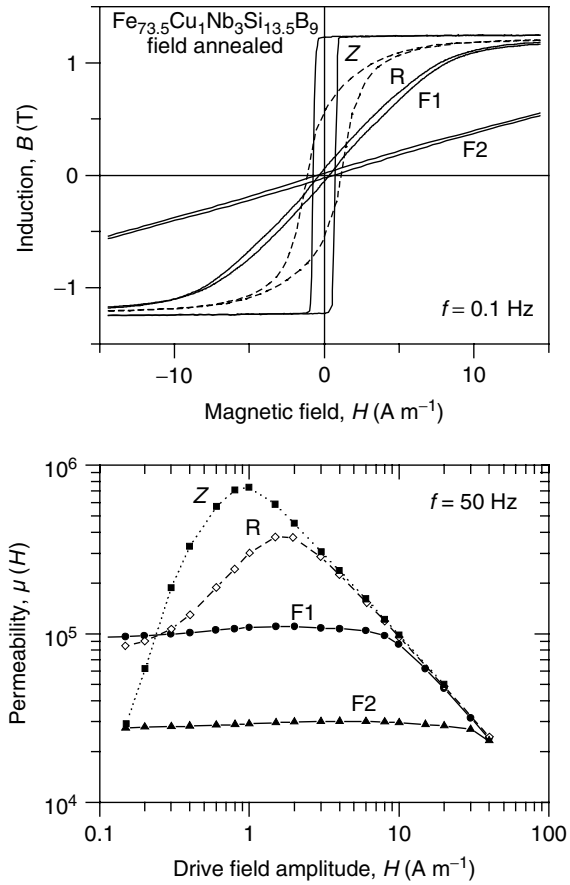

Figure 21. Quasistatic hysteresis loops and 50 Hz permeability of nanocrystalline $Fe_{73.5}Cu_1Nb_3Si_{13.5}B_9$ annealed for 1 h at 540 °C without (R) and with a magnetic field applied parallel (Z) and transverse (F2; $K_u \approx 20\,J\,m^{-3}$, $\mu \approx 30 \times 10^3$) to the magnetic path. Sample F1 ($K_u \approx 6\,J\,m^{-3}$, $\mu \approx 100 \times 10^3$) was first crystallized at 540 °C and subsequently transverse field annealed at 350 °C. (Reprinted from *Handbook of Magnetic Materials*, Vol 10, Buschow, K.H.J., Nanocrystalline Soft Magnetic Alloys, Elsevier Science B.V., pp 415–462, 1997, with permission from Elsevier.)

The *flat-shaped* loops (F1, F2) are obtained by transverse field annealing, that is, by inducing a uniaxial anisotropy perpendicular to the ribbon axis. The magnetization process is determined by rotation of the magnetization vectors from the easy direction toward the ribbon axis. This results in a permeability, μ, practically constant up to ferromagnetic saturation which by

$$\mu = \frac{J_s^2}{2\mu_0 K_u} \tag{19}$$

is directly related to the induced anisotropy energy constant, K_u.

The *rectangular* loop (Z) results after longitudinal field annealing. The uniaxial anisotropy is parallel to the ribbon axis and, thus, the magnetization process is dominated by

180° domain wall displacements. Highest maximum permeabilities can be achieved this way. Since the domain wall energy is proportional to the square root of K_u, low induced anisotropies in this case facilitate domain refinement which results in good dynamic properties like reduced anomalous eddy current losses (cf. Petzold, 2002; Flohrer *et al*., 2006).

The *round* loop (R) results after conventional annealing without magnetic field. The magnetization process is a mixture of magnetization rotation and domain wall displacements. Characteristic features of the round loop are a high initial and high maximum permeability. Still, annealing without magnetic field does not mean that there are no induced anisotropies. The latter are always induced along the local direction of the spontaneous magnetization within a ferromagnetic domain as long as the annealing temperature is lower than Curie temperature. One should therefore more precisely speak of *magnetization-induced* instead of *field-induced* anisotropies. A magnetic field during annealing just aligns the magnetization which leads to a uniform anisotropy. Correspondingly, zero field annealing yields a distribution of uniaxial anisotropies reflecting the domain structure during the heat treatment. The remanence to saturation ratio of around 50%, typical for randomly oriented uniaxial anisotropies, indicates that these randomly induced anisotropies are fluctuating on a scale larger than the exchange length and, hence, control the soft magnetic properties at small grain sizes. These induced anisotropy fluctuations can be reduced by rotating field annealing which results in a significantly reduced coercivity and an enhanced remanence (Ito and Suzuki, 2005). Similarly, the field annealed samples typically reveal a smaller coercivity than the samples annealed without field which can be understood from the simpler domain configuration due to the more homogeneously induced anisotropy. Correspondingly, proper transverse field annealing allows higher initial permeabilities than obtained by the conventional heat treatment without a magnetic field.

The almost perfectly rectangular- or flat-shaped hysteresis loops after field annealing indicate that the field-induced anisotropy clearly dominates over the residual contributions from magnetocrystalline and magnetoelastic anisotropies. Still, the induced anisotropy constant, K_u, can be tailored small enough in order to achieve highest permeabilities (e.g., $K_u \approx 6\,\mathrm{J\,m^{-3}}$ and $\mu \approx 100\,000$ as for the F1 loop shown in Figure 21). Figure 22 summarizes the dependence of K_u on the annealing condition and on the alloy composition for nanocrystalline Fe–Cu–Nb–Si–B alloys annealed in a transverse magnetic field.

If the material is nanocrystallized first without applied field and subsequently field annealed at lower temperatures, the resulting induced anisotropy depends on the field annealing temperature, T_a, and the annealing time, t_a, but less sensitively than, for example, in amorphous alloys (cf. Yoshizawa and Yamauchi, 1990). The dependence of K_u on the annealing conditions (cf. Figure 22a) allows to tailor hysteresis loops with different levels of permeability as exemplified by the F1 and F2 loops shown in Figure 21. Linear, low remanence hysteresis loops with highest permeabilities up to $\mu \approx 200 \times 10^3$ ($K_u \approx 3\,\mathrm{J\,m^{-3}}$) can be achieved in this manner. Only if the induced anisotropies fall below about $K_u \approx 2\text{–}4\,\mathrm{J\,m^{-3}}$ the random magnetocrystalline anisotropies start dominating again which is indicated by nonlinear hysteresis loops with high remanence (Herzer, 2005b). In comparison, amorphous Co-based alloys still show a low remanence and a linear hysteresis loop for induced anisotropies of $K_u \approx 0.5\,\mathrm{J\,m^{-3}}$ and even smaller values because of their virtually negligible magnetocrystalline anisotropy.

If the field annealing is performed during nanocrystallization, the induced anisotropy reaches a maximum value which is relatively insensitive to the precise annealing conditions and, thus, corresponds to the equilibrium value characteristic for the alloy composition (Herzer, 1994a). As shown in

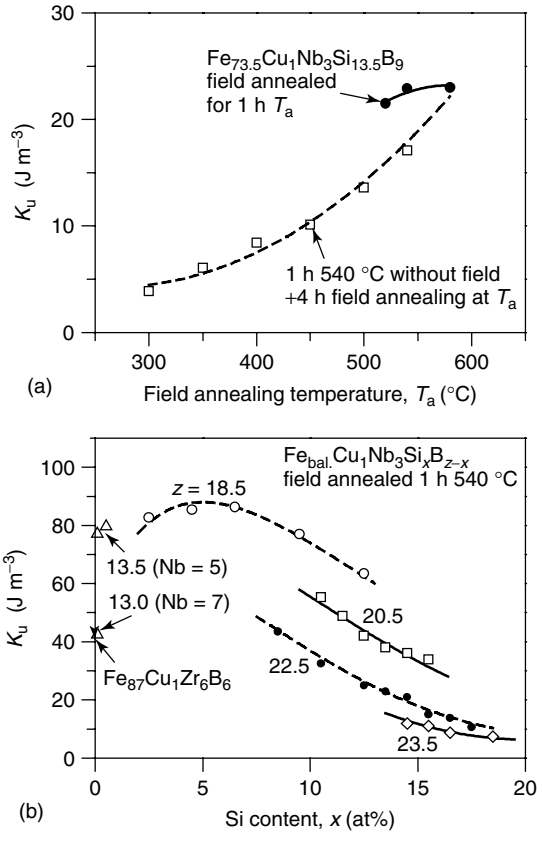

Figure 22. Field-induced anisotropy, K_u, in nanocrystalline Fe–Cu–Nb–Si–B alloys: (a) Influence of the annealing conditions and (b) role of the composition in the nanocrystalline state. (Reprinted from *Handbook of Magnetic Materials*, Vol 10, Buschow, K.H.J., Nanocrystalline Soft Magnetic Alloys, Elsevier Science B.V., pp 415–462, 1997, with permission from Elsevier.)

Figure 22(b), the induced anisotropy energy decreases with increasing metalloid contents and, in particular, with increasing Si/(Si + B) ratio. Accordingly, the lowest anisotropy energies and, thus, the highest permeabilities are found for the high Si-content alloys. The effect of the copper and niobium concentration on K_u is only minor as long as both elements are chosen such that a homogeneous nanocrystalline structure is formed. However, the influence of niobium or other refractory elements on K_u can become significant for alloy compositions with very low silicon and correspondingly high boron contents. Such compositions tend to reveal traces of boride compounds which may significantly contribute to K_u. The latter is supported by the decrease of K_u upon reducing the boron content and increasing the Nb or Zr content which suppresses the formation of such compounds.

The anisotropy induced by a magnetic field applied during nanocrystallization primarily originates from the bcc grains (Herzer, 1994a) and can be understood from the directional ordering of Si-atom pairs (cf. Sixtus, 1970). In particular, the decrease of K_u with increasing Si content is related to the simultaneously increasing long-range order (DO_3 superlattice structure) of the bcc grains. Thus, the necessary degrees of freedom for an induced directional ordering are reduced as the composition of the grains approaches completely ordered Fe_3Si where the lattice sites for the Fe and Si atoms are entirely determined by chemical interactions (cf. Néel, 1954). This mechanism is the key factor that nanocrystalline Fe–Cu–Nb–Si–B alloys exhibit lowest induced anisotropies and, hence, highest permeability despite of their high saturation magnetization.

The mechanisms of anisotropy formation also determine the thermal aging of the soft magnetic properties. Thus, thermal aging can be basically understood as the formation or reorientation of induced anisotropies along the local magnetization directions at application temperatures. The reduced degrees of freedom for anisotropy formation due to the superlattice structure and the high Curie temperature allow to stabilize low anisotropies, that is, high permeabilities, at annealing temperatures much higher than it is possible for amorphous alloys or permalloys. This essentially reduces the kinetics for anisotropy changes at application temperatures. In comparison with amorphous metals, the thermal stability is additionally improved by the more stable crystalline structure. As a consequence, nanocrystalline alloys exhibit an excellent thermal stability of their soft magnetic properties surpassing by far that of amorphous alloys and even that of permalloys (Herzer, 1997). This allows higher continuous service temperatures up to 150 °C.

The tremendous practical impact of field-induced anisotropies is evident. Their understanding is ultimately the key for the reproducible control of the soft magnetic properties. By appropriate choice of alloy composition and annealing conditions, transverse field annealing of nanocrystalline Fe–Cu–Nb–Si–B alloys, thus, allows to induce anisotropies in the range of $K_u \approx 3$–$100\,\mathrm{J\,m^{-3}}$. This corresponds to initial permeabilities of about $\mu_i \approx 10^4$–2×10^5 which perfectly covers the need of applications like common mode chokes or earth leakage circuit breakers (Petzold, 2002). More recent investigations try to expand the property spectrum of nanocrystalline alloys toward lower permeabilities in the order of several hundreds to several thousands as they are useful, for example, for energy storage chokes or current transformers. This can be achieved by adding Co and/or Ni, which like in amorphous metals (cf. Fujimori, 1983), significantly enhances the field-induced anisotropy due to pair ordering of Fe and Co or Ni atoms. Yoshizawa *et al*. (2003), for example, showed that the field-induced anisotropy in nanocrystalline $Fe_{78.8-x}Co_xCu_{0.6}Nb_{2.6}Si_9B_9$ ($x = 0$ to 78.8) is enhanced from $\sim 100\,\mathrm{J\,m^{-3}}$ at $x = 0$ to $\sim 600\,\mathrm{J\,m^{-3}}$ at $x = 50$. Ni has a similar effect on K_u like Co, but the coercivity increases drastically for Ni concentrations above about 10–15 at%. Yet, with the combined addition of Co and Ni like in $Fe_{66.8-x}Co_xNi_{10}Cu_{0.8}Nb_{2.9}Si_{11.5}B_8$ (Herzer and Otte, 2004), one can obtain similarly high field–induced anisotropies but with only about half the amount of Co, that is, at lower raw material cost. In any case, the drawback of increasing the field-induced anisotropy either by reduction of the metalloid contents (cf. Figure 11) or by adding Co and/or Ni is a disadvantageous increase of saturation magnetostriction. Müller *et al*. (1996), for example, showed that the saturation magnetostriction of nanocrystalline $Fe_{73.5-x}Co_xCu_1Nb_3Si_{15.5}B_7$ and $Fe_{86-y}Co_yZr_7B_6Cu_1$ alloys increases from near zero to maximum values of about $\lambda_s \approx 20$ ppm (for $x = 30$ at%) and $\lambda_s \approx 40$ ppm (for $y = 60$ at%), respectively, when substantial amounts of Co are added.

4.3.2 Creep-induced anisotropies

Annealing under tensile stress causes an anelastic or plastic deformation of the material and, as a consequence, an easy or hard magnetic axis along the stress axis. The basic characteristics of this creep-induced anisotropy in Fe–Cu–Nb–Si–B alloys (Kraus *et al*., 1992; Herzer, 1994b; Hofmann and Kronmüller, 1996) are essentially the same as they are well known from amorphous alloys.

Figure 23 shows some typical hysteresis loops after crystallization under tensile stress. The creep-induced anisotropy constant is proportional to the tensile stress σ_a applied during annealing, that is,

$$K_u = -\tfrac{3}{2} k \sigma_a \qquad (20)$$

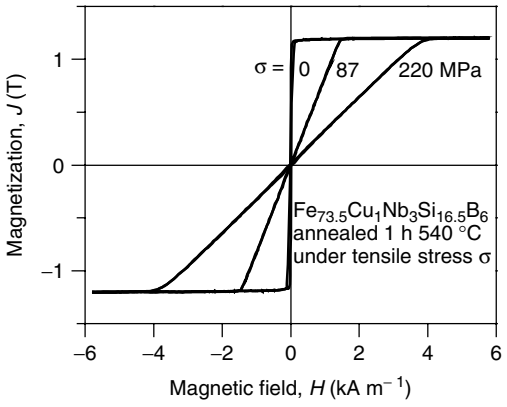

Figure 23. Dc-hysteresis loops of $Fe_{73.5}Cu_1Nb_3Si_{16.5}B_6$ nanocrystallized by annealing for 1 h at 540 °C under tensile stress σ. (Reproduced by permission of IEEE, Creep Induced Magnetic Anisotropy in Nanocrystalline Fe–Cu–Nb–Si–B Alloys, G. Herzer (1994) © 1994 IEEE.)

The anisotropy parameter k is a dimensionless proportionality constant being introduced in formal analogy to the magnetostriction constant in equation (17). By definition $k > 0$ denotes a magnetic easy axis parallel to the stress axis while $k < 0$ denotes a magnetic hard axis, that is, an easy plane perpendicular to the stress axis.

Figure 24 depicts the variation of the creep-induced anisotropy with the annealing temperature, T_a and the composition (Herzer, 1994b). The decrease of k for $T_a \geq 480\,^{\circ}C$ coincides with the transformation from the amorphous to the nanocrystalline state which is completed for $T_a \geq 500\,^{\circ}C$. The creep-induced anisotropy in the amorphous state is comparable to that typically observed in other amorphous alloy systems. However, upon devitrification, its absolute value significantly increases. Within the range where the nanocrystalline state is formed, the anisotropy induced during crystallization is fairly insensitive to the annealing time and temperature and, thus, corresponds to an equilibrium value mainly determined by the Si concentration. In particular, the magnetic hard ribbon axis ($k < 0$) observed for high Si contents turns over to an easy ribbon axis ($k > 0$) for alloys with Si concentrations below about 10 at%. An anisotropy of similar order of magnitude can also be induced in samples previously crystallized without stress. However, in this case the induced anisotropy is more sensitive to the annealing temperature since the kinetics of anisotropy formation is considerably slower (cf. Hofmann and Kronmüller, 1996).

The comparison of Figures 20 and 24 reveals that the variation with annealing temperature or alloy composition, in a way, is similar for both the creep-induced anisotropy parameter, k, and the saturation magnetostriction, λ_s, respectively. However, there are also significant differences. In particular, both quantities pass through zero at different Si concentrations. As a consequence, a strong creep-induced

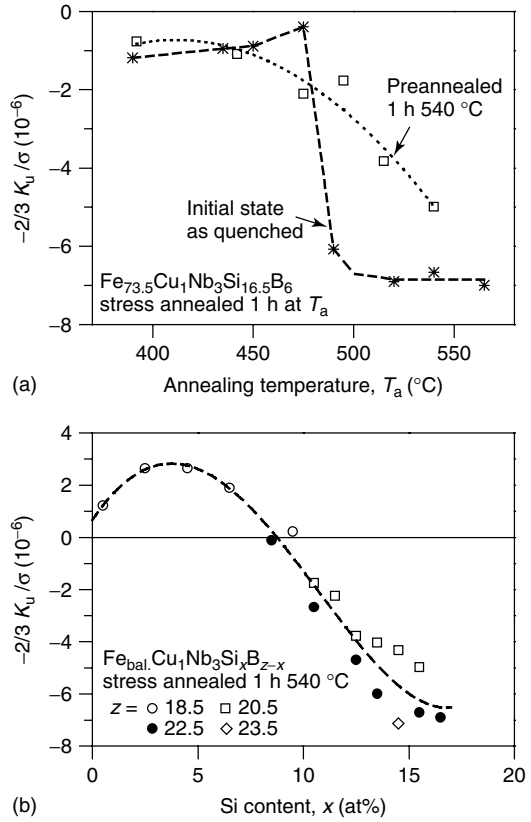

Figure 24. Creep-induced anisotropy parameter, $k = -2/3 \cdot K_u/\sigma$, of Fe–Cu–Nb–Si–B alloys: (a) Influence of the annealing conditions and (b) role of the composition in the nanocrystalline state. (Reprinted from *Handbook of Magnetic Materials*, Vol 10, Buschow, K.H.J., Nanocrystalline Soft Magnetic Alloys, Elsevier Science B.V., pp 415–462, 1997, with permission from Elsevier.)

anisotropy is found for the near-zero magnetostrictive compositions. It appears that the equilibrium value of the anisotropy parameter k differs from the saturation magnetostriction λ_s only by the lack of the positive contribution from the amorphous matrix. A closer analysis of the experimental data indeed confirms that the normalized anisotropy parameter k/x_{cr} (x_{cr} is the crystalline volume) approximately equals to the local saturation magnetostriction constant, λ_s^{FeSi}, of the bcc-FeSi grains (Herzer, 1994b). This suggests that the creep-induced anisotropy in the nanocrystalline state mainly originates from the local magnetoelastic anisotropy of the bcc grains due to an elongation induced by the stress annealing. The mechanism was confirmed by Ohnuma *et al.* (2003a,b) who directly showed by means of transmission X-ray diffractometry that the lattice spacing of the Fe(Si) nanocrystallites is elongated along the stress direction after the stress annealing. The amorphous matrix itself gives only a minor contribution to the anisotropy energy. This can be understood from (i) the comparably low magnitude of the creep-induced magnetic anisotropy generally observed in amorphous alloys

which (ii) in the nanocrystalline state is still weighted by the relatively small volume fraction of the amorphous matrix.

Creep-induced anisotropies, in principal, allow to tailor linear hysteresis loops by annealing under controlled tensile stress. The advantage over field annealed Co-doped alloys is that one can combine low magnetostriction and high anisotropies. Alves *et al*. (2002, 2005), for example, have prepared toroidally wound cores of near-zero magnetostrictive nanocrystalline $Fe_{74.5}Cu_1Nb_3Si_{15.5}B_6$ with induced anisotropies up to about $K_u \approx 2000\,J\,m^{-3}$ (i.e., $\mu \approx 300$) by (i) continuously annealing the material for a short time (10–60 s) at elevated temperatures around 650 °C under a tensile stress of 270 MPa and (ii) subsequently winding toroidal cores. However, the practical application of this technique is most challenging due to the severe embrittlement after nanocrystallization.

Yet, the practical impact of creep-induced anisotropy in nanocrystalline materials often is of more disturbative nature. For example, thin SiO_2 layers give rise to small tensile stresses during the anneal treatment which yield an unwanted creep-induced anisotropy perpendicular to the ribbon plane and, thus, a degradation of the soft magnetic properties even for zero-magnetostrictive compositions (cf. del Real, Prados, Conde and Hernando, 1994). This is a particular problem for the nanocrystalline material, since its creep-induced anisotropy is more than one order of magnitude larger than, for example, in near-zero magnetostrictive, amorphous Co-based alloys. The uncontrolled formation of such oxide layers contributes to the decrease of permeability toward high Si contents (cf. Figure 11) where both the creep-induced anisotropy and the driving force for the formation of a SiO_2 layer are particularly large.

5 CONCLUSIONS

The key to the soft magnetic properties of nanocrystalline alloys is that their structural correlation length is much smaller than the ferromagnetic exchange length. Thus, similar to the case of amorphous metals, the local magnetocrystalline anisotropies are randomly averaged out owing to the smoothing effect of exchange interaction. This averaging mechanism also applies to the fluctuations of magnetoelastic anisotropy associated with the local magnetostriction coefficients of the individual structural phases. The result is an isotropic magnetostrictive behavior characterized by a single magnetostriction coefficient λ_s which vanishes for particular compositions like nanocrystalline $Fe_{73.5}Cu_1Nb_3Si_{15.5}B_7$. For such optimized compositions, the contribution of magnetocrystalline and magnetoelastic anisotropies is ultimately negligible and the soft magnetic properties are largely determined by field-induced anisotropies which play a tremendously important role in tailoring the hysteresis loop according to the requirements of the application.

Lowest coercivities ($H_c \approx 0.5$–$1\,A\,m^{-1}$) and highest permeabilities ($\mu \approx 10^5$) are found around the originally proposed compositions, that is, $Fe_{\sim 74}Cu_1Nb_3Si_{13-16}B_{6-9}$ which are commercially available under the trade names FINEMET® (cf. Hitachi Metals Ltd, 1993) and VITROPERM® (cf. Vacuumschmelze GmbH, 1993). The soft magnetic properties are comparable with the excellent properties possessed by established materials such as permalloys or Co-based amorphous alloys. The advantages, however, are a higher saturation induction of about 1.2–1.3 T and a significantly better thermal stability of the soft magnetic properties allowing higher continuous service temperatures up to 150 °C. Similar to amorphous metals, the production inherent low thickness around 20 µm and a high electrical resistivity around 115 µΩcm minimize eddy current losses in nanocrystalline ribbons. Accordingly, the frequency dependence of permeability and the core losses of nanocrystalline Fe–Cu–Nb–Si–B alloys are comparable to those of amorphous Co-based alloys and surpass by far the properties of conventional materials, even that of ferrites, over the whole frequency range up to several 100 kHz. A corresponding comparison is given in Figure 25. The combination of high saturation magnetization and high permeability together with good high-frequency behavior, low losses, and the good thermal stability allows reductions in the size and weight of magnetic components used in, for example, switched mode power supplies or telecommunications.

Apart from its technical performance the material is based on the inexpensive raw materials iron and silicon. The

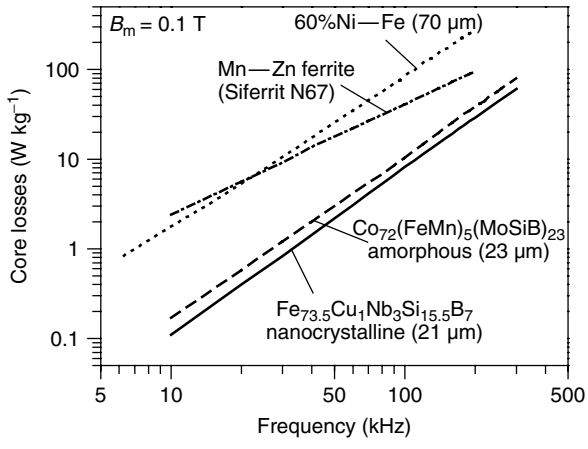

Figure 25. Core losses versus frequency for transverse field annealed nanocrystalline $Fe_{73.5}Cu_1Nb_3Si_{15.5}B_7$ and other low remanence, soft magnetic materials used for high-frequency power transformers. (Reprinted from *Handbook of Magnetic Materials*, Vol 10, Buschow, K.H.J., Nanocrystalline Soft Magnetic Alloys, Elsevier Science B.V., pp 415–462, 1997, with permission from Elsevier.)

Figure 26. Toroidal wound cores and components of VITROPERM 800F ($Fe_{73.5}Cu_1Nb_3Si_{15.5}B_7$).

amorphous precursor material for the Fe–Cu–Nb–Si–B alloys, is furthermore easily accessible by rapid solidification from the melt – a well-established technique for large-scale production of amorphous metals.

The combination of the above factors has rendered the nanocrystalline solution competitive, not only with amorphous Co-based alloys but also with classical crystalline alloys and ferrites. The consequence is a steadily increasing level of applications in magnetic cores for ground fault interrupters, common mode chokes and high-frequency transformers. Figure 26 shows some typical examples. The worldwide production rate meanwhile approaches an estimated 1000 tons/year and with increasing trend. The only drawback of the nanocrystalline materials appears to be the embrittlement that occurs upon crystallization, which requires final shape annealing and, thus, restricts application mainly to toroidally wound cores.

The second family of near-zero magnetostrictive, nanocrystalline alloys based on $Fe_{\sim 84-91}(Cu_1)-(Zr,Nb)_{\sim 7}B_{2-9}$ appears even more interesting due to their still higher saturation magnetization up to 1.7 T. However, their application so far is limited to smaller quantities. One of the major reasons is that they require a much more sophisticated production technology due to their limited glass-forming ability and or the oxygen reactivity of the Zr addition.

REFERENCES

Alben, R., Becker, J. and Chi, M.C. (1978). Random anisotropy in amorphous ferromagnets. *Journal of Applied Physics*, **49**, 1653–1658.

Alves, F., Desmoulins, J.B., Herisson, D., *et al*. (2002). Procédé de frabrication d'une bande en matériau nanocristallin, procédé et dispositif de fabrication d'un tore magnétique, tore magnétique et utilisatio du tore magnétique comme élément d'un composant inductif. French Patent Application, 2823507A1.

Alves, F., Simon, F., Kane, S.N., *et al*. (2005). Influence of rapid stress annealing on magnetic and structural properties of nanocrystalline $Fe_{74.5}Cu_1Nb_3Si_{15.5}B_6$ alloy. *Journal of Magnetism and Magnetic Materials*, **294**, e141–e144.

Arai, K., Tsutsumitakae, I. and Ohmori, K. (1984). Grain growth of rapid quenching high silicon-iron alloys. *IEEE Transactions on Magnetics*, **MAG-20**, 1463–1465.

Bozorth, R.M. (1951). *Ferromagnetism*, D. Van Nostrand Company: Princeton.

Buschow, K.H. (1997). Magnetism and processing of permanent magnet materials. In *Handbook of Magnetic Materials*, Buschow, K.H.J. (Ed.), Elsevier Science B.V., pp. 463–593, Vol. 10.

Flohrer, S., Schäfer, R., McCord, J., *et al*. (2006). Dynamic losses and domain refinement in nanocrystalline tape wound cores. *Acta Materialia*, **54**, 3253–3259.

Flohrer, S., Schäfer, R., Polak, Ch. and Herzer, G. (2005). Interplay of uniform and random anisotropy in nanocrystalline soft magnetic alloys. *Acta Materialia*, **53**, 2937–2942.

Fujimori, H. (1983). Magnetic anisotropy. In *Amorphous Metallic Alloys*, Luborsky, F.E. (Ed.), Butterworths: London, pp. 300–316.

Fujimori, H. (1995). Structure and 100 MHz soft magnetic properties in multilayers and granular thin films. *Scripta Metallurgica*, **33**, 1625–1636.

Gengnagel, H. and Wagner, H. (1961). Magnetfeldinduzierte anisotropie an FeAl- und FeSi-einkristallen. *Zeitschrift Fur Angewandte Physik*, **8**, 174–177.

Guo, H-Q., Reininger, T., Kronmüller, H., *et al*. (1991). Magnetism and microstructure in nanocrystalline FeCoZr ferromagnets. *Physica Status Solidi (a)*, **127**, 519–527.

Hasegawa, N., Kataoka, N. and Fujimori, H. (1992). Soft magnetic properties of carbide-dispersed nanocrystalline Fe-Si-Hf-C films. *IEEE Transactions on Magnetics in Japan*, **7**, 880–885.

Hasegawa, N. and Saito, M. (1991). Structural and soft magnetic properties of carbide-dispersed microcrystalline films with high thermal stability. In *Proceedings of the International Symposium on 3d Transition-Semi Metal Thin Films, Magnetism and Processing*, Japan Society for the Promotion of Science, 131 Committee: Sendai, pp. 165–174.

Hernando, A. and Kulik, T. (1994). Exchange interactions through amorphous paramagnetic layers in ferromagnetic nanocrystals. *Physical Review B*, **49**, 7064–7067.

Herzer, G. (1989). Grain structure and magnetism of nanocrystalline ferromagnets. *IEEE Transactions on Magnetics*, **25**, 3327–3329.

Herzer, G. (1990). Grain size dependence of coercivity and permeability in nanocrystalline ferromagnets. *IEEE Transactions on Magnetics*, **26**, 1397–1402.

Herzer, G. (1991). Magnetism and microstructure of nanocrystalline Fe-base alloys. In *Proceedings of the International Symposium on 3d Transition-Semi Metal Thin Films: Magnetism and Processing*, Japan Society for the Promotion of Science: 131 Committee (Thin Film) Sendai, Japan, pp.130–138.

Herzer, G. (1994a). Magnetic field induced anisotropy in nanocrystalline Fe-Cu-Nb-Si-B alloys. *Materials Science and Engineering*, **A181/A182**, 876–879.

Herzer, G. (1994b). Creep induced magnetic anisotropy in nanocrystalline Fe-Cu-Nb-Si-B alloys. *IEEE Transactions on Magnetics*, **30**, 4800–4802.

Herzer, G. (1995). Soft magnetic nanocrystalline materials. *Scripta Metallurgica*, **33**, 1741–1756.

Herzer, G. (1997). Nanocrystalline soft magnetic alloys. In *Handbook of Magnetic Materials*, Buschow, K.H.J. (Ed.), Elsevier Science B.V., pp. 415–462, Vol. 10.

Herzer, G. (2005a). The random anisotropy model – a critical review and update. In *Properties and Applications of Nanocrystalline Alloys from Amorphous Precursors*, surIdzikowski, B., Svec, P. and Miglierini, M. (Eds.), Kluwer Academic Publishers, pp. 15–34.

Herzer, G. (2005b). Anisotropies in soft magnetic nanocrystalline alloys. *Journal of Magnetism and Magnetic Materials*, **294**, 99–106.

Herzer, G. and Otte, D. (2004). Magnet core, method for the production of such a magnet core, uses of such a magnet core especially in current transformers and current-compensated inductors, and alloys and bands used for producing such a magnet core. PCT Patent Application WO 2004/088681 A2.

Herzer, G. and Warlimont, H. (1992). Nanocrystalline soft magnetic materials by partial crystallization of amorphous alloys. *Nanostructured Materials*, **1**, 263–268.

Hitachi Metals Ltd. (1993). New materials from the Nano-world, Magnetic Cores. *Data sheet* 9. Y-930415.

Hofmann, B. and Kronmüller, H. (1996). Stress-induced magnetic anisotropy in nanocrystalline FeCuNbSiB. *Journal of Magnetism and Magnetic Materials*, **152**, 91–98.

Hono, K., Hiraga, K., Wang, Q., *et al*. (1992). The microstructural evolution of a $Fe_{73.5}Si_{13.5}B_9Nb_3Cu_1$ nanocrystalline soft magnetic material. *Acta Metallurgica*, **40**, 2137–2147.

Hono, K. and Ohnuma, M. (2002). Microstructure and properties of nanocrystalline and nanogranular magnetic materials. In *Magnetic Nanostructures*, Nalwa, H.S. (Ed.), American Scientific Publishers, pp. 327–358.

Hono, K., Ping, D.H., Ohnuma, M. and Onodera, H. (1999). Cu clustering and Si partitioning in the early crystallization stage of an $Fe_{73.5}Si_{13.5}B_9Nb_3Cu_1$ amorphous alloy. *Acta Materialia*, **47**, 997–1006.

Iga, A., Tawara, Y. and Yanase, A. (1966). Magnetocrystalline anisotropy of Fe_2B. *Journal of the Physical Society of Japan*, **21**, 404.

Ito, N. and Suzuki, K. (2005). Improvement of magnetic softness in nanocrystalline soft magnetic materials by rotating magnetic field annealing. *Journal of Applied Physics*, **97**, 10F503–10F503-3.

Kataoka, N., Inoue, A., Masumoto, T., *et al*. (1989a). Effect of additional Cu element on structure and crystallization behavior of amorphous Fe-Nb-Si-B. *Alloys, Japan. Journal of Applied Physics*, **28**, L1820–L1823.

Kataoka, N., Matsunaga, T., Inoue, A. and Masumoto, T. (1989b). Soft magnetic properties of bcc Fe-Au-X-Si-B (X = Early Transition Metal) alloys with fine grain structure. *Materials Transactions JIM*, **30**, 947–950.

Kneller, E. (1969). Fine particle theory. In *Magnetism and Metallurgy*, surBerkowitz, A.E. and Kneller, E. (Eds.), Academic Press: New York, pp. 365–471.

Kraus, L., Závěta, K., Heczko, O., *et al*. (1992). Magnetic anisotropy in as-quenched and nanocrystalline $Fe_{73.5}Cu_1Nb_3Si_{13.5}B_9$ alloys. *Journal of Magnetism and Magnetic Materials*, **112**, 275–277.

Lachowicz, H.K. and Slawska-Waniewska, A. (1994). Coexistence of various magnetic phases in nanocrystalline Fe-based metallic glasses. *Journal of Magnetism and Magnetic Materials*, **133**, 238–242.

Luborsky, F.E. (1961). High coercive materials. *J. Appl. Phys.*, **32**, 171S–183S.

Müller, M., Grahl, H., Mattern, N., *et al*. (1996). The influence of Co on the structure and magnetic properties of nanocrystalline FeSiB-CuNb and FeZrBCu-based alloys. *Journal of Magnetism and Magnetic Materials*, **160**, 284–286.

Müller, M. and Mattern, N. (1994). The influence of refractory element additions on the magnetic properties and on the crysatllization behaviour of nanocrystalline soft magnetic Fe-B-Si-Cu alloys. *Journal of Magnetism and Magnetic Materials*, **136**, 79–87.

Müller, M., Mattern, N. and Illgen, L. (1991). The influence of the Si/B content on the microstructure and on the magnetic properties of magnetically soft nanocrystalline FeBSi-CuNB alloys. *Zeitschrift Fur Metallkunde*, **82**, 895–901.

Néel, L. (1954). Anisotropie magnétique et superficielle et surstructures d'orientation. *Journal of Physical Radium*, **15**, 225–239.

O'Handley, R.C., Megusar, J., Sun, S-W., *et al*. (1985). Magnetization process in devitrified glassy alloy. *Journal of Applied Physics*, **57**, 3563–3565.

Ohnuma, M., Hono, K., Linderoth, S., *et al*. (2000). Small-angle neutron scattering and differential scanning calorimetry studies on the copper clustering stage of Fe-Si-B-Nb-Cu nanocrystalline alloys. *Acta Materialia*, **48**, 4783–4790.

Ohnuma, M., Hono, K., Yanai, T., *et al*. (2003a). Direct evidence for structural origin of stress-induced magnetic anisotropy in Fe-Si-B-Nb-Cu nanocrystalline alloys. *Applied Physics Letters*, **83**, 2859–2861.

Ohnuma, M., Ping, D.H., Abe, T., *et al*. (2003b). Optimization of the microstructure and properties of co-substituted Fe-Si-B-Nb-Cu nanocrystalline soft magnetic alloys. *Journal of Applied Physics*, **93**, 9186–9194.

Petzold, J. (2002). Advantages of soft magnetic nanocrystalline materials for modern electronic applications. *Journal of Magnetism and Magnetic Materials*, **242–245**, 84–89.

Pfeifer, F. (1992). Nickel-iron alloys. In *Concise Encyclopedia of Magnetic and Superconducting Materials*, Evetts, J. (Ed.), Pergamon Press: Oxford, pp. 349–356.

Pfeifer, F. and Radeloff, C. (1980). Soft magnetic Ni-Fe and Co-Fe alloys – some physical and metallurgical aspects. *Journal of Magnetism and Magnetic Materials*, **19**, 190–207.

del Real, R.P., Prados, C., Conde, F. and Hernando, A. (1994). Magnetic anisotropy induced by nanocrystallization of a coated amorphous alloy. *Journal of Magnetism and Magnetic Materials*, **131**, 183–188.

Sawa, T. and Takahashi, Y. (1990). Magnetic properties of FeCu (3*d* transition metals) SiB alloys with fine grain structure. *Journal of Applied Physics*, **67**, 5565–5567.

Schäfer, R., Hubert, A. and Herzer, G. (1991). Domain observation on nanocrystalline material. *Journal of Applied Physics*, **69**, 5325.

Sixtus, K. (1970). Anisotropie in Eisen-Silizium-Einkristallen nach Glühen im Magnetfeld. *Zeitschrift für Angewandte Physik*, **28**, 270–274.

Slawska-Waniewska, A., Nowicki, P., Lachowicz, H.K., *et al*. (1994). Magnetic interactions in Fe-Zr-B-Cu nanocrystalline materials at elevated temperatures. *Physical Review B*, **50**, 6465–6467.

Suzuki, K. and Cadogan, J.M. (1998a). Random magnetocrystalline anisotropy in two-phase nanocrystalline systems. *Physical Review B*, **58**, 2730–2738.

Suzuki, K., Herzer, G. and Cadogan, J.M. (1998b). The effect of coherent uniaxial anisotropies on the grain-size dependence of coercivity in nanocrystalline soft magnetic alloys. *Journal of Magnetism and Magnetic Materials*, **177–181**, 949–950.

Suzuki, K., Kataoka, N., Inoue, A., *et al*. (1990). High saturation magnetization and soft magnetic properties of bcc Fe-Zr-B alloys with ultrafine grain structure. *Materials Transactions JIM*, **31**, 743–746.

Suzuki, K., Makino, A., Inoue, A. and Masumoto, T. (1994). Formation of nanocrystalline structures by crystallization of amorphous Fe-M-B (M = IVa to VIa Group Metal) alloys. *Science Reports RITU*, **A39**, 133–140.

Suzuki, K., Makino, A., Kataoka, N., *et al*. (1991a). Soft magnetic properties of nanocrystalline bcc Fe-Zr-B and Fe-M-B-Cu (M = transition metal) alloys with high saturation magnetization. *Journal of Applied Physics*, **70**, 6232–6237.

Suzuki, K., Makino, A., Kataoka, N., *et al*. (1991b). High saturation magnetization and soft magnetic properties of bcc Fe-Zr-B and Fe-Zr-B-M (M = Transition Metal) alloys with nanoscale grain size. *Materials Transactions JIM*, **32**, 93–102.

Suzuki, K., Makino, A., Kataoka, N., *et al*. (1993). Low core losses of nanocrystalline Fe-M-B (M = Zr, Hf or Nb) alloys. *Journal of Applied Physics*, **74**, 3316–3322.

Ueda, Y., Ikeda, S. and Minami, K. (1994). Precipitation of α-Fe and structure fro amorphous $Fe_{74}Cu_1Nb_3Si_xB_{22-x}$ alloys by annaleing. *Materials Science and Engineering*, **A181/A182**, 992–996.

Vacuumschmelze GmbH. (1990). *Weichmagnetische Werkstoffe*, Boll, R. (Ed.), Siemens AG Verlag: Berlin and Munich.

Vacuumschmelze GmbH. (1993). *Toroidal Cores of VITROPERM*, data sheet PW-014.

Yamamoto, T. (1980). *The Development of Sendust and Other Ferromagnetic Alloys*, Komiyama Printing Company: Chiba, Japan.

Yoshizawa, Y. (1999). Magnetic properties and microstructure of nanocrystalline Fe-based alloys. *Materials Science Forum*, **307**, 51–62.

Yoshizawa, Y., Fuji, S., Ping, D.H., *et al*. (2003). Magnetic properties of nanocrystalline FeMCuNbSiB allos (M: Co, Ni). *Scripta Materialia*, **48**, 863–868.

Yoshizawa, Y., Oguma, S. and Yamauchi, K. (1988). New Fe-based soft magnetic alloys composed of ultrafine grain structure. *Journal of Applied Physics*, **64**, 6044.

Yoshizawa, Y. and Yamauchi, K. (1990). Induced magnetic anisotropy and thickness dependence of magnetic properties in nanocrystalline alloy "Finemet". *IEEE Translation Journal on Magnetics*, **5**, 1070–1076.

Yoshizawa, Y. and Yamauchi, K. (1991a). Magnetic properties of nanocrystalline Fe-based soft magnetic alloys. *Materials Research Society Symposium Proceedings*, **232**, 183–194.

Yoshizawa, Y. and Yamauchi, K. (1991b). Magnetic properties of Fe-Cu-M-Si-B (M = Cr, V, Mo, Nb, Ta, W) alloys. *Materials Science and Engineering*, **A133**, 176–179.

APPENDIX

The objective of this appendix is to illustrate in some more detail how random anisotropies are averaged out. We start with a simple analytical model calculation and subsequently generalize the results to uniaxial and cubic anisotropies oriented randomly over all spherical angles.

The way how anisotropies are averaged can be illustrated by a simplified planar model where we assume that the magnetization vector and the anisotropy axes are lying in a plane. In order to keep the model three dimensional, we still allow the in-plane anisotropy axes to fluctuate along the coordinate perpendicular to the plane. This simple approach may be physically justified for a typical ribbon shaped sample where the large out-of-plane demagnetizing factor forces the magnetization mainly into the ribbon plane. Accordingly, the local anisotropy energy density of an individual grain is assumed to be

$$\phi_{\mathrm{K}}^{(i)}(\theta) = K_1 \sin^2(\theta - \psi_i) \tag{A1}$$

The angle ψ_i denotes the orientation of the local easy axis and is randomly fluctuating from grain to grain. The angle θ describes the orientation of the magnetization which is assumed to be constant on a scale $L_{\mathrm{ex}} > D$. Further model assumptions are that each grain has the same size D and the same local anisotropy constant K_1. The average anisotropy energy density over the volume $V_{\mathrm{ex}} = L_{\mathrm{ex}}^3$ can then be evaluated as

$$\begin{aligned}\overline{\phi}_{\mathrm{K}}(\theta) &= \frac{1}{V_{\mathrm{ex}}} \int_{V_{\mathrm{ex}}} K_1 \sin^2(\theta - \psi(\underline{x}))\, \mathrm{d}^3x \\ &= K_1 \frac{1}{N} \sum_{i=1}^{N} \sin^2(\theta - \psi_i) \\ &= k_N \sin^2(\theta - \Psi_N) \\ &\quad + \frac{K_1 - k_N}{2}\end{aligned} \tag{A2}$$

with

$$k_N = K_1 \cdot \sqrt{\frac{1}{N} + \frac{1}{N^2} \sum_i \sum_{j(\neq i)} \cos\left(2(\psi_i - \psi_j)\right)} \qquad \text{(A3)}$$

In the last step of equation (A2), the sum over the $N = (L_{ex}/D)^3$ coupled grains has hereby been rewritten as one anisotropy expression with magnitude k_N and orientation Ψ_N using trigonometric relations. The calculation is illustrated in Figure A1.

If we look at a statistical ensemble with independent sets of each N coupled grains, both Ψ_N and k_N are still random numbers. In a more physical picture this means that the easiest orientation Ψ_N of N coupled grains is randomly fluctuating on the scale of L_{ex} from one exchange-coupled region to the neighboring one. Similarly the anisotropy constants k_N are fluctuating around an average value

$$\langle k_N \rangle = \frac{\beta K_1}{\sqrt{N}} \qquad \text{(A4)}$$

with a standard deviation

$$\sigma_K := \sqrt{\langle k_N^2 \rangle - \langle k_N \rangle^2} = \eta \cdot \langle k_N \rangle \qquad \text{(A5)}$$

The fluctuations arise from the second expression under the square root in equation (A3), that is, from the sum over all anisotropy cross terms between grains at different sites. Their relative orientation $(\psi_i - \psi_j)$ is a *random phase* and the individual anisotropy cross terms therefore largely cancel. The parameters β and η involve higher order angular moments like $\langle \cos^{2n}(\psi_i - \psi_j) \rangle$ originating from the anisotropy fluctuations within the ensemble. Numerical simulations yield $\beta \approx 0.90_{\pm 0.04}$ and $\eta \approx 0.50_{\pm 0.05}$ for an ensemble with 2000 statistical independent sets of each $N(= 2 - 2^{19})$ grains. The simulations show that the results apply already for an ensemble with statistically independent sets of only two coupled grains.

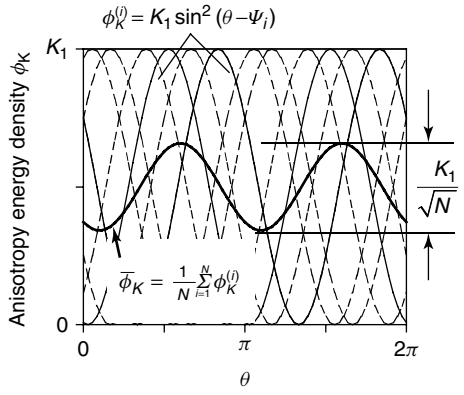

Figure A1. Local and randomly averaged anisotropy density ϕ_K as a function of the magnetization direction θ.

While the angular dependence of the anisotropy expressions given in equations (A1–A3) is specific to the above model, numerical simulations show that the relations for the ensemble averages, that is, equations (A4) and (A5), also apply very well for uniaxial or cubic anisotropies oriented randomly over all spherical angles. If the average anisotropy constant $\langle k_N \rangle$ in equation (A4) is understood as the difference between the maximum and minimum of the average anisotropy energy density, we accordingly find $\beta \approx 1.06_{\pm 0.03} (\eta \approx 0.31_{\pm 0.05})$ for uniaxial and $\beta \approx 0.393_{\pm 0.003} (\eta \approx 0.22_{\pm 0.03})$ for cubic anisotropies, respectively. The indicated errors arise from the finite ensemble size which was about 4000 statistical independent sets of N coupled grains. The rather distinct value of β for the *cubic* case is largely a consequence of common conventions for the anisotropy energy. The latter result in $\Delta\phi_K = |K_1|/3$ for cubic and $\Delta\phi_K = |K_1|$ for uniaxial anisotropies where $\Delta\phi_K = \phi_K^{max} - \phi_K^{min}$ is the difference of the anisotropy energy density between the hardest and easiest axis.

Figure A2 demonstrates that in the general case the energy surface of randomly oriented *coupled* grains no longer has the high symmetry exhibited by a pure uniaxial or cubic anisotropy. This is unlike our simplified model calculation, where the angular dependence is the same for the local and averaged anisotropy.

Random *uniaxial* anisotropies can be largely characterized analytically. The anisotropy energy density can be written as $\phi_K = \underline{m} \cdot \underline{\underline{K}}_1 \cdot \underline{m}$, where $\underline{\underline{K}}_1$ is a symmetric second rank tensor with zero trace and $\underline{m} = \underline{M}/M_s$ is the normalized magnetization vector. The average over the N coupled grains assumes the magnetization $\underline{m}$ to be constant and, hence, simply results in $\langle \phi_K \rangle_N = \underline{m} \cdot \underline{\underline{K}}_N \cdot \underline{m}$ with $\underline{\underline{K}}_N$ being still a symmetric second rank tensor with zero trace. The eigenvectors of the anisotropy tensors $\underline{\underline{K}}$ define the anisotropy axis and the eigenvalues the anisotropy constants. In a coordinate system defined by its eigenvectors, $\underline{\underline{K}}_N$ can always be represented as

$$\underline{\underline{K}}_N = k_N \cdot \begin{bmatrix} u & 0 & 0 \\ 0 & 1-2u & 0 \\ 0 & 0 & u-1 \end{bmatrix} \qquad \text{(A6)}$$

The coordinates have been hereby chosen such that the x axis is defined by the magnetic hardest and the z axis by the easiest axis. The anisotropy constant k_N denotes the energy difference between the hardest and easiest direction and, hence, is positive by definition. For a single grain we would simply have $k_1 = |K_1|$, while for N grains the ensemble average is given by $\langle k_N \rangle = \beta |K_1| / N^{1/2}$ with $\beta \approx 1.06$ as just discussed. The parameter u describes the symmetry and,

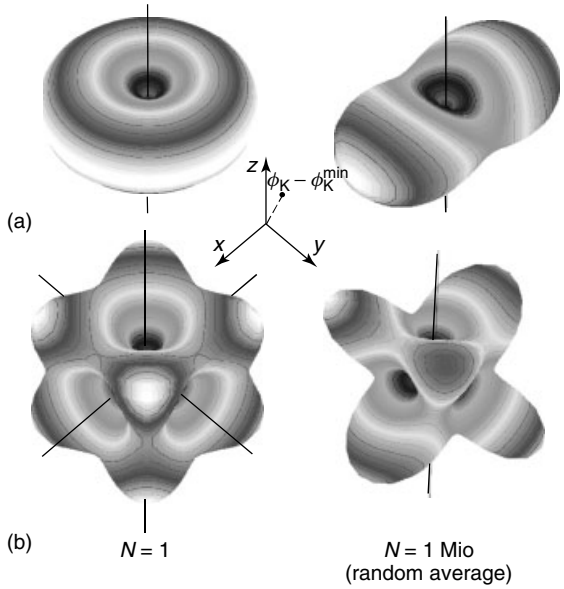

Figure A2. Energy surfaces for (a) uniaxial and (b) cubic anisotropies. The distance from the origin corresponds to the anisotropy energy difference $\phi_K - \phi_K^{min}$ for a certain orientation of the magnetization vector. The scale of each plot is different and adopted to the maximum energy difference. The thin black lines indicate the easiest magnetic axes.

with the above choice of the coordinate axis, is restricted to the range $1/3 \leq u \leq 2/3$. The boundaries $u = 1/3$ and $u = 2/3$ correspond to a magnetic easy axis with a hard plane and a magnetic hard axis with an easy plane, respectively. In the more traditional notation, this distinction is made by the sign of K_1, where $K_1 > 0$ corresponds to $u = 1/3$. However for N coupled grains, we find from our numerical simulations that u is distributed around an average value given by $\langle u \rangle \approx 0.50$ with a standard deviation of $\sigma_u \approx 0.07$, no matter if we start from an easy ($u = 1/3$) or a hard axis ($u = 2/3$). As illustrated in Figure A2 we thus deal with three preferred axes, perpendicular to each other, corresponding to a minimum, a saddle point and a maximum of the anisotropy energy.

For *cubic* anisotropies the corresponding arguments would involve the more complicated analysis of a fourth rank tensor which still has to be done. We can therefore only discuss the still somewhat preliminary numerical results. For one single *cubic* grain we have three easy axes along the $\langle 100 \rangle$ directions and four hard axes along the $\langle 111 \rangle$ directions for $K_1 > 0$ and vice versa for $K_1 < 0$. However, this distinction gets lost for randomly oriented grains. A random energy surface produced by a set of N grains with $K_1 > 0$ can always be reproduced by another set of N grains with $K_1 < 0$. The random average, thus, again breaks the high original symmetry and ultimately results in only one easiest axis and one hardest axis forming an average angle of about 50° with each other. Yet, there are a number of intermediate easy and hard directions which still remind one of the original cubic symmetry. These various easy axes typically form an angle of about $80–90^\circ$ with each other and their energies are relatively close together, differing only by about 10–20%.

Soft Magnetic Bulk Glassy and Bulk Nanocrystalline Alloys

Akihisa Inoue[1], Akihiro Makino[1] and Teruo Bitoh[2]

[1] *Tohoku University, Sendai, Japan*
[2] *Akita Prefectural University, Yurihonjo, Japan*

1 INTRODUCTION

Since the first synthesis of a ferromagnetic amorphous alloy was achieved in a vacuum deposited Co–Au system in 1965 (Mader and Nowick, 1965), a large number of Fe- and Co-based ferromagnetic amorphous alloys have been developed in the order of Fe–P–C (Duwez and Lin, 1967), Fe–P–B (Yamauchi and Nakagawa, 1971), (Fe, Co, Ni)–P–B (Hasegawa, 1972), (Fe, Co)–P–B–Al (Sherwood *et al*., 1975), (Fe, Co, Ni)–B–Si (Masumoto, Kimura, Inoue and Waseda, 1976), (Fe, Co, Ni)–B (O'Handley, Hasegawa, Ray and Chou, 1976), (Fe, Co, Ni)–(Cr, Mo, W)–C (Inoue, Masumoto, Arakawa and Iwadachi, 1978), (Fe, Co, Ni)–Zr (Nose and Masumoto, 1980), (Fe, Co, Ni)–Hf (Inoue, Kobayashi and Masumoto, 1980a), and (Fe, Co, Ni)–(Zr, Hf, Nb)–B (Inoue, Kobayashi, Nose and Masumoto, 1980b) systems. Furthermore, good soft magnetic properties have been reported simultaneously by three different research groups for Fe–P–C (Chen, 1974; Fujimori, Masumoto, Obi and Kikuchi, 1974), Fe–P–B (Egami, Flanders and Graham, 1975), and (Co, Fe)–B–Si (Kikuchi, Fujimori, Obi and Masumoto, 1975) systems between 1974 and 1975. The (Fe, Co)–P–B and (Fe, Co)–B–Si amorphous alloys have been used as soft magnetic materials named *METGLAS*. Subsequently, there had been no data on the synthesis of new soft magnetic amorphous alloys for almost 15 years between 1981 and 1995, though Fe–B–Si–Nb–Cu (FINEMET) (Yoshizawa, Oguma and Yamauchi, 1988), Fe–Zr–B (Suzuki *et al*., 1990), and Fe–M–B (M = Zr, Hf, Nb) (NANOPERM) (Makino, Inoue and Masumoto, 1995) nanocrystalline alloys were developed as a new type of soft magnetic material. It is well known that the Fe- and Co-based amorphous alloys described previously required a high cooling rate above $10^5\,\mathrm{K\,s^{-1}}$ and the resultant melt-spun alloys have been limited to a small thickness range less than about 50 μm (Chen, 1980; Masumoto, 1982; Liebermann, 1993). If we can find a new Fe- or Co-based soft magnetic alloy with much higher glass-forming ability (GFA), the resultant bulk amorphous alloys are expected to extend their field of application as soft magnetic materials. Since 1995, a new class of Fe- and Co-based glassy alloys with a supercooled liquid region beyond 50 K before crystallization and a high GFA have been found, and bulk glassy alloys (BGAs) have been synthesized in a thickness range of up to 6 mm by the copper mold casting method (Inoue, Zhang, Itoi and Takeuchi, 1997a; Inoue, Zhang and Takeuchi, 1998c; Inoue, 2000).

Handbook of Magnetism and Advanced Magnetic Materials. Edited by Helmut Kronmüller and Stuart Parkin. Volume 4: *Novel Materials*. ISBN: 978-0-470-02217-7.

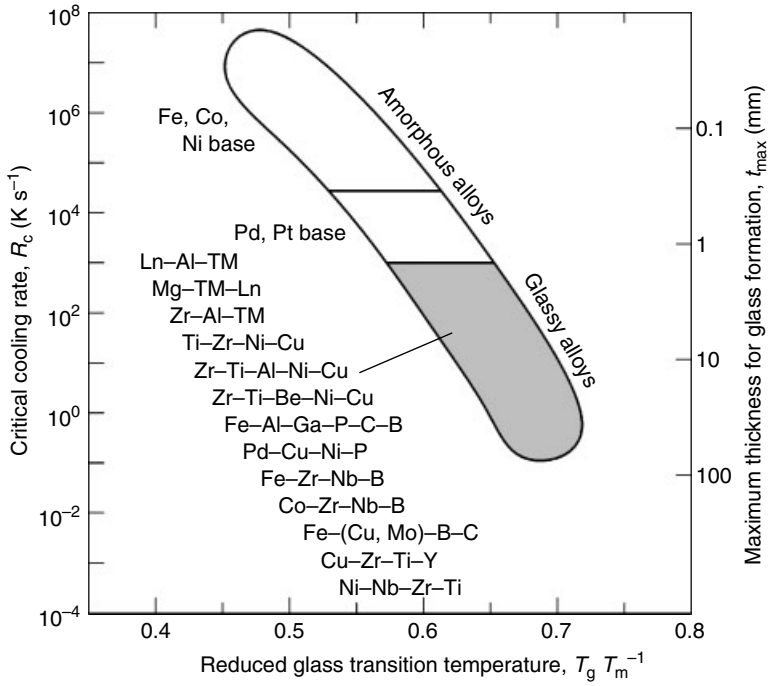

Figure 1. Relationship between critical cooling rate (R_c) for glass formation, maximum sample thickness (t_{max}) for glass formation, and reduced glass transition temperature ($T_gT_m^{-1}$; T_g and T_m are glass transition and melting temperatures, respectively) for bulk glassy alloys. The data for ordinary amorphous alloys, which require high cooling rate for glass formation, are also shown for comparison. Ln: lanthanide metal; TM: VI–VIII group transition metal.

Figure 1 shows the relationship between the critical cooling rate (R_c), the maximum sample thickness (t_{max}) for glass formation, and the reduced glass transition temperature ($T_gT_m^{-1}$; here, T_g and T_m are the glass transition and the melting temperatures, respectively) for amorphous and glassy alloys reported to date (Inoue, 1995, 1997, 1998; Inoue, Takeuchi and Zhang, 1998b,c). The lowest R_c is as low as $0.10\,K\,s^{-1}$ (Inoue and Nishiyama, 1997) for the $Pd_{40}Cu_{30}Ni_{10}P_{20}$ alloy and t_{max} reaches a value as large as approximately 100 mm. It is also noticed that the recent improvement of GFA reaches 6–7 orders for R_c and 3–4 orders for t_{max}. There is a clear tendency for GFA to increase with increasing $T_gT_m^{-1}$. Figure 2 shows the relationship between R_c, t_{max}, and the temperature interval of a supercooled liquid (ΔT_x) defined by the difference between T_g and the crystallization temperature (T_x) (Inoue, 1995, 1997, 1998; Inoue, Takeuchi and Zhang, 1998b,c). One can see a clear tendency for GFA to increase with increasing ΔT_x. The value of ΔT_x exceeds 100 K for several glassy alloys in Zr–Al–Ni–Cu(–Pd) and Pd–Cu–Ni–P systems.

It is generally known that a variety of BGAs have been synthesized using various solidification methods such as water quenching, copper mold casting, high-pressure die casting, and so on, for the past 17 years since 1988. Table 1 summarizes typical BGA systems and the calendar years when their alloy systems were reported. The alloy components can be classified into nonferrous and ferrous alloy systems. When we look at the features of the alloy components in more detail, they can be classified into five groups as summarized in Figure 3. The first group consists of early transition metals (ETMs: IV–VI group transition metals in the periodic table) or lanthanide metals (Ln), Al, and late transition metals (LTMs: VIII group transition metals) as exemplified by Zr–Al–(Ni, Cu) (Inoue, Zhang and Masumoto, 1990) and Ln–Al–(Ni, Cu) (Inoue, Zhang and Masumoto, 1989) systems. The second group is composed of LTMs, ETMs, and metalloids that are typical for Fe–(Zr, Hf, Nb)–B (Inoue, Koshiba, Zhang and Makino,1998a) and Co–(Zr, Hf, Nb, Ta)–B (Itoi and Inoue, 1998) systems. The third group is exemplified by the Fe–(Al, Ga)–metalloid system (Inoue and Gook, 1995) and the fourth group is expressed by Mg–Ln–LTM (Inoue, Ohtera, Kita and Masumoto, 1988) and ETM–Be–LTM (Peker and Johnson, 1993) systems. However, the Pd–Cu–Ni–P (Inoue, Nishiyama and Matsuda, 1996a) and Pd–Ni–P (Drehman and Greer, 1984) systems (group V) are composed of only two kinds of group elements (LTMs and metalloids), and hence are different from the alloys belonging to the four previous groups, which are made up of a combination of three types of group elements. All the alloys belonging to groups

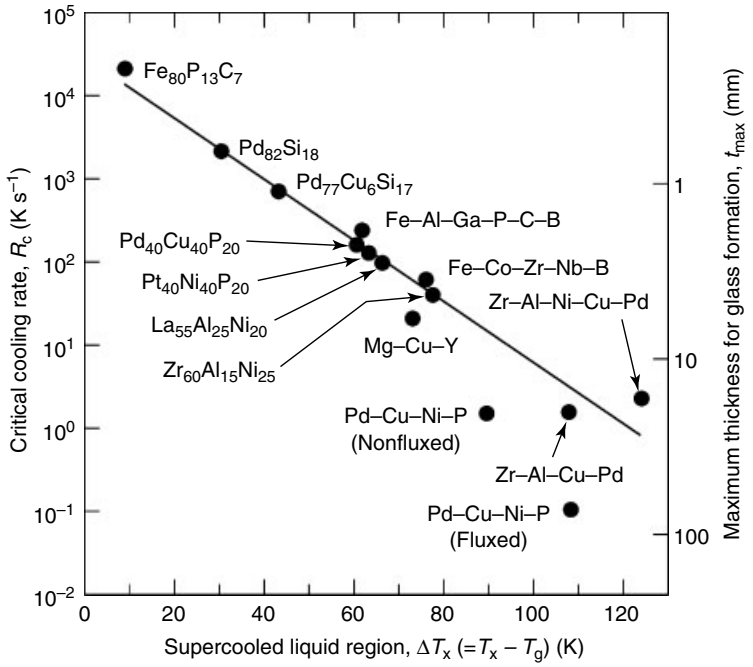

Figure 2. Relationship between critical cooling rate (R_c) for glass formation, maximum sample thickness (t_{max}) for glass formation, and temperature interval of supercooled liquid region ($\Delta T_x = T_x - T_g$; T_x and T_g are crystallization and glass transition temperatures, respectively) for bulk glassy and ordinary amorphous alloys.

Table 1. Bulk glassy alloy systems and calendar years when details about each alloy system were first published.

Nonferrous alloy systems	Years	Ferrous alloy systems	Years
Mg–Ln–M	1988	Fe–(Al, Ga)–(P, C, B, Si, Ge)	1995
(Ln = lanthanide metal, M = Ni, Cu, Zn)		Fe–(Nb, Mo)–(Al, Ga)–(P, B, Si)	1995
Ln–Al–TM	1989	Co–(Al, Ga)–(P, B, Si)	1996
(TM = VI–VIII group transition metal)		Fe–(Zr, Hf, Nb)–B	1996
Ln–Ga–TM	1989	Co–(Zr, Hf, Nb)–B	1996
Zr–Al–TM	1990	Ni–(Zr, Hf, Nb)–B	1996
Ti–Zr–TM	1993	Fe–Co–Ln–B	1998
Zr–Ti–TM–Be	1993	Fe–(Nb, Cr, Mo)–(C, B)	1999
Zr–(Ti, Nb, Pd)–Al–TM	1995	Ni–(Nb, Cr, Mo)–(P, B)	1999
Pd–Cu–Ni–P	1996	Co–Ta–B	1999
Pd–Ni–Fe–P	1996	Fe–Ga–(P, B)	2000
Pd–Cu–B–Si	1997	Ni–Zr–Ti–Sn–Si	2001
Ti–Ni–Cu–Sn	1998	(Fe, Co)–B–Si–(Nb, Zr)	2002
Cu–(Zr, Hf)–Ti	2001		
Cu–(Zr, Hf)–Ti–(Y, Be)	2001		

I–IV have three simple rules of alloy formation which can be stated as (i) multicomponent – consisting of three or more elements, (ii) significant atomic size mismatch of 12% or more, and (iii) negative heats of mixing (Inoue, 1995, 2000; Inoue, Zhang and Takeuchi, 1997b). It has subsequently been reported that the alloys with the three empirical rules can have a new structure that has the following features: a higher degree of dense random packed atomic configurations, new local atomic configurations, and long-range homogeneity with attractive interactions as summarized in Figure 4 (Inoue, 1995, 2000; Inoue, Zhang and Takeuchi, 1997b). It is also summarized that the multicomponent alloys with such a new structure can suppress the nucleation reaction of a crystalline phase and have difficulty of atomic rearrangements leading to the suppression of the growth reaction of a crystalline phase, as shown in Table 2.

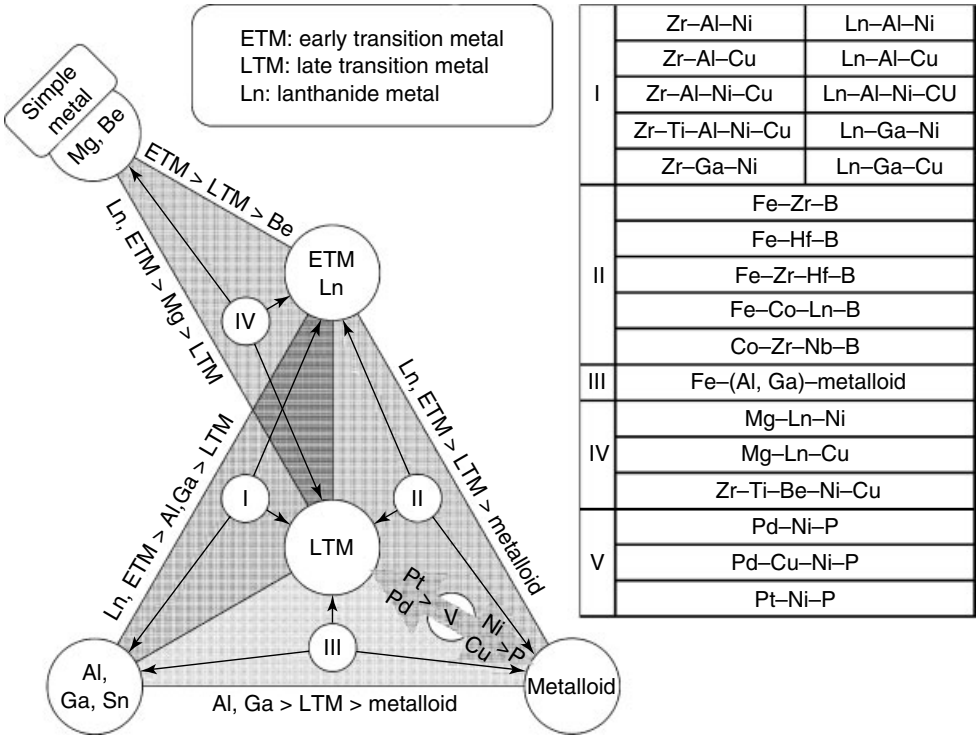

I	Zr–Al–Ni	Ln–Al–Ni
	Zr–Al–Cu	Ln–Al–Cu
	Zr–Al–Ni–Cu	Ln–Al–Ni–CU
	Zr–Ti–Al–Ni–Cu	Ln–Ga–Ni
	Zr–Ga–Ni	Ln–Ga–Cu
II	Fe–Zr–B	
	Fe–Hf–B	
	Fe–Zr–Hf–B	
	Fe–Co–Ln–B	
	Co–Zr–Nb–B	
III	Fe–(Al, Ga)–metalloid	
IV	Mg–Ln–Ni	
	Mg–Ln–Cu	
	Zr–Ti–Be–Ni–Cu	
V	Pd–Ni–P	
	Pd–Cu–Ni–P	
	Pt–Ni–P	

Figure 3. Features of alloy components for bulk glassy alloys reported to date. The alloy components can be divided into five groups.

Table 2. Mechanism for reduced instability of metallic supercooled liquid and formation of bulk glassy alloys.

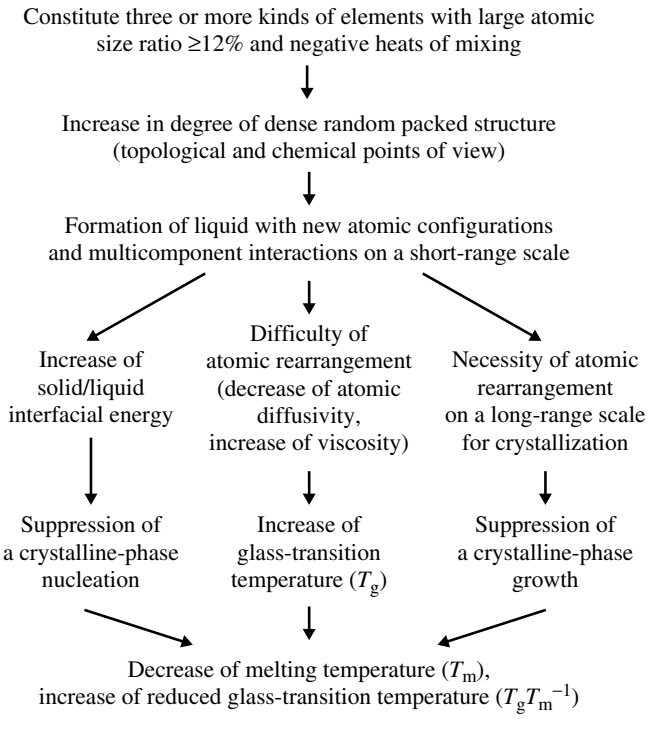

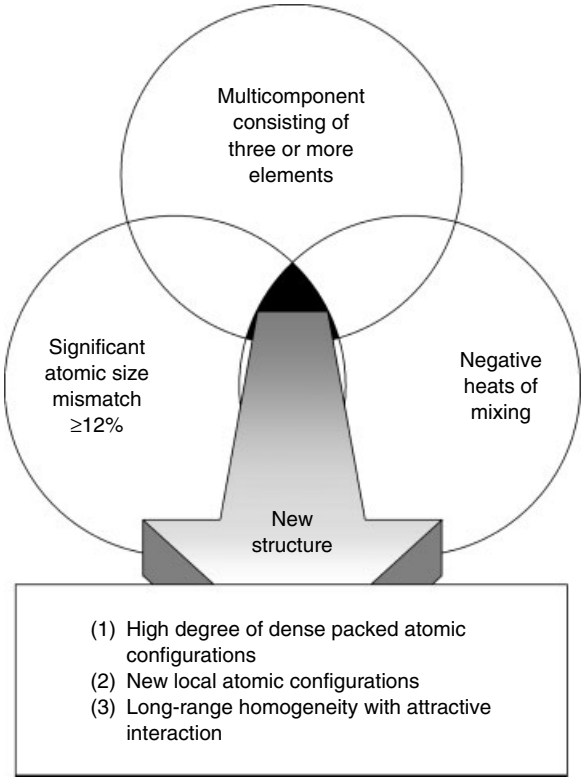

Figure 4. Features of alloy components for reduced instability of supercooled liquid and high glass-forming ability.

Table 3. Examples of soft magnetic glassy alloys and their properties.

Groups		T_g (K)	ΔT_x (K)	$T_g T_m^{-1}$	I_s (T)	H_c (A m^{-1})	λ_s (10^{-6})	μ_i (10^3)		ρ_{RT} (μΩ m)	d_{max} (mm)	References
								1 kHz	1 MHz			
(1)	$Fe_{72}Al_5Ga_2P_{10}C_6B_4Si_1$	732	53	–	1.14	0.5	–	–	–	–	2.0	Inoue *et al.* (1996b)
	$Fe_{70}Al_5Ga_2P_{9.65}C_{5.75}B_{4.6}Si_3$	748	59	–	1.2	2.2	–	–	–	–	1.0[b]	Mizushima, Ikarashi, Makino and Inoue (1999a)
	$Fe_{76}Al_4P_{12}B_4Si_4$	738	46	–	1.24	2.6	30	21.0	–	–	–	Inoue and Park (1996)
	$Fe_{73}Al_5Ga_2P_{10}B_6Ge_4$	717	49	–	1.09	2.4	33	23.5	–	–	–	Park and Inoue (1999)
	$Fe_{67}Cr_4Mo_4Ga_4P_{11}C_5B_5$	730	56	0.59	0.9	1.6	–	–	–	–	–	Shen and Schwarz (1999)
	$Fe_{65.5}Cr_4Mo_4Ga_4P_{12}C_5B_{5.5}$	723	61	0.58	–	–	–	–	–	–	4.0[c]	Shen and Schwarz (1999)
	$Fe_{77}Ga_3P_{9.5}C_4B_4Si_{2.5}$	750	48	0.60[a]	1.36	4.3	–	–	–	–	2.5	Shen and Inoue (2002)
	$Fe_{78}Ga_2P_{9.5}C_4B_4Si_{2.5}$	735	40	0.59[a]	1.40	3.4	–	–	–	–	2.0	Shen and Inoue (2002)
(2)	$Fe_{56}Co_7Ni_7Zr_8Nb_2B_{20}$	828	86	–	0.75	1.1	13	25.0	–	–	2.0	Inoue, Zhang and Takeuchi (1997b)
	$Fe_{56}Co_7Ni_7Zr_8Ta_2B_{20}$	827	88	–	0.74	2.6	14	12.0	–	–	2.0	Inoue, Zhang and Takeuchi (1997b)
	$Fe_{60}Co_8Zr_{10}Mo_5W_2B_{15}$	898	64	0.63	–	–	14	–	–	–	6.0	Inoue, Zhang and Takeuchi (1997b)
	$Fe_{52}Co_{10}Nb_8B_{30}$	907	87	–	0.63	2.1	7	21.0	4.4	2.32	–	Itoi and Inoue (1999)
	$Co_{40}Fe_{22}Nb_8B_{30}$	895	81	–	0.41	2.0	2	29.3	7.5	2.37	–	Itoi and Inoue (1999)
	$Co_{40}Fe_{22}Nb_6Zr_2B_{30}$	903	98	0.57	0.41	1.2	3	32.0	–	–	1.0	Itoi and Inoue (2000)
(3)	$Fe_{68.5}Co_{10}Sm_{1.5}B_{20}$	762	19	–	1.66	5.0	58	–	–	–	–	Inoue and Zhang (1999)
	$Fe_{62}Co_{9.5}Nd_3Dy_{0.5}B_{25}$	843	56	0.58	1.37	4.6	18	–	–	–	0.75	Zhang and Inoue (2000)
(4)	$Fe_{45}Cr_{16}Mo_{16}C_{18}B_5$	856	58	0.62	–	–	–	–	–	–	–	Pang, Zhang, Asami and Inoue (2001)
	$(Fe_{0.75}B_{0.15}Si_{0.10})_{99}Nb_1$	815	43	0.56[a]	1.50	3.7	–	–	–	–	0.5	Inoue and Shen (2002)
(5)	$(Fe_{0.75}B_{0.15}Si_{0.10})_{96}Nb_4$	835	50	0.61[a]	1.47	2.9	–	–	–	–	1.5	Inoue and Shen (2002)
	$[(Fe_{0.5}Co_{0.5})_{0.75}B_{0.20}Si_{0.05}]_{96}Nb_4$	820	50	0.587[a]	–	–	–	–	–	–	5.0	Inoue, Shen and Chang (2004)

T_g: glass transition temperature; ΔT_x: supercooled liquid region; $T_g T_m^{-1}$: reduced glass transition temperature (T_m: melting temperature); I_s: saturation magnetization; H_c: coercivity; λ_s: saturation magnetostriction constant; μ_i: initial permeability (part of complex permeability); ρ_{RT}: electrical resistivity at room temperature; d_{max}: maximum sample diameter for glass formation of copper mold cast cylinder.

[a] $T_g T_l^{-1}$ (T_l: liquidus temperature).

[b] Maximum sample thickness of copper mold cast ring.

[c] Mechanical alloying/fluxing/water quenching method.

2 ALLOY SYSTEMS AND STRUCTURE

Table 3 shows examples of the soft magnetic BGAs and their properties. The soft magnetic BGA systems are also classified into five groups as exemplified by (i) Fe–(Al, Ga)–metalloid (Inoue and Gook, 1995), Fe–(Cr, Mo)–Ga–metalloid (Shen and Schwarz, 1999), and Fe–Ga–metalloid (Shen, Koshiba, Mizushima and Inoue, 2000b); (ii) (Fe, Co)–(Zr, Hf, Nb, Ta)–B (Inoue, Koshiba, Zhang and Makino, 1998a; Itoi and Inoue, 2000); (iii) (Fe, Co)–Ln–B (Inoue and Zhang, 1999); (iv) Fe–(Cr, Mo, W)–C–B (Pang, Zhang, Asami and Inoue, 2001); and (v) (Fe, Co)–B–Si–(Zr, Nb) (Inoue and Shen, 2002; Inoue, Shen and Chang, 2004) systems.

As the most important alloy systems in which Fe-based BGAs are obtained, one can list the Fe–M–B (M = Zr, Hf, Nb, Ta) and Fe–Co–Ln–B systems. Atomic configurations in these alloy systems were examined using anomalous and ordinary X-ray scattering techniques (Imafuku *et al*., 1999, 2000; Matsubara *et al*., 2000), in comparison with ordinary Fe–Cr–B and Fe–Co–B amorphous alloys, which require a high cooling rate above $10^5\,\mathrm{K\,s^{-1}}$ for glass formation. On the basis of the radial distribution function data, the atomic distance and coordination numbers of each constituent atomic pair are summarized for Fe–(Zr or Nb)–B and Fe–Co–Ln–B glassy alloys in Tables 4 and 5, respectively. On the basis of the data generated by the structural analysis, local atomic configuration models of the Fe-based glassy alloys are shown in Figure 5. The construction of a network of atomic configurations consisting of triangle prisms, which are connected with each other through glue atoms comprising Zr, Nb, or a lanthanide metal, is a feature of this type of glassy alloys. Such a linkage structure is an important factor for stabilization of the supercooled liquid in the Fe–M–B type glassy alloys. The crystallization behavior of the Fe–Nb–B (Imafuku *et al*., 1999) and Fe–Co–Ln–B

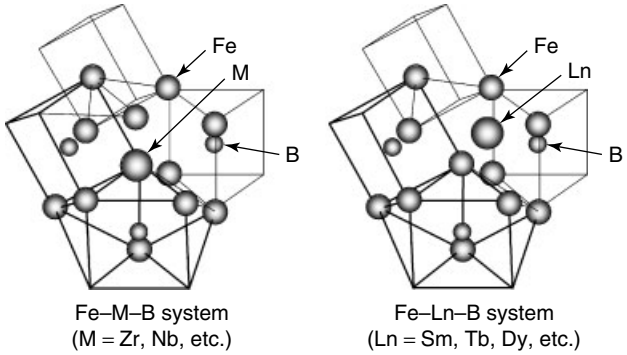

Figure 5. Local atomic structure models for Fe-based glassy alloys.

Table 4. Atomic distances (r) and coordination numbers (N) of glassy $Fe_{70}M_{10}B_{20}$ (M = Zr or Nb) and amorphous $Fe_{70}Cr_{10}B_{20}$ alloys. The subscripts of 1 and 2 for the pairs indicate the first and second neighboring Fe–Fe and Fe–M pairs. The structural parameters calculated from the crystalline Fe_3B structure are also tabulated for comparison.

Pairs	M = Zr		M = Nb	
	r^a (nm)	N^b	r^a (nm)	N^b
Fe–B	0.212	1.4	0.214	1.4
B–Fe	0.212	4.9	0.214	4.9
M–B	0.244	1.3	0.240	1.6
B–M	0.244	0.65	0.240	0.80
Fe–Fe_1	0.254	8.1	0.253	8.0
Fe–Fe_2	0.285	2.6	0.283	2.7
Fe–M_1	0.290	1.0	0.281	1.1
M–Fe_1	0.290	7.0	0.281	8.0
Fe–M_2	0.336	0.50	0.335	0.44
M–Fe_2	0.336	3.5	0.335	3.1
Pairs	M = Cr		Fe_3B crystal (calculated)	
	r^a (nm)	N^b	r^a (nm)	N^b
(Fe, Cr)–B	0.212	1.6	0.207	2.0
B–(Fe, Cr)	0.212	6.3	0.207	6.0
(Fe, Cr)–$(Fe, Cr)_1$	0.251	8.8	0.258	8.7
(Fe, Cr)–$(Fe, Cr)_2$	0.283	3.0	0.281	2.7

[a]Error = ±0.002 nm.
[b]Error = ±0.2.

Table 5. Atomic distances (r) and coordination numbers (N) of amorphous $Fe_{70}Co_{10}B_{20}$ and glassy $Fe_{67}Co_{10}Ln_3B_{20}$ (Ln = Sm, Tb, or Dy) alloys.

	Fe–B		Fe–Fe		Fe–Co		Fe–Ln	
	r (nm)	N	r (nm)	N	r (nm)	N	r (nm)	N
$Fe_{70}Co_{10}B_{20}$	0.205 ± 0.005	2.0 ± 0.4	0.255 ± 0.001	7.8 ± 0.2	0.281 ± 0.001	1.8 ± 0.1	–	–
$Fe_{67}Co_{10}Sm_3B_{20}$	0.205 ± 0.004	2.2 ± 0.5	0.248 ± 0.000	6.4 ± 0.2	0.266 ± 0.001	2.6 ± 0.1	0.296 ± 0.001	0.6 ± 0.0
$Fe_{67}Co_{10}Tb_3B_{20}$	0.197 ± 0.004	1.6 ± 0.4	0.246 ± 0.001	6.5 ± 0.3	0.272 ± 0.001	2.7 ± 0.1	0.305 ± 0.001	0.7 ± 0.0
$Fe_{67}Co_{10}Dy_3B_{20}$	0.198 ± 0.003	2.7 ± 0.4	0.243 ± 0.001	5.4 ± 0.4	0.268 ± 0.001	3.0 ± 0.1	0.303 ± 0.001	0.7 ± 0.0

(Inoue and Zhang, 1999) glassy alloys was also examined. It has been recognized that the primary crystalline phase is a metastable complex fcc $(Fe, Nb)_{23}B_6$ phase with a large lattice parameter of 1.1 nm and a unit volume consisting of 96 atoms and including icosahedral clusters. As is evident from the distinct difference in the atomic configurations between the glassy phase and the primary crystalline phase, the necessity of long-range atomic configurations to construct the primary crystalline phase with a large unit volume from the glassy phase causes retardation of the crystallization reaction. This mechanism is concluded to be one of the reasons for the stability of the supercooled liquid and the formation of BGAs.

3 THERMAL STABILITY AND SOFT MAGNETIC PROPERTIES

When the ferrous alloys summarized in Table 1 are chosen, one can detect a large supercooled liquid region beyond 50 K before crystallization on the differential scanning calorimetry (DSC) curve. In the case of Fe–Al–Ga–P–C–B system, BGAs in a cylindrical rod form are produced in the diameter range of up to 2.5 mm by the copper mold casting method (Inoue, 1997). It has also been confirmed that there is no distinct difference in T_g, ΔT_x, and crystallization behavior among the BGA cylinders with different diameters ranging from 0.5 to 2.5 mm. Figure 6 shows the outer morphology and the surface appearance of the cast Fe–Al–Ga–P–C–B bulk glassy cylinders (Inoue, Shinohara and Gook, 1995). The BGAs possess good soft magnetic properties combined with a rather large saturation magnetization (I_s) of 1.23 T. It has been confirmed that the coercivity (H_c) is less than $5\,A\,m^{-1}$ in an optimum annealed state. The use of the $Fe_{70}Al_5Ga_2P_{9.65}C_{5.75}B_{4.6}Si_3$ alloy enables us to produce a

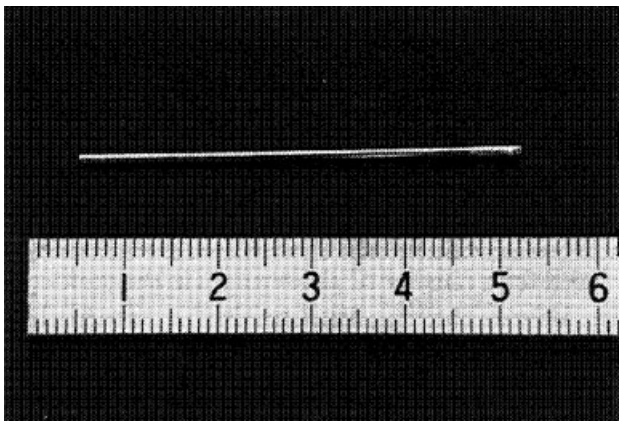

Figure 6. Outer morphology and surface appearance of a cast $Fe_{73}Al_5Ga_2P_{11}C_5B_4$ glassy alloy cylinder with a diameter of 1 mm.

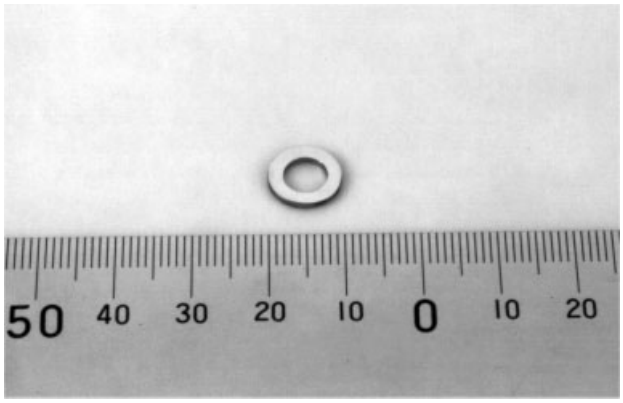

Figure 7. Outer morphology and surface appearance of a cast $Fe_{70}Al_5Ga_2P_{9.65}C_{5.75}B_{4.6}Si_3$ glassy alloy ring with a thickness of 1 mm, an outer diameter of 10 mm, and an inner diameter of 6 mm.

ring-shaped glassy alloy with a thickness of 1 mm, an outer diameter of 10 mm, and an inner diameter of 6 mm, as shown in Figure 7 (Mizushima, Ikarashi, Makino and Inoue, 1999a). The ring-shaped alloy shows the same DSC curve as that for the melt-spun glassy sheet with a thickness of 20 μm. The magnetization curves also show that the ring-shaped alloy has an I_s of 1.2 T, which is the same as that for the melt-spun sheet. Very interestingly, H_c and maximum permeability (μ_m) of the ring-shaped alloy are $2.2\,A\,m^{-1}$ and 110×10^3, respectively, which are far superior to those for the same ring-shaped sample ($3.7\,A\,m^{-1}$ and 27×10^3, respectively) made from the melt-spun glassy sheet, as shown in their $B-H$ hysteresis curves in Figure 8. Such a significant enhancement of the soft magnetic properties of the cast ring–shaped sample is presumably due to the formation of a well-arranged domain structure along the circumference. It has more recently been reported that the use of $Fe_{65}Co_{10}Ga_5P_{12}C_4B_4$ alloy without Al leads to an increase in I_s in a cast cylindrical rod form with a diameter up to 2 mm (Shen, Kimura, Inoue and Mizushima, 2000a; Shen, Koshiba, Mizushima and Inoue, 2000b).

A similar large supercooled liquid region beyond 60 K was found to be obtained in a wide composition range of 0–53 atom % of Co and 0–28 atom % of Ni in a completely different alloy system of $(Fe, Co, Ni)_{70}Zr_{10}B_{20}$ (Inoue, Zhang, Itoi and Takeuchi, 1997a). This glassy alloy system also shows good soft magnetic properties as is evident from high permeability, more than 20×10^3 at 1 kHz, and small saturation magnetostriction constant (λ_s), less than 15×10^{-6}. Furthermore, it is noticed that nearly zero λ_s is obtained in the Co-rich composition range, as shown in Figure 9. By choosing an appropriate alloy composition in the Fe–Co–Ni–Zr–Nb–B alloy series, BGAs have been produced in the diameter range of up to 6 mm by the copper mold casting process, exemplified in Figure 10.

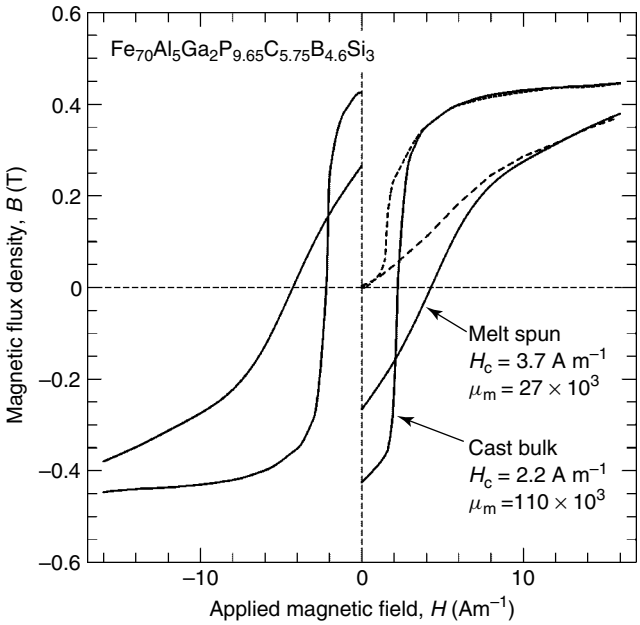

Figure 8. $B-H$ hysteresis loop, coercivity (H_c) and maximum permeability (μ_m) of cast ring-shaped $Fe_{70}Al_5Ga_2P_{9.65}C_{5.75}B_{4.6}Si_3$ glassy alloy, together with the data on a similar alloy made by stacking melt-spun sheets with a thickness of approximately 20 μm.

The increase of B content to 30 atom % in the (Fe, Co, Ni)$_{62}$Nb$_8$B$_{30}$ alloy series causes a further extension of the supercooled liquid region to more than 80 K in the (Fe, Co)-rich alloy composition range (Inoue, Zhang, Koshiba and Itoi, 1999b). Figure 11 shows the compositional dependence of ΔT_x in melt-spun (Fe, Co, Ni)$_{62}$Nb$_8$B$_{30}$ glassy alloys. It is seen that the Co-rich $Co_{40}Fe_{22}Nb_8B_{30}$ alloy shows a large supercooled liquid region at 81 K (Inoue, Itoi, Koshiba and Makino, 1999a). The Fe- and Co-based glassy alloys with 20–30 atom % of B exhibited a high electrical resistivity of 2.2–2.4 μΩ m and hence we expected to obtain good high-frequency permeability. Figure 12 shows the permeability of the melt-spun Fe- and Co-based glassy alloys with 20 atom % of B and 30 atom % of B, together with the data of commercial Fe- and Co-based amorphous sheet samples. It is clearly seen that the Fe- and Co-based glassy alloys possess much better high-frequency permeability as is evidenced form high permeability of 7×10^3 at a high frequency of 1 MHz.

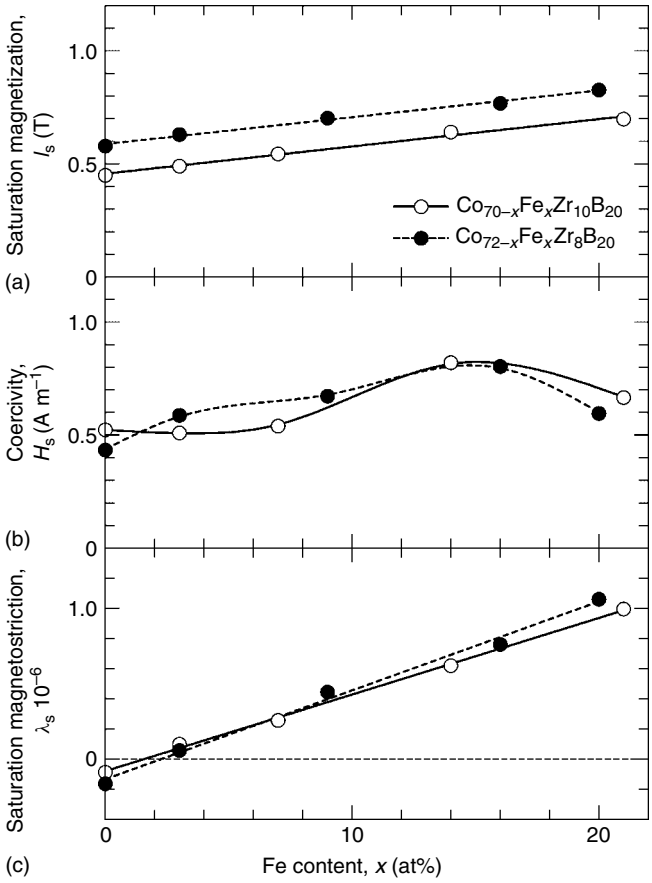

Figure 9. (a) Saturation magnetization (I_s), (b) coercivity (H_c), and (c) saturation magnetostriction constant (λ_s) as a function of Fe content for glassy $Co_{70-x}Fe_xZr_{10}B_{20}$ and $Co_{72-x}Fe_xZr_8B_{20}$ alloys subjected to annealing for 600 s at 800 K.

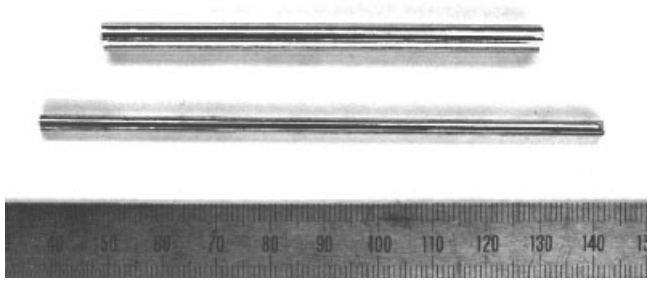

Figure 10. Outer morphology and surface appearance of cast $Fe_{60}Co_8Zr_{10}Mo_5W_2B_{15}$ glassy alloy cylinders with diameters of 3 and 5 mm.

4 CONSOLIDATED BULK ALLOYS

In addition to BGAs synthesized by copper mold casting (Inoue, Shinohara and Gook, 1995) and thick glassy sheets prepared by controlling the wheel speed in the melt-spinning process (Mizushima, Makino, Yoshida and Inoue, 1999b), an Fe-based BGA can be produced by the consolidation technique (Inoue, Yoshida, Mizushima and Makino, 2001). When we consider the Fe–Al–Ga–metalloid alloy, a fully dense BGA was produced at the pressing temperature of 703 K, which is the lowest processing temperature as compared with those for the other Fe-based

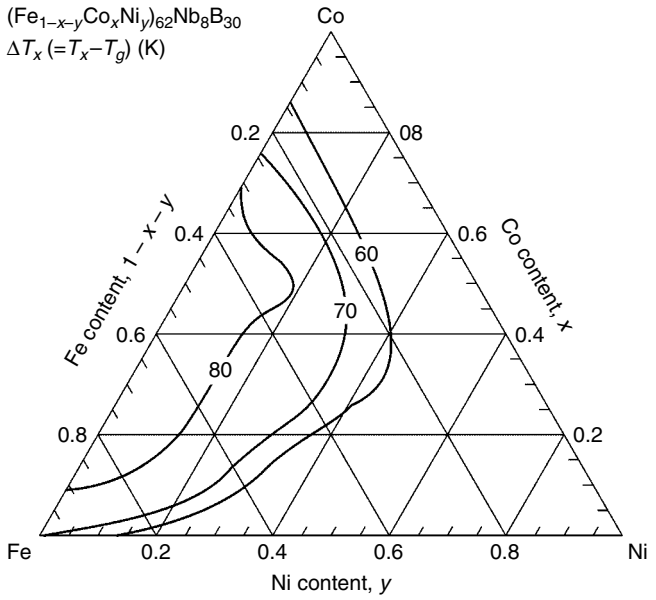

Figure 11. Compositional dependence of supercooled liquid region ($\Delta T_x = T_x - T_g$; T_x and T_g are crystallization and glass transition temperatures, respectively) for $(Fe_{1-x-y}Co_xNi_y)_{62}Nb_8B_{30}$ glassy alloys.

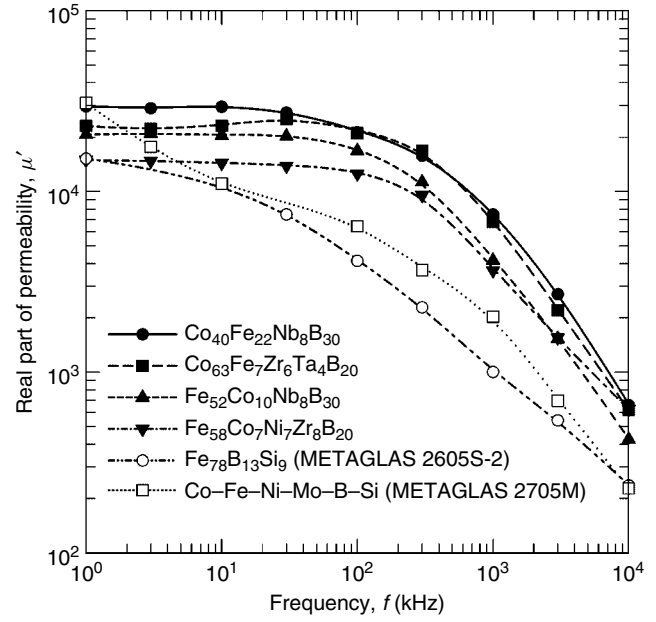

Figure 12. Frequency (f) dependence of the real part of complex permeability (μ') for melt-spun Fe- and Co-based glassy alloys. The data of commercial $Fe_{78}B_{13}Si_9$ and Co–Fe–Ni–Mo–B–Si amorphous alloys are also shown for comparison.

glassy alloys. Figure 13 shows the outer morphology and the surface appearance of Fe–Al–Ga–P–C–B–Si BGAs prepared by the warm consolidation technique. Figure 14

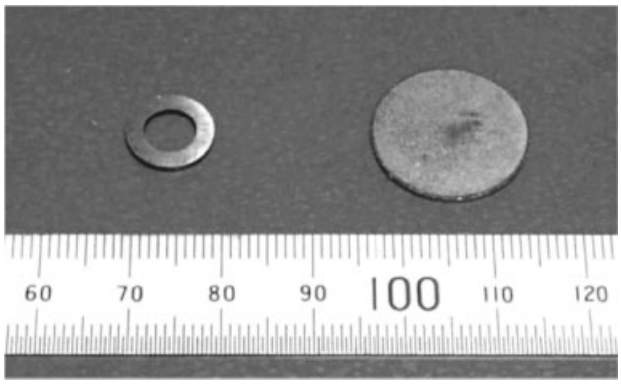

Figure 13. Outer morphology and surface appearance of bulk glassy $Fe_{70}Al_5Ga_2P_{9.65}C_{5.75}B_{4.6}Si_3$ alloys with a thickness of 1 mm prepared by warm consolidation for 480 s at 703 K under an applied pressure of 570 MPa.

shows the change in the magnetic flux density (B_{800}) under an applied magnetic field of 800 A m^{-1} (H_c), the initial permeability (μ_i) at 1 kHz, and the core loss ($W_{5/50}$) at 0.5 T (5 kOe) and 50 Hz with annealing temperature for the Fe–Al–Ga–P–C–B–Si consolidated BGAs (Inoue, Yoshida, Mizushima and Makino, 2001). The consolidated BGA exhibits a rather high B_{800} of 1.17 T, rather low H_c of 12 A m^{-1}, rather high μ' of 2.5×10^3, and low $W_{5/50}$ of 0.11 W kg^{-1}. Table 6 summarizes the soft magnetic properties of the consolidated Fe–Al–Ga–P–C–B–Si BGA, together with the data of the other consolidated Fe-based bulk glassy (Fe–Co–Ni–Hf–Nb–B and Co–Fe–Zr–B) and amorphous (Fe–B–Si) alloys. It is noticed that the Fe–Al–Ga–metalloid bulk alloy exhibits much better soft magnetic properties compared with the other Fe-based bulk glassy and amorphous alloys. The much better soft magnetic properties are presumably due to the formation of a BGA with truly full density. It is believed that if the soft magnetic properties can be improved slightly, the consolidated BGA will surely be used as a practical soft magnetic material.

5 BULK NANOCRYSTALLINE ALLOYS

The BGAs in Fe–B–Si–(Nb or Zr) systems are very attractive as a new type of soft magnetic bulk alloy because of their high I_s, exceeding 1.5 T (Inoue and Shen, 2002; Inoue, Shen and Chang, 2004). Recently, a cast amorphous alloy cylinder with a diameter of 0.5 mm was formed in the Fe–B–Si–Nb–Cu system by copper mold casting (Inoue, Shen and Ohsuna, 2002). The amorphous Fe–B–Si–Nb–Cu alloy cylinder exhibits a multistage crystallization process in which the first stage is due to the precipitation of the bcc-Fe phase and the following stages are attributed to the transition of bcc-Fe + amorphous to bcc-Fe + $Fe_{23}B_6$ + Fe_2B +

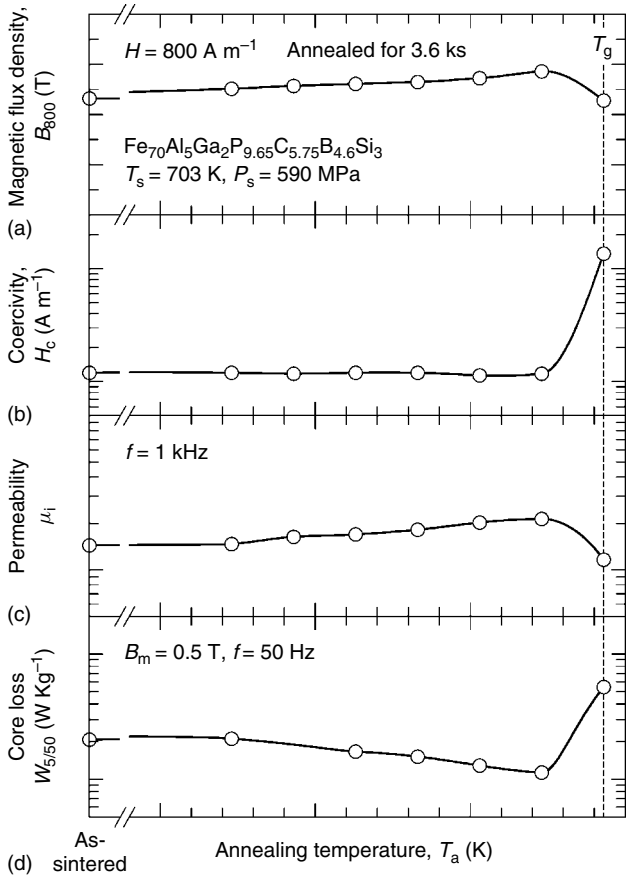

Figure 14. Changes in (a) magnetic flux density (B_{800}) at 800 A m^{-1}, (b) coercivity (H_c), (c) initial permeability (μ_i) at 1 kHz, and (d) core loss ($W_{5/50}$) at 0.5 T (5 kOe) and 50 Hz with annealing temperature (T_a) for bulk glassy $Fe_{70}Al_5Ga_2P_{9.65}C_{5.75}B_{4.6}Si_3$ alloy prepared by warm consolidation for 480 s at 703 K under an applied pressure of 570 MPa. The vertical dashed line indicates the glass transition temperature (T_g) of the alloy.

$Fe_3Si + Fe_2Nb$ phases. Figure 15 shows the bright- and dark-field transmission electron microscopy (TEM) images and the selected-area electron diffraction pattern of the $Fe_{72.5}B_{12.5}Si_{10}Nb_4Cu_1$ cast cylinder with a diameter of

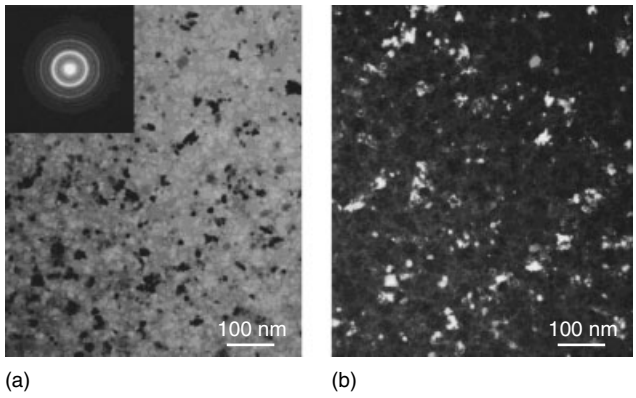

Figure 15. (a) Bright- and (b) dark-field transmission electron microscopy images and selected-area electron diffraction pattern of cast $Fe_{72.5}B_{12.5}Si_{10}Nb_4Cu_1$ amorphous alloy cylinder with a diameter of 0.5 mm annealed for 300 s at 883 K.

0.5 mm annealed for 300 s at 883 K, which is a temperature between the first (T_{x1} = 841 K) and the second ($T_{x2} \approx$ 940 K) crystallization temperatures. It is seen that bcc-Fe grains with a size of approximately 10 nm disperse homogeneously in the remaining amorphous phase matrix. The nanobeam energy-dispersive spectroscopy (EDS) reveals that the Si element is enriched in the bcc-Fe phase, while the Nb element is rejected. A similar tendency is also obtained in the $Fe_{73.5}B_9Si_{13.5}Nb_3Cu_1$ melt-spun alloy (FINEMET) (Hono, Inoue and Sakurai, 1991; Hono *et al.*, 1992). The decrease in Si content and the increase in Nb content in the remaining amorphous phase cause an increase in the thermal stability of the remaining amorphous phase in conjunction with the nanoscale bcc-Fe particles. Table 7 summarizes the thermal stability and soft magnetic properties of the nanocrystalline $Fe_{72.5}B_{12.5}Si_{10}Nb_4Cu_1$ alloy cylinder consisting of the mixed bcc-Fe and amorphous phases obtained by annealing the cast amorphous alloy cylinder. The data of the nanocrystalline $Fe_{73.5}B_9Si_{13.5}Nb_3Cu_1$ melt-spun alloy (FINEMET) are also presented for comparison (Yoshizawa, Oguma and Yamauchi, 1988). It is noticed that the nanocrystalline alloy cylinder exhibits good soft magnetic properties, that is, a high I_s

Table 6. Magnetic flux density (B_{800}) at 800 A m^{-1}, coercivity (H_c), maximum permeability (μ_m), initial permeability (μ_i) at 1 kHz and core loss ($W_{5/50}$) at 0.5 T (5 kOe) and 50 Hz of bulk glassy $Fe_{70}Al_5Ga_2P_{9.65}C_{5.75}B_{4.6}Si_3$ alloy prepared by warm consolidation for 480 s at 703 K under an applied pressure of 570 MPa. The data of other bulk glassy ($Fe_{56}Co_7Ni_7Hf_8Nb_2B_{20}$ and $Co_{56}Fe_{16}Zr_8B_{20}$) and amorphous ($Fe_{78}B_{13}Si_9$) alloys prepared by the same consolidation technique are also shown for comparison.

	B_{800} (T)	H_c (A m^{-1})	μ_m (10^3)	μ_i at 1 kHz (10^3)	$W_{5/50}$ (W kg^{-1})
$Fe_{70}Al_5Ga_2P_{9.65}C_{5.75}B_{4.6}Si_3$	1.17	12	2.5	2.5	0.11
$Fe_{56}Co_7Ni_7Hf_8Nb_2B_{20}$	0.76	28	1.6	1.1	0.17
$Co_{56}Fe_{16}Zr_8B_{20}$	0.57	24	1.9	1.1	0.21
$Fe_{78}B_{13}Si_9$	0.52	59	0.53	0.53	0.31

Table 7. First crystallization temperature (T_{x1}), saturation magnetization (I_s), coercivity (H_c), and initial permeability (μ_i) at 1 kHz of cast $Fe_{72.5}B_{12.5}Si_{10}Nb_4Cu_1$ alloy cylinder with a diameter (d) of 0.5 mm annealed for 300 s at T_a. The data of melt-spun $Fe_{72.5}B_{12.5}Si_{10}Nb_4Cu_1$ and $Fe_{73.5}B_9Si_{13.5}Nb_3Cu_1$ (FINEMET) alloys with thicknesses (t) of 40 and 18 mm, respectively, are also shown for comparison.

	t or d (mm)	T_a (K)	T_{x1} (K)	I_s (T)	H_c (A m^{-1})	μ_i at 1 kHz (10^3)
$Fe_{72.5}B_{12.5}Si_{10}Nb_4Cu_1$ (bulk)	0.5	883	841	1.21	1.8	32
$Fe_{72.5}B_{12.5}Si_{10}Nb_4Cu_1$ (melt-spun)	0.040	883	841	1.23	0.71	80
$Fe_{73.5}B_9Si_{13.5}Nb_3Cu_1$ (melt-spun) (Yoshizawa *et al*., 1988)	0.018	823	775	1.24	0.53	100

of 1.21 T, a low H_c of 1.8 A m^{-1}, and a high μ_i of 32×10^3 (Inoue, Shen and Ohsuna, 2002). One can notice clearly the achievement of good soft magnetic properties in the nanocrystalline structure state even for the bulk alloy cylindrical rod form.

6 ORIGIN OF LOW COERCIVITY OF GLASSY ALLOYS

6.1 Coercivity of amorphous and glassy alloys

In crystalline materials, H_c is determined by dislocations and grain boundaries. In amorphous materials these defects do not exist. Nevertheless, the observed H_c has values of the order of magnitude 0.5–10 A m^{-1}. The origins of H_c have been identified and discussed (Kronmüller, 1981a,b). In the order of increasing importance in amorphous alloys these are:

1. Intrinsic fluctuations of exchange energies and local anisotropy (10^{-4}–0.1 A m^{-1}), H_c^i.
2. Clusters of chemical short-range ordered regions (<0.1 A m^{-1}), H_c^{SO}.
3. Surface irregularities (<0.5 A m^{-1}), H_c^{surf}.
4. Volume pinning of domain walls by defect structures in magnetostrictive alloys (1–10 A m^{-1}), H_c^{σ}.

The observed H_c is considerably larger than the expected ones for intrinsic fluctuations or short-range ordered regions. The typical value for the contribution of the surface irregularities H_c has been estimated to be 0.5 A m^{-1} for Fe-based amorphous alloys and thus represents one of the limiting factors for H_c of the amorphous alloys (Kronmüller, 1981a; Kronmüller and Gröger, 1981). It is therefore suggested that inhomogeneities exist in amorphous alloys, acting as strong pinning centers for domain walls. These pinning centers were found to correspond to stress sources.

Stress sources are supposed to have their origin in the partial instability of the free volume below the melting point. The free volume may exist in dispersed form as agglomerates in the melt off. By a relaxation of the atomic network, the vacancy clusters may collapse, thus generating planar defects, which act as stress sources (Kronmüller *et al*., 1979; Kronmüller, 1980, 1981b). Figure 16 shows a model for the formation of the quasi-dislocation dipole (QDD)-type defects in amorphous alloys by agglomeration of vacancy-type point defects (Kronmüller, 1979, 1981b). The QDDs are characterized by the dipole width (D), the dipole length (L), and an effective Burgers vector ($\boldsymbol{b}$).

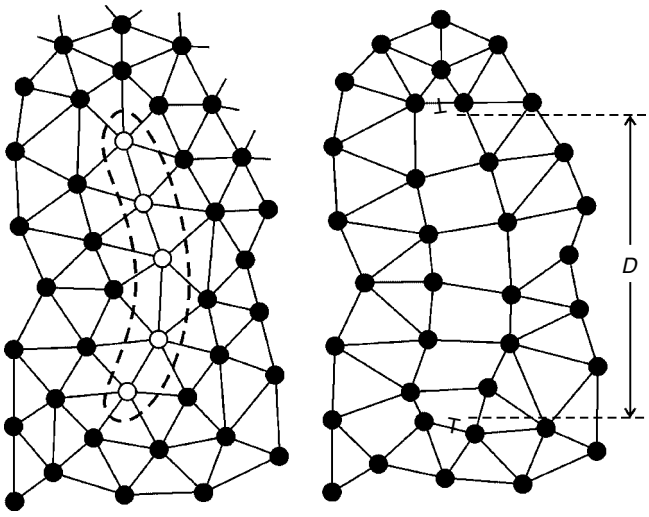

Figure 16. Schematic two-dimensional model for formation of quasi-dislocation dipoles in amorphous alloys by agglomeration of vacancy-type point defects in planar regions. The quasi-dislocation dipole is characterized by dipole width (D), dipole length (L) perpendicular to the drawing plane, and an effective Burgers vector ($\boldsymbol{b}$).

The coercivity of a random distribution of the QDD-type defects of density ρ_d is given as (Kronmüller, 1981a,b; Kronmüller and Gröger, 1981)

$$H_c^{\sigma} = \frac{12G\Delta V}{\sqrt{30F\delta}} \sqrt{\pi \rho_d \ln\left(\frac{\pi d}{2\delta}\right)} \frac{\lambda_s}{I_s} \qquad (1)$$

where G is the shear modulus, $\Delta V = DLb$ corresponds to the local volume contraction due to the QDDs, F is the domain-wall area, δ is the domain-wall thickness, and d is the domain width. The factor of $\ln\{\pi d(2\delta)^{-1}\}$ in equation (1) takes into account the statistical fluctuations

due to the $\pi d(2\delta)^{-1}$ independent positions of the domain wall within the domain width. Numerical calculations based on equation (1) predict values of the right order of magnitude for H_c in magnetostrictive alloys, while measurements of the temperature dependence of $H_c I_s \lambda_s^{-1}$, which should correspond to $\delta^{-1/2} \propto K^{1/4}$ (where K is the effective anisotropy energy density), in a number of Fe-based amorphous alloys have provided convincing proof for the existence and role of the QDDs (Kronmüller, 1981a,b; Kronmüller and Gröger, 1981).

If G, F, δ, and d are independent of the alloy system, H_c^σ can be written as

$$H_c^\sigma \propto \Delta V \sqrt{\rho_d} \frac{\lambda_s}{I_s} \tag{2}$$

Figure 17 shows H_c as a function of $\lambda_s I_s^{-1}$ for the melt-spun glassy Fe–(Al, Ga)–(P, C, B, Si, Ge) alloys and ordinary amorphous alloys with a thickness of 20–35 μm subjected to annealing (Bitoh, Makino and Inoue, 2003). Here, the contribution of the surface irregularities to H_c is assumed to be 0.5 A m^{-1} (Kronmüller, 1981a; Kronmüller and Gröger, 1981). It should be noted that the glassy Fe–(Al, Ga)–(P, C, B, Si, Ge) alloys exhibit lower H_c than the ordinary amorphous alloys with the same $\lambda_s I_s^{-1}$. The gradient of the H_c versus $\lambda_s I_s^{-1}$ plot for the glassy alloys is smaller than

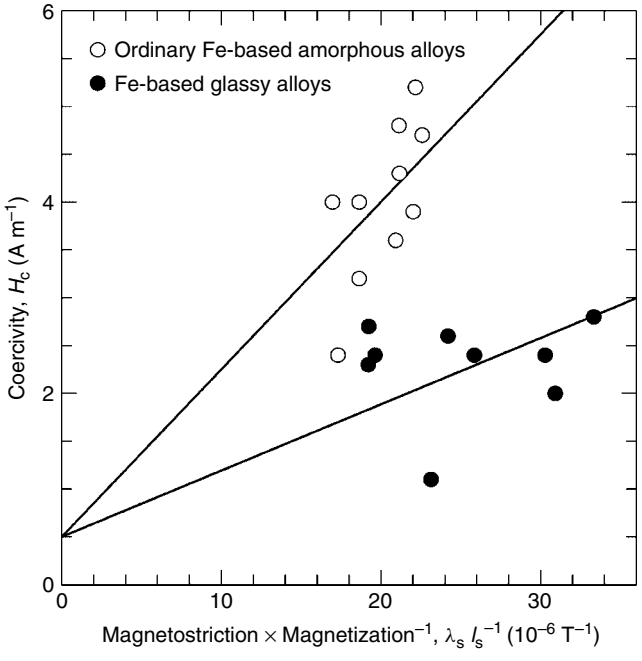

Figure 17. Coercivity (H_c) after annealing as a function of saturation magnetostriction constant and saturation magnetization ($\lambda_s I_s^{-1}$) for melt-spun Fe-based glassy alloys with a thickness of 20–35 μm and ordinary amorphous alloys. Contribution of surface irregularities to H_c is assumed to be 0.5 A m^{-1}.

that for the ordinary amorphous alloys. This result indicates that $\Delta V \rho_d^{1/2}$ of the glassy alloys is approximately 0.4 times that of the ordinary amorphous alloys; that is, ρ_d and/or ΔV of the glassy alloys are much smaller than those of the ordinary amorphous alloys. Here, the decrease of ΔV means the decrease in the pinning force due to the elastic stress (Kronmüller, 1981a,b; Kronmüller and Gröger, 1981). It should be noted that ΔV and ρ_d strongly depend on the quenched-in free volume described in the preceding text. Table 8 shows the mass density (ρ) of the typical Fe-based glassy and ordinary amorphous alloys (Bitoh, Makino and Inoue, 2004). It should be noted that the differences of ρ between the crystalline and the glassy or amorphous phases ($\Delta\rho_c$) of the glassy alloys (0.06–1.11%) are much smaller than those of the ordinary amorphous alloys (2.64–2.94%).

6.2 Magnetization process and low coercivity of glassy alloys

The magnetization curve of amorphous or glassy ferromagnetic alloys is similar to that of the crystalline materials in many aspects. In the low magnetic field (H) region, the magnetization process is governed by domain-wall movement. Sufficiently above the anisotropy field (H_K), the alloy is homogeneously magnetized. Further magnetization is due to an alignment of microscopic inhomogeneous spin states around inhomogeneities of the atomic network. In this so-called field range of approach to ferromagnetic saturation, the field dependence of magnetization is described fairly well by (Kronmüller, 1979, 1981b; Kronmüller *et al.*, 1979)

$$I = I_s - \Delta I(H) + \Delta I_{para}(H) \tag{3}$$

where the last term in equation (3) describes the increase of magnetization due to the so-called spin-wave paraprocess and

$$\Delta I(H) = \frac{a_p}{H^p} \tag{4}$$

Since the effect of intrinsic inhomogeneities on $\Delta I(H)$ is negligibly small (Kronmüller, 1979), the inhomogeneity term ($a_p H^{-p}$) is due to spin inhomogeneities induced by the magnetoelastic interactions between the elastic stress (σ) and the magnetization. Equation (4) may be attributed to certain types of stress sources as follows (Kronmüller *et al.*, 1979; Kronmüller, 1979, 1980, 1981b):

$$\text{point-like defects}: \ \sigma \propto r^{-3} \longrightarrow H^{-1/2}$$

$$\text{quasi-dislocation dipoles}: \ \sigma \propto r^{-2} \longrightarrow H^{-1}$$

$$\text{isolated quasi-dislocations}: \ \sigma \propto r^{-1} \longrightarrow H^{-2}$$

where r is the distance from the stress center.

Table 8. Mass densities (ρ) of as-quenched and annealed glassy ($Fe_{77}Al_{2.14}Ga_{0.86}P_{8.4}C_5B_4Si_{2.6}$ and $Fe_{73}Al_5Ga_2P_{11}C_5B_4$) or amorphous ($Fe_{80}B_{20}$ and $Fe_{78}B_{13}Si_9$) samples and crystalline samples (mother alloys). T_c and T_g are Curie and glass transition temperatures, respectively.

	Annealing condition	ρ^a (kg m^{-3})	$\Delta\rho_r{}^b$ (%)	$\Delta\rho_c{}^c$ (%)
$Fe_{77}Al_{2.14}Ga_{0.86}P_{8.4}C_5B_4Si_{2.6}$	As-quenched	7139	–	1.11
	603 K ($\approx 0.95T_c$) for 7.2 ks	7153	0.20	0.91
	713 K ($\approx 0.97T_g$) for 600 s	7163	0.34	0.77
	Crystal (mother alloy)	7218	–	–
$Fe_{73}Al_5Ga_2P_{11}C_5B_4$	As-quenched	7023	–	0.46
	583 K ($\approx 0.95T_c$) for 7.2 ks	7035	0.17	0.28
	713 K ($\approx 0.97T_g$) for 600 s	7051	0.40	0.06
	Crystal (mother alloy)	7055	–	–
$Fe_{80}B_{20}$	As-quenched	7388	–	2.71
	593 K ($\approx 0.90T_c$) for 7.2 ks	7393	0.07	2.64
	Crystal (mother alloy)	7588	–	–
$Fe_{78}B_{13}Si_9$	As-quenched	7179	–	2.94
	653 K ($\approx 0.95T_c$) for 7.2 ks	7195	0.22	2.72
	Crystal (mother alloy)	7390	–	–

[a]Relative error $\approx 0.02\%$.
[b]$\Delta\rho_r = (\rho_{\text{annealed}} - \rho_{\text{as-quenched}})/\rho_{\text{as-quenched}}$.
[c]$\Delta\rho_c = (\rho_{\text{crystal}} - \rho_{\text{amorphous}})/\rho_{\text{amorphous}}$.

The range of spin inhomogeneities is governed by the so-called exchange length (Kronmüller, 1979; Kronmüller *et al*., 1979)

$$L_H = \sqrt{\frac{2A}{HI_s}} \tag{5}$$

where A is the exchange stiffness constant. The role of L_H is most clearly demonstrated by the field dependence of the inhomogeneity terms due to dislocation dipoles. If D is smaller than L_H, the magnetization detects a dipole; however, for $L_H < D$, the magnetization detects the two opposite monopoles (dislocations) of the dipole separately, and a H^{-2} low is measured. Therefore, it is possible to obtain the mean dipole width, which is given for $\langle D\rangle = L_H(H_t)$, by the transition field (H_t) from the H^{-1} law to the H^{-2} law. The length of the effective Burgers vector ($\boldsymbol{b}$) can be evaluated from the coefficient (a_2) of the H^{-2} term (Kronmüller, 1979; Kronmüller *et al*., 1979).

Figure 18 shows I as a function of H^{-1} for the melt-spun Fe–(Al, Ga)–(P, C, B, Si) glassy alloys with a thickness of 25–30 μm (Bitoh, Makino and Inoue, 2004). The H^{-1}–power law behavior of $\Delta I(H)$ is observed for all the alloys in the range of $20 \lesssim (\mu_0 H)^{-1} < 40$–$50\,T^{-1}$ (20–$25 < \mu_0 H \lesssim 50$ mT, where μ_0 is the permeability of a vacuum). In the higher magnetic field range, $\Delta I(H)$ of the glassy alloys obeys the H^{-2} power law (Bitoh, Makino and Inoue, 2004). These results indicate that the QDD-type defects are the main sources of the elastic stress.

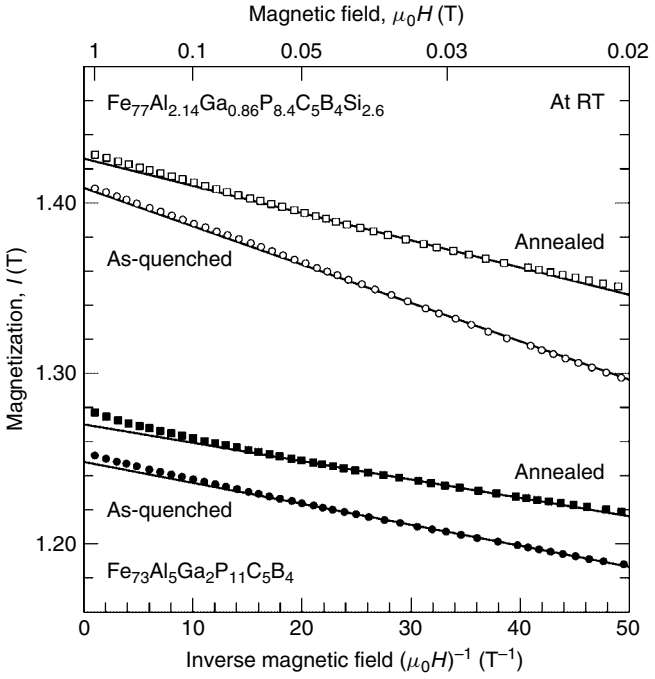

Figure 18. Magnetization (I) as a function of inverse magnetic field ($(\mu_0 H)^{-1}$) of as-quenched and annealed (for 600 s at $0.97T_g$; T_g is glass transition temperature) melt-spun glassy $Fe_{77}Al_{2.14}Ga_{0.86}P_{8.4}C_5B_4Si_{2.6}$ and $Fe_{73}Al_5Ga_2P_{11}C_5B_4$ alloys.

The analysis of the magnetization curves yields the following results: that is, both the Fe–(Al, Ga)–(P, C, B, Si) glassy alloys and the Fe–B(–Si) amorphous alloys have almost the

same $\langle D \rangle$ ($\approx$14 nm), b ($\approx$0.05 nm), and δ ($\approx$80 nm) values (Bitoh, Makino and Inoue, 2004). It can be considered that all the alloys also have almost the same value for G. The QDD-type defects are formed by the agglomeration of vacancy-type point defects in planar regions. Therefore, ρ_d is proportional to $\Delta\rho_c \Delta V^{-1}$ because $\Delta\rho_c$ denotes the amount of the free volume in the amorphous or glassy alloys. Let us further consider that L is proportional to $\langle D \rangle$. Then all the alloys have almost the same ΔV. Under these assumptions, H_c^σ can be expressed as follows:

$$H_c^\sigma = p_c(F, d)\sqrt{\Delta\rho_c}\frac{\lambda_s}{I_s} \tag{6}$$

where p_c, the prefactor, depends on F and d. Figure 19 shows the observed $H_c^\sigma I_s \lambda_s^{-1}$ as a function of $(\Delta\rho_c)^{1/2}$. This figure clearly shows that $H_c^\sigma I_s \lambda_s^{-1}$ is proportional to $(\Delta\rho_c)^{1/2}$. The prefactor of the annealed alloys is approximately 0.4 times smaller than that of the as-quenched ones. It is considered that F is increased by the structural relaxation (Schroeder, Schäfer and Kronmüller, 1978). These results suggest that low ρ_d, which corresponds to low density of the domain-wall pinning centers, is the origin of the low H_c of the Fe–(Al, Ga)–(P, C, B, Si) glassy alloys.

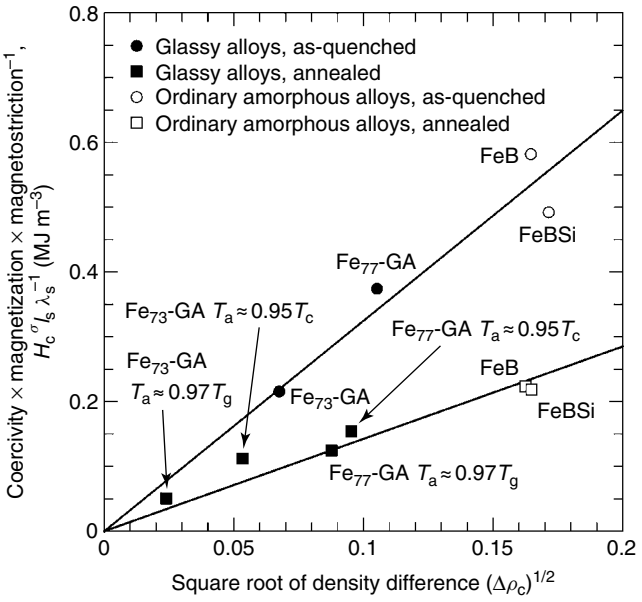

Figure 19. Coercivity times saturation magnetization divided by saturation magnetostriction constant ($H_c^\sigma I_s \lambda_s^{-1}$) as a function of square root of density differences ($(\Delta\rho_c)^{1/2}$) between crystalline and amorphous phases. Fe_{73}-GA: $Fe_{73}Al_5Ga_2P_{11}C_5B_4$; Fe_{77}-GA: $Fe_{77}Al_{2.14}Ga_{0.86}P_{8.4}C_5B_4Si_{2.6}$; FeB: $Fe_{80}B_{20}$; FeBSi: $Fe_{78}B_{13}Si_9$; T_a: annealing temperature; T_c: Curie temperature; T_g: glass transition temperature.

7 APPLICATIONS AND FUTURE TRENDS

Table 9 summarizes the advantages and disadvantages of soft magnetic properties, comparing those of Fe- and Co-based ordinary amorphous alloys. Advantages to be noted are (i) much higher GFA leading to the formation of thicker sheets and plates, larger diameter wires, and thick rings, (ii) higher electrical resistivity of 2.2–2.4 μΩ m at room temperature, (iii) more homogeneous glassy structure without clusters for crystal nucleation, (iv) appearance of a large supercooled liquid region before crystallization, (v) lower H_c, (vi) higher μ_i, (vii) intentional arrangement of domain-wall structure caused by control of casting and/or cooling condition, (viii) better high-frequency μ_i, (ix) good microforming ability in the supercooled liquid region, and (x) warm consolidation into a highly dense bulk form.

Because of these unique advantages, the soft magnetic glassy alloy powder (Liqualloy™) has already been developed as a core material for choke coils used in switching-mode power supplies. The choke coil is one of the largest components in a current switcher, and has been an obstacle to the creation of smaller units. When current is passed through a choke coil, inductance is lowered due to direct current (DC) magnetic saturation in the core material, the degree of which is commonly referred to as its DC superposition characteristic. Previously, the main core material used was ferrite, popular because of its low cost, but a major drawback of this material was its low DC magnetic saturation point. The demand for smaller choke coils is strong, and Fe-based metallic materials that are not easily subject to DC magnetic saturation have steadily come into use. However, the metallic core materials have a high degree of core loss, which leads to less efficient switching power supplies owing to heat generation in the core or power dissipation. The Fe-based magnetic glassy alloys exhibit rather high I_s, low core losses, and high electrical resistivity, simultaneously. It is difficult to produce the ordinary amorphous alloy powder with low GFA, because high-pressure gas atomization or mechanical grinding of melt-spun tapes must be used. Since the glassy alloys also have high GFA and good corrosion resistance, the glassy alloy powder can be produced easily by water atomization, which reduces manufacturing costs remarkably. Figure 20 shows the core loss (W) at 100 kHz, which is a typical operational frequency of the switching-mode power supplies with a Fe–Cr–P–C–B–Si glassy alloy dust core (Koshiba, 2003). The mixture of the near spherical glassy powder (98 mass %) with diameters ranging from 350 to 800 μm, reign for the electrical insulation of each powder and the lubricant were molded into a toroidal shape by applying a static pressure. The molded core was annealed for 3.6 ks at 763 K in a nitrogen atmosphere. The data of the commercial dust cores made of pure Fe, sendust (Fe–Al–Si), and Mo

Table 9. Advantages and disadvantages of soft magnetic properties, comparing those of Fe- and Co-based ordinary amorphous alloys.

Advantages	Disadvantages
Much higher glass-forming ability	Higher material cost
Higher electrical resistivity	Lower saturation magnetization
More homogeneous glassy structure	
Appearance of a large supercooled liquid region	
Lower coercivity	
Higher initial permeability	
Intentional arrangement of domain-wall structure	
Better high-frequency permeability	
Good microforming ability	
Warm consolidation into a highly dense bulk form	

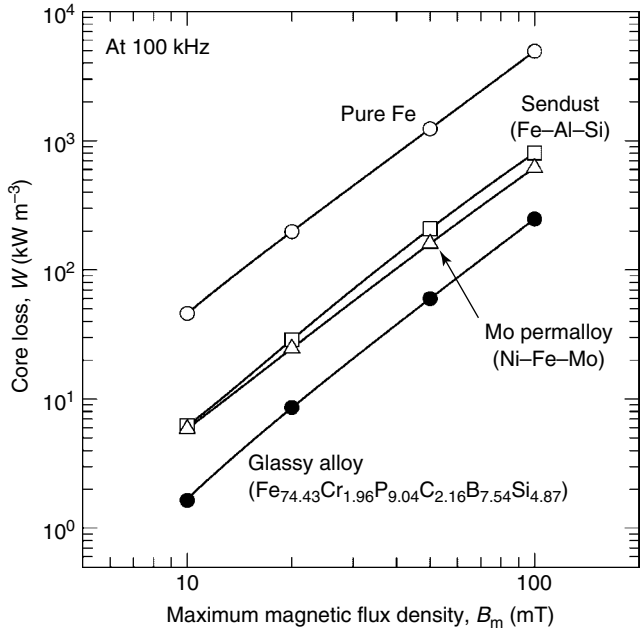

Figure 20. Core loss (W) at 100 kHz of glassy alloy ($Fe_{74.43}Cr_{1.96}P_{9.04}C_{2.16}B_{7.54}Si_{4.87}$) dust core as a function of maximum magnetic flux density (B_m). The data for commercial dust cores are also shown for comparison.

permalloy (Ni–Fe–Mo) are also shown for comparison in Figure 20. The core loss of the glassy alloy dust core is considerably lower than that of the commercial ones. The low core loss and excellent DC superposition characteristics of the glassy alloy dust core will contribute to highly efficient switching.

On the other hand, the disadvantages are (i) higher material cost due to the necessity of using special solute elements to obtain an increase in GFA and (ii) lower I_s due to the addition of larger amounts of solute elements. In particular, the lower I_s for soft magnetic glassy alloys is a serious obstacle to future use in power transformers. Consequently, a great deal of time and effort have been devoted to increasing I_s, though there exists a trade-off between the decrease in the solute contents for an increase in I_s and the increase in the solute content for an increase in GFA. However, owing to the attractive properties described earlier, it is strongly believed that the present soft magnetic BGAs will become practical magnetic materials in the near future.

REFERENCES

Bitoh, T., Makino, A. and Inoue, A. (2003). Origin of low coercivity of Fe–(Al, Ga)–(P, C, B, Si, Ge) bulk glassy alloys. *Materials Transactions*, **44**, 2020–2024.

Bitoh, T., Makino, A. and Inoue, A. (2004). Magnetization process and coercivity of Fe–(Al, Ga)–(P, C, B, Si) soft magnetic glassy alloys. *Materials Transactions*, **45**, 1219–1227.

Chen, H.S. (1974). Thermodynamic considerations on the formation and stability of metallic glasses. *Acta Metallurgica*, **22**, 1505–1511.

Chen, H.S. (1980). Glassy metals. *Reports on Progress in Physics*, **43**, 353–432.

Drehman, A.J. and Greer, A.L. (1984). Kinetics of crystal nucleation and growth in $Pd_{40}Ni_{40}P_{20}$ glass. *Acta Metallurgica*, **32**, 323–332.

Duwez, P. and Lin, S.C.H. (1967). Amorphous ferromagnetic phase in iron–carbon–phosphorus alloys. *Journal of Applied Physics*, **38**, 4096–4097.

Egami, T., Flanders, P.J. and Graham, C.D. Jr. (1975). Amorphous alloys as soft magnetic materials. In *AIP Conference Proceedings, Vol. 24, Magnetism and Magnetic Materials*, Graham, C.D. Jr., Lander G.H. and Rhyne, J.J. (Eds.) American Institute of Physics: New York, pp. 697–701.

Fujimori, H., Masumoto, T., Obi, Y. and Kikuchi, M. (1974). On the magnetization process in an iron-phosphorus-carbon amorphous ferromagnet. *Japanese Journal of Applied Physics*, **13**, 1889–1890.

Hasegawa, R. (1972). Spin-fluctuation resistivity in alloys. *Physics Letters A*, **38**, 5–7.

Hono, K., Hiraga, K., Wang, Q., *et al*. (1992). The microstructure evolution of a $Fe_{73.5}Si_{13.5}B_9Nb_3Cu_1$ nanocrystalline soft magnetic material. *Acta Metallurgica et Materialia*, **40**, 2137–2147.

Hono, K., Inoue, A. and Sakurai, T. (1991). Atom probe analysis of $Fe_{73.5}Si_{13.5}B_9Nb_3Cu_1$ nanocrystalline soft magnetic material. *Applied Physics Letters*, **58**, 2180–2182.

Imafuku, M., Sato, S., Koshiba, H., *et al*. (2000). Crystallization behavior of amorphous $Fe_{90-x}Nb_{10}B_x$ ($x = 10$ and 30) Alloys. *Materials Transactions, JIM*, **41**, 1526–1529.

Imafuku, M., Yaoita, K., Sato, S., *et al*. (1999). Effect of lanthanide element on glass-forming ability and local atomic structure of Fe–Co–(Ln)–B amorphous alloys. *Materials Transactions, JIM*, **40**, 1144–1148.

Inoue, A. (1995). High strength bulk amorphous alloys with low critical cooling rates. *Materials Transactions, JIM*, **36**, 866–875.

Inoue, A. (1997). Bulk amorphous alloys with soft and hard magnetic properties. *Materials Science and Engineering A*, **226–228**, 357–363.

Inoue, A. (1998). *Bulk Amorphous Alloys – Preparation and Fundamental Characteristics*, Trans Tech Publications: Zurich.

Inoue, A. (2000). Stabilization of metallic supercooled liquid and bulk amorphous alloys. *Acta Materialia*, **48**, 279–306.

Inoue, A. and Gook, J.S. (1995). Fe-based ferromagnetic glassy alloys with wide supercooled liquid region. *Materials Transactions, JIM*, **36**, 1180–1183.

Inoue, A., Itoi, T., Koshiba, H. and Makino, A. (1999a). High-frequency permeability characteristics of Fe- and Co-based amorphous alloys with high B concentrations. *IEEE Transactions on Magnetics*, **35**, 3355–3357.

Inoue, A., Zhang, T., Koshiba, H. and Itoi, T. (1999b). Synthesis and properties of ferromagnetic bulk amorphous alloys. In *Materials Research Society Symposium Proceedings*, Johnson, W.L., Inoue, A. and Liu C.T. (Eds.), Materials Research Society: Warrendale, pp. 251–262, Vol. 554.

Inoue, A., Kobayashi, K. and Masumoto, T. (1980a). Mechanical properties and thermal stability of Hf-poor (Fe, Co, Ni)-Hf binary amorphous alloys. In *Proceedings of the Conference on Metallic Glasses, Science and Technology*, Hargitai, C., Bakonyi, I. and Kemény T. (Eds.), Hungarian Academy of Science: Budapest, pp. 217–222, Vol. II.

Inoue, A., Kobayashi, K., Nose, M. and Masumoto, T. (1980b). Mechanical properties of (Fe, Co, Ni)–M–B (M = Ti, Zr, Hf, V, Nb, Ta and Mo) amorphous alloys with low boron concentration. *Journal de Physique*, **41**, C8, 831–834.

Inoue, A., Koshiba, H., Zhang, T. and Makino, A. (1998a). Wide supercooled liquid region and soft magnetic properties of $Fe_{56}Co_7Ni_7Zr_{0-10}Nb$ (or Ta)$_{0-10}B_{20}$ amorphous alloys. *Journal of Applied Physics*, **83**, 1967–1974.

Inoue, A., Takeuchi, A. and Zhang, T. (1998b). Ferromagnetic bulk amorphous alloys. *Metallurgical and Materials Transactions A*, **29**, 1779–1793.

Inoue, A., Zhang, T. and Takeuchi, A. (1998c). Ferrous and nonferrous bulk amorphous alloys. *Materials Science Forum*, **269–272**, 855–864.

Inoue, A., Masumoto, T., Arakawa, S. and Iwadachi, T. (1978). Mechanical properties and thermal stability of new type amorphous high-carbon alloy steels. In *Rapidly Quenched Metals III*, Cantor, B. (Ed.), The Metals Society: London, pp. 265–272, Vol. I.

Inoue, A. and Nishiyama, N. (1997). Extremely low critical cooling rates of new Pd–Cu–P base amorphous alloys. *Materials Science and Engineering A*, **226–228**, 401–405.

Inoue, A., Nishiyama, N. and Matsuda, T. (1996a). Preparation of bulk glassy $Pd_{40}Ni_{10}Cu_{30}P_{20}$ alloy of 40 mm in diameter by water quenching. *Materials Transactions, JIM*, **37**, 181–184.

Inoue, A., Takeuchi, A., Zhang, T., *et al*. (1996b). Soft magnetic properties of Fe-based amorphous alloys prepared by copper mold casting. *IEEE Transactions on Magnetics*, **32**, 4866–4871.

Inoue, A., Ohtera, K., Kita, K. and Masumoto, T. (1988). New amorphous Mg–Ce–Ni alloys with high strength and good ductility. *Japanese Journal of Applied Physics*, **27**, L2248–L2251.

Inoue, A. and Park, R.E. (1996). Soft magnetic properties and wide supercooled liquid region of Fe–P–B–Si base amorphous alloys. *Materials Transactions, JIM*, **37**, 1715–1721.

Inoue, A. and Shen, B. (2002). Soft magnetic bulk glassy Fe–B–Si–Nb alloys with high saturation magnetization above 1.5 T. *Materials Transactions*, **43**, 766–769.

Inoue, A., Shen, B.L. and Chang, C.T. (2004). Super-high strength of over 4000 MPa for Fe-based bulk glassy alloys in $[(Fe_{1-x}Co_x)_{0.75}B_{0.2}Si_{0.05}]_{96}Nb_4$ system. *Acta Materialia*, **52**, 4093–4099.

Inoue, A., Shen, B. and Ohsuna, T. (2002). Soft magnetic properties of nanocrystalline Fe–Si–B–Nb–Cu rod alloys obtained by crystallization of cast amorphous phase. *Materials Transactions*, **43**, 2237–2341.

Inoue, A., Shinohara, Y. and Gook, J.S. (1995). Thermal and magnetic properties of bulk Fe-based glassy alloys produced by copper mold casting. *Materials Transactions, JIM*, **36**, 1427–1433.

Inoue, A., Yoshida, S., Mizushima, T. and Makino, A. (2001). Structure and soft magnetic properties of bulk Fe–Al–Ga–P–C–B–Si glassy alloys prepared by consolidating glassy powders. In *Materials Research Society Symposium Proceedings*, Inoue, A., Yavari, A.R., Johnson, W.L. and Dauskardt, R.H. (Eds.), Materials Research Society: Warrendale, L12–13–1–L12–13–6, Vol. 644.

Inoue, A. and Zhang, W. (1999). New Fe-based amorphous alloys with large magnetostriction and wide supercooled liquid region before crystallization. *Journal of Applied Physics*, **85**, 4491–4493.

Inoue, A., Zhang, T. and Masumoto, T. (1989). Al–La–Ni amorphous alloys with a wide supercooled liquid region. *Materials Transactions, JIM*, **30**, 965–972.

Inoue, A., Zhang, T. and Masumoto, T. (1990). Zr–Al–Ni amorphous alloys with high glass transition temperature and significant supercooled liquid region. *Materials Transactions, JIM*, **31**, 177–183.

Inoue, A., Zhang, T., Itoi, T. and Takeuchi, A. (1997a). New Fe–Co–Ni–Zr–B amorphous alloys with wide supercooled liquid regions and good soft magnetic properties. *Materials Transactions, JIM*, **38**, 359–362.

Inoue, A., Zhang, T. and Takeuchi, A. (1997b). Bulk amorphous alloys with high mechanical strength and good soft magnetic properties in Fe–TM–B (TM = IV-VIII group transition metal) system. *Applied Physics Letters*, **71**, 464–466.

Itoi, T. and Inoue, A. (1998). Soft magnetic properties of Co-based amorphous alloys with wide supercooled liquid region. *Materials Transactions, JIM*, **39**, 762–768.

Itoi, T. and Inoue, A. (1999). High-frequency permeability of (Fe, Co, Ni)$_{62}$Nb$_8$B$_{30}$ amorphous alloys with a wide supercooled liquid region. *Applied Physics Letters*, **74**, 2510–2512.

Itoi, T. and Inoue, A. (2000). Thermal stability and soft magnetic properties of Co–Fe–M–B (M = Nb, Zr) amorphous alloys with large supercooled liquid region. *Materials Transactions, JIM*, **41**, 1256–1262.

Kikuchi, M., Fujimori, H., Obi, Y. and Masumoto, T. (1975). New amorphous ferromagnets with low coercive force. *Japanese Journal of Applied Physics*, **14**, 1077–1078.

Koshiba, H. (2003). *Production of Ferromagnetic Glassy Alloys and Application to Magnetic Dust Core*, Ph.D. thesis, Tohoku University: Sendai.

Kronmüller, H. (1979). Micromagnetism in amorphous alloys. *IEEE Transactions on Magnetics*, **MAG-15**, 1218–1225.

Kronmüller, H. (1980). Magnetization process and the microstructure in amorphous metals. *Journal de Physique*, **41**, C8, 618–625.

Kronmüller, H. (1981a). Theory of the coercive field in amorphous ferromagnetic alloys. *Journal of Magnetism and Magnetic Materials*, **24**, 159–167.

Kronmüller, H. (1981b). Micromagnetism and microstructure of amorphous alloys. *Journal of Applied Physics*, **52**, 1859–1864.

Kronmüller, H., Fähnle, M., Domann, M., *et al*. (1979). Magnetic properties of amorphous ferromagnetic alloys. *Journal of Magnetism and Magnetic Materials*, **13**, 53–70.

Kronmüller, H. and Gröger, B. (1981). Domains, domain walls and the coercive filed of amorphous ferromagnets. *Journal de Physique*, **42**, 1285–1292.

Liebermann, H.H. (Ed). (1993). *Rapidly Solidified Alloys: Process, Structures, Properties, Applications*, Marcel Dekker: New York.

Mader, S. and Nowick, A.S. (1965). Metastable Co–Au alloys: example of an amorphous ferromagnet. *Applied Physics Letters*, **7**, 57–59.

Makino, A., Inoue, A. and Masumoto, T. (1995). Nanocrystalline soft magnetic Fe–M–B (M = Zr, Hf, Nb) alloys produced by crystallization of amorphous phase. *Materials Transactions, JIM*, **36**, 924–938.

Matsubara, E., Sato, S., Imafuku, M., *et al*. (2000). Anomalous x-ray scattering study of amorphous Fe$_{70}$M$_{10}$B$_{20}$ (M = Zr, Nb, and Cr) alloys. *Materials Transactions, JIM*, **41**, 1379–1384.

Masumoto, T. (Ed). (1982). *Materials Science of Amorphous Metals*, Ohmu Publications: Tokyo.

Masumoto, T., Kimura, H., Inoue, A. and Waseda, Y. (1976). Structural stability of amorphous metals. *Materials Science and Engineering*, **23**, 141–144.

Mizushima, T., Ikarashi, K., Makino, A. and Inoue, A. (1999a). Structure and magnetic properties of bulk Fe–Al–Ga–P–C–B–Si glassy alloys in a ringed form prepared by copper mold casting. *IEEE Transactions on Magnetics*, **35**, 3361–3363.

Mizushima, T., Makino, A., Yoshida, S. and Inoue, A. (1999b). Low core losses and soft magnetic properties of Fe–Al–Ga–P–C–B–Si glassy alloy ribbons with large thicknesses. *Journal of Applied Physics*, **85**, 4418–4420.

Nose, M. and Masumoto, T. (1980). Amorphous phase formation in the zirconium-poor corner of (Fe, Co, Ni)–Zr systems. *The Science Reports of the Research Institutes, Tohoku University A*, **28**, 232–241.

O'Handley, R.C., Hasegawa, R., Ray, R. and Chou, C.-P. (1976). Ferromagnetic properties of some new metallic glasses. *Applied Physics Letters*, **29**, 330–332.

Pang, S., Zhang, T., Asami, K. and Inoue, A. (2001). New Fe–Cr–Mo–(Nb, Ta)–C–B glassy alloys with high glass-forming ability and good corrosion resistance. *Materials Transactions*, **42**, 376–379.

Park, R.E. and Inoue, A. (1999). Preparation and soft magnetic properties of Fe–P–B–Ge amorphous alloys. *Materials Transactions, JIM*, **40**, 1444–1449.

Peker, A. and Johnson, W.L. (1993). A highly processable metallic glass: Zr$_{41.2}$Ti$_{13.8}$Cu$_{12.5}$Ni$_{10.0}$Be$_{22.5}$. *Applied Physics Letters*, **63**, 2342–2344.

Schroeder, G., Schäfer, R. and Kronmüller, H. (1978). Magneto-optical investigation of the domain structure of amorphous Fe$_{80}$B$_{20}$ alloys. *Physica Status Solidi A*, **50**, 475–481.

Shen, B. and Inoue, A. (2002). Bulk glassy Fe–Ga–P–C–B–Si alloys with high glass-forming ability, high saturation magnetization and good soft magnetic properties. *Materials Transactions*, **43**, 1235–1239.

Shen, B., Kimura, H., Inoue, A. and Mizushima, T. (2000a). Bulk glassy Fe–Co–Ga–P–C–B alloys with high glass-forming ability, high saturation magnetization and good soft magnetic properties. *Materials Transactions, JIM*, **41**, 1675–1678.

Shen, B., Koshiba, H., Mizushima, T. and Inoue, A. (2000b). Bulk amorphous Fe–Ga–P–B–C alloys with a large supercooled liquid region. *Materials Transactions, JIM*, **41**, 873–876.

Shen, T.D. and Schwarz, R.B. (1999). Bulk ferromagnetic glasses prepared by fluxing and water quenching. *Applied Physics Letters*, **75**, 49–51.

Sherwood, R.C., Gyorgy, E.M., Chen, H.S., *et al*. (1975). Ferromagnetic behavior of metallic glasses. In *AIP Conference Proceedings, Vol. 24, Magnetism and Magnetic Materials*, Graham, C.D. Jr., Lander G.H. and Rhyne J.J. (Eds.), American Institute of Physics: New York, pp. 745–746.

Suzuki, K., Kataoka, N., Inoue, A., *et al*. (1990). High saturation magnetization and soft magnetic properties of bcc Fe–Zr–B alloys with ultrafine grain structure. *Materials Transactions, JIM*, **31**, 743–746.

Yamauchi, K. and Nakagawa, Y. (1971). Amorphous ferromagnetic Fe–P–B alloys prepared by a new technique of splat cooling. *Japanese Journal of Applied Physics*, **10**, 1730–1730.

Yoshizawa, Y., Oguma, S. and Yamauchi, K. (1988). New Fe-based soft magnetic alloys composed of ultrafine grain structure. *Journal of Applied Physics*, **64**, 6044–6046.

Zhang, W. and Inoue, A. (2000). Formation and magnetic properties of bulk glassy Fe–Co–Nd–Dy–B alloys with high boron concentration. *Materials Transactions, JIM*, **41**, 1679–1682.

Advanced Soft Magnetic Materials for Power Applications

Anthony J. Moses
Cardiff University, Cardiff, UK

1 INTRODUCTION

Electrical steels are traditional, mature magnetic materials that are in an ongoing state of incremental development. They comprise over 97% of the volume of all soft magnetic materials currently produced, amounting to a value of around £5000 million per annum. This represents around 1% of all steel production and amounts to over 8 million tonnes per annum. Coupled to this, over 5% of all the electrical energy we generate is consumed as iron losses when electrical steels are used as the magnetic core of electrical equipment, mainly motors and transformers. This costs the UK economy alone around £800 million per year, apart from the considerable detrimental effect on the environment as the by-product of generation of this wasted energy (Moses, 2002).

Handbook of Magnetism and Advanced Magnetic Materials. Edited by Helmut Kronmüller and Stuart Parkin. Volume 4: *Novel Materials*. ISBN: 978-0-470-02217-7.

Recently, soft magnetic iron composite cores produced by powder metallurgy routes are finding some niche applications. Their 3-D characteristics, physical shapes, and magnetic properties are very different to those of electrical steel which are produced in thin sheet form. Hence, it is important to include composite material here to recognize the possible option for using this form of material for a growing range of medium frequency applications, in particular. It should also be pointed out that development continues on other important magnetic materials such as soft ferrites and iron–cobalt alloys which are used in small volume, but critical, power applications. These are not covered here but reviews can be found elsewhere, for example, (Buschow, 1995; Fish, 1989; Boll, 1978). In this article, the reference to material properties, characterization, and so on, refer specifically to *electrical steels* rather than to the *soft magnetic composite* (SMC) materials unless otherwise stated because of their far greater importance in today's context.

Nonoriented and grain-oriented electrical steels are produced in strip form up to over 1 m in width, and normally between 0.1 and 0.65 mm in thickness. Silicon is added to increase the electrical resistivity, which in turn reduces losses under ac magnetization. Silicon does, however, reduce the saturation magnetization and can cause brittleness but it does beneficially reduce the magnetostriction and crystal anisotropy. The materials are produced by conventional steel making followed by a complex series of thickness reduction by hot and cold rolling together with annealing and coating to develop the desired magnetic and mechanical properties (Moses, 1990). The coating on grain-oriented and nonoriented steel must be uniform in thickness and sufficiently thin to minimize the building factor of assembled cores.

Grain-oriented steel contains around 3% silicon (weight) and comprises a strong [001](110) texture with grains up to 10 mm in diameter, which are developed by a critical secondary recrystallization process. The grain-oriented material has losses and permeability several times better than those of nonoriented steel when magnetized along its rolling direction which is the predominant direction of the ⟨100⟩ axes of the grains. The properties of grain-oriented silicon steel depend on the strongly anisotropic magnetic characteristics of iron and some of its alloys which tend to cause low loss and high permeability when magnetized along ⟨100⟩ directions of individual grains or crystals. Because of its texture, the domain structure mainly comprises antiparallel bar domains separated by 180° walls in the demagnetized state. Grain-oriented material is also referred to as *Goss textured steel* named after its prime developer, N.P. Goss, and should not be confused with other grain-oriented steels such as [001](100) textured or *Cubex* material which has been produced only in small quantities (Moses, 1990).

Nonoriented steel is an iron alloy with up to 3% silicon which has a mainly isotropic, random texture with grains around 10–100 μm in diameter and a very complex domain structure. They are far cheaper than grain-oriented material, and magnetic properties are reasonably uniform (isotropic) in all directions in the plane of the strip. They are broadly divided into two groups: fully processed, where the magnetic properties are fully developed by the manufacturer, and semiprocessed, where the user gives the material a final anneal after assembly or forming to complete the development of the magnetic properties. The material is covered with a nonmagnetic coating which not only has to provide electrical insulation between layers or turns in assembled cores but also needs to be of a form to give suitable punching or welding characteristics.

The magnetic properties of electrical steels depend on the static domain structure and the manner in which various types of domain walls move under the influence of ac fields. In practice, the domain structure is more complicated than the idea pattern in a well-oriented grain of steel as referred to earlier (Shilling and Houze, 1974). Much of the present understanding of the properties of electrical steel has been developed from the knowledge of static and dynamic domain structures observed on the surface of electrical steel. Figure 1 shows a typical pattern in grain-oriented material compared with the far more complicated structure typical of nonoriented steel (Hubert and Schafer, 1998).

Conventional grain-oriented (CGO) steel was developed during the 1950–1960s based on the Armco Steel Inc. process for secondary recrystallization. In the 1970s, Nippon Steel Corporation used a modified technology and production route to produce so-called high permeability, grain-oriented (HGO) steel with a better distribution of well-oriented, larger

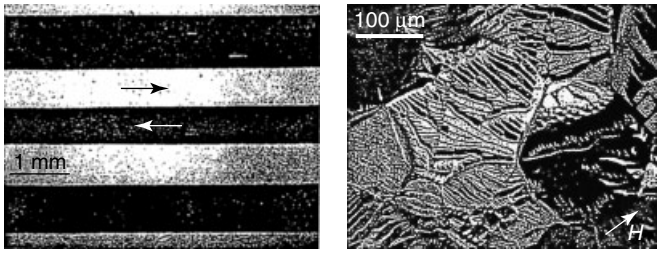

Figure 1. Typical static domain images in (a) grain-oriented and (b) nonoriented electrical steel. (Reproduced from Hubert *et al*., 1998. With permission from Springer-Verlag GmbH. © 1998.)

grains, up to around 10 mm in diameter compared with around 0.3 mm for CGO steel. Such large grains normally have wide domains and higher associated losses when magnetized, but a high-stress coating is applied to ensure that the benefit of better orientation is realized (Moses, 1990). The coating process is complex. A thin layer of magnesium oxide is first applied which reacts with the steel surface at high temperatures to produce a glass film or *Forsterite* layer (Mg_2SiO_4 glass film). A phosphate layer is applied later in the production process to produce the necessary surface electrical insulation and also to induce a high surface tensile stress along the rolling direction of the steel strip which in turn changes the static domain structure in a beneficial manner to cause a significant improvement in the stress sensitivity of the magnetic properties (Moses, Pegler and Thompson, 1972).

A further improvement in losses is achieved by additional surface treatment in grain-oriented, *domain-refined steels* (Kubota, Fujikura and Ushigami, 2000). Here, a beneficial surface stress is induced by either laser or mechanical treatment to cause further refinement, or narrowing, of the mean width of static domains with a corresponding reduction in loss. Such material normally cannot be stress-relief annealed after domain refining treatment because the beneficial surface stress is then removed.

2 LOSSES IN ELECTRICAL STEELS

Micro and macro eddy currents occur due to domain wall motion in soft magnetic materials subjected to ac magnetization. This produces the internal heating commonly referred to as *iron loss*. Traditionally, the loss is divided into three components, namely, *hysteresis*, *classical eddy current*, and *anomalous* (*excess*) *loss*. For commercial grading, these losses are quantified in terms of power ($W\,kg^{-1}$), but the same quantities are expressed, often for scientific research,

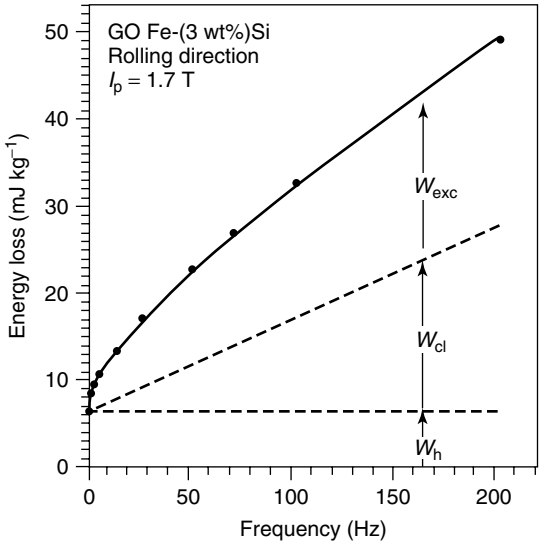

Figure 2. Energy loss per cycle as a function of magnetizing frequency in grain-oriented electrical steel at 1.7 T. (Reproduced from F. Fiorillo, 2004, with permission from TU Bergakademie Freiberg. © 2004.)

as energy components in J kg^{-1} to represent the energy loss per cycle of magnetization.

Figure 2 shows the traditional way of expressing the measured variation of these energy loss components with magnetizing frequency at a fixed sinusoidally time varying flux density of peak value $\hat{B}$ (Fiorillo, 2004).

As can be seen from Figure 2, hysteresis loss per cycle is independent of frequency. It cannot be calculated theoretically from first principles but is proportional to the area enclosed by the static $B-H$ loop. From measurements on many different types of material, it is found to depend mainly on the composition, nature, and distribution of impurities, texture, grain size, and internal stress. It is associated with the pinning of domain walls at imperfections in the material, so high-purity material will have relatively low hysteresis loss. Domain wall motion, particularly in grain-oriented materials, is also impeded close to lamination surfaces by factors such as roughness and coating-induced stress. The following empirical equation is often quoted for the total hysteresis power loss at a given magnetizing frequency f.

$$P_h = K_h f \left(\hat{B}\right)^x \tag{1}$$

where $\hat{B}$ is the peak flux density, and K_h and x are parameters that depend on the material factors referred to earlier as well as the specific magnetizing conditions.

The classical eddy current power loss in a thin lamination at magnetizing frequency f is calculated from

$$P_e = \frac{K_c \left(\hat{B} f d\right)^2}{\rho} \tag{2}$$

where K_c is a material-dependent constant, d is the lamination thickness, and ρ is its electrical resistivity. It should be noted that this commonly used equation assumes constant permeability, that is, a linear $B-H$ curve, which is true only at low induction in silicon iron. It assumes no skin effect which implies a low ratio of the product of permeability and frequency to resistivity, and it assumes sinusoidally time varying flux throughout the thickness of the lamination (Brailsford, 1966). Noting that approximations are made when deriving equation (2), it still shows the need for thin, high-resistivity laminations to minimize P_e.

The measured loss such as that shown in Figure 2 is always greater than the sum of P_h and P_e by an amount P_a, the anomalous loss, which is attributed to loss mechanisms occurring during domain wall motion. Many experimental studies have been carried out in attempts to identify and quantify the causes of P_a in electrical steels. Undoubtedly, mechanisms such as domain wall bowing, wall nucleation and annihilation, nonuniform wall mobility, and nonrepetitive wall motion from cycle to cycle contribute to the cause of the anomalous loss. A commonly used equation for estimating the anomalous loss under sinusoidal flux is written as, (Bertotti, 1998),

$$P_a = 8.8\sqrt{\sigma G S V_o}\left(\hat{B} f\right)^{3/2} \tag{3}$$

where σ is the conductivity, S is the cross-sectional area of the material, and G and V_o are parameters which are material and magnetization dependent. The numerical constant allows for waveform dependence of the expression (e.g., for a triangular waveform, it assumes a value of 8).

The components depicted in Figure 2 could be written in terms of energy loss per cycle as

$$P/f = C_0 + C_1 f + C_2 f^2 \tag{4}$$

where C_0, C_1, and C_2 are constant for a given flux density and frequency. Equation 4, of course, represents the loss variation of the components with frequency as shown in Figure 2. In nonoriented, low silicon alloys, at 50 Hz, the hysteresis loss accounts for 30–60% of the total loss, P_e accounts for 40–60%, and P_a accounts for 10–20% depending on the magnitude of flux density. In high-silicon materials, P_h becomes relatively higher. In grain-oriented materials, hysteresis loss drops from around 33 to 25%

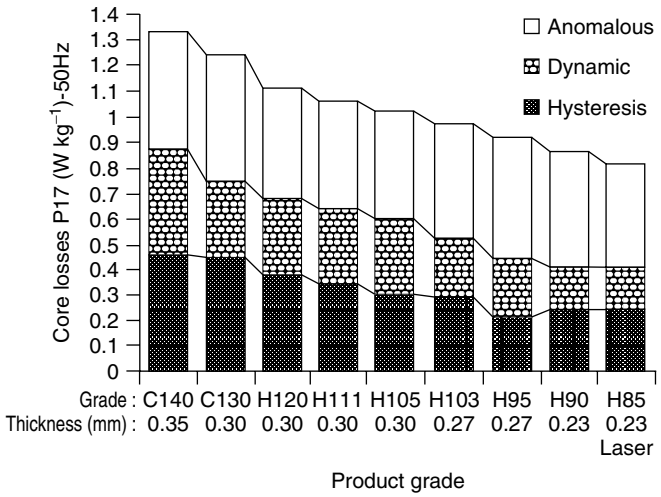

Figure 3. Evolution of best-grade commercial grain-oriented electrical steel. (Reproduced from S. Fortunati, with permission from TU Bergakademie Freiberg.)

of the total as the thickness is decreased from 0.35 to 0.23 mm, whereas the anomalous loss component increases from around 33 to 49%, although its absolute value only drops by about 10% as seen in Figure 3 (Fortunati, 2004).

3 FACTORS AFFECTING MAGNETIC PROPERTIES OF ELECTRICAL STEELS

Many factors affect the domain structure of electrical steel, which in turn controls the magnetic properties. In the previous section, it was pointed out that impurities, lamination thickness, composition, frequency, and peak flux density affect the loss components. In any engineering application, the iron loss in a magnetic core can be as much as 40% greater than that extrapolated from laboratory tests on laminations of the same grade of steel from which the core is assembled. This deterioration is defined and measured as the core *building factor* whose origin and importance is described elsewhere (Moses, 1984). In this section, effects of some of the parameters that directly affect the magnetic properties of the steel are briefly outlined.

3.1 Magnetizing flux density and frequency

The variation of loss with both flux density and frequency is well characterized under sinusoidal flux conditions and is well understood from the basic knowledge of domain activity. Equations (1–4) give a good indication of the parameters controlling the rate of increase of loss which occurs with increasing flux density or frequency. These equations cannot give quantitative values and are unreliable for prediction under extreme or complex magnetization conditions, so laboratory measurements of material loss characterization are needed for design and performance prediction of advanced machine cores. However, loss and permeability measurements on electrical steels magnetized at the increasingly higher frequencies and flux densities demanded by users requires complex, expensive equipment with skilled operators in order to obtain reproducible, reliable data.

3.2 Stress and temperature

Mechanical stress can have either a beneficial or an adverse effect on the properties of electrical steels (Moses and Phillips, 1978). Figure 4 shows the variation of loss and magnetostriction with stress at 50 Hz in grain-oriented steel when magnetized along its rolling direction at 1.5 T, 50 Hz. It

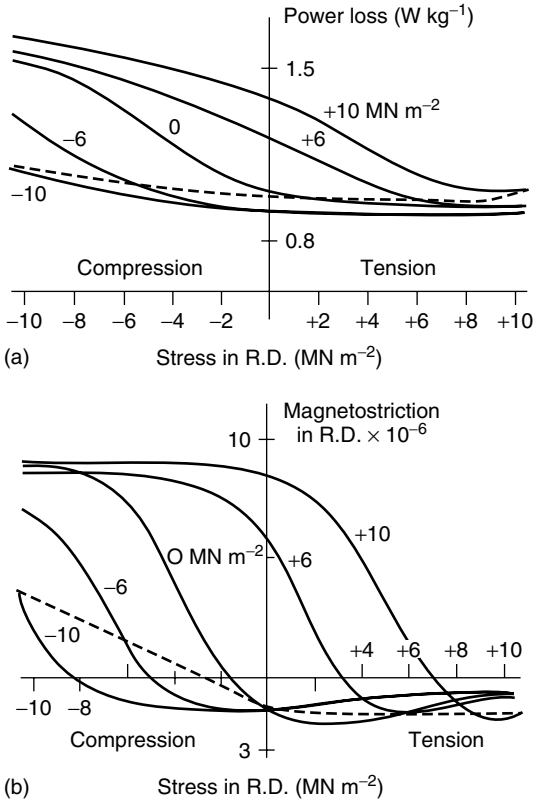

Figure 4. Variation of loss and magnetostriction with stress applied along the rolling direction of grain-oriented electrical steel. (Reproduced from A.J. Moses *et al*., 1978, with permission from IEEE. © 1978.)

should be noted that the magnetostriction, that is, the change of dimensions of the steel, which occurs with change of magnetization, is an important parameter in some applications, because it is the primary cause of acoustic noise output from static electrical equipment. Tension and compression indicated on the graph refers to stress applied along the rolling direction with different values of transverse stress simultaneously applied. For example, when no transverse stress is present (the curve labeled 0 on graph), both magnetostriction and power loss rise rapidly with compressive stress applied along the rolling direction, whereas tensile stress applied along the same direction has comparatively little effect. The characteristics change significantly when transverse stress is simultaneously applied. For example, a high transverse compressive stress of −10 MPa considerably reduces the sensitivity of loss and magnetostriction to longitudinal compression, whereas a transverse tensile stress makes the magnetic properties far worse.

The presence of mechanical stress introduces magnetoelastic energy into the material, and domains are redistributed even in the demagnetized state to minimize the free magnetic energy again. Domains in electrical steel tend to line up in ⟨100⟩ directions closest to a tensile stress direction or furthest from a compressive stress direction which is the reason for the large detrimental effect of compressive stress or the small effect of tensile stress applied along the magnetizing direction seen in Figure 4.

Because of the complex domain structure and the random nature of building stress in magnetic cores, it is impossible to calculate the effect of stress on the magnitude of loss, permeability, or magnetostriction. The results in Figure 4 also indicate that it is over simplistic and even misleading to say that compressive stress will seriously degrade the magnetic properties of grain-oriented material. Although this is often the case in practice, the importance of stress direction and whether it is unidirectional or not should be noted in any practical core assembly.

The coating applied to the surface of grain-oriented steel reduces the sensitivity of the magnetic properties to compressive stress (Moses, Pegler and Thompson, 1972). High permeability steel has lower stress sensitivity partly because of the specially chosen *high-stress coating*. The coating-induced stress in grain-oriented material effectively causes the stress sensitivity curves of the type shown in Figure 4 to shift to the right due to a large tensile component along the rolling direction. These stress sensitivity characteristics can be qualitatively estimated from the predicted reorganization of the magnetic domain structure, which occurs to minimize the total free energy in response to the introduction of the induced magnetoelastic energy. The magnitude of the magnetoelastic energy relative to other magnetic free energy sources determines the form and the nature of stress sensitivity under any given magnetization conditions. In theory, the magnetoelastic energy depends on the magnitude of the stress, its direction relative to ⟨100⟩ directions of individual grains and the magnitude of the saturation magnetostriction constants (λ_{100} and λ_{111}). These constants change with composition in such a way that the stress sensitivity of loss and magnetostriction drops with increasing silicon content to a minimum at around 6.5% (weight) silicon.

Magnetic properties such as loss, permeability, and magnetostriction of electrical steel are temperature sensitive to varying degrees (Nakaoka *et al*., 2005). Saturation magnetization drops with increasing temperature until it reaches zero at the Curie point, which varies with silicon content and is 770 °C in alloy-free iron. The domain structure which determines the magnetic properties is partly established according to the magnitudes of the magnetocrystalline anisotropy constants, electrical resistivity, and magnetostriction constants, all of which are temperature sensitive (Chen, 1958).

The losses drop by a few percent as the temperature rises from ambient to 100 °C (Bullingham, 1971), but the permeability also falls (Jenkins, 2004). In grain-oriented material, the effectiveness of the stress-inducing coating drops with increasing temperature, so the stress sensitivity of loss, magnetostriction, and permeability will increase. If the temperature is reduced below ambient, the magnetic properties do not change, but reports suggest that at cryogenic temperatures the losses increase significantly (Nakata *et al*., 1992). This is possibly due to microstructural changes, which particularly affect the hysteresis.

3.3 Losses under distorted magnetization

Both nonoriented and grain-oriented electrical steels are being used in increasing quantities in applications where they are magnetized under nonsinusoidal flux conditions. Harmonic components in the flux density waveform increase the losses considerably. The loss, P_{d}, occurring under such conditions can be analyzed as a Fourier sum of contributions from each set of flux density and field harmonic component present as

$$P_{\mathrm{d}} = \pi n f \sum_{n=1}^{\infty} \hat{B}_n \hat{H}_n \sin \phi_n \tag{5}$$

where $\hat{B}_{\mathrm{n}}$ and $\hat{H}_{\mathrm{n}}$ are the peak values of the nth harmonic components of flux density and field respectively, and ϕ_{n} is the time phase angle between corresponding harmonics of the b and h waveforms. This inherent frequency dependence of the harmonic losses indicates the advantage of high-resistivity, thin-gauge material when flux distortion is present.

In typical transformer and rotating machine applications, flux distortion can be responsible for half of the additional core losses included in the machine building factor or around 10–20% of the total core loss depending on geometry, assembly, and nominal flux density.

The more widespread use of electronically generated voltage sources to excite rotating machines in variable-speed drive systems is of increasing interest and importance. For example, in *pulse width modulation (PWM)* drive systems, machine core losses can increase by 50% or more because of the very high order harmonics present (Boglietti, Ferraris, Lazzari and Profumo, 1991). Figure 5 shows the influence of material thickness and silicon content on losses under PWM conditions in nonoriented steels (Moses and Leicht, 2005). The harmful effect of reducing the waveform modulation index from 1.0 to 0.5 shown in Figure 5 is important in variable-speed drive systems where such a range is often used in practice. The beneficial influence of using thinner-gauge or higher-resistivity steel can also be appreciated.

3.4 Rotational losses

Magnetization commonly rotates in the plane of parts of laminations assembled in electrical machine cores and is claimed to increase stator losses in some cases by up to 25% (Werner, 1991). The process, commonly referred to as *rotational* or $2-D$ magnetization, has been known and studied for many years (Moses, 1992b). It is rare for any part of a machine core to be magnetized under *pure rotational flux*, which we define as a magnetization condition when the flux density vector, B_r, at a point in a lamination is constant in magnitude and rotates at constant speed, ω. The rotational loss, P_r, can be written as

$$P_r = \frac{1}{T}\int_o^T \left\{ h_x \frac{db_x}{dt} + h_y \frac{db_y}{dt} \right\} dt \qquad (6)$$

where T is the magnetization period, h_x and h_y, db_x/dt and db_y/dt are orthogonal components of instantaneous tangential component of surface field and spatial rates of change of flux density, respectively. Figure 6 shows typical variation of rotational loss with flux density in grain-oriented and nonoriented silicon steels compared to characteristics under sinusoidal, unidirectional flux density along the rolling direction (Zurek, 2005). The rotational loss of the nonoriented steel is seen to be up to three times higher than that under the same magnitude of unidirectional (ac) flux. The difference for the grain-oriented material is far less but still significant. In general, it is found that the ratio of rotational loss to ac loss becomes higher as material texture or anisotropy increases (Arabi and Moses, 1984). The reduction of rotational loss at high flux density occurs because of fewer and fewer domain walls existing as the material approaches saturation.

Rotational losses can be analyzed in terms of hysteresis, eddy current, and excess loss components in order to study the influence of factors such as grain size, thickness, composition, and so on, which generally play very similar roles as under ac conditions. Likewise, the effect of flux harmonics, stress, and temperature on P_r follows similar trends as with unidirectional magnetization. Domain observations (Ledingham, Broadbent and Radley, 1989) demonstrate that rotational magnetization is very complex compared to unidirectional processes. It should be noted that the magnetization process is quite different under ac magnetization compared to rotational conditions, so care must be taken if attempting to infer or predict rotational loss from the value under unidirectional magnetization. Indeed, materials with

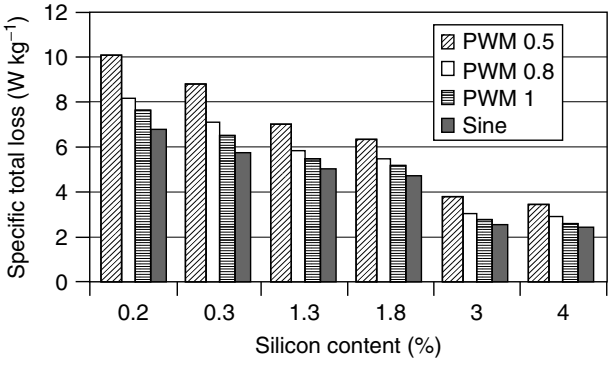

Figure 5. Effect of thickness and silicon content of nonoriented electrical steel on losses under PWM conditions at 1.5 T (peak) and 50 Hz (first harmonic). (Reproduced from Moses *et al*., 2005, with permission from the American Institute of Physics. © 2005.)

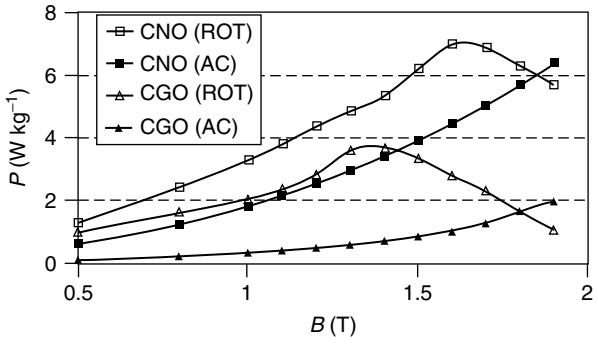

Figure 6. Variation of rotational loss (ROT) with flux density in nonoriented (CNO) and grain-oriented (CGO) electrical steel and comparison with corresponding ac losses (AC) when magnetized along rolling directions.

the 'best' magnetic properties under unidirectional magnetization need not necessarily be better than others under rotational conditions.

It is debatable whether it would be more useful for engineering applications to characterize materials under a *pure rotational field* as the reference magnetization condition than *pure rotating flux density* as is generally the case today. The research community is striving to characterize materials at very high flux densities but there are questions over the practical relevance to normal machine applications where rotational levels are generally far lower (Moses, 2004a).

3.5 High-silicon steels

Addition of silicon to steel is attractive as it increases electrical resistivity, hence reducing the eddy current losses; it reduces magnetostriction to around zero at 6.5% Si, hence tending to reduce acoustic noise of machines; it reduces the sensitivity to mechanical stress and reduces the magnetocrystalline anisotropy, hence improving the usability of the steel. However, these benefits have to be weighed up against the disadvantages of lower saturation magnetization and permeability, and most important, as far as production and operation are concerned, increased brittleness, which makes the material very difficult to manufacture and process.

Various processes have been tried over the years to produce steel containing up to around 6.5% silicon (Moses, 1992a). The method that was eventually commercialized in 1993 involves adding silicon to strips already containing around 3% silicon to increase the content to 6.5% by a chemical vapor diffusion process (Takada, Abe, Masuda and Inagaki, 1988). Here, combining the beneficial effects of silicon addition with thinner gauge (around 0.1 mm) gives low core loss at 6.5% silicon in a sufficiently ductile, nonoriented product. A comparison between flux density produced by a 50 Hz, 800 A m^{-1} field (B8), magnetostriction, and losses at various flux density/frequency combinations is shown in Table 1. Typical data for Mn–Zn ferrite and iron-based amorphous materials are included for comparison. Under some magnetizing conditions, the high-silicon alloy is seen to have the lowest core loss, but for any particular application many other factors must of course be taken into account when selecting a material.

Another attraction of high-alloy electrical steel is the possibility of creating a resistivity gradient through the thickness of the sheet by controlling the concentration of silicon or the additional alloying element. This phenomenon has been demonstrated and quantified in the laboratory using several techniques, for example, diffusion from silicon-bearing coatings (Moses and Thursby, 1983). Even under sinusoidal flux conditions, it is claimed that concentration gradients can lead to loss reductions of 50% or more (Barros Lorenzo, Ros-Yanez, De Wulf and Houbaert, 2004). High-silicon steel with controlled silicon gradient is today commercially produced using the CVD process by JFE in Japan, and large scale development to produce similar material by a hot dipping process is well advanced in Europe (Houbaert, 2004).

A further potential advantage of the material with a silicon concentration gradient is the anticipated improved performance under PWM conditions. PWM magnetizing waveforms contain low magnitude, but very high frequency harmonics. For example, a typical waveform might comprise a dominant 50 Hz component with a modulation index of 15 giving flux harmonics around 35 and 15% of the fundamental, clustered around frequencies of 1.5 and 3.0 kHz, respectively. These high-harmonic components, although small in magnitude, produce additional close-to-surface eddy currents, which, in theory, can be reduced by the presence of a resistivity gradient where the resistivity is highest at the surface. This effect has been demonstrated in the laboratory where the relative increase in loss under PWM conditions compared to sinusoidal magnetization has been found to be lower in material with a resistivity gradient. The relative effect depends on the annealing conditions which control the gradient profile (Anayi, Moses and Jenkins, 2003).

High-silicon steels are finding niche markets in high-frequency applications up to around 20 kHz, in cores subjected to distorted flux where losses or acoustic noise in conventional electrical steel may become excessive. If the material is to be used to its full technical potential as an important component in energy saving systems, development of the expensive and complex siliconizing processes is necessary to ensure that consistently uniform magnetic and mechanical properties are achieved.

4 OPTIMIZATION OF MAGNETIC PROPERTIES

The losses and permeability of the best grades of electrical steels have improved considerably over the last decades as, for example, shown in Figure 7 (Gunther, Abbruzzese, Fortunati and Ligi, 2005). Much of the improvement has been incremental and apart from achieving greater product consistency, it is possible that there is little scope for further improvement of the CGO materials (Jenkins, 2004).

A major challenge with nonoriented steels has been to simultaneously optimize losses and permeability in the same material. Generally speaking, low alloy content and small grain size are necessary to achieve high permeability, whereas low loss is normally achieved in steel with high alloy content and large grain size.

Table 1. Comparison of magnetic properties of typical core materials for medium-frequency power applications.

				Core loss (W kg^{-1}) at given B/f combination					
Material	Thickness (mm)	B8 (T)	Magnetostriction n ($\times 10^{-7}$) (1 T/400 Hz)	1 T, 50 Hz	1 T, 400 Hz	0.1 T, 10 kHz	0.05 T, 20 kHz	0.2 T, 5 kHz	Maximum permeability
6.5% Si–Fe (nonoriented)	0.10	1.25	0.1	0.7	7.3	9.7	9.1	12	18 000
	0.30	1.30	0.1	0.5	10	24.5	18	25.5	25 000
3% Si–Fe (nonoriented)	0.10	1.47	7.8	0.8	8.6	13.3	–	16.5	12 500
	0.35	1.50	7.8	0.7	14.4	33	30	38	18 000
3% Si–Fe (grain oriented)	0.10	1.85	−0.5	0.7	7.2	18	13.2	19.5	24 000
	0.35	1.93	−0.5	0.4	12.3	46	48.5	49	94 000
Amorphous (Fe–B) ribbon	0.03	1.38	27	0.13	1.5	4	3.8	4	300 000
Ferrite (Mn–Zn)	n/a	0.37	21	–	–	–	3	3	12 000

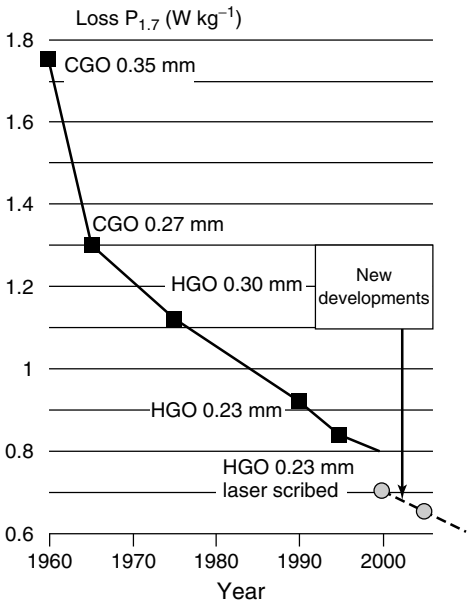

Figure 7. Recent improvements in grain-oriented electrical steels. (Reproduced from K. Gunther *et al*., 2005, with permission from Verlag Stahleisen GmbH. © 2005.)

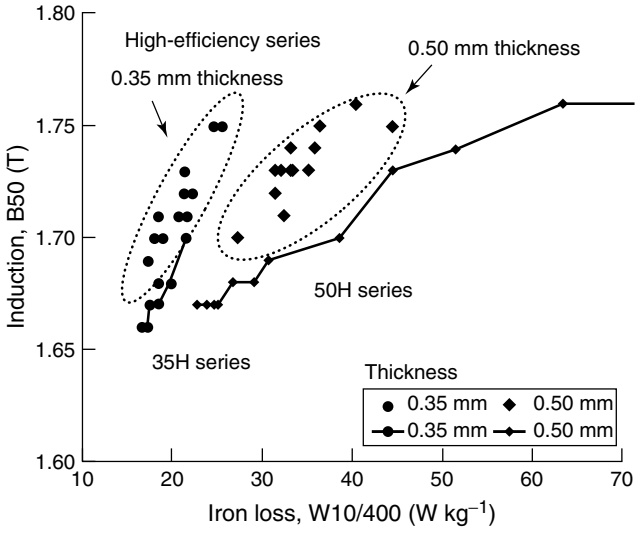

Figure 8. Magnetic properties of high efficiency, nonoriented silicon steels. (Reproduced from T. Kubota, 2005, with permission from Verlag Stahleisen GmbH, Düsseldorf, Germany. © 2005.)

Figure 8 illustrates a typical set of characteristics of commercial nonoriented steels which have been developed to have high permeability and low loss in the same products. The steel makers have achieved this by greater texture control made possible with the advent of cleaner steel produced with the aid of improved desulfurization, decarburization, and vacuum degassing (Kubota, 2005). Such findings have led to it now becoming well established that texture control for enhancement of magnetic properties is as important in nonoriented steels as in grain-oriented steels.

Reduction of thickness is an option to reduce eddy currents, and technology has already been established for commercial production of grain-oriented material, 0.1 mm thick. This usually involves rerolling strips from a thicker gauge, which, combined with other necessary extra processing, makes the material cost effective only for special applications. It is quite feasible to produce nonoriented steel even thinner but cost becomes a more major component, so it is normally restricted to high alloy grades. It is well known that for a given composition, there is an optimum thickness and optimum average grain size that gives minimum loss. The optimum condition is related to the ratio of eddy current loss to hysteresis loss. However the optimum condition depends on the form of magnetization, for example, it will vary with peak flux density, frequency, and harmonic content of the flux waveform.

The challenge of competition at power frequency from iron-based amorphous ribbon was one reason for the trend to the development of thinner grades of electrical steel. Figure 9 (Kubota, Fujikura and Ushigami, 2000) shows how the move to thinner steels, in this case 0.23–0.15 mm, can be combined with other advances to develop thin grade material whose magnetic properties can potentially surpass those of iron-based amorphous materials. Domain refining is combined with large grains to reduce hysteresis loss. Reduced density

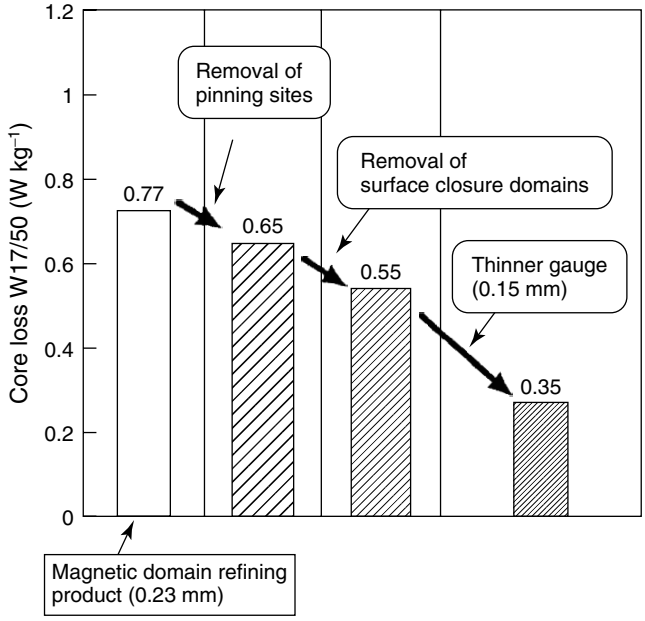

Figure 9. Future prospects for low loss grain-oriented silicon steel. (Reproduced from Kubota *et al*., 2000, with permission from Elsevier. © 2000.)

of defects in cleaner steels leads to removal of pinning sites and consequently lower hysteresis loss. Removal of surface closure domains by surface treatment has a similar effect. The reduced thickness itself reduces the eddy current component of loss.

In contrast to the focus on thickness reduction, there are incentives for assessing the possibility of developing thick materials which are attractive to core manufacturers because of benefits in core handling and assembly. If various major technical challenges in the production process can be overcome, it may be feasible, by appropriate processing, to increase the permeability of thick material without experiencing the anticipated increase in loss (Fortunati, 2004).

Another area where there is scope for development of grain-oriented steels is improvement in the complex interface between the coating and the steel. So-called surface pinning of domain walls, for example, which is believed to increase eddy current losses by 20% or more, is very much influenced by the nature of this interface. The influence of the disturbed layer close to the surface becomes proportionately more important as its thickness relative to the sheet thickness decreases. This is probably the reason why the anomalous loss shown in Figure 2 becomes a more significant contribution in thin-gauge material. There is scope for modification of the surface topology and the coating on grain-oriented steel to attempt to reduce their contribution to the anomalous loss. The steel surface needs to be as smooth as possible and near-surface oxidation should be minimal to cut down surface domain wall pinning or drag.

A further opportunity lies with the development of glassless coatings for grain-oriented steel (Ushigami, Nakayama, Arai and Kubota, 2004). These would remove many close-to-surface magnetic problems completely, as well as improve the mechanical punching quality. In the case of domain-refined steels, there is scope for better scribing by laser or other surface treatment.

4.1 Recent developments

Development of electrical steels is market driven. The main technological driving forces are to reduce losses and lower magnetostriction. All manufacturers are striving to improve the production process of both nonoriented and grain-oriented steels. It is now possible, with the availability of cleaner steels, to improve texture control, even of nonoriented steels, using elements other than silicon or aluminum. For example, manganese or tin additions can result in high permeability combined with low losses. This approach would enable the steel manufacturer to produce other combinations of desirable properties for specific applications such as low loss and very high mechanical strength (Kubota, 2005). This builds on comprehensive work carried out in the 1960s on a wide composition range of single crystals of mainly iron-based alloys to identify optimum combinations of resistivity and magnetic saturation (Foley *et al*., 1970). Today's better steel production technology does enable this prior knowledge to be exploited.

An ongoing problem in producing grain-oriented steel is that improved texture is associated with larger grain size implying higher losses without the aid of stress-inducing coatings. However, it is now becoming more feasible to reduce grain size while maintaining good orientation. One recent attempt is to introduce chromium to reduce power loss but at the expense of reduced saturation and permeability (Huppi, 1996).

An area of great interest is the introduction of *low slab reheat* in the production process for grain-oriented material (Fortunati, 2004). This route is compact and time saving, and offers the opportunity to develop new thin or thick products with a sharp Goss texture. Normal practice requires a very high slab temperature prior to hot rolling to allow the formation of precipitates essential in the Goss secondary recrystallization process. Not only is the high-temperature process energy demanding but it can also cause other technical problems (Jenkins, 2004; Gunther, Abbruzzese, Fortunati and Ligi, 2005).

A process that would significantly reduce manufacturing cost of all electrical steels is *thin strip casting*. If casting direclty from the melt to hot rolling thickness is successfully implemented, it will result in an enhanced produce with the extra benefit of the complete elimination of the high costs of continuous casting, slab reheating, and hot rolling (Gunther, Abbruzzese, Fortunati and Ligi, 2005).

Another major achievement to aim for in the production of grain-oriented steel is the replacement of the high-temperature box anneal, in which the secondary recrystallization process occurs, by a continuous annealing process. The continuous process has been demonstrated on the laboratory scale as being technically feasible and is claimed to have many benefits making it, together with strip casting, the most innovative route for future generations of grain-oriented steel products (Fortunati, 2004).

Major advances in coating technology for nonoriented steels have been made over the last few years (Lindenmo, Coombs and Snell, 2000). These have mainly been in the areas of the use of more environmentally suitable materials, better uniformity of coating composition and thickness, as well as improved punching and welding characteristics. Combined, these not only improve the basic magnetic properties of the steel but also the building factors of machine cores.

Although not directly a material property, it should be noted that different grades of fully processed, nonoriented

material have different sensitivities to deterioration of magnetic properties during material processing by the core builder, which in some applications needs to be offset against the magnetic benefits high alloy content brings (Schoppa, Schneider and Wuppermann, 2000).

5 LOSS PREDICTION

Several approaches have been developed in attempts to predict losses of electrical steel laminations magnetized uniformly at a known sinusoidal flux density under ideal laboratory conditions. The present status of some methods for predicting losses in electrical steel laminations is summarized in this section. To consider the even greater challenge of predicting losses of assembled electrical machine cores rather than sheets or strips of material under ideal conditions, factors such as localized magnetization, stress, and temperature need to be taken into account. These are described elsewhere (Moses, 2004b).

Most methods of predicting losses of laminations under given magnetizing conditions depend on knowledge of dc $B-H$ characteristics, conductivity, and thickness of the material. In order to quantify the frequency dependence of the loss, at least one value of loss at a given flux density and magnetizing frequency is needed as a reference condition. It is only possible to predict losses empirically because of the complex material-structural factors, which determine the magnitude of the hysteresis component of loss, in particular.

A widely used approach is a statistical theory of domain wall displacement based on a concept of *magnetic objects* whose activity, together with the db/dt variation in a lamination, is used in the loss prediction (Bertotti, 1988). The *magnetic objects* are defined as regions of one or more domain walls that move in a correlated fashion during ac magnetization. The energy loss, P_p, predicted under sinusoidal magnetization using this approach can be written as

$$P_\mathrm{p} = K_\mathrm{h}\hat{B}f + \frac{\pi^2}{6}\sigma d^2(\hat{B}f)^2 + 8.8\sqrt{\sigma GSV_\mathrm{o}}\left(\hat{B}f\right)^{3/2} \quad (7)$$

This is closely related to equations (1–3). The first term represents the hysteresis, where the loss per cycle is assumed to be independent of frequency. The second term is calculated from Maxwell's equations assuming homogeneous, isotropic, linear material. The third term is calculated from the *Bertotti–Fiorillo* model using a dynamic Preisach approach which simulates the excess loss by a finite switching rate of hypothetical magnetic dipoles (Bertotti, 1988). Measured or known values of loss at two frequencies are needed to calculate the terms V_o and K_h for a given material and magnetizing conditions. The term G is a geometrical factor introduced in the theory related to the eddy current density around moving domain walls (Bertotti, 1998).

The same approach can be used to predict loss under non-sinusoidal conditions provided the skin effect is negligible (Fiorillo and Novikov, 1990). A further refinement enables the same concept to be used to develop a general equation to represent losses under highly distorted flux conditions such as those occurring in devices operated under *PWM* excitation without reference to loss under sinusoidal magnetization. However, again the method neglects the skin effect and the influence of minor $B-H$ loops which may occur under distorted flux waveforms, so the range of application is restricted (Kaczmarek, Amar and Protat, 1996). The loss under such distorted flux can be written as

$$P_\mathrm{d} = K_\mathrm{h}\hat{B}f + \frac{2\sigma d^2\left(\hat{B}\right)^2}{3m\Sigma\tau} + 4\sqrt{\frac{2\sigma SGV_\mathrm{o}}{m\sqrt{\Sigma\tau}}}\left(\hat{B}\right)^{3/2} \quad (8)$$

where S is the cross-sectional area of the lamination, m is its density, τ is a wave-shape-dependent constant, and G and V_o are the material-dependent parameters that can be calculated from measurement of loss under two sine wave magnetization conditions.

It is claimed that the loss separation and analysis using the concept of *magnetic objects* is a natural and general consequence of the magnetization process (Fiorillo, 2004). The approach apparently gives a good measure of relative differences in loss versus frequency characteristics of various materials, but use as a tool for loss prediction over the wide range of magnetization conditions experienced in machine cores needs to be fully demonstrated. Also, some doubt in the approach exists because of the question over the validity of the assumption of constant hysteresis loss per cycle (Ban, 1998).

Another approach is to obtain a voltage-driven solution of the diffusion equation using a history-dependent hysteresis model (Zirka, Moroz, Marketos and Moses, 2002). A transplantation method is used together with a model for simulation of excess loss from the Landau–Lifshitz–Gilbert equations for magnetic viscosity. Apart from the material thickness and conductivity, the only other necessary input data is a family of first-order dc $B-H$ reversal curves and one reference value of loss at a given frequency and peak flux density, for example, 1.5 T, 50 Hz. A novel feature is the use of a parameter enabling accurate reproduction of the frequency dependence of the excess loss. The model is claimed to include constants which can be directly related to the material microstructure and it is claimed to predict losses in nonoriented and grain-oriented material to within 2% of the measured values (Marketos, Moroz, Moses and Zirka, 2002).

A similar approach based on the viscosity principle is to use a dynamic hysteresis model together with a 2-D magnetic potential finite element formulation. This models static $B-H$ loops, traditional eddy currents, and anomalous loss. It has been used to predict the $B-H$ trajectory and hence the losses for an electrical steel lamination with PWM excitation. Good agreement with experimental results has been claimed (Leonard, Marketos, Moses and Lu, 2006).

Other methods are based on predicting loss at a given flux density, magnetizing frequency, and waveform from prior measurements taken over a specified range of magnetizing conditions on Epstein strips, single sheets, or wound toroidal cores. Artificial neural networks have been used for this purpose to predict loss or permeability of toroids wound from grain-oriented steel with uncertainty typically less than 5% over a wide magnetization range (Moses and Leicht, 2004). This approach would be of maximum utility if it were combined with a method to go a stage further and predict localized losses in machine cores. It does require a large amount of training data over a wide range of magnetization conditions, compositions, and thicknesses to make it of any real practical use.

A recently developed *mathematical approach* is based on linear relationships found experimentally between loss measured under sinusoidal flux density and that under PWM waveforms with a given total harmonic distortion (THD) at the same fundamental frequency (Moses and Leicht, 2005). Again, as with neural network approaches, a series of measurement data under sinusoidal flux conditions is necessary as a starting point. However, the formation of the polynomial linear equations linking loss under PWM conditions to that under more readily accessible sinusoidal conditions for a given material composition and thickness avoids the need to produce data under the complex waveforms.

6 IRON POWDER CORE MATERIAL

There is an increasing interest in SMC materials because of the demand for miniaturization of cores for power electronic applications. For very high-frequency operation, ferrite cores are the main option based on cost and performance in spite of their low saturation magnetization and permeability. However for dc, and increasingly medium frequency, operation, there is growing use of cores formed by compacting iron, silicon iron, and other iron alloy powders. The compositions of commercial composite cores are essentially similar to those of common conventional bulk materials but each has a broader range of potential applications due to the possibility of true 3-D electromagnetic design and higher frequency operation than is feasible using even thin laminations.

Grain size, sintering temperature, and the degree of porosity need to be carefully controlled in order to optimize structure-sensitive properties such as maximum permeability and low coercive force. The dc magnetic properties of hot-pressed, high-purity, atomized iron powder compacts can be as good as or better that those of conventional high-purity iron (Moyer, McDermott, Topolski and Kearney, 1980). Such sintered products are not normally suitable for *ac applications* since eddy currents will normally be excessive. However for *dc applications,* the careful control of sintering conditions, in particular, leads to products with high permeability and low coercivity which could satisfy growing demands for tighter specifications and complex core shapes for electromagnetic actuators for use in transport and industrial sectors (Taylor, Mingard and Bell, 1998).

During the 1990s, advances in powder production and powder metallurgy, in general, drew more attention to magnetic powder cores suitable for *ac applications* because of their potential for use in novel 3-D topologies for electrical rotating machines offering performance or cost advantage over conventional laminated cores. Magnetic powder parts, today, are produced from high-purity powder particles each covered by insulating organic or inorganic coatings, which cause a barrier to global eddy current paths under ac magnetization. The coated powder particles, typically of 0.1-mm diameter, are mixed with less than 1% volume of binding material prior to conventional compaction into near-final-shape components. This is followed by low temperature (typically 150 °C) curing to cross-link the resin binder and produce high mechanical strength. The binding material acts as a lubricant in the pressing process and increases the mechanical strength of the composite core. Often a final anneal at 300–500 °C is carried out to develop the best combination of strength and magnetic properties. Such materials are referred to as *soft magnetic composites* or sometimes, although misleadingly, *bonded iron cores.*

The insulating coating on the powder particles in SMCs eliminates particle-to-particle eddy current paths hence minimizing eddy current losses, but it reduces the permeability and to a small extent the saturation magnetization. Internal stress caused by particle deformation during compaction is the main cause of dominant hysteresis loss in SMCs but a subsequent anneal can reduce this. Care is needed in compaction and annealing to avoid breaking down the particle coatings, otherwise eddy current loss increases.

The choice of the alloying element controls the resistivity of the individual powder particles, hence the local eddy current loss. Low resistivity material is used for dc applications but alloys with inherent high resistivity are needed to minimize eddy current loss for high-frequency operation. Permeability and coercivity are structure sensitive and

depend on factors such as powder size and shape, porosity, purity, and internal stress just as for sintered materials. Generally the permeability of a bulk SMC can be expressed as (Yanagimoto, Majima, Sunada and Aikawa, 2004)

$$\mu \propto \frac{B_s^n}{aK + b\sigma\lambda} \tag{9}$$

where B_s is the saturation induction, λ is the magnetostriction, K is an anisotropy factor, σ is the internal stress; a, b, and n are constants whose values depend on the material. The internal compaction stress in metallic powder cores is much higher than in ferrites and tends to dominate over the anisotropy. Fine powder can lead to composites with constant permeability/frequency characteristics and lower loss at high frequency than course powder, but the course powder composites generally have higher permeability and saturation induction.

Powder shape and size affects the final magnetic properties of an SMC and many combinations have been tried. One interesting approach for making high-performance SMCs has been demonstrated using anisotropic properties of elongated particles pressed by a conventional powder metallurgical process. The particles, up to over 5 mm long, are either coated or uncoated for ac and dc use, respectively (Bularzik, Krause and Kokal, 1998). Figure 10 shows the variation of core loss with flux density and frequency of such coated powder compacts compared with that of phosphorus- and silicon-bearing steel laminations. Figure 10(a) shows that even at 60 Hz, where the eddy current loss of the powder core is only 5% of the total compared to 50% in nonsilicon steel, the material could be efficient in power frequency applications such as PWM systems where high harmonic flux is present. The low eddy current loss of the powder core makes its high-frequency loss lower than that of the high-silicon material as can be seen in Figure 10(b). The loss characteristics do depend on the particle size and the ratio of their length to width/thickness as well as on the material density, which in turn depends on the thickness of the insulating coating. As with most SMCs, the compact needs to be annealed to reduce the high hysteresis loss caused by pressing-induced strain within particles without thermally breaking down the particle coating. The material, although apparently technically feasible, has not been produced commercially.

Figure 11 shows the variation of loss with frequency in other types of annealed and unannealed SMCs compared to that of a pure iron grade 1018 lamination with the same loss at 0.5 T, 50 Hz (Persson, Jansson, Jack and Mecrow, 1995). At magnetizing frequencies higher than 300 Hz, the loss of the laminated steel exceeds that of the SMCs. In general, SMCs are competitive in performance with laminated steels in the frequency range from 50 Hz to 100 kHz. In another

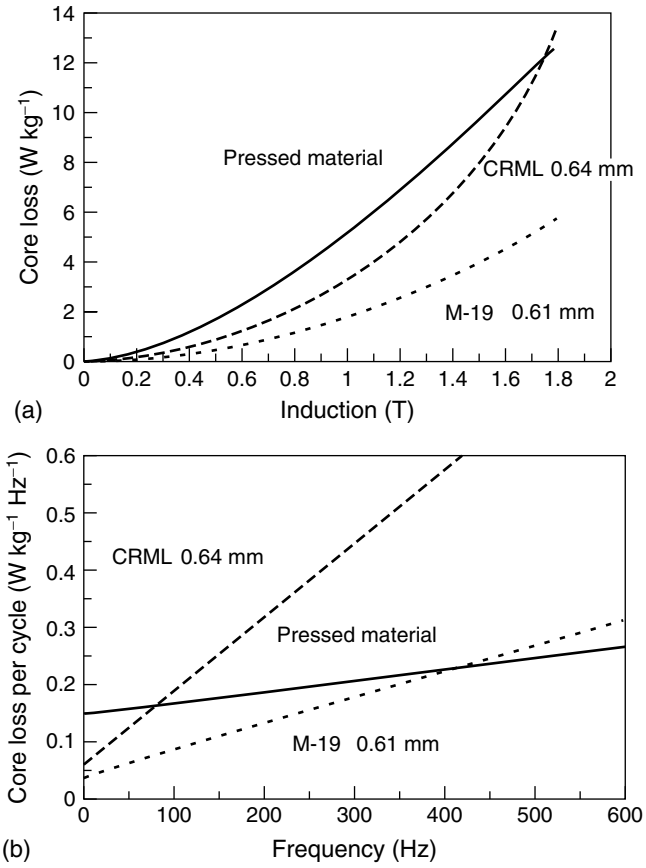

Figure 10. Loss variation with flux density (a) and frequency (b) of pressed iron powder material compared to that of phosphorous (CRML) and silicon (M-19) bearing steels at 60 Hz. (Reproduced from J.H. Bularzik *et al*., 1998, with permission from EDP Sciences. © 1998.)

example, it is quoted that the loss of coated iron powder composites is normally significantly higher than that of electrical steel at magnetizing frequencies up to around 1 kHz, but in the range 10–100 kHz it is considerably less (Goldman, 1995). Unfortunately, the permeability is not high at any magnetizing frequency and more development is needed to overcome this problem if the material is to make an impact in a wider range of electrical machine applications (Persson, Jansson, Jack and Mecrow, 1995).

Table 2 compares dc $B-H$ data of two iron SMCs from different sources with lamination materials (West, 1998). This illustrates the much larger permeability of conventional steel compared with that of the SMCs, and shows that the difference does drop at high flux density. Table 3 compares losses of similar materials with that of a higher-specification nonoriented steel over a wide frequency and flux density range (West, 1998). For the 'degraded' lamination, the performance data includes an allowance to estimate the degradation of the lamination properties when built into a

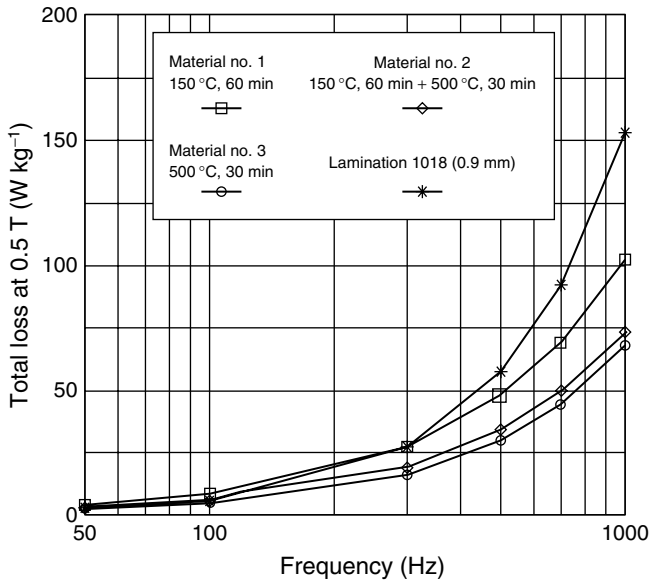

Figure 11. Comparison of losses of insulated powder and laminated steel. (Reproduced from M. Persson *et al*., 1995, with permission from IEE Publishing. © 1995.)

Table 2. Comparison of dc fields (A m^{-1}) to produce given flux density in SMC powder cores with those of typical electrical steel laminations.

Flux density	1 T	1.5 T	1.75 T	2 T
Somaloy 500	3	13	30	86
Accucore	1.4	4.8	10.7	n/a
Typical laminations	0.1	0.4	5	n/a

core due to punching shorts and rotational loss. It is perhaps more practicable to use these 'degraded' lamination figures rather than ideal laboratory data when comparing lamination performance with that of SMCs. At 400 Hz, the loss of one SMC is comparable with that of the high-grade lamination.

It can be appreciated from this snapshot comparison of permeability and losses that if SMCs are to compete with laminations in electrical machine applications, their 3-D properties must be exploited, since magnetic characteristics of laminations at low to medium frequency are generally better. Hence, the main advantage of such powder parts is the possibility for machine designers to fully exploit 3-D flux paths in machine topologies aimed at producing cores with unique electromagnetic properties combined with low material and manufacturing costs, good dimensional tolerances, and satisfactory temperature stability (Jansson, Persson, Jack and Mecrow, 1996). The magnetic and thermal properties are claimed to be isotropic and therefore very suitable for such 3-D topologies (Jansson and Persson, 1998).

Figure 12 shows an example where the 3-D versatility of the SMC is used in the design of a complex three phase claw pole, brushless motor incorporating permanent magnet material together with the SMC to optimize a complex, magnetically efficient, flux path where use of laminations would be impracticable (Viarouge, 2004).

It is interesting to note that the acoustic noise output of powder cores can be less than that of equivalent laminated assemblies (Cros, Perin and Viarouge, 2002). Another potential advantage of SMCs is that an integrated approach to the design of electrical machine core and windings can be taken to facilitate manufacturing as well as to increase the scope for novel topologies due to thermal as well as electromagnetic options. End-of-life recycling also becomes more convenient as it is easier to separate copper and iron powder parts when an SMC is used. It is important when comparing the effectiveness of SMC cores with that of a conventional lamination assembly, for any machine core application, that full use is made of the novel features and opportunities offered by SMC parts, which would not be realized fully by direct substitution of one for another.

Loss predictions in powder cores should be made with due regard to the very different structure compared to electrical steels, in particular, the 3-D nature of the materials, which makes equation 2 invalid and the eddy current path in the material more complex. A monotonic decrease of resistivity

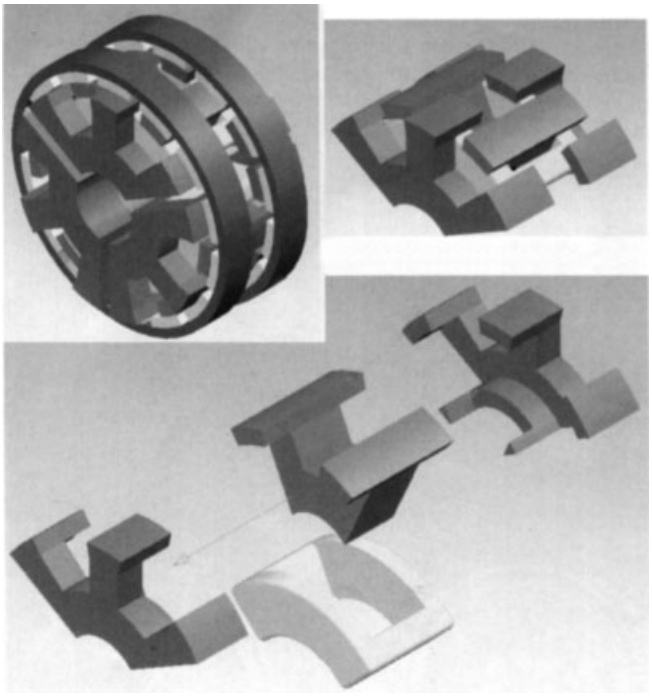

Figure 12. Complex 3-D geometry of core parts for a claw pole motor. (Reproduced from P. Viarouge, 2004, with permission from the UK Magnetics Society. © 2004.)

Table 3. Comparison of losses ($W\,kg^{-1}$) at various flux density/frequency ($T\,Hz^{-1}$) combinations in SMC cores and lamination steels.

T Hz^{-1}	1/60	1/100	1/400	1.5/60	1.5/100	1.5/100	1.75/60	1.75/100	1.75/400
Somaloy 500 (SMC)	10	18	100	19	35	205	n/a	n/a	n/a
Accucore SMC	5.2	9	44	10	17	90	12	21	n/a
0.4-mm lamination	3.5	n/a	n/a	8.7	n/a	n/a	12	n/a	n/a
0.4-mm degraded lamination	7.5	n/a	n/a	17.1	n/a	n/a	24	n/a	n/a
0.5-mm polycore lamination	2.0	4	40	3.5	10	101	7	20	n/a

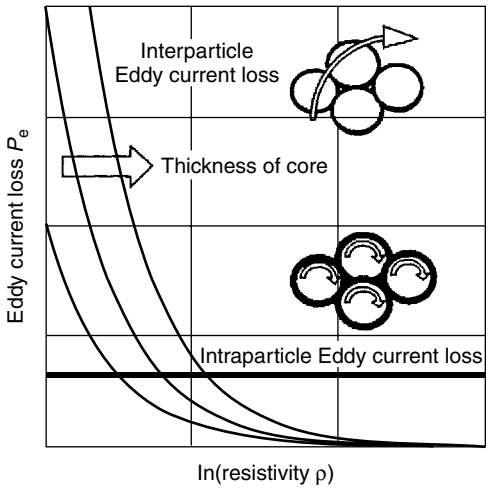

Figure 13. Schematic illustration of relationship between resistivity and eddy currents in SMC material. (Reproduced from Saito *et al*., 2005, with permission from IEEE. © 2005.)

with annealing temperature and variation of eddy currents with core size has been postulated to be due to the breakdown of surface insulation (Saito, Takemoto and Iriyama, 2005). It is assumed that two kinds of eddy currents are present as illustrated in Figure 13: firstly, circulating within the individual insulated particles and secondly, circulating around clusters of particles.

Any model for predicting the ac magnetic properties of SMCs must take account of the frequency dependent skin depth and the two eddy current mechanisms referred to earlier. Until now, no empirical approach has been reported which will take these accounts into effect. To make consistently accurate predictions of losses in SMC cores over a wide magnetizing range, models capable of accounting for core shape and size dependence of eddy current loss in complex geometries will be needed. It has not been necessary for these to be included in the development of models for predicting losses in thin laminations because of their 2-D nature.

One approach to loss prediction in SMCs assumes losses can be separated into hysteresis and eddy current components. The eddy current loss is separately calculated by finite element analysis (FEA) for a homogeneous isotropic core with known resistivity and combined with a Steinmetz model which estimates the basic hysteresis component (Nord, Pennander and Jack, 2004). Unexplained size dependence of eddy current loss was observed in the eddy current simulation, which might be related to the micro and macro eddy current paths being followed simultaneously at some frequencies. The FEA approach does lead to close agreement between measured and predicted results but the calculations depend on fitting arbitrary material constants into the expression for the hysteresis component, so the physical basis of the approach is not clear.

REFERENCES

Anayi, F., Moses, A.J. and Jenkins, K. (2003). Effect of aluminium diffusion into electrical steel on power loss under flux distortion conditions. *Journal of Magnetism and Magnetic Materials*, **254–255**, 36–38.

Arabi, M.A. and Moses, A.J. (1984). An improved method for measuring rotational power loss in electrical steels. *Journal of Magnetism and Magnetic Materials*, **41**, 227–229.

Ban, G. (1998). Investigation of the limit of statistical power loss model for 3.2% SiFe electrical steel. 1. Role of hysteresis. *Journal de physique IV (France)*, **8**, 503–504.

Barros Lorenzo, J., Ros-Yanez, T., De Wulf, M. and Houbaert, Y. (2004). Magnetic properties of electrical steel with Si and Al concentration gradients. *IEEE Transactions on Magnetics*, **40**(4), 2739–2741.

Bertotti, G. (1988). General properties of power losses in soft ferromagnetic materials. *IEEE Transactions on Magnetics*, **24**(1), 621–630.

Bertotti, G. (1998). *Hysteresis in Magnetism for Physicists, Material Scientists and Engineers*, Academic Press: San Diego.

Boglietti, A., Ferraris, P., Lazzari, M. and Profumo, F. (1991). Iron losses in magnetic materials with six–step and PWM inverter supply. *IEEE Transactions on Magnetics*, **27**(6), 5334–5336.

Boll, R. (Ed.) (1978). *Soft Magnetic Materials. The Vacuumschmelze Handbook*, Heyden & Son Ltd: London.

Brailsford, F. (1966). *Physical Principles of Magnetism*, D. Van Nostrand: London.

Bularzik, J.H., Krause, R.F. and Kokal, H.R. (1998). Properties of a new soft magnetic material for AC and DC motor applications. *Journal de physique IV (France)*, **8**, 747–753.

Bullingham, J.M. (1971). Effects of temperature on silicon iron at low frequencies. *Proceedings of the IEE*, **118**(9), 1318.

Buschow, K.H.J. (Ed.) (1995). *Handbook of Magnetic Materials*, Elsevier Science B. V.: Amsterdam.

Chen, C.W. (1958). Temperature dependence of magnetic properties of silicon-iron. *Journal of Applied Physics*, **29**(9), 1337–1343.

Cros, J., Perin, A.J. and Viarouge, P. (2002). Soft magnetic composites for electromagnetic components in lightning applications, *37th IAS Annual Meeting*, Pittsburg, USA, 13-18, pp. 342–347.

Fiorillo, F. (2004). Power losses in soft magnetic laminations. *Proceedings of Workshop on Metallurgy and Magnetism*, Technische Universitat Bergakademie: Freiberg, Chapter 15.

Fiorillo, F. and Novikov, A. (1990). An improved approach to power losses in magnetic laminations under non-sinusoidal induction waveform. *IEEE Transactions on Magnetics*, **26**(5), 2904–2910.

Fish, G.E. (1989). Soft magnetic materials. *Proceedings of the IEEE*, **78**(6), 947–961.

Foley, T.F., Leak, D.A., Newbury, R.A., *et al*. (1970). A study of ferrous based soft magnetic materials for transformers and similar applications. *Journal of the Iron and Steel Institute*, **208**, 147–156.

Fortunati, S. (2004). Grain oriented electrical steels: status and trends. *Proceedings of Workshop on Metallurgy and Magnetism*, Technische Universitat Bergakademie: Freiberg, Chapter 7.

Goldman, A. (1995). The magnetic applications choice among ferrite, ceramics, metallic strip, or powder cores. *Journal of Materials Engineering and Performance*, **4**, 395–400.

Gunther, K., Abbruzzese, G., Fortunati, S. and Ligi, G. (2005). Recent technology developments in the production of grain-oriented electrical steel. *Steel Research International*, **76**(6), 413–421.

Houbaert, Y. (2004). Properties and characteristics of high Si-steels up to 6.5% wt-% Si. *Proceedings of Workshop on Metallurgy and Magnetism*, Technische Universitat Bergakademie: Freiberg, Chapter 9.

Hubert, A. and Schafer, R. (1998). *Magnetic Domains*, Springer-Verlag: Berlin.

Huppi. G.S. (1996) *Grain Oriented Electrical Steel Having High Volume Resistivity and Method for Producing Same*, Patent number EP 0743370, Applicant ARMCO Inc.

Jansson, P. and Persson, M. (1998). Advances in insulated powder technology. *Journal de physique IV (France)*, **8**, 269–272.

Jansson, P., Persson, M., Jack, A.G. and Mecrow, B.C. (1996). Powdered soft magnetic materials for medium frequency applications. *Proceedings of Soft Magnetic Materials '96 Conference*, MPIF: San Francisco.

Jenkins, K.W. (2004). Recent progress in electrical steels. *Proceedings of Workshop on Metallurgy and Magnetism*, Technische Universitat Bergakademie: Freiberg, Chapter 8.

Kaczmarek, R., Amar, M. and Protat, F. (1996). Iron loss under PWM voltage supply in Epstein frame and in induction motor core. *IEEE Transactions on Magnetics*, **32**(1), 189–194.

Kubota, T. (2005). Recent progress on non-oriented silicon steel. *Steel Research International*, **76**(6), 464–469.

Kubota, T., Fujikura, M. and Ushigami, Y. (2000). Recent progress and future trends on grain-oriented silicon steel. *Journal of Magnetism and Magnetic Materials*, **215–216**, 69–73.

Ledingham, S., Broadbent, K. and Radley, G.S. (1989). Apparatus for measurement of velocity of domain boundaries in two dimensions in grain-oriented silicon iron. *Physica Scripta*, **40**, 526–528.

Leonard, P.J., Marketos, P., Moses, A.J. and Lu, M. (2006). Iron losses under PWM excitation using a dynamic hysteresis model and finite elements. *IEEE Transactions on Magnetics*, **42**(4), 907–910.

Lindenmo, M., Coombs, A. and Snell, D. (2000). Advantages, properties and types of coating on non-oriented electrical steels. *Journal of Magnetism and Magnetic Materials*, **215–216**, 79–81.

Marketos, P., Moroz, Y.I., Moses, A.J. and Zirka, S. (2002). A novel approach to modelling losses in electrical steel laminations, *Proceedings of IEE 4th International Conference on Computation in Electromagnetics. CEM 2002*, Bournmouth.

Moses, A.J. (1984). Factors effecting the localised flux and iron loss distribution in laminated magnetic cores. *Journal of Magnetism and Magnetic Materials*, **41**, 409–414.

Moses, A.J. (1990). Electrical steels: past, present and future development. *IEE Proceedings*, **137**(Pt A, 5), 233–245.

Moses, A.J. (1992a). Development of alternative magnetic core materials and incentives for their use. *Journal of Magnetism and Magnetic Materials*, **112**, 150–155.

Moses, A.J. (1992b). Importance of rotational losses in rotating machines and transformers. *Journal of Materials Engineering and Performance*, **1**(2), 235–244.

Moses, A.J. (2002). Opportunities for exploitation of magnetic materials in an energy conscious world. *Interdisciplinary Science Reviews*, **22**(2), 100–113.

Moses, A.J. (2004a). The case for characterisation of rotational losses under pure rotational field conditions, *8th International Workshop on 1 & 2-Dimensional Magnetic Measurements and Testing*, Ghent, paper 03, pp. 1–7.

Moses, A.J. (2004b). Loss prediction in electrical steel laminations and motor cores. *Steel Research International*, **76**(6), 455–460.

Moses, A.J. and Leicht, J. (2004). Iron loss prediction under sinusoidal and non-sinusoidal excitation using a neural network approach, *Proceedings of Soft Magnetic Materials Conference (SMM16)*, Stahleisen, pp. 329–334.

Moses, A.J. and Leicht, J. (2005). Iron loss prediction under PWM conditions. *Journal of Applied Physics*, **97**, 10R507-1–10R507-3.

Moses, A.J., Pegler, S.M. and Thompson, J.E. (1972). Role of the phosphate coating in determining the magnetic properties of Goss-oriented silicon-steel. *Proceedings of the IEE*, **119**(8), 1222–1228.

Moses, A.J. and Phillips, P.S. (1978). Some effects of stress in Goss-oriented silicon-iron. *IEEE Transactions on Magnetics*, **14**(5), 353–355.

Moses, A.J. and Thursby, G.J. (1983). Improvement of magnetic properties of electrical steel using a surface diffusion technique. *Journal of Materials Science*, **18**, 1657–1665.

Moyer, K.H., McDermott, M.J., Topolski, M.J. and Kearney, D.F. (1980). Magnetic properties of iron alloys, *Energy Efficient Electrical Steels AIME Meeting*, Pittsburgh, pp. 93–130.

Nakaoka, M., Fukuma, A., Nakaya, H., *et al*. (2005). Examination of temperature characteristics of magnetic properties using a single sheet tester. *IEEJ Transactions on Fundamentals and Materials*, **125**(1), 63–68.

Nakata, T., Takahashi, N., Fujiwara, K., *et al*. (1992). Magnetic characteristics of magnetic materials at very low temperature and their application to transformers. *Journal of Magnetism and Magnetic Materials*, **112**, 174–176.

Nord. G., Pennander, L-O. and Jack, A.G. (2004). Loss calculation for soft magnetic composites, *16th ICEM Conference*, Cracow, September 2004.

Persson, M., Jansson, P., Jack, A.G. and Mecrow, B.C. (1995). Soft magnetic composite materials–use for electrical machines, *Electrical Machines and Drives*, Conference publication 412 IEE, Durham, UK, pp. 242–246.

Saito, T., Takemoto, S. and Iriyama, T. (2005). Resistivity and core size dependencies of eddy current loss for Fe-Si compressed cores, *Technical Digest of Intermag 2000*, Toronto, Canada, paper ER-03.

Schoppa, A., Schneider, J. and Wuppermann, C-D. (2000). Influence of the manufacturing process on the magnetic properties of non-oriented electrical steels. *Journal of Magnetism and Magnetic Materials*, **215–216**, 74–78.

Shilling, J.W. and Houze, G.L. (1974). Magnetic properties and domain structures in grain-oriented 3% Si-Fe. *IEEE Transactions on Magnetics*, **M10**, 195–223.

Takada, Y., Abe, M., Masuda, S. and Inagaki, J. (1988). Commercial scale production of Fe-6.5 wt. % Si sheet and its magnetic properties. *Journal of Applied Physics*, **64**, 5367.

Taylor, J., Mingard, K. and Bell, I. (1998). High temperature sintered soft magnetic components, *IEE Seminar 'New Magnetic Materials' IEE Savoy Place*, London.

Ushigami, Y., Nakayama, T., Arai, S. and Kubota, T. (2004). Modeling and computer simulation of secondary recrystallization in grain-oriented silicon steel, *Proceedings of Soft Magnetic Materials Conference (SMM16)*, Stahleisen, pp. 487–492.

Viarouge, P. (2004). Experience with ATOMET soft magnetic composites: properties, pressing conditions and applications. *Magnews Winter 2004*, Magnetics Society: Wantage, UK, pp. 14–19.

Werner, F.E. (1991). Steels for laminations in energy efficient motors. *EPRI Center for Materials Production*, EPRI Power Research Institute, Inc. Pittsburg USA, CMP Report 91-11.

West, G.J. (1998). Automotive applications: will bonded iron replace laminations? *Soft Magnetic Materials 98*, Gorham/ Intertech Consulting: Barcelona, pp. 1–18.

Yanagimoto, K., Majima, K., Sunada, S. and Aikawa, Y. (2004). Effect of Si and Al content on core loss in Fe-Si-Al powder cores. *IEEE Transactions on Magnetics*, **40**(3), 1691–1694.

Zirka, S.E., Moroz, Y.I., Marketos, P. and Moses, A.J. (2002). Modelling losses in electrical steel laminations. *IEE Proceedings-Science Measurement and Technology*, **149**(5), 218–221.

Zurek, S. (2005). *Two-Dimensional Magnetisation Problems in Electrical Steels*, Ph.D. Thesis, Cardiff University, Cardiff.

FURTHER READING

Kaczmarek, R., Protat, F., Duan, X. and Huneus, H. (1998). The Kerr effect observations in the non oriented steel laminations. *Journal de physique IV (France)*, **8**, 311–314.

McCurie, R.A. (1994). *Ferromagnetic Materials, Structure and Properties*, Academic Press: London.

SOREL TRACY, QUEBEC CANADA, Quebec Metal Powder Ltd. (2000). Atomet EM-1 Ferromagnetic composite Powder.

Rare-earth Intermetallics for Permanent Magnet Applications

Josef Fidler[1], Dieter Suess[1] and Thomas Schrefl[2]

[1] *Vienna University of Technology, Vienna, Austria*
[2] *University of Sheffield, Sheffield, UK*

1 INTRODUCTION

Binary and ternary intermetallic compounds between rare-earth (RE) elements, such as samarium (Sm) and neodymium (Nd) with transition metals (TMs), like cobalt (Co) and/or iron (Fe), and with boron (B) have become the basis for a wide spectrum of RE permanent-magnet materials. A large number of phases have been synthesized, exhibiting different stoichiometries and a variety of crystal structure types since the 1970s. In many cases, their physical properties turned out to be of the high technical importance and these compounds are manufactured on an industrial scale. The Sm–Co phases, which also show a variety of crystal structure types, have been studied for more than 40 years and have recently become of interest for the high-temperature permanent-magnet applications. Belonging to another family of phases, which has been intensively studied for more than 20 years, are the $RE_2TM_{14}B$ (Herbst, 1991) and $RETM_{12-x}X_x$ with X = Ti, V, Si (Buschow, 1988).

The unique magnetic properties of the RE series from lanthanum to lutetium plus yttrium result from the incomplete filling of the 4f shell. The 4f orbitals are rather compact and well localized on the atom and there are both spin and orbital contributions to the magnetic moment. The orbital moment leads to the behavior of uniaxial magnetocrystalline anisotropy, which is indispensable for the development of magnetic hysteresis. Magnetic interactions between the localized 4f electrons are weak and the RE metals themselves have low Curie temperatures. By combining them with one of the ferromagnetic 3d elements where the magnetic 3d electrons occupy the outermost orbitals of the atom and interact strongly, it is possible to combine the advantages of 4f and 3d magnetism. The particular RE element needed for uniaxial anisotropy is determined by the symmetry of the site it occupies in the crystal structure. High-performance magnets are based on compounds of the magnetic light RE (Pr, Nd, Sm) for anisotropy and a 3d TM element (Co, Fe) for high magnetization and high Curie temperature. The most promising phases are $SmCo_5$, $Sm_2(Co,Fe)_{17}$, $Nd_2Fe_{14}B$ and $Sm_2Fe_{17}N_3$.

Up to now a large number of RE–TM intermetallic compounds are known and have been investigated intensively by many authors. The complex interactions of the 3d and 4f electrons lead to a wide range of intermetallics with different stoichiometries and variable RE elements that modify the magnetic properties of the 3d TM and 4f RE elements. Basic concepts related to the intrinsic magnetic properties of the 3d-rich RE–TM intermetallic compounds are summarized

Handbook of Magnetism and Advanced Magnetic Materials. Edited by Helmut Kronmüller and Stuart Parkin. Volume 4: *Novel Materials*. ISBN: 978-0-470-02217-7.

in various review articles (Franse and Radwanski, 1993; Buschow, 1986). Buschow (1977) surveys the physical properties, composition, and crystal structure of intermetallic compounds formed between RE elements and 3d transition elements. Apart from binary compounds the results of pseudobinary series are also considered. The magnetic properties determined by the exchange interactions involving 4f as well as 3d electrons, are discussed together with experimental results available on magnetovolume effects and various resonance techniques such as nuclear magnetic resonance (NMR) and the Mössbauer effect.

However, the excellent intrinsic properties, such as large magnetocrystalline uniaxial anisotropy, high saturation magnetization and Curie temperature are not the only prerequisite for high-quality permanent magnets. The coercive field, remanence and maximum energy product depend also sensitively on microstructural properties such as grain size, particle shape, grain boundary type, and the distribution of secondary phases. Magnetic and microscopic investigations of permanent magnets show that microstructural features affect the magnetic properties of permanent magnets in a characteristic manner (Fidler, Knoch, Kronmueller and Schneider, 1989; Rabenberg, Fidler and Bernardi, 1992; Hirosawa and Tsubokawa, 1990; Khlopkov *et al*., 2004; Gutfleisch *et al*., 2006; Kronmüller, Durst and Sagawa, 1988). In addition to these experimental studies, the theoretical treatment of microstructural effects is beneficial for the improvement of permanent magnets. The theoretical background for the study of magnetization processes in ferromagnetic materials is the continuum theory of micromagnetics (Brown, 1963, 1978). Micromagnetic calculations show that microstructural effects considerably deteriorate the coercive field of single hard magnetic particles and grains (Schrefl, Schmidts, Fidler and Kronmuller, 1993; Kronmüller, 1987; Kronmüller and Schrefl, 1994; Schmidts and Kronmüller, 1991). Besides the magnetic behavior of the individual particles and grains also the intergrain interactions determine the magnetic properties of nucleation-controlled hard magnetic materials (Martinek and Kronmueller, 1990; Pastushenkov, Forkl and Kronmueller, 1991; Fukunaga and Inoue, 1992). Static computational micromagnetics of demagnetization processes in nanoscaled permanent magnets (Fischer and Kronmüller, 1996) quantitatively predicts experimental results (Manaf, Buckley and Davies, 1993). The expansion and pinning behavior of magnetic domains strongly depends on the intrinsic properties of the various phases and precipitates in the multiphase magnets, such as in the $Sm(Co,Cu)_5/Sm_2(CoFe)_{17}$-type magnets (Goll, Kronmuller and Stadelmaier, 2004; Streibl, Fidler and Schrefl, 2000; Scholz *et al*., 2003; Hadjipanayis *et al*., 2000).

A combination of the intrinsic properties of the material, such as saturation polarization J_s, magnetic exchange, and magnetocrystalline anisotropy of various phases and the influence of the microstructure on the magnetization reversal process governs the hysteresis properties of the magnets. The intergranular structure between the grains plays a significant role determining the magnetic properties, thus a detailed understanding of the microstructure and grain boundaries is necessary. The microstructural features directly influence magnetic domain structures, which are a result of the occurrence of magnetic stray fields. The direct observation of microstructure and magnetic domain structure leads to a deeper insight of the reasons for coercivity of RE magnets. Advanced analytical methods, such as high-resolution electron microscopy, force microscopy, position sensitive 3D-atom probe and other techniques have been used to study RE magnets. Modeling of magnetic materials is performed at various levels and becomes more important as computer power is improved. Nowadays, numerical 3D-micromagnetic simulations of the magnetization reversal process incorporate realistic microstructures. Advanced analytical investigations and future simulations should be able to predict optimal microstructures and properties for given hard and soft magnetic materials (Fidler and Schrefl, 2000). Special emphasis of the present review is laid on the discussion of the extrinsic magnetic hysteresis properties that are related to the microstructure of the various types of RE permanent magnets. The crystal structures of the most important RE–Co and RE–TM–B compounds as basis for permanent magnets are described in Chapter 2 "Crystal structures and magnetic properties of RE-Co intermetallics" and Chapter 3 "Crystal structures and magnetic properties of RE-TM-B intermetallics", whereas Chapter 4 "Microstructure and coercivity of rare-earth permanent magnets", describes the role of microstructure on the hysteresis properties, such as coercive field and energy density product of Sm–Co and Nd–Fe–B-based permanent magnets.

2 CRYSTAL STRUCTURES AND MAGNETIC PROPERTIES OF RE–Co INTERMETALLICS

The large values of coercivities of RE–Co and RE–(Co,Fe)–B intermetallics derive from the uniaxial magnetocrystalline anisotropy. The RE atoms provide most of the magnetocrystalline anisotropy, while the magnetization arises principally from the TM sublattice. Investigations of magnetization and anisotropies of promising candidates for permanent-magnet materials by Strnat and coworkers led to the discovery of large magnetocrystalline anisotropies of $RECo_5$ compounds with the hexagonal $CaCu_5$ crystal structure (Hoffer and Strnat, 1966, 1967; Strnat *et al*., 1967). For

these compounds in which the 4f shell has a nonzero orbital magnetic moment, theoretical analyses demonstrated that the behavior of the RE ion under the combined influence of the exchange and crystalline electric field controls the easy magnetization direction and accounts for much of the large uniaxial anisotropy (Buschow, van Diepen and de Wijn, 1974; Sankar *et al*., 1975; Hummler and Faehnle, 1996)

The metallic phases present in the Sm–Co-based permanent magnets are all derivative of the binary intermetallic phases appearing in the Sm–Co binary phase diagram. For the understanding of the metallurgical behavior and the magnetic properties of these magnets, it is therefore essential to understand the alloying behavior and crystal structure of the compounds appearing in the Sm–Co binary system. The difference between the atomic radii of the Sm atom (0.1994 nm) and the Co atom (0.1383 nm) precludes, according to the Hume–Rothery rules (Cahn, 1996) any significant solid solubility between the two types of atoms. This results in the appearance of a series of intermetallic compounds in the binary phase diagram for different ratios of the Sm–Co concentrations. The phases that are important for Sm–Co-type magnets appear in the region of high Co concentration. The Sm–Co_5 phase occurs at 83.3 at% of Co and Sm_2Co_{17} phase occurs at 89.5 at% of Co. The Co-rich side of the Sm–Co binary phase diagram shows that both phases, $SmCo_5$ and Sm_2Co_{17}, exhibit no solubility at room temperature although some solubility region can be observed at higher temperature above 800 °C (Strnat, 1988; Buschow and van der Goot, 1968). Besides this fact also the Sm_2Co_7 phase has to be taken into account in the preparation of single-phase $SmCo_5$ alloys. The homogeneity range for $SmCo_5$ phase at 1200–1300 °C has been reported to exist between about 14.5 and 17 at% of Sm (Buschow and van der Goot, 1968). Almost no solubility of excess Sm exists in the $SmCo_5$ phase even at higher temperature. In the case of the Sm_2Co_{17} phase a homogeneity range is obtained toward an excess of Sm at higher temperature, while almost no solubility of excess Co can be observed at any temperature. This behavior is explained in terms of the crystallographic structure considerations for both phases.

Several other RE–TM lattices are derived from $RETM_5$ by judicious replacement of RE and TM atoms (Buschow, 1971). These include the $RETM_2$ (cubic Laves phase; $MgCu_2$-type) structure formed by the extremely magnetostrictive compounds (Clark, 1993), the $RETM_3$ (rhombohedral; $PuNi_3$-type) structure, the $RETM_{12}$ (tetragonal; $ThMn_{12}$-type) structure characterizing a class of magnetically anisotropic materials such as $REFe_{10}TM_2$ (de Boer, Ying-Kai, de Mooij and Buschow, 1987; de Mooij and Buschow, 1988) and the rhombohedral RE_2TM_{17} (Th_2Zn_{17}-type) structure. Representatives of the rhombohedral RE_2TM_{17} class include the hard-magnet compound Sm_2Co_{17} including the interstitial nitride phase $Sm_2Fe_{17}N_3$ exhibiting a large high Curie temperature ($T_C \approx 750$ K), a large room-temperature magnetization, and uniaxial anisotropy (Coey and Sun, 1990).

According to the binary Sm–Co phase diagram six ordered intermetallic compounds: $SmCo_2$, $SmCo_3$, Sm_2Co_7, Sm_5Co_{19}, $SmCo_5$, Sm_2Co_{17} appear in the composition range 67–89 at% Co: (Massalski, 1990). The crystal structure of the binary Sm–Co phases are summarized in Table 1. The Sm_2Co_7 and $SmCo_5$ exist as hexagonal structures with the $P6_3/mmc$ and the $P6/mmm$ space group symmetries, respectively. The Sm_2Co_{17} phase occurs in two modifications, as the rhombohedral structure ($R\bar{3}m$ symmetry) and the hexagonal structure ($P6/mmc$ symmetry).

Other RE elements form also isomorphic structures of type $CaCu_5$. This $RECo_5$ structure is formed by the two types of layers one formed solely of Co atoms and another mixed layer formed by RE and Co. This layer stacks in a hexagonal sequence giving a unit cell as shown in Figure 1.

The $RECo_5$ structure of $CaCu_5$ is a result of an ordered substitution of Co atoms by RE atoms in the hexagonal close-packed (hcp) Co structure (Khan, 1973). Hexagonal close-packed structures are formed by the alternate stacking of layers in two different positions ABABAB. . .. By replacing three Co atoms, which form an almost equilateral triangle, by an RE atom the $RECo_5$ structure is formed. This transformation is described by

$$\begin{aligned} 3\mathrm{Co(B)} + 5\mathrm{Co(A)} \quad &\Rightarrow \quad 2\mathrm{Co(B)} + 3\mathrm{Co(A)} + \mathrm{RE(A)} \\ &\quad -1\mathrm{Co(B)} \\ &\quad -2\mathrm{Co(A)} \\ &\quad +1\mathrm{RE(A)} \\ \equiv \mathrm{RECo_5} \end{aligned} \tag{1}$$

As a result of this substitution the interlayer distance diminishes with respect to the pure hcp structure. The change of the interlayer distance is explained by the different atomic radii of the various RE elements. The normal shrinkage with increasing atomic number inside the series is found, corresponding to a smaller radio of the involved RE atom. This explains the different tendency of the various RE atoms to form disordered stacking sequences and leading to planar stacking faults and twin boundaries.

The crystal structures from the $SmCo_2$- until the $SmCo_5$-phase are closely related with each other and are based on a regular stacking of two kinds of layers, one is a layer of $SmCo_2$-Laves phase structure and the other is that of $SmCo_5$. For compounds between $RETM_5$ and TM, a fully ordered structure is derived from the 1:5 compound by replacing some RE atoms with TM-atom pairs. The two-index formula for the expected compositions was derived by Stadelmaier (1984):

$$\mathrm{RE}_{m-n}\mathrm{TM}_{5m+2}$$

Table 1. Crystal structure data of binary Sm–Co compounds. (Reprinted with permission Buschow *et al*., copyright 1968, Elsevier.)

Compound	Lattice constant (nm)	Structure type	Space group	Space group number
Sm_3Co	$a = 0.7090$ $b = 0.9625$ $c = 0.6342$	Fe_3C	$Pnma$	62
$SmCo_2$	$a = 0.5050$	$MgCu_2$	$Fd3m$	227
Sm_5Co_2	$a = 1.6282$ $b = 0.6392$ $c = 0.7061$	Pd_5B_2	$C2/c$	15
$SmCo_3$	$a = 0.5050$ $c = 2.4359$	$NbBe_3$	$R3m$	166
Sm_2Co_7	$a = 0.5047$ $c = 2.4326$	Ce_2Ni_7	Pb_3/mmc	194
Sm_5Co_{19}	$a = 0.5035$ $c = 4.8450$	Ce_5Co_{19}	$R3m$	166
$SmCo_5$	$a = 0.5002$ $c = 0.3964$	$CaCu_5$	$P6/mmm$	191
Sm_2Co_{17}	$a = 0.4856$ $c = 0.4081$	$TbCu_7$	$P6/mmm$	191
Sm_2Co_{17}	$a = 0.8360$ $c = 0.8515$	Th_2Ni_{17}	Pb_3/mmc	194
Sm_2Co_{17}	$a = 0.8395$ $c = 1.2216$	Th_2Zn_{17}	$R3m$	166
$SmTiCo_{11}$	$a = 0.8406$ $c = 0.4730$	$ThMn_{12}$	$I4/mmm$	139

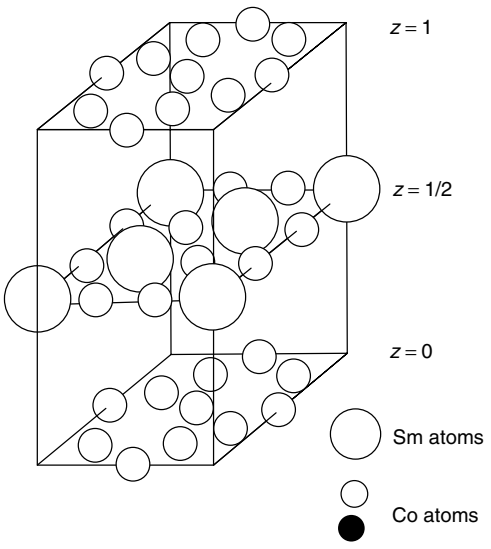

Figure 1. $SmCo_5$ crystalline structure, hexagonal, hP6, $CaCu_5$ structure type, $a = 0.5002$ nm, $c = 0.3964$ nm, $P6/mmm$.

where m is the number of $RETM_5$ units making up the new structure, and n is the total number of RE atoms being replaced.

From the technical point of view only compounds with a Curie temperature exceeding 400 °C are of interest. From the possible Sm–Co binaries, this is only fulfilled for Sm_2Co_7, Sm_5Co_{19}, $SmCo_5$ and Sm_2Co_{17} (Strnat, 1988). In view of their richer cobalt content and, hence, higher magnetization the RE_2Co_{17} compounds were also heavily investigated as hard-magnet materials. The light RE members of the series have the rhombohedral Th_2Zn_{17} structure, which is closely related to the $CaCu_5$ structure. In contrast to the $RECo_5$ series, the cobalt sublattice in the RE_2Co_{17} phases is characterized by basal plane rather than uniaxial anisotropy, and the total anisotropy is lower (Radwanski, Franse and Sinnema, 1985). The size difference between the Sm and Co atoms makes the solubility of additional Sm in this structure difficult. Pairs of Co atoms, on the other hand, can substitute Sm in the $SmCo_5$ structure to some extent. The substitution of Sm atoms occurs when pairs of Co atoms forming dumbbells replace the Sm position. When Sm atoms are randomly substituted by Co pairs, a disordered Co-rich phase sometimes referred as an $SmCo_7$ structure of type $TbCu_7$ ($P6/mmm$) is formed (Khan, 1973). When 22% of the Sm atoms have been substituted by Co pairs, the $TbCu_7$ structure becomes unstable and a phase separation occurs into the two nearest phases, $SmCo_5$ and Sm_2Co_{17} structures.

The Sm_2Co_{17} in its two modifications is the result of the ordered substitution of 1/3 of the Sm by two Co atoms lying above and below the former Sm position (Figure 2). If the stacking for the mixed planes follows an ABABA. . . hexagonal sequence, the Th_2Ni_{17} structure is formed. If the stacking follows an ABCABC. . . sequence, the Th_2Zn_{17}

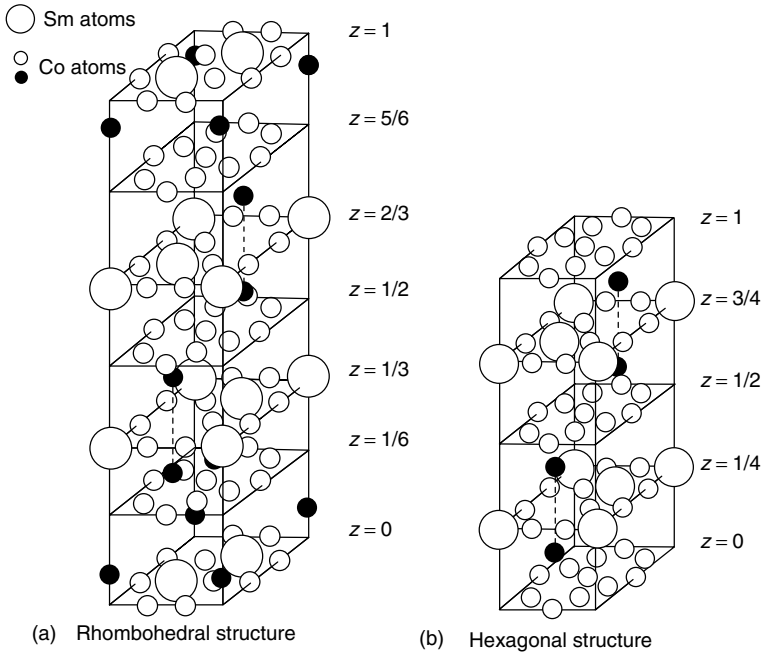

Figure 2. Sm_2Co_{17} structures. (a) rhombohedral, hR19, Th_2Zn_{17}structure type, $a = 0.8395\,\text{nm}$, $c = 1.2216\,\text{nm}$, $R\bar{3}m$ and (b) hexagonal, hP38,Th_2Ni_{17} structure type, $a = 0.8360\,\text{nm}$, $c = 0.8515\,\text{nm}$, $P6_3/mmc$.

structure is formed (Figure 3). In order to compare the structures $SmCo_5$, $SmCo_7$, Sm_2Co_{17}-R and Sm_2Co_{17}-H, the lattice parameters of each structure is related to each other according (Figure 4).

$$c_{1:5} = c_{1:7} = \frac{1}{3}c_{2:17\text{R}} = \frac{1}{2}c_{2:17\text{H}} \tag{2}$$

$$a_{1:5} = a_{1:7} = \frac{1}{\sqrt{3}}a_{2:17\text{R}} = \frac{1}{\sqrt{3}}a_{2:17\text{H}} \tag{3}$$

With the random substitution of Sm atoms by Co pairs a linear increase of the c parameter is found while the a parameter reduces slightly (Khan, 1973). In the $RECo_5$, structure the RE atoms give the main contribution to the valence electron density. As more Sm atoms are substituted by Co pairs the number of valence electrons reduces, while the reduced volume of the cell increases. The order transformation that leads to the Sm_2Co_{17} structure can be viewed as result of the better packing obtained by the Sm_2Co_{17} structure compared to the corresponding disordered $TbCu_7$-type structure.

The occurrence of a particular stacking sequence determines the stable phase at room temperature in the SmCo-magnets and therefore has important significance on the magnetic properties of the magnet. It has been found by Khan (1973) and Ray (1986) that in the Sm–Co binary phase diagram, Sm_2Co_{17} hexagonal Th_2Ni_{17} does not really occur even at high temperatures and instead a $TbCu_7$ disordered structure is formed.

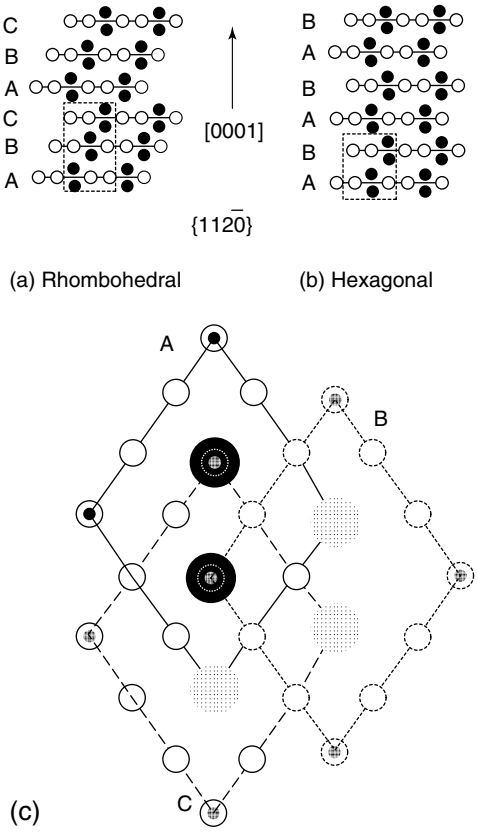

Figure 3. Stacking sequences for the (a) Th_2Zn_{17} type structure, (b) Th_2Ni_{17} structure. (c) A view along the c direction showing the different stacking positions.

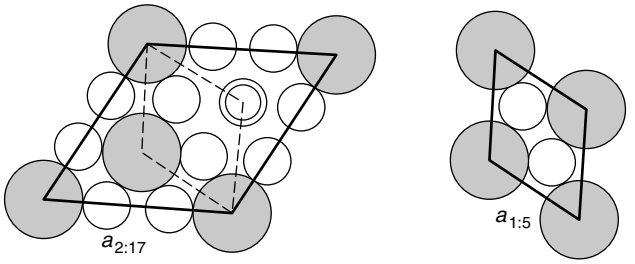

Figure 4. Basal plane of the unit cells of $SmCo_5$ and the Sm_2Co_{17} crystal structures.

The occurrence of a particular stacking sequence in a layer structure is explained in terms of energetic differences between two stacking configurations. Blandin, Friedel and Saada (1966) have shown that long-range oscillatory forces occur in metallic crystals that are related to the valence electron density. For a closed-packed structure, the different modifications only differ in the order of stacking of identical layers. This allows considering only the energy difference between closed-packed layers in different stacking environments. The difference between the energies should be enough to determine the stable stacking sequence.

Any mistake in the stacking sequence of an otherwise perfect ordered Sm_2Co_{17} layer structure will lead to a stacking fault and changes the crystallographic dependent properties around the fault. In Sm_2Co_{17}-R structure, the stacking planes are the (0001)-basal planes. When one layer of the basic structural unit is missing from the normal sequence, an intrinsic stacking fault is formed as shown in Figure 5. From the stacking fraction, the intrinsic stacking fault leads to the appearance of a hexagonal sequence of one unit cell height running as a platelet with normal parallel to the *c* axis. If instead of a missing layer, the stacking fault originates from the addition of one layer of the basic structural unit to the normal sequence, an extrinsic stacking fault is formed as shown Figure 6. In this case, the extrinsic stacking fault can lead to the formation of a hexagonal sequence running perpendicular to the c direction. Coherent twinning formed by a multiple shearing operation on the (0001) plane with the displacement vector $\frac{1}{3}\left[10\bar{1}0\right]$ also occurs, which leads to a hexagonal platelet (Figure 7).

Efforts to improve the magnetic properties of the Sm_2Co_{17} drove to the use of different substitutions for part of the Co and Sm in the magnet. To understand the effect of the substitutions in the magnetic properties of the magnet, an understanding of the anisotropy and magnetization mechanism of the Sm_2Co_{17} magnet is necessary. In $SmCo_5$ magnets the Co sublattice gives an important contribution to the total magnetic anisotropy, favoring the easy-axis anisotropy of the structure. In the case of Sm, the RE sublattice contributes significantly to the easy-axis anisotropy observed.

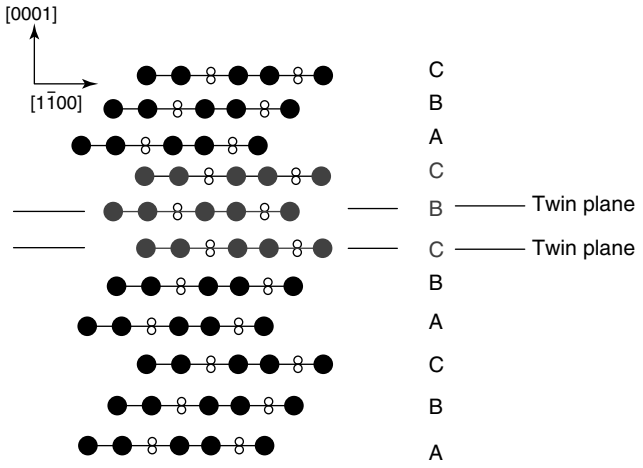

Figure 5. Intrinsic stacking fault formed by the missing of one A layer. It should be noted that, in this case, a hexagonal sequence CBC is formed with one unit cell height (Estevez-Rams, 1996).

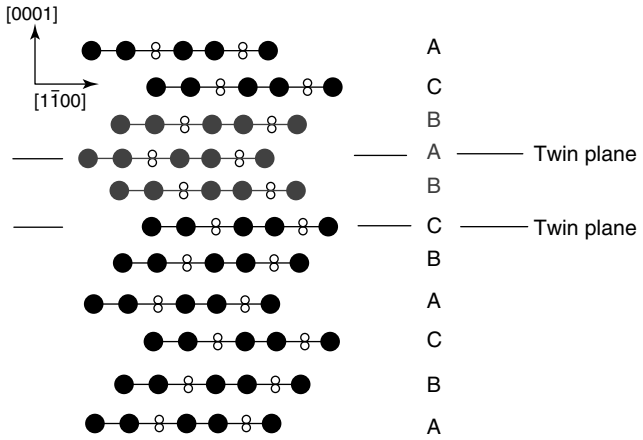

Figure 6. Extrinsic stacking fault formed by the addition of a B layer. In this case also a hexagonal stacking sequence BAB is formed (Estevez-Rams, 1996).

As temperature rises the Co contribution prevails since Sm sublattice contribution is rapidly diminished with temperature. The formation of the previously described dumbbells by substituting Sm by Co pairs, the easy-axis anisotropy decreases owing to the dumbbell contribution to easy plane anisotropy. The Sm sublattice is responsible for a strong contribution to the uniaxial anisotropy in Sm_2Co_{17} (Kumar, 1988).

Iron has been used to improve the saturation magnetization of the Sm_2Co_{17} magnets. One Fe atom is thought to preferentially substitute one Co at the dumbbell site (Perkins and Fischer, 1976; Nagamine, Rechenberg and Ray, 1990). The increased substitution of Co by iron results in a precipitation of a Co–Fe phase and in a loss of coercivity (Perry and Menth, 1975). It is also known that Sm_2Fe_{17} has an

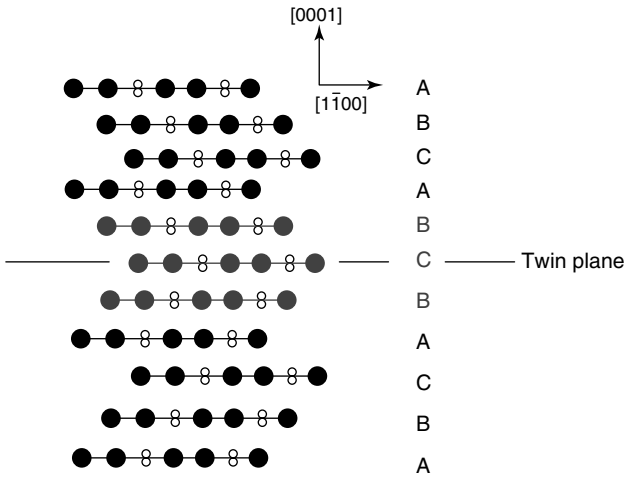

Figure 7. Coherent twinning formed by a mirror operation over a C layer. This defect also leads to a hexagonal sequence BCB (Estevez-Rams, 1996).

easy-plane anisotropy (Kumar, 1988). The Fe in the dumbbell site has a strong negative exchange interaction, which also causes a large expansion of the *c* axis with Fe content (Ray, 1986). The addition of a small amount of Zr has been found to favored a higher amount of Fe without the precipitation of the Co–Fe phase detrimental for the magnetic properties (Ojima, Tomizawa, Yoneyama and Hori, 1977). There is an on-going discussion about the exact behavior of Zr in the Sm_2Co_{17} magnets. Although it has been argued that Zr enters substituting the Sm, it is somehow accepted that Zr is substituting Co, but the exact Co position where Zr goes is still subject to discussion. Rabenberg *et al*. (1991) argues, based on extended X-ray-absorption fine-structure spectroscopy that Zr goes to the mixed plane substituting the 12j Co position. On the other hand, Ray has argued that in Fe-doped Sm_2Co_{17} magnets, Zr-vacancy pairs substitute the Fe–Fe dumbbells, based on size considerations (Ray, 1986) and in indirect evidence from Mössbauer spectroscopy (Nagamine, Rechenberg and Ray, 1990). Neutron and X-ray experiments directly support this idea showing a preference of Zr for the 6c dumbbell site (Ying-chang *et al*., 1985). Satyanarayana, Fujii and Wallace (1982) reported an alloy of $Sm_2Co_{17}Zr_1$ having the 2:17-H hexagonal modification with lattice parameters $a = 0.8558\,\text{nm}$ $c = 0.8123$ which corresponds to an interlayer distance of 0.2031 nm. This interlayer distance is below the same value for the rhombohedral structure in the Sm_2Co_{17}-R. The substitution of the Co–Co dumbbell site by a pair of Zr-vacancies will reduce the overall interlayer distance in spite of the larger size of the Zr atom compared with the Co one. The distance of the Co dumbbell from the mixed layer is influenced by the interaction between the Co pair. A Zr-vacancy pair will lie closer to the mixed plane and a smaller interlayer distance should be expected. From the analysis already made of the stability of the Sm_2Co_{17} hexagonal and rhombohedral modification, the diminishing of the interlayer distance could well explain the transformation from the rhombohedral to the hexagonal structure upon the addition of Zr. The influence of Zr in the valence electron concentration and the modification of the Fermi surface and band structure could also influence the observed behavior. In commercial Sm_2Co_{17}-type magnets, a platelet phase enriched in Zr appears upon a lengthily heat treatment precipitated inside the Sm_2Co_{17} rhombohedral matrix (Mishra *et al*., 1981). Fidler and Skalicky (1982) have indexed such phase as the hexagonal Sm_2Co_{17} structure with Zr substitution. This hexagonal structure agrees with the former analysis and appears as a result of the energetic favoring of the hexagonal stacking. The later being a result of the reduction of the interlayer distance with the substitution of the dumbbell site by Zr-vacancy pairs according to Ray proposal. Zr substitution also increases the anisotropy field (Satyanarayana, Fujii and Wallace, 1982), which is a further evidence that Zr could be substituting the Co dumbbell. The Co pair is responsible for favoring the easy plane anisotropy in the Sm_2Co_{17} structure (Kumar, 1988).

Cu improves the coercivity of the Sm_2Co_{17} magnets inducing the precipitation of a fine scale microstructure formed by cells of Sm_2Co_{17}-R surrounded by a $SmCo_5$ wall (Livingston and Martin, 1977). The improvement in coercivity is associated to a pinning mechanism on the cell walls (Nagel, 1979). Cu is considered to be completely soluble in $SmCo_5$ and an isostructural $SmCu_5$ is known (Nishida and Uehara, 1974; Katayama and Shibata, 1973). Others have reported a decomposition into two 1:5 structures (Hofer, 1970). Careful studies of the phase diagram for the ternary Sm–Co–Cu system were carried out by Perry (1977), who demonstrated that Cu stabilizes the $SmCo_5$ structure changing the peritectic line for the $SmCo_5$ to a eutectic one. He also found that Cu inhibits the appearance of Sm_2Co_{17} phases. Little solubility of Cu in this structure is also been shown. The destabilization of the Sm_2Co_{17} structures with Cu can be a result of the transformation of the band structure and valence electron density upon the addition of Cu in the Sm_2Co_{17} material. The binary phase diagram of Fe–Cu and Co–Cu shows little to no solubility of Cu in Co and Fe. The later, has been taken as indication that the atoms of Cu and Fe have a repulsive interaction.

Real Sm_2Co_{17} magnets are complex system formed by at least five components and with a complicated metallurgical behavior. Figure 8 shows a heavily faulted rhombohedral $Sm_2(Co,Fe)_{17}$ matrix phases. The magnetic properties of these magnets strongly depend on the composition and processing conditions of the alloy. Morita and coworkers

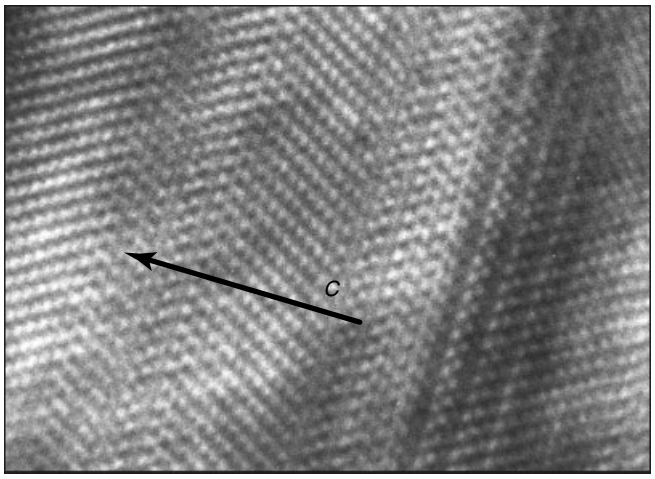

Figure 8. TEM images showing the heavily faulted regions within the rhombohedral $Sm_2(Co,Fe)_{17}$ matrix phase in a $Sm(Co,Fe,Cu,Zr)_{7.5}$ hard-magnet material.

have studied the $Sm(Co, Cu, Fe)_z$ and $Sm(Co, Cu, Fe, Zr)_z$ phase diagrams (Morita, Umeda and Kimura, 1987). According to their result, it is obvious that with the increase of Zr the homogeneity range of the Th_2Ni_{17} hexagonal structure increases. The extension of the homogeneity range for the 2:17 phase in both sides of the stoichiometry 10.5 at% Sm, while observing that with the increase of Sm, the Th_2Ni_{17} structure transforms to the disordered $TbCu_7$. At the solutionizing temperature the alloy is in a disordered $TbCu_7$ state. This state is a complex state retaining the $R\bar{3}m$ symmetry but with random occupation of dumbbell sites by TM pairs, Zr-vacancy pairs and excess Sm atoms. Such metastable state can be retained by a sufficiently quick cooling from the solutionizing temperature in order to avoid the segregation of more energetically favorable equilibrium phases upon cooling. The step aging allows the precipitation of a 1:5 cell boundary phase enriched in Cu, while precipitating a Zr-rich platelet phase believed to be a Th_2Ni_{17} hexagonal structure. The cell phase is a Sm_2Co_{17}-R, Th_2Zn_{17}, Fe enriched phase. The platelet phase and the cell boundary phase are believed to be formed cooperatively, acting the platelets as diffusion path for the Cu. The binary phase diagram shows no solubility of Co in Fe this indicates an unfavorable mixing enthalpy for both atoms and a repulsion interaction. We therefore believe that the platelet Th_2Ni_{17} phase where Fe dumbbell pairs are substituted by Zr-vacancy pairs can effectively act as diffusion path. The platelet cell c parameter was determined by Fidler, Skalicky and Rothwarf (1983) to be 0.8 nm. In the rhombohedral structure, were Fe–Fe pairs occupy the dumbbell site, the repulsive interaction between Fe atoms and Cu atoms impedes an effective diffusion of Cu.

3 CRYSTAL STRUCTURES AND MAGNETIC PROPERTIES OF RE–TM–B INTERMETALLICS

Besides the binary phases also ternary RE–TM intermetallic compounds are candidates for hard magnetic phases. Considerable technological interest has centered on $RE_2Fe_{14}B$ compounds because of their excellent intrinsic properties, such as saturation magnetization and magnetocrystalline anisotropy over Sm–Co materials. Practically magnets with energy products up to the $450\,kJ\,m^{-3}$ ($\approx 56,7$ MG Oe) range, have been prepared from melt-spun (Lee, Brewer and Schaffel, 1985; Croat, 1989) and sintered (Sagawa *et al*., 1987; Kaneko and Ishigaki, 1994; Rodewald, Wall, Katter and Uestuener, 2002) alloys. The spectrum of applications for Nd–Fe–B magnets continues to expand. On the scientific side, the existence of an entire $RE_2Fe_{14}B$ series has stimulated a great deal of research on their properties and the physics underlying those properties (Herbst, 1991).

The ternary Nd–Fe–B phase diagram was investigated by Schneider, Henig, Petzow and Stadelmaier (1986) following investigations of Stadelmaier, Elmasry, Liu and Cheng (1984) and Matsuura *et al*. (1985). The original nominal composition for the preparation of $Nd_2Fe_{14}B$-based sintered permanent magnet is $Nd_{15}Fe_{77}B_8$ (Sagawa *et al*., 1984a,c) which is richer in Nd than the stoichiometric composition of the hard magnetic phase $Nd_2Fe_{14}B$. This composition lies in the liquid plus $Nd_2Fe_{14}B$ plus $Nd_{1+\varepsilon}Fe_4B_4$ region. The crystal structure of $Nd_2Fe_{14}B$ is a tetragonal phase belonging to space group $P4_2/mnm$ with crystal parameters $a = 0.88$ nm and $c = 1.21$ nm whose crystallographic unit cell is shown in Figure 9 (Fuerst, Herbst and Alson, 1985; Herbst, Croat and Yelon, 1985). The excess of Nd in the starting material is provides the liquid Nd-rich phase at sintering temperature which enables the densification of the magnet by liquid phase sintering process. The phase forms an intergranular nonmagnetic phase during the cooling process, which magnetically decouples the $Nd_2Fe_{14}B$ grains. According the ternary phase diagram a third phase is formed which is $Nd_{1+\varepsilon}Fe_4B_4$($P4_2/ncm$, tP328, $a = 0.7117$ nm, $c = 3.507$ nm). This phase is detrimental to the hard magnetic properties of the magnet due to the further reduction of remanence and originating strong internal demagnetizing stray fields.

Comparable hard magnetic properties can be also obtained with $Pr_2Fe_{14}B$, but the Nd compound has received more attention as a magnet material, because it has higher saturation magnetization leading to higher remanence and energy density product. Table 2 compares the saturation magnetization J_s, anisotropy field H_A, easy direction of magnetocrystalline anisotropy and Curie temperature T_C of the $RE_2Fe_{14}B$

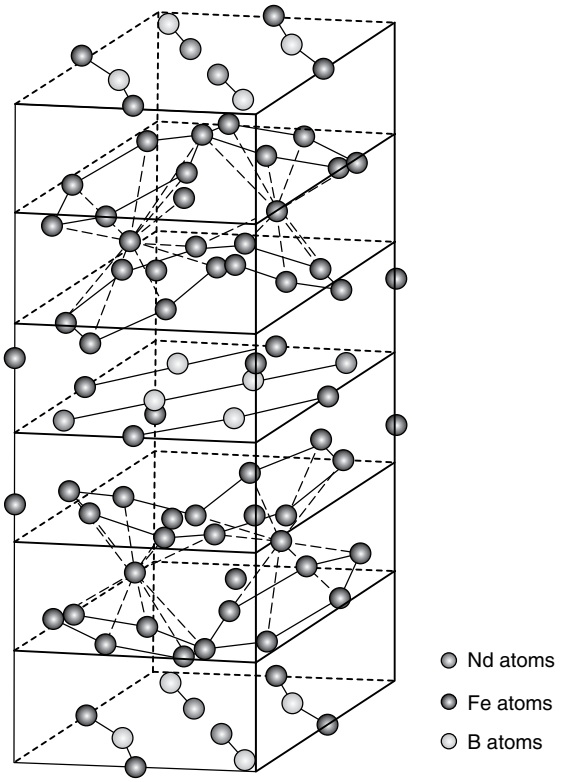

Figure 9. Crystal structure of the $Nd_2Fe_{14}B$ phase (tetragonal, $P4_2/mnm$ tP68).

Table 2. Intrinsic magnetic properties of $RE_2Fe_{14}B$-compounds at room temperature (Herbst, 1991).

Alloy	J_s(T)	H_A(kA m^{-1})	Anisotropy direction	T_c(K)
$La_2Fe_{14}B$	1.38	1600	[001]	530
$Ce_2Fe_{14}B$	1.17	2080	[001]	424
$Pr_2Fe_{14}B$	1.56	6000	[001]	565
$Nd_2Fe_{14}B$	1.60	5840	[001]	585
$Sm_2Fe_{14}B$	1.52	>12000	<100>	616
$Gd_2Fe_{14}B$	0.89	1920	[001]	661
$Tb_2Fe_{14}B$	0.70	17600	[001]	620
$Dy_2Fe_{14}B$	0.71	12000	[001]	598
$Ho_2Fe_{14}B$	0.81	6000	[001]	573
$Er_2Fe_{14}B$	0.90	640	<100>	554
$Tm_2Fe_{14}B$	1.15	640	<100>	541
$Yb_2Fe_{14}B$	1.20		[001]	524
$Lu_2Fe_{14}B$	1.17	2080	[001]	535
$Y_2Fe_{14}B$	1.41	2080	[001]	565
$Th_2Fe_{14}B$	1.41	2080	[001]	481

compounds (Herbst, 1991). It is obvious that all, except the Sm, Er, and Tm compounds show easy-axis anisotropy at room temperature.

In addition to the similarities with simpler TM-metalloid materials, many structural parallels exist between $RE_2Fe_{14}B$ and other RE–TM systems. Analogies with the hexagonal $CaCu_5$ structure characterizing the permanent-magnet compound $SmCo_5$ and a variety of other RE–TM phases include the hexagonal arrays of Fe atoms in $R_2Fe_{14}B$ are the cognates of the TM arrays in $RETM_5$. Both form hexagonal prisms enclosing the RE atoms. Givord, Li and Moreau (1984) have emphasized that the B and Fe sites of $RE_2Fe_{14}B$ correspond to the TM and RE sites, respectively, in $RETM_5$. Given the similarities of $RETM_5$ and $RE_2Fe_{14}B$ on the one hand and of $RETM_5$ and RE_2TM_{17} on the other, it is not surprising that many parallels exist between $RE_2Fe_{14}B$ and RE_2TM_{17}, especially the presence of hexagonal TM nets surrounding RE atoms in each structure.

The $RE_2Fe_{14}B$ structure has been found to form with yttrium, thorium, and all the rare-earth elements except europium and radioactive promethium (Herbst, 1991). Lattice parameter measurements show that the effect of the lanthanide contraction, the decrease in the radii of the trivalent lanthanide ions with increasing atomic number, is apparent in the decrease of the *c*lattice parameter through the RE (La–Lu) series. As the atomic number increases, the addition of another electron to the 4f shell does not completely screen the larger nuclear charge, and the radius of the RE ion contracts. The crystallographic work on $Nd_2Fe_{14}B$ and neutron studies indicate that the nuclear position parameters change minimally through the series. Only two families of $Nd_2Fe_{14}B$-type compounds are known in which Fe or B is totally replaced by another element, namely, $RE_2Co_{14}B$ (Buschow, van Noort and de Mooij, 1985) and $RE_2Fe_{14}C$ (de Boer *et al.*, 1988). Partial substitution of RE, Fe, or B with maintenance of the $RE_2Fe_{14}B$ structure is possible with many other elements, and $RE_2Fe_{14}BH_C$ and $RE_2Co_{14}BH_x$ interstitial hydride series exist (Cadogan and Coey, 1986; Gutfleisch and Harris, 1996).

4 MICROSTRUCTURE AND COERCIVITY OF RARE-EARTH PERMANENT MAGNETS

Magnetic materials and their applications have been known for many centuries. Nowadays permanent magnets are used in numerous domestic and professional appliances such as consumer electronics, computer peripherals, and telecommunications. The growing demand for miniaturization in modern technology requires the further development of permanent magnets. Smaller and stronger permanent magnets allow the construction of small devices by replacing electromagnets or less powerful permanent magnets.

The increase in applications of permanent magnets goes hand in hand with the discovery and development of progressively more powerful permanent magnets during this century. The most common figure of merit for the performance of a permanent magnet is the maximum energy density product $(BH)_{max}$, which is proportional to the magnetic field that is produced outside a unit volume of magnetic material. Thus $(BH)_{max}$ is a measure for the potential to reduce the size and weight of a magnetic device. The greater $(BH)_{max}$ the smaller the magnet to produce a field of a given value. The enormous reduction in the size of permanent magnets achieved owing to the discovery of new classes of materials that exhibit increasing $(BH)_{max}$ values. The resulting magnetic field in the air gap H_{ag} is direct proportional to the volume of the magnet V_m and the stored energy density product $(B_m \cdot H_m)$ and indirect proportional to the volume of the air gap V_{ag} according to

$$H_{ag} \approx \sqrt{\frac{V_m \cdot (B_m \cdot H_m)}{\mu_0 \cdot V_{ag}}} \tag{4}$$

A magnet should be shaped for the most efficient use in such a way that its operating point is close to the $(BH)_{max}$ point. It is evident that the increase of the energy density product reduces besides the volume also the weight of the permanent magnet-containing device, and new designs of static, such as charged beam guiding systems, and dynamic devices are possible.

Besides the Curie temperature, the energy density product, also the remanence that determines the maximum flux density within the air gap of a magnetic circuit and the coercive field are necessary to distinguish and describe different permanent-magnet materials. For practical applications also the temperature coefficients of the remanence and the coercive field are important parameters, which considerably vary in different types of magnets. The RE–intermetallic phases with a high uniaxial magnetocrystalline anisotropy, such as $SmCo_5$, Sm_2Co_{17} and $Nd_2Fe_{14}B$ are the basis for high-performance RE magnets (Strnat *et al*., 1967; Sagawa *et al*., 1984a; Croat, Herbst, Lee and Pinkerton, 1984b; Herbst, 1991). Sm–Co magnets exhibit the highest coercive fields ${}_JH_C$ and $Nd_2Fe_{14}B$-based magnets show the highest value of remanence B_r and energy density product $(BH)_{max}$, obtained so far. RE magnets are divided into the group of the so-called single-phase, nucleation-controlled magnets, based on the $SmCo_5$ or $Nd_2Fe_{14}B$ hard magnetic phases, and into the group of domain wall pinning controlled, multiphase magnets. Two-phase magnets, which are nowadays also used in high-temperature advanced power applications consist of a continuous $Sm(Co,Cu)_{5-7}$ cellular precipitation structure within a $Sm_2(Co,Fe)_{17}$ matrix phase. Nanocrystalline RE magnets exhibit microstructures of single-phase, two-phase, and multiphase character, in which the inhomogeneous magnetization behavior near the intergranular regions creates remanence enhancement. Table 3 compares the magnetocrystalline anisotropy K_1 and saturation polarization J_s together with the maximum theoretical energy density product $(BH)^{th}_{max}$ and Curie temperature of the most important RE–intermetallic compounds for hard magnets.

Table 3. Comparison of the magnetocrystalline anisotropy K_1, saturation polarization J_s, the maximum theoretical energy density product $(BH)^{th}_{max}$, and Curie temperature T_C of the most important rare-earth–intermetallic compounds for hard magnets.

Hard phase	K_1(MJ m^{-3})	J_s(T)	(BH^{th}_{max}) (kJ m^{-3})	T_C(°C)
$Nd_2Fe_{14}B$	4.9	1.61	516	310
$Sm_2Fe_{17}N_3$	8.9	1.54	472	477
$SmCo_5$	17.0	1.05	219	727
Sm_2Co_{17}	3.9	1.30	336	916

In Hoffer and Strnat (1966) discovered a new family of magnetic materials for permanent magnets that showed an extremely high magnetocrystalline anisotropy, an important requirement for obtaining a high coercivity. The new family of material based on $RECo_5$ was the first family of the RE–intermetallic magnets. For the $RECo_5$, the most important representative was $SmCo_5$. In RE–intermetallic magnets the RE provides mainly the magnetocrystalline anisotropy necessary for achieving high coercivities, while the TM mainly raises the magnetization. A second family of RE–TM magnets was soon discovered being the main representative Sm_2Co_{17}. The increase of Co in the Sm_2Co_{17} compared with the $SmCo_5$ compound had the advantage of raising the magnetization, but the crystalline anisotropy lacked behind the $SmCo_5$, efforts were then directed to raise the coercivity of magnets based on such compound in order to increase the $(BH)_{max}$ energy product. The coercivity was improved by a time consuming and complex heat treatment, after the addition of minor amounts of Cu and Zr that also allowed the raise of the magnetization by the substitution of part of the Co by Fe. A review on Sm–Co-based permanent-magnet material based on RE–Co is given by Strnat (1988) and Kumar (1988). The expensiveness of Co together with the scarcity of Sm led to efforts toward the substitution of both elements, Fe was the best candidate due to its larger contribution to magnetization than Co. This leads in 1983 to the discovery of a new family of materials showing large magnetocrystalline anisotropy and therefore good candidates for permanent magnets. The new material discovered by Sagawa *et al*. (1984b,c), Croat, Herbst, Lee and Pinkerton (1984a,b), and Hadjipanayis, Hazelton and Lawless (1983) was based in the ternary compound $Nd_2Fe_{14}B$

and large energy products, higher than 360 kJ m^{-3} at room temperature, was achieved in 1984. Nowadays the maximum energy density product of $Nd_2Fe_{14}B$-based permanent magnets have been gradually increased to values exceeding 450 kJ m^{-3} (Kaneko, 2000; Rodewald, Wall, Katter and Uestuener, 2002, 2003; Khlopkov *et al*., 2004). Figure 10 shows the increase of the maximum energy density product together with the increase of coercive field achieved during the last 100 years. It should also be noted that the low Curie temperature of the $Nd_2Fe_{14}B$ hard magnetic phase strongly determines the maximum application temperature of the magnet.

The characteristic property of permanent magnets is the magnetic 'hardness', the extent to which the material retains its magnetization in opposing fields. A measure for the magnetic hardness is the coercive field $_JH_C$, which has been drastically increased by the invention of the RE-based permanent magnets (Figure 10). To obtain a large energy product, both a high coercive field and a high spontaneous magnetization are required. Magnetic hardening is either obtained by shape anisotropy or by magnetocrystalline anisotropy. Permanent magnets up to the beginning of this century had consisted mainly in magnetic steels containing cobalt, carbon, tungsten additives and exhibited a low coercivity and low-energy products. In 1930, the Alnico magnets with $(BH)_{max}$ were introduced, made mainly of a combination of nickel, cobalt, and aluminum while in 1950 the ferrites were developed with a lower coercivity than the Alnico magnets but also at a lower production cost. The magnetic hardness of Alnico magnets (Enz, 1982; Kneller, 1962) originates from shape anisotropy. They are based on the precipitation of elongated ferromagnetic FeCo particles in a less magnetic AlNi matrix. The magnetocrystalline anisotropy of Ba hexaferrites (Rathenau, 1953) is considerably larger than the shape anisotropy of Alnicos. Because of their high coercive field and their low price, they are the most commonly used magnets nowadays. A disadvantage of the ferrites is their small spontaneous magnetization. Excellent candidates for high-quality magnets are RE–TM compounds where the RE component accounts for the high magnetocrystalline anisotropy and the TM provides a high magnetization. Sintered magnets based on Sm–Co compounds show excellent magnetic properties (Strnat, 1988). Because of the higher content of cobalt, the spontaneous magnetization also increases and therefore the energy density product of Sm_2Co_{17}-based magnets is even higher than the one of $SmCo_5$ magnets. $Nd_2Fe_{14}B$-based magnets exhibit a large uniaxial anisotropy as well as a high spontaneous magnetization that leads to the largest energy density products measured so far.

The direction of magnetization of a permanent magnet can be reversed either continuously, through coherent or incoherent rotation processes, or discontinuously, through dynamic domain processes. The coercivity is determined by the easiest of these processes. In modern RE permanent magnets, the magnetization rotation is impeded by the magnetocrystalline anisotropy. The nucleation field (Stoner and Wohlfarth, 1948)

$$H_{nuc} = \frac{2K_1}{J_s} \tag{5}$$

determines the maximum coercivity. As the coercive field of a real magnet is limited by the fact that the grain diameter exceeds the theoretical single-domain diameter, it is clear that the magnetization reversal process is controlled by the nucleation and expansion of reversed magnetic domains and not by rotation processes only.

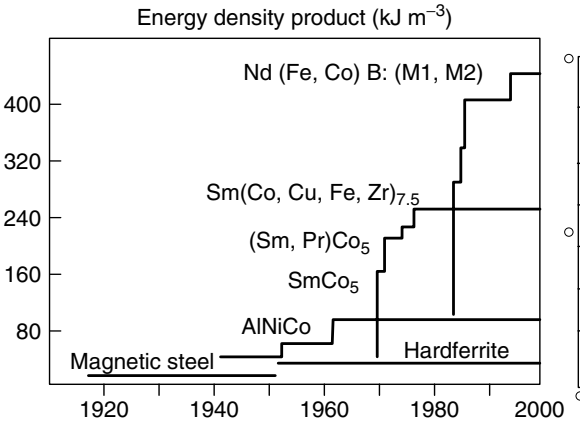

Magnet	Year	$_JH_c$ (kA m^{-1})	T_c (°C)
Magnetic steel	1890	1	
AlNiCo	1955	100	850
Hardferrite	1960	200	450
Sm Co 1:5	1975	3000	720
Sm Co 2:17	1982	2000	820
Nd Fe B	1990	1500	310

Figure 10. Historical development of the maximum energy product $(BH)_{max}$ and the coercive field $_JH_c$ in permanent-magnet materials since 1900. The low Curie temperature T_C of the $Nd_2Fe_{14}B$ limits the maximum operating temperature of Nd–Fe–B-type magnets.

The coercive field of the so-called nucleation-controlled magnets, such as $SmCo_5$ and $Nd_2Fe_{14}B$-type, is well-described by the universal relation (Kronmüller, 1987; Sagawa and Hirosawa, 1987)

$$\mu_0 H_c = \mu_0 \frac{2K_1}{J_s}\alpha - N_{eff} J_s \tag{6}$$

The first and second terms of equation (3) represent modified magnetocrystalline and demagnetizing fields, where α and N_{eff} correspond to microstructural parameters that describe the effect of the microstructure on these effective fields and which in turn may depend on the intrinsic material parameters. The parameter α mainly describes the reduction of the nucleation field due to lattice defects or the disorder at the grain surfaces (Kronmüller and Fähnle, 2003), whereas N_{eff}, accounts for the effective demagnetizing factor by internal enhanced stray fields at the grain edges and corners. Both effects lead to a reduction of H_c.

If the coercive field obeys the condition

$$|{}_J H_c| \geq \frac{1}{2 \cdot \mu_0} \cdot J_r \tag{7}$$

the maximum energy density product depends only on the remanence J_r assuming a perfectly squared demagnetization curve of the magnet, and is given by:

$$(B \cdot H)_{max}^{theor.} = \frac{1}{4 \cdot \mu_0} \cdot J_r^2 \tag{8}$$

In this case, the residual flux density $B_r = J_r$ is expressed as the following equation:

$$J_r = J_s \cdot \frac{\rho}{\rho_0} \cdot V_{hm} \cdot F_{hm} = J_s \cdot \frac{\rho}{\rho_0} \cdot V_{hm} \cdot \cos\theta \tag{9}$$

where, J_s is the saturation magnetization of the hard magnetic phase (1.61 T), V_{hm} and F_{hm} are the volume fraction and the degree of alignment of the hard magnetic grains, respectively. In order to enhance J_r and therefore the energy density product, it is necessary to avoid pores and to densify the magnets up to the theoretical value ρ_0, increase the volume fraction V_{hm} and achieve a high degree of alignment F_{hm}. The theoretical value of the maximum energy product of $Nd_2Fe_{14}B$-based magnets is calculated to be $516\,kJ\,m^{-3}$ (64 MG Oe) assuming 100% perfect alignment and 100% volume fraction of the hard phase. The origin of this magnetic property lies in the $Nd_2Fe_{14}B$ ternary tetragonal compound as a main phase. In addition, according to the ternary Nd–Fe–B phase diagram this magnet also contains a certain amount of $Nd_{1.1}Fe_4B_4$-phase and an Nd-rich phase, which is essential for sintering with liquid phase. In order to densify the magnets up to the theoretical density, it is very important to control the composition of magnets thus generating sufficient amount of liquid phase at sintering. Furthermore, controlling the volume fraction of the constituent phases is indispensable for enhancing the residual flux density (B_r) and to keep the intrinsic coercivity (${}_J H_c$) stable.

4.1 Nucleation-controlled rare-earth magnets

The coercive field of $SmCo_5$- and $Nd_2Fe_{14}B$-based magnets is determined by the high uniaxial magnetocrystalline anisotropy as well as the magnetostatic and exchange interactions between neighboring hard magnetic grains. The long-range dipolar interactions between misaligned grains are more pronounced in large-grained magnets, whereas exchange coupling reduces the coercive field in small-grained magnets. The basic microstructural feature of polycrystalline $SmCo_5$- or $Nd_2Fe_{14}B$-based magnets is the individual hard magnetic grain with its size, shape, and orientation parameters. The ideal microstructure of the so-called single-phase magnets consists of aligned single-domain hard magnetic particles. Strictly speaking, in reality these magnets show a complex, multiphase microstructure with various types of intergranular phases according to their phase diagram and phase relations. The amount of each phase and their distribution within polyphase materials are perhaps the most complex of the microstructural parameters. The occurrence of the multiphase microstructure is one of the reasons why the coercive field of the magnets according to the magnetocrystalline anisotropy field of the hard phase, such as $30.7\,MA\,m^{-1}$ for $SmCo_5$ and $6.05\,MA\,m^{-1}$ for $Nd_2Fe_{14}B$, is never reached in practice.

The microstructure of single-phase, anisotropic $SmCo_5$-type magnets consists of grains oriented parallel to the alignment direction. Most of the $SmCo_5$ grain interiors show a low defect density. The grain diameter exceeds the theoretical single-domain size and is in the order of 5–10 µm. Besides $SmCo_5$-grains also grains with densely packed, parallel stacking faults perpendicular to the hexagonal c axis are observed. Such basal stacking faults correspond to a transformation of the $SmCo_5$-crystal structure into the Sm-rich Sm_2Co_7 and Sm_5Co_{19} structure types. Using high-resolution electron microscopy together with X-ray microanalysis, the different polytypes and structural modifications of these Sm-rich phases are characterized. Incoherent precipitates with diameters up to 0.5 µm were identified as Sm_2O_3- or CaO-inclusions. In $SmCo_5$-type sintered magnets, the coercivity is determined by the nucleation field of reversed domains which is lower than the coercive field of a magnetically saturated particle with a single-domain structure and nucleation by the expansion field of the reversed domains. The nucleation of reversed domains takes place in regions

with low magnetocrystalline anisotropy. RE-rich precipitates mainly deteriorate the ${}_{\mathrm{J}}H_{\mathrm{c}}$ of the final magnet. The reason for the formation of these phases is due to the addition of a RE-rich sintering aid phase before the sintering process. The coercivity can be improved by adding small amounts of TM powders or TM oxides. Transmission electron micrographic (TEM) studies shows that the chemical composition, the size distribution and the impurity content (oxygen content) of the starting powder material are important factors for the magnetic properties of $SmCo_5$-type sintered magnets. For lower cost magnets samarium is partly substituted by a mixture of cerium-mischmetal elements or for improved magnetic properties by praseodymium, thus three groups of $SmCo_5$-type sintered magnets are distinguished, (CeMM,Sm)Co_5 with low J_{s}, and $(BH)_{\max}$, $SmCo_5$ with high ${}_{\mathrm{J}}H_{\mathrm{c}}$ and (Pr,Sm)Co_5 with high $(BH)_{\max}$ values. Microstructural investigations on sintered magnets of the type (CeMM,Sm)Co_5 and (Pr,Sm)Co_5 showed similar results as in the case of $SmCo_5$ sintered magnets. The corresponding X-ray spectra of the different phases showed a mixture of RE elements due to their ratio of the nominal composition of the magnet.

High-performance $Nd_2Fe_{14}B$-based permanent magnets are produced with different composition and various processing techniques, which influence the complex, multiphase microstructure of the magnets, such as size and shape of grains, the orientation of the easy axes of the grains, and the distribution of phases. Formation and distribution of the phases are determined by the composition of the magnets and the annealing treatment. Especially grain size and the alignment of the grains strongly depend on the processing parameters. Grain sizes in the range between 10 and 500 nm are obtained by melt-spinning, mechanical alloying, and the HDDR (hydrogenation-disproportionation-desorption-recombination) process (Harris, 1992). Sintered and hot worked magnets exhibit grain sizes above 1 µm. The powder metallurgical sintering route is the most important preparation technique for RE permanent magnets and consists of the following production steps: melting of the alloy under vacuum, crushing, milling, alignment in magnetic field, pressing, sintering, annealing, machining, and coating.

The processing route of the magnet strongly influences the grain size and grain size distribution. The coercive field in sintered magnets strongly depends on the sintering parameters, such as temperature and time. Nanocrystalline and submicron magnets are obtained by the melt-spinning route, or by mechanically alloying, or by the HDDR process (Harris, 1992; Cadogan and Coey, 1986). Hot pressing and die upsetting of Nd–Fe–B ribbon materials reveals a densely packed, anisotropic magnetic material. Platelet-shaped grains with diameters less than 1 µm are observed by TEM-investigations. The degree of orientation of the platelets, which are stacked transverse to the press direction

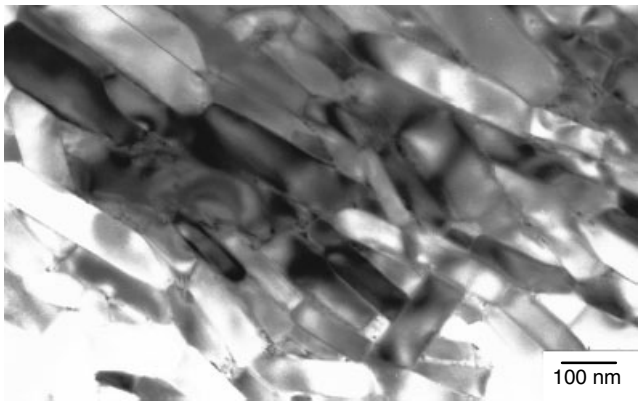

Figure 11. Microstructure of a melt-spun MQ3-type $Nd_{14}Fe_{72}Co_7B_6Ga_1$ magnet ($J_{\mathrm{r}} = 1.32\,\mathrm{T}$, ${}_{\mathrm{J}}H_{\mathrm{c}} = 1241\,\mathrm{kA\,m^{-1}}$).

with the easy c axes perpendicular to the face of each grain, determines the remanence and coercive field of the magnet (Mishra, 1987). The degree of alignment, size and shape of the grains, and the intergranular regions within the ribbons control the macroscopic magnetic properties. Die upsetting modifies the spheroidal grains after hot pressing to platelets as shown in the TEM images of Figure 11. Misaligned grains, which are clearly visible, deteriorate the remanence. The c axis for each grain runs perpendicular to the straight elongated edge. Nd-rich phase is found among the platelet-shaped grains as a fine layer between the straight edges or as pockets at the end of the platelets or between the misaligned and aligned grains. On the other hand, the magnets with a lower remanence show a microstructure with more equiaxed grains. In most of the melt-spun magnets regions with abnormally grown, large grains were found. Some of these grains were fully developed, platelet-shaped grains.

Substituent and dopant elements influence the microstructure, coercivity, and corrosion resistance of advanced (Nd,S1)-(Fe,S2)-B:(M1,M2) magnets. The replacement of the Nd-rich intergranular phase by secondary phases formed after doping by M1 and M2 type elements improves the corrosion resistance, especially in large-grained magnets. The multicomponent composition of the magnets leads to the formation of nonmagnetic and soft magnetic phases. Generally, two types of substituent elements, which replace the RE element or the transition element sites in the hard magnetic phase, and two types of dopant elements are distinguished (Fidler and Schrefl, 1996). Substituent elements mainly change the intrinsic properties such as spontaneous magnetic polarization, Curie temperature, and magnetocrystalline anisotropy. Depending on the type, the dopant elements, which show a low solubility within the hard magnetic phase, form additional intergranular rare-earth-containing or boride phases. These phases change the coupling behavior between the hard magnetic grains. Nonmagnetic intergranular

phases eliminate the direct exchange interaction and also reduce the long-range magnetostatic coupling between the hard magnetic grains; both effects lead to an increase of the coercive field. On the other hand, the decrease of the volume fraction of the hard magnetic phase within the magnet decreases the remanence. Insufficient temperature stability and poor corrosion resistance are the main factors limiting applications of $Nd_2Fe_{14}B$-based magnets. Secondary non-magnetic phases, which replace the Nd-rich intergranular phase, considerably improve the corrosion resistance and are of great technological interest.

Nd–Fe–B-based permanent magnets with a composition close to $Nd_{15}Fe_{77}B_8$ exhibit a complex multiphase microstructure. According to the ternary phase diagram at least three equilibrium phases occur, the hard magnetic $Nd_2Fe_{14}B$ phase, the boride phase $Nd_{1+\varepsilon}Fe_4B_4$ and the low melting Nd-rich phase. Other phases, such as Fe-rich and Nd oxides, and pores are found depending on the composition and processing parameters. Selected substituent elements replace the Nd atoms (S1 = Dy,Tb) and the Fe atoms (S2 = Co,Ni,Cr), respectively, in the hard magnetic phase and considerably change intrinsic properties, such as the spontaneous polarization, the Curie temperature and the magnetocrystalline anisotropy. The formation of intermetallic, soft magnetic Nd-(Fe,S2) phases, such as the Laves type $Nd(Fe,S2)_2$-phase, deteriorate the coercivity of the magnets. If dopant elements M1 or M2 are added to Nd–Fe–B, in some cases the coercivity is increased and the corrosion resistance is improved. This is the case, if the Nd-rich intergranular phase is replaced by other phases, such as $AlNd_6Fe_{13}$ and Nd_3Co. Our previous, systematic TEM-studies performed on sintered, melt-spun, mechanically alloyed, and hot worked magnets have shown that two different types of dopants can be distinguished independently of the processing route. Both types influence the microstructure in a different way (Bernardi, Fidler and Fodermayr, 1992; Bernardi and Fidler, 1994). Type 1 dopants (M1 = Al, Cu, Ga) form binary M1–Nd or ternary M1–Fe–Nd phases, and Type 2 dopants (M2 = Ti, Zr; V, Mo; Nb, W) form binary M2–B or ternary M2–Fe–B phases. The processing route of the magnet strongly influences the grain size and grain size distribution. The coercive field in sintered magnets strongly depends on the sintering parameters, such as temperature and time. Nanocrystalline and submicron magnets are obtained by the melt-spinning route, or by mechanically alloying, or by the HDDR process (Nakayama *et al*., 1994; Buschow, 1988; Gutfleisch and Harris, 1996). Hot pressing and die upsetting of Nd–Fe–B ribbon materials reveals a densely packed, anisotropic magnetic material. Platelet-shaped grains are observed by TEM-investigations. The degree of orientation of the platelets, which are stacked transverse to the press direction with the easy *c* axis perpendicular to the face of each grain, determines the remanence and coercive field of the magnet.

Nd–Fe–B sintered magnets possessing outstanding magnetic properties have developed into a major permanent-magnet material in the 20 years since their invention. The drastic increase of the energy density product of newly developed $Nd_2Fe_{14}B$-based magnets enabled the invention of many new applications of permanent magnets. In the conventional powder metallurgical sintering process it is very important to keep the processing atmosphere either in a vacuum or in an inert gas because RE elements such as Nd, Pr, and Dy, which are essential for fabrication of Nd–Fe–B magnets are easily oxidizable. Several authors have reported to obtain $Nd_2Fe_{14}B$-based magnets with energy density product $>440\,kJ\,m^{-3}$ (Kaneko, 2000; Fidler, Sasaki and Estevez-Rams, 1999; Rodewald, Wall, Katter and Uestuener, 2002, 2003) by keeping the oxygen content low (Sagawa *et al*., 1987), using the powder mixing technique (Otsuki, Otsuka and Imai, 1990), increasing the magnetizing field and reducing the pressure during compaction (Endoh and Shindo, 1994) or using the rubber isostatic pressing (RIP) technique to improve the orientation of the particles in the green compact to obtain sintered magnets with perfect orientation. The increasing demand for highest energy density magnets ($>400\,kJ\,m^{-3}$), especially for voice coil motors in hard disc drives and for magnetic circuits for magnetic resonance imaging devices, needs an efficient manufacturing process for $Nd_2Fe_{14}B$ sintered magnets with improved energy density product. A new technology–RIP–has been developed by Sagawa and Nagata (1993) and Sagawa, Nagata, Itatani and Watanabe (1994) to improve the orientation of the particles in the green compact to obtain sintered magnets with perfect orientation. RIP is one of the key technologies to approach for the theoretical limit, 64 MG0e at room temperature, of the magnets based on $Nd_2Fe_{14}B$. In RIP, magnet powder is subjected to such a strong ulsed field just before the compaction that the powder in the rubber mold is thoroughly oriented. Then the powder is compacted isostatically, while the orientation is completely held. In the conventional die pressing that uses no rubber molds, the pressure applied to the powder is uniaxial. The uniaxial pressure tends to disturb the orientation of the particles during the pressing. To prevent this orientation disturbance, the powder has to be subjected to a strong magnetic field throughout the pressing. This is one of the reasons why a pulsed field cannot be adopted for the conventional die pressing. The high orientation of the magnet produced by RIP is attributed to the application of a strong pulsed field that dissolves the agglomeration of the magnet powder particles, and then, impulsively orients the particles by isostatic pressing that holds the orientation high during the pressing. The misalignment of the hard magnetic grains with a diameter of 2–5 μm is in the best case in the order $<14\,^{\circ}C$.

The oxygen content of the magnets has to be reduced from values of 4000–6000 ppm to a value <1000 ppm. A high oxygen content is one limiting factor to decrease the Nd-content in order to improve the volume fraction of the hard magnetic phase. The squareness of the demagnetization curve and the coercive field drastically decreases as abnormal grain growth (AGG) of the $Nd_2Fe_{14}B$ grains occurs (Rodewald, Wall, Fernengel and Rodewald, 1997).

Remanence and energy product increase with decreasing Nd-content, whereas the coercive field shows its highest value at a high Nd-content. In the case when the oxygen content of the magnets was determined to be in the order of 4000–6000 ppm, a large part of the Nd was bound in the stable phase Nd_2O_3 phase. This is the why below 14 at% Nd density and hard magnetic properties of the magnets drastically deteriorated in magnets with a high oxygen content. On the contrary, low oxygen content can cause the AGG and lower the magnetic properties. The influence of oxygen on the hard magnetic properties is more complex. Kim, Camp and Stadelmaier (1994) reported that a controlled doping with oxygen improved grain alignment and resulted in an increase in remanence, coercivity, and loop squareness. One possibility to improve the alignment factor is to optimize the alignment field and/or pressure during transverse pressing. Even the sintering process influences the degree of alignment of the grains (Chin *et al*., 1988). On the other hand, several authors (Fernengel *et al*., 1996; Sagawa, Nagata, Itatani and Watanabe, 1994) found that isostatic die pressing ($\theta = 11$–$14\,^{\circ}$C) yields highest alignment followed by the transverse field die pressing (18–20 °C) and the axial field die pressing (25–27 °C). The demagnetization curve of an optimized magnet with $(BH)_{max} > 430\,kJ\,m^{-3}$ and a low oxygen content and a composition of $Nd_{13.5}Fe_{bal}B_{5.95}Cu_{0.03}Al_{0.7}$ is shown in Figure 5 and the corresponding TEM image is shown in Figure 6. The magnets produced were sintered between 960 and 1100 °C. The sintering temperature was varied to get optimum density (7.5–7.6 g cm^{-3}) and $(BH)_{max}$. The density of the samples and the remanence increased with increasing sintering temperature keeping the sintering time constant (3 h), while the squareness of the demagnetization curve only partly increased and drastically decreased as AGG of the $Nd_2Fe_{14}B$ grains occurred (Livingston, 1996). AGG of the $Nd_2Fe_{14}B$ grains occurred preferentially in magnets with low oxygen content. The oxygen content strongly affects the AGG and the magnets with higher oxygen content have the higher critical temperatures at which the AGG occurs. Figure 6 shows that the microstructure mainly consists of $Nd_2Fe_{14}B$ grains of several microns in diameter. Only a few Nd-rich phases are found as intergranular phases, especially at grain boundary junctions.

Numerical micromagnetic simulations have shown that the grain boundary phases influence the coercive field significantly (Süss, Schrefl and Fidler, 2000). The finite element simulations confirm the experimental results that nonmagnetic Nd-rich phases at grain boundary junctions increase the coercive field. Microstructural studies have characterized the complex multiphase microstructure of $Nd_2Fe_{14}B$-based permanent magnets (Fidler and Knoch, 1989). Two types of grain boundaries have been found in sintered magnets. Depending on the composition, both, grain boundaries free of any intergranular phase and also Nd-rich phases separating hard magnetic grains have been identified. Figure 12 shows a typical grain boundary junction, with only a thin layer of intergranular phase. In doped sintered magnets, the dopant element is partly dissolved in the hard magnetic phase. In the case where the solubility of the dopant is low at the sintering temperature (Nb, Mo, Zr), precipitates are formed. Dopants also form new intergranular phases and influence the wetting of the liquid phase and the smoothness of the surface $Nd_2Fe_{14}B$-grains during sintering and therefore affect the coercivity. Intergranular phases change the coupling behavior of the hard magnetic grains. Distorted grain boundary phases with reduced magnetocrystalline anisotropy favor the formation of reversed domains. The composition of these phases can be influenced by substituent and dopant elements (Bernardi, Fidler and Fodermayr, 1992). For a perfect microstructure the calculated coercive fields agree well with the Stoner–Wohlfarth theory (Stoner and Wohlfarth, 1948). The most misoriented grain, which has the largest angle between the easy axis and the alignment direction, determines the coercive field. The coercive field decreases with increasing misalignment. The values of the calculated coercive field are about 5–10% smaller than the values predicted by the Stoner–Wohlfarth theory. For sintered magnets, the measured thickness of the nonmagnetic grain boundary

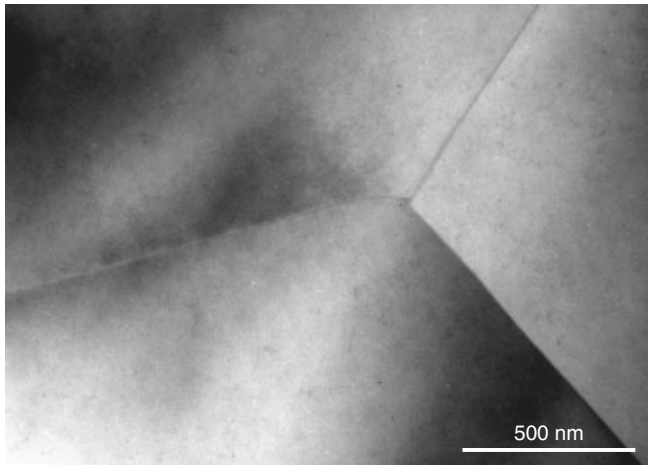

Figure 12. TEM image showing a grain boundary junction of a high energy density $Nd_{13.5}Fe_{bal}B_{5.95}Cu_{0.03}Al_{0.7}$ sintered magnet with $(BH)_{max} = 432\,kJ\,m^{-3}$, $J_r = 1.51\,T$ and ${}_JH_c = 755\,kA\,m^{-1}$.

phase varies between zero and several nanometer. This reduced magnetocrystalline anisotropy decreases the coercive field considerably, from 3200–900 kA m^{-1}, for example. The reduction of the magnetocrystalline anisotropy reverses the dependence of the coercive field on the degree of alignment (Martinek and Kronmueller, 1990). Bachmann, Fischer and Kronmüller (1998) observed a similar behavior of the coercivity on the degree of alignment for nanocrystalline magnets. The coercive field increases as the misalignment angle is changed from 8 to 16 °C misorientation. The Foucault TEM image of Figure 13 clearly shows the nucleation of reversed domains close to grain boundaries. Figure 14 compares the nucleation process for two different degrees of alignment. The micromagnetic simulations are in good agreement with the results obtained by Lorentz electron microscopic investigations (Figure 13). The isosurfaces represent the reversed nucleus. In the well-aligned sample, higher demagnetizing field initiates the nucleation of reversed domains in the defect region. The simulations are in agreement with experimental data that show a slight increase of coercivity with misalignment for Dy-free Nd–Fe–B magnets, whereas a decrease of the coercive field with increasing misalignment is observed in highly coercive, Dy-containing Nd–Fe–B magnets (Kim, Camp and Stadelmaier, 1994). The coercive field of Nd–Fe–B sintered magnet increases with increasing Nd-content (Hirosawa and Kaneko, 1998). The simulations show that the presence of the Nd-rich phase significantly changes the exchange and the magnetostatic interactions. As a consequence, the nucleation of reversed domains is suppressed.

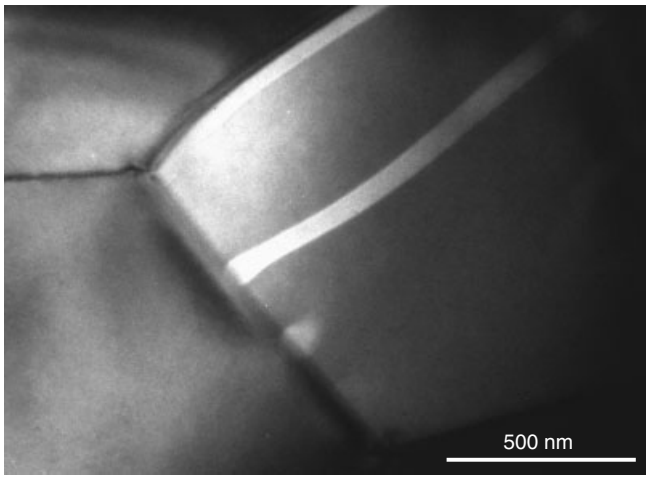

Figure 13. Foucault TEM image showing the domain nucleation at grain boundaries. Sintered $Nd_{13.5}Fe_{bal}B_{5.95}Cu_{0.03}Al_{0.7}$ magnet with $(BH)_{max} = 432\,kJ\,m^{-3}$, $J_r = 1.51\,T$ and ${}_JH_c = 755\,kA\,m^{-1}$.

4.2 Pinning controlled Sm(Co,Cu,Fe,Zr)$_{7.5-8}$ magnets

Alloys of Sm(Co, Cu, Fe, Zr)$_z$ are typically prepared by melting the respective constituents by low-frequency induction heating under an inert gas cover (Ray and Millott, 1971). Typical initial composition of the constituent elements is 10–12 Sm at%, 55–71 Co at%, 15–25 Fe at%, 3–5 Cu at%, 1–3 Zr at% for conventional applications and 11–13 Sm at%, 59–79 Co at%, 0–10 Fe at%, 8–14 Cu at%, 2–4 Zr at% for high-temperature applications (Ray, 1986).

A complex production process, which involves sintering, homogenizing, isothermal aging, and annealing, results in the formation of a cellular precipitation structure, which acts as pinning centers for magnetic domain walls (Fidler, Skalicky and Rothwarf, 1983; Livingston and Martin, 1977; Mishra *et al.*, 1981; Rabenberg, Mishra and Thomas, 1982; Nagel, 1979). The compact is first sintered between 1190 and 1210 °C in order to obtain a full dense alloy trying, at the

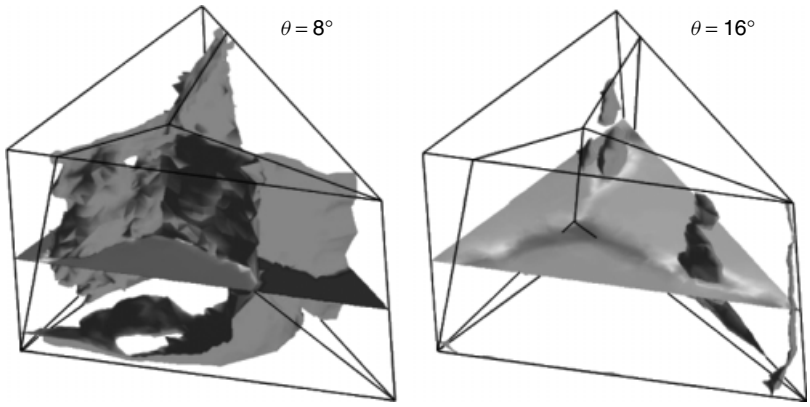

Figure 14. Numerical finite element micromagnetic simulation of the nucleation of reversed domains at a grain boundary junction in an $Nd_2Fe_{14}B$-based sintered magnet in dependence of the misalignment θ of the grains. The isosurfaces represent the regions where J_z/J_s and <0.7 and the nucleation process of reversed domains will start.

same time, to avoid excessive grain growth because of their negative effect in mechanical properties. Typical grain size is up to 50 µm. A solutionizing treatment is carried on to get a fully homogenized single-phase sample at a sufficiently high temperature and then is rapidly quenched in order to avoid phase segregation during cooling. The step aging or slow cooling heat treatment is performed at a lower temperature to obtain the precipitation of the cell boundary phase and the well formation of the continuous cell structure that accounts for the coercivity of the magnet. The two-phase magnet compound with the nominal composition $Sm(Co,Cu,Fe,Zr)_{7.5-8}$ is the best choice for high-temperature applications permanent magnets with operating temperatures above 300 °C, because of its high magnetocrystalline anisotropy, the strong domain wall pinning behavior and the high Curie temperature (Strnat, 1988; Hadjipanayis *et al*., 2000; Chen *et al*., 1998). The microstructure, which consists of the $Sm_2(Co,Fe)_{17}$ cell matrix phase, the $Sm(Co,Cu)_{5-7}$ cell boundary phase and the Zr-rich lamella phase, develops mainly during the isothermal aging (Tang *et al*., 2001). The formation of a fine cellular precipitation structure is a necessary precondition for high permanent-magnet properties at elevated temperatures, because of its behavior as pinning centers for the magnetic domain walls. However, the compositions of the distinct phases and the elemental profiles also have an even higher influence on the magnetic properties. The diffusional redistribution of the various elements during the heat treatment results in a characteristic microchemistry (Fidler *et al*., 2002; Goll, Kronmuller and Stadelmaier, 2004; Hadjipanayis *et al*., 2000; Goll, Kleinschroth, Sigle and Kronmüller, 2000). As all of the elements are placed on regular crystallographic sites, there is only diffusion of vacancies, which is very slow compared to interstitial diffusion. There are two main diffusional processes: Cu segregates to the 1:5 cell boundary phase and Fe segregates to the 2:17 matrix phase (Ray, Soffa, Blachere and Zhang, 1987). As the cell size of the precipitation structure increases with the duration of the isothermal aging, it is necessary to decrease the temperature when the desired cell size has been obtained. Diffusion continues during the following slow cooling and the subsequent annealing at 400 °C, but with a reduced rate because of the lower temperatures. Even the solutionized samples may have a microstructure and microchemistry, which have a strong influence on the duration and the profile of the heat treatment. Cu clusters within the solid solution that enabled a higher Cu diffusion rate and allowed the samples to be quenched directly after the isothermal aging (Perkins and Strässler, 1977a). The TEM images of Figure 15 show the typical cellular and lamellar precipitation structures, A high-resolution nanoprobe TEM investigation shows that the Fe content within the cell matrix phase is higher than the nominal content, which confirms that Fe mainly segregates to the

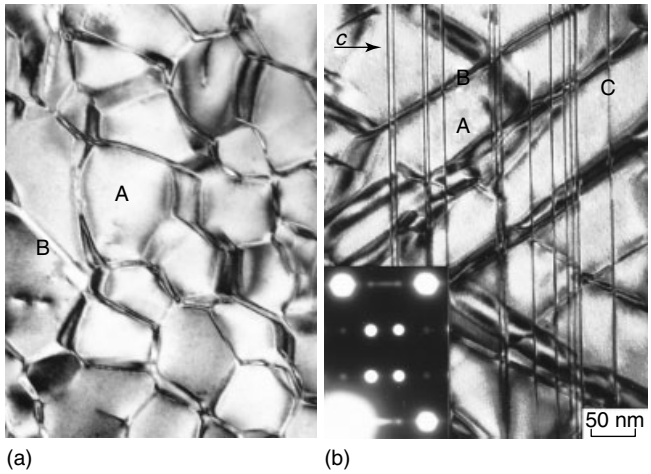

Figure 15. TEM images showing rhombic, cellular precipitation structure of a sintered Sm(Co,Cu,Fe,Zr)7.5 magnet. Views (a) parallel and (b) perpendicular to the alignment direction c. Cell boundary phase $Sm(Co,Cu)_{5-7}$ (A), cell matrix phase $Sm_2(Co,Fe)_{17}$ (B).

2:17 phase. A higher Fe/Co ratio decreases the anisotropy constant K_1 (Perkins and Strässler, 1977b) and increases the spontaneous polarization (Ray, 1984). The Zr content within the cell matrix phase lies between 1.0 and 2.4 at%. A high Zr concentration is found in the platelet phase perpendicular to the *c* axis, which presumably acts as diffusion path for the distribution of elements during the annealing procedure (Ray, 1990; Ray, Soffa, Blachere and Zhang, 1987; Rabenberg *et al*., 1991).

The magnetization reversal mechanism in Sm(Co, Fe, Cu, $Zr)_z$ magnets has been attributed to domain wall pinning at the $Sm(Co, Cu)_{5-7}$ cell boundaries (Durst, Kronmueller and Ervens, 1988a,b). Various experimental investigations, such as Kerr effect microscopy (Livingston, 1975), Lorentz electron microscopy (Fidler, 1982), analysis of initial magnetization curves (Livingston, 1981), and measurements of the irreversible susceptibility (Liu and Hadjipanayis, 1999) confirmed this assumption. Theoretical considerations (Kronmüller, 1987; Kronmüller and Fähnle, 2003) and numerical micromagnetic simulations (Streibl, Fidler and Schrefl, 2000; Scholz *et al*., 2003) reveal the details of these complex magnetization reversal processes. The Lorentz micrograph of Figure 16 shows the domain wall pinning at the continuous cell boundary phase $Sm(Co,Cu)_{5-7}$ at the remanent state at room temperature. The coercivity is determined by the difference and the gradient of the domain wall energy (Livingston and Martin, 1977; Livingston, 1996, 1981) and by the magnetoelastic coupling energy between domain wall stresses and lattice deformation strains (Fidler, 1982). The exchange constant A and the anisotropy constant K_1 of the cell boundary phase are mainly determined by

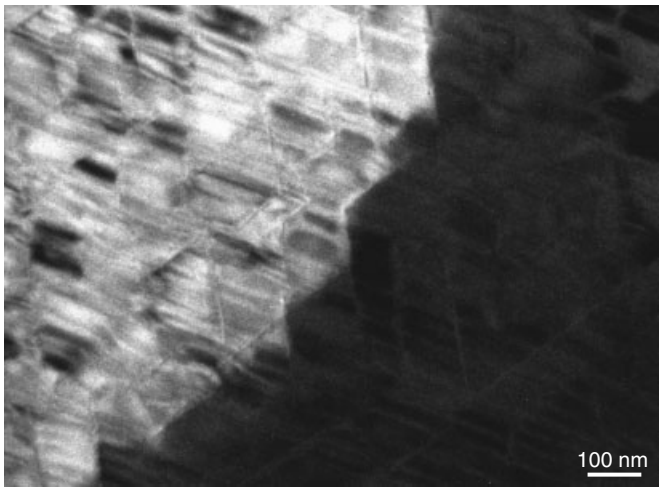

Figure 16. Foucault TEM image showing the domain pinning at the continuous cellular precipitation structure in a $Sm(Co,Cu,Fe,Zr)_z$ sintered magnet for high-temperature applications.

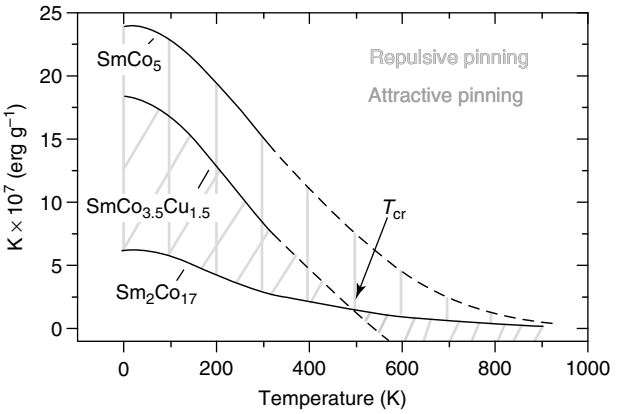

Figure 17. Temperature dependence of the anisotropy coefficients K_1 of the $Sm_2(Co,Fe)_{17}$ and $Sm(Co, Cu)_5$ phases (Tang *et al*., 2001). The coercivity of $Sm(Co,Fe,Cu,Zr)_z$ permanent magnets is determined by the gradient in domain wall energy between the different phases, which is proportional to the difference of the magnetocrystalline anisotropy constants ΔK_1. Because of the different temperature dependences of the two phases ΔK_1 is strongly dependent on the operating temperature of the magnet. (Reprinted with permission W. Tang *et al*., copyright 2001, Elsevier.)

the Cu concentration (Fidler *et al*., 2002; Goll, Kronmuller and Stadelmaier, 2004). In more detail, the different crystal structures and magnetic properties of the cell matrix and the cell boundary phase give rise to a gradient in the domain wall energy, which originates the pinning effect. There are two types of possible domain wall pinning processes. As Cu mainly segregates in the $Sm(Co, Cu)_{5-7}$ phase, the magnetocrystalline anisotropy of this phase can be tailored by the Cu content of the magnet (Lectard, Allibert and Ballou, 1994). The anisotropy constant K_1 of the cell boundary phase is either higher (low Cu concentration) or lower (high Cu concentration or high temperatures) than that of the cell matrix phase (Figure 17). As a result it is energetically favorable for a magnetic domain wall to either stay in the cell boundary phase ('attractive' domain wall pinning because of lower domain wall energy) or just inside the cells ('repulsive' domain wall pinning because of higher domain wall energy). If the cell boundary thickness is larger than the domain wall width which itself depends indirectly on the square root of K_1 the coercive field is given by Kronmüller (2000) and Kronmüller, Durst and Sagawa (1988):

$$\mu_0 H_c = \mu_0 \frac{1}{J_s \cos \psi_0} \left| \frac{d\gamma\,(z)}{dz} \right|_{max} - N_{eff} J_s \qquad (10)$$

N_{eff} denotes the effective demagnetizing factor, ψ_0 the angle between the applied field and the easy axis, z is the direction normal to the cell boundary wall and $d\gamma(z)/dz$ denotes the maximum slope of the wall energy. In the more typical case, where the boundary thickness becomes narrower than the domain wall width, the complex influence of geometrical and intrinsic magnetic parameters on the coercive field has to be determined using numerical micromagnetic simulations. Finite element reveal that the cell boundary width has a strong influence on the coercivity (Scholz *et al*., 2003). This suggests that, if an improved heat treatment resulted in larger cells with thicker cell boundaries, a higher coercivity could be achieved. A minimum thickness of 10 nm is necessary for coercivities above 1000 kA m^{-1}. Repulsive pinning enables larger coercivities than attractive pinning. For a thickness of more than 40 nm of the intercellular phase, the pinning behavior is lost again, because the domain wall sweeps through the whole intercellular phase and reverses its magnetization. As a result the unreversed cells remain until nucleation starts the reversal of their magnetization. In the case of repulsive domain wall pinning, a minimum thickness of the intercellular phase is required, too. As the thickness of the intercellular phase increases, the energy barrier becomes wider and this mechanism becomes more and more difficult. It has been shown that with increasing temperature the coercivity mechanism changes from repulsive to attractive pinning. The nucleation mechanism was found to be dominant above the Curie temperature of the cell walls (Kronmüller and Fähnle, 2003).

Recently a new series of magnets with H_c up to 1050 kA m^{-1} at 400 °C has been developed (Hadjipanayis *et al*., 2000; Chen *et al*., 1998). These magnets have low temperature coefficients of H_C and a straight line B versus H (extrinsic) demagnetization curve up to 550 °C. High Cu-, low Fe- and a higher Sm-concentration were found to contribute to high coercivity at high temperatures. In low Cu samples the magnetocrystalline anisotropy values of the 1:5

and the 2:17 phases cross at a certain temperature, which does not happen in high Cu samples. However, as a large part of the magnet consists of the 1:5 phase, the saturation polarization s strongly decreases in high Cu-containing samples. The actual domain wall pinning process in high Cu-containing magnets is rather complicated and varies from repulsive to attractive, depending on whether the magnetocrystalline anisotropy in the Cu-containing 1:5 cell boundary phase is lower or higher than in the 2:17 cell matrix phase, respectively. The shape and the thickness of the cell boundary phase and the elemental profiles across the phase determine the coercivity H_c.

4.3 Nanocrystalline, composite $Nd_2Fe_{14}B/(\alpha\text{-}Fe,Fe_3B)$ and other novel rare-earth magnets

The increasing demand for powders for bonded magnets leads to the development nitrided Sm–Fe and nanocrystalline Nd–Fe–B materials. The RE_2Fe_{17} compounds have low Curie temperatures and exhibit planar magnetic anisotropy. Substitutions or additions are needed to raise T_C and to change the magnetocrystalline anisotropy. Almost any substitution will raise T_C, but recent attention has focused on Al and Ga which also induce uniaxial anisotropy when present in modest amounts in Sm_2Fe_{17}. However, the most effective way of increasing T_C of RE_2Fe_{17} and modifying its anisotropy is to use interstitial additions (B, C, N). Interstitial modification, especially with nitrogen, has added a new dimension to the compounds that can be considered from RE permanent magnets. Besides raising T_C of iron-rich intermetallics, largely through the effect to lattice expansion (6%), interstitial atoms also control the magnetocrystalline anisotropy. Since 1990, there have been extensive studies of interstitial 2:17, 3:29, and 1:12 compounds containing nitrogen and carbon in the structures (de Boer *et al.*, 1988), but the interstitial compound that exhibits the most favorable combination of intrinsic magnetic properties remains is $Sm_2Fe_{17}N_3$ with $T_C = 470\,^{\circ}C$ (Coey and Sun, 1990). Mechanical alloying and HDDR of $Sm_2Fe_{17}N_3$ give high coercivity and good loop shape, but have so far only yielded isotropic material. The main disadvantage of nitrided powders is the dissociation at high temperature (about 600 °C) according to the reaction:

$$Sm_2Fe_{17}N_3 \rightarrow 2SmN + Fe_4N + 13\alpha\text{-}Fe \qquad (11)$$

Another useful family are the pseudobinaries Sm $(Fe_{12-x}M_x)$ where M = Ti, V, Si, which crystallize in the tetragonal $ThMn_{12}$ structure (Buschow, 1988; de Boer, Ying-Kai, de Mooij and Buschow, 1987; de Mooij and Buschow, 1988). The best of them show T_C and magnetic anisotropy similar to those of $Nd_2Fe_{14}B$, but with somewhat lower magnetization. These compounds can also be improved by interstitial modification with nitrogen or carbon.

Nanocrystalline, single-phase $Nd_2Fe_{14}B$ magnets with isotropic alignment show an enhancement of remanence that is attributed to intergrain exchange interactions, which enhance the remanence by more than 40% when compared with the remanence of noninteracting particles, if the grain size is in the order of 10–30 nm. Numerical micromagnetic calculations have revealed that the interplay of magnetostatic and exchange interactions between neighboring grains influence the coercive field and remanence considerably (Kneller and Hawig, 1991; Schrefl, Fidler and Kronmüller, 1994). Numerical micromagnetic simulation shows a large volume fraction of an inhomogeneous polarization distribution near grain boundaries in small-grained, isotropic, single-phase magnets, leading to an increase of the remanence and a decrease of the coercive field. Exchange interactions between neighboring soft and hard grains in nanocrystalline, composite magnets lead to remanence enhancement of isotropically oriented grains (Davies *et al.*, 1993; Mccallum, Kadin, Clemente and Keem, 1987; Coehoorn, de Mooij and de Waard, 1989; Hadjipanayis and Gong, 1988; Ding, Mccormick and Street, 1993; Goll, Seeger and Kronmüller, 1998). Soft magnetic grains in two- or multi-phase, composite permanent magnets cause a high polarization, and hard magnetic grains induce a large coercive field provided that the particles are small and strongly exchange coupled. The coercive field shows a maximum at an average grain size of less than 15–20 nm. Intergrain exchange interactions override the magnetocrystalline anisotropy of the $Nd_2Fe_{14}B$ grains for smaller grains, whereas exchange hardening of the soft phases becomes less effective for larger grains. The magnetization distribution at zero applied field for different grain sizes, clearly shows that the remanence enhancement and energy product increases with decreasing grain size and increases with increasing α-Fe content. Owing to the competitive effects of magnetocrystalline anisotropy and intergrain exchange interactions, the magnetization of the hard magnetic grains significantly deviates from the local easy axis for a grain size $D \leq 20$ nm. As a consequence coercivity drops, since intergrain exchange interactions help overcome the energy barrier for magnetization reversal. With increasing grain size the magnetization becomes nonuniform, following either the magnetocrystalline anisotropy direction within the hard magnetic grains or forming a flux closure structure in soft magnetic regions. Neighboring α-Fe and Fe_3B grains may make up large continuous areas of soft magnetic phase, where magnetostatic effects will determine the preferred direction of the magnetization. The large soft

magnetic regions deteriorate the squareness of the demagnetization curve and cause a decrease of the coercive field for $D > 20\,\text{nm}$. A vortex-like magnetic state with vanishing net magnetization will form within the soft magnetic phase, if the diameter of soft magnetic region exceeds 80 nm. Many of the fully dense permanent-magnet materials, especially those that are sintered, are very hard and brittle, and machining them to their final shape is often tedious. The reduction of production handling and assembly costs led to an interest in bonded magnets, which are made by consolidating a magnet powder with a polymer matrix. While machining is easy, the production processes also frequently allow parts to be made directly to their final dimensions. Thermosetting binders, such as epoxy resin, are employed for use in compression-molded magnets, thermoplastic binders like nylon for injection-molded magnets, and elastomers such as rubber are used for extruded magnets. The major drawback to bonded magnets is the reduction in their magnetic properties, relative to those that are 100% dense with magnetic material.

ACKNOWLEDGMENTS

The authors would like to thank Ernesto Estevez-Rams, Thorsten Matthias and Werner Scholz for valuable discussions and contributions.

REFERENCES

Bachmann, M., Fischer, R. and Kronmüller, H. (1998). Simulation of magnetization process in real microstructures. In *10th International Symposium on Magnetic Anisotropy and Coercivity in Rare-Earth Transition Metal Alloys*, Schultz, L. and Müller, K.H. (Eds.), Werkstoff-Informationsgesellschaft: Dresden, pp. 217–236.

Bernardi, J. and Fidler, J. (1994). Preparation and transmission electron microscope investigation of sintered $Nd_{15.4}Fe_{75.7}B_{6.7}Cu_{1.3}Nb_{0.9}$ magnets. *Journal of Applied Physics*, **76**, 6241–6243.

Bernardi, J., Fidler, J. and Fodermayr, F. (1992). The effect of V or W additives to microstructure and coercivity of Nd-Fe-B based magnets. *IEEE Transactions on Magnetics*, **28**, 2127–2129.

Blandin, A., Friedel, J. and Saada, G. (1966) *Journal of Physics*, **27**, 3–128.

de Boer, F.R., Ying-Kai, H., de Mooij, D.B. and Buschow, K.H.J. (1987). Magnetic properties of a series of novel ternary intermetallics $RFe_{10}V_2$. *Journal of the Less Common Metals*, **135**, 199–204.

de Boer, F.R., Zhang, Z-D., de Mooij, D.B., *et al*. (1988). Magnetic and crystallogrpahic properties of ternary rare-earth compounds of the type $R_2Fe_{14}C$. *Journal of Magnetism and Magnetic Materials*, **72**, 167–173.

Brown, J.W.F. (1963). *Micromagnetics*, Intersience Publishers, John Wiley & Sons: New York, London.

Brown, J.W.F. (1978). Domains, micromagnetics, and beyond: reminiscences and assessments. *Journal of Applied Physics*, **49**, 1937–1942.

Buschow, K.H.J. (1971). Intermetallic compounds of rare earth elements and Ni, Co, or Fe. *Physica Status Solidi A*, **7**, 199–210.

Buschow, K.H.J. (1977). Intermetallic compounds of rare-earth and 3d transition metals. *Reports on Progress in Physics*, **40**, 1179–1256.

Buschow, K.H.J. (1986). New permanent magnet materials. *Materials Science Reports*, **1**, 1–63.

Buschow, K.H.J. (1988). Permanent magnet materials based on 3d-rich ternary compounds. In *Handbook of Ferromagnetic Materials*, Wohlfarth, E.P. and Buschow, K.H.J. (Eds.), Elsevier, pp. 1–129, Vol. 4.

Buschow, K.H.J., van Diepen, A.M. and de Wijn, H.W. (1974). Crystal-field anisotropy of Sm_{3+} in $SmCo_5$. *Solid State Communications*, **15**, 903–906.

Buschow, K.H.J. and van der Goot, A.S. (1968). Intermetallic compounds in the system samarium-cobalt. *Journal of the Less Common Metals*, **14**, 323–328.

Buschow, K.H.J., van Noort, H.M. and de Mooij, D.B. (1985). Magnetic and structural properties of $Nd_2Fe_{14}B$, $Th_2Fe_{14}B$, $Nd2Co_{14}B$ and related materials. *Journal of the Less Common Metals*, **109**, 79–91.

Cadogan, J.M. and Coey, J.M.D. (1986). Hydrogen absorption and desorption in $Nd_2Fe_{14}B$. *Applied Physics Letters*, **48**, 442–444.

Cahn, R.W. (1996). *Physical Metallurgy*, North-Holland: Amsterdam.

Chen, C.H., Walmer, M.S., Walmer, M.H., *et al*. (1998). $Sm_2(Co,Fe,Cu,Zr)_{17}$ magnets for use at temperature $>= 400\,^{\circ}\text{C}$. *The 7th Joint MMM-Intermag Conference on Magnetism and Magnetic Materials*, *Eleventh Edition*, AIP: San Francisco, pp. 6706–6708, Vol. 83.

Chin, T.S., Hung, M.P., Tsai, D.S., *et al*. (1988). Compaction and sintering behaviors of a Nd-Fe-B permanent magnet alloy. *Journal of Applied Physics*, **64**, 5531–5533.

Clark, A.E. (1993). High power rare earth magnetostrictive materials. *Journal of Intelligent Material Systems and Structures*, **4**, 70–75.

Coehoorn, R., de Mooij, D.B. and de Waard, C. (1989). Meltspun permanent magnet materials containing Fe3B as the main phase. *Journal of Magnetism and Magnetic Materials*, **80**, 101–104.

Coey, J.M.D. and Sun, H. (1990). Improved magnetic properties by treatment of iron-based rare earth intermetallic compounds in ammonia. *Journal of Magnetism and Magnetic Materials*, **87**, 251–254.

Croat, J.J. (1989). Manufacture of Nd-Fe-B permanent magnets by rapid solidification. *Journal of the Less Common Metals*, **148**, 7–15.

Croat, J.J., Herbst, J.F., Lee, R.W. and Pinkerton, F.E. (1984a). High-energy product Nd-Fe-B permanent magnets. *Applied Physics Letters*, **44**, 148–149.

Croat, J.J., Herbst, J.F., Lee, R.W. and Pinkerton, F.E. (1984b). Pr-Fe and Nd-Fe-based materials: a new class of high-performance

permanent magnets (invited). *Journal of Applied Physics*, **55**, 2078–2082.

Davies, H.A., Manaf, A., Leonowicz, M., *et al*. (1993). Nanocrystalline structures and the enhancement of remanence and energy product in melt spun iron-rare earth-boron alloys for permanent magnets. *Nanostructured Materials*, **2**, 197–203.

Ding, J., Mccormick, P.G. and Street, R. (1993). Remanence enhancement in mechanically alloyed isotropic Sm_7Fe_{93}-nitride. *Journal of Magnetism and Magnetic Materials*, **124**, 1–4.

Durst, K.D., Kronmueller, H. and Ervens, W. (1988a). Investigation of the magnetic properties and demagnetization processes of an extremely high coercive Sm(Co,Cu,Fe,Zr)7.6 permanent magnet. I. Determination of intrinsic magnetic material parameters. *Physica Status Solidi A: Applied Research*, **108**, 403–416.

Durst, K.D., Kronmueller, H. and Ervens, W. (1988b). Investigations of the magnetic properties and demagnetization processes of an extremely high coercive Sm(Co, Cu, Fe, Zr)7.6 permanent magnet: II. The coercivity mechanism. *Physica Status Solidi A: Applied Research*, **108**, 705–719.

Endoh, M. and Shindo, M. (1994). Material design and fabrication of high energy Nd-Fe-B sintered magnets. In *13th International Workshop on Rare Earth Magnets and their Applications*, Manwaring, C.A.F., Jones, D.F.G., Williams, A.J. and Harris, I.R. (Eds.), Werkstoff-Informationsgesellschaft: Dresden, pp. 397, Vol. 1.

Enz, U. (1982). Magnetism and magnetic materials: historical developments and present role in industry and techololy. In *Ferromagnetic Materials*,Wohlfarth, E.P. (Ed.), Elsevier, pp. 1–36, Vol. 3.

Estevez-Rams, E. (1996). *Transmission Electron Microscope Study of the Relation between Microstructure and Magnetic Properties of New Hard Magnetic and Soft Magnetic Materials*, Ph.D. Thesis, Vienna University of Technology, Vienna.

Fernengel, W., Lehnert, A., Katter, M., *et al*. (1996). Examination of the degree of alignment in sintered Nd-Fe-B magnets by measurements of the remanent polarizations. *Journal of Magnetism and Magnetic Materials*, **157–158**, 19–20.

Fidler, J. (1982). Coercivity of precipitation hardened cobalt rare earth 17:2 permanent magnets. *Journal of Magnetism and Magnetic Materials*, **30**, 58–70.

Fidler, J. and Knoch, K.G. (1989). Electron microscopy of Nd-Fe-B based magnets. *Journal of Magnetism and Magnetic Materials*, **80**, 48–56.

Fidler, J., Knoch, K.G., Kronmueller, H. and Schneider, G. (1989). Analytical TEM study of Al-doped, 'two-phase' Nd-Fe-B sintered magnets. *Journal of Materials Research*, **4**, 806–814.

Fidler, J., Matthias, T., Scholz, W., *et al*. (2002). The role of the precipitation structure on the coercivity of $Sm(Co,Fe,Cu,Zr)_z$ magnets for HT applications. In *17th Rare Earth Magnets Workshop*, Hadjipanayis, G. and Bonder, M.J. (Eds.), University of Newark (USA), p. 853.

Fidler, J., Sasaki, S. and Estevez-Rams, E. (1999). High performance magnets–microstructure and coercivity. *Materials Research Society Symposium Proceedings*, **577**, 291–302.

Fidler, J. and Schrefl, T. (1996). Overview of Nd-Fe-B magnets and coercivity (invited). *Journal of Applied Physics*, **79**, 5029–5034.

Fidler, J. and Schrefl, T. (2000). Micromagnetic modelling–the current state of the art. *Journal of Physics D: Applied Physics*, **33**, R135–R156.

Fidler, J. and Skalicky, P. (1982). Microstructure of precipitation hardened cobalt rare earth permanent magnets. *Journal of Magnetism and Magnetic Materials*, **27**, 127–134.

Fidler, J., Skalicky, P. and Rothwarf, F. (1983). High resolution electron microscope study of $Sm(Co, Fe, Cu, Zr)_{7.5}$ magnets. *IEEE Transactions on Magnetics*, **19**, 2041–2043.

Fischer, R. and Kronmüller, H. (1996). Static computational micromagnetism of demagnetization processes in nanoscaled permanent magnets. *Physical Review B: Condensed Matter and Materials Physics*, **54**, 7284–7294.

Franse, J.J.M. and Radwanski, R.J. (1993). Magnetic properties of binary rare-earth 3d-transition-metal intermetallic compounds. In *Handbook of Magnetic Materials*, Buschow, K.H.J. (Ed.), Elsevier, pp. 307–501, Vol. 7.

Fuerst, C.D., Herbst, J.F. and Alson, E.A. (1985). Magnetic properties of Nd//2(Co//xFe//1// minus //x)//1//4B alloys. *Journal of Magnetism and Magnetic Materials*, **54–57**, 567–569.

Fukunaga, H. and Inoue, H. (1992). Effect of intergrain exchange interaction on magnetic properties in isotropic Nd-Fe-B magnets. *Japanese Journal of Applied Physics*, **31**, 1347–1352.

Givord, D., Li, H.S. and Moreau, J.M. (1984). Magnetic properties and crystal structure of $Nd_2Fe_{14}B$. *Solid State Communications*, **50**, 497–499.

Goll, D., Kleinschroth, I., Sigle, W. and Kronmüller, H. (2000). Melt-spun precipitation-hardened $Sm_2(Co, Cu, Fe, Zr)_{17}$ magnets with abnormal temperature dependence of coercivity. *Applied Physics Letters*, **76**, 1054–1056.

Goll, D., Kronmuller, H. and Stadelmaier, H.H. (2004). Micromagnetism and the microstructure of high-temperature permanent magnets. *Journal of Applied Physics*, **96**, 6534–6545.

Goll, D., Seeger, M. and Kronmüller, H. (1998). Magnetic and micro structural properties of nanocrystalline exchange coupled PrFeB permanent magnets. *Journal of Magnetism and Magnetic Materials*, **185**, 49–60.

Gutfleisch, O. and Harris, I.R. (1996). Fundamental and practical aspects of the hydrogenation, disproportionate, desorption and recombination process. *Journal of Physics D: Applied Physics*, **29**, 2255–2265.

Gutfleisch, O., Müller, K.H., Khlopkov, K., *et al*. (2006). Evolution of magnetic domain structures and coercivity in high-performance SmCo 2:17-type permanent magnets. *Acta Materialia*, **54**, 997–1008.

Hadjipanayis, G.C. and Gong, W. (1988). Magnetic hysteresis in melt-spun Nd-Fe-Al-B-Si alloys with high remanence. *Journal of Applied Physics*, **64**, 5559–5561.

Hadjipanayis, G.C., Hazelton, R.C. and Lawless, K.R. (1983). Cobalt-free permanent magnet materials based on iron-rare-earth alloys. *Journal of Applied Physics*, **55**, 2073–2077.

Hadjipanayis, G.C., Tang, W., Zhang, Y., *et al*. (2000). High temperature 2:17 magnets: relationship of magnetic properties to microstructure and processing. *IEEE Transactions on Magnetics*, **36**, 3382–3387.

Harris, I.R. (1992). The use of hydrogen in the production of Nd-Fe-B type magnets and the assessment of Nd-Fe-B type alloys and

permanent magnets–an update. In *12th International Workshop on Rare Earth Magnets and their Applications*, Street, B. (Ed.), The University of Western Australia: Perth, p. 347.

Herbst, J.F. (1991). $R_2Fe_{14}B$ materials: intrinsic properties and technological aspects. *Reviews of Modern Physics*, **63**, 819–898.

Herbst, J.F., Croat, J.J. and Yelon, W.B. (1985). Structural and magnetic properties of Nd[sub 2]Fe[sub 14]B (invited). *Journal of Applied Physics*, **57**, 4086–4090.

Hirosawa, S. and Kaneko, Y. (1998). Rare earth magnets with high energy products. In *15th International Workshop on Rare-Earth Magnets and their Applications*, Schultz, L. and Müller, K.H. (Eds.), Werkstoff-Informationsgesellschaft: Dresden, p. 43.

Hirosawa, S. and Tsubokawa, Y. (1990). Nd-Fe-B materials for permanent magnets. *Journal of Magnetism and Magnetic Materials*, **84**, 309–316.

Hoffer, G. and Strnat, K. (1966). Magnetocrystalline anisotropy of YCo_5 and Y_2Co_{17}. *IEEE Transactions on Magnetics*, **2**, 487–489.

Hoffer, G. and Strnat, K. (1967). Magnetocrystalline anisotropy of two Yttrium-Cobalt compounds. *Journal of Applied Physics*, **38**, 1377–1378.

Hofer, F. (1970). Physical metallurgy and magnetic measurements of $SmCo_5$-$SmCu_5$ alloys. *IEEE Transactions on Magnetics*, **6**, 221–224.

Hummler, K. and Faehnle, M. (1996). Full-potential linear-muffin-tin-orbital calculations of the magnetic properties of rare earth-transition-metal intermetaliics. I. Description of the formalism and application to the series RCo_5 (R = rare-earth atom). *Physical Review B: Condensed Matter and Materials Physics*, **53**, 3272–3289.

Kaneko, Y. (2000). Highest performance of Nd-Fe-B magnet over 55 MGOe. *IEEE Transactions on Magnetics*, **36**, 3275–3278.

Kaneko, Y. and Ishigaki, N. (1994). Recent developments of high-performance NEOMAX magnets. *Journal of Materials Engineering and Performance*, **3**, 228–233.

Katayama, T. and Shibata, T. (1973). Annealing effect on magnetic properties of permanent magnet materials based on $Sm(Co, Cu)_5$. *Japanese Journal of Applied Physics*, **12**, 319–320.

Khan, Y. (1973). On the crystal structures of the R_2Co_{17} intermetallic compounds. *Acta Crystallographica Section B*, **29**, 2502–2507.

Khlopkov, K., Gutfleisch, O., Eckert, D., *et al*. (2004). Local texture in Nd-Fe-B sintered magnets with maximised energy density. *Journal of Alloys and Compounds*, **365**, 259–265.

Kim, A.S., Camp, F.E. and Stadelmaier, H.H. (1994). Relation of remanence and coercivity of Nd,(Dy)-Fe,(Co)-B sintered permanent magnets to crystallite orientation. *Journal of Applied Physics*, **76**, 6265–6267.

Kneller, E. (1962). *Ferromagnetismus*, Springer.

Kneller, E.F. and Hawig, R. (1991). The exchange-spring magnet: a new material principle for permanent magnets. *IEEE Transactions on Magnetics*, **27**, 3588–3600.

Kronmüller, H. (1987). Theory of nucleation Fields in inhomogeneous ferromagnets. *Physica Status Solidi B: Basic Research*, **144**, 385–396.

Kronmüller, H. (2000) Review of coercivity mechanisms and the microstructure of nanocrystalline permanent magnets. In *11th International Symposium on Magnetic Anisotropy and Coercivity in Rare-Earth Transition Metal Alloys*, Kaneko, H., Homma, M. and Okada, M. (Eds.), Sendai, pp. 83–92.

Kronmüller, H., Durst, K.D. and Sagawa, M. (1988). Analysis of the magnetic hardening mechanism in RE-Fe-B permanent magnets. *Journal of Magnetism and Magnetic Materials*, **74**, 291–302.

Kronmüller, H. and Fähnle, M. (2003). *Micromagnetism and the Microstructure of Ferromagnetic Solids*, Cambridge University Press: Cambridge.

Kronmüller, H. and Goll, D. (2003). Analysis of the temperature dependence of the coercive field of Sm_2Co_{17} based magnets. *Scripta Materialia*, **48**, 833–838.

Kronmüller, H. and Schrefl, T. (1994). Interactive and cooperative magnetization processes in hard magnetic materials. *Journal of Magnetism and Magnetic Materials*, **129**, 66–78.

Kumar, K. (1988). RE_2TM_{17} permanent magnets development. *Journal of Applied Physics*, **63**, R13–R57.

Lectard, E., Allibert, C.H. and Ballou, R. (1994). Saturation magnetization and anisotropy fields in the $Sm(Co_{1-x}Cu_x)_5$ phases. *Journal of Applied Physics*, **75**, 6277–6279.

Lee, R.W., Brewer, E.G. and Schaffel, N.A. (1985). Processing of neodymium-iron-boron melt-spun ribbons to fully dense magnets. *IEEE Transactions on Magnetics*, **MAG-21**, 1958–1963.

Liu, J.F. and Hadjipanayis, G.C. (1999). Demagnetization curves and coercivity mechanism in $Sm(CoFeCuZr)_z$ magnets. *Journal of Magnetism and Magnetic Materials*, **195**, 620–626.

Livingston, J.D. (1975). Domains in sintered Co-Cu-Fe-Sm magnets. *Journal of Applied Physics*, **46**, 5259–5262.

Livingston, J.D. (1981). A review of coercivity mechanisms (invited). *Journal of Applied Physics*, **52**, 2544–2548.

Livingston, J.D. (1996). Rare-earth magnets. *MRS Bulletin*, **21**, 55–59.

Livingston, J.D. and Martin, D.L. (1977). Microstructure of aged $(Co,Cu,Fe)_7Sm$ magnets. *Journal of Applied Physics*, **48**, 1350–1354.

Manaf, A., Buckley, R.A. and Davies, H.A. (1993). New nanocrystalline high-remanence Nd-Fe-B alloys by rapid solidification. *Journal of Magnetism and Magnetic Materials*, **128**, 302–306.

Martinek, G. and Kronmueller, H. (1990). Influence of grain orientation on the coercive field in Fe-Nd-B permanent magnets. *Journal of Magnetism and Magnetic Materials*, **86**, 177–183.

Massalski, T.B. (1990). *Binary Alloy Phase Diagrams*, ASM International, The Materials Information Society, Materials Park, Ohio.

Matsuura, Y., Hirosawa, S., Yamamoto, H., *et al*. (1985). Phase diagram of the Nd-Fe-B ternary system. *Japanese Journal of Applied Physics, Part 2: Letters*, **24**, 635–637.

Mccallum, R.W., Kadin, A.M., Clemente, G.B. and Keem, J.E. (1987). High performance isotropic permanent magnet based on Nd-Fe-B. *Journal of Applied Physics*, **61**, 3577–3579.

Mishra, R.K. (1987). Microstructure of hot-pressed and die-upset NdFeB magnets. *Journal of Applied Physics*, **62**, 967–971.

Mishra, R.K., Thomas, G., Yoneyama, T., *et al*. (1981). Microstructure and properties of step aged rare earth alloy magnets. *Journal of Applied Physics*, **52**, 2517–2519.

de Mooij, D.B. and Buschow, K.H.J. (1988). Some novel ternary $ThMn_{12}$ type compounds. *Journal of the Less Common Metals*, **136**, 207–215.

Morita, Y., Umeda, T. and Kimura, Y. (1987). Phase transformation at high temperature and coercivity of $Sm(Co,Cu,Fe,Zr)_{7-9}$ magnet alloys. *IEEE Transactions on Magnetics*, **23**, 2702–2704.

Nagamine, L.C.C.M., Rechenberg, H.R. and Ray, A.E. (1990). Fe site populations in $Sm_2(Co, Fe)_{17}$ and Sm(Co, Fe, Cu, $Zr)_{8.35}$ alloys. *Journal of Magnetism and Magnetic Materials*, **89**, L270–L272.

Nagel, H. (1979). Coercivity and microstructure of $Sm(Co_{0.87}$ $Cu_{0.13})_{7.8}$. *Journal of Applied Physics*, **50**, 1026–1030.

Nakayama, R., Takeshita, T., Itakura, M., *et al*. (1994). Microstructures and crystallographic orientation of crystalline grains in anisotropic Nd-Fe-Co-B-(Ga or Zr) magnet powders produced by the hydrogenation-decomposition-desorption-recombination process. *Journal of Applied Physics*, **76**, 412–417.

Nishida, I. and Uehara, M. (1974). Study of the crystal structure and stability of pseudobinary compounds $SmCo_{5-x}Cu_x$. *Journal of the Less Common Metals*, **34**, 285–291.

Ojima, T., Tomizawa, S., Yoneyama, T. and Hori, T. (1977). Magnetic properties of a new type of rare-earth cobalt magnets $Sm_2(Co, Cu, Fe, M)_{17}$. *IEEE Transactions on Magnetics*, **13**, 1317–1319.

Otsuki, E., Otsuka, T. and Imai, T. (1990).Processing and magnetic properties of sintered Nd-Fe-B magnets. In *11th International Workshop on Rare Earth Magnets and their Applications*, Shankar, S.G. (Ed.), Carnegie Mellon University, Pittsburgh, p. 328, Vol. 1.

Pastushenkov, J., Forkl, A. and Kronmueller, H. (1991). Magnetic domain structure of sintered Fe-Nd-B type permanent magnets and magnetostatic grain interaction. *Journal of Magnetism and Magnetic Materials*, **101**, 363–366.

Perkins, R.S. and Fischer, P. (1976). Deviations from statistical site occupancy in substituted RE_2Co_{17}. *Solid State Communications*, **20**, 1013–1018.

Perkins, R.S. and Strässler, S. (1977a). Interpretation of the magnetic properties of pseudobinary $Sm_2(Co,M)_{17}$ compounds. I. Magnetocrystalline anisotropy. *Physical Review B*, **15**, 477.

Perkins, R.S. and Strässler, S. (1977b). Interpretation of the magnetic properties of pseudobinary $Sm_2(Co,M)_{17}$ compounds. II. Magnetization. *Physical Review B*, **15**, 490.

Perry, A.J. (1977). The constitution of copper-hardened samarium-cobalt permanent magnets. *Journal of the Less Common Metals*, **51**, 153–162.

Perry, A. and Menth, A. (1975). Permanent magnets based on $Sm(Co, Cu, Fe)_z$. *IEEE Transactions on Magnetics*, **11**, 1423–1425.

Rabenberg, L., Barrera, E.V., Maury, C.E., *et al*. (1991). Extended x-ray-absorption fine-structure study of the position of Zr within the unit cell of Sm_2Co_{17}. *Journal of Applied Physics*, **69**, 5568–5570.

Rabenberg, L., Fidler, J. and Bernardi, J. (1992). Observation and characterization of a twined monoclinic phase as a product of the solid state decomposition of Nd2Fe14B. *Journal of Materials Research*, **7**, 1762–1768.

Rabenberg, L., Mishra, R.K. and Thomas, G. (1982). Microstructures of precipitation hardened SmCo permanent magnets. *Journal of Applied Physics*, **53**, 2389–2391.

Radwanski, R.J., Franse, J.J.M. and Sinnema, S. (1985). Exchange interactions and basal-plane magnetocrystalline anisotropy in R_2Co_{17} intermetallics. *Journal of Magnetism and Magnetic Materials*, **51**, 175–182.

Rathenau, G.W. (1953). Saturation and magnetization of hexagonal iron oxide compounds. *Reviews of Modern Physics*, **25**, 297–301.

Ray, A.E. (1984). Metallurgical behavior of $Sm(Co,Fe,Cu,Zr)_z$ alloys. *Journal of Applied Physics*, **55**, 2094–2096.

Ray, A.E. (1986). Soft and hard magnetic materials with applications. *Soft and Hard Magnetic Materials with Applications*, ASM: Lake Buena Vista, pp. 105–117.

Ray, A.E. (1990). A revised model for the metallurgical behavior of 2:17-type permanent magnet alloys. *Journal of Applied Physics*, **67**, 4972–4974.

Ray, A. and Millott, H. (1971). The preparation of RCo_5 permanent magnet alloys. *IEEE Transactions on Magnetics*, **7**, 423–426.

Ray, A.E., Soffa, W.A., Blachere, J.R. and Zhang, B. (1987). Cellular microstructure development in $Sm(Co,Fe,Cu,Zr)_{8.35}$ alloys. *IEEE Transactions on Magnetics*, **MAG-23**, 2711–2713.

Rodewald, W., Wall, B., Fernengel, W. and Rodewald, W. (1997). Grain growth kinetics in sintered Nd-Fe-B magnets. *IEEE Transactions on Magnetics*, **33**, 3841–3843.

Rodewald, W., Wall, B., Katter, M. and Uestuener, K. (2002). Top Nd-Fe-B magnets with greater than 56 MGOe energy density and 9.8 kOe coercivity. *IEEE Transactions on Magnetics*, **38**, 2955–2957.

Rodewald, W., Wall, B., Katter, M. and Uestuener, K. (2003). Topology of Nd-Fe-B magnets with a high energy density. *IEEE Transactions on Magnetics*, **39**, 2932–2934.

Sagawa, M., Fujimura, S., Togawa, N., *et al*. (1984a). New material for permanent magnets on a base of Nd and Fe. *Journal of Applied Physics*, **55**, 2083–2087.

Sagawa, M., Fujimura, S., Togawa, N., *et al*. (1984b). New material for permanent magnets on a base of Nd and Fe (invited). *Journal of Applied Physics*, **55**, 2083–2087.

Sagawa, M., Fujimura, S., Yamamoto, H., *et al*. (1984c). Permanent magnet materials based on the rare earth-iron-boron tetragonal compunds. *IEEE Transactions on Magnetics*, **MAG-20**, 1584–1589.

Sagawa, M. and Hirosawa, S. (1987). Coercivity and microstructure of RFeB sintered permanent magnets. *Journal de Physique (Paris), Colloques*, **49**, 617–622.

Sagawa, M., Hirosawa, S., Yamamoto, H., *et al*. (1987). Nd-Fe-B permanent magnet materials. *Japanese Journal of Applied Physics, Part 1: Regular Papers and Short Notes*, **26**, 785–800.

Sagawa, M. and Nagata, H. (1993). Novel processing technology for permanent magnets. *IEEE Transactions on Magnetics*, **29**, 2747–2751.

Sagawa, M., Nagata, H., Itatani, O. and Watanabe, W. (1994). Improvement of manufacturing process for Nd-Fe-B sintered magnets. In *13th International Workshop on Rare Earth Magnets and their Applications*, Manwaring, C.A.F., Jones, D.F.G.,

Williams, A.J. and Harris, I.R. (Eds.), The University of Birmingham, Birmingham, p. 13.

Sankar, S.G., Rao, V.U.S., Segal, E., *et al*. (1975). Magnetocrystalline anisotropy of $SmCo_5$ and its interpretation on a crystal-field model. *Physical Review B*, **11**, 435.

Satyanarayana, M.V., Fujii, H. and Wallace, W.E. (1982). Magnetic properties of substituted $Sm_2Co_{17-x}T_x$ compounds (T = V, Ti, Zr, and Hf). *Journal of Applied Physics*, **53**, 2374–2376.

Schmidts, H.F. and Kronmüller, H. (1991). Size dependence of the nucleation field of rectangular ferromagnetic parallelepipeds. *Journal of Magnetism and Magnetic Materials*, **94**, 220–234.

Schneider, G., Henig, E-T., Petzow, G. and Stadelmaier, H.H. (1986). Phase relations in the system Fe-Nd-B. *Zeitschrift fur Metallkunde/Materials Research and Advanced Techniques*, **77**, 755–761.

Scholz, W., Schrefl, T., Fidler, J., *et al*. (2003). Micromagnetic simulation of the pinning and depinning process in permanent magnets. *IEEE Transactions on Magnetics*, **39**, 2920–2922.

Schrefl, T., Fidler, J. and Kronmüller, H. (1994). Remanence and coercivity in isotropic nanocrystalline permanent magnets. *Physical Review B*, **49**, 6100.

Schrefl, T., Schmidts, H.F., Fidler, J. and Kronmuller, H. (1993). Role of exchange and dipolar coupling at grain boundaries in hard magnetic materials. *Journal of Magnetism and Magnetic Materials*, **124**, 251–261.

Stadelmaier, H.H. (1984). Structural classification of transition metal-rare earth compounds between T and T_5R. *Zeitschrift fur Metallkunde/Materials Research and Advanced Techniques*, **75**, 227–230.

Stadelmaier, H.H., Elmasry, N.A., Liu, N.C. and Cheng, S.F. (1984). Metallurgy of the iron-neodymium-boron permanent magnet system. *Materials Letters*, **2**, 411–415.

Stoner, E.C. and Wohlfarth, E.P. (1948). A mechanism of magnetic hysteresis in heterogeneous alloys. *Philosophical Transactions of the Royal Society of London*, **240**, 599–642.

Streibl, B., Fidler, J. and Schrefl, T. (2000). Domain wall pinning in high temperature $Sm(Co, Fe, Cu, Zr)_{7-8}$ magnets. *Journal of Applied Physics*, **87**, 4765–4767.

Strnat, K.J. (1988). Rare earth-cobalt permanent magnets. In *Handbook of Magnetic Materials*, Wohlfarth, E.P. and Buschow, K.H.J. (Eds.), Elsevier, pp. 131–209, Vol. 4.

Strnat, K., Hoffer, G., Olson, J., *et al*. (1967). A family of new Cobalt-base permanent magnet materials. *Journal of Applied Physics*, **38**, 1001–1002.

Süss, D., Schrefl, T. and Fidler, J. (2000). Micromagnetics simulation of high energy density permanent magnets. *IEEE Transactions on Magnetics*, **36**, 3282–3284.

Tang, W., Zhang, Y., Goll, D., *et al*. (2001). New $Sm(Co, Fe, Cu, Zr)_z$magnets with better temperature stability. *Journal of Magnetism and Magnetic Materials*, **226–230**, 1365–1366.

Ying-Chang, Y., Hai-Ying, C., Feng, X., *et al*. (1985). Neutron and X-ray diffraction study of $Y_2Co_{17-x}Zr_x$ and $Y_2Co17_{1-y}Mn_y$ compounds. *IEEE Transactions on Magnetics*, **21**, 1987–1989.

Rare-earth Transition-metal Magnets

Werner Rodewald

Vacuumschmelze GmbH & Co. KG, Hanau, Germany

1 HISTORICAL REVIEW OF PERMANENT MAGNET MATERIALS

Permanent magnets have been attracting the attention of mankind since more than a thousand years. The application of lodestone, a fine mixture of ferrimagnetic magnetite (Fe_3O_4) and antiferromagnetic maghemite (γ-Fe_2O_3), in geomancy and in compasses by Chinese experts is well documented (Livingston, 1996). Since the coercivity H_{cJ} of lodestone amounts to only several $1\,kA\,m^{-1}$, these magnets had to be handled very carefully. Since the sixteenth century, needle-shaped strips of iron–carbon alloys with coercivities H_{cJ} of approximately $4\,kA\,m^{-1}$ were used by sailors of European countries. In the beginning of the nineteenth century, tungsten steel or cobalt–chromium steels were developed. These magnetic materials enable the manufacture of horseshoe magnets with maximum energy densities of about $8\,kJ\,m^{-3}$ (O'Handley, 2000).

In 1932, Mishima reported the hard magnetic properties of Fe–Al–Ni–Co alloys (Mishima, 1932), which are denoted by the tradename *Alnico*. The coercivity H_{cJ} of these magnets is determined by shape anisotropy. During a heat treatment at temperatures in the range 750–850 °C, a precipitation of ferromagnetic elongated α-(Fe,Co) rods in a Ni–Al-enriched matrix occurs by spinodal decomposition. Isotropic Alnico magnets achieve coercivities H_{cJ} in the range of $0.5–150\,kA\,m^{-1}$ and maximum energy densities between 8 and $80\,kJ\,m^{-3}$. In order to achieve anisotropic Alnico magnets, a texture in the polycrystalline microstructure was induced by directional solidification. Subsequent annealing in a magnetic field resulted in precipitation of elongated α(Fe,Co) rods parallel to the magnetic field (De Voss, 1969). Anisotropic Alnico magnets achieve coercivities H_{cJ} between 0.5 and $170\,kA\,m^{-1}$ and maximum energy densities between 40 and $75\,kJ\,m^{-3}$, see Figure 1. Single-crystal Alnico 5 magnets have a maximum energy density of $80\,kJ\,m^{-3}$, owing to the optimized alignment of the α(Fe,Co) precipitates.

In 1952, Went *et al*. detected the hard magnetic properties of the hexagonal ferrites based on $MeO{\cdot}6Fe_2O_3$, Me: Ba, Sr, Pb (Went, Rathenau, Gorter and Van Oosterhaut, 1952). The coercivity of the hexaferrites is due to a strong magnetocrystalline anisotropy, which aligns the magnetic moments of the Fe ions parallel to the hexagonal axis. In order to reverse the polarization of a magnet, in principle, a reversed magnetic domain must be nucleated in each grain by the external field. The coercivities of isotropic Ba hexaferrites range from 210 to $270\,kA\,m^{-1}$. Within a unit cell, a third of the magnetic moments of the 24 Fe^{3+} ions are aligned antiparallel to the remaining Fe^{3+} ions, so that a small

Handbook of Magnetism and Advanced Magnetic Materials. Edited by Helmut Kronmüller and Stuart Parkin. Volume 4: *Novel Materials*. © 2007 John Wiley & Sons, Ltd. ISBN: 978-0-470-02217-7.

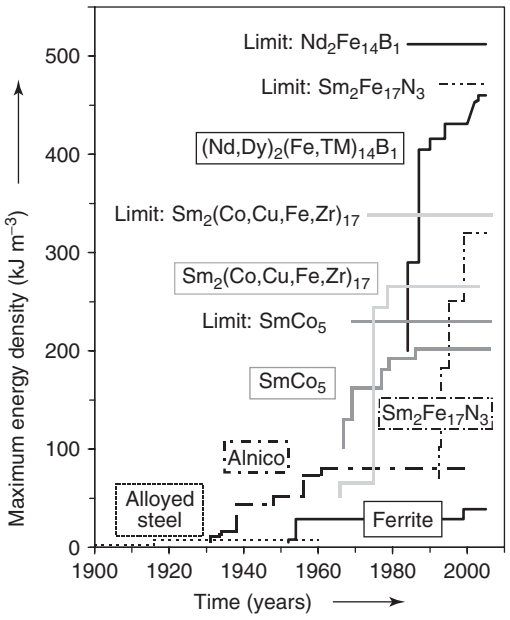

Figure 1. Progress in the maximum energy density of permanent magnets. For RE–TM magnet materials, the theoretical limits are indicated.

remanent polarization results. The maximum energy densities of isotropic $BaO{\cdot}6Fe_2O_3$ range between 6.5 and 9 kJ m^{-3}.

The uniaxial anisotropy of the hexaferrites enables the production of anisotropic magnets by powder metallurgy. After calcination, the material is milled to a fine alloy powder. The powder particles can be aligned by a magnetic field, compacted, and sintered to dense magnets. The coercivities of anisotropic Ba hexaferrites range between 130 and 340 kA m^{-1}. Owing to the increased magnetic polarization, much higher maximum energy densities between 20 and 30 kJ m^{-3} result, see Figure 1.

Even for these well-known magnetic materials, an essential improvement in the magnetic properties has been achieved lately. By a partial substitution of Sr by La and of Fe by Co, the remanent polarization and the coercivity could be increased by 4.4 and 7.5% respectively (Ogata *et al*., 1999).

In 1966, Strnat noticed the magnetocrystalline anisotropy of the rare earth (RE)–cobalt compounds $RECo_5$ (Hoffer and Strnat, 1966). The RE metals comprise the elements with the atomic numbers 58 (cerium) to 71 (lutetium), in which the 4f orbitals are filled with electrons. Owing to similar chemical properties, Y and La are also often included. Fortunately, these metals are rather abundant. For instance, the concentration of Ce in the earth's crust amounts to 46 ppm and is as available as the common metals Co (23 ppm), Sn (40 ppm), Pb (16 ppm), or Mg (15 ppm), (Vendel, 1984). Within the RE metals, Nd (24 ppm), Sm (6.5 ppm), and Dy (5 ppm) are rather abundant, see Figure 2.

In particular, the $SmCo_5$ compound has a very strong magnetocrystalline anisotropy. Hence, it was thought that anisotropic magnets should be prepared by powder metallurgy, similar to the production of the anisotropic hexaferrites. However, the RE–Co alloy powders are very sensitive to oxidation, and it took 3 years before Das succeeded in the preparation of anisotropic $SmCo_5$ magnets by powder metallurgy (Das, 1969). The coercivity of sintered $SmCo_5$ magnets is determined by nucleation of reversed domains, similar to the hexaferrites, but ranges between 1500 and 2400 kA m^{-1}. As a consequence of the high magnetic polarization, which results from the ferromagnetically coupled Co and RE^{3+} moments, the maximum energy densities amount to 160 up to 200 kJ m^{-3}, see Figure 1.

Since the concentration of Co atoms in the RE_2Co_{17} compounds is increased, a higher magnetic polarization results. However, the high saturation polarization of the RE_2Co_{17} compounds could not be exploited for increasing the maximum energy density of sintered magnets, since most of the RE_2Co_{17} compounds had a planar anisotropy. Only Sm_2Co_{17} and Er_2Co_{17} compounds have a uniaxial anisotropy (Ray and Strnat, 1972). On the basis of the Sm_2Co_{17} compound, Ojima *et al*. prepared magnets with a maximum energy density of 240 kJ m^{-3} and a coercivity of 500 kA m^{-1} (Ojima, Tomizawa, Yoneyama and Hori, 1977), which is too small for technical applications. Hence, another route for achieving strong coercivities had to be developed. By partial substitution of Co by Fe, Cu, and Zr and an appropriate heat treatment, a cellular microstructure of $Sm_2(Co,Fe)_{17}$ cells in a $Sm(Co,Cu)_5$ matrix could be achieved (Mishra *et al*., 1981). Since the intrinsic magnetic properties of these phases differ, magnetic domain walls are pinned at the phase boundaries. Hence, the pinning force determines the coercivity of such multiphase $Sm_2(Co,Cu,Fe,Zr)_{17}$ magnets (Fidler and Skalicky, 1982; Katter *et al*., 1996a,b; Katter, 1998). The coercivities H_{cJ} of sintered $Sm_2(Co,Cu,Fe,Zr)_{17}$ magnets can be tailored to meet the requirements of an application and range between 800 and 2100 kA m^{-1}. The maximum energy densities vary between 200 and 240 kJ m^{-3}, see Figure 1.

By increasing the Co content at the expense of the Fe concentration and by adjusting the Cu concentration $Sm_2(Co,Cu,Fe,Zr)_{17}$, magnets with a coercivity H_{cJ} of about 700 kA m^{-1} at a temperature of 500 °C were developed (Liu *et al*., 1999; Walmer *et al*., 2000a,b; Goll, Sigle, Hadjipanayis and Kronmüller, 2000; Zhang *et al*., 2000). With an appropriate coating, such magnets can be applied at high temperatures up to 550 °C.

Because of the successful application of RE–Co magnets, RE–Fe alloys were examined for intermetallic compounds with superior hard magnetic properties. Besides alloying and powder metallurgy (Sagawa *et al*., 1984a,b), the alternative processing route of rapid solidification or melt spinning,

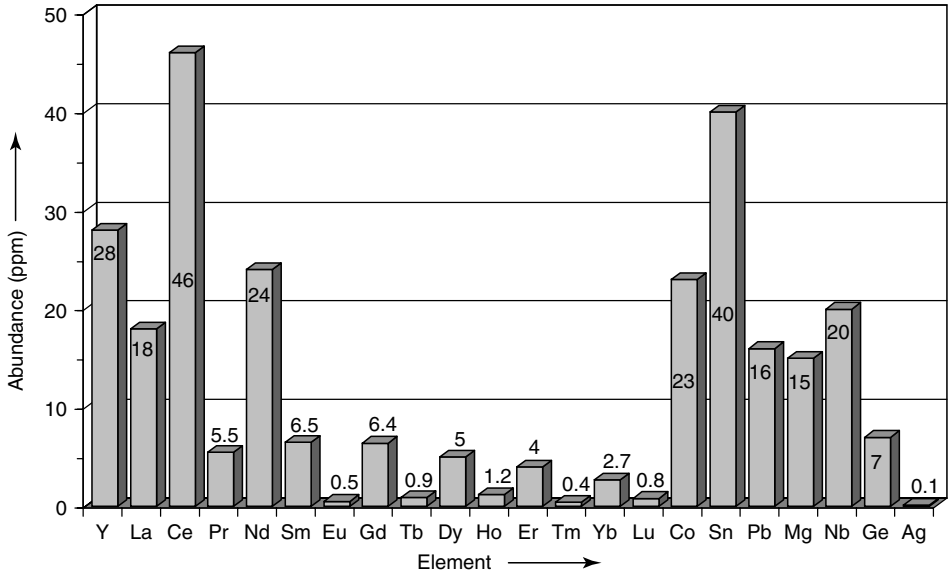

Figure 2. Abundance of rare-earth metals in comparison to some commercial metals.

respectively, has been investigated (Koon and Das, 1981; Croat, 1981a,b; Croat *et al*., 1984a,b; Hadjipanayis, Hazelton and Lawless, 1983, 1984). The efforts resulted in the development of different production routes for Nd–Fe–B magnets on the basis of the hard magnetic $Nd_2Fe_{14}B$ compound. The crystallographic positions of the different atoms in this new unit cell and their magnetic moments were determined exactly by neutron diffraction (Herbst, Croat, Pinkerton and Yelon, 1984). In this compound, the Nd atoms can be replaced by any other RE atom that influences the intrinsic magnetic properties (Sagawa *et al*., 1984; Herbst and Yelon, 1985). By a partial substitution of Nd by Dy, the coercivity of (Nd,Dy)–Fe–B magnets can be increased due to the enhanced magnetocrystalline anisotropy of the $Dy_2Fe_{14}B$ compound (Sagawa *et al*., 1984; Rodewald, 1985). Hence, the coercivities of Nd–Fe–B magnets can be adjusted to the application and now range between 950 and 2860 kA m^{-1}, the maximum energy densities being extend from 415 to 225 kJ m^{-3}, see Figure 1.

Some years later, promising hard magnetic properties were also detected in novel interstitial RE–Fe–N and RE–Fe–C compounds, the properties of which are presented by J. M. D. Coey in a separate chapter of this handbook (See also **Dilute Magnetic Oxides and Nitrides, Volume 4**).

The various production technologies for Nd–Fe–B magnets by powder metallurgy and their impact on the hard magnetic properties are presented in Section 2. In 2003, about 25.290 tons of Nd–Fe–B magnets were produced by powder metallurgy globally (Luo, 2004). Additional informations on the status of the magnet industry are presented in **Current Status and Future Development of the Magnetic Materials Industry in China, Volume 4**. The magnetizing behavior and the temperature stability of sintered Nd–Fe–B magnets are reviewed in Sections 3 and 4. A lot of research and development activities have been focused on the improvement of the corrosion behavior of sintered Nd–Fe–B magnets, which is decisive for many applications. The basic results and the progress in RE–TM magnet materials are summarized in Section 5. In many applications, the RE–TM magnets also experience mechanical stress besides magnetic stress. Some basic mechanical properties of sintered RE–TM magnets are compiled in Section 6. Some conclusions on the exploitation of the intrinsic magnetic properties of the different RE–TM compounds by commercial RE–TM magnet grades or by paramount laboratory magnets finish this review.

2 PRODUCTION OF SINTERED RE–TM MAGNETS BY POWDER METALLURGY AND THE IMPACT ON THE PROPERTIES

Most of the RE magnets with a high remanent polarization J_r or a strong coercivity H_{cJ}, respectively, are produced by powder metallurgy on a large scale in many shapes and dimensions. The processing route of RE–TM magnets starts with alloying. The alloys are melted from RE metals, transition metals (TMs), master alloys, and specific additions in vacuum induction furnaces since the RE metals are very sensitive to oxidation, in particular, at high temperatures.

An alternative processing route is the calciothermic reduction. RE oxides, TM powders, additions, and a reducing

agent, for instance, Ca hydride, are intensively mixed and compacted. During heating in a sealed container up to 1200 °C, the Ca metal evaporates and reduces the RE oxides to small RE particles, which immediately start to alloy with the TM and the additions, respectively (Herget, 1985). Finally, an RE–TM alloy powder in a matrix of Ca oxide results. After cooling to room temperature, the Ca oxide and excess Ca metal are separated from the alloy powder by leaching. Qualitatively, the calciothermic reaction and the leaching process can be described by equations (1) and (2), according to Herget (1985):

$$7.5Nd_2O_3 + 72Fe + 0.133Fe_{40}B_{60} + 22.5Ca \longrightarrow Nd_{15}Fe_{77}B_8 + 22.5CaO \quad (1)$$

$$Ca + CaO + 2H_2O \longrightarrow 2Ca(OH)_2 \quad (2)$$

The cast ingots or the calciothermic alloy powders have a multiphase polycrystalline microstructure. The hard magnetic $Nd_2Fe_{14}B$ grains are in equilibrium with Nd-rich constituents and some $Nd_{1.1}Fe_4B_4$ grains (Matsuura *et al.*, 1985). The magnetic moments of the $Nd_2Fe_{14}B$ grains are aligned parallel to the tetragonal axis by strong crystalline electric fields and hence are distributed randomly. In order to achieve a well-defined texture, powder metallurgy is applied. The alloys are crushed and milled to a fine alloy powder, see Figure 3. The powder particles must consist of single crystals or fragments thereof. In general, alloy powders with a particle size in the range between 3 and 5 µm meet this condition very well. For the production of anisotropic magnets, there exist different routes, which determine the magnetic properties, the dimensional tolerances, and the processing costs. After compaction of the alloy powders by different pressing technologies, the green parts are sintered to compact magnets. At sintering temperature, the fraction of the Nd-rich constituents is melted, so that liquid-phase sintering occurs and magnets with a density of approximately 98% of the theoretical density can be achieved. Afterward, a heat treatment is applied in order to optimize the microstructure with respect to the coercivity H_{cJ} of the magnets. Finally, the magnets are machined to dimensions, according to customer specifications, see Figure 3.

The maximum energy density is determined by the remanent polarization J_r and the reversible permeability μ_{rev}, see equation (3):

$$(BH)_{max} = \frac{J_r^2}{4 \cdot \mu_o \cdot \mu_{rev}} \quad (3)$$

In order to achieve a high maximum energy density, the remanent polarization and the reversible permeability have to be optimized. The remanent polarization J_r is determined

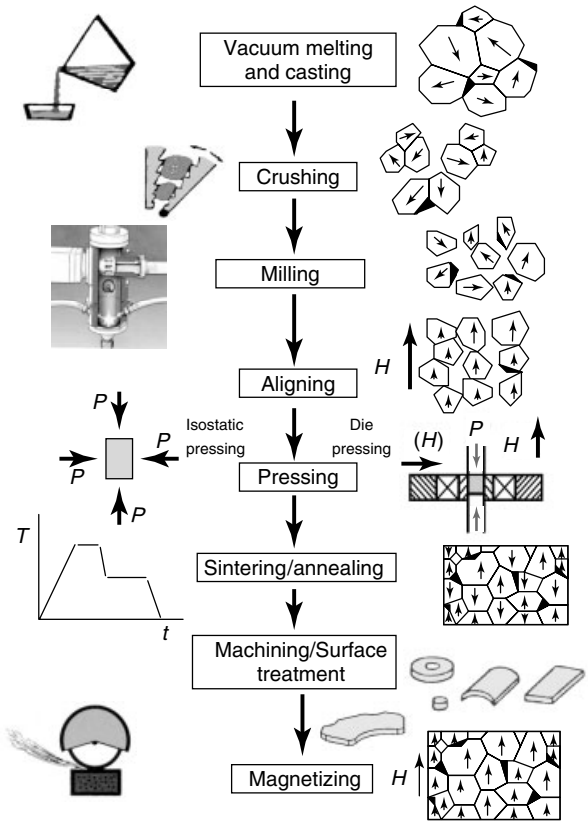

Figure 3. Processing of anisotropic RE magnets by powder metallurgy.

by equation (4):

$$J_r(20\,^\circ C) = J_s(20\,^\circ C) \cdot \frac{\rho}{\rho_0} \cdot (1 - V_{nonmag}) \cdot 0.01 \cdot f_\varphi \quad (4)$$

where $J_s(20\,^\circ C)$, ρ/ρ_0, V_{nonmag}, and f_φ denote the saturation polarization of the $Nd_2Fe_{14}B$ compound at 20 °C, the density related to the theoretical density of the alloy, and the fraction of nonmagnetic constituents and the alignment coefficient respectively.

The alignment coefficient is defined by Fernengel *et al.* (1996)

$$f_\varphi = (100\% \cdot \cos\varphi) \quad \text{with} \quad \varphi = \arctan\left(2\frac{J_{r\perp}}{J_{r\parallel}}\right) \quad (5)$$

and represents the average misalignment angle φ of the grains with respect to the easy axis, see Figure 4. The precondition is a cylindrical symmetrical distribution of the misaligned grains. Magnets pressed isostatically or in an axial magnetic field, respectively, meet this precondition fairly well. For magnets pressed in a transverse magnetic field (see Section 2.3), the perpendicular components of the remanent polarization $J_{r\perp}$ parallel or transverse to the pressing direction are different. Hence, for transversely

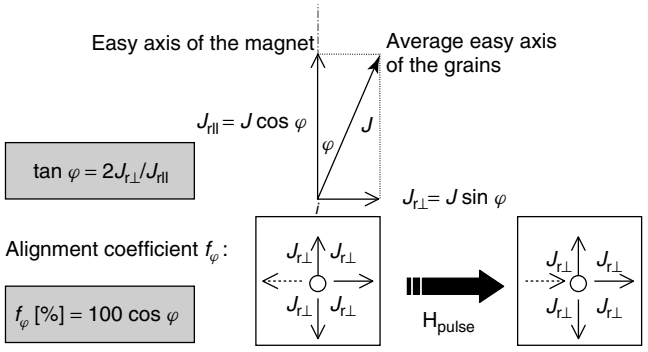

Figure 4. Schematic representation of the distribution of the components $J_{r\perp}$ of the magnetic polarization after magnetizing an anisotropic magnet perpendicular to its easy axis and definition of the alignment coefficient f_φ. Precondition is a homogeneous axial distribution of the misaligned grains, such as in cold isostatically pressed magnet blocks, axial field die pressed, or rubber isostatically pressed net-shaped magnets.

pressed magnets, two alignment coefficients have to be distinguished. The alignment coefficients can be easily determined from the remanent polarization measured parallel $J_{r\|}$ and perpendicular $J_{r\perp}$ with respect to the easy axis of an anisotropic magnet by a pair of Helmholtz coils after appropriate magnetization (Fernengel *et al.*, 1996).

The impact of different processing routes on the magnetic properties is reviewed in detail.

2.1 Cold isostatic pressing of magnet blocks (CIP)

For the production of big blocks, the alloy powder is sealed in a mold, aligned by a magnetic field, and pressed isostatically. Since the pressure increases homogeneously from all directions, the alignment of the powder particles is not disturbed significantly during compaction, see Figure 5. The isostatically pressed blocks are sintered to >98% of the theoretical density. Hence, isostatically pressed blocks have an excellent texture and achieve a high remanent polarization J_r. The alignment coefficient f_φ ranges between 96 and 99%. After sintering, the magnet blocks are annealed in order to optimize the coercivity.

Figure 6 gives the demagnetization curves $J(H)$ and $B(H)$ of isostatically pressed Nd–Fe–B magnets with a high remanent polarization at different temperatures. At room temperature, the typical remanent polarization and the coercivities amount to 1.46 T and 955 kA m^{-1} for H_{cJ} or to 915 kA m^{-1} for H_{cB}, respectively. With a recoil permeability of 1.03, a maximum energy density of 415 kJ m^{-3} results for this commercial magnet grade VACODYM® 722 HR.

Isotatically pressed blocks of $Sm_2(Co,Cu,Fe,Zr)_{17}$ magnets achieve remanent polarizations of 1.12 or 1.10 T with

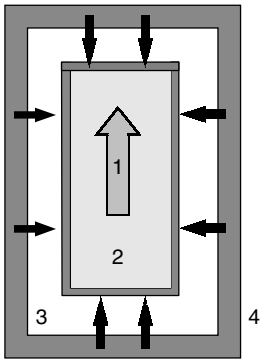

Figure 5. Principle of cold isostatic pressing of large magnet blocks: (1) alignment field, (2) alloy powder, (3) mold, (4) pressure container. Dimensions up to 105 mm in diameter and approximately 300 mm in length can be produced.

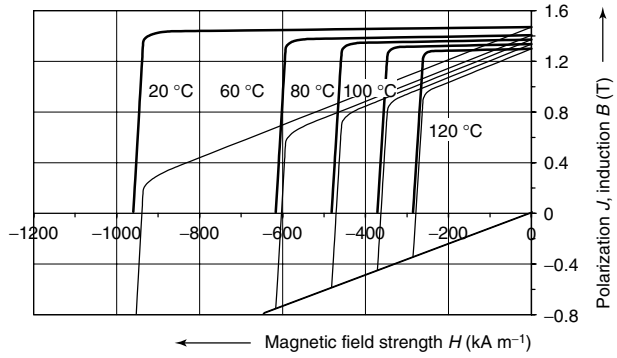

Figure 6. Demagnetization curves $J(H)$ and $B(H)$ of isostatically pressed Nd–Fe–B magnet blocks, grade VACODYM 722 HR, depending on the temperature. The typical magnetic properties at room temperature amount to $J_r = 1.46$ T, $H_{cJ} = 955$ kA m^{-1}, $(BH)_{max} = 415$ kJ m^{-3}.

coercivities H_{cJ} of 800 or 2070 kA m^{-1}, respectively, which results in maximum energy densities of 240 or 225 kJ m^{-3}. The lower Co concentration in isostatically pressed blocks of $SmCo_5$ magnets results in a smaller remanent polarization of 1.01 T and a maximum energy density of 200 kJ m^{-3}. Owing to the extraordinarily strong magnetocrystalline anisotropy of the $SmCo_5$ compound, a strong coercivity H_{cJ} of >1500 kA m^{-1} results.

2.2 Net-shaped magnets by axial field die-pressing (AP)

The manufacture of parts from isostatically pressed RE magnet blocks takes a lot of machining and therefore increases the processing costs. An alternative route is the production of net-shaped parts by die-pressing. The alloy powder is filled into the cavity of a die, aligned by an axial magnetic field, and compacted, see Figure 7. Since the easy axes

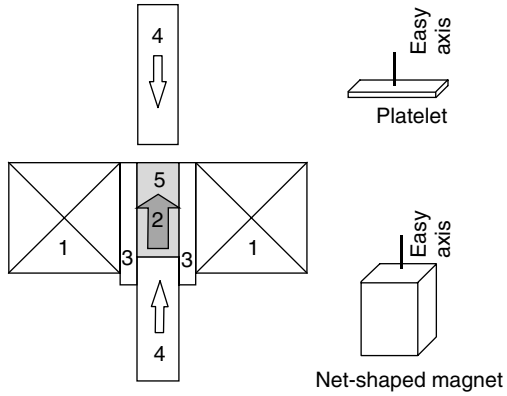

Figure 7. Principle of axial field die-pressing of large net-shaped magnets: (1) alignment coil, (2) magnetic field, (3) mold, (4) punches, and (5) alloy powder.

of the powder particles are aligned parallel to the pressing direction, the alignment is disturbed during compaction due to friction between the powder particles and the die. Hence, the remanent polarization of axial field die-pressed magnets is about 6–8% lower than isostatically pressed magnet blocks. By axial field die-pressing, a large variety of shapes with different dimensions can be manufactured economically.

Axial field die-pressed magnets based on Nd–Dy–Fe–Co–B alloys can achieve very high coercivities H_{cJ}. For instance, the typical demagnetization curves $J(H)$ and $B(H)$ at room temperature demonstrate a remanent polarization of 1.08 T and coercivities of 2.865 kA m^{-1} for H_{cJ} and 830 kA m^{-1} for H_{cB}, see Figure 8. With increasing temperature, a decrease in the coercivity H_{cJ} cannot be prevented, but at a temperature of 150 °C the coercivity H_{cJ} still amounts to 1.200 kA m^{-1}. Such magnets resist strong reversed magnetic fields even at elevated temperatures. This is a decisive benefit for many motor applications. The maximum energy density of such magnets with a strong coercivity amounts to 225 kJ m^{-3}.

Net-shaped magnets produced by axial field die-pressing from $Sm_2(Co,Cu,Fe,Zr)_{17}$ alloy powders achieve remanent polarizations and coercivities H_{cJ} in the range of 0.97–1.05 T and 2070–800 kA m^{-1}. The maximum energy density of such magnets varies between 170 and 210 kJ m^{-3}. Owing to the lower saturation polarization of the $SmCo_5$ compound, the remanent polarizations and the coercivities H_{cJ} of net-shaped $SmCo_5$ magnets amount to 0.85–0.95 T and 2400–1200 kA m^{-1}. The maximum energy densities of axial field die-pressed $SmCo_5$ magnets range between 140 and 180 kJ m^{-3}.

In general, net-shaped Sm–Co magnets are more brittle than Nd–Fe–B magnets and are sensitive to chipping, but have a superior temperature and corrosion stability.

2.3 Net-shaped magnets by transverse field die-pressing (TP)

Another possibility is the pressing of parts in a transverse magnetic field, see Figure 9. In this case, the alignment of the powder particles is not disturbed very strongly during compaction; therefore, it results in remanent polarizations similar to isostatically pressed magnet blocks. Hence, in sintered transverse field die-pressed magnets, alignment coefficients, f_φ, vary between 94 and 96% in general.

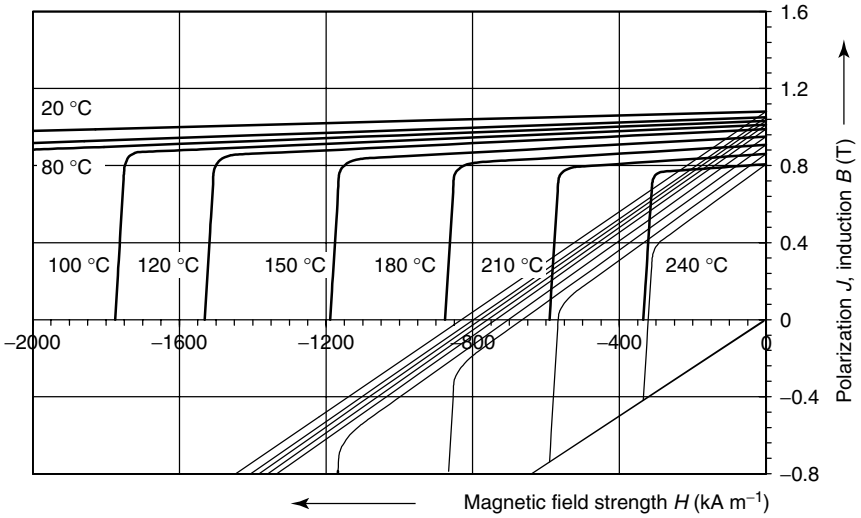

Figure 8. Demagnetization curves $J(H)$ and $B(H)$ of isostatically pressed Nd–Fe–B magnet blocks, grade VACODYM 688 AP, depending on the temperature. The typical magnetic properties at room temperature amount to $J_r = 1.08$ T, $H_{cJ} = 2865$ kA m^{-1}, $(BH)_{max} = 225$ kJ m^{-3}.

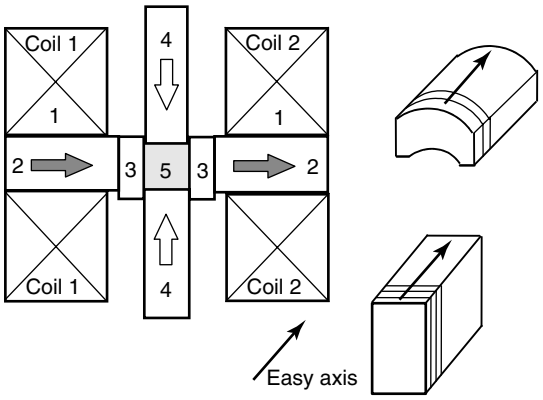

Figure 9. Principle of transverse field die-pressing of near net-shaped magnets: (1) alignment coils, (2) magnetic field, (3) mold, (4) punches, and (5) alloy powder.

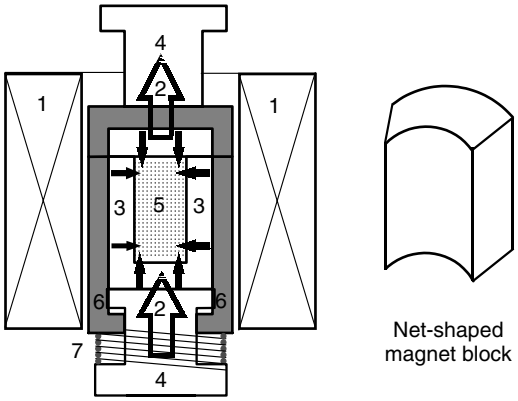

Figure 10. Principle of rubber isostatic pressing of net-shaped magnets: (1) pulse field alignment coil, (2) magnetic field, (3) thick rubber mold, (4) punches, (5) alloy powder, (6) support die, and (7) support spring.

By transverse field die-pressing, mainly rectangular blocks or near net-shaped parts are manufactured. After sintering, the blocks are cut into thin magnet plates according to customer specifications. However, near net-shaped parts may need some contour grinding before cutting. Hence, the machining costs increase in comparison to axial field die-pressed magnets.

The typical magnetic properties of transverse field die-pressed Nd–Fe–B magnets range from 1.14 up to 1.43 T for the remanent polarization and from 2865 to 955 kA m^{-1} for the coercivity H_{cJ} or from 885 to 915 kA m^{-1} for the coercivity H_{cB}, respectively, which depends on the alloy composition. Accordingly, the maximum energy densities vary between 250 and 395 kJ m^{-3}.

2.4 Net-shaped magnets by rubber isostatic pressing (RIP)

A new pressing technology, which combines the benefits of cold isostatic pressing (CIP) – an almost perfect alignment – and die-pressing net-shaped parts, is rubber isostatic pressing (RIP) (Sagawa and Nagata, 1993; Sagawa, Nagata, Watanabe and Itani, 2000; Nagata and Sagawa, 2002). The alloy powder is tapped into a thick rubber mold up to a well-defined density and then the die is closed by the upper punch. Afterwards, the powder particles are aligned by strong magnetic field pulses with a peak field strength of 2.400 kA m^{-1}. Finally, the alloy powder is compacted by axial pressing, see Figure 10. However, by the thick rubber mold, the pressing forces are diverted, so that an almost isostatic compaction occurs. Hence, near net-shaped parts with alignment coefficients comparable to isostatically pressed blocks can be manufactured.

By RIP, near net-shaped blocks with a remanent polarization of 1.47 T and a coercivity of 920 kA m^{-1} could be manufactured. The maximum energy density of such blocks amounts to 424 kJ m^{-3}, see Figure 11. Such magnets achieve alignment coefficients $f > 96\%$, which implies an average misalignment angle of $<16^{\circ}$ related to the easy axis of the magnet.

The almost perfect alignment of the grains results in strong demagnetizing local stray fields, which decrease the coercivity of such magnets (Rodewald *et al.*, 2000). Owing to the small coercivity H_{cJ}, the maximum continuous operating temperature amounts to about 60 °C for a load line $B/\mu_0 H = -2$.

2.5 Review of alternative processing routes

Besides the production of anisotropic RE–TM magnets by powder metallurgy, several alternative processing routes have been developed, in particular, for Nd–Fe–B magnets. Main objectives have been the elimination of some processing steps in order to simplify the production route and to reduce the processing costs; in particular, the handling of fine and pyrophoric RE–TM alloy powders. However, in most cases, isotropic magnet materials with inferior magnetic properties result. For the manufacture of anisotropic magnets, additional processing steps, such as hot deformation or hot rolling are needed. Besides, some alternative processing routes only enable the production of magnets with special shapes, for instance, ring magnets, thick layers, or thin films.

2.5.1 Rapid solidification and compaction of RE–TM magnets

Alloy powders for polymer-bonded magnets are produced in large quantities by rapid solidification or melt spinning

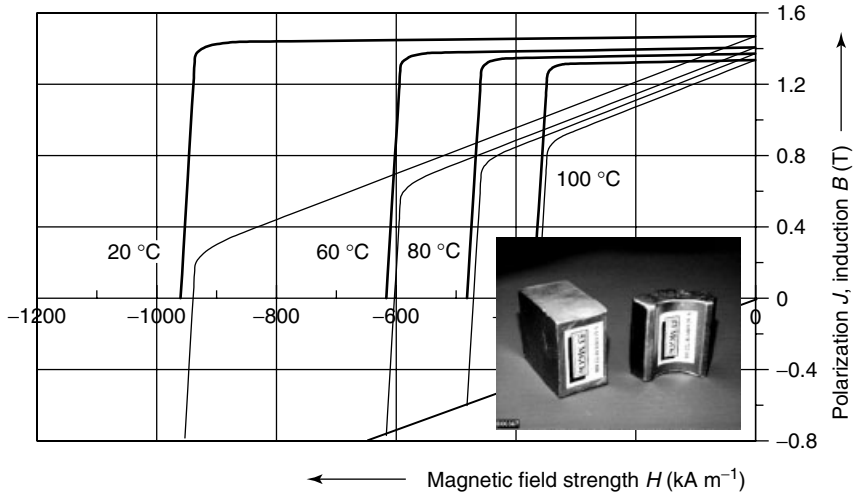

Figure 11. Demagnetization curves $J(H)$ and $B(H)$ of Nd–Dy–Fe–B magnets manufactured by rubber isostatic pressing (RIP®) at different temperatures. ®: registered trademark of Intermetallics Co. Ltd.

of Nd–Fe–B alloys. The molten alloy is chilled onto a fast rotating wheel surface, so that amorphous or submicrocrystalline ribbons with a thickness between 30 and 50 µm result (Croat *et al*., 1984). Since the easy axes of the crystals are distributed randomly, the alloy powders of such submicrocrystalline ribbons are isotropic with respect to the magnetic polarization. The remanent polarization and the coercivities of annealed and crushed alloy powders, made from Nd–Fe–B ribbons, range from 0.78 to 1.0 T and 510 to 1430 kA m^{-1}, depending on the composition of the alloy powders. The maximum energy densities, related to the theoretical density, vary from 95 to 140 kJ m^{-3}.

Compact isotropic Nd–Fe–B magnets can be manufactured by hot-pressing at temperatures of about 750 °C (Croat *et al*., 1984). The remanent polarization and the coercivities of compact isotropic hot-pressed net-shaped magnets range from 0.8 to 0.83 T for the remanent polarization, from 1440 to 1400 kA m^{-1} for the coercivity H_{cJ}, and from 112 to 120 kJ m^{-3} for the maximum energy density.

By an additional hot-deformation process at a temperature of about 750 °C, anisotropic Nd–Fe–B magnets can also be manufactured (Lee, Brewer and Schaffel, 1985). Owing to a pressure-induced anisotropic grain growth of these grains, the easy axes of which are aligned parallel to the pressing force, a texture of hot-deformed magnets is obtained (Mishra, Brewer and Lee, 1988; Li and Graham, 1990). The magnetic properties of compact anisotropic hot-deformed Nd–Fe–B magnets amount to 1.15–1.3 T for the remanent polarization, to 1600–1000 kA m^{-1} for the coercivity H_{cJ}, and to 250–340 kJ m^{-3} for the maximum energy density.

Similar principles are exploited for the production of radially aligned ring magnets by hot-backward extrusion (Yoshikawa *et al*., 1994, 1999; Grünberger, 1998). The magnetic properties of radially aligned Nd–Fe–B ring magnets strongly depend on the inner and outer diameters. Radially anisotropic Nd–Fe–B magnets with a remanent polarization between 1.08 and 1.32 T, coercivities H_{cJ} between 1990 and 1110 kA m^{-1}, and maximum energy densities between 230 and 330 kJ m^{-3} are commercially available.

2.5.2 *Gas atomization of RE–TM alloys*

Another economic route for the production of isotropic alloy powders with strong coercivities H_{cJ} is inert gas atomization (Yamamoto, Inoue and Masumoto, 1989; Lewis, Sellers and Panchanathan, 1995, 1996; Sellers *et al*., 1997; Branagan, Burch, Sellers and Hyde, 1998). The RE–TM alloy is melted by an electric arc and dispersed by a gas stream, which in general results in a wide particle size distribution (Yamamoto, Inoue and Masumoto, 1989; Lewis, Sellers and Panchanathan, 1995). The magnetic properties of the alloy powder depend on the microstructure of the particles, which can be optimized by appropriate quenching rates (Branagan, Burch, Sellers and Hyde, 1998; Kramer *et al*., 2003), subsequent heat treatments (Yamamoto, Inoue and Masumoto, 1989), or alloying additions, for instance, TiC (Branagan, Hyde, Sellers and Lewis, 1996). The research and development activities focus on the production of alloy powders with small dimensions, a narrow particle size distribution, and a submicrocrystalline microstructure in order to improve the coercivity H_{cJ} and the squareness of the demagnetization curve $J(H)$.

Commercial gas-atomized Nd–Fe–B alloy powders for the manufacture of bonded RE–TM magnets, in particular, by injection molding, with a remanent polarization and coercivity H_{cJ} of 0.73–0.76 T and 670–750 kA m^{-1} are available.

The maximum energy density of such alloy powders ranges between 80 and 92 kJ m^{-3}.

2.5.3 *Mechanical alloying and compaction of RE–TM magnets*

Mechanical alloying is a powder metallurgical processing route, originally developed for the production of oxide dispersion–strengthened materials. In general, it is well suited for the preparation of any type of nonequilibrium phases, such as amorphous or nanocrystalline materials. A powder blend consisting of elemental powders is milled in a ball mill in an inert atmosphere. Mechanical alloying was applied for the preparation of hard magnetic Nd–Fe–B powders first by Schultz, Wecker and Hellstein (1987). Elemental Nd, Fe, and B powders were milled in a ball mill in an inert atmosphere. The individual powder particles were cold worked by collisions with the balls or by friction. Heavy deformation, repeated cold welding, and fracture produced a nanocrystalline composite, which consisted of an amorphous Nd-rich phase and α-Fe crystals after prolonged milling. After a subsequent heat treatment, at a temperature between 600 and 750 °C, the hard magnetic $Nd_2Fe_{14}B$ compound was crystallized. Mechanically alloyed and heat-treated Nd–Fe–B alloy powders have a nanocrystalline microstructure. Each particle consists of many randomly aligned grains with dimensions of less than 100 nm. Similar to rapidly solidified ribbons, mechanically alloyed Nd–Fe–B alloy powders can be applied for the manufacture of polymer-bonded magnets. Typical magnetic properties of mechanically alloyed Nd–Fe–B powders amount to 0.8–0.92 T for the remanent polarization, 1200–1000 kA m^{-1} for the coercivity H_{cJ}, and 102–140 kJ m^{-3} for the maximum energy density (Schultz, Wecker and Hellstein, 1987; Bollero, Gutfleisch, Müller and Schultz, 2002).

Nanocrystalline two-phase Nd–Fe–B powders with enhanced remanent polarizations up to 1.2 T and smaller coercivities H_{cJ} in the range between 336 and 480 kA m^{-1} could be prepared by mechanical alloying and annealing (Neu and Schultz, 2001). Intensive milling of Nd–Fe–B powders, which are much easier to crush and to mill, also resulted in isotropic alloy powders with remanent polarizations and coercivities of about 0.68 T and 1.200 kA m^{-1} (Daniel, 1995).

Compact isotropic magnets can be produced by hot pressing, and an additional hot-deformation process enables the manufacture of anisotropic magnets (Schultz, Schnitzke and Wecker, 1988).

Mechanical alloying of SmF_3, Co, and Ca powders resulted after a heat treatment at a temperature between 600 and 750 °C in isotropic $SmCo_5$ powders with an extremely high coercivity H_{cJ} of 5240 kA m^{-1} (Liu, Dallimore and McCormick, 1992).

2.5.4 *Hot rolling of RE–TM magnet materials*

There are some research and development activities on the production of anisotropic RE–TM magnets directly from cast Pr–Fe–Cu–B or Nd–Fe–Cu–B alloys in order to minimize the number of processing steps. In general, cast ingots get a heat treatment at temperatures of about 1000 °C in order to homogenize the microstructure. By hot rolling such ingots, anisotropic magnet plates with a thickness up to a few millimeters have been produced (Shimoda, Akioka, Kobayashi and Yamagami, 1988, 1989; Shimoda, Akioka and Kobayashi, 1990; Hinz, Schumann, Helming and Schäfer, 1994; Rivoirard *et al*., 2000). During hot rolling, a grain refinement and an alignment occurs. Similar to the hot-deformation process, the easy axes of the grains align parallel to the deformation force and hence orientate the easy axis perpendicular to the rolling plane (Hinz, Schumann, Helming and Schäfer, 1994). Typical thickness reductions range between 75 and 95%. The optimal magnetic properties are achieved after proper annealing at temperatures between 1000 and 500 °C (Arai *et al*., 1994). In general, the magnetic properties of hot-rolled Pr–Fe–Cu–B or Nd–Fe–Cu–B magnets range between 0.9 and 1.2 T for the remanent polarization, between 800 and 1300 kA m^{-1} for the coercivity H_{cJ}, and between 120 and 290 kJ m^{-3} for the maximum energy density.

2.5.5 *Plasma spraying of RE–TM magnet layers*

A very straightforward processing route for manufacturing RE–TM magnet layers with a thickness up to some millimeters is plasma spraying. In principle, plasma spraying needs only three processing steps: alloying, crushing to an alloy powder with a particle size in the range 40–100 µm, and plasma spraying. The coarse alloy powder is melted in a gas plasma, in which the temperatures can be as high as 20 000 °C. The molten RE–TM particles are accelerated and are consolidated onto a substrate. Parts with complicated shapes can be manufactured, for instance, thin-walled hollow cylinders. The cooling rates are estimated to amount to about 10^6 K s^{-1}. Hence, amorphous or very fine crystalline microstructures result. In order to prevent oxidation, plasma spraying has to be performed in vacuum or in an inert atmosphere.

Without preheating the substrate, low coercivities of some 10 kA m^{-1} result in the as-deposited Nd–Dy–Fe–B layers, which increase substantially after appropriate annealing. The $Nd_{16}Dy_1Fe_{76}B_7$ layers have got the best magnetic properties after annealing: remanent polarizations and coercivities

H_{cJ} are in the range 0.66–0.7 T and 1210–1250 kA m^{-1}. Maximum energy densities from 80 to 82.4 kJ m^{-3} are obtained (Willson, Bauser, Liu and Huang, 2003).

Preheating the substrate to temperatures of about 600 °C, $Nd_{16}Dy_1Fe_{76}B_7$ layers achieve remanent polarizations of 0.55–0.59 T and coercivities of 960–1600 kA m^{-1}. The maximum energy densities of the almost isotropic layers amount to 44–61 kJ m^{-3} (Overfelt, Anderson and Flanagan, 1986; Rieger *et al*., 2000; Willson, Bauser, Liu and Huang, 2003).

In Nd–Fe–B plasma-sprayed layers, consolidated onto Cu substrates, which were heated to temperatures in the range 500–800 °C, some magnetic anisotropy could be obtained (Wyslocki, 1992b). Owing to the partial alignment of the $Nd_2Fe_{14}B$ grains, a remanent polarization of 0.9 T could be obtained. The very fine microstructure of the layer results in a strong coercivity H_{cJ} of 1200 kA m^{-1}. Both features, alignment of the grains and the fine microstructure, contribute to a high maximum energy density, which amounts to 180 kJ m^{-3}.

Plasma-sprayed layers, prepared form $SmCo_5$ alloy powders, achieve thin isotropic magnets with huge coercivities from 3750 up to 5400 kA m^{-1} (Kumar, Das and Wettstein, 1978). Owing to the low remanent polarizations between 0.5 and 0.56 T, maximum energy densities from 43 to 61 kJ m^{-3} are obtained.

2.5.6 *Liquid dynamic compaction of RE–TM magnet layers*

Similar to plasma spraying is the formation of RE–TM magnet layers with a thickness from 1 to 10 mm by liquid dynamic compaction. The RE–TM alloy with the final composition is melted and dispersed into small droplets by ultrasonic gas atomization. The droplet stream is consolidated onto a substrate. Growth rates up to 1 cm min^{-1} were achieved (Chin *et al*., 1986). The solidification rates were estimated to range between 100 and 1000 K s^{-1}. Owing to the almost amorphous microstructure of as-deposited Nd–Fe–B layers, only coercivities from 240 to 400 kA m^{-1} resulted. However, by annealing at temperatures between 600 and 700 °C, a fine-grained microstructure and improved magnetic properties of the isotropic layers could be achieved. Remanent polarizations and coercivities H_{cJ} of 0.53–0.7 T and 620–1250 kA m^{-1} are reported (Chin *et al*., 1986; Harada, Ando, O'Handley and Grant, 1990). The maximum energy density of these isotropic layers amount to 48–80 kJ m^{-3}.

2.5.7 *Preparation of thin RE–TM films*

For some micromechanic devices, such as miniature motors, pumps, actuators, sensors, hard magnetic films with a thickness of a few micrometers may be required. Such films can be prepared by sputtering or by laser ablation. A lot of research and development activities are going on in order to optimize the processing conditions, such as the substrate material and the temperature, the sputtering gas atmosphere, the target composition, the target–substrate distance, or even the application of a magnetic field parallel to the substrate plane (Cadieu *et al*., 1987; Parhofer, Gieres, Wecker and Schultz, 1996; Parhofer *et al*., 1998; Araki, Nakanishi and Umemura, 1999; Neu and Shaheen, 1999; Jiang and O'Shea, 2000; Castaldi, Gibbs and Davies, 2003). The films deposited onto the substrates at ambient temperatures are amorphous and need annealing at temperatures between 400 and 700 °C for crystallization. By consolidation of the sputtered material onto heated substrates, microcrystalline films can be achieved directly (Cadieu *et al*., 1987; Parhofer, Gieres, Wecker and Schultz, 1996).

About 1- to 2-μm-thick Nd–Dy–Fe–B films with a texture perpendicular to the film plane could be prepared by sputtering. In general, the magnetic properties range from 0.9 to 1.3 T for the remanent polarization, 200 to 800 kA m^{-1} for the coercivity H_{cJ}, and 150 to 190 kJ m^{-3} for the maximum energy density (Sun, Tomida, Hirosawa and Maehara, 1996; Parhofer, Gieres, Wecker and Schultz, 1996; Parhofer *et al*., 1998; Araki, Nakanishi and Umemura, 1999; Castaldi, Gibbs and Davies, 2003).

In contrast, sputtered $SmCo_5$ or $Sm_2(Co,Cu,Fe,Zr)_{17}$ films with a thickness between 1 and 2 μm crystallize with their easy axis in the film plane. The magnetic properties range from 0.6 to 0.8 T for the remanent polarization, 1000 to 1200 kA m^{-1} for the coercivity H_{cJ}, and to about 120 kJ m^{-3} for the maximum energy density (Cadieu *et al*., 1987; Neu and Shaheen, 1999).

Lately, some research and development projects have been focusing on the preparation of thin RE–TM films by pulsed-laser deposition. The thickness of such films, in general, ranges from 0.1 to 0.3 μm. The crystallization onto heated substrates with temperatures in the range 400–550 °C result in anisotropic films with a remanent polarization of about 0.6 T and a coercivity H_{cJ} of 800 kA m^{-1} for Sm–Co films (Neu *et al*., 2002b) and remanent polarizations between 0.9 and 1 T and coercivities H_{cJ} between 400 and 1000 kA m^{-1} for Nd–Fe–B films (Hannemann *et al*., 2002; Fähler *et al*., 2003; Neu *et al*., 2002a).

Isotropic Nd–Fe–B films with a thickness from about 10 to 120 μm could be prepared by high-speed pulsed-laser deposition (Nakano *et al*., 2003). The magnetic properties range between 0.4 and 0.68 T for the remanent polarization, 800 and 1200 kA m^{-1} for the coercivity H_{cJ}, and up to 77 kJ m^{-3} for the maximum energy density.

Although some improvements are to be expected by optimization of the pulsed-laser deposition, the sputtering

process seems to be more promising for the preparation of RE–TM hard magnetic films.

2.5.8 Amorphous hard magnetic RE–TM materials

In RE–Fe–Al systems, RE: Pr and Nd, there is a wide composition range for the formation of an amorphous phase, which enables the preparation of bulk amorphous alloys by conventional solidification methods (Inoue *et al*., 1996a,b; Inoue, Zhang and Takeuchi, 1997). Cylindrical rods with diameters up to 3 or 12 mm for Pr–or Nd–Fe–Al alloys respectively could be manufactured by injection casting into a Cu mold with a small pressure of 0.05 MPa or by sucking the molten alloy into a Cu mold. X-ray spectra indicate that the cylindrical rods consist of an amorphous phase. Detailed analyses of the microstructure reveal that the samples consist of Nd nanocrystals in an amorphous matrix. Indeed, the amorphous matrix contains two amorphous phases with a different composition and some short-range order (Sun *et al*., 2003).

The magnetic properties amount to 0.089 or 0.112 T for the remanent polarization, 300 or 288 kA m^{-1} for the coercivity H_{cJ}, and 13 or 19 kJ m^{-3} for the maximum energy density of $Pr_{60}Fe_{30}Al_{10}$ or $Nd_{60}Fe_{30}Al_{10}$ rods (Inoue *et al*., 1996; Inoue, Zhang and Takeuchi, 1997). The squareness of the demagnetization curve $J(H)$ depends on the diameter of the rods. This result indicates that the hard magnetic properties are sensitive to the disordered structure in the amorphous phase. There seems to be a tendency that the hard magnetic properties increase with the development of a short-range order. Annealing of cast cylinders at a temperature of 330 °C for 10 min increases the remanent polarization by about 5%, but no significant change of the coercivity H_{cJ} occurs. Heating beyond the crystallization temperature of about 510 °C results in $NdAl_2$ and $Nd_3Fe_{1-x}Al_x$ crystals in an Nd matrix. As a consequence, the hard magnetic properties decrease substantially (Inoue *et al*., 1996).

Investigation of the temperature dependence of the coercivity of $Nd_{60}Fe_{30}Al_{10}$ and of $Nd_{60}Fe_{20}Co_{10}Al_{10}$ ribbons or of cast ingots demonstrates a strong increase in the coercivity at low temperatures with a maximum between 2640 and 3200 kA m^{-1} at temperatures between 50 and 77 K (Turtelli *et al*., 2002). At temperatures below 77 K, the coercivities decrease again. The magnetization curves $J(H)$ and the linear temperature dependence of the coercivity indicate a pinning-type behavior. Probably the magnetic domain walls are pinned at the nanocrystals in the amorphous matrix (Turtelli *et al*., 2002).

In order to increase the glass-forming ability, $Nd_{60-x}Fe_{30}Al_{10}B_x$ rods, $x = 0$, 1, 3, 5, were prepared by low-pressure Cu-mold casting. For $Nd_{59}Fe_{30}Al_{10}B_1$ rods with a diameter of 1 mm, a small increase of the remanent polarization and of the maximum energy density to 0.154 T and 4.2 kJ m^{-3} results, whereas the coercivity H_{cJ} does not change significantly and amounts to 340 kA m^{-1} (Kong, Li and Ding, 2000).

By addition of B, B and Cu, or Dy to $Nd_{60}Fe_{30}Al_{10}$ alloys, the coercivity of 3-mm ingots, which were cast into a Cu mold, could be improved up to 388 kA m^{-1} for a $Nd_{41.2}Pr_{13.8}Dy_5Fe_{20}Al_{10}$ at the expense of the remanent polarization (Betancourt and Valenzuela, 2003).

However, the coercivity mechanism in amorphous RE–Fe–Al alloys is still under investigation.

3 MAGNETIZING OF RE–TM MAGNETS

After sintering, RE–TM magnets are in the thermally demagnetized state. Hence, the grains contain different magnetic domains, the dimensions of which are determined by the minimization of the magnetic stray field energy at the surface of the magnet. The magnetic domains are separated by domain walls, which can either move easily within the grains or be pinned at phase boundaries, precipitates, or planar crystal defects (Kronmüller, 1978).

Perfect magnetization of anisotropic magnets to saturation implies that all grains must be magnetized in the easy direction and no multidomain grains exist anymore. The saturation of magnets can be achieved by strong magnetic field pulses. The required magnetic field strength depends on the coercivity mechanism, the saturation polarization of the magnetic material, and the load line of the magnet or of the magnet assembly, respectively. The following coercivity mechanisms are dominant in RE–TM magnet materials with strong coercivities:

- nucleation of reversed domains in every saturated grain or
- pinning of the magnetic domain walls at phase boundaries, precipitates, or planar crystal defects.

The magnetizing curve of a magnet material from the thermally demagnetized state indicates which coercivity mechanism prevails, see Figure 12. In nucleation-type magnets, for instance, Nd–Fe–B, $SmCo_5$, or hard ferrites, the magnetic domain walls can be moved easily within the grains, so that the polarization increases steeply already in small magnetizing fields, see Figure 12(a). But, perfect saturation requires a magnetizing field strength of at least twice the saturation polarization of the magnet material (Blank, Rodewald and Schleede, 1989).

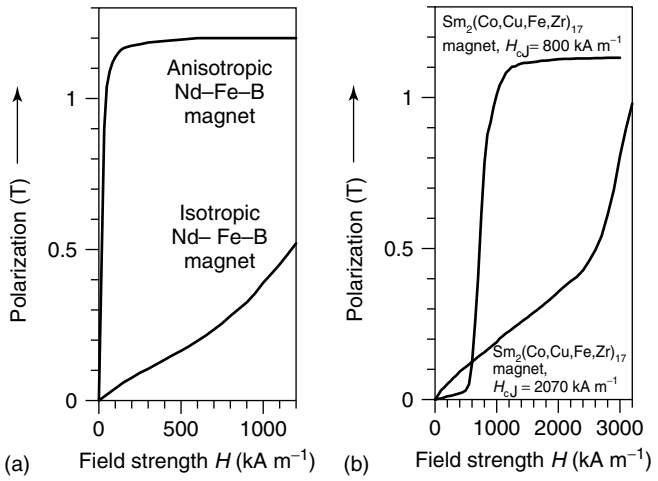

Figure 12. Principal magnetizing behavior of thermally demagnetized RE–TM magnets. (a) Nucleation-type anisotropic RE–TM magnets, for instance, Nd–Fe–B or $SmCo_5$ magnets, or isotropic RE–TM magnets, for instance, rapidly solidified Nd–Fe–B ribbons, (b) pinning-type RE–TM magnets, for instance, $Sm_2(Co,Cu,Fe,Zr)_{17}$ magnets with coercivities H_{cJ} of 800 or 2070 kA m^{-1}, respectively.

However, in isotropic Nd–Fe–B magnets, for instance, magnets made from rapidly solidified Nd–Fe–B ribbons, there is only a flat increase in the polarization from the thermally demagnetized state, see Figure 12(a). Probably only those grains, whose easy axes are aligned parallel to the magnetizing field strength, are easily saturated, whereas in all other grains the polarization must be rotated parallel to the magnetizing field. The rotation of the polarization against the magnetocrystalline fields requires strong magnetizing fields. In principle, saturation of isotropic magnets needs a magnetizing field strength similar to the anisotropy field strength.

The coercivity mechanism in nucleation-type magnets has been described by the micromagnetic theory for nucleation of reversed domains (Kronmüller, 1985, 1987; Adler and Hamann, 1985; Kronmüller, Durst and Sagawa, 1988; Sagawa and Hirosawa, 1988; Kou, Kronmüller, Givord and Rossignol, 1994) or by an empirical model for the existence and expansion of nuclei of reversed domains (Givord, Tenaud and Viadieu, 1988; Givord and Rossignol, 1996; Barthem, Givord, Rossignol and Tenaud, 2002; Givord, Rossignol and Barthem, 2003).

In pinning-type magnets, the magnetic domain walls are pinned at phase boundaries, for instance, in $Sm_2(Co,Cu,Fe,Zr)_{17}$ magnets with coercivities H_{cJ} between 500 and 800 kA m^{-1}. In order to saturate a pinning-type magnet, the domain walls must be removed from the pinning sites, which requires magnetizing fields larger than the pinning field strength, see Figure 12(b). Saturation of such magnets needs magnetizing field strengths of at least twice the coercivity H_{cJ}, see Section 3.2. Microscopic models for the coercivity mechanism of pinning-type magnets have been compiled by several authors (Durst and Kronmüller, 1987; Katter *et al*., 1996; Katter, 1998).

However, in some magnet materials, the pinning field strength is not well defined, for instance, in $Sm_2(Co,Cu,Fe,Zr)_{17}$ magnets with strong coercivities above 1600 kA m^{-1}, see Figure 12(b).

In Alnico magnets, the coercivity is determined by the shape anisotropy of the ferromagnetic Fe–Co rods in the nonmagnetic matrix. The coercivity is determined by the difference of the demagnetizing coefficient $N_|$ parallel to the easy axis and $N_\perp$ perpendicular to the easy axis of the magnet, see equation (6).

$$\mu_0 H_{cJ} = -J \cdot (N_| - N_\perp) \cdot f(q) \tag{6}$$

where $f(q)$ denotes a distribution function, which takes into account the nonideal alignment of the easy axes of the Fe–Co rods (Buschow, 1998). For the case of noninteracting uniaxial single domain particles, $f(q)$ amounts to 0.5.

For magnetization of permanent magnets, the internal magnetic field strength H_{int} in the magnet is decisive. The internal field strength is determined by the applied field strength H_{appl} and the demagnetizing field strength H_{demag} of the magnet or the magnet assembly. The demagnetizing field strength depends on the dimensions of the magnet or the load line of a magnet assembly, respectively, and the polarization of the magnet materials, see equation (7):

$$H_{int} = H_{appl} - H_{demag} = \frac{H_{appl} - 1}{\mu_0 \times N \times J} \tag{7}$$

where N denotes the demagnetization coefficient and J the polarization of the magnet material.

Most of the advanced magnets are magnetized by a short pulse field, which is achieved by discharging a capacitor bank over a Cu coil. The duration of the field pulse must last sufficiently long in order to overcome the eddy currents at the surface of the magnets, in particular, for large blocks. In general, a pulse width in the range between 5 and 10 ms is sufficient for a complete field penetration. The penetration depth λ (see equation 8) depends on the electrical resistance ρ and the permeability μ of the magnet material and the frequency f of the field pulse (Parker, 1990):

$$\lambda = \text{constant} \cdot \sqrt{\frac{\rho}{\mu \cdot f}} \tag{8}$$

In general, magnets are magnetized after assembly, since handling of not-magnetized magnets is easier and prevents

contamination by ferromagnetic particles. In addition, chipping of magnet edges due to the mutual attraction of magnet parts is avoided.

3.1 Magnetization of nucleation-type magnets

Magnetization of nucleation-type magnets, for instance, sintered anisotropic ferrites, $SmCo_5$, or Nd–Fe–B magnets, is fairly easy from the thermally demagnetized state. Since the magnetic domain walls in the individual grains can be moved easily, a polarization of about 95% of the saturation polarization results even after magnetization by a small magnetizing field strength of about 200 kA m^{-1}. However, removal of the magnetizing field strength decreases the polarization, since there is no significant coercivity. In the multidomain grains, the domain walls are moved back in order to minimize the magnetic stray field energy, see Figure 13.

Magnetization by a field strength of about 500 kA m^{-1} saturates some grains, so that some coercivity results. Such grains do not contain domain walls anymore. Since most of the grains are still multidomain grains, the demagnetization curves $J(H)$ of such partially magnetized magnets demonstrate a very poor squareness, see Figure 13.

Complete magnetization requires a strong internal field strength >1600 kA m^{-1}. In that case, every grain is saturated. There are hardly any grains that contain small reversed domains.

The coercivity of nucleation-type magnets is determined by the nucleation of reversed magnetic domains in each grain, since the grains are decoupled magnetically by nonmagnetic Nd-rich constituents. The minimal volume of such a reversed magnetic domain is proportional to the domain wall thickness cubed (Givord, Tenaud and Viadieu, 1988; Givord and Rossignol, 1996). In general, the nucleation occurs at crystal defects, where the magnetocrystalline anisotropy is reduced or at edges of grains, where strong local stray fields assist the nucleation. At edges of grains, local stray fields up to about 2.5 times the saturation polarization can occur (Adler and Hamann, 1985; Blank, Rodewald and Schleede, 1989). In order to overcome such strong local stray fields, the magnetization field strength should be at least twice the saturation of the magnet material.

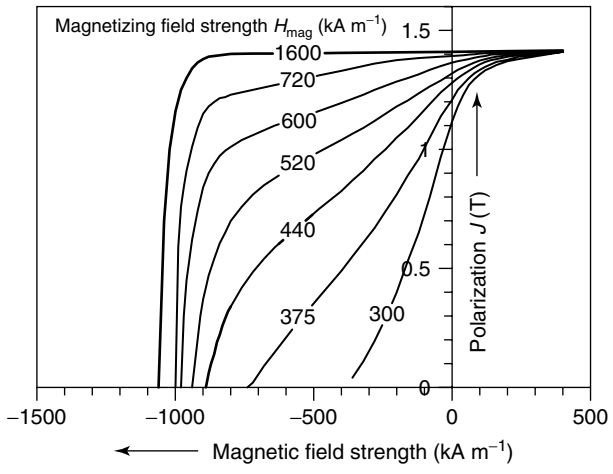

Figure 13. Magnetizing behavior of sintered Nd–Dy–Fe–B magnets. The demagnetization curves $J(H)$ were measured on different samples, each in the thermally demagnetized state, after magnetization by the indicated field strengths H_{mag}. For complete magnetization an applied field of 2000 kA m^{-1} is recommended.

There is a dominant impact of the microstructure of a magnet on the coercivity. Besides, on a strong nucleation field strength H_n, which is mainly determined by the magnetocrystalline anisotropy, the coercivity depends on local demagnetizing stray fields, which are described by an effective demagnetizing coefficient N_{eff} (Adler and Hamann, 1985; Durst and Kronmüller, 1985; Kronmüller, Durst and Sagawa, 1988; Kou, Kronmüller, Givord and Rossignol, 1994), see equation (9).

$$H_{cJ} = \frac{H_n - N_{eff}}{\mu_0 \times J} \tag{9}$$

where H_n denotes the nucleation field strength, J the polarization of the magnet material, and N_{eff} presents an effective demagnetization coefficient, which depends on the local microstructure.

3.2 Magnetization of pinning-type magnets

Magnetization of pinning-type magnets, for instance, sintered $Sm_2(Co,Cu,Fe,Zr)_{17}$ magnets with coercivities in the range 600–800 kA m^{-1}, need an internal magnetizing field strength, which is strong enough to overcome the pinning forces. If a small magnetizing field strength is applied, the magnetic domain walls are not moved and there is only a negligible increase in the polarization, see Figure 14. For internal magnetizing field strengths of about the coercive field strength, the domain walls can be pulled away from the pinning sites and the domains with a polarization parallel to the magnetic field grows significantly. Since the strength of the pinning sites may vary within the microstructure, the complete magnetization requires a magnetizing field strength of at least twice that of the coercive field strength.

Magnetization of $Sm_2(Co,Cu,Fe,Zr)_{17}$ magnets with strong coercivities in the range 1500 up to 2100 kA m^{-1} demonstrate a more heterogeneous pinning behavior. For magnetizing field strengths, which are lower than the coercivity, there is an increase in the polarization up to about a third of the remanent polarization, see Figure 15. Probably not all pinning

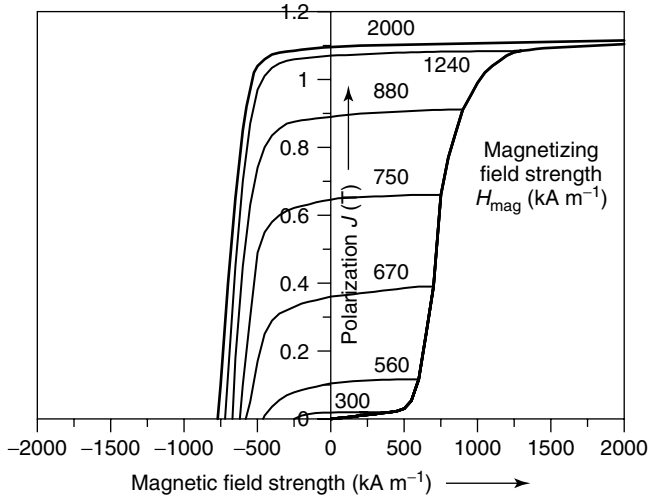

Figure 14. Magnetizing behavior of sintered $Sm_2(Co,Cu,Fe,Zr)_{17}$ magnets with a coercivity H_{cJ} of about 800 kA m^{-1}. The demagnetization curves $J(H)$ were measured on different samples, each in the thermally demagnetized state, after magnetization by the indicated field strengths H_{mag}. For complete magnetization, an applied field of 2000 kA m^{-1} is recommended.

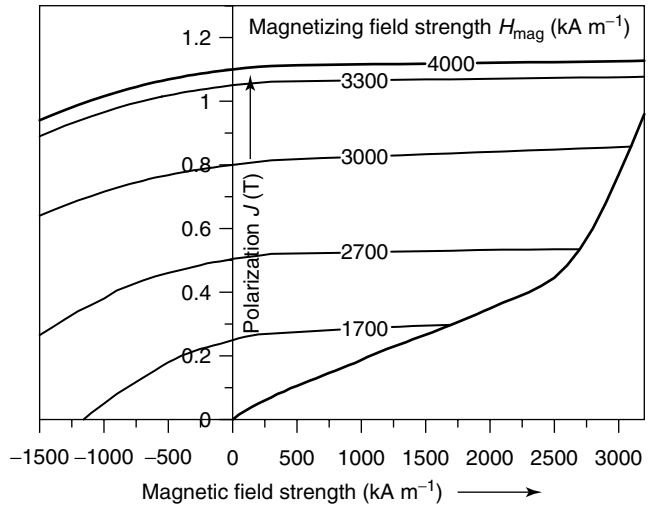

Figure 15. Magnetizing behavior of sintered $Sm_2(Co,Cu,Fe,Zr)_{17}$ magnets with a coercivity H_{cJ} of about 2070 kA m^{-1}. The demagnetization curves $J(H)$ were measured on different samples, each in the thermally demagnetized state, after magnetization by the indicated field strengths H_{mag}. For complete magnetization, an applied field of 3650 kA m^{-1} is recommended.

sites exert the same pinning strength on the magnetic domain walls. In fact, in well-annealed $Sm_2(Co,Cu,Fe,Zr)_{17}$ magnets with strong coercivities, there exist two kinds of pinning sites with different pinning strengths (Katter *et al.*, 1996). The different pinning sites were revealed by the different temperature dependences of the corresponding coercivities. Increasing the internal magnetizing field strength beyond the coercive field strength results in a strong increase in the polarization, see Figure 15. However, complete saturation of $Sm_2(Co,Cu,Fe,Zr)_{17}$ magnets requires a magnetizing field strength of at least twice the coercive field strength.

4 TEMPERATURE STABILITY OF SINTERED RE–TM MAGNETS

The magnetic properties of sintered RE magnets depend on temperature. For a proper design of magnet assemblies, their temperature dependence has to be taken into account. In particular, the maximum operating temperature of a magnet grade must not be exceeded in order to prevent degradation of a magnet assembly.

The maximum continuous operating temperature of permanent magnets depends on the temperature coefficients $TC(J_r)$ of the remanent polarization, $TC(H_{cJ})$ of the coercivity, and the load line $B/\mu_0 H$ of the magnet or the magnet assembly. In general, the maximum operating temperature T_{op} of the different permanent magnets increases proportional to the Curie temperature T_C of the magnet material, see Figure 16.

As far as the RE–TM magnets are concerned, the remanent polarization of Nd–Fe–TM–B, TM: TMs, as well as Nd–Dy–Fe–TM–B magnets, with strong coercivities $H_{cJ} > 2400$ kA m^{-1}, is larger than the remanent polarizations J_r of $SmCo_5$ or $Sm_2(Co,Cu,Fe,Zr)_{17}$ magnets, see Figure 17. But, at temperatures above 200 °C, $SmCo_5$ magnets are superior to Nd–Dy–Fe–TM–B magnets and, at temperatures above 230 °C, $Sm_2(Co,Cu,Fe,Zr)_{17}$ magnets exceed the remanent polarization of Nd–Fe–TM–B magnets. The temperature dependence of the remanent polarization is mainly determined by the Curie temperatures of the different hard magnetic compounds, $T_C(Nd_2Fe_{14}B) \cong 312$ °C, $T_C(SmCo_5) \cong 720$ °C and $T_C(Sm_2Co_{17}) \cong 820$ °C (Gutfleisch, 2000).

The temperature dependence of the coercivities of RE–TM magnets is mainly determined by the temperature dependence of the anisotropy field strength H_A. Since the anisotropy field strength of the $Nd_2Fe_{14}B$ compound, $H_A \cong 52$ kA m^{-1}, is significantly smaller than that of $SmCo_5$ compounds, $H_A \cong 320$ kA m^{-1} (Gutfleisch, 2000), the coercivity of Nd–Fe–TM–B magnets decreases more strongly with increasing temperature than the coercivity of $SmCo_5$ magnets, see Figure 18. At temperatures >150 °C, the coercivity of Sm–Co magnets exceeds the coercivities of Nd–Dy–Fe–TM–B magnets. The coercivity of the multiphase $Sm_2(Co,Cu,Fe,Zr)_{17}$ magnets is determined by pinning of the magnetic domain walls and depends only on the square root of the anisotropy field strength, which reduces the temperature dependence of the coercivity H_{cJ}.

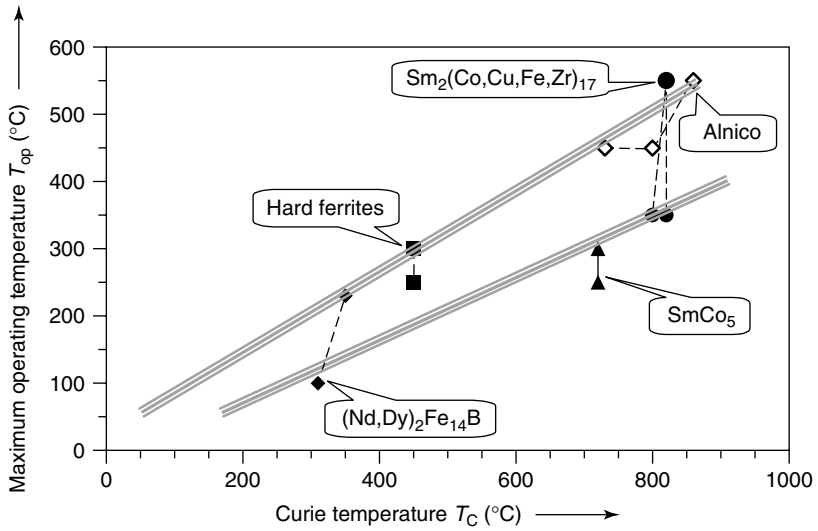

Figure 16. Maximum continuous operating temperatures T_{op} of permanent magnet materials, depending on their Curie temperatures T_C. The shaded lines indicate the lowest or highest operating temperatures, respectively, for the different permanent magnet materials.

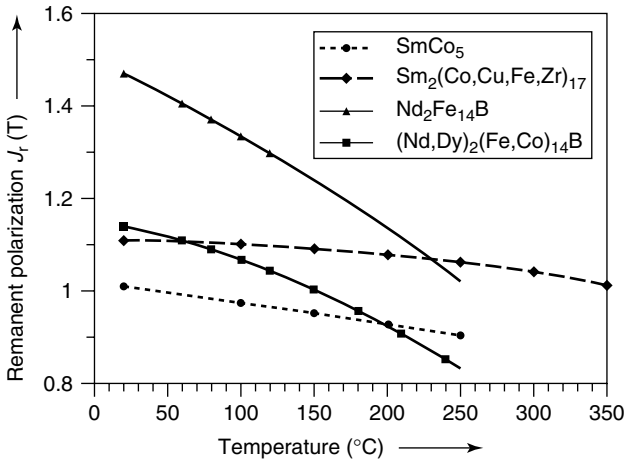

Figure 17. Remanent polarization J_r of RE–TM magnets, depending on the temperature.

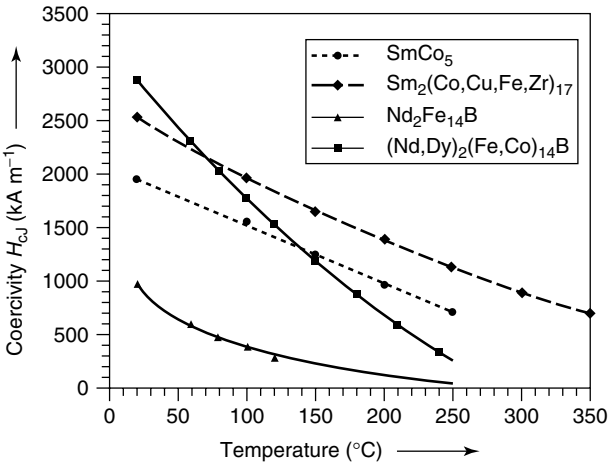

Figure 18. Coercive field strength H_{cJ} of RE–TM magnets, depending on the temperature.

As a consequence, sintered Nd–Fe–B magnets achieve maximum energy densities at 20 °C in the range 224–424 kJ m^{-3}, but, at temperatures of approximately 120 °C, sintered $Sm_2(Co,Cu,Fe,Zr)_{17}$ magnets are superior, see Figure 19.

The temperature stability of permanent magnets is determined by reversible and irreversible polarization losses. The reversible polarization changes are represented by the temperature coefficient of the remanent polarization TC(J_r).

Irreversible polarization losses are mainly caused by the temperature dependence of the coercivity H_{cJ} and the thermal aftereffect. With increasing temperature, the coercivity H_{cJ} of Nd–Fe–B magnets decreases and as a consequence the polarization of grains that have smaller coercivities may be reversed. Such irreversible polarization losses do not depend on time.

Minor polarization losses are due to the thermal aftereffect or magnetic viscosity, respectively, and depend on time logarithmically (Néel, 1951). The polarization losses due to the temperature dependence of the coercivity H_{cJ} and to the thermal aftereffect can be recovered by remagnetization.

However, polarization losses due to the deterioration of the magnet surface, for instance, by oxidation or by improper cutting and grinding (Blank and Adler, 1987) or by changes of the mircostructure due to high operating temperatures cannot be eliminated by remagnetization. The basic features that affect the temperature stability of RE–TM magnets are compiled in Table 1.

Table 1. Principle terms, which affect the temperature stability of RE–TM magnets.

Reversible polarization losses	Irreversible polarization losses	Irreversible polarization losses by microstructural changes
Reversible temperature coefficient TC(J_r)	Temperature coefficient TC(H_{cJ}) Thermal aftereffect, determined by the coefficient S_v	Surface oxidation Changes in the microstructure due to temperature

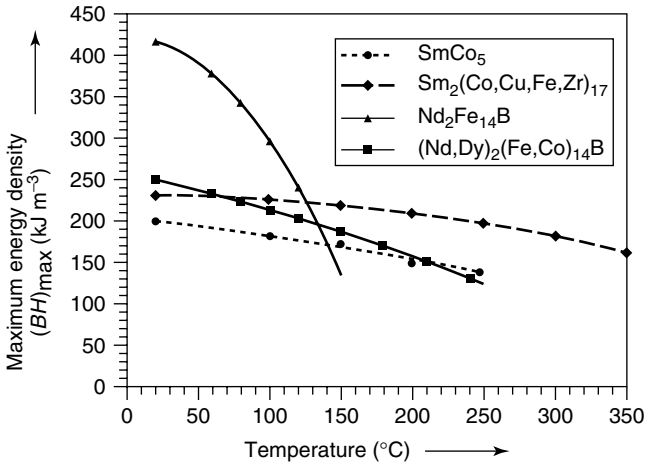

Figure 19. Maximum energy density $(BH)_{max}$ of RE–TM magnets, depending on the temperature.

4.1 Temperature coefficients of the remanent polarization J_r and of the coercivity H_{cJ}

The remanent polarization J_r and the coercivity H_{cJ} of RE magnets decrease continuously with increasing temperature. The monotonous decrease is characterized quantitatively by the temperature coefficient of the remanent polarization TC(J_r) or of the coercivity TC(H_{cJ}) respectively according to equations (10) and (11).

$$\mathrm{TC}(J_r) = \frac{J_r(T_1) - J_r(T_0)}{J_r(T_0) \cdot (T_1 - T_0)} \times 100\ \mathrm{in\%/K}$$
$$\text{for the temperature range } T_0 < T < T_1 \qquad (10)$$

$$\mathrm{TC}(H_{cJ}) = \frac{H_{cJ}(T_1) - H_{cJ}(T_0)}{H_{cJ}(T_0) \cdot (T_1 - T_0)} \times 100\ \mathrm{in\%/K}$$
$$\text{for the temperature range } T_0 < T < T_1 \qquad (11)$$

where T_0 and T_1 denote the lower and the higher temperature, very often T_0 amounts to 20 °C. $J_r(T_0)$, $J_r(T_1)$, and $H_{cJ}(T_0)$, $H_{cJ}(T_1)$ represent the remanent polarizations or the coercivities at these temperatures. The temperature coefficients describe the temperatures dependences only in small temperature ranges $T_0 < T < T_1$ fairly well. However, remanent polarizations calculated by means of the temperature coefficient TC(J_r) are a little bit smaller because the temperature dependence of the polarization is a convex graph, see Figure 20(a), whereas coercivities interpolated by means of the temperature coefficient TC(H_{cJ}) are too large, since the temperature dependence of the coercivity is a concave graph, see Figure 20(b). The deviations between the polynomial regression curves of the measurements and the interpolations by the temperature coefficients amount to <0.5% for the remanent polarization, but up to 15% for the coercivity H_{cJ}. The difference reflects the different values of the temperature coefficients. For instance, at a temperature of 120 °C, the coercivity amounts to 608 kA m^{-1} estimated by the temperature coefficient TC(H_{cJ}) and to 524 kA m^{-1} calculated by the regression polynom, see Figure 20(b). Hence, an error of about 15% results.

Typical temperature coefficients of some RE–TM magnet grades for the temperature ranges 20–100 °C and 20–150 °C are compiled in Table 2.

4.2 Irreversible polarization losses due to the temperature dependence of the coercivity H_{cJ} and the thermal aftereffect

The decrease in the coercivity H_{cJ} with increasing temperatures results in the reversal of the polarization of those grains that experience strong demagnetizing fields. The demagnetizing field strength is the sum of the applied field strength and local stray fields. Local stray fields of pores or impurities may amount to twice the polarization of the magnet material (Blank, Rodewald and Schleede, 1989). Owing to the opposite local fields, the magnetization of some grains in the magnet may be reversed, so that irreversible polarization losses result. Such irreversible polarization losses do not depend on time and occur as soon as the temperature in the magnet increases.

Irreversible polarization losses, which are caused by the temperature dependence of the coercivity, can be anticipated by an annealing treatment of the magnetized magnets or the magnetized magnet assembly. As a rule of thumb, such aging treatments for the stabilization of a magnetized magnet are performed at temperatures 10–50 K above the maximum operating temperature (Adler and Marik, 1981).

Table 2. Temperature coefficients TC(J_r) of the remanent polarization and TC(H_{cJ}) of the coercivity H_{cJ} of some RE magnet grades for the temperature ranges 20–100 °C and 20–150 °C.

Temperature range		20–100 °C		20–150 °C	
Magnet grade	(J_r in T/H_{cJ} (kA m^{-1}))	TC(J_r) (%/K)	TC(H_{cJ}) (%/K)	TC(J_r) (%/K)	TC(H_{cJ}) (%/K)
$SmCo_5$	(0.90/2400)	−0.040	−0.14	−0.045	−0.15
$SmCo_5$	(1.01/1500)	−0.040	−0.24	−0.045	−0.25
$Sm_2(Co,Cu,Fe,Zr)_{17}$	(1.12/800)	−0.030	−0.15	−0.035	−0.16
$Sm_2(Co,Cu,Fe,Zr)_{17}$	(1.10/2070)	−0.030	−0.18	−0.035	−0.19
$Nd_2Fe_{14}B$	(1.47/955)	−0.115	−0.77	–	–
$Nd_2Fe_{14}B$	(1.18/2465)	−0.085	−0.55	−0.095	−0.50
$Nd_2Fe_{14}B$	(1.08/2865)	−0.080	−0.51	−0.090	−0.46

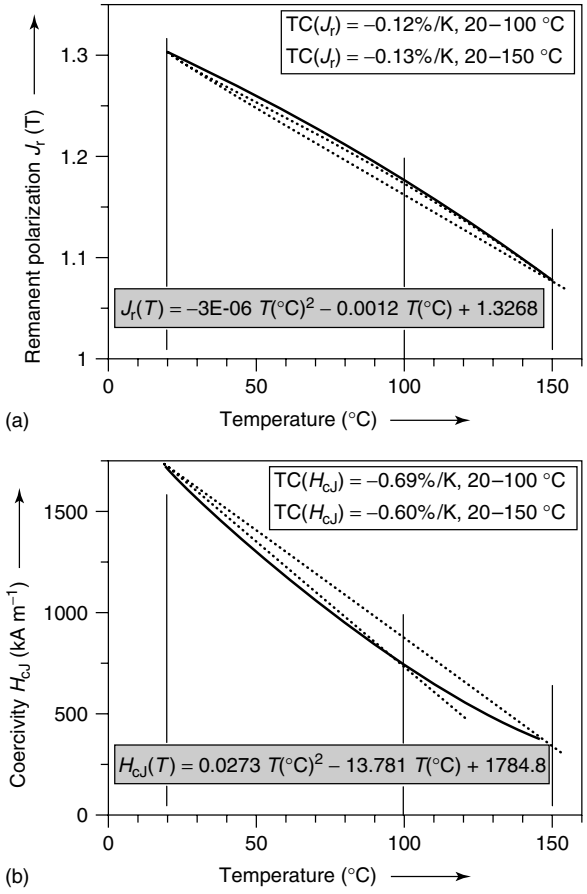

Figure 20. Temperature dependence of (a) the remanent polarization $J_r(T)$ and of (b) the coercivity $H_{cJ}(T)$ of sintered Nd–Dy–Fe–TM–B magnets. The deviation between the polynomial regression curves of the measurements and the interpolations by the temperature coefficients TC(J_r) or TC(H_{cJ}), respectively, for the different temperature intervals 20–100 °C and 20–150 °C are demonstrated.

Minor and time-dependent polarization losses may result from the thermal aftereffect or the magnetic viscosity, respectively. As soon as the sum of the external field and of internal stray fields becomes strong enough, the polarization of some grains decreases by nucleation of reversed domains. Hence, there are some multidomain grains, which contain magnetic domain walls. Even if the external magnetic field is kept constant, the domain walls can be moved by thermal activation in order to further decrease the energy of local magnetic stray fields. This results in minor decreases of the polarization dJ and is denoted as the thermal aftereffect or magnetic viscosity, respectively. Figure 21 demonstrates the principle of the aftereffect on a demagnetization curve at a constant reversed magnetic field strength.

The decrease in the polarization depends on time logarithmically and has been analyzed in detail by Néel. The

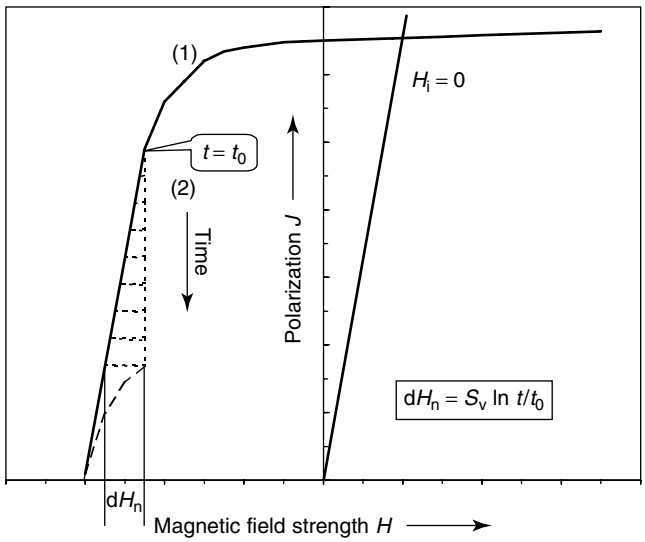

Figure 21. Procedure for the measurement of the coefficient S_v of the thermal aftereffect: (1) at first the demagnetization curve $J(H)$ is measured with a fixed sweep rate dH/dt, (2) after remagnetization of the magnet by a strong pulse field, the demagnetization curve was measured again, but, at the time $t = t_0$, the external field was kept constant and the decrease in the polarization, depending on time, was recorded.

polarization losses by the thermal aftereffect can be simulated by a small additional reversed external field dH (Néel, 1951), see equation (12):

$$dH \approx S_v \cdot \ln \frac{t}{t_0} \tag{12}$$

where S_v and dH denote the coefficient of the thermal aftereffect and the field increment that is needed for simulating the same polarization losses, t gives the time in reference to the moment at which the external magnetic field is applied and kept constant, $t_0 \approx 10^{-11}$ s, is the characteristic time for lattice vibrations (Coey, 1996). The coefficient of the thermal aftereffect is proportional to the coercivity H_{cJ} for many magnet materials. This implies that the coefficient of the thermal aftereffect decreases with increasing temperature, since the coercivities H_{cJ} decrease as well. The coefficient of the thermal aftereffect in dependence of the polarization (Street, Day and Dunlop, 1987), of the coercivity (Liu and Luo, 1990; Nishio and Yamamoto, 1993), and of the temperature has been examined by several teams (Stieler, Heiden, Kuntze and Kohake, 1984; Rodewald, 1985; Givord *et al*., 1987a,b; Singleton and Hadjipanyis, 1990). In order to determine the influence of the microstructure on the magnetic viscosity, the temperature dependence of the viscosity coefficient S_v has been examined on single-phase and multiphase nanocrystalline Nd–Fe–B or Pr–Fe–B magnets, respectively, by M. Becher *et al*. Whereas multiphase Nd–Fe–B or Pr–Fe–B magnets with a high coercivity have got high viscosity coefficients with a strong temperature dependence, exchange-coupled RE–Fe–B magnets with low coercivities have got smaller viscosity coefficients with a small temperature dependence (Becher, Seeger and Bauer, 1998).

For sintered Nd–Dy–Fe–B magnets, the coefficient of the thermal aftereffect S_v ranges from 8 to 10 kA m^{-1} at a temperature of 20 °C and decreases to about 2 kA m^{-1} at a temperature of 200 °C, probably due to the decrease in the coercivity (Rodewald, 1985). For sintered Sm–Co magnets, the coefficient of the thermal aftereffect varies between 2 and 12 kA m^{-1} and depends on the coercivity H_{cJ}.

Figure 22 gives the relative irreversible polarization losses $\Delta J_{irr}/J$, depending on the exposure time at a temperature of 130 °C in air for sintered Nd–Dy–Fe–TM–B magnets. Owing to the small coercivity and the strong temperature coefficient of the coercivity TC(H_{cJ}), such magnets experience irreversible polarization losses between 1 and 3% for small load lines, but suffer irreversible polarization losses from about 15 to 18% for a load line of $B/\mu_0 H = -0.5$. The irreversible polarization losses can be reduced by increasing the coercivity or by improving the squareness of the demagnetization curve $J(H)$ of the sintered magnets.

The irreversible polarization losses of typical Sm–Co magnets at temperatures between 100 and 200 °C amount to some percent only, due to the stronger coercivities H_{cJ} and the smaller temperature coefficient TC(H_{cJ}), see Figure 23.

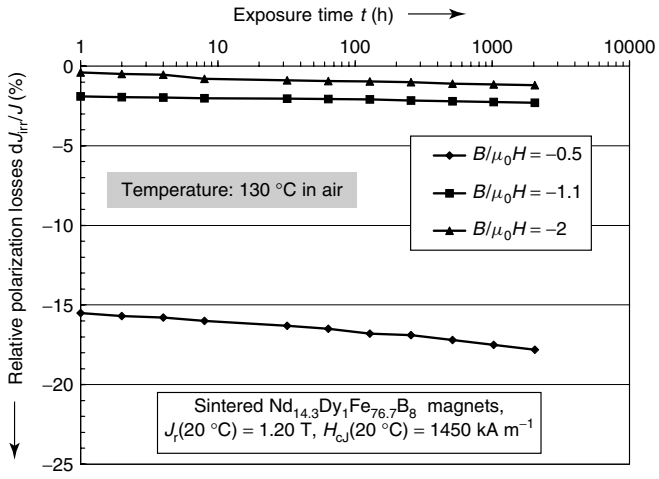

Figure 22. Irreversible polarization losses of sintered $Nd_{14.3}Dy_1Fe_{76.7}B_8$ magnets with different load lines $B/\mu_0 H$ at a temperature of 130 °C, depending on the exposure time.

In principle, the irreversible polarization losses due to the temperature dependence of the coercivity H_{cJ} and the thermal aftereffect can be recovered by remagnetization.

4.3 Irreversible polarization losses due to microstructural changes

However, irreversible polarization losses due to the deterioration of the RE–TM magnet surface, for instance, by improper cutting and grinding (Nishio, Yamamoto, Nagakura and Uehara, 1990), by oxidation (Adler and Marik, 1981; Blank and Adler, 1987) or by changes of the microstructure due to high temperatures, cannot be eliminated by remagnetization. The inset of Figure 24 demonstrates the microstructure of an oxidized surface and the impact on the demagnetization curve $J(H)$. By oxidation, the surface of the Nd–Fe–B grains is converted to a mixture of Nd oxide (hexagonal Nd_2O_3) and α-Fe (Schrey, 1986). The thickness of such a selectively oxidized surface layer may amount to some 10 nm only and hence cannot be detected by light microscopy. Only for extreme heat treatments in air, the oxidized layer increases up to the grain size of the sintered magnets.

In a demagnetizing field, the polarization of the selectively oxidized surface layer is reversed at a much lower field strength than the bulk magnet because the coercivity $H_{cJ,surf}$ ranges between 1800 and 800 kA m^{-1}, for instance, and is much lower than the coercivity of the magnet (Givord, Tenaud and Viadieu, 1986; Blank and Adler, 1987). Since the demagnetization of sintered Nd–Fe–B magnets is

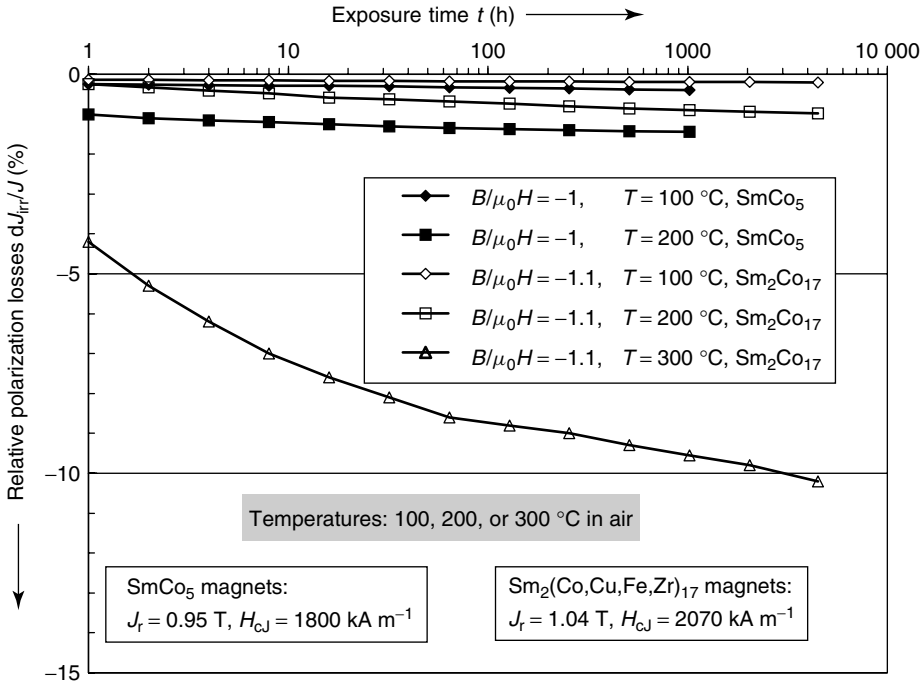

Figure 23. Irreversible polarization losses of sintered $SmCo_5$ and $Sm_2(Co,Cu,Fe,Zr)_{17}$ magnets with different load lines $B/\mu_0 H$ at different temperatures of 100, 200, and 300 °C, respectively, depending on the exposure time.

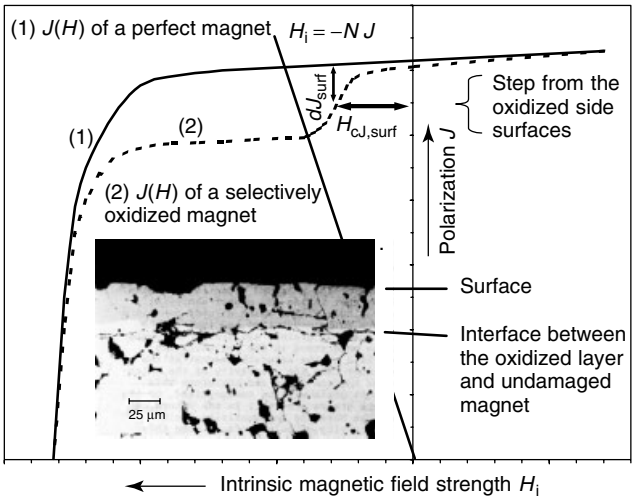

Figure 24. Influence of a selectively oxidized surface grain layer on the demagnetization curve $J(H)$ of a sintered RE–TM magnet. The enlarged microstructure of a severely oxidized layer of a Nd–Dy–Fe–B magnet after annealing in air at 500 °C for 23 h demonstrates that about one layer of grains is deteriorated.

determined by nucleation of reversed domains, not only the oxidized surface layer but the whole layer of surface grains with a thickness between 10 and 20 μm is reversed. Hence, a distinct step in the demagnetization curve $J(H)$ occurs.

The height dJ_{surf} of such a step is given by twice of the ratio of the volume V_{surf} of the reversed grain layer at the side surface to the total volume of the magnet, see equation (13):

$$dJ_{surf} = \frac{2 \cdot J_s \cdot V_{surf}}{V} = \frac{2 \cdot J_s \cdot A_{surf} \cdot d}{V} \qquad (13)$$

where J_s denotes the saturation polarization of the reversed layer, A_{surf} the area of the side surface of the magnet, d the thickness of the reversed layer, and V the total volume of the magnet.

The coefficient 2 results from the reversal of the polarization from the positive to the negative direction.

The height $dJ_{surf}/2$ is defined by the difference between the inflection point of the step in the demagnetization curve and the demagnetization curve of the unspoiled magnet. The coercivity $H_{cJ,surf}$ of the selectively oxidized surface layer is defined as the field difference between the inflection point of the step in the demagnetization curve and the ordinate, see Figure 24. The demagnetization curve has to be corrected by the demagnetizing field strength $N/\mu_0 \cdot J$.

Increasing the thickness of the selectively oxidized layer by annealing for longer times or at higher temperatures results in an increase in the height of the step dJ_{surf} and in a reduction of the coercivity $H_{cJ,surf}$ of the oxidized surface layer (Blank and Adler, 1987).

By surface treatments, the coercivity $H_{cJ,surf}$ and the height dJ_{surf} of the step can be influenced. By etching or by proper annealing, the step can almost be removed, but, after aging the magnets in air, the step may reappear.

4.4 Long-term stability of sintered Nd–Dy–Fe–B magnets

In general, the magnetic flux of sintered RE–TM magnets is constant, provided that strong temperature loads, corrosion of the magnet, and any other damages are prevented. The irreversible polarization losses due to the temperature dependence of the coercivity H_{cJ} depend on the magnet material and can be taken into account in any designed application.

The time-dependent irreversible polarization losses due to the thermal aftereffect decrease logarithmically with time. The corresponding reversed field increment can be calculated from equation (12). Then the polarization losses can be deduced from the demagnetization curves $J(H)$ of the magnet material.

Figure 25 presents measurements of the irreversible polarization losses on sintered Nd–Dy–Fe–B magnets with coercivities of 1200 or 2460 kA m^{-1}, respectively, and different load lines after aging at a temperature of 100 °C over a period of 766 days (2.1 years). The dimensions of the magnets were chosen in a way that irreversible polarization losses due to the temperature dependence of the coercive field strength are negligible. Hence, the polarization losses are mostly determined by the thermal aftereffect. After aging the Nd–Dy–Fe–B magnets for 1 year, irreversible polarization losses of about 1% result. The measurements are fairly well described by the logarithmic regression curves, see Figure 25.

With these regression equations, the irreversible polarization losses for aging periods of 3, 5, and 10 years have been calculated for example. The results are compiled in Table 3. Owing to the logarithmic time dependence, the irreversible polarization losses increase only up to <2%, provided increase in temperature beyond 100 °C, corrosion, or any other microstructural changes at the magnet surfaces are prevented.

4.5 Stability of RE–TM magnets against radiation

RE–TM magnets are often applied in focusing devices for particle beams in accelerators or in spectrometers. In such an environment, the RE–TM magnets may be exposed to γ

Table 3. Long-term irreversible polarization losses of sintered Nd–Dy–Fe–B magnets with different load lines $B/\mu_0 H$ after aging at a temperature of 100 °C in air, calculated from the regression curves in Figure 25. The regression curves are deduced from measurements over a period of 766 days (2.1 years).

Aging of Nd–Dy–Fe–B magnets at 100 °C in air	1 year	3 years	5 years	10 years
$H_{cJ} = 2460$ kA m^{-1}, $B/\mu_0 H = -0.9$	−1.03	−1.12	−1.16	−1.22
$H_{cJ} = 2460$ kA m^{-1}, $B/\mu_0 H = -0.6$	−1.04	−1.15	−1.19	−1.26
$H_{cJ} = 1150$ kA m^{-1}, $B/\mu_0 H = -6.1$	−1.20	−1.34	−1.40	−1.48

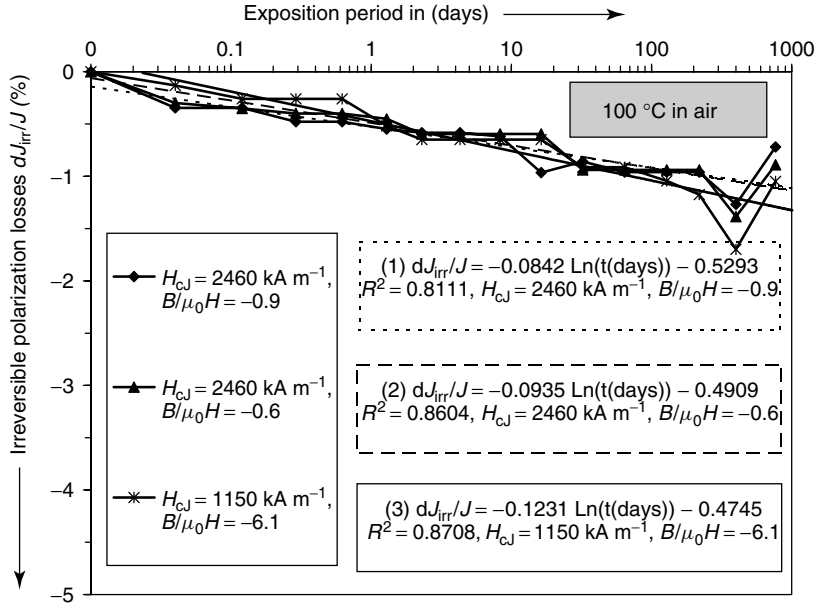

Figure 25. Long-term irreversible polarization losses of sintered Nd–Dy–Fe–B magnets with different load lines $B/\mu_0 H$ after aging at a temperature of 100 °C in air. The regression curves are deduced from measurements over a period of 766 days (2.1 years).

radiation as well as to irradiation of neutrons or other charged particles. While direct irradiation of RE–TM magnets by neutrons or charged particles may be avoided, in many cases, the magnets are often exposed to γ radiation. The effect of γ radiation from a ^{60}Co source on the magnetic properties of RE–TM magnets has been examined on five similar sets of $SmCo_5$, $Sm_2(Co,Cu,Fe,Zr)_{17}$, and Nd–Dy–Fe–B magnets at a constant temperature (Boockmann *et al.*, 1991). The magnetic properties and the load lines of the magnets amount to $J_r = 0.95\,T$, $H_{cJ} = 1800\,kA\,m^{-1}$, and $B/\mu_0 H = -0.7$ for $SmCo_5$ magnets, $J_r = 1.1\,T$, $H_{cJ} = 1400\,kA\,m^{-1}$, and $B/\mu_0 H = -0.71$ for $Sm_2(Co,Cu,Fe,Zr)_{17}$ magnets, and $J_r = 1.2\,T$, $H_{cJ} = 1520\,kA\,m^{-1}$, and $B/\mu_0 H = -0.61$ for Nd–Dy–Fe–B magnets. The magnets were supported on nonmagnetic plates with a distance of about 2 cm between every magnet, so that there was hardly any influence from the magnetic stray fields of the neighboring magnets. All magnets were exposed to γ radiation from a ^{60}Co-source emitting γ photons with energies of 1.17 and 1.33 MeV. The irradiation rate amounts to 1 krad min^{-1}. During the irradiation, the temperature was controlled by a thermocouple and could be kept constant at $(22 \pm 4)\,^{\circ}C$. After an accumulated dose of about 10 Mrad, one set of five magnets of each grade was always removed. The remanent polarization of every magnet and the demagnetization curves $J(H)$ of selected magnets were measured. The difference between the remanent polarization before and after the irradiation $dJ_{r,rad}$, related to J_r, and the standard deviations are presented in Figures 26–28 in dependence on the accumulated dose of the γ radiation.

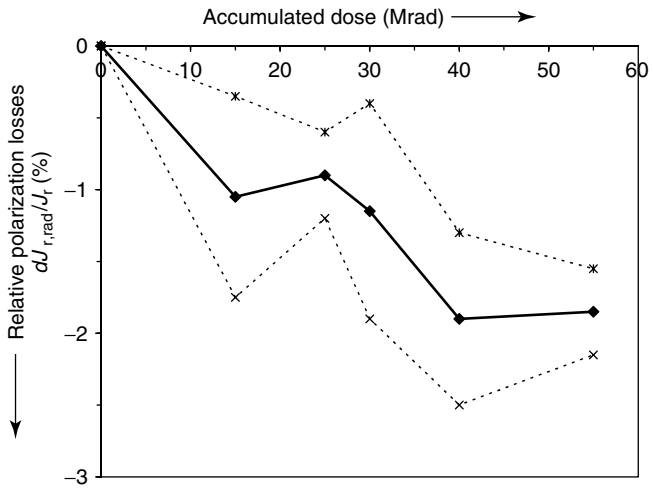

Figure 26. Dependence of the polarization losses $dJ_{r,rad}/J_r$ on the accumulated dose of γ radiation for sintered $SmCo_5$ magnets with a load line $B/\mu_0 H = -0.7$ at a temperature of about 22 °C. The data present the average of five measurements and the standard deviations.

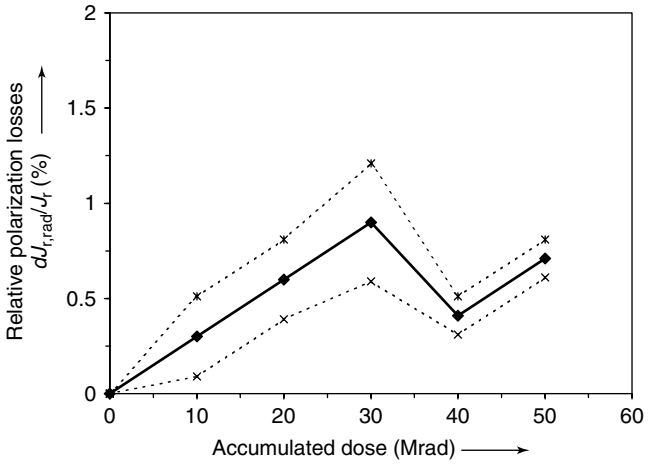

Figure 27. Dependence of the polarization changes $dJ_{r,rad}/J_r$ on the accumulated dose of γ radiation for sintered $Sm_2(Co,Cu,Fe,Zr)_{17}$ magnets with a load line $B/\mu_0 H = -0.71$ at a temperature of about 22 °C. The data present the average of five measurements and the standard deviations.

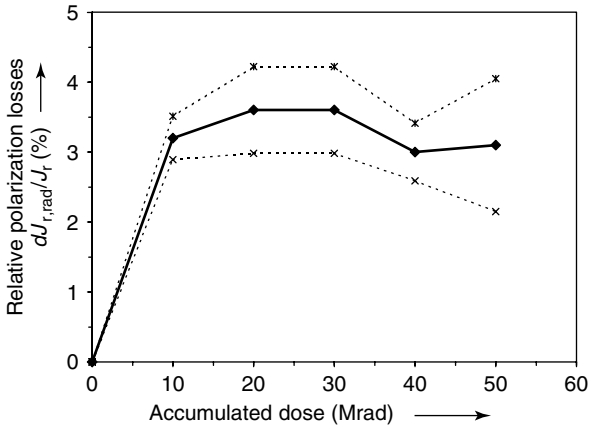

Figure 28. Dependence of the polarization changes $dJ_{r,rad}/J_r$ on the accumulated dose of γ radiation for sintered Nd–Dy–Fe–B magnets with a load line $B/\mu_0 H = -0.61$ at a temperature of about 22 °C. The data present the average of five measurements and the standard deviations.

For sintered $SmCo_5$ magnets, there seems to be a small decrease in the average remanent polarization by about 1–2%, see Figure 26. However, this was mainly caused by some oxidation at the edges of the magnets. After removal of the edges, no significant changes of the remanent polarization could be detected, which is in agreement with other results (Zeller and Nolen, 1987). The coercivity H_{cJ} of the irradiated $SmCo_5$ magnets has not been changed within an accuracy of the measurements of about 4%.

For sintered $Sm_2(Co,Cu,Fe,Zr)_{17}$ magnets, the changes in the remanent polarization $dJ_{r,rad}$ are less than 1% up to an accumulated dose of about 50 Mrad, see Figure 27.

Comparison of the demagnetization curves before and after the irradiation revealed no significant changes of the coercivity H_{cJ} within an accuracy of the measurements of about 2%.

The remanent polarization of γ-irradiated Nd–Dy–Fe–B magnets increased by about 3%, see Figure 28. The increase does not seem to depend on the accumulated dose; the origin is not known till now. A similar effect is also reported by Cost *et al*., who detected an increase in the remanent polarization of Nd–Dy–Fe–B magnets by about 0.8% after an accumulated dose of 48.8 Mrad (Cost, Brown, Giorgi and Stanley, 1987). However, Zeller *et al*. found a decrease in the remanent polarization of Nd–Fe–B magnets by about 1.5% after an accumulated γ dose of 50 Mrad and no significant changes in the remanent polarization of Nd–Dy–Fe–B magnets (Zeller *et al*., 1988). Since the coercivity H_{cJ} and the temperature stability of Nd–Fe–B magnets are inferior to Nd–Dy–Fe–B magnets, which have a stronger coercivity H_{cJ}, such polarization losses may be caused by aging due to an increase in the local temperature. In conclusion, the remanent polarization of sintered Nd–Dy–Fe–B magnets with coercivities $H_{cJ} > 1300\,\mathrm{kA\,m^{-1}}$ is not affected by γ radiation up to an accumulated dose of 50 Mrad.

Irradiation of sintered Nd–Fe–B magnets with a low coercivity of $890\,\mathrm{kA\,m^{-1}}$ and a load line $B/\mu_0 H = -0.35$ with 20 MeV protons results in polarization losses of −17% at 15 K and in almost total demagnetization after an irradiation at a temperature of 300 K. However, alloyed Nd–Dy–Fe–B magnets with a higher coercivity of $1357\,\mathrm{kA\,m^{-1}}$ and a small load line $B/\mu_0 H = -10$ experience hardly any polarization losses at room temperature even after a dose of 100 Mrad of 20 MeV protons (Talvitie *et al*., 1991). This indicates that the polarization losses may be caused by local heating in the collision cascade during irradiation, which results in the nucleation and expansion of reversed magnetic domains (Kähkönen *et al*., 1992a,b). Measurements of the demagnetization curves $J(H)$ before and after the irradiation tests by 20 MeV protons do not reveal any changes of the microstructure.

In contrast, $SmCo_5$ and $Sm_2(Co,Cu,Fe,Zr)_{17}$ magnets proved to be quite stable even after irradiation with 500 MeV protons. Polarization losses $dJ_{r,rad}$ of less than 1% were measured after irradiation by 5 Grad at a temperature of less than 120 °C (Blackmore, 1985). Remagnetization of the irradiated magnets resulted in the original magnetic properties and proved that no microstructural changes had occured.

Similar results were obtained after irradiation by 106 MeV deuterons. $SmCo_5$ and $Sm_2(Co,Cu,Fe,Zr)_{17}$ magnets did not experience significant polarization losses up to a dose of 3 Mrad, whereas Nd–Dy–Fe–B magnets were more sensitive to irradiation by 106 MeV deuterons (Zeller and Nolen, 1987).

Irradiation of Nd–Dy–Fe–B magnets with fast neutrons >0.1 MeV resulted in remanent polarization losses of about 4.5% for magnets with a coercivity $>1560\,\mathrm{kA\,m^{-1}}$ and a very small load line $B/\mu_0 H = -36$ after a total neutron fluence of 1.5×10^{16} neutrons $\mathrm{cm^{-2}}$. During irradiation, a temperature of 77 °C was measured (Brown and Cost, 1989). Nd–Dy–Fe–B magnets with lower coercivities or stronger load lines experienced much stronger polarization losses. Remagnetization after the irradiation resulted in a full recovery of the remanent polarization and an increased coercivity (Cost, Brown, Giorgi and Stanley, 1988). Hence, neutron irradiation has a similar effect on the polarization losses as a temperature load. By irradiation, nucleation of reversed domains is induced, but no changes occur in the microstructure.

$SmCo_5$ and $Sm_2(Co,Cu,Fe,Zr)_{17}$ magnets are much more stable with respect to neutron irradiation. Irradiation with fast neutrons (>0.1 MeV) up to a total fluence of 2.61×10^{18} neutrons $\mathrm{cm^{-2}}$ at a temperature of 77 °C results only in small polarization losses of less than 2% (Cost, Brown, Giorgi and Stanley, 1987). Owing to higher coercivities, $SmCo_5$ and $Sm_2(Co,Cu,Fe,Zr)_{17}$ magnets have a superior irradiation stability.

5 CORROSION BEHAVIOR OF SINTERED RE–TM MAGNETS

In many applications, RE–TM magnets are exposed to hot and humid atmospheres. In such climates, the surfaces of the RE–TM magnets may be oxidized, in particular, the RE components are preferentially oxidized.

In comparison to sintered Sm–Co magnets, Nd–Fe–B magnets are more sensitive to corrosion. As a consequence, all finished magnets get a final surface treatment. Such magnets have been applied at ambient conditions, for instance, room temperature, humidity up to 50%, no condensation of moisture, for more than 10 years in telephone transducers, without any corrosion problems.

However, in hot and humid climates, conventional Nd–Fe–B magnets, which do not contain Co additions, corrode heavily. For instance, in an accelerated test at 130 °C and 95% relative humidity, such magnets experience substantial mass losses by corrosion, whereas alloyed Nd–Dy–Fe–Co–TM–B magnets with some additions of TM: Cu, Ga, Al, and an appropriate microstructure are not affected significantly. Indeed, the weight of such magnets increases a little bit due to the formation of a passivating surface layer (Katter *et al*., 2001).

5.1 Basic principles

The microstructure of sintered Nd–Dy–Fe–B magnets consists of grains of the hard magnetic $(Nd,Dy)_2Fe_{14}B$ compound, which are separated from each other by Nd-rich constituents, in general, a Nd–Fe solid solution. Besides, there are some Nd oxides embedded or occasionally some $Nd_{1.1}Fe_4B_4$ grains may occur.

In a hot and humid climate, the Nd-rich constituents are preferentially converted to Nd hydroxides and some hydrogen is released. The hydrogen reacts immediately with the Nd-rich constituents and forms Nd hydrides. In such a hot and humid environment, Nd hydrides are not stable, react with water vapor, and are transformed into Nd hydroxides. Since this chemical reaction releases additional hydrogen, the reaction cycle continues (Katter *et al*., 2001). The microstructure of sintered Nd–Fe–B magnets and the basic constituents are presented in Figure 29.

The formation of Nd hydrides results in a strong volume increase of the Nd-rich constituents, so that cracks occur along the grain boundaries. Such microscopic cracks accelerate the corrosion. In the worst case, the surface of the sintered Nd–Fe–B magnets disintegrates. Almost white Nd oxides and grains of $Nd_2Fe_{14}B$ peel off from the surfaces of the magnets.

The corrosion rate of sintered Nd–Dy–Fe–B magnets depends on the composition of the magnet, in particular, on the electrochemical potential of the RE-rich constituents, and on the microstructure, for instance, on the fraction and on the distribution of the RE-rich phases.

By proper addition of some TMs, for instance Co, Nb, V, Mo, Cu, Ga, to the alloy, the corrosion stability of sintered Nd–Dy–Fe–B magnets can be improved substantially (Ohashi, Tawara, Yokoyama and Kobayashi, 1987; Hirosawa, Mino and Tomizawa, 1991; Kim and Camp, 1996; Grieb, 1997; Fernengel *et al*., 1999). Some of these additions transform the Nd-rich constituents into more noble intermetallic compounds, for instance, $Nd_3(Co,Cu)$, $(Nd,Dy)_5(Co,Cu,Ga)_3$, $Nd_6(Fe,Co)_{13}Ga$, see inset in Figure 29. Since the free electrochemical potentials of these compounds were determined to be about 800 mV higher than that of pure Nd metal, such Nd–Dy–Fe–Co–TM–B magnets, TM: Cu, Al, Ga, are much more stable in hot and humid climates (Katter *et al*., 2001). For such alloyed Nd–Dy–Fe–Co–TM–B magnets, the corrosion rate is substantially reduced. Depending on the total RE content, such magnets can be stable in hot and humid climates. For magnets with an appropriate total RE content, there is a passivation of the surface in the beginning and, after a prolonged exposure, the magnets start to rust similar to pure iron. However, magnets with a higher total RE concentration experience some mass losses, which depends on the exposure period in hot and humid climate (Kaszuwara and Leonowicz, 1999; Katter *et al*., 2001) or on the total RE content, if a fixed exposure period for the corrosion test is applied (Tokuhara and Hirosawa, 1991).

The sequence of the corrosion attack has been confirmed by measurements of the electrochemical potential of the constituents by scanning probe microscopy. The measurements demonstrate a correlation between the electrostatic potential and the corrosion rate. The hard magnetic $Nd_2Fe_{14}B$ grains

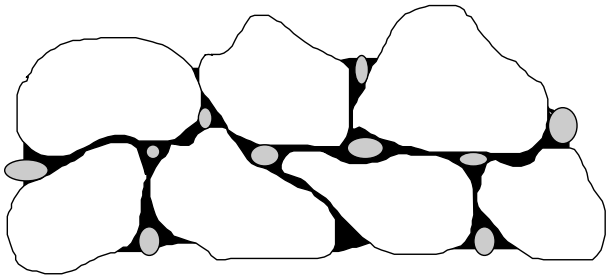

	Nd—Dy—Fe—B	Nd—Dy—Fe—Co—TM—B
Matrix	$(Nd,Dy)_2Fe_{14}B$	$(Nd,Dy)_2(Fe,Co)_{14}B$
Oxide	Nd_2O_3	Nd_2O_3
Nd-rich constituents	Nd(Fe)	$Nd_x(Co,TM)_y$

Figure 29. Model of the microstructure of sintered standard Nd–Dy–Fe–B magnets or alloyed Nd–Dy–Fe–Co–TM–B magnets, TM: Cu, Al, Ga. The inset indicates that the replacement of Nd-rich constituents Nd(Fe) by more noble $Nd_x(Co,TM)_y$ compounds improves the corrosion resistance substantially.

have a superior corrosion stability compared to $Nd_{1.1}Fe_4B_4$ borides or to the Nd–Fe solid solutions (Bala, Pawlowska, Szymura and Rabinovich, 1998; Schultz, El-Aziz, Barkleit and Mummert, 1999; Mummert *et al*., 2000; El-Aziz, 2003).

5.2 Typical corrosion tests

There are many different corrosion tests, in particular, in hot and humid climates at different temperatures. Other tests focus on more aggressive media, such as sulfuric acid in order to measure electrochemical potentials (Bala, Pawlowska, Szymura and Rabinovich, 1998; Schultz, El-Aziz, Barkleit and Mummert, 1999; Mummert *et al*., 2000), salt spray tests for automotive applications (Katter *et al*., 2001), seawater test for marine applications, and so on.

A very common test is the highly accelerated stress test (HAST), according to the standard IEC 68-2-66. The test samples are stored at 130 °C, 95% relative humidity, and 2.6 bar water vapor pressure. Under these conditions, no condensation of vapor occurs. The mass losses per surface area of the magnets are monitored, depending on the exposure time. Standard Nd–Fe–B magnets suffer mass losses of about 10–100 mg cm^{-2} after 10 days, whereas the mass losses of alloyed Nd–Dy–Fe–Co–TM–B magnets, TM: Cu, Al, Ga, with an improved corrosion stability amount to <1 mg cm^{-2}, see Figure 30. If some condensation occurs, such alloyed Nd–Dy–Fe–Co–TM–B magnets start to rust similar to iron.

The results of the accelerated corrosion tests could be confirmed by a long-term corrosion test in dry air with a relative humidity of about 50% over a period of 2 years. Sintered Nd–Fe–B magnets with an extremely high total RE content corrode faster than magnets with a lower RE content. The improvements were achieved by a controlled oxidation of RE-rich alloy powders in air before sintering (Ma *et al*., 1994; Kaszuwara and Leonowicz, 1999) or by addition of Co, Cu, Al, Zr, or C to Nd–Fe–B alloys (Kim and Camp, 1996; Kaszuwara and Leonowicz, 1999).

Since sintered $SmCo_5$ and $Sm_2(Co,Cu,Fe,Zr)_{17}$ magnets only contain a few isolated intergranular RE-rich constituents, they are much more stable in hot and humid climates than Nd–Dy–Fe–Co–TM–B magnets. Figure 31 compares the mass losses of alloyed Nd–Dy–Fe–Co–TM–B, $SmCo_5$, and $Sm_2(Co,Cu,Fe,Zr)_{17}$ magnets, depending on the exposure period in a HAST test. $SmCo_5$ and $Sm_2(Co,Cu,Fe,Zr)_{17}$ magnets form a passivation layer, which sometimes increases their weight. Hence, they are rather stable in such a hot and humid climate, whereas Nd–Dy–Fe–Co–TM–B magnets experience small mass losses of <1 mg cm^{-2} after 10 days and some milligram per square centimeter after an exposure period of 50 days.

By performing the stress test at 130 °C and a humidity of 100%, often denoted as pressure cooker test (PCT) or autoclave test, the corrosion stress can be accelerated by a factor of about 10. Since condensation of water vapor occurs,

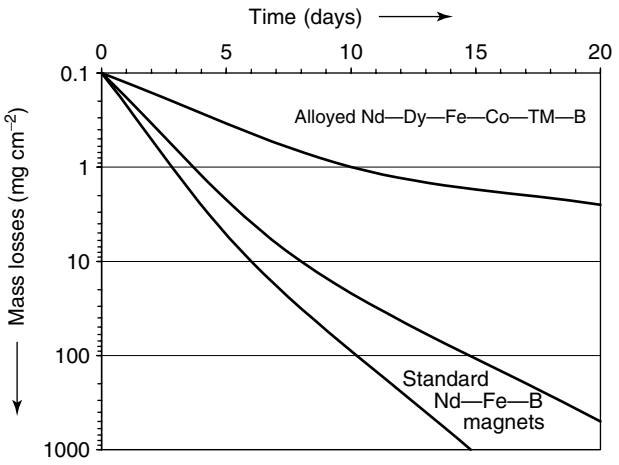

Figure 30. Mass losses per surface area of standard sintered Nd–Dy–Fe–B or alloyed Nd–Dy–Fe–Co–TM–B magnets with an improved corrosion resistance, depending on the exposure time. The highly accelerated stress test (HAST) is performed at 130 °C, 95% relative humidity, and 2.6 bar vapor pressure.

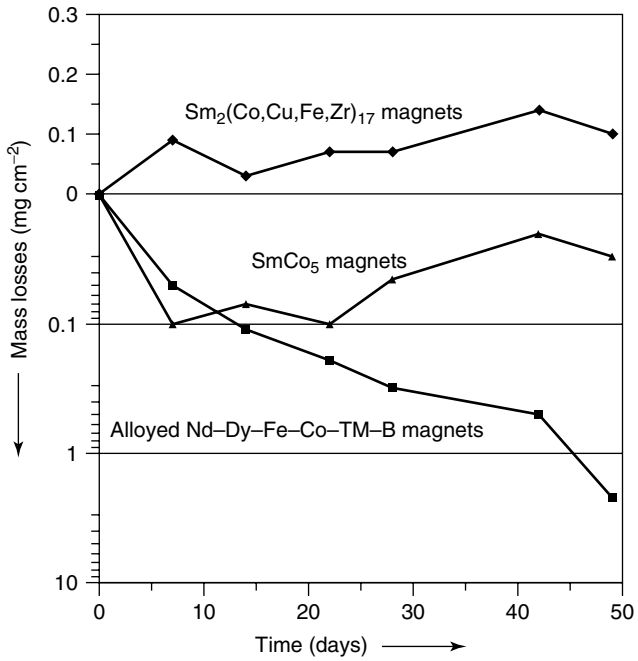

Figure 31. Comparison of mass losses per surface area of sintered $SmCo_5$, $Sm_2(Co,Cu,Fe,Zr)_{17}$, and alloyed Nd–Dy–Fe–Co–TM–B magnets in dependence on the exposure time. The highly accelerated stress test (HAST) has been performed at 130 °C, 95% relative humidity, and 2.6 bar vapor pressure.

the alloyed Nd–Dy–Fe–Co–TM–B magnets are covered with red rust after some days, but no disintegration of the magnet surface occurs (Katter *et al*., 2001).

Under salt spray conditions, according to the standard DIN 50021, the magnets are covered by red rust after an exposure time of 24 h in general.

5.3 Coating of RE–TM magnets

In applications where condensation of humidity occurs or other corrosive media exist, sintered Nd–Fe–B magnets must be protected by metallic or organic coatings. Typical commercial coatings for sintered Nd–Fe–B magnets, their color, hardness, and maximum operating temperatures are compiled in Table 4. Such coatings also facilitate the handling and cleaning of sintered magnets, for instance, for applications in clean-room workshops.

6 MECHANICAL PROPERTIES OF SINTERED RE–TM MAGNETS

Sintered RE–TM magnets are applied in many devices, for instance, motors, generators, couplings, bearings, separators, sensors, and so on in order to optimize the efficiency of the device or in order to reduce the weight or the volume of the magnet assemblies. In general, magnets operate as functional materials, but, in dynamic applications, mechanical properties may also become important.

Some mechanical properties of sintered Nd–Fe–B magnets have been examined in dependence of different processing routes (Horton, Wright and Herchenroeder, 1996; Horton *et al*., 1997), on the composition, for instance, the Co content (Rabinovich *et al*., 1996; Jiang *et al*., 2001) or different RE-rich constituents (Ohashi, Tawara, Yokoyama and Kobayashi, 1987; Otsuki, Sato and Fujiwara, 1989) or various additions of Al, Cr, Nb, Zr (Szymura, Wyslocki, Rabinovich and Bala, 1994; Rabinovich *et al*., 1996).

Besides, on the composition, the mechanical properties may also depend on the microstructure, characterized by the average grain size. There are different routes for manufacturing Nd–Dy–Fe–Co–TM–B magnets, TM: Cu, Al, Ga, with various grain sizes. For instance, Nd–Dy–Fe–TM–B magnets with various fractions of RE-rich constituents can be sintered from appropriate alloy powder blends. Owing to the different volumes of the liquid phase at the sintering temperature, the average grain size of $Nd_{12.8-x}Dy_{0.74}Fe_{bal}TM_{1.3}B_{5.6}$ magnets, TM: Co, Cu, Al, Ga, $x = 0$, 0.1, 0.3, 0.9, 1.4, 2.0, varies between 6.5 and 9.5 µm (Rodewald, Katter and Üstüner, 2004).

Another route is the sintering of $Nd_{12.9}Dy_{0.74}Fe_{bal}TM_{1.3}B_{5.6}$ magnets from alloy powders with different average particle sizes, according to Fisher sub sieve seizer (FSSS), for instance, 2.1, 2.6, 3.1, 3.5, 3.7, and 4.1 µm. By adjusted sintering conditions, dense magnets with an average grain size between 4.0 and 6.5 µm could be achieved (Rodewald, Katter and Üstüner, 2004).

The densities of the sintered magnets are controlled by the Archimedes principle. Owing to the liquid-phase sintering, Nd–Dy–Fe–TM–B magnets easily achieve densities between 7.55 and 7.6 g cm^{-3} or $\rho/\rho_0 > 99\%$, where ρ_0 denotes the density of the $Nd_2Fe_{14}B$ compound. The typical magnetic properties amount to $J_r = (1.42 \pm 0.02)$ T and $H_{cJ} = (12 \pm 1)$ kA m^{-1}. The maximum energy densities range between 360 and 400 kJ m^{-3}. The average grain

Table 4. Typical commercial surface coatings of sintered Nd–Fe–B magnets for protection against corrosion or for handling in clean rooms.

Surface	Thickness	Method	Color	Hardness	Corrosion resistance	Temperature range (°C)
Sn	>15 µm	Galvanic	Silver semibright	HV 20	Humid climate	<160
Ni	>10 µm	Galvanic	Silver semibright	HV 350	Humid climate	<200
Ni + Sn	>5 µm Ni+ >10 µm Sn	Galvanic	Silver semibright	HV 20	Humid climate	<160
Al spray coating	>5 µm	Spray coating	Yellow semibright	4 H	Excellent climatic, salt spray resistance	<180
Al yellow chromate	>5 µm	IVD	Yellow semibright	HV 20	Excellent climatic, salt spray resistance	<500
Electrocoating	>15 µm	EPP	Black	4 H	Excellent climatic, salt spray resistance	<130
	>6 µm	EPP	Black	4 H	Excellent climatic, salt spray resistance	<150

IVD, Ion Vapor Deposition; EPP, Electrophoretic Paint

size was determined by the three circular intercept method, according to the standard ASTM E112. The following mechanical properties were determined by standardized tests: the compressive and the bending strength, the fracture toughness, the Young's modulus, and the Vickers hardness.

6.1 Compressive strength f_{comp}

In general, the compressive f_{comp} strength is determined on cubes with dimensions of approximately $5 \times 5 \times 5\,mm^3$, which are cut from sintered Nd–Dy–Fe–TM–B magnets parallel to the easy axis by diamond grinding. The ram speed of the press amounts to $0.15\,mm\,min^{-1}$. Of each batch, the measurements are performed on five samples, the averages of the results and their standard deviation are compiled in Figure 32. Overall, the compressive strength f_{comp} amounts to $(960 \pm 50)\,N\,mm^{-2}$ on the average and does not depend on the grain size of the sintered magnets within the accuracy of the measurements. These results are in fair agreement with measurements on Nd–Dy–Fe–Co–B magnets with different alloying additions of Cr, Al, Nb, or Zr, the compression strength of which ranges between 860 and $1120\,N\,mm^{-2}$ (Rabinovich *et al.*, 1996).

Measurements of the compressive strength perpendicular to the easy axis result in about 4–8% smaller values. Hence, there is only a negligible anisotropy of the compressive strength in sintered Nd–Dy–Fe–TM–B magnets.

In addition, the temperature dependence of the compressive strength of $Nd_{12.9}Dy_{0.4}Fe_{bal}TM_{1.3}B_{5.6}$ magnets, TM: Co, Cu, Al, Ga, with a high remanent polarization of 1.45 T, a coercivity H_{cJ} of $1000\,kA\,m^{-1}$, and an average grain size of 8.4 µm has been examined. On the average, the compression strength decreases by about 7%, when the temperature increases by 100 K, see Figure 33.

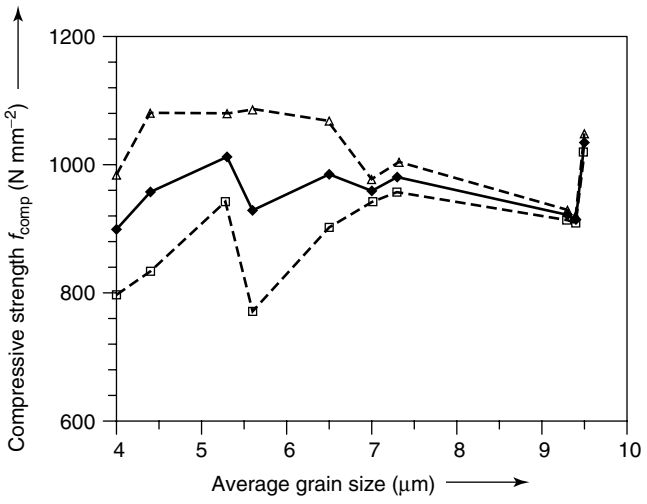

Figure 32. Compressive strength of $Nd_{12.9}Dy_{0.74}Fe_{bal}TM_{1.3}B_{5.6}$ magnets, TM: Co, Cu, Al, Ga, depending on the average grain size. The dashed graphs represent the compressive strength $f_{comp} \pm \sigma$, σ denotes the standard deviation.

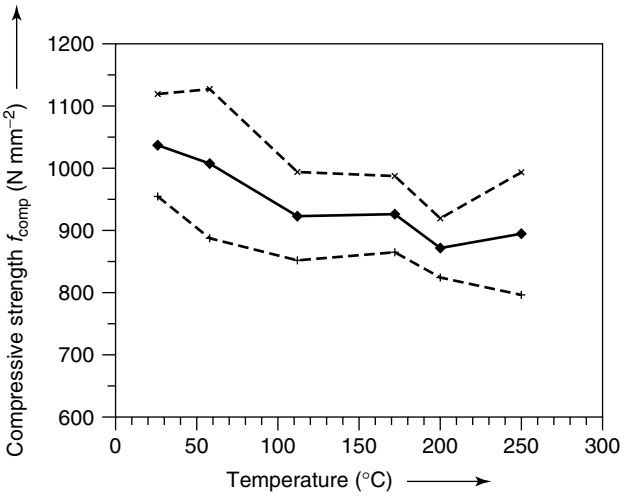

Figure 33. Compressive strength of $Nd_{12.9}Dy_{0.4}Fe_{bal}TM_{1.3}B_{5.6}$ magnets, TM: Co, Cu, Al, Ga, depending on the temperature. The dashed graphs represent the compressive strength $f_{comp} \pm \sigma$, σ denotes the standard deviation.

The compressive strength of sintered $SmCo_5$ or $Sm_2(Co,Cu,Fe,Zr)_{17}$ magnets amounts to approximately 1000 or $650\,N\,mm^{-2}$ respectively. In particular, $Sm_2(Co,Cu,Fe,Zr)_{17}$ magnets are more sensitive to compression forces and must be handled carefully in order to prevent chipping or cracks.

6.2 Bending strength f_{bend}

The bending strength f_{bend} of Nd–Dy–Fe–TM–B magnets, TM: Co, Cu, Al, Ga, was measured by the three-point bending test on bars with dimensions of approximately $5 \times 2 \times 50\,mm^3$, for instance, according to the standard ASTM 314-64, depending on the grain size. On the average, the bending strength perpendicular to the easy axis amounts to about $(330 \pm 20)\,N\,mm^{-2}$ and does not depend on the grain size of the sintered magnets within the accuracy of the measurements, see Figure 34.

There is a little anisotropy of the bending strength. In general, the bending strength perpendicular to the easy axis results in 4–10% smaller values than when it is parallel to the easy axis.

However, the bending strength of Nd–Dy–Fe–TM–B magnets, TM: Co, Cu, Al, Ga, with Co concentrations >3% or with different alloying additions of Cr, Al, Nb, or Zr, ranges only between 160 and $280\,N\,mm^{-2}$ (Rabinovich *et al.*, 1996; Jiang *et al.*, 2001).

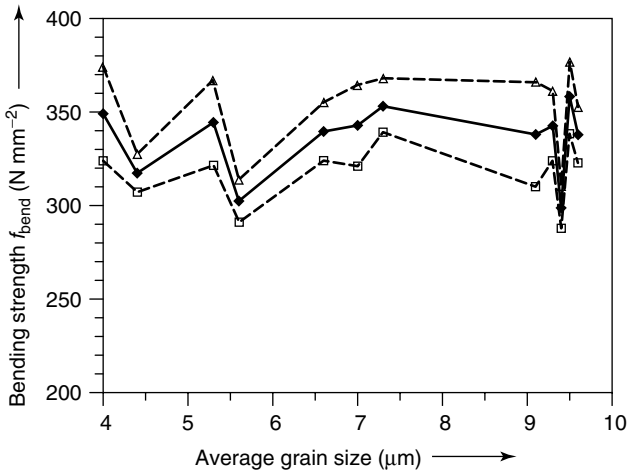

Figure 34. Bending strength of $Nd_{12.9}Dy_{0.74}Fe_{bal}TM_{1.36}B_{5.6}$ magnets, TM: Co, Cu, Al, Ga, depending on the average grain size. The dashed graphs represent the bending strength $f_{bend} \pm \sigma$, σ denotes the standard deviation.

In addition, the bending strength was examined on magnetized bars perpendicular to the easy axis, which resulted in about 10–15% smaller values. Probably the repulsive magnetic forces promote the crack formation and propagation (Rodewald, Katter and Üstüner, 2004).

Finally, the bending strength of $Nd_{12.9}Dy_{0.4}Fe_{bal}TM_{1.3}B_{5.6}$ magnets, TM: Co, Cu, Al, Ga, with a high remanent polarization of 1.45 T, a coercivity H_{cJ} of 1000 kA m^{-1} and an average grain size of 8.4 µm was examined, depending on the temperature. On the average, the bending strength decreases only by about 5%, when the temperature increases by 100 K, see Figure 35.

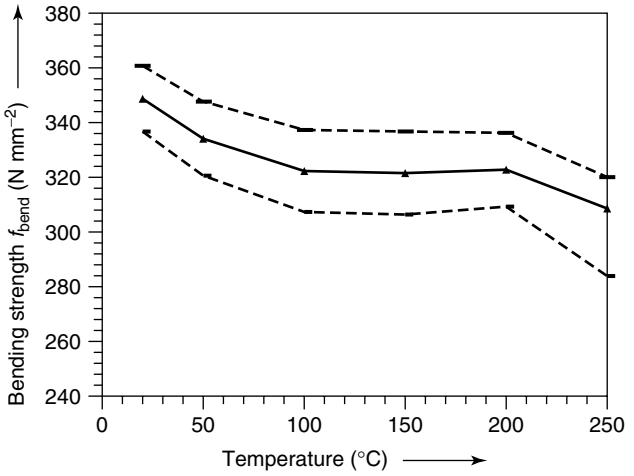

Figure 35. Bending strength of $Nd_{12.9}Dy_{0.4}Fe_{bal}TM_{1.3}B_{5.6}$ magnets, TM: Co, Cu, Al, Ga, depending on the temperature. The dashed graphs represent the bending strength $f_{bend} \pm \sigma$, σ denotes the standard deviation.

The bending strength of sintered $SmCo_5$ magnets amounts to approximately 120 N mm^{-2}, whereas the bending strength of sintered $Sm_2(Co,Cu,Fe,Zr)_{17}$ magnets ranges between 90 and 150 N mm^{-2} in general. The smaller bending strengths of Sm–Co magnets reflect rather well their high sensitivity to cracking.

6.3 Fracture toughness K_{IC}

The fracture toughness K_{IC} of $Nd_{12.9}Dy_{0.74}Fe_{bal}TM_{1.3}B_{5.6}$ magnets, TM: Co, Cu, Al, Ga, sintered of alloy powders with different average particle sizes at adjusted temperatures was examined on bars, $3 \times 6 \times 30$ mm^3, for instance, depending on the grain size. The bars had a notch of 0.2 mm in width and 3 mm in length in the middle of the bar, made by spark erosion wire cutting, in order to achieve a well-defined starting point for the cracks. The fracture force was determined by a three-point bending test according to ASTM 314-64. The cracks always started at the notch and extended symmetrically. On the average, the fracture toughness perpendicular to the easy axis amounted to (184 ± 10) N mm$^{-3/2}$. There was only a small decrease in the fracture toughness with decreasing grain size, see Figure 36. The fracture toughness K_{IC} was not affected significantly by the fraction of RE-rich constituents in the sintered magnets.

Measurements of the fracture toughness parallel to the easy axis resulted in 10–15% smaller values. Within the accuracy of the measurements there was only a small anisotropy of the fracture toughness K_{IC}.

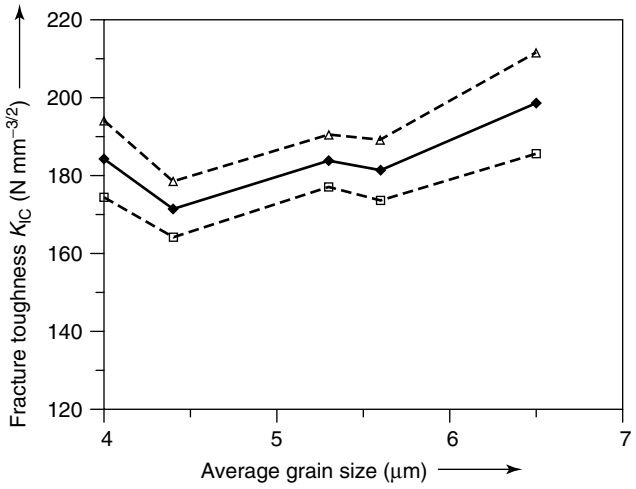

Figure 36. Fracture toughness K_{IC} of $Nd_{12.9}Dy_{0.74}Fe_{bal}TM_{1.3}B_{5.6}$ magnets, TM: Co, Cu, Al, Ga, sintered of alloy powders with different average particle sizes at adjusted temperatures, depending on the average grain size. The dashed graphs represent the fracture toughness $K_{IC} \pm \sigma$, σ denotes the standard deviation.

The fracture toughness K_{IC} was sensitive to the processing route of the magnets. The data ranged from about $60\,N\,mm^{-3/2}$ for Nd–Fe–B magnets prepared from TiC-containing gas-atomized alloy powders up to $175\,N\,mm^{-3/2}$ for sintered Nd–Fe–B magnets (Horton *et al.*, 1997). For sintered Nd–Dy–Fe–B magnets, most of the data ranged between 90 and $175\,N\,mm^{-3/2}$ (Otsuki, Sato and Fujiwara, 1989; Horton, Wright and Herchenroeder, 1996; Jiang *et al.*, 2001), whereas for Nd–Dy–Fe–Co–B magnets with a Co concentration >3%, the fracture toughness decreased to a range between 100 and $110\,N\,mm^{-3/2}$ (Jiang *et al.*, 2001).

Lately, the fracture toughness K_{IC} of $Nd_{12.9}Dy_{0.4}Fe_{bal}TM_{1.3}B_{5.6}$ magnets, TM: Co, Cu, Al, Ga, with a high remanent polarization of 1.45 T, a coercivity H_{cJ} of $1000\,kA\,m^{-1}$, and an average grain size of 8.4 µm was determined, depending on the temperature. On the average, the fracture toughness decreased by about 4–6% when the temperature increased by 100 K, see Figure 37.

The fracture toughness K_{IC} of $SmCo_5$ magnets varies between 50 and $70\,N\,mm^{-3/2}$ (Horton, Wright and Herchenroeder, 1996). Sintered $Sm_2(Co,Cu,Fe,Zr)_{17}$ magnets have an even smaller fracture toughness between 40 and $50\,N\,mm^{-3/2}$, which corroborates their sensitivity to chipping.

6.4 Young's modulus *E*

The Young's modulus E of sintered $Nd_{12.9}Dy_{0.74}Fe_{bal}TM_{1.3}B_{5.6}$ magnets, TM: Co, Cu, Al, Ga, with an average grains size of 9.8 µm was determined on bars, $3 \times 4 \times 50\,mm^3$, by ultrasound attenuation. The Young's modulus E amounted to $(160 \pm 3)\,kN\,mm^{-2}$ perpendicular to the easy axis. Measurements of the Young's modulus parallel to the easy axis yielded insignificant larger values. Within the accuracy of the measurements, there was only a negligible anisotropy of <3%.

The Young's modulus E did not seem to be very sensitive to the composition of the magnets. Data of magnets with different Co concentrations or different alloying additions of Cr, Al, Nb, or Zr, ranged between 130 and $160\,kN\,mm^{-2}$ (Szymura, Wyslocki, Rabinovich and Bala, 1994; Rabinovich *et al.*, 1996).

Measurements of the Young's modulus of sintered $Nd_{12.9}Dy_{0.74}Fe_{bal}TM_{1.3}B_{5.6}$ magnets at temperatures between 20 and 200 °C proved only a small decrease by about 2.5% when the temperature was increased by 100 K, see Figure 38.

The Young's modulus E of sintered $SmCo_5$ magnets amounted to approximately $110\,kN\,mm^{-2}$. However, the Young's modulus of sintered $Sm_2(Co,Cu,Fe,Zr)_{17}$ magnets was comparable to Nd–Dy–Fe–TM–B magnets and amounted to $150\,kN\,mm^{-2}$.

6.5 Vickers hardness HV 1

The Vickers hardness HV 1 was examined on polished surfaces of $Nd_{12.9}Dy_{0.74}Fe_{bal}TM_{1.3}B_{5.6}$ magnets, TM: Co, Cu, Al, Ga, depending on the grain size. The indenter load amounted to 10 N. There is no significant dependence of the Vickers hardness on the average grain size, see Figure 39.

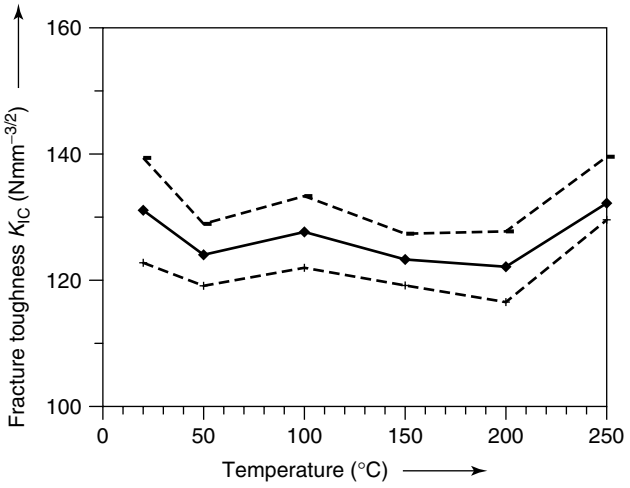

Figure 37. Fracture toughness K_{IC} of $Nd_{12.9}Dy_{0.4}Fe_{bal}TM_{1.3}B_{5.6}$ magnets, TM: Co, Cu, Al, Ga, depending on the temperature. The dashed graphs represent the fracture toughness $K_{IC} \pm \sigma$, σ denotes the standard deviation.

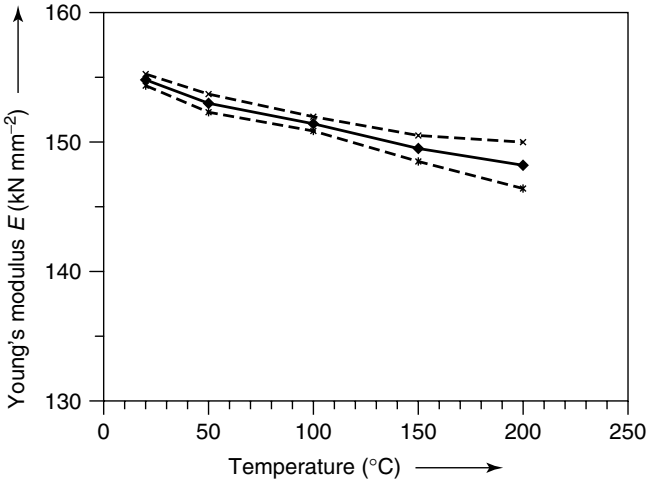

Figure 38. Young's modulus E of sintered $Nd_{12.9}Dy_{0.74}Fe_{bal}TM_{1.3}B_{5.6}$ magnets with an average grains size of 9.8 µm, depending on the temperature. The dashed graphs represent the Young's modulus $E \pm \sigma$, σ denotes the standard deviation.

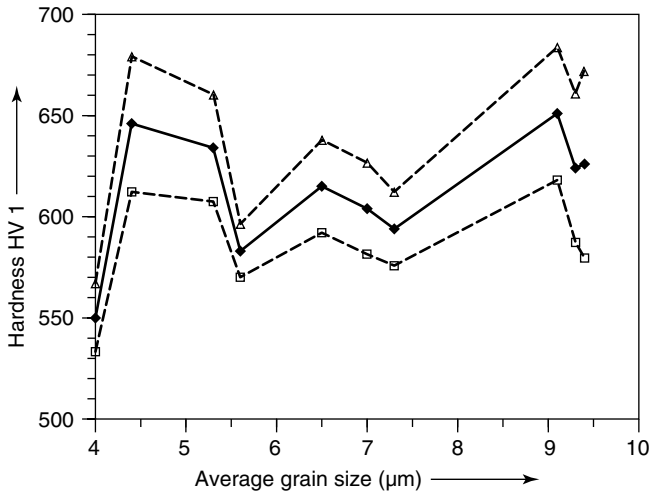

Figure 39. Vickers hardness HV 1 of $Nd_{12.9}Dy_{0.74}Fe_{bal}TM_{1.3}B_{5.6}$ magnets, TM: Co, Cu, Al, Ga, depending on the average grain size. The dashed graphs represent the Vickers hardness HV $1 \pm \sigma, \sigma$ denotes the standard deviation.

This may be due to the wide distribution of the dimensions of the grains in sintered magnets. For instance, even magnets with an average grain size of about 5 μm still contain some large grains with dimensions up to 20 μm. On the average, the Vickers hardness HV 1 amounts to (610 ± 30).

The Vickers hardness does not seem to be sensitive to the composition or to the microstructure of the magnets. Typical data range from 530 to 600 HV 1 for magnets with different RE contents (Otsuki, Sato and Fujiwara, 1989) or different Co contents (Jiang *et al.*, 2001).

The Vickers hardness HV 1 of sintered Sm–Co magnets is quite similar to Nd–Dy–Fe–TM–B magnets and amounts to 550 HV 1 for $SmCo_5$ magnets and to 640 HV 1 for $Sm_2(Co,Cu,Fe,Zr)_{17}$ magnets.

6.6 Other thermal, caloric, or electrical properties of RE–TM magnets

Additional thermal, caloric, or electrical properties of sintered RE–TM magnets can be retrieved from data sheets of magnet producers.

Very often, RE–TM magnets are glued onto soft magnetic parts, for instance, pole plates, rotor laminations of motors, casings, yokes, and so on. In particular, at increased operating temperatures, magnets with a large pole area may experience a shearing stress due to the different coefficients of the thermal expansion of the magnet and the support material. Under extreme conditions, the shearing stress may result in loosening of the bond. Hence, the coefficients of the thermal expansion should be taken into account.

For Nd–Dy–Fe–TM–B magnets, TM: Co, Cu, Al, Ga, there is a significant anisotropy of the coefficients of the thermal expansion, which range between 5 and $7.5 \times 10^{-6}\,K^{-1}$ parallel to the easy axis and between -0.5 and $-1 \times 10^{-6}\,K^{-1}$ perpendicular to the easy axis of the Nd–Dy–Fe–TM–B magnets.

For sintered Sm–Co magnets, the anisotropy of the coefficients of the thermal expansion is less pronounced. For $SmCo_5$ magnets, the coefficients of the thermal expansion amount to $7 \times 10^{-6}\,K^{-1}$ parallel and to $13 \times 10^{-6}\,K^{-1}$ perpendicular to the easy axis of the $SmCo_5$ magnets and vary from 8 to $10 \times 10^{-6}\,K^{-1}$ parallel and from 11 to $12 \times 10^{-6}\,K^{-1}$ perpendicular to the easy axis of $Sm_2(Co,Cu,Fe,Zr)_{17}$ magnets.

The thermal conductivity of sintered Nd–Dy–Fe–TM–B magnets amounts to approximately $9\,W\,m^{-1}\,K^{-1}$, which is about 11% of the thermal conductivity of iron, which amounts to $80.2\,W\,m^{-1}\,K^{-1}$, but is rather similar to the thermal conductivity of neodymium metal, which amounts to $16.5\,W\,m^{-1}\,K^{-1}$. The thermal conductivity of sintered $SmCo_5$ magnets is 10% larger than the thermal conductivity of Nd–Dy–Fe–TM–B magnets and amounts to about $10\,W\,m^{-1}\,K^{-1}$. Owing to the high Co content, the thermal conductivity of sintered $Sm_2(Co,Cu,Fe,Zr)_{17}$ magnets increases to $12\,W\,m^{-1}\,K^{-1}$, which is only 12% of the thermal conductivity of cobalt metal, which amounts to $100\,W\,m^{-1}\,K^{-1}$, but is similar to the thermal conductivity of samarium metal, which amounts to $13.3\,W\,m^{-1}\,K^{-1}$.

The specific heat of sintered RE–TM magnets is rather constant. The data range between 440 and $500\,J\,kg^{-1}\,K^{-1}$ for Nd–Dy–Fe–TM–B magnets, between 370 and $420\,J\,kg^{-1}\,K^{-1}$ for $SmCo_5$ magnets, and between 370 and $390\,J\,kg^{-1}\,K^{-1}$ for $Sm_2(Co,Cu,Fe,Zr)_{17}$ magnets. There are only minor differences to the specific heat of iron metal, $452\,J\,kg^{-1}\,K^{-1}$, or cobalt metal, $456\,J\,kg^{-1}\,K^{-1}$.

The electrical resistivity of sintered Nd–Dy–Fe–TM–B magnets ranges between 1.1 and $1.6\,\Omega\,mm^2\,m^{-1}$. In general, the electrical resistivity parallel to the easy axis is about 10–20% larger than the resistivity perpendicular to the easy axis of the Nd–Dy–Fe–TM–B magnets. There is only a small increase in the electrical resistivity of approximately $2.8 \times 10^{-2}\,\Omega\,mm^2\,m^{-1}\,K^{-1}$ in the temperature range between 20 and 100 °C.

By alloying additions to Nd–Dy–Fe–TM–B magnets, the electrical resistivity cannot be changed significantly. The electrical resistivity of Nd–Dy–Fe–TM–B magnets is about 10 times larger than the electrical resistivity of iron metal, which amounts to $0.10\,\Omega\,mm^2\,m^{-1}$.

The electrical resistivity varies between 0.5 and $0.6\,\Omega\,mm^2\,m^{-1}$ for sintered $SmCo_5$ magnets and between 0.75 and $0.85\,\Omega\,mm^2\,m^{-1}$ for sintered $Sm_2(Co,Cu,Fe,Zr)_{17}$ magnets, which is similar to the electrical resistivity

of samarium metal, $0.94\,\Omega\,mm^2\,m^{-1}$, and an order of magnitude larger than the electrical resistivity of cobalt metal, $0.06\,\Omega\,mm^2\,m^{-1}$.

7 CONCLUSIONS

Permanent magnets have become a key component in many devices. Owing to the high maximum energy density, RE–TM magnets are able to drive small motors in watches as well as strong motors in electric vehicles or huge motors for the propulsion of ships. There are miniature motors with a diameter of 1.9 mm, a length of 5 mm, which rotate at a speed of 100 000 rpm and achieve a power of 60 mW. On the other hand, there are motors with a diameter up to 3.2 m, a length up to 9.5 m, which rotate at 120 rpm. The power of such machines amounts to 5 MW and there are designs for motors with a power up to 18 MW for the propulsion of ships.

In addition, heavy and large hydraulic devices are going to be replaced by permanent magnet motors, for instance, in electronic power steering of vehicles or electronically assisted braking. In such motors, the cogging torque must be minimized. Novel and economic butterfly-shaped Nd–Dy–Fe–TM–B magnets meet such specifications.

For the design and engineering of magnet assemblies, a large variety of RE–TM magnets are commercially available. Most economic is of course the application of net-shaped parts produced by axial field die-pressing. The dimensional tolerances depend on the dimensions and on the shape of the magnets. For instance, parts with nominal dimensions up to 7 mm perpendicular to the pressing direction tolerances of ± 0.10 mm can be achieved. For larger blocks with dimensions up to 60 mm perpendicular to the pressing direction, the tolerances range between ± 0.45 and ± 0.90 mm. More precise tolerances down to ± 0.02 mm can be manufactured by grinding, but such a treatment consumes more machining time in the workshops.

Typical magnetic properties of axial field die-pressed Nd–Dy–Fe–TM–B magnets range from 1.08 to 1.36 T for the remanent polarization, 2865 to 955 kA m^{-1} for the coercivity H_{cJ}, and 225 to 350 kJ m^{-3} for the maximum energy density, see Figure 40. The maximum continuous operating temperatures range from 60 °C for magnets with a high energy density up to 230 °C for magnets with a high coercivity.

As discussed in Section 2.3, near net-shaped Nd–Dy–Fe–TM–B magnets with improved energy densities can be manufactured by transverse field die-pressing. In general, such magnets require some machining in order to meet the dimensional tolerances. Typical magnetic properties range from 1.14 to 1.43 T for the remanent polarization, 2865 to 955 kA m^{-1} for the coercivity H_{cJ}, and 250 to 395 kJ m^{-3} for the maximum energy density. The maximal continuous operating temperatures are similar to axial field die-pressed magnets.

The optimal magnetic properties and the largest parts can be produced by cold isostatic pressing of Nd–Dy–Fe–TM–B blocks. The magnetic properties range from 1.18 to 1.47 T for the remanent polarization, 2230 to 875 kA m^{-1} for the coercivity H_{cJ}, and from 270 to 415 kJ m^{-3} for the maximum energy density. The maximum continuous operating temperatures of isostatically pressed magnets range from 50 °C for magnets with the highest maximum energy density to 190 °C for magnets with the highest coercivity.

A superior temperature stability of magnet assemblies can be achieved by the application of Sm–Co magnets. For net-shaped $SmCo_5$ parts or isostatically pressed blocks, the remanent polarization varies between 0.9 and 1.01 T with coercivities H_{cJ} between 2400 and 1500 kA m^{-1} and maximum energy densities between 160 and 200 kJ m^{-3}, see Figure 40. In general, maximum continuous operating temperatures up to 250 °C can be applied.

Even higher operating temperatures up to 300 or 350 °C can be achieved for magnet assemblies of $Sm_2(Co,Cu,Fe,Zr)_{17}$ magnets. Typical magnetic properties of $Sm_2(Co,Cu,Fe,Zr)_{17}$ magnets with moderate or high coercivities range between 1.04 up to 1.12 T for the remanent polarization, 2070 or 800 kA m^{-1} for the coercivity H_{cJ}, and 205 or 240 kJ m^{-3} for the maximum energy density, see Figure 40. With respect to the temperature and corrosion stability, Sm–Co magnets are the most stable RE–TM magnets. Recently developed $Sm_2(Co,Cu,Fe,Zr)_{17}$ magnets can even be applied at temperatures up to 550°, but such

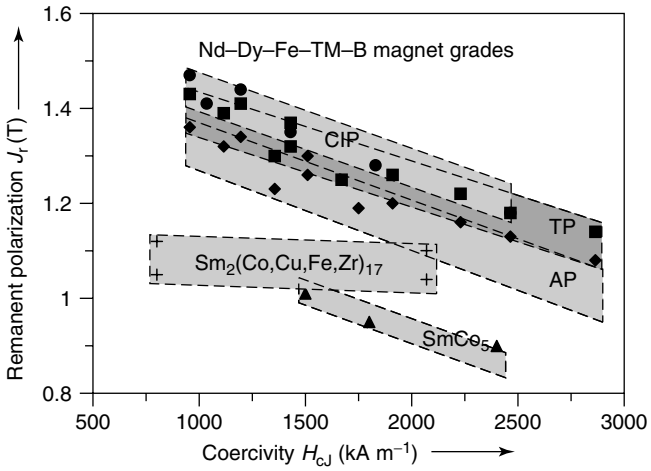

Figure 40. Remanent polarization J_r of sintered Nd–Dy–Fe–TM–B and Sm–Co magnets, depending on the coercivity H_{cJ}.

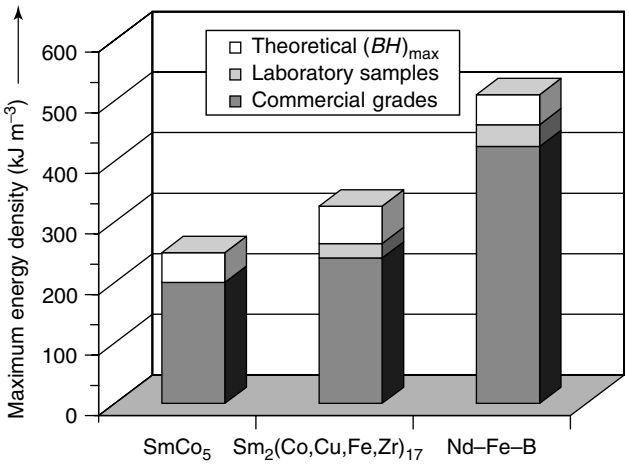

Figure 41. Exploitation of the maximum energy density of sintered RE–TM magnets based on $SmCo_5$, $Sm_2(Co,Cu,Fe,Zr)_{17}$ or $Nd_2Fe_{14}B$ compounds by commercial RE–TM magnet grades.

magnets achieve only a remanent polarization of 0.85 T and a maximum energy density of 127 kJ m^{-3} at room temperature (Walmer, 2002).

By optimization of the alloy composition, by improving the processing route, and by refining the microstructure, Nd–Dy–Fe–TM–B magnets can be tailored to meet the requirements of many different applications. As indicated in Figure 1, the maximum energy density of RE–TM magnets could be increased step by step and is now approaching the technical limits. The remanent polarization of commercial Sm–Co magnets reaches 94% of the theoretical limit and the remanent polarization of commercial Nd–Dy–Fe–TM–B magnets achieves 92% of the theoretical limit, see Figure 41.

By refined manufacturing conditions in laboratory facilities, almost ternary Nd–Fe–B magnets now achieve a remanent polarization of 1.533 T, a coercivity H_{cJ} of 784 kA m^{-1}, and a maximum energy density of 460 kJ m^{-3} (Kaneko, 2004).

Besides optimization of the processing routes of RE–TM magnets, future research and development activities should be focused on the search for new hard magnetic RE–TM compounds.

REFERENCES

Adler, E. and Hamann, P. (1985). A contribution to the understanding of coercivity and its temperature dependence in sintered $SmCo_5$ and $Nd_2Fe_{14}B$ magnets. In *Proceedings of the 4th International Symposium on Magnetic Anisotropy and Coercivity in RE-TM Alloys*, Strnat, K.J. (Ed.), University of Dayton: Ohio, pp. 747–760.

Adler, E. and Marik, H.J. (1981). Stability of samarium-cobalt magnets. In *Proceedings of the 5th International Workshop on RE-Co Permanent Magnets and Their Applications*, Strnat, K.J. (Ed.), University of Dayton: Ohio, pp. 335–356.

Arai, A., Kobayashi, O., Takagi, F., *et al*. (1994). Mechanical properties of hot-rolled Pr-Fe-B-Cu magnets. *Journal of Applied Physics*, **75**, 6631–6633.

Araki, T., Nakanishi, T. and Umemura, T. (1999). Texture of Nd-Fe-B thin films prepared by magnetron sputtering. *Journal of Applied Physics*, **85**, 4877–4879.

Bala, H., Pawlowska, G., Szymura, S. and Rabinovich, Yu.M. (1998). Electrochemical corrosion characterization of intermetallic phases occuring in Nd-Fe-B type magnets. *British Corrosion Journal*, **33**, 37–41.

Barthem, V.M.T.S., Givord, D., Rossignol, M.F. and Tenaud, P. (2002). An analysis of coercivity in various hard magnetic materials relating coercive field and activation volume. *Journal of Magnetism and Magnetic Materials*, **242–245**, 1395–1398.

Becher, M., Seeger, M., Bauer, J. (1998). Magnetic viscosity measurements on nanocrystalline NdFeB and PrFeB magnets. In *Proceedings of the 10th International Symposium on Magnetic Anisotropy and Coercivity in RE TM Alloys*, Schultz, L. and Müller, K-H. (Eds.), Werkstoff-Informationsgesellschaft: Dresden, pp. 307–316.

Betancourt, I. and Valenzuela, R. (2003). Enhanced coercivity in RE-Fe-Al based bulk amorphous alloys. *Journal of Applied Physics*, **93**, 6933–6935.

Blackmore, E.W. (1985). Radiation effects of protons on samarium-cobalt permanent magnets. *IEEE Transactions on Nuclear Science*, **NS-32**, 3669–3671.

Blank, R. and Adler, E. (1987). The effect of surface oxidation on the demagnetization curve of sintered Nd-Fe-B permanent magnets. In *Proceedings of the 9th International Workshop on RE Magnets and Their Applications*, Herget, C. and Poerschke, R. (Eds.), DPG GmbH: Bad Honnef, pp. 537–544.

Blank, R., Rodewald, W. and Schleede, B. (1989). Microscopic model for the enhancement of reversed magnetic fields in RE magnets. In *Proceedings of the 10th International Workshop on RE Magnets and Their Applications*, Shinjo, T. (Ed.), Society of Non-Traditional Technology: Tokyo, pp. 353–361.

Bollero, A., Gutfleisch, O., Müller, K.H. and Schultz, L. (2002). High-performance nanocrystalline Pr-Fe-B based magnets produced by intensive milling. *Journal of Applied Physics*, **91**, 8159–8161.

Boockmann, K., Liehr, M., Rodewald, W., *et al*. (1991). Effect of γ-radiation on Sm-Co and Nd-Dy-Fe-B magnets. *Journal of Magnetism and Magnetic Materials*, **101**, 345–346.

Branagan, D.J., Burch, J.V., Sellers, C.H. and Hyde, T.A. (1998). Processing of Nd-Fe-B alloys by inert gas atomisation. *Powder Metallurgy*, **41**, 165–167.

Branagan, D.J., Hyde, T.A., Sellers, C.H. and Lewis, L.H. (1996). A new generation of gas atomized powder with improved levels of energy product and processability. *IEEE Transactions on Magnetics*, **32**, 5097–5099.

Brown, R.D. and Cost, J.R. (1989). Radiation-induced changes in magnetic properties of Nd-Fe-B permanent magnets. *IEEE Transactions on Magnetics*, **25**, 3117–3120.

Buschow, K.H.J. (1998). *Permanent-magnet Materials and Their Applications*, Trans Tech Publications Ltd: Switzerland, p. 52.

Cadieu, F.J., Cheung, T.D., Wickramasekara, L., *et al*. (1987). The magnetic properties of high H_{cJ} Sm-Co, Nd-Fe-B, and Sm-Ti-Fe films crystallized from amorphous deposits. *Journal of Applied Physics*, **62**, 3866–3872.

Castaldi, L., Gibbs, M.R.J. and Davies, H.A. (2003). Deposition of hard magnetic rare-earth-Fe-B thin films by magnetron sputtering. *Journal of Applied Physics*, **93**, 9165–9169.

Chin, T.S., Hara, Y., Lavernia, E.J., *et al*. (1986). (Fe,Co)-Nd-B permanent magnets by liquid dynamic compaction. *Journal of Applied Physics*, **59**, 1297–1300.

Coey, J.M.D. (1996). *Rare Earth Iron Permanent Magnets*, Clarendon Press: Oxford, p. 267.

Cost, J.R., Brown, R.D., Giorgi, A.L. and Stanley, J.T. (1987). Radiation effects in RE permanent magnets. *Materials Research Society Symposium Proceedings*, **96**, 321–327.

Cost, J.R., Brown, R.D., Giorgi, A.L. and Stanley, J.T. (1988). Effects of neutron irradiation on Nd-Fe-B magnetic properties. *IEEE Transactions on Magnetics*, **24**, 2016–2019.

Croat, J.J. (1981a). Observation of large room-temperature coercivity in melt-spun $Nd_{0.4}Fe_{0.6}$. *Applied Physics Letters*, **39**, 357–358.

Croat, J.J. (1981b). Crystallization and magnetic properties of melt-spun neodymium-iron alloys. *Journal of Magnetism and Magnetic Materials*, **24**, 125–131.

Croat, J.J., Herbst, J.F., Lee, R.W. and Pinkerton, F.E. (1984a). High-energy product Nd-Fe-B permanent magnets. *Applied Physics Letters*, **44**, 148–149.

Croat, J.J., Herbst, J.F., Lee, R.W. and Pinkerton, F.E. (1984b). Pr-Fe and Nd-Fe-based materials: a new class of high-performance permanent magnets. *Journal of Applied Physics*, **55**, 2078–2082.

Daniel, B. (1995). The development of a production technique for magnets from mechanically-alloyed Fe-Nd-B powder. *Journal of Materials Processing Technology*, **54**, 60–63.

Das, D.K. (1969). Twenty million energy product samarium-cobalt magnet. *IEEE Transactions on Magnetics*, **MAG-5**, 214–216.

De Voss, K.J. (1969). Alnico permanent magnet alloys. In *Magnetism and Metallurgy*, Berkowitz, A. and Kneller, E. (Eds.), Academic Press: New York, pp. 473–512.

Durst, K.D. and Kronmüller, H. (1985). Magnetic hardening mechanisms in sintered Nd-Fe-B and $Sm_2(Co,Cu,Fe,Zr)_{17}$ permanent magnets. In *Proceedings of the 4th International Symposium on Magnetic Anisotropy and Coercivity in RE-TM Alloys*, Strnat, K.J. (Ed.), University of Dayton: Ohio, pp. 725–735.

Durst, K.D. and Kronmüller, H. (1987). The coercive field of sintered and melt-spun Nd-Fe-B magnets. *Journal of Magnetism and Magnetic Materials*, **68**, 63–75.

El-Aziz, A.M. (2003). Corrosion resistance of Nd-Fe-B permanent magnetic alloys. *Materials and Corrosion*, **54**, 88–92.

Fähler, S., Hannemann, U., Oswald, S., *et al*. (2003). Corrosion of highly coercive, highly textured Nd-Fe-B films. *IEEE Transactions on Magnetics*, **39**, 2950–2952.

Fernengel, W., Lehnert, A., Katter, M., *et al*. (1996). Examination of the degree of alignment in sintered Nd-Fe-B magnets by measurements of the polarizations. *Journal of Magnetism and Magnetic Materials*, **157–158**, 19–20.

Fernengel, W., Rodewald, W., Blank, R., *et al*. (1999). The influence of Co on the corrosion resistance of sintered Nd-Fe-B magnets. *Journal of Magnetism and Magnetic Materials*, **196–197**, 288–290.

Fidler, J. and Skalicky, P. (1982). Microstructure of precipitation hardened cobalt rare earth permanent magnets. *Journal of Magnetism and Magnetic Materials*, **27**, 127–134.

Givord, D., Lienard, A., Tenaud, P. and Viadieu, T. (1987). Magnetic viscosity in Nd-Fe-B sintered magnets. *Journal of Magnetism and Magnetic Materials*, **67**, L281–L285.

Givord, D. and Rossignol, M.F. (1996). Coercivity. In *Rare-earth Iron Permanent Magnets*, Coey, J.M.D. (Ed.), Clarendon Press: Oxford, pp. 218–285.

Givord, D., Rossignol, M. and Barthem, V.M.T.S. (2003). The physics of coercivity. *Journal of Magnetism and Magnetic Materials*, **258–259**, 1–5.

Givord, D., Tenaud, P. and Viadieu, T. (1986). Analysis of hysteresis loops in Nd-Fe-B sintered magnets. *Journal of Applied Physics*, **60**, 3263–3265.

Givord, D., Tenaud, P. and Viadieu, T. (1988). Coercivity mechanisms in ferrite and rare earth transition metal sintered magnets ($SmCo_5$, Nd-Fe-B). *IEEE Transactions on Magnetics*, **24**, 1921–1923.

Givord, D., Tenaud, P., Viadieu, T. and Hadjipanayis, G. (1987). Magnetic viscosity in different Nd-Fe-B magnets. *Journal of Applied Physics*, **61**, 3454–3456.

Goll, D., Sigle, W., Hadjipanayis, G.C. and Kronmüller H., (2000). Micromagnetic and microstructural analysis of the temperature dependence of the coercive field of $Sm_2(Co,Cu,Fe,Zr)_{17}$ permanent magnets. In *Proceedings 16th International Workshop on RE Magnets and Their Applications*, Kaneko, H., Homma, M. and Okada, M. (Eds.), Japan Institute of Metals, pp. 61–70.

Grieb, B. (1997). New corrosion resistant materials based on neodymium-iron-boron. *IEEE Transactions on Magnetics*, **33**, 3904–3906.

Grünberger, W. (1998). The solution-precipitation creep – a model for deformation and texturing mechanisms of nanocrystalline Nd-Fe-B alloys. In *Proceedings 15th International Workshop on RE Magnets and Their Applications*, Schultz, L. and Müller, K-H. (Eds.), Werkstoff-Informationsgesellschaft: Dresden, pp. 333–348.

Gutfleisch, O. (2000). Controlling the properties of high energy density permanent magnetic materials by different processing routes. *Journal of Physics D: Applied Physics*, **33**, R157–R172.

Hadjipanayis, G.C., Hazelton, R.C. and Lawless, K.R. (1983). New iron-rare-earth based permanent magnet materials. *Applied Physics Letters*, **43**, 797–799.

Hadjipanayis, G.C., Hazelton, R.C. and Lawless, K.R. (1984). Cobalt-free permanent magnet materials based on iron-rare-earth alloys. *Journal of Applied Physics*, **55**, 2073–2077.

Hannemann, U., Fähler, S., Oswald, S., *et al*. (2002). Effect of Cr and Ta buffers on hard magnetic $Nd_2Fe_{14}B$ films. *Journal of Magnetism and Magnetic Materials*, **242–245**, 1294–1296.

Harada, T., Ando, T., O'Handley, R.C. and Grant, N.J. (1990). The magnetic properties of Nd-Fe-B magnets by liquid dynamic compaction. *Journal of Applied Physics*, **67**, 4233–4237.

Herbst, J.F., Croat, J.J., Pinkerton, F.E. and Yelon, W.B. (1984). Relationships between crystal structure and magnetic properties in $Nd_2Fe_{14}B$. *Physical Review B*, **29**, 4176–4178.

Herbst, J.F. and Yelon, W.B. (1985). Crystal and magnetic structure of $Pr_2Fe_{14}B$ and $Dy_2Fe_{14}B$. *Journal of Applied Physics*, **57**, 2343–2345.

Herget, C. (1985). Metallurgical ways to Nd-Fe-B alloys. Permanent magnets from Co-reduced Nd-Fe-B. In *Proceedings of the 8th International Workshop on Rare-earth Magnets and Their Applications*, Strnat, K.J. (Ed.), University Press Dayton: Dayton, pp. 407–424.

Hinz, D., Schumann, R., Helming, K. and Schäfer, D. (1994). Texture in hot-rolled Nd-Fe-B ingots. In *Proceedings 13th International Workshop on RE Magnets and Their Applications*, Manwarning, C.A.F., Jones, D.G.R., Williams, A.J. and Harris, I.R. (Eds.), The University of Birmingham. Birmingham, pp. 581–590.

Hirosawa, S., Mino, S. and Tomizawa, H. (1991). Improved corrosion resistance and magnetic properties of Nd-Fe-B-type sintered magnets with Mo and Co. *Journal of Applied Physics*, **70**, 6609–6611.

Hoffer, G. and Strnat, K.J. (1966). Magnetocrystalline anisotropy of YCo_5 and Y_2Co_{17}. *IEEE Transactions on Magnetics*, **MAG-2**, 487–489.

Horton, J.A., Wright, J.L. and Herchenroeder, J.W. (1996). Fracture toughness of commercial magnets. *IEEE Transactions on Magnetics*, **32**, 4374–4376.

Horton, J.A., Heatherly, L., Branagan, D.J., *et al*. (1997). Consolidation, magnetic and mechanical properties of gas atomized and HDDR $Nd_2Fe_{14}B$ powders. *IEEE Transactions on Magnetics*, **33**, 3835–3837.

Inoue, A., Zhang, T. and Takeuchi, A. (1997). Hard magnetic bulk amorphous alloys. *IEEE Transactions on Magnetics*, **33**, 3814–3816.

Inoue, A., Zhang, T., Takeuchi, A. and Zhang, W. (1996a). Hard magnetic bulk amorphous Nd-Fe-Al alloys of 12 mm in diameter made by suction casting. *Materials Transactions, JIM*, **37**, 636–640.

Inoue, A., Zhang, T., Zhang, W. and Takeuchi, A. (1996b). Bulk Nd-Fe-Al amorphous alloys with hard magnetic properties. *Materials Transactions, JIM*, **37**, 99–108.

Jiang, H. and O'Shea, M.J. (2000). Structure and magnetic properties of Nd-Fe-B thin films with Cr, Mo, Nb, Ta, and V buffer layers. *Journal of Magnetism and Magnetic Materials*, **212**, 59–68.

Jiang, J., Zeng, Z., Yu, J., *et al*. (2001). The effect of Co additions on the fracture strength of Nd-Fe-B sintered magnets. *Intermetallics*, **9**, 269–272.

Kähkönen, O.P., Kautto, E., Manninen, M. and Talvitie, M. (1992a). Effects of high temperature irradiation on Sm-Co permanent magnets. *Journal of Applied Physics*, **72**, 2075–2076.

Kähkönen, O.P., Mäkinen, S., Talvitie, M. and Manninen, M. (1992b). Radiation damage in Nd-Fe-B magnets: temperature and shape effects. *Journal of Physics: Condensed Matter*, **4**, 1007–1014.

Kaneko, Y. (2004). Technological evolution and application trends of Nd-Fe-B sintered magnets in Japan. In *Proceedings of the 18th International Workshop of High Performance Magnets and Their Applications*, Dempsey, N.M. and de Rango, P. (Eds.), Centre National de la Recherche Scientifique (CNRS). Annecy, pp. 40–51, Vol. 1.

Kaszuwara, W. and Leonowicz, M. (1999). Long-term corrosion tests on Nd-Fe-B sintered magnets. *Materials Letters*, **40**, 18–22.

Katter, M. (1998). Coercivity calculation of $Sm_2(Co,Cu,Fe,Zr)_{17}$ magnets. *Journal of Applied Physics*, **83**, 6721–6723.

Katter, M., Weber, J., Assmus, W., *et al*. (1996a). Evidence for two different kinds of pinning sites in $Sm_2(Co,Cu,Fe,Zr)_{17}$ magnets. In *Proceedings of the 14th International Workshop on RE Magnets and Their Applications*, Missell, F.P., Villas-Boas, V., Rechenberg, H.R. and Landgraf, F.J.G. (Eds.), World Scientific: New Jersey, pp. 194–202.

Katter, M., Rodewald, W., Fernengel, W., *et al*. (2001). Corrosion mechanism of RE-Fe-Co-Cu-Ga-Al-B magnets. *IEEE Transactions on Magnetics*, **37**, 2474–2476.

Katter, M., Weber, J., Assmus, W., *et al*. (1996b). A new model for the coercivity mechanism of $Sm_2(Co,Cu,Fe,Zr)_{17}$ magnets. *IEEE Transactions on Magnetics*, **32**, 4815–4817.

Kim, A.S. and Camp, F.E. (1996). High performance Nd-Fe-B magnets. *Journal of Applied Physics*, **79**, 5035–5039.

Kong, H.Z., Li, Y. and Ding, J. (2000). Effect of boron additions to the hard magnetic bulk $Nd_{60}Fe_{30}Al_{10}$ amorphous alloy. *Journal of Magnetism and Magnetic Materials*, **217**, 65–73.

Koon, N.C. and Das, B.N. (1981). Magnetic properties of amorphous and crystallized $(Fe_{0.82}B_{0.18})_{0.9}Tb_{0.05}La_{0.05}$. *Applied Physics Letters*, **39**, 840–842.

Kou, X.C., Kronmüller, H., Givord, D. and Rossignol, M.F. (1994). Coercivity mechanism of sintered $Pr_{17}Fe_{75}B_8$ and $Pr_{17}Fe_{53}B_8$ permanent magnets. *Physical Review B*, **50**, 3849–3860.

Kramer, M.J., Xu, Y., Dennis, I.E., *et al*. (2003). Development of improved powder for bonded permanent magnets. *IEEE Transactions on Magnetics*, **39**, 2971–2973.

Kronmüller, H. (1978). Micromagnetism in hard magnetic materials. *Journal of Magnetism and Magnetic Materials*, **7**, 341–350.

Kronmüller, H. (1985). The nucleation fields of uniaxial ferromagnetic crystals. *Physica Status Solidi B*, **130**, 197–203.

Kronmüller, H. (1987). Theory of nucleation fields in inhomogeneous ferromagnets. *Physica Status Solidi B*, **144**, 385–396.

Kronmüller, H., Durst, K.D. and Sagawa, M. (1988). Analysis of the magnetic hardening mechanism in RE-Fe-B permanent magnets. *Journal of Magnetism and Magnetic Materials*, **74**, 291–302.

Kumar, K., Das, D. and Wettstein, E. (1978). High coercivity, isotropic plasma sprayed samarium-cobalt magnets. *Journal of Applied Physics*, **49**, 2052–2054.

Lee, R.W., Brewer, E.G. and Schaffel, N.A. (1985). Processing of neodymium-iron-boron melt-spun ribbons to fully dense magnets. *IEEE Transactions on Magnetics*, **MAG 21**, 1958–1963.

Lewis, L.H., Sellers, C.H. and Panchanathan, V. (1995). Phase composition and magnetic characteristics of inert gas-atomized RE-Fe-B based powders. *IEEE Transactions on Magnetics*, **31**, 3641–3643.

Lewis, L.H., Sellers, C.H. and Panchanathan, V. (1996). Annealing-induced property improvements in 2-14-1 powders produced by inert gas atomization. *IEEE Transactions on Magnetics*, **32**, 4371–4373.

Li, L. and Graham, C.D. Jr. (1990). Mechanism of texture formation by hot deformation in rapidly quenched Fe-Nd-B. *Journal of Applied Physics*, **67**, 4756–4758.

Liu, Y., Dallimore, M.P. and McCormick, P.G. (1992). High coercivity $SmCo_5$ synthesized by chemical reduction during mechanical alloying. *Journal of Magnetism and Magnetic Materials*, **116**, L320–L324.

Liu, J.F. and Luo, H.L. (1990). On the relationship between coercive force H_c and magnetic viscosity parameter S_v in magnetic materials. *Journal of Magnetism and Magnetic Materials*, **86**, 153–158.

Liu, J., Ding, Y., Zhang, Y., *et al*. (1999). New rare-earth permanent magnets with an intrinsic coercivity of 10 kOe at 500 °C. *Journal of Applied Physics*, **85**, 5660–5662.

Livingston, J.D. (1996). *Driving Force – The Natural Magic of Magnets*, Havard University Press: Cambridge, Massachusetts, and London, p. 13.

Luo, Y. (2004). Current status of global Nd-Fe-B magnet industry. In *Proceedings of the 18th International Workshop on High Performance Magnets and Their Applications*, Dempsey, N.M. and de Rango, P. (Eds.): Centre National de la Recherche Scientifique (CNRS). Annecy, pp. 28–39.

Ma, B.M., Liang, Y.L., Scott, D.W., *et al*. (1994). A new aspect on the corrosion resistance of sintered Nd-Fe-B magnets – is high oxygen content necessary? In *Proccedings 13th International Workshop on RE Magnets and Their Applications*, Manwarning, C.A.F., Jones, D.G.R., Williams, A.J. and Harris, I.R. (Eds.): The University of Birmingham. Birmingham, pp. 309–318.

Matsuura, Y., Hirosawa, S., Yamamoto, H., *et al*. (1985). Phase diagram of the Nd-Fe-B ternary system. *Japanese Journal of Applied Physics*, **24**, L635–L637.

Mishima, T. (1932). New high magnetic M. K. Steel. *OHM*, **19**, 353.

Mishra, R.K., Brewer, E.G. and Lee, R.W. (1988). Grain growth and alignment in hot deformed Nd-Fe-B magnets. *Journal of Applied Physics*, **63**, 3528–3530.

Mishra, R.K., Thomas, G., Yoneyama, T., *et al*. (1981). Microstructure and properties of step aged rare earth alloy magnets. *Journal of Applied Physics*, **52**, 2517–2519.

Mummert, K., El-Aziz, A.M., Barkleit, G., *et al*. (2000). Corrosion behaviour of Nd-Fe-B permanent magnets. *Materials and Corrosion*, **51**, 13–19.

Nagata, H. and Sagawa, M. (2002). Toward an ideal process for the Nd-Fe-B sintered magnets. In *Proceedings of the 17th International Workshop on RE Magnets and Their Applications*, Hadjipanayis, G.C. and Bonder, M.J. (Eds.), Rinton Press: Newark, Delaware, pp. 354–359.

Nakano, M., Katoh, R., Fukunaga, H., *et al*. (2003). Fabrication of Nd-Fe-B thick-film magnets by high-speed PLD method. *IEEE Transactions on Magnetics*, **39**, 2863–2865.

Néel, L. (1951). Le Traînage Magnétique. *Journal de Physique et le Radium*, **12**, 339–351.

Neu, V. and Schultz, L. (2001). Two-phase high-performance Nd-Fe-B powders prepared by mechanical milling. *Journal of Applied Physics*, **90**, 1540–1544.

Neu, V. and Shaheen, S.A. (1999). Sputtered Sm-Co films: microstructure and magnetic properties. *Journal of Applied Physics*, **86**, 7006–7009.

Neu, V., Hannemann, U., Fähler, S., *et al*. (2002a). Effect of rare earth content on microstucture and magnetic properties of Sm-Co and Nd-Fe-B thin films. *Journal of Applied Physics*, **91**, 8180–8182.

Neu, V., Thomas, J., Fähler, S., *et al*. (2002b). Hard magnetic Sm-Co thin films prepared by pulsed laser deposition. *Journal of Magnetism and Magnetic Materials*, **242–245**, 1290–1293.

Nishio, H. and Yamamoto, H. (1993). Magnetic aftereffect of Nd-Fe-Co-B-V compression bonded magnets. *IEEE Translation Journal on Magnetics in Japan*, **8**, 16–20.

Nishio, H., Yamamoto, H., Nagakura, M. and Uehara, M. (1990). Effects of machining on magnetic properties of Nd-Fe-B system sintered magnets. *IEEE Transactions on Magnetics*, **26**, 257–261.

Ogata, Y., Kubota, Y., Takami, T., *et al*. (1999). Improvements of magnetic properties of Sr ferrite magnets by substitutions of La and Co. *IEEE Transactions on Magnetics*, **35**, 3334–3336.

O'Handley, R.C. (2000). *Modern Magnetic Materials – Principles and Applications*, John Wiley & Sons: New York, p. 474.

Ohashi, K., Tawara, Y., Yokoyama, T. and Kobayashi, N. (1987). Corrosion resistance of Co-containing Nd-Fe-Co-B magnets. In *Proceedings of the 9th International Workshop on RE Magnets and Their Applications*, Herget, C. and Poerschke, R. (Eds.), DPG GmbH: Bad Honnef, pp. 355–361.

Ojima, T., Tomizawa, S., Yoneyama, T. and Hori, T. (1977). Magnetic properties of a new type of rare earth cobalt magnets. *IEEE Transactions on Magnetics*, **MAG-13**, 1317–1319.

Otsuki, E., Sato, T. and Fujiwara, T. (1989). Fracture strength of rare earth magnets. In *Proceedings of the 10th International Workshop on RE Magnets and Their Applications*, Shinjo, T. (Ed.), Society of Non-Traditional Technology: Tokyo, pp. 373–381.

Overfelt, R.A., Anderson, C.D. and Flanagan, W.F. (1986). Plasma sprayed $Fe_{76}Nd_{16}B_8$ permanent magnets. *Applied Physics Letters*, **49**, 1799–1801.

Parhofer, S., Gieres, G., Wecker, J. and Schultz, L. (1996). Growth characteristics and magnetic properties of sputtered Nd-Fe-B thin films. *Journal of Magnetism and Magnetic Materials*, **163**, 32–38.

Parhofer, S., Kuhrt, C., Wecker, J., *et al*. (1998). Magnetic properties and growth texture of high-coercive Nd-Fe-B thin films. *Journal of Applied Physics*, **83**, 2735–2741.

Parker, R.J. (1990). *Advances in Permanent Magnetism*, John Wiley & Sons: New York, p. 293.

Rabinovich, Yu.M., Sergeev, V.V., Maystrenko, A.D., *et al*. (1996). Physical and mechanical properties of sintered Nd-Fe-B type permanent magnets. *Intermetallics*, **4**, 641–645.

Ray, A.E. and Strnat, K.J. (1972). Easy directions of magnetization in ternary $R_2(Co,Fe)_{17}$ phases. *IEEE Transactions on Magnetics*, **MAG-8**, 516–518.

Rieger, G., Wecker, J., Rodewald, W., *et al*. (2000). Nd-Fe-B permanent magnets (thick films) produced by a vacuum-plasma-spraying process. *Journal of Applied Physics*, **87**, 5329–5331.

Rivoirard, S., Chateigner, D., de Rango, P., *et al*. (2000). Texture investigation of hot-forged Nd-Fe-B magnets. *Philosophical Magazine A*, **80**, 1955–1966.

Rodewald, W. (1985). Magnetic properties of $Nd_{15-x}Dy_xFe_{77}B_8$ alloys. In *Proceedings 4th International Symposium on Magnetic Anisotropy and Coercivity in RE-TM Alloys*, Strnat, K.J. (Ed.), University of Dayton, pp. 737–745.

Rodewald, W., Katter, M. and Üstüner, K. (2004). Coercivity and mechanical properties of Nd-Fe-B magnets in dependence on the average grain size. In *Proceedings of the 18th International Workshop on High Performance Magnets and Their Applications*, Dempsey, N.M. and de Rango, P. (Eds.): Centre National de la Recherche Scientifique (CNRS). Annecy, pp. 486–492.

Rodewald, W., Katter, M., Wall, B., *et al*. (2000). Dependence of the coercivity H_{cJ} of high energy Nd-Fe-B magnets on the alignment coefficient. *IEEE Transactions on Magnetics*, **36**, 3279–3281.

Sagawa, M., Fujimura, S., Togawa, N., *et al*. (1984a). New material for permanent magnets on a base of Nd and Fe. *Journal of Applied Physics*, **55**, 2083–2087.

Sagawa, M., Fujimura, S., Togawa, N., *et al*. (1984b). Permanent magnet materials based on the rare earth-iron-boron tetragonal compounds. *IEEE Transactions on Magnetics*, **MAG 20**, 1584–1589.

Sagawa, M. and Hirosawa, S. (1988). Magnetic hardening mechanism in sintered RE-Fe-B permanent magnets. *Journal of Materials Research*, **3**, 45–54.

Sagawa, M. and Nagata, H. (1993). Novel processing technology for permanent magnets. *IEEE Transactions on Magnetics*, **29**, 2747–2751.

Sagawa, M., Nagata, H., Watanabe, T. and Itani, O. (2000). Ruber isostatic pressing (RIP) of powders for magnets and other materials. *Materials and Design*, **21**, 243–249.

Schrey, P. (1986). TEM studies of sintered Fe-Nd-B magnets. *IEEE Transactions on Magnetics*, **MAG-22**, 913–915.

Schultz, L., El-Aziz, A.M., Barkleit, G. and Mummert, K. (1999). Corrosion behaviour of Nd-Fe-B permanent magnet alloys. *Materials Science and Engineering*, **A 267**, 307–313.

Schultz, L., Schnitzke, K. and Wecker, J. (1988). Mechanically alloyed isotropic and anisotropic Nd-Fe-B magnet material. *Journal of Applied Physics*, **64**, 5302–5304.

Schultz, L., Wecker, J. and Hellstein, E. (1987). Formation and properties of Nd-Fe-B prepared by mechanical alloying and solid-state reaction. *Journal of Applied Physics*, **61**, 3583–3585.

Sellers, C.H., Hyde, T.A., Branagan, D.J., *et al*. (1997). Microstructure and magnetic properties of inert gas atomized rare earth permanent magnet materials. *Journal of Applied Physics*, **81**, 1351–1357.

Singleton, E.W. and Hadjipanayis, G.C. (1990). Magnetic viscosity studies in hard magnetic materials. *Journal of Applied Physics*, **67**, 4759–4761.

Shimoda, T., Akioka, K. and Kobayashi, O. (1990). Current situation in development of hot-rolled RE-Fe-B magnets. In *Proccedings 11th International Workshop on RE Magnets and Their Applications*, Sankar, S.G. (Ed.), Carnegie Mellon University: Pittsburgh, pp. 17–27.

Shimoda, T., Akioka, K., Kobayashi, O. and Yamagami, T. (1988). High-energy cast Pr-Fe-B magnets. *Journal of Applied Physics*, **64**, 5290–5292.

Shimoda, T., Akioka, K., Kobayashi, O. and Yamagami, T., (1989). Hot worked anisotropic Pr-Fe-B magnets. *Proceedings 10th International Workshop on Rare Earth Magnets and Their Applications*. Shinjo, T. (Ed.), Society of Non-Traditional Technology, Tokyo, Vol. 1, pp. 399–408.

Stieler, S., Heiden, C., Kuntze, K. and Kohake, D. (1984). Investigation of magnetization creep of Co_5Sm samples. *IEEE Transactions on Magnetics*, **MAG-20**, 1581–1583.

Street, R., Day, R.K. and Dunlop, J.B. (1987). Magnetic viscosity in Nd-Fe-B and $SmCo_5$ alloys. *Journal of Magnetism and Magnetic Materials*, **69**, 106–112.

Sun, H., Tomida, T., Hirosawa, S. and Maehara, Y. (1996). Magnetic properties and microstructure studies of Nd-Fe-B thin films. *Journal of Magnetism and Magnetic Materials*, **164**, 18–26.

Sun, Z.G., Löser, W., Eckert, J., *et al*. (2003). Effect of cooling rate on microstructure and magnetic properties of $Nd_{60}Fe_{30}Al_{10}$ hard magnetic alloys. *Journal of Magnetism and Magnetic Materials*, **261**, 122–130.

Szymura, S., Wyslocki, J.J., Rabinovich, Yu.M. and Bala, H. (1994). Domain structure, magnetic and mechanical properties of Nd-Fe-B magnets with different grain size. *Physica Status Solidi A*, **141**, 435–443.

Talvitie, M., Kähkönen, O.P., Mäkinen, S., *et al*. (1991). Magnetic flux loss in Nd-Fe-B magnets irradiated with 20 MeV protons. *Journal of Magnetism and Magnetic Materials*, **102**, 323–330.

Tokuhara, K. and Hirosawa, S. (1991). Corrosion resistance of Nd-Fe-B sintered magnets. *Journal of Applied Physics*, **69**, 5521–5523.

Turtelli, R.S., Triyono, D., Grössinger, R., *et al*. (2002). Coercivity mechanism in $Nd_{60}Fe_{30}Al_{10}$ and $Nd_{60}Fe_{20}Co_{10}Al_{10}$ alloys. *Physical Review B*, **66**, 054441-1–054441-8.

Vendel, B. (1984). *Rare Earths Reminder*, The Rhône Poulenc Company.

Walmer, M.H. (2002). Recent developments and applications of sintered Sm-Co based magnets. In *Proceedings of the 17th International Workshop on RE Magnets and Their Applications*, Hadjipanayis, G.C. and Bonder, M.J. (Eds.), Rinton Press: Delaware, pp. 39–51.

Walmer, M.S., Chen, C.H., Walmer, M.H., *et al*. (2000a). Magnetic hardening, thermal stability, and microstructures for a new class of Sm-TM high temperature magnets. In *Proceedings 16th International Workshop on RE Magnets and Their Applications*, Kaneko, H., Homma, M. and Okada, M. (Eds.), Japan Institute of Metals, pp. 41–59.

Walmer, M.S., Chen, C.H. and Walmer, M.H. (2000b). A new class of Sm-TM magnets for operating temperatures up to 550 °C. *IEEE Transactions on Magnetics*, **36**, 3376–3381.

Went, J.J., Rathenau, G.W., Gorter, E.W. and Van Oosterhaut, G.W. (1952). Ferroxdure, eine Gruppe neuer Werkstoffe für Dauermagnete. *Philips Technische Rundschau*, **13**, 361–376.

Willson, M., Bauser, S., Liu, S. and Huang, M. (2003). Plasma sprayed Nd-Fe-B permanent magnets. *Journal of Applied Physics*, **93**, 7987–7989.

Wyslocki, J.J. (1992a). Magnetic properties, microstructures and domain structures of arc-plasma sprayed Nd-Fe-B permanent magnet. *Journal of Materials Science*, **27**, 3777–3781.

Wyslocki, J.J. (1992b). Domain structure of the arc-plasma sprayed Nd-Fe-B anisotropic permanent magnet. *Journal of Magnetism and Magnetic Materials*, **104–107**, 363–364.

Yamamoto, M., Inoue, A. and Masumoto, T. (1989). Production of Nd-Fe-B alloy powders using high-pressure gas atomization and their hard magnetic properties. *Metallurgical Transactions A*, **20A**, 5–11.

Yoshikawa, N., Iriyama, T., Yamada, H., *et al*. (1999). Radially oriented high energy product ring magnets. *IEEE Transactions on Magnetics*, **35**, 3268–3270.

Yoshikawa, N., Yamada, H., Iwasaki, Y., *et al*. (1994). Magnetic properties and multi-pole magnetizability of a huge radially oriented Nd-Fe-B ring magnet for EV driving motors. In *Proccedings 13th International Workshop on RE Magnets and Their Applications*, Manwarning, C.A.F., Jones, D.G.R., Williams, A.J. and Harris, I.R. (Eds.): The University of Birmingham. Birmingham, pp. 635–644.

Zeller, A.F. and Nolen, J.A. (1987). Radiation and temperature effects of Sm-Co and Nd-Fe-B magnets in low permeance configurations. In *Proceedings 9th International Workshop on RE Magnets and Their Applications*, Herget, C. and Pörschke, R. (Eds.), Deutsche Physikalische Gesellschaft e. V: Bad Soden, pp. 157–162.

Zeller, A.F., Nolen, J.A., Tanaka, S., *et al*. (1988). An adjustable permanent magnet focussing system for heavy ion beams. *IEEE Transactions on Magnetics*, **MAG-25**, 990–993.

Zhang, Y., Tang, T., Hadjipanayis, G.C., *et al*. (2000). Evolution of microstructure and microchemistry in the high temperature $Sm(Co,Cu,Fe,Zr)_z$ magnets. In *Proceedings 16th International Workshop on RE Magnets and Their Applications*, Kaneko, H., Homma, M. and Okada, M. (Eds.), Japan Institute of Metals, pp. 169–177.

FURTHER READING

Kronmüller, H., Fischer, R., Seeger, M. and Zern, A. (1996). Micromagnetism and microstructure of hard magnetic materials. *Journal of Physics D: Applied Physics*, **29**, 2274–2283.

Lai, J.K.L., Shao, Y.Z., Shek, H., *et al*. (2002). Investigation on bulk Nd-Fe-Al amorphous/nanocrystalline alloy. *Journal of Magnetism and Magnetic Materials*, **241**, 73–80.

Ohki, T., Miyagawa, M. and Yuri, T. (1989). Hot working behaviour of cast Pr-Fe-B magnets. *IEEE Transactions on Magnetics*, **25**, 4099–4104.

Schultz, L. and Wecker, J. (1988). Hard magnetic properties of Nd-Fe-B formed by mechanical alloying and solid state reaction. *Materials Science and Engineering*, **99**, 127.

Rare-earth Nanocrystalline and Nanostructured Magnets

Melania Marinescu, Alexander Gabay and George C. Hadjipanayis
University of Delaware, Newark, DE, USA

1 INTRODUCTION

In polycrystalline anisotropic magnetic materials, the coercivity H_c is strongly dependent on the size of particles or grains. The often suggested correlation between H_c and the single domain particle size has no theoretical ground (Aharoni, 1986; Brown, 1945) and, in the case of hard-magnetic materials, it contradicts experimental observations (Grönefeld and Kronmüller, 1990). It is an empirical fact, however, that with decreasing particle size, the coercivity increases. When approaching the superparamagnetic size, which is of the order of a few nanometers in anisotropic materials, H_c decreases again because of the increasing effect of thermal fluctuations. This general dependence offers a relatively simple way to convert the high anisotropy into a high coercivity by producing materials with particles or grains of the size of tens to hundreds of nanometers.

The general equation that proved to be applicable to a vast majority of hard-magnetic materials, whose coercivity is controlled by the nucleation of reversed magnetic domains, presents the coercivity as a function anisotropy field H_A and the saturation magnetization M_s as:

$$H_c = \alpha H_A - N_{eff} M_s \quad (1)$$

where the parameters α and N_{eff} describe the effects of microstructure (including the grain size) and the local stray fields (which are also dependent on the microstructure), respectively. Theoretical derivations (Kronmüller, 1987) replace the anisotropy field from equation (1) ($H_A = 2K_1/\mu_0 M_s$) with the nucleation field (see equation (2)). On the other hand, the theoretical maximum energy product $(BH)_{max}$ (which characterizes an energy conserved by a permanent magnet with a perfectly square hysteresis loop and $H_c \geq M_s/2$) is equal to $\mu_0 M_s^2/4$ (Cullity, 1972). Table 1 shows the room-temperature intrinsic magnetic properties of some rare-earth (R) intermetallic compounds. In addition to M_s and H_A, the table includes the Curie temperature T_c, which is important for estimating a temperature stability of the permanent magnet (it is not, however, sufficient for finding the maximum operating temperature but the temperature dependence of H_A is also very important).

As it can be seen from the data in Table 1, the $Nd_2Fe_{14}B$, $Pr_2Fe_{14}B$, $Nd_2Fe_{14}C$, and $Sm_2Fe_{17}N_{2.3}$ compounds promise the highest $(BH)_{max}$ due to their high values of M_s, but the magnets based on the 2:14:1 compounds have very limited application temperature range because of their low T_c.

Handbook of Magnetism and Advanced Magnetic Materials. Edited by Helmut Kronmüller and Stuart Parkin. Volume 4: *Novel Materials*. ISBN: 978-0-470-02217-7.

Table 1. Intrinsic magnetic properties of some magnetically hard compounds.

Compound	$\mu_0 M_s$ (T)	H_A (MA m^{-1})	T_C (°C)	References
$Nd_2Fe_{14}B$	1.6	5.36	312	Buschow (1991)
$Pr_2Fe_{14}B$	1.56	6.96	292	Buschow (1991)
$Nd_2Fe_{14}C$	1.5	7.60	262	Buschow (1991)
$Sm_2Fe_{17}N_{2.3}$	1.54	11.20	476	Coey and Sun (1990)
$Sm_2Fe_{17}C$	1.24	4.24	279	DeMooij and Buschow (1988)
$Sm_2Fe_{15}Ga_2C$	≈1	>7.20	346	Shen *et al*. (1994)
$Sm_2Fe_{15}Si_2C$	≈1	7.20	305	Shen *et al*. (1994)
$SmFe_{11}Ti_1$	1.16	7.36	312	Buschow (1991)
$SmFe_{10}V_2$	1.10	4.80	337	Buschow (1991)
$SmFe_{10}Mo_2$	0.97	>4	187	Buschow (1991)
$NdFe_{11}TiN_{0.5}$	≈1.30	6.40	467	Yang *et al*. (1991)
$SmFe_3$	0.81	11.20	377	Buschow (1977) and Wecker, Katter, Schnitzke and Schultz (1991)
Sm_2Co_{17}	1.25	5.20	920	Strnat (1988)
$Sm_2(Co_{0.7}Fe_{0.3})_{17}$	1.45	8	840	Strnat (1988)
$Pr_2(Co_{0.53}Fe_{0.47})_{17}$	1.56	2.56	760	Satyanarayana, Fujii and Wallace (1984)
$SmCo_5$[a]	1.14	≤35.20	681–747	Korolev *et al*. (1975) and Buschow (1977)
$PrCo_5$	1.20	13.60	620	Strnat (1988)
$LaCo_5$	0.91	14	567	Strnat (1988)
YCo_5	1.06	10.40	630	Strnat (1988)
$SmCo_4B$	≈0.5	96[b]	237	Ido, Ogata and Maki (1993)
$SmCo_2Fe_2B$	≈0.7	12	509	Ido, Ogata and Maki (1993)

[a]Reference data vary because of a wide homogeneity range for the alloy.
[b]At 4.2 K.

Despite the high M_s, $Pr_2(Co_{0.53}Fe_{0.47})_{17}$ will not likely make a good magnet because of the low H_A. On the other hand, the compounds with very high H_A and modest M_s, like $SmCo_5$ and $SmCo_4B$, can potentially develop exceptionally high H_c, but not likely the record values of $(BH)_{max}$.

The most obvious way to decrease particle size is by milling. This route seems even more attractive since it may produce single crystals, which can be aligned by a magnetic field. Unfortunately, mechanical milling cannot produce particles smaller than 0.5–1 μm. Moreover, the coercivity of single crystals is very sensitive to the state of their surface. The surface of as-milled particles is always damaged and often oxidized leading to easy nucleation of domain walls and to a low H_c. Most of the contemporary nanocrystalline hard-magnetic materials are produced by either rapid solidification or high-energy mechanical milling. In the case of rapid solidification, the molten alloy is ejected onto a chilled metal surface, usually a rotating copper wheel. Depending on a quenching rate (which is usually controlled by the wheel speed) the method produces fine nanocrystalline, partially amorphous, or fully amorphous structures. Subsequent annealing may also be needed to form grains of the desired size. Melt spinning, which is the most widely used method of rapid solidification, is capable of producing both laboratory-scale and industrial-scale quantities of materials in the form of flakes or ribbons. An intensive mechanical milling diminishes the size of crystallites *inside* the particles by introducing an increasing number of lattice defects and developing subgrains. The process eventually leads to a complete destruction of a long-range atomic order. The high-energy milling which starts from several components with different composition is called *mechanical alloying*. Similar to overquenched ribbons, the amorphous powders must be annealed. Both the rapid solidification and mechanical milling/alloying can lead to metastable compounds–sometimes having better magnetic properties than the stable ones.

Most of the as-prepared nanocrystalline hard-magnetic materials are quasi-isotropic (the melt-spun $SmCo_5$ is one of the few exceptions, Li *et al*., 2002): their grains have no preferred crystallographic orientations, so the easy magnetization directions (EMDs) are oriented randomly. In this case, even if every grain has a perfectly square hysteresis loop parallel to the EMD, the magnets, as a whole, are not expected to have a remanence higher than half the saturation magnetization. However, for very small crystallites the intergranular exchange interaction can be strong enough to 'pull' the magnetization of the adjacent crystallites together (Callen, Liu and Cullen, 1977). This 'remanence enhancement' phenomenon is often used in single-phase nanocrystalline magnets (Hadjipanayis and Gong, 1988).

If the magnet consists of two phases with different magnetic properties, the exchange interaction between the

nanograins forces them to change their magnetizations in accord. The 'exchange coupling' allows us to benefit from the high coercivity of the anisotropic compounds (like those listed in Table 1) and the high magnetization of magnetically soft materials (like pure iron) combining them in one nanocomposite magnet. The potential of this phenomenon, which had been observed for the first time in melt-spun Nd–Fe–B alloys (Coehoorn, DeMooij and DeWaard, 1989), was fully understood after one-dimensional modeling (Kryukov, Manakov, Sadkov and Sakhaev, 1989; Kneller and Hawig, 1991). According to Kneller and Hawig, for an effective coupling, the size of soft magnetic grains should be less than twice the domain wall width of the hard phase. Two-dimensional (Feutrill, McCormick and Street, 1994) and three-dimensional (Fukunaga and Inoue, 1992; Schrefl, Fischer, Fidler and Kronmüller, 1994) models were later developed. The latest description of the magnetic hardening mechanism in Pr–Fe–B nanocrystalline magnets was proposed by Goll, Seeger and Kronmuller (1998) and Kronmüller and Goll (2002b).

Skomski and Coey (1993) predicted giant energy product values for certain exchange-coupled nanostructures, for example, 120 MGOe in a multilayer composed of alternating 2.4-nm hard-magnetic $Sm_2Fe_{17}N_3$ layers and 9-nm $Fe_{65}Co_{35}$ layers. Since the highest theoretical $(BH)_{max}$ for a single-phase $Nd_2Fe_{14}B$ magnet is 64 MGOe, and this value is nearly achieved by now (∼85%) in sintered magnets, it is hardly surprising that the exchange-coupled nanocomposites are sometimes referred to as the *next generation permanent magnets*. It should be noted, however, that the giant values of $(BH)_{max}$ given earlier were derived under the assumption that the hard-magnetic phase in the nanocomposite is crystallographically oriented. Obtaining texture in the magnets produced by rapid solidification requires considerable efforts even in systems where it is possible.

Another distinct group of rare-earth nanocomposite magnets is that of precipitation-hardened R–Co–Cu–Fe–Zr magnets. In these alloys, the structure of nanoscale $Sm_2(Co,Fe)_{17}$ cells develop in the bulk state through an elaborate heat treatment. Unlike most of nanocrystalline materials, these 'bulk-hardened' magnets retain alignment of the EMD for their nanophases. Also, the coercivity of these magnets is believed to be controlled by pinning of domain walls, rather than by domain wall nucleation as suggested in equation (1).

In the following sections, we review specific nanocrystalline and nanocomposite magnets. The magnets are classified according to their component phases. Within this division, we discuss separately the different preparation methods.

2 RARE-EARTH–TRANSITION METAL–METALOID-BASED NANOCRYSTALLINE MAGNETS

2.1 R–Fe–B phase diagrams and crystallization of R–Fe–B alloys

The R–Fe–B phase diagrams have been intensively studied since 1970s (Chaban *et al*., 1979; Stadelmaier, Elmasry and Cheng, 1983; Stadelmaier, Elmasry, Liu and Cheng, 1984; Matsuura *et al*., 1985; Oesterreicher, 1985; Schneider, Henig, Petzow and Stadelmair, 1986; Grieb, Henig, Schneider and Petzow, 1989; Landgraf *et al*., 1991; Givord, Nozieres, Sanchez-Lazamares and Leccabue, 1992; Knoch, Reinsch and Petzow, 1994). From the phase constitution point of view, the R–Fe–B alloys for permanent magnets are categorized according to the R content: (i) alloys with low R content that contain the $R_2Fe_{14}B$ hard-magnetic phase and a soft magnetic phase: α-Fe or Fe_3B; (ii) near stoichiometric alloys that correspond to $R_2Fe_{14}B$ single phase ($R_{11.77}Fe_{82.23}B_6$ in at%); and (iii) high R content alloys that contain the $R_2Fe_{14}B$ phase and a R-rich phase.

At a slow cooling rate, a stoichiometric $Nd_2Fe_{14}B$ alloy solidifies according to the following sequence (Schneider, Henig, Petzow and Stadelmair, 1986):

$$\text{Liquid} \xrightarrow[\text{(liquidus point)}]{1280\,^\circ\text{C}} \text{Fe} \xrightarrow[\text{(peritectic reaction)}]{1180\,^\circ\text{C}} \text{Nd}_2\text{Fe}_{14}\text{B}$$

The $Nd_2Fe_{14}B$ crystals develop around the initially formed Fe nuclei and hinder diffusion between the primary Fe crystals and the rest of the Fe-depleted liquid matrix. In this way, the as-cast $Nd_2Fe_{14}B$ ingot consists of $Nd_2Fe_{14}B$ grains, α-Fe residual crystals, and an Nd-rich phase close to the $Fe_{30}Nd_{70}$ stoichiometry.

Branagan and McCallum (1995) gave a model CCT (continuous cooling transformation) diagram for the stoichiometric $Nd_2Fe_{14}B$ alloy system showing the phase transformation upon solidification at different cooling rates (i.e., by the melt-spinning process). A vertical section of the Nd–Fe–B phase diagram along the tie line between Fe and $Nd_2Fe_{14}B$ is presented in Figure 1.

Liao and Altounian (1989) showed that $(Nd_xFe_{1-x})_{100-y}B_y$ alloy systems present a glass-forming ability for Fe content less than 87.5 at%, while the thermal stability of these alloys increases with boron concentrations and is dependent on the Nd:Fe atomic ratio.

Rapidly solidified $Nd_2Fe_{14}B$ alloys may display different microstructure features depending on the thermal history of the melt before ejection. Large superheating of the melt (above 1723 K) can prevent the early precipitation of nuclei,

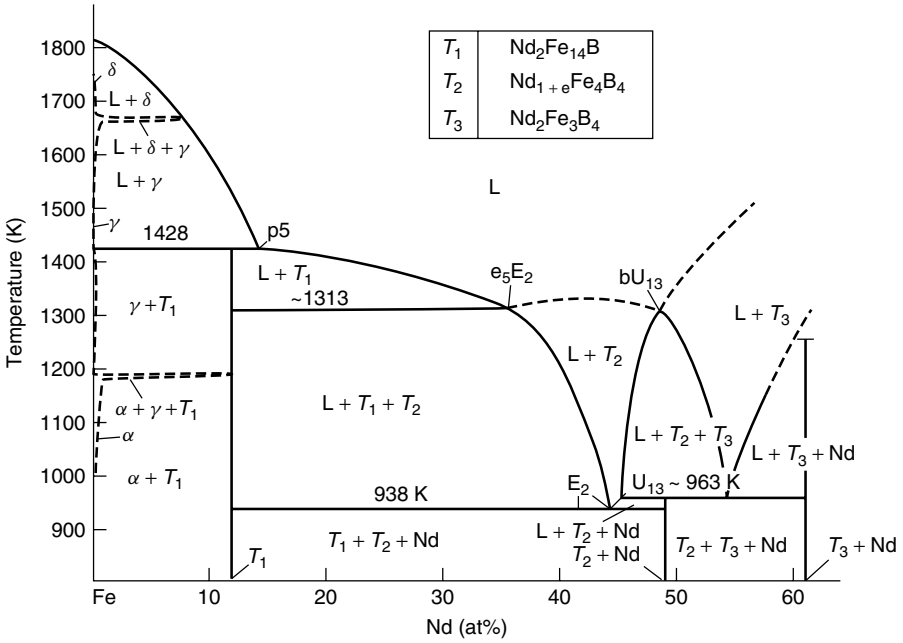

Figure 1. A vertical section of the Nd–Fe–B phase diagram along the tie line between Fe and $Nd_2Fe_{14}B$. (Reprinted with permission Branagan *et al*., copyright 1995, Elsevier.)

whereas a lower ejection temperature (1573 K) induces a nanocrystalline structure (Tang *et al*., 2003).

For each category of the R–Fe–B alloy systems, R lean, 2:14:1 stoichiometric, and R rich, the magnetic properties are different and strongly related to the grain size. For the first two categories, as the scale of the structure decreases to a certain level down to the nanometer range (but not below the critical superparamagnetic size), magnetizing-like interactions over short distances determine the enhancement of the remanence and the energy product while the coercivity may increase due to the increased density of grain boundaries.

2.2 Single-phase and R-rich nanocrystalline R–Fe–B alloys

The first studies on nanophase hard-magnetic systems were made on RFe_2 (R = Tb, Sm) alloys initially in a vitreous state, which upon crystallization develops a nanocrystalline structure with large coercivity at room temperature (Clark, 1973; Koon and Das, 1981). Hadjipanayis, Hazelton and Lawless (1983) and Croat, Herbst, Lee and Pinkerton (1984) obtained large coercivity on melt-spun Pr–Fe–B(Si) and Nd–Fe–B alloys, respectively. The large coercivity was due to the highly anisotropic $R_2Fe_{14}B$ tetragonal phase, which was produced in the nanoscale size during melt spinning or after crystallization. Coercivity of nanocrystalline $R_2Fe_{14}B$-based alloys is much larger than that of the corresponding bulk alloys, including sintered magnets. For example, melt-spun stoichiometric $Nd_2Fe_{14}B$ magnets can easily attain a coercivity of 1.15 MA m^{-1} (see Table 2) whereas the coercivity of Nd–Fe–B sintered magnets reaches only 960 kA m^{-1} (Sagawa *et al*., 1984). Table 2 summarizes the main intrinsic and extrinsic magnetic properties of $R_2Fe_{14}B$ nanocrystalline magnets. Large values of coercivity can also be obtained in the $R_2Fe_{14}C$ system, but their metallurgy is more complicated because of a phase transformation from $Nd_2Fe_{17}C_x$ to $Nd_2Fe_{14}C$ (Coehoorn, Duchateau and Demissen, 1989).

Besides melt spinning, other rapid solidification techniques like vapor deposition (Sellmyer, 1992; Fullerton *et al*., 1998), atomization (Narasimhan, Willman and Dulis, 1986), mechanical alloying (Schultz, 1990), and liquid dynamic compaction (Harada, Ando, O'Handley and Grant, 1990) have been employed for the fabrication of $R_2Fe_{14}B$ nanocrystalline magnets. By using the rapid solidification route, the nanocrystalline structure can be obtained either *in situ* by varying the cooling rate during solidification or by crystallizing the amorphous products. When using mechanical alloying, a subsequent annealing is always required to crystallize the amorphous or partially amorphous structure.

2.2.1 $R_2Fe_{14}B$ nanocrystalline ribbons obtained directly by quenching

The microstructure of the ribbons prepared by melt spinning is dependent on the quench rate (which in turn is determined by the speed of the spinning wheel). For a given composition

Table 2. Magnetic properties of $R_2Fe_{14}B$ nanocrystalline magnets.

Magnet	$\mu_0 M_s$ (T)	H_A (MA m^{-1})	T_C (°C)	H_c (MA m^{-1})	References
$Nd_2Fe_{14}B$	1.6	5.34	315	1.19	Croat, Herbst, Lee and Pinkerton (1984)
$Pr_2Fe_{14}B$	1.56	6.94	292	0.95	Goll, Seeger and Kronmuller (1998)
$Tb_2Fe_{14}B$	0.66	17.55	356	7.66	Pinkerton and Van Wingerden, (1986)
$Dy_2Fe_{14}B$	0.71	11.97	320	5.1	Pinkerton and Van Wingerden, (1986)
$Pr_2Co_{14}B$	0.97	7.98	717	1.99	Buschow, Demooij and Coehoorn, (1988)

M_s: saturation magnetization, H_A: anisotropy field, T_C: Curie temperature, H_c: coercive field.

and temperature of a melt, the best combination of magnetic hysteresis parameters can be obtained in a narrow range of the wheel speed (e.g., in the case of Nd–Fe–B alloys, the optimum wheel speed is 20–21 m s^{-1}, (Pinkerton, 1987), while the Nd–Fe–B ribbons quenched at 32 m s^{-1} are entirely amorphous (Mishra, 1986)). The best magnetic properties (coercive fields) in isotropic specimens were obtained for an optimum structure of the ribbons consisting of small polyhedral $Nd_2Fe_{14}B$ crystallites surrounded by a thin (2–3 nm) shell of a paramagnetic Nd-rich phase (Croat, Herbst, Lee and Pinkerton, 1984). Though the typical average grain size d is of the order of the single domain size d_{sd}, which was reported to vary from 150 nm (Mishra, 1986) to 300 nm (Livingston, 1985), it is not necessary to have $d < d_{sd}$ (Grönefeld and Kronmüller, 1990). On the other hand, the magnetic insulation provided by the grain-boundary phase is always favorable for the high coercivities.

Remanence of a magnet consisting of randomly oriented noninteracting uniaxial grains is limited by $J_r = J_s/2$. For the single-phase $Nd_2Fe_{14}B$ ribbons with $d \leq 26$ nm the remanence may exceed $J_s/2$ because of exchange coupling between the 2:14:1 nanocrystallites (Clemente, Keem and Bradley, 1988). The absence of the Nd-rich grain-boundary phase is the other necessary condition of the remanence enhancement phenomenon. The higher remanence leads to the higher maximum energy product: $Nd_2Fe_{14}B$ ribbons with $(BH)_{max} = 150$ kJ m^{-3}, $H_c = 960$ kA m^{-1} (Clemente, Keem and Bradley, 1988) and $(BH)_{max} = 170$ kJ m^{-3}, $H_c = 800$ kA m^{-1} (Bauer, Seeger, Zern and Kronmuller, 1996) were reported. Values of J_r up to 1.42 T and $(BH)_{max} = 180.7$ kJ m^{-3} were reported in Pr–Fe–B composite ribbons with Fe-rich composition (Goll, Seeger and Kronmuller, 1998).

Since anisotropic magnets present higher values of the energy product because of the high remanence, efforts have been made to prepare anisotropic $R_2Fe_{14}B$ ribbons via the directional solidification process (melt spinning at low wheel speed) and directional solidification combined with hot deformation (twin-roller melt spinning) that leads to the formation of columnar or dendritic structures, respectively (Dadon, Gefen and Daniel, 1987; Coehoorn and Duchateau, 1988; Chin, Huang and Yau, 1992, 1993). Anisotropic Nd–Fe–B nanocrystalline alloys were produced also by splat quenching (Harada, Ando, O'Handley and Grant, 1991). Coarse columnar structures in ribbons melt spun at low wheel speed led to a low coercivity, which undermined benefits of the obtained texture. Splats with columnar dendritic structures showed sufficiently high coercivity but only modest magnetic anisotropy.

2.2.2 *$R_2Fe_{14}B$ nanocrystalline ribbons obtained by annealing of amorphous precursors*

Calorimetric studies indicate that crystallization of amorphous $Nd_2Fe_{14}B$ alloys starts at about 580 °C with some variation when other additive elements are included (Figure 2). The optimum annealing temperature for the overquenched Nd–Fe–B and PR–Fe–B ribbons, however, is much higher, 700–800 °C. The higher annealing temperature leads to the formation of an optimum microstructure for magnetic hardening; particularly it eliminates α-Fe, which is usually the first product of crystallization. Nevertheless, unless the alloy contains a significant excess of R, a small amount of the soft

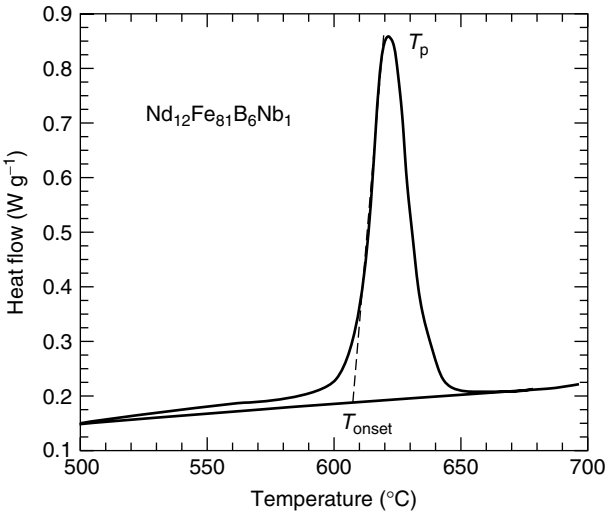

Figure 2. Calorimetric study of crystallization in amorphous $Nd_{12}Fe_{81}B_6Nb_1$ melt-spun alloy (Hadjipanayis, 1999).

magnetic phase always remains. Because of this, the magnetic properties of overquenched and subsequently annealed R–Fe–B ribbons are generally lower than those of directly quenched ribbons (Manaf, Leonowicz, Davies and Buckley, 1991). The kinetics of devitrification of overquenched $Nd_{13.5}Fe_{81.7}B_{4.8}$ and $Nd_{13.9}Fe_{78.3}B_{7.8}$ alloys has been studied by Jha, Davies and Buckley (1989). The glass-forming ability can be enhanced by the addition of TiC: the optimum wheel speed for $(Nd_{2.17}Fe_{14.17}B_{1.17})_{100-x}(TiC)_x$ was reduced as compared to the TiC-free composition (Branagan and McCallum, 1995; Branagan, Hyde, Sellers and McCallum, 1996).

The crystallization of the amorphous phase into the tetragonal $R_2Fe_{14}B$ phase and the magnetic hysteresis have been also examined in melt-spun alloys by Tao and Hadjipanayis (1984). The crystallization temperatures were found to be much higher (~650 °C) for Fe–Y–B and the heavy rare-earth alloys than in the light rare-earth Fe–R–M up to Gd (~560 °C). The crystallized samples have coercivities up to 480 kA m^{-1}. The tetragonal $La_2Fe_{14}B$ phase was found to be formed both in as-cast and crystallized melt-spun La–Fe–B alloys. This phase, however, is not stable and transforms into α-Fe and La–B upon annealing at higher temperatures (Hadjipanayis, Tao and Gudimetta, 1985).

2.2.3 *$R_2Fe_{14}B$ nanocrystalline powders*

Nanocrystalline single-phase isotropic powders can be prepared by high-energy ball milling of either single precursor alloys or several precursors with different compositions. The latter technique known as *mechanical alloying* involves a solid-state reaction between the elemental powder components, leading to the formation of composite particles with a layered morphology. In accordance with the mechanical characteristics of the starting powders and the thermodynamics of the alloy system, the reaction corresponding to the formation of 2:14:1 compound can take place during the milling or during the subsequent heat treatment (Wecker *et al*., 1994; Gong, Hadjipanayis and Krause, 1994; Chen *et al*., 1995). Coercivity values as high as $H_c = 840$ kA m^{-1} were obtained for $Nd_{15}Fe_{77}B_8$ powders (Chen *et al*., 1995). The optimum grain size of the $Nd_2Fe_{14}B$ phase was found to be about 50 nm.

Intensive milling of off-stoichiometric PR–Fe–B alloys with Dy and Zr additions lead to coercivity values as high as $H_c = 2.12$ MA m^{-1} in $Pr_{15}Dy_1Fe_{75.9}B_8Zr_{0.1}$ powders, whereas the reduction of R content and the presence of Co lead to excellent properties, $\mu_0 M_r = 0.92$ T, $H_c = 1$ MA m^{-1}, and $(BH)_{max} = 140$ kJ m^{-3}, supposedly originating from a microstructure with a mean grain size of 20 nm (Bollero *et al*., 2002).

2.3 Exchange-coupled nanocomposite R–TM–M alloys

2.3.1 *Nanocomposite α-Fe/$R_2Fe_{14}B$ alloys obtained by direct quenching*

In the early 1990s, Davies *et al*. (1992) showed that when decreasing the Nd content below 11 at% in nanocomposite $Nd_xFe_{94-x}B_6$ alloys, the α-Fe phase precipitates in an increasing amount up to 35 vol% for $x = 8$ at%. Owing to the high saturation magnetization of α-Fe and exchange coupling between the α-Fe and $N_2Fe_{14}B$ grains, this resulted in an additional enhancement of remanence, though H_c was gradually lowered. Manaf, Buckley and Davies (1993) and Manaf *et al*. 1993 reported a remanence larger than 1 T, a coercivity of 485 MA m^{-1} and $(BH)_{max} > 160$ kJ m^{-3} for the Nd-lean alloys with 8–10 at% Nd. The alloys consisted of a magnetically hard $Nd_2Fe_{14}B$ phase with an average grain size of less than 30 nm and α-Fe phase grains with an average particle grain size of less than 10 nm.

A systematic study of the two-phase α-Fe/$Nd_2Fe_{14}B$ magnets by Bauer, Seeger, Zern and Kronmuller (1996) showed that the remanence increases up to $\mu_0 M_r = 1.25$ T with increasing the content of α-Fe phase to approximately 30 vol%. This remanence value represents an enhancement of 56% as compared to that of the $Nd_2Fe_{14}B$ exchange-decoupled magnet without Fe. However, because the squareness of the hysteresis loop deteriorates with increasing α-Fe content, $(BH)_{max}$ is nearly constant for α-Fe amounts between 0 and 30 vol%, with only a weak maximum (186.4 kJ m^{-3}) at 30 vol%. In melt-spun α-Fe/$Pr_2Fe_{14}B$ magnets, Goll, Seeger and Kronmuller, (1998) obtained a pronounced maximum of $(BH)_{max}$ equal to 180.7 kJ m^{-3} for about 30 vol% of α-Fe phase. For α-Fe amounts exceeding this value, the coercivity of the magnet falls below $J_r/2$ and the $(BH)_{max}$ values start decreasing (Mendoza-Suarez, Davies and Escalante-Garcia, 2000).

The variation of the magnetic properties with the wheel speed of $Pr_xFe_{94-x}B_6$ nanocomposite ribbons with $6 \leq x \leq 10$ was studied by Mendoza-Suarez *et al*. (1999). The largest remanence enhancement was associated with the wheel speed that led to a grain size of ~30 nm for the 2:14:1 phase and of ~20 nm for the α-Fe phase. Values of the energy product as high as $(BH)_{max} = 170$ kJ m^{-3} were obtained for $x = 9$, 10 at%.

A *c*-axis orientation of the 2:14:1 phase has been observed by Jin *et al*. (2002b) (Figure 3) in the free surface of $(Pr,Tb)_2(Fe,Nb,Zr)_{14}B/\alpha$-Fe exchange-coupled nanocomposite ribbons spun at speeds below 10 m s^{-1}.

A crystallographic texture with the *c* axis perpendicular to the plane of the specimens in $Nd_{3.6}Pr_{5.4}Fe_{83}Co_3B_5$ ribbons prepared at a low wheel speed (10 m s^{-1}) has also been

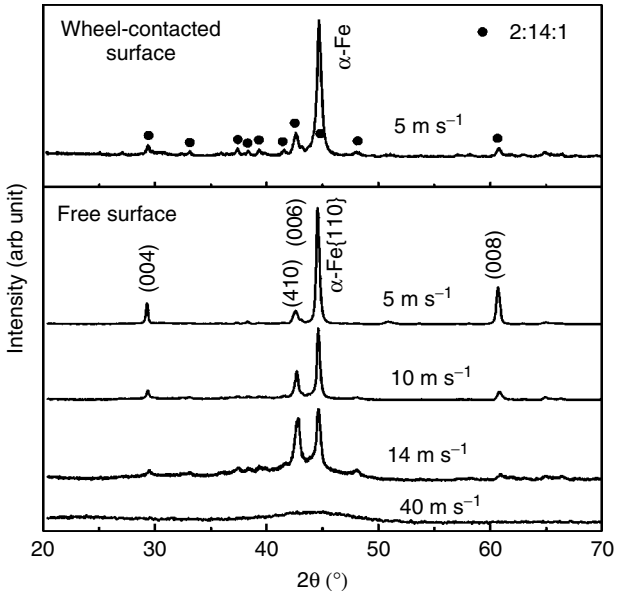

Figure 3. X-ray diffraction patterns of as-spun $Pr_7Tb_1Fe_{87}Nb_{0.5}Zr_{0.5}B_4$ ribbons indicating a trend for a *c*-axis texture of 2:14:1 phase perpendicular to the ribbon plane. (Reprinted with permission Z. Jin *et al*., copyright 2002, Elsevier.)

reported by Zhang, Guan, Yang and Zhang (2001). The orientation of the *c* axis switches to the ribbon plane for a higher wheel speed ($20\,m\,s^{-1}$) in which case, a high remanence of 0.74 M_s and a larger energy product $(BH)_{max} = 194\,kJ\,m^{-3}$ have been obtained.

2.3.2 *Nanocomposite α-Fe/$R_2Fe_{14}B$ alloys obtained by recrystallization*

In the α-Fe/$R_2Fe_{14}B$ two-phase magnets, the small size of the grains, especially those of the α-Fe phase, is essential for the intergranular exchange coupling. To avoid the overgrowth of α-Fe soft crystalline phase during annealing, high rates of heating and cooling, as well as a short isothermal stage are required. The whole annealing procedure usually lasts for only a few minutes, often seconds. This may, in particular, complicate reproducing the experimental results reported by different groups.

Most of the researchers agree that crystallization of amorphous R-lean R–Fe–B alloys occurs in several states. Among the observed metastable intermediate phases were: $R_2Fe_{23}B_3$, $RFe_{11}B_6$, and $R_3Fe_{62}B_{14}$ (Buschow, Demooij and Coehoorn, 1988); $R_3Fe_{81}B_{16}$ and $R_6Fe_{77}B_{17}$ (Gu *et al*., 1989; Gu, Shen and Zhai, 1990, 1994); R_2Fe_{17} (Linetsky, Raigorodsky and Tsvetkov, 1992); and RFe_7 (Withanawasam *et al*., 1995; Gabay *et al*., 1996).

The typical fully amorphous $Pr_8Fe_{86}B_6$ ribbons present a multistage microstructural evolution upon crystallization. From the amorphous matrix, the metastable $TbCu_7$-type phase precipitates initially and then it transforms into the metastable $Pr_2Fe_{23}B_3$ prior to the formation of $Pr_2Fe_{14}B$ and α-Fe phases (Jin *et al*., 2002a). It has been found that a more homogeneous and finer microstructure is obtained if the as-spun precursors were partially amorphous. The typical dependence of coercivity of as-spun and annealed R–Fe–B ribbons on the wheel speed is presented in Figure 4. The annealing is effective above a certain wheel speed.

Wang *et al*. (2000) studied the effect of the quenching rate during the ribbon formation, on the phase transformation and magnetic properties of $Pr_8Fe_{86}B_6$ ribbons subsequently annealed. It has been shown that the magnetic properties of the ribbons deteriorate with increasing the quenching rate followed by annealing. The directly spun ribbons present a remanence of 1.2 T and a coercivity of about $432\,kA\,m^{-1}$, whereas ribbons spun at 22 and $30\,m\,s^{-1}$ and optimally annealed show remanence values of 1.08 and 0.88 T and coercivity values of about 408 and $280\,kA\,m^{-1}$, respectively. The decrease of the magnetic hysteresis properties was attributed to the formation of coarser and more irregular microstructure.

A comprehensive study on the effect of various substitutions M (M = Cr, Nb, Ti, and Zr) for Fe, on the magnetic and structural properties of $Pr_8Fe_{84}M_2B_6$ melt-spun nanocomposites, has been done by Chen, Okumura, Hadjipanayis and Chen (2001). All these substitutions were found to make the microstructure finer and to improve the magnetic properties. The largest enhancement was obtained in Nb-substituted $Pr_8Fe_{84}Nb_2B_6$ magnets showing

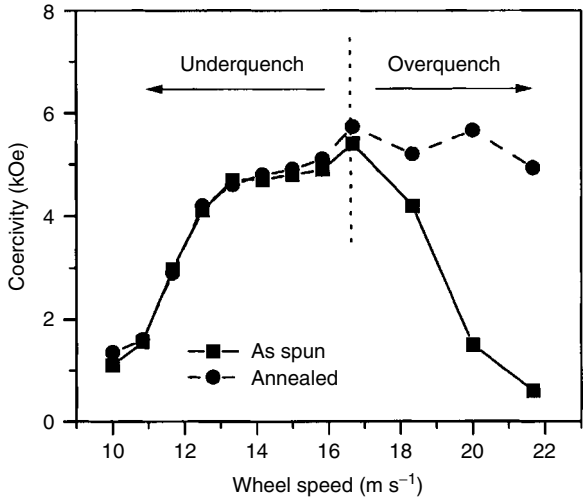

Figure 4. Coercivity of $Pr_8Fe_{86}B_6$ as a function of the wheel speed (Chen *et al*., 1999). The annealing was performed at 800 °C for 0.5–1.5 min. (Reprinted with permission Chen *et al*., copyright 1999, American Institute of Physics.)

$H_c = 518.7\,kA\,m^{-1}$, $(BH)_{max} = 143.2\,kJ\,m^{-3}$, with a grain size in the range of 10–20 nm.

Addition of Nb and Zr to $Pr_7Tb_1Fe_{88}B_4$ nanocomposite ribbons was reported (Jin *et al*., 2002b) to suppress the grain growth resulting in a large improvement of the magnetic properties with ~50% enhancement of the coercivity and a considerable increase of $(BH)_{max}$ from $441\,kA\,m^{-1}$ and $117\,kJ\,m^{-3}$ to $646\,kA\,m^{-1}$ and $162\,kJ\,m^{-3}$, respectively.

The effect of Al, Ti, or Hf additions on the magnetic properties of $Pr_{8.5}(Fe_{0.9}Co_{0.1})_{84.5}M_1B_6$ ribbons was reported by Wang and Davies (2003). In particular, the addition of Al slightly increases the coercivity whereas Ti or Hf increases the coercivity and energy product as a result of enhanced exchange coupling induced by the finer microstructure.

In contrast to the single-phase $Pr_{12}(Fe_{100-x}Co_x)_{82}B_6$ (with $x \leq 20$) nanocrystalline ribbons, which present good hard-magnetic properties ($(BH)_{max} = 220\,kJ\,m^{-3}$) by overquenching followed by annealing without any addition of grain growth inhibitor element, the two-phase Pr-lean ribbons have been found to benefit greatly with the addition of 1 at% Zr. This addition to the $Pr_{10}Fe_{84}B_6$ alloy resulted in an improved loop shape and H_c up to $550\,kA\,m^{-1}$ while $(BH)_{max}$ was increased to $140\,kJ\,m^{-3}$ compared with $80–110\,kJ\,m^{-3}$ for Zr-free ribbons (Harland and Davies, 2000).

Ga substitution for Fe was found to refine the microstructure of the $Pr_9Fe_{74}Co_{12}GaB_5$ ribbons and lead to an improvement of the magnetic properties from $J_r = 1.14\,T$ and $(BH)_{max} = 136\,kJ\,m^{-3}$ in Ga-free samples and $J_r = 1.22\,T$ to $(BH)_{max} = 177.6\,kJ\,m^{-3}$ in Ga-added samples (Zhang, Chang, Chiu and Chang, 2004). Overstoichiometric Nd–Fe–Ga–Nb–B melt-spun ribbons were studied by Bauer, Seeger and Kronmuller (1995) who reported that the coercivity is not significantly changed in samples with grain size within the range of 10 nm–1 μm.

The partitioning behavior of Co within the component phases and the Curie temperature of $Pr_2Fe_{14}B$/α-Fe nanocomposite ribbons with the nominal compositions $Pr_{9.7}Fe_{76.6}Co_{7.8}B_{5.9}$ and $Pr_{9.2}Fe_{69.4}Co_{15.4}B_{6.0}$ have been studied by Zhang *et al*. (2001a) using three-dimensional atom probe and transmission electron microscopy (TEM). It has been found that Co is dissolved uniformly, with no difference in concentration between the two component phases. For the nanocomposite samples, the Curie temperature was found to increase more rapidly with increasing overall Co content than for single-phase alloys as the Co/(Co + Fe) ratio in the 2:14:1 phase, when part of the nanocomposite system, is higher than the overall ratio.

Table 3 lists some of the best $R_2Fe_{14}B$/α-Fe nanocomposite magnets with $(BH)_{max} > 160\,kJ\,m^{-3}$.

Nanocomposite materials were also prepared in Pr–Co–Nb–B systems (Withanawasam, Panagiotopoulos and Hadjipanayis, 1996). The final microstructure consisting of a mixture of $Pr_2Co_{14}B$ and Co is formed after annealing the melt-spun ribbons through an intermediate transformation to the metastable $TbCu_7$-type structure.

2.3.3 Nanocomposite α-Fe/$R_2Fe_{14}B$ powders

Another versatile technique to produce $R_2Fe_{14}B$/α-Fe nanocomposite magnets is intensive milling of R-lean alloys or stochiometric alloys blended with different fractions of α-Fe. A 25 wt% Fe addition gave the optimum combination of the hysteresis magnetic parameters: $J_r = 1.19\,T$, $H_c = 528\,kA\,m^{-1}$, and $(BH)_{max} = 178\,kJ\,m^{-3}$ (Bollero *et al*., 2002).

Mechanically milled $Nd_{8-x}Sm_xFe_{88}B_4$ ($x = 0–2.5$) alloys have been studied by Zhang *et al*. (2004). The optimum magnetic properties of the powder milled for 5 h were achieved after annealing at 630 °C for 20 min. The reduced remanence was found to increase from 0.680 to 0.806 with increasing Sm content. Gong, Hadjipanayis and Krause (1994) obtained a remanence enhancement ($M_r/M_s = 0.60–0.68$) for R–Fe–Nb–B mechanically alloyed samples, with 5–15 at% R (R = Nd, Tb).

Neu *et al*. (1996) analyzed the influence of different additions to α-Fe/$Nd_2Fe_{14}B$ powders starting with the $Nd_8Fe_{88}B_4$ based composition. For Zr and Si addition, $\mu_0 M_r$ of approximately 1.1 T and $H_c = 320–344\,kA\,m^{-1}$ were obtained. Comparison of the magnetic properties of magnets produced by mechanical alloying of elemental powders and

Table 3. Magnetic properties of the best $R_2Fe_{14}B$/α-Fe nanocomposite magnets (ribbons).

Composition	Process route	Grain size	$\mu_0 M_r$(T)	H_c(kA m^{-1})	$(BH)_{max}$(kJ m^{-3})	References
$Pr_{8.5}(Fe_{0.8}Co_{0.2})_{86}Cu_{0.5}B_5$	Annealed	15–20 nm	10.9	583	160	Wang *et al*. (2000)
$Pr_9Fe_{74}Co_{12}GaB_5$	As-spun	15 nm	1.22	497	177.6	Zhang, Zhang and Shen (2002)
$Nd_{3.6}Pr_{5.4}Fe_{83}Co_3B_5$	As-spun	13–16 nm	0.74 M_s	450	194	Zhang *et al*. (2001)
$Pr_8Fe_{87}B_5$	As-spun	Hard-magnetic grains: 20–30 nm Soft magnetic grains: 15 nm	1.17	472	180.7	Goll, Seeger and Kronmuller (1998)

by intensive milling of precursor alloys (Neu and Schultz, 2001) showed that the latter technique is in some ways superior. The $Nd_9Fe_{77}Co_{8.5}Si_1B_{4.5}$ milled and annealed magnet had $H_c = 480\,kA\,m^{-1}$, $J_r = 1.11\,T$, and $(BH)_{max} = 147\,kJ\,m^{-3}$, if made from the precursor alloy, as compared to $H_c = 464\,kA\,m^{-1}$, $J_r = 1.07\,T$, and $(BH)_{max} = 139\,kJ\,m^{-3}$, if made from the elemental powders.

2.3.4 *Nanocomposite $Fe_3B/R_2Fe_{14}B$ alloys*

Coehoorn, DeMooij and DeWaard (1989) reported for the first time $Nd_4Fe_{78}B_{18}$ nanocomposite magnets, containing Fe_3B as the main phase and $Nd_2Fe_{14}B$ as a secondary phase, prepared by crystallization of melt-spun amorphous precursor. Because of the high boron content, an amorphous alloy is easily formed in the $Nd_2Fe_{14}B/Fe_3B$ system during melt spinning even under a relatively low wheel speed. Shen *et al*. (1994a) analyzed the thermal stability of $Nd_y(Fe_{1-x}B_x)_{100-y}$ alloys and found a very strong rise of crystallization temperature with x. In other words, boron remarkably increases the thermal stability of amorphous Nd–Fe–B alloys.

The addition of Hf and Ga in $Nd_4Fe_{76}Co_3(Hf_{1-x}Ga_x)B_{16}$ ($x = 0$, 0.5, and 1) melt-spun ribbons was found to improve the magnetic properties via improving the shape of grains. The values of remanence and coercivity of some $Fe_3B/R_2Fe_{14}B$ optimally heat-treated ribbons with various additions (Fe, Al, Si, Cu, Ga, Ag, and Au) are reported by Kanekiyo, Uehara and Hirosawa (1993), and presented in Figure 5.

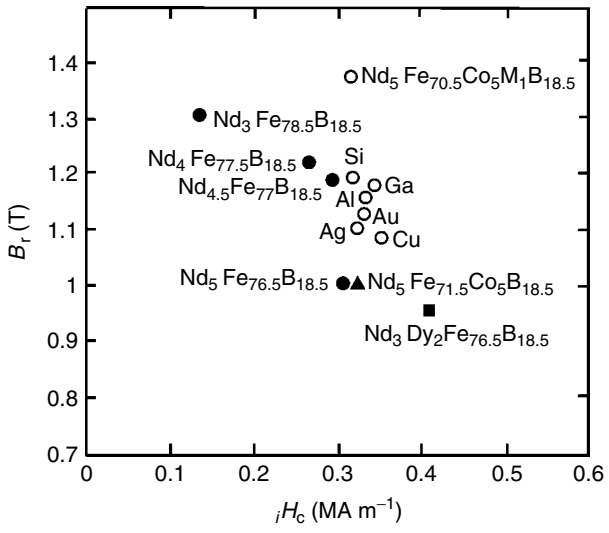

Figure 5. Remanence and coercivity of $Fe_3B/R_2Fe_{14}B$ optimally heat-treated ribbons with additions M = Fe, Al, Si, Cu, Ga, Ag, and Au (Kanekiyo, Uehara and Hirosawa, 1993).

Systematic studies on the effects of different alloying additions on Nd–Fe–B alloy with 3–5 at% Nd and 18.5 at% B have been also presented in reports of Hirosawa, Kanekiyo and Uehara (1993), Kanekiyo, Uehara and Hirosawa (1994), and Hirosawa and Kanekiyo (1996). It was found that combined additions of Co and Ga are particularly effective for improving the remanence, coercivity, and energy product. On the basis of TEM observations, it was concluded that these improvements result from a smaller grain size after the crystallization reaction. Ping, Hono and Hirosawa (1998) studied the distribution of Co and Ga atoms in $Nd_{4.5}Fe_{73}B_{18.5}Co_3Ga_1$ at various stages of crystallization. In the early stage of crystallization, Co and Ga atoms are rejected from the primary particles of the soft magnetic Fe_3B phase and are partitioned to the amorphous matrix phase. In the fully crystallized $Fe_3B/Nd_2Fe_{14}B$ nanocomposites, Co and Ga atoms are partitioned into the $Nd_2Fe_{14}B$ phase. Evidence for a slight enrichment of Ga atoms at the $Nd_2Fe_{14}B/Fe_3B$ interface has been found.

Gao, Zhu, Yang and Park (1998) found that the additions of Hf and Ga slowdown the crystallization rate in the $Nd_4Fe_{76}Co_3Hf_{0.5}Ga_{0.5}B_{16}$ amorphous alloy compared to the $Nd_4Fe_{80}B_{16}$ alloy. The optimum magnetic properties reported on annealed ribbons were $(BH)_{max} = 122.4$ and $116.8\,kJ\,m^{-3}$, respectively, while the remanence ratio M_r/M_s exceeded 0.8.

The coercivity of the nanocomposite magnets consisting of magnetically soft and magnetically hard phases is usually adjusted by varying the amount of the latter. However, in the $Fe_3B/Nd_2Fe_{14}B$ system, the room for adjustment is very small: when the Nd content exceeds 4.5 at%, the intermediate $Nd_2Fe_{23}B_3$ phase appears upon heating and it transforms into α-Fe and $Nd_1Fe_4B_4$, which are all magnetically soft. The addition of Cr extends the range for the formation of the magnetically hard $Nd_2Fe_{l4}B$ phase. Uehara *et al*. (1998) showed that in $Nd_5Fe_{77}B_{l8}$, the $Nd_2Fe_{23}B_3$ phase crystallizes along with Fe_3B from the amorphous phase and at the higher temperatures it decomposes into a mixture of α-Fe and $Nd_1Fe_4B_4$, whereas in $Nd_5Fe_{74}Cr_3B_{18}$, the $Nd_2Fe_{23}B_3$ phase breaks up into $Nd_2Fe_{l4}B$, Fe_3B, and α-Fe. According to Zhang, Matsushita and Inoue (2001), the optimum values of the magnetic properties obtained in the annealed $Nd_3Dy_{0.5}Fe_{67}Co_{9.5}B_{20}$ ribbons correspond to the four-phase structure of $Nd_2Fe_{14}B$, Fe_3B, α-Fe, and a residual amorphous phase ferromagnetic at room temperature.

An external magnetic field, applied during the annealing of melt-spun $Nd_4Fe_{73.5}Co_3Hf_{1-x}Ga_xB_{18.5}$ alloys, induced a grain refinement of about 20% and led to an increase of remanence and energy product by 30% (Yang and Park, 1995). The alloy having $x = 0.5$ exhibited $J_r = 1.25\,T$, $H_c = 225\,kA\,m^{-1}$, and $(BH)_{max} = 126.4\,kJ\,m^{-3}$. A similar effect of the magnetic field annealing was reported by Gao *et al*.

(1999) for $Nd_4Fe_{76}Co_3$ $(Hf_{1-x}Ga_x)B_{16}$ ($x = 0$, 0.5, and 1) melt-spun ribbons.

Besides the above traditional view on the $Fe_3B/R_2Fe_{14}B$ magnets, unconventional opinion exists (Li *et al*., 2004), that the hard-magnetic properties observed in these alloys may be induced in the Fe_3B phase not by the exchange interaction with the $Nd_2Fe_{14}B$ phase but rather by the partial substitution of Nd for Fe in the Fe_3B structure.

Another group of Nd–Fe–B-based nanocomposites combines the features of $Fe_3B/R_2Fe_{14}B$ and α-Fe/$R_2Fe_{14}B$. In the alloys containing approximately 9 at% Nd and 8–12 at% B, the magnetically soft metastable $Pr_2Fe_{23}B_3$ phase transforms into $Pr_2Fe_{14}B$, α-Fe, and Fe_3B by annealing at temperatures higher than 750 °C (Chen *et al*., 2003b). The phase evolution and magnetic properties of such Fe_3B/α-Fe/$R_2Fe_{14}B$ nanocomposite magnets were studied by Chang *et al*. (2002) for the $(Nd_{0.7}Pr_{0.25}La_{0.05})_xFe_{bal}Co_{10}Ti_2B_y$ alloys with $x = 4.5$–10.7 and $y = 10.9$–18.6. The best magnetic properties were obtained in the $(x, y) = (10.7, 10.9)$ alloy with $J_r = 0.8$ T, $H_c = 1.41\,MA\,m^{-1}$, and $(BH)_{max} = 104.8\,kJ\,m^{-3}$. An intrinsic coercivity $H_c > 800\,kA\,m^{-1}$, and $(BH)_{max} > 128\,kJ\,m^{-3}$ were developed in melt-spun ribbons with compositions of $(Nd_{0.95}La_{0.05})_{11}Fe_{bal}Co_{10}M_2B_{10-10.5}$ with M = Cr, V, Mo, Ti (Chang *et al*., 1999; Chang, Wang, Chang and Chen, 2000).

2.3.5 *Nanocomposite Nd–Fe carbides*

Alloys based on $R_2Fe_{14}C$ compound were also reported as a promising group of permanent magnet materials (Hellwig *et al*., 1991).

Nanocomposite Nd–Fe carbide ribbons

A study of the effect of C substitution for B on the magnetic and structural properties in nanocomposite $Nd_{10}Fe_{82}B_{8-x}C_x$ ($x = 0$, 2, 4, 5, 6, 7) ribbons in correlation with their crystallization behavior have been presented by Daniil, Okumura, Hadjipanayis and Sellmyer (2003). For $x \leq 4$, the crystallization of Nd_2Fe_{14}(B,C) and α-Fe occurs in one single stage. For $x > 4$, two structural transitions take place; the final stable structure consisting of Nd_2Fe_{14}(B,C) and α-Fe is formed from the intermediate $Nd_2Fe_{17}C_x$ and α-Fe structures. The coercivity has a maximum of $696\,kA\,m^{-1}$ for $x = 2$. With decreasing x, the formation of 2:14:1 phase is accelerated. From qualitative evaluation of X-ray diffraction (XRD) patterns it was derived that Nb and Zr additions reduce the amount of α-Fe significantly in as-spun and annealed $Nd_{10}Fe_{82}C_6B_2$ ribbons (Daniil *et al*., 2002).

Quenching of $Nd_{11}Fe_{72}Co_8(B_{0.8}C_{0.5})_9$ alloys at the optimum wheel speed allowed $(BH)_{max} = 140.5\,kJ\,m^{-3}$ (Yamamoto and Yamaguchi, 1991). Zhang, Chang, Chiu and Chang (2004) reported that ribbons with the stoichiometry $Pr_{11-x}DyFe_{72+x}Co_{10}C_4B_2$ ($x = 0$–3) consist of 2:14:1, α-Fe, 2:17 phases and a small amount of paramagnetic rare-earth 1:2 carbide. The highest values of the magnetic hysteresis parameters were obtained in $Pr_{10}DyFe_{73}Co_{10}C_4B_2$ ($B_r = 0.94$ T, $H_c = 861\,kA\,m^{-1}$).

Nanocomposite Nd–Fe carbide powders

The phase transformation and magnetic properties of mechanically alloyed $Nd_{16}Fe_{77-x}C_x$ ($x = 7$–11) and $Nd_{16}Fe_{84-x}C_{x-y}$ ($y = 0$–x and $x = 7$, 8, 9) alloys, were studied by Sui *et al*. (1996). More carbon than the stoichiometric content for $Nd_2Fe_{14}C$ was necessary to stabilize the tetragonal 2:14:1 structure. Substitution of boron for carbon can accelerate the phase transformation from $Nd_2Fe_{17}C_x$ to Nd_2Fe_{14}(C, B) and lead to an improvement of the magnetic properties. The Nd-rich phase with an fcc structure was reported to coexist with $Nd_2Fe_{14}C$ in mechanically alloyed Nd–Fe–C samples (Sui *et al*., 1996), but it was not found in melt-spun samples. The best properties were achieved in the $Nd_{16}Fe_{76}B_5C_3$ mechanically alloyed powders with $B_r = 0.71$ T, $H_c = 1.48\,MA\,m^{-1}$, and $(BH)_{max} = 91.5\,kJ\,m^{-3}$.

2.4 Bulk nanocrystalline magnets

As discussed earlier, the nanocrystalline R–Fe–B magnets are typically produced in the form of thin ribbons or fine powders. There are two exceptions to this observation: (i) the $R_xFe_{80-x-y}Co_yB_{20}$ alloys (R = Nd, Pr, Dy; $x = 3.5$–4.5; y = 10–13.5; in some reports with a small addition of Zr), which because of their remarkable glass-forming ability, can be cast into tubes or rods with 0.5–1 mm in diameter in amorphous state followed by crystallization annealing (Zhang and Inoue, 2002; Pawlik and Davies, 2003; Marinescu, Pawlik, Davies and Chiriac, 2004) and (ii) bulk nanocrystalline R–Fe–B alloys formed by room-temperature severe plastic deformation under pressure and subsequent annealing, with H_c up to $1.52\,MA\,m^{-1}$ (Popov, Gynderov and Stolyarov, 1996). As for the melt-spun R–Fe–B ribbons and intensively milled R–Fe–B powders, for most of the applications they must be consolidated before use. The most common technique is the binding of the hard-magnetic powder with a polymer or metal (usually Zn or Al). Though the nonmagnetic binder inevitably dilutes the magnetization, the bonded magnets with intermediate $(BH)_{max}$ of 80–144 $kJ\,m^{-3}$ are relatively inexpensive and can be formed into intricate net shapes (Brown, Ma and Chen, 2002). Fully dense nanocrystalline R–Fe–B magnets are commercially produced by compacting the R-rich melt-spun ribbons (≥13.5 at% R) at 700–750 °C

(Lee, 1985). Alternatively, a shock compaction can consolidate the amorphous or nanocrystalline R–Fe–B precursors without any microstructural changes (Leonowicz *et al*., 1998; Saito, 2001). Both the hot- and shock-compacted nanocrystalline magnets are isotropic.

Hot plastic deformation of R–Fe–B magnets aligns the EMDs of the 2:14:1 grains parallel to the applied pressure. This remarkable transformation can be observed in different kinds of R–Fe–B materials–cast, sintered, and so on. In the case of nanocrystalline magnets, it was first reported for hot-pressed melt-spun alloys (Lee, 1985) and later for mechanically alloyed powders (Wecker *et al*., 1994). The hot plastic deformation is usually done by either extrusion or upsetting the magnets in a loose die. The latter method is often referred to as *die upsetting*. In one of the versions of the die-upsetting technique (Yang *et al*., 1997), the hot compaction and hot deformation were performed in a single step. In the typical die-upset R–Fe–B magnets (Wecker *et al*., 1994; Leonowicz *et al*., 1994), the 2:14:1 grains are platelet shaped with a height of 50–100 nm and a diameter of 100–300 nm and the R-rich phase can be found in the form of thin grain-boundary layers. The hot-compacted specimens are isotropic while the hot-deformed ones are anisotropic due to the developed texture (Figures 6 and 7). In the model by Li and Graham (1992), the R-rich phase, which is liquid at the temperature of deformation, provides a mass transport necessary for growth of favorably oriented grains. Other studies (Grünberger *et al*., 1997) suggested that the liquid grain-boundary phase is not required for deformation and texturing, but it is rather necessary for a crack-free deformation at high strain rates. The commercially available die-upset R–Fe–B magnets have a $(BH)_{max}$ up to 360 kJ m^{-3}. The highest energy product values, up to 435.2 kJ m^{-3}, were reported for magnets made of amorphous shock-compacted precursors (Harada, Fujita and Kuji, 1996; Saito *et al*., 1998).

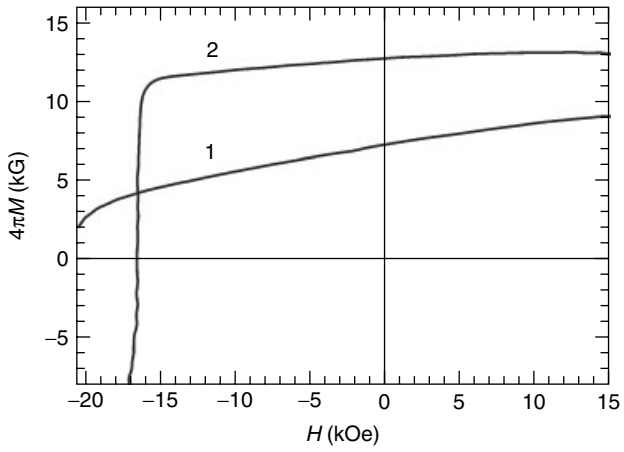

Figure 6. Demagnetization curves of hot-compacted (1) and hot-deformed (2) $Nd_{16}Fe_{77.5}Ga_{0.5}B_6$ magnets produced from intensively milled powders.

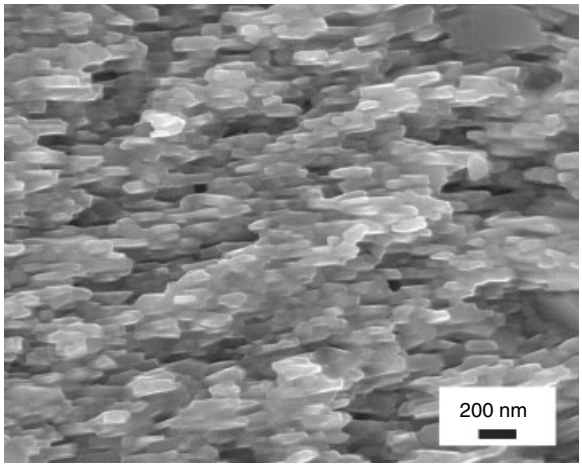

Figure 7. Elongated $Nd_2Fe_{14}B$ grains in the hot-deformed $Nd_{15.5}Fe_{77}Ga_{0.5}B_6$ magnet (scanning electron microscopy (SEM) image of the fractured surface of the magnet). Pressure had been applied in vertical direction.

While the typical R–Fe–B alloys for die upsetting contain more than 12 at% R (to provide the R-rich phase), considerable efforts were recently made to obtain *anisotropic* die-upset nanocomposites. In one of the attempts (Gabay, Zhang and Hadjipanayis, 2004), the R-rich and R-lean ribbons were blended and die upset together. The resulting magnets consisted of alternating layers of the two starting alloys arranged perpendicularly to the pressing direction (Figure 8). In the R-rich layers, the $R_2Fe_{14}B$ grains were crystallographically aligned, while the $R_2Fe_{14}B$ and α-Fe grains in the R-lean layers retained the random orientation. Though anisotropic magnets with less than 12 at% R have been obtained, their properties (see Figure 9) were far inferior to those of the traditional α-Fe-free die-upset magnets. In another recent study (Lee *et al*., 2004), die-upset anisotropic $(Nd,Pr,Dy)_2Fe_{14}B$/α-Fe magnets were reported with $(BH)_{max}$ of 336 kJ m^{-3}. The highest maximum energy product in composite magnets reported to date is $(BH)_{max} \sim 432$ kJ m^{-3} and was obtained for die-upset specimens fabricated with composite powder synthesized by coating (Liu *et al*, 2006). However, in this case, the soft magnetic phase exceeds by far the nanometer scale.

2.5 Magnetization reversal mechanism in nanostructured magnets

The magnetic hysteresis in the nanocrystalline $R_2Fe_{14}B$ alloys is difficult to model because the real microstructures are not only refined but are rather nonhomogeneous (Herbst and Croat, 1991). The pinning of domain walls at grain

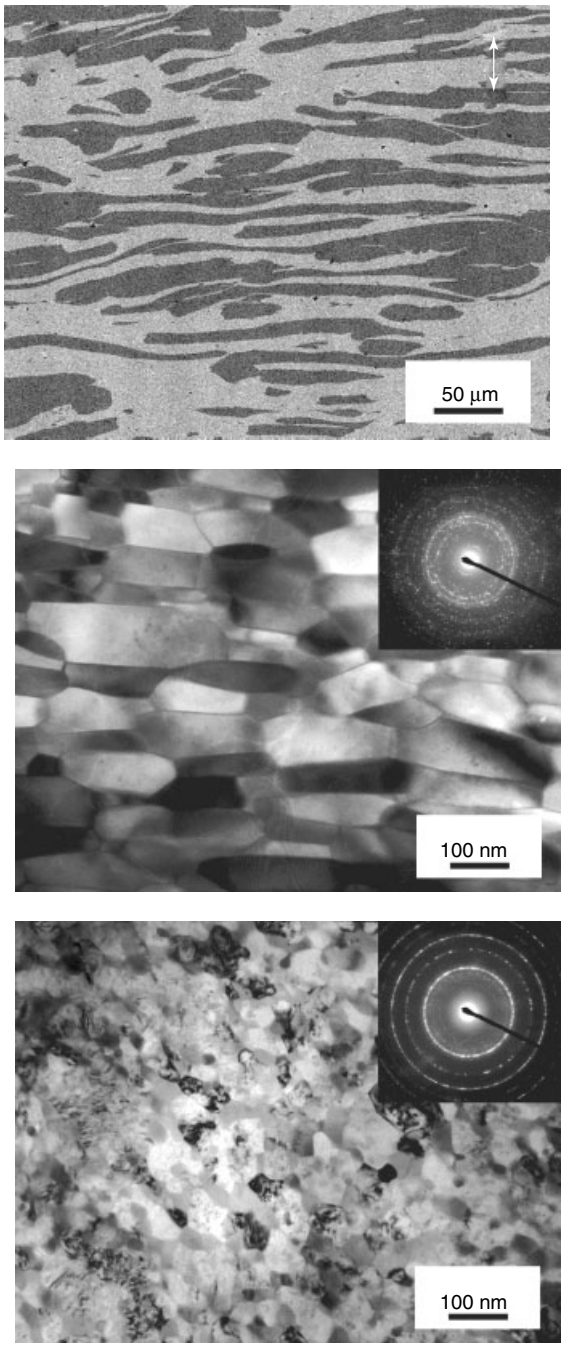

Figure 8. Microstructure of a composite magnet made from equal weight percent of $Pr_{13.5}Fe_{68}Co_{12}Ga_{0.5}B_6$ and $Pr_{3.5}Tb_1Fe_{89.5}B_6$: (a) SEM back scattered electron (BSE) image with the arrow showing the pressure direction and TEM images of areas with (b) platelet-like $R_2Fe_{14}B$ grains, (c) equiaxed $R_2Fe_{14}B$ and α-Fe grains. (Reprinted with permission Gabay *et al*., copyright 2004, American Institute of Physics.)

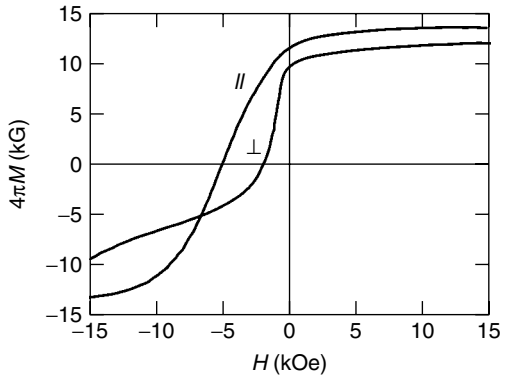

Figure 9. Demagnetization curves of die-upset magnet $(Pr,Tb)_{8.72}Fe_{85.04}Ga_{0.24}B_6$ made from equal weight percent of $Pr_{13.5}Fe_{80}Ga_{0.5}B_6 + Pr_{3.5}Tb_1Fe_{89.5}B_6$. The curves were measured parallel and perpendicular to the pressure direction.

boundaries has been suggested based on the shape of initial curves and field and temperature dependencies of the coercivity (Hadjipanayis, Dickerson and Lawless, 1986; Pinkerton and Van Wingerden, 1986). On the other hand, the coercivity controlled by nucleation of reversed domains has been proposed by Durst and Kronmuller (1987) based on the variation of the coercivity with temperature data. This mechanism is also supported by measurements of the initial magnetization and remanence showing that the magnetization reversal occurs by rotation of the magnetic moments of neighboring grains at a time. In later studies, the magnetization reversal process in the fine-grained magnets was explained better using the random anisotropy model (Givord and Rossignol, 1996). When the grains are smaller than 20 nm, the strong intergranular interactions lead to the formation of 'interaction domains'.

In nanocrystalline magnets without exchange coupling, H_c can be described by a modified form of equation (1) (Kronmüller, 1987; Martinek and Kronmuller, 1990):

$$\mu_0 H_c = \alpha_K \mu_0 H_N^{min} - N_{eff} J_s \qquad (2)$$

with H_N^{min} – the smallest nucleation field of reversed domains and α_K and N_{eff} – the microstructure parameters describing the variation of the magnetocrystalline anisotropy at the grain surface due to imperfections and the local demagnetizing coefficient, respectively. The microstructure parameters can be obtained by analyzing the temperature dependence of H_c. In the case of decoupled grains, the α_K parameter varies in the range $0.7 < \alpha_K < 0.9$. The exchange interaction between the magnetic moments of adjacent grains can be described by introducing the coefficient α_{ex} attached to α_K. The $\alpha_{ex}\alpha_K$ value of the exchange-coupled magnets is substantially lower than α_K of the magnets with decoupled grains. In the two-phase magnet containing 46.9% α-Fe, $\alpha_{ex}\alpha_K$ was found to be as low as 0.06 (Goll, Seeger and Kronmuller, 1998; Kronmüller and Goll, 2002b). The microstructural parameter N_{eff} is 0.1–0.16 in stochiometric and two-phase nanocrystalline magnets compared to 0.75–1

for magnets with decoupled grains (Bauer, Seeger, Zern and Kronmuller, 1996; Kronmüller and Goll, 2002b) indicating smaller internal stray fields in the exchange-coupled nanocomposites.

Micromagnetic analysis by Kronmüller and Goll (2002b) has showed three main sources of the reduction of H_c in nanocrystalline R–Fe–B magnets with the nucleation-controlled coercivity: (i) misaligned grains, (ii) imperfect grain boundaries, and (iii) exchange coupling between neighboring grains which induces cooperative demagnetization processes of clusters of grains.

3 RARE-EARTH–COBALT NANOSTRUCTURED AND NANOCRYSTALLINE MAGNETS

3.1 Bulk-hardened nanostructured R–Co magnets

The bulk-hardened (or precipitation-hardened) Sm–Co magnets were developed in the 1970s (Tawara and Senno, 1973; Ojima, Tomizawa, Yoneyama and Hori, 1977). They are also often called the *2:17* magnets after their major component, the Sm_2Co_{17} phase. These magnets are particularly attractive due to their excellent temperature stability and good corrosion resistance. However, these magnets are rather expensive because of their high-priced raw materials and typical heat-treatment processing which is long and complicated. Because of its 'bulk' nature, the magnetic hardening in the 2:17 Sm–Co alloys can be achieved in various types of materials. Sintered magnets, that is, those produced via a powder metallurgy, are anisotropic and show the best magnetic performance. Cast isotropic magnets are less expensive; they can be further crushed and used for manufacturing anisotropic polymer-bonded magnets. Recently bulk hardening has been realized in $Sm(Co,Fe,Cu,Zr)_z$ melt-spun ribbons (Goll, Kleinschroth, Sigle and Kronmuller, 2000; Yan, Bollero, Müller and Gutfleisch, 2002; Yan, Sun, Han and Shen, 2002). These ribbons can be potentially used for large-scale manufacturing of isotropic and partially anisotropic polymer-bonded magnets.

3.1.1 Crystallography and phase relations

The binary Sm–Co phase diagram depicts the coexistence of the Sm_2Co_{17} phase with another important phase, $SmCo_5$. The structures of the two compounds are related (Buschow and Van der Goot, 1968): Sm_2Co_{17} can be considered as $SmCo_5$ with one-third of the Sm atoms replaced by pairs (so-called dumbbells) of the Co atoms stretched along the [001] direction. There are two modifications of the Sm_2Co_{17} structure, both with the Co dumbbells ordered: the rhombohedral one (the Th_2Zn_{17} type) often referred to as *2:17R* and the hexagonal one (the Th_2Ni_{17} type), *2:17H*. It is the 2:17R structure that is stable at room temperature and is the primary phase of the 2:17 magnets. Random substitution of the Co dumbbells for the Sm atoms in the $SmCo_5$ structure results in the off-stoichiometric $SmCo_{5+\delta}$ structure. In the binary Sm–Co alloys, this structure is stable at high temperatures within a limited range of compositions. The addition of certain elements (most notably, Cu and Zr) greatly extends the range of the off-stoichiometric $SmCo_{5+\delta}$ structure. In Sm–Co–Zr system, this range stretches all the way to the Sm_2Co_{17} composition (Derkaoui, Valignat and Allibert, 1996). Thus, in the doped Sm–Co alloys, a third 2:17 structure exists–the hexagonal one with disordered dumbbells. Historically, this structure is known as that of the $TbCu_7$ type (Buschow and Van der Goot, 1971) or simply '1:7'. The commercial 2:17 magnets usually contain Cu, Zr, and Fe in addition to Sm and Co. The traditional way to express the magnet compositions is $Sm(Co,Fe,Cu,Zr)_z$. This approach, however, is misleading when referring to the above crystallographic relations; when forming any of the three 2:17 structures from the parent 1:5 compound a dumbbell of *two* Co, Fe, or Cu atoms, but only *one* Zr atom occupy the Sm site. Also it should be noted that because of the evaporation loss of Sm, in the 2:17 magnets prepared via a powder metallurgy, the effective z value is larger than the nominal one by 0.6–0.8 atoms (Liu *et al*., 2000).

3.1.2 Microstructure evolution

In general, the microstructure of the 2:17 magnets (Figures 10 and 11) develops in three-step processing. The alloys have to be annealed at 1150–1190 °C to form a single-phase hexagonal structure (2:17H or 1:7; Ray (1984) considered this structure as 'disordered rhombohedral'). The subsequent isothermal aging at 800–850 °C forms a submicron size microstructure consisting of the 2:17R cells surrounded by 1:5 layers.

According to Melton and Nagel, the cellular morphology minimizes the strain induced by a *c*-axis misfit between the coherent 2:17 and 1:5 structures (Melton and Nagel, 1977). It is still disputable how the cellular structure is actually formed. Livingston and Martin suggested that the cells evolve by precipitation and growth of the 2:17R particles, while the remnants of the 1:7 matrix phase form the 1:5 cell boundaries (Livingston and Martin, 1977). According to another model (Melton and Nagel, 1977), the cell boundaries arise from binding of isolated 1:5 particles during coarsening. Stadelmaier, Goll and Kronmüller (2005) who also considered the cell boundaries as precipitates compared them with the Widmannstätten pattern. In this model (Stadelmaier,

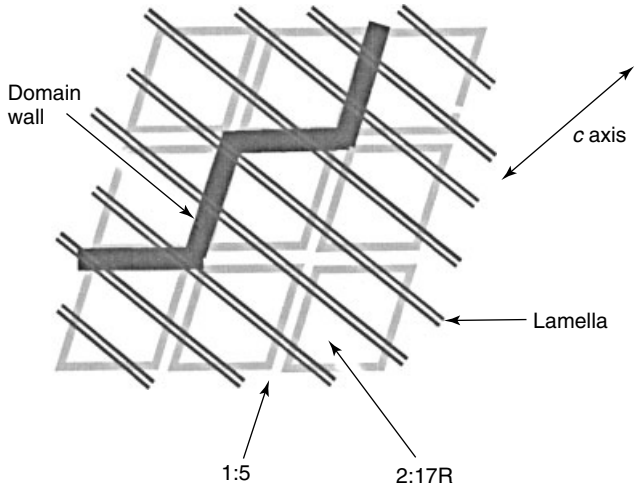

Figure 10. Schematic representation of microstructure in fully heat-treated 2:17 bulk-hardened Sm–Co magnets.

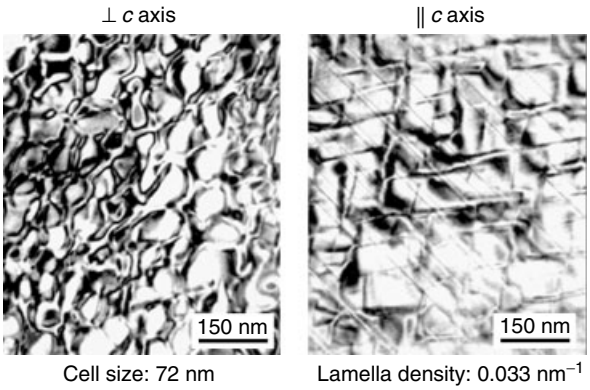

Figure 11. Typical cellular and lamellar mircostructure in 2:17 magnets along parallel and perpendicular direction to the c axis.

Goll and Kronmüller, 2005), the regular geometric pattern of the cells is caused by a low-index crystallographic interface between the 2:17 and 1:5 phases rather than by the minimum strain energy. In $Sm(Co,Fe,Cu,Zr)_z$ magnets, the 2:17/1:5 cellular structure is intersected by Zr-rich lamellae, which have been recently identified (Xiong *et al*., 2004) as $(Zr,Sm,Cu)_1(Co,Fe)_3$ with the Be_3Nb structure. After aging, the alloys have to be cooled to 350–400 °C at the rate 0.7–1 °C per min. The slow cooling is accompanied by an exchange of atoms between the phases, notably by diffusion of the Cu atoms into the 1:5 cell boundaries (Figure 12). A noticeable coercivity appears only at this stage, though for certain alloys, the aging (Yan, Bollero, Müller and Gutfleisch, 2002) or slow cooling (Tang *et al*., 2001) stages can be omitted. One should also mention that the highest concentration of Cu was found in the so-called *triple junctions*, that is the junction of three neighboring cells (Figure 12).

The above mechanism of the microstructure evolution in 2:17 magnets with heat treatment has been formulated in the early 1980s (Mishra *et al*., 1981; Fidler, Skalicky and Rothwarf, 1983). Some very recent findings (Goll, Kronmüller and Stadelmaier, 2004; Stadelmaier, Goll and Kronmüller, 2005) suggested that, opposite to the conventional view, the cell boundaries first consist of a mixture of 2:17, 2:7, and 5:19 phases, and the 1:5 structure forms only at the cooling stage.

The cellular/lamellar microstructure of the 2:17 magnets strongly depends on both the alloy composition and processing parameters. These effects were summarized in recent review by Hadjipanayis *et al*. (2000). Smaller z values in $Sm(Co,Fe,Cu,Zr)_z$ result in larger volume fraction of the 1:5 cell-boundary phase and, therefore in a smaller average cell size (Figure 13). Because the coercivity is associated with the Cu concentration in the cell-boundary phase, more Cu is required to achieve the same coercivity in the alloy with the larger volume fraction of the 1:5 phase. *Cu*, being a nonmagnetic element, decreases the magnetization of the magnet. Iron, on the contrary, increases the saturation magnetization. It also increases the average cell size (in part, probably, by stabilizing the 2:17 phase) and promotes a uniform and well-developed cellular structure. Though the cellular structure can be developed without Zr, addition of this element increases the coercivity dramatically, up to 3.20 MA m^{-1}, in the alloys with high z values. Density of the Zr-rich lamellar phase increases with Zr. It is certain that Zr assures the high-temperature single-phase structure and controls its separation into 2:17R and 1:5 during aging. The role of the lamellar phase is not that clear. It may stabilize a uniform cellular structure and/or provide diffusion paths for the Cu atoms during the slow cooling.

3.1.3 Recent advances in 2:17 magnets

Though sintered 2:17 magnets may have a room-temperature maximum energy product of more than 240 kJ m^{-3}, they are used almost exclusively for high-temperature applications (for room-temperature applications, the 2:17 magnets cannot compete with the more powerful and less expensive Nd–Fe–B magnets). However, the 2:17 magnets with the highest room temperature $(BH)_{max}$ have a weaker performance above 300 °C (Ma *et al*., 1996). During the 1990s, most of the studies in the 2:17 magnets were focused on the high-temperature properties. As a result of these concentrated efforts the maximum operating temperature of the 2:17 magnets has been increased to 450–500 °C (Liu, Chui, Dimitrov and Hadjipanayis, 1998; Chen *et al*., 1998). In general, the $Sm(Co,Fe,Cu,Zr)_z$ magnets with smaller z have better temperature stability (Figure 14, Hadjipanayis *et al*., 2000). In

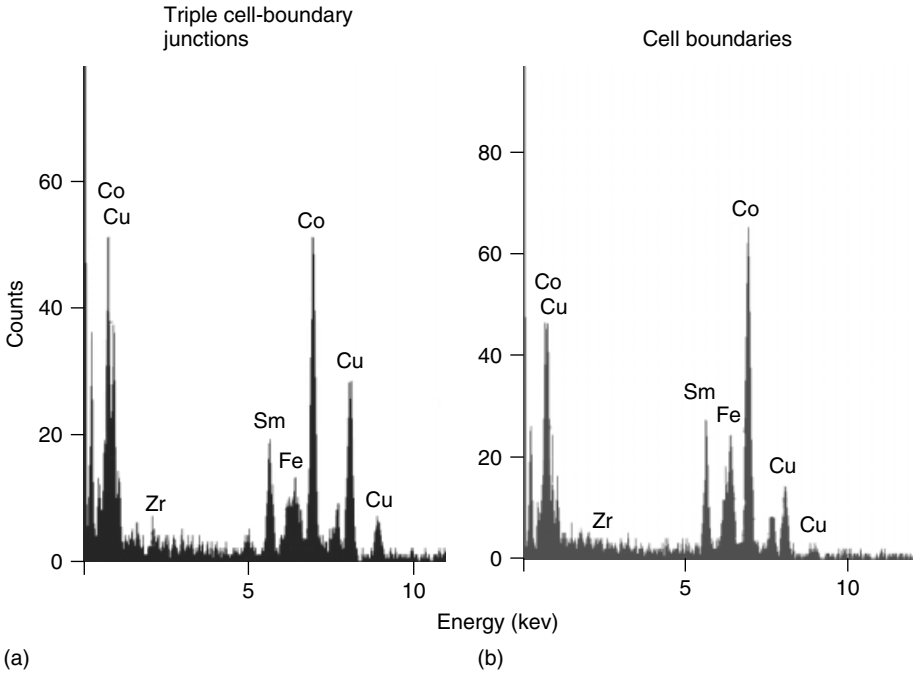

Figure 12. Nanoprobe energy dispersive X-ray (EDX) patterns of $Sm(CoCuFeZr)_z$ magnets homogenized at 1185 °C, aged at 700 °C for 24 h and followed by slow cooling to 400 °C; (a) triple cell-boundary junction, chemical composition (at%): Sm: 20.5, Cu: 29.4, Co: 37.7, Fe: 11.3, Zr: 1.1; (b) regular cell boundaries, chemical composition (at%): Sm: 13.4, Cu: 14.4, Co: 53.1, Fe: 17.8, Zr: 1.3.

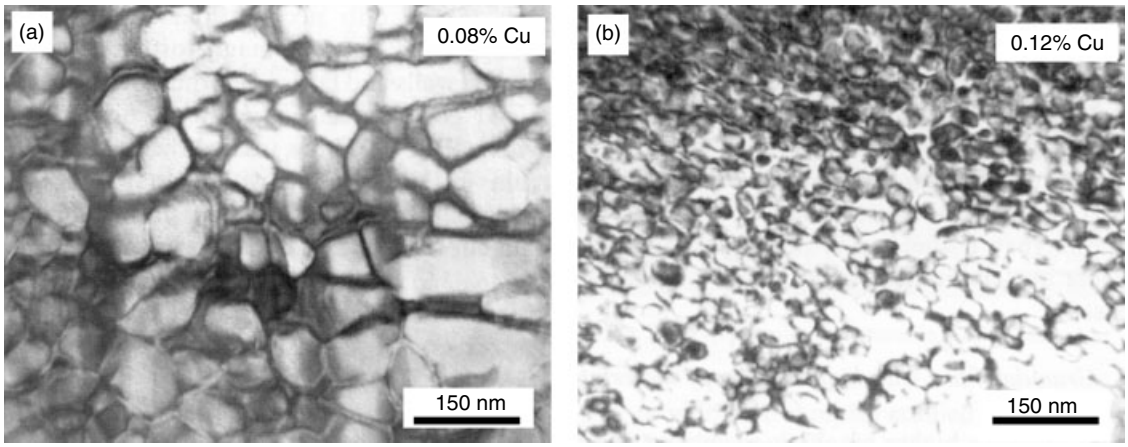

Figure 13. Effect of Cu content on cellular microstructure in $Sm(Co, Fe, Cu, Zr)_7$ (Hadjipanayis, 1999).

fact, certain 2:17 magnets show the unusual positive temperature coefficient of coercivity (Popov, Korolev and Shchegoleva, 1990).

The effect of bulk magnetic hardening in the Sm–Co–Fe–Cu–Zr alloys is not a unique feature of this system. In addition to the long-known inexpensive Ce-based magnets, there were a number of recent attempts to replace the crucial alloy components. Bulk-hardened magnets with Sm replaced by Y and Pr (Gabay, Zhang and Hadjipanayis, 2001) show a room-temperature coercivity of 640 kA m^{-1}. However, they require more Cu and Zr than the Sm-based magnets and, therefore, have inferior overall magnetic properties. Sm can also be replaced by Gd (Rong *et al*., 2004). Ti was long considered as an alternative to Zr. Recently, Sm–Co–Cu–Ti (Zhou *et al*., 2000) and Pr–Co–Cu–Ti (Zhang *et al*., 2003) magnets were found to have a significant coercivity at 400–500 °C, despite poor properties at room temperature. Similar behavior was observed when Cu in the traditional magnets had been replaced by Ni (Tang, Zhang and Hadjipanayis, 2002a). The problem with Ti and Ni is that unlike Zr and Cu they have significant room-temperature solubility in the

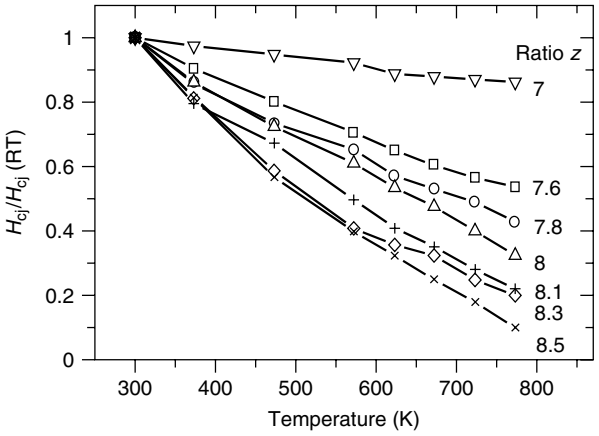

Figure 14. Temperature dependence of coercivity in $Sm(Co,Fe,Cu,Zr)_z$ magnets with different z (Hadjipanayis *et al*., 2000).

2:17R structure reducing the magnetic properties of this phase which is the primary phase in the magnets. The phenomenon of bulk magnetic hardening was even observed in the Pr–Co–Zr alloys (Gabay, Zhang and Hadjipanayis, 2000) despite the absence of Cu(Ni) and the fact that magnetocrystalline anisotropy of the main Pr_2Co_{17} phase is not uniaxial.

3.1.4 Coercivity mechanism

The predominant magnetization reversal model suggested for the 2:17 Sm–Co magnets is that of domain wall pining where the domain walls are pinned at the cell boundaries owing to a large gradient of domain wall energy (Livingston and Martin, 1977). Indeed, magnetic domain observations show that in the highly coercive 2:17 magnets, domain walls are waved and follow the cell boundaries (Figure 15). However, there is no agreement on the nature of this gradient. Figure 16 shows schematically the most typical profiles of the anisotropy constant (domain wall energy) suggested to explain the coercivity in the bulk-hardened magnets.

The profile shown in Figure 16(a) was suggested for $Sm(Co,Fe,Cu)_7$ sintered magnets (Livingston and Martin, 1977). When the domain wall energy of the cell-boundary phase is higher than that of the cell, the boundary is a repulsive pinning site–a barrier for moving domain walls. The K_1 profile shown in Figure 16(b) has been proposed for the first time by Kronmüller (1984) and was quantified later by Goll (2002) and Kronmüller and Goll (2002a). The profile was also obtained experimentally for $Sm(Co,Fe,Cu,Zr)_{7.4-7.5}$ sintered magnets (Goll, 2002; Xiong *et al*., 2004). The problem with the repulsive pinning model is that the largest difference between the higher domain wall energy of the 1:5 phase and the lower energy of the 2:17 phase must be expected at the end of the isothermal aging. The coercivity, however, appears only during the subsequent slow cooling when this difference is expected to decrease as Cu diffuses from the 2:17 cells into the 1:5 cell boundaries. To resolve this controversy, more complicated compositional profiles were suggested. According to one of the models (Yan, Gutfleisch, Gemming and Müller, 2003) the Cu-poor outer layers of the 1:5 phase result in the profile shown in Figure 16(c) and act as repulsive pinning sites. However, this model is not compatible with the experimentally determined atomic distribution within the boundary between the cell and the cell wall phases. The recent idea that the 1:5 phase itself

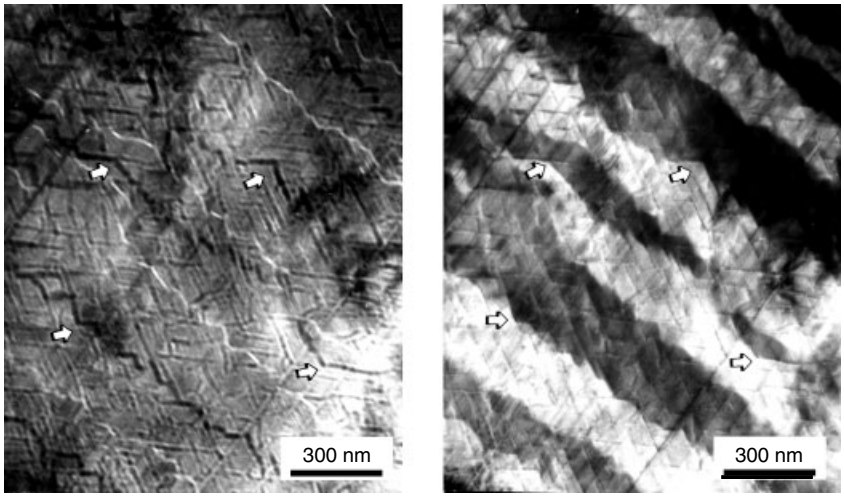

Figure 15. Typical magnetic domain structure in the fully heat-treated 2:17 Sm–Co magnets: (a) Fresnel and (b) Foucault modes of Lorentz microscopy.

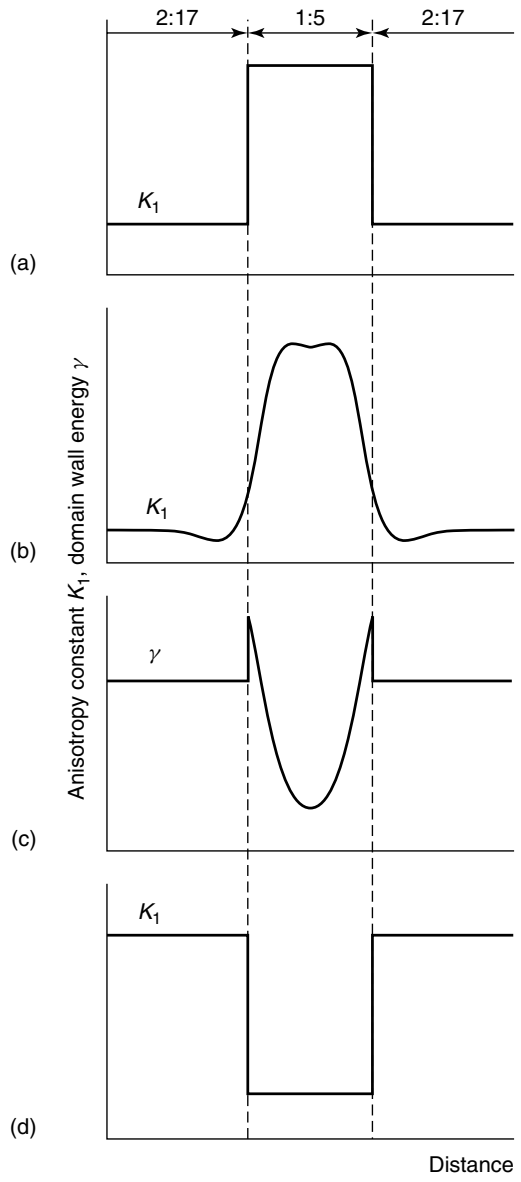

Figure 16. Profiles of the anisotropy constant K_1 or domain wall energy γ at the 1:5 cell-boundary phase as (a) suggested by Livingston and Martin (1977), (b) estimated by Goll (2002) and Xiong *et al*. (2004), (c) proposed by Yan, Gutfleisch, Gemming and Müller (2003), and (d) assumed by Liu *et al*. (2001) and Rong *et al*. (2004). (Reprinted with permission Rong *et al*., copyright 2004, American Institute of Physics.)

forms only during the slow cooling (Goll, Kronmüller and Stadelmaier, 2004; Stadelmaier, Goll and Kronmüller, 2005) may also explain why the coercivity appears only at the latter stage.

If the domain wall energy of the cell-boundary phase is lower than that in the cell, the boundary is an attractive pinning site, that is, a trap for domain walls. The attractive pinning models, in which the 1:5 phase is uniform (Figure 16d) were recently used for qualitative (Liu *et al*., 2001) and quantitative (Rong *et al*., 2004) simulations. The same experimental K_1 profile as shown in Figure 16(b) can be interpreted (Xiong *et al*., 2004) in favor of the attractive pinning, with the domain walls trapped at the Cu-rich layers of the 2:17 phase adjacent to the cell boundaries. The other model (Popov, Gaviko, Magat and Ivanova, 1990) states that attractive pinning sites appear during the slow cooling at the 2:17/1:5 interface, when the Cu atoms diffuse to the interface in order to accommodate the interphase stress.

The 2:17/1:5 interface is not the only pinning site ever considered. According to Katter *et al*., 1996, the very strong domain wall pinning in the $Sm(Co,Fe,Cu,Zr)_z$ magnets might be expected at the intersections of the 1:5 grain-boundary phase and the Zr-rich lamellar phase. However, this contribution to the coercive field is debated since the lamellar phase exists after the high-temperature treatment when the coercive field is still small.

It should be also noted that the cell-boundary $Sm(Co,Cu)_5$ phase itself is known to have a high room-temperature coercivity (Nesbitt *et al*., 1968). With increasing temperature, the domain wall energy of the 1:5 phase decreases more rapidly than that of the 2:17 phase. This means that any repulsive pinning model implies a transition to the attractive pinning at a certain elevated temperature. The 1:5 grain-boundary phase has a lower Curie temperature. At this temperature, a maximum of the coercivity is observed in the magnets with an 'anomalous' temperature dependence of H_c (Popov, Korolev and Shchegoleva, 1990; Gabay, Tang, Zhang and Hadjipanayis, 2001; Zhang *et al*., 2003). Once the grain-boundary phase becomes paramagnetic, the magnetization reversal occurs in the separated 2:17 cell either via uniform magnetization rotation or via nucleation of domain walls. It has been pointed out (Gabay, Tang, Zhang and Hadjipanayis, 2001) that, if the Cu concentration in the cell boundaries is high enough, the 2:17 cell can be magnetically separated even at room temperature (Figure 17). In such magnets, the coercivity has a 'normal' monotonic temperature dependence and it is always nucleation controlled. Neither domain wall observations nor the low initial magnetic susceptibility traditionally associated with the pinning-controlled coercivity contradict the magnetization reversal in the magnetically separated 2:17 cells. Since the cells still interact magnetostatically, the magnetic domain structure similar to the one shown in Figure 13 can be formed by interaction domains. In this case, the initial magnetic susceptibility is expected to be low, if the cells are smaller than the single domain particle size. The anomalous temperature dependence of coercivity was also reported in 2:17 melt-spun ribbons (Goll, Kleinschroth, Sigle and Kronmuller, 2000).

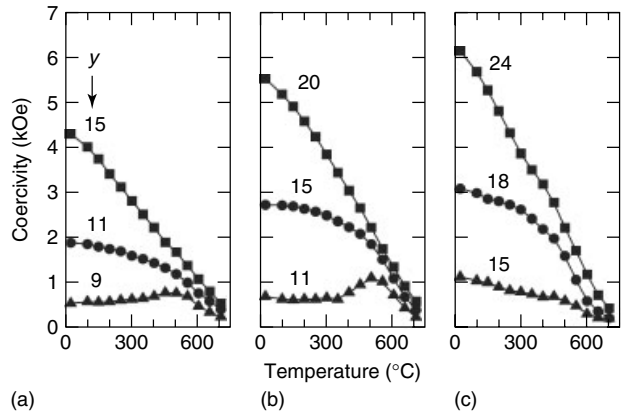

Figure 17. Temperature dependence of coercivity of the $Y_xZr_{2.5}Co_{89.5-x-y}Fe_8Cu_y$ for (a) $x = 11.5$, (b) $x = 12.5$, and (c) $x = 13.5$. (Reprinted with permission Gabay *et al*., copyright 2001, American Institute of Physics.)

3.2 Nanocrystalline R–Co magnets

3.2.1 Melt-spun R–Co magnets

Owing to their large magnetocrystalline anisotropy, $SmCo_5$ and related compounds have been obvious candidates for developing coercivity through decreasing the grain size. Melt-spun $SmCo_5$ ribbons showed coercivity values lower than that expected for a material with such a large anisotropy field (Takahashi *et al*., 1985). Since the Co-rich part of the Sm–Co phase diagram does not have a deep eutectic, the melt spinning does not lead to an amorphous structure. Most of the recent efforts in the melt-spun $SmCo_5$ were focused on solidification at relatively low speeds. The $SmCo_5$ ribbons melt spun at the wheel speed of $5–6\,m\,s^{-1}$ crystallize directionally with their EMDs preferentially laying in the ribbon plane (Ding, McCormick and Street, 1995; Li *et al*., 2002). Owing to this texture, the performance of the ribbons is comparable with that of the anisotropic sintered $SmCo_5$ magnets with the remanence, coercivity, and maximum energy product values of 0.91 T, $1.296\,MA\,m^{-1}$, and $145.6\,kJ\,m^{-3}$, respectively (Yan, Zhang, Zhang and Shen, 2000).

The $PrCo_5$ compound has a higher theoretical energy product than $SmCo_5$ because of its higher magnetization. Melt-spun Pr–Co alloys show coercivity values of more than $800\,kA\,m^{-1}$ but very poor squareness of the hysteresis loop (Morimoto, Yagi and Takeshita, 1991). Their hard-magnetic properties can be markedly improved by additions of C (Fuerst, Herbst, Murphy and Van Wingerden, 1993) or C and Ti (Branagan, Kramer, Tang and McCallum, 2000). In both cases, the additions were believed to inhibit grain growth: in the first case, by facilitating quenching, whereas in the second case, by forming TiC grain-boundary precipitates. The maximum energy product $(BH)_{max}$ of the melt-spun ribbons still did not exceed $64–72\,kJ\,m^{-3}$. The RCo_5 compounds with R = Y, Ce, Gd, Er (all having high magnetocrystalline anisotropy) were found to be even less suitable for manufacturing melt-spun permanent magnets (Fuerst, Herbst, Murphy and Van Wingerden, 1993). Although, partial Gd substitutions for Sm (Zhang W.Y. *et al*., 2001) and Pr (Meacham and Branagan, 2003) were found to be beneficial for the hard-magnetic properties.

In the Sm–Co alloys with compositions between 1:5 and 2:17, melt spinning generates the metastable '1:7' structure (which can be equally called the *Co-rich 1:5* and *Co-depleted disordered 2:17*). Since the Sm_2Co_{17} (and especially $Sm_2(Co,Fe)_{17}$) has a saturation magnetization substantially higher than that of $SmCo_5$, it seems natural to increase $(BH)_{max}$ of the $SmCo_5$ ribbons by shifting their composition toward Sm_2Co_{17}. Unfortunately, the coercivity of the melt-spun $SmCo_z$ and $Sm(Co,Fe)_z$ alloys rapidly decreases with increasing z from 5 to 8.5 (Chen *et al*., 2003a). This trend might be expected, since the anisotropy field decreases with increasing z (the anisotropy field of Sm_2Co_{17} is about one-fourth of that of $SmCo_5$). However, the major reason for the poor hard-magnetic properties of the melt-spun Sm–Co ribbons appears to be related to a coarse dendritic microstructure of the crystallized alloys (Ding, McCormick and Street, 1995; Yan *et al*., 2002). Since Crabbe, Davies and Buckley (1994) showed that melt spinning of the $Sm(Co_{0.704}Fe_{0.209}Cu_{0.061}Zr_{0.025})_{7.61}$ alloy produces a single-phase microstructure with a grain size of about 30 nm, various additions were tried to refine the microstructure of melt-spun $SmCo_z$ alloys. Carbon in combination with either Zr (Du *et al*., 2003) or Nb (Hsiao, Aich, Lewis and Shield, 2004) produces a fine 1:7 microstructure with a coercivity of $1.12–1.44\,kA\,m^{-1}$. A room-temperature coercivity of $3.08\,MA\,m^{-1}$ was reported for a B-containing melt-spun $Sm(Co,Fe,Cu,Zr,B)_{7.5}$ alloy (Makridis *et al*., 2002). It should be noted that, although the boron-added $Sm_2(Co,Fe,Mn)_{17}$ melt-spun and annealed alloys show improved temperature stability, excessive amount of B may lead to deterioration of the hard-magnetic properties because of the formation of the magnetically soft $Sm_2Fe_{14}B$ phase (Kim and Hadjipanayis, 1998).

3.2.2 Mechanically alloyed and intensively milled R–Co magnets

In contrast to the melt-spinning technique, the high-energy ball milling easily produces an amorphous $SmCo_5$ material without C or B additions. A subsequent crystallization annealing at about 600 °C leads to a uniform nanocrystalline microstructure. After milling together elemental Sm and Co, Wecker, Katter and Schultz (1991) obtained $SmCo_5$ magnets with the coercivity of $2.40\,MA\,m^{-1}$, while Liu,

Dallimore, McCormick and Alonso (1992) (they started from SmF_3, Co and Ca) achieved a coercivity of $5.20\,MA\,m^{-1}$. However, the same microstructure of RCo_5 nanograins can be realized when a single-phase RCo_5 precursor is subjected to the high-energy milling. In this case, the amorphization during milling can be accomplished in a shorter time reducing the risk of alloy oxidation and contamination by the materials of the milling media. By this route, high-performance isotropic nanocrystalline $PrCo_5$ (Chen, Meng-Burany and Hadjipanayis, 1999), YCo_5 (Tang *et al.*, 2000), and $LaCo_5$ (Okumura, Zhang and Hadjipanayis, 2002) magnets with $H_c = 1.28–1.92\,MA\,m^{-1}$ were successfully produced (Figures 18 and 19). A certain excess of R over the nominal 1:5 stoichiometry is required to obtain the maximum H_c. This fact is apparently related to the partial oxidation of the rare earth during the milling (which, of course, must be done in a protective environment, e.g., under argon).

Nanocrystalline Sm_2Co_{17} magnets also can be produced via the mechanical alloying (Wecker, Katter and Schultz, 1991). In this case, the highest reported H_c values are lower than those of $SmCo_5$ (up to $768\,kA\,m^{-1}$ has been reported by Chen, Meng-Burany, Okumura and Hadjipanayis (2000)). This is not surprising, since the nucleation-controlled coercivity of the nanocrystalline magnets is expected to be proportional to the anisotropy field H_A (Sm_2Co_{17} has a lower H_A than $SmCo_5$) reduced by the effective internal demagnetization field $N_{eff}M_s$ (Sm_2Co_{17} has a higher $N_{eff}M_s$ because of the higher M_s). In the amorphous intensively milled $SmCo_z$ ($5 < z < 8.5$) alloys, annealing at 500–650 °C leads to the formation of a metastable 1:7 phase, whose magnetic properties vary with z with values between those of $SmCo_5$ and Sm_2Co_{17}. Though the material is isotropic, the

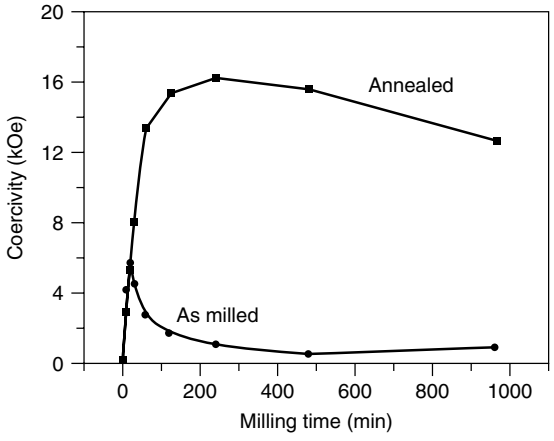

Figure 18. Coercivity of as-milled and annealed, at 800 °C for 1 min, $PrCo_5$ powders as a function of milling time. (Reprinted with permission Chen *et al.*, copyright 1999, American Institute of Physics.)

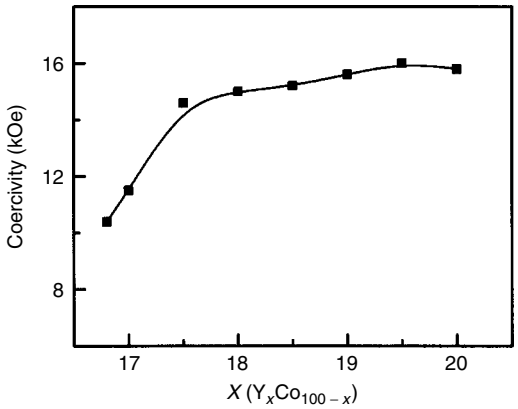

Figure 19. Coercivity of Y_xCo_{100-x} ($x = 16.8–20$) powders as a function of Y content. The powders were milled for 4 h and annealed at 950 °C for 1 min. (Reprinted with permission N. Tang *et al.*, copyright 2000, Elsevier.)

nanocrystalline structure demonstrates an enhanced remanence due to intergranular exchange coupling (Ding, Liu, McCormick and Street, 1993). Annealing at higher temperatures leads to the equilibrium 1:5 and 2:17 phases. This does not immediately lead to deterioration of the hard-magnetic properties, since the average grain size remains small. With further increase of the annealing temperature the grains coarsen and the remanence enhancement disappears. A maximum energy product of $144\,kJ\,m^{-3}$ was reported for the optimally heat-treated $Sm_{12.5}Co_{87.5}$ alloy (Ding, Liu, McCormick and Street, 1993). Similar studies performed with the Pr–Co alloys (Chen, Zhang and Hadjipanayis, 2000) also led to an increase of $(BH)_{max}$ from $72\,kJ\,m^{-3}$ for $PrCo_5$ to $94.4\,kJ\,m^{-3}$ for the alloy with 70% $PrCo_5$ and 30% Pr_2Co_{17} (at the annealing temperature of 800 °C used in that work, only the equilibrium phases could be expected).

Addition of Fe to the Sm–Co alloys leads to the formation of an additional metastable phase, bcc Co–Fe, after intensive milling (Ding, McCormick and Street, 1994). This phase remains in the microstructure after annealing at temperatures below 800 °C, that is, it may coexist with the hard-magnetic phases 1:7, 2:17, 1:5, and 2:7. The exchange-coupled nanocomposites consisting of a mixture of magnetically hard grains and magnetically soft bcc grains demonstrate even higher enhanced remanence than the single-phase alloy with hard nanograins. For mechanically alloyed and annealed $Sm_{13}(Co,Fe)_{87}$ magnets, a $(BH)_{max}$ of $160\,kJ\,m^{-3}$ has been reported (Ding, McCormick and Street, 1994).

Recently, various alloying elements were examined in an attempt to extend the temperature range of the nanocrystalline Sm–Co magnets. It was found, in particular, that the $Sm(Co,Ti,Zr,B)_7$ magnets show an increased thermal stability of the 1:7 phase (Rhen, Venkatesan, Harris and Coey, 2003).

3.2.3 Anisotropic nanocrystalline $PrCo_5$ magnets

Despite their high coercivities, the nanocrystalline magnets produced from amorphous precursors do not show high remanence and $(BH)_{max}$ values, because the EMDs of the individual crystallites are orientated randomly. In the case of Nd–Fe–B alloys, the EMDs may be almost perfectly aligned by a hot plastic deformation. Fuerst and Brewer (1993) observed a similar effect when subjecting to die-upsetting hot-compacted Pr–Co and Pr–Co–C nanocrystalline ribbons with the $PrCo_5$ as the major phase. Although imperfect, the induced texture markedly increased the remanence. For unknown reasons, the Sm–Co alloys with much higher H_c values do not develop texture during die upsetting. The optimum combination of the remanence and coercivity has been achieved for the Pr–Sm–Co–C alloys with the $(BH)_{max}$ up to 152 kJ m^{-3} (Fuerst and Brewer, 1994). Recently, Gabay, Zhang and Hadjipanayis (2005) showed that, because the intensive milling route provides better $PrCo_5$ nanocomposite magnets than melt spinning, the anisotropic die-upset magnets can be produced from intensively milled $PrCo_5$ powder using less (if any) additions. Figure 20 shows the properties of intensively milled $Pr_{0.9}Sm_{0.1}(Co_{0.98}Cu_{0.02})_5$ alloy after hot compaction and after hot deformation. Texture induced by the 75% deformation increases the remanence from 0.64 to 0.89 T and $(BH)_{max}$ from 89.6 to 133.6 kJ m^{-3}, while the coercivity decreases from 1.28 to 0.84 MA m^{-1}. The die-upset magnet consists of 1:5 and 2:17 grains with a size 20–200 nm (Figure 21). The smaller grains are more or less equiaxed, but many of the larger grains are elongated similar to those in the die-upset Nd–Fe–B magnets.

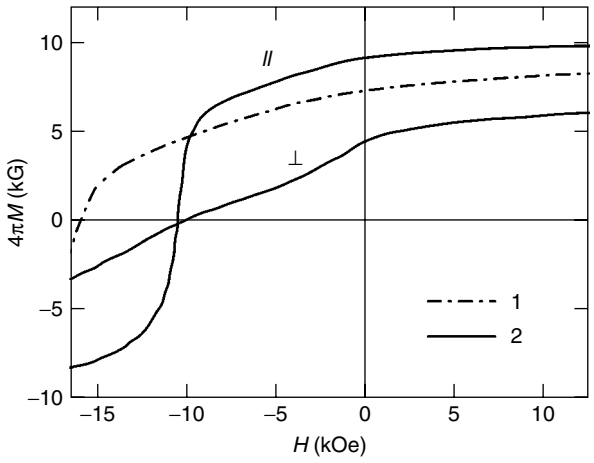

Figure 20. Demagnetization curves of hot-pressed (1) and die-upset (2) $Pr_{0.9}Sm_{0.1}(Co_{0.98}Cu_{0.02})_5$ magnets. Curves for the die-upset magnet were measured parallel and perpendicular to the pressure direction. (Reprinted with permission A.M. Gabay *et al*., copyright 2005, Elsevier.)

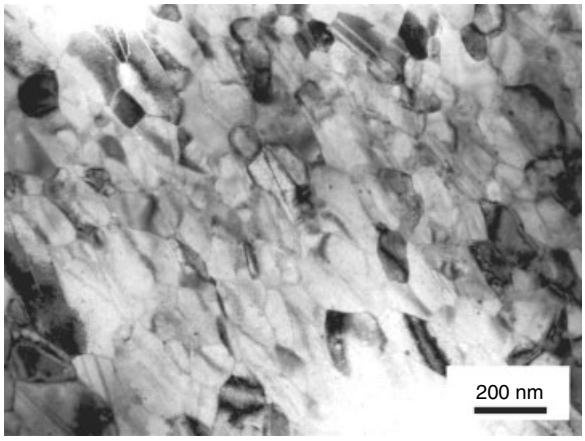

Figure 21. TEM image of die-upset $Pr_{0.9}Sm_{0.1}(Co_{0.98}Cu_{0.02})_5$ magnet. (Reprinted with permission A.M. Gabay *et al*., copyright 2005, Elsevier.)

3.2.4 Nanocrystalline $Sm(Co,Fe,B)_5$ magnets

Boron can be used not only as an element that promotes amorphization in rapidly solidified Sm–Co alloys but also to promote the formation of Sm–Co boride structures. The $SmCo_4B$ compound, in which the B atoms replacing Co in the parent $SmCo_5$ structure are ordered along the *c* axis, has a magnetocrystalline anisotropy even higher than $SmCo_5$. This makes $SmCo_4B$ a promising candidate for nanocrystalline hard magnet. Unfortunately, the Curie temperature of $SmCo_4B$ is only 197 °C. It can be increased by additional Fe substitution for Co. Gong and Hadjipanayis (1996) achieved the coercivity of 1.28 MA m^{-1} for $SmCo_2Fe_2B$ via intensive milling and subsequent annealing. However, their melt-spinning experiments yielded H_c values lesser than 400 kA m^{-1}. On the other hand, Saito *et al*. have found that melt spinning can stabilize the disordered $SmCo_{5-x}B_x$ structure with $x < 1$ and with H_c larger than $SmCo_5$ (Saito, Takahashi and Wakiyama, 1987). There is, therefore, a possibility of optimum combination of the hard-magnetic properties in metastable $Sm(Co,Fe)_{5-x}B_x$ nanocrystalline alloys, though the realization of high $(BH)_{max}$ values is not likely to happen in these materials.

4 SAMARIUM–IRON NANOCRYSTALLINE MAGNETS

4.1 Nanocrystalline $Sm(Fe,M)_{12}$ alloys

Out of the numerous $R(Fe,M)_{12}$ compounds with the tetragonal $ThMn_{12}$ structure, only those with R = Sm and M = Ti, V, Mo, and Si possess a room-temperature magnetocrystalline anisotropy which is uniaxial and large enough

for the development of permanent magnet materials. The few studies made so far have been reported on Mo- and Si-containing alloys (Schultz and Wecker, 1988; Ding and Rosenberg, 1990), whereas the majority studies were focused on the alloys with Ti and V. Both melt spinning and high-energy milling were employed to manufacture nanocrystalline $Sm(Fe,Ti)_{12}$ and $Sm(Fe,V)_{12}$ magnets. The $SmFe_{12-x}M_x$ magnets with the desired 1:12 structure can be obtained for $x \geq 1$, if M = Ti and for $x \geq 1.5$, if M = V. This assures a higher saturation magnetization and theoretical energy product for the alloys with Ti. However, the $SmFe_{11}Ti$ compound is metastable below 1000 °C, and, therefore, relatively high annealing temperatures are required to obtain this phase in the amorphous precursors. This, in turn, results in excessive grain growth and evaporation loss of Sm (this element has a high vapor pressure). At room temperature, an H_c of 448 kA m^{-1} has been obtained for melt-spun $Sm_{1.04}Fe_{10.79}Ti_{1.17}$ (Wang *et al.*, 1990) and 624 kA m^{-1} for melt-spun $Sm_{0.95}Fe_{10}V_2$ (Pinkerton and Van Wingerden, 1989); even a higher coercivity, 936 kA m^{-1}, was reported for the mechanically alloyed $Sm(Fe,V)_{12}$ alloy (Schultz, Schnitzke and Wecker, 1990). For melt-spun ribbons, the highest coercivity values appear to be reached in alloys containing both Ti and V, with values of 816 kA m^{-1} for $Sm_{1.04}Fe_{9.88}Ti_{1.04}V_{1.04}$ (Wang *et al.*, 1990) and 960 kA m^{-1} in $SmFe_{10}TiV$ ribbons annealed in Sm atmosphere (Okada, Kojima, Yamagishi and Homma, 1990). Such an annealing technique aimed to prevent the evaporation losses of Sm is, of course, too expensive for a commercial application. In fact, despite a number of advantages (the low rare-earth content, good corrosion resistance, and reasonably high coercivity), the nanocrystalline $Sm(Fe,M)_{12}$ magnets have never been commercialized, since they have a lower remanence than the isotropic Nd–Fe–B magnets.

4.2 Nanocrystalline $SmFe_3$ and $Sm_5(Fe,M)_{17}$ alloys

The hexagonal $SmFe_3$ compound (with $PuNi_3$ structure) has a room-temperature anisotropy field of 11.20 MA m^{-1}. Wecker, Katter, Schnitzke and Schultz (1991) prepared the nanocrystalline $SmFe_3$ alloys by mechanical alloying followed by annealing and obtained a room-temperature coercivity of 840 kA m^{-1}. Further improvement has been achieved via partial Zr substitution for Sm: the melt-spun Sm–Zr–Fe with the 1:3 structure showed H_c of 1.024 MA m^{-1} (Wecker, Katter, Schnitzke and Schultz, 1991), and up to 1.184 MA m^{-1} in mechanically alloyed samples (Schultz, Schnitzke, Wecker and Katter, 1991). Unfortunately, the saturation magnetization of the $(Sm,Zr)Fe_3$ alloy does not exceed 1.05 T and the typical remanence value of the isotropic nanocrystalline 1:3 magnets is only 0.4–0.5 T.

Another Sm–Fe compound with exceptional magnetic hardness, isostructural to the hexagonal Nd_5Fe_{17}, was first discovered in sputtered Sm–Fe–Ti films (Kamprath, Liu, Hegde and Cadieu, 1988). Though it can be obtained in the binary Sm–Fe alloys (Cadieu *et al.*, 1991), partial replacement of Fe by Ti and/or V greatly favors the formation of this phase (Yang, Wang and Sun, 1997). The ternaries around $Sm_{20}Fe_{70}Ti_{10}$ (Schnitzke, Schultz, Wecker and Katter, 1990a) are the most studied alloys with the 5:17 structure. Melt-spun and mechanically alloyed nanocrystalline magnets show room-temperature H_c values up to 4.64 MA m^{-1} (Katter, Wecker, Schultz and Grössinger, 1990) and 6 MA m^{-1} (Yang *et al.*, 1994), respectively. However, similar to $SmFe_3$, the $Sm_5(Fe,Ti)_{17}$ magnets did not find practical applications because of their low saturation magnetization.

5 NANOCRYSTALLINE AND NANOCOMPOSITE RARE-EARTH–IRON NITRIDES AND CARBIDES

5.1 Magnets based on Sm_2Fe_{17} nitrides

Interstitial modification of the R_2Fe_{17} compounds dramatically changes their magnetic properties (Coey and Sun, 1990). Owing to a volume expansion of the atomic lattice caused by the absorbed N, C, or H atoms, the Curie temperature and saturation magnetization increase significantly. In Sm_2Fe_{17}, the interstitial N (or C) also induces a strong uniaxial magnetocrystalline anisotropy. The saturation magnetization of the resulting Sm_2Fe_{17} nitride is almost as high as that of $Nd_2Fe_{14}B$, whereas the anisotropy field and T_c are substantially higher (see Table 1). These excellent magnetic properties were immediately realized in high-performance isotropic magnets, both in the nanocrystalline and nanocomposite form.

A room-temperature coercivity of up to 2.40 MA m^{-1} has been obtained for mechanically alloyed Sm_2Fe_{17} powders subjected to crystallization, annealing, and subsequent nitriding at 400–550 °C in N_2 gas (Schnitzke, Schultz, Wecker and Katter, 1990b). The room-temperature remanence and $(BH)_{max}$ were equivalent to those of similarly prepared Nd–Fe–B, while their performance at the elevated temperatures was better. By lowering the Sm content from the stoichiometric 10.5–7 at% and using the same mechanical alloying–annealing–nitriding technique O'Donnell, Kuhrt and Coey (1994) obtained a nanocomposite magnet consisting of 20-nm-sized $Sm_2Fe_{17}N_3$ and α-Fe grains. Owing to

intergranular exchange interaction an enhanced remanence of 1.2 T (and a coercivity of 320 kA m^{-1}) had been achieved.

Pinkerton and Fuerst (1992) obtained H_c of 1.84 MA m^{-1} for melt-spun Sm–Fe ribbons annealed in vacuum and then in N_2 gas. To facilitate the uptake of nitrogen, the ribbons were ground down to less than 25 µm. Katter, Wecker and Schultz (1991) have pointed out that the melt-spun Sm–Fe alloys may have two crystalline modifications: the rhombohedral 2:17 structure formed at the lower quenching speeds and higher Sm concentrations and the disordered hexagonal 1:7 structure formed at higher speeds and lower Sm concentrations. The 1:7 structure can also be stabilized by Nb or Zr additions (Moukarika *et al*., 1996). The melt-spun nanocomposites consisting of fine 1:7 Sm–Zr–Fe–N grains and α-Fe grains showed a remanence of 0.99 T, a coercivity of 656 kA m^{-1}, and $(BH)_{max} = 140$ kJ m^{-3} (Hidaka, Yamamoto, Nakamura and Fukuno, 1998). Even better properties were obtained for a single-phase 1:7 structure: the melt-spun nanocrystalline $(Sm_{0.7}Zr_{0.3})(Fe_{0.8}Co_{0.2})_9B_{0.1}N_x$ alloy reportedly showed a remanence of 1.07 T, a coercivity of 784 kA m^{-1}, and $(BH)_{max} = 180.8$ kJ m^{-3} (Sakurada *et al*., 2000).

The coercivity of nitrogenated melt-spun Sm_2Fe_{17} alloys can be further improved by zinc coating (Fukunaga, Aikawa, Nagaoka and Kanai, 1996).

5.2 Magnets based on Sm_2Fe_{17} carbides

Though the effect of interstitial carbon on Sm_2Fe_{17} is similar to that of the nitrogen atoms, the number of the C atoms per formula unit after a solid–gas carburization usually does not exceed 2. This means a lesser volume expansion of the 2:17 lattice and lesser gain in the magnetic properties. Nevertheless, a coercivity of 1.856 MA m^{-1} was reported for $Sm_2Fe_{17}C_2$ obtained by annealing mechanically-alloyed Sm_2Fe_{17} powders in acetylene gas (Kuhrt *et al*., 1992). By mechanically alloying Sm, Fe, and graphite powders Geng *et al*. (2001) prepared nanocomposite magnets consisting of the Sm–Fe carbide with the disordered 1:7 structure and α-Fe. Similar to the 2:17 nitrides, these carbides are structurally unstable above 700 °C.

A simpler way of manufacturing the 2:17 carbides was found after discovering that, if Fe in Sm_2Fe_{17} was partially replaced by Ga, Si, (Shen *et al*., 1994), Al (Zhang, Cheng and Shen, 1996), Cr (Chen, Ni, and Hadjipanayis, 1998), V, Ti, Nb, and Zr (Daniel *et al*., 1998) a sufficient amount of carbon (more than 1.5 atoms per the 2:17 formula) can be introduced directly during melting. The melt-spun and annealed $Sm_2Fe_{14}Ga_3C_{\leq 2.5}$ nanocrystalline ribbons show H_c values of 1.04–1.20 MA m^{-1} (Kong *et al*., 1994; Hadjipanayis *et al*., 1995). A similar H_c value of 960 kA m^{-1} had been reported for nanocrystalline $Sm_2Fe_{15}Ga_2C_2$ prepared via mechanical milling (Cao *et al*., 1996). A small excess of Sm over the 2:17 stoichiometry increases the coercivity up to 1.76 MA m^{-1} (van Lier, Seeger and Kronmüller, 1997). Additional doping with Cu, Mo, Nb, and Zr can further improve the hard-magnetic properties of the $Sm_2(Fe,Si)_{17}C_x$, $Sm_2(Fe,Al)_{17}C_x$, and $Sm_2(Fe,Ga)_{17}C_x$ ribbons (Zhang, Zhang, Shen and Zhang, 1998; Tang *et al*., 1998a,b; Zhang *et al*., 2000). van Lier *et al*. (1998) succeeded in preparing an isotropic hot-deformed magnet with the energy product of 60.8 kJ m^{-3} from melt-spun $Sm_2(Fe,Ga)_{17}C_2$ ribbons.

5.3 Magnets based on $Nd(Fe,M)_{12}$ nitrides and carbides

Interstitial modification of the $Nd(Fe,M)_{12}$ compounds changes their intrinsic magnetic properties in a way similar to that of Sm_2Fe_{17} (Yang *et al*., 1991; Wang and Hadjipanayis, 1991).

However, even the best properties of the 1:12 nitrides (those of $NdFe_{11}TiN_x$) are inferior to the properties of $Sm_2Fe_{17}N_{2.3}$ (see Table 1). Correspondingly, nanocrystalline magnets made out of these materials show only modest performance. By nitriding melt-spun and annealed $Nd(Fe,Mo)_{12}$ ribbons in N_2 gas, room-temperature coercivities in the range of 480–640 kA m^{-1} can be obtained (Tang, Singleton and Hadjipanayis, 1993; Pinkerton, Fuerst and Herbst, 1994). The melt-spun and nitrided $Nd(Fe,M)_{12}N_x$ with M = Ti, V, W, as well as the carbides obtained by treating the $Nd(Fe,Mo)_{12}$ in methane showed worse properties (Endoh, Nakamura and Mikami, 1992; Tang, Singleton and Hadjipanayis, 1993). Nitriding mechanically alloyed $Nd(Fe,M)_{12}$ powders leads to higher H_c values (Endoh, Nakamura and Mikami, 1992). While the coercivity of $Nd(Fe,Mo)_{12}N_x$ powder was about the same–up to 640 kA m^{-1} (Gong and Hadjipanayis, 1992), higher H_c values, 720–880 kA m^{-1} were reported for $Nd(Fe,V)_{12}N_x$ (Yang, Mao and Altounian, 1996; Tang *et al*., 1998c).

REFERENCES

Aharoni, A. (1986). Perfect and imperfect particles. *IEEE Transactions on Magnetics*, **22**, 478–483.

Bauer, J., Seeger, M. and Kronmuller, H. (1995). Magnetic properties and microstructural analysis of rapidly quenched FeNdB-GaNb permanent magnets. *Journal of Magnetism and Magnetic Materials*, **139**, 323–334.

Bauer, J., Seeger, M., Zern, A. and Kronmuller, H. (1996). Nanocrystalline FeNdB permanent magnets with enhanced remanence. *Journal of Applied Physics*, **80**, 1667–1673.

Bollero, A., Gutfleisch, O., Muller, K.H., *et al*. (2002). High-performance nanocrystalline PrFeB-based magnets produced by intensive milling. *Journal of Applied Physics*, **91**, 8159–8161.

Branagan, D.J., Hyde, T.A., Sellers, C.H. and McCallum, R.W. (1996). Developing rare earth permanent magnet alloys for gas atomization. *Journal of Physics D: Applied Physics*, **29**, 2376–2385.

Branagan, D.J., Kramer, M.J., Tang, Y. and McCallum, R.W. (2000). Achieving optimum loop shapes in quaternary Pr-Co alloys. *Journal of Applied Physics*, **87**, 6737–6739.

Branagan, D.J. and McCallum, R.W. (1995). Altering the cooling rate dependence of phase formation during rapid solidification in the $Nd_2Fe_{14}B$ system. *Journal of Magnetism and Magnetic Materials*, **146**, 89–102.

Brown, W.F. Jr. (1945). Virtues and weaknesses of the domain concept. *Reviews of Modern Physics*, **17**(1), 15–19.

Brown, D., Ma, B.M. and Chen, Z.M. (2002). Developments in the processing and properties of NdFeB-type permanent magnets. *Journal of Magnetism and Magnetic Materials*, **248**, 323–328.

Buschow, K.H.J. (1977). Intermetallic compounds of rare earth and 3d transition metals. *Reports on Progress in Physics*, **54**, 1123–1213.

Buschow, K.H.J. (1991). New developments in hard magnetic materials. *Reports on Progress in Physics*, **40**, 1179–1256.

Buschow, K.H.J. and Van der Goot, A.S. (1968). Intermetallic compounds in the system Sm-Co. *Journal of Less-Common Metals*, **14**, 323–328.

Buschow, K.H.J., Demooij, D.B. and Coehoorn, R. (1988). Metastable ferromagnetic materials for permanent magnets. *Journal of Less-Common Metals*, **145**(1–2), 601–611.

Buschow, K.H.J. and Van der Goot, A.S. (1971). Composition and crystal structure of hexagonal Cu-rich rare earth-copper compounds. *Acta Crystallographica*, **B27**, 1085–1088.

Cadieu, F.J., Hegde, H., Rani, R., *et al*. (1991). Cell-volume expansion in $Sm_5(Fe,T)_{17}$, T = Ti, V, magnetic phases. *Materials Letters*, **11**, 284–285.

Callen, E., Liu, Y.J. and Cullen, J.R. (1977). Initial magnetization, remanence, and coercivity of the random anisotropy amorphous ferromagnet. *Physical Review B*, **16**, 263–270.

Cao, L., Handstein, A., Grünberger, W., *et al*. (1996). Highly coercive $Sm_2Fe_{15}Ga_2C_2$ magnets made by intense ball milling. *Applied Physics Letters*, **68**, 129–131.

Chaban, N.F., Kuzma, Y.B., Bilonizhko, N.S., *et al*. (1979). Ternary (Nd,Sm,Gd)-Fe-B systems. *Doklady Akademii Nauk SSSR Series A, Fiziko-Matematichni Ta Technichni Nauki*, **10**, 873.

Chang, W.C., Wang, S.H., Chang, S.J. and Chen, Q. (2000). Magnetic and microstructure studies of boron-enriched $(Nd_{0.95}La_{0.05})_{11}Fe_{76.5-x}Co_xTi_2B_{10.5}$(x = 0–15) melt-spun ribbons. *IEEE Transactions on Magnetics*, **36**, 3312–3314.

Chang, W.C., Wang, S.H., Chang, S.J., *et al*. (1999). The effects of refractory metals on the magnetic properties of alpha-$Fe/R_2Fe_{14}B$-type nanocomposites∼. *IEEE Transactions on Magnetics*, **35**, 3265–3267.

Chang, W.C., Wen, J.F., Chang, H.W., *et al*. (2002). Phase evolution and magnetic properties of boron enriched $(Nd_{0.7}Pr_{0.25}La_{0.05})_{(x)}Fe_{bal}.Co_{10}Ti_2B_y$ (x = 4.5–10.7; y = 10.9–18.6) nanocomposites. *Journal of Magnetism and Magnetic Materials*, **239**, 433–436.

Chen, Z., Meng-Burany, X. and Hadjipanayis, G.C. (1999). High coercivity in nanostructured $PrCo_5$-based powders produced by mechanical milling and subsequent annealing. *Applied Physics Letters*, **75**, 3165–3167.

Chen, Z.M., Meng-Burany, X., Okumura, H. and Hadjipanayis, G.C. (2000). Magnetic properties and microstructure of mechanically milled $Sm_2(Co,M)_{17}$-based powders with M = Zr, Hf, Nb, V, Ti, Cr, Cu and Fe. *Journal of Applied Physics*, **87**, 3409–3414.

Chen, Z.M., Ni, C.Y. and Hadjipanayis, G.C. (1998). Microstructure and magnetic properties of melt-spun $Sm_2Fe_{15-x}Co_xCr_2C_2$ ($x = 0$–4) nanocomposite magnets. *Journal of Magnetism and Magnetic Materials*, **186**, 41–48.

Chen, Z., Okumura, H., Hadjipanayis, G.C. and Chen, Q. (2001). Microstructure refinement and magnetic property enhancement of nanocomposite $Pr_2Fe_{14}B/\alpha$-Fe magnets by small substitution of M fro Fe (M = Cr, Nb, Ti and Zr). *Journal of Alloys and Compounds*, **327**, 201–205.

Chen, Z., Zhang, Y. and Hadjipanayis, G.C. (2000). Nanocomposite $PrCo_5/Pr_2Co_{17}$ magnets with enhanced maximum energy product. *Journal of Magnetism and Magnetic Materials*, **219**, 178–182.

Chen, S.K., Huang, T.A., Duh, C.S., *et al*. (1995). Structure and magnetic properties of low-neodymium Nd-Fe-B powders by mechanical alloying. *IEEE Transactions on Magnetics*, **31**, 3644–3646.

Chen, Z.M., Zhang, Y., Hadjipanayis, G.C., *et al*. (1999). Effect of wheel speed and subsequent annealing on the microstructure and magnetic properties of nanocomposite $Pr_2Fe_{14}B/\alpha$-Fe magnets. *Journal of Magnetism and Magnetic Materials*, **206**, 8–16.

Chen, C.H., Kodat, S., Walmer, M.H., *et al*. (2003a). Effects of grain size and morphology on the coercivity of $Sm_2(Co_{1-x}Fe_x)_{17}$ based powders and spin cast ribbons. *Journal of Applied Physics*, **93**, 7966–7968.

Chen, Z.M., Smith, B.R., Ma, B.M., *et al*. (2003b). Formation of metastable $Pr_2Fe_{23}B_3$ phase and its effect on magnetic properties in rapidly quenched $Pr_9Fe_{91-x}B_x$ nanocomposites. *IEEE Transactions on Magnetics*, **39**, 2938–2940.

Chen, C.H., Walmer, M.S., Walmer, M.H., *et al*. (1998). $Sm_2(Co,Fe,Cu,Zr)_{17}$ magnets for use at temperature $\geq 400\,^{\circ}C$. *Journal of Applied Physics*, **83**, 6706–6708.

Chin, T.S., Huang, S.H. and Yau, J.M. (1992). Preferred crystalline orientation of melt-spun Nd-Fe-M-B flakes (M = Ti/Zr/Hf/V/Nb/Ta). *IEEE Transactions on Magnetics*, **28**, 2136–2138.

Chin, T.S., Huang, S.H. and Yau, J.M. (1993). As-melt-spun anisotropy of Nd-Fe-B-M flakes (M = Cr or Mo/W/Mn/Co/Ni). *IEEE Transactions on Magnetics*, **29**, 2791–2793.

Clark, A.E. (1973). High-field magnetization and coercivity of amorphous Rare-Earth–Fe_2 alloys. *Applied Physics Letters*, **23**, 642–644.

Clemente, G.B., Keem, J.E. and Bradley, J.P. (1988). The microstructural and compositional influence upon HIREM behavior in $Nd_2Fe_{14}B$. *Journal of Applied Physics*, **64**, 5299–5301.

Coehoorn, R., DeMooij, D.B. and DeWaard, C. (1989). Melt-spun permanent magnet materials containing Fe_3B as the main phase. *Journal of Magnetism and Magnetic Materials*, **80**, 101–104.

Coehoorn, R. and Duchateau, J. (1988). Preferrential crystallite orientation in melt-spun Nd-Fe-B permanent magnet materials. *Materials Science and Engineering*, **99**, 131–135.

Coehoorn, R., Duchateau, J.P.W.B. and Demissen, C.J.M. (1989). Permanent magnet materials based on $Nd_2Fe_{14}C$ prepared by melt-spinning. *Journal of Applied Physics*, **65**, 704–709.

Coey, J.M.D. and Sun, H. (1990). Improved magnetic properties by treatment of iron-based rare earth intermetallic compounds in anmonia. *Journal of Magnetism and Magnetic Materials*, **87**, L251–L254.

Crabbe, M.W., Davies, H.A. and Buckley, R.A. (1994). Remanence enhancement in nanostructured melt spun Sm $(Fe_{0.209}Cu_{0.061}Zr_{0.025}Co_{0.704})_{7.61}$. *IEEE Transactions on Magnetics*, **30**, 696–698.

Croat, J.J., Herbst, J.F., Lee, R.W. and Pinkerton, F.E.J. (1984). Pr-Fe and Nd-Fe- based materials–a new class of high-performance permanent magnets. *Journal of Applied Physics*, **55**, 2078–2082.

Cullity, B.D. (1972). *Introduction to Magnetic Materials*, Addison-Wesley: Reading.

Dadon, D., Gefen, Y. and Daniel, M.P. (1987). The texture of melt-spun $Fe_{76}Nd_{16}B_8$ ribbons. *IEEE Transactions on Magnetics*, **23**, 3605–3606.

Daniil, M., Okumura, H., Hadjipanayis, G.C. and Sellmyer, D.J. (2003). Effect of carbon substitution on the magnetic properties of Nd-Fe-(B,C) nanocomposite magnets. *Journal of Magnetism and Magnetic Materials*, **267**, 316–324.

Daniel, M., Digas, M., Moukarika, A., *et al*. (1998). Effects of substitutions M on the formation, structure and magnetic properties of $Sm_2Fe_{15}M_2C_2$ (M = V, Cr, Ti, Nb, Zr, Mn and Mo) compounds. *Journal of Magnetism and Magnetic Materials*, **177–181**, 1109–1110.

Daniil, M., Zhang, Y., Okumura, H., *et al*. (2002). Effect of grain growth inhibitors on the hysteresis properties of $Nd_{10}Fe_{82}C_6B_2$ melt-spun alloys. *IEEE Transactions on Magnetics*, **38**, 2973–2975.

Davies, H.A., Manaf, A., Leonovicz, M., *et al*. (1992). *Journal of Magnetism and Magnetic Materials*, **115**, 211–216.

DeMooij, D.B. and Buschow, K.H.J. (1988). Formation and magnetic properties of the compound $R_2Fe_{14}C$. *Journal of the Less-Common Metals*, **142**, 349–357.

Derkaoui, S., Valignat, N. and Allibert, C.H. (1996). Phase equilibria at 1150 °C in the Co-rich alloys Sm-Co-Zr and structure of the 1:7 phase. *Journal of Alloys and Compounds*, **232**, 296–301.

Ding, J., Liu, Y., McCormick, P.G. and Street, R. (1993). Remanence enhancement in isotropic Sm-Co powders. *Journal of Magnetism and Magnetic Materials*, **123**, L239–L242.

Ding, J., McCormick, P.G. and Street, R. (1994). A study of $Sm(Co_{1-x}Fe_x)_{87}$ prepared by mechanical alloying. *Journal of Magnetism and Magnetic Materials*, **135**, 200–204.

Ding, J., McCormick, P.G. and Street, R. (1995). A study of melt-spun $SmCo_5$ ribbons. *Journal of Alloys and Compounds*, **228**, 102–104.

Ding, J. and Rosenberg, M. (1990). Magnetic properties of melt spun and crystallized $SmFe_{10}M_2$. *Journal of Magnetism and Magnetic Materials*, **83**, 257–258.

Du, X.B., Zhang, H.W., Rong, C.B., *et al*. (2003). Magnetic properties of melt-spun $Sm(Co_{0.9}Fe_{0.1})_{6.8}Zr_{0.2}C_x$ ribbons with $TbCu_7$ structure. *Journal of Physics D: Applied Physics*, **36**, 2432–2434.

Durst, K.D. and Kronmuller, H. (1987). The coercive field of sintered melt-spun NdFeB magnets. *Journal of Magnetism and Magnetic Materials*, **68**, 63–75.

Endoh, M., Nakamura, K. and Mikami, H. (1992). $Nd(Fe,Mo)_{12}N_x$ compounds and magnets. *IEEE Transactions on Magnetics*, **28**, 2560–2562.

Feutrill, E.H., McCormick, P.G. and Street, R. (1994). Simulation of magnetization reversal in 2-phase exchange-coupled nanocrystalline materials. *Journal of Applied Physics*, **75**, 5701–5703.

Fidler, J., Skalicky, P. and Rothwarf, F. (1983). High resolution electron microscope study of $Sm(Co,Fe,Cu,Zr)_{7.5}$ magnets. *IEEE Transactions on Magnetics*, **19**, 2041–2043.

Fuerst, D.D. and Brewer, E.G. (1993). Die-upset $PrCo_5$-type magnets from melt-spun ribbons. *Journal of Applied Physics*, **74**, 6907–6911.

Fuerst, D.D. and Brewer, E.G. (1994). Die-upset $PrCo_5$-type magnets: enhanced coercivities. *Journal of Applied Physics*, **75**, 6637–6639.

Fuerst, C.D., Herbst, J.F., Murphy, C.B. and Van Wingerden, D.J. (1993). Melt-spun $PrCo_5$ and related magnet materials: coercivity enhancement by carbon addition. *Journal of Applied Physics*, **74**, 4651–4659.

Fukunaga, H., Aikawa, T., Nagaoka, S. and Kanai, Y. (1996). Improvement in hard magnetic properties of rapidly quenched Sm-Fe-N flakes by Zn-coating. *Journal of Magnetism and Magnetic Materials*, **157/158**, 105–106.

Fukunaga, H. and Inoue, H. (1992). Efect of intergrain exchange interaction on magnetic properties in isotropic Nd-Fe-B magnets. *Japanese Journal of Applied Physics Part 1*, **31**, 1347–1352.

Fullerton, E., Jang, J.S., Grimsditch, M., *et al*. (1998). Exchange-spring behavior in epitaxial hard/soft magnetic bilayers. *Physical Review B*, **58**, 12193–12200.

Gabay, A.M., Tang, W., Zhang, Y. and Hadjipanayis, G.C. (2001). Anomalous temperature dependence of coercivity and reversal mechanism in bulk-hardened rare earth-cobalt magnets. *Applied Physics Letters*, **78**, 1595–1597.

Gabay, A.M., Zhang, Y. and Hadjipanayis, G.C. (2000). Pr-Zr-Co precipitation-hardened magnet. *Applied Physics Letters*, **76**, 3786–3788.

Gabay, A.M., Zhang, Y. and Hadjipanayis, G.C. (2001). Bulk-hardened magnets based on Y_2Co_{17}. *Journal of Applied Physics*, **90**, 882–890.

Gabay, A.M., Zhang, Y. and Hadjipanayis, G.C. (2004). Die-upset hybrid Pr-Fe-B nanocomposite magnets. *Applied Physics Letters*, **85**, 446–448.

Gabay, A.M., Zhang, Y. and Hadjipanayis, G.C. (2005). Hot-pressed and die-upset Pr-Co magnets produced from mechanically activated alloys. *Journal of Magnetism and Magnetic Materials*, **294**(3), 287–293.

Gabay, A.M., Popov, A.G., Gaviko, V.S., *et al*. (1996). Investigation of phase composition and remanence enhancement in rapidly quenched $Nd_9(Fe,Co)_{85}B_6$ alloys. *Journal of Alloys and Compounds*, **237**, 101–107.

Gao, Y., Zhu, J., Yang, C. and Park, E. (1998). Thermomagnetic behaviors of $Nd_2Fe_{14}B/Fe_3B$ based nanocomposite magnets. *Journal of Magnetism and Magnetic Materials*, **186**, 97–103.

Gao, Y.Y., Zhu, J.J., Weng, Y.Y., *et al*. (1999). The enhanced exchange coupled interaction in nanocrystalline $Nd_2Fe_{14}B/Fe_3B$+Fe alloys with improved microstructure. *Journal of Magnetism and Magnetic Materials*, **191**, 146–152.

Geng, D.Y., Zhang, Z.D., Cui, B.Z., *et al*. (2001). Nano-composite $SmFe_7C_x/\alpha$-Fe permanent magnet. *Journal of Magnetism and Magnetic Materials*, **224**, 33–38.

Givord, D., Nozieres, J.P., Sanchez-Lazamares, J.L. and Leccabue, F. (1992). Magnetization and anisotropy in the hard ferromagnetic phase observed in Nd100-xFex (x > 25) as-cast alloys. *Journal of Magnetism and Magnetic Materials*, **111**, 164–170.

Givord, D. and Rossignol, M.F. (1996). Coercivity. In *Rare Earth Iron Permanent Magnets*, Coey, J.M.D. (Ed.), Oxford University Press, Inc.: Oxford, pp. 218–285.

Goll, D. (2002). Micromagnetism and microstructure–tailoring of high-performance permanent magnets. *Zeitschrift für Metallkunde*, **93**, 1009–1018.

Goll, D., Kleinschroth, I., Sigle, W. and Kronmuller, H. (2000). Melt-spun precipitation-hardened $Sm_2(Co, Cu, Fe, Zr)_{17}$ magnets with abnormal temperature dependence of coercivity. *Applied Physics Letters*, **76**, 1054–1056.

Goll, D., Kronmüller, H. and Stadelmaier, H.H. (2004). Micromagnetism and the microstructure of high-temperature permanent magnets. *Journal of Applied Physics*, **96**, 6534–6545.

Goll, D., Seeger, M. and Kronmuller, H. (1998). Magnetic and microstructural properties of nanocrystalline exchange coupled PrFeB permanent magnets. *Journal of Magnetism and Magnetic Materials*, **185**, 49–60.

Gong, W. and Hadjipanayis, G.C. (1992). Nitrogenated 1:12 compounds prepared by mechanical alloying. *IEEE Transactions on Magnetics*, **28**, 2563–2565.

Gong, W. and Hadjipanayis, G.C. (1996). Nanocrystalline and nanocomposite $SmCo_2Fe_2B$ magnets. *IEEE Transactions on Magnetics*, **32**, 4392–4394.

Gong, W., Hadjipanayis, G.C. and Krause, R.F. (1994). Mechanically alloyed nanocomposite magnets. *Journal of Applied Physics*, **75**, 6649–6651.

Grieb, B., Henig, E.Th., Schneider, G. and Petzow, G. (1989). Phase relations in the systems Fe-Dy-B and Fe-Tb-B. *Zeitschrift für Metallkunde*, **80**, 95–100.

Grönefeld, M. and Kronmüller, H. (1990). Initial magnetization curve and hardening mechanism in rapidly quenched Nd-Fe-B magnets. *Journal of Magnetism and Magnetic Materials*, **88**, L267–L274.

Grünberger, W., Hinz, D.D., Kichner, A., *et al*. (1997). Hot deformation in nanocrystalline Nd-Fe-B alloys. *Journal of Alloys and Compounds*, **257**, 293–301.

Gu, B.X., Shen, G.B. and Zhai, H.R. (1990). Magnetic properties and crystallization of amorphous $Nd_{14}Fe_{81}B_5$ alloys. *Physica Status Solidi*, **117**, 283–289.

Gu, B.X., Shen, G.B. and Zhai, H.R. (1994). A metastable ternary Nd-Fe-B compound. *Journal of Applied Physics*, **75**, 6955–6957.

Gu, B.X., Zhai, H.R., Shen, G.B., *et al*. (1989). Magnetic properties if heat treated $Nd_3Fe_{81}B_{16}$ alloys. *Chinese Physics Letters*, **6**, 221–224.

Hadjipanayis, G.C. (1999). Nanophase hard magnets. *Journal of Magnetism and Magnetic Materials*, **200**(1–3), 373–391.

Hadjipanayis, G.C., Dickerson, R.C. and Lawless, K.R. (1986). The microstructure and magnetic properties of melt-spun $Fe_{76}Nd_{16}B_8$ magnetic materials. *Journal of Magnetism and Magnetic Materials*, **54–57**, 557–558.

Hadjipanayis, G.C. and Gong, W. (1988). Magnetic hysteresis in melt-spun Nd-Fe-Al-B-Si alloys with high remanence. *Journal of Applied Physics*, **64**, 5559–5561.

Hadjipanayis, G.C., Hazelton, R.C. and Lawless, K.R. (1983). Iron-rare earth based permanent magnet materials. *Applied Physics Letters*, **43**, 797–799.

Hadjipanayis, G.C., Tao, Y.F. and Gudimetta, K. (1985). Formation of $Fe_{14}La_2B$ phase in as-cast and melt-spun samples. *Applied Physics Letters*, **47**, 757–758.

Hadjipanayis, G.C., Tang, W., Zhang, Y., *et al*. (2000). High temperature 2:17 magnets: relationship of magnetic properties to microstructure and processing. *IEEE Transactions on Magnetics*, **36**, 3382–3387.

Hadjipanayis, G.C., Zheng, Y.H., Murthy, A.S., *et al*. (1995). Recent developments in rare-earth nitrides and carbides. *Journal of Alloys and Compounds*, **222**, 49–56.

Harada, T., Ando, T., O'Handley, R.C. and Grant, N.J. (1990). The magnetic properties of Nd-Fe-B magnets produced by liquid dynamic compaction. *Journal of Applied Physics*, **67**, 4233–4237.

Harada, T., Ando, T., O'Handley, R.C. and Grant, N.J. (1991). Microstructure and magnetic properties of anisotropic Nd-Fe-B magnets produced by splat-quenching. *Journal of Applied Physics*, **70**, 6468–6470.

Harada, T., Fujita, M. and Kuji, T. (1996). Nd-Fe-B die upset magnets produced from amorphous bulk materials. *Journal of Alloys and Compounds*, **243**, 139–143.

Harland, C.L. and Davies, H.A. (2000). Effect of Co and Zr on magnetic properties of nanophase PrFeB alloys. *Journal of Applied Physics*, **87**, 6116–6118.

Hellwig, C., Girgis, K., Schefer, J., *et al*. (1991). Crystall and magnetic structure of the permanent magnet material $Tb_2Fe_{14}C$. *Journal of the Less-Common Metals*, **169**, 147–156.

Herbst, J.F. and Croat, J.J. (1991). Neodymium Iron Boron permanent magnets. *Journal of Magnetism and Magnetic Materials*, **100**, 57–78.

Hidaka, T., Yamamoto, T., Nakamura, H. and Fukuno, A. (1998). High remanence (Sm, Zr)$Fe_7N_x + \alpha$-Fe nanocomposite magnets through exchange coupling. *Journal of Applied Physics*, **83**, 6917–6919.

Hirosawa, S. and Kanekiyo, H. (1996). Nanostructure and magnetic properties of chromium-doped Fe_3B-$Nd_2Fe_{14}B$ exchange-coupled permanent magnets. *Materials Science and Engineering A-Structural Materials Properties Microstructure and Processing*, **217/218**, 367–370.

Hirosawa, S., Kanekiyo, H. and Uehara, M. (1993). High-coercivity iron-rich rare-earth permanent magnet material based on $(Fe, Co)_3$B-Nd-M (M = Al, Si, Cu, Ga, Ag, Au). *Journal of Applied Physics*, **73**, 6488–6490.

Hsiao, A., Aich, S., Lewis, L.H. and Shield, J.E. (2004). Magnetization processes in melt-spun Sm-Co-based alloys with the $TbCu_7$-type structure. *IEEE Transactions on Magnetics*, **40**, 2913–2915.

Ido, H., Ogata, H. and Maki, K. (1993). Magnetic characteristics of the $Sm_{1-x}Pr_xCo_{4-y}Fe_yB$ system. *Journal of Applied Physics*, **73**, 6269–6271.

Jha, A., Davies, H.A. and Buckley, R.A. (1989). Glass forming ability and kinetics of crystallization of rapidly quenched Nd-Fe-B alloys. *Journal of Magnetism and Magnetic Materials*, **80**, 109–114.

Jin, Z.Q., Okumura, H., Muñoz, J.S., *et al*. (2002a). Multi-step crystallization evolution in nanocomposite $Pr_8Fe_{86}B_6$ alloys. *Journal of Physics D: Applied Physics*, **35**, 2893–2896.

Jin, Z.Q., Okumura, H., Zhang, Y., *et al*. (2002b). Microstructure refinement and significant improvements of magnetic properties in $Pr_2Fe_{14}B/\alpha$-Fe. *Journal of Magnetism and Magnetic Materials*, **248**, 216–222.

Kamprath, N., Liu, N.C., Hegde, H. and Cadieu, F.J. (1988). Magnetic properties and synthesis of high iHc Sm-Ti-Fe. *Journal of Applied Physics*, **64**, 5720–5722.

Kanekiyo, H., Uehara, M. and Hirosawa, S. (1993). Microstructure and magnetic properties of high-remanence $Nd_5Fe_{71.5}Co_5B_{18.5}M$ (M= Al, Si, Ga, Ag, Au) rapidly solidified and crystallized alloys for resin-bonded magnets. *IEEE Transactions on Magnetics*, **29**, 2863–2865.

Kanekiyo, H., Uehara, M. and Hirosawa, S. (1994). Magnetic properties and microstructure of V-and M-added, Fe_3B-based, Nd-Fe-B nanocrystalline permanent magnets (M = Al, Si). *Materials Science and Engineering A-Structural Materials Properties Microstructure and Processing A*, **181/182**, 868–870.

Katter, M., Wecker, J. and Schultz, L. (1991). Structural and hard magnetic properties of rapidly solidified Sm–Fe–N. *Journal of Applied Physics*, **70**, 3188–3196.

Katter, M., Wecker, J., Schultz, L. and Grössinger, R. (1990). Preparation of highly coercive Sm-Fe-Ti by rapid quenching. *Applied Physics Letters*, **56**, 1377–1379.

Katter, M., Weber, J., Assmus, W., *et al*. (1996). A new model for the coercivity mechanism of $Sm_2(Co,Fe,Cu,Zr)_{17}$ magnets. *IEEE Transactions on Magnetics*, **32**, 4815–4817.

Kim, D.H. and Hadjipanayis, G.C. (1998). Magnetic properties of melt-spun $Sm_{2+Y}(Co_{0.8}Fe_{0.1}Mn_{0.1})_{17}B_X$ alloys. *Journal of Magnetism and Magnetic Materials*, **190**, 240–244.

Kneller, E.F. and Hawig, R. (1991). The exchange-spring magnet: a new material principle for permanent magnets. *IEEE Transactions on Magnetics*, **27**, 3560–3588.

Knoch, K.G., Reinsch, B. and Petzow, G. (1994). $Nd_2Fe_{14}B$-Its region of primary solidification. *Zeinschrift fur Metallkunde*, **85**(5), 350–353.

Kong, L.S., Shen, B.G., Wang, F.W., *et al*. (1994). High-coercivity Sm–Fe–Ga–C compounds with Th_2Zn_{17} structure by melt spinning. *Journal of Applied Physics*, **75**, 6250–6252.

Koon, N.C. and Das, B.N. (1981). Magnetic properties of amorphous and crystallized $(Fe_{0.82}B_{0.18})_{0.9}Tb_{0.05}La_{0.05}$. *Applied Physics Letters*, **39**, 840–842.

Korolev, A.V., Yermolenko, A.S., Yermakov, A.Ye., *et al*. (1975). Influence of deviation from stoichiometric composition on the magnetic properties of the compounds YCo_5 and $SmCo_5$. *Fizika Metallov i Metallovedenie*, **39**, 1107–1109.

Kronmüller, H. (1984). Micromagnetic analysis of precipitation-hardened permanent magnets. *IEEE Transactions on Magnetics*, **20**, 1569–1571.

Kronmüller, H. (1987). Theory of nucleation fields in inhomogeneous ferromagnets. *Physica Status Solidi B*, **144**, 385–396.

Kronmüller, H. and Goll, D. (2002a). Micromagnetic analysis of pinning-hardened nanostructured, nanocrystalline Sm_2Co_{17} based alloys. *Scripta Materialia*, **47**, 545–550.

Kronmüller, H. and Goll, D. (2002b). Micromagnetic analysis of the nucleation-hardened nanocrystalline PrFeB magnets. *Scripta Materialia*, **47**, 551–556.

Kryukov, I.I., Manakov, N.A., Sadkov, V.B. and Sakhaev, K.S. (1989). Potentiality of increase of constant magnetic energy. *Pisma v Zhurnal Tekhnicheskoi Fiziki*, **15**, 50–54, (in Russian).

Kuhrt, C., Katter, M., Wecker, J., *et al*. (1992). Mechanically alloyed and gas-phase carbonated highly coercive $Sm_2Fe_{17}C_x$. *Applied Physics Letters*, **60**, 2029–2031.

Landgraf, F.J.G., Missell, F.P., Knoch, K.G., *et al*. (1991). Binary Fe-Nd metastable phases in the solidification of Fe-Nd-B alloys. *Journal of Applied Physics*, **70**, 6107–6109.

Lee, R.W. (1985). Hot-pressed neodymium-iron-boron magnets. *Applied Physics Letters*, **46**, 790–791.

Lee, D., Hilton, J.S., Chen, C.H., *et al*. (2004). Bulk isotropic and anisotropic nanocomposite rare-earth magnets. *IEEE Transactions on Magnetics*, **40**, 2904–2906.

Leonowicz, M., Davies, H.A., Al-Khafaji, M.A., *et al*. (1994). Properti enhancement for hot deformed Fe-Nd-B magnets by modification of composition of the Nd-rich phase. *IEEE Transactions on Magnetics*, **30**, 651–653.

Leonowicz, M., Kaszuwara, W., Jezierska, E., *et al*. (1998). Application of the shock compaction technique for consolidation of hard magnetic powders. *Journal of Applied Physics*, **83**, 6634–6636.

Li, L. and Graham, C.D. (1992). The origin of crystallographic texture produced during hot deformation in rapidly-quenched NdFeB permanent magnets. *IEEE Transactions on Magnetics*, **28**, 2130–2132.

Li, S., Bi, H., Xie, G., *et al*. (2004). Magnetic hardening effect of Fe_3B alloy by partial substitution of Fe by Nd. *Journal of Magnetism and Magnetic Materials*, **282**, 202–205.

Li, L., Zhang, W.Y., Zhou, Y.Q., *et al*. (2002). Structural properties of magnetically anisotropic $SmCo_5$ ribbons. *Applied Physics Letters*, **80**, 2660–2662.

Liao, L.X. and Altounian, Z. (1989). Formation, crystallization, and magnetic properties of Nd-fe-B glasses. *Journal of Applied Physics*, **66**, 768–771.

van Lier, J., Seeger, M. and Kronmüller, H. (1997). Magnetic and microstructural properties of melt-spun FeGaSmC permanent magnets. *Journal of Magnetism and Magnetic Materials*, **167**, 43–46.

van Lier, J., Kubis, M., Grünberger, W., *et al*. (1998). High performance $Sm_{2+\delta}Fe_{15}Ga_2C_2$ permanent magnets made by melt spinning and hot pressing. *Journal of Applied Physics*, **83**, 5549–5551.

Linetsky, Y.L., Raigorodsky, V.M. and Tsvetkov, V.Y. (1992). Phase transformations in sputtered Nd-Fe-B alloys. *Journal of Alloys and Compounds*, **184**, 35–42.

Liu, J.F., Chui, T., Dimitrov, D. and Hadjipanayis, G.C. (1998). Abnormal temperature dependence of intrinsic coercivity in Sm(Co, Fe, Cu, Zr)$_z$ powder materials. *Applied Physics Letters*, **73**, 3007–3009.

Liu, Y., Dallimore, M.P., McCormick, P.G. and Alonso, T. (1992). High coercivity $SmCo_5$ synthesized by chemical reduction during mechanical alloying. *Journal of Magnetism and Magnetic Materials*, **116**, L320–L324.

Liu, S., Doyle, G., Kuhl, G.E., *et al*. (2001). Temperature dependence of coercivity in Sm_2TM_{17} magnets and domain wall motion in magnetic materials. *IEEE Transactions on Magnetics*, **37**, 2521–2524.

Liu, S., Potts, G., Doyle, G., *et al*. (2000). Effect of z value on high temperature performance of Sm(Co,Fe,Cu,Zr)$_z$ with $z =$ 7.14–8.10. *IEEE Transactions on Magnetics*, **36**, 3297–3299.

Liu, S., Don, L., Huang, M.Q., *et al*. (2006). Research and development of bulk anisotropic nanograin composite rare earth permanent magnets. *Journal of Iron and Steel Research International*, **13**(Suppl. 1), 123–135.

Livingston, J.D. (1985). Magnetic domains in sintered Fe-Nd-B magnets. *Journal of Applied Physics*, **57**, 4137–4139.

Livingston, J.D. and Martin, D.L. (1977). Microstructure of aged (Co,Cu,Fe)$_7$Sm magnets. *Journal of Applied Physics*, **48**, 1350–1354.

Ma, B.M., Liang, Y.L., Patel, J., *et al*. (1996). The effect of Fe content on the temperature dependent magnetic properties of Sm(Co,Fe,Cu,Zr)$_z$ and $SmCo_5$ sintered magnets at 450 °C. *IEEE Transactions on Magnetics*, **32**, 4377–4379.

Makridis, S.S., Litsardakis, G., Panagiotopoulos, I., *et al*. (2002). High coercivity in boron substituted Sm-Co melt-spun magnets. *IEEE Transactions on Magnetics*, **38**, 2922–2924.

Manaf, A., Buckley, R.A. and Davies, H.A. (1993). New nanocrystalline high-remanence Nd-Fe-B alloys by rapid solidification. *Journal of Magnetism and Magnetic Materials*, **128**, 302–306.

Manaf, A., Leonowicz, M., Davies, H.A. and Buckley, R.A. (1991). Effect of grain size and microstructure on magnetic properties of rapidly solidified $Fe_{82.4}Nd_{13.1}B_{4.5}$ alloy. *Journal of Applied Physics*, **70**, 6366–6368.

Manaf, A., Al-Khafaji, M., Zhang, P.Z., *et al*. (1993). Microstructure analyses of nanocrystalline Fe-Nd-B ribbons with enhanced hard magnetic properties. *Journal of Magnetism and Magnetic Materials*, **128**, 307–312.

Marinescu, M., Pawlik, P.C., Davies, H.A. and Chiriac, H. (2004). Bulk nanocomposite RE-TM-M permanent magnets. *Journal of Optoelectronics and Advanced Materials*, **6**, 603–608.

Martinek, G. and Kronmuller, H. (1990). Influence of grain orientation on the coercive field in Fe-Nd-B permanent magnets. *Journal of Magnetism and Magnetic Materials*, **86**, 177–183.

Matsuura, Y., Hirosawa, S., Yamamoto, H., *et al*. (1985). Phase diagram of the Nd-Fe-B ternary system. *Japanese Journal of Applied Physics Part 2-Letters*, **24**, L635–L637.

Meacham, B.E. and Branagan, D.J. (2003). Developing highly coercive microstructures in Pr-Co magnets by Gd substitution. *Journal of Applied Physics*, **93**, 7963–7965.

Melton, K.N. and Nagel, H. (1977). An electron microscope study of Sm-Co-Cu–based magnetic materials with the Sm_2Co_{17} structure. *Journal of Applied Physics*, **48**, 2608–2611.

Mendoza-Suarez, G., Davies, H.A. and Escalante-Garcia, J.I. (2000). $_jH_c$, J_r and $(BH)_{max}$ relationship in PrFeB melt spun alloys. *Journal of Magnetism and Magnetic Materials*, **218**, 97–102.

Mendoza-Suarez, G., Escalante-Garcia, J.I., Lopez-Cuevas, J., *et al*. (1999). Effect of roll speed on the magnetic properties of nanocomposite PrFeB magnets prepared by melt-spinning. *Journal of Magnetism and Magnetic Materials*, **206**, 37–44.

Morimoto, K., Yagi, M. and Takeshita, T. (1991). High coercivity in rapidly quenched ribbons of Pr-Co binary alloys. *Materials Transactions, JIM*, **6**, 562–565.

Moukarika, A., Papaefthymiou, V., Bakas, T., *et al*. (1996). X-ray and Mössbauer studies of Sm-Fe-Nb(Zr) (2:17:2) alloys and their nitrides. *Journal of Magnetism and Magnetic Materials*, **163**, 109–116.

Mishra, R.K. (1986). Microstructure of melt-spun Nd-Fe-M Magnequench magnets. *Journal of Magnetism and Magnetic Materials*, **54–57**, 450–456.

Mishra, R.K., Thomas, G., Yoneyama, T., *et al*. (1981). Microstructure and properties of step aged rare earth alloy magnets. *Journal of Applied Physics*, **52**, 2517–2519.

Narasimhan, K., Willman, C. and Dulis, E.J. (1986). Oxygen containing permanent magnet alloy. US Patent No. 4,588,439.

Nesbitt, E.A., Willens, R.H., Sherwood, R.C., *et al*. (1968). New permanent magnet materials. *Applied Physics Letters*, **12**, 361–362.

Neu, V. and Schultz, L. (2001). Two-phase high-performance Nd-Fe-B powders prepared by mechanical milling. *Journal of Applied Physics*, **90**, 1540–1544.

Neu, V., Crespo, P., Schäfer, R., *et al*. (1996). High remanence Nd-Fe-B-X (X = Cu, Si, Nb3Cu, Zr) powders by mechanical alloying. *Journal of Magnetism and Magnetic Materials*, **158**, 61–62.

O'Donnell, K., Kuhrt, C. and Coey, J.M.D. (1994). Influence of nitrogen content on coercivity in remanence-enhanced mechanically alloyed Sm-Fe-N. *Journal of Applied Physics*, **76**, 7068–7070.

Oesterreicher, H. (1985). In *Proceedings of the 8th Workshop on Rare-Earth Permanent Magnets and Their Applications*, Strnat, K.J. (Ed.), University of Dayton: Dayton, pp. 705–724.

Ojima, T., Tomizawa, S., Yoneyama, T. and Hori, T. (1977). Magnetic properties of a new type of rare-earth cobalt magnets. *IEEE Transactions on Magnetics*, **13**, 1317–1319.

Okada, M., Kojima, A., Yamagishi, K. and Homma, M. (1990). High coercivity in melt-spun $SmFe_{10}(Ti,M)_2$ ribbons (M = V/Cr/Mn/Mo). *IEEE Transactions on Magnetics*, **26**, 1376–1378.

Okumura, H., Zhang, F. and Hadjipanayis, G.C. (2002). Magnetic properties and microstructure of LaCo5-based powders produced by mechanical milling and subsequent annealing. *Journal of Applied Physics*, **91**, 6147–6153.

Pawlik, P. and Davies, H.A. (2003). Glass formability of Fe-Co-Pr-Dy-Zr-B alloys and magnetic properties following devitrification. *Scripta Materialia*, **49**, 755–760.

Ping, D.H., Hono, K. and Hirosawa, S. (1998). Partitioning of Ga and Co atoms in a $Fe_3B/Nd_2Fe_{14}B$ nanocomposite magnet. *Journal of Applied Physics*, **83**, 7769–7775.

Pinkerton, F.E. (1986). High coercivity in melt-spun Dy-Fe-B and Tb-Fe-B alloys. *Journal of Magnetism and Magnetic Materials*, **54–57**, 574–582.

Pinkerton, F.E. (1987). High performance permanent magnet materials. *Materials Research Society Symposium Proceedings*, Sankar, G., Herbst, J.F. and Koon, N.C. (eds). Materials Research Society, vol. 96 65–81.

Pinkerton, F.E. and Fuerst, C.D. (1992). Magnetically hard $Sm_2Fe_{17}N_x$ prepared by nitriding melt-spun ribbons. *Applied Physics Letters*, **60**, 2558–2560.

Pinkerton, F.E., Fuerst, C.D. and Herbst, J.F. (1994). Nitriding of melt-spun Nd-Fe-Mo alloys. *Journal of Applied Physics*, **75**, 6015–6017.

Pinkerton, F.E., and Van Wingerden, D.J. (1986). Magnetization process in rapidly solidified neodymium-iron-boron permanent magnet materials. *Journal of Applied Physics*, **60**(10), 3685–3690.

Pinkerton, F.E. and Van Wingerden, D.J. (1989). Magnetic hardening of $SmFe_{10}V_2$ by melt-spinning. *IEEE Transactions on Magnetics*, **25**, 3306–3308.

Popov, A.G., Gaviko, V.S., Magat, L.M. and Ivanova, G.V. (1990). Influence of copper concentration on the magnetic properties and structure of $Sm(Co,Fe,Cu,Zr)_z$ alloys. *Physics of Metals and Metallography*, **70**, 18–27.

Popov, A.G., Gynderov, D.V. and Stolyarov, V.V. (1996). Method of formation of a high coercivity state in PrFeBCu alloy. *Journal of Magnetism and Magnetic Materials*, **158**, 33–34.

Popov, A.G., Korolev, A.V. and Shchegoleva, N.N. (1990). Temperature dependence of the coercive force of $Sm(Co,Fe,Cu,Zr)_{7.3}$ alloys. *Physics of Metals and Metallography*, **69**, 100–106.

Ray, A.E. (1984). Metallurgical behavior of $Sm(Co,Fe,Cu,Zr)_z$ alloys. *Journal of Applied Physics*, **55**, 2094–2096.

Rhen, F.M.F., Venkatesan, M., Harris, I.R. and Coey, J.M.D. (2003). Effect of ZrB_2 addition on SmCo-1: 7 high temperature magnets. *Journal of Applied Physics*, **93**, 8683–8685.

Rong, C.B., Zhang, H.W., Zhang., J., *et al*. (2004). Micromagnetic simulation of the coercivity mechanism in $Sm(Co,Fe,Cu,Zr)_z$ magnets. *Journal of Applied Physics*, **95**, 1351–1356.

Sagawa, M., Fujimura, S., Togawa, N., *et al*. (1984). New material for permanent magnets on a base of Nd and Fe. *Journal of Applied Physics*, **55**, 2083–2087.

Saito, T. (2001). Production of bulk materials of an $Nd_4Fe_{77.5}B_{18.5}$ alloy and their magnetic properties. *IEEE Transactions on Magnetics*, **37**, 2561–2563.

Saito, H., Takahashi, M. and Wakiyama, T. (1987). Hard magnetic properties of the rapidly quenched $Sm(Co\text{-}Fe\text{-}B)_5$ alloy ribbons. *IEEE Transactions on Magnetics*, **23**, 2725–2727.

Saito, T., Fujita, M., Kuji, T., *et al*. (1998). The development of high-performance Nd-Fe-Co-Ga-B die-upset magnets. *Journal of Applied Physics*, **83**, 6390–6392.

Sakurada, S., Nakagawa, K., Kawashima, F., *et al*. (2000). Isotropic Sm-Zr-Fe-Co-B-N bonded magnets with high $(BH)_{max}$. In *Proceedings of the 16th International Workshop on Rare Earth Magnets and Their Applications*, Kaneko, H., Homma, M. and Okada, M. (Eds.), The Japan Institute of Metals, pp. 719–726.

Satyanarayana, M.V., Fujii, H. and Wallace, W.E. (1984). Magnetic and structural investigation on substituted $Pr_2Co_{17-x}T_x$ systems (T = Fe, Mn, Cr, Cu and Al). *Journal of Magnetism and Magnetic Materials*, **40**, 241–246.

Schneider, G., Henig, E.T., Petzow, G. and Stadelmair, H.H. (1986). Phase relations in the system Fe-Nd-B. *Zeitschrift für Metallkunde*, **77**, 755–771.

Schnitzke, K., Schultz, L., Wecker, J. and Katter, M. (1990a). Sm-Fe-Ti magnets with room-temperature coercivities above 50 kOe. *Applied Physics Letters*, **56**, 587–589.

Schnitzke, K., Schultz, L., Wecker, J. and Katter, M. (1990b). High coercivity in $Sm_2Fe_{17}N_x$ magnets. *Applied Physics Letters*, **57**, 2853–2855.

Schrefl, T., Fischer, R., Fidler, J. and Kronmüller, H. (1994). 2-dimensional and 3-dimensional calculation of remanence enhancement of rare-earth based composite magnets. *Journal of Applied Physics*, **76**, 7053–7058.

Schultz, L. (1990). In *Science and Technology of Nanostructured Materials*, *NATO ASI Series, Vol. 259*, Hadjipanayis, G.C. and Prinz, G.A. (Eds.), Springer, p. 583.

Schultz, L., Schnitzke, K. and Wecker, J. (1990). High coercivity in mechanically alloyed Sm-Fe-V magnets with a $ThMn_{12}$ crystal structure. *Applied Physics Letters*, **56**, 868–870.

Schultz, L., Schnitzke, K., Wecker, J. and Katter, M. (1991). High coercivities in mechanically alloyed Sm-Fe-X magnets. *Materials Science and Engineering A*, **133**, 143–146.

Schultz, L. and Wecker, J. (1988). Coercivity in $ThMn_{12}$-type magnets. *Journal of Applied Physics*, **64**, 5711–5713.

Sellmyer, D.J. (1992). Magnetism of nanostructured rare-earth multilayers and films. *Journal of Alloys and Compounds*, **181**, 397.

Shen, B.G., Yang, L.Y., Guo, H.G. and Zhao, J.G. (1994a). Magnetic properties and crystallization of amorphous Fe-Nd-B alloys at constant Nd concentration. *Journal of Applied Physics*, **75**, 6312–6314.

Shen, B.G., Wang, F.W., Kong, L.S., *et al*. (1994b). A novel hard magnetic material for sintering permanent magnets. *Journal of Applied Physics*, **75**, 6253–6255.

Skomski, R. and Coey, J.M.D. (1993). Giant energy product in nanostructured two-phase magnets. *Physical Review B*, **48**, 15812–15816.

Stadelmaier, H.H., Elmasry, N.A. and Cheng, S. (1983). Cobalt-free and samarium-free permanent magnet materials based on an iron–rare earth boride. *Materials Letters*, **2**(2), 169–172.

Stadelmaier, H.H., Elmasry, N.A., Liu, N.C. and Cheng, S.F. (1984). The metallurgy of the iron–neodymium–boron permanent magnet system. *Materials Letters*, **2**(5A), 411–415.

Stadelmaier, H.H., Goll, D. and Kronmüller, H. (2005). Permanent magnet alloys based on Sm_2Co_{17}; phase evolution in the quinary system Sm-Zr-Fe-Co-Cu. *Zeitschrift für Metallkunde*, **96**, 17–23.

Strnat, K.J. (1988). Rare earth–cobalt permanent magnets. In *Ferromagnetic Materials*, Wohlfarth, E.P. and Buschow, K.H.J. (Eds.), North-Holland: Amsterdam, pp. 131–209, Vol. 4.

Sui, Y.C., Zhang, Z.D., Xiao, Q.F., *et al*. (1996). Nd-Fe-(C,B) permanent magnets made by mechanical alloying and subsequent annealing. *Journal of Physics: Condensed Matter*, **8**, 11231–111242.

Takahashi, M., Saito, H., Takakura, K., *et al*. (1985). Structure and hard magnetic properties of rapidly quenched Sm-Co alloy ribbons. *Journal of the Japan Institute of Metals*, **49**, 177–186.

Tang, Z.X., Singleton, E.W. and Hadjipanayis, G.C. (1993). Hard magnetic properties of melt-spun $Nd(Fe,M)_{12}$ nitrides and carbides. *Journal of Applied Physics*, **73**, 6254–6256.

Tang, N., Chen, Z., Zhang, Y., *et al*. (2000). Nanograined YCo_5-based powders with high coercivity. *Journal of Magnetism and Magnetic Materials*, **219**, 173–177.

Tang, Y.L., Kramer, M.J., Dennis, K.W., *et al*. (2003). On the control of microstructure in rapidly solidified Nd-Fe-B alloys through melt treatment. *Journal of Magnetism and Magnetic Materials*, **267**, 307–315.

Tang, W., Lu, L.Y., Jin, Z.Q., *et al*. (1998a). Formation, structure and magnetic hardening of Zr added $Sm_2(Fe,Al,Zr)_{17}C_{1.5}$ compounds. *Journal of Magnetism and Magnetic Materials*, **184**, 209–214.

Tang, W., Jin, Z.Q., Yin, J.H., *et al*. (1998b). Influence of Mo addition on the microstructure and magnetic properties of $Sm_2(Fe, Al, Mo)_{17}C_{1.5}$ alloys. *Journal of Magnetism and Magnetic Materials*, **186**, 115–120.

Tang, S.L., Wu, C.H., Jin, X.M., *et al*. (1998c). Magnetic hardening of mechanically alloyed $NdFe_{12-x}V_x$ $(1 \leq \times \leq 2)$ and their nitrides. *Journal of Magnetism and Magnetic Materials*, **189**, 202–206.

Tang, W., Zhang, Y., Goll, D., *et al*. (2001). New Sm(Co, Fe, Cu, $Zr)_z$ magnets with better temperature stability. *Journal of Magnetism and Magnetic Materials*, **226**, 1365–1366.

Tang, W., Zhang, Y. and Hadjipanayis, G.C. (2002a). Effect of Ni substitution on the microstructure and coercivity of $Sm(Co_{bal}Fe_{0.1}Ni_yZr_{0.04})_{8.5}$ magnets. *Journal of Applied Physics*, **91**, 7896–7898.

Tao, Y.F. and Hadjipanayis, G.C. (1984). Magnetic and structural studies in rapidly quenched iron-rare earth–metalloid alloys, Presented at the *Conference on Magnetism and Magnetic Materials*, San Diego, November 1984.

Tawara, Y., and Senno, H. (1973). Bulk hardened magnet of non-stoichiometric rare-earth cobalt. *Japanese Journal of Appied Physics*, **12**, 761–762.

Uehara, M., Hirosawa, S., Kabakiyo, H., *et al*. (1998). Effect of Cr-doping on crystallization sequence and magnetic properties of $Fe_3B/Nd_2Fe_{14}B$ nanocomposite permanent magnets. *Nanostructured Materials*, **10**, 151–160.

Wang, Z.C. and Davies, H.A. (2003). Magnetic property enhancement in $Pr_2(Fe,Co)_{14}B$ / α-(Fe,Co)–based nanocomposite magnets through Hf, Ti or Al additions. *Scripta Materialia*, **48**, 845–850.

Wang, Y.Z. and Hadjipanayis, G.C. (1991). Effect of nitrogen on structural and magnetic properties of intermetallic compounds with the $ThMn_{12}$ structure. *Journal of Applied Physics*, **70**, 6009–6011.

Wang, Y.Z., Hadjipanayis, G.C., Kim, A., *et al*. (1990). Magnetic and structural studies in Sm-Fe-Ti magnets. *Journal of Applied Physics*, **67**, 4954–4956.

Wang, Z., Zhou, S., Qiao, Y., *et al*. (2000). Effects of quenching rate on the phase transformation and magnetic properties of melt-spun $Pr_8Fe_{86}B_6$ ribbons during annealing. *Journal of Magnetism and Magnetic Materials*, **218**, 72–80.

Wecker, J., Katter, M., Schnitzke, K. and Schultz, L. (1991). Magnetic hardening of $(Sm,Zr)Fe_3$ alloys. *Journal of Applied Physics*, **69**, 5847–5849.

Wecker, J., Katter, M. and Schultz, L. (1991). Mechanically alloyed Sm-Co materials. *Journal of Applied Physics*, **69**, 6058–6060.

Wecker, J., Cerva, H., Kuhrt, C., *et al*. (1994). Microstructure and magnetic properties of mechanically alloyed anisotropic Nd-Fe-B. *Journal of Applied Physics*, **76**, 6238–6240.

Withanawasam, L., Panagiotopoulos, I. and Hadjipanayis, G.C. (1996). Melt-spun $Pr_2Co_{14}B/Co$ nanocomposite magnets. *Journal of Applied Physics*, **79**, 4837–4839.

Withanawasam, L., Murphy, A.S., Hadjipanayis, G.C., *et al*. (1995). Melt-spun $Pr_2Co_{14}B/Co$ nanocomposite magnets. *Journal of Magnetism and Magnetic Materials*, **140**(144), 1057–1058.

Xiong, X.Y., Ohkubo, T., Koyama, T., *et al*. (2004). The microstructure of sintered $Sm(Co_{0.72}Fe_{0.20}Cu_{0.055}Zr_{0.025})_{7.5}$ permanent magnet studied by atom probe. *Acta Materialia*, **52**, 737–748.

Yamamoto, H. and Yamaguchi, T. (1991). Magnetic properties of high-quality melt-spun Nd-Co-B-C ribbons and their bonded magnets. *Journal of Applied Physics*, **70**, 6597–6599.

Yan, A., Bollero, A., Müller, K.H. and Gutfleisch, O. (2002). Fast development of high coercivity in melt-spun $Sm(Co,Fe,Cu,Zr)_z$ magnets. *Applied Physics Letters*, **80**, 1243–1245.

Yan, A., Gutfleisch, O., Gemming, T. and Müller, K-H. (2003). Microchemistry and magnetization reversal mechanism in melt-spun 2: 17-type Sm-Co magnets. *Applied Physics Letters*, **83**, 2208–2210.

Yan, A.R., Sun, Z.G., Han, B.S. and Shen, B.G. (2002). Magnetic anisotropy of $Sm(Co_{0.68}Fe_{0.22}Cu_{0.08}Zr_{0.02})_{7.7}$ ribbons produced by melt spinning. *Journal of Materials Research*, **17**, 648–652.

Yan, A.R., Zhang, W.Y., Zhang, H.W. and Shen, B.G. (2000). Melt-spun magnetically anisotropic $SmCo_5$ ribbons with high performance. *Journal of Magnetism and Magnetic Materials*, **210**, L10–L14.

Yan, A., Bollero, A., Gutfleisch, O., *et al*. (2002). Influence of Fe, Zr and Cu on the microstructure and crystallographic texture of melt-spun 2:17 Sm-Co ribbons. *Journal of Applied Physics*, **91**, 8825–8827.

Yang, J., Mao, O. and Altounian, Z. (1996). Structure and magnetic properties of mechanically alloyed $Nd(Fe,V)_{12}N_x$ compounds. *Journal of Applied Physics*, **79**, 5519–5521.

Yang, C.J. and Park, E.B. (1995). The effect of magnetic field treatment on enhanced exchange coupling of $Nd_2Fe_{14}B/Fe_3B$ magnet. *IEEE Transactions on Magnetics*, **32**, 4428–4430.

Yang, J., Wang, Q. and Sun, X. (1997). The structures and magnetic properties of mechanically alloyed Sm-Fe-T (T = Ti, Ti + V, V)

systems. *Journal of Magnetism and Magnetic Materials*, **166**, 216–222.

Yang, J.P., An, K.S., Song, C.Y., *et al*. (1997). A new method for preparation of anisotropic Nd-Fe-B-based magnets. *IEEE Transactions on Magnetics*, **33**, 3820–3822.

Yang, J., Wang, Q., Sun, X.K., *et al*. (1994). The structure and magnetic hardening in mechanically alloyed Sm-Fe-Ti systems. *Journal of Magnetism and Magnetic Materials*, **132**, 197–206.

Yang, Y.C., Zhang, X.D., Ge, S.L., *et al*. (1991). Magnetic and crystallographic properties of novel Fe-rich rare-earth nitrides of the type $RTiFe_{11}N_{1-\delta}$. *Journal of Applied Physics*, **70**, 6001–6005.

Zhang, W.Y., Chang, H.W., Chiu, C.H. and Chang, W.C. (2004). Phase evolution, magnetic properties, and coercivity mechanism of melt-spun Pr_2Fe_{14}(C,B)/alpha-Fe-type ribbons. *Physical Review B: Condensed Matter*, **344**, 201–205.

Zhang, J.X., Cheng, Z.H. and Shen, B.G. (1996). High coercivity of melt–spun $Sm_2Fe_{15}Al_2C_{1.5}$ compound. *Journal of Applied Physics*, **79**, 5528–5529.

Zhang, X.Y., Guan, Y., Yang, L. and Zhang, J.W. (2001). Crystallographic texture and magnetic anisotropy of α-Fe/$Nd_2Fe_{14}B$ nanocomposites prepared by controlled melt spinning. *Applied Physics Letters*, **79**, 2426–2428.

Zhang, W. and Inoue, A. (2002). Bulk nanocomposite permanent magnets produced by crystallization of (Fe,Co)-(Nd,Dy)-B bulk glassy alloy. *Applied Physics Letters*, **80**, 1610–1612.

Zhang, W., Matsushita, M. and Inoue, A. (2001). Hard magnetic properties of Fe-Co-Nd-Dy-B nanocrystalline alloys containing residual amorphous phase. *Journal of Applied Physics*, **89**, 492–495.

Zhang, W.Y., Zhang, S.Y. and Shen, B.G. (2002). Large effect of Ga addition on the magnetic properties of $Pr_2Fe_{14}B$/alpha-Fe-type ribbons. *Solid State Communications*, **122**, 641–643.

Zhang, H.W., Zhang, S.Y., Shen, B.G. and Zhang, L.G. (1998). The magnetic properties of Cu-doped Sm–Fe–Si–C ribbons prepared by melt spinning. *Journal of Applied Physics*, **83**, 4838–4842.

Zhang, J., Kleinschroth, I., Cuevas, F., *et al*. (2000). Effect of additives on the structure and magnetic properties of 1:7 type $Sm_2Fe_{15}Ga_2C_3$ permanent magnets. *Journal of Applied Physics*, **88**, 6618–6622.

Zhang, J., Liu, H., Rong, C.B., *et al*. (2003). Anomalous temperature dependence of coercivity in precipitation hardened Pr-Co-Cu-Ti magnets. *Applied Physics Letters*, **83**, 1172–1174.

Zhang, W.Y., Shen, B.G., Cheng, Z.H., *et al*. (2001). Beneficial effect of Gd substitution on magnetic properties of magnetically anisotropic $SmCo_5$ ribbons. *Applied Physics Letters*, **79**, 1843–1845.

Zhang, Y., Warren, P.J., Cerezo, A., *et al*. (2001a). Partitioning behavior and the effect of Co on the Curie temperature of nanocomposite PrFeCoB hard magnetic alloys. *Applied Physics Letters*, **79**, 797–799.

Zhang, J., Zhang, S.Y., Zhang, H.W., *et al*. (2001b). Structure and magnetic properties of Sm_xCo_5/α-Fe ($x = 0.65–1.3$) prepared by mechanical milling and subsequent annealing. *Journal of Applied Physics*, **89**, 2857–2860.

Zhang, M., Zhang, Z.D., Sun, X.K., *et al*. (2004). Remanent enhancement of nanocomposite $(Nd,Sm)_2Fe_{14}B$/α-Fe magnets. *Journal of Alloys and Compounds*, **372**, 267–271.

Zhou, J., Skomski, R., Chen, C., *et al*. (2000). Sm-Co-Cu-Ti high-temperature magnets. *Applied Physics Letters*, **77**, 1514–1516.

FURTHER READING

Daniil, M., Digas, M., Moukarika, A., *et al*. (1998). Effects of substitutions M on the formation, structure and magnetic properties of $Sm_2Fe_{15}M_2C_2$ (M = V, Cr, Ti, Nb, Zr, Mn and Mo) compounds. *Journal of Magnetism and Magnetic Materials*, **177–181**, 1109–1110.

Huang, M.Q., Turgut, Z., Smith, B.R., *et al*. (2004). Magnetic properties of $Sm(Co_{bal}Fe_{0.31}Zr_{0.05}Cu_{0.04}B_x)_z$ alloys and their melt-spun materials ($x = 0.02–0.04$, $z = 7.5–12$). *IEEE Transactions on Magnetics*, **40**, 2934–2936.

Rong, C.B., Zhang, H.W., Zhang, J., *et al*. (2005). Coherent precipitation in the $TbCu_7$-type GdCo-based ribbons prepared by simple processing. *Journal of Applied Physics*, **97**, 033907.

Tang, W., Zhang, Y. and Hadjipanayis, G.C. (2002b). The relationship between the composition and the abnormal temperature dependence of coercivity in $Sm(Co,Fe,Cu,Zr)_z$. *IEEE Transactions on Magnetics*, **38**, 2940–2942.

Tang, W., Zhang, Y. and Hadjipanayis, G.C. (2002c). Microstructure, magnetic properties and magnetic hardening in 2: 17 Sm-Co magnets. *Zeitschrift für Metallkunde*, **93**, 1002–1008.

Tang, W., Zhang, Y., Gabay, A.M. and Hadjipanayis, G.C. (2002d). Anomalous temperature dependence of coercivity in rare earth cobalt magnets. *Journal of Magnetism and Magnetic Materials*, **242**, 1335–1337.

Wang, W., Matsushita, M. and Inoue, A. (2001). Hard magnetic properties of Fe-Co-Nd-Dy-B nanocrystalline alloys containing residual amorphous phase. *Journal of Applied Physics*, **89**, 492–495.

Xiao, Q.F., Zhang, Z.D., Zhao, T., *et al*. (1997). Crystallographic transformations of rapidly quenched $Sm_{10}Fe_{90-x}Ti_x$ and magnetic properties of their nitrides. *Journal of Applied Physics*, **82**, 6170–6176.

Current Status and Future Development of the Magnetic Materials Industry in China

Yang Luo
Permanent Magnet Technical Committee TC-15 IEEE, Beijing, China

Handbook of Magnetism and Advanced Magnetic Materials. Edited by Helmut Kronmüller and Stuart Parkin. Volume 4: *Novel Materials*. ISBN: 978-0-470-02217-7.

1 GENERAL SITUATION OF THE CHINESE MAGNET INDUSTRY

Commercial magnetic materials consist of two parts (IEC, 1973; Luo, 1991): soft magnetic materials (SMMs) and hard magnetic materials (HMMs). According to the material nature, magnetic materials may be metallic or nonmetallic (ferrite), crystalline, or amorphous. There are mainly two types of SMMs: soft ferrite (SF) and amorphous (or nanocrystalline) material. The three major commercially available magnets are Alnico, hard ferrite (HF), and rare-earth magnets (NdFeB, SmCo).

The output, sales value, and averaged price of SMMs (Luo, 1995; Chen, 2004; Zhou and Lu, 1999; Zhou, 2001) and HMMs (Jia *et al*., 1998; Jia, Jia and Li, 2004; Luo, 2000a,b; Zhang, 2002, 2004) produced in China during 1990–2005 are summarized in Table 1.

Output changes of both soft (SMM) and hard magnets (HMM) made in China during 1990–2005 are shown in Figure 1. Outputs of both SMMs and HMMs have been increasing every year; the only difference is in their annual growth rate. The portion between them depends on the difference in their growth rate. The averaged output growth rate of SMMs and HMMs during 1990–2005 was +16.1 and +17.6% respectively, that is, the growth rate of HMMs was higher than that of SMMs. In 1990, the percentage of SMM/T was 28.8%; it reduced to 23.3% in 1998. Then it became 29% in 2003 and dropped to 22.8 in 2004. Generally speaking, the output of SMMs is one-fourth of the total.

The output percentage of SMMs and HMMs is around one-fourth and three-fourths of the total, respectively. The ratio between the sales value of SMMs and HMMs is around 50 to 50% all the time. The sales value

($\$ \times 10^6$) of SMMs and HMMs made in China during 1990–2005 is shown in Figure 2. The portion of SMMs was >50% during 1993–1996. It became <43% during 2003–2005.

Averaged sales prices of SMMs, HMMs, and the averaged price of TMMs are summarized in Figure 3.

General speaking, the price of SMMs is much higher than that of HMMs. Although the material and processing cost for different magnets is different, it is not the deciding factor for price. The key point is that most SMMs are sold as final products or devices, but hard magnets are sold as blocks. Consequently, all magnet producers have to provide devices

Table 1. Output (tons), sales value ($\$\times 10^6$), and averaged price ($/kg) of SMM, HMM, and total magnetic materials (TMMs) made in China (1990–2005).

		1990	1991	1992	1993	1994	1995
Output (tons)	SMM	15 150	17 580	20 210	23 150	26 610	30 880
	Δ(%)	+16	+16	+15	+15	+15	+16
	SMM/T (%)	28.8	28.4	27.6	27.3	26.6	25.4
	HMM	37 405	44 217	53 069	61 749	73 523	90 686
	Δ(%)	+18	+18	+20	+16.4	+19	+23.3
	HMM/T (%)	71.2	71.6	72.4	72.7	73.4	74.6
	TMM	52 555	61 797	73 279	84 899	100 133	121 566
	Δ(%)	+17	+17.6	+18.6	+15.9	+17.9	+21.4
Value ($\$\times 10^6$)	SMM	132.2	162	196.2	238.5	287.3	351.4
	Δ(%)	+20	+22.6	+21	+21.6	+20.5	+22
	SMM/T (%)	44.2	47.9	49.6	50.3	50.9	50.9
	HMM	166.7	176.3	199.3	236.1	277.3	338.8
	Δ(%)	+	+5.8	+16.5	+14.9	+17.5	+22
	HMM/T (%)	55.8	52.1	50.4	49.7	49.1	49.1
	TMM	298.9	338.3	395.5	474.6	564.6	689.9
	Δ(%)	+	+13.2	+16.9	+20	+19	+22.1
Price ($/kg)	SMM	8.72	9.22	9.71	10.3	10.8	11.38
	Δ(%)	–	+5.7	+5.3	+6	+4.9	+5.4
	HMM	4.46	3.99	3.76	3.82	3.77	3.74
	Δ(%)	–	−11.8	−6.1	+1.6	−1.3	−0.8
	TMM	5.69	5.47	5.40	5.59	5.64	5.675
	Δ(%)	–	−4	−1.3	+3.5	+0.9	+0.6
		1996	1997	1998	1999	2000	2001
Output (tons)	SMM	35 480	40 600	46 780	55 010	63 250	73 500
	Δ(%)	+15	+14.4	+15	+17.6	+15	+16
	SMM/T (%)	24.7	23.7	23.3	23.6	24.6	26.1
	HMM	108 270	130 935	154 265	178 200	194 085	222 910
	Δ(%)	+19.4	+20.9	+17.8	+15.5	+8.9	+14.9
	HMM/T (%)	75.3	76.3	76.7	76.4	75.4	73.9
	TMM	143 750	171 535	201 045	233 210	257 335	296 410
	Δ(%)	+18.2	+19.3	+17.2	+16	+10.3	+15.2
Value ($\$\times 10^6$)	SMM	428.2	489.8	564.3	663	761.6	869.9
	Δ(%)	+22	+14.4	+15.2	+17.5	+14.9	+14.2
	SMM/T (%)	50.7	48.98	47.3	46.1	45.8	47.4
	HMM	416.9	510.3	628.4	776.2	901.5	964.7
	Δ(%)	+23.2	+22.4	+23.1	+23.5	+16.1	+7
	HMM/T (%)	49.3	51.02	52.7	53.9	54.2	52.6
	TMM	845.1	1000.1	1192.7	1439.2	1663.1	1834.6
	Δ(%)	+22.5	+18.3	+19.3	+20.7	+15.6	+11.1
Price ($/kg)	SMM	12.07	12.06	12.06	12.05	12.04	11.84
	Δ(%)	+6	−0.08	0	−0.08	−0.08	−1.69
	HMM	3.85	3.9	4.07	4.36	4.6	4.47
	Δ(%)	+3.2	+1.3	+4.4	+7.1	+5.5	−2.9
	TMM	5.88	5.83	5.93	6.17	6.46	6.19
	Δ(%)	+3.7	−0.9	+1.7	+4	+4.7	−4.4

Table 1. (*Continued*).

		2002	2003	2004	2005
Output (tons)	SMM	83 800	101 660	128 000	164 000
	Δ(%)	+14	+21.3	+25.9	+28.1
	SMM/T (%)	27.7	29	22.8	24.7
	HMM	254 660	317 870	432 660	500 360
	Δ(%)	+14.2	+24.8	+24.8	+15.6
	HMM/T (%)	72.3	71	77.1	75.3
	TMM	338 460	419 530	560 660	664 360
	Δ(%)	+14.2	+23.9	+33.65	+18.5
Value ($\$\times 10^6$)	SMM	966	1140.8	1428.5	1777.2
	Δ(%)	+11	+18.1	+25.2	+24.4
	SMM/T (%)	46.7	42.2	40.7	42.6
	HMM	1102.3	1563.5	2084.3	2398.4
	Δ(%)	+14.3	+41.8	+33.3	+15.1
	HMM/T (%)	53.3	57.8	59.3	57.4
	TMM	2068.3	2704.3	3512.8	4175.6
	Δ(%)	+12.7	+30.7	+29.9	+18.9
Price ($/kg)	SMM	11.53	11.22	10.94	10.64
	Δ(%)	+4.2	−4.3	−2.6	−2.85
	HMM	4.33	4.92	4.817	4.793
	Δ(%)	+3.4	+2.4	−2.1	−0.5
	TMM	6.11	6.446	6.265	6.285
	Δ(%)	−1.3	+5.5	−2.9	+0.3

SMM: soft magnetic material; HMM: hard magnetic material; TMM: total magnetic material; T: magnetic materials in total; **Δ**: annual growth rate (%).

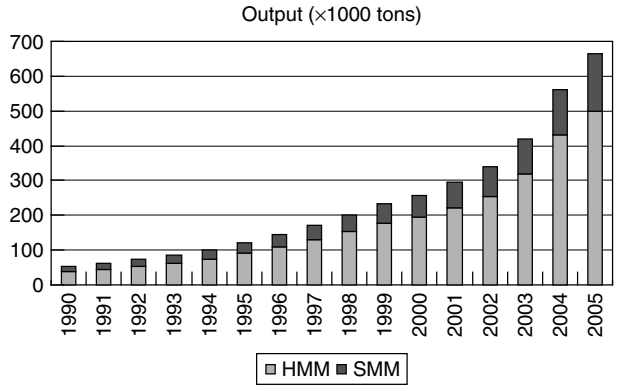

Figure 1. Output ($\times 10^3$ tons) of SMMs and HMMs made in China during 1990–2005.

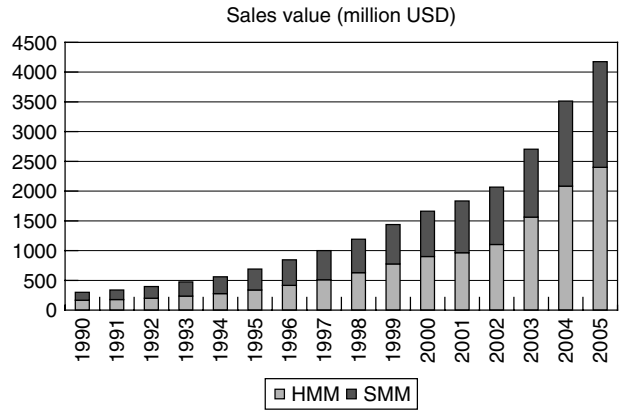

Figure 2. Sales value (million USD) of SMMs and HMMs made in China during 1990–2005.

or final products of high grade with precise tolerance to their customers to gain more added value, rather than gross blocks. This way, the needed profit can be guaranteed.

2 IMPORTANCE OF MAGNETIC MATERIALS IN MODERN COMMUNITY

Silicon-based semiconductors and magnetic materials are two of the cornerstones of the modern world economy. The importance of magnetic materials is obvious. Magnetic materials are widely used not only in computers, electronics, communication, transportation, automotives, aviation, and aerospace industries but they also penetrate into the daily lives of common people.

Whereas in the past the measure of the level of development of an industrialized country was its output of iron and steel, today this measure for a modern economy is the consumption of magnetic and other high-tech materials, since this more accurately reflects the standard of living of the citizens in each country.

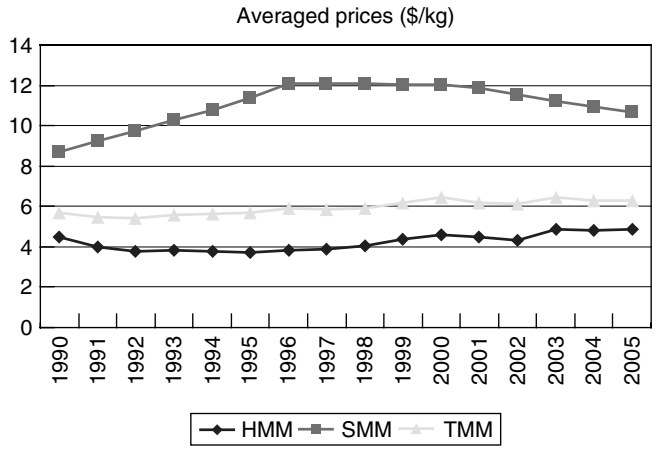

Figure 3. Averaged prices of SMMs, HMMs, and TMMs in China during 1990–2005.

In the early 1990s, the statistics showed that the consumption of magnetic materials per capita for developed countries such as the United States, Japan, and Europe was \$4.5/capita. In developing countries, such as India, this number is only \$0.25/capita, that is, 5.5% of that of developed countries. Per capita consumption in developed countries is 18 times higher than that in developing countries. The gap between developed and developing countries is so significant!

Owing to the policy of birth control, the annual growth rate of Chinese population has reduced from 2% in 1960s to less than 1% in the late 1980s. The average annual growth rate of population in China during the last 15 years since 1990 is 0.755%. The population in 2004 was 11.95% higher than that of 1990, that is, the net growth of population was 0.1398 billion. Obviously, the policy of birth control has helped in strengthening the national economy. While the annual growth rate of the sales value and per capita consumption of magnetic materials averaged was +17.85 and +14.89% respectively, the growth of both, the sales value and per capita consumption of magnetic materials, in 2004 was 11.75 and 8.06 times higher than that in 1990, respectively. The consumption value per capita in China in 1990 was \$0.217, which was only 87% of that in India. It became \$1.555 in 2004. The average annual growth rate of per capita consumption during 1990–2004 was +15.1%. On the basis of this measure, the living standard of China has improved almost seven times since 1990. This is the result of the national economic development, but the contribution of birth control policy should not be ignored. If there was no birth control and the population growth rate kept as high as 2% since 1970s, then 0.5–0.6 billion population would have been added to the current number, which is the denominator, and the per capita consumption as quotient would have been reduced by 50% or more! The situation in India will give the evidence of the importance of birth control as evidenced in another country, where the increased GDP is misappropriated by the growing population.

The population, sales value, domestic consumed value of magnetic materials (both hard and soft) made in China, and per capita consumption during 1990–2004 are listed in Table 2. The percentage of produced magnets consumed domestically is in brackets.

The average annual growth rate of population during 1990–2004 was 0.81%. It further reduced to 0.64% during 2000–2004. The average annual growth rate of the sales value of magnetic materials, its consumption domestically, and consumption per capita during the same period is +19.24, +16.034, and +15.1%, respectively. It is worth mentioning that the annual growth rate of consumption per capita since 1997–2002 was around +12.06%. In 2003 and 2004, it reached +27.8 and +26.9% respectively, which is much higher than the averaged growth rate of +15.1% during 1990–2004. The per capita consumption in 2004 reached \$1.555/capita, while it was \$0.959/capita in 2002. In other words, it has increased 62% during the last two years! The reason is obvious: sales value was significantly increased in 2003 and 2004: its annual growth rate was around +30% in 2003 and 2004, which is much higher than its averaged value of +19.24%.

The growth of consumption per capita in China during 1990–2004 is shown in Figure 4.

Population ($\times 10^9$), sales value ($\$ \times 10^9$), and domestic consumption ($\$ \times 10^9$) of magnetic materials during 1990–2004 is shown in Figure 5.

The growth rate of per capita consumption in developed countries will also continue to rise, although the growth rate will likely be quite low in comparison to that of China. If we assume a growth rate of +2% annually for developed countries (the actual annual growth rate is less then 2%), then the growth trend for developed countries will follow the dashed line in Figure 6.

It should be noted that the vertical coordinate axis in Figure 3 is logarithmic (log \$/capita), which generates a straight line under the assumption of constant growth rate. As shown in Figure 6, if the annual growth rate of per capita consumption for China averages 10, 8, or 7% instead of the current growth rate of +15%, then the logarithmic curve will cross the dashed line that represents the corresponding data for developed countries in 2021, 2028, and 2034, respectively. According to the last statistics published by the Chinese government, the annual GDP growth rate for China was 9.5% during 1985–2004. The annual economic growth rate for China will be kept around ~8% in the foreseeable future. Consequently, the gap between China and developed countries will be eliminated by 2040! In other words, the

Table 2. Population ($\times 10^9$), sales value ($\$\times 10^9$), domestic consumption ($\$\times 10^9$), and per capita consumption ($/capita) of magnetic materials.

	1990	1991	1992	1993	1994
Population ($\times 10^9$)	1.170	1.181	1.1918	1.2025	1.213
Δ(%)	+0.98	+0.94	+0.91	+0.90	+0.91
Sales value ($\$\times 10^9$)	0.2988	0.3383	0.39024	0.4617	0.55912
Δ(%)	+18	+13.2	+15.3	+18.3	+21.1
Domestic consumption ($\$\times 10^9$)	0.25398	0.2774	0.31219	0.3555	0.41375
(%)	(85)	(84)	(80)	(77)	(74)
Consumption, $/capita	0.217	0.235	0.262	0.296	0.341
Δ(%)		+8.3	+11.5	+12.8	+15.4
	1995	1996	1997	1998	1999
Population ($\times 10^9$)	1.224	1.235	1.246	1.257	1.267
Δ(%)	+0.86	+0.89	+0.89	+0.88	+0.8
Sales value ($\$\times 10^9$)	0.69024	0.8451	0.99294	1.1802	1.4105
Δ(%)	+23.5	+22.4	+19	+18.9	+19.5
Domestic consumption ($\$\times 10^9$)	0.49697	0.59157	0.6752	0.76713	0.88862
(%)	(72)	(70)	(68)	(65)	(63)
Consumption ($/capita)	0.406	0.479	0.542	0.61	0.701
Δ(%)	+19.1	+18	+13.1	+12.6	+14.9
	2000	2001	2002	2003	2004
Population ($\times 10^9$)	1.277	1.286	1.294	1.302	1.3098
Δ(%)	+0.79	+0.7	+0.625	+0.62	+0.6
Sales value ($\$\times 10^9$)	1.6176	1.8346	2.0683	2.7043	3.512
Δ(%)	+14.7	+13.4	+12.7	+30.7	+29.9
Domestic consumption ($\$\times 10^9$)	1.0029	1.1191	1.24098	1.5955	2.03696
(%)	(62)	(61)	(60)	(59)	(58)
Consumption ($/capita)	0.785	0.870	0.959	1.2254	1.555
Δ(%)	+11.2	+10.8	+10.2	+27.8	+26.9

Δ: annual changing rate (%).

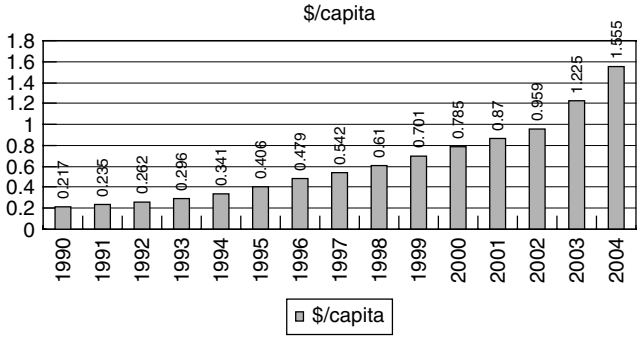

Figure 4. Per capita consumption value of magnetic materials in China (1990–2004).

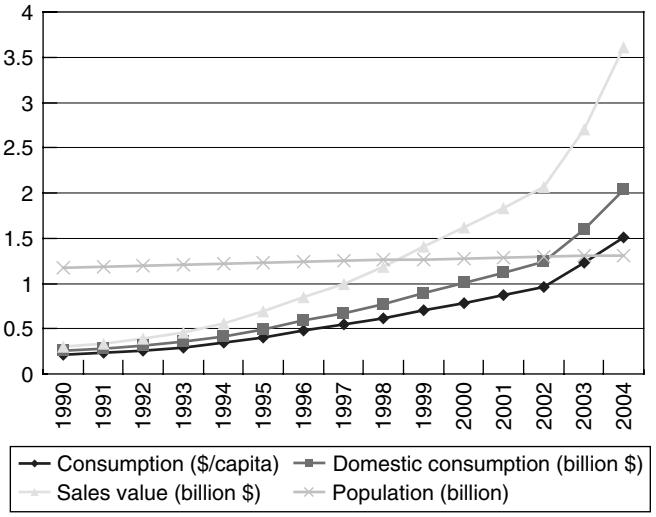

Figure 5. Population ($\times 10^9$), sales value ($\$ \times 10^9$), and domestic consumption ($\$ \times 10^9$), and consumption per capita ($/capita) of magnetic materials in China during 1990–2004.

living standard of China will be the same as that of developed countries by 2040.

A similar analysis was made by me in 2002. At that time, the cross with the dashed line representing developed countries was in 2025, 2033, and 2039, respectively. In

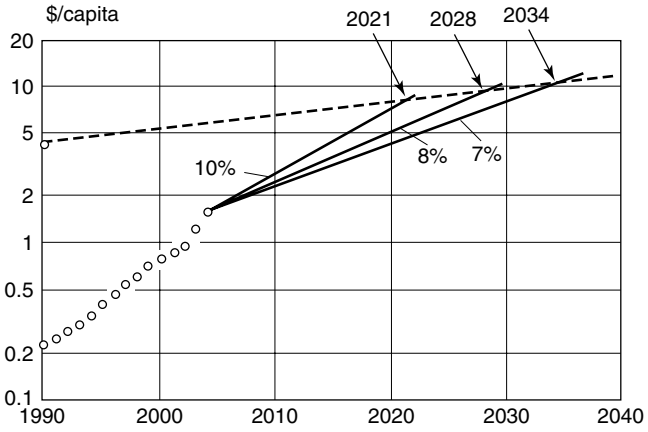

Figure 6. Changing trend of per capita consumption between China and developed countries.

fact, the time required to catch up with developed countries may be shortened by 4 years due to the unusual growth of consumption per capita during the last 2 years.

The per capita consumption value of \$1.555 means that the living standard of China has improved seven times in comparison with that in 1990; nevertheless, it is still only one-third of that of developed countries. Obviously, Chinese people still have a long way to go in order to eliminate the economic gap with developed countries completely.

The Communist Party of China announced in the 16th National Congress that within the first 20 years of the new century, a relatively comfortable life will be made possible for Chinese people, then it will take another 30 years to catch up with the developed countries in living standard. All data concerning the development of the magnet industry in China during the last decade since 1990 can be used as evidence for the reality and reasonability of such a plan.

3 SOFT MAGNETIC MATERIALS IN CHINA

All materials, which can be magnetized to saturation in a relatively low magnetic field, but lose high induction completely once the magnetic field is moved away, are called *soft magnetic materials*. Owing to historical reasons, types of magnetic materials are numerous and their branding names or grades are quite confusing. The International Electrotechnical Committee (IEC) worked on classification and technical terms of magnetic materials for many years and proposed a solution in 1973 (IEC, 1973), according to which magnetic materials are divided into two classes based on their coercive force and application: SMMs and HMMs. Each type of magnetic material can be further divided according to its nature, structural characteristics, and compositions. According to such classification, there are seven types of SMMs (Luo, 1991). Five of them are traditional metallic crystalline SMMs, namely, pure iron and low carbon steel, silicon steel, Fe–Ni (permalloy), Fe–Co, Fe–Al/Fe–Si–Al. The sixth one is nonmetallic SMM–SF. All the six SMMs mentioned earlier are crystalline materials. The final seventh type of SMMs developed in late 1960s are rapidly solidified (RS) amorphous or nanocrystalline (developed in 1980s).

Pure iron and low carbon steel and silicon steel are classified as electrotechnical steel traditionally, which are produced in mass scale and are not related to electronic materials. Thus, the traditional metallic SMMs only include Fe–Ni, Fe–Co, and Fe–Al/Fe–Si–Al alloys.

Current major commercial SMMs are SF and RS materials (Luo, 1995). As for the traditional metallic SMMs, there are Fe–Ni, Fe–Co, and Fe–Al/Fe–Si–Al alloys, which are mostly replaced either by SF or by amorphous/nanocrystalline materials, respectively. Anyway, the sales value of these metallic SMMs is a small part of the total. Consequently, SF and RS materials are solely discussed in the present paper. The traditional metallic SMMs have been ignored. Of course, this way the estimated total output and sales value of SMMs produced in China will be less than what it exactly is, but the tolerance will be less than 2% of the total.

3.1 Chinese soft ferrite industry

3.1.1 General situation

SF has developed from the study on spinel oxide started in 1947. Its permeability is high enough, the electric resistance is 10^4 times higher than that of metallic material; consequently, its power loss is much less and can be used at a higher frequency. Such materials have been commercialized since the 1950s. Now it is widely used in consumer electronics, such as radio, TV, audio, computer, and communication.

There are two groups of SF: $(Mn,Zn)Fe_3O_4$-based, that is, Mn–Zn ferrite; $(Ni,Zn)Fe_3O_4$-based, that is, Ni–Zn ferrite. The resistance of Mn–Zn ferrite $<10^2\,\Omega\,cm$, both permeability and magnetization is higher, it is used as an inductor, working at a frequency of $\sim$100 kHz. The resistance of Ni–Zn ferrite is as high as 10^4–$10^6\,\Omega\,cm$, so it can be used at higher frequencies of up to 100 kHz–100 MHz.

The production of SF in China started in the middle of 1950s. The products were of low grade, which were mainly used for radio. Both the process and the equipment were out of date. With the development of economy in China, the SF industry improved considerably. Significant progress was achieved in the 1990s, both quantitatively and qualitatively, which can be seen by the improvement in TVs,

PCs, and mobile phones made in China. The booming of the electronics sector and the involvement of foreign companies and investors has given much help in the development of the SF industry in China: TDK, FDK, Nippon-Ceramic Co., Ltd., Philips. Some companies from Taiwan have set up plants in main land either jointly or independently. The total output of SF in 2004 reached 120 000 tons. In 1980, it was 3500 tons only.

3.1.2 Current status

Producers of SF in China are estimated to be around 100. The output in 2003 was 90 000 tons, among which Mn–Zn ferrite was 60 000 tons, Ni–Zn ferrite was 25 000 tons, and the rest was about 5000 tons.

There are three types of producers: state owned, private, and foreign invested. The output of state-owned companies is 15 000 tons, which is 17% of the total; the output of private companies is 50 000 tons, that is, 55% of the total; the output of foreign-invested companies is 25 000 tons, that is, 28% of the total. The state-owned portion will be reduced, but the portion of both private- and foreign-invested companies will increase in the future.

The number, location, and production capacity of SF producers are listed in Table 3 (Chen, 2004).

The output (tons), sales value ($\$ \times 10^6$), and price ($/kg) of SF made in China during 1990–2005 are listed in Table 4.

Usually, the price of magnetic materials reduces with their output growth. However, SF seems to be an exception; its price increased continuously until 1996. The performance of products was much improved during this period. Moreover, SF is sold as devices or final products with complex shape and precise tolerance. It is quite different from HF, which is sold as gross blocks. In other words, the price of SF is

Table 3. Location, capacity (tons/year) of Chinese soft ferrite producers.

Location	Company number	Capacity (2003) (tons/year)	Capacity (2005) (tons/year)	Output of powder (tons)
Shanghai	10	31 060	27 350	11 200
Zhejiang	17	31 060	48 500	6000
Jiangsu	16	23 700	31 600	3000
Guangdong	8	14 400	22 000	–
Siquang	8	14 600	38 500	6200
Middle South	3	2000	3000	1000
North China	10	5000	10 000	–
Foreign invested	11	18 500	20 000	–
Total	83	122 760	200 950	–
Powder contained		23 200 tons	37 000 tons	
Actual output of soft ferrite		99 560 tons	163 900 tons	

Table 4. Output (tons), value ($\$\times 10^6$), and price ($/kg) of soft ferrite made in China (1990–2005).

	1990	1991	1992	1993	1994	1995	1996	1997
Output (tons)	15 000	17 400	20 000	22 900	26 300	30 500	35 000	40 000
Δ(%)	–	+16	+14.9	+14.5	+14.8	+16	+14.8	+14.3
Value ($\$\times 10^6$)	129	158.3	192	233.6	281.4	344.6	420	480
Δ(%)	–	+22.7	+21.3	+21.7	+20.5	+22.5	+21.9	+14.35
Price ($/kg)	8.6	9.1	9.6	10.2	10.7	11.3	12	12
Δ(%)	–	+5.8	+5.5	+6.3	+4.9	+5.6	+6.2	0
	1998	1999	2000	2001	2002	2003	2004	2005
Output (tons)	46 000	54 000	62 000	72 000	82 000	99 500	128 000	164 000
Δ(%)	+15	+17.4	+14.8	+16.1	+13.95	+21.3	+28.6	+28.1
Value ($\$\times 10^6$)	552	648	744	849.6	943	1114.4	1395.2	1738.4
Δ(%)	+15	+17.45	+14.8	+14.2	+11	+18.2	+25.2	+24.6
Price ($/kg)	12	12	12	11.8	11.5	11.2	10.9	10.6
Δ(%)	0	0	0	−1.7	−2.6	−2.7	−2.7	−2.8

Δ: annual changing rate (%).

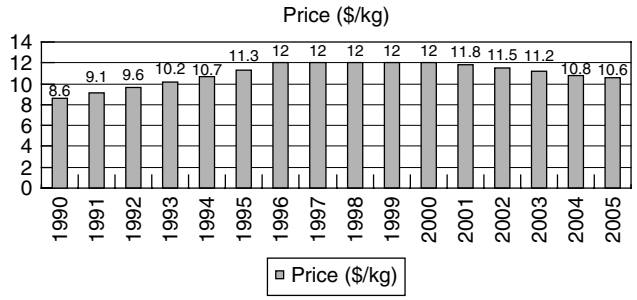

Figure 7. Price variation of soft ferrite made in China during 1990–2005.

not just the material cost, it includes partially added value for devices. Thus, the price of SF is much higher than that of HF. Starting from the new century, the promotion of the SF industry as a whole has stopped. The price has declined slightly since 2000. One can learn about this by comparison of prices of SF and HF. In order to get a higher price to guarantee the needed profit, magnet producers should make final products with high performance and higher tolerance, instead of gross blocks. Following this method, the magnet manufacturers in developed countries have been successful for years. The Chinese magnet manufacturers should also follow the same method.

The price change in SF made in China during 1990–2005 is shown in Figure 7.

The output ($\times 10^2$ tons) and sales value ($\$ \times 10^6$) of SF produced in China during 1990–2005 are shown in Figure 8.

The average annual growth rate of output and sales value of SF during the last decade was around +15.2 and +18% respectively. The growth rates of both have increased considerably during 2002–2005, which reached +28 and +25%. Curves of output and sales value are parallel in principle. The value curve exceeded the output curve due to the increase in price during 1990–1996, with an average annual growth rate of +5%. They became closer due to the reduction in price after 2000, with an average reducing rate of −2.5%.

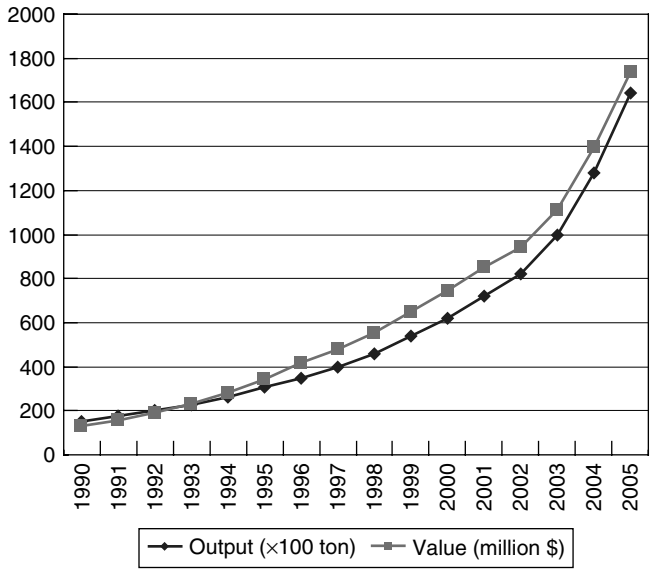

Figure 8. Output ($\times 10^2$ tons), sales value ($\$ \times 10^6$) of soft ferrite made in China.

3.2 Chinese rapidly solidified material industry

Rapidly solidification, RS, or rapidly quenching (RQ) is a technology that was developed in the late 1960s, cooling rates of which range from 10^2 to 10^{10} K s^{-1}. Many new materials with peculiar structures and excellent properties have been prepared by this technique. Structures of these materials ranged from microcrystalline (grain size of approx micrometers), nanocrystalline (grain size of approx micrometers) to amorphous (noncrystalline).

Research on amorphous metals and related RQ technology started in China in 1976, and has since spread to most universities and research institutes. From the 1980s, many metal plants have been involved in the commercialization of amorphous. As a result of R & D works, >100 grades of RS materials were developed, among which 28 grades are included in the Chinese National Standards. Different RS materials, including Fe-based (Fe ≥ 65 wt%), Co-based (Co ≥ 50 wt%), Ni-based (Ni ≥ 60 wt%), Fe–Ni-based (Fe + Ni ≥ 65 wt%), Fe–Co-based (Fe + Co ≥ 60 wt%), and Co–Ni-based (Co + Ni ≥ 60 wt%) amorphous materials have been developed and are commercially available in China now. Since both RS process and its products are quite different from the traditional metallurgy, rapidly solidification and RS materials are considered as a revolutionary development in the last century.

3.2.1 Historical review of the development of RS materials in China

In 1976, RS materials were first prepared in the laboratory. The historical development of RS materials in China is summarized as follows (Luo, 1995; Zhou and Lu, 1999; Zhou, 2001):

1976–1980, fundamental research: Studies on RQ or RS materials were started in 1967. They became quite popular in all universities and research institutes all over China in the 1970s and were commercialized in the 1980s. Some metallurgy plants were also involved in preparing RQ and RS materials. More than 100 grades RS materials were established. The commercialized RS materials included iron based (Fe > 65 wt%), cobalt based (Co > 50 wt%), nickel based (Ni > 60 wt%), iron–nickel based (Fe + Ni > 65 wt%), copper based (Cu > 70 wt%), and so on.

1981–1985, development of applied technology: In order to produce RS materials, much efforts have been made to develop the needed melt spinner or jet caster for the ribbon:

- Before 1982, jet caster with batch melt of several kilograms was developed.
- In 1983, jet caster with double ladles of 50 kg volume were developed and the width of the melt spun ribbon was 50 mm.
- In 1985, jet caster with three ladles of 50 kg capacity for each was developed and the width of melt spun ribbon was 100 mm.
- Development of 50 grades RS materials has been finished.
- Fe–Ni-based ribbon was successfully used to make induction cores for current leakage protectors. This development was invaluable for the rural area of China, where 85% of serious electric shock accidents occurred. Since Ni content in Fe–Ni amorphous ribbon is only half of that in permalloy, its price is also only half of that of permalloy. Consequently, the market demand for such materials sharply increased in the late 1980s. The success of Fe–Ni RS materials has promoted further development of production of RS materials in China. Its total output was around 10 tons in 1985.

1986–1990, building of the pilot-producing line of RS materials:

- In 1989, the melt spinner with three ladles of 100–200 kg volume was set up.
- On-line ribbon automatic catching/wounding mechanism was developed successfully.
- Fourteen sets of transformers (3–100 kVA) with amorphous ribbon cores were built and put into test.
- RS materials were used as welding material, catalyst, and construction fiber.
- Twenty-eight Stat Standards of RS materials were established and nine invention patents were issued.

1991–1995, starting pilot production of core devices:

- Pilot production of million pieces core was built up in 1993.
- c-type, r-type, o-type cores were prepared in mass scale for electronic transformer, choke, inductor, magnetic amplifier, and so on.
- Seventy-five sets of distribution transformers were built by using Fe-based RS ribbon and put into electricity net for test in comparison with that made by grain-oriented Si steel; the power loss under zero load was 60% lower. They worked stably, reliably, with lower temperature rising, and higher ability against overload.

1996–2000, further industrialization:

- In 1996, 'Engineering Center of Amorphous and Nanocrystalline Materials' was established in CISRI with the support of the Stat Science and Technology Committee.
- Producing line of Fe-based RS materials with annual output of 3000–5000 tons and an assembling line of transformer and cores was built. The ribbon width was 220 mm.

2001 – present, further development of RS industry:

The evolution of domestic melt spinner for melt spun ribbon is summarized in Table 5.

3.2.2 *Chinese amorphous and nanocrystalline materials*

RS has been included in the Stat Standard as commercial materials. The conventional RS materials are listed in the following tables as samples. Characteristics of FeCuM (M = Nb, Mo, Cr + V)SiB nanocrystalline soft magnetic alloys are listed in Table 6.

The characteristics of Fe–Ni-based, Fe-based, Co-based, and Co–Ni-based RS SMMs are listed in Tables 7–11 (Luo, 1995; Zhou and Lu, 1999; Zhou, 2001), respectively. Their major applications are also shown in these tables.

According to their nature, RS materials can be divided into two groups: SMMs and nonmagnetic materials. The nonmagnetic RS materials are used as welding, heating, and construction materials. They are also used in other minor applications, which are listed in Tables 12–14 as samples (Luo, 1995).

The SMMs include both crystalline (nanocrystalline) and noncrystalline (amorphous) materials. Amorphous or nanocrystalline materials are used for power transformers that work at several hundreds of hertz, pulse transformers, switch power sources, mutual inductors, and so on. But the main use of amorphous ribbons is for distribution power

Table 5. The evolution of melt spinner and ribbon width produced in China.

	1981	1983	1985	1987	1989	1991	1992	1993	1999
Capacity (kg/batch)	2	10	30	50	100	–	100–200	–	500–1000
Fe-based amorphous width (mm)	<10	10–20	40	50	100[a]	–	–	100[b]	220[b]
Fe-based nanocrystalline ribbon width (mm)	–	–	–	–	–	<10	20–30	60	100

[a]On-line fully automatic winding system of amorphous ribbons.
[b]On-line fully automatic winding system of amorphous ribbon and with automatic roll changing.

Table 6. Characteristics of FeCuM (M = Nb, Mo, Cr + V)SiB nanocrystalline soft magnetic alloys.

	$\mu_{0.08}$ ($\times 10^3$)	μ_m ($\times 10^3$)	H_c (A m^{-1})	B_r (T)	B_s (T)	P (W kg^{-1})
FeCuNbSiB (NMF)	17.5	64	0.48	–	1.18	$P_{5/20k}$ = 14.34 $P_{2/200k}$ = 128
$Fe_{73.5}Cu_1Nb_3Si_{13.5}B_9$ (TMF)	1.5	168	0.38	1.02	1.20	$P_{10/400k}$ = 0.52 $P_{10/1k}$ = 1.89
FeCuNbSiB (TMF)	5	–	0.64	0.06	1.16	$P_{10/1k}$ = 0.81 $P_{10/400k}$ = 0.23
$Fe_{74}Cu_1Mo_3Si_{13}B_8$ (NMF)	10	37.3	1.36	0.87	1.33	$P_{5/20k}$ = 16
$Fe_{74}Cu_1Mo_{2.5}Si_{13.5}B_9$ (LMF)	2.5	134	0.648	1.16	1.31	$P_{10/400k}$ = 0.43 $P_{10/1k}$ = 1.52
$Fe_{74}Cu_1Mo_3Si_{13}B_9$ (TMF)	2.5	3.34	1.44	0.08	1.33	$P_{5/20k}$ = 14.3
FeCuCrVSiB (NMF)	11	51	0.96	0.58	1.05	$P_{2/200k}$ = 79.3
FeCuCrVSiB (LMF)	0.56	82	0.4	0.93	1.02	$P_{2/200k}$ = 459
FeCuCrVSiB (TMF)	4.3	6.1	0.96	0.05	1.03	$P_{2/200k}$ = 73.8

NMF: annealing without magnetic field; LMF: annealing with longitudinal magnetic field; TMF: annealing with transverse magnetic field.

Table 7. Fe–Ni-based RS soft magnetic materials.

Composition (at%)	B (T)		R' (A m^{-1})	H_c (A m^{-1})	μ_m ($\times 10$)^3	P (W kg^{-1})			T_C (°C)	T_x (°C)	ρ (g cm^{-3})	Major applications
	B_s	B_{80}				$P_{1/400}$	$P_{1/5k}$	$P_{0.2/20k}$				
$Fe_{29-50}Ni_{30-44}(P,B,C)_{15-24}$	0.75	0.6	–	1.2	400	1.5	65	15	243	410	7.5	Leakage current protector Switch power source, sensor
$Fe_{29-50}Ni_{30-44}(P,B,C)_{15-24}$	0.75	–	0.1	1.6	3	–	–	15	258	421	7.5	Switch power source High-frequency inductor
$Fe_{45-50}Ni_{28-30}V_{1-2}Si_{7-8}B_{14-15}$	0.9	0.8	–	1.2	400	–	–	–	300	500	7.4	Magnetic amplifier Mutual inductor

transformers working at an industrial frequency of 50–60 Hz. Output percentages of different types of RS materials made in China (1997) are shown in Figure 9. Fe–Ni-based and FeCuNbSiB are all SMMs, the former being mainly amorphous and the latter nanocrystalline. The rest are non-magnetic materials.

3.2.3 General situation of Chinese RS materials

The output (tons), sales value ($\$ \times 10^6$), and price ($/kg) of RS materials made in China during 1990–2005 are summarized in Table 15.

The annual changing rate $\Delta(\%)$ of related data is included in the Table 15. The sales price change of RS materials is shown in Figure 10.

The output of RS materials has been increasing continuously since 1990. The growth rate during the last decade has been around +20% annually. Accordingly, its price has been declining with an annual reducing rate of −5%. Now the price is only half of that of 10 years ago! The significant increase in price since 2003–2004 is the result of increase in price of raw materials. The output ($\times 10^2$ tons) and sales value ($\$ \times 10^6$) of RS materials made in China during 1990–2005 are summarized in Figure 11.

3.3 General status of Chinese soft magnets

The output (tons), sales value ($\$ \times 10^6$), and price ($/kg) of SF, RS materials, and SMMs in total (T) made in China during 1990–2005 are summarized in Table 16.

As mentioned earlier, there are two types of SMMs in China: SF and RS materials (amorphous and nanocrystalline). Also, there are some metallic soft magnetic alloys, which are very few in quantity; these have therefore been ignored in the present paper. The error in output and sales value should be less than 2% due to such ignorance.

The output of RS materials has been increasing continuously from 1% of the total in 1990 to 2.2% in 2003. This tendency would be the same in future, especially if Fe-based

Table 8. Fe-based RS soft magnetic materials.

Composition (at%)	B_S (T)	B_{30} (T)	R' ($A\,m^{-1}$)	H_{cl} ($A\,m^{-1}$)	μ_m ($\times10^3$)	$\mu\rho(\times10^3)$ $\Delta B = 0.6\,T$	$\mu\rho(\times10^3)$ $\Delta B = 1.5\,T$	P ($W\,kg^{-1}$) $P_{1/60k}$	P ($W\,kg^{-1}$) $P_{1/400K}$	P ($W\,kg^{-1}$) $P_{1/1K}$	T_C (°C)	T_x (°C)	ρ ($g\,cm^{-3}$)	Applications
$Fe_{76-81}(SiB)_{19-24}$	1.55	1.0	–	6.4	120	–		0.2	1.7	3	390	455	7.3	Power transformer Pulse transformer Switch converter
$Fe_{75-81}Si_{3-5}$ $B_{13-19}C_{1-2.6}$	1.6	1.1	–	8	120	–		–	3.5	35	420	490	7.3	Middle-high-frequency transformer Switch power source
$Fe_{75-81}Si_{3-5}$ $B_{13-19}C_{1-2.6}$	1.6	1.3	≥0.8	6.4	6.4	–	4.7	0.16	2	30	420	490	7.3	Bipolar pulse transformer
$Fe_{75-81}Si_{3-5}$ $B_{13-19}C_{1-2.6}$	1.6	–	≤0.2	8	–	4	–	0.3	2	25	420	490	7.3	Single pole pulse transformer
$Fe_{71-74}Ni_{6-10}$ $B_{10-5}(Si,P,C)_{8-12}$	1.4	1.2	–	4	250	–	–	–	1.5	35	435	450	7.4	Magnetic amplifier Power transformer (400 Hz)
$Fe_{73-77}Si_{1-3.3}B_{14-17}$ $Ni_{4.5-5}Mo_{2.5-5.5}$	1.3	1.1	–	5	100	–	–	–	–	25	318	528	7.5	Transformer core (high frequency)
$Fe_{75-76}Si_{8-11}B_{10-24}(Cr,Nb,Mo)_3$	1.32	–	–	6.4	–	–	5	–	1.8	–	312	550	7.3	Pulse transformer Power transformer (400 Hz)
$Fe_{75-76}Si_{8-11}B_{10-24}(Cr,Nb,Mo)_3$	1.32	1	≥0.8	3.2	–	–	–	–	1.4	–	310	550	7.3	Transformer (0.4–10 kHz)
$Fe_{77-81}Si_{4-6}$ $B_{15-17.5}$	1.58	1	–	8	200	–	–	–	1.5	20	405	515	7.3	High/middle frequency Transformer

R': residual magnetization ratio; $\mu\rho$: relative pulse permeability; T_C: Curie temperature; T_x: crystallization temperature.

Table 9. Co-based RS soft magnetic materials.

Composition	B(T)		R'	H_c	μ_m	$\mu\rho$	P (W kg^{-1})		T_C	T_x	ρ	Major
	B_s	B_{30}	(A m^{-1})	(A m^{-1})	($\times 10^3$)	($\times 10^3$)	$P_{0.5/20\,k}$	$P_{0.3/100\,k}$	($^\circ$C)	($^\circ$C)	(g cm^{-3})	applications
$Co_{67-69}Fe_{3.5-5}$ $Si_{17-10}B_{16-19}$ $M_{1.2-2.2}$	0.7	0.5	$\leq$0.1	1.2	–	4	25	–	340	530	7.8	Pulse transformer High-frequency converter
$Co_{61-65}Fe_{4-4.5}$ $Si_{9-14}B_{12-18}M_{2-7}$	0.68	0.5	$\geq$0.85	1.2	400	–	35	–	320	510	7.8	Magnetic amplifier Mutual inductor Leakage current protector
$Co_{66-72}Fe_{1.5-4}$ $Si_{15-13}B_{10-20}M_{3-7}$	0.8	0.6	–	1.2	–	–	20	–	320	530	7.9	Switch power source (20 kHz)
$Co_{67-70}Fe_{2.5-3.5}$ $Si_{10-12}B_{12-19}M_{2-5}$	0.6	0.5	–	1.6	200	–	–	110	300	540	8	Switch power source (100–200 kHz)
$Co_{65-86}Fe_{1-7}B_{3-20}$ $Si_{10-14}M_{2-15}$	0.6	–	–	1.2	–	–	20	–	260	480	7.9	Magnetic head and sensor of high frequency
$Co_{66-68}Fe_{4-5}$ $Si_{6-10}B_{15-26}M_{2-7}$	0.53	–	–	1.6	150	–	–	–	320	520	7.9	Magnetic shielding (as quenched)

M: one or more metals

Table 10. Co–Ni-based RS soft magnetic materials.

Compositions (at%)	B(T)		R'	H_c	μ_m	P (W kg^{-1})		T_c	T_x	ρ	Major applications
	B_s	B_{80}	(A m^{-1})	(A m^{-1})	($\times 10^3$)	$P_{0.1/20\,k}$	$P_{0.3/1000\,k}$	($^\circ$C)	($^\circ$C)	(g cm^{-3})	
$Co_{24-40}Ni_{28-39}$ $Fe_{6-14}Si_{5-9}B_{7-16}$	0.55	–	–	1.3	100	40	–	220	460	7.9	Switch power source
$Co_{24-40}Ni_{28-39}$ $Fe_{6-14}Si_{5-9}B_{7-16}$	0.6	0.55	0.9	1.2	400	50	–	319	443	7.9	Magnetic amplifier Sensor

Table 11. Fe-based RS corrosion resistant alloy.

Composition (at%)	Dimension (mm)	B_s(T)	S (cm^2 g^{-1}) (thickness 0.03 mm)	Corrosion resistance	Applications
$Fe_{74-79}Cr_{4-9}$	Thickness 0.02–.03	1.1	90–130	Better than Cr-stainless steel	Magnetic separation
$P_{10-15}C_{6-10}$	Width 0.5 mm				Water treatment Cathode for gold extraction

S: specific surface.

Table 12. Ni-based RS elastic alloy and its application.

Composition (at%)	E (Mpa)	σ (Mpa)	H_v	ρ (10^{-7} Ω-m)	Major application
$Ni_{89.5-93}Si_{5-6}B_{2.5-3.5}$	7.8×10^4	3.4×10^3	850	15	Membrane of sensor

E: Young's module; σ: shearing module.

ribbon is used as cores for distribution transformer. The output (tons) of both SF and RS materials made in China during 1990–2005 is shown in Figure 12.

Although the output of RS materials has been increasing continuously, its price has been reducing significantly; therefore, the percentage of its sales value is only 2% of the total. Sales value ($\$ \times 10^6$) of both SF and RS made in China during 1990–2005 are shown in Figure 13.

Prices of SF, RS materials, and averaged price for SMMs in total (averaged) made in China during 1990–2005 are shown in Figure 14.

Because of the improvement in performance, SF was sold as a final product and its price had been increasing slightly before 1997. In contrast, the price of RS materials had been declining continuously. The increase in the price in 2003–2004 was the result of the increase in price of raw materials. Since the portion of SF is about 98% of the total, the averaged price of soft magnets in total is almost the same as that of SF.

4 GENERAL STATUS OF HARD MAGNET INDUSTRY

The sales value ($\$ \times 10^9$) of SMMs, HMMs, and global TMMs during 1960–2010 is listed in Table 17.

Data of 1960–1990 are taken from (Luo, 1996), data of 2000 are actual, and the forecast of 2010 is based on actual data of 2002–2004. The annual average growth rate $\Delta(\%)$ is included in the same table. The data in the brackets are in percentage related to the total value.

Sales value of SMMs was higher than that of HMMs until the middle of 1990s. Since 1994, the sales value of hard magnets exceeded that of SMMs. It is worth noting that the averaged annual growth rate of TMMs during last 50 years has been around +6.1% (6.1075%). During the last 50 years, the average annual growth rates of SMMs and HMMs have been quite different: they have been around +3.8% (3.81248%) and +9.6% (9.5513%), respectively. Thus, every decade the value of SMM and HMM would increase 1.45 and 2.49 times, respectively. Such tendencies will continue. Consequently, the value of HMM has exceeded that of SMM since 1994. In 2010, the value of HMM is expected to be more than two times that of SMM. The change in the global sales value ($\$ \times 10^9$) of magnetic materials since 1960 is summarized in Figure 15. The changing trend of both SMMs and HMMs mentioned above can be seen clearly from Figure 15.

5 STRUCTURE CHANGE OF THE MAGNET INDUSTRY

There are four major commercially available magnets: Alnico developed in the late 1930s; HF developed in the early 1950s; first and second generation of rare-earth magnets: $SmCo_5$ (1968) and Sm_2Co_{17} (late 1970s); and third generation of rare-earth magnet developed in 1983–NdFeB.

The global output T (tons), sales price P (\$/kg), and sales value V ($\$ \times 10^9$) of Alnico, ferrite, SmCo, and NdFeB magnets since 1985–2010 are listed in Table 18. The sales values V ($\$ \times 10^9$) of each type of magnets during 1985–2010 are shown in Figure 16.

As seen in Figure 16, the value of HF is more than half of the total until 1999; till then it was the majority of the magnet market. Starting from 2000, the value of rare-earth magnet (NdFeB + SmCo) exceeded that of HF. Such tendencies would continue in the foreseeable future; consequently, rare-earth magnets would certainly be the majority of magnets sold in the twenty-first century.

Both performance and price of each type of magnets are rather different. However, we cannot evaluate each type of magnets solely by its performance or its price. The energy stored in unit volume of magnet–energy product E (kJ m^{-3})–is an important parameter in characterizing a magnet. The price of unit energy stored in a magnet is called *price performance* W (\$/J) of such magnet. The price performance W (\$/J) can be expressed by following formula:

$$W = \frac{P\rho}{E} \tag{1}$$

Where W is the price performance (\$/J), P is the price (\$/tons), ρ is the density (tons m^{-3}), and E is the energy product (kJ m^{-3}) of the magnet.

The price performance of different magnets is listed in Table 19. The densities of magnets are also included in the same table.

The market share of certain magnets could not be evaluated by its tonnage output (T) solely, but could be evaluated by the energy stored in such magnets (J). If energy stored in all magnets in total globally is J_{tot}, then J/J_{tot} (%) will be the market share of such magnets. Energy stored in a certain magnet J is expressed by the following formula:

$$J = \frac{TE}{\rho} \tag{2}$$

Where J is the total energy stored (joule), T is the tonnage output (tons), E is the energy product (kJ m^{-3}), and ρ is the density (tons m^{-3}) of the magnet.

Market shares of different magnets during 1985–2010 are listed in Table 20.

Data for 1985, 1990, and 1995 in Table 20 were referred from (Luo, 1997), the data of 2005 and 2010 are estimated on the actual data of 2002–2004.

The structure change of the global magnet market (1985–2010) is summarized in Figure 17.

Table 13. The composition (%) and applications of Ni-based and Cu-based welding materials.

Composition (at%)	T_m (°C)	T_w (°C)	σ (Mpa)	T_{work} (°C)	ρ (10^{-7} Ω-m)	Major application
$Ni_{79.5-85.5}Cr_{6-8}B_{2.75-3.5}$ $Si_{4-5}Fe_{2-4}C_{0.1-0.2}$	960–990	1040–1100	137–156	<850	8.7	Welding stainless steel and supper alloy
$Cu_{77-88}Si_{10-20}Ni_{2-3}$	830–870	900–920	205–402	<850	8.7	Welding steel/steel and steel/Cu to replace Ag-based material
$Cu_{75-79}Ni_{5-15}Si_{4-12}P_{5-10}$	560–640	700–750	98–137	<850	8.7	For welding Cu/Cu, Cu/Ag–Cd, Cu/Ag to replace Ag foil
$Cu_{80-90}Ag_{8-12}Si_{1-3}P_{2-4}$	560–640	700–750	98–137	<850	8.7	To replace Ag-based welding material

T_m: melting point; T_w: welding temperature; T_{work}: working temperature; σ: shear strength in welding area.

Table 14. Fe-based RS metallic fiber and its application.

Composition (at%)	Scale (mm)	T_{work} (°C)	η (10^{-6}/°C)	T_m (°C)	ρ (g cm^3)	Application
$Fe_{30-60}Ni_{20-40}$(Cr, Si,Mn)$_{15-30}$	Φ0.4–0.6 Length 20–35	1000–1350	17.64–18.54	1380–1420	7.72	To strengthen furnace body

η: lineal expansion coefficient.

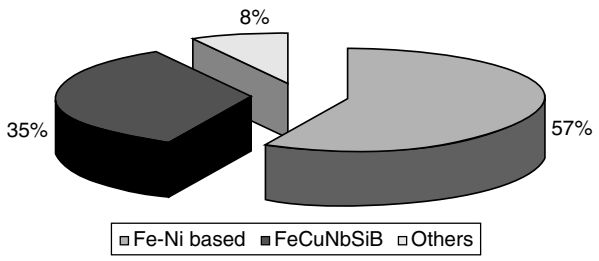

Figure 9. Output distribution of different RS materials made in China (1997).

Both vertical and horizontal coordinate axes in Figure 17 are given in logarithm because the changes in both market share J/J_{tot} and price performance W (\$/J) have covered quite big ranges: from 0.003 to 0.916 for J/J_{tot} (%) and from 0.8 to 11.4 for W (\$/J).

The market share of SmCo was 2% in 1985. Owing to strong competition from NdFeB, the market share of SmCo declined significantly since the middle of 1980s: it reduced to 1.54 and 1% in 1990 and 1995 respectively. As a result of significant reduction in the cost of both Co and Sm since 1995, the market share of SmCo has increased gradually in recent years; it was 1.1 and 1.4% in 2000 and 2005 and it will be 1.2% in 2010.

The price performance of SmCo magnet was the highest among all others: it was \$11.4/J in 1985, it reduced to \$4.7/J in 2000, and it will be \$3.2/J in 2010. It has reduced 3.5 times in comparison with that in 1985.

Market shares of different magnets changed considerably during 1985–2010: Positions of all traditional magnets, such as Alnico, HF, and SmCo are moving from upper right down toward lower left. NdFeB goes exactly in the opposite direction: moving from lower right toward upper left. Obviously, NdFeB is just like a gradually rising sun in the new century! The market share of ferrite, Alnico, and SmCo in 1985 was 91.6, 6.06, and 2.04% respectively. NdFeBs market share in 1985 was a negligible 0.3%! It has jumped to 5% in 1990, which has exceeded that of Alnico and SmCo in the same year. The market share of NdFeB was 12 and 22% in 1995 and 2000 respectively and it will be 32.8 and 47.5% in 2005 and 2010 respectively.

Alnico magnet had the majority share of the global magnet market before 1970. Since then, the market share of Alnico has been declining steadily. It dropped from 6% in 1985 to 1.8% in 2000 and it will be 0.4% or less in 2010! HF has the current majority share of the magnet market. Owing to the competition from NdFeB, its price performance has reduced gradually: It was \$0.94/J in 1985, it became \$0.96/J since the late 1980s until late 1990s due to performance improvement, then it dropped to \$0.9/J in 2000 and it will be \$0.8/J in 2010. The market share of ferrite is also shrinking: it was 91.6, 89, 84, and 75 in 1985, 1990, 1995, and 2000 respectively. It will drop to 51% by 2010.

Table 15. Output (tons), sales value ($\$ \times 10^6$), price ($/kg) of RS materials made in China during 1990–2005.

	1990	1991	1992	1993	1994	1995	1996	1997
Output (tons)	150	180	210	250	310	380	480	600
Δ(%)	+23	+20	+17	+19	+24	+23	+26	+25
Value ($\$ \times 10^6$)	3.2	3.7	4.2	4.9	5.9	6.8	8.2	9.8
Δ(%)	+19	+16	+14	+17	+20	+15	+21	+20
Price ($/kg)	21.3	20.5	20	19.6	19.1	18	17.1	16.4
Δ(%)	−3.5	−3.9	−2.5	−2	−2.6	−6	−5.3	−4.3
	1998	1999	2000	2001	2002	2003	2004	2005
Output (tons)	780	1010	1250	1500	1800	2160	2600	3100
Δ(%)	+30	+29	+24	+20	+20	+20	+20	+20
Value ($\$ \times 10^6$)	12.3	15	17.6	20.3	23	26.4	33.28	38.75
Δ(%)	+25.5	+22	+17	+15.3	+13.3	+15	+26	+16
Price ($/kg)	15.8	14.9	14.1	13.5	12.8	12.2	12.8	12.5
Δ(%)	−3.8	−6	−5.7	−4.4	−5.5	−4.9	+4.9	−2.4

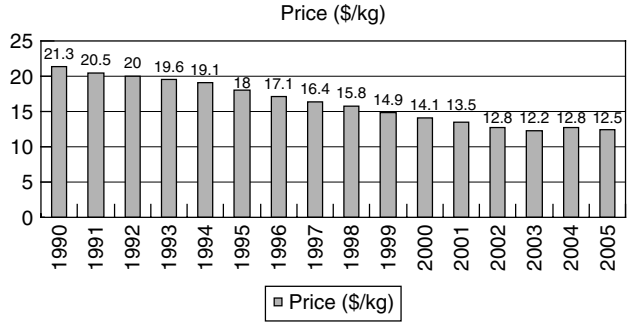

Figure 10. Price change of RS materials made in China during (1990–2005).

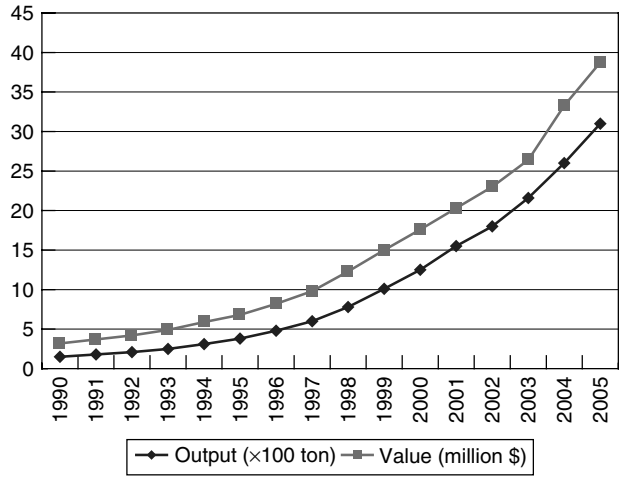

Figure 11. Output ($\times 10^2$ tons) and sales value ($\$ \times 10^6$) of RS materials made in China during (1990–2005).

The price performance of ferrite is the lowest among all magnets. It will be $0.8/J in 2010. The price performance of NdFeB was $5.83/J in 1985. It is estimated to be $1.73/J in 2010, that is, it is 2.1 times that of ferrite. In 2010, the price performance of SmCo and Alnico will be $3.23/J and $3.39/J respectively, that is, it will be 4 and 4.2 times that of ferrite.

6 GLOBAL MAGNET INDUSTRY CENTER SHIFTING

Magnets as functional materials and their development and applications are closely related to both fundamental research and booming of modern industry. Generally speaking, if half of the global total output of magnets is produced in a certain country or area, and where the research activity on magnetic materials is rather dynamic, then this country or area would become the 'Center of Global Magnet Industry'. Europe was such a center before World War II. After World War II, the Center of Global Magnet Industry shifted to the United States. Since late 1960s of last century, this center has shifted to Japan. With the beginning of the new century, the Center of Global Magnet Industry has finally shifted to China, which is evidenced by outputs of different types of magnets produced in China.

It is worth mentioning that China has a long history and tradition on magnetism and magnetic materials and their applications. There are many engineers and technicians working in the fields of magnetism and magnetic materials. Statistics showed that more than 1000 students graduated from the department of universities related to

Table 16. Output (tons), sales value ($\$ \times 10^6$), price ($/kg) of SF, RS, and soft magnetic materials in total (T) made in China during 1990–2003.

		1990	1991	1992	1993	1994	1995	1996	1997
Output (tons)	SF	15 000	17 400	20 000	22 900	26 300	30 500	35 000	40 000
	Δ(%)	+15	+16	+15	+14.5	+14.8	+16	+14.8	+14.3
	SF/T (%)	99	99	99	98.92	98.84	98.77	98.65	98.52
	RS	150	180	210	250	310	380	480	600
	Δ(%)	+23	+20	+17	+19	+24	+23	+26	+25
	RS/T (%)	1	1	1	1.08	1.16	1.23	1.35	1.48
	T	15 150	17 580	20 210	23 150	26 610	30 880	35 480	40 600
	Δ(%)	+15	+16	+15	+14.5	+14.9	+16	+14.9	+14.4
Value ($\$ \times 10^6$)	SF	129	158.3	192	233.6	281.4	344.6	420	480
	Δ(%)	+21	+22.7	+21.3	+21.7	+20.5	+22.5	+21.9	+14.3
	SF/T (%)	97.58	97.72	97.86	97.95	97.95	98.06	98.09	98
	RS	3.2	3.7	4.2	4.9	5.9	6.8	8.2	9.8
	Δ(%)	+19	+16	+14	+17	+20	+15	+21	+20
	RS/T (%)	2.42	2.28	2.14	2.05	2.05	1.94	1.91	2
	T	132.2	162	196.2	238.5	287.3	351.4	428.2	489.8
	Δ(%)	+21	+22.5	+21.1	+21.5	+20.5	+22.3	+21.8	+14.4
Price ($/kg)	SF	8.6	9.1	9.6	10.2	10.7	11.3	12	12
	Δ(%)	+5.5	+5.8	+5.5	+6.3	+4.9	+5.6	0	0
	RS	21.3	20.5	20	19.6	19.1	18	17.1	16.4
	Δ(%)	−3.5	−3.9	−2.5	−2	−2.6	−6	−5.3	−4.3
	T	8.73	9.22	9.71	10.3	10.8	11.38	12.07	12.06
	Δ(%)	+5.3	+5.6	+5.3	+6	+4.9	+5.4	+6.06	−0.8

		1998	1999	2000	2001	2002	2003	2004	2005
Output (tons)	SF	46 000	54 000	62 000	72 000	82 000	99 500	128 000	164 000
	Δ(%)	+15	+17.4	+14.8	+16.1	+13.9	+21.3	+28.6	+28.1
	SF/T (%)	98.33	98.16	98.02	97.96	97.85	97.73	98	98.14
	RS	780	1010	1250	1500	1800	2160	2600	3100
	Δ(%)	+30	+29	+24	+20	+20	+20	+20	+20
	RS/T (%)	1.67	1.84	1.98	2.04	2.15	2.22	2	1.86
	T	46 780	55 010	63 250	73 500	83 800	101 660	130 600	167 100
	Δ(%)	+15.2	+17.6	+15	+16.2	+14	+21.3	+28.5	+27.9
Value ($\$ \times 10^6$)	SF	552	648	744	849.6	943	1114.4	1395.2	1738.4
	Δ(%)	+15	+17.4	+14.8	+14.2	+11	+18.2	+25.2	+24.6
	SF/T (%)	97.82	97.74	97.69	97.67	97.62	97.78	97.67	97.82
	RS	12.3	15	17.6	20.3	23	26.4	33.28	38.75
	Δ(%)	+25.5	+22	+17	+15.3	+13.3	+15	+26	+16
	RS/T (%)	2.18	2.26	2.31	2.33	2.38	2.22	2.33	2.18
	T	564.3	663	761.6	869.9	966	1140.8	1428.5	1777.15
	Δ(%)	+15.2	+17.5	+14.9	+14.2	+11	+18.1	+25.2	+24.4
Price ($/kg)	SF	12	12	12	11.8	11.5	11.2	10.9	10.6
	Δ(%)	0	0	0	−1.7	−2.6	−2.7	−2.7	−2.8
	RS	15.8	14.9	14.1	13.5	12.8	12.2	12.8	12.5
	Δ(%)	−3.8	−6	−5.6	−4.4	−5.5	−4.9	+4.9	−2.4
	T	12.06	12.05	12.04	11.84	11.53	11.22	10.94	10.64
	Δ(%)	0	−0.08	−0.08	−1.7	−2.7	−2.8	−2.5	−2.8

magnetism annually. Many conferences concerning magnetism and magnetic materials are held in China every year. All of these promote the Chinese magnet industry. Tonnage outputs of magnets made in different countries in 2004 are summarized in Table 21. Distributions of NdFeB, ferrite, and Alnico magnet outputs in 2004 in different countries are summarized in Figures 18–20, respectively.

In short, outputs of different magnets made in China are the highest in the world since the beginning of the new

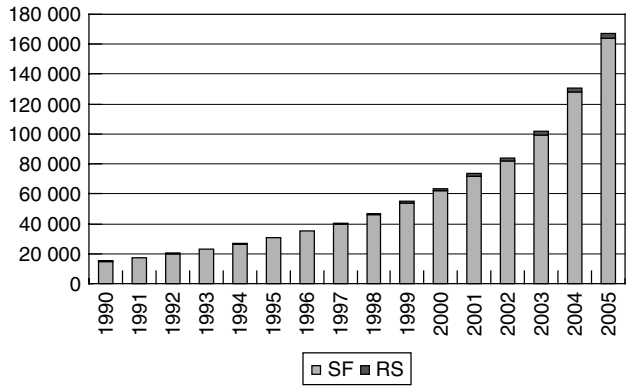

Figure 12. Output (tons) of both SF and RS materials made in China during 1990–2005.

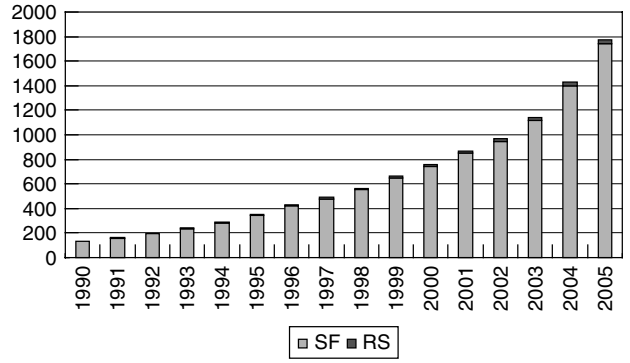

Figure 13. Sales value ($\$ \times 10^6$) of both SF and RS made in China during 1990–2005.

century. The position of China in the global magnet market will be further strengthened in the future. Discussing the position of China in the global magnet market and the future trend someone with breadth of vision in the West said that 'China would be the center of the global magnet industry in the twenty-first century. Owing to her abundant natural resources, wide territory, large population, and huge domestic market, China would keep such a position much longer than Europe, The United States of America and Japan did!' (Port Wheeler, private communication, May, 2002).

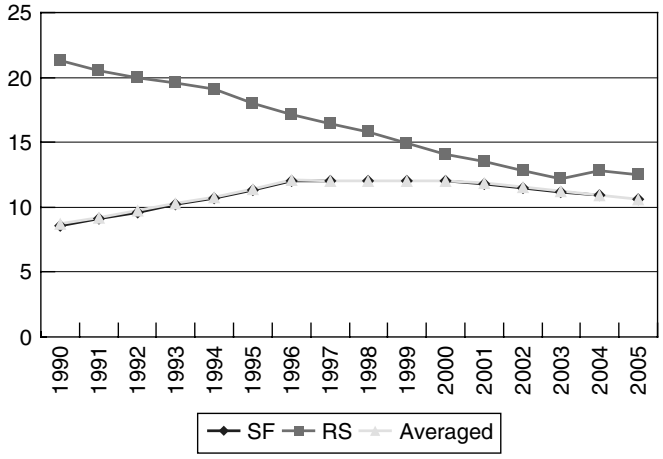

Figure 14. Price ($/kg) of SF, RS, and soft magnet in total (averaged) made in China.

Along with providing the majority of produced magnets, the Global Center of the Magnet Industry should provide magnets that are cheaper and better to all customers globally. On the basis of the abundant natural resources, huge manpower, and excellent expertise, China will surely be able to play the role of Global Center in the twenty-first century.

In view of the fact that China becomes the Center of Global Magnet Industry, there are two opinions: one is rather pessimistic, the other is quite optimistic.

The pessimist asked: 'As NdFeB magnets are so important, and are used in all high tech applications, including IT, computer, and consumer electronics, then it is hard to understand why USA and Europe agreed to stop their NdFeB magnet production?' They strongly suggested 'Do not shift all production lines to China, at least you have to keep the most advanced one for your own country!' They are afraid that China will have a monopoly in this area just as someone else has had in the past. Of course, monopoly is not good for the healthy development of the magnet industry.

The optimist said: 'Now the economy globalization becomes reality, where can make magnets better and cheaper,

Table 17. Global sales value ($\$ \times 10^9$) change of magnetic materials.

	1960	1970	1980	1990	2000	2010
SMM	0.77	1.39	1.89	2.69	3.55	5
Δ(%)	~+6	+6.0846	+3.121	+3.5921	+2.8129	+3.48423
SMM/T (%)	(85.6)	(82)	(70)	(57.4)	(44.2)	(28.7)
HMM	0.13	0.31	0.81	2	4.48	12.44
Δ(%)	~ +9	+9.0792	+10.081	+9.4587	+8.4	+10.7528
HMM/T (%)	(14.4)	(18)	(30)	(42.6)	(55.8)	(71.3)
TMM	0.9	1.7	2.7	4.69	8.03	17.44
Δ(%)	~ +6	+6.6	+4.7	+5.7	+5.6	+8.1

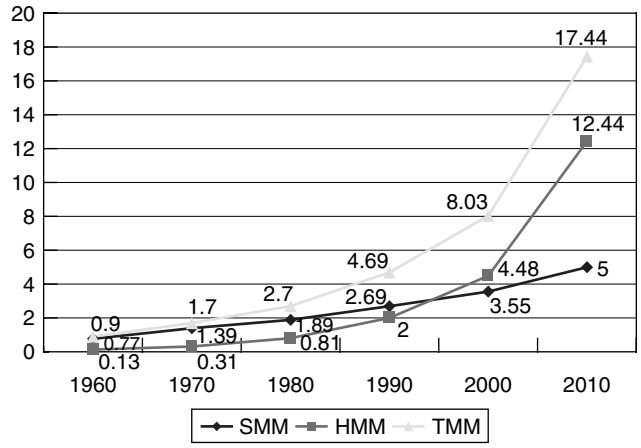

Figure 15. Global sales value ($\$ \times 10^9$) changes of magnetic materials since 1960.

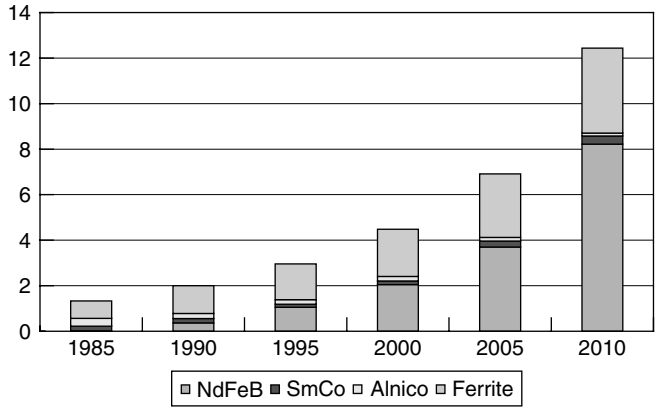

Figure 16. Sales value V ($\$ \times 10^9$) of each type of magnet (1985–2010).

then we have to shift all production activities there, it is natural and no one should complain. In fact, we have to thank China, without her contribution who can imagine that the price of sintered NdFeB magnets would drop from \$350/kg in 1983 to \$60–70/kg. Without significant price dropping of magnets, the popularization of magnet application is impossible.' I believe that the latter opinion reflects the truth and fact more than the former.

There are a lot of samples to show whether a business can be kept only due to 'strategy reason' or not. The rare-earth deposit in Mountain Pass, California, USA kept its pivotal position in the world market before the rising of the Chinese rare-earth industry until 1980s. In the late 1980s and early 1990s, there was a certain possibility for Molycorp to cooperate with China in rare-earth business in some way. But it was stopped due to 'national security', when it was clear that the mining in Mountain Pass only lost money in early 1990s. Again, it was forced to continue this business only because of 'strategic consideration'. Unfortunately, in a duration of 5 years, no single 'patriot' could be found in the United States who was willing to buy the expensive rare earth from Molycorp and refused to use rare earth from China. Finally, mining in Mountain Pass was closed in 1997. This is the result of market economy!

Table 18. Global output T (tons), sales price P (\$/kg), and sales value V ($\$ \times 10^9$) of different magnets.

	1985			1990			1995		
	T (tons)	P (\$/kg)	V ($\$ \times 10^9$)	T (ton)	P (\$/kg)	V ($\$ \times 10^9$)	T (ton)	P (\$/kg)	V ($\$ \times 10^9$)
NdFeB	75	200	0.015	2170	170	0.37	7040	150	1.056
SmCo	800	260	0.208	900	210	0.19	700	185	0.13
Alnico	7000	35	0.245	7300	30	0.22	7150	28	0.2
Ferrite	2×10^5	3.8	0.76	2.9×10^5	4.2	1.22	3.5×10^5	4.5	1.575
Total	207 875		1.228	300 370		2	364 790		2.96

	2000			2005			2010		
	T (tons)	P (\$/kg)	V ($\$ \times 10^9$)	T (tons)	P (\$/kg)	V ($\$ \times 10^9$)	T (tons)	P (\$/kg)	V ($\$ \times 10^9$)
NdFeB	18 640	110	2.05	41 100	90	3.7	102 700	80	8.216
SmCo	1200	134	0.16	2400	110	0.264	3800	95	0.36
Alnico	7300	28	0.2	6000	26	0.156	5000	26	0.13
Ferrite	4.6×10^5	4.5	2.07	6.2×10^5	4.5	2.79	8.3×10^5	4.5	3.735
Total	486 540		4.48	669 500		6.91	941 500		12.441

Table 19. Variation of price performance of magnets during 1985–2010.

	ρ (tons m^{-3})	1985			1990			1995		
		P (\$/tons)	E (kJ m^{-3})	W (\$/J)	P (\$/tons)	E (kJ m^{-3})	W (\$/J)	P (\$/tons)	E (kJ m^{-3})	W (\$/J)
NdFeB	7.4	200 000	254	5.83	185 000	279	4.91	150 000	295	3.76
SmCo	8.4	260 000	190	11.49	210 000	207	8.52	185 000	223	6.97
Alnico	7.3	35 000	56	4.56	30 000	56	3.91	28 000	56	3.65
Ferrite	5.1	3800	20.7	0.94	4200	22.3	0.96	4500	23.9	0.96
	ρ (tons m^{-3})	2000			2005			2010		
		P (\$/tons)	E (kJ m^{-3})	W (\$/J)	P (\$/tons)	E (kJ m^{-3})	W (\$/J)	P (\$/tons)	E (kJ m^{-3})	W (\$/J)
NdFeB	7.4	110 000	310	2.63	90 000	326	2.04	80 000	342	1.73
SmCo	8.4	134 000	238.8	4.71	110 000	242	3.82	95 000	246.8	3.23
Alnico	7.3	28 000	56	3.65	26 000	56	3.39	26 000	56	3.39
Ferrite	5.1	4500	25.5	0.9	4500	27	0.85	4500	28.7	0.8

7 HARD MAGNET INDUSTRY IN CHINA

All materials, which can be magnetized in a magnetic field, are called *magnetic materials*. The magnetization of HMM can be kept without a magnetic field. There are three commercially available magnets: Alnico, HF, and rare-earth magnets (SmCo, NdFeB etc.). Along with fully dense sintered magnets (S), bonded magnets (B) are also being developed. Bonded ferrite magnets are the majority at the current time, but bonded NdFeB magnets are also developing rather fast. The data for bonded NdFeB(B) magnets is in two parts: Chinese domestic company made, the production of which was started from 1993, and the output of foreign joint venture companies (started from 1996). The details are discussed later. There are bonded SmCo and Alnico magnets as well, but they are very few.

The output (tons), sales value ($\$ \times 10^6$), and price (\$/kg) of different type of hard magnets made in China during 1990–2005 are summarized in Table 22.

With the development of the economy in China, her magnet industry has developed considerably since the late 1980s. Owing to excellent scientists and engineers, R & D on magnets is rather popular here. Moreover, China herself is a huge market, which absorbs all kind of magnets, from Alnico, ferrite to highest grade of SmCo and NdFeB.

8 ALNICO MAGNET INDUSTRY IN CHINA

In 1932, 25Ni10Al–Fe was discovered by Mishima in Japan (Luo, 1991). On the basis of Fe–Ni–Al, Alnico was developed. It was an Fe-based alloy, which later became a major commercial magnet in the early 1940s, especially after Neel's important work of annealing in the magnetic field (1947), which changed Alnico from an isotropic magnet to an anisotropic one. Consequently, its magnetic properties have improved considerably. Alnico magnets developed significantly in 1950s and 1960s, and their global production reached the peak value of 40 000 tons in the late 1960s.

AlNi permanent magnet was first made in Shanghai, China in 1947. Chinese Alnico magnet industry developed rather late in comparison with developed countries. However, based on inexpensive labor cost, excellent expertise, and huge domestic market, Alnico magnet industry in China developed rather fast, The total output of Alnico in China was around 1000 tons annually in 1960s. It was more than 2000 tons annually during 1970s and 1980s. The number of Alnico manufacturers was around 70. During the last decade, numerous small Alnico manufacturers were consolidated into a few big ones. Now China is at the top in the world in the production of Alnico. Although there is very serious competition from different types of magnets, such as ferrite and rare-earth magnets, due to its excellent thermal stability, Alnico is still widely used for meters (watt-hour meter, voltmeter, ampere meter, mileage meter), acoustic devices, motors, and sensors used for automobiles and motorcycles.

8.1 Current status of Alnico magnet industry in China

With the fast development of ferrite and rare-earth magnets in China during the last decade, Alnico had serious competition from them. HF took most low-cost market shares, and rare-earth magnets took market shares of high-performance products. Fortunately, Alnico kept its position in the market

Table 20. Variation of market shares for different magnets (1985–2010).

	1985				1990			
	T (tons)	E (kJ m^{-3}) (MGOe)	J ($\times 10^7$ J)	J/J_{tot} (%)	T (ton)	E (kJ m^{-3}) (MGOe)	J ($\times 10^7$ J)	J/J_{tot} (%)
Knife (S)	75	(254)32	0.26	0.3	1860	(279)35	7.01	5.15
Knife (B)	–	–	–	–	310	(56)7	0.29	–
SmCo	800	(190)24	1.81	2.04	887	(207)26	2.19	1.54
Alnico	7000	(56)7	5.37	6.06	7300	(56)7	5.6	3.95
Ferrite	2×10^5	(20.7)2.6	81.18	91.6	2.9×10^5	(22.3)2.8	126.8	89.36
Total	207 875		88.62	100	300 370		141.9	100
	1995				2000			
	T (tons)	E (kJ m^{-3}) (MGOe)	J ($\times 10^7$ J)	J/J_{tot} (%)	T (tons)	E (kJ m^{-3}) (MGOe)	J ($\times 10^7$ J)	J/J_{tot}(%)
NdFeB (S)	5500	(295)37	21.93	12.1	15 100	(310)39	63.25	22
Knife (B)	1540	(64)8	1.62	–	3540	(71.6)9	4.16	–
SmCo	700	(223)28	1.86	1	1200	(239)30	3.41	1.1
Alnico	7150	(56)7	5.48	2.8	7300	(56)7	5.6	1.8
Ferrite	3.5×10^5	(23.9)3	164	84.1	4.6×10^5	(25.5)3.2	230	75.1
Total	364 790		194.9	100	486 540		306.4	100
	2005				2010			
	T (tons)	E (kJ m^{-3}) (MGOe)	J ($\times 10^7$ J)	J/J_{tot} (%)	T (tons)	E (kJ m^{-3}) (MGOe)	J ($\times 10^7$ J)	J/J_{tot} (%)
NdFeB (S)	360 00	(326)41	158.6	32.8	90 000	(342)43	415.9	47.5
Knife (B)	5100	(75.6)9.5	5.3	–	12 700	(79.6)10	19.4	–
SmCo	2400	(242)30.5	6.9	1.4	3800	(246.8)31	11.16	1.2
Alnico	6000	(56)7	4.6	0.9	5000	(56)7	3.84	0.4
Ferrite	6.2×10^5	(27)3.4	328.2	64.9	8.3×10^5	(28.7)3.6	467.1	50.9
Total	669 500		505.7	100	941 500		917.4	100

Note: Density of sintered NdFeB $\rho = 7.5\,\text{tons m}^{-3}$; density of bonded NdFeB $\rho = 6.1\,\text{tons m}^{-3}$.

due to its excellent magnetic performance. Its absolute output tonnage has increased slightly, although its output percentage has significantly reduced.

The thermal stability of different magnets is compared in Table 23.

The price of Alnico is reducing steadily. The rate of reduction in price of Alnico was quite high before 1995 ($\geq$10%), mainly due to the reduction in the cost of cobalt. The price stabilized after 1995.

The output of Alnico was almost around 2000 tons annually from 1990 until 1998. The output of Alnico increased to 3000 tons till 1999, after which it was around the same level, probably until 2005. The biggest application of produced Alnico is in the watt-hour meter. In order to save electricity, a policy of '1 Wh m for each family' was started by the Chinese government in 1998. Obviously, this policy, in fact, gave big support to the Chinese Alnico magnet industry. The Alnico output growth of 40% since 1999–2002 is the direct result of this!

The sales value of Alnico dropped significantly from $\$79.2 \times 10^6$ (1990) to $\$41.4 \times 10^6$ (1995). It was almost half of that of 1990. During the same period of time, its price dropped from \$36/kg to \$20.2/kg. The output was kept the same at around 2000 tons annually. The growth of sales value during 1998–2005 is the result of the output growth during the same period of time, because the price was kept almost the same at \$20/kg. The significant growth of sales value in 2003–2004 was mainly due to rise in both output and price, especially the increase in the price of Co.

The output ($\times$100 tons), sales value ($\$ \times 10^6$), and price (\$/kg) of Alnico made in China during 1990–2005 are shown in Figure 21.

The price of Alnico magnets declined from \$36/kg in 1990 to \$20/kg in 1998 with average annual reducing rate

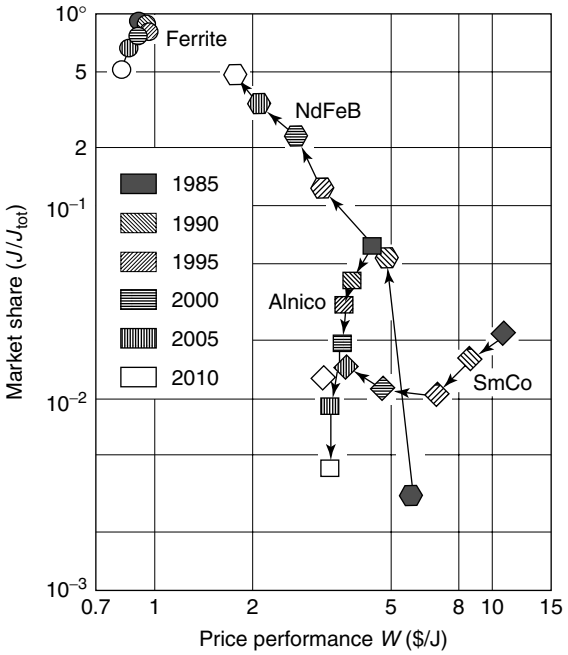

Figure 17. Structure change of global magnet market.

Table 21. Tonnage outputs of magnets made in different countries (2004).

Country/area	Alnico	Hard ferrite	Nd–Fe–B
China	3500t (56%)	(S) 350 000t (51%)	(S) 27 510t (81%)
		(B) 50 000t (32%)	(B) 1350t (35%)
		(T) 400 000t (47%)	(T) 28 860t (77%)
Japan	300t (5%)	(S) 196 000t (28%)	(S) 60 000t (18%)
		(B) 12 995t (8%)	(B) 565t (15%)
		(T) 208 995t (25%)	(T) 6565t (17%)
USA	700t (11%)	(S) 38 873t (5%)	(S) –
		(B) 40 300t (26%)	(B) 210t (5%)
		(T) 79 173t (9%)	(T) 210t (1%)
Europe	750t (12%)	(S) 46 700t (7%)	(S) 300t (1%)
		(B) 42 200t (27%)	(B) 345t (9%)
		(T) 88 900t (11%)	(T) 645t (2%)
Others	1000t (16%)	(S) 60 000t (9%)	(S) –
		(B) 10 500t (7%)	(B) 1365t (36%)
		(T) 70 500t (8%)	(T) 1365t (3%)
Global total	6250t	(S) 691 573t	(S) 33 810t
		(B) 155 995t	(B) 3835t
		(T) 847 568t	(T) 37 645t

Note: Data in brackets are percentages of the global total. S: sintered magnet; B: bonded magnet; T: global total.

of −7.63%. The price reduced slowly from $20/kg in 1998 to $19.1 in 2003 with an annual reducing rate of −0.9% (0.92513). The price was increased to $/20/kg in 2004 due to the increase in the price of raw materials in 2004. The sales value variation is similar to that of the output.

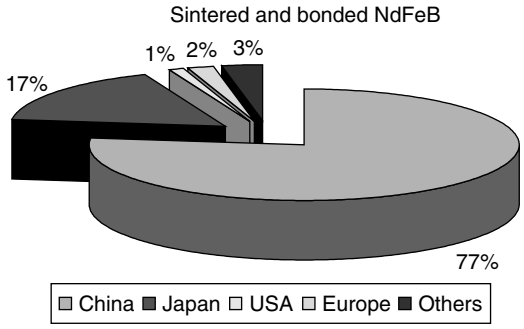

Figure 18. Distribution of global output of NdFeB magnets (S + B) in 2004.

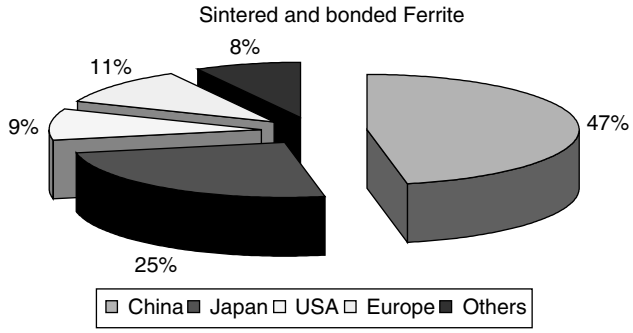

Figure 19. Distribution of global output of hard ferrite (S + B) in 2004.

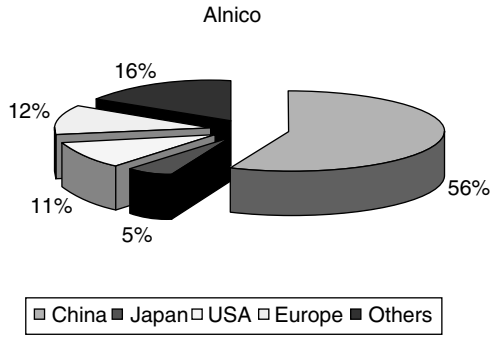

Figure 20. Distribution of global output of Alnico magnets in 2004.

8.2 Global output of Alnico magnets

The output of Alnico in Japan was 8300 tons in 1970. It reduced to 3400 tons in 1980, it became less than 2000 tons in 1990, and was only 1100 tons in 2000. The situation in the United States and Europe is similar to that in Japan. The output of Alnico magnets from 1994 to 2005 in Japan, the United States, Europe, China, others, and the global total is listed in Table 24.

Table 22. Output (tons), sales value ($\$ \times 10^6$), and price ($/kg) of various magnets made in China (1990–2005).

	1990	1991	1992	1993	1994	1995
Alnico	2200	2100	2400	2450	2300	2050
HF (S)	31 500	38 000	46 000	54 000	65 000	80 000
HF (B)	3500	3800	4200	4600	5100	7000
Output HF (T)	35 000	41 800	50 200	58 600	70 100	87 000
(tons) SmCo	55	57	59	61	63	66
NdFeB (S)	150	260	410	620	1020	1500
NdFeB (B)	–	–	–	18	40	70
RE (T)	205	317	469	699	1123	1636
Total	37 405	44 217	53 069	61 749	73 523	90 686
Alnico	79.2	67.2	68.4	63.2	51.3	41.4
HF (S)	56.7	69.2	85.1	102.6	124.8	156.8
HF (B)	11.9	12.5	13.4	14.7	15.9	21
Value HF (T)	68.6	81.7	98.5	117.3	140.7	177.8
($\times 10^6$) SmCo	6.05	6.1	6.1	6.1	6.1	6.2
NdFeB (S)	12.8	21.3	32.4	47.7	75.5	106.5
NdFeB (B)	–	–	–	2.2	4.3	6.9
RE (T)	18.85	27.4	38.5	56	85.9	119.6
Total	166.7	176.3	199.3	236.5	277.9	338.8
Alnico	36	32	28.5	25.8	22.3	20.2
HF (S)	1.8	1.82	1.85	1.9	1.92	1.96
HF (B)	3.4	3.3	3.2	3.2	3.1	3
Price HF	1.96	1.95	1.96	1.99	2	2.04
($/kg) SmCo	110	107	104	100	97	94
NdFeB (S)	85	82	79	77	74	71
NdFeB (B)	–	–	–	120	108	98
REM	92	86.4	82.1	80.1	76.5	73.1

	1996	1997	1998	1999	2000	2001
Alnico	2000	1900	2100	3000	3200	3040
HF (S)	95 000	115 000	135 000	155 000	168 000	180 000
HF (B)	9000	11 200	13 500	15 400	16 500	21 500
Output HF (T)	104 000	126 200	148 500	170 400	184 500	201 500
(tons) SmCo	70	85	105	120	135	170
NdFeB (S)	2100	2550	3260	4200	5550	6400
NdFeB (B)	100	200	300	480	700	800
RE (T)	2270	2835	3665	4800	6385	7370
Total	108 270	130 935	154 265	178 200	194 085	211 910
Alnico	40.4	38.4	42	59.1	62.4	58.7
HF (S)	190	241.5	297	356.5	403.2	432
HF (B)	27.9	35.8	47.3	57	64.5	87
Value HF (T)	217.9	277.3	344.3	413.5	467.7	519
($\$ \times 10^6$) SmCo	6.3	7	8.9	9.8	10	11.6
NdFeB (S)	142.8	165.8	202.1	243.6	288.6	281.6
NdFeB (B)	9.5	21.8	31.1	50.2	72.9	73.6
RE (T)	158.6	194.6	242.1	303.6	371.5	366.8
Total	416.9	510.3	628.4	776.2	901.6	944.5
Alnico	20.2	20.2	20	19.7	19.5	19.3
HF (S)	2	2.1	2.2	2.3	2.4	2.4
HF (B)	3.1	3.2	3.5	3.7	3.9	4.05
Price HF	2.1	2.2	2.32	2.43	2.53	2.55
($/kg) SmCo	90	87	85	82	74	68
NdFeB (S)	68	65	62	58	52	44
NdFeB (B)	95	105	103.7	104.6	104.1	92
REM	69.9	68.6	66.1	63.3	58.2	49.8

Table 22. (*Continued*)

	2002	2003	2004	2005
Alnico	3000	3000	3500	3500
HF (S)	190 000	200 000	350 000	395 000
HF (B)	27 700	33 500	51 500	67 500
Output HF (T)	208 000	218 600	401 500	462 500
(tons) SmCo	220	265	330	400
NdFeB (S)	7900	18 460	27 510	35 000
NdFeB (B)	1140	1300	1350	1500
RE (T)	9260	19 760	28 860	36 500
Total	220 260	232 645	433 860	502 500
Alnico	57.6	57.3	70	70
HF (S)	456	480	840	869
HF (B)	113	135.5	211.4	279.4
Value HF (T)	569	615.5	1051.4	1148.4
($\$\times 10^6$) SmCo	13.6	15.9	19.8	24
NdFeB (S)	300.2	646.1	935.3	1120
NdFeB (B)	100.3	110.5	112.1	120
RE (T)	400.5	756.6	1047.4	1240
Total	1027.1	1429.4	2168.8	2458.4
Alnico	19.2	19.1	20	20
HF (S)	2.4	2.4	2.4	2.2
HF (B)	4.1	4.04	4.1	4.14
Price HF (T)	2.74	2.87	2.59	2.43
($/kg) SmCo	62	60	60	60
NdFeB (S)	38	35	34	32
NdFeB (B)	88	85	83	80
REM	43.25	38.29	36.29	34

HF: hard ferrite; REM: rare-earth magnets; (S): sintered; (B): bonded; (T): total.

Table 23. Comparison of thermal stability between various magnets.

	Curie temperature		Reversible temperature coefficient (%/K)		Maximum working temperature, T_m (K)
	T_C (K)	($^\circ$C)	Near Br (273–373 K)	Near H_c (273–373 K)	
Alnico	1030–1180	757–907	−0.02	+0.03–0.07	823
$SmCo_5$	1000	727	−0.045	−0.3	523
Sm_2Co_{17}	1000	727	−0.03	−0.2	523
NdFeB	583	310	−0.1	−0.8	393
Ferrite	723	450	−0.2	0.2–0.5	358

The Alnico output variation in China, Japan, the United States, Europe, others, and the global total is summarized in Figure 22.

As seen in Figure 22, the output of Alnico magnets in all developed countries has been decreasing steadily during 1994–2005. China is the only exception, whose output is at the same level and has even shown certain growth during the same period. So it is follows that increase in total global output of Alnico is the same as the output of China.

The electricity system in urban areas of China was very old. Most of them were built in 1920s or 1930s of the last century, that is, before World War II. They have long been out of date and should be reconstructed immediately. Moreover, with the development of the national economy, a project of 'rural electrification' started in the middle of the 1990s. In order to save electricity, a policy of '1 Wh m for each family' was started by the Chinese government in 1998. This project concerns a population of around one billion and covers 90% territory of China. This project would last more than one decade. One can image how big the demand for magnetic materials will be in order to realize such a project as the biggest application of produced Alnico is watt-hour meter. Obviously, this project in fact provides an opportunity for the further development of the Chinese magnet industry,

Table 24. Alnico output in China, Japan, USA, Europe, and others (1994–2005).

	1994	1995	1996	1997	1998	1999
China	2300	2050	2000	1900	2100	3000
Δ(%)	6.2	−12	−2.5	−5.3	+7.7	+42.8
Japan	1700	1600	1500	1400	1200	1100
Δ(%)	−6	−6	−6.3	−7	−14	−8.4
USA	1000	1000	1000	1000	1000	950
Δ(%)	0	0	0	0	0	−5
Europe	1550	1500	1450	1300	1200	1100
Δ(%)	−3.2	−3.3	−3.4	−10.4	−7.7	8.4
Others	1000	1000	980	900	900	1000
Δ(%)	0	0	−2	−8.2	0	+11
Global total	7550	7150	6930	6600	6400	7150
Δ(%)	–	−5.3	−3.1	−4.8	−3.1	+11.7

	2000	2001	2002	2003	2004	2005
China	3200	3040	3000	3000	3500	3500
Δ(%)	+6.7	−5.2	−1.4	0	+14.3	0
Japan	1100	750	600	450	300	220
Δ(%)	0	−32	−20	−25	−33	−27
USA	950	900	850	800	700	610
Δ(%)	0	−5.3	−5.5	−5.9	−12.5	−12.8
Europe	1000	1000	900	900	750	620
Δ(%)	−10	0	−10	0	−16.7	−17.3
Others	1000	1100	1100	1000	1000	1000
Δ(%)	0	+10	0	−10	0	0
Global total	7250	6790	6450	6150	6250	5950
Δ(%)	+1.4	−6.3	−5	−4.7	+1.6	−4.8

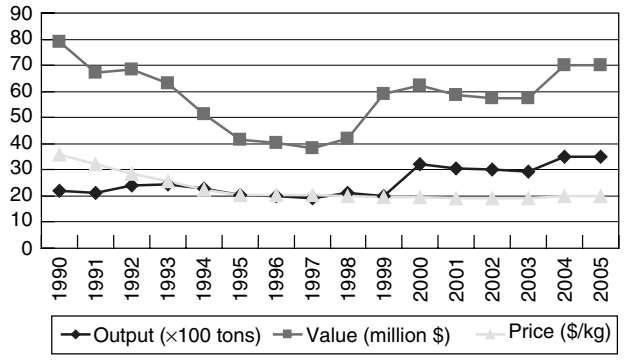

Figure 21. Output ($\times 10^2$ tons/year), sales value ($\$ \times 10^6$), and average price ($/kg) of Alnico magnets made in China during 1990–2005.

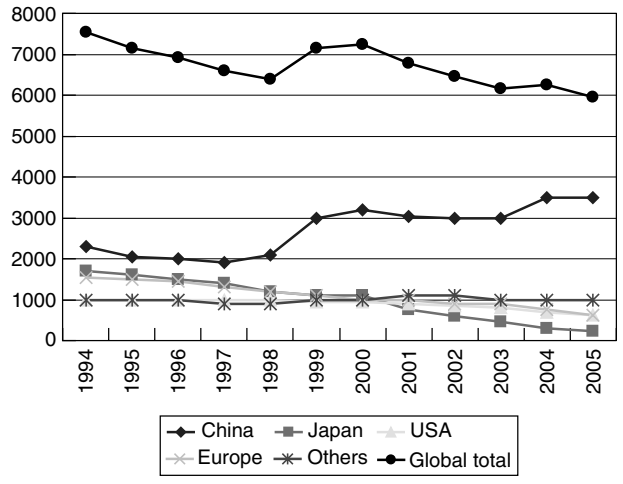

Figure 22. Output of Alnico (tons) in China, Japan, the United States, Europe, others, and global total.

including the Alnico industry. The Alnico output growth of 40% since 1999–2005 is the direct result of this!

9 HARD FERRITE INDUSTRY IN CHINA

HF, developed in the early 1950s, became major commercially available magnets in the 1960s. Their sales value exceeded that of Alnico in the early 1980s. In spite of competition from rare-earth magnets, the global output growth of HF was around +5% annually. The production of HF in developed countries becomes very difficult due to the increase in the cost of production. Now, the HF output in developed countries is only one-sixth of the global total.

Table 25. Content comparison of powder made from iron scales and oxide.

	Fe_2O_3 (%)	SiO_2 (%)	Cl (%)	Other impurity	(m^2/g)[b]	Powder size (μm)[c]	R. H. (%)
Ruthner[a]	98–99.8	0.005–1	0.08–0.9	Rest	1.7–3	–	–
H_2SO_4[a]	99.1	0.21	–	Rest	3	–	–
Hematite[a]	98–99.2	0.15–1	0–0.06	Rest	0.6–0.7	–	–
Iron scales	>99	<0.3	0	Rest	–	<10	<1

R.H.: relative humidity.
[a]Iron oxide.
[b]Specific surface.
[c]Average powder size.

9.1 Raw materials of hard ferrite

Iron oxide has been long and widely used as a raw material for HF by major magnet manufacturers in the world. The advantage of iron oxide lies in its constant and pure chemical composition. Unfortunately, China does not have iron oxide in abundance. All the iron oxide available in China is used only for steel making. Thus, instead of iron oxide, China has to use iron scales to make HF magnets, which are waste that come from hot rolling during steel making. Steel output of China in 2004 was 270 million tons, which exceeded that of the United States and Japan put together. Obviously, China has enough iron scales to meet the increasing demand of the HF industry. Iron scales are abundant and stably available in China with a very low price.

There are at least two problems in using iron scale as raw material. First, chemical composition of iron scale is unstable and fluctuates from batch to batch, because materials processed during hot rolling always vary. Secondly, the oxidation of iron during hot rolling process is not uniform with high content of Fe_3O_4 and FeO. It took more than 20 years' R & D work by Chinese researchers and engineers to solve many theoretical and practical problems they faced while using iron scale as raw material for making HF. A unique technology of using iron scale to replace iron oxide has been developed by the Beijing General Research Institute of Metallurgy Mining (BGRIMM) successfully (Bian and Li, 2001). This process has already been put to use for mass production in China. Owing to replacement of iron oxide by iron scale, the material cost is reduced by at least one-third.

BGRIMM is the biggest producer of presintering powder of ferrite in China. BGRIMM develops most advanced kilns and its operation is fully controlled by computers. It has an annual yield capacity of 8000 tons per set. Ten kilns were built in Beijing at BGRIMM's base. Such equipment and technology has now spread to different parts of China. The composition of presintered powder produced by BGRIMM and products made by other process are compared in Table 25.

With the development of the metallurgy industry in China, more and more iron oxide made from steel plants is available. The location distribution of presintered powder makers in China is listed in Table 26. The number of BGRIMM's kiln and output of powder made by such kiln is shown in brackets in this table.

9.2 Brief review on the global sintered ferrite industry

With global economic development, the demand for magnetic materials is increasing simultaneously. The price of magnets is declining all the time. The developed countries are finding it difficult to continue the production of ferrite due to low profit margins. Thus, the shifting of the production line

Table 26. Location distribution of presintered powder makers in China.

Region	Province city	Number of kiln	Capacity ($\times 10^3$ tons/year)
North	Beijing (BGRIMM)	10 (10)	80 (80)
	Tianjin	1	3
	Shanxi	2 (2)	16 (16)
Subtotal		13 (12)	99 (96)
Northeast	Liaonin	6 (3)	35 (15)
East	Shanghai	1 (1)	8 (8)
	Jiangsu	6	40
	Anhui	4 (1)	28 (8)
	Zhejiang	11 (9)	88 (72)
Subtotal		22 (11)	164 (88)
Mid-south	Henan	3 (1)	15 (8)
	Hubei	9 (5)	63 (40)
	Hunan	1	5
	Kuandong	2	10
Subtotal		15 (6)	93 (48)
Southwest	Sichuan	3	16
Total		59 (32)	402 (242)

Note: Data in brackets are related to that produced by kiln BGRIMM developed.

Table 27. Volume portion of hard ferrite used for each application in China.

Year	Output ($\times 10^3$ tons)	Used tonnage/acoustics ($\times 10^3$ tons) (%)	Used for motor ($\times 10^3$ tons) (%)	Used for holding instrument ($\times 10^3$ tons) (%)
1990	31.5	27.72 (88)	630 (2)	3150 (10)
1991	38	32.68 (86)	1140 (3)	4180 (11)
1992	46	38.64 (84)	1840 (4)	5250 (12)
1993	54	43.20 (80)	3240 (6)	7560 (14)
1994	65	48.75 (75)	5200 (8)	11 050 (17)
1995	80	56.00 (70)	8000 (10)	16 000 (20)
1996	95	63.65 (67)	14 250 (15)	17 100 (18)
1997	115	74.75 (65)	23 000 (20)	17 250 (15)
1998	135	86.40 (64)	28 350 (21)	20 250 (15)
1999	155	93.00 (60)	38 750 (25)	23 250 (15)
2000	168	100.80 (60)	42 000 (25)	25 200 (15)
2001	180	108 (60)	45 000 (25)	27 000 (15)
2002	190	114 (60)	47 500 (25)	28 500 (15)
2003	200	120 (60)	50 000 (25)	30 000 (15)

to developing countries started in the 1980s. The output of HF in developed countries reached its peak value in early 1980s. Before 1985, the average annual growth rate >40%, in 1985–1990, the average annual growth rate was around 4–10%, after 1990, the average annual growth rate became negative to: −1 to −8%. Outputs of HF made in Japan, the United States, and Europe in total were only one-sixth of the global total in 2004. Total outputs in developing countries, such as China, India, and SEA are five-sixth of the global total.

The growth of global total output of HF has continued due to the increase in the global market demand. The average annual growth rate of global output of HF is more than 5%. This growth will continue in the twenty-first century.

9.2.1 Application of sintered hard ferrite

Applications of HF are quite different in different countries. There are three applications in China: acoustics (rings), motor (segments), and holding instruments (including magnet separator). The volume of used magnets for each application is changing; these are listed in Table 27 and summarized in Figure 23. Only one portion is used for application in a motor, which is expanding among other applications. Portions for acoustics and holding instrument have reduced.

9.3 Bonded ferrite magnets

Owing to the demand of refrigerator door sealing, TV tube focusing, and so on, bonded ferrite magnet was developed in the United States and Europe by mixing magnetic powder with polymer binder in the 1960s. Such bonded magnets are called *LEEP*. Later, bonded magnets with higher

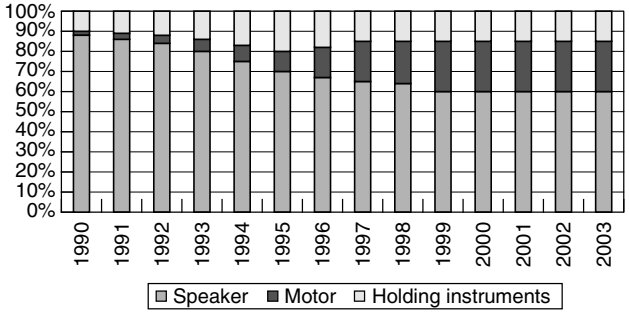

Figure 23. Percentages of hard ferrite output for different applications.

performance were developed and were called *HEEP*. On the basis of their applications and magnetic performances, Japanese bonded magnet producers divided such magnets into two groups: flexible and rigid. We follow this classification in the present paper. With the development of the electronic industry, the bonded magnet industry in China has improved considerably since the late 1980s.

9.3.1 General review on global bonded ferrite magnets

With the increase in the cost of producing bonded ferrite magnets, the industry has shifted from developed countries to developing countries including China, similar to the industries for producing other types of magnets. The use of bonded magnets in each country is different; therefore, the direction in which they develop is definitely different. For example, LEEP in Europe is mainly used as sound-damping materials for the automotive industry, in the United States, LEEP is used for advertisements, and, in Japan, it is used for medicinal purposes.

The output (tons), sales value ($\$ \times 10^6$), price ($/kg) of bonded ferrite magnets produced in China, Japan, the United States, Europe, SEA, and others during 1995–2005 are listed in Table 28. Data, except for China, are mainly taken from the publication by JABM and from discussion at the meeting of the JABM Marketing Committee (Tokyo, Japan, December 2, 2004) (JABM, 2004).

9.3.2 Bonded ferrite magnet industry in China

In the 1970s, injection equipment and technology were imported to China to produce bonded isotropic magnets mainly used for refrigerator seals and adjusting the core magnet plate for the TV tube. Since then, the producing technology, inspecting, and magnetizing equipment have been improving continuously during the 1980s. Almost 70% bonded ferrite is isotropic, whose energy products are 0.7–1 MGOe. The anisotropic bonded ferrite with energy products around 1.4–1.6 MGOe is less then 30% of the total. The forming process of anisotropic bonded ferrite requires an orientation field, which is rather expensive in comparison with that of the isotropic one. Moreover, the anisotropic magnet is used for the micromotor, which requires a magnet with special shape and precise tolerance; therefore, the price of the anisotropic bonded ferrite is much higher than that of the isotropic one. In the early 1990s, with further development of the electronic industry in China, the demand for higher-grade bonded ferrite magnets became more urgent. Such magnets require more qualified powder, which had to be imported into China in the early 1990s.

In order to solve this problem, BGRIMM developed a special grade of powder to meet the demand of bonded ferrite magnets. Now BGRIMM is able to provide powder for bonded ferrite. The specifications of the powder for bonded ferrite made by BGRIMM are listed in Table 29.

With the development of bonded ferrite magnet industry, a lot of new advanced technology and equipment has been imported into China recently. These include injection machines with orientation magnet field and automatic press with magnet field for warm compressing. Magnets prepared by calendering, rolling, and extruding have also been introduced. In order to get some idea on the price of bonded ferrite magnets, the average prices of bonded ferrite in the China market are summarized in Table 30 and are shown in Figure 24.

Preparing rigid bonded ferrite magnets in China started in 1993. Its price reduced with growth in output. Especially, its price reduced due to the replacement of the imported powder by the domestic one. The price has been stable since 2001, with improvement in the producing process. The totally averaged price of bonded ferrite magnets is the average of both flexible and rigid magnets.

10 SINTERED NdFeB PRODUCERS IN THE UNITED STATES, EUROPE, AND JAPAN

In the United States, there were three (3) NdFeB magnet producers before 1997:

Hitachi Magnets (USA): In the early 1970s, Hitachi Metals acquired former General Electric (GE) hard ferrite plant in Edmore, MI, USA. Then it expanded to China Grove, NC, where NdFeB were partly made.
CRUMAX (VAC): This was an old local magnet producer in the middle of 1990s. It was owned by YBM, it was sold to Morgan Crucible (UK) and was managed by VAC in 1999. It was fully closed in 2003.
UGIMAG (MQI): Indiana Technology was the first sintered NdFeB magnet producer in the United States. It was sold to UGIMAG in 1992, and then it was resold to MQI in 2000. Recently, its production activity has been transferred to China.

The ownership of the last two companies has changed quite frequently; nevertheless, none of them could avoid the stopping of magnet production. In fact, they had already announced the closure of their production activities in the United States by the end of 2003.

In Europe, there were four (4) sintered NdFeB magnet manufacturers:

Philips Components (UK): The production activity of this company stopped in middle of the 1990s.
VAC (Germany): The biggest producer in Europe – VAC – was sold to Morgan Crucible in 1999, and then it made a joint venture with the Chinese magnet producer, Sanhuan, in 2004.
Magnetfabrik Schramberg (Germany): This company is still working with a small output.
REOREM (Finland): This company is still working with a small output.

In Japan, there were 'five and half' (5.5) NdFeB magnet manufacturers:

Sumitomo Special Metals Co. (SSMC)
Hitachi Metals Co., Ltd. (HML)
Shin-Etsu Chemical Co.
TDK
Dowa Mining Co.: Dowa had to stop its NdFeB production in 2002 due to a sharp reduction in the sales price in the market. Dowa got the license from SSMC in the same year.
Toking Co.: Located in Sendai, Japan, it produces all kinds of magnets, including Alnico, hard ferrite, Sm-Co and NdFeB magnets, but due to patent restriction this company stopped NdFeB magnet production in early 1990s. So this company can be considered as a "half NdFeB magnet producer" solely, but not a real one.

Table 28. Output (tons), value ($\$\times^6$, price ($/kg) of bonded ferrite made in China, Japan, the United States, Europe, SEA, others, and global total.

	1995	1996	1997	1998	1999
China Flex	6600t ($2.6/kg) $17 × 10^6	8350t ($2.6/kg) $22.1 × 10^6	10 400t ($2.8/kg) $28.8 × 10^6	12 550t ($3.1/kg) $39.2 × 10^6	14 300t ($3.37/kg) $48.2 × 10^6
Rig.	400t ($10/kg) $4 × 10^6	650t ($9/kg) $5.8 × 10^6	800t ($8.7/kg) $7 × 10^6	950t ($8.5/kg) $8.1 × 10^6	1100t ($8/kg) $8.8 × 10^6
Total	7000t ($3/kg) $21 × 10^6	9000t ($3.1/kg) $27.9 × 10^6	11 200t ($3.2/kg) $35.8 × 10^6	13 500t ($3.5/kg) $47.3 × 10^6	15 400t ($3.7/kg) $57 × 10^6
Japan Flex	10 500t ($5.85/kg) $61.4 × 10^6	10 338t ($5.07/kg) $52.4 × 10^6	9626t ($5.52/kg) $53.1 × 10^6	9491t ($5.36/kg) $50.9 × 10^6	9166t ($5.61/kg) $51.4 × 10^6
Rig.	9100t ($14.95/kg) $136 × 10^6	9827t ($14.72/kg) $144.7 × 10^6	10 370t ($14.1/kg) $146.2 × 10^6	10 562t ($14.03/kg) $148.2 × 10^6	8179t ($15.28/kg) $125 × 10^6
Total	19 600t ($10/kg) $197.4 × 10^6	20 165t ($9.78/kg $197.2 × 10^6	19 996t ($9.97/kg) $199.3 × 10^6	20 053t ($9.92/kg) $199 × 10^6	17 345 ($10.17/kg) $176.4 × 10^6
USA Flex	3400t ($7.5/kg) $25.5 × 10^6	5000t ($5.84/kg) $29.2 × 10^6	9000t ($5.83/kg) $52.5 × 10^6	10 800t ($5.83/kg) $63 × 10^6	23 400t ($4.19/kg) $98.1 × 10^6
Rig.	1200t ($18.58/kg) $22.3 × 10^6	1800t ($16.67/kg $30 × 10^6	2250t ($16.67/kg) $37.5 × 10^6	2475t ($16.69/kg $41.3 × 10^6	4900t ($16.67/kg) $81.7 × 10^6
Total	4600t ($10.39/kg) $47.8 × 10^6	6800t ($8.7/kg) $59.2 × 10^6	11 250t ($8/kg) $90 × 10^6	13 275t ($7.2/kg) $104.3 × 10^6	28 300t ($6.33/kg) $179.8 × 10^6
Euro. Flex	1130t ($8.14/kg) $9.2 × 10^6	1300t ($6.77/kg) $8.8 × 10^6	1365t ($6.81/kg) $9.3 × 10^6	1406t ($6.3/kg) $9.6 × 10^6	35 000t ($2.67/kg)[a] $93.6 × 10^6[a]
Rig.	360t ($15.83/kg) $5.7 × 10^6	320t ($16.56/kg) $5.3 × 10^6	480t ($16.67/kg) $8 × 10^6	528t ($15.2/kg) $8.8 × 10^6	2000t ($16.65/kg) $33.3 × 10^6
Total	1490t ($10/kg) $14.9 × 10^6	1620t ($10.3/kg) $14.1 × 10^6	1845t ($9.38/kg) $17.3 × 10^6	2100t ($9/kg) $19 × 10^6	37 000t ($3.43/kg)[a] $126.9 × 10^6
SEA Flex	3320t ($4.49/kg) $14.9 × 10^6	3840t ($3.75/kg) $14.4 × 10^6	4224t ($3.76/kg) $15.9 × 10^6	5400t ($3.5/kg) $20 × 10^6	9900t ($3.1/kg) $30.3 × 10^6[a]
Rig.	3340t ($9.5/kg) $31.7 × 10^6	4000t ($8.33/kg) $33.3 × 10^6	4800t ($8.33/kg) $40 × 10^6× 10^6	4000t ($7.6/kg) $33.3 × 10^6	4900t ($8.33/kg) $40.8 × 10^6
Total	6660t ($7/kg) $46.6 × 10^6	7840t ($6.8/kg) $53.06 × 10^6	9024t ($6.19/kg) $55.9 × 10^6	10 000t ($5.7/kg) $56.8 × 10^6	14 800t ($4.8/kg) $71.1 × 10^6
Other Flex	2100t ($5.81/kg) $12.2 × 10^6	2478t ($6.68/kg) $11.6 × 10^6	2602t ($4.65/kg) $12.1 × 10^6	2602t ($4.4/kg) $12.1 × 10^6	10 800t ($3/kg)[a] $32.6 × 10^6[a]
Rig.	1200t ($14.4/kg) $17.3 × 10^6	1895t ($9.44/kg) $23.4 × 10^6	2274t ($12.36/kg) $28.1 × 10^6	2274t ($11.5/kg) $28.1 × 10^6	900t ($12.3/kg) $11.1 × 10^6
Total	3300t ($8.9/kg) $29.5 × 10^6	4373t ($8/kg) $35 × 10^6	4876t ($8.26/kg) $40.3 × 10^6	5440t ($7.9/kg) $42.9 × 10^6	6100t ($7.4/kg) $45.2 × 10^6
G. T. Flex	27 050t ($5.18/kg) $140.2 × 10^6	31 306t ($4.8/kg) $138.5 × 10^6	37 217t ($4.61/kg) $171.7 × 10^6	42 249t ($4.61/kg) $194.8 × 10^6	102 566t ($3.45/kg $354.2 × 10^6
Rig.	15 600 ($13.9/kg) $217 × 10^6	18 492 ($13.7/kg) $242.5 × 10^6	20 974t ($12.72/kg) $266.8 × 10^6	20 789 ($12.88/kg) $267.8 × 10^6	21 979t ($11.5/kg) $608.8 × 10^6
Total	42 650t ($8.38/kg) $357.2 × 10^6	49 798t ($7.65/kg) $381 × 10^6	58 191t ($7.54/kg) $438.5 × 10^6	630 38t ($7.34/kg) $462.6 × 10^6	124 545t ($6.7/kg) $963 × 10^6

	2000	2001	2002	2003	2004
China Flex	15 000t ($3.6/kg) $54 × 10^6	19 500t ($3.6/kg) $70.2 × 10^6	25 000t ($3.6/kg) $90 × 10^6	30 000t ($3.5/kg) $105 × 10^6	46 500t ($3.6/kg) $167.4 × 10^6
Rig.	1500t ($7/kg) $10.5 × 10^6	1995t ($8.4/kg) $16.8 × 10^6	2700t ($8.5/kg) $23 × 10^6	3500t ($8.7/kg) $30.45 × 10^6	5000t ($8.8./kg) $44 × 10^6
Total	16 500t ($3.9/kg) $64.5 × 10^6	21 495t ($4.05/kg) $87 × 10^6	27 700t ($4.1/kg) $113 × 10^6	33 500t ($4.04/kg) $135.45 × 10^6	51 500t ($4.1/kg) $211.4 × 10^6
Japan Flex	9350t ($5.5/kg) $51.4 × 10^6	9078t ($5.3/kg) $47.8 × 10^6	6740t ($5.6/kg) $37.8 × 10^6	6005t ($5.5/kg) $33.3 × 10^6	5775t ($5.7/kg) $33.2 × 10^6
Rig.	9487t ($14.1/kg) $133.8 × 10^6	7310t ($12.3/kg) $89.8 × 10^6	6820t ($14.7/kg) $100.2 × 10^6	7350t ($12.9/kg) $95 × 10^6	7220t ($13.4/kg) $97 × 10^6
Total	18 837t ($9.8/kg) $185.2 × 10^6	16 388t ($8.4/kg) $137.8 × 10^6	13 560t ($10/kg) $138 × 10^6	13 355t ($9.5/kg) $126.3 × 10^6	12 995t ($10/kg $130 × 10^6
USA Flex	25740t ($4.2/kg) $107.9 × 10^6	28 314t ($4.2/kg) $118.7 × 10^6	30 000t ($4.17/kg) $125 × 10^6	26 000t ($3/kg) $78 × 10^6	33 600t ($3/kg) $100.8 × 10^6
Rig.	5145t ($16.7/kg) $85.8 × 10^6	5402 ($16.7/kg) $90 × 10^6	5600t ($16.4/kg) $91.7 × 10^6	3750t ($12/kg) $45 × 10^6	4300t ($12/kg) $45 × 10^6
Total	30 885t ($6.27/kg) $193.7 × 10^6	33 716t ($6.19/kg) $208.7 × 10^6	35 600t ($6.08/kg) $216.7 × 10^6	29 750t ($4.1/kg) $123 × 10^6	36 300t ($3.5/kg) $127.2 × 10^6
Euro. Flex	34 650t ($2.67/kg) $92.7 × 10^6	34 304t ($2.67/kg) $91.7 × 10^6	34 000t ($2.67/kg)$90.8 × 10^6	41 000t ($2.5/kg) $102 × 10^6	40 850t ($2.5/kg) $102.1 × 10^6
Rig.	2100t ($16.7/kg) $35 × 10^6	2205t ($16.7/kg) $36.8 × 10^6	2300t ($16.5/kg) $37.9 × 10^6	1300t ($13/kg) $17 × 10^6	1360t ($13/kg) $17.7 × 10^6
Total	36 750t ($3.47/kg) $127.7	36 509t (3.5/kg) $128.5 × 10^6	36 300t ($5.97/kg) $216.7 × 10^6	42 300t ($2.8/kg) $119 × 10^6	42 200t ($2.8/kg) $119.8 × 10^6

	2000	2001	2002	2003	2004
SEA Flex	10 692t ($3/kg) $32.7 × 10^6	11 547t ($3/kg) $35.4 × 10^6	12 000t ($3/kg) $36.3 × 10^6	12 200t ($3/kg) $36.7 × 10^6	12 500t ($3/kg) $37.5 × 10^6
Rig.	5145t ($8.3/kg) $42.9 × 10^6	5402t ($8.3/kg) $45 × 10^6	5600t ($8.3/kg) $46.2 × 10^6	6700t ($8.1/kg) $54.4 × 10^6	6700t ($8/kg) $53.8 × 10^6
Total	15 837t ($4.8/kg) $75.6 × 10^6	16 950t ($4.7/kg) $80.4 × 10^6	17 600t ($4.7/kg) $82.5 × 10^6	18 900t ($4.9/kg) $91.1 × 10^6	19 200t ($4.7/kg) $91.1 × 10^6
Other Flex	10 800t ($3/kg) $32.6 × 10^6	10 800t ($3/kg) $32.6 × 10^6	10 800t ($3/kg) $32.5 × 10^6	9600t ($3/kg) $28.9 × 10^6	9600t ($3/kg) $28.9 × 10^6
Rig.	900t ($12.3/kg) $11.1 × 10^6	900t ($12.3/kg) $11.1 × 10^6	900t ($12/kg) $10.8 × 10^6	900t ($11.9/kg) $10.7 × 10^6	900t ($11.7/kg) $10.5 × 10^6
Total	11 700t ($3.7/kg) $43.8 × 10^6	11 700t ($3.7/kg) $43.8 × 10^6	11 700t ($3.7/kg) $43.3 × 10^6	10 500t ($3.8/kg) $39.6 × 10^6	10 500t ($3.7/kg) $39.4 × 10^6
G. T. Flex	106 232t ($3.3/kg) $354.8 × 10^6	113 543t ($3.2/kg) $367.8 × 10^6	118 540t ($3.5/kg) $412.4 × 10^6	124 805t ($3.1/kg) $383.9 × 10^6	148 825 ($3.1/kg) $465 × 10^6
Rig.	24 277t ($13.1/kg) $318.8 × 10^6	23 215t ($12.3/kg) $286.5 × 10^6	23 920t ($12.7/kg) $304.3 × 10^6	25 000t ($10.5/kg) $263.6 × 10^6	21 880t ($10.8/kg) $236.2 × 10^6
Total	130 509 ($5.2/kg) $673.7 × 10^6	136 757t ($4.8/kg) $654.3 × 10^6	142 460t ($5/kg) $716.7 × 10^6	149 805t ($4/kg) $647.5 × 10^6	171 195t ($4.1/kg) $701.2 × 10^6

	1990	1991	1992	1993	1994
China Flex	3500t ($3.4/kg) $11.9 × 10^6	3800t ($3.3/kg) $12.54 × 10^6	4200t ($3.2/kg) $13.44 × 10^6	4500t ($3/kg) $13.5 × 10^6	4900t ($2.8/kg) $13.7 × 10^6
Rig.	–	–	–	100t ($12/kg) $1.2 × 10^6	200t ($11/kg) $2.2 × 10^6
Total	3500t ($3.4/kg) $11.9 × 10^6	3800t ($3.3/kg) $12.5 × 10^6	4200t ($3.2/kg) $13.4 × 10^6	4600t ($3.2/kg) $14.7 × 10^6	5100t ($3.1/kg) $15.9 × 10^6

Flex: flexible bonded ferrite; Rig.: rigid bonded ferrite; G. T.: global total Euro.: Europe; SEA: South-East Asia; other: other countries.

It was announced jointly by HML and SSMC on December 18, 2003 (Jia *et al*., 1998; Jia, Jia and Li, 2004) that both companies will join together to establish a new company – 'NEOMAX Co. Ltd'. It was informed that NEOMAX is running quite well and its high-grade magnets meet the demands of newly developed applications, such as automotive motor, VCM for HDD less than 1 in., lift, and so on.

The others have had to slow down their production due to the impact from China. In order to reduce the price pressure, they are now focusing on assembling or devices making, instead of magnet production solely. Shin-Etsu Co. is in a better financial situation among all others, because it imports very cheap rare-earth concentrates from China, instead of rare-earth metal. After separation, the highly purified single rare-earth oxides can be sold in the international market at a rather high price. Shin-Etsu uses Nd oxide as starting materials to prepare Nd metal and then to make NdFeB magnets. Obviously, in this way, Shin-Etsu is in a better position than other Japanese magnet producers to compensate the reduction in magnet price.

11 OUTPUT, PRICE, AND SALES VALUE OF NdFeB MAGNETS

The output of sintered NdFeB magnets in Japan, the United States, Europe, and China during 1987–2000 was presented in my report (Luo, 2000c) at the 16th International Workshop on REM held in Sendai, Japan (September 2000). Data for China and Japan are more accurate because associations of the magnet industry in these countries publish relatively good data annually. Although there is an Association of Magnet Manufacturers in the United States, the data published by this association are definitely incomplete because some major magnet producers are not members. It is even more difficult to get data for Europe. Many participants from different countries were interested in these data and we had many interesting and important discussions during the conference.

Some Japanese experts told me that the published production of sintered NdFeB magnets in Japan is always underestimated by around 20–30% due to a number of reasons, particularly the reluctance of certain companies to provide their actual production. These experts made their estimate based on data given by master alloy producers. According to the opinion of experts from the United States and Europe, the outputs in the United States and Europe are actually 20–30% less than what is given in my table. This is because the ownership of magnet companies in the United States and Europe has changed quite frequently in last few years, thus their sales have dropped significantly and the data in my table are out of date. As for NdFeB production in China, usually they are related to blocks but not final magnets. In order to make consistency with data for other countries, data for China would have to be converted to final products, that is, the data should be reduced by 20–30% as well.

On the basis of these inputs, the tonnage outputs (tons), sales value ($\$ \times 10^8$), and price ($/kg) of sintered NdFeB magnets made in China, Japan, the United States, and Europe during 1995–2004 are reestimated and listed in Table 31.

Owing to the increased production cost in developed countries and the sharp decrease in the sales price of magnets in the international market, it will be rather difficult to continue magnet production in these countries. Consequently, the growth of production in these countries will also be rather difficult in future. The annual growth rate of the global total output of sintered NdFeB was more than +20% until 2000, it became negative in 2001 (−6%), and it again became positive after 2002 ($\geq +10\%$).

The output changes of sintered NdFeB magnet made in China, Japan, the United States, and Europe since 1995 are summarized in Figure 25. The curve with triangles in Figure 25 is related to data given by JEMA for Japan, which is −20% lower, as mentioned before. According to the data given by JEMA, the output of China exceeds that of Japan in 2000, but not in 2001. The outstanding feature in Figure 25 is the big jump in the output by China after 2002, since production in both the United States and Europe has almost stopped and 80% of global output is now concentrated in China!

The year 2001 was a 'nightmare' for global magnet industries. Owing to the global economic recession, business for both IT and computer industries was very bad. Both IT and computer industries are major customers of NdFeB magnets; consequently, the purchase of magnets dropped sharply in 2001. Statistics showed that in 2001 the output of sintered NdFeB magnets in Japan was 20% lower in comparison with that of 2000 and the sales value dropped by 36%! The situation in the United States and Europe was similar: their outputs dropped by 28 and 18%, respectively. China is the only exception in the world, where the output growth of NdFeB is continuing, although its growth rate was much reduced, from +33% (2000) to +16% (2001).

Owing to the sharp output reduction in the West, the curve of global output had declined in 2001. Owing to the reduction in the output of sintered NdFeB in Japan, China became the number one producer of sintered NdFeB in the world in 2001.

The prices in Japan, the United States, and Europe are different, but they are more or less at the same level. The price of China magnets is only half of that in western market. This is the most attractive factor of China magnets! The price changes of sintered NdFeB magnets made in China,

Table 29. Powder specifications for bonded ferrite made by BGRIMM.

Grade	Type of ferrite	Powder size (μm)	Density ($G\,cm^{-3}$)	B_r kg	$_bH_c$ (kOe)	$_iH_c$(kOe)	$(BH)_{max}$(MGOe)
XSF-1	Ba ferrite	2–4	3.7	1.5	1.2	2.4	0.50
XSF-2A	Ba ferrite	1.1–1.4	3.6	1.8	1.5	2.2	0.75
XSF-2B	Ba ferrite	1.5–1.8	3.6	1.8	1.4	1.9	0.70
XSF-2S	Sr ferrite	1.5–1.8	3.6	1.8	1.4	2	0.70
XSF-3	Sr ferrite	1–1.4	3.6	2.4	2	2.6	1.30
XSF-4	Sr ferrite	1.2–1.5	3.6	2.45	2	2.8	1.40

Table 30. Prices ($/kg) of bonded ferrite magnets in China market during 1990–2005.

	1990	1991	1992	1993	1994	1995	1996	1997
Flexible ($/kg)	3.4	3.3	3.2	3	2.8	2.6	2.6	2.8
Rigid ($/kg)	–	–	–	12	11	10	9	8.7
Totally averaged ($/kg)	3.4	3.3	3.2	3.2	3.1	3	3.1	3.2
	1998	1999	2000	2001	2002	2003	2004	2005
Flexible ($/kg)	3.1	3.4	3.6	3.6	3.6	3.5	3.6	3.6
Rigid ($/kg)	8.5	8	7	8.4	8.5	8.7	8.8	8.8
Totally averaged ($/kg)	3.5	3.7	3.9	4.05	4.1	4.04	4.1	4.14

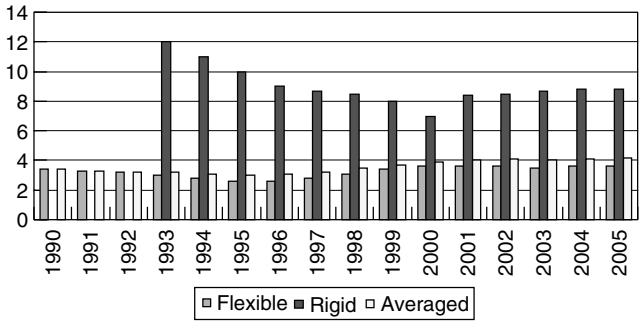

Figure 24. Price ($/kg) variation of bonded ferrite made in China (1990–2005).

Japan, the United States, Europe, and the global average are compared in Figure 26 (1995–2004).

The annual growth rate of sales value in Japan kept rather high >50% until 1990. Starting from 1991, it declined by ~20% annually. In 1992, the growth rate of sales value in Japan became negative, then it remained <20% until 1999. It declined again in 2000. In 2001, sales values of sintered NdFeB declined in all countries, the only difference being in their reducing rate: they were −36, −41, −32, and −6% for Japan, the United States, Europe, and China respectively. Since 2000, sales values in the United States and Europe have declined steadily. The sales value in Japan had increased a bit after 2001, but even in 2003, it was still much lower than its peak value of 2000.

The sales value of China in 2002 had exceeded that of 2000 with an annual growth rate of +17%. It increased even more in 2003 (with an annual growth rate of +93%) due to unusual output expansion (with annual growth rate of +109.7%), although the annual price reduction rate was around −8% (see Table 32).

Value ($\$ \times 10^8$) of NdFeB in China, Japan, the United States, Europe, and global total is shown in Figure 27.

The global total value of sintered NdFeB magnets in 2003 was still less than its peak value in 2000, in spite of its unusual increase in 2003. The same situation was seen in Japan. Its sales value in 2004 was far less than its peak value in 2000. As for China, her sales value in 2002 already exceeded that in 2000. Her sales value in 2004 was almost three times higher than that in 2000 due to her output growth of five times during the same time, although her price in 2004 was 39% less than that of 2000.

The output percentage change of sintered NdFeB made in China, Japan, the United States, and Europe during 1995–2004 is summarized in Figure 28.

Now, the output of sintered NdFeB made in China is 79.7% of the global total. The output from Japan, Europe, and the United States is 19.4, 0.9, and 0% respectively. As for the distribution of sales value, the picture is quite different: in 2004, value percentages were 63.6, 34.8, and 1.6% for China, Japan, and Europe respectively.

The gap between output and sales value is the main problem faced by the Chinese NdFeB magnet industry. The only

Table 31. Output (tons), sales value ($\$ \times 10^8$), price ($/kg) of sintered NdFeB magnets in China, Japan, the United States, and Europe (1995–2004).

	1995	1996	1997	1998	1999
China output (tons)	1820 (+48%)	2100 (+15%)	2550 (+21%)	3260 (+28%)	4200 (+29%)
Value ($\$ \times 10^8$)	1.2922 (+42%)	1.428 (+11%)	1.658 (+16%)	2.0212 (+22%)	2.436 (+21%)
Price ($/kg)	$71/kg (−4%)	$68/kg (−4%)	$65/kg (−5%)	62 (−5%)	58 (−7%)
Japan output (tons) (JEMA)	2200 (+24%)	2600 (+18%)	3800 (+46%)	4500 (+18%)	5300 (+18%)
	–	–	3200	4000	4700
Value ($\$ \times 10^8$)	3.036 (+20%)	3.51 (+16%)	4.98 (+42%)	5.76 (+15%)	6.625 (+15%)
Price ($/kg)	138 (−3%)	135 (−2%)	131 (−3%)	128 (−3%)	125 (−2%)
USA output (tons)	520 (+16%)	640 (+23%)	750 (+17%)	710 (−6%)	810 (+14%)
Value ($\$ \times 10^8$)	0.7322 (+12%)	0.87 (+19%)	0.99 (+14%)	0.909 (−9%)	0.972 (+7%)
Price ($/kg)	141 (−3%)	136 (−4%)	132 (−3%)	128 (−3%)	120 (−6%)
Europe output (tons)	410 (+24%)	510 (+24%)	580 (+14%)	630 (+9%)	680 (+8%)
Value ($\$ \times 10^8$)	0.5576 (+21%)	0.673 (+21%)	0.7424 (+10%)	0.7812 (+5%)	0.782 (+0.1%)
Price ($/kg)	136 (−3%)	2 (−3%)	128 (−3%)	124 (−3%)	115 (−7%)
Global output (tons)	4950 (+30%)	5850 (+18%)	7680 (+31%)	9100 (+18%)	10 990 (+21%)
Value ($\$ \times 10^8$)	5.619 (+23%)	6.549 (+11%)	8.406 (+28%)	9.471 (+13%)	10.875 (+15%)
Price ($/kg)	113.5 (−6%)	112 (−1%)	109 (−3%)	104 (−5%)	99 (−5%)

	2000	2001	2002	2003	2004
China output (tons)	5600 (+33%)	6500 (+16%)	8800 (+35.4%)	18 460 (+109.7%)	27 510 (+49)
Value ($\$\times 10^8$)	3.03 (+24.4%)	2.86 (−5.6%)	3.344 (+17%)	6.461 (+93.2%)	9.078 (+40.5%)
Price ($/kg)	54 (−6.9%)	44 (−18.5%)	38 (−13.6%)	35 (−7.9%)	33 (−5.7%)
Japan output (tons) (JEMA)	6400 (+20.8%)	5100 (−20.3%)	5600 (+9.8%)	6200 (+10.7%)	6700 (+8%)
	5250 (+11.7%)	4650 (−11.4%)	4750 (+2.1%)	5250 (+10.5%)	5950 (+13.3%)
Value ($\$\times 10^8$)	7.04 (+6.3%)	4.49 (−36.2%)	4.59 (+2.2%)	4.712 (+2.7%)	4.824 (+2.4%)
Price ($/kg)	110 (−12%)	88 (−20%)	82 (−6.8%)	76 (−7.3%)	72 (−5.3%)
USA output (tons)	850 (+5%)	610 (−28.2%)	280 (−54%)	100 (−64.3%)	<10 (−90%)
Value ($\$\times 10^8$)	0.935 (−6.2%)	0.55 (−52.4%)	0.24 (−43.6%)	0.08 (−66.7%)	–
Price ($/kg)	110 (−8.3%)	90 (−18%)	85 (−5.5%)	80 (−5.9%)	–
Europe output (tons)	750 (+10.3%)	640 (−14.7%)	580 (−9.4%)	460 (−20.7%)	300 (−34.8%)
Value ($\$\times 10^8$)	0.83 (+6.1%)	0.54 (−34.9%)	0.46 (−14.8%)	0.34 (−26%)	0.222 (−34.7%)
Price ($/kg)	105 (−8.7%)	85 (−19%)	80 (−5.9%)	74 (−7.5%)	74 (0%)
Global output (tons)	13 600 (+25%)	12 850 (−6.2%)	15 260 (+19%)	25 220 (+65%)	34 520 (+36.9%)
Value ($\$\times 10^8$)	11.835 (+8.8%)	8.44 (−29.4%)	8.634 (+2.3%)	11.593 (+34.3%)	14.124 (+21.8%)
Price ($/kg)	87 (−12%)	66.1 (−24%	57.9 (−12%)	46.1 (−20.4%)	40.9 (−11.3%)

way to solve this problem is to eliminate the technical gap that exists between China and developed countries, that is, to improve the performances of Chinese products.

It is well known that the prices of magnets are quite different, depending on their grades and performances. Generally speaking, the better the magnet, the higher its price would be. The price gap between Chinese and international magnet markets is rather big. As a sample, the averaged prices for different grades are shown in Figure 29.

The vertical coordinate axis shows magnet price ($/kg) and the horizontal coordinate axis shows energy products (MGOe) of magnet. There are two group curves: A – China market; B – international market. Each group contains two curves: one relates to 1998 and the other relates to 2003. The following are worth noting from Figure 29:

1. The price of magnets is rising with their energy products extensively. For example, now magnets with 40 MGOe can be sold for $40/kg in the Chinese market, magnets with 44 MGOe and 48 MGOe can be sold for as high as $55/kg and $80/kg respectively. Obviously, only higher-grade magnets can be sold at a better price. This is the only way to get rid off the problem of low economic efficiency (profit) of the NdFeB magnet industry in China.
2. Prices in Chinese and international markets are quite different as they belong to a different curve group. In general, the price in the Chinese market is only 65–70% of that in the international market.
3. Prices in both international and Chinese markets are reducing with time. The reducing rate in the international market seems even more than that in the Chinese market due to the price gap between them.

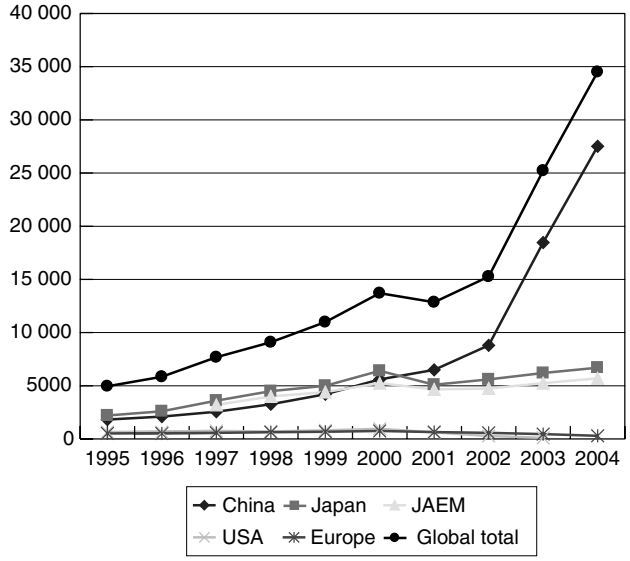

Figure 25. Output of sintered NdFeB in China, Japan, the United States, and Europe (1995–2004).

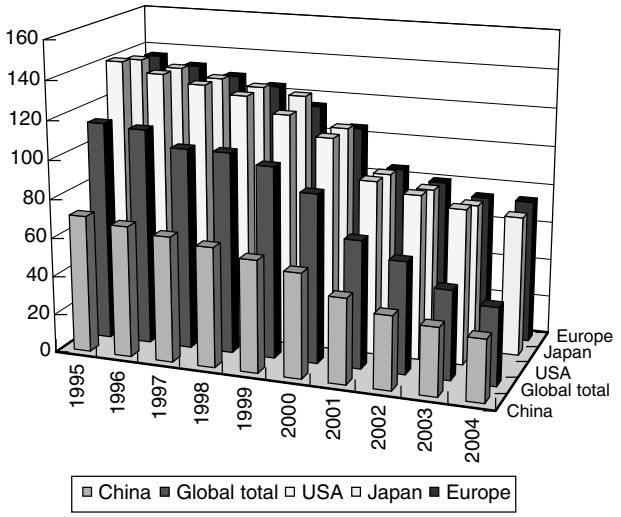

Figure 26. Sales price ($/kg) of sintered NdFeB magnets in China, Japan, the United States, Europe, and global average during 1995–2004.

Moreover, if magnet manufacturers want more value added to their magnets, they should manufacture magnets with high tolerance and accuracy, instead of block magnets, and should also do magnet assembling to make devices. This way, the magnet manufacturers in developed countries can compensate the pressure of price reduction successfully. Considering that the use of NdFeB in motor application will considerably increase in the near future, we have to focus on the development of NdFeB with high-energy products and a high coercive force, lower temperature coefficient, that is, which are suitable for motor use. In order to realize the use of NdFeB for motors more quickly, magnet manufacturers should work with motor designers and motor makers more closely.

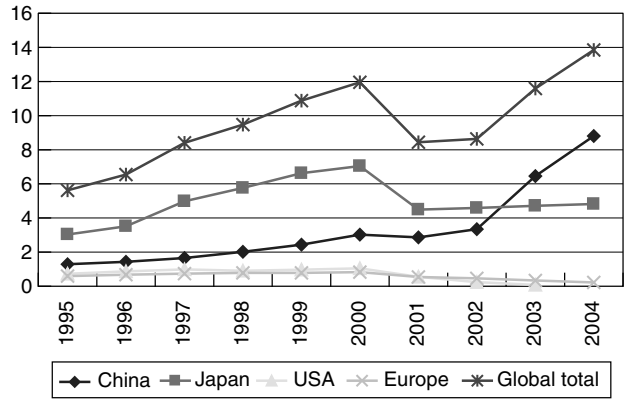

Figure 27. Value ($\$ \times 10^8$) of sintered NdFeB magnets made in China, Japan, the United States, Europe, and global total.

12 APPLICATION EXPANSION OF NdFeB MAGNETS

Since the middle of the 1990s, the market demand of NdFeB has increased so significantly that it has pushed the production expansion to a higher pace. Owing to expansion in production of NdFeB, its sales price has reduced sharply. The global economic recession has made the situation for the NdFeB magnet industry even worse; this situation may continue until 2005. On the other hand, the price reduction helps in NdFeB being used for many new applications such as motors, especially electric vehicle (EV), hybrid car, power generators, and magnetic refrigerator, whereas this was impossible earlier due to the high price of NdFeB.

In order to show the expansion of NdFeB, we take some samples from recent applications of NdFeB magnets in China.

12.1 Electric bicycle (EB)

Electric Bicycle (EB) has a permanent magnet motor (36 V/180 W) in the wheel center of bicycle and a rechargeable battery, electron monitor, with total weight ≤ 40 kg, and its speed ≤ 20 km/hr. The running distance per charge is in the range of 40–60 km. This type of EB is suitable for urban transportation in cities with population of several millions. This type of EB has been gaining popularity in south China in recent years. For example, Suzhou city with a population of half million has 180 000 EBs in the down town area. One and a half million EBs were sold in 2002. Three and a half million EBs were made in 2003. A total of around 5 million EBs were made in China in 2004.

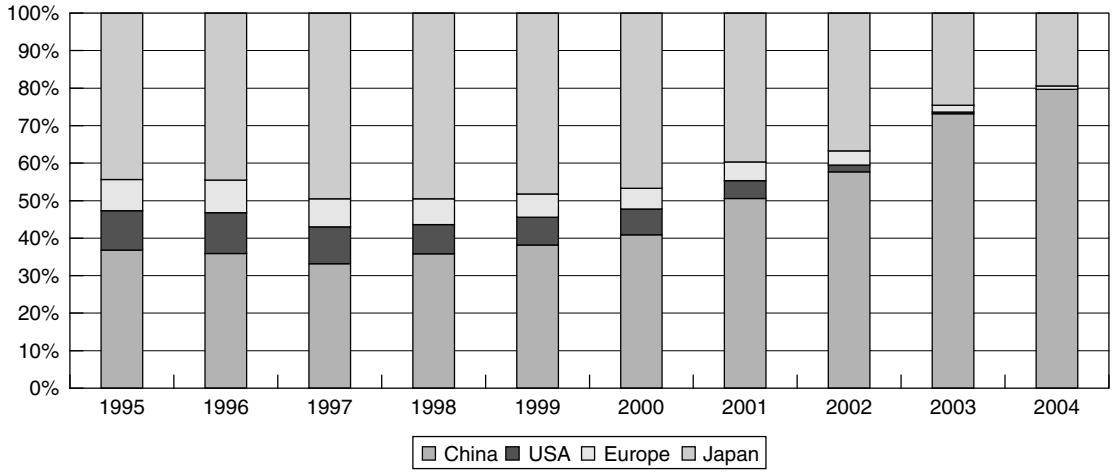

Figure 28. Output percentage change of sintered NdFeB magnets made in China, Japan, the United States, and Europe during 1995–2004.

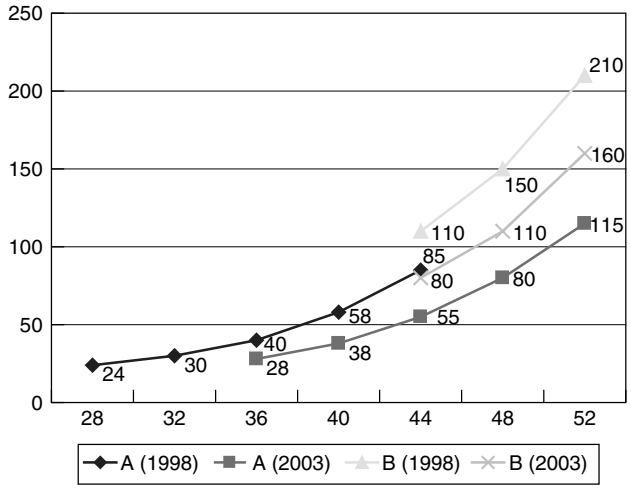

Figure 29. Average prices of sintered NdFeB depending on their grades in international (B) and China (A) market in 1998 and 2003.

The photograph of EB made in Suzhou is shown in Figure 30 as a sample.

The motor used for EB is an NdFeB magnet motor of 36 V/180 W. Three hundred and eighty grams of sintered NdFeB is used for each motor. The NdFeB that is used is of 38SH or 40H grades, the price of which is around \$38/kg. There are two types of motors: high speed and low speed, their prices are ¥350–420/pics and ¥240–280/pics, and it is \$42/pics on average. The price of EB ranges from ¥1800–2500/pics, that is, \$260/pics on average.

In order to show the value addition with product stream, we have taken data of 2003: total output of EBs is 1.5 million pieces. One thousand three hundred and thirty tons of sintered NdFeB magnets were used. It needs 653 tons of Nd_2O_3 with a value of 8.16 million USD (the price of Nd_2O_3 is \$12.5/kg). The value of used NdFeB magnets, motors, and EBs is 46.55 million USD, 147 million USD, and 910 million USD respectively. If we take the value of Nd_2O_3 as 1, then the value of the NdFeB magnet, value of NdFeB motor, and value of EB will be 6.2, 18, and 111 respectively!

Figure 30. Electric bicycle using NdFeB motor made in Suzhou.

The sharp increase in the output of EBs and used sintered NdFeB magnets is shown in Figure 31.

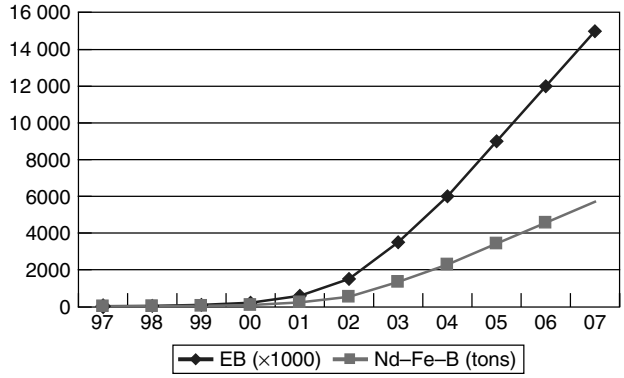

Figure 31. Output of EB ($\times 10^3$ pics) and used NdFeB magnets (tons) in China (1997–2007).

The total output of EBs will be 15 million pieces and the NdFeB magnets needed for such an application will be around 6000 tons in 2007. The annual EB output growth rate of 12 was rather high in the initial stage ($> +100\%$). It will be reduced to a normal range of within $+30\%$ annually, when the annual output reaches 15 million pieces or more.

12.1.1 Why EB has become popular in China

The EB originated in Japan, the most famous one with the trade mark PAS is made by Yamaha Co. Statistics show that in 2003 the total output of EBs in the world was 600 000 pieces. The distribution on locations is as follows:

Japan – 250 000 pieces; USA – 150 000 pieces; Europe – 100 000 pieces;

Taiwan – 100 000 pieces.

In the same year, 3.5 million EBs were made in China, which is almost six times higher than the global total! Why has the use of EBs spread so quickly in China? Some of the reasons are as follows:

1. The income of people in China is not very good as it is a developing country. The car is not affordable for every family. But, due to its low price, the EB is able to meet the needs of the common people. According to the published economic statistics in 2001, the cost of one EB (¥1800–2500/pics) is equal to the monthly income of a family in the city, or equal to the three-month income of a family in rural area. Anyway, the EB is economically available for Chinese people. Moreover, the service fee for EB is low: charging fee and depreciation of battery −¥0.9/charge. Consequently, the EB has become very popular in China recently.
2. Because of its huge population, the car did not become very popular in China, simply because of lack of oil supply and parking space. But electricity is much cheaper and easily available in China. Moreover, there is no pollution caused by using EB.
3. The people of China are used to using the bicycle to commute to various places. There is a very strong network for producing bicycles and all related parts, which can also be used for EB production. This is the reason why the EB industry has become so strong in China within the last couple of years.

12.2 Low-grade NdFeB to replace ferrite

At the end of 2003, I made a business trip to south China and visited the biggest magnet producers of bonded NdFeB (Galaxy in Chengdu), sintered NdFeB (Yunsheng in Ningbo), ferrite (DMEGC in Dongyang), and Alnico magnet (Hangzhuo Permanent Magnet Group in Hangzhuo, HPMG). I saw 'the explosion expansion of sintered NdFeB' everywhere in Zhejiang province with my own eyes, especially in the area of Ninbo city and around.

Rare-earth magnets are considered to be high-tech materials, which need high volume of investment, high technology, and highly qualified employees. But, to my surprise, what I saw in Cixi city was exactly opposite of this! There are neither big workshop buildings with modern equipment, nor are there qualified technicians. Half of the raw materials used are taken from the recycled material without any special treatment. They do not intend to make high-grade NdFeB, but only aim to replace HF. Their products are small disk magnets used as buttons for clothes, boxes, and bags. Because their magnetic force is much stronger than that of HF, such products are extremely popular among customers. Here there is mass production of NdFeB, with trucks waiting outside the plants. At one of the plants, the output of the small disk magnet per day is 12 tons, that is, $\geq$6 million pieces per day! Such products are widely used in China and abroad. The economic efficiency of such plants is much higher than that of traditional magnet producers, which make higher-grade magnets. Statistics showed that that there are 6–8 such plants in Cixi and the total annual output is $\geq$5000 tons. This is rather confusing: which way should the China NdFeB magnet industry go? Should it follow the developed countries, or should it follow Cixi?

The major applications of NdFeB magnets as high-tech and new materials are in modern high-tech industries including IT, computer, communication, automotive, and small appliances, for example, cordless tools. The total amount of magnets used for such new applications would be thousands of tons!

Therefore, the quality of products is most important for long-term development. The 'Way of Cixi' is only an appearance of certain conditions and period; it is surely not the main stream!

12.3 Application distribution of sintered NdFeB magnets

12.3.1 Distribution of sintered NdFeB magnets on applications in China

Applications of sintered NdFeB magnets in China can be divided into three groups:

1. High-tech application, such as MRI, VCM, CD pickup, CD-ROM/DVD-ROM, mobile phone, cordless tools, EB/EAV, etc.
2. Traditional application, such as speaker, magnetic separator, magnetizer including dewaxer used in oil fields and the petroleum industry.

Table 32. Output ($\times 10^3$), used NdFeB (tons), value ($\$ \times 10^8$) of NdFeB, motors, and EB (Miao, 2004).

Year	Output ($\times 10^3$pics), (Δ(%))	Used NdBeF (tons), (Price ($/kg))	Value of needed NdFeB ($\$ \times 10^6$)	Value of motor ($\$ \times 10^8$) A. P. ($42/pics)	Value of EB ($\$ \times 10^8$) A. P. ($260/pics)
1997	10	3.8 (65)	0.247	0.0042	0.026
1998	30 (200)	11.4 (62)	0.707	0.0126	0.078
1999	80 (166)	30.4 (58)	1.76	0.0336	0.208
2000	200 (150)	76 (52)	3.95	0.084	0.52
2001	580 (190)	220 (44)	9.68	0.244	1.51
2002	1500 (158)	570 (38)	21.66	0.63	3.9
2003	3500 (133)	1330 (35)	46.55	1.47	9.1
2004	6000 (71)	2280 (33)	75	2.52	15.6
2005	9000 (50)	3420 (32)	109	3.87	23.4
2006	12 000 (33)	4560 (31)	141	5.04	31.2
2007	15 000 (25)	5700 (30)	171	6.3	39

A. P.: averaged price.

Table 33. Application distribution of sintered NdFeB in China in 2003.

High-tech application MRI	360 tons	2.0%
VCM	210 tons	1.1%
CD pickup	940 tons	5.1%
DVD-ROM + CD-ROM	1500 tons (5650 tons)	8.1% (30.7%)
Mobile phone	360 tons	2.0%
Cordless tools	940 tons	5.1%
EB + EAV	1340 tons	7.3%
Traditional application Speaker	4000 tons	21.7%
Magnetic separator	2500 tons (8500 tons)	13.5% (46%)
Magnetizer (dewaxer etc.)	2000 tons	10.8%
Low-grade use (Cixi)	3000 tons	16.2%
Others	1310 tons	7.1%
Total	18 460 tons	100%

3. Low-grade uses such as magnets made in Cixi.

The distribution of used NdFeB in China (2003) is listed in Table 33 and shown in Figure 32.

The section of high-tech application is 31% of the total, considering the use for motors. This section will grow in future. The section of traditional application is 46% of the total and may reduce slightly. The use of low-grade magnets, similar to that made in Cixi, may remain steady for a certain period of time, its absolute tonnage may even increase, but its percentage would decline in the long term. In 2007, the need for sintered NdFeB magnets for EB and EAV will be 5700 and 2385 tons, respectively. The need in EB and EAV will exceed 8000 tons, and that in EV has not yet been included. It should be noted that all these demands appeared only after 1997. If the low-grade use is included, then the total demand would exceed 20 000 tons, which shows a sharp increase in the market demand for NdFeB in future!

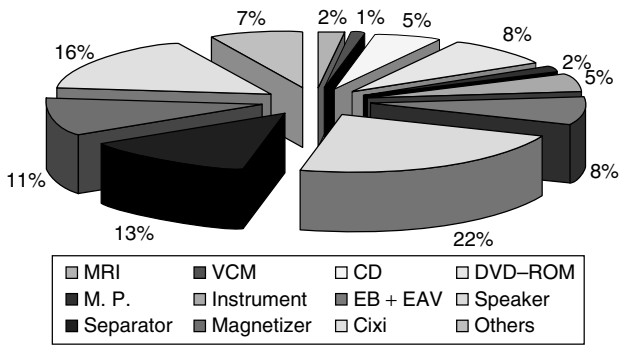

Figure 32. Application distribution of sintered NdFeB made in China (2003).

In the twenty-first century, one would see numerous improvements and growth in the NdFeB magnet industry. In particular, the next decade will see great improvement in the quality and capability of the NdFeB magnet industry in China. This will result in better and cheaper magnets for customers all over the world.

12.3.2 Application of sintered NdFeB magnets in Japan

There are three major applications of sintered NdFeB magnets in Japan: VCM, MRI, motor/generator. The portions used for certain applications vary every year. The changes during 1996–2003 are listed in Table 34 and summarized in Figure 33.

Sintered NdFeB magnets are widely used in the HDD of computers and consumer electronics. VCM is the biggest application of NdFeB magnets, but its weight percentage is reducing continuously from 57% of the total in 1996 to 35% in 2003 because the most advanced magnets with energy

Table 34. Percentage changes of used sintered magnets for certain application in Japan (1996–2003).

	VCM (%)	Motor/generator (%)	MRI (%)	Acoustics (%)	Communication (%)	Others (%)
1996	57	14	16	3	5	5
1997	58	15	14	3	6	4
1998	55	15	14	3	8	5
1999	50	20	14	3	10	3
2000	47	24	13	2	11	3
2001	43	29	16	2	9	2
2002	36	32	17	4	9	2
2003	35	34	15	8	8	2

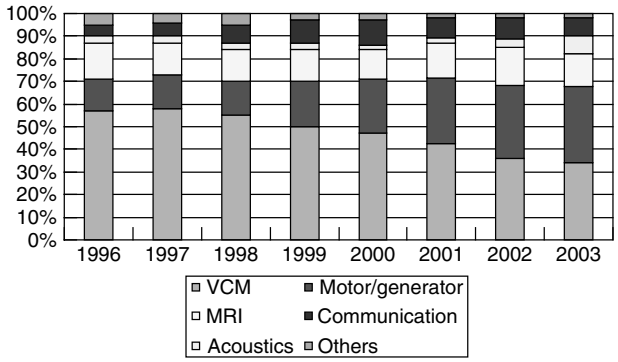

Figure 33. Percentage change of used NdFeB magnets for different applications in Japan during 1996–2003.

products ≥48 MGOe are used. Consequently, the weight per piece is much reduced. Now HDD is not only widely used for PC but is also used as a memory unit for video systems of TVs, car navigation systems, mobile phones with large memories, and so on. These 1-in. HDDs are very minute in size. The size of its VCM magnet is $3 \times 2 \times 0.8$ mm with an unsymmetrical shape, which is rather difficult to prepare.

The portion of magnets used for MRI is relatively stable; it ranges between 13 and 17%. It is not only used for medicinal purpose, but the digital MRI can also be used for quality control of agricultural products, space-orientation application, and so on (Asfour, Raoof and Fournier 2004).

The usage of small-sized magnets, such as microspeakers, pickups of CD and DVD, vibration motors of mobile phones, and audio systems for automobiles, has increased in acoustic devices and communications in recent years instead of ferrite magnets.

A remarkable increase has been observed in motor application since 1995. The driving force behind such an increase is closely related not only to improvement in performance of magnets but also to the progress in motor designs such as SPM (surface permanent magnet) type and IPM (interior permanent magnet) type by using high-performance magnets.

SPM type is mainly applied in servomotors for fabric automation and office automation, elevator lifting motor, and so on. The use of IPM type is expanding in many applications, including compressor motors. The IPM type is being increasingly used because the simple rectangular-shaped magnets can be used, which are significantly less expensive in comparison to segment magnets while preparing and assembling. IPM-type motor has been adopted by Toyota and Honda for their hybrid electric vehicle (HEV). The magnets used are 38UH grade with (BH) max = 38 MGOe, ${}_{\mathrm{i}}H_{\mathrm{c}} =$ 25 kOe, which can be used at a temperature as high as 180 °C.

13 LOCATION DISTRIBUTION OF NdFeB MAGNET MANUFACTURERS IN CHINA

The total output of sintered NdFeB magnets in China in 2004 was 27 510 tons. The magnet plant locations cover 12 provinces and Beijing–Tianjin cities. The output distribution of sintered NdFeB magnets made in China on their locations is shown in Figure 34.

In general, sintered NdFeB magnet production in China is concentrated in three areas: Zhejiang province takes the first place with 47.1% of the total output; Shanxi province takes the second place with 21.7% of the total; Beijing–Tianjin area takes the third with 11.7% of the total. The rest 19.5% of the total production is spread over nine provinces.

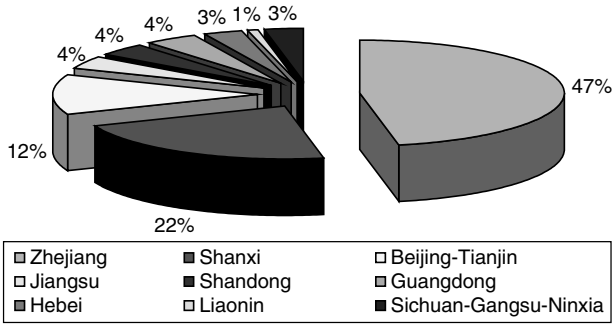

Figure 34. Location distribution of sintered NdFeB magnets made in China (2004).

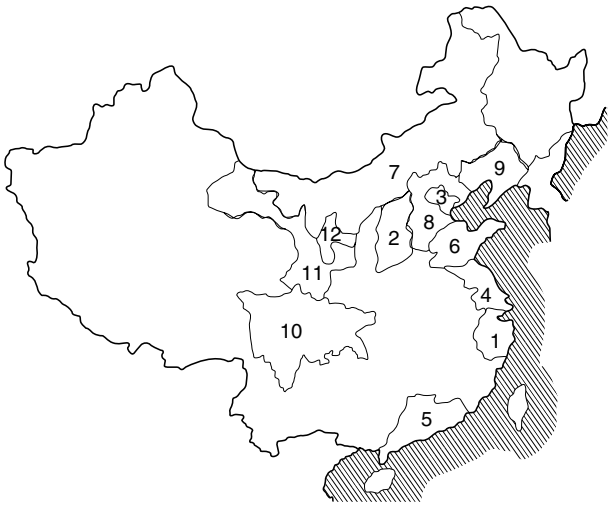

Figure 35. Location distribution of NdFeB magnet manufacturers in China. 1–Zhejiang province; 2–Shanxi province; 3–Beijing/Tianjin area; 4–Jiangsu province; 5–Kuangdong province; 6–Inner Mongolia; 7–Shiannxi province; 8–Ninxia province; 9–Gangsu province; 10–Shandong province; 11–Sichuang province; 12–Liaonin province.

Since NdFeB magnets are rather sensitive to corrosion, and it is quite hot and humid during summer in south China, the weather conditions here are unfavorable for making NdFeB magnets, especially the high-grade magnets. Thus, the NdFeB production volume in Zhejiang province is the highest, but the quality is not very good. Magnets of higher grade are produced in north China: Beijing–Tianjin area and Shanxi province (see Figure 35).

Of course, the quality of magnets depends on the process and equipment used, that is, both software and hardware used for manufacturing. The magnet plants equipped with the most advanced processes and equipment are located in the Shandong province. Therefore, the best magnets are produced there.

The actual statistical data of sintered NdFeB magnets made in China between 2003 and 2006 are given in the appendix.

REFERENCES

Asfour, A., Raoof, K. and Fournier, J.-M. (2004). Digital MRI at low-field: promising New Avenues for permanent Flux Sources, *Proceedings of 18th workshop on high performance magnets and their applications*, Annecy, France, August 2004, Vol. 2, pp. 609–615.

Bian, S. and Li, S. (2001). Current status and its future of pre-sintered ferrite powder and bonded magnets in China. *Proceedings of 2nd Bilateral Symposium on Magnetic Materials*, Taibei, Taiwan, July 16, 2001.

Chen, G. (2004). The status and future of soft ferrites in China. *Proceedings of 2004 China Magnet Symposium*, Xian, China, May 2004, pp. 187–197.

IEC Publication (1973). **50**, 901.

Japan Association of Bonded Magnet Industry (2004).

Jia, G., *et al*. (1998). Today and tomorrow of Chinese alnico industry. *Magnetic Materials and Devices*, **6**, 22.

Jia, G.-Y., Jia, Y.-Y. and Li, M.-G. (2004). Alnico magnet industry in China, *Proceedings of 2004 China magnet symposium*, Xian, China, May 2004, pp. 181–186.

Luo, Y. (1991). *Encyclopedia of Chemical Industry*, Chemical Industry Publisher: Beijing, pp. 627–636, 661–692, Vol. 2, December 1991.

Luo, Y. (1995). Development of rapidly quenched (RQ) materials in China, *Proceedings of Intertech Conference on Magnetic Materials*, San Francisco, May 1995.

Luo, Y. (1996). Magnet industry: a booming global business, *Proceeding of Gorham/Intertech's 2nd China Conference*, Guilin, 7–10, October 1996.

Luo, Y. (1997). The changing trend of NdFeB magnets, *Proceedings of 10th International NdFeB Conference*, Hyatt Regency O'Hare, Chicago, April 14–16, 1997.

Luo, Y. (2000a). Hard ferrite industry in China and its future, *Proceedings of 8th International Conference on Ferrite (8ICF)*, Kyoto, 18-21 September 2000, pp. 445–453.

Luo, Y. (2000b). Further development of rare earth magnet industry in China, *Proceedings of the 16th International Workshop on REM and Their Applications*, Sendai, September 2000, Vol. 1, pp. 31–38.

Luo, Y. (2000c). Further development of rare earth magnet industry in China, *Proceedings of the 16th International workshop on Rare Earth Magnets and their Applications*, The Japan Institute of Metals, Sendai, August 2000, pp. 31–38. vol. 1.

Miao H. (2004). Golden opportunity for NdFeB magnets due to the rise of electric bicycle in China, *Proceedings of 2004 China Magnet Symposium*, Xian, May 2004, pp. 223–231.

Zhang, J.-L. (2002). BIGRIMM new products and furue. *Proceedings of 2002 BM Symposium*, Tokyo, Lungwood Hotel, December 6, 2002.

Zhang, J. (2004). Current status of hard ferrite magnet market and raw materials in China, *Proceedings of 2004 BM Symposium*, Tokyo, 3 December 2004.

Zhou, S.-X. and Lu, Z.-C. (1999). Recent development of amorphous materials in China. *Proceedings of 1st Bilateral Symposium on Magnetic Materials*, Taibei, Taiwan, June 1999.

Zhou, S.-X. (2001). Development of amorphous and nano-crystalline soft magnetic materials in China. *Proceedings of 2nd Bilateral Symposium on Magnetic Materials*, Taibei, Taiwan, July 16, 2001.

FURTHER READING

Kaneko, Y. (2004). *Proceedings of the 18th International Workshop on HPMA'04*, Annecy, August 2004, Vol. 1, pp. 40–51.

Luo, Y. (2003). *Proceedings of 2003 Techno Frontier Symposium*, Tokyo, 18 April 2003.

Luo, Y. (2004). *Proceedings of 2004 China Magnet Symposium*, Xian, May 2004.

APPENDIX A

Table 1A. Statistics of Sintered NdFeB Made in China (data in brackets are blocks).

	2003	2004	2005	2006
Zhejiang	7 510 (48.3%) (12 750t)	10 470t (45.7%) (17 480t)	14 290t (47.4%) (22 540t)	18 240t (47.7%) (27 990t)
Shanxi	3 250 (20.9%) (5 500t)	4 960t (21.7%) (8 050t)	5 710t (18.9%) (8 950t)	7 010t (18.3%) (10 050t)
Beijing/Tianjin	2 540 (16.3%) (4 200t)	3 420t (14.9%) (5 600t)	4 770t (15.8%) (7 450t)	6 280t (16.5%) (9 390t)
The rest	2 250 (14.5%) (3 980t)	4 060 (17.7%) (6 610t)	5 390t (17.9%) (8 260t)	6 690t (17.5%) (10 440t)
Total	15 550 (+77%) (26 430t)	22 910 (+47.3%) (37 790t +43%)	30 160t (+31.7%) (47 200t +25%)	38 220t (+26.7%) (57 87t +22.6%)
Zhejiang province	2003	2004	2005	2006
Block	12 750t	17 480t (+37%)	22 540t (+29%)	27 990t (+24.2%)
Magnet	7 510t	10 470t (+39%)	14 290t (+36%)	18 240t (+27.6%)
Ninbo area	2003	2004	2005	2006
Ningbo area	2003	2004	2005	2006
Konit Mag. Co.	800 (1200)t	1080 (1800)t	1 450 (2 200)t	1 280 (2 050)t
Yunsheng Mag. Co	1600 (2650)t	1440 (2400)t	1 700 (2 700)t	2 400 (3 530)t
Ketian Mag. Co.	300 (500)t	720 (1200)t	950 (1 400)t	940 (1 400)t
Yongjiu Mag. Co.	600 (1000)t	650 (1 050)t	720 (1 150)t	1 080 (1 480)t
Zaobao Mag. Co.	400 (700)t	550 (900)t	570 (950)t	700 (1 080)t
Jinji Strong Magn.	240 (400)t	420 (700)t	450 (700) t	620 (950)t
Juyou Mag. Co.	240 (400)t	360 (560)t	380 (600)t	500 (720)t
Sanhuan Nd Mag.	180 (300)t	180 (300)t	150 (300)t	120 (180)t
Tonchuang Mag.	–	–	250 (350)t	350 (500)t
Huahui Mag. Co.	–	–	150 (240)	360 (520)t
YinXin Mag. Co.	–	–	200 (300)t	280 (400)t
Xiangyang Mag.	–	–	150 (240)t	250 (360)t
Tonsheng Mag. Co	–	–	200 (320)t	160 (250)t
Songke Mag. Co.	300 (500)t	330 (550)t	380 (600)t	450 (650)t
Cixi Heli Mag. Co.	1400 (2500)t	1800 (3200)t	2 000 (3 300)t	1 980 (3 200)t
Cixi Xinli	300 (500)t	330 (550)t	410 (640)t	380 (600)t
Cixi Yongsi	–	–	200 (320)t	350 (550)t
Cixi Hesheng	–	–	150 (250)t	260 (380)t
Subtotal: Block	10 650t	13 210t	16 560t	18 800t
Magnet	6 360t	7 860t	10 460t	12 460t
Hangzhou HPMG	300 (500)t	300 (500)t	340 (500)t	360 (550)t
Zhongke Maigao	200 (400)t	250 (420)t	300 (480)t	320 (500)t
Shenghua	100 (200)t	300 (450)t	360 (600)t	820 (1 370)t
Pengcheng	–	–	250 (400)t	350 (560)t
Subtotal: Block	1 100t	1 370t	1 980t	2 980t
Magnet	600t	850t	1 250t	1 850t
Dongyang area	2003	2004	2005	2006
Innovo Magnetics	300 (500)t	1320 (2200)t	1 400 (2 200)t	2 250 (3 600)t
Dongyang DMEGC	150 (300)t	140 (200)t	240 (350)T	450 (680)t
Zhongyuan Mag. Co.	–	–	240 (350)t	370 (560)t
Dongyang Baijian Mag.	–	–	200 (300)t	210 (320)t
Other	100 (200)t	300 (500)t	500 (800)t	650 (1 050)t

(*continued overleaf*)

Table 1A. (*Continued*).

Subtotal: Block	1 000t	2 900t	4 000t	6 210t
Magnet	550t	1 760t	2 580t	3 930t
Shanxi province	2003	2004	2005	2006
Block	5 500t	8 050t (+46.4%)	8 950t (+11.2%)	10 900t (+12.3%)
Magnet	3 250t	4 960t (+52.6%)	5 710t (+15.1%)	7 010t (+12.3%)
Taiyuan area	2003	2004	2005	2006
Tongli Magn. Co.	480 (800)t	540 (850)t	580 (900)t	750 (1 200)t
Jinshan Magn. Co.	240 (400)t	450 (700)t	450 (700)t	550 (860)t
Tianhe Magn. Co.	240 (400)t	800 (1300)t	650 (800)t	450 (600)t
Hongri Magn. Co.	180 (300)t	240 (400)t	200 (350)t	350 (620)t
Huiqiang Magn. Co.	120 (200)t	180 (300)t	200 (350)t	460 (800)t
33 Research Institute	120 (200)t	120 (200)t	80 (100)t	350 (450)t
Hengao Magn. Co.	120 (200)t	180 (300)t	190 (300)t	300 (480)t
Taiyuan Innovo	–	–	400 (600)t	580 (900)t
Subtotal: Block	2 500t	4 050t	4 100t	5 910t
Magnet	1 500t	2 510t	2 750t	3 790t
Rest of Shanxi	2003	2004	2005	2006
Hengci Keji	600 (1 000)t	800 (1 200)t	800 (1 300)t	520 (830)t
Jingyu Magn. Co.	350 (500)t	400 (700)t	460 (750)t	980 (1 400)t
Sanhuan Jingxiu	300 (500)t	350 (600)t	500 (800)t	680 (1 060)t
Luyuan Magn. Co.	–	–	–	240 (400)t
Other	500 (1 000)t	900 (1 500)t	1 200 (2 000)t	800 (1 300)t
Subtotal: Block	3 000t	4 000t	4 850t	4 990t
Magnet	1 750t	2 450t	2 960t	3 220t
Beijing-Tianjin-Tangshan	2003	2004	2005	2006
Block	4 200t	5 600t	7 450t	9 390t
Magnet	2 540t	3 420t	4 770t	6 280t
	2003	2004	2005	2006
BJMT	300 (500)t	270 (450)t	340 (500)t	400 (600)t
THINOVA	250 (400)t	350 (600)t	400 (650)t	460 (720)t
Sanhuan Eng. Center	250 (400)t	400 (600)t	430 (700)t	450 (730)t
Xinhuan Co.	120 (200)t	120 (200)t	150 (250)t	–
Gaoxiao Innovo	180 (300)t	400 (700)t	400 (650)t	1 100 (1 600)t
AT & T	240 (400)t	280 (450)t	250 (400)t	920 (1 300)t
Sanhuan Lucky	850 (1400)t	1000 (1600)t	1 170 (1 800)t	1 350 (1 950)t
Tianjin Tianhe Go.	–	–	350 (500)t	450 (640)t
Tangshan Huida Co.	–	–	420 (650)t	500 (770)t
Langfang Zhongci	–	–	160 (250)t	250 (380)t
Other	350 (600)t	600 (1000)t	700 (1100)t	400 (700)t
Jiangsu province				
Block	1 000t	2 000t	2 850t	3 080t
Magnet	500t	1 200t	1 860t	2 000t (5.2%)
	2003	2004	2005	2006
Shanghai Roke	–	–	430 (650)t	350 (530)t
Shanghai Zhenbao	–	–	380 (600)t	450 (750)t
Other	500 (1000)t	1200 (2000)t	1050 (1600)t	1200 (1800)t

Table 1A. (*Continued*).

Guangdong province				
Block	1 300t	1 600t	1 740t	2 220t
Magnet	800t	950t	1 060t	1 370t (3.6%)
	2003	2004	2005	2006
Jingyue Mag. Plant	300 (500)t	450 (700)t	520 (900)t	650 (1 120)t
Meizhou Mag. Co.	–	–	80 (120)t	120 (180)t
Other	500 (800)t	500 (900)t	460 (720)t	600 (920)t
Shandong province				
Block	380t	1 060t	1 550t	1 880t
Magnet	190t	660t	1 020t	1 280t (3.3%)
	2003	2004	2005	2006
Yantai Shougang	60 (120)t	240 (380)t	350 (550)t	620 (880)t
Yantai Zhenghai	30 (60)t	170 (280)t	250 (400)t	300 (480)t
Other	100 (200)t	250 (400)t	420 (600)t	360 (520)t
Hebei province				
Block	400t	500t	600t	700t
Magnet	200t	320t	380t	460t (1.2%)
	2003	2004	2005	2006
Other	200 (400)t	320 (500)t	380 (600)t	460 (700)t
Inner Mongolia				
Block			600t	1 000t
Magnet			400t	620t (1.6%)
	2003	2004	2005	2006
Baotou Ruefuxin Co.	–	–	400 (600)t	620 (1 000)t
Liaonin province				
Block	360t	450t	320t	510t
Magnet	250t	270t	220t	320t (0.8%)
	2003	2004	2005	2006
Shenyang Zhongbei	250 (360)t	270 (450)t	220 (350)t	320 (510)t
Sichuan/Gansu/ Ninxia provinces				
Block	600t	1 100t	600t	1 050t
Magnet	310t	660t	450t	640t (1.6%)
	2003	2004	2005	2006
Sichuan/Gansu/Ninxia	310 (600)t	660 (1 100)t	450 (600)t	640 (1 050)t

APPENDIX B

B1 Development History of the China NdFeB Magnet Industry

NdFeB magnet industry appeared in China in the late 1980s, which was much later in comparison with developed countries. Although the numbers of NdFeB magnet plants were more than 100, most of them were small workshops with producing capacities of less than 5 tons/year. Plants with producing capacities $\geq$100 tons/year appeared only in early 1990s. The quality of their products was unstable and the economic efficiency of these plants was not high enough.

B1.1 1987–1996 – initial stage of the developing NdFeB magnet industry in China

'Low start point' was the character of this period because of low initial investment, all equipment was locally made and simple. Chinese engineers were forced to work out a special process to prepare NdFeB magnets by using simple hardware. Middle-grade NdFeB magnets can be prepared by using the 'Chinese process' successfully. On the whole, the NdFeB magnet industry in China was much behind compared to that in developed countries. Along with a technical gap, a big gap existed in the management and quality control systems between China and developed countries. The questions were whether to build the magnet industry in an intensive way or still keep the small-scale peasant economy? Whether to build modern quality control systems or still keep the quality systems random and out of control? Most of the owners of magnet plants in this period had some background of materials science and machinery, but none of them were familiar with the modern management and quality control systems. Owing to the huge market demand, the NdFeB magnet industry in China developed rather fast, in spite of the many difficulties that existed. Consequently, many investors who got a lot of money from other businesses looked at the NdFeB magnet industry as a better business for new investment. Thus, the second stage of development of the NdFeB magnet industry in China started.

B1.2 1997–2002 – second stage of the developing NdFeB industry in China

'Higher starting point' was the character of this stage: the volume of investment in this period was much higher than that in the initial stage. It was at least 30–50 million RMB, while it was only 1 million RMB or less in the initial stage. The biggest investment in this period reached 280 million RMB! Using the big investment, the plant built in this stage was equipped with best domestic equipment following advanced processes, some plants even imported all the equipment from Japan, Germany, and the United States. The producing capacity was usually $\geq$200 tons/year, some reaching even 2000 tons/year. The products were of middle and high grades.

The technology, including both software and hardware, and know-how are a top secret for magnet manufacturers, which they never disclose to others, especially to competitors from developing countries. But the situation dramatically changed while China became the global manufacturing center since the beginning of the new century. Equipment producers in developed countries could not find customers for their new products in their own countries. They have to seek potential customers in China now. What looked impossible a couple years ago now seemed realistic and practical. Last year, some Japanese equipment manufacturers jointly developed a new fully closed and automatic producing line for manufacturing sintered NdFeB magnets with a capacity of 500 tons of final magnets/year (equivalent to 800 tons block magnet/year). They guaranteed to make highest-grade magnets with energy products of 50 ± 2 MGOe, and oxygen content in magnet $\leqslant$ 1000 ppm. It is especially worth mentioning here that the total price of such a producing line is $\leqslant$60% of the sum of the individual equipment!

Now, an advanced producing line for high-grade NdFeB magnets is under construction. All the equipments being used are made in China. Of course, its total cost is only 1/3–1/5 of the imported one. Considering economic globalization and continuously increasing market demand for NdFeB, a new stage for the development of the NdFeB magnet industry is starting in China now.

B1.3 2003 – a new stage of the developing NdFeB magnet industry in China

The character of this stage will be 'three highs': high start point; high investment; high reward. Thus, the project will be run as follows: (i) To get the most advanced producing line by using high investment to guarantee high grade of produced magnets for special uses. (ii) To follow most advantageous processes to make magnets in an intensive way: to divide producing process into two parts–master alloy/powder production and magnet manufacturing, to reduce investment and increase economic efficiency. (iii) To run the business according to the way of capital management, in order to guarantee a high reward of investment.

In this way, the China NdFeB magnet industry would mature and would match with international standards finally. As a member of new materials, the NdFeB magnet industry in China would march forward further.

Ferrimagnetic Insulators

Victor A.M. Brabers
Eindhoven University of Technology, Eindhoven, The Netherlands

1 INTRODUCTION

Ferrimagnetism is the phenomenon that a compound shows a resultant magnetization, which originates from the antiparallel orientation of two or more nonequivalent sublattice magnetizations. This implies that ferrimagnetism can only occur in certain crystal structures consisting of two or more crystallographic nonequivalent sublattices, which are occupied by paramagnetic ions in sufficiently high concentrations. The first materials which were identified to be ferrimagnetic were the ferrites MFe_2O_4, which crystallize in the spinel structure and for which the molecular field was applied for the first time (Néel, 1948). A compound AB_2O_4 with the spinel structure contains two cation sublattices, the tetrahedral (A) and the octahedral sites (B). In Néel's theory of ferrimagnetism, the effective inter- and intra-sublattice interactions A–B, A–A and B–B are introduced, which are in fact super-exchange interactions, that is, indirect exchange via the anion p orbitals. The strength of these super-exchange interactions depends on the electronic structure of the cations, as well as on the geometry of the relative configuration of the interacting cations and the intermediate anion. In particular it appears that the antiferromagnetic A–B interaction between Fe^{3+} ions in the spinel structure is very strong, resulting in ferrimagnetic ordering with high ordering temperatures for the spinel ferrites. In addition to the spinel structure, Fe^{3+} ions can also be substituted in a number of other crystal structures, of which the most important are the garnet structure, $R_3Fe_5O_{12}$, the perovskite structure $RFeO_3$, and hexagonal structures like the magnetoplumbite structure $MFe_{12}O_{19}$ and related structures. Although a large number of 3d-metal oxide compounds may exhibit ferrimagnetic behavior at low temperatures, the focus in this paper is on oxide compounds with a high concentration of iron because of the possible applications, that is, the ferrites, which show a substantial magnetization at room temperature. The electrical resistance of ferrites is highly dependent on the chemical composition; even if a small amount of the Fe^{3+} ions is reduced to Fe^{2}, the resulting mixed valence of iron accounts for a relatively high conductivity. The electrical conductivity is usually thermally activated, which is indicative of the semiconducting or insulating nature of these materials. If there are no mixed Fe-valences, the ferrites are highly resistive materials.

Handbook of Magnetism and Advanced Magnetic Materials. Edited by Helmut Kronmüller and Stuart Parkin. Volume 4: *Novel Materials*. ISBN: 978-0-470-02217-7.

2 SPINEL FERRITES

2.1 Magnetite

The most prominent and well-known ferrimagnetic compound is magnetite, Fe_3O_4, a magnetic mineral, which is an important ore of iron and occurs abundantly in nature as octahedral spinel crystals and as a common constituent of igneous and metamorphic rocks. Magnetite is named after an old finding place, Magnesia, an ancient city in west Turkey.

A peculiar variety of natural magnetite, lodestone, exhibits a permanent magnetization and consists of oxidized and Ti-substituted magnetite. The origin of this permanent magnetization is attributed to the microstructure developed during the formation of this mineral or is supposed to be induced by the strong magnetic field caused by lightning impact (Wasilewski and Kletetschka, 1999; Mills, 2004). Because of the magnetic properties of magnetite containing rocks, magnetite is often used as a probe in geomagnetism as well as in extraterrestrial research. In particular, the research of certain characteristics of magnetite containing minerals on Mars by the Spirit Rover was designed to determine whether liquid water was present on Mars or not (Bertelsen *et al*., 2004; Morris *et al*., 2004). The analysis of Martian meteorites is also leading to the discussion whether the magnetic particles in the meteorites are magnetosomes in origin, that is, four-billion-year-old fossils of magnetotactic bacteria, indicative of ancient extraterrestrial life, or that these particles are exclusively from inorganic origin: the decomposition of Fe-rich carbonates (Weiss *et al*., 2004). The magnetic properties of a number of Martian meteorites containing magnetite are also used to probe the enhanced ancient Martian magnetic field (Collinson, 1997).

Magnetite can be met in still several other domains of sciences. In archaeology, ancient ceramics are characterized by the detection of magnetite by magnetization measurements (van Klinken, 2001), whereas mineral magnetic analysis at archaeological sites can give information about the decomposition of organic remainders, which affects the magnetism of the soil (Linford, 2004).

Recent environmental studies monitored the heavy metal pollution of surface water by the magnetism of magnetite in sediments (Desenfant, Petrovsky and Rochette, 2004); magnetite particles accumulated on pine needles are indicative of airborne pollutants (Urbat, Lehndorff and Schwark, 2004). Airborne subway particles, which consist mainly of magnetite have been shown to be highly genotoxic, partly due to the relatively high concentration in subways (Karlsson, Nilsson and Moller, 2005).

In biological and medical sciences, the magnetism of magnetite is prominently present. A few examples are as follows: Magnetotactic bacteria can orient along magnetic lines due to the magnetization of small magnetite and greigite (Fe_3S_4) particles inside these bacteria (Frankel, 2003). The navigation system over long distance of some vertebrates, like migratory birds and fishes, is supposed to be related to the magnetism of magnetite particles (Walker *et al*., 1997). The human brain contains biogenic magnetite, which triggers the dispute whether the interaction of mobile phone RF radiation with these particles may cause health problems (Cranfield, Wieser, Al Madan and Dobson, 2003). Furthermore, nanoparticles of magnetite are very effective in the study of human cancer cells for diagnosis and therapy (Zhang, Kohler and Zhang, 2002).

Although magnetite is one of the best known ferrimagnetic materials, the investigation of the physical properties is still an intriguing field and raises sometimes more problems than giving answers as is shown in the recent reviews on the Verwey transition (Brabers, 1995; Walz, 2002; Garcia and Subias, 2004). Especially for applications of magnetite in which the nanoscale structures are important (i.e., particulate magnetic media, thin films, multilayer structures etc.), the structure of the crystal surface as well as the defect structure of the reduced dimensions are decisive for the physical properties of these nanoscale structures. In both cases, the typical crystal structure of magnetite plays an important role. The room-temperature structure of magnetite is the inverted spinel structure (space group O_h^7–Fd3m). The tetrahedral A sites are occupied by one-third of the iron ions as Fe^{3+} ions and the remaining Fe ions are located on the octahedral B sites as mixed valence Fe ions with an average charge of 2.5+. Table 1 gives the coordinates of the equivalent positions of this space group as relevant for the spinel structure. The first column is the number of equivalent positions in the set, identified by a character in the second column. The third is the point symmetry of the position of each set and the last column presents the coordinates of all equivalent positions in fractions of the lattice parameter. The unit cell contains 8 'molecules' of AB_2O_4; 32 oxygen ions occupying the position e, 16 B ions in the position d, which are in the center of an oxygen octahedron and 8 A ions in the position a, which are in the center of an oxygen tetrahedron. The positions f and b are interstitial tetrahedral sites and the position c-interstitial octahedral sites. In real spinels like magnetite the closed cubic packing of the oxygen ions is disturbed by the displacement of the oxygen ions from their ideal position into a ⟨111⟩ direction, away from the central tetrahedral ions, because of the large size of the A-site ions. A measure for this displacement is the oxygen parameter u, which determines the position e of the oxygen lattice sites (Table 1). For the undisturbed structure $u = 0.375$.

Hornstra (1960) recognized that twinning in the spinel structure can occur by stacking faults in which the b and c sites are occupied instead of the a and d positions, leading to the presence of twins. The twin or antiphase boundaries are responsible for the anomalous magnetic behavior observed for single-crystalline magnetite thin films. The reduced magnetic moment as well as the nonsaturation at high fields are due to the changes in the configuration of the interacting cations across the antiphase boundary (Margulies *et al*., 1996; Heijden *et al*., 1996). Owing to the different angles between the cations, the AB interaction is strongly decreased, whereas the intra-sublattice A–A and B–B interactions are increased, reversing the dominant interaction found in

Table 1. The sets of the equivalent symmetry points of the space group $Fd3m - O_h^7$ relevant for the spinel structure. The origin is taken at the A-site and $u \approx 3/8$ (Reproduced from N.F.M. Henry *et al*., 1965, with permission from thr International Union of Crystallography. © 1965).

	48	f	mm	u,0,0;	$\overline{u}$,0,0;	$1/4+u$,$1/4$,$1/4$;	$1/4-u$,$1/4$,$1/4$;
				0,u,0;	0,$\overline{u}$,0;	$1/4$,$1/4+u$,$1/4$;	$1/4$,$1/4-u$,$1/4$;
				0,0,u;	0,0,$\overline{u}$;	$1/4$,$1/4$,$1/4+u$;	$1/4$,$1/4$,$1/4-u$
O^{2-} sites	32	e	3 m	u,u,u;	$1/4-u$,$1/4-u$,$1/4-u$;		
				u,$\overline{u}$,$\overline{u}$;	$1/4-u$,$1/4+u$,$1/4+u$;		
				$\overline{u}$,u,$\overline{u}$;	$1/4+u$,$1/4-u$,$1/4+u$;		
				$\overline{u}$,$\overline{u}$,u;	$1/4+u$,$1/4+u$,$1/4-u$;		
B sites	16	d	$\overline{3}$ m	$5/8$,$5/8$,$5/8$;	$5/8$,$7/8$,$7/8$;	$7/8$,$5/8$,$7/8$;	$7/8$,$7/8$,$5/8$;
	16	c	$\overline{3}$ m	$1/8$,$1/8$,$1/8$;	$1/8$,$3/8$,$3/8$;	$3/8$,$1/8$,$3/8$;	$3/8$,$3/8$,$1/8$;
A sites	8	b	$\overline{4}3$ m	$1/2$,$1/2$,$1/2$;	$3/4$,$3/4$,$3/4$;		
	8	a	$\overline{4}3$ m	0,0,0;	$1/4$,$1/4$,$1/4$;		

bulk material (Margulies *et al*., 1997). The result is a low magnetization at low fields and nonsaturation at high fields.

The second topic of interest for nanostructures, which is related to the peculiar structure of magnetite, concerns the Verwey transition at 124 K, where the cubic structure transforms into a monoclinic C_c structure. The low-temperature unit cell corresponds to the cubic spinel structure with $a\sqrt{2}.a\sqrt{2}.2a$ and additional small deformations to arrive at the monoclinic symmetry. The lattice parameters at 10 K are $a = 11.868$ Å; $b = 11.851$ Å; $c = 16.752$ Å and $\beta = 90.20^\circ$ (Iizumi *et al*., 1982). The transition was attributed by Verwey (1939) to an electronic ordering of Fe^{2+} and Fe^{3+} ions on the B sites causing a decrease in the electrical conductivity of about two orders of magnitude. A similar electronic ordering was also supposed to exist at room temperature on the (100) crystal surface, which was evidenced by magnetic-sensitive scanning tunneling microscopy (STM) through the observation of a certain structure with periodicity of 1.2 nm on a natural crystal (Wiesendanger *et al*., 1992). The reconstruction of the (100) surface $(\sqrt{2} \times \sqrt{2})$ R 45°, observed on synthetic nonstoichiometric crystals was also proposed as evidence for an electron ordering in the form of Fe^{2+}–Fe^{2+} and Fe^{3+}–Fe^{3+} pairs along the ⟨110⟩ B-site rows (Shvets *et al*., 2004). Moreover, on (100) surfaces of high-quality stoichiometric synthetic crystals a long-distance 1.2-nm corrugation has been observed in the ⟨110⟩ B-site rows, which could indicate that the surface may be a Wigner crystal rather than a Wigner glass (Koltun, Hermann, Güntherodt and Brabers, 2001; Coey, Shvets, Wiesendanger and Güntherodt, 1993). Also on (110) as well as on (111) surfaces reconstruction and peculiar structures have been observed with STM techniques (Jansen, Brabers, van Kempen, 1995; Lennie *et al*., 1996; Oda *et al*., 1998). A remarkable superstructure has been found on an oxygen-rich (111) surface with quasi-hexagonal symmetry and 4.2-nm periodicity, which is supposed to be of electronic origin. It is obvious that the surface structure of magnetite will be perceptive to modifications of the electronic structure due to the presence of the mixed valence iron ions at the B sites. The observed 4.2-nm superstructure has been suggested to be related either to a polaronic or to a charge-density wave electron-lattice instability (Berdunov, Murphy, Mariotto and Shvets, 2004b).

Besides the electronic effects, chemical effects are important as well for the surface structure of magnetite. For instance, in a reducing environment, the appearance of a phase segregation of wüstite ($Fe_{1-x}O$) is observed on a (111) Fe_3O_4 surface (Condon *et al*., 1997). Further it has to be noted that for interfaces with magnetite in thin-film structures, the surface structure can be modified in an even more complex way. Interdiffusion between the layers occurs like in MgO–Fe_3O_4 interfaces, where $MgFe_2O_4$ is formed in the entire magnetite layer at relatively low temperatures around 400 °C (Anderson *et al*., 1997). This is not surprising, since the cation exchange between octahedral and tetrahedral sites is for the magnesium ferrite system at this temperature already substantial in the bulk material (Brabers and Klerk, 1977a). For other metal ions like Cu and Mn even diffusion at 300 °C and lower temperatures is expected to go on (Brabers, 1971; Brabers and Klerk, 1977b). Moreover, from magnetic aftereffect experiments, it is evidenced that in magnetite even at room-temperature migration of iron ions takes place by mediation of cation vacancies on the B sites (Walz, 2002). Because interfaces are usually stressed due to lattice misfit and lattice defects, the stability of well-defined interfaces in which magnetite is involved might be problematical. In particular this plays an important role in spin electronics application, in which the electronic structure of magnetite at the interface has to comply with certain requirements. For example, it has been shown that the structure and the defects on the surface modifies the spin transport significantly, which in turn spoils the wanted tunneling magnetoresistance effect (Berdunov, Murphy, Mariotto and Shvets, 2004a).

It is clear that if one succeeds in constructing a spin electronic device based on magnetite films, the deterioration

of spin-polarized transport by a possible aging of the magnetite films is a major technological challenge. Because the ionic diffusion is in particular at the interface already substantial at room temperature, thermodynamically stable structures have to be fabricated to prevent aging.

2.2 The Verwey transition

An enigma concerning magnetite is the continuous discussion on the mechanism of the Verwey transition and the real electronic structure of the low-temperature phase. Around 124 K, magnetite undergoes a first-order phase transition, which was originally related to an ordering of Fe^{2+} and Fe^{3} ions on the octahedral sites (Verwey, 1939). In fact, the transition can be considered as an electronic phenomenon, because all the octahedral sites are occupied by Fe^{3+} ions, over which a number of electrons is distributed equal to half of the number of available sites. The main question is now if these electrons are localized on specific sites in the low and the high-temperature phase as well, or if these electrons are itinerant. In Verwey's picture, the structure is purely ionic. While at temperatures above the transition temperature T_v the localized electrons are rather mobile, hopping from one site to another, the electrons below T_v are frozen in rows along the $\langle 110 \rangle$ direction, resulting in an orthorhombic structure. This ordering scheme has to be modified in such a sense that the pure ionic nature of the ordering is replaced by a partial ionic ordering. On the basis of electron diffraction experiments, Zuo, Spence and Petuskey (1990) proposed an ionic charge-ordering scheme with C_c-symmetry in which a characteristic charge-density wave is present. A refined analysis of the structure with high-resolution neutron and X-ray diffraction showed a dominant $[001]_c$ charge-density wave with a secondary $[00^1/_2]_c$ modulation (Wright, Attfield and Radaelli, 2001, 2002). The four B-site sublattices in this model are split into pairs of large and small sites, indicative for charge order. However, the difference in size is small and is provided as evidence for a not complete ionic separated charge order of Fe^{2+}/Fe^{3+} ions but for apparent partial local charges of 2.4 and 2.6, with a modulation in the *c* direction. From X-ray resonant-scattering studies of the 'forbidden' reflections near the Fe–K-α absorption edge, even a complete renunciation of ionic ordering has been proposed. For the (002) reflection, no difference was observed in the energy dependence below and above T_v (Hagiwara *et al*., 1999). Similar behavior was also observed for the (006) reflection, which led Garcia *et al*. (2000) to the conclusion that all the octahedral sites must have identical anomalous scattering factors, that means there is no difference between Fe^{2+} and Fe^{3+} sites within the time window of the X-ray radiation, 10^{-16} s.

Consequently, no charge fluctuation above or charge ordering below T_v would exist. Nevertheless, the same forbidden reflections were also observed in cobalt ferrite (Subias *et al*., 2004b), in which the B sites are populated by Co and Fe ions, because of the inverse spinel structure of cobalt ferrite. This implies that Co and Fe ions, which have irrefutably a different scattering factor for the resonant diffraction, do not disturb the coherence.

With this in mind, one cannot exclude that charge disproportion on the octahedral Fe sites, leading to two distinct B-site Fe ions, will have no effect upon the resonant diffraction, which makes the conclusion about the nonexistence of the charge ordering doubtful. The finite intensity of the X-ray resonant scattering for the forbidden reflections is caused by the anisotropic environment of the resonant ions. The asymmetry of the local sites can be an intrinsic property of the crystal structure or induced by several other factors. The magnetic interactions do not play a dominant role in the resonant scattering in spinel ferrites as is shown by the results on the nonmagnetic zinc ferrite (Kanazawa, Hagiwana, Kokubun and Ishida, 2002) and the experiments on magnetite above the Néel temperature (Subias *et al*., 2004b). Besides the intrinsic anisotropy of the crystal structure (the trigonal symmetry of the B site) point defects can also contribute to the resonant scattering (Dmitrienko and Ovchinikova, 2003). Magnetite can have a highly defective structure due to the oxygen nonstoichiometry.

Subias *et al*. (2004a) reported the absence of resonant scattering for certain superstructure reflections which was taken as evidence for the absence of charge order below T_v. Although, Toyoda *et al*. (1999) observed in a similar experiment super-lattice reflections, which they took as evidence for the valence contrast between the Fe ions.

Very recently, Huang *et al*. (2006) reported O–K-edge resonant X-ray scattering experiments, which proved the existence of charge-orbital ordering vanishing abruptly above the Verwey temperature. A definitive proof of this orbital ordering in magnetite, which is also imperative for the existence of charge ordering, is given by Su *et al*. (2006), which reported an extended study of single crystal X-ray resonant scattering. This conclusion is based on the observation of the giant resonant enhancement of superstructure reflections, characteristic of the Verwey transition at all relevant absorption edges (i.e., Fe–K, Fe–L_3 and O–K) and *ab initio* band structure calculations.

The charge/orbital ordering is well described by a superstructure $a/\sqrt{2} \times a\sqrt{2} \times 2a$, with the charge modulation in the *c* direction (Su *et al*., 2006; Huang *et al*., 2006).

The use of refined anomalous scattering coefficients for the octahedral iron ions gave direct evidence for a high degree of 46% Fe^{2+}/Fe^{3+} charge order in magnetite at 90 K (Goff, Wright, Attfield and Radaelli, 2005).

A nuclear resonance study on Fe^{57} in magnetite around T_v revealed 8 A-site NMR lines and 15 B-site lines for the

low-temperature phase (Novak *et al*., 2000). According to the C_c-symmetry the number of B lines must be 16. One line coincides with the A spectrum and was indeed found in an additional NMR study (Mizoguchi, 2001). Since the nucleus acts as a probe on an atomic scale, the effect of differences in charge must be easy detectable. However, the observed B-site lines could not be split into two sets of lines on the basis of the NMR parameters like the spin–lattice relaxation time T_1 and the spin–spin relaxation time T_2. This is not consistent with the presence of Fe^{2+} because the Fe^{2+} relaxation is usually much faster, and suggests strong mixing of the $3d^5$ and $3d^6$ configurations of the B-site ions. This means that a complete ionic ordered structure is not supported by the NMR results.

A number of band structure calculations have been published for magnetite to elucidate the electronic structure above as well below T_v. Depending on the method which is used the results are diverse, as expected. The self-consistent spin-polarized augmented plane wave (APW) method with the local spin density approximation (LSDA) revealed that the majority-spin electrons are semiconducting with a sizeable energy gap, whereas the minority spin electrons are present at the Fermi energy, which indicates that the $3d^6$ electrons of the iron ions are itinerant above T_v (Yanase and Siratori, 1984; Pénicaud, Siberchicot, Sommers and Kubler, 1992). The LSDA band structure calculations render always a metallic solution without charge ordering. Zhang and Satpathy (1991) tried to obviate this problem by suggesting a three-band model Hamiltonian to describe the motion of the electrons on the B sites. However, a critical parameter for itinerant or localized character of the 3d electrons is U/t, where U is the electron–electron Coulomb interaction and t the 3d bandwidth (Hubbard, 1963, 1964a,b, 1965). Modification of the LSDA method, introducing a Coulomb interaction correction, the so-called LSDA + U method, gives indeed a stable solution with a charge ordering and an energy gap of 0.19 (Antonov *et al*., 2001) and 0.34 eV (Anisimov, Elfimov, Hamada and Terakura, 1996). Unfortunately, in both studies the orthorhombic Verwey-ordering scheme was taken as starting point, which has been shown to be unrealistic (Wright, Attfield and Radaelli, 2001). With electronic structure LSDA + U calculations based on the low symmetry monoclinic structure of magnetite, a periodic charge disproportion along the c axis was found, in agreement with the experimental X-ray structure determination (Madsen and Novak, 2005). LSDA + U calculations in the tight-binding linear muffin-tin orbital calculation scheme for the P_2/c structure of magnetite unveiled a strong charge as well as an orbital ordering for the low-temperature phase, with an energy gap of 0.18 eV. However, the obtained total 3d charge disproportion is rather small (Leonov *et al*., 2004). The results show that the charge order has a pronounced $\langle 100 \rangle$ modulation, which is not compatible with the so-called Anderson criterion. It was pointed out by Anderson (1956) that nearest-neighbor Coulomb interactions in magnetite led to a T_v higher than 10^4. The Verwey transition is exceptional in the sense that if only the Coulomb interaction is the driving force for the transition, substantial short-range order must be present in the disordered structure to explain the low $T_v = 124$ K. The octahedral sites in the spinel structure are arranged in tetrahedrons, with each site belonging to two tetrahedrons. In this arrangement, it is possible to create substantial short-range order, imposed by the Anderson criterion: the total ionic charge of the individual tetrahedrons must be constant, which means an occupation by $2Fe^{2+}$ and $2Fe^{3+}$ ions per tetrahedron.

The violation of Anderson's point charge criterion in the outcome of the LSDA + U band calculation explicitly explained by the t_{2g} orbital ordering, would lead to additional Coulomb interactions stabilizing a charge-ordered structure, which does not comply with Anderson's criterion (Jeng, Guo and Huang, 2004). From a theoretical point of view, charge order combined with orbital ordering seems to be a realistic description of the mechanism of the Verwey transition, notwithstanding the denial of any charge ordering, based on X-ray resonant scattering (Garcia *et al*., 2001). This controversy on the existence of a long-range order of different electronic states on octahedral sites has been discussed recently using a number of experimental and theoretical results (Fähnle, Kronmuller and Walz, 2005).

The electronic structure and the mechanism of the Verwey transition are important for deciding whether magnetite can be useful in spin electronics. If the material can be considered as a semimetal, there is a 100% spin polarization of the charge carriers, which is very attractive for spin electronics (de Groot and Buschow, 1986). Unfortunately, the various reports on spin-polarized photoelectron spectroscopy do not give a fixed result but show a scattering of the spin-polarization degree of the conduction electrons, which might be caused by the variation of the surface structure of the thin films used in the experiments (Morton *et al*., 2002; Dedkov, Rudiger and Güntherodt, 2002; Huang *et al*., 2002; Fonin *et al*., 2003). That the surface structure modifies indeed the photoelectron emission has been shown by the temperature dependence around T_v of the onset energy near the Fermi level at which the emission starts. Depending on the crystal plane of the single crystal and surface treatment, a gradual shift of the spectral onset energy or a small jump at T_v superimposed on an overall gradual dependence occurs (Schrupp *et al*., 2004). This implies that for certain surfaces an energy gap is formed at T_v, indicative of a clear metal–insulator transition as was earlier deduced from photoelectron spectra (Chainani *et al*., 1995). For other surfaces, the gap does not disappear at T_v but is reduced by a

step from 0.10 to 0.05 eV. A similar step and the persistence of the gap above T_v was also reported for a cleaved surface (Park *et al*., 1997). Soft X-ray photoemission experiments gave evidence of the existence of strongly bound small polarons, which supports a picture for the Verwey transition in which elastic effects (like Jahn–Teller effects) interplay with local Coulomb interactions (Schrupp *et al*., 2005). The local structure of the octahedral sites, detected by EXAFS measurements shows indeed distortions, which are in favor of this picture (Subias, Garcia and Blasco, 2005).

X-ray absorption spectroscopy (XAS) and magnetic circular dichroism (MCD) experiments, which are not so surface sensitive as photoelectron spectroscopy, proved the B-site spin moment to be noninteger, in contrast to the predicted half-metallic feature. Evidence was found for a substantial average orbital moment of the B-site iron ions, $0.33\,\mu_B$ (Huang *et al*., 2004). However, XMCD experiments, taking into account self-absorption and other spurious experimental effects reveal vanishing orbital moments and nearly integer spin values (Goering *et al*., 2005; Goering, Gold, Lafkioti and Schütz, 2006)! From the preceding discussion it might be clear that the intrinsic electronic and magnetic structure of bulk magnetite is not yet completely settled.

Additional experimental data which can give insight into this problem concern the influence of impurities on the Verwey transition (Brabers, Walz and Kronmüller, 1998) and magnetic aftereffects, caused by electronic processes (Walz, 2002). The magnetic disaccommodation (DA) spectra of highly perfect single-crystalline magnetite are shown in Figure 1 (Walz *et al*., 1982). DA is defined as the relative difference of the reciprocal susceptibility $1/\chi$ measured at two times t_1 and t_2 after the demagnetization of the sample:

$$DA = [\chi^{-1}(t_2) - \chi^{-1}(t_1)]/\chi^{-1}(t_1) \qquad (1)$$

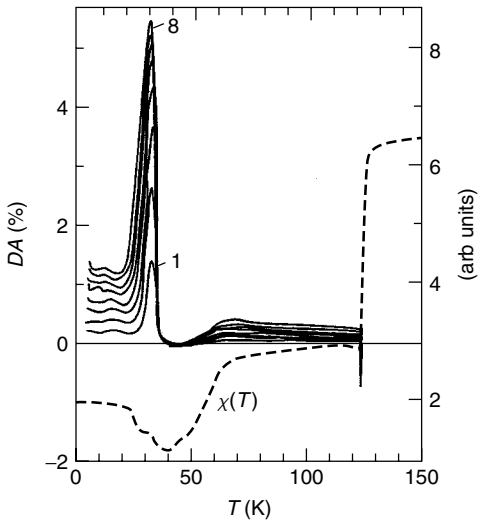

Figure 1. The isochronal disaccommodation (DA) spectra of perfect single-crystalline magnetite in the low-temperature range as measured, $t_1 = 1$ s after demagnetization and at the following times: $t_2 = 2, 4, 8, 16, 32, 64, 128$ and 180 s, yielding the curves $1, \ldots 8$, respectively. (Reproduced from Walz *et al*., 1982, with permission from Wiley-VCH. © 1982.)

The DA reflects the stabilization of the domain wall after demagnetization, which is achieved by reorientation of the local configuration, intermediate by ionic or electron transport processes. The low-temperature DA spectra in Figure 1 are most clearly structured for perfect single crystals but are modified and even complete suppressed by lattice imperfections like nonstoichiometry, mechanical stresses, impurities etc. (Walz, 2002). The conclusion is evident that the DA spectra below T_v are electronic of origin and represent intrinsic properties of bulk magnetite. A detailed analysis of the DA spectra explains the observed spectra as follows: the extended relaxation zone of logarithmic time dependence in the $4\,K < T < 30\,K$ range, together with the exponential Debye-type relaxation peak at 30 K are assigned to coherent electron tunneling processes and local electronic excitations (Walz, Weidner and Kronmüller, 1980; Walz *et al*., 1982; Kronmüller and Walz, 1980).

The 30 K peak is composed of a narrow superposition of two single Debye-type processes, as clearly indicated in the initial permeability plot in Figure 1 and which results from the thermal excitation between the doublet and singlet of the d_ε level (Kronmüller and Walz, 1980). Between 35 and 50 K, a relaxation gap occurs, accompanied by a dip in the initial susceptibility. In the 50–125 K range an extended relaxation area with logarithmic time dependency appears, which is caused by thermally activated variable range hopping processes further supported by a $T^{-1/4}$ dependence of the logarithm of the conductivity (Lenge, Kronmüller and Walz, 1984; Mott, 1990). Further evidence for the assignment to thermal activated variable range hopping was brought on by the DA spectra of electron-irradiated magnetite, which showed a splitting of the extended logarithmic relaxation zone into separated Debye processes (Walz and Kronmüller, 1990). Essential for the existence of a thermally activated magnetic relaxation is the presence of localized magnetic-anistropic species, which can reorientate under the influence of the (de)magnetization process. For the low-temperature electronic relaxation in magnetite it is obvious that Fe^{2+} ions, due to their residual orbital moment, represent such anisotropic species. Consequently, processes contributing to the DA must be linked to the electron transitions between octahedral Fe sites by means of thermal activated hopping or incoherent tunneling, which implies charge localization on the Fe^{2+}.

An interesting feature of the Verwey transition is that the transition temperature is very sensitive for the perfection

of the crystal, that is, the oxygen stoichiometry and the cation impurities. It turned out that the T_v shifting with the concentration of the cation impurity depends on the charge and the size of the substituent, as well as on the A or B site on which the substitution takes place (Brabers, Walz and Kronmüller, 1998). In Figure 2, the shifting of T_v for stoichiometric magnetite substituted with various cations is plotted against the substituent concentration. Substitution with bivalent ions (Ni, Mg, Co) on the B sites reveals a nearly identical shift with impurity concentration and even for the trivalent Ga an identical behavior is found, if the cation distribution is taken into account, one-third of Ga on B sites (Kohout *et al*., 2005). The ionic size of the impurities does fit in the range of the two and trivalent octahedral iron ions, which means that the crystal lattice is not extremely deformed by these substitutions. However, the substitution with bivalent zinc on the A sites resulted in a shift twice as large as observed for the above mentioned substitutions (Schwenk *et al*., 2000), which is also the case for Ti^{4+} on B sites and cation vacancy doping by changing the oxygen content of the crystals. In the latter cases the ratio of the concentration of the octahedral two and three valent ions is deviating from one, which seems to be more effective to retard the Verwey transition than an octahedral impurity with a similar charge as the iron ions, which leaves this ratio untouched. From these findings one could arrive at the conclusion that the charges of the B-site ions, that is, the Coulomb interactions between the B sites are the dominant driving force for the Verwey transition. Although it must be noted that the small trivalent Al ions also have a rather strong effect upon the shifting, indicating that lattice or phonon effects may play an additional role. In a first

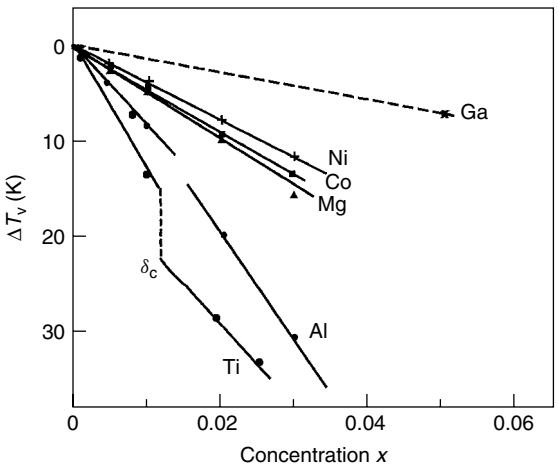

Figure 2. The shift of T_v for substituted stoichiometric magnetites $Fe_{3-x}M_xO_4$ as function of the concentration x. (Reprinted figure from Brabers *et al*., 1958, with permission from the American Physical Society. © 1958.)

approximation with a two-state mean-field model, accounting for Coulomb short- and long-range interactions only, a number of experimental results on the impurity and pressure dependence and even the value of the transition temperature were explained satisfactorily (Brabers, Walz and Kronmüller, 1999a,b, 2000). The effect of the cation substitutions on the octahedral lattice consists of a (partial) blocking of the electron exchange mechanism necessary to establish the long-range ordering scheme. The result is that a fraction of the 2+ or 3+ ions is localized, limiting the number of sites to participate in the ordering–disordering process. With the proposed model the transition temperature was calculated: $T_v = W/8\,k$ in which W represents an energy gap separating the electronic subbands of the two-state model. Taking a value of $W \sim 0.10\,eV$ (Kuipers and Brabers, 1979) one arrives at a value around 145 K, in reasonable agreement with the experimental value of 124 K. The model describes the linear T_v shifting $\Delta T_v = -\alpha x T_v$ in which x the substituent concentration M in $Fe_{3-x}M_xO_4$, T_v the Verwey temperature of the perfect magnetite crystal and $\alpha = 3$ for bivalent and trivalent substitutions on B sites or $\alpha = 9$ for Zn^{2+} on A and Ti^{4+} on B sites (Brabers, Walz and Kronmüller, 1999a). With a refinement of the model, in which the dependence of the interionic potential on the unit cell dimensions is taken into account, an expression for the pressure dependence of T_v is found (Brabers, Walz and Kronmüller, 1999b):

$$dT_v/dp = -6/7\, v/N \cdot k \tag{2}$$

v is the relative volume change at T_v and atmospheric pressure ($\Delta V/V = 6 \times 10^{-4}$); N, the number of Fe^{2+}-type ions per m^3 ($N = 1.35 \times 10^{28}\,m^{-3}$); and k, the Boltzmann constant.

The calculated value of $dT_v/dp = kGPa^{-1}$ agrees fairly well with the experimental data, which varies between -2.0 and $-5.0\,kGPa^{-1}$ for pressures up to 6 GPa.

A further refinement of the two-state mean-field model is the replacement of the two distinct levels by two bands of finite width (Brabers, Walz and Kronmüller, 2000). This provides the explanation of the discontinuity in the relation of T_v upon the impurity content at higher concentration, and also marks the transition from first to second order (Shepherd *et al*., 1991). Fitting the model parameters yields a Coulomb gap of 0.04 eV and a bandwidth of 0.01 eV, which are typical values for localized electron systems and supports a small polaronic band picture (Brabers, Walz and Kronmüller, 2000).

The IR optical conductivity is also consistent with a small-polaron nature of the charge carriers (Degiorgi, Wachter and Ihle, 1987; Pimenov *et al*., 2005). This suggests that the charge order is not only driven by electrostatic Coulomb interactions, but that elastic lattice contributions are also

relevant for the localization of the electrons on the Fe^{2+} ions and the nature of the Verwey transition. An interplay of an electron ordering with elastic lattice effects is very likely, which point of view is also put forward by Su *et al*. (2006) by introducing the Jahn–Teller distortions of the high spin Fe^{2+} ions.

2.3 Mixed spinel ferrites

A large variety of metal ions can be incorporated into the oxide spinel structure, which implies that the physical properties of the technical applied spinel ferrites like permeability, high induction, temperature and time stability, low losses and operating frequency can be tuned by a proper choice of the composition. It must be noted that spinel ferrites are usually soft magnetic, with the exception of magnetite and maghemite (γ-Fe_2O_3) in particulate media. In Table 2 some basic magnetic properties of a number of simple ferrites are given. From these data predictions can be made for the relevant magnetic properties of the mixed ferrites, useful for applications. For instance, the mixed series of the simple ferrites with $ZnFe_2O_4$ are important because of the phenomenon that the magnetization increases upon substitution as shown in Figure 3. The nonmagnetic Zn ions are located on the A sites, which results in the enhancement of the spontaneous magnetization as a consequence of the antiferromagnetic coupling between the tetrahedral and the octahedral sublattice. However, with increasing Zn concentration the Néel temperature decreases and above a concentration of $x \sim 0.5$, the antiparallel magnetic structure of the A and B sublattices is replaced by spin-canting and spin-glass structures. The spinel ferrites, which are important for applications are based on a limited number of chemical systems. The basic

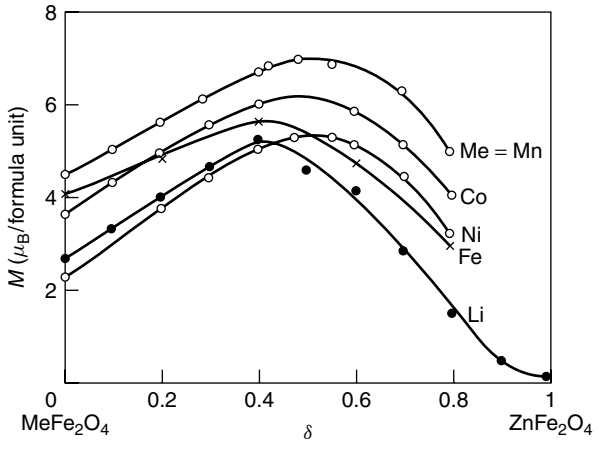

Figure 3. The magnetic moment at 0 K per formula unit of the $Me_{1-\delta}Zn_\delta Fe_2O_4$ mixed series.

composition of a soft ferrite for a specific application is first of all determined by the frequency and the power level at which the material is used. Mn–Zn ferrites are suitable up to 1 MHz for low and high power level. For frequencies above 1 MHz, the Ni–Zn ferrite system is more appropriate, because of the high electrical resistance, due to the absence of Fe^{2+}, which lowers the losses. At microwave frequencies the electrical conductivity must be very low, so that microwave ferrites are found in the Ni–Al ferrite system. An illustrative example that the choice of a basic ferrite composition for a specific application is determined by the operation frequency is given by the ferrites for deflection yokes. Because of the higher sweep frequency in high-definition *T*V and the higher resolution and the larger screen in display monitors, the original Mg–Mn ferrites are gradually replaced by the more high resistive ferrites like Mn–Mg–Zn and Ni–Zn–Cu ferrites.

Another new field in soft ferrites is the multilayer ferrite chip inductor, which consists of thin ferrite layers between silver strips which form the internal windings in the final assembly of the ferrite layer inductor. Because ferrite layers and silver strips are sintered together, low-temperature sintering is required, which limits this technique to the low-melting Ni–Zn–Cu ferrite system (Ohiai, 1997).

In addition to the basic composition, which represents only the main components of the ferrites, several types of additives are used to achieve a fine-tuning of the final properties. Depending on the objectives three types of additives can be distinguished. The first class of additives comprises of those which substitute for the main components and which control the intrinsic properties like magnetostriction, magnetic anisotropy and electrical resistance. For instance in high-permeability Mn–Zn ferrite, the presence of Fe^{2+} is essential to obtain zero magnetic anisotropy. To decrease the electrical conductivity, simultaneously with the introduction of Fe^{2+} four valent ions like Ti or Ge are substituted (Stijntjes, Klerk and Broese van Groenou, 1970). In Ni–Zn ferrites the anisotropy is tuned by the substitution of bivalent cobalt (Vogel, Gyorgy, Johnson and Sherwood, 1986). The second type concerns additives designed to segregate at the grain boundaries like Si, Zr, Ca and Ta, in order to increase the grain-boundary resistance and to reduce eddy-current losses (Otsuki, 1992; Drofenik, Žnidarsič and Zajč, 1997). Ca and Si are already present in the raw materials as impurities. In addition to the formation of the high-resistance grain boundary, Ca and Si promote the sintering of the polycrystalline ferrite by the formation of a 'glass' phase at the boundary. Sintering can be carried out at lower temperatures, preventing exaggerated grain growth. The third class of additives promotes or prevents grain growth. Grain growth is usually promoted by a liquid phase at the grain boundary by additives like CaO, SrO, V_2O_5, Nb_2O_5, Sb_2O_5, PbO, and CuO (Yan and Johnson, 1978). TiO_2 and SiO_2

Table 2. Magnetic properties of simple ferrites at room temperature and magnetic moment at 0 K.

Compound	T_c K	σ at 300 K G.cm^3 g^{-1}	$M_s^o \mu_B$/F.U	$K_1 10^5$ erg cm^{-3}	$\lambda_{100} \times 10^{-6}$	$\lambda_{111} \times 10^{-6}$	$\lambda_s \times 10^{-6}$
Fe_3O_4	860	95.5	4.1	−1.2	−19.5	+77.5	–
γ-Fe_2O_3	1020	87.3	–	−0.46	–	–	+22
$CoFe_2O_4$	790	80–94	3.4–4.0	+18 +30	−650	+170	–
$Cu_{0.5}Fe_{2.5}O_4$	575–630	–	4.0–5.4	–	–	–	–
$CuFe_2O_4$	725–775	20–30	1.3–2.7	−0.6	−65–100	+7 +15	–
Fe_2CrO_4	430	28	2.45	–	–	–	–
$Li_{0.5}Fe_{2.5}O_4$	943	69	2.60	−0.8–0.9	−25–28	+3 +4	–
$MgFe_2O_4$	605–710	31–62	0.82–2.38	−0.25–0.45	−10–14	+2	–
$MnFe_2O$	550–620	80	4.5–4.8	−0.25	−50–55	+1 +3	–
$NiFe_2O_4$	860–870	56	2.2	−0.68	−45–63	−25–34	–
$ZnFe_2O_4$	10–15	–	–	–	–	–	–
Fe_2TiO_4	120	–	–	–	–	–	–

sustain also the exaggerated grain growth but without a liquid phase; this effect is caused by the formation of cation vacancies and the diffusion of Ti and Si into the grains. Ta_2O_5 and ZrO_2 inhibit particle growth (Ishino *et al*., 1992). However, depending on the processing parameters like sinter temperature and atmosphere, additives can show opposing effects upon the grain growth. Ta_2O_5 dissolves in the spinel lattice above 1250 °C leading to an increased grain growth, below 1250 °C grain growth is inhibited by Ta_2O_5 segregation at the grain boundary (Žnidarsič, Limpel, Dražič and Drofenik, 1992). Similar to BaO, segregating in the solid grain boundary below 1240 °C preventing grain growth, at higher temperature a liquid phase is formed promoting grain growth (Drofenik, Besiničar and Kolar, 1984).

The properties of ferrites are not only determined by the chemical composition; the polycrystalline microstructure and the cation distribution between the tetrahedral and octahedral sites determine the properties as well. Because of the temperature dependence of the cation distribution, for example, in Mn, Mg, and Cu ferrites, the magnetic properties can vary within the range as indicated in Table 2, which is due to the differences in cation distribution, which are frozen during the cooling after the sinter process. The microstructure, that is, the nature of the grain boundary and the grain size does affect the magnetic susceptibility. Ferrites have an advantage that the electrical conductivity is lower than for metallic materials, but for high-permeability Mn–Zn ferrites it is desirable to choose compositions with some excess of iron. This excess of iron is present as Fe^{2+} and sets the magnetic anisotropy and magnetostriction to zero, which gives rise to a large secondary maximum in the permeability (Stijntjes and Roelofsma, 1986). Unfortunately, the mixed valence of the iron ion also gives rise to an increased electronic conductivity, which increases the eddy-current loss. By an appropriate ceramic processing, the grain boundaries can be oxidized preferentially, which increases the grain-boundary resistance and causes a frequency dependence of the effective conductivity (Koops, 1951), which means a reduction of the losses in the low frequency range. As will be discussed in the section on the magnetic permeability, the grain-boundary characteristics play an important role in the development of high-quality ferrites. The grain-boundary chemistry and structure of various commercial-grade Mn–Zn ferrites were investigated with high-resolution-transmission-electron-microscopy and Auger analysis. It was shown that glassy phases are present on a nanoscale in 1-MHz ferrites, while for 100-kHz ferrites no such phases are present, but only an enrichment of the grain boundary occurs with impurities like Ca, Si, Ti and Sn. Simultaneously, a 5–10-nm mosaic structure occurs near the grain boundary, with low angle tilts in the order of a few tenths of a degree (Nomura, 1992). Also, residual stresses, due to the grain-boundary structure and stresses induced by the thermal processing alter the permeability and losses, which is convincingly proved in the case of the excessive silver addition to Ni–Cu–Zn multilayer ferrite chip inductors. The deterioration of the magnetic properties is caused by the comprehensive stress, originating from silver precipitates at the grain boundary (Nakano, Momoi and Nomura, 1992).

2.4 Maghemite

An outstanding ferrite material is maghemite, γ-Fe_2O_3, which at room temperature is a metastable phase of ferric oxide. The stable α-Fe_2O_3 phase, hematite, has a corundum-type crystal structure; maghemite has a cation-deficient spinel structure $Fe[\theta_{0.33}Fe_{1.67}]O_4$, with the cation vacancies at the B sites. Maghemite can only be prepared at temperatures below 450 °C by oxidation of magnetite or dehydration of ferric hydroxides because above 450 °C γ-Fe_2O_3 transforms to the stable α-phase. Because of the low-temperature preparation, poorly crystallized particles are formed in which the

Fe^{3+} cations and the vacancies are distributed in a disordered way. An ordered structure of maghemite is also known, in which the vacancies and Fe^{3+} ions are 1:5 ordered on the B sites, forming a tetragonal structure with $a = 8.3396$ Å and $c = 24.9663$ Å. The cubic lattice parameter of the disordered structure is 8.3363 Å (Greaves, 1983). γ-Fe_2O_3 is applied in magnetic recording in the form of particulate media and as thin films. An important property for this application is the coercive force H_c. For iron-based recording particles, the H_c is increased by improving the acicular form of the particles, which increases the shape anisotropy (range of H_c 250–450 Oe). A second possibility is the increase of the magnetocrystalline anisotropy by Co^{2+} doping. The most effective way to increase H_c turned out to be the absorption of Co^{2+} in the surface of the particles, which results in materials known as surface Co-modified iron oxides ($H_c \sim 1000$ Oe). Besides the shape and the magnetocrystalline anisotropy, the surface anisotropy is another factor determining the size of the coercive force of the ferrite particles. Because of the large specific surface, the balance of the exchange interactions at the surface will be different from that in the bulk. A magnetic surface reconstruction might occur where the spin system lowers its energy by adopting a noncollinear structure at the surface. The concept of surface spin canting explains the particle size dependence of the magnetization and spin canting has been experimentally proved to exist by the nondisappearance of the second and fifth line in the Mössbauer spectra in an external longitudinal field (Coey, 1971). However, spin canting in small particles has not been restricted to the surface layer as was theoretically described by a simple mean-field model, but is a routine manifestation of the response of a uniaxial magnetic particle to an applied field. Consequently, a ferrimagnetic particle will not saturate by a large magnetic field (Pankhurst and Pollard, 1991). Experimental evidence for the spin canting throughout the particle has been given by the Mössbauer study of ^{57}Fe surface enriched γ-Fe_2O_3 particles (Parker and Berkowitz, 1991; Parker, Foster, Margulies and Berkowitz, 1993). Notwithstanding the importance of Co-modified γ-Fe_2O_3 as recording medium, the mechanism of the increase of H_c by the surface treatments is not clear. Co absorption onto the γ-Fe_2O_3 acicular particles increases the uniaxial anisotropy of the precursor particles, originally mainly due to the shape anisotropy. Since acicular γ-Fe_2O_3 particles are elongated along the $\langle 110 \rangle$ axis, the large single-ion anisotropy of Co^{2+} in the $\langle 100 \rangle$ direction should introduce a multiaxial anisotropy in the epitaxial oriented cobalt ferrite layers on the particle surface. The result has to be an anisotropic axis at the surface not collinear with those of the interior. An explanation for the observed uniaxial anisotropy of the whole particle is not found. The demagnetization field of the particle has been suggested to induce a uniaxial cobalt ferrite coating by establishing a local reorientation of the anisotropic Co^{2+} ions like in the DA phenomena. Another possibility is the migration of Co^{2+} into the lattice sites with a symmetry axis close to the field direction. The crystal defects at the surface created by the cobalt absorption have to be considered in more detail as possible explanation of the enhanced anisotropy. It has been shown that other 'chemistry' effects at the surface layer change the anisotropy as well (Slonczewski, 1992).

2.5 The magnetic permeability of polycrystalline ferrites

For designing components based on polycrystalline soft ferrites, the magnetic permeability as function of frequency, temperature, and magnetic field as well as the magnetic losses are significant factors. For polycrystalline ferrites two magnetization processes are of importance: rotation of the spontaneous magnetization in the domains and the domain wall displacement. In general the domain wall displacement gives a larger component to the permeability than the rotational process and accounts for the high permeability of a certain class of nonmicrowave ferrites. For microwave ferrites (>100 MHz) the rotational process is the dominant mechanism. On the basis of the natural spin resonance (NSR), which occurs at a resonance frequency $\omega_r = \gamma H^A$ (Landau and Lifshitz, 1935), in which H^A is the anisotropy field. A relation between the static permeability and the resonance frequency of the NSR has been derived:

$$f_r(\mu_i - 1) = \tfrac{4}{3}\gamma M_s \tag{3}$$

in which M_s represents the saturation magnetization and $\gamma = g \times e/2mc$. (Snoek, 1948).

For a series of polycrystalline $Ni_xZn_{1-x}Fe_2O_4$, the dispersion frequency in the permeability spectrum could be well explained by the NSR according to formula (3), which suggests that these ferrites are magnetized by the rotational process (Smit and Wijn, 1959).

The initial permeability of a material originating from rotational magnetization is given by:

$$(\mu_i - 1) = c \times M_s^2/K_1 \tag{4}$$

The coefficient c depends on the sign of the anisotropy ($c = \frac{1}{3}$ for positive K_1, $c = \frac{1}{2}$ for negative K_1). The rotational permeability does not depend on the microstructure of a polycrystalline ferrite, but for a large number of ferrites the permeability turned out to be linearly dependent on the grain size D. This microstructure dependence can easily be understood by the domain wall displacements if one considers the pinning effect of the grain boundaries upon the walls.

Because of the crystallographic disorder in the grain boundary and the porosity of the ceramic ferrites, domain walls are pinned at the periphery of the grain and can only bulge out when a small external field is applied. In equilibrium, the gain in field energy is in balance with the increased wall energy caused by the increased wall area and the demagnetization energy because of the magnetic poles formed on the bulged wall. By considering the demagnetization energy as the main effect, μ_i can be approximated by

$$(\mu_i - 1) \approx 20\, M_s^4 \times D/K_1^2 \times d \tag{5}$$

with d being the distance between the domain walls (Smit and Wijn, 1959).

A linear grain size dependence of the permeability was found with a simple but elegant model of spherical bulging of a domain wall, pinned to the grain boundary in a spherical grain with diameter $D = 2r$. The responding spherical bulging upon a weak magnetic field is schematically shown in Figure 4; the increased wall surface is $\pi \times (r^2 + x^2)$ and the volume of the black spherical segment is $\pi/6 \times x(3r^2 + x^2)$. Minimization of the magnetostatic energy of the reversed magnetization in this segment and the wall energy gives for the permeability:

$$(\mu_i^c - 1) = {}^3\!/_4\pi \times M_s^2 \times D/\gamma \tag{6}$$

in which γ represents the wall energy (Globus, 1977) and μ_i^c the experimental μ_i, corrected for the porosity $\mu_i^c = \mu_i \times d_x/d$, with d_x, the X-ray density and d the density of the polycrystalline material. The frequency dependence of the wall susceptibility can also be derived from the equation of motion of a unit surface of a 180° domain wall in an infinite medium (Döring, 1948)

$$m\ddot{z} + \beta\dot{z} + \alpha z = 2M_s \times H \tag{7}$$

m represents the domain wall mass, β the damping and α the restoring force per unit surface. Supposing that the damping is dominant and the response of the domain wall is linear, equation (6) can be derived for the wall permeability and for the relaxation frequency $f_o = 4\gamma/\pi\beta r^2$ (Guyot, Merceron, Cagan and Messekher, 1988). For polycrystalline $NiFe_2O_4$ a relaxation frequency proportional to $1/D^2$ was found and the maximum in the frequency dependence of the magnetic losses was found to be proportional with D_m, the mean grain size diameter (Gieraltowski and Globus, 1977). A practical impact of these findings is that the dispersion of the permeability can be shifted to higher frequencies and the magnetic losses be suppressed by tailoring the microstructure that is, lowering the grain size. Bulging of the domain wall in a weak magnetic field is a reversible process, which is supposed to cause no losses up to a critical field H_{cr} above which a sudden increase is observed. A typical example of the field dependence of the permeability for polycrystalline Ni–Zn ferrite is given in Figure 5 (Globus and Duplex, 1971). The appearance of the critical field H_{cr} is attributed to the depinning of the domain walls from the grain boundary. The result is an irreversible displacement of the domain wall with hysteresis losses (Guyot and Globus, 1973, 1977). Hysteresis losses within Globus' model are ascribed to the continuous pinning and depinning of the domain wall at the grain boundaries, which can be considered as a friction force causing an energy loss. A second contribution to the losses is proportional with the wall energy in that part of the domain wall, which is created and annihilated during the wall displacements. The same wall displacement is also related to the magnetoacoustic emission (MAE). MAE is the phenomenon when bursts of stress waves

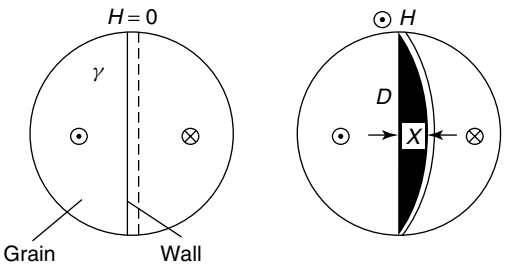

Figure 4. Schematic presentation of a domain wall pinned to the grain boundary in a spherical grain.

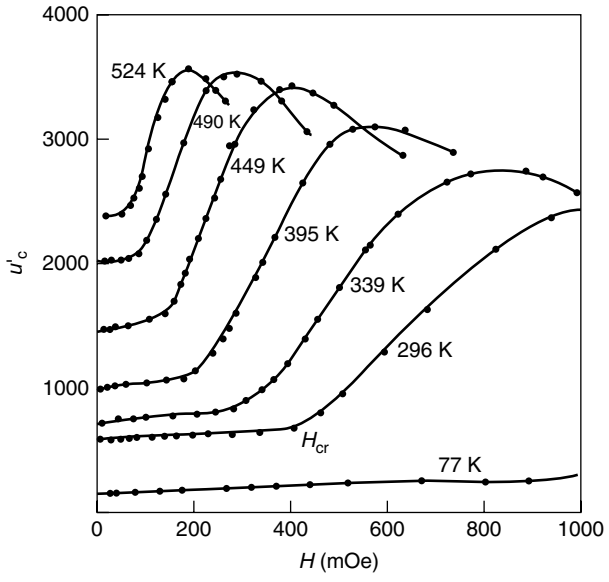

Figure 5. The permeability of polycrystalline $Ni_{0.5}Zn_{0.5}Fe_2O_4$ (grain size $D = 3.0\,\mu m$ and porosity = 0.03) as function of the measuring field H at various temperatures. (Reproduced from A. Globus *et al.*, 1971, with permission from EDP Sciences. © 1971.)

are generated during the irreversible magnetization process, originating from magnetoelastic interactions. The MAE is usually attributed to the release of magnetoelastic energy associated with the jumping of non -180° domain walls, because the displacement of a 180° wall does not change the magnetoelastic energy; the linear magnetostriction is an even function of the magnetization. In particular, for 180° domain walls, the release of the elastic energy by the creation and annihilation of these walls is supposed to cause the MAE, which can in turn be the mechanism for the hysteresis loss in ferrites (Guyot and Cagan, 1991, 1993).

The microstructure of ceramic ferrites is not only specified by the grain size, but nonmagnetic inclusions like closed pores and the finite thickness of the grain boundaries modify the physical properties significantly. In addition for the low anisotropy Mn–Zn ferrites, indications are found that also for ferrites with mainly rotational magnetization processes, a large grain size effect upon the permeability exists (Visser, Roelofsma and Aaftink, 1989). An explanation for this apparent controversy is found in the magnetic inhomogeneity of the ferrite materials.

If the demagnetizing fields caused by the nonmagnetic closed pores and the low-permeability grain boundaries are taken into consideration, the apparent μ_e for a polycrystalline matrix is given by Rikukawa (1982):

$$\mu_e = (1 - P)\mu_i/(1 + P/2) \times (1 + 0.75^{\delta}/_{D} \times \mu_i/\mu_b) \quad (8)$$

with μ_e the apparent permeability, P the porosity, δ the width of the grain boundary, D the grain size, μ_i the permeability of the grain and μ_b the permeability of the grain boundary, which is supposed to be much lower than μ_i. Since equation (8) contains only μ_i, irrelevant which mechanism is accountable for the magnetization, ferrites with rotational permeability can show a grain size effect. Most high-quality ferrites have very low porosity, which means that only low-permeability grain boundaries have to be considered which simplifies equation (8) to (Johnson, Noordermeer, Severin and Meeuwissen, 1992):

$$\mu_e = \mu_i \times D/(\mu_i\delta + D) \quad (9)$$

This is known as the nonmagnetic grain-boundary model (NMGB). The experimental results on certain polycrystalline Mn–Zn ferrites show a good fit with equation (9) as is shown in Figure 6, indicating that in these ferrites the rotational mechanism cannot be excluded. The observed decrease of the resonance frequency with increasing grain size is another point in favor of the rotational permeability for these ferrites (Visser and Johnson, 1991). However, a serious drawback of the NMGB model is that the loss factor $\mu''/(\mu')^2$ and

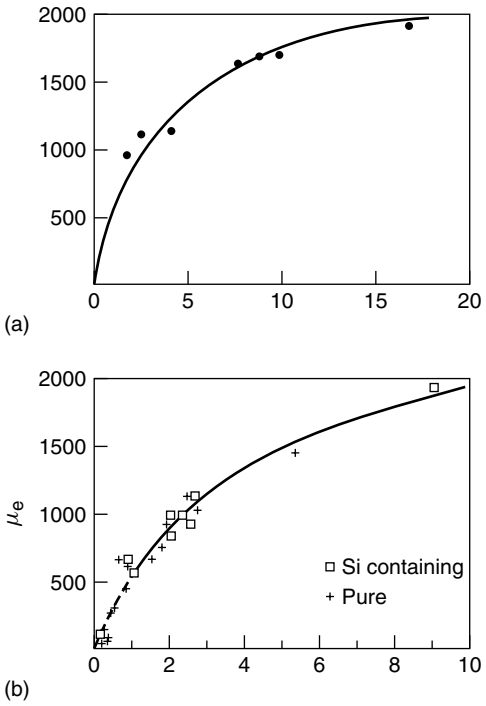

Figure 6. (a) Grain size dependence of the rotational permeability of polycrystalline $Mn_{0.68}Zn_{0.24}Fe_{2.08}O_4$. The grains contain no domain walls because of the small size of the grains. The solid curve fits equation (9) with $\mu_i = 2500$ and $\delta = 1.5$ nm. (Reprinted from Johnson *et al*., 1991, with permission from Elsevier. © 1991.) (b) Similar plot as (a) for $Mn_{0.60}Zn_{0.35}$ $Fe_{2.05}O_4$. (Reprinted from Johnson *et al*., 1992, with permission from Elsevier. © 1992.)

the temperature factor $1/\mu^2 \mathrm{d}\mu/\mathrm{d}T$ are independent of the grain size, which is not in agreement with experiment (Visser and Johnson, 1991). Both factors are strongly affected by the microstructure (Snelling, 1988). In fact the Globus wall size model and the NMGB model can be combined in a transition region, as was shown by the analysis of the permeability data of coarse-grained Mn–Zn ferrites, these models also have mutually excluding regions of validity (Visser, Johnson and van der Zaag, 1992). However, in the design of ferrites, these models are useful as guidelines to produce materials with improved properties for particular specifications.

Besides the permeability, the magnetic losses are an important quality factor of a magnetic ferrite. The magnetic loss is composed of three contributions: hysteresis losses, eddy-current loss and the residual loss, which can be represented by a total loss factor (Snelling, 1988):

$$\begin{aligned}\tan\delta_t/\mu &= \mu''/(\mu')^2 = \tan\delta_h/\mu + \tan\delta_e/\mu + \tan\delta_r/\mu \\ &= {}^4\!/_3 \nu B/\mu_o\mu^3 + \pi\mu_o d^2 f/16\rho + \tan d\delta_r/\mu \\ &= a \times B + b \times f + c \end{aligned} \quad (10)$$

with ν the Rayleigh coefficient ($\mu(H) = \mu_i + \nu H$), B the peak value of the flux density perpendicular to the cross section of a cylinder of the ferrite material with radius d, f the frequency, and ρ the bulk resistance. The coefficients a and c are the hysteresis and residual loss coefficients and are pure material properties, b is the eddy-current loss coefficient also depending on the geometry of the component.

The total power loss can be determined from the loss factor by the relation:

$$P = (\tan\delta/\mu) \times \pi \times f \times B^2/\mu_o \quad \text{Watt/m}^3 \qquad (11)$$

The eddy-current loss in ferrites is usually small compared with the total loss because of the low electrical conductivity. However to produce high-permeability Mn–Zn ferrites, which means low anisotropy, compensation by substitution of Fe^{2+}–Ti^{4+} is often used. The introduction of Fe^{2+} enhances the electrical conductivity in the grain, which increases the eddy-current loss. By a proper addition of Ca and Si to the grain boundary, a higher effective resistance in the low frequency range is obtained, which lowers the eddy-current loss again, but also the permeability according to the NMGB model.

The largest contribution to the total loss originates from the hysteresis losses, caused by the irreversible domain wall displacements, which increase with increasing amplitude of the ac field and which are determined by the wall pinning. A possibility of decreasing the hysteresis loss is to suppress the wall permeability and to promote the rotation permeability, which can be achieved by small grains in which no wall can exist or by domain wall pinning by anisotropic ions like Co^{2+} ions. Specifically, ferrites with low power losses at high frequencies are indispensable for the size reduction of power supplies operating at high frequencies. For Mn–Zn power ferrites applied up to 500 kHz, substantial improvements of the losses have been realized by simultaneous substitution with Co^{2+} and Ti^{4+} and an optimization of the thermal processing of the ceramic production by which the Ca segregates preferentially at the grain boundary. If the large Ca ion is incorporated in the grain, the lattice stresses cause additional losses (Stijntjes and Roelofsma, 1986). The hysteresis losses provoke a loss tangent proportional to the magnetic induction and the eddy-current loss a tangent proportional with frequency. The third loss contribution, the residual loss, is the remaining loss, measured at low frequencies and small field, where hysteresis and eddy-current losses are going to zero.

The residual loss is partly associated with the magnetic aftereffects due to thermally activated domain wall motions.

3 MAGNETIC IRON GARNETS

The garnet structure has been for the first time found for a series of silicates with the general formula $(A_3)_c(B_2)_a(Si_3)_d\ O_{12h}$; the space group is $O_h^{10} - Ia3d$, containing 8 'molecules' per unit cell (Menzer, 1926, 1928). There are three different cation sublattices given by the subscripts c, a and d, indicating the Wyckoff positions and which are composed of 24 dodecahedral, 16 octahedral, and 24 tetrahedral sites, respectively. The garnet structure can accommodate a large variety of cations in variable concentrations and an extended range of mixed series is known. Magnetic iron-based synthetic garnets were first synthesized by Bertaut and Forrat (1956). The prototype of the magnetic garnet is yttrium iron garnet (YIG), which can be presented by the formula $(Y_3^{3+})_c\ (Fe_2^{3+})_a\ (Fe_3^{3+})_d\ O_{12h}$. The Y^{3+} are located on the dodecahedral sublattice and the octahedral a and tetrahedral d lattices are occupied by Fe^{3+} ions. Substitution of Y^{3+} by a rare-earth (RE) ion gives a series of iron garnets all with a lattice parameter in the order of 12 Å and with remarkable temperature dependence of the saturation magnetization, as shown in Figure 7 (Bertaut and Pauthenet, 1957). The magnetization of the iron garnet is the resultant of the magnetization vectors of the three sublattice magnetizations, $M_s = M_a + M_d + M_c$, in which the iron sublattice magnetizations M_a and M_d are antiparallel and the RE sublattice M_c is parallel with M_d for the light RE (Ce, Pr, Nd) and parallel with M_a for the heavier RE ions (Eu, . . . , Yb). The antiferromagnetic coupling of the RE with the Fe^{3+} ions is weaker than between the iron ions, which results in a quick drop of the RE magnetization at low temperature. Because of the large moment of the RE ions, the RE magnetization prevails at low temperature and the Fe^{3+} magnetization at higher temperature. The result is the presence of a compensation point in the T dependence of the magnetization. For all the RE iron garnets, T_c is determined by the super-exchange interaction of the Fe^{3+} lattices and is almost identical for all the RE iron garnets ($\pm$560 K). At room temperature the complete antiparallel arrangements of the magnetizations as mentioned before occur, but at low temperatures the RE moments itself are arranged in a noncollinear structure. The point symmetry of the dodecahedral RE site is D_2, rhombic. The local symmetry on these sites is formed by three perpendicular twofold axes for which there are six different orientations possible with reference to the cubic crystal structure axis. In principle there are now six magnetic sublattices possible of which the magnetization can be canted with respect to each other. For instance, the umbrella structure has been reported for $Er_3Fe_5O_{12}$ (Hock, Fuess and Bonnet, 1991), whereas the double umbrella structure has been reported for holmium and terbium iron garnets (Hock, Fuess, Vogt and Bonnet,

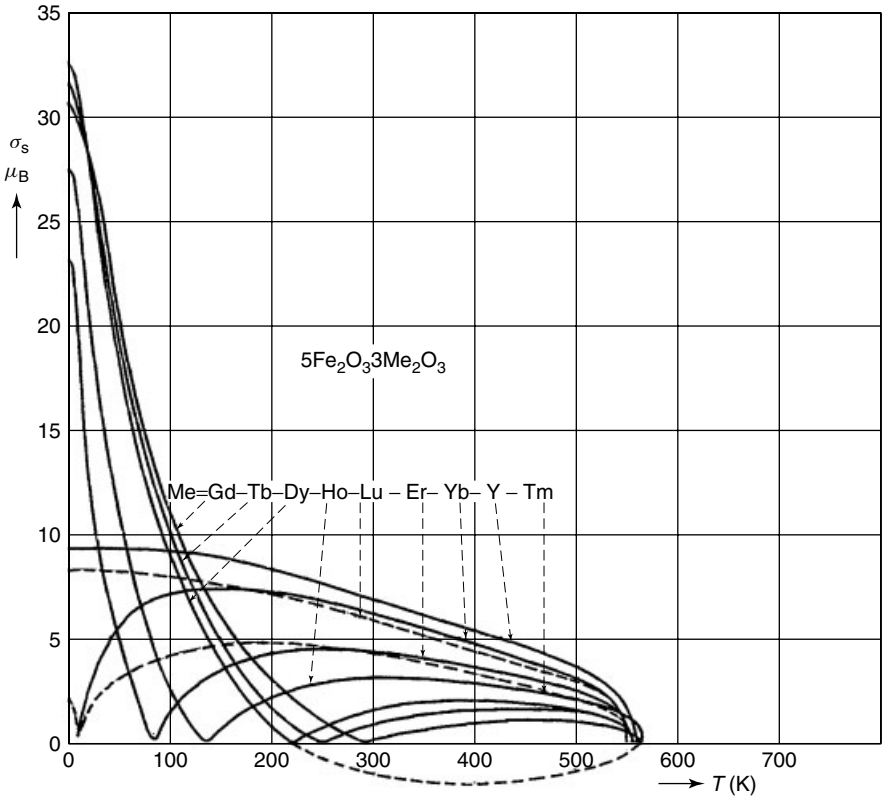

Figure 7. Spontaneous magnetization of a number of rare-earth garnets and yttrium iron garnet in μ_B per formula unit as function of temperature. (Reproduced from Bertaut *et al.*, 1957, with permission from IEE. © 1957.)

1990; Guillot, Tcheou, Marchand and Feldmann, 1984). If the resultant magnetization is directed along the ⟨111⟩ direction the magnetic moments of the RE ions are divided into two sets of three, which lie on two cones, forming the double umbrella structure. For the magnetization parallel to the ⟨100⟩ direction two of the six RE moments lie along the magnetization direction and the other four lie again on one cone, the so-called umbrella structure. The exchange interactions of the RE ions are weaker than the iron interactions, which makes it easy to change the direction of their magnetic moments, especially close to the compensation temperature. Spin orientation transitions can occur by a temperature variation or an external magnetic field. A survey of this type of transitions is given by Balestrino and Geller (1985). Iron garnets are excellent materials for microwave frequencies because of the narrow resonance line. Thin films are favorable for their magneto-optic properties. In particular the substitution of the RE ion by Bi and the iron by other metals gives the opportunity to tune the properties for special purposes. However, the substitution of iron by other magnetic or nonmagnetic metal ions lowers the Curie temperature and the spontaneous magnetization; if diamagnetic cations are involved, local canting of the Fe^{3+} magnetic moments may occur, which can generate even more magnetic phase transitions. A survey on the numerical data of the magnetic properties of RE iron garnets is given by Novak (1991).

4 HEXAGONAL FERRITES

$PbFe_{12}O_{19}$ is the archetype of a class of ferrites, which are indicated as M-type hexaferrites. These ferrites crystallize into the hexagonal magnetoplumbite structure, which is characterized by the space group $P6_3/mmc(D^4_{6h})$. The basis of this lattice is formed by a hexagonal closed packed array of oxygen ions, where in every fifth layer one-quarter of the oxygen ions is substituted by a Pb^{2+} ion. The Fe ions are located on five different interstitial sublattices, three with octahedral sites (indicated by 12k, 2a and $4f_2$), one with tetrahedral ($4f_1$) and one with bipyramidal sites (2b). The symbol of these sites includes the number of sites per unit cell. The lattice parameters of the magnetoplumbite structure are $a \approx 5.88$ Å and $c \approx 32.1$ Å. The unit cell contains two formula units. A variety of M-type ferrites can be produced by part or complete substitution of the Pb^{2+} cations by Ba^{2+}, Sr^{2+} or Ca^{2+}. The Fe^{3+} ions can be substituted by trivalent ions like Al^{3+}, Ga^{3+}, Mn^{3+}, or by a combination of divalent and four valence ions, such as Co^{2+}–Ti^{4+}.

$BaFe_{12}O_{19}$ was the first M-type ferrite employed as hard-magnetic material (Went, Rathenau, Gorter and van Oosterhout, 1952). The magnetic structure is ferrimagnetic with the magnetizations of the three sublattices 12k, 2a and 2b antiparallel with the remaining $4f_1$ and $4f_2$, which by complete alignment gives a spontaneous magnetization of $(16-8)\cdot 5 = 20\,\mu_B$ per formula unit (Gorter, 1957). The high coercive force is caused by the large uniaxial anisotropy along the *c* axis, which is caused by the hexagonal structure and the typical oxygen coordination of the bipyramidal sites (Smit and Wijn, 1959). Permanent magnets based on $BaFe_{12}O_{19}$ are produced by a ceramic technology, in which two objectives are essential. In the first place the grain size must be small (about 1 μm) in order to be a single domain to obtain high coercivity. Secondly, the grains must be aligned during a wet-pressing process by a magnetic field, in order to get an anisotropic magnet with an enhanced effective magnetization. The temperature dependence of the saturation magnetization around room temperature is high, which makes the M-type ferrites not suited for high precision applications (Shirk and Buessem, 1969). The ceramic processing of the production of permanent hexaferrite magnets plays a crucial role in the final performance of the magnets. The basic properties of the M-hexaferrites are not very distinct for the various compositions, as long as the iron concentration is high. The microstructure, that is, the grain size, alignment and the grain boundary determine to a great extent the hard-magnetic properties. The Sr-based M-ferrites have the advantage of a higher coercive force at some level of remnant magnetization, because the ceramic processing is easier to control for this composition (Cochardt, 1966). The ceramic techniques have been optimized in such a way that further improvement of the performance of the permanent ferrite magnets is very limited. However, some improvements seem still to be possible by improving the intrinsic properties by a chemical modification. An increase of the anisotropy in the Sr-based M-ferrite is possible, if Sr^{2+} and Fe^{3+} are replaced by La^{3+} and Co^{3+}, which results in a strong increase of anisotropy and coercivity, without a negative effect on the remnant magnetization (Tenaud *et al*., 2004).

Table 3. Compositions of hexagonal ferrites.

Type	Chemical formula	Short symbol
M	$BaFe_{12}O_{19}$	BaM
W	$BaMe_2Fe_{16}O_{27}$	Me_2W
Y	$Ba_2Me_2Fe_{12}O_{22}$	Me_2Y
Z	$Ba_3Me_2Fe_{24}O_{41}$	Me_2Z
X	$Ba_2Me_2Fe_{28}O_{46}$	Me_2X
U	$Ba_4Me_2Fe_{36}O_{60}$	Me_4U

Besides the M-type hexaferrites, a number of other hexaferrites exist which have strongly related crystal structures because they are built from similar crystal blocks as the M-structure (Smit and Wijn, 1959). In Table 3 the chemical formulas of the various types are given, in which Me stands for a bivalent transition-metal ion or Mg and Zn. In all these ferrites the hexagonal axis settles the magnetization in the sense that the magnetization is strongly aligned into the *c* direction, which means hard-magnetic materials. A second possibility is that the magnetization is aligned in a plane perpendicular to the *c* axis, which means high magnetic permeability in the plane but low in the other directions, the so-called ferroxplana materials. The W-, X- and Z-type compounds show uniaxial anisotropy in the *c* direction, but because of their problematic processing in the production, they are not attractive for the production of permanent magnets. The Y compounds, showing the ferroxplana behavior, are materials very well suited for high frequencies up to 1 GHz (Jonker, Wijn and Braun, 1957).

REFERENCES

Anderson, P.W. (1956). Ordering and antiferromagnetism in ferrites. *Physical Review*, **102**, 1008–1013.

Anderson, J.F., Kuhn, M., Diebold, U., *et al*. (1997). Surface structure and morphology of Mg-segregated epitaxial Fe_3O_4 (001) thin films on MgO (001). *Physical Review B*, **56**, 9902–9909.

Anisimov, V.I., Elfimov, I.S., Hamada, N. and Terakura, K. (1996). Charge-ordered insulating state of Fe_3O_4 from first principles electronic structure calculations. *Physical Review B*, **54**, 4387–4390.

Antonov, V.N., Harmon, B.N., Antropov, V.P., *et al*. (2001). Electronic structure and magneto-optical Kerr-effect of Fe_3O_4 and Mg^{2+} or Al^{3+} substituted Fe_3O_4. *Physical Review B*, **64**, 134410.

Balestrino, G. and Geller, S. (1985). Magnetic phase transitions in garnets. *Journal of Magnetism and Magnetic Materials*, **49**, 225–234.

Berdunov, N., Murphy, S., Mariotto, G. and Shvets, I.V. (2004a). Atomically resolved spin-dependent tunneling on the oxygen terminated Fe_3O_4 (111). *Physical Review Letters*, **93**, 057201.

Berdunov, N., Murphy, S., Mariotto, G. and Shvets, I.V. (2004b). Room temperature study of a strain-induced electronic superstructure on a magnetite (111) surface. *Physical Review B*, **70**, 085405.

Bertaut, F. and Forrat, F. (1956). The structure of the ferrimagnetic rare earth ferrites. *Comptes Rendus de l'Academie des Sciences (Paris)*, **242**, 382–384.

Bertaut, F. and Pauthenet, R. (1957). Crystalline structure and magnetic properties of ferrites having the general formula $5Fe_2O_3.3M_2O_3$. *Proceedings of the Institution of Electrical Engineers*, **B104**, 261–264.

Bertelsen, P., Goetz, W., Madsen, M.B., *et al*. (2004). Magnetic properties experiments on the mars exploration rover spirit at Gusev Crater. *Science*, **30**, 827–829.

Brabers, V.A.M. (1971). Cation migration, cation valencies and the cubic-tetragonal transition in $Mn_xFe_{3-x}O_4$. *Journal of Physics and Chemistry of Solids*, **32**, 2181–2191.

Brabers, V.A.M. (1995). Progress in spinel ferrite research. In *Handbook of Ferromagnetic Materials*, Buschow, K. (Ed.), Elsevier Science B.V.: Amsterdam, pp. 189–324, Vol. 8.

Brabers, V.A.M. and Klerk, J. (1977a). Kinetics of the cation redistribution in magnesium ferrite. *Journal de Physique, Colloque*, **38**(Suppl. 1), 207–209.

Brabers, V.A.M. and Klerk, J. (1977b). Dilatometric investigation of the phase transition in copper ferrite. *Thermochimica Acta*, **18**, 287–294.

Brabers, V.A.M., Walz, F. and Kronmüller, H. (1998). Impurity effect on the Verwey transition in magnetite. *Physical Review B*, **58**, 14163–14167.

Brabers, J.H.V.J., Walz, F. and Kronmüller, H. (1999a). A model for the Verwey transition based on an effective interionic potential. *Physica B: Physics of Condensed Matter*, **266**, 321–331.

Brabers, J.H.V.J., Walz, F. and Kronmüller, H. (1999b). The role of volume effects in the Verwey transition in magnetite. *Journal of Physics: Condensed Matter*, **11**, 3679–3686.

Brabers, J.H.V.J., Walz, F. and Kronmüller, H. (2000). The influence of a finite bandwidth on the Verwey transition in magnetite. *Journal of Physics: Condensed Matter*, **12**, 5437–5452.

Chainani, A., Yokoya, T., Moritomo, T., *et al*. (1995). High resolution photoemission spectroscopy of the Verwey transition in Fe_3O_4. *Physical Review B*, **51**, 17976–17979.

Cochardt, A. (1966). Recent ferrite magnet developments. *Journal of Applied Physics*, **40**, 1112–1114.

Coey, J.M.D. (1971). Noncollinear spin arrangement in ultrafine ferrimagnetic crystallites. *Physical Review Letters*, **27**, 1140–1142.

Coey, J.M.D., Shvets, I.V., Wiesendanger, F. and Güntherodt, J. (1993). Charge freezing and surface anisotropy on magnetite (100). *Journal of Applied Physics*, **73**, 6742–6744.

Collinson, D.W. (1997). Magnetic properties of Martian meteorites: implications for an ancient magnetic field. *Meteoritics and Planetary Science*, **32**, 803–811.

Condon, N.G., Leibsle, F.M., Parker, T., *et al*. (1997). Biphase ordering on Fe_3O_4 (111). *Physical Review B*, **55**, 15885–15894.

Cranfield, C., Wieser, H.G., Al Madan, J. and Dobson, J. (2003). Preliminary evaluation of nanoscale biogenic magnetite-based ferromagnetic transduction mechanisms for mobile phone bioeffects. *IEEE Transactions on Nanobioscience*, **2**, 40–43.

Dedkov, Y.S., Rudiger, U. and Güntherodt, G. (2002). Evidence for the half-metallic ferromagnetic state of Fe_3O_4 by spin-resolved photoelectron spectroscopy. *Physical Review B*, **65**, 064417.

Degiorgi, L., Wachter, P. and Ihle, D. (1987). Small-polaron conductivity in magnetite. *Physical Review B*, **35**, 9259–9265.

Desenfant, F., Petrovsky, E. and Rochette, P. (2004). Magnetic signature of industrial pollution of stream sediments and correlation with heavy metals: case study from South-France. *Water, Air, and Soil Pollution*, **152**, 297–312.

Dmitrienko, V.E. and Ovchinikova, E.N. (2003). Point defect induced forbidden reflections in resonant X-ray scattering. *Journal of Synchrotron Radiation*, **10**, 376–379.

Döring, W. (1948). Ueber die Trägheit der Wände zwischen Weißschen Bezirken. *Zeitschrift fur Naturforschung*, **3A**, 374–379.

Drofenik, M., Besiničar, S. and Kolar, F. (1984). Influence of BaO additions on the microstructure and magnetic properties of Co-Ni, Zn ferrites. *American Ceramic Society Bulletin*, **63**, 699–670.

Drofenik, M., Žnidarsič, A. and Zajč, I. (1997). Highly resistive grain boundaries in doped MnZn ferrites for high frequency power ferrites. *Journal of Applied Physics*, **82**, 333–340.

Fähnle, M., Kronmuller, H. and Walz, F. (2005). Time-scales of electronic processes in Fe_3O_4–an attempt to resolve a recent accentuated controversy. *Physica B*, **369**, 177–180.

Fonin, M., Dedkov, Y.S., Mayer, J., *et al*. (2003). Preparation, structure and electronic properties of Fe_3O_4 films on the Fe (110) Mo/Al_2O_3 (1120) substrate. *Physical Review B*, **68**, 045414.

Frankel, R.B. (2003). Biological permanent magnets. *Hyperfine Interactions*, **151**, 145–153.

Garcia, J. and Subias, G. (2004). The Verwey transition-a new perspective. *Journal of Physics: Condensed Matter*, **16**, R145–R178.

Garcia, J., Subias, G., Proietti, M.G., *et al*. (2000). Resonant "forbidden" reflections in magnetite. *Physical Review Letters*, **85**, 578–581.

Garcia, J., Subias, G., Proietti, M.G., *et al*. (2001). Absence of the charge ordering below the Verwey temperature in magnetite. *Physical Review B*, **63**, 054110.

Gieraltowski, J. and Globus, A. (1977). Domain wall size and magnetic losses in frequency spectra of ferrites and garnets. *IEEE Transactions on Magnetics*, **MAG-13**, 1357–1358.

Globus, A. (1977). Some physical considerations about the domain wall size theory of magnetization mechanisms. *Journal de Physique, Colloques*, **38**(Suppl. C-1), 1–15.

Globus, A. and Duplex, P. (1971). Dispersion des courbes de première aimantation par la diamètre des cristallites et le champs d'anisotropie. *Journal de Physique, Colloques*, **32**(Suppl. C-1), 261–262.

Goering, E., Gold, S., Lafkioti, M. and Schütz, G. (2006). Vanishing Fe 3d orbital moments in single-crystalline magnetite. *Europhysics Letters*, **73**, 97–103.

Goering, E., Gold, S., Lafkioti, M., *et al*. (2005). Oxygen K-edge shift at the Verwey transition of magnetite. *Physical Review B*, **72**, 033112.

Goff, R.J., Wright, J.P., Attfield, J.P. and Radaelli, P.G. (2005). Resonant X-ray diffraction study of the charge order in magnetite. *Journal of Physics: Condensed Matter*, **17**, 7633–7642.

Gorter, E.W. (1957). Saturation magnetization of some ferrimagnetic oxides with hexagonal structure. *Proceedings of the Institution of Electrical Engineers*, **104B**, 257–260.

Greaves, C. (1983). A powder neutron diffraction investigation of vacancy ordering and covalence in γ-Fe_2O_3. *Journal of Solid State Chemistry*, **49**, 325–333.

de Groot, R.A. and Buschow, K.H.J. (1986). Recent developments in half-metallic magnetism. *Journal of Magnetism and Magnetic Materials*, **54–57**, 1377–1380.

Guillot, M., Tcheou, F., Marchand, A. and Feldmann, P. (1984). Temperature evolution of the umbrella structure in holmium iron garnet. *Zeitschrift für Physik B: Condensed Matter*, **56**, 29–39.

Guyot, M. and Cagan, V. (1991). The acoustic emission along the hysteresis loop of various ferro-and ferrimagnets. *Journal of Magnetism and Magnetic Materials*, **101**, 256–262.

Guyot, M. and Cagan, V. (1993). The magnetoacoustic emission. *Journal of Applied Physics*, **73**, 5348–5353.

Guyot, M. and Globus, A. (1973). Determination of the domain wall energy from hysteresis loops in YIG. *Physica Status Solidi B*, **59**, 447–454.

Guyot, M. and Globus, A. (1977). Determination of the domain wall energy and the exchange constant from hysteresis in ferrimagnetic polycrystals. *Journal de Physique, Colloques*, **38**(Suppl. C-1), 157–162.

Guyot, M., Merceron, Th., Cagan, V. and Messekher, A. (1988). Mobility and /or damping of the domain wall: comparison between experimental and theoretical values in ferrimagnets. *Physica Status Solidi A*, **106**, 595–612.

Hagiwara, K., Kanazawa, M., Horie, K., *et al*. (1999). Measurements of ATS scattering from magnetite near the Fe K-α absorption edge in the temperature range of 290 K −90 K. *Journal of the Physical Society of Japan*, **68**, 1592–1597.

van der Heijden, P.A.A., Bloemen, P., Gaines, J.M., *et al*. (1996). Magnetic interface anisotropy of MBE grown ultrathin (001) Fe_3O_4layers. *Journal of Magnetism and Magnetic Materials*, **159**, L293–L298.

Henry, N.F.M. and Lonsdale, K. (1965). *International Tables for X-ray Crystallography*, *Volume I, Symmetry Groups*, The Kynoch Press: Birmingham, p. 340.

Hock, R., Fuess, H. and Bonnet, M. (1991). Low temperature magnetic structure of erbium garnet. *Zeitschrift für Physik B: Condensed Matter*, **82**, 283–294.

Hock, R., Fuess, H., Vogt, T. and Bonnet, M. (1990). Crystallographic distortion and magnetic structure of terbium iron garnet at low temperatures. *Journal of Solid State Chemistry*, **84**, 39–51.

Hornstra, J. (1960). Dislocations, stacking faults and twins in the spinel structure. *Journal of Physics and Chemistry of Solids*, **15**, 311–323.

Huang, D.J., Chang, C.F., Chen, J., *et al*. (2002). Spin-resolved photoemission studies of epitaxial Fe_3O_4 (100) thin films. *Journal of Magnetism and Magnetic Materials*, **239**, 261–265.

Huang, D.J., Chang, C.F., Jeng, H.T., *et al*. (2004). Spin and orbital moment of Fe_3O_4. *Physical Review Letters*, **93**, 077204.

Huang, D.J., Lin, H.J., Okamoto, J., *et al*. (2006). Charge-orbital ordering and Verwey transition in magnetite measured by resonant soft X-ray scattering. *Physical Review Letters*, **96**, 096401.

Hubbard, J. (1963). Electron correlations in narrow energy bands. *Proceedings of the Royal Society*, **A 284**, 238–259.

Hubbard, J. (1964a). Electron correlations in narrow energy bands. II. The degenerate band case. *Proceedings of the Royal Society*, **A 277**, 237–259.

Hubbard, J. (1964b). Electron correlation in narrow energy bands. III. An improved solution. *Proceedings of the Royal Society*, **A 281**, 401–419.

Hubbard, J. (1965). Electron correlation in narrow energy bands. IV. The atomic presentation. *Proceedings of the Royal Society*, **A 285**, 542–560.

Iizumi, M., Koetzle, T.F., Shirane, G., *et al*. (1982). Structure of magnetite Fe_3O_4 below the Verwey transition temperature. *Acta Crystallographica. Section B*, **38**, 2121–2133.

Ishino, K.H., Satoh, Y., Takahashi, K., *et al*. (1992). A Low-loss Ferrite for High Frequency Switching Power Supplies, *Ferrites, Proceedings of the Sixth International Conference on Ferrites*, Tokyo, pp. 1173–1176.

Jansen, R., Brabers, V.A.M. and van Kempen, H. (1995). One-dimensional reconstruction observed on Fe_3O_4 (110) by scanning-tunneling-microscopy. *Surface Science*, **328**, 237–247.

Jeng, H.T., Guo, G.Y. and Huang, D.J. (2004). The charge-orbital ordering and Verwey transition in magnetite. *Physical Review Letters*, **93**, 156403.

Johnson, M.T., Noordermeer, A., Severin, M.M.E. and Meeuwissen, W.A.M. (1992). Microstructural dependence of the complex permeability in fine grained MnZn ferrites. *Journal of Magnetism and Magnetic Materials*, **116**, 169–176.

Jonker, G.H., Wijn, H.P.J. and Braun, P.B. (1957). Ferroxplana, hexagonal ferromagnetic iron oxide compounds for very high frequencies. *Philips Technische Rundschau*, **18**, 249–258.

Kanazawa, M., Hagiwana, K., Kokubun, J. and Ishida, K. (2002). ATS scattering from the tetrahedral and octahedral site in magnetite and franklenite. *Journal of the Physical Society of Japan*, **71**, 1765–1770.

Karlsson, H.L., Nilsson, L. and Moller, L. (2005). Subway particles are more genotoxic than street particles and induce oxidative stress in cultured human lung cells. *Chemical Research in Toxicology*, **18**(1), 19–25.

van Klinken, J. (2001). Magnetization of ancient ceramics. *Archaeometry*, **43**, 49–57.

Kohout, J., Gamaliya, E., Stepankova, H., *et al*. (2005). NMR of Fe-57, Ga-69 and Ga-71 in Ga substituted magnetite. *Journal of Magnetism and Magnetic Materials*, **290**, 1018–11020.

Koltun, R., Hermann, M., Güntherodt, G. and Brabers, V.A.M. (2001). Enhanced atomic-scale contrast on Fe_3O_4 (100) observed with a Fe-STM tip. *Applied Physics A-Materials Science and Processing*, **73**, 49–53.

Koops, C.G. (1951). Dispersion of the resistivity and dielectric constant of some semiconductors at audiofrequencies. *Physical Review*, **83**, 121–124.

Kronmüller, H. and Walz, F. (1980). Magnetic after-effects in Fe_3O_4 and vacancy-doped magnetite. *Philosophical Magazine B*, **42**, 433–452.

Kuipers, A.J.M. and Brabers, V.A.M. (1979). Electrical transport in magnetite near the Verwey transition. *Physical Review B*, **20**, 594–600.

Landau, L. and Lifshitz, E. (1935). On the theory of the dispersion of magnetic permeability in ferromagnetic bodies. *Physikalische Zeitschrift der Sowjetunion*, **8**, 153–169.

Lenge, N., Kronmüller, H. and Walz, F. (1984). The relation between electrical conductivity mechanisms and magnetic after-effects in single crystal magnetite. *Journal of the Physical Society of Japan*, **53**, 1406–1414.

Lennie, A.R., Condon, N.G., Leibsle, F.M., *et al*. (1996). Structure of Fe_3O_4 (111) surfaces observed by scanning-tunneling-microscopy. *Physical Review B*, **53**, 10244–10253.

Leonov, I., Yaresko, A.N., Antonov, V.N., *et al*. (2004). Charge and orbital order in Fe_3O_4. *Physical Review Letters*, **93**, 146404.

Linford, N.T. (2004). Magnetic ghost: mineral magnetic measurements on Roman and Anglo-Saxon graves. *Archaeological Prospection*, **11**, 167–180.

Madsen, G.K.H. and Novak, P. (2005). Charge order in magnetite. An LDA + U study. *Europhysics Letters*, **69**, 777–783.

Margulies, D.T., Parker, F.T., Rudee, M.L., *et al*. (1997). Origin of the anomalous magnetic behavior in single crystal Fe_3O_4 films. *Physical Review Letters*, **79**, 5162–5165.

Margulies, D.T., Parker, F.T., Spada, F.E., *et al*. (1996). Anomalous moment and anisotropy behavior in Fe $_3O_4$ films. *Physical Review B*, **53**, 9175–9187.

Menzer, G. (1926). The crystal structure of garnet. *Zeitschrift für Kristallographie, Kristallgeometrie, Kristallphysik, Kristallchemie*, **63**, 157–158.

Menzer, G. (1928). The crystal structure of garnet. *Zeitschrift für Kristallographie, Kristallgeometrie, Kristallphysik, Kristallchemie*, **69**, 300–396.

Mills, A.A. (2004). The lodestone: history, physics and formation. *Annals of Science*, **61**, 273–319.

Mizoguchi, M. (2001). Charge and orbital ordering structure of Fe_3O_4 in the low temperature phase as deduced from NMR studies. *Journal of the Physical Society of Japan*, **70**, 2334–2344.

Morris, R.V., Klingelhofer, G., Bernhardt, B., *et al*. (2004). Mineralogy at Gusev Crater from the Mössbauer spectrometer on the spirit rover. *Science*, **305**, 833–836.

Morton, S.A., Wadill, G.D., Kim, S., *et al*. (2002). Spin–resolved photoelectron spectroscopy of Fe_3O_4. *Surface Science*, **513**, L451–L457.

Mott, N.F. (1990). *Metal Insulator Transitions*, *Second Edition*, Taylor and Francis: London.

Nakano, A., Momoi, H. and Nomura, T. (1992). Effect of Ag on the Microstructure of the Low Temperature Sintered NiCuZn Ferrites, *Ferrites. Proceedings of the Sixth International Conference on Ferrites*, Tokyo, pp. 1225–1228.

Néel, L. (1948). Propriétés magnétiques des ferrites: ferrimagnétisme et antiferromagnétisme. *Annales de Physique*, **3**, 137–198.

Nomura, T. (1992). Micro- and Nanostructure-property Relationships in Soft Ferrites, *Ferrites. Proceedings of the Sixth International Conference on Ferrites*, Tokyo, pp. 65–70.

Novak, P. (1991). *Landolt Bornstein, Numerical Data and Fundamental Relationships in Science and Technology*, Springer-Verlag, Vol. III-27e.

Novak, P., Stepankova, H., Englich, J., *et al*. (2000). NMR in magnetite below and round the Verwey transition. *Physical Review B*, **61**, 1256–1260.

Oda, Y., Mizuno, S., Todo, S., *et al*. (1998). Surface structure of magnetite Fe_3O_4 (110). *Japanese Journal of Applied Physics Part 1*, **37**, 4518–4521.

Ohiai, T. (1997). Current status of soft ferrites in Japan. *Journal of Physical IV, Colloques*, **7**(Suppl C-1), 27–30.

Otsuki, E. (1992). Nanostructures and Magnetic Properties of MnZn Ferrites, *Ferrites, Proceedings of the Sixth International Conference on Ferrites*, Tokyo, pp. 59–64.

Pankhurst, Q.A. and Pollard, R.J. (1991). Origen of the spin-canting anomaly in small ferrimagnetic particles. *Physical Review Letters*, **67**, 248–250.

Park, J.H., Tjeng, L.H., Allen, J.W., *et al*. (1997). Single particle gap above the Verwey transition. *Physical Review B*, **55**, 12813–12817.

Parker, F.T. and Berkowitz, A.E. (1991). Field response of surface spins on Co-adsorbed γ-Fe_2O_3. *Physical Review B*, **44**, 7437–7443.

Parker, F.T., Foster, M.W., Margulies, D.T. and Berkowitz, A.E. (1993). Spin canting, surface magnetization and finite size effects. *Physical Review B*, **47**, 7885–7891.

Pénicaud, M., Siberchicot, B., Sommers, C.B. and Kubler, J. (1992). Calculated electronic band-structure and magnetic moments of ferrites. *Journal of Magnetism and Magnetic Materials*, **103**, 212–220.

Pimenov, A., Tachos, S., Rudolf, T., *et al*. (2005). Terahertz conductivity at the Verwey transition in magnetite. *Physical Review B*, **72**, 035131.

Rikukawa, H. (1982). Relationship between microstructure and magnetic properties of ferrites containing closed pores. *IEEE Transactions on Magnetics*, **Mag-18**, 1535–1537.

Schrupp, D., Sing, M., Tsunekawa, M., *et al*. (2004). Surface electronic structure and Verwey-transition of magnetite studied by photoemission spectroscopy. *Annalen der Physik*, **13**, 78–80.

Schrupp, D., Sing, M., Tsunekawa, M., *et al*. (2005). High-energy photo-emission on Fe_3O_4. Small polaron physics and the Verwey transition. *Europhysics Letters*, **70**, 789–795.

Schwenk, H., Bareiter, S., Hinkel, C., *et al*. (2000). Charge ordering and elastic constants in $Fe_{3-x}Zn_xO_4$. *The European Physical Journal B*, **13**, 491–494.

Shepherd, J.P., Koenitzer, J.W., Aragon, R., *et al*. (1991). Heat capacity and entropy of nonstoichiometric $Fe_{3(1-\delta)}O_4$: thermodynamic nature of the Verwey transition. *Physical Review B*, **43**, 8461–8471.

Shirk, B.T. and Buessem, W.R. (1969). Temperature dependence of M_S and K_1 of $BaFe_{12}O_{19}$ and $SrFe_{12}O_{19}$ single crystals. *Journal of Applied Physics*, **40**, 1294–1296.

Shvets, I.V., Mariotto, G., Jordan, K., *et al*. (2004). Long-range charge order on the Fe_3O_4(100) surface. *Physical Review B*, **70**, 155406.

Slonczewski, J.C. (1992). Theory of surface anisotropy and coercivity in γ-Fe_2O_3. *Journal of Magnetism and Magnetic Materials*, **117**, 368–378.

Smit, J. and Wijn, H.P.J. (1959). *Ferrites*, Philips Technical Library: Eindhoven.

Snelling, E.C. (1988). *Soft Ferrites*, *Second Edition*, Butterworths: London.

Snoek, J. (1948). Dispersion and absorption in magnetic ferrites at frequencies above one megacycle. *Physica*, **14**, 207–217.

Stijntjes, Th.G.W., Klerk, J. and Broese van Groenou, A. (1970). Permeability and conductivity of Ti-substituted MnZn-ferrites. *Philips Research Reports*, **25**, 95–107.

Stijntjes, Th.G.W. and Roelofsma, J.J. (1986). Low loss power ferrite for frequencies up to 500 kHz. *Advances in Ceramics*, **16**, 493–499.

Su, Y., Li, H., Claessen, R., *et al*. (2006). Definitive evidence for orbital ordering in magnetite. *Nature*, Submitted to.

Subias, G., Garcia, J., Blasco, J., *et al*. (2004a). Magnetite, a model system for mixed-valence oxides, does not show charge ordering. *Physical Review Letters*, **93**, 156408.

Subias, G., Garcia, J., Proietti, M.G., *et al*. (2004b). X-ray resonant scattering of (0 0 4n + 2) forbidden reflections in spinel ferrites. *Physical Review B*, **70**, 155105.

Subias, G., Garcia, J. and Blasco, J. (2005). EXAFS spectroscopy analysis of the Verwey transition in Fe_3O_4. *Physical Review B*, **71**, 155103.

Tenaud, P., Morel, A., Kools, F., *et al*. (2004). Recent improvements of hard ferrite permanent magnets based on La-Co substitution. *Journal of Alloys and Compounds*, **370**, 331–334.

Toyoda, T., Sasaki, S. and Tanaka, M. (1999). Evidence of charge ordering of $Fe^{2+}$and Fe^{3+} in magnetite observed by synchrotron X-ray anomalous scattering. *The American Mineralogist*, **84**, 294–298.

Urbat, M., Lehndorff, E. and Schwark, L. (2004). Biomonetoring of air quality in the Cologne conurbation using pine needles as a passive sampler–Part 1-magnetic properties. *Atmospheric Environment*, **38**, 3781–3792.

Verwey, E.J.W. (1939). Electronic conduction of magnetite (Fe_3O_4) and its transition point at low temperature. *Nature*, **144**, 327–328.

Visser, E.G. and Johnson, M.T. (1991). A novel interpretation of the complex permeability in polycrystalline ferrites. *Journal of Magnetism and Magnetic Materials*, **101**, 143–147.

Visser, E.G., Johnson, M.T. and van der Zaag, P.J. (1992). A New Interpretation of the Permeability of Ferrite Polycrystals, *Ferrites. Proceedings of the Sixth International Conference on Ferrites*, Tokyo, pp. 807–811.

Visser, E.G., Roelofsma, J.J. and Aaftink, G.J.M. (1989). Domain wall loss and rotational loss in high frequency power ferrites. *Proceedings of the Fifth International Conference on Ferrites, Bombay. Crystal –Properties and Preparation*, **27–30**, 605–610.

Vogel, E.M., Gyorgy, E.M., Johnson, D.W. and Sherwood, D.W. (1986). The dependence of the critical field on the induced anisotropy in Ni-Zn-Co ferrites. *Advances in Ceramics*, **16**, 131–138.

Walker, M.M., Diebel, C.E., Haugh, C.V., *et al*. (1997). Structure and function of the vertebrate sense. *Nature*, **390**, 371.

Walz, F. (2002). The Verwey transition-a topical review. *Journal of Physics: Condensed Matter*, **14**, R285–R340.

Walz, F. and Kronmüller, H. (1990). Point defects in electron irradiated magnetite. *Physica Status Solidi B*, **160**, 661–671.

Walz, F., Weidner, M. and Kronmüller, H. (1980). Investigation of magnetic after-effects in magnetite at low temperatures (4 to 35 K). *Physica Status Solidi A*, **59**, 171–182.

Walz, F., Brabers, V.A.M., Chikazumi, S., *et al*. (1982). Magnetic after-effects in single and polycrystalline magnetite. *Physica Status Solidi B*, **110**, 471–478.

Wasilewski, P. and Kletetschka, G. (1999). Lodestone: natures only permanent magnet –what it is and how it gets charged. *Geophysical Research Letters*, **26**, 2275–2278.

Weiss, B.P., Kim, S.S., Kirschvink, J.L., *et al*. (2004). Magnetic test for magnetosome chains in Martian meteorite ALH 84001. *Proceedings of the National Academy of Sciences of the United States of America*, **101**, 8281–8284.

Went, J.J., Rathenau, G.W., Gorter, E.W. and van Oosterhout, G.W. (1952). Ferroxdure, a class of permanent magnetic materials. *Philips Technical Review*, **13**, 194–208.

Wiesendanger, R., Shvets, I.V., Burgler, D., *et al*. (1992). Topographic and magnetic-sensitive scanning tunneling microscope study of magnetite. *Science*, **255**, 583–586.

Wright, J.P., Attfield, J.P. and Radaelli, P.G. (2001). Long range charge ordering in magnetite below the Verwey transition. *Physical Review Letters*, **87**, art 266401.

Wright, J.P., Attfield, J.P. and Radaelli, P.G. (2002). Charge ordered structure of magnetite Fe_3O_4 below the Verwey transition. *Physical Review B*, **66**, art 214422.

Yan, M.F. and Johnson, D.W. (1978). Impurity-induced exaggerated grain growth in Mn-Zn ferrite. *Journal of the American Ceramic Society*, **61**, 342–349.

Yanase, A. and Siratori, K. (1984). Band structure in the high temperature phase of Fe_3O_4. *Journal of the Physical Society of Japan*, **53**, 312–317.

Zhang, Y., Kohler, N. and Zhang, M.Q. (2002). Surface modification of superparamagnetic magnetic monoparticles and their intercellular uptake. *Biomaterials*, **33**, 1553–1561.

Zhang, Z. and Satpathy, S. (1991). The electron states, magnetism and the Verwey transition in magnetite. *Physical Review B*, **44**, 13319–13331.

Žnidarsič, A., Limpel, M., Dražič, G. and Drofenik, M. (1992). Microstructural Control in Low Loss Power Ferrite, *Ferrites. Proceedings of the Sixth International Conference on Ferrites*, Tokyo, pp. 333–336.

Zuo, J.M., Spence, C.H. and Petuskey, W. (1990). Charge ordering in magnetite at low temperatures. *Physical Review B*, **42**, 8451–8464.

FURTHER READING

Adelsköld, V. (1938). X-ray studies on magnetoplumbite $PbO.6Fe_2O_3$ and other substances resembling "beta-alumina" $Na_2O.11Al_2O_3$. *Arkiv for Kemi Mineralogi och Geologi*, **12A**(29), 1–9.

Yoshida, Y. and Iida, S. (1979). X-ray study of the phase transition in magnetite. *Journal of the Physical Society of Japan*, **47**, 1627–1633.

Crystallography and Chemistry of Perovskites

Mats Johnsson[1] and Peter Lemmens[2]

[1] *Stockholm University, Stockholm, Sweden*
[2] *Technische Universität Braunschweig, Braunschweig, Germany*

1 INTRODUCTION

The structural family of perovskites is a large family of compounds having crystal structures related to the mineral perovskite $CaTiO_3$. In the ideal form, the crystal structure of cubic ABX_3 perovskite can be described as consisting of corner sharing $[BX_6]$ octahedra with the A cation occupying the 12-fold coordination site formed in the middle of the cube of eight such octahedra. The ideal cubic perovskite structure is not very common and also the mineral perovskite itself is slightly distorted. The perovskite family of oxides is probably the best-studied family of oxides. The interest in compounds belonging to this family of crystal structures arises from the large and ever surprising variety of properties exhibited and the flexibility to accommodate almost all of the elements in the periodic system. Pioneering structural work on perovskites were conducted by Goldschmidt and coworkers in the 1920s that formed the basis for further exploration of the perovskite family of compounds (Bhalla, Guo and Roy, 2000). Distorted perovskites have reduced symmetry, which is important for their magnetic and electric properties. Owing to these properties, perovskites have great industrial importance, especially the ferroelectric tetragonal form of $BaTiO_3$.

Handbook of Magnetism and Advanced Magnetic Materials. Edited by Helmut Kronmüller and Stuart Parkin. Volume 4: *Novel Materials*. ISBN: 978-0-470-02217-7.

2 THE CRYSTAL STRUCTURE OF PEROVSKITE

If the large oxide ion is combined with a metal ion having a small radius, the resulting crystal structure can be looked upon as close-packed oxygen ions with metal ions in the interstitials. This is observed for many compounds with oxygen ions and transition metals of valence +2, for example, NiO, CoO, and MnO. In these crystal structures, the oxygen ions form a cubic close-packed (ccp) lattice with the metal ion in octahedral interstitials (i.e., the rock salt structure). Replacing one-fourth of the oxygen with a cation of approximately the same radius as oxygen (e.g., alkali, alkaline earth, or rare earth element) reduces the number of octahedral voids, occupied by a small cation, to one-fourth. The chemical formula is written as ABX_3 and the crystal structure is called *perovskite*. X is often oxygen but other large ions such as F^- and Cl^- are also possible.

The idealized cubic structure is realized, for example, in $CaRbF_3$ and $SrTiO_3$. The latter can be described as Sr^{2+} and O^{2-} ions forming a ccp lattice with Ti^{4+} ions occupying the octahedral holes created by the oxygen ions. The perovskite structure has a three-dimensional net of corner sharing $[TiO_6]$ octahedra with Sr^{2+} ions in the 12-fold cavities in between the polyhedra (see Figure 1).

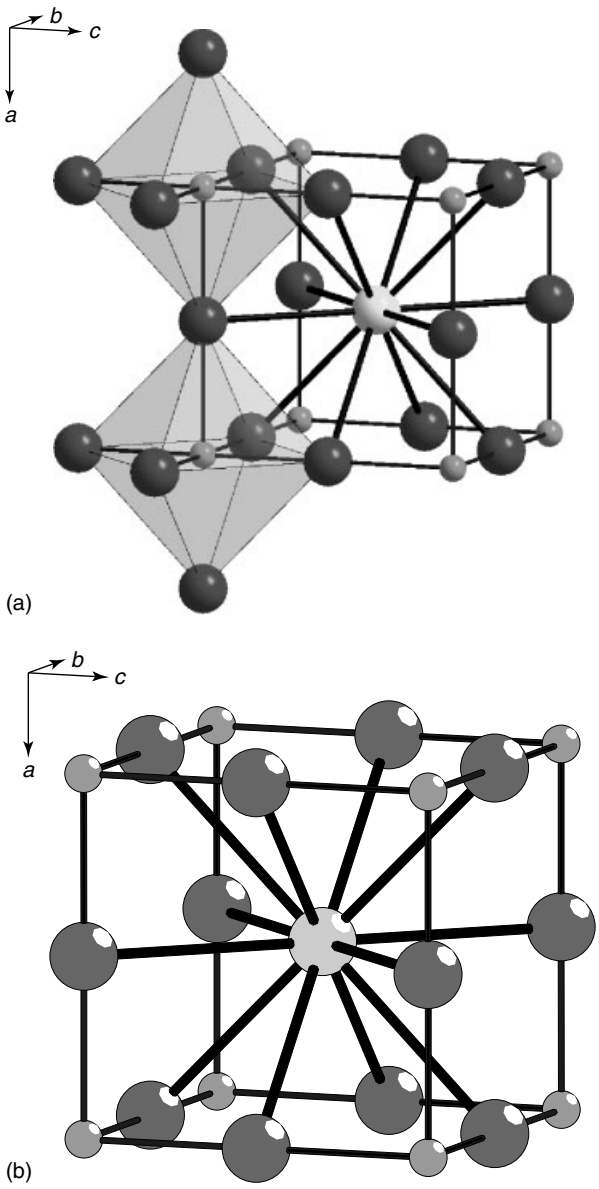

Figure 1. Outline of the ideal cubic perovskite structure $SrTiO_3$ that has (a) a three-dimensional net of corner sharing $[TiO_6]$ octahedra with (b) Sr^{2+} ions in the twelve fold cavities in between the polyhedra.

In the cubic ABX_3 perovskite structure ($a = 3.905$ Å, space group $Pm3m$, $Z = 1$), the A atoms are in Wyckoff position 1b, ½,½,½; the B atoms in 1a, 0,0,0; and the X atoms in 3d ½,0,0; 0,½,0; 0,0,½, all being special positions. If the position of the Sr^{2+} ion (A) is vacant, the remaining framework is that of the ReO_3 type. Partial occupation of the A position occurs in the cubic tungsten bronzes A_xWO_3 (A = alkali metal, $0.3 \leq x \leq 0.93$). The ReO_3 structure type can be converted to a denser packing by rotating the octahedra until a hexagonal close packing of the RhF_3 type is obtained. The void in the center has then an octahedral surrounding. If this octahedral hole is occupied we have the ilmenite structure, $FeTiO_3$. The perovskite structure is known to be very flexible, and the A and B ions can be varied leading to the large number of known compounds with perovskite or related structures. Most perovskites are distorted and do not have the ideal cubic structure.

Three main factors are identified as being responsible for the distortion: size effects, deviations form the ideal composition, and the Jahn–Teller effect. It is rare that a distortion of a certain perovskite compound can be assigned to a single effect. In most cases several factors act on the structure. As an example of the complexity, $BaTiO_3$ has four phase transitions on heating: rhombohedral ($R3m$), $-90\,^{\circ}C \rightarrow$ orthorhombic ($Amm2$), $5\,^{\circ}C \rightarrow$ tetragonal ($P4mm$), $120\,^{\circ}C \rightarrow$ cubic ($Pm3m$).

2.1 Size effects

In the ideal cubic case, the cell axis, a, is geometrically related to the ionic radii (r_A, r_B, and r_O) as described in equation (1):

$$a = \sqrt{2}(r_A + r_O) = 2(r_B + r_O) \tag{1}$$

The ratio of the two expressions for the cell length is called the *Goldschmidt's tolerance factor* t, and it allows us to estimate the degree of distortion. It is based on ionic radii, that is, purely ionic bonding is assumed, but can be regarded as an indication for compounds with a high degree of ionic bonding; it is described in equation (2).

$$t = \frac{(r_A + r_O)}{\sqrt{2}(r_B + r_O)} \tag{2}$$

The ideal cubic perovskite $SrTiO_3$ has $t = 1.00$, $r_A = 1.44$ Å, $r_B = 0.605$ Å, and $r_O = 1.40$ Å. If the A ion is smaller than the ideal value then t becomes smaller than 1. As a result, the $[BO_6]$ octahedra will tilt in order to fill space. However, the cubic structure occurs if $0.89 < t < 1$ (Wells, 1995; Müller, 1993). Lower values of t will lower the symmetry of the crystal structure. For example, $GdFeO_3$ (ICSD, 2005) with $t = 0.81$ is orthorhombic ($r_A = 1.107$ Å and $r_B = 0.78$ Å) (see Figure 2a). Also the mineral perovskite $CaTiO_3$ itself, has this structure. With values less than 0.8, the ilmenite structure is more stable.

On the other hand, if t is larger than 1 due to a large A or a small B ion then hexagonal variants of the perovskite structure are stable, for example, $BaNiO_3$ type structures. In this case, the close-packed layers are stacked in a hexagonal

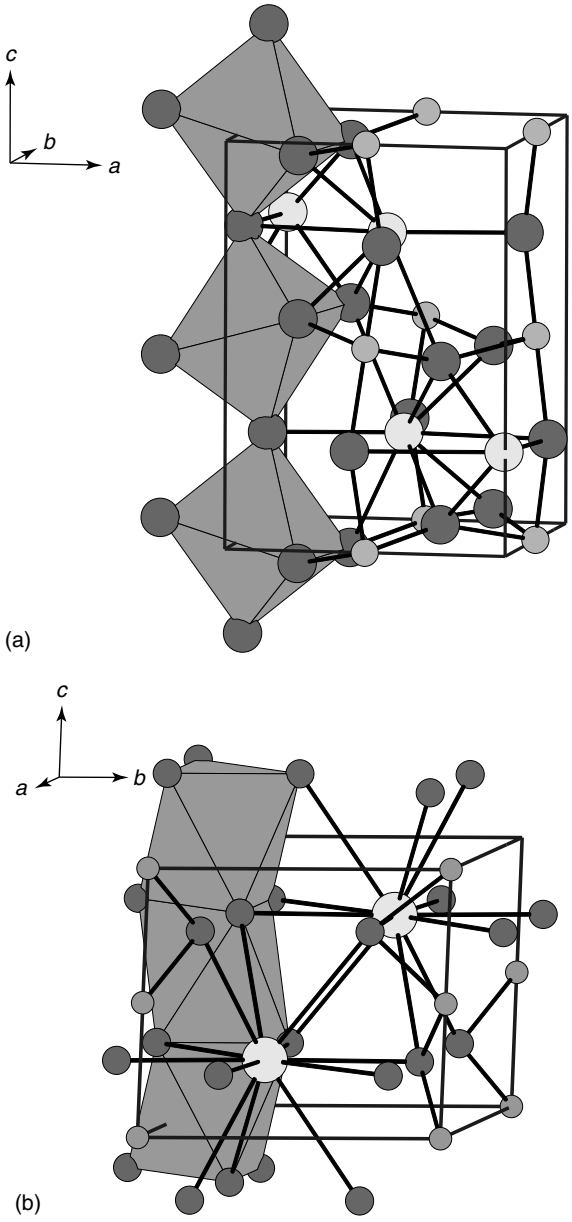

Figure 2. (a) Low values of the tolerance factor t will lower the symmetry of the crystal structure. $GdFeO_3$ with $t = 0.81$ have tilted $[FeO_6]$ octahedra and crystallize in the orthorhombic system ($r_A = 1.107$ Å and $r_B = 0.78$ Å). (b) If t is larger than 1 due to a large A or a small B ion then hexagonal variants form of the perovskite structure. The t value for $BaNiO_3$ is 1.13 ($r_A = 1.61$ Å and $r_B = 0.48$ Å).

manner in contrast to the cubic one found for $SrTiO_3$, leading to face sharing of the $[NiO_6]$ octahedra, (see Figure 2b). The t value for $BaNiO_3$ is 1.13 ($r_A = 1.61$ Å and $r_B = 0.48$ Å). Since perovskites are not truly ionic compounds and the t values also depend on the values that are taken for the ionic radii, the tolerance factor is only a rough estimate.

2.2 Changing the composition from the ideal ABO_3

An example is the family of compounds $SrFeO_x$ ($2.5 \leq x \leq 3$). The valency of the Fe ions can be changed by heating the sample in either an oxidizing or a reducing environment. As a result, the oxygen content can vary between 2.5 and 3. For example, in $SrFeO_{2.875}$ some Fe ions can be assigned to the oxidation state +3 and others to +4. The oxygen vacancies order so that FeO_5 square pyramids are formed (see Figure 3). The $SrFeO_x$ compounds are examples of defective perovskites. Their chemistry can be described according to the homologous series $A_nB_nO_{3n-1}$, $n = 2 - \infty$. Several other types of vacancy orderings are known, for example, the structures of $Ca_2Mn_2O_5$ and $La_2Ni_2O_5$ having $n = 2$ are shown in Figure 4(a–b).

2.3 Jahn–Teller effects

In some perovskites, the distortion of the structure can be assigned to Jahn–Teller active ions at the B position. For example, in $LnMnO_3$ (Ln = La, Pr, or Nb) with Mn^{3+} ions the $3d^4$ electrons divide up into $3\,t_g$ and $1\,e_g$ electron. The odd number of electrons in the e_g orbital cause an elongation of the $[MnO_6]$ octahedron.

3 SUPERSTRUCTURES RELATED TO THE PEROVSKITE STRUCTURE

If we double all three unit cell edges of the cubic perovskite structure, it is possible to occupy equivalent positions with atoms of different elements (see Figure 5). In K_2NaAlF_6, the K^+ and the F^- ions take the Ca^{2+} and the O^{2-} positions, respectively, of the perovskite. The one-to-one relation can be recognized by comparing with the doubled formula of perovskite. The comparison also shows how the octahedral Ti^{4+} position shifts into two sites for Na^+ and Al^{3+} (Müller, 1993). In kryolite, Na_3AlF_6, the Na^+ ions occupy two different positions, namely the Sr^{2+} and the Ti^{4+} positions of the doubled perovskite cell, that is, positions with coordination numbers of 6 and 12. Since this is not convenient for ions of the same size, the structure experiences some distortion.

Perovskites of the type $ACuO_{3-\delta}$ which have Cu atoms in the octahedral sites are deficient in oxygen; alkaline earth, and trivalent ions (Y^{3+}, lanthanoids, Bi^{3+}, Tl^{3+}) occupy the A site. A typical composition is $YBa_2Cu_3O_{7-x}$ with $x \approx 0.04$. These compounds are high-temperature superconductors. The structure is a superstructure of perovskite, but

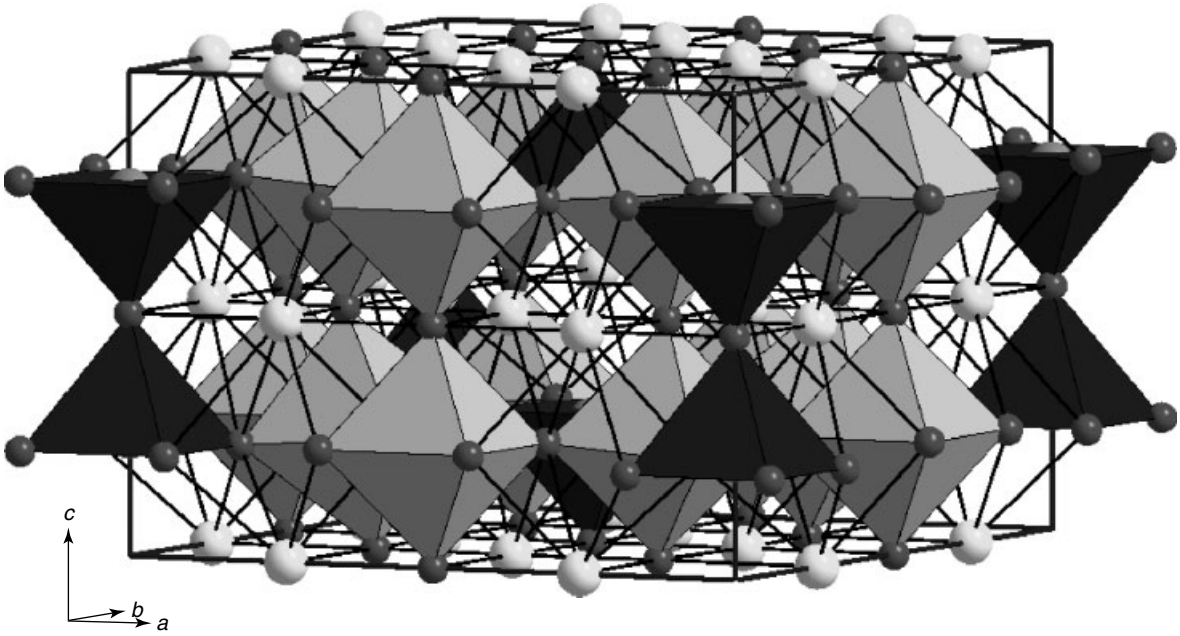

Figure 3. Ordering of oxygen vacancies in $SrFeO_{2.875}$ (=$Sr_8Fe_8O_{23}$). Fe ions are located in both square pyramids and in octahedra.

with approximately two-ninth of the oxygen positions vacant, in such way that two-third of the Cu atoms have square pyramidal coordination and one-third have square-planar coordination (see Figure 6). The cobaltite $GdBaCo_2O_{5.5}$ is another example of an oxygen-deficient perovskite-related structure where the Co^{3+} ions have octahedral and square pyramidal coordination (Frontera, Garcia-Munoz, Llobet and Aranda, 2002) (see Figure 7).

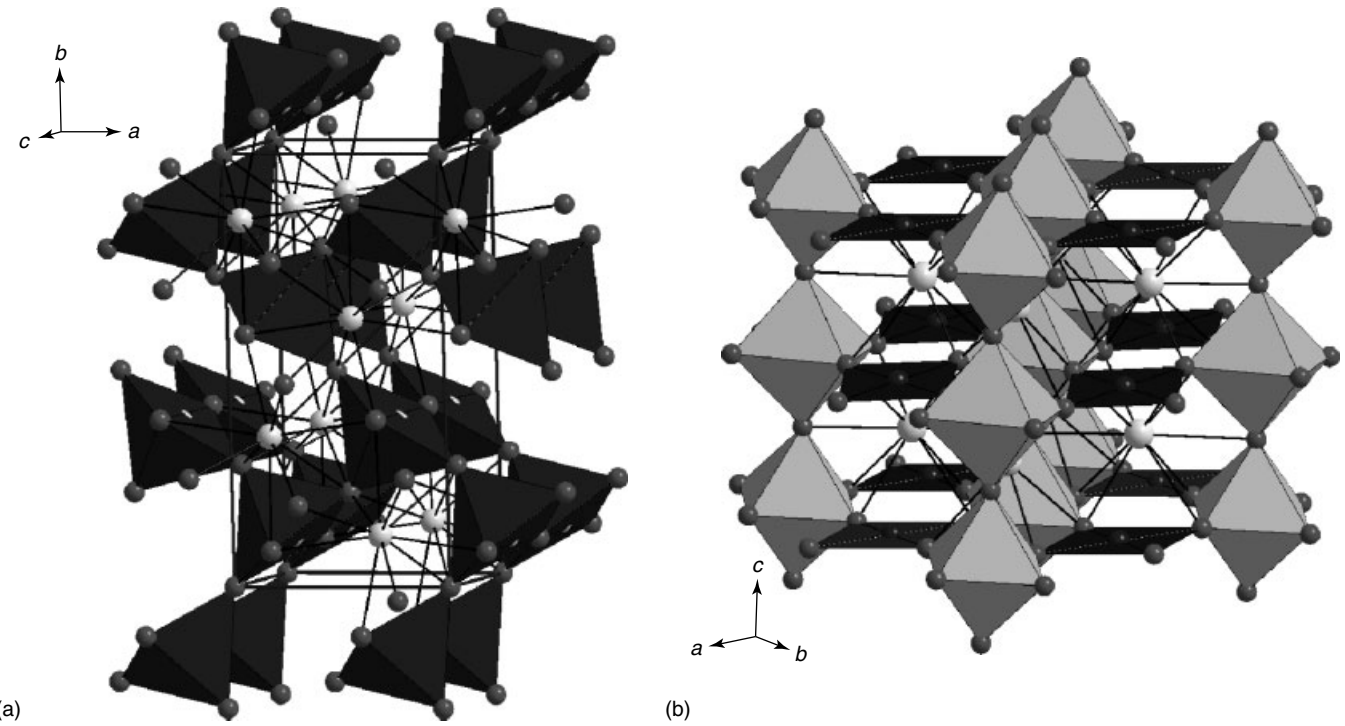

Figure 4. Ordering of oxygen vacancies in (a) $Ca_2Mn_2O_5$ having [MnO_5] square pyramides and (b) $La_2Ni_2O_5$ having [NiO_6] octahedra and [NiO_4] square planes.

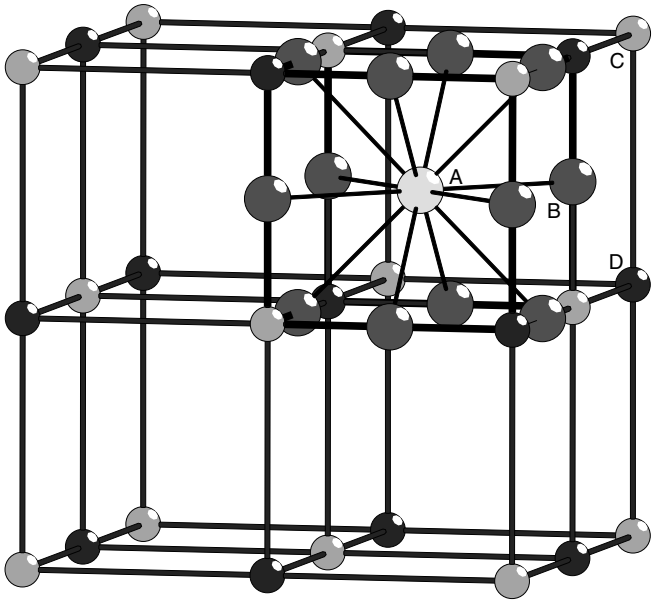

Figure 5. Superstructures of the perovskite type. If the unit cell edges are doubled, it is possible to occupy equivalent positions with atoms of different elements. The one-to-one relation can be recognized by comparing with the doubled formula of perovskite.

Structure type	Example	A(Yellow)	B(Red)	C(Green)	D(Blue)
Perovskite	$SrTiO_3$	Sr^{2+}	O^{2-}	Ti^{4+}	Ti^{4+}
Elpasolite	K_2NaAlF_6	K^+	F^-	Na^+	Al^{3+}
Kryolite	$(NH_4)_3AlF_6$	NH_4^+	F^-	NH_4^+	Al^{3+}
K_2PtCl_6	–	K^+	Cl^-	–	Pt^{4+}

Also the brownmillerite structure is an oxygen-deficient superstructure of cubic perovskite with an ordering of oxygen vacancies. Ruddlesden and Popper designed a series of homologous compounds with the general formula $AO(ABO_3)_n$, where AO represent a rock salt structure layer separating blocks of perovskite layers characterized by $n = 1, 2, 3, \ldots, \infty$. Examples are the high T_c superconductor prototype La_2CuO_4 and the 2D quantum antiferromagnet La_2NiO_4.

4 ELECTRONIC AND MAGNETIC PROPERTIES OF PEROVSKITES

Perovskites with transition metal ions (TMIs) on the B site show an enormous variety of intriguing electronic or magnetic properties. This variety is not only related to their chemical flexibility but also, to a large extent, to the complex character that TMIs play in certain coordinations with oxygen or halides (Lemmens and Millet, 2004). While magnetism

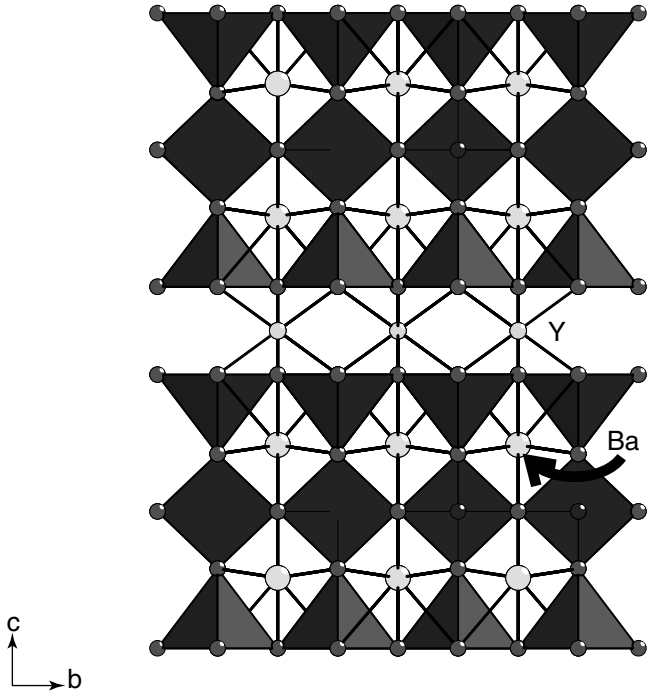

Figure 6. The high-temperature superconductor $YBa_2Cu_3O_{6.96}$. The structure is a superstructure of perovskite with approximately two-ninth of the oxygen positions vacant, in such way that two-third of the Cu atoms have $[CuO_5]$ square pyramidal coordination and one-third have square-planar $[CuO_4]$ coordination. The perovskite structure is attained by inserting oxygen atoms in between the yttrium atoms (gray) and in between the $[CuO_4]$ square planes.

and electronic correlations are usually related to unfilled 3d electron shells of the TMI, pronounced dielectric properties are connected with filled 3d electron shells. Multiferrocity, a coexistence of spontaneous ferroelectric and ferromagnetic moments, is a rare phenomenon due to the small number of low-symmetry magnetic point groups that allow a spontaneous polarization (Schmid, 1994). Nevertheless, in the presence of competing interactions (Hemberger *et al.*, 2005), canted moments (Kimura *et al.*, 2003; Higashiyama *et al.*, 2004), or in composites (Zheng *et al.*, 2004) large magneto-capacitive couplings have been reported (Fiebig, 2005).

In the following section, we will discuss examples of material properties in which transition metal perovskites and related structures prove to be outstanding. To some extent, these aspects also touch application areas, such as capacitors, transducers, actuators, sensors, and electro-optical switches.

4.1 Dielectric and ferroelectric perovskites

High dielectric permittivity (ε) or ferroelectric materials are of enormous importance as electroceramics for engineering and electronics. Perovskites, for example, titanium or

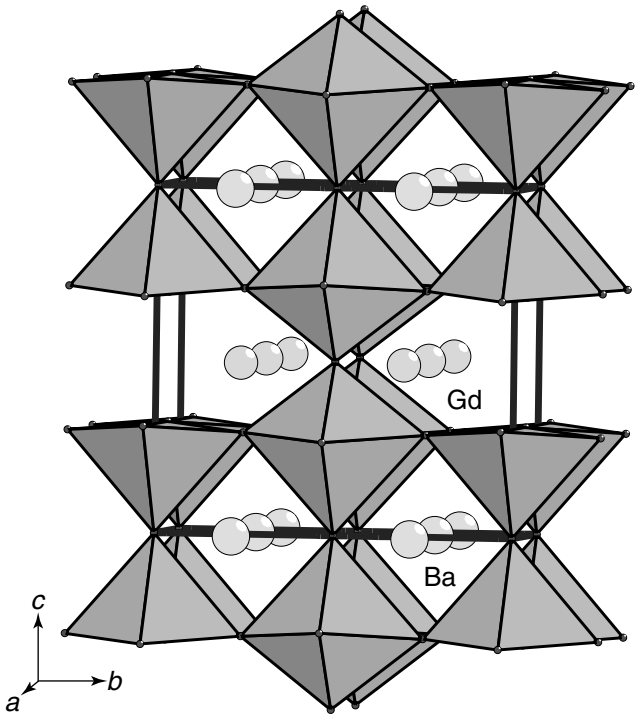

Figure 7. The cobaltite $GdBaCo_2O_{5.5}$ has a perovskite related structure were 1/12 of the oxygen atoms are missing leading to that 50% of the Co atoms have square pyramidal [CoO_5] coordination and 50% of the Co atoms have octahedral [CoO_6] coordination.

niobium perovskites, $BaTiO_3$, and $LiNbO_3$, have been intensively studied in the past (Cross and Newnham, 1987; Cross, 1987). A large ε is based on collective polar displacements of the metal ions with respect to the oxygen sublattice and is a highly nonlinear and anisotropic phenomenon. The phase transition that leads to ferroelectricity is usually described by a soft-mode model (Shirane, 1974).

To optimize dielectric and mechanical properties, several routes have been followed from the structurally simple $BaTiO_3$ via the solid solution system $Pb(Zr,Ti)O_3$ to other distinct families of materials. These routes explicitly take into account the flexibility for chemical manipulation and "docility" of the perovskites (Cross and Newnham, 1987; Cross, 1987). One of them is the relaxor ferroelectric. It is genuinely based on a multielement substituted Pb titanate ($PbTiO_3$) with the composition A(B'B")O_3 with a random occupation of the A and B sites by metal ions of different valence.

Relaxor ferroelectrics show enormously large dielectric constants, a pronounced frequency dispersion and variation of ε as function of temperature. These effects are due to slow relaxation processes for temperatures above a glass transition (Lunkenheimer, Schneider, Brand and Loidl, 2000). The length scales of fluctuating composition and spontaneous polarization are 2–5 nm, that is, the effects are based on electronic inhomogeneities and the existence of polar nanoregions. The lattice part of the response is considered to be a local softening of transverse-optical phonon branch that prevents the propagation of long-wavelength ($q = 0$) phonons. It is interesting to note that the fundamental limit, the superparaelectric state, is still not reached for such small length scales (Spaldin, 2004). Generic examples for relaxor ferroelectrics are PZT: $Pb(Zn_{1/3}Nb_{2/3})O_{3-x}PbTiO_3$ and PMN: $Pb(Mg_{1/3}Nb_{2/3})O_{3-x}PbTiO_3$, with PZT having a higher temperature scale compared to PMN.

Incipient ferroelectrics or quantum paraelectrics can be regarded as almost ferroelectric crystals (Höchli, Knorr and Loidl, 1990). Examples are $KTaO_3$ and $SrTiO_3$ (Bednorz and Müller, 1984). Pronounced quantum fluctuations of ions suppress the phase transition into the ferroelectric state and stabilize the soft transverse-optical mode. The dielectric susceptibility shows a divergence in the limit $T = 0\,K$ together with pronounced phonon anharmonicities (Bednorz and Müller, 1984). In these systems, even minor substitutions or doping can induce phase transitions into ferroelectric states. Finally, we mention perovskite-related oxides with giant dielectric constants (GDCs) where no evidence for a ferroelectric instability exists. These nonintrinsic permittivities are attributed to barrier layers and surface effects (Lunkenheimer *et al.*, 2002). Examples are $CaCu_3Ti_4O_{12}$, (Ramirez *et al.*, 2000) and the Li-ion conductor material $La_{0.67}Li_{0.25}Ti_{0.75}Al_{0.25}O_3$ (Garcia-Martin, Morata-Orrantia, Aguirre and Alario-Franco, 2005).

4.2 Magnetism and electronic correlations

Magnetism or orbital (electronic) ordering phenomena of various kinds are observed in perovskites with TMI that have unfilled 3d electron shells. Electronic correlations (Fazekas, 1999) of such 3d states are generally strong, as the ratio U_d/W of the Coulomb repulsion energy U_d versus the bandwidth W is larger compared to other electronic states, that is, they have a more local character and a tendency for insulating states or metal-insulator transitions (Imada, Fujimori and Tokura, 1998). Hopping and superexchange of these electrons takes place via oxygen sites due to the overlap of the respective wave function. Thereby, the properties and phase diagrams of a perovskite strongly depend on nonstoichiometries and, even more, on tilting or distortions of the [BO_6] octahedra. Further aspects rely on order/disorder processes of the orbital part of the 3d wave function, charge doping and charge/orbital inhomogeneous states that lead to colossal response, for example, to external magnetic fields (Tokura, 2003).

However, before considering such effects, the properties of the system are given by a hierarchy of energies based on the electronic structure, that is, the number of 3d electrons, the Hund's rule coupling, the crystalline electric field or Jahn–Teller splitting of the 3d electron states, and finally due to exchange energies.

4.3 Cuprates, Jahn–Teller distortions and high-temperature superconductors

This hierarchy of energies is well established for cuprates with Cu^{2+} in a $3d^9$ configuration. The hole in the d shell has $e_g x^2 - y^2$ symmetry and contributes to an $s = 1/2$ spin moment. The orbital moment is quenched due to the crystalline electric field of the surrounding oxygen. The e_g electron is Jahn–Teller active, that is, local or collective configurations with oxygen in distorted octahedra are energetically preferable. Extreme limits are pyramidal [CuO_5] or even a planar [CuO_4] configuration of the oxygen neighbors. Thereby, the superexchange and magnetic interactions between the $s = 1/2$ spin moments are restricted to a plane or, if building blocks are shifted by half a unit cell within the plane, to a quasi-one-dimensional path. There are numerous realizations of such low-dimensional magnetic systems as in Sr_2CuO_3 (spin chain system) or $SrCu_2O_3$ (spin ladder system) (Lemmens, Güntherodt and Gros, 2003). Owing to the small coordination number of the spin moments in one dimension and pronounced quantum fluctuations related to the small magnitude of the spin, such compounds generally do not show long-range ordering. Strong fluctuations are evident as broad maxima in the magnetic susceptibility and continua in inelastic neutron scattering.

Superexchange and electronic correlations – restricted to a two-dimensional, weakly doped plane – are the key ingredients of high-temperature superconductors. The crystal structure of the prototype and perovskite-related compound $YBa_2Cu_3O_{7-x}$ is shown in Figure 6. For $x \approx 1$, the resulting Cu^{2+} with $s = 1/2$ moments show long antiferromagnetic range ordering with a Néel temperature of more than 500 K. This high ordering temperature marks the exceptionally large energy scales and strong correlations involved in these materials. With smaller x, doping is induced that leads to a drastic drop of the Néel temperature and the onset of high-temperature superconductivity. The maximum superconducting transition temperature is $T_{cmax} = 92\,K$ for this system.

Electronic correlations are essential to understand the effect of doping. The electronic structure of cuprates in the vicinity of the Fermi level is given by an occupied low-energy and an unoccupied high-energy band, the lower and the upper Hubbard band, separated by the Coulomb repulsion energy U_d of the 3d electrons. High-temperature superconductors are charge transfer insulators, that is, the oxygen is included in this scheme as an occupied, nonbonding 2p band separated by a smaller charge transfer energy Δ from the upper Hubbard band ($\Delta < U_d$). The doping process consists of introducing a novel correlated electron state, the Zhang–Rice singlet state (Imada, Fujimori and Tokura, 1998), in the proximity of the oxygen band. This state of hybridized Cu and O character leads to a transformation from a long-range Néel state to a high-temperature superconductor. Although the number of known high-temperature superconductors seem to be large (of the order of 20 compounds), they all rely on this scheme of a doped, two-dimensional perovskite-related structure with pronounced electronic correlations (Imada, Fujimori and Tokura, 1998; Dagotto, 1994; Orenstein and Millis, 2000).

4.4 Cobaltates, spin state transitions and oxygen deficiency

If the hierarchy of energies, mentioned in the preceding text, is not well defined, the compound chooses certain ways to lift degeneracies of the electronic system. Important are spin state transitions or crossover behavior, a partial metallization of 3d electrons, or charge disproportionation of the TMI sites. Perovskites based on cobalt and vanadium serve as model systems for such effects and the resulting interplay of electronic and structural degrees of freedom. In the following text, we will discuss briefly two cobaltates to give an example for the resulting complexities.

In the cobalt perovskite $LaCoO_3$, with the same crystal structure as is shown in Figure 1, all three spin states of Co^{3+} ($3d^6$) are close to degenerate. As these states correspond to slightly different ionic radii with decreasing temperatures, a crossover of the dominant populations from high spin ($s = 2$), intermediate spin ($s = 1$) to low spin ($s = 0$) Co^{3+} $3d^6$ states takes place. This process is mainly controlled by temperature and has no evident collective character. The magnetic susceptibility shows a broad maximum and a strong decrease at low temperatures (Korotin *et al.*, 1996). The different ionic radii of the spin states also couple the electronic configurations of the TMIs only weakly to other properties of the compound.

An ordered oxygen deficiency leads to a multiplication of the unit cell volume. It also has a profound influence on the electronic and magnetic properties of the compound (Vidya *et al.*, 2004). Owing to the smaller coordination number of some TMI sites, the respective bandwidth is reduced, and with increasing electronic correlations, the tendencies for charge/orbital ordered states is enhanced. In Figure 7

the perovskite cobaltite $GdBaCo_2O_{5.5}$ is depicted. Oxygen defects form chains of $[CoO_5]$ pyramids and $[CoO_6]$ octahedra along the crystallographic *a* axis. Compared to the ideal perovskite $LaCoO_3$, the behavior is rather complex and highly collective. The phase diagram contains a metal-insulator transition and three different magnetic phases that include spin state ordering (Fauth, Suard, Caignaert and Mirebeau, 2002; Chernenkov *et al*., 2005; Plakhty *et al*., 2005).

4.5 Manganites and orbital degrees of freedom

In the manganite $(La,Sr)MnO_3$, the ratio La^{3+}/Sr^{2+} determines the oxidation state of Mn and thus the ratio Mn^{3+}/Mn^{4+}. This corresponds to the number of Mn sites with a single 3d e_g orbital occupied. Double exchange describes the situation where these states simultaneously hop via Mn^{4+} ions. The remaining $3\,t_{2g}$ electrons on each Mn ion sum up to $s = 3/2$ due to Hund's rule coupling and form a 'rigid background'. The bandwidth and charge transport are solely given by e_g state dependents on the spin and orbital orientation of the exchange partners.

As a function of composition, different magnetic ground states and orbitally/charge ordered structures are observed. These degrees of freedom react rather cooperative because of the strong interlink of the octahedra in the perovskite structure (Choi *et al*., 2005). Pronounced effects are observed in all physical quantities. However, most spectacular is the colossal magnetoresistance (CMR) at the borderline between a ferromagnetic insulating and ferromagnetic metallic phase. For a more complete treatment of this increasingly rich field of research including a discussion of relevant vanadium and titanium perovskites, we refer to reviews (Imada, Fujimori and Tokura, 1998; Tokura, 2003; Tokura and Tomioka, 1999; Salamon and Jaime, 2001; Dagotto, 2002) and recent focus issues (Keimer and Oles, 2004) of international journals.

5 SYNTHESIS

Many perovskites are synthesized by solid-state reactions giving polycrystalline samples. The starting materials are then usually simple binary oxides or pure elements made to react at relatively high temperatures. This synthesis technique involves problems due to the fact that certain starting oxides (e.g., PbO) may vaporize. The reaction temperature can be lowered by applying microwave synthesis techniques, thus minimizing the loss of volatile starting components. Hydrothermal synthesis techniques have been applied to manufacture nanopowders of, for example, $BaTiO_3$. Powders and thin films with controlled levels of dopants have been prepared with the sol–gel technique using metal alkoxides as precursors. Thin films of ferroelectrics have been successfully prepared by physical vapor deposition (PVD) or pulsed laser deposition (PLD).

During recent years, several research groups have succeeded in growing single crystals of several families of perovskite-related compounds from molten alkali carbonates or other fluxes such as hydroxides or halides. Large single crystals (>10 cm long) of manganites and other oxides have been grown by utilizing optically heated floating zone techniques with oxygen injected into the furnace around the molten zone (see Figure 8). The review (Bhalla, Guo and Roy, 2000) and references therein are referred for further aspects of synthesis techniques.

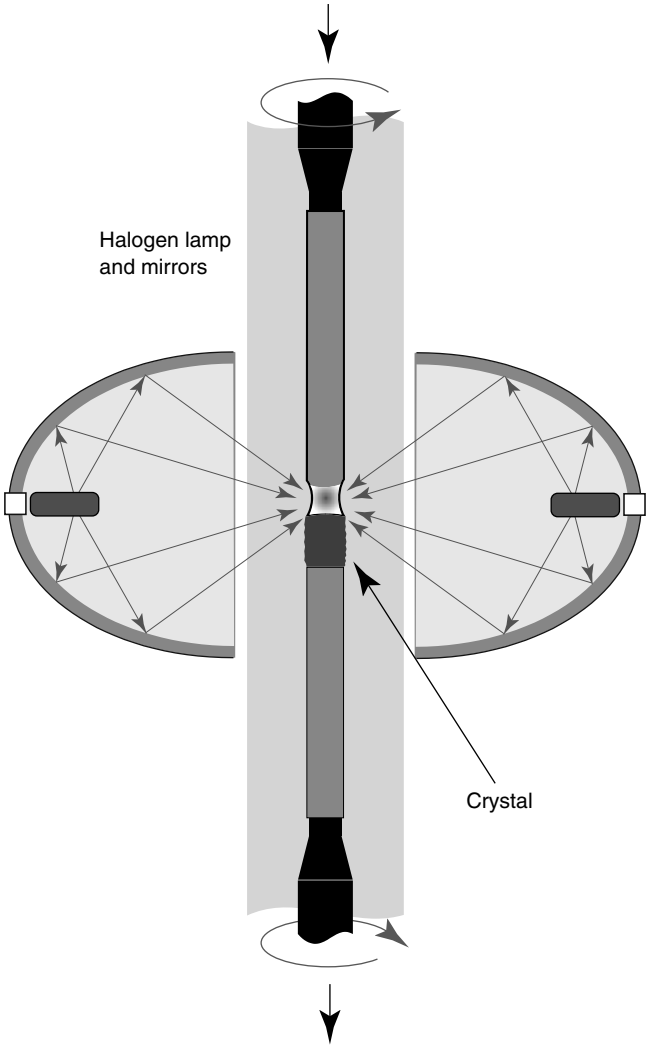

Figure 8. Outline of the principles for a floating zone mirror furnace. The crystal is grown by moving sintered powder rods through an optically heated floating zone.

ACKNOWLEDGMENTS

We acknowledge discussions with Rainer Waser and support from the Swedish Research Council, the German Science foundation (DFG), and the European Science Foundation (ESF).

REFERENCES

Bednorz, J.G. and Müller, K.A. (1984). Strontium calcium titanate ($Sr_{1-x}Ca_xTiO_3$): an XY quantum ferroelectric with transition to randomness. *Physical Review Letters*, **52**, 2289–2292.

Bhalla, A.S., Guo, R. and Roy, R. (2000). The perovskite structure – a review of its role in ceramic science and technology. *Materials Research Innovations*, **4**, 3–26.

Chernenkov, Yu.P., Plakhty, V.P., Fedorov, V.I., *et al*. (2005). X-ray diffraction study of superstructure in $GdBaCo_2O_{5.5}$. *Physical Review B*, **71**, 184105/1–184105/5.

Choi, K.-Y., Lemmens, P., Sahaoui, T., *et al*. (2005). Existence of orbital polarons in ferromagnetic insulating La1-xSrxMnO3 ($0.11 \leq x \leq 0.14$) revealed by giant phonon softening. *Physical Review B*, **71**, 174402/1–174402/7.

Cross, L.E. (1987). Relaxor ferroelectrics. *Ferroelectrics*, **76**, 241–267.

Cross, L.E. and Newnham, R.E. (1987). *The Ceramics and Civilization – High-Technology Ceramics – Past, Present, and Future*, Vol. 111, The American Ceramic Society.

Dagotto, E. (1994). Correlated electrons in high-temperature superconductors. *Reviews of Modern Physics*, **66**, 763–840.

Dagotto, E. (2002). *Phase Separation and Collossal Magnetoresitance*, Springer-Verlag: Berlin.

Fauth, F., Suard, E., Caignaert, V. and Mirebeau, I. (2002). Spin-state ordered clusters in the perovskite $NdBaCo_2O_{5.47}$. *Physical Review B*, **66**, 184421/1–184421/5.

Fazekas, P. (1999). *Lecture Notes on Electron Correlations and Magnetism*, *Series in Modern Condensed Matter Physics – Vol. 5*, World Scientific Publishing: Singapore.

Fiebig, M. (2005). Revival of the magnetoelectric effect *Journal of Physics D: Applied Physics*, **38**, R123–R152.

Frontera, C., Garcia-Munoz, J.L., Llobet, A. and Aranda, M.A.G. (2002). Selective spin-state switch and metal-insulator transition in $GdBaCo_2O_{5.5}$. *Physical Review B*, **65**, 180405/1–180405/4.

Garcia-Martin, S., Morata-Orrantia, A., Aguirre, M.H. and Alario-Franco, M.A. (2005). Giant barrier layer capacitance effects in the lithium ion conducting material $La_{0.67}Li_{0.25}Ti_{0.75}Al_{0.25}O_3$. *Applied Physics Letters*, **86**, 043110/1–043110/3.

Hemberger, J., Lunkenheimer, P., Fichtl, R., *et al*. (2005). Relaxor ferroelectricity and colossal magnetocapacitive coupling in ferromagnetic $CdCr_2S_4$. *Nature*, **434**, 364–367.

Higashiyama, D., Kida, N., Miyasaka, S., *et al*. (2004). Control of the ferroelectric properties of $DyMn_2O_5$ by magnetic fields. *Physical Review B*, **70**, 174405/1–174405/7.

Höchli, U.T., Knorr, K. and Loidl, A. (1990). Orientational glasses. *Advances in Physics*, **39**, 405–615.

Imada, M., Fujimori, A. and Tokura, Y. (1998). Metal-insulator transitions. *Reviews of Modern Physics*, **70**, 1039–1263.

Inorganic Crystallographic Structure Database (ICSD). (2005). Copyright © 2005 by FIZ Karlsruhe, Germany. http:www.fiz-karlsruhe.de/ecid/Internet/en/DB/icsd/index.html.

Keimer, B. and Oles, A.M. (2004). Editorial and contributions to the *Focus on Orbital Physics*, *New Journal of Physics*, **6**, 1367–2630. http://www.iop.org/EJ/abstract/1367-2630/6/1/E05.

Kimura, T., Goto, T., Shintani, H., *et al*. (2003). Magnetic control of ferroelectric polarization. *Nature*, **426**, 55–58.

Korotin, M.A., Ezhov, S.Yu., Solovyev, I.V., *et al*. (1996). Intermediate-spin state and properties of $LaCoO_3$. *Physical Review B*, **54**, 5309–5316.

Lemmens, P., Güntherodt, G. and Gros, C. (2003). Magnetic light scattering in low-dimensional quantum systems. *Physics Reports*, **375**, 1–103.

Lemmens, P. and Millet, P. (2004). Spin – orbit – topology, a triptych. In *Quantum Magnetism – Lecture Notes in Physics*, Schollwöck, U., Richter, J., Farell, B.J.J. and Bishop, R.F. (Eds.), Springer-Verlag: Heidelberg.

Lunkenheimer, P., Bobnar, V., Pronin, A.V., *et al*. (2002). Origin of apparent colossal dielectric constants. *Physical Review B*, **66**, 052105/1–052105/4.

Lunkenheimer, P., Schneider, U., Brand, R. and Loidl, A. (2000). Glassy dynamics. *Contemporary Physics*, **41**, 15–36.

Müller, U. (1993). *Inorganic Structural Chemistry*, John Wiley & Sons: Chichester.

Orenstein, J. and Millis, A.J. (2000). Advances in the physics of high-temperature superconductivity. *Science*, **288**, 468–474.

Plakhty, V.P., Chernenkov, Yu.P., Barilo, S.N., *et al*. (2005). Spin structure and magnetic phase transitions in $TbBaCo_2O_{5.5}$. *Physical Review B*, **71**, 214407/1–214407/14.

Ramirez, A.P., Subramanian, M.A., Gardel, M., *et al*. (2000). Giant dielectric constant response in a copper titanate. *Solid State Communications*, **115**, 217–220.

Salamon, M.B. and Jaime, M. (2001). The physics of manganites: structure and transport. *Reviews of Modern Physics*, **73**, 583–628.

Schmid, H. (1994). Multi-ferroic magnetoelectrics. *Ferroelectrics*, **162**, 665–686.

Shirane, G. (1974). Neutron scattering studies of structural phase transitions at Brookhaven. *Reviews of Modern Physics*, **46**, 437–449.

Spaldin, N.A. (2004). Materials science: fundamental size limits in ferroelectricity. *Science*, **304**, 1606–1607.

Tokura, Y. (2003). Correlated-electron physics in transition-metal oxides. *Physics Today*, **56**, 50–55.

Tokura, Y. and Tomioka, Y. (1999). Colossal magnetoresistive manganites. *Journal of Magnetism and Magnetic Materials*, **200**, 1–23.

Vidya, R., Ravindran, P., Vajeeston, P., *et al*. (2004). Effect of oxygen stoichiometry on spin, charge, and orbital ordering in manganites. *Physical Review B*, **69**, 092405/1–092405/4.

Wells, A.F. (1995). *Structural Inorganic Chemistry*, Oxford Science Publications: London.

Zheng, H., Wang, J., Lofland, S.E., *et al*. (2004). Multiferroic $BaTiO_3$-$CoFe_2O_4$ nanostructures. *Science*, **303**, 661–663.

Dilute Magnetic Oxides and Nitrides

John Michael David Coey and Karsten Rode
Trinity College, Dublin 2, Ireland

1 INTRODUCTION

The magnetism of oxides was long regarded as an important, but well understood and uninspiring branch of magnetism from which little that was new could be expected. The sources of magnetism in transition-metal and rare-earth oxides are the metal cations, which bear a magnetic moment due to unpaired electrons in the 3d shells, or sometimes in the 4d shell. The number of electrons per cation is integral, and the moments are well localized on the ions. The oxides are usually insulators or wide-gap semiconductors. Electrons or holes, introduced by doping or nonstoichiometry, are often trapped, and do not contribute to the conductivity.

The crystal structures of oxides are frequently based on a close-packed lattice of oxygen anions (ionic radius 140 pm) where the 3d cations occupy the octahedral interstices with six oxygen neighbors, or the tetrahedral interstices with four oxygen neighbors. The larger cations show some preference for the octahedral sites. The 4f ions have a greater coordination number, and may even take the place of an anion in the close-packed oxygen lattice.

The primary band gap E_p in 3d oxides is between the filled oxygen 2p valence band, corresponding to O^{2-} ions, and the empty conduction band of 4s character, formed from the transition-metal states. The localized 3d levels lie in the gap (see Figure 1). The magnitude of E_p decreases on moving along the 3d series from 8.1 eV for TiO_2 or 5.7 eV for Sc_2O_3 to 3.4 eV for ZnO or 4.9 eV for Ga_2O_3. The measured band gap E_g can be much less than E_p because of the possibility of p–d, or d–s transitions. A list of common 3d cations, for which a localized electron picture is appropriate is given in Table 1.

The wave functions of the 3d cations have exponentially decaying tails, which ensures that there is negligible overlap between cations which are not nearest neighbors. These neighbors share one or more common coordinating oxygen anion. Hence the magnetic exchange coupling is essentially an affair of nearest-neighbor cations, with an intervening oxygen. These are known as *superexchange interactions*.

A dilute oxide has the general formula

$$(M_xN_{1-x})O_n \tag{1}$$

where M is a magnetic cation, N is a nonmagnetic cation, n is an integer or rational fraction, and x is the magnetic doping level $0 \leq x \leq 1$, which will usually be expressed here in percent. An important limit is x_p, the percolation threshold (Stauffer, 1985), where continuous nearest-neighbor paths first appear which link M cations throughout the crystal. Below x_p there are only isolated cations, and small clusters of nearest-neighbor pairs, triplets, and so on. Above x_p there is a bulk cluster, which encompasses most of the magnetic cations. Whenever the exchange interactions only involve nearest neighbors, there is no possibility of long-range order below x_p, the percolation threshold, approximately $2/Z_0$

Handbook of Magnetism and Advanced Magnetic Materials. Edited by Helmut Kronmüller and Stuart Parkin. Volume 4: *Novel Materials*. ISBN: 978-0-470-02217-7.

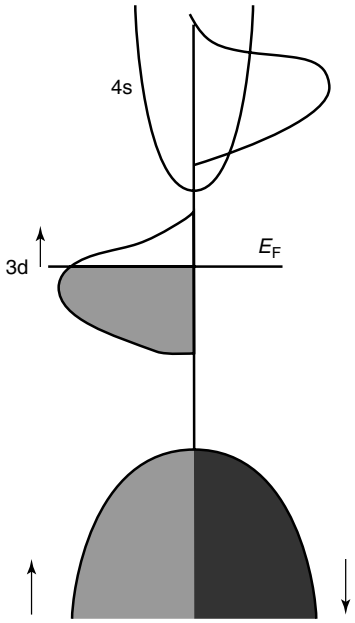

Figure 1. Generic electronic structure diagram for a 3d metal oxide.

Table 1. Charge state, electronic configuration, ionic radius in O_h coordination for common magnetic and nonmagnetic cations in oxides.

Cation	Charge state	Configuration	Ionic radius (pm)
Sc	3^+	$3d^0$	83
Ti	$3^+/4^+$	$3d^0/3d^1$	61/69
V	2^+	$3d^3$	72
Cr	3^+	$3d^3$	64
Mn	$2^+/3^+/4^+$	$3d^5/3d^4/3d^3$	83/65/53
Fe	$2^+/3^+$	$3d^6/3d^5$	82/65
Co	$2^+/3^+$	$3d^7/3d^6$	82/61
Ni	$2^+/3^+$	$3d^8/3d^7$	78/69
Cu	2^+	$3d^9$	72

(Deutscher, Zallen and Adler, 1983), where Z_0 is the cation coordination number. Depending on the structure, Z_0 lies between 6 and 12, which means that x_p is in the range 16 to 33%.

It therefore came as a surprise when a series of reports, beginning with that of Masumoto *et al*. (2001a), claimed that oxides with only a few percent of magnetic cations, usually 1–10%, were ferromagnetically ordered at room temperature. The first samples were all *thin films*. Table 2 lists some of these early reports.

These results were surprising for at least three reasons:

1. The magnetic order appears in films where the doping is far below x_p.
2. The magnetic order is ferromagnetic, whereas the superexchange in oxides is usually antiferromagnetic.
3. The films are ferromagnetic at room temperature and above, although no such dilute magnetic oxide or semiconductor, and no dilute magnetic metal had ever been found to be magnetically ordered at room temperature. (An exception is Pd, which has a greatly enhanced Pauli paramagnetism and by itself almost satisfies the Stoner criterion for the appearance of magnetism.)

In these circumstances the claims of ferromagnetism in these films were regarded with scepticism, and the conviction that high-temperature ferromagnetism must somehow be associated with a segregated impurity phase. In some of the samples, secondary phases in the form of cobalt clusters, Mn–Ga alloys or nanoparticles of Fe_3O_4 were indeed found. In other systems such a V-doped ZnO there are no known ferromagnetic phases in the ternary system. For this, and other reasons discussed below, one is led to consider the high-temperature ferromagnetism of dilute oxides and nitrides as a new and significant magnetic phenomenon.

2 MAGNETIC INTERACTIONS IN OXIDES

The principal magnetic interaction in oxides is superexchange. The coupling between the spins of two cations occurs via the intervening oxygen, as shown schematically for the $Mn^{2+} - O^{2-} - Mn^{2+}$ bond in Figure 2. The Mn has a half-filled 3d shell, so only minority-spin electron transfer from the oxygen to the manganese is possible. A 2p electron with $\downarrow$ is transferred to the Mn on the left, leaving a $2p\downarrow$ hole, which can be filled by an electron from the other Mn, provided it is $\downarrow$. Superexchange theory leads to a Heisenberg-type Hamiltonian

$$H = -2J\mathbf{S}_i \cdot \mathbf{S}_j \tag{2}$$

where the exchange constant $J = J_0 \cos^2\theta$ where θ is the superexchange bond angle and $J_0 = t^2/U$, where t is the M–O transfer integral and U is the on-site Coulomb interaction for the M ion. Typically, $t \approx 0.1$ eV and $U \approx 5$ eV. Hence the order of magnitude of the exchange constant is 2 meV or 20 K.

The expression for the Curie temperature in mean-field theory is

$$T_C = \frac{2ZJS(S+1)}{3k} \tag{3}$$

Hence, if $S = 5/2$, the largest value possible in the 3d series, and the cation coordination number $Z = 8$, we find

Table 2. Dilute ferromagnetic oxide thin films with T_C above room temperature.

Material	E_g (eV)	Doping	Moment (μ_B)	T_C (K)	Reference
GaN	3.5	Mn – 9%	0.9	940	Sonoda *et al*. (2002)
		Cr	–	>400	Hashimoto, Zhou, Kanamura and Asahi (2002)
		Gd – 6%		>400	Teraguchi *et al*. (2002)
AlN	4.3	Cr – 7%	1.2	>600	Wu *et al*. (2003)
TiO_2	3.2	V – 5%	4.2	>400	Hong *et al*. (2004)
		Co – 1–2%	0.3	>300	Masumoto *et al*. (2001a)
		Co – 7%	1.4	>650	Shinde *et al*. (2003)
		Fe – 2%	2.4	300	Wang *et al*. (2003)
SnO_2	3.5	Fe – 5%	1.8	610	Coey, Douvalis, Fitzgerald and Venkatesan (2004)
		Co – 5%	7.5	650	Ogale *et al*. (2003)
ZnO	3.3	V – 15 %	0.5	>350	Saeki, Tabata and Kawai (2001)
		Mn – 2.2%	0.16	>300	Sharma *et al*. (2003)
		Fe – 5%, Cu – 1%	0.75	550	Han *et al*. (2002)
		Co – 10%	2.0	280–300	Ueda, Tabata and Kawai (2001)
		Ni – 0.9%	0.06	>300	Radovanovic and Gamelin (2003)
Cu_2O	2.0	Co – 5%, Al – 0.5%	0.2	>300	Kale *et al*. (2003)

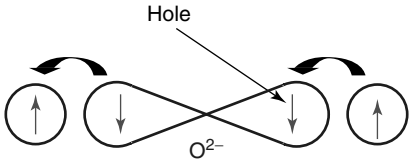

Figure 2. Superexchange interaction between ions with more than half-filled d shells via an O^{2-} anion.

$T_C \approx 800$ K. In practice, the superexchange interactions are often frustrated – the antiparallel coupling of all nearest neighbors cannot be achieved for geometric reasons imposed by the topology of the lattice. Furthermore, equation (3) is known to overestimate T_C by about 30%. In practice, the magnetic ordering temperatures of oxides do not exceed 1000 K. Hematite – α-Fe_2O_3 – has a Néel temperature of 960 K. In most cases the magnetic ordering temperatures of oxides are a few hundred kelvin, at best. When they are diluted with nonmagnetic cations, the coordination number $Z = Z_0x$ is reduced, and T_C varies as x above the percolation threshold (Figure 3).

The validity of the Heisenberg model in oxides has been amply demonstrated by fitting the exchange constants to the spin-wave dispersion relations determined by inelastic neutron scattering. Complete data sets have been obtained for Fe_2O_3, Cr_2O_3, and Fe_3O_4, among others (Samuelsen and Shirane, 1970; Samuelsen, Hutchings and Shirane, 1970; Bourdonnay *et al*., 1970). The values of the exchange constants range from -30 K to $+6$ K in α-Fe_2O_3. Negative interactions are for superexchange bonds involving the same ions, with large bond angles. Positive values are for bonds involving ions in different valence states, or near 90° bonds between ions in the same valence state.

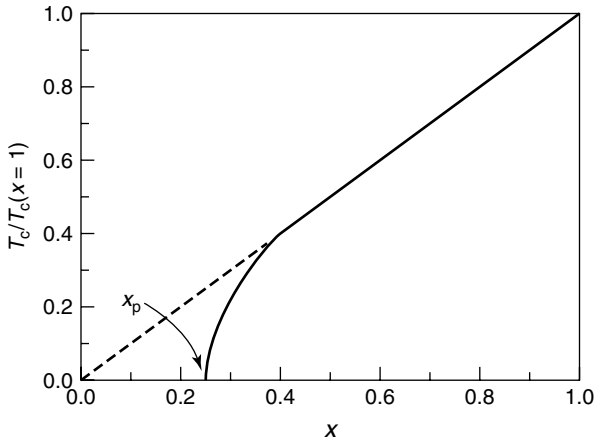

Figure 3. Variation of the magnetic ordering temperature in a dilute magnetic oxide with nearest-neighbor superexchange interactions. The dotted line is the prediction of mean-field theory for long-range interactions.

During the 1960s, a wealth of information was accumulated on the nature of the exchange interactions between different cations for different superexchange bond angles. An extensive set of rules was formulated by Goodenough (1955) and Kanamori (1959). These rules were simplified by Anderson (1963), as follows:

1. 180° exchange between half-filled orbits is strong and antiferromagnetic.
2. 90° exchange between half-filled orbits is ferromagnetic, and rather weak.
3. Exchange between a half-filled and an empty orbital of different symmetry is ferromagnetic and rather weak.

To summarize, concentrated magnetic oxides are well described in terms of the *m*-J paradigm: there are localized magnetic moments *m* on the cations, and superexchange interactions couple them together. The paradigm provides a good account of the magnetic order and the spin waves. Magnetocrystalline anisotropy in oxides is also well understood, in terms of crystal-field theory. The electric field acting on the localized electron shell of a 3d ion can be expressed as a multipole expansion where the second derivatives of the potential couple with the electric quadrupole moment of the ionic charge distribution, and the fourth derivatives with the hexadecapole moments (Hutchings, 1964). The leading term in the expansion is

$$H_{\mathrm{cf}} = \theta_2 < r_2 > A_2{}^0 \hat{\mathbf{O}}_2{}^0 \approx D\hat{\mathbf{S}}_{\mathbf{Z}}{}^2 \tag{4}$$

where $\hat{\mathbf{O}}_n{}^m$ is the Stevens operator equivalent, a method used to evaluate the matrix element of the wave function corresponding to a particular value of J (described in some detail in Hutchings (1964)). In a site with uniaxial anisotropy, $\hat{\mathbf{O}}_2{}^0$ is equivalent to $(3\mathbf{J}_{\mathbf{Z}} - J(J+1))$. θ_2 is the reduced matrix element known as the *Stevens parameter*. For the 4f series, J is a good quantum number, and the sixth order terms may need to be taken into account for ions with $J > 5/2$. Typically, the crystal-field parameter D, the zero field spin-orbit splitting of the ground state, for non-S-state ions is of order λ^2/Δ, where λ is the spin-orbit coupling and Δ is the crystal-field splitting. This ratio is of order 1 K. The small magnitude of this interactions means that an applied magnetic field of order 1 T will suffice to saturate the magnetization in a hard direction.

Nitrides are rather different, in that the ionic model does not suit them so well. The large, highly charged N^{3+} ion does not really exist. Such configurations are inevitably screened, and have a strongly covalent character. The ionic model is a plausible starting point for compounds such as RN, where R is a trivalent 4f cation, or an ion such as Ga^{3+} or Al^{3+}. In interstitial compounds such as Fe_4N, the nitrogen is in an uncharged, atomiclike state, where it is actually smaller than the surrounding iron atoms.

3 MAGNETIC PROPERTIES OF DILUTE OXIDES AND NITRIDES

First, it is useful to summarize the behavior which is normally expected from a dilute magnetic oxide. A random distribution of magnetic dopant ions is illustrated schematically in Figure 4(a). At low concentrations, most of the dopants are isolated, with no magnetic nearest neighbors, and a Curie-law susceptibility is expected.

$$\chi = \frac{\mu_0 N x g^2 \mu_{\mathrm{B}}{}^2 S(S+1)}{3kT} \tag{5}$$

As the concentration increases, there will be an increasing proportion of dimers and larger groups. The dimers and other even-membered groups have a Curie–Weiss susceptibility

$$\chi = \frac{\mu_0 N x_2 g^2 \mu_{\mathrm{B}}{}^2 S(S+1)}{3k(T-\theta)} \tag{6}$$

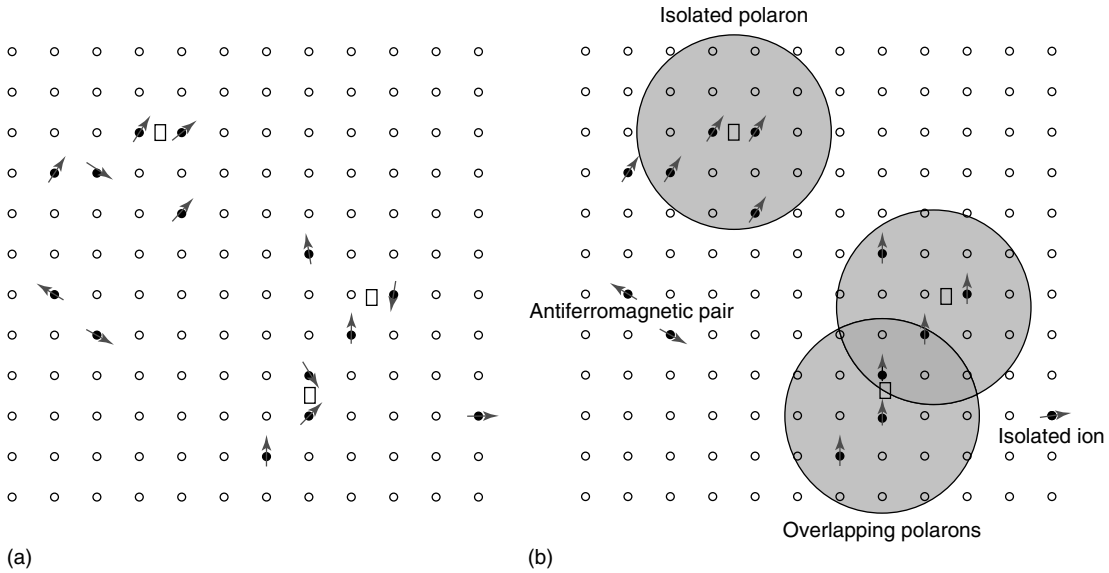

Figure 4. (a) Schematic representation of distribution of dopant ions in a dilute magnetic semiconductor. (b) The same, but with donor defects which create magnetic polarons where the dopant ions are coupled ferromagnetically.

where θ is a negative constant of order 10–100 K, which is proportional to the antiferromagnetic exchange coupling J_0. The odd-membered groups with a net moment contribute a modified Curie-law susceptibility. With all this, deviations from a linear response to an applied field of up to 1 T, for example, are only perceptible below about 10 K. The room-temperature dimensionless susceptibility is of order $10^{-3}x$. Such is the behavior normally expected of a dilute magnetic oxide. This is what is actually found in bulk crystalline materials and in well-crystallized, defect-free thin films. There are numerous examples in the literature of this 'normal' behavior, for example, Sati *et al*. (2006), Pacuski *et al*. (2006), and Rao and Deepak (2005).

We now present experimental results on the dilute oxides and nitrides, which can exhibit an anomalous ferromagnetic behavior when they are in thin-film or nanocrystalline form. The crystal structures of host materials are presented in Figure 5. Some structural details are given in Table 3, including the percolation threshold x_p and the cation site symmetry. The band gap E_g is listed, together with the high-frequency dielectric constant. The main systems will be discussed in turn.

Magnetization measurements on thin films deposited on substrates, which are the samples of most interest in the present context, present something of a challenge. There is a huge mismatch between mass of the thin-film sample – typically some tens of micrograms – and that of the substrate – which is about a thousand times greater. Commonly used substrates include sapphire (Al_2O_3), MgO, $SrTiO_3$, $LaAlO_3$, and Si. The problem is illustrated in Figure 6. The substrate presents a diamagnetic signal, which is perhaps reproducible to within 1% given the uncertainties in positioning and centering the substrate in the superconducting quantum interference device (SQUID) magnetometer, vibrating-sample magnetometer (VSM), or alternating-gradient force magnetometer (AGFM) used to measure the hysteresis loop. It is therefore practically impossible to determine the diamagnetic susceptibility of the undoped film. A Curie-law signal due to paramagnetic dopant ions can be readily detected at low temperatures, but it is difficult to measure any high-field slope that may be associated with the ferromagnetic signal. The diamagnetic susceptibility of some common substrate materials is listed in Table 4.

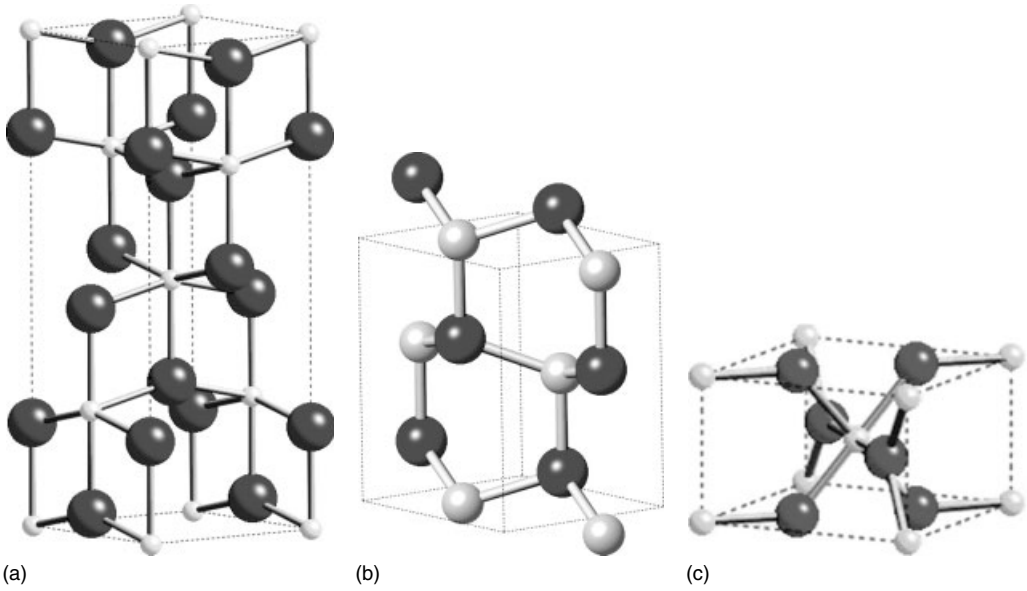

Figure 5. Crystal structures of host semiconductors: (a) TiO_2 (anatase), (b) ZnO or GaN (wurtzite), (c) SnO_2 or TiO_2 (rutile). Oxygen in dark spheres, cations in light spheres.

Table 3. Parameters for some oxides.

Material	Structure	n_c (10^{28} m^{-3})	ε	m^*/m	E_g (eV)	C	x_p
ZnO	Wurtzite	3.94	4.0	0.28	3.4	Tetrahedral	0.18
TiO_2	Anatase	2.93	9.0	1.0	3.2	Octahedral	0.25
SnO_2	Rutile	2.80	3.9	0.24	3.6	Octahedral	0.25

n_c: cation density; ε: high-frequency dielectric constant; E_g: optical band gap; C: cation coordination; x_p: cation percolation threshold.

Table 4. Diamagnetic susceptibility of some substrate materials (room temperature) $\chi = \mathrm{M/H}$ is the dimensionless SI susceptibility. To obtain the mass susceptibility (units $\mathrm{m^3\,kg^{-1}}$) divide by the density. To convert to dimensionless cgs susceptibility (emu $\mathrm{cm^{-3}}$) divide χ by 4π.

Material	Density (kg $\mathrm{m^{-3}}$)	χ (10^{-6})
Al_2O_3	3960	−19
MgO	3600	−14
$SrTiO_3$	5120	−7.1
$LaAlO_3$	6510	−18
Si	2329	−4.1
SiC	3210	−13

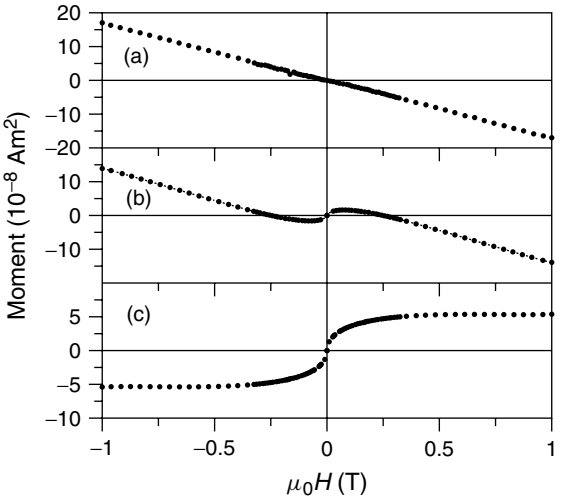

Figure 6. Data reduction for magnetization measurements on a thin film of a dilute magnetic oxide or nitride. (a) Diamagnetic substrate, (b) ferromagnetic thin film with diamagnetic substrate, (c) ferromagnetic component isolated from (b).

The measured response for a ferromagnetic thin film is shown in Figure 6(b). The magnetization appears to saturate in a field of order 1 T, and the high-field slope becomes that of the substrate, within experimental error. The procedure is then to suppose that the magnetization is indeed saturated and to subtract the high-field diamagnetic slope as the substrate correction, yielding the magnetization curve for the film shown in Figure 6(c). Typically, these 'ferromagnetic' hysteresis loops for dilute magnetic oxides exhibit little coercivity (≈ 10 mT), and a small remanence ratio ($M_\mathrm{r}/M_\mathrm{s} \approx$ 5–10%) [1]. The magnetization of the samples is often given in units of Bohr magnetons per transition metal (TM) ion by normalizing the measured magnetic moment by the number of TM ions supposedly in the sample. This unit is useful when comparing different doping concentrations and also when comparing different host materials, if the TM concentration is accurately known.

3.1 ZnO

ZnO is a promising semiconductor material with a band gap of 3.37 eV. It has a natural tendency to be n-type on account of oxygen vacancies or interstitial zinc atoms in the wurtzite structure. Recently, it has been possible to make nitrogen-doped p-type material, which opens the way to producing light-emitting diodes and laser diodes. An extensive review of the semiconducting properties of ZnO is available (Ozgur *et al*., 2005).

Various cations can replace zinc in the structure. The Co^{2+} ion gives a characteristic pattern of optical absorption in the band gap, due to crystal-field transitions of the ion in tetrahedral coordination. Studies of the magnetic properties of bulk material doped with Co (Rao and Deepak, 2005; Bouloudenine *et al*., 2005) or Mn (Alaria *et al*., 2005) show only the paramagnetism expected for isolated ions and small antiferromagnetically coupled nearest-neighbor clusters which arise statistically at a low doping level, as discussed above (Figure 5a).

The range of solid solubility of cations of the 3d series in ZnO films prepared by pulsed-laser deposition was established by Jin *et al*. (2001); solubility limits as high as 15% were found for Co, but most other cations could be introduced at the 5% level. None of these films were found to be magnetic, but following Ueda, Tabata and Kawai, (2001), who were the first to report high-temperature ferromagnetism in films doped with Co at the 10% level, there have been numerous reports of ferromagnetic moments in films doped with Co (See among others Janisch, Gopal and Spaldin, 2005; Prellier, Fouchet and Mercey, 2003; Pearton *et al*., 2004 and references therein), as well as almost every other 3d dopant from Sc to Ni (Sharma *et al*., 2003; Venkatesan *et al*., 2004b; Saeki, Tabata and Kawai, 2001; Radovanovic and Gamelin, 2003) (Figure 7). It must be emphasized that there are no reports of magnetism in undoped ZnO films,

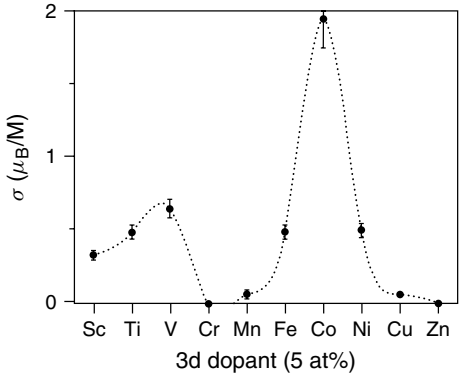

Figure 7. Magnetic moment measured at room temperature for ZnO with various 3d dopants. (Reprinted with permission M. Venkatesan *et al*., copyright 2004, Nature Publishing Group.)

however, prepared. There are also numerous counterexamples where no room-temperature moment has been found in doped films. Negative results tend to be underreported in the literature, so the observation of ferromagnetism in ZnO films is probably less prevalent than one might imagine. It is very sensitive to the deposition conditions (Ozgur *et al*., 2005). However, nanoparticles and nanorods of ZnO with cobalt and other dopants have also been found to be magnetic under certain process conditions (Martinez *et al*., 2005), although the moments per cobalt atom are an order of magnitude less than those found for the thin films, which are typically $0.1-1\ \mu_B$/Co.

Some progress has been made toward providing a systematic experimental account of the phenomenon. Narrow process windows have been delimited where ferromagnetism can be observed, depending on the deposition method – pulsed-laser deposition, sputtering, evaporation, organometallic chemical vapor deposition, and others. With Cr and Mn, for example, it is difficult to produce ferromagnetic moments in n-type material, whereas p-type samples can exhibit the symptoms (Kittilstved, Liu and Gamelin, 2006) (Figure 8). The substrate temperature required for ferromagnetism is often around 400 °C, where the films are not of the best crystalline quality. This points to a defect-related origin of the magnetism (Khare *et al*., 2006). Other evidence in this sense comes from the appearance of magnetism in Zn-doped (Halliburton *et al*., 2005; Schwartz and Gamelin, 2004), or in oxygen-deficient (Patterson, 2006) films.

The evidence that Co-doped ZnO is an intrinsically ferromagnetic semiconductor is rather sparse. No magnetoresistance has been observed at room temperature, despite the high T_C, nor is there clear evidence of an anomalous Hall effect. Magnetoresistance can, however, be observed below

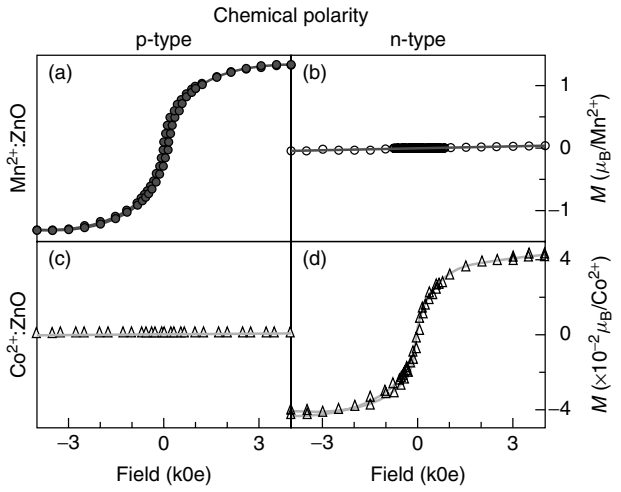

Figure 8. Development of magnetism in n-type ZnO with Co or p-type ZnO with Mn. (Reprinted with permission K.R. Kittilstved *et al*., copyright 2006, Nature Publishing Group.)

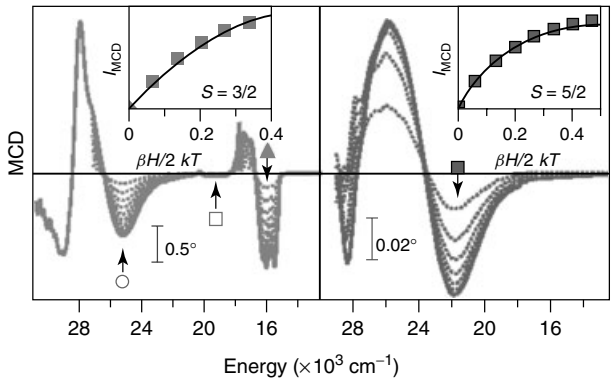

Figure 9. MCD spectra and the magnetic field dependence of the intensity of the MCD signal (insets) recorded at different energies in ZnO doped with Co (left) and Mn (right). (Reprinted with permission K.R. Kittilstved *et al*., copyright 2006, Nature Publishing Group.)

about 30 K (Stamenov *et al*., 2006). Furthermore, there is a band-edge magnetic dichroism which exhibits ferromagnetic response (Kittilstved, Liu and Gamelin, 2006; Neal *et al*., 2006), as well as a paramagnetic dichroic response from the dilute Co^{2+} ions in tetrahedral sites in the wurtzite lattice, Figure 9 (Kittilstved, Liu and Gamelin, 2006). The ferromagnetic dichroism has been observed for Ti and Co (Figure 10) and also for V and Mn doping (Neal *et al*., 2006). The interaction between the conduction electrons and the Co spins seems to be rather weak, and the magnetic properties are little influenced by changing the carrier concentration, by Al doping, for example Venkatesan *et al*. (2006).

A problem in interpreting the magnetic data for some dopants is the tendency to form ferromagnetic impurity phases, which may escape detection by X rays. For cobalt, in particular, absence of evidence cannot be taken as evidence of absence. There is a tendency for nanometric coherent cobalt precipitates to appear in the ZnO films which exhibit ferromagnetic properties (Park *et al*., 2004). An impurity-based explanation ($Mn_{2-x}Zn_xO_3$) has been advanced also for Mn-doped material (Kundaliya *et al*., 2004). For other dopants, such as vanadium, contamination by high-temperature ferromagnetic impurity phases seems improbable.

In some cases, there are features of the data which make an impurity-phase explanation untenable. These are (i) observation of a moment per transition-metal ion greater than that of any possible ferromagnetic impurity phase based on the dopant ion, and which may exceed the spin-only moment of the cation, and (ii) observation of an anisotropy of the magnetization, measured in different directions relative to the crystal axes of the film, which is not a feature of any known ferromagnetic phase at room temperature. An example is shown in Figure 11.

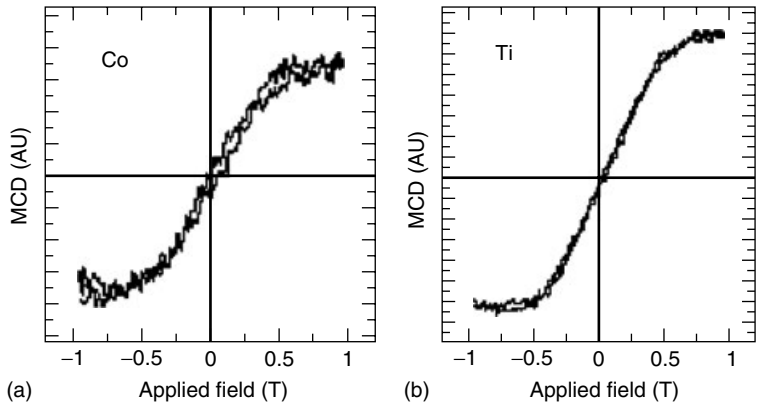

Figure 10. Magnetic field dependence of the intensity of the MCD signal recorded at the ZnO band edge. Co-doped ZnO (a) and Ti-doped ZnO (b). (Reprinted with permission Neal *et al*., copyright 2006, American Physical Society.)

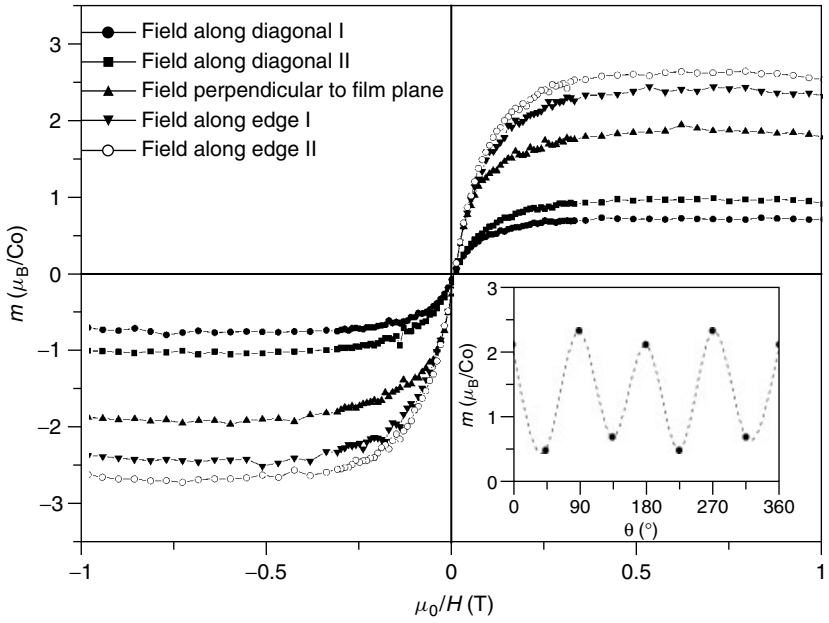

Figure 11. Anisotropy of the magnetization of a film of $(Zn_{0.95}Co_{0.05})O$.

The tunnel spin polarization of transition-metal-doped ZnO has been measured (Rode, 2006). Although poorly reproducible, these results are in line with the observation of magnetic circular dichroism (MCD) on the band edge as discussed above. The possibility of obtaining and manipulating a spin current in ZnO could be of great interest, as the spin lifetime in ZnO is rather long (Ghosh *et al*., 2005).

3.2 TiO_2

Anatase with 1–2% Co doping was the first example of high-temperature ferromagnetism in a dilute oxide film (Masumoto *et al*., 2001a). The same group reported ferromagnetism in rutile films (Masumoto *et al*., 2001b). The solubility of aliovalent Co in these oxides is low, and there is the possibility of cobalt-metal clustering (Kim *et al*., 2003; Stampe, Kennedy, Xin and Parker, 2003). But films can be prepared which are apparently free of clusters, and exhibit ferromagnetism (Shinde *et al*., 2003; Bryan, Heald, Chambers and Gamelin, 2004). Other evidence that Co-doped TiO_2 may be intrinsically ferromagnetic, and carrier mediated include electric-field modulation of the magnetization (Zhao *et al*., 2005), observation of band-edge optical dichroism (Toyosaki *et al*., 2005a), anomalous Hall effect (Toyosaki *et al*., 2004) as well as tunnel magnetoresistance (Toyosaki *et al*., 2005b).

Other cation dopants reported to make TiO_2 ferromagnetic include V (Hong *et al*., 2004) and Cr (Chambers and Farrow, 2003). It is found that highly perfect Cr-doped TiO_2 films are

not ferromagnetic, whereas films with structural defects may be (Kaspar *et al*., 2005). The Cr is trivalent in TiO_2 films, and the magnetization is highly anisotropic (Osterwalder *et al*., 2005).

TiO_2, unlike ZnO or SnO_2 is usually quite insulating in thin-film form, which indicates that delocalized, conduction electrons are not necessary for the high-temperature ferromagnetism.

3.3 SnO_2

First reports of high-temperature ferromagnetism in SnO_2 films came from Ogale *et al*. (2003), who reported a Curie temperature of 650 K and a huge moment of 7.5 μ_B/Co for films doped with 5%. Subsequently, ferromagnetism was observed for films doped with V, Cr Mn, Fe, and Ni, as well as Co, (Hong *et al*., 2005b; Coey, Douvalis, Fitzgerald and Venkatesan, 2004; Hong *et al*., 2005c), and in some of these cases the moments also exceed the cation spin-only values (Ogale *et al*., 2003; Fitzgerald *et al*., 2006). In the case of V doping, for example, the results have been shown to depend rather critically on the substrate employed (Hong *et al*., 2005c; Fitzgerald *et al*., 2006). The anisotropic magnetization and weak hysteresis found for doped ZnO or TiO_2 is also found for SnO_2. It seems to be a characteristic signature of the ferromagnetism in dilute oxides.

In the case of Fe-doped SnO_2 films, nanocrystalline Fe_3O_4 forms in some conditions, but it cannot be the complete explanation of ferromagnetism, when the moment exceeds 1.33 μ_B/Fe.

3.4 Other oxides

Room-temperature ferromagnetism has been reported in thin films of Cu_2O produced by sputtering (Kale *et al*., 2003) or electrodeposition (Liu *et al*., 2005).

Indium oxide doped with Cr is a promising system. Moments of 1.5 μ_B/Cr are found, and there seems to be little prospect of contamination of the films by ferromagnetic impurities. (CrO_2 is ferromagnetic, with $T_C = 390$ K, but T_C is reported as 900 K). An anomalous Hall signal is observed at room temperature, and the magnetism is related to the carrier concentration (Philip *et al*., 2006).

Indium tin oxide, the well-known transparent conductor is ferromagnetic when doped with Mn (Philip *et al*., 2004).

Ferromagnetic behaviour has been observed for HfO_2 doped with Fe or Co doping (Coey *et al*., 2005; Hong *et al*., 2005a). HfO_2 is an example of a material which is magnetic in thin-film form even when undoped (Coey *et al*., 2005; Venkatesan *et al*., 2004a). See the following text.

Another interesting oxide is $LaSrTiO_3$. This metallic oxide is ferromagnetic when doped with Co and also shows tunnel spin polarization (Herranz *et al*., 2006a,b).

3.5 d^0 systems

There is some evidence that it is possible to achieve ferromagnetism an *undoped* defective oxides. Thin films of HfO_2 show weakly hysteretic ferromagnetism when prepared on various substrates, with magnetizations of up to 30 k Am^{-1}. (Hong *et al*., 2005a; Coey *et al*., 2005). This is perhaps misleading, as the magnetization does not scale with substrate thickness. Typically it can be 200–400 μ_B nm^{-2}. Other systems where ferromagnetism has been reported in thin films include anatase-TiO_2 (Hong, Sakai, Poirot and Brizé, 2006), CaB_6, SrB_6 (Dorneles *et al*., 2004), and reduced powders of HfO_2 and WO_3. On the other hand, investigations of alkaline earth oxides MgO, CaO, SrO, BaO, some of which have been predicted to exhibit ferromagnetism related to the presence of cation vacancies (Elfimov, Yunoki and Sawatzky, 2002), have thus far shown no sign of being magnetic.

3.6 Nitrides

The first reports of ferromagnetism in a dilute nitride were from Sonoda *et al*., who found $T_C = 960$ K in a film of GaN doped with 9% Mn (Sonoda *et al*., 2002). Such high doping makes one wary of Ga–Mn phases, which have high Curie points. Nevertheless, Cr-doped GaN and AlN are also reported to be high-temperature ferromagnets (Park *et al*., 2002; Wu *et al*., 2003), and there are no plausible ferromagnetic impurity phases in these systems.

More striking are the reports of ferromagnetism in GaN films grown by molecular-beam epitaxy and doped with Gd. First reports, which showed $T_C > 400$ K were for films with $x = 6\%$ (Dhar *et al*., 2005a). Subsequently, films were doped with Gd at the level of 10^{16}–10^{19} atoms/cm^3, which corresponds to $2 \times 10^{-7} < x < 0.0002$, and the system appears to order ferromagnetically, with a moment per Gd atom as high as 10^4 μ_B in the most dilute films (Dhar *et al*., 2005b). Here the Gd atoms are separated by an average distance of 4.5 to 45 nm, in a matrix which is nonconducting, yet they exhibit room-temperature ferromagnetism. The Gd, whether substitutional or interstitial, creates large strains in the piezoelectric GaN matrix.

4 DISCUSSION

The experimental picture is obscured by the difficulty in reproducing some of the experimental results, and the

difficulties in characterizing defects and interface states in the thin films, as well as the difficulty in detecting small amounts (≈ 1 wt%) of secondary phases. The anomalous ferromagnetism is not a feature of highly perfect films or bulk crystalline material.

The presence of ferromagnetic nanoparticles of a second phase with a high T_C is an important factor, and possibly the complete explanation of the ferromagnetism in certain cases. Co nanoparticles are difficult to detect, but Fe and Fe_3O_4 are readily picked up by Mossbauer spectroscopy. Other high-temperature ferromagnets are spinel phases, where the antiferromagnetic interactions lead to ferromagnetic structures where the moment does not exceed $1.5\,\mu_B$/magnetic cation. High-temperature nitride ferromagnets include Mn_4N, $MnGa_2$, and $MnGa_3$. Nevertheless, it seems improbable that impurity phases can be a general explanation. In some systems, there are no plausible candidates for ferromagnetic impurities, other than ubiquitous iron introduced by careless sample handling. Other arguments were given in Section 3.1.

Insofar as it is possible to generalize from the data at hand, the characteristic features of the high-temperature ferromagnetism in dilute oxides and nitrides are as follows:

The ferromagnetism exhibits very little hysteresis. The loop in Figure 6(c) is practically the same for any of the systems we have been discussing.

The films may be insulating or semiconducting; the semiconductors are usually n-type. They may be partially compensated, semiconducting, or degenerate. Coupling between the magnetism and the conduction electrons is weak.

The moment does not depend obviously on the film thickness or doping level when $x < x_p$. It is often $100–400\,\mu_B\,nm^{-2}$. The moment per dopant ion increases as x decreases, and it may exceed the spin-only value for the ion at low concentrations.

The ferromagnetism is already present in *some* undoped films, and in all films at concentrations that lie far below the percolation threshold associated with nearest-neighbor cation coupling. T_C can be far above RT.

The magnetism is highly anisotropic, in a way unrelated to the dopant, but dependent on the film/substrate combination.

The conventional picture of magnetism in insulators or magnetic semiconductors is at a loss to account for these observations. The Curie or Néel temperatures of oxides are plotted on a histogram in Figure 12. None of them exceed the Néel point of α-Fe_2O_3, which is 960 K. The ordering temperatures in solid solutions vary as x or as $x^{1/2}$. No order is expected at room temperature when $x < 10\%$, or in insulators when $x < x_p$. The magnetic behavior we would normally expect from the m-J paradigm is a superposition of Curie-law paramagnetism for isolated ions and Curie–Weiss behavior for the small, antiferromagnetically coupled groups of two, three, or more ions. Indeed, this is what is found in well-crystallized, bulk material (Rao and Deepak, 2005), but not in the ferromagnetic thin films of interest here.

Next we consider carrier-mediated exchange. In the first generation of n-type rare-earth magnetic semiconductors such as EuS, studied in the 1960s and 1970s (Methfessel and Mattis, 1968), the carriers are electrons in the spin-split

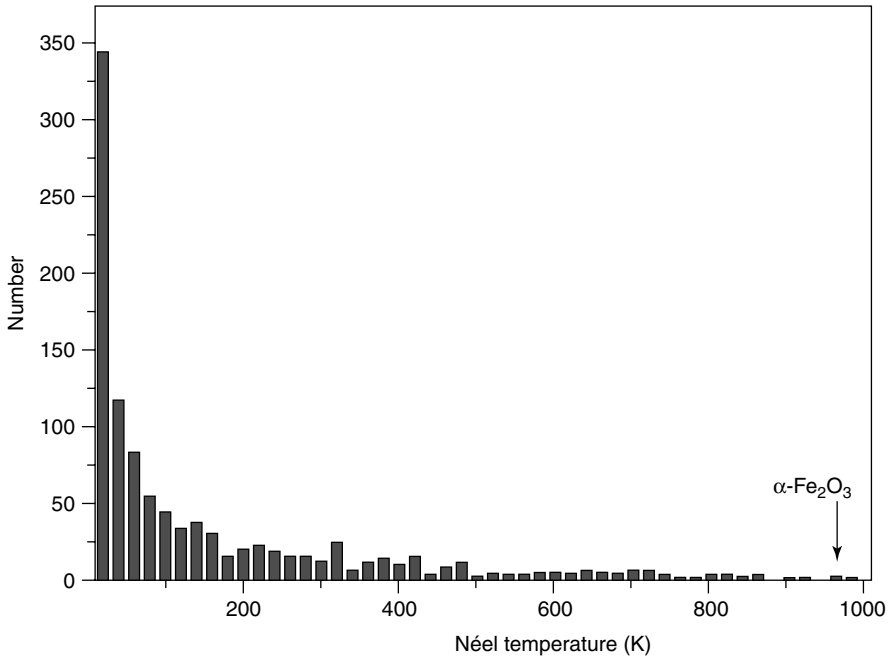

Figure 12. Histogram of the Néel temperature of a selection of magnetic oxides.

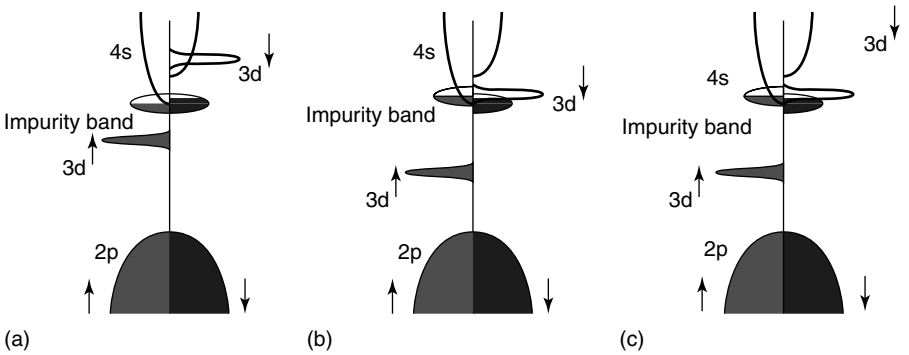

Figure 13. Spin-split impurity band model for dilute magnetic semiconductors. The electronic structure diagrams are drawn for cases where the impurity band is separated from (a), or resonant with (b and c) the d bands of the dopant.

5d/6s conduction band. In the next generation of p-type materials such as (GaMn)As, the carriers are holes in a spin-split 4p valence band. In an influential paper, Dietl *et al*. (2000) suggested that high Curie temperatures might be obtained in this way in p-type Mn-doped ZnO or GaN. These materials are usually n-type, however, and the s–d exchange interaction α is usually weaker than the p–d exchange interaction β.

A newer a model of magnetic semiconductors is one where exchange is propagated by a spin-split impurity band (Figure 13) derived from donor or acceptor defect states, which form magnetic polarons (Figure 5b). This has the virtue of yielding simple expressions for the Curie temperature when treated by molecular field theory (Coey, Venkatesan and Stamenov, 2005; Priour and Das Sarma, 2006)

$$T_{\mathrm{C}} = \left[\frac{S(S+1)s^2 x\delta}{3}\right]^{1/2} \frac{J_{\mathrm{sd}}\omega_{\mathrm{c}}}{k_{\mathrm{B}}} \tag{7}$$

Where S and s are the cation core spin and the donor spin respectively. δ is the donor or acceptor defect concentration and the cation volume fraction in the oxide $\omega_{\mathrm{c}} \approx 8\%$.

The problem is that, knowing the values of the parameters in the model, especially $J_{\mathrm{sd}} \approx 1\,\mathrm{eV}$, the predicted Curie temperatures are again of the order of 10 K, which are 1 or 2 orders of magnitude too low. The model can be modified by introducing hybridization and charge transfer from the donor orbitals to those of the dopants, but at some point in the dilute limit it has to fail, and a different approach is needed.

Small concentrations of conduction electrons do provide ferromagnetic coupling via the RKKY interaction, but an estimate of the magnitude of the magnetic ordering temperature due to this interaction is

$$T_{\mathrm{C}} \approx \frac{Z_0 n^{5/3} m^* \delta x^{1/3} J_{\mathrm{sf}}^2 S(S+1)}{(96\eth\hbar^2 n_{\mathrm{c}}^{2/3} k_{\mathrm{B}})} \tag{8}$$

The Curie temperature at elevated carrier concentrations, corresponding to about $10^{21}\,\mathrm{cm}^{-3}$, does not exceed a few tens of kelvin.

Some insight into the problem is provided by first-principles calculations for specific defects. Early calculations by Elfimov *et al*. for CaO (Elfimov, Yunoki and Sawatzky, 2002) indicated that a Ca vacancy could stabilize a moment on the adjacent oxygen ions where two holes coupled with parallel spin to form a triplet state. These extended molecular magnetic states were then shown to couple ferromagnetically to produce long-range order. A similar calculation for CaB_6 led to the prediction of defect-related ferromagnetism there too (Monnier and Delley, 2001), which has been observed in powders (Lofland *et al*., 2003) and amorphous films (Dorneles *et al*., 2004). In HfO_2, Das Pemmaraju and Sanvito (2005) have shown that an Hf vacancy induces a moment of $4\,\mu_{\mathrm{B}}$ on holes in the surrounding oxygen ions, and the coupling of these extended molecular magnetic objects is again ferromagnetic. Although no evidence of ferromagnetism in defective CaO has yet been found, the idea of oxygen-hole-related molecular magnetism has much to commend it.

Electronic defects associated with oxygen or nitrogen appear to be the most plausible source of the anomalous ferromagnetism in doped and undoped material. These holes are strongly correlated, and can form extended molecular orbitals. At least the *m* part of the *m*-J paradigm has to be revised. It is unclear whether the extended spin moments overlap sufficiently to provide the exchange necessary for high-temperature magnetism, or whether a quite different mechanism must be sought, based, for example, on elastic strain.

There have been numerous calculations in doped systems (Janisch, Gopal and Spaldin, 2005; Patterson, 2006; Gopal and Spaldin, 2006 and references therein). A critical feature in these systems is the position of the different 3d charge states relative to the primary band gap, which is difficult

to obtain accurately by density-functional theory methods. Some insight is provided by phenomenological theory (Kittilstved, Liu and Gamelin, 2006).

5 CONCLUSIONS

The magnetism of dilute magnetic oxides and nitrides is one of the most intriguing and potentially important open questions in magnetism at present. There is sufficient evidence that the observations are not, in most cases attributable to artifacts or trivial impurities. There is something to explain.

There appear to be two sources of the magnetism, defects and dopants. Both are usually necessary, but in the d^0 systems, the former suffice. The nature of the magnetic order and the coupling mechanism has to be explained, but it seems that the *m*-J paradigm for magnetism in solids is unable to encompass these materials.

On present evidence, the coupling between the 3d dopants and the conduction electrons in these systems is weak. There is evidence of intrinsic ferromagnetism, but useful magnetoresistive effects, for example, are not observed at room temperature. Applications of this new class of materials, which exhibit some sort of ferromagnetism above room temperature, optical transparency, and a wide range of transport properties ranging from degenerate semiconductor to insulator, remain to be identified.

NOTES

[1] $1\,\mathrm{Am^2} = 10^3\,\mathrm{emu}$; $1\,\mathrm{Am^2\,kg^{-1}} = 1\,\mathrm{emu\,g^{-1}}$; $1\,\mathrm{Am^{-1}} = 10^{-3}\,\mathrm{emu\,cm^{-3}}$; $1\,\mu_\mathrm{B}\ \mathrm{fu^{-1}} = 5585/\mathrm{MW\,Am^2\,kg^{-1}}$.

ACKNOWLEDGMENTS

This work was supported by Science Foundation Ireland and the EU, as part of the MANSE and Dynamics projects, respectively.

REFERENCES

Alaria, J., Turek, P., Bernard, M., *et al*. (2005). No ferromagnetism in Mn-doped ZnO semiconductors. *Chemical Physics Letters*, **415**, 337.

Anderson, P.W. (1963). Theory of magnetic exchange interactions: exchange in insulators and semiconductors. *Solid State Physic-solid State Physics*, **14**, 99.

Bouloudenine, M., Viart, N., Colis, S., *et al*. (2005). Antiferromagnetism in bulk $Zn_{1-x}Co_xO$ magnetic semiconductors prepared by the coprecipitation technique. *Applied Physics Letters*, **87**, 052501.

Bourdonnay, H., Bousquet, A., Cotton, J.P., *et al*. (1970). Experimental determination of exchange integrals in Magnetite. *Journal de Physique*, **32**(2–3), C1–1182.

Bryan, J.D., Heald, S.M., Chambers, S.A. and Gamelin, D.R. (2004). Strong room-temperature ferromagnetism in Co^{2+}-Doped TiO_2 made from colloidal nanocrystals. *Journal of the American Chemical Society*, **126**, 11640–11647.

Chambers, S.A. and Farrow, R.F. (2003). New possibilities for ferromagnetic semiconductors. *MRS Bulletin*, **28**(10), 729–733.

Coey, J.M.D., Douvalis, A.P., Fitzgerald, C.B. and Venkatesan, M. (2004). Ferromagnetism in Fe-doped SnO_2 thin films. *Applied Physics Letters*, **84**, 1332–1334.

Coey, J.M.D., Venkatesan, M. and Fitzgerald, C.B. (2005). Donor impurity band exchange in dilute ferromagnetic oxides. *Nature Materials*, **4**, 173–179.

Coey, J.M.D., Venkatesan, M., Stamenov, P., *et al*. (2005). Magnetism in hafnium dioxide. *Physical Review B*, **72**, 024450.

Das Pemmaraju, C. and Sanvito, S. (2005). Ferromagnetism driven by intrinsic point defects in HfO_2. *Physical Review Letters*, **94**, 217205.

Deutscher, G., Zallen, R. and Adler, J. (Eds.) (1983). *Percolation Structures and Processes*, Adam Hilger: Bristol.

Dhar, S., Brandt, O., Ramsteiner, M., *et al*. (2005a). Colossal magnetic moment of Gd in GaN. *Physical Review Letters*, **94**, 037205.

Dhar, S., Pérez, L., Brandt, O., *et al*. (2005b). Gd-doped GaN: a very dilute ferromagnetic semiconductor with a Curie temperature above 300 K. *Physical Review B*, **72**, 245203.

Dietl, T., Ohno, H., Matsukura, F., *et al*. (2000). Zener model description of ferromagnetism in Zinc-blende magnetic semiconductors. *Science*, **287**, 1019.

Dorneles, L.S., Venkatesan, M., Moliner, M., *et al*. (2004). Magnetism in thin films of CaB_6 and SrB_6. *Applied Physics Letters*, **85**, 6377.

Elfimov, I.S., Yunoki, S. and Sawatzky, G.A. (2002). Possible path to a new class of ferromagnetic and half-metallic ferromagnetic materials. *Physical Review Letters*, **89**, 216403.

Fitzgerald, C.B., Venkatesan, M., Dorneles, L.S., *et al*. (2006). Magnetism in dilute magnetic oxide thin films based on SnO_2, *Physical Review B*, **74**, 115307.

Ghosh, S., Sih, V., Lau, W.H., *et al*. (2005). Room-temperature spin coherence in ZnO. *Applied Physics Letters*, **86**, 232507.

Goodenough, J. (1955). Theory of the role of covalence in the perovskite-type manganites [La, M(II)]MnO_3. *Physical Review*, **100**, 564.

Gopal, P. and Spaldin, N.A. (2006). Magnetic interactions in transition-metal-doped ZnO: An ab initio study. *Physical Review B*, **74**, 094418.

Halliburton, L.E., Giles, N.C., Garces, N.Y., *et al*. (2005). Production of native donors in ZnO by annealing at high temperature in Zn vapor. *Applied Physics Letters*, **87**, 172108.

Han, S-J., Song, J.W., Yang, C-H., *et al*. (2002). A key to room-temperature ferromagnetism in Fe-doped ZnO: Cu. *Applied Physics Letters*, **81**(22), 4212–4214.

Hashimoto, M., Zhou, Y-K., Kanamura, M. and Asahi, H. (2002). High temperature (>400 K) ferromagnetism in III-V-based diluted magnetic semiconductor GaCrN grown by ECR molecular-beam epitaxy. *Solid State Communications*, **122**(1), 37–39.

Herranz, G., Basletic, M., Bibes, M., *et al*. (2006a). Full oxide heterostructure combining a high-TC diluted ferromagnet with a high-mobility conductor. *Physical Review B*, **73**, 064403.

Herranz, G., Ranchal, R., Bibes, M., *et al*. (2006b). Co-doped (La,Sr)$TiO_{3-\delta}$: a high-Curie temperature diluted magnetic system with large spin-polarization. *Physical Review Letters*, **96**(2), 027207.

Hong, N.H., Sakai, J., Poirot, N. and Brizé, V. (2006). Room-temperature ferromagnetism observed in undoped semiconducting and insulating oxide thin films. *Physical Review B*, **73**, 132404.

Hong, N.H., Sakai, J., Poirot, N. and Ruyter, A. (2005a). Laser ablated Ni-doped HfO_2 thin films: room temperature ferromagnets. *Applied Physics Letters*, **86**, 242505.

Hong, N.H., Sakai, J., Prellier, W. and Hassini, A. (2005b). Transparent Cr-doped SnO2 thin films: ferromagnetism beyond room temperature with a giant magnetic moment. *Journal of Physics. Condensed Matter*, **17**(10), 1697.

Hong, N.H., Sakai, J., Huong, N.T., *et al*. (2005c). Role of defects in tuning ferromagnetism in diluted magnetic oxide thin films. *Physical Review B*, **72**, 045336.

Hong, N.H., Sakai, J., Prellier, W., *et al*. (2004). Ferromagnetism in transition-metal-doped TiO_2 thin films. *Physical Review B*, **70**, 195204.

Hutchings, M.T. (1964). Point-charge calculation of energy levels of magnetic ions in crystalline electric fields. *Solid State Physics*, **16**, 227–273.

Janisch, R., Gopal, P. and Spaldin, N.A. (2005). Transition metal-doped TiO_2 and ZnO – present status of the field. *Journal of Physics. Condensed Matter*, **17**, R657.

Jin, Z., Fukumura, T., Kawasaki, M., *et al*. (2001). High throughput fabrication of transition-metal-doped epitaxial ZnO thin films: a series of oxide-diluted magnetic semiconductors and their properties. *Applied Physics Letters*, **78**(24), 3824–3826.

Kale, S.N., Ogale, S.B., Shinde, S.R., *et al*. (2003). Magnetism in cobalt-doped Cu_2O thin films without and with Al, V, or Zn codopants. *Applied Physics Letters*, **82**(13), 2100–2102.

Kanamori, J. (1959). Superexchange interaction and symmetry properties of electron orbitals. *Journal of Physics and Chemistry of Solids*, **10**, 87.

Kaspar, T.C., Heald, S.M., Wang, C.M., *et al*. (2005). Negligible magnetism in excellent structural quality $Cr_xTi_{1-x}O_2$ anatase: contrast with high-T_C ferromagnetism in structurally defective $Cr_xTi_{1-x}O_2$. *Physical Review Letters*, **95**, 217203.

Khare, N., Kappers, M.J., Wei, M., *et al*. (2006). Defect induced ferromagnetism in Co-doped ZnO. *Advanced Materials*, **18**, 1449–1452.

Kim, J-Y., Park, J-H., Park, B-G., *et al*. (2003). Ferromagnetism induced by clustered Co in Co-doped anatase TiO_2 thin films. *Physical Review Letters*, **90**, 017401.

Kittilstved, K.R., Liu, W.K. and Gamelin, D.R. (2006). Electronic origins of polarity-dependent high T_C ferromagnetism in oxide diluted magnetic semiconductors. *Nature Materials*, **5**, 291.

Kundaliya, D.C., Ogale, S.B., Lofland, S.E., *et al*. (2004). On the origin of high-temperature ferromagnetism in the low-temperature processed Mn–Zn–O system. *Nature Materials*, **3**, 709.

Liu, Y.L., Harrington, S., Yates, K.A., *et al*. (2005). Epitaxial, ferromagnetic $Cu_{2-x}Mn_xO$ films on (001) Si by near-room-temperature electrodeposition. *Applied Physics Letters*, **87**, 222108.

Lofland, S.E., Seaman, B., Ramanujachary, K.V., *et al*. (2003). Defect driven magnetism in calcium hexaboride. *Physical Review B*, **67**, 020410(R).

Martinez, B., Sandiumenge, F., Balcells, L., *et al*. (2005). Role of the microstructure on the magnetic properties of Co-doped ZnO nanoparticles. *Applied Physics Letters*, **86**(10), 103113.

Masumoto, Y., Murakami, M., Shono, T., *et al*. (2001a). Room-temperature ferromagnetism in transparent transition metal-doped titanium dioxide. *Science*, **291**, 854–856.

Matsumoto, Y., Takahashi, R., Murakami, M., *et al*. (2001b). Ferromagnetism in Co-doped TiO_2 rutile thin films grown by laser molecular beam epitaxy. *Japanese Journal of Applied Physics*, **40**, L1204–L1206.

Methfessel, S. and Mattis, D.C. (1968). Magnetic semiconductors. In *Handbuch der Physik*, Flügge, S. (Ed.), Freiburg, Springer-Verlag: Berlin, Vol. 18/1.

Monnier, R. and Delley, B. (2001). Point defects, ferromagnetism, and transport in calcium hexaboride. *Physical Review Letters*, **87**, 157204.

Neal, J.R., Behan, A.J., Ibrahim, R.M., *et al*. (2006). Room temperature magneto-optics of ferromagnetic transition-metal doped ZnO thin films. cond-mat/0604307.

Ogale, S.B., Choudhary, R.J., Buban, J.P., *et al*. (2003). High temperature ferromagnetism with a giant magnetic moment in transparent Co-doped $SnO_{2-\delta}$. *Physical Review Letters*, **91**, 077205.

Osterwalder, J., Droubay, T., Kaspar, T., *et al*. (2005). Growth of Cr-doped TiO_2 films in the rutile and anatase structures by oxygen plasma assisted molecular beam epitaxy. *Thin Solid Films*, **484**, 289–298.

Ozgur, U., Alivov, Y.I., Liu, C., *et al*. (2005). A comprehensive review of ZnO materials and devices. *Journal of Applied Physics*, **98**, 041301.

Pacuski, W., Ferrand, D., Cibert, J., *et al*. (2006). Effect of the s, p-d exchange interaction on the excitons in $Zn_{1-x}Co_xO$ epilayers. *Physical Review B*, **73**, 035214.

Park, J.H., Kim, M.G., Jang, H.M., *et al*. (2004). Co metal clustering as the origin of ferromagnetism in Co-doped ZnO thin films. *Applied Physics Letters*, **84**(8), 1338.

Park, S.E., Lee, H-J., Cho, Y.C., *et al*. (2002). Room-temperature ferromagnetism in Cr-doped GaN single crystals. *Applied Physics Letters*, **80**(22), 4187–4189.

Patterson, C.H. (2006). Role of defects in ferromagnetism in $Zn_{1-x}Co_xO$: A hybrid density-functional study. *Physical Review B*, **74**, 144432.

Pearton, S.J., Heo, W.H., Ivill, M., *et al*. (2004). Dilute magnetic semiconducting oxides. *Semiconductor Science and Technology*, **19**, R59.

Philip, J., Punnoose, A., Kim, B.I., *et al*. (2006). Carrier-controlled ferromagnetism in transparent oxide semiconductors. *Nature Materials*, **5**, 298.

Philip, J., Theodoropoulou, N., Berera, G., *et al*. (2004). High-temperature ferromagnetism in manganese-doped indium–tin oxide films. *Applied Physics Letters*, **85**(5), 777–779.

Prellier, W., Fouchet, A. and Mercey, B. (2003). Oxide-diluted magnetic semiconductors: a review of the experimental status. *Journal of Physics. Condensed Matter*, **15**, R1583.

Priour, D.J. Jr. and Das Sarma, S. (2006). Clustering in disordered ferromagnets: the Curie temperature in diluted magnetic semiconductors. *Physical Review B*, **73**, 165203.

Radovanovic, P.V. and Gamelin, D.R. (2003). High-temperature ferromagnetism in Ni^{2+}-doped ZnO aggregates prepared from colloidal diluted magnetic semiconductor quantum dots. *Physical Review Letters*, **91**, 157202.

Rao, C.N.R. and Deepak, F.L. (2005). Absence of ferromagnetism in Mn- and Co-doped ZnO. *Journal of Materials Chemistry*, **15**, 573–578.

Rode, K. (2006). *Contribution a L'etude des Semiconducteurs Ferromagnetiques Dilues: Cas des Films Minces D'oxyde de Zinc Dope au Cobalt*, Ph.D. Thesis, Universite Paris XI Orsay, France.

Saeki, H., Tabata, H. and Kawai, T. (2001). Magnetic and electric properties of vanadium doped ZnO films. *Solid State Communicationsolid State Communications*, **120**, 439.

Samuelsen, E.J., Hutchings, M.T. and Shirane, G. (1970). Inelastic neutron scattering investigation of spin waves and magnetic interactions in Cr_2O_3. *Physica (Utrecht)*, **48**(1), 13.

Samuelsen, E.J. and Shirane, G. (1970). Inelastic neutron scattering investigation of spin waves and magnetic interactions in alpha-Fe_2O_3. *Physica Status Solidi*, **42**, 241.

Sati, P., Hayn, R., Kuzian, R., *et al*. (2006). Magnetic anisotropy of Co^{2+} as signature of intrinsic ferromagnetism in ZnO:Co. *Physical Review Letters*, **96**, 017203.

Schwartz, D.A. and Gamelin, D.R. (2004). Reversible 300 K ferromagnetic ordering in a diluted magnetic semiconductor. *Advanced Materials*, **16**, 2115–2119.

Sharma, P., Gupta, A., Rao, K.V., *et al*. (2003). Ferromagnetism above room temperature in bulk and transparent thin films of Mn-doped ZnO. *Nature Materials*, **2**, 673.

Shinde, S.R., Ogale, S.B., Das Sarma, S., *et al*. (2003). Ferromagnetism in laser deposited anatase $Ti_{1-x}Co_xO_{2-\delta}$ films. *Physical Review B*, **67**, 115211.

Sonoda, S., Shimizua, S., Sasakib, T., *et al*. (2002). Molecular beam epitaxy of wurtzite (Ga,Mn)N films on sapphire(0 0 0 1) showing the ferromagnetic behaviour at room temperature. *Journal of Crystal Growth*, **237–239**, 1358–1362.

Stamenov, P., Venkatesan, M., Dorneles, L.S., *et al*. (2006). Magnetoresistance of Co-doped ZnO thin films. *Journal of Applied Physics*, **99**, 08M124.

Stampe, P.A., Kennedy, R.J., Xin, Y. and Parker, J.S. (2003). Investigation of the cobalt distribution in the room temperature ferromagnet TiO_2:Co. *Journal of Applied Physics*, **93**(10), 7864–7866.

Stauffer, D. (1985). *Introduction to Percolation Theory*, Taylor and Francis: London and Philadelphia.

Teraguchi, N., Suzuki, A., Nanishi, Y., *et al*. (2002). Room-temperature observation of ferromagnetism in diluted magnetic semiconductor GaGdN grown by RF-molecular beam epitaxy. *Solid State Communication*, **122**(12), 651–653.

Toyosaki, H., Fukumura, T., Yamada, Y. and Kawasaki, M. (2005a). Evolution of ferromagnetic circular dichroism coincident with magnetization and anomalous Hall effect in Co-doped rutile TiO_2. *Applied Physics Letters*, **86**, 182503.

Toyosaki, H., Fukumura, T., Ueno, K., *et al*. (2005b). A ferromagnetic oxide semiconductor as spin injection electrode in magnetic tunnel junction. *Japanese Journal of Applied Physics*, **44**(28), L896–L898.

Toyosaki, H., Fukumura, T., Yamada, Y., *et al*. (2004). Anomalous Hall effect governed by electron doping in a room-temperature transparent ferromagnetic semiconductor. *Nature Materials*, **3**, 221–224.

Ueda, K., Tabata, H. and Kawai, T. (2001). Magnetic and electric properties of transition-metal-doped ZnO films. *Applied Physics Letters*, **79**(7), 988–990.

Venkatesan, M., Fitzgerald, C.B. and Coey, J.M.D. (2004a). Unexpected magnetism in a dielectric oxide. *Nature (London)*, **430**, 630.

Venkatesan, M., Fitzgerald, C.B., Lunney, J.G. and Coey, J.M.D. (2004b). Anisotropic ferromagnetism in substituted zinc oxide. *Physical Review Letters*, **93**, 177206.

Venkatesan, M., Gunning, R.D., Stamenov, P., *et al*. (2006). Tuning of magnetic, magnetotransport and optical properties in Al codoped Zn-Co-O thin films. Unpublished.

Wang, Z., Wang, W., Tang, J., *et al*. (2003). Extraordinary Hall effect and ferromagnetism in Fe-doped reduced rutile. *Applied Physics Letters*, **83**(3), 518–520.

Wu, S.Y., Liu, H.X., Gu, L., *et al*. (2003). Synthesis, characterization, and modeling of high quality ferromagnetic Cr-doped AlN thin films. *Applied Physics Letters*, **82**(18), 3047–3049.

Zhao, T., Shinde, S.R., Ogale, S.B., *et al*. (2005). Electric field effect in diluted magnetic insulator anatase Co: TiO_2. *Physical Review Letters*, **94**, 126601.

Heusler Alloys

Robert A. de Groot[1,2]

[1] *Radboud University Nijmegen, Nijmegen, The Netherlands*
[2] *Rijks Universiteit Groningen, Groningen, The Netherlands*

1 INTRODUCTION

In the beginning of the twentieth century, Heusler studied the magnetic properties of ternary alloys containing both transition and main-group metals (Heusler, 1903). The motivation for this work was the mysterious observation that magnetic alloys could be formed from nonmagnetic elements. (Antiferromagnetism was not discovered yet, so chromium and manganese were considered as nonmagnetic elements.) More than a century later, these alloys, named after Heusler, are still an area of active research. A number of them possess the unique property of exhibiting metallic behavior for one spin direction only. Half-metals (as these alloys have been baptized) are the ultimate materials in spintronics, where besides the charge, the spin of the electron plays an essential role – conceptually in some cases and indispensably as components of an actual device in other cases. Also, half-metals form an interesting area for fundamental research in materials science. Electronic structure calculations have played an important role in the area of half-metallic properties of Heusler alloys and beyond. Part of the reason for this is the degree of refinement these calculations have today, which make them a reliable instrument in materials science, especially in areas where little experimental data is at hand. There is hardly any direct experimental observation of half-metallicity possible. The most direct way of observing half-metallic magnetism is spin-resolved positron annihilation, an expensive measurement requiring dedicated equipment and single crystals. The possibility of extracting 100% spin-polarized electrons from a half-metal has been taken as a proof of half-metallic magnetism, but this requires electrons to cross a surface or an interface. Only recently, we have began to realize that surfaces and interfaces are distinct objects with distinct properties. They require special studies, both computationally as well as experimentally. Unfortunately, the understanding of interfaces is not nearly as advanced as that of bulk properties. This chapter follows more or less the historic developments of the half-metallic properties of Heusler alloys. This implies that computational studies form its backbone. However, experimental studies are essential and will be discussed.

Today we know two classes of alloys named after Heusler: the $C1_b$ structure and the $L2_1$ structure, sometimes referred to as the *half Heuslers* and the *full Heuslers*, respectively. Both structures are closely related with each other as well as with the zinc-blende structure. All three are based on a face centered cubic Bravais lattice. Whereas the zinc-blende structure has the 0, 0, 0 and 1/4, 1/4, 1/4 positions, the three constituents in the Heusler $C1_b$ structure occupy the 0, 0, 0; 1/4, 1/4, 1/4; and 1/2, 1/2, 1/2 positions. The full-Heusler structure is identical with the half-Heusler structure, furthermore, the element occupying the 1/4, 1/4, 1/4 position also occupies the 3/4, 3/4, 3/4

Handbook of Magnetism and Advanced Magnetic Materials. Edited by Helmut Kronmüller and Stuart Parkin. Volume 4: *Novel Materials*. ISBN: 978-0-470-02217-7.

position. Thus, the $C1_b$ structure lacks the inversion symmetry that the $L2_1$ structure has. These differences and similarities are essential and at the same time almost sufficient to understand the quite different, rich physics of both classes of alloys.

Two groups initially studied the electronic structure of Heusler alloys independently and at the same time. NiMnSb, a half-Heusler, showed semiconducting behavior exclusively for the minority-spin direction and was baptized a 'half-metallic ferromagnet' (de Groot, Mueller, van Engen and Buschow, 1983). At the same time, several full Heuslers were studied (Kübler, Williams and Sommers, 1983), and it was noticed by these authors that for Co_2MnAl and Co_2MnSn, 'the minority-spin state density nearly vanished'. Both groups realized the consequences of controlling the electron spin in electrical conduction, an area known as *spintronics* today. Kübler remarks 'This should lead to peculiar transport properties in these Heusler alloys', while the publication of the Dutch group was delayed by half a year because of a patent application using half-metals as a source of spin-polarized electrons in a transistor containing two layers of half-metal separated by a nonmagnetic layer.

The similarities of both Heusler structures and the occurrence of half-metallic magnetism in both types of alloys suggest a common origin. These similarities are misleading, however. The origin of half-metallic magnetism in the two structures is quite distinct. Also, the defect chemistry, important for the robustness of the half-metallicity, is different, as we will see.

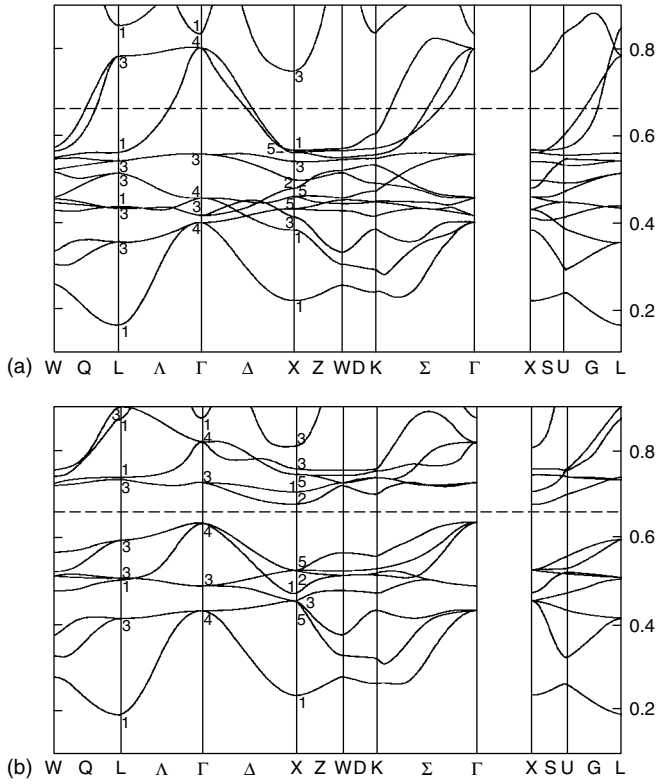

Figure 1. Band structure of NiMnSb for (a) the majority-spin direction and (b) the minority-spin direction.

2 HEUSLER $C1_b$s

2.1 Nickel–manganese–antimonide

2.1.1 General

Since NiMnSb is a half-metal that has been studied for a long time, both computationally as well as experimentally, it will be treated here in detail. The band structure is shown in Figure 1 for both spin directions. The majority-spin panel shows that three bands cross the Fermi level with sizable slope. This is a consequence of the rather large bandwidths of the bands. The minority-spin direction shows an energy gap at the Fermi level with valence and conduction bands that closely resemble those of many zinc-blende semiconductors with an indirect band gap. The similarity is even more pronounced if we remove the Ni d states from the Hamiltonian (but not their interaction with the antimony and manganese states) and compare the valence band with that of GaSb (Figure 2). This observation is important. One can analyze band structures in terms of tight-binding interactions as described by Slater and Koster. An interaction between two atoms in real space contributes a cosine to the band structure in the corresponding direction of k space. The strength of the interaction determines the dispersion, while the wavelength of the cosine is determined by the inverse of the distance between the interacting atoms in real space. Therefore similarities of band structures directly reflect similarities in chemical bonding. Much of this information is lost if one considers quantities derived from Brillouin zone integrals like densities of states. So, the essential ingredients are the trivalent manganese with tetrahedral coordination interacting with the pentavalent antimony, which is also tetrahedrally coordinated (as long as no inversion center is present, even d wave functions of manganese in NiMnSb can play the same role as the odd p functions in a zinc-blende semiconductor). Whereas this interaction is direct in the zinc-blende semiconductors, it is indirect through the nickel atoms in the half Heuslers; to quote Kübler: 'a nickel *induced* Mn–Sb *covalent interaction*' (Kübler, 2000). Whereas the zinc-blende semiconductors show a band gap for 8 valence electrons, 18 electrons are required here in order to keep the nickel d shell filled. Thus, the magnetic moment of NiMnSb is

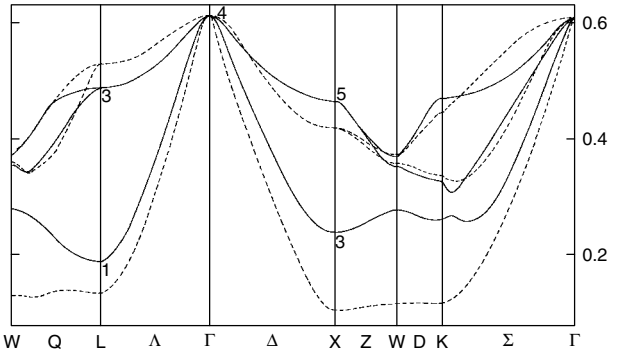

Figure 2. Valence-band structure of minority-spin (semiconducting) NiMnSb ($C1_b$ structure) where the Ni-d states were deliberately removed from the Hamiltonian (full lines). For comparison the valence-band structure of GaSb (calculated with the same method) is shown (broken lines).

$4\,\mu_B$, of which manganese carries 90%, while the remaining moment resides on the nickel atom. The interactions for the majority-spin direction are quite different. Because the manganese d states are much lower in energy as compared to the minority-spin d states, these electrons are practically degenerate with the antimony electrons they interact with. Consequently, the bandwidths are larger when compared to the semiconducting spin direction and no band gap occurs, either at the Fermi energy or in the vicinity of it. Note that this is a very different case from the strongly magnetic half-metals, the manganites with colossal magnetoresistance, or, for example, CrO_2. In these cases, the majority and minority bands are to a good approximation shifted in a ridged bandlike fashion by the exchange interaction. The Fermi level intersects the majority band while the corresponding minority band is still empty. This situation is practically determined by the valence of the ion carrying the magnetic moment only. Thus, very little influence is to be expected from disorder, surfaces, and interfaces, as long as the proper valence of the magnetic species is conserved. NiMnSb, on the other hand, requires the correct crystal structure and site occupancy, as shown in the next paragraph. Since the role of nickel is so passive, one wonders whether it is needed at all. Manganese–antimonide does exist, but it crystallizes in the nickel–arsenide structure. This structure has a deformed octahedral coordination of the metal and a trigonal prismatic coordination of the pnictide. Consequently it is not half-metallic. But manganese–antimonide in the zinc-blende structure is a half-metal, very much like nickel–manganese–antimonide. The magnetic moments are identical. So the role of nickel in NiMnSb is to stabilize it in the crystal structure with the required coordination of manganese and antimony. It is very efficient in doing so: the lattice parameter of NiMnSb is actually smaller than that of zinc-blende manganese–antimonide.

Let us return to the issue of point defects in nickel–manganese–antimonide. A proper site occupancy is essential (Helmholdt *et al.*, 1984). For example, nickel–manganese interchange deprives the manganese of its tetrahedral coordination and consequently does not show any half-metallic properties. Even a 1% interchange is enough to destroy the band gap (Orgassa, Fujiwara, Schulthess and Butler, 2000). However, such an interchange is energetically very unfavorable. It costs 2.8 eV per interchanged Ni–Mn pair, more than the heat of evaporation. Similar considerations hold for nickel–antimony interchange. This is consistent with nuclear magnetic resonance (NMR) measurements on cold-worked Heusler alloys. All investigated full Heuslers showed broadening of the manganese line, but even severe crushing in the case of NiMnSb left the NMR spectrum unaffected (Schaf, Le Dang, Veillet and Campbell, 1983). The trivalent behavior of manganese for the minority-spin direction implies that minority-spin d electrons are involved in the chemical bonds and the valence-band formation. Magnetic materials can be classified as strong magnets or weak magnets. Strong magnets are defined as magnets, where an increase in the spin-up, spin-down splitting in energy (the exchange interaction) does not lead to an increase in magnetic moment. Clearly, the magnetic moment is not limited by the strength of the exchange interaction, but by a lack of available electron states. For transition metals, this implies a full majority d shell or an empty minority d shell. In the case of a weak magnet, the moment is not determined by a lack of available states but by balancing the energy gain of magnetic moment formation (the exchange interaction) against the cost of transferring electrons from one spin direction to the opposite one (band energy). The involvement of the manganese d electron in the valence band for the minority-spin direction classifies NiMnSb as a *weak* magnet. One can force NiMnSb into becoming a strong magnet by artificially increasing the exchange interaction till the magnetic moment has obtained the value of $5\,\mu_B$, characteristic of a strong magnet in this case. The resulting band structure is shown in Figure 3. NiMnSb has evolved into a normal metal. Clearly half-metallicity and strong magnetism are mutually exclusive in NiMnSb.

2.1.2 Experimental bulk properties

A striking, but trivially proven property of half-metals is the occurrence of integral magnetic moments. This property follows directly from the fact that the number of electrons of the semiconducting spin direction and the total number of electrons are integers. This gives a direct indication of whether a compound could be a half-metal. It should be applied with caution, however. An integral magnetic moment is no proof of half-metallicity: integral magnetic

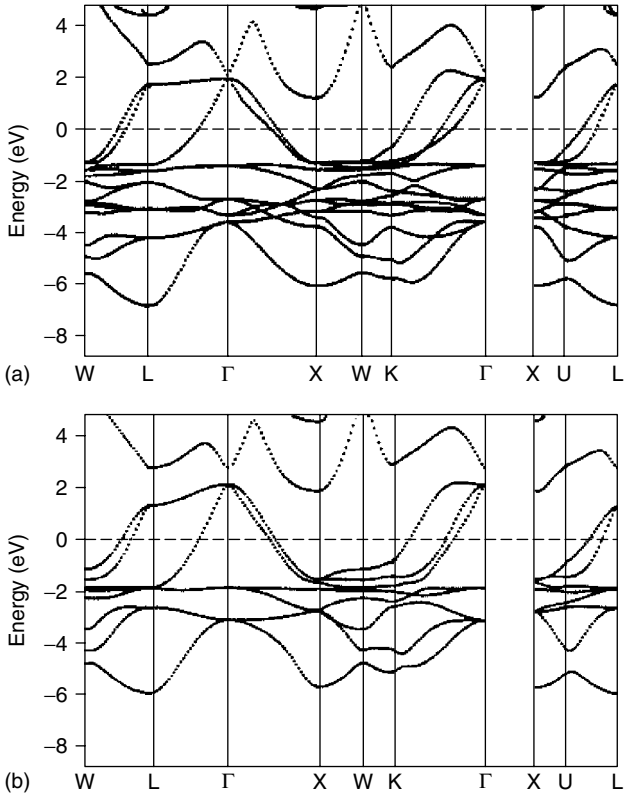

Figure 3. Band structure of NiMnSb with an artificially increased exchange splitting: (a) majority-spin channel and (b) minority-spin channel.

moments can occur accidentally within the precision of the experiment. The sulfospinel greigite is *not* half-metallic in spite of its integer magnetic moment of $2\,\mu_B$. The opposite case can also occur. An integral number of electrons (per formula unit) occurs only for an integral number of atoms. So, a nonintegral magnetic moment does *not* disprove half-metallicity if deviations from stoichiometry occur, for example, in the form of vacancies. These imperfections are more difficult to measure than a magnetic moment. (Chemical analyses of a sample will not help if the missing element is present in the sample in the form of another phase, which is frequently the case. X-ray diffraction is insensitive in detecting smaller fractions of other phases.) The magnetic moment at a low temperature for NiMnSb agrees with the expected $4\,\mu_B$.

The most direct proof of half-metallicity is provided by positron annihilation. This method measures the Fermi surfaces for the two spin directions independently and can also detect the absence of a Fermi surface for a particular spin direction. These are genuine bulk measurements. This way, the half-metallic properties of NiMnSb were confirmed experimentally to the precision of 0.01 electrons (Hanssen and Mijnarends, 1986; Hanssen, Mijnarends, Rabou and Buschow, 1990). (Another attractive feature of positron annihilation is that it can be applied on a broad range of temperatures, unlike methods such as de Haas–van Alphen or cyclotron resonance.)

Fingerprints of half-metallicity are expected to show up in transport properties like the temperature dependence of electrical resistivity, the (anomalous) Hall effect, and so on. The situation here is remarkably complex, however, and a simple consistent picture is missing. The first study specifically addressing these points is the work of Otto *et al*. for NiMnSb (as well as PtMnSb, AuMnSb, CoMnSb, and PtMnSn). In a half-metal, no spin-flip scattering (one magnon scattering) is possible. The characteristic T^2 term in the temperature dependence of resistivity at low temperatures is indeed missing for NiMnSb (as well as for PtMnSb and CoMnSb, see the following text). The normal Hall effect shows a strong linear decrease from 4 to 90 K by a factor of 7, after which it saturates. Otto explains this remarkable feature as resulting from a complex Fermi surface comprising three sheets of mixed hole/electron character. Otto *et al*. report a strong anomalous Hall effect for all cases they investigated. Assuming a degree of spin polarization of the conduction electrons that is proportional to the magnetization (both as a function of temperature), a linear behavior is observed in all systems investigated for the anomalous Hall effect divided by the normal resistivity as a function of resistivity. NiMnSb follows this trend above 97 K only. The temperature dependence of the resistivity in half-metals was reviewed and studied theoretically by Irkhin and Katsnelson. The expected temperature dependence of the resistivity is $T^{9/2}$, which has not been reported experimentally. On the other hand, these authors also considered the nonquasiparticle contribution to the temperature dependence of the resistivity and obtained $T^{\sim 1.65}$, very close to the experimentally observed $T^{3/2}$, above a temperature of 100 K (Irkhin and Katsnelson, 1994, 2002). Strong evidence exists that a transition takes place in NiMnSb, but a complete understanding is still missing. An interesting scenario considers the thermal excitation of electrons at the Fermi energy level to the bottom of the conduction band (Hordequin, Ristoiu, Ranno and Pierre, 2000). This excitation transfers a majority-spin electron to the minority-spin direction. It reduces the magnetic moment and thus the exchange splitting, lowering the activation energy for more excitations of this type. A catastrophe occurs, the bottom of the conduction band drops below the Fermi level and the half-metallic properties are lost. Basically, this is a magnetic analog of the semiconductor–metal transition as described by Falicov. Such a phase transition could happen for any half-metal, but it requires the Fermi level to be positioned asymmetrically in the band gap, closer to the conduction band for half-metals with a band gap in the minority-spin direction. More recently, evidence has been obtained that around a temperature of

90 K, a reordering of the magnetic moments occurs, with loss of the half-metallic properties (Borca *et al*., 2001). The low temperature of these transitions is somewhat unexpected. Naively one would expect the spin polarization of the conduction electrons as a function of temperature to roughly follow the magnetization. Clearly more work is needed in order to obtain a full understanding here. Why was this transition not noticed in measurements of the magnetization? How does the transition depend on details of the magnon spectrum and could it be suppressed by doping with lanthanide atoms (Attema *et al*., 2004)? Half-metals with a band gap in the majority-spin direction, an area practically unexplored till now, could greatly contribute to our understanding of finite temperature properties.

2.1.3 Surfaces and interfaces

The majority of the techniques that measure the degree of spin polarization of the conduction electrons are actually surface-sensitive techniques. It is important to have an understanding of the physical properties of the surface of NiMnSb and half-metals in general. Also, knowledge and understanding of interfaces of half-metals with semiconductors, in particular, is of importance in spintronics. Ideally, a *bona fide* energy gap exists for one spin direction in the half-metal throughout the interface into the semiconductor. Such an interface is an exception. Designing an interface that fulfills all requirements requires proper insight into the interactions at the interface. Strongly magnetic half-metals have fundamentally different surface and interface properties compared to weak magnetic half-metals. In the case of strong magnetic half-metals, the magnetic properties are essentially determined by the ion carrying the magnetic moment and its valence. As long as this valence is conserved, the half-metallic properties are conserved, even at the surface. Figure 4 shows a comparison of the surface electronic structure with the bulk for the strongly magnetic half-metal CrO_2 (van Leuken and de Groot, 1995). In both cases, remarkably little influence of the surface on the electronic properties is found. In the case of weak magnets, additional strict requirements on the structure need to be fulfilled in order to maintain half-metallic properties. These conditions are violated at the surfaces. Experimentally, spin-dependent photoemission did not show 100% polarization (Bona *et al*., 1985), but inverse photoemission (probing the empty electron states) showed a very high degree of spin polarization (Ristoiu *et al*., 2000). Photoemission is a very surface-sensitive technique. A drawback is the possibility that it does not measure the entire Brillouin zone. For this reason Andreev reflection is superior. The spin polarization obtained this way is only 60% (Soulen *et al*., 1998). Originally, Andreev reflection was not considered as a particularly surface-sensitive technique, but

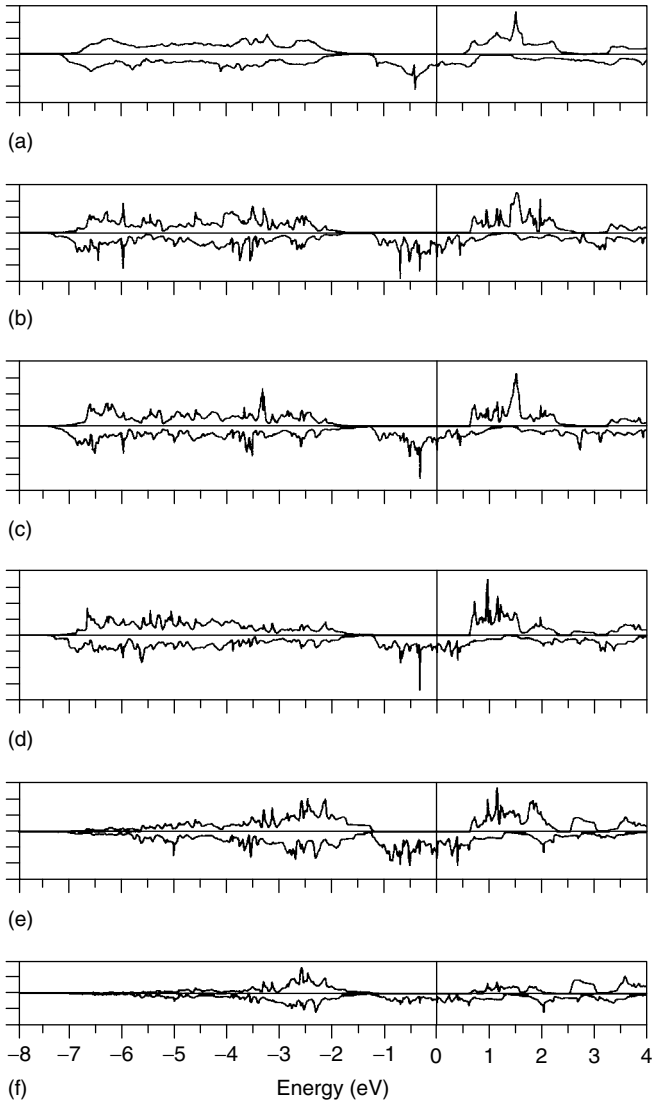

Figure 4. Comparison of the density of states of bulk CrO_2 (a) with the density of states per layer of the CrO_2(001) slab: central CrO_2 layer (b), sub-subsurface layer (c), subsurface layer (d), surface layer (e), and first vacuum layer (f). Vertical scale: 2 states per eV formula unit per division and 0.2 states per eV formula unit per division for (f).

this question is still under debate (Eschrig, Kopu, Cuevas and Schoen, 2003), and its interpretation is sometimes subtle (Auth, Jakob, Block and Felser, 2003). Electronic structure calculations on all the possible surfaces of low index (100, 110, 111) showed that none of them exhibited half-metallic surfaces, independent of the termination, and there are no reasons to assume that more complex surfaces would not interpolate between these cases (see e.g., Galanakis, 2002 for the (001) surfaces). The most detailed calculations find two metallic minority-spin surface states for the (001) surface (Jenkins and King, 2001). The same is found for the (111)

surface (Jenkins, 2004). This study also gives detailed information on the thermodynamic stability of the various (111) surfaces. An important conclusion is the stability of the antimony-terminated surface. For details we refer to the original literature.

The breakdown of half-metallicity at the surface of NiMnSb could be a reason to abolish NiMnSb and Heuslers, in general, as candidates for spin injection into semiconductors. However, it should be realized that the surface of NiMnSb is quite different from the interface with a semiconductor in view of the similarity in electronic structure between NiMnSb and III–V semiconductors. Also, the application of a strong magnetic half-metal like CrO_2 on a III–V semiconductor may very well introduce metallic behavior in the *semiconductor* for the spin direction in which the half-metal itself is semiconducting.

The properties of an interface are even more complex than those of a surface. Experimentally, few techniques are available to directly measure interface properties as compared to those available for measurements at the surface. Computationally also, the situation is much more complicated than is generally realized. Even if no lattice mismatch exists between the two materials and interdiffusion of atoms from the neighboring materials can be neglected, the number of possible interfaces is still infinite, since the lateral orientation of one material with respect to the other is undetermined. Also, the structure at the interface and its volume need to be determined. This requires a careful and very expensive structure optimization. But it should be realized that actual interfaces are not determined by thermodynamic equilibrium alone. These optimizations are essential: the value of the spin polarization of the conduction electrons at the interface can change by hundreds of percent as compared with the guessed geometry. Structural relaxations in the stacking direction can be calculated quite straightforwardly. But relaxations in the lateral directions require very large unit cells and can be performed for relatively easy cases only. An early study of interfaces of low index of NiMnSb with InP and CdS showed (de Wijs and de Groot, 2001; Figure 5) that only one interface maintained semiconducting properties for the half-metal throughout the interface into the semiconductor. It is the 111 interface where both half-metal and semiconductors are anion terminated with a displacement of the lattices with respect to each other in the lateral directions in such a way that the two anions are positioned on top of each other in the stacking direction. In the first inspection, such an interface may look unstable, but such anion–anion bonds do occur in minerals like costabite and paracostabite, which have crystal structures very much related to the interfaces described here. Minerals are stable on a geological timescale. Much can be learned from the reason for this being the only half-metallic interface. The 111 direction in NiMnSb is the only

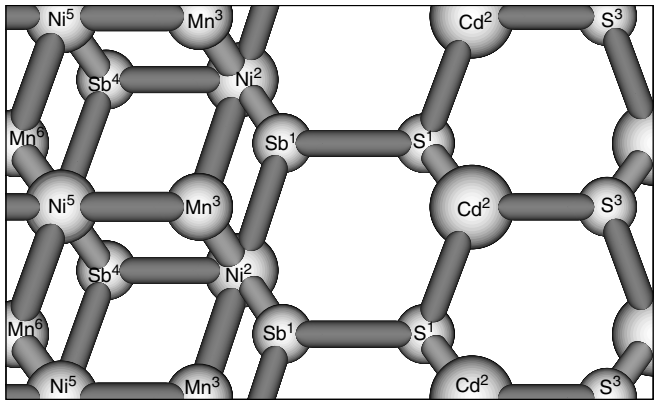

Figure 5. Structure of the half-metallic NiMnSb(111)/CdS(111) interface. The [111] axis runs horizontally, form left to right. Notice the Sb–S bond at the interface ($d_{Sb1-S1} = 2.7$ Å).

direction in which one finds layers of one element only, the 100 and 110 directions already show at least one plane with more than one component. The origin of the band gap in NiMnSb is very much like that in a III–V semiconductor, where the trivalent manganese can play a role similar to that of a trivalent metal like gallium in the corresponding semiconductor. But there is a difference between the two. In Ga–pnictide semiconductors, the contribution of Ga to the valence bands consists of 4s and 4p electrons, whereas Mn in NiMnSb contributes 4s and 3d electrons, with different main quantum numbers. Each element separately (Ga or Mn) gives a band structure with a *bona fide* band gap, *but a mixture of them does not.* The double-anion-terminated 111 interface is the only interface without anions coordinated by both transition and main-group metals. These findings are confirmed by calculations on $Ga_{(1-x)}$ Mn_xSb. The limited solubility of Mn in, for example, GaAs as known in dilute magnetic semiconductors, is not unrelated with the problems of a NiMnSb/semiconductor interface. Experimental work has been focused mainly on (100) interfaces. The best surface morphology and crystal quality was obtained for NiMnSb grown on GaAs, which was 20% deficient in antimony (van Roy *et al*., 2000, 2001). A (111) NiMnSb–GaAs B interface of good quality was realized (van Roy *et al*., 2003). This interface did not show a high degree of polarization, possibly because of the lattice mismatch.

2.2 Heusler alloys isoelectronic with nickel–manganese–antimonide

2.2.1 General

The band structures of PdMnSb and PtMnSb show strong similarities with that of NiMnSb. In PdMnSb, the Fermi energy straddles the top of the valence band. PtMnSb shows

major differences in the conduction band as compared with NiMnSb. The origin of these differences is relativistic: they originate from the mass–velocity and Darwin terms. The result is that the platinum 6s states are positioned much lower in energy than the 4s states of Ni in NiMnSb. This has a direct influence on the nature of the band gap. The direct gap for PtMnSb is very much like NiMnSb, the bottom of the conduction band at the Γ point, however, is a single degenerate band in which Pt s states contribute substantially. This possibly influences the magneto-optic Kerr effect.

The very high magneto-optic Kerr effect in PtMnSb spurred interest in this compound and in Heusler alloys, in general. The 2.5° (double) rotation at room temperature was a record (van Engen, Buschow and Jongebreur, 1983). A simple model related this observation to the half-metallic properties as the complement of the optical generation of spin-polarized electrons in semiconductors: where an optical transition with circularly polarized light from a spin-orbit split valence band generates spin-polarized electrons in the conduction band, the absorption of light from a 100% spin-polarized, spin-orbit split top of a valence band is possible for one (circular) polarization only. This uncompensated excitation gives a peak in the magneto-optic spectrum at a remarkably good position (de Groot, Mueller, van Engen and Buschow, 1984). The differences between PtMnSb and NiMnSb could be explained by the much higher position of the final state in the latter compound caused by the absence of strong scalar relativistic effects, leading to a second peak at much higher energy (Wijngaard, Haas and de Groot, 1989). On the other hand, the importance of a very small diagonal part, which enters the denominator in the expression of the Kerr effect, was stressed (Feil and Haas, 1987).

The first calculations of magneto-optical spectra based on first-principles calculations appeared in the beginning of the 1990s (Halilov and Kulatov, 1991; Kulatov, Uspenkii and Halilov, 1995). The magneto-optical properties of PtMnSb were reproduced very well. The results for NiMnSb showed a discrepancy of 0.5 eV in the position of spectral features and peaks that are more than twice as strong as compared with experiment. The latter point is of no importance, since any defects in samples and temperature reduce spectral features. A very thorough study on the background of magneto-optics in NiMnSb, PdMnSb, and PtMnSb analyzed in detail the effects of spin-orbit coupling, the magnetic moment, the degree of hybridization, the half-metallic character, the plasma frequency, and the crystal structure. This was accomplished by calculations on a large number of (sometimes hypothetical) compounds, in which these factors could be controlled separately. All factors contributed in the case of PtMnSb (Antonov *et al*., 1997). Regrettably, no analyses were made as to whether a specific part of the Brillouin zone contributed to the observed effect. Recent measurements on the (magneto-)optical properties of NiMnSb (Gao *et al*., 1999) were interpreted using the calculations of Antonov *et al*. and very good agreement was obtained. On the other hand, recent measurements on the *temperature* dependence of the Kerr effect in PtMnSb showed that there still remains an aspect to be understood: the Kerr effect increases by more than a factor of 3 on cooling down to 100 K (Carey, Newman and Wears, 2000). The diagonal part of the dielectric tensor is responsible for this unexpected result.

2.3 Other half-metals in the $C1_b$ structure

2.3.1 Slater–Pauling curves

If one plots the magnetic moment per formula unit of a large collection of compounds as a function of the number of valence electrons, many linear dependences are obtained. A unique curve with slope -1 is obtained for high electron concentrations, at the right side of what has been baptized the *Slater–Pauling* (SP) curve (Figure 6). This particular behavior is obtained if the number of majority electrons is constant; in practically all cases, this implies that the majority d bands are completely filled, for example, it is an implication of strong magnetism. The situation at the left-hand side of the SP curve is more complex. One could imagine that strong magnetism based on empty minority-spin bands is the origin. But low electron concentrations necessarily imply atoms from the left side of the transition-metal series, and the delocalized behavior of their d electrons does not favor magnetism (Kübler, 2000). An exception is found in the strongly ionic, strongly magnetic compounds like the colossal magnetoresistance materials and oxides like CrO_2. They are half-metals, but are not the subject of this chapter. Several different curves with a positive slope are found at the left side of the SP diagram, each representing a different mechanism for keeping the number of minority-spin electrons constant. One such mechanism is half-metallic magnetism.

In NiMnSb, if we were to substitute Ni with other 3d metals, the resulting compounds would follow the SP curve as long as the half-metallic magnetism persists. As mentioned before, the presence of minority-spin d electrons in the valence-band complex causes NiMnSb to be a weak magnet. Consequently, the maximal magnetic moment in a possible *series* of half-metals based on it is $4\,\mu_B$. This marks NiMnSb as the end of the series. Indeed, compounds with electron concentrations beyond NiMnSb are not half-metallic. In NiFeSb, the reduction in magnetic moment is accomplished by the occupation of minority-spin d states in the conduction band with the inevitable loss of half-metallicity. The required loss of half-metallicity and reduction of magnetic moments is energetically, more favorably realized by adopting an

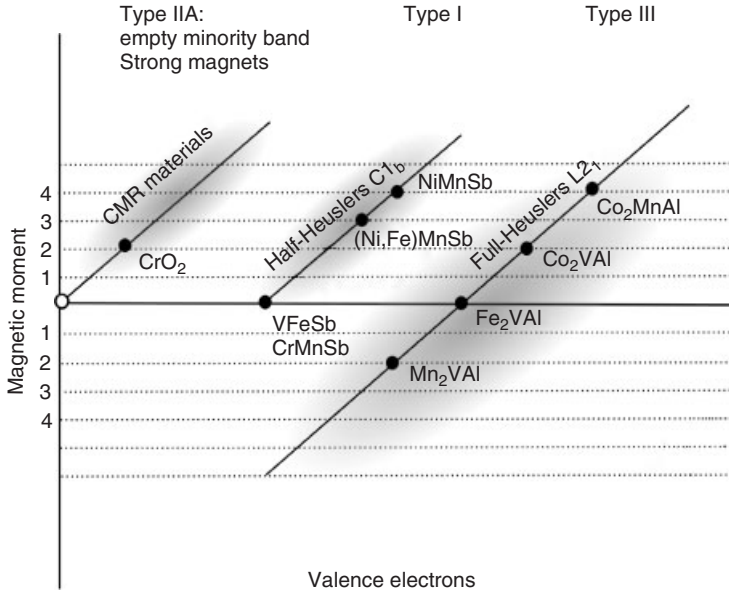

Figure 6. Slater-Pauling curves showing the relation between several classes of half-metals.

antiferromagnetic magnetic structure by doubling the unit cell (CuMnSb). A *reduction* of the electron density leads to CoMnSb calculated to be a half-metal indeed (Kübler, 1984). The band structure for the minority (semiconducting)-spin direction has hardly changed. The metallic spin direction is more strongly affected and the magnetic moment is reduced to $3\,\mu_B$. Following the SP curve, the next compound is FeMnSb. Calculations show a half-metallic electronic structure here as well (de Groot, van der Kraan and Buschow, 1986). Consequently, the magnetic moment is reduced to $2\,\mu_B$, which is quite a small moment for iron and manganese to share in a magnetic alloy. This is actually not the case. FeMnSb is a *ferrimagnet*, so $2\,\mu_B$ represents the *difference* of the moments on iron and manganese. This way, both the energy gain of the energy gap as well as the maximal gain in exchange energy can be obtained: the ferromagnetic solution can accommodate the larger moments as well, but at the expense of the energy gain associated with the band gap. This constitutes an exchange coupling mechanism unique for half-metals and is expected to occur for band gaps exceeding the exchange coupling strengths, which rarely exceed 0.1 eV. The next case is MnMnSb (this notation is used to accentuate the very different crystallographic point group symmetries of the two manganese atoms). It is a half-metallic ferrimagnet with a net moment of $1\,\mu_B$. Another way of reducing the number of charge carriers is the substitution of nickel with 4d or 5d elements like osmium, iridium, or rhodium. In these cases, the exchange interaction of the introduced elements is not strong enough to maintain half-metallic properties. Instead a rigid band like that of the Fermi energy occurs. The band gap is maintained, but the Fermi level is positioned below the top of the valence band. PtMnSn shows a similar behavior (de Groot van der Kraan and Buschow, 1986).

The results discussed in the previous paragraph are only partially confirmed experimentally, mainly because of the fact that these systems adopt different crystal structures. Experimentally a magnetic moment different from $3\,\mu_B$ is found for CoMnSb. The explanation for this discrepancy is that CoMnSb actually shows a tetragonal superstructure related to the Heusler $C1_b$ structure but with partial occupation of cobalt on the empty sites (Szytula *et al*., 1972). The situation for FeMnSb is also more complex. Partial substitution of Ni by Fe in NiMnSb leads initially to the theoretically expected behavior. But beyond 10%, a second non-half-metallic phase similar to CoMnSb shows up. No calculations have been reported on iron-substituted NiMnSb yet. Mn_2Sb does exist and is experimentally found to be a ferrimagnet with a magnetic moment of $1\,\mu_B$. However, it crystallizes in the Cu_2Sb structure, quite different from the Heusler structure. Band structure calculations in the actual structure are consistent with the magnetic properties, but do not show any sign of half-metallicity (Wijngaard, Haas and de Groot, 1992).

Potentially, other half-metals could exist by substituting both transition metals in NiMnSb. CoVSb has been seriously considered, but has been rejected on the basis of neutron scattering work (Heyne *et al*., 2005).

2.3.2 CrMnSb, half-metallic antiferromagnetism

The SP curve described in Section 2.3.1 intersects the ordinate for CrMnSb. Usually, the intersection of the SP curve

is an indication of a nonmagnetic solution. But in this particular case, we have seen that the reduction of magnetization following the SP curve is energetically more favorably realized by adopting an antiparallel ordering of the magnetic moments of the two different magnetic atoms. Following this trend toward CrMnSb, a fundamentally new type of material is encountered: There is no net magnetization, *but the conduction electrons remain completely spin polarized.* This was baptized half-metallic antiferromagnetism (de Groot, 1991). It is a situation quite distinct from traditional antiferromagnets, in which magnetization vanishes because of a symmetry operator or a spin-density wave. As a matter of fact, the half-metallic antiferromagnetism is so different from conventional antiferromagnetism, that its name is controversial. The reason we use the name is that the cancellation of the moments on *different* atoms (Cr and Mn in this case) on *different* Wyckoff positions is, nevertheless, *exact.* It follows from the requirement of integral magnetic moments for half-metals and this is zero here. Unfortunately, CrMnSb actually crystallizes in the same crystal structure as Mn_2Sb, and although it is antiferromagnetic for some range of composition it is not half-metallic. Isoelectronic VFeSb does adopt the Heusler $C1_b$ structure, but it is a nonmagnetic semiconductor. Clearly, the energy gain of having a band gap for the second spin direction exceeds the gain in exchange energy of a magnetic solution here. The half-metallic antiferromagnetic solution could be stabilized in a calculation by partially replacing the more delocalized d metal vanadium by manganese (van Leuken and de Groot, 1995). The required electron count was maintained by modifying the occupation of the main-group element: $(VFeSb)_{(1-x)}(MnFeIn)_x$. We are not aware of any attempts to synthesize this compound. A practical realization, whether as a Heusler alloy or other, would be important. Not only has it been predicted that half-metallic antiferromagnets show a novel form of superconductivity ('single-spin superconductivity') (Pickett, 1996) but also that applications of systems with 100% spin polarization without magnetization are easily imagined.

3 HEUSLER $L2_1$ STRUCTURE

The Heusler $L2_1$ structure is obtained by occupation of the remaining open position of the $C1_b$ structure by the element with cube coordination already present in this structure. This introduces an inversion center in the crystal structure and eliminates the tetrahedral coordination of the two atoms in the half-Heusler structure. The strong interatomic interaction responsible for the well-defined band gaps in the half Heuslers is forbidden by symmetry in the full Heuslers. The relation with zinc-blende semiconductors is lost, as evidenced by the distinct band gap topologies. Half-metals in the $L2_1$ show narrower bands, and a band gap opens up simply because the bandwidth is not always larger than a ligand-field splitting. This process is quite independent of the structure; a continuing decrease of interatomic interactions with respect to crystal-field and intra-atomic interactions leads through various other possible type of half-metals to magnetite in the end (Yanase and Siratori, 1984), at which point a Mott insulating state occurs. This is case 3 of half-metallicity in the classification scheme of half-metals (Fang, de Wijs and de Groot, 2002). The fact that both classes of half-metals ($C1_b$ and $L2_1$) share the *same* SP curve should not be interpreted as an indication of a common detailed mechanism in both cases; it merely reflects the fact that bonding–antibonding interactions are strongest near half-filled electron shells, independent of the specific details of these interactions. (Several different versions of the SP curves exist. Both classes of Heuslers fall only on the same SP curve if the unit of the ordinate is the average number of charge carriers per atom.)

The number of known full-Heusler alloys as well as the number of potential half-metals is larger than those for the half Heuslers. Much of the systems investigated at this moment go back to the early experimental work of Ziebeck and Webster (1974). From a computational point of view, besides the early work of Kübler, important early work came from the Japanese group (Fujii, Sugimura, Ishida and Asano, 1990; Ishida, Fujii, Kashiwagi and Asano, 1995; Fujii, Ishida and Asano, 1995). An important aspect is the occurrence of disorder in full Heuslers. The type of disorder that can occur and the influence of disorder, particularly, in connection with the integrity of the band gap is a subject of active research. There seems to be a trend that the most damaging types of disorder are also the energetically less favorable ones. This justifies some optimism in terms of applications, but the amount of disorder is not always determined by thermodynamics alone, in particular, in cases where samples are prepared at low temperatures. Annealing afterwards is sometimes difficult because of the risk of interdiffusion from or to a neighboring layer already present.

The physics of half-metals in the full-Heusler alloys is best displayed in an SP curve shown in Figure 7 (Galanakis, Dederichs and Papanikolaou, 2002). Galanakis, Dederichs, and Papanikolaou (2002) also compiled much of the experimental and computational results on full Heuslers. For this reason we will concentrate on more recent work here. Much work has been done on the alloys in the upper right corner of the SP curve. Magnetic moments are relatively large here, but more importantly, the Curie temperatures are also high. Several groups have addressed the problem of impurities in Co_2MnSi. A strong dependence on the impurity concentration was found depending on the preparation condition as inferred from residual resistance ratios (RRRs) (Raphael

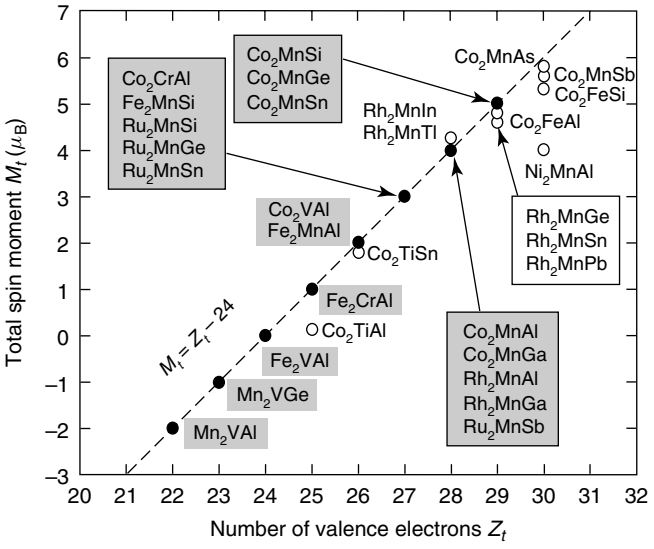

Figure 7. Calculated total spin moments for all the studied Heusler alloys. The dashed line represents the Slater–Pauling behavior. With open circles we present the compounds deviating from the SP curve.

et al., 2002). Single crystals showed an RRR of 6.5, arc melted samples 2.7, while the best films had an RRR of 1.4. Neutron diffraction on polycrystalline bulk samples showed the presence of Co–Mn disorder. Electronic structure calculations (Picozzi, Continenza and Freeman, 2004) showed a Mn antisite to be harmless, but a Co antisite induces a strong peak in the density of states at the Fermi level for the majority spin. It is considered of rather localized character, however. The effect of imperfections, strain, and impurities were investigated for Co_2MnGe, isoelectronic with the silicon analog (Carey, Block and Gurney, 2004). The effect of strain on the spin polarization of the conduction electrons was negligible up to 3%. On the other hand, the presence of impurities and, in particular, oxygen has a devastating effect. Nevertheless, Co_2MnSi showed 61% tunneling magnetoresistance at a temperature of 10 K, using an aluminum oxide barrier (Kammerer, Thomas, Huetten and Reiss, 2004). The effect decreases rather fast, but is continuous with temperature, which is explained in nonperfect interfaces.

Half-metallic behavior was predicted for Co_2CrAl, with the magnetic moment of $3\,\mu_B$ expected from the SP curve. Experimentally a magnetic moment of $1.55\,\mu_B$ was obtained, which would disprove half-metallicity (Buschow and van Engen, 1981). However, later work showed variations of the magnetic moment between 1.5 and $3\,\mu_B$. Reproducible moments in line with a half-metallicity are obtained by partially substituting Cr by Fe (Elmers *et al.*, 2003 and reference 7 therein). Electronic structure calculations proved that a low iron concentration was most effective (Miura, Nagao and Shirai, 2004). Two detailed studies of interfaces with III–V semiconductors were reported recently. Although half-metallicity was lost, a very high degree of spin polarization (estimated at ∼90% from Figure 1) was obtained for the (110) interface with GaAs – higher than (100) interfaces (Nagao, Shirai and Miura, 2004). For InP, on the other hand, the (001) surface showed more than 80% majority-spin contribution at the Fermi level (Galanakis, 2004), corresponding to over 60% spin polarization.

Finally, we consider the half-metals with low electron concentration, which are found in the lower left part of the SP curve. The half-metallic properties of Fe_2CrAl could not be confirmed experimentally. The magnetic moment derived from the saturation magnetization was $1.75\,\mu_B$ rather than the $1\,\mu_B$ expected from the SP curve. Also, the band structure did not show half-metallic properties, when calculated with the experimental lattice constant (Zhang, Bruck, de Boer and Wu, 2004).

A most interesting phenomenon, at least from a scientific point of view, occurs when following the SP curve further to the left. One step to the left of Fe_2CrAl, one arrives at Fe_2VAl, where the SP curve crosses the ordinate. Consequently, no distinction between majority spin and minority spin exists anymore, which implies either a half-metallic antiferromagnet or a nonmagnetic solution, where the preservation of the band gap along the SP curve suggests semiconducting behavior. Experimentally, it is a nonmagnetic semiconductor with exotic properties, which are outside the scope of this review. *But the SP curve continues beyond this point.* The crossing of the ordinate in the SP curve indicates a transition from half-metals with a minority-spin gap to half-metals with a majority-spin gap for Mn_2VAl (Weht and Pickett, 1999). Half-metals with a majority-spin gap are rare. Other examples are found in the double perovskites (Kobayashi *et al.*, 1998) and magnetite (Fe_3O_4), but the half-metallic properties of the latter compound are seriously challenged. The many-body physics at finite temperature of half-metals with a band gap for majority-spin electrons is distinct from that of ordinary half-metals (Irkhin and Katsnelson, 1994). The prospect of studying these differences in a series of similar chemical compounds is a challenge for the future.

REFERENCES

Antonov, V.N., Opponeer, P.M., Yaresko, A.N., *et al.* (1997). Computationally based explanation of the peculiar magneto-optical properties of PtMnSb and related ternary compounds. *Physical Review B*, **56**, 13012–13025.

Attema, J.J., Fang, C.M., Chioncel, L., *et al.* (2004). Defects in half-metals and finite temperatures. *Journal of Physics: Condensed Matter*, **16**, S5517–S5524.

Auth, N., Jakob, G., Block, T. and Felser, C. (2003). Spin polarization of magnetoresistive materials by point contact spectroscopy. *Physical Review B*, **68**, 024403-1–024403-6.

Bona, G.L., Meier, F., Taborelli, M., *et al*. (1985). Spin Polarized Photoemission from NiMnSb. *Solid State Communications*, **56**, 391.

Borca, C.N., Komesu, T., Jeong, H-K., *et al*. (2001). Evidence for temperature dependent moments ordering in ferromagnetic NiMnSb(100). *Physical Review B*, **64**, 052409-1–052409-4.

Buschow, K.H.J. and van Engen, P.G. (1981). Magnetic and magneto-optical properties of Heusler alloys based on aluminium and gallium. *Journal of Magnetism and Magnetic Materials*, **25**, 90–96.

Carey, M.J., Block, T. and Gurney, B.A. (2004). Band-structure calculations of imperfect Co2MnGe Heusler compounds. *Applied Physics Letters*, **85**, 4442–4444.

Carey, R., Newman, D.M. and Wears, M.L. (2000). Giant low-temperature enhancement of magneto-optic Kerr effects in PtMnSb. *Physical Review B*, **62**, 1520–1523.

Elmers, H.J., Fecher, G.H., Valdaitsev, D., *et al*. (2003). Element-specific magnetic moments from core-absorption magnetic circular dichroism of the doped Heusler alloy Co2Cr0.6Fe0.4Al. *Physical Review B*, **76**, 104412-1–104412-8.

van Engen, P.G., Buschow, K.H.J. and Jongebreur, R. (1983). PtMnSb, a material with very high magneto-optical Kerr effect. *Applied Physics Letters*, **42**, 202–204.

Eschrig, M., Kopu, J., Cuevas, J.C. and Schoen, G. (2003). Theory of half-metal/superconductor heterostructures. *Physical Review Letters*, **90**, 137003-1–137003-4.

Fang, C.M., de Wijs, G.A. and de Groot, R.A. (2002). Spin-polarization in half-metals. *Journal of Applied Physics*, **91**, 8340–8344.

Feil, H. and Haas, C. (1987). Magneto-optical Kerr effect, enhanced by plasma resonance of charge carriers. *Physical Review Letters*, **58**, 65–68.

Fujii, S., Ishida, S. and Asano, S. (1995). A half-metallic band-structure and Fe(2)MnZ (Z=Al,Si,P). *Journal of the Physical Society of Japan*, **64**, 185–191.

Fujii, S., Sugimura, S., Ishida, S. and Asano, S. (1990). Hyperfine fields and electronic structure of the Heusler alloys Co2MnAl, Co2MnGa, Co2MnSi, Co2MnGe, Co2MnSn. *Journal of Physics: Condensed Matter*, **2**, 8583–8589.

Galanakis, I. (2002). Surface properties of the half- and full-Heusler alloys. *Journal of Physics: Condensed Matter*, **14**, 6329–6340.

Galanakis, I. (2004). Towards half-metallic interfaces: Co2CrAl/InP contacts. *Journal of Physics: Condensed Matter*, **16**, 8007–8014.

Galanakis, I., Dederichs, P.H. and Papanikolaou, N. (2002). Slater-Pauling behavior and the origin of the half-metallicity of the full-Heusler alloys. *Physical Review B*, **66**, 174429-1–174429-9.

Gao, X., Woollam, J.A., Kirby, R.D., *et al*. (1999). Dielectric tensor for magneto-optic NiMnSb. *Physical Review B*, **59**, 9965–9971.

de Groot, R.A. (1991). Halfmetallic magnetism in the 1990's. *Physica B*, **172**, 45.

de Groot, R.A., van der Kraan, A.M. and Buschow, K.H.J. (1986). FeMnSb, a half-metallic ferrimagnet. *Journal of Magnetism and Magnetic Materials*, **61**, 330–336.

de Groot, R.A., Mueller, F.M., van Engen, P.G. and Buschow, K.H.J. (1983). New class of materials: half-metallic ferromagnets. *Physical Review Letters*, **50**, 2024–2027.

de Groot, R.A., Mueller, F.M., van Engen, P.G. and Buschow, K.H.J. (1984). Half-metallic ferromagnets and their magneto-optical properties (invited). *Journal of Applied Physics*, **55**, 2151–2155.

Halilov, S.V. and Kulatov, E.T. (1991). Electron and magneto-optical properties of half-metallic ferromagnets and uranium monochalcogenide. *Journal of Physics: Condensed Matter*, **3**, 6363–6374.

Hanssen, K.E.H. and Mijnarends, P.E. (1986). Positron-annihilation study of the half-metallic ferromagnet NiMnSb-theory. *Physical Review B*, **34**, 5009–5016.

Hanssen, K.E.H., Mijnarends, P.E., Rabou, P.L.L.M. and Buschow, K.H.J. (1990). Positron-annihilation study of the half-metallic ferromagnet NiMnSb-experiment. *Physical Review B*, **42**, 1533–1540.

Helmholdt, R.B., de Groot, R.A., Mueller, F.M., *et al*. (1984). Magnetic and crystallographic properties of several $C1_b$ type Heusler compounds. *Journal of Magnetism and Magnetic Materials*, **43**, 249–255.

Heusler, Fr. (1903). Ueber die synthese ferromagnetischer manganlegierungen. *Verhandlungen der Deutschen Physikalischen Gesellschaft*, **5**, 219–223.

Heyne, L., Igarashi, T., Kanomata, T., *et al*. (2005). Atomic and magnetic order in the weak ferromagnet CoVSb: is it a half-metallic ferromagnet? *Journal of Physics: Condensed Matter*, **17**, 4991–4999.

Hordequin, C., Ristoiu, D., Ranno, L. and Pierre, J. (2000). On the cross-over from half-metal to normal metal in NiMnSb. *European Physical Journal B*, **16**, 287–293.

Irkhin, V.Y. and Katsnelson, M.I. (1994). Half-metallic ferromagnets. *Physics Uspekhi*, **37**, 659–676.

Irkhin, V.Y. and Katsnelson, M.I. (2002). Temperature dependences of resistivity and magnetoresistivity for halfmetallic ferromagnets. *European Physical Journal B*, **30**, 481–486.

Ishida, S., Fujii, S., Kashiwagi, S. and Asano, S. (1995). Search for half-metallic properties of new Heusler alloys Ru(2)MnZ (Z=Ge, Sn and Sb). *Journal of the Physical Society of Japan*, **64**, 2152–2157.

Jenkins, S.J. (2004). Ternary half-metallics and related binary compounds: Stoichiometry, surface states, and spin. *Physical Review B,* **70**, 245401.

Jenkins, S.J. and King, D.A. (2001). Minority metallic surface states of a half-metallic ferrimagnet. *Surface Science*, **494**, 159.

Kammerer, S., Thomas, A., Huetten, A. and Reiss, G. (2004). Co2MnSi Heusler alloy as magnetic electrodes in magnetic tunnel junctions. *Applied Physics Letters*, **85**, 79–81.

Kobayashi, K.L., Kimura, T., Sawada, H., *et al*. (1998). Room temperature magnetoresistance in an oxide material with an ordered double-perovskite structure. *Nature*, **395**, 677–680.

Kübler, J. (1984). First principles theory of metallic magnetism. *Physica*, **127B**, 257–263.

Kübler, J. (2000). *Theory of Itinerant Electron Magnetism*, Clarendon Press: Oxford.

Kübler, J., Williams, A.R. and Sommers, C.B. (1983). Formation and coupling of magnetic moments in Heusler alloys. *Physical Review B*, **28**, 1745.

Kulatov, E., Uspenkii, Yu. and Halilov, S. (1995). Ab initio calculated magneto-optical spectra of half-metallic ferromagnets. *Journal of Magnetism and Magnetic Materials*, **145**, 395–397.

van Leuken, H. and de Groot, R.A. (1995). Half-metallic antiferromagnets. *Physical Review Letters*, **74**, 1171–1173.

Miura, Y., Nagao, K. and Shirai, M. (2004). Atomic disorder effects on half-metallicity of the full-Heusler alloys Co2(Cr1-xFex)Al: a first principles study. *Physical Review B*, **69**, 144413-1–144413-7.

Nagao, K., Shirai, M. and Miura, Y. (2004). *Ab initio* calculations of spin polarization at Co_2CrAl/GaAs interfaces. *Journal of Physics: Condensed Matter*, **16**, S5725–S5728.

Orgassa, D., Fujiwara, H., Schulthess, T.C. and Butler, W.H. (2000). Disorder dependence of the magnetic moment of the half-metallic ferromagnet NiMnSb from first principles. *Journal of Applied Physics*, **87**, 5870–5871.

Pickett, W.E. (1996). Single spin superconductivity. *Physical Review Letters*, **77**, 3185–3188.

Picozzi, S., Continenza, A. and Freeman, A.J. (2004). Role of structural defects on the half-metallic character of Co2MnGe and Co2MnSi Heusler alloys. *Physical Review B*, **69**, 094423.

Raphael, M.P., Ravel, B., Huang, Q., *et al*. (2002). Presence of antisite disorder and its characterization in the predicted half-metal Co2MnSi. *Physical Review B*, **66**, 104429-1–104429-6.

Ristoiu, D., Nozieres, J.P., Borca, C.N., *et al*. (2000). The surface composition and spin polarization of NiMnSb epitaxial thin films. *Europhysics Letters*, **49**, 624–630.

Schaf, J., Le Dang, K., Veillet, P. and Campbell, I.A. (1983). Extended and local effects of cold work in Heusler alloys. *Journal of Physics F: Metal Physics*, **13**, 1311–1316.

Soulen, R.J., Byers, J.M., Osofsky, M.S., *et al*. (1998). Measuring the spin polarization of a metal with a superconducting point contact. *Science*, **282**, 85–88.

Szytula, A., Szelag, J., Todorovi, J., *et al*. (1972). Atomic and magnetic study of Heusler alloys NiMnSb and CoMnSb. *Physica Status Solidi A: Applied Research*, **9**, 97–103.

Van Roy, W., Borghs, G. and De Boeck, J. (2001). Epitaxial growth of the half-metallic ferromagnet NiMnSb on GaAs(001). *Journal of Crystal Growth*, **227**, 862.

Van Roy, W., De Boeck, J., Brijs, B. and Borghs, G. (2000). Epitaxial NiMnSb films on GaAs(001). *Applied Physics Letters*, **77**, 4190.

Van Roy, W., Wojcik, M., Jedryka, E., *et al*. (2003). Very low chemical disorder in epitaxial NiMnSb films on GaAs(111)B. *Applied Physics Letters*, **83**, 4214.

Weht, R. and Pickett, W.E. (1999). Half-metallic ferrimagnetism in Mn2VAl. *Physical Review B*, **60**, 13006.

Wijngaard, J.H., Haas, C. and de Groot, R.A. (1989). Origin of the differences in the magneto-optical Kerr effect between PtMnSb and NiMnSb. *Physical Review B*, **40**, 9319–9320.

Wijngaard, J.H., Haas, C. and de Groot, R.A. (1992). Ferrimagnetic-antiferromagnetic phase transition in $Mn_{2-x}Cr_xSb$: electronic structure and electrical and magnetic properties. *Physical Review B*, **45**, 5359–5405.

de Wijs, G.A. and de Groot, R.A. (2001). Towards 100% spin-polarized charge-injection: the half-metallic NiMnSb/CdS interface. *Physical Review B*, **64**, 020402-1–020402-4.

Yanase, A. and Siratori, K. (1984). Band structure in the high temperature phase of Fe_3O_4. *Journal of the Physical Society of Japan*, **53**, 312–317.

Zhang, M., Bruck, E., de Boer, F.R. and Wu, G.G. (2004). Electronic structure, magnetism and transport properties of the Heusler alloy Fe_2CrAl. *Journal of Magnetism and Magnetic Materials*, **283**, 409–414.

Ziebeck, K.R.A. and Webster, P.J. (1974). Neutron-diffraction and magnetization study of Heusler alloys containing Co and Zr, Hf or Nb. *Journal of Physics and Chemistry of Solids*, **35**, 1–7.

Half-metals

M. Venkatesan
Trinity College, Dublin 2, Ireland

1 INTRODUCTION

Half-metallic ferromagnets are solids that are metals with a Fermi surface in one spin channel, but for the opposite spin there is a gap in the spin-polarized density of states (DOS), like a semiconductor or insulator (O'Handley, 2000). The gap may occur in either the majority or minority channel. In general, half-metals are ferromagnetic but a ferromagnet is not necessarily a half-metal. Half-metals are the extreme case of strong ferromagnets where not only $3d$ electrons are fully polarized, but also other (sp) down-spin bands do not cross the Fermi level. As a result of this, only electrons of one spin direction contribute toward conduction yielding 100% spin polarization at the Fermi energy, E_F. This unusual property could have significant implications for applications related to magnetism and spin electronics. Electrically conducting ferromagnetic materials where the conduction electrons have a high mobility and are fully spin polarized are desirable for realizing future thin-film spin electronic devices. Since the devices will probably be expected to work around and above room temperature, the new ferromagnets should have Curie temperatures in excess of 500 K. Half-metallic ferromagnetic electrodes can serve as ideal spin injectors and detectors, because they can carry current in only one spin direction under moderate voltage. They also constitute ideal components for giant magnetoresistance (GMR) and tunneling magnetoresistance (TMR) devices.

Half-metallicity yields features of the solid that are quite different from conventional ferromagnetic metals. It is not an easy property to detect experimentally, unlike superconductors, metals, semiconductors, or insulators where there is a clear indication in electrical transport. It has therefore been customary to rely on electronic structure calculations to identify half-metals. One of the features is flat high-field susceptibility at low temperature, but it is impractical to measure the intrinsic high-field susceptibility of a ferromagnet accurately to assert that it is zero. The response of a half-metal to an electric and magnetic field is quite different. There is electric conductivity, but no high-field magnetic susceptibility. The application of an external magnetic field only shifts the up- and down-spin bands by $\pm g\mu_B H$ with no change in net spin moment. Hence, the spin susceptibility vanishes, like an insulator. The best indication of a half-metal is metallic conduction in a solid with a spin moment at $T = 0$ which is *precisely an integral number of Bohr magnetons per unit cell*. In a stoichiometric compound, the number of electrons per unit cell $n = n^{\uparrow} + n^{\downarrow}$ is an integer. On account of the gap in one of the spin-polarized bands, $n^{\uparrow}$ or $n^{\downarrow}$ is also an integer. It follows that both $n^{\uparrow}$ and $n^{\downarrow}$ are integers, and so

Handbook of Magnetism and Advanced Magnetic Materials. Edited by Helmut Kronmüller and Stuart Parkin. Volume 4: *Novel Materials*. ISBN: 978-0-470-02217-7.

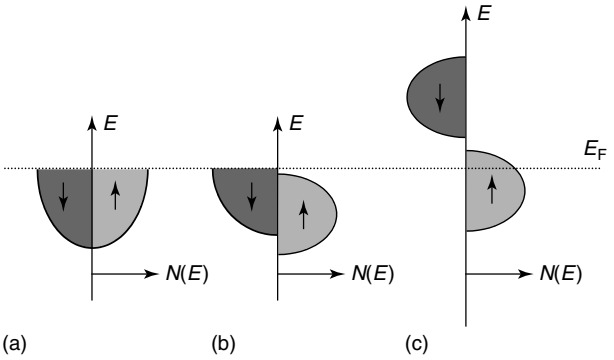

Figure 1. Schematic densities of states of (a) a normal metal, (b) a ferromagnetic metal, and (c) a half-metal.

is the difference $n^{\uparrow} - n^{\downarrow}$ which is the spin moment in units of the Bohr magneton. The integer spin moment criterion, or an extension of it to cover the case of a solid solution, is a necessary but not a sufficient condition for half-metallicity.

The schematic diagram of a normal metal, ferromagnetic metal, and half-metal is shown in Figure 1. Normal and conventional ferromagnets such as Fe, Co, Ni are not half-metals. The conduction electrons in the 3*d* ferromagnets are not fully spin polarized, even when the d band is strongly spin split, because of the simultaneous presence of 4*s* electrons at the Fermi level. Cobalt and nickel, for example, are strong ferromagnets with fully spin-polarized d bands and fully occupied majority spin states (↑ 3*d* band), and only ↓ 3*d* electrons at E_F (O'Handley, 2000). However, the Fermi level also crosses the unpolarized 4*s* band, which carries most of the current. So there are both the spin-up and spin-down densities of states present at E_F. In order to obtain only ↑ or ↓ electrons at E_F, it is necessary to reorder the 3*d* and 4*s* bands. This is done by hybridization, pushing the bottom of the 4*s* band up above E_F or depressing the Fermi level in the d band below the bottom of the 4*s* band. Therefore, all half-metals consist of more than one element – they are alloys or compounds. Most known examples are oxides, sulfides, or Heusler alloys. Some are stoichiometric compounds, others are solid solutions.

2 CLASSIFICATION OF HALF-METALS

Half-metals can be classified (Coey, Venkatesan and Bari, 2001; Coey and Sanvito, 2004) into four categories, types I–IV, as presented in Figure 2. Type IA (IB) half-metals (Figure 2a and b) only have majority (minority) spin electrons appearing at E_F. In type II half-metals (Figure 2c), the electrons lie in a band that is sufficiently narrow for them to be localized. The heavy carriers may then form polarons, where conduction takes place via electron hopping between spin-polarized sites. Type III half-metals (Figure 2d) have localized ↑ carriers and delocalized ↓ carriers or vice versa (also known as *transport half-metal*). A DOS exists for *both* subbands at E_F, but the carriers in one band have a much larger effective mass than those in the other. As far as electronic transport properties are concerned, only one sort of carriers contributes significantly to the conduction. Type IV half-metals (Figure 2f) are semimetallic – magnetically ordered semimetals with a great difference in effective masses between electrons and holes. There is a big difference between a half-metal and a semimetal. A semimetal (Figure 2e) like bismuth, graphite, or antimony is usually nonmagnetic with small and equal numbers of electrons and holes (≈ 0.01 per atom) due to a small overlap between valence and conduction bands. Table 1 summarizes the various types of half-metals in detail (Coey, Venkatesan and Bari, 2001; Coey and Sanvito, 2004).

3 HALF-METALLIC MATERIALS

In this section, we will review some materials that are claimed to be half-metals before discussing the experimental techniques needed to measure spin polarization and other half-metallic characteristics. There are two main classes of materials – oxides and Heusler alloys. The crystal structures of a few representative materials are presented in Figure 3. Table 2 summarizes the list of different types of half metallic materials with predicted spin moment per formula unit, deduced from band structure calculations, and the Curie temperature.

3.1 Oxides

3.1.1 CrO_2

Chromium dioxide crystallizes in the tetragonal rutile structure (Barry, 1999; Coey and Venkatesan, 2002) and it is the best-studied half-metal in the literature (Barry, 1999; Coey and Venkatesan, 2002). The formal electronic configuration is $(t_{2g}^2)^{\uparrow}$ for Cr^{4+}, and $2p^6$ for O^{2-} although there is some $O^{2-} \rightarrow Cr^{4+}$ charge transfer and strong mixing of oxygen hole and chromium electron states at E_F (Lewis, Allen and Sasaki, 1997; Korotin, Anisimov, Khomski and Sawatzky, 1998). Band-structure calculations (Schwarz, 1986) have shown that CrO_2 is a half-metallic system (Figure 4a) with the spin-spilt band structure of a type IA half-metal and a spin gap $\Delta_{\downarrow} > 1$ eV. The half-metallic character is maintained up to the surface (van Leuken and de Groot, 1995). The calculations generally show a t_{2g} bandwidth of 2.5–3.0 eV, with a trident structure including a narrow peak in the DOS due to the d_{xy} electrons. All the calculations and experimental

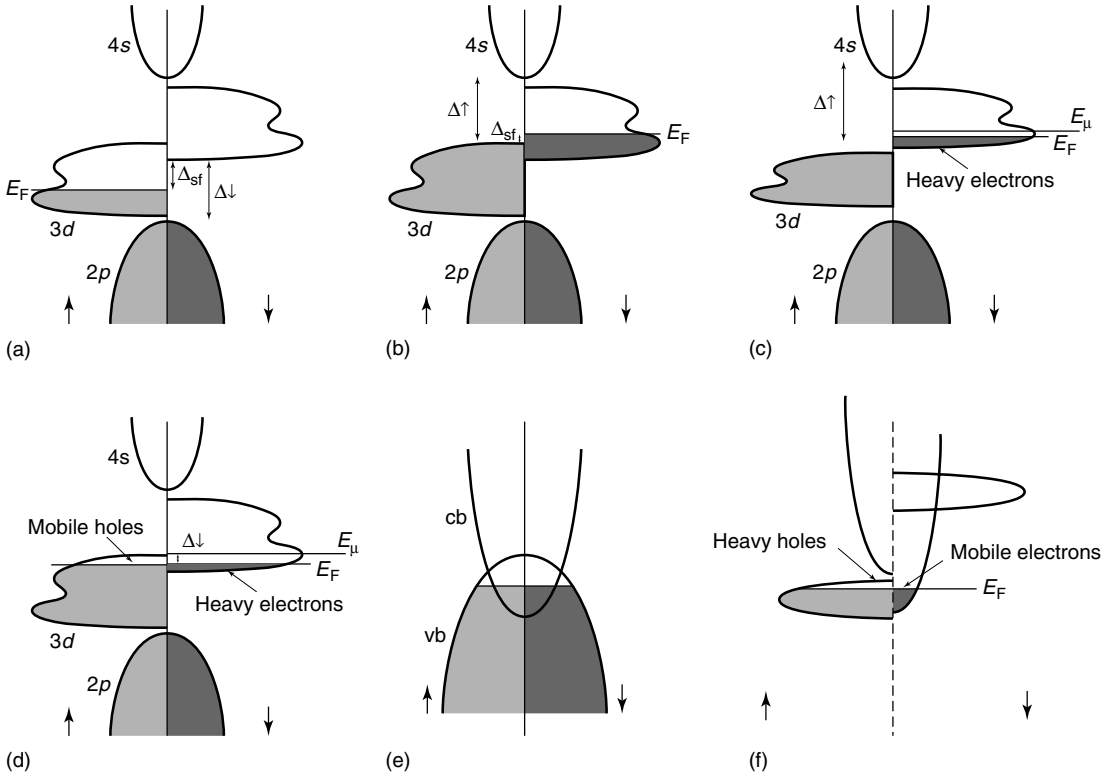

Figure 2. Schematic density of states for a half-metal. (a) Type IA with only ↑ electrons at E_F, (b) type IB with only ↓ electrons at E_F, (c) type II, (d) type III, (e) semimetal, (f) type IV, half-metallic semimetal. The symbols Δ_{sf}, $\Delta_{\uparrow,\downarrow}$, and E_μ refer to the spin-flip excitation energy, spin gap, and the mobility edge, respectively (Coey, Venkatesan and Bari, 2001; Coey and Sanvito, 2004).

Table 1. Summary of the classification of half-metals (Coey, Venkatesan and Bari, 2001; Coey and Sanvito, 2004).

Type	Density of states	Conductivity	↑ electrons at E_F	↓ electrons at E_F
1A	Half-metal	Metallic	Itinerant	None
1B	Half-metal	Metallic	None	Itinerant
IIA	Half-metal	Nonmetallic	Localized	None
IIB	Half-metal	Nonmetallic	None	Localized
IIIA	Metal	Metallic	Itinerant	Localized
IIIB	Metal	Metallic	Localized	Itinerant
IVA	Semimetal	Metallic	Itinerant	Localized
IVB	Semimetal	Metallic	Localized	Itinerant
VA	Semiconductor	Semiconducting	Few, itinerant	None
VB	Semiconductor	Semiconducting	None	Few, itinerant

results yield a low-temperature magnetic moment of $\sigma = 133\,\mathrm{Am^2\,kg^{-1}}$ corresponding to an integral moment of $2.0\,\mu_B$ per formula unit (Chamberland, 1977). The Curie temperature of CrO_2 is about 395 K. The transport properties (resistivity, magnetoresistance) exhibit a syndrome where spin-flip scattering seems to be suppressed below a temperature $\Delta \approx 0.2T_C$. This is related to spin-wave excitations and not to the spin-flip gap Δ_{sf}, which is many times greater than Δ. A series of Andreev reflection measurements (Soulen *et al.*, 1998; Ji *et al.*, 2001) have been carried out on CrO_2 – superconductor point contacts. These indicate a very high spin polarization, $P \approx 80$–96% for CrO_2 at low temperatures (<2 K).

3.1.2 Fe_3O_4

Magnetite, the most famous magnetic mineral, is a spin-polarized, Fe^{2+}–Fe^{3+} mixed-valence metal. It is the half-metal with the highest Curie temperature (860 K) among oxides. The B sites of the spinel structure (Figure 3b) are populated by an equal mixture of Fe^{3+} and Fe^{2+}, so the average B-site configuration is $(t_{2g}^3 e_g^2)^\uparrow\ (t_{2g}^{0.5})^\downarrow$. The

Table 2. Half-metallic materials.

Material	Type	↑ electrons	↓ electrons	T_C (K)	$M = (N_\uparrow - N_\downarrow)$ μ_B	References
CrO_2	IA	Cr (t_{2g})	–	396	2	Coey and Venkatesan (2002), Lewis, Allen and Sasaki (1997) and Korotin, Anisimov, Khomski and Sawatzky (1998)
Sr_2FeMoO_6	IB	–	Mo (t_{2g})	420	4	Kobayashi *et al*. (1998)
Fe_3O_4	IIB	–	Fe (t_{2g})	860	4	Penicaud, Silberchiot, Sommers and Kubler (1992) and Zhang and Satpathy (1991)
$La_{0.7}Sr_{0.3}MnO_3$	IIIA	Mn (e_g)	Mn (t_{2g})	390	<3.7	Nadgorny *et al*. (2001)
$Tl_2Mn_2O_7$	IVB	Mn (t_{2g})	Tl (6*s*)	120	6	Singh (1997)
$(Co_{1-x}Fe_x)S_2$	IA	Co (e_g)	–	∼100	$(1-x)$	Jarrett *et al*. (1968) and Mazin (2000)
NiMnSb	IA	Ni (e_g)	–	730	4	de Groot, Mueller, van Engen and Buschow (1983)
PtMnSb	IA	Pt (e_g)	–	572	4	de Groot, Mueller, van Engen and Buschow (1983)
Co_2MnSi	IB	Co (t_{2g})	–	985	5	Fujii, Ishida and Asano (1995)
$Co_2(Cr_{0.6}Fe_{0.4})Al$	IA	Co (t_{2g})	–	690	<3.7	Block *et al*. (2003) and Felser, Elmers and Fecher (2005)
Mn_2VAl	IB	Mn (t_{2g})	–	760	2	Weht and Pickett (1999)

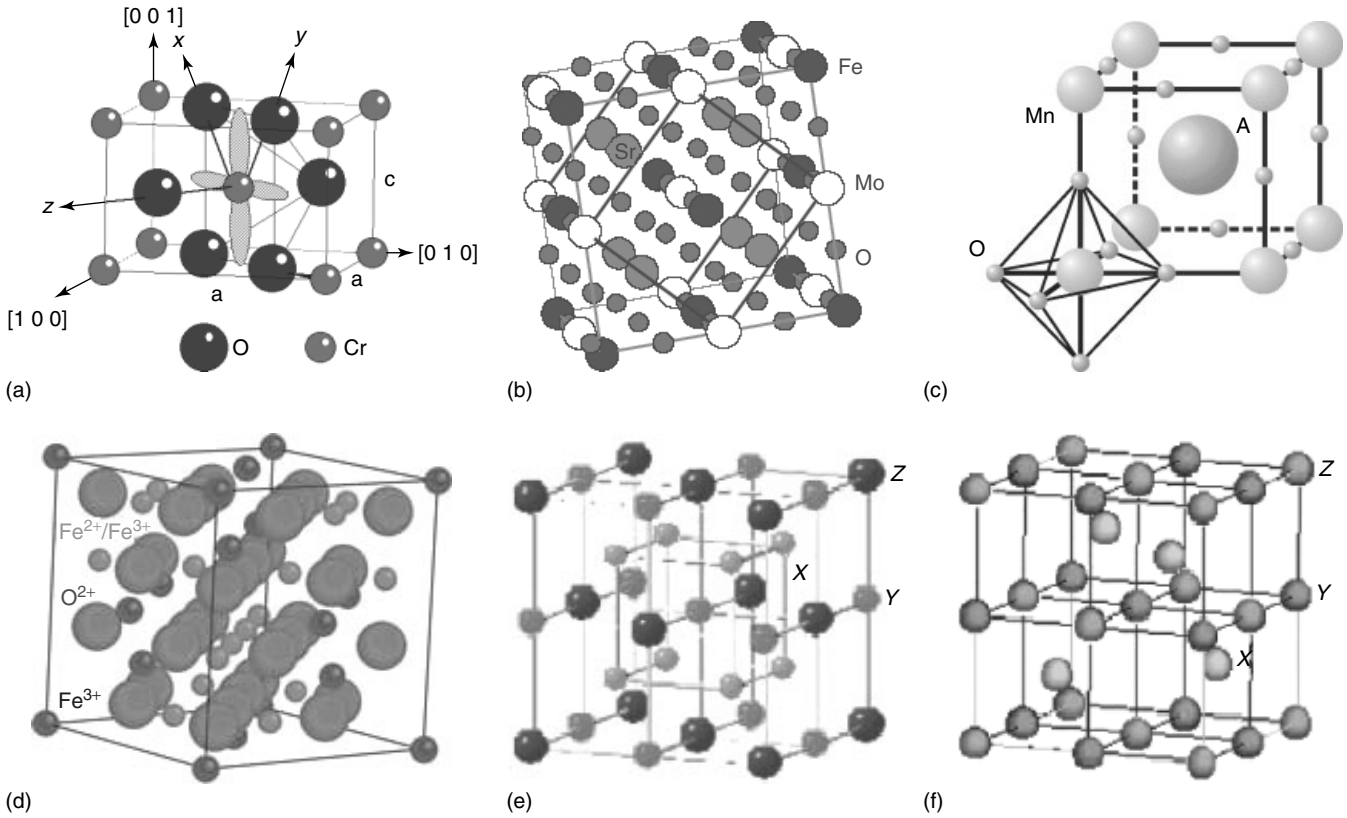

Figure 3. Crystal structure of (a) CrO_2, (b) Fe_3O_4, (c) (La,Sr)MnO_3, (d) Sr_2FeMoO_6, (e) half-Heusler, and (f) full-Heusler.

A sites contain oppositely magnetized $Fe^{3+}(t_{2g}^3 e_g^2)^\downarrow$ cores. The ↓ B-site electrons form small polarons which hop among the B sites (Brabers, 1995). Magnetite undergoes a metal–insulator phase transition below about 120 K in which the conductivity abruptly decreases by a factor ∼100 (Verwey, 1939). Resistivity at 120 K, where the B-site charges order, is $\sim 10^{-4}\,\Omega$m. High-quality films and crystals have a spin moment of $4.0\,\mu_B$ at this temperature, reflecting the ferrimagnetic structure of A and B sites. Magnetite is a type IIB half-metal with a spin gap in the majority DOS (Penicaud, Silberchiot, Sommers and Kubler, 1992; Zhang and Satpathy, 1991) as shown by the band structure in Figure 4(b). Despite the strong belief that magnetite should exhibit a large spin polarization owing to its half-metallicity,

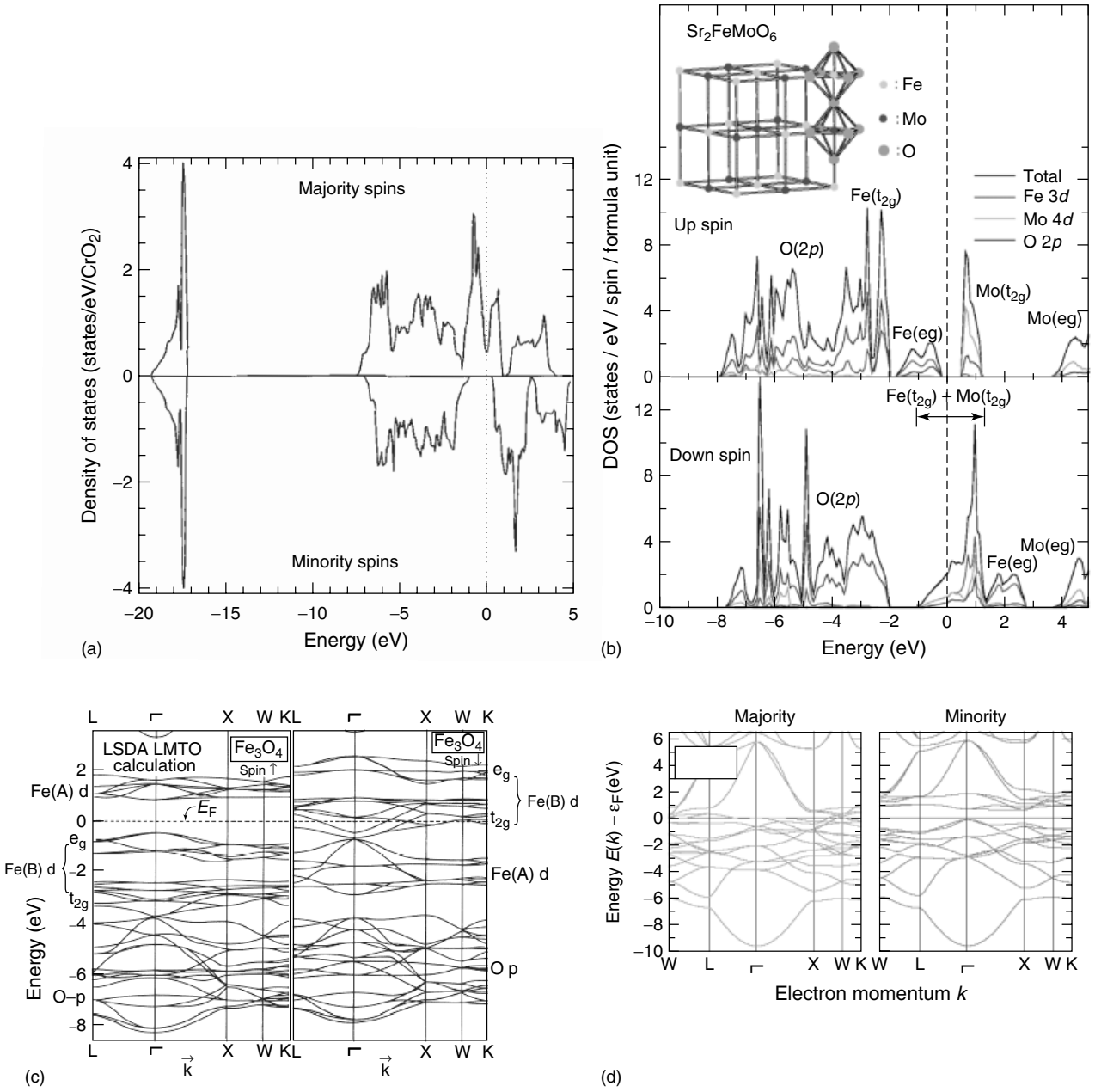

Figure 4. Density of state for majority and minority spins in (a) CrO_2 (Lewis, Allen and Sasaki, 1997; Korotin, Anisimov, Khomski and Sawatzky, 1998), (b) Fe_3O_4 (Penicaud, Silberchiot, Sommers and Kubler, 1992; Zhang and Satpathy, 1991), (c) Sr_2FeMoO_6 (Kobayashi *et al*., 1998), and (d) Co_2CrAl (Felser, Elmers and Fecher, 2005).

no concrete manifestation has been reported as yet and the low magnetoresistance values in TMR junctions is still not properly understood.

3.1.3 $La_{0.7}Sr_{0.3}MnO_3$

Optimally doped $La_{1-x}Sr_xMnO_3$ (LSMO) is a half-metallic material and potential candidate for spin electronics applications, although LSMO ($x = 0.3$–0.4) has a Curie temperature around 360–380 K, which is probably too low for any room-temperature devices. It crystallizes into a rhombohedrally distorted perovskite structure. The substitution of Sr for La creates a mixture of Mn^{3+} $(t_{2g}^3 e_g)^{\uparrow}$ and Mn^{4+} $(t_{2g}^3)^{\uparrow}$ on the B sites of the structure (Figure 3c) (Coey, Viret and von Molnar, 1999). The hopping $e_g^{\uparrow}$ electron produces ferromagnetic coupling by double exchange. The electronic structure of LSMO, as described by band theory, is completely

spin polarized reflecting the type III, transport half-metallic behavior (Nadgorny *et al*., 2001). Electronic structure calculations on this (Nadgorny *et al*., 2001) and the isostructural phase $(La_{0:67}Ca_{0:33})MnO_3$ (Pickett and Singh, 1996) place the Fermi level slightly above the bottom of the $t_{2g}^{\downarrow}$ band. The ferromagnetic moment is consistently reported as slightly less than the $3.7\,\mu_B$ when $x = 0.3$. $(La_{0.7}Sr_{0..3})MnO_3$ is a type IIIA half-metal, with both mobile $Mn(e_g)\uparrow$ electrons and immobile $Mn(t_{2g})\downarrow$ electrons at E_F having very different mobilities for the two spins.

3.1.4 Sr_2FeMoO_6

In the ordered double perovskites $A_2BB'O_6$, the transition-metal sites are occupied alternatively by different cations B and B' (Figure 3d). Oxygen atoms bridge between B and B', forming alternating octahedra with B or B' as central atom. The double perovskite Sr_2FeMoO_6 (SFMO) crystallizes in a tetragonal structure, space group $P4_2/n$, with NaCl-type order of Fe and Mo. Here, Fe and Mo ions alternate on the B and B' sites. In all the proposed models, its electronic structure is composed of localized up-spins borne by the Fe^{3+} ($S = 5/2$) ions and a conduction band partially occupied by the single itinerant down-spin electron provided by the Mo^{5+} ions. Formal electronic configurations are Fe^{3+} $(t_{2g}^3 e_g^2)^{\uparrow}$ and $Mo^{5+}(t_{2g}^1)^{\downarrow}$, although the Mo and Fe $t_{2g}^{\downarrow}$ orbitals are strongly mixed. A half-metallic structure (Figure 4c) is predicted (Kobayashi *et al*., 1998). The compound is ferrimagnetic with $T_C = 420\,K$ and a saturation magnetic moment of $4\,\mu_B$. It is a type IB half-metal. Some good-quality films have moments approaching this value (Westerburg, Reisinger and Jakob, 2000), but moments measured in single crystals are generally lower (Tomioka *et al*., 2000) which is usually attributed to antisite disorder of Fe and Mo. X-ray magnetic circular dichroism (XMCD) (Besse *et al*., 2002) confirms the presence of a finite spin moment on Mo together with only very small orbital moments on both Fe and Mo suggesting that the predicted half-metallicity is due to a configuration with five localized d electrons forming a high-spin moment on Fe and one antiparallel delocalized electron shared between the Mo and the other sites.

3.1.5 $Tl_2Mn_2O_7$

The pyrochlore manganite $Tl_2Mn_2O_7$ is a cubic compound with an interesting electronic structure and unexpected magnetic properties (Shimakawa, Kubo and Manako, 1996; Subramanian *et al*., 1996). In a simple ionic picture, the material would be an insulator containing Mn^{4+} ($3d^3$) and Tl^{3+} ($5d^{10}$) cations. Only the former bear the magnetic moment of $3\,\mu_B$ due to a $t_{2g}^{3\uparrow}$ configuration. The thallium compound, however, is a ferromagnetic semimetal with a small number of heavy holes at the top of a narrow $\uparrow$ band of mainly Mn (t_{2g}) character and an equal number of mobile $\downarrow$ electrons in a broadband of mixed Tl ($6s$), O ($2p$), and Mn ($3d$) character (Shimakawa *et al*., 1999; Singh, 1997; Mishra and Sathpaty, 1998). The number of carriers has been estimated at 0.086 per unit cell (Imai, Shimakawa, Sushko and Kubo, 2000) or 0.005 per manganese from LSDA-LAPW calculations. Other calculations (Shimakawa *et al*., 1999; Singh, 1997; Mishra and Sathpaty, 1998) give 0.04 or 0.24 carriers per unit cell, but all agree on the ferromagnetic semimetallic structure. The mobile $\downarrow$ electrons are expected to dominate the conduction, while the heavy $\uparrow$ holes, for which the Fermi energy lies just 0.07 eV below the top of the band, will be easily localized by any impurities or disorder that may be present in the compound. $Tl_2Mn_2O_7$ can also be regarded as a half-metal insofar as the $\uparrow$ holes do not contribute significantly to the conduction; it is therefore a type IVB half-metal (Coey and Sanvito, 2004). Measurements of the Hall effect confirm the electronic structure predictions to the extent that the Hall coefficient is negative, and corresponds, in a one-band model, to 0.01–0.05 electrons per unit cell (Shimakawa, Kubo and Manako, 1996; Imai, Shimakawa, Sushko and Kubo, 2000).

3.2 Heusler alloys

Another promising class of materials for spin electronic applications is the Heusler alloys, a number of which have been predicted to be half-metallic ferromagents (de Groot, Mueller, van Engen and Buschow, 1983; Pickett and Moodera, 2001; Irkhin and Katsnel'son, 1994; Galanakis and Dederichs, 2005). The Heusler structures consist of four interpenetrating fcc sublattices, some of which may or may not be filled. Full-Heusler alloy, A_2BC, crystallizes in the $L2_1$ structure (Figure 3f) and all the sublattices are filled. Half-Heusler alloy, ABC, crystallizes in the Cl_b crystal structure (Figure 3e) and the A_1 sublattice is empty. The Cl_B structure is closely related to the zinc-blende structure. Some of these alloys exhibit very high Curie temperatures (as high as 1100 K) and integral spin moments required for half-metallicity. Both Heusler and half-Heusler compounds show the Slater–Pauling behavior (Kübler, 1984) of the binary transition-metal alloys. The total spin magnetic moment per unit cell scales with the total number of valence electrons following a simple electron counting scheme (Galanakis and Dederichs, 2005). The total number of electrons Z_t is the sum of the number of spin-up and spin-down electrons, while the total spin moment M_t is given by the difference ($Z_t = N_\uparrow + N_\downarrow$; $M_t = N_\uparrow - N_\downarrow \rightarrow M_t = Z_t - 2N_\downarrow$). The minority band contains 9 electrons for half-Heusler and 12 electrons for full-Heusler alloys. Therefore, the total spin moment is given by the relation $M_t = Z_t - 18$ (Figure 5a)

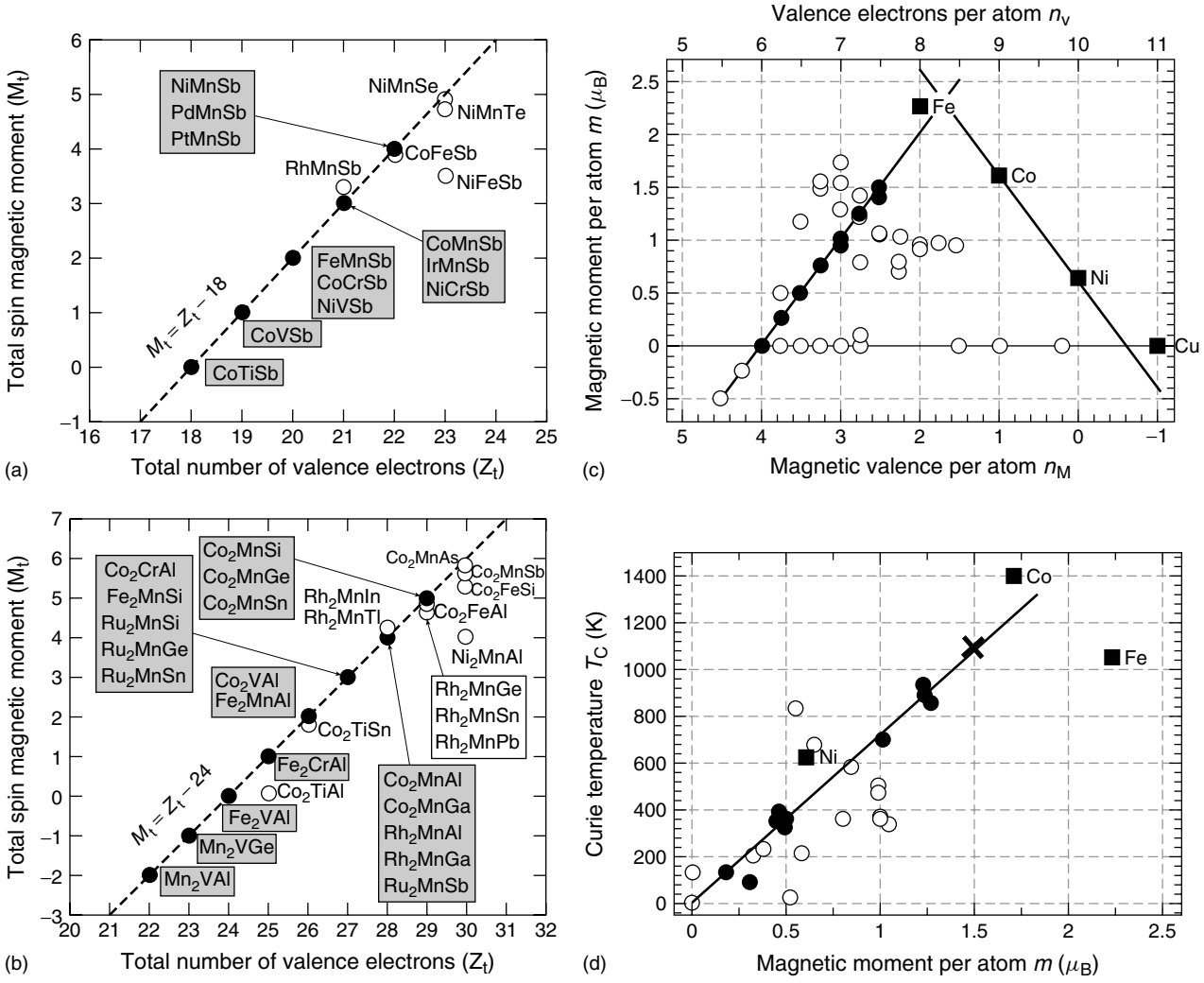

Figure 5. Calculated total spin moments for some (a) half-Heusler and (b) full-Heusler alloys. The dashed line represents the Slater–Pauling behavior (Galanakis and Dederichs, 2005). Scaling of (c) magnetic moments and (d) Curie temperature of Heusler compounds (Wurmehl *et al*., 2005). The heavy 3*d* transition metals are given for comparison. Solid symbols correspond to Co_2-based full-Heusler alloys and open symbols refer to other Heusler compounds.

or $M_t = Z_t - 24$ (Figure 5b) for the half- and full-Heusler alloys respectively (Galanakis and Dederichs, 2005). The variation of magnetic moment and Curie temperature with the number of valence electrons (Wurmehl *et al*., 2005) is shown in Figure 5(c) and (d). Typical examples that fall in this half-metallic category include the half-Heusler alloys NiMnSb (de Groot, Mueller, van Engen and Buschow, 1983), PtMnSb (de Groot, Mueller, van Engen and Buschow, 1983) and the full-Heusler alloys Co_2MnSi (Fujii, Ishida and Asano, 1995), Co_2(Cr,Fe)Al (Block *et al*., 2003; Felser, Elmers and Fecher, 2005). Theoretical calculations predict the critical dependence of magnetic properties on structure, atomic ordering, number of electrons per unit cell, and defects. Half-metallicity is sensitive to the composition and surface structure and atomic disorder (Palmstrøm, 2003).

3.2.1 NiMnSb

Many groups have intensively studied the NiMnSb alloy because of its high-spin polarization (de Groot, Mueller, van Engen and Buschow, 1983). This half-Heusler alloy has atoms ordered on three of the four sublattices of the fcc structure and crystallizes in the Cl_b structure, with the fourth remaining vacant. A self-consistent spin-polarized calculation of energy bands in NiMnSb was performed by de Groot, Mueller, van Engen and Buschow (1983), who first predicted half-metallicity in this material. In the majority spin-up band, the Mn d states are shifted to lower energies and form a common d band with the Ni d states, while in the minority spin-down band the Mn states are shifted to higher energies and are unoccupied, so that a band gap

at E_F is formed separating the occupied d bonding from the unoccupied d antibonding states. NiMnSb is a type IA half-metal with ↑ electrons of Ni(e_g) character at E_F and the calculated magnetic moment is $4\,\mu_B$ per formula unit. Presence of small quantities of other phases and modest amounts of atomic disorder can destroy the half-metallicity (Orgassa, Fujiwara, Schulthess and Butler, 1999).

3.2.2 PtMnSb

Considerable interest has focused on the half-Heusler alloy PtMnSb, which crystallizes in the Cl_B structure. Self-consistent electronic structure calculations by de Groot, Mueller, van Engen and Buschow (1983) and de Groot, Mueller, van Engen and Buschow (1984) revealed half-metallic behavior, and the spin-spilt band structure is that of a type IA half-metal. The results are very similar to those for NiMnSb. The calculated magnetic moment was again $4\,\mu_B$ per formula unit. The main contribution to the magnetic moment comes from the Mn atoms ($4\,\mu_B$), which have their minority d band shifted E_F. The partial Pt moment ($0.18\,\mu_B$) is quite small and the even smaller Sb moment ($-0.04\,\mu_B$) couples antiferromagnetically to the Mn moments. The compound shows a very large magneto-optical Kerr rotation. The Kerr rotation has a maximum in excess of 2.5° at 720 nm (van Engen, Buschow, Jongebreur and Erman, 1983). The vanishing spin-down density at E_F leads to a noncancellation of the optical transitions arising from up- and down-spin bands. The half-metallic properties also lead to a small plasma frequency enhancing the Kerr effect. The effect derives from the large spin-orbit coupling of Pt together with the large magnetic moment on Mn and the strong hybridization of Mn, Pt, and Sb orbitals.

3.2.3 Co_2MnSi

Half-metallic behavior has also been predicted for Co_2MnSi (Fujii, Ishida and Asano, 1995) in which both the cobalt and manganese atoms carry magnetic moments. The magnetic properties depend sensitively on the degree of atomic order and the conduction electron concentration. Spin-polarized band-structure calculations (Fujii, Asano and Ishida, 1984) indicate that the moments are predominantly $3d$ in origin and the shapes of the DOS for Co and Mn are similar. This ternary intermetallic full-Heusler alloy is predicted to be half-metallic with a minority spin Co $3d$ gap of 0.4 eV. In addition, Co_2MnSi is a type IB half-metal with a $T_C = 985$ K, the highest among those of all known Heusler alloys containing manganese. The saturation magnetic moment is $5\,\mu_B$ per formula unit.

3.2.4 Co_2(Cr,Fe)Al

Co_2CrAl has 27 valence electrons and is in the ordered $L2_1$ structure. Its electronic structure shows a gap for minority spin electrons at the Fermi energy. It is thus a type IA half-metal (Figure 4d). Block *et al.* (2003) have recently argued that the electron count 27.8 for the compound $Co_2Cr_{0.6}Fe_{0.4}Al$ leads to a DOS peak in the majority spin electrons due to Fermi surface nesting. The magnetization curves show the alloy to be a soft ferromagnet with a low-temperature saturated moment of $3.65\,\mu_B$ per formula unit (Felser, Elmers and Fecher, 2005; Clifford, Venkatesan, Gunning and Coey, 2004), very close to the value of $3.7\,\mu_B$ per formula unit predicted from the band-structure calculations (Block *et al.*, 2003; Felser, Elmers and Fecher, 2005). The Curie temperature of the alloy was found to be 660 K. Disorder is known to destroy the half-metallic property.

3.2.5 Mn_2VAl

Mn_2VAl has a ferrimagnetic structure with a moment of roughly $1.5\,\mu_B$ on each Mn and $-0.9\,\mu_B$ on V. The DOS within nearly 0.5 eV of the Fermi level, both above and below, is dominated by Mn t_{2g} character (Weht and Pickett, 1999). At stoichiometry, the saturation moment is reported to be $2.0\,\mu_B$ per formula unit, close to the integral value of the spin moment and the Curie temperature is 760 K (Jiang, Venkatesan and Coey, 2001). It is not a robust half-metal because any changes in stoichiometry as well as incomplete atomic order will greatly affect the structural stability and magnetic properties of the system and can eliminate the spin gap, introducing light ↓ holes at the Fermi level. The Fermi level lies exactly in the minority spin band. In the system $Mn_2V_{1+x}Al_{1-x}$, although V and Al atoms may substitute each other's sublattice, the structure remains the Heusler one from x between -0.3 and $+0.2$, with linearly varying saturation moment (Yoshida, Kawakami and Nakamichi, 1981). The ideal compound is predicted to be a type IB half-metal with Mn (t_{2g}) ↓ electrons at E_F.

3.2.6 Other half-metals

FeS_2 is a nonmagnetic semiconductor with the Fe^{2+} in a low-spin state $(t_{2g}^3)^{\uparrow}(t_{2g}^3)^{\downarrow}$ and a gap between the t_{2g} and e_g states, in agreement with the band-structure calculations (Eyert, Hock, Fiechter and Tributsch, 1998; Opahle, Koepernik and Eschrig, 1999). On the other hand, CoS_2 is an itinerant ferromagnet and the Fermi level sits on a steep slope of the DOS. On substitution of Co (∼0.1%), it becomes a ferromagnetic metal and remains ferromagnetic all the way through to CoS_2. The solid solutions are ferromagnetic with

$T_C \propto x$ and $m \approx x\mu_B$ for $x > 0.1$ in an extremely wide concentration range (Jarrett *et al*., 1968). This seems to be a robust half-metal of type IA (Mazin, 2000).

In the case of Mn_4N, where the Mn occupies an fcc lattice the DOS at E_F is zero for the Mn(I) positions and has a deep minimum at the Mn(II) position which resembles that of a half-metal (Matar, Mohn, Demazeau and Siberchicot, 1988; Fujii, Ishida and Asano, 1992). Investigations of the isostructural ferromagnetic system Fe_4N which has a high saturation magnetization ($2.2\,\mu_B$ per Fe) revealed the same result, an absence of DOS at E_F at the Fe(I) positions (Matar, Mohn, Demazeau and Siberchicot, 1988; Sakuma, 1991).

Theoretical calculations on half-metals with zinc-blende transition-metal chalcogenides and pnictides are reviewed in detail by Liu (2005). Half-metallic ferromagnetism is also achieved while doping some transition-metal atoms into the semiconductors ZnTe and CdTe. In some cases, half-metallicity is robust when these materials are subject to large deformations. Zinc-blende-type CrAs, CrSb, and MnAs are theoretically predicted to be half-metals (Akinaga, Manago and Shirai, 2000; Shirai, 2001).

4 SPIN POLARIZATION

There is no clear experimental signature or property which allows us to identify a material as a half-metal. This is in contrast to metals, semiconductors, and superconductors where there is a clear electrical signature.

Spin polarization is a measure of the ratio of the electron density for each spin at the Fermi energy, and is given by the expression,

$$P_0 = (N^{\uparrow} - N^{\downarrow})/(N^{\uparrow} + N^{\downarrow}) \tag{1}$$

where $N^{\uparrow,\downarrow}$ are the densities of states of majority ($\uparrow$) or minority ($\downarrow$) at E_F, but this parameter is not necessarily the one measured experimentally. In the case of ballistic or diffusive transport, the densities of states must be weighted by the Fermi velocity of the electrons, or its square, respectively (Mazin, 1999).

$$P_n = (\langle N^{\uparrow} v_F^{\uparrow n}\rangle - \langle N^{\downarrow} v_F^{\downarrow n}\rangle)/(\langle N^{\uparrow} v_F^{\uparrow n}\rangle + \langle N^{\downarrow} v_F^{\downarrow n}\rangle) \tag{2}$$

P_1 or P_2 may be large for transport half-metals (type III – $La_{0.7}Sr_{0.3}MnO_3$ and type IV – $Tl_2Mn_2O_7$), but P_0 can be small for the same materials. The densities of states in tunneling experiments should be weighted by the appropriate spin-dependent tunneling matrix element to give tunneling spin polarization P_T. Mazin shows that P_T is equal to P_2 in the case of a specular barrier with low transparency (Mazin, 1999). One of the major problems with the above definition is that it is only valid at 0 K – the actual value of the spin polarization drastically reduced with increasing temperature due to spin-flip processes. Another argument is that the spin polarization of a ferromagnet in a heterostructure is not simply a property of the ferromagnet alone, but it is a joint property of the materials used in the heterostructure. In epitaxial tunnel junctions, for example, the effective spin polarization depends on the barrier oxide and the applied bias. There is mounting evidence that the spin polarization in a tunnel junction is critically dependent on the interface with the barrier and can even change sign for a given ferromagnetic electrode according to the nature of the barrier (de Teresa *et al*., 1999). This leads to doubts of claims that the polarization is an intrinsic property of a material, except when $P = 100\%$.

Measuring the spin polarization poses lots of challenges. All the techniques for measuring spin polarization somehow involve extracting electrons from the surface of the material, with the chance that its inherent polarization will be modified in the process. But, until now, there are no measurements that identify a material as a half-metal without removing electrons. Several methods have been explored to measure the spin polarization of ferromagnetic metals as summarized in Figure 6. Table 3 lists a number of measurements of spin polarization for half metallic materials including elemental ferromagnets Fe, Co and Ni. The spin polarization is weighted differently in each technique. Photoemission experiments (Park *et al*., 1998) measure the unweighted spin polarization P_0 of a ferromagnet. Tedrow and Meservey's technique of spin-polarized tunneling (Meservey and Tedrow, 1994) measures the tunneling spin polarization P_t directly. Andreev reflection (Soulen *et al*., 1998; Upadhyay, Palanisami, Louie and Burman, 1998) measures the transport spin polarization directly, weighted by $v_F^{\uparrow,\downarrow}$ or its square, but is not sensitive to the sign of the polarization. Spin-polarized scanning tunneling microscopy (Bode, 2003) gives the tunneling spin polarization P_t through a vacuum barrier. In addition to these direct measurements, transport measurements in point contacts (Versluijs, Bari and Coey, 2001; Garcia, 2000) and tunnel junctions (Moodera and Mathon, 1999) with two ferromagnetic electrodes separated by a thin insulating barrier are used to determine the spin polarization indirectly through magnetoresistance measurements (Figure 6). There are several experimental difficulties in all these measurement methods and they rarely yield 100% polarization.

When the electrons are fully spin polarized, $N^{\uparrow}$ or $N^{\downarrow} = 0$ and $P_0 = P_1 = P_2 = 100\%$, but they will be different for any other polarization. For example, for $(La_{0.67}Ca_{0.33})MnO_3$ (Pickett and Singh, 1996), $N^{\uparrow}$ and $N^{\downarrow}$ are 0.58 and 0.27 states eV^{-1} fu^{-1}, respectively, and $v_F^{\uparrow}$ and $v_F^{\downarrow}$ are 0.76×10^6

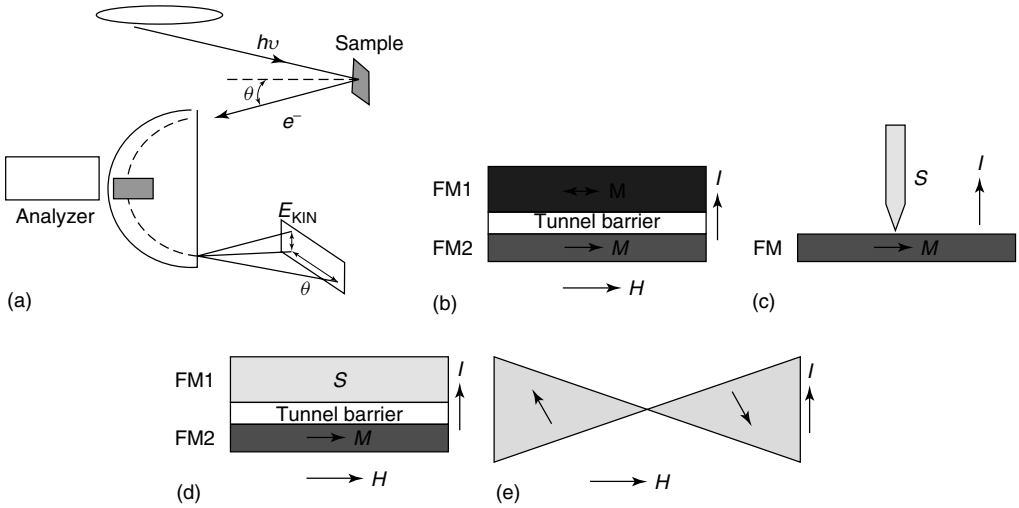

Figure 6. Experimental techniques for measuring spin polarization. (a) Photoemission, (b) tunnel junction, (c) Andreev reflection, (d) Tedrow–Meservey, and (e) point contact (*M* denotes ferromagnetic electrode and *S* represents superconducting electrode).

Table 3. Measured spin polarization in various systems.

Material	Method	T (K)	P (%)	References
Fe	Andreev	4.2	43	Soulen *et al*. (1998)
	Tedrow–Meservey	0.2	45	Monsma and Parkin (2000)
	Tedrow–Meservey	0.2	77	Parkin *et al*. (2004)
Co	Andreev	4.2	40	Soulen *et al*. (1998)
	Tedrow–Meservey	0.2	42	Monsma and Parkin (2000)
Ni	Andreev	4.2	42	Soulen *et al*. (1998)
	Tedrow–Meservey	0.2	31	Monsma and Parkin (2000)
CrO_2	Photoemission	300	95	Kämper *et al*. (1987)
	Andreev	4.2	94–98	Soulen *et al*. (1998) and Ji *et al*. (2001)
	Tunnel junction	4.2	8	Gupta, Li and Xiao (2001)
	PMR	4.2	82	Barry (1999) and Coey and Venkatesan (2002)
Fe_3O_4	Photoemission	300	80	Dedkov, Rüdiger and Güntherodt (2002)
	Tunnel junction	4.2	43	Seneor *et al*. (1999)
	Point contact	300	84	Versluijs, Bari and Coey (2001)
$La_{0.7}Sr_{0.3}MnO_3$	Photoemission	40	100	Park *et al*. (1998)
	Andreev	4.2	58–92	Nadgorny *et al*. (2001)
	Tunnel junction	4.2	85–95	Viret *et al*. (1997) and Bowen *et al*. (2003)
	Tedrow–Meservey	4.2	72	Worledge and Geballe (2000)
Sr_2FeMoO_6	Tunnel junction	4.2	90	Bibes *et al*. (2003)
	Point contact	300	11	Clifford (2005)
NiMnSb	Photoemission	300	50–67	Ristoiu *et al*. (2000) and Bona *et al*. (1985)
	Andreev	4.2	58	Soulen *et al*. (1998)
	Tunnel junction	4.2	25	Tanaka, Nowak and Moodera (1999)
	Tedrow–Meservey	0.4	28	Tanaka, Nowak and Moodera (1999)
Co_2MnSi	Tunnel junction	10	61	Kämmerer, Thomas, Hütten and Reiss (2004)
	Andreev	300	20	Clifford (2005)
$Co_2(Cr,Fe)Al$	Tunnel junction	300	42–47	Marukame *et al*. (2005) and Okamura *et al*. (2005)
	Point contact	300	80	Clifford (2005)

and 0.22×10^6 m s^{-1}, hence $P_0 = 36\%$, $P_1 = 76\%$ but $P_2 = 92\%$. In the case of $3d$ ferromagnets in the diffusive limit, the value of P is always positive and close to 40% (Monsma and Parkin, 2000) despite the fact that the $3d^{\uparrow}$ bands are full for the strong ferromagnets cobalt and nickel, and the Fermi level lies in the $3d^{\downarrow}$ band. The positive spin polarization is actually associated with the more mobile $4s$ electrons, which are polarized by hybridization with the $3d$ states.

In the case of point contacts or tunnel junction geometry, the magnetoresistance is defined as

$$MR = \Delta R/R_{\uparrow\downarrow} = (R_{\uparrow\downarrow} - R_{\uparrow\uparrow})/R_{\uparrow\downarrow} = 2P_1P_2/(1 + P_1P_2) \quad (3)$$

where $R_{\uparrow\downarrow}(R_{\uparrow\uparrow})$ is the resistance in antiparallel (parallel) state and P_1 and P_2 are polarizations of the two electrodes. Note that MR cannot exceed 100%. Since the conductance is $G = 1/R$, $\Delta R/R$ is also equal to $(G_{\uparrow\uparrow} - G_{\uparrow\downarrow})/G_{\uparrow\uparrow}$. It is often used in conjunction with the Julliere model (Julliere, 1975) to infer the spin polarization if the electrodes are identical ($P_1 = P_2$) or if the polarization of one of them is known.

5 MEASUREMENTS OF SPIN POLARIZATION

5.1 Spin-resolved photoemission

Spin-resolved photoemission measurements (Figure 6a) directly manifest the half-metallic nature of materials (Park *et al*., 1998). For the majority (minority) spin, the photoemission spectrum showed a metallic Fermi cutoff, whereas for the minority (majority) spin, it showed an insulating gap. The spin polarization of ejected photoelectrons can be measured for different incident photon energies. This method provides a rather direct image of the spin-polarized DOS near E_F, but it lacks the necessary energy resolution ($\sim$1 meV) and requires very careful surface preparation as the photoelectrons that carry the information are coming from a thin layer at the surface. The surface or interface states may have a critical influence on the result. The measured polarization is weighted by the absorption cross section for $\uparrow$ and $\downarrow$ electrons.

The stoichiometric or near-stoichiometric ordered NiMnSb alloy, with MnSb surface termination, exhibits high polarization in normal-incidence spin-polarized inverse photoemission. The polarization at the Fermi level is 67% (Ristoiu *et al*., 2000). This is significantly higher than the polarization asymmetry of 50%, at room temperature, measured from a polycrystalline sample using spin-polarized photoemission (Bona *et al*., 1985). Careful studies (Park *et al*., 1998) on $La_{0.7}Sr_{0.3}MnO_3$ shows that the spectrum for the majority spin extends up to E_F and shows the metallic Fermi cutoff, while that for the minority spin decreases rapidly at $\sim$1 eV binding energy. The spin polarization is found to be $\sim$100%. Typical data for $La_{0.7}Sr_{0.3}MnO_3$ (Park *et al*., 1998) is shown in Figure 7(a).

5.2 Andreev reflection

Andreev reflection is a process which occurs when a current passes between a superconductor and a normal metal through a point contact (Figure 6c). For an electron to pass from a normal metal to a superconductor it must form a Cooper pair with another electron. The $\uparrow$ electrons injected from the normal metal into the superconductor must form Cooper pairs, and this is achieved by the simultaneous injection of a $\downarrow$ hole from the superconductor back into the metal. The injected current is doubled in this way for a normal metal, when the junction is biased within the superconducting gap, Δ. If a normal metal is replaced by a half-metal, Cooper pairs are unable to form since electronics of both spin are required to form a pair. For a half-metallic ferromagnet, there are no states available, and the current is then zero (Soulen *et al*., 1998; Upadhyay, Palanisami, Louie and Burman, 1998). The effect depends on the degree of spin polarization, which may be deduced from data at $T = 0$ using $P_1 = 1 - G_0/2G_n$ where G_0 is the conductance at zero bias and G_n is the conductance when the applied voltage is much greater than the energy gap. The data (Ji *et al*., 2001) for CrO_2 is presented in Figure 7(b). This technique is simple to implement – no special surface preparation is necessary and there are no limits on sample geometry. Point contact Andreev reflection (PCAR) technique, by creating a nanocontact by depositing through a nanohole made through a layer of PMMA, was recently established to measure the spin polarization of various half-metals (Clifford, 2005).

5.3 Tunnel junctions

Magnetic tunnel junctions (MTJs) generally consist of ferromagnet/insulator/ferromagnet (FIF) structures (Figure 6c). Spin-polarized tunneling in ferromagnetic junctions has been recently reviewed by Moodera and Mathon (1999). These are usually made up of thin film of ferromagnetic electrodes separated by a thin layer of insulating barrier oxide. The most important part of junction preparation is the formation of the tunnel barrier. Up to now, Al_2O_3 has been the most commonly used tunnel barrier material. Thin layers of this material are amorphous and as a result the TMR is predominantly determined by spin polarization of the ferromagnetic electrodes. However, it was recently shown that much higher TMR values can be obtained with crystalline MgO tunnel barriers (Parkin *et al*., 2004; Yuasa *et al*., 2004) as shown in Figure 8(a,b). The reason is that the tunneling matrix elements for crystalline MgO are spin dependent, so the barrier acts as an efficient *spin filter*.

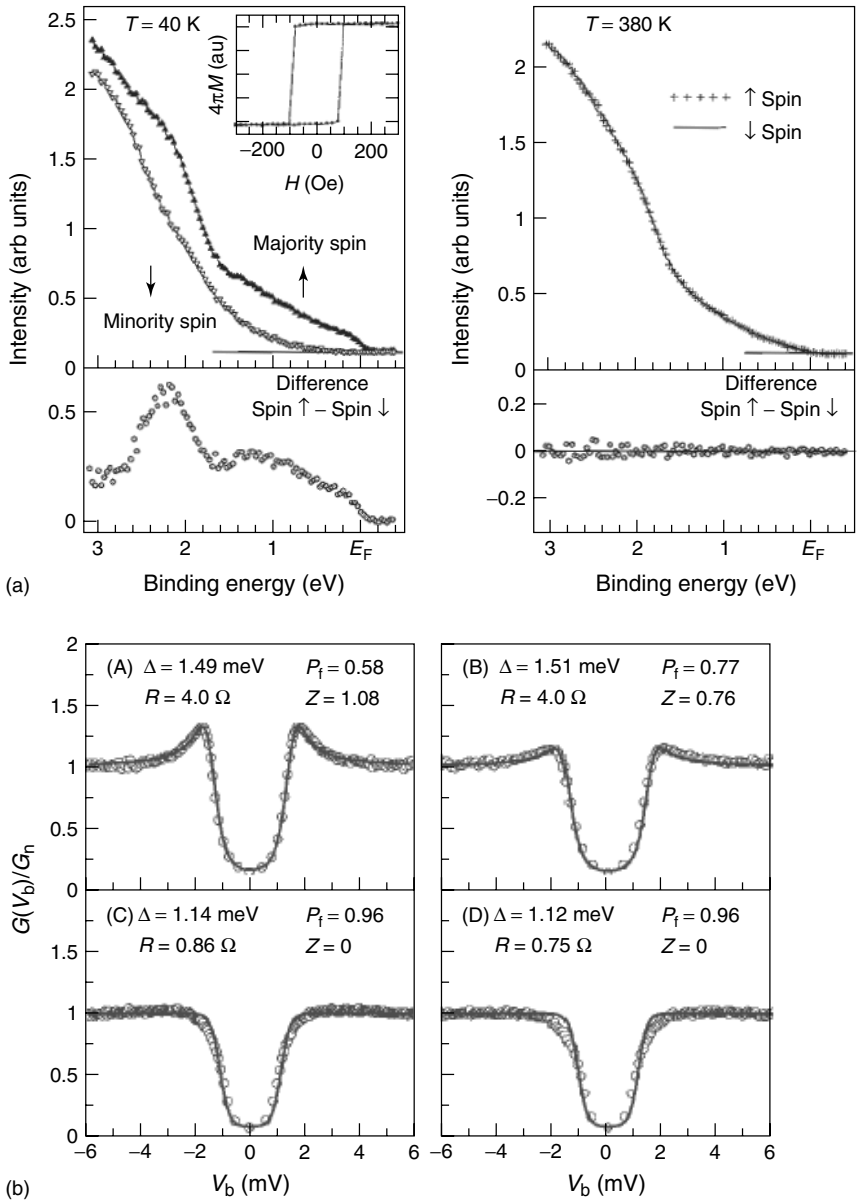

Figure 7. (a) Spin-resolved photoemission spectra of $La_{0.7}Sr_{0.3}MnO_3$ thin film (Park *et al*., 1998) and (b) normalized conductance $G(V_b)/G_n$ versus bias voltage V_b for Pb/CrO_2 point contacts at 1.85 K for different contact resistances (Ji *et al*., 2001). The solid lines are fits to the data, with the BTK model resulting in P, Z, and Δ as shown in the panel.

The magnitude of the TMR is related to the spin polarization P of the individual FM electrodes: $(R_{\uparrow\downarrow} - R_{\uparrow\uparrow})/R_{\uparrow\downarrow} = 2P_1P_2/(1 + P_1P_2)$, where $R_{\uparrow\downarrow}$ and $R_{\uparrow\uparrow}$ are the resistance of the MTJ corresponding to antiparallel and parallel orientation of the FM electrodes, respectively. For best results, the junction area should be small, so the ferromagnetic electrodes can be deposited as two perpendicular stripes using shadow masks, or else the films are patterned using a lithographic technique. The electrode shapes are chosen so that they have different switching fields, and the magnetoresistance is measured from the difference in resistance between the parallel and antiparallel configurations. While the magnetoresistance is sensitive to applied voltage, falling rapidly with increasing bias, the polarization is sensitive to temperature and decreases rapidly with increasing temperature.

5.4 Tedrow–Meservey method

Meservey and Tedrow (1994) measured the conduction electron spin polarization of magnetic metals and compounds using the Zeeman-split quasiparticle DOS in a

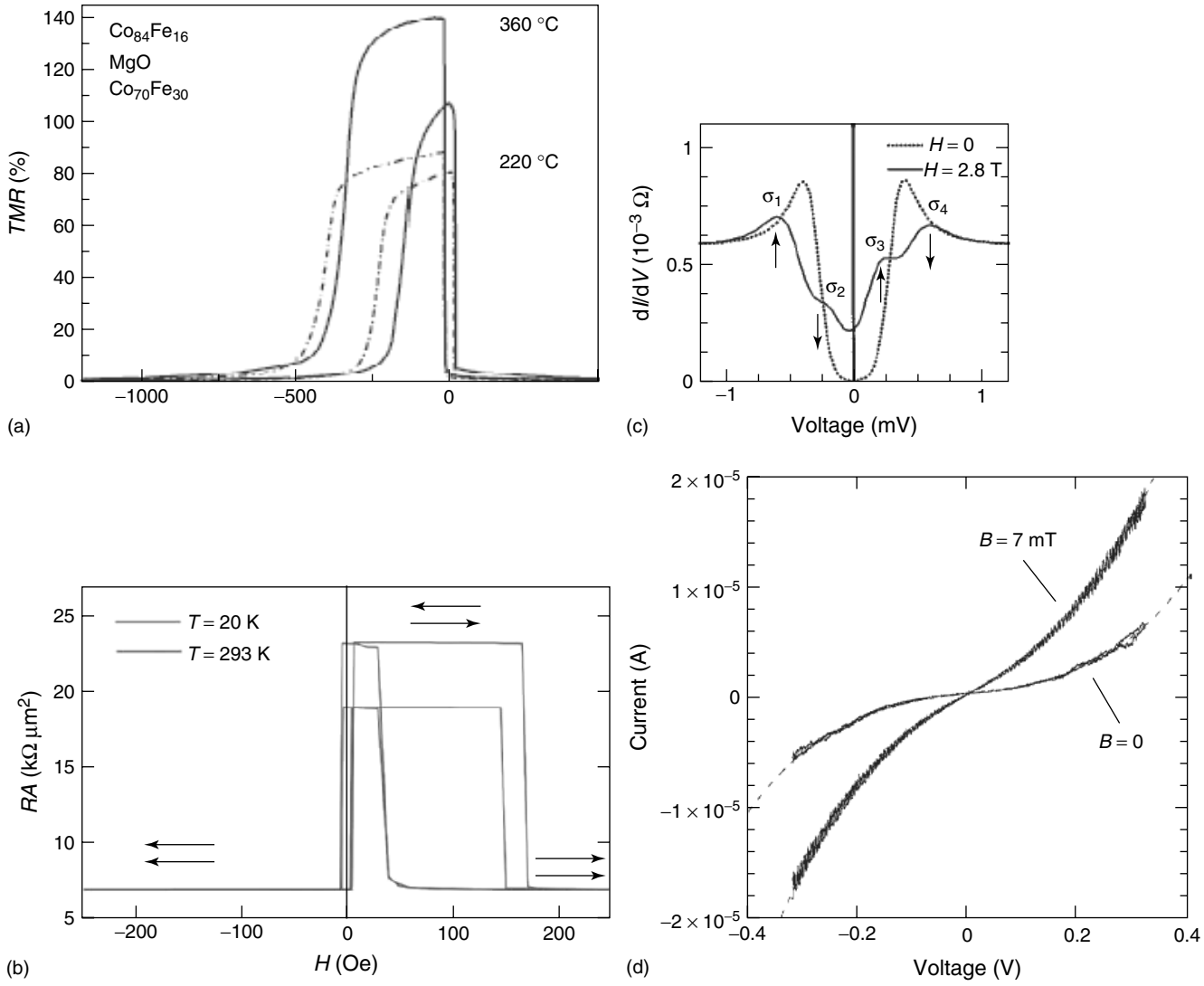

Figure 8. (a) TMR versus field for MTJs with structures (all thicknesses in Å): 100 TaN/250 IrMn/8 Co84Fe16/30 Co70Fe30/29 MgO/150 Co84Fe16/100 Mg (Parkin *et al.*, 2004). (b) Tunnel magnetoresistance of Fe(001)/MgO(001)/Fe(001) junctions (Yuasa *et al.*, 2004). (c) Spin-polarized differential tunnel conductance versus voltage in NiMnSb/Al_2O_3/Al at 0.4 K (Tanaka, Nowak and Moodera, 1999). (d) Typical magnetic field effect on a Fe_3O_4 nanocontact showing the I:V curves with and without a magnetic field (Versluijs, Bari and Coey, 2001).

superconductor. This technique involves a tunnel barrier where the second electrode is a thin layer of superconducting aluminum (Figure 6d). The superconducting electrode serves as an analyzer of the spin polarization of the tunneling current. They showed that the conduction electrons in ferromagnetic metals are spin polarized and that the spin is conserved in the tunneling process. Tunneling from a ferromagnetic film, with its unequal spin distribution at the Fermi level (E_F), into such a spin-split superconducting Al film reflects the spin polarization of the tunneling electrons coming from the ferromagnet. The superconducting transition of Al is 1.2 K, but there is a high critical field because the penetration depth in a type I superconductor can be much greater than the film thickness. Figure 8(c) compares the field dependence of dI/dV for the first reported half-metal, NiMnSb (Tanaka, Nowak and Moodera, 1999).

The normal tunneling characteristic from a ferromagnet to a superconductor in zero field is shown in Figure 8(c). It depends on the convolution of the ferromagnetic and superconducting densities of states, and the twin peaks are separated by the superconducting energy gap; for Al, $2\Delta \approx 0.25$ meV. In an applied field, the superconductor quasiparticle DOS are Zeeman split, allowing the tunnel current to be clearly resolved into spin-up and spin-down parts and the curve becomes asymmetric, as shown in Figure 8(c). The spin polarization is usually inferred from

the conductivity at the four points labeled σ_1 to σ_4, using the formula

$$P = [(\sigma_1 - \sigma_3) - (\sigma_2 - \sigma_4)] = [(\sigma_1 - \sigma_3) + (\sigma_2 - \sigma_4)] \quad (4)$$

5.5 Point contacts

Point contact phenomena, like quantum conductance, are best studied in nanocontacts formed when two macroscopic electrodes are put into contact and then slowly pulled apart. Precise control over the movements of the electrodes is desirable for the formation of a stable nanocontact. In this technique, a stable conducting contact is established between two crystallites of the ferromagnetic material, and the magnetoresistance of the contact is measured (Figure 6e). Normally, there is no method of controlling the magnetization directions in the initial contact before applying the magnetic field, so the experiment involves making many contacts and selecting those with the largest magnetoresistance. Typical data for Fe_3O_4 are illustrated in Figure 8(d) (Versluijs, Bari and Coey, 2001). A related structure is a nanowire between two spin-polarized electrodes. Provided the transfer of the electron across the contact does not interfere with its spin (the transport may be ballistic, by hopping, or by tunneling) the magnetoresistance for classical spins is still given by equation (3) (Julliere, 1975).

6 TRANSPORT PROPERTIES

In view of the difficulties in measuring P directly, it is worth exploring other experimental signatures, apart from the integral spin moment and metallic conduction, which can throw some light on half-metallicity. The transport properties of some half-metallic systems show unique features, though it is not generalized to all half-metallic systems. In conventional metallic ferromagnets, generally a T^2 dependency of the resistivity is found in the low-temperature region (Wohlfarth, 1980; Meaden, 1971). This quadratic term is usually ascribed to the electron-scattering process called *one-magnon scattering* (Mannari, 1959), where an electron undergoes a spin flip in an inelastic process involving creation or annihilation of a magnon. In half-metallic ferromagnets, spin-flip one-magnon scattering at low temperatures is not possible, because only states with one spin direction are present at E_F at $T = 0\,K$. This will lead to the absence of T^2 dependence of resistivity and to an increase in the mobility of the charge carriers. The first available magnetic scattering processes involve two magnons, which give rise to a term in the resistivity varying as $T^{9/2}$ (Kubo and Ohata, 1972). Unfortunately, such a term is very difficult to disentangle from regular scattering processes involving phonons. However, the absence of a T^2 term forms only a necessary and not sufficient condition for complete spin polarization of current carriers at low temperatures. For example, if the Fermi surfaces of spin-up and spin-down carriers are spheres with a large radius difference (in k space), magnons with wave vectors shorter than this difference do not contribute to the scattering of these current carriers, and a T^2 term cannot be observed. In addition, there is no contribution of one-magnon processes to the anomalous Hall effect ($R_s(T) \propto aT^3 + bT^4$). It follows that magnetic scattering in half-metals should be dominated by two-magnon processes. Careful studies on NiMnSb and PtMnSb (Otto *et al.*, 1989) reveal that the resistivity varies linearly with temperature below 15 K (Figure 9a,b). However, electron–electron and electron–photon scattering processes can also lead to such behavior and creates difficulty to ascribe the dependence entirely to a half-metal. The most dominant magnetic scattering processes involve two magnons, which give rise to a term in the resistivity varying as $T^{9/2}$ is reported by Kubo and Ohata (1972) based on a rigid band electronic structures of half-metals. Unfortunately, such a term is very difficult to disentangle from regular scattering processes involving phonons. Irkhin and Katsnel'son (2002) showed that the resistivity is proportional to $T^{9/2}$ for $T < T^*$ and to $T^{7/2}$ for $T > T^*$, T^* being the crossover temperature for longitudinal scattering processes. The $T^{7/2}$ behavior also plays an important role in magnetoresistance. At finite temperatures, however, it is necessary to take into account the effect of spin fluctuations, which breaks down the perfect spin polarization. In the absence of spin gaps, magnetization deviates from its saturation values as $\delta M \propto T^{3/2}$ in three dimensions. In the strong Hund's coupling limit, spin polarization of the conduction electrons are proportional to the total spin polarization. At finite temperatures, the half-metallic structure of conduction electrons breaks down and as a consequence, the rigid band approaches cannot be justified. Taking into account the nonrigid band behavior due to spin fluctuations, it was established (Furukawa, 2000) that the most dominant contribution for the low-temperature resistivity is from an unconventional one-magnon scattering process in which case the resistivity is proportional to the product of the following two quantities – magnon population δM and the DOS of the minority spin quasiparticles which should also scale as δM. Therefore, $\rho(T) \propto (\delta M)^2 \propto T^3$. This T^3 behavior is demonstrated experimentally for mixed valent manganite $La_{0.7}Sr_{0.3}MnO_3$ single crystals (Figure 9c) (Furukawa, 2000).

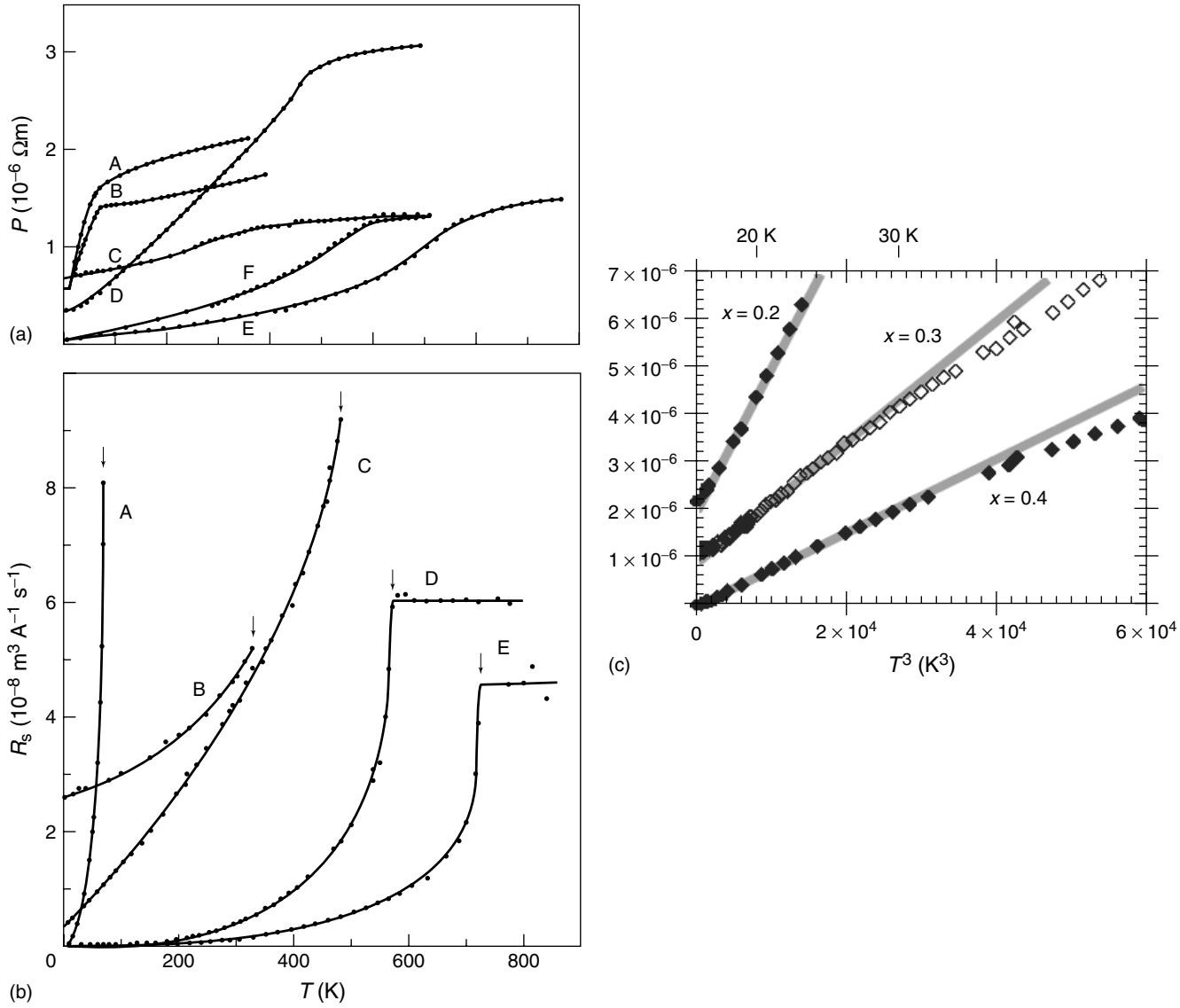

Figure 9. Temperature dependences of the (a) electric resistivity of the half-Heusler alloys TMnSb (T = Cu (A), Au (B), Co (D), Ni (E), Pt (F)) and PtMnSn (C) (Otto *et al*., 1989), (b) spontaneous Hall coefficient of TMnSb (T = Au (A), Co (C), Pt (D), Ni (E)) and PtMnSn (B) (Otto *et al*., 1989), and (c) T^3 behavior of resistivity in $La_{1-x}Sr_xMnO_3$ single crystals (Furukawa, 2000).

7 SURFACE/INTERFACE STATES

The DOS and exchange interactions at the surface/interface may be very different from those of the bulk. It was well established that spin disorder has a profound effect on the half-metallic nature (Skomski and Dowben, 2002; Dowben and Skomski, 2003). Opposite spin surface states (Jenkins and King, 2001; de Wijs and de Groot, 2001; Jenkins and King, 2002) in half-metals can develop into interface states (de Wijs and de Groot, 2001; Jenkins and King, 2002; Picozzi, Continenza and Freeman, 2003) and destroy the half-metallic behavior. The increase in the number of interfaces enhances the spin minority population, which in turn decreases the spin polarization. At finite temperature, thermally activated spin-flip scattering such as spin waves will also induce states within the gap (Dowben and Skomski, 2003). Even in an ideally prepared single crystal at zero temperature, the spin-orbit coupling will introduce states in the half-metallic gap of minority states, which are produced by spin-flip scattering of the majority states. Magnon excitations tend to decrease the polarization at low temperature for many half-metallic systems viz $La_{0.7}Sr_{0.3}MnO_3$ (Obata, Manako, Shimakawa and Kubo, 1999), CrO_2 (Coey and Venkatesan, 2002; Watts *et al*.,

2000) and NiMnSb (Borca *et al*., 2001; Hordequin, Ristoiu, Ranno and Pierre, 2000). The low-energy transverse and longitudinal optical modes (phonon modes) can couple to spin-wave modes and reduce the net magnetization in half-metals (Dowben and Skomski, 2003).

The best-studied half-metal CrO_2 with nearly 100% spin polarization possesses stoichiometric (001) surface. Calculations reveal two oxygen-derived surface states in the band gap for the minority spin direction. However, these states lie well below E_F and do not affect the half-metallicity at the surface (van Leuken and de Groot, 1995). For magnetite, the loss of half-metallicity could be due to the presence of disorder above the Verwey transition temperature ($T_V = 120\,K$), which results in smearing of the energy gap in the minority subbands. Manganites and double perovskites show nonstoichiometry surfaces which lead to surface reconstructions. In half-Heusler NiMnSb, the random disorder, in particular, Ni−Mn interchange greatly affects the half-metallic property and hence the spin polarization (Helmholdt *et al*., 1984). First-principles band theory calculations have demonstrated that antisite disorder can destroy the half-metallic character of a number of Heusler alloys (Orgassa, Fujiwara, Schulthess and Butler, 1999). Major challenges remain in controlling the composition, defects, atomic ordering both in the bulk and at the interface.

8 APPLICATION OF HALF-METALS IN SPIN ELECTRONICS

High-spin polarization half-metallic materials are promising candidates for integration into the GMR multilayers, first discovered by Fert *et al*. (Baibich *et al*., 1988), as the spins of the current carriers are predominantly aligned in the same direction (Figure 10a). They are ideal sources of spin-polarized electrons and can act as spin injectors, detectors, and magnetically controllable spin filters. The emerging science of spin electronics seeks to exploit the two separate spin channels in increasingly sophisticated electronic devices. So far, these expectations have not been fully realized in practical applications.

8.1 Spin valves

The basic element of a spin valve is two ferromagnetic layers separated by a nonmagnetic spacer (Figure 10b). The electrical resistance of the structure is low when the magnetization directions of the ferromagnetic layers are aligned parallel and high when they are antiparallel. One of the ferromagnetic layers, the free layer, switches magnetization direction close to zero field. The other layer, the pinned layer, is grown next to an antiferromagnet and its magnetization direction is pinned at low fields. Switching of the free layer at low fields, therefore, results in a transition from the parallel to antiparallel state and a change in resistance. Hence the exchange-biased spin valve is a highly sensitive magnetic field sensor and can be used in several applications. Improvements in spin valve performance (GMR, exchange field, sensitivity) are continually pursued both through the development of new materials and thin-film stacks, in particular, using high spin-polarized half-metallic electrodes, and the design of new spin valve geometries. The basic FM/NM/FM/AF spin valve has evolved into many variants (Dieny, 2004; Coehoorn, 2003). For example, dual spin valves essentially consist of three FM layers separated by two nonmagnetic spacers. The magnetization of the outer two FM layers are pinned by an AFM layer, whereas the inner FM layer is free. GMR ratios as large as 25% have been reported (Egelhoff *et al*., 1995, 1996) for these structures but the increased thickness of the structure may make it unsuitable for read-head applications. A further advance in spin valve design was the development of the synthetic antiferromagnet (SAF) (Parkin, More and Roche, 1990). The pinning fields in the SAF spin valve can be twice as large as that of the standard spin valve. Another advantage of using the SAF is that, in a patterned device, stray field created by the pinned layer on the sensing layer is reduced because of the antiparallel alignment of the two FM layers in the pinned layer. Spin valves with nano-oxide layers (NOLs) were introduced in Kamiguchi *et al*. (1999) resulting in enhanced MR ratios of up to 18%. An overwhelming amount of spin valve research has been driven by the interests of the magnetic storage industry. Less than a decade after their discovery, spin valves were introduced as sensor materials in hard disk read heads. Other applications include position, speed and velocity sensors, and electronic compasses.

8.2 Magnetic tunnel junction

The basic two terminal device is an MTJ (Figure 10c) (Moodera, Kinder, Wong and Meservey, 1995) where two ferromagnetic half-metallic electrodes are separated by a thin insulating barrier. In a configuration where the magnetic moments are aligned parallel in top and bottom half-metallic electrodes, current will pass by tunneling of the majority spin electrons. There is no tunneling event in the antiparallel configuration because spin-up electrons can only tunnel into spin-up empty states, which lead to high resistance state. The schematic band profile in TMR and GMR junctions (Mavropoulos, Ležaić and Blügel, 2005) is compared in Figure 11. This simple ideal half-metal based spin-controlled switch (MTJs) device finds interesting applications in the

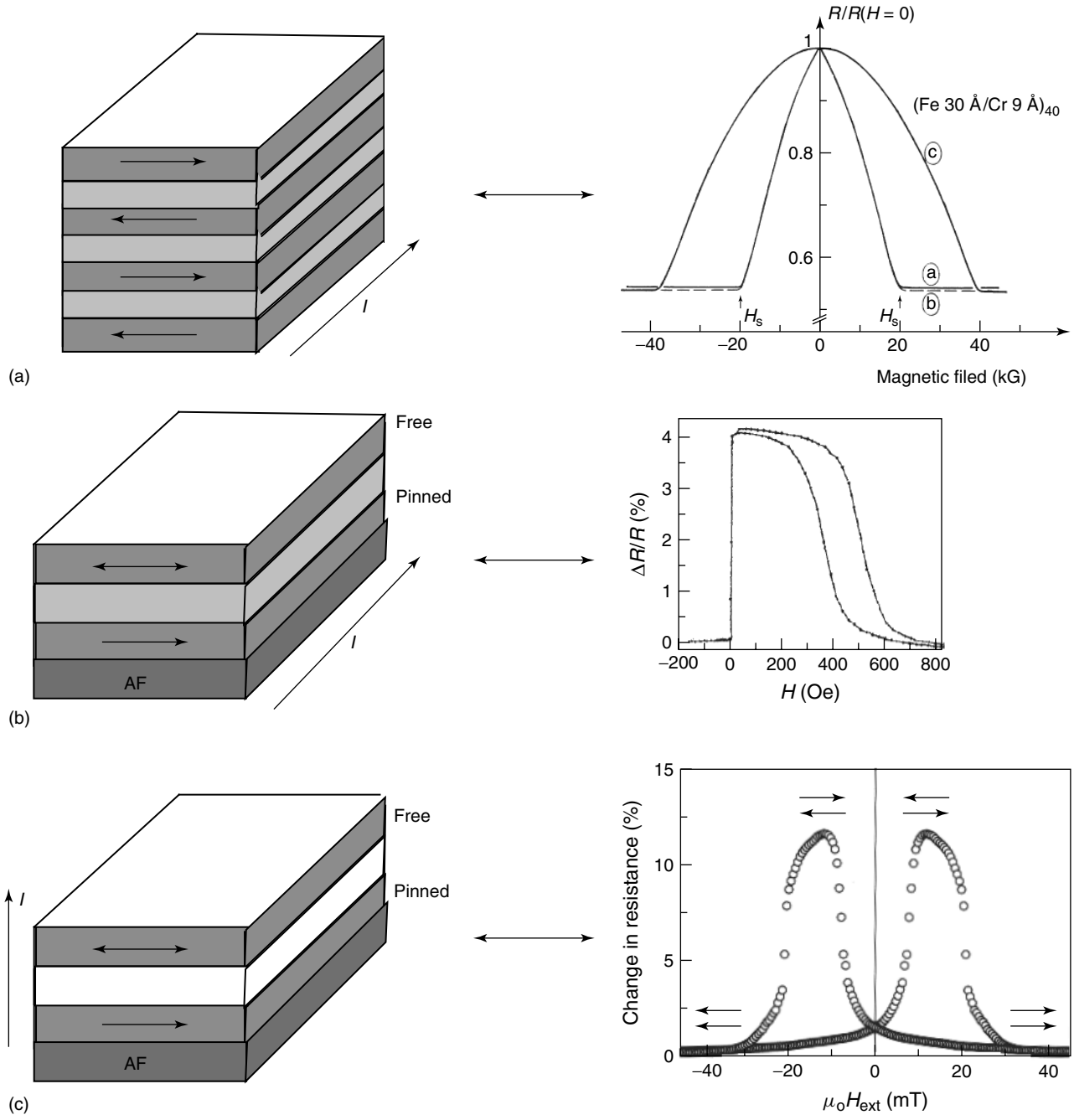

Figure 10. Schematic diagram of (a) GMR structure (Baibich *et al*., 1988), (b) spin valve (Dieny, 2004), and (c) magnetic tunnel junction (Moodera, Kinder, Wong and Meservey, 1995) and the corresponding magnetoresistance behavior.

area of magnetic memories (MRAMs) and also read heads for magnetic hard disk drives (Prinz, 1998; Wolf *et al*., 2001). These devices are nonvolatile with high speed, high density, and low power consumption. They are promising replacements for the present semiconductor RAMs. As a result, there exists a great potential market for these applications. Spin polarization measured via MTJ is the realistic limit for spin electronics applications. Moreover, the tunnel junction area is precisely controllable and so is the magnetic orientation of the two magnetic electrodes. Other applications include sensors, contactless potentiometer, and so on. A huge TMR ratio will certainly help to realize sensors with enhanced sensitivities in small field ranges.

The theoretical prediction of spin polarization in the half-Heusler (de Groot, Mueller, van Engen and Buschow, 1983) and as full-Heusler (Fujii, Ishida and Asano, 1995; Block

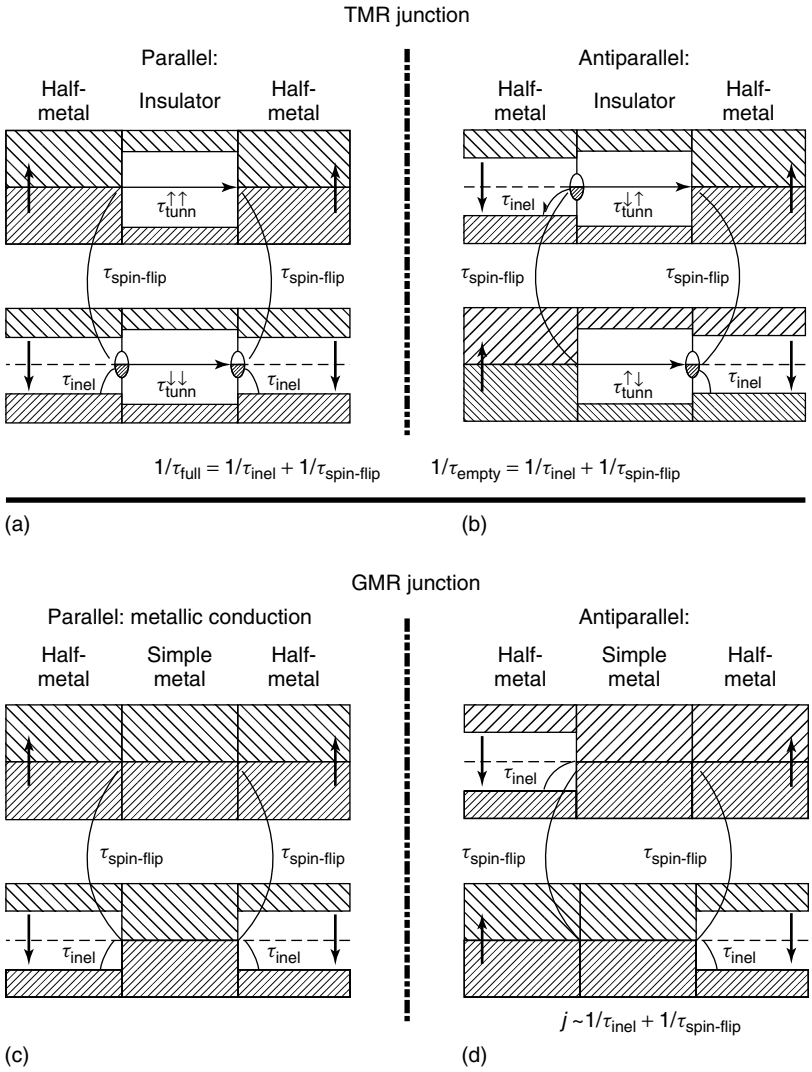

Figure 11. Schematic band picture in TMR (a and b) and GMR (c and d) junction using half-metallic electrodes. E_F is shown as a dashed line. Dark shaded, light shaded, and unshaded regions correspond to filled bands, empty bands, and band gaps respectively. Interface states contribute to the tunneling current and is controlled by the tunneling rate as shown in the figure (Mavropoulos, Ležaić and Blügel, 2005).

et al., 2003; Felser, Elmers and Fecher, 2005) alloys is currently the driving force for evaluating the potential of MTJs. Experimental attempts to realize MTJs with Heusler alloy did not yield any enhancement till recently. NiMnSb based MTJ exhibit spin polarization of 25% at 4.2 K and 9% at 300 K. Recently, MTJs based on full-Heusler alloy of type $Co_2Cr_{0.6}Fe_{0.4}Al$ showed promising results, reaching spin polarization values of 42–47% at room temperature (Marukame *et al*., 2005; Okamura *et al*., 2005). Another interesting candidate is half-metallic Co_2MnSi ($T_C = 985$ K). It was found that the temperature dependence of the spin polarization scales with the magnetic moment (Meservey, Pereskevopoulus and Tedrow, 1976) as described by the Bloch $T^{3/2}$ behavior (O'Handley, 2000) and consequently, materials with large Curie temperatures should have a high remanent spin polarization at room temperature. Recent experimental results on MTJs with $Co_{70}Fe_{30}$ and Co_2MnSi electrodes separated by a AlO_x barrier yields 66% spin polarization at 20 K (Kämmerer, Thomas, Hütten and Reiss, 2004). This value clearly exceeds that of the 3*d*-based magnetic elements or their alloys but is also well below the predicted 100%.

According to Butler, Zhang, Schulthess and MacLaren (2001), it is possible to obtain huge TMR values at room temperature in epitaxial Fe(100)/MgO(100)/Fe(100) with thick MgO tunnel barriers. This has been realized to some extent in CoFe/MgO (Parkin *et al*., 2004) and Fe/MgO/Fe (Yuasa *et al*., 2004) based MTJs. These MTJs based on MgO tunnel barrier will certainly have an immense impact on spin electronic devices operable at room temperature.

Moreover, they exhibit high temperature stability which makes them suitable for integration with CMOS circuits for MRAM applications (Parkin *et al*., 2004). In particular, Parkin *et al*. showed that these devices would have dramatic effect on MRAMs with read performance better than the current prototypes and eases the implementation of advanced MRAM architectures with ultradense cross-point random access memory (Reohr *et al*., 2002).

Half-metallic electrodes also constitute ideal components for GMR with half-metallic electrodes sandwiching a non-magnetic metal (Figure 10a). While half-metallic property of materials can be exploited fully in GMR-based junctions, the presence of interface states dramatically affect the TMR junctions as the tunneling rate is slower compared to the spin-flip rate (Mavropoulos, Ležaić and Blügel, 2005).

8.3 Spin transistor

Another proposed application of half-metal is in the *spin* MOSFET with an Si channel, MOS gate, and ferromagnetic source and drain electrodes as described by Tanaka (2005). The source/channel and drain/channel contacts, made up of half-metallic ferromagnets, are Schottky barriers, which allow for efficient spin injection and detection. The typical device structure is shown in Figure 12(a). The spin MOSFET behaves similar to Si-MOSFETs but with an additional spin-dependent transport functionality. Spin-polarized charge carriers are injected through the Schottky barrier by tunneling into the Si channel. The half-metallic drain selectively extracts the spin-polarized carriers from the channel, only when the spin configuration between the ferromagnetic source and drain is parallel. Thus, the output current depends on the relative magnetic configuration of the source and drain (Tanaka, 2005) as shown in Figure 12(b). Experiments showed that Schottky barriers can be used as spin aligners in reverse bias (Zhu *et al*., 2001; Hanbicki *et al*., 2002). However, under reverse bias, it is difficult to incorporate two Schottky barriers in series in GMR injector/detector configuration as one of them will lose its spin dependence (Schmidt, 2005).

8.4 Spin filters

A different approach to polarized spin injection is the *spin filter* (Hao, Moodera and Meservey, 1990), a tunnel barrier with different barrier heights, and therefore greatly different transmission coefficients for ↑ and ↓ electrons. Barrier heights are sufficiently different for almost fully spin-polarized currents to emerge on the far side of a barrier with unpolarized incident current. This can be realized using the

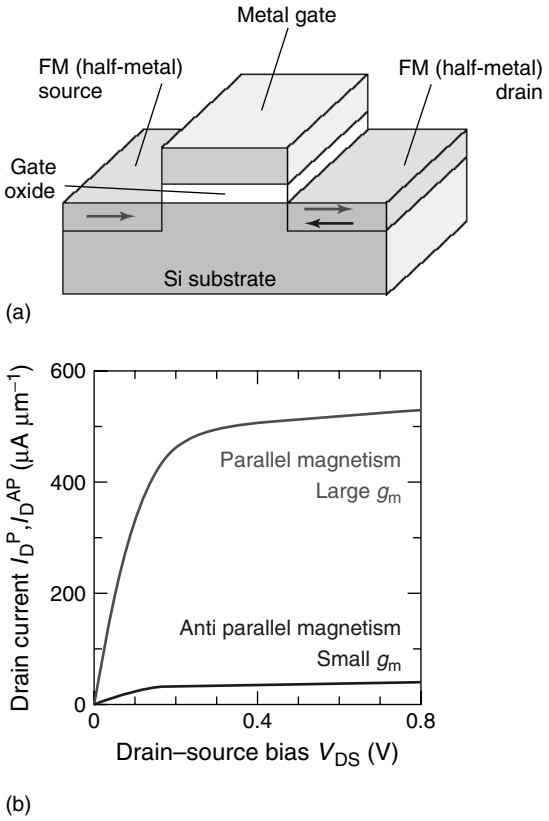

Figure 12. (a) The structure of spin MOSFET device and (b) calculated drain currents in parallel and antiparallel configurations (Tanaka, 2005).

half-metallic ferromagnetic materials with the majority spin channel with the lower resistance carries the entire current and minority channel acts as a barrier. The spin-filter effect may be used to provide a low-energy spin-polarized electron source.

9 CONCLUSIONS

The classification of half-metals is discussed taking account of both itinerant and localized electrons. For many potential applications, we need half-metals, which are compatible with semiconductors. In order to obtain useful materials operable at room temperature, it is quite important to explore new half-metallic compounds and structures through band-structure calculations and seek the highest possible Curie temperatures. The growth of high-quality single-crystalline epitaxial films of various half-metallic ferromagnets must be controlled. The effect of interfacial states on semiconductors needs to be studied in detail. Interface engineering will be critical for device operation, for example, making use of multiple reflection as in spin tunnel junctions. There are

dramatic developments in the search for new semiconductor-compatible half-metals such as Heusler alloys. However, growth temperature must be reduced to match the semiconductor integration. Studies should be focused on new half-metallic oxides and nitrides with high Curie temperature to enable them to be introduced in tunnel junctions or spin valves to attain huge TMR values at room temperature. The half-metallic oxides, nitrides, sulfides, Heusler alloys, and the novel magnetic semiconducting oxides, in the form of ultrathin films or layered samples, should be sufficient for future nanoscale applications. The ability to pattern in a subnanometer range today suggests that the role of half-metals in spin electronic applications is reaching a new stage. The difficulties in measuring the spin polarization directly forced to explore other experimental techniques to identify a half-metal, apart from an integral spin moment, metallic conduction criteria and band-structure calculations.

ACKNOWLEDGMENTS

This work was supported by Science Foundation Ireland as part of the CINSE and MANSE programs. The author is grateful to Prof. J.M.D. Coey for fruitful discussions and helpful comments.

REFERENCES

Akinaga, H., Manago, T. and Shirai, M. (2000). Material design of half-metallic zinc-blende CrAs and the synthesis by molecular-beam epitaxy. *Japanese Journal of Applied Physics*, **39**, L1118–L1120.

Baibich, M.N., Broto, J.M., Fert, A., *et al*. (1988). Giant magnetoresistance of (001)Fe/ (001)Cr magnetic superlattices. *Physical Review Letters*, **61**, 2472–2475.

Barry, A. (1999). *CrO_2: A general study*, Ph.D. Thesis, Trinity College, University of Dublin .

Besse, M., Cros, V., Barthélémy, A., *et al*. (2002). Experimental evidence of the ferrimagnetic ground state of Sr_2FeMoO_6 probed by X-ray magnetic circular dichroism. *Europhysics Letters*, **60**, 608–614.

Bibes, M., Bouzehouane, K., Barthélémy, A., *et al*. (2003). Tunnel magnetoresistance in nanojunctions based on Sr_2FeMoO_6. *Applied Physics Letters*, **83**, 2629–2631.

Block, T., Felser, C., Jakob, G., *et al*. (2003). Large negative magnetoresistance effects in $Co_2Cr_{0.6}Fe_{0.4}Al$. *Journal of Solid State Chemistry*, **176**, 646–651.

Bode, M. (2003). Spin-polarized scanning tunnelling microscopy. *Reports on Progress in Physics*, **66**, 523–582.

Bona, G.L., Meier, F., Taborelli, M., *et al*. (1985). Spin polarized photoemission from NiMnSb. *Solid State Communications*, **56**, 391–394.

Borca, C.N., Komesu, T., Jeong, H., *et al*. (2001). Evidence for temperature dependent moments ordering in ferromagnetic NiMnSb(100). *Physical Review B*, **64**, 052409.

Bowen, M., Bibes, M., Barthélémy, A., *et al*. (2003). Nearly total spin polarization in $La_{2/3}Sr_{1/3}MnO_3$ from tunneling experiments. *Applied Physics Letters*, **82**, 233–235.

Brabers, V.A.M. (1995). In *Ferromagnetic Materials*, Buschow, K.H.J. (Ed.), Elsevier, Vol. 8.

Butler, W.H., Zhang, X-G., Schulthess, T.C. and MacLaren, J.M. (2001). Spin-dependent tunneling conductance of Fe/MgO/Fe sandwiches. *Physical Review B*, **63**, 054416.

Chamberland, B.L. (1977). *CRC Critical Reviews in Solid State and Materials Sciences*, **7**, 1.

Clifford, E. (2005). *A Study of Spin-polarization in Potential Half-metals*, Ph.D. Thesis, Trinity College, University of Dublin.

Clifford, E., Venkatesan, M., Gunning, R. and Coey, J.M.D. (2004). Magnetoresitance in point contacts of the Heusler alloy $Co_2Cr_{0.6}Fe_{0.4}Al$. *Solid State Communications*, **131**, 61–64.

Coehoorn, R. (2003). *Handbook of Magnetic Materials*, Elsevier, pp. 1–197, Vol. 15.

Coey, J.M.D. and Sanvito, S. (2004). Magnetic semiconductors and half-metals. *Journal of Physics D: Applied Physics*, **37**, 988–993.

Coey, J.M.D. and Venkatesan, M. (2002). Half-metallic ferromagnetism: example of CrO_2. *Journal of Applied Physics*, **91**, 8345–8350.

Coey, J.M.D., Venkatesan, M. and Bari, M.A. (2001). In *High Magnetic Fields: Applications in Condensed Matter Physics and Spectroscopy*, Berthier, C., Levy, L.P. and Martinez, G. (Eds.), Springer: Berlin, p. 377.

Coey, J.M.D., Viret, M. and von Molnar, S. (1999). Mixed valence manganites. *Adv. Phys.*, **48**, 167–293.

Dedkov, Y.S., Rüdiger, U. and Güntherodt, G. (2002). Evidence for the half-metallic ferromagnetic state of Fe_3O_4 by spin-resolved photoelectron spectroscopy. *Physical Review B*, **65**, 064417.

Dieny, B. (2004). In *Chapter 1: Spin Valves Magnetoelectronics*, Johnson, M. (Ed.), Elsevier.

Dowben, P.A. and Skomski, R. (2003). Finite-temperature spin polarization in half-metallic ferromagnets. *Journal of Applied Physics*, **93**, 7948–7950.

Egelhoff, W.F., Chen, P.J., Powell, C.J., *et al*. (1996). Optimizing the giant magnetoresistance of symmetric and bottom spin valves. *Journal of Applied Physics*, **79**, 5277–5281.

Egelhoff, W.F., Ha, T., Misra, R.D.K., *et al*. (1995). Magnetoresistance values exceeding 21 percent in symmetrical spin valves. *Journal of Applied Physics*, **78**, 273–277.

van Engen, P.G., Buschow, K.H.J., Jongebreur, R. and Erman, M. (1983). PtMnSb, a materials with very high magneto-optical Kerr effect. *Applied Physics Letters*, **42**, 202–204.

Eyert, V., Hock, K.H., Fiechter, S. and Tributsch, H. (1998). Electronic structure of FeS_2: the crucial role of electron-lattice interaction. *Physical Review B*, **57**, 6350–6359.

Felser, C., Elmers, H.J. and Fecher, G.H. (2005). *The Properties of $Co_2Cr_{1-x}Fe_xAl$ Al Heusler Compounds*, Lecture Notes in Physics, Vol. 667, Springer-Verlag: Berlin, Heidelberg, P. 113.

Fujii, S., Asano, S. and Ishida, J. (1984). Bandstructures and hyperfine fields of Heusler alloys. *Journal of the Physical Society of Japan*, **53**, 2718–2725.

Fujii, S., Ishida, S. and Asano, S. (1992). Band calculations for Mn_4N and body-centered cubic Mn, fixing local spin directions. *Journal of Physics. Condensed Matter*, **4**, 1575–1580.

Fujii, S., Ishida, S. and Asano, S. (1995). A half-metallic band structure and Fe_2MnZ (Z=AL, SI, P). *Journal of the Physical Society of Japan*, **64**, 185–191.

Furukawa, N. (2000). Unconventional one-magnon scattering resistivity in half-metals. *Journal of the Physical Society of Japan*, **69**, 1954–1957.

Galanakis, I. and Dederichs, P.H. (2005). *Half-metallicity and Slater-pauling Behaviour in the Ferromagnetic Heusler Alloys*, Lecture Notes in Physics, Vol. 667, Springer-Verlag: Berlin, Heidelberg, p. 1.

Garcia, N. (2000). Conducting ballistic magnetoresistance and tunneling magnetoresistance: pinholes and tunnel barriers. *Applied Physics Letters*, **77**, 1351–1353.

de Groot, R.A., Mueller, F.M., van Engen, P.G. and Buschow, K.H.J. (1983). New class of materials: half-metallic ferromagnets. *Physical Review Letters*, **50**, 2024–2027.

de Groot, R.A., Mueller, F.M., van Engen, P.G. and Buschow, K.H.J. (1984). Half-metallic ferromagnets and their magneto-optical properties. *Journal of Applied Physics*, **55**, 2151–2154.

Gupta, A., Li, X.W. and Xiao, G. (2001). Inverse magnetoresistance in chromium-dioxide-based magnetic tunnel junctions. *Applied Physics Letters*, **78**, 1894–1896.

Hanbicki, A.T., Jonker, B.T., Itskos, G., *et al*. (2002). Efficient electrical spin injection from a magnetic metal/tunnel barrier contact into a semiconductor. *Applied Physics Letters*, **80**, 1240–1242.

Hao, X., Moodera, J.S. and Meservey, R. (1990). Spin-filter effect of ferromagnetic europium sulfide tunnel barriers. *Physical Review B*, **42**, 8235–8243.

Helmholdt, R.B., de Groot, R.A., Mueller, F.M., *et al*. (1984). Magnetic and crystallographic properties of several Cl_b type heusler compounds. *Journal of Magnetism and Magnetic Materials*, **43**, 249–255.

Hordequin, Ch., Ristoiu, D., Ranno, L. and Pierre, J. (2000). On the cross-over from half-metal to normal ferromagnet in NiMnSb. *European Physical Journal B*, **16**, 287–293.

Imai, H., Shimakawa, Y., Sushko, Yu.V. and Kubo, Y. (2000). Carrier density change in the colossal-magnetoresistance pyrochlore $Tl_2Mn_2O_7$. *Physical Review B*, **62**, 12190–12194.

Irkhin, V.Y. and Katsnel'son, M.I. (1994). Half-metallic ferromagnets. *Physics Uspekhi*, **37**, 659–677.

Irkhin, V.Y. and Katsnel'son, M.I. (2002). Temperature dependences of resistivity and magnetoresistivity for half-metallic ferromagnets. *European Physical Journal B*, **30**, 481–486.

Jarrett, H.S., Cloud, W.H., Bouchard, R.J., *et al*. (1968). Evidence for itinerant d-electron ferromagnetism. *Physical Review Letters*, **21**, 617–620.

Jenkins, S.J. and King, D.A. (2001). Minority metallic surface states of a half-metallic ferrimagnet. *Surface Science*, **494**, L793–L798.

Jenkins, S.J. and King, D.A. (2002). Formation of interface states on a half-metal surface. *Surface Science*, **501**, L185–L190.

Ji, Y., Strijkers, G.J., Yang, F.Y., *et al*. (2001). Determination of the spin polarization of half-metallic CrO_2 by point contact Andreev reflection. *Physical Review Letters*, **86**, 5585–5585.

Jiang, C., Venkatesan, M. and Coey, J.M.D. (2001). Transport and magnetic properties of Mn_2VAl: search for half-metallicity. *Solid State Communications*, **118**, 513–516.

Julliere, M. (1975). Tunneling between ferromagnetic films. *Physics Letters A*, **54**, 225–226.

Kamiguchi, Y., Saito, K., Koui, K., *et al*. (1999). *Multi-layered thin-film functional device and magnetoresistance effect element*, US patent 6,303,218 B1.

Kämmerer, S., Thomas, A., Hütten, A. and Reiss, G. (2004). Co_2MnSi Heusler alloy as magnetic electrodes in magnetic tunnel junctions. *Applied Physics Letters*, **85**, 79–81.

Kämper, K.P., Schmitt, W., Güntherodt, G., *et al*. (1987). CrO_2 – a new half-metallic ferromagnet. *Physical Review Letters*, **59**, 2788–2791.

Kobayashi, K.I., Kimura, T., Sawada, H., *et al*. (1998). Room-temperature magnetoresistance in an oxide material with an ordered double-perovskite structure. *Nature*, **395**, 677–680.

Korotin, M.A., Anisimov, V.I., Khomski, D.I. and Sawatzky, G.A. (1998). CrO_2: a self-doped double exchange ferromagnet. *Physical Review Letters*, **80**, 4305–4308.

Kübler, J. (1984). 1st principle theory of metallic magnetism. *Physica B*, **127**, 257–263.

Kubo, K. and Ohata, N.A. (1972). Quantum theory of double exchange. *Journal of the Physical Society of Japan*, **33**, 21–32.

Lewis, S.P., Allen, P.B. and Sasaki, T. (1997). Band structure and transport properties of CrO_2. *Physical Review B*, **55**, 10253–10260.

van Leuken, H. and de Groot, R.A. (1995). Electronic structure of the chromium dioxide (001) surface. *Physical Review B*, **51**, 7176–7178.

Liu, B-G. (2005). *Half-Metallic Ferromagnetism and Stability of Transition Metal Pnictides and Chalcogenides*, Lecture Notes in Physics, Vol. 667, Springer-Verlag: Berlin, Heidelberg, p. 267.

Mannari, I. (1959). Electrical resistance of ferromagnetic metals. *Progress of Theoretical Physics*, **22**, 335–343.

Marukame, T., Kasahara, T., Matsuda, K.I., *et al*. (2005). High tunnel magnetoresistance in epitaxial $Co_2Cr_{0.6}Fe_{0.4}Al$/MgO/CoFe tunnel junctions. *IEEE Transactions on Magnetics*, **41**, 2603–2605.

Matar, S., Mohn, P., Demazeau, G. and Siberchicot, B. (1988). The calculated electronic and magnetic structures of Fe_4N and Mn_4N. *Journal de Physique (France)*, **49**, 1761–1768.

Mavropoulos, P., Ležaić, M. and Blügel, S. (2005). Half-metallic ferromagnets for magnetic tunnel junctions by *ab*-initio calculations. *Physical Review B*, **72**, 174428.

Mazin, I.I. (1999). How to define and calculate the degree of spin polarization in ferromagnets. *Physical Review Letters*, **83**, 1427–1430.

Mazin, I.I. (2000). Robust half metalicity in $Fe_xCo_{1-x}S_2$. *Applied Physics Letters*, **77**, 3000–3002.

Meaden, G.T. (1971). Conduction electron scattering and resistance of magnetic elements. *Contemporary Physics*, **12**, 313–316.

Meservey, R., Pereskevopoulus, D. and Tedrow, P.M. (1976). Correlation between spin polarization of tunnel currents from 3*d* ferromagnets and their magnetic moments. *Physical Review Letters*, **37**, 858–860.

Meservey, R. and Tedrow, P.M. (1994). Spin-polarized electron tunneling. *Physics Reports*, **238**, 173–243.

Mishra, S.K. and Sathpaty, S. (1998). Electronic structure and exchange interactions in the manganese-based pyrochlore oxides. *Physical Review B*, **58**, 7585–7592.

Monsma, D.J. and Parkin, S.S.P. (2000). Spin polarization of tunneling current from ferromagnet/Al_2O_3 interfaces using copper-doped aluminum superconducting films. *Applied Physics Letters*, **77**, 720–722.

Moodera, J.S., Kinder, L.R., Wong, T.M. and Meservey, R. (1995). Large magnetoresistance at room temperature in ferromagnetic thin film tunnel junctions. *Physical Review Letters*, **74**, 3273–3276.

Moodera, J.S. and Mathon, G. (1999). Spin polarized tunneling in ferromagnetic junctions. *Journal of Magnetism and Magnetic Materials*, **200**, 248–273.

Nadgorny,B., Mazin, I.I., Osofsky, M., *et al*. (2001). The origin of high transport spin polarization in $La_{0.7}Sr_{0.3}$ MnO_3: direct evidence for minority spin states. *Physical Review B*. **63**, 184433.

Obata, T., Manako, T., Shimakawa, Y. and Kubo, Y. (1999). Tunneling magnetoresistance at up to 270 K in $La_{0.8}Sr_{0.2}MnO_3$/$SrTiO_3$/$La_{0.8}Sr_{0.2}MnO_3$ junctions with 1.6 nm thick barriers. *Applied Physics Letters*, **74**, 290–292.

O'Handley, R.C. (2000). *Modern Magnetic Materials*, Wiley: New York.

Okamura, S., Miyazaki, A., Sugimoto, S., *et al*. (2005). Large tunnel magnetoresistance at room temperature with a Co_2FeAl full-Heusler alloy electrode. *Applied Physics Letters*, **86**, 232503.

Opahle, I., Koepernik, K. and Eschrig, H. (1999). Full-potential band-structure calculation of iron pyrite. *Physical Review B*, **60**, 14035–14041.

Orgassa, D., Fujiwara, H., Schulthess, T.C. and Butler, W.H. (1999). First-principles calculation of the effect of atomic disorder on the electronic structure of the half-metallic ferromagnet NiMnSb. *Physical Review B*, **60**, 13237–13240.

Otto, M.J., Feil, H., van Woerden, R.A.M., *et al*. (1989). Half-metallic ferromagnets. II: transport properties of NiMnSb and related intermetallic compounds. *Journal of Physics. Condensed Matter*, **1**, 2351–2360.

Palmstrøm, C. (2003). Epitaxial Heusler alloys: new materials for semiconductor spintronics. *MRS Bulletin*, **10**, 725–728.

Park, J.H., Vescovo, E., Kim, H.J., *et al*. (1998). Direct evidence for a half-metallic ferromagnet. *Nature*, **392**, 794–796.

Parkin, S.S.P., More, N. and Roche, K.P. (1990). Oscillations in exchange coupling and magnetoresistance in metallic superlattice structures – Co/Ru, Co/Cr and Fe/Cr. *Physical Review Letters*, **64**, 2304–2307.

Parkin, S.S.P., Kaiser, C., Panchula, A., *et al*. (2004). Giant tunnelling magnetoresistance at room temperature with MgO (100) tunnel barriers. *Nature Materials*, **3**, 862–867.

Penicaud, M., Silberchiot, B., Sommers, C.B. and Kubler, J. (1992). Calculated electronic band-structure and magnetic moments of ferrites. *Journal of Magnetism and Magnetic Materials*, **103**, 212–220.

Pickett, W.E. and Moodera, J.S. (2001). Half metallic magnets. *Physics Today*, **54**, 39–44.

Pickett, W.E. and Singh, D.J. (1996). Electronic structure and half-metallic transport in the $La_{1-x}Ca_xMnO_3$ system. *Physical Review B*, **53**, 1146–1160.

Picozzi, S., Continenza, A. and Freeman, A.J. (2003). First principles study of electronic and magnetic properties of Co_2MnGe/GaAs interfaces. *Journal of Physics and Chemistry of Solids*, **64**, 1697–1701.

Prinz, G.A. (1998). Device physics – magnetoelectronics. *Science*, **282**, 1660–1663.

Reohr, W., Honigschmid, H., Robertazzi, R., *et al*. (2002). Memories of tomorrow. *IEEE Circuits and Devices*, **18**, 17–27.

Ristoiu, D., Nozières, J.P., Borca, C.N., *et al*. (2000). The surface composition and spin polarization of NiMnSb epitaxial thin films. *Europhysics Letters*, **49**, 624–630.

Sakuma, A. (1991). Electronic and magnetic structure of Fe_4N. *Journal of the Physical Society of Japan*, **60**, 2007–2012.

Schmidt, G. (2005). Concepts for spin injection into semiconductors – a review. *Journal of Physics D: Applied Physics*, **38**, R107–R122.

Schwarz, K. (1986). CrO_2 predicted as a half-metallic ferromagnet. *Journal of Physics F: Metal Physics*, **16**, L211–L215.

Seneor, P., Fert, A., Maurice, J-L., *et al*. (1999). Large magnetoresistance in tunnel junctions with an iron oxide electrode. *Applied Physics Letters*, **74**, 4017–4019.

Shimakawa, Y., Kubo, Y. and Manako, T. (1996). Giant magnetoresistance in $Tl_2Mn_2O_7$ with the pyrochlore structure. *Nature*, **379**, 53–55.

Shimakawa, Y., Kubo, Y., Hamada, N., *et al*. (1999). Crystal structure, magnetic and transport properties, and electronic band structure of $A_2Mn_2O_7$ pyrochlores (A = Y, In, Lu, and Tl). *Physical Review B*, **59**, 1249–1254.

Shirai, M. (2001). Electronic and magnetic properties of 3*d* transition-metal-doped GaAs. *Physica E*, **10**, 143–147.

Singh, D.J. (1997). Magnetoelectronic effects in pyrochlore Tl2Mn2O7: role of Tl–O covalency. *Physical Review B*, **55**, 313.

Skomski, R. and Dowben, P.A. (2002). The finite-temperature densities of states for half-metallic ferromagnets. *Europhysics Letters*, **58**, 544–548.

Soulen, R.J., Byers, J.M., Osofsky, M.S., *et al*. (1998). Measuring the spin polarization of a metal with a superconducting point contact. *Science*, **282**, 85–88.

Subramanian, M.A., Toby, B.H., Ramirez, A.P., *et al*. (1996). Colossal magnetoresistance without Mn^{3+}/Mn^{4+} double exchange in the stoichiometric pyrochlore $Tl_2Mn_2O_7$. *Science*, **273**, 81–84.

Tanaka, M. (2005). Spintronics: recent progress and tomorrow's challenges. *Journal of Crystal Growth*, **278**, 25–37.

Tanaka, C.T., Nowak, J. and Moodera, J.S. (1999). Spin-polarized tunneling in a half-metallic ferromagnet. *Journal of Applied Physics*, **86**, 6239–6242.

de Teresa, J.M., Bethelemy, A., Fert, A., *et al*. (1999). Inverse tunnel magnetoresistance in Co/$SrTiO_3$/$La_{0.7}Sr_{0.3}$ MnO_3: new

ideas on spin-polarized tunneling. *Physical Review Letters*, **82**, 4288–4291.

Tomioka, Y., Okuda, T., Okimoto, Y., *et al*. (2000). Magnetic and electronic properties of a single crystal of ordered double perovskite Sr_2FeMoO_6. *Physical Review B*, **61**, 422–427.

Upadhyay, S.K., Palanisami, A., Louie, R.N. and Burman, R.A. (1998). Probing ferromagnets with Andreev reflection. *Physical Review Letters*, **81**, 3247–3250.

Versluijs, J.J., Bari, M.A. and Coey, J.M.D. (2001). Magnetoresistance of half-metallic oxide nanocontacts. *Physical Review Letters*, **87**, 026601.

Verwey, E.J.W. (1939). Electronic conduction of magnetite (Fe_3O_4) and its transition point at low temperatures. *Nature*, **144**, 327–328.

Viret, M., Drouet, M., Nassar, J., *et al*. (1997). Low-field colossal magnetoresistance in manganite tunnel spin valves. *Europhysics Letters*, **39**, 545–549.

Watts, S.M., Wirth, S., von Molnár, S., *et al*. (2000). Evidence for two-band magnetotransport in half-metallic chromium dioxide. *Physical Review B*, **61**, 9621–9628.

Weht, R. and Pickett, W.E. (1999). Half-metallic ferrimagnetism in Mn_2VAl. *Physical Review B*, **60**, 13006–13010.

Westerburg, W., Reisinger, D. and Jakob, G. (2000). Epitaxy and magnetotransport of Sr_2FeMoO_6 thin films. *Physical Review B*, **62**, R767–R770.

de Wijs, G.A. and de Groot, R.A. (2001). Towards 100% spin-polarized charge-injection: the half-metallic NiMnSb/CdS interface. *Physical Review B*, **64**, 020402.

Wohlfarth, E.P. (1980). In *Iron, Cobalt and Nickel, in Ferromagnetic Materials*, Wohlfarth, E.P. (Ed.), North Holland: Amsterdam.

Wolf, S.A., Awschalom, D.D., Buhrman, R.A., *et al*. (2001). Spintronics: a spin-based electronics vision for the future. *Science*, **294**, 1488–1495.

Worledge, D.C. and Geballe, T.H. (2000). Spin-polarized tunneling in $La_{0.67}Sr_{0.33}MnO_3$. *Applied Physics Letters*, **76**, 900–902.

Wurmehl, S., Fecher, G.H., Kandpal, H.C., *et al*. (2005). Geometric, electronic, and magnetic structure of Co_2FeSi: curie temperature and magnetic moment measurements and calculations. *Physical Review B*, **72**, 184434.

Yoshida, Y., Kawakami, M. and Nakamichi, T. (1981). Magnetic properties of a ternary alloy $Mn_{0.5}V_{0.5-y}Al_y$. *Journal of the Physical Society of Japan*, **50**, 2203–2208.

Yuasa, S., Nagahama, T., Fukushima, A., *et al*. (2004). Giant room-temperature magnetoresistance in single-crystal Fe/MgO/Fe magnetic tunnel junctions. *Nature Materials*, **3**, 868.

Zhang, Z. and Satpathy, S. (1991). Electron-states, magnetism and the verwey transition in magnetite. *Physical Review B*, **44**, 13319.

Zhu, H.J., Ramsteiner, M., Kostial, H., *et al*. (2001). Room-temperature spin injection from Fe into GaAs. *Physical Review Letters*, **87**, 16601.

FURTHER READING

Singh, D.J., Harris, V.G., Arsenov, A. and Mukovskii, Ya. (2001). Origin of high transport spin polarization in $La_{0.7}Sr_{0.3}MnO_3$: direct evidence for minority spin states. *Physical Review B*, **63**, 184433.

Superparamagnetic Particles

Steen Mørup and Mikkel Fougt Hansen
Technical University of Denmark, Kongens Lyngby, Denmark

1 INTRODUCTION

Magnetic nanoparticles have attracted much attention because of their unique magnetic properties, which, in several respects, differ considerably from those of bulk materials, and because of their many technological applications. Magnetic nanoparticles play a crucial role in information technology as they are used for data storage in, for example, hard disks in modern computers. Apart from this very important application, they are applied, for example, in ferrofluids and catalysts, for magnetic targeted drug delivery and MRI contrast imaging, and in biotechnology. Moreover, magnetic nanoparticles are commonly found in nature, including, for example, in sediments, in living organisms, and in primitive meteorites. It has been shown that a variety of different animals can navigate on the basis of a magnetic sense, which can be ascribed to magnetic nanoparticles in their bodies. The preparation, properties, and applications of magnetic nanoparticles have been the subject of several review papers (Bean and Livingston, 1959; Mørup, Dumesic and Topsøe, 1980; Mørup, 1990; Tronc, 1996; Leslie-Pelecky and Rieke, 1996; Murad, 1996, 1998; Dormann, Fiorani and Tronc, 1997; Kodama, 1999; Garcia-Palacios, 2000; Walker, Diebel and Green, 2000; Battle and Labarta, 2002; Pankhurst, Connolly, Jones and Dobson, 2003; Tartaj *et al*., 2003; Jönsson, 2004; Willard *et al*., 2004; Bansmann *et al*., 2005).

Usually, crystals of ferromagnetic and ferrimagnetic crystals spontaneously split up in magnetic domains as this reduces the magnetic energy. The domain walls, in which the spin directions gradually chance from the magnetization direction of one domain to that of the next, typically have widths of the order of 100 atomic layers. Because it costs exchange energy to form a domain wall, it is not energetically favorable to form domain walls in particles with dimension below a certain critical size. The critical size for single domain behavior is typically in the range 10–1000 nm, depending on the material.

A very significant difference between bulk materials and nanoparticles is that the magnetization direction may be unstable in magnetic nanoparticles because the thermal energy may be sufficient to overcome the energy barrier separating the easy directions of magnetization. This phenomenon, termed *superparamagnetic relaxation*, is particularly crucial in the development of high-density magnetic data storage media. The continued increase in the data storage density requires a reduction of the particle size, but the onset of superparamagnetic relaxation in very small particles makes them useless for data storage and this ultimately sets an upper limit for the density of stored data in magnetic recording media.

Handbook of Magnetism and Advanced Magnetic Materials. Edited by Helmut Kronmüller and Stuart Parkin. Volume 4: *Novel Materials*. ISBN: 978-0-470-02217-7.

In this chapter, we discuss the properties of magnetic nanoparticles with special emphasis on superparamagnetic relaxation, and we show how a number of different experimental techniques can elucidate these phenomena. The aim of this chapter is to give an introduction to the field for nonspecialists rather than presenting a comprehensive review. In Section 2, a general introduction to magnetic relaxation phenomena in nanoparticles is given. In Section 3, we present a brief review of some of the common preparation techniques, and, in Section 4, we discuss some of the most important (nonmagnetic) characterization techniques. Section 5 deals with the most important techniques used for studies of magnetic relaxation phenomena in nanoparticles with an emphasis on studies of noninteracting particles. In Section 6, we show how the magnetic relaxation phenomena can be influenced by interparticle interactions. Finally, in Section 7, we give a brief discussion of the magnetic structure of nanoparticles, spin canting, and the related transverse relaxation.

2 MAGNETIC RELAXATION IN NANOPARTICLES

Single domain particles are characterized by two or more easy directions of magnetization, that is, directions of the magnetization, which give minimum magnetic energy. If the magnetocrystalline anisotropy is predominant, the easy directions are defined by the crystal symmetry. However, in nanoparticles, it is commonly found that other contributions to the magnetic anisotropy are more important (Mørup, Dumesic and Topsøe, 1980; Dormann, Fiorani and Tronc, 1997). For ferromagnetic and ferrimagnetic particles, shape anisotropy may be significant if the particle shape deviates from the spherical shape. The lower symmetry of the surface atoms compared to bulk can result in surface anisotropy, which may be predominant for particle sizes below about 10 nm. Furthermore, if a particle is exposed to stress, this may also result in a contribution to the magnetic anisotropy. For these reasons, the magnetic anisotropy of nanoparticles is complex, but commonly it is assumed that nanoparticles have a dominating uniaxial anisotropy with a magnetic energy given by the simple expression

$$E = KV \sin^2 \theta \tag{1}$$

where K is an effective magnetic anisotropy constant, V is the particle volume, and θ is the angle between the magnetization direction and the easy axis of magnetization. In this case, there are energy minima at $\theta = 0^\circ$ and $\theta = 180^\circ$ separated by an energy barrier of height KV. In very small particles at a finite temperature, the energy barrier may be comparable to the thermal energy, and the particles then perform superparamagnetic relaxation, that is, spontaneous fluctuations of the magnetization direction between the easy directions of magnetization. The superparamagnetic relaxation time, τ, is approximately given by the Néel–Brown expression (Néel, 1949; Brown, 1963)

$$\tau = \tau_0 \exp(KV/k_B T) \tag{2}$$

where τ_0 is typically in the range 10^{-12}–10^{-9} s, k_B is Boltzmann's constant, and T is the temperature. τ_0 depends on material parameters such as the magnetization, the magnetic anisotropy constant, the particle volume, and also weakly on temperature (Néel, 1949; Brown, 1963; Dormann, Fiorani and Tronc, 1997). Equation (2) is valid for particles that are well separated, such that interparticle magnetic interactions are negligible. The influence of interparticle interactions on the magnetic relaxation is discussed in Section 6.

Superparamagnetic relaxation can be studied using several different experimental techniques. In experimental studies, the timescale of the experimental technique is crucial. If the superparamagnetic relaxation time is longer than the timescale of the experimental technique, the magnetization appears static, but, if it is shorter, one may instead observe an average value of the magnetization. The temperature at which the superparamagnetic relaxation time is equal to the timescale of the experimental technique is called the *blocking temperature*, T_B. It is noteworthy that the blocking temperature of a sample is not uniquely defined, but, for each applied experimental technique, a related blocking temperature can be defined.

In practice, samples of superparamagnetic particles have a particle size distribution, and the magnetic anisotropy constants may also vary from particle to particle because of differences in, for example, particle size, shape, stress, and the surface state. Therefore, there will be a distribution of energy barriers, which can lead to a very broad distribution of relaxation times due to the exponential dependence of the superparamagnetic relaxation time, τ, on the energy barrier, KV. In a sample with an energy barrier distribution, the (median) blocking temperature can be defined as the temperature at which half the volume of the particulate material has relaxation times shorter than the timescale of the experimental technique and half of it has longer relaxation times.

In DC magnetization measurements, the timescale is of the order of seconds or longer. In AC magnetization measurements, one can choose the timescale by choosing the frequency. For studies of nanoparticles with short relaxation times, Mössbauer spectroscopy, with a timescale of the order of a few nanoseconds, is often used. Even shorter relaxation times may be studied by inelastic neutron scattering. The

use of these techniques for studies of magnetic relaxation in nanoparticles is discussed in Section 5. In a few studies, it has been demonstrated that muon spin relaxation (μ-SR) also can be used for studies of superparamagnetic relaxation. This technique can be used to study relaxation phenomena with frequencies in the range 10^4–10^{11} s^{-1} (Bewley and Cywinski, 1998; van Lierop, Ryan, Pumarol and Roseman, 2001; Ucko *et al*., 2001).

Below the blocking temperature, where the superparamagnetic relaxation is negligibly slow, there may still be thermal excitations, which affect the magnetic properties. For a particle with magnetic energy given by equation (1), the probability that the magnetization direction forms an angle in the range between θ and $\theta + \mathrm{d}\theta$ with the easy direction of magnetization is given by Mørup and Topsøe (1976) and Mørup (1983)

$$p(\theta)\mathrm{d}\theta = \frac{\exp(-E(\theta)/k_\mathrm{B}T)\sin\theta}{\int_0^{\pi/2}\exp(-E(\theta)/k_\mathrm{B}T)\sin\theta\mathrm{d}\theta}\mathrm{d}\theta \qquad (3)$$

Thus, even well below the blocking temperature, the magnetic properties may be influenced by fluctuations of the magnetization direction close to the easy axis. These fluctuations are uniform, that is, the magnetic moments of all the ionic spins are parallel and they have been termed *collective magnetic excitations*. Collective magnetic excitations can be described in terms of precession of the (sublattice) magnetization vector in the anisotropy field in combination with transitions between precession states with different precession angles (Mørup *et al*., 2002). In Mössbauer spectroscopy studies, the fluctuations can be considered fast compared to the timescale, and, as discussed in Section 5.3, one measures a magnetic hyperfine field, which is proportional to the average magnetization, which is given by Mørup and Topsøe (1976), Mørup (1983), and Mørup and Hansen (2005)

$$\langle M\rangle_T = M_0\langle\cos\theta\rangle_T = M_0\int_0^{\pi/2}\cos\theta\, p(\theta)\,\mathrm{d}\theta \approx M_0(1 - k_\mathrm{B}T/2\,KV) \qquad (4)$$

where M_0 is the saturation (or nonrelaxing) magnetization and the approximation is valid for $k_\mathrm{B}T \ll KV$. In inelastic neutron-scattering experiments, which have a shorter timescale, one can measure the transition energy for transitions between the precession states. This is discussed in Section 5.4.

In nanoparticles of antiferromagnetic materials, the sublattice magnetization directions may fluctuate in a way that is similar to the fluctuations of the magnetization direction of ferromagnetic and ferrimagnetic nanoparticles. Ideally, the net magnetic moment of an antiferromagnetic particle should be negligible. However, in practice, nanoparticles of antiferromagnetic materials have nonzero magnetic moments. This can be explained by uncompensated magnetic moments due to different numbers of ions with spin up and spin down at the surface and possibly also in the interior of the particles (Néel, 1961; Richardson *et al*., 1991; Kodama, 1999). It has recently been suggested that thermal excitations of the uniform mode in a nanoparticle of an antiferromagnetic material can result in a contribution to the magnetic moment (thermoinduced magnetization), which increases with increasing temperature (Mørup and Frandsen, 2004; Mørup and Hansen, 2005).

Apart from the thermally activated relaxation discussed in the preceding text, it has been suggested that quantum tunneling between the energy minima may take place (Chudnovsky and Gunther, 1988; Barbara and Chudnovsky, 1990). Since quantum tunneling is temperature independent, one should expect that it gives rise to a temperature-independent relaxation time below the temperature where the thermally activated relaxation is slow compared to quantum tunneling.

3 SAMPLE PREPARATION TECHNIQUES

Magnetic nanoparticles can be synthesized by using numerous different techniques. Here, we present a brief overview of some of the most commonly applied preparation methods and give some examples of the occurrence of magnetic nanoparticles in nature.

3.1 Chemical synthesis and thermal decomposition

Wet chemical synthesis methods are among the most-used techniques for preparation of magnetic nanoparticles (Willard *et al*., 2004). For example, nanoparticles of iron oxides, such as maghemite (γ-Fe_2O_3), magnetite (Fe_3O_4) (Jolivet, Tronc and Chanéac, 2000), and hematite (α-Fe_2O_3) (Sugimoto, Wang, Itoh and Maramatsu, 1998), are conveniently prepared by precipitation from aqueous solutions of iron salts. By varying the preparation conditions, it is possible to vary the average particle size. Thermal decomposition of, for example, (oxy)hydroxides or hydrated salts is another commonly used technique for preparation of nanoparticles (Richardson *et al*., 1991; Bødker *et al*., 2000). By varying the decomposition temperature, one can vary the average particle size. Precipitation and thermal decomposition techniques usually result in rather broad size distributions. Narrow size distributions can be obtained using the so-called inverse micelle technique (O'Conner *et al*., 2001; Willard *et al*., 2004). Thermal decomposition of, for example, $Fe(CO)_5$ in organic liquids containing appropriate surfactant molecules

can also lead to very narrow particle size distributions (Fisker *et al*., 2000; Sun *et al*., 2000), and three-dimensional ordered arrays of nanoparticles can be prepared by drying suspensions of such monodisperse particles (Bentzon *et al*., 1989).

3.2 Preparation of metallic nanoparticles by reduction

Metallic nanoparticles can be prepared by reduction of, for example, metal oxide nanoparticles in hydrogen at elevated temperatures. Often, there is a strong tendency for the particles to sinter during the reduction. Therefore, the reduction is often carried out using samples of particles, that are well dispersed on a high-surface-area support, such as silica, carbon black, alumina, or others (Topsøe, Dumesic and Mørup, 1980; Bødker, Mørup and Linderoth, 1994; Bødker *et al*., 1998). Metallic nanoparticles are very reactive and may even burn when exposed to air. Therefore, studies of their magnetic properties must be performed in a controlled environment, and sophisticated *in situ* cells have been constructed for such studies (Bødker and Mørup, 1996).

3.3 Chemical reduction using $NaBH_4$

Nanoparticles of amorphous $TM_{1-x}B_x$ alloys, where TM is a transition metal (Fe, Co, or Ni), can be prepared by reduction of the transition-metal ions in aqueous solution using $NaBH_4$ (or KBH_4). It has been shown that the boron content can be varied by changing the pH value of the solution in which the reaction takes place (van Wonterghem *et al*., 1986; Linderoth and Mørup, 1991).

3.4 Evaporation techniques

Evaporation of metals in inert atmospheres has also been used to produce nanoparticles and, by varying the gas composition and pressure, it is possible to vary the particle size (Granqvist and Buhrman, 1976). In some studies, this preparation technique has been combined with separation in a mass spectrometer such that one can select particles with a well-defined size (Billas, Becker, Chatelain and de Heer, 1993).

3.5 Ball milling

For large-scale production of nanoparticles, high-energy ball milling may be used (Koch, 1991; Suryanarayana, 2001). With this technique, one can typically reduce the crystal size to around 10–20 nm within hours. Further milling does not result in smaller particles because ball milling of very small particles also can result in growth of crystallites (Mørup, Jiang, Bødker and Horsewell, 2001). Ball-milled samples usually contain many defects, and the crystallites of nanometer size often form large agglomerates. Besides, material from the balls and vials usually contaminate the ball-milled samples. A very interesting feature of ball milling is that one can make chemical reactions by high-energy ball-milling mixtures of different materials. In this way, it appears possible to produce nanocrystals of metastable materials, which cannot be produced by traditional techniques (Koch, 1991; Suryanarayana, 2001; Principi, 2001).

3.6 Coating of nanoparticles

As discussed in Section 6, magnetic interactions between nanoparticles can have a significant influence on the magnetic relaxation. Therefore, it is often important that one is able to control the distance between the particles. Coating the nanoparticles with surfactant molecules such as oleic acid reduces the magnetic interaction, and, for antiferromagnetic particles, this may be sufficient to ensure that the interactions are negligible. For nanoparticles of ferromagnetic or ferrimagnetic materials, further separation may be necessary to reduce the interactions because of the long-range dipole interactions. In several studies, coated particles have been suspended in a liquid to form a stable suspension (a ferrofluid). One may then ideally control the strength of the interactions by diluting the liquid, and studies of the magnetic properties can be performed on frozen samples. In other studies, particles have been prepared in a matrix of polyvinyl alcohol (PVA), which is a solid at room temperature (Tronc, 1996; Tronc *et al*., 2000).

3.7 Magnetic nanoparticles in biological samples

The iron storage protein ferritin has been used in many studies of the fundamental magnetic properties of nanoparticles. Ferritin consists of a core of iron oxyhydroxide surrounded by a protein shell. It can be extracted from, for example, horse spleen, and it is commercially available. Ferritin has the advantage that the particle size distribution is relatively narrow, and the protein shell ensures that the interparticle interactions are negligible. Several different animals utilize magnetic nanoparticles for navigation. Magnetotactic bacteria contain a chain of, for example, single domain magnetite particles, which have superparamagnetic blocking temperatures well above room temperature. This chain of particles acts as a compass needle (Blakemore, 1975).

Homing pigeons have a magnetic sense, which is based on arrays of superparamagnetic nanoparticles in the tissue of the upper-beak skin. These arrays are deformed by the Earth's magnetic field and, via complex mechanisms, this enables the pigeons to navigate (Davila, Fleissner, Winklhofer and Petersen 2003).

3.8 Magnetic nanoparticles in geological samples

Nanoparticles of iron oxides and oxyhydroxides are widespread in soils and are responsible for the reddish color of, for example, tropical soils. Superparamagnetic behavior in geological samples can have important implications in studies of geomagnetism (Néel, 1949). The magnetic properties of soils have been extensively studied by, for example, Mössbauer spectroscopy (Murad, 1998; Vandenberghe *et al*., 2000).

4 CHARACTERIZATION OF NANOPARTICLES

4.1 Structural characterization

In studies of magnetic nanoparticles, it is essential that they are well characterized with respect to purity, size, shape, and so on. It is, for example, noteworthy that even tiny amounts of a strongly magnetic impurity phase may dominate the magnetization of an antiferromagnetic material.

A standard technique for characterization of nanoparticles is X-ray diffraction, which is used to identify the crystalline phases in a sample. Furthermore, this technique can also be used to estimate the particle size since the diffraction lines of nanoparticles are broadened with a line broadening that is inversely proportional to the particle size (Langford, Louër and Scardi, 2000). X-ray diffraction is less suitable for characterization of amorphous and poorly crystalline materials.

Transmission electron microscopy is another standard technique for characterization of nanoparticles. It gives information about both the particle size and the particle morphology. In studies of crystalline nanoparticles, electron diffraction can be used to determine the crystal structure. High-resolution transmission electron microscopy often allows observation of the lattice planes, and, in this way, the crystal structure can also be studied. Often, nanoparticles have a tendency to agglomerate, and it may then be difficult to obtain information on individual particles. Well-separated particles can be prepared by coating with appropriate surfactant molecules, and, by analyzing them in large numbers, one can estimate the particle size distribution. Figure 1(a) shows an example of a transmission electron microscope image of surfactant-coated amorphous Fe–C particles with a very narrow size distribution. The particles were prepared by thermal decomposition of $Fe(CO)_5$. Figure 1(b) shows the corresponding size distribution obtained from a computer analysis of an image containing about 4500 particles (Fisker *et al*., 2000).

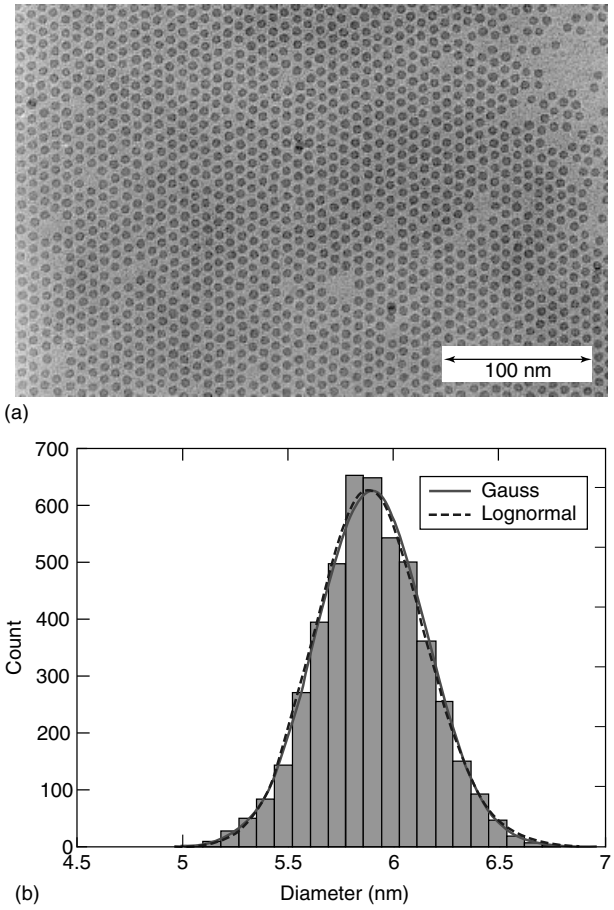

Figure 1. (a) Transmission electron microscopy image of amorphous Fe–C nanoparticles. (b) Size distribution of the same particles determined by a computer analysis of approximately 4500 particles in an image. The mean diameter is 5.9 nm with a standard deviation of 0.3 nm. (Kluwer Academic Publishers, *Journal of Nanoparticle Research* **2**(3), 2000, pp 267–277, Estimation of Nanoparticle size distributions by image analysis, R. Fisker, J.M. Carstensen, M.F. Hansen, F. Bødker, S. Mørup, figure 6, with kind permission of Springer Science and Business Media.)

Other techniques that can be employed for the morphological characterization of nanoparticles are small-angle neutron scattering (SANS) and small-angle X-ray scattering (SAXS). For samples with nearly uniform particle sizes, these techniques can give information on the size distribution and the structural and magnetic (for SANS) correlations between particles.

4.2 Particle size distributions

As discussed in Section 2, the exponential dependence of the superparamagnetic relaxation time on the energy barrier, KV, implies that the particle size distribution can have a great influence on the magnetic behavior of a sample, even for narrow size distributions. It is therefore important to know and include the particle size distribution when experimental data are analyzed. Let the number-weighted particle volume distribution be $f_{\mathrm{N}}(V)\,\mathrm{d}V$. Thus, the number of particles with volumes between V and $V+\mathrm{d}V$ is $f_{\mathrm{N}}(V)\,\mathrm{d}V$. If the signal from a particle of size V is $g(V,x)$, where x is the experimental parameter that will be varied in the measurements, the resulting signal, $G(x)$, from the entire sample is

$$G(x)=\int_0^\infty g(V,x)\,f_{\mathrm{N}}(V)\,\mathrm{d}V \tag{5}$$

Often, the normalized number-weighted or volume-weighted volume distribution is represented by a log-normal distribution

$$f_{\mathrm{LN}}(V)\,\mathrm{d}V=\frac{1}{\sqrt{2\pi}\sigma V}\exp\left(-\frac{\ln^2(V/V_{\mathrm{m}})}{2\sigma^2}\right)\mathrm{d}V \tag{6}$$

where V_{m} is the median particle volume and σ is the logarithmic standard deviation (Granqvist and Buhrman, 1976). This distribution function has been used to describe the size distribution of nanoparticles in numerous publications.

5 EXPERIMENTAL STUDIES OF NONINTERACTING MAGNETIC PARTICLES

5.1 DC magnetization measurements

When a sample of superparamagnetic particles is exposed to an applied magnetic field above the blocking temperature, the measured magnetization equals its thermal equilibrium value, that is, the particles are magnetized in a way that is similar to a paramagnetic material. However, the magnetic moments that interact with the applied magnetic field are the moments of whole particles, which can be hundreds or thousands of Bohr magnetons. This is in contrast to paramagnetic materials in which only the magnetic moments of individual ions (typically a few Bohr magnetons) interact with the field. Therefore, at a given temperature, the magnetization of a sample of superparamagnetic particles will approach the saturation value much faster than for a paramagnetic material. Often, the magnetic anisotropy energy can be considered negligible compared to the Zeeman energy, and the magnetic energy is then given by

$$E=-\boldsymbol{\mu}\cdot\mathbf{B}+KV\sin^2\theta\approx-\boldsymbol{\mu}\cdot\mathbf{B} \tag{7}$$

where $\boldsymbol{\mu}$ is the magnetic moment of the particle, $\mathbf{B}=\mu_0\mathbf{H}$ is the applied magnetic induction, and $\mathbf{H}$ is the intensity of the applied magnetic field. To ease the language in the following, we refer to $\mathbf{B}(=\mu_0\mathbf{H})$ as the applied magnetic field as it is common in the literature. The average magnetization along the applied field in thermal equilibrium is proportional to the Langevin function $L(\mu B/k_{\mathrm{B}}T)$:

$$\begin{aligned}\langle M\rangle &= M_0L(\mu B/k_{\mathrm{B}}T)\\ &\equiv M_0[\coth(\mu B/k_{\mathrm{B}}T)-k_{\mathrm{B}}T/\mu B]\end{aligned} \tag{8}$$

Thus, if the magnetization is plotted as a function of B/T, curves obtained at different temperatures should be identical in a temperature range where M_0 and μ can be considered temperature independent. This behavior is often taken as a fingerprint of a superparamagnetic sample.

In a detailed analysis of magnetization data, one has to take the particle size distribution into account. The average magnetic moment of a particle in a small applied magnetic field is $m(V,T)=\chi(V,T)VH$, where $\chi(V,T)$ is the initial magnetic susceptibility and T is the temperature. The total initial susceptibility of the sample is by definition the total magnetic moment divided by H and the total sample volume, that is,

$$\chi(T)=\frac{\int_0^\infty\chi(V,T)Vf_{\mathrm{N}}(V)\,\mathrm{d}V}{\int_0^\infty Vf_{\mathrm{N}}(V)\,\mathrm{d}V}\equiv\int_0^\infty\chi(V,T)\,f_{\mathrm{V}}(V)\,\mathrm{d}V \tag{9}$$

Here, we have defined the volume-weighted size distribution function $f_{\mathrm{V}}(V)\,\mathrm{d}V=Vf_{\mathrm{N}}(V)\,\mathrm{d}V/\int_0^\infty Vf_{\mathrm{N}}(V)\,\mathrm{d}V$, which is conveniently used in experimental studies where the sample signal is proportional to the particle volume.

When the magnetic anisotropy is not negligible, the field dependence of the magnetization deviates from the Langevin function. An analysis of the magnetization curves may then be used to estimate the magnetic anisotropy constant (Hanson, Johansson and Mørup, 1993; Respaud, 1999).

Below the blocking temperature, the magnetization curves exhibit hysteresis. It is characteristic that the coercivity decreases with increasing temperature and vanishes at the blocking temperature. The temperature dependence of the coercivity has in several cases been found to be in accordance with the expression (Bean and Livingston, 1959)

$$H_{\mathrm{c}}\approx 2\,KV(1-5\sqrt{k_{\mathrm{B}}T/KV})/\mu \tag{10}$$

Often, the superparamagnetic relaxation in samples of magnetic nanoparticles is studied by measuring the so-called zero-field-cooled (ZFC) and the field-cooled (FC) magnetization curves. A ZFC magnetization curve is obtained by cooling the sample in zero applied magnetic field from a temperature, where the entire sample shows a superparamagnetic response. Then a small field is applied and the magnetization of the sample is measured as a function of temperature during heating. The FC magnetization curve is measured as a function of increasing temperature after cooling the sample in the applied magnetic field. A typical example is shown in Figure 2. At temperatures well below the blocking temperature, the ZFC magnetization is small because the sample is not in thermal equilibrium and the magnetization directions of the particles in a small applied field are mainly governed by the randomly oriented easy directions of magnetization. With increasing temperature, first the smaller particles become superparamagnetic, and the probability of finding the particles with their magnetization directions close to that of the applied field increases, resulting in an increase in the magnetization. With further increasing temperature, more and more particles become superparamagnetic, resulting in an increasing magnetization until the net effect of the thermal energy is a decrease in the magnetization. In the FC state, the magnetization in the blocked state is preferably frozen in directions close to that of the applied field. Therefore, the magnetization is considerably larger than that in the ZFC state. The ZFC and the FC curves coincide above the bifurcation temperature, which is the temperature above which all particles are superparamagnetic.

The ZFC magnetic susceptibility curves are often modeled in the following manner: Well below the blocking temperature, the magnetic moments are frozen in random easy directions and the effect of an applied external field in this case is to slightly change the directions of minimum energy. For particles with uniaxial anisotropy and randomly oriented easy axes, a minimization of the energy yields the low-field magnetic susceptibility

$$\chi_0 = \frac{\mu_0 M_0^2}{3K} \tag{11}$$

Well above the blocking temperature, the thermal effects dominate and the susceptibility at low fields is obtained using the fact that the Langevin function fulfills $L(x) \approx x/3$ for $x < 1$. The result is

$$\chi_\infty = \frac{\mu_0 M_0^2 V}{3k_B T} \tag{12}$$

In the analyses of ZFC susceptibility curves for real samples, it is often assumed that the response of a particle of a given size is described by equation (11) for $T < T_B$ and equation (12) for $T \geq T_B$ as the effects of the particle size distribution on the relaxation time significantly smear out the assumed sharp transition between the blocked and superparamagnetic state. A typical timescale of such measurements is $\tau_m \approx 100\,\mathrm{s}$. It should be noted that the peak in the ZFC magnetization curve corresponds to the blocking temperature for a sample of particles of the same size. However, for a particle size distribution, the peak temperature can be up to a factor of 2 larger than the blocking temperature (Gittleman, Abeles and Bozowski, 1974; Chantrell, El-Hilo and O'Grady, 1991).

To elucidate the energy barrier distribution and to reveal information on interparticle interactions, it is useful to study the remanent magnetic moment after exposing the sample to different temperature and field conditions. These different conditions lead to the so-called thermoremanent magnetization (TRM), isothermal remanent magnetization (IRM), and the direct current demagnetization (DCD) magnetization. These techniques have especially been used for studies of magnetic recording media, where the stability of the remanent state after exposure to a magnetic field is essential for the ability to read the stored information. For an introduction and further references on these techniques, see Dormann, Fiorani and Tronc (1997).

Magnetic viscosity measurement is another useful technique for studies of superparamagnetic relaxation (Labarta, Iglesias, Balcells and Badia, 1993; Iglesias, Badia, Labarta and Balcells, 1996). In such measurements, one measures the approach to equilibrium magnetization as a function of time. For example, the sample can be cooled in an applied magnetic field and the field is switched off at a selected temperature. Subsequently, the time dependence of the magnetization $M(t)$ is measured as a function of time. The magnetic

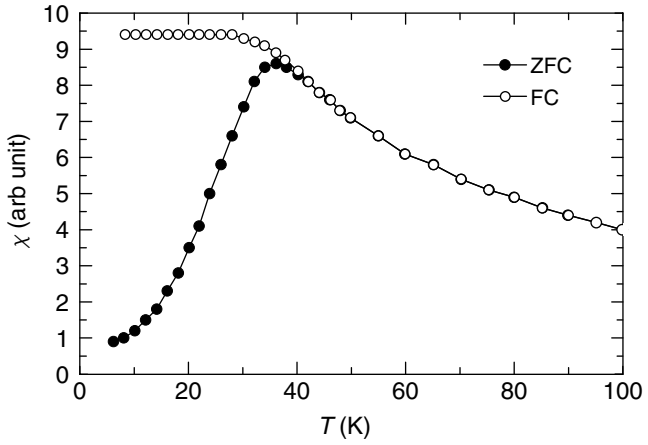

Figure 2. ZFC and FC magnetization curves measured on a ferrofluid of the Fe–C particles from Figure 1 with a concentration of 0.05 vol% in an applied field of $\mu_0 H = 0.5\,\mathrm{mT}$.

viscosity is defined as

$$S = \frac{\partial M(t)}{\partial \ln t} \tag{13}$$

In several studies, it has been found that the magnetic viscosity becomes temperature independent at very low temperatures (Zhang, Tejada, Hernandez and Ziolo, 1997; Tejada, Zhang and Chudnovsky, 1993). This has been taken as evidence for quantum tunneling. It has, however, been pointed out that if the distribution of energy barriers, ΔEs, diverges approximately inversely proportional to ΔE for $\Delta E \to 0$, this will also lead to an apparently temperature-independent relaxation time (Barbara *et al*., 1992). Both computer simulations (Kodama, Berkowitz, McNiff and Foner, 1996) and analytical calculations (Mørup, 2003) have shown that there may be energy barrier distributions due to localized magnetic defects that diverge for $\Delta E \to 0$. It can be shown that a plot of $S/k_{\mathrm{B}}T$ against $k_{\mathrm{B}}T\ln(t)$ gives information about the distribution of energy barriers (Iglesias, Badia, Labarta and Balcells, 1996). In a study of ferritin, St. Pierre *et al*. (2001) have shown experimentally that the energy barrier distribution in fact seems to diverge for $\Delta E \to 0$. The origin of such an energy barrier distribution is further discussed in Section 7.

5.2 AC magnetization measurements

The applied magnetic field intensity in the AC magnetization measurements is $H(t) = H_0 \cos(\omega t)$, where $\omega = 2\pi f$ and f is the frequency of the applied magnetic field. The response of the magnetic moments of the particles may be phase shifted compared to the applied field and is therefore conveniently described as a complex number. The complex magnetic susceptibility is written as

$$\chi_{\mathrm{AC}}(\omega, T) = \chi'(\omega, T) + \mathrm{i}\chi''(\omega, T) \tag{14}$$

where χ' and χ'' are the in-phase and out-of-phase components of the measured susceptibility, respectively. A simple expression for χ_{AC} has been given by Gittleman, Abeles, and Bozowski (1974). They wrote the time-dependent magnetic susceptibility as

$$\chi_{\mathrm{AC}}(t, T) = \chi_0 + (\chi_\infty - \chi_0) \cdot (1 - \mathrm{e}^{-t/\tau}) \tag{15}$$

where χ_0 is the magnetic susceptibility in the absence of thermal fluctuations (equation 11), χ_∞ is the equilibrium susceptibility (equation 12), and τ is the superparamagnetic relaxation time (equation 2). This expression is a good approximation to more accurate and complicated expressions for a random distribution of easy axes (Svedlindh, Jonsson and García-Palacios, 1997). By Fourier transformation, one obtains

$$\chi_{\mathrm{AC}}(\omega, T) = \frac{\chi_\infty + \mathrm{i}\omega\tau\chi_0}{1 + \mathrm{i}\omega\tau} = \frac{\chi_\infty + \chi_0(\omega\tau)^2}{1 + (\omega\tau)^2} + \mathrm{i}\frac{\omega\tau(\chi_0 - \chi_\infty)}{1 + (\omega\tau)^2} \tag{16}$$

AC susceptibility measurements have the advantage that the timescale is well defined and that it can be varied over several orders of magnitude ranging from $\sim 10^{-2}$ to 10^5 s^{-1}. The in-phase susceptibility shows a behavior similar to $\chi_{\mathrm{ZFC}}(T)$. The out-of-phase susceptibility is nonzero when the relaxation time of a significant fraction of the particles is of the order of ω^{-1} and peaks at the blocking temperature. It should be noted that, for a size distribution of particles, which is not too narrow, the out-of-phase susceptibility mirrors the distribution of superparamagnetic relaxation times (Jonsson, Mattsson, Nordblad and Svedlindh, 1997). Figure 3 shows AC susceptibility curves of samples of noninteracting and interacting γ-Fe_2O_3 nanoparticles. For the noninteracting sample, it is seen that both the in-phase and out-of-phase susceptibility curves are shifted toward higher temperatures as the frequency is increased and also that the peak height of the out-of-phase susceptibility curve depends only weakly on the frequency. The curves for the interacting sample are discussed in Section 6.

5.3 Mössbauer spectroscopy

Mössbauer spectroscopy has been widely used for studies of the magnetic properties of nanoparticles. The technique can be used for several isotopes of which the most important one, which we have also focused on here, is ^{57}Fe. An introduction to Mössbauer spectroscopy can be found in, for example, Greenwood and Gibb (1971). The technique is very sensitive to relaxation phenomena with relaxation times of the order of nanoseconds and can therefore be used for studies of relaxation phenomena that cannot be studied by, for example, AC and DC susceptibility measurements.

^{57}Fe Mössbauer spectra of bulk magnetic materials consist of one or more sextets, depending on the number of different Fe atomic sites. The distance between the lines is proportional to the magnetic field acting at the nucleus. In Mössbauer studies of magnetic nanoparticles, superparamagnetic relaxation can have a dramatic influence on the shape of the spectra, depending on the relaxation time. The timescale of Mössbauer spectroscopy, τ_{M}, is related to the Larmor precession time of the nuclear magnetic moment in the magnetic hyperfine field. In ^{57}Fe Mössbauer spectroscopy studies, τ_{M} is typically of the order of a few nanoseconds. The spectra

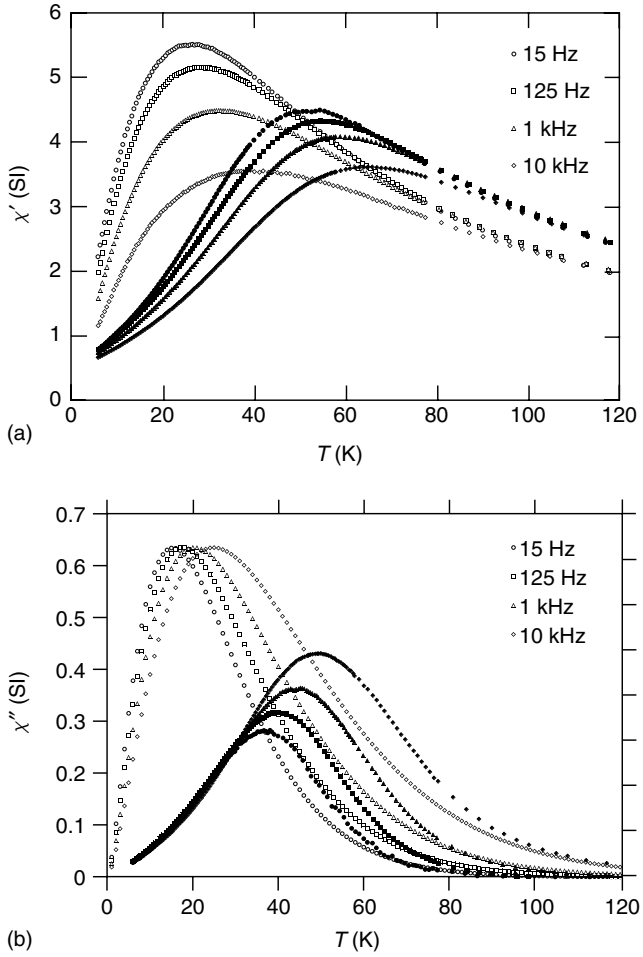

Figure 3. In-phase (a) and out-of-phase (b) AC susceptibilities versus temperature at different frequencies ranging from 15 Hz to 10 kHz for a noninteracting 0.03 vol% ferrofluid (open symbols) and an interacting 17 vol% ferrofluid (filled symbols) of 8-nm γ-Fe_2O_3 nanoparticles. (Reprinted figure from T. Jonsson, P. Nordblad, P. Svedlindh, *Phys. Rev.*, **B57**, pp 497–504 (1998).)

consist of sextets for relaxation times that are long compared to τ_M. For relaxation times close to τ_M, the lines are broadened and the magnetic splitting gradually collapses. For very short relaxation times ($<10^{-10}$ s), only a singlet or a doublet component is observed. This is illustrated in Figure 4, which shows theoretical ^{57}Fe Mössbauer spectra for different relaxation times.

Since the inevitable particle size distribution results in a broad distribution of relaxation times, the spectra of samples of magnetic nanoparticles consist of superpositions of components with different relaxation times. In nanoparticles, for which τ_0 is small compared to τ_M, a typical particle size distribution results in a very broad distribution of relaxation times at temperatures where the average relaxation time is close to τ_M. Therefore, close to the blocking temperature,

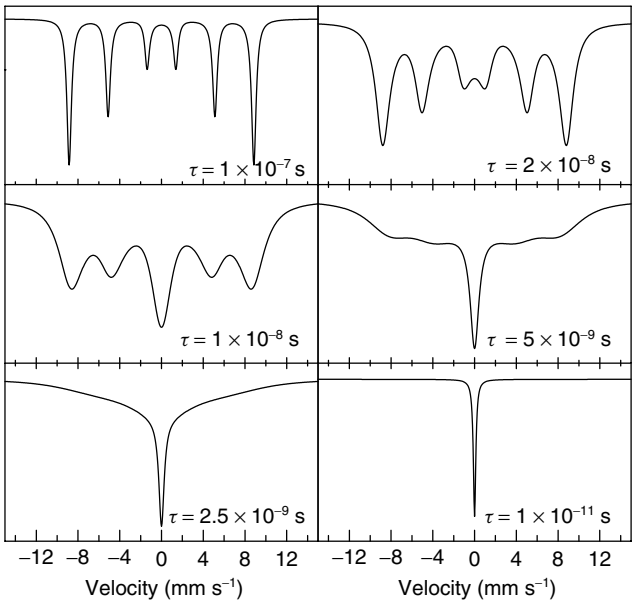

Figure 4. Theoretical Mössbauer spectra calculated for different superparamagnetic relaxation times and a hyperfine field fluctuating between ±55 T.

only a very small fraction of the particles have relaxation times close to τ_M. Thus, the spectra mainly consist of a superposition of a sextet with narrow lines, due to particles that are well below their blocking temperature ($\tau \gg \tau_M$), and a sharp central doublet or singlet, due to particles that exhibit fast superparamagnetic relaxation ($\tau \ll \tau_M$) (Kündig, Bömmel, Constabaris and Lindquist, 1966; Mørup *et al.*, 2002). Figure 5 shows Mössbauer spectra of α-Fe nanoparticles for which τ_0 is of the order of 10^{-10} s (Bødker *et al.*, 1998), and the spectra therefore mainly consist of a sextet and a doublet with relatively narrow lines. Broad components due to particles with relaxation times of the order of 10^{-8}–10^{-9} s only give a minor contribution. In nanoparticles of α-Fe_2O_3, τ_0 is of the order of 10^{-11} s (Bødker and Mørup, 2000) and, in Mössbauer spectra obtained near the blocking temperature, the contributions from particles with relaxation times of the order of 10^{-8}–10^{-9} s are barely visible. This is illustrated in the spectra of noninteracting 9-nm hematite particles shown in Section 6 (Figure 8a). In samples of nanoparticles for which τ_0 is of the order of 10^{-10}–10^{-9} s, a larger fraction of the particles have relaxation times comparable to the timescale of Mössbauer spectroscopy in a temperature range where KV/k_BT is small. This results in spectra with broadened lines around the blocking temperature. This is the case for spectra of γ-Fe_2O_3 nanoparticles with sizes of the order of 5–10 nm (Mørup, Bødker, Hendriksen and Linderoth, 1995; Frandsen *et al.*, 2004) for which $\tau_0 \approx 4 \times 10^{-10}$ s (Jonsson, Mattsson, Nordblad and Svedlindh, 1997).

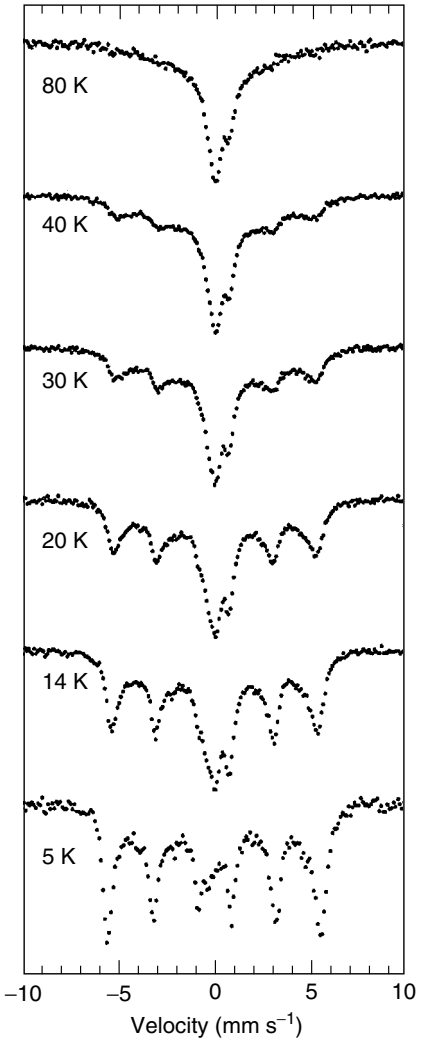

Figure 5. Mössbauer spectra of 3-nm α-Fe particles obtained at the indicated temperatures. (Reprinted from *Journal of Magnetism and Magnetic Materials*, vol 177–181, Bodker *et al.*, 'Superparamagnetic relaxation in α-Fe particles', pp 925–927 (1998), with permission from Elsevier.)

Below the blocking temperature, the magnetic hyperfine splitting of the spectra is reduced owing to collective magnetic excitations. For a particle with magnetic anisotropy energy given by equation (1), the observed magnetic hyperfine field is proportional to $\langle M \rangle$ (equation 4) and is given by Mørup and Topsøe (1976) and Mørup (1983)

$$B_{\text{obs}} \approx B_0(1 - k_{\text{B}}T/2\,KV) \tag{17}$$

where B_0 is the magnetic field acting on the nucleus in the absence of superparamagnetic relaxation. For antiferromagnetic particles, B_{obs} is proportional to the average value of the sublattice magnetizations, but can also be expressed by equation (17) (Mørup and Hansen, 2005).

Studies of the temperature dependence of the Mössbauer spectra of nanoparticles allow the parameters KV and τ_0 to be estimated. Often, the particle volume, V, is known from, for example, X-ray diffraction or transmission electron microscopy. In such cases, the magnetic anisotropy constant can be estimated. Mössbauer studies of magnetic nanoparticles of α-Fe (Bødker, Mørup and Linderoth, 1994), γ-Fe_2O_3 (Tronc, 1996), and α-Fe_2O_3 (Bødker and Mørup, 2000) have shown that the magnetic anisotropy constant increases with decreasing particle size. This has been explained by a contribution from the surface to the magnetic anisotropy, which is expected to increase with decreasing particle size.

In the presence of an applied magnetic field **B**, the magnetic energy of a ferro- or ferrimagnetic particle is given by equation (7) and, if the magnetic anisotropy is negligible, the magnetic field at the nucleus is given by

$$\mathbf{B}_{\text{obs}} \approx \mathbf{B}_0 L(\mu B/k_{\text{B}}T) + \mathbf{B} \tag{18}$$

Figure 6 shows room-temperature Mössbauer spectra of 7.5-nm maghemite nanoparticles in different applied magnetic fields (Mørup, Bødker, Hendriksen and Linderoth, 1995). It can be seen that even moderate applied fields result in a substantial splitting. The lines are relatively broad, mainly because of the distribution of magnetic moments due to the particle size distribution, which gives rise to a distribution in the values of B_{obs}. For values of $\mu B/k_{\text{B}}T$ larger than 2–3, one may use the high-field approximation $L(x) \approx 1 - x^{-1}$ and we then find

$$B_{\text{obs}} \approx B_0(1 - k_{\text{B}}T/\mu B) - B \tag{19}$$

The minus in front of the last term is because the magnetic hyperfine field in iron compounds is usually opposite to the magnetization. It can be seen from equation (19) that a plot of the induced hyperfine field, $B_{\text{ind}} = B_{\text{obs}} + B$, as a function of B^{-1} should give a straight line with intercept B_0 and slope $B_0 k_{\text{B}}T/\mu$ from which the magnetic moment of the particles can be estimated (Mørup, Dumesic and Topsøe, 1980; Mørup, 1983). When the magnetization is known, the average particle size can be estimated.

5.4 Neutron scattering

Neutron scattering is another technique that has appeared useful in studies of the magnetic properties of nanoparticles. Neutrons can be scattered by both nuclei and ionic magnetic moments. Therefore, neutron diffraction gives information not only about both the crystal structure (as X-ray diffraction) but also about the magnetic structure. Thus, one can

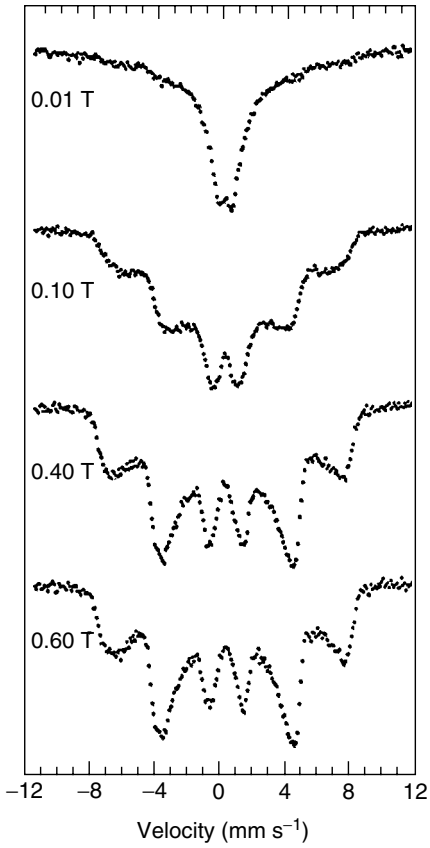

Figure 6. Mössbauer spectra of coated 7.5-nm maghemite nanoparticles obtained at 295 K with the indicated values of magnetic fields applied perpendicular to the γ-ray direction. (Reprinted figure from S. Mørup, F. Bødker, P.V. Hendriksen, S. Linderoth, *Phys. Rev.* **B52**, pp 287–294 (1995).)

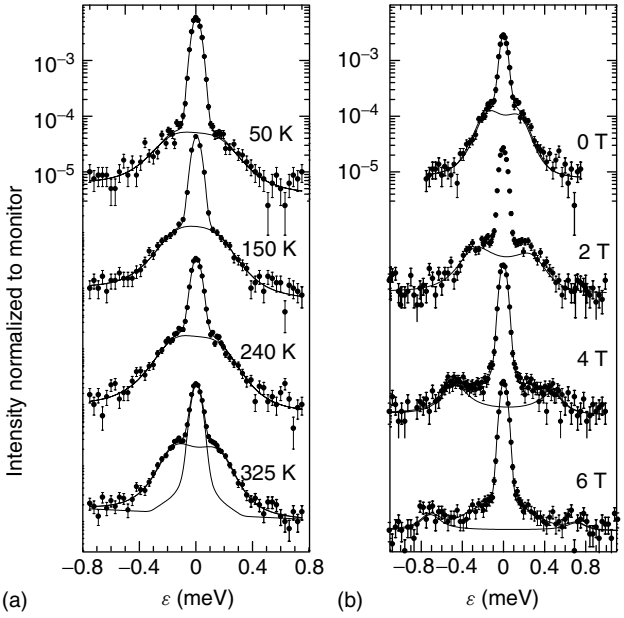

Figure 7. (a) Typical inelastic neutron-scattering data on 15-nm α-Fe_2O_3 nanoparticles obtained at zero field at the indicated temperatures. (b) Inelastic neutron-scattering data obtained at $T = 268$ K at the indicated applied magnetic fields. (Reprinted figure from M.F. Hansen, F. Bødker, S. Mørup, K. Lefmann, K.N. Clausen, P.A. Lindgärd, *Phys. Rev. Lett.* **79**, pp 4910–4913 (1997).)

study, for example, how the magnetic structure and the magnetic transition temperature of nanoparticles may depend on particle size. In a neutron diffraction study of plate-shaped nanoparticles of NiO with a thickness of a few nanometers (Klausen *et al.*, 2002), it was found that the Néel temperature was considerably lower than the bulk value, in accordance with theoretical estimates.

In inelastic neutron-scattering experiments, one analyzes the energy distribution of neutrons that are diffracted at a certain diffraction angle using a so-called triple-axis neutron spectrometer (Hansen *et al.*, 2000). By choosing a diffraction angle corresponding to a purely magnetic reflection, the energy distribution of the scattered neutrons gives information about the energy of magnetic excitations in the sample. As an example, Figure 7 shows energy scans from a triple-axis neutron spectrometer taken around the pure hexagonal (001) antiferromagnetic reflection for 15-nm hematite nanoparticles (Hansen *et al.*, 1997). The zero field scans (a) show a relatively narrow, quasielastic peak centered at zero energy transfer and two broad inelastic peaks at energy transfers around $\varepsilon \approx \pm 0.2$ meV. The width of the quasielastic peak increases with increasing temperature because of the finite lifetime of the magnetization orientations in superparamagnetic particles. Thus, the superparamagnetic relaxation time can be estimated from the line width of the quasielastic peak. Neutron scattering is sensitive to fluctuations at the timescale $10^{-14}\,\mathrm{s} > \tau > 10^{-7}\,\mathrm{s}$, that is, it is suitable for the study of superparamagnetic relaxation, which is so fast that Mössbauer spectroscopy becomes insensitive to the relaxation frequency. The inelastic peaks are caused by collective magnetic excitations and their positions correspond to the energy change associated with a transition between two neighboring precession states. The position of the inelastic peaks is at $\varepsilon = \pm\hbar\omega_{\mathrm{AF}}$, where $\omega_{\mathrm{AF}} \approx \hbar^{-1} g\mu_{\mathrm{B}}(2B_{\mathrm{A}}B_{\mathrm{E}})^{1/2}$ is the antiferromagnetic resonance frequency, g is the gyromagnetic ratio, μ_{B} is the Bohr magneton, $B_{\mathrm{A}} = K/M_{\mathrm{s}}$ is the anisotropy field, M_{s} is the sublattice saturation magnetization, and B_{E} is the exchange field (Hansen *et al.*, 1997, 2000). It can be seen that the area of the inelastic peaks increases with increasing temperature. This is due to the temperature dependence of the population of the precession states. When magnetic fields are applied, the inelastic peaks move to higher energies (Figure 7b) because the magnetization vectors precess in an effective field, which has contributions from both the anisotropy field and the applied field.

6 INTERPARTICLE INTERACTIONS

The magnetic properties of samples of nanoparticles are often strongly influenced by interparticle interactions. In particular, interactions can have a significant influence on the superparamagnetic relaxation. In some cases, the interactions result in faster relaxation and, in other cases, they result in some suppression of the relaxation. These apparently contradicting results have given rise to some debate in the literature (Hansen and Mørup, 1998; Dormann, Fiorani and Tronc, 1999). Both dipole interaction and exchange interaction between magnetic nanoparticles can be significant.

6.1 Dipole interactions

In samples with ferromagnetic or ferrimagnetic nanoparticles, the magnetic dipole interaction between neighboring particles is of the order of $E_{\mathrm{dd}} = \mu_0 \mu^2/(4\pi d^3)$, where d is the average distance between neighboring particles. If the concentration of particles is high, the interaction energy may be comparable to both the anisotropy energy and also to the thermal energy for temperatures up to about 100 K or more (Hansen and Mørup, 1998). In samples with weak interactions, the dipole fields modify the energy barriers separating the easy directions of magnetization. Dormann, Bessais, and Fiorani (1988) have proposed a model according to which the energy barriers always increase because of the dipole interactions. This model can qualitatively explain many experimental observations of suppression of superparamagnetic relaxation in samples with interparticle interactions. However, in some Mössbauer spectroscopy studies, the opposite behavior has been observed (Prené *et al*., 1994; Tronc *et al*., 1995). Simple analytical calculations (Mørup and Tronc, 1994; Hansen and Mørup, 1998) have shown that the net effect of weak dipole interactions is to reduce the average value of the energy barriers, and this can explain the increase in the relaxation frequency with increasing interaction strength. Later theoretical work has confirmed that the net effect of weak dipole interactions is to reduce the average energy barriers and thereby increase the relaxation frequency (Jönsson and García-Palacios, 2001; Iglesias and Labarta, 2004; Berkov, 1998).

In samples of ferro- and ferrimagnetic nanoparticles, it has been found that strong dipole interactions may result in a divergence of the superparamagnetic relaxation time at a finite temperature, which depends on the strength of the interactions. This has been investigated using, for example, AC magnetization measurements (Zhang, Boyd and Luo, 1996; Djurberg *et al*., 1997; Dormann *et al*., 1999). Both theoretical estimates and experimental studies have indicated that the critical temperature is of the order of $E_{\mathrm{dd}}/k_{\mathrm{B}}$ (Mørup, 1994; Hansen and Mørup, 1998). Below this critical temperature, such samples may exhibit complex nonequilibrium phenomena that are similar to those observed in spin glasses (Djurberg *et al*., 1997; Mamiya, Nakatani and Furubayashi, 1998; Jönsson, 2004). In ZFC magnetization measurements, interactions are observed to shift the peak of the curve toward higher temperatures. In AC susceptibility measurements, the peaks of the in-phase and out-of-phase susceptibility curves are typically shifted toward higher temperatures and, for strong interactions, the shape of the susceptibility curves may change significantly with frequency. In Figure 3, which shows AC susceptibility data for both noninteracting and strongly interacting γ-Fe_2O_3 nanoparticles, it is seen that the interactions shift all peaks toward higher temperatures and that the shape and height of the out-of-phase susceptibility curves have a stronger dependency on the frequency than the corresponding curves for the noninteracting particles. It is noteworthy that, because of the longer timescale of magnetization measurements compared to that of Mössbauer spectroscopy, the decrease in the relaxation time due to weak interactions may not be clearly visible in magnetization measurements (Mørup, 1994).

In summary, it is found that for weak magnetic dipole interactions the superparamagnetic relaxation time decreases with increasing strength of the interactions, but, for stronger interactions, the relaxation time increases when approaching a spin-glass-like ordered (collective) state.

6.2 Exchange interaction between nanoparticles

Because nanoparticles of antiferromagnetic materials have magnetic moments that are much smaller than those of typical ferromagnetic and ferrimagnetic particles, the magnetic dipole interaction between them is much weaker. Anyway, it has been found in several Mössbauer spectroscopy studies that interactions between antiferromagnetic nanoparticles can significantly suppress the superparamagnetic relaxation. This has been attributed to exchange interactions between surface atoms of neighboring particles (Mørup *et al*., 1983; Hansen, Bender Koch and Mørup, 2000; Bødker, Hansen, Bender Koch and Mørup, 2000; Frandsen and Mørup, 2003). As an example, Figures 8(a) and (b) show Mössbauer spectra of noninteracting and interacting 9-nm hematite particles, respectively. The particles in the two samples were from the same batch. The noninteracting particles were coated with oleic acid and suspended in heptane, whereas the interacting particles were uncoated, suspended in water, and then dried at room temperature allowing them to interact. The large differences between the spectra in Figures 8(a) and (b) show that interactions can have a substantial influence

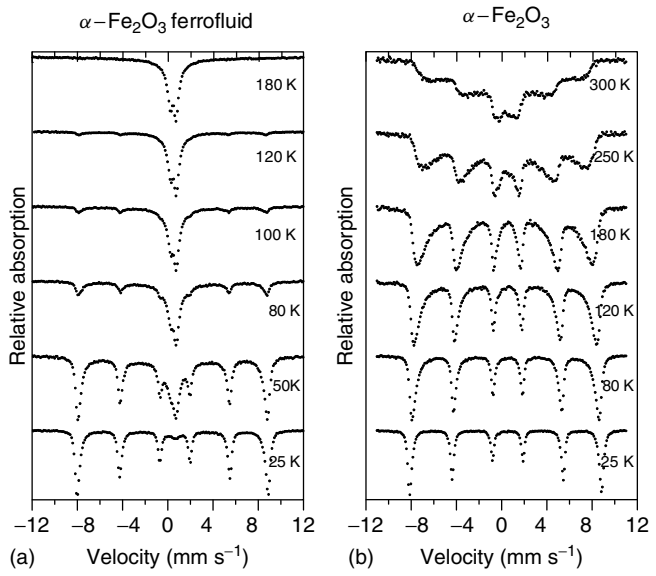

Figure 8. Mössbauer spectra obtained at the indicated temperatures of (a) noninteracting 9-nm α-Fe_2O_3 particles and (b) interacting 9-nm α-Fe_2O_3 particles. (Reprinted from the *Journal of Magnetism & Magnetic Materials*, vol 266, Frandsen *et al*., Inter-particle interactions in composites of antiferromagnetic nanoparticles, pp 36–48, 2003, with permission from Elsevier.)

on the relaxation. The observations can be explained by a simple model in which the magnetic energy of a particle, i, which interacts with its neighbors, j, is written (Mørup *et al*., 1983; Hansen, Bender Koch and Mørup, 2000; Frandsen and Mørup, 2003)

$$E_i = K V_i \sin^2 \theta - \mathbf{M}_i \cdot \sum_j K_{ij} \mathbf{M}_j \qquad (20)$$

where $\mathbf{M}_i$ and $\mathbf{M}_j$ represent the (sublattice) magnetization of the particles i and j, respectively and K_{ij} is an effective exchange coupling constant due to exchange coupling between surface atoms belonging to neighboring particles. If the first term in equation (20) is predominant, superparamagnetic relaxation may take place between the easy directions close to $\theta = 0$ and $\theta = \pi$ and, as discussed in Section 5.3, this results in spectra consisting of superimposed sextets and doublets. Strong interactions can result in an ordered (collective) state at temperatures where noninteracting particles would be superparamagnetic (Mørup *et al*., 1983; Hansen, Bender Koch and Mørup, 2000; Frandsen and Mørup, 2003). The magnetic properties may then be calculated using a simple mean-field model in which the summation in the second term in equation (20) is replaced by an average value (Mørup *et al*., 1983; Hansen, Bender Koch and Mørup, 2000; Frandsen and Mørup, 2003). Equation (20) then has a form similar to equation (7), that is, the effect of interactions is described in terms of an effective interaction field. If the interaction term in equation (20) is predominant, there is only one energy minimum. At finite temperatures, the (sublattice) magnetization then fluctuates around the direction corresponding to this energy minimum. If the fluctuations of the sublattice magnetization directions are fast compared to the timescale of Mössbauer spectroscopy, the magnetic splitting in the spectra is proportional to the average value of the magnetic hyperfine field. Variations of the magnitude and direction of the interaction field in the sample results in a distribution of magnetic hyperfine splittings, which leads to broadened sextets, like those seen in Figure 8(b), as it is also the case in spectra of superparamagnetic particles in applied magnetic fields (Figure 6). If the neighboring particles are randomly oriented, one might expect that the contributions from different neighboring particles in the summation of equation (20) partially cancel, and therefore the interaction field should be small. However, it has been shown that interacting nanoparticles of α-Fe_2O_3 nanoparticles may not be randomly oriented, but can form chains of particles with a common [001] axis. Neutron diffraction studies have shown that both structural and magnetic correlations exist across the interfaces along this direction. This can explain the substantial exchange coupling between the particles (Frandsen *et al*., 2005).

In recent studies, it has been found that exchange interactions between nanoparticles of different magnetic materials can have unexpected effects on the superparamagnetic relaxation time (Frandsen and Mørup, 2003; Frandsen *et al*., 2004). For example, the superparamagnetic relaxation of iron oxide particles was to some extent suppressed when they were mixed with nanoparticles of CoO, whereas the opposite effect was found when the iron oxide particles were mixed with nanoparticles of NiO. The studies indicate that there can be a strong exchange interaction between nanoparticles of iron oxide and nanoparticles of CoO and NiO. The different effect of mixing with CoO and NiO can be explained by differences in magnetic anisotropy of the nanoparticles of the two materials (Frandsen and Mørup, 2003; Frandsen *et al*., 2004).

7 MAGNETIC STRUCTURE AND TRANSVERSE RELAXATION IN NANOPARTICLES

Several studies have shown that the magnetic structure of nanoparticles may deviate from that of the corresponding bulk materials. Computer simulations have suggested that nanoparticles of NiO may have a complicated antiferromagnetic structure with eight sublattices instead of

the simple two-sublattice structure that is found in bulk (Kodama, Makhlouf and Berkowitz, 1997). In bulk hematite, the magnetic structure changes at the Morin temperature, $T_M \approx 263$ K. Above T_M, the sublattice magnetization is perpendicular to the [001] axis of the hexagonal structure. Below this temperature, the sublattice magnetization is parallel to this direction. However, in particles with diameters less than about 20 nm, the sublattice magnetization direction remains perpendicular to the [001] axis at all temperatures (Kündig, Bömmel, Constabaris and Lindquist, 1966; Schroeer and Nininger, 1967; Bødker and Mørup, 2000). Neutron-scattering studies have shown that the Néel temperature of NiO nanoparticles can be lowered compared to the bulk value (Klausen *et al*., 2002). It has recently been shown that interparticle interactions on powders of hematite nanoparticles can rotate the sublattice magnetization directions because of exchange coupling between differently oriented neighboring nanoparticles (Frandsen and Mørup, 2005).

In many defect-free macroscopic crystals of ferrimagnetic and antiferromagnetic materials, the spins in the sublattices are antiparallel. However, if a sample has defects in the interior, magnetic frustration may result in localized noncollinear magnetic structures. Noncollinear (canted) spin structures are commonly found in diamagnetically substituted ferrites and garnets (Coey, 1987; Dormann and Nogues, 1990). Similar spin-canting effects may be found at surfaces, and may therefore be important in nanoparticles. Experimental studies have revealed a rich variation of the dependence of spin canting on composition, temperature, particle size, and applied magnetic fields (Coey, 1971, 1987; Morrish and Haneda, 1983; Parker, Foster, Margulies and Berkowitz, 1993; Kodama, Berkowitz, McNiff and Foner, 1996; Tronc *et al*., 1998, 2000; Mørup, 2003). In particular, spin canting in maghemite (γ-Fe_2O_3) nanoparticles has been extensively studied because of their importance in magnetic data storage media.

Spin canting is conveniently studied by Mössbauer spectroscopy with large magnetic fields applied parallel to the γ-ray direction. In ^{57}Fe Mössbauer spectra, obtained in this way, the relative intensities of lines 2 and 5 in the six-line spectra are proportional to $\sin^2\theta_0/(1+\cos^2\theta_0)$, where θ_0 is the angle between the γ-ray direction and the total magnetic field at the nucleus. If the magnetic hyperfine field is large compared to the applied field, one finds that $\theta_0 \approx \theta_c$, where θ_c is the canting angle. Figure 9 shows, as an example, Mössbauer spectra of maghemite nanoparticles obtained at various temperatures with a magnetic field of 6 T applied parallel to the γ-ray direction (Tronc *et al*., 2000). In a perfect ferrimagnetic material, lines 2 and 5 would have zero intensity. The finite intensity of the lines in the spectra obtained at 9 K thus show that there is a noncollinear spin

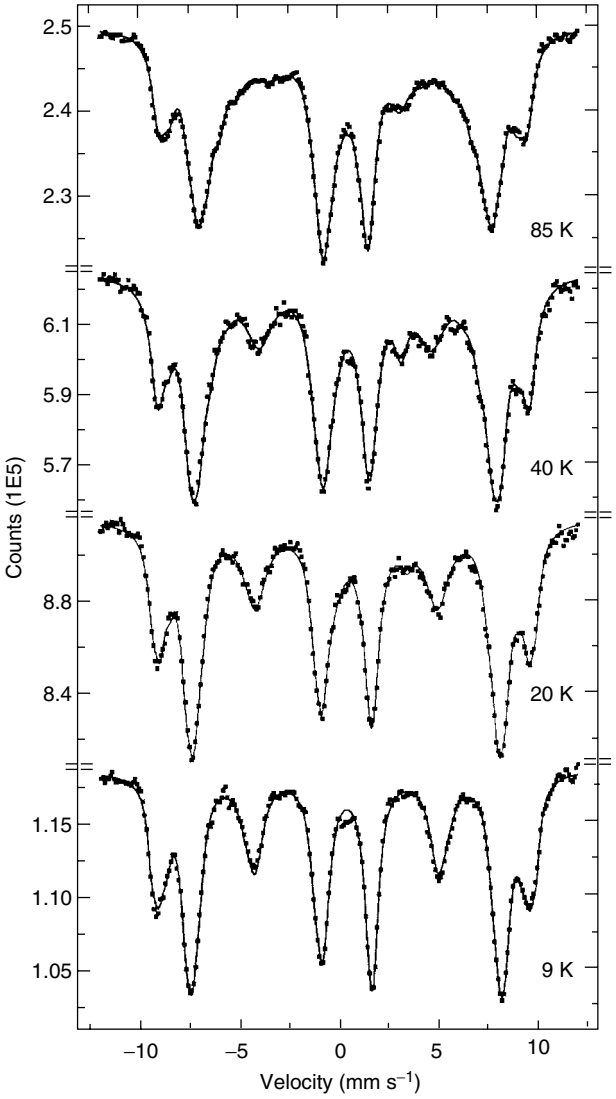

Figure 9. Mössbauer spectra of maghemite nanoparticles with a mean diameter of 2.7 nm. The spectra were obtained at the indicated temperatures with a magnetic field of 6 T applied parallel to the γ-ray direction. (Reprinted from the *Journal of Magnetism & Magnetic Materials*, vol 221, Tronc *et al*., pp 63–79, Surface-related properties of γ-Fe_2O_3 nanoparticles, 2000, with permission from Elsevier.)

structure in the sample. At higher temperatures, the intensity of lines 2 and 5 gradually disappears. This may be explained as follows: Let θ_c be the angle between a canted spin and the spin direction in defect-free environments. Owing to symmetry, a canted state with a canting angle θ_c is usually accompanied by an equivalent state with canting angle $-\theta_c$ (Mørup, 2003). The energy barriers that separate such equivalent states may be quite small and at finite temperatures there may therefore be transitions between such equivalent canted states. If the relaxation time of this so-called

transverse relaxation is of the order of nanoseconds, lines 2 and 5 in the Mössbauer spectrum are broadened (Helgason, Rasmussen and Mørup, 2006). If the transverse relaxation is fast compared to the timescale of Mössbauer spectroscopy, the nucleus only experiences the average magnetic hyperfine field, which is parallel to the applied magnetic field and the intensity of lines 2 and 5 therefore vanishes, as seen in the Mössbauer spectra in Figure 9. It has been shown that the energy barriers, ΔE, separating equivalent states with canting angles θ_c and $-\theta_c$, may have a distribution, which diverges for $\Delta E \rightarrow 0$ (Mørup, 2003). This may explain some of the observations of an apparently temperature-independent relaxation at low temperatures, discussed in Section 5.1.

In several studies, it has been assumed that spin canting is restricted to the surface, and the thickness of the canted surface layer has been calculated. However, this simple model cannot explain the irregular variation of the degree of canting with particle size (Linderoth *et al*., 1994). In fact, it has been shown that maghemite particles with similar size may have different degrees of canting, depending on the preparation method (Morales, Serna, Bødker and Mørup, 1997; Serna *et al*., 2001). This indicates that defects in the interior of the nanoparticles also can play an important role.

Extensive spin canting results in a diminished saturation magnetization. This makes the particles less useful for many applications such as data storage, biotechnology, and so on. Therefore, it is important to use preparation techniques, which lead to particles with low defect concentrations.

REFERENCES

Bansmann, J., Baker, S.H., Binns, C., *et al*. (2005). Magnetic and structural properties of isolated and assembled clusters. *Surface Science Reports*, **56**, 189–275.

Barbara, B. and Chudnovsky, E.M. (1990). Macroscopic quantum tunneling in antiferromagnets. *Physics Letters A*, **145**, 205–208.

Barbara, B., Paulsen, C., Sampaio, L.C., *et al*. (1992). Observation of quantum tunnelling of the magnetization vector in small particles with or without domain walls. In *Studies of Magnetic Properties of Fine Particles and Their Relevance to Materials Science*, Dormann, J.L. and Fiorani, D. (Eds.), Elsevier Science Publishers, pp. 235–242.

Battle, X. and Labarta, A. (2002). Finite size effects in fine particles: magnetic and transport properties. *Journal of Physics D: Applied Physics*, **35**, R15–R42.

Bean, C.P. and Livingston, J.D. (1959). Superparamagnetism. *Journal of Applied Physics*, **30**, S120–S129.

Bentzon, M.D., van Wonterghem, J., Mørup, S., *et al*. (1989). Ordered aggregates of ultrafine iron oxide particles: super crystals. *Philosophical Magazine B*, **60**, 169–178.

Berkov, D.V. (1998). Numerical calculation of the energy barrier distribution in disordered many-particle systems: the path integral method. *Journal of Magnetism and Magnetic Materials*, **186**, 199–213.

Bewley, R.I. and Cywinski, R. (1998). Muon spin relaxation in a superparamagnet: field dynamics in $Cu_{98}Co_2$. *Physical Review B*, **58**, 11544–11551.

Billas, I.M.L., Becker, J.A., Chatelain, A. and de Heer, W.A. (1993). Magnetic moments of iron clusters with 25 to 700 atoms and their dependence on temperature. *Physical Review Letters*, **71**, 4067–4070.

Blakemore, R.P. (1975). Magnetotactic bacteria. *Science*, **19**, 377–379.

Bødker, F., Hansen, M.F., Bender Koch, C. and Mørup, S. (2000). Particle interaction effects in antiferromagnetic NiO nanoparticles. *Journal of Magnetism and Magnetic Materials*, **221**, 32–36.

Bødker, F. and Mørup, S. (1996). *In situ* cell for Mössbauer spectroscopy between 5 and 800 K in applied magnetic fields. *Nuclear Instruments and Methods in Physical Research Section B*, **108**, 413–416.

Bødker, F. and Mørup, S. (2000). Size dependence of the properties of hematite nanoparticles. *Europhysics Letters*, **52**, 217–223.

Bødker, F., Mørup, S. and Linderoth, S. (1994). Surface effects in metallic iron nanoparticles. *Physical Review Letters*, **72**, 282–285.

Bødker, F., Hansen, M.F., Bender Koch, C., *et al*. (2000). Magnetic properties of hematite nanoparticles. *Physical Review B*, **61**, 6826–6838.

Bødker, F., Mørup, S., Pedersen, M.S., *et al*. (1998). Superparamagnetic relaxation in α-Fe particles. *Journal of Magnetism and Magnetic Materials*, **177–181**, 925–927.

Brown, W.F. Jr. (1963). Thermal fluctuations of a single domain particle. *Physical Review*, **130**, 1677–1686.

Chantrell, R.W., El-Hilo, M. and O'Grady, K. (1991). Spin-glass behaviour in a fine particle system. *IEEE Transactions on Magnetics*, **27**, 3570–3578.

Chudnovsky, E.M. and Gunther, L. (1988). Quantum tunneling of magnetization in small ferromagnetic particles. *Physical Review Letters*, **60**, 661–664.

Coey, J.M.D. (1971). Noncollinear spin arrangement in ultrafine ferromagnetic crystallites. *Physical Review Letters*, **27**, 1140–1142.

Coey, J.M.D. (1987). Noncollinear spin structures. *Canadian Journal of Physics*, **65**, 1210–1232.

Davila, R.F., Fleissner, G., Winklhofer, M. and Petersen, N. (2003). A new model for a magnetoreceptor in homing pigeons based on interacting clusters of superparamagnetic magnetite. *Physics and Chemistry of the Earth*, **28**, 647–652.

Djurberg, C., Svedlindh, P., Nordblad, P., *et al*. (1997). Dynamics of an interacting particle system: evidence of critical slowing down. *Physical Review Letters*, **79**, 5154–5157.

Dormann, J.L., Bessais, L. and Fiorani, D. (1988). A dynamic study of small interacting particles: superparamagnetic model and spin-glass laws. *Journal of Physics C*, **21**, 2015–2034.

Dormann, J.L., Fiorani, D. and Tronc, E. (1997). Magnetic relaxation in fine-particle systems. *Advances in Chemical Physics*, **98**, 283–494.

Dormann, J.L., Fiorani, D. and Tronc, E. (1999). On the models for interparticle interactions in nanoparticle assemblies: comparison with experimental results. *Journal of Magnetism and Magnetic Materials*, **202**, 251–267.

Dormann, J.L. and Nogues, M. (1990). Magnetic structures of substituted ferrites. *Journal of Physics. Condensed Matter*, **2**, 1223–1237.

Dormann, J.L., Fiorani, D., Cherkaoui, R., *et al*. (1999). From pure superparamagnetism to glass collective state in γ-Fe_2O_3 nanoparticle assemblies. *Journal of Magnetism and Magnetic Materials*, **203**, 23–27.

Fisker, R., Carstensen, J.M., Hansen, M.F., *et al*. (2000). Estimation of nanoparticle size distributions by image analysis. *Journal of Nanoparticle Research*, **2**, 267–277.

Frandsen, C. and Mørup, S. (2003). Inter-particle interactions in composites of antiferromagnetic nanoparticles. *Journal of Magnetism and Magnetic Materials*, **266**, 36–48.

Frandsen, C. and Mørup, S. (2005). Spin rotation in α-Fe_2O_3 nanoparticles by interparticle interactions. *Physical Review Letters*, **94**, 027202-1–027202-4.

Frandsen, C., Bahl, C.R.H., Lebech, B., *et al*. (2005). Oriented attachment and exchange coupling of α-Fe_2O_3 nanoparticles. *Physical Review B*, **72**, 214406-1–214406-7.

Frandsen, C., Ostenfeld, C.W., Xu, M., *et al*. (2004). Interparticle interactions in composites of nanoparticles of ferrimagnetic (γ-Fe_2O_3) and antiferromagnetic (CoO,NiO) materials. *Physical Review B*, **70**, 134416-1–134416-7.

Garcia-Palacios, J.L. (2000). On the statics and dynamics of magnetoanisotropic nanoparticles. *Advances in Chemical Physics*, **112**, 1–210.

Gittleman, J.I., Abeles, B. and Bozowski, S. (1974). Superparamagnetism and relaxation effects in granular Ni-SiO_2 and Ni-Al_2O_3 films. *Physical Review B*, **9**, 3891–3897.

Granqvist, C.G. and Buhrman, R.A. (1976). Ultrafine metal particles. *Journal of Applied Physics*, **47**, 2200–2219.

Greenwood, N.N. and Gibb, T.C. (1971). *Mössbauer Spectroscopy*, Chapman & Hall: London.

Hansen, M.F., Bender Koch, C. and Mørup, S. (2000). The magnetic dynamics of weakly and strongly interacting hematite nanoparticles. *Physical Review B*, **62**, 1124–1135.

Hansen, M.F. and Mørup, S. (1998). Models for the dynamics of interacting magnetic nanoparticles. *Journal of Magnetism and Magnetic Materials*, **184**, 262–274.

Hansen, M.F., Bødker, F., Mørup, S., *et al*. (1997). Dynamics of magnetic nanoparticles studied by neutron scattering. *Physical Review Letters*, **79**, 4910–4913.

Hansen, M.F., Bødker, F., Mørup, S., *et al*. (2000). Magnetic dynamics of fine particles studied by inelastic neutron scattering. *Journal of Magnetism and Magnetic Materials*, **221**, 10–25.

Hanson, M., Johansson, C. and Mørup, S. (1993). The influence of magnetic anisotropy on the magnetization of small ferromagnetic particles. *Journal of Physics. Condensed Matter*, **5**, 725–732.

Helgason, Ö., Rasmussen, H.K. and Mørup, S. (2006). Spin-canting and transverse relaxation in maghemite nanoparticles and in tin-doped maghemite. *Journal of Magnetism and Magnetic Materials*, **302**, 413–420.

Iglesias, O., Badia, F., Labarta, A. and Balcells, Ll. (1996). Energy barrier distributions in magnetic systems from the $\mathrm{Tln}(t/\tau_0)$ scaling. *Zeitschrift fur Physik B*, **100**, 173–178.

Iglesias, O. and Labarta, A. (2004). Magnetic relaxation in terms of microscopic energy barriers in a model of dipolar interacting nanoparticles. *Physical Review B*, **70**, 144401-1–144401-10.

Jolivet, J.P., Tronc, E. and Chanéac, C. (2000). Synthesis of iron oxide- and metal-based nanomaterials. *European Physical Journal of Applied Physics*, **10**, 167–172.

Jönsson, P.E. (2004). Superparamagnetism and spin glass dynamics of interacting magnetic nanoparticle systems. *Advances in Chemical Physics*, **128**, 191–248.

Jönsson, P.E. and García-Palacios, J.L. (2001). Relaxation time of weakly interacting superparamagnets. *Europhysics Letters*, **55**, 418–424.

Jonsson, T., Mattsson, J., Nordblad, P. and Svedlindh, P. (1997). Energy barrier distribution of a noninteracting nano-sized magnetic particle system. *Journal of Magnetism and Magnetic Materials*, **168**, 269–277.

Jonsson, T., Nordblad, P. and Svedlindh, P. (1998). Dynamic study of dipole-dipole interaction effects in a magnetic nanoparticle system. *Physica Review B*, **57**, 497–504.

Klausen, S.N., Lindgård, P-A., Lefmann, K., *et al*. (2002). Temperature dependence of the magnetization of disc shaped NiO nanoparticles. *Physical Status Solidi A*, **189**, 1039–1042.

Koch, C.C. (1991). Mechanical milling and alloying. In *Materials Science and Technology*, Cahn, R.W., Haasen, P. and Kramer, E.J. (Eds.), VCH Publishers: Weinheim, pp. 193–245.

Kodama, R.H. (1999). Magnetic nanoparticles. *Journal of Magnetism and Magnetic Materials*, **200**, 359–372.

Kodama, R.H., Berkowitz, A.E., McNiff, E.J. and Foner, S. (1996). Surface spin disorder in $NiFe_2O_4$ nanoparticles. *Physical Review Letters*, **77**, 394–397.

Kodama, R.H., Makhlouf, S.A. and Berkowitz, A.E. (1997). Finite size effects in antiferromagnetic NiO particles. *Physical Review Letters*, **79**, 1393–1396.

Kündig, W., Bömmel, H., Constabaris, G. and Lindquist, R.H. (1966). Some properties of supported small α-Fe_2O_3 particles determined with the Mössbauer effect. *Physical Review*, **142**, 327–333.

Labarta, A., Iglesias, O., Balcells, Ll. and Badia, F. (1993). Magnetic relaxation in small-particle systems: $\mathrm{Tln}(t/\tau_0)$ scaling. *Physical Review B*, **48**, 10240–10246.

Langford, J.I., Louër, D. and Scardi, P. (2000). Effect of a crystallite size distribution on X-ray diffraction line profiles and whole-powder-pattern fitting. *Journal of Applied Crystallography*, **33**, 964–974.

Leslie-Pelecky, D.L. and Rieke, R.D. (1996). Magnetic properties of nanostructured materials. *Chemistry of Materials*, **8**, 1770–1783.

van Lierop, J., Ryan, D.H., Pumarol, M.E. and Roseman, M. (2001). Muon spin relaxation study of spin dynamics in a polysaccharide iron complex. *Journal of Applied Physics*, **89**, 7645–7647.

Linderoth, S. and Mørup, S. (1991). Amorphous $TM_{1-x}B_x$ alloy particles prepared by chemical reduction. *Journal of Applied Physics*, **69**, 5256–5261.

Linderoth, S., Hendriksen, P.V., Bødker, F., *et al*. (1994). On spin canting in maghemite particles. *Journal of Applied Physics*, **75**, 6583–6585.

Mamiya, H., Nakatani, I. and Furubayashi, T. (1998). Blocking and freezing of magnetic moments for iron nitride fine particle systems. *Physical Review Letters*, **80**, 177–180.

Morales, M.P., Serna, F., Bødker, F. and Mørup, S. (1997). Spin-canting due to vacancy disorder in maghemite. *Journal of Physics. Condensed Matter*, **9**, 5461–5467.

Morrish, A.H. and Haneda, K. (1983). Surface magnetic properties of fine particles. *Journal of Magnetism and Magnetic Materials*, **35**, 105–113.

Mørup, S. (1983). Magnetic hyperfine splitting in Mössbauer spectra of microcrystals. *Journal of Magnetism and Magnetic Materials*, **37**, 39–50.

Mørup, S. (1990). Mössbauer effect in small particles. *Hyperfine Interactions*, **61**, 959–974.

Mørup, S. (1994). Superparamagnetism and spin glass ordering in magnetic nanocomposites. *Europhysics Letters*, **28**, 671–676.

Mørup, S. (2003). Spin canting and transverse relaxation at surfaces and in the interior of ferrimagnetic particles. *Journal of Magnetism and Magnetic Materials*, **266**, 110–118.

Mørup, S., Bødker, F., Hendriksen, P.V. and Linderoth, S. (1995). Spin-glass-like ordering of the magnetic moments of interacting nano-sized maghemite particles. *Physical Review B*, **52**, 287–294.

Mørup, S., Dumesic, J.A. and Topsøe, H. (1980). Magnetic microcrystals. In *Applications of Mössbauer Spectroscopy*, Cohen, R.L. (Ed.), Academic Press: New York, pp. 1–54, Vol. 2.

Mørup, S. and Frandsen, C. (2004). Thermoinduced magnetization in nanoparticles of antiferromagnetic materials. *Physical Review Letters*, **92**, 217201-1–217201-4.

Mørup, S. and Hansen, B.R. (2005). Uniform magnetic excitations in nanoparticles. *Physical Review B*, **72**, 024418-1–024418-6.

Mørup, S., Jiang, J.Z., Bødker, F. and Horsewell, A. (2001). Crystal growth and the steady-state grain size during high-energy ball-milling. *Europhysics Letters*, **56**, 441–446.

Mørup, S. and Topsøe, H. (1976). Mössbauer studies of thermal excitations in magnetically ordered microcrystals. *Applied Physics*, **11**, 63–66.

Mørup, S. and Tronc, E. (1994). Superparamagnetic relaxation of weakly interacting nanoparticles. *Physical Review Letters*, **72**, 3278–3281.

Mørup, S., Frandsen, C., Bødker, F., *et al*. (2002). Magnetic properties of nanoparticles of antiferromagnetic materials. *Hyperfine Interactions*, **144/145**, 347–357.

Mørup, S., Madsen, M.B., Franck, J., *et al*. (1983). A new interpretation of Mössbauer spectra of microcrystalline goethite: "Superferromagnetism or super-spin-glass behaviour". *Journal of Magnetism and Magnetic Materials*, **40**, 163–174.

Murad, E. (1996). Magnetic properties of microcrystalline iron(III) oxides and related materials as reflected by their Mössbauer spectra. *Physics and Chemistry of Minerals*, **23**, 248–262.

Murad, E. (1998). Clays and clay minerals: what can Mössbauer spectroscopy do to help understand them? *Hyperfine Interactions*, **117**, 39–70.

Néel, L. (1949). Théorie du trainage magnétique des ferromagnétiques en grains fins avec applications aux terres cuites. *Annales de Géophysique*, **5**, 99–136.

Néel, L. (1961). Superparamagnétisme des grains très fins antiferromagnétiques. *Comptes Rendus*, **252**, 4075–4080.

O'Conner, C.J., Kolesnichenko, V., Carpenter, E., *et al*. (2001). Fabrication and properties of magnetic particles with nanometer dimensions. *Synthetic Metals*, **122**, 547–557.

Pankhurst, Q.A., Connolly, J., Jones, S.K. and Dobson, J. (2003). Applications of magnetic nanoparticles in biomedicine. *Journal of Physics D: Applied Physics*, **36**, R167–R181.

Parker, F.T., Foster, M.W., Margulies, D.T. and Berkowitz, A.E. (1993). Spin canting, surface magnetization, and finite-size effects in γ-Fe_2O_3 nanoparticles. *Physical Review B*, **47**, 7885–7891.

Prené, P., Tronc, E., Jolivet, J.P., *et al*. (1994). Mössbauer investigation of non-aggregated γ-Fe_2O_3 particles. *Hyperfine Interactions*, **93**, 1409–1414.

Principi, G. (2001). High-energy ball-milling of some intermetallics. *Hyperfine Interactions*, **134**, 53–67.

Respaud, M. (1999). Magnetization process of noninteracting cobalt nanoparticles in the superparamagnetic regime: deviation from Langevin law. *Journal of Applied Physics*, **86**, 556–561.

Richardson, J.T., Yiagas, D.I., Turk, B., *et al*. (1991). Origin of superparamagnetism in nickel oxide. *Journal of Applied Physics*, **70**, 6977–6982.

Schroeer, D. and Nininger, R.C. (1967). Morin transition in α-Fe_2O_3 microcrystals. *Physical Review Letters*, **19**, 632–634.

Serna, C.J., Bødker, F., Mørup, S., *et al*. (2001). Spin frustration in maghemite nanoparticles. *Solid State Communications*, **118**, 437–440.

St. Pierre, T.G., Gorham, N.T., Allen, P.D., *et al*. (2001). Apparent magnetic energy-barrier distribution in horse-spleen ferritin: evidence for multiple interacting magnetic entities per ferrihydrite nanoparticle. *Physical Review B*, **65**, 024436-1–024436-7.

Sugimoto, T., Wang, Y., Itoh, H. and Maramatsu, A. (1998). Systematic control of size, shape and internal structure of monodisperse α-Fe_2O_3 particles. *Colloids and Surfaces A: Physicochemical and Engineering Aspects*, **134**, 265–279.

Sun, S., Murray, C.B., Weller, D., *et al*. (2000). Monodisperse FePt nanoparticles and ferromagnetic FePt nanocrystal superlattices. *Science*, **287**, 1989–1992.

Suryanarayana, C. (2001). Mechanical alloying and milling. *Progress in Materials Science*, **46**, 1–184.

Svedlindh, P., Jonsson, T. and García-Palacios, J.L. (1997). Intrapotential-well contribution to the AC susceptibility of a noninteracting nano-sized magnetic particle system. *Journal of Magnetism and Magnetic Materials*, **169**, 323–334.

Tartaj, P., Morales, M.P., Veintemillas-Verdaguer, S., *et al*. (2003). The preparation of magnetic nanoparticles for applications in biomedicine. *Journal of Physics D: Applied Physics*, **36**, R182–R197.

Tejada, J., Zhang, X.X. and Chudnovsky, E.M. (1993). Quantum relaxation in random magnets. *Physical Review B*, **47**, 14977–14987.

Topsøe, H., Dumesic, J.A. and Mørup, S. (1980). Catalysis and surface science. In *Applications of Mössbauer Spectroscopy*, Cohen, R.L. (Ed.), Academic Press: New York, pp. 55–188, Vol. 2.

Tronc, E. (1996). Nanoparticles. *Nuovo Cimento D*, **18**, 163–180.

Tronc, E., Ezzir, A., Cherkaoui, R., *et al*. (2000). Surface-related properties of γ-Fe_2O_3 nanoparticles. *Journal of Magnetism and Magnetic Materials*, **221**, 63–79.

Tronc, E., Prené, P., Jolivet, J.P., *et al*. (1995). Magnetic dynamics of γ-Fe_2O_3 particles. *Nanostructured Materials*, **6**, 945–948.

Tronc, E., Prené, P., Jolivet, J.P., *et al*. (1998). Spin canting in γ-Fe_2O_3 nanoparticles. *Hyperfine Interactions*, **112**, 97–100.

Ucko, D.H., Pankhurst, Q.A., Barquín, L.F., *et al*. (2001). Magnetic relaxation in the nanoscale granular alloy $Fe_{20}Cu_{20}Ag_{60}$. *Physical Review B*, **64**, 104433-1–104433-13.

Vandenberghe, R.E., Barrero, C.A., da Costa, G.M., *et al*. (2000). Mössbauer characterization of iron oxides and oxyhydroxides: the present state of the art. *Hyperfine Interactions*, **126**, 247–259.

Walker, M.M., Diebel, C.E. and Green, C.R. (2000). Structure, function and use of the magnetic sense in animals. *Journal of Applied Physics*, **87**, 4653–4658.

Willard, M.A., Kurihara, L.K., Carpenter, E.E., *et al*. (2004). Chemically prepared magnetic nanoparticles. *International Materials Reviews*, **49**, 125–170.

van Wonterghem, J., Mørup, S., Koch, C.J.W., *et al*. (1986). Formation of ultra-fine amorphous alloy particles by reduction in aqueous solution. *Nature*, **322**, 622–623.

Zhang, J., Boyd, C. and Luo, W. (1996). Two mechanisms and a scaling relation for dynamics in ferrofluids. *Physical Review Letters*, **77**, 390–393.

Zhang, X.X., Tejada, J., Hernandez, J.M. and Ziolo, R.F. (1997). Quantum tunneling of magnetization in mesoscopic systems. *Nanostructured Materials*, **9**, 301–310.

Novel Nanoparticulate Magnetic Materials and Structures

David J. Sellmyer, Yingfan Xu, Yucheng Sui and Ralph Skomski
University of Nebraska, Lincoln, NE, USA

1 INTRODUCTION

Magnetic nanoparticles, clusters, and particulate thin films have many present or future applications, for example, as permanent magnets, soft magnets, and sensors. However, in recent years, the most active area of research has been *magnetic recording*, and this trend is likely to continue in the foreseeable future. Magnetic recording media, such as hard disks and magnetic tapes, are widely used for data storage in computers and in audiovisual technology. Key criteria for magnetic recording media are areal density, signal-to-noise ratio, and thermal stability. Nanoparticulate thin films are ideally suited for this application because factors such as grain size, grain-size distribution, texture, magnetization, grain isolation, and film smoothness can be controlled with considerable precision. This is an important aspect of the fascinating increase in hard-disk storage density since about 1990, when thin-film media were introduced on an industrial scale. In addition, nanoparticulate thin films and related materials, such as fine particles and ferrofluids, have present or potential uses in many other areas including biomedical imaging and treatment applications.

This chapter deals with various aspects of nanoparticulate magnetic thin films and of the particles they contain. Emphasis is on magnetic recording media, due to their special importance in advanced data storage. Furthermore, we focus on the processing of nanoparticles of different shape, size, chemical composition, and texture, and on magnetic properties and phenomena directly related to the structures of interest. For information about basic magnetic phenomena, bulk properties, experimental and theoretical methods, and applications beyond magnetic recording media we refer to other articles of this handbook and to the references quoted in the following text. Similarly, structures produced from ultrathin films, such as dots and antidots, geometries created by ion-beam milling and lithography, and top-down approaches such as scanning tunneling microscopy (STM) deposition go beyond the scope of this article.

1.1 Basic concepts of magnetic recording

A key figure of merit of magnetic recording media is the areal storage density, measured in bits per square centimeter (b cm^{-2}) or bits per square inch (1 b $in.^{-2} = 6.452$ b cm^{-2}). Figure 1 shows schematically the development of the areal storage density in recent decades. Since its invention, magnetic recording has developed rapidly, competing with and often outperforming other storage media, from vinyl records and punch cards to advanced electronic and optical

Handbook of Magnetism and Advanced Magnetic Materials. Edited by Helmut Kronmüller and Stuart Parkin. Volume 4: *Novel Materials*. ISBN: 978-0-470-02217-7.

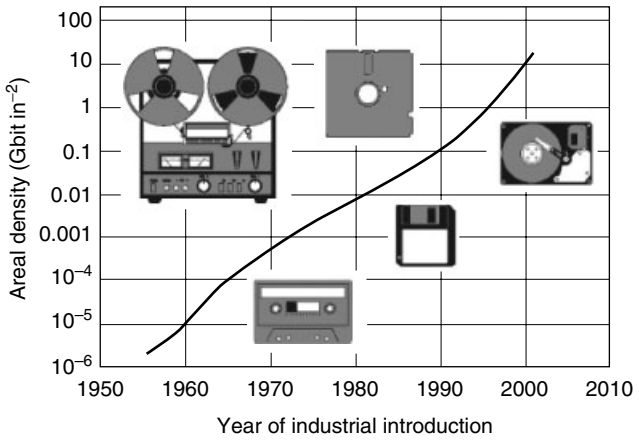

Figure 1. Increase in areal storage density since the 1950s (schematic). Modern audiovisual and data recording would be unthinkable without this development of storage media.

storage media such as CD-ROMs and flash memory. The main advantages of magnetic storage are the potential density and cost. The bit size of optical and magneto-optical media is limited by the wavelength of the used light, whereas semiconductor devices can be slow and/or volatile.

Defining an effective bit size as the square root of the inverse areal density, the progress shown in Figure 1 corresponds to a bit-size reduction from 250 µm in 1960 to 250 nm in 2000. The recent trend is likely to continue in the next few years, with terabit recording at the horizon. An upper limit to the recording density is provided by the thermal stability of the stored information, which makes it difficult to realize room-temperature magnetic recording using bit sizes smaller than several nanometers (Section 1.2).

A condition for magnetic recording is magnetic hysteresis, as epitomized by coercivity, remanence, and loop shape. In a sense, magnetic recording media are intermediate between soft and hard magnets. Typical media exhibit moderate but well-controlled coercivities. The coercivity H_c must be sufficiently large to ensure the long-time stability of the stored information, but very high coercivities complicate the recording process, because they require excessive writing fields. Very small particles obey the coherent rotation or Stoner–Wohlfarth theory, and for uniaxial anisotropy the coercivity approaches the anisotropy field $H_a = 2K_1/\mu_o M_s$. In this expression, K_1 is the first uniaxial anisotropy constant and M_s is the spontaneous magnetization. In most systems, H_c is much smaller than H_a. This is due to real-structure imperfections (Section 1.2).

The first magnetic recording medium was the magnetic wire, invented by Valdemar Poulsen in Denmark in 1898. Until the early 1940s, steel wires were used quite extensively for dictation, telephone recording, and radio broadcasting. Tape recording was pioneered in Germany, leading from a patent for iron-coated paper (!) and polymer film strips in 1928 to the first portable tape recorder (Volk, 1935). This was the starting point for various developments in sound and audiovisual magnetic recording, including the introduction of the tape cassette system in 1963 and of the VHS videocassette system in 1976.

A very important application of magnetic recording is *data storage* (Mee and Daniel, 1996; Comstock, 1999; Wood, 2000). Data storage using magnetic tapes is cheap but slow and therefore not suitable for applications where fast access is important. The first data-storage tapes, used in the United States in 1951, had bit lengths of about 200 µm and areal storage densities of the order of 0.002 Mb in.$^{-2}$. Tape storage systems range from ordinary audiocassettes to large reel-to-reel systems for mass storage. Audiocassettes were a popular choice for some home computers in the 1980s but are no longer used. By contrast, reel-to-reel and sophisticated cartridge systems continue to be used for purposes such as data backup. For example, present-day tapes have capacities of up to 320 GB.

Diskettes or *floppy disks* are a very convenient storage medium with moderate capacity. The first floppy disks, introduced in 1971, had a diameter of 8 in. and a storage capacity of 0.08 MB. Early personal computers used 51/4″ floppy disks, whereas single-sided single-density 51/4″ disks, first produced in 1976, had a capacity of 0.18 MB. The 31/2″ disk format was introduced by Sony in 1981. The widely used 31/2″ DS/HD disks, which date back to 1987, have a storage capacity of 1.44 MB and an areal density of more than 2.4 Mb in.$^{-2}$, as compared to about 0.3 Mb in.$^{-2}$ in early 51/4″ disks (1 MB in.$^{-2}$ = 0.155 GB cm^{-2}). The traditional way of producing floppy discs was to start from magnetic thin films that were isotropic in the plane. The disks were then obtained by cutting.

Today, *hard disks* are the most powerful data-storage medium for personal computers. Early hard disks, introduced by IBM in 1973, had a capacity of 30 MB but were large and cumbersome. Designed for use in data centers and large offices, they often required special power supplies and equipment racks. Since the 1980s, internal and external hard disks have been used in personal computers. The first PC hard disks had a capacity of only 5 MB, increasing to typically about 1 GB (1000 MB) in the mid-1990s and about 100 GB in 2005. This increase has been made possible by advances in magnetic nanotechnology, defining an effective bit size as the square root of bit width (track spacing) and bit length (inverse linear bit density). This underlines the role of nanostructuring in advanced magnetic recording: areal densities of 1 Mb in.$^{-2}$, 1 Gb in.$^{-2}$, and 1 Tb in.$^{-2}$ correspond roughly to bit sizes of 25 µm, 800 nm, and 25 nm, respectively. The physics of ultrahigh-density magnetic recording has recently been reviewed by Plumer, van Ek and Weller (2001).

1.2 Recording materials and limits

Early magnetic storage media used ferromagnetic 3d metals, especially iron and nickel, in the form of powders, wires, and thin films. They were soon complemented or superseded by magnetic oxides in the form of elongated small particles. Widely used oxides are γ-Fe_2O_3, CrO_2, and $BaFe_{12}O_{19}$, with typical particle lengths between 1 and 2 μm and coercivities of order of 50 mT (500 Oe). These media have the magnetization in the disk or tape plane, as contrasted to perpendicular recording. The latter, presently in a development stage, is more difficult to realize than longitudinal recording but has greater potential for ultrahigh-density recording (Wood, 2000).

The coercivity of typical magnetic particles is much smaller than the Stoner–Wohlfarth prediction $H_a = 2K_1/\mu_o M_s$. This is because real-structure imperfections give rise to incoherent magnetization reversal, even if the particle size is smaller than the critical single domain size (Skomski, 2003). Furthermore, for particle diameters larger about 20 nm, there are incoherent curling or 'vortex' modes, irrespective of the presence of imperfections. It is therefore necessary to have a sufficiently high anisotropy K_1. The leading contribution to the anisotropy involves spin-orbit coupling and crystal-field interactions. It depends on the local chemistry and on the atomic coordination of the magnetic moments and can be tuned quite easily by chemical substitutions (Skomski and Coey, 1999).

However, with decreasing particle size the coercivity increases and becomes more Stoner–Wohlfarth like. In fact, for some materials, the coercivity of small particles is actually too high for convenient writing, and coercivity tuning is more important that mere anisotropy enhancement. Aside from chemical substitutions, this may be done by exploiting the strong temperature dependence of the anisotropy and magnetization of some magnetic alloys (thermally assisted writing) and by using hard-soft composites.

An upper limit to the room-temperature areal density is given by the thermal stability of the stored information. Small hard grains of uniaxial anisotropy K_1 and volume V exhibit magnetic energy barriers $E_a = K_1 V$. When the volume is too small, thermal excitations reverse the spin direction and destroy the stored information. In a different context, this phenomenon is known as *superparamagnetism*. As analyzed by Becker and Döring (1939) and later popularized by Néel and Brown, thermally activated magnetization processes obey the Arrhenius law $\tau = \tau_o \exp(E_a/k_B T)$. In terms of the thermal stability factor $\xi = \ln(\tau/\tau_o)$, stability is achieved for volumes larger than

$$V = \xi k_B T/K_1 \tag{1}$$

Since $\tau_o \sim 10^{-10}$ s for a wide range of materials, safe information storage for more than 10 years implies $\xi \approx 60$. Room-temperature anisotropies of very hard materials are of order 10 MJ m^{-3} (Skomski and Coey, 1999), so that V cannot be made arbitrarily small. Making particles elongated, $V = b^2 t$ where the film thickness $t \gg b$, does not solve the problem, because very thin particles are susceptible to thermally activated domain formation. The domain-wall energy $\gamma = 4\sqrt{AK_1}$, where $A \sim 10$ pJ m^{-1} is the exchange stiffness, so that the energy barrier for a double wall is of order $8b^2\sqrt{AK_1}$. This energy is independent of t and means that the room-temperature bit size cannot be much smaller than about 2 nm. Exchange coupling to other phases, such as antiferromagnets, stabilizes the stored information at the expense of areal density and does not represent a viable way of overcoming the superparamagnetic limit.

The high anisotropy of materials helps to improve thermal stability and coercivity. For this reason, hard magnetic materials are increasingly used in magnetic recording, although extremely high coercivities complicate writing. A typical example is $L1_0$ materials, such as FePt. Advanced high-density recording media, characterized by more than 10 Gb in.$^{-2}$ (1.55 Gb cm^{-2}), are based on materials such as Co–Cr–Pt–B, where Pt improves anisotropy. Other classes of materials, such as rare-earth transition-metal (RE-TM) nanocomposite films are also being considered.

1.3 New magnetic recording media

Magnetic thin films have been used as recording media in hard-disk drives since about 1990. Together with the development of recording-head technology, from the early inductive read heads and magnetoresistive (MR) heads since 1990 to the recent giant magnetoresistive (GMR) heads, this has been the key factor in the enhancement of the storage density in recent years (Mee and Daniel, 1996). The head development is accompanied by a shift of emphasis from read-back signal amplitude to signal-to-noise ratio, with focus on questions such as grain-size distribution and grain-size refinement. This includes grain isolation by chemical or physical means, in order to reduce intergranular coupling.

There are several approaches forwards the development of new recording media: Sputtering is a well-established method, but it is rapidly approaching its grain size and noise limits. Another approach is to use patterned media where each grain acts as a recording bit. This has the potential to increase the recording density beyond 1 Tb in.$^{-2}$, but it is very difficult to fabricate large-area patterned media and to read and write signals on such media. A third approach is to use patterned perpendicular recording media. This makes it possible to stabilize the magnetic structure by using

elongated particles, but there are various technical challenges involved in this and all recording schemes that approach 1Tb in.$^{-2}$.

1.3.1 Sputtered media

The first generation of magnetic media for hard disks used particulate media consisting of γ-Fe_2O_3 particles dispersed in polymeric binders. The coating was spun onto the substrates, and the magnetic particles were aligned by a circumferential magnetic field before the solvents had completely evaporated. To improve the mechanical durability and to separate the recording head from the polymeric binder, aluminum oxide particles with diameters larger than the coating thickness were added. Since adequate mechanical properties require a particle volume fraction of less than 30%, relatively thick coatings are necessary. Thin coatings with good uniformity are very difficult to obtain and the nonmagnetic aluminum oxide particles degrade the signal-to-noise ration.

Today, most magnetic recording media for hard-disk drives are thin films, which are deposited by *sputtering*. The advantages of the sputtered film media over particle-coated media are their superior magnetic properties in much thinner films and smoother surfaces. Smooth surfaces allow low flying heights that reduce spacing between the head and the medium, thereby increasing the areal density. In addition, by modifying the sputtering parameters, the microstructure can be controlled and magnetic properties can be tailored to satisfy desired recording requirements. Advantageous magnetic properties of sputtered thin films are high magnetization, high anisotropy, and adjustable coercivity. In particular, the enhanced magnetization allows the use of thin recording layers without loss in read-back signal, and the high anisotropy enhances the thermal stability.

Figure 2 shows the basic structure of a thin-film medium, which consists of a substrate, an underlayer, a magnetic layer, an overcoat, and a lubricant. An Al–Mg alloy with a thick plated amorphous NiP layer is used as the substrate. The hard NiP layer allows easy polishing and provides a surface for resistance to mechanical damage. The underlayers develop a necessary texture, which controls the grain size and hexagonal *c*-axis alignment of the magnetic layer.

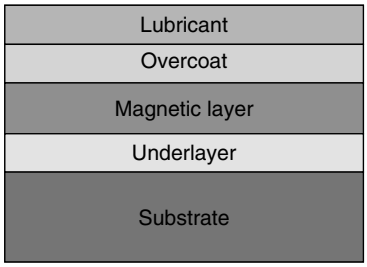

Figure 2. Basic structure of a thin-film medium.

The underlayers, Cr or body-centered cubic Cr alloys such as Cr–Mo and Cr–W, promote the epitaxial growth of magnetic layer. To reduce the grain size and orientation, an additional nucleation or seed layer is deposited before the Cr-alloy underlayer, because it is difficult to nucleate the necessary Cr texture on glass or glass-ceramic surfaces. Examples of seed-layer materials are MgO (Lee, Cheong, Laughlin and Lambeth, 1995) and AlN (Mirzamaani and Doerner, 1996).

Most *magnetic layers* for the present longitudinal recording are pseudoternary and -quaternary alloys based on hcp cobalt. Typical examples are Co–Cr–Ta, Co–Cr–Pt, Co–Ni–Pt, Co–Ta–Ni, Co–Cr–Pt–Ta, and Co–Pt–Cr–X (X = Ni, B, or Si). Another material of potential interest is Co–Cr–Pt–Ta–Nb. A key issue in magnetic recording is media noise. In thin-film media, a major consideration is transition noise, which strongly depends on the grain size and on whether the grains are exchange coupled. Reducing intergranular interactions by physically isolating or chemically segregating the grains helps reduce the media noise. The chromium yields grain boundaries that decouple the grains and improve the corrosion resistance. Elements such as Ta, B, Nb, P, Pt, W, Si, Ir, and Sm are added to Co to improve the signal-to-noise ratio by realizing optimized nanostructures. A similar effect is obtained by adjusting deposition parameters. For example, using high gas pressure to sputter Co alloy can create voided grain boundaries, which helps to isolate the grains physically (Yogi *et al*., 1990).

1.3.2 $L1_0$ alloys

Unlike most other additives, Pt enhances the magnetocrystalline anisotropy of the magnetic alloys, improving both the coercivity and the thermal stability (Ishikawa and Sinclair, 1996). Magnets with equiatomic compositions, such as FePt and CoPt, crystallize in the tetragonal CuAu(I) and $L1_0$ structure. These materials, discovered by Graf and Kussmann (1935) and Jellinghaus (1936), are characterized by very high magnetic anisotropies of several megajoule per cubic meter and have long been used as specialty permanent magnets. Recently, this fascinating class of materials has attracted considerable attention in magnetic recording. Figure 3 shows that the $L1_0$ structure consists of alternating monolayers of different atoms. The magnetic $L1_0$ magnets contain a 3d or iron-series transition-metal element, such as Fe or Co, and a 4d or 5d transition-metal element, such as Pt or Pd.

A challenge is that nearly equiatomic FePt and CoPt form both the disordered fcc and ordered $L1_0$ structure. The cubic anisotropy of the fcc is very low, and a proper heat treatment of the as-deposited fcc films is necessary to form the $L1_0$

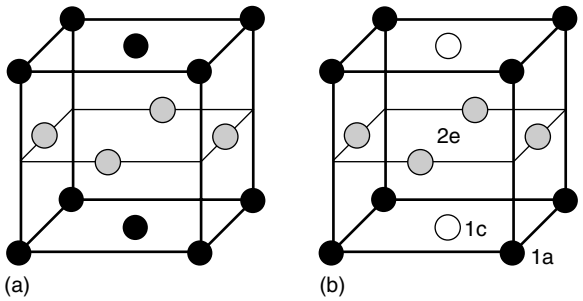

Figure 3. Structure of $L1_0$-type magnets: (a) equiatomic composition and (b) general composition (ABC_2). (Reproduced from R. Skomski *et al*., 2005, with permission from Elsevier. © 2005.)

phase. The coercivities of appropriately grown FePt films, about 2 T, are in fact too high for convenient writing. Current research aims at tuning the coercivity by methods such as random or site-specific substitutions on 1a, 1c, and 2e sites.

A promising approach is to embed CoPt and FePt particles in a nonmagnetic matrix, such as C, SiO_2, Ag, Al_2O_3, and B_2O_3. Most of these films are deposited in a multilayered film and subsequently annealed to obtain the desired nanocomposite structure. For example, the anisotropy of FePt in nanocomposite FePt:B_2O_3 films can be controlled by varying the total film thickness, initial B_2O_3 layer thickness, and the Fe concentration (Luo *et al.,* 2000). Yan *et al*. (2003) have fabricated nonepitaxially grown, double-layered FePt:C/FeCoNi thin films with excellent perpendicular anisotropy on a soft underlayer.

1.3.3 Rare-earth transition-metal compounds

A potentially important class of materials for magnetic recording is RE-TM intermetallics. By rare-earth and transition-metal substitutions it is possible to tune the properties such as magnetization, Curie temperature, and anisotropy over a wide range (Skomski and Coey, 1999). The room-temperature anisotropy of $SmCo^5$ is as high as 17 MJ m^{-3}, as compared to 0.53 MJ m^{-3} for hcp Co. This large anisotropy would allow grain sizes down to a few nanometers, without losing the thermal stability. This corresponds to areal densities in excess of 1 Tb in.$^{-2}$.

However, RE-TM films with the desired properties are usually difficult to produce, as deposited RE-TM films are amorphous and do not have large crystalline anisotropy when they are sputtered below 600 °C. This leads to unfavorably high processing temperatures during growth or post annealing, which is difficult to realize on an industrial scale. Furthermore, rare earths are very corrosive and need special care during processing. Among the considered alloys are Sm-Co and Pr-Co, and the resulting structures are granular. For example, room-temperature deposition of Pr-Co films on Cr underlayers yields essentially amorphous films with coercivities of about 30–40 mT. Subsequent annealing for 20 min at 400 °C causes the Pr-Co to crystallize, and high-resolution transmission electron microscopy (TEM) reveals grain sizes of about 10 nm. The coercivity reaches 200–800 mT, depending on film thickness and deposition conditions (Malhotra *et al*., 1996).

1.3.4 Particulate and other structured media

Advanced magnetic recording technology requires new magnetic nanostructures, such as nanoparticle-based media with great uniformity in both particle size and particle properties (Weller and Moser, 1999). This includes the limit of patterning the media so that each grain represents one bit (White *et al*., 1997). Methods to produce suitable nanostructured thin-film materials include artificial structuring, template-assisted assembly (Sun, Fullerton, Weller and Murray, 2001), and self-assembly. A comprehensive treatment of these methods goes far beyond the scope of this chapter, and we will restrict ourselves to a few examples and then address some material issues in more detail.

E-beam and focused ion-beam lithography, which work for feature sizes down to 50 nm or less, are slow and cumbersome. By contrast, optical lithography and related methods, such as laser-interference lithography (Zheng *et al*., 2001), can be used to pattern large areas; but the feature size is limited by the wavelength. Template methods, such as electrodeposition into porous anodic alumina, combine small feature sizes, and large-area processing (Sellmyer, Zheng and Skomski, 2001). They can also be used to produce structures such as nanocylinders (Section 3).

In some cases, the exchange interaction of the heavy (4d or 5d) transition-metal atoms is antiferromagnetic. This is exploited in *antiferromagnetically coupled* or AFC media, where Co-based magnetic layers are separated by ultrathin ruthenium layers (Fullerton *et al*., 2000). For some thickness, the Pauli-paramagnetic ruthenium layer yields an antiferromagnetic RKKY-type coupling between the Co layers, and the recording signal is the staggered magnetization of the structure.

One way of producing arrays of monodisperse particles is *chemical synthesis*. The nanoparticle dispersions are stabilized toward aggregation and oxidation by a layer of organic stabilizers. It is then deposited on a solid substrate and the solvent is allowed to evaporate. In the films, the grains or nanoparticles are separated by a nonmagnetic coating (Figure 4), which minimizes exchange coupling between adjacent grains. As an example, decomposition of $Fe(CO)_5$ and using polymer stabilizers is a common way to make Fe nanoparticles (see e.g., Johansson, Hanson, Hendriksen and Mørup, 1993). It is also possible to produce binary-alloy

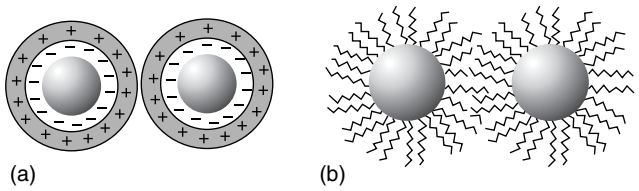

Figure 4. Chemically processed nanoparticles: (a) coating by ionic compounds and (b) steric repulsion due to long-chain surfactants. (Reproduced from David Sellmyer *et al*., Advanced Magnetic Nanostructures, Chapter 9, 2006, with permission from Springer. © 2006.)

nanoparticles, such as CoPt and FePt, but the preparation of nanoparticles with well-controlled stoichiometry is quite complicated (Sun *et al*., 2000).

2 METALLIC NANOCLUSTERS

Magnetic nanoclusters, which have diameters from 1 to 10 nm, are of great scientific and technological interest. An example are the magnetic moments of free Fe, Co, and Ni clusters whose size dependence was determined by measuring their Stern–Gerlach deflections (Bucher, Douglass and Bloomfield, 1991; Billas, Becker, Châtelain and de Heer, 1993; Apsel, Emmert, Deng and Bloomfield, 1996; Edmonds *et al*., 1999). At a low temperature of 120 K, small Fe clusters ($25 \leq N \leq 130$ atoms) have a moment of $3\,\mu_B$ per atom, as compared to the bulk value of $2.2\,\mu_B$; which is reached at about $N = 500$ atoms (Billas, Becker, Châtelain and de Heer, 1993). This moment reduction, which reflects the reduced atomic coordination of surface atoms, and other features, such as pronounced surface anisotropy, make clusters attractive for potential applications such as high-density data storage, spin electronics, memory devices, and high-performance magnetic materials.

Traditionally, CoPt and FePt nanoparticles are prepared by normal magnetron sputtering or electron beam evaporation techniques (Stavroyiannis *et al*., 1998; Yu *et al*., 1999; Bian, Sato and Hirotsu, 1999; Suzuki, Kiya, Honda and Ouchi, 2001). Here we focus on a relatively recently developed gas-aggregation technique, where magnetron sputtering is employed in the source (Haberland, Karrais, Mall and Thurner, 1992; Haberland *et al*., 1994) for the preparation of magnetic nanoclusters and of cluster-assembled nanocomposites. This cluster-deposition technique can produce a range of mean cluster sizes from 3 to 12 nm with high deposition rate (can be as high as 5 Å s^{-1}), and a well-controlled cluster size and size distribution. A major advantage is that the clusters have size dispersions much smaller than that of grains in a typical vapor-deposition system.

2.1 Cluster source and gas aggregation

The formation of metal clusters by gas aggregation, where metal atoms are either evaporated or sputtered into a cooled inert gas flow at relatively high pressure, has been well established for the last two decades. By repeated collisions with the carrier gas, the supersaturated metal vapor nucleates and forms clusters. In some cases, this method is used in combination with mass selectors or time-of-flight (TOF) spectrometers (Baker *et al*., 2000).

Sputtering-based cluster sources have three advantages: (i) they can produce a large range of mean cluster sizes from 200 to 15 000 atoms per cluster, (ii) they have a high degree of ionization, from 20 to 50%, depending on the target material, and (iii) a wide variety of elements and alloys can be used as source materials. Usually, the deposition rate is about 3 Å s^{-1} for the total flux of the cluster beam. Sputtering-based gas-aggregation sources are now widely used in laboratories and commercially available from Oxford Applied Research and Mantis Deposition.

Figure 5 shows a modern cluster-deposition system with a sputtering-based gas-aggregation source (Xu, Sun, Qiang and Sellmyer, 2003a,b). It consists of five chambers: (i) the chamber for cluster formation containing a LN_2 cooled aggregation tube with a magnetron sputter discharge, (ii) a chamber containing a quadrupole mass selection and e-beam deposit in system for particle coating, (iii) the deposition chamber with a substrate holder, (iv) a sample load-lock

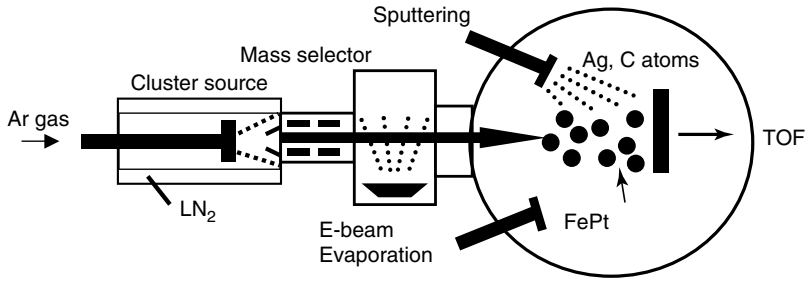

Figure 5. Cluster-deposition system (schematic). (Reproduced from D.J. Sellmyer *et al*., 2005. With permission from IEEE. © 2005.)

chamber (not shown) for rapid substrate change, and (v) a chamber (not shown) containing the TOF mass spectrometer. Briefly, the clusters are generated in the aggregation tube, go through two apertures, and are then deposited onto the substrate. The cluster size can be adjusted by varying the source parameters: gas-aggregation tube temperature, gas pressure, gases Ar to He flux ratio, magnetron power, and the condensation length in which the clusters aggregate. If a very narrow cluster size distribution is needed, the mass selector can be employed; in this case the ratio of rms diameter deviation to average diameter can be made as small as $\sigma/d \approx 3\%$. Figure 6 shows an example of Fe clusters produced with the quadruple mass selector.

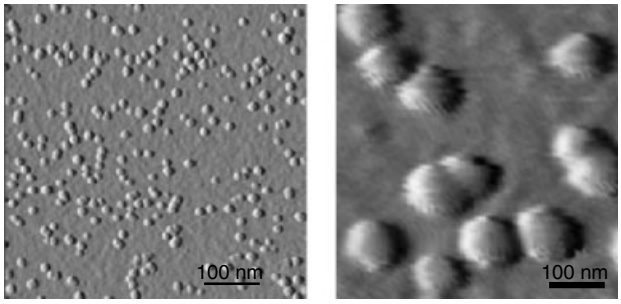

Figure 6. (a) Atomic-force (AFM) images of Fe clusters. (b) Enlarged Fe clusters with size about 8 nm.

2.2 $L1_0$ FePt and CoPt nanoclusters

This section deals with the size distribution and nanostructure of FePt and CoPt clusters prepared by the gas-aggregation technique (Xu, Sun, Qiang and Sellmyer, 2003a,b).

2.2.1 Size distribution and nanostructure of clusters

For cluster films deposited on a substrate, the determination of the structure are mostly done by using TEM. For the TEM observations, the FePt and CoPt nanoclusters are directly deposited onto carbon-coated films supported by Cu grids.

The TEM images in Figure 7 show CoPt clusters with average size of 4.9 nm ($\sigma = 0.46$ nm, $\sigma/d = 0.09$), prepared with sputtering power of 160 W (Xu, Sun, Qiang and Sellmyer, 2003a). The high-resolution image indicates that the CoPt clusters have faceted surfaces. Similar results were obtained for FePt clusters (Xu, Sun, Qiang and Sellmyer, 2003b). The cluster size follows a Gaussian distribution rather than the lognormal one observed in Fe clusters (Upward *et al*., 2000). This distinction is important but not yet understood in terms of the cluster formation mechanism.

The formation of $L1_0$-ordered FePt clusters naturally requires a high-temperature postdeposition annealing. However, postdeposition annealing leads to subsequent crystallite growth and concurring agglomeration of the clusters on the substrate. Rellinghaus, Stappert, Acet and Wassermann (2003) used a sintering oven between the cluster source and the deposition chamber, allowing preparation and thermal sintering of FePt nanoclusters in the gas phase prior to their deposition.

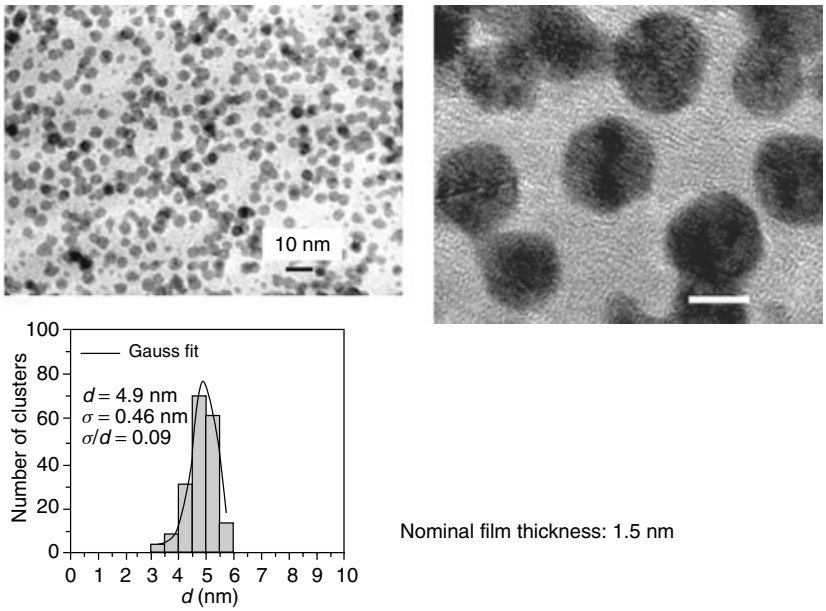

Figure 7. TEM images of CoPt clusters with cluster size distribution. Right: Larger magnification of the clusters. (Reproduced from D.J. Sellmyer *et al*., 2005. With permission from IEEE. © 2005.)

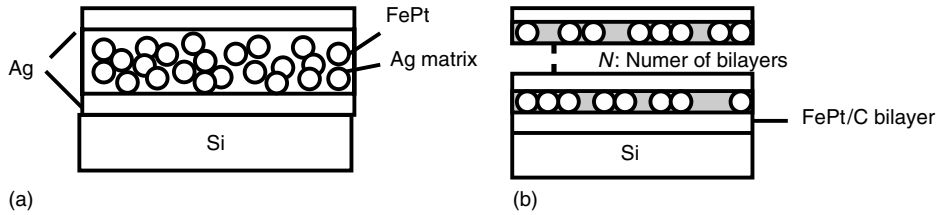

Figure 8. Cluster film structures: (a) codeposition and (b) multilayers.

2.2.2 FePt:C cluster films

For most applications, *embedded* clusters are more important than free clusters. The matrix material may be magnetic or nonmagnetic and metallic or nonmetallic. A cluster beam combined with an atomic beam from normal magnetron sputtering guns is used for matrix materials deposition, such as Ag, C, and so on. Figure 8 shows two examples: clusters embedded in matrix by codeposition (a) and isolated by a matrix via multilayers (b).

Figure 9 shows TEM images for annealed FePt:C nanocluster films prepared by the multilayer method. Alternating FePt cluster and C layers were deposited onto a Si substrate. The average FePt cluster size is about 4.5 nm, and the thickness of carbon layer was adjusted to yield C volume fractions changing from 7 to 45% (Xu, Yan and Sellmyer, 2004). The carbon serves to isolate the clusters and to avoid cluster aggregation during thermal annealing. After annealing, the FePt clusters remained well separated by the amorphous carbon, Figure 9(b).

As verified by X-ray diffraction, the grains have the $L1_0$ structure. Both in-plane and perpendicular coercivities increase with annealing temperature. A perpendicular coercivity larger than 13 kOe was achieved in the films annealed at a temperature of 700 °C for 10 min. The same method was also used to prepare dilute FePt:C cluster films with a FePt volume fraction of 5%. The low-temperature coercivity is 4.0 T, corresponding to an anisotropy field of 8.3 T. This indicates that the individual FePt particles are Stoner–Wohlfarth like.

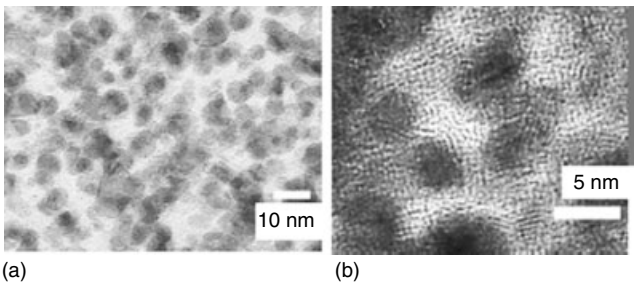

Figure 9. TEM images of FePt:C cluster film with 45 vol% C, annealed at 650 °C for 10 min. (Reproduced from Y. Xu *et al.*, 2004, with permission from IEEE. © 2004.)

3 CHEMICALLY DEPOSITED NANOPARTICLES AND NANOTUBES

There are three main bottom-up approaches in making isolated magnetic clusters: chemical reaction (molecular clusters), evaporation or sputtering and condensation (gas phase clusters), and matrix isolation (solution phase and template synthesis). Matrix isolation is the most widely used method in creating magnetic nanostructure. In this section, the main focus is on (i) the creation of nanostructures through solution processes and (ii) template synthesis.

3.1 Chemical reaction mechanisms

3.1.1 Cluster formation by solution reaction

Cluster synthesis by solution phase reaction is a thermodynamic quasiequilibrium approach and follows the well-established theory of crystal growth. It consists of three consecutive processes: supersaturation, nucleation, and growth (Murray, Kagan and Bawendi, 2000). Solvents ensure that the chemical reaction proceeds homogeneously and act as a flexible isolating matrix to keep the clusters apart. To produce monodispersed clusters, it is highly desirable that nuclei with identical size be created at the same time in supersaturated solution. In many cases, the supersaturation is technically achieved through the rapid injection of organometallic compounds into a hot solution. Either thermal decomposition or chemical reduction at the high temperature, combined with the rapid drop of processing temperature, induces a sharp nucleation followed by slow growth at low concentration.

Both the inhibition of additional nucleation during growth and the controlled growth of nuclei are important to obtain monodispersed clusters. When the concentration of growth species is lower than the specific concentration after the explosive nucleation, additional nucleation is inhibited. The organic capping agents on cluster surfaces act as a diffusion

barrier to control the growth of the nuclei. The polymeric layers covering the clusters also prevent agglomeration and oxidation, and define the minimum intercluster separation after self-assembly. Further growth, named *Ostwald ripening*, is observed in many systems at a late stage of growth. The main characteristic of Ostwald ripening is that the larger clusters keep growing at the expense of smaller ones, driven by the difference of their surface free energy. Ostwald ripening also helps to narrow the size distribution if it is properly exploited.

3.1.2 Template-mediated synthesis

If the isolating matrix is a solid nanostructure instead of a liquid, the matrix isolation approach is called *template-mediated synthesis*, rather than solution phase synthesis. A wide variety of materials covering both organics and inorganics have been built into nanostructures by template-engaged processes (Hulteen and Martin, 1997; Sellmyer, Zheng and Skomski, 2001; Sui, Skomski, Sorge and Sellmyer, 2004a; Sui *et al*., 2004b). The only requirement seems to be the proper method to load the pores with the desired materials, as long as the template is stable with respect to the nanomaterials and chemical reactions inside these pores.

Most of the work in this area is based on porous films such as anodized alumina, track-etched polycarbon, and self-assembled block copolymers (Hulteen and Martin, 1997). The common feature of these templates is nanopores having their axis perpendicular to the film plane, but pore diameters, densities, distributions, thermal and chemical stabilities, surface chemical characteristics differ from one template to another. For nanostructures deposited by electrochemical, electroless, sol–gel and electrophoretic process, the templates are involved physically rather than chemically and have a similar isolating effect for all the typical templates. For nanostructures produced by high-temperature chemical reaction – chemical vapor deposition (CVD) or hydrogen reduction – anodized alumina film becomes the only option, due to its heat resistance (Sui *et al*., 2002; Sui, Skomski, Sorge and Sellmyer, 2004a).

3.2 Magnetic clusters produced by solution phase reaction

The decomposition of organometallic precursors in an inert atmosphere (Section 3.1.1) has long been employed to produce Co, Fe, and Ni clusters (Thomas, 1966; Hoon, Kilner, Russell and Tanner, 1983), but with a relatively large size distribution. A modification of this technique, namely, the rapid injection of organometallic reagents into a hot coordinating solvent, has led to the synthesis of monodispersed clusters of transition metals and their alloys with controllable size and shape. The synthesis of FePt cluster by the combination of $Pt(acac)_2$ reduction and $Fe(CO)_5$ thermal decomposition in dioctylether under airless condition is a typical chemical synthesis via solution phase reaction (Sun *et al*., 2000). The cluster size is controlled by the explosive nucleation and the slow seed-mediated growth. For example, 10-nm FePt clusters are produced first by growing 3-nm clusters *in situ* and then adding more reagents to enlarge the existing seeds to 10 nm. The alloy composition can be adjusted by changing the molar ratio of iron carbonyl to the platinum salt. Postannealing is necessary to transform the FePt clusters from the disordered face-centered cubic to the ordered $L1_0$ structure. Following a similar recipe, clusters of both transition-metal oxides and a RE-TM alloy ($SmCo_5$) with narrow size distributions have also been synthesized. However, the low anisotropy of the Sm-Co, $0.2\,MJ\,m^{-3}$ indicates incomplete phase transformation, leaving much room for improvement by the solution phase reaction.

One of the oldest techniques for the synthesis of magnetic clusters is the precipitation of oxides from the solution. For example, Fe_3O_4 nanoparticles were produced via coprecipitation from a $FeCl_3$ and $FeCl_2$ water solution by NaOH or $NH_3{\cdot}H_2O$ base. The advantage of the precipitation reaction is that large quantities of clusters can be produced by controlling the pH value and the metal cation concentration properly. However, it is difficult to tailor the size and shape of the particles. This problem has been solved by a recently developed organic-phase synthesis approach. Either metal or oxide clusters can be generated by the decomposition of organometallic compounds in the presence of polymeric stabilizers. The type of the organometallic precursors and the solvents, the decomposition and growth condition are critical in determining whether metal or oxide clusters will be produced (Park *et al*., 2004). For example, 5-nm clusters of iron oxides are produced by the decomposition of iron-oleate complex in 1-hexadecene at 350 °C > 280 °C for 30 min. When the same iron-oleate complex is processed in trioctylamine at 380 °C, 20-nm iron cubes are synthesized. Both iron cubes and spherical iron oxide clusters have size variations of less than 4.1%, without applying size-selection process. This technique can be extended to produce monodispersed manganese ferrite and cobalt ferrite clusters also.

Magnetic clusters made by solution reaction provide not only a good opportunity to explore the basic physics and chemistry of nanomaterials, but also supply a rich source of building blocks to construct macrosystems with controlled nanostructure. Such structures are of importance, for example, in permanent magnetism (Skomski and Coey, 1999; Sellmyer, 2002). When FePt and Fe_3O_4 clusters of similar size (about 4 nm) assembled together

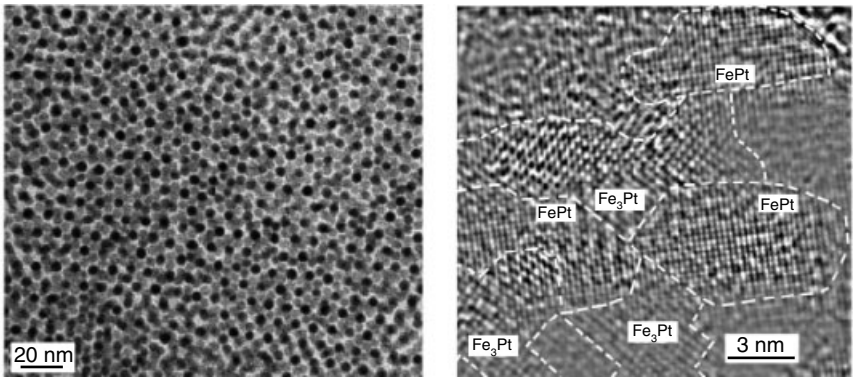

Figure 10. TEM image of binary particulate thin films: (a) FePt and Fe_3O_4 nanoparticles and (b) annealed FePt–Fe_3Pt nanocomposite. (Reprinted by permission from Macmillan Publishers Ltd: Nature 420, H. Zeng *et al*., 2002. © 2002.)

in specific mass ratio, and heated in a gas mixture (Ar + 5% H_2) at 650 °C for 1 h, the binary system is transformed into a homogeneous mixture of hard tetragonal FePt phase and a high magnetization soft Fe_3Pt phase (Zeng *et al*., 2002). Figure 10 shows typical TEM images of (a) assembled binary FePt and Fe_3O_4 nanoparticles, and (b) of the annealed FePt–Fe_3Pt nanocomposite. The latter structure exhibits effective exchange coupling between hard and soft magnetic phases to enhance the energy product of the nanocomposite.

3.3 Magnetic nanostructures created by template-mediated reaction

3.3.1 Magnetic nanotubes and one-dimensional nanocomposites

Magnetic nanostructures may be produced in a wide range of shapes, sizes, and materials (Skomski, 2003). This includes not only thin films, particles, and nanowires but also structures such as nanotubes and nanorings. Transition-metal nanotubes and nanowires have been produced by electroless or electrodeposition guided by various porous templates (Tourillon *et al*., 2000; Sellmyer, Zheng and Skomski, 2001). Nanochannels of porous alumina are used as nanoreactors to create both nanotubes and nanoparticles. However, it is difficult to tune the magnetic properties of one-dimensional structures generated by electrochemical methods. This refers, in particular, to magnetic compounds, such as intermetallics and ferrimagnetic oxides.

Nanoporous alumina templates have been loaded with a mixture of $H_2PtCl_6 \cdot 6H_2O$ and $FeCl_3 \cdot 6H_2O$ and heated in hydrogen for 1.5 h at 560 °C. This led to the formation of FePt nanotubes inside the pores of the template. Similarly, Fe_3O_4 nanotubes arrays were produced by loading the template with alcohol solution of 65% $Fe(NO_3)_3 \cdot 9H_2O$ and processing at 250 °C for 2.5 h in flowing hydrogen (Sui, Skomski, Sorge and Sellmyer, 2004a). The porous alumina film simply serves as a skeleton in which FePt or Fe_3O_4 are generated *in situ* by hydrogen reduction and shaped into nanotubes with their morphologies complementary to the nanochannels of the anodized alumina. Figure 11 shows the results of the procedure: TEM micrographs of (a) FePt and (b) Fe_3O_4 nanotubes, and hysteresis loops of (c) FePt and (d) Fe_3O_4. The magnetic properties can be explained in terms of a tubular random-anisotropy model (Sui, Skomski, Sorge and Sellmyer, *et al*., 2004a).

Hysteresis in very small particles is realized by coherent or Stoner–Wohlfarth rotation. In practice, this applies to particles with diameters of less than 5–20 nm, depending on factors such as particle shape and real structure (defect structure). In larger particles, there is a broad range of incoherent spin configurations such as spin waves and curling modes or 'vortices'. Figure 12 shows some examples for nanotubes and nanorings (Sui, Skomski, Sorge and Sellmyer, 2004a). The physical origin of these nonuniform spin states and the corresponding length scales have been reviewed by Skomski (2003, 2004), and there is also a discussion of incoherent magnetization states in nanoparticles of various shapes (Skomski, Kashyap, Sorge and Sellmyer, 2004).

The technique of chemical reactions in nanochannels can be extended to the creation of quasi-one-dimensional nanocomposites of transition metals in carbon by the combination of hydrogen reduction with carbon deposition using CVD (Sui *et al*., 2002). Figure 13 shows TEM micrograph of a composite FePt:C nanofiber. The FePt $L1_0$ clusters were formed by hydrogen reduction at 650 °C, followed by carbon deposition using C_2H_2 pyrolysis at the same temperature. The FePt:C nanocomposite exhibits a coercivity of 29.0 kOe after heating at 900 °C in nitrogen.

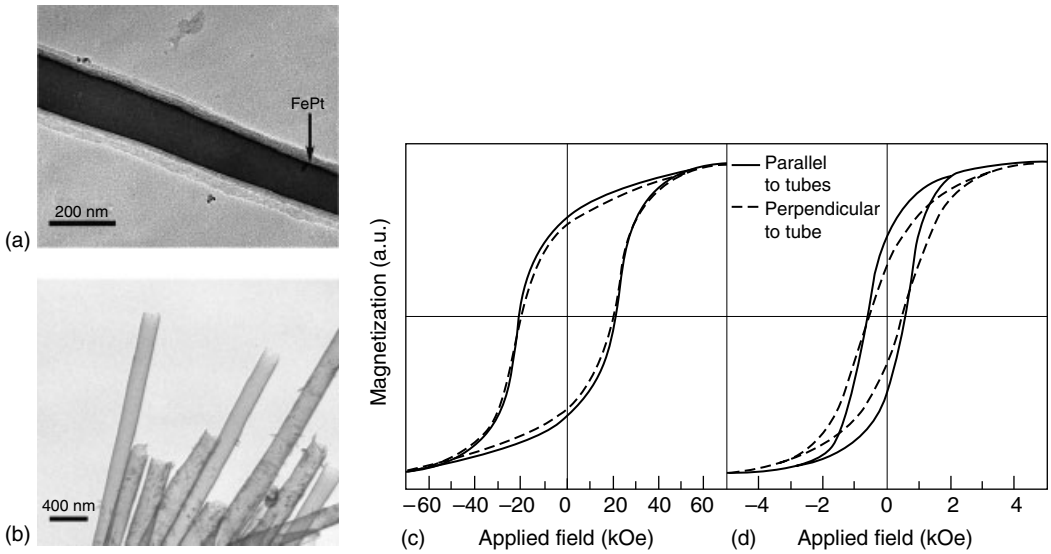

Figure 11. TEM micrographs and room-temperature hysteresis loops of magnetic nanotubes: (a) isolated FePt nanotube surrounded by alumina and (b) Fe_3O_4 nanotubes released from the matrix, (c) hysteresis of FePt and (d) Fe_3O_4. In the loops, the external field is parallel (solid lines) and perpendicular (dashed lines) to the tubes axes. (Reproduced from Y.C. Sui *et al*. 2004, with permission from the American Institute of Physics. © 2004.)

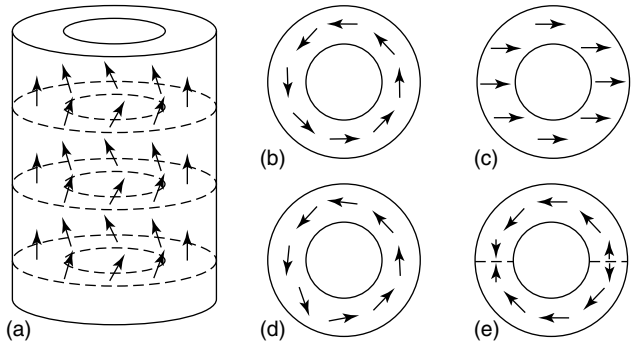

Figure 12. Some spin structures in magnetic nanotubes and nanorings: (a) and (b) curling, (c) coherent rotation, (d) curling modified by random anisotropy, and (e) excited spin-wave mode. (Reproduced from Y.C. Sui *et al*., 2004, with permission from American Institute of Physics. © 2004.)

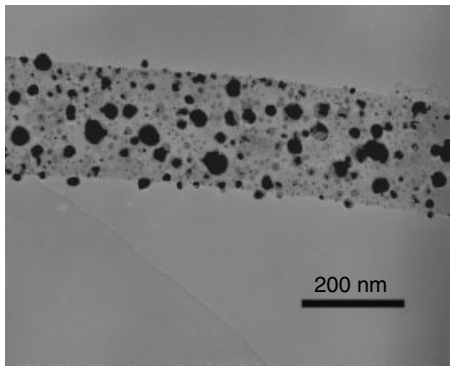

Figure 13. TEM micrograph of a nanofiber-like FePt:C nanocomposite.

3.3.2 Template-mediated self-assembly

FePt $L1_0$ nanoparticles produced within the pores of the templates by hydrogen reduction can be extracted and capped with organic surfactants. These clusters have a relatively large size distribution. After size selection via chemical processing, clusters with average diameter of 11 nm precipitated out. Figure 14 shows a TEM image of the selected FePt cluster assembled on a copper grid with 10 nm carbon coating, which demonstrates a narrow size distribution with standard size deviation (σ/d) of about 7%. Those clusters form a suspension in hexane and behave as a liquid under the influence of capillary action.

Figure 15 depicts an alumina template with ordered pore array. The barrier layer consists of a regular hexagonal array of hemispherical cells above the pores. Two-step anodization of aluminum foils can create similar structures (Sui *et al*., 2002). The pore array of the alumina template tunes the self-assembly process when the FePt cluster suspension is drop cast over the template, and a magnetic pattern matching the hexagonal pore distribution is generated. This simple and fast technique is called *template-mediated self-assembly* (TMSA). An external magnetic field applied at the same time aligns the magnetic clusters during assembly.

The result of the TMSA process is shown in Figure 16. The images show the barrier layer after TMSA cluster suspension of FePt $L1_0$ in an external magnetic field. The

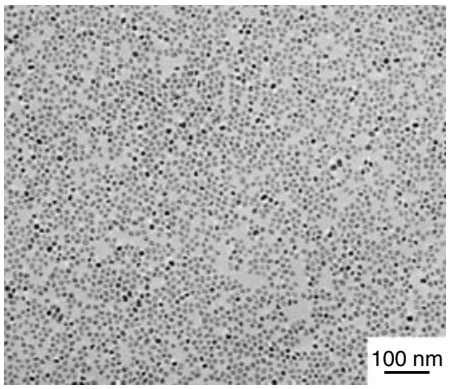

Figure 14. TEM image of the selected FePt cluster assembled on a copper grid with 10-nm carbon coating. (Reproduced from Y.C. Sui *et al*., 2005, with permission from American Institute of Physics. © 2005.)

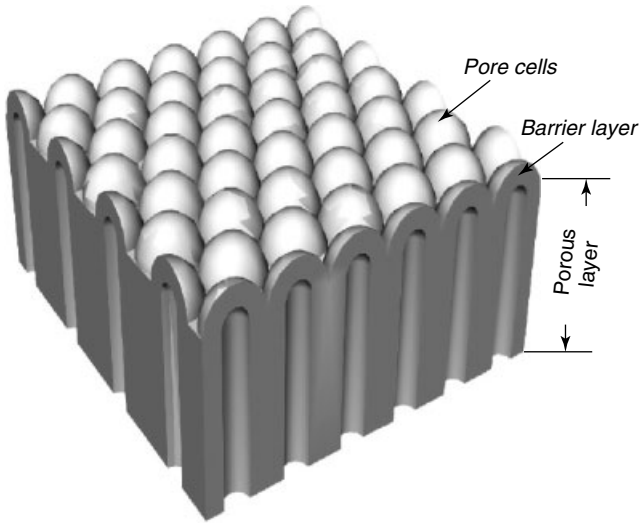

Figure 15. Alumina template with ordered pore array (schematic). (Reproduced from Y.C. Sui *et al*., 2002 with permission from Elsevier. © 2002.)

average pore diameter is 50 nm, which lead to the formation of 50-nm FePt dots arrays. The advantages of this technique over traditional self-assembly are that it can generate ordered cluster arrays up to centimeter scales or larger, and that the magnetic dots can be aligned by a magnetic field. This technique has a high potential for nanofabrication of arrays for high-density magnetic recording or other nanodevices.

4 CONCLUDING REMARKS

For two reasons, the focus of this article has been on nanoparticles and particulate thin films for recording media. Firstly, the recording industry has been the major driving force in recent magnetism research, and this trend is likely to continue in the near to medium future. Secondly, various aspects of experimental, theoretical, and industrial magnetism relevant to particulate magnets are treated in other parts of this handbook. However, it is important to keep in mind that many other present or future materials, such as soft magnets, permanent magnets, ferrofluids, and sensors, are nanoparticulate magnets. Examples are isotropic permanent magnets (Coehoorn, de Mooij and de Waard, 1989) and nanocrystalline soft magnets (Yoshizawa, Oguma and Yamauchi, 1988). Furthermore, particulate systems often combine features of nanoparticles or clusters with those of thin-film and bulk magnets (Zhou *et al*., 2004).

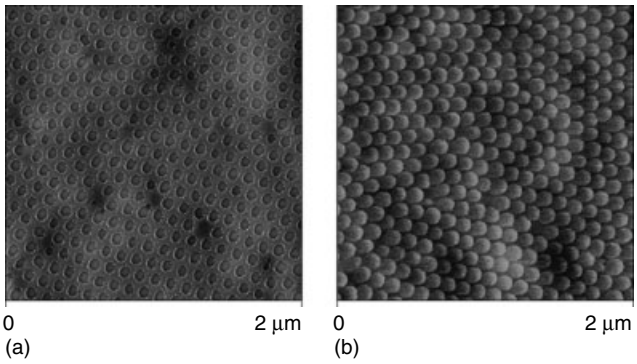

Figure 16. Self-assembled template-mediated $L1_0$ FePt: (a) atomic-force microscopy and (b) magnetic-force microscopy. Images are taken from the closed end of the pores (top side in Fig. 15). (Reproduced from Y.C. Sui *et al*., 2005, with permission from American Institute of Physics. © 2005.)

There are various methods to fabricate free and embedded ensembles of nanoparticles for magnetic recording. Key requirements for storage densities approaching 1 Tb in.$^{-2}$ are nanoparticles with well-controlled sizes, size distributions, separations, and crystalline orientations, and there has been an unprecedented search for artificial granular nanostructures that satisfy these criteria. The balance of room-temperature anisotropy and cluster or grain size is becoming increasingly important as the superparamagnetic limit is approached.

Our specific emphasis has been on cluster deposition of magnetic particles and deposition into porous templates. Chemical deposition is not as versatile as vacuum deposition technologies, such as sputtering. A combination of conventional thin-film technology and self-assembly may be a viable route to overcome these limitations.

ACKNOWLEDGMENTS

The authors are grateful to NSF-MRSEC, DOE, ARO, INSIC, and the W. M. Keck Foundation for supporting their work.

REFERENCES

Apsel, S.E., Emmert, J.W., Deng, J. and Bloomfield, L.A. (1996). Surface-enhanced magnetism in nickel clusters. *Physical Review Letters*, **76**, 1441–1444.

Baker, S.H., Thornton, S.C., Edmonds, K.W., *et al*. (2000). The construction of a gas aggregation source for the preparation of size-selected nanoscale transition metal clusters. *Review of Scientific Instruments*, **71**, 3178–3183.

Becker, R. and Döring, W. (1939). *Ferromagnetismus*, Springer: Berlin.

Bian, B., Sato, K. and Hirotsu, Y. (1999). Ordering of island-like FePt crystallites with orientations. *Applied Physics Letters*, **75**, 3686–3688.

Billas, I.M.L., Becker, J.A., Châtelain, A. and de Heer, W.A. (1993). Magnetic moments of iron clusters with 25 to 700 atoms and their dependence on temperature. *Physical Review Letters*, **71**, 4067–4070.

Bucher, J.P., Douglass, D.C. and Bloomfield, L.A. (1991). Magnetic properties of free cobalt clusters. *Physical Review Letters*, **66**, 3052–3055.

Coehoorn, R., de Mooij, D.B. and de Waard, C. (1989). Meltspun permanent magnet materials containing Fe_3B as the main phase. *Journal of Magnetism and Magnetic Materials*, **80**, 101–104.

Comstock, R.L. (1999). *Introduction to Magnetism and Magnetic Recording*, John Wiley & Sons: New York.

Edmonds, K.W., Binns, C., Baker, S.H., *et al*. (1999). Doubling of the orbital magnetic moment in nanoscale Fe clusters. *Physical Review B*, **60**, 472–476.

Fullerton, E.E., Margulies, D.T., Schabes, M.E., *et al*. (2000). Antiferromagnetically coupled magnetic media layers for thermally stable high density recording. *Applied Physics Letters*, **77**, 3806–3808.

Graf, L. and Kussmann, A. (1935). Equilibrium diagram and magnetic properties of Pt-Fe alloys. *Physikalische Zeitschrift*, **36**, 544–551.

Haberland, H., Karrais, M., Mall, M. and Thurner, Y. (1992). Thin film from energetic cluster impact: a feasibility study. *Journal of Vacuum Science and Technology A*, **10**, 3266–3271.

Haberland, H., Mall, M., Moseler, M., *et al*. (1994). Filling of micron-sized contact holes with copper by energetic cluster impact. *Journal of Vacuum Science and Technology A*, **12**, 2925–2930.

Hoon, S.R., Kilner, M., Russell, G. and Tanner, B.K. (1983). Preparation and properties of nickel ferrofluids. *Journal of Magnetism and Magnetic Materials*, **39**, 107–110.

Hulteen, J.C. and Martin, C.R. (1997). A general template-based method for the preparation of nanomaterials. *Journal of Materials Chemistry*, **7**, 1075–1087.

Ishikawa, A. and Sinclair, R. (1996). Effects of Pt addition on the magnetic and crystallographic properties of Co-Cr-Pt thin-film media. *Journal of Magnetism and Magnetic Materials*, **152**, 265–273.

Jellinghaus, W. (1936). New alloys with high coercive force. *Zeitschrift für technische Physik*, **17**, 33–36.

Johansson, C., Hanson, M., Hendriksen, P.V. and Mørup, S. (1993). The magnetization of magnetic liquids containing amorphous $Fe_{1-x}C_x$ particles. *Journal of Magnetism and Magnetic Materials*, **122**, 125–128.

Lee, L.L., Cheong, B.K., Laughlin, D.E. and Lambeth, D.N. (1995). MgO seed layers for CoCrPt/Cr longitudinal magnetic recording media. *Applied Physics Letters*, **67**, 3638–3640.

Luo, C.P., Liou, S.H., Gao, L., *et al*. (2000). Nanostructured FePt:B_2O_3 thin films with perpendicular magnetic anisotropy. *Applied Physics Letters*, **77**, 2225.

Malhotra, S.S., Liu, Y., Shan, Z.S., *et al*. (1996). High coercivity PrCoCr thin film for longitudinal magnetic recording media. *Journal of Magnetism and Magnetic Materials*, **161**, 316–322.

Mee, C.D. and Daniel, E.D. (Eds.) (1996). *Magnetic Storage Handbook*, McGraw-Hill.

Mirzamaani, M. and Doerner, M.F. (1996). Magnetic performance and tribology of sputter-textured thin-film disks. *IEEE Transaction on Magnetics*, **32**, 3638–3641.

Murray, C.B., Kagan, C.R. and Bawendi, M.G. (2000). *Annual Review of Materials Science*, **30**, 545–610.

Park, J., An, K.J., Hwang, Y.S., *et al*. (2004). Ultra-large-scale synthesis of monodisperse nanocrystals. *Nature Materials*, **3**, 891–895.

Plumer, M.L., van Ek, J. and Weller, D. (2001). *The Physics of Ultra-High-Density Magnetic Recording*, Springer: Berlin.

Rellinghaus, B., Stappert, S., Acet, M. and Wassermann, E.F. (2003). Magnetic properties of FePt nanoparticles. *Journal of Magnetism and Magnetic Materials*, **266**, 142–154.

Sellmyer, D.J. (2002). Strong magnets by self-assembly. *Nature*, **420**, 374–375.

Sellmyer, D. and Skomski, R. (Eds.) (2006). *Advanced Magnetic Nanostructures*, Springer: New York.

Sellmyer, D.J., Zheng, M. and Skomski, R. (2001). Magnetism of Fe, Co and Ni nanowires in self-assembled arrays. *Journal of Physics: Condensed Matter*, **13**, R433–R460.

Skomski, R. (2003). Nanomagnetics. *Journal of Physics: Condensed Matter*, **15**, R841–R896.

Skomski, R. (2004). Nanomagnetic scaling. *Journal of Magnetism and Magnetic Materials*, **272–276**, 1476–1481.

Skomski, R. and Coey, J.M.D. (1999). *Permanent Magnetism*, Institute of Physics: Bristol.

Skomski, R., Kashyap, A., Sorge, K.D. and Sellmyer, D.J. (2004). Multidomain and incoherent effects in magnetic nanodots. *Journal of Applied Physics Letters*, **95**, 7022–7024.

Stavroyiannis, S., Panagiotopoulos, I., Niarchos, D., *et al*. (1998). CoPt/Ag nanocomposites for high density recording media. *Applied Physics Letters*, **73**, 3453–3455.

Sui, Y.C., Cui, B.Z., Martinez, L., *et al*. (2002). Pore structure, barrier layer topography and matrix alumina structure of porous anodic alumina film. *Thin Solid Films*, **406**, 64–69.

Sui, Y.C., Skomski, R., Sorge, K.D. and Sellmyer, D.J. (2004a). Nanotube magnetism. *Applied Physics Letters*, **84**, 1525–1527.

Sui, Y.C., Zhou, J., Li, X.Z., *et al*. (2004b). Growth and magnetism of FePt:C composites in nanoscale channels. *Journal of Applied Physics Letters*, **95**, 6741–6743.

Sun, S., Fullerton, E.E., Weller, D. and Murray, C.B. (2001). Compositionally controlled FePt nanoparticle materials. *IEEE Transaction on Magnetics*, **37**, 1239–1243.

Sun, S., Murray, C.B., Weller, D., *et al*. (2000). Monodisperse FePt nanoparticles and ferromagnetic FePt nanocrystal superlattices. *Science*, **287**, 1989–1992.

Suzuki, T., Kiya, T., Honda, N. and Ouchi, K. (2001). Fe-Pt perpendicular double-layered media with high recording resolution. *Journal of Magnetism and Magnetic Material*, **235**, 312–318.

Thomas, J.R. (1966). Preparation and magnetic properties of colloidal cobalt particles. *Journal of Applied Physics*, **37**, 2914–2915.

Tourillon, G., Pontonnier, L., Levy, J.P. and Langlais, V. (2000). Electrochemically synthesized Co and Fe nanowires and nanotubes. *Electrochemical and Solid State Letters*, **3**, 20–23.

Upward, M.D., Cotier, B.N., Moriarty, P., *et al*. (2000). Deposition of Fe clusters on Si surface. *Journal of Vacuum Science and Technology B*, **18**, 2646–2649.

Volk, T. (1935). Magnetophon, das neue Tonaufzeichnungsgerät der AEG. *AEG-Mitteilungen*, **25**, 199–201.

Weller, D. and Moser, A. (1999). Thermal effect limits in ultrahigh density magnetic recording. *IEEE Transaction on Magnetics*, **35**, 4423–4439.

White, R.L., New, R.M.H. and Pease, R.F.W. (1997). Patterned media: a viable route to 50 Gbit/in2 and up for magnetic recording. *IEEE Transaction on Magnetics*, **33**, 990–995.

Wood, R. (2000). The feasibility of magnetic recording at 1 terabit per square inch. *IEEE Transaction on Magnetics*, **36**, 36–42.

Xu, Y., Sun, Z.G., Qiang, Y. and Sellmyer, D.J. (2003a). Preparation and magnetic properties of CoPt and CoPt:Ag nanocluster films. *Journal of Magnetism and Magnetic Materials*, **266**, 164–170.

Xu, Y., Sun, Z.G., Qiang, Y. and Sellmyer, D.J. (2003b). Magnetic properties of $L1_0$ FePt and FePt:Ag nanocluster films. *Journal of Applied Physics*, **93**, 8289–8291.

Xu, Y., Yan, M.L. and Sellmyer, D.J. (2004). Nanostructure and magnetic properties of FePt:C cluster films. *IEEE Transaction on Magnetics*, **40**, 2525–2527.

Yan, M.L., Li, X.Z., Gao, L., *et al*. (2003). Fabrication of nonepitaxially grown, double-layered fept:c/feconi thin films for perpendicular recording. *Applied Physics Letters*, **83**, 3332–3334.

Yogi, T., Nguyen, T.A., Lambert, S.E., *et al*. (1990). Role of atomic mobility in the transition noise of longitudinal media. *IEEE Transaction on Magnetics*, **26**, 1578–1580.

Yoshizawa, Y., Oguma, S. and Yamauchi, K. (1988). New Fe-based soft magnetic alloys composed of ultrafine grain structure. *Journal of Applied Physics*, **64**, 6044–6046.

Yu, M., Liu, Y., Moser, A., *et al*. (1999). Nanocomposite CoPt:C films for extremely high-density recording. *Applied Physics Letters*, **75**, 3992–3994.

Zeng, H., Li, J., Liu, J.P., *et al*. (2002). Exchange-coupled nanocomposite magnets by nanoparticle self-assembly. *Nature*, **420**, 395–398.

Zheng, M., Yu, M., Liu, Y., *et al*. (2001). Magnetic nanodot arrays produced by direct laser interference lithography. *Applied Physics Letters*, **79**, 2606–2608.

Zhou, J., Kashyap, A., Liu, Y., *et al*. (2004). Magnetization reversal and giant coercivity in Sm-Co/Cu-Ti particulate films. *IEEE Transactions on Magnetics*, **40**, 2940–2942.

FURTHER READING

Weller, D., Moser, A., Folks, L., *et al*. (2000). High Ku materials approach to 100 Gbits/in^2. *IEEE Transaction on Magnetics*, **36**, 10–15.

Advanced Magnetic Microwires

Manuel Vázquez
Instituto de Ciencia de Materiales, Madrid, Spain

1 INTRODUCING AMORPHOUS MAGNETIC MICROWIRES

Amorphous microwires, being among the softest magnetic materials, present outstanding peculiarities. Those with large and positive magnetostriction, exhibit bistable behavior with magnetization reversal through a giant Barkhausen jump originating in the propagation of a single-domain wall. On the other hand, microwires with vanishing magnetostriction show giant magnetoimpedance (GMI) effect. And both types show natural ferromagnetic resonance (NFMR) at microwave frequencies. Recently, a combination of fabrication methods has enabled the design of new bimagnetic multilayer microwire materials with novel properties, thus opening new generation of magnetic microwires. All these properties, and many others, make amorphous magnetic microwires very attractive for unique technological applications, and also provide opportunities for fundamental micromagnetic studies due mainly to their simple magnetic domain structure.

Magnetic microwires with disordered atomic structure belong to the large family of amorphous alloys. From the early development of amorphous metallic alloys, researchers have been looking to obtain amorphous microstructured materials with specific shapes and magnetic properties designed for applications, in particular, devices. Such developments have been running in a parallel way with the development of new techniques of fabrication. In this regard, for example, amorphous alloys are prepared, in the shape of ribbons, by rapid solidification techniques (usually directly labelled as metallic glasses), as thin films by sputtering methods, and as bulk materials, by optimized nonequilibrium techniques. Among these materials, amorphous thin films are readily integrated into thin-film and semiconductor technology but their magnetic character is not as soft as that of the others. Metallic glasses are commonly fabricated in ribbon form with specific applications in cores of small transformers or elements in sensor devices. For general information about amorphous alloys, the reader is referred to the chapter **Amorphous Alloys, Volume 4**. Here, we focus on a particular family of metallic glasses with cylindrical shape. What is actually an amorphous magnetic microwire? and what are the conditions determining their technically exciting behavior? Their same name provides the reader with a detailed description of the nature of microwires: *amorphous magnetic microwires*. Firstly, due to their ferromagnetic behavior, the largest energy term among magnetic interactions to be considered is *exchange coupling*. Secondly, their nature being structurally amorphous, magnetocrystalline anisotropy can be neglected so that *magnetoelastic anisotropy* plays a major role. And thirdly, their

Handbook of Magnetism and Advanced Magnetic Materials. Edited by Helmut Kronmüller and Stuart Parkin. Volume 4: *Novel Materials*. ISBN: 978-0-470-02217-7.

cylindrical symmetry induces a very characteristic magnetic *shape anisotropy*.

In fact, all of the above three factors are influenced by the *rapid solidification* method employed in the fabrication. Firstly, composition, as in other magnetic amorphous alloys obtained by melt spinning is mainly restricted to various FeCo-based alloys. Of particular relevance is the fact that the alloy composition determines the *magnetostriction* constant, λ_s. Secondly, the quenching technique determines the possibility to achieve amorphous structure, but in turn introduces unique distribution of strong internal *mechanical stresses*, σ. Thus, magnetostriction and stresses determine the strength of magnetoelastic anisotropy. And finally, the particular fabrication method determines the cylindrical shape. Here, for simplicity, we will consider the term *microwire* for kinds of amorphous and nanocrystalline wires with diameter ranging between 1 and 100 μm.

In summary, the magnetic behavior of amorphous magnetic microwires is determined by exchange interaction, plus shape and magnetoelastic anisotropy energy terms. Major scientific and technological relevance of amorphous alloy microwires are associated either with their characteristic single-domain structure determining their bistable behavior, or with their ultrasoft magnetic behavior in connection with the GMI effect.

Magnetic wires with polycrystalline structure have been fabricated by metallurgical procedures for many years with diameter from millimeter to hundred of microns. Typically, such procedures induce large mechanical stresses that, combined with the shape anisotropy, determine their magnetic response of interest in various sensing applications. In particular, the so-called Wiegand wires were introduced in the beginning of the 1980s exhibiting quite large Barkhausen jump that can be employed for pulse sensors (Wiegand, 1981).

The production of amorphous wires with diameter in the range of hundred microns was first enabled by the development of modified melt-spinning processes in the 1970s. The first successful method to produce amorphous wires, based on a process of liquid solidification into water, was developed by Kavesh (1976). There, the metallic molten alloy was directly injected into a confluent cooling fluid (normally water) with viscosity nearly equal to that of the molten alloy. The first work on the attractive magnetic behavior of such amorphous wires was reported by O'Handley (1975). Further development of quenching technique into rotating water was subsequently achieved in Japan by Ohnaka *et al.* (1982) and Masumoto, Ohnaka, Inoue and Hagiwara (1981) and particularly by technical researchers at Unitika Ltd, allowing the commercialization of amorphous microwires, produced in a continuous way, with a diameter restricted to around 100 μm. Relevant scientific work in the 1980s was performed by the researchers Mohri in Japan and Humphrey *et al.* (1987) in United States. In the 1990s, other groups have been actively involved in the research of these microwires particularly paying attention to preparation and structure characterization by Olofinjana and Davies (1992) in Sheffield, magnetic domain observation by Yamasaki (1992) and Yajako, Yamasaki and Humphrey (1993) in Kyushu, magnetic bistability by Mitra and Vázquez (1990) and Vázquez, Gómez-Polo, Chen and Hernando (1994) in Madrid, magnetoelastic behavior by Squire, Atkinson, Gibbs and Atalay (1994) in Bath, and other groups in Japan mainly involved in development of various sensor devices. Additionally, in 1994, the GMI effect was rediscovered in nonmagnetostrictive amorphous wires simultaneously by Panina and Mohri (1994) in Nagoya and Beach and Berkowitz (1994) in San Diego. Recent activities are mainly related to their adoption as sensing elements by several groups in Europe and particularly in Japan.

The story on the development of the amorphous microwires prepared by quenching and drawing method is even longer. These microwires covered by an insulating Pyrex coat are fabricated by a technique that, in essence, was introduced in the 1920s by Taylor (1924) in United States. After modifications of this method, first glass-coated microwires were prepared in the former Soviet Union in the 1950s by Ulitovsky (1957). First reports on such materials were dealing with their mechanical properties by Nixdorf (1967) in Germany and by Goto (1977) in Japan, and on magnetic properties by a number of researchers in former Eastern Europe (i.e., Schneider in East Germany, and Kraus in Checkoslovakia (Kraus, Schneider and Wiesner, 1976)). The interesting radar absorption properties attracted much interest in the Soviet Union during the 1980s, and the work was developed somehow independently by different groups in Kishinev, Moscow, and Leningrad. By the beginning of the 1990s, first reports in western journals were introduced by Chiriac in Romania and Vázquez in Spain (Chiriac, Pop, Barariu and Vázquez, 1994; Zhukov *et al.*, 1995) through their contacts with Larin and Torcunov in Amotec Ltd in Moldova (Baranov *et al.*, 1989). This interest was related to the fact that exhibiting similar outstanding properties as wires prepared by liquid quenching into water, they offered additional possibilities to be used as sensing elements due to their reduced diameter, ranging between 1 and 30 μm, and protecting insulating glass coating. Additionally, interest was also related to their real possibilities as outstanding materials at microwave frequencies derived from the so-called NFMR effect that make them attractive in radar absorption coatings or even as left-handed materials (LHMs).

From the original studies of the Russian school, other families of similar fibers have been investigated by a group in Montrèal leaded by Ström-Olsen, and then Yelon (Rodkowski *et al.*, 1995), or by Kraposhin in Saint Petersburg. Other works around Moscow have been reported by Shalyguina

(Moscow State University), Antonov (Theoretical and Applied Electrodynamics) and Usov (Troistsky Institute) in Moscow, and by Manov (Advanced Metal Technologies Ltd) in Israel.

Nowadays, various attempts are being performed to fabricate novel microwires with new or optimized properties. In this regard, the recent introduction of so-called multilayered microwires consisting of several cylindrical microlayers with different magnetic behavior offers promising perspectives owing to the observed biphase magnetic behavior of interest for the spin-valve-like magnetic or the asymmetric magnetoimpedance responses (Pirota *et al*., 2004). In parallel, latest attempts are focused on the preparation of magnetically harder, although structurally not amorphous, microwires by introducing anisotropic hard phases. All these attempts are related to the employment of new metallurgical or combined techniques. The present trends can be thus summarized considering the path of methods used to prepare microwire materials: from metallurgical traditional methods enabling the production 'typically' of millimeter diameter fibers, to the rapid solidification techniques for producing micrometric diameter wires, and, in the next stage leading probably to the controlled production of submicrometric and nanometric wires which require different fabrication procedures.

Specific international workshops and meeting have been devoted to amorphous microwires. The first one was organized by Unitika Ltd in London, 1991, chaired by Ogasawara and Humphrey. Next one was held in Albuquerque, New Mexico, in 1994 chaired by Hasegawa and Ramanan, and their proceedings appeared as a special issue of *IEEE Transactions on Magnetics* (1995). In 1999, Mohri organized a symposium at the University of Nagoya. Vázquez, González, Zhukov, and Gómez-Polo chaired in 2001 the International Workshop on Magnetic Wires in San Sebastián, Spain, the papers later appeared in a special issue of the *Journal of Magnetism and Magnetic Materials* (2002).

The general aspects of advanced microwires are described in this chapter to give the reader a general overview with a particular emphasis on the magnetization processes, in which lies the origin of their technological applications.

2 AMORPHOUS MICROWIRES: PRODUCTION AND PROCESSING

Magnetic alloys composition that can be produced with amorphous structure, similarly as for metallic glass ribbons, can be given as $TM_xM_{(1-x)}$ with x typically between 70 and 80%. Transition metals (TMs), Fe, Co, and Ni and their combinations determine the magnetic character. Many other TMs have been investigated, such as Ti, V, Nb, Ta, Cr, Mo, W, Mn, Pd, or Al (Hagiwara, Inoue and Masumoto, 1982). As for the metalloids, those typically considered are Si and B, although others such as C, P, Al, and so on, can be employed.

Intrinsic magnetic properties such as saturation magnetization or Curie temperature exhibit similar values as amorphous alloy in ribbon shape having the same composition. The technical magnetic behavior of microwires can be classified into three groups according to their magnetostriction, λ:

1. FeSiB alloys with large and positive magnetostriction (in the order of $1-3 \times 10^{-5}$).
2. FeSiBCuNb alloys with similar λ, but which notably reduces its value and eventually changes sign upon nanocrystallization process.
3. CoFeSiB alloys with balanced magnetostriction for the Fe/Co rate at around 5%.
4. CoSiB alloys with negative and slightly reduced magnetostriction $\lambda \approx -1 \times 10^{-6}$.

Mechanical or electrical properties are quite similar to those of amorphous ribbons. The reader is referred to review articles (Donald, 1987) for in-water-quenched wires and (Goto, 1980) for glass-coated microwires.

2.1 Fabrication techniques

General information about the fabrication of amorphous microwires can be found in Ogasawara and Ueno (1995) on in-water-quenched wires, (Zhukov *et al*., 2003) on glass-coated microwires, and (Ogasawara and Ueno, 1995; Hagiwara and Inoue, 1993) on both types of amorphous materials. Figure 1 shows views of the in-rotating-water-quenching (1a and 1b) and glass-coating (1c) units at ICMM/CSIC laboratories as well as a glass-coated microwire (1d).

2.1.1 In-rotating-water-quenching production technique

In this method, experimentally introduced and patented by Ohnaka (1980), a molten metal stream is ejected through the orifice of a quartz tube into a water layer formed by centrifugal force on the internal surface of a rotating drum. The equipment and the process itself essentially consists of the following elements and steps:

1. A *rotating drum unit*, typically 0.5 m diameter, which rotates at around 350 rpm. Owing to centrifugal force, water previously bombed at the drum forms a tiny layer approximately 2 mm deep onto its internal surface.
2. A *microwave coil heater* of the metallic mother alloy. This is previously prepared by pressing of powders and preheated for homogenization, or alternatively prepared

by arc melting. Such mother alloy is placed inside a vertical quartz nozzle tube having a small orifice, typically 0.1–0.3 mm diameter, at its bottom. The temperature of the molten alloy can be controlled by means of a thermocouple.

3. An *ejection system* of the molten alloy by argon overpressure, around 0.5 MPa, on the top quartz tube. Once the convenient temperature is reached, in the range between 1250 and 1300 °C, and with the help of a pneumatic system, the whole quartz tube is lowered so that the mentioned orifice gets quite close to the surface of the rotating water layer. This proceeds simultaneously to the injection of the argon overpressure so that a molten lead stream crosses the quartz orifice and plunges into water.
4. A *cooling system* that consists of the rotating water. The quenching rate is of the order of $10^5\,\mathrm{K\,s^{-1}}$.
5. A microwire *collector system*. Typically, a continuous production of several tens of meters can be produced at laboratory scale (depending on the weight of mother alloy). Then the drum stops and the microwire is collected manually. Commercial equipments incorporate an additional winding system to enhance the production of amorphous wire.

The quenching rate (about $10^5\,\mathrm{K\,s^{-1}}$) required to achieve amorphous structure restricts the diameter in a range typically from 80 to 200 µm. The production of a continuous wire is solved by controlling a number of fabrication parameters such as the following: (i) Diameter of the orifice at the bottom of the quartz tube; allowing for shrinkage during solidification, typically 3–4 vol%, this parameter determines the final wire diameter. (ii) Temperature of molten alloy. (iii) Argon overpressure. (iv) Distance from the orifice to water layer during injection. (v) Tangential velocity at the surface of the rotating drum and drum diameter itself. (vi) Ejection angle between the jet of molten metal and the rotating water layer.

2.1.2 Quenching and drawing procedure: glass-coated microwires

As introduced previously, this technique is based on early works by Taylor, Ulitovsky and others (Ulitovsky, 1957; Goto, 1977; Nixdorf, 1967; Kraus, Schneider and Wiesner, 1976; Donald, 1987; Ohnaka, 1980; Larin *et al*., 2002), and it has had an emerging interest in recent years. By this method, it is possible to fabricate composite microwires consisting of a metallic nucleus with diameter ranging between 1 and 30 µm and an insulating coating 2–10 µm thick (see Figure 1d). The main differences with previously described wires are (i) the smaller diameter of the metallic nucleus with interesting possibilities in miniaturization and (ii) the presence of the insulating coating, which offers protection against corrosion and electrical insulation, but also induces additional strong mechanical stresses to the nucleus.

The main steps of this process of fabrication (see Figure 1c) are as follows:

1. A *vertically moving system* with controlled velocity to ensure the continuous production, at around $400\,\mathrm{m\,min^{-1}}$, of microwire. This allows the vertical displacement of the Pyrex tube that contains the pellet of metallic mother alloy, previously prepared as mentioned earlier.
2. A *microwave coil heater* surrounding the Pyrex tube with the metallic pellet. It induces the melting of the metallic alloy, at 1200–1300 °C, which generates sufficient heating for practical melting of the Pyrex, or similar insulating glass. The metallic alloy and insulating external layer then remain as a very viscous melt.
3. A *drawing and quenching* system that essentially consists in a first starting manual process by which that viscous melt is drawn down. By this procedure, the melt rapidly solidifies into a metallic nucleus with surface Pyrex coating. This rapid solidification is enhanced by a running water jet allowing a quenching rate of about $10^5\,\mathrm{K\,s^{-1}}$. The solidified microwire gets down with a

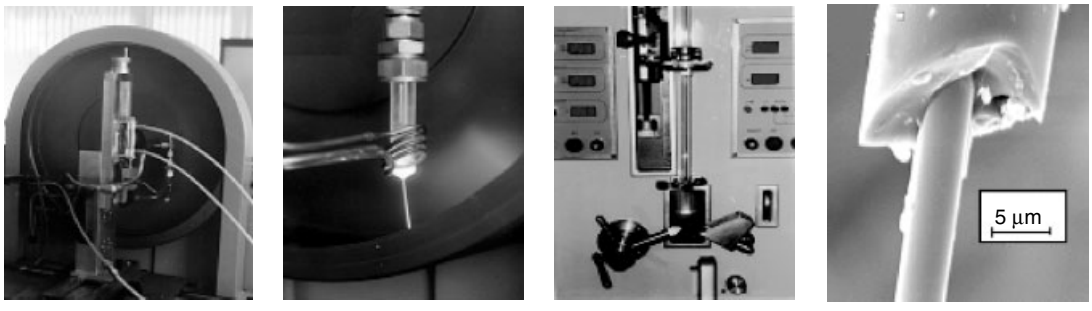

(a) (b) (c) (d)

Figure 1. In-rotating-water-quenching unit: general view (a), and during the melting process (b). Quenching and drawing unit (c) and glass-coated microwire (d).

total mass vertical displacement coupled to the vertical moving system.

4. A microwire *collector system*, enabling a continuous production of around 400 m min^{-1} with typically several kilometer-long microwire produced at laboratory scale. The system consists of a rotating cylinder collecting the drawn microwire whose rotating velocity is coupled to the vertical displacement mentioned above. It also has a lateral displacement to allow winding of several kilometers of microwires around a bobbin. Additionally, the continuous production of microwire is automatically controlled by a microwave sensor detecting the presence of microwire below the heater units.

A number of parameters determine the geometrical dimensions of the final microwire as, for example: (i) vertical drawing stress and velocity, (ii) insulating tube thickness (typically 0.5–2 mm), (iii) temperature of the melt, (iv) vacuum underpressure inside the Pyrex tube in order to control the diameter of the metallic core.

Usually, the insulating coating is made out of Pyrex, but other insulators as Ursan can be employed. Controlled tailoring of the coating thickness is also important as described later because of the different internal stresses induced in the nucleus during the fabrication process.

Finally, we should mention an alternative method developed by the group in Montréal (Ström-Olsen and Rudkowsky, Piotr, 1991). In this method, the rapid solidification method is based on the melt extraction from a continuous stream of liquid alloy. The molten material wets the edge of a fast rotating metallic wheel. The molten tip is placed under the center of the sharp edge of the wheel to wet symmetrically and finally extract small fibers. The surface below the line of contact transfers heat to the casting wheel and permits a thin layer of liquid to be pulled from the molten tip. The cross section of the fibers is nearly circular, with diameter in the range of 5–25 μm, while their continuous length may reach up to several meters.

2.2 Distributed mechanical stresses due to quenching

Different attempts have been performed to determine the complex distribution of internal mechanical stresses, σ_{int}, arising from the casting technique for both in-water-quenched and glass-coated microwires:

1. *In-water-quenched microwires:* Stresses are frozen in as a consequence of thermal gradient inside the wire during quenching. According to the classical theory of elasticity and considering that the cooling front corresponds to a cylindrical surface, there appears a thermal gradient in the radial direction (Boley and Weiner, 1990). A general assumption is that the cooling process takes place steeply in differential tubular shells inwards from the surface where the cooling rate should be higher. Complex stress distributions have been reported (Madurga and Hernando, 1990; Liu, Malmhäll, Arnberg and Savage, 1990; Costa and Rao, 1991; Velázquez *et al*., 1991). Essentially, three components of stresses: radial, σ_{r}, azimuthal, σ_ϕ, and axial, σ_{z}, appear being radially distributed. Whereas radial stress remains always tensile (positive) in character, circular and axial stresses change sign from tensile at the inner part to negative at the outer part having maximum value at the surface, so defining two main regions within the wires: the *inner core* and the *outer shell* where the interface remains at a radius $r \approx 0.7\,R$(R being the microwire radius). Some refinements of the stress distribution have been considered more recently, in order to account for the stresses around the axis of the wire (Chen *et al*., 2001), the result of which is given in Figure 2. Estimated average value of stresses is in the order of 50–100 MPa.
2. *Glass-coated microwires:* The case of glass-coated microwires is even more complex since now we have to consider the stresses arising from three different contributions: (i) *thermoelastic stresses* from the temperature gradient during quenching, which are essentially similar to those as for in-water-quenched microwires; (ii) *drawing stresses*, tensile in nature, originated by the extraction process; and (iii) stresses coming from the *different thermal expansion coefficients* of metallic nucleus and insulating coating.

Different authors have calculated the stress distributions. Baranov *et al*. (1989) considered that most stresses actually arise from the differential thermal expansion coefficients so

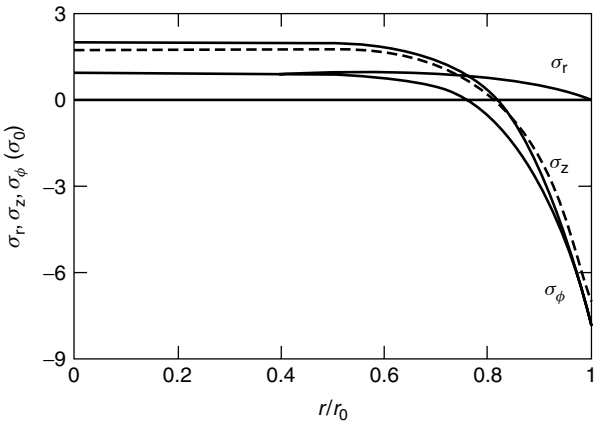

Figure 2. Radial distribution of stresses frozen in during quenching: radial, σ_{r}, azimuthal, σ_ϕ, and axial, σ_{z}. (Reproduced from D.-X. Chen *et al*., 2001, with permission from IEEE. © 2001.)

obtaining complex axial, σ_{zz}, radial, σ_{rr}, and azimuthal, $\sigma_{\phi\phi}$, stress contributions:

$$\sigma_{rr} = \sigma_{\phi\phi} = \frac{3E_r S_r}{(E_r + 3)\, S_r + 4}\varepsilon E_m$$
$$\sigma_{zz} = \sigma_{rr}\frac{(E_r + 1)\, S_r + 2}{E_r S_r + 1} \quad (1)$$

with $\epsilon = (\alpha_g - \alpha_m)\Delta T$, ($\Delta T$ being the temperature change), where $E_r = E_g/E_m$, $S_r = S_g/S_m$, and α denote, Young's modulus, cross section, and thermal expansion coefficient, respectively, and subscripts m and g indicate metallic and glassy coating, respectively. Other models (Chiriac and Ovari, 1996; Velázquez, Vázquez and Zhukov, 1996) consider all three origins for stresses. Nevertheless, the final distribution of stress depends on the prevailing relative contribution either from the drawing stresses or from the coating stresses arising from the differential thermal expansion coefficient. Average value of stresses in glass-coated microwires is of the order of 400–500 MPa.

2.3 Controlled processing: how to tailor properties

In a search to adjust to desired magnetic behavior, as-cast amorphous microstructure can be modified by mechanical, chemical, or thermal processing. Most noticeable methods are given in the following sections.

2.3.1 Cold drawing and chemical etching

These processes are aimed at the modification of the geometry of the microwires. Cold drawing was developed by Unitika Ltd and other groups in Japan (Malmhäll *et al*., 1987; Kakuno, Masuda, Yamada and Mochida, 1987) with a final objective of reducing the diameter of such amorphous wires in order to miniaturize the sensing elements made out of such materials. The diameter of the wires is reduced continuously step by step through a large number of drawing processes. In this way, the microwire diameter can be reduced from around 120 µm down to typically 30 µm. Although the amorphous microstructure is maintained, strong mechanical inelastic stresses are induced by this process which usually hardens its magnetic behavior. Cold-drawn microwires are subjected subsequently to thermal processing that reduces such stresses, thus recovering and even optimizing the soft properties of precursor microwires.

Glass coating of microwires can be either fully or partially reduced by suitable chemical etching (Chiriac, Pop, Bararíu and Vázquez, 1994; Zhukov *et al*., 1995; Catalán *et al*., 1997; Chiriac, Ovari, Marinescu and Nagacevschi, 1996). Diluted acids (i.e., HF, HCl, and others) are employed to proceed with a careful coating removal, which also modifies the stress state of the metallic nucleus resulting in a significant magnetic softening.

2.3.2 Inducing particular short-range ordering: thermal annealing

Amorphous microstructure can be modified by different thermal processes which relax and induce particular short range ordering (Fujimori, 1983; Hernando and Vázquez, 1993; Nielsen, 1985). Further information can be found in the chapter corresponding to amorphous ribbons. For amorphous microwires, simple thermal treatments at low temperatures result in a relaxed more stable amorphous microstructure with partial annihilation of structural defects and significant reduction of the mechanical stresses induced during the quenching fabrication process.

On the other hand, thermomagnetic annealing gives rise to internal stress relaxation and, when annealing below the Curie point, it induces short range ordering with an associated induced magnetic anisotropy with easy magnetization direction lying along the orientation of the field during annealing. The thermal treatment can be done either in a conventional furnace or by current annealing, making an electrical current flow along the microwire. In the latter case, it generates a circumferential field and a circular induced anisotropy by itself when the current is not high enough to overcome the Curie temperature of the alloy. Finally, thermomechanical annealing also induces noticeable anisotropies as for the case of amorphous ribbons. Experimental results concerning all these types of annealing for in-water-quenched microwires and on glass-coated microwires can be found in Gómez-Polo and Vázquez (1993), Zhukov *et al*. (2000) and Zhukov (2006).

3 AXIAL MAGNETIZATION PROCESS AND MAGNETIC BISTABILITY

All the outstanding magnetic characteristics of amorphous microwires and particularly their magnetization processes derive from the unique stress distribution and from the magnetostriction constant, in turn determined by the alloy composition. The corresponding magnetoelastic anisotropy together with the shape anisotropy determines the magnetization process for each type of microwires. A number of review papers dealing with magnetization process of in-water-quenched (Humphrey *et al*., 1987; Vázquez and Chen, 1995; Squire, Atkinson, Gibbs and Atalay, 1994), and glass-coated microwires (Vázquez and Zhukov, 1996; Chiriac and Ovari, 1996; Vázquez, 2001a; Zhukov, 2002)

have been previously reported. Here, most important characteristics are collected and the latest results introduced and discussed. In this first section, we analyze the magnetization process of magnetostrictive microwires exhibiting bistable behavior and its consequences.

3.1 Domain structure and axial hysteresis loops of Fe-based magnetostrictive microwires

3.1.1 Axial hysteresis loops and main domain structure

General information about the distribution of magnetization in the wire can be straightforwardly extracted from combined information from axial loops and domain observation (see Figure 3). The low-frequency low-field longitudinal hysteresis loop of Fe-based microwire, prepared by the techniques described previously, is astonishingly simple. It takes a square shape with a single giant Barkhausen jump at switching field of around 5–30 A m^{-1} for in-water-quenched and glass-coated microwires, respectively. From this simple experimental fact and assuming a domain wall displacement magnetization process (confirmed by additional experiments), we can derive some important information: the axial magnetization reversal takes place by the displacement of *a single-domain wall*.

Complementary information can be obtained from magnetic domain observation in the case of in-water-quenched microwires (i.e., by magnetooptic Kerr effect, or Bitter technique) (Reininger, Kronmüller, Gómez-Polo and Vázquez, 1993): at the surface, domain patterns are relatively complex with a number of zigzag walls denoting some complex distribution of magnetization direction at that region. In turn, the domain structure of the inner part is much simpler as observed after careful polishing of the microwire: at zero field, no domain wall can be detected indicating the homogeneous distribution of magnetization in a large single domain axially magnetized.

At higher applied fields (not observed in Figure 3), magnetization process takes place in a nearly reversible way until approaching magnetic saturation at fields of the order of units or tens of kiloamperes per meter for in-water-quenched and glass-coated microwires, respectively. In fact, for in-water-quenched wires, remanence, M_r, to saturation magnetization, M_s, squareness ratio, $m_r = M_r/M_s$, is nearly $m_r \approx 0.5$ (see Figure 4a) (for an analysis of the correlation between remanence and fractional volumes of core and shell, see Fujimori, 1983; Hernando and Vázquez, 1993; Nielsen, 1985). This

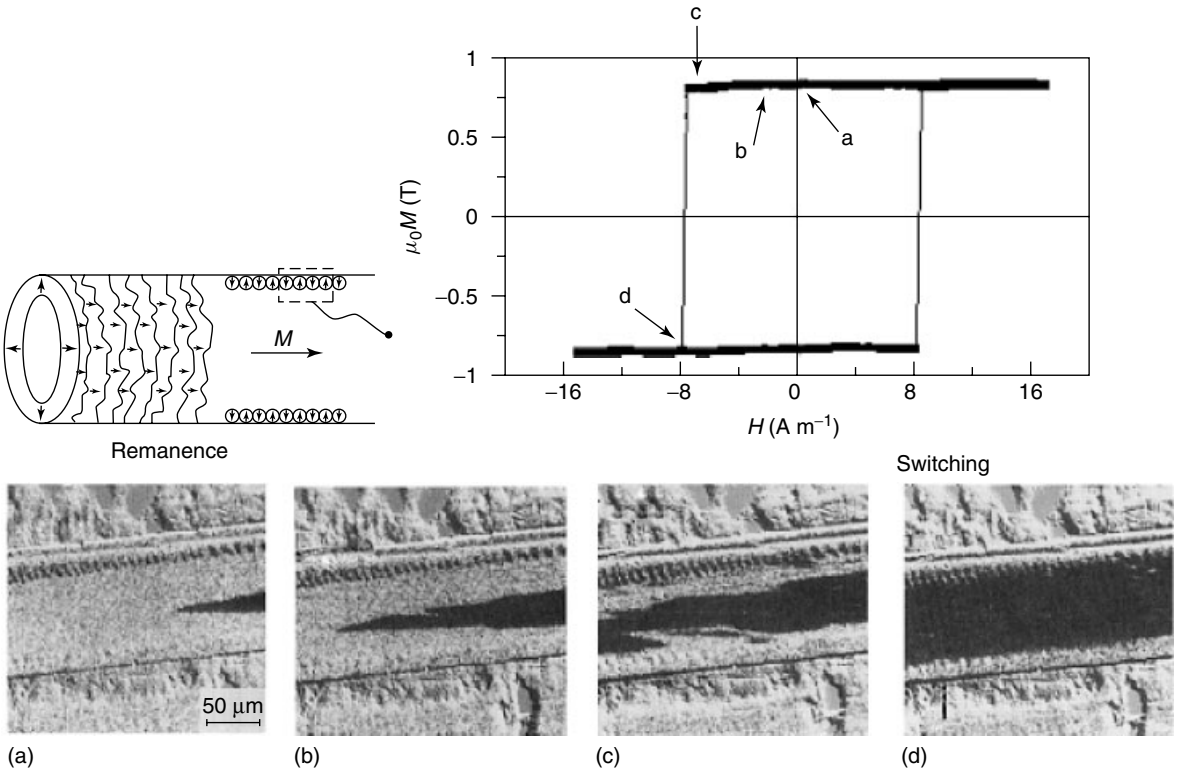

Figure 3. $Fe_{75}Si_{15}B_{10}$ in-water-quenched microwire: correlation between low-field bistable hysteresis loop (top right) and main domain structure (schematic view, top left). Evolution of inner core domain between remanence and switching, as observed by Kerr effect, during magnetization reversal (bottom). (Reproduced from T. Reininger *et al.*, 1993, with permission from American Institute of Physics. © 1993.)

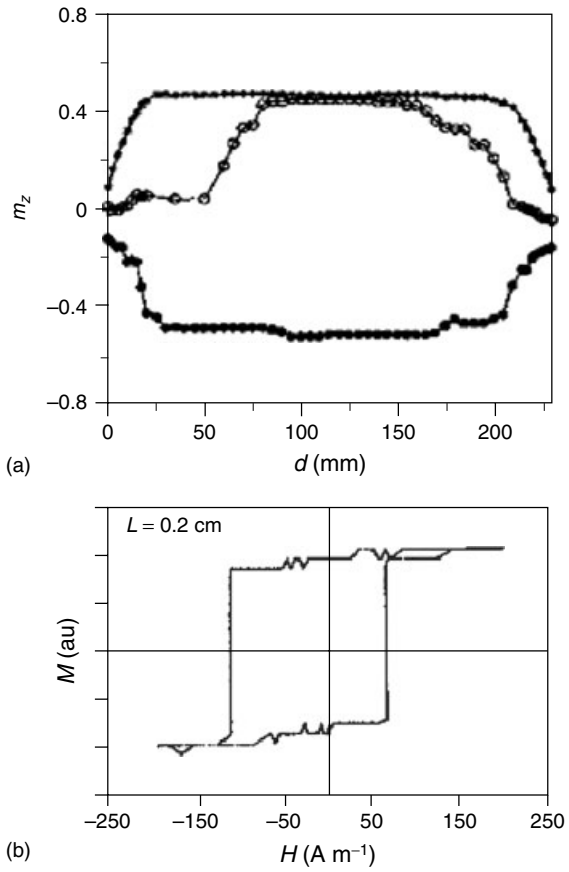

Figure 4. (a) Magnetization profile at the remanence (*), just before (○) and after (●) switching for an Fe-rich amorphous wire (a). (Reproduced from M. Vázquez *et al*., 1995, with permission from IEEE. *copyright* 1995.) The evidence of bistability in glass-coated Fe-rich wires in samples of very short lengths (b). (Reproduced from M. Vázquez *et al*., 1996, with permission from Elsevier. © 1996.)

indicates that the fractional volume involved in the giant Barkhausen jump, that is, the inner core is nearly one-half of the wire and, consequently, its radius is $r \approx 0.7\,R$ (note that this corresponds to the distance to the wire axis in Figure 2 where axial stress is no longer predominant). The outer shell consists of a multidomain structure with magnetization radially oriented and additional closure structures at the very surface (see schematic view in Figure 3), all of that magnetizing reversibly at high field. This is consistent with the distribution of stresses obtained in the previous section. From its analysis, we conclude that the easy magnetization direction from magnetoelastic origin is axial at the core where axial tensile stresses dominate. At the shell, maximum stresses are azimuthal and axial and their compressive character in the surface of the wire results in a Poisson contraction and radial easy axis. This radial easy axis, in competition against the transverse demagnetizing field, gives rise to the complex domain structure at the surface of microwires, as schematically drawn in Figure 3.

The case of glass-coated microwires is very similar, although the domain structure is much more difficult to observe owing to their reduced dimension. Figure 4(b) shows how the bistability is preserved in glass-coated microwires even at very short sample lengths.

3.1.2 Fine domain structure of microwires

Finer domain structure at the inner part of in-water-quenched microwires has been thoroughly studied by Yamasaki (Mitra and Vázquez, 1990; Vázquez, Gómez-Polo, Chen and Hernando, 1994). A careful polishing of microwires allows one to observe a finer domain structure at the border between core and shell.

Closure domain structures also appear at the ends of microwires to reduce the large magnetostatic energy associated with magnetic charges that would otherwise appear (Vázquez, Gómez-Polo and Chen, 1992; Gómez-Polo, Vázquez and Chen, 1993). This fine domain structure has been directly observed by magneto-optic Kerr effect and Bitter technique in in-water-quenched microwires (Reininger, Kronmüller, Gómez-Polo and Vázquez, 1993; Vázquez, Gómez-Polo and Chen, 1992; Gómez-Polo, Vázquez and Chen, 1993; Vázquez, Theuss and Kronmüller, 1999) (see Figure 3, bottom). The existence of those closure structures is also derived from the profiles of magnetization and susceptibility close to the ends in both types of microwires. Figure 4(a) shows the reduced-remanence regions at the ends of the wire. Such reduction is ascribed to the closure structures (note those enlarged regions just before the switching) (Vázquez, Theuss and Kronmüller, 1999; Zhukova, Usov, Zhukov and González, 2002). The length of such closure structures is of about 3 cm and 1 mm for in-water-quenched and glass-coated microwires, respectively, that gives us a hint of half the minimum length of microwires to observe bistable magnetic behavior: around 6 cm and 2 mm for in-water-quenched and glass-coated Fe-rich microwires, respectively. The loop for a 2-mm-long glass-coated microwire is shown in Figure 4(b). Figure 5(a) shows the hysteresis loop for a 5-cm-long in-water-quenched microwire that now consists of two Barkhausen jumps. This indicates that the inner core at its center is not a single-domain structure, which is confirmed by the corresponding domain structure (after careful polishing) showing the presence of two antiparallel domains (Figure 5b).

3.2 Bistable reversal mechanism and its dynamics

The very existence of the closure structure at the microwire ends is very important for understanding the magnetization

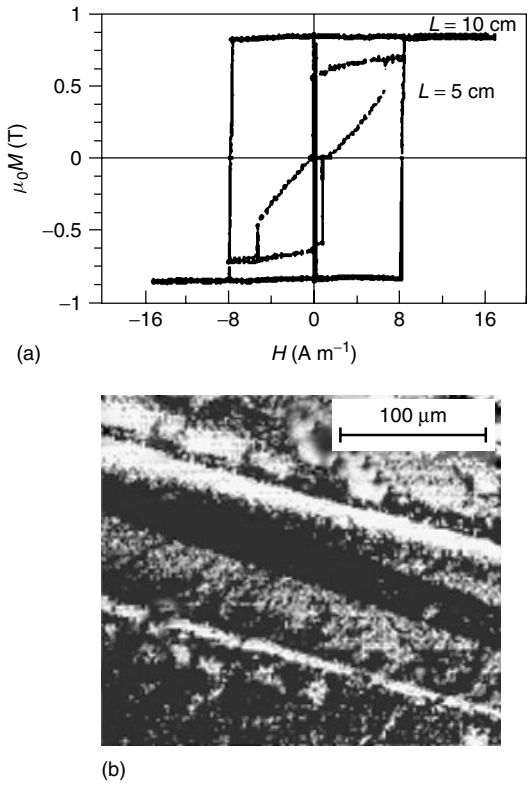

Figure 5. Hysteresis loops for a 10- and 5-cm-long wires (a), and the domain structure of a microwire shorter than the critical length for bistability (b). (Reproduced from T. Reininger *et al*., 1993, with permission from American Institute of Physics. © 1993.)

reversal process under homogeneous axial field. At the bottom of Figure 3, a set of images shows the domain structure at 1-cm distance from the end of a microwire between the remanence and the switching: at the inner core, there is a main single domain (light) and the tip of a closure domain. At the left, only the expanded closure domain (dark) can be observed. As the reverse applied field increases, the closure domain structure increases in size. At a given applied field, the energy stored at the main domain becomes large enough so that, the magnetic configuration becomes unstable and a single wall depins from the closure structure and propagates along the wire until reaching the closure structure at the opposite end. Note that the enlargement of the closure domain before the switching is not detected in the hysteresis loop of Figure 3(a) because the tiny coil is placed at the center of the wire. A simple expression for the switching field, H_{sw}, is

$$H_{sw} \sim [1/(\mu_0 M_s \nu_{cr})](\alpha E_\gamma + \beta E_{sf}) \qquad (2)$$

where E_γ denotes the wall energy and E_{sf} is the stray field energy from the charges at the wire end, ν_{cr} is the fractional volume of the enlarged closure structure at the depinning, and α and β are geometric parameters. The general mechanism of reversal can be seen as nucleation of reverse domain plus depinning and propagation of a single wall, with the particularity, as discussed later, that the reverse domain may exist at any finite field.

The magnetization reversal process and its dynamics has been studied in several works for the two types of microwires from the early work by O'Handley (1975). More recent studies are connected with the investigations on the closure structures at the wire ends for in-water-quenched microwires (del Real *et al*., 1993; Chen, Dempsey, Vázquez and Hernando, 1995), and glass-coated microwires (Zhukov, 2001; Neagu *et al*., 2001a). It was firstly shown that evolution of the reversal process was unidirectional irrespective of the initial remanent state, possibly owing to the slightly different closure structures at each end (Vázquez, Gómez-Polo and Chen, 1992; Gómez-Polo, Vázquez and Chen, 1993). Experimental methods similar to those of Sixtus and Tonks, in which a long solenoid drives the magnetization drives the magnetization process and two peak-up coils where peak signals are induced upon the passing of the propagating wall. A careful analysis of the symmetric shape of the induced peaks (see Figure 6a) revealed that the shape of the wall is rather quasiplanar not only for in-water-quenched (del Real *et al*., 1993; Chen, Dempsey, Vázquez and Hernando, 1995) but also for glass-coated microwires (Varga, García, Vázquez and Vojtanik, 2005) (note that the time constant of the circuit should be shorter than the peak width). Moreover, from the width of the induced peaks it is also possible to deduce the length of the wall to be of the order of few centimeters and millimeters for in-water-quenched and glass-coated microwires, respectively.

The motion equation of the wall during propagation can be written as

$$m\frac{d^2x}{dt^2} + \beta\frac{dx}{dt} + \alpha x = 2\mu_0 M_s H \qquad (3)$$

where β represents the damping coefficient, m is an effective mass of the wall, α the restoring force constant, and $2M_sH$ the driving force supplied by the applied field. Once the wall propagates at constant velocity, equation (3) reduces to $v = (2\mu_0 M_s/\beta)(H - H_0)$, where H_0 is generally taken as the critical propagation field. The velocity of the wall is thus experimentally deduced from the flight time between those two peaks. Figure 6(b) shows the evolution of the wall velocity, v, with the applied field, H, for a range of measuring temperatures. For large enough field, $H \geq H_{sw}$, the velocity increases as expected linearly with the applied field and the switching field, H_{sw}, depends on the measuring temperature. Note the high speed of the propagating wall reaching up to 500 m s^{-1} at applied fields of 200 A m^{-1}.

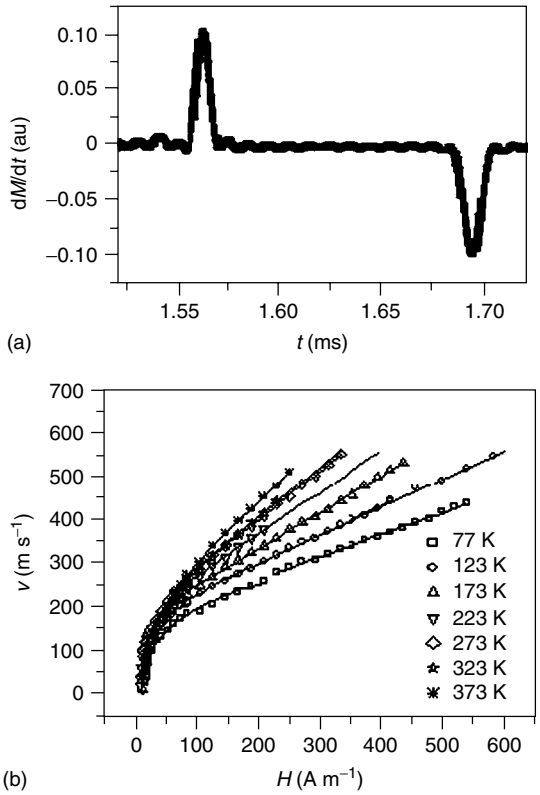

Figure 6. Induced peaks at two coils during wall propagation for a Fe-based glass-coated microwire (a). (Reproduced from L. Sampaio *et al*., 2000, with permission from the American Physical Society. © 2000.) Dependence of the propagating wall on constant applied axial field during propagation for a range of indicated temperatures (b). (After Varga *et al*., to be published.)

A first astonishing fact is that the extrapolation of that linear behavior to zero velocity gives a negative field. According to classical nucleation–propagation theory, square loops are obtained when nucleation field, H_n (typically provided by an extra local exciting coil), is larger than the propagation field, H_p, so that, once the reverse domain is formed, it immediately enlarges and propagates along the entire microwire ($H_n > H_p$): the propagation field is the linear extrapolation value to zero velocity, while the switching field corresponds to the nucleation field. In the present case, something singular happens, at negative fields the closure structures at the ends of the wire existing to reduce the stray fields energy play the role of the reverse domain, but a wall does not depin and propagates until reaching the propagation or switching field. Thus, we reach a reversal mode of square loop by which a reverse domain is first nucleated even at negative applied field but does not move until reaching the propagation field ($H_p > H_n$): the extrapolated figure corresponds to an effective nucleation field while the switching field corresponds to the propagation or depinning field.

Further studies on the domain wall dynamics in glass-coated microwires in the low-field regime have been performed in order to obtain deeper information. As observed in Figure 6(b), in the low-field regime, a nonlinear behavior is observed whose analysis has allowed one the experimental confirmation of the scaling behavior of the single-domain wall propagating on large distance (Varga *et al*., to be published). Three regions can be then distinguished for the propagating wall: (i) Below some critical field, H_{cr}, the domain wall is pinned at the wire end; (ii) just above that field, the domain wall propagates in the adiabatic regime, interacting with the defects during its propagation, with an average velocity that scales as $v \sim (H - H_{cr})^q$, with q the scaling factor; and (iii) at higher fields, $H > H_{sw}$, the domain wall propagates in the viscous regime and its average velocity is proportional to the applied magnetic field as considered above. The scaling law is an universal law valid on a wide range of scales where crackling noise is detected: from meter (earthquake-tectonic plates rub past one to another), decimeter (movement of the car on the landscape full of holes), centimeter (splitting the piece of paper), millimeter (drop of the water moving around the dirty glass) down to the micrometer scale for the domain wall movement or for dislocation propagation under small tension (Sethna, Dahmen and Myers, 2001; Zapperi, Castellano, Colairoi and Durin, 2005; Nakatani, Thiaville and Miltat, 2003). Fitted values of scaling factor to experimental results are close although not exceeding 1/2, and they reflect the correlation length of the domain wall with the defects (the lower the q, the longer is the correlation length).

With regard to the damping of domain wall motion, two mechanisms are commonly considered (O'Handley, 1975; del Real *et al*., 1993; Chen, Dempsey, Vázquez and Hernando, 1995): eddy current and spin relaxation. An additional contribution from structural relaxation/spin origin has been recently experimentally and theoretically introduced (Varga, García, Vázquez and Vojtanik, 2005). A general expression for the temperature dependence of damping coefficient β has been then proposed as the sum of eddy current, β_e, spin relaxation, β_r, and interaction with the mentioned defects, β_s, damping mechanisms:

$$\beta = \beta_e + \beta_r + \beta_s = \frac{k_1 M_s(T)^2}{\rho(T)} + k_2(M_s(T)^3(1 + r\Delta T))^{1/2} + k_3\frac{\tau}{T} \qquad (4)$$

where k_1 is a geometrical parameter, k_2 is proportional to mechanical stresses induced during fabrication, σ_r, and k_3 reflects the interaction between the wall and local structural defects, ρ is the resistivity, $r \approx E(\alpha_g - \alpha_m)/\sigma_r$, and τ the relaxation time.

3.3 Magnetoelastic effects

3.3.1 Influence of applied tensile, torsional, and bending stresses

Magnetoelastic anisotropy plays an important role owing to the relatively high magnetostriction, λ_s, of Fe-based amorphous microwires, of the order of $1-3 \times 10^{-5}$. The application of mechanical stress induces an extra magnetoelastic anisotropy with energy density $K_{m.elas} = (3/2)\lambda_s \sigma_{ap}$ that reinforces or balances the anisotropy arising from stresses frozen in during fabrication. In the case of applied tensile axial stress, it is observed that the remanence increases continuously until saturation as a consequence of the increase of the fractional volume of the inner core with axial easy direction at the expense of the outer shell. This evolution supplies complementary information on the distribution of the internal stresses at the shell. For example, the applied stresses at which remanence saturates are of the order of 100 and 400 MPa for in-water-quenched and glass-coated microwires, respectively.

From equation (2), a simple expression can be derived for the dependence of the switching field on applied stress, σ_{ap}, (Severino, Gómez-Polo, Marín and Vázquez, 1992):

$$H_{sw} = \gamma \sqrt{\lambda(\sigma_{ap} - \sigma_r)} - \mu_0 N_{eff}(L) M_s \qquad (5)$$

where γ is a parameter containing mainly geometrical factors, and the effective demagnetizing factor N_{eff} is a function of the length-to-diameter ratio of the wire. Actually, H_{sw} is determined by a term proportional to the energy stored in the depinned wall which is proportional to the applied stress.

The fitting of that expression to experimental results is very reasonable as observed in Figure 7(a) for several microwires with different lengths (Severino, Gómez-Polo, Marín and Vázquez, 1992). At low applied tensile axial stress, it balances internal stress in the outer shell which reduces the energy stored in the wall and the switching field according to equation (5). Note also, that for the shortest microwire, bistability is only observed after applying large-enough stresses. When applied and internal stresses nearly balance each other, and the effective demagnetizing field becomes more important, the formation of a number of walls is possible. This hinders the formation of a large domain and consequently the observation of bistable behavior.

Application of torsional stresses induces distributed tensile and compressive stresses following a helical path at 45° with the wire axis. Figure 7(b) shows the domain structure of an in-water-quenched wire subjected to torsional stress, where the helical path denotes the easy magnetization direction at 45° (Hernando *et al*., to be published). Torsional

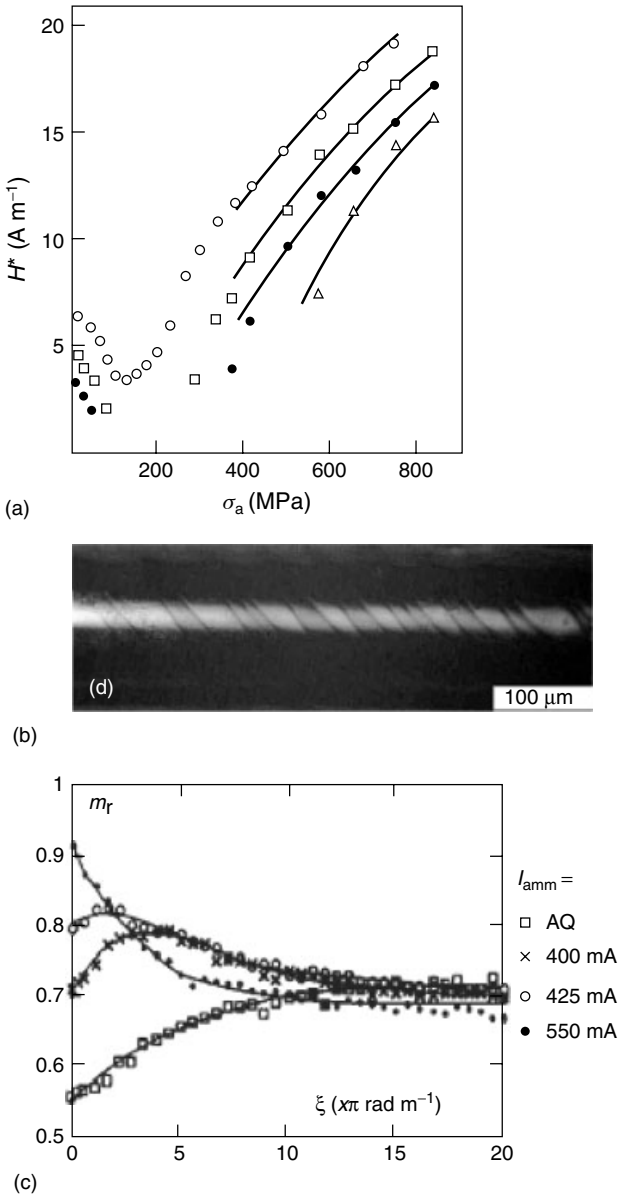

Figure 7. Dependence of switching field on applied tensile stress for a FeSiB in-water-quenched microwire (length = 12, 9.9, 8.4, and 6 cm) (a). (Reproduced from A.M. Severino *et al*., 1992, with permission from Elsevier. © 1992.) Bitter image of the domain structure at the surface of a torqued microwire (after Hernando *et al*., to be published), and torsional dependence of remanence for a bistable Fe-based microwire (b). (Reproduced from M. Vázquez *et al*., 1991, with permission from Elsevier. © 1991.)

stress, $\tau = \mu \xi r$, with μ the shear modulus, and ξ the angular displacement per unit length, induces inhomogeneous stresses so that, the corresponding magnetoelastic anisotropy is given by:

$$K_{m.elas}(r) = \frac{3}{2}\lambda_s \mu \xi r \qquad (6)$$

One should also consider the different response to applied torsion of the inner core and the outer shell because each region exhibits a different internal magnetoelastic easy axis. Upon twisting, ξ, the magnetization rotates toward the helix at 45° from the axial direction in the core and from the transverse direction at the shell. For large enough torsion, the magnetization orientates along the helical direction in the whole microwire, resulting in a reduced remanence of $m_r = 0.7$. An expression for the evolution of reduced remanence, $m_r = M_r/M_s$, with torsion has been proposed elsewhere (Vázquez *et al*., 1991; Chiriac *et al*., 1997) considering the evolution of the fractional volumes of the core and the shell with applied torsion as well as that of the magnetization direction in each region:

$$m_r = \frac{1}{\sqrt{2}} v_{os} \left(\frac{K_\tau}{K_{os}} \right) + \frac{1}{\sqrt{2}} v_{ic} \left[1 + \left(1 + \frac{K_\tau^2}{K_{ic}^2} \right)^{-1/2} \right] \quad (7)$$

Where K_τ, K_{ic}, and K_{os} denote the average magnetoelastic anisotropy constant induced by torsion, and those internally at the inner core and the outer shell, respectively, and v_{ic} and v_{os} are the fractional volumes of the core and shell, respectively. The experimental evolution with applied torsion is fitted to that expression, as observed in Figure 7(b), for a series of microwires that have been thermally treated inducing variations of the fractional volumes.

Applying bending stresses gives rise to distributed tensile and compressive stresses for convex and concave curvature regions of the wire, respectively. For the convex region with tensile component, the magnetization easy axis parallel to the wire axis is reinforced, while the compressive stress at the concave region induces a transverse easy axis. For large enough bending (small radius of curvature) the domain structure consists of an asymmetric inner core with axial magnetization and the residual region with transverse easy axis (Vázquez, Gómez-Polo, Theuss and Kronmüller, 1996; Vázquez, Gómez-Polo, Velázquez and Hernando, 1994). That asymmetric core is then responsible for the bistable behavior in bent microwires (Figure 8).

3.3.2 Thermally induced stresses in glass-coated microwires

An expression for the stresses induced during the fabrication in glass-coated microwires by the coating is given in equation (1). The strength of their effect on the magnetic behavior of microwires can be straightforwardly derived by comparing hysteresis loops (see Figure 9) for microwires with different metallic radius to total radius ratio, $\rho = r_{met}/R_{tot}$

Glass coating plays an important role to determine stresses not only in the as-prepared state, but also as a source of additional stresses when the measuring temperature is modified owing to the different thermal expansion coefficients, α_m and α_g, of metallic nucleus and glass coating, respectively (Vázquez *et al*., 2004b, 2006b). A general expression for the stresses arising from the coating and induced by a temperature change, ΔT, is

$$\sigma(T) = E(\alpha_g - \alpha_m)\Delta T + \sigma_r \quad (8)$$

where σ_r denotes the internal stresses induced during fabrication. An estimation of the effective thermally induced tensile stresses when decreasing temperature down to around 10 K is of the order of 200–300 MPa (Vázquez *et al*., 2004b, 2006b).

Recently, experiments have been performed to evaluate the temperature dependence of the switching field and its fluctuations in glass-coated microwires. In fact, previous studies were reported on the jitter of induced pulses by the reversal of magnetization that in principle should be avoided for technological purposes (Mohri, Humphrey, Yamasaki and Okamura, 1984; Zhukova *et al*., 2002). Figure 10(a) shows the distribution of the switching field as a function of temperature. It can be observed that not only the average switching field but also the width of the distribution decreases with increasing temperature. Such studies have allowed us to evaluate the contributions to the switching field: the magnetostrictive term (mostly relevant at high temperatures and containing the temperature dependence of magnetostriction and that of coating stresses), and the structural fluctuations term (relevant at low temperatures as indicated for the damping parameter) (Varga, García, Vázquez and Vojtanik, 2003, 2005; García, Varga and Vázquez, 2005).

The fitting to this temperature dependence has been done considering the magnetoelastic and structure contributions (see Figure 10b). Note that temperature dependence of magnetoelastic term arises from that of mechanical stresses induced by the coating, and from the magnetostriction. The switching field can be then expressed as (Varga, García, Vázquez and Vojtanik, 2003; García, Varga and Vázquez, 2005):

$$H_{sw} = p\left\{\left[\alpha(x)M_s^3(T) + \beta(x)M_s^2(T)\right](1 + r(\Delta T))\right\}^{1/2} + \frac{nG(T,t)}{M_s(T)} \quad (9)$$

where p is a constant, $r \approx E(\alpha_g - \alpha_m)/\sigma_r$, α and β the relative contributions to magnetostriction from single-ion and two-ion mechanisms, $\lambda(T) = \alpha M_s^3(T) - \beta M_s^2(T)$, n is the density of structural defects interacting with the propagating wall, and G is a relaxation function with relaxation time τ. It should be mentioned that the magnetostriction is sensitive not only to modification of temperature but also to applied mechanical stresses and to thermal treatments in

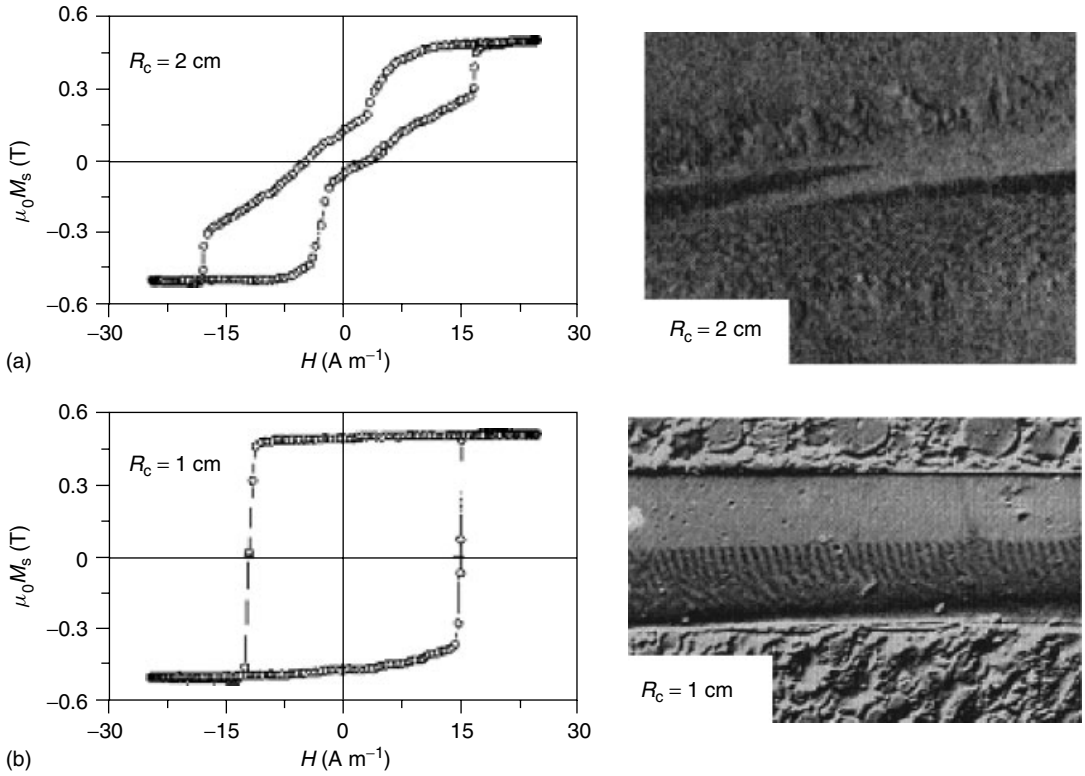

Figure 8. Hysteresis loops and corresponding domain structure images observed by Kerr effect of a 10-cm-long Fe-rich bent mirowires with radius of curvature $R_c = 2$ cm (a) and $R_c = 1$ cm (b). (Reproduced from M. Vázquez *et al.*, 1996, with permission from Elsevier. © 1996.) Note the reappearance of bistability in strongly bent wire.

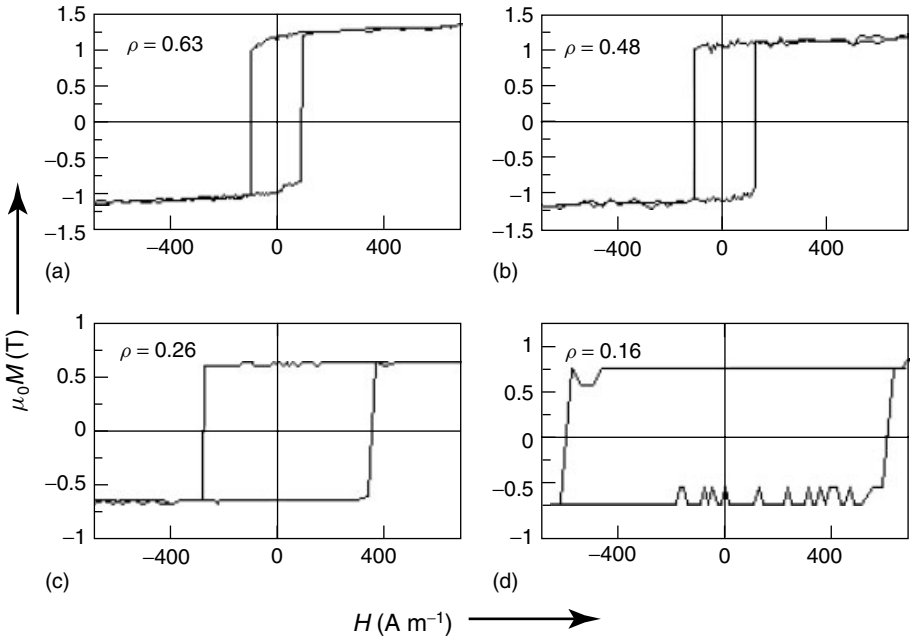

Figure 9. Hysteresis loops for glass-coated microwires as a function of the ratio metallic to total diameter, $\rho = r_{met}/R_{tot}$. (Reproduced from M. Vázquez *et al.*, 1996, with permission from Elsevier. © 1996.)

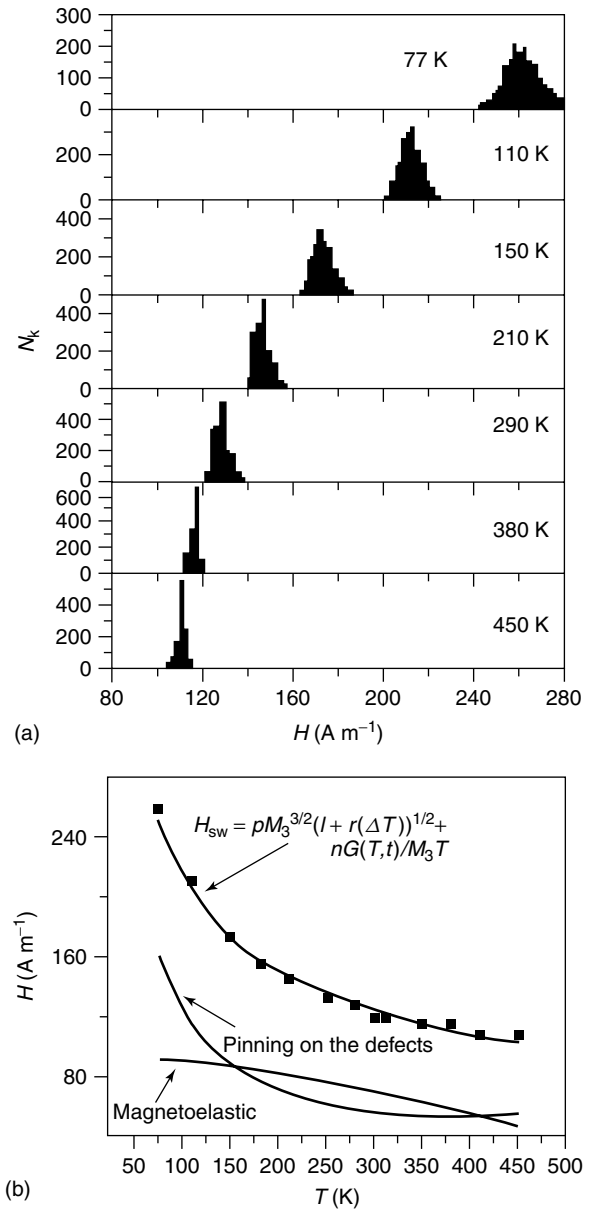

Figure 10. Temperature dependence of fluctuating switching field of glass-coated microwire (a), and of fitted contributions to its average value (b). (Reproduced from F. Castaño *et al*., 1999, with permission from the American Institute of Physics.)

a similar way as amorphous ribbons (Zhukov *et al*., 2003; Barandiarán *et al*., 1987). Such changes, $\Delta\lambda$, can reach values up to 10^{-7} so that, they are relevant for Co-base non-magnetostrictive alloys.

3.3.3 Magnetoelasticity and elastic moduli

Applied magnetic fields produce magnetostrictively induced deformation that gives rise to modification of effective elastic Young and shear *moduli* of magnetostrictive microwires, and to variations of the sound velocity. Several reports have been published on magnetoelastic properties related to ΔE effect and sound velocity effect for both types of microwires, where the role played by thermal treatments and/or the application of stress is shown (Squire, 1994; Kakuno, Masuda, Yamada and Mochida, 1987; Chiriac *et al*., 2000). The induced torsional deformation has also been reported where dc axial and ac circular field were applied simultaneously (Velázquez *et al*., 1995; Navarro, Garcia-Beneytez, Vázquez and Hernando, 1996). Forced and free oscillations are detected for the torsional magnetoelastic resonance where resonant peaks at given frequencies are accounted for by considering the existence of two main domain regions, and its connection to the variations of shear modulus. Complex bifurcation modes have also been detected.

3.3.4 Field-induced rotation of magnetostrictive wires

Exciting a vertically standing Fe-based microwire with a longitudinal ac field (of the order of kilohertz frequency), supplied by a solenoid or coil, results in spontaneous rotation of the wire with frequency of the order of units or tens of hertz. Such a rotation is only observed for given values of the exciting field frequency (see Figure 11a), and the most important characteristics of this unusual effect recently rediscovered in bistable amorphous microwires (Chiriac, Marinescu and Ovari, 1997; Castaño *et al*., 1999; Sugino, Takezawa, Honda and Yamasaki, 2001) are as follows: (i) It is observed for different types of wires (even ribbons) with amorphous or polycrystalline microstructure (e.g., until 3-mm-diameter commercial Ni cylindrical rods (Luna, Raposo, Rauscher and Vázquez, 2002). (ii) A minimum threshold field amplitude is needed for proper rotation the sense of which depends in a complex way on the field itself. (iii) Typical rotation frequency of microwire is of the order of units or tens of hertz, much lower than that of the exciting field, and it depends on mechanical friction to the capillary or tube surrounding the wire. (iv) Such rotation can be accompanied by levitation of the wire, when allowed by the sustaining force from the gradient field acting exerted by the exciting coil (see Figure 11b).

The origin of this phenomenon is quantitatively not well known, but it must be connected with the magnetostrictive character of the samples because the only requirement to be observed is a sufficiently large value of magnetostriction of the wire. Apparently, longitudinal vibrations of the wire, induced by the magnetostrictive elongations due to the exciting field, transform into coherent rotation through the friction with the surrounding tube or capillary. This phenomenon exhibiting some peculiar characteristics related to lack of symmetry and chaos as well as a kind of magnetic

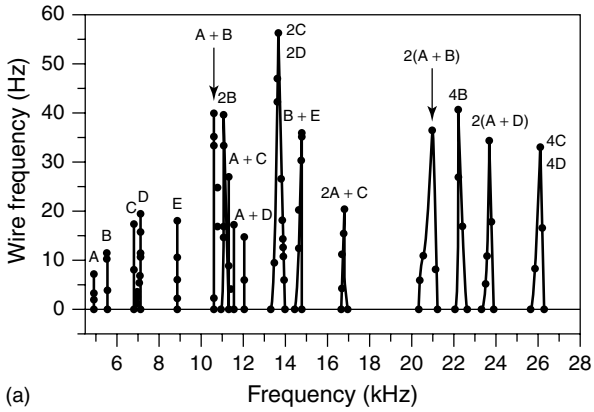

(a)

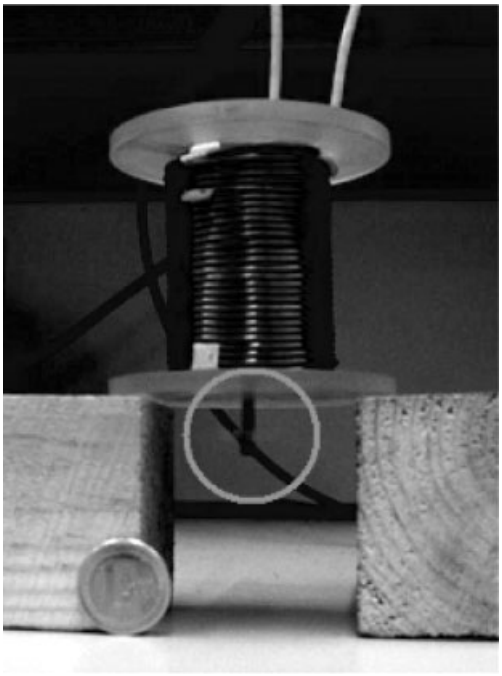

(b)

Figure 11. Rotation frequency of a Fe-based magnetostrictive microwire as a function of the frequency of the ac exciting field (note the discrete values of this frequency) (a). (Reproduced from M. Vázquez *et al*., 1999, with permission from the American Institute of Physics. © 1999.) Field-induced rotation in a levitating magnetostrictive wire (rotation is shown by the movement of a small flag in the circle) (b). (Reproduced from Luna *et al*., 2003, with permission from Elsevier. © 2003.)

ratchet was, nevertheless, studied for many years without final full understanding (Barnett and Kenny, 1952).

3.4 Arrays of bistable microwires: magnetostatic interactions and chaotic behavior

An interesting possibility for bistable microwires is its employment as memory units in magnetic labels (Hernando *et al*., 1996). There, a set of parallel bistable microwires are placed in a tag, each one with different switching field so that, when magnetized under an increasing field, each microwire reverses at its characteristic switching field. In order to increase the capability of storing information, it is desirable to reduce the size of sensing units (wire length and interwire separation), place them as close as possible, and reduce, when possible, the differential switching field among all of them. Experimental results indicate, nevertheless, that when they are spaced too closely, the intrinsic switching field of each wire is shifted indicating that some magnetostatic interaction takes place, and the magnetic information can be lost.

Bistable magnetic microwires are characterized by a nearly single-domain structure with a large axial domain with closure structures at the ends that appear to reduce the stray field energy. It seems likely that closure structures are either perturbed and/or they do not close completely their stray fields so that, each microwire can be taken as an effective dipole creating a stray field at the neighboring microwires modifying their switching field. Several studies have been reported on the magnetostatic interactions in sets of magnetic microwires (Velázquez, García, Vázquez and Hernando, 1996, 1999). From the experimental point of view, the hysteresis loop of a set of nearly identical microwires is characterized by as many Barkhausen jumps as the number of microwires, as observed in Figure 12(a) (Sampaio *et al*., 2000).

The modeling to quantify such hysteresis loops has been done considering the total magnetic energy, E_{mag}, that contains the Zeeman, dipolar, and anisotropy contributions and can be given by the general expression:

$$E = -\sum_j \vec{m}_j \cdot \vec{H}_{\mathrm{ap}} - \sum_{i>j} \frac{\vec{m}_i \cdot \vec{m}_j - 3(\vec{m}_i \cdot \vec{n}_{ij})(\vec{m}_j \cdot \hat{n}_{ij})}{r_{ij}^3} - \sum_j k_j \left(\frac{\vec{m}_j}{m_j} \cdot \hat{z}\right)^2 \tag{10a}$$

where m_i denote the dipolar magnetic moment of each microwire, r_{ij} is the distance between neighboring microwires, and k_j is the magnetic anisotropy constant with longitudinal easy axis. The final expression of magnetization and the effective switching field are determined by the Monte Carlo method. Alternatively, the problem can be solved by iteration, considering the expression for the magnetization of each wire as a function of the applied field plus the interactions with the surrounding microwires as

$$M_i(H_i) = M_i\left(H_{\mathrm{ap}} - \sum_{j=1}^{j=N} K_{ij} M_j\right) \tag{10b}$$

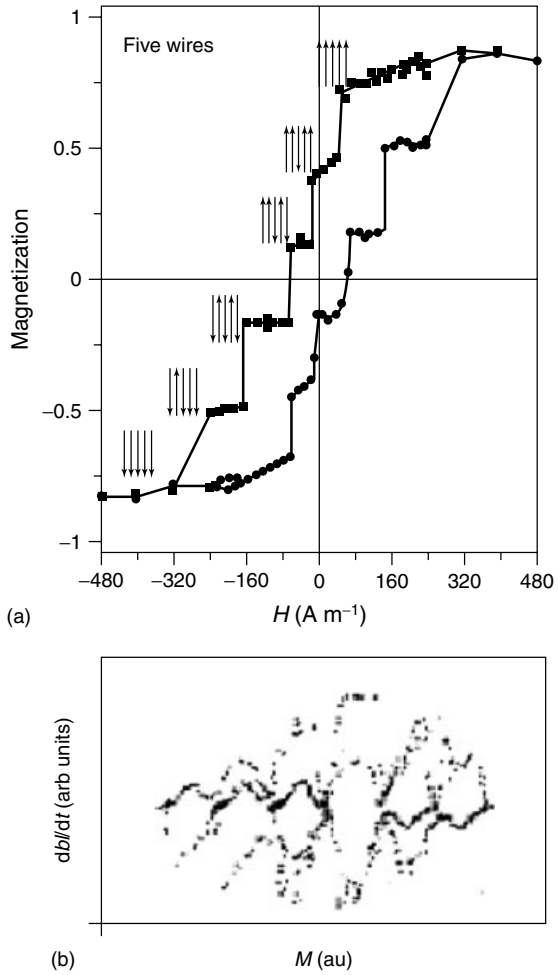

Figure 12. Hysteresis loops for a set of five bistable microwires (a). (Reproduced from L. Sampaio *et al*., 2000, with permission from American Institute of Physics. © 2000.) Reconstruction of the attractor in the magnetization phase diagram of a set of five microwires (b). (Reproduced from J. Velázquez *et al*., 1996, with permission from the American Physical Society. © 1996.)

The later contribution depends on their geometrical arrangement, which being dependent on the distances between individual microwires, r_{ij}, is reflected in the constant K_{ij}. To start the process, initial values are introduced in a first iteration (Vázquez *et al*., 2004a).

Several different modeled configurations of microwires arrays have been considered as linear, cubic, or hexagonal configurations (Vázquez and Velázquez, 2002). Particularly, the hexagonal configuration is of interest regarding the similarities with the case of nanowires in nanoporous alumina membranes.

Finally, it should be mentioned that the switching field of individual microwires, although very close, cannot be taken as identical. As a consequence of that, a complex behavior with weak-chaos characteristics has been found when analyzing the magnetic stability of the set of microwires. The reader is referred to previous references for further details (Velázquez, García, Vázquez and Hernando, 1996, 1999; Vázquez and Velázquez, 2002), and as an example, Figure 12(b) shows the temporal evolution of magnetization of a set of two microwires showing the reconstruction of the corresponding attractor.

3.5 Applications of Fe-based magnetostrictive microwires

3.5.1 Applications based on magnetic bistability

A number of applications can be found from the unique magnetization reversal of bistable microwires (Vázquez and Hernando, 1996). Some of them are related to sharp jitterless voltage induced in pick-up coils wound around the microwires during the magnetization reversal, with improved response with regard to Wiegand wires (Mohri, 1994a; Rauscher and Radeloff, 1989). Applications using bistable microwire as sensing elements include switchers, rotation counters, and position and velocity sensors among others. Sensors employed in security systems making use of the sharp induced voltage also include those based on the high harmonic response (Humphrey, 1987) such as an identification magnetic tag where codification is related to the multipeak induced signal in a set of bistable microwires with different switching fields.

3.5.2 Applications based on magnetoelasticity

The magnetostrictive character of Fe-based microwires is very suitable for various magnetoelastic sensing applications. Among others, some examples are mentioned in the following. Delay lines and sound velocity sensors using magnetostrictive Fe-based microwires have been proposed by Hristoforou (1997) and Hristoforou and Niarchos (1992). Digitizers, dc current sensor, and noncontact torsional stress sensors have been proposed based on inverse Wiedemann effect and torsion (Meydan and Elshebani, 1992; Pulido *et al*., 1991). A thermoelastic sensor makes use of differential thermal expansion coefficients of glass-coated microwires (Vázquez *et al*., 2006a). A novel viscometer is based on the field-induced rotation effect of magnetostrictive wires discussed above (Vázquez *et al*., 2001). A magnetoelastic sensor for signature identification based on the magnetoelastic behavior of magnetostrictive microwires has also been proposed (Zhukov, Vázquez and Beneytez, 1998; Zhukov, Garcia Beneytez and Vázquez, 1996). As an example of its possibilities for signature identification and authentication, a

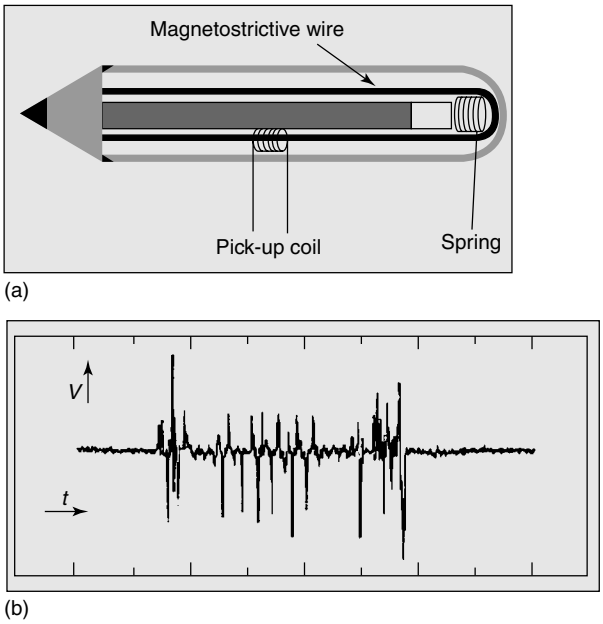

Figure 13. Schematic view and principle of operation of the magnetoelastic sensor (a), and a typical magnetoelastic signature defined by a number of pulses with given serial time interval (b). (Reproduced from A. Zhukov *et al*., 1998, with permission from EDP Sciences. © 1998.)

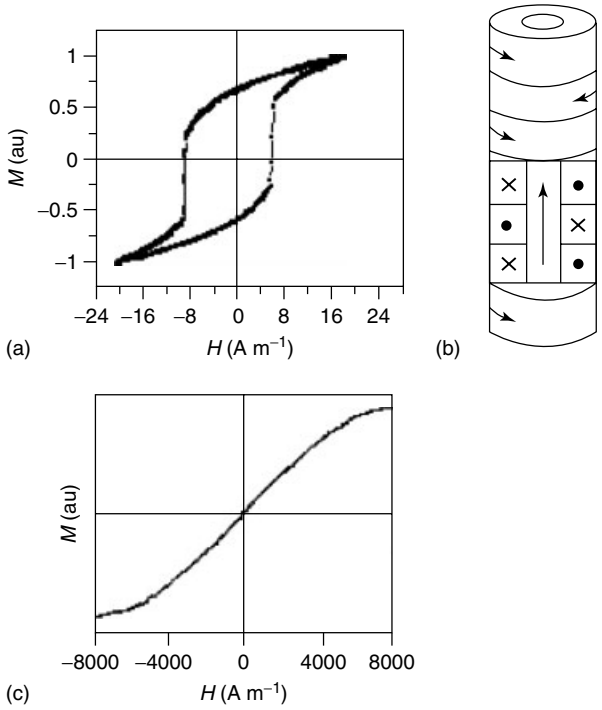

Figure 14. Axial hysteresis loop (a) and schematic view of domain structure (b) for an as-cast negative magnetostriction CoSiB in-water-quenched microwire, and for an as-prepared glass-coated microwire with similar composition (c).

schematic view of the sensor is shown in Figure 13(a). A typical magnetoelastic signature before digitalizing is depicted in Figure 13(b), where the voltage peaks, proportional to the mechanical stress are plotted as a function of time. An individual magnetoelastic signature is characterized by the number of peaks, their trend, and time intervals, while amplitude of peaks typically depend on the mood of the signatory.

4 CIRCULAR MAGNETIZATION PROCESS AND GIANT MAGNETOIMPEDANCE

4.1 Magnetization process of microwires with circumferential easy axis

4.1.1 Axial magnetization process of Co-based negative magnetostriction microwires

The axial hysteresis loop of as-cast negative magnetostriction Co-base CoSiB-like amorphous microwires obtained by in-water quenching consists, as for positive magnetostriction microwires, of a low-field giant Barkhausen jump and a reversible magnetization process at higher fields until reaching saturation (see Figure 14a). While it looks similar to the bistable loops of Fe-based microwires and the coercivity takes similar values, there are some differences: (i) reduced remanence at stable magnetic states takes smaller values of around $m_r \sim 0.36$ and (ii) differential susceptibility around remanence takes higher values of around 1 order of magnitude. These experimental results (Humphrey *et al*., 1987) together with the direct observation of domains by magneto-optical Kerr effect (Yamasaki, 1992; Yajako, Yamasaki and Humphrey, 1993), allow us to assume that the domain structure consists, as for Fe-based microwires, of two main regions: (i) an inner core with easy magnetization direction diverging from the wire axis by a small angle that depends on the radial coordinate and (ii) a shell domain structure with mostly circumferential easy axis giving rise to the so-called bamboolike structure. This domain structure is schematically depicted in Figure 14(b).

Upon applying an axial magnetic field, magnetization reverses at the core with a Barkhausen jump not so large as for Fe-based wires owing to the reduced axial component of the magnetization. A critical length to observe bistability is again observed (Zhukova, Usov, Zhukov and González, 2002). At a higher field, magnetization rotates at the shell toward the axial direction until the disappearance of the circumferential domains.

A typical axial hysteresis loop of Co-based glass-coated microwire is shown in Figure 14(c). In this case, there is no large Barkhausen jump, and magnetization process can be

interpreted as taking place by magnetization rotation from a circumferential orientation toward the longitudinal direction. This denotes the existence of a spontaneous circumferential anisotropy throughout the whole microwire, practically without inner core (Zhukov, 2001; Neagu *et al*., 2001a; Varga, García, Vázquez and Vojtanik, 2005). This indicates that the whole cross section should consist of a circumferentially magnetized shell, with a well-defined transverse magnetic anisotropy, K_ϕ, whose anisotropy field, $H_{\kappa\phi}$, can be experimentally evaluated as the field required to reach saturation in Figure 14(c). The average effective axial stress built in during rapid solidification can be determined from the anisotropy field expression $H_{\phi\kappa} = 2K_\phi/\mu_0 M_s = 3\lambda\sigma/\mu_0 M_s$. Taking the experimental values of the anisotropy field, $H_{\phi\kappa}$, the saturation magnetization, M_s, and the magnetostriction constant of this alloy composition ($\lambda \sim -1 \times 10^{-6}$), one reaches an average effective axial stress of 400 MPa.

A similar all-radii circumferential anisotropy can be also observed in nonmagnetostrictive CoFe-based in-water-quenched microwires induced by suitable stress-annealing treatments (Freijo *et al*., 1999). As observed in Figure 15(a) for the axial hysteresis loop after stress annealing, a circumferential anisotropy with circular anisotropy field of around 6 Oe is deduced. In spite of this circumferential anisotropy, a vortex micromagnetic structure with axial magnetization should appear at the very axis of the wire to reduce the otherwise significant exchange energy that would be stored. An effective radius of that vortex can be calculated by minimization of the total exchange (circular, ϕ, and radial, r, terms) plus circular anisotropy, K_ϕ, energies, leading to the Euler equation:

$$(d^2\Theta/dr^2) + (1/r)(d\Theta/dr) + [K_\Theta/A - 1/2r^2]\sin 2\Theta = 0 \tag{11}$$

In the example shown in Figure 15(a), a vortex diameter of around 0.3 µm is calculated which gives an almost negligible contribution to the whole axial hysteresis loop. A similar evaluation for an as-prepared negative magnetostriction (-2×10^{-6}) Co-based glass-coated microwire results in a vortex diameter of about 0.2 µm.

4.1.2 Crossed nonaxial magnetization processes

In cylindrical coordinates, suitable to the shape of our samples, the magnetization vector (considering axial and circular

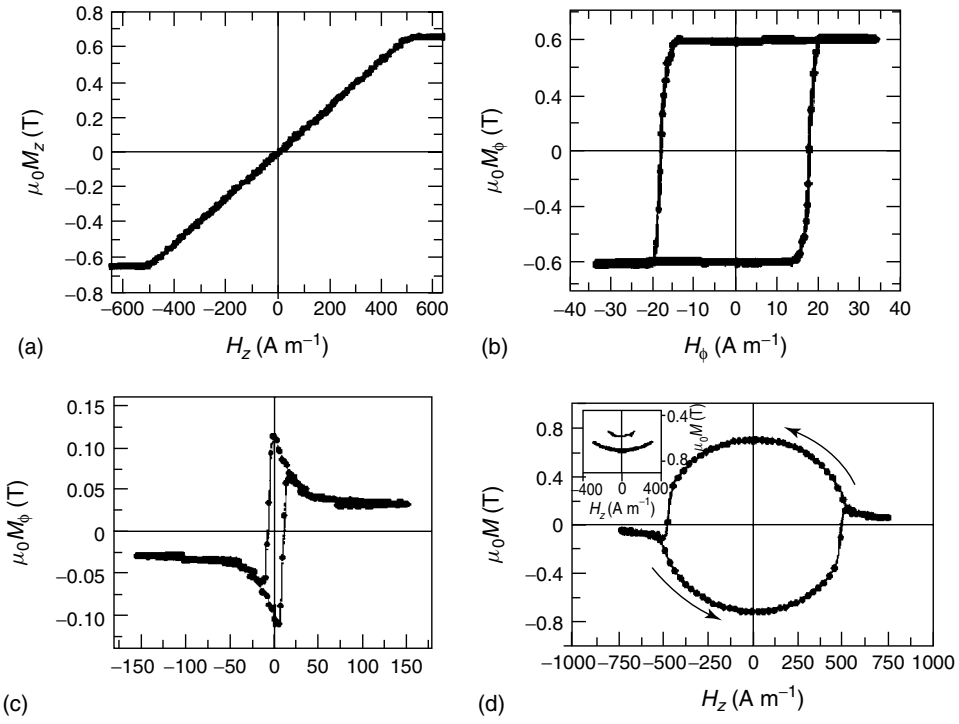

Figure 15. Axial, M_z versus M_z (a), circular, M_ϕ versus M_ϕ, (reproduced from J.J. Freijo *et al*., 1999, with permission from the American Institute of Physics. © 1999) (b), Matteucci, M_ϕ versus H_z, (reproduced from J.J. Freijo *et al*., 1999, with permission from the American Institute of Physics. © 1999) (c) and inverse Wiedemann, M_z versus H_ϕ, (reproduced from *Journal of Applied Physics*, 1999, 5450, with permission from the American Institute of Physics) (d) hysteresis loops corresponding to the four terms of susceptibility tensor in equation 12 for a CoFe-based microwire after annealing under stress. (Reproduced from J.J. Freijo *et al*., 1999, with permission from the American Institute of Physics. © 1999.) Note the induced circular anisotropy.

components) can be expressed through the susceptibility tensor as:

$$\left(M_z M_\phi\right) = \begin{pmatrix} \chi_{zz} & \chi_{z\phi} \\ \chi_{\phi z} & \chi_{\phi} \end{pmatrix} \begin{pmatrix} H_z \\ H_\phi \end{pmatrix} \tag{12}$$

which is useful particularly when the magnetization has nonvanishing components along the two orthogonal directions. Axial and circular hysteresis loops gives rise to χ_{zz} and $\chi_{\phi\phi}$ susceptibility terms, respectively. The Matteucci effect consists of the observation of a circular component of magnetization (or equivalently of a voltage induced at the ends of microwires) when axially magnetizing the wire (the corresponding susceptibility term is $\chi_{\phi z}$). The inverse Wiedemann effect consists of the existence of an axial magnetization component when the wire is subjected to a circular field (susceptibility term $\chi_{z\phi}$).

Figure 15 shows the four hysteresis loops corresponding to the 4 susceptibility terms in equation (12) for a CoFe nonmagnetostrictive wire after stress annealing, inducing a circular anisotropy. Axial, circular, Matteucci and inverse Wiedemann hysteresis loops are given respectively in Figure 15(a–d).

These effects are typically observed when the magnetization exhibits some helical component so that, when magnetizing axially or circularly, crossed circular or axial magnetization processes are observed, respectively (Kraus *et al*., 1994). Such a helical component can be induced by applying torsion or annealing under torsion. In fact, a spontaneous helical component of magnetization is experimentally deduced from both types of crossed loops in as-cast microwires (Velázquez *et al*., 1991), and actually it arises from the departure from parallelism between the magnetization in the core and the shell and/or just from interface between both regions. Recent studies suggest that the core/shell model should be modified with the introduction of some helical component at the core of negative magnetostriction in-water-quenched wires (Chen *et al*., 2001).

4.1.3 Circular magnetization process and magnetoinductive effect

The circular magnetization process, M_ϕ versus H_ϕ, is relevant when the microwires exhibit a circular component of magnetization, and in the case of the GMI effect considered in the next section. The circular magnetic field, H_ϕ, is supplied by the flow of ac current, I, along the microwire (as in the case of the inverse Wiedemann effect), and is radially inhomogeneous, $H_\phi = Ir/R$. Circular magnetization, M_ϕ is evaluated by integration of the voltage induced at the ends of the microwire, as a consequence of the changes in circular component of magnetization after subtracting the voltage coming from the ac current itself, that is, $M_\phi \approx \int \mathrm{d}M_\phi/\mathrm{d}t \approx \int (V - V_I)\mathrm{d}t$. As an example, Figure 15(b) shows the circular hysteresis loop, M_ϕ versus H_ϕ, corresponding to a stress-annealed nonmagnetostrictive CoFe-based in-water-quenched microwire (Pulido *et al*., 1991). Alternatively, circular magnetization reversal can be studied by magneto-optical Kerr effect (Chizhik, González, Zhukov and Blanco, 2002; Kabanov, Zhukov, Zhukva and González, 2005), thus obtaining direct information on the magnetization process at the very surface of the microwires.

The circular hysteresis loop in Figure 15(b) is obtained at a low ac field frequency (at 80 Hz). An increase of the working frequency gives rise to a noticeable enhancement of the voltage induced at the ends arising from the circular magnetization process. This circular magnetization process is sometimes labelled as magnetoinductive effect, which has been studied by several authors specially for in-water-quenched microwires (Mohri *et al*., 1992; Velázquez, Vázquez, Chen and Hernando, 1994). The magnetoinductive voltage, ΔV_{ind}, can be expressed as:

$$\Delta V_{\mathrm{ind}} \approx \sqrt{1 + \left(\pi \mu_0 r^2 \chi_{\phi\,\mathrm{max}} f/2\rho\right)^2} \tag{13}$$

where r and ρ are the radius and resistivity of the microwire, and $\chi_{\phi\mathrm{max}}$ denotes the maximum circular susceptibility, which is achieved for an ac current circulating through the wire that generates a magnetic field corresponding to the circular coercivity. Note that magnetoinductive voltage increases with the frequency, f, of the exciting circular field and with the circular susceptibility, but it decreases with resistivity of the wire. Concerning the later, circular susceptibility shows maximum values just around the circular switching field or circular coercivity. While the frequency range for this magnetoinductive effect is of the order of kilohertz, at higher frequencies it is overcome by a new phenomenon: the magnetoimpedance effect.

4.2 Giant magnetoimpedance effect

4.2.1 Magnetization process of nonmagnetostrictive CoFe microwires

Nonmagnetostrictive amorphous CoFe-based microwires exhibit the softest behavior when magnetizing along both axial and circular directions. The intrinsic magnetoelastic anisotropy, being now much smaller owing to the reduced magnetostriction (of the order of 10^{-7}), enables the formation of a larger number of walls, and magnetic bistability is no longer observed: within the core, a multidomain structure is present that destroys bistability but in turn, results in the largest values of initial permeability (up to about 10^5).

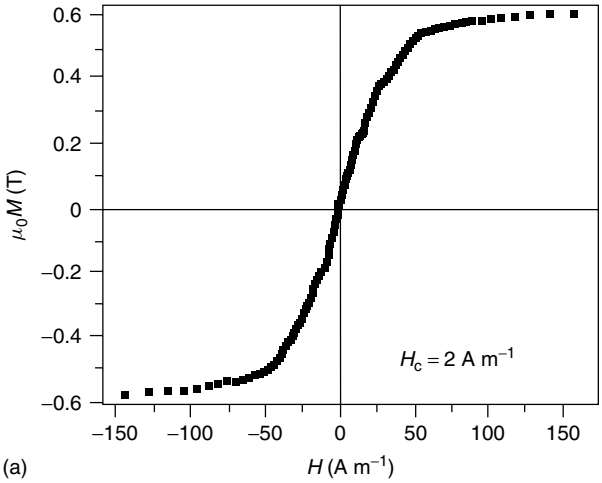

(a)

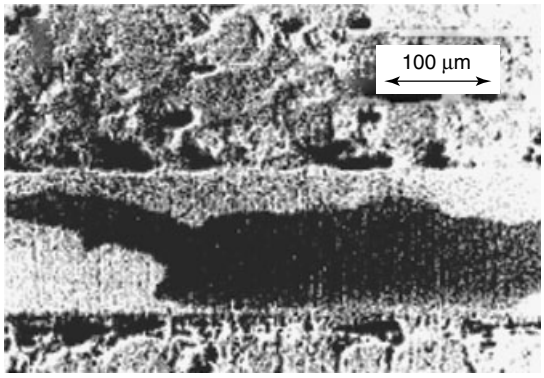

(b)

Figure 16. A nearly nonhysteretic loop of a nonmagnetostrictive as-cast CoFe-based in-water-quenched microwire (a). (Courtsey of G.A. Badini Confalonieri, Thesis, University of Sheffield, 2005.) Kerr effect image showing the multidomain structure in its core (b). (Reproduced from H. Theuss *et al*., 1995, with permission from Elsevier. © 1995.)

Figure 16 shows the axial hysteresis loop for an as-prepared in-water-quenched CoFe-based microwire.

Bistability can be, nevertheless, observed at low temperature as a consequence of the increase in magnetostriction (Theuss *et al*., 1995). It should also be mentioned that magnetostriction of such nonmagnetostrictive microwires is significantly modified by thermal treatments as well as by the application of mechanical stress. In fact, as for ribbon-shaped amorphous alloys, magnetostriction decreases linearly with applied stress, and a change of sign can even be observed as has been reported for the two families of microwires (Gómez-Polo and Vázquez, 1993; Zhukov *et al*., 2000; Zhukov, 2006; González *et al*., 2000; Neagu *et al*. 2001b).

4.2.2 Phenomenology of giant magnetoimpedance

The phenomenon of GMI, consists of the modification of impedance, both real and imaginary components, of a metallic conductor upon the action of a static magnetic field. Although this phenomenon was first reported many years ago (Harrison, Turney and Rowe, 1935), it did not attract much attention until its rediscovery in the 1990s (Panina and Mohri, 1994; Beach and Berkowitz, 1994) in nonmagnetostrictive CoFe-based in-water-quenched microwires. The most important characteristics of GMI for microwires are: (i) that they must show a magnetic character as soft as possible, (ii) the largest relative changes of impedance with static field reaches up to around 600%, and (iii) the static field required to observe GMI is typically of the order of few units or tens of oersted, with a maximum sensitivity of around 300% Oe^{-1} at very low fields. A number of review articles have been recently published covering the different aspects of magnetoimpedance (Knobel, Vázquez and Kraus, 2003; Vázquez, 2001b; Mohri *et al*., 2001). Here, we will only summarize some interesting effects related to microwires while further detailed information can be found in those review articles.

The common experimental method to evaluate GMI is very simple: the impedance of a microwire is typically evaluated through the four-points technique by which the voltage at the ends of the microwire is measured as a function of a low-amplitude ac current flowing along the microwire. A modification of the impedance is then observed when the sample is subjected to a static magnetic field. The GMI ratio is usually defined as:

$$\frac{\Delta Z}{Z} = \frac{\left|Z(H_0)\right| - \left|Z(H_{0,\max})\right|}{\left|Z(H_{0,\max})\right|} \tag{14}$$

where the impedance $Z = R + iX$.

Figure 17 shows the frequency dependent GMI effect for two as-cast amorphous microwires. The larger values of GMI are observed for in-rotating-water microwire at frequencies of the order of about 1 MHz or less, while glass-coated microwires show their maxima at higher frequency of around 10 MHz (Vázquez *et al*., 1998; Chiriac, Ovari and Marinescu, 1998).

GMI actually depends not only on frequency but also on a number of additional parameters characterizing the microwire and particularly the circular magnetization process. These factors include: (i) current flowing through the microwire (specially, depending on whether it creates a circular field overcoming the circular coercivity, or not), (ii) alloy composition (and consequently magnetostriction), (iii) the actual magnetic domain structure, and (iv) thermal treatments relaxing the amorphous microstructure or inducing anisotropies. For further information on the phenomenology of GMI the reader is referred to the review articles mentioned earlier.

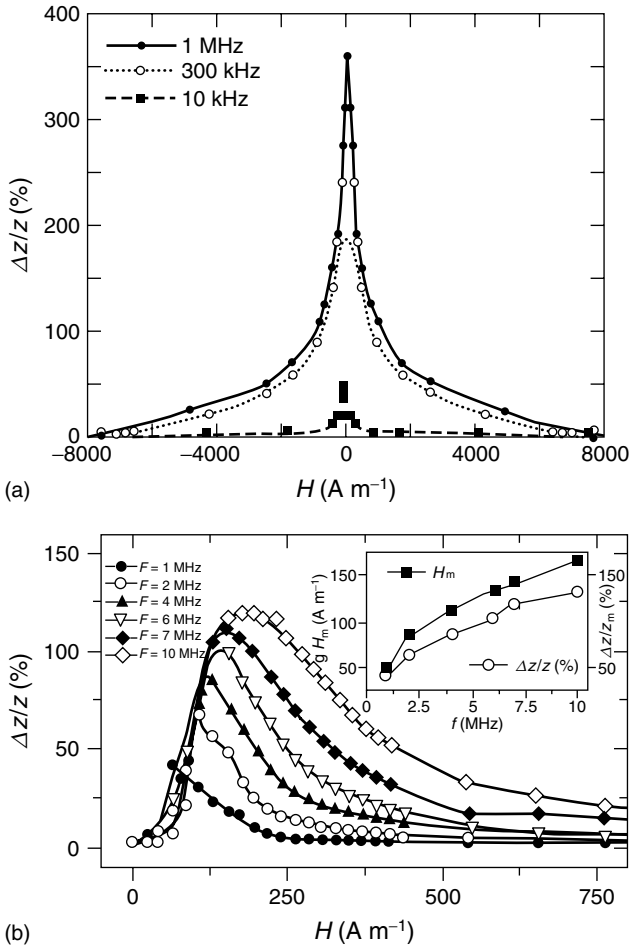

Figure 17. Giant magnetoimpedance ratio (GMI), as a function of static magnetic field for a range of measuring frequencies for a CoFe nonmagnetostrictive in-rotating-water microwire (a) (reproduced from M. Vázquez *et al*., 1996, with permission from IOP Publishing Ltd. © 1996) and for a CoFe based glass-coated amorphous microwire (b). (Reproduced from M. Vázquez *et al*., 2000, with permission from Materials Research Society. © 2000.)

4.2.3 The skin effect and the giant magnetoimpedance: circular permeability

The origin of GMI is related to the classical electromagnetic skin effect (Knobel, Vázquez and Kraus, 2003; Vázquez, 2001b; Mohri *et al*., 2001). When an ac current of sufficient high frequency flows along a metallic sample, it concentrates in a thin layer at the surface as a consequence of the induced eddy currents. The skin depth, δ, over which the current flows is given by

$$\delta = \sqrt{\frac{\rho}{\pi f \mu_\phi}} \tag{15}$$

which in turn determines the impedance of the sample that can be expressed as

$$Z = R_{\mathrm{DC}} \left(\frac{ka}{2}\right) \frac{J_0(ka)}{J_1(ka)} \tag{16}$$

Here, J_i is the Bessel functions, and $k = (1+i)/\delta$. Typically, the penetration depth, δ, in metallic nonmagnetic samples depends only on their conductivity and on the frequency of the ac current. Nevertheless, in ultrasoft magnetic materials, the skin effect is strongly enhanced through the transverse permeability as deduced in equations (14) and (15). The effect of the static applied field is thus simply that of modifying the effective circular permeability of the microwire. Actually, GMI can be regarded as a consequence of the circular magnetization process generated by the high-frequency ac circular field, the circular permeability can be modified and to some extent tailored by the static magnetic field.

Particularly, the domain structure existing in the microwires determines the $Z(H)$ profile of the impedance response to static applied fields. Two main GMI profiles are directly correlated with the domain structure and magnetization process of microwires: (i) single-peak (SP) behavior consists of a continuous decrease of GMI ratio from a maximum nearly at zero applied field, $H_{\max} \approx 0$, and (ii) two-peak (TP) behavior, which maximum GMI is observed at a given static field, $H_{\max} \neq 0$. Figure 18 shows examples of each of those behaviors. SP behavior is observed in those microwires with an effective axial anisotropy, while TP behavior appears in those microwires with an effective circular anisotropy which corresponds to the field, $H_{\max}$, for which maximum GMI is observed. The correlation between GMI shape and the corresponding magnetization process has been discussed further elsewhere (Vázquez, Sinnecker and Kurlyandskaya, 1999).

4.2.4 Stress-impedance and magnetoelastic effects

Because the GMI response is determined by the circular susceptibility, it is clear that it will be modified magnetostrictively by the application of mechanical stresses. A number of works have been published concerning the influence of applied stresses, particularly tensile and torsional stresses, on the GMI response (Knobel, Vázquez, Sánchez and Hernando, 1997; Li, Vázquez and Chen, 2003; Prida *et al*., 2003). An example is given in Figure 19(a) for applied torsion. The stress-impedance (SI) ratio, under a given applied dc field, for any kind of applied mechanical stress, can be defined as

$$\left(\frac{\Delta Z}{Z}\right)_{H_0} = \frac{|Z(\sigma)| - |Z(\sigma_{\max})|}{|Z(\sigma_{\max})|} \tag{17}$$

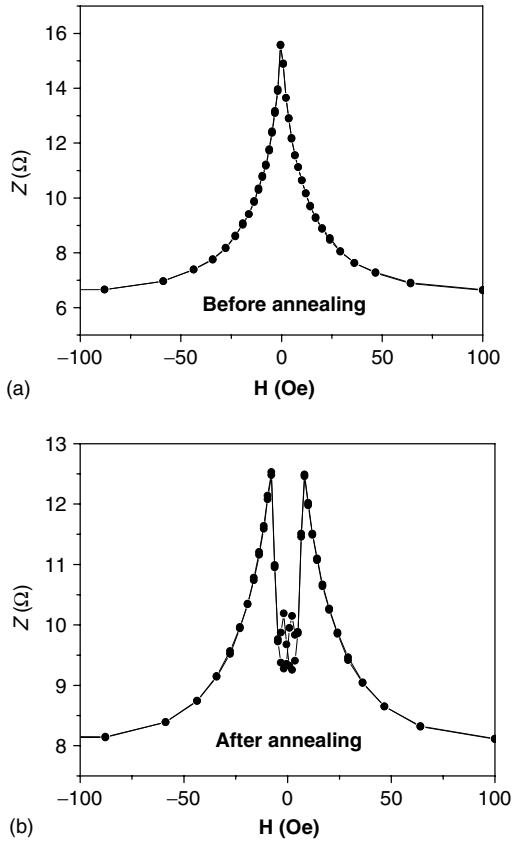

Figure 18. Single peak (a) and two peaks (b) GMI behavior (900 KHz, 5 mA) for a $(Co_{0.947}Fe_{0.053})_{70}Si_{12}B_{18}$ nonmagnetostrictive in-water-quenched microwire in its as-cast state (a), and after thermal annealing (b) exhibiting effective axial and circular anisotropy, respectively. (Reproduced from M. Vázquez *et al*., 1999, Materials Science Forum, pp. 209. © 1999.)

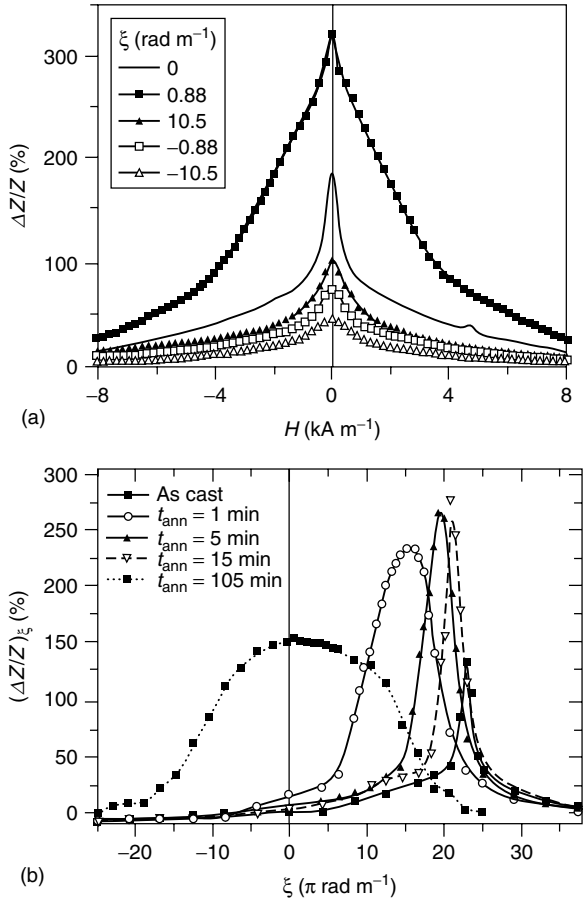

Figure 19. Evolution of magnetoimpedance response of a microwire under applied torque (a). (Reproduced from Y.F. Li *et al*., 2003, with permission from the American Institute of Physics. © 2003.) Asymmetric torsion impedance after a helical anisotropy is induced by torsion annealing (b). (Reproduced from M. Knobel *et al*., 2003, with permission from Elsevier. © 2003.)

Additionally, GMI has also been proved to be a useful tool to determine a number of magnetic characteristics of magnetoimpedive samples. For example, from the dependence on applied stress, σ, of the field, H_{max}, at which maximum GMI is observed, it is possible to derive quantitatively the magnetostriction of the microwire (Knobel, Vázquez, Sánchez and Hernando, 1997) as

$$\lambda_s = -\left(\mu_0 \frac{M_s}{3}\right)\left(\frac{\Delta H_{max}}{\Delta \sigma}\right) \tag{18}$$

There is particular technological interest in the possibility of obtaining asymmetric GMI that enable a continuous reading of impedance with field (Panina, 2002; Kraus, Freit, Pirota and Chiriac, 2003). Such asymmetry can be obtained by superimposing an additional static field, or inducing a helical anisotropy either by applying a torque or by mechanical torsion stress annealing (Zhukov *et al*., 2000; Panina, Mohri and Makhnovskiy, 1999; Kim, Jang, Kim and Yoon, 1999; Gómez-Polo, Vázquez and Knobel, 2001). Figure 19(b) shows the asymmetric GMI obtained after current annealing under torsion for different annealing times. It should be mentioned that particular real enhancement of GMI is to be expected by suitable thermal treatment and smoothening of the sample surface (Kraus, 1999). Another characteristic of GMI is the appearance of hysteresis as a consequence of the irreversibility in the circular magnetization process. Such hysteresis should be avoided as much as possible for technological applications (Knobel, Vázquez and Kraus, 2003; Vázquez, 2001b; Mohri *et al*., 2001).

4.2.5 Giant magnetoimpedance and ferromagnetic resonance

At frequencies higher than few tens of megahertz, the evaluation of impedance is no longer reliable by the four-point technique due to uncertainties in parasitic and cable impedances. To determine the effective impedance at microwave frequencies, several experimental methods

are employed including guided waves in cavities, the insertion of microwires into coaxial lines for determination of transmission coefficients, or through studies on the real and imaginary components of permeability (Lofland, García-Miquel, Vázquez and Baghat, 2002; García-Miquel, García, García-Beneytez and Vázquez, 2001; Jacquart and Acher, 1996). The electromagnetic field configuration at microwave frequencies is the same as for radiofrequencies where orthogonal electrical field and magnetic field are acting on the sample, and now the impedance has to be considered as the relation between both fields. In the microwave frequency range, the magnetoimpedance effect has been theoretically correlated with ferromagnetic resonance phenomena (Yelon, Menard, Britel and Ciureanu, 1996; Melo, Menard, Ciureanu and Yelon, 2002) where one should consider the correlation between surface impedance and the skin effect. Under particular biasing field, H_0, the ferromagnetic resonance frequency can be approximated by García-Miquel *et al*. (2001) and García *et al*. (2000):

$$f_r = \gamma\mu_0\sqrt{(H_0 + M_s)\left(H_0 - \frac{2k}{\mu_0 M_s}\right)} \cong \gamma\mu_0\sqrt{M_s(H_0 - H_k)} \tag{19}$$

where γ is the gyromagnetic ratio and $H_k = 2k/\mu_0 M_s$ is the transverse anisotropy field. The resonance frequency can be experimentally evaluated also through the scattering parameter S_{11} correlating to the incident, P_{in}, reflected, P_{ref}, and absorbed, P_{abs}, powers as: $|S_{11}|^2 = P_{ref}/P_{in} = 1 - P_{abs}/P_{in}$. As an example, Figure 20(a) shows the evolution of the square of the scattering parameter with the frequency for a series of increasing applied field values, allowing us to determine the field dependence of the resonance frequency (as determined from the minimum square scattering parameter). Figure 20(b) shows the field dependence of the square resonance frequency, following equation (19), for a series of glass-coated microwires. Extrapolation of observed linear behavior gives us values of anisotropy fields, while saturation magnetization can be extracted from the corresponding slopes.

Several experiments have been performed on the correlation between absorption spectra and magnetization process for amorphous and nanocrystalline microwires (Ovari, Chiriac, Vázquez and Hernando, 2000; Lofland *et al*., 1999; Montiel *et al*., 2005). In these reports, the observed low-field absorption peak has been ascribed to the magnetization reversal process of the microwires. All the outstanding microwave phenomena are actually a consequence of the so-called NFMR, which in these glass-coated microwires appears in this frequency range. In CoFe and Fe-based microwires NFMR frequencies are of around 2–3 GHz and 8–12 GHz for nonmagnetostrictive CoFe-based and magnetostrictive

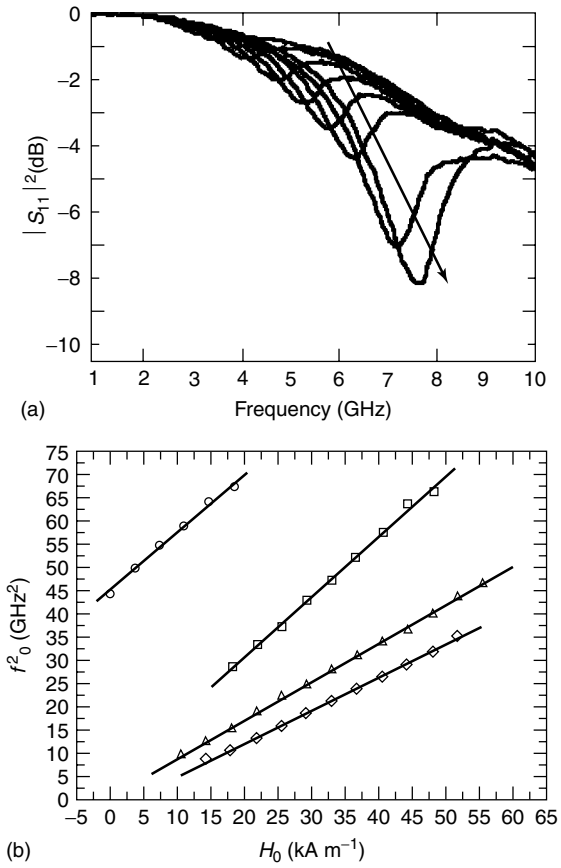

Figure 20. Evolution of the square scattering parameter, $|S_{11}|^2$ with the working frequency for a range of increasing applied field values up to 700 Oe as indicated by the arrow (a). (Reproduced from H. García-Miquel *et al*., 2001, with permission from IEEE. © 2001.) Applied field dependence of the square resonance frequency, f^2, for a series of glass-coated microwires (b) with compositions: (◇) $Co_{72.5}Si_{12.5}B_{15}$, (△) $(Co_{0.94}Fe_{0.06})_{72.5}Si_{12.5}B_{15}$, (○) $(Co_{50}Fe_{50})_{72.5}Si_{12.5}B_{15}$, (□) $Fe_{72.5}Si_{12.5}B_{15}$. (Reproduced from H. Garcia *et al*., 2000, with permission from Sociedad Española de Cerámica y Vidrio. © 2000.)

Fe-based microwires, respectively as a consequence of the intrinsic magnetoelastic anisotropy (Baranov, Zotov, Larin and Torkunov, 1991).

4.3 Applications based on ultrasoft behavior and microwave absorption

4.3.1 Ultrasoft magnetic behavior and giant magnetoimpedance

Nonmagnetostrictive CoFe-based amorphous microwires are among the softest magnetic materials and consequently, they can be used in a broad spectrum of sensing devices. A first application of such wires is as magnetic tips for a particular near field microscopy. The CoFe-based in-water-quenched microwire is subjected to a particular chemical

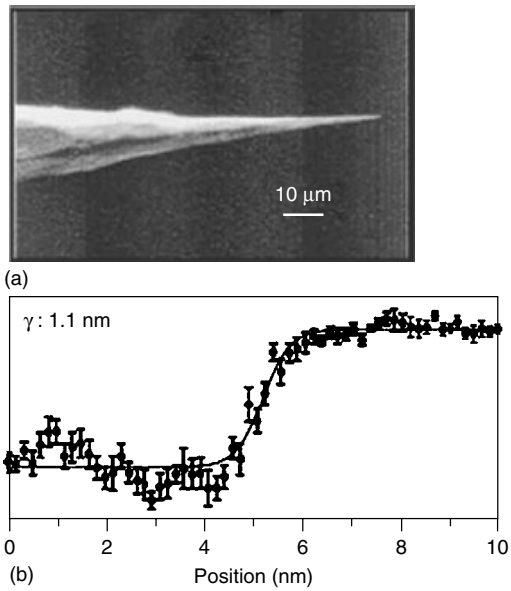

Figure 21. Sharpened microwire (a) used as magnetic tip in spin-polarized scanning tunneling microscopy, and high sensitivity fine structure of the domain wall in a Co sample (b). (Reproduced from W. Wulfhekel *et al*., 2001, with permission from Springer-Verlag. © 2001.)

etching resulting in sharpening of the microwire end (see Figure 21a). As an example, Figure 21(b) shows the high sensitivity fine structure of the domain wall in a Co sample obtained in a spin-polarized scanning tunneling microscope (Wulfhekel *et al*., 2001). An additional advantage of these wires is the significant reduction of magnetostrictively induced vibrations at the tip.

Nevertheless, the large number of applications where non-magnetostrictive microwires are usefully employed include sensing elements based on the GMI effect. They have been extensively developed in Japan mainly around the group led by Mohri (1994b), Mohri, Uchiyama and Panina (1997), and Mohri *et al*. (2002). Most of the sensors use CMOS-type circuitry where tiny pieces of amorphous microwires (1–2 mm long) showing GMI effect are employed as elements to sense static field. Magnetic field sensors are characterized by low power consumption and high low-field sensitivity (around 100% change in impedance, up to 1 nT). Several sensors, as developed by Aichi Steels (3D magnetic field sensors, GPS compass, etc.) (Cai, Yamamoto and Honkura, 2005 Private Communication), are currently used in car industry or car traffic monitoring. Other related applications include the record of the car magnetic signature in parking places and on moving cars (Valenzuela, Vázquez and Hernando, 1996; Uchiyama *et al*., 2000).

Stress-impedance effect is being used as principle of work in other families of sensors (Cobeño *et al*., 2001): in biomedical applications as, for example, to detect cancer tumors, biomechanical movements (as eyelid or articulator movements (Mohri, 1994b; Mohri, Uchiyama and Panina, 1997; Mohri *et al*., 2002; Sonoda, 1995), or as biomolecular labels when coated to specific antibody (Kurlyandskaya and Levit, 2005).

4.3.2 Electromagnetic field absorption

Probably one of the most interesting technological applications of glass-coated microwires is their employment as absorbers to the electromagnetic radiation, as has been theoretically studied and experimentally demonstrated (Baranov, 1998, 2003; Belozorov, Derkach and Tarapov, 2002). This is very important for electromagnetic shielding of military and civil vehicles, planes, and ships, in civil airports or for mobile phones and similar technologies. These types of experiments were already performed years ago but not well publicized. Particularly, arrays of glass-coated microwires in suitable dielectric matrix are most interesting for such shielding. As can be observed in Figure 22(a), there is a broad frequency spectrum for the absorption, with maximum value of around 30 dB (equivalent to 99.9% absorption). Recent studies (Makhnovskiy, Panina and Sandacci, 2005; Makhnovskiy *et al*., 2006; Acher *et al*., 2000) show that the microwave behavior (i.e., scattering spectra) of this type of composite materials based on glass-coated microwires can be suitably tuned by relatively small applied field and mechanical stress. This is particularly relevant for applications in remote non-destructive evaluation of structural materials.

Finally, the potential exists to use glass-coated microwires to develop *LHMs*, where the wave vector, k, the electric field, E, and the magnetic, H, field would form a left-handed rather than a right-handed vectors set. Such materials exhibit negative index of refraction as proposed in Veselago (1967), and this behavior has attracted much attention owing to recent theoretical and experimental reports (Pendry, 2000; Smith, Pendry and Wiltshire, 2004). Particularly, such phenomenon is predicted in the case when both permeability and permitivity show negative values simultaneously, which can be achieved in arrays of glass-coated microwires under particular conditions of frequency and field (Baranov and Vázquez, to be published; Engelvin-Adenot, Dudek, Toneguzzo and Acher, 2007). As shown in Figure 22(b), negative permeability can be found just above the FMR frequency, which combined with appropriate dielectric matrix would result in an LHM.

5 NOVEL ADVANCED MICROWIRES

Until now, we have been considering microwires with amorphous microstructure. They exhibit outstanding properties

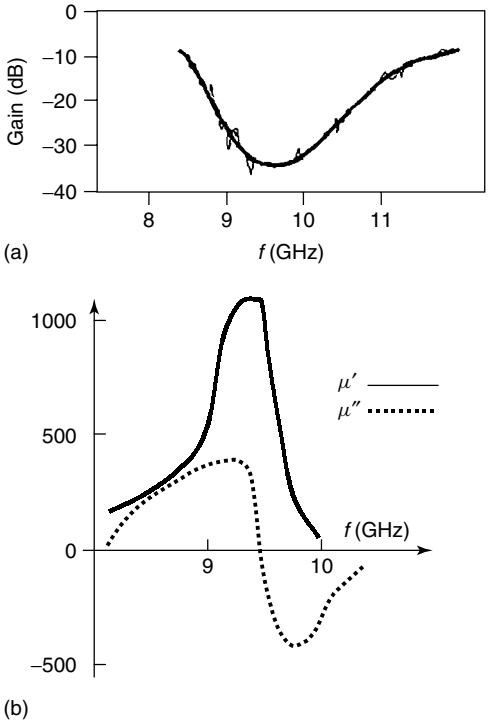

Figure 22. Electromagnetic absorption spectrum of a composite radioabsorbing screen containing short pieces of glass-coated microwires, (a) and frequency dependence of real, μ and imaginary, μ components of permeability in a Fe-based glass-coated microwire (b). (After Baranov and Vázquez, to be published.)

derived from the out-of-equilibrium fabrication processes. Once these rapid solidification methods have been completed, further processing can be done to achieve extraordinary properties of interest, in particular, appreciations. In this section, we review information on different processing methods used to optimize some particular properties or even resulting in a novel family of microwire material with unique magnetic behavior. First, we analyze microwires exhibiting inhomogeneous structure, with a characteristic structure length of the order of nm (e.g., either nanocrystals or grains embedded in matrix). Later on, we consider multilayer microwires with homogeneous characteristics within each layer.

5.1 Composite microwires

5.1.1 Nanocrystalline microwires: optimizing soft magnetic behavior

Owing to their metastable nature, amorphous microwires thermally treated at elevated temperature can crystallize, which often results in drastic magnetic hardening. However, as shown by Yoshizawa, Oguma and Yamauchi (1988) for FeSiB amorphous alloy ribbons with small addition of elements as Cu and Nb, a stable and homogeneous microstructure with soft magnetic properties can be attained after suitable thermal treatments (for detailed information, see chapter **Soft Magnetic Materials – Nanocrystalline Alloys, Volume 4**). A similar effect has been reported for in-water-quenched microwires (Gómez-Polo *et al*., 1993; Vázquez, Marín, Davies and Olofinjana, 1994) and glass-coated microwires (Arcas *et al*., 1996; Chiriac, Ovari, Pop and Bararіu, 1997).

Microwires showing high magnetostriction exhibit bistable behavior in their as-cast state, which is later destroyed by the thermal treatments. Figure 23(a) shows the evolution of coercivity for a $Fe_{75}Si_{11}B_{10}Cu_1Nb_3$ in-water-quenched microwire (Gómez-Polo *et al*., 1993; Vázquez, Marín, Davies and Olofinjana, 1994), where different magnetic stages can be detected: (i) a first reduction after annealing up to 440 °C is ascribed to the relaxation of internal

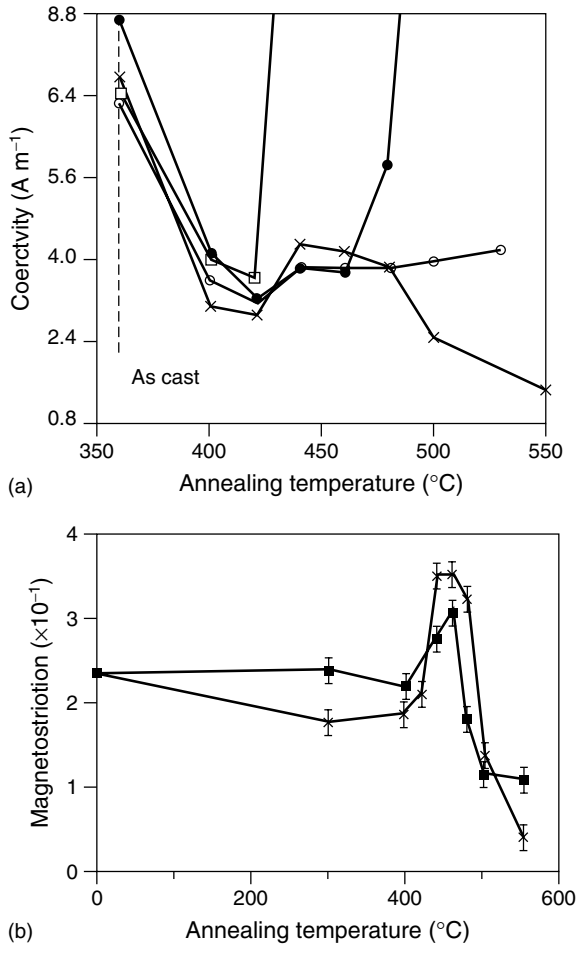

Figure 23. Annealing temperature dependence of coercivity for $Fe_{73.5}Si_{13.5}B_{13}$ (●), $Fe_{73.5}Si_{13.5}B_{13}Cu_1$ (□), $Fe_{73.5}Si_{13.5}B_{10}Nb_3$ (○), and $Fe_{73.5}Si_{13.5}B_9Cu_1Nb_3$ (×) microwires (a); and of magnetostriction for a FeSiBCuNb ribbon (×) and nanocrystalline microwires (○) (b). (Reproduced from C. Gómez-Polo *et al*., 1994, with permission from the American Institute of Physics. © 1994.)

mechanical stresses in the amorphous structure, (ii) annealing near 460 °C results in a relative increase in coercivity, which is ascribed to a first nucleation of Cu-rich clusters that act as pinning centers, (iii) optimum ultrasoft behavior is obtained by annealing at 530 °C when the composite nanostructure consists of α-Fe(Si) nanograins, around 10 nm in grain size, embedded in a residual amorphous matrix, and (iv) further crystallization with the growth of grain size and appearance of new phases (borides) with harder character results in increased coercivity. For glass-coated microwires, a similar evolution of coercivity is observed although at slightly more elevated temperatures, perhaps due to a difference in the effective temperature of the microwire owing to the protective coating (Arcas *et al*., 1996; Chiriac, Ovari, Pop and Bararíu, 1997).

A general expression for the coercivity considering its proportionality with the energy stored in a wall is:

$$H_c \propto \frac{\sqrt{A(3\lambda\sigma + \langle K_{crys}\rangle)}}{\mu_0 M_s} \tag{20}$$

Here, all λ, σ and $\langle K_{crys}\rangle$ (the average magnetocrystalline anisotropy of treated microwire) are modified by the thermal treatments. The ultrasoft character is ascribed to reduction of the average anisotropy constant, $\langle K_{crys}\rangle$, due to the reduced size of nanocrystals, 10–12 nm in average, smaller than the exchange correlation length, as well as to the significant reduction of the magnetostriction. The evolution of the magnetostriction with annealing temperature can be observed in Figure 23(b). Here, the final reduction of magnetostriction after annealing at 540 °C has been ascribed to the balance between contribution between nanocrystalline and residual amorphous phases, while intermediate relative increase seems to be related to first structural modifications as mentioned previously.

It is to be mentioned that besides ultrasoft magnetic character, nanocrystalline microwires exhibit improved mechanical behavior with respect to ribbon-shaped samples (Olofinjana and Davies, 1995). Because the bistability is lost at the optimum nanocrystalline state owing to the reduced effective anisotropy, the most interesting issue is that of improved magnetoimpedance behavior due to its soft character (Knobel *et al*., 1996). Nevertheless, optimum GMI does not reach the results obtained with soft amorphous microwires.

5.1.2 Nanocomposite hard and granular microwires

Whereas the amorphous state results in magnetic softening, some different attempts have been made to prepare hard magnetic microwires. First attempts have been done simply by crystallizing precursors soft amorphous microwires for the alloy compositions considered so far. This gives rise to magnetic hardness and enhanced coercivity of the order of 100 Oe.

Later attempts have been made by adding suitable elements in order to induce magnetic hardening either by forming new hard phases or just by enhancing pinning mechanism of magnetization reversal (Wang *et al*., 1997; Sinnecker *et al*., 1999; Zhukov *et al*., 1999). Several glass-coated microwires containing immiscible elements have been prepared by quenching and drawing technique followed by thermal treatments so that final granular systems are formed. We mention three series of alloys Fe–Co–Cr (with coercivity of 16 kA m^{-1}), Fe–Ni–Cu (50 kA m^{-1}), or Co–Ni–Cu–Mn (60 kA m^{-1}). Some technical difficulties arise, nevertheless, to fabricate these microwires owing to the higher temperature required to melt such alloys as well as their high tendency toward oxidation. Despite these works, reported values of coercivities of several hundreds of oersted, the net magnetization is unfortunately significantly reduced in comparison with that of soft phases. Latest results performed on FePt rich microwires have allowed coercivities of around 100 kA m^{-1} (Badini, Torcunov, García and Vázquez, to be published).

Finally, some recent works have been reported in granular microwires showing that they exhibit some magnetotransport properties, particularly magnetoresistance, which are of interest for sensing applications although so far being relatively modest in amplitude (Zhukov *et al*., 2004a,b; Zhukov, González and Zhukova, 2005).

5.2 Multilayer microwires

Owing to the cylindrical symmetry, the preparation of multilayered microwires by adding external layers or microtubes to existing wires has been studied. First, attempts were reported in Rauscher and Radeloff (1991) where composite microwires were prepared consisting of a soft NiFe-based core and a hard CrCoFe shell. There, the magnetic interactions between components play an important role to determine the bistable magnetic behavior of the core.

Attempts were performed by electrochemical deposition of CoP, CoFeNi, and CoNi alloys onto Cu-rich microwires which was used as electrode (Kurlyandskaya *et al*., 1999; Vázquez *et al*., 2000; Sinnecker *et al*., 2000; Atalay and Atalay, 2005). The objectives for fabrication of these microtubes onto metallic nonmagnetic microwires were related to their magnetoimpedance properties. Owing to the differential conductivity and especially their permeability, the magnetoimpedance behavior was expected to show a particular response. In fact, quite large variations of the imaginary component of impedance were reported (see Figure 24a). Additionally, interest lies in the preparation technique itself

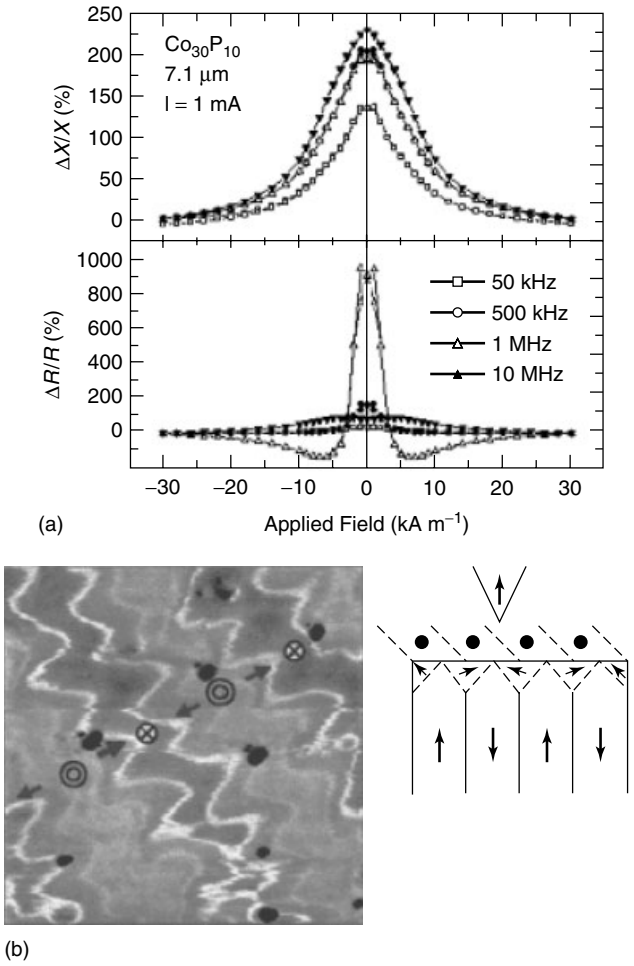

Figure 24. Large giant magnetoimpedance (GMI), effect in a CoP microtube electroplated onto a Cu microwire (a) (reproduced from J.M. García *et al*., 2000, with permission from the American Institute of Physics. © 2000) with corresponding schematic interpretation of domains (b). (Reproduced from J.M. García *et al*., 2001, with permission from the American Institute of Physics. © 2001.)

that allowed the fabrication of novel materials with nonstandard properties. Electrodeposition of outer layers to microwires opens new possibilities for controlled behavior such as modifiable easy magnetization axis (from radial to in plane of the layer) depending on thickness and electroplating parameters. Figure 24(b) shows the domain structure at the surface of a Co microlayer onto Cu microwire where the existence of radial anisotropy is deduced. A correlation between the frequency dependence of the impedance and the penetration of the surface closure structure was found that enabled the evaluation of the thickness of such closure structure (García *et al*., 2001).

More recently, multilayered microwire structure has been achieved employing the two families of amorphous microwires considered in previous sections as precursors and combining sputtering and electrodeposition techniques. For this purpose, a specific electrodeposition cell is to be designed because of the particular geometry of the electroplating (Pirota *et al*., 2004). Sputtering of a nanolayer by commercial sputtering is first required in the specific case of glass-coated microwires to provide a conducting path for electroplating. For example, Ti, Ag, or Au layer, several tens of nanometer thickness, is first sputtered onto the Pyrex-like coating. This nanotube actually acts as an electrode for the subsequent electrodeposition of metallic elements and alloys, magnetic or nonmagnetic, thus obtaining a multilayered microwire.

The influence of these additional coatings on the magnetic behavior of multilayer microwire is really impressive as is given in Figure 25 as an example. The shape of a hysteresis loop can be tailored for particular purposes: after just sputtering a Ti nanolayer in Figure 25(a), the nearly nonhysteretic

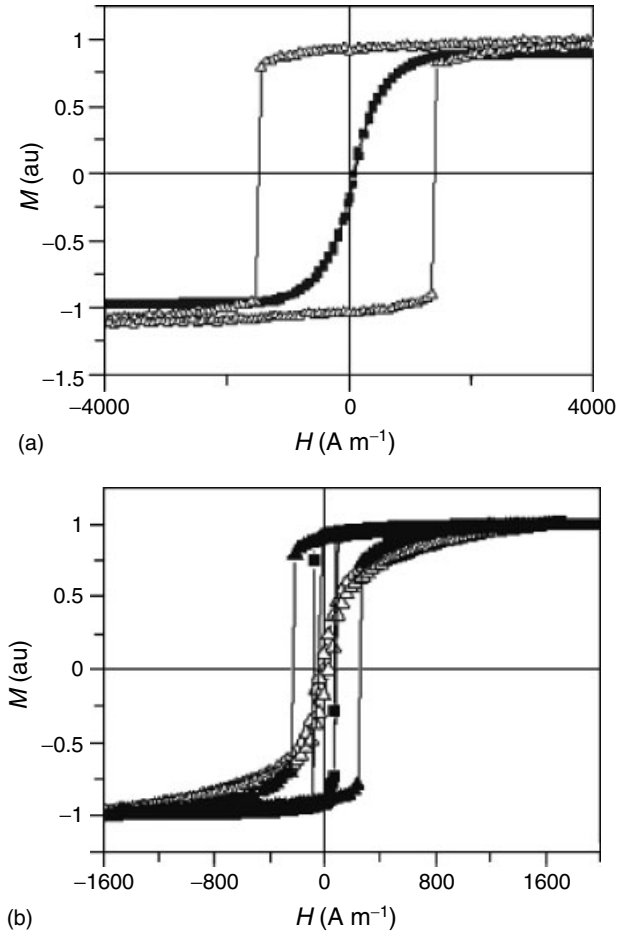

Figure 25. Hysteresis loops of multilayer microwires consisting of a $(CoFeNi)_{75}Si_{10}B_{15}$ glass-coated microwire (■) and after (△) sputtering a 10-nm-thick Ti nanolayer (a), and for a $Fe_{72.5}Si_{12.5}B_{15}$ glass-coated microwire (■), after sputtering a 30-nm-thick Au nanolayer (▲) and after subsequent electroplating (△) of a 14-m-thick Ag microlayer (b). (Reproduced from K. Pirota *et al*., 2005, with permission from Elsevier. © 2005.)

loop of a CoFeNi-based nonmagnetostrictive microwire, typical of a circular anisotropy becomes square denoting the axial anisotropy ascribed to the compressive stresses induced by the Ti nanolayer. In turn, in Figure 25(b), the square loop of a Fe-based magnetostrictive microwire becomes finally nearly nonhysteretic after sputtering and subsequent electroplating two nano- and microlayers, respectively.

An interesting possibility is to obtain multiphase magnetic microwires by suitable electroplating of magnetic material (Pirota *et al*., 2005), which was recently exploited in the production of biphase magnetic multilayer microwires. In the case shown in Figure 26(a), the internal core is a nonmagnetostrictive ultrasoft Co-rich alloy, and the externally electroplated microlayer consists of a magnetically harder CoNi alloy. The hysteresis loops show the biphase hysteresis loop characterized by two giant Barkhausen jumps: the first one at the very low-field region (observed at around $20\,\mathrm{A\,m^{-1}}$) corresponding to the magnetization reversal at the magnetically ultrasoft Co-rich ultrasoft amorphous alloy, while the second one is observed at higher field (of around $20\,\mathrm{kA\,m^{-1}}$) and is ascribed to magnetization reversal at the external semihard CoNi microlayer.

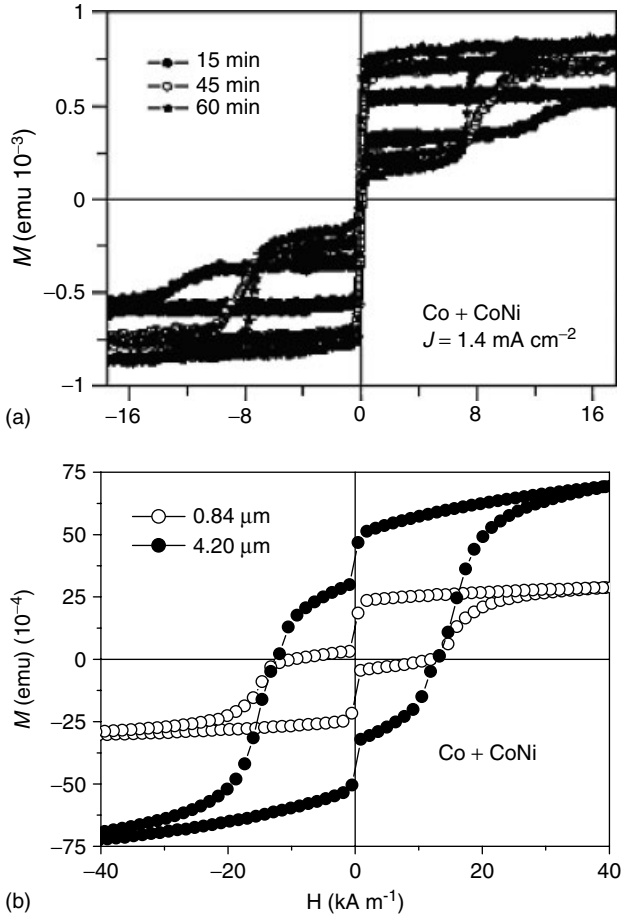

Figure 26. High-field hysteresis loops for a soft/hard biphase magnetic multilayer microwire consisting of an ultrasoft Co-based nonmagnetostrictive glass-coated microwire, coated by an intermediate sputtered 10-nm-thick Au nanolayer, and an outer electroplated CoNi microlayer shell with increasing thickness (a) (reproduced from K. Pirota *et al*., 2005, with permission from Elsevier. © 2005), and one branch of the low-field hysteresis loops after premagnetizing to saturation (b). (After Torrejón, Badini, Pirota and Vázquez, 2007.)

The existence of a magnetic coupling between the soft core and the hard layer has been recently confirmed (Torrejón, Badini, Pirota and Vázquez, 2007). Figure 26(b) shows the shifted low-field magnetization curves of the ultrasoft core after premagnetizing in a saturating magnetic field for a range of thicknesses of the electroplated hard shell. This shifting or bias field, H_b, is parallel to the premagnetizing field direction similar to antiferromagnetic-like coupling in exchange FM/AFM biased thin films used in spin valves. In the present case, where the bias field depends on the geometrical characteristics (i.e., length and thickness of each phase), its origin has been ascribed to the magnetostatic field created by unbalanced charges at the ends of the hard layer which remains in its remanence state after premagnetizing. A similar effect has been found in the case of electroplating directly onto an in-water-quenched microwire (Vázquez *et al*., 2006a,b, 2007; Torrejón, Badini, Pirota and Vázquez, 2007).

The possibility of tailoring multilayer microwires is particularly interesting regarding some technological applications. One, based on the magnetoelastic behavior of the multilayer microwires, makes use of the mechanical stresses induced by the new coatings and of their different magnetic response upon temperature changes. This principle has been used for sensitive quick-response thermal sensors (Vázquez *et al*., 2001).

Other applications are based on the magnetic coupling between phases. The field created by the hard phase can be employed as the additional dc field required to obtain asymmetric magnetoimpedance which is used for magnetic field sensing. The magnetostatic bias between soft and hard phases giving rise to a spin-valve effect, similar to exchange coupling in planar multilayer structures, opens new applications deriving from the cylindrical symmetry of the multilayer microwires.

6 FINAL REMARKS

We conclude the chapter with a mention of the large number of fields where magnetic microwires are relevant, from fundamental aspects as exhibiting simple, nearly ideal domain structure for suitable micromagnetic static and dynamic calculations, weak-chaos behavior induced by magnetic interaction, or the scaling law in low-field propagating

single-domain wall, to interesting fabrication and processing techniques, to engineering materials, or to a variety of sensor applications profiting, for instance, of their excellent magnetoelastic or microwave properties. Present challenges are related to the search of novel microwires with optimized hard, soft, or multiphase magnetic behavior, as well as to fabricate, in a controlled way, wires with more reduced dimensions, that is, nanoscale diameter which is the topic of the next chapter.

REFERENCES

Acher, O., Engelvin-Adenot, A.L. and Duverger, F. (2000). Fresnel coefficients at an interface with a lamellar composite material. *Physical Review B*, **62**, 3890.

Arcas, J., Gómez-Polo, C., Zhukov, A., *et al*. (1996). Magnetic properties of amorphous and devitrified FeSiBCuNb glass-coated microwires. *Nanostructured Materials*, **7**, 823.

Atalay, F.E. and Atalay, S. (2005). Giant magnetoimpedance effect in NiFe/Cu plated wire with various plating thicknesses. *Journal of Alloys and Compounds*, **392**, 322.

Badini Confalonieri, G.A. (2005). *Thesis Vanishing magnetostriction amorphous alloy wires for sensor applications*, University of Sheffield.

Badini, G., Torcunov, A., García, K. and Vázquez, M., to be published.

Barandiarán, J.M., Hernando, A., Madurga, V., *et al*. (1987). Temperature, stress, and structural-relaxation dependence of the magnetostriction in $(Co_{0.94}/BFe_{0.06})_{75}/BSi_{15}B_{10}$ glasses. *Physical Review B*, **35**, 5066.

Baranov, S.A. and Vázquez, M., Engineering microwave properties of glass-coated microwires for radio-absorption screens. to be published.

Baranov, S.A. (1998). Magnetic properties of an amorphous microconductor in the microwave range. *Technical Physics*, **43**, 122.

Baranov, S.A. (2003). Permeability of an amorphous microwire in the microwave band. *Journal of Communications Technology and Electronics*, **48**, 226.

Baranov, S.A., Zotov, S.K., Larin, V.S. and Torkunov, A.V. (1991). Features of natural ferromagnetic resonance in an amorphous microwire (in Russian). *Fizika Metallov i Metallovedenie*, **69**, 172.

Baranov, S.A., Berzhanskii, V.N., Zotov, S.K., *et al*. (1989). Ferromagnetic resonance in amorphous magnetic wires (in Russian). *Fizika Metallov i Metallovedenie*, **67**, 73.

Barnett, S.J. and Kenny, G.S. (1952). Gyromagnetic ratios of iron, cobalt, and many binary alloys of iron, cobalt and nickel. *Physical Review B*, **87**, 723.

Beach, R.S. and Berkowitz, A.E. (1994). Giant magnetic field dependent impedance of amorphous FeCoSiB wire. *Applied Physics Letters*, **64**, 3652.

Belozorov, D.P., Derkach, V.N. and Tarapov, S.I. (2002). High frquency absorption and magnetoimpedance of amorphous microwires. *Advances in Modern Radio Science*, **12**, 48.

Boley, B.A. and Weiner, J.H. (1990). Theory of Thermal Stresses. *Theory of Thermal Stresses*, John Wiley & Sons: New York.

Cai, C.M., Yamamoto, M. and Honkura, Y. (2005). Private communication. Intermag. the press.

Castaño, F., Vázquez, M., Chen, D-X., *et al*. (1999). Magnetomechanical rotation of magnetostrictive amorphous wires. *Applied Physics Letters*, **75**, 2117.

Catalán, C., Prida, V.M., Alonso, J., *et al*. (1997). Effect of glass coating on magnetic properties of amorphous microwires. *Materials Science and Engineering A*, Rapidly Quenched & Metastable Materials, (suppl.) 438–441.

Chen, D.X., Dempsey, N.M., Vázquez, M. and Hernando, A. (1995). Propagating domain wall shape and dynamics in iron-rich amorphous wires. *IEEE Transactions on Magnetics*, **31**, 781.

Chen, D-X., Pascual, L., Castaño, F., *et al*. (2001). Revised core-shell domain model for magnetostrictive amorphous wires. *IEEE Transactions on Magnetics*, **37**, 994–1002.

Chiriac, H., Marinescu, C.S. and Ovari, T.A. (1997). Comparative study of the giant magneto-impedance effect in CoFeSiB glass-covered and cold-drawn amorphous wires. *IEEE Transactions on Magnetics*, **33**, 3349.

Chiriac, H. and Ovari, T.A. (1996). Amorphous glass-covered magnetic wires: Preparation, properties, applications. *Progress in Materials Science*, **40**, 333.

Chiriac, H., Ovari, A.T. and Marinescu, C.S. (1998). Giant magneto-impedance effect in nanocrystalline glass-covered wires. *Journal of Applied Physics*, **83**, 6584.

Chiriac, H., Ovari, T.A., Marinescu, S.C. and Nagacevschi, V. (1996). Magnetic anisotropy in FeSiB amorphous glass-covered wires. *IEEE Transactions on Magnetics*, **32**, 4755.

Chiriac, H., Ovari, T.A., Pop, Gh. and Barariu, F. (1997). Magnetic behavior of nanostructured glass covered metallic wires. *Journal of Applied Physics*, **81**, 1.

Chiriac, H., Pop, G., Barariu, F. and Vázquez, M. (1994). Magnetic behavior of the amorphous wires covered by glass. *Journal of Applied Physics*, **75**, 6949.

Chiriac, H., Hristoforou, E., Neagu, M., *et al*. (1997). A new magnetic field sensor based on magnetostrictive delay lines. *Sensors and Actuators, A*, **59**, 79.

Chiriac, H., Hristoforou, E., Neagu, M., *et al*. (2000). Stress dependence of sound velocity in Fe-based amorphous wires. *IEEE Transactions on Magnetics*, **36**, 3436.

Chizhik, A., González, J., Zhukov, A. and Blanco, J.M. (2002). Magnetization reversal of Co-rich wires in circular magnetic field. *Journal of Applied Physics*, **91**, 537.

Cobeño, A.F., Zhukov, A., Blanco, J.M., *et al*. (2001). Magnetoelastic sensor based on GMI of amorphous microwire. *Sensors and Actuators*, **A91**, 95.

Costa, J.L. and Rao, K.V. (1991). Induced anisotropy in as-quenched amorphous wires. In *Physics of Magnetic Materials*, Gorzkowski, W., Gutowski, M., Lachowicz, H. and Szymczak, H. (Eds.), World Scientific: Singapore, p. 279.

Donald, I.W. (1987). Production, properties and applications of microwire and related products. *Journal of Materials Science*, **22**, 2661.

Engelvin-Adenot, A.L., Dudek, C., Toneguzzo, P. and Acher, O. (2007). Microwave properties of ferromagnetic composites and metamaterials. *Journal of European Ceramic Society*, **27**, 1029.

Freijo, J.J., Hernando, A., Vázquez, M., *et al*. (1999). Exchange biasing in ferromagnetic amorphous wires: A controllable micromagnetic configuration. *Applied Physics Letters*, **74**, 1305.

Fujimori, H. (1983). Magnetic anisotropy. In *Amorphous Metallic Alloys*, Luborsky, F.E. (Ed.), Butterworths: London, p. 300.

García, H., García, J.M., García-Beneitez, J.M., *et al*. (2000). Resonancia ferromagnética en vidrios metálicos. *Boletin de la Sociedad Espanola de Ceramica y Vidrio*, **39**, 367.

García, K., Varga, R. and Vázquez, M. (2005). Influence of the magnetoelastic mechanism on the fluctuating switching field of Fe-based amorphous microwires. *IEEE Transactions on Magnetics*, **41**, 3256.

García, J.M., Asenjo, A., Vázquez, M., *et al*. (2001). Determination of closure domain penetration in electrodeposited microtubes by combined magnetic force microscopy and giant magnetoimpedance techniques. *Journal of Applied Physics*, **89**, 3888.

García-Miquel, H., Esbrí, M.J., García, J.M., *et al*. (2001). Power absorption and ferromagnetic resonance in Co-rich metallic glasses. *IEEE Transactions on Magnetics*, **37**, 561.

García-Miquel, H., García, J.M., García-Beneytez, J.M. and Vázquez, M. (2001). Surface magnetic anisotropy in glass-coated amorphous microwires as determined from ferromagnetic resonance measurements. *Journal of Magnetism and Magnetic Materials*, **231**, 38.

Gómez-Polo, C. and Vázquez, M. (1993). Structural relaxation and magnetic properties of Co-rich amorphous wire. *Journal of Magnetism and Magnetic Materials*, **118**, 86.

Gómez-Polo, C., Vázquez, M. and Chen, D-X. (1993). Directionally alternating domain wall propagation in bistable amorphous wires. *Applied Physics Letters*, **62**, 108.

Gómez-Polo, C., Vázquez, M. and Knobel, M. (2001). Rotational giant magnetoimpedance in soft magnetic wires: modelization through Fourier harmonic contribution. *Applied Physics Letter*, **78**, 111.

Gómez-Polo, C., Olofinjana, A.O., Marin, P., *et al*. (1993). The influence of nanocrystalline microstructure on the magneticproperties of a wire shaped ferromagnetic alloy. *IEEE Transactions on Magnetics*, **29**, 2673.

González, J., Zhukov, A., Blanco, J.M., *et al*. (2000). Evaluation of the saturation magnetostriction in nearly zero magnetostrictive glass-coated amorphous microwires. *Journal of Applied Physics*, **87**, 5950.

Goto, T. (1977). Mechanical properties of amorphopus FePCB filament produced by glass-coated melt spinning. *Bulletin of the Japan Institute of Metals*, **15**, 633.

Goto, T. (1980). Fe-B and Fe-Si-B system ally filaments produced by glass-coated melt spinning. *Transactions of the Japan Institute of Metals*, **21**, 219.

Hagiwara, M. and Inoue, A. (1993). Production techniques of alloy wires by rapid solidification. In *Rapidly Solidified Alloys*, Liebermann, H.H. (Ed.), Marcel Dekker: New York, p. 139.

Hagiwara, M., Inoue, A. and Masumoto, T. (1982). Mechanical properties of Fe-Si-B amorphous wires produced by in-rotating-water spining method. *Metallurgical Transactions A*, **13A**, 373.

Harrison, E.P., Turney, G.L. and Rowe, H. (1935). Electrical properties of wires of high permeability. *Nature*, **135**, 961.

Hernando, A. and Vázquez, M. (1993). In *Rapidly Solidified Alloys*, Liebermann, H.H. (Ed.), Marcel Dekker: New York, p. 139.

Hernando, B., Olivera, J., Sánchez, M.L., *et al*. Magnetic Domain Structure and Impedance of Amorphous Microwires under Torsional Stress (to be published).

Hernando, A., Zhukov, A., Vázquez, M., *et al*. (1996). Método de codificación y marcado magnético de objetos. ES Patent: P9601993.

Hristoforou, E. (1997). Magnetostrictive delay lines and their applications. *Sensors and Actuators*, **A59**, 183.

Hristoforou, E. and Niarchos, D. (1992). Amorphous wires in displacement sensing techniques. *Journal of Magnetism and Magnetic Materials*, **116**, 177.

Humphrey, F.B. (1987). Article surveillance magnetic marker having an hysteresis loop with large Barkhausen discontinuities. US Patent 4660025.

Humphrey, F.B., Mohri, K., Yamasaki, J., *et al*. (1987). In *Proceedings of the Symposium on Magnetic Properties of Amorphous Metals*, Hernando, A., Madurga, V., Sánchez M.C., and Vázquez, M. (Eds.), North-Holland: Amsterdam, p. 110.

Issue devoted to magnetic wires (1995), *IEEE Transactions on Magnetics*, **31**(2),.

Jacquart, P.M. and Acher, O. (1996). Permeability measurement on composites made of oriented metallic wires from 0.1 to 18 GHz. *IEEE Transactions on Microwave Theory and Techniques*, **44**, 2116.

Issue devoted to magnetic wires (2002), *Journal of Magnetism and Magnetic Materials*, **249**(1–2),.

Kabanov, Yu., Zhukov, A., Zhukva, V. and González, J. (2005). Magnetic domain structure of wires studied by using the magneto-optical indicator film method. *Applied Physics Letters*, **87**, 142507.

Kakuno, K., Masuda, S., Yamada, T. and Mochida, H. (1987). Effects of wire-drawing and annealing on propagation of magnetoelsatic waves in amorphous wires. *IEEE Transactions on Magnetics*, **23**, 2554.

Kavesh, S. (1976). Apparatus for liquid quenching of free jet spun metal. US Patent 3 960 200.

Kim, C.G., Jang, K.J., Kim, D.Y. and Yoon, S.S. (1999). Analysis of asymmetric giant magnetoimpedance in field-annealed Co-based amorphous ribbon. *Applied Physics Letters*, **75**, 2114.

Knobel, M., Sánchez, M.L., Gómez-Polo, C., *et al*. (1996). Giant magneto-impedance effect in nanostructured magnetic wires. *Journal of Applied Physics*, **79**, 1646.

Knobel, M., Vázquez, M. and Kraus, L. (2003). Giant magnetoimepdance. In *Handbook of Magnetic Materials*, Buschow, K.H.J. (Ed.), Elsevier, p. 497, Vol. 15.

Knobel, M., Vázquez, M., Sánchez, M.L. and Hernando, A. (1997). Effect of tensile stress on the field response of impedance in low magnetostriction amorphous wires. *Journal of Magnetism and Magnetic Materials*, **169**, 89.

Kraus, L. (1999). Theory of giant magneto-impedance in the planar conductor with uniaxial magnetic anisotropy. *Journal of Magnetism and Magnetic Materials*, **196–197**, 354.

Kraus, L., Freit, Z., Pirota, K. and Chiriac, H. (2003). Giant magnetoimpedance in glass-covered amorphous microwires. *Journal of Magnetism and Magnetic Materials*, **254–255**, 3.

Kraus, L., Schneider, J. and Wiesner, H. (1976). Ferromagnetic-resonance in amorphous in amorphous alloys prepared by rapid quenching from melt. *Czechoslovak Journal of Physics, Section B*, **26**, 601.

Kraus, L., Kane, S., Vázquez, M., *et al*. (1994). Tensor Components of the magnetization in a twisted Fe-rich amorphous wire. *Journal of Applied Physics*, **75**, 6952.

Kurlyandskaya, G. and Levit, V. (2005). Magnetic Dynabeads detection by sensitive element based on giant magnetoimpedance. *Biosensors and Bioelectronics*, **20**, 1611.

Kurlyandskaya, G., Barandiarán, J.M., González, J., *et al*. (1999). Magnetoimpedance effect in CoFeNi plated wire with ac field annealing destabilized domain structure. *Journal of Applied Physics*, **85**, 5438.

Larin, V.S. Torkunov, A.V., Panina, L.V., *et al*. (2002). Micro wires and a process for their preparation. UK Patent GB0108373.2.

Li, Y.F., Vázquez, M. and Chen, D-X. (2003). Torsion-dependent magnetoimpedance in FeCuNbSiB nanocrystalline wires with vanishing or transverse anisotropy. *Journal of Applied Physics*, **93**, 9839.

Liu, J., Malmhäll, R., Arnberg, L. and Savage, S.J. (1990). Theoretical-analysis of residual-stress effects on the magnetostrictive properties of amorphous wires. *Journal of Applied Physics*, **67**, 4238.

Lofland, S.E., Baghat, S.M., García-Beneytez, J.M., *et al*. (1999). Low field microwave magnetoimpedance in amorphous microwires. *Journal of Applied Physics*, **85**, 4442.

Lofland, S.E., García-Miquel, H., Vázquez, M. and Baghat, S.M. (2002). Microwave magnetoabsorption in glass-coated amorphous microwires with radii close to skin depth. *Journal of Applied Physics*, **92**, 2058.

Luna, C., Raposo, V., Rauscher, G. and Vázquez, M. (2002). AC Magnetic field-induced rotation in levitating magnetostrictive wire. *IEEE Transactions on Magnetics*, **38**, 3180.

Luna, C., Raposo, V. Garshelis, I. *et al*., (2003). Inducing rotation and levitation in magnetostrictive wires and rods. *Sensors and Actuators A*, **106**, 274.

Madurga, V. and Hernando, A. (1990). Radial stress-distribution generated during rapid solidification of amorphous wires. *Journal of Physics: Condensed Matter*, **2**, 2127.

Makhnovskiy, D.P., Panina, L.V. and Sandacci, S.I. (2005). Field and Stress -Tuneable Microwave Composite Materials Based on Ferromagnetic Wires. In *Progress in Ferromagnetism Research*, Murray, V.N. (Ed.), Nova Science Publishers: Hauppauge.

Makhnovskiy, D.P., Panina, L.V., García, C., *et al*. (2006). Experimental demonstration of tunable scattering spectra at microwave frequencies in composite media containing CoFeCrSiB glass-coated amorphous ferromagnetic wires and comparison with theory. *Physical Review B*, **74**, 064205.

Malmhäll, R., Mohri, K., Humphrey, F.B., *et al*. (1987). Bistable magnetization revehersal in 50-mum diameter annealed cold-drawn amorphous wires. *IEEE Transactions on Magnetics*, **23**, 3242.

Masumoto, T., Ohnaka, I., Inoue, A. and Hagiwara, M. (1981). Production of Pd-Cu-Si amorphous wires by melt spinning method using rotating water. *Scripta Materialia*, **15**, 293.

Melo, L., Menard, D., Ciureanu, P. and Yelon, A. (2002). Influence of surface anisotropy on magnetoimpedance in wires. *Journal of Applied Physics*, **92**, 7272.

Meydan, T. and Elshebani, M.S. (1992). Displacement transducers using magnetostrictive delay-line principle in amorphous materials. *Journal of Magnetism and Magnetic Materials*, **112**, 344.

Mitra, A. and Vázquez, M. (1990). Stress-Dependent and annealing-dependent magnetic-properties of amorphous wires. *Journal of Physics D: Applied Physics*, **23**, 228.

Mohri, K. (1994a). Review on recent advances in the field of amorphous-metal sensors and transducers. *IEEE Transactions on Magnetics*, **20**, 942.

Mohri, K. (1994b). Aplication of amorphous magnetic wires to computer peripherals. *Materials Science and Engineering A*, **185**, 141.

Mohri, K., Humphrey, B.B., Yamasaki, J. and Okamura, K. (1984). Jitter-less pulse-generator elements using amorphous bistable wires. *IEEE Transactions on Magnetics*, **20**, 1409.

Mohri, K., Uchiyama, T. and Panina, L.V. (1997). Recent advances of micro magnetic sensors and sensing application. *Sensors and Actuators, A*, **59**, 1.

Mohri, K., Kohzawa, T., Kawasima, K., *et al*. (1992). Magnetoinductive effect (MI effect) in amorphous wires. *IEEE Transactions on Magnetics*, **28**, 3150.

Mohri, K., Uchiyama, T., Shen, L.P., *et al*. (2001). Sensitive micro magnetic sensor family utilizing magneto-impedance (MI) and stress-impedance (SI) effects for intelligent measurements and controls. *Sensors and Actuators*, **A91**, 85.

Mohri, K., Uchiyama, T., Shen, L.P., *et al*. (2002). Amorphous wire and CMOS IC-based sensitive micromagnetic sensors utilizing magnetoimpedance (MI) and stress-impedance (SI) effects. *IEEE Transactions on Magnetics*, **38**, 3063.

Montiel, H., Alvarez, G., Betancourt, I., *et al*. (2005). Correlations between low-field microwave absorption and magnetoimpedance in Co-based amorphous ribbons. *Applied Physics Letters*, **86**, 072503.

Nakatani, Y., Thiaville, A. and Miltat, J. (2003). Faster magnetic walls in rough wires. *Nature Materials*, **2**, 521.

Navarro, E., Garcia-Beneytez, J.M., Vázquez, M. and Hernando, A. (1996). Bifurcations in highly magnetostrictive amorphous wires. *Journal of Applied Physics*, **79**, 9231–9235.

Neagu, M., Chiriac, H., Hristoforou, E., *et al*. (2001a). Domain wall propagation in Fe-rich glass covered amorphous wires. *Journal of Magnetism and Magnetic Materials*, **226–230**, 1516.

Neagu, M., Chiriac, H., Vázquez, M., *et al*. (2001b). Saturation magnetostriction of Co-rich glass-covered amorphous wires. *Journal of Magnetism and Magnetic Materials*, **254**, 472.

Nielsen, O.V. (1985). Effects of longitudinal and torsional stress annealing on the magnetic anisotropy in amorphous ribbon materials. *IEEE Transactions on Magnetics*, **21**, 2008.

Nixdorf, J. (1967). Ein neues Verfahren zur Herstellung dünner Drähte mit Durchmessern im µm-Bereich. *Draht-Welt*, **53**, 696.

Ogasawara, I. and Ueno, S. (1995). Preparation and properties of amorphous wires. *IEEE Transactions on Magnetics*, **31**, 1219.

O'Handley, R.C. (1975). Domain wall kinetics in soft ferromagnetic metallic glasses. *Journal of Applied Physics*, **46**, 4996.

Ohnaka, I. (1980). Melt-spinning into liquid cooling medium. *Japanese Patent*, **64**, 948.

Ohnaka, I., Fukusako, T., Ohmichi, T., *et al*. (1982). In *Proceedings of the 4th International Conference Rapidly Quenched Metals*, Masumoto, T. and Suzuki, K. (Eds.): The Japan Institute of Metals, Sendai, p. 31.

Olofinjana, A.O. and Davies, H.A. (1992). Voids in directly cast amorphous alloy wire. *Scripta Metallurgica et Materialia*, **27**, 1679.

Olofinjana, A.O. and Davies, H.A. (1995). Preparation and mechanical properties of of Fe-Si-B-Nb-Cu nanocrystalline alloy wire. *Nanostructured Materials*, **6**, 465.

Ovari, T.A., Chiriac, H., Vázquez, M. and Hernando, A. (2000). Correlation between the magneto-impedance and ferromagnetic resonance responses in nanocrystalline microwires. *IEEE Transactions on Magnetics*, **36**, 3445.

Panina, L.V. and Mohri, K. (1994). Magneto-impedance effect in amorphous wires. *Applied Physics Letters*, **65**, 1189.

Panina, L.V., Mohri, K. and Makhnovskiy, D. (1999). Mechanism of asymmetrical magnetoimpedance in amorphous wires. *Journal of Applied Physics*, **85**, 5444.

Panina, L.V. (2002). Asymmetrical giant magneto-impedance (AGMI) in amorphous wires. *Journal of Magnetism and Magnetic Materials*, **249**, 278.

Pendry, J.B. (2000). Negative refraction makes a perfect lens. *Physical Review Letters*, **85**, 3966.

Pirota, K., Hernández-Vélez, M., Navas, D., *et al*. (2004). Multilayer microwires: Tailoring magnetic behaviour by sputtering and electroplating. *Advanced Functional Materials*, **14**, 266.

Pirota, K., Provencio, M., García, K., *et al*. (2005). Bi-magnetic microwires: a novel family of materials with controlled magnetic behaviour. *Journal of Magnetism and Magnetic Materials*, **290–291**, 68.

Prida, V.M., Hernando, B., Sánchez, M.L., *et al*. (2003). Torsional impedance effect in Fe-rich amorphous wires. *Journal of Magnetism and Magnetic Materials*, **258**, 158.

Pulido, E., del Real, R.P., Conde, F., *et al*. (1991). Amorphous wire magnetic-field and DC current sensor based on the inverse wiedemann effect. *IEEE Transactions on Magnetics*, **27**, 5241.

Rauscher, G. and Radeloff, C. (1989). Wiegand and pulse-wire sensors. In *Magnetic Sensors*, Boll, R. and Overshott, K.J. (Eds.), VCH Weinheim, p. 315.

Rauscher, G. and Radeloff, C. (1991). Large Barkhausen jump in composite wires. *IEEE Transactions on Magnetics*, **27**, 5238.

del Real, R.P., Prados, C., Chen, D-X., *et al*. (1993). Eddy-current damping of planar domain wall in bistable amorphous wires. *Applied Physics Letters*, **63**, 3518.

Reininger, T., Kronmüller, H., Gómez-Polo, C. and Vázquez, M. (1993). Magnetic domain observation in amorphous wires. *Journal of Applied Physics*, **73**, 5357.

Rodkowski, P., Strom-Olsen, J.O., Rudkowska, G., *et al*. (1995). Ultra-fine, ultra-soft metallic fibers. *IEEE Transactions on Magnetics*, **31**, 1224.

Sampaio, L., Sinnecker, E., Cernichiaro, G., *et al*. (2000). Magnetic microwires as macrospins in a long-range dipole-dipole interaction. *Physical Review B*, **61**, 8976.

Sethna, J.P., Dahmen, K.A. and Myers, C.R. (2001). Crackling noise. *Nature*, **410**, 242–250.

Severino, A.M., Gómez-Polo, C., Marín, P. and Vázquez, M. (1992). Influence of the sample length on the switching process of magnetostrictive amorphous wire. *Journal of Magnetism and Magnetic Materials*, **103**, 117.

Sinnecker, J.P., García, J.M., Asenjo, A., *et al*. (2000). Giant magnetoimpedance in CoP electrodeposited microtubes. *Journal of Materials Research*, **15**, 751.

Sinnecker, E., Páramo, D., Larin, V., *et al*. (1999). Glass coated microwires with enhanced coercivity. *Journal of Magnetism and Magnetic Materials*, **203**, 54.

Smith, D.R., Pendry, J.B. and Wiltshire, M.C.K. (2004). Metamaterials and negative refractive index. *Science*, **305**, 788.

Sonoda, Y. (1995). Applications of magnetometer sensors to observing bio-mechanical movements. *IEEE Transactions on Magnetics*, **31**, 1283.

Squire, P.T. (1994). Magnetomechanical measurements of magnetically soft amorphous materials. *Measurement Science and Technology*, **5**, 67.

Squire, P.T., Atkinson, D., Gibbs, M.R.J. and Atalay, S. (1994). Amorphous wires and their applications. *Journal of Magnetism and Magnetic Materials*, **132**, 10.

Ström-Olsen, J.O. and Rudkowsky, Piotr Z. (1991). Ferromagnetic fibers having use in electronical surveillance and method of making same. US Patent No 5,003,291.

Sugino, T., Takezawa, M., Honda, T. and Yamasaki, J. (2001). Basic load characteristics of magnetostrictive amorphous wire micromotor. *IEEE Transactions on Magnetics*, **37**, 2871–2873.

Taylor, G.F. (1924). A method of drawing metallic filaments and a discussion of their properties and uses. *Physical Review*, **23**, 655.

Theuss, H., Hofmann, B., Gómez-Polo, C., *et al*. (1995). Temperature dependence of the magnetization process of nearly non-magnetostrictive Co-rich amorphous wires. *Journal of Magnetism and Magnetic Materials*, **145**, 165.

Torrejón, J., Badini, G., Pirota, K. and Vázquez, M., (2007, accepted for publication). Design of multilayer microwires with controllable magnetic properties: magnetostatic and magnetoelastic coupling. *Acta Materialia*.

Uchiyama, T., Itoh, T., Mohri, K., *et al*. (2000). Car sensing method using amorphous wire CMOS IC sensor built into a disk installed on a road. *Journal of the Magnetics Society of Japan*, **24**, 775.

Ulitovsky, A.V. (1957). *Pribory I Technika Eksperimenta*, **3**, 115.

Valenzuela, R., Vázquez, M. and Hernando, A. (1996). A position sensor based on magnetoimpedance. *Journal of Applied Physics*, **79**, 6549.

Varga, R., García, K., Vázquez, M. and Vojtanik, P. (2003). Temperature dependence of the switching field and its distribution

function in Fe-based bistable microwires. *Applied Physics Letters*, **83**, 2620.

Varga, R., García, K., Vázquez, M. and Vojtanik, P. (2005). Single-Domain Wall Propagation and Damping Mechanism during Magnetic Switching of Bistable Amorphous Microwires. *Physical Review Letters*, **94**, 017201.

Varga, R., Torrejon, J., Kostyk, Y. *et al*., to be published.

Vázquez, M. (2001a). Soft magnetic wires. *Physica B*, **299**, 302.

Vázquez, M. (2001b). Giant magneto-impedance in soft magnetic Wires. *Journal of Magnetism and Magnetic Materials*, **226–230**, 693.

Vázquez, M. and Chen, D-X. (1995). The magnetization reversal process in amorphous wires. *IEEE Transactions on Magnetics*, **31**, 1229.

Vázquez, M., Gómez-Polo, C. and Chen, D-X. (1992). Switching mechanism and domain structure of bistable amorphouswires. *IEEE Transactions on Magnetics*, **28**, 3147.

Vázquez, M., Gómez-Polo, C., Chen, D-X. and Hernando, A. (1994). Magnetic bistability of amorphous wires and sensor applications. *IEEE Transactions on Magnetics*, **30**, 907.

Vázquez, M., Gómez-Polo, C., Theuss, H. and Kronmüller, H. (1996). Domain structure and magnetization process of bent Fe-rich amorphous wires. *Journal of Magnetism and Magnetic Materials*, **164**, 319.

Vázquez, M., Gómez-Polo, C., Velázquez, J. and Hernando, A. (1994). Bending stresses and bistable behavior in Fe-rich amorphous wire. *Journal of Applied Physics*, **75**, 5791.

Vázquez, M. and Hernando, A. (1996). A soft magnetic wire for sensor applications. *Journal of Physics D: Applied Physics*, **29**, 939.

Vázquez, M., Marín, P., Davies, H.A. and Olofinjana, A.O. (1994). Magnetic hardening of FeSiBCuNb ribbons and wires during the 1st stage of crystallization to a nanophase structure. *Applied Physics Letters*, **64**, 310.

Vázquez, M., Sinnecker, J.P. and Kurlyandskaya, G. (1999). Hysteretic behaviour and anisotropy fields in the magnetoimpedance effect. *Materials Science Forum*, Trans Tech Publications: Switzerland, p. 209, Vols. 302–303.

Vázquez, M., Theuss, H. and Kronmüller, H. (1999). Susceptibility profile in soft magnetic wires. *IEEE Transactions on Magnetics*, **35**, 573.

Vázquez, M. and Velázquez, J. (2002). An analysis of interacting bistable magnetic microwires: from ordered to chaotic behaviours. *Physica B*, **320**, 230.

Vázquez, M. and Zhukov, A. (1996). Magnetic properties of glass-coated amorphous and nanocrystalline microwires. *Journal of Magnetism and Magnetic Materials*, **160**, 223.

Vázquez, M., Badini-Confalonieri, G., Kraus, L., *et al*. (2007). Magnetostatic bias in soft/hard layered materials based on amorphous ribbons and microwires. *Journal of Non-crystalline Solids*, **353**, 763.

Vázquez, M., Castaño, F., Ovari, T.A., *et al*. (2001). New viscosimeter based on the ac field induced rotation of magnetostrictive amorphous wires. *Sensors and Actuators*, **A91**, 112.

Vázquez, M., García-Beneytez, J.M., García, J.M., *et al*. (2000). Giant magneto-impedance in heterogeneous microwires. *Journal of Applied Physics*, **88**, 6501.

Vázquez, M., González, J., Blanco, J.M., *et al*. (1991). Torsion dependence of the magnetization process in magnetostrictive amorphous. *Journal of Magnetism and Magnetic Materials*, **96**, 321.

Vázquez, M., Nielsch, K., Vargas, P., *et al*. (2004a). Modelling hysteresis of interacting nanowires arrays. *Physica B*, **343**, 395.

Vázquez, M., Zhukov, A., García, K., *et al*. (2004b). Dependencia térmica del proceso de inversión de la imanación en microhilos magnéticos biestables. *Boletin de la Sociedad Espanola de Ceramica y Vidrio*, **43**, 532.

Vázquez, M., Pirota, K., Badini, G., *et al*. (2006a). Sensor multifuncional basado en microhilos magnéticos multicapas con acoplamiento magnetoelástico. Patent PCT/ES2006/070173.

Vázquez, M., Pirota, K., Torrejón, J., *et al*. (2006b). Magnetoelastic interactions in multilayer microwires. *Journal of Magnetism and Magnetic Materials*, **304**, 197.

Vázquez, M., Zhukov, A., Aragoneses, P., *et al*. (1998). Magnetoimpedance in glass-coated CoMnSiB amorphous microwires. *IEEE Transactions on Magnetics*, **34**, 724.

Velázquez, J., García, C., Vázquez, M. and Hernando, A. (1996). Dynamic magnetostatic interaction between amorphous ferromagnetic wires. *Physical Review B*, **54**, 9903.

Velázquez, J., García, C., Vázquez, M. and Hernando, A. (1999). Interacting amorphous ferromagnetic wires: A complex system. *Journal of Applied Physics*, **85**, 2768.

Velázquez, J., Vázquez, M., Chen, D.X. and Hernando, A. (1994). Giant magnetoimpedance in nonmagnetostrictive amorphous wires. *Physical Review B*, **50**, 16737.

Velázquez, J., Vázquez, M. and Zhukov, A. (1996). Magnetoelastic anisotropy distribution in glass-coated microwires. *Journal of Materials Research*, **11**, 2499.

Velázquez, J., Navarro, E., Vázquez, M., *et al*. (1995). Torsional mode magnetoelastic resonance in ferromagnetic amorphous wire. *Journal of Applied Physics*, **77**, 5819.

Velázquez, J., Vázquez, M., Hernando, A., *et al*. (1991). Magnetoelastic anisotropy in amorphous wires due to quenching. *Journal of Applied Physics*, **70**, 6525.

Veselago, V.G. (1967). Properties of materials having simultaneously negative values of dielectric (XI) and magnetic (MU) susceptibilities. *Soviet Physics Solid State*, **8**, 2854.

Wang, K.Y., Chen, D-X., Arcas, J., *et al*. (1997). Formation and magnetic properties of compounds Er(Fe1-xCox)(11.35)Nb-0.65 ($0 \Leftarrow x \Leftarrow 0.4$). *Journal of Physics: Condensed Matter*, **9**, L573.

Wiegand, J.R. (1981). Switchable magnetic device. US Patent 4247 601.

Wulfhekel, W., Ding, H., Lutzke, W., *et al*. (2001). High-resolution magnetic imaging by local tunneling magnetoresistance. *Applied Physics*, **A72**, 463.

Yajako, M., Yamasaki, J. and Humphrey, F.B. (1993). Domain observations of Fe and Co based amorphous wires. *IEEE Transactions on Magnetics*, **29**, 3484.

Yamasaki, J. (1992). Domain structure of Co base wire with zero magnetostriction. *Journal of the Magnetics Society of Japan*, **16**, 14.

Yelon, A., Menard, D., Britel, M. and Ciureanu, P. (1996). Calculations of giant magnetoimpedance and of ferromagnetic resonance response are rigorously equivalent. *Applied Physics Letters*, **69**, 3084.

Yoshizawa, Y., Oguma, S. and Yamauchi, K. (1988). New Fe-based soft magnetic-alloys composed of ultrafine grain-structure. *Journal of Applied Physics*, **64**, 6044.

Zapperi, S., Castellano, C., Colairoi, F. and Durin, G. (2005). Signature of effective mass in crackling-noise asymmetry. *Nature Physics*, **1**, 46.

Zhukov, A. (2001). Domain wall propagation in a Fe-rich glass-coated amorphous microwire. *Applied Physics Letters*, **78**, 3106.

Zhukov, A. (2002). Glass-coated magnetic microwires for technical applications. *Journal of Magnetism and Magnetic Materials*, **242–244**, 216.

Zhukov, A. (2006). Design of the magnetic properties of Fe-rich, glass-coated microwires for technical applications. *Advanced Functional Materials*, **16**, 675.

Zhukova, V., Blanco, J.M., Zhukov, A. and Gonzáles, J. (2001). Studies of the magnetostriction of as-prepared and annealed glass-coated Co-rich amorphous microwires by SAMR method. *Journal of Physics D*, **34**, L113.

Zhukov, A., González, J. and Zhukova, V. (2005). Magneto resistance in thin wires with granular structure. *Journal of Magnetism and Magnetic Materials*, **294**, 165.

Zhukov, A., Garcia Beneytez, J.M., and Vázquez, M., (1996). Dispositivo magnetoelástico para la identificación y autentificación de firmas. Patent ES 9600172.

Zhukova, V., Usov, N.A., Zhukov, A. and González, J. (2002). Length effect in a Co-rich amorphous wire. *Physical Review B*, **65**, 134407.

Zhukov, A., Vázquez, M. and Beneytez, J.M. (1998). Magnetoelastic sensor for signature identification based on mechanomagnetic effect in amorphous wires. *Journal de Physique IV*, **8**, Pr−763.

Zhukov, A., González, J., Blanco, J.M., *et al*. (2000). Induced magnetic anisotropy in Co-Mn-Si-B amorphous microwires. *Journal of Applied Physics*, **87**, 1402.

Zhukov, A., González, J., Vázquez, M., *et al*. (2003). Nanocrystalline and Amorphous Magnetic Microwires. In *Encyclopedia of Nanoscience and Nanotechnology*, Nalwa, H.S. (Ed.), American Scientific Publishers, p. 1, Vol. X.

Zhukov, A., Luna, C., Martínez, J.L., *et al*. (2004a). Magnetoresistance in Co−Ni−Cu glass coated microwires. *Journal of Magnetism and Magnetic Materials*, **272–276**, 389.

Zhukov, A., Martín, D., Batallan, F., *et al*. (2004b). Studies of magnetoresistence and structure in CoNiCu thin wires. *Physical Status Solidi C*, **1**, 3717.

Zhukov, A., Sinnecker, E., Páramo, D., *et al*. (1999). Fabrication and magnetic properties of glass-coated microwires from immiscible elements. *Journal of Applied Physics*, **85**, 4482.

Zhukov, A.P., Vázquez, M., Velázquez, J., *et al*. (1995). The remagnetization process in thin and ultra-thin Fe-rich amorphous wires. *Journal of Magnetism and Magnetic Materials*, **151**, 132.

Zhukova, V., Zhukov, A., Blanco, J.M., *et al*. (2002). Switching field fluctuations in a glass-coated Fe-rich amorphous microwire. *Journal of Magnetism and Magnetic Materials*, **249**, 131.

Zhukov, A., Zhukova, V., Blanco, J.M., *et al*. (2003). Magnetostriction in glass-coated magnetic microwires. *Journal of Magnetism and Magnetic Materials*, **258–259**, 151.

Template-based Synthesis and Characterization of High-density Ferromagnetic Nanowire Arrays

Kornelius Nielsch[1] and Bethanie J. H. Stadler[2]

[1] *Max-Planck-Institut für Mikrostrukturphysik, Halle, Germany*
[2] *University of Minnesota, Minneapolis, MN, USA*

1 INTRODUCTION

Nanoscale arrays of ferromagnetic materials have an exciting future in a wide range of applications, including magnetic storage and nanoelectromechanical systems (NEMS) sensors and actuators. The motivation for studying nanowire arrays is that they hold much promise in fast-moving technologies such as magnetic storage. In addition, nanowire arrays inherently provide a high density of sensors, which will enable completely new applications, such as compact, high-bandwidth NEMS sensors. Several of these applications are discussed in this introduction, but the principles can be applied to many other important technologies.

One of the best examples of a fast-moving technology is magnetic storage, which has played a key role in the development of information technology since IBM built the original hard disk drive, known as random access method of accounting and control (RAMAC), in 1956. RAMAC had an areal density of 2 kbit $in.^{-2}$ and stored 5 MB of information on 50 24-in. disks. From 1956 to 1991, the areal density progressed at an average rate of 23% per year. After 1991, the annual increase in storage density for commercially available hard disks increased to 60%. By 2006, IBM was selling 2.5-in. hard disks with areal densities of 30 Gbit $in.^{-2}$, and a number of companies had demonstrated densities ranging up to 120 Gbit $in.^{-2}$ in their laboratories. If nanowire arrays were used as perpendicular magnetic storage media (O'Barr *et al*., 1997; Ross *et al*., 1999), an areal density of about 1 Tbit $in.^{-2}$ could be achieved using a hexagonally arranged array of nanomagnets with a lattice constant of about 25 nm (Figure 1; see also Section 7).

Nanowire arrays can be fabricated more cost-effectively by electrodeposition into nanoporous templates than by traditional fabrication methods, such as nanopatterning using focused ion beam or electron-beam lithography (Routkevitch *et al*., 1996). Moreover, these arrays of magnetic nanowires can be easily fabricated over areas of several square centimeters. Although a variety of nanoporous templates are reviewed here, hexagonally arranged porous

Handbook of Magnetism and Advanced Magnetic Materials. Edited by Helmut Kronmüller and Stuart Parkin. Volume 4: *Novel Materials*. ISBN: 978-0-470-02217-7.

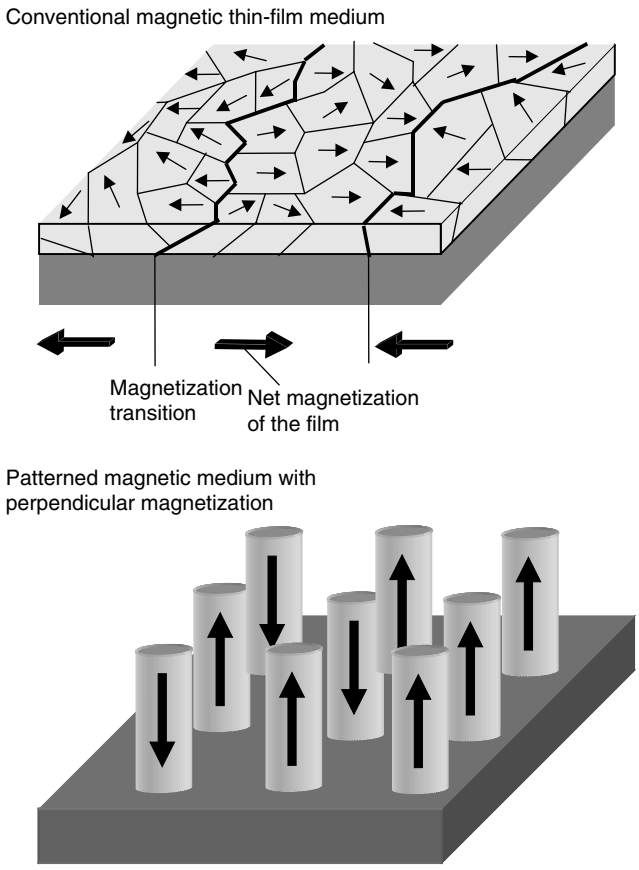

Figure 1. Principle of a conventional magnetic media based on longitudinal thin films and the principal of a patterned magnetic media based on single-domain nanowires.

alumina templates are most important for the following discussion on nanowire arrays.

Since 1975, numerous articles on disordered porous alumina templates filled with ferromagnetic materials have been published (Kawai and Ueda, 1975; Kaneko, 1981; Almawlawi, Coombs and Moskovits, 1991; Feiyue, Metzger and Doyle, 1997; Strijkers *et al*., 1999; Zeng *et al*., 2000). These structures had large distributions in both their pore sizes and their interpore spacings, and the degree of pore filling was usually not specified in the literature. On the basis of an approach by Masuda and Fukuda (1995) (see also Section 3), several groups have obtained ordered porous alumina arrays with sharply defined pore sizes and interpore spacings using two-step electrochemical anodization of aluminum (Li *et al*., 1998; Nielsch *et al*., 2002a; Stadler *et al*., 2005). Using this technique, the pores had excellent short-ranged order, leading to a polydomain structure where typical domain sizes were on the microscale. Monodomain pore arrays have also been obtained by electron-beam lithography (Li, Müller and Gösele, 2000) and nanoimprint techniques (Masuda *et al*., 1997; Tan, 2005; Stadler *et al*., 2005; McGary *et al*., 2006).

The first attempts at developing metal-filled alumina membranes for magnetic media were made by a Japanese company in the middle 1970s (Kawai and Ueda, 1975; Kaneko, 1981). At that time, disordered membranes were used and information was stored like conventional media (1 bit $\equiv$ 10–100 magnetic wires). At the turn of the century, two major Japanese companies (Canon and Fujitsu Technology) restarted research activities on the development of a high-density magnetic media based on perfectly ordered alumina membranes with the hope of obtaining patterned magnetic media with a storage capacity in the terabits per square inch range, where each magnetic nanowire could be addressed and store 1 bit of information.

In sensor applications, clusters of nanowires have often been used in order to make contact between the wires and microfabricated electronics (Lindeberg and Hjort, 2003). Track-etched, templated Ni nanowire clusters have been used in this way to measure magnetoresistance (MR) as high as 1% ($\Delta R/R$) caused by a strong field (7 kOe). Because of the potential of individual nanowire sensors, many groups have made magnetic nanowires and are studying the magnetic properties of the wires as a function of size, template, composition, temperature, and external fields (Liu, Wang, Yan and Xue, 2004; Chiriac, Moga, Urse and Ovari, 2003; Nielsch *et al*., 2002b,c; Skomski, 2003; Kelcher, Park, Yoo and Myung, 2005). Magnetotransport in Bi nanowires has also been studied at low temperatures (Zhang *et al*., 1998). In addition to the cluster measurements, copolymer templates have been made with sufficiently spaced wires to allow MR measurements of single wires at a time (Gravier *et al*., 2004).

However, for some innovative sensor applications, such as artificial cilia transducers which mimic the cilia in the ear, it is essential to have dense arrays of parallel wires that are perpendicular to the substrate (Figure 2a). This requirement is also present in magnetic random access memory in order to achieve high density (each bit a single nanowire) combined with thermal stability (Figure 2b). For applications like these, template-based nanomagnets are the best option.

This article discusses several templates that can be used in the fabrication of nanomagnet arrays in Section 2, with an emphasis on nanoporous anodic alumina. Next, two methods for the fabrication of nanomagnets are explained in Section 3. The magnetic properties of Co, Ni, and permalloy nanowires arrays are described in Section 4, followed by some modeling results of these properties in Section 5. Sections 6 and 7 present arrays with perfect large-scale order and some key applications. Finally, a summary of the fundamentals presented here is given in the concluding remarks.

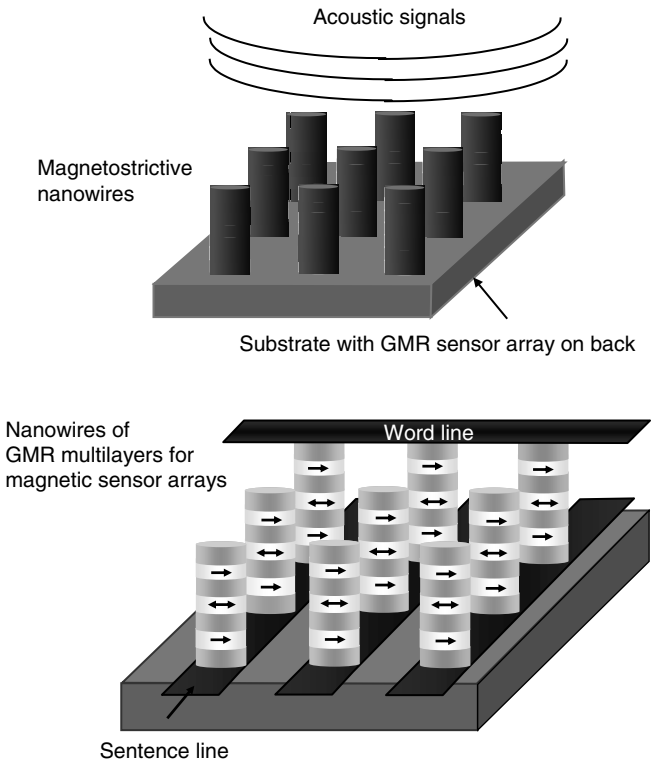

Figure 2. Schematics of acoustic and magnetic sensors based on magnetic nanowire arrays.

2 GENERAL SYNTHESIS TECHNIQUES FOR MAGNETIC NANOWIRE ARRAYS

Although this chapter primarily focuses on fabrication using anodic alumina templates, several nanoporous templates can be used to make nanowires. Self-assembled nanoporous templates include both anodic alumina and diblock copolymers. Another template involves pores that are defined inside certain polymers using ion tracks. Once a nanoporous template is obtained, nanowires can be grown inside the pores via electrochemical deposition. If the nanowires are grown to extend out of the pores, the exposed sides will induce lateral growth, which may be undesirable. For example, in many applications, the nanowires are removed from their template, and lateral outgrowths on the surface will inhibit the template etching. In magnetic nanowires, outgrowth will also alter the measured magnetic properties of the sample, such as anisotropy.

For completeness, the reader should be aware that there are several other methods of growing nanowires that do not involve templates, including fabrication of individual nanowires via step-edge decoration (Petrovykh, Himpsel and Jung, 1988; Tokuda *et al*., 2004), aqueous growth using electrical fields (Cheng, Gonela, Gu and Haynie, 2005), and the vapor–liquid–solid technique (Morales and Lieber, 1998). Also, in addition to the 'bottom-up' approaches of self-assembly discussed here, some experimentalists have fabricated ferromagnetic nanowires using 'top-down' approaches such as lithography. Although some interesting studies on ferromagnetic nanowires fabricated this way have been reported (Florez, Krafft and Gomez, 2005; Dumpich, Krome and Hausmanns, 2002; Castano *et al*., 2002), the nanowires are strictly limited to parallel configurations with the substrate in order to obtain high aspect ratios (10–100). Therefore, two-dimensional arrays, such as those discussed here, are not possible.

The most common nanoporous templates are discussed in detail below, including anodic aluminum oxide, selectively etched block copolymers, and ion-track-etched polymers. Another template that is less common involves phase-separated Al–Si alloys from which the Al has been etched (Fukutani, Tanji, Motoi and Den, 2004).

2.1 Anodic alumina templates

The main advantage of anodic alumina nanoporous templates is that the nanopores can be made to self-assemble strictly parallel to each other and perpendicular to the substrate (Figure 3), using a two-step anodization process that was developed initially by Masuda and Satoh (Masuda and Fukuda, 1995; Masuda, Tanaka and Baba, 1990). The pores are grown inside an oxide that forms during the anodization of either Al foil or Al films for integrated nanopores (Rabin *et al*., 2003). The process of anodization involves applying

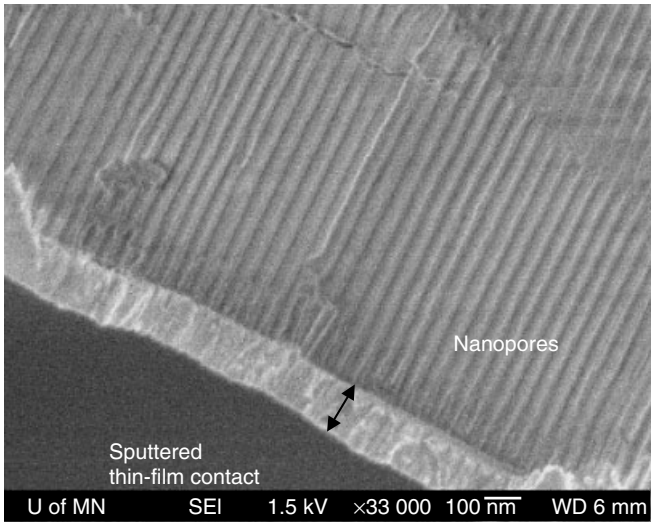

Figure 3. As seen in this fractured side view of anodic alumina nanopores, the pores are strictly parallel to each other. A Cu contact has been sputtered onto one side for electrodeposition of wires into the other side of the pores.

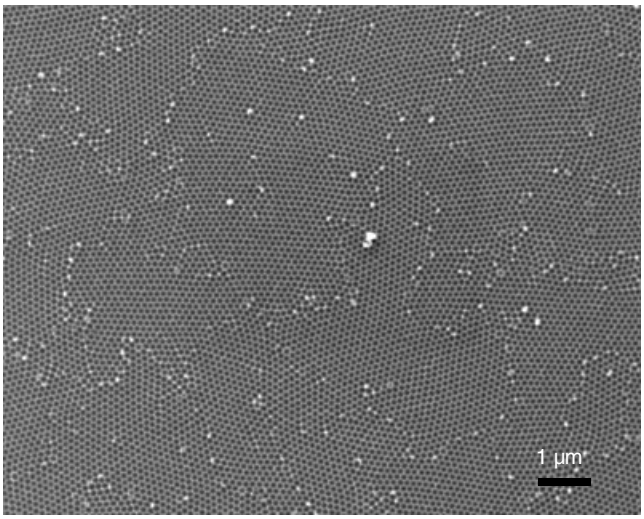

(a)

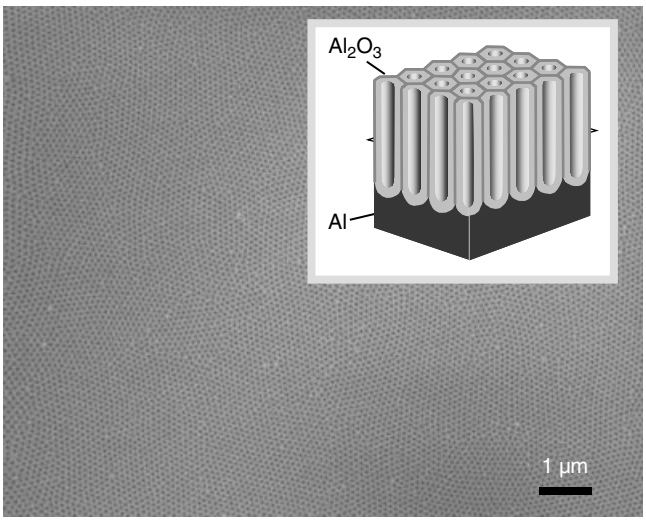

(b)

Figure 4. Self-assembled anodic alumina nanopores with typical short-range order: (a) Al surface after first oxide is etched away and (b) top of oxide after second anodization.

a voltage to a clean, smooth surface of aluminum while exposing it to an acid. The pores appear to form owing to mechanical stresses in the thickness-limited passive oxide that grows as a result of the anodization (Li *et al*., 1998). The pore ordering occurs at the oxide/Al interface, so the electrolyte/oxide interface, or top interface, will be less ordered than the bottom interface in self-assembled pores. Also, the bottom of the as-grown pores will be closed off by the passive oxide layer, which is called the *barrier layer*.

The two-step process (Masuda and Fukuda, 1995; Masuda, Tanaka and Baba, 1990) involves an initial, long anodization (∼16 h) to establish order at the oxide/metal interface. This nanoporous oxide is then etched away, leaving a clean Al

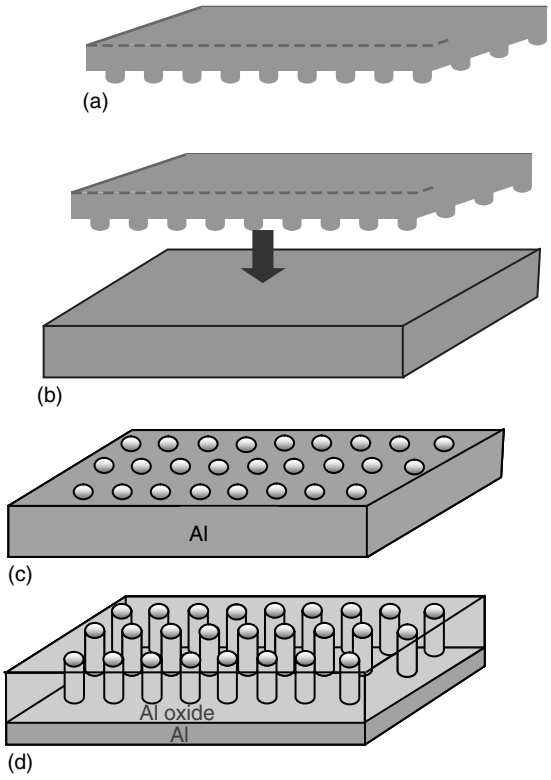

Figure 5. Process for directed self-assembly of nanopore arrays by nanoimprint method: (a) master stamp with ordered array of posts, (b) molding on the Al using an oil press, (c) patterned Al sheet, (d) anodization and growth of high-order nanopore arrays.

substrate that is textured where the bottoms of the now-etched nanopores had been (Figure 4a). A second oxide is then grown under the same conditions, and the new pores form at the already organized sites of the first anodization because of variations in mechanical stress at the textured Al surface (Figure 4b). These nanopores are parallel to each other since they will grow at the same location from top to bottom.

The dimensions of the nanoporous arrays are determined by the temperature of the electrochemical bath, the choice of electrolyte, and the voltage. The latter two parameters are especially important, and it has been shown that the interpore spacing (a) varies linearly from 10 to 500 nm with applied voltage (V) from 5 to 195 V according to

$$a(\text{nm}) \sim -b + mV(V) \tag{1}$$

where researchers have found values of b and m to be in the range of 0–1.7 and 2.5–3, respectively (Li *et al*., 1998; Cobian, 2004). Sulfuric acid is the common electrolyte for a less than 30 nm, oxalic acid is used for $30 < a < 70$ nm, and phosphoric acid is used for $a > 100$ nm. Pore diameters are typically a third to a half of the interpore spacings.

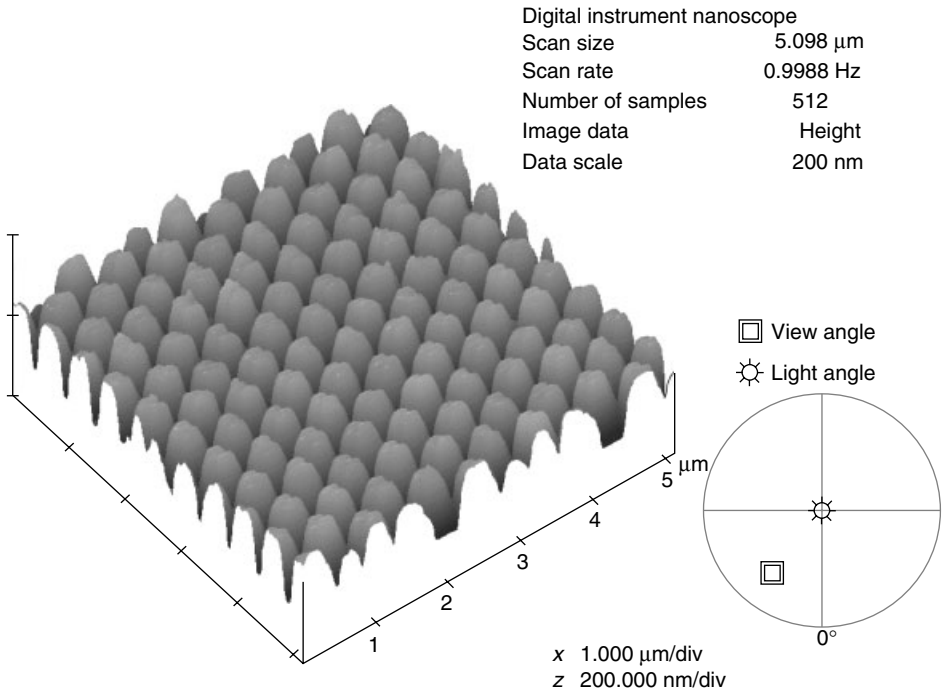

Figure 6. Atomic force micrograph of Si_3N_4 posts defined by electron-beam lithography for use as an imprint nanostamp.

With self-organization, the nanopores are hexagonally ordered with short-range order (Figure 4) (Tan, 2005; Stadler *et al*., 2005). However, a mechanical texture to the surface of the aluminum prior to anodization can be introduced to encourage long-range order (Figure 5). This has been done either by direct nanolithography and etching of the Al surface (Li *et al*., 1998) or by imprinting the Al with lithographically defined stamps of either SiC (Masuda *et al*., 1997; Masuda, Nishio and Baba, 1993) or Si_3N_4 (Stadler *et al*., 2005; Nielsch *et al*., 2003; Choi *et al*., 2003). Figures 6–8 show atomic force micrographs of a nitride stamp and an imprinted Al surface, and an scanning electron microscopy (SEM) photo of the resulting pores with long-range order, respectively (Tan, 2005; Stadler *et al*., 2005; McGary *et al*., 2006). Another stamp, and the resulting array of perfectly ordered Ni nanowires, is described in Section 6.

After growing the nanopores, the barrier layer is etched in phosphoric acid and a metallic contact is deposited on one side for electrodeposition of metal into the other end of the pores, Section 3.1. However, the barrier oxide presents a difficulty when trying to integrate nanowires onto convenient substrates, such as Si or glass (Rabin *et al*., 2003). Some researchers have tried to etch the whole sample in phosphoric acid, but the pores widened and lost their shape when the barrier layer was being removed. For short pores, for example those used for nanopattern transfer, the barrier layer can be removed by reactive ion etching with an inductively coupled plasm head (Zou, Qi, Tan and Stadler, 2006). This technique combines the speed of reactive ion etching (RIE) with the directionality of ion milling (Horst *et al*., 1997). Alternatively, electrodeposition techniques have also been used with a thinned barrier layer, see Section 3.2. In this case the barrier layer was not removed, but by an exponential reduction of the anodization potential over time the barrier layer was thinned down to less than 5 nm and dendrite pores were formed at the pore bottoms.

2.2 Diblock copolymer templates

Diblock copolymer membranes are an alternative to anodic alumina templates. Their advantages include the lack of a barrier layer and the ease of dissolution of the template to expose the wires, if desired for a specific application. However, the possible diameters (14–50 nm with $a = 24$–89 nm) are limited, and they are more difficult to align completely perpendicular to the substrate for subsequent electrodeposition of nanowires.

Diblock copolymers have two different types of polymers (e.g., polystyrene and polymethylmethacrylate) that are attached at one end (Xu *et al*., 2001; Gates, Mayers, Cattle and Xia, 2002; Thurn-Albrecht *et al*., 2000). Close-packed arrays can be achieved when the ratio of the minor to the major component is 0.3:0.7, then the minor phase is removed to make a nanoporous membrane (Olayo-Valles *et al*., 2005; Guo *et al*., 2006). An electric field can be used to help

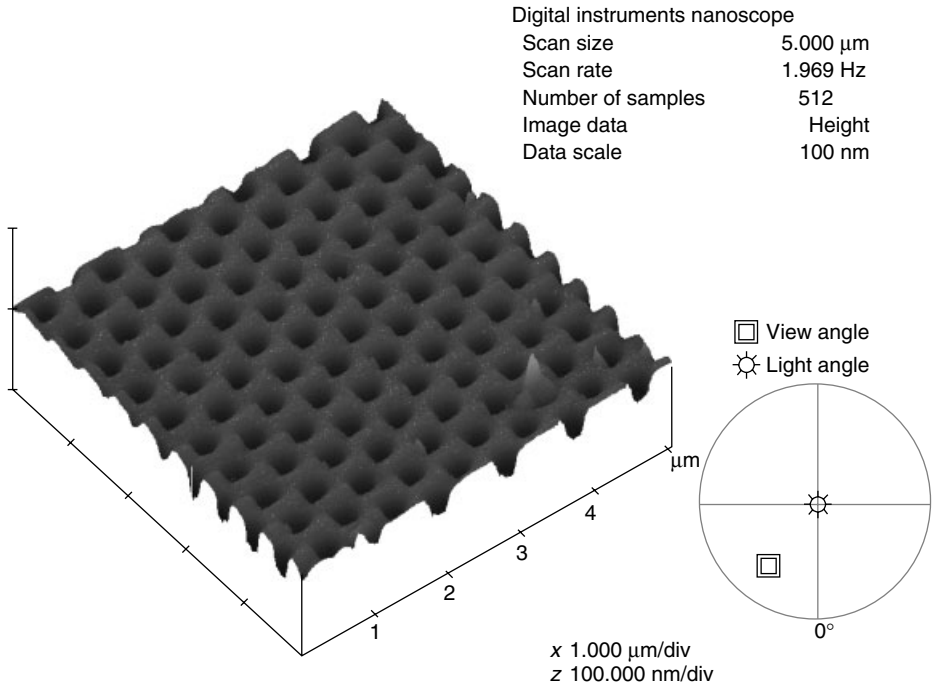

Figure 7. Atomic force micrograph of a polished Al surface that has been imprinted using a nanostamp.

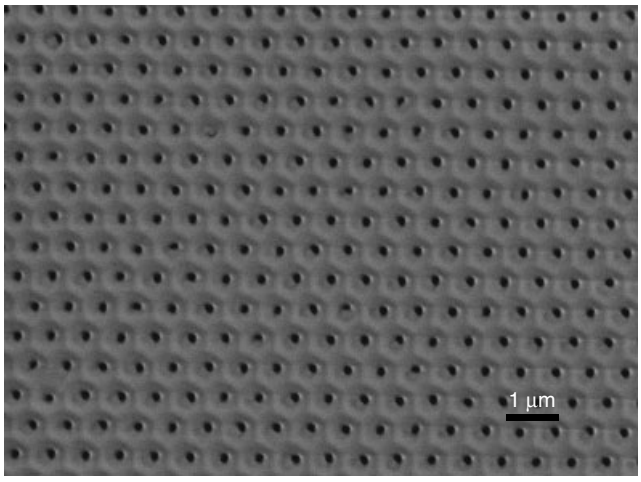

Figure 8. Scanning electron micrograph of nanopores that grew inside the oxide as an imprinted Al surface was anodized. The stamp was used to induce long-range order.

align the columns perpendicular to the substrate using surface charges between the blocks (Morkved *et al*., 1996; Amundson *et al*., 1994). However, the substrate can introduce competing interfacial interactions that encourage the cylindrical nanodomains to align parallel to the substrate if the voltage is not above a specific threshold (Thurn-Albrecht, DeRouchey, Russell and Jaeger, 2000).

Interestingly, nanowires can be grown directly by phase separation of a mixture of metal salt and polymer, but they will not be aligned. Au nanowires have been embedded directly into poly(ethylene oxide)–poly(propylene oxide)–poly(ethylene oxide) block copolymer by mixing gold salt ($HAuCl_4$) into the block copolymer medium and reducing the salt via UV irradiation and thermal reduction (Kim *et al*., 2004). Variations of styrene and vinylpyridine diblock copolymers have produced cylindrical nanostructures which have either been coated with metals or semiconductors or have been filled with metals through photoreduction (Fahmi, Braun and Stamm, 2003; Djalali, Li and Schmidt, 2002).

2.3 Etched ion-track templates

Nanowires can also be grown in ion tracks that have been etched in polycarbonate (Whitney, Jiang, Searson and Chien, 1993; Ferain and Legras, 1997; Schonenberger *et al*., 1997; Mbindyo *et al*., 2002; Dauginet-De Pra, Ferain, Legras and Demoustier-Champagne, 2002; Attenborough *et al*., 1995; Valizadeh, George, Leisner and Hultman, 2002). This technique produces a lower density of nanopores, even down to a single nanopore (Enculescu *et al*., 2003; Chtanko, *et al*., 2004; Toimil Molares *et al*., 2003), so that single wires can be measured. For this, 10–50-μm-thick polymer membranes are irradiated with heavy ions, such as Ar, Xe, Au, or Pb, with energies of 8–12 MeV/nucleon for single-ion tracks or 0.2–2 GeV with fluences between 10^6 and 10^9 ions/cm^2 for multiple tracks. The tracks left by the ions can

then be chemically etched in aqueous NaOH, sometimes after UV irradiation, to make pores as small as 15 nm. Occasionally, the polycarbonate membrane is spun-coated onto a substrate for convenient integration (Dauginet-De Pra, Ferain, Legras and Demoustier-Champagne, 2002), but the resulting pores tend to be conically shaped.

3 PREPARATION OF MAGNETIC NANOWIRES

Two approaches will be presented for the electrodeposition of magnetic nanowires in alumina membranes. First, electroplating directly onto a metallic electrode will be discussed where the barrier layer at the bottom of the pores has been removed. Second, a pulsed plating technique will be described in which the nanowires can be grown onto a thinned barrier layer.

3.1 Deposition directly onto contact electrodes

Once the nanoporous templates discussed above are fabricated, electrochemical deposition is the best method for nanowire growth due to the high aspect ratios involved. For direct deposition, the barrier oxide at the bottom of the pores is removed by floating the template on phosphoric acid with the bottom down in order to avoid pore widening. A contact film can then be sputtered onto one side of the template, but care must be taken that the film covers up the pores. Sometimes, rf sputtering can yield films that penetrate the pores a short distance, and they will not provide good electrical contact for growing wires. The use of oblique-angle sputtering can provide a solution. Films of copper, silver, gold, or any metal can be used, but precious metals usually require a thin initial coating of Ti or Cr to provide adhesion to the nanoporous oxide because of the high surface energetics. Contact-coated nanopores are submerged into an electrolyte containing metal ions and a voltage is applied that is sufficient to reduce the ions (Figure 9). The back of the sample is insulated so that only the contact at the bottom of the nanopores is exposed to the electrolyte, and wires grow as the metal reduces there.

The nanowires grow most evenly using potentiostatic deposition, where a constant voltage is applied to the electrode with respect to a reference electrode that is placed in close proximity to the working surface. This voltage must be less than the reduction potential of the metal, and overpotentials (η) increase current density (J) according to Erying's equation:

$$J = nFA\left(C_O e^{-\alpha nF\eta/k_B T} - C_R e^{(1-\alpha)nF\eta/k_B T}\right) \qquad (2)$$

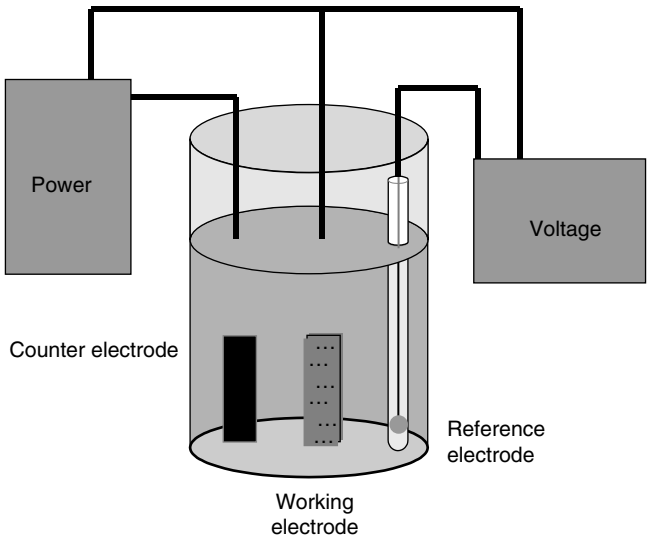

Figure 9. Schematic of electrodeposition apparatus used to grow nanowires inside templates.

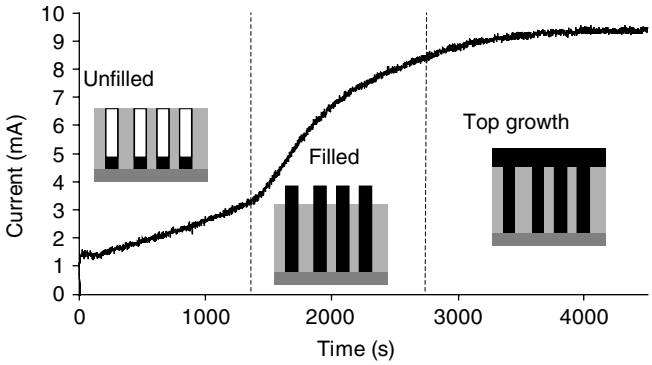

Figure 10. A plot of the current density versus growth time for potentiostatic electrodeposition of nanowires. The schematics show the progress of the growth of the nanowires with time.

where F is Faraday's constant, A is the electrode area, α is an empirical constant, k_B is Boltzmann's constant, and T is the temperature. The deposition rate is proportional to J, so it will scale exponentially with overpotential, so this overpotential can dramatically affect the resulting morphology, for example, grain size (Paunovic and Schlesinger, 1998). Also, the current density can be monitored during the growth in order to reach the desired lengths of the nanowires (Figure 10).

The most common electrolyte is a Watts bath, which is composed of metal sulfates and boric acid (a Lewis acid) to control the pH both in the bulk electrolyte and at the working surface. A typical recipe for Ni nanowires is $26\,g\,l^{-1}$ nickel sulfate heptahydrate, $45\,g\,l^{-1}$ boric acid (using -1.5 V vs a Ag/AgCl reference electrode at room temperature (RT) and sonication). For Fe nanowires, $80\,g\,l^{-1}$

$FeSO_4 \cdot 7H_2O$, 30 g l^{-1} H_3BO_3 can be used, and a new magnetostricitve alloy, $Fe_{1-x}Ga_x$ or Galfenol, can be obtained by adding 25 g l^{-1} $Ga_2(SO_4)_3 \cdot 18H_2O$. Voltages of -1 to -1.5 V versus Ag/AgCl can be used at RT with sonication, and sometimes complexing agents are added to the electrolyte (McGary, 2006). For growth of alloy nanowires, the overpotential for the two constituents will be different at a specific growth voltage. This is a good thing when one wants to control composition according to equation (2) using the standard reduction potentials. However, for nanowires, it can lead to great variations in nanowire composition as the wire grows closer to the reference electrode. Therefore, somewhat dilute electrolytes can be advantageous (McGary, 2006). X-ray diffraction (XRD) has shown that these bcc metals grow with the [110] direction parallel to the wire axis, and energy dispersive spectroscopy (EDS) or wavelength dispersive spectroscopy (WDS) can be used to study compositional variations along the wires.

A typical bath for Co nanowires is 75–250 g l^{-1} $CoSO_4$ with 0–50 g l^{-1} H_3BO_3 and sometimes NaOH is used to adjust the pH (3.3–6.5) (Cobian, 2004). As discussed in Section 4, the crystallography of several electrodeposited metals, especially hcp Co, has been shown to be dependent on pH. A high pH yields wires with the *c* axis parallel to the wire axes and low pH yields wires with the *c* axis perpendicular to the wire axes, as shown by XRD and ferromagnetic resonance (Cobian, 2004; Darques, Encinas, Vila and Piraux, 2004). This makes titration and the choice of whether to use Lewis acids matters of importance because the magnetocrystalline anisotropy of Co is large. Finally, for Co/Cu multilayered nanowires, 250 g l^{-1} $CoSO_4$ and 12.5 g l^{-1} $CuSO_4$ can be used. The reduction potential of copper (+0.14 V vs Ag^+/AgCl) is much higher than the reduction potential of cobalt (−0.48 vs Ag^+/AgCl). Therefore a dilution of Cu^{2+} in the bath enables deposition of Co primarily at more negative overpotentials and Cu primarily at potentials between the standard reduction potentials. The optimal potentials for depositing cobalt and copper were determined by cyclic voltammetry to be -1 and -0.5 V, respectively (Cobian, 2004; Tan and Stadler, 2006). For the thin multilayers required to produce MR (1–20 nm), transmission electron microscopy (TEM) must be used to analyze the layers (Tan and Stadler, 2006).

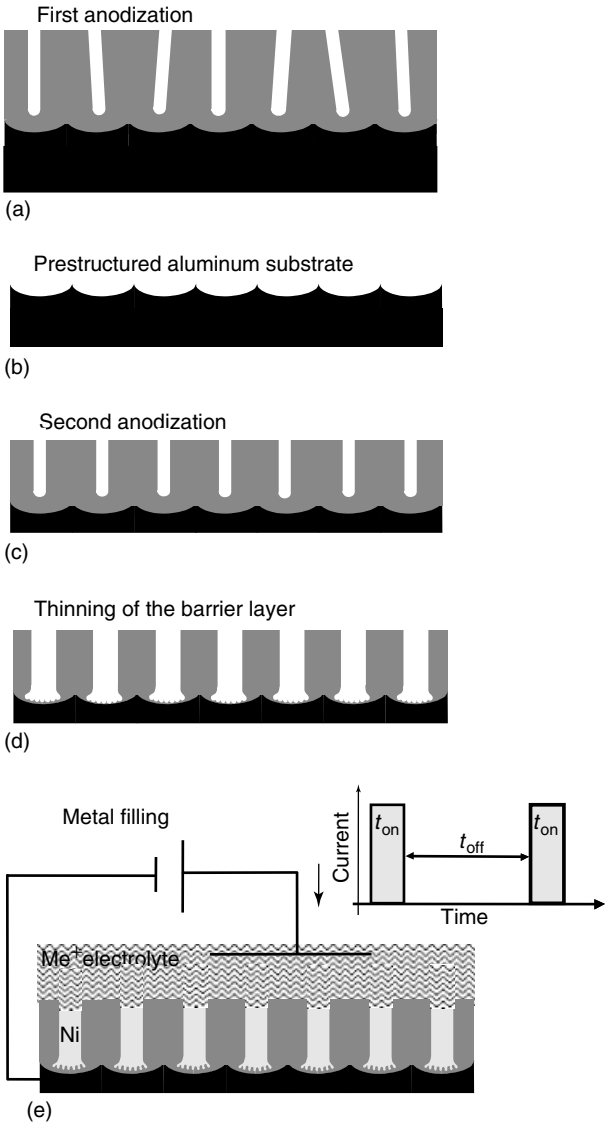

Figure 11. Schematic diagram demonstrating the fabrication of a highly ordered porous alumina matrix and the preparatory steps necessary for the subsequent filling of the structure. The Al substrate was prestructured by a long-time anodization and by removing the oxide (a,b). A second anodization step yielded a highly ordered alumina pore structure (c). The barrier layer was thinned and the pores were widened by isotropic chemical etching (d). To thin the barrier layer further, two current-limiting anodization steps followed, with dendrite pores forming at the barrier layer. Pulsed electrodeposition of nickel in the pores is shown in (e).

3.2 Pulsed electrodeposition on the oxide barrier

As mentioned above, the alumina membranes can be prepared via a two-step anodization process (Figure 11). When depositing wires without removing the barrier layer (e.g., for integrated templates), the quality and homogeneity of the deposition process has been significantly improved by thinning the barrier layer (Figure 11d). This thinning is done by chemical pore widening and by current-limited anodization (Nielsch *et al.*, 2000a). Firstly, growth electrolyte (oxalic acid) is heated to 30 °C to decrease the thickness of the barrier layer and to widen the pores chemically. After 3 h, the barrier layer is decreased from 45 to 30 nm and the mean pore diameter is increased from 30 nm to approximately 50 nm.

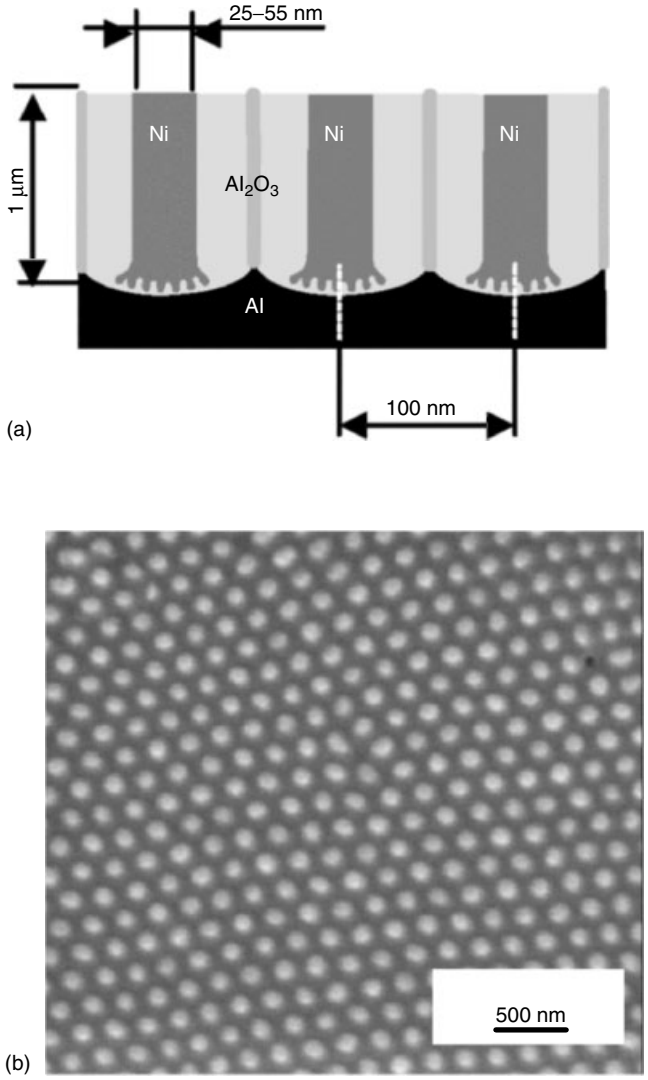

Figure 12. (a) Sketch of the magnetic structure. Nickel nanowires are arranged in a hexagonal array perpendicular to a silicon substrate and embedded in an aluminum oxide matrix. (b) Top-view SEM micrograph of a nickel-filled alumina matrix, with an interpore distance of 105 nm, fixed on a silicon substrate. The Ni columns have a diameter $D_P = 35$ nm and a length of ∼700 nm.

Afterward, the electrolyte is cooled down to 2 °C to interrupt the widening process. Secondly, the structure is anodized twice for 15 min using constant-current conditions of 290 and 135 mA cm^{-2}, respectively. During these anodization steps, the anodization potential decreases and the pores branch out at the formation front such that the thickness of the barrier layer is significantly reduced. Finally, the anodizing potential reaches 6–7 V, which corresponds to a barrier oxide thickness of less than 10 nm (Figure 11d) (Nielsch *et al*., 2000a).

Ferromagnetic materials can then be electrodeposited from aqueous electrolytes at the pore tip of these high-aspect-ratio porous templates (Figure 11e). A highly concentrated Watts-bath electrolyte is used to achieve a high concentration of metal ions in each pore. For example, a typical recipe for a nickel electrolyte is 300 g l^{-1} $NiSO_4 \cdot 6H_2O$, 45 g l^{-1} $NiCl_2 \cdot 6H_2O$, 45 g l^{-1} H_3BO_3, pH = 4.5, $T = 35$ °C (Nielsch *et al*., 2000a,b). The typical electrolyte for a cobalt deposition is similar, except that it contains Co salts and has a pH of 4.3 (Nielsch *et al*., 2000a,b). Frequently, an alternating current (AC) signal is used for the deposition (Almawlawi, Coombs and Moskovits, 1991; Feiyue, Metzger and Doyle, 1997; Choi *et al*., 2003; Nielsch *et al*., 2000a) when a porous alumina structure is kept on its aluminum substrate for the filling process. The metal is directly deposited onto the nearly insulating oxide barrier layer at the pore tips. It has been demonstrated that a pulsed electrodeposition (PED) is more suitable for a direct and homogeneous filling of the porous alumina structures, as described briefly in the following text (Nielsch *et al*., 2002a).

Nielsch found that pore filling was based on modulated pulse signals in the milliseconds range. During a relatively long pulse of negative current (8 ms, $I_{pulse} = -70$ mA cm^{-2}), metal was deposited in the bottom of the pore (Nielsch *et al*., 2002a). The measured voltage varied between −8 and −12 V. After the deposition pulse, a short pulse of positive polarization (2 ms, $U_{pulse} = +4$ V) followed to interrupt the electric field at the deposition interface immediately. A relatively long break time (0.3–1 s) was allowed between the deposition pulses to refresh the ion concentration at the deposition interface, to let the deposition by-products diffuse away from the pore bottoms, and to ensure a stable pH in each pore during the deposition. Consequently, the delay time t_{off} improved the homogeneity of the deposition. For the deposition of nickel $t_{off} = 990$ ms was selected. The deposition continued until the nanowires began to grow out of the pores.

For the characterization of these metal-filled templates (Figure 12a) and their magnetic properties, the tips of the nanowires closest to the substrate must be removed. To do this, the top of the template structure is fixed to a silicon substrate by conducting glue. Next, the aluminum substrate is removed by a saturated solution of HgCl and the structure is turned upside down. After removing ∼200 nm from the top of the sample using a focused ion beam, the top ends of the nanowires become visible at the surface and a relatively smooth surface can be obtained.

As an example, Figure 12(b) shows an SEM image of a nickel sample with a nanowire diameter of 35 nm and a 105-nm interpore distance (Nielsch *et al*., 2000a). Ferromagnetic nanowires (white) with a monodisperse diameter were embedded in the porous alumina matrix (black). Because of the self-organization process, the nanowires were arranged in a hexagonal pattern. Nearly 100% pore filling was obtained for all of the samples, demonstrating that the metallic filling extended over the whole length of the pores.

The crystallinity of these samples was further analyzed by XRD. From the 2θ scan, the average crystallite size was estimated using the Scherrer equation for round particles, yielding an average grain size $D_{Gr} = 10–15$ nm. Analysis by transmission electron microscopy has been performed on individual Ni nanowires that have been released from the alumina matrix by selective chemical etching. The nanowires consist of nanocrystallites of between 20 and 100 nm most of which have tetrahedral shapes, a face-centered cubic (fcc) lattice, and preferential ⟨110⟩ orientation perpendicular to the nanowire axis (Nielsch *et al*., 2001). Before magnetic characterization, the nanowire arrays embedded in the alumina matrix were transferred onto a silicon substrate and the dendrite structure of the magnetic nanowire was removed by ion bombardment (Nielsch *et al*., 2002c).

4 MAGNETIC PROPERTIES OF MAGNETIC NANOWIRE ARRAYS

Although many magnetic materials have been grown in nanoporous templates, the following discussion focuses on Co, Ni, and permalloy in order to review several different aspects of magnetic nanowires. In particular, magnetic anisotropy is best studied using Co because the crystallographic and shape anisotropies are comparable. Controlling coercivity is particularly interesting in Ni and permalloy. These chosen properties are interesting for applications in sensors and recording applications, respectively, but they also give the reader a sense of what properties are present in magnetic nanowires for many applications.

4.1 Arrays of cobalt nanowires

Cobalt is an especially interesting ferromagnetic material for nanowires because it has a large magnetocrystalline anisotropy. In fact, when comparing energy densities, this anisotropy ($K_u = 4.1 \times 10^5\ J\,m^{-3}$) is comparable to the magnetostatic shape anisotropy ($\mu_0 M_s^2/2 = 1.3 \times 10^6\ J\,m^{-3}$) (O'Handley, 2000). Therefore, aligning the *c* axis of the unit cell parallel and perpendicular to the wire axis enables control of a variety of interrelated magnetic properties, such as effective anisotropy, coercivity, and remanent magnetization.

This crystallographic alignment can be controlled using deposition parameters such as the pH of the solution, including the local pH at the growth surface, the deposition rate, applied magnetic fields, and the nanowire size. For example, Co will deposit in either the fcc or hcp phase depending on pH, where very low pH (<2.3) yields fcc (Cobian, 2004). Crystallographic alignment of magnetic hcp cobalt has been shown through the use of a magnetic field (Cobian, 2004; Stadler *et al*., 2005), but the pH is a stronger determinant of crystallographic alignment. For this reason, if Lewis acids, such as boric acid, are used to buffer the local pH, an applied magnetic field will have little effect on the crystallographic alignment. This has been shown in electrolytic solutions that contain boric acid, but are subsequently titrated to achieve controlled pH (Cobian, 2004; Darques, Encinas, Vila and Piraux, 2004). As mentioned in Section 3.1, low pH (3.3–5.3) will yield (100) alignment and high pH (>5.8) will yield (002) alignment, which means the hcp *c* axis is aligned perpendicular and parallel to the wire axis, respectively. Finally, deposition rate can be controlled using the Co^{2+} ion concentration in the electrolyte. If the rate is too fast, or too slow, an applied field will not affect the alignment. For example, with no boric acid (pH = 3.5) and 250 g l^{-1} $CoSO_4$, the alignment was (002) as expected for high pH solutions for all applied magnetic fields (Figure 13a). However, with a medium concentration of $CoSO_4$ (155 g l^{-1}) and no boric acid, a perpendicular applied field caused (100) alignment as the Co nanowires grew (Figure 13b) (Cobian, 2004).

The effects of the crystallographic alignment on magnetic properties can be seen from the hysteresis loops taken by vibrating sample magnetometry (VSM) of the resulting nanowires arrays. Although shape anisotropy will dominate, as predicted by the energy densities, a fivefold increase in the remnant magnetization and a threefold increase in the coercivities of the nanowires whose anisotropy axes were aligned parallel to each other can be obtained (Figure 14a).

Magnetostatic interactions between the nanowires can limit the overall control of the magnetic properties of the array, and templates that enable larger spacing between the nanowires may extend control. Also, if Co/Cu multilayers are grown along the nanowires, the shape anisotropy of each Co layer can be controlled when its thickness is comparable to the diameters of the nanowires (Stadler *et al*., 2005; Tan and Stadler, 2006). Finally, the parameters discussed in the preceding text have similar affects on crystallography over a wide range of diameters. However, the diameter itself will have a large effect on the magnetic properties, with the coercivity increasing with decreasing diameter until the diameter reaches about 30 nm, after which the coercivity will sharply decrease (Figure 14b) (Stadler *et al*., 2005).

4.2 Nickel and permalloy nanowire arrays

4.2.1 SQUID characterization and effects of Ni volume fraction

In addition to the vibration sample magnetometer (VSM) mentioned above, a superconducting quantum interference device (SQUID) magnetometer can also be used to measure

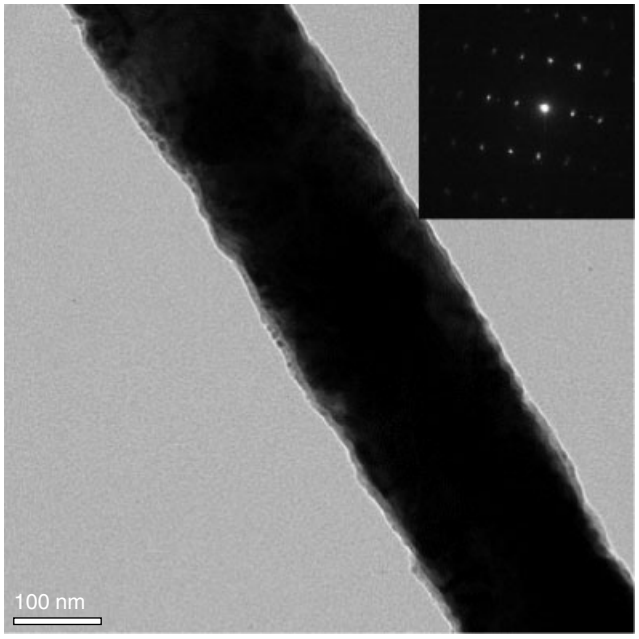

(a)

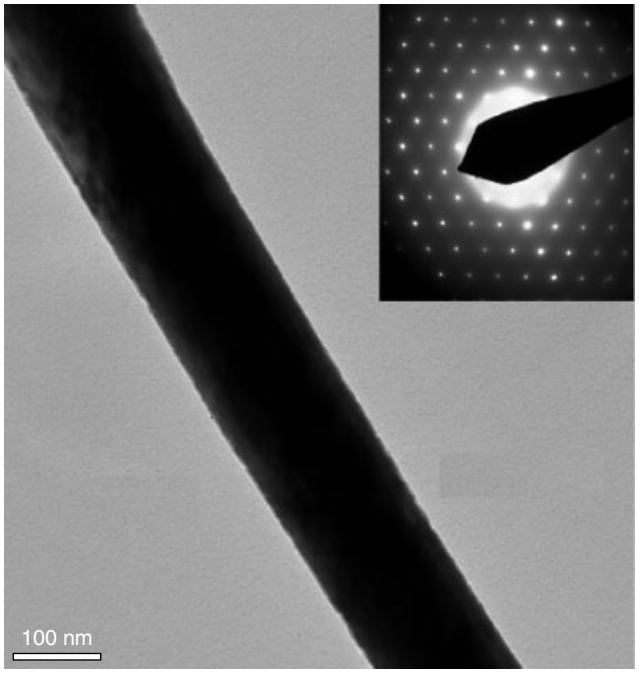

(b)

Figure 13. TEM micrographs and diffraction patterns of Co nanowires grown from a solution (pH $\sim$ 3.5) with no pH buffering agent. (a) High concentrations of Co^{2+} ions yielded expected [001] alignment along the wire axis, so side view is (100). (b) Slower deposition rates enabled the crystallographic alignment to be controlled by an applied magnetic field, and perpendicular fields caused the *c* axis to be aligned perpendicular to the nanowires axis (Cobian, 2004). (Reprinted with permission T. Xu *et al*., copyright 2001, Eslevier.)

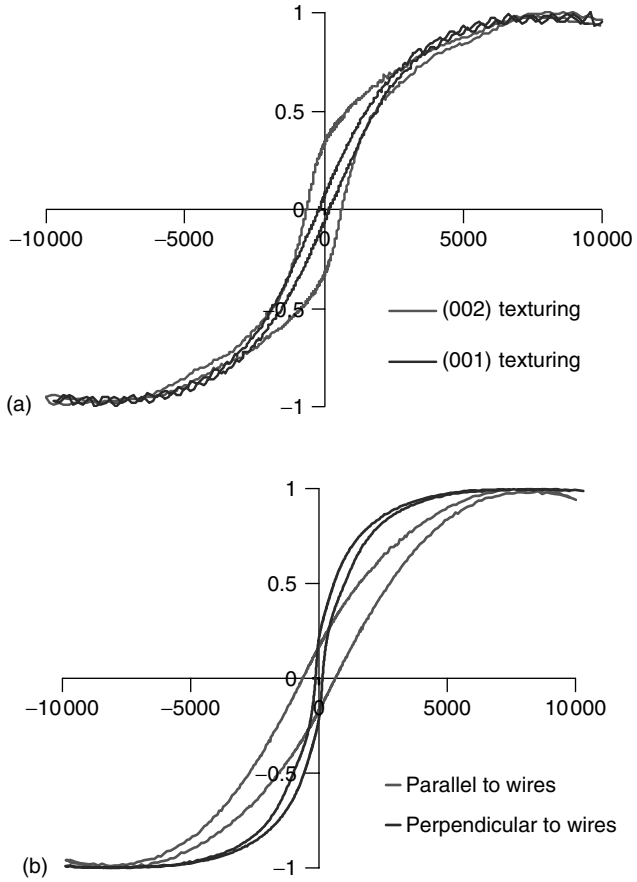

Figure 14. (a) Hysteresis loops parallel to the nanowire axes ((002) texturing: $H_c = 630\,\text{Oe}$, $M_r/M_s = 0.33$; (100) texturing: $H_c = 190\,\text{Oe}$, $M_r/M_s = 0.065$). (b) Hysteresis loops for (100) 40-nm-diameter nanowires (parallel: $H_c = 650\,\text{Oe}$, $M_r/M_s = 0.167$; perpendicular: $H_c = 130\,\text{Oe}$, $M_r/M_s = 0.21$).

the magnetic properties of nanowire arrays. Figure 15 shows a hysteresis loop for a sample with an interpore distance $D_{\text{int}} = 65\,\text{nm}$, a nanowire diameter $D_P = 25\,\text{nm}$, and a column length $L = 700\,\text{nm}$ (Nielsch *et al*., 2002c). When an applied field was parallel to the axis of these Ni nanowires, the hysteresis loop exhibited a coercivity $H_c^{\parallel} \approx 1100\,\text{Oe}$ and a squareness of 96%. In the perpendicular direction, the coercivity was small ($H_c^{\perp} \approx 150\,\text{Oe}$), large magnetic fields were required for a complete magnetization, and the loop showed a nearly reversible behavior. Therefore, this sample had its preferential magnetic orientation along the wire axis.

For this arrangement each Ni nanowire was a single-domain particle, and its anisotropy was determined by the particle shape (Nielsch *et al*., 2001). When this magnetic array was saturated along the magnetic easy axis, the average internal stray field between the nanowires was $H_D^{\parallel} = 2\pi^{3/2}(D_P/D_{\text{int}})^2 \cdot M_s = 770\,\text{Oe}$ (Nielsch *et al*., 2001) and thus it was smaller than $H_c^{\parallel}$. Each Ni nanowire had

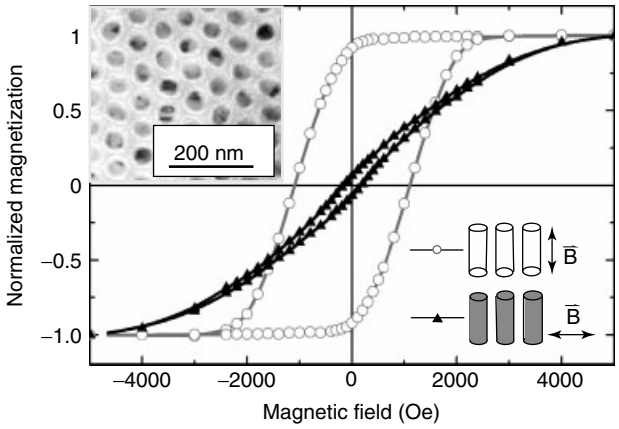

Figure 15. SQUID hysteresis loops of the nickel nanowire array with a pitch of 65 nm, a column length of about 700 nm, and a wire diameter of 25 nm measured with an applied field parallel (○) and perpendicular (▲) to the column axis. The inset shows a micrograph image of the corresponding sample recorded by transmission electron microscopy. The Ni nanowires embedded in the alumina matrix can be clearly seen.

on average a switching field $H_{sw} \approx H_c^{\parallel}$ with a standard deviation ΔH_{sw}, due to the diameter variation. After the sample had been saturated along the nanowire axis and the magnetic field had been switched off, a very small fraction of nanowires reversed their magnetization, because locally $(H_{sw} - \Delta H_{sw}) < H_D$. This explains the small deviation of the measured squareness (96%) from the expected value of 100% for $H_D^{\parallel} < H_c^{\parallel}$.

In these Ni samples, the volume fraction of the ferromagnetic material in the oxide matrices was usually around 10% (Nielsch *et al*., 2001). Even with this relatively low volume fraction, the dipolar interaction seemed to have significant impact on total magnetic anisotropy of the nanowire arrays. The effect of the volume fraction of magnetic material in the alumina membrane on the total magnetic anisotropy and the hysteresis loops was investigated in detail (Nielsch *et al*., 2001). A set of three Ni samples with fixed interpore distances of 105 nm and column lengths of about 800–1000 nm was prepared. Figure 15 shows the hysteresis loops for the nickel arrays measured with an applied field parallel (∥) and perpendicular (⊥) to the wire axis. In this experiment, the Ni nanowire arrays had wire diameters of 55 (sample A), 40 (B), and 30 nm (C), which corresponded to volume fractions of magnetic material of $P = 24.5$, 13, and 7.5%, respectively.

The hysteresis loop for sample A measured in the ∥ direction showed a coercive field of $H_c^{\parallel} \approx 600$ Oe and squareness of about 30% (Figure 16a). For the ⊥ direction, the hysteresis showed a low coercive field of $H_c^{\perp} \approx 100$ Oe. The hysteresis for both directions exhibited similar saturation fields ($H_s \approx 4000$ Oe). Therefore, this sample did not have a preferential magnetic orientation. In contrast, sample

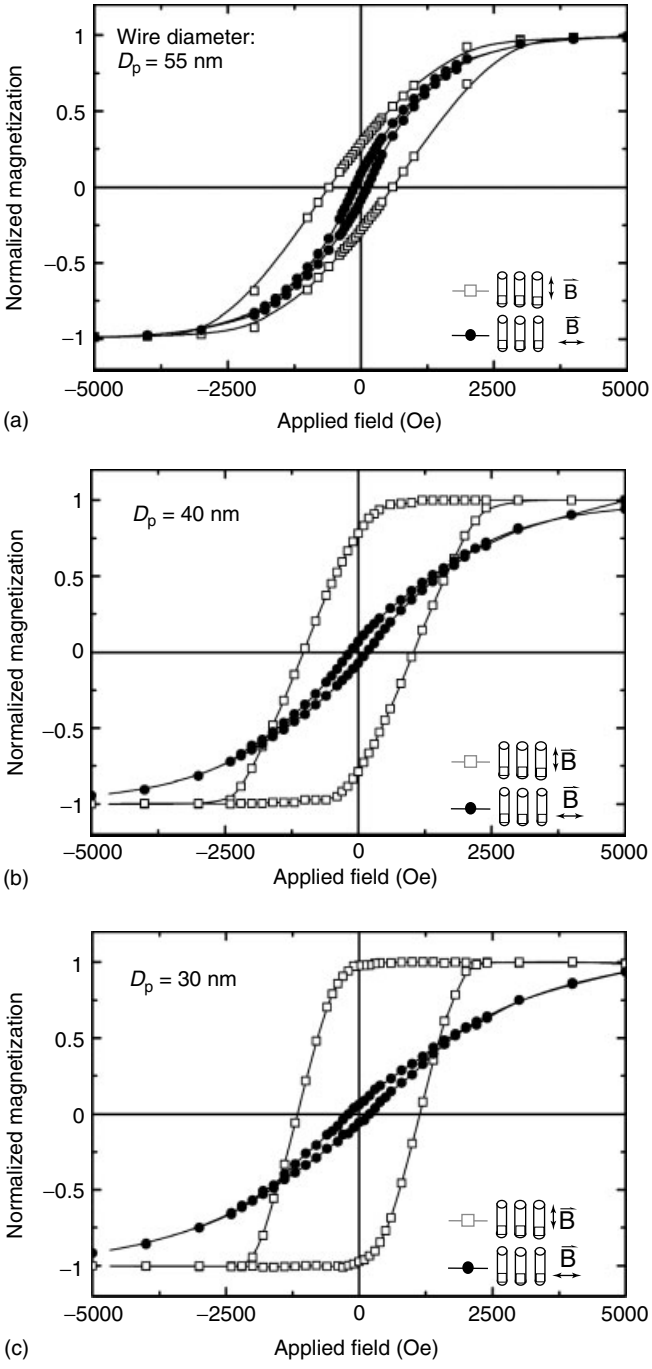

Figure 16. SQUID hysteresis loops for hexagonally ordered Ni nanowire arrays with a pitch of 105 nm and pore diameters of D_P 55 nm (a), 40 nm (b), and 30 nm (c).

B ($D_P = 40$ nm; Figure 16b) exhibited increased coercive fields of about $H_c^{\parallel} \approx 1000$ Oe and improved magnetic hardness, ∼80% squareness. This sample had a magnetic easy axis along the wire axis ($H_s^{\parallel} \approx 2500$ Oe, $H_s^{\perp} \approx 5500$ Oe, and $H_c^{\parallel} \gg H_c^{\perp}$). For sample C ($D_P = 30$ nm), a squareness of 98% and the highest coercive field $H_c^{\parallel} \approx 1200$ Oe

(Figure 16c) were measured. This is the highest reported coercivity for a high-density ($D_{\text{int}} < 120\,\text{nm}$) Ni nanowire array (Kawai and Ueda, 1975; Kaneko, 1981; Zeng *et al*., 2000; Hwang *et al*., 2000a; Chou, Wie, Krauss and Fischer, 1994). Samples B (40 nm) and C (30 nm) had similar magnetic anisotropies. The bulk value of the saturation magnetization $M_s \approx 484\,\text{emu cm}^{-3}$ was used. By determining the absolute amount of nickel in the pores using atomic absorption spectroscopy and relating it to the absolute magnetization by SQUID magnetometry, these samples were determined to have $M_s = 480\,\text{emu cm}^{-3}$.

The magnetic anisotropy of arrays of thin magnetic wires results from the interplay of a series of effective fields. In the case of a single-domain wire, which is expected for Ni with diameters smaller than 55 nm, three contributions must be considered. First is the macroscopic demagnetization field due to the average magnetic charges of the wires at the surface. For Ni in the geometry of a hexagonal pore structure, the average derived demagnetization field ($-4\pi M_s P$; $P >$ porosity of the template structure) is about -1750 Oe for 55 nm pores, -920 Oe for 40 nm pores, and -520 Oe for 30 nm pores. Second, the shape anisotropy of the individual wire if magnetized parallel to the pore axis is of the order of $2\pi M_s \approx 3200$ Oe. Third, a contribution results from the magnetocrystalline anisotropy energy, given by ($-4K_1/3M_s > 120$ Oe for Ni where K_1 is the magnetocrystalline anisotropy. When reducing the pore diameter from 55 to 30 nm while keeping the interpore distance constant ($D_{\text{int}} = 105$ nm), the remanence increased up to nearly 100% and the coercive field shifted toward 1200 Oe. Sample B with $D_P = 40$ nm and sample C with $D_P = 30$ nm, mentioned above, were single-domain wires, which were preferentially magnetized in the $\parallel$ direction because the shape anisotropy of 3200 Oe easily overcame the crystal field of 120 Oe. Theoretically, the effective coercive field of a single infinitely extended cylinder magnetized parallel to the $\langle 111 \rangle$ easy direction of the Ni cylinder axis for homogeneous rotation is given by $H_c = 4K_1/3M_s - 2\pi M_s$. This holds if the cylinder diameter is smaller than the critical diameter D_{crit} for the curling process (Aharoni and Shtrikman, 1958), $D_P < D_{\text{crit}} \approx 3.68 \times \sqrt{(\pi M_s^2)}$ ($A = 8.6 \times 10^7$) erg cm^{-1} for Ni yielding for Ni $D_{\text{crit}} = 40$ nm. Therefore, the curling mode is not an appropriate description for the magnetization of samples with $D_P = 40$ and 55 nm (Nielsch *et al*., 2001).

As single-domain particles, the magnetic reversal process of these Ni nanomagnets appears to occur by inhomogeneous switching modes, as discussed in the micromagnetic modeling by Hertel (2001, 2002). The small size distribution in the pore diameter ($\Delta D_P/D_P < 10\%$) (Nielsch *et al*., 2002a; Masuda and Fukuda, 1995) has a positive impact on the magnetic properties. The highest measured coercive field ($H_c \sim 1200$ Oe for a close-packed nickel nanowire array embedded in a membrane matrix) has been reported when $P = 7.5\%$. Earlier work on unarranged nickel nanowire arrays demonstrated lower coercive fields, about 1000 Oe or less along the easy axis (Kawai and Ueda, 1975; Kaneko, 1981; Zeng *et al*., 2000; Ounadjela *et al*., 1997). The large size distributions (up to $\Delta D_P/D_P > 50\%$) (Strijkers *et al*., 1999) in the pore diameters and the interwire distances enhanced the magnetic interactions in the nanowire arrays and reduced the squareness of the hysteresis loop.

4.2.2 Dynamic properties of nickel nanowires

The dynamic properties of Nickel nanowires have been investigated by a few groups. M.H. Kuok *et al*. from the National University of Singapore have investigated spin-wave modes in Ni nanowire arrays by inelastic Brillouin light scattering experiments in zero magnetic fields (Wang *et al*., 2003). They detected three so-called bulk magnon modes in Ni nanowires and observed an increase in the mode frequencies with decreasing nanowire diameter ($f \sim 1/D_P^2$), which can be labeled as a magnetic quantum size effect. In contrast, on lithographically patterned magnetic films, only surface spin-wave modes have been detected (Jorzick *et al*., 1999a,b; Mathieu *et al*., 1998).

Riccardo Hertel from the Max Planck Institute in Halle has simulated the dynamic properties and the switching modes of Ni nanowires by micromagnetic simulations. He showed that magnetic switching does not occur via coherent rotation (Stoner–Wohlfarth model) or via classic curling. If a nanowire is 60 nm in diameter and more than 1 μm in length, the switching event happens at a timescale of a few hundred picoseconds after a reversed field is applied. In this case switching happens by the propagation of a vortex domain wall (local curling mode) along the nanowire axis (Hertel, 2002; Hertel and Kirschner, 2004). If the nanowire diameter is reduced, the magnetic stiffness increases, for example, for 40 nm diameter the switching process is accomplished after a few nanoseconds. In this case, a 180° head-to-head wall starts at one end of the nanowire and propagates along the length of the wire (Hertel and Kirschner, 2004). The writing speed of conventional magnetic media is currently in the range of a few hundred picoseconds. We can assume that Ni nanowires with sub-30 nm diameter will experience slower switching (>5 ns), and therefore their application to patterned magnetic media, may be restricted.

4.2.3 Permalloy nanowire arrays

A further enhancement of the coercive fields of the Ni nanowire arrays was obtained by adding a small amount of iron sulfate (0.8 g l^{-1} $FeSO_4 \cdot 7H_2O$) to the Ni electrolyte, see Section 3.2. The resulting magnetic nanowire contained

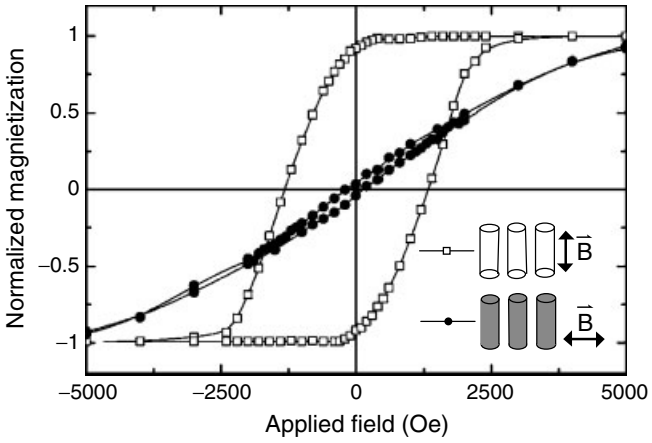

Figure 17. SQUID hysteresis loops of the permalloy ($Ni_{83}Fe_{17}$) nanowire array with a pitch of 105 nm, a column length of about 1000 nm, and a wire diameter of 30 nm measured with an applied field parallel (□) and perpendicular (●) to the column axis.

83% Ni and 17% Fe, which is the nearly ideal composition for permalloy (80% Ni, 20% Fe). Although there was a negligible effect of magnetic anisotropy in the Ni nanowires, this will be even smaller for permalloy nanowires than for Ni nanowires. On the other hand permalloy (M_s = 800–900 emu cm^{-3}) has a higher saturation magnetization than nickel (480 emu cm^{-3}). For a permalloy nanowire array with 30 nm wire diameter, 105 nm interwire distance, and 800 nm wire length, the preferential magnetic orientation was parallel to the wire axis (Figure 17). This hysteresis loop for the parallel direction (∥) had coercive fields of 1350 Oe and a squareness of 96%. The hysteresis loop for the perpendicular direction (⊥) exhibited a small coercive field (100 Oe) and higher saturation fields, up to 7500 Oe. If Figure 17 is compared with Figure 14(a), the permalloy nanowire array had a higher coercivity but a slightly reduced remanence. The additional amount of iron led to an enhancement of the total saturation magnetization M_s of each nanowire. The coercivity and the saturation field increased because of the rise of the theoretical shape effect factor for a nanowire ($2\pi M_s$). On the other hand, the interactions between the nanowires increased because of the enhancement of the average demagnetization fields ($-4\pi M_s \cdot P$: $P \equiv$ metal filling fraction in the oxide matrix), which led to the reduction of the remanence. In conclusion, all these investigations suggest that Ni nanowires and permalloy nanowires are suitable for patterned perpendicular magnetic media. Although, coercive fields of $H_c^{\parallel} = 1200–1350$ Oe were obtained, and the squareness of the hysteresis loop was in the range of 95 to 100%, the estimated demagnetization field inside the magnetic array was still in the range $H_D = 0.5 - 0.7 \times H_c^{\parallel}$. For application as storage media, the dipolar interactions inside the nanowire arrays have to be further reduced, for example, $H_D = 0.1 - 0.2 \times H_c^{\parallel}$. In principle, this can be obtained by reducing the ratio between nanowire diameter (D_P) and interpore distance (D_{int}) by 50–65%, whereby the filling fraction of magnetic material inside the oxide matrix will decrease to less than 3%.

5 MODELING OF THE MAGNETIC PROPERTIES

5.1 Switching field of individual nanowires

Ideally nanowires have a uniaxial anisotropy and the magnetization prefers to align parallel to the nanowire axis (z direction). This anisotropy depends on the aspect ratio of these one-dimensional nanostructures. Here, two simple analytical models for the calculation of the switching field and coercive field for an isolated magnetic nanowire are described.

5.1.1 Stoner and Wohlfarth model

In the classical model based on (Stoner, Wohlfarth and Wohlfarth, 1948), a homogeneously magnetized 3D ellipsoid is used as an approximation for a cylindrical shaped nanowire (Figure 18). In this simple model, any effects related to the crystal structure of the nanowires are excluded. The energy term of the stray field E_D is determined by the aspect ratio $a = L/D_P$ (length/diameter) and the alignment (ϑ) of the magnetization toward the nanowire axis.

$$E_D = \pi M_s^2 \left[1 + \frac{3}{a^2}\left[1 - \ln(2a)\right]\right] \sin^2 \vartheta \qquad (3)$$

When the magnetic dipole is aligned along the nanowire axis, the stray field is in the lowest energetic state. On the basis of the energy term E_D, the maximum switching field H_D of a homogeneous magnetized cylinder can be calculated.

$$H_D = 2\pi M_s \left[1 + \frac{3}{a^2}\left[1 - \ln(2a)\right]\right] \qquad (4)$$

Most of the experimental data presented in the Chapter 4 were taken from magnetic nanowires that exhibited aspect ratios >10. Therefore equation (2) can be simplified for the case $a \gg 1$. The approximated switching field for 180° rotation of the magnetization is given by equation (3).

$$H_D = 2\pi M_s \qquad (5)$$

For Ni, Co, and Fe nanowires, the theoretic switching fields have been calculated on the basis of the model of Stoner and Wohlfarth as H_D = 3260, 8900, and 10 800 Oe, respectively.

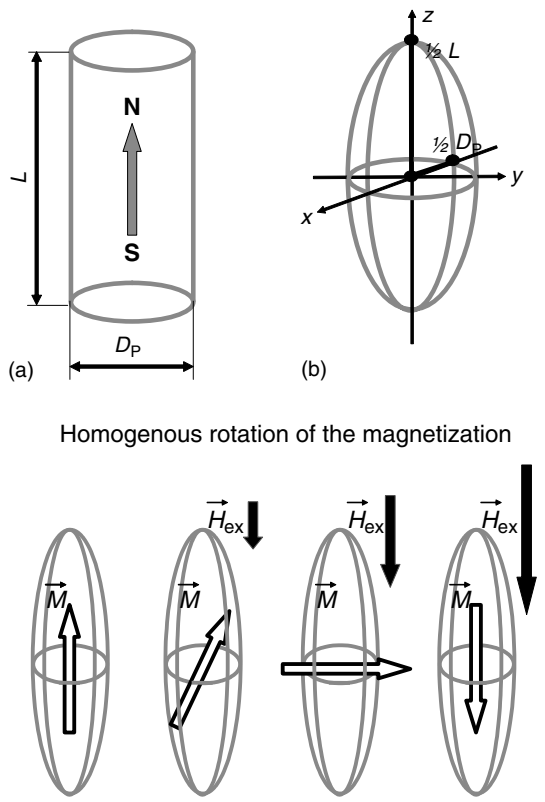

Figure 18. In Stoner–Wohlfarth model a homogeneous magnetized cylinder (a) is approximated by a elongated ellipsoid (b). During the switching process the magnetization is homogenous at any stage of the rotation process.

These values are more than two times higher than the maximum coercivities measured on magnetic nanowires up to now. Contrary to the Stoner–Wohlfarth model, the magnetic nanowires tend to be inhomogeneously magnetized. Micromagnetic simulations provide a more realistic picture of the magnetization inside the nanowire and their switching behaviors. An alternative analytic model has been suggested by Jacobs and Bean (1955).

5.1.2 Jacobs and Bean model

In the simple model by Jacobs and Bean (1955) a chain of an integer number a, of magnetic spheres is used for the calculation of the switching field (Figure 19). Each sphere

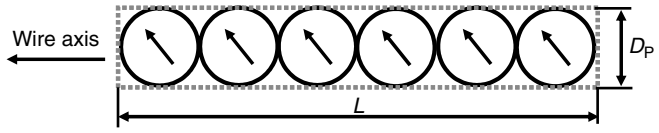

Figure 19. Jacobs and Bean Model: A chain of homogeneous magnetized spheres is used as an approximation for a single-domain nanowire.

is homogeneously magnetized and the magnetization vector in each sphere is pointing in the same direction. On the basis of the dipolar interactions between the magnetic spheres the stray field energy E_D is calculated depending on the orientation angle (ϑ) of the magnetization M toward the nanowire axis.

$$E_D = \frac{1}{2}\pi M_s^2 \left(\sum_{j-1}^{a} \frac{a-j}{aj^3} \right) \sin^2 \vartheta \tag{6}$$

On the basis of (6) the coercive field H_D for an infinitely long nanowire ($a \to \infty$) has been calculated as follows:

$$H_D \approx 1.2\pi M_s \tag{7}$$

The calculated switching field for an isolated nanowire based on the model of Jacobs and Bean is about 40% lower than the Stoner–Wohlfarth approximation.

5.1.3 Curling model

The Curling model (Aharoni, 1999) is a noncoherent calculation that minimizes the total magnetic energy. Curling is often suggested as the reversal mechanism for ferromagnetic nanowires when their diameters are several times larger than the magnetic exchange length $\lambda_{ex} = (2A/\mu_0 M_s^2)^{1/2}$ (where A is the exchange stiffness constant, M_s is the saturation magnetization of the ferromagnetic material, and μ_0 is the permittivity of free space). For Ni, Co, permalloy, and Fe the magnetic exchange lengths are $\lambda_{ex} = 8.3$, 2.9, 5, and 2.3 nm, respectively. When magnetic reversal occurs via curling, a magnetic vortex structure is formed at the nanowire ends and for magnetic cylinders with an infinite length, an analytic solution can be calculated. In contrast to the Stoner–Wohlfarth model where the exchange energy is minimized, in curling the stray field energy is minimized and this leads to an inhomogeneous and vortex-type magnetization. The analytic solution for the nucleation field, H_{sw}, is given as

$$H_{sw} = \frac{27A}{M_s \cdot D_P^2} - \frac{2K_1}{M_s} \tag{8}$$

where K_1 is the magnetocrystalline anisotropy constant. If the nanowire diameters are $D_P \geq \sqrt{27A/2\pi \cdot M_s^2}$ the Curling approximation is a very useful approximation for the theoretic switching field. At smaller diameters the Stoner–Wohlfarth approximation is a more suitable model. If we calculate the theoretic switching field for nickel nanowires with 40 nm (55 nm) diameters and zero magnetocrystalline anisotropy ($K_1 = 0$), the results with Stoner–Wohlfarth, Jacobs–Bean, and Curling are 3200 Oe

(3200 Oe), 1795 Oe (1778 Oe), and 2650 Oe (1310 Oe), respectively. Unfortunately, these theoretic values all have large discrepancies with each other and the experimental data (Figure 16): 1000 Oe (600 Oe) coercivity for $D_P = 40$ nm ($D_P = 55$ nm).

5.2 Dipolar interactions inside the nanowire arrays

Each saturated nanowire produces a dipolar magnetic field, which interacts with the neighboring nanowires. The sum of the dipolar fields from each nanowire inside a magnetic array is called stray or demagnetization field. When an external magnetic field $\vec{H}_{ex}$ is applied, the effective field $\vec{H}_{eff}$, which acts on each nanowire, is the difference between $\vec{H}_{ex}$ and the sum of the dipolar fields originated by the neighboring nanowires.

$$\vec{H}_{eff} = \vec{H}_{ex} - \sum_i \vec{H}_{D,i} \tag{9}$$

In the case that the whole magnetic nanowire array is saturated parallel to the nanowire axis and the external magnetic field is pointing in the same direction, the effective magnetic field $\vec{H}_{eff}$ within the nanowire array is lower than the applied external magnetic field $\vec{H}_{ex}$.

The average demagnetization field of a nanowire array can be calculated under the assumption that the nanowire array is a magnetic thin film with an effective saturation magnetization per volume M_{eff}. When a porous alumina membrane with a pore diameter D_P and an interpore distance D_{int} is filled completely with a ferromagnetic material, M_{eff} can be calculated on the basis of the ratio of the volume of the ferromagnetic material versus the matrix volume.

$$M_{eff} = \frac{\pi}{\sqrt{12}} \left(\frac{D_P}{D_{int}} \right)^2 M_s \tag{10}$$

The average dipolar field H_D inside a saturated nanowire array (magnetic field parallel to nanowire axis) can be estimated as shown in equation (11):

$$H_D = 4\pi M_{eff} = \frac{2\pi^2}{\sqrt{3}} \left(\frac{D_P}{D_{int}} \right)^2 M_s \tag{11}$$

A more accurate model for the demagnetization field inside a saturated nanowire array with a hexagonal arrangement has been proposed by Samwel, Bissel and Lodder (1992). A magnetostatic field $H_{A\to B}$ acts from nanowire A toward nanowire B from a distance D_{int}, and both nanowires have length L. The dipolar field at the top of nanowire B, which is pointing parallel to the nanowire axis, can be calculated by the following equation:

$$H_{A\to B} = \frac{\pi D_P^2 M_s}{2L} \left[\frac{1}{D_{int}} - \frac{1}{\sqrt{D_{int}^2 + L^2}} \right] \tag{12}$$

For a hexagonal arrangement of an infinite large nanowire array the average stray field has been calculated on the basis of the approach of Samwel, Bissel and Lodder (1992).

$$H_D = \frac{3\pi D_P^2 M_s}{L D_{int}} \sum_{i=1}^{\infty} \sum_{j=0}^{i-1} \left(\frac{1}{\sqrt{\left(i^2 - ij + j^2\right)}} - \frac{1}{\sqrt{\left(i^2 - ij + j^2 + (L/D_{int})^2\right)}} \right) \tag{13}$$

The indices i and j are explained by Figure 20. In equation (13), the total dipolar field is summed for a 60° section of the magnetic array and is multiplied by 6. Equation (13) can be written as a function of the average demagnetization H_D:

$$H_D = 4\pi M_{eff} \gamma \tag{14}$$

in this case γ can be interpreted as a correction factor for equation (11):

$$\gamma = \frac{3\sqrt{3}}{2\pi} \frac{D_{int}}{L} \sum_{i=1}^{\infty} \sum_{j=0}^{i-1} \left(\frac{1}{\sqrt{\left(i^2 - ij + j^2\right)}} - \frac{1}{\sqrt{\left(i^2 - ij + j^2 + (L/D_{int})^2\right)}} \right) \tag{15}$$

For magnetic arrays with a high-aspect-ratio nanowires ($L/D_P > 10$) the correction factor γ is in the range of 0.95–0.98. Therefore we can conclude that equation (10) is a relatively accurate approximation for the calculation of the average stray field inside a saturated nanowire array (nanowire axis parallel to applied field).

5.3 Monte Carlo simulation of the hysteresis loop

In the past Hwang *et al*. (2000b) and Zheng, Pardavi-Horvath and Vertesy (1997) have worked on the numerical simulation of the hysteresis loops when the magnetic field is applied parallel to the nanowire axis. An Ising-type approach is used, where each nanowire is a single-domain magnet (i) with a

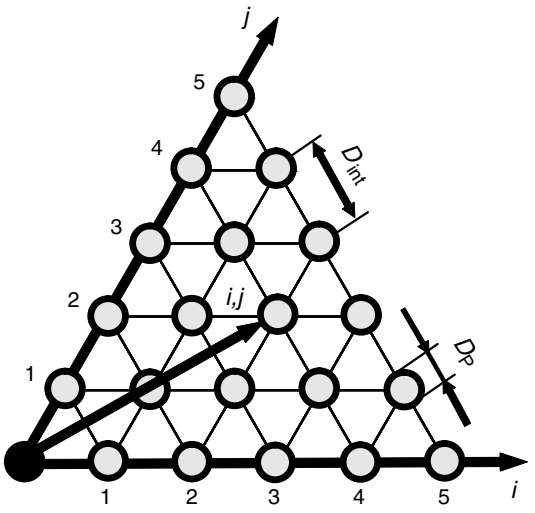

Figure 20. Map of a magnetic nanowire array for the calculation of the dipolar interactions. On the basis of the hexagonal symmetry only one-sixth part of the array is plotted, which is sufficient for the calculations.

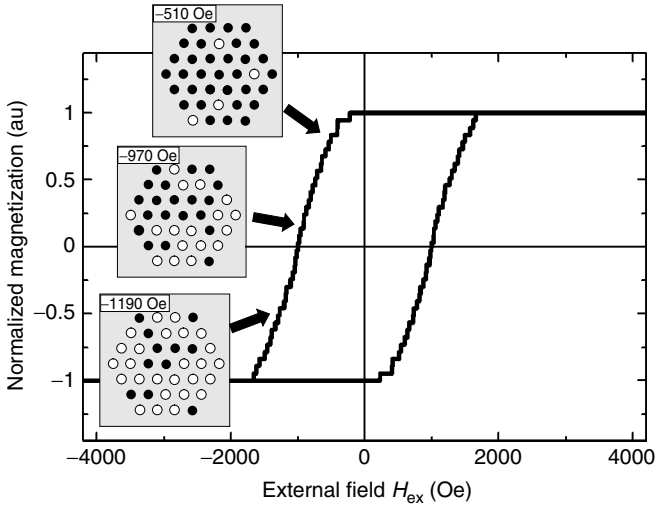

Figure 21. As an example, a numerical simulation of the hysteresis loop is shown for an array of 37 Ni nanowires with a nanowire diameter of 45 nm, an interwire distance of 105 nm, and a wire length of 800 nm.

boxlike hysteresis loop, when the magnetic field is applied parallel to the wire axis, and an individual switching $H_{sw}(i)$. The average switching field $\overline{H_{sw}}(i)$ of the whole magnetic array corresponds to the measured coercive field H_c of a nanowire array with identical geometrical parameters, for example, L, D_{int}, D_P. The variation of $H_{sw}(i)$ follows a classical Gaussian distribution. $\Delta H_{sw}(i)$ is used as a fitting parameter for the simulation and defines the variation width of $H_{sw}(i)$.

Usually, Monte Carlo simulations are started with a saturated array of nanomagnets ($M_{(i)} = +M_s$). At the beginning, the external magnetic field H_{ex} is significantly larger than the saturation field of the whole array. The effective field $H_{eff}(i)$ is calculated by adding up the stray field contributions for each nanomagnet i from all neighboring nanowires j with the magnetic polarization $p(j) = +1$.

$$H_{eff}(i) = H_{ex} - \frac{\pi D_P^2 M_s}{2L} \sum_{j \neq i} \left[\frac{1}{D(i,j)} - \frac{1}{\sqrt{D(i,j)^2 + L^2}} \right] p(j) \qquad (16)$$

The external field H_{ex} is reduced in infinitely small steps until the first nanowire is found where the local effective field is smaller than the individual switching field: $|H_{eff}(i)| > |H_{sw}(i)|$. After that the polarization of the nanomagnet i becomes negative ($p(i) = -1$), the local effective magnetic field $H_{eff}(j)$ is recalculated for each nanomagnet j and the external field H_{ex} is reduced until another nanomagnet k is found that fulfills the criteria $|H_{eff}(k)| > |H_{sw}(k)|$. This iterative procedure is repeated until the whole array of single-domain magnets has totally changed its polarization ($p(i) = -1$). The complete hysteresis loop is simulated by varying the external field H_{ex} from $+H_s \rightarrow -H_s \rightarrow +H_s$ stepwise and calculating the magnetization of the entire magnetic array as a function of the external field.

As an example, the hysteresis loop (nanowire parallel to H_{ex}) of a miniarray composed of 37 magnetic nanowires was simulated. For the simulation an average switching field $\overline{H_{sw}} = 1000$ Oe and a distribution width of $\Delta H_{sw} = 250$ Oe were selected. The following geometric parameters were used for this calculation: nanowire diameter $D_P = 45$ nm, interwire distance $D_{int} = 105$ nm, and nanowire length $L = 800$ nm. The simulated hysteresis loop and the domain pattern for three different external fields $H_{ex} = 510$, 970, and 1190 are plotted in Figure 21. Since the number of nanowires in this test simulation was small, the Barkhausen jumps, which originate from the switches of single wires, can be detected in this hysteresis loop.

In these Monte Carlo simulations (Figure 22) the distribution width of the switching field ΔH_{sw} was a very essential parameter. In order to visualize the effect of ΔH_{sw} on the simulated hysteresis loops, a second test calculation was performed for an array composed of 37 nanowires (with the same geometric parameters, $\overline{H_{sw}} = 1000$ Oe, and $\Delta H_{sw} = 20$, 100, 250, and 400 Oe). For low ΔH_{sw} the hysteresis loop looked similar to a parallelogram. When the distribution width ΔH_{sw} was enhanced, the shearing effect on the hysteresis loop increased and the edges of the loop became rounded. In the past, only the stray field interactions

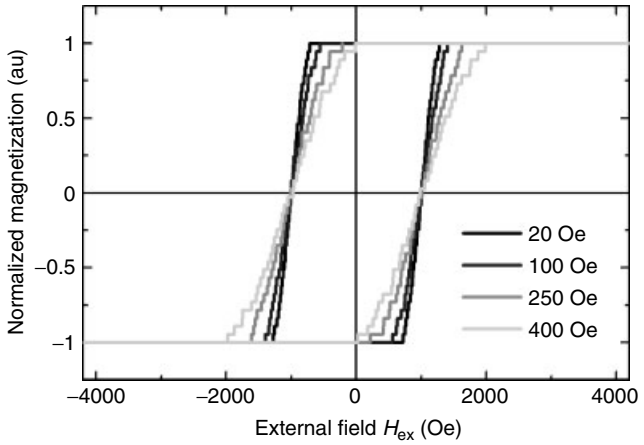

Figure 22. This simulation demonstrates the influence of the switching field distribution on the hysteresis loop when the magnetic field is applied parallel to the nanowire axis. The geometric parameters of this simulation are identical to the simulation shown in Figure 21.

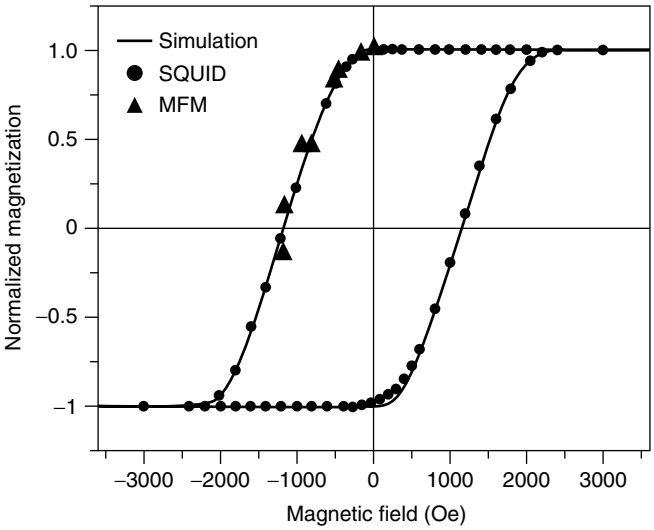

Figure 23. Comparison of a numerical simulation and a SQUID hysteresis loops of a nickel nanowire array with a pitch of 100 nm, column length of about 700 nm, and a wire diameter of 30 nm measured with an applied field parallel and perpendicular to the column axis. Additionally the statistical results from MFM investigations while an external magnetic field H was applied to the sample are also plotted in this figure.

have been considered, but shearing effects in the hysteresis loops of magnetic nanowires have been discussed in the literature (Hwang *et al*., 2000b). As demonstrated in Section 6, the ordering degree of the nanowire array has an important influence on the coercive fields and the shearing effect of the hysteresis. Disordered nanowire arrays have a broad distribution in nanowire diameter. Therefore less-ordered nanostructures have a broader distribution of the switching field ΔH_{sw} and their hysteresis loops exhibit stronger shearing effects. Briefly, the dipolar interactions between the nanomagnets and the distribution width of the switching field are responsible for the shearing of the hysteresis loops.

For comparison with the experimental measurement, Monte Carlo simulations were performed on magnetic arrays with up to 65 269 nanowires. In Figure 23, the experimental data of a nickel nanowire array (wire diameter $D_P = 30$ nm, periodicity $D_{int} = 105$ nm, wire length $L = 800$ nm, $H_c = \overline{H_{sw}} = 1150$ Oe) was measured by a SQUID magnetometer and the statistical analysis of the magnetic force microscopy (MFM) investigations (Nielsch *et al*., 2001, 2002b) were compared with the corresponding Monte Carlo simulation. Here an excellent fit to experimental data was obtained for $\Delta H_{sw} = 150$ Oe. ΔH_{sw} corresponds to 13% of H_c.

In this analysis, a Ni nanowire array within a self-ordered alumina template with an average deviation in pore diameter of about 8% was used. If we assume further that $2\Delta D_P/\overline{D_P} \approx \Delta H_{sw}/\overline{H_{sw}} \approx 16\%$, we can presume that the factor ΔH_{sw} in this simulation is in good agreement with the variation of the cross-section area of the magnetic nanowires. The experimental data presented by Nielsch *et al*. (2001, 2002b) and the Monte Carlo simulations give clear evidence that a perfectly ordered nanowire array with a well-defined pore diameter will have a higher magnetic anisotropy than a self-ordered nanowire array with a larger distribution in pore diameter.

6 FERROMAGNETIC NANOWIRE ARRAYS WITH PERFECT ARRANGEMENT ON LARGE (CM^2)-SCALE ORDER

For the application of magnetic nanowire arrays as a magnetic media and as magnetic field sensors, a perfect arrangement of the array on a large scale is necessary in order to be able to address each individual nanowire. Additionally, a perfect arrangement narrows the distribution of the nanowire diameters and interpore distances, and this will reduce the switching field distribution of the individual nanowires ΔH_{sw}. As demonstrated in Section 5.3, a low ΔH_{sw} will improve the total anisotropy of the whole magnetic array. This assumption has been proved experimentally, by measurement of the hysteresis loops of nickel-filled alumina membranes with a different degree of self-ordering (Nielsch *et al*., 2002c; Vázquez *et al*., 2004).

Using imprint lithography as a tool for prepattering aluminum surfaces, alumina templates with a perfect hexagonal pore arrangement on a square centimeter scale can be achieved using a single anodization process. Initially,

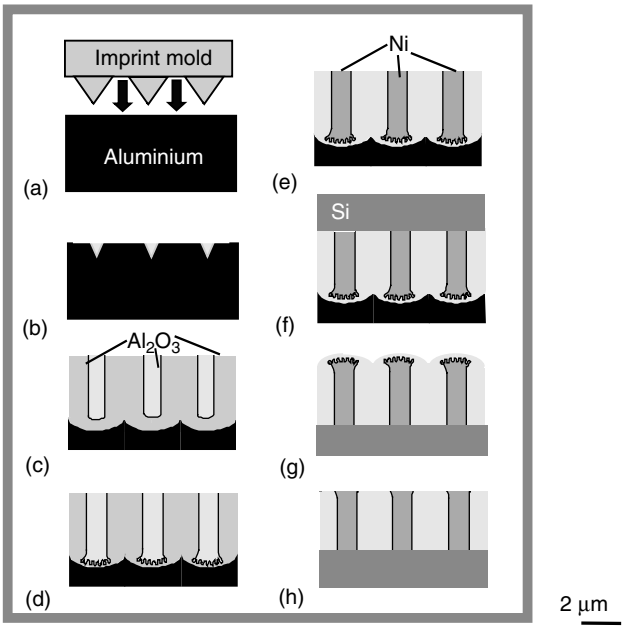

Figure 24. The sketch shows the fabrication process for a perfect ordered magnetic nanowire array.

Masuda *et al*. (1997) used this technique for the fabrication of perfectly ordered, unfilled alumina membranes on a small scale.

In this section, the fabrication of Ni nanowire arrays on a square centimeter scale based on imprint lithography is presented. First, mechanically polished Al substrates were patterned by an imprint master mold, or stamp, described elsewhere (Choi *et al*., 2003). The stamp consisted of hexagonal arrays of Si_3N_4 pyramids with a pitch of $a = 500\,\text{nm}$ (Figure 24a). The imprinted etch pits on the Al surface acted as nucleation sites for pore formation (Figure 24b). The prestructured Al surface was anodized with 1 wt% H_3PO_4 at 195 V for 75 min. Alumina templates (Figure 24c) with a perfect hexagonal arrangement of pores on a square centimeter scale were obtained. Subsequently, the barrier layer was thinned at the pore bottom (Figure 24d) from about 250 nm to less than 7 nm, which resulted in the formation of small dendrite pores at the pore bottom, as described in Section 3.2. Nickel was directly plated onto the nearly insulating barrier by current pulses (Figure 24e). Subsequently, Si substrates were fixed on top of the area (Figure 24f), the Al substrate was selectively removed by chemical etching and the sample was turned upside down (Figure 24g). Finally, the barrier layer and the dendritic part of the nanowires were removed by etching with a focused ion beam (Figure 24h), in order to reduce the stray field interactions between the nanowires. Scanning electron images (Figure 25a) of the nanowire structure revealed $h \approx 4\,\mu\text{m}$, $a = 500\,\text{nm}$, and $D_\text{P} = 180\,\text{nm}$ with a dispersion $\Delta D_\text{P}/D_\text{P} < 2\%$. In comparison, Figure 25(b)

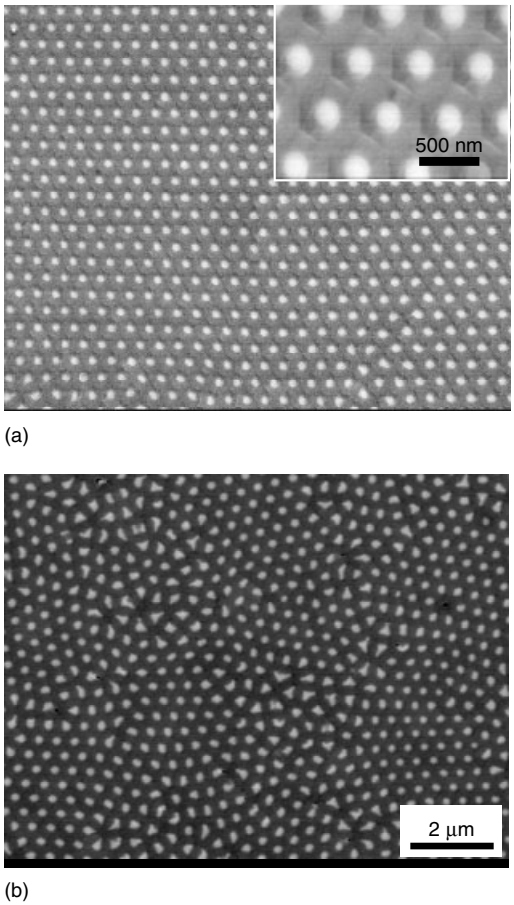

Figure 25. SEM micrographs of nickel nanowire arrays with a 2D monocrystalline (a) and 2D polycrystalline (b) arrangement of the magnetic columns fabricated by imprint lithography and self-organization, respectively. Both arrays have 500-nm interwire distance and 180-nm column diameter. The length of the magnetic columns is ∼5 μm. The inset in (a) shows a higher magnification of the same Ni nanowire array with the perfect arrangement.

shows a nickel nanowire array with a 2D polycrystalline arrangement. The latter array, which was fabricated by the classical two-step anodization process, had a medium-range ordering and a larger dispersion $\Delta D_\text{P}/D_\text{P} \approx 10\%$. Both samples were fabricated under identical electrochemical conditions.

The hysteresis loops were measured for both samples in the direction of nanowire axes and perpendicular to the nanowire axes (Figure 26). In the case when the nanowires had a monodisperse pore diameter and monocrystalline arrangement, a coercive field of 250 Oe and a remanence of 42% were detected. The second sample exhibited a reduced coercivity of 160 Oe and a remanence of 30% because of larger dipolar interactions caused by larger deviations in the nanowire diameters and higher disorder in the magnetic array. In contrast to earlier results on Ni nanowires with

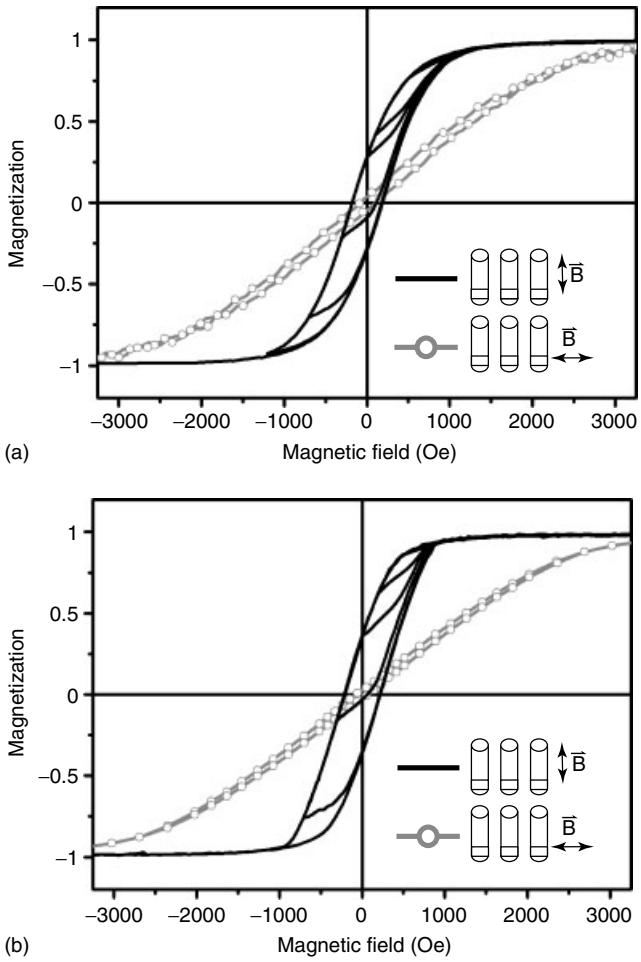

Figure 26. SQUID hysteresis loops of the nickel nanowire arrays with a 2D monocrystalline (a) and 2D polycrystalline (b) arrangement measured with an applied field parallel and perpendicular to the column axis.

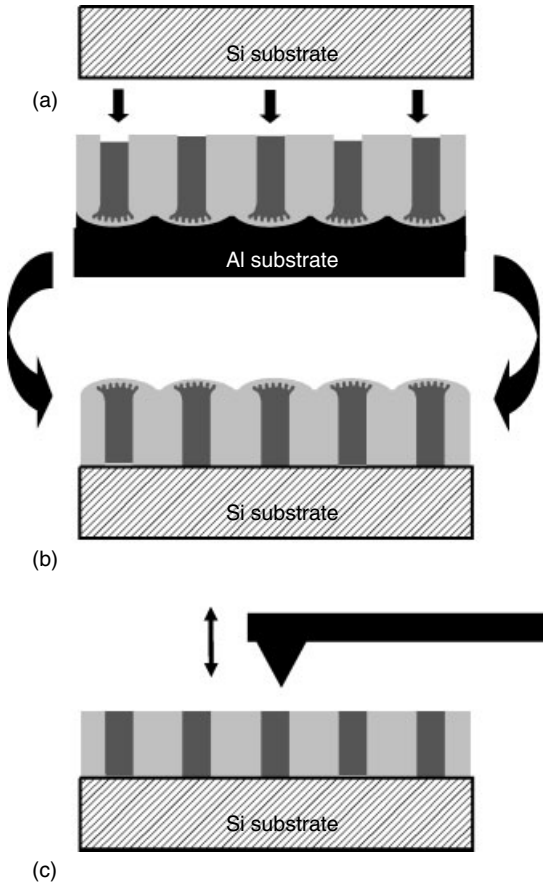

Figure 27. Schematic diagram demonstrating the preparation steps for the subsequent magnetic force microscopy. The filled template was attached to a Si substrate (a). The Al substrate was removed by selective chemical etching (b) and the structure was turned upside down. By focussed ion beam milling the barrier layer and dendrite structure were removed and a smooth surface was obtained (c).

$D_P < 55$ nm (Figure 26a), a single Ni nanowire with $D_P = 180$ nm diameter does not exhibit a boxlike magnetization loop. The reduced remanence of an array of nanowires appears to be due to dipolar interactions, and the sample with the 2D monocrystalline arrangement (Figure 26a) has a narrower distribution of the nanowire switching fields ($\Delta H_{sw}/H_{sw} \approx 2\Delta D_P/D_P$).

7 APPLICATIONS

7.1 Recording application and magnetic force microscopy

One of the promising applications of nanowire arrays is in recording, where one bit of information would correspond to one single-domain, nanosized particle, or one nanomagnet. These nanomagnets would have large aspect ratios to maintain thermal stability rather than the ∼1000 grains required by longitudinal media as discussed in Section 1. The following section discusses an atomic probe technique that can be used in evaluating these nanowire arrays for recording.

In contrast to the bulk measurements of VSM and SQUID, MFM can be used to image the magnetic polarization at the top end of each magnetic nanowire (Figure 27) (Nielsch *et al.*, 2001, 2002b). Figure 28 demonstrates the domain structure of an array of nickel columns in the demagnetized state. First, the topographic image of the Ni nanowire array embedded in the alumina matrix was measured by atomic force microscopy as shown in Figure 28(a). The geometric parameters of the sample were the same as in Figure 16(b) ($D_P = 40$ nm). Dark spots in the magnetic image (Figure 28b) imply that the magnetization was pointing up and bright spots imply that the magnetization was pointing down. Up magnetization may be interpreted as a binary '1', and down magnetization as a binary '0'. It can

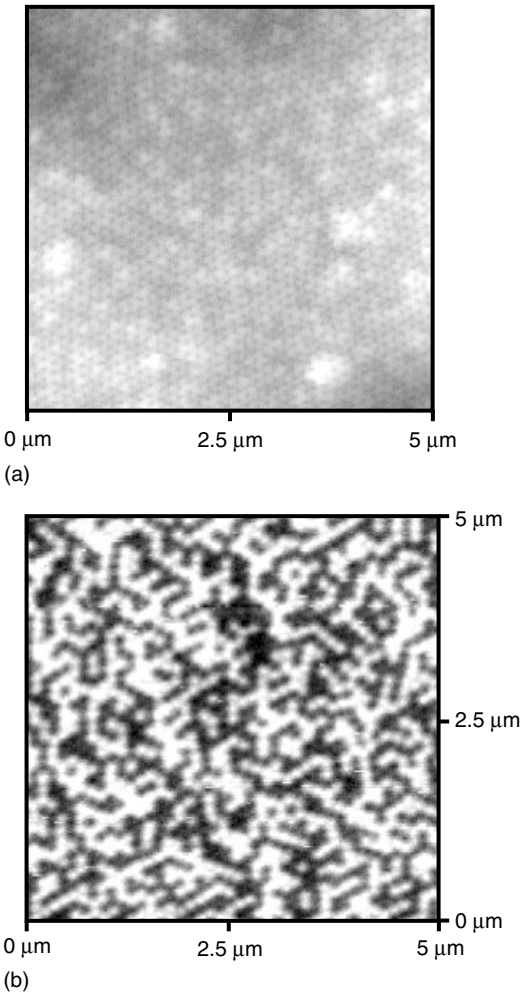

Figure 28. (a) Topographic image recorded by atomic force microscope of an array of magnetic nanowires with 105 nm interwire distance and 40 nm wire diameter embedded in the alumina membranes. (b) Magnetic force microscopic image of the corresponding nanowire array in the demagnetized state, showing the magnetic polarization of the pillars alternately 'up' (white) and 'down' (black).

be deduced from the picture that the Ni pillars were single-domain nanomagnets aligned perpendicular to the surface. The patterned domain structure was due to an antiferromagnetic alignment of pillars influenced by the weak magnetic interaction between these nanomagnets.

The labyrinth pattern (Figure 28b) of the domain structure was characteristic for hexagonally arranged single-domain magnetic particles with a perpendicular magnetic orientation in the demagnetized state. In the case of a quadratic lattice, each of the four nearest neighbors will be aligned antiparallel, and the domain structure exhibits a checkerboard pattern (Ross *et al*., 1999). In a hexagonal lattice, two of the six nearest neighbors will align their magnetization parallel and four will be magnetized antiparallel if the stray field has only nearest-neighbor interaction. In Figure 28(b), it can be seen that an average of 2.5 nanomagnets were aligned parallel and that 3.5 were magnetized antiparallel. Therefore, the stray field interaction appeared to extend over several lattice periods D_{int}, because of the high aspect ratio of the magnetic nanowires. The stray field interactions for sample B with $D_{\text{P}} = 40\,\text{nm}$ therefore appeared moderate, as has been shown using the simple approximation of the demagnetization field H_{D}.

Additionally, MFM investigations with applied magnetic field can be used to study the switching behavior of the individual nanowires in the array (Nielsch *et al*., 2002b). Low moment magnetic tips should be used for MFM scans, in order to prevent switching of the magnetization in the nanowires by the dipole field of the magnetic tip ($H_{\text{tip}} \approx 50\,\text{Oe}$). Here, the sample was saturated by an external magnetic field of about 5000 Oe along the wire axes. The first scan was performed without an external field (Figure 29a). In order to get a better impression of the magnetic polarization of each pillar, the MFM images were numerically enhanced. Even though $H_{\text{ex}} = 0\,\text{Oe}$ and the maximum demagnetization field of $H_{\text{D}} = -920\,\text{Oe}$ was smaller than the coercive field, a few pillars had already switched their polarization, because of the dipolar interactions between the nanowires and the distribution of the switching field of the individual nanowires. Next the external magnetic field was increased to -300, -600, and $-900\,\text{Oe}$ (Figure 29b–d) in the direction opposite to the magnetization. The stray field of the sample appeared to increase, $H_{\text{eff}} = H_{\text{D}} + H_{\text{ex}}$. For $H_{\text{ex}} = -300\,\text{Oe}$, the effective field in the nanowire array was already smaller than the coercive field, therefore a significant number of nanowires had reversed their magnetizations. Increasing the external field led to an increased number of reverse-magnetized pillars (Figure 29b–d). The enhancement of H_{eff} was partly compensated by the reduced dipole interactions from the reversed pillars. In the final image (Figure 29d), the applied external field had nearly reached the coercive field $H_{\text{c}}^{\parallel} = 1000\,\text{Oe}$. The number of switched (black) and unswitched (white) nanowires was nearly equal. In this case, the average demagnetization field in the sample was reduced nearly to a minimum and $H_{\text{ex}} \approx H_{\text{eff}} \approx H_{\text{c}}^{\parallel}$.

The suitability of nickel nanowire arrays for patterned perpendicular magnetic media has been studied in more detail. For this experiment sample A ($D_{\text{P}} = 30\,\text{nm}$) with the best magnetic performances in terms of squareness (100%) and coercivity (1200 Oe) was used (see Figure 16c). An attempt was made to saturate a defined area of a demagnetized sample by a strong magnetic MFM tip ($H_{\text{tip}} \approx 250\,\text{Oe}$) and an external magnetic field ($H_{\text{ex}} = -1200\,\text{Oe}$). The amount of the applied external field was nearly equal to the average switching field (H_{sw}) of the individual nanowire ($H_{\text{c}}^{\parallel} = 1200\,\text{Oe}$)

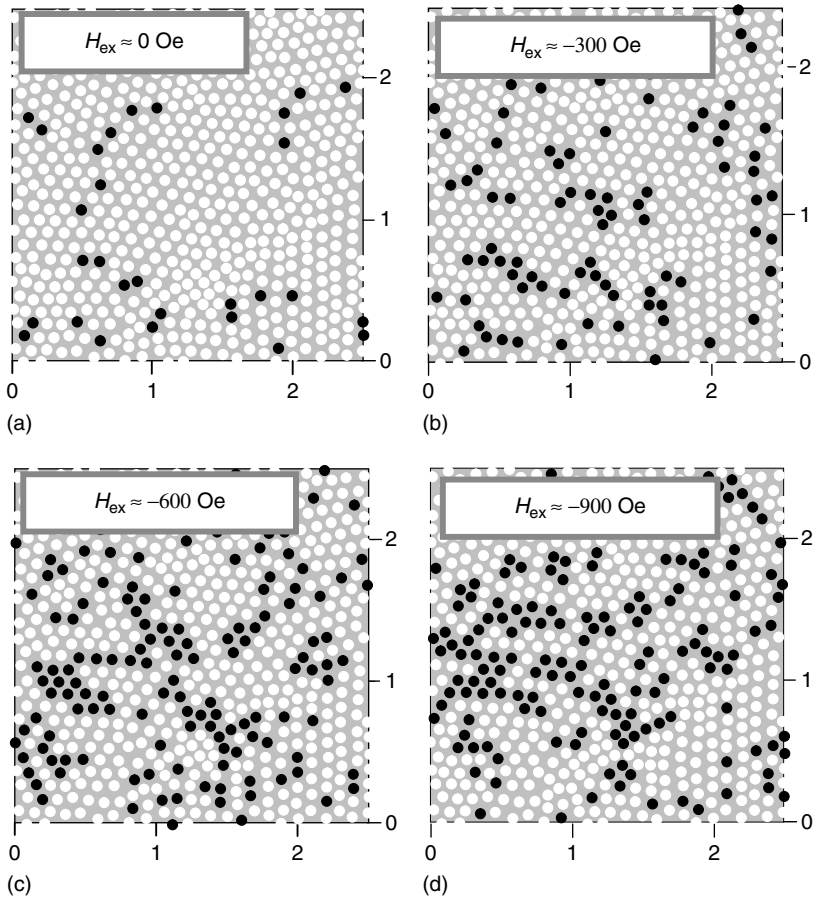

Figure 29. An external magnetic field was applied perpendicular to the sample surface. (a) The MFM image of the saturated nanowire array. Numerically enhanced MFM images recorded with an applied magnetic field of $H_{ex} = 0$ (a), -300 (b), -600 (c), and -900 Oe (d).

and was applied in the direction of the nanowire axis. Starting in the upper region of Figure 30 the strong magnetic tip was scanned over an area of $5 \times 5\,\mu m^2$. Hereby, a total external field of about $H'_{ex} = H_{ex} + H_{tip} = -1450$ Oe was locally applied on this selective area. Subsequently, the external magnetic field was switched off. An enlarge area of $10 \times 10\,\mu m^2$ (Figure 30) was scanned with the magnetic tip in order to measure the domain pattern of the manipulated area in the nanowire array. Inside the area of the first scan, nearly every nickel column ($\sim$93%) was magnetized in the same direction. Figure 30 shows the local impact (dark quadratic region) of the external magnetic field and the strong magnetic tip during the first MFM scan on the magnetization of nanowires. Around the magnetized region of $5 \times 5\,\mu m^2$, the nickel nanowire array remained in the demagnetized state and exhibited the labyrinth-like domain pattern (Figure 28). The border between the magnetized area and the surrounding demagnetized area is clearly visible. From this picture, it can be concluded that the applied magnetic field ($H_{sw} \approx H_c$) alone was not strong enough for the switching of magnetic polarization in the Ni columns. Hence, the additional field contribution from the strong MFM tip (H_{tip}) enabled the local switching process in the Ni nanowire array. The probability for a nickel nanowire to remain unswitched (light spots) increased in the lower region of the magnetically manipulated area (Figure 30, first scan). In the upper region, where the first magnetic scan procedure was started, the first five or six horizontal nanowire rows had been saturated in the same direction. During the first scan procedure when the area of the saturated nanowires was growing, the probability for a nanomagnet to remain unswitched increased. It can be assumed that the stray field interactions between the demagnetized and the magnetized area can be neglected and the net stray field in the demagnetized area is zero. By increasing the area of parallel-magnetized nanowires, the dipole interactions between the magnetic elements were enhanced and the applied local field ($H_{tip} + H_{ex}$) was becoming less sufficient for a complete magnetic alignment of magnetization in a horizontal row of nickel columns. At the left and right border of the magnetically manipulated area, the stray field interactions were weak and a lower number of unswitched magnetic columns were observed there. From this experiment, it can

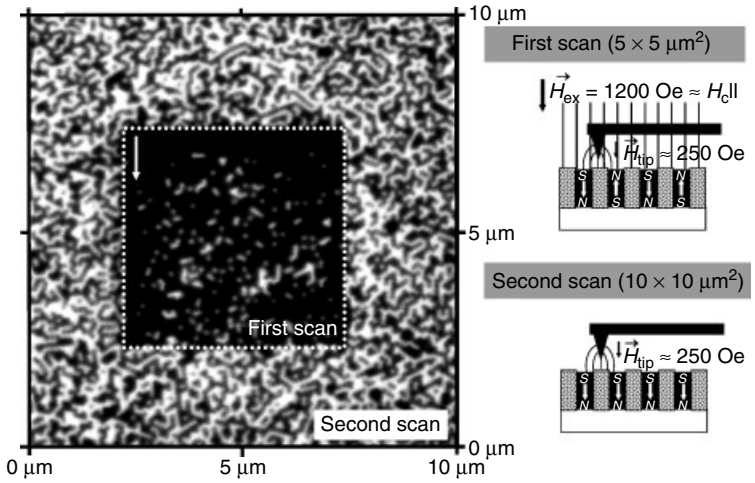

Figure 30. Local magnetic switching of a demagnetized sample area ($5 \times 5\,\mu m^2$, first scan) by a strong magnetic MFM tip ($H_{tip} \approx -250$ Oe) and an external magnetic field ($H_{ex} = -1200$ Oe). This image of the domain pattern ($10 \times 10\,\mu m^2$) was recorded by a second subsequent MFM scan without an external magnetic field.

be concluded that the stray field dipole interactions between the nanowires were extended over several interwire distances because of their high aspect ratio (nanowire length to interwire distance $L/D_{int} \approx 7$). In principle, a single nanowire can store 1 bit of information and can be locally switched independently of the magnetization of its nearest neighbors.

Researchers from Fujitsu Laboratories in Japan (Kikuchi *et al*., 2005) have preformed reading and writing tests on cobalt-filled porous alumina structures with 63-nm pitch on 2.5-in. disks, recently. Although they performed these experiments on disordered porous alumina structures, they demonstrated the data readout of the magnetic polarization of individual nanowires with a standard head for perpendicular recording. Currently, the Fujitsu researchers performing these tests on ferromagnetic materials filled alumina pore arrays with short and long range ordering.

7.2 Nanoelectromechanical systems (NEMS) and magnetic sensors

Other applications for magnetic nanowires include magnetic and mechanical sensors, where the nanowires can essentially be used as magnetoelectronic systems and/or NEMS with advantages that scale indirectly with size. In particular, NEMS sensors involve nanowire motion. Typically the force to be sensed moves the nanowires, and this motion is then detected by another means. Similar size advantages are already commercially achieved with microelectromechanical systems (MEMS), which began to attract interest in the middle of the last century (Feynman, 1992). Advantages of MEMS include reduced mass, increased resonant frequencies, lower force constants, and ease of 'manufacturing' large numbers of devices simultaneously using silicon (Si) planar processing. MEMS are now seen commercially in applications such as mirrors for optical communications (Lin and Goldstein, 2002; Ermolov *et al*., 2002), accelerometers (Beliveau, Spencer, Thomas and Roberson, 1999), medical devices (Maluf, Gee, Petersen and Kovacs, 1996), and flow control in ink-jet printers (Brünahl and Grishin, 2002; Lee, Kim, Kuk and Oh, 2002), and acoustic sensor arrays (Arnold, Nishida, Cattafesta and Sheplak, 2003).

Several groups are taking the MEMS-like 'top-down' approach to new limits in the nanoscale through novel lithography techniques using ion and electron-beam etching (Abadal *et al*., 1999; Yang *et al*., 2001; Roukes, 2001; Sundararajan and Bhushan, 2002). These novel non-silicon-specific techniques enable new materials to be used, which further increases the potential functionality of NEMS. However, owing to the limitations of lithography, they are limited in that the devices must usually have their largest dimension in plane and, as mentioned above, the processing is expensive with small areal coverage. Arrays of magnetic nanowires enable 'bottom-up' fabrication of NEMS, which offers the advantage of low-cost, high-density arrays.

Two applications of magnetic nanowire sensors can be classified as NEMS. The first involves layered nanowires to be used for atomic resolution in magnetic resonance force microscopy using layers of Ni, Au, and Pt (Valizadeh, George, Leisner and Hultman, 2002). A nanoreflector of Ag is preferentially grown on top of the Au layers at various locations along the wire depending on the sensor design (Barbic and Scherer, 2005). The resonance of such wires has been studied as well (Husain *et al*., 2003).

The second NEMS application of magnetic nanowires involves magnetostrictive nanowires for acoustic sensors (Stadler *et al*., 2005; McGary and Stadler, 2005; McGary *et al*., 2006; Downey and Flatau, 2005). These magnetostrictive nanowires are being tailored to dimensions that will resonate at a variety of frequencies for applications in sonar, hearing, and ultrasound. Because they are magnetostrictive, the nanowires will generate a magnetic field when they change dimension because of the acoustic signal. This field will then be detected by a magnetic sensor, ideally this sensor will be a nanowire giant magnetoresistance (GMR) sensor that is integrated directly into the base of each nanowire. In this way, a very small array will be produced for sensing the magnitude and phase of the incoming sound. Resonant frequencies can range from kilohertz to gigahertz for 20 nm nanowires by varying the lengths from 0.5 to 100 μm (Stadler *et al*., 2005). Arrays of shorter wires will therefore be useful in medical applications, for example, in echocardiography, and the arrays can be polished at an angle to produce varying lengths, which will enable high spatial resolution imaging. Longer nanowires will be useful in applications such as ultrasound, sonar, and hearing.

In addition to NEMS, nanowires can be used as magnetic sensors, which use MR to sense external fields. This property can be intrinsic to the nanowire material, for example, Ni, or it can be optimized by designing multilayers inside the wires. An example of the latter is Co/Cu/Co stacks in which one of the Co layers is fabricated to have a higher coercivity than the other, perhaps by altering its thickness. Most magnetic nanowires studies involve template-grown arrays, although sometimes step decoration has been used, for example, Fe wires on sapphire steps (Westphalen, Zabel and Theis-Brohl, 2004).

These Co/Cu/Co multilayers are an example of GMR structures. These structures involve passing current through two ferromagnetic layers that have different coercivities (such as Co), and they are separated by a nonmagnetic spacer (such as the Cu). The ferromagnetic layer that is more coercive is considered to have a 'fixed' magnetization direction and the magnetization of the other ferromagnet is designed to be soft so that it can point in the direction of the magnetic field to be sensed. When these two layers are aligned (which occurs when the sensed field is aligned with the fixed layer), the resistance of the structure is low. However, when the ferromagnets are not aligned, the electrons become polarized in one layer, and they are less likely to be able to conduct through the other layer due to interfacial scattering.

This phenomenon of GMR is mostly studied using Co/Cu/Co layers (McGary, 2006; Piraux *et al*., 1997; Blondel, Meir, Doudin and Ansermet, 1994; Liu, Nagodawithana, Searson and Chien, 1995), which have yielded MR of 20% or higher at RT (Liu, Nagodawithana, Searson and Chien, 1995; Doudin, Blondel and Ansermet, 1996). The exact MR ratio depends on the total length of the nanowire, which often includes long Cu ends that contribute to the total resistance, but not to the MR, so the absolute MR of the multilayers will be higher than the measured MR. Figure 31 shows a 100-nm nanowire from an array grown with the recipe given in Section 3 with (30 nm) Co/(50 nm) Cu layers. Similar wires with 150 nm diameters and (5 nm) Co/(5 nm) Cu yielded 7% MR at RT using the recipe given (Stadler and Tan, 2006). Several other configurations have been studied in which the pure Co ferromagnetic layers are replaced by CoNiCu (Heydon *et al*., 1997), NiFe (Blondel, Meir, Doudin and Ansermet, 1994; Dubois *et al*., 1997), CoNi (Attenborough *et al*., 1995), Ni (Wang *et al*., 1996; Chen, Searson and Chien, 2003), and Fe (Piraux *et al*., 1997). The Cu nonmagnetic spacer can also be replaced by other metals, such as Ag (Valizadeh, George, Leisner and Hultman, 2002), Pt (Chu, Inoue, Wada and Kurashima, 2004), or Pb (Dubois *et al*., 1999). Most groups use single electrochemical baths which contain sulfates or other salts of all of the desired metals, but some groups use separate baths for each layer (Blondel, Doudin and Ansermet, 1997). In growing these GMR structures, it is difficult to obtain ferromagnetic layers with the required differences in coercivity. In patterned thin-film sensors, this is usually done using an antiferromanget next to one of the ferromagnets in order to fix its magnetization. However, antiferromagnets are often oxides or alloys that are difficult to deposit (e.g., IrMn), and the other option, synthetic antiferromagnets, involves stacks of up to five elements which can require additional metal ions in the electrolyte, and hence complicate the deposition of each layer. As mentioned above, the coercivity can be altered by varying the thickness of one of the ferromagnetic layers, but this has a limited effect.

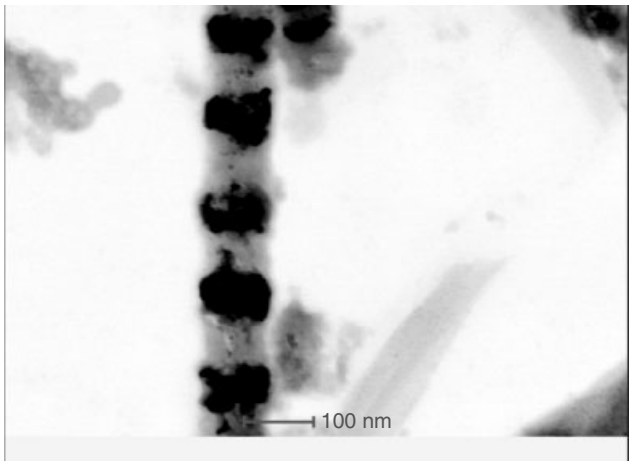

Figure 31. High-resolution TEM image of a Co/Cu/Co multilayered nanowire.

Another method is to vary the crystallographic alignment of Co in the various layers using an external applied magnetic field as shown in Figure 13 (Cobian, 2004). This allows one bath for all of the layers as long as the nanowires can be deposited inside a double-axes magnet.

8 CONCLUSIONS

About 10 years ago, Masuda and Fukuda discovered the self-ordered growth of nanoporous alumina membranes via anodization. Since this time, highly ordered anodized alumina has attracted many international groups as a template material for the synthesis of magnetic nanowires. Classical ferromagnetic materials, such as iron, cobalt, and nickel, as well as novel magnetic materials, such as CoPt and GaFe alloys, have been electrodeposited by constant or pulsed electrical signals inside the nanopores of these alumina membranes. The monodisperse nanowires are then in a strictly parallel hexagonal arrangement that is perpendicular to the substrate. The diameters have been tailored from 10 to 350 nm by varying the anodization conditions, such as electrolyte, voltage, and temperature.

The magnetic properties of the nanowires and arrays have been modified through the choice of material, diameter, spacing, and applied fields during growth. For Co nanowires the anisotropy has been controlled by balancing the strong crystallographic anisotropy of Co with the shape anisotropy of the wires. Multilayered nanowires of Co/Cu/Co with controlled anisotropy in the Co are well suited for magnetic sensors and magnetic random access memory (MRAM). For $Fe_{1-x}Ga_x$ alloys (Galfenol), the magnetostriction varies with composition, which has been controlled via deposition parameters. Nanowire arrays of Galfenol are essentially NEMS that can be used as cilia for sensors of acoustic and other mechanical signals. For Ni and NiMn nanowires, large coercivities have been obtained with weak dipolar interactions between wires due to small magnetocrystalline anisotropy and small magnetic moment. These materials are therefore particularly suitable for patterned perpendicular magnetic media.

Numerical simulations were presented that showed that the independent magnetization reversal of individual nanowires inside a close-packed array was possible. Also, perfectly ordered magnetic nanowire arrays have been demonstrated on the square centimeters scale by nanoimprinting the Al precursor prior to anodization. Significant improvement of the magnetic performance was obtained, because the nanomagnets had a very narrow size distribution, as well as perfect order.

The fabrication of large-scale, perfectly ordered nanowire arrays with sub-100 nm periodicity and very monodisperse magnetic nanowires with sub-10 nm diameters are still a great challenge, and further developments of these nanostructures are necessary. Also, the growth of novel magnetic materials, especially new alloys, will be a frontier for this field that must be reached in order to realize the potential of many applications. New applications continue to be developed, including multilayer nanotubes, self-assembled 3D nanostructures based on multilayer magnetic nanowires, nanowires with specific binding sites for molecules or DNA, and more. With many fundamentals understood, we are only seeing the tip of the iceberg in the impact of magnetic nanowires.

ACKNOWLEDGMENTS

We are grateful to T. Schweinböck, H. Kronmüller, S. F. Fischer, D. Weiss, D. Navas, M. Vazquez, Ryan Cobian, Patrick McGary, Liwen Tan, and Na hyoung Kim for support, experimental measurements, or fruitful discussions. We also like to thank Professor U. Gösele and Professor J. Kirschner for supporting this activity. Partial funding of some results was provided by the US Office of Naval Research and the US National Science Foundation, including the University of Minnesota's Materials Research Science and Engineering Center.

REFERENCES

Abadal, G., Boisen, A., Davis, Z.J., *et al*. (1999). Combined laser and atomic force microscope lithography on aluminum: mask fabrication for nanoelectromechanical systems. *Applied Physics Letters*, **74**, 3206–3208.

Aharoni, A. (1999). Incoherent magnetization reversals in elongated particles. *Journal of Magnetism and Magnetic Materials*, **196–197**, 786–790.

Aharoni, A. and Shtrikman, S. (1958). Magnetization curve of the infinite cylinder. *Physical Review*, **109**, 1522–1528.

Almawlawi, D., Coombs, N. and Moskovits, M. (1991). Magnetic properties of Fe deposited into anodic aluminum oxide pores as a function of particle size. *Journal of Applied Physics*, **70**, 4421–4425.

Amundson, K., Helfand, E., Quan, X., *et al*. (1994). Alignment of lamellar block copolymer microstructure in an electric field. 2: mechanisms of alignment. *Macromolecules*, **27**, 6559–6570.

Arnold, D.P., Nishida, T., Cattafesta, L.N. and Sheplak, M. (2003). A directional acoustic array using silicon micromachined piezoresistive microphones. *The Journal of the Acoustical Society of America*, **113**, 289–298.

Attenborough, K., Hart, R., Schwarzacher, W., *et al*. (1995). Superlattice nanowires. *Materials Research Society Symposium Proceedings: Magnetic Ultrathin Films, Multilayers, and Surfaces*, **384**, 3–8.

Barbic, M. and Scherer, A. (2005). Composite nanowire-based probes for magnetic resonance force microscopy. *Nano Letters*, **5**, 187–190.

Beliveau, A., Spencer, G.T., Thomas, K.A. and Roberson, S.L. (1999). Evaluation of MEMS capacitive accelerometers. *IEEE Design and Test of Computers*, **16**, 48–56.

Blondel, A., Doudin, B. and Ansermet, J.P. (1997). Comparative study of the magnetoresistance of electrodeposited Co/Cu multilayered nanowires made by single and dual bath techniques. *Journal of Magnetism and Magnetic Materials*, **165**, 34–37.

Blondel, A., Meir, J.P., Doudin, B. and Ansermet, J.P. (1994). Giant magnetoresistance of nanowires of multilayers. *Applied Physics Letters*, **65**, 3019–3021.

Brünahl, J. and Grishin, A.M. (2002). Piezoelectric shear mode drop-on-demand inkjet actuator. *Sensors And Actuators A: Physical*, **101**, 371–382.

Castano, F.J., Haratani, S., Hao, Y., *et al*. (2002). Giant magnetoresistance in 60-150-nm-wide pseudo-spin-valve nanowires. *Applied Physics Letters*, **81**, 2809–2811.

Chen, M., Searson, P.C. and Chien, C.L. (2003). Micromagnetic behavior of electrodeposited Ni/Cu multilayer nanowires. *Journal of Applied Physics*, **93**, 8253–8255.

Cheng, C., Gonela, R.K., Gu, Q. and Haynie, D.T. (2005). Self-assembly of metallic nanowires from aqueous solution. *Nano Letters*, **5**, 175–178.

Chiriac, H., Moga, A.E., Urse, M. and Ovari, T.A. (2003). Preparation and magnetic properties of electrodeposited magnetic nanowires. *Sensors and Actuators A:Physical*, **106**, 348–351.

Choi, J., Nielsch, K., Reiche, M., *et al*. (2003). Fabrication of monodomain alumina pore arrays with an interpore distance smaller than the lattice constant of the imprint stamp. *Journal of Vacuum Science and Technology B*, **21**, 763–766.

Chou, S.Y., Wie, M.S., Krauss, P.R. and Fischer, P.B. (1994). Single-domain magnetic pillar array of 35 nm diameter and 65 Gbits/in^2. density for ultrahigh density quantum magnetic storage. *Journal of Applied Physics*, **76**, 6673–6675.

Chtanko, N., Molares, M.E.T., Cornelius, T., *et al*. (2004). Etched single-ion-track templates for single nanowire synthesis. *Journal of Physical Chemistry B*, **108**, 9950–9954.

Chu, S-Z., Inoue, S., Wada, K. and Kurashima, K. (2004). Fabrication and structural characteristics of nanocrystalline Fe-Pt thin films and Fe-Pt nanowire arrays embedded in alumina films on ITO/Glass. *Journal of Physical Chemistry B*, **108**, 5582–5587.

Cobian, R. (2004). *Tuning the Structural and Magnetic Properties of Cobalt and Cobalt/Copper Multilayered Nanowires. Masters of Science in Electrical Engineering* Thesis, University of Minnesota.

Darques, M., Encinas, A., Vila, L. and Piraux, L. (2004). Tailoring of the c-axis orientation and magnetic anisotropy in electrodeposited Co nanowires. *Journal of Physics: Condensed Matter*, **16**, S2279–S2286.

Dauginet-De Pra, L., Ferain, E., Legras, R. and Demoustier-Champagne, S. (2002). Fabrication of a new generation of track-etched templates and their use for the synthesis of metallic and organic nanostructures. *Nuclear Instruments and Methods in Physics Research Section B: Beam Interactions With Materials and Atoms*, **196**, 81–88.

Djalali, R., Li, S-Y. and Schmidt, M. (2002). Amphipolar core-shell cylindrical brushes as templates for the formation of gold clusters and nanowires. *Macromolecules*, **35**, 4282–4288.

Doudin, B., Blondel, A. and Ansermet, J.P. (1996). Arrays of multilayered nanowires. *Journal of Applied Physics*, **79**, 6090–6094.

Downey, P. and Flatau, A. (2005). Magnetoelastic bending of Galfenol for sensor applications. *Journal of Applied Physics*, **97**, 10R505.

Dubois, S., Marchal, C., Beuken, J.M., *et al*. (1997). Perpendicular giant magnetoresistance of NiFe/Cu multilayered nanowires. *Applied Physics Letters*, **70**, 396–398.

Dubois, S., Michel, A., Eymery, J.P., *et al*. (1999). Fabrication and properties of arrays of superconducting nanowires. *Journal of Materials Research*, **14**, 665–671.

Dumpich, G., Krome, T.P. and Hausmanns, B. (2002). Magnetoresistance of single Co nanowires. *Journal of Magnetism and Magnetic Materials*, **248**, 241–247.

Enculescu, I., Siwy, Z., Dobrev, D., *et al*. (2003). Copper nanowires electrodeposited in etched single-ion track templates. *Applied Physics, A*, **77**, 751–755.

Ermolov, V., Nieminen, H., Nybergh, K., *et al*. (2002). MEMS for mobile communications. *Circuits Assembly*, **13**, 46–44.

Fahmi, A.W., Braun, H.G. and Stamm, M. (2003). Fabrication of metallized nanowires from self-assembled diblock copolymer templates. *Advanced Materials*, **15**, 1201–1204.

Feiyue, L., Metzger, R.M. and Doyle, W.D. (1997). Influence of particle size on the magnetic viscosity and activation volume of α-Fe nanowires in alumite films. *IEEE Transactions on Magnetics*, **33**, 3715–3717.

Ferain, E. and Legras, R. (1997). Characterisation of nanoporous particle track etched membrane. *Nuclear Instruments and Methods in Physics Research Section B*, **131**, 97–102.

Feynman, R.P. (1992). There's plenty of room at the bottom [data storage]. *Journal of Microelectromechanical Systems*, **1**, 60–66.

Florez, S.H., Krafft, C. and Gomez, R.D. (2005). Spin-current-induced magnetization reversal in magnetic nanowires with constrictions. *Journal of Applied Physics*, **97**, 10C705.

Fukutani, K., Tanji, K., Motoi, T. and Den, T. (2004). Ultrahigh pore density nanoporous films produced by the phase separation of eutectic Al-Si for template-assisted growth of nanowire array. *Advanced Materials*, **16**, 1456–1460.

Gates, B., Mayers, B., Cattle, B. and Xia, Y. (2002). Synthesis and characterization of uniform nanowires of trigonal selenium. *Advanced Functional Materials*, **12**, 219–227.

Gravier, L., Fabian, A., Rudolf, A., *et al*. (2004). Spin-dependent thermopower in Co/Cu multilayer nanowires. *Journal of Magnetism and Magnetic Materials*, **271**, 153–158.

Guo, S., Rzayev, J., Bailey, T.S., *et al*. (2006). Nanopore and nanobushing arrays from ABC triblock thin films containing two etchable blocks. *Chemistry of Materials*, **18**, 1719–1721.

Hertel, R. (2001). Micromagnetic simulations of magnetostatically coupled nickel nanowires. *Journal of Applied Physics*, **90**, 5752–5758.

Hertel, R. (2002). Computational micromagnetism of magnetization processes in nickel nanowires. *Journal of Magnetism and Magnetic Materials*, **249**, 251–256.

Hertel, R. and Kirschner, J. (2004). Magnetization reversal dynamics in nickel nanowires. *Physica B: Condensed Matterhysica B: Condensed Matter*, **343**, 206–210.

Heydon, G.P., Hoon, S.R., Farley, A.N., *et al*. (1997). Magnetic properties of electrodeposited nanowires. *Journal of Physics D: Applied Physics*, **30**, 1083–1093.

Horst, S.C., Agarwala, S., King, O., *et al*. (1997). GaAs/AlGaAs ridge lasers with etched mirrors formed by an inductively coupled plasma reactor. *Applied Physics Letters*, **71**, 1444–1445.

Husain, A., Hone, J., Postma, H.W.C., *et al*. (2003). Nanowire-bades very-high-frequency electromechanical resonator. *Applied Physics Letters*, **83**, 1240–1242.

Hwang, M., Abraham, M.C., Savas, T.A., *et al*. (2000a). Magnetic force microscopy study of interactions in 100 nm period nanomagnet arrays. *Journal of Applied Physics*, **87**, 5108–5110.

Hwang, M., Farhoud, M., Hao, Y., *et al*. (2000b). Major hysteresis loop modeling of two-dimensional arrays of single domain particles. *IEEE Transactions on Magnetics*, **36**, 3173–3175.

Jacobs, L.S. and Bean, C.P. (1955). An approach to elongated fine-particle magnets. *Physical Review B*, **100**, 1060–1067.

Jorzick, J., Demokritov, S.O., Hillebrands, B., *et al*. (1999a). Spin-wave quantization and dynamic coupling in micron-size circular magnetic dots. *Applied Physics Letters*, **75**, 3859–3861.

Jorzick, J., Demokritov, S.O., Mathieu, C., *et al*. (1999b). Brillouin light scattering from quantized spin waves in micron-size magnetic wires. *Physical Review B*, **60**, 15194–15200.

Kaneko, M.P. (1981). Magnetization reversal mechanism of nickel alumite films. *IEEE Transactions on Magnetics*, **17**, 1468–1471.

Kawai, S. and Ueda, R. (1975). Magnetic properties of anodic oxide coatings on aluminium containing electrodeposited Co and Co-Ni. *Journal of the Electrochemical Society*, **122**, 32–36.

Kelcher, S., Park, D-Y., Yoo, B-Y. and Myung, N.V. (2005). Film stress and magnetic properties of nickel, cobalt, iron and iron-cobalt alloy electrodeposits. *Plating and Surface Finishing*, **92**, 24–29.

Kikuchi, H., Nakao, H., Yasui, K., *et al*. (2005). Fabrication of head-flyable nanohole patterned media and dynamic write/read measurement with GMR head. *IEEE Transactions on Magnetics*, **41**, 3226–3228.

Kim, J.U., Cha, S.H., Shin, K., *et al*. (2004). Preparation of gold nanowires and nanosheets in bulk block copolymer phases under mild conditions. *Advanced Materials*, **16**, 459–464.

Lee, S-W., Kim, H-C., Kuk, K. and Oh, Y.S. (2002). A monolithic inkjet print head: DomeJet. *Sensors and Actuators A: Physical*, **95**, 114–119.

Li, A.P., Müller, F., Birner, A., *et al*. (1998). Hexagonal pore arrays with a 50–420 nm interpore distance formed by self-organization in anodic alumina. *Journal of Applied Physics*, **84**, 6023–6026.

Li, A.P., Müller, F. and Gösele, U. (2000). Polycrystalline and monocrystalline pore arrays with large interpore distance in anodic alumina. *Electrochemistry and Solid State Letters*, **3**, 131–134.

Lin, L.Y. and Goldstein, E.L. (2002). Opportunities and challenges for MEMS in lightwave communications. *IEEE Journal of Selected Topics in Quantum Electronics*, **8**, 163–172.

Lindeberg, M. and Hjort, K. (2003). Interconnected nanowire clusters in polyimide for flexible circuits and magnetic sensing applications. *Sensors and Actuators A: Physical*, **105**, 150–161.

Liu, K., Nagodawithana, K., Searson, P.C. and Chien, C.L. (1995). Perpendicular giant magnetoresistance of multilayered Co/Cu nanowires. *Physical Review B*, **51**, 7381–7384.

Liu, Q.F., Wang, J.B., Yan, Z.J. and Xue, D.S. (2004). The effect of diameter on micro-magnetic properties of Fe0.68Ni0.32 nanowire arrays. *Journal of Magnetism and Magnetic Materials*, **278**, 323–327.

Maluf, N.I., Gee, D.A., Petersen, K.E. and Kovacs, G.T.A. (1995). Medical applications of MEMS, *WESCON/95 Conference Record*, San Francisco, CA, pp. 300–306.

Mathieu, C., Jorzick, J., Frank, A., *et al*. (1998). Lateral quantization of spin waves in micron size magnetic wires. *Physical Review Letters*, **81**, 3968–3971.

Masuda, H. and Fukuda, K. (1995). Ordered metal nanohole arrays made by A 2-step replication of honeycomb structures of anodic alumina. *Science*, **268**, 1466–1468.

Masuda, H., Nishio, K. and Baba, N. (1993). Preparation of microporous metal membranes by two-step replication of the microstructure of anodic alumina. *Thin Solid Films*, **223**, 1–3.

Masuda, H., Tanaka, H. and Baba, N. (1990). Preparation of porous material by replacing microstrucutre of anodic alumina film with metal. *Chemistry Letters*, **4**, 621–622.

Masuda, H., Yamada, H., Satoh, M., *et al*. (1997). Highly ordered nanochannel-array architecture in anodic alumina. *Applied Physics Letters*, **71**, 2770–2772.

Mbindyo, J.K.N., Mallouk, T.E., Mattzela, J.B., *et al*. (2002). Template synthesis of metal nanowires containing monolayer molecular junctions. *Journal of the American Chemical Society*, **124**, 4020–4026.

McGary, P. (2006). *Masters of Science in Electrical Engineering*, Thesis, University of Minnesota.

McGary, P.D. and Stadler, B.J.H. (2005). Electrochemical deposition of $Fe_{1-x}Ga_x$ nanowire arrays. *Journal of Applied Physics*, **97**, 10R503.

McGary, P.D., Tan, L., Zou, J., *et al*. (2006). Magnetic nanowires for acoustic sensors. *Journal of Applied Physics*, **99**, 08B310.

Morales, A.M. and Lieber, C.M. (1998). A laser ablation method for the synthesis of crystalline semiconductor nanowires. *Science*, **279**, 208–211.

Morkved, T.L., Lu, M., Urbas, A.M., *et al*. (1996). Local control of microdomain orientation in diblock copolymer thin films with electric fields. *Science*, **273**, 931–933.

Nielsch, K., Choi, J., Hertel, R., *et al*. (2003). Intermag Conference 2003. *Digests of the Intermag Conference*, Boston, GC11.

Nielsch, K., Choi, J., Schwirn, K., *et al*. (2002a). Self-ordering regimes of porous alumina: the 10% porosity rule. *Nano Letters*, **2**, 677–680.

Nielsch, K., Wehrspohn, R.B., Fischer, S.F., *et al*. (2002b). High density hexagonal nickel nanowire array. *Journal of Magnetism and Magnetic Materials*, **249**, 234–240.

Nielsch, K., Hertel, R., Wehrspohn, R.B., *et al*. (2002c). Switching behavior of single nanowires inside dense nickel nanowire arrays. *IEEE Transactions on Magnetics*, **38**, 2571–2573.

Nielsch, K., Müller, F., Li, A.P. and Gösele, U. (2000a). Uniform nickel deposition into ordered alumina pores by pulsed electrodeposition. *Advanced Materials*, **12**, 582–586.

Nielsch, K., Müller, F., Wehrspohn, R.B., *et al*. (2000b). Magnetic nanowire arrays obtained by electrodeposition in ordered alumina templates. *The Electrochemical Society Proceedings Series*, **8**, 13–22.

Nielsch, K., Wehrspohn, R.B., Barthel, J., *et al*. (2001). Hexagonally ordered 100 nm period nickel nanowire arrays. *Applied Physics Letters*, **79**, 1360–1362.

O'Barr, R., Yamamoto, S.Y., Schultz, S., *et al*. (1997). Fabrication and characterization of nanoscale arrays of nickel columns. *Journal of Applied Physics*, **81**, 4730–4732.

O'Handley, R.C. (2000). *Modern Magnetic Materials: Principles and Applications*. John Wiley & Sons, New York.

Olayo-Valles, R., Guo, S., Lund, M.S., *et al*. (2005). Perpendicular domain orientation in thin films of polystyrene – Polylactide diblock copolymers. *Macromolecules*, **38**, 10101–10108.

Ounadjela, K., Ferre, R., Louail, L., *et al*. (1997). Magnetization reversal in cobalt and nickel electrodeposited nanowires. *Journal of Applied Physics*, **81**, 5455–5457.

Paunovic, M. and Schlesinger, M. (1998). *Fundamentals of Electrochemical Deposition*, John Wiley & Sons: New York.

Petrovykh, D.Y., Himpsel, F.J. and Jung, T. (1988). Width distribution of nanowires grown by step decoration. *Surface Science*, **407**, 189–199.

Piraux, L., Dubois, S., Duvail, J.L., *et al*. (1997). Arrays of nanowires of magnetic metals and multilayers: perpendicular GMR and magnetic properties. *Journal of Magnetism and Magnetic Materials*, **175**, 127–136.

Rabin, O., Herz, P.R., Lin, Y.M., *et al*. (2003). Formation of thick porous anodic alumina films and nanowire arrays on silicon wafers and glass. *Advanced Functional Materials*, **13**, 631–638.

Roukes, M. (2001). Nanoelectromechanical systems face the future. *Physics World*, **14**, 25–31.

Routkevitch, D., Tager, A.A., Haruyama, J., *et al*. (1996). Nonlithographic nano-wire arrays: fabrication, physics, and device applications. *IEEE Transactions on Electron Devices*, **147**, 1646–1658.

Ross, C.A., Smith, H.I., Savas, T.A., *et al*. (1999). Fabrication of patterned media for high density magnetic storage. *Journal of Vacuum Science and Technology B*, **17**, 3168–3176.

Samwel, E.O., Bissel, P.R. and Lodder, J.C. (1992). Internal field corrections in perpendicular columnar structured Alumite films. *Journal of Magnetism and Magnetic Materials*, **115**, 327–332.

Schonenberger, C., van der Zande, B.M.I., Fokkink, L.G.J., *et al*. (1997). Template synthesis of nanowires in porous polycarbonate membranes: electrochemistry and morphology. *Journal of Physical Chemistry B*, **101**, 5497–5505.

Skomski, R. (2003). Nanomagnetics. *Journal of Physics: Condensed Matter*, **15**, R841–R896.

Stadler, B.J.H., Kim, N.H., Tan, L.W., *et al*. (2005). Nanowire Arrays with Specialized Geometries for Magnetoelectronics (Invited). MRS Proceedings: Fabrication and Applications of Nanomagnetic Structures, Boston, MA, I6.3.

Stoner, E.C., Wohlfarth, F.R.S. and Wohlfarth, E.P. (1948). A mechanism of magnetic hysteresis in heterogeneous alloys. *Philosophical Transactions of the Royal Society of London, Series A*, **240**, 599–642.

Strijkers, G.J., Dalderop, J.H.J., Broeksteeg, M.A.A., *et al*. (1999). Structure and magnetization of arrays of electrodeposited Co wires in anodic alumina. *Journal of Applied Physics*, **86**, 5141–5145.

Sundararajan, S. and Bhushan, B. (2002). Development of AFM-based techniques to measure mechanical properties of nanoscale structures. *Sensors and Actuators A: Physical*, **101**, 338–351.

Tan, L., (2005). *Directed Self-Assembly of Magnetic Nanowire Arrays with Long Range Order*. Doctor of Philosophy in Materials Science Dossier, University of Minnesota.

Tan, L. and Stadler, B.J.H. (2006). Fabrication and magnetic behavior of Co/Cu multilayered nanowires. *Journal of Materials Research*, **21**, 2870–2875.

Thurn-Albrecht, T., DeRouchey, J., Russell, T.P. and Jaeger, H.M. (2000). Overcoming interfacial interactions with electric fields. *Macromolecules*, **33**, 3250–3253.

Thurn-Albrecht, T., Schotter, J., Kastle, G.A., *et al*. (2000). Ultrahigh-density nanowire arrays grown in self-assembled diblock copolymer templates. *Science*, **290**, 2126–2129.

Toimil Molares, M.E., Hohberger, E.M., Schaeflein, Ch., *et al*. (2003). Electrical characterization of electrochemically grown single sopper nanowires. *Applied Physics Letters*, **82**, 2139–2141.

Tokuda, N., Watanabe, H., Hojo, D., *et al*. (2004). Fabrication of Cu nanowires along atomic step edge lines on Si(1 1 1) substrates. *Applied Surface Science*, **237**, 529–532.

Valizadeh, S., George, J.M., Leisner, P. and Hultman, L. (2002). Electrochemical synthesis of Ag/Co multilayered nanowires in porous polycarbonate membranes. *Thin Solid Films*, **402**, 262–271.

Vázquez, M., Nielsch, K., Vargas, P., *et al*. (2004). Modelling hysteresis of interacting nanowires arrays. *Physica B: Condensed Matter*, **343**, 395–402.

Wang, Z.K., Kuok, M.H., Ng, S.C., *et al*. (2003). Spin-wave quantization in ferromagnetic nickel nanowires. *Physical Review Letters*, **89**, 027201.

Wang, L., Yu-Zhang, K., Metrot, A., *et al*. (1996). TEM study of electrodeposited Ni/Cu multilayers in the form of nanowires. *Thin Solid Films*, **288**, 86–89.

Westphalen, A., Zabel, H. and Theis-Brohl, K. (2004). Magnetic nanowires on faceted sapphire surfaces. *Thin Solid Films*, **449**, 207–214.

Whitney, T.M., Jiang, J.S., Searson, P.C. and Chien, C.L. (1993). Fabrication and magnetic properties of arrays of metallic nanowires. *Science*, **261**, 1316–1316.

Xu, T., Kim, H.C., DeRouchey, J., *et al*. (2001). The influence of molecular weight on nanoporous polymer films. *Polymer*, **42**, 9091–9095.

Yang, Y.T., Ekinci, K.L., Huang, X.M.H., *et al*. (2001). Monocrystalline silicon carbide nanoelectromechanical systems. *Applied Physics Letters*, **78**, 162–164.

Zhang, Z., Sun, X., Dresselhaus, M.S., *et al*. (1998). Magneto-transport investigations of ultrafine single-crystalline bismuth nanowire arrays. *Applied Physics Letters*, **73**, 1589–1591.

Zeng, H., Zheng, M., Skomski, R., *et al*. (2000). Magnetic properties of self-assembled Co nanowires of varying length and diameter. *Journal of Applied Physics*, **87**, 4718–4720.

Zheng, G., Pardavi-Horvath, M. and Vertesy, G. (1997). Major loop reconstruction from switching of individual particles. *Journal of Applied Physics*, **81**, 5591–5593.

Zou, J., Qi, X., Tan, L. and Stadler, B.J.H. (2006). Large-scale ordering of porous Si using anodic aluminum oxide grown by directed self-assembly. *Applied Physics Letters*, **89**, 093106.

Magnetic Carbon

Pablo Esquinazi
University of Leipzig, Leipzig, Germany

1 INTRODUCTION

Not long ago, carbon allotropes like graphite, diamond, carbon nanotubes, and fullerenes were accepted to be basically diamagnetic. In Short, the diamagnetic signal is the counter-response to an applied magnetic field from localized electrons, as in diamond, or from delocalized π-band electrons, as in graphite for fields normal to the graphene layers, or from a mixture of the diamagnetism of localized electrons and the so-called van Vleck paramagnetic (magnetic dipole interband transitions due to the asymmetry of the chemical bond) contributions, as in fullerenes and nanotubes. This magnetic response was reviewed some years ago by Haddon (1995). On the other hand, it was a common belief that any ferromagnetic-like signal measured at room temperature in a carbon structure is due to magnetic impurities. Apart from a few publications at the end of the 1980s and in the 1990s (some of them will be reviewed in Section 2), the scientific community did not take the possibility that a carbon structure could show magnetic order at room temperature seriously. The main problem scientists have to convince themselves on such a phenomenon in a material with only s and p electrons is that magnetic impurities, like Fe or Ni, may contribute to the magnetic response substantially in case the 'intrinsic' magnetic signals are relatively small.

Paradoxically, the overall success of the pioneer model of ferromagnetism in metals contributed substantially to create some kind of 'magnetic prejudice' for more than 60 years. In his original article, Heisenberg (1928) rejected the possibility of magnetic order in elements with main quantum number $n < 3$ (for the electrons responsible for the ferromagnetism). Elements like Fe, Ni, or Co have a net magnetic moment $\mathbf{m}$ in the solid state due to unpaired 3d electrons. Through exchange interactions between them characterized by a constant J, compounds based on these elements belong to the restricted family of ferromagnets with Curie temperature above room temperature. In contrast, carbon in the atomic state has $\mathbf{m} = 0$ and in the solid state shows strong covalent bondings that suppress any unpaired-electron spin. It is therefore understandable that judging the 'sometimes unclear' experimental evidence in the past the possibility of magnetic order in carbon-based materials was tacitly denied by the main stream of scientists working in magnetism.

From the basic research point of view the existence of a room-temperature magnet containing only s and p electrons is of great significance for the physics of magnetism, especially because of the expected interesting correlation effects between electrons. We note that macroscopic magnetic order in metal-free organic materials has been reported in 1991 in the open-shell radical *p*-nitrophenylnitronyl nitroxide (*p*-NPNN) (Turek *et al*., 1991; Tamura *et al*., 1991) and

Handbook of Magnetism and Advanced Magnetic Materials. Edited by Helmut Kronmüller and Stuart Parkin. Volume 4: *Novel Materials*. ISBN: 978-0-470-02217-7.

in tetrakis(dimethylamino)ethylene (TDAE) + C_{60} charge-transfer salt (Allemand *et al*., 1991) with Curie temperatures $T_c = 0.6$ and 16 K, respectively. These findings were recognized by the community, in clear contrast to the few, rather unnoticed works where evidence for magnetic order in carbon was reported before 1991 (see Section 2). A number of studies on molecular magnets with low Curie temperatures ($T_c < 30$ K) have been done in the last 10 years (Veciana, 2001; Blundell and Pratt, 2004). We also note that antiferromagnetic order has been observed in a material with only s or p electrons, as probably the first example for an s-electron antiferromagnet reported in the compound $(Na/K)_8(AlSiO_4)_6$ below 50 K by Srdanov, Stucky, Lippmaa and Engelhardt (1998) indicates; see also Madsen, Iversen, Blaha and Schwarz (2001).

To the best of our knowledge, we are not aware of any physical law that prohibits the existence of a room-temperature ferromagnet in a compound with only s or p electrons. Therefore, and taking into account experimental data, there are no reasons to deny *a priori* its existence. In this article we review in Section 2 a few early publications that indicate the possible existence of unusual magnetic order in carbon. In Section 3, we discuss the characterization of the magnetic impurities, an important issue when the intrinsic magnetic signals of the studied compounds are relatively weak. In Section 4, we review different magnetic phenomena observed in carbon structures, that is, diamagnetism (Section 4.1), paramagnetism (Section 4.2), as well as recent observations of magnetic order in well-characterized carbon-based samples prepared under special conditions (Section 4.3). In the last section of this article, we review the possible origins for a magnetic order in carbon, discussed nowadays in the literature.

2 EARLY REPORTS ON FERROMAGNETIC-LIKE BEHAVIOR IN CARBON STRUCTURES

Till the end of the last millennium nearly 100 papers and 30 patents describing ferromagnetic structures containing either pure carbon or carbon combined with first-row elements were published. Many of these publications, some of them unknown to the main stream of magnetism experts, was reviewed recently by Makarova (2003, 2004). Unfortunately, in several of these early published studies the concentration of impurities is not clarified, perhaps not even determined. Therefore, it is not easy to provide a rigorous evaluation for most of them, also because the reproducibility of those results was apparently not reported in later work. Taking into account the experience of the author with the contribution of magnetic impurities (mainly Fe), we cannot assume that those early observations were free from systematic errors. Nevertheless, some of these results attract our attention. In this section, we restrict ourselves to discuss chronologically only a few of them.

Apparently, one of the first room-temperature organic ferromagnets was synthesized by Oostra and Torrance (1984) and reported in a symposium that took place in Honolulu. Three years later, these authors published a paper in which they showed that the reaction of symmetrical triaminobenzene ($C_6H_9N_3$) with iodine produces a black, insoluble polymer. This polymer showed, in some of the runs, ferromagnetism up to ∼600–700 K, which is near its decomposition temperature (Torrance, Oostra and Nazzal, 1987). The observed magnetization in that sample remains unknown since only the magnetic moment was reported without providing any information on the sample mass or volume. Although some trace quantities of Fe were found, neither its amount nor the irreversibility observed with temperature, implies that magnetic impurities may be the possible source for the magnetism. Apparently, a lack of reproducibility of the results reported by these authors remained in the years to come.

Korshak *et al*. (1986) (see also Korshak, Medvedeva, Ovchinnikov and Spektor, 1987) found a spontaneous magnetization $M = 0.02\,\text{emu g}^{-1}$ ($1\,\text{emu g}^{-1} = 1\,\text{Am}^2\,\text{kg}^{-1}$) in a chain of interacting radicals obtained by polymerization of a BIPO polydiacetylene crystal (BIPO: 1,4-bis-(2,2,6,6-tetramethyl-4-oxy-4-piperidyl-1-oxyl)-butadiene). The apparent magnetic order vanished at temperatures between 420 and 460 K. The value reported for the spontaneous magnetization is not high enough to assure negligible contributions from transition-metal impurities. However, the relatively low, apparent Curie temperature of less than 500 K does not imply pure iron or iron oxide (magnetite) magnetic contribution. One cannot rule out, however, that an Fe–C or another magnetic element–C alloy may show such a Curie temperature.

An extraordinary saturation magnetization value of $M_s \sim 150\,\text{emu g}^{-1}$ was reported [1] by Ovchinnikov and Spector (1988) for the pyrolytic decomposition at 1300 ± 100 K of polyacrylonitril (PAN) with a Curie temperature near 800 K. The impurity concentration reported in that publication does not seem to account for the large magnetization value. To the best of our knowledge, apparently nobody could reproduce those results.

Murata, Ushijima, Ueda and Kawaguchi (1991) measured the magnetization of amorphous-like carbons prepared from tetraaza compounds by chemical vapor deposition (CVD) method. The starting, commercially available materials (tetraaza) were organic monomers with different amounts of carbon, hydrogen, and nitrogen. The carbon-based material was heated in vacuum at 950 °C for 30 min. The aza-carbon

showed a remnant magnetization value (measured not at 0 but at 50 Oe applied field) $M_r \simeq 0.45\,\text{emu g}^{-1}$ at room temperature. Murata, Ushijima, Ueda and Kawaguchi (1991) further showed that at room temperature M_s increased as a function of the ratio between hydrogen and carbon (H/C) of the starting material. For H/C $\simeq$ 2.8 the authors obtained $M_s \simeq 2\,\text{emu g}^{-1}$. Although this work gave no information on the impurity concentration in the final samples, the systematic increase of M_s with H/C does not seem to support an impurity magnetic contribution. The role of hydrogen on the magnetic order was not clear.

The same authors (Murata, Ushijima, Ueda and Kawaguchi, 1992) later showed that the amorphous-like carbon compound prepared by direct pyrolysis of 1,2-diaminopropane (H/C = 3.3) was ferromagnetic with $M_s \simeq 10\,\text{emu g}^{-1}$ at room temperature (a factor 10 smaller than magnetite Fe_3O_4) (see Figure 1). A complete elemental analysis of impurities for the magnetic sample was not reported in that work, but only 3 wt% nitrogen and an unknown amount of hydrogen. If we assume that the signal is due to Fe impurities, then to obtain a magnetization at saturation of $10\,\text{emu g}^{-1}$ the carbon sample should have several weight percent of Fe! Not only does this number appear to be too large but the temperature dependence of the magnetization (see Figure 1) does not also show any sign of magnetism of small ferromagnetic particles, nor a Curie or Curie–Weiss behavior. The superparamagnetism effect is expected in case the Fe (or Fe_3O_4) grains are small enough and are randomly distributed in the sample. It shows a strong temperature dependence in the magnetization for fields of the order of those shown in Figure 1. As an example for superparamagnetism of Fe in carbon, see Figure 9 in Esquinazi *et al*. (2002) where a graphite crystal with an average Fe concentration of $500\,\mu\text{g g}^{-1}$ has been measured. The observed dependence is in clear contrast to that in Figure 1 as well as in highly oriented pyrolytic graphite samples with concentrations of Fe impurities in the $10\,\mu\text{g g}^{-1}$ region (Esquinazi *et al*., 2002).

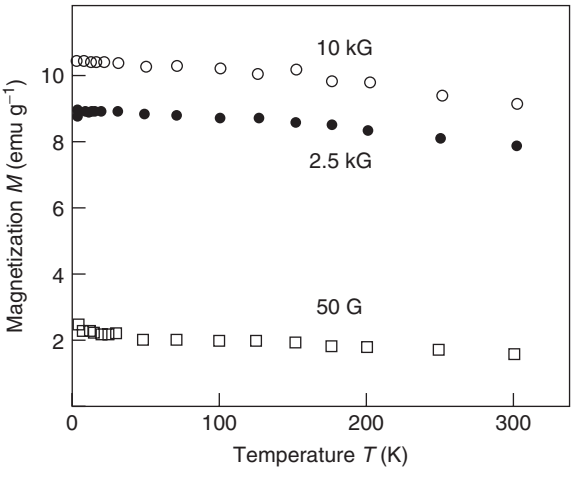

Figure 1. Temperature dependence at three different applied fields of the magnetization of an amorphous-like carbon compound prepared by direct pyrolysis of 1,2-diaminopropane with a ratio between hydrogen and carbon, H/C = 3.3. (Reproduced from Murata *et al*. 1992, with permission from the Royal Society of Chemistry. © 1992.)

Murata, Ushijima, Ueda and Kawaguchi (1992) speculated that atomic hydrogen may have led to the formation of a three-dimensional network of both sp^3- and sp^2-carbons, which according to theoretical predictions (Ovchinnikov and Spector, 1988) (see also Section 5) may originate a spin-ordered state in the (dangling) π electrons from the sp^2-carbons. As Murata, Ushijima, Ueda and Kawaguchi (1991) and Mizogami, Mizutani, Fukuda and Kawabata (1991) observed, ferromagnetic behavior in pyrolytic carbon is obtained from adamantane as a raw material by CVD method under low-temperature growth. Clear hysteresis loop was observed at room temperature. The authors stressed that the highly oriented structure and a large number of unpaired electrons appeared to play an important role in the observed ferromagnetism. Ferromagnetic impurities like Fe were not detected within experimental accuracy.

An interesting experiment was performed by Murakami and Suematsu (1996) inducing magnetic ordering in fullerene C_{60} crystals exposing them to light irradiation from a xenon lamp in the presence of oxygen. Before irradiation the pristine fullerene crystals showed the usual temperature-independent diamagnetic signal with a susceptibility $\chi \simeq -2.7 \times 10^{-7}\,\text{emu (gOe)}^{-1}$, state (a) in Figure 2. This diamagnetism is overwhelmed by a para- and ferromagnetic response after irradiation of the sample under xenon light in oxygen for 2.5 h, state (b) in Figure 2. After annealing the sample (after state (b)) at 400 °C in vacuum to remove physisorbed oxygen (O_2, usually the origin for the paramagnetic response in some carbon-based samples) the paramagnetic contribution decreased but an enhancement of the ferromagnetic-like contribution was observed, state (c) in Figure 2. After leaving the sample in air for three months, the ferro- and paramagnetic contributions increased as can be seen in Figure 2, state (d). Figure 3 shows in more detail the ferromagnetic hysteresis loop of the C_{60} crystal in the state (c) at room temperature. Note that the magnetization plotted in the figures were calculated by dividing the measured magnetic moment by the total sample mass and not by the ferromagnetic mass of the sample. The authors separated the ferromagnetic part from the sample and obtained an increase of 100 in the magnetic moment ($0.1\,\mu_B$) per C_{60} molecule.

From the work of Murakami and Suematsu (1996) the following is worth noting. (i) The temperature dependence of the saturation magnetization indicates an extraordinarily high

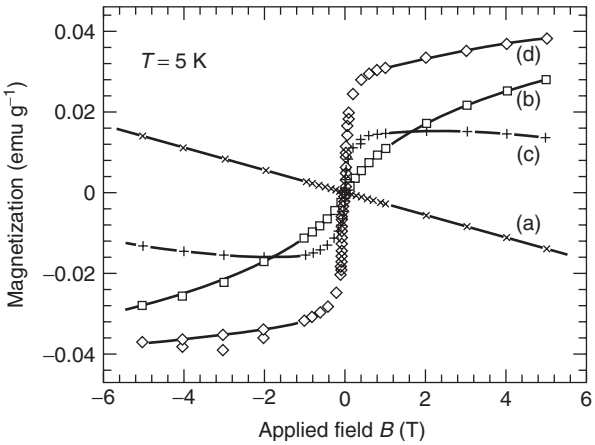

Figure 2. Magnetic field dependence of the magnetization at 5 K for (a) a pristine C_{60} powder crystals, (b) the same sample exposed to xenon light in oxygen for 2.5 h, (c) after annealing it at 400 °C for 2.5 h and (d) after leaving it in air for three months. (Reproduced from Y. Murakami *et al*., Pure & Appl. Chem., 1996, with permission from the International Union of Pure and Applied Chemistry. © 1996.)

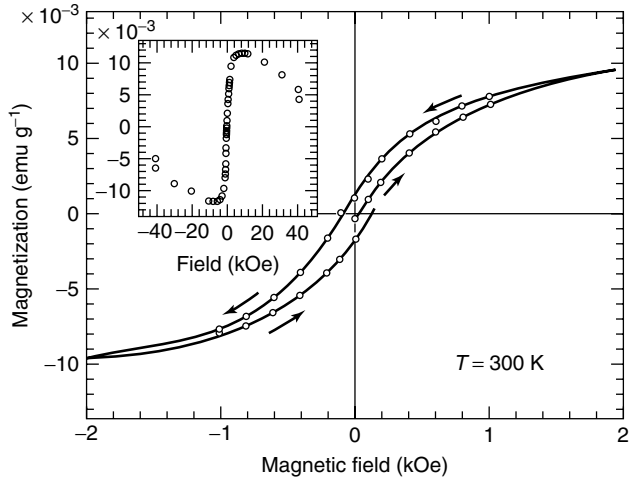

Figure 3. Magnetization hysteresis loop at room temperature of a C_{60} sample corresponding to state (c) in Figure 2 at low fields. The inset shows the results in a larger field scale. (Reproduced from Y. Murakami *et al*., Pure & Appl. Chem., 1996, with permission from the International Union of Pure and Applied Chemistry. © 1996.)

Curie temperature $T_c \sim 800$ K. (ii) No elemental analysis of the samples at the different preparation steps were reported in that work, although with the used procedure one does not expect the introduction of impurities. On the other hand Makarova *et al*. (2003) recently reported similar effects by photopolymerization of fullerene films (see Section 4.3.2). (iii) The temperature dependence of the magnetic moment at fixed fields shows the contribution of small particle magnetism, which is in part the origin for the Curie-like term measured at low temperatures ($T < 40$ K). (iv) The room-temperature hysteresis loops (see Figure 3) indicate a saturation field of the order of 2 kOe and a remanence magnetization of the order of 10% of its saturation value. It is remarkable that similar values are also obtained for different ferromagnetic carbon-based samples produced by different methods (see Section 4.3). From this study it remains unclear whether polymerized fullerene or a disordered graphitic structure is responsible for the observed magnetic order.

For completeness we also note the reports on the ferromagnetic behavior of micrographitic structures with high surface area ($\sim 3110\ m^2\ g^{-1}$) (Ishii, Matsumura and Kaneko, 1995; Ishii, Shindo and Kaneko, 1995). The magnetic properties of activated mesocarbon microbead (a-MCMB) were examined over the temperature range 1.7–285 K. Magnetic hysteresis and a saturation and residual magnetization of 0.032 and 0.016 emu g^{-1} at 1.7 K were observed. Although the magnetic hysteresis loop became small while increasing temperature, it still remained at 285 K. The Fe impurity concentration was 80 ppm. In the case that this quantity of Fe would be ferromagnetic at low temperatures one expects a saturation magnetization at least two times larger than the measured one. Therefore, neither the absolute values of the measured magnetization nor its temperature dependence (Ishii, Matsumura and Kaneko, 1995) can be taken as evidence against an extrinsic origin for the observed magnetism. Although low-surface-area carbon ($570\ m^2\ g^{-1}$) showed no ferromagnetism (Ishii, Shindo and Kaneko, 1995), the unknown impurity contribution always casts a doubt and this is the main reason for the scepticism and the lack of interest that the scientific community showed in the past on all the results involving magnetic order in metal-free materials.

3 MEASUREMENT OF THE IMPURITY CONCENTRATION

There are several methods for a quantitative determination of the impurity concentration of a sample. They are as follows: (i) Particle-induced X-ray emission (PIXE). This is a standard-free, quantitative, nondestructive multielemental analysis, which provides a 0.1–100 μg g^{-1} detection limit depending on the matrix and element to be analyzed. It requires a proton beam in the megaelectron volt energy range. (ii) Energy dispersion X-ray (EDX) analysis spectroscopy using electrons. This method is similar to PIXE. However, its detection limit is at least a factor of 100 larger due to strong bremsstrahlung background. (iii) X-ray fluorescence (XRF) analysis. This method is similar to PIXE; however, for bulk analysis a large sample mass >100 mg is required for good sensitivity. XRF microbeam usually requires a synchrotron.

(iv) Methods like Inductively-Coupled-Plasma-Spectrometry (ICP-MS), Secondary Neutral Mass Spectrometry (SNMS), and Secondary Ion Mass Spectroscopy (SIMS) need standard samples for quantification. Very low detection limits can be achieved, depending on the element to be analyzed. The disadvantage is, however, that these methods are destructive. (v) Neutron activation analysis (NAA) is a very sensitive method but needs a relatively large amount of sample and a (large) neutron source to make the nucleus of the impurities radioactive. A study that was recently done has checked the accuracy of the PIXE method by comparing its results with those obtained from XRF and NAA on the same samples. Very good agreement has been found between the three methods (Barzola-Quiquia *et al*., 2007).

For carbon-based materials the preferred method is PIXE. It uses protons to get a map for all relevant impurity elements within a sample depth of 30 µm for a proton energy of ∼2 MeV in carbon. A systematic and full characterization of the magnetic impurity content in each of the samples, and after each treatment or handling (it makes no sense to start with a highly pure sample and then cut it with a steel knife afterwards), is of primary importance and absolutely necessary specially because in several samples, due to their small magnetization and/or small mass, the magnetic moment at saturation is very small ($m_s \lesssim 10^{-5}$ emu). The reader can get more details on this method in the papers by Butz *et al*. (2005) and Esquinazi *et al*. (2006). Here we would like to make a few remarks. A total charge of 0.5 µC suffices to obtain with a proton microbeam a minimum detection limit for Fe impurities below 1 µg g^{-1}. The advantage of using a microbeam for PIXE analysis, compared to a broad beam, is that a distribution map for all relevant impurity elements can be obtained contrary to the integral value from the broad-beam method, which is a rather important issue considering the grossly inhomogeneous distribution of impurities like Fe which we have encountered in some samples (see, e.g., Figure 1 in Spemann *et al*., 2003). A typical broad-beam PIXE spectrum for a highly oriented pyrolytic graphite (HOPG) sample is shown in Figure 4. It shows the presence of a number of impurities, the Fe content being (0.45 ± 0.04) ppm. Taking into account experimental (see Sections 2 and 4.3) as well recent theoretical studies (see Section 5), hydrogen, as well as oxygen, may be related to the origin of the magnetic signals in carbon-based materials. However, hydrogen content measurements with a sensitivity in the parts per million range are a rather difficult experimental task. Butz *et al*. (2005) briefly discuss the methods available for this kind of measurement.

A recent study done by Reichart *et al*. (2006) using a proton–proton scattering method analyzed the hydrogen distribution of pristine as well as irradiated HOPG samples, which were implanted with micrometer-sized spots and

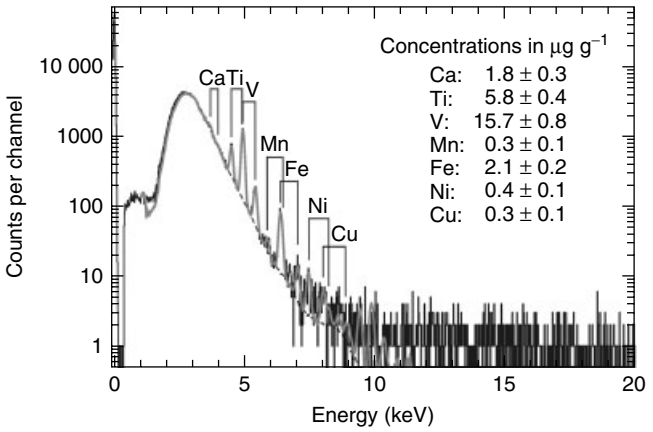

Figure 4. Typical broad-beam PIXE spectrum from a HOPG sample. The main impurities are Ti, V, and Fe. The minimum detection limit for other elements heavier than Si is ∼0.3 µg g^{-1}. Note that 2.1 µg g^{-1} iron in the carbon matrix means a concentration of 0.45 ppm Fe. (Reproduced from T. Butz *et al*., 2005, with permission from Springer. © 2005.)

extended areas with various doses of 2.25 MeV protons at the Leipzig microprobe LIPSION (see Section 4.3.3). For this study a sensitive three-dimensional hydrogen microscopy system at the Munich microprobe SNAKE was used. The background hydrogen level in pristine HOPG was determined to be about 0.3 at-ppm. About 4.8×10^{15} H atoms/cm^2 were observed in the near-surface region (∼4 µm-depth resolution). The depth profiles of the implants showed hydrogen located within a confined peak at the end of the penetration range, in agreement with SRIM Monte Carlo simulations and no evidence of diffusion broadening along the *c* axis. For the sample with microspots, up to 36 at-% of the implanted hydrogen was not detected, providing support for a lateral hydrogen diffusion.

3.1 The role of iron

Iron is usually the main magnetic impurity that one finds in carbon-based materials. Owing to its relatively large para- and ferromagnetic contributions, the measurement of its concentration is of main importance. As an example and assuming that 1 µg Fe per gram carbon for a sample with the density of graphite would be ferromagnetic, its contribution would be $\simeq 2.2 \times 10^{-4}$ emu g^{-1} to the magnetization in the case of Fe clusters or $\simeq 1.4 \times 10^{-4}$ emu g^{-1} in the case of Fe_3O_4 clusters. Usually such small amounts of impurities are diluted in the sample and one does not measure a ferro- but a paramagnetic or superparamagnetic behavior because of small particle magnetism. For an example see Figure 9 in Esquinazi *et al*. (2002) where the magnetization of a graphite sample with an average concentration of Fe ∼500 µg g^{-1}

has been measured. Instead of a ferromagnetic behavior, a superparamagnetic-like behavior was measured with a strong temperature dependence. From the saturation of the magnetic moment at very high fields and low temperatures one can estimate that $\sim 840\,\mu g\,g^{-1}$ Fe in the graphite matrix contributes to the magnetic response. Interestingly, this relatively large amount of Fe in carbon did not show ferromagnetism. Nevertheless, the influence of ferromagnetic impurities, specially that of Fe and magnetite (Fe_3O_4), has to be carefully checked because the ferromagnetic signals of the carbon-based samples are (still) relatively small.

Measurements of the magnetization of graphite nodules from a meteorite (Coey *et al*., 2002) and of the magnetic force gradients of carbon nanotubes in contact with ferromagnetic substrates (Cespedes *et al*., 2004) suggest that magnetic ordering in graphite might be induced by a proximity effect. A relatively large magnetization-decay length (identical to the spin-diffusion length) $\lambda_s \approx 5\,nm$ was estimated for the graphite–magnetite interface by Coey *et al*. (2002). However, there is no direct evidence yet for such a large magnetization-decay length. Local ferromagnetism in C/Fe multilayers was observed by resonant magnetic reflectivity of circularly polarized synchrotron radiation (Mertins *et al*., 2004). The thickness of the carbon layers was 0.55 nm in comparison with 2.55 nm for the Fe layers. Taking into account an average roughness of 0.35 nm at the interface where a mixture of C and Fe exists, the induced ferromagnetism appears within a penetration depth of less than 0.5 nm. This result would agree with the results of Höhne, Ziese and Esquinazi (2004) in which by studying the magnetization of graphite–magnetite composites a $\lambda_s \lesssim 0.4\,nm$ was inferred with no indication of an induction of bulk ferromagnetism in graphite through the contact with magnetite. More experiments are necessary for a conclusion about the existence of a large magnetic proximity effect in certain carbon structures.

4 MAGNETIC STATES IN CARBON STRUCTURES

4.1 Diamagnetism

Usually, a diamagnetic signal is measured in carbon-based materials. The absolute value of this signal depends on the contribution of the core electrons, valence electrons, and a van Vleck paramagnetic term mentioned in the introduction. The total susceptibility of natural IIa diamond single crystal at room temperature is $\chi \simeq -5.9 \times 10^{-7}\,emu\,(gOe)^{-1}$. This value is only a few percent from that of oriented graphite, which shows the largest diamagnetic susceptibility for fields applied parallel to the *c* axis. In a simple but successful model the diamagnetic response is proportional to an effective area of the electronic current loop (see Haddon (1995) and references therein). Therefore, one can derive an effective radius for the electronic circulation, which goes from the closed-shell atom confinement as in diamond to current flows along several bonds in conjugated rings. With this concept it is possible to understand the increase in the ring π electron's current diamagnetic response for planar aromatic organic compounds. To understand the susceptibility of fullerenes, however, a constrained movement of the π electrons and the van Vleck paramagnetic contribution should be taken into account.

Owing to the increasing importance of single-wall and multiwall carbon nanotubes in basic and applied research, there has been a renewed interest in the properties of oriented graphite. Interestingly, the transport and magnetic properties of graphite are still not well understood (see, e.g., Kopelevich *et al*. (2003a) and references therein). Measurements of highly oriented pyrolytic graphite samples with rocking curve width at half maximum full-width half-maximum (FWHM) $\leq 0.4^\circ$ provide a value for the susceptibility $\chi_{||} = -(2.4 \pm 0.1) \times 10^{-5}\,emu\,(gOe)^{-1}$ at 300 K and for fields applied parallel to the *c* axis (Esquinazi *et al*., 2002). This large diamagnetism stems from 'fast-moving' electrons (McClure, 1956) with a small effective mass $m^* \sim 0.05\,m_0$ (here m_0 is the free electron mass). Within a tight-binding picture the small effective mass is due to the large π-bonding overlap of the neighboring C atoms in a single layer given by the band parameter $\gamma_0 \propto 1/m^*$. For the calculation of χ the linear dispersion relation for two-dimensional (2D) graphene $E(k) \propto k$ was assumed (Wallace, 1947). The main contribution to the T-dependence of $\chi(T)$ at $T \gtrsim 150\,K$ is given by $\partial f/\partial E|_{E=E_F}$ (f is the Fermi–Dirac distribution function) due to the condensation of fermions into the Landau level with $n = 0$ after the application of a magnetic field (McClure, 1956). Although experimental results are, in general, in agreement with this theory, to explain the saturation of $\chi(T)$ at low T a series of additional band parameters has to be included (see Dresselhaus *et al*. (1988) and references therein). We note, however, that this further developed theory does not account for the measured anisotropy of the g factors (Dresselhaus *et al*., 1988).

High-resolution magnetization measurements in different HOPG samples indicate that at low temperatures χ does not saturate but has a shallow, well-defined and field-dependent minimum at $T \lesssim 30\,K$ (see, e.g., Kopelevich, Lemanov, Moehlecke and Torres, 1999; Huber, Urbano, Sercheli and Rettori, 2004). This minimum is not due to magnetic impurities. The origin for this minimum is not yet clarified and no attempt has been made to check whether it is compatible with elaborate theories for the diamagnetism in graphite.

Owing to the available sample quality, the measurement of the anisotropy in the carrier diamagnetism of graphite is difficult. Taking into account recent measurements of the electrical anisotropy that indicates a ratio (parallel to perpendicular to the c axis) of the order of or larger than 10^4 for well-ordered samples, we expect to have a susceptibility $|\chi_\perp|$ smaller than the atomic susceptibility $|\chi_{at}|$ of carbon in graphite, which is of the order of $|-5 \times 10^{-7}|$ emu (gOe)$^{-1}$ according to literature. We have to also take into account internal misalignments of the crystallites in the sample. At room temperature and for a sample with FWHM $= 0.4^\circ$, owing to the $\chi_{||}$ component a value of the order of $|-1.7 \times 10^{-7}|$ emu (gOe)$^{-1}$ would be measured for fields applied nominally parallel to the planes. The effect of this internal misalignment has been verified by electrical conductivity measurements (Kempa, Semmelhack, Esquinazi and Kopelevich, 2003).

4.2 Paramagnetism in disordered carbon

The response of free, independent magnetic moments under an applied magnetic field B and without interaction between them gives rise to paramagnetism. As a function of field and temperature the magnetization M due to this effect follows the Brillouin function $B_J(y)$ where J is the total angular moment of the magnetic ion and $y \propto B/k_B T$. For $y \ll 1$ the susceptibility $\chi = M/B$ follows the Curie law $\chi = C/T$, C, being the Curie constant. At low-enough temperatures the paramagnetic response follows a s-like curve with saturation of M at high-enough magnetic fields, that is, at $y \gg 1$. This kind of behavior is observed in carbon samples when some kind of disorder exists. In disordered carbon structures, apart from the intrinsic van Vleck paramagnetism due to nonspherical potential, paramagnetic signals due to localized spins from unpaired electrons associated with the existence of broken σ-dangling bonds or the mixture of sp^2–sp^3 bonds are measured. In this case the density of paramagnetic centers is related to the disorder of the carbon structure. Interestingly, in earlier work (see Delhaès and Carmona (1981) and references therein) this density was also correlated with the hydrogen concentration. Although this paramagnetic phenomenon is well known one should not confuse it with the s-like response of ferromagnets. In general the paramagnetic response follows a Curie law (it scales with H/T) and shows no hysteresis in the magnetization loop.

According to theoretical work zigzag (Fujita) edges of ordered graphene layers may also contribute to the paramagnetic response due to electron spin localization at the sp^2 free bond of the edge carbon atoms (Fujita, Wakabayashi, Nakada and Kusakabe, 1996). Although no direct evidence for this contribution has been reported yet, scanning tunneling microscopy (STM) measurements on this kind of edges indeed indicate an increase in the electronic density of states (Esquinazi *et al*., 2002; Kobayashi, Fukui, Enoki and Kusakabe, 2006) as predicted.

If we increase the disorder in a graphite structure the main diamagnetic signal decreases in absolute value and turns paramagnetic when the disorder is large enough. An example of this behavior can be seen in Figure 5 where the temperature dependence of the magnetization of a target made of an ultrapure graphite powder and of the material obtained from disordered carbon films prepared by pulsed-laser deposition (PLD) on Si substrates are shown (Höhne *et al*., 2004b; Esquinazi and Höhne, 2005).

In general, disordered carbon material shows a Curie-like dependence added to a Pauli-like contribution (T-independent paramagnetism) (see Figure 5). The inset in Figure 5 shows the field dependence of the magnetization for the carbon film material at 5 K. These data can be described by the classical Langevin expression from which we obtain a spin density $n_s \sim 10^{19}\,g^{-1}$. Annealing the disordered carbon material at 1000 °C for 10 h in vacuum clearly reduces the temperature-dependent paramagnetic part (see Figure 5). Note that the observed behavior with annealing is not in favor of a magnetic impurity contribution. Within experimental

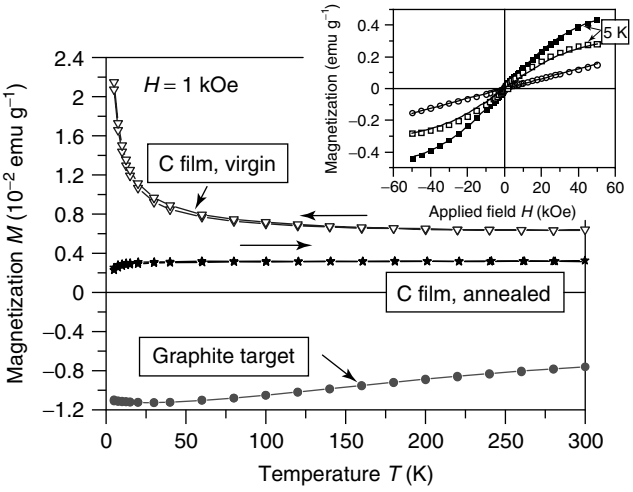

Figure 5. Temperature dependence of the magnetization at 1 kOe obtained for graphite target made from an ultrapure graphite powder and disorder carbon films, before and after annealing at 1000 °C for 10 h in vacuum. Inset: Field dependence of the magnetization of the carbon films at 5 K (■), and after subtraction of the Pauli-like term (□) given by the straight line through the points (○) $M = 3.1 \times 10^{-6} H$ emu (gOe)$^{-1}$ where H is the applied field in oersted. In the scale of the figure the Pauli-like magnetization curves measured at 300 K (before and after annealing) and at 5 K (after annealing) (○) practically coincide. The continuous lines through the points (■, □) are fits to the classical Langevin expression. (Reproduced from Esquinazi *et al*., 2005, with permission from Elsevier. © 2005.)

Table 1. Paramagnetic-like properties of disordered carbon samples at different years. The samples are (a) different noncrystalline carbons (Delhaès and Carmona, 1981), (b) activated carbon fibers (low-T annealing) (Shibayama, Sato, Enoki and Endo, 2000), (c) PLD-carbon films (nonannealed) (Höhne *et al*., 2004b), (d) Nanofoam (Rode *et al*., 2004), and (e) PLD-carbon films (nonannealed) (Takai *et al*., 2004).

Year	. . .1981	2000	2003	2003	2004
Sample	(a)	(b)	(c)	(d)	(e)
$n_s(g^{-1})$	10^{19}–10^{20}	$\sim 4 \times 10^{19}$	$\sim 2 \times 10^{19}$	$\sim 10^{20}$	$\sim 2 \times 10^{20}$
M_s(emu g^{-1})	$\lesssim 0.5$	~ 0.2	~ 0.4	~ 0.35	~ 1.5

n_s: spin density; M_s: magnetization at saturation measured at $T < 10$ K.

error the hysteresis loops for the disordered carbon films above 5 K are reversible. This indicates that a disordered mixture of sp^2–sp^3 bonds, which exists in the disordered carbon films, does not automatically trigger ferromagnetism.

A quick look at the published literature shows that the paramagnetic response of disordered carbon is a 'time-independent' general phenomenon. Table 1 shows the spin density n_s and the magnetization at saturation M_s of very different disordered carbon samples. In their virgin, nonannealed states, carbon fibers, nanofoams, or amorphous carbon films prepared by PLD, show similar values for both n_s and M_s and their overall behavior as a function of temperature follows a Curie-like dependence added to a Pauli-like contribution. One should be careful to associate magnetic ordering to this paramagnetic response. Nevertheless, at low-enough temperatures and for high-enough spin density nonsimple magnetic behavior was reported in nanofoams (Rode *et al*., 2004; Arčon *et al*., 2007) where a small ferromagnetic-like hysteresis loop was superposed to the main paramagnetic response. Also, the observed behavior of some activated carbon fibers (Shibayama, Sato, Enoki and Endo, 2000) or nanographite (Enoki and Takai, 2006) suggests that interactions between localized spins may exist. The localized spins at the edges can have an exchange interaction between them mediated by π electrons. The paramagnetic response of disordered carbon is being rediscovered nowadays owing to its sensitivity to guest molecules. It is believed that physisorption of guest molecules in the micropore space of nanographite (or nanofoam) network can produce a magnetic switching effect of the edge-state spins, an effect that can be used for molecular device applications of nanographite as gas-sensing probe (Enoki and Takai, 2006).

4.3 Magnetic order

At the beginning of this millennium there were a few new reports on magnetic order in carbon-based structures that began to finally attract the interest of the community. In this section we will review mainly those works published since the year 2000.

4.3.1 In highly oriented pyrolytic graphite

According to theoretical ideas that are described in Section 5 a perfect graphite sample should show nil or at most very weak ferro- or ferrimagnetic signal. In fact well-annealed graphite powder of high purity and high degree of orientation (which indicates a small defect density) does not show any evidence for such a phenomenon within experimental accuracy. Most, but not all, of the oriented bulk graphite samples, however, show weak ferromagnetic-like signals. It should not be surprising if somebody measures a non-ferromagnetic-like signal in an oriented graphite sample, because this signal depends on the properties of each sample. In general, the measurement of these signals is not simple since their magnitude is overwhelmed by the giant diamagnetic one. The subtraction of this diamagnetic contribution is, in general, simple since it depends linearly on applied field. However, for the signal levels we are discussing (ferromagnetic-like magnetic moment of the order of 10^{-5} emu or less; see, e.g., Esquinazi *et al*. (2002)) the available magnetometers (in general superconducting quantum interference devices, SQUIDs) may produce in some cases hysteresis curves that do not come from the samples but are artifacts of different origins. One should spend enough time to characterize those artifacts.

After a first report on ferromagnetic- and superconducting-like behavior in the magnetization of some HOPG samples by Kopelevich, Esquinazi, Torres and Moehlecke (2000) Esquinazi *et al*. (2002) studied in detail several HOPG samples from different sources with concentration of Fe impurities between $<0.3\,\mu g\,g^{-1}$ and $\sim 19\,\mu g\,g^{-1}$. The concentration of other magnetic metallic impurities were below $2\,\mu g\,g^{-1}$. Figure 6(a) shows that the magnetization at 2 kOe, after subtraction of background contributions, does not show a correlation with the Fe concentration. The results also indicate that the ferromagnetic-like hysteresis loops are weakly temperature dependent between 5 and 300 K, see inset in (b). A naive estimate assuming that the Fe concentration behaves as ferromagnetic Fe- or Fe_3O_4-bulk in the carbon matrix would give the two lines shown in Figure 6(a). Except for three HOPG samples the others show magnetization values below the ones expected from those lines. This figure clearly shows how much care is needed with the sample handling in all these studies. The assumption that such a small amount of Fe distributed in the carbon matrix behaves ferromagnetically is not consistent with the behavior we observed in graphite samples with much larger Fe concentrations (Esquinazi *et al*., 2002) nor in 4d–5d metals, where paramagnetism as well as

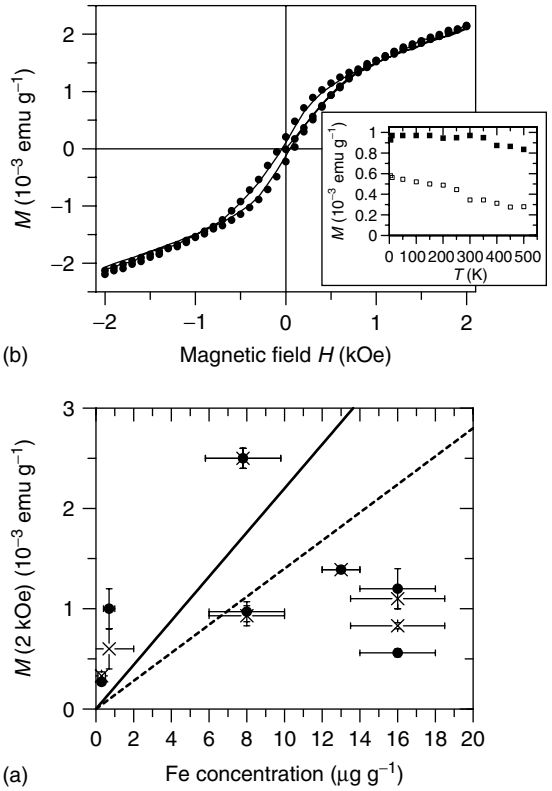

Figure 6. (a)Magnetization at 2 kOe as a function of Fe concentration at two temperatures ((*X*): 300 K, (●): 5 K) for different HOPG and Kish graphite samples. The solid line represents the expected magnetization if Fe contained in the samples was in a ferromagnetic state. The dashed line represents the analogous relation for Fe_3O_4. (b) Hysteresis loops at 5 K (●) and 300 K (continuous line) of a HOPG sample (FWHM $\sim 1.3^\circ$) for fields applied parallel to the graphene planes. No background was subtracted from the data. The inset shows the T-dependence of the magnetization at saturation (■) and its remanence (□) after annealing for 16 h at 700 K. (Reproduced from Esquinazi *et al*., 2005, with permission from Elsevier. © 2005.)

spin glass behaviors are measured for Fe concentrations of $\sim$100 ppm or larger (Peters *et al*., 1984).

Figure 6(b) shows two hysteresis loops for a HOPG sample. We note that in this field range no sign of diamagnetism is measured but a paramagnetic behavior is added to the hysteresis. This is one of some fortuitous cases where the diamagnetic component is small enough owing to the small misalignment of the sample in the SQUID. The observed behavior in Figure 6 is in clear contrast with the T-dependent paramagnetic contribution measured in samples with a larger amount of Fe impurities (Esquinazi *et al*., 2002). The reason for the temperature-independent (between 5 and 300 K) Pauli-like paramagnetism is probably related to the intrinsic lattice disorder as in disordered carbon samples (see Section 4.2). The results shown in Figure 6 belong to a relatively disordered HOPG sample with FWHM $\simeq 1.3^\circ$ and a Pauli-like susceptibility $\chi \sim 5 \times 10^{-7}$ emu (gOe)$^{-1}$, smaller than that obtained for disordered carbon $\chi \sim 3 \times 10^{-6}$ emu (gOe)$^{-1}$ (Höhne *et al*., 2004b). We expect that by increasing the lattice disorder a Curie-like paramagnetic contribution will appear. The overall results suggest that special lattice disorder and probably the influence of a light atom like hydrogen may be related to the origin of the observed ferromagnetism. A review of the recent theoretical ideas on this topic is given in Section 5.

4.3.2 In fullerenes

Reports on magnetic order in fullerenes, either pressure polymerized (Makarova *et al*., 2001; Wood *et al*., 2002; Narozhnyi *et al*., 2003), hydrofullerite $C_{60}H_{24}$ (Antonov *et al*., 2002) or photopolymerized fullerene powder and films in the presence of oxygen (Makarova *et al*., 2003) triggered a renaissance of interest in the magnetism in carbon structures. Neutral C_{60} can be polymerized into phases in which the cages are linked by cyclic C_4 units by photoirradiation, an electron beam, or by pressure. Polymerized fullerenes can exist in a variety of one-, two-, or three-dimensional phases. According to the original reports, polymerization of C_{60} at temperatures and pressures near the cage collapse and graphitization of the anisotropic 2D rhombohedral Rh-C_{60} phase leads to ferromagnetism with $T_c \gtrsim 500$ K (Makarova *et al*., 2001; Wood *et al*., 2002; Narozhnyi *et al*., 2003). The systematic work of Wood *et al*. (2002) indicates a maximum in the magnetization for samples prepared at conditions near the cage collapse. We should note, however, that neither the amount of magnetic samples nor the studied condition-parameters range (temperature, pressure, and time) are sufficient to give a clear phase diagram for the occurrence of ferromagnetism in polymerized fullerenes. There is not enough experimental evidence that assures that the magnetic order does depend primordially on a specific lattice structure of the polymerized fullerene. This fact added to the non-negligible impurity concentration (see below in this section) found in those samples (Spemann *et al*., 2003) casts doubts about the intrinsic nature of most of the ferromagnetic signals (Höhne and Esquinazi, 2002). The measured Curie temperature for the pressure-polymerized samples E16 and E17 was 500 K (Makarova *et al*., 2001; Höhne and Esquinazi, 2002). Samples prepared in a similar way, however, revealed Curie temperatures above 800 K (Wood *et al*., 2002; Narozhnyi *et al*., 2003).

Four pressure-polymerized phases have been identified as rhombohedral (Rh), tetragonal (T), orthorhombic (O), and dimeric (D) phases (Davidov *et al*., 2000). The details of the $p - T$ phase diagram are rather complicated and can be seen in Figure 18 in the review of Makarova (2004). The R phase is thought to be stabilized between 700 and $\sim$1100 K in the

pressure range between ∼3 and ∼9 GPa. The speculation that the magnetism in polymerized fullerene is related to the Rh structure near the cage collapse at the phase transition line between rhombohedral and disordered structure, as depicted in Makarova *et al*. (2003) and Makarova (2003, 2004), cannot be confirmed at present. The polymerized samples studied by Makarova *et al*. (2001) and Höhne and Esquinazi (2002) (with the names E16, E17, and E20) were actually produced at 1125 K (T phase with disordered graphite), 973 K (mostly Rh phase), and 1073 K (Rh phase with disordered graphitized fullerite) and at pressures of 2.5 and 6 GPa where this last pressure corresponds to the last two samples; see also Makarova *et al*. (2005).

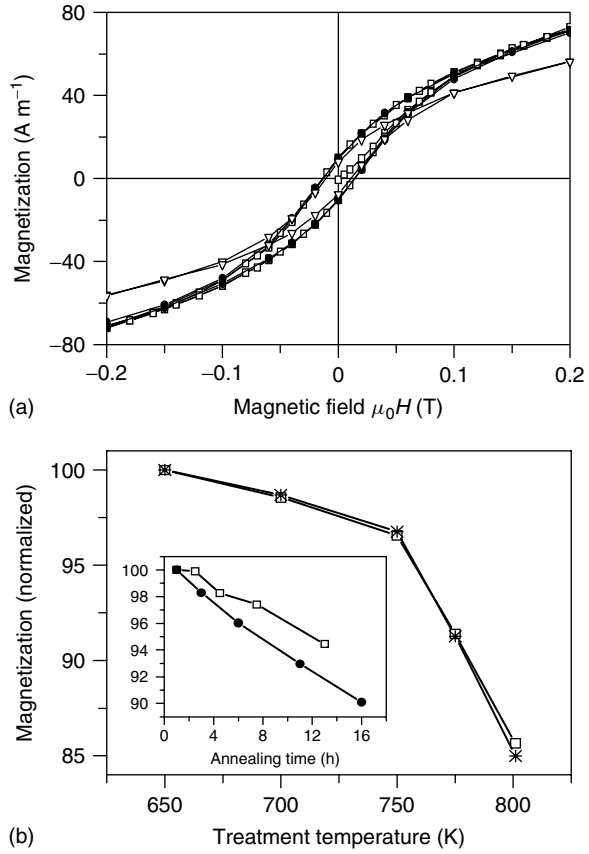

Figure 7. (a) Hysteresis loops of the magnetization measured at $T = 400$ K in the virgin state (□), and after heat treatment for 3 h at 700 K (●) and for 16 h at 800 K (▽). To convert the magnetization unit A m^{-1} into emu g^{-1} divide the first by the density of the sample $\sim 1.75 \times 10^3$ kg m^{-3}. (b) Magnetization values measured at 400 K in magnetic fields of 0.2 (□) and 1 T (∗) after heat treatment for 3 h at different temperatures. The values measured after treatment at 650 K were set to 100. Inset: Normalized magnetization values measured at 400 K and a magnetic field of 0.2 T as a function of annealing time at 750 K (□) and 800 K (●); these annealing studies were performed first at 750 K and then at 800 K. All measurements were done on sample E17. (Reproduced from R. Höhne *et al*., 2002, with permission from Wiley VCH-Verlag. © 2002.)

Indirect evidence for the absence of a correlation between the Rh phase and the magnetism in fullerenes is given by the annealing behavior of the samples studied by Höhne and Esquinazi (2002). Figure 7(a) shows the magnetization loop at 400 K of sample E17 (the same sample included in Makarova *et al*., 2001) at different annealing stages. Figure 7(b) shows the evolution of the magnetization (at fixed applied field of 2 kOe and a temperature of 400 K) with annealing temperature (after leaving the sample for 3 h at each temperature). There are no changes of the magnetic state after treatments up to 650 K even after 10 h. After a treatment at 700 K weak changes on the magnetic state were observed. After 3 h treatment at 700 K the magnetization (at 400 K and at a field of 1 T) had 98.5% of the virgin value, decreasing to 79% after 16 h at 800 K.

Korobov *et al*. (2003) showed that the Rh phase prepared at $T = 1025-1050$ K and $p = 6$ GPa rapidly decomposed at 520–570 K for 5 min and did not demonstrate additional thermal stability. Comparing this result with the evolution with annealing shown in Figure 7 we conclude that there is no evidence of a relation between the Rh phase and the magnetic signal. Recently published band structure calculations of Rh-C_{60} performed in the local-spin-density approximation found no magnetic solution for Rh-C_{60} and energy bands with different spins are found to be identical and not split, concluding that the rhombohedral distortion of C_{60} itself cannot induce magnetic ordering in polymerized fullerene in agreement with magnetization, X-ray emission, and absorption spectra measurements performed in Rh-C_{60} samples (Boukhvalov *et al*., 2004). These results suggest that the magnetic ordering is related to other carbon structures that are formed before the fullerene cages collapse, as the work of Wood *et al*. (2002) indicates; see Figure 8.

An important issue is the impurity concentration in the fullerene samples polymerized under pressure. Apparently the pressure cells used by Makarova *et al*. (2001) were not clean enough according to the measured impurity concentration through PIXE measurements (Höhne and Esquinazi, 2002; Spemann *et al*., 2003) that reaches values of the order of 400 μg g^{-1} of iron, nonhomogeneously distributed across the sample within 30 μm depth from the surface. Because the pristine C_{60} powder has a much smaller impurity concentration, the impurities should have been incorporated during some sample preparation steps. Owing to the iron concentration one may speculate that Fe_3C may have been synthesized during the preparation conditions. Such an alloy shows a Curie temperature of the order of 500 K similar to the measured one in some of the samples (Makarova *et al*., 2001). In fact, polymerized C_{60} samples mixed with iron before polymerization show a similar Curie temperature (500 K) as those reported by Makarova *et al*. (2001), owing to the presence of the compound Fe_3C (Talyzin *et al*., 2007). Taking into

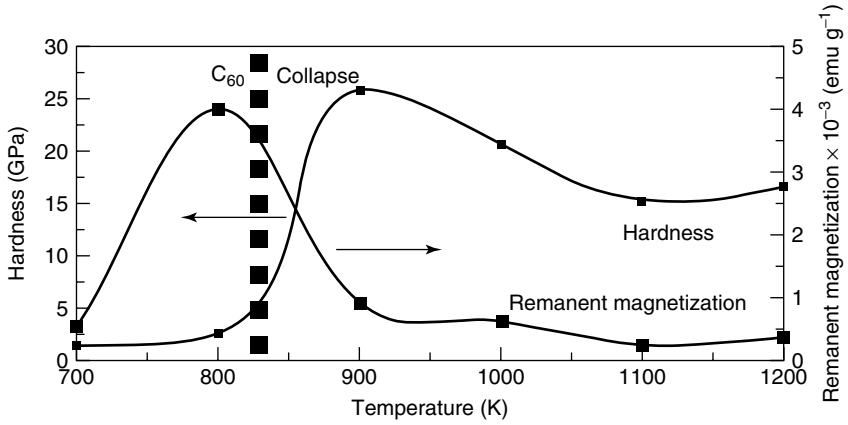

Figure 8. Hardness and remanent magnetization as a function of the preparation temperature for fullerene samples treated at 9 GPa, indicating the region of radical center generation. According to Wood *et al*. (2002) a pressure of 9 GPa was applied to all the samples before heating. The samples were then heated to preparation temperatures in the range 700–1200 K where they were held for 1 min. X-ray diffraction work (Bennington *et al*., 2000) indicates that this isobar will go through an almost pure rhombohedral phase straight into the graphitic hard carbon phase. Note that a maximum remanent magnetization was obtained near the cage collapse. (Reproduced from R.A. Wood *et al*., 2002, with permission from IOP Publishing Ltd. © 2002.)

account this result and the amount of Fe found in the original samples (Höhne and Esquinazi, 2002; Spemann *et al*., 2003), one concludes that the main magnetic signal and the ferromagnetic transition reported by Makarova *et al*. (2001) likely originated from Fe_3C (Makarova *et al*., 2006). We note that recent experimental study (Han *et al*., 2005) performed on samples prepared from fullerenes with lower impurity content and after high pressure high temperature (HPHT) treatment showed vanishingly small bulk magnetization, indicating that the pressure polymerization of fullerenes is not an appropriate method to produce magnetic carbon.

In spite of the results discussed above we would like to comment on a combined experiment with PIXE and magnetic force microscopy (MFM) done in the pressure-polymerized fullerenes (Han *et al*., 2003b; Spemann *et al*., 2003). In one piece of the E16 sample described above, a region of area $\sim 500 \times 250\,\mu m^2$ with a concentration of magnetic impurities below $1\,\mu g\,g^{-1}$ was selected and characterized with MFM. Around 30% of the pure region showed magnetic domains, indicating that only a small fraction ($\sim$10%) of the sample contributes to the magnetic signal measured by the SQUID. Figure 9 shows one kind of MFM images obtained in such pure region where apparent magnetic domains were observed (Han *et al*., 2003b, 2003c). The MFM image changes clearly when it is measured under a magnetic field; see Figure 9. It remains unclear, however, how large the total magnetic moment and mass of the impurity-free magnetic region are.

We should note that in the work of Wood *et al*. (2002) no detailed impurity measurements were provided although we would naively rule out such a contribution because a maximum in the magnetization is obtained only at a particular

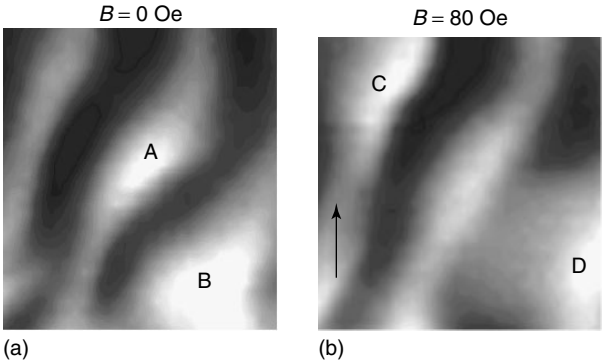

Figure 9. Magnetic force gradient images taken at room temperature from the pure region of the E16 bulk sample without (a) and with (b) magnetic field of 80 Oe. The scan size was $2.5 \times 2.5\,\mu m^2$ and the tip-sample distance was 100 nm. The arrow shows the direction of applied magnetic field. Note the clear change in the phase shift signal at the regions denoted by letters before and under a magnetic field. (Reproduced from Han *et al*., 2003, with permission from Elsevier. © 2003.)

point of the phase diagram; see Figure 8. However, as the work of Talyzin *et al*. (2007) indicates, there appears to be a chemical reaction of Fe with C_{60} at the used temperature and pressure treatment, which forces the cage structure to collapse with a $\sim$15% volume shrinking. Owing to this collapse it is possible that the pressure cell breaks and contamination from outside penetrates the sample. This may be a possible explanation for the behavior shown in Figure 8.

In Section 2 we have noted that Murakami and Suematsu (1996) produced magnetic order in C_{60} crystals exposing them to xenon-light radiation in the presence of oxygen. Similar to polymerization by pressure, oxygen-free C_{60} films

and crystals can be photopolymerized under the action of UV and visible light (Rao *et al*., 1993a,b). Two processes occur when C_{60} is simultaneously exposed to oxygen and light: a photoassisted diffusion of molecular oxygen into solid C_{60} and oxidation of C_{60} (Rao *et al*., 1993a). The oxygen phototransformed phase has, in general, the formula $C_{60}(O_2)_x$ with x depending on the light wavelength and intensity as well as the crystallinity of the sample. There is indirect evidence that the photoassisted reaction of oxygen with C_{60} may lead to the opening and breaking of the C_{60} cages (Wohlers, Bauer and Schlögl, 1997; Matsuishi *et al*., 1997). Whether after the opening of the cages the oxygen atoms or other light atoms like hydrogen play a main role in the magnetic order remains to be studied.

Makarova *et al*. (2003) repeated the experiment of Murakami and Suematsu (1996) transforming C_{60} bulk samples by white light for several days and C_{60} films by Ar-ion laser and electron beam with different wavelengths. More details on the preparation conditions as well as the penetration depths of the irradiation can be found in the original publication. The change in the magnetic signal has been characterized by ac susceptibility and SQUID measurements for the bulk samples and through MFM measurements of the fullerene films. Fullerene irradiated in the presence of oxygen showed clear ferromagnetic hysteresis loops with a saturation magnetization that increased with the exposition time. Figure 10 shows the topography and the magnetic field gradient images of the laser-illuminated spot region of a fullerene film. The magnetic signals (maxima and minima in the force gradient) coincide with the topography. The irradiation-driven transition from a van der Waals–bonded solid to a chemically bonded one contracts the lattice, creating grains as seen in the atomic force microscopy (AFM) images (see Figure 10). These grains or the surface of the grains turned out to be magnetic. No magnetic signals are measured at the nonexposed areas even when topography irregularities exist (Makarova *et al*., 2003). A nonexposed region of the same C_{60} film was irradiated with protons (20 spots pairwise separated by 20 μm at different fluences and 2.5 MeV energy); see Figure 10. Although no change in topography was observed, the irradiated region reveals clear phase constrast. Since the penetration depth of the protons at the energy used is much larger than the thickness of the C_{60} film (∼0.25 μm) it is not expected that those protons remain in the film. As we will discuss in the next sections, the defects produced by the proton irradiation and the hydrogen atoms already in the sample may trigger magnetic order. In summary, we may conclude that fullerenes do not show magnetic order and serve only as an auxiliary unit for the formation of magnetic carbon defects.

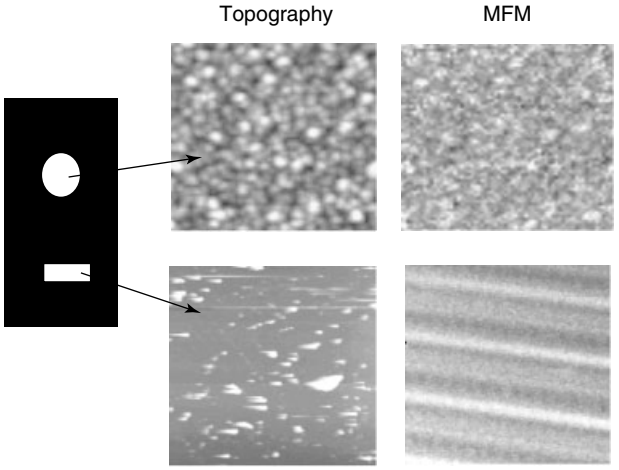

Figure 10. Left-side sketch shows the fullerene film with the two irradiated regions: the upper ellipse corresponds to the laser-illuminated region in air (2.6 eV and 200 mW cm^{-2} intensity) (Makarova *et al*., 2003) and the lower rectangle, to the region where 20 spots of 1.8 μm diameter each where irradiated with a proton microbeam with a current of 500 pA and fluences between 0.068 and 68 nC μm^{-2}. In contrast to the clear change in topography at the laser-irradiated spot (due to the grain formation) and at the proton-irradiated spots in HOPG (see Section 4.3.3) no change in the topography is detected after proton irradiation of the spots in the fullerene film. All images correspond to an area of $5 \times 5\,\mu m^2$. (Reproduced from Esquinazi *et al*., 2005, with permission from Elsevier. © 2005.)

4.3.3 In proton-irradiated carbon structures

Although irradiation effects in graphite were a major research area in the past, their influence on the magnetic properties were only noted through the increase in the spin density and a decrease in the diamagnetism owing to the introduction of lattice defects (Kelly, 1981). Recently, induced magnetic order by proton irradiation was found in graphite and disordered carbon and fullerene films (Esquinazi *et al*., 2003; Höhne *et al*., 2004a; Han *et al*., 2003a; Esquinazi *et al*., 2006). In this section we will briefly review some of the obtained results, mainly on the effects produced by proton irradiation in HOPG samples. For a detailed review on these effects in carbon structures and other irradiation characteristics, the reader should refer to a recently published article (Esquinazi *et al*., 2006).

The early literature on magnetism in carbon structures tends to indicate that apparently hydrogen (or maybe another light atom like oxygen) plays a role in the reported ferromagnetism. As we have described in Section 2, especially the work of Murata, Ushijima, Ueda and Kawaguchi (1991, 1992) suggests a correlation between hydrogen concentration and magnetic order in carbon. Proton irradiation provides us with the unique possibility to implant hydrogen, produce lattice defects in the carbon structure, and simultaneously

have a complete elemental analysis of the sample. Protons in the megaelectron volt energy range have a penetration depth of several tens of micrometers inside a carbon structure (Spemann *et al*., 2004). The defect formation process by high-energy protons is a nonequilibrium athermal process and it appears rather unlikely that ordered arrays of defects are formed by migration of interstitial carbon atoms or vacancies, maybe with the exception of interstitials across the gallery. According to Banhart (1999) and from electron irradiation studies, the essential types of radiation damage up to intermediate temperatures are the rupture of basal planes (due to shift of the C atoms out of the plane) and the aggregation of interstitials into small dislocation loops between the graphene layers. The protuberances measured at the irradiated surface of microspots (Han *et al*., 2003a) result from the creation of interstitials. The migration energy of the interstitial depends on whether it is bounded. Di-interstitials were proposed to explain the irradiation-induced amorphization of graphite with a migration energy of 0.86 eV (Niwase, 1995). The interstitial loops are stable up to rather high temperatures, probably to 1000 °C (Banhart, 1999).

Irradiation changes the ratio of sp^2 to sp^3 bonding leading to cross-links between the graphene layers and the formation of sp^3 clusters (Tanabe, 1996). These clusters appear to be stable and do not anneal at high temperatures. Raman and X-ray photoemission spectroscopy (XPS) measurements indicate an additional disorder mode peak 'D' at 1360 cm^{-1}. Experimental results after proton irradiation in HOPG samples indicate that with increasing fluence the E_2g_2 and D modes become broader and the ratio of their intensities $I(D)/I(E_2g_2)$ increases as a measure of the degree of disorder (Höhne *et al*., 2004a). Monte Carlo simulations (Ziegler, 1977–1985) indicate that the vacancy and interstitial number produced by the megaelectron volt protons is about 15 times larger than the number of implanted ions. For fluences 0.001–75 nC μm^{-2} we get in the near-surface region between 4.7×10^{-6} and 0.35 displacements per carbon atom, that is, complete amorphization for the highest fluence, using a displacement energy of 35 eV for Frenkel pairs in HOPG, in agreement with recently published studies of the damage cascades by irradiation on graphite (Abe, Naramoto, Iwase and Kinoshita, 1997). For a fluence of 75 nC μm^{-2} we have $\sim 5 \times 10^{11}$ protons/μm^2, that is, the regions where defects are created by each individual proton overlap heavily. A dangling bond at the vacancy position in the carbon structure could trap a hydrogen atom – not necessarily from the proton implantation but already present as impurity in the sample. Theoretical estimates (Lehtinen *et al*., 2004) indicate (see Section 5) that certain H-vacancy complexes as well as hydrogen bonded to carbon adatoms (just above a graphene layer) have a magnetic moment; each hydrogen would provide an average magnetic moment of $\sim 1\,\mu_B$.

'Magnetic spots' of micrometer size

With a proton microbeam of energy in the megaelectron volt range directed onto the HOPG surface parallel to the *c* axis of the sample without beam scanning (excepting line scans, see the following text) it is possible to 'magnetically write' on a graphite surface, leading to the formation of micron-sized spots with enhanced defect density, as measured by micro-Raman (Höhne *et al*., 2004a; Esquinazi *et al*., 2006). In general, two spots separated by a distance of 20 μm were irradiated with the same ion fluence and several ion fluences were used. For large-enough fluences the swelling at the spots can be directly observed with an optical microscope (Spemann *et al*., 2004; Esquinazi *et al*., 2005). The height of this swelling depends on the irradiated fluence and on the mass of the ions. The swelling in the *c* direction occurs together with the contraction in the graphene layer; the newly formed interstitial planes push the existing planes apart leading to a protuberance at the sample surface. The dependence of the maximum swelling height h, measured by AFM (see Figure 11), with the fluence for proton irradiation f follows the function $h = 27.5 f^{0.61}$ nm with f in nC μm^{-2}. With an MFM one can measure the phase change of the, eventually magnetic, signal on the spots; see Figure 11. Whether these phase changes at the surface of the spots are of magnetic origin should be further checked since electrostatic effects, partially related to changes in the work function of the irradiated area, may provide a nonnegligible contribution.

The maximum amplitude of the signal (maximum phase shift) as a function of the fluence has a more complicated, nonmonotonic dependence, which depends also on the proton current used (Esquinazi *et al*., 2006). The units of the phase signal from the MFM are 'degrees'; a relation of this phase shift of the tip vibration to the force gradient can be found in Lohau *et al*. (1999, 2000). Examples for the magnetic moment calculated from measurements of the phase shift in carbon samples can be found in Han *et al*. (2003b, 2003c); Han and Esquinazi (2004). The dependence of the phase signal amplitude with the tip-to-sample distance can be used to estimate roughly the local magnetization of a micrometer region assuming a specific thickness (usually of the order of 1 μm). For the magnetic spots a relatively large magnetization was estimated (Han and Esquinazi, 2004). However, in those measurements the influence of electric potential differences (e.g., difference in contact potentials (work functions) between tip and sample surface or circuit-induced potential differences) was not taken into account and appropriately checked. Therefore, we may doubt the estimated values as well as the magnetic origin of the phase contrast at and in the surroundings of an irradiated spot till clear evidence from other experimental techniques is obtained. SQUID measurements done on thousands of

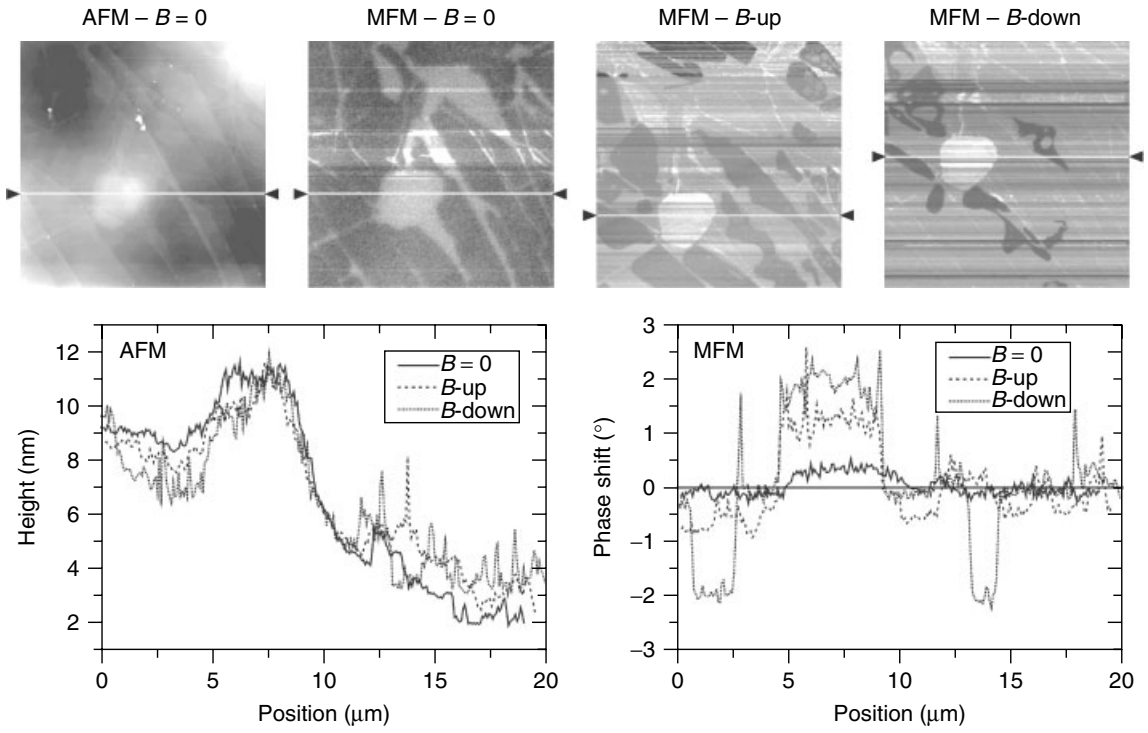

Figure 11. AFM (top left) and MFM images (scan size: $20 \times 20\,\mu m^2$) for a $2 \times 2\,\mu m^2$ spot irradiated with 2.25 MeV protons at a fluence of $7.5 \times 10^{16}\,cm^{-2} \simeq 0.115\,nC\ \mu m^{-2}$. The AFM and MFM line scans shown below were extracted from the images as indicated by the black triangles. The images show the results of the spot measured after irradiation ($B = 0$), after exposing it to a field of $\sim$1 kOe in the c direction (B-up) or $-c$-direction (B-down). The measurements were done, however, at zero applied field. Since the sample had to be removed from the MFM for the exposure to an external magnetic field, the subsequent repositioning of the spot in the MFM was accurate to $\sim$2 μm. Note that the phase changes in these images may be partially influenced by electrostatic as well as aging effects, since there was a certain time lag between the measurements at different applied magnetic fields. (Reproduced from Han *et al*., 2003a, with permission from Wiley VCH-Verlag. © 2003.)

spots in HOPG confirm that there show magnetic order (Barzola-Quiquia *et al*., 2007) The recently performed X-ray circular dichroism absorption measurements at proton-irradiated spots produced on 200-nm-thick carbon films suggest the presence of magnetic order at the carbon K-edge (Ohldag, *et al*., 2006). These kinds of experiments are very important to rule out impurity contributions as well as to confirm the magnetic order at the proton-irradiated regions.

With an α particle microbeam of 1.5 MeV energy similar topological spots were produced on HOPG surfaces (Han *et al*., 2003a). In contrast to the phase contrast obtained at the spots produced with the proton microbeam, those spots showed a much smaller contrast indicating that disorder alone does not trigger the observed signals. Nevertheless, more experiments using α particles in a broader range of parameters are still necessary because we cannot rule out that other effects, like local annealing, adversely influence the development of the observed phenomena.

Proton irradiation of large areas

Eventually, in order to visualize magnetic domain patterns as well as to increase the induced magnetization to reach the minimum range of commercial SQUIDs (typical magnetic moment resolution $\sim 10^{-7}$ emu or better) it is necessary to increase the irradiation area as well as the total irradiated charge. Figures 12 and 13 show the magnetic moment data and magnetic images obtained for a HOPG sample irradiated in a broad area (Esquinazi *et al*., 2003).

The increase of the saturation magnetic moment with the total irradiated charge has been reproduced in other HOPG samples (Esquinazi *et al*., 2003, 2006; Barzola-Quiquia *et al*., 2007). However, irradiation can lead also to negligible change or even to a reduction of the total magnetic moment upon the selected irradiation parameters and sample characteristics. The parameters that influence the magnetic order are (i) the total implanted charge; (ii) the input energy; (iii) the fluence, the irradiated charge per unit area; (iv) the ion current, large currents might heat the sample and nonsystematic effects are then possible; (v) micro- or

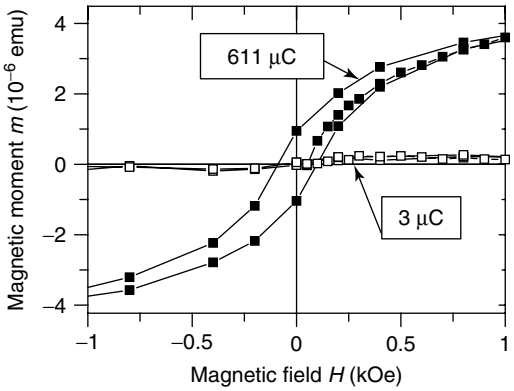

Figure 12. Magnetic moment as a function of applied field of a HOPG sample proton irradiated with a total charge of 3 μC and 611 μC (stage No. 1 and 2 + 3, respectively, described in Esquinazi *et al*. (2003)). The field was applied parallel to the graphene planes. (Reproduced from Esquinazi *et al*., 2004, with permission from Elsevier. © 2004.)

macroirradiation; (vi) sample temperature; and (vii) the initial state of the sample, namely, the density and type of defects, as well as the concentration of hydrogen before irradiation. Computer simulation results of the effects of adsorbed hydrogen on the band structure of a graphene layer indicate that metallization caused by specific defects can quench a spin-polarized state (Duplock, Scheffler and Lindan, 2004).

Clear proton irradiation effects on the magnetic response of thin carbon and fullerene films were reported (see Höhne *et al*. (2004a) and Esquinazi *et al*. (2006) and Figure 10), although the thickness of those films ($\lesssim 1\,\mu m$) were much smaller than the proton penetration depth at the used energies, that is, most of the protons should go through the material. These experimental facts indicate either that the hydrogen concentration in the sample or surrounding before irradiation might be relevant (the measured H concentration at the surface of HOPG samples is rather high; see Reichart *et al*. (2006)) and/or that the defect concentration in the first micrometer from the sample surface and produced by the proton beam is not negligible.

4.3.4 In other carbon-based structures

Kapton® is a tough, aromatic polyimide material, generally used in the form of a composite film (of amber color) in a wide variety of applications. The molecular structure is composed of an imide part, polymellitic dianhydride, and a bridging part, 4,4′-oxydianiline, that is, it contains basically the elements C, N, O, and H. Kapton has been (and apparently is still) used as wiring insulation, although it is suspected to be involved in several aircraft disasters owing to its tendency to arc. Kapton and some other polymer films with heat resistance transform into graphite films with high crystallinity after heat treatment at high temperatures ($T >$ 2000 K). For polyimide films the degree of graphitization increases for thinner films (Hatori, Yamada and Shiraishi, 1992, 1993). Low-temperature annealing of polymers leads to the formation of porous structures with a high density of radical molecules. Therefore, it is tempting to think that through the exchange interaction between unpaired electrons on free radicals one may trigger magnetic order. Note, however, that this assumption does not always work as the magnetization of disordered carbon revealed; see Section 4.2.

Kaburagi and Hishiyama (2002) observed an interesting behavior of the magnetization of Kapton when it starts decomposing around 770 K. Figure 14 shows the magnetization loops at 300 K measured for Kapton samples kept for 1 h at each of the temperatures shown in the figure and under nitrogen flow. The results clearly show that Kapton's magnetization behavior changes from the usual diamagnetic one to a ferromagnetic one at annealing temperatures around 500 °C. A maximum saturation magnetization at room temperature of 0.06 emu g^{-1} (coincidentally a value observed for some of the polymerized fullerene samples) was reached after an annealing temperature of 520 °C. Note that the ferromagnetic behavior vanishes for annealing temperatures above 520 °C. Taking into account that annealing dramatically decreases the concentration of light elements (a 70% weight loss was measured after a heat treatment at 540 °C (Kaburagi and Hishiyama, 2002)) the results suggest that a specific balance between graphitic-like order plus a certain amount of light atoms are necessary to trigger the magnetic order. The coercive field at 300 K was of the order of 0.005 T and a remanent magnetization of the order of a few percent of its saturation value. The magnetic response of the annealed samples shows the contribution of three components, that is, diamagnetism, paramagnetism (clearly observed when M is measured as a function of temperature at fixed field), and ferromagnetism. We expect that the magnetic order is not homogeneously distributed in the annealed sample. In spite of the clear magnetic order demonstrated by the SQUID measurements, the authors did not find evidence of magnetic domains using MFM, nor any sign for an anisotropic response within experimental error. Measurements done after five months revealed a slight decrease of M and increase of the paramagnetic part. This aging effect of the magnetic order appears to be a general feature observed in different carbon-based samples; see Section 4.3.5. We should note, however, that several groups could not still reproduce the results of Kaburagi and Hishiyama (2002) shown in Figure 14. Therefore we may doubt whether the observed effects are intrinsic to the measured samples.

Kopelevich *et al*. (2003b) reported on local ferromagnetism in microporous carbon with the structural regularity of zeolite Y. The authors observed clear hysteresis loops

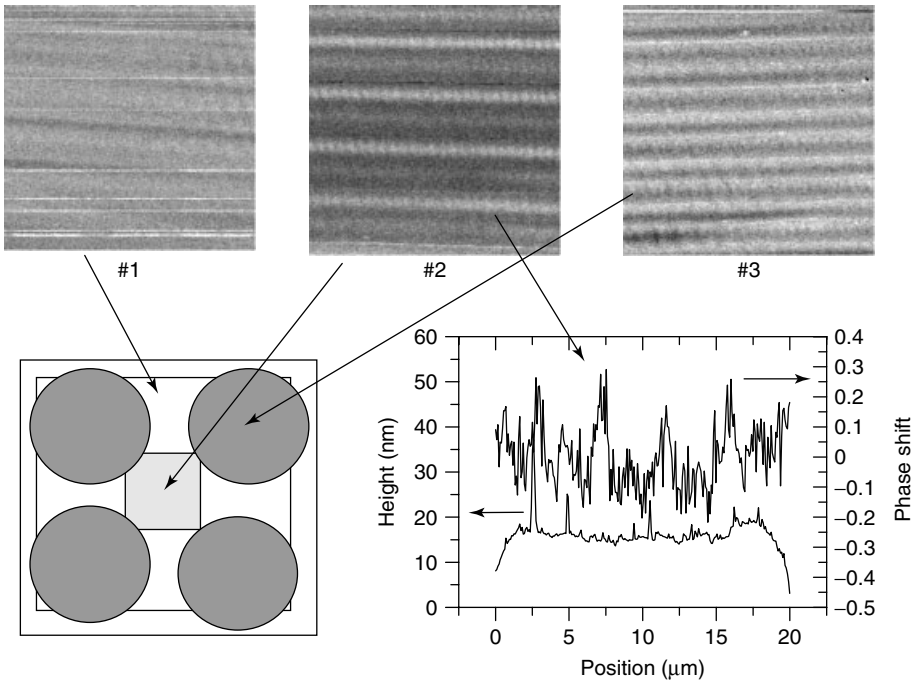

Figure 13. Top: Phase gradient images obtained at room temperature from MFM at three surfaces of a HOPG sample at three irradiation stages as described in Esquinazi *et al*. (2003). Bottom right: Topography and phase gradient line scans of the MFM image at the stage No. 2. As in Figure 11 the possible influence of electrostatic effects may play a role in the observed phase contrast and should be checked in future experiments. (Reproduced from Esquinazi *et al*., 2003, with permission from the American Physical Society. © 2003.)

added to a paramagnetic contribution. Subtracting this contribution at low temperatures, the saturation magnetization of this sample is $\lesssim 0.04\,\mathrm{emu\,g^{-1}}$. This value should be compared to $\sim 0.06\,\mathrm{emu\,g^{-1}}$, which is the maximum expected saturation magnetization due to the Fe concentration in the samples (Kopelevich *et al*., 2003b). In contrast to the behavior observed in most of the carbon-based samples reported above, this microporous carbon revealed a rather complicated temperature and field dependence added to clear difference between field and zero-field cooled samples at low-enough temperatures and fields. Following the experimental work of Harris, Burian and Duber (2000) that indicates that microporous carbon may have a fullerene-related structure, in which pentagons and heptagons are distributed randomly throughout a hexagonal network, Kopelevich *et al*. (2003b) proposed that the origin of magnetism may be related to topological disorder and curved graphene sheets, whereas the behavior at low temperatures may be due to a percolative-type transition of isolated magnetic clusters. This proposal agrees with the *ab initio* density functional theoretical calculations on carbon nanostructures with negative Gaussian curvature and without undercoordinated carbon atoms that reveal a net magnetic moment in the ground state of these structures (Park *et al*., 2003). It would be interesting to repeat these measurements with samples of higher purity and to study the evolution with annealing.

4.3.5 Aging and annealing effects

Depending on the sample and the origin of the magnetic order, it is possible to observe aging effects in the magnetization. Taking into account previous reports on the behavior and diffusion of hydrogen in graphite (Atsumi, 2002) one may expect to observe some time dependence in the magnetic response in some of the magnetic samples if hydrogen is involved in its origin. We note, however, that in general it is not simple to separate a pure hydrogen diffusion effect from structural relaxation because both may always be correlated.

Aging effects at room temperature in the magnetization has been observed in the fullerene $C_{60}H_{24}$ by Antonov *et al*. (2002). Hydrofullerites $C_{60}H_x$ synthesized at hydrogen pressures of 0.6 and 3 GPa were found to be ferromagnetic at room temperature (Antonov *et al*., 2002) with a magnetization at saturation of the order of $1\,\mathrm{emu\,g^{-1}}$. Figure 15 shows that the magnetization of a ferromagnetic sample decreases when the sample is stored at ambient conditions.

Different measurements were done in irradiated samples to test the possible influence of hydrogen diffusion in the observed magnetism. Measurements were done in irradiated spots in HOPG as well as in disordered carbon films just after irradiation and after several months of leaving the sample at ambient conditions. After a period of more than six months the magnetic signals decreased (Esquinazi *et al*.,

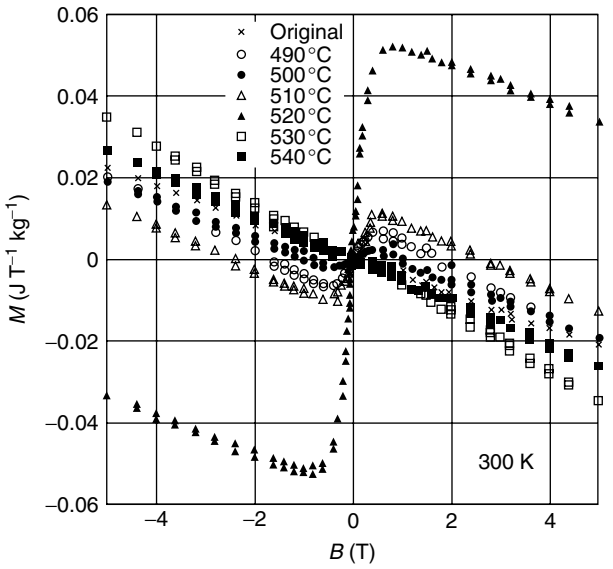

Figure 14. Magnetization ($J\,T^{-1}\,kg^{-1} = emu\,g^{-1}$) as a function of magnetic field at room temperature for Kapton after annealing for 1 h at the indicated temperatures in a nitrogen flow. (Reproduced from Y. Kaburagi *et al*., 2002, with permission from Materials Research Society. © 2002.)

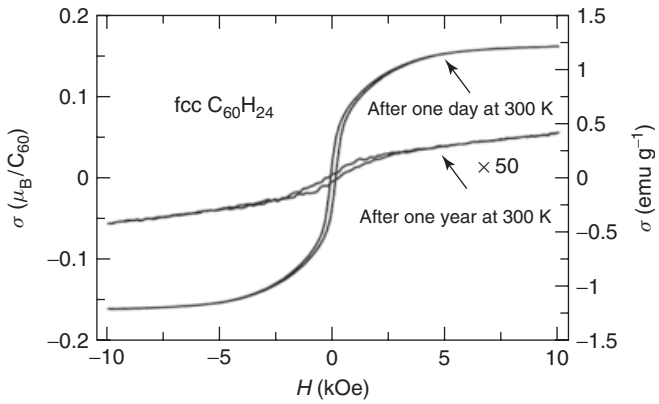

Figure 15. Magnetization as a function of magnetic field at room temperature for a $C_{60}H_{24}$ sample synthesized at a hydrogen pressure of 0.6 GPa and at $T = 350\,^{\circ}C$ and exposed to ambient conditions for 1 day and 1 year. (Reproduced from Antonov *et al*., 2002, with permission from Elsevier. © 2002.)

2006). Figure 16 shows the magnetic moment of a disordered carbon sample before, just after proton irradiation, and after one year at room temperature (after irradiation). It is clearly seen that the ferromagnetic-like hysteresis vanishes after one year. A clear decrease of the maximum phase shift of the MFM signal at the magnetic spot positions as well as changes in the topography with time have also been observed (Esquinazi *et al*., 2006). Annealing irradiated samples at high temperatures (∼1000 °C) makes the phase contrast vanish at room temperature (Esquinazi *et al*., 2006).

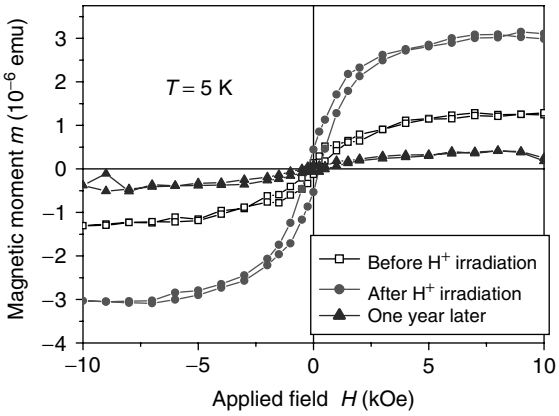

Figure 16. Magnetic moment (the diamagnetic background was subtracted) as a function of applied field for the disordered carbon film CH577a after preparation by PLD (before irradiation (□)), after irradiation (●) and one year later, leaving the sample at room temperature (▲). (Reproduced from Esquinazi *et al*., 2005, with permission from Elsevier. © 2005.)

The oxygen effect on the magnetic properties of graphite has been explored by Kopelevich, Moehlecke and da Silva (2006). In their experiments, an activated graphite powder was prepared by cutting and grinding an ultraclean graphite rod at $T = 300$ K in oxygen atmosphere by means of a virgin diamond saw blade. It is found that whereas the starting sample demonstrated a diamagnetic (nonhysteretic) response, measurements performed on the oxidized graphite powder revealed a pronounced ferromagnetic signal. It has also been found that the ferromagnetism vanishes with time after taking the sample out from the oxygen atmosphere, providing indirect evidence that the ferromagnetism is triggered by the adsorbed oxygen and not by a possible trace of magnetic impurities.

5 POSSIBLE ORIGINS OF THE MAGNETIC ORDER

In general, magnetic order in solids at low-enough temperatures, that is, below the Curie temperature, is characterized by a microscopic arrangement of magnetic moments, which are related to atoms containing partially filled electron shells, like in elements (and their alloys) with 3d or 4f electrons. To account for the 'order' one needs an exchange interaction (given by a constant J) of electrostatic origin between the localized magnetic moments or, in case of itinerant electron magnetism, an effective exchange energy for the unpaired, delocalized electrons. What makes the room-temperature carbon-based magnetic order unusual is the absence of d and f electrons, that means an apparent absence of localized magnetic moments. In this section we review several

proposals for a magnetic order in carbon structures and their correlations with experimental results. We would like to mention that due to the still inhomogeneous distribution (actually unknown) of magnetic material in the reported carbon structures, it makes little sense to speak about a specific amount of Bohr magneton per carbon atom or per fullerene cage. Any correlation of this number with theoretical predictions should be dealt with carefully.

(a) Can ferromagnetism occur in a perfect graphene layer? Itinerant ferromagnetism in graphite: It has been pointed out that the low dimensionality and density of carriers in graphite ($n_{2D} = 1 \ldots 2.4 \times 10^{11}\,\mathrm{cm}^{-2}$) may give rise to itinerant ferromagnetism (Khveshchenko, 2001a,b). This phenomenon is related to the large electron–electron interaction expected for a two-dimensional system with a low density of carriers. The strength of this interaction can be estimated through the Coulomb coupling constant

$$r_\mathrm{s} = \frac{e^2 m^*}{\hbar^2 \epsilon \epsilon_0 \sqrt{\pi n_{2D}}} \tag{1}$$

where $m^* = 0.04$–$0.06\,m$ (Sharma, Johnson and McClure, 1974) is the effective mass of the carriers (m is the free electron mass), $\epsilon = 12$–15 the dielectric constant. Using these values we get $r_\mathrm{s} = 7$–21. The constant r_s is given by the ratio between potential Coulomb energy (between carriers) and the Fermi (kinetic) energy. If $r_\mathrm{s} \gtrsim 1$ and within a rough picture, it may be possible that the ground state of an electron pair is not given by spin-up and spin-down but both with the same spin direction because in this case the Coulomb interaction decreases (the effective distance between the two electrons increases) and therefore a magnetic order appears.

In case the main carriers are massless Dirac fermions, as it is assumed for graphite due to the linear dispersion relation of the carriers near the Fermi energy, then the strength of the Coulomb interaction is characterized by

$$g = \frac{e^2}{\epsilon_0 v_\mathrm{F} \hbar} \tag{2}$$

With $v_\mathrm{F} \sim 2 \times 10^6\,\mathrm{m\,s}^{-1}$, $g \sim 10$ and therefore the strong Coulomb interaction can open an excitonic gap in the spectrum of the Dirac fermions (Khveshchenko, 2001a,b). Theory indicates that the occurrence of a gap is accompanied by the appearance of a small magnetic moment due to the band anisotropy.

Indirect experimental evidence for the importance of the Coulomb interaction between carriers and the opening of a gap with field may be given by the field-induced metal-insulator transition in the magnetoresistance of HOPG for fields applied normal to the layers (Kempa *et al*., 2000, 2003; Kopelevich *et al*., 2003a). Direct experimental evidence for the existence of a gap in the band structure of graphite is still missing and therefore the existence and further details of the long-range itinerant ferromagnetic order remain unclear.

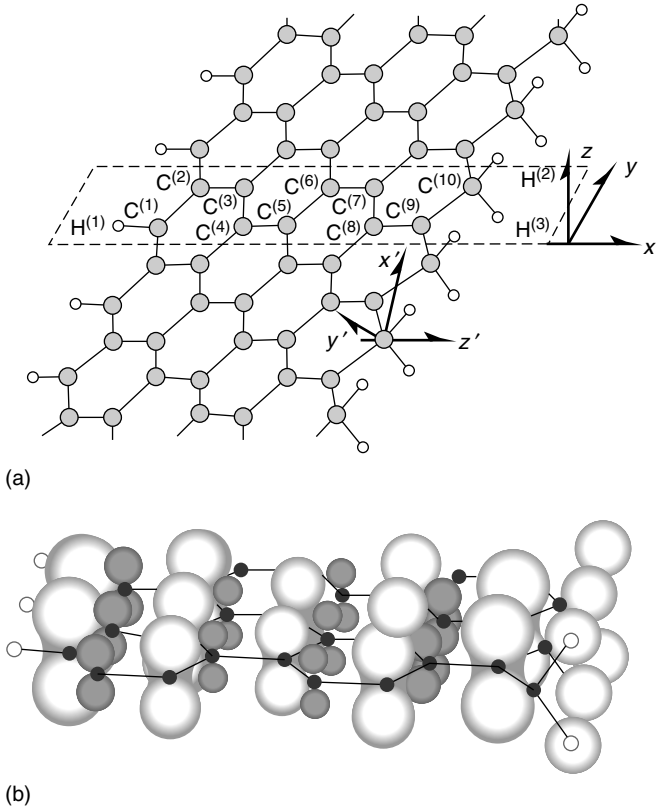

Figure 17. (a) The structure of a magnetic graphene ribbon. Dark circles represent carbon atoms and open circles, hydrogen. The unit cell contains 10 carbon and 3 hydrogen atoms, represented by dashed lines in the x, y plane. The monohydrogenated $C^{(1)}$ carbon atom forms sp^2 bonding, whereas the dihydrogenated $C^{(10)}$ carbon atom, an sp^3 bonding. (Reproduced from Kusakabe *et al*., 2003, with permission from the American Physical Society. © 2003.) (b) Spin density represented by isosurfaces. Bright and gray surfaces represent spin-up and spin-down densities. (Reproduced from Kusakabe *et al*., 2003, with permission from the American Physical Society. © 2003.)

(b) Magnetic properties of graphene with zigzag edges: Fujita, Wakabayashi, Nakada and Kusakabe (1996) categorized two-dimensional graphitic structures in nanometer scale as a novel graphitic material with properties different from bulk graphite or small aromatic molecules due to the influence of the open edges. Depending on the shape and termination of the edges a magnetic instability may occur in the graphitic structure. One distinguishes between three types of edges: zigzag (monohydrogenated Fujita's edge, edges similar to the position $C^{(1)}$ in Figure 17(a), dihydrogenated zigzag edges, Klein's edge (Klein, 1994), edges similar to the

position $C^{(10)}$ in Figure 17(a)), or armchair edges. Theoretical predictions (Fujita, Wakabayashi, Nakada and Kusakabe, 1996) indicate that the electronic states at Fujita's zigzag edges (terminated with one hydrogen atom, i.e., sp^2-bonded carbon atoms) are strongly localized with the nonbonding unpaired electrons having a localized magnetic moment with $S = 1/2$. These states, characterized by nearly flat dispersion in a certain range of momentum space and whose density of states has a sharp peak around the Fermi energy, would decay exponentially into the bulk of the 2D sheet (Nakada, Fujita, Dresselhaus and Dresselhaus, 1996). The edge states are believed to be responsible for the paramagnetic as well as the unconventional behavior observed in activated carbon fibers by Shibayama, Sato, Enoki and Endo (2000) (see also Enoki and Takai (2006)). Evidence for an increase of the density of states at the Fermi level at zigzag edges has been obtained by STM studies (Giunta and Kelty, 2001; Esquinazi *et al*., 2002; Kobayashi, Fukui, Enoki and Kusakabe, 2006).

Although a dihydrogenated zigzag edge behaves as Klein's edge and becomes magnetically ordered as Fijuta's edge (Kusakabe and Maruyama, 2003), a graphene ribbon with both edges either mono- or dihydrogenated *cannot* be magnetic, unless they are uncompensated. This is expected because of the effective antiferromagnetic compensation (net moment zero) of the localized magnetic moments at the opposite edges of the graphene ribbon. This situation agrees with the so-called Lieb's theorem (Lieb (1989b) see also Lieb (1989a)), which states that the ground state of a lattice like graphene is magnetic with a total spin given by $S = |N_A - N_B|/2$, where $N_A(N_B)$ is the number of A (B) sites or stared (unstared) carbon atoms, if a short-range interelectron repulsion U is assumed. A similar result has been obtained already for hydrocarbon molecules by Ovchinnikov (1978). If the π-electron system is described by this bipartite network with only nearest-neighbor electron transfer paths (electrons hop from a lattice position A to B without direct A–A or B–B hopping) then a flat band appears at E_F if the orbital energy is the same for every site. A couple of examples on how to estimate S for two hydrocarbon networks are given by Maruyama *et al*. (2004).

A finite magnetic moment per unit cell is obtained in graphene if both Fujita's and Klein's edges exist in the same ribbon. In this case the spin balance cancels owing to the existence of an sp^2- and an sp^3-bonded carbon atoms ($C^{(1)}$ and $C^{(10)}$ in Figure 17(a)) at the edges. The flat band is destroyed and an energy difference appears between the spin-up and spin-down bands. This spin gap is estimated with local-spin-density-approximation (LSDA) to be of the order of 0.2 eV for the unit cell of Figure 17(a) (Kusakabe and Maruyama, 2003) (note that the calculation is done at $T = 0$ K). The LSDA results indicate a net magnetic moment of $1\,\mu_B$ per unit cell of the ribbon. Similar calculations substituting hydrogen by fluor and oxygen as well as the addition of methylene indicate that the net magnetic moment depends on the bonded atom at the edges (Maruyama and Kusakabe, 2004; Maruyama *et al*., 2004). Note that the sp^2–sp^3 unbalance of carbon-bonded atoms plays a crucial role in triggering the finite magnetic moment. Note that this is not localized at the edges but distributed in the whole cell. The structure and energy spectra of different classes of large hydrocarbons ($\sim 10^4$ carbon atoms) with different edge structures and semiconducting properties have been studied theoretically by Dietz, Tyutyulkov, Madjarova and Müllen (2000). The main results of this work indicate that defects in polycyclic aromatic hydrocarbons change their energy spectra and in some cases the defect state energy levels are situated within the energy gap as n or p state in conventional semiconductors. In some cases the defects can lead to a high-spin state (ferro- or antiferromagnetic order) in the aromatic hydrocarbon.

Since electron–electron interactions play a main role in the development of a spontaneous spin-polarized state at the zigzag edges, one may doubt the use of certain theoretical approximations to solve this problem. Therefore, controlled approximations are always necessary to understand and clarify their influence on the calculated low-energy properties of the small graphitic structures. Hikihara, Hu, Lin and Mou (2003) studied the effects of the electron–electron interactions and showed that (i) in the presence of a Hubbard interaction the ground state is a spin singlet with finite charge and spin gaps without spontaneous spin polarization. (ii) Electrons at the zigzag edges correlate ferromagnetically composing effective spins that are easily polarizable by an external field. (iii) The localization at the zigzag edges of the effective spins are robust against electron–electron interactions. Regarding the question of interaction between graphene layers (interlayer interaction) in a 3D graphite structure, Harigaya (2001) showed that the magnetic properties change drastically depending on the type of stacking geometry; for the simple stacking there is apparently no magnetic solution.

(c) Three-dimensional structures of full carbon magnets: Mataga (1968) and Tyutyulkov and Bangov (1974) were probably the first authors to propose organic ferromagnets with unpaired electrons in nonbonding π-molecular orbital, in particular, in hydrocarbon molecules and nonclassical π-conjugated polymers. A few years later Ovchinnikov (1978) published similar ideas. A magnetic all-carbon structure with a mixture of sp^2 and sp^3 bonds was proposed by Ovchinnikov and Shamovsky (1991) (see also the references therein). These authors suggested that a three-dimensional all-carbon structure with the highest magnetization would contain an equal number of sp^2 and sp^3 hybridized carbon

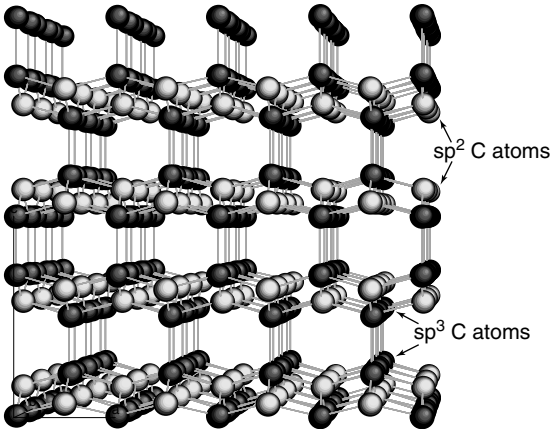

Figure 18. The theoretical structure of 'ferrocarbon' that contains equal numbers of sp^2 and sp^3 hybridized carbon atoms. This structure is intermediate between the graphite and diamond structures and contains 50% of unpaired-electron carriers. The lattice parameters were determined by energy minimization by Ovchinnikov and Shamovsky (1991). (Reproduced from A.A. Ovchinnikov *et al*., 1991, with permission from Elsevier. © 1991.)

atoms, that is, a mixture of the diamond and graphite structures. Note that the structure is obtained by shifting some of the sp^2 carbon atoms out from the planar graphene layer and hybridizing them to an sp^3 state with the next carbon neighbors from the top or bottom graphene layers. Through this sp^3 hybridization a singlet state is achieved for the former π electrons. Every sp^2 carbon atom with one unpaired electron is surrounded by three sp^3 carbon atoms. The elementary cell of the structure proposed by Ovchinnikov and Shamovsky (1991) and shown in Figure 18 has eight carbon atoms with a maximum magnetic moment of $4\,\mu_B$ per unit cell. The authors' estimations suggest that an exchange interaction between all pairs of nearest unpaired electrons localized on the sp^2 carbon atoms might be possible and the triplet, ferromagnetic electronic configuration should be the ground state of the structure. In spite of some reports in literature (see Shulg'a, Boldyrev and Ovchinnikov (1992) and references therein) it is unclear whether such a structure has been realized and how large its intrinsic magnetization was since nobody apparently could reproduce those results.

Unpaired spins in an all-carbon structure can be also found in special cases like nanostructures with negative Gaussian curvature, see Figure 19(a), as suggested by Park *et al*. (2003). The carbon radicals are those depicted by the gray spheres in one of the four phases of the tetrapod, see Figure 19(b). Note that in this structure the radicals are not undercoordinated but sterically protected by heptagons (gray areas in Figure 19(b)) and hexagons. These radicals are the source for the spin polarization. According to Park *et al*. (2003) the decomposition of the calculated electronic density of states for the sp^2 terminated tetrapod suggests that 4 of 12 unpaired spins are not localized and originate a magnetic ground state. Although such negative Gaussian curvatures are unlikely to be the origin of the magnetic order in graphite structures, the authors speculate that this building block may exist in carbon foams giving rise to its anomalous magnetic behavior (Rode *et al*., 2004).

(d) Magnetic properties of vacancies and adatoms on certain carbon structures: Till the end of the 1990s there was basically consensus that disorder in a graphite or other carbon-based structure produces a paramagnetic behavior due to the formation of nonbonding electrons (dangling bonds). Owing to the expected electron–electron interactions in graphene, González, Guinea and Vozmediano (2001) suggested that topological defects enhance the density of states and induce electronic instabilities, giving rise to the possibility of ferromagnetism as well as *p*-wave superconductivity. Quantitative treatments of the magnetic properties of vacancies and adatoms using spin-polarized density-functional simulations have been published recently. Experimental evidence for ferromagnetic behavior in carbon structures with some kind of disorder, like proton-irradiated graphite (Esquinazi *et al*., 2003), suggests that vacancies and adatoms, possibly with the influence of light atoms like hydrogen or oxygen, play an important role in the magnetic order. *Ab initio* calculations indicate that a carbon adatom on a graphene sheet can have equilibrium positions with a finite magnetic moment of the order of $0.5\,\mu_B$ (Lehtinen *et al*., 2003). This moment can be understood if we consider that the hybridization state is different for the two surface atoms attached to the adatom and this last one (sp^2–sp^3 vs sp^2 hybridization, respectively); the half p_z electron of the adatom provides the $0.5\,\mu_B$.

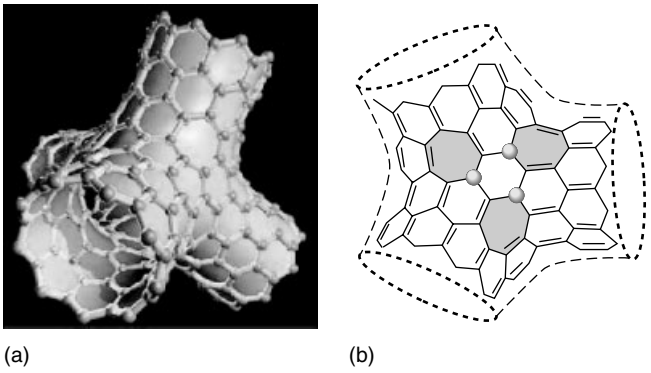

Figure 19. (a) Structure of the building block of schwarzite, the 'tetrapod'. (Reproduced from Park *et al*., 2003, with permission from the American Physical Society. © 2003.) (b) Three trivalent carbon radicals are represented by the gray spheres. The tetrapod contains 12 trivalent radicals. The gray areas indicate the heptagons to which the radicals are associated. (Reproduced from Park *et al*., 2003, with permission from the American Physical Society. © 2003.)

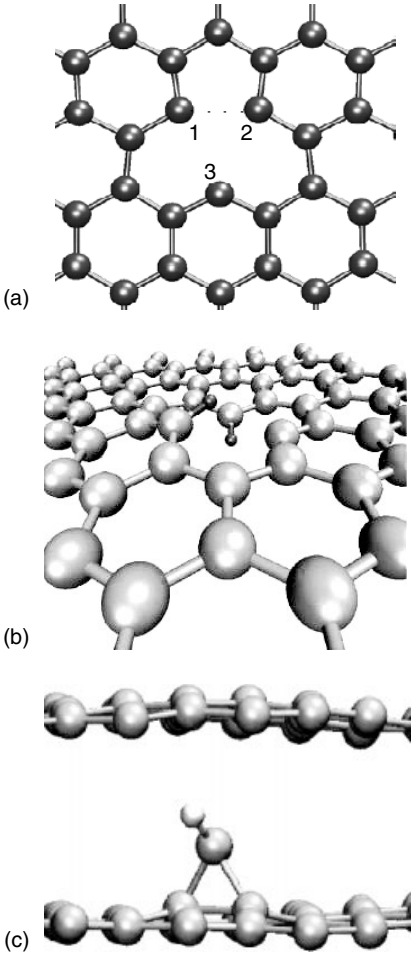

Figure 20. (a) Atomic structure of a vacancy in a graphene layer. (Reproduced from Y. Ma *et al*., 2004, with permission from IOP Publishing Ltd. © 2004.) (b) Structure of a vacancy surrounded by two hydrogens. (Reproduced from Lehtinen *et al*., 2004, with permission from American Physical Society. © 2004.) (c) Structure of a C–H group adsorbed between two graphene layers. (Reproduced from Lehtinen *et al*., 2004, with permission from American Physical Society. © 2004.)

Ma, Lehtinen, Foster and Nieminen (2004) analyzed the magnetic state of a vacancy in a graphene sheet as that shown in Figure 20(a). Their result indicates that the vacancy undergoes a Jahn–Teller distortion moving the atoms 1 and 2 together in Figure 20(a). This deformed pentagon saturates the sp^2 electrons of the atoms 1 and 2, leaving number 3 with a dangling bond that is responsible for the $1.04\,\mu_B$ magnetic moment. Ma, Lehtinen, Foster and Nieminen (2004) also studied the dependence of the electronic structure and magnetic properties on the vacancy concentration of carbon nanotubes. Their results indicate that vacancies can change the electronic structure of the nanotube and, in case it is metallic, the vacancy may trigger ferro- or ferrimagnetism.

The calculations of Lehtinen *et al*. (2004) indicate that if an hydrogen encounters an empty vacancy, then it compensates the dangling bond, and the magnetic moment of Figure 20(a) vanishes. However, if a vacancy is saturated by a hydrogen atom, a second hydrogen atom can bond to the other side of the vacancy (see Figure 20(b)). This configuration with one H-atom above the graphene plane and one below has a magnetic moment of $1.2\,\mu_B$ localized on the dangling sp^2 bond. The other possibility to have a magnetic moment of the order of $0.9\,\mu_B$ is when the hydrogen atom bonds to the C adatom in between two graphene layers (see Figure 20(c)). Lehtinen *et al*. (2004) estimated the total magnetic moment produced in the irradiation experiments made by Esquinazi *et al*. (2003) taking into account the amount of hydrogen atoms, vacancies, and C adatoms obtaining reasonable agreement. We note, however, that the magnetic order is not demonstrated by these calculations but is implicitly assumed through defect–defect interactions.

Chan *et al*. (2004) used density-functional theory and reactive force field molecular dynamics to study the magnetic order in fullerenes with defect rhombohedral structure. They found that if a hydrogen bonds a C atom near a vacancy of the C_{60} cage, a ferromagnetic ground state is found with a moment of $3.0\,\mu_B$ per cage. In contrast to the graphene case mentioned above, this bonding of hydrogen in the curved fullerene structure does not quench the magnetic moment but one of two possible states, destroying the spin balance. To account for the measured magnetization the authors estimated a ratio $H{:}C_{60} \sim 10\%$. Inelastic neutron scattering experiments performed by the same authors indicated a similar concentration of hydrogen as the theoretical estimate.

(e) The influence of hydrogen: In the previous section we saw that bonding of hydrogen with carbon atoms near vacancies or at the edges of graphene layers may be of advantage for the formation of a magnetically ordered state in certain carbon structures. In this section we would like to emphasize some results from literature that indicate that the coupling of hydrogen to carbon atoms in graphite-like structures can have a strong influence in the electric and magnetic properties of the carbon structure.

Ruffieux *et al*. (2000) combined AFM and STM measurements to study the topography and the electronic changes in the vicinity of defects produced by chemisorbed hydrogen or atomic vacancy formation on the basal plane of graphite. HOPG samples were irradiated with a low proton flux of $10^{12}\,cm^{-2}\,s^{-1}$ and 10 eV energy. In the region where chemisorbed hydrogen was present, these authors found superlattice-type modifications of the electronic properties over a distance of 25 lattice ($\sim$6 nm range) constants without modifications in the topography. These results are the first to show a long-range modification of the electronic structure produced by a hydrogen atom.

A positive muon (μ^+) is an elementary particle with a mass (1/9)th that of a proton and therefore much larger than that of an electron. The electronic structure around a (μ^+) in a solid is virtually identical to that of hydrogen in the same solid. After implantation in a solid these particles occupy interstitial sites and are a convenient way to simulate the behavior of hydrogen impurity. The study of the spin-relaxation rate and Knight shift, within the 2.2 μs lifetime of the muon, provides a valuable way to characterize the local electronic structure one would expect around a hydrogen atom in the implanted solid structure. Evidence for local magnetic moment formation on the carbon atoms of a graphene layer around a positive muon in graphite was obtained by Chakhalian *et al*. (2002) supported by the unusually large and temperature-dependent Knight shift. The muon-spin-relaxation rate is also anomalously large and deviates from the Korringa relaxation for normal metals. Chakhalian *et al*. (2002) noted that this result is compatible with the strong energy dependence in the density of states and the small Fermi energy of graphite.

First-principles calculations of the electronic density of states of graphene done by Duplock, Scheffler and Lindan (2004) showed that the adsorption of atomic hydrogen opens a substantial gap of 1.25 eV inducing a spin-polarized state. This result agrees, in principle, with the experimental results from Chakhalian *et al*. (2002) described above. The results of Duplock, Scheffler and Lindan (2004) further showed that the spin state is quenched when hydrogen is adsorbed either on a Stone–Wales defect (pentagon and a heptagon pair on the graphene layer) or on a layer containing this defect. This amazing result appears to be due to the metallization induced by this kind of defect on the band structure of the graphene layer.

6 CONCLUSION

Defects undoubtedly alter the magnetic properties of carbon-based structures. The simplest, well-reproducible example is the increase of the paramagnetic contribution with disorder in a graphite structure. There are several publications that indicate that in certain carbon-based structures a magnetic order exists, which remains even above room temperature and without the influence of metal ions. This interesting behavior was overseen by the main stream of experts in magnetism partially because of the unclear characterization of the magnetic impurity contribution in several, earlier publications and also due to the lack of sensitivity in earlier studies. This situation has been improved by systematic and careful studies of the magnetism in graphite, disordered carbon, and fullerenes, especially after proton irradiation in which an overall impurity characterization was performed. On the basis of the results obtained recently, the author is convinced that room-temperature ferromagnetism in metal-free carbon-based materials is a much more general phenomenon than one ever thought. Impurities remain a problem because in several of the not-yet optimized materials the signals are rather weak and can be easily overwhelmed by a few tens of parts per million of ferromagnetic iron or other magnetic ion. This unwanted contribution added to aging effects and poor reproducibility of the methods used to produce magnetic order in carbon systems are the main problems faced by researchers nowadays. A large number of open questions will keep researchers busy in the years to come, namely, the origin for the magnetic order; the range of Curie temperature; the maximum achievable saturation magnetization in carbon structures; the contribution to the magnetic order from lattice defects and their influence as H-trapping centers; the electrical conductivity of the ferromagnetic structures; the influence of the ion current, fluence, and energy of the irradiated particle and the sample temperature on the magnetic order; the hydrogen and oxygen coverage in the first micrometers from the surface before and after irradiation; the defect relaxation and hydrogen, or other light element, diffusion, and their influence on the magnetic order.

NOTES

[1] In the manuscript from Ovchinnikov and Spector (1988) the absolute value of magnetization is in units of $\mathrm{G\,g^{-1}}$, a unit that does not match the usual magnetization units. In that publication, however, there is a figure where the magnetization in G and in $\mathrm{emu\,g^{-1}}$ for the same sample are given. From that figure we infer that the used '$\mathrm{G\,g^{-1}}$' should be equivalent to $\mathrm{emu\,g^{-1}}$.

ACKNOWLEDGMENTS

The author thanks all his collaborators from the Institute for Experimental Physics II of the University of Leipzig, especially R. Höhne, D. Spemann, K. Schindler, A. Setzer, M. Ziese, H. Schmidt, M. Diaconu, and T. Butz. Without their permanent contributions the work done in the last five years would not have been possible. Useful discussions with Y. Kopelevich, A. Talyzin, F. Guinea, M. A. Vozmediano, K. Kusakabe, T. Enoki, and A. V. Krasheninnikov are gratefully acknowledged. The author acknowledges the support by the Deutsche Forschungsgemeinschaft through Grant ES 86/11-1 and the European Union Project 'Ferrocarbon'.

REFERENCES

Abe, H., Naramoto, H., Iwase, A. and Kinoshita, C. (1997). Effect of damage cascades on the irradiation-induced amorphization in graphite. *Nuclear Instruments and Methods in Physical Research Section B*, **127/128**, 681–684.

Allemand, P.M., Khemani, C., Koch, A., *et al*. (1991). Organic molecular soft ferromagnetism in a fullerene-C_{60}. *Science*, **253**, 301–303.

Antonov, V.E., Bashkin, I.O., Khasanov, S.S., *et al*. (2002). Magnetic ordering in hydrofullerite $C_{60}H_{24}$. *Journal of Alloys and Compounds*, **330–332**, 365–368.

Arčon, D., Jagličič, Z., Zorko, A., *et al*. (2006). Origin of magnetic moments in carbon nanofoams. *Physical Review B*, **74**, 014438-1–014438-9.

Atsumi, H. (2002). Hydrogen bulk retention in graphite and kinetics of diffusion. *Journal of Nuclear Materials*, **307–311**, 1466–1470.

Banhart, F. (1999). Irradiation effects in carbon nanostructures. *Reports on Progress in Physics*, **62**, 1181–1221.

Barzola-Quiquia, J., Esquinazi, P., Rothermel, M., *et al*. (2007). Proton-induced magnetic order in carbon: SQUID measurements. *Nuclear Instruments and Methods in Physical Research Section B*, doi:10.1016/j.nimb.2006.12.036 (in press).

Bennington, S.M., Kitamura, N., Cain, M.G., *et al*. (2000). In situ diffraction measurement of the polymerization of c_{60} at high temperatures and pressures. *Journal of Physics: Condensed Matter*, **12**, L451–L456.

Blundell, S.J. and Pratt, F.L. (2004). Organic and molecular magnets. *Journal of Physics: Condensed Matter*, **16**, R771–R828.

Boukhvalov, D.W., Karimov, P.F., Kurmaev, E.Z., *et al*. (2004). Testing the magnetism of polymerized fullerene. *Physical Review B*, **69**, 115425-1–115425-4.

Butz, T., Spemann, D., Han, K-H., *et al*. (2005). The role of nuclear nanoprobes in inducing magnetic ordering in graphite. *Hyperfine Interactions*, **160**, 27–37.

Cespedes, O., Ferreira, M.S., Sanvito, S., *et al*. (2004). Contact induced magnetism in carbon nanotubes. *Journal of Physics: Condensed Matter*, **16**, L155–L161.

Chakhalian, J.A., Kiefl, R.F., Dunsiger, S.R., *et al*. (2002). Evidence for local moment formation around a positive muon in graphite. *Physical Review B*, **66**, 155107-1–155107-8.

Chan, J.A., Montanari, B., Gale, J.D., *et al*. (2004). Magnetic properties of polymerized C_{60}: the influence of defects and hydrogen. *Physical Review B*, **70**, 041403(R)-1–041403(R)-4.

Coey, J., Venkatesan, M., Fitzgerald, C., *et al*. (2002). Ferromagnetism of a graphite nodule from the canyon diablo meteorite. *Nature*, **420**, 156–159.

Davidov, V.A., Kashevarova, L.S., Rakhmanina, A.V., *et al*. (2000). Spectroscopic study of pressure-polymerized phases of C_{60}. *Physical Review B*, **61**, 11936–11945.

Delhaès, P. and Carmona, F. (1981). *Physical Properties of Non-crystalline Carbon*, Marcel Dekker: New York, pp. 89–174, Vol. 17, chapter 2.

Dietz, F., Tyutyulkov, N., Madjarova, G. and Müllen, K. (2000). Is 2-d graphite an ultimate large hydrocarbon? II. structure and energy spectra of polycyclic aromatic hydrocarbons with defects. *Journal of Physical Chemistry*, **104**, 1746–1761.

Dresselhaus, M.S., Dresselhaus, G., Sugihara, K., *et al*. (1988). *Graphite Fibers and Filaments*, Springer-Verlag: Berlin.

Duplock, E.J., Scheffler, M. and Lindan, P.J.D. (2004). Hallmark of perfect graphite. *Physical Review Letters*, **92**, 225502-1–225502-4.

Enoki, T. and Takai, K. (2006). Unconventional magnetic properties of nanographite. In *Carbon-Based Magnetism: An Overview of the Magnetism of Metal-Free Carbon-Based Compounds and Materials*, Makarova, T. and Palacio, F. (Eds.), Elsevier Science, chapter 17.

Esquinazi, P. and Höhne, R. (2005). Magnetism in carbon structures. *Journal of Magnetism and Magnetic Materials*, **290–291**, 20–27.

Esquinazi, P., Han, K-H., Höhne, R., *et al*. (2005). Examples of room-temperature magnetic ordering in carbon-based structures. *Phase Transitions*, **78**, 155–168.

Esquinazi, P., Höhne, R., Han, K.H., *et al*. (2004). Magnetic carbon: explicit evidence of ferromagnetism induced by proton irradiation. *Carbon*, **42**, 1213–1217.

Esquinazi, P., Höhne, R., Han, K-H., *et al*. (2006). In *Carbon-Based Magnetism: An Overview of the Magnetism of Metal-Free Carbon-Based Compounds and Materials*, Makarova, T. and Palacio, F. (Eds.), Elsevier Science, pp. 437–462, chapter 19.

Esquinazi, P., Setzer, A., Höhne, R., *et al*. (2002). Ferromagnetism in oriented graphite samples. *Physical Review B*, **66**, 024429-1–024429-10.

Esquinazi, P., Spemann, D., Höhne, R., *et al*. (2003). Induced magnetic ordering by proton irradiation in graphite. *Physical Review Letters*, **91**, 227201-1–227201-4.

Fujita, M., Wakabayashi, K., Nakada, K. and Kusakabe, K. (1996). Peculiar localized state at zigzag graphite edge. *Journal of the Physical Society of Japan*, **65**, 1920–1923.

Giunta, P.L. and Kelty, S.P. (2001). Direct observation of graphite layer edge states by scanning tunneling microscopy. *Journal of Chemical Physics*, **114**, 1807–1812.

González, J., Guinea, F. and Vozmediano, M.A.H. (2001). Electron-electron interactions in graphene sheets. *Physical Review B*, **63**, 134421-1–134421-8.

Haddon, R.C. (1995). Magnetism of the carbon allotropes. *Nature*, **378**, 249–255.

Han, K-H. and Esquinazi, P. (2004). Quantitative determination of the magnetization of proton irradiated spots in graphite with magnetic force microscopy. *Journal of Applied Physics*, **96**, 1581–1584.

Han, K-H., Spemann, D., Esquinazi, P., *et al*. (2003a). Ferromagnetic spots in graphite produced by proton irradiation. *Advanced Materials*, **15**, 1719–1722.

Han, K-H., Spemann, D., Höhne, R., *et al*. (2003b). Observation of intrinsic magnetic domains in C_{60} polymer. *Carbon*, **41**, 785–795, see also 2425.

Han, K-H., Spemann, D., Höhne, R., *et al*. (2003c). Observation of intrinsic magnetic domains in C_{60} polymer. *Carbon*, **41**, 2425.

Han, K-H., Talyzin, A., Dzwilewski, A., *et al*. (2005). Magnetic properties of carbon phases synthesized using high-pressure high-temperature treatment. *Physical Review B*, **72**, 224424-1–224424-7.

Harigaya, K. (2001). New type of antiferromagnetic state in stacked nanographite. *Chemical Physics Letters*, **340**, 123–128.

Harris, P.J.F., Burian, A. and Duber, S. (2000). High-resolution electron microscopy of a microporous carbon. *Philosophical Magazine Letters*, **80**, 381–386.

Hatori, H., Yamada, Y. and Shiraishi, M. (1992). In-plane orientation and graphitizability of polyimide films. *Carbon*, **30**, 763–766.

Hatori, H., Yamada, Y. and Shiraishi, M. (1993). In-plane orientation and graphitizability of polyimide films: II. Film thickness dependence. *Carbon*, **31**, 1307–1312.

Heisenberg, W. (1928). Zur theorie des ferromagnetismus. *Zeitschrift fur Physik*, **49**, 619–636.

Hikihara, T., Hu, X., Lin, H-H. and Mou, C-Y. (2003). Ground-state properties of nanographite systems with zigzag edges. *Physical Review B*, **68**, 035432-1–035432-9.

Höhne, R. and Esquinazi, P. (2002). Can carbon be ferromagnetic? *Advanced Materials*, **14**, 753–756.

Höhne, R., Esquinazi, P., Han, K-H., *et al*. (2004a). Ferromagnetic structures in graphite and amorphous carbon films produced by high energy proton irradiation. In *Proceedings of the 16 International Conference of Soft Magnetic Materials*, Raabe, D. (Ed.), Dierk Raabe pp. 185–190 (ISBN 3-514-00711-X).

Höhne, R., Han, K-H., Esquinazi, P., *et al*. (2004b). Magnetism of pure, disordered carbon films prepared by pulsed laser deposition. *Journal of Magnetism and Magnetic Materials*, **272–276**, e839–e840.

Höhne, R., Ziese, M. and Esquinazi, P. (2004). Searching for a magnetic proximity effect in magnetite-carbon structures. *Carbon*, **42**, 3109–3114.

Huber, D.L., Urbano, R.R., Sercheli, M.S. and Rettori, C. (2004). Fluctuating field model for conduction electron spin resonance in graphite. *Physical Review B*, **70**, 125417-1–125417-5.

Ishii, C., Matsumura, Y. and Kaneko, K. (1995). Ferromagnetic behavior of superhigh surface area carbon. *Journal of Physical Chemistry*, **99**, 5743–5745.

Ishii, C., Shindo, N. and Kaneko, K. (1995). Random magnetism of superhigh surface area carbon having minute graphitic structures. *Chemical Physics Letters*, **242**, 196–201.

Kaburagi, Y. and Hishiyama, Y. (2002). Ferromagnetism discovered on heat-treating the aromatic polyimide film Kapton. *Journal of Materials Research*, **17**, 2000–2006.

Kelly, B.T. (1981). *Physics of Graphite*, Applied Science Publishers: London.

Kempa, H., Semmelhack, H.C., Esquinazi, P. and Kopelevich, Y. (2003). Absence of metal-insulator transition and coherent interlayer transport in oriented graphite in parallel magnetic fields. *Solid State Communications*, **125**, 1–5.

Kempa, H., Kopelevich, Y., Mrowka, F., *et al*. (2000). Magnetic field driven superconductor-insulator-type transition in graphite. *Solid State Communications*, **115**, 539–542.

Khveshchenko, D.V. (2001a). Ghost excitonic insulator transition in layered graphite. *Physical Review Letters*, **87**, 246802-1–246802-4.

Khveshchenko, D.V. (2001b). Magnetic-field-induced insulating behavior in highly oriented pyrolitic graphite. *Physical Review Letters*, **87**, 206401-1–206401-4.

Klein, D.J. (1994). Graphitic polymer strips with edge states. *Chemical Physics Letters*, **217**, 261–265.

Kobayashi, Y., Fukui, K., Enoki, T. and Kusakabe, K. (2006). Edge state on hydrogen-terminated graphite edges investigated by scanning tunneling microscopy. *Physical Review B*, **73**, 125415-1–125415-8.

Kopelevich, Y., Esquinazi, P., Torres, J. and Moehlecke, S. (2000). Ferromagnetic- and superconducting-like behavior of graphite. *Journal of Low Temperature Physics*, **119**, 691–702.

Kopelevich, Y., Lemanov, V., Moehlecke, S. and Torres, J. (1999). Landau level quantization and possible superconducting instabilities in highly oriented pyrolitic graphite. *Physics of the Solid State*, **41**, 1959–1962.

Kopelevich, Y., Moehlecke, S. and da Silva, R.R. (2006). Ferromagnetic and superconducting instabilities in graphite. In *Carbon-Based Magnetism: An Overview of the Magnetism of Metal-Free Carbon-Based Compounds and Materials*, Makarova, T. and Palacio, F. (Eds.), Elsevier Science, chapter 18.

Kopelevich, Y., Esquinazi, P., Torres, J.H.S., *et al*. (2003a). Graphite as a highly correlated electron system. *Advances in Solid State Physics*, **43**, 207–222.

Kopelevich, Y., da Silva, R.R., Torres, J.H.S., *et al*. (2003b). Local ferromagnetism in microporous carbon with the structural regularity of zeolite Y. *Physical Review B*, **68**, 092408-1–092408-4.

Korobov, M.V., Senyavin, V.M., Bogachev, A.G., *et al*. (2003). Phase transformations in pressure polymerized C_{60}. *Chemical Physics Letters*, **381**, 410–415.

Korshak, Y.V., Medvedeva, T.V., Ovchinnikov, A.A. and Spektor, V.N. (1987). Organic polymer ferromagnet. *Nature*, **326**, 370–372.

Korshak, Y.V., Ovchinnikov, A.A., Shapiro, A.M., *et al*. (1986). Organic polymer ferromagnet. *JETP Letters*, **43**, 399–402.

Kusakabe, K. and Maruyama, M. (2003). Magnetic nanographite. *Physical Review B*, **67**, 092406-1–092406-4.

Lehtinen, P.O., Foster, A.S., Ayuela, A., *et al*. (2003). Magnetic properties and diffusion of adatoms on a graphene sheet. *Physical Review Letters*, **91**, 017202-1–017202-4.

Lehtinen, P.O., Foster, A.S., Ma, Y., *et al*. (2004). Irradiation-induced magnetism in graphite: a density-functional study. *Physical Review Letters*, **93**, 187202-1–187202-4.

Lieb, E.H. (1989a). Two theorems on the Hubbard model, (Erratum). *Physical Review Letters*, **62**, 1927.

Lieb, E.H. (1989b). Two theorems on the Hubbard model. *Physical Review Letters*, **62**, 1201–1204.

Lohau, J., Kirsch, S., Carl, A. and Wassermann, E. (2000). Quantitative determination of the magnetization and stray field of a single domain Co/Pt dot with magnetic force microscopy. *Applied Physics Letters*, **76**, 3094–3096.

Lohau, J., Kirsch, S., Carl, A., *et al*. (1999). Quantitative determination of effective dipole and monopole moments of magnetic force microscopy tips. *Journal of Applied Physics*, **86**, 3410–3417.

Ma, Y., Lehtinen, P.O., Foster, A.S. and Nieminen, R.M. (2004). Magnetic properties of vacancies in graphene and single-walled carbon nanotubes. *New Journal of Physics*, **6**, 68-1–68-15.

Madsen, G.K.H., Iversen, B.B., Blaha, P. and Schwarz, K. (2001). Electronic structure of the sodium and potassium electrosodalites $(Na/K)_8(AlSiO_4)_6$. *Physical Review B*, **64**, 195102-1–195102-6.

Makarova, T. (2003). *Magnetism of Carbon-Based Materials*, *Vol. 45 of Studies of High Temperature Superconductors*, NOVA Science Publishers, pp. 107–169.

Makarova, T. (2004). Magnetic properties of carbon structures. *Semiconductors*, **38**, 615–638.

Makarova, T., Han, K., Esquinazi, P., *et al*. (2003). Magnetism in photopolymerized fullerenes. *Carbon*, **41**, 1575–1584.

Makarova, T., Sundqvist, B., Höhne, R., *et al*. (2001). Magnetic carbon. *Nature*, **413**, 716–718.

Makarova, T., Sundqvist, B., Höhne, R., *et al*. (2005). Magnetic carbon. *Nature*, **436**, 1200. Corrigendum to the paper in Nature 413, 716 (2001).

Makarova, T., Sundqvist, B., Höhne, R., *et al*. (2006). Magnetic carbon. *Nature*, **440**, 707. Retraction to the paper in Nature, 413, 716 (2001).

Maruyama, M. and Kusakabe, K. (2004). Theoretical prediction of synthesis methods to create magnetic nanographite. *Journal of the Physical Society of Japan*, **73**, 656–663.

Maruyama, M., Kusakabe, K., Tsuneyuki, S., *et al*. (2004). Magnetic properties of nanographite with modified zigzag edges. *Journal of Physics and Chemistry of Solids*, **65**, 119–122.

Mataga, N. (1968). Possible "ferromagnetic states" of some hypothetical hydrocarbons. *Theoretica Chimica Acta (Berlin)*, **10**, 372–376.

Matsuishi, K., Ohno, T., Yasuda, N., *et al*. (1997). Photo-induced transformation of C_{60} films and single crystals by laser irradiation. *Journal of Physics and Chemistry of Solids*, **58**, 1747–1752.

McClure, J.W. (1956). Diamagnetism of graphite. *Physical Review*, **104**, 666–671.

Mertins, H-C., Valencia, S., Gudat, W., *et al*. (2004). Direct observation of local ferromagnetism on carbon in C/Fe multilayers. *Europhysics Letters*, **66**, 743–748.

Mizogami, S., Mizutani, M., Fukuda, M. and Kawabata, K. (1991). Abnormal ferromagnetic behavior for pyrolytic carbon under low temperature growth by cvd method. *Synthetic Metals*, **43**, 3271–3274.

Murakami, Y. and Suematsu, H. (1996). Magnetism of C_{60} induced by photo-assisted oxidation. *Pure and Applied Chemistry*, **68**, 1463–1467.

Murata, K., Ushijima, H., Ueda, H. and Kawaguchi, K. (1991). Magnetic properties of amorphous-like carbons prepared by tetraaza compounds by the chemical vapour deposition (CVD) method. *Journal of the Chemical Society, Chemical Communications*, 1265–1266.

Murata, K., Ushijima, H., Ueda, H. and Kawaguchi, K. (1992). A stable carbon-based organic magnet. *Journal of the Chemical Society, Chemical Communications*, 567–569.

Nakada, K., Fujita, M., Dresselhaus, G. and Dresselhaus, M.S. (1996). Edge state in graphene ribbons: nanometer size effect and edge shape dependence. *Physical Review B*, **54**, 17954–17961.

Narozhnyi, V.N., Müller, K-H., Eckert, D., *et al*. (2003). Ferromagnetic carbon with enhanced Curie temperature. *Physica B: Physics of Condensed Matter*, **329**, 1217–1218.

Niwase, K. (1995). Irradiation-induced amorphization of graphite. *Physical Review B*, **52**, 15785–15798.

Ohldag, H., Höhne, R., Spemann, D. *et al*. (2006), e-print arXiv.org/cond-mat/0609478.

Oostra, S. and Torrance, J.B. (1984). Symposium on Horizons in the Properties of Low Dimensional Compounds, Honolulu, December 20, 1984 (unpublished), see also Torrance, J.B., Oostra, S. and Nazzal, A. 1987.

Ovchinnikov, A.A. (1978). Multiplicity of the ground state of large alternant organic molecules with conjugated bonds. *Theoretica Chimica Acta (Berlin)*, **47**, 297–304.

Ovchinnikov, A.A. and Shamovsky, I.L. (1991). The structure of ferromagnetic phase of carbon. *Journal of Molecular Structure (Theochem)*, **251**, 133–140.

Ovchinnikov, A.A. and Spector, V.N. (1988). Organic ferromagnets – new results. *Synthetic Metals*, **27**, B615–B624.

Park, N., Yoon, M., Berber, S., *et al*. (2003). Magnetism in all-carbon nanostructures with negative gaussian curvature. *Physical Review Letters*, **91**, 237204-1–237204-4.

Peters, R.P., Buchal, C., Kubota, M., *et al*. (1984). Palladium-iron: a giant-moment spin-glass at ultralow temperatures. *Physical Review Letters*, **53**, 1108–1111.

Rao, A.M., Wang, K.A., Holden, J.M., *et al*. (1993a). Photoassisted oxygen doping of C_{60} films. *Journal of Materials Research*, **8**, 2277–2281.

Rao, A.M., Zhou, P., Wang, K.A., *et al*. (1993b). Photoinduced polymerization of solid C_{60} films. *Science*, **259**, 955–957.

Reichart, P., Spemann, D., Hauptner, A., *et al*. (2006). 3d-hydrogen analysis of ferromagnetic microstructures in proton irradiated graphite. *Nuclear Instruments and Methods in Physical Research Section B*, **249**, 286–291.

Rode, A.V., Gamaly, E.G., Christy, A.G., *et al*. (2004). Unconventional magnetism in all-carbon nanofoam. *Physical Review B*, **70**, 054407-1–054407-9.

Ruffieux, R., Gröning, O., Schwaller, P., *et al*. (2000). Hydrogen atoms cause long-range electronic effects on graphite. *Physical Review Letters*, **84**, 4910–4914.

Sharma, M.P., Johnson, L.G. and McClure, J.W. (1974). Diamagnetism of graphite. *Physical Review B*, **9**, 2467–2475.

Shibayama, Y., Sato, H., Enoki, T. and Endo, M. (2000). Disordered magnetism at the metal-insulator threshold in nano-graphite-based carbon materials. *Physical Review Letters*, **84**, 1744–1747.

Shulg'a, Y.M., Boldyrev, A.I. and Ovchinnikov, A.A. (1992). Auger electron spectroscopy and electron energy-loss spectroscopy study of ferromagnetic carbon. *Chemical Physics Letters*, **189**, 577–580.

Spemann, D., Han, K-H., Esquinazi, P., *et al*. (2004). Ferromagnetic microstructures in highly oriented pyrolytic graphite created by high energy proton irradiation. *Nuclear Instruments and Methods in Physical Research Section B*, **219–220**, 886–890.

Spemann, D., Han, K-H., Höhne, R., *et al*. (2003). Evidence for intrinsic weak ferromagnetism in a C_{60} polymer by PIXE and MFM. *Nuclear Instruments and Methods in Physical Research Section B*, **210**, 531–536.

Srdanov, V.I., Stucky, G.D., Lippmaa, E. and Engelhardt, G. (1998). Evidence for an antiferromagnetic transition in a zeolite-supported cubic lattice f centers. *Physical Review Letters*, **80**, 2449–2452.

Takai, K., Oga, M., Aoki, S., *et al*. (2004). Unconventional electronic and magnetic properties of sp^2/sp^3 mixed disordered carbon. In *Proceedings of the Carbon 2004 International Conference*, Calo, J.M. (Ed.), Brown University, p. 63, 11–16 July 2004.

Talyzin, A., Dzwilewski, A., Dubrovinsky, L., *et al*. (2007). Structural and magnetic properties of polymerized C60 with Fe. *European Physical Journal B*, **55**, 57–62.

Tamura, M., Nakazawa, Y., Shiomi, D., *et al*. (1991). Bulk ferromagnetism in the β-phase crystal of the *p*-nitrophenyl nitronyl nitroxide radical. *Chemical Physics Letters*, **186**, 401–404.

Tanabe, T. (1996). Radiation damage of graphite – degradation of material parameters and defect structures. *Physica Scripta*, **T64**, 7–16.

Torrance, J.B., Oostra, S. and Nazzal, A. (1987). A new, simple-model for organic ferromagnetism and the first organic ferromagnet. *Synthetic Metals*, **19**, 709–714.

Turek, P., Nozawa, K., Shiomi, D., *et al*. (1991). Ferromagnetic coupling in a new phase of the *p*-nitrophenyl nitronyl nitroxide radical. *Chemical Physics Letters*, **180**, 327–331.

Tyutyulkov, N. and Bangov, I. (1974). Electronic structure of some hypothetical polymeric nonclassical hydrocarbons. *Comptes Rendus de l'Academie Bulgare des Sciences*, **27**, 1517–1524.

Veciana, J. (2001). *π-Electron Magnetism: From Molecules to Magnetic Materials*, Springer-Verlag: Berlin.

Wallace, P.R. (1947). The band theory of graphite. *Physical Review*, **71**, 622–634.

Wohlers, M., Bauer, A. and Schlögl, R. (1997). Oxidation of fullerene materials. *Mikrochimica Acta*, **14**, 267–270.

Wood, R.A., Lewis, M.H., Lees, M.R., *et al*. (2002). Ferromagnetic fullerene. *Journal of Physics: Condensed Matter*, **14**, L385–L391.

Ziegler, J.F. (1977–1985). *The Stopping and Range of Ions in Matter*, Pergamon Press: New York.

Magnetic Ultrathin Films

Bretislav Heinrich and John Francis Cochran
Simon Fraser University, Burnaby, British Columbia, Canada

1 THIN-FILM GROWTH

Ultrathin magnetic films have been extensively investigated since early 1980. In ultrathin films the interfaces play a crucial role. In ultrathin structures, the exchange energy between electrons maintains the same orientation of the atomic magnetic moments across the film. The magnetic properties of interface atoms are often different from those in the bulk. These properties in ultrathin films are shared by the atoms inside the film because of the very strong exchange forces. As a result, ultrathin films behave like giant magnetic molecules that are characterized by unique magnetic properties absent in the bulk. In order to fully benefit from the unique behavior of interface atoms on thin-film magnetic properties, one is compelled to prepare ultrathin-film structures having the best possible quality of interfaces. The deposition of the film material on a suitable substrate is usually carried out close to room temperature (RT) where the film growth is controlled by the interplay of thermodynamics and kinetics. The atomic layers are formed by nucleation of flat atomic islands and the deposited atoms are incorporated into these islands by surface diffusion. However, this is a nonequilibrium kinetic process that affects the growth mode. In general, one can say that perfect interfaces cannot be achieved, but by choosing suitable growth conditions one can create ultrathin-film structures in which the interfaces have a dominant effect. In fact, a reasonable degree of interface roughness can result in novel magnetic properties which would be absent in structures having perfect interfaces. In the following, we will demonstrate the wealth and depth of studies obtained by using ultrathin-film homoepitaxial and heteroepitaxial structures grown in a quasi layer by layer mode where the interface roughness is mainly limited to a few atomic layers.

The growth of ultrathin metallic structures has been mainly carried out using three major deposition techniques: thermal deposition (TD), laser pulse deposition (LPD), and sputtering.

1.1 Thermal deposition (TD)

Deposition rates are usually between 1 and 10 atomic layers/min. That slow rate automatically requires that the growth be carried out in stringent ultrahigh vacuum (UHV) conditions: a vacuum pressure lower than a few times 10^{-10} Torr is a necessity which can't be compromised. Interface diffusion and segregation usually limits the substrate temperatures to the vicinity of 300–400 K, but in some cases one has to resort to the use of cryogenic substrate temperatures at the initial stages of the growth. In that case, it has been found useful to eventually increase the substrate temperature to the highest allowable temperature in order to avoid excessive lattice defects, achieve large atomic terraces, and improve the overall interface roughness. One has to realize that interface diffusion and intermixing are characterized by significantly lower energy barriers compared with the bulk.

Handbook of Magnetism and Advanced Magnetic Materials. Edited by Helmut Kronmüller and Stuart Parkin. Volume 4: *Novel Materials*. ISBN: 978-0-470-02217-7.

Therefore once several atomic layers have been deposited the substrate temperature can be increased without having an adverse effect on the interface quality. There are no universal rules to follow. It depends on the individual substrates and deposited films. It is crucial to be able to follow the film growth *in situ* by means of some surface science techniques. Scanning tunneling microscopy (STM), reflection high-energy electron diffraction (RHEED), low-energy electron diffraction (LEED), angular resolved Auger electron spectroscopies (ARAES), and X-ray photoelectron spectroscopies (XPS) are most commonly employed as *in situ* UHV tools. The growth of heteroepitaxial structures can be affected by a number of problems related to interface thermodynamics and lattice mismatch.

1.1.1 Surface segregation and interdiffusion

Surface segregation can be important in the growth of heteroepitaxial structures especially at elevated temperatures. It is often thought that alloys like CoCu or FeAu are not formed naturally because their heats of alloying is endothermic. This does not necessarily apply to surfaces. In many cases, the thermodynamics favors surface segregation (mixing of film and substrate atoms) on a low surface free energy substrate and as a result metastable alloys can be formed (Steigerwald, Jacobs and Egelhoff, 1988). The effect of segregation was nicely demonstrated by Egelhoff (1989) using Ni grown on a Cu(001) substrate. Rapid segregation was observed at 450 K. Bulk diffusion was not possible at these temperatures. A lattice site hop via the vacancy mechanism would happen on a timescale of 10^7 years at 450 K. The Cu/Ni interface provides a much lower activation energy allowing an effective segregation of Cu on the top of the deposited Ni film (Egelhoff, 1994a). A possible process is exchange diffusion often referred to as the place-exchange atomic mechanism. In this process, surface diffusion proceeds by the combined motion of an adatom moving down into the substrate surface at the same time that a substrate surface atom moves up to form a new film atom (Chambliss, Wilson and Ching, 1992; Grass, 2003). Interface exchange diffusion can dramatically affect the magnetic properties. A typical example is an Fe-whisker/Cr/Fe(001) structure which has played a crucial role in the study of exchange coupling between two ferromagnets separated by a spin density wave (SDW) Cr(001) layer. Scanning electron microscopy with polarization analysis (SEMPA) (Unguris, Celotta and Pierce, 1991; Unguris, Celotta and Pierce, 1992) and magneto-optic Kerr effect (MOKE) measurements (Purcell *et al.*, 1991) showed that the exchange coupling oscillates with the thickness of the Cr film with a short-wavelength period of $\sim$2 atomic layers. Heinrich and coworkers have carried out quantitative studies (Heinrich and Cochran, 1993; Heinrich, Cochran, Monchesky and Urban, 1999). They found that the coupling is extremely sensitive to small variations in the growth conditions. In addition it was also established that the phase of the coupling in this system was shifted by 180°. The bilinear exchange coupling strength was found to oscillate between ferromagnetic and antiferromagnetic for an even and odd number of the Cr atomic layers. This is exactly opposite to that expected for a SDW in Cr(001). This study showed that the strength of the bilinear coupling constant J_1 was very sensitive to the initial growth conditions: a lower initial substrate temperature resulted in a larger exchange coupling strength. This behavior indicated that the atomic formation of the Cr layer is more complex than had been previously acknowledged. ARAES (Venus and Heinrich, 1996), STM (Davis, Stroscio, Pierce and Celotta, 1996), and proton induced AES (Pfandzelter, Igel and Winter, 1996) have shown that the formation of the Fe/Cr(001) interface is strongly affected by an interface exchange atom diffusion. The ARAES studies showed that interface alloying during the growth starts at the low temperature of 100 °C. Interface alloying increases with increasing temperature. It is driven by the difference in binding energies between the substrate and the adatoms. Interface alloying has been observed in those systems for which the substrates have a lower melting point than the adatom solids. Therefore this effect is not symmetric. It happens at the Fe/Cr interface but it is absent at the Cr/Fe(001) interface (Heinrich, Cochran, Monchesky and Urban, 1999). Freyss, Stoeffler and Dreysse (1997) used a tight-binding d-band Hamiltonian to show that the interface alloying indeed results in the reversal of the phase of the bilinear exchange coupling in agreement with the experimental studies. The interface roughness of Fe/Cr/Fe(001) and Fe/Cr(001) structures has a profound effect on the SDW even in thick Cr layers. In Fe/Cr/Cr(001) superlattices grown on MgO(001) substrates (Fullerton, Bader and Robertson, 1996), the neutron scattering data have shown that the transverse SDW (with the magnetic moment parallel to the film and the single Q wave vector oriented perpendicular to the layers) orders symmetrically in the Cr layers with the nodes near the Fe–Cr interfaces. This is in agreement with the Stoeffler and Gautier theoretical calculations (Stoeffler and Gautier, 1995) showing that the magnetic moment in Cr is primarily stabilized by SDW order. The magnetic moment in Cr can be easily decreased, even quenched, by interface disorder. The SDW in Cr depends strongly on the degree of interface roughness. Cr(001) films grown on $(1\bar{1}02)$ oriented Al_2O_3 substrates having a Nb(001) buffer layer (Boedeker, Schreuer and Zabel, 1999) and covered by an Fe(001) layer showed a different behavior. For thicknesses less than 25 nm a transverse incommensurate SDW with the magnetic moment of Cr perpendicular to the film was

observed. In this case, the interface disorder was accommodated by orienting the magnetic moment of the Cr atoms perpendicular to the in-plane Fe magnetic moments. There is no preference for the Cr moments to be parallel or antiparallel to the surrounding Fe atomic moments. Commensurate SDWs were obtained by limiting the Cr thickness to values less than the SDW wavelength, see further details in Boedeker, Schreuer and Zabel (1999).

1.1.2 Surfactants in epitaxy

An absorbate can modify the balance of surface and interface free energies and can have a pronounced effect on surface morphology. That was nicely demonstrated by the Egelhoff and Chambliss groups (Steigerwald, Jacobs and Egelhoff, 1988; Chambliss, Wilson and Ching, 1992). Transition metals (TMs) such as Fe and Ni have the tendency to conglomerate and intermix on Cu(001) substrates. An absorbate such as oxygen forms stronger bonds with Fe and Ni than with Cu. This significantly decreases the TM surface energy and leads to an appreciable reshuffling of the Ni and Fe atoms resulting in a flattening of the Fe, Ni/vacuum interface (Egelhoff, 1994b). Egelhoff *et al*. (1997) have used oxygen as a surfactant in the growth of Co/Cu/Co spin valve structures. Their spin valve structures were fabricated using sputtering (see Section 1.3 below). Single Co/Cu/Co specimens grown on a NiO substrate in 2 mTorr of Ar, oxygen free, exhibited a giant magnetoresistance (GMR) effect of 14%: Egelhoff *et al*. refer to this structure as a 'bottom spin valve'. Bottom spin valves grown in an atmosphere of 2 mTorr Ar plus 5×10^{-9} Torr of oxygen exhibited an increase in GMR from 14 to 19%. This increase in GMR is thought to be due to the growth of smoother Co/Cu interfaces resulting in an increased specular scattering of the conduction electrons at those interfaces. The GMR effect could be further increased by postgrowth oxidation of the top Co layer. A surface film of oxidized Co led to a smoother Co/CoO interface which further increased the level of specular scattering of electrons. The Egelhoff *et al*. procedure (Egelhoff *et al*., 1997), considerably increased the efficiency of GMR sensors and has become a part of the processing steps for commercially made spin valve sensors.

Not all surfactants lead to smooth interfaces. Fe films grown on GaAs(001) substrates are known to incorporate approximately 0.6 monolayer (ML) of As as a surfactant. This limits the size of Fe terraces to 3 nm. In this particular case the As likes to become attached to the Fe atomic steps. In fact, the As floats on the top of metallic layers deposited over the Fe films. The surface reconstruction of Au(001) (grown on Fe(001)) is 2×2 instead of the well-known 5×1 reconstruction of a clean Au(001) surface, see Figure 1. STM images have shown that the Au terraces are

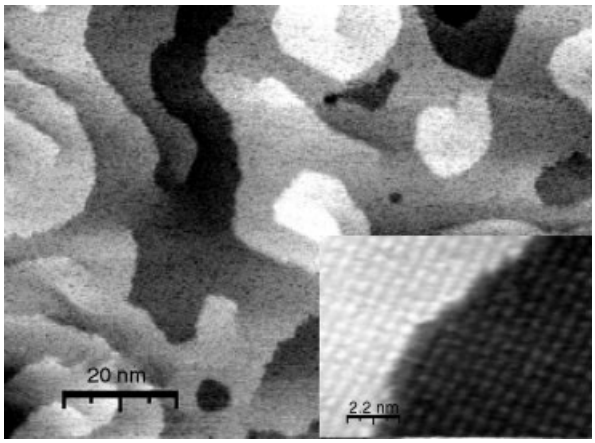

Figure 1. STM image of the top Au(001) layer in a GaAs/Fe/Au(001) structure prepared by thermal deposition. Lower right inset: Note that the Au(001) film has a 2×2 surface reconstruction. This reconstruction is triggered by surfactant As. Notice that the atomic terraces are rounded and decorated by 2×2 atomic kinks.

not of a rectangular shape as is the case of a clean Au surface, but are rounded and are terminated by a high density of atomic kinks consisting of 2×2 Au atoms: the surface of the 5×1 reconstruction consists of rectangular shaped terraces. (Recent measurements carried out together with the Max Planck Institute, Halle, and the Technical University, Krakow.) A well-known 5×1 reconstruction of Au(001) was observed in GaAs/Fe/Au(001) structures prepared by LPD, see Figure 2. This suggests that LPD does not allow surfactant As to float on the top of the metallic layers.

It was found possible to increase the size of atomic terraces of Fe grown on GaAs(001) by removing the surfactant As by sputtering using grazing incidence 500 eV Ar^+ ions. Subsequent annealing and the growth of Fe at 200 °C markedly improved the film conductivity (Monchesky *et al*., 1999). This indicated that the removal of As and subsequent annealing and growth at 200 °C repaired the defects created by the sputtering and improved the surface smoothness: this resulted in a greater specular electron reflectivity at the Fe/vacuum interface (Enders *et al*., 2001).

1.1.3 Lattice strain

In heteroepitaxy the lattice mismatch can be significant and can result in ordered structural defects which can profoundly modify the magnetic properties of ultrathin-film structures.

Pd/Fe(001)

A typical example is Pd grown on Fe(001) templates. Because of a high density of states at the Fermi surface, the magnetic properties of Pd are sensitive to structural changes. Several authors have predicted the onset of ferromagnetism

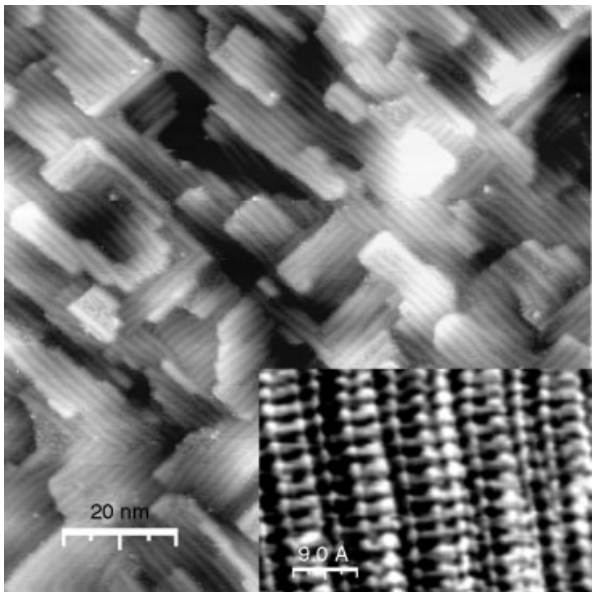

Figure 2. STM image of the top Au(001) layer in a GaAs/Fe/Au(001) structure prepared by laser pulse deposition (LPD). The STM image corresponds to a well-known 5×1 reconstruction of a clean Au(001) surface. The Au(001) surface is terminated by a corrugated atomic (111) plane, see the lower right inset. Notice that the atomic terraces are square shaped with the atomic steps oriented along the ⟨110⟩ crystallographic directions.

in fcc Pd having a lattice expanded by 6% (Moruzzi and Marcus, 1989a,b). Molecular beam epitaxy (MBE) makes it possible to explore the interplay of structure and magnetism in ultrathin Pd layers by creating metastable phases and manipulating the atomic structure via epitaxial strain. In the Fe/Pd(001) system, the lattice strain results from the 4.2% mismatch between the bcc Fe(001) and the Pd(001) surface nets. Ultrathin Pd(001) films grown on Fe(001) are expanded laterally to match the Fe mesh (Celinski *et al*., 1990). The structure and magnetism of Pd in Fe/Pd/Fe (001) trilayers grown on Ag(001) substrates were studied in Celinski *et al*. (1990). The main result of the magnetic measurements was that the Pd was ferromagnetic only for two adjacent Pd atomic layers at the Fe/Pd and Pd/Fe interfaces. By increasing the thickness of Pd by one additional atomic layer (a total thickness of 5 ML) the long-range ferromagnetic order in Pd was lost. Using RHEED and X-ray diffraction it could be shown that the Pd ultrathin films grew on Fe(001) with a 4.2% latterly expanded lattice accompanied by an out-of-plane contraction of 7.2% ($c/a = 0.89$). The ultrathin films of Pd grown on Fe(001) had a pronounced face-centered tetragonal (fct) structure (Fullerton *et al*., 1995). Theoretical *ab initio* studies of the interfacial structure showed that the structural ground state of the epitaxially strained Pd layer was well described by a fct structure which maintained the bulk Pd atomic volume (Fullerton *et al*., 1995). This was in agreement with the results of RHEED and X-ray diffraction measurements.

Ab initio theoretical studies of Fe_3Pd_n superlattices (where n is the number of Pd atomic layers) with fct Pd found that indeed the first two atomic layers of Pd at the Fe/Pd and Pd/Fe interfaces are ferromagnetic but the magnetic moment in the third atomic layers abruptly disappears (Fullerton *et al*., 1995). The spin polarization in Pd is mainly induced by the Fe moments and does not have an intrinsic character. The magnetic moment in the Pd atomic layer adjacent to Fe was found to be 0.29 Bohr magnetons (μ_B). Polarized neutron reflectivity results on an Fe(5.6 ML)/Pd(7 ML)/Au(20 ML) sample determined the average moment per Fe atom to be $2.66\,\mu_B$ (Fullerton *et al*., 1995). Calculations for the same structure showed that this value is consistent with the observed induced Pd polarization. It is interesting to point out that metallic fcc Pd having a lattice expansion of 4.2% would result in long-range ferromagnetic order (Fullerton *et al*., 1995). Clearly the lattice vertical relaxation has to be taken into account in order to explain the real magnetic properties of strained epitaxial structures.

Lattice strain is eventually relaxed by the introduction of a network of misfit dislocations. Crystalline Au/Pd/Fe(001) and Au/Fe/Pd/Fe(001) epitaxial layers grown on GaAs(001) represent typical cases. Pd has a lateral lattice mismatch of 4.2% with respect to the Fe(001) and 4.9% with respect to the Au(001) atomic meshes, and therefore samples with a sufficiently thick Pd layer are influenced by the presence of lattice strain induced defects. Using plan view transmission electron microscopy (TEM), (Woltersdorf, Heinrich, Woltersdorf and Scholz, 2004), a self-assembled network of misfit dislocations was found to be oriented along the ⟨100⟩ crystallographic axes of Fe, see Figure 3.

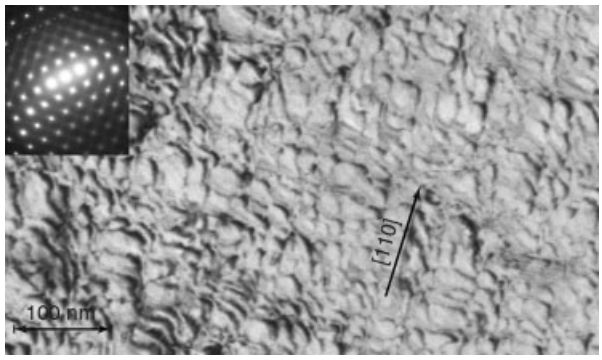

Figure 3. Plan view TEM image of the 90Au/9Pd/16Fe/GaAs(001) sample exposing the misfit dislocation network (Woltersdorf, Heinrich, Woltersdorf and Scholz, 2004). The upper left inset shows the corresponding diffraction pattern. The fourfold symmetry of defects is evident in the presence of reciprocal sheets. The mean separation between dislocation lines was ∼15 nm. (Reprinted with permission B. Heinrich *et al*., copyright 2004, American Physical Society.)

The onset of a rectangular network of misfit dislocations resulted in a strong extrinsic magnetic damping. This damping could be described by a two-magnon scattering process (Woltersdorf, Heinrich, Woltersdorf and Scholz, 2004; Woltersdorf and Heinrich, 2004). The lattice defects associated with misfit dislocation slip planes created a rectangular network of uniaxial anisotropies having an overall fourfold in-plane symmetry oriented along the ⟨100⟩ axes of the Fe(001) template. No overall average uniaxial anisotropy was observed indicating that the distribution of the uniaxial anisotropies along the misfit dislocation slip planes was highly symmetric. Due to inhomogeneities in the induced in-plane network of uniaxial anisotropies the ferromagnetic resonance (FMR) linewidth exhibited a strong fourfold angular dependence on the direction of the saturation magnetization with respect to the Fe crystallographic axes. The maximum two-magnon scattering occurred with the magnetization directed along the ⟨100⟩ axes, while the two-magnon scattering contribution was absent when the magnetization was directed along the ⟨110⟩ axes.

An angular dependent extrinsic damping created by a rectangular network of defects appears to be a common phenomenon.

Ni/Fe and Heusler alloy films

The creation of a network of lattice defects satisfying the in-plane crystalline fourfold symmetry has also been observed in metastable bcc Ni/Fe(001) bilayers grown on Ag(001) substrates (Heinrich *et al*., 1988), Fe(001) films grown on bcc Cu(001) (Celinski and Heinrich, 1991), and in Fe/V superlattices (Lindner *et al*., 2003). After depositing 3 ML of Ni on Fe(001) to form a Ni/Fe(001) bilayer the bcc Ni went through a major structural change. Mijiritskii *et al*. (1998), showed that the Ni underwent a bcc to fcc martensitic transition creating a mosaic of four fcc Ni domains with the fcc Ni{110} planes parallel with the bcc Fe{110} planes and the Ni⟨211⟩ crystallographic directions along the Fe⟨110⟩ axes. The lattice defects created by the martensitic transition again resulted in local anisotropies having the overall symmetry of the Fe(001) template (Lindner *et al*., 2003). This resulted in two strong magnetic effects: firstly, an additional average in-plane fourfold anisotropy field in Ni/Fe, $2K/M_s$, was created and exceeded the cubic anisotropy field of the bulk Fe by nearly an order of magnitude. Secondly, the inhomogeneous part of the magnetic anisotropy resulted in a strong extrinsic damping with the damping maxima occurring when the magnetization was directed along ⟨110⟩ and the damping minima occurring when the magnetization was directed along the ⟨100⟩ crystallographic axes of the Fe. Coercive fields of several hundred oersted were observed due to the enhanced anisotropy and lattice defects (Heinrich *et al*., 1993; Przybylski *et al*., 2002).

A similar situation occurs for semimetals. Half-Heusler compound NiMnSb(001) films were grown in UHV, MBE, on (In,Ga)As/InP (001) wafers for possible applications in spin injection devices, (Bach *et al*., 2003). A quasicontinuous network of defects closely aligned with the ⟨100⟩ in-plane directions (Koveshnikov *et al*., 2005) resulted in strong two-magnon scattering which led to an extrinsic magnetic damping exceeding the intrinsic damping by two orders of magnitude (Heinrich *et al*., 2004). The ability to control the damping by means of a network of misfit dislocations could be attractive to promote a fast convergence to the steady state of magnetic memory pixels where the rotation of the magnetic moment in the time domain is of the order of nanoseconds.

Fe/MgO

The role of lattice mismatch and chemistry at interfaces is exemplified by the growth of MgO on Fe(001). The growth of high quality crystalline layers of MgO on Fe is attractive for use in Fe/MgO/Fe(001) spin polarized tunneling junctions (Klaua *et al*., 2001). It also represents an interesting case of interface formation involving a TM (Fe), and an oxide (MgO) having a large tunneling barrier. The structural studies were particularly simplified by using perfect Fe whiskers for substrates: the Fe whiskers were prepared by chemical vapor deposition (CVD). Single-crystal Fe(001) discs were also used. The MgO layers were deposited on a substrate at 295 K using electron beam evaporation. MgO grows pseudomorphically on Fe(001) for thicknesses up to 6 ML with the epitaxial relationship of Fe(001)[110]/MgO(001)[100] and a 3.8% compression of the MgO lattice. A partial lattice relaxation sets in for MgO films thicker than 6 ML, resulting in an increased lattice spacing. The most convincing indication of the pseudomorphic growth and subsequent sharp onset of misfit dislocations can be seen in the LEED patterns.

The LEED and RHEED spots were very sharp on a clean bcc Fe(001) whisker indicating a superb surface quality. Similar sharp spots were observed from the MgO(001) surface after the growth of 6 ML of MgO. For thicknesses greater than 7 ML the MgO LEED pattern showed four additional satellite spots around each main MgO diffraction spot, see Figure 4. The four lines connecting any given set of satellite spots and their central diffraction spot were directed along equivalent ⟨100⟩ in-plane crystallographic directions of the MgO lattice. This splitting decreased with increasing thickness of MgO. This behavior can be explained using a model which includes edge dislocation formation at the Fe/MgO interface. The MgO lattice warps in a narrow region above the misfit dislocation lines. The warped surfaces created tilted reciprocal-space rods which satisfied the fourfold in-plane symmetry of the Fe(001) template. The LEED satellite

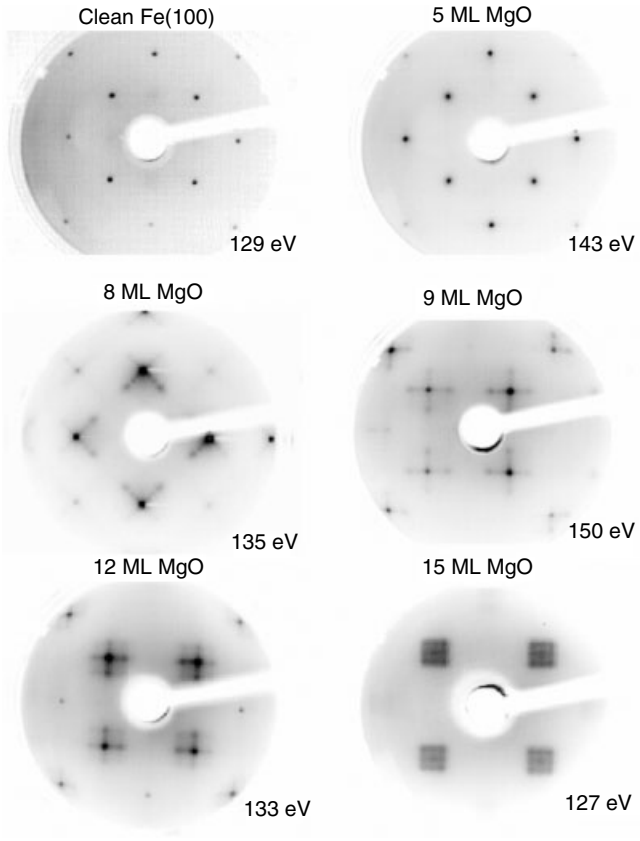

Figure 4. LEED patterns of MgO(001) films grown on a nearly perfect Fe(001) whisker template (prepared by chemical vapor deposition). Notice that the MgO(001) starts to grow with the lattice spacing of Fe and having nearly perfect LEED diffraction spots like those of the Fe(001) whisker. At 8 ML the MgO(001) partly releases its lattice strain (compression) by creating a network of misfit dislocations. The dislocation glide planes result in surface corrugations leading to inclined reciprocal rods. Each main diffraction spot is surrounded by four satellite spots reflecting the fourfold symmetry of the Fe(001) template, see the text. Notice that the satellite spots decrease their separation with increasing thickness of the MgO film which indicates that the core of the dislocation network remains confined to the Fe/MgO(001) interface.

spots were caused by the tilted reciprocal-space rods. STM images revealed nearly perfect layer-by-layer growth. Electron diffraction and STM studies revealed an overall surface topography and orientation but they did not provide one with details of the chemistry at the Fe/MgO interface. *Ab initio* calculations by Butler, Zhanh, Schulthess and MacClaren (2001) for Fe/MgO/Fe(001) trilayers have provided evidence for the importance of lattice perfection at the Fe/MgO interface. They showed that tunneling magnetoresistance (TMR) can become as large as several 1000% due to a strongly peaked conductance in the majority channel for a parallel alignment of the Fe magnetic moments, while the minority channel conductance is dominated by interface states. Clearly the transmission magnetoresistance, the TMR ratio, will be strongly affected by the chemistry and lattice configuration at the Fe/MgO interface. Meyerheim *et al*. have addressed this question by using surface X-ray diffraction (SXRD) measurements (Meyerheim *et al*., 2001). They found that, contrary to common belief, MgO is not formed in direct contact with the Fe. They found that a FeO interface layer is formed between the Fe substrate and the growing MgO layer, see Figure 5. This oxide layer clearly must affect the formation of interface states and the corresponding TMR ratio.

The Fe-whisker/MgO/Fe/Au(001) structure provided an ideal opportunity to investigate tunneling through a nearly perfect crystalline tunneling junction. The tunneling in Fe-whisker/MgO and Fe-whisker/MgO/Fe/Au(001) structures was investigated by means of an STM tip (Klaua *et al*., 2001). The tunneling *I–V* characteristics were found to be very asymmetric. For a negative bias no tunneling current was observed due to the large tunneling barrier in MgO. The *I–V* curves for a positive bias showed an abrupt increase in the tunneling current when the Fermi level of the STM tip was lined up with the conduction band states of MgO. In fact in that way it was possible to determine the potential barrier of the Fe/MgO/Fe system. For 2 ML of MgO the tunneling barrier was already 2.5 eV. The tunneling barrier reached the bulk value of 3.5 eV at an MgO thickness of 5 ML. The relationship between the MgO layer thickness and the electron transport

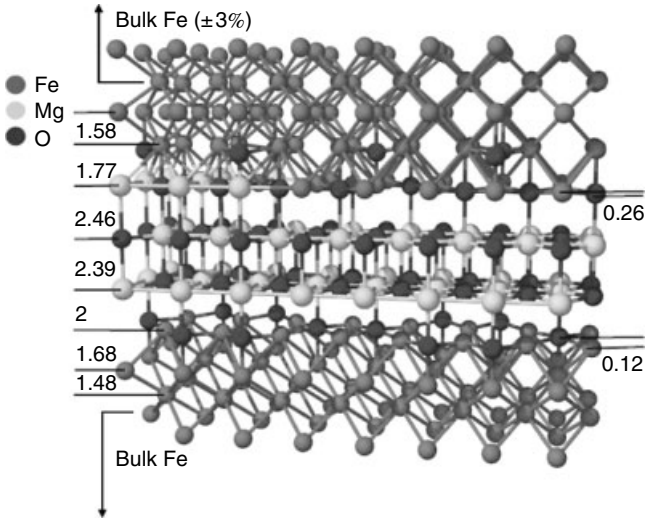

Figure 5. A model of atomic layers of a crystalline Fe/MgO/Fe(001) structure prepared on a Fe(001) whisker. This model was obtained by interpreting the surface X-ray diffraction (SXRD) measurements, see Meyerheim *et al*. (2001). Notice that the first oxide layer is mostly FeO with the oxygen atoms located on the fourfold hollow sites of the top Fe(001) atomic layer. The integers on the left side describe the interplanar distances in angstroms. (Reprinted with permission Meyerheim *et al*., copyright 2001, American Physical Society.)

through the MgO layers was obtained by taking STM topographic images and acquiring tunneling *I–V* characteristics simultaneously. These images showed that the tunnel barriers were homogeneous across a large area of the sample, and they revealed a low density of localized defects (a few nanometers across) that correlated neither with substrate steps nor with misfit dislocations. These defects were most likely caused by localized defect states located midway between the valence and conduction bands of MgO (Klaua *et al*., 2001). The same *I–V* images were obtained for the Fe/MgO and the Fe/MgO/Fe/Au samples. Both samples exhibited mainly perfect tunneling characteristics and a low density of localized defects. This was an important observation. It can be concluded that the electron transport in high quality crystalline MgO tunneling junctions proceeds by ballistic tunneling.

The magnetization behavior of single crystalline Fe-whisker/20MgO/20Fe/20Au(001) films was investigated by depth-selective Kerr microscopy (Schaefer *et al*., 2002). No magnetic coupling through the MgO was observed. It was demonstrated that a moving 180° whisker domain wall acts on the Fe film by writing domains in the film that are magnetized transverse to the wall direction. The sign of the transverse domains depends on the internal rotation sense of the whisker wall, not on its surface rotation. The change in sign of the transverse domains was always accompanied by a Bloch line. This clearly indicated that the residual fringing fields emerging from the whisker wall must be responsible for the interaction. The sign of these fringing fields depends on the internal rotation alignment of the whisker wall.

Fe/GaAs

The importance of growth of metallic structures on semiconductor substrates has been realized right at the advent of MBE studies of 3d TM elements. The early development in this field is well described in Prinz (1994). The Fe/GaAs(001) interfaces became very attractive for spintronics devices using electrical spin injection into semiconductors. See review chapters on Spin-Light Emitting Diodes (SLED) by Jonker (2005) and Optical Studies of Electron Spin Transmission by Bland, Steinmueller, Hirohata and Taniyama (2005). The magnetic properties of GaAs/Fe(001) will be further discussed in Section 2.5. The Naval research laboratory (NRL) group has carried out extensive studies of GaAs/Fe(001) and GaAs/AlGaAs/Fe(001) interfaces. They were able to find plausible Fe/AlGaAs(001) interface structures (Zega *et al*., 2006) by employing high-angle annular-dark-field (HAADF) imaging, the highest resolution chemically sensitive TEM technique. The results were interpreted by means of using computer simulations based on density-functional theory. It was found that the Fe films grown at the substrate temperature of 10–15 °C results in a structurally disordered Fe_3GaAs compound interface that is about 5 atomic layers in thickness. By means of low temperature annealing at 200 °C the interface becomes ordered and coherent with intermixing of the Fe and AlGaAs occurring on a single atomic plane. This marked improvement in the interface structure results in an appreciable increase in spin injection polarization going from 18% for grown samples to 25% for annealed samples. The interface structure strongly affects carrier lifetimes and perfectness of Schottky barriers. The Fe films grown at 175 °C on a GaAs(001) template terminated by an As rich 2×4 reconstruction resulted in an appreciable enhancement of carrier lifetimes and a decrease in the density of midgap states (depinning of the Fermi level) compared to the Fe films grown on S-passivated, AlGaAs, and native oxide GaAs(001) templates (Jonker, Glembocki, Holm and Wagner, 1997). The STM study of a submonolayer growth of Fe on a (2×6) reconstructed GaAs(001) template was carried out by Ionescu *et al*. (2005). The (2×6) reconstruction is a Ga-rich As terminated surface. They have shown that in the early stages the growth of Fe clusters mainly occurs atop the As-dimer rows. At 0.3 ML of Fe a transition from the 3D cluster growth to a 2D island nucleation takes place. At 1 ML the coalescence of several islands leads to a large distribution of island sizes and decreased island density. The STM images indicated that during deposition some of the Fe penetrates into the GaAs(001) substrate. Fe atoms substitute for Ga atoms in the second layer displacing them into an interstitial position. In addition, it is suggested that the Fe atoms inside the top As layer together with the top Fe layer form Fe_2As antiferromagnetic compound seed crystals for the bcc Fe growth. The following Fe growth is GaAs(001)‖Fe_2As(001)‖Fe(001) and within the plane GaAs[110]‖Fe_2As[100]‖Fe[110]. The substitution of Ga atoms by Fe is in agreement with the recent Mössbauer studies (Kardasz *et al*., 2007). A low hyperfine field component was found in the TD Fe films on GaAs(001) − (2×6). The low hyperfine field (0.65 T) component corresponds to approximately 6% of the relative intensity.

1.2 Laser pulse deposition (LPD)

LPD turned out to be particularly useful for the growth of high T_c material compounds (Chrisey and Hueber, 1994). The main advantage of this method is that any material can be deposited, and the stoichiometry of any material is preserved. It turns out that the popular view is not always true. In magnetically doped TM oxides, such as Co-doped TiO_2, when the film composition has been independently measured, it has been found to be different from that in the target. In the LPD method repeatable short pulses from a high-power laser impinge on the surface of a target material. The evaporation takes place within the very short time of

a few nanoseconds. The material does not melt but it is ablated. The resulting vapor consists mostly of atoms and dimers. The laser pulse is usually longer than the time required for evaporation and this results in absorption of the light by the vapor. The absorption of light leads to ionization of the evaporated atoms and the formation of a visible so-called plasma plume which expands toward the target. The evaporated material in the plasma reaches an energy of $\sim$1 eV, much higher than that obtained by thermal evaporation. A recoil plasma plume and target macroscopic and microscopic surface irregularities after repeated exposure to high-energy laser pulses lead to the so-called splashing in which particles and droplets are deposited on the substrate. The particles and droplets are of the order of a micron in size and are absolutely undesirable in the growth of ultrathin films. There are a number of modifications of the LPD system that allow one to minimize the effect of splashing (Gavignan, 1991; Holzapfel *et al*., 1996). Generally a large distance between the target and the substrate, rotation of the target during deposition, and keeping the laser power slightly above the ablation threshold help to minimize the role of splashing (Jenniches *et al*., 1999).

The LPD average deposition rate is not high: usually a fraction of a monolayers per minute, similar, but even lower than the deposition rate for TD films. However, during the laser pulse the evaporation rate is very high and one obtains the so-called instantaneous deposition (Cheung and Sankur, 1988). The deposition rate during the pulse can be in the range of 10^4 ML s^{-1} which is 6–7 orders of magnitude higher than the deposition rate associated with TD (Jenniches *et al*., 1999). This large deposition rate leads to a substantial increase in the density of condensation nuclei compared with TD. After applying the laser pulse the atoms in the plasma plume are deposited over a period of the order of 1 μs, the duration time of the plasma plume. This leads to a very high rate of deposition. Each laser pulse deposits between 10^{-3} and 10^{-2} ML of atoms/μs. It is known that the number of nuclei scales with the flux as $(F/D)^c$, where F is the flux, D is the diffusion constant, and $c \sim 0.5$ (Villain, Pimpinelli and Wolf, 1992). Therefore during the first laser pulse a significantly larger density of nuclei is formed than is established during TD. Small critical nuclei consist only of two atoms. After the next laser pulse the burst of deposited single atoms is available to participate in the growth. Between laser pulses the deposited adatoms have time to diffuse and to become attached to the closely spaced nuclei. In this way a full atomic layer is slowly filled. In TD the deposition is continuous and the flux is 6–7 orders of magnitude smaller than that obtained using LPD. This means that the density of TD nuclei is much lower. The nuclei are larger and more separated. The deposited atoms have a much longer time to get attached to existing nuclei than is the case for LPD. This can profoundly affect the growth of structures where it can be expected that a fast incorporation of atoms into a continuous layer is important for maintaining a metastable structure.

Jenniches *et al*. (1999) found that using LPD one can grow metastable fcc Fe(001) on Cu(001) layer by layer up to 10 ML. The growth was carried out at RT. The fcc Fe(001) films thicker than 10 ML underwent a phase transition to bcc Fe. Fcc Fe forms a high magnetic moment state that increases with thickness up to 3 ML. Between 5 and 7 ML the film experiences an inverse spin reorientation from a magnetization oriented in plane to an out-of-plane magnetization orientation in which the easy axis is perpendicular to the film plane. The TD films showed no layer-by-layer growth for the first 2 ML: a layer-by-layer growth appeared only after an average thickness of 2 ML. The LPD films grew in the fcc structure, whereas the TD films grow in a fct structure. The LPD films have the lattice constant of Cu in both directions. The fct films were found to be unstable with increasing temperature (Zharnikov *et al*., 1997), while the LPD films were found to be stable. Improved morphology and structure for films grown by LPD was also observed in the growth of Fe(111) on a Cu(111) substrate. The deposition was carried out at 220 K in order to eliminate a significant interdiffusion of Cu and Fe. Two monolayers thick Fe/Cu(111) films grown by TD exhibited a conglomerated structure where the surface coverage ranged from 0 to 5 ML with a considerable presence of ridgelike features (Ohresser *et al*., 1999). TD deposited films of Fe on Cu(001) had a critical thickness of 3 ML for the fcc to bcc lattice transformation. The LPD films grew with a better structural quality than the TD grown films. In the low thickness range, 3 ML, the LPD films have a long-range order and a large magnetic moment while the TD films have a short range order and low magnetic moment (Ohresser *et al*., 1999).

LPD is not always a winner. The bcc Fe(001) films grown by TD on a GaAs(001) substrate exhibit a smoother GaAs/Fe interface than those grown by LPD. Mössbauer studies have shown that the LPD films have a high degree of Fe incorporated into the GaAs while the TD films incorporated only a small amount of Fe into the GaAs substrate and these incorporated atoms exhibited a small hyperfine field (Kardasz *et al*., 2007). The rough Fe/GaAs interface obtained using LPD is most likely caused by the high kinetic energy of the LPD atoms. Layer-by-layer growth is only observed using TD, but the average size of terraces is similar in the LPD and TD grown films. The interface magnetic properties are profoundly affected by the method of deposition. The LPD deposited films exhibit nearly zero in-plane uniaxial anisotropy, whereas the TD deposited films exhibit a large uniaxial anisotropy of 1 KOe for Fe(001) films 10 ML thick (Monchesky *et al*., 1999).

1.3 Magnetron sputtering

Sputtering differs from MBE growth techniques due to the difference in the kinetic energy of the deposited atoms. The energy of the sputtered atoms depends on many factors (Eric E. Fullerton private communication). It depends on the relative potential of the target, the masses of the sputtering gas, target atoms, the product of the gas pressure and the target-to-substrate distance. The latter is particularly important because the sputter gas thermalizes the sputtered atoms. The greater the gas pressure and/or target-to-substrate distance the more the atoms are thermalized and can be characterized by a temperature that approaches ambient temperature, see Schuller and Falco (1981), Fullerton (1993), and Windischmann (1992). The energy of the adatoms impinging on a substrate in sputtering can have a profound effect on the deposited film morphology. Crystalline TM films, rare-earth (RE) and oxide epitaxial layers have been grown using sputtering in which the sputtered atoms are deposited on epitaxial buffer layers grown on single-crystal substrates. Epitaxial crystalline films prepared by the use of sputtering include Fe (Yaegashi, Kurihara and Segawa, 1993; Fuke, Sawabe and Mizoguchi, 1993; Fullerton *et al*., 1993; Mattson, Fullerton, Sowers and Bader, 1995); Pt and FePt (Lairson *et al*., 1992; Lairson, Visokay, Sinclair and Clements, 1993); Co (Morawe *et al*., 1991); Cu (Giron *et al*., 1993); $SmFe_{12}$, Sm_2Co_7, Sm_2Co_{17} (Fullerton, Sowers, Pearson and Bader, 1997) and MgO (Park, Fullerton and Bader, 1995).

MgO(111), MgO(110), and MgO(001) substrates have been employed to grow different orientations of the bcc TMs Nb, Mo, Fe, and Cr (Mattson, Fullerton, Sowers and Bader, 1995). Nb, Mo, Cr, and Fe films have been grown with the (001), (112), and (110) crystallographic orientations on MgO(001), MgO(110), and MgO(111) substrates, respectively. Fe/Cr(001) and Fe/Cr(211) superlattices have been grown on MgO(001) and MgO(110) substrates covered by a 10-nm Cr buffer layer which was deposited at 600 °C (Fullerton *et al*., 1993). The subsequent Fe/Cr superlattices were grown at 180 °C. The epitaxial orientation of the Fe/Cr(211) superlattices was found to be $\mathrm{Fe/Cr}\left[0\bar{1}1\right] \| \mathrm{MgO}\left[1\bar{1}0\right]$ while for Fe/Cr(001) the epitaxial orientation was found to be Fe/Cr[001]||MgO[011]. These orientations correspond to a 3.8 and a 16.7% lattice mismatch of the Cr with MgO, respectively. The crystalline lattice coherence was found to be ∼43 nm. A 10-nm Cr buffer layer was found to be sufficiently thick to relieve most of the epitaxial strain prior to the growth of the superlattice films. XRD measurements showed that the Fe/Cr superlattices sputtered on MgO appeared to be comparable in crystalline quality to those grown on MgO using MBE. The Fe/Cr superlattices were used to investigate the strength of the exchange coupling between the iron films. The exchange coupling exhibited an oscillatory dependence on the Cr film thickness. Only long wavelength oscillations were observed indicating that the interface roughness of the sputtered films was worse than those prepared on good single crystalline lattice matched substrates using MBE (Heinrich and Cochran, 1993; Heinrich, Cochran, Monchesky and Urban, 1999 and references within). In the sputtered Fe/Cr superlattices the strength, oscillation period, and phase of the long wavelength exchange coupling strength were found to be identical for both superlattice orientations. The crystalline magnetic volume anisotropies were found to be nearly the same as those observed for bulk Fe.

Ultrathin films of MgO (5–30 nm) were grown epitaxially onto 15-nm-thick Fe(001) which was used as a seed layer on MgO(001). The LEED spot patterns were observed to be broad and diffused even for 0.5-nm-thick MgO. This indicated that sputtering results in a more disordered MgO(001) lattice structure than that observed for MgO films grown on bulk Fe(001) substrates using TD, see the preceding text. However, the long-range lattice order improved with an increasing MgO thickness. This suggested that the lattice strain in the sputtered films was released already in the initial stages of growth. X-ray forward scattering measurements on sputtered MgO films revealed peaks corresponding to the main crystallographic directions of bulk crystalline MgO.

Epitaxial RE-TM thin films were grown using sputtering onto a buffer layer of 10–20-nm-thick W deposited on MgO(001) (Fullerton, Sowers, Pearson and Bader, 1997). The W(001) buffer layer was sputtered onto a substrate held at a temperature of 600 °C. The W mosaic spread was found to be ∼1°. The epitaxial relationship was found to be W[100]||MgO[110]. This resulted in *c*-axis tetragonal $SmFe_{12}$ films and a *c*-axis growth of hexagonal Sm–Co films. The magnetization in Co-rich Sm_2Co_{17} films was found to be reversible on thermal cycling to 800 K and showed only a 13% reduction in magnetic moment from RT to 800 K. The in-plane coercivity was observed to be 1 T at 300 K and retained the quite high value of 0.42 T at 500 K.

Sputtering has been extensively employed in the preparation of spintronics devices. These systems will be described in separate Chapters.

2 MAGNETIC ANISOTROPIES IN FERROMAGNETIC THIN FILMS

2.1 Anisotropies in bulk single-crystal ferromagnets

Most of our understanding of the properties of ultrathin ferromagnetic films is derived from experimental studies carried

out on films of the TMs Fe, Co, and Ni. Consequently this article will concentrate on a discussion of films composed of those three metals and their alloys. In their bulk form, and in thermal equilibrium at RTs, iron is a body-centered cubic metal (bcc), cobalt is a hexagonal close-packed metal (hcp), and nickel is face-centered cubic metal (fcc). The ferromagnetic state is characterized by a magnetic moment per unit volume, M_s, that is independent of an applied magnetic field to a good approximation (Chikazumi, 1964; Brown, 1978). This magnetization density does depend upon the temperature, and obtains its maximum value at $T = 0\,\mathrm{K}$. The magnetization vanishes at the Curie temperature in zero applied magnetic field. The Curie temperatures of iron, cobalt, and nickel are 1044, 1390, and 631 K (Crangle and Goodman, 1971). It is known from experiment that the free energy of a ferromagnet depends upon the orientation of the magnetization, M_s, with respect to the crystalline axes that define its crystal structure. The origin of this magnetic anisotropy is spin-orbit coupling between the atomic spin moment and the atomic orbital moments (Kittel, 1949; Chikazumi, 1964). On the basis of symmetry arguments the variation of the free energy contribution due to anisotropy in a cubic crystal can be written, to lowest order in the magnetization components,

$$F_a = -\frac{K_1}{2}\left[\left(\frac{M_x}{M_s}\right)^4 + \left(\frac{M_y}{M_s}\right)^4 + \left(\frac{M_z}{M_s}\right)^4\right] \tag{1}$$

where K_1 is an empirical temperature dependent parameter and M_x, M_y, and M_z are the components of $\vec{M}_s$ along the three cube axes. Note that the dependence of F_a on the magnetization components can also be written in the form

$$F_a = \frac{K_1}{M_s^4}\left[M_x^2 M_y^2 + M_x^2 M_z^2 + M_y^2 M_z^2\right] \tag{2}$$

The equivalence of equations (1) and (2) follows from the relation $M_s^2 = M_x^2 + M_y^2 + M_z^2$.

For hexagonal crystal symmetry the anisotropic free energy can be expressed in lowest orders by

$$F_a = K_2 \sin^2(\phi) + K_4 \sin^4(\phi) \tag{3}$$

where

$$\sin^2(\phi) = 1 - \left(\frac{M_z}{M_s}\right)^2$$

and ϕ is the angle between $\vec{M}_s$ and the c axis of the crystal. K_2 and K_4 are temperature dependent parameters, see Chikazumi (1964).

The variation of the free energy density with magnetization direction in the crystal results in a torque density that acts so as to align the magnetization along a direction that minimizes the free energy density. This torque density can be written as

$$\vec{L} = \vec{M}_s \times \vec{H}_a \tag{4}$$

where

$$\vec{H}_a = -\left(\frac{\partial F_a}{\partial M_x}\right)\hat{u}_x - \left(\frac{\partial F_a}{\partial M_y}\right)\hat{u}_y - \left(\frac{\partial F_a}{\partial M_z}\right)\hat{u}_z \tag{5}$$

is an effective magnetic field that exerts the same torque on the magnetization as does a real magnetic field (Brown, 1978).

2.2 Ultrathin ferromagnetic crystals

Consider a very thin crystal whose thickness t is very small compared with its lateral dimensions and which is uniformly magnetized. The magnetization in such thin films is uniform for internal magnetic fields that are comparable to, or larger than, typical anisotropy fields: the same exchange interaction between spins that results in the ferromagnetic state makes any spatial variation of the magnetization density relatively costly in free energy (Brown, 1978). It is clear that the free energy density of this film is likely to be quite different when the magnetization is directed along the film normal as compared with the case in which the magnetization lies in the film plane. The most important source of this free energy difference is due to the magnetic fields generated by the shape of the film. When the magnetization lies in the plane of a film a few mm in lateral dimensions but a few nm thick the magnetic field generated by the magnetization density, discontinuity at the film edges can be ignored (the approximation of infinite lateral dimensions). However, when this same uniform magnetization has a component, M_z, directed along the film normal the discontinuity in magnetization at the film surfaces generates an internal demagnetizing field $H_d = -4\pi M_z$. The interaction between this demagnetizing field and the magnetization density contributes a term to the free energy density having the form

$$F_d = 2\pi M_z^2 \tag{6}$$

Another important source of difference between a bulk magnetic crystal and a magnetic thin film comes about because the thin film must necessarily be supported on a substrate. If the crystal structure of the thin film is not exactly matched to the crystal structure of the substrate, the bonding between the film and substrate must result in deformation of the film. In general, the film structure becomes distorted both in plane and out of plane. The simplest case is that in which the film retains fourfold symmetry in plane but the lattice

spacing in the perpendicular direction becomes different from the in-plane spacing so that the thin film adopts a tetragonal symmetry. For tetragonal symmetry the magnetocrystalline free energy density can be written as

$$F_{\mathrm{a}} = -\frac{K_1^{\mathrm{par}}}{2}\left[\left(\frac{M_x}{M_{\mathrm{s}}}\right)^4 + \left(\frac{M_y}{M_{\mathrm{s}}}\right)^4\right] - \frac{K_1^{\mathrm{perp}}}{2}\left(\frac{M_z}{M_{\mathrm{s}}}\right)^4 - K_{\perp}\left(\frac{M_z}{M_{\mathrm{s}}}\right)^2 \tag{7}$$

where K_1^{par}, K_1^{perp}, and $K_{\perp}$ are anisotropy parameters having the dimensions of energy per unit volume. An example of this case is that of a thin crystal of Fe(001) grown on the (001) surface of a silver substrate (Heinrich *et al*., 1988, 1991; Heinrich and Cochran, 1993, Section 1.4.1). The atoms in the fcc Ag(001) surface net form a square array 2.889 Å on a side. The atoms on the bcc Fe(001) surface planes form a square array 2.866 Å on a side. Thus the fourfold hollows on the silver surface can accommodate the Fe(001) surface atoms if the iron net is expanded by 0.8% in plane. At the same time the spacing between iron atomic layers is reduced by 1.5%: see Section 1.4.1 Heinrich and Cochran (1993).

It may happen that the thin ferromagnetic film is grown on a substrate template that does not exhibit in-plane fourfold symmetry. In that case the free energy density should include a term of lower symmetry having the form of an in-plane uniaxial anisotropy in addition to the terms of equation (7):

$$F_{\mathrm{u}} = -\frac{K_{\mathrm{u}}}{M_{\mathrm{s}}^2}\left(\vec{M}_{\mathrm{s}}\cdot\hat{u}\right)^2 \tag{8}$$

In equation (8) K_{u} is a uniaxial anisotropy parameter and $\hat{u}$ is a unit vector that specifies the orientation of the in-plane twofold axis.

It is an experimental fact that the magnetocrystalline anisotropy parameters of equations (7) and (8) depend upon thickness and temperature. It has been observed that each of the parameters in equations (7) and (8) usually exhibits a thickness dependence such that

$$K_i = K_{iV} + \left(\frac{K_{iS}}{t}\right) \tag{9}$$

where K_{iV} is a thickness independent volume coefficient that has the units of energy per unit volume, and K_{iS} is a coefficient that has the units of energy per unit area, (Heinrich and Cochran, 1993). K_{iS} has the dimensions of a surface anisotropy term. In fact the anisotropy coefficients K_{iS} are found to be sensitive to the structure and chemical composition of the film surfaces and their interfaces with the substrate and any cover layer that may be present: often the film is covered by a nonmagnetic layer either because it forms part of a multilayer, or because the film is covered by an inert film such as gold in order to protect the magnetic film from corrosion if the specimen must be removed from the vacuum system. It should be noted, however, that an inverse dependence of the anisotropy parameter on thickness can also result from the inclusion in the film of a network of dislocations generated in order to relieve stresses in the magnetic film due to lattice mismatches between film and substrate (Chappert and Bruno, 1988, Section IVB).

2.3 The measurement of ultrathin-film anisotropies

The variation of the film free energy with magnetization orientation means that torques are exerted on the magnetization vector due to the effective fields of equation (5). Thus any experimental technique that permits one to measure torques on the magnetization can be used to obtain the anisotropy coefficients of equations (7) and (8). There are two main methods for the investigation of these torques: (i) FMR experiments and (ii) experiments designed to measure the orientation of the magnetization vector as a function of the strength and orientation of an applied magnetic field.

FMR is a dynamic technique in which the frequency is measured when the magnetization, having been perturbed from equilibrium, precesses around its equilibrium orientation. The precessional frequency depends upon all of the magnetic fields to which the magnetization is subject, including the dipolar and anisotropy effective fields:

$$H_\alpha = -\frac{\partial F_{\mathrm{sum}}}{\partial M_\alpha} \tag{10}$$

where $F_{\mathrm{sum}} = F_{\mathrm{d}} + F_{\mathrm{a}} + F_{\mathrm{u}}$ from equations (6–8). A study of how the precessional frequency depends upon applied magnetic field strength and orientation enables one to determine the effective fields due to magnetocrystalline anisotropy. In FMR experiments the precessional frequencies are determined from the resonant absorption of microwave radiation; see the review articles by Heinrich (1994), Farle (1998), and Poulopoulos and Baberschke (1999).

A related technique is Brillouin light scattering (BLS). In BLS the magnetization oscillates around its equilibrium orientation as the result of thermal agitation. The optical constants of the magnetic thin-film material are modulated at the magnetization precessional frequency, ω, and this modulation results in a frequency shift of $\pm\omega$ in the frequency of light reflected from the film; see the articles by Cochran (1994), and by Hillebrands and Güntherodt (1994). FMR and BLS have approximately the same sensitivity.

FMR requires larger specimens than does BLS, but the frequency discrimination is so fine that one can measure effective fields with a precision of 1 Oe in a 10 Å thick iron film having an area of 1 mm^2. The frequency resolution of the BLS technique is between 10 and 100 times less than that for FMR but it can be used to investigate specimens whose dimensions are as small as a few microns on a side. Note that both FMR and BLS measurements yield effective fields. It is therefore necessary to know M_s in order to obtain the anisotropy coefficients K_i. Usually the saturation magnetization must be measured in a separate experiment using a sensitive magnetometer such as a superconducting quantum interference device (SQUID). However, the strength of the FMR absorption signal is proportional to M_s, and it proves to be possible to obtain M_s with an accuracy of a few percent by means of very careful absorption measurements (Celinski, Urquhart and Heinrich, 1997).

A second class of experiments designed to evaluate anisotropy coefficients is based upon the measurement of magnetization curves. Anisotropy coefficients can be deduced from a series of measurements of the magnetization component directed along the applied magnetic field, M_H, as the applied field is varied from zero to a field large enough to ensure that $M_H = M_s$. The free energy difference between the zero field state and the saturated state is given by

$$\Delta F = \int_0^{M_s} H \, \mathrm{d}M_H \tag{11}$$

The change in ΔF with the direction of the applied magnetic field is a direct measure of the variation of the free energy density with the orientation of the magnetization vector, and therefore it can be used to determine the various anisotropy parameters. A very sensitive magnetometer is required to measure the magnetization density in ultrathin magnetic films. Usually the magnetic moment of a specimen of known thickness and area is measured using a SQUID or an alternating-gradient magnetometer (AGM): see Flanders (1988). Absolute magnetic moment measurements are difficult and rather slow, therefore in most cases the magnetometer is used only to measure the saturation magnetization, M_s, and the magneto-optic Kerr effect, MOKE, is used to measure the ratio M_H/M_s as a function of applied magnetic field. For a discussion of the physics of MOKE see Bader and Erskine (1994). These authors also discuss the use of MOKE to investigate anisotropy in ultrathin films. MOKE is a particularly convenient tool for finding the orientation of easy and hard magnetic axes. The optical beam used to measure MOKE can be focused to a very small spot a few microns in diameter so that MOKE can be used to investigate specimens having small lateral dimensions. The use of MOKE to measure anisotropy coefficients is discussed by de Jonge, Bloeman and den Broeder (1994), and by Johnson, Bloeman, den Broeder and de Vries (1996). Bayreuther *et al.* (2003), have discussed the use of hard axis magnetization curves to deduce the in-plane magnetic anisotropy coefficients for Fe(001) films grown on GaAs(001) substrates. They were able to evaluate K_1^{par} and $K_\perp$ (see equation (7)) from a comparison of the M_H versus H data with a theory based upon continuous rotation of the magnetization vector, $\vec{M}_s$.

A very useful modification of the M_H versus H technique has been described by Weber, Allenspach and Bischof (1997). These authors provide a fixed bias magnetic field, H_b, applied along a direction perpendicular to the variable magnetic field, H. The bias field guarantees a reversible rotation of the magnetization vector over an extended range of the field, H. The method has been shown to be particularly useful for the measurement of in-plane anisotropy coefficients when the variable field is aligned with an in-plane easy axis.

Finally, Gradmann and his coworkers have developed a torsion magnetometer that can be used to measure the magnetic properties of thin magnetic films in the UHV system in which the films are grown (Gradmann, Kümmerle and Tham, 1976). These authors have shown that the torsion data can be used to measure the specimen magnetic moment and the anisotropy parameters at the same time. This technique has been used to measure the magnetic moment of Ni(111) films, in UHV, grown on a Re(0001) crystal, (Gradmann and Bergholz, 1984). The magnetic moment of a Ni film only 2.5 MLs thick and having an area of 0.1 cm^2 could be measured with an uncertainty of approximately 1%. See also the review article by Gradmann (1993).

2.4 The origin of magnetocrystalline anisotropy

2.4.1 First-principles electronic band calculations

First-principles calculations of magnetic anisotropies are based upon the solution of Schrödinger's equation for interacting electrons with spin. The forms of the equations to be solved are discussed by Gay and Richter (1994). In order to calculate anisotropies it is necessary to calculate the ground state energy of the system under investigation for various orientations of the magnetization vector with respect to the crystalline axes. This is a formidable task since the energy differences in question, in the order of millielectron volts per atom, are very small compared with the total ground state energy of the order of Volts per atom. Nevertheless, in their pioneering articles Gay and Richter (1986, 1987), calculated the magnetic anisotropy coefficients for Fe, Ni, V, and Co monolayers having the lattice spacing of the

Ag(001) surface. They also calculated the perpendicular uniaxial anisotropy coefficients for freestanding (001) iron films 3, 5, 7, and 9 layers thick. The calculations indicated that Fe and V monolayers should have a magnetization vector oriented perpendicular to the film plane, whereas Ni and Co film magnetizations should lie in the film plane. The success of these calculations in predicting a perpendicular magnetization for Fe(001) in agreement with experiment stimulated a great deal of theoretical and experimental work on thin-film magnetic anisotropies. The precision with which the ground state energies could be calculated improved with time until it is now claimed that anisotropy energies for Fe, Ni, and Co monolayers, which are of the order of 1 meV/atom, can be calculated with an uncertainty of the order of 0.001 meV/atom. (1 meV/atom corresponds to a surface energy of 2.45 ergs cm^{-2} for atoms arranged on a Cu(001) surface net – a square net 2.56 Å on a side.) See the review article by Wu and Freeman (1999).

In all of the above calculations the variation of the ground state energy with orientation of the magnetization is due to spin-orbit coupling. In many cases the calculated thin-film perpendicular anisotropy coefficients are in agreement with experimental observations. However, the calculations are usually carried out for smooth and perfect surface interface planes, whereas in real specimens these interface planes are usually rough on a scale of at least ±1 atomic layer. Moreover, in many cases of interest there is some intermixing between substrate or overlayer atoms with the thin magnetic film atoms (Schurer, Celinski and Heinrich, 1995). Therefore, one cannot expect perfect agreement between calculated and observed anisotropy coefficients no matter how exactly solved the theoretical model may be.

2.4.2 *The Néel model*

In 1954 L. Néel introduced a phenomenological model for the ferromagnetic state based upon the sum of pairwise interactions between ferromagnetic atoms. This model was meant to help understand the origin of surface anisotropies as well as to elucidate the physics of magnetoelastic phenomena (Néel, 1954). The pair interaction was written as the sum of Legendre polynomials:

$$W(r,\theta) = L(r)P_2(\cos\theta) + g(r)P_4(\cos\theta) + \cdots \tag{12}$$

where r is the separation of the atom pair, $L(r)$ and $g(r)$ are phenomenological parameters, and θ is the angle between the magnetization direction and the line that joins the atom pair. Usually only the first term of the above series is used to discuss magnetic anisotropies and magnetoelastic effects. Thus, ignoring the constant term, the pair interaction can be written as

$$W(r,\theta) = L_f(r)\left(\hat{u}_r \cdot \hat{m}\right)^2 \tag{13}$$

where $\hat{u}_r$ is a unit vector directed along the line joining the atom pair, and $\hat{m}$ is a unit vector in the direction of the magnetization vector. This simple model can be used to calculate the free energy density for an ultrathin film in terms of the parameter L_f. Such a free energy function will consist of the sum of a term proportional to the film thickness, a volume term, plus a term independent of film thickness, a surface term. It is clear that the free energy density must depend upon any strains introduced by film growth on a lattice mismatched substrate because it depends upon the angles between magnetization direction and the orientation of the lines joining nearest-neighbor atoms. Chapter 8 of Chikazumi (1964) demonstrates the use of the Néel model to deduce the form of the magnetoelastic coupling energy for cubic crystals. For a (001) oriented cubic lattice whose in-plane lattice parameter has been altered by $\epsilon_1 = \Delta a/a$, and whose lattice parameter perpendicular to the plane has been altered by $\epsilon_2 = \Delta c/a$ the magnetoelastic energy density is given by:

$$F_{\text{me}} = \text{const} + B_1\left[\epsilon_1\left(\frac{M_x}{M_s}\right)^2 + \epsilon_1\left(\frac{M_y}{M_s}\right)^2 + \epsilon_2\left(\frac{M_z}{M_s}\right)^2\right] \tag{14}$$

B_1 is a magnetoelastic coupling constant. From the condition that the film must be stress free along the film normal one has

$$\frac{\epsilon_2}{\epsilon_1} = -\frac{2C_{12}}{C_{11}} \tag{15}$$

where C_{11}, C_{12} are elastic constants such that the elastic energy density is given by

$$F_{\text{el}} = \frac{C_{11}}{2}\left(2\epsilon_1^2 + \epsilon_2^2\right) + C_{12}\left(\epsilon_1^2 + 2\epsilon_1\epsilon_2\right) \tag{16}$$

see Sander (1999). From equations (14) and (15), and the condition $M_x^2 + M_y^2 + M_z^2 = M_s^2$ the strain contribution to the free energy density can be written as

$$\begin{aligned} F_{\text{me}} &= \text{const} + B_1\left[\epsilon_2 - \epsilon_1\right]\left(\frac{M_z}{M_s}\right)^2 \\ &= \text{const} - B_1\left(1 + \frac{2C_{12}}{C_{11}}\right)\epsilon_1\left(\frac{M_z}{M_s}\right)^2 \end{aligned} \tag{17}$$

For iron $C_{11} = 2.41 \times 10^{12}$ ergs cm^{-3}, $C_{12} = 1.46 \times 10^{12}$ ergs cm^{-3}, and $B_1 = -34.3 \times 10^6$ ergs cm^{-3}. Therefore, if an iron film is stretched in plane, the magnetoelastic coupling acts so as to orient the magnetization in the film

plane. For a strain of 1% the magnetoelastic contribution to the effective perpendicular uniaxial anisotropy would be $-K_\perp = 7.6 \times 10^5\,\mathrm{ergs\,cm^{-3}}$, see equation (7). This can be compared with the dipole–dipole energy $F_\mathrm{d} = 2\pi M_\mathrm{s}^2 = 18.2 \times 10^6\,\mathrm{ergs\,cm^{-3}}$. Sander (1999) describes in detail how to calculate the magnetoelastic contribution to the effective uniaxial anisotropy coefficient for cubic and hexagonal films having various surface plane orientations.

The above Néel model results in an anisotropic free energy density that is independent of the substrate or overlayer materials. In order to correct this defect MacLaren and Victora (1993) and Victora and MacLaren (1993a,b) have proposed an extension of the Néel theory that includes a pair interaction between ferromagnetic atoms and nonmagnetic nearest-neighbor atoms having the form

$$W(r,\theta) = L_m(r)\left(\hat{u}_r \cdot \hat{m}\right)^2 \tag{18}$$

where $\hat{u}_r$ is a unit vector in the direction of the line joining a ferromagnetic atom with a nonmagnetic atom, and $\hat{m}$ is a unit vector parallel with the magnetization vector. In this version of the theory at least two interaction parameters are required, L_f and L_m. MacLaren and Victora have determined these two parameters for the Co(001)/Pd system by comparison of the resulting anisotropic free energy expression with the free energy obtained from first-principles calculations using the experimentally observed strained lattice spacings as measured by Engel *et al*. (1991). The results of their first principles calculations were in good agreement with experiment. They used the values of L_f, L_m so determined to calculate the anisotropy coefficients for (111) and (110) oriented Co/Pd surfaces. The results were in reasonable agreement with the experimental data of Engel *et al*. (1991).

The Victora and MacLaren extension of the Néel model has been applied to Co/Cu(001) and Co/Pd(001) structures by Heinrich, Kowalewski and Cochran (1998). These authors used measured lattice strains and measured surface anisotropy energies to deduce that $L_f = 9.0 \times 10^{-16}$ and $L_m = 2.3 \times 10^{-16}$ ergs for the Cu/Co interface compared with $L_f = 7.1 \times 10^{-16}$ and $L_m = 6.9 \times 10^{-16}$ ergs for the Co/Pd interface. Thus the interaction energy between Co and Pd atoms was found to be approximately three times larger than the interaction energy between Co and Cu atoms. This difference is not unexpected given the tendency of Pd to form a magnetic moment when placed at an interface with a ferromagnet.

In an interesting application of the Néel model, equation (12), Bayreuther *et al*. (2003) were able to show that the fourth order in-plane volume anisotropy coefficient should be correlated with the fourth order in-plane surface anisotropy coefficient (see the notation of equations (7) and (9)). Indeed, the ratio $\left(K_{1S}^\mathrm{par}/K_{1V}^\mathrm{par}\right)$ was found to be independent of composition for a series of $Fe_{1-x}Co_x$ alloy films grown on a GaAs(001) substrate. The experimental ratio was found to correspond to a thickness of 6 MLs.

2.4.3 Vicinal surfaces

If a crystal is cut so that the surface plane makes a small angle with respect to a principle crystallographic plane the result is a surface containing many monatomic steps. Such a surface is called a vicinal surface. In a series of experiments in which Fe films and Fe films covered by Ni films were grown on vicinal Ag substrates it was discovered that the specimens exhibited an in-plane twofold magnetic anisotropy in which the direction of the uniaxial anisotropy axis was correlated with the orientation of the vicinal surface steps (Heinrich *et al*., 1988). A few years later systematic studies of the anisotropies introduced by growing Fe and Co films on deliberately miscut vicinal substrates were initiated by Chen and Erskine (1992), who studied Fe films grown on W substrates, and by Krams *et al*. (1993), who studied Co films grown on Cu substrates. In these studies the substrates exhibited a well-defined surface roughness consisting of parallel monatomic steps separated by a distance that depended on the relatively small angle between the surface normal and the crystalline [001] direction. In the case of Fe grown on a W(1 1 14) surface the uniaxial easy axis was found to be perpendicular to the step edges. In the case of Co grown on Cu(1 1 13) the easy axis was found to be parallel with the step edges. In the case of Co/Cu the uniaxial anisotropy parameter was found to be quite strong: $K_\mathrm{u} = 6 \times 10^5\,\mathrm{ergs\,cm^{-3}}$ and therefore comparable in strength with the in-plane fourfold anisotropy parameter $K_1^\mathrm{par} = -6.5 \times 10^5\,\mathrm{ergs\ cm^{-3}}$. Albrecht *et al*. (1992), also studied anisotropies deliberately introduced by substrate steps for Fe(110) films grown on W(110). They showed that their experimental results were in good agreement with calculations based upon the Néel pair model of anisotropies (Néel, 1954).

According to Krams *et al*. (1993) and Krams, Hillebrands, Güntherodt and Oepen (1994), the uniaxial anisotropy due to a stepped surface is a consequence of the lattice mismatch between the magnetic thin film and the substrate upon which it has been grown. Chuang, Ballentine and O'Handley (1994), ascribe the step-induced uniaxial anisotropy partly due to magnetoelastic effects and partly due to the missing bonds at the step edges and corners. The latter authors have applied the Néel model (Néel, 1954), to derive expressions for the effect of steps on the (001), (110), and (111) surfaces of simple cubic, bcc, and fcc crystals. Their models do correctly predict the orientation of the easy in-plane magnetic anisotropy axes, but they tend to overestimate the strength of the anisotropy parameters for the Co/Cu and Fe/W systems.

Arias and Mills (1999), have also discussed the problem of step-induced anisotropies, see Section 2.4.4. They have concluded that the contribution of surface steps to the in-plane uniaxial anisotropy energy due to stray magnetic fields is consistent with observations on Fe(001) films grown on a vicinal substrate.

More recent studies carried out on Co and Fe films grown on vicinal substrates can be found in the articles by Mikuszeit, Pütter and Oepen (2004), and by Rickart *et al*. (2004).

2.4.4 Surface roughness

1. The expression for the magnetostatic contribution to the free energy density, $F_{\rm d}$ of equation (6), has been written for a uniformly magnetized continuum. In a real thin film the magnetization density is localized near atomic positions. This nonuniform magnetization distribution may be better modeled by a collection of point dipoles situated at the atomic positions. The magnetostatic energy density of a lattice of point magnetic dipoles has been studied by Draaisma and Draaisma and de Jonge (1988), and is dealt with in the appendix of Heinrich *et al*. (1988). These authors have shown that the correction to $F_{\rm d}$ can be described as a surface contribution to the perpendicular uniaxial anisotropy having the form

$$F_{\rm corr} = -\frac{K_{\rm s}}{t}\left(\frac{M_z}{M_{\rm s}}\right)^2 \tag{19}$$

per surface, where $K_{\rm s}$ depends upon the crystal structure and upon the surface plane of the film. For cubic structures the correction is largest for the bcc(001) surface, and amounts to $0.05\,{\rm ergs\,cm^{-2}}$ per surface for iron. The correction, equation (19), favors alignment of the magnetization vector along the film normal. This contribution to the perpendicular uniaxial surface anisotropy parameter is approximately a factor of 10 smaller than the surface energy parameter measured for the Fe(001)/Au interface (Heinrich and Cochran, 1993).

2. The above correction to the uniaxial surface free energy contribution treats surface roughness whose dimensions are the interatomic spacing. Any real thin-film specimen will exhibit surface roughness on a much larger lateral scale as a result of the mode of growth, or as a result of growth on a substrate whose chemical composition varies from place to place on the surface, or as a result of growth on a substrate whose surface consists of flat smooth areas bounded by steps. Dieny and Vedyayev (1994), have pointed out that lateral variations of the uniaxial surface energy parameter around the average value, $\Delta K_{S\rm perp}$, will generate a fourfold surface free energy term having the form

$$\Delta F_{S\rm perp} = -K_{4S}\ \sin^2(\theta)\cos^2(\theta) \tag{20}$$

where θ is the angle between the average magnetization vector and the normal to the film plane. Note that the angular variation of $\Delta F_{S\rm perp}$ corresponds to a fourfold variation of the anisotropy energy with angle. Dieny and Vedyayev have calculated the surface energy parameter K_{4S} for a periodic array consisting of square mesas of length on a side and repeated with a two-dimensional spatial period of length L. The key finding is that K_{4S} is proportional to the square of the fluctuation of the uniaxial surface energy parameter around the average value. This means that the easy axes of the fourfold surface energy term are oriented at 45° to the film normal. They have also shown that for reasonable estimates of the uniaxial surface energy parameter fluctuations the effective anisotropy field, $2K_{4S}/M_{\rm s}D$, where D is the film thickness, can become comparable to fourfold volume anisotropy effective fields, $2K_1^{\rm par}/M_{\rm s}$, for films a few monolayers thick. Thus the fourfold free energy term generated by the lateral variation of the twofold surface energy term may be expected to play an important role in specimens for which the dipolar field, $4\pi M_{\rm s}$, is nearly cancelled by the uniaxial surface energy effective field $2K_{\perp S}/M_{\rm s}D$. Under those circumstances the magnetization vector may be canted so that it is neither oriented perpendicular to the film nor parallel with the film surface: see Allenspach, Stampanoni and Bischof (1990).

Heinrich, Monchesky and Urban (2001), have also investigated the effect of lateral variations of any of the magnetic anisotropy parameters. Their calculation was modeled on the Slonczewski treatment of the effect of spacer thickness variations on the interlayer exchange coupling between two ferromagnetic films separated by a nonmagnetic spacer layer (Slonczewski, 1991). They concluded that any system that exhibits a lateral variation of the anisotropic free energy characterized by a particular angular power will exhibit an effective anisotropic free energy corresponding to a higher angular power as a consequence of exchange averaging over the lower order term. Specifically, Heinrich *et al*. have shown that, under simplifying but reasonable assumptions, lateral variations of the uniaxial anisotropy parameter $K_{\rm u}$ results in a fourfold anisotropy energy having the form

$$\Delta F_4 \cong -2\Delta K_{\rm u}\left[\frac{\Delta K_{\rm u}/M_{\rm s}}{(2A/M_{\rm s})\,k_{\rm eff}^2}\right]\sin^2(\phi)\,\cos^2(\phi) \tag{21}$$

where ϕ is the average angle that the magnetization direction makes with the direction of the uniaxial axis, A is the exchange stiffness parameter, $k_{\rm eff} = \pi/L$, and L is the characteristic spatial period of the inhomogeneities. Note that the above expression is proportional to $(\Delta K_{\rm u})^2$ so that

fluctuations of either sign contribute to easy axes that are oriented 45° to the original twofold axis. This is in agreement with the calculations of Dieny and Vedyayev. Note that if K_u is the average uniaxial surface energy parameter then $\Delta K_u/M_s$ in the brackets in equation (21) must be replaced by the effective field $(\Delta K_u/M_s D)$. For the case in which the thickness of the film fluctuates around the mean thickness, D, by an average value ΔD the fluctuations in the surface free energy parameter can be written $\Delta K_u = K_u(\Delta D/D)$. It follows that the resulting fourfold surface free energy term will not be independent of film thickness as is required of a true surface energy term unless $(\Delta D/D)$ is proportional to $\sqrt{D}$.

It should be noted that the fourfold in-plane anisotropy measured by Bayreuther *et al*. (2003), in Fe/Co alloy films grown on GaAs(001) can also be explained as the result of fluctuations in the strength of the in-plane twofold anisotropy parameter; see the last paragraph of Section 2.4.2.

3. It has been pointed out by Bruno (1988), that the magnetostatic contribution to the free energy density, F_d, see equation (6), must be corrected to take into account stray fields when the film thickness varies from place to place. Any film roughness may be expected to affect the magnetostatic energy density which is calculated from the expression

$$F_d = -\frac{1}{2}\int_{\text{Volume}} \vec{M}\cdot\vec{H}\,dV \tag{22}$$

where $\vec{H}$ is the magnetic field generated by the magnetization distribution. Bruno finds that for a stepped surface the correction to F_d of equation (6) can be described as a contribution to the uniaxial surface anisotropy parameter corresponding to a free energy contribution proportional to $\sin^2(\theta)$, where θ is the angle between the magnetization vector and the film normal. For a step height of one atomic layer separating flat areas 10 atomic spacings wide, this contribution to the surface energy parameter can be as large as $0.15\,\text{ergs cm}^{-2}$, per surface, for a Fe(110) interface. This form of surface roughness favors alignment of the magnetization along the film normal. Arias and Mills (1999), discuss in detail the calculation of the contribution to the free energy density for the case of an external magnetic field, H_0, applied in the film plane so that in the absence of surface roughness the magnetization density, M_s, would everywhere be parallel to the applied magnetic field and the contribution to the free energy density would be $-M_s H_0$. For an external magnetic field applied along the z direction in the film plane these authors show that the correction to the free energy density caused by surface roughness is given by

$$\Delta F = -\frac{M_s}{2}\int_{\text{Volume}} dV\; h_z(\vec{r}) \tag{23}$$

where h_z is the z component of the magnetic field generated by the surface roughness, and the integral is taken over the volume of the film taking the roughness into account. Arias and Mills applied their theory to the case of equally spaced steps generated by growth of the film on a vicinal surface. They show that the correction to the magnetostatic energy density is a uniaxial anisotropy in which the easy axis is parallel with the step edges. The strength of the step-induced uniaxial free energy calculated for Fe(001) and a vicinal angle of a few degrees was found to be in the range $0.02-0.04\,\text{ergs cm}^{-2}$, values similar to those found experimentally.

2.5 Anisotropy data

RT uniaxial perpendicular anisotropy coefficients, plus references to the relevant articles, are listed in the review article by Johnson, Bloeman, den Broeder and de Vries (1996). Their Table 3 lists data for Fe films grown on various substrates; Table 4 lists data for Co films grown on various substrates; and Table 5 lists data for Ni films grown on various substrates. More detailed data and discussion are provided in the review article by Heinrich and Cochran (1993): in particular, refer to their Table 1 for anisotropy parameters measured for the interface between Fe(001) and vacuum, Ag, Cu, Au, and Pd. The review article by Farle (1998), contains extended discussions of the Ni/Cu(001) and the Gd/W(001) systems. The case of Fe grown on GaAs(001) has become very interesting because the small mismatch between the Fe(001) and the GaAs(001) interface makes this combination an obvious choice for devices based on a hybrid ferromagnetic/semiconductor system. The Fe/GaAs(001) system is exhaustively discussed in the monumental review article by Wastlbauer and Bland (2005). Their article includes a compilation of measured anisotropy coefficients plus relevant references.

It is interesting to point out complexities related to the in-plane uniaxial anisotropy in GaAs(001) structures. The origin of the large in-plane interface uniaxial anisotropy in GaAs/Fe(001) has so far not been clearly understood. The hard magnetic axis lies along the $[1\bar{1}0]$ crystallographic direction which is parallel to the dangling bonds of As terminated (2×6) and pseudo (4×6) reconstructed GaAs(001) substrates (Monchesky *et al*., 2000). However Moosbuehler, Bensch, Dumm and Bayreuther (2002) have shown that the strength and sign of the in-plane uniaxial surface anisotropy is not affected by a particular reconstruction of the GaAs template. A genuine Ga rich (4×6) reconstruction results in almost the same uniaxial anisotropy as that observed in the (2×6) As rich reconstruction. Therefore it is hard to believe that the source of this anisotropy lies in chemical

bonding between the dangling bonds of As and the Fe. This point of view is further supported by recent results obtained by Aktas *et al*. (submitted). They found that a Cr(001) layer grown over a 15 ML thick Fe(001) film grown on GaAs(001) can significantly decrease, or even entirely remove, the in-plane uniaxial anisotropy. This observation implies that the interface chemistry between As and Fe cannot be the source of the in-plane anisotropy. Calculations by Mirbt, Sanyal, Isheden and Johansson (2003), have suggested that an interface in-plane shear (of the order of 2%) can be stabilized at the GaAs/Fe(001) interface. A significant interface shear was observed in InAs/Fe(001) structures by Xu, Freeland, Tselepi and Bland (2002). However, recent work by Gordon and Crozier (2006), using the technique of polarization dependent X-ray absorption fine structure (XAFS) has shown that an interface shear of approximately 1% is present in 2 ML thick Fe films grown on GaAs(001) substrates and, without a capping layer, measured *in situ* at pressures in the mid-10^{-10} Torr. The in-plane shear strain was found to be $\epsilon_6 = -0.013$ (The notation used here is that used by Sander (1999), and by Thomas *et al*. (2003), in which the displacement of an atom originally at (x_1, x_2, x_3) in a Cartesian coordinate system is given by $dx_m = \sum_{n=1}^{3} \epsilon_{m,n} x_n$ where $\epsilon_{m,n}$ are the components of the strain tensor. In the present application to a strained Fe(001) film in which x_1, x_2 are taken to be along the in-plane cube axes, and following Thomas *et al*. (2003), $\epsilon_{11} = \epsilon_{22} = \epsilon_1$, $\epsilon_{33} = \epsilon_3$, $\epsilon_{12} = \epsilon_{21} = \epsilon_6/2$, and $\epsilon_{13} = \epsilon_{31} = \epsilon_{23} = \epsilon_{32} = 0$. The in-plane uniaxial anisotropy contribution to the free energy density is given by $(B_2\epsilon_6/2)\sin(2\phi)$ where ϕ is the angle between the magnetization vector and the [100] direction and, following Thomas *et al*., $B_2 = 7.62 \times 10^6\,\mathrm{J\,m^3}$.) Thus the surface cell length along [110] was observed to be smaller than the surface cell length along $[1\bar{1}0]$. No interface shear could be detected within experimental error in a 5 ML thick Fe sample: this observation suggests that in their samples the lattice shear was located only at the GaAs/Fe interface. The in-plane lattice shear leads to a uniaxial anisotropy due to the magnetoelastic parameter B_2, (Sander, 1999), with the uniaxial magnetic axis oriented along one of the $\langle 110 \rangle$ directions, (Urban, Woltersdorf and Heinrich, 2001). Thomas *et al*. (2003) have observed in-plane shear in relatively thick Fe(001) layers grown on GaAs(001) and capped with aluminum. The in-plane shear component ϵ_6 was clearly resolved for films thicker than 4 nm. The shear component $\epsilon_6 = 0.002$ at 13 nm, became unobservably small at a film thickness of 2 nm. In this case the sign of the in-plane shear was reversed compared to that in the ultrathin films investigated by Gordon and Crozier (2006). In the measurements reported by Thomas *et al*. (2003), the strength and sign of the in-plane uniaxial anisotropy energy associated with the in-plane shear follows closely the predictions of the equation

$$f_{\mathrm{me}} = \left(\frac{B_2\epsilon_6}{2}\right)\sin(2\phi) \tag{24}$$

where ϕ is the angle between the magnetization vector and the [100] direction and, following Thomas *et al*., $B_2 = 7.62 \times 10^6\,\mathrm{J\,m^{-3}}$. In this case the easy in-plane uniaxial anisotropy axis was directed along the $[1\bar{1}0]$ crystallographic direction.

Using the interface shear from the XAFS measurements and the value $B_2 = 7.62 \times 10^7\,\mathrm{ergs\,cm^{-3}}$ for bulk iron (Thomas *et al*., 2003), multiplied by 2.87×10^{-8} cm results in an interface anisotropy of approximately $-0.014\,\mathrm{ergs\,cm^{-2}}$: this surface energy is approximately a factor of 5 smaller than the observed anisotropy (Urban, Woltersdorf and Heinrich, 2001; Moosbuehler, Bensch, Dumm and Bayreuther, 2002). However it leads to the correct orientation for the easy magnetic axis, (Rickart *et al*., 2004). In order to explain the strength of the observed in-plane uniaxial anisotropy at the GaAs/Fe[001] interface one would require a larger interface shear and perhaps an enhanced value of the magnetoelastic coefficient B_2.

Seki *et al*. (2003), have shown that thin films of the alloy $Fe_{38}Pt_{62}$ having a uniaxial perpendicular anisotropy parameter as large as $K_\perp = 1.8 \times 10^7\,\mathrm{ergs\,cm^{-3}}$ can be grown on an MgO(001) substrate at substrate temperatures as low as 300 °C. These films, 18 nm thick, were grown by means of codeposition of Fe and Pt by sputtering on a (1-nm Fe + 40-nm Pt) buffer layer deposited on the MgO(001) crystal at RT. The films exhibited long-range intermetallic order having the $L1_0$ structure. Such films may be useful for ultrahigh density recording media. It is very interesting that Fe and Pt codeposited on a clean MgO(001) substrate at temperatures ranging from 500 to 700 °C formed isolated islands of the alloy $Fe_{52}Pt_{48}$ consisting of crystals having a tetragonal structure with the *c* axis oriented along the normal to the substrate (Shima *et al*., 2003). Films composed of islands 10 nm thick not only exhibited a very large uniaxial perpendicular anisotropy but they were characterized by coercive fields as large as 40 KOe!

Finally, the attention of the reader is directed to the article by Tian *et al*. (2005). These authors have discovered how to grow films of bcc Ni up to a thickness of 3.5 nm on GaAs(001). Body-centered Ni does not occur in nature. Their bcc(001) Ni films are characterized by a Curie temperature of 456 K, a lattice constant of $a = 0.282$ nm, and an atomic magnetic moment of $0.52\,\mu_{\mathrm{B}}$. Their films exhibited an in-plane fourfold anisotropy parameter of strength $K_1^{\mathrm{par}} = 4.0 \times 10^5\,\mathrm{ergs\,cm^{-3}}$, with the easy axis along $\langle 100 \rangle$.

ACKNOWLEDGMENTS

The authors would like to thank their colleagues Dr G. Woltersdorf, Dr H. Meyerheim, Mr B. Kardasz, and O. Mosendz for their invaluable help in the preparation of this chapter. We would like to thank to Dr Eric E. Fullerton for his input in the section on magnetron sputtering, and Dr Berend T. Jonker and Dr Daryl Crozier for their input on the atomic formation of Fe/GaAs interfaces. We would like to thank especially the Natural Science Engineering Research Council (NSERC) of Canada, and the Canadian Institute for Advanced Research (CIAR) for continued research funding which makes our work possible.

REFERENCES

Aktas, B., Heinrich, B., Woltersdorf, G., *et al*. Magnetic Anisotropies Ultra-thin Iron Films Grown on Surface Reconstructed GaAs Substrates, Au/Fe/GaAs, Cr/Fe/GaAs(001) Structures. Submitted to the journal of applied physics.

Albrecht, M., Furubayashi, T., Przybylski, M., *et al*. (1992). Magnetic step anisotropies. *Journal of Magnetism and Magnetic Materials*, **113**, 207–220.

Allenspach, R., Stampanoni, M. and Bischof, A. (1990). Magnetic domains in thin epitaxial Co/Au(111) films. *Physical Review Letters*, **65**, 3344–3347.

Arias, R. and Mills, D.L. (1999). Theory of roughness-induced anisotropy in ferromagnetic films: The dipolar mechanism. *Physical Review*, **B59**, 11871–11881.

Bach, P., Rüster, C., Gould, C., *et al*. (2003). Molecular-beam epitaxy of the half-Heusler alloy NiMnSb on (In,Ga)As/InP (001). *Applied Physics Letters*, **83**, 521–523.

Bader, S.D. and Erskine, J.L. (1994). Magneto-optical effects in ultrathin magnetic structures. *Ultrathin Magnetic Structures (II)*, Heinrich, B. and Bland, J.A.C. (Eds.), Springer-Verlag: Berlin, Heidelberg, p. 297.

Bayreuther, G., Dumm, M., Uhl, B., *et al*. (2003). Magnetocrystalline volume and interface anisotropies in epitaxial films: universal relation and Neel's model. *Journal of Applied Physics*, **93**, 8230–8235.

Bland, J.A.C., Steinmueller, S.J., Hirohata, A. and Taniyama, T. (2005). Optical studies of electron spin transmission. *Ultrathin Magnetic Structures (IV)*, Heinrich, B. and Bland, J.A.C. (Eds.), Springer-Verlag: Berlin, Heidelberg, Chapter 4.

Boedeker, P., Schreuer, A. and Zabel, H. (1999). Spin-density waves and reorientation effects in thin epitaxial Cr films covered with ferromagnetic and paramagnetic layers. *Physical Review*, **B59**, 9408.

Brown, W.F. Jr. (Ed.) (1978). *Micromagnetics*, Robert E. Krieger Publishing: Huntington, New York.

Bruno, P. (1988). Dipolar magnetic surface anisotropy in ferromagnetic thin films with interfacial roughness. *Journal of Applied Physics*, **64**, 3153–3156.

Butler, W.H., Zhanh, X.G., Schulthess, T.C. and MacClaren, J. (2001). Spin-dependent tunneling conductance of Fe—MgO—Fe sandwiches. *Physical Review*, **B63**, 54416.

Celinski, Z. and Heinrich, B. (1991). Ferromagnetic resonance linewidth of Fe ultrathin films grown on a BCC Cu substrate. *Journal of Applied Physics*, **70**, 5935.

Celinski, Z., Heinrich, B., Cochran, J.F., *et al*. (1990). Growth and magnetic studies of lattice expanded Pd in ultrathin Fe(001)/Pd(001)/Fe(001) structures. *Physical Review Letters*, **65**, 1156.

Celinski, Z., Urquhart, K.B. and Heinrich, B. (1997). Using ferromagnetic resonance to measure the magnetic moments of ultrathin films. *Journal of Magnetism and Magnetic Materials*, **166**, 6–26.

Chambliss, D.D., Wilson, R.J. and Ching, S. (1992). Nucleation and growth of ultrathin Fe and Au films on Cu(100) studied by scanning tunneling microscopy. *Journal of Vacuum Science and Technology*, **B10**, 1993.

Chappert, C. and Bruno, P. (1988). Magnetic anisotropy in metallic ultrathin films and related experiments on cobalt films. *Japanese Journal of Applied Physics*, **64**, 5736–5741.

Chen, J. and Erskine, J.L. (1992). Surface-step-induced magnetic anisotropy in thin epitaxial Fe films on W(001). *Physical Review Letters*, **68**, 1212–1215.

Cheung, J.T. and Sankur, H. (1988). Growth of thin films by laser-induced evaporation. *CRC Critical Reviews in Solid State and Materials Sciences*, **15**, 63.

Chikazumi, S. (Ed.) (1964). *Physics of Magnetism*, John Wiley & Sons: New York, Chapter 7.

Chrisey, D.B. and Hueber, G.K. (Eds.) (1994). *Pulsed Laser Deposition of Thin Films*, Wiley.

Chuang, D.S., Ballentine, C.A. and O'Handley, R.C. (1994). Surface and step magnetic anisotropy. *Physical Review*, **B49**, 15084–15095.

Cochran, J.F. (1994). Light Scattering from Ultrathin Magnetic Layers and Bilayers. *Ultrathin Magnetic Structures (II)*, Heinrich, B. and Bland, J.A.C. (Eds), Springer-Verlag: Berlin, Heidelberg, p. 222.

Crangle, J. and Goodman, G.M. (1971). The magnetization of pure iron and nickel. *Proceedings of the Royal Society of London*, **A321**, 477–491.

Davis, A., Stroscio, J.A., Pierce, D.T. and Celotta, R.J. (1996). Atomic-scale observations of alloying at the Cr-Fe(001) interface. *Physical Review Letters*, **76**, 4175.

Dieny, B. and Vedyayev, A. (1994). Crossover from easy-plane to perpendicular anisotropy in magnetic thin films: canted anisotropy due to partial coverage or interfacial roughness. *Europhysics Letters*, **25**, 723–728.

Draaisma, H.J.G. and de Jonge, W.J.M. (1988). Surface and volume anisotropy from dipole-dipole interactions in ultrathin ferromagnetic films. *Journal of Applied Physics*, **64**, 3610–3613.

Egelhoff, W.F. Jr. (1989). X-ray photoelectron forward scattering studies of surface segregation in epitaxial Ni-Cu-Ni(100) sandwich structures. *Journal of Vacuum Science and Technology*, **A7**, 2060.

Egelhoff, W.F. Jr. (1994a). Surface Segregation. *Ultrathin Magnetic Structures (I)*, Bland, J.A.C. and Heinrich, B., (Eds.), Springer-Verlag: Berlin, Heidelberg, Section 5.2.33.

Egelhoff, W.F. Jr. (1994b). Surfactans in Epitaxy. *Ultrathin Magnetic Structures (I)*, Bland, J.A.C. and Heinrich, B. (Eds.), Springer-Verlag: Berlin, Heidelberg, Section 5.2.36.

Egelhoff, W.F. Jr., Chen, P.J., Powell, C.J., *et al*. (1997). Oxygen as a surfactant in the growth of giant magnetoresistance spin valves. *Journal of Applied Physics*, **82**, 6142.

Enders, A., Monchesky, T.L., Myrtle, K., *et al*. (2001). The role of interfaces in the magnetoresistance of Au/Fe/Au/Fe/GaAs(001). *Journal of Applied Physics*, **89**, 7110.

Engel, B.N., England, C.D., van Leeuwen, R.A., *et al*. (1991). Magnetocrystalline and magnetoelastic anisotropy in epitaxial Co/Pd superlattices. *Journal of Applied Physics*, **70**, 5873–5875.

Farle, M. (1998). Ferromagnetic resonance of ultrathin metallic layers. *Reports on Progress in Physics*, **61**, 755–826.

Flanders, P.J. (1988). An alternating-gradient magnetometer. *Journal of Applied Physics*, **63**, 3940–3945.

Freyss, M., Stoeffler, D. and Dreysse, H. (1997). Interfacial alloying and interfacial coupling in Cr/Fe(001). *Physical Review*, **B56**, 6047.

Fuke, H., Sawabe, A. and Mizoguchi, T. (1993). Structural and magnetic properties of (001) Fe films. *Japanese Journal of Applied Physics*, **32**, L1137.

Fullerton, E.E. (1993). Interfacial roughness of sputtered multilayers: Nb/Si. *Physical Review*, **B48**, 17432.

Fullerton, E.E., Bader, S.D. and Robertson, J.L. (1996). Spin-density-wave antiferromagnetism of Cr in Fe/Cr (001) superlattices. *Physical Review Letters*, **77**, 1382.

Fullerton, E.E., Conover, M.J., Mattson, J.E., *et al*. (1993). Oscillatory interlayer coupling and giant magnetoresistance in epitaxial Fe/Cr(211) and (100) superlattices. *Physical Review*, **B48**, 15755.

Fullerton, E.E., Sowers, C.H., Pearson, J.E. and Bader, S.D. (1997). Structure and magnetism of epitaxial rare-earth-transition-metal films. *Journal of Applied Physics*, **81**, 5637.

Fullerton, E.E., Stoeffler, D., Ounadjela, K., *et al*. (1995). Structure and magnetism of epitaxially strained Pd(001) films on Fe(001): experiment and theory. *Physical Review*, **B51**, 6364.

Gavignan, J.P. (1991). *Science and Technology of Nanostructured Magnetic Materials*, Hadjipanayis, G.C. and Prinz, G.A. (Eds.), Plenum Publishing.

Gay, J.G. and Richter, R. (1994). Electronic structure of Magnetic thin Films. *Ultrathin Magnetic Structures (I)*, Bland, J.A.C. and Heinrich, B. (Eds.), Springer-Verlag: Berlin, Heidelberg, p. 22.

Gay, J.G. and Richter, R. (1986). Spin anisotropy of ferromagnetic films. *Physical Review Letters*, **56**, 2728–2731.

Gay, J.G. and Richter, R. (1987). Spin anisotropy of ferromagnetic slabs and overlayers. *Journal of Applied Physics*, **61**, 3362–3365.

Giron, E., Boher, P., Houdy, P., *et al*. (1993). Growth and structure of fcc (100) Co/Cu and Fe/Cu multilayers. *Journal of Magnetism and Magnetic Materials*, **121**, 24.

Gordon, R.A. and Crozier, E.D. (2006). In-plane structural anisotropy of ultrathin Fe films on GaAs(001)-4 × 6: X-ray absorption fine-structure. *Physical Review*, **B74**, 165405.

Gradmann, U. (1993). *Magnetism in Ultrathin Transition Metal Films, Handbook of Magnetic Materials*, Buschow, K.H.J. (Ed.), Elsevier: Amsterdam, pp. 1–96, Vol. 7.

Gradmann, U. and Bergholz, R. (1984). Magnetization of Pd(111) films by contact with ferromagnetic Ni(111) film. *Physical Review Letters*, **52**, 771–774.

Gradmann, U., Kümmerle, W. and Tham, R. (1976). High sensitivity torsion magnetometers for oligatomic films. *Applied Physics*, **10**, 219–225.

Grass, A. (2003). *Theoretical Surface Science, A Microscopic Perspective*, Springer-Verlag: Berlin, Heidelberg, Section 7.2.

Heinrich, B. (1994). Radio frequency techniques. *Ultrathin Magnetic Structures (II)*, Heinrich, B. and Bland, J.A.C. (Eds.), Springer-Verlag: Berlin, Heidelberg, p. 195.

Heinrich, B., Celinski, Z., Cochran, J.F., *et al*. (1991). Magnetic anisotropies in single and multilayered structures. *Japanese Journal of Applied Physics*, **70**, 5769–5774.

Heinrich, B. and Cochran, J.F. (1993). Ultrathin metallic magnetic films: magnetic anisotropies and exchange interactions. *Advances in Physics*, **42**, 523–639.

Heinrich, B., Cochran, J.F., Monchesky, T. and Urban, R. (1999). Exchange coupling through spin-density waves in Cr(001) structures: Fe-whisker/Cr/Fe(001) studies. *Physical Review*, **59**, 14520.

Heinrich, B., From, M., Cochran, J.F., *et al*. (1993). Ultrathin films, multilayers and surfaces, interfaces and characterization. *Materials Research Society Symposium Proceedings*, **313**, 119–128.

Heinrich, B., Kowalewski, M. and Cochran, J.F. (1998). Engineering of magnetic properties using ultrathin metallic structures prepared by molecular beam epitaxy. *Canadian Journal of Chemistry*, **76**, 1595–1605.

Heinrich, B., Monchesky, T. and Urban, R. (2001). Role of interfaces in higher order angular terms of magnetic anisotropies: ultrathin film structures. *Journal of Magnetism and Magnetic Materials*, **236**, 339–346.

Heinrich, B., Purcell, S.T., Dutcher, J.R., *et al*. (1988). Structural and magnetic properties of ultrathin Ni/Fe bilayers grown epitaxially on Ag(001). *Physical Review*, **B38**, 12879.

Heinrich, B., Woltersdorf, G., Urban, R., *et al*. (2004). Magnetic properties of NiMnSb(001) films grown on InGaAs/InP(001). *Journal of Applied Physics*, **95**, 7462.

Heinrich, B., Urquhart, K., Dutcher, J.R., *et al*. (1988). Large surface anisotropies in ultrathin films of bcc and fcc Fe(001). *Journal of Applied Physics*, **63**, 3863–3868.

Hillebrands, B. and Güntherodt, G. (1994). Brillouin light scattering in magnetic superlattices. *Ultrathin Magnetic Structures (II)*, Heinrich, B. and Bland, J.A.C. (Eds.), Springer-Verlag: Berlin, Heidelberg, p. 258.

Holzapfel, B., Roas, B., Schultz, L., *et al*. (1996). Off-axis laser deposition of $YBa_2Cu_3O_7$? thin films. *Applied Physics Letters*, **61**, 3178.

Ionescu, A., Tselepi, M., Gillingham, D.M., *et al*. (2005). Submonolayer growth of Fe on a GaAs(100)-2 × 6 reconstructed surface. *Physical Review*, **B72**, 125404.

Jenniches, H., Shen, J., Mohan, Ch.V., *et al*. (1999). Structure and magnetism of pulsed-laser-deposited ultrathin films of Fe on Cu(100). *Physical Review*, **B59**, 1196.

Johnson, M.T., Bloeman, P.J.H., den Broeder, F.J.A. and de Vries, J.J. (1996). Magnetic anisotropy in metallic multilayers. *Reports on Progress in Physics*, **59**, 1409–1458.

de Jonge, W.J.M., Bloeman, P.J.H. and den Broeder, F.J.A. (1994). *Ultrathin Magnetic Structures (I)*, Bland, J.A.C. and Heinrich, B. (Eds.), Springer-Verlag: Berlin, Heidelberg, p. 65.

Jonker, B.T. (2005). Experimental investigations of magnetic anisotropy. *Ultrathin Magnetic Structures (IV)*, Heinrich, B. and Bland, J.A.C. (Eds.), Springer-Verlag: Berlin, Heidelberg, Chapter 3.

Jonker, B.T., Glembocki, O.J., Holm, R.T. and Wagner, R.J. (1997). Enhanced carrier lifetimes and suppression of midgap states in GaAs at a magnetic metal interface. *Physical Review Letters*, **79**, 4886.

Kardasz, B., Zukrowski, J., Mosendz, O., *et al*. (2007). Interface atomic structure and magnetic anisotropy in ultrathin Fe films grown by TD and PLD on GaAs(001). *Journal of Applied Physics*, **101**, to be published.

Kittel, C. (1949). Physical theory of ferromagnetic domains. *Reviews of Modern Physics*, **21**, 541–583.

Klaua, M., Ullmann, D., Bathel, J., *et al*. (2001). Growth, structure, electronic, and magnetic properties of MgO/Fe(001) bilayers. *Physical Review*, **B64**, 134411.

Koveshnikov, A., Woltersdorf, F., Liu, J.G., *et al*. (2005). Structural and magnetic properties of NiMnSb/InGaAs/InP(001). *Journal of Applied Physics*, **97**, 3906.

Krams, P., Hillebrands, B., Güntherodt, G. and Oepen, H.P. (1994). Magnetic anisotropies of ultrathin Co films on Cu(1 1 13) substrates. *Physical Review*, **B49**, 3633–3636.

Krams, P., Lauks, F., Stamps, R.L. *et al*. (1993). Magnetic anisotropies of ultrathin Co films on Cu(0 0 1) and Cu(1 1 13) substrates. *Journal of Magnetism and Magnetic Materials*, **121**, 483–486.

Lairson, B.M., Visokay, M.R., Sinclair, R., *et al*. (1992). Epitaxial Pt(00l), Pt(110), and Pt(l11) films on MgO(001), MgO(110), MgO(111), and $A1_20_3$(0001). *Applied Physics Letters*, **61**, 1390.

Lairson, B.M., Visokay, M.R., Sinclair, R. and Clements, B.M. (1993). Epitaxial PtFe(001) thin films on MgO(001) with perpendicular magnetic anisotropy. *Applied Physics Letters*, **62**, 639.

Lindner, J., Leng, K., Kosubek, E., *et al*. (2003). Non-Gilbert-type damping of the magnetic relaxation in ultrathin ferromagnets: importance of magnon-magnon scattering. *Physical Review*, **B68**, 60102(R).

MacLaren, J.M. and Victora, R.H. (1993). Theoretical predictions for magnetic interface anisotropy. *IEEE Transactions on Magnetics*, **29**, 3034–3039.

Mattson, J.E., Fullerton, E.E., Sowers, C.H. and Bader, S.D. (1995). Epitaxial growth of body-centered-cubic transition metal films and superlattices onto MgO (111), (011), and (001) substrates. *Journal of Vacuum Science and Technology*, **A13**, 276.

Meyerheim, H.L., Popescu, R., Kirschner, J., *et al*. (2001). Geometrical and compositional structure at metal-oxide interfaces: MgO on Fe(001). *Physical Review Letters*, **87**, 76102.

Mijiritskii, A.V., Smulders, P.J.M., Chumanov, V.Ya., *et al*. (1998). Structure of Ni overlayers on bcc Fe(100). *Physical Review*, **B58**, 8960.

Mikuszeit, N., Pütter, S. and Oepen, H.P. (2004). Thickness dependent magnetization canting in Co on Cu (1 1 13). *Journal of Magnetism and Magnetic Materials*, **268**, 340–347.

Mirbt, S., Sanyal, B., Isheden, C. and Johansson, B. (2003). First-principles calculations of Fe on GaAs(100). *Physical Review*, **B67**, 155421.

Monchesky, T.L., Heinrich, B., Urban, R., *et al*. (1999). Magnetoresistance and magnetic properties of Fe/Cu/Fe/GaAs(100). *Physical Review*, **B60**, 14.

Monchesky, T.L., Urban, R., Heinrich, B., *et al*. (2000). Giant magnetoresistance of Fe/Cu/Fe(001) trilayers grown directly on GaAs(001). *Journal of Applied Physics*, **87**, 5167–5169.

Moosbuehler, R., Bensch, F., Dumm, M. and Bayreuther, G. (2002). Epitaxial Fe films on GaAs(001): Does the substrate surface reconstruction affect the uniaxial magnetic anisotropy?. *Journal of Applied Physics*, **91**, 8757–8759.

Moruzzi, V.L. and Marcus, P.M. (1989a). Magnetism in fcc rhodium and palladium. *Physical Review*, **B39**, 471.

Moruzzi, V.L. and Marcus, P.M. (1989b). Magnetism in bcc 3d transition metals: onset and approach to the Hund's-rule limit. *Physical Review*, **B38**, 1613.

Morawe, C., Stierle, A., Metoki, N., *et al*. (1991). Optimization of sputtered Co films. *Journal of Magnetism and Magnetic Materials*, **102**, 223.

Néel, L. (1954). Magnetic surface anisotropy and superlattice formation by orientation. *Journal de Physique et le Radium*, **15**, 225–239.

Ohresser, P., Shen, J., Barthel, J., *et al*. (1999). Growth, structure, and magnetism of fcc Fe ultrathin films on Cu(111) by pulsed laser deposition. *Physical Review*, **B59**, 3696.

Park, Yongsup., Fullerton, E.E. and Bader, S.D. (1995). Epitaxial growth of ultrathin MgO films on Fe(001) seed layers. *Journal of Vacuum Science and Technology*, **A13**, 301.

Pfandzelter, R., Igel, T. and Winter, H. (1996). Intermixing during growth of Cr on Fe(100) studied by proton- and electron-induced Auger-electron spectroscopy. *Physical Review*, **B54**, 4496.

Poulopoulos, P. and Baberschke, K. (1999). Magnetism in thin films. *Journal of Physics: Condensed Matter*, **11**, 9495–9515.

Prinz, G.A. (1994). Magnetic metal films on semiconductor substrates. *Ultrathin Magnetic Structures (II)*, Bland, J.A.C. and Heinrich, B. (Eds.), Springer-Verlag: Berlin, Heidelberg, Chapter 1.

Przybylski, M., Grabowski, J., Zavaliche, F., *et al*. (2002). Structural and magnetic characterization of single-crystalline Fe/MgO/Fe magneto-tunnel junctions grown on GaAs(001) and InP(001). *Journal of Physics D: Applied Physics*, **35**, 1821.

Purcell, S.T., Folkerts, W., Johnson, M.T., *et al*. (1991). Oscillations with a period of two Cr monolayers in the antiferromagnetic exchange coupling in a (001) Fe/Cr/Fe sandwich structure. *Physical Review Letters*, **67**, 903–906.

Rickart, M., Mewes, T., Demokritov, S.O., *et al*. (2004). Correlation between topography and magnetic surface anisotropy in

epitaxial Fe films on vicinal-to-(001) Au surfaces with different step orientation. *Physical Review*, **B70**, 06048-1–06048-4.

Sander, D. (1999). The correlation between mechanical stress and magnetic properties of ultrathin films. *Reports on Progress in Physics*, **62**, 809–858.

Schaefer, R., Urban, R., Ullmann, D., *et al*. (2002). Domain wall induced switching of whisker-based tunnel junctions. *Physical Review*, **B65**, 144405.

Schuller, I. and Falco, Ch. (1981). Thermalization of sputtered atoms. *Journal of Applied Physics*, **52**, 5803.

Schurer, P.J., Celinski, Z. and Heinrich, B. (1995). Mossbauer investigation of the growth of the Fe multilayer in Fe(100)/Ag(100) structures. *Physical Review*, **51**, 2506–2514.

Seki, T., Shima, T., Takanashi, K., *et al*. (2003). $L1_0$ ordering of off-stoichiometric FePt (001) thin films at reduced temperature. *Applied Physics Letters*, **82**, 2461–2463.

Shima, T., Takanashi, K., Takahashi, Y.K., *et al*. (2003). High coercivity and magnetic domain observation in epitaxially grown particulate FePt thin films. *Journal of Magnetism and Magnetic Materials*, **266**, 171–177.

Slonczewski, J.C. (1991). Fluctuation mechanism for biquadratic exchange coupling in magnetic multilayers. *Physical Review Letters*, **67**, 3172–3175.

Steigerwald, D.A., Jacobs, I. and Egelhoff, W.F. Jr. (1988). Structural study of the epitaxial growth of fcc-Fe films, sandwiches, and superlattices on Cu(100). *Surface Science*, **202**, 472.

Stoeffler, D. and Gautier, F. (1995). Theoretical investigations of the magnetic behaviour of Cr monolayers deposited on a Fe(001) substrate: role of a mono-atomic step. *Journal of Magnetism and Magnetic Materials*, **147**, 260.

Thomas, O., Shen, Q., Schieffer, P., *et al*. (2003). Interplay between anisotropic strain relaxation and uniaxial interface magnetic anisotropy in epitaxial Fe films on (001) GaAs. *Physical Review Letters*, **90**, 17205.

Tian, C.S., Qian, D., Wu, D., *et al*. (2005). Body-centered-cubic Ni and its magnetic properties. *Physical Review Letters*, **94**, 137210-1–137210-4.

Unguris, J., Celotta, R.J. and Pierce, D.T. (1991). Observation of two different oscillation periods in the exchange coupling of Fe/Cr/Fe(100). *Physical Review Letters*, **67**, 140.

Unguris, J., Celotta, R.J. and Pierce, D.T. (1992). Magnetism in Cr thin films on Fe(100). *Physical Review Letters*, **69**, 1125.

Urban, R., Woltersdorf, G. and Heinrich, B. (2001). Gilbert damping in single and multilayer ultrathin films: role of interfaces in nonlocal spin dynamics. *Physical Review Letters*, **87**, 217204.

Venus, D. and Heinrich, B. (1996). Interfacial mixing of ultrathin Cr films grown on an Fe whisker. *Physical Review*, **B53**, R1733.

Victora, R.H. and MacLaren, J.M. (1993a). Theory of anisotropy in strained superlattices. *Journal of Applied Physics*, **73**, 6415–6417.

Victora, R.H. and MacLaren, J.M. (1993b). Theory of magnetic interface anisotropy. *Physical Review*, **B47**, 11583–11586.

Villain, J., Pimpinelli, A. and Wolf, D.E. (1992). Layer by layer growth in molecular beam epitaxy. *Comments on Condensed Matter Physics*, **16**, 1.

Wastlbauer, G. and Bland, J.A.C. (2005). Structural and magnetic properties of ultrathin epitaxial Fe films on GaAs(001) and related semiconductor substrates. *Advances in Physics*, **54**, 137–219.

Weber, W., Allenspach, R. and Bischof, A. (1997). Determining magnetic anisotropies from hysteresis loops. *Applied Physics Letters*, **70**, 520–522.

Windischmann, H. (1992). Intrinsic stress in sputter-deposited thin films. *CRC Critical Reviews in Solid State and Materials Sciences*, **17**(6), 547.

Woltersdorf, G. and Heinrich, B. (2004). Two-magnon scattering in a self-assembled nanoscale network of misfit dislocations. *Physical Review*, **B69**, 4417.

Woltersdorf, G., Heinrich, B., Woltersdorf, J. and Scholz, R. (2004). Spin dynamics in ultrathin film structures with a network of misfit dislocations. *Journal of Applied Physics*, **95**, 7007.

Wu, R. and Freeman, A.J. (1999). Spin-orbit induced magnetic phenomena in bulk metals and their surfaces and interfaces. *Journal of Magnetism and Magnetic Materials*, **200**, 498–514.

Xu, Y.B., Freeland, D.J., Tselepi, M. and Bland, J.A.C. (2002). Anisotropic lattice relaxation and uniaxial magnetic anisotropy in Fe/InAs(100)-4 $\times$ 2. *Physical Review*, **B62**, 1167–1170.

Yaegashi, S., Kurihara, T. and Segawa, H. (1993). Epitaxial growth and magnetic properties of Fe(211). *Journal of Applied Physics*, **74**, 4506.

Zega, T.J., Handbicki, A.T., Erwin, S.C., *et al*. (2006). Determination of interface atomic structure and its impact on spin transport using Z-contrast microscopy and density-functional theory. *Physical Review Letters*, **96**, 196101–1.

Zharnikov, M., Dittschar, A., Kuch, W., *et al*. (1997). Interplay between structure and magnetism in Fe/Cu(100) upon temperature variation. *Journal of Magnetism and Magnetic Materials*, **174**, 40.

Hard Magnetic Films

Toshiyuki Shima[1] and Koki Takanashi[2]

[1] *Tohoku Gakuin University, Sendai, Japan*
[2] *Tohoku University, Sendai, Japan*

1 INTRODUCTION

Future development of magnetic devices strongly depends on the progress of the performance of hard magnetic films. Recently, a lot of work has been reported for nanoscale patterned or particulate magnets (Carl *et al*., 1999; Sun *et al*., 2000; Chen *et al*., 2003), since they are believed to be good candidates for future magnetic devices such as next-generation ultra-high-density magnetic storage media and biasing nanomagnets in micro-electromagnetic devices. However, all ferromagnetic materials are characterized by a critical grain size where thermal fluctuations become dominant at room temperature. In order to reduce this critical grain size, materials with high magnetocrystalline anisotropy (K_u) have attracted much attention. In this chapter, firstly, the fundamental phenomena and models which are important for the understanding of hard magnetic properties in thin films will be described. Secondly, the recent developments of hard magnetic films and their potential applications will be mentioned.

Handbook of Magnetism and Advanced Magnetic Materials. Edited by Helmut Kronmüller and Stuart Parkin. Volume 4: *Novel Materials*. ISBN: 978-0-470-02217-7.

1.1 High K_u materials

It is well known that the magnetocrystalline anisotropy is a key factor to determine the nature of magnetic materials. For soft magnetic materials (SMs), many studies have been made to reduce the effective magnetic anisotropy by amorphization (Hoffmann, 1964) or nanocrystallization (Yoshizawa, Oguma and Yamauchi, 1988; Hasegawa and Saito 1992; Suzuki *et al*., 1991; Herzer, 1989). On the other hand, for hard magnetic materials (HMs), a lot of effort has been made for exploring new materials, since the origin for a large magnetocrystalline anisotropy is due to the asymmetry of crystal structure. For instance, Sm–Co alloy (Buschow, 1969; Senno and Tawara, 1975; Ojima, Tomizawa, Yoneyama and Hori, 1977) and Nd–Fe–B alloy (Sagawa *et al*., 1984; Croat, Herbst, Lee and Pinkerton, 1984) magnets with complex crystal structures, which were discovered in the last few decades, exhibit a large uniaxial magnetic anisotropy K_u. Representative high K_u materials are summarized in Figure 1 (Weller and Moser, 1999). It is well known that $L1_0$ ordered alloys (CuAu-type crystal structure) such as MnAl, CoPt, FePd, and FePt possess large K_u, which arise from a breakdown of the crystal symmetry from a cubic structure to a tetragonal one. For example, it has been reported that the K_u of $L1_0$ FePt almost reaches a value of the order of $10^8\,\mathrm{erg\,cm^{-3}}$ which is close to that of Sm–Co alloy and about 20 times larger than that of pure Co. The large K_u of $L1_0$ FePt offers thermally stable grains with diameters down to a few nanometers, as compared with about 10 nm for pure Co.

1.2 Magnetization process and coercivity

A lot of features of magnetic materials are implied in the magnetization curves (M–H curves); in other words, the

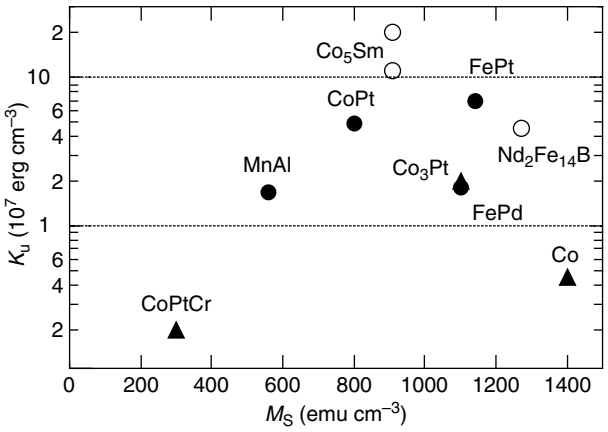

Figure 1. Saturation magnetization (M_S) and magnetocrystalline anisotropy energy (K_u) in representative high K_u materials; ●: $L1_0$ ordered alloys, ○: rare-earth–transition-metal alloys, ▲: Co and Co alloys (Weller and Moser, 1999).

response of the magnetization of the material to an applied field. The curves with the field applied along either the hard or easy axis contain important information regarding the behavior of hard magnets. This may be associated with the concept of nucleation and domain wall displacement. By measuring the initial magnetization curve (virgin magnetization curve) after demagnetization, two different kinds of qualitative behavior are observed. These are classified into nucleation-type (a) and pinning-type (b) magnets as shown in Figure 2. In a nucleation-type magnet, the initial curve is steep and the saturation of magnetization is reached at a field much lower than the coercive field (H_c). Domain walls are present in the initial state and they are free to move and do not feel pinning effects, leading to the easy saturation of magnetization. Once the domain walls are swept away from the specimen, it is difficult to nucleate reversed domains. In a pinning-type magnet, on the other hand, a field of the order of the coercive field ($H \approx H_c$) is required to saturate the magnetization of the specimen from the initial state. This indicates that domain wall pinning is the main mechanism for coercivity.

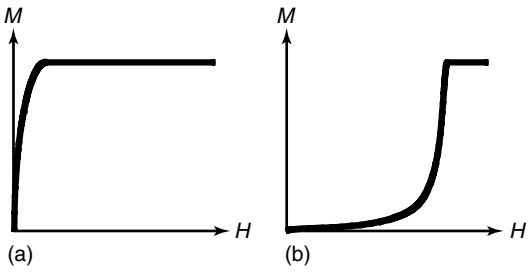

Figure 2. Schematic illustration of initial magnetization curves in (a) nucleation-type and (b) pinning-type magnets.

When the specimen size is reduced, single domain (SD) states become stable, and then, the magnetization rotation becomes a dominant process. However, an SD particle does not necessarily reverse the magnetization by coherent rotation, because incoherent rotation such as curling and buckling owing to morphological defects is not excluded. The transition from coherent rotation to incoherent rotation occurs at a particle diameter of about 10 nm, which is of the order of 5 $(A/\mu_0 M_S^2)^{1/2}$, independent of the magnetic anisotropy energy K. With increasing particle size, multidomain (MD) particles are formed. The critical boundary between MD and SD particles with a spherical shape is given by the critical diameter of particles $D_{crit} = 9\gamma_B/\mu_0 M_S^2$, where γ_B is the specific wall energy ($E4(AK)^{1/2}$) (Kronmüller and Fähnle, 2003). A qualitative relation between H_c and the particle diameter D is given in Figure 3.

1.3 Exchange-spring magnet

Kneller and Hawig (1991), proposed the exchange-spring magnet as a way to create a next-generation, high-performance permanent magnet. Such systems are based on the interfacial exchange coupling of two suitably dispersed nanostructured ferromagnetic phases. One of the two phases is an HM in order to provide a high coercive force, while the other is an SM to provide high saturation magnetization. Theoretical treatment of such systems predicts the improvement of hard magnetic properties such as a high maximum energy product ($(BH)_{max}$), a reversible demagnetizing curve (exchange spring) and high remanence (B_r) ratio. For instance, such exchange-spring characteristics can be realized by preparing a nanostructured composite of fine HM grains separated by a thin SM layer. However, it is noted that particles must not be exchange coupled to each other in order not

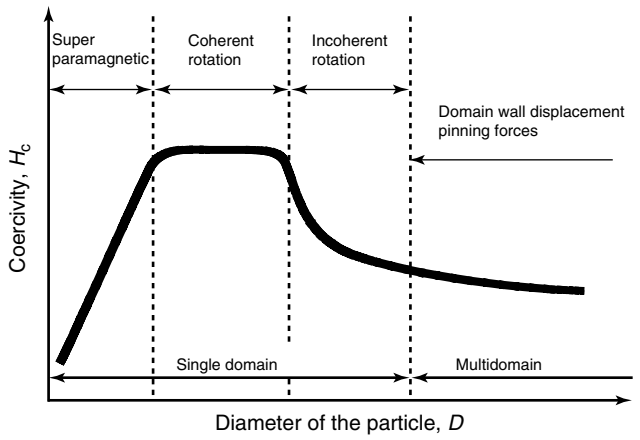

Figure 3. Schematic qualitative relation between coercivity H_c and particle diameter.

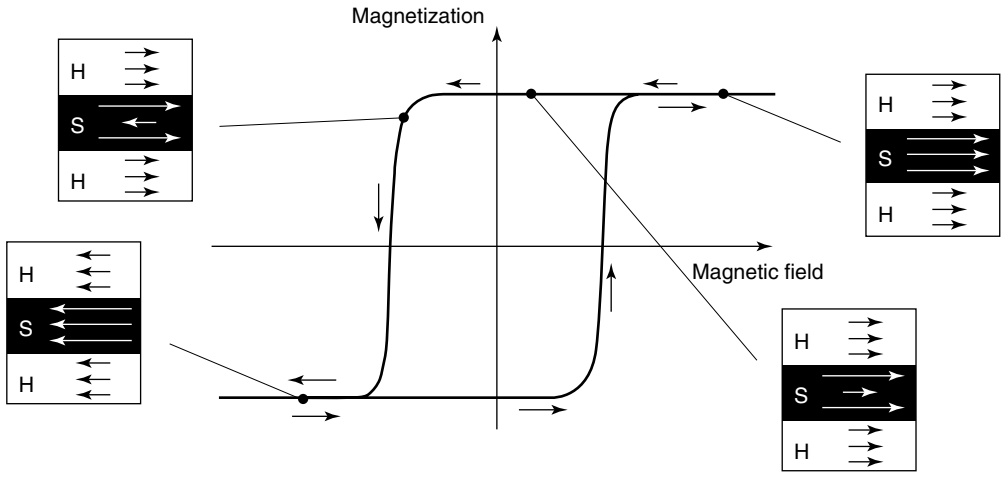

Figure 4. A schematic illustration of the exchange-coupling behavior of the magnetization curve. H: hard magnetic layer; S: soft magnetic layer.

Table 1. K and exchange length l_{ex} of Fe, Co, and Ni. $l_{ex} = (A/K_u)^{1/2}$, $A = 10^{-11}$ (J m^{-1}).

	K (10^3 J m^{-3})	l_{ex}(nm)
Fe	48	14
Ni	4.5	47
Co	410	5

to switch collectively. In appropriate systems, the magnetization of SM may be exchange coupled to that of magnetically hard nanocrystalline grains; the coupling then tends to hold the moment of SM parallel to those of the nearest grain over an exchange length (l_{ex}). A schematic illustration of exchange-coupled behavior in magnetization curves is shown in Figure 4. The values of K and l_{ex} are summarized for representative SM such as Fe, Ni, and, for reference, also Co in Table 1. If the thickness of the SM layer is larger than l_{ex}, no additional moment enhancement is expected. In order to realize high-performance permanent magnets that are greater than existing magnets, magnetic thin-film multilayers may be a promising candidate as an exchange-spring system. Skomski and Coey (1993) predicted that the remanent enhanced magnets, in other words, materials with giant $(BH)_{max}$, of 1090 kJ m^{-3} (137 MGOe) could be realized for $Sm_3Fe_{17}N_3/Fe_{65}Co_{35}$ multilayer films, assuming alignment of the hard-phase easy axes and development of sufficient coercivity.

2 FABRICATION OF THIN FILMS

In order to prepare hard magnetic films, many kinds of deposition techniques are used. Here, conventional and typical deposition techniques such as sputtering and thermal evaporation are briefly described.

2.1 Sputtering

Sputtering is a most widely used technique for preparing thin films. The benefit of this method is that both metals and insulators can easily be deposited. Besides, a lot of sputtering parameters, such as pressure during deposition, distance between target and substrate, input power, deposition rate, and so on, can easily be changed. Since the operation of a sputtering system is simple, it has become a conventional and convenient technique for thin-film preparation, not only for academic but also for practical use. Moreover, if an important report on the process is revealed, it can be mutually transferred between the laboratory and the industry. The definition of sputtering is as follows:

Sputtering is the process in which atoms are ejected from the surface of a material (target) when the surface is bombarded by energetic particles (ions). Sputtering can often be operated using inert gases like Ar, Kr, or Xe, since there is no chemical reaction between the sputtering gas and the target. The inert gas is ionized in a strong electric field, creating a plasma above the target. When a subtle amount of reactive gas such as oxygen or nitrogen is mixed with the sputtering gas and introduced into the sputtering chamber during deposition, compound films of oxide or nitride can be prepared. This process is called *reactive sputtering*. When a composite (multicomponent) target or multiple targets are used, alloy films can be prepared. Several sputtering systems are proposed for thin-film deposition including dc diode, RF diode, magnetron, and ion-beam sputtering. The basic construction of sputtering is shown in Figure 5(a). The

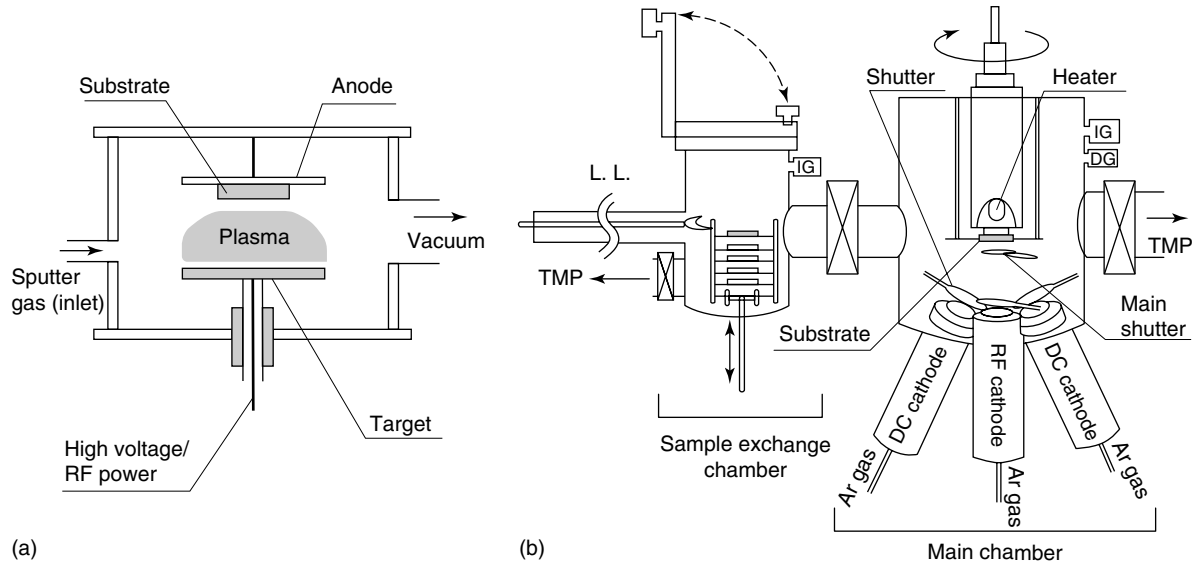

Figure 5. A schematic illustration of sputtering systems.

base pressure for most sputtering systems is in the range from 10^{-6} to 10^{-4} Pa. This relatively high vacuum (HV) is achieved with diffusion, turbo molecular, or cryogenic pumps. Recently, in order to improve the quality of films, sputtering systems with a base pressure in ultrahigh vacuum (UHV) region are being used. The working pressure during deposition is in the range of 10^{-2}–1 Pa. A typical sputtering system with a UHV chamber is illustrated in Figure 5(b).

2.2 Thermal evaporation

Materials to be deposited are thermally evaporated and then deposited onto a substrate. The thermal evaporation process is conventionally called *vacuum evaporation*. There are a lot of ways to evaporate the material. The simplest way is to heat the source materials in a crucible up to approximately its evaporation temperature by passing electrical current through a filament, which surrounds the crucible. The filament is generally made of refractory metals such as W, Mo, or Ta, with or without ceramic coating. Another method consists of bombarding the surface of the material with electron beam (EB) created by an electron gun (EB deposition). The heating of the material is much more localized in this case. Crucibles of graphite, alumina, beryllia, boron nitride, zirconia, and some refractory metals are used with indirect heating.

EB evaporation is carried out in a vacuum chamber with a pressure of the order of 10^{-4}–10^{-6} Pa. The operation pressure during deposition depends strongly on the quality of the equipment and deposition materials. Figure 6 shows a schematic illustration of a typical EB evaporation system with three independent EB guns. Ingots (source material)

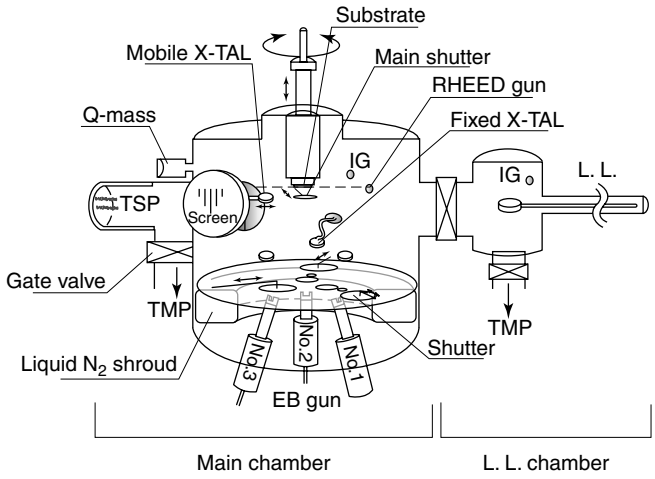

Figure 6. Schematic representation of an EB deposition system.

are melted by the EB created by an electron gun powered from several kilowatts to several hundred kilowatts. The high-energetic EB is directed onto the melting crucible, where the source material is located. The multilayered structure is prepared by controlling shutters above crucibles. If necessary, the thickness is controlled in the unit of monatomic layer and monitored by reflection high-energy electron diffraction (RHEED) oscillation. A thin film is then deposited on a substrate with a variety of temperatures by heating the substrate.

Another method is pulsed-laser deposition (PLD, also known as *laser molecular-beam epitaxy*, *MBE*), in which the material is locally heated with a laser beam. PLD is an improved process used for the deposition of alloys

and/or compounds with a precisely controlled chemical composition. A high-power pulsed laser such as KrF excimar laser or YAG laser is irradiated onto the target of source materials through the quartz window.

The MBE system is a complicated but most reliable deposition process in thermal evaporation and it works at relatively higher vacuum, in other words, UHV atmosphere (i.e., 10^{-9}–10^{-7} Pa). In order to get high-quality samples, the growth chamber is usually combined with *in situ* characterization equipment. This is an excellent preparation technique for fundamental studies; however, it is now difficult to transfer the fundamental results directly into industry except for semiconductor fields.

2.3 Thin-film growth process

In general, depending on the thermodynamic parameters of the deposit and the substrate surface, film growth processes are classified as follows: (a) Volmer-Weber mode (island growth), (b) Frank-van der Merwe mode (layer growth), and (c) Stranski-Krastanov mode (mixed growth). The Volmer-Weber mode is schematically described in Figure 7. In the first stage, a thin film is grown with the island-growth mode (island state). The lateral grain size is expected to increase with increasing the surface mobility of the adsorbed species; in other words, large grains are formed at high substrate temperature. With increasing the volume fraction of the material, that is, increasing the nominal thickness of the film, the islands grow and coalesce forming an interconnected mazelike pattern (discontinuous state). Finally, percolation occurs and the film changes from a discontinuous to a continuous state, and leads to the reduction of the bare substrate surface. However, the coalescence is strongly affected by the deposition temperature. The morphology tends to show the continuous state when the film is fabricated at low temperature, while it tends to show the island state at high deposition temperature. The tendency to form an island state is enhanced by increasing the surface mobility of the adsorbed species by increasing the substrate temperature.

The understanding of magnetization processes in the magnets of nanometer scale is of great technological and scientific interest. Since the early work of Kittel (1946) and Stoner and Wohlfarth (1948), the magnetization processes of fine particles and their assemblies have been investigated extensively (Jacobs and Bean, 1995). The magnetization reversal process, and therefore the coercivity should depend strongly on the characteristic size and the morphology of materials. Up to now, only a few studies have been devoted to the discussion about the relationship between experimentally measured magnetization behavior and actual nanostructural observations of thin films. However, recent development of the fabrication technique for thin films has enabled the preparation of nanoscaled magnetic materials and recent progress of the characterization technique also has enabled the evaluation of magnetic properties on the nanoscale.

Figure 7. Growth process of thin film.

3 RARE-EARTH–TRANSITION-METAL ALLOY THIN FILMS

3.1 High-performance rare-earth magnets

Hard magnets based on $SmCo_5$ possess the highest uniaxial anisotropy $K_u \approx 10^8\,\mathrm{erg\,cm^{-3}}$ of all the magnets, as shown in Figure 1. On the other hand, magnets based on Sm_2Co_{17} phase exhibit higher saturation magnetization and Curie temperature. Besides, recently developed magnets based on $Nd_2Fe_{14}B$ exhibit the highest energy products $(BH)_{max}$. These permanent magnets are called *high-performance permanent magnets* and their magnetic properties are summarized in Table 2 (Evetts, 1992; Schrefl and Fidler, 1992; Skomski and Coey, 1993; Hu, Li, Gavigan and Coey, 1989).

It is well known that a particular nanostructure is required to obtain the hard magnetic properties in these materials. Important aspects of this structure involve the size, shape, and crystal orientation of grains, and the intergrain coupling. Recent improvement of microfabrication and thin-film preparation technique enables these permanent magnets to have reduced dimensions down to a micrometer region to fit the

Table 2. Several magnetic properties on rare-earth–transition-metal magnets (Evetts, 1992; Schrefl and Fidler, 1992; Skomski and Coey, 1993; Hu, Li, Gavigan and Coey, 1989).

Material	$4\pi M_S$ (kG)	K_u ($\times 10^7\,\mathrm{erg\,cm^{-3}}$)	T_C(K)
$SmCo_5$	10.7	17.2	1020
Sm_2Co_{17}	12	3.3	1190
$Nd_2Fe_{14}B$	16.1	4.3	588
$Sm_2Fe_{17}N_3$	15.4	8.9	749
$Sm_2Fe_{11}Ti_1$	12.1	4.8	584

micromagnetic device applications. One potential application of hard magnetic films is micro-electromechanical systems (MEMS), that are prepared from relatively thick films of the order of several micrometers and the high $(BH)_{max}$ of rare-earth magnets promises small lateral dimensions. Several MEMS components such as a submillimeter electric motor and a stepper motor were successfully prepared (Yamashita, Yamasaki, Ikeda and Iwabuchi, 1991; Lemke, Lang, Göddenhenrich and Heiden, 1995). Another application is the creation of a bias magnetic field on the monolithic microwave integrated circuits (MMICs).

Furthermore, there is a huge application area of hard magnetic films for consumer electronics, such as a magnetic data storage on computer hard disks (HDs), HD video recorders, portable music players, and so on. The present conventional CoCr-based materials are facing the superparamagnetic limit, where the information stored in the small magnetic dots tends to become thermally unstable. In order to overcome the limit of areal recording density, the substitution of present recording system to a perpendicular regime is being implemented and materials with a higher K_u are of great interest. Compared to other applications, small film thicknesses ($5 \sim 20$ nm) are required for magnetic recording.

In this section, the magnetic properties of rare-earth-based permanent magnet films are briefly reviewed particularly focusing on their improvement through the introduction of underlayers and the adoption of the concept of an exchange-spring magnet.

3.2 Sm–Co thin films

The first report on the fabrication of rare-earth-based permanent magnet films was performed by Theuerer, Nesbitt and Bacon (1969). A getter sputtering technique was used to prepare $SmCo_5$ thin films and a large coercivity exceeding 20 kOe was obtained in the in-plane direction at the substrate temperature T_S of 600 °C. They also reported that a large coercivity of 30 kOe was obtained for $SmCo_{3.65}Cu_{1.35}$ thin films at $T_S = 500$ °C. Cadieu *et al*. investigated the synthesis and the magnetic anisotropy of $SmCo_5$ and $Sm_2(Co, Fe, Zr)_{17}$ thin films (Cadieu *et al*., 1982; Cadieu, Cheung and Wickramasekera, 1985; Cadieu, 1987; Hegde *et al*., 1994; Rani *et al*., 1997). In order to apply these films to recording media, the effect of Cr underlayer on the magnetic properties and microstructure were investigated, firstly by Velu and Lambeth (1992) and Okumura *et al*. (1995). They reported that the introduction of Cr underlayer plays an important role for getting high coercivity on Sm–Co films. Fullerton *et al*. (1996, 1997) studied the microstructures and the magnetic properties of epitaxial rare-earth–transition-metal films on a Cr underlayer and its effects were investigated (Mishra *et al*., 1981). They observed strong in-plane anisotropies that reflect the symmetry of the Cr buffer layers. Malhotra *et al*. (1996) reported that H_c as high as 31 kOe was obtained for 100-nm-thick Sm–Co films with a Cr underlayer of 20 nm after annealing at 500 °C. They also reported that high H_c of 20 kOe was obtained for several 10-nm-thick Sm–Co films with a Cr underlayer. They concluded that the reason for the large enhancement in coercivity after annealing is due to the crystallization of SmCo grains. Many studies on $SmCo_5$ films exhibiting in-plane magnetic anisotropy have been carried out. However, in order to influence the progress on high-density magnetic recording, the study of Sm–Co films with perpendicular magnetic anisotropy is strongly needed. Recently, Chen, Hegde, Jen and Cadieu (1993) reported that Sm–Co films, which were sputter deposited at a high Ar pressure and postannealed at a high temperature, showed perpendicular magnetic anisotropy, but these Sm–Co films were amorphous and the perpendicular magnetic anisotropy was insufficient. Recent investigation enabled the improvement of the perpendicular magnetic anisotropy by controlling the crystal orientation (Sayama, Mizutani, Asahi and Osaka, 2004).

3.3 NdFeB thin films

The fabrication of NdFeB thin films was firstly demonstrated by Cadieu, Cheung and Wickramasekara (1986). They prepared NdFeB films by using a slow deposition rate together with applying bias field in the in-plane direction, and high H_c of 16 kOe was achieved. However, in order to consider a practical use, some drawbacks were pointed out: the substrate temperature during deposition, 750 °C, was too high and the easy magnetization axis was aligned in the in-plane direction. Since then, many studies have been made in order to control the crystal orientation and to improve the magnetic properties. Table 3 summarizes representative studies on NeFeB thin films reported so far (Aylesworth, Zhao, Sellmyer and Hadjipanayis, 1988; Yamashita, Yamasaki, Ikeda and Iwabuchi, 1991; Lemke, Muller, Göddenhenrich and Heiden, 1995; Shindo *et al*., 1996; Parhofer, Gieres, Wecker and Schultz, 1996; Shima, Kamegawa, Hono and Fujimori, 2001).

Aylesworth, Zhao, Sellmyer and Hadjipanayis (1988) studied the effect of an Fe underlayer on NdFeB films and a coercive field of 5 kOe measured in the perpendicular direction was obtained. They concluded that Fe underlayer plays an important role for suppressing the formation of Nd–O phase. Yamashita, Yamasaki, Ikeda and Iwabuchi (1991) studied the effect of composition and substrate temperature during deposition. High H_c of 7 kOe measured in the perpendicular direction and large $(BH)_{max}$ of more than 20 MGOe were obtained. Furthermore, by using the NdFeB films, the

Table 3. Representative studies on NdFeB thin films (Cadieu, Cheung and Wickramasekara, 1986; Aylesworth, Zhao, Sellmyer and Hadjipanayis, 1988; Yamashita, Yamasaki, Ikeda and Iwabuchi, 1991; Lemke, Muller, Göddenhenrich and Heiden, 1995; Shindo *et al*., 1996; Parhofer, Gieres, Wecker and Schultz, 1996; Shima, Kamegawa, Hono and Fujimori, 2001).

Author	Heat treatment (°C)	Underlayer	Composition	H_c (kOe) [Direction]	Notes	Year
Cadieu	$T_{sub} = 750$	–	Unknown	16 [//]	UHV-sputtering bias field	1986
Aylesworth	$T_{sub} = 500$	Fe(200)	Unknown	5 [⊥]	Multiple-gun sputtering, bias field	1988
Yamashita	$T_{sub} = 450$	–	$Nd_{13}Fe_{76}B_{11}$	7 [⊥]	–	1991
Lemke	$T_{sub} = 620$	Unknown	–	2.1 [⊥]	–	1995
Shindo	$T_{ann} = 700$	Ti	$Nd_{13-15}Fe_{bal}B_{7-11}$	5 [//]	–	1996
Parhofer	$T_{sub} = 550$	–	$Nd_{32.2}Fe_{62.1}B_{5.7}$	18 [⊥]	UHV sputtering	1996
Shima	$T_{sub} = 650$	Cr	$Nd_{12.7}Fe_{73.5}B_{13.8}$	5.5 [⊥]	Cr overlayer	2001

T_{sub} and T_{ann} means substrate and annealing temperature.
Marked // is in plane and ⊥ is perpendicular to the plane.

operation of small-sized pulsed motors was demonstrated as one of the possible applications. Shindo *et al*. (1996) studied the effect of postannealing for the films consisting mainly of the $Nd_2Fe_{14}B$ phase and a coercive field of 5 kOe in the in-plane direction was obtained. Parhofer, Gieres, Wecker and Schultz (1996) studied the relationship between the magnetic properties and the composition and high H_c of 18 kOe in the perpendicular direction was achieved. In order to achieve hard magnetic properties, the $Nd_2Fe_{14}B$ phase should be sufficiently crystallized. Here, two methods have been considered: one is the postannealing that transforms the amorphous phase into the crystallized phase; the other is the deposition on heated substrates. However, it is hard to change the in-plane oriented *c* axis of the NdFeB phase to the perpendicular oriented one by postannealing. Shima, Kamegawa, Hono and Fujimori (2001) studied the effect of Cr overlayer on NdFeB films and the highly oriented $Nd_2Fe_{14}B$ phase was achieved on a glass substrate. They concluded that Cr overlayer plays a significant role in developing crystallographically textured $Nd_2Fe_{14}B$ grains, and they also assume that the developed texture is due to the seeding effect of the overlayer to induce the crystallization of the amorphous underlayer.

4 FePt THIN FILMS

As described in Section 1, many studies have been focused on the $L1_0$ ordered alloys such as MnAl, CoPt, FePd, and FePt, because they possess large uniaxial magnetocrystalline anisotropy K_u. Among them, $L1_0$ ordered FePt alloy has attracted much attention in recent years as a candidate material for applications such as next-generation high-density magnetic storage, because of large K_u of the order of 10^7 erg cm^{-3} and high corrosion resistance compared to rare-earth-based alloys described in Section 3. In this section, the basic properties and recent topics of FePt thin films are described.

4.1 $L1_0$ ordered structure

The key feature which is essential for remarkable magnetic properties of FePt alloys is the chemically ordered $L1_0$ phase around the equiatomic composition in the thermal equilibrium phase diagram as shown in Figure 8 (Okamoto, 2000). Although the thermodynamic ordering temperature of $L1_0$ FePt phase is 1300 °C, the FePt films fabricated by sputtering or vacuum evaporation methods usually have disordered face centered cubic (FCC) structure. In general, high-temperature postannealing above 500 °C is necessary to transform the disordered FCC phase to the $L1_0$ structure. The crystal structure of $L1_0$ structure is basically face centered tetragonal (FCT), composed of alternating atomic planes of Fe and Pt along the *c* axis (Figure 9). The $L1_0$ ordered phase of FePt alloy exhibits a large uniaxial magnetocrystalline anisotropy along the *c* axis, with a reported bulk value of 7×10^7 erg cm^{-3} (Ovanov, Solina and Demshina, 1973). This value is the highest of all the materials including no rare-earth elements as described in Figure 1.

4.2 Film morphology and magnetization process

The magnetization process of hard magnetic films depends strongly on the film morphology. It was clearly demonstrated in FePt thin films epitaxially grown on a MgO(001) substrate (Shima, Takanashi, Takahashi and Hono, 2002a, 2004). The film morphology may be changed by deposition parameters. Here, as two representatives, the results obtained by changing the substrate temperature T_S or the nominal thickness t_N will be described.

4.2.1 Substrate temperature (T_S) dependence

Transmission electron microscopy (TEM) bright field images and selected area electron diffraction (SAED) patterns of the

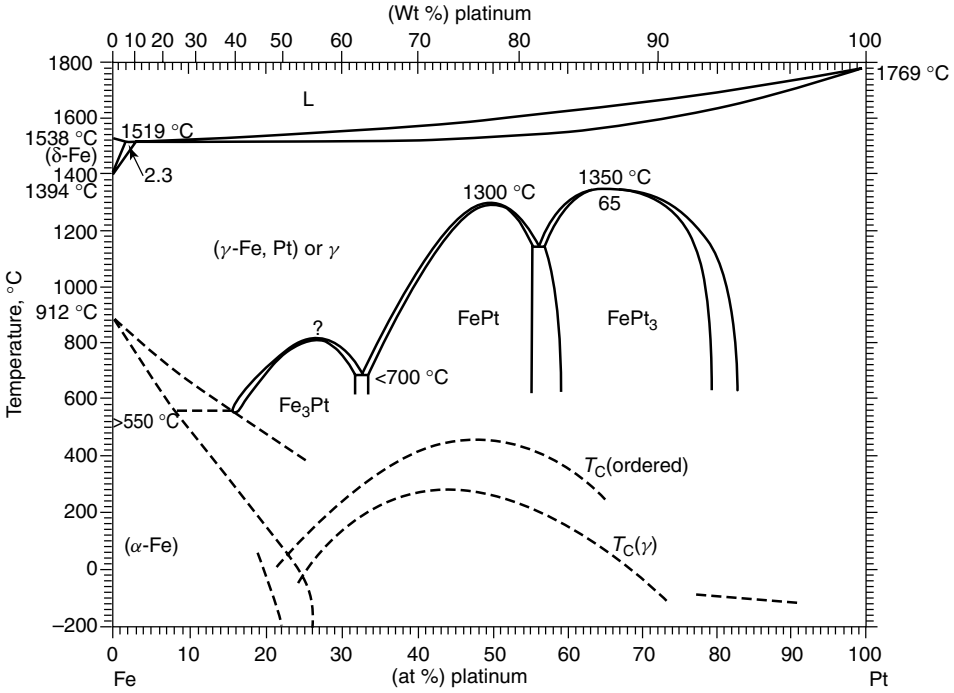

Figure 8. Phase diagram of a binary Fe–Pt alloy. (Reprinted with permission H. Okamoto, copyright 2000, ASM International.)

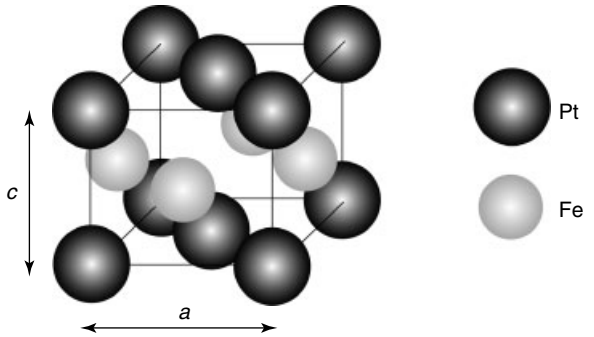

Figure 9. Crystal structure of $L1_0$ phase.

FePt films deposited on a MgO(001) substrate at various T_S in the range from 200 to 700 °C are shown in Figure 10. The nominal thickness t_N is fixed at 10 nm. In the diffraction pattern for $T_S = 200$ °C, only A1 diffraction spots are observed to be overlapped with the MgO diffraction spots from the substrate. Very weak superlattice spots are observed in the diffraction pattern for $T_S = 300$ °C, suggesting that the degree of order is still very low. The intensities of superlattice spots increase with T_S. The SAED patterns show the epitaxial growth with cube–cube orientation relationship between the FePt film and the MgO substrate, that is, $(001)_{FePt}||(001)_{MgO}$ and $<100>_{FePt}||<100>_{MgO}$.

Figure 11 shows a TEM image for $t_N = 10$ nm ($T_S = 700$ °C). The film was grown with the island-growth mode. Strongly faceted islands of FePt particles are observed with large size distribution. The major facet planes are (100) and (010), and the minor facet plane is (110), indicating that the surface energy of (100) and (010) planes is the lowest. When particles are small, the surface energy is large compared to the volume free energy, and thus the small particles would show clear faceting. The stripe contrast observed in the particles are the Moiré pattern originating from the lattice parameter difference between FePt and MgO, and the distance between neighboring stripes is approximately 2.2 nm as expected from the lattice mismatch between FePt and MgO with $a_{FePt} = 0.40$ nm and $a_{MgO} = 0.42$ nm, respectively. In cross-sectional TEM images, no structural defects, such as twins are observed and the surfaces of the particles are atomically flat. The sizes of particles are widely distributed with a typical lateral size of about 50 nm. In addition to these particles, much smaller particles are also observed. This suggests that a number of small particles were formed in the initial stage of the film deposition, and then they coalesced to form big particles.

Magnetization curves taken at 295 K for different substrate temperature T_S are shown in Figure 12. The solid and broken curves represent the magnetization measured in the direction perpendicular and parallel to the film plane, respectively. The film prepared at $T_S = 200$ °C is magnetically soft because of the low magnetocrystalline anisotropy of disordered FePt. With increasing T_S, at $T_S = 450$ °C, the easy magnetization axis changes from in plane to the direction perpendicular to the film plane. The coercivity H_c of the film increases

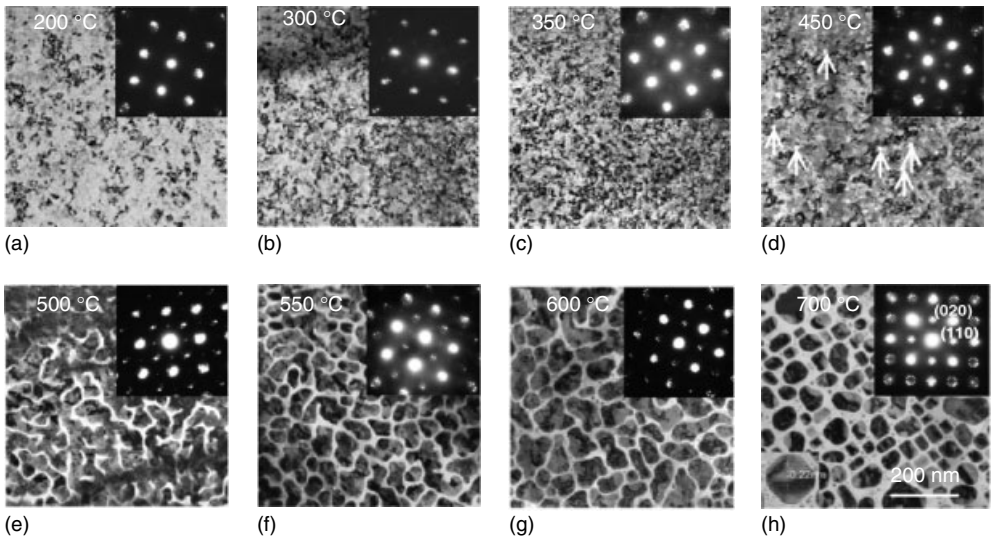

Figure 10. Bright field TEM images and SAED patterns of FePt films fabricated on MgO(001) substrates at various T_S. (Reprinted with permission Y.K. Takahashi *et al*., copyright 2003, Elsevier.)

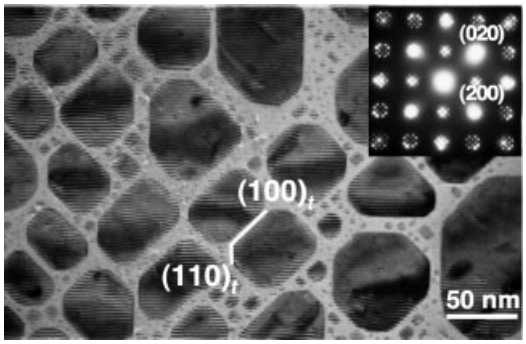

Figure 11. TEM bright field image and selected area diffraction (SAED) pattern (inset) of FePt thin film with $t_N = 10$ nm. (Reprinted with permission Shima *et al*., copyright 2002, American Institute of Physics.)

from 0.85 kOe to about 42 kOe with increasing T_S from 450 to 700 °C. The in-plane magnetization of the film prepared at $T_S = 450$ °C saturates at 20 kOe. In the film deposited above 500 °C, however, the in-plane magnetization does not saturate even at 55 kOe, indicating high uniaxial magnetic anisotropy. Since the maximum magnetic field of 55 kOe in the super conducting quantum interence device (SQUID) is not sufficient to saturate the magnetization, the real value of H_c and saturation magnetization (M_S) are even higher. From the change of the magnetization curves, it is noted that the magnetocrystalline anisotropy increases with the progress of the $L1_0$ ordering as T_S is increased.

4.2.2 Nominal thickness (t_N) dependence

A remarkable change in the morphology of the film is observed for the films with different nominal thicknesses (t_N) deposited at 700 °C. Figure 13 shows TEM images for different t_N values. With increasing t_N, the typical size of particles increases from ∼50 nm for $t_N = 10$ nm to about ∼400 nm for $t_N = 20$ nm because of the coalescence. With further increase of t_N, particles grow to form an interconnected isotropic mazelike pattern. However, the mazelike structure does not percolate for $t_N \leq 45$ nm. The percolation occurs for $t_N = 50$ nm, and the film changes from discontinuous to continuous morphology. The electronic transport measurement also reveals that there is a drastic change in electrical resistance between $t_N = 45$ and 50 nm. The resistances are 800 MΩ and 810 Ω for $t_N = 45$ and 50 nm, respectively. With further increase of t_N, the percolated network expands at the expense of the voids, and the free space between FePt diminishes.

Figure 14 shows magnetization curves for different values of t_N. The easy magnetization axis is perpendicular to the film plane for all the samples, since the [001] axis of the tetragonal $L1_0$ ordered structure is perpendicular to the film plane as shown in Figure 1. Huge H_c of about 40 kOe, measured in the direction perpendicular to the film plane, was obtained for $t_N = 10$ nm at room temperature. With increasing t_N, the coercivity decreases slowly, but still keeps a quite large value of about 25 kOe for $t_N = 45$ nm. However, a drastic change of the magnetization curves is observed (Thiele, Folks, Toney and Weller, 1998; Kooy and Enz, 1960) between $t_N = 45$ and 50 nm. This critical region corresponds to the change in the morphology of the films from a particulate to a continuous state. With further increasing t_N, the magnetization becomes easier to be saturated in the perpendicular direction.

In Figure 15, the magnetic properties obtained from the magnetization curves and electrical resistance as a function

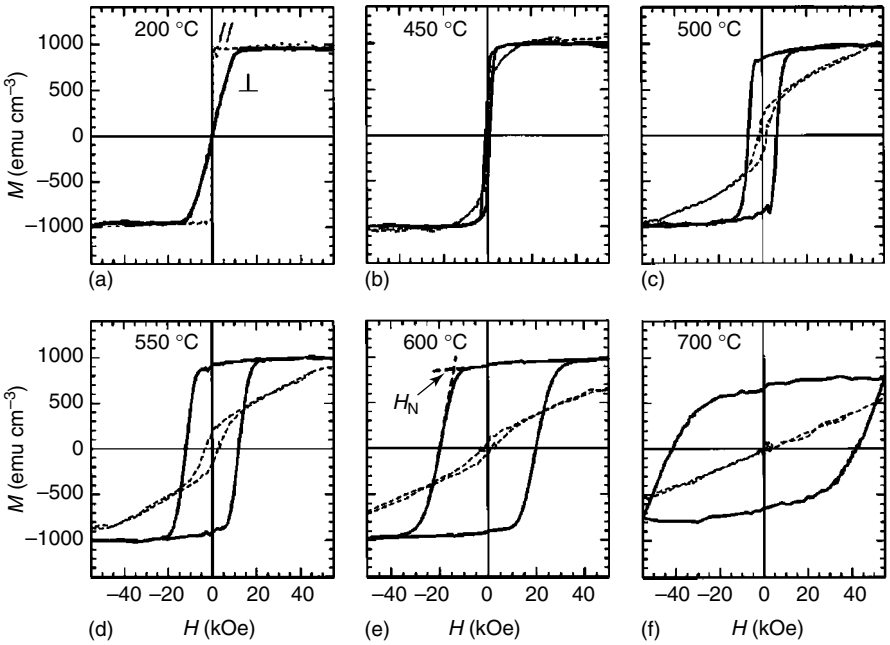

Figure 12. Magnetization curves taken at 295 K of FePt films with various T_S. Solid and broken curves represent the data with the applied field perpendicular and parallel to the film plane, respectively. (Reprinted with permission Y.K. Takahashi *et al*., copyright 2003, Elsevier.)

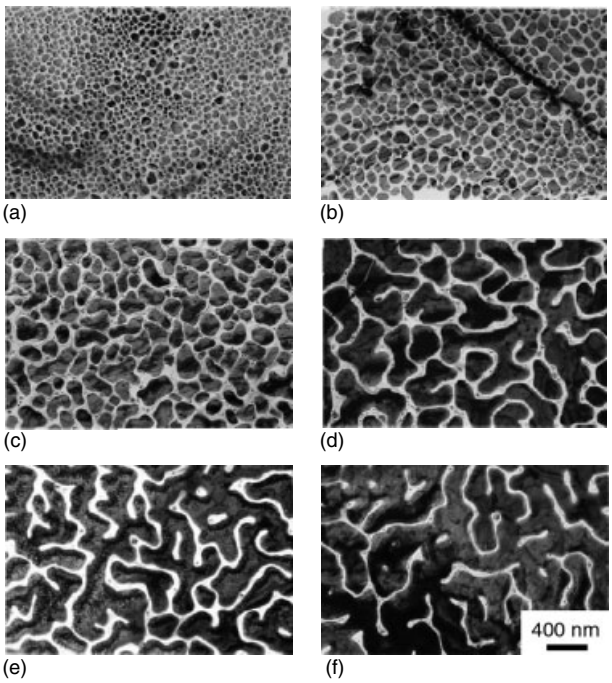

Figure 13. TEM images of FePt thin films for different film thicknesses: 10 nm (a), 20 nm (b), 45 nm (c), 50 nm (d), 60 nm (e), and 100 nm (f). (Reprinted with permission Shima *et al*., copyright 2002, American Institute of Physics.)

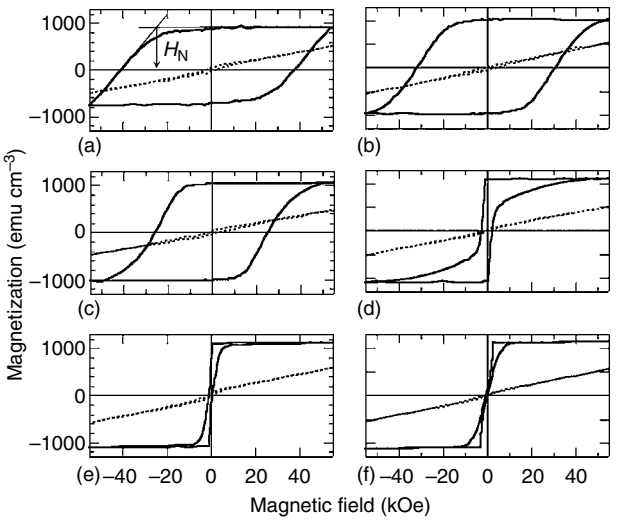

Figure 14. Room-temperature magnetization curves for FePt thin films with different film thicknesses: 10 nm (a), 20 nm (b), 45 nm (c), 50 nm (d), 60 nm (e), and 100 nm (f). The magnetic field was applied in the direction perpendicular to the film (solid line) and in the in-plane direction (broken line). (Reprinted with permission Shima *et al*., copyright 2002, American Institute of Physics.)

of t_N are summarized. Large coercivites are obtained for $t_N \leq 45$ nm, and a drastic change by 1 order of magnitude is observed between $t_N = 45$ and 50, where the electrical resistance also reveals a drastic drop showing the onset of percolation. The nucleation field (H_N), at which the magnetization begins to drop with decreasing the field after saturation, is also evaluated. In the case of the films with large coercivity, the nucleation fields are defined from the

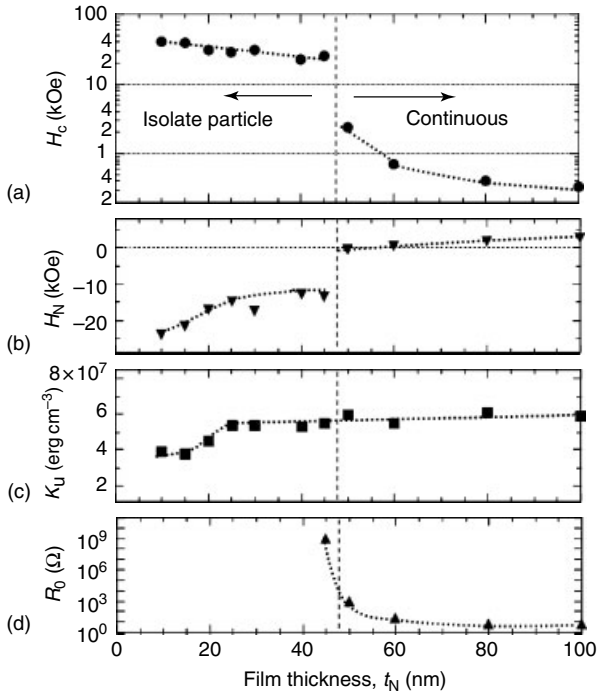

Figure 15. Magnetic properties and electrical resistance for FePt thin films as a function of the film thickness t_N. Magnetic properties are coercivity H_c (a), nucleation field H_N (b), and the uniaxial magnetic anisotropy K_u (c), respectively. (Reprinted with permission Shima *et al*., copyright 2002, American Institute of Physics.)

cross point of the extrapolation of the values of saturation magnetization and the tangential line at the coercivity. The behavior of H_N shows a tendency similar to that of the coercivity: H_N also changes drastically between $t_N = 45$ and 50 nm. The uniaxial magnetic anisotropy K_u determined from the area enclosed between the magnetization curves in applied fields parallel and perpendicular to the film plane are also shown in Figure 15(c). The films with $t_N \geq 25$ nm showed a large value of $6.0 \pm 0.5 \times 10^7$ erg cm^{-3} which is very close to the value of the fully ordered FePt alloys (7×10^7 erg cm^{-3}). No jump is seen between $t_N = 45$ and 50 nm. For $t_N \leq 25$ nm, K_u decreases gradually with t_N. This is thought to be due to the lack of magnetization saturation associated with the fact that for very small t_N, the coercivity is larger than the maximum applied field (55 kOe).

Magnetic force microscope (MFM) images superimposed with atomic force microscope (AFM) images for different t_N are shown in Figure 16. For $t_N = 10$ nm, most particles have an SD state. With increasing t_N, MD particles, which correspond to a black and white contrast inside a particle, appear. The critical size from an SD to an MD particle is estimated to be approximately 200 nm. Almost all particles have the MD state for $t_N = 45$ nm; nevertheless, the coercive force is still quite high. There is no remarkable difference in the domain structure between $t_N = 45$ and 50 nm, that is, at the percolation boundary where the coercivity shows a noticeable drop. In other words, the drastic decrease in coercivity is not associated with a change in the domain structure, but it depends only on the percolation of particles. The origin for this behavior might be considered in the following way: there are some nucleation sites where reversed domains are easily generated at a very low magnetic field. However, such nucleation sites are very few. For a discontinuous film that is not percolated, domain walls created around the nucleation site cannot propagate all over the film, resulting in high coercivity. For a percolated continuous film, on the other hand, the domain walls can propagate all over the film, once the nucleation has occurred. Therefore, the coercivity becomes very small.

The drastic change in H_c is clearly observed at the percolation boundary in association with the morphology change from discontinuous to continuous state, where the magnetic domain structure shows no remarkable change. Transition from SD to MD particles proceeds gradually for even smaller t_N below the percolation limit. The detailed magnetization process of the samples in the region $t_N <$ 40 nm is given in the case where a field high enough to saturate the magnetization is applied.

Figure 17 shows H_c as a function of t_N at room temperature and 4.5 K. H_c was obtained from the magnetization curves measured with the applied magnetic field perpendicular to the substrate plane, using a vibrating sample magnetometer (VSM) equipped with a superconducting magnet (maximum magnetic field of ±140 kOe). Huge H_c values of 70 kOe at room temperature and 105 kOe at 4.5 K are obtained for $t_N = 5$ nm. In addition, the maximum energy product $(BH)_{max}$ at room temperature reaches about 50 MGOe, which is almost equal to the ideal value $(2\pi M_S)^2$. At both room temperature and 4.5 K, H_c decreases gradually with t_N. However, it remains large (42 and 59 kOe at room temperature and 4.5 K, respectively) even for $t_N = 40$ nm. A rapid decrease of H_c for $t_N \leq 3$ nm at room temperature is caused by poor chemical order in small particles with a diameter less than a few nanometers and also by thermal instability. It has been found from MFM observation that most of the particles have the SD state for $t_N \leq 5$ nm where the particle sizes are a few tens of nanometers or smaller. As t_N increases, MD particles appear with increasing average size, and most of the particles have the MD state for $t_N \geq 25$ nm where the particle sizes are typically of the order of hundreds of nanometers. SD and MD particles are mixed in the intermediate region between $t_N = 5$ and 25 nm.

The t_N dependence of H_c shows different behavior depending on the microstructure of the film (Takahashi, Hono, Shima and Takanashi, 2003). Figure 18 shows H_c measured

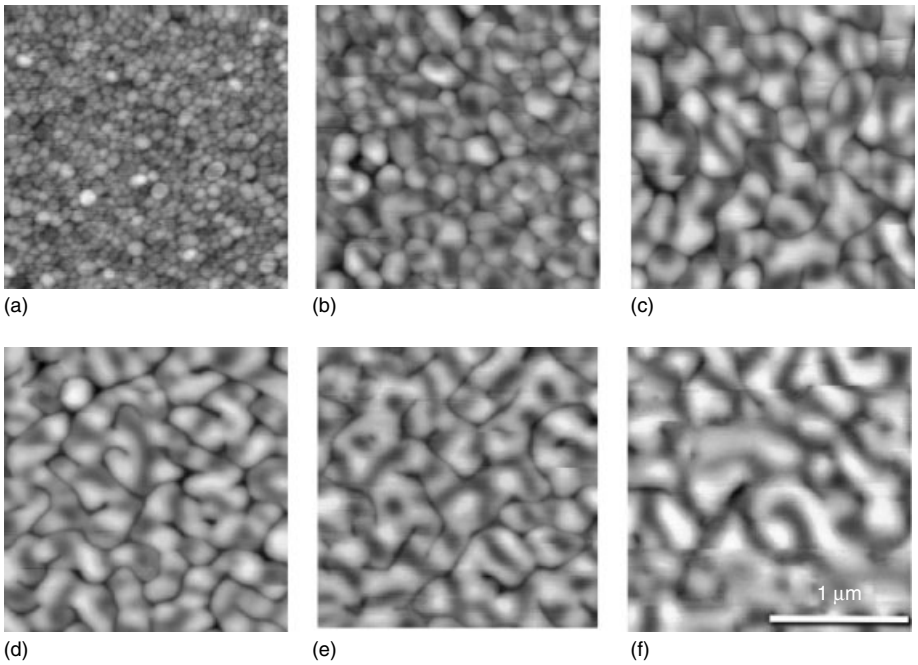

Figure 16. MFM images superimposed with AFM images of FePt thin films for different film thicknesses, $t_N = 10$ nm (a), 20 nm (b), 45 nm (c), 50 nm (d), 60 nm (e), and 100 nm (f). (Shima, Takanashi, Li and Ishio, 2003). (Reprinted with permission T. Shima *et al*., copyright 2003, Elsevier.)

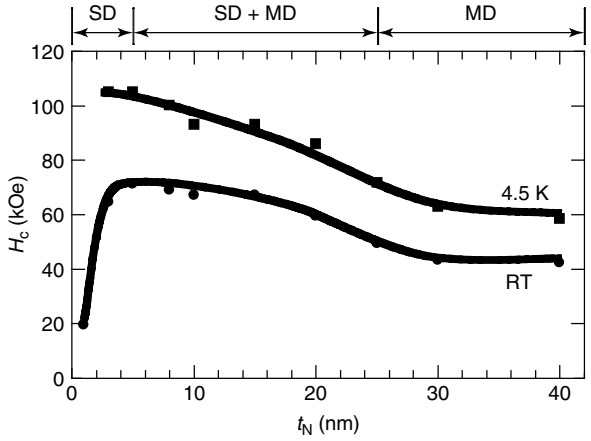

Figure 17. H_c as a function of t_N at room temperature and 4.5 K. (Reprinted with permission Shima *et al*., copyright 2004, American institute of Physics.)

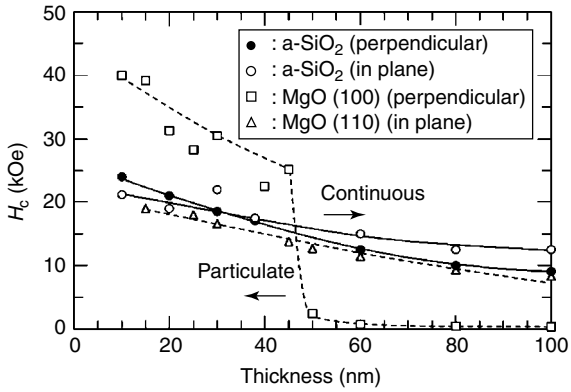

Figure 18. H_c as a function of t_N for the film on various substrates: MgO(100), MgO(110) single crystal and SiO_2 amorphous substrates. Each H_c was measured in the easy magnetization axis. (Reprinted with permission Takahashi *et al*., copyright 2004, American Institute of Physics.)

in the easy magnetization axis as a function of t_N for films deposited on various substrates: MgO(001), MgO(110) single crystal, and SiO_2 amorphous substrates (Takahashi *et al*., 2004b). The substrate temperature T_S was fixed at 700 °C. Electrical resistance measurements and TEM observations indicate that the percolation occurs between $t_N = 45$ and 50 nm for the film on any substrate. Nevertheless, in contrast to the behavior for the films on MgO(001) substrate, a gradual change of H_c was observed and no jump was seen at the critical thickness for the films on MgO(110) and SiO_2. The former indicates low resistance to the movement of the nucleated domain walls for the films on MgO(001), while the latter indicates the presence of pinning for the domain wall movement for the films on MgO(110) and SiO_2. X-ray diffraction (XRD) and TEM measurements revealed that FePt films grown on MgO(110) substrates consist dominantly of (101) texture, where twins with two different directions of the *c* axis, that is, the easy magnetization axis, exist. FePt

films grown on SiO_2 glass substrates show polycrystalline structure consisting of grains with different directions of the *c* axis. The pinning is then thought to be due to structural defects like twins and/or grain boundaries.

4.3 Magnetization process for highly oriented FePt(001) particles

FePt(001) island films grown on MgO(001) substrates at high T_S provide model systems for the assembly of hard magnetic particles because of their defect-free highly oriented structure. Figure 19 shows the initial magnetization curves starting from the demagnetized state for different values of t_N, clearly showing the difference between the magnetization processes in SD and MD particles. All the magnetization curves were measured at 295 K in the direction perpendicular to the film plane. The vertical axis indicates the magnetization normalized by the magnetization value at 140 kOe. t_N is 3, 5, 8, 10, 12, 15, 18, 20, 25, 30, and 40 nm. The films with $t_N = 3$ and 5 nm are very difficult to be magnetized, because they contain only SD particles with sizes from ten to a few tens of nanometers. Hence, the magnetization progresses only by the magnetization rotation in the particles. However, with increasing t_N (10 and 12 nm), that is, with increasing particle size, a steep increase of the magnetization at low magnetic field is observed although the complete saturation is still hard. The fractional magnetization at low magnetic field corresponds to the magnetic domain wall displacement; in other words, particles larger than 200 nm with MD structure are first magnetized at low magnetic field. With further increasing t_N (15 and 20 nm), the volume fraction of MD particles increases, and consequently, the fraction of the magnetization that is magnetized at low magnetic field increases. This figure also indicates that the particles smaller than 200 nm, that is, with SD structure, still exist for the film with $t_N = 20$ nm because a small fraction of the magnetization is still hard to saturate. However, they disappear for the films with $t_N \geq 25$ nm. In this case, the magnetization can easily be saturated at a field lower than 10 kOe by domain walls displacement process. Such initial magnetization curves are usually classified as 'nucleation type'. The coexistence of both SD and MD structures is clearly elucidated from the initial magnetization process, and is consistent with the MFM observations.

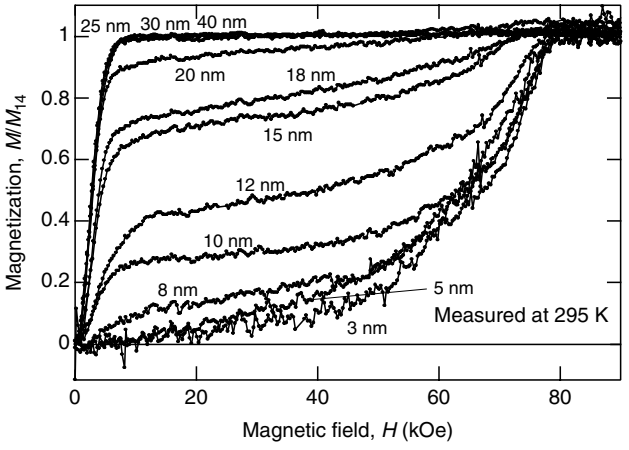

Figure 19. Initial magnetization curves for FePt films with different t_N. t_N is 3, 5, 8, 10, 12, 15, 18, 20, 25, 30, and 40 nm. (Reprinted with permission Shima *et al*., copyright 2004, American institute of Physics.)

Even in hard magnets showing so-called nucleation-type behavior to date, it is well known that a high magnetic field comparable to or larger than H_c is generally required to fully magnetize the material, because the existence of multiple phases and/or grain boundaries and interparticle dipolar interaction prevents the complete disappearance of reversed domains. However, the FePt nanoparticles are clearly different from these. Figure 20 shows the magnetization curves for $t_N = 25$ nm, with variation of the initial applied field (H_{in}) from the virgin state. H_{in} is 2 kOe (a), 3 kOe (b), 4 kOe (c), 5 kOe (d), and 6 kOe (e). The magnetic field is first increased to H_{in} from the virgin state and then reversed to −55 kOe. It is then increased again through zero to +55 kOe, and finally reversed through zero to −55 kOe. In the case of $H_{in} = 2$ kOe (Figure 20a), most of the particles have their magnetization easily reversed at low negative magnetic fields of a few kilooersteds when the magnetic field is reversed. With increasing H_{in}, the fraction of the particles showing easily reversed magnetization decreases (Figure 20b,d), before finally disappearing at $H_{in} = 6$ kOe (Figure 20e). This result indicates that 6 kOe alone is enough to fully magnetize the sample and obtain a high H_c value of more than 50 kOe. In other words, domain walls are completely wiped out from each particle at a low magnetic field, and the nucleation of reversed domains becomes very difficult; a high magnetic field is then required for magnetization reversal (Shima *et al*., 2006).

This remarkable nucleation-type behavior may be attributed to the ideal structure with defect-free, perfectly aligned, monocrystalline FePt nanoparticles, and weak dipolar interaction between particles. The wipeout of domain walls is thought to be dominated by the competition between the applied magnetic field and interparticle dipolar interaction (Durst and Kronmüller, 1987; Givord, Tenaud and Viadieu, 1988; Givord *et al*., 1992) in sintered NdFeB magnets where NdFeB grains are densely packed. Conversely, for FePt nanoparticles shown in this section, the particle density is low and the interparticle distance is considerably larger. Therefore, the interparticle dipolar interaction is significantly reduced compared to that in sintered NdFeB.

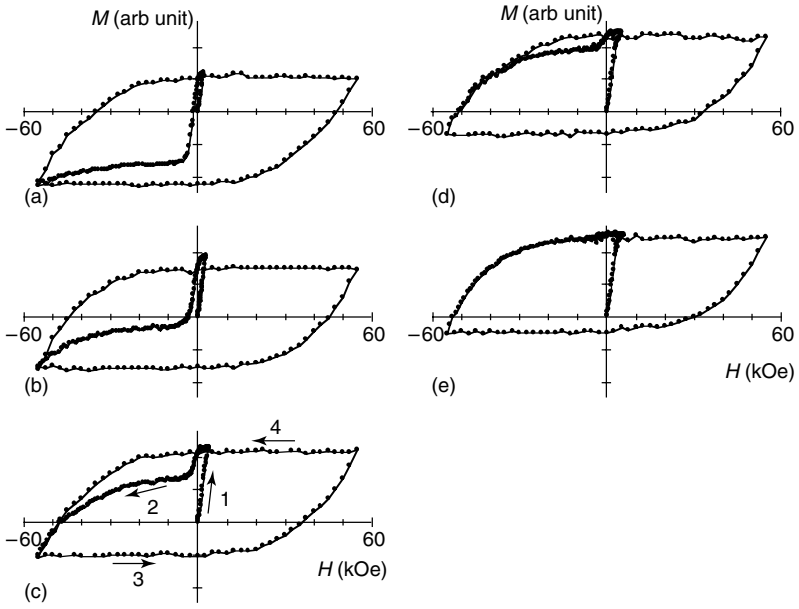

Figure 20. Magnetization curves for nominal thickness $t_N = 25$ nm, with varying the initial applied field (H_{in}) from the virgin state. H_{in} is 2 kOe (a), 3 kOe (b), 4 kOe (c), 5 kOe, (d), and 6 kOe (e). (Reprinted with permission Shima *et al*., copyright 2006, American Institute of Physics.)

4.4 Low-temperature fabrication of $L1_0$ phase

It is well known that the substrate temperature during deposition and/or the postannealing temperature are required to be high (usually more than 500 °C) for the preparation of highly ordered Fe–Pt alloy films. However, for practical use, it is essential to reduce the growth temperature. Recently, a lot of studies have focused on the reduction of the ordering temperature by several approaches as summarized in Table 4.

Maeda *et al*. (2002) reported that the addition of Cu to FePt is an effective way to reduce the ordering temperature, and H_c of about 5 kOe was obtained after annealing at 300 °C. A similar result was also reported by Takahashi, Ohnuma and Hono (2002). They confirmed that the Fe site was substituted by Cu in a FePtCu system and the decrease of the ordering temperature was thought to be attributed to faster diffusion in Cu-containing FePt alloy, owing to the depression of the melting temperature. Besides the addition of Cu, Platt *et al*. (2002) studied the effect of Au and Ag in the FePt films. The reduction of the annealing time by Zr addition (Lee, Yang, Kim and Na, 2001) and the control of the particle size by C addition were also reported (Ko, Perumal and Shin, 2003).

Ravelosona, Chappert, Mathet and Bernas (2000) actively studied the effect of ion irradiation. They have shown that the long-range order in FePt films, grown by sputtering at moderate temperatures, was enhanced by He ion irradiation. After irradiation, the perpendicular magnetic anisotropy was observed to increase. Authors believe that this irradiation technique could be a candidate for the fabrication of partially ordered granular media based on the weakly ordered alloys.

Luo and Sellmyer (1995) and Endo, Kikuchi, Kitakami and Shimada (2001) found that the rapid diffusion at Fe/Pt interface occurred at temperatures around 300 °C and the multilayer structure directly transforms to the ordered FCT phase when Fe and Pt layer thicknesses are almost equal. They also confirmed that the rapid formation of the FCT phase in the multilayers with Fe/Pt ≈1 was due to relatively rapid diffusion at the interface. Ultimate multilayer structure is an alternate stacking of monatomic layers of Fe and Pt. Shima, Moriguchi, Mitani and Takanashi (2002b) reported that the $L1_0$ phase could artificially be produced by alternating Fe(001) and Pt(001) monatomic layers on a MgO(001) substrate at temperatures below 230 °C. The samples prepared by this technique exhibited perpendicular magnetization with a large uniaxial magnetic anisotropy K_u of 3×10^7 erg cm^{-3} and high chemical ordering (long-range order parameter $S = 0.7 \pm 0.1$) even at $T_S = 200$ °C.

Furthermore, Suzuki, Harada, Honda and Ouchi (1999) reported that a high Ar pressure during deposition was very effective in promoting the chemical ordering. On the other hand, Takahashi, Ohnuma and Hono (2001) reported that the combination of the elevated substrate temperature during the deposition and postannealing was effective for the promotion of ordering even at 300 °C.

Numerous studies were made for the samples with compositions around $Fe_{50}Pt_{50}$ (in at%). However, Seki *et al*. (2003) found that $L1_0$ ordered FePt(001) films with large magnetic

Table 4. Recent studies on the reduction of the ordering temperature for FePt films (Hsu, Jeong, Laughlin and Lambeth, 2001; Maeda *et al*., 2002; Takahashi, Ohnuma and Hono, 2001, 2002; Platt *et al*., 2002; Lee, Yang, Kim and Na, 2001; Ko, Perumal and Shin, 2003; Ravelosona, Chappert, Mathet and Bernas, 2000; Luo and Sellmyer, 1995; Endo, Kikuchi, Kitakami and Shimada, 2001; Shima, Moriguchi, Mitani and Takanashi, 2002; Suzuki, Harada, Honda and Ouchi, 1999; Seki *et al*., 2003).

	Method	Substrate	Composition Fe:Pt (at%)	Temperature (°C)	Author	Year
Au underlayer	SP	Si(001)	55:45	300	Y. -N. Hsu	2001
Cu addition	SP	Glass	46.5:53.5	300	T. Maeda	2002
	SP	Glass	50:50	400	Y. K. Takahashi	2002
	SP	Si(001)	50:50	350	C. L. Platt	2002
Zr addition	SP	Glass	59:41	500	S. R. Lee	2001
C addition	SP	MgO(001)	49.5:50.5	400	S. H. Ko	2003
He^+ irradiation	SP	MgO(001)	50:50	350	D. Ravelosona	2000
Multilayering	SP	Glass	–	300	C. P. Luo	1995
	SP	Quartz	52:48	300–325	Y. Endo	2001
Monatomic layer control	MBE	MgO(001)	52:48	230	T. Shima	2002
High Ar pressure	SP	Glass/sapphire	–	450	T. Suzuki	1999
In situ annealing	SP	Glass	50:50	300	Y. K. Takahashi	2001
Off stoichiometry	SP	MgO(001)	38:62	300	T. Seki	2003

SP: sputtering.

anisotropy could successfully be prepared at $T_S = 300\,^{\circ}C$ by decreasing the Fe concentration from the equiatomic composition. This is quite a simple method for the reduction of ordering temperature, although the detailed mechanism is not elucidated yet.

4.5 Self-assembly of FePt nanoparticles

The demand for higher magnetic recording density with a low system noise stimulates the need for a medium consisting of magnetically isolated particles with a size below 10 nm. Besides, the size of ferromagnetic particles dispersed in a nonmagnetic matrix is expected to become a few nanometers even for a bit size of a 10–20 nm. This size almost reaches the superparamagnetic limit for existing materials that are unsuitable for such applications. Besides, in order to overcome thermal fluctuation and demagnetizing fields that make the magnetization of the recording bit unstable, high K_u materials are needed. A lot of studies on granular-type films consisting of $L1_0$ ordered FePt particles dispersed in a nonmagnetic matrix have been performed. Recent reports on FePt granular films, where FePt nanoparticles are embedded in the matrix materials are indicated here; oxide (MgO: Mukai, Uzumaki and Tanaka, 2003; Shima, Takanashi, Takahashi and Hono, 2006; Al_2O_3: Bian *et al*., 1999; White *et al*., 2003; Al–O: Watanabe, Masumoto, Ping and Hono, 2000; Ping *et al*., 2001; SiO_2: Saito, Kitakami and Shimada, 2002; Luo and Sellmyer, 1999; B_2O_3: Luo *et al*., 2000), nitride (BN: Daniil *et al*., 2002; Christodoulides *et al*., 2001; AlN: Chen, Luo, Lie and Hua, 2001; Si_3N_4: Kuo and Kuo, 2000), metal, and so on (Ag: Chen *et al*., 2002; Ping *et al*., 2001; C: Christodoulides *et al*., 2001; Lee *et al*., 2005). Generally, the granular structure is obtained by following preparation techniques: one of them is codeposition of Fe, Pt, and matrix material. The other consists of first depositing FePt/matrix films in a multilayer form and subsequently annealing the samples at high temperature to form granular structure. Sputtering and ion implantation techniques are used.

Among a lot of investigations on FePt granular films, Takahashi *et al*. (2004a) revealed that there exists a size dependence of the degree of chemical order in FePt–Al_2O_3 granular films. In other words, when the particle size becomes less than a few nanometers, the ordered phase becomes unstable with respect to the disordered phase. Since FePt nanoparticles cannot be coarsened when the volume fraction of FePt is low in the oxide matrix, they may not be able to be ordered to the $L1_0$ structure owing to the size effect.

Figure 21 shows a self-organized magnetic assembly (SOMA) of FePt nanoparticles (Sun *et al*., 2000) which has given a great influence on research direction as a promising candidate for an advanced future magnetic recording media. The chemically processed FePt particles are initially in the disordered state, so they must be ordered to the $L1_0$ phase by annealing. However, several problems are still to be overcome. One of these problems is that the ordered arrays of nanoparticles are deteriorated by the coalescence of the particles. The other is that aligning the *c* axis of the particles by the chemical synthesis method is not easy. Recent progress of chemical synthesis may have an answer to the first problem: it was revealed that SiO_2-coated FePt nanoparticles, which were prepared by chemical synthesis, suppress the coalescence of the particles after annealing at high temperature (Yamamoto, Morimoto, Ono and Takano, 2005). In

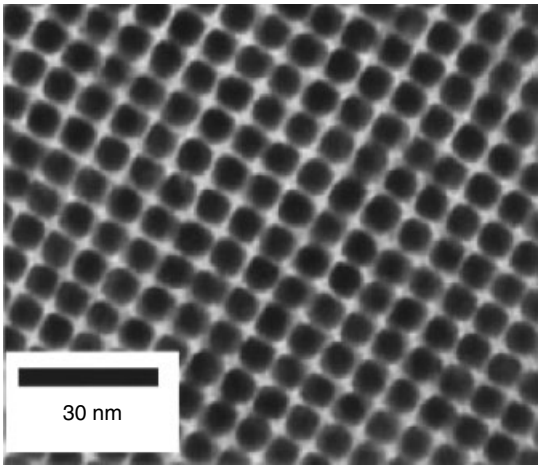

Figure 21. TEM image of a 3-D assembly of FePt nanoparticles with a diameter of 6 nm (Sun *et al*., 2000).

addition, the direct synthesis of $L1_0$ nanoparticles at low temperature using 'modified polyol method' was demonstrated and was found to be effective for reducing the ordering temperature and suppressing the coarsening (Takahashi, Ogawa, Hasegawa and Jeyadevan, 2005).

5 NANOCOMPOSITE MAGNET FILMS

Several attempts to realize an exchange-spring magnet, in other words, a nanocomposite magnet, have been performed by the mixture of a hard magnetic layer and a soft magnetic layer as described in Section 1.3. A possible combination for the nanocomposite structure is constituted by Sm–Co, Sm–Fe, Nd–Fe–B, Fe–Pt as the hard phase and α-Fe, Fe_3B, NiFe, Co as the soft phase. Theoretical energy products $(BH)_{max}$ of some nanocomposite magnets and bulk $Nd_2Fe_{14}B$ alloy, as a reference, are shown in Table 5 (Skomski 1994; Sabiryanov and Jaswal, 1998a). 'Megajoule magnet' can possibly be achieved when $Sm_2Fe_{17}N_3$ and $Fe_{65}Co_{35}$ alloys are selected. Several papers on the experimental work were published on Co/Sm–Co (Liu, Skomski, Liu and Sellmyer, 2000), Fe/FePt (Liu *et al*., 1997), Fe/Pt (Liu, Luo, Liu and Sellmyer, 1998), FePt/Fe_3Pt (Zeng *et al*., 2002), and $Ni_{80}Fe_{20}/Sm_{40}Fe_{60}$ (Yan *et al*., 2001). However, to date, magnetic properties such as remanence enhancement and energy product have not succeeded those of the best aligned 'single-phase' magnets such as $Nd_2Fe_{14}B$ with $(BH)_{max} \simeq 55$ MGOe. The key technology to achieve the improvement of magnetic properties is thought to be in the control of the direction of the easy magnetization axis and the epitaxial growth of each layer.

Table 5. Theoretical energy product $(BH)_{max}$ of some nanocomposite magnets and bulk $Nd_2Fe_{14}B$ alloy (Skomski, 1994; Sabiryanov and Jaswal, 1998a).

Material		$(BH)_{max}$	
Hard phase	Soft phase	(MGOe)	(kJ m^{-3})
$Sm_2Fe_{17}N_3$	$Fe_{65}Co_{35}$	137	1090
$Sm_2Fe_{17}N_3$	Fe	110	880
FePt	Fe	90	720
$Nd_2Fe_{14}B$	Fe	90	720
Sm_2Fe_{17}	Fe	74	592
$SmCo_5$	$Fe_{65}Co_{35}$	65	520
$Nd_2Fe_{14}B$ (bulk)		55	440

REFERENCES

Aylesworth, K.D., Zhao, Z.R., Sellmyer, D.J. and Hadjipanayis, G.C. (1988). Magnetic and structural properties of $Nd_2Fe_{14}B$ permanent-magnet films and multilayers with Fe and Ag. *Journal of Applied Physics*, **64**, 5742.

Bian, B., Hirotsu, Y., Sato, K., *et al*. (1999). Structures and magnetic properties of oriented Fe/Au and Fe/Pt nanoparticles on a-Al_2O_3. *Journal of Electron Microscopy*, **48**, 753.

Buschow, K.H.J. (1969). Preparation of $SmCo_5$ Permanent Magnets. *Journal of Applied Physics*, **40**, 4029.

Cadieu, F.J.L. (1987). High coercive force and large remanent moment magnetic films with special anisotropies. *Journal of Applied Physics*, **61**, 4105.

Cadieu, F.J., Cheung, T.D. and Wickramasekera, L. (1985). Magnetic properties of Sm-Ti-Fe and Sm-Co based films. *Journal of Applied Physics*, **57**, 4161.

Cadieu, F.J., Cheung, T.D. and Wickramasekara, L. (1986). Magnetic properties of sputtered Nd-Fe-B films. *Journal of Magnetism and Magnetic Materials*, **54–57**, 535.

Cadieu, F.J., Cheung, T.D., Aly, S.H., *et al*. (1982). Selectively thermalized sputtering for the direct synthesis of Sm–Co and Sm–Fe ferromagnetic phases. *Journal of Applied Physics*, **53**, 8338.

Carl, A., Kirsch, S., Lohau, J., *et al*. (1999). Magnetization reversal of nanostructured Co/Pt multilayer dots and films studied with magnetic force microscopy and MOKE. *IEEE Transactions on Magnetics*, **35**, 3106.

Chen, K., Hegde, H., Jen, S.U. and Cadieu, F.J. (1993). Different types of anisotropy in amorphous SmCo films. *Journal of Applied Physics*, **73**, 5923.

Chen, S.C., Luo, P.C., Lie, C.T. and Hua, J.T. (2001). Microstructure and coercivity of granular FePt–AlN thin films. *Journal of Magnetism and Magnetic Materials*, **236**, 151.

Chen, S.C., Kuo, P.C., Sun, A.C., *et al*. (2002). Granular FePt–Ag thin films with uniform FePt particle size for high-density magnetic recording. *Materials Science and Engineering B*, **88**, 91.

Chen, M., Nikles, D.E., Yin, H., *et al*. (2003). Patterning self-assembled FePt nanoparticles. *Journal of Magnetism and Magnetic Materials*, **266**, 8.

Christodoulides, J.A., Farber, P., Dannl, M., *et al*. (2001). Magnetic, structural and microstructural properties of FePt/M (M=C,BN) granular films. *IEEE Transactions on Magnetics*, **37**, 1292.

Croat, J.J., Herbst, J.F., Lee, R.W. and Pinkerton, F.E. (1984). Pr–Fe and Nd-Fe-based materials: A new class of high-performance permanent magnets. *Journal of Applied Physics*, **55**, 2078.

Daniil, M., Farber, P.A., Okumura, H., *et al*. (2002). FePt/BN granular films for high-density recording media. *Journal of Magnetism and Magnetic Materials*, **246**, 297.

Durst, K.D. and Kronmüller, H. (1987). The coercive field of sintered and melt-spun NdFeB magnets. *Journal of Magnetism and Magnetic Materials*, **68**, 63.

Endo, Y., Kikuchi, N., Kitakami, O. and Shimada, Y. (2001). Lowering of ordering temperature for fct Fe–Pt in Fe/Pt multilayers. *Journal of Applied Physics*, **89**, 7065.

Evetts, J.E. (Ed.) (1992). *Concise Encyclopedia of Magnetic and Superconducting Materials*, Paragamon: Oxford.

Fullerton, E.E., Jiang, J.S., Rehm, C., *et al*. (1997). High coercivity, epitaxial Sm–Co films with uniaxial in-plane anisotropy. *Applied Physics Letters*, **71**, 1579.

Fullerton, E.E., Sowers, C.H., Pearson, J., *et al*. (1996). A general approach to the epitaxial growth of rare-earth-transition-metal films. *Applied Physics Letters*, **69**, 2438.

Givord, D., Tenaud, P. and Viadieu, T. (1988). Coercivity mechanisms in ferrites and rare earth transition metal sintered magnets ($SmCo_5$, Nd-Fe-B). *IEEE Transactions on Magnetics*, **MAG-24**, 1921.

Givord, D., Lu, Q., Missell, F.P., *et al*. (1992). A direct study of the dipolar field in several RFeB systems. *Journal of Magnetism and Magnetic Materials*, **104–107**, 1129.

Hasegawa, N. and Saito, M. (1992). Structural and soft magnetic properties of nanocrystalline (Fe, Co, Ni)-Ta-C films with high thermal stability. *Journal of Magnetism and Magnetic Materials*, **103**, 294.

Hegde, H., Samarasekara, P., Rani, R., *et al*. (1994). Sputter synthesis of $TbCu_7$ type Sm(CoFeCuZr) films with controlled easy axis orientation. *Journal of Applied Physics*, **76**, 6760.

Herzer, G. (1989). Grain structure and magnetism of nanocrystalline ferromagnets. *IEEE Transactions on Magnetics*, **MAG-25**, 3327.

Hoffmann, H. (1964). Quantitative Calculation of the Magnetic Ripple of Uniaxial Thin Permalloy Films. *Journal of Applied Physics*, **35**, 1790.

Hsu, Y.N., Jeong, S., Laughlin, D.E. and Lambeth, D.N. (2001). Effects of Ag underlayers on the microstructure and magnetic properties of epitaxial FePt thin films. *Journal of Applied Physics*, **89**, 7068.

Hu, B.P., Li, H.S., Gavigan, J.P. and Coey, J.M.D. (1989). Intrinsic magnetic properties of the iron-rich $ThMn_{12}$-structure alloys R(Fe11Ti); R=Y, Nd, Sm, Gd, Tb, Dy, Ho, Er, Tm and Lu. *Journal of Physics: Condensed Matter*, **1**, 755.

Jacobs, J.S. and Bean, C.P. (1995). An Approach to Elongated Fine-Particle Magnets. *Physical Review*, **100**, 1060.

Kittel, C. (1946). Theory of the Structure of Ferromagnetic Domains in Films and Small Particles. *Physical Review*, **70**, 965.

Kneller, E.F. and Hawig, R. (1991). The exchange-spring magnet: a new material principle for permanent magnets. *IEEE Transactions on Magnetics*, **27**, 3588.

Ko, H.S., Perumal, A. and Shin, S-C. (2003). Fine control of $L1_0$ ordering and grain growth kinetics by C doping in FePt films. *Applied Physics Letters*, **82**, 2311.

Kooy, C. and Enz, U. (1960). Experimental and theoretical study of the domain configuration in thin layers of BaFe O. *Philips Research Reports*, **15**, 7.

Kronmüller, H. and Fähnle, M. (2003). *Micromagnetism and the Microstructure of Ferromagnetic Solids*, Cambridge University Press: Cambridge, p. 104.

Kuo, C.M. and Kuo, P.C. (2000). Magnetic properties and microstructure of FePt–Si_3N_4 nanocomposite thin films. *Journal of Applied Physics*, **87**, 419.

Lee, S.R., Yang, S., Kim, Y.K. and Na, J.G. (2001). Rapid ordering of Zr-doped FePt alloy films. *Applied Physics Letters*, **78**, 4001.

Lee, Y.H., Guo, M.S., Wur, C.S., *et al*. (2005). Magnetoresistance of FePt nanograins embedded in carbon matrix. *Journal of Magnetism and Magnetic Materials*, **286**, 113.

Lemke, H., Lang, T., Göddenhenrich, T. and Heiden, C. (1995). Micro patterning of thin Nd-Fe-B films. *Journal of Magnetism and Magnetic Materials*, **148**, 426.

Lemke, H., Muller, S., Göddenhenrich, T. and Heiden, C. (1995). Influence of preparation conditions on the properties of sputtered NdFeB films. *Physical Status Solidi (a),* **150**, 723.

Liu, J.P., Luo, C.P., Liu, Y. and Sellmyer, D.J. (1998). High energy products in rapidly annealed nanoscale Fe/Pt multilayers. *Applied Physics Letters*, **72**, 483.

Liu, J.P., Skomski, R., Liu, Y. and Sellmyer, D.J. (2000). Temperature dependence of magnetic hysteresis of RCox:Co nanocomposites (R=Pr and Sm). *Journal of Applied Physics*, **87**, 6740.

Liu, J.P., Liu, Y., Luo, C.P., *et al*. (1997). Magnetic hardening in FePt nanostructured films. *Journal of Applied Physics*, **81**, 5644.

Luo, C.P. and Sellmyer, D.J. (1995). Magnetic properties and structure of Fe/Pt thin films. *IEEE Transactions on Magnetics*, **31**, 2764.

Luo, C.P. and Sellmyer, D.J. (1999). Structural and magnetic properties of FePt:SiO_2 granular thin films. *Applied Physics Letters*, **75**, 3162.

Luo, C.P., Liou, S.H., Gao, L., *et al*. (2000). Nanostructured FePt:B_2O_3 thin films with perpendicular magnetic anisotropy. *Applied Physics Letters*, **77**, 2225.

Maeda, T., Kai, T., Kikitsu, A., *et al*. (2002). Reduction of ordering temperature of an FePt-ordered alloy by addition of Cu. *Applied Physics Letters*, **80**, 2147.

Malhotra, S.S., Liu, Y., Shan, Z.S., *et al*. (1996). High coercivity rare earth-cobalt films. *Journal of Applied Physics*, **79**, 5958.

Mishra, R.K., Thomas, G., Yoneyama, T., *et al*. (1981). Microstructure and properties of step aged rare earth alloy magnets. *Journal of Applied Physics*, **52**, 2517.

Mukai, R., Uzumaki, T. and Tanaka, A. (2003). Monolayer of physically separated FePt islands with a tetragonal $L1_0$ structure produced by thermally created mass transport. *IEEE Transactions on Magnetics*, **39**, 1925.

Ojima, T., Tomizawa, S., Yoneyama, T. and Hori, T. (1977). Magnetic properties of a new type of rare-earth cobalt magnets $Sm_2(Co, Cu, Fe, M)_{17}$. *IEEE Transactions on Magnetics*, **MAG-13**, 1317.

Okamoto, H. (2000), *Phase Diagram of Binary Alloys*, ASM International: Cleveland, USA, p. 371.

Okumura, Y., Suzuki, O., Morita, H., *et al*. (1995). Microstructure and magnetic properties of sputtered CoSm/Cr thin films with high coercivities. *Journal of Magnetism and Magnetic Materials*, **146**, 5.

Ovanov, O.A., Solina, L.V. and Demshina, V.A. (1973). Determination of the anisotropy constant and saturation magnetization, and magnetic properties of powders of an iron-platinum alloy. *Physics of Metals and Metallography*, **35**, 81.

Parhofer, S., Gieres, G., Wecker, J. and Schultz, L. (1996). Growth characteristics and magnetic properties of sputtered Nd-Fe-B thin films. *Journal of Magnetism and Magnetic Materials*, **163**, 32.

Ping, D.H., Ohnuma, M., Hono, K., *et al*. (2001). Microstructures of FePt–Al–O and FePt–Ag nanogranular thin films and their magnetic properties. *Journal of Applied Physics*, **90**, 4708.

Platt, C.L., Wierman, K.W., Svedberg, E.B., *et al*. (2002). L-1_0 ordering and microstructure of FePt thin films with Cu, Ag, and Au additive. *Journal of Applied Physics*, **92**, 6104.

Rani, R., Cadieu, F.J., Qian, X.R., *et al*. (1997). SmCo based sputtered films with $CaCu_5$ and $TbCu_7$ structures. *Journal of Applied Physics*, **81**, 5634.

Ravelosona, D., Chappert, C., Mathet, V. and Bernas, H. (2000). Chemical order induced by He + ion irradiation in FePt (001) films. *Journal of Applied Physics*, **87**, 5771.

Sabiryanov, R.F. and Jaswal, S.S. (1998a). Electronic structure and magnetic properties of hard/soft multilayers. *Journal of Magnetism and Magnetic Materials*, **177–181**, 989.

Sabiryanov, R.F. and Jaswal, S.S. (1998b). Magnetic properties of hard/soft composites: SmCo5/Co1-xFex. *Physical Review B*, **58**, 12071.

Sagawa, M., Fujimura, S., Togawa, N., *et al*. (1984). New material for permanent magnets on a base of Nd and Fe. *Journal of Applied Physics*, **55**, 2083.

Saito, T., Kitakami, O. and Shimada, Y. (2002). Grain growth and L10 ordering in FePt–SiO_2 granular films. *Journal of Magnetism and Magnetic Materials*, **239**, 310.

Sayama, J., Mizutani, K., Asahi, T. and Osaka, T. (2004). Thin films of $SmCo_5$ with very high perpendicular magnetic anisotropy. *Applied Physics Letters*, **85**, 5640.

Schrefl, T. and Fidler, J. (1992). Numerical simulation of magnetization reversal in hard magnetic materials using a finite element method. *Journal of Magnetism and Magnetic Materials*, **111**, 105.

Seki, T., Shima, T., Takanashi, K., *et al*. (2003). $L1_0$ ordering of off-stoichiometric FePt (001) thin films at reduced temperature. *Applied Physics Letters*, **82**, 2461.

Senno, H. and Tawara, Y. (1975). Magnetic Properties of Sm-Co-Fe-Cu Alloys for Permanent Magnet Materials. *Japanese Journal of Applied Physics*, **14**, 1619.

Shima, T., Kamegawa, A., Hono, K. and Fujimori, H. (2001). Overlayer-induced anisotropic alignment of $Nd_2Fe_{14}B$ nanograins. *Applied Physics Letters*, **78**, 2049.

Shima, T., Moriguchi, T., Mitani, S. and Takanashi, K. (2002b). Low-temperature fabrication of $L1_0$ ordered FePt alloy by alternate monatomic layer deposition. *Applied Physics Letters*, **80**, 288.

Shima, T., Takanashi, K., Li, G.Q. and Ishio, S. (2003). Microstructure and Magnetic Properties for Highly Coercive FePt Sputtered Films. *Materials Transactions*, **44**, 1508.

Shima, T., Takanashi, K., Takahashi, Y.K. and Hono, K. (2002a). Preparation and magnetic properties of highly coercive FePt films. *Applied Physics Letters*, **81**, 1050.

Shima, T., Takanashi, K., Takahashi, Y.K. and Hono, K. (2004). Coercivity exceeding 100 kOe in epitaxially grown FePt sputtered films. *Applied Physics Letters*, **85**, 2571.

Shima, T., Takanashi, K., Takahashi, Y.K. and Hono, K. (2006). Formation of octahedral FePt nanoparticles by alternate deposition of FePt and MgO. *Applied Physics Letters*, **88**, 063117.

Shima, T., Takanashi, K., Takahashi, Y.K., *et al*. (2006). Nucleation-type magnetization behavior in FePt (001) particulate films. *Journal of Applied Physics*, **99**, 033516.

Shindo, M., Ishizone, M., Kato, H., *et al*. (1996). Exchange-spring behavior in sputter-deposited α-Fe/Nd-Fe-B multilayer magnets. *Journal of Magnetism and Magnetic Materials*, **161**, L1.

Skomski, R. (1994). Aligned two-phase magnets: Permanent magnetism of the future?. *Journal of Applied Physics*, **76**, 7059.

Skomski, R. and Coey, J.M.D. (1993). Giant energy product in nanostructured two-phase magnets. *Physical Review B*, **48**, 15812.

Stoner, E.C. and Wohlfarth, E.P. (1948). A mechanism of magnetic hysteresis in heterogeneous alloys. *Philosophical Transactions of the Royal Society of London, Series A*, **240**, 599.

Sun, S., Murray, C.B., Weller, D., *et al*. (2000). Monodisperse FePt Nanoparticles and Ferromagnetic FePt Nanocrystal Superlattices. *Science*, **287**, 1989.

Suzuki, T., Harada, K., Honda, N. and Ouchi, K. (1999). Preparation of ordered Fe–Pt thin films for perpendicular magnetic recording media. *Journal of Magnetism and Magnetic Materials*, **193**, 85.

Suzuki, K., Makino, A., Kataoka, N., *et al*. (1991). High Saturation Magnetization and Soft Magnetic Properties of bcc Fe-Zr-B and Fe-Zr-B-M (M=Transition Metal) Alloys with Nanoscale Grain Size. *Materials Transactions, JIM* , **32**, 93.

Takahashi, Y.K., Hono, K., Shima, T. and Takanashi, K. (2003). Microstructure and magnetic properties of FePt thin films epitaxially grown on MgO(001) substrates. *Journal of Magnetism and Magnetic Materials*, **267**, 248.

Takahashi, M., Ogawa, T., Hasegawa, D. and Jeyadevan, B. (2005). Direct synthesis of Pt based $L1_0$ structured nanoparticles. *Journal of Applied Physics*, **97**, 10J307.

Takahashi, Y.K., Ohnuma, M. and Hono, K. (2001). Low-Temperature Fabrication of High-Coercivity $L1_0$ Ordered FePt Magnetic Thin Films by Sputtering. *Japanese Journal of Applied Physics*, **40**, L1367.

Takahashi, Y.K., Ohnuma, M. and Hono, K. (2002). Effect of Cu on the structure and magnetic properties of FePt sputtered film. *Journal of Magnetism and Magnetic Materials*, **246**, 259.

Takahashi, Y.K., Koyama, T., Ohnuma, M., *et al*. (2004a). Size dependence of ordering in FePt nanoparticles. *Journal of Applied Physics*, **95**, 2690.

Takahashi, Y.K., Seki, T.O., Hono, K., *et al*. (2004b). Microstructure and magnetic properties of FePt and Fe/FePt polycrystalline films with high coercivity. *Journal of Applied Physics*, **96**, 475.

Theuerer, H.C., Nesbitt, E.A. and Bacon, D.D. (1969). High-Coercive-Force Rare-Earth Alloy Films by Getter Sputtering. *Journal of Applied Physics*, **40**, 2994.

Thiele, J.U., Folks, L., Toney, M.F. and Weller, D.K. (1998). Perpendicular magnetic anisotropy and magnetic domain structure in sputtered epitaxial FePt (001) $L1_0$ films. *Journal of Applied Physics*, **84**, 5686.

Velu, E.M.T. and Lambeth, D.N. (1992). High density recording on SmCo/Cr thin film media. *IEEE Transactions on Magnetics*, **28**, 3249.

Watanabe, M., Masumoto, T., Ping, D.H. and Hono, K. (2000). Microstructure and magnetic properties of FePt–Al–O granular thin films. *Applied Physics Letters*, **76**, 3971.

Weller, D. and Moser, A. (1999). Thermal effect limits in ultrahigh-density magnetic recording. *IEEE Transactions on Magnetics*, **35**, 4423.

White, C.W., Withrow, S.P., Sorge, K.D., *et al*. (2003). Oriented ferromagnetic Fe-Pt alloy nanoparticles produced in Al_2O_3 by ion-beam synthesis. *Journal of Applied Physics*, **93**, 2656.

Yamamoto, S., Morimoto, Y., Ono, T. and Takano, M. (2005). Magnetically superior and easy to handle L10-FePt nanocrystals. *Applied Physics Letters*, **87**, 032503.

Yamashita, S., Yamasaki, J., Ikeda, M. and Iwabuchi, N. (1991). Anisotropic Nd–Fe–B thin-film magnets for milli-size motor. *Journal of Applied Physics*, **70**, 6627.

Yan, S.S., Barnard, J.A., Xu, F.T., *et al*. (2001). Critical dimension of the transition from single switching to an exchange spring process in hard/soft exchange-coupled bilayers. *Physical Review B*, **64**, 184403.

Yoshizawa, Y., Oguma, S. and Yamauchi, K. (1988). New Fe-based soft magnetic alloys composed of ultrafine grain structure. *Journal of Applied Physics*, **64**, 6044.

Zeng, H., Li, J., Liu, J.P., *et al*. (2002). Exchange-coupled nanocomposite magnets by nanoparticle self-assembly. *Nature*, **420**, 395.

Magneto-optical Materials

Wolfgang Kleemann
Universität Duisburg-Essen, Duisburg, Germany

1 INTRODUCTION

Magneto-optics was discovered in the nineteenth century. *Michael Faraday* (1791–1867) observed the rotation of the plane of light polarization in a piece of longitudinally magnetized glass in 1845 (Faraday, 1846), while *John Kerr* (1824–1907) realized the complementary effect in reflection from the poles of a magnet in 1876 (Kerr, 1877). More precisely, the magneto-optical *Kerr* effect (MOKE) is the change of polarization (ellipticity and/or rotation of the polarization axes) and/or intensity of the light being reflected by a magnetized surface. Three different geometries are distinguished (Figure 1): the polar (a), the longitudinal (b), and the transversal MOKE (c). All of these effects are linear in the magnetization and/or the magnetic field (quadratic contributions may superimpose at very high fields). Both Faraday rotation and MOKE may be classified as magnetic circular birefringence (MCB) effects, which are Kramers–Kronig related to magnetic circular dichroism (MCD). They have to be distinguished from transverse magneto-optical (MO) effects being quadratic in magnetization and/or magnetic field. The *Voigt* or *Cotton–Mouton* effect (Voigt, 1898, 1908; Cotton and Mouton, 1907) is commonly known as *magnetic linear birefringence* (MLB), which is related to the magnetic linear dichroism (MLD).

Today, the theory of magneto-optics is well understood and the development of MO materials and devices is an extremely vivid field of research. This has been documented in the last 20 years from various points of view, either focusing on materials (Buschow, 1988) or on theory (Oppeneer, 2001), or on both of them in an excellent monograph (Zvezdin and Kotov, 1997). Aspects of applications were in the focus of other reviews or monographs. Ever since, Faraday rotation and MOKE have been most popular methods to image ferro- and ferrimagnetic domain structures (Dillon, 1963; Craik and Tebble, 1965; Dillon, 1971; Hubert and Schäfer, 1998). Although MO recording materials and devices have been developed since more than 30 years, they reached maturity only in the last 10 years. In particular, the preparation of high performance MO materials and their heterostructures allowing the storage, readout, and erasure of data at very high densities were sensitively improved. This has been documented in various extensive reviews (Mansuripur, 1995; Gambino and Suzuki, 1999; Röll 2003). Thin films and nanostrucures are, meanwhile, probably the most investigated materials in MO research and development (Ferré, 1992). Even more sophisticated structures like MO light waveguides and magnetophotonic crystals (Lyubchanskii *et al*., 2003) are at the dawn of applications.

In parallel to the development of appropriate materials, the search for optimized light sources has become increasingly important. The development of the MO disc technology is intimately connected with the development of novel laser diodes emitting at shorter light wavelengths. On the

Handbook of Magnetism and Advanced Magnetic Materials. Edited by Helmut Kronmüller and Stuart Parkin. Volume 4: *Novel Materials*. ISBN: 978-0-470-02217-7.

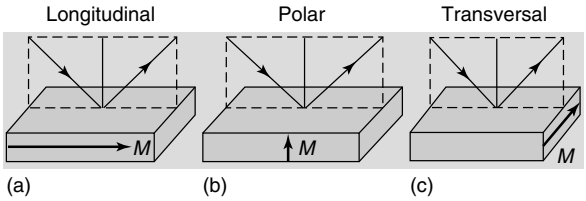

Figure 1. Schematic longitudinal (a), polar (b), and transversal Kerr effect (c) configurations.

other hand, high-power mode-locked solid-state lasers with ultrashort pulses are now playing a major role in modern materials research, where MOKE has become an indispensable tool for investigating novel nanostructured and/or very thin-film materials at high temporal resolution (Hillebrands and Ounadjela, 2002, 2003). Owing to its very fast response, high accuracy, and high temporal and spatial resolution, the MO probe has proved to be probably the most powerful method to study magnetic properties at extreme length and timescales (Rasing *et al*., 2003). The novel term *femtomagnetism* stands for temporal magnetic response on a subpicosecond timescale and substantially relies on MO spectroscopical techniques (Bigot, Guidoni, Beaurepaire and Saeta, 2004). The excellent time resolution of MOKE is also absolutely essential in spintronics research, where spin states of magnetic semiconductors are investigated at the picosecond timescale (Kimel *et al*., 2004). Finally, the development of powerful and versatile synchrotron-based light sources in the X-ray regime opened another extremely fruitful branch of magneto-optics. Magnetically dichroic signals (X-ray magnetic circular dichroism, XMCD, X-ray magnetic linear dichroism, XMLD) at resonance with spin-polarized transitions from K and L edges (Schütz *et al*., 1987) have proven to be extremely sensitive and have become widely used for investigations of quantitative aspects of magnetism, meanwhile also connected with microscopic imaging at high spatial resolution (Stoehr *et al*., 1993, Fischer *et al*., 1996).

When talking about *magnetic domains* intuitively the topography of ferromagnetic and ferrimagnetic magnetization is normally considered (Hubert and Schäfer, 1998). This view is, however, incomplete, since there are at least as many antiferromagnetic materials in nature as ferromagnetic ones. For thermodynamic reasons, they also decay into domains, the structure of which is, however, less evident than in the ferroic case. It is usually not accessible by MOKE or Faraday rotation and has never been considered as useful as the ferromagnetic one. This opinion has changed in recent years, since antiferromagnetic materials gained appreciable technological interest within the context of spin electronics (Prinz, 1998), exchange bias (Nogués and Schuller, 1999), magnetoelectric, and multiferroic systems (Fiebig, 2005). While the cumbersome method of neutron topography was previously the only direct method to verify the $\pm 180^\circ$ orientation of an antiferromagnetic uniaxial order parameter (Tanner, 1979), nonlinear MO spectroscopy is now an alternative to image antiferromagnetic domain topography at higher resolution using second harmonic generation (SHG) (Fiebig, Fröhlich, Krichevstov and Pisarev, 1994). Another very promising method utilizes the XMLD of antiferromagnets with appropriate symmetry (Nolting *et al*., 2000).

In this contribution, we shall give brief overviews on the theoretical aspects (Section 2) and the experimental techniques (Section 3) presently involved in magneto-optics. Section 4 will then deal with some MO materials and their applications, which are presently in the focus of interest: magneto-optical storage materials, magnetic semiconductors, antiferromagnets, and magnetophotonic crystals.

2 THEORETICAL ASPECTS

2.1 Linear magneto-optics

In the spectral range of visible and UV light, MO effects are linked to the dielectric permittivity tensor being perturbed by magnetic contributions. Being far above the frequencies of magnetic resonances, there is virtually no contribution from the magnetic permeability. Let us first consider a simple quasiclassic model of the axial (polar) MO effects based on the Drude–Lorentz model of elastically bound electrons (spatial coordinate $\mathbf{r} = (x, y)$, mass m, charge e, damping constant γ, eigenfrequency ω_o) under the combined action of the electrical field of the light wave, $\mathbf{E} = (E_x, E_y)\exp(i\omega t)$ and an axial external magnetic field, $\mathbf{B} = B\hat{z}$. The equation of motion reads

$$m\ddot{\mathbf{r}} + \gamma\dot{\mathbf{r}} + m\omega_o^2\mathbf{r} = e\mathbf{E} + e(\dot{\mathbf{r}} \times \mathbf{B}) \tag{1}$$

and is solved by harmonically oscillating coordinates $x = x_o \exp(i\omega t)$ and $y = y_o \exp(i\omega t)$ which enter circular coordinates,

$$x_\pm = \alpha_\pm E_\pm / e \tag{2}$$

with $x_\pm = (x_o \pm i y_o)\exp(i\omega t)$ and $E_\pm = (E_x \pm i E_y)\exp(i\omega t)$. The electric dipole moment $p_\pm = e x_\pm = \alpha_\pm E_\pm$ involves the polarizabilities

$$\alpha_\pm = \frac{e^2}{m\left(\omega_o^2 - \omega^2\right) + i\omega\gamma \mp e\omega B} \approx \frac{e^2}{m\left(\omega_o^2 - \omega^2\right) + i\omega\gamma} \times \left\{1 \pm \frac{e\omega B}{m\left(\omega_o^2 - \omega^2\right) + i\omega\gamma}\right\} \tag{3}$$

such that finally

$$\vec{p} = \begin{pmatrix} p_x \\ p_y \end{pmatrix} = \frac{1}{2} \begin{pmatrix} \alpha_+ + \alpha_- & i\,(\alpha_+ - \alpha_-) \\ -i\,(\alpha_+ - \alpha_-) & \alpha_+ + \alpha_- \end{pmatrix} \times \begin{pmatrix} E_x \\ E_y \end{pmatrix} = \vec{\alpha}\vec{E} \tag{4}$$

The tensor of the dielectric permittivity

$$\varepsilon_{ij} = \frac{N\alpha_{ij}}{\varepsilon_o} + \delta_{ij},$$
$$\vec{\varepsilon} = \frac{1}{2} \begin{pmatrix} N(\alpha_+ + \alpha_-)/\varepsilon_o + 1 & iN(\alpha_+ - \alpha_-)/\varepsilon_o \\ -iN(\alpha_+ - \alpha_-)/\varepsilon_o & N(\alpha_+ + \alpha_-)/\varepsilon_o + 1 \end{pmatrix} \tag{5}$$

is diagonal in circular polarization and yields the complex refractive indices

$$\tilde{n}_\pm = \sqrt{\varepsilon_\pm} = \sqrt{N\alpha_\pm/\varepsilon_o + 1} \equiv n_\pm + i\kappa_\pm \tag{6}$$

The *Faraday* rotation angle is readily found from the circular birefringence $n_+ - n_-$ and yields

$$\Theta_{\mathrm{F}} = \frac{\pi}{\lambda_{\mathrm{o}}} (n_+ - n_-)\, t \propto Re\,(\alpha_+ - \alpha_-) \propto B \tag{7}$$

where t is the sample thickness. The *Faraday* ellipticity is related to the circular dichroism $\kappa_+ - \kappa_-$ via

$$\varepsilon_{\mathrm{F}} = \frac{\pi}{\lambda_{\mathrm{o}}} (\kappa_+ - \kappa_-)\, d \propto \mathrm{Im}\,(\alpha_+ - \alpha_-) \propto B \tag{8}$$

In a ferromagnet, one has to replace B by the magnetization M such that

$$\Theta_{\mathrm{F}}, \varepsilon_{\mathrm{F}} \propto M \tag{9}$$

Kerr rotation and ellipticity in the polar geometry (Figure 1a) is calculated by starting from an x polarized incident wave, which contains two circularly polarized eigenmodes at longitudinal propagation,

$$\mathbf{E}_i^{\pm} = \begin{pmatrix} 1 \\ \pm i \end{pmatrix} \frac{E_i}{2} \text{ with } \mathbf{E}_i = \mathbf{E}_{\mathrm{o}} \mathrm{e}^{i(\omega t - kz)} \tag{10}$$

Making use of the dielectric tensor, equation (5), which may be written as

$$\boldsymbol{\varepsilon} = \begin{pmatrix} \varepsilon_{xx} & i\varepsilon_{xy} & 0 \\ -i\varepsilon_{xy} & \varepsilon_{xx} & 0 \\ 0 & 0 & \varepsilon_{zz} \end{pmatrix} \tag{11}$$

and of Fresnel's formulae, one obtains the reflected field components

$$\mathbf{E}_{\mathrm{r}}^{+} = \frac{1 - n_+}{1 + n_+} \begin{pmatrix} 1 \\ i \end{pmatrix} \frac{E_e}{2} \tag{12}$$

where $\mathbf{E}_{\mathrm{r}}^{-} = \frac{1-n_-}{1+n_-} \begin{pmatrix} 1 \\ -i \end{pmatrix} \frac{E_i}{2}$ and $n_\pm = \left(\varepsilon_{xx} \mp \varepsilon_{xy}\right)^{1/2}$. One thus obtains

$$E_{\mathrm{r}x} = \frac{1}{2} \left(\frac{1 - n_+}{1 + n_+} + \frac{1 - n_-}{1 + n_-} \right) E_i = \frac{-n_+ n_- + 1}{(1 + n_+)\,(1 + n_-)} E_i = A_x \mathrm{e}^{i\Phi_x} \tag{13}$$

$$E_{\mathrm{r}y} = \frac{i}{2} \left(\frac{1 - n_+}{1 + n_+} - \frac{1 - n_-}{1 + n_-} \right) E_i = i \frac{-n_+ + n_-}{(1 + n_+)\,(1 + n_-)} E_i = A_y \mathrm{e}^{i\Phi_y} \tag{14}$$

and the ratio

$$\frac{E_{\mathrm{r}y}}{E_{\mathrm{r}x}} = i \frac{n_+ - n_-}{n_+ n_- - 1} = \frac{A_y}{A_x} \mathrm{e}^{i(\Phi_y - \Phi_x)} = \frac{A_y}{A_x} \left[\cos\left(\Phi_y - \Phi_x\right) + i \sin\left(\Phi_y - \Phi_x\right) \right] \tag{15}$$

For $\Phi_y - \Phi_x = 0$ one solely obtains Kerr rotation,

$$Re \frac{E_{\mathrm{r}y}}{E_{\mathrm{r}x}} = \frac{A_y}{A_x} = \tan\theta_{\mathrm{K}} \approx \theta_{\mathrm{K}} \tag{16}$$

while for $\Phi_y - \Phi_x = \frac{\pi}{2}$ mere Kerr ellipticity is observed,

$$Im \frac{E_{\mathrm{r}y}}{E_{\mathrm{r}x}} = \frac{A_y}{A_x} = \varepsilon_{\mathrm{K}} \tag{17}$$

Since in general $0 \neq \Phi_y - \Phi_x \neq \frac{\pi}{2}$, both components as defined by equations (16) and (17) are simultaneously observed. Under the constraint $|\varepsilon_{xy}| \ll |\varepsilon_{xx}|$ a compact final formula is derived,

$$\frac{E_{\mathrm{r}y}}{E_{\mathrm{r}x}} = i \frac{n_+ - n_-}{n_+ n_- - 1} \approx \frac{\varepsilon_{xy}}{i\,(\varepsilon_{xx})^{1/2}\,(\varepsilon_{xx} - 1)} \tag{18}$$

Interestingly, a transparent solid with real tensor components ε_{xx} and ε_{xy} lacks any Kerr rotation, $\mathrm{Re}\frac{E_{\mathrm{r}y}}{E_{\mathrm{r}x}} = 0$, but reveals nonvanishing Kerr ellipticity,

$$\mathrm{Im} \frac{E_{\mathrm{r}y}}{E_{\mathrm{r}x}} = \varepsilon_K = \frac{-\varepsilon_{xy}}{(\varepsilon_{xx})^{1/2}(\varepsilon_{xx} - 1)} \tag{19}$$

Since the secondary motion of the electrons due to the Lorentz field in equation (1) is perpendicular to both the

direction of the magnetization and to the primary motion, a secondary amplitude is superimposed to the primary beam of the reflected light. This explains qualitatively the differences between the three general MOKE geometries shown in Figure 1. In the *polar* geometry, P-MOKE (a) the magnetization is perpendicular to the reflecting surface; hence, a linearly polarized wave generates a secondary component, which is strongest at perpendicular incidence. There is no dependence on the initial direction of the polarization. In the *longitudinal* configuration, L-MOKE (b) the magnetization is parallel to both the plane of incidence and to the reflecting surface. This generates a rotation of the polarization of the reflected beam both for s (= perpendicular) and p (= parallel) polarized light with respect to the plane of incidence, however, with different signs of the Kerr rotation. It vanishes for perpendicular incidence and maximizes at intermediate angles of incidence. General results for arbitrary angles of incidence have been derived by explicit use of the corresponding Fresnel's formulae (see e.g., Metzger, Pluvinage and Torguet, 1965; Dillon, 1971; Zvezdin and Kotov, 1997).

For the *transversal* geometry, T-MOKE (c) does not involve any rotation or ellipticity as is the case for P-MOKE or L-MOKE, since the secondary amplitude either vanishes (in s-wave polarization, where **M** is parallel to $\dot{\mathbf{r}}$) or adds along the propagation vector (in p-wave polarization). However, in the latter case, the reflectivity changes at oblique incidence when inverting the magnetic field (or magnetization), since the component of the electric polarization **P** perpendicular to the direction of the reflected beam changes. Thus, the *transversal* 'Kerr' effect is quite useful for observing or measuring magnetization contrast by simple intensity measurements (Voigt, 1908; Yang and Scheinfein, 1993). T-MOKE was first observed by Zeeman (1897) and is particularly suited to visualize surface magnetic domain structures (Hubert and Schäfer, 1998).

It should be mentioned that second-order contributions, that is, quadratic in the components of **M**, may be quite sizeable. They are natural ingredients from the beginning in the sense of perturbation expansions like those used in equation (3) and dominate in the transverse *Voigt* geometry. The linear dielectric tensor, equation (11), has to be supplemented by a quadratic one and reads as follows for cubic crystals (Hubert and Schäfer, 1998):

$$\boldsymbol{\varepsilon} = \varepsilon \begin{pmatrix} 1 & -iQm_z & iQm_y \\ iQm_z & 1 & -iQm_x \\ -iQm_y & iQm_x & 1 \end{pmatrix} + \begin{pmatrix} B_1 m_x^2 & B_2 m_x m_y & B_2 m_x m_z \\ B_2 m_x m_y & B_1 m_y^2 & B_2 m_y m_z \\ B_2 m_x m_z & B_2 m_y m_z & B_1 m_z^2 \end{pmatrix} \quad (20)$$

Here, **m** is the unit vector of the magnetization, $Q \propto \varepsilon_{xy}$ (*Voigt constant*), and B_1 and B_2 are material parameters. In the Faraday configuration with $m_x = m_y = 0$, Faraday effect and P-MOKE emerge linearly in m_z as anticipated above, whereas in the L-MOKE configuration with $m_x \neq 0 \neq m_y$, the Kerr rotation angle may effectively contain quadratic contributions formally described as

$$\theta_{\mathrm{K}} \propto m_y + \alpha m_x m_y + \beta m_x^2 \quad (21)$$

They were shown to depend on the angle of incidence and to give rise to asymmetric hysteresis loops as reported, for example, for the case of thin films of Fe (Postava *et al*., 1997; Yan, Schreiber, Grünberg and Schäfer, 2000) and discussed within an extended MOKE theory (Osgood, Clemens and White, 1997; Osgood, Bader, Clemens and White, 1998).

All MO spectroscopies are based on the coupling of electromagnetic waves to the orbital states of spin-polarized electron states. Since these are coupled by the spin-orbit interaction, techniques like MOKE are intimately probing the very heart of magnetism within the electronic structure of materials (Schoenes, 2003). In order to understand MOKE theoretically, basically the nondiagonal element of the dielectric tensor, ε_{xy}, which enters the pertinent formulae, equations (18) and (19), has to be calculated in a reasonable approximation. Attempts to do this without taking into account the spin-orbit interaction (Bennett and Stern, 1965) virtually failed, and an early perturbation theory (Argyres, 1955) including spin-orbit coupling was finally acknowledged to be basically correct. Direct calculations of MOKE spectra (Misemer, 1988; Oppeneer, Sticht, Maurer and Kübler, 1992) confirmed that the Kerr effect scales linearly with the spin-orbit coupling strength. Here, we restrict ourselves to give a simple picture, starting with the imaginary part of the optical conductivity, σ_{xy}, which is Kramers–Kronig related to the dielectric tensor component ε_{xy} (Bruno, Suzuki and Chappert, 1996),

$$\sigma''_{xy}(\omega) \propto \frac{1}{\omega} \sum_{i,f} f(E_{\mathrm{i}}) \left[1 - f(E_{\mathrm{f}})\right] \times \left[|\langle i|p_-|f\rangle|^2 - |\langle i|p_+|f\rangle|^2\right] \delta(\omega_{if} - \omega) \quad (22)$$

where $f(E)$ is the Fermi function, $\langle i|p_\pm|f\rangle$ the dipole matrix elements for left and right circularly polarized light, and $\hbar\omega_{if} = E_{\mathrm{f}} - E_{\mathrm{i}}$ photon energies connecting initial and final electronic states of the system under inspection. Figure 2 (Bruno, Suzuki and Chappert, 1996) shows a simplified quasiatomic energy scheme of a ferromagnetic metal, where optical absorption in the visible region is due to dipolar allowed d–p transitions. Two level splittings are essential: (i) the exchange splitting $\Delta_{\mathrm{ex}} \approx 1\text{–}2\,\mathrm{eV}$ between the

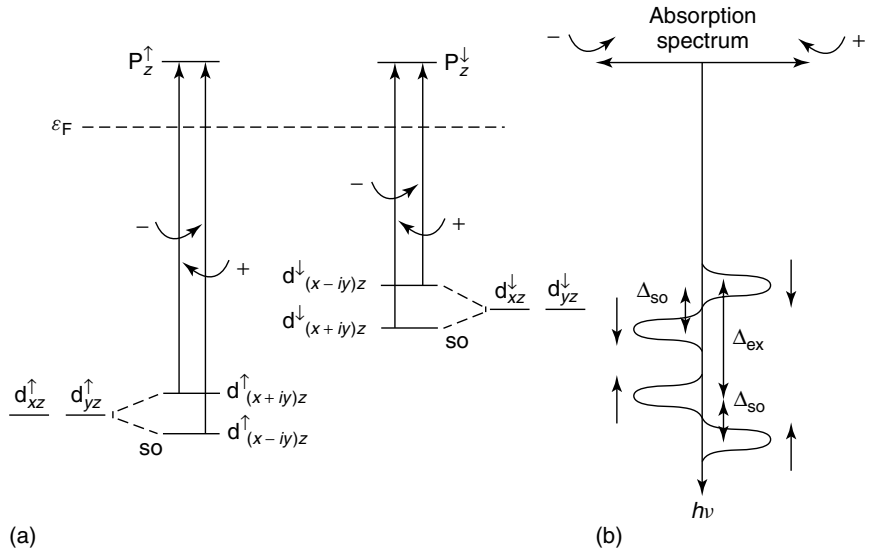

Figure 2. Energy levels of a ferromagnet, showing the electric dipolar optical transitions for left and right circular light (a) and the corresponding absorption spectra (b). (Reproduced from Bruno *et al*., 1996, with permission from the American Physical Society. © 1996.)

spin-up and spin-down electrons and (ii) the spin-orbit splitting $\Delta_{so} \approx 10-20\,\text{meV}$ between the $d_{xz,yz}$ states. The transitions from the spin-orbit split levels into the p_z state are distinguished by their photon polarization, σ_+ and σ_-, respectively. This explains the dichroism within the absorption spectrum as depicted in Figure 2(b), which reveals four differently polarized absorption lines. Clearly, this MCD would be absent without spin-orbit splitting, viz in case of degeneracy of the $d_{xz,yz}$ states. It would also be absent without the exchange splitting, since the two spin-orbit split doublets would collapse and annihilate any dichroism. It should be remarked that the spin-orbit splitting does not necessarily occur in the ground state (Schoenes, 2003). For example, the largest ever reported Faraday rotation exceeding $2 \times 10^6\,\text{deg}\,\text{cm}^{-1}$ is observed in thin films of europium monochalcogenides EuS, EuSe, and EuTe, which have a $4f^7(^8S_{7/2})$ ground state without any orbital moment. Hence, there is no spin-orbit splitting in the initial state, but in the final ones.

Realistic calculations of MOKE spectra have to take into account the full band structure of the systems involved. They require the knowledge of the single particle electron wave functions and their energies. The dielectric permittivity tensor components or, equivalently, the components of the optical conductivity are usually calculated within the Kubo formalism (Kubo, 1957), while its principal ingredients (energies and wave functions) are provided within density-functional theory (DFT) (Kohn and Sham, 1965), for example, in local spin density approximation (LSDA). Figures 3–5 show three examples of *ab initio* calculated MOKE spectra of ferromagnetic Co, CoPt (Oppeneer and Antonov, 1996), and MnBi (Oppeneer *et al*., 1996), respectively. All of them (solid lines) compare reasonably well with experimental results (Weller *et al*., 1994; Weller, 1996; Di, 1992; Harder, Menzel, Widmer and Schoenes, 1998, respectively) on bulk samples. Interestingly, the cobalt spectra turn out to depend substantially on the crystallographic directions, that is, on the magnetocrystalline anisotropy (left: fcc-Co, right: hcp-Co $[11\bar{2}0]$ and [1000]). This is another manifestation of the spin-orbit interaction. The spectra of MnBi give an example of the difficulties in obtaining reliable experimental results on a material, which is not easily prepared in perfect stoichiometry and where vacuum conditions may play a role on the absolute values of the MOKE components of Φ_K. We remark that the magnitude of Φ_K increases from Co to CoPt and MnBi. Even larger values have been found for other rare-earth (RE) elements, in particular, for Ce compounds. Record values as high as $\theta_K = 90^\circ$ were found, for example, in CeSb (Pittini, Schoenes, Vogt and Wachter, 1996). This is a consequence of the strong localization of the 4f electrons, where the 100% effects shown in Figure 2 are approximately realized. As a tribute to the high correlation of the 4f electrons, however, precise calculations of the MO spectra require the introduction of an additional Hubbard-like Coulomb interaction U (Yaresko *et al*., 1996; Oppeneer, 2001).

2.2 X-ray magneto-optics

XMCD is closely related to conventional MOKE or MCD, but is shifted down to the subnanometer wavelength regime, that is, 2 orders of magnitude smaller than visible light (Schütz *et al*., 1987). The dichroic effect occurs in the

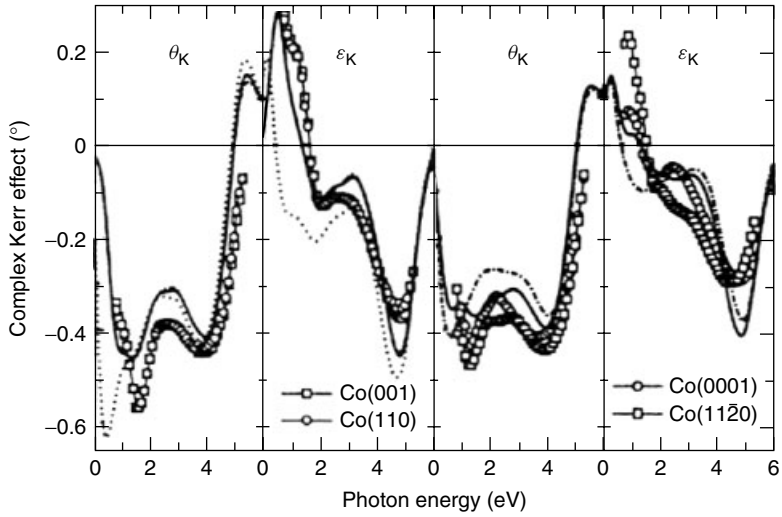

Figure 3. Polar Kerr rotation θ_K and ellipticity ε_K of (001) and (110) fcc-Co (left) and hcp-Co (0001) and (11$\bar{2}$0) (right) obtained from theory (solid lines; only interband contributions: dotted lines) and experiments (symbols: after Weller *et al*., 1994). (Reproduced from P.M. Oppeneer *et al*., 1996, with permission from Springer-Verlag GmbH. © 1996.)

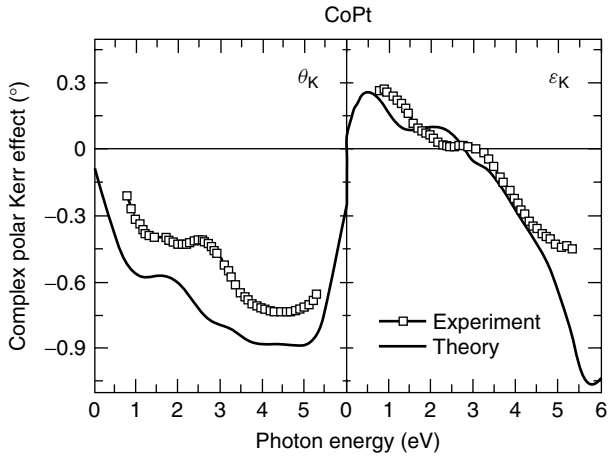

Figure 4. Polar Kerr spectra of CoPt from theory (solid lines: after Oppeneer and Antonov, 1996) and experiments (symbols: after Weller, 1996). (Reproduced from Oppeneer *et al*., 2001, with permission from Elsevier. © 2001.)

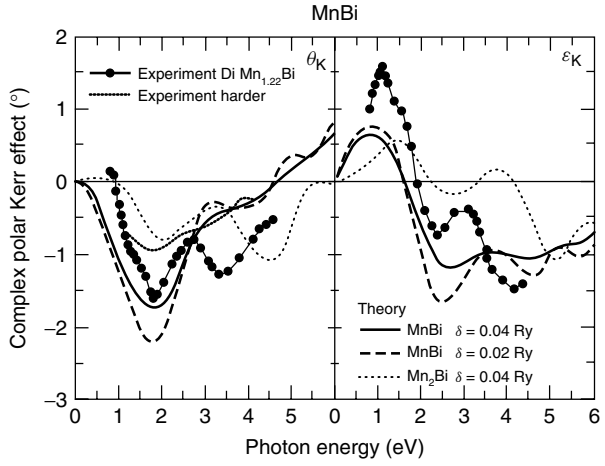

Figure 5. Polar Kerr spectra of MnBi from theory (lines; for various lifetime broadenings and for Mn_2Bi) and experiments (symbols: after Di, 1992, broken lines: after Harder, Menzel, Widmer and Schoenes, 1998). (Reproduced from Oppeneer *et al*., 2001, with permission from Elsevier. © 2001.)

vicinity of element-specific inner-core absorption edges and denotes the dependence of the absorption of circularly polarized X rays on the ferromagnetic magnetization component onto the photon wave vector (Ebert and Schütz, 1996; Starke, 2000). At L edges in 3d transition metals (TMs) relative changes in the absorption constant as large as up to 50% occur. Very similar to MOKE, as observed in the NIR/visible/UV regime (Figure 2), the physical origin of XMCD in the X-ray absorption is based on angular momentum conservation and spin-orbit interaction basically in the initial state. If the energy of the absorbed photon equals the binding energy of a particular inner-core level (e.g., $p_{3/2}$), the photoelectron is excited into an unoccupied state of d symmetry above the Fermi level, obeying dipolar selection rules. In the case of a circularly polarized absorbed photon, the emitted photoelectron acquires both an expectation value of the spin and the orbital momentum projected onto the direction of propagation of the incoming photon obeying the constraint $\Delta m_l = \pm 1$. The spin and orbital polarizations as calculated via Clebsch–Gordan coefficients are $\langle \sigma_z \rangle = 50$ and 25% at the L_2 and L_3 edges, whereas $\langle l_z \rangle = 75\%$ at both L edges. According to the Pauli principle, the photoelectron can be considered as a local probe for the spin and

orbital polarization of the absorbing atom. Just like in a spin ferromagnet, the final density of states exhibits a spin polarization owing to the exchange interaction, and the transition probability of the absorption process depends on the polarization of the final d states, which is directly related to the magnetization of the absorbing atom. In the ideal case of a completely spin-polarized final state, that is, one spin band is completely shifted below the Fermi level and the magnetic moments are fully aligned, the difference between the absorption coefficients for the direction of the magnetization parallel μ_+ and antiparallel μ_- to the photon propagation direction $(\mu_+ - \mu_-)$ normalized with respect to the unpolarized absorption $(\mu_+ + \mu_-)$ corresponds directly to $\langle \sigma_z \rangle$ provided that the corresponding orbital polarization can be neglected. Taking into account also the orbital contribution, a further increase or decrease of the dichroic signal at the L_3 and L_2 edges has to be expected.

As an example, Figure 6 shows the XMCD of Fe at the levels $2p_{3/2}$ and $2p_{1/2}$ (c), obtained as a difference spectrum of the two circularly polarized X-ray absorption spectra (XAS) (b), and after subtracting the nonmagnetic substrate background (a) (Chen *et al*., 1995). Further, the summed and the integrated XAS are shown (d). In principle, the comparison of the magnetic contrast taken at the L_3 and L_2 edges yields information on the lateral spin and orbital contributions. By applying sum rules (Thole *et al*., 1992; Carra *et al*., 1993) one can extract separately the spin and the orbital moments, whose ratio is $m_{\mathrm{orb}}/m_{\mathrm{spin}} \approx 0.04$ in the case of bcc-Fe (Figure 6). This unique feature of XMCD spectroscopy has revived appreciable interest in the orbital moments, whose role, for example, in the origin of the magnetocrystalline anisotropy energy of ferromagnets is of paramount importance (Weller *et al*., 1995; Weller, 1996). The other great advantage of XMCD is its element specificity. For example, experiments on multilayers are selective with respect to the elements involved and can reveal individual magnetic moment distributions of individual layers or at interfaces (cf. Section 3.6).

The realization of XMLD being quadratic in **M** and occurring on transversely magnetized samples in absorption geometry was demonstrated by Kuiper *et al*. (1993) on Fe_2O_3, while its dispersive counterpart, the X-ray MO Voigt effect, was first observed by Mertins *et al*. (2001) on an amorphous Co film. The ellipticity, which corresponds to the MLB in the visible region, was analyzed using the dichroic reflection at an analyzer plate. Its value agrees excellently with *ab initio* caculations, which crucially have to take into account the exchange splitting of the 2p core states. While the observed Voigt ellipticity is quite small ($\theta_V = 7.5\,\mathrm{deg}\,\mu\mathrm{m}^{-1}$), much larger effects ($\Delta R/R \approx 20\%$) were observed in reflection on antiferromagnetic NiMn and NiO (Oppeneer *et al*., 2003). Thus, reflection XMLD promises to become a versatile tool to image antiferromagnetic domains, which may sustain external magnetic fields in contrast to conventional XMLD–PEEM (photoelectron emission microscope) (Section 3.6).

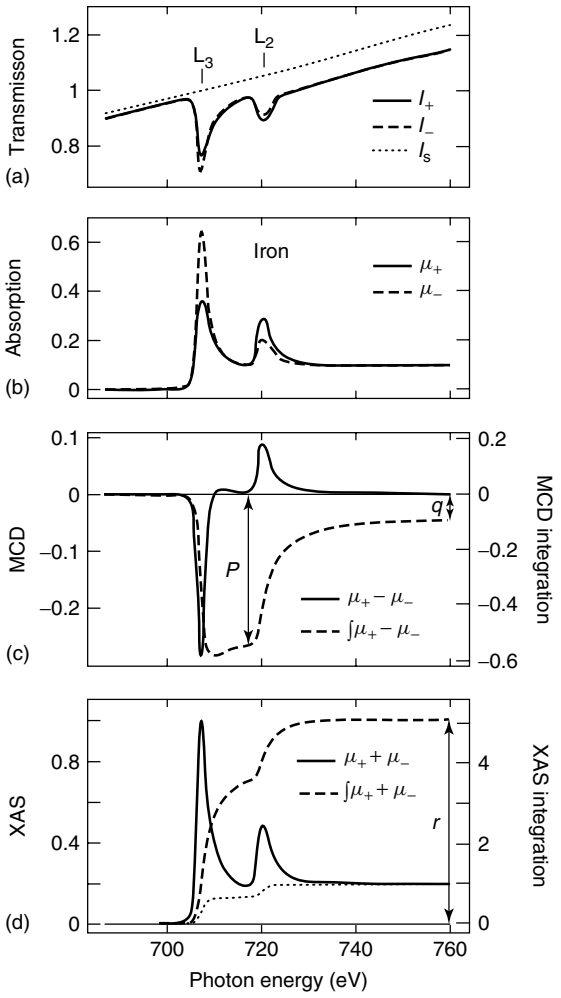

Figure 6. X-ray transmission (a), absorption (b), MCD (c), and XAS (d) spectra of Fe/parylene thin films taken at two opposite saturation magnetizations. Integrated spectra for sum-rule analysis are shown as dotted lines in (c) and (d). (Reproduced from Chen *et al*., 1995, with permission from the American Physical Society. © 1995.)

2.3 Nonlinear magneto-optics

Usually MOKE signals are observed at the same frequency as that of the incident light, hence, the name *linear* MO response. Under favorable circumstances there is, however, also a measurable fraction of frequency-doubled light due to SHG. This effect is referred to as *nonlinear,* because of its origin due to the nonlinear optical

susceptibility, which generates light at second harmonic (SH) frequency, but not on the dependence on the magnetization, which remains linear to first order as in the ordinary MOKE. SHG appears when inversion symmetry is broken (Shen, 1984) as is usually the case for every solid at its surface. A simultaneous change of the state of polarization of SH reflected light was predicted (Pan, Wei and Shen, 1989; Hübner and Bennemann, 1989) and first been observed on an Fe surface (Reif, Zink, Schneider and Kirschner, 1991). The determination of a magnetic structure from SHG is based on the relation $P_i(2\omega) = \varepsilon_0[\chi_{ijk}(i) + \chi_{ijk}(c)]E_j(\omega)E_k(\omega)$ between the induced nonlinear polarization $P_i(2\omega)$ at the doubled frequency 2ω and the electric fields $E_j(\omega)$ and $E_k(\omega)$ of the incident light at frequency ω. $\chi_{ijk}(i)$ and $\chi_{ijk}(c)$ are the nonlinear susceptibility tensor components, which couple to the crystallographic and magnetic structure, respectively. From the nonvanishing components $\chi_{ijk}(c)$ it is possible to determine the magnetic structure and interactions of a system (Birss, 1966). The theory of nonlinear MO effects was considered for metal surfaces (Pustagowa, Hübner and Bennemann, 1993; Hübner and Bennemann, 1995; Bennemann, 1998), insulating antiferromagnets (Fiebig, Fröhlich, Krichevstov and Pisarev, 1994; Qian, Dong and Xing, 2001; Iizuka-Sakano, Hanamura and Tanabe, 2001), and magnetic granular alloys (Granovsky, Kuzmichov and Clerc, 2003). The best-known phenomenon is NOMOKE (occasionally also termed *SHMOKE* = second harmonic magneto-optical Kerr effect; Crawford, Silva, Teplin and Rogers, 1999). This counterpart to MOKE has meanwhile become a popular instrument in order to characterize magnetic surfaces and interfaces, in particular, of thin films and multilayers (Rasing, 1998). Nonlinear MO spectroscopy benefits from its 'additional degrees of freedom' (Bennemann, 1998), since it can clearly distinguish between transitions of magnetic and nonmagnetic origin. In centrosymmetric materials, SHG is restricted to the symmetry-breaking surfaces and interfaces. It is therefore a highly selective sensor for surface or interface magnetism.

An illustrative comparison is drawn in Figure 7 between MOKE and NOMOKE properties obtained on a thin-film sample of Co with variant thickness t (in monolayer units, ML) (Vollmer, Jin, Regensburger and Kirschner, 1999). While the MOKE signal increases linearly with t as predicted (see Section 3 Visnovsky, 1995), the intensity $I(2\omega)$ maximizes already for 2 ML with a slightly decreasing asymmetry A between the components $I(2\omega, +B)$ and $I(2\omega, -B)$. Unfortunately, the efficiency of the SHG is very small, $I(2\omega)/I(\omega) \approx 10^{-12}$. Hence, in contrast with linear MOKE, the use of nonlinear MOKE presently rather lies in its fundamental ability to explore surfaces and interfaces, than in practical applications.

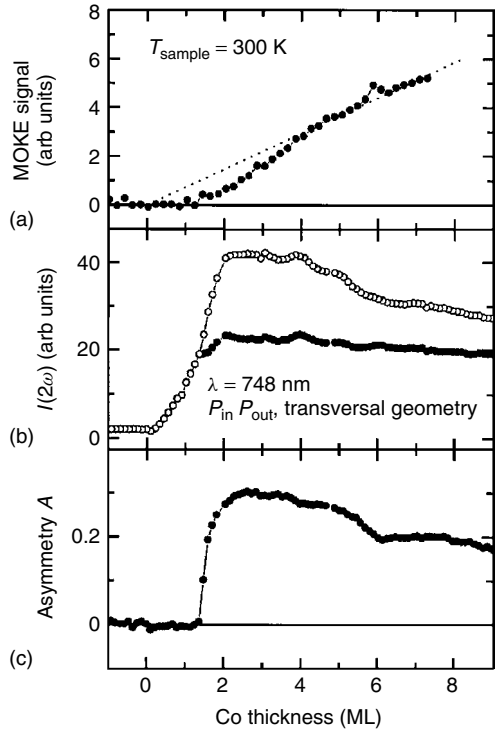

Figure 7. L-MOKE (a), SH intensity (b), and nonlinear asymmetry (c) measured on Co/Cu(001) at variant Co thickness under an angle of incidence $\alpha = 38^\circ$ with $\lambda = 633$ nm. (Reproduced from Vollmer *et al.*, 1999, with permission from Elsevier. © 1999.)

3 EXPERIMENTAL TECHNIQUES

3.1 Magneto-optic ellipsometry

In addition to conventional ellipsometry aiming at determining Kerr rotation angle θ_K and ellipticity ε_K, domain imaging by polarization optical techniques has become very important in recent years (Hubert and Schäfer, 1998). High performance experimental techniques are now available for both MO ellipsometry and domain imaging. Kerr microscopes have been developed to achieve satisfying contrast also in the case of weak MO effects ($\theta_K \approx 0.1^\circ$) by using sensitive charge coupled device cameras and sophisticated image processing (Meyer, Pommier and Ferré, 1989; Hubert and Schäfer, 1998). The measurement of rotations and ellipticities with a resolution of a few microradians is achieved, for example, with the help of a photoelastic modulator (PEM) (Jasperson and Schnatterly, 1969) driven at a fairly high frequency of $f \approx 0$ kHz. The signals at both the fundamental and the first harmonic frequency of the emerging light intensity are detected by using lock-in detection. Linear detection of the signal is achieved when placing the reflecting sample between polarizers, which are oriented 45° with respect to

each other. As a rule, ellipticity is observed at frequency f, whereas rotation emerges at $2f$. Instead of a PEM a Faraday rotation modulator may also be used. It is much easier to assemble than the photoelastic one, however, at the price of a reduced signal-to-noise ratio owing to the lower modulation frequency, $f \approx 1\,\text{kHz}$. Moreover, sensitivity to Kerr ellipticity is achieved here only when placing an additional birefringent $\lambda/4$ retarder plate into the reflected beam.

Analyses of MOKE measurement techniques utilizing different modulators, retarders, polarizing beam splitters, and so on, have been presented by various authors (Sato, 1981; Nederpel and Martens, 1985; Bader and Moog, 1987; Sato *et al*., 1993; Kim, Aderholz and Kleemann, 1993; Yang and Scheinfein, 1993; Zeidler *et al*., 1996; Berger and Pufall, 1997; Pufall, Platt and Berger, 1999; Vavassori, 2000; Teplin and Rogers, 2001; Allwood, Xiong, Cooke and Cowburn, 2003). They are usually based on the Jones matrix calculus (Azzam and Bashara, 1979) using homogeneous dielectric permittivity tensors as in our classical example of Section 2. In the following, we briefly present two methods, one being extremely simple and easy to mount, while the other one is more sophisticated, highly precise, and prepared for absolute calibration.

For many purposes, very low-cost MOKE apparatus without any polarization modulation and lock-in technique is sufficient. After deleting the PEM and one of the orthogonal magnetic fields, M(T) or M(L), in the setup shown in Figure 8, one remains with a laser diode or a HeNe laser as a light source, while a Si photodiode or a phototransistor serves as a detector (D). When orienting the analyzer (P_2) for the reflected light nearly crossed to the incident p polarization (angular mismatch $0 < \alpha \ll \pi/2$) and measuring the transmitted light intensity for both magnetization directions, I_+ and I_-, one can easily determine the Kerr angle from the asymmetry $A_K = (I_+ - I_-)/(I_+ + I_- - 2I_\text{u})$ by setting $\theta_\text{K} \approx \alpha A_\text{K}/2$ provided that $\theta_\text{K} \ll \alpha$. Here, I_u is the leakage intensity measured at $\alpha = 0$. A p-oriented quarter wave plate placed in the reflected beam makes Kerr ellipticity accessible via a related formula, $\varepsilon_\text{K} \approx \alpha A_\text{K}/2$.

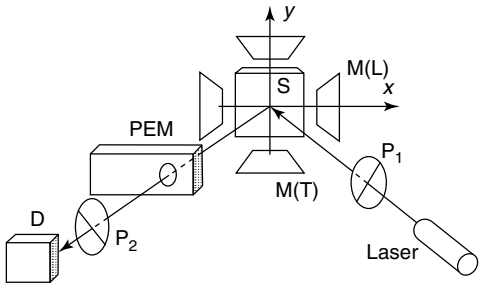

Figure 8. L- and/or T-MOKE experiment with light source (laser), polarizer (P_1), sample (S), magnet (M), photoelastic modulator (PEM), analyzer (P_2), and photodetector (D). Two pairs of magnetic pole shoes are shown for L- and T-Moke, M(L) and M(T), respectively. (Reproduced from P. Vavassori *et al*., 2000, with permission from the American Institute of Physics. © 2000.)

A spectroscopical setup for measuring θ_K and ε_K in P-MOKE configuration quantitatively and employing photoelastic polarization modulation is shown in Figure 9 (Kim, Aderholz and Kleemann, 1993). Two arrangements for light source (L) and detector (D) are in use. For routine investigations, a 5-mW HeNe laser or a laser diode is placed directly in front of the polarizer P_1 and behind the analyzer P_2, respectively. In the second case, for measurements of the spectral dependences as a function of the light wavelength $350 \leq \lambda \leq 800\,\text{nm}$, the light source L is a 50-W tungsten filament lamp, and D is a photomultiplier. Fiber optical attachments F_1 and F_2 are interfaced in order to produce a parallel white beam with diameter $d \approx 3\,\text{mm}$ at the entrance (F_1) and to collect it at the exit (F_2). Thereafter, the light is dispersed by a grating monochromator G with a spectral bandpass $\Delta\lambda \approx 2\,\text{nm}$ before reaching the photomultiplier D. The optical elements consist of two Glan air polarizing prisms (P_1, P_2), an elasto-optic modulator (M), a calcite wedge Babinet-Soleil-type phase compensator (C) and quartz lenses L_1 and L_2 for focusing the light beam onto the sample S and F_2 or D, respectively. S is placed with its surface plane perpendicular to the field **B** of an electromagnet ($|\mathbf{B}| \leq 2\text{T}$). It is hit by the light beam at near normal incidence, $\alpha_i < 3^\circ$. The light intensity emerging at D is Fourier analyzed by two lock-in amplifiers, A_1 and A_2, tuned to the first and second harmonics of the modulator frequency ω, I_1 and I_2, while a third amplifier measures the dc component, I_0. When properly setting the orientations of the light vector components and of the optical elements, I_1 and I_2 measure

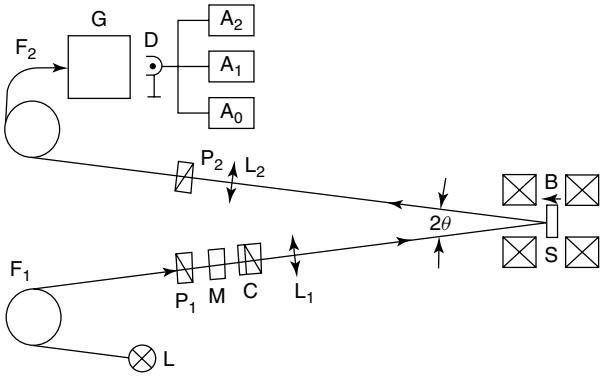

Figure 9. P-MOKE spectrometer with light source (L), optical fibers (F_1 and F_2), polarizers (P_1 and P_2), lenses (L_1 and L_2), photoelastic modulator (M; frequency ω), Babinet-Soleil compensator (C), sample (S), monochromator (G), photomultiplier (D), and amplifiers tuned to dc (A_0), ω (A_1), and 2ω (A_2). (Reproduced from W.S. Kim *et al*., 1993, with permission from Institute of Physics Publishing Ltd. © 1993.)

directly the Kerr ellipticity and the rotation, respectively, while I_0 serves for normalizing the signals and filtering noise. Absolute calibration of the signals is achieved by normalizing I_1 and I_2 to amplitudes obtained at certain calibration settings of the compensator (C) and of the analyzer (P_2), respectively (Kim, Aderholz and Kleemann, 1993). It should be noticed that the Kerr ellipticity is often the best option for measuring the magnetization of a reflecting material. On one hand, it might provide a spectral advantage with respect to rotation, as is the case, for example, for the widely used MO material Co at photon energies around 5 eV (Figure 3) (Weller *et al*., 1994). On the other hand, very often the large Faraday rotation in the windows of the vacuum vessel or cryogenic setup risks to mask tiny Kerr rotation signals.

Another problem to be addressed are interference effects owing to surface layers at bulk samples or in multilayer samples with individual layer thicknesses in the order of the optical wavelength used. The theory as sketched in Section 2.1 applies to the reflection at only one optical interface. In order to describe the MO response of layered systems, one has to account for the reflections at the inner surfaces. To this end a transfer matrix formalism has been developed, which considers the amplitude and phase conditions at the interfaces. The theory was originally developed (Yeh, 1980) for nonmagnetic birefringent multilayers. In order to include the description of magnetic anisotropic media, the dielectric tensor becomes, in general, asymmetric (due to broken time inversion symmetry) and complex (i.e., containing refraction and absorption indices). At the interfaces, continuity of amplitudes and phases has to be properly accounted for. Transfer matrices have been developed for various magnetic symmetries (polar, longitudinal, and transversal) and film sequences (Sprokel, 1984; Visnovsky, 1986a; Zak, Moog, Liu and Bader, 1990), and applied to pertinent thin-film and multilayer configurations with remarkably good success (Visnovsky, 1986b; Visnovsky *et al*., 1995).

It turns out that the multiple reflections not only inside the active MO layers but also at adjacent buffer or cap layers have to be taken into account. This may become crucial, in particular, in the vicinity of the plasma frequency of adjacent nonmagnetic metallic layers (Visnovsky *et al*., 1995). Figure 10 shows saturated P-MOKE spectra of trilayers Au(5 nm)/Co(t_{Co})/Au(25 nm)/glass for different thicknesses of the Co layer, which agree well in experiment (a,c) and theory (b,d). It has to be stressed that these caculations rely on bulk optical constants of all components, Au, Co, and even float glass, which absorbs strongly at photon energies $E > 3.8$ eV. Comparison with P-MOKE data obtained on bulk Co (Figure 3) clearly shows that the multilayer structure and its nonmagnetic components strongly suppress the Kerr angle, $|\theta_K|$ at high photon energies, $\approx$3.8 eV. This is, again, primarily due to the glass substrate, while the Au layers exert their main influence at low energies, $\approx$1.5 eV. Remarkably, in the ultrathin limit, $t < 20$ nm, the MOKE parameters depend linearly on the thickness, t, as shown in Figure 7 for the longitudinal Kerr angle of s-polarized light of wavelength $\lambda = 633$ nm incident under 38° (longitudinal) on a thin film of Co (Vollmer, Jin, Regensburger and Kirschner, 1999). This result is not intuitively expected, since reflection properties should *by definition* not depend on the thickness of the mirror. However, this is not true at thickness scales $t \ll \lambda$, because of the finite penetration length of electromagnetic waves even into strongly absorbing metals.

3.2 Vector MOKE

It is often desirable to measure not only the component of **M** along the applied field but also the orthogonal magnetization component(s) in order to reconstruct the complete magnetization vector. To this end, various 'vector MOKE' (V-MOKE for short) strategies have been developed (Florczak and Dahlberg, 1991; Yang and Scheinfein, 1993; Daboo *et al*., 1993; Berger and Pufall, 1999; Vavassori, 2000; Schmitte *et al*., 2002). In the setup chosen by Vavassori (2000) (Figure 8), complete vector magnetometry is possible without any moving element in a conventional MOKE setup. It involves a HeNe laser, whose beam passes a rotatable glan-Thomson polarizer P_1, hits the sample S under an angle of incidence of 25°, after reflection passes a *PEM* with frequency ω (Jasperson and Schnatterly, 1969), a second polarizer P_2 and is detected by a photodiode D. A magnetic field can be applied both parallel and perpendicular to the plane of incidence by means of a double-axis electromagnet M. By choosing both polarizations, s and p, detecting the modulated signal under both ω and 2ω, and rotating all optical elements (except the sample) in a second set of measurements by $\pm$45°, one can find all the data, which suffice to calculate all three vectorial components of the normalized magnetization, m_x, m_y, and m_z, as shown for the magnetic hysteresis curve of a 180-nm-thick film of CoNiO in Figure 11. This sample was prepared with an oblique out-of-plane anisotropy axis. This explains the occurrence not only of a finite transverse in-plane component m_y but also of a perpendicular component m_z while reverting the magnetization with a field parallel to the x axis.

Other setups use L-MOKE exclusively with s-polarized light, $\boldsymbol{E} \parallel y$ (coordinates as in Figure 8), while the external field **H** lies in the (xz) plane of incidence (Schmitte *et al*., 2002). Let the magnetization **M** be a vector lying in the (xy) plane. Then the MOKE signal is proportional only to its x component, M_x. The y component M_y would yield a T-MOKE signal in p polarization, but remains undetected in s polarization. It can be registered, however, by its s-polarized

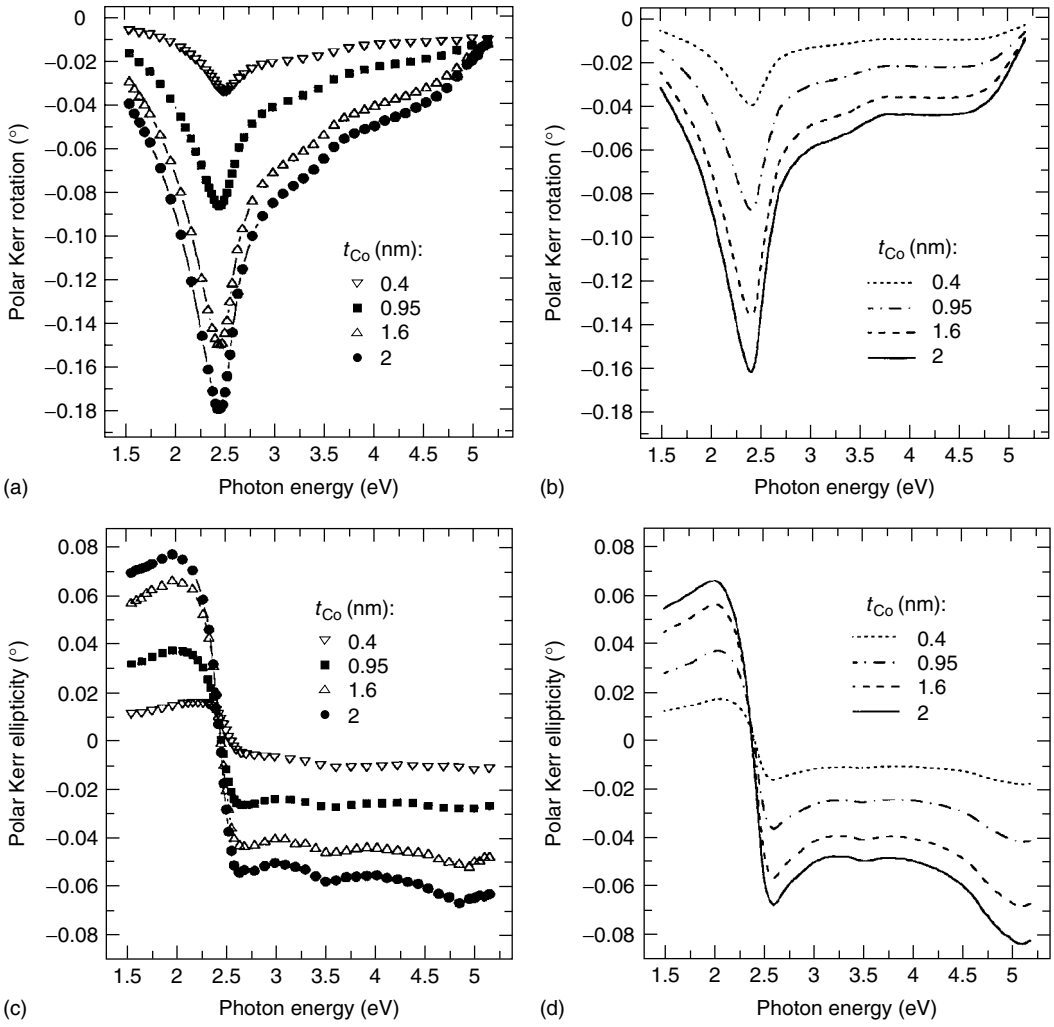

Figure 10. Saturated P-MOKE spectra of [Au (5 nm)/Co (t_{co})/Au (25 nm)]$_n$/glass (1 mm) samples for different values of t_{co} from experiments (a,c) and matrix calculations (b,d). (Reproduced from Visnowsky *et al*., 1995, with permission from the American Physical Society. © 1995.)

L-MOKE signal upon rotating the plane of incidence by 90° into the (*yz*) orientation, while keeping the sample and the field fixed. In practice, the same target is reached by keeping the plane of incidence fixed, but rotating the sample and the field together by 90°.

The rotation of the optical and magnetic components can be avoided by mounting two orthogonal s-polarized L-MOKE setups, thus realizing simultaneous vector magnetometry. Alternatively one may use a combination of L- and T-MOKE. Since the transverse Kerr effect implies an intensity change of the reflected p-polarized light, while the longitudinal Kerr effect provokes a rotation of its plane of polarization, one can unambiguously extract both quantities in a simultaneous experiment. The fact that there are no moving parts of the setup is clearly the advantage of this technique (Flocrzak and Dahlberg, 1991), but enhanced calibration efforts have to be taken, since both measured signals are not commensurate.

3.3 Diffracted MOKE

MOKE experiments are very advantageous in performing locally resolved magnetometry on a submicron level by simply focusing the light onto the desired area. Hence, Kerr magnetometry has become an indispensable tool for investigating small magnetic structures. If these structures have some periodicity, for example, either as a mechanical or a magnetic (i.e., domain) stripe pattern, another piece of information can be drawn from the reflected light. The material acts like a diffraction pattern, where the diffraction orders may contain magnetic information via the

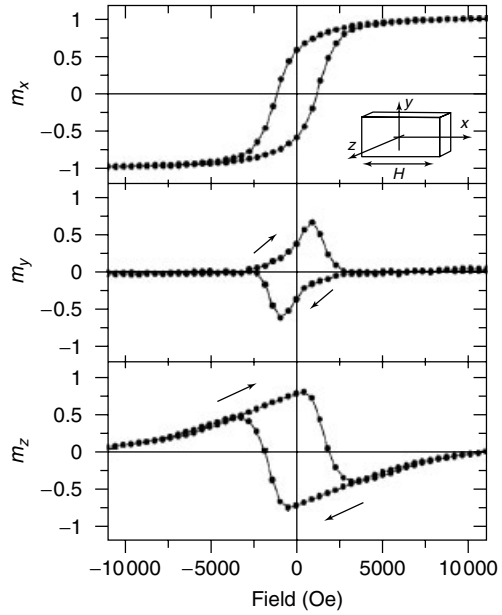

Figure 11. Normalized magnetization components m_x, m_y, and m_z obtained from V-MOKE on a CoNiO thick film as a function of the applied field H_x. (Reproduced from P. Vavassori *et al*., 2000, with permission from the American Institute of Physics. © 2000.)

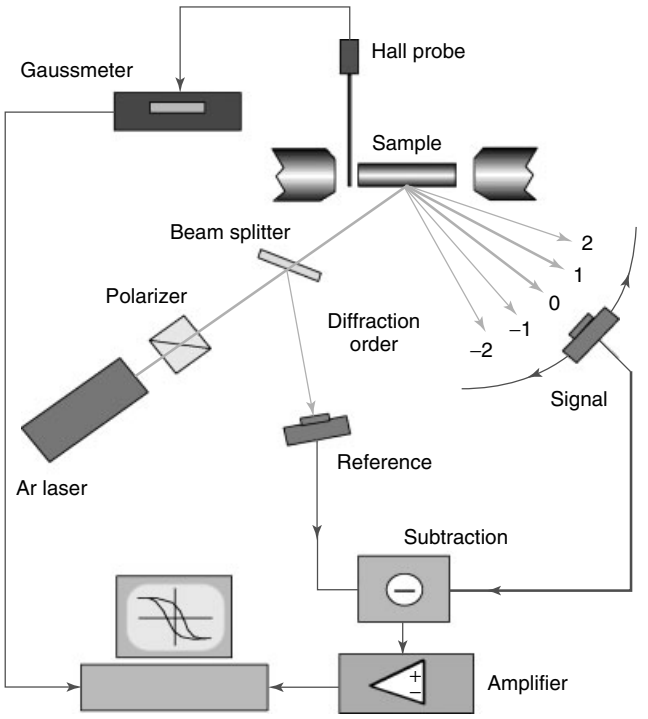

Figure 12. Block diagram of a D-MOKE setup. (Reproduced from M. Grimsditch *et al*., 2004, with permission from Institute of Physics Publishing Ltd. © 2004.)

rotation or ellipticity of the emerging light, hence, the name D-MOKE (Grimsditch and Vavassori, 2004) or, occasionally, Bragg-MOKE (Schmitte, Schemberg, Westerholt and Zabel, 2000). Figure 12 shows schematically the D-MOKE setup of Grimsditch and Vavassori (2004), where the incident beam is chosen to hit the grating under a typical L-MOKE angle α_0 and various positive and negative diffraction orders n are expected to appear at angles $\alpha_f = \alpha_0 \pm \alpha_n$. While the mechanical shape of the grating and the periodicity of its reflectivity determine the distribution of diffracted spots via Fourier transformation of the intensity distribution function, the underlying magnetization pattern contributes a magnetic form factor. The MOKE signal reflects the Fourier transform of the magnetization pattern according to

$$f_n^{(m)} = \int m(r) \exp(2\pi nir/d) \mathrm{d}S \tag{23}$$

where $m(r)$, d, and r are the normalized magnetization profile, its period, and the position inside the unit cell area, respectively (Geoffroy *et al*., 1993; Vial and van Labeke, 1998; Vavassori *et al*., 1999; Schmitte, Schemberg, Westerholt and Zabel, 2000; Schmitte, Westphalen, Theis-Bröhl and Zabel, 2003; Grimsditch and Vavassori, 2004). The electric field in the nth-order diffracted beam from a magnetic patterned surface may be written as

$$E_n = E_0 \left(r_{\mathrm{pp(ss)}} f_n + r_{\mathrm{pp(ss)}}^{(m)} f_n^{(m)} \right) \tag{24}$$

where E_0 is the incident electric field, $f_n = \int \exp(2\pi nir/d)\, \mathrm{d}S$ the structural form factor of the grating, and $r_{\mathrm{pp(ss)}}$ and $r_{\mathrm{pp(ss)}}^{(m)}$ the nonmagnetic and magnetic p(s)-polarized reflectivities of the material, respectively. It has to be noticed that both $r_{\mathrm{pp(ss)}}$ and $r_{\mathrm{pp(ss)}}^{(m)}$ are, in general, differently angular dependent according to their individual Fresnel's coefficients. Hence, it turns out that a good agreement between observed and calculated D-MOKE usually requires micromagnetic calculations (Brown, 1978). As an example, Figure 13 (Grimsditch and Vavassori, 2004) shows hysteresis curves up to diffraction order $n = 2$ obtained experimentally (upper row) on a two-dimensional periodic arrangement of square rings of permalloy, in comparison with theoretical magnetization curves (lower row) calculated on the basis of object oriented micromagnetic framework (OOMMF) (Donahue and Porter, 2000). D-MOKE is considered as a novel technique, which can yield information on the magnetic spin structure within micro- or even nanosized particles. As with every diffraction method, D-MOKE requires a periodic arrangement of exactly equal elements. Micromagnetic calculations are indispensable for a detailed understanding of the magnetic form factors. Hence, any transformation of the D-MOKE signal from Fourier space into the real space should be accompanied by simulations. If successful, the method might compete with or even surpass other magnetic imaging methods like PEEM

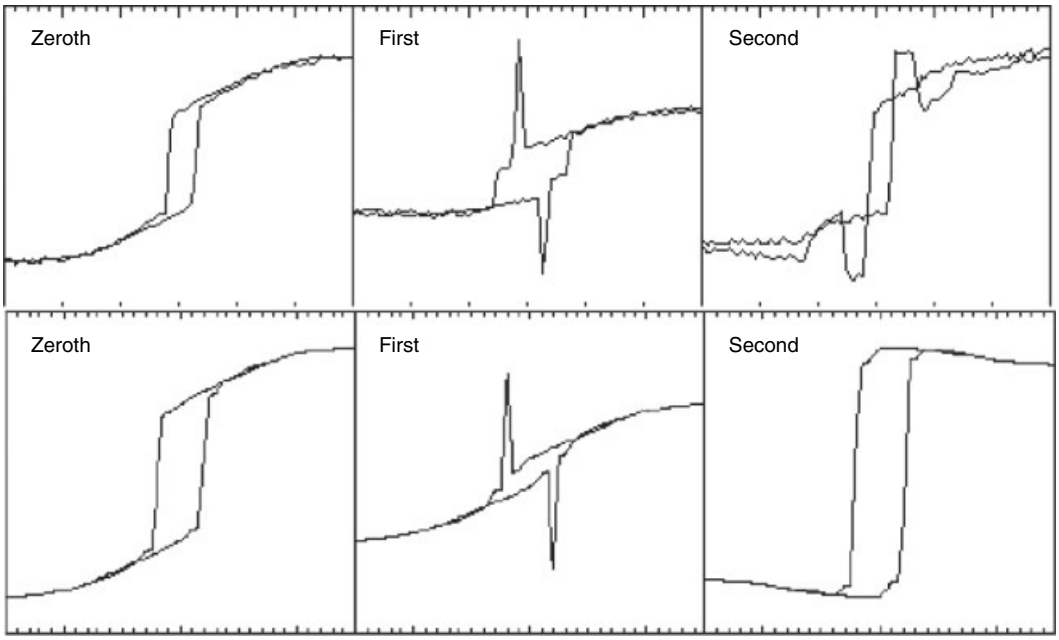

Figure 13. D-MOKE hysteresis loops of zeroth-, first-, and second-order for square rings of permalloy, periodically arranged on a square lattice obtained with an edge-parallel magnetic field (upper panels: experimental; lower panels: calculated). (Reproduced from M. Grimsditch *et al*., 2004, with permission from Institute of Physics Publishing Ltd. © 2004.)

(Section 3.6). Recently, it could be shown that periodic magnetic structures may also serve as diffraction gratings for soft X rays (Remhof *et al*., 2005). Analogous to D-MOKE, one finds diffracted beams in reflection, whose XMCD contrast mirrors the magnetic form factor (equation (23)). In combination with micromagnetic simulations, this opens another possibility to transform the element-specific magnetization patterns from Fourier into real space, with no restrictions on magnetic fields to be applied and no need for sophisticated X-ray optics.

3.4 Dynamic MOKE

The dynamics of magnetization reversal is of prime importance in magnetic and MO recording and in the context of modern magnetoelectronics (Ferré, 2001). MO diagnostics has become a leading technique being involved in three types of magnetization reversal phenomena: (i) thermomagnetic effects induced by local laser heating of the sample, (ii) photoinduced effects, which are not based on thermal heating and open a new field of research called *femtomagnetism*, and (iii) magnetic field–induced effects as evidenced by magnetization reversal or full hysteresis loops. In the latter category, MO techniques are indispensable in order to observe the field-driven dynamics of magnetization reversal from the milli- to the gigahertz region. At very low frequencies, Kerr microscopy was successfully employed, for example, on ultrathin Pt/Co/Pt trilayers in order to observe the creep of pinned domain walls under near-coercive magnetic fields, and to determine the stationary wall velocity v as a function of the field H (Lemerle *et al*., 1998) and the local wall roughening (Repain *et al*., 2004). Figure 14 shows a double exposure of a domain-wall contrast before and after a magnetic

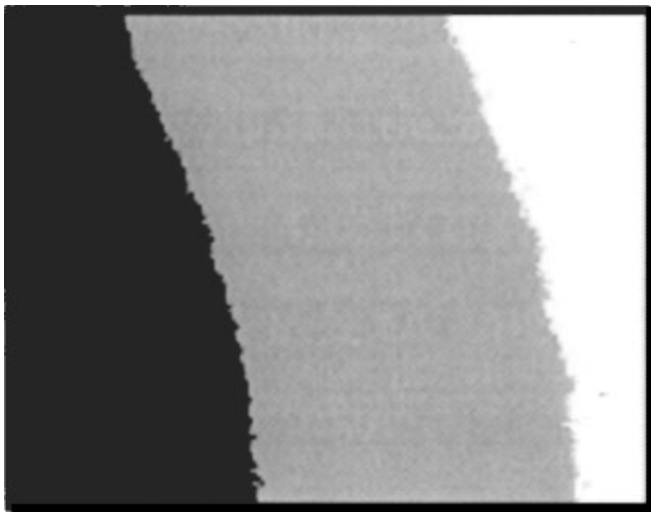

Figure 14. P-MOKE image (size $90 \times 72\,\mu m^2$) of a domain wall in Pt(1.2 nm)/Co(0.5 nm)/Pt(1.2 nm)/glass before (black) and after (gray) being swept by a perpendicular field of 46 mT during 111 µs. (Reproduced from Lemerle *et al*., 1998, with permission from the American Physical Society. © 1998.)

field pulse of 460 Oe during a time of 111 μs. Excellent agreement with creep theory (Feigel'man, Geshkenbein, Larkin and Vinokur, 1989) was obtained.

At intermediate frequencies, dynamic ferromagnetic hysteresis loops are known to broaden as the frequency f increases. In simple Ising-type systems with one leading relaxation time, τ, one even expects a dynamic phase transition at a critical frequency f_0 in the sense that the dynamic order parameter, $Q = (1/2\pi)\oint M\mathrm{d}t$, changes discontinuously from $Q = 0$ at $f < f_0$ to $Q \neq 0$ at $f > f_0$ (shift of the loop, e.g., to the upper two quadrants in the M–t plane) (Chakrabarti and Acharyya, 1999). Such processes have been studied, for example, at frequencies up to $f = 2\,\mathrm{kHz}$ on thin films of Fe/GaAs (Moore and Bland, 2004). Figure 15(g) shows the dynamic broadening of hysteresis loops recorded with L-MOKE on a *superferromagnetic* (i.e., predominantly dipolarly coupled) discontinuous multilayer of CoFe nanoparticles embedded in amorphous alumina at frequencies from 5 mHz up to 10 Hz (Bedanta *et al*., 2006). The very weak coercive field increases power law–like, $H_c = H_{c0} + b\,f^{\alpha}$, where $\mu_0 H_{c0} \approx 0.2\,\mathrm{mT}$ and $\alpha \approx 0.5$ (Figure 15h). The dynamic contribution reflects the presence of nucleation processes and domain-wall sliding motion, as confirmed by L-MOKE microscopy for $f \approx 0.1\,\mathrm{Hz}$ in Figure 15(a–f) (Bedanta *et al*., 2006) in close agreement with observations in continuous ferromagnetic films (Lee *et al*., 2000).

Finally, at high frequencies, MO techniques are indispensable either as touchless transient methods, if high magnetic field pulses are involved (Takeyama, Osada and Miura, 2004; Singleton *et al*., 2004) or as unrivaled fast speed methods, if timescales at or below the nanosecond level are to be resolved. Here, questions are posed like 'how fast can the magnetization of a magnetic medium or element be changed?' and 'what are the fundamental and practical limits of the speed of magnetic writing and reading?'. They are of paramount interest with far reaching consequences for the future of data storage and retrieval. Surely, there is large economical and technical interest in finding answers, which hopefully guarantee further applicability of Moore's law with respect to the acceleration of data transfer. However, there is also a lot of exciting fundamental research, which greatly profits from ultrafast laser pulse sources and MO pump-probe techniques.

Since the invention of the first magnetic memory disk in 1954, much effort has been put into enhancing the speed, bit density, and reliability of magnetic memory devices. Modern magnetic random access memory (MRAM) devices aim at fast coherent magnetization rotation by precession of the entire memory cell (Hiebert, Stankiewicz and Freeman, 1997; Back *et al*., 1998; Choi *et al*., 2001; Hiebert, Ballentine and Freeman, 2002; Kaka and Russek, 2002), since conventional reversal by domain-wall motion is much too slow. In principle, the fundamental limit of the switching speed via precession is given by half of the precession period. The dynamics of the magnetization then follows the Landau–Lifshitz–Gilbert equation of motion,

$$\frac{\mathrm{d}\mathbf{M}}{\mathrm{d}t} = -|\gamma|\,(\mathbf{M}\times\mathbf{H}_{\mathrm{eff}}) - \lambda\,[\mathbf{M}\times(\mathbf{M}\times\mathbf{H}_{\mathrm{eff}})] \qquad (25)$$

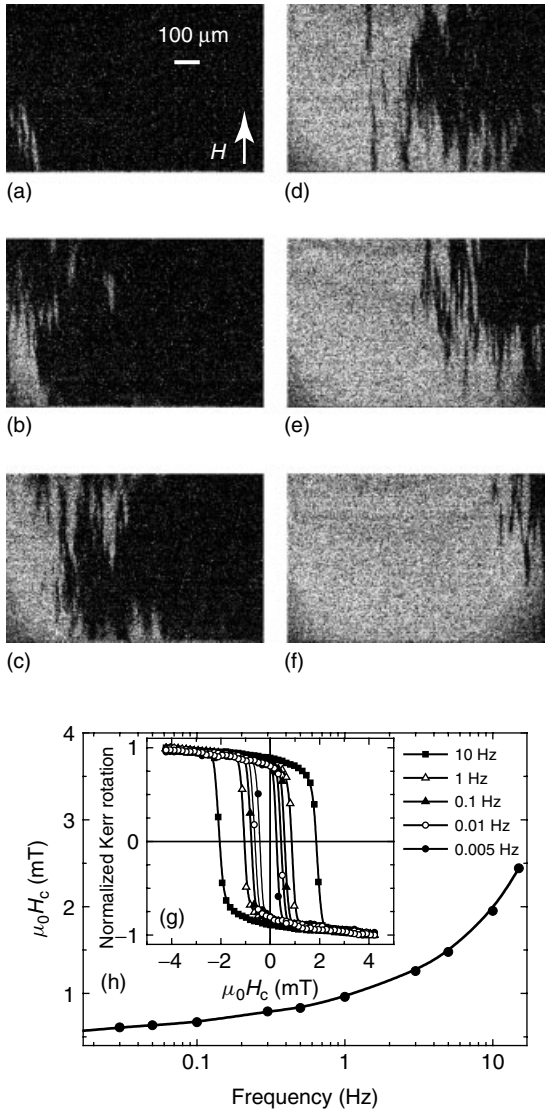

Figure 15. (a–f) Longitudinal Kerr microscopy domain images at room temperature of initially remanent $[Co_{80}Fe_{20}(1.3\,\mathrm{nm})/Al_2O_3(3\,\mathrm{nm})]_{10}$ (size $980 \times 700\,\mu\mathrm{m}^2$) under a supercoercive field, $\mu_0 H = 0.65\,\mathrm{mT}$, at $t = 1.5$ (a), 2.5 (b), 3.5 (c), 4.5 (d), 5.5 (e), and 7 s (f). (g) Normalized L-MOKE loops obtained on the same sample at $T = 294\,\mathrm{K}$ and $f = 0.005$ (1), 0.01 (2), 0.1 (3), 1 (4), and 10 Hz (5), and (h) frequency dependence of the coercive field, best fitted to power laws $H_c = H_{c0} + \mathrm{b}\,f^{\alpha}$ with $\mu_0 H_{c0} = 0.2\,\mathrm{mT}$ and $\alpha = 0.5 \pm 0.1$ (solid line). (From Bedanta *et al*., 2007.)

where the gyroscopic constant γ represents the precession frequency. The phenomenological damping factor λ drives the system toward an energy minimum. $\mathbf{H}_{\text{eff}}$ is the sum of the external field $\mathbf{H}_{\text{bias}} \cdot \mathbf{H}_{\text{pulse}}$, the anisotropy $\mathbf{H}_{\text{ani}}$ and the demagnetizing field $\mathbf{H}_{\text{dem}}$, and is decisive for the path on which the magnetization reaches a new equilibrium. Methods have been developed to reverse the magnetization in undercritically damped systems by coherent rotation of the magnetization at switching times of about 200 ps while avoiding any ringing. Here, we show one example of how to achieve this by applying specifically shaped magnetic field pulses that match the intrinsic properties of the magnetic elements. Figure 16 shows the apparatus (Gerrits *et al.*, 2002) containing a sequence of two pump-laser pulses, which are separated by a distinct time delay and excite two GaAs-photoconductive switches. The generated current pulses are superimposed to produce one short and squarelike magnetic field pulse. The field pulse is launched down a coplanar waveguide structure and excites the thin-film permalloy ($Ni_{81}Fe_{19}$) element at the end of the tapering. The inset is a micrograph of the 8-nm-thin permalloy magnetic element that has an elliptical shape with dimensions of 8×16 mm. The vector- and time-resolved element response is measured by magnetization-induced second harmonic generation (MSHG) (see Section 3.5) and P-MOKE. A high-reflectance infrared mirror (HRIR) is used to split the fundamental and SH part of the beam. A photomultiplier tube (PMT) is used to detect the SH photons. By applying proper pulse shaping the authors succeeded in achieving writing frequencies of 5 GHz.

Which kind of spin dynamics has to be expected at times far below the precession period? Again, ultrashort laser pulses are the ultimate solution for all kinds of dynamic

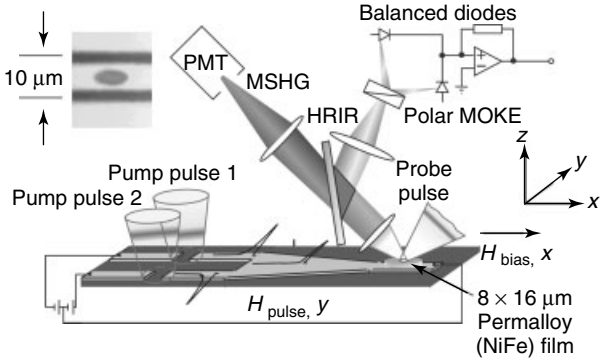

Figure 16. Experimental setup of a pump-probe experiment for measuring the *xy*- and time-resolved magnetization of a thin-film permalloy element with dimensions $8 \times 16\,\mu m^2$ (micrograph upper left corner) using 150 fs Ti:Sapphire laser pulses for switching the field and probing the magnetization by MOKE and MSHG. (Reproduced from Th. Gerrits *et al.*, 2002, with permission from Nature Publishing Group. © 2002.)

investigations in the subnanosecond regime. Mode-locked pulse lasers, which deliver light pulses with duration $\approx$10 fs, are predestinated to probe spin dynamics on this timescale. Surprisingly, at the very beginning of a typical magnetization reversal (or spin-flip?) experiment a tremendous increase of the spin temperature is observed. This was apparent with time-resolved L-MOKE on a polycrystalline Ni film (Beaurepaire, Merle, Daunois and Bigot, 1996), in which a 60-fs dye laser pulse heats the spin temperature up to nearly 600 K within 2 ps, hence, much faster than predicted for conventionally precessing spins. The dynamics of the spin excitation (demagnetization) and recovery was measured with an all-optical pump-probe experiment. In parallel, the increase of the electron temperature was measured by the dynamics of the optical transmission. It rises differently than the spin temperature in the first 2 ps, thus corroborating early 'two-temperature' models (Anisimov, Kaspeliovitch and Perel'man, 1974a,b). These findings were confirmed by spectrotemporal magneto-optics using a Ti:Sapphire pulse laser (Bigot, Beaurepaire, Guidoni and Merle, 2002; Bigot, Guidoni, Beaurepaire and Saeta, 2004). Obviously, *femtomagnetism*, that is, magnetism on a femtosecond timescale, seems to behave quite differently than conventional demagnetization processes (spin precession, magnetic domain motion and rotation). These become relevant only on the nanosecond timescale of spin-lattice, magnetic dipole, and spin–spin interactions (Zhang, Hübner, Beaurepaire and Bigot, 2002). In other experiments (Koopmans, van Kampen, Kohlhepp and de Jonge, 2000), a disproportionality of θ_K and ε_K was observed, although both quantities should be proportional to **M**. Hence, the question arises, if really the magnetization vector **M** is measured in ultrafast pump-probe demagnetization experiments? The new data seem to reveal the blocking of spin-excitation channels rather than a true change of **M**. Hence, alternatively, dichroic bleaching and nonequilibrium MOKE response have been proposed for an adequate description (Oppeneer and Liebsch, 2004). Further theoretical and experimental research is clearly needed in this novel field of magnetism.

3.5 Nonlinear MOKE

NOMOKE is a typical surface effect and in metals it is dominating, even if the material underinspection has broken inversion symmetry (Pan, Wei and Shen, 1989). Hence, it appears tempting to measure both MOKE and NOMOKE with the same apparatus and thus provide both magnetic volume and surface information simultaneously as shown in Figure 7 (Vollmer *et al.*, 1995). One apparatus toward this end was shown in Figure 16. A similar setup of Teplin and Rogers (2001) contains the V-MOKE option, in addition.

It allows to measure both L- and T-MOKE for achieving the magnetization vector components both in the bulk (via fundamental wave ellipticity) and at the surface or interface (via second harmonic wave ellipticity). Images of the spatial magnetization distribution can be measured by moving the sample across the laser focus using an *xy*-piezo scanner. The light pulses of the Ti:Sapphire laser ($\tau = 50$ fs) are further utilized to investigate bulk and surface magnetodynamics by simultaneous pump-probe strategies. As an example, Figure 17 shows the magnetization components of a permalloy film, which are precessing synchronously in a static field after application of a 100-ps field pulse (Teplin and Rogers, 2001).

3.6 Magneto-optic X-ray microscopy

The magnetic contrast occurring in XMCD can be applied to imaging techniques in the absorption mode. XMCD microscopy has been developed utilizing either (i) the primary absorption process or (ii) the subsequent emission of secondary electrons. In the latter mode, XMCD has been coupled to a PEEM, which gains a spatial resolution on samples at remanence from a few micrometers (Stöhr *et al*., 1993) to 300 nm (Schneider *et al*., 1997). Basic features of these experiments are the element specificity and the surface sensitivity, but they are restricted to studies in virtually zero magnetic field. As an example, Figure 18 shows two X-PEEM micrographs obtained on a bilayer of ferromagnetic cobalt (XMCD contrast at the Co L_3 edge) deposited on antiferromagnetic $LaFeO_3$ (XMLD contrast at the Fe L_3 edge) (Nolting *et al*., 2000). The images reveal clear correlations between the domains in both layers, which are exchange coupled and exhibit local exchange bias (Nogués and Schuller, 1999) domain by domain. The very origin of the global exchange bias, that is, the solid shift of the ferromagnetic hysteresis loop along the field axis as induced by magnetic field cooling was unraveled on the bilayer system $Ir_{20}Mn_{80}$/Co by using XMCD–PEEM in the total electron yield mode, which tolerates nonzero magnetic fields (Ohldag *et al*., 2003). Here, a fraction of about 4% of pinned excess magnetic moments on the antiferromagnetic $Ir_{20}Mn_{80}$ interface were clearly observed by Mn L_3-edge XMCD and attributed to the very heart of the observed exchange bias.

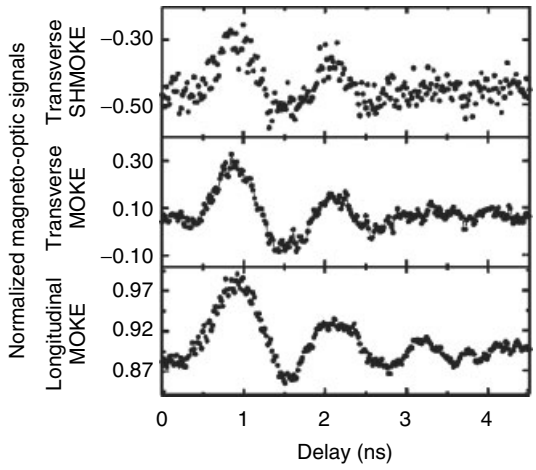

Figure 17. Normalized dynamic MOKE and NOMOKE (= SHMOKE) response of a $Fe_{80}Ni_{20}$ thin-film sample to a magnetic field pulse with 100 ps rise time in the transverse direction. Static transverse and longitudinal fields are applied so that the magnetic response of each magnetization component is linear and not hysteretic. (Reproduced from C.W. Teplin *et al*., 2001, with permission from the American Institute of Physics. © 2001.)

An alternative approach to image magnetic domains with improved parameters, viz on the nanometer length scale and permitting the application external magnetic fields uses microzone plates for lensless imaging of X rays in transmission. This was first realized at the synchrotron source BESSY I using the XMCD effect used in the complementary transmission mode (Fischer *et al*., 1996). Figure 19 shows some of the recorded magnetic X-ray micrographs of a multilayer $[Gd(0.4\,nm)/Fe(0.4\,nm)]_{75}$ (Fischer *et al*., 1998). The domain structures observed indicate magnetization vector components parallel and antiparallel to the light wave vector, respectively, at an approximate resolution of 30 nm. Different stages of the reverting magnetization from nucleation (N) to saturation (S) while passing relatively hard wormlike structures (W) are indicated. In the nucleation regime, a time-dependent magnetic aftereffect (= creep (C); cf. Figure 14 (Lemerle *et al*., 1998)) could be studied on a timescale of seconds.

4 MAGNETO-OPTICAL MATERIALS

Since more than 20 years, the two most prominent technological applications for MO effects have been optical isolators for fiber optical data transmission and MO memories. Both fields have intensely triggered the research of MO materials, whose state of the art has variously been reviewed (Dillon, 1991; Schoenes, 1992; Mansuripur, 1995; Zvezdin and Kotov, 1997; Gambino and Suzuki, 1999; Oppeneer, 2001; Röll, 2003). In the following sections, the established experience will briefly be recalled, while the focus will rather be laid onto the more recent developments.

4.1 Magneto-optical storage materials

The success of modern optical data storage devices started in 1982 with the introduction of the audio compact disc (CD).

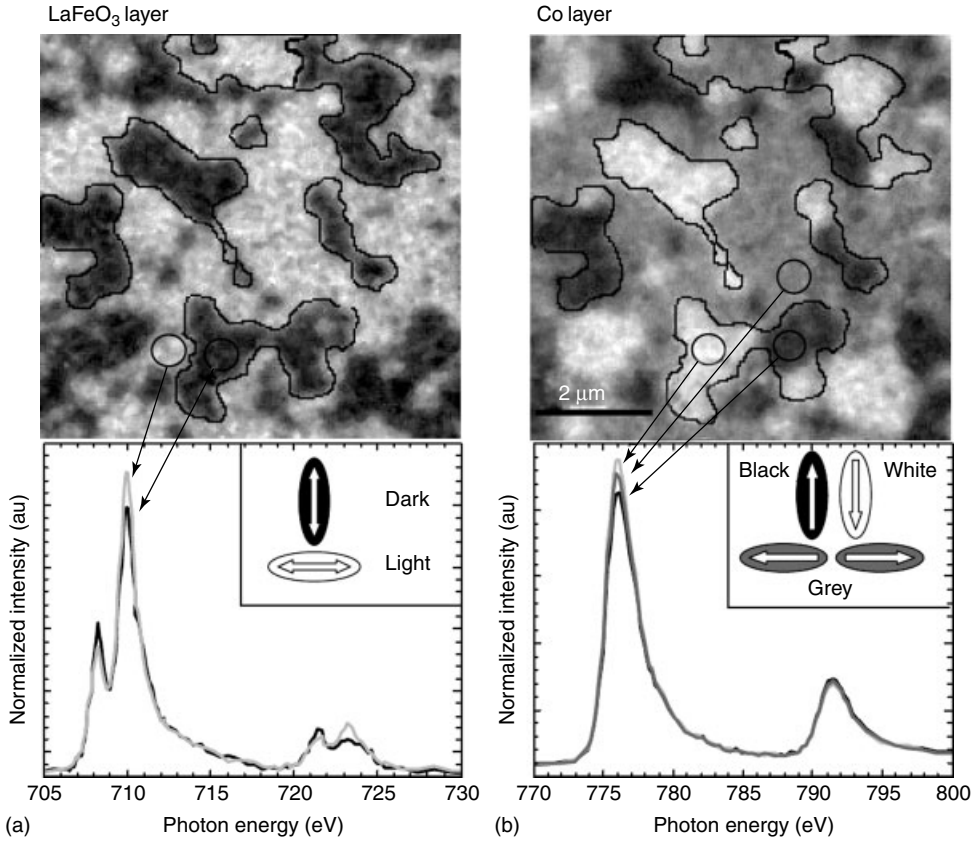

Figure 18. Fe L-edge XMLD (a) and Co L-edge XMCD images (b) and local spectra from the antiferromagnetic and ferromagnetic layers for Co(1.2 nm)/$LaFeO_3$/$SrTiO_3$(001). The contrast in the images arises from antiferromagnetic domains in (a) and ferromagnetic domains in (b) with in-plane orientations of the antiferromagnetic axis and ferromagnetic spins as indicated below the images. The X-ray spectra were recorded in the indicated areas and illustrate the origin of the intensity contrast in the PEEM images. (Reproduced from F. Nolting *et al*., 2000, with permission from Nature Publishing Group. © 2000.)

The erasable MO disc became available in 1988. The binary information is stored in small magnetic domains which are formed or erased in a magnetic layer by laser pulses in the presence of a magnetic field (thermomagnetic writing/erasing). Readout is obtained from intensity modulations of the reflected laser light caused by P-MOKE at the written domains (Mansuripur, 1995; Gambino and Suzuki, 1999; Röll, 2003).

MO storage materials are expected to undergo a very large ('unlimited') number of write/erase operations without any loss in recording/reading quality. The MO media write magnetically with thermal assist and read optically. Presently there are two standard formats, 5.5 and 3.5 in., which are protected by hard envelopes. The larger format MO disks have been capable of holding about as much as the standard CD-ROM, but under the pressure from inexpensive and relatively fast CD-R and CD-RW, more recently also DVD-RW disks, MO drives seemed to be losing ground. However, novel principles of MO recording technology like *direct overwrite* (Saito, 1999) and *magnetically induced superresolution* (MSR) (Kaneko, 1999, 2000) are now promising again to find their way back into the group of most advanced magnetic storage devices of the future.

Above their Curie temperature, T_C, any magnetic material loses its spontaneous magnetization and thus all magnetic information due to a complete disordering of their magnetic domains. Even more importantly, the material's coercivity, H_c, decreases as the temperature approaches the Curie point, and becomes zero when this temperature is exceeded. Modern MO recording systems use materials with $T_C \approx 200\,^{\circ}C$, low enough to enable the disk not to be damaged by many heating and cooling cycles, but high enough not to risk a loss of data under ambient conditions.

The fact that H_c drops at higher temperatures allows thermally assisted magnetic recording with relatively weak magnetic fields, which simplifies the drive's design. Even a relatively weak laser, $P \approx 1$ mW, can generate a high local temperature when focused onto a small spot of the order of 1 μm. When the material is heated, the magnetization of the material can easily be changed by applying a magnetic

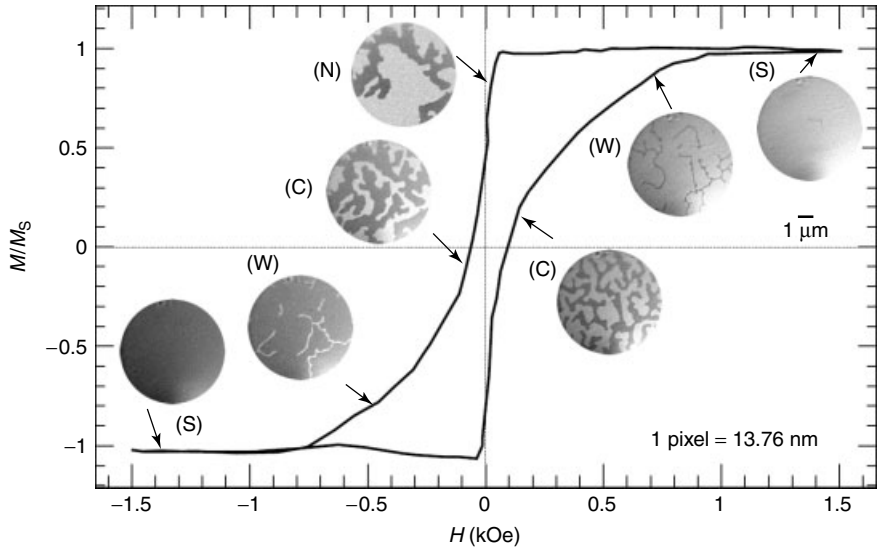

Figure 19. A sequence of XMCD micrographs at the Fe L_3 edge of a layered Gd–Fe system in an applied magnetic field covering the complete hysteresis loop. The different stages saturation (S), nucleation (N), and wormlike domains (W) are marked. The hysteresis loop, M/M_s versus H (solid line), was determined from MOKE measurements. (Reproduced from P. Fischer *et al*., 1998, with permission from Institute of Physics Publishing Ltd. © 1998.)

field from a permanent magnet. When the material is cooled to room temperature, H_c rises back to such a high level that the magnetic data cannot easily be affected by magnetic fields, which may accidentally approach the MO device from outside. The basic schematic of the recording process is illustrated in Figure 20. The disk inserted into the drive will face the magnet from the label side, whereas the transparent face will face the laser. Although longitudinal recording as is customary in most present days' hard disks might be feasible by using L-MOKE readout, MO recording has always used the perpendicular direction of the magnetization with P-MOKE readout and potentially higher density of data storage.

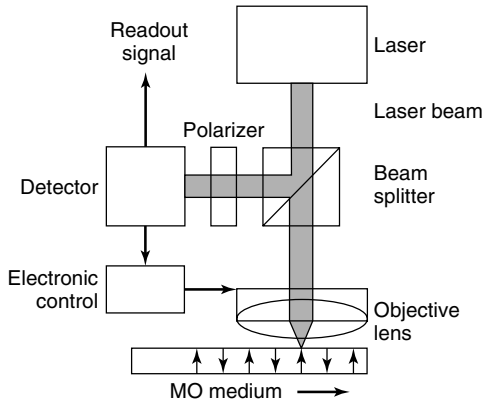

Figure 20. Optical paths and electronic control of the MOKE write and read head. (Reproduced from H. Röll *et al*., 2003, with permission from Wiley VCH. © 2003.)

For readout, the laser is operated at sufficiently low power, which does not change the stored information, viz the domain structure. The state of polarization of the reflected light is changed by P-MOKE, that is, the incident, linearly polarized light becomes elliptical with a slight tilt of the long polarization axis, $\theta_K \leq 0.5^\circ$. For opposite magnetization directions, $\pm\theta_K$ is obtained such that the light passing an analyzing polarizer encounters an intensity modulation between differently magnetized bubble domains ('bits'). The electronic control of the lens position in Figure 20 is to focus and to track the laser beam along the 'land' areas, which carry the storage material loaded with information. Usually quadrilayer stacks are used in the design of MO disks. In order to increase the optical absorption of the MO layer (thickness ≈30 nm) and thus to reduce the laser power for recording, it is coated by thin (≈100 nm) dielectric antireflection layers made from AlN or SiN. Another thin Al layer (≈50 nm) is introduced to serve both as a light reflector and as a heat sink.

The polar Kerr effect used for the readout procedure is sensitive to the magnetization component perpendicular to the film plane. In order to obtain a complete perpendicular orientation, a sufficiently large uniaxial anisotropy K_u is necessary. It must be larger than the shape anisotropy which is proportional to M_s^2,

$$K_u \geq (1/2)\mu_0 M_s^2 \tag{26}$$

Further, a large product $M_s H_c$ is required to ensure high recording density. Very low medium noise, large P-MOKE

signals and a large domain-wall stiffness minimizing wall jaggedness are to optimize the signal-to-noise ratio. Finally, high corrosion resistance is desirable.

Many different materials have been considered because of their individual promising features. For example, MnBi with its large MOKE signal, $\theta_K > 1^\circ$, has always appeared to be a good candidate. However, it was finally abandoned for MO recording purposes because of the high media noise owing to its polycrystalline structure. Only when being in a single crystalline state the MO properties of MnBi still attract interest (Brammeier *et al.*, 2004). Amorphous RE–TM alloys with extremely low media noise have finally served for the development of MO data storage systems passing three generations of media with increasing complexity:

1. binary RE–TM amorphous alloy films
2. ternary or quaternary RE–TM amorphous alloy films
3. exchange coupled ternary RE–TM alloy bilayers.

The first generation started with RE-rich RE–TM amorphous alloy films (RE = Tb, Gd and TM = Fe, Co) (Chaudhari, Cuomo and Gambino, 1973; Gambino and Suzuki, 1999). These materials, for example, $Tb_{75}Fe_{25}$, are widely used as relatively thin films (20–50 nm) in current commercial MO disks. Even better quality was obtained by materials of the second generation, ternary RE–TM alloys, where Tb and Fe can be partially substituted by other RE or TM atoms, for instance, Gd, Dy or Co, Ni, respectively. Since the films reveal antiferromagnetic coupling between the RE and the TM components, the net magnetization M_s can be small in spite of the fact, that the magnetizations of the RE and TM subnetworks are high. As the temperature dependencies of the two subnetwork magnetizations are different often a compensation temperature, T_{comp}, exists where the net magnetization is even zero (Figure 21). At T_{comp} the coercivity of the material becomes very large, since an external field cannot turn the magnetization into any given direction. This is important for the stability of the domains. At a high temperature near T_C, the coercivity is sufficiently small to form a domain by the external bias field H_b. During cooling to room temperature the coercivity increases rapidly and, as a consequence, a written domain will not be destroyed by any external stray field.

Magnetization data for different TbFeCo films are shown in Figure 22 (Greidanus, Jacobs, Spruit and Klahn, 1989). Within a small range of composition the compensation temperature changes from zero to a value above Curie temperature. For the stability of the domains a compensation temperature near room temperature is favorable. It can be obtained by a Tb content of approximately 25%. The composition influences also the Curie temperature, T_C, but in a much smaller range. A Curie temperature near 200 °C is convenient for the writing process. For a given Tb content, the

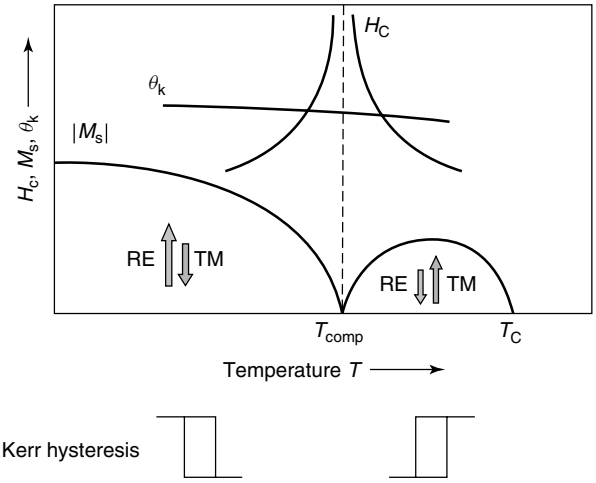

Figure 21. Magneto-optical properties of rare-earth (RE) and transition-metal (TM) thin films (M_s: saturation magnetization, θ_K: Kerr rotation angle, H_c: coercivity). (Reproduced from H. Röll *et al.*, 2003, with permission from Wiley VCH. © 2003.)

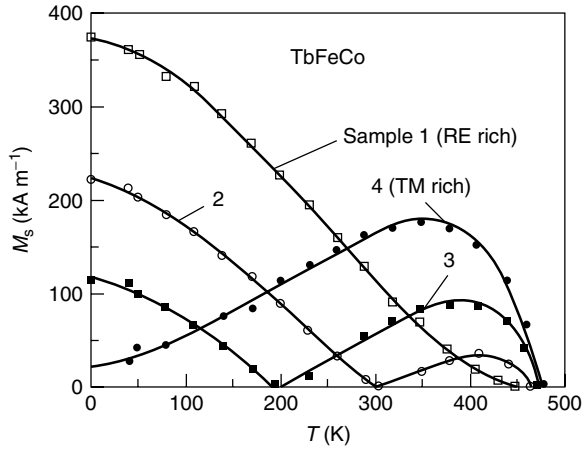

Figure 22. Magnetization curves M_s versus T of films of $Tb_{29.9}Fe_{62.6}Co_{7.5}$ (1), $Tb_{27.2}Fe_{63.5}Co_{7.3}$ (2), $Tb_{23.6}Fe_{67.6}Co_{8.8}$ (3), and $Tb_{21.2}Fe_{71.9}Co_{6.9}$ (4). (Reproduced from F.J.A.M. Greidanus *et al.*, 1989, with permission from IEEE. © 1989.)

Curie temperature can be slightly shifted to higher values by substitution of Fe by Co (Hansen, 1991). For TbFeCo films being near to the compensation point at room temperature (comparable to Figure 22, curve 2), excellent recording parameters have been achieved: $\theta_K = 0.43^\circ$ at $\lambda = 830$ nm with a carrier-to-noise ratio of greater than 60 dB at a bandwidth of 30 kHz (Hatwar, Genova and Stinson, 1990).

The Kerr effect required for readout is related to inter- and intraband transitions of the RE/TM alloy. For wavelengths between 620 and 780 nm, which are still commonly used for readout, the main contribution comes from the 3d electrons of the TMs. In the temperature range near the compensation temperature, the Kerr rotation θ_K varies only

slightly according to the variation of the magnetization of the TM subnetwork. An external field, however, acts on the net magnetization, which changes from a RE-dominated behavior below the compensation temperature to a TM dominated behavior above the compensation temperature. Hysteresis loops determined by MOKE, therefore change their sign when the temperature passes the compensation temperature T_{comp} (Figure 21).

A very important contribution to noise comes from irregularities of the written domains. They depend on the composition as well as on the writing conditions. In Figure 23, this is demonstrated for some test structures observed in Tb/Fe multilayers. Domains which are spontaneously formed usually have an irregular shape (Figure 23a). By using laser pulses of 20 µs length and various power levels, circular domains can be written in a film with $H_c = 170\,\mathrm{kA\,m^{-1}}$. Depending on the power level the diameter can be varied between 5 and 1 µm (Figure 23b). The regularity of the domains depends also on the magnitude of the bias field during the writing process (Figure 23c). For a pulse length of 10 µs and a power level of 1.8 mW, the field must exceed $15\,\mathrm{kA\,m^{-1}}$, otherwise a granular substructure is observed within the domains. In Figure 23(d), a domain structure is shown which is obtained by magnetic field modulation. A circular domain can be partially overwritten when the laser spot is slightly shifted and the bias field is reversed from one direction to the opposite. The result is a track of crescentlike domains. It is obvious, that a high recording density along the track can be obtained in spite of a relatively large diameter of the individual domain. This type of recording is applied in the present generation of the MiniDisc.

A principal limitation for the recording density is set by optical diffraction. The diameter d of the diffraction pattern produced by the objective lens during writing and reading is given by

$$D = 1.22\lambda/NA \tag{27}$$

where λ is the wavelength of the radiation (at present between 780 and 620 nm) and NA is the numerical aperture of the

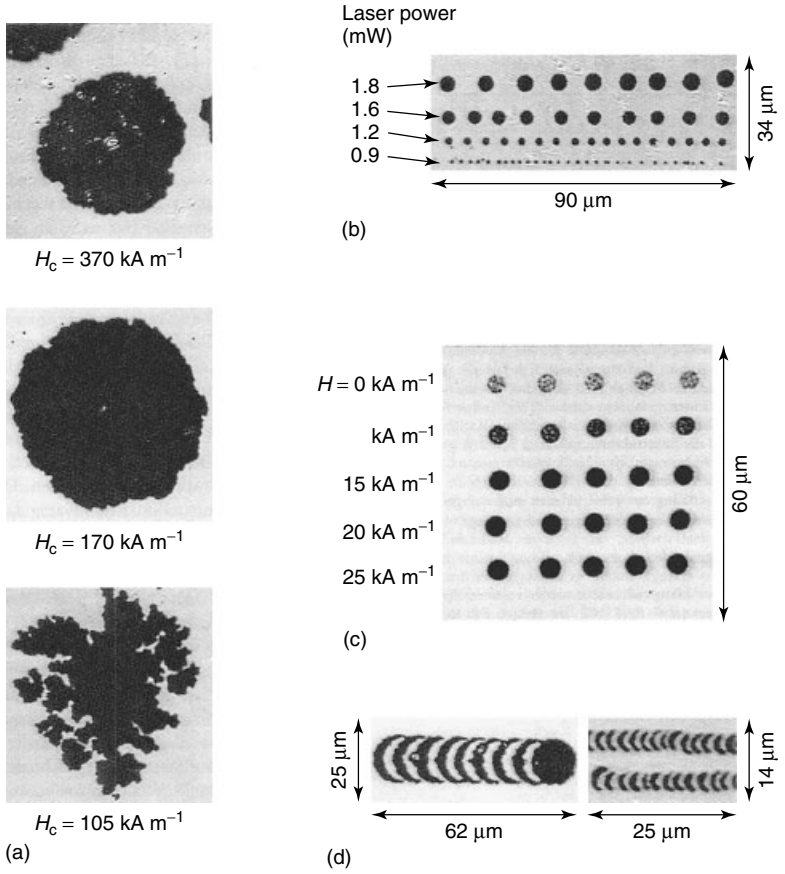

Figure 23. Magnetic domains in Tb/Fe multilayers observed by Kerr microscopy. (a) Spontaneously formed domains in films with different coercivities; (b) thermomagnetically written domains in the film with $H_c = 170\,\mathrm{kA\,m^{-1}}$ at pulse length 20 µs and variant laser power; (c) domains thermomagnetically written with laser power 1.8 mW, pulse length 10 µs, and variant bias field H_b; (d) domains written by magnetic field modulation. (Reproduced from H. Röll *et al.*, 2003, with permission from Wiley VCH. © 2003.)

objective lens of the optical head. The writing process is not so critical, because the size of the written domain depends mainly on the relation between the applied bias field H_b and the temperature distribution of H_c produced by the laser pulse (cf. Figure 23b). By appropriate conditions, domains smaller than the optical limit d can be created. The main problem originates from the reading process, since it is not possible to distinguish very small domains in a distance below (d/2). It is assumed, that the problem can be overcome in near future by MSR or related techniques (Kaneko, 1999; 2000). This principle is related to optical near-field techniques, where a narrow aperture is shifted over the sample in a very close distance and reads out the information from the center of a diffraction-broadened domain ('bit'). Its realization is closely coupled to the use of MO recording materials of the third generation, viz exchange coupled RE–TM ternary alloy films.

The original procedure to write, erase, and read out information from a MO disc is discontinuous (see the preceding text) and excludes the direct overwrite function for very high-speed real-time recording. Here exchange-coupled RE–TM alloy bilayers can help very elegantly (Saito, 1999). Figure 24 shows schematically the bilayer consisting of a TM dominated memory layer (1; e.g., sample 3 from Figure 22) and a RE-dominated reference layer (2; e.g., sample 1 from Figure 22). Layer (2) has low coercivity at room temperature and is initialized by H_{ini} (left-hand side). Interfaces appear between up-magnetized parts of layer (1) (logic '1'). Then a low-level laser pulse heats the layer (1) to T_L close to its Curie temperature such that the antiparallel ground state forms by virtue of the interlayer exchange. This sets the disc to logic '0'. Alternatively, a high-level laser pulse heats the disc to T_H close to the Curie temperature of layer (2). Now an inverted weak bias field H_b switches layer (2) down, while layer (1) being above its Curie temperature loses its information. On cooling, however, layer (1) is switched up via exchange coupling and now carries the information '1'. Thus, by low-level and high-level modulation of the laser power an arbitrary bit pattern can be recorded by direct overwrite. This principle, together with the concept of superresolution (only the center of the laser spot is used for reading and writing), has opened the breakthrough to very high density MO recording. Presently (year 2005), the highest storage levels of commercial MO discs are 9.1 GB (5.5 in.) and 2.3 GB (3.5 in.).

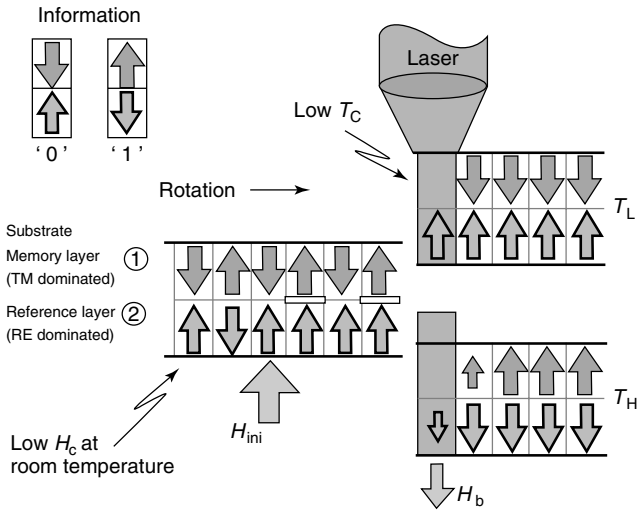

Figure 24. Principle of direct overwrite by laser intensity modulation (see text). (Reproduced from H. Röll *et al.*, 2003, with permission from Wiley VCH. © 2003.)

A more straightforward solution toward even higher storage densities would be the application of a green or blue laser instead of the present red and infrared lasers. In near future, GaInN-based semiconductor lasers will be used at wavelengths of 428 nm (blue), which would allow an increase of recording density by a factor 3.8 by a linear reduction of the dimensions. However, for the presently available RE/TM media, the figure of merit drops rapidly with decreasing wavelengths. The most promising candidates for green and blue laser radiation are Co/Pt or Co/Pd multilayer structures, for example, with a composition $25\times$ (0.4-nm Co + 1.9-nm Pt) (Carcia and Suzuki, 1999; Kaneko, 2000). Studies on TbFeCo/Pt multilayers (Itoh, Suzuki and Birukawa, 1999) have shown that the Pt component is essential for the enhanced P-MOKE angles in the violet region ($\approx$3 eV, Figure 4) and high perpendicular anisotropy. Although laboratory experiments have been successfully performed, it is an open question, if large numbers of discs with such a complicated structure can be produced on an industrial scale.

4.2 Magneto-optical semiconductors

Three classes of magnetic semiconductors have to be distinguished:

1. magnetic insulators
2. semimagnetic semiconductors
3. ferromagnetic semiconductors.

Magnetic insulators, which can also be considered as 'large gap magnetic semiconductors', comprise all magnetic ionic crystals, for example, the cubic europium chalcogenides (EuO, EuS, EuSe, and EuTe), the cubic garnets like yttrium-iron-garnet, $Y_3Fe_5O_{12}$, YIG, the (quasi)tetragonal rutile-type compounds like MnF_2, NiF_2, FeF_2, and CoF_2, the cubic TM oxides like MnO, NiO, FeO, and CoO, and the layered halides like $FeCl_2$, $FeBr_2$, and $CrCl_3$. All of these and

many more insulating compounds are well known from their magneto-optic behavior, which has been described in some detail in previous reviews (Dillon, 1971; Ferré and Gehring, 1984; Eremenko and Kharchenko, 1992; Oppeneer, 2001).

Considerable interest has recently been devoted to antiferromagnets like FeF_2 and CoO because of their key role in the appearance of exchange bias, which occurs when being exchange coupled to an adjacent ferromagnet (Meiklejohn and Bean, 1956; Nogués and Schuller, 1999) (see Section 4.3). Both constituents – the ferro- and the antiferrmagnetic component – and the evolution of domains at their interface are subject to detailed MO investigations, both in the visible (Roshchin *et al*., 2005) and in the soft X-ray regime (Ohldag *et al*., 2003). Two further classes of insulating magnets came recently into the focus of interest, the so-called magnetoelectrics and multiferroics (Fiebig, 2005; Eerenstein, Mathur and Scott, 2006). While multiferroics experience the coexistence of two types of long-range order (e.g., $TbMnO_3$ has antiferromagnetic order below $T_N = 44\,K$ and ferroelectric order below $T_C = 27\,K$ (Kimura *et al*., 2003)), magnetoelectrics have only one type of long-range order (mostly antiferromagnetic). In these compounds, magnetoelectric coupling denotes the induction of a dielectric polarization by a magnetic field and – concomitantly – the appearance of a magnetic moment induced by an electric field (O'Dell, 1970). This is prototypically realized in the antiferromagnetic insulator Cr_2O_3, whose antiferromagnetic 180° domains were imaged magneto-optically (Fiebig, Fröhlich, Krichevstov and Pisarev, 1994, see Section 4.3).

Semimagnetic semiconductors, SMS (also: diluted magnetic semiconductors, DMS) are usually II–VI semiconductors, in which TM ions of magnetic semiconductors (preferentially chalcogenides of Cr, Mn, Fe, and Co) substitute cations of the host semiconductor material (preferentially chalcogenides of Zn, Hg, and Cd) at concentrations $x \lesssim 50\%$. The fundamental difference between SMS and ordinary semiconductors, for example, between $Cd_{1-x}Mn_xTe$ and $Cd_{1-x}Zn_xTe$, is the strong field-induced magnetism in SMS, which is not observed in the absence of a magnetic field. The localized d electrons of the dopant ions strongly couple to the delocalized sp carriers of the host semiconductor. By virtue of sp–d exchange large MO effects are induced as first observed by Komarov, Ryabchenko and Terletskii (1977a,b) on $Cd_{1-x}Mn_xTe$ at microwave frequencies. Verdet constants as large as $10\,deg\,Oe^{-1}cm^{-1}$ were observed at a temperature $T = 77\,K$ and photon energy $W = 1.8\,eV$ for $x = 0.2$ (Gaj, Galazka and Nawrocki, 1978). These effects are due to a giant band splitting of the electrons, holes, and excitons, and may be observed both via MCD or via MCB (Faraday rotation). Recently, Verdet constants in the same order of magnitude were also observed in a large gap SMS, $Zn_{1-x}Co_xO$, $x = 0.042$, at UV wavelengths, $W = 3.4\,eV$, and temperature $T = 5\,K$ (Ando *et al*., 2001). These effects vanish at room temperature, but should be regained in ferromagnetically ordering $Zn_{1-x}Co_xO$ (Sato and Katayama-Yoshida, 2000).

A large amount of experimental results and steps toward a theory of the carrier-ion exchange in SMS have been compiled by Gaj (1988) and Kossut and Dobrowolski (1993). The s–d exchange is a direct ferromagnetic exchange between s and d one-electron orbitals centered at the same ion core and is virtually independent of the host and magnetic ions. On the contrary, the p–d exchange is kinetic due to p–d hybridization and can have either sign. As a rule, it is ferromagnetic for less than half-filled d shells as for $Cr(d^4)$, but antiferromagnetic for more than half-filled d shells as for $Mn(d^5)$, $Fe(d^6)$, or $Co(d^{7+})$. They have been determined in $Cd_{1-x}Cr_xS$ by free exciton spectroscopy (Twardowski *et al*., 1996). At larger concentrations, d–d exchange may give rise to collective states, for example, spin glass or antiferromagnetic, which have extensively been investigated using the MO probe (Ayadi, Ferré, Mauger and Triboulet, 1986).

The giant Faraday rotation in SMS is used to study the magnetization of the Mn^{2+} ions optically. At low x it is given by

$$\theta_F = \theta_0(\hbar\omega)B_S(H,T) + \chi(\hbar\omega) \tag{28}$$

where $\theta_0(\hbar\omega)$ and $\chi(\hbar\omega)$ are the paramagnetic contribution of Mn^{2+} and the diamagnetic contribution of the interband transitions, respectively, while $B_S(H,T)$ is the Brillouin function referring to the spin quantum number $S(= 5/2$ for $Mn^{2+})$ at the magnetic field H and the temperature T. The first term in equation (28) saturates at high fields ($\mu_0 H > 7$ T) such that only the negative second term remains. For $x > 0.01$, the d–d interaction between the magnetic ions becomes important and gives rise to quantized nearest-neighbor pair states with corresponding Zeeman levels and steps in the Faraday rotation θ_F versus B (Matsuda and Kuroda, 1996).

By exciting SMS with intense femtosecond laser pulses with circular polarization and measuring the time-resolved MOKE rotation, the Larmor precession of the Mn^{2+} spins initiated by photoinjected carriers can be observed. The pump pulse, tuned to the heavy-hole (HH) exciton resonance creates magnetic moments of electrons and HH along the growth direction in $CdTe/Cd_{1-x}Mn_xTe$ quantum wells, which is perpendicular to both the magnetic field and the sample surface (Voigt geometry). After pumping, the conduction electron spins precess with Larmor frequency amplified by the s–d exchange. In contrast, HH being quantized along the growth direction cannot precess and decay. Interestingly, as shown in Figure 25, a slower weak θ_K oscillation appears superimposed. It is due to the Mn^{2+} spins being subject to additional

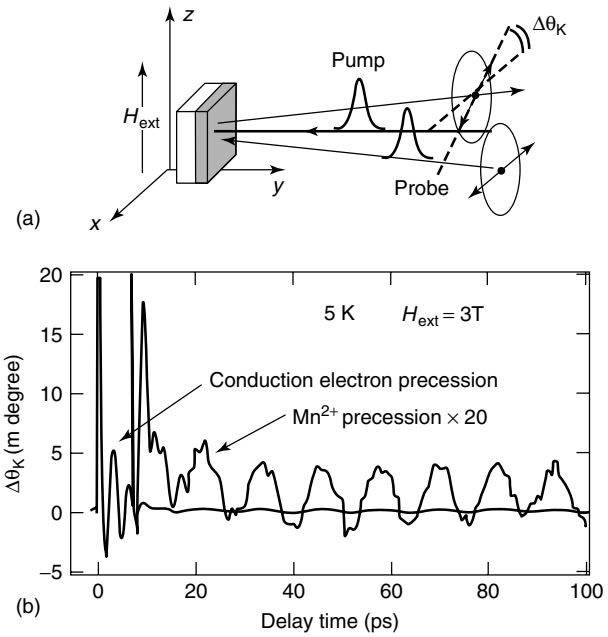

Figure 25. (a) Geometric configuration of the time-resolved magneto-optical Kerr rotation measurement. (b) Time-resolved Kerr rotation signal of $CdTe/Cd_{1-x}Mn_xTe$ quantum wells for σ^+ excitation at 3 T and 5 K. (Reproduced from Akimoto *et al.*, 1998, with permission from the American Physical Society. © 1998.)

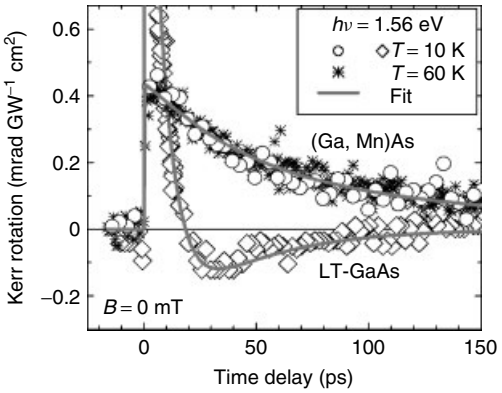

Figure 26. Temporal decay of the Kerr rotation of $Ga_{0.98}Mn_{0.02}As$ after circularly polarized excitation with 100-ps laser pulses of power 0.1 GW cm^{-2} at a photon energy of 1.56 eV and $T = 10$ and 60 K, respectively, in comparison with the behavior of a reference film of low-temperature grown-GaAs. (Reproduced from Kimel *et al.*, 2004, with permission from the American Physical Society. © 2004.)

tipping owing to the HH exchange field (Akimoto *et al.*, 1998).

Picosecond spin dynamics of photoinduced (nonequilibrium) spin polarization is also of major interest in *ferromagnetic semiconductors* of the type $Ga_{1-x}Mn_xAs$, which have recently been shown to reach Curie temperatures up to $T_C \approx 250$ K in suitable heterostructures (Nazmul *et al.*, 2005). This technique is believed to contribute to the development of ultrafast magnetic devices in spintronics. The hole-mediated ferromagnetic exchange in semiconductors opens the possibility to change the magnetic properties of $Ga_{1-x}Mn_xAs$ by modulating the hole concentration (Ohno, 1998). The magnetization dynamics of an epitaxially grown $Ga_{0.98}Mn_{0.02}As$ film of 350 nm thickness was measured by using a pump-probe MOKE technique (Kimel *et al.*, 2004). At a fluence of 10 μJ cm^{-2} the photoinduced magnetization turned out to correspond to the application of an external field of about 1 mT. The observed relaxation time of 30 ps (Figure 26) was attributed to intraconduction band relaxation and – surprisingly – was independent of the Mn^{2+} ordering.

Magneto-optics is also the proper instrument for testing the efficiency of spin-injection devices. Spin transmission across ferromagnet/semiconductor interfaces is one of the key goals for the realization of the spin transistor (Datta and Das, 1990). In order to evaluate the actual degree of spin transmission, up to 32% were reported on Fe/AlGaAs/GaAs–Schottky diodes (Hanbicki *et al.*, 2003), it was proposed to measure the changes of the magneto-optic response of the ferromagnetic component, for example, via P-MOKE while injecting charge carriers. Experiments carried out on bilayers of Co/GaAs and $Ni_{0.8}Fe_{0.2}$/GaAs (Ruggiero *et al.*, 2003) showed, however, that any change of the MOKE signal coming from the spin injection was masked by the dominating intrinsic MO activity of the bare ferromagnetic layer. More adequate are attempts analyzing the spin polarization of the current through the semiconductor component directly via the circular polarization of the light emitted at a sensing pn contact. Recently, it was demonstrated that the circular polarization of the emission from an optically pumped vertically emitting multiquantum well laser (VCSEL) is very sensitive to the spin polarization of the driving current. For example, by generating 30% spin polarization of the photoelectrons via the circular polarization of the pump light, 100% polarization of the laser radiation was obtained, thanks to the nonlinearity of the laser threshold (Hövel *et al.*, 2005). Using this sensitive MO diagnostics tool, 0.75% spin polarization could be observed at $T = 90$ K in an electrically pumped spin VCSEL when using a perpendicularly magnetized Fe/Tb multilayer in remanence as an injecting electrode (Gerhardt *et al.*, 2005).

4.3 Antiferromagnets

Only recently, the majority of the magnetism community has acknowledged antiferromagnets to be worth studying and to pay attention about. The opinion changed radically, since

antiferromagnetic materials gained appreciable technological interest with regard to the concepts of spin electronics (Prinz, 1998), exchange bias (Nogués and Schuller, 1999), magnetoelectric and multiferroic systems (Fiebig, 2005; Eerenstein, Mathur and Scott, 2006). However, although only in recent years advanced MO spectroscopical methods became available in order to determine antiferromagnetic domain topograhy (see the following text), the benefits of magneto-optics toward understanding antiferromagnetic crystals became obvious already more than 30 years ago. The quadratic MO effects, in particular, the MLB was found to be an excellent tool to determine the magnetic specific heat c_m of optically transparent materials, for example, rutile type antiferromagnets like MnF_2 and FeF_2 (Jahn and Dachs, 1971). It was soon understood (Smolenskii, Pisarev and Sinii, 1975, 1976) that the optical refractive index and the corresponding linear birefringence are sensitive to spin-correlation functions. One may consider (Borovik-Romanov, Kreines and Talaev, 1974a,b) the dependence of the electrical energy of radiation per unit volume on the spin correlations according to

$$w_e = \frac{1}{2} \sum_{i,j=x,y,z} \left[\varepsilon_{ii} E_i E_i + \frac{1}{2} \sum_{l,l'\gamma,\delta} R_{i,j,\gamma,\delta} \langle S_i^{\gamma} S_j^{\delta} \rangle E_i E_j \right] \tag{29}$$

In this relation, ε_{ii} represents the unperturbed optical permittivity tensor components, E_i the electric field of the radiation, $R_{i,j,\gamma,\delta}$ the magneto-optic tensor components, and $\langle S_i^{\gamma} S_j^{\delta} \rangle$ the spin-correlation functions, respectively. Single ion ($l = l'$) and two-ion ($l \neq l'$) contributions are included. From this one readily obtains the magnetically perturbed permittivity components

$$\varepsilon'_{ii} = \frac{\partial w_e}{\partial E_i \partial E_i}, \varepsilon'_{ij} = \frac{\partial w_e}{\partial E_i \partial E_j} \tag{30}$$

which are linear functions of the spin-correlation functions. This applies equally to the refractive indices and to the linear birefringence, when expanding the Fresnel ellipsoid given by equation (30). Thus, a comparatively simple optical method provides access to spin correlation functions, which are usually measured by neutron scattering. Surprisingly, it turned out that MLB method was capable of determining an important thermodynamic quantity, namely, the magnetic energy, $U \propto J \langle S_i S_{i+1} \rangle$. Here J and $\langle S_i S_{i+1} \rangle$ stand for the nearest-neighbor spin exchange interaction and the corresponding spin–spin correlation function. Empirically, MLB is very often dominated by the same correlation function, $\Delta n_m \propto \langle S_i S_{i+1} \rangle$, thus giving access to the magnetic specific heat $(d\Delta n_m/dT) \propto (dU/dT) \propto c_m$. It should be stressed that the same information is basically contained in the refractive indices (Markovin, Pisarev, Smolensky and Syrnikov, 1976), which are, however, usually much harder to measure at sufficient accuracy than linear birefringence. The ease of measuring MLB at very high accuracy made it an extremely popular MO method (Ferré and Gehring, 1984). It is often superior to caloric methods, where phonon contributions may mask the tiny magnetic anomalies.

By using proper modulation methods, the MLB can be measured with an utmost accuracy in the order $\delta(\Delta n) \approx 10^{-8}$ on a crystal of thickness 1 mm (Ferré and Gehring, 1984). Similarly, changes of refractive indices may be determined at an accuracy up to the order $\delta n \approx 10^{-6}$ when employing photoelastically modulated two-beam interferometry (Schäfer and Kleemann, 1985). In conjunction with polarization microscopy, the modulation method is able to determine crystal optical anisotropy with high accuracy at domains on the micrometer scale. As an example, Figure 27 shows the temperature dependence of the MLB in α-MnS, a crystal isomorphic in the cubic phase to NiO. Two anomalies are observed, where the magnitude of the MLB sharply rises in an order parameter fashion, $\Delta n_m \propto \langle S^2 \rangle$, at $T_{C1} = 152.7\,\mathrm{K}$ and at $T_{C2} = 129.5\,\mathrm{K}$ (Kleemann, Schäfer and van der Heide, 1982). Obviously two successive phase transitions occur, from the cubic into a rhombohedrally compressed (as in NiO) at T_{C1}, and into a rhombohedrally elongated phase – very probably with multi-**k** antiferromagnetic ordering due to biquadratic exchange – at T_{C2}. This conjecture is corroborated by a comparison with strain data (Figure 27). Owing to a decay of the cubic single crystal into an antiferromagnetic multidomain sample at the phase transition, which transforms

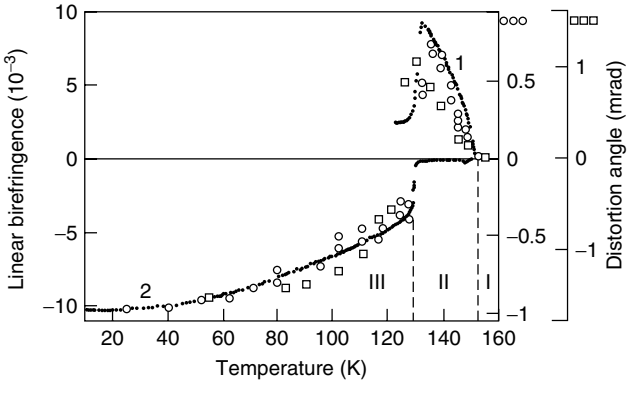

Figure 27. Linear birefringence Δn versus T (solid points) of α-MnS measured at $\lambda = 560\,\mathrm{nm}$ on single T domains selected in phase I (curve 1) and III (curve 2), respectively. Comparison is made with lattice distortion data fitted to the MLB data at low T. (Reproduced from Kleeman *et al.*, 1982, with permission from Elsevier. © 1982.)

into yet another domain network at the second one, the microscopic MLB technique is indispensable.

Antiferromagnetic domains were first postulated by Néel (1948) and first evidenced by MO methods in 1960 on NiO (Slack, 1960; Roth, 1960). These latter authors were able to map domains exhibiting MLB of different sign owing to coupling of strain to spin-pair correlation functions, which give rise to magnetostrictive distortion of the cubic lattice. Figure 28 shows the so-called T (= trigonal) domain pattern of a (111) oriented crystal plate of α-MnS under the polarizing light microscope at $T = 74\,\mathrm{K}$ (Kleemann, Schäfer and van der Heide, 1982). The pattern appears with different contrast depending on the choice of three different orientations of the crossed polarizers, $[\bar{2}11]$, $[1\bar{2}1]$, and $[11\bar{2}]$. These are projections of the three trigonal $\langle 111\rangle$ axes, which are orthogonal to the magnetic easy planes similar to the situation found in NiO (Slack, 1960; Roth, 1960), but not orthogonal to the sample plane. The T_1 domain (optically neutral for all polarizer settings) is missing because of surface compressive stress along [111] arising at the phase transition at $T_N = 129.5\,\mathrm{K}$. According to minimum strain conditions, the crystallographic orientations of the twin walls are restricted to the 110 and 100 planes. Only the walls parallel to $(\bar{1}10)$, $(10\bar{1})$, and $(0\bar{1}1)$ intersect the habit plane perpendicularly along $[\bar{2}11]$, $[1\bar{2}1]$, and $[11\bar{2}]$ (sharp borders), while all other walls are oblique with respect to the habit plane (diffuse borders). It should be noticed that the possibilities of antiferromagnetic domain topography were recently rediscovered using resonant XMLD techniques with polarized synchrotron radiation. Essentially under the same polarization selection rules as applicable to MLB (Roth, 1960), the 12 intraplanar $\langle 11\bar{2}\rangle$ oriented S (= spin) domains within the four T domains have been imaged by XMLD/PEEM on NiO (Hillebrecht *et al.*, 2001).

The intimate interplay between MO permittivity and spin correlations makes magneto-optics a versatile tool to tackle more sophisticated problems of statistical physics. For example, the famous random-field Ising model, one of the standards for microscopic disorder in spin systems (Imry and Ma, 1975), has been studied on diamagnetically diluted uniaxial antiferromagnets like $Fe_{1-x}Zn_xF_2$, $x \lesssim 0.5$, using both MLB (Belanger, Jaccarino and King, 1983) and Faraday rotation (Kleemann, King and Jaccarino, 1986). Peculiarly, both MO techniques reveal the same critical dependence, namely, $(\mathrm{d}\Delta n_\mathrm{m}/\mathrm{d}T) \propto (\mathrm{d}\theta_\mathrm{F}/\mathrm{d}T) \propto c_m$. This is in accordance with field-scaling properties of the leading singularities of all second derivatives of the free energy with respect to T and H. All of them, $(\partial^2 F/\partial H\partial T)$, $(\partial^2 F/\partial H^2)$, $(\partial^2 F/\partial T^2)$, diverge as $H^y|T - T_\mathrm{C}|^{-\alpha}$, with the same $\alpha \approx 0$, but different exponents y emerging from scaling theory (Kleemann, King and Jaccarino, 1986). This is illustrated by Figure 29, which shows the logarithmic

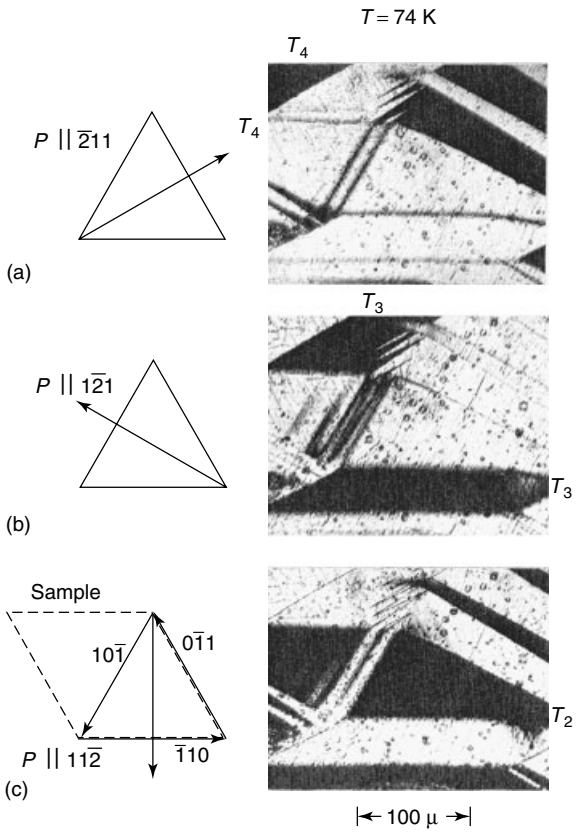

Figure 28. MLB contrast of T domains in phase III of as-grown (111) platelets of α-MnS with thickness 25 μm observed at various settings of the polarizers (left-hand panel). Optically neutral T_j domains ($j = 2$, 3, and 4) are indicated. (Reproduced from Kleeman *et al.*, 1982, with permission from Elsevier. © 1982.)

divergences of $(\mathrm{d}\Delta n_\mathrm{m}/\mathrm{d}T)$ (Belanger, Jaccarino and King, 1983) and $(\mathrm{d}\theta_\mathrm{F}/\mathrm{d}T)$ (Pollak, Kleemann and Belanger, 1988) obtained on $Fe_{0.47}Zn_{.53}F_2$ in different external magnetic fields.

MLB – or its Kramers–Kronig complement MLD – is applicable to domain topography only, whenever the spatial symmetry is broken in the antiferromagnetic phase. For example, all cubic systems become optically anisotropic as collinear spin ordering takes place. This does not hold in uniaxial single crystals, if the magnetic order parameter conserves the axial symmetry. Contrary to frequent belief, this is also valid for the resonant XMLD technique (the XMLD contrast observed on a thin film of $LaFeO_3$ in Figure 18 becomes possible only because of its inherent 'twin' structure containing crystallites with alternate in-plane c axes!). In the case of antiferromagnetic 180° domains, linear MO methods are applicable only if a magnetic field induces a net magnetization and time inversion symmetry becomes broken (Eremenko and Kharchenko, 1987; Dillon, 1991). Figure 30 shows a drastic example, namely, the metamagnetic domain

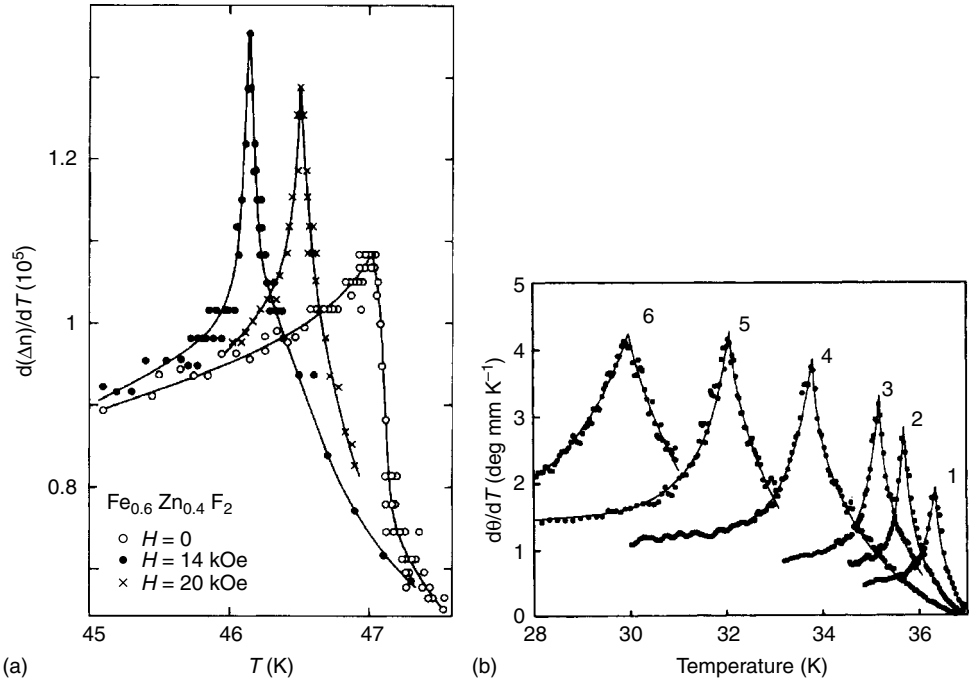

Figure 29. $d(\Delta n)/dT$ (a) and $d(\theta_F)/dT$ of $Fe_{1-x}Zn_xF_2$, $x = 0.40$ (a) and 0.53 (b) as functions of the temperature for magnetic fields $B = 0$, 1.4 and 2.0 T (a), and 1, 1.5, 2, 3, 4, and 5 T (b) applied parallel to [001]. (Reproduced from Belanger *et al.*, 1983, with permission from the American Physical Society. © 1983 (a) and Reproduced from Pollack *et al.*, 1988, with permission from the American Physical Society. © 1988 (b).)

pattern of the uniaxial antiferromagnet $FeCl_2$ in its 'mixed phase', that is, when exposed to sufficiently high axial magnetic field (Kushauer, 1995). The domains show Faraday rotation contrast between strongly magnetized metamagnetic (= paramagnetically saturated) domains (white) embedded in weakly magnetized antiferromagnetic background (black) induced by fields between the critical values, $H_{c1} = 841\,\text{kA/m} < H < H_{c2} = 1420\,\text{kA m}^{-1}$. Magnetostatically stabilized stripe domains are observed, which nucleate as bubbles close to the critical fields (a,t) and form maze-type patterns with minimal mutual distances (h–j) at intermediate fields, $H \approx 1100\,\text{kA m}^{-1}$. Similarities with stripe and bubble domain patterns in ferrimagnetic garnets and strongly perpendicular anisotropic films are obvious (Kooy and Enz, 1960; Thiele 1970; Bobeck and della Torre, 1975; Hubert and Schäfer, 1998).

Domain visualization of uniaxial antiferromagnets in its zero-field ground state has long time been possible only via neutron topograhy (Alperin, Brown, Nathans and Pickart, 1962; Schlenker and Baruchel, 1978), a tedious and time consuming technique (exposure times up to 24 h!), which has a poor spatial resolution in the order of 0.1 mm. Only recently, a purely MO technique was discovered, which is applicable to uniaxial antiferromagnetic crystals, which are based on nonreciprocal properties of the point group involved (Fiebig, Fröhlich, Krichevstov and Pisarev, 1994). It is possible by using nonlinear resonant sum frequency spectroscopy, viz by mapping the interference patterns of time-inversion and non-time-inversion symmetrical contributions to the nonlinear polarization. A model system fulfilling the above symmetry conditions is the axial magnetoelectric antiferromagnet Cr_2O_3, a sample of which shows its domain structure in Figure 31 in right (a,c) and left (b) circular SH light at a photon energy of 2.1 eV (Fiebig, 1995). The technique, although involving a setup with an optical parametric oscillator (OPO) for two-photon spectroscopy in a suitable spectral region, is less expensive than the spin-polarized neutron probe and reveals a much better spatial resolution in the order of 1 µm. It has been applied to a number of nonreciprocal materials. Presently, attention is focused on magnetoelectric and multiferroic materials (Fiebig, 2005) like $HoMnO_3$ (Goltsev, Pisarev, Lottermoser and Fiebig, 2003) and $YMnO_3$ (Fiebig *et al.*, 2002), where access to antiferromagnetic and ferroelectric domain structure was enabled by SHG spectroscopy.

4.4 Magnetophotonic crystals

Starting with the pioneering work of Yablonovich (1987) and John (1987) photonic band gap (PBG) materials or photonic crystals (PCs) have been of utmost interest among theoreticians and experimentalists because of their promising potential in applications in micro- and optoelectronics.

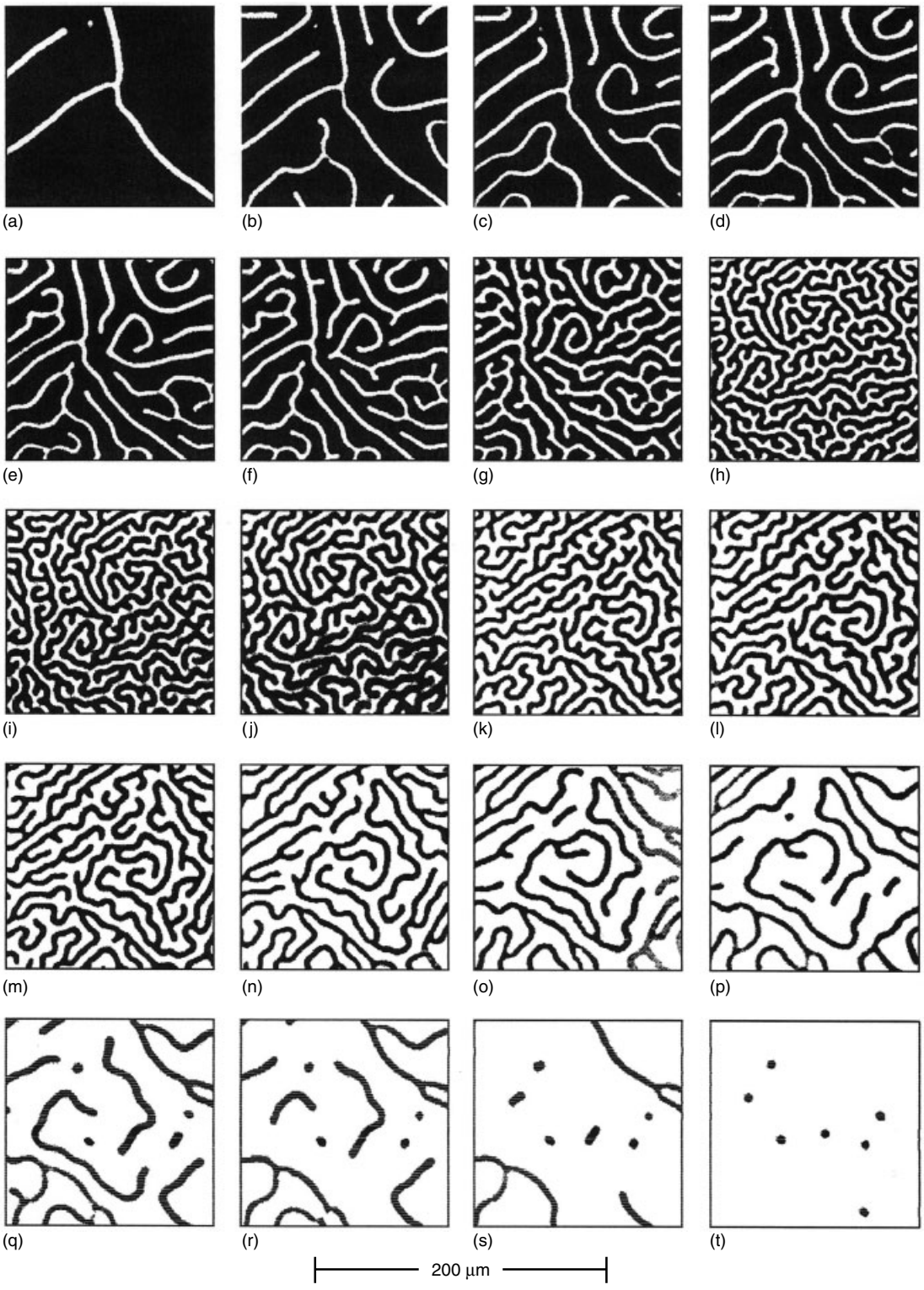

Figure 30. Faraday rotation contrast of metamagnetic domains (white) observed in a (111) platelet (thickness 170 μm) of antiferromagnetic $FeCl_2$ (black) at $T = 10\,\mathrm{K}$ under various axial magnetic fields $481.4 \leq H \leq 1407.3\,\mathrm{kA\,m^{-1}}$. (From Kushauer, 1995.)

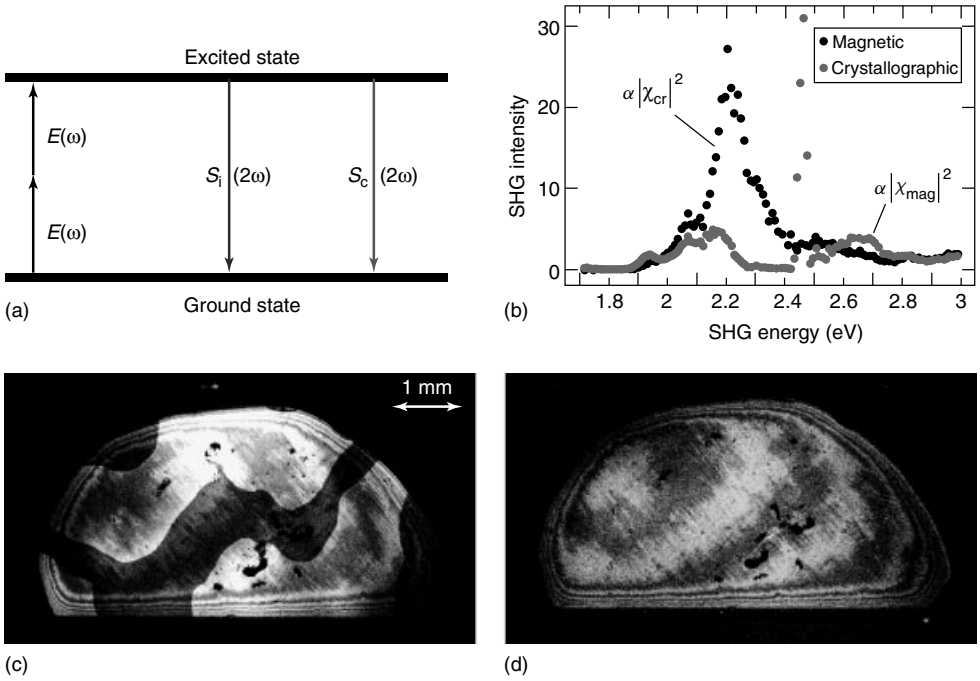

Figure 31. Antiferromagnetic domains in Cr_2O_3 (c) imaged by second harmonic generated intensity contrast due to interference of the crystallographic and magnetic two-photon scattering fields, S_i and S_c (a), respectively, at appropriate resonant frequencies (b). Above $T_N = 308$ K (d) the domain contrast vanishes. (Reproduced from M. Fiebig *et al*., 2001, with permission from Institute of Physics Publishing Ltd. © 2001.)

PCs are one- (1D), two- (2D), or three-dimensional (3D) periodically ordered structures made from materials with different refractive indices. The periods being in the order of the wavelengths of the impinging electromagnetic radiation (microwaves, infrared, or visible light) give rise to interference effects, which finally lead to band formation in the electromagnetic spectrum. A PBG may finally inhibit light propagation for certain frequencies and selected or even arbitrary polarization.

PCs, even those without a PBG, have multiple interesting and useful properties related to the dispersion, anisotropy, and polarization properties of the photonic bands (Joannopoulos, Meade and Winn, 1995). They have, for example, been demonstrated to create efficient dispersion compensation, enhanced nonlinear frequency conversion, to operate as highly efficient Bragg mirrors and to realize the localization of light (Yablonovitch, 1987). The tunability of the optical properties of PCs can open new applications of these materials in integrated-optics devices. Tunability in semiconductor structures may, among others, be achieved by use of magnetic constituents. This leads to the fabrication of magnetic photonic crystals (MPCs), which have attracted much interest in the past 10 years. Review articles about the theory and the experimental realizations of MPCs were published by Lyubchanskii *et al*. (2003), Zvezdin and Belotelov (2004), and Inoue (2006).

Incorporation of magnetic components into PCs can lead to new and interesting phenomena of magneto-optics such as enhanced MCB and MLB (Inoue and Fujii, 1997; Steel, Levy and Osgood, 2000; Levy, Yang and Steel, 2001; Saado, Golosovsky, Davidov and Frenkel, 2002; Dolgova *et al*., 2004). The first PC structures were one-dimensional multilayers with dielectric mirrors ($\lambda/4$ stacks of materials with high and low refractive index) and a transparent magnetic $\lambda/2$ Fabry–Pérot cavity (Figure 32). These '1D MPCs with stacking faults' were designed as to fulfill the optical isolator conditions, viz 45° Faraday rotation and 100% transparency at a given wavelength. This aim could be reached in a very good approximation by Kato *et al*. (2003) with a bilayer number $k = 6$, an enhancement of θ_F by a factor of 150, and an absorption in the order 10^{-6}. Figure 33 (inset) gives an impression of the high finesse of the spectral enhancement of both the optical transmission and the Faraday rotation (enhancement factor 50) of a related MPC, $(SiO_2/Ta_2O_3)_5$/Bi:YIG/$(SiO_2/Ta_2O_3)_5$ (Murzina *et al*., 2004).

The theory of 1D MPCs is related to that of magnetic multilayers (Visnovsky *et al*., 1995), although the layers are coarsened toward micrometer thickness instead of the 'conventional' nanometric periods. However, the matrix formalism to be applied is very similar. A 4×4 transfer-matrix formalism is applicable, which describes the circularly

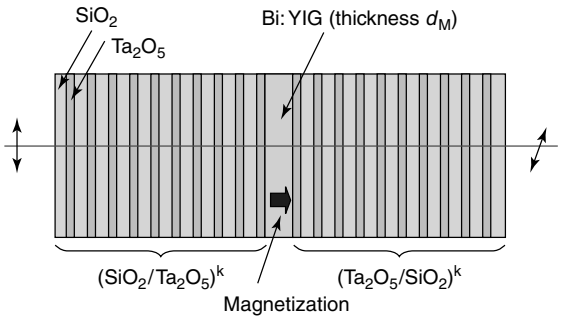

Figure 32. Schematic 1D magnetophotonic crystal containing a Bi:YIG layer as a defect and acting as a Fabry–Pérot resonator with enhanced Faraday rotation of Bi:YIG.

polarized eigenmodes with clock- and anticlock-wise rotation of the electric-field vector (Belotelov and Zvezdin, 2005). In 2D and 3D, the full eigenvalue problem has to be resolved as in classical PC theory (Sakoda, 2004). This means to solve the Helmholtz equation under the constraint of a spatially periodic dielectric constant, $\varepsilon(\mathbf{r})$, a problem which reminds of the equation of motion of electrons in the periodic potential of a crystal. Dispersion relationships, $\omega(\mathbf{k})$, and a band structure emerge for (nonexisting) quasi-longitudinal and (existing) quasitransverse modes, which are vectorial Bloch functions. Taking into account the periodic magneto-optic Voigt parameter (see equation (20)), $Q(\mathbf{r})$ changes the mode behavior in the sense that transverse electric (TE) modes adiabatically transform into transverse magnetic (TM) ones and vice versa. This is a consequence of the gyrotropy of the medium. Peculiarly for the MPC structure, it turns out that the specific Faraday rotation grows sharply, when the frequency approaches the band gap. This can be understood by the fact that the group velocity of the light decelerates appreciably close to the gap. This leads to an increased light-matter interaction (similarly as for the light in the Fabry–Pérot cavity of a 1D MPC) with enhanced MO effects. This was evidenced on a 3D colloidal MPC containing a Faraday active transparent liquid, where the Faraday rotation increases by a factor of 5 within the stop band, whereas it is virtually unaffected outside the stop band (Koerdt, Rikken and Petrov, 2003).

Self-organizing colloidal crystals with magnetic components (Xu *et al*., 2002), inverted magnetically filled opals (Gates and Xia, 2001), and structured ferrofluids(Richardi *et al*., 2002) are presently the most popular candidates of MPC growth. Apart from these artificially prepared magnetic superlattices, natural or artificially prepared magnetic domain structures have been investigated. They may occur as 1D stripe domain patterns or as 2D bubble lattices (Bobeck and della Torre, 1975; Hubert and Schäfer, 1998). Again, as in structural MPCs, mode conversion TE → TM is

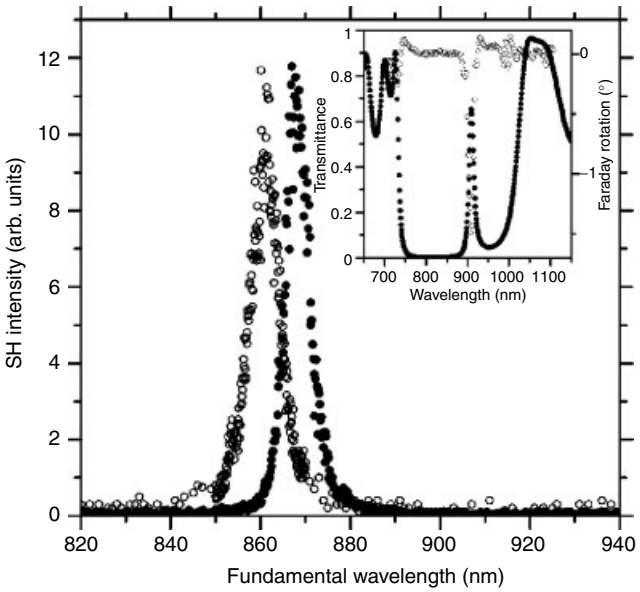

Figure 33. SHG spectra of the MPC with $\lambda_{PBG} \approx 900$ nm measured in the p-in, p-out and s-in, p-out polarization combinations, open and solid circles, respectively. Inset: Transmittance spectra (solid circles) and Faraday rotation angle (open circles) measured at normal incidence. (Reproduced from Murzina *et al*., 2004, with permission from the American Physical Society. © 2004.)

expected (Nikitov and Tailhades, 2001). Applications in MO waveguides (Dötsch *et al*., 2005) are envisaged.

A new aspect of MPCs is the use of optical nonlinearity because of their ability to enhance small effects significantly (Aktsipetrov *et al*., 2005). For example, the modification of the electromagnetic wave dispersion near to the PBG edges allows one to effectively fulfill the phase matching conditions for SHG, if either the fundamental or the SH wave is tuned toward the gap (Dumeige *et al*., 2001). A new domain of nonlinear optics appears as the second- and third-order structural nonlinearities that are combined with the broken time-reversal symmetry owing to the magnetization of ferromagnetic materials. As a result of this combination, SHG and third-harmonic generation (THG) become very sensitive to control by external magnetic impacts. MSHG has, for example, been observed in MPC microcavities formed from a half-wavelength-thick Bi:YIG film sandwiched between two high-finesse dielectric Bragg reflectors (Murzina *et al*., 2004; Fedyanina *et al*., 2004). Apart from the well-known enhancement of the Faraday rotation (Figure 33, inset), this 1D MPC reveals SHG for both s- and p-polarized fundamental radiation, which is resonance enhanced at least by a factor of 10^3 as compared to the intensity outside the PBG (Figure 33, main panel). Magnetization-induced changes of the relative phase of the SH wave are observed using SHG interferometry and reach the factor of 4 in intensity and 180° in phase for directions

opposite to the dc magnetic field. The longitudinal and polar nonlinear MOKEs manifest themselves in a considerable rotation, up to $\theta_K \approx 50^\circ$, of the SH wave polarization. This enhancement is attributed to the fulfillment of the phase-matching conditions for the MSHG effect in layered structures with periodic modulation of both optical (MO) and nonlinear optical parameters. Recently, also a 2D magnetophotonic crystal, viz a hexagonal magnetic bubble lattice, has been shown to reveal enhanced MSHG at the PBG with noticeable influence of an external magnetic field (Dadoenkova *et al*., 2005).

5 CONCLUSION

Magneto-optics in solid-state research and applications has reached a new level as an indispensable tool for magnetic research and applications. Although the traditional tasks are still vivid and most useful, viz applications in MO recording and optical isolators, new techniques have matured in the last 10 years. Partially they are based on sophisticated light sources, which make magneto-optics extremely important, if not irreplaceable. Together with ultrafast laser light sources the limits of magnetic dynamics can now be explored. In conjunction with intense, polarized, and highly resolved synchrotron radiation core level, X-ray spectroscopy has become a routine tool to separate spin from orbital magnetism, to distinguish between contributions of different magnetic elements, and to image magnetic nanodomains both in real and Fourier space. Intense laser light sources are the key to real surface sensitive magnetic explorations via MSHG and to unprecedented possibilities for MO SHG imaging of 180° domains in antiferromagnets. New materials for spintronics and magnetic storage purposes like ultrathin films, multilayers, and patterned nanostructures are preferably investigated by magneto-optic methods for obvious reasons. But there are also new devices like magneto-optic waveguides and magnetophotonic crystals, which are specially designed for magneto-optics and will certainly soon enter the market for tele and data communications. It is probably not too optimistic to predict that (Lyubchanskii *et al*., 2003) 'the use of magnetic materials in combination with dielectrics, metals, and semiconductors can lead to the creation of a new class of devices for photonics applications, and a new direction in photonics called *magnetophotonics*'.

ACKNOWLEDGMENTS

Thanks are due to Oleg Petracic for help with the bibliography and to the Deutsche Forschungsgemeinschaft through SFB 491, KL306/37, and KL306/38 for financial support.

REFERENCES

Akimoto, R., Ando, K., Sasaki, F., *et al*. (1998). Larmor precession of Mn^{2+} moments initiated by the exchange field of photoinjected carriers in CdTe/$Cd_{1-x}Mn_xTe$ quantum wells. *Physical Review B*, **57**, 7208–7213.

Aktsipetrov, O.A., Dolgova, T.V., Fedyanin, A.A., *et al*. (2005). Magnetization-induced second- and third-harmonic generation in magnetophotonic crystals. *Journal of the Optical Society of America B*, **22**, 176–186.

Allwood, D.A., Xiong, G., Cooke, M.D. and Cowburn, R.P. (2003). Magneto-optical Kerr effect analysis of magnetic nanostructures. *Journal of Physics D: Applied Physics*, **36**, 2175–2182.

Alperin, H.A., Brown, P.J., Nathans, A. and Pickart, S.J. (1962). Polarized neutron study of antiferromagnetic domains in MnF_2. *Physical Review Letters*, **8**, 237–239.

Ando, K., Saito, H., Jin, Z-W., *et al*. (2001). Large magneto-optical effect in an oxide diluted magnetic semiconductor $Zn_{1-x}Co_xO$. *Applied Physics Letters*, **78**, 2700–2702.

Anisimov, S.I., Kaspeliovitch, B.L. and Perel'man, T.L. (1974a). Emission of electrons from the surface of metals induced by ultrashort laser pulses. *Zhurnal Eksperimentalnoi I Teoreticheskoi Fiziki*, **66**, 776–781.

Anisimov, S.I., Kaspeliovitch, B.L. and Perel'man, T.L. (1974b). Emission of electrons from the surface of metals induced by ultrashort laser pulses. *Soviet Physics - JETP*, **39**, 375.

Argyres, P.N. (1955). Theory of the Faraday and Kerr effects in ferromagnets. *Physical Review*, **97**, 334–345.

Ayadi, M., Ferré, J., Mauger, A. and Triboulet, R. (1986). Spin-freezing process in a spin-glass: $Cd0.6Mn_{0.4}Te$. *Physical Review Letters*, **57**, 1165–1168.

Azzam, R.M.A. and Bashara, N.M. (1979). *Ellipsometry and Polarized Light*, North-Holland: Amsterdam.

Back, C.H., Weller, D., Heidmann, J., *et al*. (1998). Magnetization reversal in ultrashort magnetic field pulses. *Physical Review Letters*, **81**, 3251–3254.

Bader, S. (1991). Smoke. *Journal of Magnetism and Magnetic Materials*, **100**, 440–454.

Bader, S.D. and Moog, E.R. (1987). Magnetic properties of novel epitaxial films. *Journal of Applied Physics*, **61**, 3729.

Beaurepaire, E., Merle, J-C., Daunois, A. and Bigot, J-Y. (1996). Ultrafast spin dynamics in ferromagnetic nickel. *Physical Review Letters*, **76**, 4250–4253.

Bedanta, S., Eimüller, T., Kleemann, W., *et al*. (2007). Overcoming dipolar disorder in dense ensembles of CoFe nanoparticles: Superferromagnetism. *Physical Review Letters* (in press).

Belanger, D.P., Jaccarino, V. and King, A.R. (1983). Random-field critical behavior of a $d = 3$ Ising system. *Physical Review B*, **28**, 2522–2526.

Belotelov, V.I. and Zvezdin, A.K. (2005). Magneto-optical properties of photonic crystals. *Journal of the Optical Society of America B*, **22**, 286–292.

Bennemann, K-H. (ed.) (1998). Nonlinear optics in metals, In *International Series of Monographs in Physics*, Oxford University Press: New York, Vol. 98.

Bennett, H.S. and Stern, E.A. (1965). Faraday effect in solids. *Physical Review*, **137**, A448–A461.

Berger, A. and Pufall, M.R. (1997). Generalized magneto-optical ellipsometry. *Applied Physics Letters*, **71**, 965–967.

Berger, A. and Pufall, M.R. (1999). Quantitative vector magnetometry using generalized magneto-optical ellipsometry. *Journal of Applied Physics*, **85**, 4583–4585.

Bigot, J.Y., Beaurepaire, E., Guidoni, L. and Merle, J-C. (2002). Magnetization dynamics on the femtosecond time-scale in metallic ferromagnets. In *Magnetism: Molecules to Materials III*, Miller, J.S. and Drillon, M. (Eds.), Wile-VCH: Weinheim.

Bigot, J.Y., Guidoni, L., Beaurepaire, E. and Saeta, P.N. (2004). Femtosecond spectrotemporal magneto-optics. *Physical Review Letters*, **93**, 077401.

Birss, R.R. (1966). *Symmetry and Magnetism*, North-Holland: Amsterdam.

Bobeck, A.H. and della Torre, E. (1975). *Magnetic Bubbles*, North Holland: Amsterdam.

Borovik-Romanov, A.S., Kreines, N.M., Pankov, A.A. and Talaev, M.A. (1974a). Magnetic birefringence of light in antiferromagnetic substances M_nCO_3, $CoCO_3$ and $CsMnF_3$. *Soviet Physics -JETP*, **39**, 378.

Borovik-Romanov, A.S., Kreines, N.M., Pankov, A.A. and Talaev, M.A. (1974b). Magnetic birefringence of light in antiferromagnetic substances M_nCO_3, $CoCO_3$ and $CsMnF_3$. *Zhurnal Eksperimentalnoi I Teoreticheskoi Fiziki*, **66**, 782–791.

Brammeier, D.P., Park, J.M., Olson, C.G., *et al*. (2004). Magneto-optic spectrum and electronic structure of single-crystal MnBi. *Journal of Magnetism and Magnetic Materials*, **283**, 95–102.

Brown, W.F. Jr. (1978). *Micromagnetics*, Krieger: New York.

Bruno, P., Suzuki, Y. and Chappert, C. (1996). Magneto-optical Kerr effect in a paramagnetic overlayer on a ferromagnetic substrate: a spin-polarized quantum size effect. *Physical Review B*, **53**, 9214–9220.

Buschow, K.H.J. (1988). Magneto-optical properties of alloys and intermetallic compounds. In *Ferromagnetic Materials - A Handbook on the Properties of Magnetically Ordered Substances*, Wohlfarth, E.P. and Buschow, K.H.J. (Eds.), North Holland: Amsterdam, pp. 493–595.

Carcia, P.F. and Suzuki, T. (1999). New MO recording media based on Pt/Co and Pd/Co multilayers and Pt-Co alloys. In *Magneto-Optical Recording Materials*, Gambino, R.J. and Suzuki, T. (Eds.), IEEE Press: New York.

Carra, P., Thole, B.T., Altarelli, M. and Wang, X. (1993). X-ray circular dichroism and local magnetic fields. *Physical Review Letters*, **70**, 694.

Chakrabarti, B.K. and Acharyya, M. (1999). Dynamic transitions and hysteresis. *Reviews of Modern Physics*, **71**, 847–859.

Chaudhari, P., Cuomo, J.J. and Gambino, R.J. (1973). Amorphous metallic films for magneto-optic applications. *Applied Physics Letters*, **22**, 337–339.

Chen, C.T., Idzerda, Y.U., Lin, H-J., *et al*. (1995). Experimental confirmation of the X-ray magnetic circular dichroism sum rules for iron and cobalt. *Physical Review Letters*, **75**, 152–155.

Choi, B.C., Belov, M., Hiebert, W.K., *et al*. (2001). Ultrafast magnetization reversal dynamics investigated by time domain imaging. *Physical Review Letters*, **86**, 728–731.

Cotton, A. and Mouton, H. (1907). Sur les propriétés magnéto-optiques des colloides et des liqueurs hétérogènes. *Annales de Chimie et de Physique*, **11**, 145–203.

Craik, D.J. and Tebble, R.S. (1965). *Ferromagnetism and Ferromagnetic Domains*, North-Holland: Amsterdam.

Crawford, T.M., Silva, T.J., Teplin, C.W. and Rogers, C.T. (1999). Subnanosecond magnetization dynamics measured by the second-harmonic magneto-optic Kerr effect. *Applied Physics Letters*, **74**, 3386–3388.

Daboo, C., Bland, J.A.C., Hicken, R.J., *et al*. (1993). Vectorial magnetometry with the magneto-optic Kerr effect applied to Co/Cu/Co trilayer structures. *Physical Review B*, **47**, 11852–11859.

Dadoenkova, N.N., Lyubchanskii, I.L., Lyubchanskii, M.I., *et al*. (2005). Influence of magnetic field on nonlinear magneto-optical diffraction on two-dimensional hexagonal magnetic bubble lattice. *Journal of the Optical Society of America B*, **22**, 215–219.

Datta, S. and Das, B. (1990). Electronic analog of the electro-optic modulator. *Applied Physics Letters*, **56**, 665–667.

Di, G.Q. (1992). The giant magneto-optical effect in MnBiAl alloy films (in Japanese). PhD Thesis, Nagoya University.

Dillon, J.F. Jr. (1963). Domains and domain walls. In *Magnetism*, Rado, G.T. and Suhl, H. (Eds.), Academic Press: New York, pp. 429–453, Vol. 3.

Dillon, J.F. Jr. (1971). Magneto-optical properties of magnetic crystals. In *Magnetic Properties of Materials*, Smit, J. (Ed.), McGraw-Hill: New York, pp. 108–148.

Dillon, J.F. Jr. (1991). Magnetooptics. *Journal of Magnetism and Magnetic Materials*, **100**, 425–439.

Dolgova, T.V., Fedyanin, A.A., Aksipetrov, O.A., *et al*. (2004). Nonlinear magnetooptical Kerr effect in garnet magnetophotonic crystals. *Journal of Applied Physics*, **95**, 7330–7332.

Donahue, M. and Porter, D. (2000). *OOMMF User's Guide, Version 1.0, Interagency Report NISTIR 6376*, National Institute of Standards and Technology: Gaithersburg.

Dötsch, H., Bahlmann, N., Zhuromskyy, O., *et al*. (2005). Applications of magneto-optical waveguides in integrated optics. *Journal of the Optical Society of America B*, **22**, 240.

Dumeige, Y., Vidakovi, P., Sauvage, S., *et al*. (2001). Enhancement of second-harmonic generation in a one-dimensional semiconductor photonic bandgap. *Applied Physics Letters*, **78**, 3021–3023.

Ebert, H. and Schütz, G. (1996). *Spin-Orbit-Influenced Spectroscopies of Magnetic Solids: Proceedings of an International Workshop*, Springer: Berlin, New York.

Eerenstein, W., Mathur, N.D. and Scott, J.F. (2006). Multiferroic and magnetoelectric materials. *Nature (London)*, **442**, 759–765.

Eremenko, V.V. and Kharchenko, N.F. (1992). Magneto-optics of antiferromagnets. *Physics Reports*, **155**, 379–401.

Faraday, M. (1846). On the magnetization of light and the illumination of magnetic lines of force. *Philosophical Transactions of the Royal Society of London*, **136**, 1–20.

Fedyanina, A.A., Aktsipetrova, O.A., Kobayashi, D., *et al*. (2004). Enhanced Faraday and nonlinear magneto-optical Kerr effects in magnetophotonic crystals. *Journal of Magnetism and Magnetic Materials*, **282**, 256–259.

Feigel'man, M.V., Geshkenbein, V.B., Larkin, A.I. and Vinokur, V.M. (1989). Theory of collective flux creep. *Physical Review Letters*, **63**, 2303.

Ferré, J. (1992). Magnetooptics in ultra-thin magnetic films and multilayers. *Magnetism, Magnetic Materials and their Applications*, IOP Publishing: Bristol, pp. 167–194.

Ferré, J. (2001). Dynamics of the magnetization reversal: from continuous to patterned ferromagnetic films. In *Spin Dynamics in Confined Magnetic Structures I*, *Topics in Applied Physics*, Hillebrands, B. and Ounadjela, K. (Eds.), Springer: Heidelberg, New York, pp. 127–166, Vol. 83.

Ferré, J. and Gehring, G. (1984). Linear optical birefringence of magnetic crystals. *Reports on Progress in Physics*, **47**, 513–611.

Ferré, J., Penissard, G., Marlière, C., *et al*. (1991). Magneto-optical studies of Co/Au ultrathin metallic films. *Applied Physics Letters*, **56**, 1588–1590.

Fiebig, M. (1995). *Nichtlineare Spektroskopie und Topographie an antiferromagnetischen Domänen PhD Thesis*, Universität Dortmund.

Fiebig, M. (2005). Revival of the magnetoelectric effect. *Journal of Physics D: Applied Physics*, **38**, R132–R152.

Fiebig, M., Fröhlich, D., Krichevstov, B.B. and Pisarev, R. (1994). Second harmonic generation and magnetic-dipole-electric dipole interference in antiferromagnetic Cr_2O_3. *Physical Review Letters*, **73**, 2127–2130.

Fiebig, M., Lottermoser, T., Fröhlich, D., *et al*. (2002). Observation of coupled magnetic and electric domains. *Nature (London)*, **419**, 818–820.

Fischer, P., Eimüller, T., Schütz, G., *et al*. (1998). Imaging of magnetic domains by transmission X-ray microscopy. *Journal of Physics D: Applied Physics*, **31**, 649–655.

Fischer, P., Schütz, G., Schmahl, G., *et al*. (1996). Imaging of magnetic domains with the X-ray microscope at BESSY using X-ray magnetic circular dichroism. *Zeitschrift Fur Physik B: Condensed Matter*, **101**, 313–316.

Florczak, J.M. and Dahlberg, E.D. (1991). Magnetization reversal in (100) Fe thin films. *Physical Review B*, **44**, 9338–9347.

Gaj, J.A. (1988). Magneto-optical properties of large-gap diluted magnetic semiconductors. In *Semiconductors and Semimetals*, *Diluted Magnetic Semiconductors*, Furdyna, J.K. and Kossut, J. (Eds.), Academic Press: San Diego, pp. 275–309, Vol. 25.

Gaj, J.A., Galazka, R.R. and Nawrocki, M. (1978). Giant exciton Faraday rotation in $Cd_{1-x}Mn_xTe$ mixed crystals. *Solid State Communications*, **25**, 193–195.

Gates, B., and Xia, Y. (2001). Photonic crystals that can be addressed with an external magnetic field. *Advanced Materials* **13**, 1695–1608.

Gambino, R.J. and Suzuki, T. (1999). *Magneto-Optical Recording Materials*, IEEE Press: New York.

Geoffroy, O., Givord, D., Otani, Y., *et al*. (1993). T-MOKE hysteresis loops in Bragg diffraction from 2D patterns. *Journal of Magnetism and Magnetic Materials*, **121**, 513–515.

Gerhardt, N.C., Hövel, S., Brenner, C., *et al*. (2005). Electron spin injection into GaAs from ferromagnetic contacts in remanence. *Applied Physics Letters*, **87**, 032502.

Gerrits, Th., van den Berg, H.A.M., Hohlfeld, J., *et al*. (2002). Ultrafast precessional magnetization reversal by picosecond magnetic field pulse shaping. *Nature(London)*, **418**, 509–511.

Goltsev, A.V., Pisarev, R.V., Lottermoser, T. and Fiebig, M. (2003). Structure and interaction of antiferromagnetic domain walls in hexagonal $YMnO_3$. *Physical Review Letters*, **90**, 177204.

Granovsky, A.B., Kuzmichov, M.V. and Clerc, J.P. (2003). Effective medium theory for nonlinear magneto-optics in magnetic granular alloys. *Journal of Magnetism and Magnetic Materials*, **258**, 103–105.

Greidanus, F.J.A.M., Jacobs, B.A.J., Spruit, J.H.M. and Klahn, S. (1989). Recording experiments on rare-earth transition-metal thin-films studied with Lorentz microscopy. *IEEE Transactions on Magnetics*, **MAG-25**, 3524–3529.

Grimsditch, M. and Vavassori, P. (2004). The diffracted magneto-optic Kerr effect: what does it tell you? *Journal of Physics: Condensed Matter*, **16**, R275–R294.

Hanbicki, A.T., van 't Erve, O.M.J., Magno, R., *et al*. (2003). Analysis of the transport process providing spin injection through an Fe/AlGaAs Schottky barrier. *Applied Physics Letters*, **82**, 4092–4094.

Hansen, P. (1991). Magnetic amorphous alloys. In *Handbook of Magnetic Materials*, Buschow, K.H.J. (Ed.), Elsevier: Amsterdam, pp. 292–452, Vol. 16.

Harder, H-U., Menzel, T., Widmer, D. and Schoenes, J. (1998). Structure, magnetic, and magneto-optical properties of MnBi films grown on quartz and (001)GaAs substrates. *Journal of Applied Physics*, **84**, 3625–3629.

Hatwar, T.K., Genova, D. and Stinson, D.G. (1990). Correlation of composition and angular uniformity with performance in magneto-optic disks prepared from alloy targets. *Journal of Applied Physics*, **67**, 5304–5306.

Hiebert, W.K., Ballentine, G.E. and Freeman, M.R. (2002). Comparison of experimental and numerical micromagnetic dynamics in precessional switching and modal oscillations. *Physical Review B*, **65**, R140404.

Hiebert, W.K., Stankiewicz, A. and Freeman, M.R. (1997). Direct observation of magnetic relaxation in small permalloy disk by time-resolved scanning Kerr microscopy. *Physical Review Letters*, **79**, 1134–1137.

Hillebrands, B. and Ounadjela, K. (Eds.) (2002). *Spin Dynamics in Confined Magnetic Structures I*, *Topics in Applied Physics*, Springer-Verlag: Berlin, Heidelberg, Vol. 83.

Hillebrands, B. and Ounadjela, K. (Eds.) (2003). *Spin Dynamics in Confined Magnetic Structures II*, *Topics in Applied Physics*, Springer-Verlag: Berlin, Heidelberg, Vol. 87.

Hillebrecht, F.U., Ohldag, H., Weber, N.B., *et al*. (2001). Magnetic moments at the surface of antiferromagnetic NiO(100). *Physical Review Letters*, **86**, 3419–3422.

Hövel, S., Gerhardt, N., Hofmann, M., *et al*. (2005). Spin controlled optically pumped vertical cavity surface emitting laser. *Electronics Letters*, **41**, 251.

Hübner, W. and Bennemann, K-H. (1989). Nonlinear magneto-optical Kerr effect on a nickel surface. *Physical Review B*, **40**, 5973–5979.

Hübner, W. and Bennemann, K-H. (1995). Electronic theory for the nonlinear magneto-optical response of transition metal at surfaces and interfaces: dependence of the Kerr rotation on the polarization and magnetic easy axis. *Physical Review B*, **52**, 13411–13418.

Hubert, A. and Schäfer, R. (1998). *Magnetic Domains*, Springer-Verlag: Berlin-Heidelberg, New York.

Iizuka-Sakano, T., Hanamura, E. and Tanabe, Y. (2001). Second-harmonic-generation spectra of the hexagonal manganites $RMnO_3$. *Journal of Physics: Condensed Matter*, **13**, 3031–3055.

Imry, Y. and Ma, S-K. (1975). Random-field instability of the ordered state of continuous symmetry. *Physical Review Letters*, **35**, 1399–1401.

Inoue, M., Fujikawa, R., Baryshev, A., *et al*. (2006). Magnetophotonic crystals. *Journal of Physics D: Applied Physics*, **39**, R151–R161.

Inoue, M. and Fujii, T. (1997). Magneto-optical properties of one-dimensional magnetic and dielectric layers. *Journal of Applied Physics*, **81**, 5659–5665.

Itoh, Y., Suzuki, T. and Birukawa, M. (1999). Magnetic and magneto-optical properties of TbFeCo/(Pt,Pd) multilayers optimized for short wavelength recording. *Journal of Applied Physics*, **85**, 5091–5093.

Joannopoulos, J.D., Meade, R.D. and Winn, J.N. (1995). *Photonic Crystals: Molding the Flow of Light*, Princeton University Press: Princeton.

Jahn, I.R. and Dachs, H. (1971). Change of the optical birefringence associated with the antiferromagnetic ordering of MnF_2, FeF_2, CoF_2, and NiF_2. *Solid State Communications*, **99**, 1617–1620.

Jasperson, S.N. and Schnatterly, S.E. (1969). An improved method for high reflectivity ellipsometry based on a new polarization modulation technique. *Review of Scientific Instruments*, **40**, 761–767.

John, S. (1987). Strong localization of photons in certain disordered dielectric superlattices. *Physical Review Letters*, **58**, 2486–2489.

Kaka, S. and Russek, S.E. (2002). Precessional switching of submicrometer spin-valves. *Applied Physics Letters*, **86**, 2958–2960.

Kaneko, M. (1999). Magnetically induced superresolution. In *Magneto-Optical Recording Materials*, Gambino, R.J. and Suzuki, T. (Eds.), IEEE Press: New York, pp. 350–384.

Kaneko, M. (2000). Faraday and Kerr effects in ferromagnets. In *Magneto-Optics*, *Springer Series in Solid-State Sciences*, Sugano, S. and Kojima, N. (Eds.), Springer-Verlag: Berlin, Heidelberg, p. 271, Vol. 128.

Kato, H., Matsushita, T., Takayama, A., *et al*. (2003). Theoretical analysis of optical and magneto-optical properties of one-dimensional magnetophotonic crystals. *Journal of Applied Physics*, **93**, 3906–3911.

Kerr, J. (1877). On rotation of the plane of polarization by reflection from a pole of a magnet. *Philosophical Transactions of the Royal Society*, **3**, 321–343.

Kim, W.S., Aderholz, M. and Kleemann, W. (1993). Calibration of polar Kerr rotation and ellipticity measurements. *Measurement Science and Technology*, **4**, 1275–1280.

Kimel, A.V., Astakhov, G.V., Schott, G.M., *et al*. (2004). Picosecond dynamics of the photoinduced spin polarization in epitaxial (Ga,Mn)As films. *Physical Review Letters*, **92**, 237203.

Kimura, T., Goto, T., Shintani, H., *et al*. (2003). *Nature (London)*, **426**, 55–57.

Kleemann, W., King, A.R. and Jaccarino, V. (1986). Critical behavior of the magnetization of a $d = 3$ random-field Ising system. *Physical Review B*, **34**, 479–482.

Kleemann, W., Schäfer, F.J. and van der Heide, H. (1982). Linear optical anisotropy and domain structures at two successive antiferromagnetic phase transitions in α-MnS. *Journal of Magnetism and Magnetic Materials*, **25**, 317–334.

Koerdt, C., Rikken, G.L.J.A. and Petrov, E.P. (2003). Faraday effect of photonic crystals. *Applied Physics Letters*, **82**, 1538–1540.

Kohn, W. and Sham, L. (1965). Self-consistent equations including exchange and correlation effects. *Physical Review*, **140**, A1133–A1138.

Komarov, A.V., Ryabchenko, S.M. and Terletskii, O.V. (1977a). Magneto-optical studies and double opticomagnetic resonance of the exciton band in CdTe single crystals doped with Mn^{2+} ions. *Soviet Physics JETP*, **46**, 318–325.

Komarov, A.V., Ryabchenko, S.M. and Terletskii, O.V. (1977b). Magneto-optical studies and double opticomagnetic resonance of the exciton band in CdTe single crystals doped with Mn^{2+} ions. *Zhurnal Eksperimentalnoi I Teoreticheskoi Fiziki*, **73**, 608–618.

Koopmans, B., van Kampen, M., Kohlhepp, J.T. and de Jonge, W.J.M. (2000). Ultrafast magneto-optics in nickel: magnetism or optics? *Physical Review Letters*, **85**, 844–847.

Kooy, C. and Enz, U. (1960). Experimental and theoretical study of the domain configuration in thin layers of $BaFe_{12}O_{18}$. *Philips Research Reports*, **15**, 7–29.

Kossut, J. and Dobrowolski, W. (1993). Diluted magnetic semiconductors. In *Handbook of Magnetic Materials*, Buschow, K.H.J. (Ed.), Elsevier: Amsterdam, p. 231, Vol. 7.

Kubo, R. (1957). Statistical-mechanical theory of irreversible processes. I. General theory and simple applications to magnetic and conduction problems. *Journal of the Physical Society of Japan*, **12**, 570.

Kuiper, P., Searle, B.G., Rudolf, P., *et al*. (1993). X-ray magnetic circular dichroism of antiferromagnet Fe_2O_3: the orientation of magnetic moments observed by Fe $2p$ X-ray absorption spectroscopy. *Physical Review Letters*, **70**, 1549–1552.

Kushauer, J. (1995). Magnetische Domänen in verdünnten uniaxialen Antiferromagneten PhD Thesis, Gerhard-Mercator-Universität, Duisburg, Germany.

Lee, W.Y., Xu, Y.B., Gardiner, S.M., *et al*. (2000). Sweep rate-dependent magnetization reversal in epitaxial Fe/GaAs(001) and Fe/InAs(001) thin films. *Journal of Applied Physics*, **87**, 5926–5928.

Lemerle, S., Ferré, J., Chappert, C., *et al*. (1998). Domain wall creep in an Ising ultrathin magnetic film. *Physical Review Letters*, **90**, 177204.

Levy, M., Yang, H.C. and Steel, M.J. (2001). Flat top response in one-dimensional magnetic photonic band gap structures with Faraday rotation enhancement. *Journal of Lightwave Technology*, **19**, 1964–1969.

Lyubchanskii, I.L., Dadoenkova, N.N., Lyubchanskii, M.I., *et al*. (2003). Magnetic photonic crystals. *Journal of Physics D*, **36**, R277–R287.

Mansuripur, M. (1995). *The Physical Properties of Magneto-Optical Recording*, Cambridge University Press: Cambridge.

Markovin, P.A., Pisarev, R.V., Smolensky, G.A. and Syrnikov, P.P. (1976). Observation of isotropic magnetic contribution to the refractive index of ABF_3-type cubic crystals. *Solid State Communications*, **19**, 185–188.

Matsuda, Y. and Kuroda, N. (1996). High-pressure effects on high-field magnetophoto-luminescence in $Cd_{1-x}M_xSe$ (M = Mn, Co). *Physical Review B*, **53**, 4471–4478.

Meiklejohn, W.H. and Bean, C.P. (1956). New magnetic anisotropy. *Physical Review*, **102**, 1413–1414.

Mertins, H-Ch., Oppeneer, P.M., Kunes, J., *et al*. (2001). Observation of the x-ray magneto-optical Voigt effect. *Physical Review Letters*, **87**, 047401.

Metzger, G., Pluvinage, P. and Torguet, R. (1965). Linear and quadratic terms in the magneto-optical Kerr effect. *Annalen der Physik*, **10**, 5–12.

Meyer, P., Pommier, J. and Ferré, J. (1989). Magnetooptic observation of domains at low temperature in the transparent ferromagnet $LiHoF_4$. *SPIE International Society for Optical Engineering*, **1126**, 93–98.

Misemer, D.K. (1988). The effect of spin-orbit interaction and exchange splitting on magneto-optic coefficients. *Journal of Magnetism and Magnetic Materials*, **72**, 267–274.

Moore, T.A. and Bland, J.A.C. (2004). Mesofrequency dynamic hysteresis in thin ferromagnetic films. *Journal of Physics: Condensed Matter*, **16**, R1369–R1386.

Murzina, T.V., Kapra, R.V., Dolgova, T.V., *et al*. (2004). Magnetization-induced second-harmonic generation in magnetophotonic crystals. *Physical Review B*, **70**, 012407.

Nazmul, A.M., Amemiya, T., Shuto, Y., *et al*. (2005). High temperature ferromagnetism in GaAs-based heterostructures with Mn doping. *Physical Review Letters*, **95**, 017201.

Nederpel, P.O.J. and Martens, J.W.D. (1985). Magneto-optical ellipsometer. *Review of Scientific Instruments*, **56**, 687–690.

Néel, L. (1948). Propriétés magnétiques des ferrites: ferrimagnétisme et antiferromagnétisme. *Annals of Physics*, **3**, 137–198.

Nikitov, S.A. and Tailhades, Ph. (2001). Optical modes conversion in magneto-photonic crystal waveguides. *Optics Communication* **199**, 389–397.

Nogués, J. and Schuller, I.K. (1999). Exchange bias. *Journal of Magnetism and Magnetic Materials*, **192**, 203–232.

Nolting, F., Scholl, A., Stöhr, J., *et al*. (2000). Direct observation of the alignment of ferromagnetic spins by antiferromagnetic spins. *Nature (London)*, **405**, 767–769.

O'Dell, T.H. (1970). *The Electrodynamics of Magneto-Electric Media*, North-Holland: Amsterdam.

Ohldag, H., Scholl, A., Nolting, F., *et al*. (2003). Correlation between exchange bias and pinned interfacial spins. *Physical Review Letters*, **91**, 017203.

Ohno, H. (1998). Making nonmagnetic semiconductors ferromagnetic. *Science (London)*, **281**, 951–956.

Oppeneer, P.M. (2001). Magneto-optical Kerr spectra. In *Handbook of Magnetic Materials*, Buschow, K.H.J. (Ed.), North Holland: Amsterdam, pp. 229–424, Vol. 13.

Oppeneer, P.M. and Antonov, V.N. (1996). Energy-band theory of the magneto-optical Kerr effect of selected ferromagnetic materials. In *Spin-Orbit-Influenced Spectroscopies of Magnetic Solids,*, Ebert, H. and Schütz, G. (Eds.), Springer: Berlin, pp. 29–48.

Oppeneer, P.M., Antonov, V.N., Kraft, T., *et al*. (1996). First-principles study of the giant magneto-optical Kerr effect in MnBi and related compounds. *Journal of Applied Physics*, **80**, 1099–1105.

Oppeneer, P.M. and Liebsch, A. (2004). Ultrafast demagnetization in Ni: theory of magneto-optics for non-equilibrium electron distributions. *Journal of Physics: Condensed Matter*, **16**, 5519–5530.

Oppeneer, P.M., Mertins, H-Ch., Abramsohn, D., *et al*. (2003). Buried antiferromagnetic films investigated by x-ray magneto-optical reflection spectroscopy. *Physical Review B*, **67**, 052401.

Oppeneer, P.M., Sticht, J., Maurer, T. and Kübler, J. (1992). Ab initio investigation of microscopic enhancement factors in tuning the magneto-optical Kerr effect. *Zeitschrift Fur Physik*, **88**, 309–315.

Osgood, R.M., Bader, S.D., Clemens, B.M. and White, R.L. (1998). Second-order magneto-optic effects in anisotropic thin films. *Journal of Magnetism and Magnetic Materials*, **182**, 297–323.

Osgood, R.M., Clemens, B.M. and White, R.L. (1997). Asymmetric magneto-optic response in anisotropic thin films. *Physical Review B*, **55**, 8990–8996.

Pan, R.P., Wei, H.D. and Shen, Y.R. (1989). Optical second-harmonic generation from magnetized surfaces. *Physical Review B*, **39**, 1229–1234.

Pittini, R., Schoenes, J., Vogt, O. and Wachter, P. (1996). Discovery of 90 degree magneto-optical polar Kerr rotation in CeSb. *Physical Review Letters*, **77**, 944–947.

Pollak, P., Kleemann, W. and Belanger, D.P. (1988). Metastability of the uniform magnetization in three-dimensional random-field Ising model systems: II. $Fe_{0.47}$ $Zn_{0.53}Cl_2$. *Physical Review B*, **38**, 4773–4780.

Postava, K., Jaffres, H., Schuhl, A., *et al*. (1997). Linear and quadratic magneto-optical measurements of the spin reorientation in epitaxial Fe films on MgO. *Journal of Magnetism and Magnetic Materials*, **172**, 199–208.

Prinz, G.A. (1998). Magnetoelectronics. *Science*, **282**, 1660–1663.

Pufall, M.R., Platt, C. and Berger, A. (1999). Layer-resolved magnetometry of a bilayer using the magneto-optical Kerr effect with varying angle of incidence. *Journal of Applied Physics*, **85**, 4818–4820.

Pustagowa, U., Hübner, W. and Bennemann, K.H. (1993). Theory for the magneto-optical Kerr effect at ferromagnetic transition-metal surfaces. *Physical Review B*, **48**, 8607–8618.

Qian, M., Dong, J. and Xing, D.Y. (2001). Optical properties of the ferroelectromagnet $YMnO_3$ studied from first principles. *Physical Review B*, **63**, 155101.

Rasing, T. (1998). Nonlinear magneto-optical studies of ultrathin films and multilayers. In *Nonlinear Optics in Metals*, Bennemann, K.H. (Ed.), Clarendon: Oxford, pp. 132–218.

Rasing, Th., van den Berg, H., Gerrits, Th. and Hohlfeld, J. (2003). Ultrafast magnetization and switching dynamics. In *Spin Dynamics in Confined Magnetic Structures II*, Hillebrands, B. and Ounadjela, K. (Eds.), Springer-Verlag: Berlin-Heidelberg. *Topics in Applied Physics*, p. 213–251, Vol. 87.

Reif, J., Zink, J.C., Schneider, C.M. and Kirschner, J. (1991). Effects of surface magnetism on optical second harmonic generation. *Physical Review Letters*, **67**, 2878–2881.

Remhof, A., Bircan, C., Westphalen, A., *et al*. (2005). Shining light on magnetic microstructures. *Superlattices and Microstructures*, **37**, 353–363.

Repain, V., Bauer, M., Jamet, J-P., *et al*. (2004). Creep motion of a magnetic wall: avalanche size divergence. *Europhysics Letters*, **68**, 460–466.

Richardi, J., Ingert, D. and Pileni, M.P. (2002). Theoretical study of the field-induced pattern formation in magnetic liquids. *Physical Review E*, **66**, 046306.

Röll, H. (2003). Magneto-optical discs. In *Nanoelectronics and Information Technology*, Waser, R. (Ed.), Wiley-VCH GmbH & Co KG: Weinheim, pp. 635–643.

Roshchin, I.V., Petracic, O., Morales, R., *et al*. (2005). Lateral length scales in exchange bias. *Europhysics Letters*, **71**, 297–303.

Roth, W.I. (1960). Neutron and optical studies in NiO. *Journal of Applied Physics*, **31**, 2000–2011.

Ruggiero, S.T., Williams, A., Tanner, C.E., *et al*. (2003). Magneto-optic effects in spin-injection devices. *Applied Physics Letters*, **82**, 4599–4601.

Saado, Y., Golosovsky, M., Davidov, D. and Frenkel, A. (2002). Tunable photonic bandgap in self-assembled clusters of floating magnetic particles. *Physical Review B*, **66**, 195108.

Saito, J. (1999). Light intensity modulation direct overwrite. In *Magneto-Optical Recording Materials*, Gambino, R.J. and Suzuki, T. (Eds.), IEEE Press: New York, pp. 320–349.

Sakoda, K. (2004). *Optical Properties of Photonic Crystals*, *Second Edition*, Springer-Verlag: New York.

Sato, K. (1981). Measurement of magneto-optical Kerr effect using piezo-birefringent modulator. *Japanese Journal of Applied Physics*, **20**, 2403–2409.

Sato, K., Hongu, H., Ikekame, H., *et al*. (1993). Magnetooptical Kerr spectrometer for 1.2-5.9 eV region and its application to FePt/Pt multilayers. *Japanese Journal of Applied Physics*, **32**, 989–995.

Sato, K. and Katayama-Yoshida, H. (2000). Material design for transparent ferromagnets with ZnO-based magnetic semiconductors. *Japanese Journal of Applied Physics*, **39**, L555–L558.

Schäfer, F.J. and Kleemann, W. (1985). High-precision refractive index measurements revealing order parameter fluctuations in $KMnF_3$ and NiO. *Journal of Applied Physics*, **57**, 2606–2612.

Schlenker, M. and Baruchel, J. (1978). Neutron techniques for the observation of ferromagnetic and antiferromagnetic domains. *Journal of Applied Physics*, **49**, 1996–2001.

Schmitte, T., Schemberg, T., Westerholt, K. and Zabel, H. (2000). Magneto-optical Kerr effects of ferromagnetic Ni-gratings. *Journal of Applied Physics*, **87**, 5630–5632.

Schmitte, T., Theis-Bröhl, K., Leiner, V., *et al*. (2002). Magneto-optical study of the magnetization reversal process of Fe nanowires. *Journal of Physics: Condensed Matter*, **14**, 7525–7538.

Schmitte, T., Westphalen, A., Theis-Bröhl, K. and Zabel, H. (2003). The Bragg-MOKE: magnetic domains in Fourier space. *Superlattices and Microstructures*, **34**, 127–136.

Schneider, C.M., Frömter, R., Swiech, W., *et al*. (1997). Magnetic spectromicroscopy and microspectroscopy with submicrometer resolution. *Journal of Applied Physics*, **81**, 5020.

Schoenes, J. (1992). Magneto-optical properties of metals, alloys and compounds. In *Materials Science and Technology*, Buschow, K.H.J. (Ed.), VCH: Weinheim, p. 149, Vol. 3A.

Schoenes, J. (2003). On the role of spin-orbit splitting in magneto-optics. *Journal of Physics: Condensed Matter*, **15**, S707–S708.

Shen, Y.R. (1984). *The Principles of Nonlinear Optics*, Wiley: New York.

Schütz, G., Wagner, W., Wilhelm, W., *et al*. (1987). Absorption of circularly polarized X-rays in iron. *Physical Review Letters*, **58**, 737–740.

Singleton, J., Mielke, C.H., Migliori, A., *et al*. (2004). *The National High Magnetic Field Laboratory Pulsed-Field Facility at Los Alamos National Laboratory*. *Physica B - Cond. Matter*, **346**, 614–617.

Slack, G.A. (1960). Crystallography and domain walls in antiferromagnetic NiO crystals. *Journal of Applied Physics*, **31**, 1571–1582.

Smolenskii, G.A., Pisarev, R.V. and Sinii, I.G. (1975). Birefringence of light in magnetically ordered crystals. *Uspekhi Fizicheskikh Nauk*, **116**, 231–270.

Smolenskii, G.A., Pisarev, R.V. and Sinii, I.G. (1976). Birefringence of light in magnetically ordered crystals. *Soviet Physics Uspekhi*, **18**, 410–429.

Sprokel, G.J. (1984). Reflectivity, rotation and ellipticity of magneto-optic film structures. *Applied Optics*, **23**, 3983–3989.

Starke, K. (2000). *Magnetic dichroism in Core-Level Photoemission*, Springer-Verlag: Berlin, New York.

Steel, M.J., Levy, M. and Osgood, R.M. (2000). High transmission enhanced Faraday rotation in one-dimensional photonic crystals with defects. *IEEE Photonics Technology Letters*, **12**, 1171–1173.

Stöhr, J., Wu, Y., Hermsmeier, B.D., *et al*. (1993). Element-specific magnetic microscopy with circularly polarized X-rays. *Science (London)*, **259**, 658–661.

Takeyama, S., Osada, T. and Miura, N. (2004). Solid-state physics towards pulsed ultra-high magnetic fields at ISSP. *Physica B - Condensed Matter*, **346**, 576–581.

Tanner, B.K. (1979). Antiferromagnetic domains. *Contemporary Physics*, **20**, 187–210.

Teplin, C.W. and Rogers, C.T. (2001). Simultaneous measurement of the surface and bulk magnetization in thin magnetic films. *Journal of Applied Physics*, **89**, 7168–7170.

Thiele, A.A. (1970). The theory of cylindrical magnetic domains. *Journal of Applied Physics*, **41**, 1139–1145.

Thole, B.T., Carra, P., Sette, F. and van der Laan, G. (1992). X-ray circular dichroism as a probe of orbital magnetization. *Physical Review Letters*, **68**, 1943.

Twardowski, A.D., Heiman, M.T., Liu, M.T., *et al*. (1996). Raman spectroscopy of $Cd_{1-x}Cr_xS$. *Physical Review B*, **53**, 10728–10731.

Vavassori, P. (2000). Polarization modulation technique for magneto-optical quantitative vector magnetometry. *Applied Physics Letters*, **77**, 1605–1607.

Vavassori, P., Methlushko, V., Osgood, R.M. III., *et al*. (1999). Magnetic information in the light diffracted by a negative dot array of Fe. *Physical Review B*, **59**, 6337–6343.

Vial, A. and van Labeke, D. (1998). Diffraction hysteresis loop modelisation in transverse magneto-optical Kerr effect. *Optics Communications*, **153**, 125–133.

Visnovsky, S. (1986a). Magneto-optical ellipsometry. *Czechoslovak Journal of Physics B*, **36**, 625–650.

Visnovsky, S. (1986b). Magneto-optical polar Kerr effect in a film-substrate system. *Czechoslovak Journal of Physics B*, **36**, 834–847.

Visnovsky, S., Nyvlt, M., Prosser, V., *et al*. (1995). Polar magneto-optics in simple ultrathin magnetic film structures. *Physical Review B*, **52**, 1090–1106.

Voigt, W. (1898). Doppelbrechung von im magnetfeld befindlichen natriumdampf in der richtung normal zu den kraftlinien. *Nachrichten der Königlichen Gesellschaft der Wissenschaften zu Göttingen, Mathematisch-Physikalische Klasse*, **4**, 335–359.

Voigt, W. (1908). *Magneto- und Elektro-Optik*, Teubner: Leipzig.

Vollmer, R., Jin, Q.Y., Regensburger, H. and Kirschner, J. (1999). Second harmonic generation from magnetic surfaces and thin films. *Journal of Magnetism and Magnetic Materials*, **198–199**, 611–616.

Vollmer, R., Kirilyuk, A., Schwabe, H., *et al*. (1995). Direct comparison of nonlinear and linear Kerr-effect measurements on thin Co films on Cu(001). *Journal of Magnetism and Magnetic Materials*, **148**, 295–297.

Weller, D. (1996). Magneto-optical Kerr spectroscopy of transition metal alloy and compound films. In *Spin-orbit-influenced Spectroscopies of Magnetic Solids*, Ebert, H. and Schütz, G. (Eds.), Springer-Verlag: Berlin, pp. 1–28.

Weller, D., Harp, G.R., Farrow, R.F.C., *et al*. (1994). Orientation dependence of the polar Kerr effect in fcc and hcp Co. *Physical Review Letters*, **72**, 2097–2100.

Weller, D., Stöhr, J., Nakajima, R., *et al*. (1995). Microscopic origin of magnetic anisotropy in Au/Co/Au probed with X-ray magnetic circular dichroism. *Physical Review Letters*, **75**, 3752–3755.

Xu, X., Majetich, S.A. and Asher, S.A. (2002). Mesoscopic monodisperse ferromagnetic colloids enable magnetically controlled photonic crystals. *Journal of American Chemical Society*, **124**, 13864–13868.

Yablonovitch, E. (1987). Inhibited spontaneous emission in solid-state physics and electronics. *Physical Review Letters*, **58**, 2059–2062.

Yan, S.S., Schreiber, R., Grünberg, P. and Schäfer, R. (2000). Magnetization reversal in (001)Fe thin films studied by combining domain images and MOKE hysteresis loops. *Journal of Magnetism and Magnetic Materials*, **210**, 309–315.

Yang, Z.J. and Scheinfein, M. (1993). Combined three-axis surface magneto-optical Kerr effects in the study of surface and ultrathin-film magnetism. *Journal of Applied Physics*, **74**, 6810–6823.

Yaresko, A.N., Oppeneer, P.M., Perlov, A.Y., *et al*. (1996). On the nature of the absolute maximal observable magneto-optical Kerr rotation of CeSb. *Europhysics Letters*, **36**, 551–556.

Yeh, P. (1980). Optics of anisotropic layered media: A new 4×4 matrix algebra. *Surface Science*, **96**, 41–53.

Zak, J., Moog, E.R., Liu, C. and Bader, S.D. (1990). Universal approach to magneto-optics. *Journal of Magnetism and Magnetic Materials*, **89**, 107–123.

Zeeman, P. (1897). The effect of magnetisation on the nature of light emitted by substance. *Nature*, **55**, 347.

Zeidler, Th., Schreiber, F., Zabel, H., *et al*. (1996). Reorientational transition in Co/Cr (001) superlattices. *Physical Review B*, **53**, 3256–3262.

Zhang, G.P., Hübner, W., Beaurepaire, E. and Bigot, J-Y. (2002). Laser-induced ultrafast demagnetization: femtomagnetism, a new frontier? In *Spin Dynamics in Confined Magnetic Structures I*, Hillebrands, B. and Ounadjela, K. (Eds.), Springer-Verlag: Berlin, Heidelberg, *Topics in Applied Physics*, p. 245–288, Vol. 83.

Zvezdin, A.K. and Belotelov, V.I. (2004). Magneto-optical properties of photonic crystals. *European Physical Journal B*, **37**, 479–487.

Zvezdin, A.K. and Kotov, V.A. (1997). *Modern Magneto-Optics and Magneto-Optical Materials*, IOP Publishing: Bristol, Philadelphia.

FURTHER READING

Borovik-Romanov, A.S., Kreines, N.M. and Talaev, M.A. (1971). Magnetic birefringence in antiferromagnetic MnF_2. *JETP Letters*, **13**, 54–57.

Brändle, H., Weller, D., Parkin, S.S.P., *et al*. (1992). Magneto-optical properties of CrO_2. *Physical Review B*, **46**, 13889–13895.

Dillon, J.F. Jr. (1958). Observation of domains in the ferrimagnetic garnets by transmitted light. *Journal of Applied Physics*, **29**, 1286–1291.

Eremenko, V.V., Kharchenko, N.F., Litvinenko, Yu.G. and Naumenko, V.M. (1992). *Magneto-Optics and Spectroscopy of Antiferromagnets*, Springer-Verlag: Berlin, Heidelberg, New York.

Hasegawa, R., Gambino, R.J. and Ruf, M. (1975). Magnetic properties of amorphous Gd-Co-Au films. *Applied Physics Letters*, **27**, 512–513.

Kryder, M.H. (1993). Magneto-optical storage materials. *Annual Review of Material Science*, **23**, 411–436.

Magnetocaloric Materials

Vitalij K. Pecharsky and Karl A. Gschneidner, Jr.
Iowa State University, Ames, IA, USA

1 INTRODUCTION

Modern society is highly dependent on reliable refrigeration technology. Without this technology: the food supply would be seasonal and limited to locally produced nonperishable items; comfortable living conditions would be impossible everywhere; and many medical advancements, for example, MRI, organ transplantation, organ and tissue cryostorage, and cryosurgery would be impossible. It is startling that all these and other developments in achieving and maintaining temperatures lower than ambient are supported by the technology which remains essentially unchanged from the time it was invented more than a century ago.

Handbook of Magnetism and Advanced Magnetic Materials. Edited by Helmut Kronmüller and Stuart Parkin. Volume 4: *Novel Materials*. ISBN: 978-0-470-02217-7.

Near-room-temperature refrigeration today is almost entirely based on a vapor-compression refrigeration cycle. Over the years, all parts of a commercial refrigerator, that is, the compressor, heat exchangers, refrigerant, and packaging, were considerably improved due to extended research and development efforts carried out by the academia and industry. Both recently achieved and anticipated improvements in the technology, however, are incremental since conventional refrigeration is already near its fundamental limit of energy efficiency. Furthermore, chlorofluorocarbons (CFCs), hydrofluorocarbons (HFCs), and other chemicals used as refrigerants eventually escape into the environment promoting ozone layer depletion and global warming, and therefore, liquid chemical–based refrigeration is a major factor contributing to deleterious, cumulative changes in the global climate.

Refrigeration is defined as the use of a working body that changes its temperature in response to certain thermodynamic triggers to cool an object. These variations must be achieved quickly, repeatedly, reversibly, and with minimum energy losses. Since a magnetic field easily and effectively couples to magnetic moments of individual atoms in a solid, the magnetic field is one of the common thermodynamic variables that can alter the temperature of a magnetic solid. For instance, heating (but not cooling) of ferromagnetic materials having a measurable hysteresis by a low frequency ac magnetic field is a well-known magnetothermal effect, and this so-called hysteresis heating has been successfully utilized in treating certain tumors by hyperthermia (Borelli, Luderer and Panzarino, 1984). Both heating and cooling of soft ferromagnetic materials in response to increasing and decreasing magnetic fields, respectively, has been known since the latter part of the nineteenth century when Warburg (1881) reported a small but measurable, reversible temperature changes in pure iron in response to magnetic field changes. Today,

this phenomenon is recognized as the *magnetocaloric effect* (MCE) and materials exhibiting large, reversible temperature changes in response to changing magnetic fields are usually referred to as *magnetocaloric materials*.

2 THE MAGNETOCALORIC EFFECT AND ITS SIGNIFICANCE

The magnetocaloric effect – commonly abbreviated as MCE – is one of the most fundamental physical properties of magnetic materials. The MCE describes the behavior of a magnetic solid when it is exposed to a changing magnetic field: its temperature may be appreciably increased or decreased, with both the sign and the extent of the temperature difference between the final and the initial states of the material being dependent on numerous intrinsic and extrinsic factors. The chemical composition, the crystal structure, and the magnetic state of a compound are among the most important intrinsic material parameters that determine its MCE. The extrinsic factors include the temperature, the surrounding pressure, and the sign of the magnetic field change, that is, whether the magnitude of the magnetic field has been raised or lowered. These variables affect the magnetic field–induced temperature changes and therefore play a role in defining the MCE.

The MCE is inherent to every magnetic solid, and has extraordinary fundamental importance because it spans many orders of magnitude over length, energy, and timescales: from quantum mechanics to micromagnetics, from statistical to macroscopic thermodynamics, and from spin dynamics to bulk heat flow and thermal conductivity. Understanding and, ultimately, controlling this vast, many-body and many-parameter landscape is an enormously challenging task, yet even partial successes along the way facilitate greater precision and better control over the design of novel magnetocaloric solids. In other words, knowing how changes in the chemical composition, the crystal structure, and the microstructure affect the physical behavior of solids helps to create an environment in which a material could be tailored to exhibit a specific combination of magnetic and thermal properties.

In addition to its basic scientific significance, the MCE is the cornerstone of near-room-temperature magnetic cooling, which is poised for commercialization in the foreseeable future and may soon become an energy efficient and environmentally friendly alternative to vapor-compression refrigeration technology (Pecharsky and Gschneidner, 1999a; Zimm *et al*., 1998; Zimm, 2003, Tishin and Spichkin, 2003; Gschneidner, Pecharsky and Tsokol, 2005). Practical applications of the MCE, therefore, have the potential to reduce the global energy consumption, and eliminate or minimize the use of ozone depleting compounds, greenhouse gases, and hazardous chemicals.

Among several alternatives to conventional refrigeration (thermoelectric cooling is probably the best known and well developed, yet it remains an energy inefficient technology), *magnetic cooling* has been in and out of the limelight for many decades. Its first application was suggested in late 1920s by Debye (1926) and, independently, by Giauque (1927). One-step cooling from 1.5 to 0.25 K by adiabatically demagnetizing gadolinium sulfate octahydrate was successfully demonstrated by Giauque and MacDougall (1933). Since then, adiabatic demagnetization refrigeration has been and still remains a great tool in achieving ultralow temperatures in many research laboratories. The potential of the magnetic cooling for the near-room-temperature applications, however, remained uncertain before the late 1990s despite two well-known demonstrations that were undertaken in the last quarter of the twentieth century, that is, those by Brown (1976) and Green, Chafe, Stevens and Humphrey (1990).

Today, following a seminal work of Zimm *et al*. (1998), near-room-temperature magnetic refrigeration has quickly caught the attention of both scientists and engineers, and by the end of 2006 more than 20 laboratory-scale magnetic cooling units have been built and tested. Various degrees of success in implementing magnetic refrigeration as a near-room-temperature cooling technology have been reported by Bohigas *et al*. (2000), Hirano *et al*. (2002), Rowe and Barclay (2002a,b), Blumenfeld, Prenger, Sternberg and Zimm (2002), Hirano (2003), Wu (2003), Zimm (2003), Richard, Rowe and Chahine (2004), Clot *et al*. (2004), Shir *et al*. (2005), Lu, Xu, Wu and Jin (2005), Okamura, Yamada, Hirano and Nagaya (2005), Rowe, Dikeos and Tura (2005), Vasile and Müller (2005), and Zimm, Boeder and Chell (2005). Furthermore, as far as the authors of this chapter are aware, a few more units have been built and either tested or are undergoing rigorous evaluation as of the time of writing this article, yet to date there have been no publication concerning these units in any kind of broadly available medium.

Among the many components that need to come together in order to make a successful operating magnetic refrigerator shown schematically in Figure 1 (for more information see recent reviews by Pecharsky and Gschneidner 1999a; Gschneidner, Pecharsky and Tsokol 2005 and a monograph by Tishin and Spichkin 2003), the magnetocaloric compound (the magnetic refrigerant material) is of utmost importance. First, its MCE must be large for a given, usually relatively small magnetic field change, and it should occur in the temperature range between that of the hot and cold heat exchangers of a device. Second, the magnetocaloric material must be chemically stable, noncorrosive, nonflammable, and nontoxic. Third, the compound or alloy must be composed

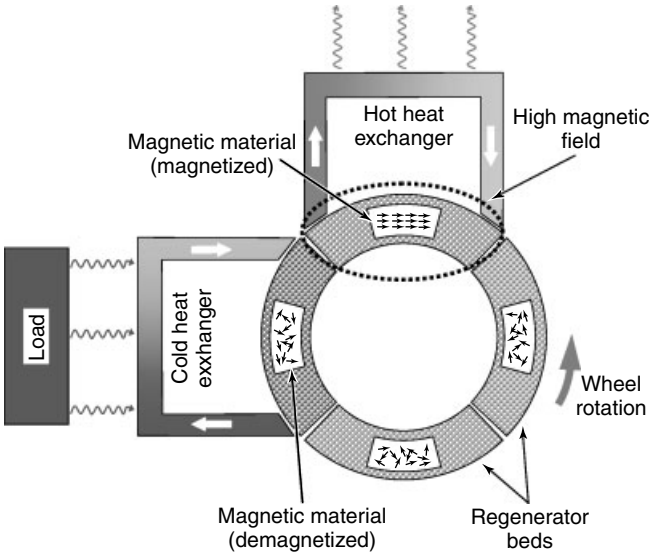

Figure 1. Schematic of a magnetic refrigerator. The wheel consists of regenerator beds packed with a magnetic material. As the wheel rotates, one of the beds (top) enters the high-magnetic-field volume, heating up due to the magnetocaloric effect. Heat exchange fluid flows through the bed removing heat via hot heat exchanger. Previously magnetized and already cooled by the heat exchanged fluid bed exits the high-magnetic-field area (left), cooling down due to reverse magnetocaloric effect. Heat exchange fluid flows through the bed, thereby removing heat from a load.

from readily available, inexpensive components. Fourth, the manufacturing of the material should be economical without adding too much to the cost of the final product, which is a regenerator bed. Finally, in addition to chemical stability, the magnetocaloric material should exhibit sufficient mechanical stability to ensure that the life span of a magnetic refrigerator is comparable to the life span of a modern conventional refrigeration device.

Over the last decade, basic research on the magnetocaloric materials enjoyed nearly explosive growth (Gschneidner, Pecharsky and Tsokol, 2005). As a result, a variety of advanced magnetocaloric materials have been discovered and we are certain that more exciting breakthroughs lie ahead. Magnetocaloric compounds have extended far beyond the prototypical elemental Gd to include binary rare-earth-based alloys, oxide perovskite materials, complex intermetallics, and chalcogenides and pnictides. Recently, novel magnetocaloric materials have been reviewed in detail by Gschneidner, Pecharsky and Tsokol (2005), and therefore, we refer the reader to this review for an exhaustive list of materials along with a large body of numerical MCE data. Instead, this chapter is intended as a primer about the current state of the art in magnetocaloric materials, concentrating on compounds that have a good chance of commercial success in the near future. Even though predictions in science maybe quite unreliable, we will conclude this work with our thoughts on how the science of near-room-temperature magnetocaloric materials will develop and where we are most likely to see the biggest breakthroughs in the next few years to a decade.

3 MAGNETOCALORIC EFFECT: THE FUNDAMENTALS

The MCE arises from the coupling of a magnetic sublattice with an external magnetic field, which affects the magnetic part of the total entropy of a solid. Similar to isothermal compression of a gas, during which positional disorder and the corresponding component of the total entropy of a gaseous system are suppressed, exposing a paramagnet near absolute zero temperature or a ferromagnet near its Curie temperature, T_C, to a change of a magnetic field (B) from zero to any nonzero value, or in general, from any initial value B_i to a final higher value $B_f(\Delta B = B_f - B_i > 0)$ greatly reduces disorder of a spin system. Thus, the magnetic part (S_M) of the total entropy (S) is substantially lowered. In a reversible process, which resembles the expansion of a gas at constant temperature, isothermal demagnetization ($\Delta B < 0$) restores the zero-field magnetic entropy of a system. The MCE, therefore, can be quantified as an extensive thermodynamic quantity, which is the isothermal magnetic entropy change, ΔS_M. The latter is illustrated in Figure 2 as the difference between entropy functions determined at a common given temperature and is marked by a vertical arrow.

When a gas is compressed adiabatically, its total entropy remains constant, whereas velocities of the constituent molecules, and therefore, the temperature of the gas both increase. Likewise, the sum of the lattice and electronic entropies of a solid must change by $-\Delta S_M$ as a result of adiabatic magnetization (or demagnetization) of the material, thus leading to an increase (decrease) of the vibrational entropy of the lattice. This brings about an adiabatic temperature change, ΔT_{ad}, which is an intensive thermodynamic quantity that is also used to measure and quantify the MCE.

In Figure 2, ΔT_{ad} is illustrated as the difference between the two entropy functions determined at the same entropy and is indicated using a horizontal arrow. It is worth noting that in the case of a refrigeration cycle employing a gas, it is a *change of pressure* that results either in the adiabatic temperature change, or the isothermal entropy change, while in the case of a magnetic solid it is a *change of magnetic field* that brings about the entropy or temperature change. No matter how strong the magnetic field is around the sample, the MCE will remain zero as long as the field is kept constant.

For a given material at a constant pressure, the two quantitative characteristics of the MCE, ΔS_{M} and ΔT_{ad}, are functions of the absolute temperature, T, and the magnetic field change, ΔB. The MCE can be easily computed provided the behavior of the total entropy of a compound is known as a *function of temperature* in both the initial and final magnetic fields, for example, see Figure 2:

$$\Delta S_{\mathrm{M}}(T,\Delta B)_{\Delta B} = S(T,B)_{B=B_{\mathrm{f}}} - S(T,B)_{B=B_{\mathrm{i}}} \quad (1)$$

$$\Delta T_{\mathrm{ad}}(T,\Delta B)_{\Delta B} = T(S,B)_{B=B_{\mathrm{f}}} - T(S,B)_{B=B_{\mathrm{i}}} \quad (2)$$

Equation (2), in which the entropy is the independent variable and the temperature is the dependent variable, is straightforwardly employed in direct measurements of the adiabatic temperature change ΔT_{ad}. The temperature of a sample is measured in both B_{i} and B_{f}, that is, before and after the magnetic field has been altered. The difference between the two temperatures yields the intensive MCE value, for example, see Gopal, Chahine, Földeaki and Bose (1995), Gopal, Chahine and Bose (1997), and Dan'kov, Tishin, Pecharsky and Gschneidner (1997), which is usually reported as a function of temperature for $B_{\mathrm{i}} = 0$.

At equilibrium, both ΔS_{M} and ΔT_{ad} are correlated with the magnetization (M), magnetic flux density (B), heat capacity at constant pressure (C_P), and absolute temperature by one of the following fundamental equations derived from the well-known Maxwell relationships and general thermodynamics:

$$\Delta S_{\mathrm{M}}(T,\Delta B)_{\Delta B} = \int_{B_{\mathrm{i}}}^{B_{\mathrm{f}}} \left(\frac{\partial M(T,B)}{\partial T}\right)_B \mathrm{d}B \quad (3)$$

$$\Delta T_{\mathrm{ad}}(T,\Delta B)_{\Delta B} = -\int_{B_{\mathrm{i}}}^{B_{\mathrm{f}}} \left(\frac{T}{C_P(T,B)} \times \frac{\partial M(T,B)}{\partial T}\right)_B \mathrm{d}B \quad (4)$$

As immediately follows from equations (1)–(4), materials whose total entropy is strongly influenced by a magnetic field and whose magnetization varies rapidly with temperature in any magnetic field are expected to exhibit an appreciable MCE. The MCE usually peaks when $|(\partial M(T,B)/\partial T)_B|$ is the greatest, that is, around T_{C} in a conventional ferromagnet or near absolute zero temperature in a paramagnet. The MCE of a simple ferromagnet is gradually lowered both below and above T_{C}, as is clearly seen in Figure 3.

Equations (3) and (4) are applicable to ferromagnets that magnetically order via a second-order phase transformation and they give correct estimates of the MCE for the first-order phase transition materials, yet both equations fail to describe the MCE in the vicinity of a truly discontinuous first-order phase transition when either or both $|[\partial M(T,B)/\partial T]_B|$ and $[T/C_P(T,B)]_B$ do not exist or cannot be accurately measured [1]. Equations (1) and (2), on the other hand, define

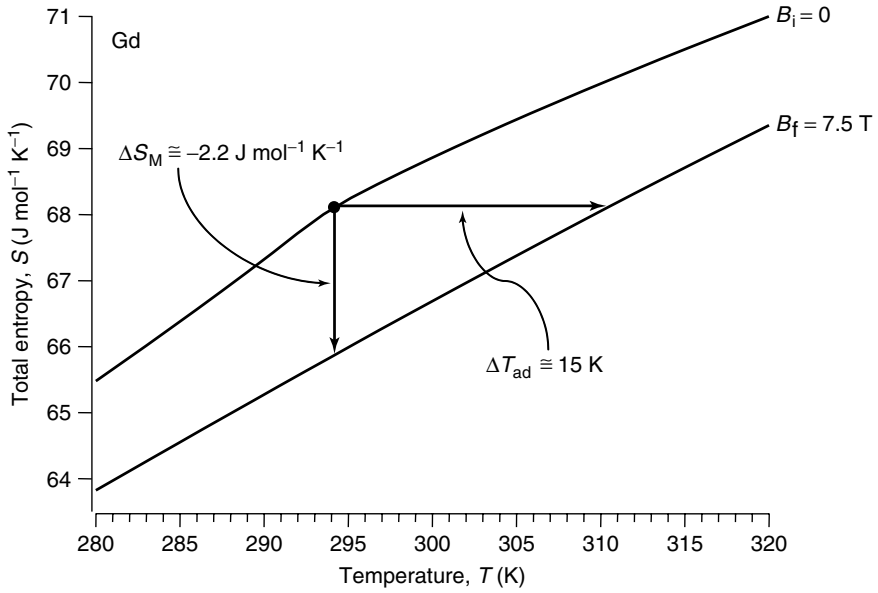

Figure 2. The total entropies of Gd shown as functions of temperature in 0 and 7.5 T magnetic fields near the Curie temperature of the metal ($T_{\mathrm{C}} = 294$ K). The vertical arrow represents the isothermal magnetic entropy change, ΔS_{M}, while the horizontal arrow is the adiabatic temperature change, ΔT_{ad}, both for the case when Gd is magnetized at T_{C}.

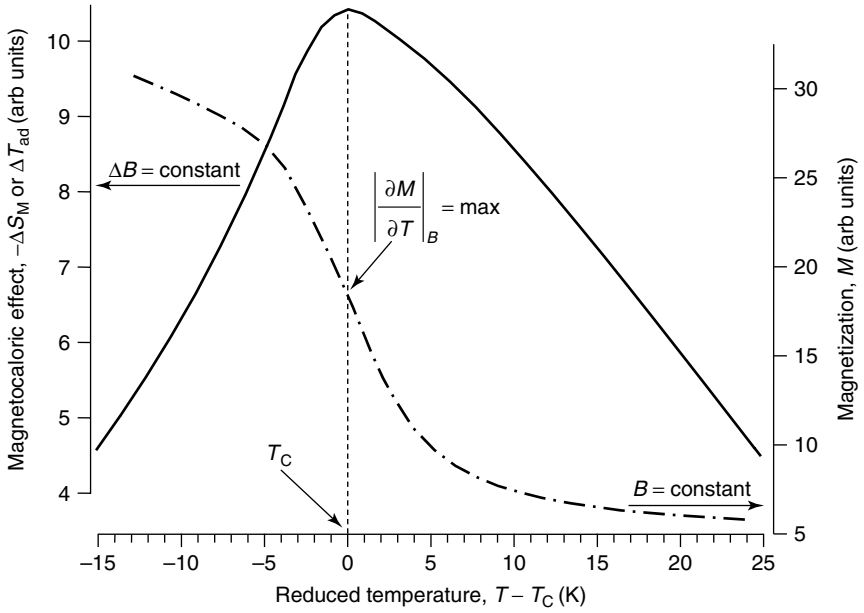

Figure 3. The characteristic temperature dependencies of the magnetocaloric effect (for a fixed magnetic field change ΔB, solid line, left-hand scale) and the magnetization (for a constant magnetic field B, dash-dotted line, right-hand scale) of a soft ferromagnetic material near its Curie temperature, T_C.

the MCE regardless of the thermodynamic nature of the phase transformation that occurs, if any, in a material.

For a first-order phase transition, it is also possible to employ an approximation, which is based on the Clausius–Clapeyron equation to determine the entropy change, ΔS:

$$\left(\frac{\mathrm{d}B}{\mathrm{d}T}\right)_{\mathrm{eq}} = -\left(\frac{\Delta S}{\Delta M}\right)_T \tag{5}$$

In equation (5), the left-hand-side derivative is taken under equilibrium conditions, that is, when the Gibbs free energies of the two phases are identical. For the right-hand side, $\Delta S = S_2 - S_1$ and $\Delta M = M_2 - M_1$, where the subscripts 1 and 2 correspond to the states of the material in the initial and final magnetic fields, respectively. Obviously, equation (5) is only applicable when B_f is strong enough to complete the transformation from state 1 to state 2 and when the quantity $\mathrm{d}B/\mathrm{d}T$ at equilibrium is known. In other words, the $B - T$ phase diagram for the system must be well established. By combining equations (3) and (4) with equation (5) and postulating that $T/C_P(T,B)$ is constant (for a true first-order phase transition the magnetic field has no effect on the heat capacity other than shifting the transition temperature), the following proportionality can be written for the adiabatic temperature change:

$$\Delta T_{\mathrm{ad}} \propto \left(\frac{T}{C_P(T,B)}\right)_B \left(\frac{\mathrm{d}B}{\mathrm{d}T}\right)_{\mathrm{eq}} \Delta M \tag{6}$$

The extensive measure of the MCE is indeed an irreplaceable tool enabling a quick and reasonably accurate way of gauging whether or not a compound is suitable as a magnetocaloric material (e.g., see Földeaki, Chahine and Bose, 1995). In this context, it is worthwhile to remind the reader that while a good magnetocaloric material must have as large ΔS_M as possible, it must also have the largest possible ΔT_{ad} to be competitive with known prototypic MCE materials. In other words, one must be careful when comparing the cooling potential of closely related materials (e.g., two metallic alloys containing different lanthanides or two perovskite-type oxide materials) exhibiting similar ΔS_M over vastly different temperature ranges or chemically dissimilar materials (such as a lanthanide-containing intermetallic compound with a perovskite-type oxide) over the same range of temperatures based solely on the magnitudes of ΔS_M. Caution should be exercised because absolute temperature and heat capacity are both factored in the definition of the adiabatic temperature change, see equations (4) and (6). Furthermore, one should always be aware of both random and systematic errors, which when combined may reach 25%, depending on the temperature range and the experimental technique that was employed to measure the magnetocaloric properties of a material. These and other related subjects have been extensively discussed in the past and we refer the reader to critical assessments written by Pecharsky and Gschneidner (1999b, 2001) and Pecharsky, Gschneidner, Pecharsky and Tishin (2001).

4 THE BENCHMARK MCE MATERIAL – GADOLINIUM

As far as near-room-temperature applications are concerned, the rare-earth metal Gd is truly a benchmark magnetic refrigerant material. It exhibits excellent magnetocaloric properties, which are difficult to improve upon. Not surprisingly, the metal has been employed in each of the early demonstrations of near-ambient cooling by the MCE (Brown, 1976; Green, Chafe, Stevens and Humphrey, 1990). Gadolinium was indeed used as the refrigerant powering the first successful proof-of-principle refrigerator device (Zimm *et al*., 1998). Metallic gadolinium has constituted the whole or at least a major part of every magnetic regenerator bed in every near-room-temperature magnetic cooling machine built and tested to date (Bohigas *et al*., 2000; Hirano *et al*., 2002; Rowe and Barclay, 2002a,b; Blumenfeld, Prenger, Sternberg and Zimm, 2002; Hirano, 2003; Wu, 2003; Zimm, 2003; Richard, Rowe and Chahine, 2004; Clot *et al*., 2004; Shir *et al*., 2005; Lu, Xu, Wu and Jin, 2005; Okamura, Yamada, Hirano and Nagaya, 2005; Vasile and Müller 2005; Zimm, Boeder and Chell, 2005).

Pure Gd metal adopts the simplest, hexagonal close-packed crystal structure, and it orders ferromagnetically at $T_C = 294\,K$ (this value is representative of a 99.95+ wt% pure metal, but can be lower in an impure metal (see Dan'kov, Tishin, Pecharsky and Gschneidner, 1998). Below its Curie temperature, the magnetic moments of all Gd atoms align parallel to the c axis of the crystal (the easy magnetization direction) but for $T < 232\,K$ the moment direction begins to deviate from the c axis reaching a maximum of $\sim 65^\circ$ for $T = 180\,K$ (Cable and Wollan, 1968). The moments can be realigned with the c axis by a weak magnetic field. Since magnetization and heat capacity are two most relevant physical properties defining the MCE, see equations (1)–(4), these are displayed for reference in Figures 4 and 5, respectively, for a Gd single crystal (Dan'kov, Tishin, Pecharsky and Gschneidner, 1998). Even though, the magnitude of $|\partial M/\partial T|_B$ decreases with the increasing magnetic field (Figure 4), the absolute value of the derivative is always maximized in the immediate vicinity of T_C and remains substantial in magnetic fields of 5 T and higher. The zero-field heat capacity (Figure 5) exhibits a λ-type maximum, which is typical for many second-order ferromagnetic ordering transitions. As the magnetic field increases, the sharp peak in heat capacity becomes more and more rounded, that is, the heat capacity below the zero-field peak is suppressed, while it becomes enhanced above T_C.

Large $|\partial M/\partial T|_B$ and large changes of the heat capacity induced by the magnetic field imply the presence of the large MCE in Gd. The isothermal magnetic entropy change, calculated using equations (1) and (3) from the heat capacity and magnetization data, respectively, is shown in Figure 6. This figure indicates that the MCE computed from the two different types of experimental data (compare the results for a 2 and 5 T magnetic field changes) match well, provided experimental measurements have been performed with sufficient accuracy. Furthermore, the results of Figure 6 clearly show that as the magnetic field increases, the derivative of the MCE with respect to the magnetic field decreases (both ΔT_{ad} and ΔS_M are nearly proportional to

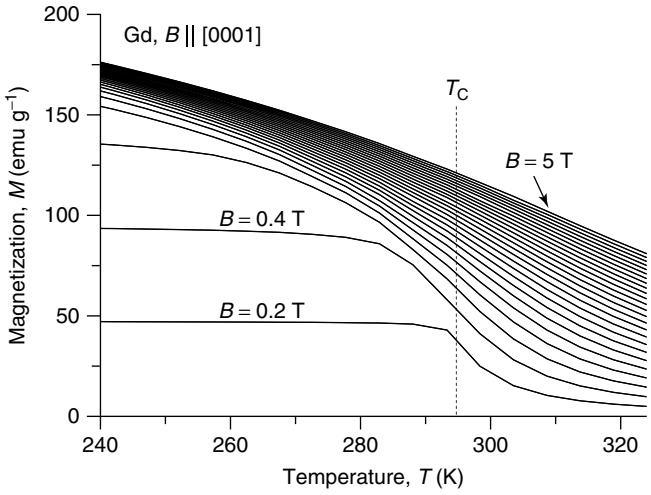

Figure 4. The magnetization of Gd single crystal measured in magnetic fields ranging from 0.2 to 5 T. Every $M(T)$ curve is separated from its nearest neighbor(s) by a fixed difference in the magnetic field, that is, $\Delta B = 0.2\,T$. The magnetic field vector was parallel to the [0001] direction during each measurement.

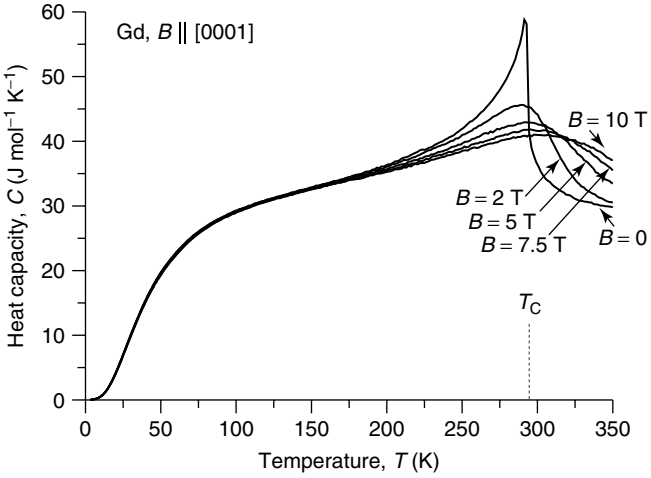

Figure 5. The heat capacity of single crystal Gd measured in various constant dc magnetic fields with the magnetic field vector parallel to the [0001] direction.

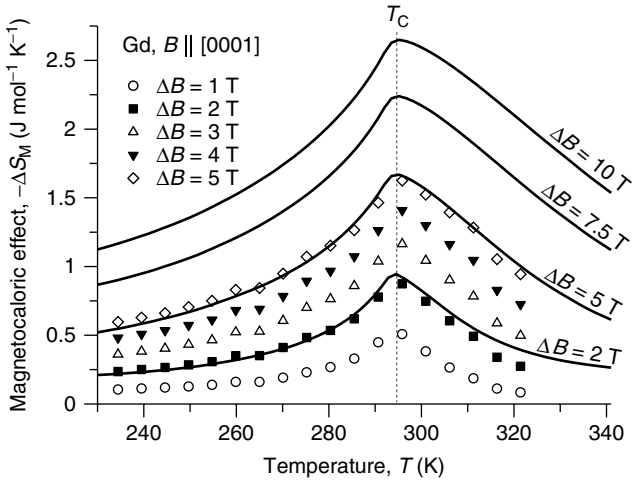

Figure 6. A comparison of the magnetocaloric effect (isothermal magnetic entropy change) of single crystalline Gd calculated from the magnetization data shown in Figure 4 (symbols) and the heat capacity data shown in Figure 5 (solid lines).

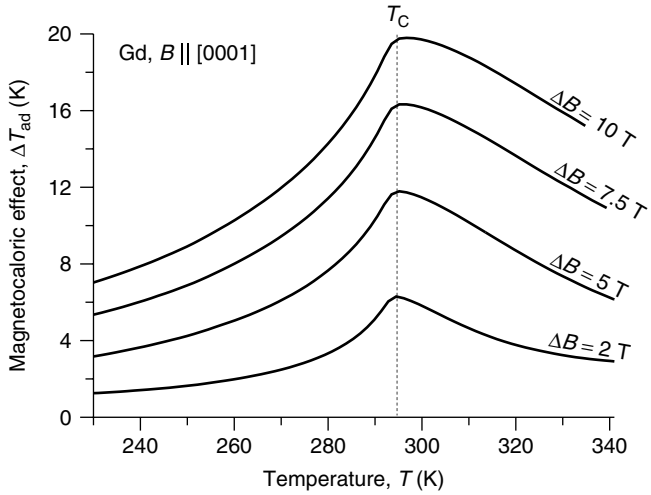

Figure 7. The magnetocaloric effect (adiabatic temperature change) of single crystalline Gd calculated from the heat capacity data shown in Figure 5.

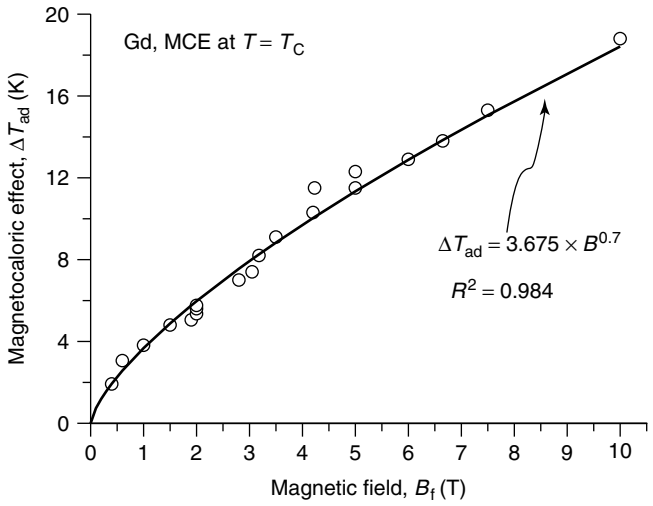

Figure 8. The magnetocaloric effect of Gd at its Curie temperature, shown as a function of the final magnetic field, B_f, for $B_i = 0$, both measured directly and calculated from heat capacity data by different authors (symbols) and the least squares fit assuming power-law dependence of the MCE on the magnetic field. See Dan'kov, Tishin, Pecharsky and Gschneidner (1998) and Gschneidner and Pecharsky (2000) for a list of references and sources of the experimental MCE data.

$B^{2/3}$, that is, d(MCE)/d$B \propto B^{-1/3}$, see Oesterreicher and Parker, 1984). In other words the highest specific MCE (i.e., the MCE per unit field change) always occurs near zero magnetic field. The intensive MCE of Gd, calculated using equation (2) from the data presented in Figure 5, is illustrated for four different magnetic field changes in Figure 7. Similar to ΔS_M, ΔT_{ad}, peaks at T_C and d(ΔT_{ad})/dB is also substantially reduced as B increases. The nearly $B^{2/3}$ dependence of the ΔT_{ad} of Gd is illustrated in Figure 8, where experimental measurements reported by numerous authors (see Dan'kov, Tishin, Pecharsky and Gschneidner, 1998; Gschneidner and Pecharsky, 2000) exhibit an excellent fit of the MCE data to the $B^{0.7}$ behavior.

It is worth noting that the magnetocrystalline anisotropy of Gd in fields exceeding a few tenths of a tesla is negligible (Dan'kov, Tishin, Pecharsky and Gschneidner, 1998), and therefore, the results shown in Figures 4–7 change little when the magnetic field is applied along a different crystallographic direction, or even for a polycrystalline Gd, provided the latter is as pure as the single crystal used to collect these data (the purity of the metal was 99.98 wt%). The behavior of the MCE of Gd illustrated in Figures 6 and 7 is quite universal for materials with second-order paramagnetic–ferromagnetic phase transformations. The differences between the MCE of Gd and those of other second-order phase transition materials mainly lie in differences in the absolute values of the MCE for the same magnetic field change, the temperature of the peak, and how quickly the derivative, d(MCE)/dB, is suppressed by the increasing magnetic field. To illustrate this universality, we show in Figure 9 the adiabatic temperature change of five different magnetocaloric materials, all of which order magnetically via second-order transformations at various temperatures ranging from ∼14 to ∼294 K. One of the five materials – elemental dysprosium – orders antiferromagnetically but magnetic fields exceeding ∼2 T transform the metal into a collinear ferromagnet, thus the behavior of the MCE

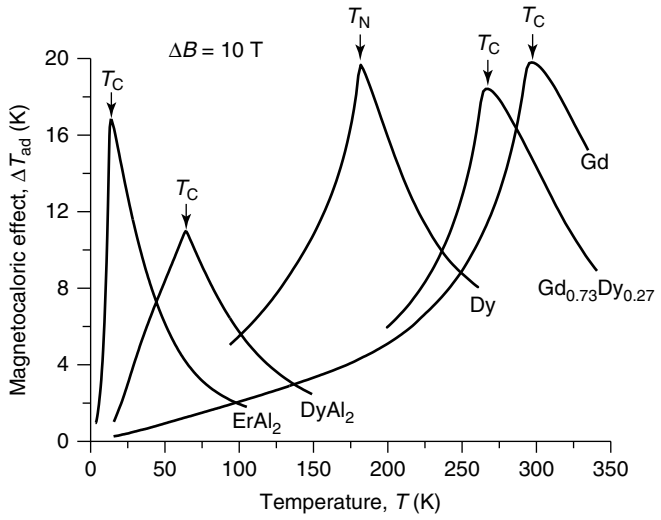

Figure 9. The magnetocaloric effect of polycrystalline $ErAl_2$ (Gschneidner, Pecharsky and Malik, 1996), polycrystalline $DyAl_2$ (Gschneidner, Pecharsky and Malik, 1996), single crystalline Dy with the magnetic field vector parallel to the *a* axis (Chernyshov *et al*., 2005), polycrystalline $Gd_{0.73}Dy_{0.27}$ (Pecharsky and Gschneidner, 1995), and single crystalline Gd with the magnetic field vector parallel to the *c* axis (Dan'kov, Tishin, Pecharsky and Gschneidner, 1998) as calculated from heat capacities measured in a 0 and 10 T magnetic field.

near the Neél temperature of Dy is nearly identical to that of other ferromagnets [2].

5 THE GIANT MAGNETOCALORIC EFFECT

Rising interest in both the fundamental science and potential applications of advanced magnetocaloric materials has been sparked by recent discoveries of new compounds exhibiting a MCE much larger than those found in the vast majority of previously known compounds, including elemental Gd. The most notable examples that originated a modern pool of advanced magnetocaloric materials are FeRh (Annaorazov *et al*., 1992), $La_{0.8}Ca_{0.2}MnO_3$ (Guo *et al*., 1997), and $Gd_5Si_2Ge_2$ and related $Gd_5(Si_xGe_{4-x})$ alloys (Pecharsky and Gschneidner, 1997a,b,c); the latter references also coined the phrase 'the giant magnetocaloric effect' (GMCE) materials. A few years later, several other families of materials have been shown to also exhibit a GMCE at temperatures close to ambient. These include $Tb_5Si_2Ge_2$ (Morellon *et al*., 2001), MnAs and $MnAs_{1-x}Sb_x$ compounds (Wada and Tanabe, 2001; Gama *et al*., 2004), $La(Fe_{1-x}Si_x)_{13}$ alloys (Hu *et al*., 2001) and their hydrides $La(Fe_{1-x}Si_x)_{13}H_y$ (Fujita, Fujieda, Hasegawa and Fukamichi, 2003), $MnFeP_{0.45}As_{0.55}$ and related $MnFeP_xAs_{1-x}$ alloys (Tegus, Brück, Buschow and de Boer, 2002; Brück *et al*., 2003), and $Ni_{2\pm x}Mn_{1\pm x}Ga$ ferromagnetic shape memory alloys (Albertini *et al*., 2004; Pasquale, Sasso and Lewis, 2004; Zhou, Li, Kunkel and Williams, 2004).

Today, it has been well established that the GMCE arises from magnetic field–induced magnetostructural first-order transformations. Upon the application of a magnetic field, the magnetic state of a compound changes from a paramagnet or an antiferromagnet to a nearly collinear ferromagnet simultaneously with either a martensitic-like structural change (e.g., see Morellon *et al*., 1998; Choe *et al*., 2000), or is accompanied by a phase volume discontinuity but without a clear crystallographic modification (Fujita, Fukamichi, Koyama and Watanabe, 2004). When the system undergoes a first-order phase transition, then the behavior of the total entropy as a function of temperature reflects a discontinuous (in reality almost always continuous except for some ultrapure lanthanides, see Pecharsky, Gschneidner and Fort, 1996; Gschneidner, Pecharsky and Fort, 1997) change of entropy at a critical temperature, T_t. Figure 10 shows a schematic $T - S$ diagram modeling discontinuous entropy changes in a $Gd_5Si_2Ge_2$ compound near the magnetostructural transition in a 0 and 2 T magnetic fields. A magnetic field has a small effect on the heat capacity both below and above the first-order phase transition temperature, but T_t increases with the increasing magnetic field at a rate of approximately $4\,K\,T^{-1}$ (Pecharsky, Gschneidner and Pecharsky, 2003). The phase transition in the magnetic field B_i occurs at temperature T_{t,B_i}, and the enthalpy of this transformation is ΔH_{B_i}. The discontinuous equilibrium change of the entropy at T_{t,B_i} totals $\Delta S_{B_i} = \Delta H_{B_i}/T_{t,B_i}$. Likewise, the phase transition in the magnetic field B_f occurs at T_{t,B_f}, the enthalpy of this transformation is ΔH_{B_i}, and the equilibrium entropy change is $\Delta S_{B_f} = \Delta H_{B_f}/T_{t,B_f}$. It was shown by Pecharsky, Gschneidner, Pecharsky and Tishin (2001) that for relatively small magnetic fields, that is, those that are most suitable for commercial near-room-temperature magnetic refrigeration applications, the maximum MCE in a first-order phase transition material can be defined as follows:

$$\Delta S_M \cong \frac{\Delta H_{B_i}}{T_{t,B_i}} \cong \frac{\Delta H_{B_f}}{T_{t,B_f}} \tag{7}$$

$$\Delta T_{ad} \cong \frac{\partial T_t}{\partial B}(B_f - B_i) \tag{8}$$

Equation (8) additionally assumes that the derivative, $\partial T_t/\partial B$, is constant.

Comparing the schematics presented in Figures 10 and 2 and considering equations (7) and (8) it is easy to see that for *first-order system*s one has to be careful when evaluating the magnetocaloric properties of different materials in relatively small magnetic fields. Thus, a compound with a large ΔS_M

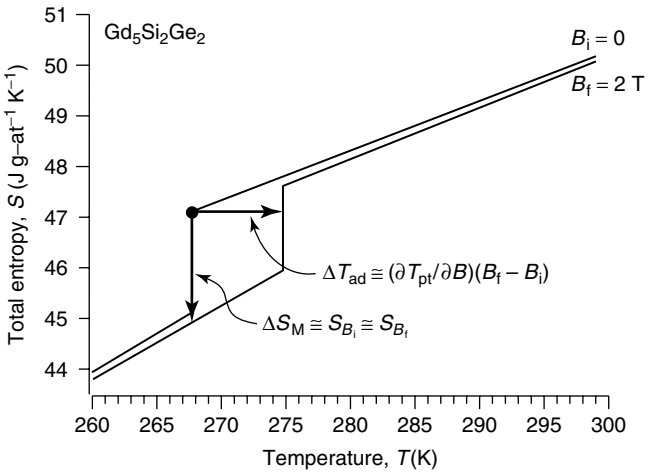

Figure 10. The idealized schematic of the $S-T$ diagrams of $Gd_5Si_2Ge_2$ in the vicinity of the magnetostructural transition in magnetic fields of 0 and 2 T. The thick arrows designate two measures of the magnetocaloric effect at T_C.

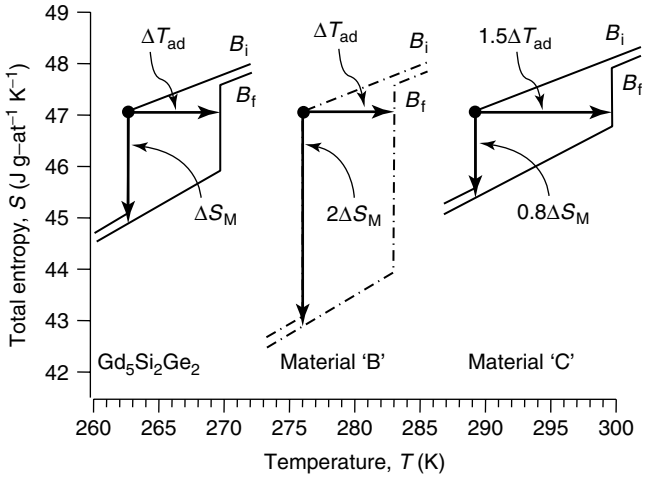

Figure 11. Schematic $S-T$ diagrams of three different materials illustrating independence of both the extensive and intensive magnetocaloric effects in small magnetic fields.

may not necessarily be a compound with a large ΔT_{ad}. Quite to the contrary, it is possible that among the two, the compound exhibiting a smaller ΔS_M has a larger ΔT_{ad}. To illustrate these situations, we show in Figure 11 schematic $T-S$ diagrams of two hypothetical materials 'B' and 'C' together with the same for $Gd_5Si_2Ge_2$. Material 'B' has ΔS_M twice as large as that of the $Gd_5Si_2Ge_2$, yet the adiabatic temperature changes of both materials are identical. Material 'C' has a ΔS_M, which is smaller by 20% but its ΔT_{ad} is 1.5 times that of $Gd_5Si_2Ge_2$.

The behavior of both the extensive and intensive measures of the GMCE in first-order phase transition materials is different when compared to the conventional MCE in second-order phase transition compounds, as can be easily seen from Figure 12 when compared to Figures 3, 6, 7 and 9. First, especially for small magnetic fields, the GMCE is much larger than the conventional MCE (also see Figure 3 in a review by Gschneidner, Pecharsky and Tsokol, 2005). Second, the width of the GMCE becomes broader as ΔB increases, but it broadens asymmetrically toward one side, away from the phase transition temperature. Third, as ΔB increases, both the ΔS_M and the ΔT_{ad} increase rapidly for small fields with the corresponding derivatives ($\partial \Delta S_m/\partial \Delta B$ and $\partial \Delta T_{ad}/\partial \Delta B$) exhibiting a clear tendency toward saturation. As a matter of fact, when the magnetic field is strong enough to complete the transformation, the magnitudes of the ΔS_M discontinuities remain truly identical (see the left-hand sides of the peaks in Figure 12(a) at $\Delta B = 5$ and 7.5 T). Considering Figure 10, these discontinuities correspond to $\Delta S_{B_i} = \Delta H_{B_i}/T_{t,B_i}$ and the observed modest rise of the background under ΔS_M peaks is due to magnetic field effects on the magnetic entropy of the material in the ferromagnetic state, just as in other materials exhibiting conventional MCE. As was shown recently by Chernyshov *et al.* (2005), the calculated magnetic entropy change in Dy in the vicinity of its first-order magnetic phase transition at $T = 90$ K matches the entropy change of the spontaneous ferromagnetic FM $\rightarrow$ antiferromagnetic AFM phase transformation measured directly in a zero magnetic field (Pecharsky, Gschneidner and Fort, 1996) to within 2%.

6 ROLE OF THE STRUCTURAL CHANGE IN THE GMCE

Although crystallographic details of the magnetic field–induced structural changes are well-documented at least for some of the GMCE materials (Pecharsky, Holm, Gschneidner and Rink, 2003; Holm *et al.*, 2004), the contribution of crystallographic changes to the MCE presents an interesting basic science question. *Ab initio* calculations of the entropies involved in the magnetostructural phase changes are difficult, to say the least, and therefore, we will provide insight into this question using some of the available experimental data. We concentrate on $R_5(Si_{4-x}Ge_x)$ compounds, where R is a rare-earth element, because alloys with R = Gd that have nearly the same composition (x), and therefore, have closely spaced Curie temperatures, can be prepared in two different crystal structures around $x = 2$ in the paramagnetic state (Pecharsky *et al.*, 2003). The magnetic ordering in these materials occurs via a second-order phase transformation when $x < 1.91$ because both the paramagnetic and ferromagnetic $Gd_5(Si_{4-x}Ge_x)$ phases have the same orthorhombic Gd_5Si_4-type structure and these alloys exhibit

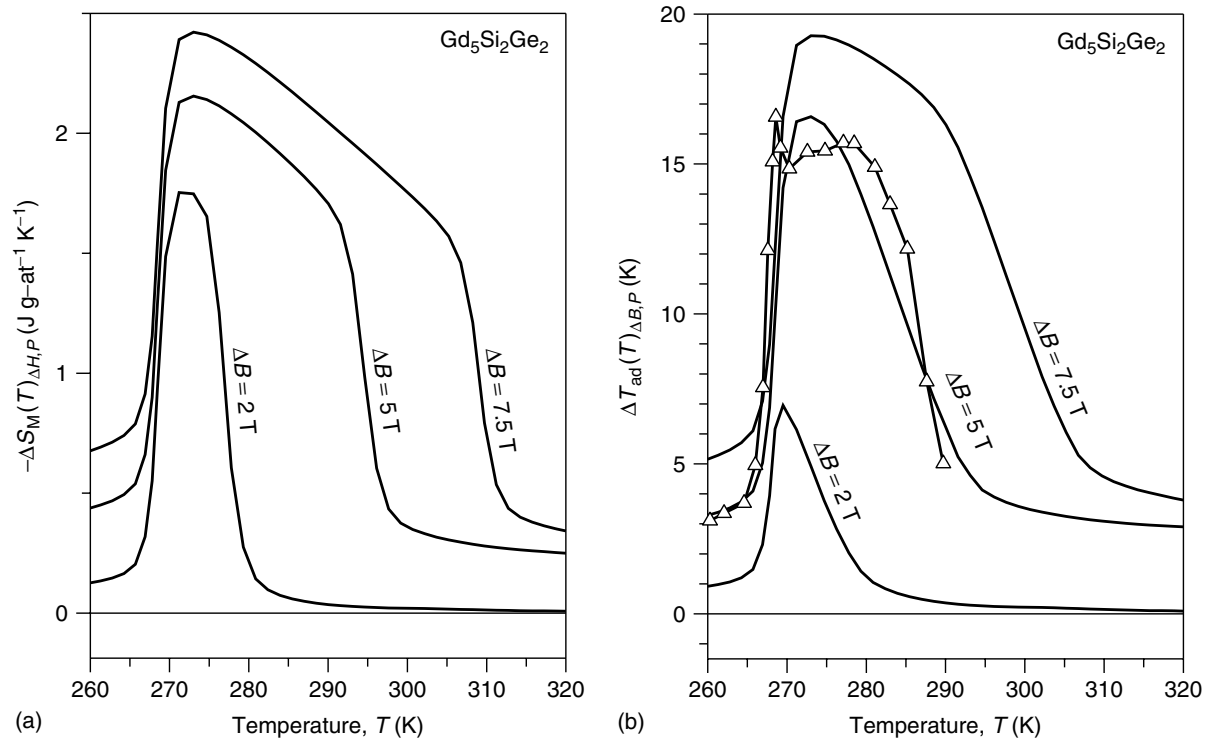

Figure 12. The magnetocaloric effects of $Gd_5Si_2Ge_2$ shown as functions of temperature for three different magnetic field changes: from 0 to 2 T, from 0 to 5 T, and from 0 to 7.5 T calculated from heat capacity data. The open triangles represent the MCE measured directly for a magnetic field change from 0 to 5 T.

a conventional MCE. When $x \geq 1.91$, the paramagnetic $Gd_5(Si_{4-x}Ge_x)$ phases adopt the monoclinic $Gd_5(Si_2Ge_2)$-type structure and order ferromagnetically concurrently with a structural change to the orthorhombic Gd_5Si_4-type structure. This results in a first-order paramagnetic to ferromagnetic transformation and yields the GMCE, see Figure 12.

Taking into consideration this difference in the thermodynamic nature of phase transitions occurring in closely related intermetallic phases, in Figure 13 we illustrate the behavior of the total entropies of $Gd_5(Si_{2.5}Ge_{1.5})$ and $Gd_5(Si_2Ge_2)$ in 0 and 7.5 T magnetic fields. The former compound orders ferromagnetically in a conventional second-order manner at $T_C = \sim 312$ K, while the latter material undergoes a first-order magnetostructural transition at $T_C = \sim 270$ K. Since the Curie temperatures of the two materials are slightly different, all data in Figure 13 are plotted as functions of the reduced temperature, $T - T_t$, where T_t is taken just above T_C as the temperature at which the magnetostructural transformation in $Gd_5(Si_2Ge_2)$ is complete. For clarity, the total entropy functions of $Gd_5(Si_{2.5}Ge_{1.5})$ were also reduced by subtracting a constant value of ~ 5.5 J/g-at K to match the total zero magnetic field entropy of $Gd_5(Si_2Ge_2)$ just below the magnetostructural transition temperature.

As expected from the similarity of the chemical compositions, identical crystallography, and ferromagnetism, the total entropy functions of the two materials after normalization show nearly indistinguishable behavior in a zero magnetic field immediately below their respective Curie temperatures. A major deviation between the two entropy functions occurs in the vicinity of T_C, where the entropy of $Gd_5(Si_2Ge_2)$ is increased by the change in structural entropy $\Delta S_{str} = \Delta H_{str}/T_t$, where ΔH_{str} is the enthalpy or latent heat of a first-order structural phase transformation. As is easily seen from Figure 13, the two zero magnetic field entropy functions continue to behave very similarly above the T_C; in fact, the difference between them remains nearly constant and is equal to ΔS_{str}. Once again, we relate this similarity in the behavior of the two entropies to close relationships between crystallography and magnetism of these two compounds.

The total entropies of the two materials after the application of the magnetic field do not match as well as the zero magnetic field entropies do, as is also clearly seen in Figure 13. This mismatch is related to different effects of the magnetic field on conventional ferromagnets, such as $Gd_5(Si_{2.5}Ge_{1.5})$, when compared to $Gd_5(Si_2Ge_2)$, which has a first-order magnetic-martensitic phase change. In fact, since

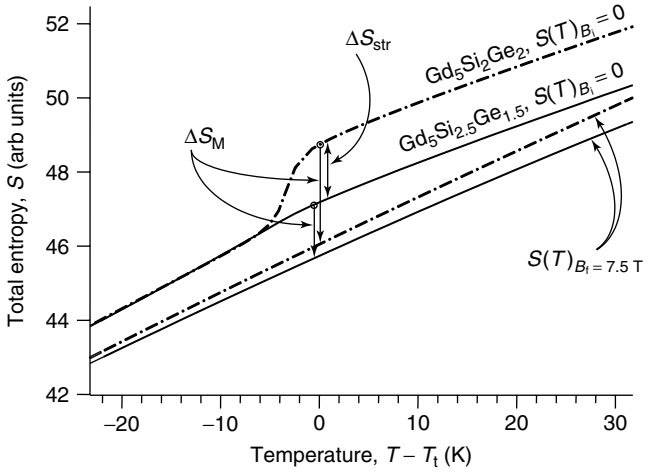

Figure 13. The behavior of the total entropies of $Gd_5Si_{2.5}Ge_{1.5}$, where ferromagnetic ordering at T_C is a second-order phase transformation (solid lines), and of $Gd_5Si_2Ge_2$ where ferromagnetic ordering is a first-order phase transformation (dash-dotted lines) in the vicinities of their respective Curie temperatures in 0 and 7.5 T magnetic fields. The three vertical arrows around T_t indicate the magnitudes of the magnetocaloric effects of the two materials, and entropy of the first-order phase transition in $Gd_5Si_2Ge_2$, all at $T = T_t$.

the crystal structure is decoupled from a magnetic sublattice in the case of $Gd_5(Si_{2.5}Ge_{1.5})$, the magnetic field does not actually transform the system into a nearly collinear ferromagnet, nor does it raise the Curie temperature of the material. Conversely, in the case of $Gd_5(Si_2Ge_2)$, where the magnetic field induces a magnetostructural phase change, the Curie temperature is increased nearly linearly with the field. Furthermore, first-principles calculations indicate that the conventional ferromagnetic ordering of the orthorhombic paramagnetic $Gd_5(Si_2Ge_2)$ occurs at a much higher temperature than a conventional ferromagnetic ordering of the monoclinic paramagnetic $Gd_5(Si_2Ge_2)$ if the monoclinic structure can be maintained in a ferromagnetic state (Pecharsky *et al*., 2003; Paudyal, Pecharsky, Gschneidner and Harmon, 2006). This difference in the Curie temperatures of the two structures and the fact that the magnetostructural transition between the monoclinic paramagnetic and orthorhombic ferromagnetic phases of $Gd_5(Si_2Ge_2)$ occurs at $T_C^{\text{monoclinic}} < T_t < T_C^{\text{orthorhombic}}$ may explain the suppression spin fluctuations and ferromagnetic clustering above T_t in the case of $Gd_5(Si_2Ge_2)$, while both should be present in $Gd_5(Si_{2.5}Ge_{1.5})$.

The MCEs at T_C are shown in Figure 13 as arrows for both compounds (the arrows are offset along the temperature axis for clarity). Obviously, the two MCEs are considerably different and the difference between them should be primarily ascribed to the absence and the presence of a structural change in $Gd_5(Si_{2.5}Ge_{1.5})$ and $Gd_5(Si_2Ge_2)$, respectively. Even though the magnetic field has slightly different effect on the total entropies of the two compounds, the difference in ΔS_M at the T_C is nearly identical to ΔS_{str}. The large magnetic field–induced phase volume and chemical bonding changes, observed in $Gd_5Si_2Ge_2$ and other $R_5Si_{4-x}Ge_x$ materials, therefore, indicate that the GMCE is achieved due to the concomitant change of the entropy during the structural transformation, designated in Figure 13 as ΔS_{str}. As a result, it is possible to speculate that the observed GMCE is the sum of the conventional magnetic entropy-driven process (ΔS_m, which is the same as ΔS_M in a material without a structural change as defined by equation (3) and the difference in the entropies of the two crystallographic modifications (ΔS_{str}) of a solid:

$$\Delta S_M(T, \Delta B)_{\Delta B = B_f - B_i} = \Delta S_{str} + \Delta S_m \tag{9}$$

Although the first factor in the right-hand side of equation (9) is a hidden parameter in conventional magnetization, heat capacity, and direct MCE measurements because any of these properties reflect both the magnetic and crystallographic states of the material, an estimate of ΔS_{str} based on comparing the MCEs exhibited by these two members of the $Gd_5(Si_{4-x}Ge_x)$ family is possible. This situation is illustrated in Figure 14, where we plot the isothermal magnetic entropy changes of $Gd_5Si_2Ge_2$ and of $Gd_5(Si_{2.5}Ge_{1.5})$ for field changes from 2 to 10 T (both sets of data have been taken from Pecharsky, Gschneidner and Pecharsky, 2003). Considering equation (9) and recalling that ΔS_{str} is independent of the magnetic field, provided that the entire volume of the material retains the low field crystal structure at B_i and it is completely converted into the high-field allotrope by B_f, the difference between the peak values of ΔS_M should remain constant regardless of the field change. This constant difference, indeed, is approximately equal to ΔS_{str}. A simple calculation based on the data presented in Figure 14 results in $\Delta S_{str} = 1.08(4)\ \text{J/g–at}^{-1}\,\text{K}^{-1}$ (or $9.8 \pm 0.3\ \text{J kg}^{-1}\,\text{K}^{-1}$) for $Gd_5Si_2Ge_2$.

Recently, Morellon *et al*. (2004) were able to establish the role of the lattice in bringing about the GMCE by using a different approach. They employed a single compound – $Tb_5Si_2Ge_2$ – in which the magnetic and structural transitions are separated by about 10 K under normal pressure. After applying hydrostatic pressure, the two transition temperatures were superimposed and the two transformations were recoupled, resulting in a GMCE and in an estimated ΔS_{str} on the order of $9\ \text{J kg}^{-1}\,\text{K}^{-1}$ (or $\sim 1\ \text{J/g–at}^{-1}\,\text{K}^{-1}$). Considering that the structural transition in $Tb_5Si_2Ge_2$ (Ritter *et al*., 2002) is the same as that found in the $Gd_5Si_2Ge_2$ the agreement between the two values was expected and is indeed very good.

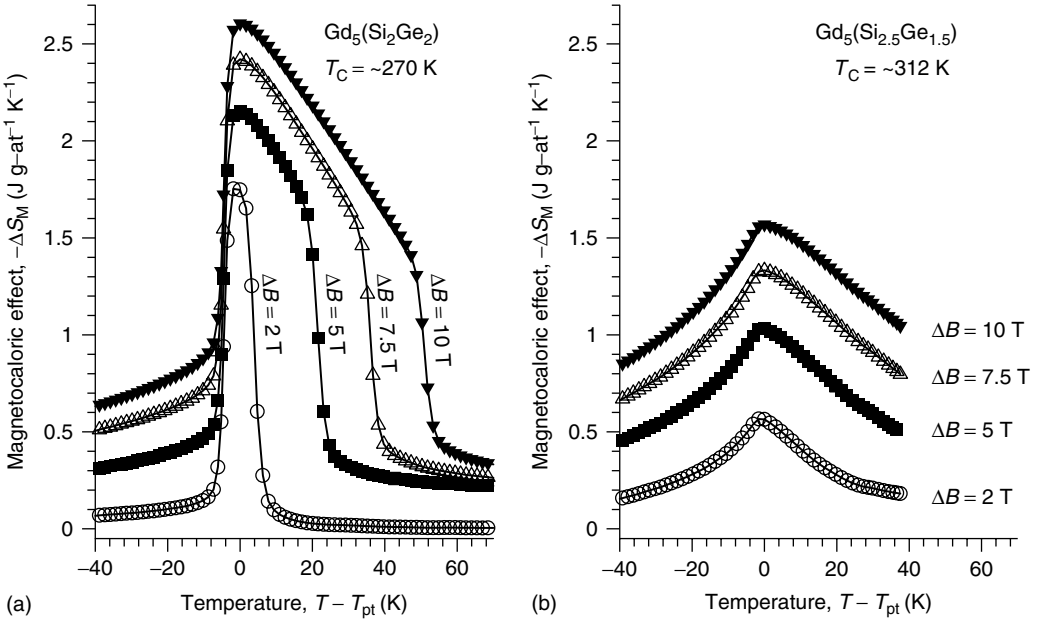

Figure 14. The magnetocaloric effects of $Gd_5Si_2Ge_2$ (a) $Gd_5Si_{2.5}Ge_{1.5}$ (b) calculated from heat capacity data allowing for the calculation of the contribution from the structural transition to the observed isothermal magnetic entropy change of $Gd_5Si_2Ge_2$.

7 CONCLUSIONS: WHAT DOES THE FUTURE HOLD?

The discovery of the GMCE and extensive characterization of multiple families of GMCE materials are indeed extremely important developments both in the science of the MCE and, potentially, in its application to near-room-temperature cooling. As described above, the overlapping contribution from the crystallographic and related electronic changes in the lattice may account for 50% or more of the total MCE (as quantified by the isothermal magnetic entropy change) in magnetic fields of 5 T and below. More significantly, the relative contribution from the structural entropy change ΔS_{str} to ΔS_M increases as the magnetic field decreases so long as the final magnetic field (B_f) is strong enough to complete the magnetostructural transition. A chart schematically comparing the MCEs in first-order phase transition compounds (GMCE materials) and second-order phase transition compounds (MCE materials) is shown in Figure 15. At any temperature, the GMCE materials have much larger magnetic field–induced entropy changes compared to conventional MCE compounds. As far as near-room-temperature applications are of concern, elemental Gd and $Gd_5Si_2Ge_2$ remain the leaders in their respective groups of compounds.

Advanced magnetocaloric materials, no doubt, should exist in other solid systems where structural changes are coupled with ferromagnetic ordering, and therefore, can be triggered by a magnetic field. Considering equation (9), the strongest MCEs in the weakest magnetic fields are anticipated to be found in novel materials designed to maximize the entropy differences of the low-magnetic-field and high-magnetic-field phases that includes the large entropy of a structural transformation, ΔS_{str}, in addition to a large magnetic entropy change ΔS_m. Furthermore, it is important that these materials also have a large ΔT_{ad}, which can be achieved by maximizing the effect of a magnetic field on the phase transition temperature.

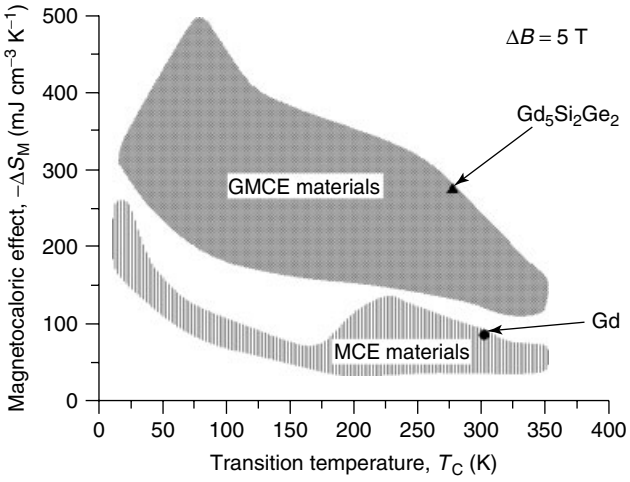

Figure 15. A map showing the magnitudes of the magnetocaloric effect in first-order (GMCE materials) and second-order (MCE materials) phase transition materials. (Adopted from Gschneidner, Pecharsky and Tsokol 2005, Figure 3.)

Where shall one look for such materials? Although no one at this point can give a definitive recipe, we believe that the most useful magnetocaloric materials

- will have large densities in order to support maximum cooling power in a small volume;
- will be first-order phase transition materials exhibiting GMCEs to provide maximum cooling power at the lowest energy cost;
- will order ferromagnetically to minimize internal entropy losses from realignment of spins in ferromagnets, antiferromagnets, spin glasses, and so on;
- will be metals because metals usually have much better thermal conductivities than ceramics;
- will contain a lanthanide, most likely Gd, and will have 50% or more magnetic atoms in order to minimize inactive thermal mass of the solid;
- and will finally, likely be crystalline bulk materials, not nanostructures or amphorous materials for near-room temperature.

Although nanostructures offer numerous potential benefits, such as large surface areas, control of geometry, and good thermal conductivity, nanoparticles normally do not order magnetically since the blocking temperatures are usually well below the temperature range useful for consumer applications. Amorphous alloys, which offer superior mechanical properties over brittle intermetallic alloys, have magnetocaloric properties which are distinctly inferior to the crystalline materials, primarily because the atoms and thus the spins of the magnetic atoms are randomly orientated causing an entropy loss due to the energy required to align the spins by the applied magnetic field (Gschneidner and Pecharsky, 2000).

In summary, much remains to be done to better understand, and therefore, achieve a better control over known magnetic materials to maximize their magnetocaloric properties and performance. A clear path forward will remain highlighted by thorough experiments coupled with theory, where the latter is tested and refined against the former, thus resulting in discoveries of new and improved materials and bringing near-room-temperature magnetic refrigeration technology to fruition in the not-so-distant future.

NOTES

[1] By definition, partial first derivatives of the Gibbs free energy with respect to intensive thermodynamic variables, for example, T, P, or B, vary discontinuously at the first-order phase transition. As a result, the bulk magnetization is expected to undergo a discontinuous change at constant temperature, and the heat capacity is expected to be infinite during a first-order phase transformation. Thus, in theory, $[\partial M(T,B)/\partial T]_B$ and $[T/C_P(T,B)]_B$ do not exist at the temperature of the first-order transition. In reality, these changes occur over a few kelvin wide temperature range and both functions can be measured experimentally.

[2] When a magnetic field varies between zero and a certain nonzero value that is lower than the critical field needed to induce a metamagnetic transition in an antiferromagnetic system, a 'negative' of 'reverse' magnetocaloric effect is commonly observed, specifically, ΔT_{ad} becomes negative and ΔS_{M} positive when $\Delta B > 0$.

ACKNOWLEDGMENTS

This work was supported by the Office of Basic Energy Sciences, Materials Sciences Division of the United States Department of Energy under contract No. DE-AC02-07CH11358 with Iowa State University.

REFERENCES

Albertini, F., Canepa, F., Cirafici, S., *et al*. (2004). Composition dependence of magnetic and magnetothermal properties of Ni-Mn-Ga shape memory alloys. *Journal of Magnetism and Magnetic Materials*, **272–276**, 2111–2112.

Annaorazov, M.P., Asatryan, K.A., Myalikgulyev, G., *et al*. (1992). Alloys of Fe-Rh system as a new class of working material for magnetic refrigerators. *Cryogenics*, **32**, 867–872.

Blumenfeld, P.E., Prenger, F.C., Sternberg, A. and Zimm, C.B. (2002). High temperature superconducting magnetic refrigeration. *Advances in Cryogenic Engineering*, **47**, 1019–1026.

Bohigas, X., Molins, S., Roig, A., *et al*. (2000). Room-temperature magnetic refrigerator using permanent magnets. *IEEE Transactions on Magnetics*, **36**, 538–544.

Borelli, N.F., Luderer, A.A. and Panzarino, J.N. (1984). Hysteresis heating for the treatment of tumours. *Physics in Medicine and Biology*, **29**, 487–494.

Brown, G.V. (1976). Magnetic heat pumping near room temperature. *Journal of Applied Physics*, **47**, 3673–3680.

Brück, E., Tegus, O., Li, X.W., *et al*. (2003). Magnetic refrigeration – towards room-temperature applications. *Physica B: Condensed Matter*, **327**, 431–437.

Cable, J.W. and Wollan, E.O. (1968). Neutron diffraction study of the magnetic behavior of gadolinium. *Physical Review*, **165**, 733–734.

Chernyshov, A.S., Tsokol, A.O., Tishin, A.M., *et al*. (2005). Magnetic and magnetocaloric properties and the magnetic phase diagram of single-crystal dysprosium. *Physical Review B*, **71**, 184410/1–184410/17.

Choe, W., Pecharsky, V.K., Pecharsky, A.O., *et al*. (2000). Making and breaking covalent bonds across the magnetic transition in the giant magnetocaloric material $Gd_5(Si_2Ge_2)$. *Physical Review Letters*, **84**, 4617–4620.

Clot, P., Viallet, D., Allab, F., *et al*. (2004). A magnet-based device for active magnetic refrigeration. *IEEE Transactions on Magnetics*, **39**, 3349–3351.

Dan'kov, S.Yu., Tishin, A.M., Pecharsky, V.K. and Gschneidner, K.A. Jr. (1997). Experimental device for studying the magnetocaloric effect in pulse magnetic fields. *The Review of Scientific Instruments*, **68**, 2432–2437.

Dan'kov, S.Yu., Tishin, A.M., Pecharsky, V.K. and Gschneidner, K.A. Jr. (1998). Magnetic phase transitions and the magnetothermal properties of gadolinium. *Physical Review B*, **57**, 3478–3490.

Debye, P. (1926). Einige Bemerkungen zur Magnetisierung bei tiefer Temperatur. *Annalen der Physik (Leipzig)*, **81**, 1154–1160.

Földeaki, M., Chahine, R. and Bose, T.K. (1995). Magnetic measurements: a powerful tool in magnetic refrigerator design. *Journal of Applied Physics*, **77**, 3528–3537.

Fujita, A., Fujieda, S., Hasegawa, Y. and Fukamichi, K. (2003). Itinerant-electron metamagnetic transition and large magnetocaloric effects in $La(Fe_xSi_{1-x})_{13}$ compounds and their hydrides. *Physical Review B*, **67**, 104416/1–104416/12.

Fujita, A., Fukamichi, K., Koyama, K. and Watanabe, K. (2004). X-ray diffraction study of magnetovolume effect in itinerant-electron metamagnetic $La(Fe_{0.88}Si_{0.12})_{13}$ compound. *Journal of Applied Physics*, **95**, 6687–6689.

Gama, S., Coelho, A.A., de Campos, A., *et al*. (2004). Pressure-induced colossal magnetocaloric effect in MnAs. *Physical Review Letters*, **93**, 237202/1–237202/4.

Giauque, W.P. (1927). A thermodynamic treatment of certain magnetic effects. A proposed method of producing temperatures considerably below 1° absolute. *Journal of the American Chemical Society*, **49**, 1864–1870.

Giauque, W.P. and MacDougall, D.P. (1933). Attainment of temperatures below 1° absolute by demagnetization of $Gd_2(SO_4)_3{\cdot}8H_2O$. *Physical Review*, **43**, 786.

Gopal, B.R., Chahine, R. and Bose, T.K. (1997). Sample translatory type insert for automated magnetocaloric effect measurements. *The Review of Scientific Instruments*, **68**, 1818–1822.

Gopal, B.R., Chahine, R., Földeaki, M. and Bose, T.K. (1995). Noncontact thermoacoustic method to measure magnetocaloric effect. *The Review of Scientific Instruments*, **66**, 232–238.

Green, G., Chafe, J., Stevens, J. and Humphrey, J. (1990). A gadolinium-terbium active regenerator. *Advances in Cryogenic Engineering*, **35**, 1165–1174.

Gschneidner, K.A. Jr. and Pecharsky, V.K. (2000). Magnetocaloric Materials. *Annual Reviews in Materials Sciences*, **30**, 387–429.

Gschneidner, K.A. Jr., Pecharsky, V.K. and Fort, D. (1997). Novel thermal effects at the first order magnetic phase transition in erbium and a comparison with dysprosium. *Physical Review Letters*, **78**, 4218–4284.

Gschneidner, K.A. Jr., Pecharsky, V.K. and Malik, S.K. (1996). The $(Dy_{1-x}Er_x)Al_2$ alloys as active magnetic regenerator materials. *Advances in Cryogenic Engineering*, **42A**, 465–474.

Gschneidner, K.A. Jr., Pecharsky, V.K. and Tsokol, A.O. (2005). Recent developments in magnetocaloric materials. *Reports on Progress in Physics*, **68**, 1479–1539.

Guo, Z.B., Du, Y.W., Zhu, J.S., *et al*. (1997). Large magnetic entropy change in perovskite-type manganese oxides. *Physical Review Letters*, **78**, 1142–1145.

Hirano, N. (2003). Room temperature magnetic refrigerator using permanent magnets, Paper No. K7.002, presented at the *American Physical Society Meeting*, Austin, March 4. http://www.aps.org/meet/MAR03/baps/tocK.html.

Hirano, N., Nagaya, S., Takahashi, M., *et al*. (2002). Development of magnetic refrigerator for room temperature application. *Advances in Cryogenic Engineering*, **47**, 1027–1034.

Holm, A.P., Pecharsky, V.K., Gschneidner, K.A. Jr., *et al*. (2004). X-ray powder diffractometer for in situ structural studies in magnetic fields from 0 to 35 kOe between 2.2 and 315 K. *The Review of Scientific Instruments*, **75**, 1081–1088.

Hu, F.X., Shen, B.G., Sun, J.R., *et al*. (2001). Influence of negative lattice expansion on magnetic entropy change in the compounds $LaFe_{11.4}Si_{1.6}$. *Applied Physics Letters*, **78**, 3675–3677.

Lu, D.W., Xu, X.N., Wu, H.B. and Jin, X. (2005). A permanent-magnet magneto-refrigerator study using Gd/Gd-SiGe/Gd-SiGe-Ga alloys. In *Proceedings of the 1st International Conference on Magnetic Refrigeration at Room Temperature*, Montreux, 27–30 September, 2005, Egolf, P.W. (Ed.), International Institute of Refrigeration: Paris, pp. 291–296.

Morellon, L., Algarabel, P.A., Ibarra, M., *et al*. (1998). Magnetic-field-induced structural phase transition in $(Gd_5Si_{1.8}Ge_{2.2})$. *Physical Review B*, **58**, R14721–R14724.

Morellon, L., Arnold, Z., Magen, C., *et al*. (2004). Pressure enhancement of the giant magnetocaloric effect in $Tb_5(Si_2Ge_2)$. *Physical Review Letters*, **93**, 137201/1–137201/4.

Morellon, L., Magen, C., Algarabel, P.A., *et al*. (2001). Magnetocaloric effect in $Tb_5(Si_xGe_{1-x})_4$. *Applied Physics Letters*, **79**, 1318–1320.

Oesterreicher, H. and Parker, T.F. (1984). Magnetic cooling near Curie temperatures above 300 K. *Journal of Applied Physics*, **55**, 4334–4338.

Okamura, T., Yamada, K., Hirano, N. and Nagaya, N. (2005). In *Proceedings of the 1st International Conference on Magnetic Refrigeration at Room Temperature*, Montreux, 27–30 September, 2005, Egolf, P.W. (Ed.), International Institute of Refrigeration: Paris, pp. 319–324.

Pasquale, M., Sasso, C.P. and Lewis, L.H. (2004). Magnetic entropy change in Ni_2MnGa single crystals. *Journal of Applied Physics*, **95**, 6918–6920.

Paudyal, D., Pecharsky, V.K., Gschneidner, K.A. Jr. and Harmon, B.N. (2006). Electron correlation effects on the magnetostructural transition and magnetocaloric effect in $Gd_5Si_2Ge_2$. *Physical Review B*, **73**, 144406/1–144406/12.

Pecharsky, V.K. and Gschneidner, K.A. Jr. (1995). Magnetocaloric effect of polycrystalline $Gd_{0.73}Dy_{0.27}$. Unpublished.

Pecharsky, V.K. and Gschneidner, K.A. Jr. (1997a). Giant magnetocaloric effect in $Gd_5(Si_2Ge_2)$. *Physical Review Letters*, **78**, 4494–4497.

Pecharsky, V.K. and Gschneidner, K.A. Jr. (1997b). Tunable magnetic regenerator alloys with a giant magnetocaloric effect

for magnetic refrigeration from ∼20 to ∼290 K. *Applied Physics Letters*, **70**, 3299–3301.

Pecharsky, V.K. and Gschneidner, K.A. Jr. (1997c). Effect of alloying on the giant magnetocaloric effect of $Gd_5(Si_2Ge_2)$. *Journal of Magnetism and Magnetic Materials*, **167**, L179–L184.

Pecharsky, V.K. and Gschneidner, K.A. Jr. (1999a). Magnetocaloric effect and magnetic refrigeration. *Journal of Magnetism and Magnetic Materials*, **200**, 44–56.

Pecharsky, V.K. and Gschneidner, K.A. Jr. (1999b). Magnetocaloric effect from indirect measurements: magnetization and heat capacity. *Journal of Applied Physics*, **86**, 565–575.

Pecharsky, V.K. and Gschneidner, K.A. Jr. (2001). Some common misconceptions concerning magnetic refrigerant materials. *Journal of Applied Physics*, **90**, 4614–4622.

Pecharsky, V.K., Gschneidner, K.A., Jr. and Fort, D. (1996). Superheating and other unusual observations regarding the first order phase transition in Dy. *Scripta Materialia*, **35**, 843–848.

Pecharsky, A.O., Gschneidner, K.A. Jr. and Pecharsky, V.K. (2003). The giant magnetocaloric effect of optimally prepared $Gd_5Si_2Ge_2$. *Journal of Applied Physics*, **93**, 4722–4728.

Pecharsky, V.K., Gschneidner, K.A. Jr., Pecharsky, A.O. and Tishin, A.M. (2001). Thermodynamics of the magnetocaloric effect. *Physical Review B*, **64**, 144406/1–144406/10.

Pecharsky, V.K., Holm, A.P., Gschneidner, K.A. Jr. and Rink, R. (2003). Massive magnetic-field-induced structural transformation in Gd_5Ge_4 and the nature of the giant magnetocaloric effect. *Physical Review Letters*, **91**, 197204/1–97204/4.

Pecharsky, V.K., Samolyuk, G.D., Antropov, V.P., *et al*. (2003). The effect of varying the crystal structure on the magnetism, electronic structure and thermodynamics in the $Gd_5(Si_xGe_{1-x})_4$ system near x = 0.5. *Journal of Solid State Chemistry*, **171**, 57–68.

Richard, M.A., Rowe, A.M. and Chahine, R. (2004). Magnetic refrigeration: single and multimaterial active magnetic regenerator experiments. *Journal of Applied Physics*, **95**, 2146–2150.

Ritter, C., Morellon, L., Algarabel, P.A., *et al*. (2002). Magnetic and structural phase diagram of $Tb_5(Si_xGe_{1-x})_4$. *Physical Review B*, **65**, 094405/1–094405/10.

Rowe, A.M. and Barclay, J.A. (2002a). Design of an active magnetic regenerator test apparatus. *Advances in Cryogenic Engineering*, **47**, 995–1002.

Rowe, A.M. and Barclay, J.A. (2002b). Static and dynamic force balancing in reciprocating active magnetic refrigerators. *Advances in Cryogenic Engineering*, **47**, 1003–1010.

Rowe, A., Dikeos, A. and Tura, A. (2005). Experimental studies of a near-room temperature magnetic refrigeration. In *Proceedings of the 1st International Conference on Magnetic Refrigeration at Room Temperature*, Montreux, 27–30 September, 2005, Egolf, P.W. (Ed.), International Institute of Refrigeration: Paris, pp. 325–334.

Shir, F., Bennet, L.H., Della Torre, E., w*et al*. (2005). Transient Response in magnetocaloric refrigeration. *IEEE Transactions on Magnetics*, **41**, 2129–2134.

Tegus, O., Brück, E., Buschow, K.H.J. and de Boer, F.R. (2002). Transition-metal-based magnetic refrigerants for room-temperature applications. *Nature (London)*, **415**, 150–152.

Tishin, A.M. and Spichkin, Y.I. (2003). *The Magnetocaloric Effect and its Applications*, Institue of Physics Publishing: Bristol.

Vasile, C. and Müller, C. (2005). A new system for a magnetocaloric refrigerator. In *Proceedings of the 1st International Conference on Magnetic Refrigeration at Room Temperature*, Montreux, 27–30 September, 2005, Egolf, P.W. (Ed.), International Institute of Refrigeration: Paris, pp. 357–366.

Wada, H. and Tanabe, Y. (2001). Giant magnetocaloric effect of $MnAs_{1-x}Sb_x$. *Applied Physics Letters*, **79**, 3302–3304.

Warburg, E. (1881). Magnetische Untersuchungen. *Annalen der Physik (Leipzig)*, **13**, 141–164.

Wu, W. (2003). Development of a magnetic refrigeration prototype for operation at ambient temperature, Paper No. K7.004, presented at the *American Physical Society Meeting*, Austin, March 4. http://www.aps.org/meet/MAR03/baps/tocK.html.

Zhou, X., Li, W., Kunkel, H.P. and Williams, G. (2004). A criterion for enhancing the giant magnetcaloric effect: (Ni-Mn-Ga) – a promising new system for magnetic refrigeration. *Journal of Physics: Condensed Matter*, **16**, L39–L44.

Zimm, C. (2003). Development of a magnetic refrigeration prototype for operation at ambient temperature, Paper No. K7.003, presented at the *American Physical Society Meeting*, Austin, March 4. http://www.aps.org/meet/MAR03/baps/tocK.html.

Zimm, C., Boeder, A., Chell, J., *et al*. (2005). Design and performance of a permanent magnet rotary refrigerator. In *Proceedings of the 1st International Conference on Magnetic Refrigeration at Room Temperature*, Montreux, 27–30 September, 2005, Egolf, P.W. (Ed.), International Institute of Refrigeration: Paris, pp. 367–376.

Zimm, C., Jastrab, A., Sternberg, A., *et al*. (1998). Description and performance of a near room temperature magnetic refrigerator. *Advances in Cryogenic Engineering*, **43**, 1759–1766.

Chalcogenides and Pnictides

Daniel Fruchart and Pierre Wolfers
CNRS, Grenoble, France

1 PNICTIDES

Transition-metal-rich phosphides and arsenides or antimonides (X = P, As, Sb) exhibit very peculiar but strongly related crystal structures, leading to fairly marked magnetic characteristics. Both the magnetic ordering temperatures and the local magnetic moments of transition elements (T) usually do not range very far from those of the metals and alloys, respectively. In fact, the main series of TT′X and TX metal–type compounds display nearest metal–metal distances 10–20% larger than only those in pure metal compounds (Fruchart, 1982). Contrary to halides, oxides, and chalcogenides, the size of the nonmetal element X in this case is effectively smaller, the ionic–covalent character of the T–X bonds is less marked, to the benefit of the metal character of phosphides and arsenides. This peculiarity stands for the classes of closely structured TT′X and TX compounds as well, where X = Si, Ge, Sn, Sb,. . ., for example, with MnAlGe on one side and MnSb on the other.

It also exists as a ternary pnictides series, for example, as skutterudites phosphides or antimonides (Leithe-Jasper *et al*., 2004), or more complex systems, for example, $Zr_2Fe_{32}P_8$ (Le Sénéchal *et al*., 1999) of the generic formula $\square_{n(n+1)}R_{n(n-1)}T_{6(n^2+1)}X_{2(2n^2+1)+1}$ (where R is a rare-earth element and $\square$ is a vacancy), that most of the time exhibit either magnetic properties at low temperature only or are weakly polarized with a small moment, if any. These are not discussed here since they exhibit weak magnetic characteristics, often disperse and also peculiar magnetic components and couplings. Also, the binary and ternary transition-metal nitrides are not considered here since the marked interstitial character of X = N in many metal lattices is better compared to those in parent metal carbides, even borides. The coordination polyhedron of nitrogen in transition-metal nitrides is quite different from that in compounds with a less metallic type such as phosphides, arsenides, antimonides.

Nevertheless, the magnetic properties of the two main series TX and TT′X considered here remain dominated by direct metal–metal interactions (Fruchart, 1982); however, the T–X bonds lead to a reduction in the magnetic polarization reference to the orbital scheme of a pure ionic state and support marked competition of exchange forces. Additionally, for several compounds, rather strong magnetic moments (larger than $\sim 3\,\mu_B$ for Mn) have been measured. In fact, the classes of TX and TT′X materials are also characterized by instabilities of the local magnetic polarization, with a possible impact on long-range magnetic ordering that, in most cases, are accompanied by structural transitions.

Handbook of Magnetism and Advanced Magnetic Materials. Edited by Helmut Kronmüller and Stuart Parkin. Volume 4: *Novel Materials*. ISBN: 978-0-470-02217-7.

Earlier, J.B. Goodenough had focused his interest on these two series of peculiar compounds, thus establishing conceptual phase diagrams (Goodenough, 1973, 1976) and had proposed a general analysis of the subtle physical and magnetic aspects of T-metal pnictides in terms of electron filling orbitals, with regard to characteristics that were intermediate between metal and ionic types.

Such singular behaviors led to the renewal of a marked interest in both series of TT′X and TX metal phosphides and arsenides since high-performance magnetocaloric properties have been revealed quite recently. Promisingly, their corresponding magnetic transitions spread over a wide range of temperature for large changes in magnetization, moreover being induced by moderate magnetic fields, as delivered by the modern permanent magnet, for example, the NdFeB-type of magnet.

2 CRYSTAL STRUCTURE RELATIONSHIPS

The TT′X series of compounds exhibit peculiar structural arrangements as a consequence of sensitive T–T′ metal interactions. From a unique pseudo unit cell (block) containing one formula unit (fu), the very rich series of polytype structures labeled T2 (tetragonal, 2 fu/cell), H3 (hexagonal, 3 fu/cell), O4 (orthorhombic, 4 fu/cell), O8, H12, and so on, are derived (Artigas, Fruchart, Boursier and Fruchart, 1990). The elementary block is defined as a pseudorhombic unit cell, where the X atoms form two types of interstices, two with tetrahedral coordination, *T*, and two of fivefold coordination with the shape of square-based pyramids, *P*. The three fundamental polytype members crystallize with the Cu_2Sb (SG: P4/*nmm*), the Fe_2P (SG: P$\bar{6}$2*m*), or the Co_2P (SG: P*nma*)-type of structure. These structures are strongly related since the different point symmetry groups allow one to build compact but different arrangements of blocks with respect to the fourfold, threefold, and twofold symmetries, respectively. The three main TT′X structures are represented in Figure 1, along with the rhombic pseudo unit cell containing one formula unit that is defined from a triangular channel formed by the X atoms.

Analogies can be established between the different crystal structures of the former series and those of the T′X one. Here, one of the metal atoms (T′) is 'missing', the corresponding tetrahedron, *T*, being empty; thus the T-metal atom occupies the center of the octahedron formed from two neighboring pyramids, *P*. The corresponding crystal structures are of the NiAs hexagonal type (H2, SG: P-3/*mmc*) and the MnP orthorhombic type (O4, SG: P*nma*), as seen in Figure 2. Both the TX crystal structures are directly related since the second

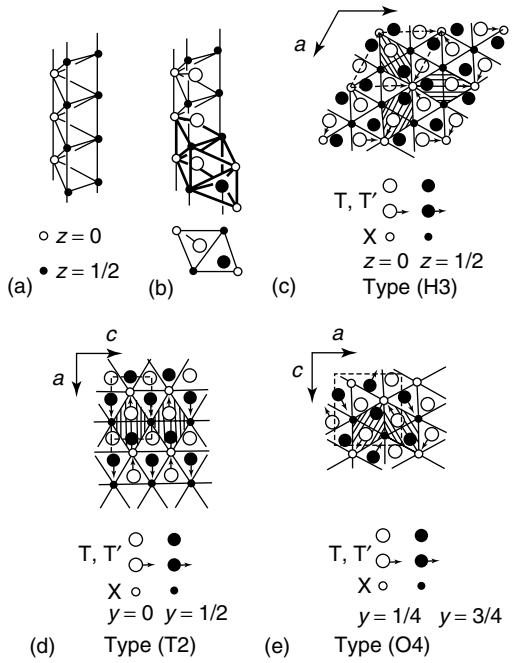

Figure 1. Structures (c) – type Fe_2As (T2), (d) – type Fe_2P (H3), and (e) – type Co_2P (O4) of the TT′X compounds as projected along axes to evidence the *T* (tetrahedral) and *P* (pyramidal) sites, the latter identified by arrows toward the apical X site. Above are represented fragments illustrating the triangular channel (a), hosting the pseudorhombohedral TT′X cell (b). (Fruchart, R., 1982, *Annales De Chimie*, **7**(6–7), 572; Artigas, M., PhD, Grenoble, 1992, p. 30.)

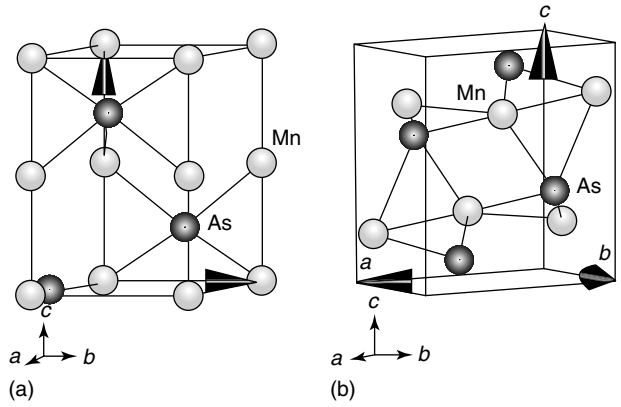

Figure 2. MnAs crystal structures in hexagonal (a) and orthorhombic (b) types. (Nascimento, F.B., *Materials Research*, **9**(1), (2006) 113.)

one can be considered to be the orthohexagonal distorted variant, the T atom being shifted from the center of the octahedron as a bipyramid, alternately in one or the other of the two pyramids. In fact, the series of TX and TT′X pnictides derive from the NiAs or are filled from Ni_2In via displacive or distortive types of transformations.

For both series TT′X and TX, more dense structures (shorter and shorter metal–metal distances) are obtained by application of external pressure or chemical pressure (Krumbugel-Nylund *et al*., 1974) following the succession T2 (TT′X) to H3 (TT′X and TX) to O4 (TT′X and TX). Since the magnetic coupling forces are intimately related to the metal-to-metal distances and directly depend on the crystal structure taken by the TT′X or TX compounds, magnetoelastic transitions take place systematically with changes in both the crystal and magnetic structures (e.g., ferro to antiferro (AF) in the MnAs–FeAs system Krumbugel-Nylund, 1974). The competing magnetic interactions promote the presence of metastable noncollinear, long-range ordering arrangement, leading to metamagnetic behavior versus the applied magnetic field. Also, instabilities of the electronic origin are commonly observed, and abrupt changes in the metal atom magnetization level can accompany the structure transition, which is often of the first-order type.

3 GENERAL OVERVIEW ON MAGNETIC PROPERTIES

The structural and magnetic characteristics of most intermetallic compounds of transition elements, namely, the pnictides formed with P, As, and Sb, had been extensively reviewed 15 years ago by Beckman and Lundgren (1991). The reader is invited to refer to this excellent review for information on most of the compounds mentioned earlier. As mentioned in the preceding text, one can easily recall the most pertinent phase diagrams, as reported versus composition, stoichiometry, or external pressure, thus well illustrating the dramatic interplays between crystal structures and opposite magnetic couplings.

Both the series of pnictides discussed here reveal optimal magnetic properties corresponding well to a peculiar valence electron concentration (VEC) that leads to extreme ordering temperatures or (and) large magnetization levels. Whatever the crystal structure of the considered TT′X polytypes may be, the maximum T_C of most compounds takes place close to the d^6 configuration (Fe), as for Fe_2P, MnCoP, MnCoAs, CrNiAs, and so on (Fruchart, 1982). This also applies to the solid solutions and multinaries. For example, Figure 3 presents the huge variation of both Curie temperature in the $Mn_{1-x}Co_xP$ system and magnetization, as reported earlier (Fruchart, Martin-Farrugia, Rouault and Sénateur, 1980). For the optimized VEC value, ferromagnetic couplings are, most of the time, dominating but with a slight change in composition or application of pressure (chemical or external pressure), dramatic changes take place with abrupt drops in magnetization. Then, AF couplings control the long-range magnetic ordering, which is often incommensurate

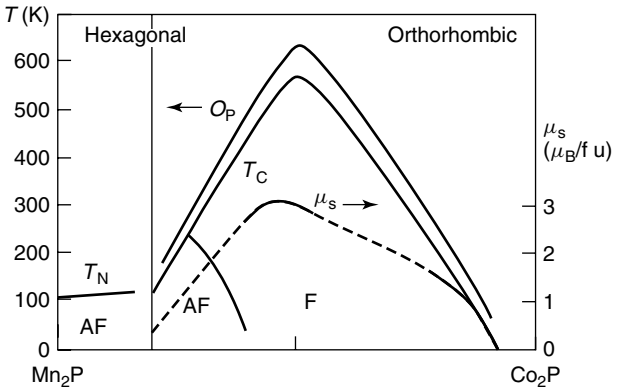

Figure 3. Magnetic phase diagram of the system Mn_2P–Co_2P. (After Fruchart, D., *et al*. Phys. Stat. Sol. (a) 57 675–682. *Handbook of Magnetic Materials*, Buschow (Ed.), Vol. 6, O. Beckman and L. Lundgren, p. 236.)

with the crystal cell. The situation is perfectly illustrated in Figure 4(a–c), all related to Fe_2P. In the vicinity of the change in ordering, both the ferro-antiferromagnetic and the ferro-paramagnetic transitions are accompanied either by a change in the crystal structure or at least by discontinuities of the cell parameters. Simultaneously, the magnetic moment of the T (T′) element can vary abruptly as the electronic state becomes modified (Bacmann *et al*., 1994). Additionally, in the paramagnetic state, short-range magnetic ordering effects have been observed with a regime of high-temperature correlation of up to $3T_C$ (Zach *et al*., 1994, 1995; Zach, Guillot, Picoche and Fruchart, 1995a).

Very similar instability effects, also of electronic origin, have been pointed out in the TX series, as illustrated in Figure 5 for the CrP–MnP–FeP system (Sénateur, Roger, Fruchart and Chappert, 1969; Beckman and Lundgren, 1991). The well-known lattice and magnetic instability of MnAs (Goodenough and Kafalas, 1967) versus temperature, composition, and application of pressure are more particularly illustrated in Figure 6(a) versus composition and Figure 6(b) versus application of an external pressure.

More recent fundamental investigations on the properties of the TT′X series have been reported from the 1990s up to now, mostly by T. Kanomata *et al*. in Japan, R. Zach *et al*. in Poland, D. Fruchart *et al*. in France, J. Bartolomé *et al*. in Spain, for a part under crossed collaborations, and by E. Brück *et al*. in The Netherlands. After the discovery of the very important magnetocaloric effect (MCE) in MnAs by H. Wada *et al*. in Japan, S. Gama *et al*. in Brazil have evidenced colossal MCE properties of $MnAs_{1-x}Sb_x$ systems under pressure.

These contributions can be classified relative to their main objectives and interests as follows:

1. Investigation of the magnetic and electronic structures.

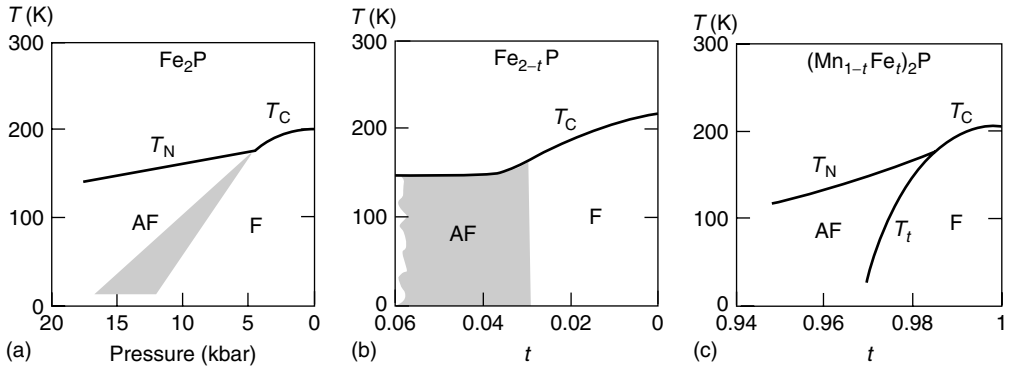

Figure 4. (a) (T, P) Phase diagram for Fe_2P, (b) (T, t = □) diagram for $Fe_{2-x}P$, (c) diagram for $(Mn_{1-x}Fe_x)_2P$. (After Roger, A. PhD Thesis, Paris–Orsay, (1970); or *Handbook of Magnetic Materials*, Buschow (Ed.), Vol. 6, Beckman, O. and Lundgren, L. p. 230.)

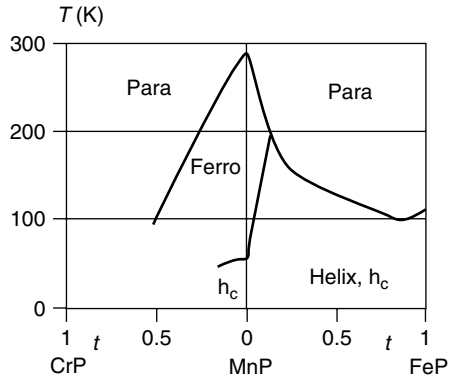

Figure 5. Magnetic phase diagram of the systems CrP–MnP–FeP. (After Sénateur, Roger, Fruchart and Chappert, 1969; *Handbook of Magnetic Materials*, Buschow Ed., vol. 6, Beckman, O. & Lundgren, L. p. 203.)

2. Correlation of the typical magnetoelastic behaviors with the crystal and magnetic transformations at specific transitions.
3. Transformations induced by applying external pressure or high magnetic fields.
4. Specific analysis of the change in entropy at transition in terms of MCE.

3.1 Investigation of the magnetic and electronic structures

3.1.1 TT′X pnictides

Fe_2P remains a material of reference because of the multiple magnetic and physical sensitive characteristics obtained with the pure and substituted compounds. Band structure calculations using a KKR-CPA (Korringa Kohn Rostoker-Coherent Potential Approximation) method were performed to compare with the experimental results obtained by a combination of magnetization and neutron diffraction measurements on Fe_2P (Koumina *et al.*, 1998) and on $FeMnP_{1-x}As_x$ compounds (Tobola *et al.*, 1996). A fairly good agreement was reached in determining the magnetic moments from experience and calculations. The reentrant spin glass SP (Spin Glass)–type transition at T ∼ 125 K of Fe_2P substituted with small amounts (5%) of both Cr and Ni was studied by dc magnetization and ac susceptibility (Srivastava *et al.*, 1994). The critical exponent of the freezing phenomenon was determined, thus ranging well with values observed for ordinary paramagnetic SP transitions. The magnetic phase diagram of slightly Cr-substituted Fe_2P samples was determined from magnetization and neutron diffraction experiments. Three different regions were identified with reference to an intermediate range ($50 < T < 120$ K), where negative interaction forces reveal an important comparison made with low and high ranges of temperatures respectively, both exhibiting ferromagnetic-type orderings (Sudish-Kumar, Srivastava, Krishnamurthy and Sahni, 1999).

The dependence of the thermopower Seebeck coefficient S(T) (Nakama *et al.*, 1998) was measured versus polarization of the magnetic structure by application of high magnetic fields up to 15 T. A large field dependence was found with a shoulder between 60 and 70 K and a discontinuity at 'T_C'; a first-order-type transition.

The magnetic phase diagram of MnRhAs (H3 type) was reanalyzed using single-crystal and ac susceptibility technique in order to make the metastable character of a so-called *ferro-AF multistep transition* taking place between 127 and 176 K more precise. Three zones with different behaviors were evidenced to relate to the spin canting phenomena (Rillo *et al.*, 1992).

The ferromagnetic $(Fe_{1-x}Ru_x)_2P$ (H3 type) system was investigated using the same technique as in the preceding text, thus revealing two magnetic transitions, the role of increasing Ru content being interpreted similar to the application of high pressure on the binary Fe_2P (Artigas *et al.*,

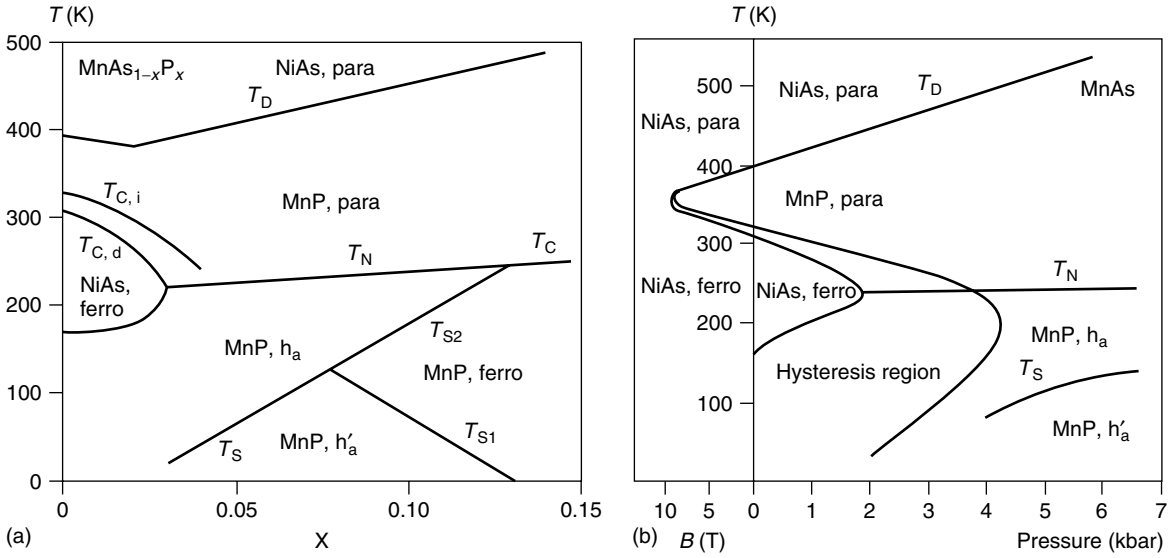

Figure 6. (a) Phase diagram of the pseudobinary compounds $MnAs_{1-x}P_x$ on the MnAs rich side, indicating the transition lines from NiAs to MnP-type structure, and first-order transition from ferromagnetic NiAs to paramagnetic MnP. (*Handbook of Magnetic Materials*, Buschow (Ed.), Vol. 6, Beckman, O. and Lundgren, L. p. 209.) (b) Influence on magnetic field and pressure on the crystal and magnetic structure of MnAs. (*Handbook of Magnetic Materials*, Buschow (Ed.), Vol. 6, Beckman, O. and Lundgren, L. p. 205.)

1992), the latter being reanalyzed by neutron diffraction and band structure calculations (Tobola *et al*., 1996). A comparison was established with the parent $MnFeP_{0.7}As_{0.3}$ where a drop in the magnetic moment of Fe was evidenced earlier at ferro-AF transition.

Following the phase diagram reinvestigation (Bacmann *et al*., 1990) of the $(Mn_{1-x}Fe_x)_2P$ (H3 type) by ac susceptibility, new magnetic phases were detected, in agreement with a parallel neutron diffraction analysis. The system $(Mn_{1-x}Co_x)_2P$ (O4 type) isoelectronic to Fe_2P (H3 type) for $x = 0.5$ was analyzed parallel to magnetization measurements and band structure calculations (Sredniawa *et al*., 2002). In agreement with the magnetic arrangements, as determined elsewhere by neutron diffraction, the rapid drop in phase transitions induced by much higher Mn contents was correlated with a marked enhancement of density of states (DOS) close to the Fermi level. Complementary to the two preceding ternary systems, analysis of the pseudo-quaternary $MnFe_{1-x}Co_xP$ systems by different experimental techniques and band structure calculations (Sredniawa *et al*., 2001) reveals a very interesting phase diagram with a first-order AF-ferro transition sensitive to composition. This orthorhombic phase diagram appears quite similar to the hexagonal part of the MnFeP–MnFeAs hexagonal system (Bacmann *et al*., 1994; Tobola *et al*., 1996). Substitution of Si to P in MnFeP was shown to be possible up to $x \sim 0.4$; however, the thermal treatment history dependence reveals unexpected and puzzling effects in terms of Curie temperature (Zhang *et al*., 2005).

Magnetization curves measured in an H3 (MnRuP) and in T2 (MnZnSb and MnGaGe) systems around Curie temperature to determine the critical exponents (Ono *et al*., 2001) lead to the conclusion that the two-dimensional magnetic character applies well for the later T2-type compounds, contrary to the H3-type MnRuP. Systematic computational KKR-CPA analyses of tetragonal arsenides, binary, and ternary antiferromagnets (Cr_2As, CrMnAs, Mn_2As, CrNiAs) were performed (Tobola *et al*., 1997), revealing an excellent agreement with the previous magnetic structure determination, namely, using neutron diffraction. However, the hexagonal CrNiAs compound, isoelectronic to Fe_2P, reveals strong competition between AF and ferromagnetic couplings, and it was anticipated that pressure effects or substitution should increase the magnetic moment of Cr up to more than $2\,\mu_B$. The pressure effects have been studied in detail by Ohta *et al*., as reported in Section 3.3. The reports given by this group are parallel to the high-field magnetization performed on $(Cr_{1-x}Ni_x)_2As$ with $x = 0.5$, 0.7, concluding that the low temperature anomalous magnetization attributed to the spin glass–like behavior related to band magnetism (Ohta *et al*., 1995a). From a band structure analysis, they concluded that CrTX systems with T = Fe, Co, Ni, X = P, As, Cr are magnetically ordered but Cr carries only a magnetic moment (Ishida, Takiguchi, Fujii and Asano, 1996). Finally, a study based on neutron diffraction (Bacmann, Fruchart, Koumina and Wolfers, 2004) revealed that the low-temperature phase of CrNiAs (up to ∼110 K) consists of a sine-modulated structure with moments on both Cr

and Ni, but up to $T_C \sim 210$ K, only Cr carries a moment, forming a simple collinear structure.

More recently, all possible magnetic exchange couplings that could take place in the tetragonal series of TT′X pnictides were reviewed from theoretical symmetry approaches (Fruchart, 2005). Contrary to most magnetic arrangements established up to now, which form AF collinear magnetic structures, long-range noncollinear structures are basically allowed in complete agreement with a first experimental result (Yamagishi *et al*., 1999). Here also, potential magnetoelastic couplings must be accounted to fully understand the magnetic phase diagram, as anticipated earlier (Shirakawa and Ido, 1976).

Definitively, a systematic analysis of the magnetic couplings versus the metal–metal distances in some TT′X with T = Cr and Mn, T = 4d elements (Ru, Rh, Pd) phosphides and arsenides leads to the conclusion that the physical behavior should also be interpreted in terms of itinerant–electron magnetism (Ohta, Kanomata and Kaneko, 1990; Kanomata *et al*., 1991), as revealed by fitting the susceptibility traces.

3.1.2 TX pnictides

For TX pnictides, similar fundamental analyses were performed in order to better understand the subtle equilibrium state between ferromagnetic and AF phase regions.

Symmetric and antisymmetric anisotropic exchange energies were considered for the relative stability of the different modulated magnetic phases existing in the monopnictides MnP, FeP, CrAs, MnAs (Sjöstrøm, 1992). The results, based on a band model analysis, confirm that the shape of the Fermi surface and the antisymmetric interactions is crucial for the stability of the helical magnetic structure, for example, in MnP.

The magnetic couplings supported by conduction carriers were demonstrated to be of relative importance in correlating the transport and magnetic properties (Barner, 1987). Also, the canted and helicoidal equilibrium spin structure was attributed to mixed couplings, with peculiar field and temperature dependence in MnP_xAs_{1-x} and $Cr_xMn_{1-x}Sb$ systems (Kohnke *et al*., 1996).

MnP (O4 type) is one of the few magnetic systems in which a uniaxial Lifshitz point (LP) has been identified, occurring at the confluence of modulated, ferromagnetic, and paramagnetic phases. Experiments were performed by applying the magnetic field along the main direction of the orthorhombic cell, thus allowing the evaluation of the critical exponent parameters, for example, susceptibility and specific heat (Becerra, Bindilatti and Oliveira, 2000). The results have been successfully interpreted in terms of a 3-D Ising model. Besides, from the analysis of the wave vector dependence q(H) with the applied field of all the modulated magnetic structures (helix, fan, cone), the shape of the magnetization curves realized while applying the field along the lattice vectors was explained along with the nature of the cone-phase-type transition (Zieba, Slota and Kucharczyk, 2000). The characteristics of the LP, triple point, and critical end point were derived on the basis of an axial next nearest-neighbor Heisenberg model (ANNNH), thus appearing in semiquantitative agreement with the experiments. Effective values for the crossover exponent, wave vector exponent, and magnetization discontinuity provide explanations of the deviation to experimental results. Apart from the mechanisms of phase transformation, the nature of the O4–MnP-type magnetic structure was requestioned theoretically by density-functional determination (Niranjan, Sahu and Kleinman, 2004). The high-temperature magnetic state was shown to be antiferromagnetic and the absence of any Curie–Weiss-type magnetic susceptibility was justified by the lack of long-range ordering, according to the model.

3.2 Typical magnetoelastic behaviors

A peculiar system $MnFeP_{1-x}As_x$ revealed to be very interesting since it contains the three main structure polytypes O4 for the P-rich side, T2 for the As-rich side, and H3 for intermediate compositions, as shown in Figure 7. By analyzing the dependence of magnetic couplings versus the metal–metal distances ('densification' effect from T2 to H3 to O4), the intermediate H3 part of the phase diagram reveals

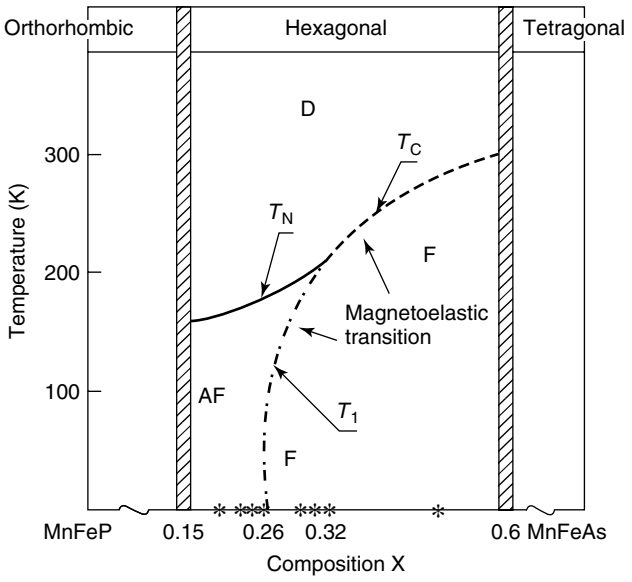

Figure 7. Magnetic phase diagram of the MnFeP–MnFeAs system. (A., Krümbugel-Nylund PhD University of Paris–Orsay, 1974; M., Bacmann *et al*. *Journal of Magnetism and Magnetic Materials* **134**, (1994), 59–67.)

the existence of a singular transition T_T at $x \sim 0.27$ between a ferromagnetic domain and an antiferromagnetic one. The so-called *Curie temperature* 'T_C' from ferro to 'paramagnetic' *P* state appeared to have similar trends: first-order transition type with a magnetoelastic character, as the F–AF transition. The influence of high magnetic fields was measured in the range 0–20 T from 4 to 400 K, thus inducing magnetic phase transformations with magnetoelastic characters (Zach, Guillot and Fruchart, 1990). Then the magnetic ordering was checked for using several complementary techniques such as X-ray and neutron diffraction versus temperature, Mössbauer spectroscopy, and magnetic measurements (Bacmann *et al*., 1994; Zach *et al*., 1995). The ***a*** cell parameter drops down by ∼1% at the F–AF and F–P transitions T_T and 'T_C'; conversely, the ***c*** cell parameter increases by ∼2.5%, thus almost no change in volume is observed. Crystal structure refinements indicate that, starting from the ferromagnetic state, the magnetoelastic transitions T_T and 'T_C' led to the mean ⟨Mn–Mn⟩ (pyramidal sites) distance remaining unchanged, the ⟨Fe–Fe⟩ (tetrahedral sites) distance dropped by 0.1 Å, conversely to the ⟨Mn–Fe⟩, which increased by the same value. A high-field X-ray diffraction investigation performed on $MnFeP_{0.5}As_{0.5}$ confirms the same change in the ***a*** and ***c*** cell parameters when applying high field just above 'T_C'; however, the cell volume slightly and continuously decreases with increasing magnetic field through the transformation (Koyama, Kanomata, Matsukawa and Watanabe, 2005), thus realizing the reverse behavior of the volume expansion when temperature increases. Solving the complex noncollinear and incommensurate AF structure using both neutron diffraction and ^{57}Fe Mössbauer spectroscopy indicate that at T_T (and accordingly at 'T_C') the magnetic moment drops down by ∼50% (0.6 μ_B), the magnetic moment of Mn remaining unaffected, close to 3 μ_B. All these trends were confirmed later by KKR-CPA electronic structure calculations. The confirmation of most of the characteristics of the $MnFeP_{1-x}As_x$ magnetic system was achieved more recently using ^{57}Fe Mössbauer spectroscopy, but applied to close compositions as those previously analyzed (Hermann *et al*., 2004).

Both competing positive and negative interactions and a reduction in the Fe–M exchange forces induce a ferromagnetic–paramagnetic magnetoelastic transition with a marked loss of long-range correlation just above 'T_C', as indicated by the important diffuse scattering at large ***q*** vectors (Bacmann *et al*., 1994). A magneto-resistance study was realized on $MnFeP_{0.55}As_{0.45}$ on a polycrystalline sample prepared by a solid-state reaction (Tegus, Brück, Buschow and de Boer, 2002). The extremum of the derivative of $\rho(T)$ coincides well with 'T_C'. The increase in resistivity, which is almost constant in the room-temperature (RT) range, approaching the magnetic ordering temperature may be related to the existence of AF spin fluctuations. This appears in agreement with what was proposed by Zach *et al*. (1995).

The critical field behavior was investigated experimentally (Zach, Guillot, Picoche and Fruchart, 1995a), allowing to propose a Landau type of thermodynamic model as seen in Figure 8(a–c). This model was shown to be supported well by systematic magnetic measurements under pressure, allowing to build a (T, B, P) diagram (Zach, 1997).

Recently, a model description of the first-order phase transition in $MnFeP_{1-x}As_x$ was proposed (Tegus *et al*., 2005b) on the basis of the Bean–Rodbell model. Exchange interactions, elastic energy, entropy, pressure terms and, finally, the Zeeman energy were used to minimize the Gibbs free energy with respect to the volume and magnetization. The fit of pertinent parameters to experimental data confirms that the magnetoelastic couplings play a very important role in the mechanism of the phase transition.

Besides, the magnetoelastic properties and electronic structure analysis for a similar H3 system $(Fe_{1-x}Ni_x)_2P$ were determined recently (Zach *et al*., 2004). Once more, the tetrahedral site where preferentially Ni substitutes for Fe loses its magnetic polarization rapidly.

In both cases, similar to the other ones of the TT′X series, the magnetoelastic character of the first-order-type transitions is directly related to magnetic instabilities of electronic origin, induced by chemical pressure effects.

3.3 Transformations induced by external pressure or high magnetic fields

Since the TT′X (and TX) systems of magnetic transition-metal pnictides reveal very dramatic competitions of coupling forces, with correlated magnetoelastic phenomena, an external pressure technique was used along with a high magnetic field to better understand the nature of the transitions.

The MnRhAs (H3 type) compound first proved to be very attractive with regard to the successive complex noncollinear structure, AF at low temperature, transforming to a F + AF state via a first-order transition at $T_T = 158$ K, then losing long-range ordering at $T_C \sim 200$ K (Chenevier *et al*., 1984; Bacmann *et al*., 1986). Moreover, antiphase magnetic arrangements occurred immediately down to T_T, as specially confirmed later by neutron diffraction and topography (Chenevier *et al*., 1992). The pressure dependence of the different transitions was first investigated by Kanomata, Shirakawa and Kaneko (1987), indicating the stabilization of the AF domain at the expense of the F + AF one. This was confirmed in more detail with the (T, B, P) phase diagram determined on the extended $MnRhAs_{1-x}P_x$ system (Zach *et al*., 1992, 1995; Zach, 1997). Critical field exponent as well as triple point and end point were evidenced

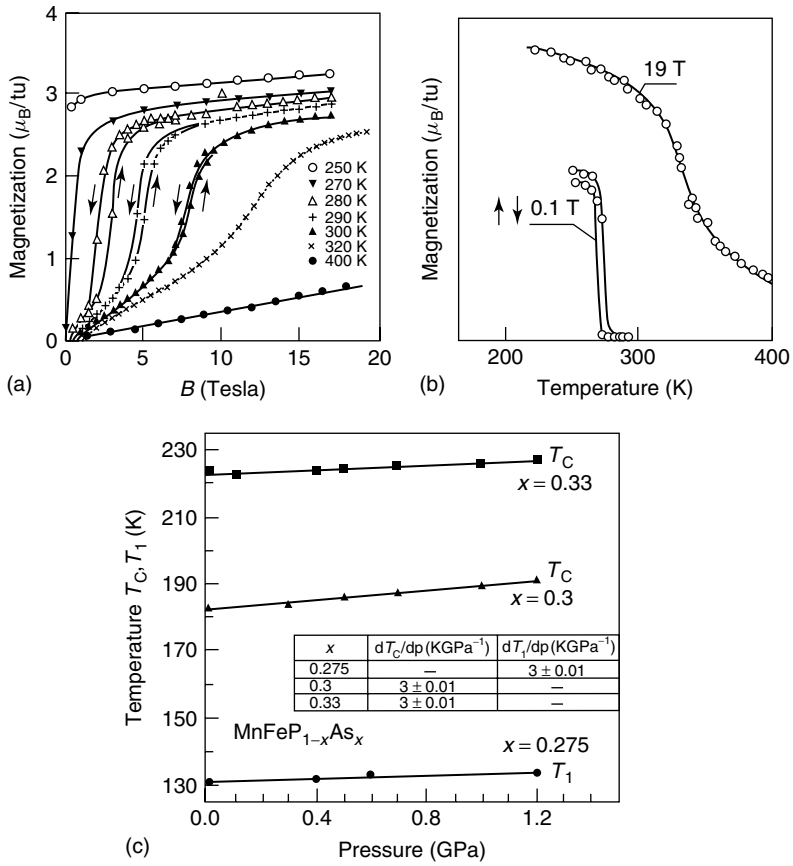

x	dT_C/dp (KGPa^{-1})	dT_1/dp (KGPa^{-1})
0.275	–	3 ± 0.01
0.3	3 ± 0.01	–
0.33	3 ± 0.01	–

Figure 8. (a) Isothermal $M_T(B)$ magnetization of $MnFeP_{0.5}As_{0.5}$; (b) isofield $M_B(T)$ magnetization of $MnFeP_{0.5}As_{0.5}$; (c) (P, T) magnetic phase diagram of $MnFeP_{1-x}As_x$, $x = 0.275$ (T_{F-AF}), $x = 0.3$ ('T_C'), $x = 0.33$ ('T_C'). (Zach, R., Hab Thesis, D., Politecknika Krakowska, Zeszyt Naukowy NR 2 Krakow 1997.)

and interpreted using a Landau-type thermodynamic model as for the $MnFeP_{1-x}As_x$ system (Zach, 1997).

Pressure-induced structural transition in the ferromagnet MnRhP (H3 type) and MnRhAs at RT by using an *in situ* experiment (Eto *et al*., 2000). A transformation to an orthorhombic (more dense) structure occurred under 34 GPa. Another unidentified transformation also occurred for MnRhAs under 25 GPa. The Curie temperature dependence of the former and ferromagnetic compound was checked under pressure, revealing a c-plane dependence of the exchange forces (Nishino *et al*., 2000). The magnetic characteristics of the second compound, as submitted to external pressure, but in a weaker pressure range than for the X-ray investigation, were determined by Fujii *et al*. (2001). This experiment has allowed to establish a singular behavior, as reported in Figure 9, but in good agreement with earlier studies (Zach *et al*., 1997). For a pressure larger than 5 GPa, an almost ferromagnetic phase was stabilized. Similarly, a ferromagnetic state was stabilized under pressure up to 12 GPa in the $MnRhAs_{0.5}P_{0.5}$as a part of reanalysis of the $MnRhAs_{1-x}P_x$ system with $x = 0.4$, 0.5, 0.6 (Zach *et al*., 1992; Fujii *et al*., 2002a). Finally, the related but more complex system $MnRh_{1-x}Co_xAs$ was investigated up to 8 GPa for magnetic properties and using *in situ* experiments for X-ray analysis (Fujii *et al*., 2002b). MnCoAs (O4 type) is a ferromagnet and from substitution of Rh to Co, a reinforced ferromagnetic state can be expected at the expense of the low-temperature AF state. A comparison of the results in terms of magnetic couplings acting along the *c* axis with those recorded on parent compounds (MnRhP, MnRuP, MnRhAs, $MnRhAs_{1-x}P_x$, MnZnSb) allowed the authors to conclude that RKKY-type interactions play an important role in the exchange mechanism in the TT′X system, as illustrated in Figure 10.

Other sensitive TT′X systems were investigated under pressure, with CrNiAs and CrRhAs (both H3 type) for a similar phenomenology anticipated with both the $Co_xMn_{1-x}P$ and $MnRhAs_{1-x}P_x$, systems. A decrease in the ordering temperature T_C and T_N respectively was induced by application of pressure (Ohta *et al*., 1995b; Ohta and Onmayashiki, 1998).

Interestingly, MnFeAs (T2 type) transforms and is stabilized to MnFeAs (H3 type) by using high pressure (6 GPa)

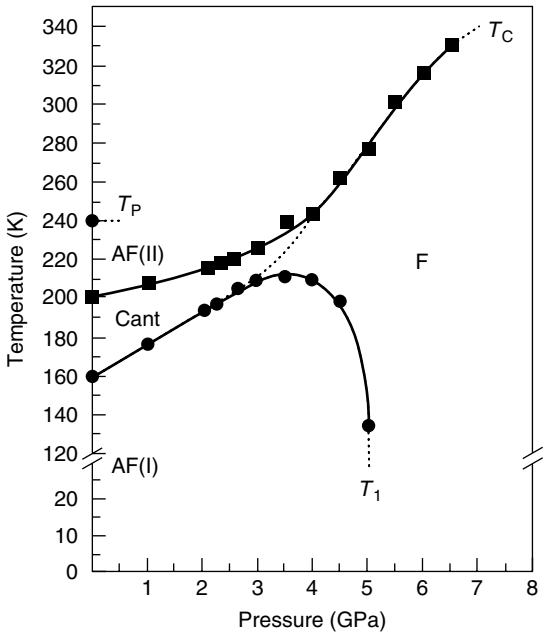

Figure 9. The (P–T) phase diagram determined from the present experiment. A pressure-induced phase transition from AF(I) to F takes place at around 5 GPa. T_P was not detected in this experiment. The dotted line was drawn according to Kanomata, Shirakawa and Kaneko, (1987). (Fujii, N., *et al*. *Journal of Magnetism and Magnetic Materials*, **224**(1) (2001) 15.)

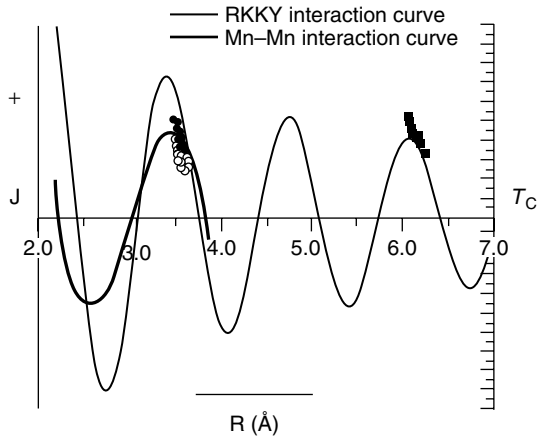

Figure 10. Mn–Mn interaction curves in MnMX-type intermetallic compounds calculated from RKKY theory and estimated from refs. (30–32) in Fujii *et al*., (2002b) for Mn alloys. Observations of T_C for MnRuP (●), MnRhAs (○), MnZnSb (■) are also plotted. (Fujii, N., *et al*. *Journal of Alloys and Compounds*, **345**, (2002b), 66.)

at a temperature of 800 °C. X-ray analysis of the cell parameters, neutron diffraction to analyze both the crystal and magnetic structures, ^{57}Fe Mössbauer spectroscopy studies, and KKR-CPA electronic structure calculations were undertaken (Tobola *et al*., 2001). All results were in fair agreement

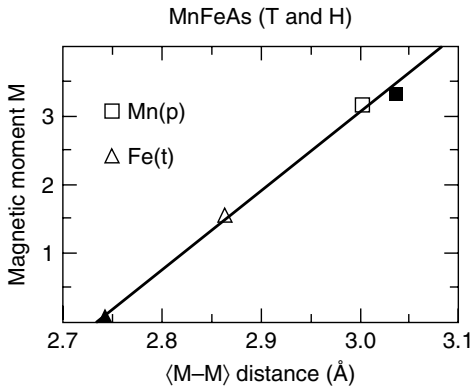

Figure 11. Experimental magnetic moments of Fe (triangle) and Mn (square) in tetragonal (T2-filled symbols) and hexagonal (H3-empty symbols) structures of MnFeAs. (Tobola, J., *et al*. *Journal of Alloys and Compounds*, 317–318, (2001), 279.)

with the fact that the Mn magnetic moment (pyramidal site) was weakly reduced from T2 to H3 type, but, for Fe (tetrahedral site), it was almost zero as T2 was comprised between 1.1 and 1.54 μ_B, respectively, deduced from the calculations and the experiments. This supports well the specific instable character of the magnetic moment of Fe sitting in the tetrahedral site of the TT′X compounds similar to $MnRhAs_{1-x}P_x$ in the H3 range of compositions. Figure 11 represents the position of the Mn and Fe magnetic moment versus the mean metal–metal distance.

Niziol *et al*. have primarily studied the $(Co_{1-x}Mn_x)_2P$ system ($x = 0.6$ and 0.75), namely, using ac susceptibility measurement under external pressure (Niziol *et al*., 1993). The metastable character of the ferromagnetic state with reference to the low-temperature incommensurate AF structure was correlated with a magnetovolume effect. The results led to the proposition of a localized/delocalized picture of magnetism.

In the past, the tetragonal compound Mn_2Sb (T2 type) has got attention for its ferrimagnetic characteristics up to relatively high temperature, as reported in Beckman and Lundgren (1991). Under external pressure and using neutron diffraction, the ferri-antiferromagnetic transition initiated when applying pressure for many of the parent-substituted compounds was not evidenced in pure Mn_2Sb (Ryzhkovskii *et al*., 2002). Under a pressure of 2.8 GPa, the pure binary antimonide is only characterized by a spin reorientation phenomenon. Besides, it was shown earlier on a parent system (Val'kov and Khapalyuk, 1997) that cycles of thermal treatments applied on substituted $Fe_{0.5}Mn_{1.1}As$ (T2 type) allowed to suppress the low-temperature phase down to 77 K, the material still being ferromagnetic, contrary to the sample prepared in a conventional way.

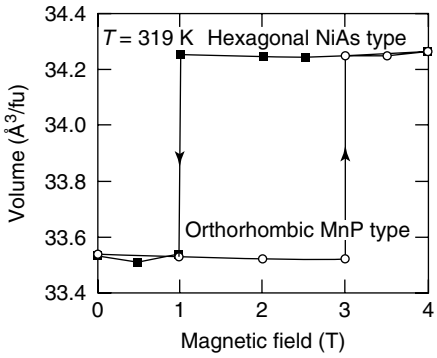

Figure 12. Field dependence of the lattice volume/fu for MnAs. (○) and (■) indicate the volume in increasing and decreasing fields, respectively. (Ishikawa, F., *et al*. *Journal of Applied Physics*, **42**, (2003), L 920.)

In terms of field-induced structural and magnetic transformations, the monopnictide series provides a very interesting result with MnAs (Ishikawa, Koyama, Watanabe and Wada, 2003; Ishikawa, Koyama and Watanabe, 2004). From both magnetization measurements and X-ray diffraction performed under a magnetic field, a metamagnetic transition from paramagnetic to ferromagnetic state was induced above T_C. From the X-ray profile analysis, the forced magnetic state was stabilized at ∼3.5 T, and the first-order crystalline and magnetic transition was deduced from a particularly squared hysteresis loop, as reported in Figure 12.

4 MAGNETOCALORIC PROPERTIES OF THE TT′X AND TX SERIES

4.1 Thermodynamics of magnetocaloric materials

In order to understand the physical origin of the MCE, it is useful to recall briefly the thermodynamic properties of a magnetic material plunged in a magnetic field B. Under constant pressure, the full entropy is given by

$$S(T, B) = S_{\text{lat}}(T) + S_{\text{e}}(T) + S_{\text{m}}(T, B) \tag{1}$$

where S_{lat}, S_{e}, and S_{m} represent respectively the lattice entropy, the electronic entropy, and the magnetic entropy. The MCE can be related to the magnetic properties of the material through the thermodynamic Maxwell's equation

$$\left(\frac{\partial S}{\partial B}\right)_T = \left(\frac{\partial M}{\partial T}\right)_B \tag{2}$$

According to the magnetization measurements versus temperature and applied magnetic field, the magnetic-entropy change of a material can be calculated using this relation as

$$\Delta S_{\text{m}}(T, 0 \rightarrow B) = \int_0^B \left(\frac{\partial M}{\partial T}\right)_{B'} \mathrm{d}B' \tag{3}$$

Considering the temperature variation $M(T)$ and equation (3), it is concluded that a homogeneous magnetic material having a definite magnetic phase transition temperature is not suitable for use as the refrigerant because $(\partial M/\partial T)$ varies considerably with temperature change near T_C and, as a result, entropy change is maximum accordingly.

Using magnetization measurement made at discrete temperature intervals and by numerical integration of equation (3), ΔS_{m} can be approximated as

$$\Delta S_{\text{m}} = \sum_i \frac{M_{i+1} - M_i}{T_{i+1} - T_i} \Delta B_i \tag{4}$$

where M_{i+1} and M_i are the magnetization values measured in a field B, at temperature T_{i+1} and T_i respectively.

In the classical mean-field theory, the relative magnetization is given by

$$\sigma = B_j(y) = \frac{2j+1}{2j} \coth\left(\frac{2j+1}{2j} y\right) - \frac{1}{2j} \coth\left(\frac{1}{2j} y\right) \tag{5}$$

where B_j is the Brillouin function and j is the total angular momentum. The argument y is the solution to the simultaneous equations

$$\sigma = B_j(y)$$

$$y = \frac{1}{T}\left[3T_C\left(\frac{j}{j+1}\right)\sigma + \frac{g\mu_B j}{k} B\right] \tag{6}$$

where k is the Boltzmann constant, g the Landé factor, and μ_B the Bohr magneton.

According to principles of magnetism, the magnetic entropy is derived from

$$S_{\text{m}} = R\left[\ln\left(\frac{\sinh\left(\frac{2j+1}{2j} y\right)}{\sinh\left(\frac{y}{2j}\right)}\right) - y B_j(y)\right] \tag{7}$$

where R is the universal gas constant, and the changes of magnetic entropy caused by a variation of magnetic field $\Delta B = B_f - B_i$ are given by

$$\Delta S_{\text{m}}(T, \Delta B = B_f - B_i) = S_{\text{m}}(T, B_f) - S_{\text{m}}(T, B_i) \tag{8}$$

For deeper analyses, one can refer, for example, to the analytical model developed by von Ranke *et al*. (2005) to

understand the colossal MCE, or, more extensively, to the recent book by Tishin and Spichkin (2003).

From the preceding considerations, it can be expected that the best magnetocaloric materials in terms of application for refrigeration close to RT must undergo first-order-like magnetic transition that is easy to handle under rather low magnetic fields (e.g., 1–2 T), with a limited hysteresis effect to be effectively activated reversibly, with a high density of atom magnetization. Transition-metal-rich magnetic materials, such as the T-pnictides, herein reviewed can fulfill these specifications, since they often exhibit tunable both lattice and ferromagnetic characteristics, along with being good thermal conductors and being formed with rather inexpensive elements.

Reports with more technical details and systems are available in more specific papers such as (Lebouc, Allab, Fournier and Yonnet, 2005).

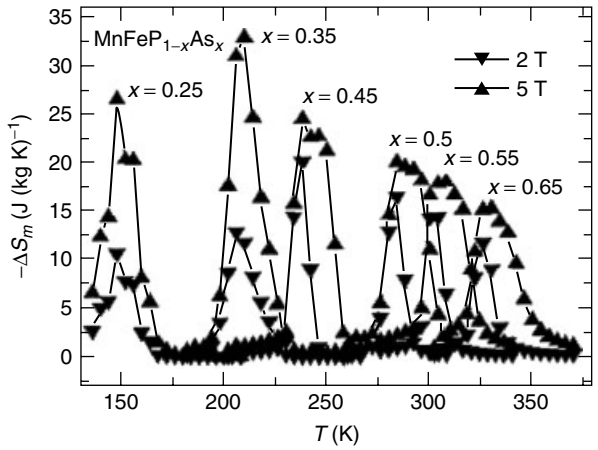

Figure 13. Magnetic-entropy change for different compounds of the $MnFeP_{1-x}As_x$ system for applied field change of 2 and 5 T. (Brück, E., *et al*. *Journal of Alloys and Compounds*, **383**, (2004), 34.)

4.2 Magnetocaloric properties in the TT′X series

Up to 2002, the best promising magnetocaloric material close to RT belonged to the series deriving from the $Gd_5(Si_{1-x}Ge_x)_2$-type compounds (Pecharsky and Gschneidner, 1997).

The $MnFeP_{1-x}As_x$ series was revealed by Tegus, Brück, Buschow, and de Boer (2002) as a performing MCE challenger of the gadolinium intermetallics in terms of effectiveness, also with reference to the cost of elements. Tunability of their MCE characteristics in interesting temperature ranges for application was demonstrated soon after by the same group when selecting different compositions by substitution of As to P (Tegus, Brück, de Boer and Buschow, 2002) or of Mn to Fe (Brück *et al*., 2003; Tegus, 2003). Interestingly, high values of magnetic-entropy changes for different compounds of the $MnFeP_{1-x}As_x$ series were measured up to $-\Delta S_m \sim 35\,J\,kg^{-1}\,K^{-1}$, in rather moderate applied magnetic field, the temperature of activation ranging from ∼150 to 350 K, as shown in Figure 13. However, the best performances remained a little far from RT, better results were recorded close to RT when a moderate part of Ge to As was substituted, thus forming $MnFeP_{0.5}As_{0.5-x}Ge_x$ with a smaller c/a ratio of the hexagonal cell parameter (Brück *et al*., 2004). This point proved to be of importance for the corresponding increase in the corresponding so-called *Curie temperature* 'T_C' and amplitude of the magnetoelastic effect at transition. Further, the maximal magnetic-entropy change was derived from little more complicated formulas such as $Mn_{1.1}Fe_{0.9}P_{0.7}As_{0.3-x}Ge_x$ (Tegus *et al*., 2005a). A more overall analysis of the properties of the MnFeX series was established first by E. Brück *et al*. (Brück *et al*., 2004; Brück, Ilyn, Tishin and Tegus, 2005). Complementary to these specific papers, reports were made on the same series of TT′X materials (Fruchart *et al*., 2005). This particularly concerns systems exhibiting sensitive magnetic properties with magnetoelastic transitions $(Mn_{1-x}Co_x)_2P$, $Fe(Fe_{1-x}M_x)P$, MnRhAs, as well as MnAs.

Besides, a model description of the first-order phase transition in $MnFeP_{1-x}As_x$ was built by the same group (Tegus *et al*., 2005b), based on the Bean–Rodbell model. Another type of approach was proposed a little earlier (von Ranke *et al*., 2004) based on the Landau theory as well as in (Zach, Guillot and Tobola, 1998; Zach *et al*., 1997) to derive the conditions of a first-order transition and then to evaluate ΔS_m and ΔS_{lat}, the magnetic and lattice contribution to change in entropy. All the results appear to fit correctly with the experimental data (Tegus *et al*., 2005b; von Ranke *et al*., 2004; Zach, 1997; Zach, Guillot and Tobola, 1998). However, the electronic part of entropy change at transition ΔS_e was not accounted for.

4.3 Magnetocaloric properties in the TX series

The discovery of giant MCE in $MnAs_{1-x}Sb_x$ samples was made by Wada and coworkers and was reported in 2001–2002. This was a major step in the utilization of T-intermetallics as magnetic refrigerant materials (Wada and Tanabe, 2001; Wada, Taniguchi and Tanabe, 2002). The magnetic-entropy change was rapidly fixed up to $-\Delta S_m \sim 30\,J\,kg^{-1}\,K$ for $x \sim 0.3$ (Wada *et al*., 2003). These were unusual characteristics in the vicinity of the first-order phase transition between the ferromagnetic low-temperature NiAs-type structure and the nonmagnetic MnP-type structure, as illustrated in Figures 2 and 14. Substitution of Sb to As

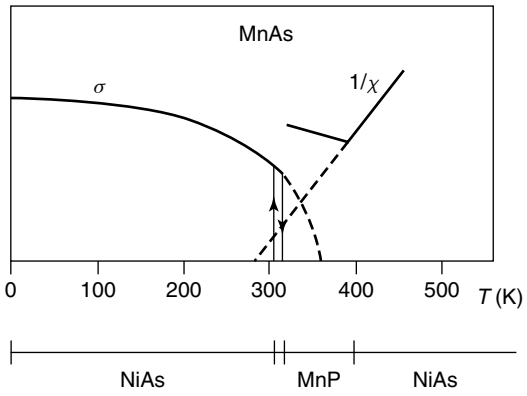

Figure 14. Magnetization and inverse susceptibility of MnAs showing the temperature region of different NiAs and MnP crystal structures. (*Handbook of Magnetic Materials*, Buschow (Ed.), Vol. 6, Beckman, O. and Lundgren, L. p. 204.)

appeared interesting since this decreases the transition temperature, with a reduction of the strong hysteresis effect related to the very abrupt character of the first-order transition of MnAs. A theoretical analysis of the giant MCE in $MnAs_{1-x}Sb_x$ compounds, based on the Landau theory of phase transition, using a Bean–Rodbell-type model, the critical dependence of the transition temperature first versus second order was deduced and also the temperature dependence of ΔS_m was derived in a fair agreement with experience (von Ranke *et al*., 2004). Then a composite system was anticipated for an optimal design and process to work in an Erickson mode near RT.

The parallel effect of deviation from stoichiometry of $MnAs_{1-x}Sb_x$ materials was analyzed on the magnetic and MCE properties, and excess iron content was related to some decrease in the optimal magnetization level (Morikawa and Wada, 2004). Interstitial iron resulting from excess composition was proposed as the parameter controlling the 'T_C' well, the nature (order) of the phase transition, the amplitude of the hysteresis at transition, and finally the force of the MCE, in relation to the increase in the c/a cell parameter ratio. Because of a certain lack of miscibility with Sb additions, the single-phase region was ascribed to compositions $Mn_{1+\delta}As_{1-x}Sb_x$ with δ ranging from 0.05 to 0.11 (Morikawa, Wada, Kogure and Hirosawa, 2004). Then a specific heat treatment determined to get the best composition and element distribution, parallel to the high value of $-\Delta S_m \sim 34\,J\,kg^{-1}\,K$ field ranging in (0–5 T), and a Clausius–Clapeyron analysis (first-order transition) was demonstrated to fit fairly well to the estimate of $-\Delta S_m$ plotted versus T built according to the Maxwell relation (Wada and Asano, 2005). A further analysis of the heat treatment process was made more recently, thus allowing to determine the condition for homogeneous materials with sharp transition (Wada, Funaba and Asano, 2006), when quenching the $Mn_{1+\delta}As_{1-x}Sb_x$ samples directly from the melt instead of slow cooling down as done earlier. Besides, using a high-pressure resistive furnace (5.5 MPa applied during synthesis), high quality MnAs samples were prepared (Nascimento *et al*., 2006), thus exhibiting high variation of entropy well, up to $-\Delta S_m \sim 47\,J\,kg^{-1}\,K$ for 0–5 T applied field.

Application of external pressure on MnAs was experienced, leading to colossal MCE levels, the change in entropy at transition exceeding $-\Delta S_m \sim 260\,J\,kg^{-1}\,K$ from 0 to 5 T under 0.223 GPa as shown on Figure 15, effectively more than six times stronger than without application of pressure (Gama *et al*., 2004). From such experiments and analysis, the authors have concluded that, if generally admitted, the assumption of field independence of Δ_l and Δ_e is certainly not valid. Similar pressure experiences were undertaken on well-known $Gd_5Si_2Ge_2$-type compounds by the same group (Magnus *et al*., 2005), with a reverse behavior for the entropy variation in spite of preserving the magnetization level, even increasing the transition temperature. A complete model allowing the description of the colossal entropy variation of MCE material was developed and specifically applied to MnAs (von Ranke *et al*., 2006). It includes the exchange interactions (β-parameter), the magnetoelastic contributions (η-parameter), the external pressure effects (via the Grünesein relation, γ-parameter), the magnetic field dependence of the lattice entropy, but neglecting the electronic contribution. By adjusting the phenomenological parameters β, γ, η to experimental results, the model allows to determine the temperature dependence without and under applied field of the total entropy Δ_T. However, the authors consider that if the model does not reproduce exactly the shape of the ΔT traces versus temperature and pressure, the fair agreement in

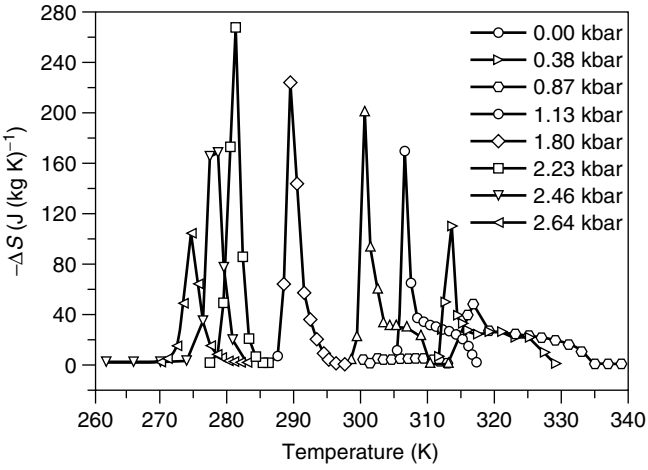

Figure 15. The MCE of MnAs as a function of temperature and pressure. (Gama, S., *et al*. PRL 93, 237202 (2004) p. 3.)

amplitude value leads to ascribe the colossal MCE effect to marked increase in the lattice entropy under pressure. Theoretical analyses of the fundamental behavior and of the (T, H, P) phase diagram of MnAs have been made parallel to the experimentations of the S. Gama's group by de Oliveira (2004) and Nascimento *et al*. (2006).

4.4 Magnetocaloric properties in another series of pnictides

Another series of intermetallic compounds also reveals interesting features in terms of sensitivity to temperature, magnetic field, pressure, chemical composition. . . ferromagnetic phases, with first- or second-order magnetoelastic coupled transitions, as, for example, related to Mn_3GaC, $LaSi_{13-x}Si_x$, $Ce(Fe_{1-x}Co_x)_2$, MnTGe, $MnCoSi_{1-x}Ge_x$. . . all different type compounds. Also, in the series of transition-metal compounds, other families were checked for, as part of an extended list, for example, $Mn_5Ge_{3-x}Sb_x$ (Songlin *et al*., 2002a), $Mn_{5-x}FeSi_xSi_3$ (Songlin *et al*., 2002b), NdP and NdAs (Plaza *et al*., 2004). . . with medium to rather high variations of magnetic entropy at transition. However, the reference book by Tishin and Spichkin (2003) exposes deeply the basic concepts and displays unique sets of data on all of the known systems exhibiting MCE properties. A comparative review of the main characteristics of the most promising MCE alloys and compounds has been reported more recently by Brück (2005).

Other types of materials are interesting to consider in terms of potentially high ferromagnetic but switchable properties, for example, the ternary iron germanium pnictides (X = P, As, Sb) where, apart from MnP and NiAs-type compounds, the systems reveal rich ferromagnetic but switchable properties with different types of structures (Mills and Mar, 2000).

5 CONCLUSION

Two main series of transition-metal-rich pnictides, TT′X and TX, reveal a wide panel of various magnetic properties, but critical situations are confronted owing to strong magnetoelastic couplings associating crystal structure peculiarities and instabilities of magnetic configurations. These series prove to be very attractive with the recent evidence of a marked magnetocaloric character to the many existing transitions. Presently, the renewed interest in the TT′X and TX pnictides covers large fields from fundamental analyses to performances of materials and systems. In fact, the need of alternative solutions to solve the double problem of energy and of environment preservation promotes more research efforts, for example, for room-temperature refrigeration and air conditioning. Anyway, it is worth noting that, exactly 40 years ago, early but determining fundamental characterizations devoted to the just-discovered series of transition-metal pnictides were thus achieved (Goodenough and Kafalas, 1967). This made a milestone lecture of very unusual physical properties versus temperature, magnetic field, and pressure, exhibited by the herein discussed series. The need for a deeper but detailed knowledge led to renewed investigations on magnetic pnictides to better understand the various but interdependent overall contributions to MCE.

6 CHALCOGENIDES

The following part of the chapter is a short review of the knowledge of magnetic chalcogenides compounds. We limit the field of this review to the really new and unusual properties of compounds. The most important event in magnetic compounds is the new interest on the diluted ferromagnetic semiconductors (DMSs) compounds that should be the basic materials for a new kind of electronic components: the 'spintronic' components, in which information is carried by the spins of charge carriers. The first compound family is a zinc-blende compound family in which the metal can be substituted by a magnetic ion. These materials are intensively studied for their epitaxial compatibility with the more classical semiconductors such as GaAs or Si. In complement, the half-metallic ferromagnetic compounds can help to create a basic set of spintronic materials.

After a brief presentation on some layered ferromagnetic compounds and on a 'new class of alkali metal–transition metal chalcogenides', we present recently studied rare-earth and copper chalcogenides that exhibit some structural similarity with high T_C superconductor structures. We finish our discussion of magnetic chalcogenides with two studies on magnetic actinide (essentially uranium) compounds that always constitute an important research activity.

7 NEW MATERIALS FOR SPINTRONICS

Experimental studies on Fe/Cr multilayers (Baibich *et al*., 1988) have made it obvious that the spin drives the conductivity in these structures and led to a new solid state physic concept: spin-based electronic, so-called spintronic, is presently the subject of intensive developments in the world. The first applications, for the magnetic hard disk reading heads, use the giant magnetoresistance (GMR) and tunneling magnetoresistance (TMR) (Barthélémy, Fert and Petroff, 1999; Tsymbal, Mryasov and LeClair, 2003) allowing the actual data storage capacities being reached.

The actual spintronic challenge is now to find convenient materials to construct a real spin-based electronic device in parallel with the conventional ones based on IV, III–V, and II–VI semiconductors. For this purpose, both ferromagnetic semiconductors and half-metallic ferromagnetic compounds are explored.

7.1 The diluted ferromagnetic semiconductors (DMS)

This materials class is derived from the classical semiconductors III–V and II–VI with zinc-blende or wurtzite crystallographic structure. The ferromagnetism is obtained with a partial substitution of the cations by magnetic ions as 3d or 4f metal where the ferromagnetic interaction will be mediated by the holes (Dietl, Haury and Merle d'Aubigné, 1997; Dietl, Ohno and Matsukura, 2001). These material series constitute the diluted magnetic compounds, called *DMS*.

The most relevant feature of DMS, which attracted considerable interest, is the coexistence and interaction of two different electronic subsystems: unlocalized conduction (s type) and valence (p type) band electrons and localized (d or f type) electrons of magnetic ions. In particular the s, p–d exchange interaction leads to strong band splittings, which result in giant magneto-optical effects (Chang and Xia, 2002). On the other hand, the randomly distributed magnetic ions with the d–d exchange interaction can induce formation of antiferromagnetic or spin-glass phases instead of the ferromagnetic one, depending on the magnetic ion concentration and temperature (de Jonge and Swagten, 1991; Twardowski, 1995).

After about three decades of investigation, many devices were synthesized by molecular-beam epitaxy (MBE) technology for DMS growth with various magnetic ions (like Mn, Fe, Co, and recently Cr). Figure 16 displays computed ferromagnetic ordering temperatures (Dietl, Haury and Merle d'Aubigné, 1997) and evidences a possibility to reach room-temperature ferromagnetism for some compounds. This prediction was confirmed by the observed ordering temperature of (Ga,Mn)As that has reached 100 K on one hand (Ohno *et al*., 1996) and, on the other hand, the recent studies starting from the ZnO thin films present some ferromagnetic properties at room temperature (Yan, Ong and Rao, 2004; Shi-Shen e*t al*., 2004) as displayed in Figure 17. Table 1, displays some recent experimental results collected by Hebard *et al*. (2004). It includes the results for the (Ga,Mn)As sample (Ohno *et al*., 1996).

Hebard *et al*. (2004), in their paper, discuss the meaning of high T_C ferromagnetism in DMS and make clear the various disturbing effects during the sample synthesis and their consequences on the final apparent properties.

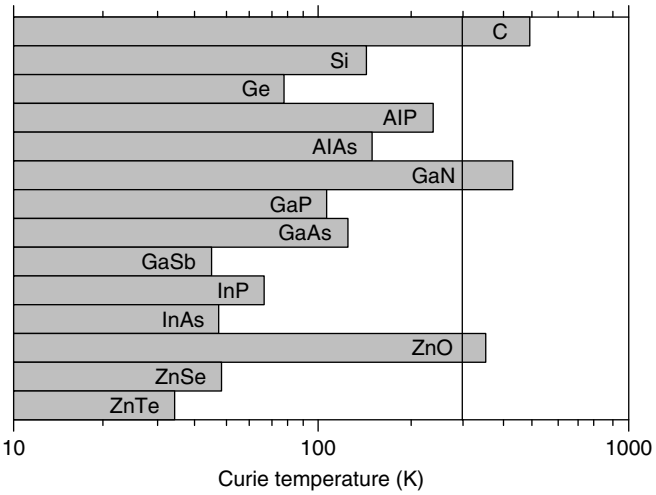

Figure 16. Computed values of the Curie temperatures T_C for various p-type IV, III–V, and II–VI semiconductors containing 5% of Mn by cation and 3.5×1020 holes/cm^3. (After Dietl, T. *et al*., 2001 and Dietl, T., 2002.)

The electronic structure of these compounds was intensively studied by several authors with various methods. Two recent papers (Sanyal, Bengone and Mirbt, 2003; Erikson *et al*., 2004) present a fine analysis of the electronic structure of these compounds. In the first step, starting from self-consistent electronic structure calculation, including a collinear spin arrangement, an electronic structure is determined. Then, the deduced exchange interactions are used in Monte Carlo simulations to take into account the statistical mechanics part of the problem. The results for several representative groups III–V and II–VI DMSs are found to agree nicely with the experimental data particularly for the ordering temperatures.

As pointed out by many authors in recent studies of these materials, it is difficult to get reproducible results which are very sensitive to the methods (MBE, pulsed-laser deposition, metallo organic chemical vapour deposition, etc.) and conditions of compound film elaboration. It seems that it is rather difficult to obtain homogeneous distributions of the magnetic cations in the sample and, the observed Curie temperature is often markedly lower than the predicted one. Finally, the semiconductor properties are depending of the nature and the magnetic ions concentration which affect the strength of exchange interactions that stabilize the ferromagnetic state.

In conclusion, it seems, these semiconductors are actually difficult to use for electronic application so that a very important characteristic of these compounds is the possibility to insert them in devices using standard III–V or II–VI semiconductors. In addition, as known from Tomasz Dietl: 'With no doubt, search for functional ferromagnetic semiconductor

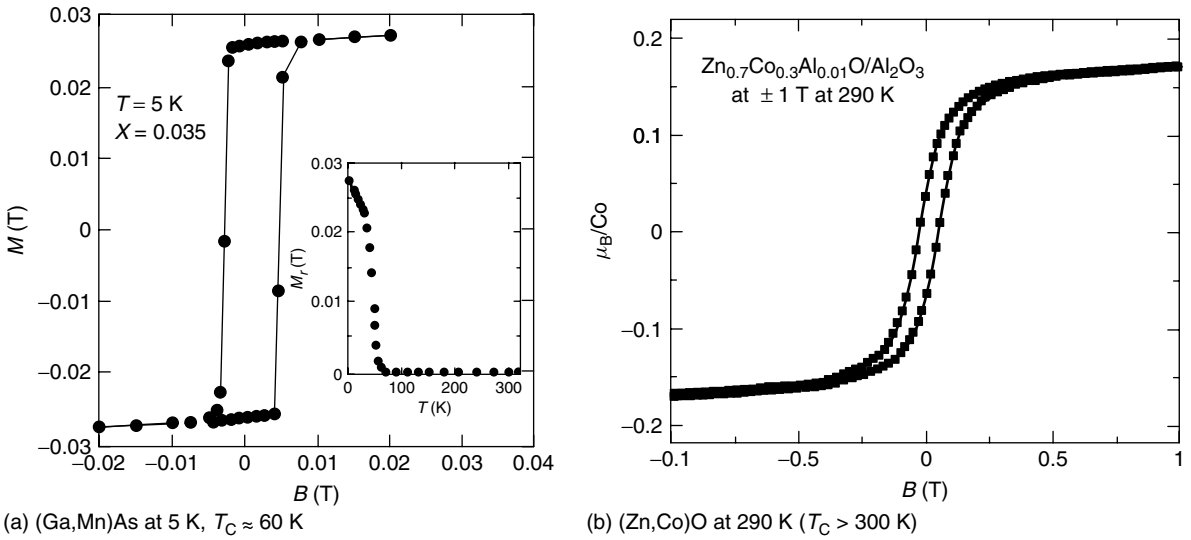

Figure 17. Two Hysteresis cycles for (a) (Ga,Mn)As and (b) (Zn,Co)O films. (After (a) Ohno *et al*., 1996 and (b) Yan *et al*., 2004.)

Table 1. Experimental results on some diluted magnetic semiconductors $A_xM_{1-x}B$ samples as collected by Hebard *et al*. (2004), except for GaAs line that was given by Ohno *et al*. (1996). T_C denotes, the observed Curie temperature by field (H_a) cooling and H_{co} is the coercitive field as observed at the temperature T_o.

Host material	Carrier concentration (cm^{-3})	Magnetic ion	T_C (K)/H_a (Oe)	H_{co} (Oe)/T_o (K)
GaAs	p type, 7.7×10^{20}	3.5% Mn	60/NA	50/5
GaP:C	p type, 1×10^{20}	3% Mn	330/500	50/300
		5% Mn	40/500	NA
GaP	n type, 1×10^{16}	3% Mn	60/1000	NA
GaN:Mg	p type, 3×10^{17}	3% Mn	250/100	25/100
		3% Fe	250/500	100/10
		5% Fe	<200/500	125/10
		3% Ni	200/500	NA
		5% Ni	40/500	NA
SiC:Al	p type, 1×10^{17}	5% Fe	250/500	50/10
		5% Mn	250/500	150/10

nanostructures and their theoretical modeling have evolved into an important branch of today's materials science and condensed matter physics.'

7.2 The half-metallic ferromagnetic compounds

Half-metallic ferromagnets (HMFs) are metals having 100% spin-polarized electrons at the Fermi level. The high Curie temperature and very small lattice mismatch with widely employed semiconductors are the useful features that are suitable for spintronic applications.

Some Heusler compounds, like NiMnSb, PtMnSb, PdMnSb, or PtMnSn, were found to possess this necessary combination of properties with a ground state (de Groot, Mueller, van Engen and Bushow, 1983) characterized by a 100% spin polarization of charge carriers.

Recently, Akinaga and coworkers (Akinaga, Manago and Shirai, 2000) have grown a new zinc-blende phase of CrAs. The epitaxial growth was performed by MBE on a GaAs substrate. This zinc-blende CrAs layer was identified as a room-temperature ferromagnet (Figure 18). Studies by several authors seem to indicate that this metastable zinc-blende structure is possible for thin layers

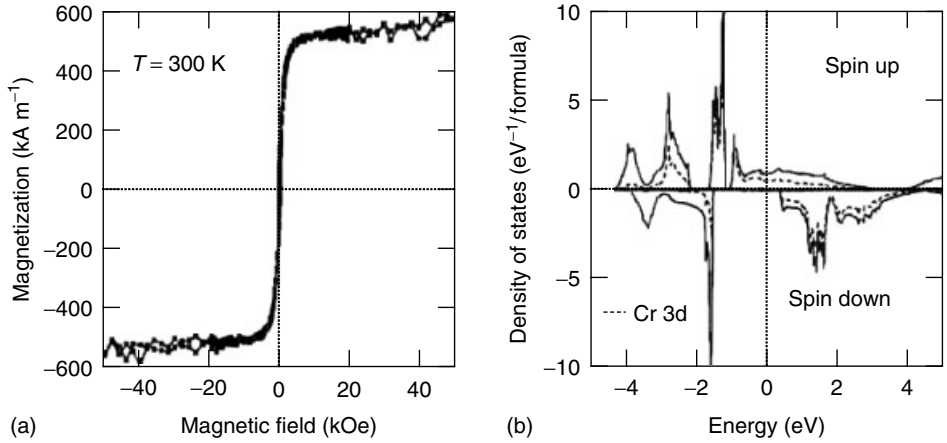

Figure 18. Film of zinc-blende film zb-CrAs/GaAs: Magnetization hysteresis loop at 300 K with applied magnetic field in the film plane (a), and density of states (DOS) where the broken lines denotes the Cr 3d component. The vertical dotted line denotes the Fermi energy (b) (Akinaga *et al*., 2000).

of other similar compounds such as VAs, CrAs, CrSb, MnAs (Kübler, 2003 and their referenced papers). The zinc-blende HMFs would exhibit a high Curie temperature of the same order as the Heusler HMF NiMnSb with $T_C = 701$ K (Kübler, 2003). As for DMS compounds previously described, the main interest of these zinc-blende HMFs is their ability to form thin films (few nanometers) by epitaxy on the traditional III–V and II–VI semiconductors which is combined with their high Curie temperatures.

These half-metallic ferromagnetic compounds should be difficult to use because there are basically instable phases that can be stabilized only by the constraints of substrate with the zinc-blende structure. This fact can make the design of future spintronic devices complicated and therefore, to date, it is difficult to evaluate their future impact on applications.

8 TRANSITION-METAL CHALCOGENIDES

8.1 Magnetic properties of the lamellar compound $Cr_2Ge_2Te_6$

$Cr_2Ge_2Te_6$ is a recently studied layered material belonging to the lamellar ternary $M_2X_2Te_6$ chalcogenides family (where M is a +3 oxidation state metal such as V, Mn, Fe, Co, Ni, Zn, Cd, or Hg and X_2 a silicon or a germanium pair). The crystallographic structures of these compounds can be described as hexagonal compact stackings of Te atoms in which M atoms and the X_2 pair occupy octahedrons in the different layers. The different layers are attached by empty slabs, so-called van der Walls gap. As some other compound family member, $Cr_2Ge_2Te_6$ exhibits a ferromagnetic state at low temperature with a Curie point of 61 K that is significantly higher than for other compounds as $Cr_2Si_2Te_6$ ($T_C = 32$ K) (Carteaux, Brunet, Ouvrard and André, 1995).

8.2 New class of alkali metal–transition metal chalcogenides

The chalcogenides $A_xM_yX_z$ (A = alkali metal, M = transition metal, X = S, Se, or Te) crystallize in structures that, depending upon the stoichiometry, contain isolated groups, dimers, chains, or layers, where the anionic building units M_yX_{zx} are formed by linkage of the $[MX_4]$ tetrahedrons via their edges. The particularity of this study is the use of magnetic properties as an indication of transition between separated or linked together building units (Bronger and Müller, 1997). When the building units are linked together, the compound exhibit some antiferromagnetic orderings while in the other case the paramagnetic susceptibilities are exhibited (Bronger and Müller, 1997).

9 R(4f), X COMPOUNDS

The ternary R–T–X (R = rare earth, T = transition metal, X = chalcogen) including rare-earth and transition-metal (3d or 4d) elements form a very wide space of formulas that exhibit a large panel of physical properties. To illustrate a typical series of compounds, we briefly present the properties of rare-earth with copper chalcogenides.

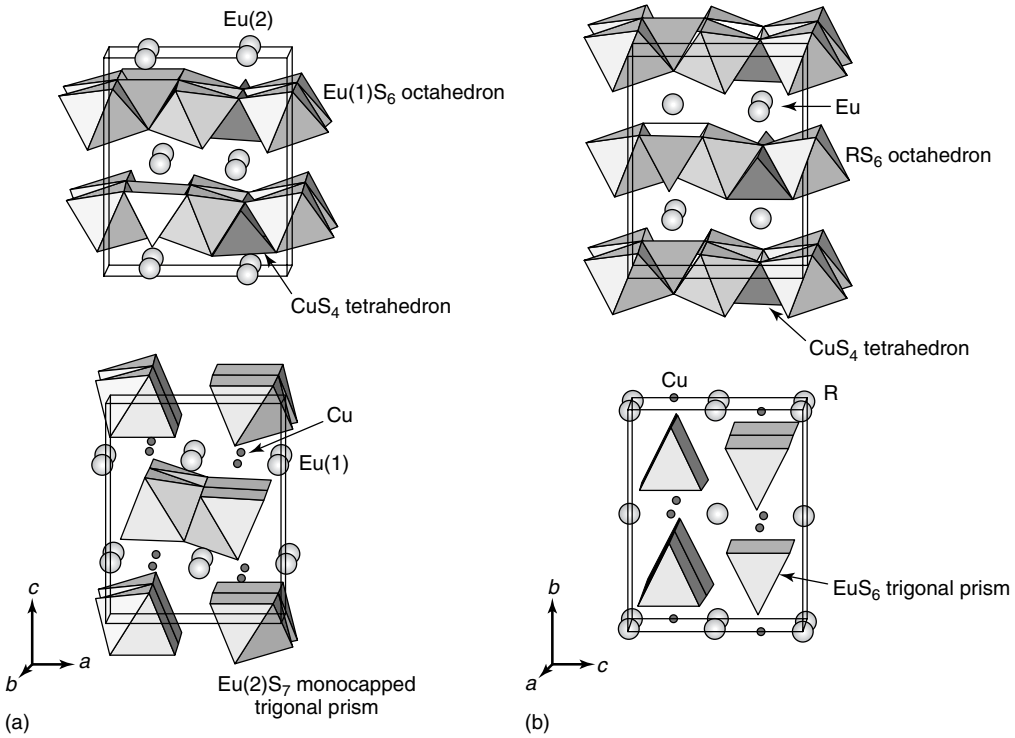

Figure 19. Polyhedral representations of the two types of structures: $EuRCuS_3$ crystallize in the Eu_2CuS_3 (a) except for R = Tm, Yb, and Lu where the type structure is $KZrCuS_3$ (b).

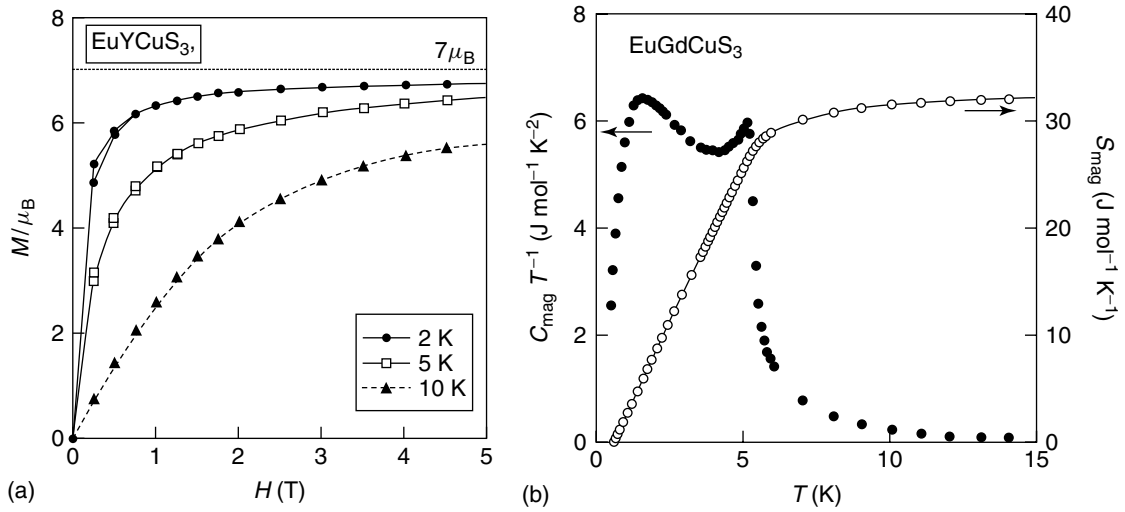

Figure 20. Magnetization curves of (a) $EuYCuS_3$ and (b) $EuGdCuS_3$.

9.1 The $EuRCuS_3$(R = Y, Gd–Lu) compound series

The $EuRCuS_3$ (R = Y, Gd–Lu) compounds series (Wakeshima, Furuuchi and Hinatsu, 2004) is derived from europium sulfide Eu_2CuS_3 (space group *Pnma*) (Lemoine, Carré and Guittard, 1986) in which the Eu^{3+} cations (not magnetic at ground state) are replaced by other rare-earth atoms while the magnetic Eu^{2+} are kept. These substitutions do not change the crystallographic structure except for the smallest atoms, R = Tm, Yb, and Lu, for which the structural type is $KZrCuS_3$ (space group *Bbmm*) that is a supergroup of *Pnma*. The structure of these compounds can be displayed as stack of layers of CuS_4 tetrahedrons and RS_6 octahedrons spaced

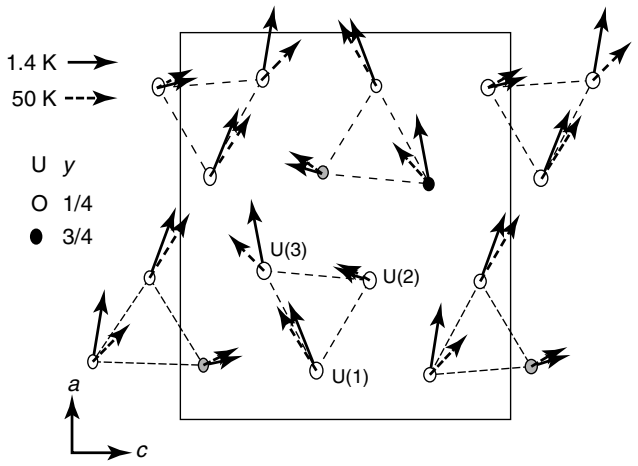

Figure 21. Superposition of the magnetic structures of U_3Te_5 at 1.4 and 50 K in the (a, c) projection plane.

by Eu planes (Figure 19). These systems of layers can be considered as close to high-T_C superconductor compounds with the substitution of oxygen by the sulfur atoms.

These compounds exhibit ferromagnetic behavior for R = Y or Lu (nonmagnetic rare-earth atoms) and ferrimagnetic ones for the magnetic rare-earth atoms. The ordering temperature is close to 5 K for all compounds. The susceptibility, magnetization (Figure 20a) and specific heat (C_p) measurements on the Y and Lu compounds reveal that the ferromagnetic ordering is induced only by the Eu^{2+} (in the eightfold degeneracy ground state). In Figure 20 the magnetization curves for $EuYCuS_3$ and $EuGdCuS_3$ show the contribution of the gadolinium atom as equal to that the europium atoms. This is consistent with the same state $4^8S_{7/2}$ for both atoms and for all these compounds the magnetic moments are close to the classical ionic values if we take in account the crystal-field anisotropy for an isotropic powder sample.

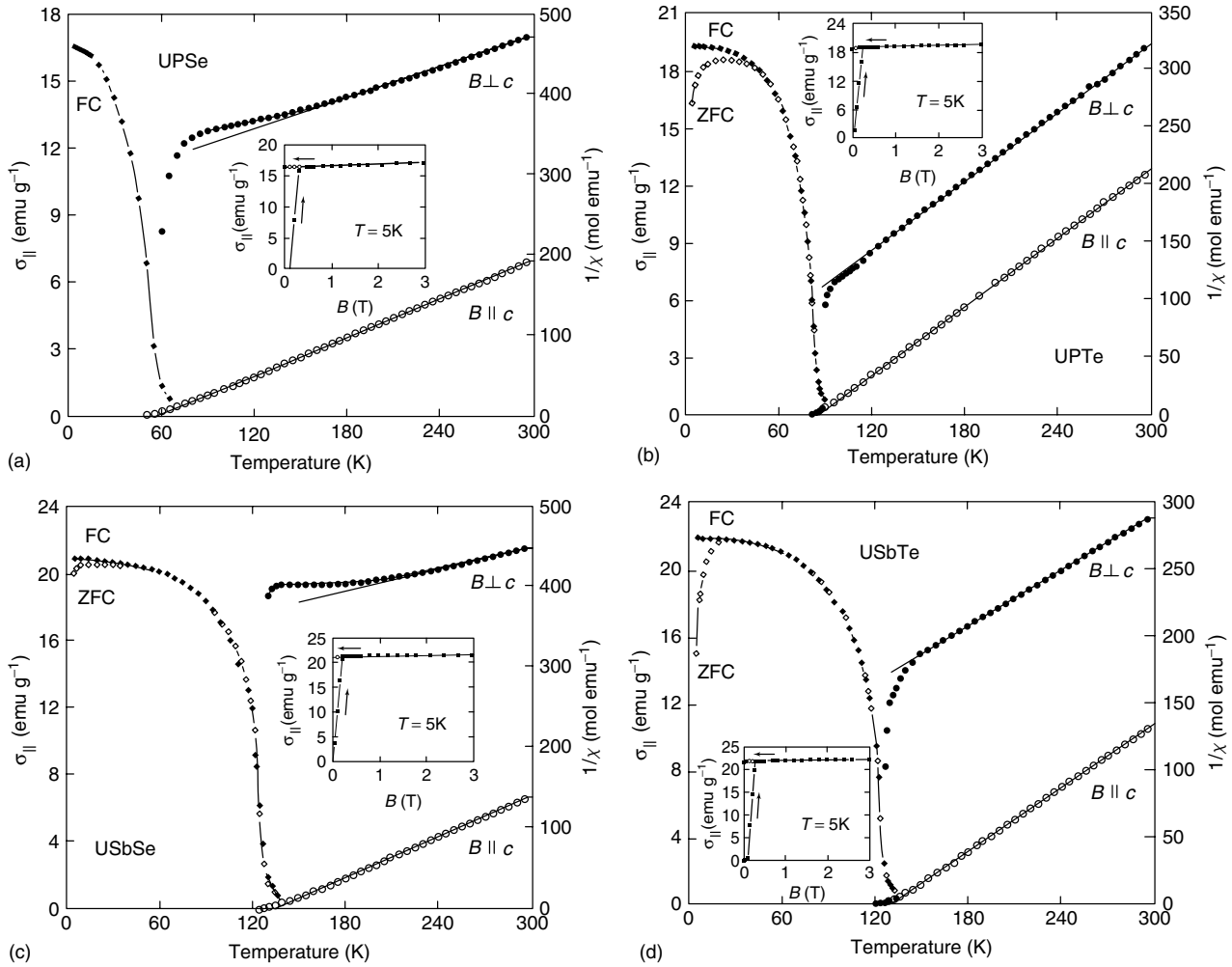

Figure 22. Spontaneous magnetizations and reciprocal of magnetic susceptibility versus the temperature for single crystals of (a) UPSe, (b) UPTe, (c) USbSe, and (d) UsbTe. The magnetic susceptibility was measured in parallel and perpendicularly of c axis that is the spontaneous magnetization direction.

10 Ac(5f), X COMPOUNDS

Actually, the chalcogenides including uranium (and also some other actinides, particularly thorium) form a significant part of the recent metal chalcogenides studies. Here, we briefly describe some typical studies of magnetic uranium chalcogenides: U_3Te_5, U_2Te_3. Moreover the compounds of formula UXY (X = chalcogen, Y = P, As, or Sb) form an other family which displays particularly high anisotropy of uraniums compounds, even in the paramagnetic state.

U_3Te_5, U_2Te_3

As detailed in the previous reference, the U_3Te_5 compounds crystallize in the orthorhombic space group *Pnma* with three uranium nonequivalent atom sites U(1), U(2), U(3). Their respective magnetic moments lie in the $a-c$ plane with a F_xC_z-type structure, with different magnetic moments for U(1), U(2), U(3). A spin reorientation toward the c direction occurs around $T = 45$ K. Both magnetic structures are displayed in Figure 21 (Tougait, André, Bourée and Noel, 2001).

Neutron diffraction data for U_2Te_3 (*Pnmn* space group) are consistent with an antiferromagnetic not collinear G_xA_z-type structure. The magnetic moments of uranium atoms in both crystallographic sites U(1) and U(2) are in the $a-c$ plane with different magnitudes. A slight spin reorientation on the U(2) site occurs also around $T = 45$ K. Close to the ordering temperature ($T = 95$ K, $T_N = 95$ K), some small neutron diffraction lines indicate a complex magnetic structure.

In both compounds, these results are correlated with the macroscopic magnetic measurements.

10.1 UXY compounds

The compounds UPSe, UPTe, USbSe, and USbTe are ferromagnetic with the ordering temperature of $T_C = 55$, 85, 128, and 127 K respectively (Kaczorowski, Noël and Zygmunt, 1995). The authors have measured the susceptibilities and magnetizations on single crystals that display a very large anisotropy of uranium (Figure 22).

The compound UAsSe is ferromagnetic with a ordering temperature T_C close to 113 K (Henkie, Fabrowski, Wojakowski and Zaleski, 1995). This magnetic state disappears at low temperature while the resistivity increases (Kondo effect).

REFERENCES

Akinaga, H., Manago, T. and Shirai, M. (2000). Material design of half-metallic zinc-blende CrAs and the synthesis by molecular-beam epitaxy. *Japanese Journal of Applied Physics*, L1118–L1120.

Artigas, M., Fruchart, D., Boursier, D. and Fruchart, R. (1990). Généralisation du modèle cristallochimique des phases métalliques MM'X à base de sous motifs pseudorhomboèdriques. Prévisions structurales. *Comptes Rendus de l' Academie des Sciences*, **310**, série II, 1621–1627.

Artigas, M., Fruchart, D., Rillo, C., *et al*. (1992). Magnetic phase transitions in $(Fe_{1-x}Ru_x)_2P$ $(0.25 < x < 0.6)$. *Journal of Magnetism and Magnetic Materials*, **104–107**(3), 1993–1994.

Bacmann, M., Chenevier, B., Fruchart, D., *et al*. (1986). Magnetic structures and magnetoresistivity of MnRhAs. *Journal of Magnetism and Magnetic Materials*, **54–57**(3), 1541–1542.

Bacmann, M., Fruchart, D., Chenevier, B., *et al*. (1990). Magnetic phase diagram of the $(Fe_{1-x}Mn_x)_2P$ system. *Journal of Magnetism and Magnetic Materials*, **83**(1–3), 313–314.

Bacmann, M., Fruchart, D., Koumina, A. and Wolfers, P. (2004). In *Low Temperature Magnetic Structure of CrNiAs. The Proceedings of EPDIC8*, Andersson, Y., Mittemeijer, E.J. and Welzel, U. (Ed.), Trans Tech Publications, Materials Science Forum, pp. 179–182.

Bacmann, M., Soubeyroux, J.L., Barrett, R., *et al*. (1994). Magnetoelastic transition and antiferromagnetic ordering in the system $MnFeP_{1-y}As_y$. *Journal of Magnetism and Magnetic Materials*, **134**(1), 59–67.

Baibich, M.N., Broto, J.M., Fert, A., *et al*. (1988). Giant magnetoresistance of (001)Fe/(001)Cr magnetic superlattice. *Physical Review Letters*, **61**, 2472.

Barner, K. (1987). Correlation of magnetic and transport properties for some mixed magnetic transition metal pnictides. *Journal of Magnetism and Magnetic Materials*, **70**(1–3), 268–270.

Barthélémy, A., Fert, A. and Petroff, F. (1999). Giant magnetoresistance in magnetic multilayers. In *Handbook of Magnetic Materials*, Bushow, K.H.J. (Ed.), North-Holland, p. 1, Vol. 12.

Becerra, C.C., Bindilatti, V. and Oliveira, N.F. Jr. (2000). Evidence for the Ising-Lifshitz crossover in MnP. *Physical Review B. Condensed Matter*, **62**(13), 8965–8968.

Beckman, O. and Lundgren, L. (1991). In *Compounds of Transition Elements with Nonmetals. Handbook Magnetic Materials*, Buschow, K.H.J. (Ed.), Elsevier Science Publishers, Chapter 3, pp. 181–287, Vol. 6.

Bronger, W. and Müller, P. (1997). The magnetochemical characterisation of the bonding features in ternary chalcogenides of manganese, iron and cobalt with low dimensional structural units. *Journal of Alloys and Compounds*, **246**, 27–36.

Brück, E. (2005). Developments in magnetocaloric refrigeration. *Journal of Physics D: Applied Physics*, **38**, R381–R391.

Brück, E., Ilyn, M., Tishin, A.M. and Tegus, O. (2005). Magnetocaloric effects in $MnFeP_{1-x}As_x$ based compounds. *Journal of Magnetism and Magnetic Materials*, **290–291**(1), 8–13.

Brück, E., Tegus, O., Li, X.W., *et al*. (2003). Magnetic refrigeration towards room-temperature applications. *Physica B: Condensed Matter*, **327**(2–4), 431–437.

Brück, E., Tegus, O., Zhang, L., *et al*. (2004). Magnetic refrigeration near room temperature with Fe_2P-based compounds. *Journal of Alloys and Compounds*, **383**, 32–36.

Carteaux, V., Brunet, D., Ouvrard, G. and André, G. (1995). Crystallographic, magnetic and electronic structures of a new layered ferromagnetic compound $Cr_2Ge_2Te_6$. *Journal of Physics: Condensed Matter*, **7**, 69–87.

Chang, K. and Xia, J.B. (2002). Magneto-optical properties of diluted magnetic semiconductor quantum dots. *Journal of Physics: Condensed Matter*, **14**, 13661–13665.

Chenevier, B., Baruchel, J., Bacmann, M., *et al*. (1992). Neutron diffraction and topographic investigation of the multiphase magnetic transition in MnRhAs. *Journal of Alloys and Compounds*, **179**, 147–156.

Chenevier, B., Fruchart, D., Bacmann, M., *et al*. (1984). Propriétés magnétiques de MnRhAs. *Physica Status Solidi A*, **84**, 199–206.

Dietl, T. (2002). Ferromagnetic semiconductors. *Semiconductor Science and Technology*, **17**, 377–392.

Dietl, T., Haury, A. and Merle d'Aubigné, Y. (1997). Free carrier_induced ferromagnetism in structures of diluted magnetic semiconductors. *Physical Review B*, **55**, R3347–R3350.

Dietl, T., Ohno, H. and Matsukura, F. (2001). Hole-mediated ferromagnetism in tetrahedrally coordinated semiconductors. *Physical Review B*, **63**, 195205.

Erikson, O., Bergqvist, L., Sanyal, B., *et al*. (2004). Electronic structure and magnetism of diluted magnetic semiconductors. *Journal of Physics: Condensed Matter*, **16**, S5481–S5489.

Eto, T., Yamagishi, M., Ishizuka, M., *et al*. (2000). Pressure induced structural transition in intermetallic compounds MnRhP and MnRhAs. *Journal of Alloys and Compounds*, **307**, 96–100.

Fruchart, R. (1982). Effets d'électronégativité et interactions métalliques dans les phosphures et arséniures ternaires des éléments de transition 3d, 4d, 5d de type métallique. *Annales de Chimie*, **7**(6–7), 563–604.

Fruchart, D. (2005). Magnetic couplings in MM'X compounds of Cu_2Sb type of structure (M, M′ = d-metals, X = p-elements as P, As, Sb. . .). *Solid State Sciences*, **7**, 767–775.

Fruchart, D., Allab, F., Balli, M., *et al*. (2005). On the magnetocaloric effect in d-metal pnictides. *Physica A*, **358**, 123–135.

Fruchart, D., Martin-Farrugia, C., Rouault, A. and Sénateur, J.P. (1980). Etude structurale et magnétique de CoMnP. *Physical Status Solidi A*, **57**, 675–682.

Fujii, N., Zach, R., Ishizuka, M., *et al*. (2001). Pressure-induced magnetic transition in MnRhAs. *Journal of Magnetism and Magnetic Materials*, **224**(1), 12–16.

Fujii, N., Zach, R., Ishizuka, M., *et al*. (2002a). Pressure dependence of the magnetic properties of MnRhX (X = P, As). *Journal of Physics: Condensed Matter*, **14**(44), 11135–11138.

Fujii, N., Zach, R., Kanomata, T., *et al*. (2002b). Effect of pressure on the magnetic properties of $MnRh_{1-x}Co_xAs$. *Journal of Alloys and Compounds*, **345**, 59–67.

Gama, S., Coelho, A.A., de Campos, A., *et al*. (2004). Pressure-induced colossal magnetocaloric effect in MnAs. *Physical Review Letters*, **93**(237202), 1–4.

Goodenough, J.B. (1973). Interpretation of structure and magnetism in transition metal pnictides M_2X and $(M_{1-x}M'_x)_2X$. *Journal of Solid State Chemistry*, **7**(4), 428–447.

Goodenough, J.B. (1976). Conceptual phase diagrams and their applications to itinerant electron magnetism. In *Magnetism in Metals and Metallic Compounds*, Lopuszanski, J.T., Pekalski, A. and Przystawa, J. (Eds.), Plenum Publishing Corporation: New York, pp. 35–90.

Goodenough, J.B. and Kafalas, J.A. (1967). High-pressure study of the first-order phase transition in MnAs. *Physical Review*, **157**(2), 389–395.

de Groot, R.A., Mueller, F.M., van Engen, P.G. and Bushow, K.H.J. (1983). *New class of Materials; Half-metallic Ferromagnets*.

Hebard, A.F., Rairigh, R.P., Kelly, J.G., *et al*. (2004). Mining for high Tc ferromagnetism in ion-iplanted dilute magnetic semiconductors. *Journal of Physics D: Applied Physics*, **37**, 511–517.

Henkie, Z., Fabrowski, R.A., Wojakowski, A. and Zaleski, A.J. (1995). Suppression of the ferromagnetic state by disorder in the anisotropic Kondo lattice system UAsSe. *Journal of Magnetism and Magnetic Materials*, **140–144**(Part 2), 1433–1434.

Hermann, R.P., Tegus, O., Brück, E., *et al*. (2004). Mössbauer spectral study of the magnetocaloric $FeMnP_{1-x}As_x$ compounds. *Physical Review B. Condensed Matter and Materials Physics*, **70**(21), 214425-1–214425-9.

Ishida, S., Takiguchi, T., Fujii, S. and Asano, S. (1996). Magnetic properties and electronic structures of CrMZ (M = Fe, Co, Ni; Z = P, As). *Physica B*, **217**, 87–96.

Ishikawa, F., Koyama, K. and Watanabe, K. (2004). X ray diffraction study of the structural phase transition in MnAs under high magnetic fields. *Physica B, Condensed Matter*, **346**, 408–412.

Ishikawa, F., Koyama, K., Watanabe, K. and Wada, H. (2003). Field induced structural transformation in MnAs. *Journal of Applied Physics*, **42 L**, 918–920.

de Jonge, W.J.M. and Swagten, H.J.M. (1991). Magnetic properties of diluted magnetic selmiconductors. *Journal of Magnetism and Magnetic Materials*, **100**, 322.

Kaczorowski, D., Noël, H. and Zygmunt, A. (1995). Magnetic studies on UXY (X = P, Sb; Y = Se, Te) single crystals. *Journal of Magnetism and Magnetic Materials*, **140–144**(Part 2), 1431–1432.

Kanomata, T., Kawashima, T., Utsugi, H., *et al*. (1991). Magnetic properties of the intermetallic compounds MM′X (M = Cr, Mn, M' = Ru, Rh, Pd, and X = P, As). *Journal of Applied Physics*, **69**(8), pt. 2A, 4639–4641.

Kanomata, T., Shirakawa, K. and Kaneko, T. (1987). Giant pressure derivative of the magnetic transition temperature for $Fe_{2.1-x}Mn_xAs$ (x = 1.30 and 1.35). *Physics Letters A*, **124**(1–2), 100–102.

Kohnke, H.J., Kleeberg, Ch., Dankelmann, V., *et al*. (1996). Anisotropic magnetization of some ferromagnetic and canted transition metal pnictides. *Journal of Alloys and Compounds*, **239**, 150–157.

Koumina, A., Bacmann, M., Fruchart, D., *et al*. (1998). Crystallographic and magnetic properties of Fe_2P. *Annales de Chimie - Science des Matériaux*, **23**(1–2), 177–180.

Koyama, K., Kanomata, T., Matsukawa, T. and Watanabe, K. (2005). Magnetic field effect on structural property of $MnFeP_{0.5}As_{0.5}$. *Materials Transactions*, **46**(8), 1753–1756.

Krumbugel-Nylund, A. (1974). Etude Structurale et Magnétique des Arséniophosphures MM'$(P_{1-y}As_y)$ et des Solutions Solides

entre Arséniures M_2As des Métaux de Transition de la Première Série (M, M' = Cr, Mn, Fe, Co, Ni), PhD Thesis. University of Paris–Orsay.

Krumbugel-Nylund, A., Boursier, D., Rouault, A., *et al*. (1974). Magnetic structural properties of arseniophosphides $Co_2(P_{1-y}As_y)$, $Mn_2(P_{1-y}As_y)$ and $MnCo(P_{1-y}As_y)$. *Material Research Bulletin*, **9**(1), 21–34.

Kübler, J. (2003). Curie temperature of zinc-blende half-metallic ferromagnets. *Physical Review B*, **67**, 220403.

Lebouc, A., Allab, F., Fournier, J-M. and Yonnet, J.P. (2005). Réfrigération magnétique. *Technique de l'Ingénieur*, **RE 28**, 1–16.

Leithe-Jasper, A., Schnelle, W., Rosner, H., *et al*., (2004). Weak itinerant ferromagnetism and electronic and crystal structures of alkali-metal iron antimonides: $NaFe_4Sb_{12}$ and KFe_4Sb_{12}. *Physical Review B, Condensed Matter and Materials Physics*, **70**(21), 214418-1–214418-12.

Lemoine, P., Carré, D. and Guittard, M. (1986). Structure du Sulfure d'Europium et de Cuivre Eu_2CuS_3. *Acta Crystallographica*, **C42**, 390–391.

Le Sénéchal, C., Babizhet'ky, V., Deputier, S., *et al*. (1999). Crystal chemistry of defective intermetallics with empty triangular metalloid channels: the new phosphide $Zr_6Cr_{60}P_{39}$. *Journal of Solid State Chemistry*, **144**(2), 277–286.

Magnus, A., Carvalho, G., Alves, C.S., *et al*. (2005). The magnetic and magnetocaloric properties of $Gd_5Ge_2Si_2$ compound under hydrostatic pressure. *Journal of Applied Physics*, **97**(10M320), 1–3.

Mills, A.M. and Mar, A. (2000). Structures of the ternary iron germanium pnictides $FeGe_{1-x}Pn_x$ (Pn = P, As, Sb). *Journal of Alloys and Compounds*, **298**(1–2), 82–92.

Morikawa, T. and Wada, H. (2004). Effect of deviation from stoichiometry on magnetic and magnetocaloric properties in $MnAs_{1-x}Sb_x$. *Journal of Magnetism and Magnetic Materials*, **272–276**(1), 583–584.

Morikawa, T., Wada, H., Kogure, R. and Hirosawa, S. (2004). Effect of concentration deviation from stoichiometry on the magnetism of $Mn_{1+\delta}As_{0.75}Sb_{0.25}$. *Journal of Magnetism and Magnetic Materials*, **283**(2–3), 322–328.

Nakama, T., Kohama, T., Shimoji, T., *et al*. (1998). Thermopower of Fe_2P in magnetic fields up to 15 T. *Journal of Magnetism and Magnetic Materials*, **177–181**(2), 1369–1370.

Nascimento, F.C., dos Santos, A.O., de Campos, A., *et al*. (2006). Structural and magnetic study of the MnAs magnetocaloric compound. *Materials Research*, **9**(1), 111–114.

Niranjan, M.K., Sahu, B.R. and Kleinman, L. (2004). Density functional determination of the magnetic state of β-MnAs. *Physical Review B*, **70**(180406), 1–4.

Nishino, M., Fujii, N., Endo, S., *et al*. (2000). Anomalous pressure dependence of the Curie temperature in MnRhP. *Physics Letters A*, **276**, 133–136.

Niziol, S., Zach, R., Fruchart, D., *et al*. (1993). New magnetic properties of $(Co_{1-x}Mn_x)_2P$. *Journal of Magnetism and Magnetic Materials*, **127**(1–2), 103–108.

Ohno, H., Shen, A., Matsukura, F., *et al*. (1996). (Ga,Mn)As: a new diluted magnetic semiconductor based on GaAs. *Applied Physics Letters*, **69**(3), 363–365.

Ohta, S., Kumada, T., Fukushima, T., *et al*. (1995a). High-field magnetization in $(Cr_{1-x}Ni_x)_2As$ with x = 0.5 and 0.7. *Journal of Magnetism and Magnetic Materials*, **139**(3), 292–298.

Ohta, S., Kaneko, T., Yoshida, H., *et al*. (1995b). Pressure effect of the magnetic transition temperatures and thermal expansion in chromium ternary pnictides CrMAs (M = Ni, Rh). *Journal of Magnetism and Magnetic Materials*, **150**(2), 157–164.

Ohta, S., Kanomata, T. and Kaneko, T. (1990). Magnetic properties of CrRhAs and CrRuAs. *Journal of Magnetism and Magnetic Materials*, **90–91**, 171–172.

Ohta, S. and Onmayashiki, H. (1998). Antiferromagnetic stability and structural trend of transition-metal phosphides containing Co. *Physica B: Condensed Matter*, **253**(3–4), 193–202.

de Oliveira, N.A. (2004). Magnetocaloric effect in transition metals based compounds: a theoretical approach. *The European Physical Journal B*, **40**, 259–264.

Ono, F., Inoue, H., Wei, S., *et al*. (2001). Magnetization curves in MnRhP around the curie temperature. *Journal of Alloys and Compounds*, **317–318**, 254–257.

Pecharsky, V.K. and Gschneidner, K.A. Jr. (1997). Tunable magnetic regenerator alloys with a giant magnetocaloric effect for magnetic refrigeration from ~20 to ~290 K. *Applied Physics Letters*, **70**(24), 3299–3301.

Plaza, E.J.R., Alves, C.S., Coelho, A.A., *et al*. (2004). Magnetic and magnetocaloric properties of Nd monopnictides. *Journal of Magnetism and Magnetic Materials*, **272–276**(3), 2373–2374.

Rillo, C., Bartolomé, J., Bacmann, M., *et al*. (1992). Magnetic phase transition in MnRhAs single crystal: an ac susceptibility study. *Journal of Magnetism and Magnetic Materials*, **104–107**(3), 1995–1996.

Ryzhkovskii, V.M., Glazkov, V.P., Goncharov, V.S., *et al*. (2002). Neutron diffraction investigation of the magnetic structure of the Mn_2Sb pnictide at high pressures. *Physics of the Solid State*, **44**(12), 2281–2286.

Sanyal, B., Bengone, O. and Mirbt, S. (2003). Electronic structure and magnetism of Mn-doped GaN. *Physical Review B*, **68**, 205210.

Sénateur, J.P., Roger, A., Fruchart, R. and Chappert, J. (1969). *Comptes Rendus de l' Academie des Sciences Série C*, **269**, 1385.

Shirakawa, K. and Ido, H. (1976). Magnetic transition of the Mn_2Sb-Mn_2As system. *Journal of the Physical Society of Japan*, **30**(3), 1782.

Shi-Shen, Y., Ren, C., Wang, X., *et al*. (2004). Ferromagnetism and magnetoresistance of Co-ZnO inhomogeneous magnetic semiconductors. *Applied Physics Letters*, **84**(13), 2376–2378.

Sjöstrøm, J. (1992). Symmetric and antisymmetric anisotropic exchange energies as crucial factors for the magnetic structures in MnP, FeP, CrAs and MnAs. *Journal of Physics: Condensed Matter*, **4**(26), 5723–5734.

Songlin, D.W., Tegus, O., Brück, E., *et al*. (2002a). Magnetic and magnetocaloric properties of $Mn_5Ge_{3-x}Sb_x$. *Journal of Alloys and Compounds*, **337**, 269–271.

Songlin, D.W., Tegus, O., Brück, E., *et al*. (2002b). Magnetic phase transition and magnetocaloric effect in $Mn_{5-x}Fe_xSi_3$. *Journal of Alloys and Compounds*, **334**, 249–252.

Sredniawa, B., Zach, R., Chajec, W., *et al*. (2002). Magnetism and electronic structure of the $(Co_{1-x}Mn_x)_2P$ system. *Journal of Magnetism and Magnetic Materials*, **242–245**(Part 2), 931–934.

Sredniawa, B., Zach, R., Fornal, P., *et al*. (2001). Crystal structure, magnetic and electronic properties of $Co_xFe_{1-x}MnP$ system. *Journal of Alloys and Compounds*, **317–318**, 266–273.

Srivastava, B.K., Krishnamurthy, A., Ghose, V., *et al*. (1994). Reentrant spin glass like behaviour of $(Fe_{0.90}Cr_{0.05}Ni_{0.05})_2P$. *Journal of Magnetism and Magnetic Materials*, **132**(1–3), 124–130.

Sudish-Kumar, P.S.K., Srivastava, B.K., Krishnamurthy, A. and Sahni, V.C. (1999). Magnetic structure of $(Fe_{0.97}Cr_{0.03})_2P$. *Pramana, Journal of Physics*, **52**(1), 111–120.

Tegus, O. (2003). *Novel Materials for Magnetic Refrigeration*. PhD. Thesis, University of Amsterdam.

Tegus, O., Brück, E., de Boer, F.R. and Buschow, K.H.J. (2002). Magneto-resistance of MnFe(As, P). Intermag Europe 2002 Digest of Technical Papers. 2002 *IEEE International Magnetic Conference*, Roma-Italy, Cat. No. 02CH37323, AC7.

Tegus, O., Brück, E., Buschow, K.H.J. and de Boer, F.R. (2002). Transition-metal-based magnetic refrigerants for room-temperature applications. *Nature*, **415**, 150–152.

Tegus, O., Fuquan, B., Dagula, W., *et al*. (2005a). Magnetic-entropy change in $Mn_{1.1}Fe_{0.9}P_{0.7}As_{0.3-x}Ge_x$. *Journal of Alloys and Compounds*, **396**(1–2), 6–9.

Tegus, O., Lin, G.X., Dagula, W., *et al*. (2005b). A model description of the first order phase transition in $MnFeP_{1-x}As_x$. *Journal of Magnetism and Magnetic Materials*, **290–291**(1), 658–660.

Tishin, A.M. and Spichkin, Y.I. (2003). *The Magnetocaloric Effect and its Application*, *Series in Condensed Matter Physics*, Institute of Physics, ISBN 0-7503-0922-9.

Tobola, J., Bacmann, M., Fruchart, D., *et al*. (1996). Magnetism of Fe_2P investigated by neutron experiments and band structure calculations. *Journal of Magnetism and Magnetic Materials*, **157–158**, 708–710.

Tobola, J., Bacmann, M., Fruchart, D., *et al*. (2001). Structure and magnetism in the polymorphous MnFeAs. *Journal of Alloys and Compounds*, **317–318**, 274–279.

Tobola, J., Kaprzyk, S., Fruchart, D., *et al*. (1997). Electronic and magnetic structure of ternary transition metal arsenides related to the Fe_2X type (X = P, As). *Journal of Alloys and Compounds*, **262–263**, 65–70.

Tougait, O., André, G., Bourée, F. and Noel, H. (2001). Neutron diffraction study of magnetic ordering of two binary uranium tellurides U_3Te_5 and U_2Te_3. *Journal of Alloys and Compounds*, **317–318**, 227–232.

Tsymbal, E.Y., Mryasov, O.N. and LeClair, P.R. (2003). Spin-dependent tunnelling in magnetic tunnel junctions. *Journal of Physics: Condensed Matter*, **15**, 109.

Twardowski, A. (1995). Recent development of diluted magnetic semiconductors. *Chinese Journal of Physics*, **33**(4), 375.

Val'kov, V.I. and Khapalyuk, E.A. (1997). Features of magnetic phase transitions in iron-manganese arsenides of the type $Fe_{a-x}Mn_xAs$ (a approximately = 1.6). *Physics of the Solid State*, **39**(5), 791–795.

von Ranke, P.J., de Campos, A., Caron, L., *et al*. (2004). Calculation of the giant magnetocaloric effect in $MnFeP_{0.45}As_{0.55}$ compound. *Physical Review B*, **70**(094410), 1–5.

von Ranke, P.J., Gama, S., Coelho, A.A., *et al*. (2006). Theoretical description of the colossal magnetocaloric effect: application to MnAs. *Physical Review B*, **73**(014415), 1–5.

von Ranke, P.J., de Oliveira, N.A., Mello, A., *et al*. (2005). Analytical model to understand the colossal magnetocaloric effect. *Physical Review B*, **71**(054410), 1–6.

Wada, H. and Asano, T. (2005). Effect of heat treatment on giant magnetocaloric properties of $Mn_{1+\delta}As_{1-x}Sb_x$. *Journal of Magnetism and Magnetic Materials*, **290–291**(1), 703–705.

Wada, H., Funaba, C. and Asano, T. (2006). Effects of heat treatment on the magnetic phase transition and magnetocaloric properties of $Mn_{1+\delta}As_{1-x}Sb_x$. *Materials Transactions*, **47**(3), 486–491.

Wada, H., Morikawa, T., Taniguchi, K., *et al*. (2003). Giant magnetocaloric effect of $MnAs_{1-x}Sb_x$ in vicinity of first-order magnetic transition. *Physica B*, **328**(1–2), 114–116.

Wada, H. and Tanabe, Y. (2001). Giant magnetocaloric effect of $MnAs_{1-x}Sb_x$. *Applied Physics Letters*, **79**(20), 3302–3304.

Wada, H., Taniguchi, K. and Tanabe, Y. (2002). Extremely large magnetic entropy change of $MnAs_{1-x}Sb_x$ near room temperature. *Materials Transactions*, **43**(1), 73–77.

Wakeshima, M., Furuuchi, F. and Hinatsu, Y. (2004). Crystal structures and magnetic properties of novel rare-earth copper sulfides, $EuRCuS_3$ (R = Y, Gd-Lu). *Journal of Physics: Condensed Matter*, **16**, 5503–5518.

Yamagishi, Y., Ohoyama, K., Kanouchi, T., *et al*. (1999). Multi-magnetic modes in $(Cr_{1-x}Mn_x)_2As$. *Journal of Physics and Chemistry of Solids*, **60**, 1229–1231.

Yan, L., Ong, C.K. and Rao, X.S. (2004). Magnetic order in Co-dopped and (Mn, Co) codoped ZnO thin films by pulsed laser deposition. *Journal of Applied Physics*, **96**(1), 508–511.

Zach, R. (1997). Magnetic Properties and Magnetoelastic Phases Transitions of $MnFeP_{1-x}As_x$ ($0.15 < x < 0.66$) and $MnRh_{1-x}As_x$ isostructural series of solid solutions. D. Hab Thesis, Politecknika Krakowska, Zeszyt Naukowy NR 2 Krakow, Poland, ISSN 0137-136X.

Zach, R., Bacmann, M., Fruchart, D., *et al*. (1994). Neutron diffraction studies of $MnFeAs_yP_{1-y}$ system. *Acta Physica Polonica*, **A85**, 229–231.

Zach, R., Fruchart, R., Fruchart, D., *et al*. (1992). High pressure study of $MnRhAs_{1-x}P_x$ system. *Journal of Magnetism and Magnetic Materials*, **104–107**(3), 1929–1930.

Zach, R., Guillot, M. and Fruchart, R. (1990). The influence of high magnetic fields on the first order magneto-elastic transition in $MnFeP_{1-y}As_y$system. *Journal of Magnetism and Magnetic Materials*, **89**(1–2), 221–228.

Zach, R., Guillot, M., Picoche, J.C. and Fruchart, R. (1995a). Critical field behaviour in $MnFeAs_yP_{1-y}$. *Journal of Magnetism and Magnetic Materials*, **140–144**, 1541–1542.

Zach, R., Guillot, M., Picoche, J.C. and Fruchart, R. (1995b). High dc field magnetic properties of $MnRhAs_{1-x}P_x$ system. *Journal of Magnetism and Magnetic Materials*, **140–144**(1), 143–144.

Zach, R., Guillot, M. and Tobola, J. (1998). Semiquantitative analysis of magnetic phase transitions in the $MnRhAs_{1-x}P_x$ series of compounds. *Journal of Applied Physics*, **83**(11), 7237–7239.

Zach, R., Kaprzyk, S., Niziol, S., *et al*. (1997). Magnetoelastic properties of $MnRhAs_{1-x}P_x$ and band structure results from KKR-CPA. *Acta Physica Polonica A*, **91**(2), 471–474.

Zach, R., Malaman, B., Bacmann, M., *et al*. (1995). Magnetic study of the hexagonal $MnFeP_{1-x}As_x$ system. *Journal of Magnetism and Magnetic Materials*, **147**(3), 201–204.

Zach, R., Tobola, J., Sredniawa, B., *et al*. (2004). Magneto-elastic properties and electronic structure analysis of the $(Fe_{1-x}Ni_x)_2P$ system. *Journal of Alloys and Compounds*, **383**, 322–327.

Zhang, L., Moze, O., Prokes, K., *et al*. (2005). Neutron diffraction study of history dependence in $MnFeP_{0.6}Si_{0.4}$. *Journal of Magnetism and Magnetic Materials*, **290–291**(1), 679–681.

Zieba, A., Slota, M. and Kucharczyk, M. (2000). Modulated phases, magnetic phase diagrams, and the Lifshitz point in MnP from the mean field theory. *Physical Review B: Condensed Matter*, **61**(5), 3435–3449.

FURTHER READING

Balli, M., Fruchart, D., Hlil, E.K., *et al*. (2005). A magnetocaloric effect in some Fe_2P like compounds. In *Refrigeration Science and Technology*, Egolf, P.W. (Ed.), International Institute of Refrigeration, IIR: Paris, ISSN 0151. 1637, pp. 211–219.

Roger, A. (1970). *Etude Cristallographique et Magnétique des Phosphures MP et M_2P de la Série du Fer et de leurs Solutions Solides*, PhD. Thesis, University of Paris Sud - Orsay, Orsay, France.

Tegus, O., Brück, E., Li, X.W., *et al*. (2004). Tuning of the magnetocaloric effects in MnFe(P,As) by substitution of elements. *Journal of Magnetism and Magnetic Materials*, **272–276**(3), 2389–2390.

Tougait, O., Potel, M. and Noël, H.J. (1998). Crystal structure and magnetic properties of the binary triuranium pentatelluride U_3Te_5. *Journal of Solid State Chemistry*, **139**, 356.

Wakeshima, M., Taira, N., Hinatsu, Y., *et al*. (2003). Specific heat and neutron diffraction study on quaternary sulfides $BaNd_2CoS_5$ and $BaNd_2ZnS_5$. *Journal of Solid State Chemistry*, **174**(1), 159–164.

Magnetostrictive Materials and Magnetic Shape Memory Materials

Robert C. O'Handley
Massachusetts Institute of Technology, Cambridge, MA, USA

1 INTRODUCTION

Among the most interesting and technically important properties of any class of materials are its couplings with other phenomena. Examples include piezoelectricity, thermoelectricity, electro-optics, magneto-optics, and magnetomechanical effects. Magnetostriction refers to the deformation of a material owing to changes in its state of magnetization. The magnetostrictive deformation can be isotropic (magnetovolume effect), or anisotropic (Joule magnetostriction). A large volume change is often observed on cooling a magnetic material through its Curie temperature (Figure 1). In the case of Ni, this volume expansion is over 4% (Gschneider, 1964; Stoelinga, Gersdorf and deVries, 1965; Kollie, 1977).

This volume change allows the material to accommodate the increased energy of the spins in the magnetically ordered state; when electrons are no longer equally distributed between spin-up and spin-down states, their kinetic energy increases (Janak and Williams, 1976). In the ferromagnetic state, increasing a field beyond the anisotropy field may also induce a small isotropic strain associated with the high-field susceptibility. This chapter will focus more on the Joule magnetostriction, an anisotropic strain of lower symmetry than the crystal itself that arises from a *change in direction of the magnetization* (Figure 1, inset circle) as well as on a related phenomenon, the large field-induced strain in magnetic shape-memory alloys such as Ni–Mn–Ga. This latter effect is *not* due to the rotation of the magnetization but rather to *field-induced twin-boundary motion*.

Magnetostrictive strains are typically less than 10^{-4} except for certain rare-earth and rare-earth/transition-metal alloys. The net volume change during anisotropic magnetostriction is often close to zero, so $\lambda_\perp \approx -0.5\lambda_\parallel$, where $\lambda_\perp(\lambda_\parallel)$ is measured in the direction perpendicular (parallel) to the field-induced, saturation magnetization. Not only is the magnetostrictive strain tensor anisotropic about the magnetization direction but it can also have very different components depending on the crystallographic direction in which the magnetization is oriented. The inverse effect, whereby an imposed stress changes the state of magnetization, is important for a variety of sensors. In addition, magnetostrictive materials under certain conditions can appear to have a reduced elastic stiffness, called the ΔE effect, and hence reduced sound velocity. These phenomena will be discussed. Other useful references on magnetostriction include the following: Del Moral (2006); O'Handley (2000); Cullen, Clark and Hathaway (1997); Lacheisserie (1993); Kittel and Galt (1967); Kanamori (1963); and Kittel (1949).

Handbook of Magnetism and Advanced Magnetic Materials. Edited by Helmut Kronmüller and Stuart Parkin. Volume 4: *Novel Materials*. ISBN: 978-0-470-02217-7.

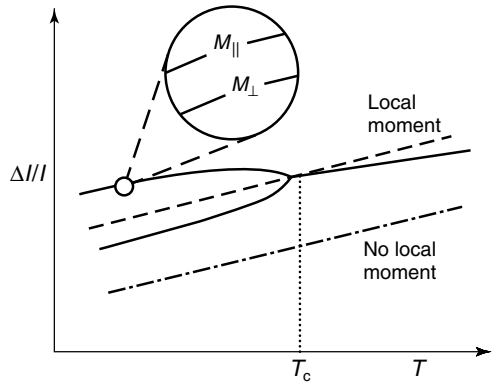

Figure 1. Schematic of the thermal expansion of a magnetic material as a function of temperature illustrating the increased volume due to the presence of a local magnetic moment and the onset of magnetic anomalies below the Curie temperature. A small anisotropic strain, depending on the direction of magnetization (circled inset), is also observed below T_C. The latter is usually referred to as *anisotropic magnetostriction*. (Reprinted with permission O'Handley R.C., copyright 2000, John Wiley & Sons Inc.)

Magnetostriction is an *elastic* deformation. Time-reversal invariance of physical phenomena requires that the strain be the same if the magnetization direction reverses along the same axis. Hence, there is no change in strain for 180° domain-wall motion. There is change in magnetostrictive strain for 90° domain-wall motion and for magnetization rotation.

Historically, Ni was the most widely used magnetostrictive material. Though it has a magnetostrictive strain of only 30 or 40×10^{-6}, the low magnetic anisotropy of Ni allows this strain to be achieved in relatively weak fields. In the 1960s and 1970s, the magnetostriction of many rare-earth transition-metal intermetallic compounds and alloys was studied. This led to the development of the highly magnetostrictive alloy, $Fe_2(Tb_{0.3}Dy_{0.7})$, called *Terfenol-D*, having $\lambda_{\|} - \lambda_{\perp} \approx 2400 \times 10^{-6}$ and relatively low magnetic anisotropy, $\mu_0 H_a \approx 0.1$T (Abbundi and Clark, 1977; Clark, 1980). But these intermetallic compounds are brittle and hard to grow with the proper texture. A new class of ductile, high-magnetostriction alloys based on BCC solid solutions of Fe–Ga has shown $\lambda_{100} \approx 400 \times 10^{-6}$ in fields of order 0.01 T (Clark *et al*., 2000; Guruswamy *et al*., 2000). (λ_{100} is the change in length relative to the dimensions of the demagnetized crystal, measured parallel to the crystallographic [100] direction when $\boldsymbol{M}$ is saturated in that direction.)

In was noted three decades ago that the large field-induced strain in Dy appears to be associated with twin-boundary motion (Liebermann and Graham, 1976). It had long been speculated that similar large strains could be observed in a subclass of shape-memory alloys that are also ferromagnetic shape memory alloys (FSMAs). Examples of such materials include Fe–Pd and Ni_2MnGa. It was expected that an applied field could either move crystallographic twin boundaries in the martensitic state to produce a large strain, or change the temperature of the transformation from the untwined, high-symmetry (austenite) phase to the twinned, low-symmetry (martensite) phase. Thus, application of a field at a temperature close to the transformation could control the large deformation energy there (Ullakko 1996; James and Wuttig, 1996). Experimental evidence of magnetic-field-induced strain by motion of twin boundaries began to accumulate (Ullakko *et al*., 1996; James and Wuttig, 1998; Tickle *et al*., 1999). The full field-induced strain of $1 - c/a = 6\%$ in tetragonal Ni–Mn–Ga (Murray *et al*., 2000) and 10% in its orthorhombic phase (Sozinov, Likhachev, Lanske and Ullakko, 2002) have been observed.

Field-induced strain in FSMAs has two components. First, there is the usual *elastic* magnetostrictive strain that increases quadratically with applied field as the magnetization direction changes; it is of the order -150×10^{-6} in Ni–Mn–Ga alloys (Tickle *et al*., 1999). Second, when mobile twin boundaries are present, there is a much larger *plastic* strain, of order 6 or 10% in tetragonal or orthorhombic Ni–Mn–Ga, respectively. This strain starts to appear when the applied field exceeds a threshold field, and initially increases linearly with the field, then saturates gradually as H approaches $H_a \approx 0.55 \times 10^6\,\mathrm{A\,m^{-1}}$. There are several recent review articles on FSMAs (O'Handley and Allen, 2000; O'Handley *et al*., 2000; Kostorz and Müllner, 2005; Söderberg *et al*., 2006).

This article reviews the phenomenology and range of observed anisotropic magnetostricitve strains. It also summarizes some aspects of the current understanding of magnetic-field-induced strains in FSMAs. The two phenomena, magnetostriction and field-induced strain in FSMAs, are compared and contrasted.

2 ANISOTROPHIC MAGNETOSTRICTION

Changing the direction of magnetization in a magnetic material for $T < T_C$ generally causes it to strain anisotropically (Figure 1, circled inset); that is, the magnetization vector has associated with it a stress tensor with principal axes directed along $\boldsymbol{M}$ that causes a mechanical deformation. The field dependence of this *anisotropic strain* is shown schematically in Figure 2 for an isotropic material ($\varepsilon_{\|}$ for strain measured parallel to the field and $\varepsilon_{\perp}$ for strain measured perpendicular to the field). This anisotropic strain was first observed in 1842 by Joule in iron and is often called *Joule magnetostriction*. The fact that the magnetostrictive strain, $\varepsilon(H) = \Delta l(H)/l \equiv \lambda(H)$, saturates above a certain field, $\lambda\ (H_{sat}) \equiv \lambda_s$, indicates that the anisotropic strain is due to a field-induced change in the direction of the magnetization, not the change in the field itself.

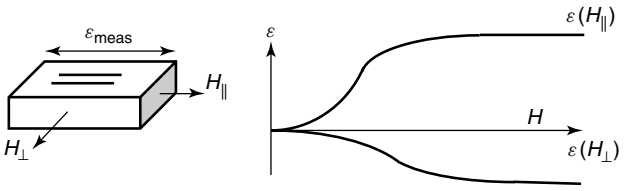

Figure 2. When a demagnetized sample is magnetized by an external field, the sample strains anisotropically. The strain in the direction of magnetization, $\varepsilon(H_\parallel)$, will be opposite in sign to the strain measured perpendicular to the direction of magnetization, $\varepsilon(H_\perp)$. The strains depicted above are those for a material with a positive magnetostriction constant: $(\Delta l/l)_\parallel > 0$.

Values of the saturation magnetostriction, λ_s, can range from zero (effectively, $\varepsilon < 10^{-7}$) to nearly $\pm 10^{-4}$ in 3d metals and alloys and to over $\pm 10^{-3}$ in some 4f metals and alloys. For Ni, which has a principal magnetostrictive stress, $B_1 = +6.2\,\text{MPa}$ and, given its Young's modulus, $E = 2 \times 10^{11}\,\text{N m}^{-2}$, we would expect to observe magnetostrictive strains of the order 30×10^{-6}. This is indeed close to the magnetostriction of polycrystalline Ni, $\lambda_s = -34 \times 10^{-6}$. The minus sign indicates that Ni tends to contract in the direction of magnetization and shows a nearly volume-conserving expansion in the two orthogonal directions, $\varepsilon_\perp = -\varepsilon_\parallel/2$.

The inverse effect is also important. Stressing or straining a magnetic material can produce a change in its preferred magnetization direction or in its M–H curve (Figure 3). These phenomena are called *inverse Joule effects*, *Villari effects*, or *piezomagnetism*. *If the saturation magnetostriction coefficient*, λ_s, *is positive, it is easier to magnetize the material in the tensile strain direction*. It is harder to magnetize a material in a direction for which $\lambda_s < 0$ and the imposed strain $\varepsilon > 0$ or for which $\lambda_s > 0$ and $\varepsilon < 0$. This implies the existence of terms in the magnetic anisotropy energy, which depend on strain as well as on the direction cosines of the magnetization: $\boldsymbol{M} = M_s(\alpha_x, \alpha_y, \alpha_z)$. These magnetic–elastic coupled terms describe the magnetoelastic (ME) anisotropy energy. The anisotropic strain effects arising from terms in the free-energy containing products of strain and magnetization direction are the focus of this chapter.

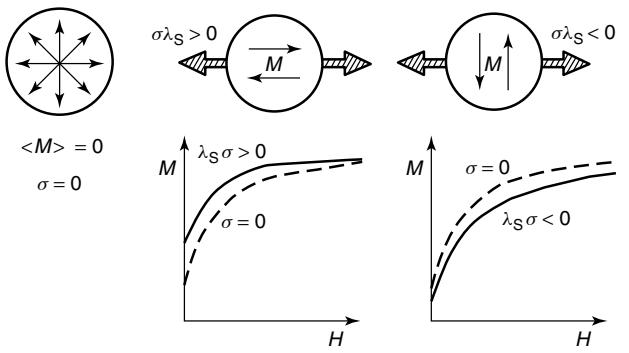

Figure 3. Imposing a strain on a magnetic material by an external mechanical stress can alter the change direction of magnetization (magnetic anisotropy) and thus alter the shape of the M–H curve below saturation. The cases above illustrate the changes observed for a polycrystalline material with a positive magnetostriction constant. (Reprinted with permission O'Handley R.C., copyright 2000, John Wiley & Sons Inc.)

2.1 Phenomenology

2.1.1 Field dependence of Joule magnetostriction

The *anisotropic magnetostrictive strain* relative to the direction of magnetization may be described for an *isotropic material* comprised of a single domain (i.e., one magnetization direction) by the relation

$$\varepsilon = \frac{3}{2}\lambda_s\left(\cos^2\theta - \frac{1}{3}\right) \tag{1}$$

Here $\varepsilon = \Delta l/l$ is the strain measured at an angle θ relative to the saturation magnetization direction and λ_s, the saturation magnetostriction coefficient, is the measure of the magnitude of the strain on changing the direction of magnetization in the material. The strain ε is sometimes called the *magnetostriction*, λ, but clearly, from equation (1), ε is a function of the direction of $\boldsymbol{M}$ or of the applied field so it should not be confused with the saturation magnetostriction λ_s which is a material constant. Figure 2 shows the variation of strain in a given direction in a material as an external field is increased either parallel or perpendicular to the strain-measuring direction.

For a uniaxial material in the absence of an external field, the magnetization lies along the 'easy axis' direction (defined by the uniaxial magnetic anisotropy). A 'hard-axis' magnetization process (in which the field is applied orthogonal to the preferred direction of magnetization) is known to be linear in the field, H and to scale with the ratio of the saturation magnetization, M_s, to the anisotropy field, H_a: $M(H) = M_s H/H_a$. This relation can be expressed in terms of the reduced magnetization, $m(H) = M(H)/M_s$, and reduced field, $h = H/H_a$ giving $m = h$. (The anisotropy field is the field at which a linear, hard-axis magnetization process saturates.) From Figure 4(a), and $m(H) = \cos[\theta(H)]$, we may write equation (1) as

$$\varepsilon = \frac{3}{2}\lambda_s\left(m^2 - \frac{1}{3}\right) \tag{2}$$

That is, the magnetostrictive strain in a hard uniaxial direction is quadratic in $m = h$, so ε is proportional to H^2 (Figure 4b), saturating at $h = 1$.

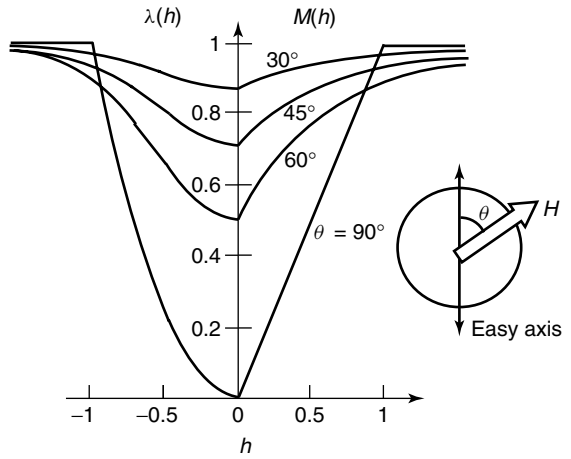

Figure 4. Reduced magnetization (b) and magnetostriction (a) versus reduced field, h, calculated for different orientations of applied field relative to easy axis. Application of a magnetic field perpendicular to the easy axis of a material causes a rotation of the magnetization direction and results in a linear M–H characteristic and a quadratic dependence of strain on field. The field-dependent strain is shown here as positive along the field direction as is the case for $\lambda_s > 0$ (O'Handley, 2000).

Above saturation, the two strain curves in Figure 2 are essentially parallel to each other (except for the presence of any high-field-susceptibility-induced volume magnetostriction) and their difference defines λ_s. From equation (1)

$$\varepsilon_{\parallel} = \frac{3}{2}\lambda_s\left(1 - \frac{1}{3}\right) = \lambda_s \; \varepsilon_{\perp} = \frac{3}{2}\lambda_s\left(0 - \frac{1}{3}\right) = -\frac{\lambda_s}{2} \quad (3)$$

That is, the saturation magnetostriction λ_s is the strain measured in the field direction relative to the randomly magnetized state ($\langle\cos^2\theta\rangle = 1/3$). However, because a completely demagnetized state is not easily achieved with certainty, measurement of *both* $\varepsilon_{\parallel}$ and $\varepsilon_{\perp}$ in equation (3) is recommended to determine λ_s in isotropic materials:

$$\varepsilon_{\parallel} - \varepsilon_{\perp} = \frac{3}{2}\lambda_s \quad \text{so that} \quad \lambda_s = \frac{2}{3}(\varepsilon_{\parallel} - \varepsilon_{\perp}) \qquad (4)$$

The significance of equation (4) for measurement of λ_s in isotropic materials can be appreciated by referring to Figure 2. Changes in the zero-field magnetization distribution may shift the origin up or down between the limits of $\varepsilon_{\parallel}$ and $\varepsilon_{\perp}$, but the difference between the two high-field strains remains fixed at $(3/2)\lambda_s$. Thus, two strains should be measured to specify λ_s in an isotropic material. More than two measurements are required to fully specify λ_{ij} for lower-symmetry materials.

The magnetostrictive strain is the same in each of two magnetic domains separated by a 180° domain wall because $\cos^2\theta$ is the same in each domain. This is due to time-reversal invariance; the energy is the same whether the microscopic currents rotate to give $\boldsymbol{M}$ in one direction or they reverse sign to give $\boldsymbol{M}$ in the opposite direction. Therefore, there is no magnetostrictive shape change associated with a magnetization process involving only 180° domain walls. (There may be a local strain about a 180° domain wall owing to the change in orientation of $\boldsymbol{M}$ there, but the elastic constraint of the material reduces this strain relative to the magnetostrictive strain of an unconstrained, saturated sample.)

2.1.2 Some data

For materials that are not isotropic, the magnetostriction constant can be different in different directions and higher-order distortions than the dipolar strain in equation (1) may also play a role. For example, magnetizing an iron crystal along ⟨100⟩ causes an elongation along ⟨100⟩ relative to the demagnetized state. Magnetizing it along ⟨111⟩ causes a contraction along the ⟨111⟩ direction relative to the demagnetized state. Nickel contracts in the direction of magnetization for any crystal orientation. This is reflected in the principal magnetostriction coefficients of Fe and Ni:

$$\text{BCC iron} \;\; \lambda_{100} = 20.5 \times 10^{-6} \;\; \text{and} \;\; \lambda_{111} = -21.5 \times 10^{-6}$$

$$\text{FCC nickel} \;\; \lambda_{100} = -46 \times 10^{-6} \;\; \text{and} \;\; \lambda_{111} = -25 \times 10^{-6}$$

It should be noted that the ⟨100⟩ directions are the easy directions of magnetization for BCC-Fe and the ⟨111⟩ directions are easy for FCC-Ni (O'Handley, 2000, Ch. 5; Lacheisserie and Monterroso, 1983). Rotating the magnetization of an iron crystal from one easy axis to a different easy axis causes an increase in length along the field axis of $(3/2)\lambda_{100} \approx 31 \times 10^{-6}$. The field at which the magnetostriction saturates is the anisotropy field (see Figure 4).

Many of the rare-earth metals and rare-earth intermetallic compounds are characterized by very strong magnetic anisotropy which makes it difficult to get an accurate measurement of saturation magnetostriction values. Some data for these materials are given in Table 1. Further data on these systems can be found in Cullity (1973) and O'Handley (2000) and in review articles (Clark, 1980; Morin and Schmitt 1990; Cullen, Clark and Hathaway, 1997). An alloy having nearly zero magnetic anisotropy at room temperature, Terfenol-D ($Fe_2[Dy_{0.7}Tb_{0.3}]$) was developed at the Naval Ordinance Laboratory (hence the name *Ter-Fe-NOL*) (Clark, 1980; Cullen, Clark and Hathaway, 1997) by combining appropriate ratios of the cubic Laves compounds Fe_2Tb ($K_1 = -7 \times 10^7\,\mathrm{J\,m^{-3}}$) with Fe_2Dy ($K_1 = 3 \times 10^7\,\mathrm{J\,m^{-3}}$).

The highly magnetostrictive rare-earth compounds are prone to oxidation and are relatively brittle (poor tensile behavior and not easily machined). Favorably textured

Table 1. Magnetostriction constants λ_{100} and λ_{111} in parts per million at 4.2 K and at room temperature for several materials. Some polycrystalline room-temperature values are also listed. The prefix *a* designates an amorphous material. For uniaxial materials (denoted by superscript 'u') where $\lambda^{\gamma,2}$ or $\lambda^{\varepsilon,2}$ was reported, their values are given in parentheses in the λ_{100} and λ_{111} column, respectively.

	$T = 4.2$ K		Room temperature		
	$\lambda_{100}(\lambda^{\gamma,2})$	$\lambda_{111}(\lambda^{\varepsilon,2})$	$\lambda_{100}(\lambda^{\gamma,2})$	$\lambda_{111}(\lambda^{\varepsilon,2})$	Polycrystal λ_s
3d metals					
BCC-Fe	26	−30	21	−21	−7
HCP-Co^u	(−150)	(45)	(−140)	(50)	(−62)
FCC-Ni	−60	−35	−46	−24	−34
BCC-Fe-Ga	–	–	400	30	–
a-$Fe_{80}B_{20}$	48	–	–	–	+32
a-$Fe_{40}Ni_{40}B_{20}$	+20	–	–	–	+14
a-$Co_{80}B_{20}$	−4	–	–	–	−4
4f metals/alloys					
Gd^u	(−175)	(105)	(−10)	0	–
Tb^u	–	(8700)	–	(30)	–
$TbFe_2$	–	4400	–	2600	1753
$Tb_{0.3}Dy_{0.7}Fe_2$	–	–	–	1600	1200
Spinel ferrites					
Fe_3O_4	0	50	−15	56	+40
$CoFe_2O_4$	–	–	−670	120	−110
Garnets					
YIG	−0.6	−2.5	−1.4	−1.6	−2

polycrystalline boules ([211] parallel to the boule axis) can be grown with modest yield. There remained a need for a less expensive and more ductile high-magnetostriction Fe-based alloy. It appears to have been found in the BCC-Fe–Ga solid solutions (appropriately named *Galfenol*) (Clark *et al*., 2000, Guruswamy *et al*., 2000). The variation of λ_{100} with Ga content is shown in Figure 5 (λ_{111} is less than 10% of λ_{100}) due, in part, to the large value of $C_{44} \approx 1.2 \times 10^{11}$ Pa over most of the Ga range studied) (Wuttig, Dai and Cullen, 2002). The peak in λ_{100} at $x_{Ga} = 26$ at% is because of the vanishing of $C_{11} - C_{12}$ there. The peak in λ_{100} at 19% Ga occurs in the solid solution range and is of technical importance; its origin is possibly due to directional ordering of Ga over a short range.

Field-dependent data are not presented here because the form of the strain versus field can depend on many factors such as sample shape, microstructure, and stress, which may obscure the predicted quadratic dependence on field for magnetization along a hard axis (Figure 4). The *typical* field dependence of magnetostriction in a variety of magnetic alloys are compared in Figure 6 on a Log–Log scale. It includes representative behavior for the very low anisotropy Fe-rich amorphous magnetic alloys (such as $Fe_{80}B_{20}$, for which $\lambda_{100} = 32 \times 10^{-6}$ (O'Handley, 1978)), BCC $Fe_{81}Ga_{19}$ and $Fe_2(Dy_{0.7}Tb_{0.3})$, Terfenol-D®. Also included in Figure 6 is the field dependence of the magnetostriction (solid line) and field-induced twin-boundary motion (dashed line) for Ni–Mn–Ga (see next section). In all cases, the magnetostriction is shown as quadratic in

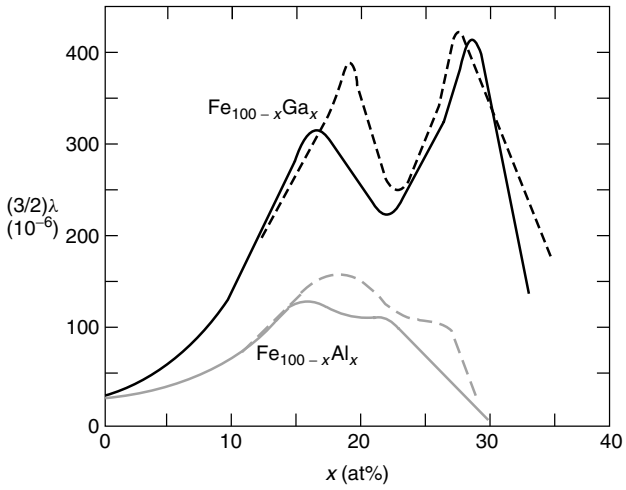

Figure 5. Dependence of λ_{100} on composition for a variety of $Fe_{1-x}Ga_x$ alloys compared with the behavior of $Fe_{1-x}Al_x$ (Hall, 1959). The solid lines are for furnace-cooled samples and the dashed lines are for quenched samples. Data for $Fe_{1-x}Be_x$ alloys is available up to 12 at% and follows that for Fe–Ga in that range. (Data assembled by M. Wun Fogle and J. Restorff, unpublished.) (Reprinted with permission R.C. Hall, copyright 1959, American Institute of Physics.)

the field up to its saturation value. Note the difference in saturation fields for the various materials. The diagonal dotted line is a guide to the eye with a slope of unity; it indicates that the saturation magnetostriction is not achieved at a field that is proportional to the saturation magnetostriction.

A quality factor for many applications is the ratio strain per unit field, λ/H. Amorphous magnetic alloys have advantage on that basis because they typically saturate in fields of order $10-100\,\mathrm{A\,m^{-1}}$ though they produce far less strain than the other materials. Terenol-D® shows about six times the magnetostrictive strain of Fe–Ga ($2400 \times 10^{-6}/400 \times 10^{-6}$) but Galfenol® magnetostriction saturates in a field of approximately about $8\,\mathrm{kA\,m^{-1}}$ while Terfenol-D requires about $80\,\mathrm{kA\,m^{-1}}$ to saturate.

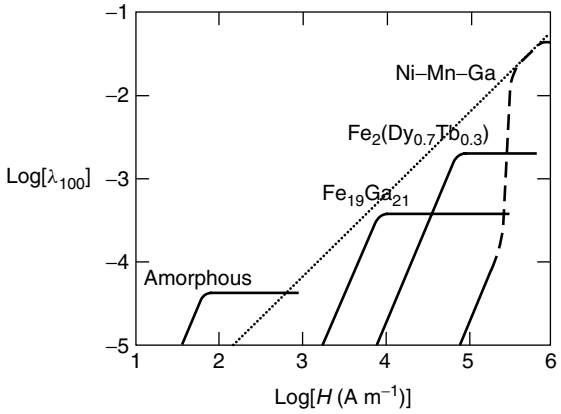

Figure 6. Log–Log representation of λ_{100} versus H typical of various classes of magnetostrictive materials. Amorphous magnetic alloys are represented by $Fe_{80}B_{20}$ and the Ni–Mn–Ga behavior is typical of its tegragonal phase (see below). The fine diagonal line represents a linear dependence of saturation magnetostriction on field indicating an advantage for amorphous alloys in terms of the quality factor, λ/H.

2.2 Cubic systems

The ME contribution to the magnetic anisotropy of a cubic material is expressed to first order as

$$f_{\mathrm{ME}} = B_1\left[e_{xx}\left(\alpha_1^2-\frac{1}{3}\right)+e_{yy}\left(\alpha_2^2-\frac{1}{3}\right)+e_{zz}\left(\alpha_3^2-\frac{1}{3}\right)\right] + B_2\left[e_{xy}\alpha_1\alpha_2+e_{yz}\alpha_2\alpha_3+e_{zx}\alpha_3\alpha_1\right]+\cdots \qquad (5)$$

Here, the direction cosines specify the direction of magnetization and the B_i's are the stresses of magnetic origin, which give rise to the components of the magnetostrictive strain tensor, ε_{ij}, by minimization of the total free energy including elastic terms:

$$(\varepsilon_{ii}) = \begin{pmatrix} -\dfrac{B_1}{(c_{11}-c_{12})}\left(\alpha_1^2-\dfrac{1}{3}\right) & -\dfrac{B_2}{c_{44}}\alpha_1\alpha_2 & -\dfrac{B_2}{c_{44}}\alpha_1\alpha_3 \\ -\dfrac{B_2}{c_{44}}\alpha_1\alpha_2 & -\dfrac{B_1}{(c_{11}-c_{12})}\left(\alpha_2^2-\dfrac{1}{3}\right) & -\dfrac{B_2}{c_{44}}\alpha_3\alpha_2 \\ -\dfrac{B_2}{c_{44}}\alpha_1\alpha_3 & -\dfrac{B_2}{c_{44}}\alpha_3\alpha_2 & -\dfrac{B_1}{(c_{11}-c_{12})}\left(\alpha_3^2-\dfrac{1}{3}\right) \end{pmatrix} \qquad (6)$$

Equation (6) makes it clear that the magnetostrictive strain, ε_{ij}, results from the action of components of the ME stress tensor, B_{ij}, on the material whose stiffness is characterized by the elastic constants, c_{ij}. The strain in any direction, β, is specified by projecting ε_{ij} on the vector $(\beta_1, \beta_2, \beta_3)$:

$$\frac{\partial \ell}{\ell} = (\beta_1,\beta_2,\beta_3)(e_{ii})\begin{pmatrix}\beta_1\\ \beta_2\\ \beta_3\end{pmatrix} = \sum e_{ii}\beta_i^2 + \sum_{i<j} e_{ij}\beta_i\beta_j \qquad (7)$$

Substituting the values of ε_{ij} given in equation (5) into equation (7), gives the strain in direction β for magnetization in direction α:

$$\frac{\partial \ell}{\ell} = -\frac{B_1}{c_{11}-c_{12}}\left(\alpha_1^2\beta_1^2+\alpha_2^2\beta_2^2+\alpha_3^2\beta_3^2-\frac{1}{3}\right) - \frac{B_2}{c_{44}}\left(\alpha_1\alpha_2\beta_1\beta_2+\alpha_2\alpha_3\beta_2\beta_3+\alpha_3\alpha_1\beta_3\beta_1\right) \qquad (8)$$

Equation (8) shows how the deformation of a magnetic sample depends on the direction of magnetization through the α's and on the strain-measuring direction through the β's. The factor of $-1/3$ in equation (8) reflects the fact that a demagnetized crystal with a perfectly random distribution of domain magnetizations is taken by convention to be in a state of zero strain, $dl/l = 0$.

For a sample *magnetized in the* [100] *direction*, the *strain measured in that direction* is defined as λ_{100}. In that case, $\alpha_1 = \beta_1 = 1$ and $\alpha_2 = \alpha_3 = \beta_2 = \beta_3 = 0$, giving:

$$\lambda_{100} = -\frac{2}{3}\frac{B_1}{c_{11}-c_{12}} \qquad (9)$$

For λ_{111}, $\alpha_i = \beta_i = (1/3)$ giving:

$$\lambda_{111} = -\frac{1}{3}\frac{B_2}{c_{44}} \tag{10}$$

Similarly, for λ_{110} we get,

$$\varepsilon_{110} = \lambda_{110} = -\frac{1}{6}\frac{B_1}{(c_{11} - c_{12})} - \frac{1}{4}\frac{B_2}{c_{44}} = \frac{1}{4}\lambda_{100} + \frac{3}{4}\lambda_{111} \tag{11}$$

For an *isotropic material*, all reference to crystallographic direction is gone, so we expect $\lambda_{100} = \lambda_{111} = \lambda_s$, and thus equation (8) reduces to equation (1).

2.3 Polycrystalline materials

For a random polycrystalline material, rotating $\boldsymbol{M}$ produces the full ME stress, B_i, in each grain, but the local strain of each grain may be incompatible with the strains of adjacent grains. The macroscopic material expresses the magnetostrictive strain that is the sum of those of its grains that are constrained and have different orientations.

When magnetostrictive strains are small, it may be adequate to neglect elastic interaction of various grains (O'Handley and Grant, 1985). For a completely *random 3-D polycrystalline material* Callen and Goldberg (1965) obtained:

$$\lambda_s = \frac{2}{5}\lambda_{100} + \frac{3}{5}\lambda_{111} \tag{12}$$

The λ_s values measured for polycrystalline nickel and iron are -34×10^{-6} and -7×10^{-6}, respectively. Use of equation (12) is justified only for an *untextured* polycrystalline material and for amorphous alloys. If a polycrystalline material is crystallographically textured or if the grains are more nearly isotropic magnetoelastically (i.e., $\lambda_{100} \approx \lambda_{111}$), then a net strain closer to the true magnetostriction value can be realized.

Values of saturation magnetostriction for several materials are listed in Table 1. The experimental notation (λ_{100}, λ_{111}) is used because of its prevalence in the literature. More universal definitions of λ, namely, $\lambda^{\alpha,2} \approx 3\lambda_{100}/2$, $\lambda^{\varepsilon,2} \approx 3\lambda_{111}/2$ (Lacheisserie, 1993), are described in the following text. Where the literature indicates that $\lambda^{\gamma,2}$ or $\lambda^{\varepsilon,2}$ was measured, those values are listed in parentheses in Table 1.

2.4 Magnetoelastic contribution to anisotropy

For a cubic material, the magnetocrystalline anisotropy energy density can be written as $f_a = K_1(\alpha_1^2\alpha_2^2 + \alpha_2^2\alpha_3^2 + \alpha_3^2\alpha_1^2) + K_2\alpha_1^2\alpha_2^2\alpha_3^2 + \cdots$. The direction cosines of the magnetization are arranged in a way that defines an energy function that reflects the crystal symmetry. The anisotropy coefficients, K_i, describe the strength of the preference for M to orient in specific crystallographic directions. Inspection of equation (5) shows that for a given value of strain, the ME energy resembles a magnetic anisotropy energy inasmuch as it is a function of the magnetization orientation. However, the first two ME terms for a *cubic* material are of lower symmetry, than the cubic magnetocrystalline anisotropy terms, K_1 and K_2. ME energy is simply that part of the magnetic anisotropy that depends on strain; it can be of lower symmetry than the strain-independent part because of the small change in symmetry imposed by the strain. Thus, isolation of the strain-dependent part of the anisotropy provides a measure of the ME coupling coefficients, B_i.

The ME contribution to the anisotropy is responsible for the inverse magnetostrictive effect illustrated in Figure 3. Inverse ME effects appear in two situations. First, an *imposed mechanical strain* alters the energy density function, $f_a(\theta, \phi)$, and hence changes the magnetization process below saturation. Second, a *magnetostrictive strain* (resulting from a change in magnetization direction) alters the free energy and hence changes the approach to saturation. The latter is a second-order effect and is most apparent in high-magnetostriction materials such as some rare-earth-containing materials.

An example of stress or strain-induced anisotropy can be found in O'Handley (2000). Essentially, tension in a positive magnetostriction material ($\lambda_s \varepsilon_{xx} > 0$ or $B_1 \varepsilon xx < 0$) makes the magnetization process easier in the tensile direction. The area to the left of a hard-axis magnetization curve gives the anisotropy energy density, K^{eff}. If one measures the magnetization curve of a sample in different known states of strain, then the change in that area indicating the energy needed to magnetize the sample changes by $B_1\varepsilon(1 + \upsilon)$. This is true even for an arbitrarily shaped magnetization curve – the strain-induced change in energy needed to magnetize a sample is the ME energy (O'Handley, Song and Ballentine, 1993).

2.5 Symmetry-invariant notation

It is important to know the form that the magnetostriction must take in hexagonal and in other low-symmetry magnetic structures. Materials with hexagonal structures include cobalt and many cobalt-rich alloys, rare-earth metals, and some rare-earth intermetallic compounds, as well as barium

hexaferrite. Presented here are the results of the general formalism for magnetic anisotropy and magnetostriction introduced by Callen and Callen (1960, 1963, 1965) and reviewed by Lacheisserie (1993).

Legendre polynomial expansions of the magnetic free energy are used widely for cubic materials; the simple expansion $f_a = \sum_{n=0,\ldots} C_n \sin^{2n}\theta$ is often used for uniaxial materials. It was noted by Callen and Callen in 1960 that it is appropriate to expand the magnetic anisotropy energy in a set of orthogonal, normalized functions based on Legendre polynomials,

$$g_\ell(\alpha) = \sum_{m=-\ell}^{\ell} A_\ell^m Y_\ell^m(\alpha) \tag{13}$$

The argument α is the direction cosine of the magnetization. The coefficients, A_l^m, of the spherical harmonics, Y_l^m, are defined so the polynomials, $g_l(\alpha)$, belong to the irreducible representation of the crystal point group to be described. The anisotropy energy density is then written:

$$f_K^{\text{hex}} = \sum_{\ell=0} k_\ell g_\ell(\alpha) = k_o + k_2\left(\alpha^2 - \frac{1}{3}\right) + k_4\left(\alpha^4 - \frac{6}{7}\alpha^2 + \frac{3}{35}\right) + \cdots \tag{14}$$

The anisotropy coefficients, k_l, based on such expansions are found more often in the literature on rare-earth materials. When these functions are used, the ME energy expression is a sum of products of strain components and direction cosines, each of which has the same symmetry. This is illustrated in Figure 7 for the cubic system where the strains and direction-cosine terms are both seen to have the familiar forms of the atomic d orbitals in cubic symmetry. These are the five irreducible representations of the cubic point group.

The form of the ME energy in cubic and uniaxial symmetry is given below to lowest order in these symmetry-invariant polynomials. This is followed by the formula for the magnetostriction. Higher-order terms and forms for other symmetries can be found in (Lacheisserie, 1993).

For cubic symmetry, the ME free energy is

$$\begin{aligned} f_{\text{me}}^{\text{cubic}} = {} & \frac{\varepsilon_{xx}+\varepsilon_{yy}+\varepsilon_{zz}}{3}[b^{\alpha,0} + \cdots] \\ & + \frac{3}{2}\left(\varepsilon_{zz} - \frac{\varepsilon_{xx}+\varepsilon_{yy}}{2}\right)\left[b^{\gamma,2}\left(\alpha_3^2 - \frac{\alpha_1^2+\alpha_2^2}{2}\right) + \cdots\right] \\ & + \frac{1}{2}(\varepsilon_{xx} - \varepsilon_{yy})\ \left[b^{r,2}(\alpha_1^2 - \alpha_2^2) + \cdots\right] \\ & + 2\varepsilon_{xy}\alpha_1\alpha_2\left\{b^{\varepsilon,2} + \cdots\right\} + \text{cycl.} \end{aligned} \tag{15}$$

The terms $b^{l,m}$ and ε_{ij} are the ME coupling (stress) coefficients and strains, respectively, in the irreducible representation. The magnetostriction for cubic crystals, to fourth order in α_i is

$$\begin{aligned} \lambda^{\text{cubic}} = {} & \frac{1}{3}\lambda^{\alpha,4}\left(\alpha_1^4 + \alpha_2^4 + \alpha_3^4 - \frac{3}{5}\right) + \sum_{i=1,2,3}\left(\beta_i^2 - \frac{1}{3}\right) \\ & \times \alpha_i^2\left[\lambda^{\gamma,2} + \lambda^{\gamma,4}\left(\alpha_i^2 - \frac{6}{7}\right) + \cdots\right] \\ & + \sum_{i<j=1,2,3} 2\beta_i\beta_j\alpha_i\alpha_j\left[\lambda^{\varepsilon,2} + \lambda^{\varepsilon,4}\left(\alpha_k^2 - \frac{1}{7}\right) + \cdots\right] \end{aligned} \tag{16}$$

The superscript α on the magnetostriction denotes volume strains, which preserve crystal symmetry. The γ and ε exponents come from the molecular-orbital notation that describe 3d orbitals as either the doublet d^γ (d_{z^2} and $d_{x^2-y^2}$) or the triplet d^ε (d_{xy}, d_{yz} and d_{zx}); see Figure 7. They are volume-conserving uniaxial strains. The index after the Greek superscript indicates the order in direction cosines (2 = uniaxial, 4 = cubic, etc.). These symmetry-based cubic magnetostriction coefficients can be expressed in terms of the older coefficients by the relations:

$$\lambda_{100} = \frac{2}{15}\lambda^{\alpha,4} + \frac{2}{3}\left(\lambda^{\gamma,2} + \frac{1}{7}\lambda^{\gamma,4} + \cdots\right) \approx \frac{2}{3}\lambda^{\gamma,2} \tag{17}$$

$$\lambda_{111} = -\frac{4}{45}\lambda^{\alpha,4} + \frac{2}{3}\left(\lambda^{\varepsilon,2} + \frac{4}{21}\lambda^{\varepsilon,4} + \cdots\right) \approx \frac{2}{3}\lambda^{\varepsilon,2} \tag{18}$$

For hexagonal symmetry, the free-energy density is given by

$$\begin{aligned} f_{\text{me}}^{\text{uniaxial}} = {} & b_1^{\alpha,0}\frac{\varepsilon_{xx}+\varepsilon_{yy}+\varepsilon_{zz}}{3} + b_2^{\alpha,0}\frac{\sqrt{2}}{3} \\ & \times\left(\varepsilon_{zz} - \frac{\varepsilon_{xx}+\varepsilon_{yy}}{2}\right) + \left[b_1^{\alpha,2}\frac{\varepsilon_{xx}+\varepsilon_{yy}+\varepsilon_{zz}}{\sqrt{2}}\right. \\ & \left. + b_2^{\alpha,2}\left(\varepsilon_{zz} - \frac{\varepsilon_{xx}+\varepsilon_{yy}}{2}\right)\right]\left(a_3^2 - \frac{1}{3}\right) \\ & + b^{\varepsilon,2}\left[\frac{1}{2}\left(\varepsilon_{xx} - \varepsilon_{yy}\right)\left(\alpha_1^2 - \alpha_2^2\right) + 2\varepsilon_{xy}\alpha_1\alpha_2\right] \\ & + 2b^{\zeta,2}\left(\varepsilon_{yz}\alpha_2\alpha_3 + \varepsilon_{xz}\alpha_1\alpha_3\right) + \cdots \end{aligned} \tag{19}$$

For crystals of hexagonal symmetry, the magnetostriction is

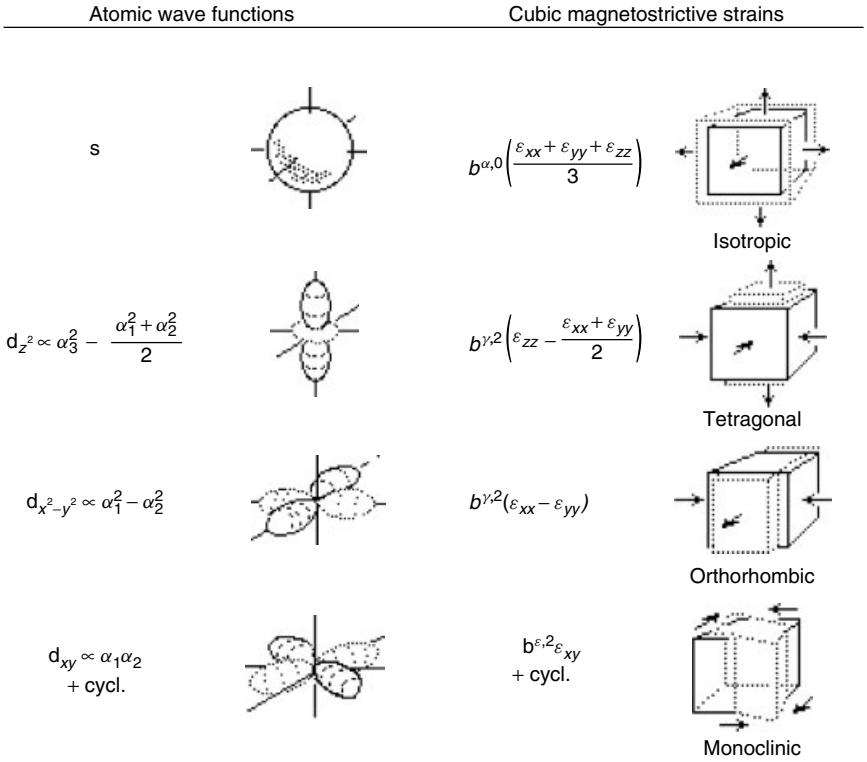

Figure 7. The first line shows the form of the isotropic s-wave function and the isotropic, volume magnetostriction. In the next three rows, the symmetry and amplitude (solid line, $\psi_d > 0$, dotted lines, $\psi_d < 0$) of the five atomic d functions are seen to be isomorphic with the five cubic Joule magnetostriction strains (equation (15)). This is because both are examples of irreducible representations of the cubic group. (Adapted from O'Handley, 2000.)

$$\begin{aligned}\lambda^{\text{hex}} = {} & \frac{1}{3}\lambda_1^{\alpha,0} + \lambda_2^{\alpha,0}\left(\beta_3^2 - \frac{1}{3}\right) \\ & + \left[\frac{1}{3}\lambda_1^{\alpha,2} + \lambda_2^{\alpha,2}\left(\beta_3^2 - \frac{\beta_1^2+\beta_2^2}{3}\right)\right]\left(\alpha_3^2 - \frac{1}{3}\right) \\ & + \lambda^{\varepsilon,2}\left[\frac{1}{2}\left(\beta_2^1 - \beta_2^2\right)\left(\alpha_1^2 - \alpha_2^2\right) + 2\beta_1\beta_2\alpha_1\alpha_2\right] \\ & + 2\lambda^{\zeta,2}\left(\beta_2\beta_3\alpha_2\alpha_3 + \beta_1\beta_3\alpha_1\alpha_3\right) + \ldots \end{aligned} \tag{20}$$

The α- and ε-labeled magnetostriction coefficients describe the same distortions in a hexagonal system as they do in cubic symmetry. ε-labeled terms distort the symmetry in the base plane; ζ terms shear over the c axis (Clark, 1980).

2.6 Temperature dependence

Proper measurement and analysis of the temperature dependence of magnetostriction can indicate a great deal about the nature of the strain-dependent, anisotropic interactions in a material and about the symmetry of the local atomic environment of the magnetic species.

Figure 8 shows the temperature dependence of the two principal magnetostriction constants in Ni. The shaded area shows the trend and scatter in data from numerous sources. The solid lines are theoretical fits that are based on the assumption of localized magnetic moments as will be described below.

The temperature dependence of magnetostriction in iron is quite different from that of nickel, with λ_{100} showing a maximum below room temperature then decreasing at lower temperatures (Tatsumoto and Okamoto, 1959; Lacheisserie and Monterroso, 1983). The temperature dependence of the magnetostriction of Ni comes closer to the theoretical than does that of iron. It is believed this is due to the lower energy of the Ni d bands (thus, more localized magnetic moment) compared to those of Fe.

In rare-earth metals, the metallic character comes from the 5d and 6s valence bands whereas the magnetic moments arise from the partially filled 4f states, which are more atomiclike, more localized; thus the magnetostriction of rare earths should be well described by theory. Figure 9 shows the temperature dependence of λ^{A} and $\lambda^{\text{C}} = \lambda^{\varepsilon,2}/2$ for single-crystal Tb. Note the steep decrease with increasing temperature for λ^{A} (cubic symmetry strain with temperature

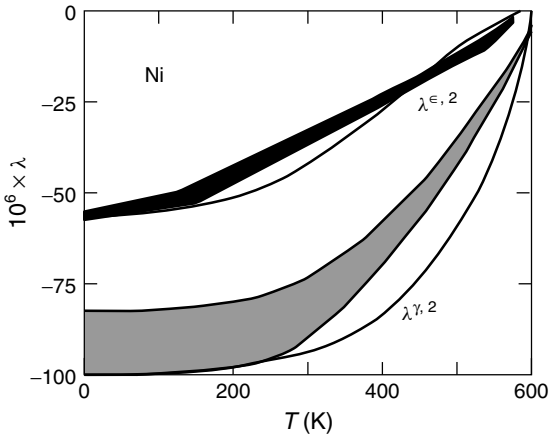

Figure 8. The shaded areas show range of experimental magnetostriction of Ni single crystals (Franse and Stolp, 1970; Lee and Asgar, 1971) and solid lines show calculated temperature dependence (Lacheisserie, 1972; Lacheisserie and Roucy, 1982).

dependence proportional to m^{10}) compared to λ^{C} (uniaxial strain with temperature dependence proportional to m^3). See theory in the following text.

In these examples, just as for magnetocrystalline anisotropy, $\lambda(T)$ drops much more sharply with increasing temperature than does $M(T)$. Here, the results of the theory developed by Callen and Callen (1966) for the temperature dependence of anisotropy and magnetostriction are outlined. To describe the *strain dependence* of the energy, the anisotropic Hamiltonian is expanded in powers of strain to first order:

$$H_{\mathrm{ME}} = \varepsilon_\mu \mathbf{S}_i \cdot \frac{\partial \mathbf{J}_{ij}}{\partial \varepsilon_\mu} \cdot \mathbf{S}_j + \varepsilon_\mu \mathbf{S}_i \cdot \frac{\partial \mathbf{D}}{\partial \varepsilon_\mu} \cdot \mathbf{S}_i + \cdots \qquad (21)$$

Here, $\mathbf{S}_i$ is a spin vector at site i. The elastic Hamiltonian is added to equation (21) and the expectation value of this strain-dependent Hamiltonian, $E = \langle H \rangle$ is minimized to allow solution for the strain components ε_u. The *two-ion* term expresses the strain dependence of the *anisotropic-exchange* interaction, $\mathbf{J}_{ij}$, between the z components of *spins at two different sites*. It gives rise in the solution to correlation functions $\langle S_i^z\, S_j^z \rangle$. (The usual Heisenberg exchange interaction, which is most responsible for the value of the Curie temperature, is an *isotropic* interaction between two spins). The *single-ion* term expresses the effect of strain on the *crystal-field anisotropy*, **D**, seen by a single magnetic ion. It leads to terms in the solution proportional to $\langle (S_i^z)^2 \rangle$. These spin-correlation functions play a central role in understanding the temperature dependence of anisotropy and magnetostriction (Callen and Callen, 1960, 1963, 1965; Lacheisserie, 1993; O'Handley, 1978; Legvold, Alstad and Rhyne, 1963; Rhyne and Legvold, 1965).

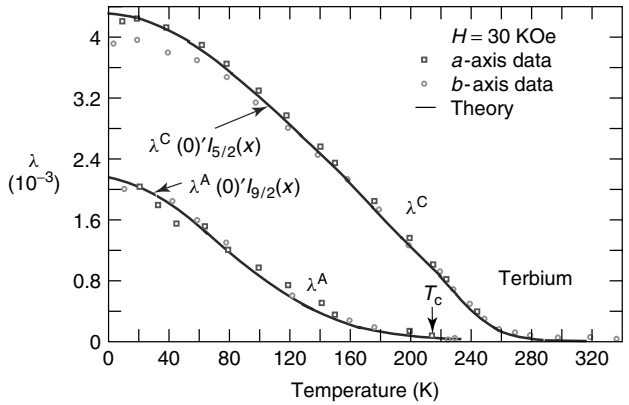

Figure 9. Temperature dependence of λ^{A} and $\lambda^{\mathrm{C}} = \lambda^{\varepsilon,2}/2$ for Tb single crystal (Rhyne and Legvold, 1965).

The exact results of the quantum statistical mechanical model of temperature dependence of ME effects owing to *single-ion effects* can be summarized as follows:

$$\frac{\lambda_\ell(T)}{\lambda_\ell(0)} \quad \text{or} \quad \frac{K_\ell(T)}{K_\ell(0)} = \kappa_\ell(T) = \frac{\left\langle [\mathbf{S}_i^z(T)]^2 \right\rangle}{\left\langle [\mathbf{S}_i^z(0)]^2 \right\rangle}$$

$$\Rightarrow \frac{I_{\ell+1/2}(X)}{I_{1/2}(X)} \equiv \hat{I}_{\ell+1/2}(X) \qquad (22)$$

Here, $I(X)$ is a modified Bessel function and $\hat{I}(X)$ is a reduced, modified Bessel function (Callen and Callen, 1960, 1963, 1965). The argument X is defined by the temperature dependence of magnetization $m(T) = I_{3/2}(X)$ so that X can be formally written as $X = I_{3/2}^{-1}(m)$.

Approximate temperature dependences of the modified Bessel functions have been calculated (Callen and Callen, 1963, 1965); they are characterized by different dependences on the reduced magnetization, m, above and below approximately 0.6 T_{C}. Table 2 shows the low-T and high-T approximations for *single-ion anisotropy* for $l = 2$ and 4.

The temperature dependence of the magnetization for the *two-ion exchange* mechanism is given more simply by the square of the reduced magnetization:

$$\frac{\left\langle S_i^z(T) S_j^z(T) \right\rangle}{\left\langle S_i^z(0) S_j^z(0) \right\rangle} \equiv m^2 \qquad (23)$$

Table 2. Approximate *single-ion* magnetization power law dependences for uniaxial ($l = 2$) and cubic ($l = 4$) systems at low and high temperatures.

Approximations to $\hat{I}_{l+1/2}(X)$		$l = 2$	$l = 4$
Low T	$\sim m^{l(l+1)/2}$	m^3	m^{10}
High T	$\sim m^l$	m^2	m^4

The two-ion exchange is sometimes weaker than the single-ion anisotropy but does play a role in many dipole-coupled rare-earth systems (Morin and Schmitt, 1990).

Lacheisserie (1972) has shown that the nickel data available in 1971 can be fit up to 300 K with a combination of single-ion and two-ion terms (solid lines, Figure 8)

$$B^{\gamma,2} = 110\{0.13\hat{I}_{5/2}(X) + 0.87m^2\} \times 10^6 \text{ erg cm}^{-3}$$
$$B^{\varepsilon,2} = 149\{2.54\hat{I}_{5/2}(X) - 1.54m^2\} \times 10^6 \text{ erg cm}^{-3} \quad (24)$$

Equation (24) indicates that the magnetostriction of nickel contains a two-ion, anisotropic-exchange term in addition to a single-ion contribution. The former plays a significant role as T/T_C approaches unity because there the more-strongly temperature-dependent, single-ion terms are very small. These nickel magnetostriction functions, equations (22) and (24), at room temperature and 4.2 K agree with the data in Table 1. The temperature dependence of magnetostriction in iron is more complex than that of Ni. This is believed to be because of the more itinerant nature of the 3d states (delocalized magnetic moments) in Fe compared to Ni (Lacheisserie and Monterroso, 1983).

The temperature dependence of $\lambda^{\gamma,2}$ in Gd follows that of a sum of single-ion and two-ion terms (Callen and Callen, 1965). Here, the two-ion term is strong enough to account for a change in sign of λ above 220 K.

A particularly simple case is that of amorphous metallic alloys. Although these materials are macroscopically isotropic, they are characterized locally by uniaxial anisotropy. The measured temperature dependence of magnetostriction in several different amorphous alloys is quite well described by the uniaxial, single-ion form of equation (22), $\hat{I}_{5/2}(X)$. Some cobalt-rich amorphous alloys show a change in sign of λ_s with increasing temperature that, as in the case of Gd, may be associated with a significant two-ion contribution (O'Handley, 1978; Lacheisserie, 1987).

2.7 Second-order effects

There are two second-order ME effects that are important to note. One is a change in the ME constants, either λ_s or B_i, when a material is strained to a significant level. In this effect, the ME energy density contains terms that are quadratic in strain and also have direction cosines of the magnetization as coefficients. The other second-order effect is a change in the elastic constant of a material owing to the presence of a magnetostrictive strain in addition to the strain produced by an external stress. This is referred to as the ΔE *effect*.

2.7.1 Strain-induced changes in ME coefficients

In highly strained materials, such as epitaxial thin films with significant lattice mismatch between the film and substrate, the ME coupling coefficient, B_1, can assume values different from bulk. Just as an external strain or stress can alter the magnetocrystalline anisotropy (equation (5)), it can also alter the ME coupling coefficient or the magnetostriction coefficient. This may be appreciated by recognizing that equation (5) is the first-order term in an expansion of the magnetic anisotropy in strain. If terms of second order in strain, such as $D_{ij}\alpha_i\alpha_j\varepsilon_{ij}$, are added to the free energy, then the terms may be regrouped to express an effective ME coupling coefficient, $B_1^{\text{eff}} = B_1 + D_1\varepsilon_{ij}$ (O'Handley and Sun, 1992; Sander, 1999).

Such second-order changes in ME coupling coefficients have been measured directly by straining a bulk material (Lacheisserie and Roucy, 1982) as well as in epitaxial thin film of Ni/Cu, (Ha and O'Handley, 1999; Ciria and O'Handley, 2002), or in polycrystalline thin films of Fe (Koch, Weber, Thürmer and Rieder, 1996; Sander, 1999). A detailed theory of these effects is under development (Fahnle and Komelj, 2002).

Values of D_1 for Ni films (Lachaeisserie, 1993; Sander, 1999; Ciria *et al.*, 2003) are of the order -2.3×10^8. Clearly when these values are multiplied by a strain of order 1%, the product is comparable to the magnitude of the first-order ME coupling coefficient, B_1, namely, 6.2×10^6 Pa and -3.4×10^6 Pa for Ni and Fe, respectively. In both of the cases cited, the second-order effect changes the sign of the ME energy density, $B_1^{\text{eff}}\varepsilon$, for positive strain but not for negative strain.

2.7.2 ΔE Effect

Application of an external mechanical stress to a magnetostrictive material induces a strain which in turn, tends to rotate the magnetization; $\boldsymbol{M}$ moves toward a tensile stress direction for $\lambda > 0$, $B < 0$ (Figure 3). The stress-induced rotation of $\boldsymbol{M}$ brings with it the *magnetostrictive strain in addition to the mechanically induced strain*. In the weak stress regime, the Joule magnetostriction makes a material appear mechanically softer than if the magnetization were not free to respond to the stress. This is illustrated in Figure 10 (from Lacheisserie, 1993). The material appears mechanically softer regardless of the sign of the magnetostriction indicating that this effect is quadratic in λ_s. The added magnetic strain, $\varepsilon_M \approx \lambda_s$, is generally insignificant compared to the elastic strain for large stresses. Thus, this ΔE effect, as it is called, is more important for acoustic waves, vibrations, and damping, than it is for mechanical strength.

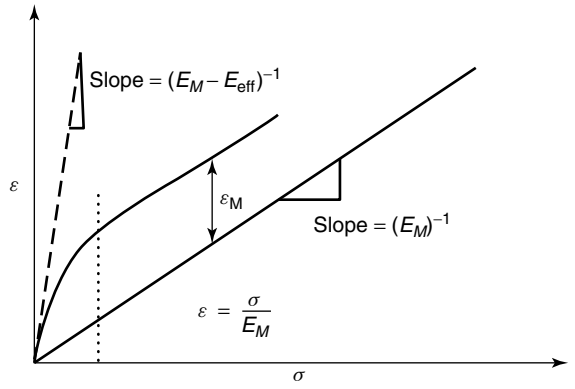

Figure 10. Strain versus stress in a magnetic material in the elastic regime. When the magnetization is fixed, the small strain behavior is purely linear. When the magnetization is free to respond to the applied stress, the material appears softer because of the additional magnetostrictive strain, ε_M. (Adapted from Lacheisserie, 1993.)

The total strain ε_{tot} that the ferromagnetic sample experiences understress, σ, can be written as a sum of the mechanical strain and the magnetostrictive strain:

$$\varepsilon_{\text{tot}} = \frac{\sigma}{E_M} + \frac{3}{2}\lambda_s\left[\cos^2\theta - \frac{1}{3}\right] \tag{25}$$

Here, E_M is the Young's modulus for *fixed magnetization* (no magnetostrictive contribution). The magnetostrictive contribution to total strain is taken from equation (1) where θ is the angle between the magnetization and the strain-measuring direction. Because $\cos\theta = m = H/H_a^{\text{eff}}$ for a hard-axis magnetization process, we can eliminate $\cos\theta$ from equation (25). The apparent modulus, $E_{\text{apparent}} = E_H = \partial\sigma/\partial\varepsilon_{\text{tot}}$, in the presence of this magnetostrictive strain is then obtained from equation (25) as:

$$\frac{1}{E_{\text{apparent}}} \equiv \frac{1}{E_H} = \frac{\partial e_{\text{tot}}}{\partial\sigma} = \frac{1}{E_M} - \frac{3\lambda_s H^2}{(H_a^{\text{eff}})^3}\frac{\partial H_a^{\text{eff}}}{\partial\sigma} \tag{26}$$

The ME contribution to the effective anisotropy field, H_a^{eff}, can be written as $3\lambda_s\sigma/M_s$ to first order, giving

$$\frac{E_M - E_H}{E_H} \equiv \frac{\Delta E}{E} = \frac{9\lambda_s^2 H^2}{M_s(H_a^{\text{eff}})^3}E_M \tag{27}$$

This formula applies when the magnetization is initially orthogonal to the stress direction.

Figure 11 shows the variation with temperature of the ΔE effect in amorphous Fe–P–C ribbons as a function of annealing condition: Z indicates zero field annealed, L and T indicate field annealed, longitudinal, and transverse to the ribbon direction, respectively. The experiments were done by measuring variations in the vibration frequency of the ribbon near 400 Hz (Berry and Pritchet, 1975). Clearly the ΔE effect

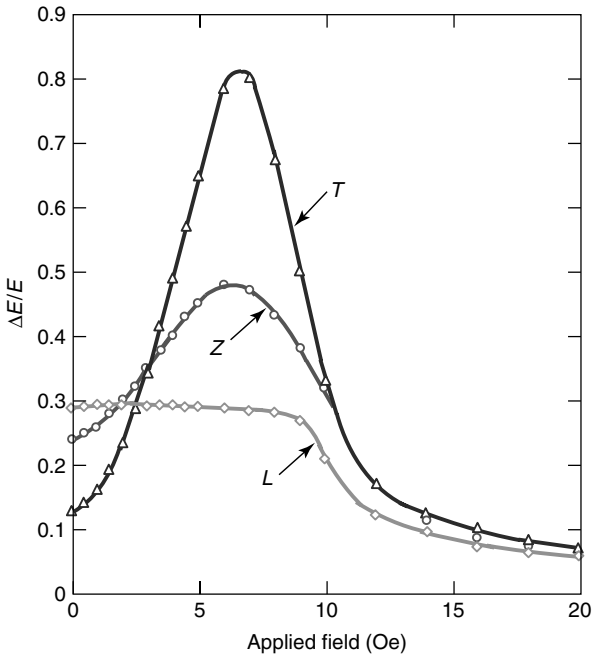

Figure 11. ΔE effect measured by the vibrating reed technique on an amorphous Fe–P–C ribbon in three annealing conditions: Z, no field, L, longitudinal field; T, transverse field. (Reprinted with permission Berry *et al*., copyright 1975, American Physical Society.)

is a function of the initial magnetization configuration of a sample. Annealing in the transverse direction gives an initial magnetization state that produces the most magnetostrictive strain under longitudinal flexure. At these low strain levels, the modulus of the amorphous ribbon is reduced by 80% in a field of about 6 Oe.

The ΔE effect is used in many magnetoacoustic devices where the resonance frequency, proportional to $E_H^{1/2}$, can be modulated by an applied field.

The relative strength of the ΔE effect is measured by a magnetomechanical coupling factor, k, which is defined as the ratio of the energy in coupled ME modes to the geometric mean of the pure elastic and pure magnetic energies:

$$k = \frac{2\mathbf{d}H\sigma}{\sqrt{\frac{1}{2}s^H\sigma^2\frac{1}{2}\chi H^2}} = \frac{4\mathbf{d}}{\sqrt{s^H\chi^\sigma}} = 4\mathbf{d}\sqrt{\frac{E^H}{\chi^\sigma}} \tag{28}$$

Here the free-energy density has the form,

$$g = \frac{1}{2}s^H\sigma^2 + 2\mathbf{d}H\sigma - \frac{1}{2}\gamma^\sigma H^2 \tag{29}$$

In equation (29), s^H is the mechanical compliance at constant field, $s^H = E_H^{-1}$, and χ^σ is the magnetic susceptibility at constant stress. This energy form expresses the partition of energy between pure elastic modes $(1/2)s^H\sigma^2$, pure

magnetic modes $(1/2)\chi^{\sigma}H^2$, and coupled ME modes, $\mathbf{d}H\sigma$. The magnetic and elastic responses for a *coupled* ME system are expressed:

$$-\partial g/\partial H = M = \chi^{sH} + \mathbf{d}\sigma$$
$$\text{and} \quad -\partial g/\partial \sigma = \varepsilon = \sigma s^{H} + \mathbf{d}H \tag{30}$$

The parameter **d**, called the *magnetostrictivity*, is defined as

$$\frac{1}{V}\frac{\partial^2 G}{\partial H \partial \sigma} = -\frac{\partial M}{\partial \sigma} = \frac{\partial e}{\partial H} \equiv \mathbf{d} \tag{31}$$

It describes the magnitude of magnetic-field-induced strain or stress-induced changes in M in a material. If the isotropic magnetostrictive strain expression in equation (1) is substituted for ε in equation (30), and $m = H/H_a$ for hard-axis magnetization is used, the magnetostrictivity can be expressed below saturation as

$$\mathbf{d} = 3\lambda_s \frac{H}{{H_a}^2} \tag{32}$$

where $\mathbf{d} = 0$ for $H > H_a$ (Livingston, 1982). Figure 12 shows the variation of $\mathbf{d}(H)$ for a material with pure transverse anisotropy (solid line) and for a more realistic M–H loop (dashed). Note that $\mathbf{d}(H)$ is the field derivative of $\lambda(H)$ shown in Figure 4 or from equation (1). Equations (27) and (32) indicate that the ΔE effect reaches a maximum when $\mathbf{d}^2$ is a maximum; **d** reaches a peak at or below the effective anisotropy field, H_a^{eff}.

The magnetostrictivity is important for transducer applications because it describes the stress sensitivity of magnetization (magnetoacoustic microphone) or the field sensitivity of strain (ME speaker or sonar projector) (equation (31)). What is needed for these applications is a material with a large value of λ_s but more importantly, a small value of H_a so that saturation is achieved in a relatively weak field. Hence, a useful figure of merit for transducer materials is the ratio $\lambda_s/K_{\text{eff}}^2$ as suggested by equation (32). Keeping in mind that the area under $\mathbf{d}(H)$ is fixed by λ_s (equation (30)), it is clear that decreasing the anisotropy field tends to increase the peak value of $\mathbf{d}(H)$.

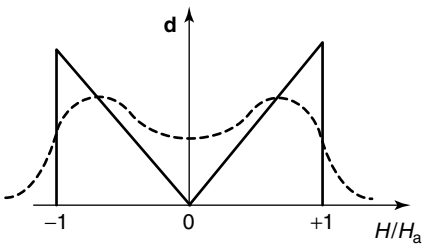

Figure 12. Magnetostrictivity versus field applied transverse to an easy axis (solid line) and for a more rounded magnetization curve (dashed line).

The magnetomechanical coupling factor, k, can take on values between zero and unity, the latter being the condition of complete coupling. In tensor notation, k_{33} pertains to longitudinal mode coupling. Similar expressions apply for shear mode coupling constants.

In terms of the ΔE effect, it can be shown that

$$k^2 = \frac{E_M - E_H}{E_M} = \frac{\Delta E}{E} \tag{33}$$

Thus, the ΔE effect can be expressed in terms of k, **d**, or the magnetostrictive strain.

2.8 Measurement techniques

The techniques for measuring magnetostriction fall into three broad categories.

1. When the sample is free to strain, that is, it is not constrained by adhesion to another material, the true magnetostrictive strain may be measured directly by a variety of means including the use of strain gauge, dilatometer, or capacitance techniques (in which the straining material displaces a capacitor plate). These are direct measurements of free strain.
2. When the magnetic sample is constrained by another body having appreciable bending modulus, Et (E is the elastic stiffness and t is the thickness of the second component), then the magnetostrictive *stress*, B_i can sometimes be measured by the deforming effect that an applied field has on the composite. Rotating $\boldsymbol{M}$ from an easy to a hard axis in a cubic material (equation (5)) generates the full ME stress, B_i. In this case, a strain less than the free magnetostriction, $|\varepsilon| < |\lambda_{ijk}|$, is generated in the constrained magnetostrictive material.

   The ME coupling coefficients of thin films on substrates have been determined from the deflection of the film-substrate cantilever upon change of the magnetization direction (Klokholm, 1976; Tam and Schroeder, 1989; Weber, Koch and Rieder, 1994). The displacement, Δy, of the end of the substrate of length L, fixed at one end (Figure 13), depends on the net in-plane stress, σ_f, generated by the appropriate ME coupling coefficient, B_f, exerted by the film as described by Stoney's equation (valid for $L > 3w$, with w being the width of the cantilever):

$$\Delta y = \frac{3t_f L^2 B_f (1 - \upsilon_s)}{t_s^2 E_s} \approx \frac{2t_f L^2 B_f}{t_s^2 E_s} \tag{34}$$

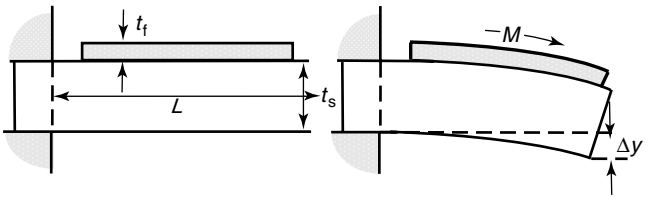

Figure 13. Schematic representation of cantilever bending owing to ME stress as the magnetization direction is changed. The case shown here is for $\lambda_s > 0$, or $B_1 < 0$.

Here t_i, E_i, and υ_i are the thickness, modulus, and Poisson's ratio of the film, $i = f$, or substrate, $i = s$, respectively. The magnetostriction constant can be determined from B_f using equations (8–10) if the elastic constants of the film are also known (but it is the *stress*, B_i, that is actually measured).

The cantilever deflection can be measured by a change in capacitance with the film acting as one plate of the capacitor (Klokholm, 1976), by differential capacitance technique with the film between two capacitor plates (Koch, Leonhard, Thurner and Abermann, 1990), or by deflection of a laser beam reflected from a point on the sample (Betz, Lachiesserie and Baczewski, 1996; Sander, Enders and Kirschner, 1995). This is a direct measurement of ME stress or of constrained strain.

The simple form of equation (34) overlooks more complex aspects of the deformation of a single-crystal cantilever such as the impact that clamping has on the deformation tensor and, particularly in shorter cantilevers, the opposite curvature across the width (due to the Poisson effect of the composite beam). Dahmen, Lehwald and Sander (2000) used analytic and finite element models to address these issues and arrived at a generalized Stoney equation that includes the effects of the dimensionality of the curvature due to an applied surface stress. These results were extended to the case of a cantilever deformed by the magnetostrictive stress due to a 90° rotation of the magnetization; the components of the ME stress tensor measured in such a case were determined for cubic, tetragonal, trigonal, and hexagonal symmetry (Dahmen, Ibach and Sander, 2001).

3. If free or bonded magnetic samples are subjected to known *strains*, then the ME coefficient, B_i, can sometimes be determined from the *strain-induced change in anisotropy* (perhaps measured from the M–H curve) of the magnetic sample of interest. This is the inverse method of measuring the ME coupling. This method can be applied to bulk (Sun and O'Handley, 1991) or thin-film samples but it is most commonly used for the latter (O'Handley, Song and Ballentine, 1993; Song, Ballentine and O'Handley, 1994; Baril, Gurney, Wilhoit and Speriosu, 1999).

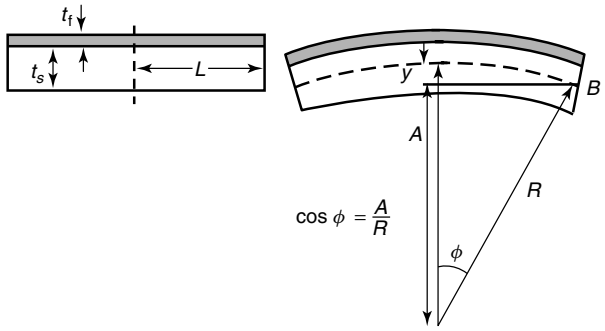

Figure 14. Geometry for determining strain in a thin film on a substrate at the circularly curved, central portion of a four-point bending jig. (Reprinted with permission O'Handley R.C., copyright 2000, John Wiley & Sons Inc.)

The magnitude of the strain in a film of thickness t_f on a substrate of thickness $t_s > t_f$ can be related to the vertical displacement, y, in a four-point bending geometry. In a four-point fixture, the bending is circular inside the inner two pressure points separated by a distance $2L$ (Figure 14). It can be shown that in the limit of circular curvature of radius R, the film strain is $\varepsilon = t_s/(2R)$. Using $\cos\,\phi = A/R = (R - y)/R$ and $\phi = L/R$, the parameters R and ϕ can be eliminated to give:

$$y = \frac{t_s}{2\varepsilon_f}\left[1 - \cos\left(\frac{2\varepsilon_f L}{t_s}\right)\right] \xrightarrow{2\varepsilon_f L/t_s \ll 1} \frac{L^2}{t_s}\varepsilon_f \qquad (35)$$

Thus, knowing the vertical displacement at a given distance, L, from the center of a film on a substrate gives the magnitude of the strain imposed on the film. In such a bending geometry, the film is essentially constrained (by the substrate) across its width, $\varepsilon_{yy} = 0$, and is free to strain normal to its surface, $\varepsilon_{zz} \neq 0$. It can be shown (O'Handley, 2000) that $\varepsilon_{zz} = -\upsilon\varepsilon_{xx}(1 - \upsilon) \approx \varepsilon_{xx}/2$. Thus, the ME contribution to the anisotropy energy of the film strained by $\varepsilon_{xx} = \varepsilon_f = yt_s/L^2$ is, from equation (5):

$$f_{\mathrm{ME}} = B_1 e_{xx}\left[\alpha_x^2 - \frac{1 - 2\upsilon}{3(1 - \upsilon)}\right] \approx B_1 e_{xx}\left(\alpha_x^2 - \frac{1}{6}\right) \qquad (36)$$

Details for various geometries are given in O'Handley, Song and Ballentine (1993).

3 MAGNETIC SHAPE-MEMORY ALLOYS

3.1 Introduction

Ni–Mn–Ga and other FSMAs show large magnetic-field-induced strains owing to twin-boundary motion in the

martensitic phase (Ullakko *et al*., 1996; James and Wuttig, 1998). The stoichiometric compound, Ni_2MnGa, transforms from a cubic austenite phase to tetragonal martensite below about 250 K. It was shown (Chernenko, Cesari, Kokorin and Vitenko, 1995; Murray *et al*., 1998; Vasil'ev *et al*., 1999) that compositions having higher electron-per-atom ratios such as $Ni_{49}Mn_{29}Ga_{22}$ have T_{mart} above room temperature and, thus, can show magnetic-field-induced twin-boundary motion at room temperature. It is in these compositions that magnetic-field-induced strain has most often been studied (Murray *et al*., 1998; O'Handley *et al*., 2000; Tickle *et al*., 1999; Wu *et al*., 1999; Heczko, Sozinov and Ullakko, 2000); the maximum field-induced strain in tetragonal martensite, given by $1 - c/a = 6\%$, was reported in 2000 (Murray *et al*., 2000). Compositions with slightly higher Mn/Ga ratios transform from the cubic austenite to *orthorhombic* martensite and can show a field-induced strain of 10% (Sozinov, Likhachev, Lanske and Ullakko, 2002).

In order to understand the magnetic-field-induced strain in these materials, it is important to clarify (i) the nature of the structure across a twin plane, (ii) the effects of an externally applied magnetic field (or stress) on the energy of two martensite variants having different orientations of their *c* axes (the magnetic easy axis), and (iii) perhaps most importantly, the relative magnitudes of the yield stress that must be overcome to initiate twin-boundary motion, the magnetic mechanism that drives the growth of a particular variant, and the thermal energy at the operating temperature.

3.1.1 Crystal structure

Figure 15 shows the evolution of the X-ray powder diffraction pattern with decreasing temperature from cubic austenite to tetragonal martensite for $Ni_{49.5}Mn_{29.5}Ga_{21}$ (Richard, 2005). For diffraction peaks satisfying $h + k + l = 4n$ (n is an integer), the splitting from single lines to doublets (with the appearance of some modulation peaks) is the important characteristic of the transformation that makes twinning and field-induced twin-boundary motion possible. The inset shows the variation of the magnetic susceptibility with temperature indicating T_C at about 360 K and the first-order martensite transformation centered at 306 K.

Well below the martensite finish temperature, the sample is fully transformed to tetragonal martensite. This single-phase, martensitic regime is of interest here; it can be twinned. Single crystals of $Ni_{50}Mn_{29}Ga_{21}$ can show large-scale twins separated by a twin boundary (Figure 16c) across which a shear displacement is observed (Murray *et al*., 1998). Ni–Mn–Ga particles of similar composition made by spark erosion (Tang *et al*., 2003) show abundant nanometer-scale twinning after annealing (Figure 16, Solomon, Smith, Tang and Berkowitz, 2004; Solomon *et al*., 2005).

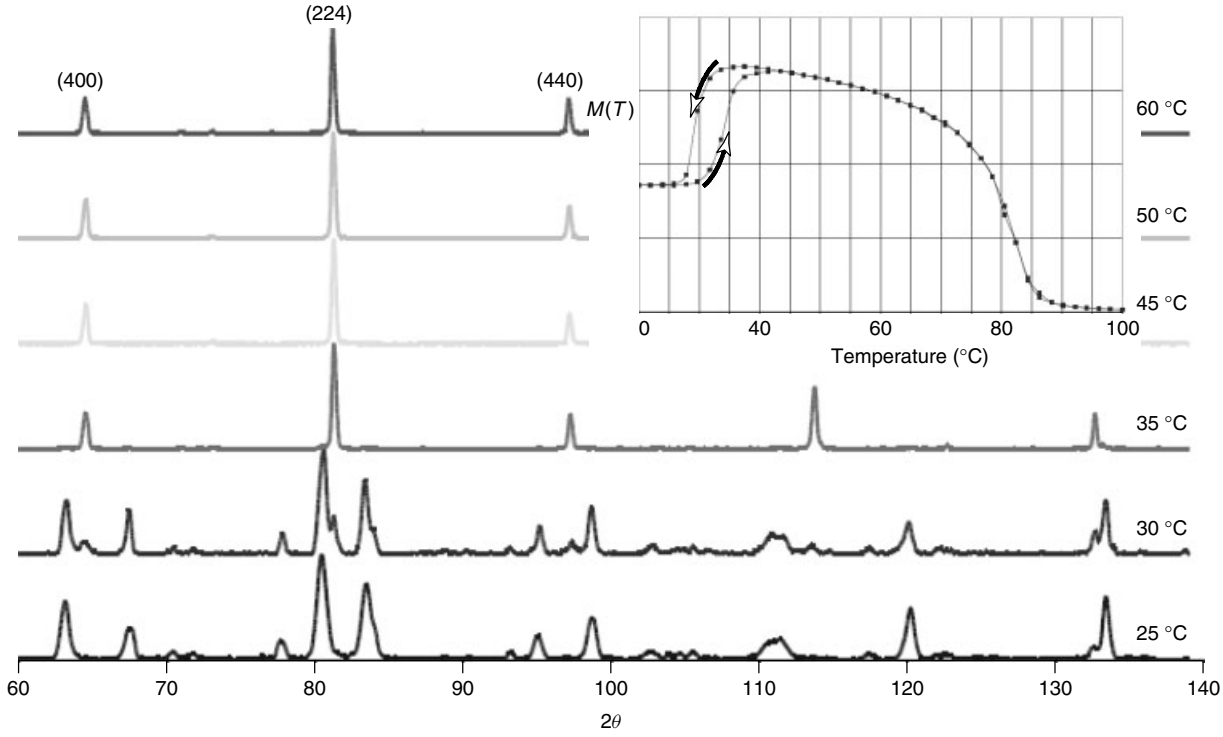

Figure 15. X-ray powder diffraction patterns for Ni–Mn–Ga alloy at selected temperatures. Splitting of peaks below 306 K indicates the transformation to tetragonal martensite. Inset: susceptibility versus temperature (Richard, 2005).

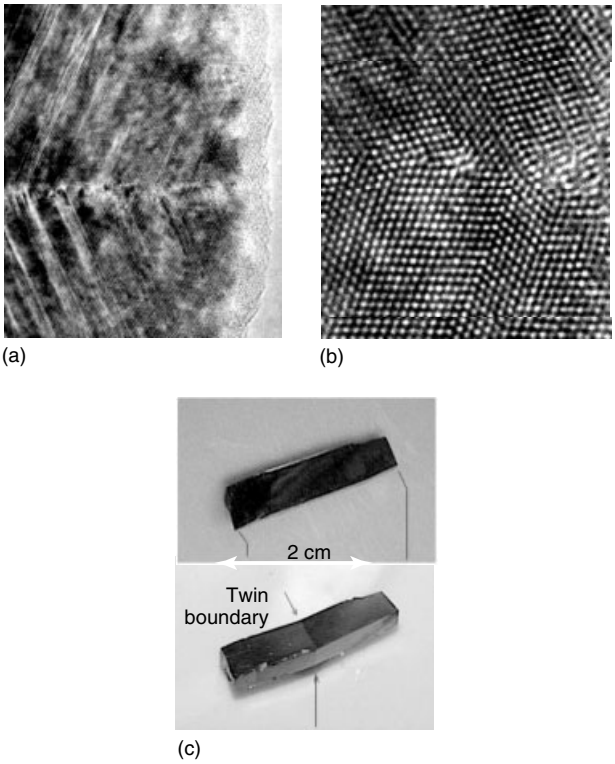

Figure 16. (a) High-resolution transmission electron microscopy images Ni–Mn–Ga particles made by spark erosion. (b) Atomic-scale five-layered martensite reflects the atomic instability along $\langle \underline{1}01 \rangle$ in {101} (Solomon, Smith, Tang and Berkowitz, 2004; Solomon *et al*., 2005). The twinning evident as a horizontal interface in (a) can also be seen in some samples on a macroscopic scale (c) (Murray *et al*., 1998). (Reprinted with permission Solomon *et al*., copyright 2004, American Institute of Physics.)

Three different twin variants (different *c*-axis orientations) are possible in tetragonal martensite; two are depicted schematically in Figure 17. The elastic energy associated with a twin plane in the martensitic phase is minimized if the plane is arranged with mirror symmetry as shown in Figure 17(a). There are only two stable positions for the atoms along the twin-plane {101} in a $\langle \underline{1}01 \rangle$ direction. The energy barrier between these two states is critical for understanding the motion of twin boundaries; the barrier height reflects changes in the lattice potential with position near defects. In fact, the atomic structure of the twin plane is more complicated than the planar form shown here. Evidence suggests that the twin plane consists of a series of terraces and steps that define not only dislocations (with a burgers vector, **b**, in the plane of the terrace) but also disconnections characterized by a height, **h**, due to the steps (Hirth and Pond, 1996). Clearly, the horizontal twin interface in Figure 16(a) shows an irregular form. For the purpose of understanding magnetic-field-induced twin-boundary motion, it is assumed here that the longer-range structure of the

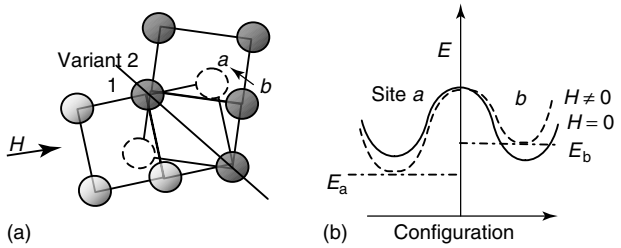

Figure 17. At temperatures below T_0, the martensitic phase is stable; it can form crystallographic twins (a) to minimize strain energy that accumulates during transformation. Panel (b) shows two possible atomic positions exist parallel to and near the twin boundary. Application of a magnetic field lowers the energy of the potential well corresponding to the variant having its *c* axis more nearly parallel to H.

twin plane depicted in Figure 17 is an adequate model because the magnetic exchange interaction ensures that the magnetization is relatively uniform over a longer range than the distance between the steps; the exchange length can be calculated from the magnetic anisotropy to be of order 14 nm (O'Handley *et al*., 2001). The external magnetic field shown as parallel to variant 1 and its effects on the free energy will be discussed in the following text.

If a tetragonal Ni–Mn–Ga crystal is cut so that the sample faces are parallel to its cubic austenite {100} planes, then it can generally be trained so that a single set of {101} twin planes is active. After suitable heat treatment to homogenize the composition, the crystal is prepared for actuation by application of a compressive bias stress, $\sigma > \sigma_0$, in the direction shown in Figure 18(a); this favors growth of twin variants having *c* parallel to the compression axis. If a second stress, orthogonal to the first, is briefly applied as in Figure 18(b) but not fully detwinning the crystal, then a twin structure like that in Figure 18(b) can be achieved. This stress is reduced (Figure 18d); then a magnetic field is applied as shown in Figure 18(d) with a weak, orthogonal bias stress; twin boundaries move back and forth as the ratio of the field energy to the stress energy, $\mu_0 M_s H/\sigma\varepsilon_0$, is greater or less than unity.

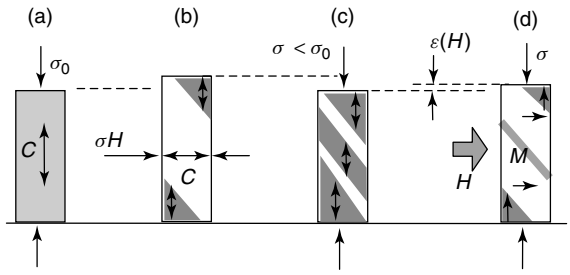

Figure 18. Panels (a) and (b) show crystal training, (c) and (d) crystal actuation. The shaded and clear regions distinguish variants having *c* axis vertical and horizontal, respectively.

3.2 Actuation

3.2.1 Strain versus field

After setting the sample in an initial state with the c axis perpendicular to the field direction, *one-time* field actuation was reported to produce the maximum field-induced strain in tetragonal martensite, $1 - c/a$ (Murray *et al*., 2000). It was demonstrated that *cyclic* actuation of FSMA crystals is possible in a system that contains a reset mechanism, such as a spring that is compressed as the sample deforms by twin-boundary motion under the action of a field directed orthogonal to the spring axis. The field-induced strain observed in such cyclic actuation is often only 2.5 or 3% (Figure 19) (Henry *et al*., 2002) in contrast to the 6% achieved under low static load. There are two reasons for this. First, when the sample ends are constrained, twin boundaries are generally inhibited from entering the constrained regions, reducing the active sample length. Second, the presence of the back stress from the spring as the sample is actuated decreases the effectiveness of the magnetic driving force.

Note also the evidence in Figure 19 of a *threshold magnetic field* below which little twin-boundary motion occurs. (The threshold field is more evident in quasistatic measurements (Murray *et al*., 2000); it is somewhat rounded out in these 2 Hz, cyclic measurements.) The threshold field is a stochastic magnetomechanical parameter, much like the coercive field below which no irreversible domain-wall motion occurs. A related threshold or *yield stress* appears in stress–strain measurements on these materials and the two are related by $\mu_0 M_s H_i = \sigma_{yield}\varepsilon_0$, where H_i is the *internal* field (applied field corrected for demagnetizing effects) above which gross twin-boundary motion initiates. In a perfect crystal, H_{thresh} depends on the local energy change when a twin boundary interacts with the Peierls potential; in a real crystal, it also depends on the much larger energy change when the twin boundary interacts with a distribution of defects (Marioni, Allen and O'Handley, 2004; Paul, O'Handley and Peterson, 2005). Threshold fields of 0.1–0.3 T are typically observed in active Ni–Mn–Ga crystals, and the field-induced strain saturates when the applied field reaches about 0.7 T.

The behavior in Figure 19 should be compared and contrasted with that of magnetostriction. Beyond the obvious difference in the magnitude of the field-induced strain in the two cases, there are two features of the FSMA behavior in Figure 19 that are different from that in magnetostriction. These are (i) the presence of a threshold field below which the large strain does not appear in FSMAs and (ii) the large hysteresis of FSMAs (magnetostriction is anhysteretic, especially in the ideal hard-axis magnetization process). Further differences will be pointed out in the following text.

3.2.2 Frequency dependence

These cyclic actuation experiments were extended to higher frequencies in order to understand the operational bandwidth of Ni–Mn–Ga crystals having a volume of about a cubic

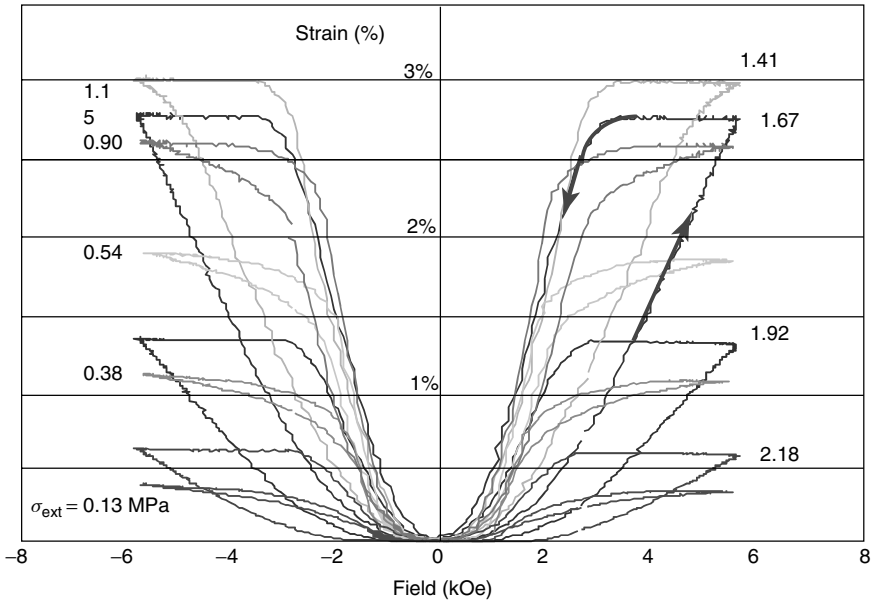

Figure 19. Cyclic strain versus field at 1 Hz for different bias stresses in Ni–Mn–Ga crystal. The bias stress values indicated are initial values and increase by as much as 20% during actuation. (Reprinted with permission Henry *et al*., copyright 2002, American Institute of Physics.)

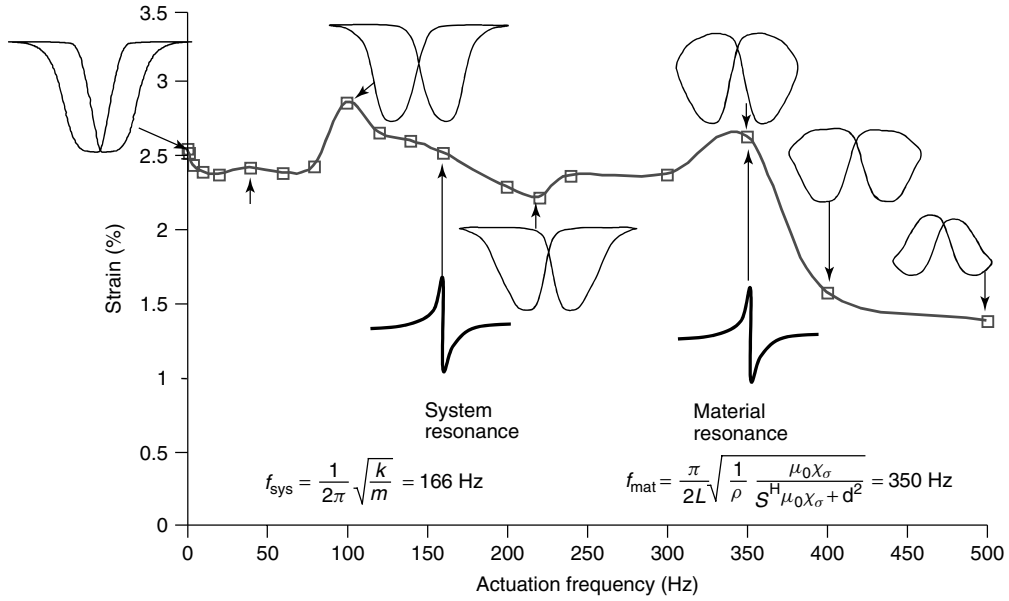

Figure 20. Field-induced strain at 4.6 kOe versus actuation frequency with overlaid ε-H loops. (Reprinted with permission C.P. Henry *et al*., copyright 2003 International Society for Optical Engineering.)

centimeter. Figure 20 shows the field-induced strain achieved at 4.6 kOe versus frequency for $Ni_{49.5}Mn_{29.5}Ga_{21}$ (Henry *et al*., 2003). Overlaid on the curve are the strain versus field loops at selected frequencies. The maximum field that could be achieved with the power supply used in these experiments drops off above 300 Hz because of the increased inductive reactance of the field coils. What is clear from the data is that (i) there is considerable structure in the strain versus frequency curve, (ii) there is a clear decrease in strain above about 350 Hz (actuation frequency is twice the drive frequency), and (iii) the strain versus field loops show more hysteresis with increasing frequency and the phase of the strain changes dramatically relative to that of the field above about 350 Hz.

The structure in the $\varepsilon(f)$ curve between 100 and 200 Hz has been determined to arise from mechanical resonances in the measuring system. The decrease in output strain above 300 Hz is due to the decreasing strength of the applied field as well as to a material resonance, as evidenced by the 180° change in phase of the strain relative to the field. The resonance centered near 350 Hz appears to be the material resonance.

Pulse field actuation experiments were carried out to probe the details of twin-boundary kinetics (Marioni, O'Handley and Allen, 2003). It was observed that the field-induced strain lags the initiation of the magnetic-field pulse by more than that expected from the need to exceed the threshold field for twin-boundary motion. An additional lag is found to be due to the inertia of the sample under the appreciable acceleration (3×10^4 m s^{-2}) it experiences in these experiments. It is also observed that the free end of the sample does not achieve a velocity greater than 6.2 m s^{-1}, regardless of the peak field strength or its rise time. This is now understood to be a consequence of the fact that the magnetic energy applied to the sample cannot exceed $K_u V$ and this limits the FSMA kinetic energy and thus, $v \leq (2K_u/\rho)^{1/2} \approx 6$ m s^{-1}. So the large displacement of actuated FSMA crystals appears to limit their bandwidth to $f < 2500$ Hz for samples of any size.

3.3 Models

Of the many models describing the field-induced motion of twin boundaries in FSMAs, four are briefly compared. They are (i) numerical micromagnetic models (James and Wuttig, 1996), (ii) thermodynamic models (O'Handley, 1998; L'vov, Gomonaj and Chernenko 1998; Likhachev and Ullakko, 2000; Kiefer and Lagoudas, 2005), (iii) analytic, micromagnetic model (Paul, Marquiss and Quattrochi, 2003; Paul, O'Handley and Peterson, 2005), and (iv) kinetic models (Paul, O'Handley and Peterson, 2005; O'Handley *et al*., 2006). These models generally include the Zeeman energy, magnetic anisotropy energy, and an external stress for each of two or sometimes three variant types. They may also include a magnetostatic energy that tends to restore the net magnetization to zero when the field vanishes or, with similar effect, an internal elastic energy that tends to restore the field-induced strain to zero when the field is removed. Energies associated with the yield stress, σ_{yield} can also be added.

Likhachev and Ullakko (2000) have taken a more general analytic approach to the problem in three dimensions. They integrate the Maxwell relation, $(\partial\varepsilon/\partial H) = -(\partial M/\partial\sigma)$, to arrive at the field-dependent strain. Experimental $M(H)$ and $\sigma(\varepsilon)$ data are used as input to allow prediction of $\varepsilon(H, \sigma)$ that includes magnetostatic effects without the need to describe them analytically.

3.3.1 Thermodynamics

A phenomenological, free-energy model for the field and temperature dependence of the magnetization in ferromagnetic martensites has been described (L'vov, Gomanaj and Chernenko, 1998). In their model, the free energy of the large strain due to twin-boundary motion is combined with the much smaller magnetostrictive strain, both as coefficients of the direction cosines of the magnetization. While the magnetostrictive strain does depend only on the direction of magnetization, the strain due to twin-boundary motion does not necessarily appear as the magnetization is rotated if the twin boundaries are pinned. Nevertheless, this model was successfully extended to describe the field dependence of stress–strain curves as well as the field dependence of the magnetostrictive stress (see Figure A1) that accumulates in a twin variant as its magnetization is rotated by the applied field even before twin-boundary motion.

Models of Paul, Marquiss and Quattrochi (2003) and Paul, O'Handley and Peterson (2005) are analytic micromagnetic treatments (exchange energy is included) that describe (i) the field-induced displacement of the 90° domain wall from the twin boundary at fields below threshold in the presence of an elastic defect, (ii) the field-induced acceleration of the twin dislocation between pinning events, and (iii) the interaction of the twin boundary with a localized, elastic defect.

In one variation of the second class of models (O'Handley, 1998), the free-energy density of a two-variant crystal takes the form:

$$\begin{aligned} g(\theta, f_1) = &-\mu_0 M_s H\left[1 + (1 - f_1)\cos\theta\right] \\ &+(1 - f_1)K_u \sin^2\theta + \frac{1}{2}C^{\text{eff}}\left[(f_1 - f_2)\varepsilon_0\right]^2 \\ &+\sigma_{\text{ext}}\varepsilon_0\left[f_1 - (1 - f_1)\cos\theta\right]\cdots \end{aligned} \tag{37}$$

Here, f_1 and $f_2 = 1 - f_1$ describe the *equilibrium* variant distribution and the term proportional to an effective elastic constant, C^{eff}, describes the effect of elastic energy stored in the crystal when twin-boundary motion occurs from the equivariant state. θ is the angle between the applied field direction and the magnetization in variant 2. The external stress term was added later (Murray *et al*., 2000). The resulting field-induced strain is given by

$$\varepsilon(H) \equiv \varepsilon_0 \delta f = \frac{2K_u h(1 - h/2) - \sigma\varepsilon}{C_{\text{eff}}\varepsilon_0} \tag{38}$$

and the field-induced magnetization is

$$m(H) \equiv \frac{M(H)}{M_s} = f_1 + hf_2 = \delta f + \frac{1}{2} + h\left(\delta f - \frac{1}{2}\right) \tag{39}$$

Here, $\delta f = f_1 - 1/2$ is the imbalance in the volume fraction of variants 1 and 2 and $h = \mu_0 M_s H/(2K_u) = \cos\theta_2$ (O'Handley, 1998).

When the field is small compared to the anisotropy field, the analytic models predict a linearly increasing twin-rearrangement strain. If an *ad hoc* yield stress is included (Murray *et al*., 2000) or if defects are incorporated in a microscopic way (Paul, Marquiss and Quattrochi, 2003), then the observed threshold behavior is accounted for. When the applied field approaches the anisotropy field, the Zeeman energy difference across the twin boundary is decreased (***M***.***H*** approaches zero everywhere in the sample) and the achievable strain saturates. The normalized driving force that describes field-induced strain (δf from the rhs of equation (38) normalized to K_u) is plotted in Figure 21 without (solid line) and with (dashed line) twin-boundary yield stress included. The effect of compressive bias stress orthogonal to the field axis would be to increase the field at which actuation initiates and decrease the strain at which actuation saturates.

A closer examination of the assumptions of the equilibrium thermodynamic models is informative. The dependence of the free-energy densities of two adjacent variants in an external magnetic field applied parallel to the c axis of one of them (variant 1 in Figure 17) is shown in Figure 22. Note

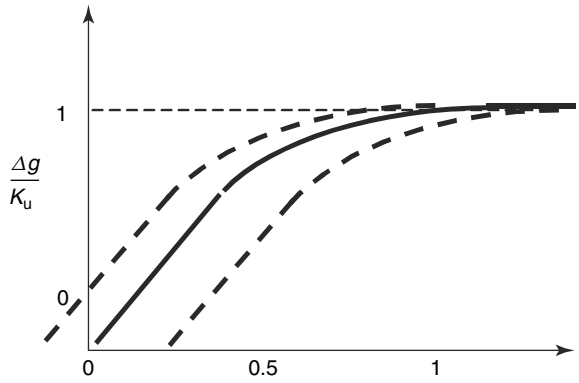

Figure 21. Output of equation (38), ε versus h with zero bias stress is shown passing through the origin. The displaced dashed lines show the effects of an *ad hoc* addition of a twin-boundary yield stress of order 1 MPa, which is equivalent to a field of 100 kA m^{-1} or 0.2 H_a.

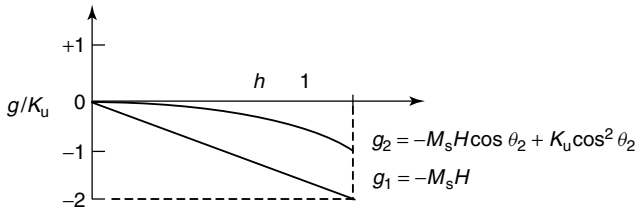

Figure 22. Variation of magnetic free energy density with field strength for two martensite variants, variant 1 having its magnetic easy axis, *c*, parallel to *H* (O'Handley *et al*., 2006).

that above h = 1, the free energy difference between the two variants does not change; the thermodynamic driving force for twin boundary motion is constant for h > 1.

3.3.2 Kinetics

While it is clear from Figure 22 that application of a magnetic field stabilizes variant 1 relative to variant 2, an energy barrier must exist between these two states because the twin boundary does not spontaneously move to expand the volume of variant 1 at the expense of variant 2 under application of a field below the threshold value. Further, the application of magnetic field also exerts *a mechanical shear stress* or torque, τ_{mag}, on the atoms along the twin plane in a direction that moves the twin plane into the unstable variant (Figure 23). This magnetic energy density difference, $g_2 - g_1$, and the torque energy density, $\tau_{\text{yield}}\gamma_0$, where γ_0 is the shear strain involved in the process ($\gamma_0 = 0.122$ for Ni–Mn–Ga (O'Handley *et al*., 2001)) are each of the order $10^5\,\text{J m}^{-3}$ corresponding to about $10\,\mu\text{eV atom}^{-1}$. These magnetic energies are much less than thermal energy per atom at room temperature $\Delta g_{\text{mag}} \leqslant K_{\text{u}} \ll (k_{\text{B}}T/V)$. Thus, it is expected that at room temperature, thermal fluctuations are capable of causing a cluster of several hundred atoms to surmount the barrier, allowing the system to sample both potential wells. But the thermal energy has no preference for direction when the two energy minima have the same potential; to change the variant configuration, the energy wells should have different energies or a shear stress must act on the atoms. The magnetic field provides the difference in energy minima as shown in Figure 22. In Figure 17, variant 1 is favored by a shear stress along [10$\underline{1}$] in (101) that acts to move some of the atoms of variant 2 into the dashed position. At $T = 0\,\text{K}$, the magnetic shear stress, τ_{mag}, would have to exceed the yield stress for twin-boundary motion (Murray *et al*., 2000; Ullakko, 1996; Müllner and Ullakko, 1998; Heczko and Ullakko, 2001):

$$\tau_{\text{mag}} \equiv \frac{K_{\text{u}}}{\gamma_0} > \tau_{\text{yield}} \tag{40}$$

Here τ_{yield} is the threshold shear stress across the twin boundary that initiates twin-boundary motion. This condition may not be met at low temperature. At nonzero temperatures, the magnetic field provides a direction for the transition between the energy minima while the thermal energy provides most of the activation energy to get over the barrier:

$$g_{\text{mag}} + \frac{k_{\text{B}}T}{V} > \tau_{\text{yield}} \tag{41}$$

Here, g_{mag} includes both the Zeeman energy difference between the two states and the magnetic torque on the atoms. Thus, the role of *thermal* activation must be considered when modeling the actuation of FSMAs. The fourth category of models (analytic micromagnetics) has begun to describe the temperature dependence of field-induced strain in FSMAs, which is now considered (Paul, O'Handley and Peterson, 2005).

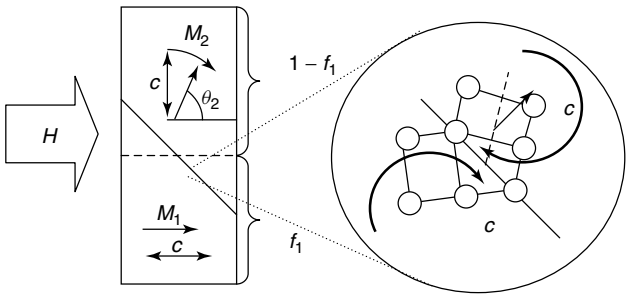

Figure 23. Simple two-variant model of twinned tetragonal martensite. Panel at right represents the change in crystallography across the twin plane and the torque on each variant for a sample constrained from rotating (O'Handley *et al*., 2006).

3.4 Temperature dependence

Magnetic-field-induced strain is generally observed to occur over a limited temperature range below the martensite transformation and above a lower cutoff temperature. Early studies on polycrystalline compositions indicated a very narrow operating range below the transformation (Murray *et al*., 1998; Heczko, Sozinov and Ullakko, 2000). Other temperature-dependent measurements on single crystals are summarized in Figure 24 (Wu *et al*., 1999; Liu *et al*., 2002); they indicate that the temperature range depends on the alloy composition, with one sample being actuated down to 160 K.

Heczko and Straka (2003) described a model that attributes the temperature dependence of field-induced twin rearrangement to the condition in equation (40). They measured the temperature dependence of the magnetic anisotropy, the lattice constants, and twin-boundary yield stress of a Ni–Mn–Ga alloy. They find that the yield stress increases sharply with decreasing temperature. Their model does

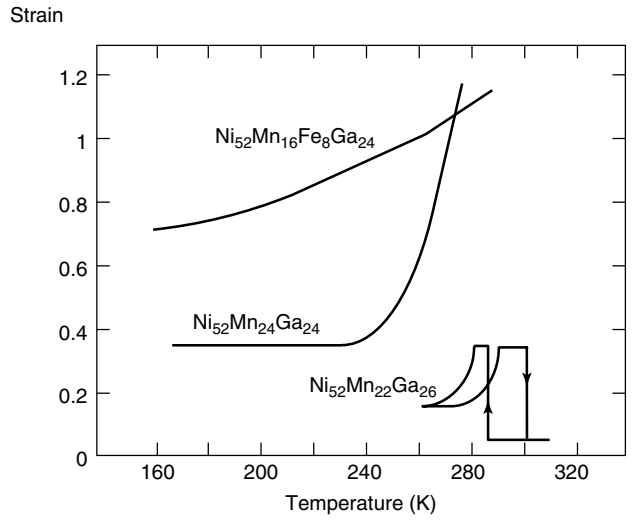

Figure 24. Experimental results for temperature dependence of field-induced strain in three different Ni–Mn–Ga martensites (Liu *et al*., 2002).

provide a basis for understanding the limited range of activation. However, the condition in equation (40) contains no magnetic-field dependence even though twin-boundary motion is observed to proceed at fields below H_a. Further, this model, like all thermodynamic models, does not contain a real physical driving mechanism between the states of the double well, nor does it account for the role of thermal activation in the twin-boundary actuation process.

More recently the temperature dependence of the mechanical torque exerted on the unfavorably oriented variants by application of a field, $T = -(\partial G_{\text{Zeeman}}/\partial\theta)$ where G_{Zeeman} is the first term in equation (37), has been considered to describe the temperature dependence at various fields of the twin-boundary activated strain (O'Handley *et al*., 2006). This model includes thermal activation and the difference in rates of transition between the two potential wells in the presence of an applied field. For Ni–Mn–Ga martensite variants having their crystallographic c axis perpendicular to the applied field (variant 2 in Figure 17), the field-dependent torque per unit volume, $\tau = \mathrm{T}/\Omega$, is given by

$$\tau_2 = -\frac{\partial(-M_s H\cos\theta_2)}{\partial\theta} = -2K_u h\sqrt{1-h^2} \qquad (42)$$

Here M_s, K_u, and h are temperature dependent. This torque on the magnetization is clockwise about the center of mass of variant 2 in Figure 17, generates a mechanical torque on variant 2 that is also clockwise. There is no torque on variant 1 because $\theta_1 = 0$, except that which is transferred from variant 2 in the presence of a physical constraint against rotation of variant 1. The shear across the twin boundary is in a direction that drives the atoms near the twin plane in variant 2 in a direction that grows variant 1 (cf. Figures 17 and 21).

The temperature dependence of the shear stress at the twin boundary is expressed in general terms by making use of the relation for uniaxial anisotropy (Akulov 1936; Callen and Callen, 1966) expressed in equation (23) for two-ion interactions and in Table 2 ($l = 2$, high T) for single-ion mechanisms. (This relation would not hold through an intermartensitic transformation in which the nature of the anisotropy changes; such transformations are often observed in the Ni–Mn–Ga system.) Further, the temperature dependence of the reduced magnetization is approximated with the scaling relation, $m = 1 - t^2 = 1 - (T/T_C)^2$. In this case, the temperature dependence of the torque density reduces to:

$$\tau(T) = -2K_u(0)h(T)(1-t^2)^2\sqrt{1-h(T)^2} \qquad (43)$$

The field dependence of the torque density rises from zero at $h = 0$ to a maximum of K_u at $h = 1/\sqrt{2}$ then decreases to zero again when the applied field reaches the temperature-dependent anisotropy field ($\theta_2 = 0$).

Figure 25 plots the thermally activated torque density, $\tau(T)\Delta R(T)$ versus t, for different values of $h(T)$. $\Delta R(T)$ is the net thermally activated transition rate for atoms moving from positions favoring variant 2 to those favoring variant 1:

$$\Delta R = A_{1\to2}\exp\left[-\frac{\Delta G_0 - \mu_0 M_s H\cos\theta}{k_B T}\right] - A_{2\to1}\exp\left[-\frac{\Delta G_0 + \mu_0 M_s H\cos\theta}{k_B T}\right] \qquad (44)$$

Here, A_{i-j} is a preexponential factor for attempt rate in the double well potential and $\Delta G_0 = 0.015\,\text{eV}$ is the defect energy barrier height in the absence of a magnetic field. An activation barrier close to this value, and the approximate

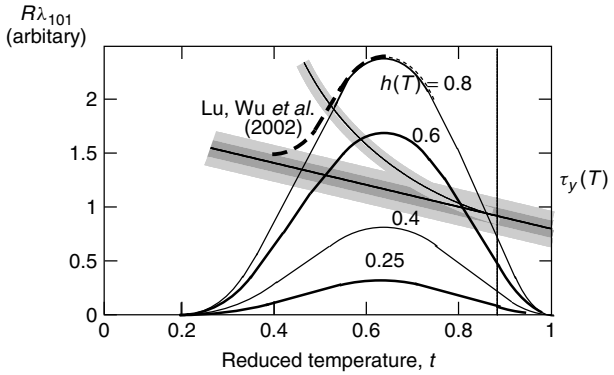

Figure 25. Dependence of thermally activated torque on reduced temperature for $\Delta G = 15\,\text{meV}$ and various values of $h(T)$. Two assumed forms for $\tau_y(T)$ are shown. (Adapted from O'Handley *et al*., 2006.)

range of the strain field about a Ni–Mn–Ga twin boundary, 2 nm, were estimated earlier (O'Handley *et al*., 2001). (See (O'Handley *et al*., 2006), for numerical values used.) Here, a preexponential factor of unity has been used in the thermal activation so the vertical scale is arbitrary. Note that the thermally activated torque is quenched as the reduced temperature, t, approaches zero and vanishes at $t = 1$ (or below $t = 1$ upon transformation to austenite where the two wells become one). The very weak thermal activation at low temperatures does not allow the relatively small magnetic energy to effect twin-boundary motion. Two forms of *threshold* shear stress are also shown in Figure 25, one a simple linear relation based on the weak temperature dependence of the elastic constants, and the other a representation of the exponential temperature dependence observed in one Ni–Mn–Ga alloy (Heczko and Straka, 2003). The shaded area around these yield-stress lines suggests the distribution of pinning strengths that is inherent in the stochastic process of twin-boundary actuation (Marioni, Allen and O'Handley, 2004). Equations (43) and (44) then indicate that field-induced twin-boundary motion occurs over a limited temperature range (between about $h = 0.5$ and 0.8 here) below the martensitic transformation temperature, T_0 (vertical dashed line), or even lower if the applied field decreases below the anisotropy field for $T < T_0$. Actuation vanishes in the temperature range where the temperature-dependent torque drops below the temperature-dependent threshold stress.

Superimposed on the calculated curves are data from Liu *et al*. (2002) showing the decrease in field-induced strain at temperatures below the maximum field-induced strain. The horizontal range of the data was scaled based on the Curie temperature; the vertical axis of the data was scaled to fit the general curve. This is not intended to be a quantitative confirmation of the model but an indication of how it is able to predict the vanishing of thermally activated, field-induced strain at low temperatures. These temperature-dependent models provide new insights into the complex processes that govern the temperature dependence of magnetic-field-induced twin-boundary motion, and show that it contrasts starkly with the temperature dependence of magnetostriction.

4 SUMMARY

ME effects arise from the strain dependence of spin-orbit and anisotropic-exchange interactions. Joule magnetostriction can be described by at least five related parameters: the ME coupling coefficients B_i (stresses of magnetic origin), the magnetostriction constants λ_i (strains of magnetic origin), the magnetostrictivity, **d** (the change in magnetization per unit stress or the change in strain per unit field), the ΔE effect, or magnetomechanical coupling factor, k. The Joule magnetostriction is the strain associated with the direction of magnetization. In an unconstrained sample, λ is proportional to a component of the magnetic stress, B_i, divided by the appropriate stiffness modulus. The inverse Joule effect brings about a change in the magnetization process or change in the anisotropy field, upon straining a sample.

The temperature dependence measured for Joule ME effects is generally steeper than that of the magnetization itself. (The same is true as for magnetic anisotropy.) The reduced magnetostriction, $\lambda^{\gamma,\alpha}(T)/\lambda^{\gamma,\alpha}(0)$, varies as the $l(l+1)/2$ power of the reduced magnetization in materials whose magnetic moments are well localized. Rare-earth metals and alloys with $L_z \neq 0$ can show much larger ME effects than most 3d transition metals and their alloys.

The large field-induced strains observed in FSMAs are due to torque-induced twin-boundary motion and hence are more closely related to (i) martensite crystallography, including compatibility between parent austenite and martensite (James

Table 3. Comparison of Joule magnetostriction and field-induced twin-boundary motion.

	Anisotropic magnetostriction	Field-induced twin-boundary motion
Strain and symmetry	Magnetostrictive strain lowers symmetry of crystal by small elastic distortion	Large strain results from reorientation of low-symmetry crystallographic twins by twin-boundary motion
Strain reference	Direction of $\boldsymbol{M}$	Crystal axes
Strain mechanism	Spin-orbit interaction or anisotropic exchange	Field-induced torque on crystal, thermal activation
Range of strain	$<10^{-4}$ in transition metals, 2×10^{-3} in rare-earth/transition metal alloys	$1 - c/a = 6\%$ tetragonal, 10% in orthorhombic Ni–Mn–Ga
Reversibility	Elastic; small hysteresis due to 90° domain-wall motion	Plastic; large hysteresis due to twin boundary threshold
Role of domain walls	Motion of 90° walls gives strain; motion of 180° walls does not	90° walls follow twin boundary 180° walls produce no strain
Temperature dependence	$\lambda(T)/\lambda(0) = m^{l(l+1)/2}$ $\lambda(0)$ generally $>$ λ (room temperature)	$\varepsilon(H)$ observed below martensite transition but not below thermal cutoff

and Hahn, 2000) as well as $1 - c/a$, which limits the strain in tetragonal martensites, (ii) defect structure, which governs the mobility of twin boundaries, and (iii) the magnetic anisotropy, which limits the torque and hence the shear stress that can be applied along a twin boundary. Table 3 summarizes some of the salient characteristics of Joule magnetostriction and magnetic-field-induced strain in FSMAs that distinguish these two magnetic-field-induced strains that arise from very different mechanisms.

In Fe, 90° domain walls separate two magnetic domains that are weakly strained by Joule magnetostriction in a twinning relation across the domain wall. Application of a field favoring one of the domains may move the domain wall; rotation of the magnetization via domain-wall motion results in a change in magnetostriction in that 'transformed' region and hence a small change in the gross shape of the crystal. In FSMAs the twin boundary is a crystallographic feature, not a result of magnetostriction. The 90° domain wall that is located at the twin boundary in zero field can be separated from the twin boundary by application of a field below the threshold for twin-boundary motion without the large strain that distinguishes these materials; a small magnetostrictive strain accompanies the rotation of the magnetization.

ACKNOWLEDGMENTS

The work from MIT on magnetostriction has been generously supported over the years by the Office of Naval Research (N00014-90J1174), Army Research Office and the National Science Foundation (DMR 94-10943). The work from MIT on FSMAs has been supported by ONR and DARPA and most recently by a Multi-University Research Initiative from ONR. Many students and colleagues have contributed to this work with their research and comments.

REFERENCES

Abbundi, R. and Clark, A.E. (1977). Anomalous thermal expansion and magnetostriction of single crystal $Tb_{0.27}Dy_{0.73}Fe_2$. *IEEE Transactions on Magnetics*, **13**, 1519–1520.

Baril, L., Gurney, B., Wilhoit, D. and Speriosu, V. (1999). Magnetostriction in spin valves. *Journal of Applied Physics*, **85**, 5139–5141.

Berry, B. and Pritchet, W. (1975). Magnetic annealing and directional ordering of an amorphous ferromagnetic alloy. *Physical Review Letters*, **34**, 1022–1025.

Betz, J., Lachiesserie, E. du Tremolet de and Baczewski, L.T. (1996). Magnetoelastic properties of nickel thin films. *Applied Physics Letters*, **68**, 132–133.

Callen, E.R. and Callen, H.B. (1960). Anisotropic magnetostriction. *Journal of Physics and Chemistry of Solids*, **16**, 310–328.

Callen, E.R. and Callen, H.B. (1963). Static magnetoelastic coupling in cubic crystals. *Physical Review*, **129**, 578–593.

Callen, E.R. and Callen, H.B. (1965). Magnetostriction, forced magnetostriction, and anomalous thermal expansion in ferromagnets. *Physical Review*, **139**, A455–A471.

Callen, H.B. and Callen, E. (1966). The present status of the temperature dependence of magneocrystalline anisotropy and the $l(l+1)/2$ power law. *Journal of Physics and Chemistry of Solids*, **27**, 1271–1285.

Callen, H.B. and Goldberg, N. (1965). Magnetostriction of polycrystalline aggregates. *Journal of Applied Physics*, **36**, 976–977.

Chernenko, V.A., Cesari, E., Kokorin, V.V. and Vitenko, N. (1995). The development of new ferromagnetic shape memory alloys in Ni-Mn-Ga system. *Scripta Metallurgica et Materialia*, **33**, 1239–1244.

Ciria, M., Arnaudas, J.I., Benito, L., *et al*. (2003). Magnetoelastic coupling in thin films with weak out-of-plane anisotropy. *Physical Review*, **B67**, 024429-1–024429-6.

Ciria, M. and O'Handley, R.C. (2002). Surface-and strain-induced anisotropy in epitaxial Cu/Ni90Fe10/Cu/Si(001) films. *Journal of Magnetism and Magnetic Materials*, **240**, 464.

Clark, A.E. (1980). Magnetostrictive rare earth-Fe_2 compounds. In *Ferromagnetic Materials*, Wohlfarth, E.P. (Ed.), North Holland: Amsterdam, pp. 531–589, Vol. 1.

Clark, A.E., Restorff, J.B., Wun-Fogle, M., *et al*. (2000). Magnetostrictive properties of b.c.c. Fe-Ga and Fe-Ga-Al alloys. *IEEE Transactions on Magnetics*, **MAG-36**, 3238–3240.

Cullen, J.R., Clark, A.E. and Hathaway, K.B. (1997). In *Handbook of Materials Science*, Buschow, K.H.J. (Ed.), VCH Publishers, Chapter 16.

Cullity, B.D. (1973). *Introduction to Magnetic Materials*, Addison-Wesley: New York.

Dahmen, K., Ibach, H. and Sander, D. (2001). A finite element analysis of the bending of crystalline plates due to anisotropic surface and film stress applied to magnetoelasticity. *Journal of Magnetism and Magnetic Materials*, **231**, 74–84.

Dahmen, K., Lehwald, S. and Ibach, H. (2000). Bending of crystalline plates under the influence of surface stress. *Surface Science*, **446**, 161–173.

Del Moral, A. (2006). *Handbook of Magnetostriction: Basic Principles and Magnetostrictive Materials*, Taylor & Francis.

Fahnle, M. and Komelj, M. (2002a). Determination of the complete set of second-order magneto-elastic coupling constants on epitaxial films. *Physical Review B*, **65**, 212410-1–212410-4.

Fahnle, M. and Komelj, M. (2002b). Second-order magnetoelastic effects. *Zeitschrift fur Metallkinde*, **10**, 970–973.

Franse, J.J.M. and Stolp, M. (1970). The magnetostriction constants of nickel. *Physics Letters A*, **32**, 316–317.

Gschneider, K. (1964). Physical properties and interrelationships of metallic and semimetallic elements. In *Solid State Physics*, Seitz, F. and Turnbull, D. (Eds.), Academic Press: New York, pp. 276–388, Vol. 16.

Guruswamy, S., Srisukhumbowornchai, N., Clark, A.E., *et al*. (2000). Strong, ductile, and low-field-magnetostrictive alloys based on Fe-Ga. *Scripta Materialia*, **43**, 239–244.

Ha, K. and O'Handley, R.C. (1999). Non-linear magnetoelastic anisotropy in Cu/Ni/Cu/Si(001) films. *Journal of Applied Physics*, **85**, 5282–5284.

Hall, R.C. (1959). Single crystal anisotrophy and magnetostriction constants of several ferromagnetic materials including alloys of NiFe, SiFe, AlFe, CoNi, and CoFe. *Journal of Applied Physics*, **30**, 816–819.

Heczko, O., Sozinov, A. and Ullakko, K. (2000). Giant field-induced reversible strain in magnetic shape memory NiMnGa alloy. *IEEE Transactions on Magnetics*, **36**, 3266–3268.

Heczko, O. and Straka, L. (2003). Temperature dependence and temperature limits of magnetic shape memory effect. *Journal of Applied Physics*, **94**, 7139–7143.

Heczko, O. and Ullakko, K. (2001). Effect of temperature on magnetic properties of Ni–Mn–Ga magnetic shape memory (MSM) alloys. *IEEE Transactions on Magnetics*, **37**, 2672–2674.

Henry, C.P., Bono, D., Feuchtwanger, J., *et al*. (2002). AC field-induced strain of single crystal Ni-Mn-Ga. *Journal of Applied Physics*, **91**, 7810–7812.

Henry, C.P., Tello, P.G., Bono, D., *et al*. (2003). Frequency response of single crystal Ni-Mn-Ga FSMAs. *SPIE Conference Proceedings*, **5053**, 207–211.

Hirth, J.P. and Pond, R.C. (1996). Steps, dislocatioins and disconnections as interface defects relating to structure and phase transformations. *Acta Materialia*, **44**, 4749–4763.

James, R.D. and Hane, K.F. (2000). Martensitic transformations and shape-memory materials. *Acta Materialia*, **48**, 197–222.

James, R.D. and Wuttig, M. (1996). Alternative smart materials. *Proceedings of SPIE*, **2715**, 420–426.

James, R.D. and Wuttig, M. (1998). Magnetostriction of martensite. *Philosophical Magazine A*, **77**, 1273–1299.

Janak, J. and Williams, A.R. (1976). Giant internal magnetic pressure and compressibility anomalies. *Physical Review B*, **14**, 4199–4204.

Kanamori, J. (1963). Anisotropy and magnetostriction in ferro and antiferromagnetic materials. In *Magnetism*, Rado, G.T. and Suhl, H. (Eds.), Academic Press: New York, pp. 127–203, Vol. 1, Chapter 4.

Kittel, C. (1949). Physical theory of ferromagnetic domains. *Reviews of Modern Physics*, **21**, 541–583.

Kittel, C. and Galt, J.K. (1967). *Introduction to Solid State Physics*, Seitz, F. and Turnbull, D. (Eds.), Academic Press: New York, pp. 437–564, Vol. 3.

Kiefer, B. and Lagoudas, D.C. (2005). Magnetic field-induced martensitic variant reorientation in magnetic shape memory alloys. *Philosophical Magazine*, **85**, 4289–4329.

Klokholm, E. (1976). Measurement of magnetostriction in thin films. *IEEE Transactions on Magnetics*, **12**, 819–821.

Koch, R., Leonhard, H., Thurner, G. and Abermann, R. (1990). A UHV-compatible thin-film stress-measuring apparatus based on the cantilever beam principle. *Review of Scientific Instruments*, **61**, 3859–3862.

Koch, R., Weber, M., Thürmer, K. and Rieder, K.H. (1996). Magnetoelastic coupling of Fe at high stress investigated by means of epitaxial Fe(001) films. *Journal of Magnetism and Magnetic Materials*, **159**, L11.

Kollie, T.G. (1977). Measurement of the thermal expansion coefficient of nickel from 300 to 1000 K and determination of the power-law constants near the Curie temperature. *Physical Review B*, **16**, 4872–4881.

Kostorz, G. and Müllner, P. (2005). Magnetoplasticity. *Zeitschrift fur Metallkinde*, **96**, 701–707.

Lacheisserie, E. du Tremolet de (1972). Thermal variations of the magnetostriction coefficients of nickel. *Physica Status Solidi (b)*, **54**, K135–K137.

Lacheisserie, E. du Tremolet de (1987). Pair model of anisotropy and magnetostriction in soft amorphous magnets. *Journal of Magnetism and Magnetic Materials*, **67**, 102–114.

Lacheisserie, E. du Tremolet de (1993). *Magnetostriction: Theory and Applications of Magnetoelasticity*, CRC Press: Boca Raton.

Lacheisserie, E. du Tremolet de and Monterroso, R.M. (1983). Magnetostriction of iron. *Journal of Magnetism and Magnetic Materials*, **31–34**, 837–838.

Lacheisserie, E du Tremolet de and Rouchy, J. (1982). The magnetoelastic coupling in nickel. *Journal of Magnetism and Magnetic Materials*, **28**, 77–87.

Lee, E.W. and Asgar, M.A. (1971). The magnetostriction of nickel. *Proceedings of Royal Society of London, A*, **326**, 73–85.

Legvold, S., Alstad, J. and Rhyne, J. (1963). Giant magnetostriction in dysprosium and holmium single crystals. *Physical Review Letters*, **10**, 509–511.

Liebermann, H.H. and Graham, C.D. (1976). *Magnetism and Magnetic Materials*, AIP Conf. Proc. 29, AIP: New York, pp. 598–600.

Likhachev, A. and Ullakko, K. (2000). Quantitative model of large magnetostrain effect in ferromagnetic shape memory alloys. *The European Physical Journal B*, **14**, 263–267.

Liu, Z.H., Zhang, M., Wang, W.Q., *et al*. (2002). Magnetic properties and martensitic transformation in quaternary Heusler alloy of NiMnFeGa. *Journal of Applied Physics*, **92**, 5006–5008.

Livingston, J.D. (1982). Magnetomechanical properties of amorphous metals. *Physica Status Solidi (a)*, **70**, 591–596.

L'vov, V.A., Gomanaj, E.V. and Chernenko, V.A. (1998). A phenomenological model of ferromagnetic martensite. *Journal of Physics: Condensed Matter*, **10**, 4587–4596.

Richard, M. (2005). Systematic analysis of the crystal structure, chemical ordering , and microstructure of Ni-Mn-Ga ferromagnetic shape memory alloys. PhD thesis, M.I.T.

Marioni, M.A., Allen, S.M. and O'Handley, R.C. (2004). Nonuniform twin-boundary motion in Ni–Mn–Ga single crystals. *Applied Physics Letters*, **84**, 4071–4073.

Marioni, M.A., O'Handley, R.C. and Allen, S.M. (2003). Pulsed magnetic field-induced actuation of Ni-Mn-Ga single crystals. *Applied Physics Letters*, **83**, 3966–3968.

Morin, P. and Schmitt, D. (1990). Quadrupolar interactions and magento-elastic effects in rare-earth intermetallic compounds. In *Ferromagnetic Materials*, Buschow, K.H.J. (Ed.), North Holland: Amsterdam, pp. 1–132, Vol. 5.

Müllner, P. and Ullakko, K. (1998). The force of a magnetic/electric field on a twinning dislocation. *Physica Status Solidi (b)*, **208**, R1–R2.

Murray, S.J., Farinelli, M., Kantner, C., *et al*. (1998). Field-induced strain under load in Ni–Mn–Ga magnetic shape memory materials. *Journal of Applied Physics*, **83**, 7297–7299.

Murray, S.J., Marioni, M., Allen, S.M., *et al*. (2000). 6% magnetic-field-induced strain by twin-boundary motion in ferromagnetic Ni–Mn–Ga. *Applied Physics Letters*, **77**, 886–888.

O'Handley, R.C. (1978). Magnetostriction of transition-metal-metalloid glasses: temperature dependence. *Physical Review B*, **18**, 930–938.

O'Handley, R.C. (1998). Model for strain and magnetization in magnetic shape-memory alloys. *Journal of Applied Physics*, **83**, 3263–3270.

O'Handley, R.C. (2000). *Modern Magnetic Materials: Principles and Applications*, John Wiley & Sons: New York.

O'Handley, R.C. and Allen, S.M. (2000). Shape-memory alloys, magnetically activated ferromagnetic shape-memory materials. In *Encyclopedia of Smart Materials*, Schwartz, M. (Ed.), John Wiley & Sons: New York, pp. 936–951.

O'Handley, R.C., Allen, S.M., Paul, D.I., *et al*. (2003). Magnetic field-induced strain in single crystal Ni-Mn-Ga. *SPIE Conference Proceedings*, **5053**, 200–206.

O'Handley, R.C. and Grant, N.J. (1985). Magnetostriction and short-range order in amorphous alloys. In *Rapidly Quenched Metals*, Steeb, S. and Warlimont, H. (Eds.), Elsevier: Amsterdam, pp. 1125–1128.

O'Handley, R.C., Murray, S.J., Marioni, M., *et al*. (2000). Phenomenology of giant magnetic-field induced strain in ferromagnetic shape memory materials. *Journal of Applied Physics*, **87**, 4712–4717.

O'Handley, R.C., Paul, D.I., Allen, S.M., *et al*. (2006). Model for temperature dependence of field-induced strain in ferromagnetic shape memory alloys. *Materials Science and Engineering*, **A438–440**, 435–439.

O'Handley, R.C., Paul, D.I., Marioni, M., *et al*. (2001). Field-induced strain in ferromagnetic shape memory alloys: from macroscopic to microscopic models. *Japan Institute of Metals*, **II**, 2945–2948.

O'Handley, R.C., Song, Oh-Sung and Ballentine, C.A. (1993). Determining thin-film magnetoelastic constants. *Journal of Applied Physics*, **74**, 6302–6307.

O'Handley, R.C. and Sun, S.W. (1992). Strained layers and magnetoelastic coupling. *Journal of Magnetism and Magnetic Materials*, **104-107**, 1717–1720.

Paul, D.I., Marquiss, J. and Quattrochi, D. (2003). Theory of magnetization: twin boundary interaction in ferromagnetic shape memory alloys. *Journal of Applied Physics*, **93**, 4561–4564.

Paul, D.I., O'Handley, R.C. and Peterson, B.W. (2005). Ferromagnetic shape memory alloys: theory of interactions. *Journal of Applied Physics*, **97**, 312–316.

Rhyne, J.J. and Legvold, S. (1965). Magnetostriction of Tb single crystals. *Physical Review*, **138**, A507–A514.

Sander, D. (1999). The correlation between mechanical stress and magnetic anisotropy in ultrathin films. *Reports on Progress in Physics*, **62**, 809.

Sander, D., Enders, A. and Kirschner, J. (1995). A simple technique to measure stress in ultrathin films during growth. *Review of Scientific Instruments*, **66**, 4734–4735.

Söderberg, O., Sozinov, A., Ge, Y., *et al*. (2006). Giant magnetostrictive materials. In: Buschow, J. (ed.) *Handbook of Magnetic Materials*. Elsevier Science: Amsterdam, Vol 16. 1–39.

Solomon, V., McCartney, M.R., Smith, D.J., *et al*. (2005). Magnetic domain configuration in spark-eroded ferromagnetic shape memory Ni-Mn-Ga particles. *Applied Physics Letters*, **86**, 192503–192505.

Solomon, V., Smith, D.J., Tang, Y.J. and Berkowitz, A.E. (2004). Microstructural characterization of Ni-Mn-Ga ferromagnetic shape memory alloy particles. *Journal of Applied Physics*, **95**, 6954–6956.

Song, O.S., Ballentine, C.A. and O'Handley, R.C. (1994). Giant surface magnetostriction in polycrystalline Ni and NiFe films. *Applied Physics Letters*, **64**, 2593–2595.

Sozinov, A., Likhachev, A.A., Lanske, N. and Ullakko, K. (2002). Giant magnetic-field-induced strain in NiMnGa seven-layered martensitic phase. *Applied Physics Letters*, **80**, 1746–1748.

Stoelinga, J.H.M., Gersdorf, R. and deVries, G. (1965). Forced magnetostriction and its temperature dependence of binary alloys between iron, cobalt and nickel. *Physica*, **31**, 349–361.

Sun, S.W. and O'Handley, R.C. (1991). Surface magnetoelastic coupling. *Physical Review Letters*, **66**, 2798–2801.

Tam, A.C. and Schroeder, H. (1989). A new high-precision optical technique to measure magnetostriction of a thin film deposited on a substrate. *IEEE Transactions on Magnetics*, **25**, 2629–2638.

Tang, Y.J., Smith, D.J., Hu, H., *et al*. (2003). Structure and phase transitions of ferromagnetic shape memory alloy $Ni_{49}Mn_{30}Ga_{21}$ fine particles prepared by spark erosion. *IEEE Transactions*, **MAG-39**, 3405–3407.

Tatsumoto, E. and Okamoto, T. (1959). Temperature dependence of the magnetostriction constants in iron and silicon iron. *Journal of the Physical Society of Japan*, **14**, 1588–1594.

Tickle, R., James, R.D., Shield, T., *et al*. (1999). Ferromagnetic shape memory in the NiMnGa system. *IEEE Transactions on Magnetics*, **35**, 4301–4310.

Ullakko, K.J. (1996). Magnetically controlled shape memory alloys: a new class of actuator materials. *Journal of Materials Engineering and Performance*, **5**, 405–409.

Ullakko, K., Huang, J.K., Kantner, C., *et al*. (1996). Large magnetic-field-induced strains in Ni_2MnGa single crystals. *Applied Physical Letters*, **69**, 1966–1968.

Vasil'ev, A.N., Bozhko, A.D., Khovailo, V.V., *et al*. (1999). Structural and magnetic phase transitions in shape-memory alloys $Ni_{2+x}Mn_{1-x}Ga$. *Physical Review*, **B59**, 1113–1120.

Weber, M., Koch, R. and Rieder, K.H. (1994). UHV cantilever beam technique for quantitative measurement of magnetization, magnetostriction and intrinsic stress of ultrathin magnetic films. *Physical Review Letters*, **73**, 1166–1169.

Wu, G.H., Yu, C.H., Meng, L.Q., *et al*. (1999). Giant magnetic-field-induced strains in Heusler alloy NiMnGa with modified composition. *Applied Physics Letters*, **79**, 2990–2992.

Wuttig, M., Dai, L. and Cullen, J. (2002). Elasticity and magnetoelasticity of Fe-Ga solid solutions. *Journal of Applied Physics*, **80**, 1135–1137.

FURTHER READING

Brown, W.F. Jr. (1966). *Magnetoelastic Interactions*, Springer Verlag: Berlin.

Callen, E. (1968). Magnetostriction. *Journal of Applied Physics*, **39**, 519–527.

Chernenko, V.A., L'vov, V.A., Müller, P., *et al*. (2004). Magnetic-field-induced superelasticity of ferromagnetic thermoelastic martensites: experiment and modeling. *Physical Review B*, **69**, 134410-1–134410-8.

Chikazumi, S. (1997). *Physics of Ferromagnetism*, Oxford University Press: Oxford.

Clark, A.E., Wun-Fogle, M., Restorff, J.B., *et al*. (2001). Effect of quenching on the magnetostriction of $Fe_{1-x}Ga_x$ ($0.13 < x < 0.21$). *IEEE Transactions on Magnetics*, **MAG-37**, 2678–2680.

Gutjahr-Löser, Th., Sander, D. and Kirschner, J. (2000). Magnetoelastic coupling in Ni and Fe monolayers on Cu(001). *Journal of Applied Physics*, **87**, 5920.

Lee, E.W. (1955). Magnetostriction and magnetomechanical effects. *Reports on Progress in Physics*, **18**, 184–229.

Rhyne, J.J., Foner, S., McNiff, E.J. and Doclo, R. (1968). Rare earth metal single crystals. I. High-field properties of Dy, Er, Ho, Tb, and Gd. *Journal of Applied Physics*, **39**, 892–893.

Slonczewski, J.C. (1960). Origin of magnetoelastic effects in cobalt-iron ferrite. *Journal of Physics and Chemistry of Solids*, **15**, 335–353.

Tickle, R. and James, R.D. (1999). Magnetic and magnetomechanical properties of Ni2MnGa. *Journal of Magnetism and Magnetic Materials*, **195**, 627–638.

APPENDIX

It is important to consider the possible role of conventional magnetostriction in the actuation process of magnetic martensites. Anisotropic magnetostriction is observed to be about -100 to -150×10^{-6} in Ni–Mn–Ga (Tickle *et al*., 1999). This small strain, quadratic in the applied field, is indicated schematically in Figure A1 for Ni–Mn–Ga by the solid line below a typical threshold field of $200\,\mathrm{kA\,m^{-1}}$. In a multivariant martensite, as the magnetization is rotated, the domains are not free to fully express their magnetostrictive strain because of the constraints of adjacent variants, sample clamping, and any imposed bias stress. In these cases, the magnetic stress (the magnetoelastic coupling coefficient, B_1 in this case) builds up inside the constrained variant. This stress can be as large or larger than the yield stress for twin-boundary motion; for Terfenol-D, $B_1 \approx 60\,\mathrm{MPa}$ and in most other magnetic materials it is of the order of 1–10 MPa. The question here concerns the role of this stress accumulation on twin-boundary motion as a field is applied to a multivariant magnetic martensite. The large field-induced strain of certain magnetic martensites is due to twin-boundary motion. Twin-boundary motion may or may not occur in a multivariant crystal upon field-induced rotation of the magnetization in unfavorably oriented variant. However, once twin-boundary motion is initiated, it will proceed to minimize the energy in the presence of the applied field and the accumulated magnetostrictive stress.

In an actuation experiment configured as in Figure 18 but having the external stress provided by a compression spring, one would expect the stress in the load path to be proportional to the strain. Figure A1 shows the output of a load cell during cyclic actuation of the Ni–Mn–Ga sample whose field-induced strain is similar to that shown in Figure 19 (O'Handley *et al*., 2003). Note that the stress increases quadratically by as much as 0.5 MPa even at fields below the threshold for twin-boundary motion. Once twin-boundary motion is initiated (the range over which hysteresis is observed), this motion proceeds with no increase in load-path stress until the magnetic driving stress exceeds the load-path stress (spring plus ME stress). There is no increase in stress above saturation at about $H_a \approx 500\,\mathrm{kA\,m^{-1}}$.

It is possible quantitatively to explain the stress versus field data in Figure A1. The free energy in equation (1) must be supplemented with the ME anisotropy energy density in cubic systems, which has the form (O'Handley, 2000):

$$g_{\mathrm{ME}} = B_1\left[\varepsilon_{xx}(\alpha_x^2 - \tfrac{1}{3}) + \varepsilon_{yy}(\alpha_y^2 - \tfrac{1}{3}) + \varepsilon_{zz}(\alpha_z^2 - \tfrac{1}{3})\right] \tag{A1}$$

Here, the ε_{ii} are the principal magnetostrictive strains and α_i are the direction cosines of the magnetization. Because the ME energies are small ($B_1\varepsilon \approx 10^3\,\mathrm{J\,m^{-3}}$) compared to the magnetic anisotropy, the magnetization direction, determined from $\mathrm{d}g/\mathrm{d}\theta = 0$, is only weakly affected by ME energy. However, to determine the stress inside a constrained crystal, the derivative of the free energy with respect to strains is taken, and the magnitude of B_1 is such that it cannot be neglected relative to the other stresses in the problem that affect twin distribution. When the magnetization in variant 2 rotates in the presence of a field, it exerts a compressive (Tickle *et al*., 1999a,b)

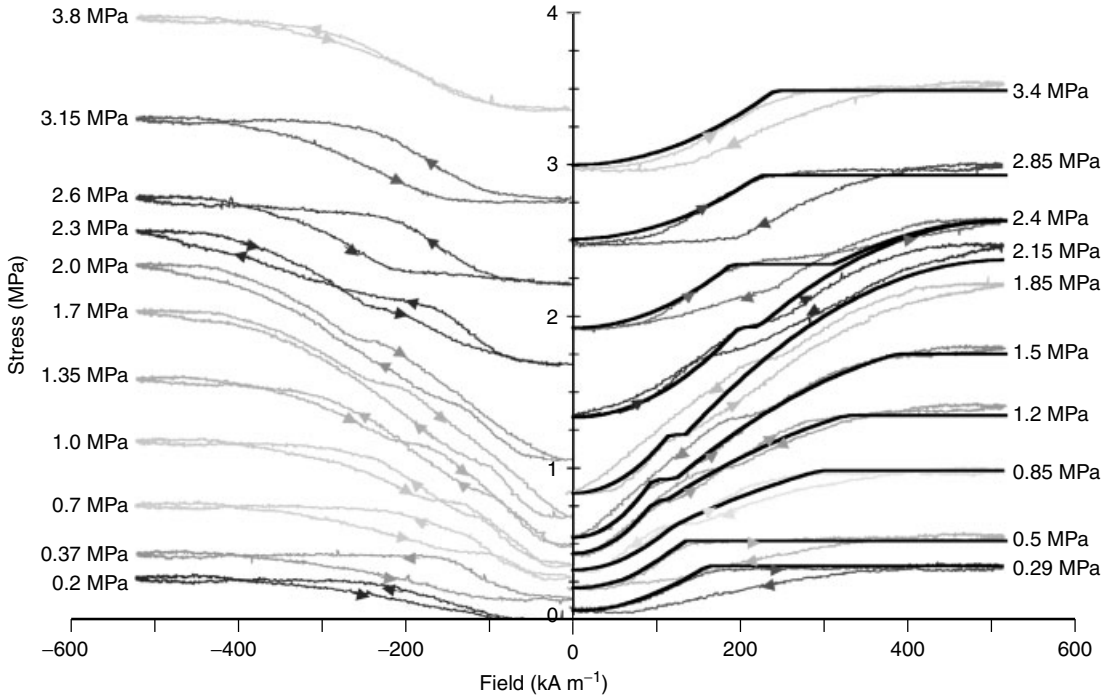

Figure A1. Magnetic-field dependence of stress measured by a load cell during actuation of Ni–Mn–Ga crystal. Theoretical results of equation (4) are plotted for the increasing field branch on half of the data set using different values of σ_0 that correspond to the initial bias stress as labeled. (Reprinted with permission R.C. O'Handley *et al*., copyright 2003 International Society for Optical Engineering.)

magnetostrictive stress on variant 1 proportional to $B_1\varepsilon \approx 10^3\,\mathrm{J\,m^{-3}}$. When the total energy density is written and minimized to find the stress, σ_y, the result is (O'Handley *et al*., 2003):

$$\sigma_y = \frac{\partial g}{\partial \varepsilon_{2y}} + \sigma_{\mathrm{ext}} = \sigma_{2y} + \sigma_{\mathrm{ext}} \tag{A2}$$

$$= \tfrac{3}{2}[B_1(f_1 - h^2) - \sigma_{\mathrm{ext}}(y_0, h)] + \sigma_{\mathrm{ext}}(y_0, h) \tag{A3}$$

The stress predicted by equation (A2) is plotted as a solid line in Figure A1. The model results correctly predict the quadratic increase in stress approaching 1 MPa before twin-boundary motion initiates. This stress is due to magnetostriction in the constrained sample. This model also expresses the absence of an increase in stress during twin-boundary motion. Finally, the saturation of magnetostrictive stress above the anisotropy field is also properly described.

Ferroelectricity in Incommensurate Magnets

A. Brooks Harris[1] and Gavin Lawes[2]

[1] *University of Pennsylvania, Philadelphia, PA, USA*
[2] *Wayne State University, Detroit, MI, USA*

1 INTRODUCTION

The interactions between long-range magnetic order and long-range ferroelectric order have been studied in depth since the first experimental confirmation of the magnetoelectric effect in the late 1950s (Dzyaloshinskii, 1959; Astrov, 1960; Folen, Rado and Stalder, 1961). We note the existence of several reviews (Smolenskii and Chupis, 1982; Schmid, 1973; Fiebig, 2005; Eerenstein, Mathur and Scott, 2006) and monographs (Birss, 1954), which give a general overview of the subject.

Handbook of Magnetism and Advanced Magnetic Materials. Edited by Helmut Kronmüller and Stuart Parkin. Volume 4: *Novel Materials*.

ISBN: 978-0-470-02217-7.

Of particular interest for this review are those materials which that exhibit a combined magnetic and ferroelectric transition. Perhaps the best known of these is Ni–I boracite ($Ni_3B_7O_{13}I$) which shows coupled ferromagnetic (FM), ferroelectric, and ferroelastic properties at a single phase transition at $T = 61.5\,\mathrm{K}$ (Ascher, Rieder and Stoessel, 1966; Toledano, Schmid, Clin and Rivera, 1985). The multiferroic behavior in this boracite arises from the fact that the magnetic transition is connected to a structural distortion, which in turn allows the development of ferroelectric order (Toledano, Schmid, Clin and Rivera, 1985). This transition can be understood in terms of a phenomenological Landau theory that couples the FM, ferroelectric, and ferroelastic order parameters to a primary antiferromagnetic (AFM) order parameter (Toledano, Schmid, Clin and Rivera, 1985). The strong coupling between magnetic and ferroelectric order parameters in systems having a simultaneous phase transition is demonstrated by the observation that in $Ni_3B_7O_{13}I$ it is possible to reverse the direction of the spontaneous polarization by applying an external magnetic field perpendicular to the direction of magnetization (Ascher, Rieder and Stoessel, 1966).

Cr_2BeO_4 also develops magnetic and ferroelectric order at a single phase transition (Newnham, Kramer, Schulze and Cross, 1978). Below $T = 28\,\mathrm{K}$, Cr_2BeO_4 orders antiferromagnetically into a state with spiral spin structure, and this AFM state shows an extremely small spontaneous polarization (approximately one million times smaller than that of $BaTiO_3$). The coupling between magnetic and ferroelectric order is expressed by a model proposing a mechanism in which the electric polarization is induced solely by the AFM order (Stefanovskii and Yablonskii, 1986). A similar model for magnetically induced ferroelectric order will be discussed in detail in the following sections.

The multiferroic behavior of $BaMnF_4$ is useful for illustrating the importance of symmetry considerations in determining magnetoelectric properties. Pyroelectric $BaMnF_4$ orders antiferromagnetically when cooled below $T = 26\,\mathrm{K}$, and there is a dielectric anomaly at this magnetic transition temperature (Samara and Richards, 1976). This decrease in dielectric constant below T_N varies like the square of the sublattice magnetization, and clearly indicates a coupling between the magnetic and ferroelectric properties of the sample. This interaction between magnetic and ferroelectric order is attributed to a magnetoelectric coupling, which causes a polarization-induced spin canting of 3 mrad (Fox and Scott, 1977). This spontaneous magnetoelectric effect is allowed by the $2'$ magnetic point group of $BaMnF_4$. Substituting 1% Co for Mn changes the magnetic point group to 2, which does not allow a spontaneous magnetoelectric effect, and no dielectric anomaly is observed in $BaCo_{0.01}Mn_{0.99}F_4$ (Fox, Tilley and Scott, 1980). While the magnetic structure in $BaMnF_4$ is strongly affected by the ferroelectric order, the very large coercive field precludes controlling the magnetization using an external electric field (Fiebig, 2005).

Until quite recently, the theoretical and experimental studies have focused on ferroelectricity in systems with simple FM or AFM order (Fox, Tilley and Scott, 1980; Toledano, Schmid, Clin and Rivera, 1985) (with studies on Cr_2BeO_4 being the notable exception). These systems are tractable from a theoretical standpoint, and allow a comparison to be made between experimental results and straightforward models based on magnetic space groups. However, limiting the scope of investigation to systems with FM or AFM order neglects a large class of materials that have more complex magnetic structures. Here, we will not consider systems (several of which are listed in Table 1 of Smolenskii and Chupis, 1982) which are ferroelectric at high temperature and then have a lower temperature magnetic phase transition (Fiebig *et al*., 2002). Instead, in this brief review article we will focus on the more recent studies in which ferroelectricity appears simultaneously (in a single combined phase transition) with long-range sinusoidally modulated magnetic order (Kimura *et al*., 2003; Hur *et al*., 2004), which we will refer to generically as 'incommensurate' magnetic order. (Commensurate systems have a wave vector q such that $aq = n/m$, where n and m are integers. If this condition is not satisfied, the system is incommensurate.) Accordingly, we will briefly summarize the experimental situation for the systems $TbMnO_3$ (TMO) (Hur *et al*., 2004; Kenzelmann *et al*., 2005) and $Ni_3V_2O_8$ (NVO) (Lawes *et al*., 2004, 2005; Kenzelmann *et al*., 2006). Then we will describe in detail the symmetry analysis developed in Lawes *et al*. (2005), Kenzelmann *et al*. (2006), and Harris (2006a) to understand the phenomenology of these systems. We believe that this theoretical approach is simple enough that it can easily be applied

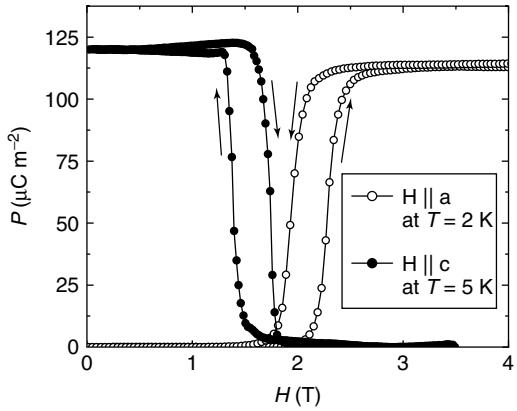

Figure 1. Experimental results for the spontaneous (i.e., in zero applied electric field) polarization **P** versus applied uniform magnetic field **H** applied along different crystallographic directions at selected temperatures for NVO. Only the *b*-component of the spontaneous polarization vector is nonzero. The arrows indicate the directions of increasing and decreasing magnetic field. (Reprinted with permission G. Lawes *et al*., copyright 2005, American Institute of Physics.)

to the ever increasing number of systems like NVO or TMO in which ferroelectricity is induced by incommensurate magnetic long-range order (For a symmetry analysis of several other systems, see Harris, 2006b).

To illustrate this phenomenon, we show, in Figure 1 some intriguing data from (Lawes *et al*., 2005) showing that the spontaneous polarization **P** depends strongly on the applied magnetic field **H**. At first glance, this data seems to have no obvious explanation. However, when viewed in combination with the magnetic phase diagram (see Figure 6) we will see that this data indicates that the spontaneous polarization is nonzero only in the magnetic phase we will call the 'low-temperature incommensurate phase'. The hysteresis is a consequence of passing through a first-order phase boundary between this phase and an AFM phase in which a spontaneous polarization is not allowed. Thus, the dramatic dependence of polarization on magnetic field has a simple explanation: ferroelectric order appears only in one specific magnetic phase whose existence depends in the value of the magnetic field. This strong coupling between magnetic and ferroelectric order is potentially important for device applications, as we will discuss in the following section. From a basic physics standpoint, these systems that exhibit a coupling between the ferroelectric moment (a polar vector) and the magnetic moment (an axial vector) are very interesting. (As we will see, such systems have order parameters whose response to both electric and magnetic fields becomes large especially near a phase transition.) A complete understanding of this coupling from a microscopic theory is not yet available. Here, we will show that the Landau expansion explains the observed phenomenology

of this interaction and that these results follow from the microscopic symmetry of the strain dependence of the exchange tensor. This explanation will serve as a guide to constructing a fully microscopic theory of magnetoelectric coupling.

Briefly, this review is organized as follows. In Section 2, we discuss some general types of applications in which the magnetoelectric coupling may be exploited to develop new types of devices. It should be emphasized that these applications are speculative, and are intended to illustrate the types of new devices that could be developed using these new materials. In Section 3, we review the Landau description of ferroelectricity. In Section 4, we give a simplified theoretical analysis of incommensurate magnetic ordering and in Section 5, we discuss how Landau theory leads to a symmetry-based description of incommensurate magnetic ordering. It is our aim to demystify the use of representation theory for the determination of magnetic structure by diffraction techniques. Understanding these incommensurate magnetic structures is crucial to developing a model for the coupling between magnetic and ferroelectric order in these systems. In Section 6, we use the results of Section 5 to analyze how symmetry restricts the form of the coupling between electric and magnetic order parameters and thereby explain the simultaneous appearance of these two kinds of order parameters in a single phase transition. The construction of this interaction is greatly simplified by the fact that it involves an expansion in powers of the order parameters relative to the paramagnetic paraelectric phase. Thus the interactions have to satisfy the invariances of the disordered paramagnetic/paraelectric phase (Dzyaloshinskii, 1957; Landau and Lifshitz, 1958) and we do not need to broach the more complicated question of analyzing the symmetry of interaction within an ordered phase. In Section 7, we analyze the symmetry of the strain dependence of the exchange tensor and show that it leads to results identical to those of Landau theory. In Section 8 we summarize the main points of this review and speculate on some future directions of research. We will discuss how our results on ferroelectric order in incommensurate magnets may offer guidance in searching for new magnetoelectric materials. Finally in Section 9, we briefly discuss results which appeared subsequent to the writing of this review.

2 DEVICE APPLICATIONS

The development of devices incorporating both charge and spin degrees of freedom, often referred to as *spintronics*, has already led to significant technological breakthroughs (Wolf *et al*., 2001). Magnetic sensors based on giant magnetoresistance (GMR) are widely used as the read heads in modern hard drives, and magnetic random access memory also relies strongly on couplings between charge and spin. Additionally, there are a wide range of proposals for devices based on controlling the spin degree of freedom in FM semiconductors, including spin valves and qubits for quantum computing. Much of the research on materials in which charge and spin are coupled has focused on metallic and semiconducting systems. However, dielectric materials exhibiting couplings between electric polarization and magnetization may also play an important role in developing the next generation of spintronic devices.

Magnetoelectrics are systems in which either applying an external magnetic field produces an electric polarization or applying an external electric field produces a magnetization. This type of coupling between charge and spin was postulated by Pierre Curie at the end of the nineteenth century (Curie, 1894), but not observed experimentally until the late 1950s (Astrov, 1960; Folen, Rado and Stalder, 1961). Materials in which two or more of ferroelectric, FM, and ferroelastic order coexist are referred to as multiferroics. This strict definition of multiferroics is often relaxed to include systems that exhibit combinations of any type of long-range magnetic, ferroelectric, or ferroelastic order. Furthermore, a fourth class of ferroic order, *ferrotoroidicity*, has been included in discussions of multiferroic materials (Fiebig, 2005; Schmid and Rivera, 1994; Ye *et al*., 1994). This review will concentrate specifically on magnetoelectric multiferroics, where the coexistence of long-range magnetic and long-range dielectric order leads to a pronounced coupling between the charge and spin degrees of freedom in these systems.

We consider two classes of devices based on magnetoelectric multiferroics. The first class of devices depend on the magnetoelectric effect – the induction of a magnetization (polarization) by an applied electric (magnetic) field. Using the magnetoelectric effect, it is possible to design a range of devices from sensors to transducers to actuators, in which magnetic and electric properties are coupled. The second class of devices exploits the fact that these materials have simultaneously appearing long-range magnetic and ferroelectric order. The underlying assumption is that multiferroics exhibit both charge and spin ordering, and because of the coupling between the two, both magnetic and ferroelectric order will be strongly affected by either magnetic or electric fields. Strictly speaking, only magnetic field control of the electric polarization has been demonstrated for the multiferroic materials with incommensurate magnetic structures discussed in this review, but magnetic phase control by an external electric field has been demonstrated in other multiferroic materials (Lottermoser *et al*., 2004). Very recently, Ederer and Spaldin have discussed the materials requirements for electrically switchable magnetic properties in thin-film multiferroics (Ederer and Spaldin, 2005).

The investigation of magnetoelectric devices is an active area of research. Prototype devices fabricated using piezoelectric–magnetostrictive composite materials to produce magnetoelectric coupling have already been tested (Bayrashev, Parker, Robbins and Ziaie, 2003; Srinivasan *et al*., 2002), and there are a range of proposals for other magnetoelectric devices. These include utilizing magnetoelectric materials as the pinning layer in GMR devices (Binek and Doudin, 2005), for low-frequency wireless power applications (Bayrashev, Parker, Robbins and Ziaie, 2003), and for developing tunable dielectric materials (Katsufuji and Takagi, 2001). One key feature of magnetoelectric materials is that they allow the design of devices controlled magnetically or electrically, as desired. Controlling the magnetic properties of materials using an *electric* field offers significant benefits in designing new devices. Using current-based methods to switch magnetic devices is relatively slow and power intensive. Voltage control of the magnetic properties is expected to offer significantly faster switching (thin-film ferroelectrics can show switching times of less than 200 ps (Li *et al*., 2004)) in a low-power device. Magnetoelectric materials offer the potential for fabricating highly tunable, fast switching, low-loss/low-power devices having very small form factors, which would be suitable for a wide range of commercial and industrial applications.

The materials property most relevant in determining the suitability of a compound for applications in magnetoelectric devices is the magnitude of the magnetoelectric susceptibility, χ_{ME}. For homogeneous materials, χ_{ME} satisfies the bound,

$$\left(\chi_{\mathrm{ME}}^2 \leq \chi_{\mathrm{E}}\chi_{\mathrm{M}}\right) \tag{1}$$

where χ_{E} and χ_{M} are the electric and magnetic susceptibilities of the system, respectively (Smolenskii and Chupis, 1982). Therefore, in order to maximize the magnitude of the magnetoelectric coupling, one should attempt to maximize the magnitudes of *both* χ_{M} and χ_{E}. Since ferroelectrics typically have large values of χ_{E} and ferromagnets typically have large values of χ_{M}, multiferroics are expected to have large values of χ_{ME}. Furthermore, since susceptibilities are largest at the ordering transition, systems developing magnetic and ferroelectric order at the same temperature should show exceptionally large magnetoelectric couplings. Understanding the microscopic origins of the magnetoelectric coupling in these multiferroic systems will have important ramifications for developing novel magnetoelectronic devices.

Beyond simply exhibiting very large magnetoelectric couplings, intrinsic multiferroics also have both long-range magnetic order and long-range ferroelectric order. The coupling between magnetization and polarization offers new possibilities for designing devices. The ability to control the magnetic or ferroelectric state of a system using either a magnetic field or an electric field would offer the ability to develop multifunctional memory elements, for example, ferroelectric memory that can be written to using magnetic fields. We will discuss two proposals for new technologies that explicitly utilize the ferroelectric and magnetic characters of magnetoelectric multiferroics. It should be emphasized that this discussion is meant only to illustrate some of the potential applications arising from the incorporation of multiferroic materials into new devices. More investigation on the specific properties of these multiferroics is required before proof-of-principle devices could be designed on the basis of these speculations. Because the spontaneous polarization in incommensurate multiferroics is small, these materials are not expected to replace conventional ferroelectrics in any type of current devices. Therefore, we will concentrate on discussing novel applications which would only be possible using multiferroic materials.

As the bit density of modern hard drives increases, the characteristic size of the magnetic structures used to store the information is decreasing. As the physical size of the bit is reduced, the anisotropy energy decreases, and the magnetic moment can begin to thermally fluctuate. Controlling these thermal fluctuations is necessary to ensure the long-term stability of stored information in ultradense magnetic recording material. For long-term magnetic storage (5+ years), the ratio of the energy barrier against these thermal fluctuations to k_{BT} should be large, roughly 55. In current devices, this is often accomplished by using materials with very large magnetic anisotropy energies or by exploiting the anisotropic difference between FM and AFM layers. One possible application for multiferroic materials is to use the coupling between ferroelectric and magnetic order in these systems to stabilize the magnetic moment against thermal fluctuations in nanoscale magnets.

In many magnetoelectric multiferroics, there is a strong coupling between the ferroelectric and magnetic order parameters. In such systems, fixing the polarization (magnetization) direction will fix the axis of the magnetization (polarization). This coupling is observed in measurements showing that the sign of the magnetically induced polarization is independent of the sign of the applied magnetic field, although the development of ferroelectric order depends strongly on the magnetic field axis. In such multiferroics, fixing the electric polarization would also fix the magnetization axis. This ferroelectrically induced magnetic anisotropy would inhibit thermally activated switching of the magnetic moments by significantly increasing the magnitude of the energy barrier to magnetization reversal. This could be accomplished, for example, by assembling multiferroic nanoparticles on a ferroelectric substrate. In this geometry, the very large ferroelectric anisotropy energy would provide a tunable

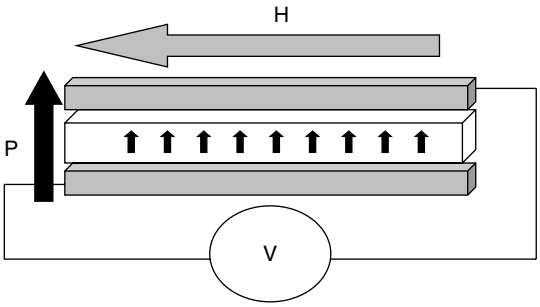

Figure 2. Schematic illustration of a device to measure magnetic fields by using the induced polarization. The middle layer (white) is a multiferroic material with strong magnetoelectric couplings and the outer layers (gray) are ferromagnetic metals. In this example, the polarization is induced in a direction perpendicular to the applied magnetic field.

barrier against thermal fluctuations of the *magnetic* moment as well.

Multiferroics may also have important applications in developing magnetic field sensors. There are a range of proposals for incorporating magnetoelectric materials in exceptionally sensitive magnetic field detectors. Even relatively small external magnetic fields will produce a voltage change in materials with very large magnetoelectric couplings. Since it is often better to measure small voltages at zero applied current rather than small magnetizations or small changes in resistivity, magnetoelectric materials offer the potential for developing greatly improved magnetic field sensors. Because multiferroics exhibiting simultaneous magnetic and ferroelectric transitions offer exceptionally large magnetoelectric couplings, these materials are particularly interesting in the context of improved sensors. Figure 2 shows a schematic for such a device (http://www.nasatech.com/Briefs/May00/NPO20523.html). The magnetization produces a spontaneous polarization directed perpendicular to the plane of the sensor. This magnetically induced voltage can be measured to a high degree of accuracy, either directly or by measuring the dielectric response of the compound. This device could also be configured to extract energy from an *alternating* magnetic field – the magnetically induced alternating voltage could be used as a supply for very low-power applications (Bayrashev, Parker, Robbins and Ziaie, 2003).

Beyond simply being used as a passive magnetic field sensor, the device illustrated in Figure 2 could also be configured as a voltage-biased magnetic memory element. One of the difficulties facing current magnetic random access memory (MRAM) devices lies in producing magnetic fields that are strong enough to cause a moment reversal in the memory element but also sufficiently localized to affect only one specific element. While identifying multiferroic materials in which applying a voltage could reverse the direction of the magnetization would certainly be beneficial for developing MRAM devices, a more modest type of voltage-assisted magnetization reversal could also be implemented in memory elements. As will be discussed in the following section, ferroelectric order can be promoted or suppressed by the application of an external magnetic field in many multiferroic materials. We expect that in these materials, applying an electric field could then suppress or promote magnetic ordering. In such a system, the coercivity of the magnetic memory element could be tuned by applying an electric field. Incommensurate multiferroics may be more suitable for devices based on voltage-tunable coercivity, rather than voltage-tunable magnetization, because of the very small spontaneous polarization typically developing in these systems.

Consider the multiferroic memory element in a FM state, which can be suppressed by applying a sufficiently large voltage. In the absence of an electric field, the coercivity of the memory element is large, so the magnetization is unaffected by stray magnetic fields. In order to reverse the magnetization direction, a bias voltage is applied to the multiferroic element, bringing the system closer to the magnetic transition, reducing the magnitude of the coercive field. In this state, the magnetization can be reversed by a relatively small external magnetic field, smaller than the coercive field of the unbiased multiferroic. When the voltage is removed, the new magnetization will be stable. This type of voltage-assisted magnetization reversal could be used to produce arrays of magnetic memory elements that could be switched by the same external magnetic field. Only those elements that have a bias voltage applied will have a sufficiently small coercivity to be switched by the magnetic field. This technique may offer advantages over transitional MRAM devices, such as a smaller sensitivity to stray fields (allowing higher bit density) and potentially faster switching times. This is schematically illustrated in Figure 3.

While multiferroics offer many exciting possibilities for designing novel magnetoelectric and magnetodielectric devices, there are several materials limitations that need to be overcome, specifically for incommensurate multiferroics. All incommensurate multiferroics identified to date have transition temperatures well below room temperature, with the possible exception of $Ba_{0.5}Sr_{1.5}Zn_2Fe_{12}O_{22}$ (T. Kimura, private communication). Additionally, the magnitude of the spontaneous polarization in incommensurate multiferroics is very small, with typical polarizations on the order of only $10^{-3}\,\mathrm{Cm}^{-2}$. Finally, incommensurate multiferroics often have a small or negligible net magnetization in the ordered state. These limitations make it difficult to identify applications in which incommensurate multiferroics could replace conventional FM or ferroelectric materials. However, the strong spin-charge coupling in multiferroic materials does

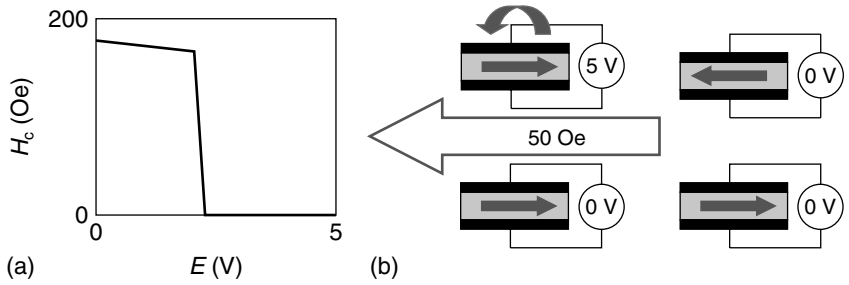

Figure 3. Voltage-assisted MRAM. (a) Schematic diagram showing a *model curve* for how the coercive magnetic field is expected to vary with voltage. (b) With the magnetization of the bits originally directed to the right, a small (50 Oe) writing field is applied. At zero voltage, this is smaller than the coercive field, so that the magnetization does not switch. However, applying 5 V across the multiferroic layer reduces the coercive field to almost zero, so that this small magnetic field is sufficient to reverse the direction of magnetization.

offer the possibility of designing new classes of devices, which would be impossible with conventional materials. Identifying incommensurate multiferroics having higher transition temperatures and larger ordered moments (both electric and magnetic) is one of the major current research objectives for multiferroic materials. Furthermore, there is some hope that the ferroelectric properties of incommensurate multiferroics may be enhanced in thin films. Recent work on $BiFeO_3$ films has shown that the magnitude of the polarization in thin films is approximately an order of magnitude larger than in bulk samples (Wang *et al*., 2003). This has been explained in terms of epitaxial strain (Li *et al*., 2004) and allows the possibility that the spontaneous polarization of incommensurate multiferroics may be enhanced in thin films.

3 FERROELECTRICITY

We start by making a few observations concerning the symmetry properties of ferroelectric systems for which magnetic ordering plays no role. In the most common scenario, ferroelectrics exhibit a high-temperature phase having spatial inversion symmetry which prevents the existence of a vector order parameter. Then, as the temperature is reduced through a critical value, T_F, a lattice instability develops in which inversion symmetry is broken cooperatively via a continuous phase transition at which a spontaneous polarization appears. Within a Landau theory this transition is described by a free energy as a function of the polarization $\mathbf{P}$ which is of the form

$$F = \frac{1}{2}\chi_E^{-1}\mathbf{P}^2 + \mathcal{O}(\mathbf{P})^4 = \frac{1}{2}a(T - T_F)\mathbf{P}^2 + \mathcal{O}(\mathbf{P})^4 \quad (2)$$

At the transition, the fact that the quadratic term in $\mathbf{P}$ becomes unstable (negative) reflects the divergence in the electric susceptibility at the ferroelectric transition. This instability is sometimes traced to a soft phonon, but whatever the mechanism, the appearance of ferroelectricity represents a broken symmetry. Conversely, as will become relevant in the following, ferroelectricity can only occur if the symmetry is broken to permit the ordering of the polarization vector. We will use this criterion to determine which types of magnetic order can possibly induce ferroelectric order. If one takes the quartic terms in equation (2) to be of the form $(b/4)[\mathbf{P}^2]^2$ (with $a > 0$ for stability), then minimization of F with respect to $\mathbf{P}$ shows that for $T < T_F$ one has $P \sim [a(T_F - T)/b]^{1/2}$, which is expected to hold as long as $T_F - T$ is not so large that sixth- and higher-order terms in F are important. Mean-field theory ignores spatial correlations that lead to modifications of critical exponents, but the scope of this review does not permit consideration of such corrections (Domb and Green, 1976).

As the temperature is further lowered it is possible for this ferroelectric system to develop long-range magnetic order (Fiebig *et al*., 2002). In this case, one does not expect significant interaction between electrical and magnetic properties because the two phenomena are essentially independent of one another. In these systems, the spontaneous polarization will depend only weakly on the applied magnetic field. In this scenario, it is well known (Lawes, Ramirez, Varma and Subramanian, 2003) that one can expect anomalies in the dielectric response of the system when the ferroelectric develops (independently) long-range magnetic order. This review is *not* concerned with such an 'accidental' superposition of electric and magnetic properties. Instead, we focus our attention on the situation when the appearance of long-range magnetic order induces ferroelectricity. Furthermore, we will consider an interesting subclass in which the long-range magnetic order is modulated with an apparently incommensurate wave vector. We will develop a Landau theory for this combined phase transition in which the fact that the wave vector does not have high symmetry (and is thus neither FM or AFM) is crucial to our analysis. Thus the development here cannot be obtained by a trivial extension of theories applicable to FM or AFM ferroelectrics. A simplifying feature of this formulation is that it is based on an expansion of the free energy in powers of the various order parameters relative

to the *paramagnetic* phase. Accordingly, each term in this expansion has to have the full symmetry of the disordered phase (Dzyaloshinskii, 1957; Landau and Lifshitz, 1958). In contrast, it is less straightforward to analyze whether the symmetry of a magnetically ordered phase permits an induced ferroelectric order. Also, the Landau formulation correctly predicts which components of the spontaneous polarization vector are induced by the magnetic ordering. In addition, the Landau expansion indicates that the spontaneous polarization is proportional to the nth power of the emerging magnetic order parameter. In the cases considered here $n = 1$, as we shall see.

4 TOY MODELS FOR INCOMMENSURATE MAGNETISM

4.1 Review of mean-field theory

In this section we review the description and phenomenology of incommensurate magnets, because the characterization of their symmetry is essential to understanding the coupling between magnetic and electric long-range order.

For the purposes of this review, it suffices to consider the description of incommensurate magnets within mean-field theory. For a system consisting of quantum spins of magnitude S on each site, we write the trial free energy as

$$F \equiv U - TS = \mathrm{Tr}[\boldsymbol{\rho}\mathcal{H} + kT\boldsymbol{\rho}\ln\boldsymbol{\rho}] \tag{3}$$

where $\mathcal{H}$ is the Hamiltonian, T the temperature, U the internal energy, S the entropy, and the actual free energy is the minimum of F with respect to the choice of $\boldsymbol{\rho}$ subject to the conditions that $\boldsymbol{\rho}$ is Hermitian with unit trace. Within mean-field theory we take the density matrix to be the product of independent single particle density matrices $\boldsymbol{\rho}(i)$ for each site i:

$$\boldsymbol{\rho} \equiv \prod_i \boldsymbol{\rho}(i) \tag{4}$$

This approximation corresponds to the intuitive idea that when correlations between spins are neglected, each spin reacts to the mean field of its neighbors.

In equation (3), the trace of $\boldsymbol{\rho}\mathcal{H}$ gives the internal energy U and that of $-k\boldsymbol{\rho}\ln\boldsymbol{\rho}$ gives the entropy S. In the absence of anisotropy it suffices to set

$$\boldsymbol{\rho}(i) = \frac{1}{2S+1}[\mathcal{I} + c\boldsymbol{\sigma}(i)\cdot\mathbf{S}_i] \tag{5}$$

where $\mathcal{I}$ is the unit matrix of dimension $(2S+1)$, c is a constant of order unity, chosen to make equation (6) true, and $\mathbf{S}_i$ is the vector spin operator for site i (here $\mathbf{S}_i$ is a $(2S+1)$ dimensional matrix). The free energy is then minimized with respect to the trial parameters $\boldsymbol{\sigma}(i)$, which physically are identified as the average spin vectors:

$$\langle\mathbf{S}(i)\rangle \equiv \mathrm{Tr}[\boldsymbol{\rho}(i)\mathbf{S}(i)] = \boldsymbol{\sigma}(i) \tag{6}$$

Thus, $\boldsymbol{\sigma}(i)$ is the vector *order parameter* at the ith lattice site. In this formulation the internal energy is quadratic in the order parameter $\boldsymbol{\sigma}$, whereas the entropic term involves both quadratic and higher powers of the order parameter. As we shall see, even without explicit calculations much information can be inferred from the symmetry of the trial free energy as a function of the order parameter(s).

As mentioned in the introduction, we will focus our attention on systems which display incommensurately modulated magnetic long-range order. We refer the reader to a comprehensive survey of such systems by Nagamiya (1967). Here we give a simplified review. To characterize an incommensurate state we consider a toy model consisting of a one-dimensional system with interparticle separation a and having isotropic AFM exchange interactions J_1 and J_2 between nearest and next-nearest neighbors, respectively. If J_2 is AFM and large enough, these two interactions compete and produce an incommensurate spin structure. Thus we are led to consider the Hamiltonian

$$\mathcal{H} = \sum_n \mathbf{S}_n \cdot [J_1\mathbf{S}_{n+1} + J_2\mathbf{S}_{n+2}] \tag{7}$$

with $J_2 > 0$. The corresponding trial free energy is

$$F = \frac{1}{2}dkT\sum_i \boldsymbol{\sigma}(i)^2 + \sum_{n=1,2} J_n\boldsymbol{\sigma}(i)\cdot\boldsymbol{\sigma}(i+n) + \mathcal{O}(\boldsymbol{\sigma}^4) \tag{8}$$

where the entropic term is scaled by a constant of order unity, d.

4.2 Wave vector selection

It is instructive to write the free energy per spin, f, in terms of Fourier variables, $\boldsymbol{\sigma}(q) = (1/N)\sum_i e^{iqx_i}\boldsymbol{\sigma}(i)$, where N is the total number of spins as

$$f \equiv \frac{F}{N} = \frac{1}{2}\sum_q \chi(q)^{-1}\boldsymbol{\sigma}(q)\cdot\boldsymbol{\sigma}(-q) + \mathcal{O}(\boldsymbol{\sigma}^4) \tag{9}$$

where $\chi(q)^{-1} = dkT + J_1\cos(qa) + J_2\cos(2qa)$ is the wave vector-dependent susceptibility. At high temperature (when $kT \gg |J_1|$ and $kT \gg |J_2|$), $\chi(q)^{-1}$ is positive for all q and the free energy is minimized by setting all the order

parameters $\boldsymbol{\sigma}(q)$ to zero. In Figure 4, we show $\chi(q)^{-1}$ as a function of wave vector q for a sequence of temperatures. As the temperature is lowered through a critical value T_c, $\chi(q)^{-1}$ becomes zero for the wave vector $q \equiv q_0$ which minimizes $\chi(q)^{-1}$:

$$\cos(q_0 a) = \frac{-J_1}{(4J_2)} \tag{10}$$

This determination of the value of q_0 is called *wave vector selection*. As the temperature is reduced through T_c the paramagnetic phase becomes unstable against the formation of long-range order at the selected wave vector q_0. If q_0 is commensurate, that is, if $q_0/(2\pi)$ is rational, then the magnetic unit cell has length $2\pi/q_0$. Otherwise the periodicity of the magnetic structure is incommensurate with the periodicity of the lattice. However, it is essentially impossible to distinguish whether a system is truly incommensurate or merely has a very large magnetic unit cell. Since the properties of systems depend very weakly on whether the magnetic unit cell is infinite, the question whether the magnetic structure is truly incommensurate is an academic one.

For $T < T_c$ the order parameter $\boldsymbol{\sigma}(q_0)$ assumes a nonzero value determined by the (negative) quadratic terms in the free energy in combination with the (positive) terms of order $\boldsymbol{\sigma}^4$, so that

$$f \sim \frac{1}{2} r\sigma(q_0)^2 + u\sigma(q_0)^4 \tag{11}$$

Within mean-field theory $r \sim a(T - T_c)$, in which case $|\boldsymbol{\sigma}(q_0)| \sim (T_c - T)^{1/2}$. Once order develops at one wave vector, other terms of order $\boldsymbol{\sigma}^4$ prevent order developing at other wave vectors. This scenario is realistic for a three-dimensional system (for which long-range order is not destroyed by thermal fluctuations). The eigenvector associated with the eigenvalue of the quadratic form which passes through zero is called the *critical eigenvector*. The critical eigenvector contains the form factor of the ordering, that is, it completely describes the pattern of spin ordering within a unit cell. In this simple model there is only one spin per unit cell, so the eigenvector specifies the spin direction, that is, the component of spin which condenses. (This concept will be better illustrated when we consider real systems that often have more than one magnetic site per unit cell.) In the present case when there is no anisotropy, the spin structure when $\boldsymbol{\sigma}(q)$ becomes nonzero for $q = q_0$ is a modulated one in which the x component of spin has a complex amplitude, A_x, so that

$$\sigma_x(i) = A_x e^{iq_0 x_i} + A_x^* e^{-iq_0 x_i} \tag{12}$$

and similarly for the other spin components. If these complex amplitudes A_x, A_y, and A_z all have the same phase (We say that two complex-valued quantities, z_1 and z_2, have the *same phase* if z_1/z_2 is *real*, but is not necessarily *positive real*.), then the spin is linearly polarized with respect to an axis determined by the ratios of A_x, A_y and A_z and with an amplitude that varies sinusoidally with position. If the complex amplitudes do not have the same phase, then the spin structure will be a helix, a spiral, or a fan, and so on.

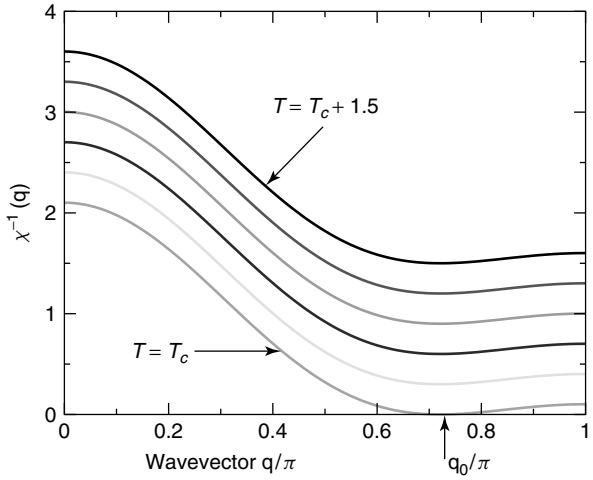

Figure 4. $\chi(q)^{-1}$ at a sequence of temperatures, $T = T_c + 0.3n$ for $n = 0, 1, 2, 3, 4, 5$ with $J_1 = 1.0$ and $J_1/J_2 = 2.56$ (as is appropriate for NVO). Here $T_c = 0.711$.

4.3 Effects of anisotropy

This toy model will not accurately capture the behavior of real magnetic systems because we have not yet included any magnetic anisotropy. As can be seen from Figure 5, the sequence of phases which appear as the temperature is reduced for zero anisotropy ($K = 0$) is not characteristic of the case when K is nonzero, even if K is small. So $K \neq 0$ is the generic scenario. In the presence of single-ion easy-axis anisotropy, the trial free energy at quadratic order assumes the form

$$f = \frac{1}{2}\sum_q \chi(q)^{-1}\boldsymbol{\sigma}(q)\cdot\boldsymbol{\sigma}(-q) - K\sum_q \boldsymbol{\sigma}_x(q)\boldsymbol{\sigma}_x(-q) + \mathcal{O}(\boldsymbol{\sigma}^4) \tag{13}$$

where K is an anisotropy energy that favors alignment of spins along the easy axis, here the x axis, and f denotes the free energy per spin. In this case, the instability (at which long-range order first appears) is one in which the spins are confined to the easy axis and have a sinusoidally varying amplitude. This type of ordered phase will be referred to as

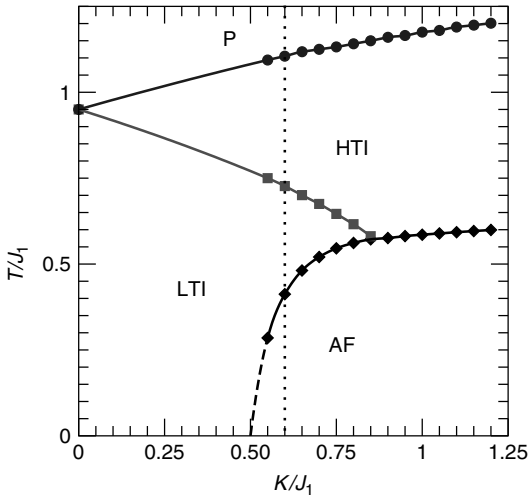

Figure 5. Zero-temperature phase diagram for the $J_1 - J_2$ ($S = 1$) model with easy-axis anisotropy scaled by K (Kenzelmann *et al.*, 2006). The points represent numerical implementation of mean-field theory except for $K = 0$ where analytic results are used. Here, 'HTI' denotes a longitudinally polarized incommensurate phase and 'LTI' an elliptically polarized incommensurate phase. In both phases, the modulation vector is given by equation (10). 'AF' denotes a two-sublattice collinear antiferromagnetic phase. For large anisotropy this model reduces to the anisotropic nearest–next-nearest neighbor Ising (ANNNI) model (Fisher and Selke, 1980a,b). The dashed line is drawn for a value of the anisotropy energy that reproduces the evolution of magnetic phases in NVO as a function of T for $H = 0$. (Reprinted with permission G. Lawes *et al.*, copyright 2006, American Physical Society.)

the high-temperature incommensurate (HTI) phase and the associated critical temperature will be denoted T_{HTI}. If the anisotropy is not too large, then, as the temperature is further reduced, the fourth-order terms in the free energy (which we have so far neglected) become important. One effect of these terms can be visualized as incorporating the constraint of 'fixed length'. In the HTI phase, the spins have a length that varies sinusoidally with position. However, in the ground state, we expect each spin to have its maximum length S but to be oriented in a direction to optimize the energy. Thus, in the extreme limit of zero temperature, the constraint of fixed spin length is fully enforced. Although the constraint is less fully realized at higher temperature, the qualitative effect is clear: when the temperature is sufficiently reduced, one has a continuous phase transition into a phase we refer to as the low-temperature incommensurate (LTI) phase. In this phase, the spins develop transverse order (in addition to the preexisting longitudinal order along the easy axis) to more nearly achieve fixed spin length. If the easy-axis anisotropy is small, the range of temperature over which the HTI phase is stable is also small. The phase diagram of such a model as a function of anisotropy energy K and temperature is shown in Figure 5 (Lawes *et al.*, 2004; Kenzelmann *et al.*, 2006).

We will mainly be concerned with the two incommensurate phases, the longitudinally modulated HTI phase and the elliptically polarized low-temperature incommensurate LTI phase. Although the details of the unit cell complicate the picture, the phenomenology of the HTI and LTI phases are usually roughly similar to that of the simplified case discussed here. In Figure 6, we show the experimentally determined phase diagrams of NVO and TMO as a function of applied magnetic field H and temperature T, with the HTI and LTI phases labeled.

4.4 Wave vector locking

From equation (10), it would seem that the wave vector q is a continuous and smooth function of J_2/J_1. Although our toy model does not give any simple explanation for the observed temperature dependence of q, a more complete analysis (as in Harris *et al.*, 2006 and Kajimoto *et al.*, 2004) leads to a small dependence on temperature which, like the dependence on J_2/J_1, might be thought to be smooth and continuous. However, there are terms which favor commensurate values of q. These terms in the free energy must conserve wave vector, but only to within a reciprocal lattice vector G (which for our one-dimensional toy model can assume the values $G_m = (2m\pi/a)$, where a is the nearest-neighbor separation). Thus one has the so-called Umklapp terms such as $\delta f = w\sigma(q)^4$, when $4q = \mathbf{G}_m$. More generally the Umklapp terms give a contribution to the free energy of the form

$$\delta f = \sum_{m,n} w_{m,n}\sigma(q)^{2n}\delta_{nq-2m\pi/a} \tag{14}$$

where the coefficient w_m is of order unity and δ_x is unity if $x = 0$ and is zero otherwise. (Within the present formulation these terms come from expanding $\mathrm{Tr}\boldsymbol{\rho}\ln\boldsymbol{\rho}$ to higher than quadratic order in the order parameter.) The effect of these Umklapp terms is to cause the wave vector to 'lock' onto a commensurate value $q = 2(m/n)\pi/a$ as J_2/J_1 is varied. Since $\sigma(q)$ is smaller than one, especially near the ordering transition, these terms become much less important as the integer denominator n increases. Thus the effect of the Umklapp terms is that the variation of q as a function of a control parameter (such as the temperature) becomes a so-called devil's staircase, which may either be complete or (if σ is small enough) incomplete, as shown in Figure 7. In the systems we will discuss here, there is no clear evidence of a devil's staircase as a function of temperature. Accordingly, we find it convenient to imagine that q is incommensurate, and does not get stuck on commensurate values by Umklapp terms. Even if this is not strictly true, the difference in properties between an incommensurate system and a commensurate system with a large integer denominator

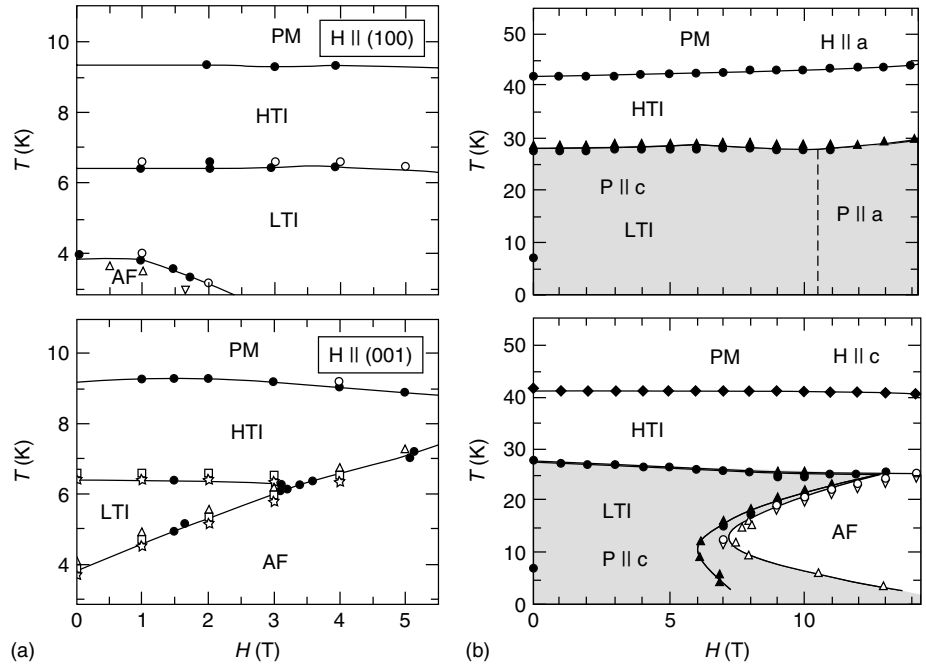

Figure 6. Phase diagram for NVO (a) and TMO (b) as a function of H and T. The HTI and LTI phases will be discussed in more detail, but correspond roughly to the scenario of our toy model. The interpretation of the H dependence of the phase boundaries for NVO is given in Kenzelmann *et al*. (2006). For NVO, AF indicates a commensurate antiferromagnetic phase with a weak ferromagnetic moment. (The NVO phase diagram is adapted from Lawes *et al*., 2004 and the TMO phase diagram is adapted from Kimura *et al*., 2005.) (Reprinted with permission T. Kimura *et al*., copyright 2005, American Physical Society.)

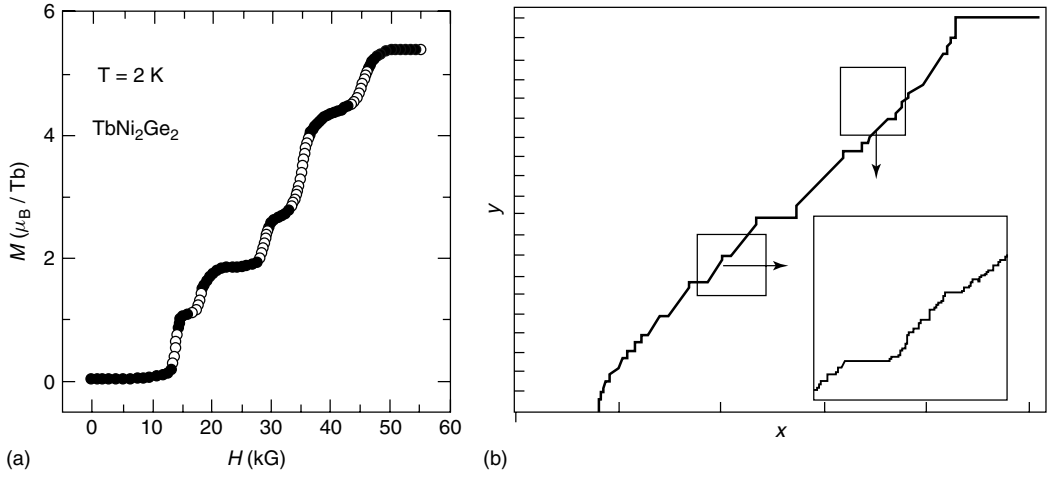

Figure 7. The devil's staircase (DS). (a) An *incomplete* DS for the dependence of the magnetization of $TbNi_2Ge_2$ as a function of magnetic field (Bud'ko *et al*., 1999). (b) Schematic example of a *complete* DS function $Y = f(X)$. In a complete DS, the function is nonconstant on a set of measure zero. For an incomplete DS, the function is nonconstant on a set of nonzero measure. (Reprinted with permission S.L. Bud'ko *et al*., copyright 1999, Elsevier.)

n is experimentally irrelevant for the large values of n ($n \sim 50$), for the systems we will discuss. Accordingly, we will refer to the systems as 'incommensurate' even though this may not be strictly accurate.

In principle, the symmetry of real systems is usually such that anisotropy also occurs in the exchange interaction, in which case the trial free energy assumes the form

$$f = \frac{1}{2}\sum_{q}\sum_{\alpha=x,y,z}\chi(q)_{\alpha}^{-1}\boldsymbol{\sigma}_{\alpha}(q)\cdot\boldsymbol{\sigma}_{\alpha}(-q) + \mathcal{O}(\boldsymbol{\sigma}^4) \tag{15}$$

where $\chi(q)_{\alpha}^{-1} = dkT + J_{1\alpha}\cos(qa) + J_{2\alpha}\cos(2qa)$. If $J_{n\alpha}$ is isotropic (i.e., if it does not depend on α), then the wave vector selected for the ordering of the α component

of spin also will not depend on α. However, in principle $J_{n\alpha}$ depends weakly on α, and therefore the selected wave vector q_0 will also depend weakly on α and the ordering will involve $\sigma_x(q_x)$, $\sigma_y(q_y)$, and $\sigma_z(q_z)$, where q_x, q_y, and q_z differ slightly from one another. Thus in the LTI phase it is possible that the two components of spin might have slightly different wave vectors, which we denote $q_{\rm HTI}$ and $q_{\rm LTI}$. But as with the Umklapp contributions, there will be quartic terms in the free energy (in this formulation coming from the entropic terms) which favor locking the two wave vectors to be equal. These terms can be of the form

$$f_{\rm lock} = a[\boldsymbol{\sigma}_{\rm HTI}(q_{\rm HTI})^2\boldsymbol{\sigma}_{\rm LTI}(-q_{\rm LTI})^2 + \boldsymbol{\sigma}_{\rm HTI}(-q_{\rm HTI})^2\boldsymbol{\sigma}_{\rm LTI}(q_{\rm LTI})^2]\delta_{q_{\rm HTI},q_{\rm LTI}} \quad (16)$$

where $\sigma_{\rm HTI}e^{i\phi_{\rm HTI}} \equiv \boldsymbol{\sigma}_{\rm HTI}(q_{\rm HTI})$ ($\sigma_{\rm LTI}e^{i\phi_{\rm LTI}} \equiv \boldsymbol{\sigma}_{\rm LTI}(q_{\rm LTI})$) is an order parameter characterizing the appearance of the HTI (LTI) phase, and for simplicity we have assumed that the constant a is real valued. This interaction only satisfies wave vector conservation if the two wave vectors are exactly equal. If, in the absence of this term, the two wave vectors are sufficiently close to one another, then this locking energy will cause the wave vectors of the two order parameters to be locked into equality with one another. (In this case, minimization of δf will also fix the relative phase $\phi_{\rm HTI} - \phi_{\rm LTI}$.) Since exchange anisotropy is usually not large, the wave vectors associated with different spin components are normally almost equal to one another. In that case, $f_{\rm lock}$ will be large enough to lock the HTI and LTI wave vectors to a common value. This 'locked' scenario is quite common and we assume it to be the case here. Indeed for the systems discussed below, the data suggests that the HTI and LTI order parameters involve a single wave vector.

5 MAGNETIC SYMMETRY

5.1 Nontrivial unit cell

There is one final refinement of our toy model which we must consider, that is the structure of the crystallographic unit cell. In the toy model considered above, the entire spin structure is characterized by a wave vector and a single complex vector amplitude. Note that the wave vector determines only how the spin wave function evolves from one unit cell to the next. However, to date, almost all magnetically incommensurate systems which have been identified as multiferroics have two or more magnetic ions per crystallographic unit cell. To describe such more general structures, one must introduce a spin wave function for the unit cell. Accordingly, we now discuss how this spin wave function for the unit cell is restricted by the symmetry of the crystal lattice. As a preliminary, we start by discussing the crystal structure of the two systems, NVO and TMO. In Table 1, we list the general equivalent positions which define the space group operations. For NVO we choose the generators of the space group to be the identity, E, a twofold rotation about the x axis, $(x, y, z) \rightarrow (x, \overline{y}, \overline{z})$, the $x - y$ glide plane, $(x, y, z) \rightarrow (x, y + \frac{1}{2}, \overline{z} + \frac{1}{2})$, spatial inversion, $(x, y, z) \rightarrow (\overline{x}, \overline{y}, \overline{z})$, and translations. For TMO, the generators are taken to be E, a mirror z plane, $(x, y, z) \rightarrow (x, y, \frac{1}{2} - z)$, the $y - z$ glide plane, $(x, y, z) \rightarrow (\frac{1}{2} - x, y + \frac{1}{2}, z)$, spatial inversion, and translations. The magnetic sites are at the positions listed in Table 2 and shown in Figure 8.

5.2 Representation theory

If there are $n_{\rm u}$ spins in a unit cell, then an incommensurate state will be described by a wave vector $\mathbf{q}$ and the complex-valued Fourier amplitudes $\mathcal{S}_{\alpha,\tau}(\mathbf{q})$, where $\alpha = x, y, z$ and $\tau = 1, 2, \ldots n_{\rm u}$, in terms of which we write the spin wave functions in the form

$$S_{\alpha,\tau}(\mathbf{R}) = \mathcal{S}_{\alpha\tau}(\mathbf{q})e^{i\mathbf{q}\cdot(\mathbf{R}+\mathbf{r}_\tau)} + \mathcal{S}_{\alpha\tau}(\mathbf{q})^*\ e^{-i\mathbf{q}\cdot(\mathbf{R}+\mathbf{r}_\tau)} \quad (17)$$

where $\mathbf{r}_\tau$ is the position of the τth site within the unit cell. For NVO $\tau = 1, s; 2, s; 3, s;$ or $4, s$ for spine (s) sites and $1, c$, or $2, c$ for cross-tie (c) sites. Thus, apart from the wave vector $\mathbf{q}$, the determination of the spin structure requires fixing the $6n_{\rm u}$ real-valued parameters that are needed to specify the $3n_{\rm u}$ complex-valued parameters $\mathcal{S}_{\alpha\tau}(\mathbf{q})$. Note that the complex amplitudes $\mathcal{S}(q)$ are defined relative to the phase, $\mathbf{q}\cdot(\mathbf{R} + \mathbf{r}_\tau)$ which would obtain if the wave were perfectly sinusoidal. (For NVO and TMO this convention will simplify later results.) One should think of the spin wave function as consisting of a superposition of sinusoidal spin distributions for each of the three Cartesian components of spin on each of the $n_{\rm u}$ sublattices. Each distribution is characterized by an amplitude and phase as encoded in the complex amplitude $\mathcal{S}_{\alpha\tau}(\mathbf{q})$.

We now discuss how symmetry restricts the possible values of the amplitudes $\mathcal{S}_{\alpha,\tau}(q)$ and how these variables are determined via diffraction experiments. The analysis of the symmetry of such systems in terms of their point groups is not developed. Accordingly, a model-independent (representation) analysis (Bertaut, 1971; Rossat-Mignod, 1987) is customarily invoked in such cases when it is assumed (as is generally the case) that the magnetic ordering transition is a continuous one. As we shall see in examples discussed later, it is essential to correctly characterize the symmetry properties of the magnetic ordering in order to understand how this ordering induces ferroelectricity. However, perhaps surprisingly, a crucial point in connection with representation

Table 1. General positions of the space groups for NVO (top), Cmca (#64 in Hahn, 1983) and for TMO (bottom), Pbnm (#62 in Hahn, 1983). For Cmca, the primitive translation vectors are $\mathbf{a}_1 = (a/2)\hat{i} + (b/2)\hat{j}$; $\mathbf{a}_2 = (a/2)\hat{i} - (b/2)\hat{j}$; and $\mathbf{a}_3 = c\hat{k}$. For Pbnm they are $\mathbf{a}_1 = a\hat{i}$; $\mathbf{a}_2 = b\hat{j}$, and $\mathbf{a}_3 = c\hat{k}$.

$\mathbf{r} = (x, y, z)$	$2_z\mathbf{r} = (\overline{x}, \overline{y} + \frac{1}{2}, z + \frac{1}{2})$	$2_y\mathbf{r} = (\overline{x}, y + \frac{1}{2}, \overline{z} + \frac{1}{2})$	$2_x\mathbf{r} = (x, \overline{y}, \overline{z})$
$\mathcal{I}\mathbf{r} = (\overline{x}, \overline{y}, \overline{z})$	$m_{xy}\mathbf{r} = (x, y + \frac{1}{2}, \overline{z} + \frac{1}{2})$	$m_{xz}\mathbf{r} = (x, \overline{y} + \frac{1}{2}, z + \frac{1}{2})$	$m_{yz}\mathbf{r} = (\overline{x}, y, z)$

$\mathbf{r} = (x, y, z)$	$m_{xy}\mathbf{r} = (x, y, \frac{1}{2} - z)$	$2_x\mathbf{r} = (x + \frac{1}{2}, \overline{y} + \frac{1}{2}, \overline{z})$	$m_{xz}\mathbf{r} = (x + \frac{1}{2}, \overline{y} + \frac{1}{2}, \frac{1}{2} + z)$
$\mathcal{I}\mathbf{r} = (\overline{x}, \overline{y}, \overline{z})$	$2_z\mathbf{r} = (\overline{x}, \overline{y}, \frac{1}{2} + z)$	$m_{yz}\mathbf{r} = (\frac{1}{2} - x, y + \frac{1}{2}, z)$	$2_y\mathbf{r} = (\frac{1}{2} - x, y + \frac{1}{2}, \frac{1}{2} - z)$

Table 2. Left: Unit cell lattice positions in NVO of the Ni^{2+} ions carrying $S = 1$ (given as fractions of the cell dimensions a, b, and c). The 'spine' sites are r_n^s and the cross-tie sites are r_n^c. Right: Positions of the Mn and Tb ion sites in the unit cell of TMO as fractions of the cell sides a, b, and c.

r_1^s	(0.25, −0.13, 0.25)
r_2^s	(0.25, 0.13, 0.75)
r_3^s	(0.75, 0.13, 0.75)
r_4^s	(0.75, −0.13, 0.25)
r_1^c	(0, 0, 0)
r_2^c	(0.5, 0, 0.5)

	$n = 1$	$n = 2$	$n = 3$	$n = 4$
Mn	$(0, \frac{1}{2}, 0)$	$(\frac{1}{2}, 0, 0)$	$(0, \frac{1}{2}, \frac{1}{2})$	$(\frac{1}{2}, 0, \frac{1}{2})$
Tb[a]	$(x, y, \frac{1}{4})$	$(x + \frac{1}{2}, \overline{y} + \frac{1}{2}, \frac{3}{4})$	$(\overline{x}, \overline{y}, \frac{3}{4})$	$(\overline{x} + \frac{1}{2}, y + \frac{1}{2}, \frac{1}{4})$

[a] $x = 0.9836$ and $y = 0.0810$ from Blasco *et al*. (2000).

theory that seems to have been universally overlooked until recently (Lawes *et al*., 2005; Kenzelmann *et al*., 2005, 2006) is that for systems such as the family of multiferroics we consider here inversion symmetry places additional constraints on the allowed magnetic structures that can appear at the ordering transition.

To explain this recent development, we first give a much simplified review of representation theory. *If the magnetic ordering transition is assumed to be continuous*, then the phase transition is signaled by an instability in the susceptibility that occurs as the temperature is lowered into the magnetically ordered phase. Alternatively, one may see this instability in the quadratic terms when the free energy is expanded in powers of the order parameters. As we have already noted, we may confine our attention to the order parameters associated with the selected wave vector **q** which first becomes unstable as the temperature is lowered. In order to conserve wave vector the quadratic terms in the Landau

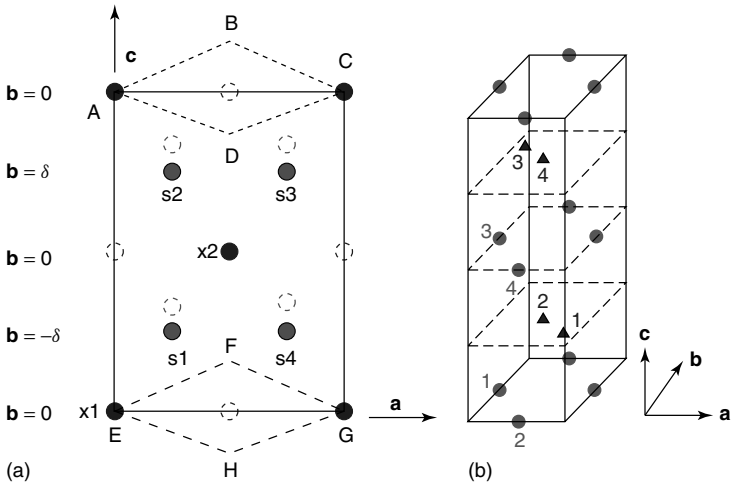

Figure 8. (a) The unit cell (ABCDEFGH) showing only Ni ions numbered as in Table 2. The **b** axis is perpendicular to the plane of the paper. Dashed circles represent spins in adjacent planes displaced from the solid symbols by $\pm\mathbf{b}/2$. (b) The unit cell of $TbMnO_3$ showing only the Mn ions (filled circles) and the Tb ions (filled triangles), numbered as in Table 2.

expansion associated with the selected wave vector **q** must be of the form

$$f_2 = \sum_{\alpha,\beta,\tau,\tau'} c_{\alpha,\tau;\beta,\tau'}(\mathbf{q})\mathcal{S}_{\alpha,\tau}(-\mathbf{q})\mathcal{S}_{\beta,\tau'}(\mathbf{q}) \qquad (18)$$

where $\mathcal{S}_{\alpha,\tau}(-\mathbf{q}) = \mathcal{S}_{\alpha,\tau}(\mathbf{q})^*$. For f_2 to be real for any choice of the complex-valued Fourier amplitudes, it is required that $c_{\alpha,\tau;\beta,\tau'}(\mathbf{q})^* = c_{\beta,\tau';\alpha,\tau}(\mathbf{q})$. Within a simple theory, such as mean-field theory, the coefficient $c_{\alpha,\tau;\beta,\tau'}$ in equation (18) is such that

$$f_2 = \sum_{\alpha,\beta,\tau,\tau'} \left[dkT\delta_{\alpha,\beta}\delta_{\tau,\tau'} - \tilde{c}_{\alpha,\tau;\beta,\tau'}(\mathbf{q})\right]\mathcal{S}_{\alpha,\tau}(-\mathbf{q})\mathcal{S}_{\beta,\tau'}(\mathbf{q}) \qquad (19)$$

where d is a constant of order unity of entropic origin, $\delta_{\alpha,\beta}$ is unity if $\alpha = \beta$ and is zero otherwise, and the $\tilde{c}_{\alpha,\tau;\beta,\tau'}(\mathbf{q})$ are temperature-independent coefficients determined by the spin–spin interactions of the system. When kT is much larger than the characteristic interaction energy, all the eigenvalues of f_2 are positive and the paramagentic phase is stable. As the temperature is lowered, one eigenvalue will become nonpositive although we do not rely on the specific form of equation (19). The stability of the resulting ordered phase is then ensured by the quartic terms of order uS^4, which were not included in equation (18).

Note that the pattern of spin ordering within the unit cell is determined by the eigenvector associated with the first eigenvalue of the quadratic free energy, which passes through zero as the temperature is lowered. (We call this eigenvalue the 'critical eigenvalue' and the associated eigenvector the 'critical eigenvector'.) This phenomenon was discussed briefly earlier in connection with wave vector selection. As we shall see, this analysis of the symmetry of the critical eigenvector is essential when one constructs the allowed couplings between magnetic and ferroelectric order parameters. (A similar, but more complicated analysis, has been developed to describe second-harmonic generation by Sa, Valenti and Gros, 2000.)

As in the case of phonons or other normal modes, the eigenvectors of this quadratic form can be labeled according to the irreducible representations (irreps) Γ_n of the paramagnetic phase, which leave invariant the selected wave vector for ordering. (This group of symmetry operations is called the *group of the wave vector* or the *little group*.) The relevant symmetry is that of the paramagnetic phase because the expansion of the free energy in powers of the order parameters is relative to this phase (Dzyaloshinskii, 1957; Landau and Lifshitz, 1958). For the orthorhombic systems, NVO and TMO, considered in this review, all the irreps are one dimensional. In such cases, the eigenvectors of f_2 must also be eigenvectors of the rotation or mirror (or glide) operations of the little group with eigenvalues of unit magnitude. (To illustrate the principles involved in the complete symmetry analysis of magnetic structures, we focus on the simplest scenario, namely when the irreps are one dimensional and each wave vector is an eigenvector of all the symmetry operations of the group of the wave vector. To use the point of view expressed here for a two-dimensional irrep, see Harris, 2006b.) We now enumerate the symmetry operations for NVO and TMO, which leave the wave vector invariant. For NVO the ordering wave vector lies along the crystal **a** axis, and the symmetry operations of the little group are 2_x, a twofold rotation about the x axis (we often refer to **a**, **b**, and **c** as x, y, and z, respectively) and m_{xy}, a glide operation which takes z into $-z$ followed by a translation of $(\mathbf{b}+\mathbf{c})/2$. For TMO the ordering wave vector lies along the crystal **b** axis and the symmetry operations are a twofold screw rotation about the y axis, 2_y and the mirror plane m_{xy}. These operations are defined in Table 1. Technically speaking, the eigenvalues of these symmetry operations (which characterize the symmetry of the irrep) are known as *characters* and their values for each irrep Γ_p and for each symmetry operation $\mathcal{O}$ are given in the so-called 'character table', which we give for NVO and TMO in Table 3. We see that (apart from a phase factor for TMO) we have four irreps, that is, four symmetries, depending on whether the spin wave function is chosen independently to be even or odd under the two mirror operations.

The result of the group theoretical analysis is that one expresses the Fourier amplitudes $\mathcal{S}_{\alpha\tau}(\mathbf{q})$ in terms of *symmetry adapted coordinates* $m_r^{(n)}$ associated with the irrep Γ_n. Thus if the spin distribution is that of irrep Γ_n, we write

$$S_{\alpha,\tau}^{\Gamma_n}(\mathbf{q}) = \sum_r m_r^{(n)} U_{\alpha,\tau}^{n,r} \qquad (20)$$

where the symmetry adapted basis functions $U_{\alpha,\tau}^{n,r}$ give the α component of spin on the τth sublattice for the rth basis function associated with irrep Γ_n. Although the symmetry adapted coordinates and basis functions are allowed to be complex, the spin vectors given by equation (17) are, of course, real valued.

To make the analysis more intuitive, we may liken it to the problem of determining allowed wave functions for a particle in a spherically symmetric potential. For illustrative purposes we consider a Coulomb potential with a weak spherically symmetric perturbation (for example, a perturbation of the form ar^4). To solve this problem, one introduces symmetry adapted basis functions for the various irreps, which in this case are s functions $\psi_n^{(s)}$, p functions $\psi_n^{(p_x)}$, $\psi_n^{(p_y)}$, $\psi_n^{(p_z)}$, and so on, where n labels the principal quantum number. As is well known, as a consequence of spherical symmetry, the potential has nonzero matrix elements only between symmetry adapted basis functions having the same symmetry label,

Table 3. Character table for the symmetry operations $\mathcal{O}$ of the group[(a)] $G_{\mathbf{k}}$ for the irreps Γ_n for incommensurate magnetic structure of (left) NVO with $\mathbf{k} = (q, 0, 0)$ and (right) TMO for $\mathbf{k} = (0, q, 0)$.

$\mathcal{O}^{a} =$	1	2_x	m_{xy}	m_{xz}
Γ^1	1	1	1	1
Γ^2	1	1	−1	−1
Γ^3	1	−1	−1	1
Γ^4	1	−1	1	−1

$\mathcal{O}^{a,b} =$	E	$\tilde{2}_y$	m_{xy}	$\tilde{m}_{yz}$
Γ_1	1	1	1	1
Γ_2	1	1	−1	−1
Γ_3	1	−1	1	−1
Γ_4	1	−1	−1	1

[a]Operators (without tildes) are defined in Table 1.
[b]For an operator $\mathcal{O}$ we define $\tilde{\mathcal{O}} = e^{iqa/2}\mathcal{O}$.

q, where q denotes (s), (p_x), and so on. Thus eigenfunctions Ψ can be characterized by a symmetry (irrep) label q and, in analogy with equation (20), $\Psi^{(q)}$ can be expressed as a linear combination of symmetry adapted basis functions $\psi_m^{(q)}$, for $m = 1, 2 \ldots$ having a given symmetry label:

$$\Psi^{(q)} = \sum_m c_m \psi_m^{(q)} \tag{21}$$

The symmetry adapted basis functions $\psi_m^{(q)}$ are determined solely by the symmetry of the system. In contrast, the coefficients c_m (which we have called the symmetry adapted coordinates, $m_r^{(n)}$) depend on the specific details of the potential. Analogously, in our magnetic structure problem, the possible eigenvectors will be linear combinations of the symmetry adapted basis functions $U_{\alpha\tau}^{nr}$ with coefficients $m_r^{(n)}$. The U's can be constructed on the basis of symmetry considerations, whereas the m's depend on the specific details of the system. An intuitive picture of the nth symmetry adapted basis function associated with irrep Γ can obtained as follows. Consider the family of symmetry operations $\mathcal{O}_p$ of the little group (which conserves the wave vector). We arbitrarily assign an amplitude $U_{\alpha\tau}^{\Gamma,n}$ to one $S_{\alpha,\tau}(\mathbf{q})$. Then, the condition that the spin wave function is to have a given symmetry under the operations $\mathcal{O}_p$, will fix the amplitude of the other sublattices that are related to the initial one (α, τ) by the operations $\mathcal{O}_p$. For NVO, for instance, if we fix the x component of the spine site $s, 1$ to be $U_{x,\tau}^{p,1}(\mathbf{q})$ (assuming irrep Γ_p to be the active irrep), then in order to have a given symmetry, the amplitudes of all the other spine sites will be given by

$$S_{x,\tau'}(\mathbf{q}) = \pm U_{x,\tau'}^{p,1}(\mathbf{q}) \tag{22}$$

with the sign chosen according to the symmetry of the basis function being constructed. As a result, in constructing allowed eigenfunctions to describe the ordered phase we generally will find that spin functions for each family of crystallographically equivalent sites will be specified by a single parameter. Using the above procedure, one can construct the spin distribution in the form of equation (20) and the results for the spin distribution on the magnetic sublattices assuming a given irrep are given subsequently in the tables.

We now give a short explanation on how to read these tables. For NVO, the first column of Table 4 gives the spin distribution $\mathbf{S}_{\alpha,\tau}^{\Gamma_1}$ for the irrep Γ_1. To specify a spin distribution we have to specify the complex amplitudes for 3 Cartesian spin components of 6 magnetic sublattices, which requires a total of 18 complex parameters. Symmetry indicates that if irrep Γ_1 is assumed to be the active irrep, then the distribution is in fact completely specified by fixing the values of the four complex amplitudes (which we have called symmetry adapted coordinates, $m_r^{(n)}$) $m_{s_x}^{(1)}$, $m_{s_y}^{(1)}$, $m_{s_z}^{(1)}$, and $m_{c_x}^{(1)}$. (Notice that here the index r assumes the values s_x, s_y, s_z, and c_x.) In our language, the symmetry adapted basis functions are the functions which multiply the m's. Thus

$$U_{x,\tau=ns}^{1,r=s_x} = \frac{\partial S_{x,\tau=ns}^{\Gamma_1}}{\partial m_{s_x}^{(1)}} = (i, i, -i, -i) \tag{23}$$

where, on the right-hand side of the equation are given the values for the x components of spin on the sublattices $\tau = 1s, 2s, 3s, 4s$. In the same way, for the y and z components one has

$$U_{y,\tau=ns}^{1,r=s_y} = \frac{\partial S_{y,\tau=n_s}^{\Gamma_1}}{\partial m_{s_y}^{(1)}} = (1, -1, 1, -1) \tag{24}$$

$$U_{z,\tau=ns}^{1,r=s_z} = \frac{\partial S_{z,\tau=n_s}^{\Gamma_1}}{\partial m_{s_z}^{(1)}} = (i, -i, -i, i) \tag{25}$$

Similarly, irreps Γ_2, Γ_3, and Γ_4 require fixing respectively four, five, and five symmetry adapted coordinates. Clearly, the fitting procedure is to try each irrep in turn and see which irrep best fits the data. Often one irrep will be vastly superior to all the others. Normally, one does not include phase factors i into the complex amplitudes, as is done in Table 4 for $m_{s_x}^{(1)}$, for instance. This inclusion cannot affect the structure determination because the best fit will determine the same value of $im_{s_x}^{(1)}$ as it would have done for $m_{s_x}^{(1)}$ had

Table 4. Symmetry adapted basis functions $U^{nr}_{\alpha\tau}$ which transform according to the irreducible representation Γ_n for the incommensurate phase associated with $\mathbf{q} = (q, 0, 0)$ for the Ni spine (s) and cross-tie (c) sites of NVO in the notation of equation (20). So $U^{nr}_{\alpha\tau} = \partial \mathbf{S}^{\Gamma_n}_{\alpha\tau}/\partial m^{(n)}_r$ The symmetry adapted coordinates $m^{(n)}_r$, where $r = s_x, s_y, s_z, c_x, c_y, c_z$, assume complex values, as discussed in the text. The numbering of sites is given in Table 2. The phase factors of i are chosen to simplify the transformation properties under spatial inversion, as is discussed later.

Site τ	$\mathbf{S}^{\Gamma_1}_{\alpha,\tau}$	$\mathbf{S}^{\Gamma_2}_{\alpha,\tau}$	$\mathbf{S}^{\Gamma_3}_{\alpha,\tau}$	$\mathbf{S}^{\Gamma_4}_{\alpha,\tau}$
1s	$(im^{(1)}_{s_x}, m^{(1)}_{s_y}, im^{(1)}_{s_z})$	$(m^{(2)}_{s_x}, im^{(2)}_{s_y}, m^{(2)}_{s_z})$	$(im^{(3)}_{s_x}, m^{(3)}_{s_y}, im^{(3)}_{s_z})$	$(m^{(4)}_{s_x}, im^{(4)}_{s_y}, m^{(4)}_{s_z})$
2s	$(im^{(1)}_{s_x}, -m^{(1)}_{s_y}, -im^{(1)}_{s_z})$	$(m^{(2)}_{s_x}, -im^{(2)}_{s_y}, -m^{(2)}_{s_z})$	$(-im^{(3)}_{s_x}, m^{(3)}_{s_y}, im^{(3)}_{s_z})$	$(-m^{(4)}_{s_x}, im^{(4)}_{s_y}, m^{(4)}_{s_z})$
3s	$(-im^{(1)}_{s_x}, m^{(1)}_{s_y}, -im^{(1)}_{s_z})$	$(m^{(2)}_{s_x}, -im^{(2)}_{s_y}, m^{(2)}_{s_z})$	$(-im^{(3)}_{s_x}, m^{(3)}_{s_y}, -im^{(3)}_{s_z})$	$(m^{(4)}_{s_x} - im^{(4)}_{s_y}, m^{(4)}_{s_z})$
4s	$(-im^{(1)}_{s_x}, -m^{(1)}_{s_y}, im^{(1)}_{s_z})$	$(m^{(2)}_{s_x}, im^{(2)}_{s_y}, -m^{(2)}_{s_z})$	$(im^{(3)}_{s_x}, m^{(3)}_{s_y}, -im^{(3)}_{s_z})$	$(-m^{(4)}_{s_x}, -im^{(4)}_{s_y}, m^{(4)}_{s_z})$
1c	$(m^{(1)}_{c_x}, 0, 0)$	$(m^{(2)}_{c_x}, 0, 0)$	$(0, m^{(3)}_{c_y}, m^{(3)}_{c_z})$	$(0, m^{(4)}_{c_y}, m^{(4)}_{c_z})$
2c	$(-m^{(1)}_{c_x}, 0, 0)$	$(m^{(2)}_{c_x}, 0, 0)$	$(0, m^{(3)}_{c_y}, -m^{(3)}_{c_z})$	$(0, -m^{(4)}_{c_y}, m^{(4)}_{c_z})$

Table 5. Symmetry adapted basis functions $U^{nr}_{\alpha\tau}$ which transform according to the irreducible representation Γ_n for the incommensurate phase associated with $\mathbf{q} = (0, q, 0)$ for the Mn sites (nM) and TB sites (nT) in TMO, numbered as in Table 2. The complex-valued symmetry adapted coordinates for the irrep Γ_n are $m^{(n)}_r$ and in this table $r = M_x, M_y, M_z, T_{1x}, T_{1y}, T_{1z}, T_{2x}, T_{2y}, T_{2z}$.

Site (τ)	$\mathbf{S}^{\Gamma_1}_{\alpha\tau}$	$\mathbf{S}^{\Gamma_2}_{\alpha\tau}$	$\mathbf{S}^{\Gamma_3}_{\alpha\tau}$	$\mathbf{S}^{\Gamma_4}_{\alpha\tau}$
1M	$(m^{(1)}_{M_x}, m^{(1)}_{M_y}, m^{(1)}_{M_z})$	$(m^{(2)}_{M_x}, m^{(2)}_{M_y}, m^{(2)}_{M_z})$	$(m^{(3)}_{M_x}, m^{(3)}_{M_y} m^{(3)}_{M_z})$	$(m^{(4)}_{M_x}, m^{(4)}_{M_y}, m^{(4)}_{M_z})$
2M	$(m^{(1)}_{M_x}, -m^{(1)}_{M_y}, -m^{(1)}_{M_z})$	$(-m^{(2)}_{M_x}, m^{(2)}_{M_y}, m^{(2)}_{M_z})$	$(-m^{(3)}_{M_x}, m^{(3)}_{M_y}, m^{(3)}_{M_z})$	$(m^{(4)}_{M_x}, -m^{(4)}_{M_y}, -m^{(4)}_{M_z})$
3M	$(-m^{(1)}_{M_x}, -m^{(1)}_{M_y}, m^{(1)}_{M_z})$	$(m^{(2)}_{M_x}, m^{(2)}_{M_y}, -m^{(2)}_{M_z})$	$(-m^{(3)}_{M_x}, -m^{(3)}_{M_y}, m^{(3)}_{M_z})$	$(m^{(4)}_{M_x}, m^{(4)}_{M_y}, -m^{(4)}_{M_z})$
4M	$(-m^{(1)}_{M_x}, m^{(1)}_{M_y}, -m^{(1)}_{M_z})$	$(-m^{(2)}_{M_x}, m^{(2)}_{M_y}, -m^{(2)}_{M_z})$	$(m^{(3)}_{M_x}, -m^{(3)}_{M_y}, m^{(3)}_{M_z})$	$(m^{(4)}_{M_x}, -m^{(4)}_{M_y}, m^{(4)}_{M_z})$
1T	$(0, 0, m^{(1)}_{T_{2z}})$	$(m^{(2)}_{T_{2x}}, m^{(2)}_{T_{2y}}, 0)$	$(0, 0, m^{(3)}_{T_{2z}})$	$(m^{(4)}_{T_{2x}}, m^{(4)}_{T_{2y}}, 0)$
2T	$(0, 0, -m^{(1)}_{T_{1z}})$	$(-m^{(2)}_{T_{1x}}, m^{(2)}_{T_{1y}}, 0)$	$(0, 0, m^{(3)}_{T_{1z}})$	$(m^{(4)}_{T_{1x}}, -m^{(4)}_{T_{1y}}, 0)$
3T	$(0, 0, m^{(1)}_{T_{1z}})$	$(m^{(2)}_{T_{1x}}, m^{(2)}_{T_{1y}}, 0)$	$(0, 0, m^{(3)}_{T_{1z}})$	$(m^{(4)}_{T_{1x}}, m^{(4)}_{T_{1y}}, 0)$
4T	$(0, 0, -m^{(1)}_{T_{2z}})$	$(-m^{(2)}_{T_{2x}}, m^{(2)}_{T_{2y}}, 0)$	$(0, 0, m^{(3)}_{T_{2z}})$	$(m^{(4)}_{T_{2x}}, -m^{(4)}_{T_{2y}}, 0)$

we not included the factor of i. Inclusion of the factor of i may appear to be an unwanted complexity. However, its inclusion will prove to be convenient later in equation (37). One can verify that the symmetry adapted basis functions given in equations (23–25) transform into themselves (with a + or − sign) under 2_x or m_{xy}, as indicated in the character table.

As for NVO, we can use Table 5 to write down the symmetry adapted basis functions for TMO. For instance,

$$U^{1,r=M_x}_{x,\tau=nM} = \frac{\partial S^{\Gamma_1}_{x,\tau=nM}}{\partial m^{(1)}_{M_x}} = (1, 1, -1, -1) \tag{26}$$

$$U^{1,r=M_y}_{y,\tau=nM} = \frac{\partial S^{\Gamma_1}_{y,\tau=nM}}{\partial m^{(1)}_{M_y}} = (1, -1, -1, 1) \tag{27}$$

$$U^{1,r=T_{2z}}_{z,\tau=nT} = \frac{\partial S^{\Gamma_1}_{z,\tau=nT}}{\partial m^{(1)}_{T_{2z}}} = (1, 0, 0, -1) \tag{28}$$

To further illustrate this, we write an explicit formula for the distribution of magnetization in NVO assuming Γ_4 to be the active irrep. Then using equations (17) and (20) we write the distribution of the x component of spin on the 1,s sublattice as

$$S_{x,1s}(\mathbf{r}) = m^{(4)}_{s_x} e^{i\mathbf{q}\cdot\mathbf{r}} + [m^{(4)}_{s_x}]^*\ e^{-i\mathbf{q}\cdot\mathbf{r}} \tag{29}$$

where $\mathbf{r} \equiv \mathbf{R} + \boldsymbol{\tau}_{1,s}$ is the actual position of the spin in the 1,s sublattice. The complex-valued symmetry adapted coordinate $m^{(4)}_{s_x}$ incorporates the amplitude and phase of the sinusoidal wave for the x component of spin on the spine sublattices. We give some (but not all) of the other results assuming Γ_4 to be the active irrep, namely,

$$S_{y,1s}(\mathbf{r}) = im^{(4)}_{s_y} e^{i\mathbf{q}\cdot\mathbf{r}} - i[m^{(4)}_{s_y}]^*\ e^{-i\mathbf{q}\cdot\mathbf{r}} \tag{30}$$

$$S_{z,1s}(\mathbf{r}) = m^{(4)}_{s_z} e^{i\mathbf{q}\cdot\mathbf{r}} + [m^{(4)}_{s_z}]^*\ e^{-i\mathbf{q}\cdot\mathbf{r}} \tag{31}$$

$$S_{x,2s}(\mathbf{r}) = -m^{(4)}_{s_x} e^{i\mathbf{q}\cdot\mathbf{r}} - [m^{(4)}_{s_x}]^*\ e^{-i\mathbf{q}\cdot\mathbf{r}} \tag{32}$$

$$S_{y,1c}(\mathbf{r}) = m_{c_y}^{(4)} e^{i\mathbf{q}\cdot\mathbf{r}} + [m_{c_y}^{(4)}]^* \; e^{-i\mathbf{q}\cdot\mathbf{r}} \tag{33}$$

and so forth. Thus, the incommensurate state is parameterized as consisting of sinusoidal waves having arbitrary amplitudes and phases for each spin component of each crystallographically inequivalent set of sites (i.e., spine sites or cross-ties, respectively). As we shall see in a moment, the recent new development (Lawes *et al*., 2005; Kenzelmann *et al*., 2005) for crystals whose paramagnetic phase is inversion symmetric is to invoke this symmetry to fix the relative phases or, in cases like TMO, the amplitudes of crystallographically inequivalent (with respect to the little group) Tb sites that are related to one another by spatial inversion.

In the above analysis, we assumed that ordering occurs via a single irrep. One might wonder if two irreps could accidentally have an instability at the same temperature. We reject the possibility of such an accidental degeneracy. However, if one adjusts an additional control parameter, such as the pressure, it is possible to reach a multicritical point where two irreps simultaneously become active. A simple example of this principle arises when one treats a ferromagnet on a tetragonal lattice. In that case, one irrep is one dimensional and corresponds to the FM order lying along the fourfold crystal (**c**) axis and the other irrep is two-dimensional and corresponds to ordering in the plane perpendicular to the **c** axis. Clearly, the mean-field transition temperatures for these two distinct orderings should be assumed to be different. If the anisotropy is easy axis, the FM moment will lie along the **c** axis and if the anisotropy is easy plane the moment will be perpendicular to the **c** axis. It is possible for the anisotropy to vanish, but only by adjusting another thermodynamic variable, such as uniaxial stress. One therefore concludes that criticality is associated with a *single* irrep. Since the transformation to symmetry adapted coordinates can be determined using only symmetry considerations, the possible patterns of spin ordering within the unit cell are strongly restricted.

When, for NVO or TMO, the temperature is lowered further and the LTI phase is entered (see Figure 6), then an additional irrep will become active via a second continuous phase transition. For NVO, the new LTI representation (in addition to Γ_4 already present in the HTI phase) is (Lawes *et al*., 2004) Γ_1 and for TMO the new LTI representation (in addition to Γ_3 already present in the HTI phase) is (Kenzelmann *et al*., 2005) Γ_2. In an appendix we discuss that when two different irreps are active, their presence does not induce the development of a third irrep. However, had there been a further phase transition from the LTI phase into yet another incommensurate phase with three irreps, then the presence of three different irreps would induce the presence of a fourth one.

As an illustration of how to apply the above results, we show, in Figure 9, typical spin configurations for NVO which result from the spin wave functions which transform according to irrep #4. The configuration shown in (a) is not allowed because, as we discuss below, it is not consistent with the inversion symmetry of the paramagnetic phase.

5.3 Effect of inversion symmetry for NVO

Until now we only used the consequences of the symmetry of the group of transformations that leave the wave vector invariant at a continuous magnetic ordering transition. According to the usual formalism (Bertaut, 1971; Rossat-Mignod, 1987), one can only exploit symmetries that conserve the wave vector. (If the wave vector were on a face of the Brillouin zone, it could be invariant under inversion). Recently (Lawes *et al*., 2005; Kenzelmann *et al*., 2005, 2006; Schweizer, Villain and Harris, 2007), it has been shown that in such systems spatial inversion plays a crucial role in reducing the number of parameters (symmetry adapted coordinates) needed to specify the magnetic structure. We now give a simplified description of how inversion symmetry restricts the allowed spin structures.

As we have observed previously, the quadratic free energy of equation (18) must be invariant under all the operations of the paramagnetic space group. In particular, the operations for the systems we consider here which are *not* in the little group of the wave vector are those generated by spatial inversion, $\mathcal{I}$. Usually when one introduces an additional symmetry, the matrix for the quadratic free energy becomes block diagonal. Here, the result of the additional symmetry is not to reduce the size of the submatrices for the quadratic free energy, but rather it places additional constraints on the symmetry adapted coordinates m which appear in Tables 4 and 5.

We first analyze the situation for NVO. We need to determine the effect of $\mathcal{I}$ on the spin wave functions listed in Table 4. Recall that the magnetic moment is a pseudovector. That means that under spatial inversion the orientation of the moment is unchanged, but it is simply transported from its initial location at $\mathbf{r}$ to the transformed location, $-\mathbf{r}$. Looking at equation (17) we see that spatial inversion interchanges $\mathcal{S}$ and $\mathcal{S}^*$, but since the orientation is unchanged, spatial inversion will not affect the spin component label α. However, spatial inversion does interchange Ni sublattices #1 and #3 and also #2 and #4. In other words, in the notation of Table 4, we have

$$\mathcal{I}\mathcal{S}_{x,s1} = \mathcal{S}^*_{x,s3}, \;\; \mathcal{I}\mathcal{S}_{x,s2} = \mathcal{S}^*_{x,s4} \tag{34}$$

and similarly for the y- and z-components. To see the consequences of these relations, consider the effect of the first of these two relations acting on the spin distribution for

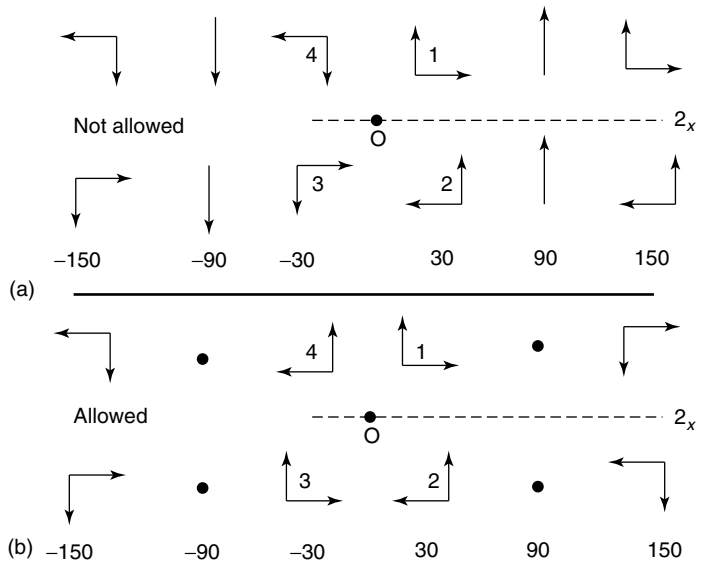

Figure 9. Two structures for spine spins in an **a**–**c** plane for NVO obtained using spin components from Table 4 which transform according to irrep Γ_4. For simplicity this figure is for the wave vector $k = 2\pi/(3a)$, where $a/2$ is the distance between sites. The axis for the twofold rotation 2_x is indicated. The glide plane, which relates spins in adjacent layers is not shown. The sites are numbered as in Table 2. At the bottom of each panel, we give (in degrees) the phase $\theta = \mathbf{q} \cdot \mathbf{r}$ of the propagation factor $\exp(i\mathbf{q} \cdot \mathbf{r})$ at each site. (a) For $m_{s_x}^{(4)} = 1$, $m_{s_z}^{(4)} = -i$ and the other parameters equal to zero. (b) For $m_{s_x}^{(4)} = m_{s_z}^{(4)} = 1$ and the other parameters equal to zero. As we shall see in equation (43), the order parameters $m_{s_x}^{(4)}$ and $m_{s_z}^{(4)}$ must have the same phase, that is, $m_{s_x}^{(4)}/m_{s_z}^{(4)}$ must be real. Only the configuration in (b) satisfies this constraint.

irrep Γ_1 given in the first column of Table 4, for instance. The first relation of equation (34) implies that

$$\mathcal{I}(im_{s_x}^{(1)}, m_{s_y}^{(1)}, im_{s_z}^{(1)}) = (-im_{s_x}^{(1)}, m_{s_y}^{(1)}, -im_{s_z}^{(1)})^* \tag{35}$$

which can be written as

$$\mathcal{I}(m_{s_x}^{(1)}, m_{s_y}^{(1)}, m_{s_z}^{(1)}) = (m_{s_x}^{(1)}, m_{s_y}^{(1)}, m_{s_z}^{(1)})^* \tag{36}$$

This same analysis can be repeated for the other representations and also for the second relation of equation (34). Then we see that the choices of the phase factors i in Table 4 leads to the simple result that for $\alpha = x$, y, or z, and independent of representation Γ_n

$$\mathcal{I}\mathbf{m}_{s_\alpha}^{(n)}(q) = \mathbf{m}_{s_\alpha}^{(n)}(q)^* \tag{37}$$

(Had we not included the phase factors i in Table 4, we would have had to keep track of which m's obey $\mathcal{I}m = m^*$ and which obey $\mathcal{I}m = -m^*$.) For the cross-tie sites, the situation is similar except that under spatial inversion each sublattice is transformed into itself. Thus, we find that

$$\mathcal{I}\mathbf{m}_{c_\alpha}^{(n)}(q) = \mathbf{m}_{c_\alpha}^{(n)}(q)^* \tag{38}$$

So, generally for NVO we have for *any representation* Γ_n

$$\mathcal{I}m_r^{(n)}(q) = m_r^{(n)}(q)^* \tag{39}$$

where $r = s_x, s_y, s_z, c_x, c_y, c_z$. (Note that this relation does not imply inversion symmetry. If the system has inversion symmetry about the origin, then $\mathcal{I}m_r^{(n)}(q) = m_r^{(n)}$, and magnetic order cannot induce ferroelectric order. Thus one cannot have ferroelectric order if all the m's are real.)

Now we invoke the invariance of the free energy with respect to spatial inversion (which, for NVO, is a symmetry of the paramagnetic lattice). For this purpose, we consider the form of the quadratic free energy written in equation (18). Since f_2 is quadratic in the $\mathcal{S}$'s, it can also be written as a quadratic form in the symmetry adapted coordinates m:

$$\begin{aligned} f_2 &= \sum_{jkn} F_{j,k}^{(n)} m_j^{(n)}(-\mathbf{q}) m_k^{(n)}(\mathbf{q}) \\ &= \sum_{jkn} F_{j,k}^{(n)} m_j^{(n)}(\mathbf{q})^*\, m_k^{(n)}(\mathbf{q}) \end{aligned} \tag{40}$$

where n refers to the irrep Γ_n. Note that there are no matrix elements connecting coefficients of different irreps. Also we used wave vector conservation which implies that $\mathbf{q}$ couples to $-\mathbf{q}$. For f_2 to be real no matter what the m's might be, one requires that the matrix $\mathbf{F}$ be Hermitian:

$$F_{j,k}^{(n)} = F_{k,j}^{(n)*} \tag{41}$$

Now we use equation (39) to see the consequence of f_2 being inversion invariant. We have that

$$\begin{aligned}\mathcal{I}f_2 &= \sum_n \sum_{jk} F_{j,k}^{(n)} \left[\mathcal{I}m_j^{(n)}(q)^* \right]\left[\mathcal{I}m_k^{(n)}(q)\right] \\ &= \sum_n \sum_{jk} F_{j,k}^{(n)} m_j^{(n)}(q) m_k^{(n)}(q)^* \\ &= f_2 = \sum_n \sum_{jk} F_{k,j}^{(n)} m_k^{(n)}(q)^* \, m_j^{(n)}(q) \end{aligned} \tag{42}$$

Thus we see that inversion invariance of $f_2^{(n)}$ implies that $F_{j,k}^{(n)} = F_{k,j}^{(n)}$. Combining this with equation (41) we see that all the coefficients of the quadratic form must be real valued. This means that all the components of the eigenvectors of the quadratic free energy, when written in terms of the variables of equation (40), can be taken to be real valued. However, this does not mean that these variables *must* be real. Rather, since these variables are allowed to be complex, we may initially take them to be real valued, but more generally one may then introduce an overall complex phase factor. So, the critical eigenvector of irrep Γ_n (which, when normalized, has components $x_j^{(n)}$), has an arbitrary overall phase, in which case the symmetry adapted coordinates in the HTI phase are given as

$$m_j^{(4)} = \boldsymbol{\sigma}_{\rm HTI} x_j^{(4)} = |\boldsymbol{\sigma}_{\rm HTI}| \, e^{i\phi_{\rm HTI}} r_j^{(4)} \tag{43}$$

in terms of the real-valued eigenvalue components $r_j^{(4)}$. As mentioned above, since the r's depend on the details of the interactions, we do not say anything about their explicit form. Also, because we have introduced an overall scale factor $\boldsymbol{\sigma}_{\rm HTI}$, we may require that $\sum_j \left[r_j^{(4)}\right]^2 = 1$. Notice that the phase of all variables of a given irrep are the same. In other words, the phases of the m's in equations (30–33) are all the same. Equation (43) shows that we are dealing with an x–y-like order parameter $\boldsymbol{\sigma} \equiv \sigma_{\rm HTI} e^{i\phi_{\rm HTI}}$ which has an amplitude and a phase. (As the temperature is varied near $T_{\rm HTI}$, Landau theory gives the approximate result $\sigma_{\rm HTI} \sim (T_{\rm HTI} - T)^{1/2}$.) In the appendix, this argument (showing that the $x_j^{(n)}$ are real apart from an overall phase factor) is extended to include fourth-order terms in the free energy. In analyzing experimental data, it is very helpful to realize that apart from the overall phase, $\phi_{\rm HTI}$, all the phases of the of the symmetry adapted coordinates $m_j^{(4)}$ are fixed. When speaking in terms of the spin components, $\mathcal{S}_{\alpha\tau}(q)$, the listing of Table 4 indicates that (for irrep #4, for instance), $\mathcal{S}_{x,1s}(q)$, $\mathcal{S}_{z,1s}(q)$, $\mathcal{S}_{y,1c}(q)$, and $\mathcal{S}_{z,1c}(q)$ will all have the same phase, but (due to the factor i), $\mathcal{S}_{y,1s}(q)$ will be out of phase with the other variables, as one sees in equation (30). As it happens, unless a huge number (several thousand) of reflections are monitored, it is impossible to use diffraction data to fix the relative phases with any degree of certainty. Thus, this theoretical development is useful to completely determine the spin structure of complicated systems such as NVO or TMO. (See note added in publication.)

We now check to see whether the HTI phase has a center of inversion symmetry, in which case, a spontaneous polarization cannot be induced in this phase. We will show that for NVO a phase with a single representation has inversion symmetry. First of all, because we assume incommensurability, we can redefine the origin to be arbitrarily close to a lattice site at R, such that $\phi - qR$ is a multiple of 2π. We have already noted that $\mathcal{I}m_\alpha^\tau = m_\alpha^{\tau *}$. But if ϕ in equation (43) is redefined to be zero, this implies that $\mathcal{I}m_\alpha^\tau = m_\alpha^\tau$, which means that the spin structure has inversion symmetry about the redefined origin. In Figure 9, we show an example of a system obeying equation (43) which does have inversion symmetry and one having an arbitrary set of parameters out of Table 4 which does not satisfy equation (43) and is therefore not allowed. This latter structure does not display inversion symmetry. Note that, as exemplified in Figure 9(b), it is possible for a structure to be noncollinear, but to have a center of inversion symmetry. So noncollinearity, in and of itself, does not guarantee having a spontaneous polarization.

The analysis of the LTI phase is similar. Here again, one can use the transformation properties of the order parameters under inversion to fix the phases of the spin amplitudes. Again, at quadratic order, one has the same result as for the HTI phase: all the LTI order parameters m_α^s for the LTI irrep Γ_1 have the same phase, $\phi_{\rm LTI}$ (which generally is not equal to $\phi_{\rm HTI}$). The analysis is extended to quartic order in the appendix. When two order parameters are nonzero, inversion symmetry will be broken if the centers of symmetry of the two irreps do not coincide, that is, if $\phi_{\rm LTI} \neq \phi_{\rm HTI}$, as is expressed in equation (61).

5.4 Effect of inversion symmetry for TMO

For TMO the nth Mn sublattice (denoted nM) is transformed into itself, so, using Table 5, we have

$$\mathcal{I}S_{\alpha,nM}^{\Gamma_n} = \left[S_{\alpha,nM}^{\Gamma_n}\right]^* \tag{44}$$

which implies that

$$\mathcal{I}m_{M_\alpha}^{(n)}(q) = \left[m_{M_\alpha}^{(n)}(q)\right]^* \tag{45}$$

For the Tb spins, inversion transforms sublattice #1 (denoted $T1$) into sublattice #3 (denoted $T3$) and #2 (denoted $T2$) into #4 (denoted $T4$), so that for them one has

$$\mathcal{I}S_{\alpha,T1}^{\Gamma_n}(q) = \left[S_{\alpha,T3}^{\Gamma_n}(q)\right]^* \ , \ \mathcal{I}S_{\alpha,T2}^{\Gamma_n}(q) = \left[S_{\alpha,T4}^{\Gamma_n}(q)\right]^* \tag{46}$$

These relations imply that

$$\mathcal{I}m^{(n)}_{T_{1\alpha}} = \left[m^{(n)}_{T_{2\alpha}}\right]^* \tag{47}$$

The situation for TMO is slightly more complicated than it was for NVO because of the presence of the lower-symmetry Tb sites. In the HTI phase, the irrep for TMO was determined to be Γ_3. One can repeat the argument used for NVO to show that all the symmetry adapted coordinates on the Mn sites, $m^{(3)}_{M_\alpha}$, have the same phase. To proceed further, we now study the quadratic free energy $f_2^{(3)}$ associated with the irrep Γ_3. In matrix notation we have the quadratic free energy in terms of symmetry adapted coordinates as

$$f_2^{(3)} = \left[m^{(3)\,*}_{M_x},\ m^{(3)\,*}_{M_y},\ m^{(3)\,*}_{M_z},\ m^{(3)\,*}_{T_{1z}},\ m^{(3)\,*}_{T_{2z}}\right] \times \begin{bmatrix} a & b & c & z_1 & z_2 \\ b & d & e & z_3 & z_4 \\ c & e & f & z_5 & z_6 \\ z_1^* & z_3^* & z_5^* & g & z_7 \\ z_2^* & z_4^* & z_6^* & z_7^* & h \end{bmatrix} \begin{bmatrix} m^{(3)}_{M_x} \\ m^{(3)}_{M_y} \\ m^{(3)}_{M_z} \\ m^{(3)}_{T_{1z}} \\ m^{(3)}_{T_{2z}} \end{bmatrix} \tag{48}$$

In writing this form, we have used the fact that the reality of $f_2^{(3)}$ requires the matrix to be Hermitian. Also the matrix elements b, c, and e are real, as can be shown from the arguments used previously for NVO. We now consider complex-valued matrix elements z_n, which have no analog for NVO. (An analogous formulation would be needed for NVO if we were to consider the effect of the minuscule moments which are induced on the lower-symmetry oxygen sites.) We see that the form of equation (48) implies a contribution to $f_2^{(3)}$ of the form

$$\delta f_2^{(3)} = z_1 \left[m^{(3)}_{M_x}\right]^*\ m^{(3)}_{T_{1z}} \tag{49}$$

Using equations (45) and (47), we have that

$$\mathcal{I}\delta f_2^{(3)} = z_1 m^{(3)}_{M_x} \left[m^{(3)}_{T_{2z}}\right]^* \tag{50}$$

Invariance under inversion symmetry indicates that this term must be the same as that, $z_2^*\ [m^{(3)}_{T_{2z}}]^*\ m^{(3)}_{M_x}$, given by equation (48). We thus conclude that $z_2^* = z_1$. Similarly, one can show that $z_4^* = z_3$ and $z_6^* = z_5$. Inversion symmetry gives no information on the phase of z_7. Thus the matrix for $f_2^{(3)}$ is of the form

$$\begin{bmatrix} a & b & c & y_1 & y_1^* \\ b & d & e & y_2 & y_2^* \\ c & e & f & y_3 & y_3^* \\ y_1^* & y_2^* & y_3^* & g & y_4 \\ y_1 & y_2 & y_3 & y_4^* & h \end{bmatrix} \tag{51}$$

where only the y's are complex valued. One can then show that any eigenvector of this matrix must be of the form

$$\psi = [M_x, M_y, M_z, T_1, T_2] = \sigma_{\rm HTI}[r_x, r_y, r_z, c, c^*\ ]e^{i\phi_{\rm HTI}} \tag{52}$$

where r_α is real, c can be complex, and we require the normalization $2|c|^2 + \sum r_\alpha^2 = 1$. As for NVO, we introduced an arbitrary overall phase $\phi_{\rm HTI}$. Note that $m^{(3)}_{M_\alpha}(q) = \sigma_{\rm HTI} r_\alpha e^{i\phi_{\rm HTI}}$, $m^{(3)}_{T_{1z}}(q) = \sigma_{\rm HTI} c e^{i\phi_{\rm HTI}}$, and $m^{(3)}_{T_{2z}}(q) = \sigma_{\rm HTI} c^*\ e^{i\phi_{\rm HTI}}$. Thus, as a result of inversion symmetry, the amplitudes of the two Tb sublattices (c and c^*), which without considering inversion symmetry were unrelated, are now equal in magnitude and have equal and opposite phases relative to the Mn sites. The value of this relative phase (of c) is not fixed by symmetry. As for NVO, one can verify that ψ is inversion invariant if ϕ is redefined to be zero, since then $\mathcal{I}r_\alpha = r_\alpha$ and $\mathcal{I}c = (c^*)^*\ = c$. (The latter relation follows from equation (47).)

5.5 Summary

Finally, we should emphasize that although we do not have a quantitative treatment of the development of magnetic long-range order, we can certainly determine the magnetic symmetry. This information is encoded in Table 3. For NVO, $\sigma_{\rm HTI}$ is associated with irrep #4 and therefore is odd under a twofold rotation about x and even with respect to the mirror plane taking z into $-z$. Likewise, $\sigma_{\rm LTI}$ is associated with irrep #1 and is therefore even with respect to both these operations. For future reference, we also give the transformation properties of $\boldsymbol{\sigma}_{\rm HTI}\boldsymbol{\sigma}_{\rm LTI}$. These results are summarized in Table 6. The symmetry of the LTI phase of NVO is illustrated in Figure 10.

For TMO, the HTI order parameter $\boldsymbol{\sigma}_{\rm HTI}$ is odd with respect to the mirror taking z into $-z$ and is even with respect to the mirror taking x into $-x$. Likewise, $\boldsymbol{\sigma}_{\rm LTI}$ is associated with irrep #2 and is even with respect to the mirror taking z into $-z$ and is odd with respect to the mirror taking x into $-x$ and these results are summarized in Table 6.

In Table 7, we give the experimentally determined values of the symmetry adapted parameters that describe the HTI and LTI phases of NVO and TMO. The results for NVO are analyzed in detail in Kenzelmann *et al.* (2006). We will make a few brief observations here. For NVO, the spine spins dominantly have order in the x direction in the HTI phase from irrep Γ_4 indicating that the x axis is the easy axis. The additional order in the LTI phase due to irrep Γ_1 is along the y direction, and the phase difference

Table 6. Transformation properties of order parameters for NVO (left) and TMO (right). In this table, $\boldsymbol{\sigma} \equiv \sigma e^{i\phi}$. and 'c.c.' denotes complex conjugation. Each column gives the result of applying the operator at the top of the column to the order parameter listed in the row.

Order Parameter	2_x	m_{xy}	$\mathcal{I}$
$\boldsymbol{\sigma}_{\rm HTI}(q)$	-1	1	c.c.
$\boldsymbol{\sigma}_{\rm LTI}(q)$	1	1	c.c.
$\boldsymbol{\sigma}_{\rm LTI}(q)\boldsymbol{\sigma}_{\rm HTI}(-q)$	-1	1	c.c.

Order Parameter	$\tilde{2}_y$	m_{xy}	$\mathcal{I}$
$\boldsymbol{\sigma}_{\rm HTI}(q)$	-1	1	c.c.
$\boldsymbol{\sigma}_{\rm LTI}(q)$	1	-1	c.c.
$\boldsymbol{\sigma}_{\rm LTI}(q)\boldsymbol{\sigma}_{\rm HTI}(-q)$	-1	-1	c.c.

Table 7. Values of the symmetry adapted parameters that describe the HTI and LTI phases of NVO (see Lawes *et al*., 2004) and TMO (see Kenzelmann *et al*., 2005). The uncertainty in the last digit quoted is given in parenthesis. Where there is no parenthesis, the entry is fixed by symmetry to be zero. For TMO, the two Tb order parameters were assumed to have the same magnitude (as predicted by Landau theory) and the phase difference between the Tb parameters $m^{(2)}_{T_{1\alpha}}$ and $m^{(2)}_{T_{2\alpha}}$ in the LTI phase was found to be $1.3(3)\pi$. For NVO, $T = 7$K is in the HTI phase and $T = 5$K is in the LTI phase. For TMO, $T = 35$K is in the HTI phase and $T = 15$K is in the LTI phase.

NVO					TMO				
T(K)	Variable	$\alpha = x$	$\alpha = y$	$\alpha = z$	T(K)	Variable	$\alpha = x$	$\alpha = y$	$\alpha = z$
7	$m^{(4)}_{s_\alpha}$	1.93(5)	0.20(5)	0.10(4)	35	$m^{(3)}_{M_\alpha}$	0.0(8)	2.90(5)	0.0(5)
7	$m^{(4)}_{c_\alpha}$	0	$-0.2(2)$	0.00(2)	35	$\lvert m^{(3)}_{T_{n\alpha}}\rvert$	0	0	0.0(4)
5	$m^{(4)}_{s_\alpha}$	2.0(1)	0.16(9)	0.01(5)	15	$m^{(3)}_{M_\alpha}$	0.0(5)	3.9(1)	0.0(7)
5	$m^{(1)}_{s_\alpha}$	0.5i(5)	-0.5i(1)	0.00i(3)	15	$m^{(2)}_{M_\alpha}$	0.0i(1)	0.0i(8)	2.8i(1)
5	$m^{(4)}_{c_\alpha}$	0	$-2.1(2)$	$-0.03(9)$	15	$\lvert m^{(3)}_{T_{n\alpha}}\rvert$	0	0	0(1)
5	$m^{(1)}_{c_\alpha}$	0.9i(5)	0	0	15	$\lvert m^{(2)}_{T_{n\alpha}}\rvert$	1.2(1)	0(1)	0

$\phi_{\rm LTI} - \phi_{\rm HTI} = \pi/2$ indicates that the spin structure is a spiral, as illustrated in Figure 10. From this figure, one sees that interactions between nearest neighboring spins in adjacent spines displaced from one another along either **c** or **b** are AFM. Since the wave vectors are the same for both types of order, we infer that the exchange interactions are nearly isotropic.

For the Mn spins in TMO, the situation is much the same. In the HTI phase, the Mn spins dominantly have order in the y direction, indicating that this axis is the easy axis. In the HTI irrep (Γ_3) one sees, from Table 5, that sites #1 and #2 (in one basal plane) have positive y components of spin and that sites #3 and #4 (in the adjacent basal plane) have negative y components of spin indicating FM in-plane interactions and AFM out-of-plane interactions. In the LTI phase of TMO, the additional irrep Γ_2 involves spins along z axis and Table 5 shows that for irrep #2 the components are again arranged ferromagnetically within basal planes but antiferromagnetically between adjacent basal planes. The fact that both components of spin are organized similarly suggests that the exchange interactions are probably nearly isotropic. As for NVO the difference in phase between the LTI and HTI order parameters is characteristic of a spiral spin structure.

6 MAGNETOELECTRIC COUPLING

6.1 Landau theory with two order parameters

Now we consider the Landau expansion for the free energy, $f_{\rm ME}$, of the combined magnetic and electric system. One might be tempted to write

$$f_{\rm ME} = a(T - T_F)\mathbf{P}^2 + b(T - T_M)|\sigma|^2 \qquad (53)$$

where σ is a magnetic order parameter and, if we wish to describe a phase transition in which both electric and magnetic order appear simultaneously, we would set $T_{\rm F} = T_{\rm M}$. There are several reasons to reject this scenario. First of all, it is never attractive to assume an accidental degeneracy ($T_F = T_M$). This degeneracy can happen, of course, but normally one would have to adjust some addition control parameter (such as pressure) to reach such a higher-order critical point. In addition, in this type of scenario magnetic and electric properties would not be interrelated. In NVO and TMO, in contrast, as shown in Figure 1, the electric polarization has a dramatic dependence on the applied magnetic field (Lawes *et al*., 2005), which such an independent scenario could not explain.

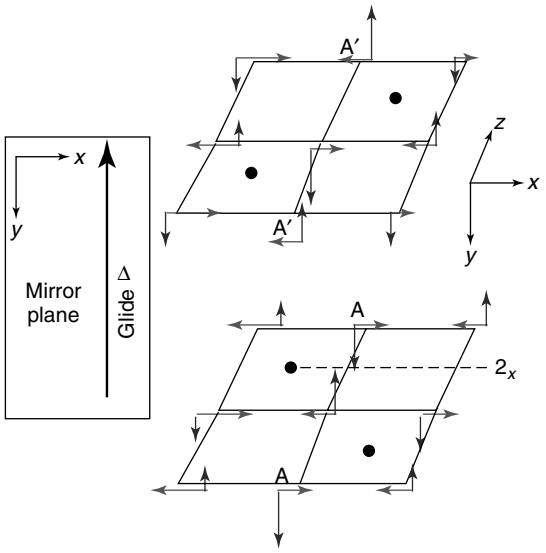

Figure 10. Schematic representation to show the symmetry of spin components for NVO. Here, we show sections of two adjacent **a**–**c** planes. The filled circles indicate the cross-tie sites whose spin components are not shown, for simplicity. The x components transform according Γ_4: they are odd under the twofold rotation 2_x about the x axis and are even under the x–y glide plane (the mirror plane is shown on the left with a subsequent displacement $\vec{\Delta}$ along $\hat{y}$). (Remember that the magnetic moment vector involves a cross product and therefore is an axial vector: under a mirror operation it picks up an extra minus sign.) The y components transform according to Γ_1: they are even under both operations. Although the x and y components have different symmetry, they can plausibly result from nearly isotropic exchange interactions.

6.2 Landau theory with two coupled order parameters

Accordingly, we turn to a formulation in which the appearance of magnetic order induces ferroelectric order. (The possibility that electric order induces magnetic order is not allowed by symmetry, by the argument in footnote 87 of Toledano, Schmid, Clin and Rivera (1985).) So we write

$$f_{\rm ME} = a\chi_{\rm E}^{-1}\mathbf{P}^2 + a(T - T_M)|\sigma|^2 + V_{\rm ME} \tag{54}$$

where $\chi_{\rm E}^{-1}$ does not approach zero and the simultaneous appearance of magnetic and electric order is due to the term $V_{\rm ME}$. As we have seen, the magnetic order is associated with a nonzero wave vector, whereas the ferroelectric order is a zero wave vector phenomenon. Accordingly, we are constrained to posit a magnetoelectric coupling of the form

$$V_{\rm ME} \sim \sigma(q)\sigma(-q)P \tag{55}$$

This term will do what we want: when magnetic order appears in $\sigma(q)$, it will then give rise to a linear perturbation in P, so that $P \sim \chi_{\rm E}|\sigma(q)|^2$. This argument is schematic, of course, and we will have to fill in the details, which must be consistent with the crystal symmetry of the specific systems involved.

The minimal phenomenological model that describes the magnetic and electric behavior of the HTI and LTI phases is therefore written as

$$\begin{aligned} f = {} & \frac{1}{2}(T - T_{\rm HTI})\boldsymbol{\sigma}_{\rm HTI}(q)\boldsymbol{\sigma}^*_{\rm HTI}(q) \\ & + \frac{1}{2}(T - T_{\rm LTI})\boldsymbol{\sigma}_{\rm LTI}(q)\boldsymbol{\sigma}^*_{\rm LTI}(q) \\ & + \mathcal{O}(|\sigma|^4) + \frac{1}{2}\chi_{\rm E}^{-1}\mathbf{P}^2 + V_{\rm ME} \end{aligned} \tag{56}$$

where

$$V_{\rm ME} = \sum_{\rm A,B\,=\,LTI,\,HTI} \sum_{\gamma=x,y,z} a_{A,B,\gamma}\boldsymbol{\sigma}_A(q)^*\,\boldsymbol{\sigma}_B(q)P_\gamma \tag{57}$$

6.3 Symmetry of magnetoelectric coupling

We now show that this free energy reproduces the observed phenomenology of ferroelectricity in NVO and TMO. First, of all, in the HTI phase (where $\boldsymbol{\sigma}_{\rm LTI} = 0$) $V_{\rm ME}$ is of the form

$$V_{\rm ME} = \sum_\gamma b_\gamma |\boldsymbol{\sigma}_{\rm HTI}(q)|^2 P_\gamma \tag{58}$$

where b_γ is real. Now we use the fact that $V_{\rm ME}$ has to be inversion invariant, since it arises in an expansion relative to the paramagnetic phase, which is inversion invariant (Dzyaloshinskii, 1957; Landau and Lifshitz, 1958). We use $\mathcal{I}\sigma_{\rm HTI}(q) = \sigma_{\rm HTI}(q)^*$ and $\mathcal{I}P_\gamma = -P_\gamma$ to show that b_γ must vanish. Indeed, we have already seen, the HTI phases of NVO and TMO are inversion invariant. So, for these situations b_γ in equation (58) must be zero and no polarization can be induced in the HTI phase.

Now we consider the situation in the LTI phase when the two order parameters $\sigma_{\rm HTI}$ and $\sigma_{\rm LTI}$ are both nonzero. The argument which indicated that $a_{\rm HTI,HTI,\gamma} = 0$ can be used to establish that $a_{\rm LTI,LTI,\gamma} = 0$. Then we write

$$\begin{aligned} V_{\rm ME} = \sum_\gamma \big[& c_\gamma \boldsymbol{\sigma}_{\rm HTI}(q)^*\,\boldsymbol{\sigma}_{\rm LTI}(q) \\ & + c^*_\gamma\,\boldsymbol{\sigma}^*_{\rm LTI}(q)\boldsymbol{\sigma}_{\rm HTI}(q)\big] P_\gamma \end{aligned} \tag{59}$$

This interaction has to be inversion invariant, so we use the transformation properties of the order parameters under inversion to write

$$V_{\rm ME} = \mathcal{I} V_{\rm ME} = -\sum_{\gamma} \left[c_\gamma \boldsymbol{\sigma}_{\rm HTI}(q) \boldsymbol{\sigma}_{\rm LTI}(q)^* + c_\gamma^* \, \boldsymbol{\sigma}_{\rm LTI}(q) \boldsymbol{\sigma}_{\rm HTI}(q)^* \right] P_\gamma \qquad (60)$$

Comparison with equation (59) indicates that c_γ must be pure imaginary: $c_\gamma = i r_\gamma$, where r_γ is real. Then

$$V_{\rm ME} = 2 \sum_{\gamma} r_\gamma \sigma_{\rm HTI}(q) \sigma_{\rm LTI}(q) P_\gamma \sin[\phi_{\rm HTI} - \phi_{\rm LTI}] \qquad (61)$$

This result shows that to get a nonzero spontaneous polarization it is necessary that two order parameters be nonzero. (A similar interaction was proposed by Frohlich, Leute, Pavlov and Pisarev, 1998 in their analysis of second-harmonic generation.) Furthermore, these two order parameters must *not* have the same phase. In fact, a more detailed analysis of Landau theory shows that the phase difference $\phi_{\rm HTI} - \phi_{\rm LTI}$ is expected to be $\pi/2$. (This result comes from an analysis of the quartic terms. As we observed earlier, the function of the quartic terms is to enforce the constraint of fixed spin length. This constraint usually means that the ordering in two representations should be out of phase, so that when one representation gives a maximum of spin lengths, the other gives a minimum of spin lengths.) The reader should be alerted to the fact that there are systems such as $TbMn_2O_5$ and YMn_2O_5 which have a magnetoelectric interaction of the form

$$V_{\rm ME} = \sum_{\gamma} r_\gamma [|\sigma_1(q)|^2 - |\sigma_2(q)|^2] P_\gamma \qquad (62)$$

and which therefore can support a ferroelectric phase in the presence of a *single* incommensurate magnetic order parameter (Harris, 2006b). (A similar magnetoelectric interaction was found in Cowley, 1980, and Sergienko, Sen and Dagotto, 2006, for *commensurately* ordered magnetic systems.)

Finally, we consider how the symmetry properties constrain the spontaneous polarization. Look at Table 6. There we see how the magnetic order parameters transform under the various symmetry operations of the paramagnetic phase. For $V_{\rm ME}$ to be an invariant, we see that for NVO, **P** must be odd under 2_x (which restricts **P** to be along y or z) and it must be even under m_{xy} (which restricts **P** to be along x or y). Thus, symmetry restricts **P** to be only along y. This is exactly what experiment shows. For TMO, **P** must be odd under both $\tilde{2}_y$ and m_{xy}. Thus, symmetry restricts **P** to lie along z at $H = 0$, as is observed in experiment. (At higher magnetic fields, the magnetic symmetry must change to explain why the polarization switches from the z axis to the x axis.) Furthermore, the temperature variation of **P**, shown in Figure 11 looks very much like that for an order parameter. But that is to be expected because if we minimize the total free energy with respect to **P**, using equation (61), we see that the spontaneous polarization is given as

$$P_\gamma \sim \chi_{\rm E} \sigma_{\rm HTI} \sigma_{\rm LTI} \qquad (63)$$

When the LTI phase is entered, $\sigma_{\rm HTI}$ is already well developed and is therefore essentially independent of temperature. Thus we expect that crudely $P_\gamma \sim \sigma_{\rm LTI}$. Indeed, although we have not undertaken a quantitative analysis, the experimental curves of P versus T look quite similar to those for an order parameter.

Finally, for TMO for a large magnetic field along **a** (see Figure 6) or along **b** (see Kimura *et al*., 2005), there is a change of orientation of the spontaneous polarization **P** to lie along **a**. Since there seems to be no analogous phase transition within the HTI phase, we attribute this reorientation to a change in the LTI spin state. Instead of the additional irrep of the LTI phase being Γ_2 (as it is at low field), we infer that the new LTI irrep is Γ_1, since this combination of irreps is consistent with having **P** along **a**. Furthermore, if we assume that the exchange coupling is isotropic, then we would expect that Γ_1 ordering would be FM within basal planes and AFM between planes. From Table 5, this constraint can only be satisfied if the ordering involves the x component of spin. So, from the polarization data we

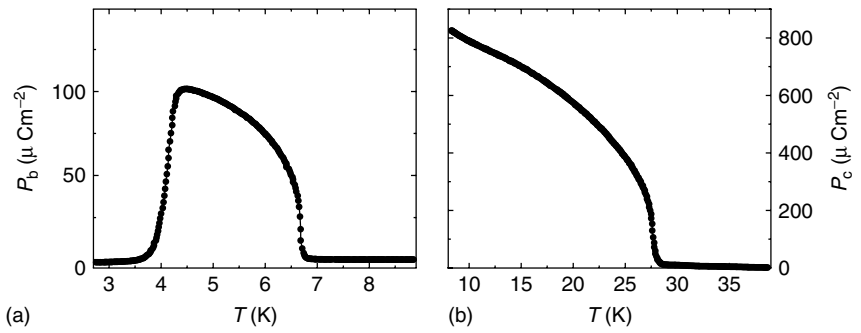

Figure 11. Temperature dependence of the spontaneous polarization at zero applied magnetic field for NVO (a) and for TMO (b). Note the different scales for **P**. (Reprinted with permission G. Lawes *et al*., copyright 2005, American Institute of Physics (a) and Reprinted with permission T. Kimura *et al*., copyright 2003, Nature Publishing Group (b).)

speculate that the Mn spin structure (which at low field is in the **b**–**c** plane) is rotated, at high field, into the **a**–**b** plane.

6.4 Spin-current model

A microscopic explanation of ferroelectricity occurring simultaneously with spiral order of the type seen in TMO or NVO was given by Katsura, Nagaosa and Balatsky (2005). (Subsequently, a similar result was obtained phenomenologically Mostovoy, 2006.) In this theory, a microscopic mechanism is invoked in which a spontaneous polarization $\mathbf{P}_{ij}$ can be induced by spins $\mathbf{S}_i$ and $\mathbf{S}_j$ which are located at respective positions $\mathbf{r}_i$ and $\mathbf{r}_j$. Assuming a noncollinear spin ordering (presumably established by competing exchange interactions), they found that

$$\mathbf{P}_{ij} = a\left[\frac{\mathbf{r}_{ij} \times (\mathbf{S}_i \times \mathbf{S}_j)}{r_{ij}}\right] \tag{64}$$

where a is a constant and $\mathbf{r}_{ij} = \mathbf{r}_i - \mathbf{r}_j$. This model successfully predicts the magnetically induced spontaneous polarization in both NVO and TMO. First of all, in the HTI phases if the spins are assumed to be collinear, this mechanism predicts that $\mathbf{P}_{ij} = 0$. In a phase in which the spins rotate a plane perpendicular to $\mathbf{n}$, one see that the vector $\mathbf{S}_i \times \mathbf{S}_j$ must be parallel to $\mathbf{n}$. If one averages over spins in planes perpendicular to the wave vector $\mathbf{q}$, one see that the net polarization must be in the direction $\mathbf{n} \times \mathbf{q}$. For the LTI phase of NVO, for instance, the vector $\mathbf{n}$ is parallel to the $\mathbf{b}$ direction and $\mathbf{q}$ is along the $\mathbf{a}$ direction. This model therefore correctly predicts a spontaneous polarization along the $\mathbf{c}$ direction. However, the predictions of this mechanism are less obvious when there are small transverse components of magnetization which are allowed within the observed irrep.

The same argument also correctly predicts the direction of the spontaneous polarization in TMO and gives the same prediction for the rotation of the plane of the magnetization when TMO is subject to a large magnetic field that rotates the direction of the spontaneous polarization.

6.4.1 Note added in Proof

Recently, the stacked triangular antiferromagnet $RbFe(MO_4)_2$ with spins confined to the plane perpendicular to the threefold axis, with each such plane forming a 120° antiferromagnet has been shown to be ferroelectric (Kenzelmann *et al*., 2007). Since the spins are perpendicular to the threefold axis, the vector $\mathbf{S}_i \times \mathbf{S}_j$ must lie along the threefold axis. The observed spontaneous polarization along the threefold axis contradicts the prediction of the spin-current model that there be no ferroelectricity induced by antiferromagnetism. So, while the spin-current model is appealing in the simplicity of its conclusion, it cannot be a universal explanation of magnetically induced ferroelectricity. In this system equation (62) is verified by showing that P_γ goes like $|\sigma_1(q)|^2$ when $\sigma_2(q)$ vanishes.

We also point out a recent paper of Sergienko and Dagotto (2006) (SD) who show that the Dzyaloshinskii–Moriya (DM) interaction can induce a combined magnetic and ferroelectric phase transition. However, in the model explicitly considered in their paper, the phenomenology seems inappropriate since the transition requires a threshold strength of the DM interaction, whereas the phenomenology we have developed here always gives ferroelectricity independent of the strength of the magnetoelectric coupling providing the symmetry is appropriate.

6.5 Broken symmetry

We should also mention some considerations concerning broken symmetry for NVO. (Clearly, a similar discussion applies to other similar systems.) Since both transitions involving the HTI phase involve broken symmetry, we assert the following. At the level of the present analysis when the temperature is reduced to enter the HTI phase, the modulated order appears with an arbitrary phase ϕ_{HTI}. Of course, if this state is truly incommensurate, then this phase will remain arbitrary. Normally, however, we would expect some perturbation to break this symmetry and this continuous symmetry should be removed. However, we do expect a degeneracy with respect to the time-reversed version of the ordered HTI phase. In that case upon performing many runs of the same experiment, both time-reversed versions of the HTI ordered phase should occur with equal probability.

One can make much the same observation about the HTI→LTI phase transition. Here, one has the additional broken symmetry associated with the irrep Γ_1. When the temperature is reduced to enter the LTI phase, the system will have two symmetry-equivalent states into which it can condense. As with the usual magnetic phase transitions, one can (in principle) select between these two phases by applying a suitably spatially modulated magnetic field. Such an experiment does not seem currently feasible (because modulation of an applied field on an atomic scale is difficult to produce). However, because the magnetic order parameters are coupled to the ferroelectric moment, one can select between the two symmetry-equivalent possibilities for the LTI order parameter by applying a small *electric* field. An interesting experiment suggests itself: compare the magnetic state as determined by, say, neutron diffraction for the two cases of a small applied electric field in the positive and negative $\mathbf{b}$ directions. According to the magnetoelectric trilinear coupling, application of such an electric field should select the sign of the product $\sigma_{\mathrm{HTI}}\sigma_{\mathrm{LTI}}$. In this context, we

remark that measurement of the spontaneous polarization **P** (as in Figure 1) is made by preparing the sample in a small symmetry-breaking electric field $\mathbf{E}_0$, which is removed once **P** becomes nonzero. The ferroelectric order is confirmed by verifying that **P** changes sign when the sign of $\mathbf{E}_0$ is changed.

7 MICROSCOPICS

Since the spontaneous polarization **P** must result from a spontaneous condensation of an optical phonon having a dipole moment, we are led to study the symmetry of the phonon excitations at zero wave vector. Neglecting nonzero wave vectors, we write the α component of the displacement of the τth ion in the unit cell at **R** as

$$u_\alpha(\mathbf{R}, \tau) = \sum_i Q_i \xi_\alpha^{(i)}(\tau) \tag{65}$$

where $\xi_\alpha^{(i)}(\tau)$ is the normalized form factor of the ith generalized displacement whose amplitude is Q_i. A comprehensive analysis is given elsewhere (Harris, Yildirim, Aharony and Entin-Wohlman, 2006), but here we confine our attention to generalized displacements in NVO which transform appropriately (like a displacement along **b**) to explain experiments. Such a (y-like) generalized displacement Q_i must be invariant under the operations (see Table 2) E, $\boldsymbol{\sigma}_x$, $\boldsymbol{\sigma}_z$, and 2_y and change sign under $\boldsymbol{\sigma}_y$, 2_x, 2_z, and $\mathcal{I}$. There are 12 such generalized displacements of the 13 ions in the primitive unit cell. Six of these are the uniform displacements along **b** of all crystallographically equivalent sites of a given type, that is Ni spine sites, Ni cross-tie sites, V sites, O_1, O_2, and O_3 sites, and these uniform displacements, denoted Q_1, $Q_2, \ldots Q_6$, give rise to a dipole moment along the **b** axis. Other generalized displacements involve, perhaps surprisingly, oppositely oriented displacements along the **a** or **c** axis within a group of crystallographically equivalent sites. We illustrate one of these (Q_7 involving Ni cross-tie sites) along with Q_2 in Figure 12. Since Q_7 has the same symmetry as $Q_1 \ldots Q_6$, it must couple to these modes. One can easily visualize this by imagining the ions to act like hard spheres. In that case, as the cross-tie ions approach spine sites #1 and #4, they cause these site (which initially were at negative y) to move to more negative y. Similarly, as the cross-tie sites move away from sites #2 and #3, these ions have more room to move closer to $y = 0$. In other words, the opposing motion of the cross-tie sites in mode Q_7 along the **c** axis interacts with the uniform motion in mode Q_1 of the spine sites along **b**. In summary, the elastic free energy as a function of displacements can be written as

$$f(\{Q_i\}) = \frac{1}{2} \sum_{i,j=1}^{12} V_{ij} Q_i Q_j \tag{66}$$

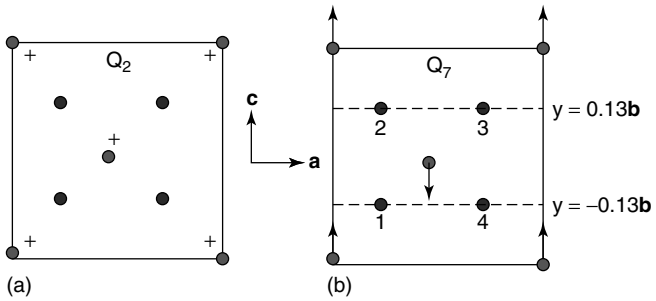

Figure 12. Pattern of two generalized displacements, Q_2 (a) and Q_7 (b), which transform under the symmetry operations of the crystal like a displacement along **b**. In (a), '+' indicates motion along the positive **b** axis. In Q_2, all the cross-tie sites move in parallel along the **b** axis and therefore this motion induces a dipole moment. As discussed in the text, the nonuniform motion of the cross-tie sites in the generalized displacement Q_7 induces uniform motion of the spine site in the **b** direction which in turn produces a dipole moment.

At the time of this writing, no calculation or neutron experiments to determine V_{ij} have appeared. Instead we have recourse to a very crude toy model, obtained by setting

$$f(\{Q_i\}) = \sum_i \frac{1}{2} M_i \omega_D^2 Q_i^2 \tag{67}$$

where M_i is the mass of ions in mode Q_i and ω_D is the Debye frequency, characteristic of phonons.

We now consider the effect of a generalized y-like displacement Q_i on the exchange interaction between nearest neighbors in the same spine. Then for spins numbered 1 and 4 in a unit cell we have the exchange interaction as a function of displacement as

$$\mathcal{H}_{14}(Q_i) = \mathcal{H}_{14}(0) + Q_i \sum_{\alpha\beta} S_\alpha(1) \frac{\mathrm{d}M_{\alpha\beta}(1,4)}{\mathrm{d}Q_i} S_\beta(4) \tag{68}$$

The existence of a mirror plane perpendicularly bisecting the 1–4 bond ($m_{\mathbf{bc}}$) implies that

$$\mathcal{H}_{14}(Q_i) = m_{\mathbf{bc}} \mathcal{H}_{14}(Q_i) \tag{69}$$

which is

$$\mathcal{H}_{14}(Q_i) = Q_i [S_{1x}, S_{1y}, S_{1z}] \frac{\mathrm{d}}{\mathrm{d}Q_i} \times \begin{bmatrix} M_{xx} & -M_{yx} & -M_{zx} \\ -M_{xy} & M_{yy} & M_{zy} \\ -M_{xz} & M_{yz} & M_{zz} \end{bmatrix} \begin{bmatrix} S_{4x} \\ S_{4y} \\ S_{4z} \end{bmatrix} \tag{70}$$

where we used $m_{\mathbf{bc}} Q_i = Q_i$, $m_{\mathbf{bc}} S_{1x} = S_{4x}$, $m_{\mathbf{bc}} S_{1y} = -S_{4y}$, and $m_{\mathbf{bc}} S_{1z} = -S_{4z}$ (the spin is a pseudovector). Thus,

to satisfy equation (69) the derivatives must satisfy the conditions

$$\frac{\mathrm{d}M_{yx}}{\mathrm{d}Q_i} = -\frac{\mathrm{d}M_{xy}}{\mathrm{d}Q_i}, \frac{\mathrm{d}M_{zx}}{\mathrm{d}Q_i} = -\frac{\mathrm{d}M_{xz}}{\mathrm{d}Q_i}, \frac{\mathrm{d}M_{zy}}{\mathrm{d}Q_i} = \frac{\mathrm{d}M_{yz}}{\mathrm{d}Q_i} \quad (71)$$

Thus the gradient of the exchange tensor must assume the form

$$\frac{\mathrm{d}M_{\alpha\beta}(1,4)}{\mathrm{d}Q_i} = \frac{\mathrm{d}}{\mathrm{d}Q_i}\begin{bmatrix} J_{xx} & D_z & -D_y \\ -D_z & J_{yy} & J_{yz} \\ D_y & J_{yz} & J_{zz} \end{bmatrix} \quad (72)$$

where $J_{\alpha\beta}$ is the symmetric exchange tensor and **D** is the Dzyaloshinskii–Moriya vector, which specifies the antisymmetric component of the exchange tensor.

We determine the other similar interactions in the unit cell using the appropriate symmetry operations. If 2_y is a rotation about an axis parallel to **b** and which passes through site #4, then

$$\mathcal{H}(4,1';y) = 2_y\mathcal{H}(1,4;y) = Q_i[S_{4x}, S_{4y}, S_{4z}]\frac{\mathrm{d}}{\mathrm{d}Q_i} \times \begin{bmatrix} J_{xx} & D_z & D_y \\ -D_z & J_{yy} & -J_{yz} \\ -D_y & -J_{yz} & J_{zz} \end{bmatrix}\begin{bmatrix} S_{1'x} \\ S_{1'y} \\ S_{1'z} \end{bmatrix} \quad (73)$$

where we used $2_y Q_i = Q_i$, and site #4′ is one unit cell to the right of site #4 in Figure 12. Also, if 2_x is a rotation about the **a** axis, then

$$\mathcal{H}(2,3;y) = 2_x\mathcal{H}(1,4;y) = Q_i[S_{2x}, S_{2y}, S_{2z}]\frac{\mathrm{d}}{\mathrm{d}Q_i} \times \begin{bmatrix} -J_{xx} & D_z & -D_y \\ -D_z & -J_{yy} & -J_{yz} \\ D_y & -J_{yz} & -J_{zz} \end{bmatrix}\begin{bmatrix} S_{3x} \\ S_{3y} \\ S_{3z} \end{bmatrix} \quad (74)$$

where we used $2_x Q_i = -Q_i$ and

$$\mathcal{H}(3,2';y) = 2_y\mathcal{H}(2,3;y) = Q_i[S_{3x}, S_{3y}, S_{3z}]\frac{\mathrm{d}}{\mathrm{d}Q_i} \times \begin{bmatrix} -J_{xx} & D_z & D_y \\ -D_z & -J_{yy} & J_{yz} \\ -D_y & J_{yz} & -J_{zz} \end{bmatrix}\begin{bmatrix} S_{2'x} \\ S_{2'y} \\ S_{2'z} \end{bmatrix} \quad (75)$$

where site #2′ is one unit cell to the right of site #3 in Figure 12.

When we consider equation (67) and neglect fluctuations, the spin–phonon interactions lead to the result

$$\langle Q_i\rangle = \left(M_i\omega_{\mathrm{D}}^2\right)^{-1}\sum_{\alpha\beta}\sum_{n,m}\langle S_\alpha(n)\rangle\frac{\mathrm{d}M_{\alpha\beta}(n,m)}{\mathrm{d}Q_i}\langle S_\beta(m)\rangle \quad (76)$$

where $\langle\ \rangle$ indicates a thermal average and (n, m) are summed over the four nearest-neighbor spine–spine interactions in a unit cell. Assuming the spins are characterized by spine spin components scaled by **a** for irrep 4 and by **b** for irrep #1, we write the spin components as

$$\begin{aligned} S_x(x_1) &= (a_x + ib_x)\mathrm{e}^{iqx_1} + (a_x^* - ib_x^*)\mathrm{e}^{-iqx_1} \\ S_x(x_2) &= (-a_x + ib_x)\mathrm{e}^{iqx_1} + (-a_x^* - ib_x^*)\mathrm{e}^{-iqx_1} \\ S_x(x_3) &= (a_x - ib_x)\mathrm{e}^{iqx_4} + (a_x^* + ib_x^*)\mathrm{e}^{-iqx_4} \\ S_x(x_4) &= (-a_x - ib_x)\mathrm{e}^{iqx_4} + (-a_x^* + ib_x^*)\mathrm{e}^{-iqx_4} \end{aligned} \quad (77)$$

$$\begin{aligned} S_y(x_1) &= (ia_y + b_y)\mathrm{e}^{iqx_1} + (-ia_y^* + b_y^*)\mathrm{e}^{-iqx_1} \\ S_y(x_2) &= (ia_y - b_y)\mathrm{e}^{iqx_1} + (-ia_y^* - b_y^*)\mathrm{e}^{-iqx_1} \\ S_y(x_3) &= (-ia_y + b_y)\mathrm{e}^{iqx_4} + (ia_y^* + b_y^*)\mathrm{e}^{-iqx_4} \\ S_y(x_4) &= (-ia_y - b_y)\mathrm{e}^{iqx_4} + (ia_y^* - b_y^*)\mathrm{e}^{-iqx_4} \end{aligned} \quad (78)$$

$$\begin{aligned} S_z(x_1) &= (a_z + ib_z)\mathrm{e}^{iqx_1} + (a_z^* - ib_z^*)\mathrm{e}^{-iqx_1} \\ S_z(x_2) &= (a_z - ib_z)\mathrm{e}^{iqx_1} + (a_z^* + ib_z^*)\mathrm{e}^{-iqx_1} \\ S_z(x_3) &= (a_z - ib_z)\mathrm{e}^{iqx_4} + (a_z^* + ib_z^*)\mathrm{e}^{-iqx_4} \\ S_z(x_4) &= (a_z + ib_z)\mathrm{e}^{iqx_4} + (a_z^* - ib_z^*)\mathrm{e}^{-iqx_4} \end{aligned} \quad (79)$$

Using these evaluations one can carry out the sum over (n, m) in equation (76) to get

$$\langle Q_i\rangle = 16(M_i\omega_{\mathrm{D}}^2)^{-1}\left[F_i^{(s)}\sin(qa/2) + F_i^{(c)}\cos(qa/2)\right] \quad (80)$$

where

$$F_i^{(c)} = \Im\left[a_x^*\, b_z + a_z^*\, b_x\right]\mathrm{d}D_y/\mathrm{d}Q_i + \sum_\alpha \pi_\alpha \Im\left[a_\alpha b_\alpha^*\right]\mathrm{d}J_{\alpha\alpha}/\mathrm{d}Q_i \quad (81)$$

and

$$F_i^{(s)} = \Im\left[a_z b_y^* + b_z a_y^*\right]\mathrm{d}J_{yz}/\mathrm{d}Q_i + \Im\left[a_x b_y^* + b_x a_y^*\right]\mathrm{d}D_z/\mathrm{d}Q_i \quad (82)$$

where $-\pi_x = \pi_y = \pi_z = 1$. Note that these terms require the presence of both order parameters **a** and **b** and hence they can only be nonzero in the LTI phase. Also these terms are only nonzero if **a** and **b** have different phases. For displacements that could give rise to a spontaneous polarization along the **a** or **c** axes, the sum over (n, m) in equation (76) gives zero (Harris, Yildirim, Aharony and Entin-Wohlman, 2006). These conclusions agree with the

result found using Landau theory. This magnon–phonon coupling also contributes to the temperature dependence of the wave vector q (Kenzelmann *et al*., 2006; Harris *et al*., 2006).

To get an order-of-magnitude estimate of the various quantities, we consider the effect of the motion of the oxygen ions, which are the lightest atoms and therefore have the largest displacements. Crudely speaking, the dipole moment, P_Q of the generalized displacement Q is given by $P_Q = q_Q \sum_{i\in Q} u_i$, where q_Q is the charge of the ions of Q and u_i is the displacement of ion i in Q. More accurately, q_Q should be replaced by an effective charge q_Q^* which takes account of the electrical relaxation that occurs as the ions move. (This is analogous to the discussion given at the end of the preceding paragraph.) Thus, even Q_7 will develop a (probably small) dipole moment in the **b** direction. However, for simplicity we set

$$\langle P\rangle = \frac{q_i\langle Q\rangle}{v_{\rm uc}} = \frac{2e\langle Q\rangle}{v_{\rm uc}} \tag{83}$$

where $v_{\rm uc} \approx 275\times 10^{-30}\mathrm{m}^3$ is the volume of the unit cell. More accurately, $\langle Q\rangle$ should be replaced by $\langle Q\rangle\sqrt{n}$, where n is the number of ions involved in the mode generalized displacement Q (So $n = 4$ or $n = 6$). So, in meters, $\langle Q\rangle \approx (275\times 10^{-30})(5\times 10^{-4})/(3.2\times 10^{-19}\sqrt{n})$, where we took $P = 5\times 10^{-4}\,\mathrm{C\,m^{-2}}$ as a typical value. Thus we estimate the ionic displacement to be of order $\langle Q\rangle \sim 0.001$ Å. (Actually, neutron diffraction indicates that the ionic displacement ought to be at most 0.001 Å.) (We thank Prof. C. Broholm for communicating this bound to us.) If $\partial J/\partial Q$ represents a typical value for $\partial M_{\alpha\beta}/\mathrm{d}Q$, then

$$\langle Q_i\rangle \sim \frac{(\hbar c)^2}{(M_i c^2)(\hbar\omega_{\rm D})^2}\frac{\partial J}{\partial Q} \tag{84}$$

Working in Åand eV and taking $\langle Q_i\rangle = 0.001$ Å, $\hbar\omega_{\rm D} \approx 0.05$ eV, $M_i c^2 \approx 1.6\times 10^{10}$ eV, and $\hbar c \approx 2000$ eV Å, we find that this mechanism requires that

$$\frac{\partial J}{\partial Q} \sim 0.01\ \mathrm{eV/Å} \tag{85}$$

This seems to be a plausible value. Obviously a first-principles calculation of $\partial M_{\alpha\beta}/\partial Q_i$ would be of interest to make this analysis more concrete.

8 SUMMARY AND OUTLOOK

The development of multiferroic materials having very large magnetoelectric couplings offers the possibility of designing new types of devices that exploit the coupling between magnetic and ferroelectric order. Furthermore, investigating the nature of the coupling between magnetic and ferroelectric order parameters in these compounds may be important in understanding other systems displaying significant interactions between different types of long-range order. We will briefly summarize the main results of the model we have presented coupling ferroelectricity with incommensurate magnetic order, and then discuss what this implies for future research on magnetoelectric multiferroics.

8.1 Summary of this review

As many of the recently identified materials exhibiting simultaneous magnetic and ferroelectric order are incommensurate magnets, we have focused on these systems. We discussed a toy model for incommensurate magnetism. In this model, we saw that, under the assumption that the magnetic anisotropy is not too large, the magnetic system will undergo a paramagnetic to a longitudinally ordered incommensurate phase we refer to as the HTI phase. On further lowering the temperature, the is another transition to a distinct incommensurate phase with additional transverse spin ordering, which we call the LTI phase.

Because knowing the detailed symmetry of the incommensurate magnetic structure is crucial for determining whether ferroelectric order is allowed, we considered the extension of this toy model to systems with nontrivial unit cells. We addressed this problem by expressing the spin order parameters in terms of irreducible representations consistent with the symmetry restrictions of the unit cell. The central observation for understanding the magnetoelectric coupling is that the free energy must be invariant under all symmetries of the paramagnetic phase, and in particular, if the paramagnetic crystal has inversion symmetry, it must be invariant under spatial inversion. This requirement was used to determine whether a particular incommensurate magnetic structure allowed the possibility of ferroelectric order. Using this approach, we are able to qualitatively explain the multiferroic behavior of both NVO and TMO, including the absence of ferroelectric order in the HTI phase, the development of ferroelectricity in the LTI phase, and the qualitative features of the spontaneous polarization (direction and temperature dependence).

It is worth noting that the magnetoelectric coupling we have described here does not reduce to the analogous coupling that can occur in a ferromagnet or in an antiferromagnet. As remarked in the review of Smolenskii and Chupis (1982), such a trilinear coupling cannot exist in structures that (like NVO or TMO) have inversion symmetry in the paramagnetic phase. Indeed, the mechanism we invoke requires that $q \neq 0$, as one can see from equation (61). (If $q = 0$, then the

order parameters are real, $\phi_{\mathrm{HTI}} = \phi_{\mathrm{LTI}} = 0$ and $V_{\mathrm{ME}} = 0$.) In that review, they also mention a coupling that involves gradients of the magnetic order parameter. That type of coupling may be related to the one used here, although in our case the symmetry properties of the unit cell play a crucial role that cannot be replaced by a continuum vector field.

We also showed that the microscopic symmetry of the derivative of the exchange tensor with respect to ionic displacement leads to results in complete agreement with the symmetry arguments based on the Landau expansion. This symmetry will have to be respected by any truly microscopic theory of magnetoferroelectrics.

8.2 Outlook for device applications

The success of the theory described in this review suggests that it may be valuable both in understanding the origins of multiferroic behavior in presently identified systems, and well as in guiding the search for new multiferroic compounds having desirable materials properties. We briefly discussed the technological drivers motivating the search for magnetoelectric materials, by illustrating the types of devices that might be possible using multiferroics. However, there are two main difficulties that must be resolved before these materials could be incorporated into fabricating next generation magnetoelectric devices. Firstly, the very low transition temperatures into the ferroelectric LTI phase (6.4 K for NVO and ∼27 K for TMO) make these materials unsuitable for many applications. Secondly, the spontaneous polarizations in these systems are typically several orders of magnitude smaller than what is found in conventional ferroelectrics. Before incommensurate multiferroics can be considered for applications, it will be necessary to engineer materials having larger spontaneous polarizations developing at higher temperatures. We discuss in the following some of the general ideas extracted from our model which may help guide the search for new multiferroics more suitable for applications.

Extending the search for multiferroics from simple ferromagnets to systems with incommensurate magnetic order is an important first step in finding materials that have a room-temperature transition into a phase, developing magnetic and ferroelectric order simultaneously. Insulating ferromagnets tend to have very low transition temperatures, but many incommensurate magnets have ordering temperatures well above room temperature (Sosnowska, Newmaier and Seichle, 1982). In fact, the incommensurate magnetic structure associated with ferroelectric order in one recently identified multiferroic (T. Kimura, private communication) persists up to $T = 320$ K. Our results suggest that insulating incommensurate magnets with high magnetic ordering temperatures may be prime candidates in the search for strongly coupled magnetoelectric multiferroics at room temperature.

The second shortcoming of currently known incommensurate multiferroics for device applications is the small value of the spontaneous polarizations. As we develop a better understanding of the microscopic mechanisms giving rise to multiferroic order, it should be possible to engineer materials with larger ferroelectric moments. Additionally, several recent studies suggest that the spontaneous polarization of certain multiferroic materials may be significantly enhanced in thin-film geometries (Wang *et al*., 2003). This offers the possibility of improving the properties of incommensurate multiferroics by preparing the thin-film samples that would be required for device applications.

8.3 Experimental outlook

Both of the systems we have considered in detail (NVO and TMO) are inversion symmetric in the paramagnetic phase, and only develop ferroelectric order by coupling the polarization to two distinct magnetic order parameters. On the surface, this might suggest that the search for new multiferroic materials should focus on systems with multiple magnetically ordered phases developing in zero field. However, as pointed out in equation (62) ferroelectricity can appear within a scenario involving the condensation of a single magnetic order parameter and very recent experiments on $RbFe(MoO_4)_2$ have shown this unambiguously (Kenzelmann *et al*., 2007).

This specific example raises the general problem of producing multiferroic order in a system that has neither magnetic nor ferroelectric order in the high-temperature phase. In particular, consider systems that lack inversion symmetry, but whose rotational symmetry elements preclude a nonzero vector order parameter. We give two families of such crystal structures. The first is that of the point group D_2 (orthorhombic space groups #16–#24 in Hahn, 1983) and the second is that of point group T (cubic space groups #195–#199 in Hahn, 1983). In the para phase, these systems have no magnetic long-range order and, because these crystal structures do not allow vector ordering, they do not display ferroelectric order. When such a system develops long-range incommensurate order with a wave vector along one of the crystallographic directions, then only rotations about this direction remain symmetric and a spontaneous polarization along the direction of the wave vector is permitted, at least in principle. This mechanism would therefore allow the development of multiferroic order at a single phase transition.

These results suggest that there are many more multiferroic materials than previously considered, and offer guidelines to identifying new multiferroics. The magnetic transition giving rise to ferroelectric order should produce a noncollinear

spin structure. Because magnetic order in geometrically frustrated magnets is often driven by anisotropic interactions, such complex spin structures often arise on frustrated triangular lattices. Furthermore, because the magnetic exchange energies at the ordering temperatures are typically large in frustrated systems (with the order temperature T_c an order of magnitude smaller than the Weiss temperature), these systems often show significant magnetoelectric coupling. Systems having low-energy phonon modes may be more susceptible to magnetically induced ferroelectric distortions, although other typical requirements for conventional ferroelectrics, specifically empty d orbitals (Seshadri and Hill, 2001), are apparently unimportant in multiferroics. Finally, while many of the magnetically induced multiferroics studied so far are in fact incommensurately ordered, it is not a necessary prerequisite, but is simply a consequence of the geometrical frustration in these systems (Kenzelmann *et al*., 2007). A recently studied commensurately ordered multiferroic is discussed in Sergienko and Dagotto (in press).

We also refer the reader to Section 6.5 where we suggest an experiment to test our assertions about broken symmetry, namely that the application of a small symmetry-breaking electric field should select states for which $\sigma_{\mathrm{HTI}}\sigma_{\mathrm{LTI}}$ has a fixed sign, although neither order parameter individually has a fixed sign.

Another experimental program which this study suggests concerns the phase diagram of these systems in the $T-E$ plane, where E is the uniform applied field. Since only the LTI phase of NVO or TMO has a spontaneous polarization, this phase is favored (relative to the HTI or AF phases) in the presence of an electric field. So we propose the schematic phase diagram shown in Figure 13. We have not specified the scale of the horizontal axis in this schematic figure, but at least for the LTI–AF transition in NVO we can estimate how thin a film would have to be to produce a 5% shift in the transition temperature for an applied voltage of 5 V. The analog of the Clausius–Clapeyron equation for the LTI–AF phase boundary in the $T-E$ plane is

$$\frac{\mathrm{d}T}{\mathrm{d}E} = \frac{-V(P_{\mathrm{LTI}} - P_{\mathrm{AF}})}{(S_{\mathrm{LTI}} - S_{\mathrm{AF}})} \tag{86}$$

Now take V to be the volume per Ni ion. The volume of the conventional unit cell is $v = abc$, so $V = abc/12$, because there are 12 Ni's per conventional unit cell. $a = 5.9$, $b = 11.4$, and $c = 8.2$, all in 10^{-10} m. For one Ni ion, the total entropy change from zero to infinite temperature is $k \ln 3$. Guided by specific heat measurements (Lawes *et al*., 2004) we set

$$(S_+ - S_-) = 0.01k \ln 3 \tag{87}$$

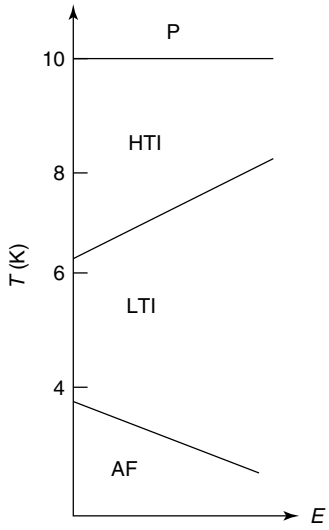

Figure 13. Schematic phase diagram for a system like NVO in the $T-E$ plane. (We do not give the scale of the E axis.)

and take $P = 5 \times 10^{-4}\,\mathrm{C\,m^{-2}}$ as a typical value. Then we find

$$\frac{\mathrm{d}T}{\mathrm{d}E} = -[(540 \times 10^{-30}\,\mathrm{m^3}/12)](5 \times 10^{-4}\,\mathrm{C\,m^{-2}})/ [1.4 \times 10^{-25}\,\mathrm{JK^{-1}}] = 1.5 \times 10^{-7}\,\mathrm{Km\,V^{-1}} \tag{88}$$

To see roughly what this means, set $\mathrm{d}T = 0.05\,T_c = 0.2\,\mathrm{K}$ and $\mathrm{d}E = 5\mathrm{V}/t$, where t is the thickness of the sample. This gives $0.2t \times 10^{-8}$, or $t \approx 1\,\mu$.

Finally, we emphasize that it would be desirable to determine the magnetic structure of TMO for high magnetic fields along the **a** or **b** direction to test whether the magnetic structure proposed below equation (63) is realized.

8.4 Theoretical outlook

It is clear that the next step for theorists is to construct a fully microscopic theory to explain the phenomenological trilinear interaction highlighted in this review. Here, we indicated how the dependence of the exchange interaction on ionic displacements gives rise to the symmetries expected from Landau theory. What is clearly missing is a microscopic calculation of the exchange constants. This sort of calculation as a function of bond angles has been pursued for Cu–O–Cu bonds (Tornow, Entin-Wohlman and Aharony, 1999). However, what is needed here is the more complicated calculation for Ni–O–Ni bonds and furthermore, it would seem that this is going to require some sort of calculation based on the local density approximation to determine the dependence of the exchange tensors on ionic displacements. Calculations of this type are being carried out.

9 RECENT DEVELOPMENTS

Subsequent to preparation of this review there have been several important studies of optical and dynamical properties of multiferroic systems. We give a very brief overview of work in these two areas.

We first consider the optical properties of phonon modes. We remind the reader of the crucial fact that for systems with inversion symmetry the modes at zero wave vector can be classified as being either even or odd under inversion symmetry. Only odd modes can be detected by absorption of electromagnetic radiation and only even modes contribute to Raman scattering (in which an outgoing photon is observed with a small shift in energy from the incoming photon due to creation or destruction of an elementary excitation of the system). Of course, when the system develops a spontaneous polarization, this selection rule is broken in a way that one can analyze by asking what ferroelectric subgroups are contained in the original centrosymmetric space group. Here, we give a simple approach to elucidate the mechanisms involved in breaking inversion symmetry. For this purpose, we construct an effective linear coupling between even and odd modes which leads to their mixing and concomitant breakdown of the even–odd selection rule due to the presence of a spontaneous polarization. We consider the expansion in terms of displacements relative to the inversion symmetric structure. In that expansion inversion symmetry does not permit the existence of a linear even–odd phonon coupling of the form

$$V = \sum_{m,n} c_{nm} Q_{\mathrm{odd},n} Q_{\mathrm{even},m} \tag{89}$$

where $Q_{\mathrm{odd},n}$ is the amplitude of the nth odd phonon mode at zero wave vector and $Q_{\mathrm{even},m}$ is that of the mth even phonon mode at zero wave vector. So we consider the anharmonic perturbation V_3 due to the interaction of three phonons:

$$V_3 = \sum_{\mathbf{k}_1,\mathbf{k}_2\mathbf{k}_3} \sum_{r,s,t} c_{rst} Q_r(\mathbf{k}_1) Q_s(\mathbf{k}_2) Q_t(\mathbf{k}_3) \times \Delta(\mathbf{k}_1 + \mathbf{k}_2 + \mathbf{k}_3) \tag{90}$$

where $Q_n(\mathbf{k})$ is the amplitude of the nth phonon at wave vector $\mathbf{k}$ and Δ expresses the conservation of wave vector modulo a reciprocal lattice vector. We replace one of these phonon amplitudes by its equilibrium value in the ferroelectric phase. For concreteness we specialize to the case of NVO where the condensed phonons which give rise to the observed spontaneous polarization along the y axis are $Q_{y_n}(0)$, the nth y like mode at zero wave vector. Thus, the coupling we seek is of the form

$$V \sim \sum_{\mathbf{k}} \sum_{r,s,t} c_{rst} Q_r(\mathbf{k}) Q_s(-\mathbf{k}) \langle Q_{y_t}(0) \rangle \tag{91}$$

where $\langle Q_{y_t}(0) \rangle$ is the amplitude of the static distortion in the phonon coordinate $Q_{y_t}(0)$. We then see that the coupling at zero wave vector is of the form

$$V \sim P_y \sum_{m,n} d_{mn} Q_{\mathrm{even},m}(0) Q_{\mathrm{odd},n}(0) \tag{92}$$

As a result of this coupling absorption active (odd) modes that transform like x, y, or z will be mixed into Raman active (even) modes that transform like xy, y^2 (A_g), and yz respectively. What this means is that Raman modes of symmetry, say, xy, will now be absorption active for radiation polarized with the electric field along x. Likewise Raman active modes that transform like xy, yz, or A_g will be mixed into absorption active modes that transform like x, z, or y, respectively. (xz Raman modes will get mixed into xyz modes that are silent modes.) As a result, modes that are absorption active with radiation polarized so that the electric field is along x will be weakly Raman active with xy symmetry. For xz symmetry Raman scattering, the polarization will not induce and new modes. This argument explains which modes may now be observed in the presence of the ferroelectric distortion. (Similar conclusions for the optical selection rules for $TbMn_2O_5$ were obtained in Aguilar *et al.*, 2006.) The cross section for distortion-induced absorption or Raman scattering is proportional to the square of the wave function induced by the distortion. Thus the induced cross sections will be proportional to the square of the spontaneous polarization, as is observed (Aguilar *et al.*, 2006). In addition, as the ferroelectric phase is entered there should also appear an anomalous temperature-dependent shift in frequency of the modes proportional to the square of the order parameter.

In addition to the mechanism of equation (90), one may have similar effects from a spin-phonon interaction treated by Fennie and Rabe (2006). This interaction is schematically of the form

$$V = \sum_{\mathbf{r},\,\mathbf{r}',\alpha\beta} \sum_{m,n} Q_m Q_n S_\alpha(\mathbf{r}) S_\beta(\mathbf{r}') Q_m Q_n \frac{\partial^2 J_{\alpha,\beta}(\mathbf{r},\mathbf{r}')}{\partial Q_m \partial Q_n} \tag{93}$$

where the Q's are phonon amplitudes and $J_{\alpha\beta}(\mathbf{r},\mathbf{r}')$ is an exchange tensor which couples the α component of spin at site $\mathbf{r}$ to the β component of spin at site $\mathbf{r}'$. When $S_\alpha(\mathbf{r}) S_\beta(\mathbf{r}')$ is replaced by its thermal expectation value, a result of the form of equation (92) is obtained, except that P_y is replaced by a spin–spin correlation function, *which has the same symmetry as* P_y.

The spontaneous polarization also has a dramatic effect on the absorption because of magnon creation or excitation. This process, which, in the absence of a spontaneous polarization, is only allowed because of magnetic dipole excitation, now has a strongly enhanced cross section due to admixing of the wave function which allows the highly dominant electric dipole excitation process (Pimenov *et al*., 2006a,b). Thus, even though the wave function of the magnon only suffers a tiny perturbation and energy shift due to magnetoelectric interaction, its absorption cross section is significantly increased because of the possibility of electric dipole excitation. A detailed calculation of this effect has appeared (Katsura, Balatsky and Nagaosa, 2007). However, a simple effective magnon-polarization coupling can be intuited from the trilinear magnetoelectric interaction which is schematically of the form

$$V \sim \sum_{\alpha\beta\gamma} c_{\alpha\beta\gamma}^{\tau\tau'} S_{\alpha\tau}(\mathbf{q}) S_{\beta\tau'}(-\mathbf{q}) P_{\gamma} \tag{94}$$

In a magnetically ordered phase (even one without a spontaneous polarization), we have the effective interaction

$$V \sim \sum_{\alpha\beta\gamma} c_{\alpha\beta\gamma}^{\tau\tau'} \langle S_{\alpha\tau}(\mathbf{q}) \rangle S_{\beta\tau'}(-\mathbf{q}) P_{\gamma} \tag{95}$$

This indicates an effective coupling that mixes the spontaneous polarization (at zero wave vector) into the spin excitation (magnon) at wave vector $\mathbf{q}$ or $-\mathbf{q}$. This would be observed by a huge enhancement of the cross section for absorption of electromagnetic radiation by magnon creation caused by the possibility of an electric dipole process in which radiation at zero wave vector couples to the low-energy magnon at wave vector $\mathbf{q}$. By the Kramers–Kronig relation, this coupling also explains (Sushkov *et al*., 2007) the anomalous enhancement which is seen in some multiferroics when spin ordering takes place.

ACKNOWLEDGMENTS

We have greatly profited from many discussions with A. Aharony, C. Broholm, H. D. Drew, O. Entin-Wohlman, M. Kenzelmann, T. Kimura, A. P. Ramirez, and T. Yildirim. We acknowledge help from B. Adhikary in preparing the figures. ABH thanks the US–Israel BSF for partial support.

REFERENCES

Aguilar, R.V., Sushkov, A.B., Park, S., *et al*. (2006). Infrared phonon signatures of multiferrocitiy in $TbMn_2O_5$, *Physical Review B* , **74**, 184404 cond-mat 0605416.

Ascher, E., Rieder, H., Schmid, H. and Stoessel, H. (1966). Some properties of ferromagnetoelectric nickel-iodine Boracite $Ni_3B_7O_{13}I$, *Journal of Applied Physics*, **37**, 1404.

Astrov, D.N. (1960). The magnetoelectric effect in antiferromagnets, *Journal of Experimental and Theoretical Physics (USSR)*, **38**, 984 [*Soviet Physics JETP*, **11**, 708 (1960)].

Bayrashev, A., Parker, A., Robbins, W. and Ziaie, B. (2003). Low frequency wireless powering of microsystems using piezoelectric-magnetostrictive laminate composites. *"Tranducers '03," 12th International Conference on Solid-State Sensors, Acutators and Microsystems. Digest of Technical Papers*, Boston, MA pt. 2, vol. 2, p. 1707.

Bertaut, E.F. (1971). Magnetic structure analysis and group theory. *Journal de Physique, Colloque C1,* **32**, 462.

Binek, Ch. and Doudin, B. (2005). Magnetoelectronics with magnetoelectrics. *Journal of Physics: Condensed Matter*, **17**, L39.

Birss, R. (1954). *Symmetry and Magnetism*, North Holland: Amsterdam.

Blasco, J., Ritter, C., Garcia, J., *et al*. (2000). Structural and magnetic study of $Tb_{1-x}Ca_xMnO_3$ perovskites. *Physical Review*, **62**, 5609.

Bud'ko, S.L., Islam, Z., Wiener, T.A., *et al*. (1999). Anisotropy and metamagnetism in the RNi_2Ge_2 (R=Y, La-Nd, Sm-Lu) series. *Journal of Magnetism and Magnetic Materials*, **205**, 53.

Cowley, R.A. (1980). Structural phase-transitions. 1. Landau theory. *Advances in Physics*, **29**, 1.

Curie, P. (1894). Sur la symetrie dans les phenomenes physique, symetrie d'un champ electrique et d'un champ magnetique. *Journal of Physics*, **3**(Ser. III), 393.

Domb, C. and Green, M.S. (Eds.) (1976). *Phase Transitions and Critical Phenomena*, Academic Press: New York,, Vol 6.

Dzyaloshinskii, I.E. (1957). Thermodynamic theory of weak ferromagnetism in antiferromagnetic substances. *Soviet Physics JETP*, **5**, 1259.

Dzyaloshinskii, I.E. (1959). On the magneto-electrical effect in antiferoomagnets. *Journal of Experimental and Theoretical Physics (USSR)*, **37**, 881 [*Soviet Physics JETP*, **10**, 628 (1960)].

Ederer, C. and Spaldin, N. (2005). Influence of strain and oxygen vacancies on the magnetoelectric properties of multiferroic bismuth ferrite. *Physical Review B*, **71**, 060401.

Eerenstein, W., Mathur, N.D. and Scott, J.F. (2006). Multiferroic and magnetoelectric materials. *Nature*, **442**, 759.

Fennie, C.J. and Rabe, K.M. (2006). Magnetically induced phonon anisotropy in $ZnCr_2O_4$ from first principles. *Physical Review Letters*, **96**, 759–205505.

Fiebig, M. (2005). Revival of the magnetoelectric effect. *Journal of Physics D*, **38**, R123.

Fiebig, M., Lottermoser, Th., Frohlich, D., *et al*. (2002). Obsevation of coupled magnetic and electric domains. *Nature*, **491**, 818.

Fisher, M.E. and Selke, W. (1980a). Infinitely many commensurate phases in a simple ising-model. *Physical Review Letters*, **44**, 1502.

Fisher, M.E. and Selke, W. (1980b). Infinitely many commensurate phases in a simple ising-model. *Physical Review Letters*, **45**, E148.

Folen, V.J., Rado, G.T. and Stalder, E.W. (1961). Anistropy of magnetoelectric effect in Cr_2O_3. *Physical Review Letters*, **6**, 607.

Fox, D.L. and Scott, J.F. (1977). Ferroelectrically induced ferromagnetism. *Journal of Physics C: Solid State Physics*, **10**, L329.

Fox, D.L., Tilley, D.R. and Scott, J.F. (1980). Magnetoelectric phenomena in $BaMnF_4$ and $BaMn_{0.99}Co_{0.01}F_4$. *Physical Review B*, **21**, 2926.

Frohlich, D., Leute, St., Pavlov, V.V. and Pisarev, R.V. (1998). Nonlinear optical spectroscopy of the two-order-parameter compound $YMnO_3$. *Physical Review Letters*, **81**, 3239..

Hahn, T. (Ed.) (1983). *International Tables for Crystallography*, D. Riedel: Boston, Vol A.

Harris, A.B. (2006a). Ferroelectricity induced by incommensurate magnetism. *Journal of Applied Physics*, **99**, 08E303.

Harris, A.B. (2006b). Symmetry of multiferroics. *Journal of Applied Physics*, **99**, 08E303. cond-mat/0610241.

Harris, A.B. Aharony, A., Entin-Wohlman, O., *et al*. (2006) unpublished.

Harris, A.B., Yildirim, T., Aharony, A. and Entin-Wohlman, O. (2006). Towards a microscopic model of magnetoelectric interactions in $Ni_3V_2O_8$. *Physical Review B*, **73**, 184433.

http://www.nasatech.com/Briefs/May00/NPO20523.html.

Hur, N., Park, S., Sharma, P.A., *et al*. (2004). Electric polarization reversal and memory in multiferroic material induced by magnetic fields. *Nature*, **429**, 392.

Kajimoto, R., Yoshizawa, H., Shintani, H., *et al*. (2004). Magnetic structure of $TbMnO_3$ by neutron diffraction. *Physical Review B*, **70**, 012401; *Physical Review B*, **70**, 219904(E) (2004).

Katsufuji, T. and Takagi, H. (2001). Coupling between magnetism and dielectric properties in quantum paraelectric $EuTiO_3$. *Physical Review B*, **64**, 054415.

Katsura, H., Balatsky, A.V. and Nagaosa, N. (2007). Dynamical magnetoelectric coupling in helical magnets. *Physical Review Letters*, **98**, 027203 cond-mat 0602547.

Katsura, H., Nagaosa, N. and Balatsky, A.V. (2005). Spin current and magnetoelectric effect in noncollinear magnets. *Physical Review Letters*, **95**, 057205.

Kenzelmann, M., Broholm, C., Rogado, N., *et al*. (2006). Field dependence of magnetic ordering in Kagomé-staircase compound $Ni_3V_2O_8$. *Physical Review B*, **74**, 014429.

Kenzelmann, M., Harris, A.B., Jonas, S., *et al*. (2005). Magnetic inversion symmetry breaking and ferroelectricity in $TbMnO_3$. *Physical Review Letters*, **95**, 087206.

Kenzelmann, M., Lawes, G., Harris, A.B., *et al*. (2007). Direct transition from a disordered to a multiferroic phase on a triangular lattice. cond-mat/0701426.

Kimura, T., Goto, T., Shintani, H., *et al*. (2003). Magnetic control of ferroelectric polarization. *Nature*, **426**, 55.

Kimura, T., Lawes, G., Goto, T., *et al*. (2005). Magnetoelectric phase diaghrams of orthorhombic $RMnO_3$ (R=Gd, Tb, and Dy). *Physical Review B*, **71**, 224425.

Landau, L.D. and Lifshitz, E.M. (1958). *Statistical Physics*, Pergamon: London.

Lawes, G., Harris, A.B., Kimura, T., *et al*. (2005). Magnetically driven ferroelectric order in $Ni_3V_2O_8$. *Physical Review Letters*, **95**, 087205.

Lawes, G., Kenzelmann, M., Rogado, N., *et al*. (2004). Competing magnetic phases on a Kagomé staircase. *Physical Review Letters*, **93**, 247201.

Lawes, G., Ramirez, A.P., Varma, C.M. and Subramanian, M.A. (2003). Magnetodielectric effects from spin fluctuations in isostructural ferromagnetic and antiferromagnetic systems. *Physical Review Letters*, **91**, 257208.

Li, J., Nagaraj, B., Liang, H., *et al*. (2004). Ultrafast polarization switching in thin-fild ferroelectrics. *Applied Physics Letters*, **84**, 1174.

Li, J., Wang, J., Wuttig, M., *et al*. (2004). Dramatically enhanced polarization in (001), (101), and (111) $BiFeO_3$ thin films due to epitaxial induced transitions. *Applied Physics Letters*, **84**, 5261.

Lottermoser, T., Lonkai, T., Amann, U., *et al*. (2004). Magnetic phase control by an electric field. *Nature*, **430**, 541.

Mostovoy, M. (2006). Ferroelectricity in spiral magnets. *Physical Review Letters*, **96**, 067601.

Nagamiya, T. (1967). In *Solid State Physics*, Seitz, F. and Turnbull, D. (Eds.), Academic Press: New York, p. 346, Vol. 29.

Newnham, R.E., Kramer, J.J., Schulze, W.A. and Cross, L.E. (1978). Magnetoferroelectricity in Cr_2BeO_4. *Journal of Applied Physics*, **49**, 6088.

Pimenov, A., Muykhin, A.A., Nanov, V.Yu., *et al*. (2006a). Possible evidence for electromagnons in multiferroic manganites. *Nature Physics*, **2**, 57.

Pimenov, A., Rudolf, T., Mayr, F., *et al*. (2006b). Coupling of phonons and electromagnons in $GdMnO_3$. *Physical Review B*, **74**, 100403 cond-mat 0605523.

Rossat-Mignod, J. (1987). Chapter 20 Magnetic structures. In *Methods of Experimental Physics*, Skold, K. and Price, D.L. (Eds.), Academic Press, Vol. 23.

Sa, D., Valenti, R. and Gros, C. (2000). A generalized Ginzburg-Landau approach to second harmonic generation. *European Physical Journal B*, **14**, 301.

Samara, G.A. and Richards, P.M. (1976). Low-temperature dielectric properties and phase transition in $BaMnF_4$. *Physical Review B*, **14**, 5073.

Schmid, H. (1973). On a magnetoelectric classification of materials. *International Journal of Magnetism*, **4**, 337.

Schmid, H. and Rivera, J.-P. (1994). Search for the piezomagnetoelectric effect in $LiCoPO_4$. *Ferroelectrics*, **161**, 91.

Schweizer, J., Villain, J. and Harris, A.B. (2007). Symmetry of magnetic structures: the case of $CeAl_2$. *European Physical Journal of Applied Physics*, **38**, 31.

Sergienko, I.A., Sen, C. and Dagotto, E. (2006). Ferroelectricity in the magnetic E-phase of orthorhombic perovskites. *Physical Review Letters*, **97**, 227204.

Sergienko, I.A. and Dagotto, E. (2006). Direct transition from a disordered to a multiferroic phase on a triangular lattice. *Physical Review B*, **73**, 094434.

Seshadri, R. and Hill, N. (2001). Visualizing the role of Bi 6s 'lone pairs' in the off-center distortion in ferromagnetic $BiMnO_3$. *Chemistry of Materials*, **13**, 2892.

Smolenskii, G.A. and Chupis, I.E. (1982). Segnetomagnetics. *Uspekhi Fizicheskikh Nauk*, **137**, 415 [*Soviet Physics Uspekhi*, **25**, 475].

Sosnowska, I., Newmaier, T.P. and Seichle, E. (1982). Spiral magnetic ordering in bismuth ferrite. *Journal of Physics C*, **14**, 4835.

Srinivasan, G., Laletsin, V.M., Hayes, R., *et al*. (2002). Giant magnetoelectric effects in layered composites of nickel zinc ferrite and lead zirconate titanate. *Solid State Communications*, **124**, 373.

Stefanovskii, E.P. and Yablonskii, D.A. (1986). Theory of electrical polarization of multisublattice orthorhombic antiferromagnets with double-exchange superstructure. *Soviet Journal of Low Temperature Physics*, **12**, 478.

Sushkov, A.B., Aguilar, R.V., Park, S., *et al*. (2007). Electromagnons in multiferoic YMn_2O_5 and $TbMn_2O_5$. *Physical Review Letters*, **98**, 027202.

Toledano, P., Schmid, H., Clin, M. and Rivera, J.P. (1985). Theory of low-temperature phases in boracites - latent antiferromagnetism, weak ferromagnetism, and improper magnetostructural couplings. *Physical Review B*, **32**, 6006.

Tornow, S., Entin-Wohlman, O. and Aharony, A. (1999). Anisotropic superexchange for nearest and next-nearest coppers in chain, ladder, and lamellar cuprates. *Physical Review B*, **60**, 10206.

Wang, J., Neaton, J.B., Zheng, H., *et al*. (2003). Epitaxial $BiFeO_3$ multiferroic thin film heterostructures. *Science*, **299**, 1719.

Wolf, S.A., Awschalom, D.D., Buhrman, R.A., *et al*. (2001). Spintronics: a spin-based electronics vision for the future. *Science*, **294**, 1488.

Ye, Z.G., Rivera, J.-P., Schmid, H., *et al*. (1994). Magnetoelectric effect and magnetic torque of choromium chlorine boracite $Cr_3B_7O_{13}Cl$. *Ferroelectrics*, **161**, 99.

APPENDICES

A QUARTIC TERMS

A.1 HTI phase of NVO

Since irrep #4 cannot induce any other irrep, the free energy only involves order parameters of that irrep. (So we will omit the superscript $n = 4$ which labels that irrep.) Then, correct to quartic order we write the free energy associated with irrep #4 as

$$\mathcal{H} = \mathcal{H}^{(2)} + \mathcal{H}^{(4)} + \ldots \tag{A1}$$

where

$$\mathcal{H}^{(2)} = \sum_{\tau\tau'} v_{\tau,\tau'} m_\tau(q)^*\, m_{\tau'}(q) \tag{A2}$$

and

$$\mathcal{H}^{(4)} = (1/4) \sum_{\tau_1,\tau_2,\tau_3,\tau_4} w_{\tau_1,\tau_2,\tau_3,\tau_4} m_{\tau_1}(q)^* \times m_{\tau_2}(q)^*\, m_{\tau_3}(q) m_{\tau_4}(q) \tag{A3}$$

where $m_{\tau=1}(q) = m_{s_x}(q)$, $m_{\tau=2}(q) = m_{s_y}(q)$, $m_{\tau=3}(q) = m_{s_z}(q)$, $m_{\tau=4}(q) = m_{c_y}(q)$, and $m_{\tau=5}(q) = m_{c_z}$, and the spin components at all the sites in the unit cell are given in Table 4 in terms of these variables. Hermiticity implies that $v_{\tau,\tau'} = v^*_{\tau',\tau}$ and

$$w_{\tau_1,\tau_2,\tau_3,\tau_4} = w^*_{\tau_3,\tau_4,\tau_1,\tau_2} \tag{A4}$$

and $\mathbf{w}$ can be taken to be symmetric under interchange of τ_1 and τ_2 and of τ_3 and τ_4. Since $\mathcal{H}^{(4)}$ must be invariant under inversion we have that

$$\begin{aligned}\mathcal{H}^{(4)} &= \frac{1}{4} \sum_{\tau_1,\tau_2,\tau_3,\tau_4} w_{\tau_1,\tau_2,\tau_3,\tau_4} \left[\mathcal{I}m_{\tau_1}(q)^*\right]\left[\mathcal{I}m_{\tau_2}(q)^*\right] \\ &\quad \times \left[\mathcal{I}m_{\tau_3}(q)\right]\left[\mathcal{I}m_{\tau_4}(q)\right] \\ &= \frac{1}{4} \sum_{\tau_1,\tau_2,\tau_3,\tau_4} w_{\tau_1,\tau_2,\tau_3,\tau_4} m_{\tau_1}(q) m_{\tau_2}(q) \\ &\quad \times m_{\tau_3}(q)^*\, m_{\tau_4}(q)^*\end{aligned} \tag{A5}$$

For this to reproduce $\mathcal{H}^{(4)}$ we must have that

$$w_{\tau_1,\tau_2,\tau_3,\tau_4} = w_{\tau_3,\tau_4,\tau_1,\tau_2} \tag{A6}$$

In conjunction with equation (A4), this indicates that all the matrix elements of $\mathbf{w}$ are real.

Now we transform to normal modes:

$$m_\tau(q) = \sum_\rho r_{\tau,\rho} \xi_\rho e^{i\phi_\rho} \tag{A7}$$

$$\boldsymbol{\xi}_{\rho'} = \sum_{\tau'} r_{\tau'\rho'} m_{\tau'}(q) e^{-i\phi_{\rho'}} \equiv \xi_{\rho'} e^{-i\phi_{\rho'}} \tag{A8}$$

where $\rho = 0, 1, 2, 3, 4$ labels the normal mode, the r's are real, and the critical mode (ρ_0) has an amplitude ξ_0 which heretofore we called σ_{HTI}. The quartic Hamiltonian is

$$\mathcal{H}_4 = \frac{1}{4} \sum_{\tau_1,\tau_2,\tau_3,\tau_4} \sum_{\rho_1,\rho_2,\rho_3,\rho_4} w_{\tau_1,\tau_2,\tau_3,\tau_4} r_{\tau_1,\rho_1} r_{\tau_2,\rho_2} r_{\tau_3,\rho_3} \times r_{\tau_4,\rho_4} \xi_{\rho_1} \xi_{\rho_2} \xi_{\rho_3} \xi_{\rho_4} e^{i\left(\phi_{\rho_3} + \phi_{\rho_4} - \phi_{\rho_1} - \phi_{\rho_2}\right)} \tag{A9}$$

This quartic term will involve contributions proportional to $\xi_0^p \equiv \sigma_{\mathrm{HTI}}^p$, where p ranges from zero to four. If we were to omit the quartic terms with $p = 3$, then the minimum of the trial free energy would be realized for $\sigma_{\mathrm{HTI}} \neq 0$, but with the other ξ_ρ's being zero. Therefore, the most important term to consider is the one cubic in σ_{HTI}, which is

$$\begin{aligned}\delta\mathcal{H}_4 &= \frac{1}{2}\sum_{\tau_1,\tau_2,\tau_3,\tau_4}\sum_{\rho=1}^{3} w_{\tau_1,\tau_2,\tau_3,\tau_4} r_{\tau_1,0} r_{\tau_2,0} r_{\tau_3,0} r_{\tau_4,\rho} \\ &\quad\times\ \xi_\rho \sigma_{\mathrm{HTI}}^3 e^{i(\phi_\rho - \phi_{\mathrm{HTI}})} + \text{c. c.} \\ &= \sum_{\rho=1}^{3} A_\rho \xi_\rho \sigma_{\mathrm{HTI}}^3 \cos[\phi_\rho - \phi_{\mathrm{HTI}}] \end{aligned} \tag{A10}$$

where A_ρ is real. The quadratic terms for the noncritical variables can be written as

$$\delta\mathcal{H}_2 = \frac{1}{2}\sum_{\rho=1}^{3} \chi_\rho^{-1} \boldsymbol{\xi}_\rho^* \, \boldsymbol{\xi}_\rho = \frac{1}{2}\sum_{\rho=1}^{3} \chi_\rho^{-1} \xi_\rho^2 \tag{A11}$$

where χ_ρ is the susceptibility of the ρth mode. Then, after minimization with respect to the noncritical variables ξ_ρ for $\rho > 0$, we see that $\cos[\phi_\rho - \phi_{\mathrm{HTI}}] = \pm 1$ (so that σ_{LTI} and σ_{LTI} are in phase) and

$$\xi_\rho = \pm \chi_\rho A_\rho \sigma_{\mathrm{HTI}}^3 \tag{A12}$$

Thus the effect of the quartic terms is to induce nonzero values for the noncritical normal modes and thereby slightly change the components of the critical eigenvector, but the quartic terms do not change the fact that all the order parameters m_τ belong to irrep #4 and that they all have the same relative phase.

A.2 LTI phase of NVO

Now we consider the LTI phase, where we have two irreps simultaneously present. There are various types of quartic terms. First, consider those quartic terms which only involve a single irrep. We can apply the analysis of the HTI phase, to state that such terms do not modify the conclusion that all the symmetry adapted coordinates of irrep #4 have the same phase, ϕ_4, and all the symmetry adapted coordinates of irrep #1 have the same phase ϕ_1.

Next consider the more general quartic terms which involve both irreps. Terms of the type $[m^{(4)}]^* \, [m^{(1)}]^* \, m^{(4)} m^{(1)}$ are independent of the phases and therefore after minimization of the trial free energy these terms do not modify the phases. There are no terms that involve three order parameters of one irrep and one order parameter of the other irrep. So the only terms that might affect the phases are terms of the form $[m^{(4)}]^* \, [m^{(4)}]^* \, m^{(1)} m^{(1)}$ and its complex conjugate. So, we consider quartic terms of the form

$$\begin{aligned} F_4 = &\sum_{\tau_1\tau_2\tau_3\tau_4} w^{(4)(4)(1)(1)}_{\tau_1\tau_2\tau_3\tau_4} m^{(4)}_{\tau_1}(q)^* \, m^{(4)}_{\tau_2}(q)^* \\ &\times\ m^{(1)}_{\tau_3}(q) m^{(1)}_{\tau_4}(q) + \text{c. c.} \end{aligned} \tag{A13}$$

Hermiticity requires that $w^{(4)(4)(1)(1)}_{\tau_1\tau_2\tau_3\tau_4} = [w^{(1)(1)(4)(4)}_{\tau_3\tau_4\tau_1\tau_1}]^*$. Then inversion symmetry indicates that the w coefficients are real. Thus these quartic terms give

$$\begin{aligned} F_4 = A\cos\big[2(\phi_4 - \phi_1)\big] &\sum_{\tau_1\tau_2\tau_3\tau_4}\sum_{\rho_1\rho_2\rho_3\rho_4} r^{(4)}_{\tau_1\rho_1} r^{(4)}_{\tau_2\rho_2} r^{(1)}_{\tau_3\rho_3} \\ &\times\ r^{(1)}_{\tau_4\rho_4} \xi^{(4)}_{\rho_1} \xi^{(4)}_{\rho_2} \xi^{(1)}_{\rho_3} \xi^{(1)}_{\rho_4} \end{aligned} \tag{A14}$$

where the r's are the real-valued transformation coefficients determined in quadratic order. All the quantities in F_4 are real. So F_4 is minimized by either setting $\cos[2(\phi_4 - \phi_1)] = \pm 1$. An explicit calculation for the actual experimentally determined values of the order parameters indicated that the correct choice of sign is the negative sign, and therefore that the two irreps are out of phase with one another. This conclusion agrees with the intuitive argument based on the idea that quartic terms tend to enforce the fixed spin length constraint. When the coordinates of one irrep are maximal, then those of the other irrep should be minimal. Thus, we conclude that $|\sin(\phi_{\mathrm{HTI}} - \phi_{\mathrm{LTI}})| = 1$ in equation (61).

B DO TWO IRREPS INDUCE A THIRD ONE?

When two irreps, $\Gamma_x(q)$ and $\Gamma_y(q)$ are simultaneously present (as happens in the LTI phase), one might ask whether their combination could then induce a third representation, $\Gamma_a(q)$, all of which are assumed to be associated with the selected wave vector q. Since $\Gamma_y(q)\Gamma_y(-q)$ is unity, it is equivalent to ask whether for some k, products like $\Gamma_x(q)^{k-1} \otimes \Gamma_y(-q)^k \otimes \Gamma_a(q)$ or $\Gamma_y(q)^{k-1} \otimes \Gamma_x(-q)^k \otimes \Gamma_a(q)$ transform like unity. (The form of this product is dictated by wave vector conservation. In this connection, we neglect the possible effects of Umklapp terms.) If one of these products satisfies this condition, then the existing order parameters can give rise to a linear field acting on $\Gamma_a(q)$, thereby inducing a nonzero value for this representation. By explicit enumeration of the various cases, one can verify that the condition to induce a third irrep cannot be satisfied. If, hypothetically, there existed a third phase transition in which a third irrep condensed, then the presence of these three irreps would induce the fourth irrep.

Magnetism and Quantum Criticality in Heavy-Fermion Compounds: Interplay with Superconductivity

Oliver Stockert[1], Michael Nicklas[1], Peter Thalmeier[1], Philipp Gegenwart[2] and Frank Steglich[1]

[1] *Max-Planck-Institut für Chemische Physik fester Stoffe, Dresden, Germany*
[2] *Georg-August-Universität Göttingen, Göttingen, Germany*

1 INTRODUCTION

Intermetallic systems with strong electronic correlations continue to be of interest since these systems can serve as model systems to study electron interactions. The strong electron interactions result in a largely enhanced effective mass of the quasiparticles, hence the name heavy-fermion (HF) systems. The electronic interactions can lead to a variety of different ground states: paramagnetic, magnetically ordered, or superconducting. Most ordered systems show antiferromagnetic (AF) order, only a few compounds order ferromagnetically. Especially the interplay between magnetic order and superconductivity (SC) attracts special interest.

Research in the two decades after first observations in $CeAl_3$ in 1975 (Andres, Graebner and Ott, 1975) and following the discovery of HF SC in $CeCu_2Si_2$ in 1979 (Steglich *et al*., 1979), by which it was verified that the low-temperature anomalies found in $CeAl_2$ are indeed due to charge carriers with very large effective mass ($m \approx 1000 m_e$ with m_e being the free electron mass, 'heavy fermions'), was driven by the discovery of new systems and the investigation of their properties. In contrast, during the last decade the research focused mainly on two topics: (i) the interplay between magnetic order and SC, and (ii) the behavior at magnetic instabilities at $T = 0$, that is, at a so-called quantum phase transition (QPT). Interplay between SC and magnetic order is an important issue since in classical superconductors magnetic impurities suppress SC while in HF superconductors the magnetic f electrons are essential and are involved in the superconducting pairing mechanism and form Cooper pairs. In contrast to phonon-mediated SC there seems to be growing evidence that in HF superconductors spin fluctuations play the role as superconducting glue. HF superconductors usually do not show an isotropic superconducting energy gap, but have unusual order parameters with an anisotropic gap and line or point nodes where the gap vanishes. Coexistence and/or competition of both phenomena, magnetism and SC, can also have important implications for the order parameters which might have to be compatible with each other. The appearance of SC is closely related to QPTs. At a

Handbook of Magnetism and Advanced Magnetic Materials. Edited by Helmut Kronmüller and Stuart Parkin. Volume 4: *Novel Materials*. ISBN: 978-0-470-02217-7.

QPT a magnetically ordered phase vanishes as a function of an external parameter, the ordering temperature is suppressed to $T_{N/c} = 0$. In the case of a continuous phase transition tuned to occur at $T = 0$, this $T = 0$ QPT is then called a *quantum critical point* (QCP). In the vicinity of such a magnetic instability unusual low-temperature behavior in thermodynamic and transport properties is observed, called *non-Fermi-liquid behavior*. Sometimes these systems become superconducting close to the QPTs. Since the transition from a nonmagnetic to a magnetically ordered state occurs at $T = 0$, quantum rather than thermal fluctuations become critical at the QPT. It is this nature of these quantum fluctuations that attracts experimentalists as well as theorists.

We focus our review on only a few typical model systems. They are prominent examples for the interplay between SC and magnetic order or for systems close to a QCP. We will present thermodynamic and transport properties and show in addition microscopic measurements like nuclear magnetic/quadrupole resonance, muon spin rotation or neutron scattering.

General reviews about the experimental situation in HF systems can be found in (Grewe and Steglich, 1991; Kuramoto and Kitaoka, 2000; Stewart, 2001) while an overview of theoretical concepts, especially on the interplay between magnetism and SC is given in (Thalmeier *et al*., 2005).

This overview is organized as follows. We first introduce the basic concept of QPTs and QCPs and present a simple microscopic model to describe HF systems (Section 2). We will then move on to the archetypal system $CeCu_2Si_2$ in Section 3. A relatively new class of materials is derived from the classical $CeIn_3$, the Ce115 systems, being close to quantum criticality and exhibiting a rich variety of magnetically ordered phases and SC. They can be described within a conventional picture of QCPs. Then theoretical aspects about different behavior at QPTs are presented. While systems showing a conventional behavior at a QCP sometimes exhibit SC, unconventional behavior seems to exclude the appearance of SC. We restrict ourselves to one important member with unconventional behavior which will be presented in Section 4: $YbRh_2Si_2$. This compound was only discovered a few years ago in contrast to the system $CeCu_{6-x}Au_x$, which has been known for roughly two decades. We end with a short summary and outlook (Section 5).

2 QUANTUM PHASE TRANSITIONS

Many strongly correlated electron (HF) systems, usually intermetallic rare-earth compounds containing mainly cerium (Ce) or ytterbium (Yb), can be tuned continuously from a magnetically ordered to a nonmagnetic ground state by means of an external control parameter such as doping x, hydrostatic pressure p, or magnetic field B. This offers the possibility to induce a $T = 0$ phase transition, a so-called QPT, separating a magnetically ordered state from a nonmagnetic ground state at $T = 0$. Instead of being driven by thermal fluctuations as for finite temperature phase transitions, a magnetic–nonmagnetic transition as a function of the control parameter at absolute zero is driven by quantum fluctuations. If a continuous phase transition is tuned to $T = 0$, we will call this special QPT in the following a QCP. Around the critical value of the control parameter where the magnetic order vanishes, that is, for $T_{N/c} = 0$ at the QCP, these systems no longer behave as Fermi liquids (FLs) like usual metals but exhibit strong deviations from FL behavior in thermodynamic and transport properties at low temperatures, called *non-Fermi-liquid* (NFL) behavior. This NFL behavior is visible for example, in the specific heat showing a specific heat coefficient $\gamma = C/T$ quite often diverging as the logarithm of the temperature, $\gamma = C/T \propto -\ln T$, or an electrical resistivity varying with temperature as $\Delta\rho \propto T^n$, $n < 2$. These T dependences are in marked contrast to the predictions for a Landau–Fermi liquid (LFL) with $\gamma = \text{const}$ or $\Delta\rho = T^2$. The general phase diagram of systems close to a QCP is displayed in Figure 1. Some compounds even become superconducting in the vicinity of the QCP with indications for unconventional SC.

However, the concept of QCPs is not restricted only to magnetic and HF systems but is a more general concept for systems where a second-order phase transition separates an ordered phase from a nonordered one and where the phase transition can be tuned to $T_c = 0$. While for finite temperature phase transitions the critical fluctuations are restricted to a region just around the ordering temperature or a small fraction in reduced temperature given by the energy scale of the transition temperature, such an energy scale does not

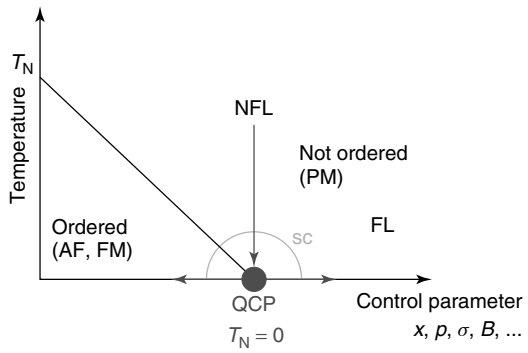

Figure 1. General phase diagram of magnetic systems close to a quantum critical point (QCP) where $T_N \to 0$. At the QCP, unusual temperature dependences in thermodynamic properties are observed (NFL). Sometimes superconductivity (SC) occurs in the vicinity of the QCP.

exist at the QCP and the temperature itself is the scale for spin excitations. These low-energy spin excitations becoming critical at the QCP are discussed as the possible origin for the NFL behavior. Here the nature and dimensionality of these critical fluctuations play a crucial role. Their character may also be responsible for the occurrence of SC in the vicinity of a QCP in some of the systems.

A simple microscopic approach to understand the physics at a QCP is the so-called Doniach model (Doniach, 1977), which starts from the competition between the Kondo effect and the Ruderman–Kittel–Kasuya–Yosida (RKKY) interaction. Here the Kondo effect describes the exchange interaction between a magnetic impurity and conduction electrons. For an AF coupling with coupling constant J the impurity spin is completely screened by conduction electrons at low temperatures, resulting in the formation of a nonmagnetic Kondo-singlet ground state. This Kondo singlet is accompanied by an energy gain of $k_{\mathrm{B}}T_{\mathrm{K}} \propto e^{-1/JN(E_{\mathrm{F}})}$ with T_{K} the Kondo temperature. In HF systems however, independent magnetic impurity spins are no longer present, but they form a periodic array of f electrons (Kondo lattice). This slightly modifies the effective T_{K}. On the other hand, the f electrons can interact with each other through the RKKY interaction. This interaction is mediated via the conduction electrons and favors a magnetically ordered ground state. As for the Kondo effect, the coupling constant between local spin and conduction electrons is important. However, it enters into the energy gain of the system in a different way from that for the Kondo effect. For the RKKY interaction the energy is then lowered by $k_{\mathrm{B}}T_{\mathrm{RKKY}} \propto J^2N(E_{\mathrm{F}})$. The ground state in HF systems is now determined by the competition between Kondo effect and RKKY interaction. If the Kondo interaction dominates, the system orders magnetically. In the case of a stronger Kondo effect, a nonmagnetic ground state is formed and usually FL behavior is observed. Since both interactions depend on the coupling constant J between the local moments and the conduction electrons and J can be changed by hydrostatic pressure, magnetic field, or chemical substitution, the ground state in these systems can be tuned from magnetically ordered to a nonmagnetic ground state. At the QCP where both interactions cancel each other, interactions that are usually weaker can become dominant and for example, SC can occur.

3 CONVENTIONAL QUANTUM CRITICALITY

3.1 $CeCu_2Si_2$

$CeCu_2Si_2$ is one of the prototypical HF compounds exhibiting antiferromagnetism and SC at low temperatures. Both phenomena are observed below 1 K and the interplay can be adjusted sensitively by very small changes in sample composition or by applying hydrostatic pressure. Especially this interplay between both ground states and the vicinity of the compound to a QCP at the disappearance of the AF order attract both experimentalists and theorists.

Although the superconducting properties of $CeCu_2Si_2$ ($T_{\mathrm{c}} \approx 600\,\mathrm{mK}$, $B_{\mathrm{c}2} \approx 1\,\mathrm{T}$) were already discovered more than 25 years ago (Steglich *et al.*, 1979), the nature of the HF SC still remains unclear. The compound forms only in a very narrow range of the ternary phase diagram Ce:Cu:Si around the 1:2:2 composition (Steglich *et al.*, 1996) and crystallizes in the tetragonal $ThCr_2Si_2$ structure (space group $I4/mmm$) with lattice constants $a = 4.1\,\text{Å}$ and $c = 9.9\,\text{Å}$. However, the ground state depends very delicately on the actual composition. Thus, Cu-rich samples exhibit only SC (S phase) and Si-rich ones only show magnetic order (A phase), while in stoichiometric samples (A/S-type) a complex interaction between SC and magnetic order occurs (Steglich, Gegenwart and Geibel, 2001). The origin of the AF order was unraveled only very recently (Stockert *et al.*, 2004). First indications of magnetic order in $CeCu_2Si_2$ were already given in the late 1980s by muon spin rotation (μSR) and nuclear magnetic resonance (NMR) measurements (Nakamura, Kitaoka, Yamada and Asayama, 1988; Uemura *et al.*, 1989). Both techniques found order with static or slowly fluctuating moments of the order of $0.1\mu_{\mathrm{B}}$. Successive neutron-scattering studies failed in detecting any magnetic intensity. Therefore this unusual ordered state, called *A phase*, was thoroughly investigated by thermodynamic and transport properties in the 1990s. The A phase forms below $T \approx 600-800\,\mathrm{mK}$ and upon applying a magnetic field at low temperatures the magnetic A phase is suppressed in a field of $B \approx 7-8\,\mathrm{T}$ giving rise to another ordered phase, called *B phase*, which first detected by ultrasound attenuation measurements (Bruls *et al.*, 1994). All these measurements revealed a complex (B, T) phase diagram (Bruls *et al.*, 1994; Steglich *et al.*, 1996; Gegenwart *et al.*, 1998) with different magnetically ordered and superconducting phases depending on the actual stoichiometry. Electrical resistivity measurements gave first hints about the origin of the A phase in $CeCu_2Si_2$ (Gegenwart *et al.*, 1997, 1998). The relative increase of the resistivity below the ordering temperature along a certain direction, while along another direction a drop in the resistivity was observed, suggested the opening of a gap. Hence, it was speculated that the A phase was a spin-density wave.

For a better understanding of the ground-state properties initial experiments have been performed under hydrostatic pressure (Yuan *et al.*, 2003; Holmes, Jaccard and Miyake, 2004; Lengyel *et al.*, 2006) in addition to experiments on the Ge-substituted system $CeCu_2(Si_{1-x}Ge_x)_2$ (Knebel *et al.*, 1996; Trovarelli *et al.*, 1997; Deppe *et al.*, 2004; Oeschler

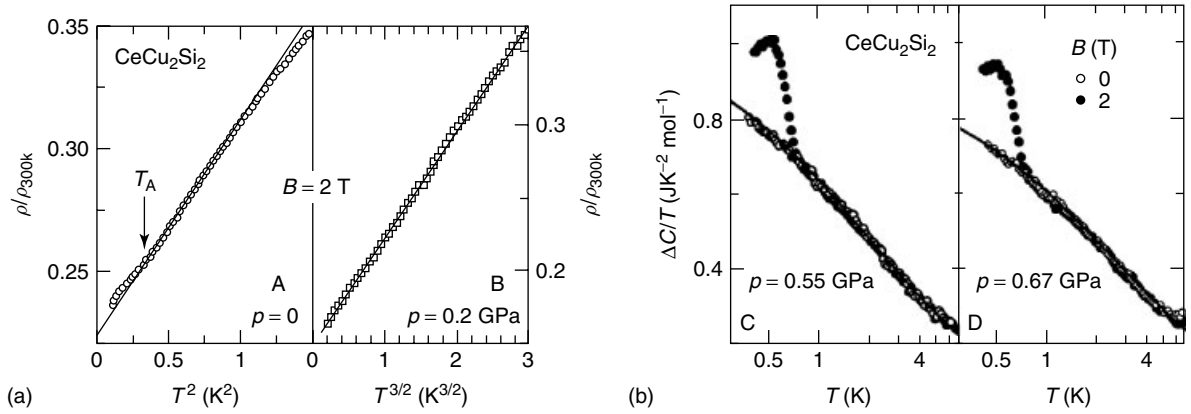

Figure 2. Non-Fermi-liquid behavior of the electrical resisitivity (A, B) and the specific heat (C, D) in pressure-tuned $CeCu_2Si_2$ when applying an overcritical magnetic field to kill superconductivity (Sparn *et al.*, 1998). At the QCP the resistivity varies as $\Delta\rho \propto T^{3/2}$, while the specific heat $\Delta C/T$ follows a $\sqrt{T}$ behavior. Note the relative increase of ρ below the ordering temperature at ambient pressure indicating the opening of a charge gap.

et al., 2005). They suggest that $CeCu_2Si_2$ is located quite close to a QCP at the disappearance of the A phase. While Ge doping expands the lattice and thus stabilizes the magnetic A-phase order (Knebel *et al.*, 1996; Trovarelli *et al.*, 1997), hydrostatic pressure acts in the opposite way, suppressing the A phase (Yuan *et al.*, 2003; Lengyel *et al.*, 2006). A-phase magnetism disappears continuously as a function of pressure and, around the QCP, SC appears in $CeCu_2Si_2$. When applying a magnetic field to kill SC, NFL behavior is observed, for example, in the specific heat or the electrical resistivity (Gegenwart *et al.*, 1998). Thus, the specific heat exhibits a temperature dependence $C/T = \gamma_0 - \alpha\sqrt{T}$ for $T \to 0$ and the electrical resistivity varies with temperature as $\Delta\rho \propto T^{3/2}$ (cf. Figure 2). These results are compatible with a three-dimensional spin-density-wave instability within the Hertz–Millis theory.

However, SC is not only detected in a narrow range around the critical pressure to suppress magnetism (up to a few tenths of GPa), but extends to very high pressures (more than 7 GPa) (cf. Figure 3). This behavior is similar to the related compound $CeCu_2Ge_2$ (Jaccard, Wilhelm, Alami-Yadri and Vargoz, 1999), but in marked contrast to other Ce-based HF systems, like $CePd_2Si_2$ or $CeIn_3$ (Mathur *et al.*, 1998), which can be tuned to a QCP by pressure. In these systems, SC is detected only in a narrow pressure range around the critical pressure, necessary to suppress magnetic order. Pressure experiments on pure $CeCu_2Si_2$ (Holmes, Jaccard and Miyake, 2004) and lightly Ge-doped $CeCu_2(Si_{1-x}Ge_x)_2$ (Yuan *et al.*, 2003) to reduce the mean free path and therefore weaken the SC, established in fact two distinct superconducting regimes at low and at high pressure. In pure $CeCu_2Si_2$ both superconducting regions merge to form one superconducting phase extending from low to high pressure. The superconducting high-pressure regime seems to coincide with a weak first-order valence transition of cerium in $CeCu_2Si_2$. Such a transition has been reported in the related compound $CeCu_2Ge_2$ by X-ray diffractometry (Onodera *et al.*, 2002). For the moderately Ge-doped $CeCu_2Si_2$ single crystals this was concluded from recent resistivity data (Yuan *et al.*, 2006). Since the critical endpoint of this first-order valence-transition phase boundary is very low ($T < 20$ K) for these alloys (Yuan *et al.*, 2006), some sufficiently soft valence fluctuations are likely to exist under the high-pressure superconducting dome where they

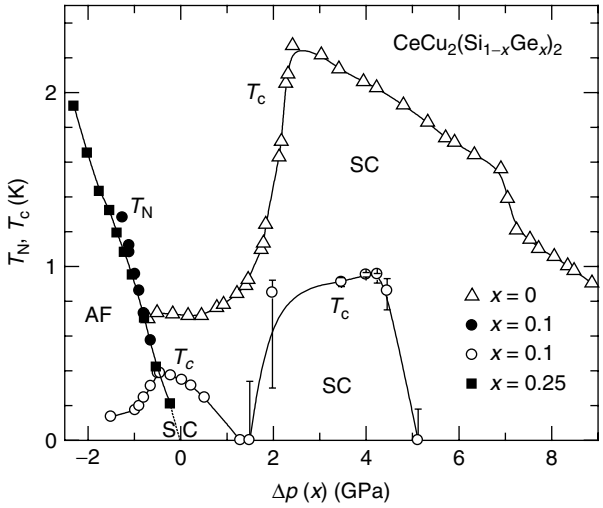

Figure 3. Temperature–pressure phase diagram of $CeCu_2(Si_{1-x}Ge_x)_2$ indicating the pressure dependence of the transitions into the antiferromagnetically ordered state (closed symbols) and the superconducting states (open symbols). The data are plotted as a function of relative pressure $\Delta p = p - p_c$ in a way that the magnetic transition lines for all Ge concentrations coincide. (Reprinted with permission Yuan *et al.*, copyright 2003, AAAS.)

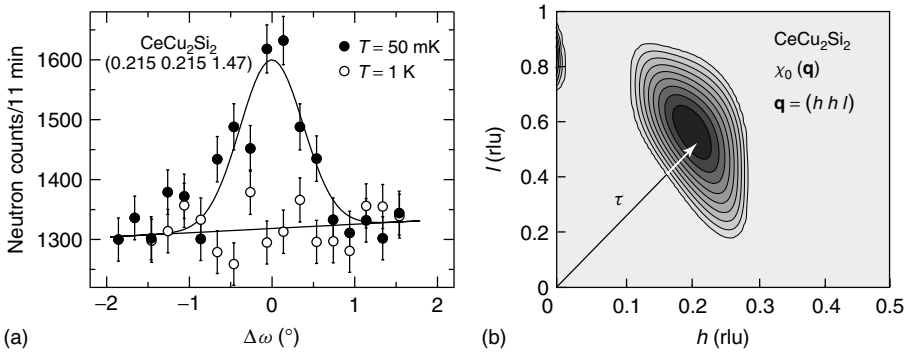

Figure 4. (a) Rocking scan across the position of a magnetic superstructure reflection in magnetically ordered A-type $CeCu_2Si_2$. (b) Comparison of the measured propagation vector with a theoretical intensity map for the wave vector–dependent magnetic susceptibility in $CeCu_2Si_2$. (Reprinted with permission Stockert *et al.*, copyright 2004, American Physical Society.)

may mediate Cooper-pair formation (Miyake, Narikiyo and Onishi, 1999). Therefore, the two distinct superconducting regimes in $CeCu_2Si_2$ may indeed arise owing to different pairing mechanisms, related to fluctuations of the spin density at low pressure and of the charge density at high pressure.

The recent availability of large $CeCu_2Si_2$ single crystals with well-defined physical properties allowed single crystal neutron diffraction to be performed for the first time (Stockert *et al.*, 2004). Incommensurate AF order was found in an A-type single crystal with a propagation vector $\mathbf{Q} = (0.215, 0.215, 0.530)$ at $T = 50\,\mathrm{mK}$ as displayed in Figure 4(a) (Stockert *et al.*, 2004). The magnetic intensity vanishes at $T_\mathrm{N} = 800\,\mathrm{mK}$ in close accordance with thermodynamic measurements and the ordered moment has been estimated to be $m_0 \approx 0.1\,\mu_\mathrm{B}$ assuming a sinusoidal modulation of the magnetic moments lying in the basal plane.

The incommensurate magnetic order is determined by nesting properties of Fermi surface as suggested by renormalized band structure calculation (Zwicknagl and Pulst, 1993; Stockert *et al.*, 2004). The Fermi surface of the heavy quasiparticles ($m^* \approx 500\,m_0$) has been calculated with the renormalized band method (Zwicknagl, 1993) and indicates nesting for the incommensurate wave vector $\mathbf{q} \approx (0.21, 0.21, 0.55)$ (Stockert *et al.*, 2004). Further hints are given by the direct calculation of the wave vector–dependent static susceptibility $\chi(\mathbf{q})$. The maximum of $\chi(\mathbf{q})$ coincides with the propagation vector observed in the neutron experiments as shown in Figure 4(b) (Stockert *et al.*, 2004). Therefore at low temperatures the renormalized Fermi surface is indeed unstable with respect to the formation of a spin-density wave. This observation of a low-moment spin-density wave explains why the pronounced NFL behavior in normal-state $CeCu_2Si_2$ satisfactorily agrees with the predictions of the Hertz–Millis–Moriya theory for three-dimensional critical AF spin fluctuations.

With the knowledge of the A-phase magnetism, A/S-type single crystals have been investigated. These crystals are located closer to the QCP as the Néel temperature is already reduced to $T_\mathrm{N} \approx 700\,\mathrm{mK}$. In elastic neutron-scattering experiments (Stockert *et al.*, 2005; Thalmeier *et al.*, 2005) magnetic intensity has been detected below T_N at the same positions as for pure A-type crystals showing that the incommensurate magnetic order is quite unaffected by slight changes in the stoichiometry. Surprisingly, the magnetic intensity vanishes inside the superconducting state well below $T_\mathrm{c} \approx 550\,\mathrm{mK}$ (cf. Figure 5). Therefore, SC and AF order do not coexist on a microscopic scale. Instead, SC expels magnetism at low temperatures. These findings are confirmed by a μSR measurements on the same A/S-type single crystal (Stockert *et al.*, 2006). The new results are in line with previous μSR and nuclear quadrupole resonance (NQR) experiments

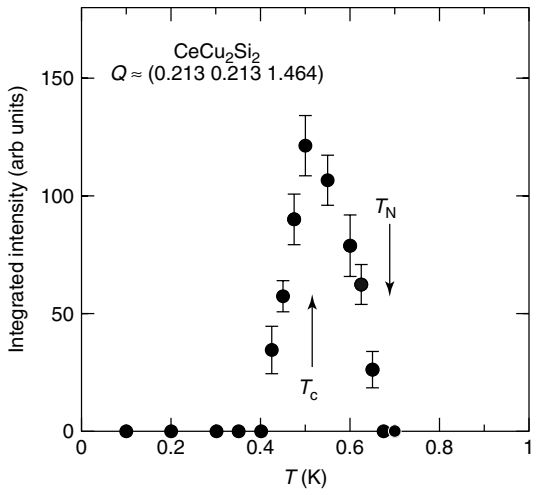

Figure 5. Temperature dependence of the intensity of a magnetic superstructure reflection in A/S-type $CeCu_2Si_2$. (Reprinted with permission Thalmeier *et al.*, copyright 2005, Springer Verlag, Berlin.)

(Feyerherm *et al*., 1997; Ishida *et al*., 1999), which were restricted at that time to polycrystalline samples, but also found phase separation between AF and superconducting phases.

Current studies on $CeCu_2Si_2$ focus on the nature of the superconducting pairing mechanism aiming to detect the charge and/or spin excitation gap and the symmetry of the order parameter in the superconducting state.

3.2 $CeTIn_5$ (T = Co, Rh, Ir)

The discovery of SC in the new class of HF compounds with the general formula $Ce_nT_mIn_{3n+2m}$ (T = Co, Ir, Rh) extended the number of unusual HF systems showing an intensive interplay of magnetism and SC.

This family of materials is composed of alternating n-fold layers of $CeIn_3$ and m-fold layers of TIn_2 crystallizing in the tetragonal $HoCoGa_5$ structure-type (space group $P4/mmm$) (Grin, Yarmolyuk and Gladyshevskii, 1979). The parent compound $CeIn_3$ ($n = \infty$), orders in a commensurate AF structure below $T_N = 10\,K$. Magnetism is suppressed to $T_N = 0\,K$ at a critical pressure of $p_c \approx 2.5\,GPa$, and right in the vicinity of p_c SC is developing below $T_c = 200\,mK$ (Mathur *et al*., 1998). At the critical pressure the low-temperature normal-state resistivity can be described by a power law $\rho = \rho_0 + A'T^{\varepsilon}$, where ρ_0 is the residual resistivity and the exponent $\varepsilon \approx 1.6$ is indicative of NFL behavior (Mathur *et al*., 1998; Knebel *et al*., 2001). The single-layered descendants consisting of $CeIn_3$ layers separated by TIn_2 exhibit a variety of fascinating physical properties caused by the intimate interrelationship of magnetism, SC, and dimensionality. $CeCoIn_5$ and $CeIrIn_5$ are superconducting below $T_c = 2.3\,K$ (Petrovic *et al*., 2001) and $T_c = 0.4\,K$ (Petrovic *et al*., 2001), respectively. $CeCoIn_5$ exhibits the highest T_c among the Ce-based HF superconductors at ambient pressure. $CeRhIn_5$ orders antiferromagnetically below $T_N = 3.8\,K$ (Hegger *et al*., 2000) at atmospheric pressure, and SC develops under hydrostatic pressure ($p > 0.9$ GPa) (Hegger *et al*., 2000; Llobet *et al*., 2004) with a maximum $T_c = 2.12\,K$ at 2.1 GPa, similar to the parent compound $CeIn_3$, but with a maximum T_c being one order of magnitude higher.

We want to start our discussion with the magnetic properties of $CeRhIn_5$. Without the existence of this magnetic representative of the $CeTIn_5$ family the role of magnetism in its nonmagnetic, superconducting compounds Co and Ir homologs would be even more in disguise. $CeRhIn_5$ orders in an incommensurate structure with a propagation vector $(0.5, 0.5, \delta = 0.297)$ (Bao *et al*., 2000, 2001) corresponding to a simple AF structure in the basal plane and a tilting by $\delta = 107^{\circ}$ between the moments in different planes along the c axis. The magnetic moment ($\mu \approx 0.8\,\mu_B$) (Llobet *et al*., 2004) (the originally published value (Bao *et al*., 2000, 2001) was corrected in (Llobet *et al*., 2004)) is only 20% smaller than the full moment obtained from crystal-electric-field (CEF) calculations ($\mu = 0.92\,\mu_B$) not taking into account the reduction of the measured moment by the Kondo effect. The ordered moment in $CeRhIn_5$ is much larger than that, for example, in $CeCu_2Si_2$ ($\mu = 0.1\,\mu_B$) (Stockert *et al*., 2004).

$CeRhIn_5$ has localized 4f electron states which are CEF split into three Kramers doublets $\Gamma_7^1(0)$, $\Gamma_7^2(6.9\,meV)$, and $\Gamma_6(23.6\,meV)$ (Christianson *et al*., 2004). Therefore, the low-temperature properties are determined exclusively by the ground-state doublet. De Haas–van Alphen (dHvA) studies and local density approximation (LDA) calculations have been carried out showing that $CeRhIn_5$ has indeed, as expected for localized 4f electrons, a Fermi surface similar to that of the reference compound $LaRhIn_5$ (Shishido *et al*., 2002; Hall *et al*., 2001a). On the other hand, the low-temperature Fermi surface in $CeCoIn_5$ (Hall *et al*., 2001b; Shishido *et al*., 2002) and $CeIrIn_5$ (Haga *et al*., 2001; Shishido *et al*., 2002) is best described by including the 4f electrons and considering them as itinerant. The layered structure produces an anisotropic electronic structure reflected in the Fermi surface by almost cylindrical shapes. Though these compounds should not be considered as purely two dimensional, their structural (electronic) anisotropy has an essential influence on their ground-state properties.

Applying pressure in $CeRhIn_5$ first leads to a slight increase of the Néel temperature T_N to a maximum value of $T_N \approx 3.9\,K$ at 0.8 GPa, before the magnetic ground state becomes less favorable and T_N drops, typical for a Ce-based magnetically ordered HF compound near its magnetic instability. The staggered magnetic moment decreases little with increasing pressure (Llobet *et al*., 2004; Majumdar *et al*., 2002). Llobet *et al*. (2004) find only a slight enhancement of the discommensuration. No magnetic order is evident at $p = 1.85\,GPa$ and $T = 1.8\,K$ in their data anymore. In contrast, a marked change of the wave vector at 1 GPa is reported by Majumdar *et al*. (2002). Zero resistance and the onset of a diamagnetic response in the susceptibility indicating the development of SC is already observed deep inside the AF phase for $p \gtrsim 0.9$ (Nicklas *et al*., 2004), while clear evidence for *bulk* SC from specific heat experiments inside the AF phase is reported only close to the pressure where T_N meets T_c (Knebel *et al*., 2004). No trace of the Néel transition appears inside the superconducting phase at zero magnetic field for $T_N < T_c$ suggesting that AF order disappears abruptly as a function of pressure. It is remarkable that at about $p_c \approx 2.3\,GPa$ a drastic change of the 4f electron nature from localized to itinerant takes place as evidenced by the disappearance of the dHvA frequencies for the main branches together with those characteristic for

the antiferromagnetism and the appearance of new branches ($p > 2.3$ GPa) (Shishido, Settai, Harima and Ōnuki, 2005). These new branches are qualitatively the same as those in $CeCoIn_5$, consistent with LDA calculation taking the 4f electrons as part of the Fermi surface (Shishido *et al.*, 2002). A magnetic field $B > 2$ T induces a magnetic transition inside the SC state which evolves smoothly from $T_N(p)$ with increasing pressure (Park *et al.*, 2006; Knebel *et al.*, 2006). The temperature, where the line of field-induced transition crosses the superconducting upper critical field in the $H-T$ phase diagram [$T_M(H = H_{c2})$], extrapolates to zero at $p_c \approx 2.25$ GPa at about the pressure where the size of the Fermi surface changes (Shishido, Settai, Harima and Ōnuki, 2005). This might be taken as evidence for a locally critical QCP (Si, Rabello, Ingersent and Smith, 2001). However, dHvA experiments are carried out at a magnetic field of the order of 10 T. At atmospheric pressure, the Kondo temperature is of the order of the Néel temperature ($T_N = 3.8$ K) corresponding to a Kondo field of about $B_K \sim 1$ T (Hegger *et al.*, 2000; Curro *et al.*, 2003). B_K is usually increasing with pressure in Ce-based HF systems and, therefore, it is conceivable that $B_K(p)$ will reach the measuring field of the dHvA experiments close to p_c. Here, it is worth noting that in HF compounds commonly both *local* Kondo and *nonlocal* magnetic (AF or ferromagnetic (FM)) correlations become frozen below $T \approx T_K(B = 0)$ and $B \approx B_K(T = 0)$, respectively (Grewe and Steglich, 1991). Thus for instance, in $CeRu_2Si_2$ (AF correlations) the Kondo temperature and the metamagnetic field show the same pressure-dependent increment (Mignot *et al.*, 1988). A similar observation was recently made for $YbRh_2Si_2$ with dominating FM correlations in wide parts of the $B-T$ phase diagram (cf. Section 4.1) (Tokiwa *et al.*, 2005). It is therefore possible that the measuring field of the dHvA experiments performed on $CeRhIn_5$ under $p \approx p_c$ has the meaning of a metamagnetic field. This would in a natural way explain the observed change of the Fermi surface: for $p < p_c$ the measuring field would be greater than B_K explaining the local character of the 4f electrons, while for $p > p_c$, with further increasing B_K the 4f electrons in dHvA experiments would appear to be part of a larger Fermi surface because of the Kondo screening. Alternatively, the divergence of the cyclotron mass when approaching the critical pressure p_c from either side (Shishido, Settai, Harima and Ōnuki, 2005) may well be taken as evidence for unconventional quantum criticality (cf. Section 4).

Substituting Rh by the isoelectronic Co or Ir, $CeRhIn_5$ slowly looses the AF phase (Pagliuso *et al.*, 2002; Zapf *et al.*, 2001). As a consequence of replacing Rh by Co the unit-cell volume shrinks and one, therefore, expects a suppression of the AF order. For $x \gtrsim 0.70$ in $CeRh_{1-x}Co_xIn_5$ no magnetic order is indeed present anymore (Zapf *et al.*, 2001). Already at a doping level of $x \gtrsim 0.35$, bulk SC occurs coexisting with AF order, and persists up to stochiometric $CeCoIn_5$. Ir doping suppresses T_N in $CeRh_{1-x}Ir_xIn_5$ at concentration $x \approx 0.65$, and an extended range of microscopic coexistence of SC and AF ($0.35 \leq x \leq 0.65$) exists (Pagliuso *et al.*, 2002). The microscopic coexistence was confirmed by susceptibility measurements conducted simultaneously with NQR (Zheng *et al.*, 2004) and μSR (Morris *et al.*, 2003) experiments. However, the SC phase does not represent an ideal dome-shape as, for example, in $CeIn_3$. In contrast to Co substitution, the unit-cell volume increases slightly on Ir-doping showing that volume is not the only relevant control parameter. A cusplike minimum in $T_c(x)$ appears at $x = 0.9$ in (Pagliuso *et al.*, 2001; Pagliuso *et al.*, 2002; Nicklas *et al.*, 2004). Under the application of hydrostatic pressure, this minimum evolves in a region where SC is removed from the $x-T$ phase diagram leaving two distinct superconducting phases, SC1 and SC2 (see Figure 6) (Nicklas *et al.*, 2004). Upon applying pressure, AF order is giving away for SC, while the maximum of T_c is roughly tracking the critical pressure p_c on the Rh-rich side of the phase diagram. At 1.75 GPa, AF order has nearly completely disappeared from the $x-T$ phase diagram and the SC1 phase extends in the whole range from $CeRhIn_5$ up to $x \approx 0.75$. This is taken as a hint to spin-fluctuation-mediated SC, whereas the nature of the SC2 phase in the immediate proximity to $CeIrIn_5$ remains unclear.

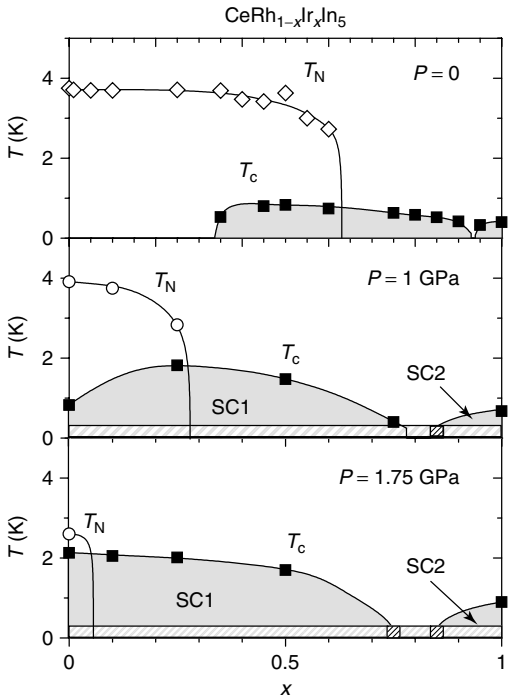

Figure 6. Evolution of the concentration–temperature ($x-T$) phase diagram of $CeRh_{1-x}Ir_xIn_5$ with pressure. (Reprinted with permission Nicklas *et al.*, copyright 2004, American Physical Society.)

$CeIrIn_5$ seems to be far away from any magnetism. No evidence for a magnetic phase transition appears in specific heat, magnetization, or susceptibility data. μSR experiments confirm the absence of any long-range magnetic order down to $T = 20\,\mathrm{mK}$ (Higemoto *et al.*, 2002; Morris *et al.*, 2003). However, strong AF spin fluctuations play an important role, and NQR studies are consistent with $CeIrIn_5$ being in the nearly AF region close to magnetic ordering (Zheng *et al.*, 2001; Kohori *et al.*, 2001). In the normal state, T_1^{-1} does not follow a Korringa law as expected from LFL theory, pointing to the NFL character of $CeIrIn_5$. Zheng *et al.* (2001) explain the unusual temperature dependence of $1/T_1T$ by the existence of anisotropic AF spin fluctuations. Recent NMR data show that hydrostatic pressure rapidly suppresses the AF spin fluctuations but enhances the superconducting transition temperature T_c (Kawasaki *et al.*, 2005). At 2.1 GPa, $T_c = 0.8\,\mathrm{K}$ is twice the value at ambient pressure. It is important to note that SC in $CeIrIn_5$ is robust over a wide pressure range where AF fluctuations are absent (Kawasaki *et al.*, 2005). These results are consistent with pressure studies of the doping series $CeRh_{1-x}Ir_xIn_5$ showing that the SC phase on the Ir-rich side close to $CeIrIn_5$ is disconnected from a second SC phase coexisting with AF in a wide range for higher Rh concentrations (Nicklas *et al.*, 2004). Recently, AF order has been reported in slightly Cd-doped $CeIrIn_5$ (Pham *et al.*, 2006), where In is partly replaced by Cd leading to a lattice contraction. This puts up the question, what provides the glue for the Cooper pairing in $CeIrIn_5$ and the role of AF spin fluctuations. In magnetic fields, LFL behavior occurs between T_c and the crossover temperature T_{LFL} (Capan *et al.*, 2004), suggesting that SC also at zero magnetic field and at ambient pressure develops in the background of a LFL state. With increasing field T_{LFL} is suppressed continuously and can be extrapolated to $T = 0$ at a critical field of $B_c \approx 26\,\mathrm{T}$. Close to this (Kim, Alwood, Kumar and Stewart, 2002) extrapolate the existence of a metamagnetic quantum critical endpoint (QCEP) inferred from (i) specific heat measurements performed at $B \geq 30\,\mathrm{T}$ and $T > 1.4\,\mathrm{K}$ and (ii) from magnetization measurements which reveal a metamagnetic transition around 42 T at 1.3 K (Takeuchi *et al.*, 2001). Detailed studies in the vicinity of this critical field are still missing, and the detailed nature of the QCEP is waiting to be unraveled. The relationship of this QCEP with the *substitution-controlled* QCP in $CeIr(In_{1-x}Cd_x)_5$ and SC in $CeIrIn_5$ is still to be explored.

$CeCoIn_5$ is the most extensively studied compound in this series. As for $CeIrIn_5$, no proof for any long-range magnetic order has yet been reported. The μSR relaxation rate is temperature independent, clearly showing the absence of magnetic order (Higemoto *et al.*, 2002). The resistivity data in the normal state exhibit a linear temperature dependence up to $T = 20\,\mathrm{K}$ (Petrovic *et al.*, 2001). Also, the coefficient of the electronic specific heat shows a logarithmic divergence (Petrovic *et al.*, 2001). The NFL behavior in both the resistivity and the specific heat extending to the lowest temperatures in the normal-state point to the presence of strong AF fluctuations in $CeCoIn_5$ usually explained in a QCP scenario. In addition, NMR and NQR experiments show the existence of strong AF spin fluctuations (Kohori *et al.*, 2001; Kawasaki *et al.*, 2003; Yashima *et al.*, 2004). Substitution studies on $CeRh_{1-x}Co_xIn_5$ substantiate the closeness of magnetic order in $CeCoIn_5$. Similar conclusions can be drawn from the comparison of the pressure–temperature ($p-T$) phase diagram of $CeRhIn_5$ (Hegger *et al.*, 2000; Llobet *et al.*, 2004; Nicklas *et al.*, 2004) and $CeCoIn_5$ (Nicklas *et al.*, 2001; Sidorov *et al.*, 2002): $CeCoIn_5$ can be considered as under an effective pressure of $p_{eff} \approx 1.6\,\mathrm{GPa}$ compared to the AF $CeRhIn_5$ (see Figure 7). This is further supported by a Cd-substitution study where, as in $CeIrIn_5$, In is partly replaced with Cd imposing a small negative chemical pressure inducing AF (Pham *et al.*, 2006). Therefore, $CeCoIn_5$ at atmospheric pressure can be considered situated close to a QCP existing at a small hypothetical negative pressure.

A detailed analysis of specific heat and resistivity data obtained on $CeCoIn_5$ in magnetic fields suggests the presence of a field-induced QCP in immediate proximity to the upper critical field for SC [$B_{c2}(T = 0)$] (Bianchi *et al.*, 2003; Paglione *et al.*, 2003; Ronning *et al.*, 2005). The temperature dependence of the normal-state specific heat and the resistivity taken to the lowest temperatures in fields $B \gtrsim B_{c2}(T = 0)$ exhibit NFL behavior for the magnetic-field orientations, parallel to the c axis (Bianchi *et al.*, 2003; Paglione *et al.*, 2003) and within the basal plane ($B \parallel ab$) (Ronning *et al.*, 2005). With further increasing field, crossovers in $C(T)/T$ from

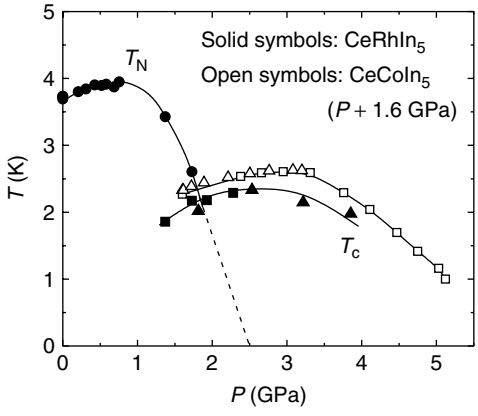

Figure 7. Pressure–temperature ($p-T$) phase diagram of $CeRhIn_5$ (solid symbols) and $CeCoIn_5$ (open symbols). $CeRhIn_5$: T_N (●) from (Llobet *et al.*, 2004) and T_c from (Llobet *et al.*, 2004) (■) and (Muramatsu *et al.*, 2001) (▲). ($CeCoIn_5$ data shifted by $\Delta p = 1.6\,\mathrm{GPa}$, T_c taken from Nicklas *et al.*, 2001 (△) and Sidorov *et al.*, 2002 (□).)

$-\ln T$ to constant behavior and in $\rho(T)$ from a linear to a quadratic temperature dependence indicate the establishment of a field-induced LFL state. An analysis of the data leads to the conclusion that an AF QCP exists close to $B_{c2}(T=0)$ for the field applied within the basal plane (Bianchi *et al.*, 2003; Paglione *et al.*, 2003) as well as in the c direction (Ronning *et al.*, 2005). This holds true despite a factor of 2.4 difference between $B_{c2}(T=0)$ for $B \parallel c$ and $B \parallel ab$. However, the existence of AF ordering at $B \lesssim B_{c2}(T=0)$ has yet to be demonstrated. The normal-state thermal-expansion coefficient $\alpha(T)$ measured at $B \gtrsim B_{c2}(T=0)$ is actually independent of temperature, $300\,\mathrm{mK} < T < 6\,\mathrm{K}$ (Donath *et al.*, 2007) (see Figure 8). These results as well as the logarithmic decrease of $C(T)/T$ (Bianchi *et al.*, 2003) and the linear T dependence of the electrical resistivity (Petrovic *et al.*, 2001) are compatible with 2D quantum critical fluctuations within the Hertz–Millis theory. Below $T^* = 300\,\mathrm{mK}$ down to 100 mK $\alpha(T)$ follows a $T^{1/2}$ dependence (Donath *et al.*, 2007), predicted for 3D quantum critical fluctuations within this itinerant theory.

In conclusion, the $CeTIn_5$ compounds are located close to QCPs, exhibit SC around the QCP, and can be described within an itinerant spin-density-wave scenario by the Hertz–Millis theory.

3.3 Theoretical concepts

The idea that tuning of a control parameter may change the magnetic state of an insulator or metal at zero temperature is indeed a very old one. The classical Stoner–Wolfarth theory of itinerant ferromagnetism (Stoner, 1938) identifies this control parameter as $x = IN(E_F)$, where I is the exchange integral of itinerant conduction electrons and $N(E_F)$ the conduction-electron density of states (DOS). For $x > x_c = 1$ a spontaneous FM moment and exchange splitting of conduction bands sets in. For x only marginally above the FM QCP $x_c = 1$ one therefore has only weak ferromagnetism (WFM) and anomalous thermodynamic and transport behavior due to paramagnon excitations (Berk and Schrieffer, 1966; Doniach and Engelsberg, 1966) was observed. The first theory to address such quantum critical phenomena were Moriya's self-consistent renormalization (SCR) theory (Moriya and Kawabata, 1973a,b; Moriya, 1985) for the WFM and the theory by Hertz (1976) on which much of the later developments are based. An alternative scenario describes lanthanide or actinide intermetallics with localized f-electron states showing a singlet–singlet CEF splitting Δ (e.g., Pr compounds) and effective RKKY exchange $J(\mathbf{Q})$ where a transition from the nonmagnetic singlet ground state to an induced moment magnetic state with modulation vector $\mathbf{Q}$ may occur. This happens if the control parameter $x = \alpha^2 J(\mathbf{Q})^2/2\Delta$ is larger than the critical $x_c = 1$ (Jensen and Mackintosh, 1991). The induced moment scenario is very similar to the Bose–Einstein condensation (BEC) picture for the field-induced AF transition below a critical field in some quasi-one-dimensional spin chain compounds (Rüegg *et al.*, 2003).

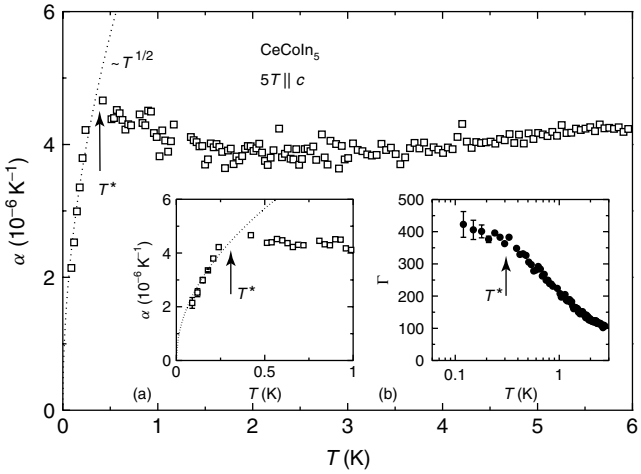

Figure 8. Temperature dependence of the linear thermal-expansion coefficient of $CeCoIn_5$ at $B = 5\,\mathrm{T}$ ($B \parallel$ c). Dotted line and arrow indicate $\alpha \propto \sqrt{T}$ and crossover temperature $T^\star$, respectively. Inset (a) enlarges low-temperature regime. Inset (b) displays temperature dependence of Grüneisen parameter $\Gamma = V_m/\kappa_T \times \alpha/C$ using $V_m = 9.57 \times 10^{-5}\,\mathrm{m^3\,mol^{-1}}$ and $\kappa_T = (3.43 \pm 0.16) \times 10^{-3}\,\mathrm{GPa^{-1}}$ (Kumar, Cornelius and Sarrao, 2004). (From Donath *et al.*, 2007.)

In this section we focus exclusively on quantum critical phenomena in HF compounds. First we discuss the basics of an empirical scaling ansatz based on naive ideas of universality and then discuss a phenomenological Gaussian type spin-fluctuation model for the nearly AF FL. Finally we briefly mention the implications of impurity effects.

The families of Ce-HF compounds discussed before show that a magnetically ordered, SDW phase may evolve continuously out of a disordered LFL phase by applying hydrostatic pressure, by varying chemical pressure via doping, or by varying an applied magnetic field. At zero temperature, pressure (or field) may be considered as control parameter of a QPT between LFL and SDW phases which meet at a QCP at the critical pressure p_c (or critical field B_c) where the total energies of the two phases become equal (Continentino, 2001; Sachdev, 1999). The notion of a QPT implies that the total energy is indeed dominated by the quantum fluctuations of the order-parameter field, the effective phase-space dimensionality is then $d_{\mathrm{eff}} = d + z$ rather than just the spatial dimensionality d because at the QCP with $T_N = 0$ quantum fluctuations develop long-range correlations in both space and time. Here z is the dynamic exponent which characterizes the rescaling of energies of quantum fluctuations with system size ($\tau \propto \xi^z$). On the other hand for a phase transition

at finite $T_N > 0$ the coherence of quantum fluctuations is destroyed by thermal fluctuations for times longer than the timescale $\tau_T = \hbar/k_B T_N$ and hence classical phase transitions are driven by thermal fluctuations of the order parameter in real space with dimension d. As a consequence right along the quantum critical line ($r = 0$) in Figure 9 anomalous NFL temperature dependence of physical quantities like $\chi(T)$, $C(T)/T$, and $\rho(T)$ emerges. Its origin and theoretical description has been the subject of much controversy. Here we briefly outline the most important predictions of those frequently applied models which treat QPT as classical ones in higher dimensions, that is, scaling theory and theories of critical spin fluctuations including disorder effects. Finally concepts of so-called local criticality are mentioned.

3.3.1 Scaling theories for the quantum critical point

A Kondo impurity in a metallic host shows all the signatures of a local LFL state (Hewson, 1993) at temperatures $T \ll T^*$, notably a scaling of the free-energy density with T/T^*. This idea has been successfully extended to the LFL phase of HF and mixed valence compounds in a phenomenological scaling ansatz (Takke *et al.*, 1981; Thalmeier and Fulde, 1986) to explain observed relations between quantities like specific heat, thermal expansion, magnetostriction, and others. It is natural to apply these ideas to the vicinity of the QCP also, where the characteristic energies $T^*(p)$ and $T_c(p)$ themselves depend on the distance r to the QCP which then appears as a further scaling variable. The associated correlation length, ξ, and timescales of quantum fluctuations, τ, diverge on approaching the phase transition. Their critical exponents are universal, depending only on dimension and the degrees of freedom of the order parameter. Defining

$$r = \frac{X - X_c}{X_c}, \qquad t = \frac{T - T_c}{T_c} \qquad (X = p \text{ or } H) \quad (1)$$

where t, r measure the distance to the transition temperature T_c and critical control parameter X_c respectively. On approaching the QCP ($T = 0$, $r = 0$) the correlation length, fluctuation time, and free-energy scale as

$$\xi \sim |r|^{-\nu}, \quad \tau \sim |r|^{-\nu z}, \quad f \sim |r|^{2-\alpha} \tilde{f}\left(\frac{T}{T^*}, \frac{H}{H^*}\right) \quad (2)$$

Here H^* has the meaning of 'metamagnetic' field scale, for fields $H \gg H^*$ the HF state is destroyed by breaking the Kondo-singlet state. For QPT the hyperscaling relation, which relates critical exponents to the effective dimension, is given by

$$2 - \alpha = \nu d_{\text{eff}}, \quad d_{\text{eff}} = d + z \quad (3)$$

In the case of the Gaussian fixed point appropriate for $d_{\text{eff}} > 4$ one has $\nu = \frac{1}{2}$. In the free energy of equation (2), which is a generalization of the one used in (Takke *et al.*, 1981; Thalmeier and Fulde, 1986), the characteristic temperature, T^*, and metamagnetic field, H^*, have scaling relations

$$T^* \sim |r|^{\nu z}, \qquad H^* \sim |r|^{\phi_h} \quad (4)$$

In the magnetically ordered regime T^* has to be replaced by the magnetic transition temperature which scales as $T_N \sim |r|^{\psi}$ where ψ is the shift exponent. Below the upper critical dimension $d_{\text{eff}} = 4$ one has $\psi = \nu z$, that is, $T_N(r)$ and $T^*(r)$ scale symmetrically around the QCP (Figure 9), however, for $d_{\text{eff}} > 4$ in general one has $\psi \neq \nu z$. This is known as *breakdown of hyperscaling*. Within a generalized Landau–Ginzburg–Wilson approach this may be understood as the effect of a dangerously irrelevant quartic interaction u (equation (6)) which, although it scales to zero for $d_{\text{eff}} > 4$, nevertheless changes the scaling behavior at finite T leading to a modified shift exponent $\psi = z/(d_{\text{eff}} - 2)$ for $d_{\text{eff}} > 4$. The zero-temperature critical exponent α in equation (3) satisfies the scaling relation $\alpha + 2\beta + \gamma = 2$ while ϕ_h is independent.

From the experimental view the most interesting aspect is the temperature dependence of physical properties at the QCP ($r = 0$) in the NFL regime. Very useful quantities are specific heat $C = (T/V)(\partial S/\partial T)_p$ and thermal expansion $\alpha = (1/V)(\partial V/\partial T)_p$ (Küchler *et al.*, 2003; Zhu, Garst, Rosch and Si, 2003). At the QCP ($r = 0$) they scale with

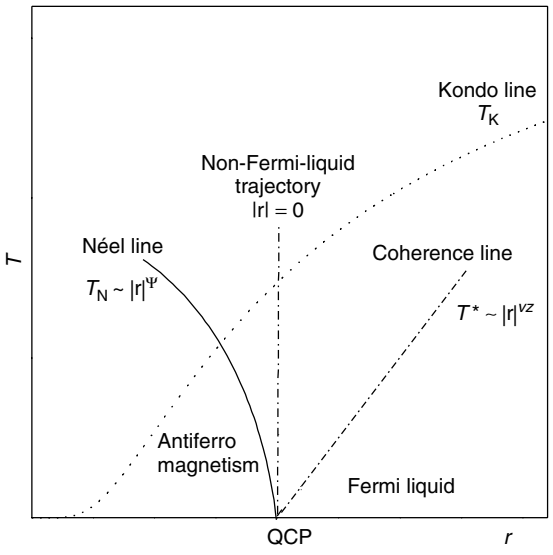

Figure 9. Schematic phase diagram for Kondo compounds with a QCP separating AF (left) and LFL (right) phases. Scaling of the characteristic temperatures is indicated (Continentino, 2004b).

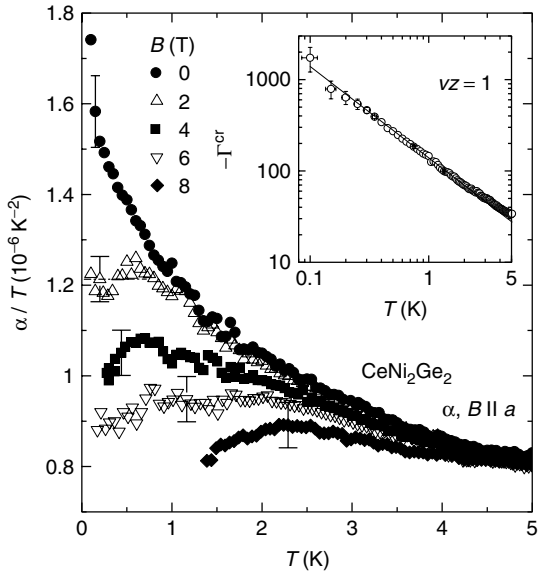

Figure 10. Thermal expansion showing the suppression of NFL behavior as a function of the field. The inset shows that for $B = 0$, the critical contribution to the Grüneisen ratio Γ of $CeNi_2Ge_2$ scales as $\Gamma \sim 1/T^{\nu z}$ with $\nu z = 1$. After equation (5), this means (assuming $z = 2$ for AF SDW) a mean-field correlation length exponent $\nu = 1/2$ which is in agreement with $d_{\text{eff}} = d + z = 5$ for the effective dimension. (Reprinted with permission Küchler *et al.*, copyright 2003, American Physical Society.)

temperature as

$$C(T) \sim T^{d/z}, \quad \alpha(T) \sim T^{(d-\frac{1}{\nu})/z} \quad \text{and}$$
$$\Gamma = \frac{\alpha}{C} \sim T^{-\frac{1}{\nu z}} \tag{5}$$

This means that the temperature dependence of the critical 'Grüneisen ratio' $\Gamma(r = 0)$ is controlled by the exponent which directly determines the timescale of quantum fluctuations (equation 2). Using this important relation a consistent explanation of experiments in the NFL compound $CeNi_2Ge_2$ can indeed be given (Figure 10). Tables of the scaling behavior of the quantities in equation (5) for various d, z have been given in (Küchler *et al.*, 2003).

The exponent νz at the same time determines the pressure scaling (equation 4) of the characteristic temperature T^* on the nonmagnetic side of the QCP. On the other hand the pressure scaling exponent of the characteristic field H^* is an independent quantity within the scaling ansatz. Experimentally it has been investigated in detail for $CeRu_2Si_2$, which has a metamagnetic field scale $H^*(p = 0) = 7.8\,\text{T}$ ($\mathbf{H} \parallel c$). It was found that empirically $\phi_h = 2 - \alpha = \nu z$ is fulfilled. According to the free energy in equation (2) this implies with $m = (\partial f/\partial H)$ that $m(H^*) =$ const independent of pressure. This was indeed found experimentally (Lacerda *et al.*, 1989). The empirical relation $2 - \alpha = \nu z$ may be interpreted as hyperscaling with dimension $d = 0$ according to equation (3). The empirical validity of such a relation points to a dimensional crossover as function of pressure close to the QCP which is caused by the different divergence of spatial and temporal correlations (Continentino, 2004a).

3.3.2 Nearly antiferromagnetic Fermi liquid

The quantum critical behavior in the nearly AF FL has been studied within two closely related approaches. Firstly the SCR theory of WFM may be extended to the weakly AF case often observed in HF compounds (Moriya and Takimoto, 1995). It starts with a parameterized phenomenological ansatz for the dynamical conduction-electron susceptibility which is expanded around the AF wave vector $\mathbf{Q}$. The moment size and spin-fluctuation spectrum is then self-consistently determined via sum rule requirements as function of microscopic model parameters and temperature. This approach has the advantage of keeping the connection to the original microscopic degrees of freedom and being also applicable away from the QCP.

For understanding only the scaling behavior close to the QCP (for $r > 0$, i.e., on the nonmagnetic side) one may start from an even more phenomenological model based on a Landau–Ginzburg–Wilson functional that contains only the spatial and temporal fluctuations $\Phi(\mathbf{q}, \omega)$ of the incipient magnetic order parameter treated within an renormalization group (RNG) approach. At this stage the fermionic degrees of freedom have already been integrated out and the frequency dependence of the Gaussian (quadratic) term of the action and the strength of the quartic interaction term of fluctuations are determined. This elimination is possible only when the Fermi surface has no nesting features for the $\mathbf{Q}$-vector of incipient magnetic order. In uranium-based HF systems this is probably the case since $\mathbf{Q}$ is mostly that of commensurate AF unrelated to nesting vectors. However for the $CeCu_2(Si_{1-x}Ge_x)_2$ series the magnetism is clearly related to nesting properties and the model described in the subsequent text may not be applicable. It was first proposed by Hertz (1976) for QPTs and extended later (Millis, 1993). The effective action functional is given by

$$S[\phi] = \sum_{\mathbf{q}, i\omega_n} (r + q^2 + \frac{|\omega_n|}{\Gamma_q}) |\Phi_{\mathbf{q}, i\omega_n}|^2$$
$$+ u \int_0^\beta d\tau \int d^d\mathbf{r} |\Phi(\mathbf{r}, \tau)|^4 \tag{6}$$
$$\text{with} \quad \Gamma_{\mathbf{q}} = \Gamma_0 q^{z-2} \tag{7}$$

An essential ingredient of the theory is the assumption of overdamped order-parameter fluctuations in the AF case which means $z = 2$ as opposed to quasi-propagating fluctuation modes in the FM case ($z = 3$) which are protected by conservation laws. The dominant mechanism is Landau damping of fluctuations via excitation of electron-hole pairs. Solution of renormalization group equations for the preceding model shows that the quartic interaction term scales with $u'/u = b^{4-(d+z)}$ ($b = L/L'$). This means that for $d_{\text{eff}} > 4$ the low-temperature behavior is determined by a Gaussian fixed point with exponent $\nu = \frac{1}{2}$ leading to ($H = 0$) scaling relations for free energy, specific heat, and so on, as described before within the scaling ansatz whose foundation becomes now clear.

It was tacitly assumed in the preceding text that the tuning to the QCP happens via application of hydrostatic or chemical pressure, that is, without breaking spatial or other symmetries. This raises the question what happens when the QCP is reached via magnetic-field tuning (Fischer and Rosch, 2004). Because the field introduces anisotropy and breaks time reversal symmetry, a different nonuniversal scaling behavior may result. It is caused by precession terms present for nonzero field that modify the dynamics of the order-parameter fluctuations and compete with the Landau damping. The relative importance of the two effects has been parameterized in (Fischer and Rosch, 2004) and the resulting nonuniversal quantum critical scaling has been studied for the thermodynamic coefficients. One interesting result of this analysis is that at the QCP ($H = H_c$) the temperature scaling of the uniform susceptibility is given by

$$\frac{1}{T}[\chi(T) - \chi(0)] \sim \xi(T) \tag{8}$$

which would be a direct experimental method to extract the (temperature) scaling exponent of the correlation length in the quantum critical regime.

3.3.3 *Impurity effects on quantum critical behavior*

Resistivity measurements are a versatile method to investigate the vicinity of a QCP. Theoretically this poses the inverse problem compared to thermodynamics. One has to eliminate the order-parameter fluctuations and study their effect on the quasiparticle scattering rate. At the same time the ordinary impurity scattering and the interference of both mechanisms has to be included. Naturally this leads to nonuniversal behavior of $\rho(T)$ above the QCP and a wide range of temperature exponents has indeed been observed. Using a phenomenological ansatz for the spin-fluctuation propagator, this problem may be treated with a standard Boltzmann equation approach (Rosch, 1999; Rosch, 2000) where the total quasiparticle scattering probability is given by

$$P(\mathbf{k}, \mathbf{k}') = g_i^2 \delta(\epsilon_{\mathbf{k}} - \epsilon_{\mathbf{k}'}) + \frac{2g_s^2}{\Gamma} n(\epsilon_{\mathbf{k}} - \epsilon_{\mathbf{k}'}) \text{Im}\chi(\epsilon_{\mathbf{k}} - \epsilon_{\mathbf{k}'}) \tag{9}$$

where g_i and g_S denote the strength of scattering by impurities or fluctuations respectively, their dimensionless ratio is defined by $x = \pi g_i^2 / 2g_S^2$. Furthermore $n(\epsilon_{\mathbf{k}} - \epsilon_{\mathbf{k}'})$ is the Bose function and $\epsilon_{\mathbf{k}}$ the quasiparticle energies. The ansatz for the order-parameter fluctuation spectrum is defined by

$$\chi_{\mathbf{q}}(\omega) \simeq \frac{1}{1/(q_0\xi)^2 + (\mathbf{q} \pm \mathbf{Q})^2/q_0^2 - i\omega/\Gamma};$$
$$1/(q_0\xi)^2 = r + c\left(\frac{T}{\Gamma}\right)^{\frac{3}{2}} \tag{10}$$

where the parameters q_0, Γ denote characteristic momentum and energy scales of fluctuations which are related via the second equation in the preceding text. The results for the scaled resistivity as a function of the reduced temperature $T/\Gamma x$ are shown in Figure 11 for various ratios of the two scattering strengths. In the pure limit $x \ll 1$ the scattering is dominated by exchange of spin fluctuations with momentum $\mathbf{Q}$, this affects only quasiparticles in the 'hot lines' of the Fermi surface (FS) shown in Figure 11(inset). In the dirty limit $x \gg 1$ where impurity scattering dominates, all quasiparticles are affected equally. For $x \simeq 1$ the two mechanisms interfere. As a consequence, the exponent α of the resistivity $\Delta\rho(T) \sim T^{\alpha}$ is nonuniversal and depends on x. As seen in Figure 11 it varies between $\alpha \sim 1$ in the pure limit and $\alpha \sim 3/2$ in the dirty limit. This is indeed the range of observed exponents for Ce-compounds near the QCP.

In the scenario of the previous sections the scattering by spin fluctuations is localized in $\mathbf{k}$ space, only quasiparticles on hot lines are affected. This is due to the construction of the model where it is assumed that the wave vector $\mathbf{Q}$ of critical fluctuations is in no way related to the FS geometry. Therefore only 'hot lines' but no finite 'nested' areas in $\mathbf{k}$-space are involved in the scattering. For this reason the QCP anomalies of specific heat and resistivity in the model discussed in the preceding text are not strong enough to explain experimental results in compounds like $YbRh_2Si_2$ and $CeCu_{6-x}Au_x$. An alternative approach of 'local quantum criticality' where all electrons on the FS develop singular scattering by construction has been proposed in (Si, Rabello, Ingersent and Smith, 2001).

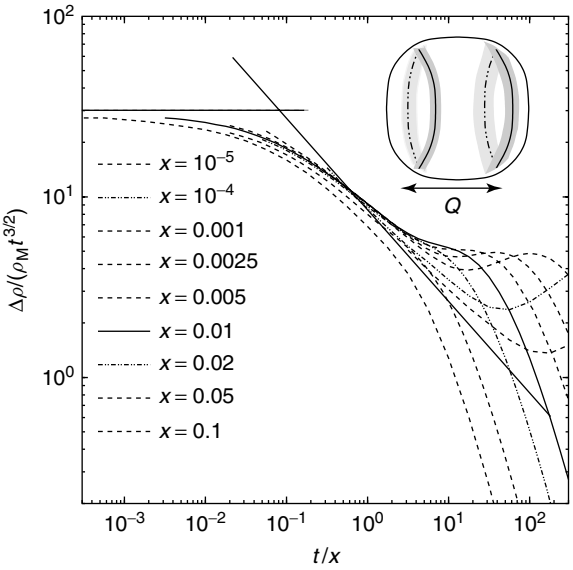

Figure 11. Temperature ($t/x = T/\Gamma x$) dependence of the scaled resistivity $\Delta\rho(t/x)/t^{3/2}$ at the QCP ($r = 0$, $d = 3$) for various scattering ratios x. Straight solid lines show $\Delta\rho \sim t^{3/2}$ for $t \ll x$ and $\Delta\rho \sim t$ for $x \ll t \ll \sqrt{T}$. Inset shows hot lines on the FS with strong quasiparticle scattering by spin fluctuations with momentum **Q**.

4 UNCONVENTIONAL QUANTUM CRITICALITY IN HEAVY-FERMION SYSTEMS

Quantum criticality in f-electron-based heavy fermion systems arises from the competition of the on-site Kondo effect with intersite RKKY exchange interaction as already stated earlier. Whereas the Kondo interaction leads to a screening of the local moments resulting in a paramagnetic ground state with itinerant f electrons, the indirect exchange coupling (RKKY interaction) can mediate long-range ordering between the local moments. By variation of the f-conduction-electron hybridization, these systems can be tuned continuously from the nonmagnetic HF state through a magnetic QCP into a long-range magnetically ordered state. The important question arises whether the heavy quasiparticles retain their itinerant character and form a spin-density wave at the QCP as for $CeCu_2Si_2$ or $CeTIn_5$ or, alternatively, decompose due to the destruction of the Kondo screening (Coleman, Pépin, Si and Ramazashvili, 2001). The first approach to capture the breakdown of the lattice Kondo effect due to quantum critical fluctuations employs an extension of the dynamical mean-field theory (DMFT) and has been worked out by Si *et al.* (2001). On the basis of the idea that the breakdown of the Kondo screening is a local phenomenon, that is, it affects each spin on the Kondo lattice independently, a 'locally critical' QCP scenario, implying Kondo-singlet destruction (Si, Rabello, Ingersent and Smith, 2001) and an electron fractionalization (Coleman, Pépin, Si and Ramazashvili, 2001; Pépin, 2005), has been proposed. An alternative proposal concerns fractionalized FLs (Senthil, Sachdev and Vojta, 2003, 2005). Details on such unconventional scenarios can be found in **Heavy Fermions: Electrons at the Edge of Magnetism, Volume 1**.

4.1 $YbRh_2Si_2$

The tetragonal $YbRh_2S_2$ has recently attracted much interest as a prototype for a clean HF compound located very close to a magnetic QCP (Trovarelli *et al.*, 2000). The low-temperature properties are determined by the CEF-derived doublet ground state which is well separated from the excited levels (Stockert *et al.*, 2006). The analysis of the magnetic entropy reveals a single-ion Kondo scale of 25 K for this lowest lying doublet (with effective spin $\frac{1}{2}$). Upon cooling to below T_K, the electronic specific heat coefficient $C_{el}(T)/T$ displayed in Figure 12(a), shows a pronounced increase which can be described by a $-\ln T$ dependence between 0.3 and 10 K. This is followed by a steep upturn which ends in a sharp phase transition at $T_N = 70$ mK (Custers *et al.*, 2003b). Magnetic measurements have proved the AF nature of this transition (Trovarelli *et al.*, 2000; Gegenwart *et al.*, 2002).

The electrical resistivity of $YbRh_2Si_2$ follows a quasilinear temperature dependence from 10 K down to T_N, below

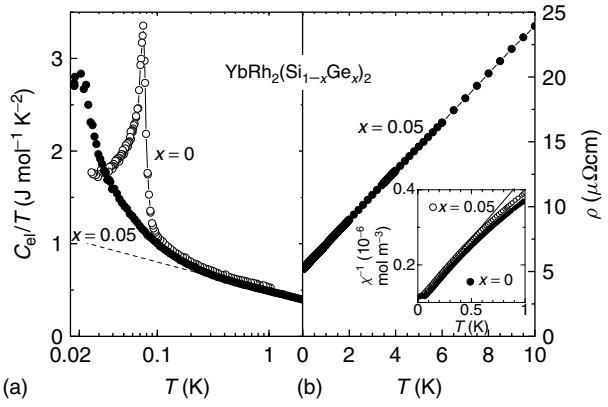

Figure 12. (a) Electronic specific heat of $YbRh_2(Si_{1-x}Ge_x)_2$ as C_{el}/T versus T (on a logarithmic scale) for $x = 0$ and $x = 0.05$ (Custers *et al.*, 2003b). C_{el} denotes the specific heat after subtraction of the nuclear and phonon contributions. (b) Electrical resistivity of $YbRh_2(Si_{0.95}Ge_{0.05})_2$ as ρ versus T (Custers *et al.*, 2003a). The inset displays the inverse susceptibility χ^{-1} versus T for $x = 0$ and $x = 0.05$. The dotted line indicates Curie–Weiss behavior $\chi^{-1} \sim (T - \Theta)$ with $\Theta - 0.3$ K. (Reprinted with permission Custers *et al.*, copyright 2003, Nature Publishing Group & Custers *et al.*, copyright 2003, IOP.)

which a sharp decrease, independent of the current direction, is observed (Gegenwart *et al.*, 2002). The AF order is very weak; muon-spin-rotation experiments have revealed an ordered moment of $2 \times 10^{-3}\,\mu_B$ (Ishida *et al.*, 2003) in accordance with the tiny entropy gain at T_N. The weakness of the AF order is also evidenced by the small critical magnetic field of 0.06 T in the easy tetragonal plane and 0.7 T along the magnetic hard direction parallel to the c axis (Gegenwart *et al.*, 2002).

Hydrostatic pressure causes an increase of T_N as expected in the case of Yb systems for which the ionic size of the magnetic Yb^{3+} configuration is smaller than that of the nonmagnetic Yb^{2+} one. Extrapolating $T_N(p)$ toward zero temperature reveals a small negative critical pressure of −0.3 GPa (Mederle *et al.*, 2002). Thus, a volume expansion induced by the partial substitution of Si with the larger but isoelectronic Ge tunes the system closer to the zero-field QCP. For a single crystal with a nominal composition $YbRh_2(Si_{0.95}Ge_{0.05})_2$, the Néel temperature is suppressed to 20 mK (cf. Figure 12a), and the electrical resistivity follows a linear temperature dependence down to lowest temperatures (Figure 12b) (Custers *et al.*, 2003b). Correspondingly, the critical magnetic field H_c within the easy plane has been reduced to about 0.025 T. At $H = H_c$ and below $T \approx 0.3$ K, the electronic specific heat coefficient follows a power-law divergence $C_{el}(T)/T \sim T^{-1/3}$. This behavior is incompatible with a SDW-type QCP, which at most (i.e., in the case of 2D critical fluctuations) could result in a logarithmic divergence (Millis, 1993; Moriya and Takimoto, 1995). The application of magnetic fields $H > H_c$ results in an LFL ground state which allows to determine the Sommerfeld coefficient $\gamma_0(H)$, Pauli susceptibility $\chi_0(H)$, as well as $A(H)$, which denotes the T^2 coefficient of the electrical resistivity contribution $\Delta\rho = AT^2$. All these properties have been studied systematically starting close to H_c up to very large fields (Custers *et al.*, 2003b; Gegenwart *et al.*, 2005). Figure 13(a) displays the evolution of the Sommerfeld coefficient as a function of the distance from the QCP, $b = B - B_c$. Its power-law dependence proves the divergence of the heavy quasiparticle mass at the QCP in this system.

As outlined before, the Grüneisen ratio, $\Gamma(T) \sim \beta(T)/C(T)$, of thermal expansion, $\beta(T)$, to specific heat, $C(T)$, is a most sensitive thermodynamic probe of quantum criticality as it has to diverge in the approach of any (pressure sensitive) QCP. The critical exponent ϵ in the divergence $\Gamma(T) \sim 1/T^{\epsilon}$ is given by $\epsilon = 1/\nu z$ (Zhu, Garst, Rosch and Si, 2003). Here ν and z are the related critical exponents for the correlation length and correlation time, respectively. For a three-dimensional (3D) AF QCP (in the 2D case, logarithmic corrections are present), the itinerant theory predicts $\nu = 1/2$ and $z = 2$ yielding $\epsilon = 1$. This was, in fact, observed for $CeNi_2Ge_2$ (Küchler *et al.*, 2003). For

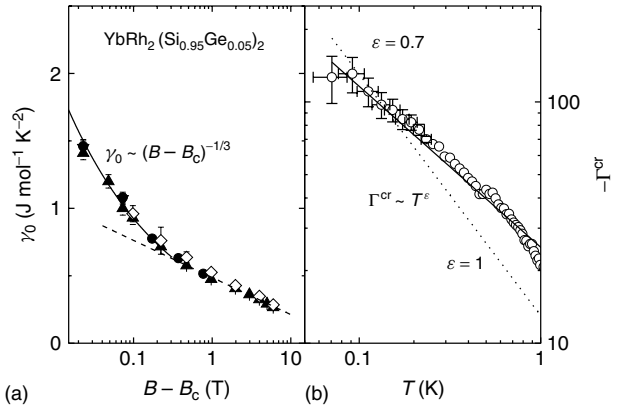

Figure 13. Magnetic-field dependence of the Sommerfeld coefficient $\gamma_0 = C_{el}(T \longrightarrow 0)/T$ of $YbRh_2(Si_{0.95}Ge_{0.05})_2$ as γ_0 versus $B - B_c$ (applied within the easy magnetic plane) with $B_c = 0.027$ T (a). Dashed and solid lines indicate logarithmic and power-law divergences, respectively (Custers *et al.*, 2003b). (b): Double-logarithmic plot of the critical Grüneisen ratio $\Gamma^{cr} = V_m/\kappa_T \cdot \beta^{cr}/C^{cr}$. Here V_m and κ_T denote the molar volume and isothermal compressibility, respectively. A normal contribution to thermal expansion, β, has been subtracted from the raw data, to determine β^{cr} (Küchler *et al.*, 2003). The critical contribution to the specific heat is obtained by subtracting nuclear and phonon contributions from the raw data. The solid and dotted lines represent $\Gamma^{cr} \sim T^{-\epsilon}$ with $\epsilon = 0.7$ and 1, respectively. (Reprinted with permission Custers *et al.*, copyright 2003, Nature Publishing Group.)

$YbRh_2(Si_{0.95}Ge_{0.05})$, by contrast, the measured Grüneisen exponent is fractional: $\epsilon = 0.7 \pm 0.1$ (Küchler *et al.*, 2003) (cf. Figure 13b). This observation provides further evidence for the failure of the itinerant theory and may hint at a locally critical QCP in this system (Küchler *et al.*, 2003). In this latter scenario, the heavy quasiparticles decompose, leading to unscreened f moments in close vicinity to the QCP (Coleman, Pépin, Si and Ramazashvili, 2001; Si, Rabello, Ingersent and Smith, 2001). Indeed, below 0.3 K the ac susceptibility (cf. inset of Figure 12b) follows a Curie–Weiss law, with negative Weiss temperature $\theta = -0.3$ K and with a surprisingly large effective moment $\mu_{eff} \approx 1.4\,\mu_B$ per Yb^{3+}. This indicates the emergence of correlated, non-Kondo-quenched spins at finite temperatures above the QCP (Custers *et al.*, 2003b). In the same temperature range, the electronic specific heat coefficient deviates toward larger values from the $-\ln T$ dependence observed above 0.3 K. For the Ge-doped system, this 'upturn' continues down to the lowest accessible temperature when the critical field H_c is applied. This intrinsically electronic feature can be attributed to the QCP as it disappears in the LFL regime at $H > H_c$. The unique power-law temperature dependence of $C_{el}(T)/T$ for $T < 0.3$ K is disparate from the linear temperature dependence of the electrical resistivity which holds all the way from 10 K to 10 mK (Figure 12b): In case of a q-independent self energy, the linear $\rho(T)$ dependence

would correspond to $C_{\rm el}(T)/T \sim -\ln T$, as in fact observed for $0.3\,K < T < 10\,{\rm K}$. Assuming that the thermodynamic quantity $C_{\rm el}(T)/T$ is probing mainly the dominating local 4f ('spin') part of the composite heavy quasiparticles, while the latter (transport) quantity is mainly probing the itinerant conduction-electron ('charge') part, the disparity between $\rho(T)$ and $C_{\rm el}(T)/T$ observed in the paramagnetic state for $T < 0.3\,{\rm K}$ may be viewed as a direct manifestation of the breakup of the heavy quasiparticles in the approach of the QCP (Custers *et al.*, 2003b).

Bulk magnetic susceptibility (Gegenwart *et al.*, 2005) as well as NMR measurements (Ishida *et al.*, 2002) have revealed strong FM fluctuations for $H > H_{\rm c}$. The Pauli susceptibility follows a power-law divergence $\chi_0(H) \sim (H - H_{\rm c})^{0.6}$ and the dimensionless Sommerfeld–Wilson ratio $R_{\rm W}$ is strongly enhanced (cf. Figure 14a). Whereas typically $R_{\rm W} \sim 2$ for HF systems, in $YbRh_2(Si_{0.95}Ge_{0.05})_2$ it equals 17.5 ± 2 away from the critical field and increases upon lowering the field toward $H_{\rm c}$ (Gegenwart *et al.*, 2005). NMR measurements, while signaling the dominance of AF fluctuations in the quantum critical regime, have also revealed enhanced FM fluctuations: the Korringa ratio $S = 1/T_1T_{\rm K}^2$, with the 4f contribution to the spin-lattice relaxation rate T_1 and isotropic Knight shift K reaches only 10% of the free electron value (Ishida *et al.*, 2002). In $YbRh_2Si_2$, a sharp electron spin resonance (ESR) has been observed at low temperatures (Sichelschmidt *et al.*, 2003). Typically, the spin-fluctuation rates of Kondo ions cause much too large ESR linewidths making ESR signals undetectable. For $YbRh_2Si_2$, the ESR signal occurs well *below* $T_{\rm K}$, and its intensity follows the temperature dependence of the bulk susceptibility which strongly increases upon cooling to low temperatures. The possible relation between the strong FM fluctuations and the occurrence of the ESR signal needs to be clarified. One may argue, that (2D) FM fluctuations explain the fractional Grüneisen exponent of $1/\nu z = 2/3$ within the itinerant theory. This picture is problematic as both the coefficient of the T^2 component of the resistivity, $A(H)$, as well as $\chi_0(H)$ diverge in the approach of the critical field. The ratio A/χ_0^2 is nearly constant (cf. Figure 14b). Since FM spin fluctuations are inefficient in affecting charge transport, the A/χ_0^2 scaling implies that the $q = 0$ fluctuations are a part of overall critical fluctuations in an extended range of wave vector scales (Gegenwart *et al.*, 2007).

The Hall-effect evolution across the field-tuned QCP in $YbRh_2Si_2$ has been studied in great detail at low temperatures (Paschen *et al.*, 2004). Most remarkably, the magnetic field-induced suppression of the weak magnetic ordering with a tiny ordered moment of $2 \times 10^{-3}\,\mu_{\rm B}$/Yb (Ishida *et al.*, 2003) leads to a large (about 30%) change of the Hall coefficient. A new line in the temperature–field phase diagram has been discovered, across which the isothermal Hall resistivity as a

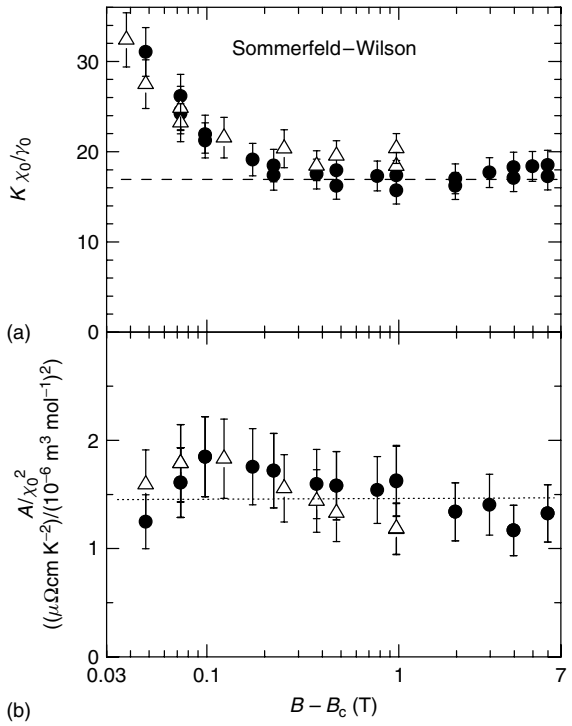

Figure 14. Field dependence of the dimensionless Sommerfeld–Wilson ratio $R_{\rm W} = K\,\chi_0/\gamma_0$, $K = \pi^2 k_{\rm B}^2/(\mu_0\mu_{\rm eff}^2)$ (a) and A/χ_0^2 (b) of $YbRh_2(Si_{0.95}Ge_{0.05})_2$ (Gegenwart *et al.*, 2005), with $A = \Delta\rho(T)/T^2$. (Reprinted with permission Genenwart *et al.*, copyright 2005, American Physical Society.)

function of the applied magnetic field changes from a phase with small Fermi-surface volume (at low fields) to a phase with larger Fermi-surface volume (at elevated fields). Upon decreasing the temperature, this crossover sharpens its width obeying a T-power-law dependence. This suggests that the crossover ends up in a sudden jump of the Fermi-surface volume at the QCP (Paschen *et al.*, 2004).

Very recently, a comparison of thermodynamic measurements with the transport properties has been performed. Figure 15(a) displays the remarkable similarity of the field dependence of the Hall resistivity with both that of the magnetostriction and magnetization. All properties can be fitted by an empirical 'crossover' function yielding a characteristic field scale $H_0(T)$ which defines a scale $T^*(H)$ in the $T-H$ phase diagram (cf. Figure 15b). This scale is seen to be distinct from either the transition temperature ($T_{\rm N}$) for the magnetic ordering at $H < H_{\rm c}$ or the scale ($T_{\rm LFL}$) for the establishment of the coherent LFL state at $H > H_{\rm c}$. For all three quantities, the width of the crossover extrapolates to zero at $T = 0$, implying that the differentials of the magnetostriction, magnetization, and Hall resistivity exhibit a jump in the zero-temperature limit (Gegenwart *et al.*, 2007). These findings contradict the conventional order-parameter fluctuation theory in at least two respects. First, the only

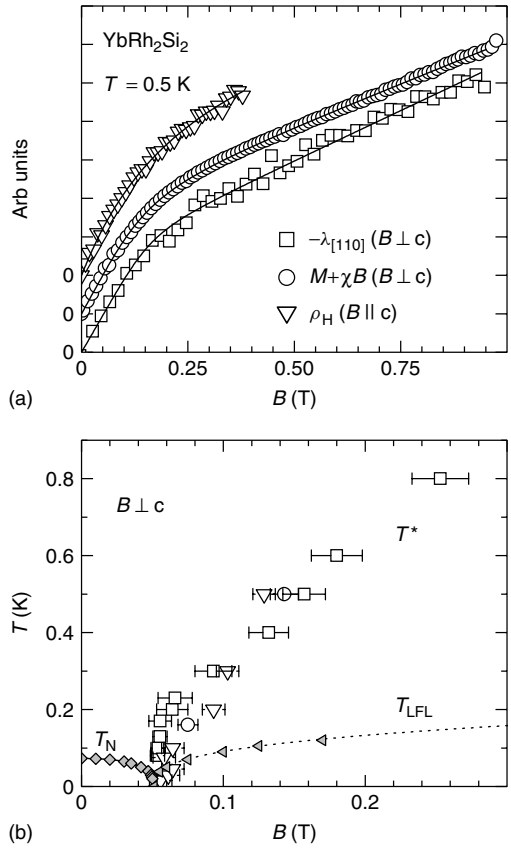

Figure 15. Comparison of the magnetic-field dependence of the Hall resistivity ($H \parallel c$), magnetostriction $\lambda(H) \perp c$), and $M + \chi H(H \perp c)$ which is the field derivative of the magnetic free-energy contribution ($-MH$), all at $T = 0.5\,\mathrm{K}$; similar behavior is observed at other temperatures (a). The solid lines indicate fits of a crossover function $f(H, T)$. (Reprinted with permission Gegenwart *et al*., copyright 2007, AAAS.) Each data set has been normalized by its initial slope. For clarity, the three data sets have been shifted by different amounts vertically. (b) Temperature versus magnetic field diagram for $YbRh_2Si_2$ ($H \perp c$). The gray diamonds and triangles represent respectively the Néel ordering temperature (T_N) and the crossover temperature (T_{LFL}) below which the electrical resistivity varies like T^2. T^* marks the characteristic energy scale determined by the crossovers in Hall resistivity, magnetization, and magnetostriction using the same symbols as in (a). For $\rho_H(T, H)$, the fields $H \parallel c$ were multiplied with the anisotropy factor 1/11. (Reprinted with permission Custers *et al*., copyright 2003, Nature Publishing Group.)

low-energy scale in that theory is associated with magnetic slowing down, which for $H > H_c$ is T_{LFL}. Second, within that theory, only kinklike features, rather than jumps, are expected in the differentials of the aforementioned thermodynamic and transport quantities. The results of Figure 15 indicate that quantum criticality in HF systems may invoke effects of Kondo disentanglement which are manifested through vanishing energy scales that add to those associated with the slowing down of the order-parameter fluctuations.

To summarize, the observed properties of $YbRh_2Si_2$ are incompatible with the predictions of the itinerant (Hertz–Millis) theory and hint at unconventional quantum criticality with multiple vanishing energy scales. Detailed inelastic neutron-scattering experiments are highly desirable to characterize the complicated magnetic fluctuation spectrum which consists of both AF and FM components. The absence of SC even in high-quality single crystals with residual resistivity of less than $0.5\,\mu\Omega\,\mathrm{cm}$ for temperatures $T > 10\,\mathrm{mK}$ is particularly striking. It is likely that SC still occurs below 10 mK. On the other hand, the formation of Cooper pairs may be prevented either by those FM quantum critical fluctuations that are dominating at elevated frequencies or by the very nature of this type of unconventional quantum criticality.

5 OUTLOOK

In contrast to several of the U-based HF compounds whose low-temperature behavior is characterized by the coexistence of AF order and SC, their Ce-based counterparts often show SC to be intimately related to an AF instability or QCP. For the prototypical system $CePd_2Si_2$ it was proposed first that the AF quantum critical fluctuations as main scatterers for the heavy-mass charge carriers not only cause the pronounced NFL effects in the normal state (e.g., $\Delta\rho \propto T^{1.2}$ below $T \approx 20\,\mathrm{K}$) but also mediate the formation of Cooper pairs (Mathur *et al*., 1998): Paramagnon-mediated SC in Ce-based NFL superconductors has meanwhile been widely accepted, although it has not yet been verified experimentally. The proposal by Mathur *et al*. implies charge carriers that keep their integrity at the QCP like 3d electrons in transition metals do, to which the theoretical models described in Section 3 had been originally applied. Since inelastic neutron-scattering and quasiparticle-tunneling experiments to directly demonstrate paramagnon-mediated SC are yet lacking in these kind of superconductors, it appears most desirable to check the *itinerant* nature of their AF ordering. In fact, in the case of $CeCu_2Si_2$ neutron-diffraction experiments, performed at ambient pressure, revealed an incommensurate SDW phase with very small ordered moment. Recalling the anomalous T-power-law dependencies of the resistivity and the Sommerfeld coefficient in the low-temperature state of $CeCu_2Si_2$ close to its QCP, the quantum critical fluctuations in this material are safely of the 3D-SDW type. Of course, neutron-diffraction measurements in other Ce-based NFL superconductors are badly needed to reveal deeper insight into the microscopics underlying Cooper-pair formation in these most interesting materials. In the case of $CeCoIn_5$, thermal-expansion measurements conducted in overcritical

magnetic fields also point to a field-induced QCP of 3D-SDW type at $B_{QCP} \leq B_{c2}(0)$. However, AF order masked by SC could not be established for this compound until now.

Turning to the nonsuperconducting lanthanide-based systems $CeCu_{5.9}Au_{0.1}$ and $YbRh_2Si_2$, it is fair to say that their QCP is indeed of an unconventional nature, that is, it differs strongly from the 3D-SDW-type QCP. It, thus, appears straightforward to relate the lack of SC in these materials to this very fact. On the other hand, it may be argued that the degree of disorder introduced into $CeCu_6$ by doping with 10 at% Au is too high for an unconventional superconducting order parameter to survive. Interestingly, this type of reasoning fails completely in the case of $YbRh_2Si_2$. Here, new high-quality single crystals with residual HRRR resistivity ratios $H \geq 140$ (residual resistivities $\rho_0 \leq 0.5\,\mu\Omega\,\mathrm{cm}$), that is, substantially smaller than those of the best superconducting $CePd_2Si_2$ single crystals (Mathur *et al*., 1998) do not show SC at least for $T > 10\,\mathrm{mK}$. Experiments at much lower temperatures are presently in preparation to check for the possible existence of SC in $YbRh_2Si_2$.

At the current state of the art the following conclusion may be formulated which should also motivate future experimental and theoretical research on strongly correlated matter: paramagnon-mediated SC is favored by a 3D-SDW QCP [1]. However, so far no SC has been observed at unconventional AF QCPs, as in $YbRh_2Si_2$, which is characterized, for example, by the destruction of the Kondo singlets and by FM quantum critical fluctuations in wide parts of the phase diagram. Therefore an unconventional AF QCP might be detrimental to SC. Undoubtedly, the interplay between SC and quantum criticality will remain in the focus of future theoretical and experimental studies of correlated matter.

NOTE

[1] This does not exclude SC in compounds that are lacking a QCP, due to the fact that the $T = 0$ transition from AF ordered to LFL, induced by varying hydrostatic pressure, is of first order. In this case, low-energy quantum critical fluctuations are absent, but SC may nevertheless occur because of higher-frequency AF spin fluctuations. Prime candidates for such a scenario are $CeCu_2Ge_2$ (Jaccard, Wilhelm, Alami-Yadri and Vargoz, 1999) and $CeRh_2Si_2$ (Movshovich *et al*., 2001).

ACKNOWLEDGMENTS

We greatly acknowledge stimulating discussions with E. Abrahams, E. D. Bauer, P. Coleman, J. Custers, J. G. Donath, Z. Fisk, C. Geibel, M. Imada, K. Ishida, Y. Kitaoka, R. Küchler, M. Loewenhaupt, H. v. Löhneysen, D. E. MacLaughlin, M. B. Maple, K. Neumaier, N. Oeschler, S. Paschen, C. Pépin, J. L. Sarrao, Q. Si, J. Sichelschmidt, V. A. Sidorov, J. D. Thompson, Y. Tokiwa, T. Vojta, T. Westerkamp, H. Q. Yuan, and G. Zwicknagl.

REFERENCES

Andres, K., Graebner, J.E. and Ott, H.R. (1975). 4f-virtual-bound-state formation in $CeAl_3$ at low temperatures. *Physical Review Letters*, **35**, 1779–1782.

Bao, W., Pagliuso, P.G., Sarrao, J.L., *et al*. (2000). Incommensurate magnetic structure of $CeRhIn_5$. *Physical Review B*, **62**, R14621–R14624. Erratum [Physical Review B, **62**, R14621 (2000)].

Bao, W., Pagliuso, P.G., Sarrao, J.L., *et al*. (2001). Incommensurate magnetic structure of $CeRhIn_5$. *Physical Review B*, **63**, 219901.

Berk, N.F. and Schrieffer, J.R. (1966). Effect of ferromagnetic spin correlations on superconductivity. *Physical Review Letters*, **17**, 433–435.

Bianchi, A., Movshovich, R., Vekhter, I., *et al*. (2003). Avoided antiferromagnetic order and quantum critical point in $CeCoIn_5$. *Physical Review Letters*, **1**, 257001.

Bruls, G., Wolf, B., Finsterbusch, D., *et al*. (1994). Unusual $B - T$ phase diagram of the heavy-fermion superconductor $CeCu_2Si_2$. *Physical Review Letters*, **72**, 1754–1757.

Capan, C., Bianchi, A., Ronning, F., *et al*. (2004). Non-Fermi-liquid behavior in $CeIrIn_5$ near a metamagnetic transition. *Physical Review B*, **70**, 180502(R).

Christianson, A.D., Bauer, E.D., Lawrence, J.M., *et al*. (2004). Crystalline electric field effects in $CeMIn_5$ ($M = $ Co,Rh,Ir): superconductivity and the influence of Kondo spin fluctuations. *Physical Review B*, **70**, 134505.

Coleman, P., Pépin, C., Si, Q. and Ramazashvili, R. (2001). How do Fermi liquids get heavy and die? *Journal of Physics: Condensed Matter*, **13**, R723–R738.

Continentino, M.A. (2001). *Quantum Scaling in Many-Body Systems*, World Scientific Publishing: Singapore.

Continentino, M.A. (2004a). *Comment on Universally Diverging Gruneisen Parameter and the Magnetocaloric Effect Close to a Quantum Critical Point*, arXiv:cond-mat/0408217.

Continentino, M.A. (2004b). *Quantum Critical Point in Heavy Fermions*, arXiv:cond-mat/0412321.

Curro, N.J., Sarrao, J.L., Thompson, J.D., *et al*. (2003). Low-frequency spin dynamics in the $CeMIn_5$ materials. *Physical Review Letters*, **90**, 227202.

Custers, J., Gegenwart, P., Neumaier, K., *et al*. (2003a). Quantum criticality in $YbRh_2Si_2$. *Journal of Physics: Condensed Matter*, **15**, S2047–S2053.

Custers, J., Gegenwart, P., Wilhelm, H., *et al*. (2003b). The break-up of heavy electrons at a quantum critical point. *Nature*, **424**, 524–527.

Deppe, M., Borth, R., Geibel, C., *et al*. (2004). Study of the magnetic order in $CeCu_2(Si_{1?x}Ge_x)_2$: evidence for a critical point at $x = 0.25$. *Journal of Magnetism and Magnetic Materials*, **272–276**, 40–41.

Donath, J.G., Gegenwart, P., Steglich, F., *et al*. (2007) *Dimensional crossover of quantum critical behavior in* $CeCoIn_5$, arXiv:cond-mat/0704.0506.

Doniach, S. (1977). The Kondo lattice and weak antiferromagnetism. *Physica B and C*, **91**, 231–234.

Doniach, S. and Engelsberg, S. (1966). Low-temperature properties of nearly ferromagnetic Fermi liquids. *Physical Review Letters*, **17**, 750–753.

Feyerherm, R., Amato, A., Geibel, C., *et al*. (1997). Competition between magnetism and superconductivity in $CeCu_2Si_2$. *Physical Review B*, **56**, 699–710.

Fischer, I. and Rosch, A. (2004). *Field-tuned Quantum Critical Point of Antiferromagnetic Metals*, arXiv:cond-mat/0412248.

Gegenwart, P., Custers, J., Geibel, C., *et al*. (2002). Magnetic-field induced quantum critical point in $YbRh_2Si_2$. *Physical Review Letters*, **89**, 056402.

Gegenwart, P., Custers, J., Tokiwa, Y., *et al*. (2005). Ferromagnetic quantum critical fluctuations in $YbRh_2(Si_{0.95}Ge_{0.05})_2$. *Physical Review Letters*, **94**, 076402.

Gegenwart, P., Langhammer, C., Geibel, C., *et al*. (1998). Breakup of heavy fermions on the brink of "Phase *A*" in $CeCu_2Si_2$. *Physical Review Letters*, **81**, 1501–1504.

Gegenwart, P., Lohmann, M., Lang, M., *et al*. (1997). Non-Fermi-liquid behavior in $CeCu_2Si_2$ at the disappearance of the presumably magnetically ordered "A-phase". *Physica B*, **230–232**, 572–575.

Gegenwart, P., Westerkamp, T., Krellner, C., *et al*. (2007). Multiple Energy Scales at a Quantum Critical Point, *Science*. **315**, 969–971.

Grewe, N. and Steglich, F. (1991). Heavy fermions. In *Handbook on the Physics and Chemistry of Rare Earths*, Gschneidner, K.A. and Eyring, L. (Eds.), Elsevier Science Publishers B. V.: Amsterdam, pp. 343–474, Vol. 14.

Grin, Y.N., Yarmolyuk, Y.P. and Gladyshevskii, E.I. (1979). Crystal-structure of the compounds $R_{10}Ga_3Co_7$(R = Y, La). *Kristallografiya*, **24**, 455–460.

Haga, Y., Inada, Y., Harima, H., *et al*. (2001). Quasi-two-dimensional Fermi surfaces of the heavy fermion superconductor $CeIrIn_5$. *Physical Review B*, **63**, 060503.

Hall, D., Palm, E.C., Murphy, T.P., *et al*. (2001a). Electronic structure of CeRhIn5: de Haas-van Alphen and energy band calculations. *Physical Review B*, **64**, 064506.

Hall, D., Palm, E.C., Murphy, T.P., *et al*. (2001b). Fermi surface of the heavy-fermion superconductor $CeCoIn_5$: the de Haas-van Alphen effect in the normal state. *Physical Review B*, **64**, 212508.

Hegger, H., Petrovic, C., Moshopoulou, E.G., *et al*. (2000). Pressure-induced superconductivity in Quasi-2D $CeRhIn_5$. *Physical Review Letters*, **84**, 4986–4989.

Hertz, J.A. (1976). Quantum critical phenomena. *Physical Review B*, **14**, 1165–1184.

Hewson, A.C. (1993). *The Kondo Problem to Heavy Fermions*, Cambridge University Press: Cambridge.

Higemoto, W., Koda, A., Kadono, R., *et al*. (2002). μSR Studies on heavy fermion superconductors $CeIrIn_5$ and $CeCoIn_5$. *Journal of the Physical Society of Japan*, **71**, 1023–1026.

Holmes, A.T., Jaccard, D. and Miyake, K. (2004). Signatures of valence fluctuations in $CeCu_2Si_2$ under high pressure. *Physical Review B*, **69**, 024508.

Ishida, K., Kawasaki, Y., Tabuchi, K., *et al*. (1999). Evolution from magnetism to unconventional superconductivity in a series of CexCu2Si2 compounds probed by Cu NQR. *Physical Review Letters*, **82**, 5353–5356.

Ishida, K., MacLaughlin, D.E., Young, B.L., *et al*. (2003). Low-temperature magnetic order and spin dynamics in $YbRh_2Si_2$. *Physical Review B*, **68**, 184401.

Ishida, K., Okamoto, K., Kawasaki, Y., *et al*. (2002). $YbRh_2Si_2$: spin fluctuations in the vicinity of a quantum critical point at low magnetic field. *Physical Review Letters*, **89**, 107202.

Jaccard, D., Wilhelm, H., Alami-Yadri, K. and Vargoz, E. (1999). Magnetism and superconductivity in heavy fermion compounds at high pressure. *Physica B*, **259–261**, 1–7.

Jensen, J. and Mackintosh, A.R. (1991). *Rare Earth Magnetism Structures and Excitations*, Clarendon Press: Oxford.

Kawasaki, Y., Kawasaki, S., Yashima, M., *et al*. (2003). Anisotropic spin fluctuations in heavy-fermion superconductor $CeCoIn_5$: in-NQR and Co-NMR studies. *Journal of the Physical Society of Japan*, **72**, 2308–2311.

Kawasaki, S., Zheng, G-q., Kan, H., *et al*. (2005). Enhancing the superconducting transition temperature of the heavy fermion compound $CeIrIn_5$ in the absence of spin correlations. *Physical Review Letters*, **94**, 037007.

Kim, J.S., Alwood, L., Kumar, P. and Stewart, G.R. (2002). Field-induced transition in the specific heat of $CeIrIn_5$ for $B \gtrsim 30\,\mathrm{T}$. *Physical Review B*, **65**, 174520.

Knebel, G., Aoki, D., Braithwaite, D., *et al*. (2006). Coexistence of antiferromagnetism and superconductivity in $CeRhIn_5$ under high pressure and magnetic field. *Physical Review B*, **74**, 020501(R).

Knebel, G., Braithwaite, D., Canfield, P.C., *et al*. (2001). Electronic properties of $CeIn_3$ under high pressure near the quantum critical point. *Physical Review B*, **65**, 024425.

Knebel, G., Eggert, C., Engelmann, D., *et al*. (1996). Phase diagram of $CeCu_2(Si_{1-x}Ge_x)_2$. *Physical Review B*, **53**, 11586–11592.

Knebel, G., Méasson, M.A., Salce, B., *et al*. (2004). High-pressure phase diagrams of $CeRhIn_5$ and $CeCoIn_5$ studied by ac calorimetry. *Journal of Physics: Condensed Matter*, **16**, 8905–8922.

Kohori, Y., Yamato, Y., Iwamoto, Y., *et al*. (2001). NMR and NQR studies of the heavy fermion superconductors $CeTIn_5$? (T = Co and Ir). *Physical Review B*, **64**, 134526.

Küchler, R., Oeschler, N., Gegenwart, P., *et al*. (2003). Divergence of the Grüneisen ratio at quantum critical points in heavy fermion metals. *Physical Review Letters*, **91**, 066405.

Kumar, R.S., Cornelius, A.L. and Sarrao, J.L. (2004). Compressibility of $CeMIn_5$ and Ce_2MIn_8 (M = Rh, Ir, and Co) compounds. *Physical Review B*, **70**, 214526.

Kuramoto, Y. and Kitaoka, Y. (2000). *Dynamics of Heavy Electrons*, Clarendon University Press: Oxford.

Lacerda, A., de Visser, A., Haen, P., *et al*. (1989). Thermal properties of heavy-fermion $CeRu_2Si_2$. *Physical Review B*, **40**, 8759–8768.

Lengyel, E., Sparn, G., Nicklas, M., *et al*. (2006). Heat capacity of $CeCu_2Si_2$ under hydrostatic pressure. *Physica B*, **378–380**, 415–416.

Llobet, A., Gardner, J.S., Moshopoulou, E.G., *et al*. (2004). Magnetic structure of $CeRhIn_5$ as a function of pressure and temperature. *Physical Review B*, **69**, 024403.

Majumdar, S., Balakrishnan, G., Lees, M.R., *et al*. (2002). Pressure-induced change in the magnetic modulation of $CeRhIn_5$. *Physical Review B*, **66**, 212502.

Mathur, N.D., Grosche, F.M., Julian, S.R., *et al*. (1998). Magnetically mediated superconductivity in heavy fermion compounds. *Nature*, **94**, 39–43.

Mederle, S., Borth, R., Geibel, C., *et al*. (2002). An unconventional metallic state in $YbRh_2(Si_{1-x}Ge_x)_2$ – a high pressure study. *Journal of Physics: Condensed Matter*, **14**, 10731–10736.

Mignot, J-M., Flouquet, J., Haen, P., *et al*. (1988). Metamagnetic $CeRu_2Si_2$: new perspectives for heavy-fermion studies in high fields. *Journal of Magnetism and Magnetic Materials*, **76–77**, 97–104.

Millis, A.J. (1993). Effect of a nonzero temperature on quantum critical points in itinerant fermion systems. *Physical Review B*, **48**, 7183–7196.

Miyake, K., Narikiyo, O. and Onishi, Y. (1999). Superconductivity of Ce-based heavy fermions under pressure: valence fluctuation mediated pairing associated with valence instability of Ce. *Physica B*, **259–261**, 676–677.

Moriya, T. (1985). *Spin Fluctuations in Itinerant Electron Magnets*, Springer-Verlag: Berlin.

Moriya, T. and Kawabata, A. (1973a). Effect of spin fluctuations on itinerant electron ferromagnetism. *Journal of the Physical Society of Japan*, **34**, 639–651.

Moriya, T. and Kawabata, A. (1973b). Effect of spin fluctuations on itinerant electron ferromagnetism. II. *Journal of the Physical Society of Japan*, **35**, 669–676.

Moriya, T. and Takimoto, T. (1995). Anomalous properties around magnetic instability in heavy electron systems. *Journal of the Physical Society of Japan*, **64**, 960–969.

Morris, G.D., Heffner, R.H., Sonier, J.E., *et al*. (2003). Magnetism and superconductivity in $CeRh_{1-x}Ir_xIn_5$ heavy fermion materials. *Physica B*, **326**, 390–393.

Movshovich, R., Jaime, M., Thompson, J.D., *et al*. (2001). Unconventional superconductivity in $CeIrIn_5$ and $CeCoIn_5$: specific heat and thermal conductivity studies. *Physical Review Letters*, **86**, 5152–5155.

Muramatsu, T., Tateiwa, N., Kobayashi, T.C., *et al*. (2001). Superconductivity of $CeRhIn_5$ under high pressure. *Journal of the Physical Society of Japan*, **70**, 3362–3367.

Nakamura, H., Kitaoka, Y., Yamada, H. and Asayama, K. (1988). Discovery of antiferromagnetic ordering above upper critical field in the heavy fermion superconductor $CeCu_2Si_2$. *Journal of Magnetism and Magnetic Materials*, **76–77**, 517–519.

Nicklas, M., Borth, R., Lengyel, E., *et al*. (2001). Response of the heavy-fermion superconductor $CeCoIn_5$ to pressure: roles of dimensionality and proximity to a quantum-critical point. *Journal of Physics: Condensed Matter*, **13**, L905–L912.

Nicklas, M., Sidorov, V.A., Borges, H.A., *et al*. (2004). Two superconducting phases in $CeRh_{1-x}Ir_xIn_5$. *Physical Review B*, **70**, 020505(R).

Oeschler, N., Deppe, M., Lengyel, E., *et al*. (2005). Magnetic phase diagram of $CeCu_2(Si_{1-x}Ge_x)_2$ measured with low-temperature thermal expansion. *Physical Review B*, **71**, 094409.

Onodera, A., Tsuduki, S., Ohishi, Y., *et al*. (2002). Equation of state of $CeCu_2Ge_2$ at cryogenic temperature. *Solid State Communications*, **123**, 113–116.

Paglione, J., Tanatar, M.A., Hawthorn, D.G., *et al*. (2003). Field-induced quantum critical point in $CeCoIn_5$. *Physical Review Letters*, **91**, 246405.

Pagliuso, P.G., Movshovich, R., Bianchi, A.D., *et al*. (2002). Multiple phase transitions in Ce(Rh,Ir,Co)In_5. *Physica B*, **312–313**, 129–131.

Pagliuso, P.G., Petrovic, C., Movshovich, R., *et al*. (2001). Coexistence of magnetism and superconductivity in $CeRh_{1-x}Ir_xIn_5$. *Physical Review B*, **64**, 100503.

Park, T., Ronning, F., Yuan, H.Q., *et al*. (2006). Hidden magnetism and quantum criticality in the heavy fermion superconductor $CeRhIn_5$. *Nature*, **440**, 65–68.

Paschen, S., Lühmann, T., Wirth, S., *et al*. (2004). Hall-effect evolution across a heavy-fermion quantum critical point. *Nature*, **432**, 881–885.

Pépin, C. (2005). Fractionalization and fermi-surface volume in heavy-fermion compounds: the case of $YbRh_2Si_2$. *Physical Review Letters*, **94**, 066402.

Petrovic, C., Movshovich, R., Jaime, M., *et al*. (2001). A new heavy-fermion superconductor $CeIrIn_5$: a relative of the cuprates? *Europhysics Letters*, **53**, 354–359.

Petrovic, C., Pagliuso, P.G., Hundley, M.F., *et al*. (2001). Heavy-fermion superconductivity in $CeCoIn_5$ at 2.3 K. *Journal of Physics: Condensed Matter*, **13**, L337–L342.

Pham, L.D., Park, T., Maquilon, S., *et al*. (2006). Reversible tuning of the heavy-fermion ground state in $CeCoIn_5$. *Physical Review Letters*, **97**, 056404.

Ronning, F., Capan, C., Bianchi, A., *et al*. (2005). Field-tuned quantum critical point in $CeCoIn_5$ near the superconducting upper critical field. *Physical Review B*, **71**, 104528.

Rosch, A. (1999). Interplay of disorder and spin fluctuations in the resistivity near a quantum critical point. *Physical Review Letters*, **82**, 4280–4283.

Rosch, A. (2000). Disorder effects on transport near AFM quantum phase transitions. *Physica B*, **280**, 341–346.

Rüegg, C., Cavadini, N., Furrer, A., *et al*. (2003). Bose-Einstein condensation of the triplet states in the magnetic insulator $TlCuCl_3$. *Nature*, **423**, 62–65.

Sachdev, S. (1999). *Quantum Phase Transitions*, Cambridge University Press: Cambridge.

Senthil, T., Sachdev, S. and Vojta, M. (2003). Fractionalized Fermi liquids. *Physical Review Letters*, **90**, 216403.

Senthil, T., Sachdev, S. and Vojta, M. (2005). Quantum phase transitions out of the heavy Fermi liquid. *Physica B*, **359–361**, 9–16.

Shishido, H., Settai, R., Aoki, D., *et al*. (2002). Fermi surface, magnetic and superconducting properties of $LaRhIn_5$ and $CeTIn_5$

(T: Co, Rh and Ir). *Journal of the Physical Society of Japan*, **71**, 162–173.

Shishido, H., Settai, R., Harima, H. and Ōnuki, Y. (2005). A drastic change of the Fermi surface at a critical pressure in $CeRhIn_5$: dHvA study under pressure. *Journal of the Physical Society of Japan*, **74**, 1103–1106.

Si, Q., Rabello, S., Ingersent, K. and Smith, J.L. (2001). Locally critical quantum phase transitions in strongly correlated metals. *Nature*, **413**, 804–808.

Sichelschmidt, J., Ivanshin, V.A., Ferstl, J., *et al*. (2003). Low temperature electron spin resonance of the Kondo ion in a heavy fermion metal: $YbRh_2Si_2$. *Physical Review Letters*, **91**, 156401.

Sidorov, V.A., Nicklas, M., Pagliuso, P.G., *et al*. (2002). Superconductivity and quantum criticality in $CeCoIn_5$. *Physical Review Letters*, **89**, 157004.

Sparn, G., Donnevert, L., Hellmann, P., *et al*. (1998). Pressure studies near quantum phase transitions in strongly correlated Ce systems. *Review of High Pressure Science and Technology*, **7**, 431–436.

Steglich, F., Aarts, J., Bredl, C.D., *et al*. (1979). Superconductivity in the presence of strong Pauli paramagnetism: $CeCu_2Si_2$. *Physical Review Letters*, **43**, 1892–1896.

Steglich, F., Gegenwart, P., Geibel, C., *et al*. (1996). New observations concerning magnetism and superconductivity in heavy-fermion metals. *Physica B*, **223–224**, 1–8.

Steglich, F., Gegenwart, P. and Geibel, C. (2001). Superconductivity and magnetism in heavy-fermions. In *More is Different: Fifty years of Condensed Matter Physics*, Ong N-P. and Bhatt R. (Eds.), Princeton University Press: Princeton, pp. 191–210.

Stewart, G.R. (2001). Non-Fermi-liquid behavior in *d*- and *f*-electron metals. *Reviews of Modern Physics*, **73**, 797–855.

Stockert, O., Andreica, D., Amato, A., *et al*. (2006). Magnetic order and superconductivity in single-crystalline $CeCu_2Si_2$. *Physica B*, **374–375**, 167–170.

Stockert, O., Faulhaber E., Prokes, K., *et al*. (2005). *Does Superconductivity Survive in the Superconducting Phase of $CeCu_2Si_2$?* Hahn-Meitner-Institut Annual Report 2004, Selected Results, HMI-B-602, pp. 38–39.

Stockert, O., Faulhaber, E., Zwicknagl, G., *et al*. (2004). Nature of the *A* phase in $CeCu_2Si_2$. *Physical Review Letters*, **92**, 136401.

Stockert, O., Koza, M.M., Ferstl, J., *et al*. (2006). Crystalline electric field excitations of the non-Fermi-liquid $YbRh_2Si_2$. *Physica B*, **378–380**, 157–158.

Stoner, E.C. (1938). Collective electron ferromagnetism. *Proceedings of the Royal Society of London Series A*, **165**, 372–414.

Takeuchi, T., Inoue, T., Sugiyama, K., *et al*. (2001). Magnetic and thermal properties of $CeIrIn_5$ and $CeRhIn_5$. *Journal of the Physical Society of Japan*, **70**, 877–883.

Takke, R., Niksch, M., Assmus, W., *et al*. (1981). Grüneisen parameter of cerium compounds with unstable 4f shells. *Zeitschrift für Physik B*, **44**, 33–39.

Thalmeier, P. and Fulde, P. (1986). Simple scaling approach to the volume magnetostriction in unstable-moment systems. *Europhysics Letters*, **1**, 367–371.

Thalmeier, P., Zwicknagl, G., Stockert, O., *et al*. (2005). Superconductivity in heavy fermion compounds. In *Frontiers in Superconducting Materials*, Narlikar A.V. (Ed.), Springer-Verlag: Berlin, pp. 109–182.

Tokiwa, Y., Gegenwart, P., Radu, T., *et al*. (2005). Field-induced suppression of the heavy-fermion state in $YbRh_2Si_2$. *Physical Review Letters*, **94**, 226402.

Trovarelli, O., Geibel, C., Mederle, S., *et al*. (2000). $YbRh_2Si_2$: pronounced non-Fermi-liquid effects above a low-lying magnetic phase transition. *Physical Review Letters*, **85**, 626–629.

Trovarelli, O., Weiden, M., Müller-Reisener, R., *et al*. (1997). Evolution of magnetism and superconductivity in $CeCu_2(Si_{1-x}Ge_x)_2$. *Physical Review B*, **56**, 678–685.

Uemura, Y.J., Kossler, W.J., Yu, X.H., *et al*. (1989). Coexisting static magnetic order and superconductivity in $CeCu_{2.1}Si_2$ found by muon spin relaxation. *Physical Review B*, **39**, 4726–4729.

Yashima, M., Kawasaki, S., Kawasaki, Y., *et al*. (2004). Magnetic citicality and unconventional superconductivity in $CeCoIn_5$: study of 115in-nuclear quadrupole resonance under pressure. *Journal of the Physical Society of Japan*, **73**, 2073–2076.

Yuan, H.Q., Grosche, F.M., Deppe, M., *et al*. (2003). Observation of two distinct superconducting phases in $CeCu_2Si_2$. *Science*, **302**, 2104–2107.

Yuan, H.Q., Grosche, F.M., Deppe, M., *et al*. (2006). Non-Fermi liquid states in the pressurized $CeCu_2(Si_{1-x}Ge_x)_2$ system: two critical points. *Physical Review Letters*, **96**, 047008.

Zapf, V.S., Freeman, E.J., Bauer, E.D., *et al*. (2001). Coexistence of superconductivity and antiferromagnetism in $CeRh_{1-x}Co_xIn_5$. *Physical Review B*, **5**, 014506.

Zheng, G., Tanabe, K., Mito, T., *et al*. (2001). Unique spin dynamics and unconventional superconductivity in the layered heavy fermion compound $CeIrIn_5$: NQR evidence. *Physical Review Letters*, **6**, 4664.

Zheng, G., Yamaguchi, N., Kan, H., *et al*. (2004). Coexistence of antiferromagnetic order and unconventional superconductivity in heavy-fermion $CeRh_{1-x}Ir_xIn_5$ compounds: nuclear quadrupole resonance studies. *Physical Review B*, **70**, 014511.

Zhu, L., Garst, M., Rosch, A. and Si, Q. (2003). Universally diverging Grüneisen parameter and the magnetocaloric effect close to quantum critical points. *Physical Review Letters*, **91**, 066404.

Zwicknagl, G. and Pulst, U. (1993). $CeCu_2Si_2$: renormalized band structure, quasiparticles and co-operative phenomena. *Physica B*, **186–188**, 895–898.

Zwicknagl, G. (1993). Quasi-particles in heavy fermion systems. *Advances in Physics*, **41**, 203–302.

Molecular Nanomagnets

Wolfgang Wernsdorfer
CNRS/UJF, Grenoble, France

1 INTRODUCTION

The interface between classical and quantum physics has always been an interesting area, but its importance has nevertheless, grown with the current explosive thrusts in nanoscience. Taking devices to the limit of miniaturization (the mesoscale and beyond) where quantum effects become important makes it essential to understand the interplay between the classical properties of the macroscale and the quantum properties of the microscale. This is particularly true in nanomagnetism, where many potential applications require monodisperse, magnetic nanoparticles.

Handbook of Magnetism and Advanced Magnetic Materials. Edited by Helmut Kronmüller and Stuart Parkin. Volume 4: *Novel Materials*. ISBN: 978-0-470-02217-7.

In order to put this review into perspective, let us consider Figure 1, which presents a scale of size ranging from macroscopic down to nanoscopic sizes. The unit of this scale is the number of magnetic moments in a magnetic system. At macroscopic sizes, a magnetic system is described by magnetic domains (Weiss, 1907; Hubert and Schäfer, 1998) that are separated by domain walls. Magnetization reversal occurs via nucleation, propagation, and annihilation of domain walls (see the hysteresis loop in Figure 1a, which was measured on an individual elliptic CoZr particle of $1 \times 0.8\,\mu m^2$ and a thickness of 50 nm (Wernsdorfer *et al.*, 1995)). Shape and width of domain walls depend on the material of the magnetic system, on its size, shape, and surface, and on its temperature (Aharoni, 1996; Wernsdorfer, 2001).

When the system size is of the order of magnitude of the domain-wall width or the exchange length, the formation of domain walls requires a large amount of energy. Therefore, the magnetization remains in the so-called single-domain state. Hence, the magnetization might reverse by uniform rotation, curling, or other nonuniform modes (see hysteresis loop in Figure 1b). For system sizes well below the domain-wall width or the exchange length, one must explicitly take the magnetic moments (spins) and their couplings into account. The theoretical description is complicated by the particle's boundaries.

Magnetic molecular clusters (also called *molecular nanomagnets* or *single-molecule magnets* (*SMMs*)) are the final point in the series of smaller and smaller units from bulk matter to atoms (Figure 1). Till date, they have been the most promising candidates for observing quantum phenomena because they have a well-defined structure with well-characterized spin ground-state and magnetic anisotropy. These molecules can be regularly assembled in

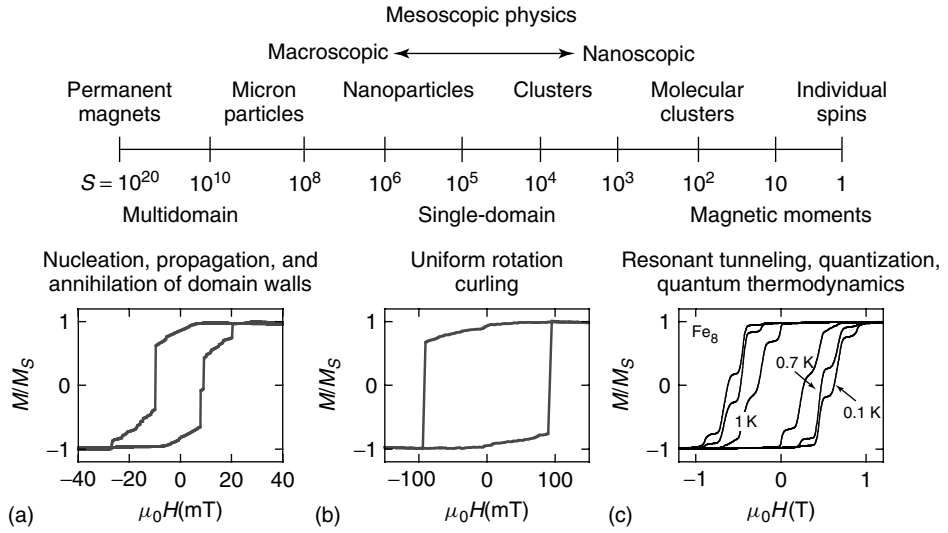

Figure 1. Scale of size that goes from macroscopic down to nanoscopic sizes. The unit of this scale is the number of magnetic moments in a magnetic system (roughly corresponding to the number of atoms). The hysteresis loops are typical examples of magnetization reversal via nucleation, propagation, and annihilation of domain walls (a), via uniform rotation (b), and via quantum tunneling (c).

large crystals where all molecules often have the same orientation. Hence, macroscopic measurements can give direct access to single-molecule properties.

This chapter introduces the basic concepts that are needed to understand the quantum phenomena observed in molecular nanomagnets. Most tunneling studies presented here were performed by magnetization measurements on single crystals using an array of micro-superconduting quantum interference devices (micro-SQUIDs) (Wernsdorfer, 2001). This chapter concludes by mentioning new trends toward molecular spintronics using junctions and nano-SQUIDs (Cleuziou *et al.*, 2006).

2 OVERVIEW OF MOLECULAR NANOMAGNETS

Molecular nanomagnets or SMMs are mainly organic molecules that have one or several metal centers with unpaired electrons. These polynuclear metal complexes are surrounded by bulky ligands (often organic carboxylate ligands). The most prominent examples are a dodecanuclear mixed-valence manganese-oxo cluster with acetate ligands, short Mn_{12} acetate (Lis, 1980), and an octanuclear iron(III) oxo-hydroxo cluster of formula $[Fe_8O_2(OH)_{12}(tacn)_6]^{8+}$ where tacn is a macrocyclic ligand, short Fe_8 (Wieghardt, Pohl, Jibril and Huttner, 1984). Both systems have a spin ground state of $S = 10$ and an Ising-type magnetic anisotropy, which stabilizes the spin states with $m = \pm 10$ and generates an energy barrier for the reversal of the magnetization of about 67 K for Mn_{12} acetate (Caneschi *et al.*, 1991; Sessoli *et al.*, 1993; Sessoli, Gatteschi, Caneschi and Novak, 1993) and 25 K for Fe_8 (Barra *et al.*, 1996).

Thermally activated quantum tunneling of the magnetization was first evidenced in both systems (Novak and Sessoli, 1995; Paulsen and Park, 1995; Friedman, Sarachik, Tejada and Ziolo, 1996; Thomas *et al.*, 1996; Sangregorio *et al.*, 1997). Theoretical discussion of this assumes that thermal processes (principally phonons) promote the molecules up to high levels with small quantum numbers $|m|$, not far below the top of the energy barrier, and the molecules then tunnel inelastically to the other (Abragam and Bleaney, 1970; Villain, Hartmann-Boutron, Sessoli and Rettori, 1994; Politi, Rettori, Hartmann-Boutron and Villain, 1995; Hartmann-Boutron, Politi and Villain, 1996; Villain, Wurger, Fort and Rettori, 1997; Garanin and Chudnovsky, 1997; Fort *et al.*, 1998; Leuenberger and Loss, 2000b). Thus the transition is almost entirely accomplished via thermal transitions and the characteristic relaxation time is strongly temperature dependent. For Fe_8, however, the relaxation time becomes temperature independent below 0.36 K (Sangregorio *et al.*, 1997; Ohm, Sangregorio and Paulsen, 1998a), showing that a pure tunneling mechanism between the only populated ground states $m = \pm S = \pm 10$ is responsible for the relaxation of the magnetization. On the other hand, in the Mn_{12} acetate system, one sees temperature-independent relaxation only for strong applied fields and below about 0.6 K (Perenboom *et al.*, 1998; Kent *et al.*, 2000). During the last few years, many new molecular nanomagnets were presented (see, for instance, Caneschi *et al.*, 1999; Aubin *et al.*, 1998; Price *et al.*, 1999; Yoo *et al.*, 2000), which also show tunneling at low temperatures. The largest molecular nanomagnet is currently a

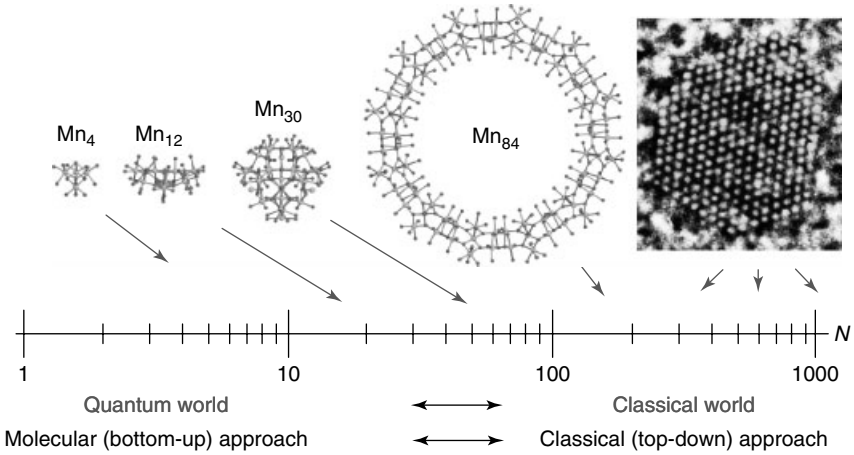

Figure 2. Size scale spanning atomic to nanoscale dimensions. On the far right a high-resolution transmission electron microscopy view along a [110] direction of a typical 3-nm-diameter cobalt nanoparticle exhibiting a face-centered cubic structure and containing about 1000 Co atoms (Jamet *et al*., 2001) is shown. The Mn_{84} molecule is a 4.2-nm-diameter particle. The indicated smaller Mn nanomagnets, which are drawn to scale, are also shown for comparison. An alternative means of comparison is the Néel vector (N), which is the scale shown. The arrows indicate the magnitude of the Néel vectors for the indicated SMMs, which are 7.5, 22, 61, and 168 for Mn_4, Mn_{12}, Mn_{30}, and Mn_{84}, respectively. (Reproduced from A. Tasiopoulos *et al*., 2004, with permission from Wiley VCH. © 2004.)

Mn_{84} molecule (Tasiopoulos *et al*., 2004) that has the size of a magentic nanoparticle (Figure 2).

3 GIANT SPIN MODEL FOR NANOMAGNETS

A magnetic molecule, which behaves like a small nanomagnet, must have a large uniaxial easy-axis-type magnetic anisotropy and a large ground-state spin. A typical example is the octanuclear iron(III) oxo-hydroxo cluster of formula $[Fe_8O_2(OH)_{12}(tacn)_6]^{8+}$, where tacn is a macrocyclic ligand (1,4,7-traiazcyclononane), short Fe_8 (Figure 3) (Wieghardt, Pohl, Jibril and Huttner, 1984).

The internal iron(III) ions are octahedrally coordinated to the two oxides and to four hydroxo bridges. The outer iron(III) ions coordinate three nitrogens and three hydroxyls. Spin polarized neutron scattering showed that all Fe ions have a spin 5/2, six spins up and two down (Pontillon *et al*., 1999). This rationalizes the $S = 10$ spin ground state that is in agreement with magnetization measurements.

In principle, a multispin Hamiltonian can be derived taking into account all exchange interactions and the single-ion magnetic anisotropies. However, the Hilbert space is very large ($6^8 \approx 10^6$) and the exchange coupling constants are not well known. Therefore, a giant spin model that describes the ground spin-state multiplet in an effective way is often used. For a nanomagnet like the Fe_8 molecular cluster, it has the following Hamiltonian:

$$\mathcal{H} = -DS_z^2 + E\left(S_x^2 - S_y^2\right) - g\mu_B\mu_0\vec{S}\cdot\vec{H} \qquad (1)$$

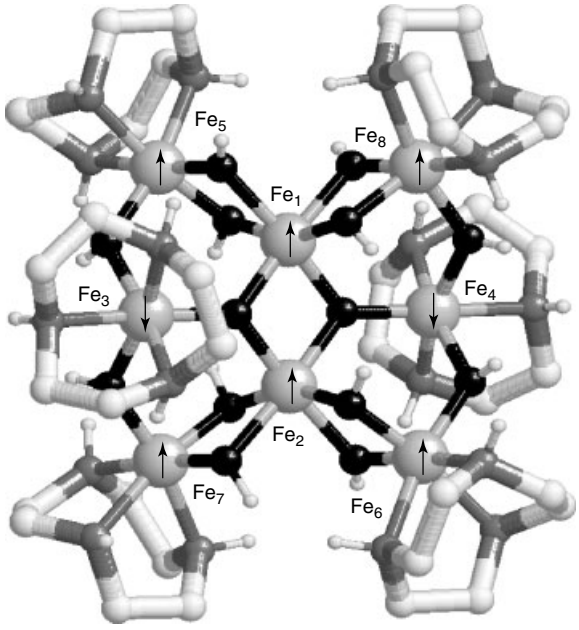

Figure 3. Schematic view of the magnetic core of the Fe_8 cluster. The oxygen atoms are black, the nitrogen atoms are gray, and carbon atoms are white. The arrows represent the spin structure of the ground state $S = 10$. (Reproduced from W. Wernsdorfer *et al*., 2000, with permission from the American Physical Society. © 2000.)

S_x, S_y, and S_z are the three components of the spin operator, D and E are the anisotropy constants, which are determined via high-frequency electron paramagnetic resonance (HF-EPR) ($D/k_B \approx 0.275$ K and $E/k_B \approx 0.046$ K (Barra *et al*., 1996)), and the last term of the Hamiltonian describes

the Zeeman energy associated with an applied field $\vec{H}$. This Hamiltonian defines hard, medium, and easy axes of magnetization in x, y, and z directions, respectively (Figure 4). It has an energy-level spectrum with $(2S+1) = 21$ values, which, to a first approximation, can be labeled by the quantum numbers $m = -10, -9, \ldots, 10$ choosing the z-axis as quantization axis. The energy spectrum, shown in Figure 5, can be obtained by using standard diagonalization techniques of the $[21 \times 21]$ matrix describing the spin Hamiltonian $S = 10$. At $\vec{H} = 0$, the levels $m = \pm 10$ have the lowest energy. When a field H_z is applied, the energy levels with $m < -2$ increase, while those with $m > 2$ decrease (Figure 5). Therefore, energy levels of positive and negative quantum numbers cross at certain fields H_z. It turns out that for Fe_8 the levels cross at fields given by $\mu_0 H_z \approx n \times 0.22\,\mathrm{T}$, with $n = 1, 2, 3, \ldots$. The inset of Figure 5 displays the details at a level crossing where transverse terms containing S_x or S_y spin operators turn the crossing into an 'avoided level crossing'. The spin S is 'in resonance' between two states when the local longitudinal field is close to an avoided level crossing. The energy gap, the so-called tunnel spitting Δ, can be tuned by an applied field in the xy plane (Figure 4) via the $S_x H_x$ and $S_y H_y$ Zeeman terms (Section 3.2).

The effect of these avoided level crossings can be seen in hysteresis loop measurements (Figure 6). When the applied field is near an avoided level crossing, the magnetization relaxes faster, yielding steps separated by plateaus. As the temperature is lowered, there is a decrease in the transition rate due to reduced thermal-assisted tunneling.

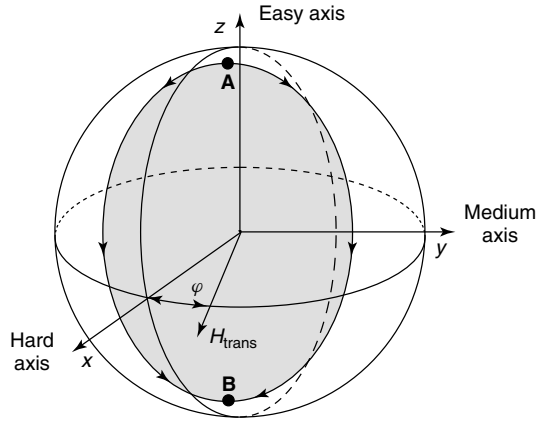

Figure 4. Unit sphere showing degenerate minima **A** and **B**, which are joined by two tunnel paths (heavy lines). The hard, medium, and easy axes are taken in x-, y-, and z-direction, respectively. The constant transverse field H_{trans} for tunnel splitting measurements is applied in the xy plane at an azimuth angle φ. At zero applied field $\vec{H} = 0$, the giant spin reversal results from the interference of two quantum spin paths of opposite direction in the easy anisotropy yz plane. For transverse fields in the direction of the hard axis, the two quantum spin paths are in a plane that is parallel to the yz plane, as indicated in the figure. By using Stokes'theorem it has been shown (Garg, 1993) that the path integrals can be converted in an area integral, yielding that destructive interference–that is a quench of the tunneling rate–occurs whenever the shaded area is $k\pi/S$, where k is an odd integer. The interference effects disappear quickly when the transverse field has a component in the y-direction because the tunneling is then dominated by only one quantum spin path. (Reproduced from A. Garg, 1993, with permission from EDP Sciences. © 1993.)

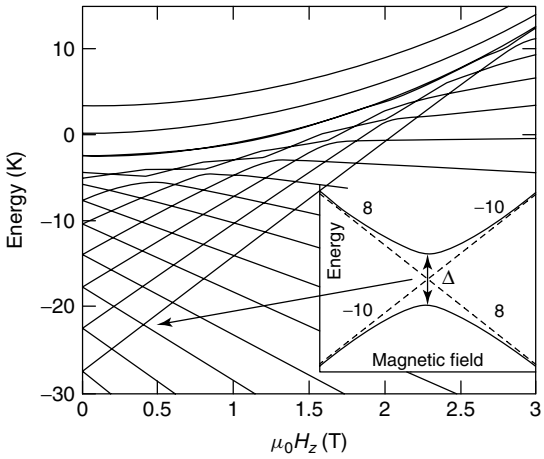

Figure 5. Zeeman diagram of the 21 levels of the $S = 10$ manifold of Fe_8 as a function of the field applied along the easy axis (equation (1)). From bottom to top, the levels are labeled with quantum numbers $m = \pm 10, \pm 9, \ldots, 0$. The levels cross at fields given by $\mu_0 H_z \approx n \times 0.22\,\mathrm{T}$, with $n = 1, 2, 3, \ldots$. The *inset* displays the detail at a level crossing where the transverse terms (terms containing S_x or/and S_y spin operators) turn the crossing into an avoided level crossing. The greater the tunnel splitting Δ, the higher the tunnel rate.

3.1 Landau–Zener tunneling in Fe_8

The nonadiabatic transition between the two states in a two-level system was first discussed by Landau (1932), Zener (1932), and Stückelberg (1932). The original work by Zener concentrates on the electronic states of a biatomic molecule, while Landau and Stückelberg considered two atoms that undergo a scattering process. Their solution of the time-dependent Schrödinger equation of a two-level system could be applied to many physical systems and it became an important tool for studying tunneling transitions. The Landau–Zener model has also been applied to spin tunneling in nanoparticles and clusters (Miyashita, 1995,1996; Rose and Stamp, 1998; Thorwart, Grifoni and Hänggi, 2000; Leuenberger and Loss, 2000a). The tunneling probability P when sweeping the longitudinal field H_z at a constant rate over an avoided energy level crossing (Figure 7) is given by

$$P_{m,m'} = 1 - \exp\left[-\frac{\pi \Delta_{m,m'}^2}{2\hbar g \mu_{\mathrm{B}} |m - m'| \mu_0 \mathrm{d}H_z/\mathrm{d}t}\right] \qquad (2)$$

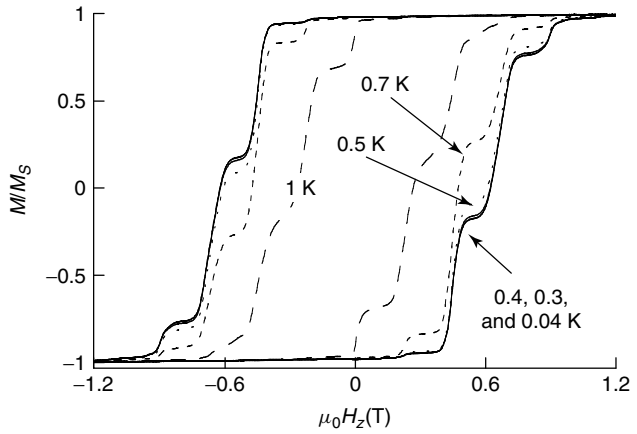

Figure 6. Hysteresis loops of a single crystal of Fe_8 molecular clusters at different temperatures. The longitudinal field (z-direction) was swept at a constant sweeping rate of $0.014\,\mathrm{T\,s^{-1}}$. The loops display a series of steps, separated by plateaus. As the temperature is lowered, there is a decrease in the transition rate due to reduced thermal-assisted tunneling. The hysteresis loops become temperature independent below 0.35 K, demonstrating quantum tunneling at the lowest energy levels. (Reproduced from W. Wernsdorfer *et al*., 1999, with permission from The American Association for the Advancement of Science. © 1999.)

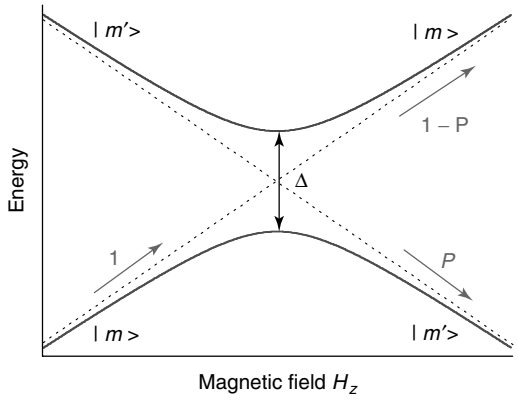

Figure 7. Detail of the energy-level diagram near an avoided level crossing. m and m' are the quantum numbers of the energy level. $P_{m,m'}$ is the Landau–Zener tunnel probability when sweeping the applied field from left to right over the anticrossing. The greater the gap Δ and the slower the sweeping rate, the higher is the tunnel rate (equation (2)).

Here, m and m' are the quantum numbers of the avoided level crossing, $\mathrm{d}H_z/\mathrm{d}t$ is the constant field sweeping rates, $g \approx 2$, μ_B is the Bohr magneton, and $\hbar$ is Planck's constant.

With the Landau–Zener model in mind, we can now start to understand the hysteresis loops qualitatively (Figure 6). Let us start at a large negative magnetic field H_z. At very low temperatures, all molecules are in the $m = -10$ ground state (Figure 5). When the applied field H_z is ramped down to zero, all molecules stay in the $m = -10$ ground state. When ramping the field over the $\Delta_{-10,10}$–region at $H_z \approx 0$, there is a Landau–Zener tunnel probability $P_{-10,10}$ to tunnel from the $m = -10$ to the $m = 10$ state. $P_{-10,10}$ depends on the sweeping rate (equation (2)), that is, the slower the sweeping rate, the larger the value of $P_{-10,10}$. This is clearly demonstrated in the hysteresis loop measurements showing larger steps for slower sweeping rates (Wernsdorfer and Sessoli, 1999). When the field H_z is now further increased, there is a remaining fraction of molecules in the $m = -10$ state that become a metastable state. The next chance to escape from this state is when the field reaches the $\Delta_{-10,9}$ region. There is a Landau–Zener tunnel probability $P_{-10,9}$ to tunnel from the $m = -10$ to the $m = 9$ state. As $m = 9$ is an excited state, the molecules in this state desexcite quickly to the $m = 10$ state by emitting a phonon. An analogous procedure takes place when the applied field reaches the $\Delta_{-10,10-n}$ regions ($n = 2, 3, \ldots$) until all molecules are in the $m = 10$ ground state, that is, the magnetization of all molecules is reversed. As phonon emission can only change the molecule state by $\Delta m = 1$ or 2, there is a phonon cascade for higher applied fields.

In order to apply the Landau–Zener formula (equation (2)) quantitatively, we first saturated the crystal of Fe_8 clusters in a field of $H_z = -1.4\,\mathrm{T}$, yielding an initial magnetization $M_\mathrm{in} = -M_\mathrm{s}$. Then, we swept the applied field at a constant rate over one of the resonance transitions and measured the fraction of molecules that reversed their spin. This procedure yields the tunneling rate $P_{-10,10-n}$ and thus the tunnel splitting $\Delta_{-10,10-n}$ (equation (2)) with $n = 0, 1, 2, \ldots$.

We first checked the predicted Landau–Zener sweeping field dependence of the tunneling rate. We found a good agreement for sweeping rates between 10 and $0.001\,\mathrm{T\,s^{-1}}$ (Wernsdorfer and Sessoli, 1999). The deviations at lower sweeping rates are mainly due to the *hole digging mechanism* (Wernsdorfer *et al*., 1999), which slows down the relaxation (Section 7.2). Our measurements showed for the first time that the Landau–Zener method is particularly adapted for molecular clusters because it works even in the presence of dipolar fields, which spread the resonance transition provided that the field sweeping rate is not too small.

3.2 Oscillations of tunnel splitting

An applied field in the xy plane can tune the tunnel splittings $\Delta_{m,m'}$ via the S_x and S_y spin operators of the Zeeman terms that do not commute with the spin Hamiltonian. This effect can be demonstrated by using the Landau–Zener method (Section 3.1). Figure 8 presents a detailed study of the tunnel splitting $\Delta_{\pm 10}$ at the tunnel transition between $m = \pm 10$, as a function of transverse fields applied at different angles φ, defined as the azimuth angle between the anisotropy

hard axis and the transverse field (Figure 4). For small angles φ, the tunneling rate oscillated with a period of $\sim$0.4 T, whereas no oscillations were present for large angles φ (Wernsdorfer and Sessoli, 1999). In the latter case, a much stronger increase of $\Delta_{\pm 10}$ with transverse field was observed. The transverse field dependence of the tunneling rate for different resonance conditions between the state $m = -10$ and $(10 - n)$ can be observed by sweeping the longitudinal field around $\mu_0 H_z = n \times 0.22\,\mathrm{T}$ with $n = 0, 1, 2, \ldots$. The corresponding tunnel splittings $\Delta_{-10,10-n}$ oscillated with almost the same period of $\sim$0.4 T (Figure 8). In addition, a comparison of quantum transitions between $m = -10$ and $(10 - n)$, with n even or odd, revealed a parity (or symmetry) effect that is analogous to the Kramers' suppression of tunneling predicted for half-integer spins (Loss, DiVincenzo and Grinstein, 1992; von Delft and Henley, 1992). A similar strong dependence on the azimuth angle φ was observed for all studied resonances.

3.2.1 Semiclassical descriptions

Before showing that the preceding results can be derived by an exact numerical calculation using the quantum operator formalism, it is useful to discuss semiclassical models. The original prediction of oscillation of the tunnel splitting was done by using the path integral formalism (Feynman, Leighton and Sand, 1970). Here (Garg, 1993), the oscillations are explained by constructive or destructive interference of quantum spin phases (Berry phases) of two tunnel paths (instanton trajectories) (Figure 4). After our experiments were reported, the Wentzel–Kramers–Brillouin theory has been used independently by Garg (1999) and Villain and Fort (2000). The surprise is that although these models (Garg, 1993,1999; Villain and Fort, 2000) are derived semiclassically, and should have higher-order corrections in $1/S$, they appear to be exactly as written! This has first been noted in Garg (1999) and Villain and Fort (2000) and then proved in Kececioglu and Garg (2001). Some extensions or alternative explications of Garg's result can be found in Barnes (1999), Liang, Mueller-Kirsten, Park and Pu (2000), Yoo and Lee (2000), and Rong *et al.* (2000).

The period of oscillation is given by (Garg, 1993)

$$\Delta H = \frac{2k_\mathrm{B}}{g\mu_\mathrm{B}}\sqrt{2E(E+D)} \tag{3}$$

where D and E are defined in equation (1). We find a period of oscillation of $\Delta H = 0.26\,\mathrm{T}$ for $D = 0.275\,\mathrm{K}$ and $E = 0.046\,\mathrm{K}$ as in Barra *et al.* (1996). This is somewhat smaller than the experimental value of $\sim$0.4 T. We believe that this is due to higher-order terms of the spin Hamiltonian, which are neglected in Garg's calculation. These terms can easily be included in the operator formalism as shown in the next section.

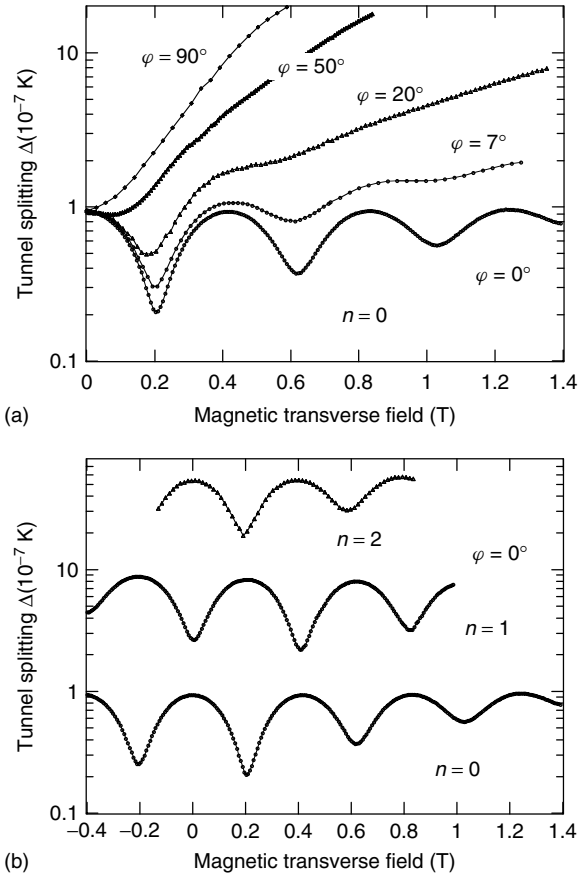

Figure 8. Measured tunnel splitting Δ as a function of transverse field for (a) several azimuth angles φ at $m = \pm 10$ and (b) $\varphi \approx 0^\circ$, as well as for quantum transition between $m = -10$ and $(10 - n)$. Note the parity effect that is analogous to the suppression of tunneling predicted for half-integer spins. It should also be mentioned that internal dipolar and hyperfine fields hinder a quench of Δ, which is predicted for an isolated spin. (Reproduced from W. Wernsdorfer *et al.*, 1999, with permission from The American Association for the Advancement of Science. © 1999.)

3.2.2 Exact numerical diagonalization

In order to quantitatively reproduce the observed periodicity we included fourth-order terms in the spin Hamiltonian (equation (1)) as employed in the simulation of inelastic neutron scattering measurements (Caciuffo *et al.*, 1998; Amoretti *et al.*, 2000) and performed a diagonalization of the $[21 \times 21]$ matrix describing the $S = 10$ system. For the calculation of the tunnel splitting we used $D = 0.289\,\mathrm{K}$, $E = 0.055\,\mathrm{K}$ (equation (1)), and the fourth-order terms as defined in Caciuffo *et al.* (1998) with $B_4^0 = 0.72 \times 10^{-6}\,\mathrm{K}$, $B_4^2 = 1.01 \times 10^{-5}\,\mathrm{K}$, and $B_4^4 = -0.43 \times 10^{-4}\,\mathrm{K}$, which are close to the values obtained by EPR measurements (Barra,

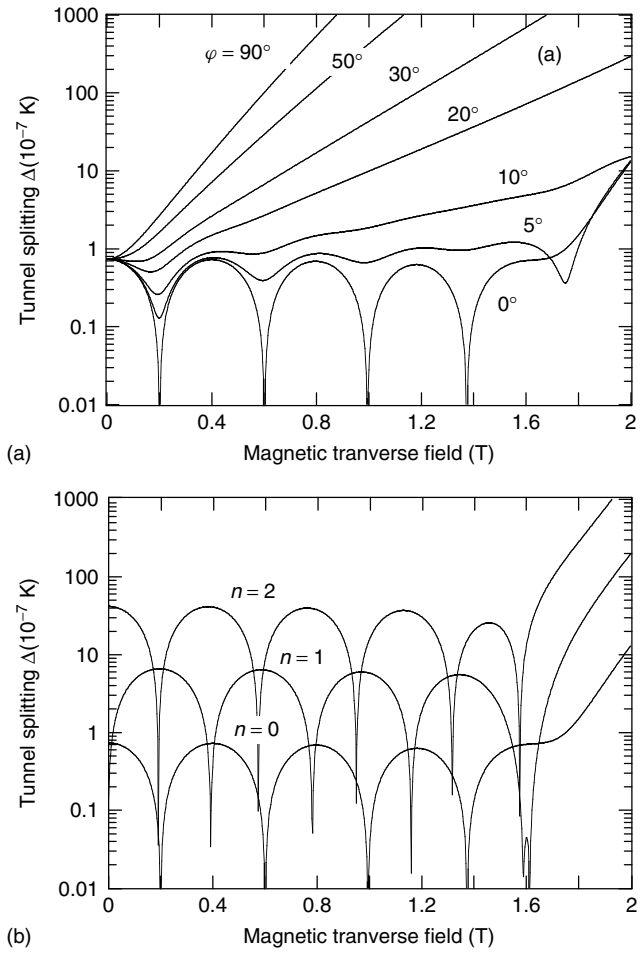

Figure 9. Calculated tunnel splitting Δ as a function of transverse field for (a) quantum transition between $m = \pm 10$ at several azimuth angles φ and (b) quantum transition between $m = -10$ and $(10 - n)$ at $\varphi = 0^{\circ}$ (Section 3.2.2). The fourth-order terms suppress the oscillations of Δ for large transverse fields $|H_x|$. (Reproduced from W. Wernsdorfer *et al.*, 1999, with permission from The American Association for the Advancement of Science. © 1999.)

Gatteschi and Sessoli, 2000) and neutron scattering measurements (Amoretti *et al.*, 2000).

The calculated tunnel splittings for the states involved in the tunneling process at the resonances $n = 0$, 1, and 2 are reported in Figure 9, showing the oscillations as well as the parity effect for odd resonances.

3.2.3 Spin-parity effect

The spin-parity effect is among the most interesting quantum phenomena that can be studied at the mesoscopic level in SMMs. It predicts that quantum tunneling is suppressed at zero applied field if the total spin of the magnetic system is half-integer but is allowed in integer spin systems. Enz and Schilling (1986), and van Hemmen and Süto (1986) were the first to suggest the absence of tunneling as a consequence of Kramers degeneracy [1].

The predicted spin-parity effect can be observed by measuring the tunnel splitting as a function of transverse field (Wernsdorfer *et al.*, 2002a). An integer spin system is rather insensitive to small transverse fields, whereas a half-integer-spin system is much more sensitive. However, a half-integer-spin system also undergoes tunneling at zero external field as a result of environmental degrees of freedom such as hyperfine and dipolar couplings or small intermolecular exchange interaction.

The best observation of the spin-parity effect has been seen for two molecular Mn_{12} clusters with a spin ground state of $S = 10$ and $S = 19/2$ showing oscillations of the tunnel probability as a function of a transverse field being due to topological quantum phase interference of two tunnel paths of opposite windings (Section 3.2.1). Spin-parity-dependent tunneling was established for the first time in these compounds by comparing the quantum phase interference of integer and half-integer-spin systems (Wernsdorfer, Chakov and Christou, 2005).

3.3 A classical approach with applications to the quantum regime

Recently, the molecular (or bottom-up) approach has reached the size regime of the classical (or top-down) approach to nanoscale magnetic materials (Tasiopoulos *et al.*, 2004). Indeed, a giant Mn_{84} SMM was reported with a 4-nm-diameter torus structure, exhibiting both magnetization hysteresis and quantum tunneling. The study of such large systems is greatly complicated by the fact that the spin Hilbert space is huge and it is impossible to treat such systems with exact matrix diagonalization methods. However, since some SMMs are now as large as some classical nanoparticles, it raises the interesting possibility that classical models commonly employed to study the latter may be used to obtain a first-order understanding of large molecular systems. Indeed, we herein propose the use of the classical Néel–Brown model (Néel, 1949; Brown, 1963; Coffey *et al.*, 1995) of thermally activated magnetization reversal of a magnetic single-domain particle in order to study large SMMs. This method allows us to determine important parameters that characterize the magnetic properties of the SMM: the energy barrier, the magnetic anisotropy constant, the spin, τ_0, and the crossover temperature from the classical to the quantum regime. The method is particularly useful for SMMs having low-lying energy states and not showing quantum tunneling steps in hysteresis loops. In such systems, electron paramagnetic resonance (EPR) measurements often exhibit

only very broad absorption peaks, which do not allow the determination of the magnetic anisotropy.

3.3.1 The Néel–Brown model of thermally activated magnetization reversal

The method is based on the Néel–Brown model of thermally activated magnetization reversal of a magnetic single-domain particle, which has two equivalent ground states of opposite magnetization separated by an energy barrier due to magnetic anisotropy (Néel, 1949; Brown, 1963; Coffey *et al.*, 1995). The system can escape from one state to the other either by thermal activation over the barrier at high temperatures or by quantum tunneling at low temperatures. At sufficiently low temperatures and at zero field, the energy barrier between the two states of opposite magnetization is much too high to observe an escape process. However, the barrier can be lowered by applying a magnetic field in the direction opposite to that of the particle's magnetization. When the applied field is close enough to the reversal field, thermal fluctuations are sufficient to allow the system to overcome the barrier, and the magnetization is reversed.

This stochastic escape process can be studied via the relaxation time method consisting of the measurement of the probability that the magnetization has not reversed after a certain time. In the case of an assembly of identical and isolated particles, it corresponds to measurements of the relaxation of magnetization. According to the Néel–Brown model, the probability that the magnetization has not reversed after a time t is given by

$$P(t) = e^{-t/\tau} \tag{4}$$

and τ (inverse of the reversal rate) can be expressed by an Arrhenius law of the form:

$$\tau(T, H) = \tau_0 e^{\Delta E(H)/k_B T} \tag{5}$$

where $\Delta E(H)$ is the field-dependent energy barrier height and τ_0 is the inverse of the attempt frequency. In most cases, $\Delta E(H)$ can be approximated by

$$\Delta E(H) \approx E_0 \left(1 - \frac{H}{H_c^0}\right)^{\alpha} \tag{6}$$

where H_c^0 is the reversal field at zero temperature, E_0 is the barrier height at zero applied field, and α is a constant of the order of unity (for most cases $1.5 \leq \alpha \leq 2$). In the case of a Stoner–Wohlfarth particle (Néel, 1947; Stoner and Wohlfarth, 1948) with uniaxial anisotropy and the field applied along the easy axis of magnetization, all constants can be determined analytically (Néel, 1947,1949): $\alpha = 2$, $E_0 = KV$, and $H_c^0 = 2K/M_s$, where K is the uniaxial anisotropy constant, V is the particle volume, and M_s is the saturation magnetization. For SMMs with dominating uniaxial anisotropy, $\alpha = 2$, $E_0 = DS^2$, and $H_c^0 = 2DS/g\mu_0\mu_B$. However, in general, all constants depend to some degree on the fine details of the magnetic anisotropy and the direction of the applied field H (Thiaville, 1998, 2000).

In order to study the field dependence of the relaxation time $\tau(T, H)$ and to obtain the parameters of the model, the decay of magnetization has to be studied at many applied fields H and temperatures T. This is experimentally very time consuming and complicated by the fact that the equilibrium magnetization is temperature dependent and difficult to obtain for long relaxation times. In addition, for fast relaxation times the initial magnetization depends on the field sweep rates to apply to the field. The number of exploitable decades for τ values is therefore limited for relaxation time measurements.

A more convenient method for studying the magnetization decay is by ramping the applied field at a given rate (Wernsdorfer *et al.*, 1997a) and measuring the coercive field H_c (the field value to obtain zero magnetization), which is then measured as a function of the field sweep rate and temperature.

The mathematical transformation from a reversal time probability (equations (4) and (5)) to a reversal field probability was first given by Kurkijärvi (1972) for the critical current in SQUIDs. Later, Gunther and Barbara calculated similar expressions for magnetic domain-wall junctions (Gunther and Barbara, 1994). A more general calculation was evaluated by Garg (1995). Here, we use a simplified version (Wernsdorfer *et al.*, 1997a) [2] and approximate the mean reversal field of an assembly of identical particles or SMMs by the coercive field H_c:

$$H_c(T, v) \approx H_c^0 \left(1 - \left[\frac{kT}{E_0} \ln\left(\frac{c}{v}\right)\right]^{1/\alpha}\right) \tag{7}$$

where the field sweeping rate is given by $v = \mathrm{d}H/\mathrm{d}t$; H_c^0 is the coercive field at zero temperature, and $c = H_c^0 k_B T / [\tau_0 \alpha E_0 (1 - H_c/H_c^0)^{\alpha-1}]$ (Wernsdorfer *et al.*, 1997a).

3.3.2 Application to Mn_{12} SMMs

The method is applied here to Mn_{12} SMMs with a spin ground state of $S = 10$ (Murugesu *et al.*, 2005). Figure 10 shows typical hysteresis loops with a series of quantum steps separated by plateaus. In order to apply the preceding method, the temperature and field sweep rate dependencies of the coercive fields H_c were measured and plotted in Figure 11. As expected for a thermally activated process, H_c increases with decreasing temperature and increasing field

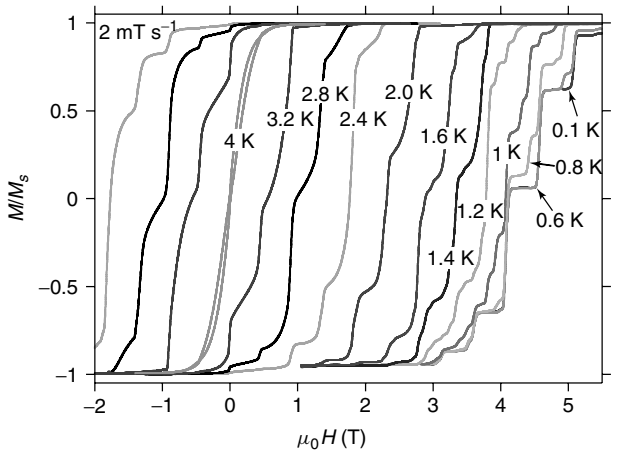

Figure 10. Hysteresis loops of single crystals of a Mn_{12} molecular cluster at different temperatures and a constant field sweep rate indicated in the figure. The loops display a series of steps, separated by plateaus. As the temperature is lowered, there is a decrease in the transition rate due to reduced thermal-assisted tunneling. The hysteresis loops become temperature independent below 0.6 K, demonstrating quantum tunneling at the lowest energy levels. (Reproduced from W. Wernsdorfer *et al.*, 2006, with permission from the American Physical Society. © 2006.)

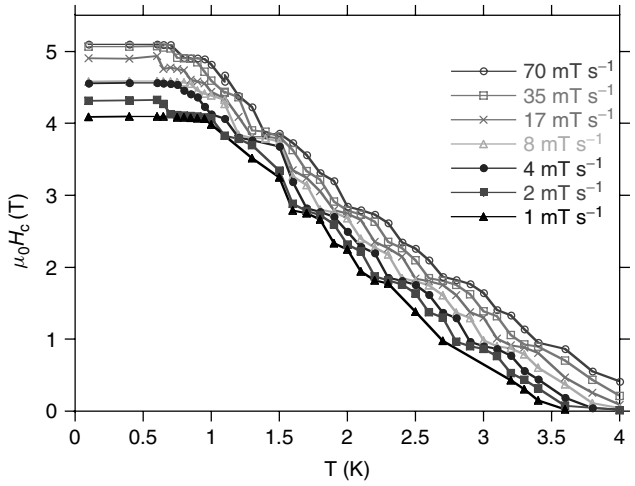

Figure 11. Coercive field H_c for Mn_{12} as a function of temperature. Note the steps of H_c coming from the resonant tunneling steps in the hysteresis loops (Figure 10). (Reproduced from W. Wernsdorfer *et al.*, 2005, with permission from the American Physical Society. © 2005.)

sweep rate. Furthermore, all measurements show an almost logarithmic dependence of H_c on the field sweep rate. H_c becomes temperature independent below about 0.6 K.

The validity of equation (7) was tested by plotting the set of $H_c(T, v)$ values as a function of $[Tln(c/v)]^{1/2}$ where $c = H_c^0 k_B T/[\tau_0 2E_0(1 - H_c/H_c^0)]$. If the underlying model is sufficient, all points should collapse onto one straight line by choosing the proper values for the constant τ_0. We found

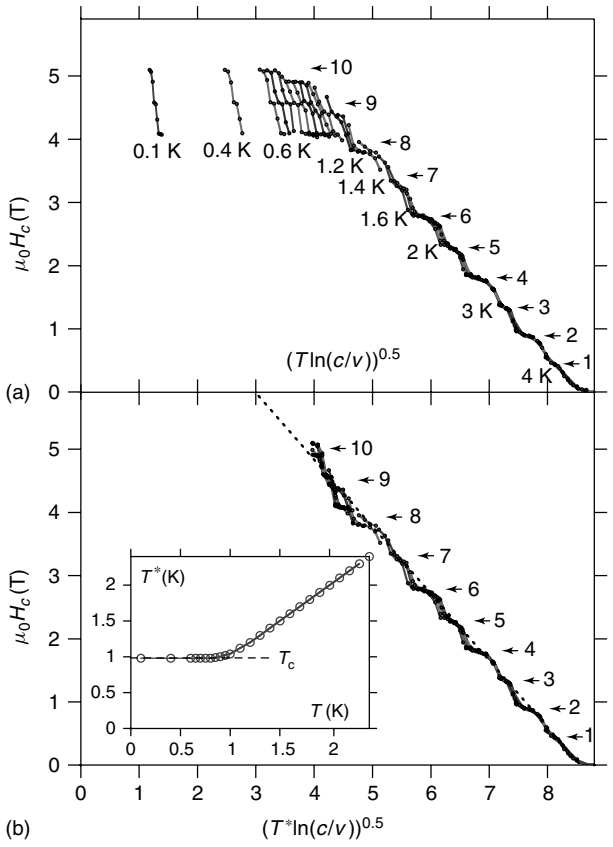

Figure 12. (a) Scaling plot of the coercive field $H_c(T, v)$ of Mn_{12} for field sweep rates between 0.0001 and 0.1 T s^{-1} and several temperatures: 0.1 K, 0.4 K, from 0.6 to 1 K in steps of 0.05 K, and from 1 to 4 K in steps of 0.1 K. The arrows indicate the step index $n = -(m + m')$ where m and m' are the quantum numbers of the corresponding level crossing. Note the parity effect of the steps: even n have larger steps than odd n. (b) Same data of $H_c(T, v)$ and same scales but the real temperature T is replaced by an effective temperature T^* (see inset), which restores the scaling below 1.1 K. (Reproduced from W. Wernsdorfer *et al.*, 2005, with permission from the American Physical Society. © 2005.)

that the data of $H_c(T, v)$ fell on a master curve provided $\tau_0 = 2.1 \times 10^{-7}$ s.

At low temperatures, strong deviations from the master curves are observed. In order to investigate the possibility that these low-temperature deviations are due to escape from the metastable potential well by tunneling, a common method for classical models is to replace the real temperature T by an effective temperature $T^*(T)$ in order to restore the scaling plot (Wernsdorfer *et al.*, 1997b). In the case of tunneling, $T^*(T)$ should saturate at low temperatures. Indeed, the ansatz of $T^*(T)$, as shown in the inset of Figure 12(b), can unequivocally restore the scaling plot demonstrated by a straight master curve (Figure 12b). The flattening of T^* corresponds to a saturation of the escape rate, which is a necessary signature of tunneling. The crossover temperature T_c can be defined as

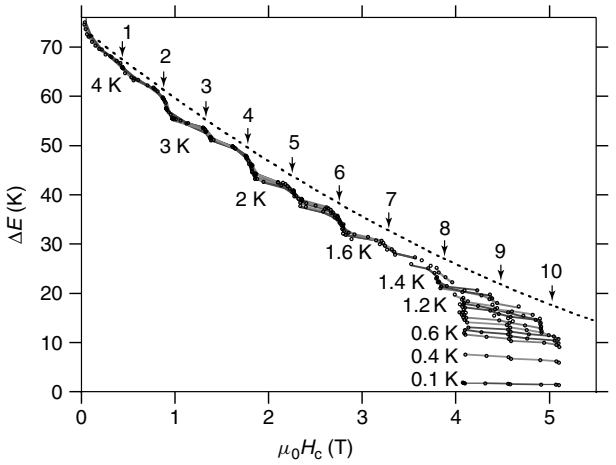

Figure 13. Field dependence of the energy barrier of Mn_{12} obtained from [2] and the set of $H_c(T, v)$ data from Figure 12. The arrows indicate the step index $n = -(m + m')$, where m and m' are the quantum numbers of the corresponding level crossing. Note the steplike reduction of the energy barrier due to resonant tunneling and the parity effect of the steps: even n have larger steps than odd n. The dotted line gives the classical barrier $\Delta E = E_0(1 - H/H_a)^2$ with $E_0 = 74\,\mathrm{K}$ and $H_a = 9.8\,\mathrm{T}$. (Reproduced from W. Wernsdorfer *et al.*, 2005, with permission from the American Physical Society. © 2005.)

the temperature where the quantum rate equals the thermal one. The inset of Figure 12(b) gives $T_c = 0.97\,\mathrm{K}$. The slopes and the intercepts of the master curves give $E_0 = 72.4\,\mathrm{K}$ and $H_c^0 = 9.1\,\mathrm{T}$. The E_0 values are in good agreement with those extracted from Arrhenius plots (69 K) (Murugesu *et al.*, 2005). This result allows us to estimate the spin ground state using $S = 2E_0/(g\mu_B\mu_0 H_c^0)$: $S = 11$. This differs slightly from $S = 10$ determined via magnetization measurements. This deviation is due to quantum effects in the thermally activated regime and is considered further in the subsequent text.

Several points should be mentioned: (i) The classical regime of the model corresponds in most SMMs to the thermally activated tunneling regime with tunneling close to the top of the energy barrier. Because all parameters are deduced from this regime, small deviations from the exact values are expected. (ii) The field dependence of the energy barrier can be obtained directly using [2] and is plotted in Figure 13. (iii) Equation (7) is not valid for fields that are close to $H = 0$ because the model only takes into account the transitions from the metastable to the stable well. However, close to $H = 0$, transitions between both wells are possible, leading to a rounding of the master curve at small fields. (iv) The method can be applied to powder samples with random orientations of the molecules. In this case, $\alpha \approx 1.5$, $vE_0 = DS^2$ where v can be calculated (Thiaville, 1998,2000), and the intercept of the master curve gives $H_c^0/2$. (v) In the case of a distribution of anisotropies, different parts of the distribution can be probed by applying the method at different M values. (vi) This method is insensitive to small intermolecular interactions when H_c is larger than the typical interaction field. (vii) The method can be generalized for 1D, 2D, and 3D networks of spins. In this case, equation (6) describes a nucleation barrier.

4 QUANTUM DYNAMICS OF A DIMER OF NANOMAGNETS

We present here a new family of dimers of nanomagnets (Wernsdorfer, Aliaga-Alcalde, Hendrickson and Christou, 2002) in which antiferromagnetic coupling between two SMMs results in quantum behavior that is different from that of the individual SMMs. Each SMM acts as a bias on its neighbor, shifting the quantum tunneling resonances of the individual SMMs. Hysteresis loop measurements on a single crystal of SMM dimers established quantum tunneling of the magnetization via entangled states of the dimer. This shows that the dimer really does behave as a quantum-mechanically coupled dimer, and also allows the measurement of the longitudinal and transverse superexchange coupling constants (Tiron *et al.*, 2003). The experimental evidence for entangled states was confirmed by an EPR study (Hill, Edwards, Aliaga-Alcalde and Christou, 2003).

The compound $[Mn_4O_3Cl_4(O_2CEt)_3(py)_3]$ crystallizes in the hexagonal space group $R3$(bar) with two Mn_4 molecules per unit cell lying head to head on a crystallographic S_6 symmetry axis (Wernsdorfer, Aliaga-Alcalde, Hendrickson and Christou, 2002) (Figure 14). Each Mn_4 monomer has a ground-state spin of $S = 9/2$, well separated from the first excited state $S = 7/2$ by a gap of about 300 K (Hendrickson *et al.*, 1992). The Mn−Mn distances and the Mn-O-Mn angles are similar, and the uniaxial anisotropy constant is expected to be the same for the two dimer systems. These dimers are held together via six C−H···Cl hydrogen bonds between the pyridine (py) rings on one molecule and the Cl ions on the other, and one Cl···Cl Van der Waals interaction. These interactions lead to an antiferromagnetic superexchange interaction between the two Mn_4 units of the $[Mn_4]_2$ dimer (Wernsdorfer, Aliaga-Alcalde, Hendrickson and Christou, 2002). Dipolar couplings between Mn_4 molecules can be easily calculated and are more than one order of magnitude smaller than the exchange interaction.

Before presenting the measurements, we summarize a simplified spin Hamiltonian describing the $[Mn_4]_2$ dimer (Wernsdorfer, Aliaga-Alcalde, Hendrickson and Christou, 2002). Each Mn_4 SMM can be modeled as a *giant spin* of $S = 9/2$ with Ising-like anisotropy (equation (1)). The corresponding Hamiltonian is given by

$$\mathcal{H}_i = -DS_{z,i}^2 + \mathcal{H}_{\mathrm{trans},i} - g\mu_B\mu_0\vec{S}_i \cdot \vec{H} \qquad (8)$$

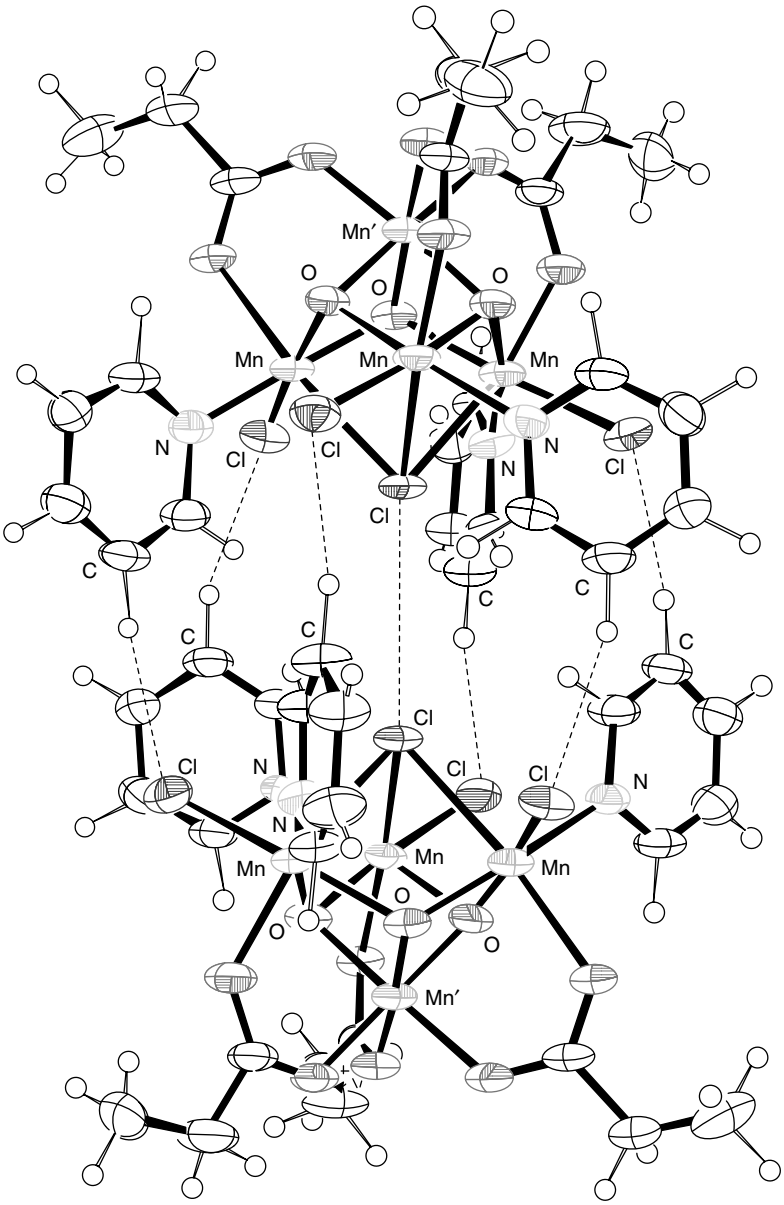

Figure 14. The structure of the $[Mn_4]_2$ dimer of $[Mn_4O_3Cl_4(O_2CEt)_3(py)_3]$. The small circles are hydrogen atoms. The dashed lines are C–H···Cl hydrogen bonds and the dotted line is the close Cl···Cl approach. The labels Mn and Mn^1 refer to Mn^{III} and Mn^{IV} ions, respectively.

where $i = 1$ or 2 (referring to the two Mn_4 SMMs of the dimer), D is the uniaxial anisotropy constant, and the other symbols have their usual meaning. Tunneling is allowed in these half-integer ($S = 9/2$) spin systems because of a small transverse anisotropy $\mathcal{H}_{\text{trans},i}$ containing $S_{x,i}$ and $S_{y,i}$ spin operators and transverse fields (H_x and H_y). The exact form of $\mathcal{H}_{\text{trans},i}$ is not important in this discussion. The last term in equation (8) is the Zeeman energy associated with an applied field. The Mn_4 units within the $[Mn_4]_2$ dimer are coupled by a weak superexchange interaction via both the six C–H···Cl pathways and the Cl···Cl approach. Thus, the Hamiltonian ($\mathcal{H}$) for $[Mn_4]_2$ is

$$\mathcal{H} = \mathcal{H}_1 + \mathcal{H}_2 + J_z S_{z,1} S_{z,2} + J_{xy}(S_{x,1} S_{x,2} + S_{y,1} S_{y,2}) \quad (9)$$

where J_z and J_{xy} are the longitudinal and transverse superexchange interactions, respectively. $J_z = J_{xy}$ is the case of isotropic superexchange. The $(2S + 1)^2 = 100$ energy states of the dimer can be calculated by exact numerical diagonalization and are plotted in Figure 15 as a function of applied field along the easy axis. Each state of $[Mn_4]_2$ can be labeled by two quantum numbers (M_1, M_2) for

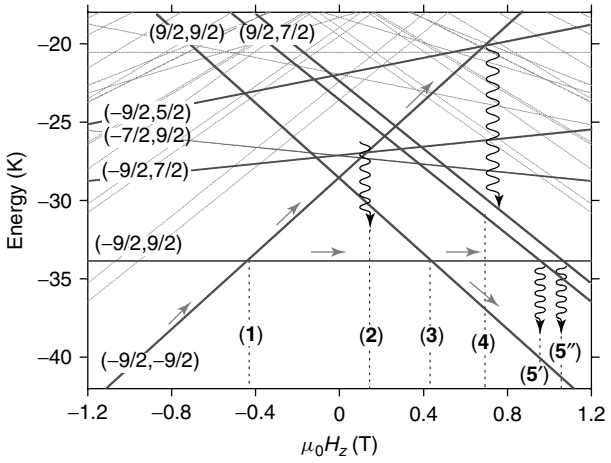

Figure 15. Low-lying spin-state energies of the $[Mn_4]_2$ dimer, calculated by exact numerical diagonalization using equation (9) with $D = 0.77$ K and $J = 0.13$ K, as a function of applied magnetic field H_z (Zeeman diagram). The bold energy levels are labeled with two quantum numbers (M_1, M_2). Dotted lines, labeled 1 to 5, indicate the strongest tunnel resonances: **1**: (−9/2,−9/2) to (−9/2,9/2); **2**: (−9/2,−9/2) to (−9/2,7/2), followed by relaxation to (−9/2,9/2); **3**: (−9/2,9/2) to (9/2,9/2); **4**: (−9/2,−9/2) to (−9/2,5/2), followed by relaxation to (−9/2,9/2); **5**: (−9/2,9/2) to (7/2,9/2), followed by relaxation to (9/2,9/2). For clarity, degenerate states such as (M, M′) and (M′, M) and lifted degenerate states such as $(M, M \pm 1)$, $(M, M \pm 2)$, and so on, are not listed. For example, the $(9/2, 7/2)$ and $(7/2, 9/2)$ states are strongly split into a symmetric (labeled **5″**) and antisymmetric (labeled **5′**) combination of $(9/2, 7/2)$ and $(7/2, 9/2)$ states. This splitting is used to measure the transverse superexchange interaction constant J_{xy}. Cotunneling and other two-body tunnel transitions have a lower probability of occurrence and are neglected (Wernsdorfer *et al*., 2002b). (Reproduced from R. Tiron *et al*., 2003, with permission from the American Physical Society. © 2003.)

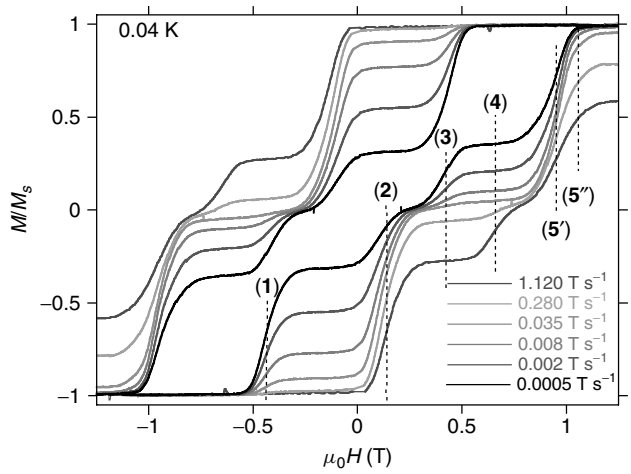

Figure 16. Hysteresis loops for the $[Mn_4]_2$ dimer at several field sweep rates and 40 mK. The tunnel transitions (manifested by steps) are labeled from **1** to **5** (see Figure 1). (Reproduced from R. Tiron *et al*., 2003, with permission from the American Physical Society. © 2003.)

the two Mn_4 SMMs, with $M_1 = -9/2, -7/2, \ldots, 9/2$ and $M_2 = -9/2, -7/2, \ldots, 9/2$. The degeneracy of some of the (M_1, M_2) states is lifted by transverse anisotropy terms. For the sake of simplicity, we mainly discuss the effect of the transverse superexchange interaction $\mathcal{J}_{\text{trans}} = J_{xy}(S_{x,1}S_{x,2} + S_{y,1}S_{y,2}) = J_{xy}(S_{+,1}S_{-,2} + S_{-,1}S_{+,2})/2$, where $S_{+,i}$ and $S_{-,i}$ are the usual spin raising and lowering operators. Because $\mathcal{J}_{\text{trans}}$ acts on $(M, M \pm 1)$ states to first order of perturbation theory, the degeneracy of these states is strongly lifted. For example, the $(9/2, 7/2)$ and $(7/2, 9/2)$ states are strongly split into a symmetric (labeled **5″**) and antisymmetric (labeled **5′**) combination of $(9/2, 7/2)$ and $(7/2, 9/2)$ states. Similar results hold for the $(-9/2, -7/2)$ and $(-7/2, -9/2)$ states. Measurement of this energy splitting allows us to determine the transverse superexchange interaction constant J_{xy} because the latter is proportional to the former.

Figure 16 shows typical hysteresis loops (magnetization vs magnetic field scans) with the field applied along the easy axis of magnetization of $[Mn_4]_2$, that is, parallel to the S_6 axis. These loops display steplike features separated by plateaus. The step heights are temperature independent below ∼0.35 K (Wernsdorfer, Aliaga-Alcalde, Hendrickson and Christou, 2002). The steps are due to resonant quantum tunneling of magnetization (QTM) between the energy states of the $[Mn_4]_2$ dimer (see captions of Figures 15 and 16 for a discussion of five tunnel transitions). QTM has been previously observed for most SMMs, but the novelty for $[Mn_4]_2$ dimers is that the QTM is now the collective behavior of the complete $S = 0$ dimer of exchange-coupled $S = 9/2$ Mn_4 quantum systems. This coupling is manifested as an exchange bias of all tunneling transitions, and the resulting hysteresis loop consequently displays unique features, such as the absence for the first time in an SMM of a QTM step at zero field (Wernsdorfer, Aliaga-Alcalde, Hendrickson and Christou, 2002).

Even though the five strongest tunneling transitions are observed in Figure 16, fine structure is not observed. For example, the hysteresis loops do not show the splitting of the $(9/2, 7/2)$ states (labeled **5′** and **5″**), which we suspected might be due to line broadening. Usually, line broadening in SMMs is caused by dipolar and hyperfine interactions (Prokof'ev and Stamp, 1998), and distributions of anisotropy and exchange parameters. In most SMMs, the zero-field resonance is mainly broadened by dipolar and hyperfine interactions because distributions of anisotropy parameters do not affect the zero-field resonance. For an antiferromagnetically coupled dimer, however, this resonance is shifted to negative fields. Therefore, a distribution of the exchange coupling parameter J_z can further broaden this resonance. In fact, we showed that the latter is the dominant source of broadening (Tiron *et al*., 2003). We used the 'quantum hole

digging' method (see Section 7.2) (Prokof'ev and Stamp, 1998; Wernsdorfer *et al*., 1999, 2000; Alonso and Fernandez, 2001; Tupitsyn, Stamp and Prokof'ev, 2004) to provide direct experimental evidence for the transitions **5′** and **5″**, which established tunneling involving entangled dimer states and allowed us to determine J_{xy} (Tiron *et al*., 2003).

5 RESONANT PHOTON ABSORPTION IN Cr_7Ni ANTIFERROMAGNETIC RINGS

Magnetic molecules are currently considered to be among the most promising electron-spin-based quantum systems for storing and processing quantum information. For this purpose, ferromagnetic (Leuenberger and Loss, 2001) and antiferromagnetic (Meier, Levy and Loss, 2003a,b) systems have attracted an increasing interest (Troiani *et al*., 2005a,b). In the latter case, the quantum hardware is thought of as a collection of coupled molecules, each corresponding to a different qubit. The main advantages would arise from the fact that they are extremely small and almost identical, allowing to obtain, in a single measurement, statistical averages of a large number of qubits. The magnetic properties can be modeled with an outstanding degree of accuracy. And, most importantly, the desired physical properties can be engineered chemically.

The suitability of Cr-based antiferromagnetic molecular rings for the qubit implementation has been proposed (Troiani *et al*., 2005a,b). The substitution of one metal ion in a Cr-based molecular ring with dominant antiferromagnetic couplings allows its level structure and ground-state degeneracy to be engineered (Overgaard *et al*., 2002; Larsen *et al*., 2003). A Cr_7Ni molecular ring was characterized by means of low-temperature specific-heat and torque-magnetometry measurements, thus determining the microscopic parameters of the corresponding spin Hamiltonian. The energy spectrum and the suppression of the leakage-inducing S-mixing render the Cr_7Ni molecule a suitable candidate for the qubit implementation (Carretta *et al*., 2005; Troiani *et al*., 2005a,b).

In this section, we report the first microsuperconducting quantum interference device (micro-SQUID) (Wernsdorfer, Müller, Mailly and Barbara, 2004) studies of the Cr_7Ni molecular ring (Wernsdorfer, Mailly, Timco and Winpenny, 2005). EPR methods are combined with high-sensitivity magnetization measurements. We found very narrow resonant photon absorption lines, which are mainly broadened by hyperfine interactions. Similar measurements were performed on Ni_4 molecules (del Barco, Kent, Yang and Hendrickson, 2004) but quantum coherence was not directly observed.

The Cr_7Ni molecular ring is based on a homometallic ring with formula $[Cr_8F_8(O_2CCMe_3)_{16}]$. The eight chromium(III) ions lie at the corners of a regular octagon (Overgaard *et al*., 2002). Each edge of the octagon is bridged by one fluoride ion and two pivalate ligands. There is a large cavity at the center of the ring. If a single chromium(III) ion is replaced by a metal(II) ion, for example, nickel(II), this makes the ring anionic and a cation can be incorporated in the cavity. Thus, we can synthesize the compound $[H_2NMe_2][Cr_7NiF_8(O_2CCMe_3)_{16}]$ (Larsen *et al*., 2003). If crystallized from a mixture of THF and MeCN, the Cr_8 and Cr_7Ni compounds are isostructural, crystallizing in the tetragonal space group, $P4$.

The measurements were made in a dilution cryostat using a single crystal of Cr_7Ni of size 20 µm. The magnetic probe was a micro-SQUID array (Wernsdorfer, 2001; Wernsdorfer, Müller, Mailly and Barbara, 2004) equipped with three coils allowing the application of a field in any direction and with sweep rates up to $10\,\mathrm{T\,s^{-1}}$. The electromagnetic radiation was generated by a frequency synthesizer triggered with a nanosecond pulse generator. This setup allows continuous variation of the frequency from 0.1 Hz to 20 GHz, with pulse lengths ∼1 ns to continuous radiation (Thirion, Wernsdorfer and Mailly, 2003). Using a gold radio frequency (RF) loop of size 50 µm, the RF radiation field was directed in a plane perpendicular to the applied static field $\mu_0 H$. The microwave power of the generator could be varied from −80 to 20 dBm (10^{-11} to 10^{-1} W). The sample absorbs only a small fraction of the generator power. This fraction is, however, proportional to the microwave power of the generator. The microwave amplitude B_{RF} can be estimated with the method described in Wernsdorfer, Müller, Mailly and Barbara (2004). We found $B_{\mathrm{RF}} \approx 1$ mT at 4 GHz and 15 dBm, which is more than 1000 times larger than that obtained in our previous work on V_{15} (Wernsdorfer, Müller, Mailly and Barbara, 2004).

Figure 17(a) shows magnetization versus applied field curves for several field sweep rates at a cryostat temperature of 0.04 K. The magnetization loops exhibit a clear hysteresis, which is characteristic of the phonon-bottleneck regime with a spin−phonon relaxation time to the cryostat of a few seconds (Chiorescu *et al*., 2000b). Note that the degeneracy of the Kramers doublet is lifted owing to internal transverse fields (mainly the transverse hyperfine fields). In order to quantify the out-of-equilibrium effect, Figure 17(b) presents the same data as in Figure 17(a) but the magnetization M is converted into a spin temperature T_S using the equation (Abragam and Bleaney, 1970)

$$M(T_S)/M_{\mathrm{s}} = \tanh\left(\frac{g\mu_{\mathrm{B}} S\mu_0 H}{k_{\mathrm{B}} T_S}\right) \tag{10}$$

with $S = 1/2$ and $g = 2.1$ (Larsen *et al*., 2003). Figure 17(b) shows clearly a strong adiabatic cooling when sweeping the

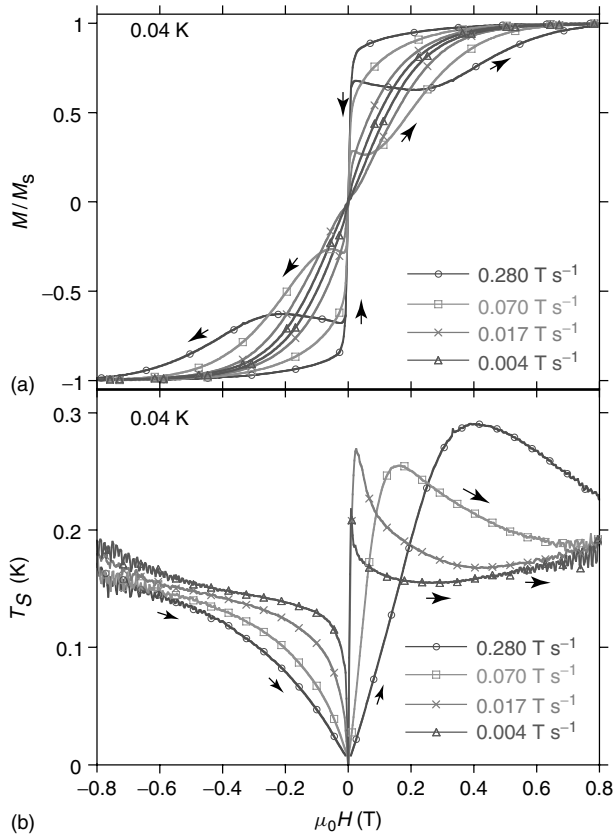

Figure 17. (a) Magnetization (M) hysteresis loops for several field sweep rates at a cryostat temperature of 0.04 K. The loops are normalized by the saturation magnetization M_s at 1.5 T. (b) Spin temperature T_S for field sweeps from negative to positive fields, obtained by inversion of equation (10), where $M(T_S)$ are the data in (a). (Reproduced from W. Wernsdorfer *et al*., 2005, with permission from the American Physical Society. © 2005.)

field down to zero field. Note that this cooling mechanism might be used before qubit operations to reach extremely low temperatures even at relatively high cryostat temperatures. High-frequency noise from the RF-loop around the sample leads to spin temperatures at 1 T being higher than the cryostat temperature.

Figure 18 shows magnetization curves $M(H)$ in the quasi-static regime with a field sweep rate slow enough ($0.14\,\mathrm{mTs^{-1}}$) to keep the system at equilibrium. During the field sweep, RF pulses are applied to the sample with a pulse length of 1 µs and a period of 4 s between each pulse. Depending on the RF frequency, clear dips are observed, which result from resonant absorptions of photons associated with spin transitions between the quantum numbers $m_s = 1/2$ and $-1/2$. After each pulse, the magnetization relaxes back to the equilibrium magnetization (see the fine structure in the inset of Figure 18).

Typical relaxation measurements at a constant applied field after RF pulses of different durations are shown in Figure 19.

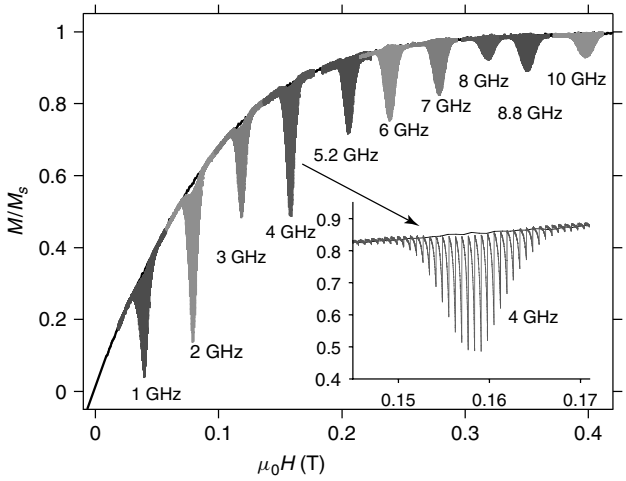

Figure 18. Magnetization curves measured with and without irradiation. The cryostat temperature was 40 mK and the field sweep rate of $0.14\,\mathrm{mT\,s^{-1}}$ was slow in order to keep the system at equilibrium. The electromagnetic radiation was pulsed with a period of 4 s and a pulse length of 1 µs. The RF frequencies are indicated and the RF amplitude is slightly frequency dependent. Inset: Enlargement of the 4 GHz resonance. The fine structure is due to the RF pulses. (Reproduced from W. Wernsdorfer *et al*., 2005, with permission from the American Physical Society. © 2005.)

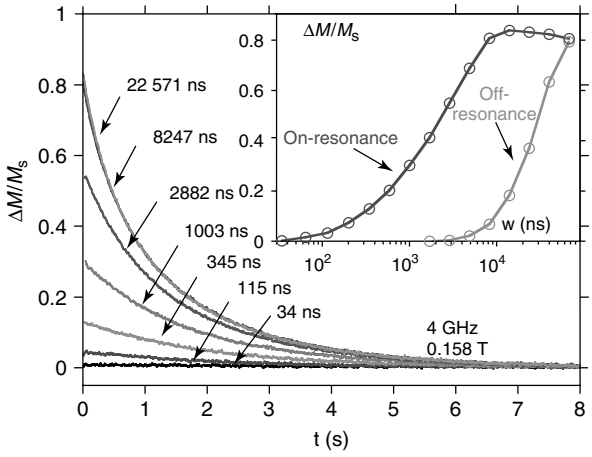

Figure 19. Relaxation of magnetization after an RF pulse of 4 GHz. The pulse lengths w are indicated. Inset: magnetization variation ΔM after a RF pulse versus the pulse length w for an on-resonance field (0.1582 T) and off-resonance field (0.1722 T). (Reproduced from W. Wernsdorfer *et al*., 2005, with permission from the American Physical Society. © 2005.)

The relaxation is exponential with the rate being independent of the pulse length. Detailed studies show that the relaxation rate is dominated by the phonon-bottleneck regime, that is, the spin–phonon relaxation time to the cryostat.

The inset of Figure 19 presents the change of magnetization ΔM between the magnetization before and after the pulse as a function of the pulse length w. ΔM increases linearly with w for short pulses of few tens of nanoseconds.

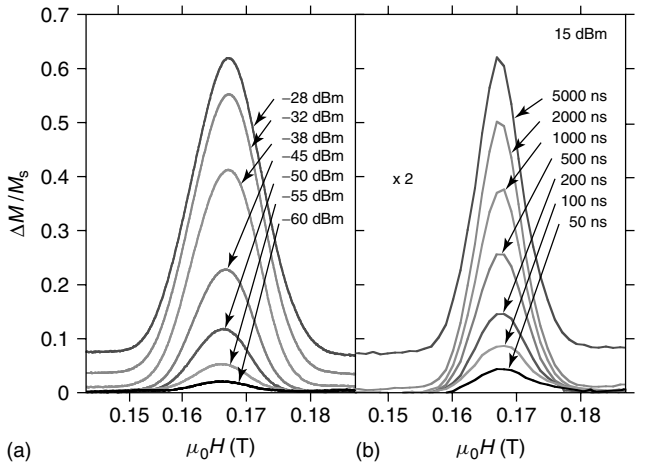

Figure 20. (a) Magnetization variation ΔM between the equilibrium curves measured without and with continuous irradiation. The microwave frequency was 4.2 GHz. The microwave powers of the generator are indicated. (b) Magnetization variation ΔM after a RF pulse of 4.2 GHz and several pulse lengths. The cryostat temperature was 40 mK. ΔM is multiplied by a factor two. (Reproduced from W. Wernsdorfer *et al.*, 2005, with permission from the American Physical Society. © 2005.)

It saturates for $w \approx 10\,\mu$s and decreases for very long pulses because of cryostat heating effects. Nonresonant photon absorption is also observed for very long pulses.

The resonant photon absorption lines are often taken to estimate a lower bound on the decoherence time of a qubit. We therefore investigated the linewidth observed in Figure 18 in more detail. Figure 20(a) presents a typical power dependence of the linewidth for continuous irradiation at 4.2 GHz. Resonant photon absorption is clearly visible for a generator power larger than −60 dBm (1 nW). The line saturated at about −20 dBm (10 μW). Figure 20(b) presents the absorption line for the pulsed technique (see Figure 18) for several pulse lengths and a generator power of 15 dBm (32 mW, $B_{\mathrm{RF}} \approx 1$ mT). The resonant photon absorption is clearly visible for pulse lengths longer than 10 ns. Note that the linewidths in Figure 20(a) are nearly twice as large as those in Figure 20(b).

In our case of an assembly of identical spins, the line broadening is mainly due to dipolar and hyperfine interactions. The dipolar coupling energy can be estimated with $E_{\mathrm{dip}}/k_{\mathrm{B}} \approx (g\mu_{\mathrm{B}}S)^2/V \approx 0.1$ mK ($S = 1/2$ and $V = 6.3\,\mathrm{nm}^3$) (Troiani *et al.*, 2005b). The hyperfine coupling with the nuclear spins can be obtained by considering the dipolar interaction of one Cr ion ($S = 3/2$) with the neighboring F nucleus having a nuclear spin $I = 1/2$. With $g_{\mathrm{F}} = +5.26$ and the distance of $d = 0.2$ nm between F and Cr ions, the interaction energy is about 0.4 mK for each of the eight F nuclear spins (Troiani *et al.*, 2005b). The hyperfine line broadening of all eight F nuclear spins is about 3 mK, which corresponds to 5 mT, in good agreement with the observed Gaussian linewidths of about $\sigma = 4$ mT in Figures 18 and 20.

Finally, we discuss the possibility of observing Rabi oscillations with the present setup. Owing to inhomogeneous broadening, only a lower bound of the coherence time τ_{c} can be estimated from the resonance lines in Figure 20: $\tau_{\mathrm{c}} \approx B_\nu/(\sigma\nu) \approx 10$ ns with $B_\nu = 0.166$ T, $\sigma = 4$ mT, and $\nu = 4.2$ GHz. The corresponding number of coherent flips of the spin system is given by $N = \tau_{\mathrm{c}}/\tau_{\mathrm{Rabi}}$ with $\tau_{\mathrm{Rabi}} = 2\pi/(\gamma B_{\mathrm{RF}}) \approx 40$ ns for $B_{\mathrm{RF}} \approx 1$ mT. We obtain $N \approx 0.25$, showing that there is possibility of seeing Rabi oscillations in the present conditions. In order to obtain $N \gg 1$, it will be necessary to further increase the radiation field B_{RF}, to substantially reduce the hyperfine broadening by substituting the F ions with OH groups, and to minimize the dipolar coupling by doping the crystal of Cr_7Ni molecules with Cr_8 molecules [3].

6 PHOTON-ASSISTED TUNNELING IN SINGLE-MOLECULE MAGNET

It has also been proposed that molecular nanomagnets could be used as quantum computers by implementing Grover's algorithm (Leuenberger and Loss, 2001). For this, it is necessary to be able to generate an arbitrary superposition of eigenstates of these systems. The method suggested was through the use of multifrequency coherent magnetic radiation in the microwave and radiofrequency range. This would first introduce and amplify the desired phase for each m_S state and this information could be finally read out by standard magnetic resonance techniques. In this approach advantage is taken from the non-equidistance of the m_S levels of the ground multiplet (arising from the large axial anisotropy of these systems), which allows coherent populations of the different m_S levels. A theoretical work pointed out that a very accurate control of pulse shape technique, both in amplitude, duration, and choice of frequency is needed to fulfill the condition to design quantum computing devices in molecular nanomagnets (Zhou, Tao, Shen and Liang, 2002). In addition to such basic difficulties, we see in the subsequent text that the total microwave power convoyed onto the samples cannot exceed a critical value above which nonlinear effects occur.

In order to investigate the feasibility of the proposed Process, any preliminary experiment should aim to understand the effects of microwave absorption on the spin dynamics of these systems at low temperatures. The measurements were performed using micro-Hall bars (Sorace *et al.*, 2003). Continuous microwave radiation was generated by a couple of Gunn diodes equipped with calibrated attenuators.

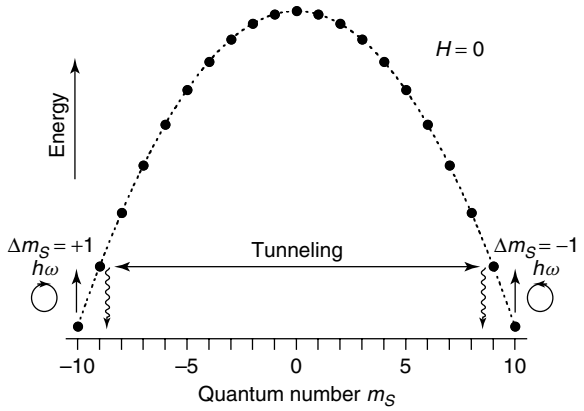

Figure 21. Schematic representation of photon-assisted tunneling. On irradiating an Fe_8 sample with a radiation of wavelength corresponding to the $m_S = -10$ to -9 splitting (vertical arrow), an enhancement of the fraction of molecules that tunnel from the first excited state is expected (horizontal arrow). The use of circularly polarized radiation allows selecting only one side of the well and distinguishing between spin–phonon and spin–photon transitions. (Reproduced from L. Sorace *et al.*, 2003, with permission from the American Physical Society. © 2003.)

With this experimental setup, which has very good stability of emitted power and a narrow bandwidth (100 kHz), only relative powers at the output of the diode can be known, which will be referred to as ρ in the following discussion. We irradiated the sample using a 6-mm waveguide equipped with infrared filters in order to reduce heating. The circular polarization was maximized around 97%. The study was performed on a 0.1-mm Fe_8 single crystal.

As schematically depicted in Figure 21, microwave radiation with a frequency of 115 GHz corresponds to the energy separation between the ground states $m_S = \pm S$ and the first excited states $m_S = \pm(S-1)$ of Fe_8 in zero applied magnetic field (Barra *et al.*, 1996; Hill *et al.*, 2002). If the radiation is linearly polarized, the populations of the first excited states ($m_S = \pm(S-1)$) in both wells will be enhanced equally (equal transition probability for $\Delta m_S = \pm 1$). On the other hand, the use of circular polarization has the advantage of distinguishing between $\Delta m_S = +1$ (left polarization, σ^- photons) or $\Delta m_S = -1$ (right polarization, σ^+ photons) (Abragam and Bleaney, 1970), and the population of only one of the two excited states will be enhanced (Figure 21). An excess of tunneling from one well to the other is then expected. Therefore, circular polarization can help distinguish between spin–phonon relaxation, and spin-phonon relaxation modified by the absorption of photons. The former equally affects the two sides of the barrier, that is, the two branches of the hysteresis loop, while the latter modifies the population of only one side of the barrier, that is, one branch of the hysteresis loop. Any difference observed between the two branches of the hysteresis loop has to be traced back to photon absorption.

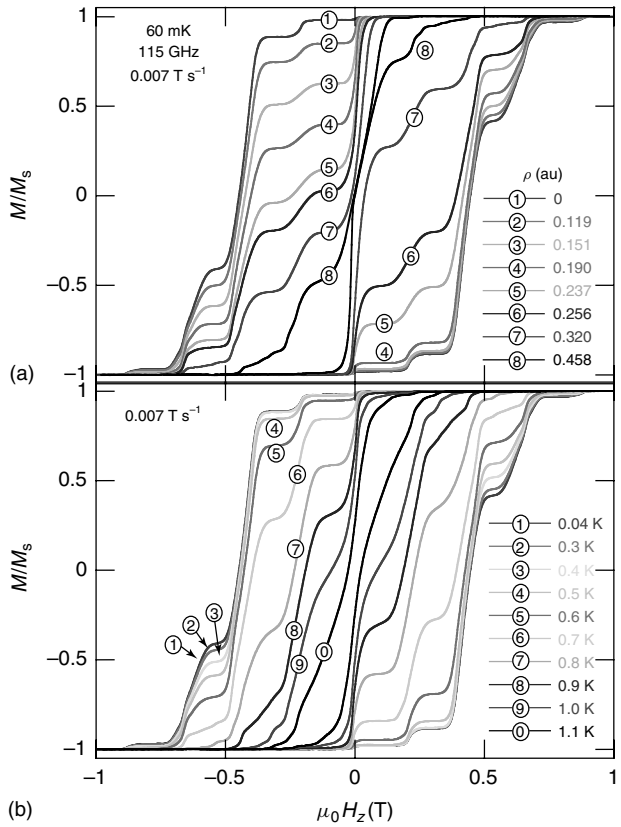

Figure 22. Magnetic hysteresis loops of Fe_8 at a field sweep rate of $0.007\,T\,s^{-1}$ and at 60 mK under irradiation with microwaves at 115 GHz and for several microwave powers ρ (a). The easy axis of the crystal is oriented along the applied field and perpendicular to the radiation oscillating magnetic field. The observed increasing of the tunneling rate at zero field, as a consequence of the absorption of photons induced by circularly polarized radiation, becomes evident by comparing the zero-field steps after positive or negative saturation. For comparison, the thermal behavior is presented in (b). (Reproduced from L. Sorace *et al.*, 2003, with permission from the American Physical Society. © 2003.)

Figure 22(a) shows the hysteresis loops of an Fe_8 single crystal with the easy axis parallel to the applied field, measured at 60 mK under irradiation. The tunneling transition near zero field is strongly enhanced for a radiation at 115 GHz. This is in agreement with a photon-induced population transfer from $m_S = 10$ to $m_S = 9$, and agrees with earlier HF-EPR studies showing strong zero field absorption at about 116 GHz (Barra *et al.*, 1996; Hill *et al.*, 2002). Figure 22(a) also shows the expected asymmetry of the hysteresis loops in the presence of circularly polarized radiation. In particular, the height of the zero-field step (first tunnel resonance, $n = 0$) obtained when sweeping the field from negative saturation is much less affected than when sweeping

from positive saturation. This behavior is completely different from phonon-assisted tunneling (Figure 22b) and clearly establishes that tunneling is assisted by photons for the matching frequency of 115 GHz. The observation of a more symmetric shape of the hysteresis curve at high microwave power can be explained both by the incomplete microwave polarization and by phonon emission, leading to relaxation on both sides of the barrier.

A detailed study showed that at lowest powers the tunnel probability increases linearly with power, whereas at higher powers a strongly nonlinear regime is observed (Sorace *et al*., 2003). The latter might be due to multispin and coherent photon transitions.

7 ENVIRONMENTAL DECOHERENCE EFFECTS IN NANOMAGNETS

At temperatures below 0.36 K, Fe_8 molecular clusters display a clear crossover from thermally activated relaxation to a temperature-independent quantum regime, with a pronounced resonance structure of the relaxation time as a function of the external field (Section 3). It was surprising, however, that the observed relaxation of the magnetization in the quantum regime was found to be nonexponential and the resonance width orders of magnitude too large (Sangregorio *et al*., 1997; Ohm, Sangregorio and Paulsen, 1998a). The key to understand this seemingly anomalous behavior involves the hyperfine fields as well as the evolving distribution of the weak dipole fields of the nanomagnets themselves (Prokof'ev and Stamp, 1998). Both effects were shown to be the main source of decoherence at very low temperature. At higher temperatures, phonons are another source of decoherence.

In the following sections, we focus on the low temperature and low field limits, where phonon-mediated relaxation is astronomically long and can be neglected. In this limit, the $m = \pm S$ spin states are coupled owing to the tunneling splitting $\Delta_{\pm S}$, which is about 10^{-7} K for Fe_8 (Section 3.2) with $S = 10$. In order to tunnel between these states, the longitudinal magnetic energy bias $\xi = g\mu_B S H_{\text{local}}$ due to the local magnetic field H_{local} on a molecule must be smaller than $\Delta_{\pm S}$, implying a local field smaller than 10^{-8} T for Fe_8 clusters. Since the typical intermolecular dipole fields are of the order of 0.05 T, at first it seems that almost all molecules should be blocked from tunneling by a very large energy bias. Prokof'ev and Stamp have proposed a solution to this dilemma by proposing that fast dynamic nuclear fluctuations broaden the resonance, and the gradual adjustment of the dipole fields in the sample caused by the tunneling brings other molecules into resonance and allows continuous relaxation (Prokof'ev and Stamp, 1998). Some interesting predictions are briefly reviewed in the following section.

7.1 Prokof'ev–Stamp theory

Prokof'ev and Stamp were the first to realize that there are localized couplings of environmental modes with mesoscopic systems that cannot be modeled with an 'oscillator bath' model (Feynman and Vernon, 1963) describing delocalized environmental modes such as electrons, phonons, photons, and so on. They found that these localized modes such as nuclear and paramagnetic spins were often strong and described them with a spin bath model (Prokof'ev and Stamp, 1996). We do not review this theory (Prokof'ev and Stamp, 2000) but focus on one particular application that is interesting for molecular clusters (Prokof'ev and Stamp, 1998). Prokof'ev and Stamp showed that, at a given longitudinal applied field H_z, the magnetization of a crystal of molecular clusters should relax at short times with a square-root time dependence, which is due to a gradual modification of the dipole fields in the sample caused by the tunneling

$$M(H_z, t) = M_{\text{in}} + (M_{\text{eq}}(H_z) - M_{\text{in}})\sqrt{\Gamma_{\text{sqrt}}(H_z)t} \qquad (11)$$

Here, M_{in} is the initial magnetization at time $t = 0$ (after a rapid field change), and $M_{\text{eq}}(H_z)$ is the equilibrium magnetization at H_z. The rate function $\Gamma_{\text{sqrt}}(H_z)$ is proportional to the normalized distribution $P(H_z)$ of molecules that are in resonance at H_z:

$$\Gamma_{\text{sqrt}}(H_z) = c\frac{\xi_0}{E_D}\frac{\Delta_{\pm S}^2}{4\hbar}P(H_z) \qquad (12)$$

where ξ_0 is the linewidth from the nuclear spins, E_D is the Gaussian half-width of $P(H_z)$, and c is a constant of the order of unity, which depends on the sample shape. If these simple relations are exact, then measurements of the short time relaxation as a function of the applied field H_z directly give the distribution $P(H_z)$, and they allow one to measure the tunnel splitting $\Delta_{\pm S}$, which is described in the next section.

7.2 Hole digging method to study dipolar distributions and hyperfine couplings

Motivated by the Prokof'ev–Stamp theory (Prokof'ev and Stamp, 1998), we developed a new technique–which we call the *hole digging method*–that can be used to observe the time evolution of molecular states in crystals of molecular clusters. It allowed us to measure the statistical distribution of magnetic bias fields in the Fe_8 system that arise from the weak dipole fields of the clusters themselves. A hole can be 'dug' into the distribution by depleting the available spins

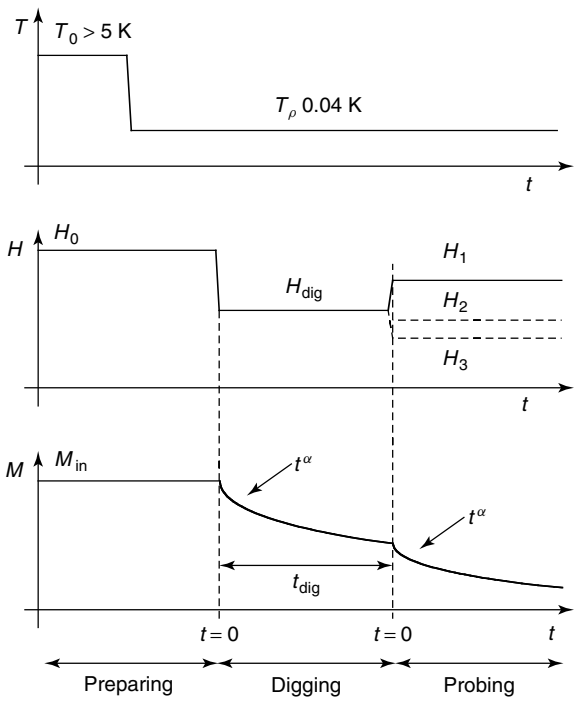

Figure 23. Schema of the hole digging method presenting the time dependence of temperature, applied field, and magnetization of the sample.

at a given applied field. Our method is based on the simple idea that, after a rapid field change, the resulting short time relaxation of the magnetization is directly related to the number of molecules that are in resonance at the given applied field. Prokof'ev and Stamp have suggested that the short time relaxation should follow a $\sqrt{t}-$relaxation law (equation (11)). However, the hole digging method should work with any short time relaxation law–for example, a power law

$$M(H_z, t) = M_{\text{in}} + (M_{\text{eq}}(H_z) - M_{\text{in}})(\Gamma_{\text{short}}(H_z)t)^{\alpha} \quad (13)$$

where Γ_{short} is a characteristic short time relaxation rate that is directly related to the number of molecules that are in resonance at the applied field H_z, and $0 < \alpha < 1$ in most cases. $\alpha = 0.5$ in the Prokof'ev–Stamp theory (equation (11)) and Γ_{sqrt} is directly proportional to $P(H_z)$ (equation (12)). The *hole digging method* can be divided into three steps (Figure 23):

1. *Preparing the initial state:* A well-defined initial magnetization state of the crystal of molecular clusters can be achieved by rapidly cooling the sample from high down to low temperatures in a constant applied field H_z^0. For zero applied field ($H_z = 0$) or rather large applied fields ($H_z > 1\,\text{T}$), a demagnetized or saturated magnetization state of the entire crystal can be obtained, respectively. When quenching the sample in a small field of few milliteslas, any possible initial magnetization M_{in} is achieved. When the quench is fast (<1 s), the sample's magnetization does not have time to relax, either by thermal or by quantum transitions. This procedure yields a frozen thermal equilibrium distribution, whereas for slow cooling rates the molecule spin states in the crystal might tend to a certain dipolar ordered ground state. Finally, a randomly disordered state can be achieved by sweeping the field back and forth over the zero-field resonance. During each sweep, few spins tunnel randomly back and fourth. When the Landau-Zener tunnel probability is small ($P_{\text{LZ}} \ll 1$), and a large number of back and forth sweeps is performed, the randomly disordered state can be complete (Wernsdorfer, Bhaduri, Vinslava and Christou, 2005).
2. *Modifying the initial state–hole digging:* After preparing the initial state, a field H_{dig} is applied during a time t_{dig}, called *digging field* and *digging time*, respectively. During the digging time and depending on H_{dig}, a fraction of the molecular spins tunnel (back and/or forth), that is, they reverse the direction of magnetization [4].
3. *Probing the final state:* Finally, a field H_z^{probe} is applied (Figure 23) to measure the short time relaxation from which one yields Γ_{short} (equation (13)), which is related to the number of spins that are still free for tunneling after step (2).

The entire procedure is then repeated many times but at other fields H_z^{probe}, yielding $\Gamma_{\text{short}}(H_z, H_{\text{dig}}, t_{\text{dig}})$, which is related to the distribution of spins $P(H_z, H_{\text{dig}}, t_{\text{dig}})$ that are still free for tunneling after the hole digging. For $t_{\text{dig}} = 0$, this method maps out the initial distribution.

7.3 Intermolecular dipole interaction in Fe_8

We applied the hole digging method to several samples of molecular clusters and quantum spin glasses. The most detailed study has been done on the Fe_8 system. We found the predicted $\sqrt{t}$ relaxation (equation (11)) in experiments on fully saturated Fe_8 crystals (Ohm, Sangregorio and Paulsen, 1998a,b) and on nonsaturated samples (Wernsdorfer *et al.*, 1999). Figure 24 displays a detailed study of the dipolar distributions, revealing a remarkable structure that is due to next-nearest-neighbor effects (Wernsdorfer *et al.*, 1999). These results are in good agreement with simulations (Cuccoli *et al.*, 1999; Tupitsyn, Stamp and Prokof'ev, 2004).

For a saturated initial state, the Prokof'ev–Stamp theory allows one to estimate the tunnel splitting $\Delta_{\pm S}$. Using equations (3), (9), and (12) of Prokof'ev and Stamp (1998),

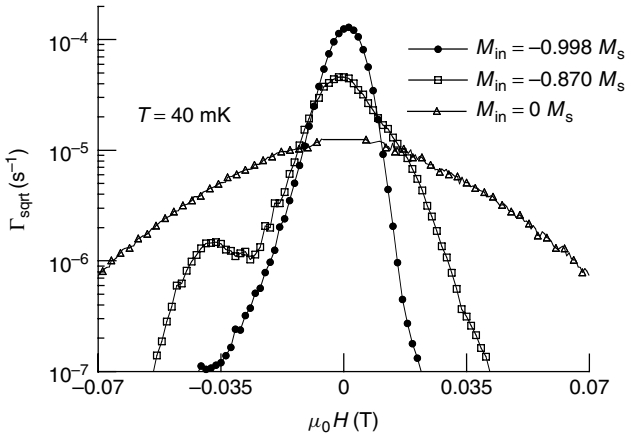

Figure 24. Field dependence of the short time square-root relaxation rates $\Gamma_{sqrt}(H_z)$ for three different values of the initial magnetization M_{in}. According to equation (12), the curves are proportional to the distribution $P(H_z)$ of magnetic energy bias due to local dipole field distributions in the sample. Note the logarithmic scale for Γ_{sqrt}. The peaked distribution labeled $M_{in} = -0.998 M_s$ was obtained by saturating the sample, whereas the other distributions were obtained by thermal annealing. $M_{in} = -0.870 M_s$ is distorted by nearest-neighbor lattice effects. The peak at −0.04 T as well as the shoulder at 0.02 T and 0.04 T are originated by the clusters that have one nearest-neighbor cluster with reversed magnetization: the peak at −0.04 T corresponds to the reversal of the neighboring cluster along the **a** crystallographic axis, which almost coincides with the easy axis of magnetization, while the shoulder at 0.02 and 0.04 T is due to the clusters along crystallographic axes **b** and **c**. (Reproduced from W. Wernsdorfer *et al.*, 1999, with permission from the American Physical Society. © 1999.)

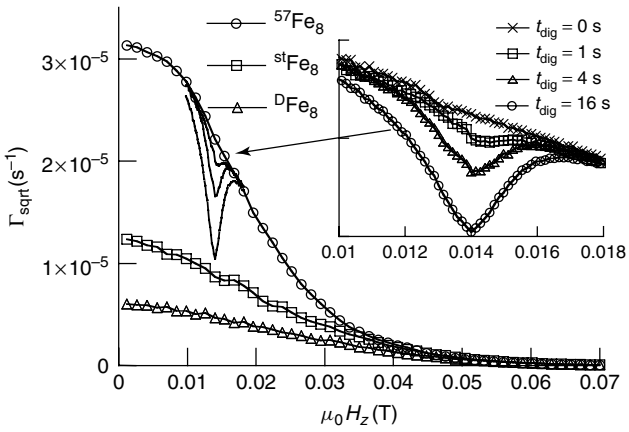

Figure 25. Comparison of the short time relaxation rates of three different Fe_8 samples at $T = 40$ mK with $H_{trans} = 0$ and $M_{init} = 0$. The inset displays a typical example of a hole that was dug into the distribution by allowing the sample to relax for the time t_{dig} at $\mu_0 H_{dig} = 14$ mT. (Reproduced from W. Wernsdorfer *et al.*, 2000, with permission from the American Physical Society. © 2000.)

along with integration, we find $\int \Gamma_{sqrt} d\xi = c \frac{\xi_0}{E_D} \frac{\Delta_{\pm S}^2}{4\hbar}$, where c is a constant of the order of unity that depends on the sample shape. With $E_D = 15$ mT, $\xi_0 = 0.8$ mT, $c = 1$, and Γ_{sqrt} (Wernsdorfer *et al.*, 1999, 2000), we find $\Delta_{\pm 10} = 1.2 \times 10^{-7}$ K, which is close to the result of $\Delta_{\pm 10} = 1.0 \times 10^{-7}$ K obtained by using a Landau–Zener method (Section 3.1) (Wernsdorfer and Sessoli, 1999).

Whereas the hole digging method probes the longitudinal dipolar distribution (H_z direction), the Landau–Zener method can be used to probe the transverse dipolar distribution by measuring the tunnel splittings Δ around a topological quench.

7.4 Hyperfine interaction in Fe_8

The strong influence of nuclear spins on resonant quantum tunneling in the molecular cluster Fe_8 was demonstrated for the first time (Wernsdorfer *et al.*, 2000) by comparing the relaxation rate of the standard Fe_8 sample with two isotopic modified samples: (i) ^{56}Fe is replaced by ^{57}Fe, and (ii) a fraction of ^{1}H is replaced by ^{2}H. By using the hole digging method, we measured an intrinsic broadening that is driven by the hyperfine fields (Figure 25). Our measurements are in good agreement with numerical hyperfine calculations (Wernsdorfer *et al.*, 2000; Tupitsyn, Stamp and Prokof'ev, 2004). For $T > 1.5$ K, the influence of nuclear spins on the relaxation rate is less important, suggesting that spin–phonon coupling dominates the relaxation rate.

8 CONCLUSION

In conclusion, we presented detailed measurements that demonstrated that molecular nanomagnets offer a unique opportunity to explore the quantum dynamics of a large but finite spin. We focused our discussion on the Fe_8 molecular nanomagnet because it is the first system where studies in the pure quantum regime were possible. The tunneling in this system is remarkable because it does not show up at the lowest orders of perturbation theory.

A new family of supramolecular, antiferromagnetically exchange-coupled dimers of SMMs has recently been reported (Wernsdorfer, Aliaga-Alcalde, Hendrickson and Christou, 2002). Each SMM acts as a bias on its neighbor, shifting the quantum tunneling resonances of the individual SMMs. Hysteresis loop measurements on a single crystal of SMM dimers have established quantum tunneling of the magnetization via entangled states of the dimer. This showed that the dimer really does behave as a quantum-mechanically coupled dimer. The transitions are well separated, suggesting long coherence times compared to the timescale of the energy splitting (Tiron *et al.*, 2003). This result is of great importance if such systems are to be used for quantum computing.

Molecules with small spin have also been studied. For example, time-resolved magnetization measurements were performed on a spin 1/2 molecular complex, the so-called V_{15} (Chiorescu *et al*., 2000a). Despite the absence of a barrier, magnetic hysteresis is observed over a timescale of several seconds. A detailed analysis in terms of a dissipative two-level model has been given, in which fluctuations and splittings are of the same energy. Spin–phonon coupling leads to long relaxation times and to a particular 'butterfly' hysteresis loop (Chiorescu *et al*., 2000b; Dobrovitski, Katsnelson and Harmon, 2000). We presented magnetization measurements on a crystal of Cr_7Ni antiferromagnetic rings with a spin 1/2. Irradiation with microwaves at frequencies between 1 and 10 GHz leads to the observation of very narrow resonant photon absorption lines, which are broadened by hyperfine and spin–spin interactions.

The use of circularly polarized microwaves allowed us to show for the first time the phenomenon of photon-assisted tunneling in magnetism, using an SMM Fe_8 (Sorace *et al*., 2003). In accordance with the selection rules for EPR spectroscopy (Abragam and Bleaney, 1970), circularly polarized radiation promotes the transition $m_S = 10$ to 9 with $\Delta m_S = -1$, giving an effect of magnetic dichroism at millimeter wavelengths. At lowest powers, the tunnel probability increases linearly with power, whereas at higher powers a strongly nonlinear regime is observed. The latter might be due to multispin and coherent photon transitions.

What remains still debated is the possibility of observing quantum coherence between states of opposite magnetization. Dipole–dipole and hyperfine interactions are source of decoherence. In other words, when a spin has tunneled through the barrier, it experiences a huge modification of its environment (hyperfine and dipolar), which prohibits the back tunneling. Prokof'ev and Stamp suggested three possible strategies to suppress the decoherence (Prokof'ev and Stamp, 1995). (i) Choose a system where the nuclear magnetic resonance (NMR) frequencies far exceed the tunnel frequencies making any coupling impossible. (ii) Isotopically purify the sample to remove all nuclear spins. (iii) Apply a transverse field to increase the tunnel rate to frequencies much larger than hyperfine field fluctuations. Several groups are currently working on such proposals.

With reference to the perspectives of the field of SMMs, we expect that chemistry will play a major role through the synthesis of novel larger spin clusters with strong anisotropy. We want to stress that there are already many other molecular nanomagnets (the largest is currently an Mn_{84}, Figure 2) that are possible model systems. We believe that more sophisticated theories that describe the dephasing effects of the environment onto the quantum system are needed. These investigations are important for studying the quantum character of molecular clusters for applications like 'quantum computers'. The first implementation of Grover's algorithm with molecular nanomagnets has been proposed (Leuenberger and Loss, 2001). Antiferromagnetic systems have attracted much interest. In this case, the quantum hardware is thought of as a collection of coupled molecules, each corresponding to a different qubit (Meier, Levy and Loss, 2003a,b; Troiani *et al*., 2005a,b). In order to explore these possibilities, new and very precise setups are currently being built and new methods and strategies are being developed. The field of molecular nanomagnets is evolving toward molecular electronics and spintronics, which are both rapidly emerging fields of nanoelectronics with a strong potential impact for the realization of new functions and devices helpful for information storage as well as quantum information. New projects aim at the merging of the two fields by the realization of molecular junctions that involve a molecular nanomagnet. In order to tackle the challenge of controlled connection at the single-molecule level, molecular self-assembly on nanojunctions obtained by the technique of electromigration was used (Heersche *et al*., 2006; Jo *et al*., 2006). Furthermore, a new nano-SQUID with carbon nanotube Josephson junctions has been developed (Cleuziou *et al*., 2006), which should be sensitive enough to study individual magnetic molecules that are attached to the carbon nanotube. Such techniques will lead to enormous progress in the understanding of the electronic and magnetic properties of isolated molecular systems and will reveal intriguing new physics.

NOTES

[1] The Kramers theorem asserts that no matter how unsymmetric the crystal field is, an ion possessing an odd number of electrons must have a ground state that is at least doubly degenerate, even in the presence of crystal fields and spin–orbit interactions (Kramers, 1930).

[2] The probability density of reversal of a stochastic process is $-\mathrm{d}P/\mathrm{d}t = P/\tau$ and the maximum of the probability density can be derived from $\mathrm{d}^2P/\mathrm{d}t^2 = P(1 + \mathrm{d}\tau/\mathrm{d}t)/\tau^2 = 0$. This gives $\mathrm{d}\tau/\mathrm{d}t = -1$. The application to equation (5) leads to $\Delta E(H) = k_\mathrm{B}T \ln\left[k_\mathrm{B}T/\left(\tau_0 \frac{\mathrm{d}E}{\mathrm{d}H}\frac{\mathrm{d}H}{\mathrm{d}t}\right)\right]$. Using equation (6) we find equation (7).

[3] Very recently measurements (Ardavan *et al*., 2007) of the dephasing time of the Cr_7Ni molecular magnets showed values up to three orders of magnitude higher than originally thought (Wernsdorfer, Mailly, Timco and Winpenny, 2005). Such a long timescale gives enough time for about a hundred manipulations, which is a promising figure for quantum computing (Wernsdorfer, 2007).

[4] The field sweeping rate to be applied $H_{\rm dig}$ should be fast enough to minimize the change of the initial state during the field sweep.

REFERENCES

Abragam, A. and Bleaney, B. (1970). *Electron Paramagnetic Resonance of Transition Ions*, Clarendon Press: Oxford.

Aharoni, A. (1996). *An Introduction to the Theory of Ferromagnetism*, Oxford University Press: London.

Alonso, J.J. and Fernandez, J.F. (2001). Tunnel Window's imprint on dipolar field distributions. *Physical Review Letters*, **87**, 097205.

Amoretti, G., Caciuffo, R., Combet, J., *et al*. (2000). Inelastic neutron scattering below 85 meV and zero-field splitting parameters in the Fe8 magnetic cluster. *Physical Review B*, **62**, 3022.

Ardavan, A., Rival, O., Morton, J.J.L., *et al*. (2007). Will spin-relaxation times in molecular magnets permit quantum information processing?. *Physical Revue Letters*, **98**, 057201.

Aubin, S.M.J., Dilley, N.R., Wemple, M.B., *et al*. (1998). Resonant magnetization tunnelling in the half-integer-spin single-molecule magnet $[Mn_{12}O_{12}(O_2CEt)_{16}(H_2O)_4]$. *Journal of the American Chemical Society*, **120**, 839.

del Barco, E., Kent, A.D., Yang, E.C. and Hendrickson, D.N. (2004). Quantum superposition of high spin states in the single molecule magnet Ni4. *Physical Review Letters*, **93**, 157202.

Barnes, S. (1999). Manifestation of intermediate spin for Fe_8. http://arxiv.org/abs/cond-mat/9907257.

Barra, A-L., Debrunner, P., Gatteschi, D., *et al*. (1996). Superparamagnetic-like behavior in an octanuclear iron cluster. *Europhysics Letters*, **35**, 133.

Barra, A., Gatteschi, D. and Sessoli, R. (2000). High-frequency EPR spectra of Fe8. a critical appraisal of the Barrier for the reorientation of the magnetization in single-molecule magnets. *Chemistry- a European Journal*, **6**, 1608.

Brown, W.F. (1963). Thermal fluctuations of a single-domain particle. *Physical Review*, **130**, 1677.

Caciuffo, R., Amoretti, G., Murani, A., *et al*. (1998). Neutron spectroscopy for the magnetic anisotropy of molecular clusters. *Physical Review Letters*, **81**, 4744.

Caneschi, A., Gatteschi, D., Laugier, J., *et al*. (1991). Alternating current susceptibility, high field magnetization, and millimeter band EPR evidence for a ground $S = 10$ state in $[Mn_{12}...]$. *Journal of the American Chemical Society*, **113**, 5873–5874.

Caneschi, A., Gatteschi, D., Sangregorio, C., *et al*. (1999). The molecular approach to nanoscale magnetism. *Journal of Magnetism and Magnetic Materials*, **200**, 182.

Carretta, S., Santini, P., Amoretti, G., *et al*. (2005). Topology and spin dynamics in magnetic molecules. *Physical Review B*, **72**,, 060403(R).

Chiorescu, I., Wernsdorfer, W., Barbara, B., *et al*. (2000a). Environmental effects on big molecule with spin 1/2. *Journal of Applied Physics*, **87**, 5496.

Chiorescu, I., Wernsdorfer, W., Müller, A., *et al*. (2000b). Butterfly hysteresis loop and dissipative spin reversal in the $S = 1/2$, V_{15} molecular complex. *Physical Review Letters*, **84**, 3454.

Cleuziou, J-P., Wernsdorfer, W., Bouchiat, V., *et al*. (2006). Carbon nanotube superconducting quantum interference device. *Nature Nanotechnology*, **1**, 53.

Coffey, W.T., D.S.F. Crothers, J.L. Dormann, *et al*. (1995). Effect of an oblique magnetic field on the superparamagnetic relaxation time. *Physical Review B*, **52**, 15951.

Cuccoli, A., Fort, A., Rettori, A., *et al*. (1999). Dipolar interaction and incoherent quantum tunneling: a Monte Carlo study of magnetic relaxation. *European Physical Journal B*, **12**, 39.

von Delft, J. and Henley, C.L. (1992). Destructive quantum interference in spin tunneling problems. *Physical Review Letters*, **69**, 3236.

Dobrovitski, V.V., Katsnelson, M.I. and Harmon, B.N. (2000). Mechanisms of decoherence in weakly anisotropic molecular magnets. *Physical Review Letters*, **84**, 3458.

Enz, M. and Schilling, R. (1986). Magnetic field dependence of the tunnelling splitting of quantum spins. *Journal of Physics C*, **19**, L711.

Feynman, R.P., Leighton, R.B. and Sand, M. (1970). *The Feynman Lectures on Physics*, Addison-Wesley: London, Vol. 3.

Feynman, R. and Vernon, F. (1963). The theory of the general quantum system interacting with a linear dissipative system. *Annals of Physics*, **24**, 118.

Fort, A., Rettori, A., Villain, J., *et al*. (1998). Mixed quantum-thermal relaxation in Mn12 acetate molecules. *Physical Review Letters*, **80**, 612.

Friedman, J.R., Sarachik, M.P., Tejada, J. and Ziolo, R. (1996). Macroscopic measurement of resonant magnetization tunneling in high-spin molecules. *Physical Review Letters*, **76**, 3830.

Garanin, D. and Chudnovsky, E. (1997). Thermally activated resonant magnetization tunneling in molecular magnets: Mn12Ac and others. *Physical Review B*, **56**, 11102.

Garg, A. (1993). Topologically quenched tunnel splitting in spin systems without Kramers' degeneracy. *Europhysics Letters*, **22**, 205.

Garg, A. (1995). Escape-field distribution for escape from a metastable potential well subject to a steadily increasing bias field. *Physical Review B*, **51**, 15592.

Garg, A. (1999). Oscillatory tunnel splittings in spin systems: a discrete Wentzel-Kramers-Brillouin approach. *Physical Review Letters*, **83**, 4385.

Gunther, L. and Barbara, B. (1994). Quantum tunneling across a domain-wall junction. *Physical Review B*, **49**, 3926.

Hartmann-Boutron, F., Politi, P. and Villain, J. (1996). Tunneling and magnetic relaxation in mesoscopic molecules. *International Journal of Modern Physics*, **10**, 2577.

Heersche, H.B., de Groot, Z., Folk, J.A., *et al*. (2006). Electron transport through single Mn12 molecular magnets. *Physical Review Letters*, **96**, 206801.

van Hemmen, J.L.V. and Süto, S. (1986). Tunnelling of quantum spins. *Europhysics Letters*, **1**, 481.

Hendrickson, D.N., Christou, G., Schmitt, E., *et al*. (1992). Photosynthetic water oxidation center: spin frustration in distorted

cubane $MnIVMnIV_3$ model complexes. *Journal of the American Chemical Society*, **114**, 2455.

Hill, S., Edwards, R., Aliaga-Alcalde, N. and Christou, G. (2003). Quantum coherence in an exchange-coupled dimer of single-molecule magnets. *Science*, **302**, 1015.

Hill, S., Maccagnano, S., Park, K., *et al*. (2002). Detailed single-crystal EPR line shape measurements for the single-molecule magnets Fe8Br and Mn12-acetate. *Physical Review B*, **65**, 224410.

Hubert, A. and Schäfer, R. (1998). *Magnetic Domains: The Analysis of Magnetic Microstructures*, Springer-Verlag: Berlin, Heidelberg, New York.

Jamet, M., Wernsdorfer, W., Thirion, C., *et al*. (2001). Magnetic anisotropy of individual cobalt clusters. *Physical Review Letters*, **86**, 4676.

Jo, M-H., Grose, J., Baheti, K., *et al*. (2006). Signatures of molecular magnetism in single-molecule transport spectroscopy. *Nano Letters*, **6**, 2014.

Kececioglu, E. and Garg, A. (2001). Diabolical points in magnetic molecules: an exactly solvable model. *Physical Review B*, **63**, 064422.

Kent, A., Zhong, Y., Bokacheva, L., *et al*. (2000). Low-temperature magnetic hysteresis in Mn_{12} acetate single crystals. *Europhysics Letters*, **49**, 521–527.

Kramers, H.A. (1930). General theory of the paramagnetic rotation in crystals. *Proceedings of the Academy of Sciences Amsterdam*, **33**, 959.

Kurkijärvi, J. (1972). Intrinsic fluctuations in a superconducting ring closed with a Josephson junction. *Physical Review B*, **6**, 832.

Landau, L. (1932). On the theory of transfer of energy at collisions II. *Physikalische Zeitschrift der Sowjetunion*, **2**, 46.

Larsen, F.K., McInnes, E.J.L., Mkami, H.E., *et al*. (2003). *Angewandte Chemie International Edition*, **42**, 101.

Leuenberger, M.N. and Loss, D. (2000a). Incoherent Zener tunneling and its application to molecular magnets. *Physical Review B*, **61**, 12200.

Leuenberger, M.N. and Loss, D. (2000b). Spin tunneling and phonon-assisted relaxation in Mn12 -acetate. *Physical Review B*, **61**, 1286.

Leuenberger, M.N. and Loss, D. (2001). Quantum computing with molecular magnets. *Nature*, **410**, 789.

Liang, J-Q., Mueller-Kirsten, H., Park, D. and Pu, F-C. (2000). Phase interference for quantum tunneling in spin systems. *Physical Review B*, **61**, 8856.

Lis, T. (1980). *Acta Crystallographica Section B*, **36**, 2042.

Loss, D., DiVincenzo, D.P. and Grinstein, G. (1992). Suppression of tunneling by interference in half-integer-spin particles. *Physical Review Letters*, **69**, 3232.

Meier, F., Levy, J. and Loss, D. (2003a). *Physical Review Letters*, **90**, 047901.

Meier, F., Levy, J. and Loss, D. (2003b). *Physical Review B*, **68**, 134417.

Miyashita, S. (1995). Dynamics of the magnetization with an inversion of the magnetic field. *Journal of the Physical Society of Japan*, **64**, 3207.

Miyashita, S. (1996). Observation of the energy gap due to the quantum tunneling making use of the Landau-Zener mechanism [uniaxial magnets]. *Journal of the Physical Society of Japan*, **65**, 2734.

Murugesu, M., Wernsdorfer, W., Abboud, K.A., *et al*. (2005). New Mn-12 single-molecule magnets from edge-sharing bioctahedra. *Dalton Transactions*, **19**, 2285.

Néel, L. (1947). *Comptes Rendus de l'Académie des Sciences*, **224**, 1550.

Néel, L. (1949). *Annales de Geophysique*, **5**, 99.

Novak, M. and Sessoli, R. (1995). AC susceptibility relaxation studies on a manganese organic cluster compound: Mn_{12}-ac. In *Quantum Tunneling of Magnetization-QTM'94*, *Vol. 301 of NATO ASI Series E: Applied Sciences*, Gunther, L. and Barbara, B. (Eds.), Kluwer Academic Publishers: London, pp. 171–188.

Ohm, T., Sangregorio, C. and Paulsen, C. (1998a). Local field dynamics in a resonant quantum tunneling system of magnetic molecules. *European Physical Journal B*, **6**, 195.

Ohm, T., Sangregorio, C. and Paulsen, C. (1998b). Non-exponential relaxation in a resonant quantum tunneling system of magnetic molecules. *Journal of Low Temperature Physics*, **113**, 1141.

Overgaard, J., Iversen, B.B., Palii, S.P., *et al*. (2002). Host-guest chemistry of the chromium-wheel complex $[Cr_8F_8(tBuCO_2)_{16}]$: prediction of inclusion capabilities by using an electrostatic potential distribution determined by modeling synchrotron x-ray structure factors at 16 K. *Chemistry- a European Journal*, **8**, 2775.

Paulsen, C. and Park, J-G. (1995). In *Quantum Tunneling of Magnetization-QTM'94*, *Volume 301 of NATO ASI Series E: Applied Sciences*. Gunther, L. and Barbara, B. (Eds.), Kluwer Academic Publishers: London, pp. 189–205.

Perenboom, J., Brooks, J., Hill, S., *et al*. (1998). Relaxation of the magnetization of Mn_{12} acetate. *Physical Review B*, **58**, 330–338.

Politi, P., Rettori, A., Hartmann-Boutron, F. and Villain, J. (1995). Tunneling in mesoscopic magnetic molecules. *Physical Review Letters*, **75**, 537.

Pontillon, Y., Caneschi, A., Gatteschi, D., *et al*. (1999). Magnetization density in an irob(III) magnetic cluster. A polarized neutron investigation. *Journal of the American Chemical Society*, **121**, 5342.

Price, D.J., Lionti, F., Ballou, R., *et al*. (1999). Large metal clusters and lattices with analogues to biology. *Philosophical Transactions of the Royal Society of London. Series A*, **357**, 3099.

Prokof'ev, N. and Stamp, P. (1995). Spin environments and the suppression of quantum coherence. In *Quantum Tunneling of Magnetization-QTM'94*, *Vol. 301 of NATO ASI Series E: Applied Sciences*, Gunther, L. and Barbara, B. (Eds.), Kluwer Academic Publishers: London, p. 369.

Prokof'ev, N. and Stamp, P. (1996). Quantum relaxation of magnetisation in magnetic particles. *Journal of Low Temperature Physics*, **104**, 143.

Prokof'ev, N. and Stamp, P. (1998). Low-temperature quantum relaxation in a system of magnetic nanomolecules. *Physical Review Letters*, **80**, 5794.

Prokof'ev, N. and Stamp, P. (2000). Theory of the spin bath. *Reports on Progress in Physics*, **63**, 669–726.

Rong Lü, Su-Peng Kou, Jia-Lin Zhu, *et al* (2000). Magnetization quantum tunneling at excited levels for a biaxial spin system in an arbitrarily direted magnetic field. *Phys. Rev. B 62*, 3346.

Rose, G. and Stamp, P. (1998). Short time AC response of a system of nanomagnets. *Journal of Low Temperature Physics*, **113**, 1153.

Sangregorio, C., Ohm, T., Paulsen, C., *et al*. (1997). Quantum tunneling of the magnetization in an iron cluster nanomagnet. *Physical Review Letters*, **78**, 4645.

Sessoli, R., Gatteschi, D., Caneschi, A. and Novak, M.A. (1993). Magnetic bistability in a metal-ion cluster. *Nature*, **365**, 141–143.

Sessoli, R., Tsai, H-L., Schake, A.R., *et al*. (1993). High-spin molecules: $[Mn_{12}O_{12}(O_2CR)_{16}(H_2O)_4]$. *Journal of the American Chemical Society*, **115**, 1804–1816.

Sorace, L., Wernsdorfer, W., Thirion, C., *et al*. (2003). Photon-assisted tunneling in a Fe8 single-molecule magnet. *Physical Review B*, **68**,, 220407(R).

Stückelberg, E. (1932). Theorie der unelastischen Stoesse zwischen Atomen. *Helvetica Physica Acta*, **5**, 369.

Stoner, E.C. and Wohlfarth, E.P. (1948). A mechanism of magnetic hysteresis in heterogeneous alloys. *Philosophical Transactions of the Royal Society of London, Series A*, **240**, 599. Reprinted in *IEEE Trans. Magn*. **MAG-27**, 3475, (1991).

Tasiopoulos, A., Vinslava, A., Wernsdorfer, W., *et al*. (2004). Giant single-molecule magnets: a Mn_{84} torus and its supramolecular nanotubes. *Angewandte Chemie International Edition in English*, **43**, 2117.

Thiaville, A. (1998). Extensions of the geometric solution of the two dimensional coherent magnetization rotation model. *Journal of Magnetism and Magnetic Materials*, **182**, 5.

Thiaville, A. (2000). Coherent rotation of magnetization in three dimensions: a geometrical approach. *Physical Review B*, **61**, 12221.

Thirion, C., Wernsdorfer, W. and Mailly, D. (2003). Switching of magnetization by nonlinear resonance studied in single nanoparticles. *Nature Materials*, **2**, 524.

Thomas, L., Lionti, F., Ballou, R., *et al*. (1996). Macroscopic quantum tunneling of magnetization in a single crystal of nanomagnets. *Nature (London)*, **383**, 145–147.

Thorwart, M., Grifoni, M. and Hänggi, P. (2000). Strong coupling theory for driven tunneling and vibrational relaxation. *Physical Review Letters*, **85**, 860.

Tiron, R., Wernsdorfer, W., Foguet-Albiol, D., *et al*. (2003). Spin quantum tunneling via entangled states in a dimer of exchange-coupled single-molecule magnets. *Physical Review Letters*, **91**, 227203.

Troiani, F., Affronte, M., Carrettaa, S., *et al*. (2005a). Proposal for quantum gates in permanently coupled antiferromagnetic spin rings without need of local fields. *Physical Review Letters*, **94**, 190501.

Troiani, F., Ghirri, A., Affronte, M., *et al*. (2005b). Molecular engineering of antiferromagnetic rings for quantum computation. *Physical Review Letters*, **94**, 207208.

Tupitsyn, I., Stamp, P. and Prokof'ev, N.V. (2004). Hole-digging in ensembles of tunneling molecular magnets. *Physical Review B*, **69**, 132406.

Villain, J. and Fort, A. (2000). Magnetic tunneling told to ignorants by two ignorants. *European Physical Journal B*, **17**, 69.

Villain, J., Hartmann-Boutron, F., Sessoli, R. and Rettori, A. (1994). Magnetic relaxation in big magnetic molecules. *Europhysics Letters*, **27**, 159.

Villain, J., Wurger, A., Fort, A. and Rettori, A. (1997). Tunnel effect in magnetic systems: from the microscopic description to the master equation. *Journal de Physique I*, **7**, 1583.

Wernsdorfer, W. (2001). Classical and quantum magnetization reversal studied in nanometer-sized particles and clusters. *Advances in Chemical Physics*, **118**, 99.

Wernsdorfer, W. (2007). A long-lasting phase. *Nature Materials*, **6**, 174.

Wernsdorfer, W., Aliaga-Alcalde, N., Hendrickson, D. and Christou, G. (2002). Exchange-biased quantum tunnelling in a supramolecular dimer of single-molecule magnets. *Nature*, **416**, 406.

Wernsdorfer, W., Bhaduri, S., Boskovic, C., *et al*. (2002a). Spin-parity dependent tunneling of magnetization in single-molecule magnets. *Physical Review B*, **65**, 180403(R).

Wernsdorfer, W., Bhaduri, S., Tiron, R., *et al*. (2002b). Spin-spin cross relaxation in single-molecule magnets. *Physical Review Letters*, **89**, 197201.

Wernsdorfer, W., Caneschi, A., Sessoli, R., *et al*. (2000). Effects of nuclear spins on the quantum relaxation of the magnetization for the molecular nanomagnet Fe_8. *Physical Review Letters*, **84**, 2965.

Wernsdorfer, W., Chakov, N.E. and Christou, G. (2005). Quantum phase interference and spin-parity in Mn_{12} single-molecule magnets. *Physical Review Letters*, **95**, 037203.

Wernsdorfer, W., Bhaduri, S., Vinslava, A. Christou G. (2005). Landau-Zener tunneling in the presence of weak intermolecular interactions in a crystal of Mn4 single-molecule magnets. *Phys. Rev. B 72*, 214429.

Wernsdorfer, W., Hasselbach, K., Mailly, D., *et al*. (1995). DC-SQUID magnetization measurements of single magnetic particles. *Journal of Magnetism and Magnetic Materials*, **145**, 33.

Wernsdorfer, W., Mailly, D., Timco, G.A. and Winpenny, R.E.P. (2005). Resonant photon absorption and hole burning in Cr_7Ni antiferromagnetic rings. *Physical Review B*, **72**, 060409(R).

Wernsdorfer, W., Müller, A., Mailly, D. and Barbara, B. (2004). Resonant photon absorption in the low-spin molecule V15. *Europhysics Letters*, **66**, 861.

Wernsdorfer, W., Ohm, T., Sangregorio, C., *et al*. (1999). Observation of the distribution of molecular spin states by resonant quantum tunneling of the magnetization. *Physical Review Letters*, **82**, 3903.

Wernsdorfer, W., Orozco, E.B., Hasselbach, K., *et al*. (1997a). Experimental evidence of the Néel–Brown model of magnetization reversal. *Physical Review Letters*, **78**, 1791.

Wernsdorfer, W., Orozco, E.B., Hasselbach, K., *et al*. (1997b). Macroscopic quantum tunneling of magnetization of single ferrimagnetic nanoparticles of barium ferrite. *Physical Review Letters*, **79**, 4014.

Wernsdorfer, W. and Sessoli, R. (1999). Quantum phase interference and parity effects in magnetic molecular clusters. *Science*, **284**, 133.

Wieghardt, K., Pohl, K., Jibril, I. and Huttner, G. (1984). Hydrolysis products of the monomeric amine complex $(C_6H_{15}N_3)FeCl_3$: the structure of the octameric Iron(III) cation of $[Fe_8...]$. *Angewandte Chemie International Edition in English*, **23**, 77–78.

Yoo, J., Brechin, E.K., Yamaguchi, A., *et al*. (2000). Single-molecule magnets; a new class of tetranuclear manganese magnets. *Inorganic Chemistry*, **39**, 3615.

Yoo, S-K. and Lee, S-Y. (2000). Geometrical phase effects in biaxial nanomagentic particles. *Physical Review B*, **62**, 3014.

Zener, C. (1932). Non-adiabatic crossing of energy levels. *Proceedings of the Royal Society of London, Series A*, **137**, 696.

Zhou, B., Tao, R., Shen, S. and Liang, J.Q. (2002). Quantum computing of molecular magnet Mn_{12}. *Physical Review A*, **66**, 010301.

Spintronic Biochips for Biomolecular Recognition

Paulo P. Freitas[1,2] and Hugo A. Ferreira[1,2]

[1] *INESC – Microsystems and Nanotechnologies, Lisboa, Portugal*
[2] *Instituto Superior Técnico, Lisboa, Portugal*

1 INTRODUCTION

The past few years have witnessed a continuously growing interest in the use of magnetic-field sensors for biological applications and, in particular, for the detection of biomolecular recognition.

Biomolecular recognition can be understood as the interaction between biomolecules that show affinity toward each other or present some sort of complementarity between them. This translates into the establishment of intermolecular forces of varying intensity either they are Van der Waals forces, salt bridges or hydrogen bonds. Examples of these interactions can be DNA–DNA hybridization, antibody–antigen recognition and general ligand–receptor binding (Voet, Voet and Pratt, 1999).

Handbook of Magnetism and Advanced Magnetic Materials. Edited by Helmut Kronmüller and Stuart Parkin. Volume 4: *Novel Materials*. ISBN: 978-0-470-02217-7.

Biomolecular recognition is in fact ubiquitous in life as it is the means through which cell 'machinery' works: the replication of the genetic code; the translation of this code into functional units, the enzymes; the fabrication and modification of biomolecular structures such as proteins, lipids, glycids, and nucleic acids; the intra and extracellular transport; cell metabolism; cell sensing and signaling pathways; just to name a few of general biological processes (Voet, Voet and Pratt, 1999; Cooper, 2000). More familiar uses of biomolecular recognition, on the other hand, include, for instance, pregnancy tests, blood type testing, genetic screening, and site-directed cancer treatments presently being developed.

It is then understandable that the detection of biomolecular recognition is becoming even more important in areas such as healthcare, pharmaceutical industry, environmental analysis, detection of biological warfare agents, and in broad biotechnological applications.

Generally, the detection of biomolecular recognition involves the use of a known biomolecule that probes a testing sample for a specific target analyte. Hence, they are given the names of probe biomolecule and target biomolecule, respectively. For instance, in pregnancy tests the presence of a specific hormone, the human Chorionic Gonadotropin (hCG), in urine indicates that the woman is most probably pregnant. In this case, the target molecule is hCG and the probe biomolecule is an antibody for hCG.

Conventional methods of detecting biomolecular recognition involve the labeling of biomolecules such that a distinct physical property can be detected or measured in the event of biomolecular recognition. As so, biomolecules are usually labeled with radioactive, colorimetric or fluorescent markers, which can be a small chemical moiety, a biomolecule, an

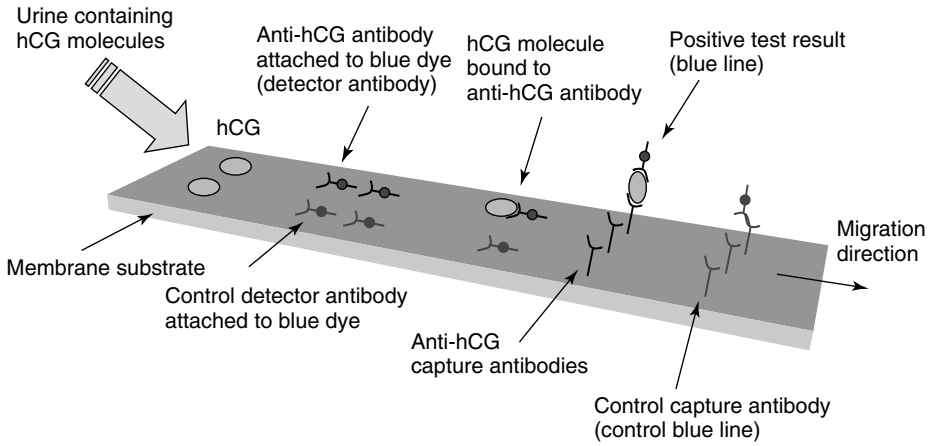

Figure 1. A familiar example of biomolecular recognition: the pregnancy test. Human Chorionic Gonadotropin (hCG) molecules present in the urine of a pregnant woman migrate through a membrane by capillarity. These molecules are first recognized by antibodies labeled with a colored dye, which are adsorbed to the membrane. The antibody-protein moves in the membrane support and are recognized by antibodies immobilized in a narrow region of the membrane. The result is a thin colored line in the test indicating that the woman is pregnant. At the same time, control antibodies also labeled with a similar dye move through the membrane and are bound to the control antibodies immobilized in the membrane indicating that the test proceeded reasonably.

enzyme, a particle or even a conjugation of several of these elements.

Again, in present pregnancy home tests the detection of the hCG hormone proceeds more or less as follows: the hCG molecules carried by the urine move by capillarity through a membrane which contains antibodies labeled with a colored dye (detector antibody). The antibodies recognize the hormone and the complex migrates along the membrane. The hCG molecule complexed with the detector antibody is then recognized by secondary antibodies immobilized in a narrow region of the membrane (capture antibodies) forming a 'sandwich' like structure. Finally, a thin colored line in the test strip appears as a result of increased concentration of blue dyes at that region (Unipath, http://www.unipath.com). The pregnancy test referred in the preceding text is an example of immunoassay, as the target is recognized by an antibody (Figure 1).

The conventional labeling methods present a series of disadvantages. In the case of biomolecular radioactive labeling, although being a sensitive technique, expensive scintillators are required for quantitative measurement. Furthermore, the great care necessary when working with radioactive compounds limits the use of this technique. These systems are presently being replaced by colorimetric- and fluorescent-based ones, which do not show this drawback.

Enzyme-label-based systems usually produce a colored compound that indicates biomolecular recognition. They offer high sensitivity and enable multiplex analysis but require additional reagents (the substrate that produces a colored compound when catalyzed by the enzyme) and the enzyme activity is sensitive to changes in the environment, namely temperature and pH, which limits the range of use of the method. The most widely used colorimetric system is the enzyme-linked immunosorbent assay (ELISA) of which the presented pregnancy test is a variation (Peruski and Peruski, 2003).

The systems that make use of fluorescent labels are also quite sensitive and also enable multiplexing but they often require expensive optical systems for signal detection, and furthermore, the labels photo bleach when exposed to light. This then limits the generalized use of these systems and limits the reproducible retesting of the assays. The most familiar systems of this kind are the real-time polymerase chain reaction (RT-PCR) systems (Cirino, Musser and Egan, 2004) and the so-called DNA chips or DNA microarrays (Ramsay, 1998) which will be discussed in more detail further in Figure 2.

Recent advances on particle synthesis and preparation, such as metal and semiconducting nanoparticles, have overcome some of the limitations of the traditional labels: radioactive, chemical, and biomolecular, such as the dangerous handling and the stability. These labels are also enabling higher biomolecular detection sensitivities and conferring new functionalities to bioanalytical assays (Katz and Willner, 2004).

Magnetic particles have been traditionally used in biological applications for biomolecular and cell separation; has a contrast agent in nuclear magnetic resonance (NMR) imaging; in hyperthermia studies for cancer treatment or even for drug, gene, or radionuclide delivery (Häfeli, Schutt, Teller and Zborowski, 1997; Pankhurst, Connolly, Jones and Dobson, 2003). More recently, they started to be used as labels

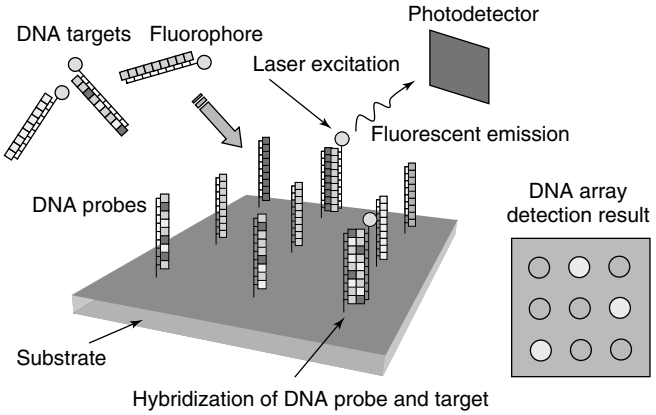

Figure 2. DNA chips or DNA microarrays are comprised of a substrate (usually glass slides) patterned with different DNA probes. These regions usually are circular spots of varying diameters (∼50 to 100 μm or more) that contain millions of copies of the same DNA sequence. In these systems, sample DNA targets are usually labeled with fluorophores and are incubated with the microarrays for several hours for hybridization to occur. DNA target and probe hybridization is detected by measuring the fluorescent emission of the labels with complex optical systems and photodetectors.

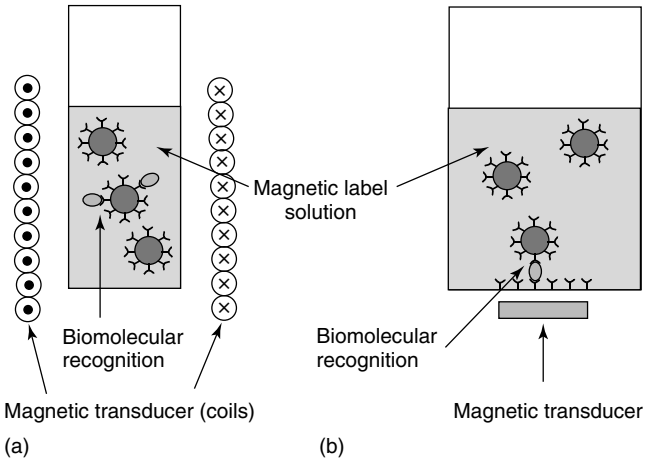

Figure 3. Two types of assays for biomolecular recognition using magnetic labels. (a) In volume detection assays, biomolecular recognition is detected by measuring the magnetic properties of a bulk solution comprised of magnetic labels functionalized with probe molecules that recognize particular targets. (b) In surface detection assays, magnetic labels bound to a surface through biomolecular recognition of probe and target molecules are detected by a nearby magnetic transducer.

or markers for the detection of biomolecular recognition. They offer a number of advantages over colorimetric or fluorescent labels: they are more stable over a broader range of experimental conditions (in temperature and pH) and more stable over time (do not photo bleach, like fluorescent labels); they enable more sensitive measurements as biological samples usually do not contain magnetic material, but often show a color or fluorescent background; they can be used to discriminate between specifically and unspecifically bound biomolecules through the application of a magnetic field (Lee *et al*., 2000); they can be transported and manipulated on chip (Gijs, 2004; Yellen, Hovorka and Friedman, 2005); and they can be readily detected using magnetic-field sensors.

The idea behind magnetic biosensors and biochips is then to use the magnetic labels instead of the conventional ones: biomolecular recognition between target and probe biomolecules is detected by a magnetic-field transducer that senses the magnetic labels bound to the target–probe complexes.

Since magnetic biosensors were first proposed as a simple and sensitive biomolecular recognition detection technique, by making use of coils and ferrofluids (Kriz, Radevik and Kriz, 1996; Kriz, Gehrke and Kriz, 1998), different assay types with different magnetic sensors and labels have been proposed and developed. Basically, two types of assays can be considered with respect to where biomolecular recognition is detected: the volume detection and the surface detection assays (Figure 3).

In volume detection assays (Figure 3a), biomolecular recognition is detected in the bulk of a solution comprised of a suspension of magnetic particles functionalized with the probe molecules of interest. Upon binding of the target analytes to the probes, the hydrodynamic radius of the magnetic particles increases causing a change in their magnetic relaxation times. As a consequence, a shift in the frequency-dependent magnetic susceptibility is observed (Connolly and St. Pierre, 2001; Astalan *et al*., 2004; Chung *et al*., 2004). In these assays, measurement devices such as ac magnetic susceptometers, that measure changes in both the inductance and resistance of an induction coil, are used.

In surface detection assays (Figure 3b), on the other hand, probe biomolecules are immobilized on a solid phase. In these assays, target biomolecules move from the bulk solution to the solid phase surface where they are recognized by the probes. Magnetic carriers bound to the target–probe complexes are then immobilized to the surface. In this case, the magnetic relaxation processes are distinct from when the carriers are free in solution (this will be discussed later on). This difference in relaxation times is used on surface detection assays based on super quantum interfering devices (SQUIDs) (Kötitz *et al*., 1997; Chemla *et al*., 2000).

Nevertheless, the generality of surface detection assays, which correspond to the majority of biosystems being developed, do not rely on measuring changes in the magnetic relaxation of carriers but simply uses the fact that the magnetic carriers create a magnetic field that can be sensed by a transducer.

Several transducers have been used so far, which vary both on physical mechanisms, geometries, properties, and applications: coils (Richardson, Hawkins and Luxton, 2001; Richardson, Hill, Luxton and Hawkins, 2001); giant magnetoimpedance (GMI) sensors (Kurlyandskaya *et al*., 2003; Kurlyandskaya and Levit, 2005; Chiriac, Tibu, Moga and Hera, 2005); SQUID magnetometers (Enpuku *et al*., 1999; Katsura *et al*., 2001); complementary metal–oxide semiconductor (CMOS) Hall-effect sensors (Besse *et al*., 2002); quantum-well Hall effect devices (Landry *et al*., 2004; Sandhu *et al*., 2004; Sandhu and Handa, 2005); and finally, magnetoresistive sensors (Graham, Ferreira and Freitas, 2004; Freitas *et al*., 2004), which are the focus of this chapter.

Coils and giant magnetoimpedance devices assess the presence of magnetic markers by changes in magnetic susceptibility, in the resonance frequency, and in the impedance of the sensing elements, respectively. These devices are simple to fabricate and are better suited for volume magnetic label detection. SQUIDs quantify the magnetic flux created by the labels and are the most sensitive of the magnetic-field sensors developed to date; they are able to sense fields in the order of 100 fT (10^{-13} T). Nevertheless, for high-transition temperature SQUID devices, they require liquid nitrogen (77 K) and vacuum to operate. As a consequence of the necessary apparatus, the separation between the sensor and the sample is usually of tens of micrometers, which results in a smaller effective sensitivity of the device. Hall effect devices do not show these constraints; they measure a voltage drop built in a transversal direction to the sense current due to the Lorentz force induced by the magnetic stray fields originated from the markers. CMOS-based sensor fabrication is relatively straightforward and CMOS-amplification circuitry can be easily integrated with the sensing component. Quantum-well based Hall devices although show a higher sensitivity than CMOS based ones, their fabrication is also more complex, and is comparable to more advanced spintronic devices. Briefly, magnetoresistive sensors are electrical resistors whose resistance value varies with an applied magnetic field, and as so they can be measured using a simple two-point probe measurement scheme. In addition, they operate at room temperature and can be made to have sensitivities down to the pT (10^{-12} T). Furthermore, there is a firmly established technology, as magnetoresistive sensors are used in magnetic reading heads, in several sensing applications (Freitas *et al*., 2000) and most recently on magnetic random access memories (MRAM) and novel magnetoelectronic devices, including biosensors (Freitas *et al*., 2006).

Magnetoelectronic sensors enable then a direct transduction of biomolecular recognition events into electrical signals, which is a considerable advantage over the systems that use colorimetric or fluorescent labels. These optical systems, in their simplest form, provide a qualitative result (yes or no), or a semiquantitative answer based on predefined scales, where interpretation most often depends on the person analyzing the test. On the other hand, more complex systems that often include multiplex testing require bench-top, complex, and expensive optical instrumentation coupled with electrical transduction mechanisms and specialized data-analysis software. Furthermore, these latter systems are usually not portable and cannot be used at the point of care.

This chapter will then review the latest developments on spintronic biosensors and biochips, which show that these devices have the potential to become highly specific and sensitive platforms for low cost, high throughput and portable bioassays. The chapter is organized as follows: first the several types of magnetoresistive sensors will be discussed, together with a comparison of their performance; second the discussion will focus on the magnetic labels or markers used and their properties; afterwards a brief discussion on biomolecular functionalization will be given, and the architectures and detection schemes will be shown next; some applications that have been targeted by several groups will be present together with detection results, while some particular considerations on the detection will be given; finally some conclusions will be drawn at the end.

2 MAGNETORESISTIVE SENSORS

The first magnetoresistive biochip platform was developed at the Naval Research Laboratory (NRL) and was called *bead array counter* (BARC) (Baselt *et al*., 1998). The BARC chip was comprised by 66 giant magnetoresistance (GMR) sensor traces of dimensions of $5 \times 80\,\mu m^2$. Sensors were grouped into eight sensing zones each comprised of eight GMR sensors, these account for 64 sensors while the remaining 2 where used as reference sensors in a half-Wheatstone bridge arrangement. The different sensing zones where later used to detect different biological warfare agents (Edelstein *et al*., 2000).

Since then, a number of research groups worldwide have been developing spintronic biochip platforms based on different magnetoresistive sensors and on distinct sensor geometries, performances, and applications: anisotropic magnetoresistance (AMR) rings (Miller, Prinz, Cheng and Bounnak, 2002); planar Hall effect (PHE) sensors (Ejsing, Hansen and Menon, 2003; Ejsing *et al*., 2004); GMR multilayer traces (Miller *et al*., 2001), serpentines (Rife *et al*., 2003) and spirals (Schotter *et al*., 2002); spin valve (SV) traces (Graham *et al*., 2002; Lagae *et al*., 2002; Li *et al*., 2003), u-shaped (Ferreira *et al*., 2005b, 2005c), or serpentine (Anguelouch, Reich, Chien and Tondra, 2004); and magnetic

tunnel junctions (MTJs) (Shen, Liu, Mazumdar and Xiao, 2005; Cardoso *et al*., 2006).

2.1 Anisotropic magnetoresistance (AMR) based sensors

AMR-based ring sensors were designed and fabricated by NRL for single micron-sized magnetic label detection (Miller, Prinz, Cheng and Bounnak, 2002). The ring sensor was fabricated in NiFe with inner and outer diameters of 3.2 and 5 µm, respectively. The ring was designed to detect the radial component of fringe field created by a single 4.3-µm-diameter $Ni_{70}Fe_{30}$ microsphere, when excited by an out-of-plane alternate current (ac) magnetic field (Figure 4a).

In the setup from NRL, two AMR ring structures (separated by 50 µm) constitute half of a Wheatstone bridge, with the other half completed off chip with resistors of approximately the same value of the resistances of the rings.

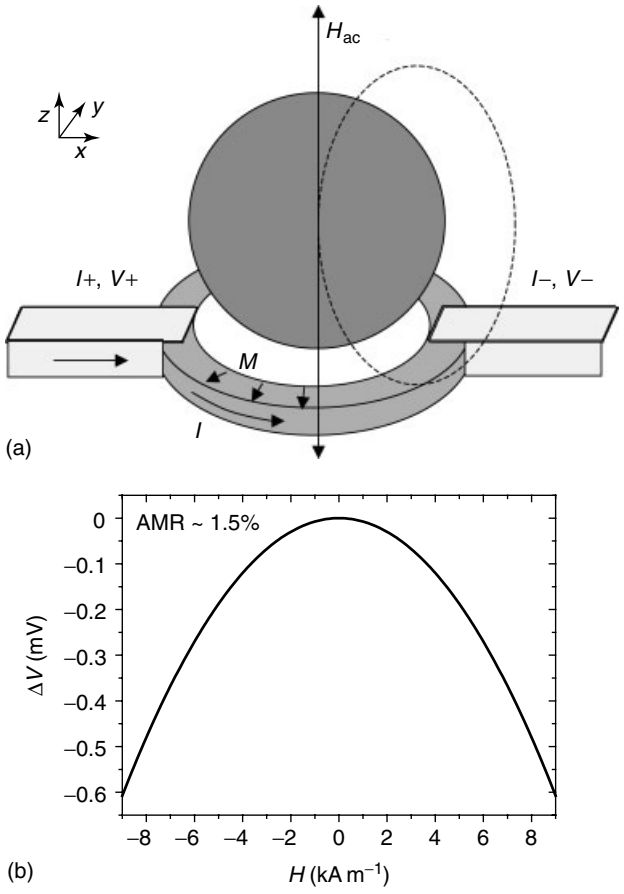

Figure 4. (a) Schematic showing an AMR ring sensor geometry, current flow, voltage measure points, and external magnetic excitation field directions. (b) Typical AMR sensor transfer curve as calculated from equation (1) and using data from Miller, Prinz, Cheng and Bounnak (2002).

An ac driven homopolar electromagnet was used to create a perpendicular-to-plane magnetizing field with typical field amplitudes H_0 between 0 and 4 kA m^{-1} (or 50 Oe), and frequencies f of 200 Hz. In most magnetic-field sensor platforms, paramagnetic or nonremanent magnetic labels are used, such that only in the presence of a magnetizing field they have a moment and thus create a field that is sensed by a particular transducer (this will be further discussed on the section on magnetic labels).

A direct current (dc) bias of ~1 V was applied to the bridge and a single microsphere was measured by scanning the label over one of the rings using an atomic force microscope (AFM) tip (to where the particle was previously glued).

The magnetoresistance of the AMR rings have roughly quadratic magnetic-field dependence around zero applied field, as can be seen from the equation for the electrical response (ΔV) of a single ring structure (Figure 4b).

$$\Delta V = -\left(\frac{\Delta R}{R}\right)_S \mathrm{I} R_{sq} \left(\frac{2\pi r_{av}}{h}\right) \left(\frac{\langle H_{labels}\rangle}{H_k}\right)^2 \qquad (1)$$

In equation (1), $(\Delta R/R)_S$ is the magnetoresistance ratio of the ring structure, which is defined by the difference in resistance between the maximum resistance state (in which the current is parallel or antiparallel to the circumferential magnetization) and the minimum resistance state (in which the current is normal to the magnetization), all divided by the minimum resistance. In this case, the AMR of the NiFe ring structures was ~1.5% (for a film thickness of 20 nm), but as a two-terminal device, the lead/contact resistances reduce the effective AMR to ~1%.

Also in equation (1), I is the sense current and R_{sq} is the sheet resistance defined as $R_{sq} = \rho/t$, with ρ the resistivity and t the thickness of the sensing layer. r_{av} is the average radius of the ring, $(r_{max} + r_{min})/2$, and h is the height of the sensor, $r_{max} - r_{min}$, with r_{max} and r_{min} being the outer and inner radius of the ring structures, respectively. $\langle H_{label}\rangle$ is the radial component of the field created by a magnetic particle averaged at the sensing layer (this issue will be discussed later on). Finally, H_k is the effective anisotropy field that include the crystalline anisotropy and shape demagnetizing fields.

Given the quadratic response of the sensor to the field created by the label, the detection was realized at $2f$, as the expansion of the magnetoresistance yields the dominant term.

Finally, this sensor was designed for the single label detection and was proposed as a sensing unit of a MRAM-like biosensor.

2.2 Planar Hall effect (PHE) based sensors

The use of PHE sensors for magnetic label detection was first proposed by the Mikroelectronik Centret (MIC) of the Technical University of Denmark (DTU) (Ejsing, Hansen and Menon, 2003). These devices are based on the spontaneous resistance anisotropy occurring in ferromagnets, just like the AMR rings.

The fabricated sensors were simple Ni crosses ($20 \times 20\,\mu m^2$ sensing area) and were used to detect 2.8-μm-diameter superparamagnetic polystyrene microspheres (Dynabeads M-280, DynalBiotech, http://www.dynalbiotech.com).

Using this cross geometry, two leads were used for driving current through a sensor, while measuring the voltage drop developed transversally to the current direction, with the other two leads (Figure 5). This voltage drop changed as a result of field created by the labels changing the direction of the magnetization of the ferromagnetic sensing layer with respect to the direction of the current, as shown in equation (2).

$$\Delta V = -\frac{1}{2}\Delta R I \frac{\langle H_{\text{labels}} \rangle}{H_{\text{k}}} \tag{2}$$

Here, $\Delta R = (\rho_{\parallel} - \rho_{\perp})/\text{t}$, with $\rho_{\parallel}$ and $\rho_{\perp}$ being the resistivity of the magnetic material with the sense current parallel or perpendicular to the material magnetization, respectively. For Ni, the resistivity variation is ∼2% (20-nm thick film). Again t is the thickness of the sensing layer, $\langle H_{\text{labels}} \rangle$ is the field created by the magnetic label averaged over the sensing area and H_{k} is the crystalline anisotropy field.

In the MIC platform, a dc sense current of 0.25 mA was used together with an in-plane magnetizing field up to $4.8\,\text{kA m}^{-1}$ (60 Oe) perpendicular to the sense current direction (Figure 5b). Particle detection was realized by measuring the sensor transfer before and after adding a magnetic label solution.

A further improvement, in collaboration with the Institute of Engineering of Systems and Computers – Microsystems and Nanotechnologies (INESC–MN), consisted of the design and fabrication of exchange-biased permalloy planar Hall sensors (Ejsing *et al*., 2004, 2005). Here a MnIr antiferromagnetic layer was used to control the anisotropy and to achieve a well-defined single-domain initial magnetization state. As a consequence, H_{k} in equation (2) represents the sum of the crystalline anisotropy field with the exchange field created by the antiferromagnetic layer.

In this case, PHE crosses of dimensions of $10\,\mu m^2 \times 10\,\mu m^2$ were used to detect in real-time 2-μm-diameter microspheres and 250-nm-diameter particles (Micromer-M and Nanomag-D labels, Micromod, http://www.micromod.de). Direct sense currents ranging from 1 to 10 mA were used together with an in-plane magnetizing field of $1.2\,\text{kA m}^{-1}$ (Ejsing *et al*., 2004); in addition, it was shown that using the sense current alone, without any external field, was sufficient to magnetize the nonremanent magnetic particles tested (Ejsing *et al*., 2005).

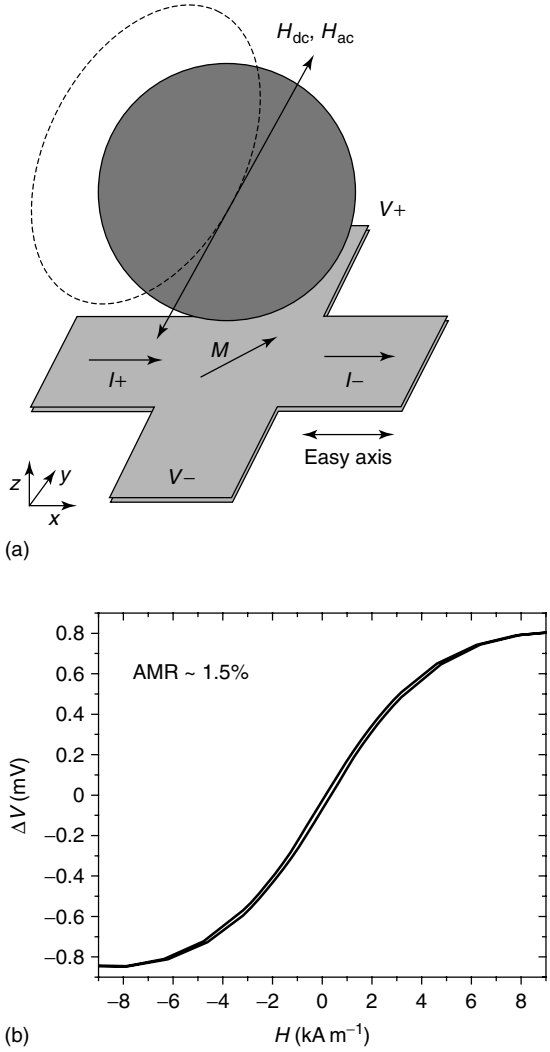

Figure 5. (a) Schematic showing a planar Hall cross sensor geometry, current flow, voltage measure points, and external magnetic excitation field directions. (b) Typical planar Hall effect sensor transfer curve. Data from INESC MN, for a $10 \times 10\,\mu m^2$ sensor with the structure Ta70Å/NiFe300Å/MnPt300Å/Ta70Å.

2.3 Giant magnetoresistance (GMR) multilayer based sensors

GMR multilayer sensors, together with SVs, are the sensing components used in the most developed biochip and

biosensing platforms. These devices are based on the spin-dependent transmission of conduction electrons between magnetic layers coupled through a nonmagnetic spacer. This transmission depends on the relative orientation of the magnetic moments of the magnetic layers (Baibich *et al.*, 1988).

GMR sensors are comprised of a multilayer of magnetic layers separated by nonmagnetic spacer layers and show typical magnetoresistance ratios $(\Delta R/R)_S$ from 5 to ~15%. The output for these sensors is given by equation (3) as is shown in Figure 6:

$$\Delta V = -\left(\frac{\Delta R}{R}\right)_S IR_{sq}\left(\frac{W}{h}\right)\frac{\langle|H_{labels}|\rangle}{H_k} \qquad (3)$$

Here $(\Delta R/R)_S$ is the magnetoresistance ratio, defined as the difference between the maximum resistance of the sensor (when the magnetic layers are antiparallel) and the minimum resistance of the sensor (when the magnetic layers are parallel), divided by the minimum resistance. W is the width of the sensor and h is its height. $|H_{labels}|$ is the absolute value of the component of the field created by the labels in the sensing direction, as the sensor response is unipolar (symmetrical with respect to the applied field, Figure 6b). Again the field created by the labels is averaged on the sensing layer and H_k is the effective anisotropy field that include the crystalline anisotropy and shape demagnetizing fields.

The BARC platform mentioned in the preceding text was the first system to be developed. In an earlier version it was comprised of $5 \times 80\,\mu m^2$ GMR sensor traces. These were arranged in a half-Wheatstone bridge, with a sensor for magnetic label detection in one arm of the bridge and one reference sensor at the other arm. The full bridge was completed with external resistors. Direct sense currents of 5 to 10 mA were used together with a perpendicular-to-plane external magnetizing field of $4\,kA\,m^{-1}$ rms at a frequency of 200 Hz was to enable lock-in detection at 400 Hz, just as in the AMR rings setup (Baselt *et al.*, 1998). The system was then used to detect biological warfare agents through the fringe field created by 2.8-μm-diameter Dynabeads that recognized the specific analytes (Edelstein *et al.*, 2000; Miller *et al.*, 2001).

In a later version, in collaboration with nonvolatile electronics (NVE), the BARC system encompassed serpentine GMR sensors, 1.6 μm wide on a 4 μm pitch, with a total length of 8 mm within a 200-μm-diameter circular zone. This was used to better fit the surface functionalized area to the sensor area (this issue will be discussed later on). A bias voltage across the bridge of 4 V was used together with magnetizing fields of 9.6 an $6.8\,kA\,m^{-1}$ rms at the same frequencies and in the same configuration as previously. Dynal

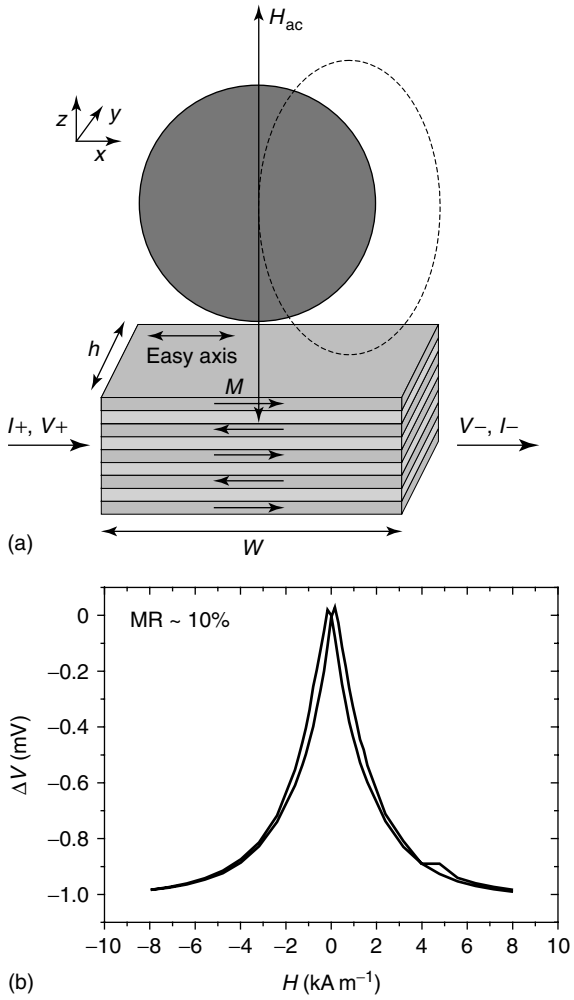

Figure 6. (a) Schematic showing a GMR sensor trace geometry, current flow, voltage measure points, and external magnetic excitation field directions. (b) Typical transfer curve for a GMR sensor. Data from INESC MN for a $2 \times 6\,\mu m^2$ GMR sensor with the stack NiFe60Å/[Cu19Å/NiFe13Å/CoFe4Å]20.

M-280 microsphere and $Ni_{30}Fe_{70}$ were detected (Rife *et al.*, 2003).

The GMR approach was followed by group at Universität Bielefeld, which used 1 μm wide spiral-shaped GMR sensors of a total of 70 μm in diameter (Schotter *et al.*, 2002, 2004). In this platform, smaller 0.35- and 0.86-μm magnetic microspheres Bangs Laboratories (http://www.bangslabs.com) were detected. As in the NRL biosystem, an out-of-plane magnetizing field is used and the sensor response is due to the in-plane components of the fringe field created by the magnetic labels. Particle detection is achieved by recording the dc sensor response from -12 to $12\,kA\,m^{-1}$ (or from -40 to $40\,kA\,m^{-1}$) with respect to a neighboring reference element in a half-Wheatstone

bridge arrangement. These platforms will be discussed more in detail later on Section 5.

2.4 Spin-valve (SV) sensors

SV based biochips were first introduced by INESC–MN (Graham *et al*., 2002) and were followed, in collaboration, by a group at Interuniversitair Micro-Elektronica Centrum (IMEC) (Lagae *et al*., 2002). Later on research laboratories at Standford University (Li *et al*., 2003) and at John Hopkins University (Anguelouch, Reich, Chien and Tondra, 2004) started independent projects on SV based biosensors.

SV sensors, in its simplest form, are comprised of only a single trilayer: two ferromagnetic layers separated by a non-ferromagnetic spacer, and they are also based on the GMR effect (Dieny *et al*., 1991). One of these ferromagnetic layers is called the *reference layer* as it is pinned by exchange coupling to an antiferromagnetic layer, and consequently is not sensitive to low applied magnetic fields. The other ferromagnetic layer is called the *free layer* as it senses even very small magnetic fields. As in GMR multilayer sensors, the spin-valve sensor resistance depends on the relative orientation of the magnetic moments of the magnetic layers. If carefully engineered, SVs can show a linear response to near zero applied fields. Shape demagnetizing effects or perpendicular easy-axis definition for the free and pinned layers during SV deposition are some means to accomplish that, for instance. The sensor response in this case is said to be bipolar and is given by equation (4) (Figure 7).

$$\Delta V = -\left(\frac{1}{2}\right)\left(\frac{\Delta R}{R}\right)_{\mathrm{S}} I R_{\mathrm{sq}} \left(\frac{W}{h}\right) \frac{\langle H_{\mathrm{labels}} \rangle}{H_{\mathrm{k}}} \qquad (4)$$

Here, symbols are the same as for the GMR sensors. Typical values for the magnetoresistance ratio for SV sensors are 7 to 15% (Dieny, 2004). Specular SVs on the other hand show higher $(\Delta R/R)_{\mathrm{S}}$ values from 15 to 20% (Dieny, 2004).

At INESC–MN $2 \times 6\,\mu\mathrm{m}^2$ SV sensors (with a full sensor length of 14 µm) were fabricated to detect single 2-µm microspheres (Micromer-M) (Graham *et al*., 2002) and several magnetic labels of different iron oxide compositions and different sizes ranging from 50 nm up to 1.5 µm (Ferreira, Graham, Freitas and Cabral, 2003). Shape demagnetization effects were used to obtain a sensor linear response (Figure 7b). Typical dc sense currents of 5 to 8 mA were used together with small $1.2\,\mathrm{kA\,m^{-1}}$ dc magnetizing fields applied in the SV sensing direction (see Figure 7a). Measurements were done in real time in a liquid medium using a simple multimeter.

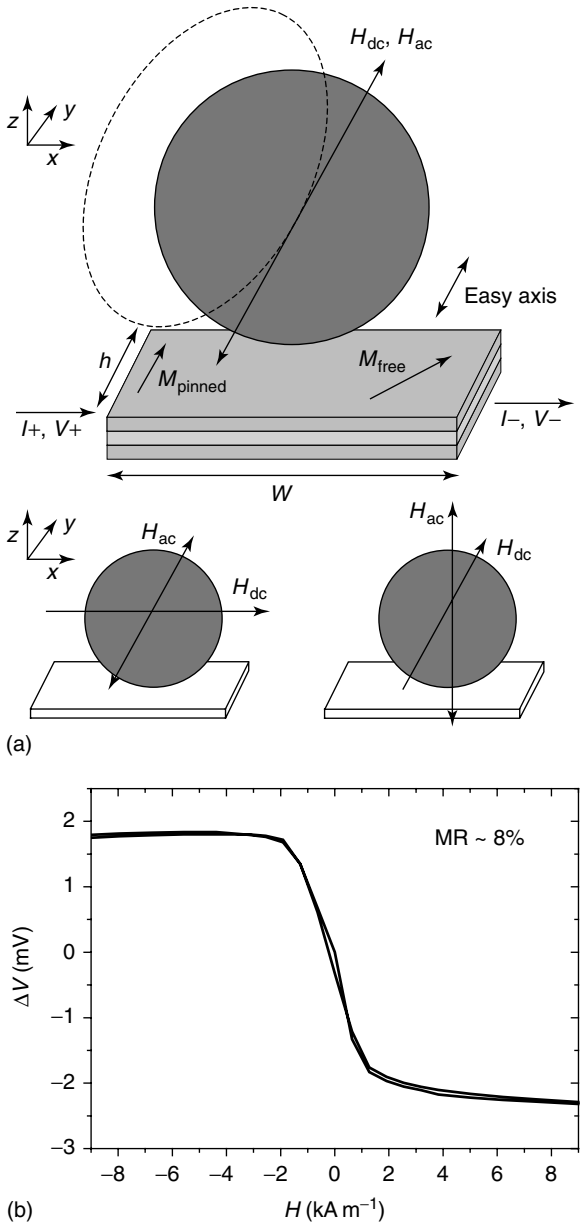

Figure 7. (a) Schematic showing a spin-valve sensor geometry, current flow, voltage measure points, and used external magnetic excitation field directions (larger scheme, INESC; smaller schemes, Stanford). (b) Typical spin valve sensor transfer curve. Data from INESC MN, for a $6 \times 2\,\mu\mathrm{m}^2$ sensor (Graham *et al*., 2005).

A differential dc measurement setup comprised of $2 \times 6\,\mu\mathrm{m}^2$ sensors in a half-Wheatstone bridge (with external resistors completing the other half) was used for detection of biomolecular recognition in the model system biotin–streptavidin (Graham, Ferreira, Freitas and Cabral, 2003). In this case, a SV sensor was functionalized with biotin and was then able to detect bound streptavidin-coated magnetic labels. Another sensor (75 µm away) was

covered with a photoresist mask and was used as a reference sensor, as biomolecular recognition was not observed over the photoresist layer (see details in Sections 5 and 6).

More recently, larger $2.5 \times 80\,\mu m^2$ u-shaped SVs were used for an increased dynamic range (higher number of particles to be detected), in applications for genetic disease diagnostics (Ferreira *et al*., 2005c; Ferreira *et al*., 2006) and for detection of pathogenic microorganisms (Martins *et al*., 2005) (see Section 6). Magnetic label detection in this case was done using a lock-in amplifier for lower noise and decreased thermal drift dependence. Direct sense currents of 1 mA were used together with a combination of external ac magnetizing fields ($\sim 1\,kA\,m^{-1}$ rms at 30 Hz) and dc bias fields (0.8 to $1.2\,kA\,m^{-1}$) applied in the sensing direction of the SVs.

Additionally, some INESC–MN sensing platforms made use of on-chip biomolecule transport using magnetic particles as carriers.

IMEC used $2 \times 16\,\mu m^2$ spin-valve sensors to detect ensembles of nanometer-sized particles. Sensors were linearized by shape anisotropy as in the INESC–MN approach. A sense current of 10 mA was used, and the magnetization of the superparamagnetic labels was achieved by the field created by two metal conductors adjacent to sensor. Current passes alternatively to one or the other conductor, resulting in particle movement over the sensor and, consequently, on label detection (Lagae *et al*., 2002).

In that respect, both approaches from INESC–MN and IMEC are unique with respect to other magnetoresistive biochip platforms and even to more general magnetic-field biosensors. Both research groups make use of on-chip conductors combined with a magnetic transducer to be able to manipulate and move magnetic labeled biomolecules on chip and to detect biomolecular recognition in almost real time.

In the case of INESC–MN, the use of tapered metal conductors (Graham *et al*., 2002) or u-shaped lines (Ferreira *et al*., 2005a) enabled the acceleration of biomolecular recognition between complementary DNA strands (Graham *et al*., 2005; Ferreira *et al*., 2005b). IMEC proposes to use on-chip tapered conductors (Lagae *et al*., 2002) for the detection of biomolecular recognition using a magnetic label cleaving process (Lagae *et al*., 2005). These issues will be further discussed in Sections 5 and 6.

Stanford University research group first used SV sensors of 2.5 to 3 μm height and ∼4 μm width (active areas) to detect a single 2.8-μm-diameter Dynabead (Li *et al*., 2003). Herein, shape demagnetization was also used to achieve a linear response from the SV. Furthermore, a half-Wheatstone bridge arrangement was used, with one active sensor and one reference sensor covered with hard-baked photoresist, just like the INESC–MN approach (Graham, Ferreira, Freitas and Cabral, 2003). Magnetizing fields were applied in plane. A dc longitudinal bias field (in the hard axis direction) was used to polarize the magnetic beads and an orthogonal ac field (in the sensing direction) was used to modulate their magnetizations. DC bias fields between 7.5 and $9.5\,kA\,m^{-1}$ were used, together with ac orthogonal fields of $\sim 3\,kA\,m^{-1}$ rms at 40 Hz.

The laboratory at Standford University detects particles after a label solution as dried out and particles remained settled over the sensor. A later stage, particles are dissolved back in water and are washed away. This contrasts with the approach followed at INESC–MN, where particle and biomolecular recognition measurements are all performed in liquid.

In a further conception of the system (Li, Wang and Sun, 2004), the Stanford group used smaller $0.3 \times 1.5\,\mu m^2$ (active area) sensors for the detection of 16-nm Fe_3O_4 magnetic nanoparticles (Sun and Zeng, 2002). The experimental setup was similar to the previous one, but in this one a dc bias field of $6.4\,kA\,m^{-1}$ was applied transversely to the sensor (in the sensing direction) to polarize the nanoparticles and ac field of $\sim 8\,kA\,m^{-1}$ at a frequency f of 208 Hz was applied perpendicular to plane, similarly to GMR sensors. Measurements were performed at $2f$. In this study, a nanoparticle monolayer was patterned over the sensor surface using a polyethilenimine mediated self-assembly method (Sun *et al*., 2002).

More recently, a collaborative work between the John Hopkins University and NVE resulted in a platform that uses serpentine or meander SV sensors in a full-Wheatstone bridge arrangement on chip (Anguelouch, Reich, Chien and Tondra, 2004). These meander lines were 4 μm wide on a 6 μm pitch, comprising active sensing areas of $100 \times 100\,\mu m^2$ or $200 \times 200\,\mu m^2$. Two of the bridge resistors were laid out as interlaced meander lines and served as the sensing elements, while the remaining sensors were covered by a protective layer 6 μm and served as compensating elements. DC currents of 1 mA were used for detection of 5 and 30 μm length ferromagnetic nanowires. These nanowires have the potential to be used as biomolecular labels and for cell manipulation (Reich *et al*., 2003).

2.5 Magnetic tunnel junction (MTJ) sensor

These devices are based on the spin-dependent tunneling of electrodes across an insulator that separates two ferromagnetic layers. As with GMR sensors, the electron tunneling through an insulating barrier depends on the relative orientation of the magnetizations of the magnetic layers (Moodera, Kinder, Wong and Meservey, 1995).

Just, the same way as SVs, MTJs can be fabricated to have a linear response. In this case, which is the most suitable for biosensing applications, the transducer output is given by:

$$\Delta V = -\left(\frac{1}{2}\right)\left(\frac{\Delta R}{R}\right)_S I \left(\frac{RA}{Wh}\right)\frac{\langle H_{\text{labels}}\rangle}{H_k} \qquad (5)$$

In equation (5), symbols hold the same meaning as for GMR and SV sensors, while *RA* represents the MTJ resistance area product. A transfer curve for the MTJ sensor is shown in Figure 8.

Of the magnetoresistive sensor family, MTJ sensors show the highest values of the magnetoresistance ratio, ∼50 to 70% for AlOx barrier junctions (Wang, 2004) and, recently, >200% for MgO tunnel barriers (Parkin *et al*., 2004; Yuasa *et al*., 2004).

MTJ based biosensors have been recently proposed (Schotter *et al*., 2002; Freitas *et al*., 2004; Wang *et al*., 2005) and magnetic label detection has been demonstrated (Shen, Liu, Mazumdar and Xiao, 2005; Cardoso *et al*., 2006).

A group from Brown University (Shen, Liu, Mazumdar and Xiao, 2005), fabricated $2 \times 6\,\mu m^2$ MTJ sensors to detect single superparamagnetic M-280 Dynabeads. The sensor was operated in an ac bridge configuration (1 V rms at 8 kHz bias voltage), and the sensor response was read using a lock-in amplifier. Two external dc applied fields in the sensing direction ($1.2\,kA\,m^{-1}$) and perpendicular to the sensing direction ($1.6\,kA\,m^{-1}$) were applied such that the MTJ sensor operated in the most sensitive and linear region of the transfer curve.

Recently, INESC–MN demonstrated the detection of 250-nm-diameter magnetic labels (Nanomag-D) using a sensing unit comprised of a AlOx barrier MTJ in series with a hydrogenated amorphous silicon (a-Si:H) thin-film diode (TFD) (Cardoso *et al*., 2006). This sensing unit is the basis for an MRAM-like biosensor as was previously proposed (Baselt *et al*., 1998), and a 16×16 MTJ-diode matrix was already fabricated (this will be further discussed in Section 5).

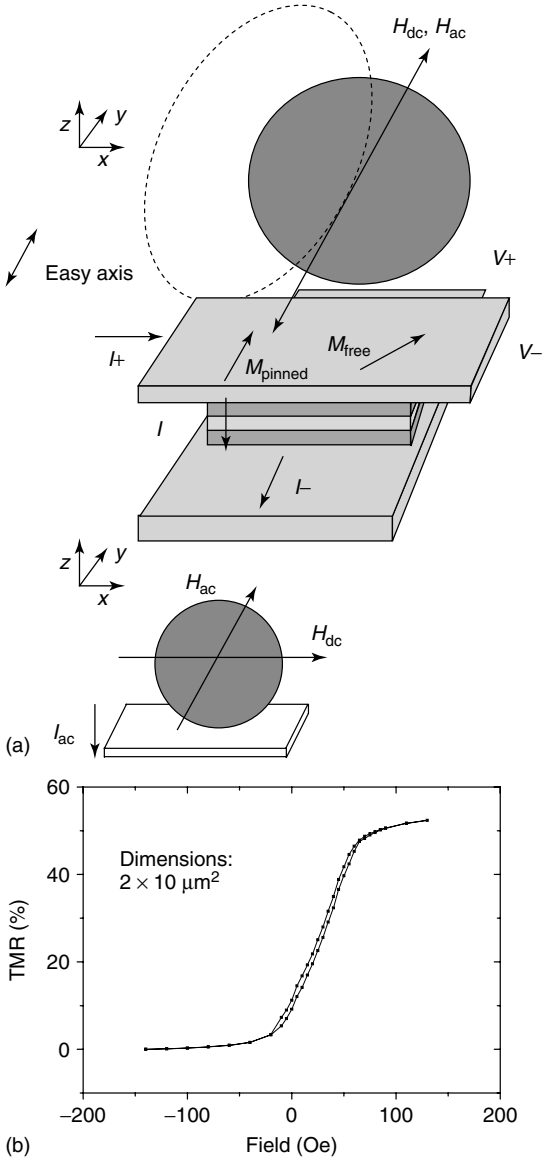

Figure 8. (a) Schematic showing a magnetic tunnel junction sensor geometry, current flow, voltage measurement points, and used external magnetic excitation field directions (larger scheme, INESC; smaller schemes, Brown). (b) Typical sensor transfer curve, $10 \times 2\,\mu m^2$ (F. Cardoso, INESC MN, 2006).

2.6 Detection of magnetic labels

In magnetic biosensing applications, it is important to quantify the number of labels that are being detected in order to determine the number of biomolecular recognition events.

In the calculation of the response of a magnetoresistive sensor to the presence of magnetic labels it is usually assumed that the sensing layers respond to an average field $\langle H_{label}\rangle$, rather than to the inhomogenous local field they create (Tondra, Porter and Lipert, 2000). In fact, a good agreement was obtained between analytical calculations, assuming this average field, and micromagnetics simulations (Li and Wang, 2003). Furthermore it is assumed that the sensing layers rotate coherently with $\langle H_{label}\rangle$, as described by the Stoner–Wohlfarth model (Stoner and Wohlfarth, 1948). Here, the sensing layers correspond to the exchanged-bias NiFe layer in planar Hall sensors; the GMR multilayers; or the free layers of the SVs and MTJs.

Although, several analytical models have been developed according to the type of sensor and to the particular detection

methods, they all consider the assumptions made in the preceding text together with the dipole field approximation in SI.

$$\boldsymbol{H}_{\text{label}}(\boldsymbol{r}) = \frac{\left(\frac{3(\boldsymbol{m}\cdot\boldsymbol{r})\boldsymbol{r}}{r^5} - \frac{\boldsymbol{m}}{r^3}\right)}{4\pi} \tag{6}$$

Here, it is assumed that the magnetic moment $\boldsymbol{m}$ of the label is located at its center, and $\boldsymbol{r}$ is the distance between the label center and the point of the sensor where the field is calculated.

The dipole field in equation (6) is inhomogeneous at the sensing layer, and consequently, the sensor response depends on the position of the magnetic label with respect to the sensor (Figure 9a). In bipolar response transducers, such as AMR rings and GMR sensors, labels adjacent to the transducer also contribute to a change in resistance, though this effect is relevant only for labels few micrometers apart

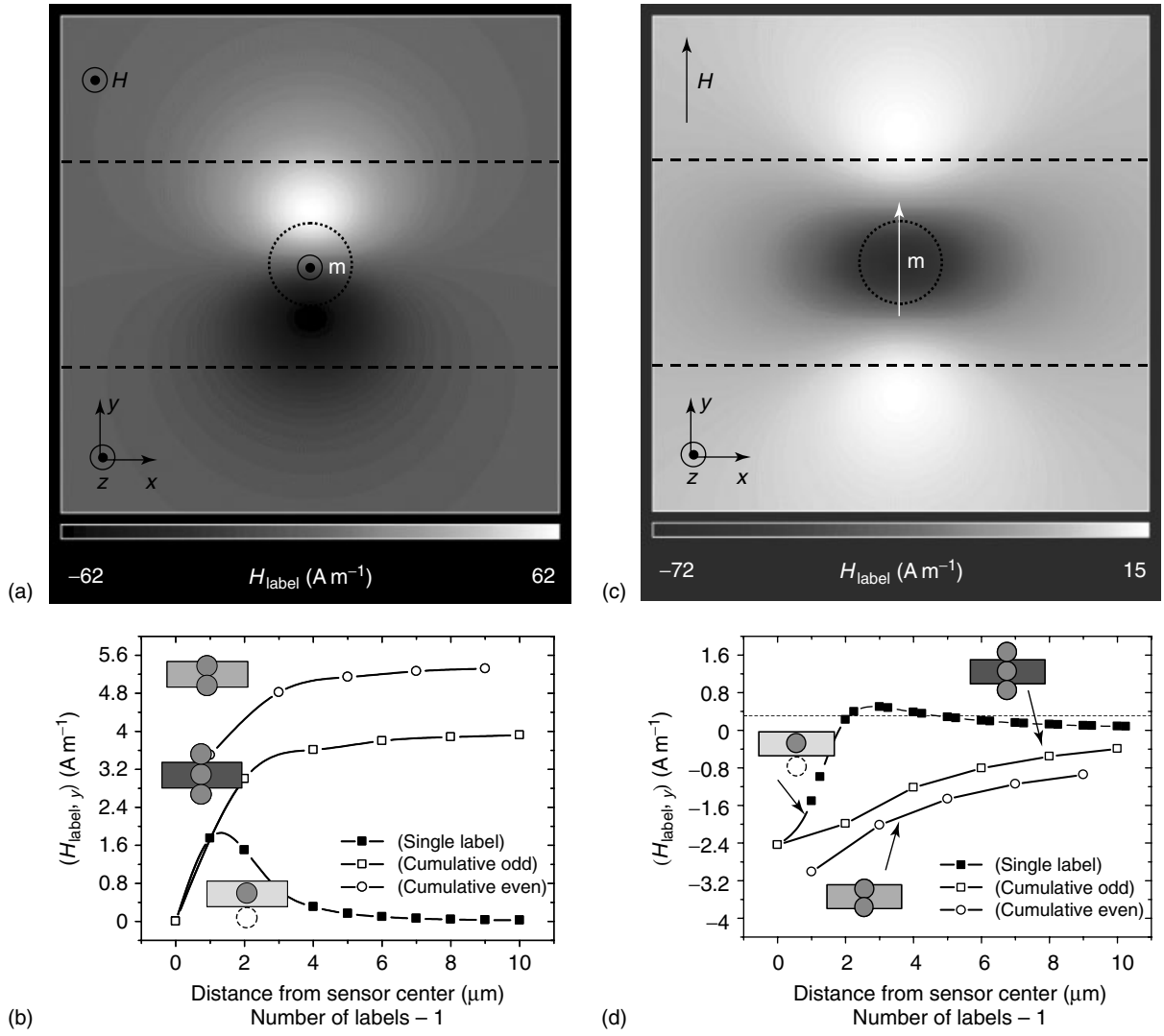

Figure 9. (a) Inhomogenous magnetic field created by a 2-μm microsphere, which shows a magnetization of 0.48 kA m^{-1} under a 1.2 kA m^{-1} external magnetizing field applied perpendicular to the plane of the sensor; 2.5-μm high sensor and particle outlines are shown in dashed lines. (b) Magnetic field created by a single label at varying distances from the center of the sensor (solid squares); also shown are the fields created by multiple labels placed on a row in two distinct arrangements (open squares and open circles) over a spin-valve sensor (the number of labels in the arrangements is indicated in the horizontal axis); fields are averaged over a $2.5 \times 40\,\mu\text{m}^2$ spin-valve trace. (c) Inhomogenous magnetic field created by a 2-μm microsphere under a 1.2 kA m^{-1} external magnetizing field applied in plane in the spin valve sensing direction. (d) Magnetic field created by a single label at varying distances from the center of the sensor and the fields created by multiple labels placed on a row in two distinct arrangements: a label at the center of the sensor and additional adjacent labels (cumulative odd); two labels over the sensor and additional labels on both sides (cumulative even).

(Figure 9a right). On the other hand, for transducers with a unipolar response such planar Hall sensors, SVs, and MTJs, adjacent labels can even have an opposite contribution to the field created by the labels on top of the sensing structures (Figure 9b). In these devices, particular care must be taken on the surface functionalized area and the estimation of the number of detected labels.

In addition, as will be discussed in Section 3, labels show usually a paramagnetic behavior, that is, they only possess a magnetic moment in presence of an externally applied magnetic field. As such, the magnetic moment of the label can be given in SI by $\boldsymbol{m} = \chi \boldsymbol{H}/V$, where χ is the susceptibility per label, $\boldsymbol{H}$ is the total applied field and V is the volume of the label.

Models have utilized several magnetizing field conditions, where the only requirement is that the induced moment on the labels gives rise to magnetic-field components in the sensing directions of the transducer (see previous sections on sensors). Nevertheless, these models only take into account the externally applied field as the magnetizing field.

It has been experimentally observed that even in the absence of an externally applied field $\mathbf{H_{ext}}$ magnetic label detection is possible. This can be attributed to either the sense current, that itself creates a magnetizing field $\boldsymbol{H_j}$ (Ejsing *et al*., 2005), or to magnetostatic field created by the magnetic layers of the sensors $\boldsymbol{H_m}$ (Ferreira, Feliciano, Graham and Freitas, 2005a). In reality, most of the times, it is the combination of the several different fields $\boldsymbol{H} = \boldsymbol{H_{ext}} + \boldsymbol{H_j} + \boldsymbol{H_m}$ that magnetizes the labels (Ferreira, Feliciano, Graham and Freitas, 2005a).

Although, the possibility to detect magnetic labels without the need of external field is advantageous, as it simplifies the experimental setup and measurement protocols, care must be taken when designing sensors and implementing the optimum detection method.

At INESC–MN a study was made on the detection of 250-nm-diameter magnetic labels using $2 \times 6\,\mu m^2$ top pinned SV sensors. These sensors were fabricated with the structure Ta 30 Å/NiFe 30 Å/CoFe 25 Å/Cu 26 Å/CoFe 25 Å/MnIr 60 Å/Ta 30 Å/TiW (N) 150 Å and showed a linear range roughly between -2.5 and $1.5\,kA\,m^{-1}$ at 8-mA sensor bias current. Values for $\boldsymbol{H_j}$ and $\boldsymbol{H_m}$, averaged along the sensitive direction of the SV (smaller dimension) and at a distance of $\sim$300 nm from the sensing layer, were $\langle H_y^j \rangle \sim -0.18\,kA\,m^{-1}$ per mA sense current and $\langle H_y^m \rangle \sim -1.0$–$1.7 \sin\theta$ (field in kA m), with θ the angle between the magnetization of the free layer and the sense current direction (for $\theta = 90^\circ$ the sensor is in the minimum resistance state as the pinned are free layers are parallel) (Bertram, 1994). As a consequence, the intensities of the several fields were comparable (Ferreira, Feliciano, Graham and Freitas, 2005a). Table 1 shows the intensities for these fields for three conditions:

Table 1. Magnetic fields acting on a 250-nm particle located on top of a spin-valve sensor ($2 \times 6\,\mu m^2$). The distance between the center of the label and the sensing layer is $\sim$300 nm. External uniform magnetic fields $\boldsymbol{H_{ext}}$ were applied in the sensing direction (y axis in Figure 9) and magnetostatic fields $\boldsymbol{H_m}$ and the field created by an 8-mA sense current $\boldsymbol{H_j}$ were averaged along the smaller dimension of the sensor. The total magnetic field $\boldsymbol{H}$ was also calculated for the three conditions presented.

	Magnetic fields ($kA\,m^{-1}$)		
H_{ext}	−1.20	0	1.20
$\langle H_y^m \rangle$	−0.56	−1.43	−2.31
$\langle H_y^j \rangle$	−1.44	−1.44	−1.44
$\langle H_y \rangle$	−3.20	−2.87	−2.55

In fact, for the external applied fields considered in Table 1, the resulting total magnetic fields acting on the labels are always negative with respect to the y axis of Figure 9 (i.e., opposite to the pinned layer magnetization direction). This means that in all these cases the stray magnetic fields created by the labels contribute to a decrease in the resistance of the transducer (see subsequent text).

The existence of magnetostatic fields had further consequences on sensor operation when using an ac external excitation field: a dc external bias field was required for optimum sensor operation (Ferreira *et al*., 2005c; Ferreira *et al*., 2006) (see Figure 10).

Without considering the effect of magnetostatic fields, an ac excitation field results in the induction of a magnetic moment in the same direction and consequently, the stray fields of the labels at the sensing layer oppose the applied field. The labels then shield the sensor from the external field, resulting in a decrease of the peak-to-peak signal or the rms output (see sensor transfer curve in Figure 10a top). Figure 10(a) in the bottom shows the rms signals obtained for a $2.5\,\mu m^2 \times 80\,\mu m^2$ spin-valve sensor with a 25% sensor coverage of 250 nm particles, by applying a dc bias and different ac excitation fields. It is observed that the sensor output increases with the magnitude of the ac field up to a maximum, where the ac field is large enough to surpass the linear regime of the sensor and move into the saturation regions.

On the other hand, when considering magnetostatic fields the induced magnetic moment of the labels is always negative, resulting in a decrease of the resistance of the sensor for all applied fields. As a consequence, the peak-to-peak signal window is shifted to lower resistances, while maintaining the magnitude of the signal in the linear region of the transfer curve. This results in a small or near zero variation of the rms signals in this regime (Figure 10b top). Applying a dc bias signal results in an increase of the sensor output to labels (25% sensor coverage) up to a

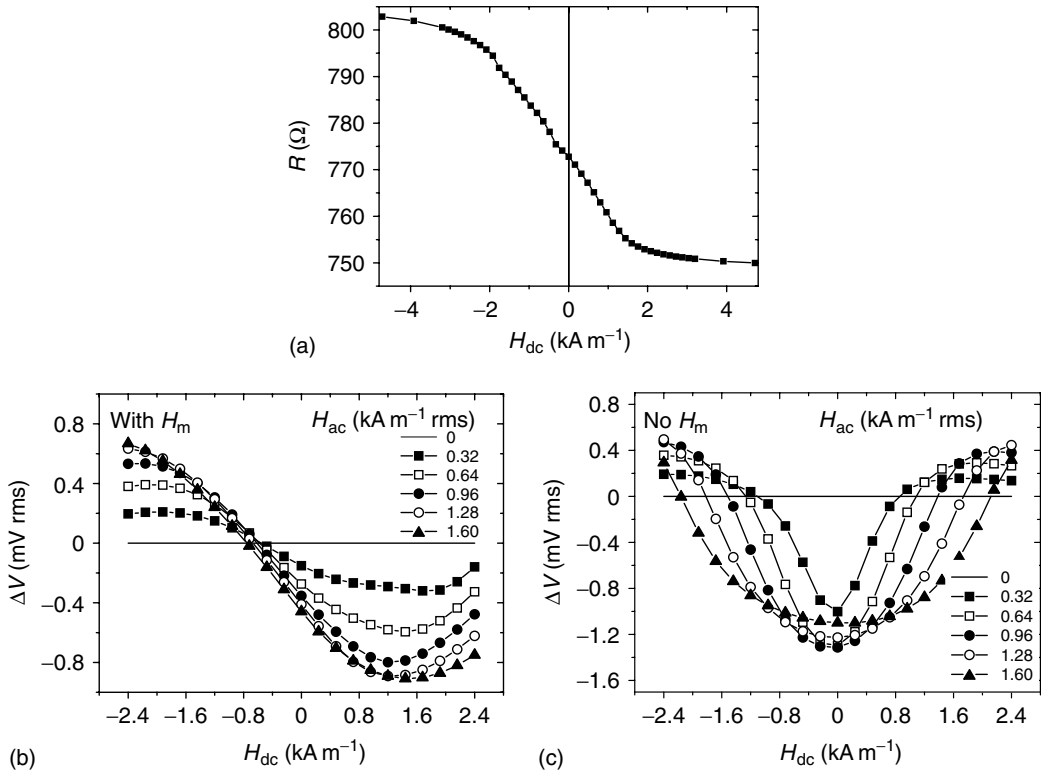

Figure 10. (a) Spin valve sensor transfer curve. (b) Sensor output (AC excitation field +DC bias field) calculated. Without taking into account sensor magnetostatic fields. (c) Sensor output (AC excitation field +DC bias field) calculated taking into account6) sensor magnetostatic fields.

maximum field where the ac excitation field goes deep into the saturation regions (Figure 10b bottom).

Finally, in order to be sensitive only to the external magnetizing field (or at least be the dominant magnetizing field) low sense currents may be used and sensors may be designed and fabricated with synthetic free (SF) and synthetic antiferromagnetic (SAF) pinned layers, such that magnetostatic fields are minimized (Guedes, Mendes, Freitas and Martins, 2006). In these conditions, the dc bias external field is no longer necessary for ac detection (see Figure 11).

2.7 Sensor performance

In sensing applications, the figure of merit to be considered is the signal-to-noise ratio (SNR), although the absolute signal is also important as the highest the signal is the lesser is the requirement for amplification steps and simpler is the detection apparatus. For instance, in earlier INESC–MN studies single magnetic microspheres were detected by simply measuring the dc voltage drop across a spin-valve resistor using a common multimeter (Graham *et al*., 2002).

For defining sensor performance is also necessary to consider the application for which the sensor is designed, that is, either it is required the detection of a great number of labels with a considerable dynamic range (number of particles to be detected) or one targets for single label and single biomolecular recognition detection (Graham, Ferreira and Freitas, 2004). As such, sensor geometry is something to take into account, not only for dynamic range (as will be discussed further in Section 5) but also in terms of sensitivity.

As sensors respond to the average field created by the labels on the sensing layer it is natural to expect that sensor sensitivity to a single label improves as the dimensions of the sensor are made comparable to those of the label (Tondra, Porter and Lipert, 2000).

On the other hand, sensor sensitivity in the broader sense depends on the magnetoresistance ratio of the bulk magnetoresistive material, on the sensor geometry (which can be used to obtain a linear response through shape demagnetizing fields) and on externally applied bias fields (which can also be used to linearize the sensors).

Here, the SNRs of the several magnetoresistive sensors are determined taking into account the detection of a single 2-μm microsphere (Freitas *et al*., 2004) and the noise levels obtained in the linear regime of the sensor. Table 2 shows

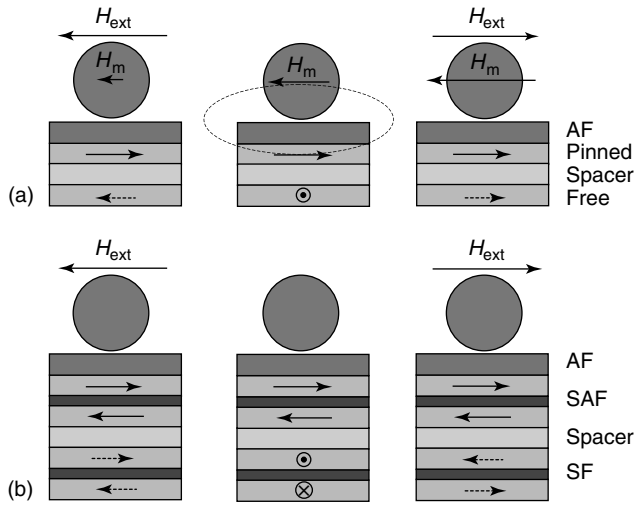

Figure 11. (a) Cross-section schematic of a top pinned spin-valve sensor showing the effects of the magnetostatic fields created by the ferromagnetic layers of the sensor. Three conditions are considered: with the external magnetic field applied in the negative direction (opposite to the magnetization of the pinned layer), without external magnetic field and with the external field applied in the positive direction (direction of the magnetization of the pinned layer). (b) Cross-section schematic of a spin-valve sensor with synthetic free (SF) and synthetic antiferromagnetic (SAF) layers. When these layers are compensated the resulting magnetostatic fields are null and labels respond only to the external magnetizing fields.

a comparison of the performance of the different types of magnetoresistive sensors mentioned in the preceding text, with respect to the signal-to-noise ratio. The magnetic properties shown are typical for these sensors and the sensor size was chosen for optimal single 2-μm microsphere under a magnetizing field of $1.2\,\mathrm{kA\,m^{-1}}$ (moment of $2 \times 10^{-15}\,\mathrm{J\,T^{-1}}$). Thermal or Johnson noise was calculated from $\sqrt{4k_bTR}$, where k_b is the Boltzmann constant ($1.38 \times 10^{-23}\,\mathrm{J\,K^{-1}}$), T is the absolute temperature (taken as 300 K) and R is the resistance of the transducer. In addition, the noise for the MTJ sensors with AlOx or MgO barriers was calculated from the summation of the thermal and shot noise $\sqrt{(4k_bTR + 2IeR^2)}$, where I is the sense current and e is the charge of the electron (1.6×10^{-19}C) (Raquet, 2001; Almeida *et al*., 2006). Finally, the minimum detectable field and the SNR was calculated for the minimum noise of these magnetoelectronic devices.

One can observe from Table 2 that due to its highest magnetoresistance ratio, the MgO barrier MTJ transducers show the highest sensitivity and consequently, highest signal per label, followed by AlOx MTJs, SVs, GMR sensors, AMR rings, and planar Hall crosses. On the other hand, for low resistance tunnel junctions (as shown), the minimum noise level is comparable to the noise levels of the other transducers, this then results in a smaller minimum detectable field and a higher SNR.

Note that in this table, the sense current was kept constant at 1 mA. Some of the sensor performances relations may differ if different currents are applied through the sensors, as the different sensors show distinct limits of operation. As an example, MTJ sensors show a decrease in tunneling magnetoresistance (TMR) with increasing sensing currents (voltage bias) and there is an increase in shot noise; while for SVs, 10-mA currents can be applied, increasing the sensor response to a single label by a factor of 10, while maintaining mostly the same thermal noise level.

MgO barrier based MTJ transducers show the promise of being the most sensitive of spintronic transducers ever, being capable of detecting magnetic fields in the picotesla range. This may enable the detection of single 10-nm magnetic particles and, consequently, of single biomolecular interactions. This shows that magnetoresistive biochips have the potential to become useful tools for molecular biology.

3 MAGNETIC LABELS

Different kinds of magnetic labels have been used in magnetic biosensing applications, ranging from nanometer to micrometer sized particles (Pankhurst, Connolly, Jones and Dobson, 2003) and nanowires (Reich *et al*., 2003). In addition, ferromagnetic, paramagnetic, or superparamagnetic labels have been chosen according to the application, transduction mechanism, and assay type.

Several ferromagnetic materials, such as Fe, Co, Ni, and their alloys, and ferrimagnetic materials, such as γ-Fe_2O_3 (maghemite) and Fe_3O_4 (magnetite), have been used in magnetic particle preparation. Nevertheless, their magnetic properties depend, not only on the material used but also on the label size. For instance, large labels, of micrometer dimensions or more, usually present a multidomain structure, as this represents a minimum magnetic energy of the system. Nevertheless for smaller labels (below the micrometer range), the energy is minimum in a single-domain state rather than including domain walls. As such, the response of these particles to an applied magnetic field is a large hysteresis loop (see Figure 12). Multidomain magnetic particles, on the other hand, show a narrow hysteresis loop, as domain walls require a smaller energy to move. Both multi- and single-domain particles show a nonzero magnetization under no applied field, and as such they are called *remanent magnetic particles*.

Smaller particles or labels, with dimensions of the order of tens of nanometers or less, have a magnetocrystalline and shape anisotropy energy that are in the order of or

Table 2. Comparison of the performance of different magnetoresistive sensors used for the detection of magnetic labels, including magnetic tunnel junctions with AlOx and MgO barriers. Typical magnetic properties for these sensors were used, and sensor geometries were chosen for the detection of a single 2-μm magnetic label of magnetization of $0.48\,\mathrm{kA\,m^{-1}}$. t* represents the magnetic sensing layer thickness. Remaining symbols are as detailed in previous sections for each of the sensor types. The field created by the label in the AMR sensor case was averaged in an annulus of radius and height of 1 μm. For the remaining sensors the label field was averaged in a squared area. The thermal noise is shown for the different sensors, while for MTJ sensors the presented noise is the summation of the thermal and shot noise (see text for details). The signal-to-noise ratio was obtained dividing the signal per 2-μm microsphere, ΔV, by the noise.

Sensor type	Width (μm)	Height (μm)	t^* (nm)	R_{sq} (Ω cm) RA (Ω μm^2)	$\Delta R/R$ (%)	H_k (kA m^{-1})	S (V T^{-1}A^{-1})
AMR ring	$r_{ext} = 1.5$ $r_{int} = 0.5$	1	20	10.5	1.5	14.5	27
Planar Hall	2.5	2.5	30	7	1.5	2.4	17
GMR	2.5	2.5	72	2.8	10	2.4	93
Spin valve	2.5	2.5	5	20	8	2.4	265
MTJ AlOx	2.5	2.5	5	80	25	2.4	531
MTJ MgO	2.5	2.5	5	150	150	2.4	5968

Sensor type	I (mA)	$\langle\mu_0 H_{label}\rangle$ (μT)	ΔV (μV)	Thermal noise/shot noise (nV Hz$^{-0.5}$)	$\langle\mu_0 H_{label}\rangle_{min}$ (nT)	SNR
AMR ring	1	60	1.6	0.7	27	2200
Planar Hall	1	28	0.5	0.3	20	1400
GMR	1	28	2.6	0.2	2.3	12 000
Spin valve	1	28	7.4	0.6	2.2	13 000
MTJ AlOx	1	28	15	0.5	1.0	29 000
MTJ MgO	1	28	170	0.8	0.1	220 000

smaller than the thermal energy (Kittel, 1996). The particles are superparamagnetic and show no remanent moment. These labels show a nonhysteretic behavior with an applied magnetic field, which is a signature of superparamagnetism (Figure12).

Under an externally applied field, magnetic labels align with the field but after the field is removed the magnetization of the particles relaxes. Relaxation occurs through two mechanisms, Néel (1955) and Brownian (Debye, 1929), and the predominance of one of the mechanism over the other depends on label size.

Néel relaxation is related to superparamagnetism, as the magnetic moment of a label fluctuates thermally inside the particle (Figure 13a), and it is characterized by the relaxation time τ_N:

$$\tau_N = \tau_0 \exp\left(\frac{\Delta E}{k_B T}\right) \tag{7}$$

In equation (7), τ_0 is usually taken as 1 to 100 ps (Brown, 1963), ΔE is the energy barrier to the moment reversal and includes the magnetocrystalline and shape anisotropies. K_B is the Boltzmann constant and T is the absolute temperature (K). Néel relaxation is dominant for particles with sizes smaller than 10–20 nm.

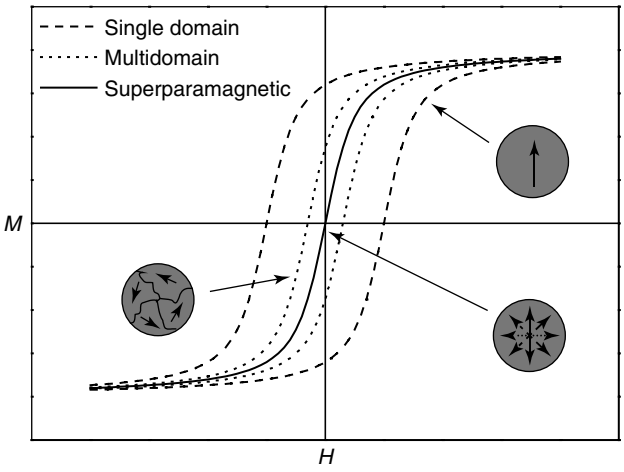

Figure 12. Magnetization versus applied field curves for single domain, multidomain and superparamagnetic labels.

Larger magnetic particles have a relaxation time τ_N in the order of tens or hundredths seconds and thus exhibit remanence. Nevertheless, their magnetization relaxes through

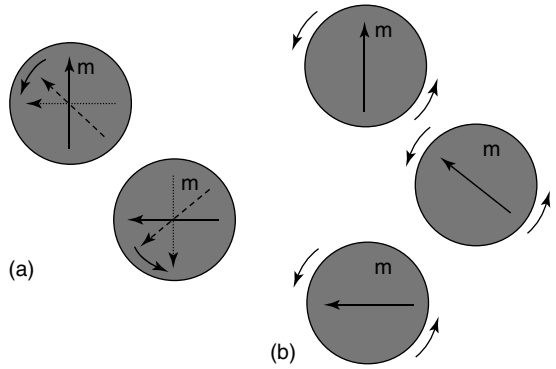

Figure 13. (a) Néel relaxation mechanism (dominant for superparamagnetic particles): labels magnetic moment, rotates with thermal energy without being accompanied by label rotation. (b) Brownian relaxation mechanism (more relevant in single-domain and multidomain particles): labels magnetic moment, relaxes together with the rotation of the whole label in the carrier liquid.

the Brownian rotation of the whole label in the carrier liquid (Figure 13b). The moment is fixed within the particle. It is characterized by the time constant τ_B:

$$\tau_B = \frac{4\pi\eta r^3}{k_B T} \tag{8}$$

Here η is the viscosity of the carrier liquid (e.g., for water, $0.001\,\mathrm{N\,s\,m^{-2}}$) and r is the hydrodynamic radius of the label.

It is these distinct magnetic properties that are used in the different biosensing approaches. Volume assays are based on Brownian relaxation of nanoparticles in solution. When labels recognize a particular analyte in solution, through probe biomolecules immobilized on the particles surfaces, their hydrodynamic radius increases. As a consequence, the ac susceptibility peak of the solution shifts to lower frequencies (Connolly and St. Pierre, 2001; Astalan *et al*., 2004; Chung *et al*., 2004).

SQUIDs, on the other hand, have been used to distinguish between surface-immobilized magnetically labeled biomolecules and particles free in solution (Kötitz *et al*., 1997; Chemla *et al*., 2000). In these cases, after removal of an applied field, surface-bond labels only show a relatively slow Néel relaxation, while unbound free-in-solution labels relax mainly via the Brownian mechanism and are distinguished by the transducers.

The remaining surface-based assays are based on the detection of magnetic stray fields created by the labels bound to the surface through the biomolecular recognition between target and probe biomolecules. Here, ∼10-nm superparamagnetic labels are used, or more frequently larger >50 nm to micrometer sized labels. The larger labels are comprised of smaller superparamagnetic labels dispersed in or coated with a polymer, metallic or oxide layer, and show a paramagnetic or a nonremanent behavior.

In magnetoresistive bioassays, magnetic labels should comply with certain requisites: have a high saturation magnetization (made of materials like Fe, Co, Ni, and their alloys) so that the signal per particle is the maximum possible; show material stability over time (like iron oxides); be biocompatible and nontoxic (like iron oxides); be monodispersed and do not cluster, that is, be superparamagnetic; show low unspecific adsorption to undesired biomolecules and surfaces; and ideally, each particle should label or tag a single biomolecule. In addition, material stability and biocompatibility requisites should apply to the encompassing matrix or the coating.

The technology of magnetic particles for biosensing applications involves several fields of knowledge, namely, inorganic and organic chemistry, materials science, and molecular biology. In fact, magnetic properties are as important as suitable coating and biomolecule functionalization chemistries.

At INESC–MN, several particles of diameters ranging from 50 nm up to 2.8 µm were studied (Ferreira, Graham, Freitas and Cabral, 2003; Freitas *et al*., 2004). Table 3 shows some of the magnetic properties of the labels tested by INESC–MN and other research laboratories.

As a notice, 130 and 250 nm (Nanomag-D) particles and 2-µm microspheres (Micromer-M) do not show a pure paramagnetic behavior at low applied fields as they do not fit the Langevin equation in this regime (Freitas *et al*., 2004).

$$M = M_S\left[\coth(gH) - \frac{1}{(qH)}\right] \tag{9}$$

In equation (9), M is the magnetization of the label, M_S is its saturation magnetization, H is the applied field and $q = \mu_0 m_p / k_B T$, where μ_0 is the magnetic permeability in vacuum and m_p is the average moment of each nanoparticle that comprises the label.

These labels show an increased magnetic susceptibility near zero, which may be the consequence of interacting smaller nanoparticles that comprise the larger ones (Figure 14).

4 BIOMOLECULAR FUNCTIONALIZATION

A magnetoresistive sensing platform can only be used for biosensing after it has been functionalized with biomolecules. This issue is as important as the magnetic transducers themselves, and implies a great control on surface and label functionalization biochemistries and assay protocols.

Table 3. Properties of several magnetic labels used in magnetoresistive biosensing platforms. Data was obtained by vibrating sample magnetometry at INESC–MN, unless indicated otherwise.

Label	Manufacturer	Diameter (nm)	Magnetization kA m^{-1})[a]	Susceptibility[b]	Material[c]
4SP NiFe powder[d]	Novamet	3300	5	4.2	$Ni_{70}Fe_{30}$(~100%)
Dynal M-280[d]	Dynal Biotech	2800	0.40	0.35	FeOx (17%)
Micromer-M	Micromod	2000	0.48	0.22	FeOx (15%)
CM01N/7228[e]	Bangs Laboratories	860	1.88	1.57	FeOx (27.5%)
CM01N/7024[e]	Bangs Laboratories	350	0.99	0.825	FeOx (45.8%)
Nanomag-D	Micromod	250	20.10	4.81	FeOx (75%)
Nanomag-D	Micromod	130	17.80	4.44	FeOx (75%)
Nanomag-D-spio	Micromod	100	0.34	0.28	FeOx (35%)
Nanomag-D-spio	Micromod	50	0.85	0.71	FeOx (35%)

[a]Magnetization per particle at an excitation field $\boldsymbol{H}$ of 1.2 kA m^{-1}.
[b]Average susceptibility for $1 < |\boldsymbol{H}| < 4$ kA m^{-1}.
[c]FeOx represents γ-Fe_2O_3 and Fe_3O_4. % values represent the magnetic content of the particles (data from supplier).
[d]Magnetization and susceptibility values were taken from magnetization curves shown on Rife *et al*. (2003).
[e]Magnetization values were estimated from data shown in Schotter *et al*. (2004) admitting a constant susceptibility from 0 to 40 kA m^{-1}.

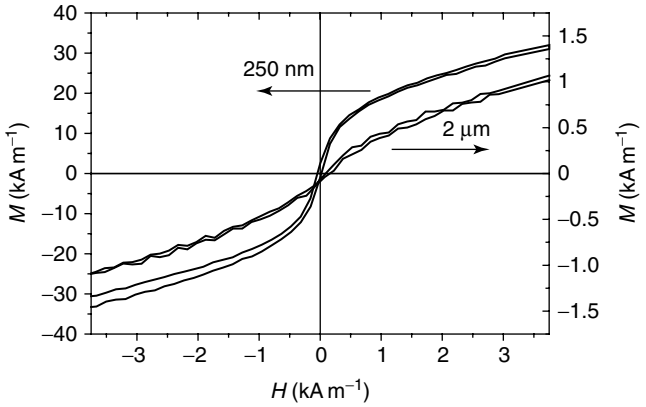

Figure 14. Magnetization curves for 2-µm microspheres and 250-nm-diameter nanoparticles in the low field regime. It is observed an increased magnetic susceptibility near zero applied field and, in particular, for smaller particles. Pure paramagnetic behavior is represented by a dashed line.

Currently, several protocols for the functionalization of nucleic acids and proteins (including antibodies and enzymes) have been developed. These methods depend on the biomolecule but also on the surface to be functionalized. Most common biochip surfaces include glass (Joos, Kuster and Cone, 1997), silicon dioxide (Chrisey, Lee and O'Ferrall, 1996), gold (Bamdad, 1998), and polymers (Fixe, Dufva, Telleman and Christensen, 2004a).

Generally, surface derivatization protocols for glass or silicon dioxide (as done in INESC–MN) consist of the following steps: activation; silanization; cross-linking; and probe biomolecule immobilization.

The activation step, may or may not be necessary, and consists in formation of reactive hydroxyl groups at the biochip surface (Figure 15a); for that several cleaning and oxidizing procedures have been developed (Cras, Rowe-Taitt, Nivens and Ligler, 1999). Nevertheless, in magnetoresistive biochip applications mild conditions are required not only for cleaning but also for all derivatization protocols. As such, low salt solutions, and weak acids or weak bases should be used; otherwise both surface as sensors may be corroded (Freitas *et al*., 2004).

The silanization protocol involves the use of trialkoxy silane derivatives containing an organic functional group such as an amine (Weetall, 1976). A silane molecule, such as triaminopropyltriethoxysilane (APTES) reacts with the hydroxyl (–OH) groups on the surface leaving amino groups available to react further (Figure 15b).

After silanization, usually a crosslinker is used to enable the covalent binding of two distinct chemical entities that are unreactive toward each other (e.g., amino $-NH_2$ and thiol –SH groups) (Figure 15c). A crosslinker serves another important purpose: it provides a physical spacer that gives a larger mobility and freedom to the immobilized biomolecules. This greater accessibility is important to facilitate biomolecular recognition. In fact, it has been shown that hybridization efficiency depends on the cross-linker size, as larger spacers enable an easier access of target molecules to the surface-immobilized probes (Southern, Mir and Shchepinov, 1999).

Cross-linking molecules are designated by homobifunctional, if they present identical reactive groups at the each end of the spacer (e.g., glutaraldehyde) or, on the other hand, they are called by heterobifunctional if they have distinct functional groups (like *N*-[ε-maleimidocaproyloxy]sulfosuccinimide ester or sulfo-EMCS) (Figure 15c). In bioarray applications, heterobifunctional cross-linkers are preferred as they diminish the potential for multipoint reactions.

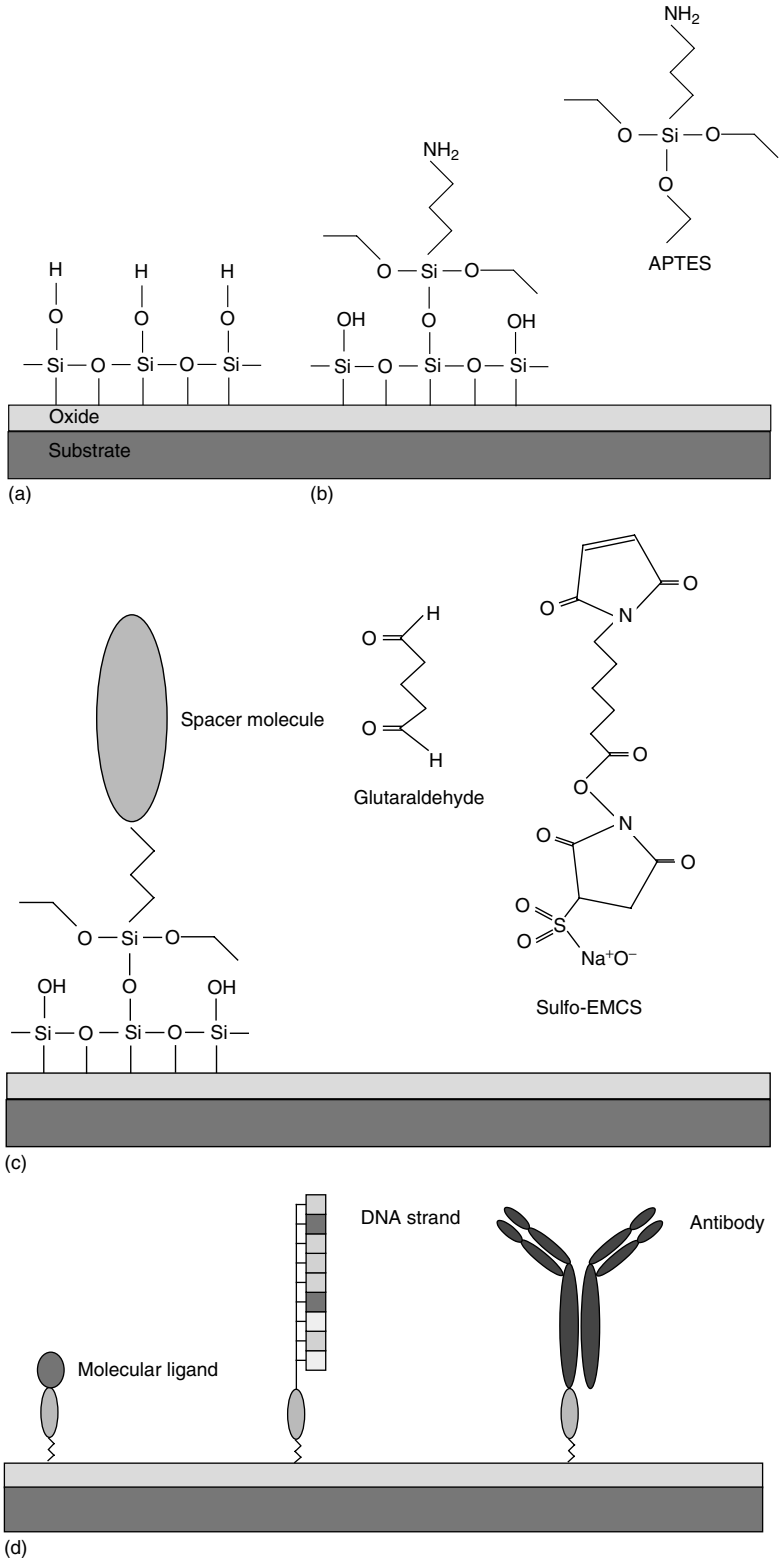

Figure 15. Oxide surface biochemical functionalization protocol: (a) Surface activation: formation of hydroxyl groups on the surface; (b) Silanization (formation of reactive amino groups) using a 3-aminopropyltriethoxysilane (APTES) solution; (c) Crosslinking with spacer molecules such as glutaraldehyde and sulfo-EMCS; and (d) Probe biomolecule (nucleic acids, proteins, etc.) immobilization to the surface through the covalent reactions between functional groups in the molecules and the cross-linkers.

Finally, probe–biomolecule immobilization can also be done using distinct protocols, depending on the biomolecule, functional groups of the spacer and the surface type. Usually, DNA probes modified at one end with an amino, carboxylic (–COOH) or thiol group are covalently bound to the cross-linker molecules (Figure 15d). In case of proteins, unreacted functional groups of aminoacid residues are used for the same end.

Biofunctionalization of gold surfaces (Bamdad, 1998) is also one of the most common approaches as the protocols are relatively straightforward. Thiolated biomolecules, such as DNA strands modified at one end with a thiol or a thiolated spacer, bind to the gold surface forming a self-assembled monolayer (SAM).

Polymer functionalization may be similar to other surfaces such as glass or silicon oxide, involving activation, amination of the surface, crosslinking, and probe immobilization (Fixe, Dufva, Telleman and Christensen, 2004a). Nevertheless, by using native functional groups in the polymer, such as methyl esters groups in poly(methylmetacrylate) (PMMA), probe immobilization can be done in on-step (Fixe, Dufva, Telleman and Christensen, 2004b). This has great advantages over traditional methods, as it is both labor time and reagent-cost saving.

Again, probe biomolecule immobilization chemistries must be optimized for each case, and in biochip applications mild conditions should be used. The surface density of bound probes is an important parameter, as low surface coverage will yield low biomolecular interaction rates and, consequently, low detection signals. High surface density of probes, on the other hand, may result on biomolecular steric hindrance and consequently low biomolecular interaction rates and detection signals may be observed. In addition, probe immobilization protocols should lead to a well-defined probe orientation accessible to the target for recognition; should be thermally and chemically stable; and finally, should be reproducible.

A bioarray is a two-dimensional set of distinct biological probes. These are designed to enable an analysis of several components in the same assay in a parallel fashion. For instance, DNA microarrays may be used to investigate the expression of genes of an ill tissue and compared it with the case of a healthy one; or they may be used to screen a particular genetic mutation related to a hereditary disease. Usually, in designing a bioarray, there is redundancy of probes (i.e., each probe is represented in several places on a chip) for statistical purposes; and both positive and negative controls are included to assess the good functioning of the assay and to determine the background noise.

Currently, there are several ways to produce a bioarray. One of the approaches is by on-chip synthesis of oligonucleotides, which uses a combination of microelectronic photolithographic techniques and combinatorial chemistry (Pease *et al*., 1994). Although, this method allows the fabrication of highly dense arrays, representing more than 100 000 genes in an area of $1.28 \times 1.28\,\mathrm{cm}^2$, the procedure is costly and time consuming, and is not applicable to proteins; these aspects prevent then a widespread use of the system (http://www.affymetrix.com). The present technology enables the fabrication of probe regions with feature sizes of $\sim 10\,\mu\mathrm{m}$.

The most common method to make DNA or protein arrays is the immobilization of pre-synthesized DNA strands and protein solutions, respectively, using devices called *microspotters* (http://www.arrayit.com), which enable the immobilization of up to 100 000 different biomolecules represented in a glass slide (Ramsay, 1998; Okamoto, Suzuki and Yamamoto, 2000). A typical biomolecule spot size is $\sim 50-100\,\mu\mathrm{m}$, but improving technologies are rapidly reaching smaller sizes, even to the nanometer scale using techniques such as dip-pen nanolithography (Demers *et al*., 2002) and supramolecular nanostamping (Yu *et al*., 2005).

Alternative methods of probe immobilization include the use of electric fields (http://www.nanogen.com), which enable much shorter probe immobilization times in comparison with the previous methods (Heller, 1996; Fixe *et al*., 2003), and the potential use of magnetic fields for biomolecular patterning (Yellen, Hovorka and Friedman, 2005).

Label functionalization protocols are similar to the ones referred in the preceding text for chip surface functionalization and, consequently, should also comply with the same requirements: mild-conditions surface biochemistries; reproducibility; thermal and chemical stability; nontoxic surface properties; and suitable biomolecular surface density.

The chemistry will depend then on the surface or coating of the particles: silica, gold, polymer, or other (del Campo, Sen, Lellouche and Bruce, 2005; Bao and Krishan, 2005; Nishibiraki *et al*., 2005; Joshi, Li, Wang and Sun, 2004) and on the biomolecule to be functionalized. This later one is related to the bioassay to be performed and the detection scheme. As such, magnetic labels may be functionalized with target molecules (e.g., analyte DNA) or with a detector biomolecule (e.g., antibody or another protein) (see Sections 5 and 6).

5 DETECTION SCHEMES AND CHIP ARCHITECTURES

Until recently, magnetoresistive biochips were being developed mostly for DNA hybridization detection in applications concerning biological warfare agent detection (Edelstein *et al*., 2000; Miller *et al*., 2001) and diagnostics of

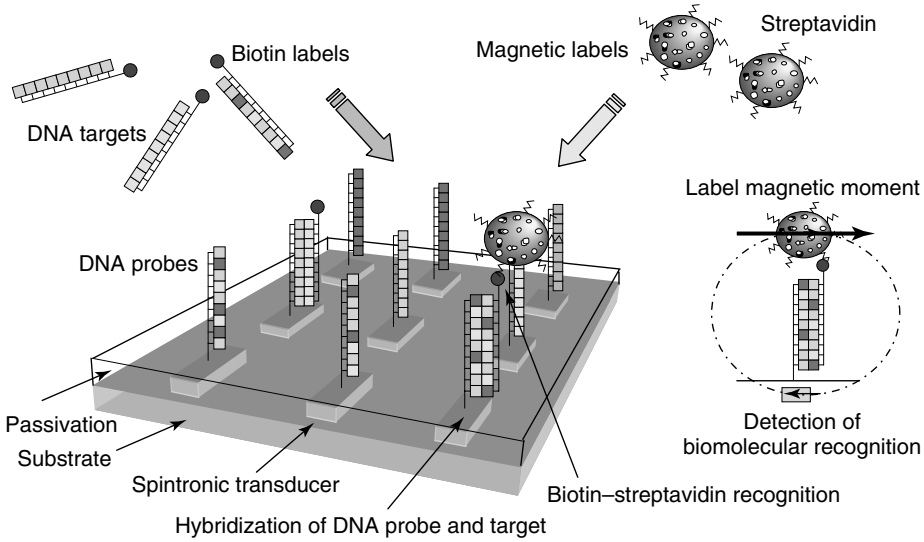

Figure 16. Post-hybridization detection method. Spintronic biochips functionalized with DNA probes are incubated usually for several hours with DNA targets labeled with a biotin reporter molecule. After hybridization has occurred, streptavidin-coated magnetic labels are dispensed over the chip. The streptavidin proteins recognized biotin molecules available where hybridization occured. Finally, magnetic labels bound to hybridized sites are detected by spintronic transducers that sense the labels stray fields.

cystic fibrosis (Graham, Ferreira and Freitas, 2004; Lagae *et al*., 2005).

Two hybridization detection strategies have been followed, the post-hybridization detection method and the magnetic-field-assisted detection method.

In the post-hybridization detection method (followed by both the NRL; the University of Bielefeld; and INESC–MN), target biomolecules are labeled with a small reporter biomolecule called *biotin*. After hybridization occurs with the probe DNA strands immobilized on the chip surface, a solution of magnetic labels is dispensed over the chip. These labels are coated with a detector protein called *streptavidin* that recognizes the reporter biotin molecules that tag the hybridized DNA targets. Subsequently, the stray field created by the magnetic labels is detected with the use of on-chip magnetoresistive sensors, indicating that hybridization has occurred (Figure 16).

In this method, the analyte solution is dispensed over the chip and the biotinylated DNA targets diffuse, passively, in solution until finding their complementary probe molecules at the chip surface. This way, hybridization times alone take usually from 3 to 12 h, which limits these systems to applications or assays were response times are not crucial.

In order to overcome this limitation, a detection method based on magnetic-field-assisted hybridization was developed at INESC–MN. In this method, DNA targets are labeled with magnetic labels and are transported to probe immobilized sensor sites by on-chip current carrying conductors that generate local magnetic-field gradients. The close proximity of target and probe biomolecules accelerates then the rate at which biomolecular recognition reactions happen. This way hybridization is detected almost in real time (Figure 17).

Using different designs, comprised of tapered on-chip conductors (Graham *et al*., 2002; Lagae *et al*., 2002; Figure 18a) or u-shaped current lines (Ferreira *et al*., 2005a; Figure 18b) enabled the detection of hybridization between complementary DNA strands in times of less than 5 min (Graham *et al*., 2005) and 30 min (Ferreira *et al*., 2005b). These systems show the potential to be used in the rapid detection of biological warfare agents, in pathogen identification or in clinical diagnostics in the point of care.

Another variant of the magnetic-field-assisted hybridization method involves the use of enzymatic cleavage of the magnetic labels bound after hybridization has occurred (Lagae *et al*., 2005). After release, labels can be detected by moving them over the sensor by alternatively applying current through tapered line structures adjacent to the sensor (Lagae *et al*., 2002) (Figure 19).

These magnetoresistive DNA chips (Freitas *et al*., 2004) have then 'evolved' in order to 'fit' with the biological requirements of the bioassays and their applications. One of such requirements is the probe-functionalized area, which, typically, has been defined by microspotting of the chip surface above the sensing elements.

The initial BARC chip from NRL (Baselt *et al*., 1998) was comprised of eight sensing zones, each containing eight GMR sensor traces of dimensions of $5 \times 80\,\mu m^2$. Each sensing zone was $\sim$250 µm in diameter and was functionalized with a particular DNA probe (Edelstein *et al*., 2000; Miller *et al*., 2001). Since magnetic labels were only

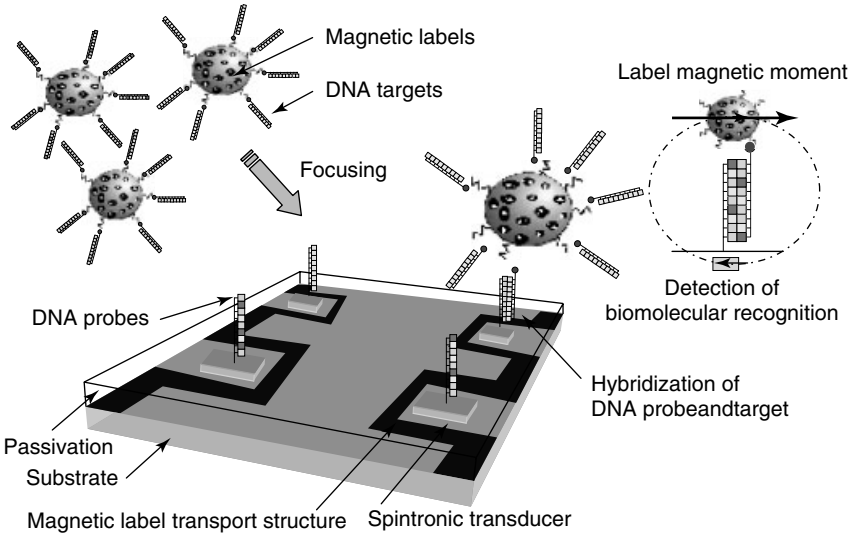

Figure 17. Magnetic-field-assisted hybridization and detection. Spintronic biochips functionalized with probe DNA are incubated with magnetically labeled DNA targets. On-chip current carrying conductors that create local magnetic-field gradients are used to attract the magnetically labeled molecules to functionalized sensing regions. The proximity of target and probe molecules accelerates the hybridization reaction rate, enabling faster hybridization times and the detection of biomolecular recognition in almost real time.

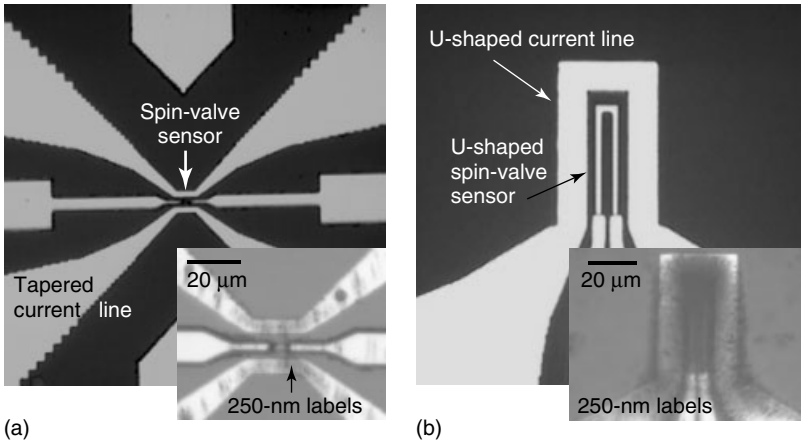

Figure 18. Optical microscope photographs of different magnetic-field guiding lines developed at INESC–MN. (a) Tapered current conductors create a maximum field gradient at the region nearest to a spin-valve sensor; inset: current passing through both top and bottom lines attract 250-nm particles closer to a $2 \times 6\,\mu m^2$ spin-valve sensor. (b) U-shaped current conductors used in combination with external magnetic fields are used to create an oscillatory magnetic-field gradient that focus labels in the inside of the line were a $2.5 \times 80\,\mu m^2$ u-shaped spin-valve sensor was fabricated; inset: 250-nm labels are concentrated at the sensing region.

detectable over or adjacent to the GMR sensors, the effective biomolecular recognition sensing area was relatively small ($\sim$10% or less) in comparison with the total functionalized area. In this case, for low DNA target concentration, target molecules could hybridize in $\sim$90% of the functionalized area and not being detected.

A later version of the BARC chip (Rife *et al.*, 2003) was designed to overcome this limitation, as the GMR sensors were fabricated in a serpentine shape that comprised a diameter of $\sim$200 μm and, consequently, fitted better the functionalized area (even so the sensing area was $<$70% of the total area with probe DNA). At the same time the number of sensing areas in the latest chip increased from 8 to 64.

One aspect to take into account is that an increase in the probe immobilized area corresponds to an increase in the biological sensitivity of the system, as the highest is the number of probe biomolecules on the surface the highest is the possibility to capture a complimentary target biomolecules that diffuses in the analyte solution being tested.

As such, an increase of the sensing area to fit the functionalized area resulted in the overall increase of the

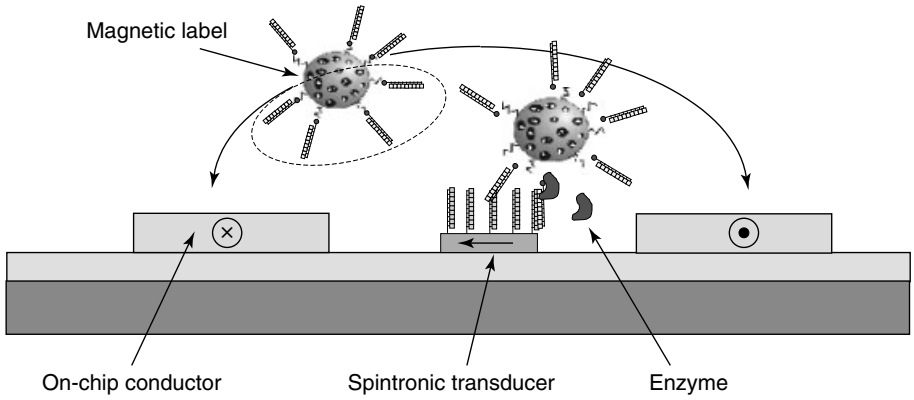

Figure 19. Variant of the magnetic-field-assisted hybridization method. After hybridization occurred, enzymes are used to cleave bound magnetic labels. Labels are then moved back and forth across the sensor using on-chip current conductors, enabling label detection.

biological sensitivity of the system. With the increase of the sensor size, the dynamic range of operation of the sensor also increases, that is, the number of magnetic labels that can be detected increases, and consequently the number of detectable biomolecular interactions also increases. Nevertheless, the sensitivity to lower number of particles or to single particles diminishes. Thus, in sensor design a compromise has to be made with respect to biological sensitivity and dynamic range with the single label sensitivity (Figure 20).

The group at the University of Bielefeld have also followed the strategy of fitting the sensor size to the probe immobilized area. In their case, they fabricated spiral-shaped GMR sensors with a diameter of 70 µm in order to fit DNA spots of 100 µm in diameter. A first version of the chip included 30 sensing elements, with half of them being used

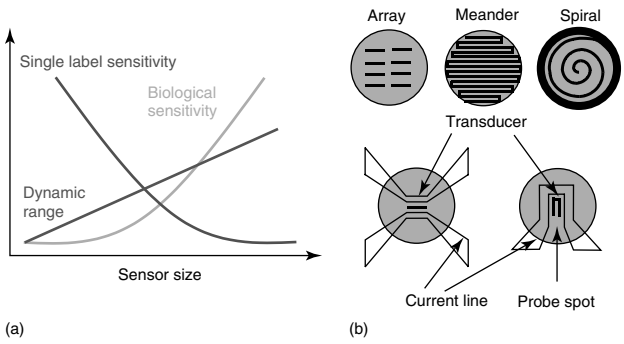

Figure 20. (a) Diagram showing the dependence on sensor size of biological sensitivity of the system, single label sensitivity and sensor dynamic range; a compromise must be found for this variables depending on the sensor and the application. (b) Different strategies for fitting the sensor size to the probe functionalized area: array of sensors and meander (NRL); and spiral sensor (University of Bielefeld). Using on-chip current conductors overcomes the large difference between sensor size and probe area by focusing the magnetically labeled targets at the sensing sites.

for reference purposes (Schotter *et al*., 2002). In a later version, where the magnetoresistive sensing platform was compared favorably with a fluorescence-based system, the chip included 206 spiral GMR sensors, with 6 of them being used as references.

Alternatively, the INESC–MN group, started to target single label detection by fabricating smaller $2 \times 6\,\mu m^2$ SV sensors (Graham *et al*., 2002), and the potential for the detection of single biomolecular recognition events (Graham, Ferreira and Freitas, 2004). These sensors had a small dynamic range of ∼200 nanoparticles of 250 nm in diameter (Graham *et al*., 2005), which seems reasonable for applications where it is necessary to distinguish between a yes or no answer more than a quantitative value. Examples of such assays are the distinction between different mutations in the same gene, including single nucleotide polymorphisms (SNPs), or the assessment of differences in the splicing of mRNA (splice-site mutations), or even the detection of a single pathogenic microorganism (see following section).

At a later stage a chip was designed to quantify differences in gene expression of an ill tissue versus a healthy one. In this case, a larger dynamic range was necessary and as a consequence larger $2.5 \times 80\,\mu m^2$ u-shaped SV sensors were fabricated (24 sensors per chip). These sensors allowed the detection up to a maximum of ∼3200 nanoparticles of 250 nm in diameter (Ferreira *et al*., 2005b).

These sensors have a very small sensing region when comparing to a typical probe spot size of 100 µm, and the comparison is even more unfavorable when considering the smaller $2 \times 6\,\mu m^2$ SVs. Nevertheless, these limitations are overcome by the use of on-chip biomolecular transport and focusing systems.

As a final note with respect to chip architecture, single sensor proof-of-concept studies from several research laboratories and more developed biochip sensing platforms all show a design limitation. These platforms comprised a small

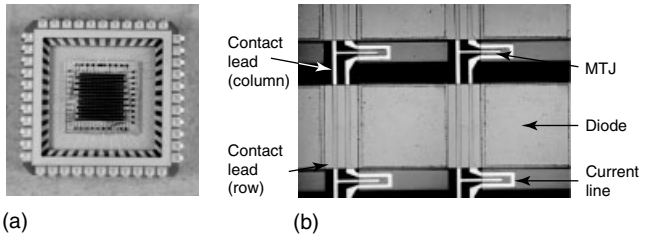

Figure 21. (a) Matrix of 256 magnetic tunnel junction (MTJ) sensing elements fabricated at INESC–MN (chip mounted on a chip carrier). (b) Photograph showing four sensing elements of the matrix. Each sensing element is addressed using thin-film diodes of amorphous-silicon. Also shown are the row and column contacts and u-shaped current lines for the focusing of magnetically labeled targets.

number of sensing elements (INESC–MN, 24 sensors; NRL, 64 serpentines; and University of Bielefeld, 200 transducers), and a further increase in the number of sensing elements is accompanied by a prohibitively large number of contacts and an off-chip multiplexing circuitry increasingly complex. These designs limit the number of different probes that can be immobilized and, consequently, the number of different analytes that can be screened in a single sample.

Recently though, a fully scalable biosensing platform was proposed and fabricated, based on a structure of a switching element and a magnetic transducer previously studied at INESC–MN for MRAM applications (Sousa, Freitas, Chu and Conde, 1999). A first prototype of a 16×16 matrix was fabricated, comprising as a sensing unit, a hydrogenated amorphous silicon (a-Si:H) TFD in series with a MTJ with a linear response (Cardoso *et al*., 2006) (Figure 21). This system can potentially be expanded to 10 000 or more sensing elements, and consequently, thousands of analytes could be analyzed simultaneously.

6 BIOASSAYS AND DETECTION RESULTS

The bioassays that have been developed concern the detection of oligonucleotides (short DNA strands) or of structural antigens from pathogenic microorganisms.

The BARC chip was used in the detection of biological warfare agents such as: *Bacillus anthracis*; *Yersinia pestis*, *Brucella suis*, *Francisella tularensis*, *Vibrio cholarae*, *Clostridium botulinum*, and *Campylobacter jejuni*. Here, DNA strands 30 nucleotides (or bases) long that represent specific bacterium, were immobilized on gold pads fabricated on top of the sensitive areas, and the chip was interrogated with a particular complementary DNA target (Edelstein *et al*., 2000; Miller *et al*., 2001).

The biochip from the University of Bielefeld, on the other hand, used polymerase chain reaction (PCR) amplified probe DNA sequences 1 kb (kilo-bases) long. The chip was immobilized with probes that were complimentary or not to a particular DNA target. The noncomplimentary probe was used to assess the background signals. In this work, a comparison with traditional fluorescence methods was made, showing that the magnetoresistive platform was more sensitive at low probe DNA concentrations (Schotter *et al*., 2004).

At INESC–MN, and within the scope of an European project, work has been focused on the development of diagnostic chips, using as a model disease cystic fibrosis (Freitas *et al*., 2004; Lagae *et al*., 2005). Cystic fibrosis is a genetic disease characterized by mutations in the cystic fibrosis conductance regulator (CFTR) gene which is localized in the chromosome 7 (Collins, 1992). Presently, more than 1000 mutations have been described (Cystic Fibrosis Mutation Database, http://www.genet.sickkids.on.ca/cftr), and their prevalence among populations varies according to race and geographical distribution. The majority of these mutations consist of variations in a small number of nucleotides of the DNA, frequently a single nucleotide is either replaced by another base, inserted, or deleted (SNPs). For instance the most common mutation, F508del, refers to the deletion of 3 nucleotides that corresponds to the deletion of a phenylalanine aminoacid at the position 508 in the CFTR protein.

Two approaches are being followed for the diagnostics of cystic fibrosis: one corresponds to screening the messenger RNA (mRNA) resulting from the transcription of the mutated CFTR gene; the other one corresponds to the analysis of genes (others than the CFTR genes) whose expression is consistently increased or diminished in cells and tissues with cystic fibrosis than in healthy ones (Clarke, Braz and Amaral, 2004).

With respect to the first approach, a study was made using the post-hybridization detection method (Graham, Ferreira and Freitas, 2004; Freitas *et al*., 2004). Here, the chip surface was immobilized with a 50-mer (50 nucleotide long) DNA probe that corresponds to the region of the gene where the F508del mutation occurs. The chip was further interrogated with PCR products either complementary to the probe or not. The noncomplementary target used was related to a proto-oncogene. Typical obtained signals are shown in Figure 22.

Later on, the same probe and targets were used in magnetic-field hybridization experiments, and hybridization times of less than 5 min were observed using the magnetoresistive biochip platform with on-chip tapered conductors (Graham *et al*., 2005). In addition, it was shown that by repeating the biomolecular recognition experiment on the same chip, an increased hybridization signal was detected,

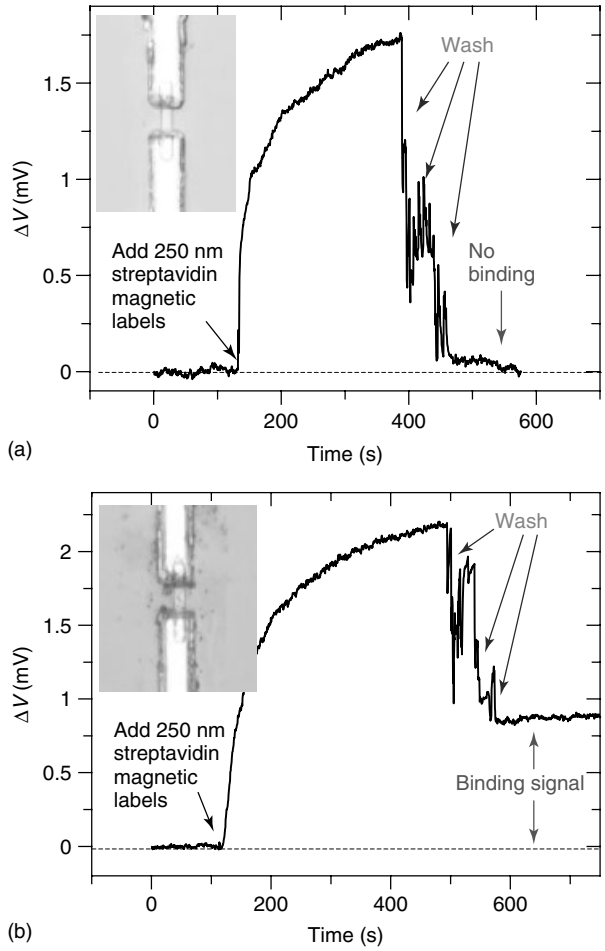

Figure 22. Post-hybridization detection experiments on chips functionalized with 50 oligomers representing the DNA sequence that spans the region where the most common in cystic fibrosis occurs. (a) The chip was incubated overnight with a biotinylated noncomplementary 75 nucleotide long target that represents the proto-oncogene *rac1*; after hybridization was attempted, streptavidin-coated magnetic labels of 250 nm in diameter were dispensed over the chip for 5 min and a change in sensor response was observed due to the presence of labels; after the chip was washed and unbound labels removed the signal returned to the baseline indicating that no hybridization occured. Inset: picture showing a $2 \times 6\,\mu m^2$ spin valve clear of particles. (b) In this case, the chip was incubated with complementary target (96 oligonucleotides) labeled with biotin reporter molecules; after introducing labels into the chip for 5 min and washing the signal did not returned to zero, indicating that hybridization between the complementary molecules occured. Inset: picture showing labels bound to the sensor surface as a result of DNA–DNA recognition.

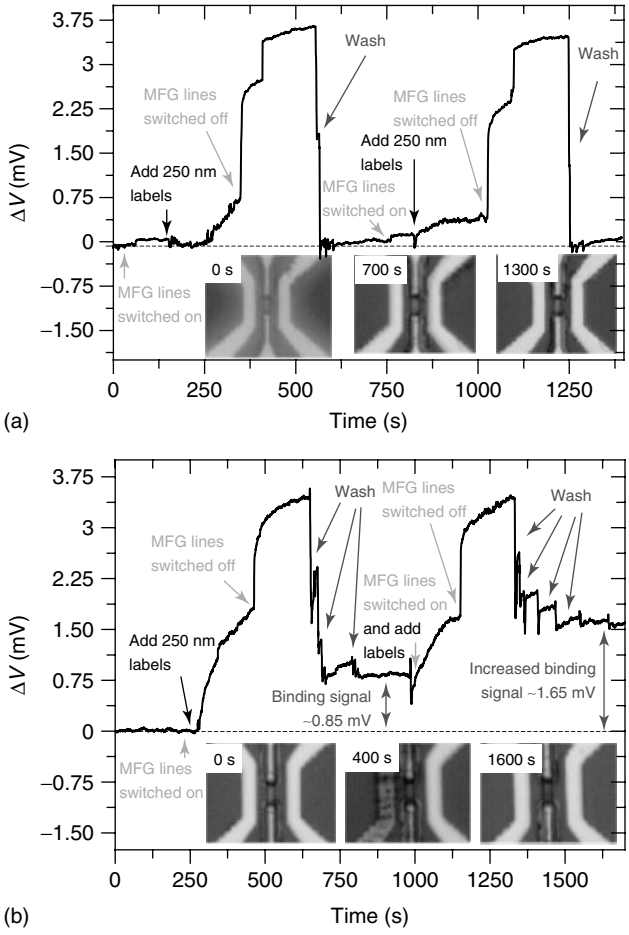

Figure 23. Magnetic-field-assisted hybridization and simultaneous detection experiments. The chips were functionalized with a cystic fibrosis-related DNA probe and were incubated with magnetically-labeled noncomplementary or complementary targets. (a) Noncomplementary targets functionalized to magnetic nanoparticles were concentrated at sensing sites using magnetic-field guiding lines with a tapered design; after ~5 min unbound labels were washed away and the signal returned to zero; later on the experiment was repeated. Insets: pictures taken from the sensor at different times during experimentation showing that no particles bound to the surface. (b) In this case, the same experiment was done for magnetically labeled complementary targets; after particle focusing and washing a residual signal was obtained indicating biomolecular recognition; later on after a second focusing step an increased signal was observed which corresponded to an increased number of hybridization events.

corresponding to an increased extension of the hybridization reaction (Figure 23).

Concerning the second approach, a new chip based on u-shaped spin-valve sensors and on u-shaped current lines for magnetic-field-assisted hybridization was used. Here, the same chip surface was spotted with distinct 50-mer probe sequences that correspond to genes that are either overexpressed or subexpressed in diseased tissues in comparison with healthy ones. A further control gene (whose expression does not change) was also spotted onto the chip. During experimentation, magnetically labeled target DNAs were focused simultaneously at 8 to 16 sensors by local magnetic filed gradients created by the u-shaped lines (Ferreira *et al*., 2005b), and hybridization signals were measured in

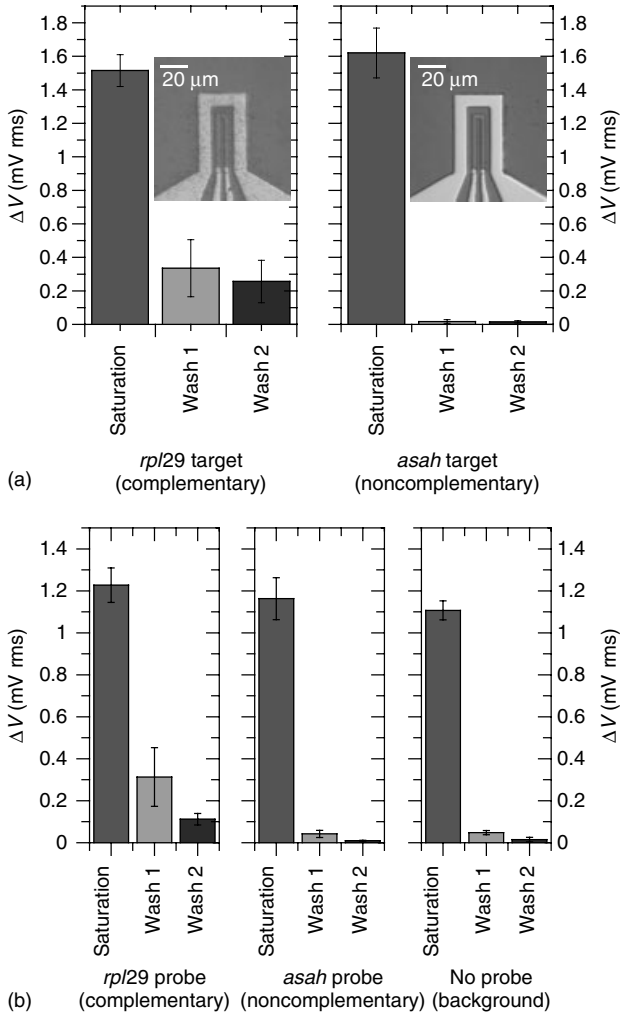

Figure 24. Magnetic-field-assisted hybridization and simultaneous detection experiments using u-shaped current lines and $2.5 \times 80\,\mu m^2$ u-shaped spin valves. (a) Spintronic biochips were functionalized with a 50-mer single-stranded DNA molecules that correspond to a gene that was found to be upregulated (*rpl29*) in cystic fibrosis-related cell lines vs healthy cell lines; in this case complementary (*rpl29*) and noncomplementary (*asah*) magnetically-labeled targets were focused for ∼15 min before washing; chips were further washed a second time with a more stringent solution to further remove weakly or unspecific bound labels; statistical data is presented for six monitored sensors. Insets show pictures for complementary and noncomplementary testing experiments. (b) Chips were functionalized with both DNA probes corresponding to upregulated (*rpl29*) and down-regulated (*asah*) genes and tested with a *rpl29* magnetically labeled target; focusing occured for about 30 min at nearly half focusing current. In these charts, saturation represents the sensor responses to labels just before washing.

less than 30 min (Ferreira *et al*., 2005c). Typical statistical results obtained are shown in Figure 24.

Furthermore, a recent study realized with 250-nm-diameter magnetic labels has shown that this platform is sensitive to particle concentrations down to 1 pM. This corresponds

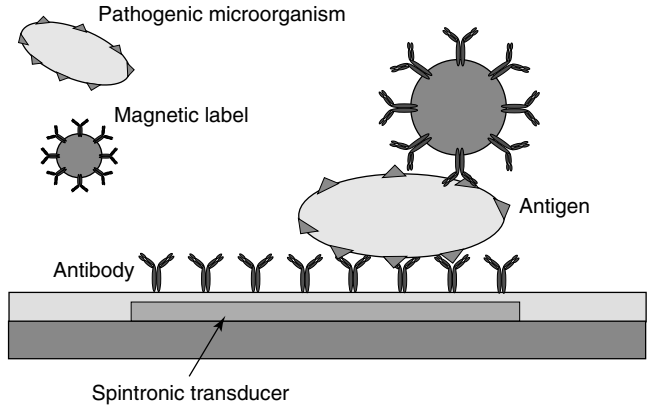

Figure 25. Schematic showing detection strategy for the detection of whole cells of pathogenic microorganisms. A sensor surface, functionalized with antibodies against a particular microorganism such as *Salmonella*, is incubated with a testing solution. In the case that the pathogen is present, the antigens present at its membrane surface are recognized by the surface bound antibodies. Later, magnetic labels functionalized with antibodies for the same microorganism bind to it, indicating its presence by measurement of the stray field of the labels.

to DNA target concentrations of 500 pM, which compares favorably with traditional DNA assays (μM concentrations). In addition, this system presents a dynamic range of at least 2 orders of magnitude, thus making these magnetoresistive DNA chips attractive for fast diagnostics of genetic diseases (Ferreira *et al*., 2006).

More recently, at INESC–MN the same biochip platform was used for the detection of pathogenic microorganisms in water (Martins *et al*., 2005). In this case, the chip surface was functionalized with antibodies against *Salmonella* species and was incubated with a solution containing viable *Salmonella* cells. Subsequently, the chip was interrogated with magnetic labels functionalized with the same antibody against the pathogen, which bound to the immobilized cells forming a 'sandwich'-like structure (see Figure 25). This showed that the chip could also successfully be used as an immunoassay, just by changing the chip surface biomolecular functionality.

7 CONCLUSIONS

Spintronics or magnetoelectronics is, in general terms, the study of devices whose operation is based not only in the electron charge like in regular electronic devices but also the electron spin (Prinz, 1998). The understanding of the underlying physics, together with advances in material science and in microelectronic processing have given rise to numerous devices that changed, are changing, and will change the day-to-day life of mankind. Such devices include

for instance, sensors in hard-disk readheads, which enable the access to practically all of man's knowledge in digital form. Among various sensing applications in position devices or in air-lock braking systems (ABS) in automobiles, magnetoelectronic devices are being developed for memories (MRAMs) and novel semiconducting hybrid devices such as spin transistors. More recently, spintronic sensors are finding new applications in the ever-growing field of biomedicine and biotechnology (Freitas *et al*., 2006).

Spintronic biochips and biosensors are presently being developed by a number of research groups and companies worldwide and they hold the promise of becoming important tools for the rapid, sensitive, high-throughput and low-cost detection of biomolecular recognition, such as in diagnostics and in the detection of pathogenic microorganisms. Its applications can span areas ranging from medicine to biotechnology and from environmental studies to the quality monitoring of beverages and food products.

Although, future seems bright a number of challenges still need to be addressed, such as thorough studies of biological assays, including the assessment of the sensitivity, the specificity, and the positive predictive and the negative predictive values of the tests. Furthermore, of quite importance is the integration of the detection platform with sample treatment procedures and data-analysis system. In this respect, hybrid systems combining magnetoresistive sensors and microfluidics are being developed (Tamanaha, Whitman and Colton, 2002; Ferreira *et al*., 2004) with the ultimate goal of fabricating a lab-on-chip system for complete sample analysis (Ahn *et al*., 2004). Finally, the simplicity of operation and the direct electronic read-out of biomolecular recognition events are pushing forward the development of portable spintronic biochip platforms that can be used at the point of care (Piedade *et al*., 2006).

ACKNOWLEDGMENTS

INESC–MN work presented in this paper was supported by the following Portuguese national projects: POCTI/BIO/34459/99, POSC/EEA-ESE/58523/2004, and POCTI/CTM/59411/2004; the the European projects CF CHIP-QLK3-CT-2001-01982, SNIP2CHIP-NMP4-CT-2005-016833, and BIOMAGSENSE-NMP4-CT-2005-017210; and also by Fundação Calouste Gulbenkian. Hugo A. Ferreira is grateful to Fundação de Ciência e Tecnologia for the grant SFRH/BD/5031/2001 for the development of his PhD studies.

REFERENCES

Ahn, C.H., Choi, J-W., Beaucage, G., *et al*. (2004). Disposable smart lab on a chip for point-of-care clinical diagnostics. *Proceedings of the IEEE*, **92**, 154–173.

Almeida, J.M., Ferreira, R., Freitas, P.P., *et al*. (2006). 1/f noise in linearized low resistance MgO magnetic tunnel junctions. *Journal of Applied Physics*, **99**, 08B314–08B316.

Anguelouch, A., Reich, D.H., Chien, C.L. and Tondra, M. (2004). Detection of ferromagnetic nanowires using GMR sensors. *IEEE Transactions on Magnetics*, **40**, 2997–2999.

Astalan, A.P., Ahrentorp, F., Johansson, C., *et al*. (2004). Biomolecular reactions studied using changes in Brownian rotation dynamics of magnetic particles. *Biosensors and Bioelectronics*, **19**, 945–951.

Baibich, M.N., Broto, J.M., Fert, A., *et al*. (1988). Giant magnetoresistance of (001)Fe/ (001)Cr magnetic superlattices. *Physical Review Letters*, **61**, 2472–2475.

Bamdad, C. (1998). A DNA self-assembled monolayer for the specific attachment of unmodified double-or single-stranded DNA. *Biophysical Journal*, **75**, 1997–2003.

Bao, Y. and Krishan, K.M. (2005). Preparation of functionalized and gold-coated cobalt nanocrystals for biomedical applications. *Journal of Magnetism and Magnetic Materials*, **293**, 15–19.

Baselt, D.R., Lee, G.U., Natesan, M., *et al*. (1998). A biosensor based on magnetoresistance technology. *Biosensors and Bioelectronics*, **13**, 731–739.

Bertram, H.N. (1994). *Theory of Magnetic Recording*, Cambridge University Press.

Besse, P-A., Boero, G., Demierre, M., *et al*. (2002). Detection of single magnetic microbead using a miniaturized silicon Hall sensor. *Applied Physics Letters*, **80**, 4199–4201.

Brown, W.F. Jr., (1963). Thermal fluctuations of a single-domain particle. *Physical Review*, **130**, 1677–1686.

del Campo, A., Sen, T., Lellouche, J-P. and Bruce, I.J. (2005). Multifunctional magnetite and silica-magnetite nanoparticles: synthesis, surface activation and applications in life sciences. *Journal of Magnetism and Magnetic Materials*, **293**, 33–40.

Cardoso, F.A., Ferreira, H.A., Conde, J.P. *et al*. (2006). Diode/ Magnetic Tunnel Junction cell for fully scalable matrix based biochip. *Journal of Applied Physics*, **99**, 08B307–08B309.

Chemla, Y.R., Grossman, H.L., Poon, Y., *et al*. (2000). Ultrasensitive magnetic biosensor for homogeneous immunoassay. *Proceedings of the National Academy of Sciences of the United States of America*, **19**, 14268–14272.

Chiriac, H., Tibu, M., Moga, A.E. and Hera, D.D. (2005). Magnetic GMI sensor for detection of biomolecules. *Journal of Magnetism and Magnetic Materials*, **293**, 671–676.

Chrisey, L.A., Lee, G.U. and O'Ferrall, C.E. (1996). Covalent attachment of synthetic DNA self-assembled monolayer films. *Nucleic Acids Research*, **24**, 3031–3039.

Chung, S.H., Hoffmann, A., Bader, S.D., *et al*. (2004). Biological sensors based on Brownian relaxation of magnetic nanoparticles. *Applied Physics Letters*, **85**, 2971–2973.

Cirino, N.M., Musser, K.A. and Egan, C. (2004). Multiplex diagnostic platforms for detection of biothreat agents. *Expert Review of Molecular Diagnostics*, **4**, 841–857.

Clarke, L.A., Braz, C. and Amaral, M.D. (2004). Cystic fibrosis-related patterns of gene expression: a genome-wide microarray approach. *Pediatric Pulmonology*, **38**(Suppl. 27), 219.

Collins, F.S. (1992). Cystic fibrosis –molecular biology and therapeutic implications. *Science*, **256**, 1149–1156.

Connolly, J. and St. Pierre, T. (2001). Proposed biosensors based on time-dependent properties of magnetic fluids. *Journal of Magnetism and Magnetic Materials*, **225**, 156–160.

Cooper, G.M. (2000). *The Cell – a Molecular Approach*, *Second Edition*, ASM Press: Washington.

Cras, J.J., Rowe-Taitt, C.A., Nivens, D.A. and Ligler, F.S. (1999). Comparison of chemical cleaning methods of glass in preparation for silanization. *Biosensors and Bioelectronics*, **14**, 683–688.

Debye, P. (1929). *Polar Molecules*, Chemical Catalog Company: New York.

Demers, L.M., Ginger, D.S., Park, S-J., *et al*. (2002). Direct patterning of modified oligonucleotides on metals and insulators by dip-pen nanolithography. *Science*, **296**, 1836–1838.

Dieny, B., Speriosu, V.S., Metin, S., *et al*. (1991). Magnetotransport properties of magnetically soft spin-valve structures. *Journal of Applied Physics*, **69**, 4774–4779.

Dieny, B. (2004). Spin valves. In *Magnetoelectronics*, Johnson, M. (Ed.), Academic Press: New York, pp. 67–149.

Edelstein, R.L., Tamanha, C.R., Sheehan, P.E., *et al*. (2000). The BARC biosensor applied to the detection of biological warfare agents. *Biosensors and Bioelectronics*, **14**, 805–813.

Ejsing, L., Hansen, M.F. and Menon, A.K. (2003). Planar Hall effect magnetic sensor for micro-bead detection, *Proceedings of the 17th European Conference on Solid-State Transducers, Eurosensors 2003*, Guimarães, 21-24 September 2003, pp. 1095–1098.

Ejsing, L., Hansen, M.F., Menon, A.K., *et al*. (2004). Planar Hall effect sensor for magnetic micro- and nanobead detection. *Applied Physics Letters*, **84**, 4729–4731.

Ejsing, L., Hansen, M.F., Menon, A.K., *et al*. (2005). Magnetic microbead detection using the planar Hall effect. *Journal of Magnetism and Magnetic Materials*, **293**, 677–684.

Enpuku, K., Minotani, T., Gima, T., *et al*. (1999). Detection of magnetic nanoparticles with superconducting quantum interference device (SQUID) magnetometer and application to immunoassays. *Japanese Journal of Applied Physics*, **38**, L1102–L1105.

Ferreira, H.A., Cardoso, F.A., Ferreira, R., *et al*. (2006) Magnetoresistive DNA chips based on ac field focusing of magnetic labels. *Journal of Applied Physics*, **99**, 08P105–08P107.

Ferreira, H.A., Feliciano, N., Graham, D.L. and Freitas, P.P. (2005a). Effect of spin-valve sensor magnetostatic fields on nanobead detection for biochip applications. *Journal of Applied Physics*, **97**, 10Q904.

Ferreira, H.A., Feliciano, N., Graham, D.L., *et al*. (2005b). Rapid DNA hybridization based on AC field focusing of magnetically-labeled target DNA. *Applied Physics Letters*, **87**, 013901.

Ferreira, H.A., Graham, D.L., Feliciano, N., *et al*. (2005c). Detection of cystic fibrosis related DNA targets using AC field focusing of magnetic labels and spin-valve sensors. *IEEE Transactions on Magnetics*, **41**, 3931–3933.

Ferreira, H.A., Graham, D.L., Freitas, P.P. and Cabral, J.M.S. (2003). Biodetection using magnetically labeled biomolecules and arrays of spin valve sensors. *Journal of Applied Physics*, **93**, 7281–7286.

Ferreira, H.A., Graham, D.L., Parracho, P., *et al*. (2004). Flow velocity measurement in microchannels using magnetoresistive chips. *IEEE Transactions on Magnetics*, **40**, 2652–2654.

Fixe, F., Cabeça, R., Chu, V., *et al*. (2003). Electric-field-pulse-assisted covalent immobilization of DNA in the nanosecond time scale. *Applied Physics Letters*, **83**, 1465–1467.

Fixe, F., Dufva, M., Telleman, P. and Christensen, C.B.V. (2004a). Functionalization of poly(methyl methacrylate) (PMMA) as a substrate for DNA microarrays. *Nucleic Acids Research*, **32**, e9.

Fixe, F., Dufva, M., Telleman, P. and Christensen, C.B.V. (2004b). One-step immobilization of aminated and thiolated DNA onto poly(methylmethacrylate) (PMMA) substrates. *Lab on a Chip*, **4**, 191–195.

Freitas, P.P., Ferreira, H.A., van Dijken, S. and Gregg, J., (2006). Nanostructures for spin electronics. In *Advanced Magnetic Nanostructures*, Sellmyer, D. and Skomski, R. (Ed.), Springer: New York, pp. 403–460.

Freitas, P.P., Ferreira, H.A., Graham, D.L., *et al*. (2004). Magnetoresistive DNA chips. In *Magnetoelectronics*, Johnson, M. (Ed.), Academic Press: New York, pp. 332–373.

Freitas, P.P., Silva, F., Oliveira, N.J., *et al*. (2000). Spin-valve sensors. *Sensors and Actuators, A*, **81**, 2–8.

Gijs, M.A.M. (2004). Magnetic bead handling on-chip: new opportunities for analytical applications. *Microfluidics and Nanofluidics*, **1**, 22–40.

Graham, D.L., Ferreira, H., Bernardo, J., *et al*. (2002). Single magnetic microsphere placement and detection on-chip using current line designs with integrated spin valve sensors: biotechnological applications. *Journal of Applied Physics*, **91**, 7786–7788.

Graham, D.L., Ferreira, H.A., Feliciano, N., *et al*. (2005). Magnetic field-assisted DNA hybridisation and simultaneous detection using mícron-sized spin-valve sensors and magnetic nanoparticles. *Sensors and Actuators, B*, **107**, 936–944.

Graham, D.L., Ferreira, H.A. and Freitas, P.P. (2004). Magnetoresistance-based biosensors and biochips. *Trends in Biotechnology*, **22**, 455–462.

Graham, D.L., Ferreira, H.A., Freitas, P.P. and Cabral, J.M.S. (2003). High sensitivity detection of molecular recognition using magnetically labelled biomolecules and magnetoresistive sensors. *Biosensors and Bioelectronics*, **18**, 483–488.

Guedes, A., Mendes, M.J., Freitas, P.P. and Martins, J.L. (2006) Study of SF-SAF structures for magnetic sensor application. *Journal of Applied Physics*, **99**, 08B703–08B705.

Häfeli, U., Schutt, W., Teller, J. and Zborowski, M. (Eds.) (1997). *Scientific and Clinical Applications of Magnetic Carriers*, Plenum Press: New York.

Heller, M.J. (1996). An active microelectronics device for multiplex DNA analysis. *IEEE Engineering in Medicine and Biology*, **15**, 100–104.

Joos, B., Kuster, H. and Cone, R. (1997). Covalent attachment of hybridisable oligonucleotides to glass supports. *Analytical Biochemistry*, **247**, 96–101.

Joshi, V., Li, G., Wang, S.X. and Sun, S. (2004). Biochemical stability of components for use in a DNA detection system. *IEEE Transactions on Magnetics*, **40**, 3012–3014.

Katsura, S., Yasuda, T., Hirano, K., *et al*. (2001). Development of a new detection method for DNA molecules. *Superconductor Science and Technology*, **14**, 1131–1134.

Katz, E. and Willner, I. (2004). Integrated nanoparticle-biomolecule hybrid systems: synthesis, properties and applications. *Angewandte Chemie International Edition*, **43**, 6042–6108.

Kittel, C. (1996). *Introduction to Solid State Physics*, *Seventh Edition*, John Wiley & Sons: New York, pp. 441–484.

Kötitz, R., Matz, H., Trahms, L., *et al*. (1997). SQUID based remanence measurements for immunoassays. *IEEE Transactions on Applied Superconductivity*, **7**, 3678–3681.

Kriz, K., Gehrke, J. and Kriz, D. (1998). Advances toward magneto immunoassays. *Biosensors and Bioelectronics*, **13**, 817–823.

Kriz, C.B., Radevik, K. and Kriz, D. (1996). Magnetic permeability measurements in bioanalysis and biosensors. *Analytical Chemistry*, **68**, 1966–1970.

Kurlyandskaya, G. and Levit, V. (2005). Magnetic Dynabeads detection by sensitive element based on giant magnetoimpedance. *Biosensors and Bioelectronics*, **20**, 1611–1616.

Kurlyandskaya, G.V., Sánchez, M.L., Hernando, B., *et al*. (2003). Giant-magnetoimpedance-based sensitive element as a model for biosensors. *Applied Physics Letters*, **82**, 3053–3055.

Lagae, L., Wirix-Speetjens, R., Das, J., *et al*. (2002). On-chip manipulation and magnetization assessment of magnetic bead ensembles by integrated spin-valve sensors. *Journal of Applied Physics*, **91**, 7445–7447.

Lagae, L., Wirix-Speetjens, R., Liu, C-X., *et al*. (2005). Magnetic biosensors for genetic screening of cystic fibrosis. *IEE Proceedings on Circuits, Devices and Systems*, **152**, 393–400.

Landry, G., Miller, M.M., Bennett, B.R., *et al*. (2004). Characterization of single magnetic particles with InAs quantum-well Hall devices. *Applied Physics Letters*, **85**, 4693–4695.

Lee, G.U., Metzger, S., Natesan, M., *et al*. (2000). Implementation of force differentiation in the immunoassay. *Analytical Biochemistry*, **286**, 261–271.

Li, G., Joshi, V., White, R.L., *et al*. (2003). Detection of single micron-sized magnetic bead and magnetic nanoparticles using spin valve sensors for biological applications. *Journal of Applied Physics*, **93**, 7557–7559.

Li, G. and Wang, S.X. (2003). Analytical and micromagnetic modeling for detection of a single magnetic microbead or nanobead by spin valve sensors. *IEEE Transactions on Magnetics*, **39**, 3313–3315.

Li, G., Wang, S.X. and Sun, S. (2004). Model and experiment of detecting multiple magnetic nanoparticles as biomolecular labels by spin valve sensors. *IEEE Transactions on Magnetics*, **40**, 3000–3002.

Martins, V.C.B., Fonseca, L.P., Ferreira, H.A., *et al*. (2005). Use of magnetoresistive biochips for monitoring of pathogenic microorganisms in water through bioprobes: oligonucleotides and antibodies, *Technical Proceedings of the 2005 NSTI Nanotechnology Conference and Trade Show*, Anaheim, 8-12 May 2005, **1**, chapter 8: Bio Micro Sensors, pp. 493–496.

Miller, M.M., Prinz, G.A., Cheng, S-F. and Bounnak, S. (2002). Detection of a micron-sized magnetic sphere using a ring-shaped anisotropic magnetoresistance-based sensor: a model for a magnetoresistance-based biosensor. *Applied Physics Letters*, **81**, 2211–2213.

Miller, M.M., Sheehan, P.E., Edelstein, R.L., *et al*. (2001). A DNA array sensor utilizing magnetic microbeads and magnetoelectronic detection. *Journal of Magnetism and Magnetic Materials*, **225**, 138–144.

Moodera, J.S., Kinder, L.R., Wong, T.M. and Meservey, R. (1995). Large magnetoresistance at room temperature in ferromagnetic thin film tunnel junctions. *Physical Review Letters*, **74**, 3273–3276.

Néel, L. (1955). Some theoretical aspects of rock magnetism. *Advances in Physics*, **4**, 191–243.

Nishibiraki, H., Kuroda, C.S., Maeda, M., *et al*. (2005). Preparation of medical magnetic nanobeads with ferrite particles encapsulated in a polyglycidyl methacrylate (GMA) for bioscreening. *Journal of Applied Physics*, **97**, 10Q919.

Okamoto, T., Suzuki, T. and Yamamoto, N. (2000). Microarray fabrication with covalent attachment of DNA using bubble jet technology. *Nature Biotechnology*, **18**, 438–441.

Pankhurst, Q.A., Connolly, J., Jones, S.K. and Dobson, J. (2003). Applications of magnetic nanoparticles in biomedicine. *Journal of Physics D: Applied Physics*, **36**, R167–R181.

Parkin, S.S.P., Kaiser, C., Panchula, A., *et al*. (2004). Giant tunneling magnetoresistance at room temperature with MgO (100) tunnel barriers. *Nature Materials*, **3**, 862–866.

Pease, A.C., Solas, D., Sullivan, E.J., *et al*. (1994). Light generated oligonucleotides arrays for rapid DNA sequence analysis. *Proceedings of the National Academy of Sciences of the United States of America*, **91**, 5022–5026.

Peruski, A.H., and Peruski, L.F. Jr. (2003). Immunologic methods for detection and identification of infectious disease and biological warfare agents. *Clinical and Diagnostic Laboratory Immunology*, **10**, 506–513.

Piedade, M., Sousa, L., Germano, J., *et al* (2006). A new hand-held microsystem architecture for biological analysis. *IEEE Trans on Circuits and Systems*, **53**, 2384–2395.

Prinz, G.A. (1998). Device physics –magnetoelectronics. *Science*, **282**, 1660–1663.

Ramsay, G. (1998). DNA-chips: state-of-the-art. *Nature Biotechnology*, **16**, 40–44.

Raquet, B. (2001). Electronic noise in magnetic materials and devices. In *Spin Electronics*, Lecture Notes in Physics, Ziese, M. and Thorton, M.J. (Eds.), Springer: Berlin, pp. 232–273.

Reich, D.H., Tanase, M., Hultgren, A., *et al*. (2003). Biological applications of multifunctional magnetic nanowires. *Journal of Applied Physics*, **93**, 7275–7280.

Richardson, J., Hawkins, P. and Luxton, R. (2001). The use of coated paramagnetic particles as a physical label in a magneto-immunoassay. *Biosensors and Bioelectronics*, **16**, 989–993.

Richardson, J., Hill, A., Luxton, R. and Hawkins, P. (2001). A novel measuring system for the determination of paramagnetic particles for use in magneto-immunoassays. *Biosensors and Bioelectronics*, **16**, 1127–1132.

Rife, J.C., Miller, M.M., Sheehan, P.E., *et al*. (2003). Design and performance of GMR sensors for the detection of magnetic microbeads in biosensors. *Sensors and Actuators, A*, **107**, 209–218.

Sandhu, A. and Handa, H. (2005). Practical Hall effect sensors for biomedical instrumentation. *IEEE Transactions on Magnetics*, **41**, 4123–4127.

Sandhu, A., Sanbonsugi, H., Shibasaki, I., *et al*. (2004). High sensitivity InSb ultra-thin film micro-hall sensors for bioscreening applications. *Japanese Journal of Applied Physics*, **43**, L868–L870.

Schotter, J., Kamp, P.B., Becker, A., *et al*. (2002). A biochip based on magnetoresistive sensors. *IEEE Transactions on Magnetics*, **38**, 3365–3367.

Schotter, J., Kamp, P.B., Becker, A., *et al*. (2004). Comparison of a prototype magnetoresistive biosensor to standard fluorescent DNA detection. *Biosensors and Bioelectronics*, **19**, 1149–1156.

Shen, W., Liu, X., Mazumdar, D. and Xiao, G. (2005). *In situ* detection of single micron-sized magnetic beads using magnetic tunnel junctions sensors. *Applied Physics Letters*, **86**, 253901.

Sousa, R.C., Freitas, P.P., Chu, V. and Conde, J.P. (1999). Vertical integration of a spin-dependent tunnel junction with an amorphous Si diode for MRAM application. *IEEE Transactions on Magnetics*, **35**, 2832–2834.

Southern, E.M., Mir, K. and Shchepinov, M. (1999). Molecular interactions on microarrays. *Nature Genetics*, **21**, 5–9.

Stoner, E.C. and Wohlfarth, E.P. (1948). A mechanism of magnetic hysterisis in heterogenous alloys. *Philosophical Transactions of the Royal Society of London, Series A*, **240**, 599–642.

Sun, S., Anders, S., Hamann, H.F., *et al*. (2002). Polymer mediated self-assembly of magnetic nanoparticles. *Journal of the American Chemical Society*, **124**, 2884–2885.

Sun, S. and Zeng, H. (2002). Size-controlled synthesis of magnetite nanoparticles. *Journal of the American Chemical Society*, **124**, 8204–8205.

Tamanaha, C.R., Whitman, L.J. and Colton, R.J. (2002). Hybrid macro-micro fluidics system for a chip-based biosensor. *Journal of Micromechanics and Microengineering*, **12**, N7–N17.

Tondra, M., Porter, M. and Lipert, R.J. (2000). Model for detection of immobilized superparamagnetic nanosphere assay labels using giant magnetoresistive sensors. *Journal of Vacuum Science and Technology A*, **18**, 1125–1129.

Voet, D., Voet, J.G. and Pratt, C.W. (1999). *Fundamentals of Biochemistry*, John Wiley & Sons: New York.

Wang, D., Nordman, C., Daughton, J.M., *et al*. (2004). 70% TMR at RT for SDT sandwich junctions with CoFeB as free and reference layers. *IEEE Transactions on Magnetics*, **40**, 2269–2271.

Wang, S.X., Bae, S-Y., Li., G., *et al*. (2005). Toward a magnetic microarray for sensitive diagnostics. *Journal of Magnetism and Magnetic Materials*, **293**, 731–736.

Weetall, H.H. (1976). Covalent coupling methods for inorganic support materials. *Methods in Enzymology*, **44**, 134–148.

Yellen, B.B., Hovorka, O. and Friedman, G. (2005). Arranging matter by magnetic nanoparticle assemblers. *Proceedings of the National Academy of Sciences of the United States of America*, **102**, 8860–8864.

Yu, A.A., Savas, T.A., Taylor, G.S., *et al*. (2005). Supramolecular nanostamping: using DNA as movable type. *Nano Letters*, **5**, 1061–1064.

Yuasa, S., Nagahama, T., Fukushima, A., *et al*. (2004). Giant room-temperature magnetoresistance in single-crystal Fe/MgO/Fe magnetic tunnel junctions. *Nature Materials*, **3**, 868–871.

FURTHER READING

Ball, J.C., Puckett, L.G. and Bachas, L.G. (2003). Covalent immobilization of beta-galactosidase onto a gold-coated magnetoelastic transducer via a self-assembled monolayer: toward a magnetoelastic biosensor. *Analytical Chemistry*, **75**, 6932–6939.

Ruan, C., Zeng, K., Varghese, O.K. and Grimes, C.A. (2003). Magnetoelastic immunosensors: amplified mass immunosorbent assay for detection of *Escherichia coli* O157: H7. *Analytical Chemistry*, **75**, 6494–6498.

Application of Magnetic Particles in Medicine and Biology

Wilfried Andrä[1], Urs Häfeli[2], Rudolf Hergt[1] and Ripen Misri[2]

[1] *Institute for Physical High Technology, Jena, Germany*
[2] *University of British Columbia, Vancouver, British Columbia, Canada*

1 INTRODUCTION

Magnetic particles (MPs) exist in our environment in greater amounts than is commonly noticed. Huge masses of sediments contain iron oxide particles of terrigenous material. A small number of these particles are formed from magnetosomes, which are special organelles of bacteria. Recent investigations have revealed interesting details of the factors governing the size and formation of these biogenic MPs (Schüler and Frankel, 1999; Scheffel *et al*., 2006).

The properties of biogenic MPs are particularly favorable for certain applications such as a heat source in local magnetic hyperthermia (see Section 4). Nevertheless, their general use in medicine and biology is restricted owing to the fact that their growth cannot be easily controlled. Moreover, their content of bacterial proteins, if not completely removed, causes problems for their medical application. Many methods have, therefore, been developed to artificially prepare particles with properties suitable for particular applications. One of the first preparation methods, chemical precipitation of particles from a mixture of a ferrous and a ferric salt reacting at a basic $pH > 8$, was described in 1938 and used for the investigation of magnetic microstructures (Elmore, 1938). This wet method of preparing an aqueous suspension of nanoparticles was later followed by a dry powder preparation, using the thermal decomposition of iron pentacarbonyl (Andrä and Schwabe, 1955). Very recently, laser evaporation has also been applied to the highly efficient production of dry iron oxide nanoparticles (Kurland *et al*., 2007). During the last few decades, different synthetic techniques have been developed, a comprehensive review of which was done by Tartaj *et al*. (2003). The most common technique, however, is still the chemical precipitation developed by Elmore, leading to well-controlled superparamagnetic particles of typically 10 nm diameter. Attempts to increase the particle diameter has generally led to broader size distributions. In order to prepare larger particles with a narrow size distribution, a separation of the nucleation stage from further particle growth has been tried. Sun and Zeng (2002) were particularly successful at this, producing well-defined particle diameters. An alternative method, used for the preparation of barium ferrite particles, is the glass crystallization method, which has recently been adapted to γ-Fe_2O_3 nanopowders (Müller, Hergt, Zeisberger and Gawalek, 2005). The mean particle size can be controlled by the parameters of the annealing procedure. In spite of these successes, further systematic investigations for optimizing preparation techniques are necessary in order to provide nanoparticles with tailored magnetic properties.

Handbook of Magnetism and Advanced Magnetic Materials. Edited by Helmut Kronmüller and Stuart Parkin. Volume 4: *Novel Materials*. ISBN: 978-0-470-02217-7.

Medical applications of magnetic powders have been known since ancient times (Häfeli, 1998), but many of these were based on superstition and irrational ideas. It is only in the last couple of decades that the scientific use of artificially prepared MPs in medicine and biology has taken off. Important medical applications include their use as contrast media, vascular occlusion agents, localized heating sources in hyperthermia and thermoablation, targeted drug and radiation sources, transfectant (magnetofection) agents, and agents to purify and separate distinct cell populations. In the sections that follow, these topics will be covered in more detail.

Another application of MPs that can only be touched upon owing to space limitations is their natural use, for example, as sensing elements in living beings. Four decades ago, the existence of biogenic magnetite as tooth capping in a primitive sea mollusc was discovered by Lowenstam (1962). Later, magnetic iron-oxide particles were found in many different animal species. Recent reports have focused on the biophysical mechanism of magnetic sensing, which is assumed to be strongly connected with MPs in higher organisms (Kirschvink and Gould, 1981; Kobayashi and Kirschvink, 1995). The role of other MPs, such as the iron cores of ferritin, is also omitted in this chapter. Interested readers should refer to Meldrum, Heywood and Mann (1992).

2 MAGNETIC LABELING OF CELLS AND BIOMOLECULES

Magnetic labeling of cells and biomolecules can be accomplished with the use of magnetic carriers, henceforth referred to as MPs. Magnetic labeling has found extensive application in life science research, clinical diagnostics, and therapeutics. MPs can have a hydrophobic or affinity ligand immobilized on their surface or can possess ion-exchange groups that act as linkers. These specific surface structures make MPs useful in the processing of a wide variety of test samples for analysis (= samples). Samples include crude cell lysates, whole blood, plasma, ascites fluid, milk, whey, urine, cultivation media, wastes from the food and fermentation industry as well as many others (Safarik and Safarikova, 2004). When the sample and MPs are mixed and allowed to incubate for some time, the target compound (i.e., analyte) binds to the MPs and the magnetic complex that is formed can be easily and rapidly removed from the sample using an appropriate magnetic separator (see Section 2.2). After washing out the contaminants, the isolated target compound can be separated and used for further work. This process is termed *positive isolation*, that is, the direct isolation of the desired compound (Figure 1a). Magnetic separation can also be used to remove unwanted compounds from a heterogeneous suspension. In this approach, the MP-bound compound is discarded and the remaining target compounds of interest recovered. This process is termed *negative isolation* (Figure 1b).

The advantages of magnetic separation far outweigh their disadvantages, as summarized in Table 1. Magnetic separation is simple to perform and flexible compared to conventional separation methods.

2.1 Magnetic carriers

Most MPs are based on inorganic magnetic materials, primarily iron oxides. For their use in biotechnology, these MPs are either coated with or embedded into matrix materials such as polymers and silica and are then typically referred to as *composite particles*. The first applications of coated MPs began in the 1970s and included enzyme immobilization, radioimmunoassay, specific cell binding, and affinity chromatography (Pouliquen, 2001). In 1978, Kronick *et al*. reported the first use of MPs for cell separation (Kronick, Campbell and Joseph, 1978). In 1979, John Ugelstad of Norway made the first uniform monosized polystyrene spheres (Ugelstad and Mork, 1980) and developed them within a few years into a highly successful commercial product, namely, monosized composite particles (Dynabeads®) (Ugelstad *et al*., 1992). Critical to their success was that Dynabeads® are superparamagnetic, which means that they can be easily resuspended once the magnetic field is removed, with no residual magnetism.

Dynabeads® are currently available in diameters of 1, 2.8, and 4.5 μm. These large-sized particles have the disadvantage that they have limited surface area per weight. Nonporous spherical beads of 50-nm diameter contain a 20 times larger surface area than 1-μm beads of the same weight; making the beads porous further adds to their surface area. Decreasing the size of MPs to 50 nm, as was done by Miltenyi (Safarik and Safarikova, 1999), will theoretically allow for a larger number of functional groups, and the binding of increased amounts of ligands, for example, antibodies. MPs of such small particle size, however, will require high-gradient magnetic fields for separation (Miltenyi, Muller, Weichel and Radbruch, 1990). Such high gradients typically exceed $100\,\mathrm{T\,m^{-1}}$.

Most applications utilize composite magnetic nano- or microparticles with sizes between 50 nm and 10 μm, although even very large MPs that are 800 μm in diameter have been used for the magnetic separation of α amylases from porcine pancreas, starch-degrading enzymes, and wheat germ (Teotia and Gupta, 2001). The largest and earliest commercial provider of MPs in the micrometer range is Dynal Biotech (bought by Invitrogen in 2005) and in the nanometer range it is Miltenyi Biotec. However, there are many smaller

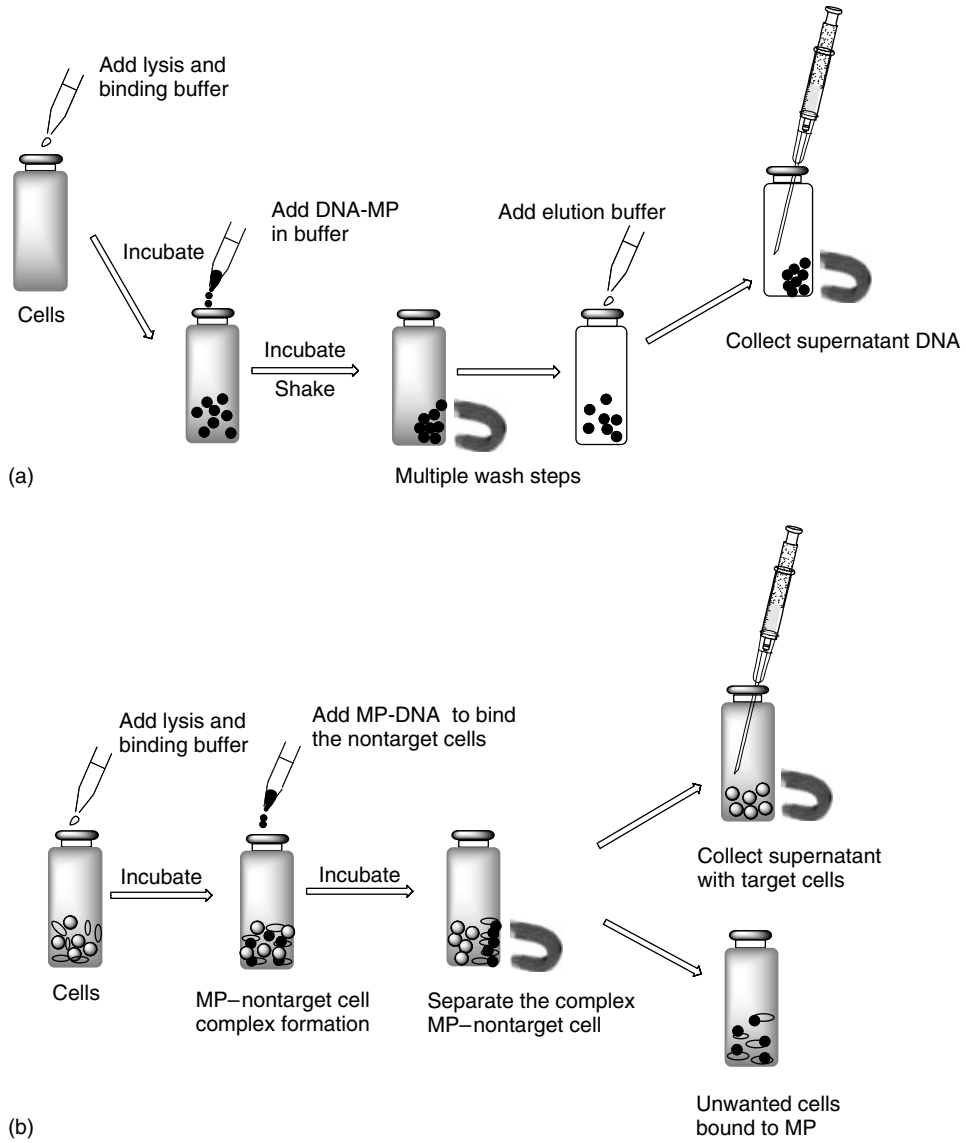

Figure 1. (a) The *positive isolation* of genomic DNA starts with the lysis and binding of DNA under nondenaturing conditions, followed by the addition of MPs with specific affinity ligands. After multiple wash steps, the purified DNA is obtained. (b) The *negative isolation* of bacterial cells begins with the addition of MPs with affinity to the nontarget cells. Bound MPs are then attracted by a magnet and the untouched target cells collected from the supernatant. Magnetic separation is indicated by the symbol of a horseshoe magnet.

companies that provide products for magnetic separation and specialty applications as well as appropriate (super)magnetic particles.

For magnetic separation, different materials can be used to prepare MPs. A partial list of matrix materials includes synthetic polymers such as poly (ethyl-2-cyanoacrylate) and poly (styrene-*co*-maleic anhydride); biopolymers such as dextran and albumin; and porous glass. The magnetic components include inorganic magnetic materials such as the iron oxides magnetite Fe_3O_4, maghemite γ-Fe_2O_3, and mixtures thereof. Metallic iron, cobalt, nickel, and alloys thereof can also be used. Since the largest use of these materials is *in vitro*, biocompatibility is not of major concern in the choice of materials.

In addition to size, structure, magnetic moment, and (superpara)magnetic properties, the most important MP parameters are surface charge, surface hydrophobicity or hydrophilicity, porosity, and the type and density of reactive surface groups. Chemically reactive groups on the surface are used for covalent immobilization of affinity ligands and target biomolecules. They must remain stable under varied temperature and pH conditions, must be correctly oriented, and must have low nonspecific binding even in complex sample types. Choosing relevant chemical groups and spacers,

Table 1. General advantages and disadvantages of magnetic cell separation using magnetic particles (MPs).

Advantages	Disadvantages
• Simple method with very few handling steps • All the steps can take place in a single test tube. No necessity for excessive instruments or equipment • Separation can be directly performed on crude samples • Total separation time can be shortened by combining the disintegration and separation steps • Magnetic absorbents can be removed easily owing to their magnetic properties • Useful for large-scale separations • Magnetic separation is usually gentle on the target proteins or peptides • Large commercial availability of MP and MP separation kits	• Insufficient and/or ineffective resuspension of the MP pellets after washing and elution steps may result in: –Lower yields –Lower purity of the separation product compared to other purification methods • Magnetic component in positive selection may interfere with subsequent procedures

adding blocking agents, and carrying out post-immobilization modifications allows for the preparation of highly specific MPs. For example, immobilization of oligonucleotides is normally achieved by introduction of specific chemical groups at the end of the oligonucleotides, thus retaining functional activity. NH_2 groups or SH groups are often used for direct covalent coupling to the MP surface, while the introduction of a biotin molecule at the 5′ or 3′ end of the oligonucleotide is used in combination with MPs coated with streptavidin. The strong streptavidin–biotin bond is temperature stable (up to 80 °C) and can withstand alkaline treatments (0.15 M NaOH), features which make streptavidin MPs a versatile tool in molecular biology (Bosnes *et al*., 1997).

Nonspecific binding of analytes to MPs during magnetic separations can be a problem. Additional preclearing steps are often carried out, particularly when extracting proteins and peptides from crude samples. By studying the characteristic MP properties such as type (hydrophilic/hydrophobic, nonporous/macroporous), size, and functional group for use of appropriate ligands, Korecka *et al*. determined the reaction conditions required to develop immobilized magnetic enzyme reactors (IMERs). These enzyme reactors consist of the immobilized proteolytic enzymes trypsin, chymotrypsin, papain, and neuraminidase immobilized on MPs (Korecka *et al*., 2005). The strategy adopted in getting minimal nonspecific sorption of proteins and peptides, without the need for any additional preclearing steps before studying heterogeneous proteins and/or glycoproteins, was the use of different MP matrix materials. The optimal materials chosen included hydrophilic cellulose and alginate, and hydrophobic polystyrene, poly(NIPAM) and poly(HEMA-*co*-GMA) (Korecka *et al*., 2005).

2.2 Magnetic separators

Magnetic separations have been used in various areas such as molecular biology, biochemistry, immunochemistry, enzymology, analytical chemistry, and environmental chemistry (Safarik and Safarikova, 2004). Magnetic separations with MPs have also been successfully studied for a wide variety of applications such as the detoxification of blood-borne toxins of humans (Mertz *et al*., 2005), the separation of pathogenic bacteria from food and environmental samples (Rotariu *et al*., 2005), and the extraction of surfactants from water (Safarikova *et al*., 2005).

Magnetic separation techniques generally consist of two steps. In the first step, solid phase affinity MPs with specific target recognition capabilities are mixed with the sample and selectively bind to the target in the sample. In the second step, the target–MP complex formed is captured by a magnetic field and removed from the separation medium. Magnetic fields for separation can be produced by permanent magnets or electromagnets. The shape and magnitude of magnetic fields determine where and how quickly the MPs separate in any given vessel. The magnetic field gradient and magnitude play important roles in separation and their product determines the strength of the magnetic force that acts on any given MP. The higher the relative force densities, the more quickly a given magnet can separate the MPs, and the smaller the MPs can be.

Magnetic separators may be either batch-wise driven or continuous driven, and one may chose between the two on the basis of the desired application. Commercially available laboratory-scale batch magnetic separators are usually made from magnets embedded in disinfectant-proof material.

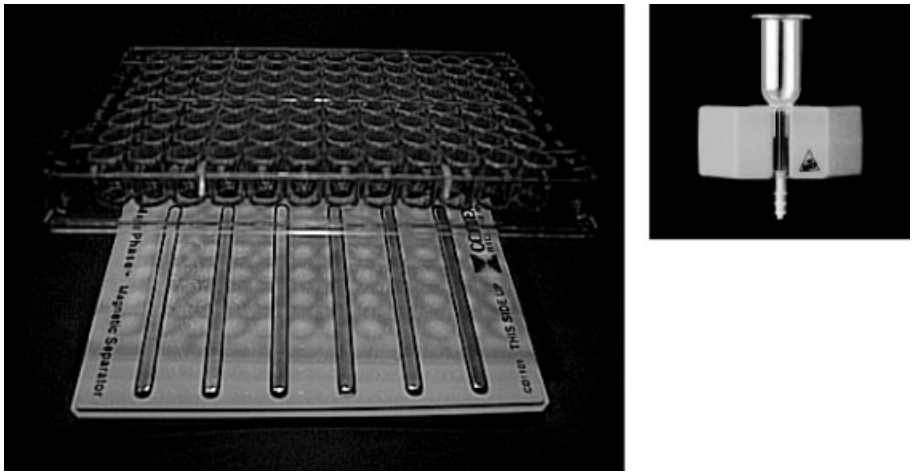

(a) (b)

Figure 2. Commercially available magnetic separators. (a) The 96-well plate laboratory-scale batch-type magnetic separator from Cortex Biochem pulls the magnetically labeled samples to the bottom of the plate, close to the long stripe-shaped NdFeB magnets. (b) The MiniMACS separator from Miltenyi Biotec is a lab scale HGMS separator, designed for extracting animal and plant cells, bacteria, viruses, cellular organelles, and molecules such as mRNA. It is designed for the positive selection of up to 10^7 labeled cells, from up to 2×10^8 unseparated cells.

The batch-type separators have racks constructed for separations and some also have a removable magnetic plate to facilitate easy washing of separated MPs (Figure 2). Other examples of batch-type magnetic separators include holders for Eppendorf microtubes, standard test tubes, and centrifugation cuvettes (Safarik and Safarikova, 2004). Simple magnet blocks in these holders typically generate field gradients in the order of 1–6 T m^{-1} across the diameter of standard 15–50-ml laboratory test tubes with wall thicknesses of 1–2 mm.

The magnetic force acting on a pointlike magnetic dipole moment m is described by the formula

$$F = m\nabla|B| \tag{1}$$

where the total magnetic dipole moment of the MPs is the result of volume magnetization of the magnetic component included in the MPs, M:

$$m = V_{\mathrm{m}}\, M \tag{2}$$

and where V_{m} is the total volume of the magnetic material in the MPs. The magnetic component is free to rotate in space (together with the MPs), and its magnetization is induced by the external magnetic field of strength H:

$$M = \Delta\chi H \tag{3}$$

where $\Delta\chi$ is the effective magnetic susceptibility of the magnetic component relative to medium. In an isotropic, weakly diamagnetic medium such as water, and for diluted MP suspensions with no free magnetic component in the solution, magnetic fields H and B differ only by a constant, the magnetic permeability of vacuum μ_0:

$$B = \mu_0 H \tag{4}$$

Combining the last four formulas and applying them to the special case of time-independent, magnetostatic fields, as is the case in the just described magnetic separators, one obtains the magnetic force acting on an MP as

$$F_{\mathrm{m}} = V_{\mathrm{m}}\Delta\chi\frac{\nabla B^2}{2\mu_0} \tag{5}$$

For small Reynolds numbers (i.e., $Re_{\mathrm{particle}} < 0.1$) the magnetic drift velocity can be derived from equation (5) when the sedimentation and buoyancy force can be neglected. Thus, the magnetic drift velocity v_{m} can be defined as

$$v_{\mathrm{m}} = \frac{V_{\mathrm{m}}\Delta\chi}{f}\frac{\nabla B^2}{2\mu_0} \tag{6}$$

where $f = 3\pi\eta D$ is the Stokes drag coefficient, η is the viscosity, and D is the MP diameter (Zborowski, 1997). The direction of the magnetic force is orthogonal to the magnetic flux.

Flow-through separations can be useful when the separation of large volumes of samples is desired or when separation involves nanosized MPs. Flow-through magnetic separations are usually carried out using a high-gradient magnetic separator (HGMS), in which optimally designed

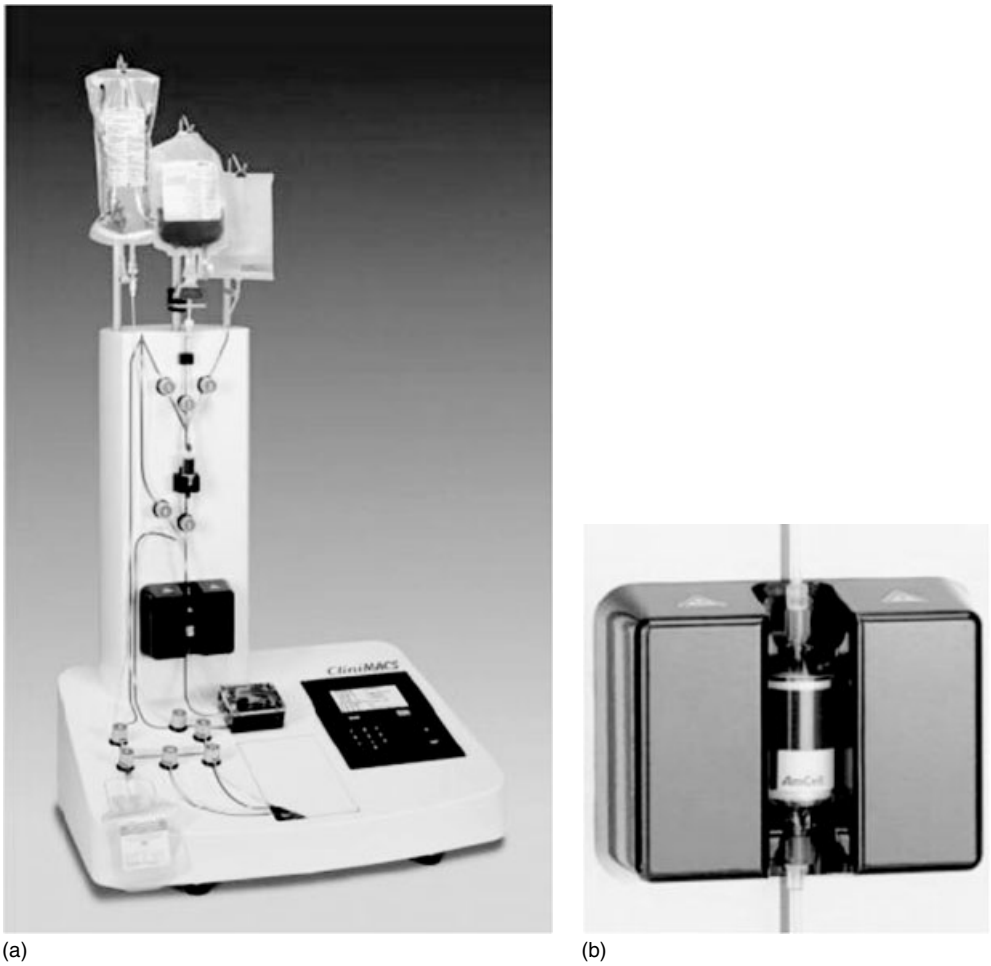

Figure 3. (a) The CliniMACS® instrument from Miltenyi Biotec with installed tubing set is a commercially available automated cell selection device, based on the HGMS principle. It enables the operator to perform large-scale magnetic cell selection in a closed and sterile system. (b) The CliniMACS® magnetic separation device (with separation column in the middle) consists of two strong permanent NdFeB magnets.

magnetic circuits generate gradients from 10 to 100 T m^{-1} across 15–50-ml test tubes (Hatch and Stelter, 2001). HGMS for laboratory-scale use consists of a column of densely packed fine magnetic grade stainless steel wool or small steel balls that is placed between the poles of a strong magnet. The MP suspension is pumped through the column and the MPs are retained within the matrix. The MPs are then recovered by gentle vibration of the column after removal of the magnetic field (Safarik, Ptackova and Safarikova, 2001). HGMSs create magnetic field gradients that can be used to attract much smaller and less magnetic MPs than those required for conventional magnetic separation techniques. The most frequently used HGMS application is the labeling of cells with submicron-sized MPs and their successful separation and/or extraction (Thomas *et al*., 1993).

The separation of pathogenic microorganisms, biological cells, or chemical compounds can be accomplished with the help of antibody-coated MPs. This separation technique is known as *immunomagnetic separation* (IMS). Current standard IMS devices use 1–8 µm MP for test volumes of 1 ml. By increasing the sample size, the sensitivity of the IMS process can be improved such that even the lowest amounts of pathogens can be extracted. A flow-through immunomagnetic separator has been designed and tested to process large volumes of samples (>50 ml) (Rotariu *et al*., 2005). The preliminary results show that between 70 and 113 times more *Escherichia coli* O157 can be recovered when compared with the standard 1-ml method.

The fast and simple handling of samples and the ability to deal with large sample volumes are major advantages of magnetic separation techniques and make them amenable to automation. The CliniMACS® system (Figure 3), marketed by Miltenyi Biotech in Europe since 1997, is an automated magnetic cell selection device based on the HGMS principle.

It enables the operator to perform large-scale magnetic cell selection of CD34, CD133 (AC133), and CD14 positive cells from human peripheral blood and bone marrow in a closed and sterile system (Campbell *et al*., 2005). CD34 and CD133 are protein complexes presented on the surface of hematopoetic and endothelial cells, and CD14 is a protein complex expressed and secreted by myeloid cells. The first commercial automated magnetic cell selection device is the Isolex 300i marketed by Baxter. It received European regulatory approval in 1995 and was also approved by the U.S. Federal Drug Administration (FDA) in 1999, for clinical selection of $CD34^+$ positive cells. A more detailed review of the MACS system and its applications has been recently published (Apel *et al*., 2006).

2.3 Magnetic isolation of proteins and DNA molecules

Magnetic isolation relies on the affinity and interaction between the MPs and the target compounds. To get the highest yields with low nonspecific binding and short separation times, appropriate ligands can be coupled to the MP with specific affinity toward the target compound(s). These MPs are added to the analysis sample, where they bind the target compounds. This method is called the *direct method*. In the *indirect method*, the affinity ligands are added to the solution or suspension without MPs being present. After binding with the target compound and forming a ligand–analyte complex, the entire complex is captured by the MPs (Safarik and Safarikova, 2004).

Magnetic separation produces superior yields of the isolates with shorter separation times. Risoen *et al*. purified two recombinant DNA binding proteins, oncoprotein Myb, and full-length yeast TFIIIA, directly from an *E. coli* cell lysate, in a single step with high purity and recovery (Risoen, Struksnes, Myrset and Gabrielsen, 1995). Holschuh *et al*. have accomplished purification of antibodies from up to 100 l of cell culture supernatant, with protein A–coated MP, called *MagPrep*^{R} *Protein A* (Merck Biosciences). The MPs were coated with 3-(2,3-epoxypropoxy)-propyltrimethoxysilane for the direct covalent immobilization of protein A. Using this technique, magnetic separation results in a similar yield and purity of product as a conventional column, but is much faster (Holschuh and Schwammle, 2005).

Various separation kits are commercially available and can be used for applications such as protein isolation, protein screening, immunoassays, purification of immunoglobulins, immunoprecipitation, and human cell separation for clinical diagnostics and research. The *geneMAG-DNA/Bacteria* kit (Chemicell, Germany) can serve as an example for these novel, simple, and highly efficient tools in molecular biology. After lysing the bacteria, adding the MPs, incubating, and washing, genomic DNA can be efficiently extracted from bacteria with magnetic silica beads (Figure 1a).

Even MPs without linker compounds can be used to separate and screen biomolecules. Magnetic separation of amino acids, using gold/iron oxide composite nanoparticles has been reported (Kinoshita *et al*., 2005). Gold firmly combines with mercapto-containing biomolecules, thus enabling the binding of functional biomolecules without the use of a special linker molecule for each different application. The sulfur-containing amino acids cystine and methionine connect to gold through Au–S bonds and can then be selectively picked up by MPs. Similarly, aspartic acid and glutamic acid have been adsorbed relatively well onto monolithic iron oxide particles, possibly owing to the presence of carboxyl groups found on these molecules (Kinoshita *et al*., 2005).

The literature is full of examples of successful extractions of cells, bacteria, enzymes, proteins, and nucleic acids as reviewed in detail by Safarik and Safarikova (2004). Table 2 gives some examples of the biologic substances that can be isolated and/or purified by magnetic separation techniques.

2.4 Magnetic gene transfection

Nucleic acids form the building blocks for living systems and are responsible for all the processes taking place within the cells. Introducing nucleic acids in a controlled and defined manner opens up an opportunity to influence the processes within living cells. One of the most effective ways to transport nucleic acids is gene therapy, where a 'normal' gene is inserted into the genome to replace an 'abnormal' disease-causing gene. This is normally done with a carrier molecule called a *vector*, which delivers the therapeutic gene to the target cells.

The most effective vectors are viruses that have been genetically altered to carry normal human DNA. After the death of Jesse Gelsinger, however, who died within two days of being injected with adenoviral vectors during a phase I clinical gene therapy trial for a life-threatening enzyme deficiency, more research efforts have focused on developing a nonviral gene transfer system, thus reducing the potential biological risks associated with viral vectors (Somia and Verma, 2000).

Irrespective of the type of vector (viral or nonviral/synthetic), the low efficiency of gene transfer poses a significant challenge in gene transfection, since the transfer process for vectors to target cells is, to a large extent, diffusion controlled (Plank *et al*., 2003b). In addition, the lack of selectivity creates a subsequent need for local targeting to achieve an effective dose at the target cells and to avoid any untoward

Table 2. Examples of magnetic separation for diagnostic and analytical applications.

Type of material	Isolated component	Source	Magnetic carrier	Affinity ligand	Applications	References
Protozoa	Toxoplasma oocysts	Oocysts from cat feces	Goat antimouse IgM coated microbeads (BM 0829)	Monoclonal antibody 3G4	Detection of protozoal cells causing toxoplasmosis	Dumetre and Darde (2005)
Nucleic acids	Viral RNA/DNA	Plasma	MPVA beads	Streptavidin	Nucleic acid testing for detection of viruses	Lutz *et al*. (2005)
Protein	Yeast transcription factor	Heparin agarose	Dynabead™ M-280 streptavidin	Biotin end labeled $tRNA^{Glu}$ gene	Drug discovery, diagnostics	Risoen, Struksnes, Myrset and Gabrielsen (1995)
Cells	Retinal astrocytes (glial cells)	Retina of transgenic mice	Sheep antirat Dynabeads™	Anti-PECAM-1	Study of retinal pathology	Scheef, Wang, Sorenson and Sheibani (2005)
Cells	Tumor cells (gliomas)	Brain tissue	Antimouse IgG beads	Anti-VE cadherin Anti-E selection Anti-CD105 Anti-CD68	Study of malignant brain tumor	Miebach *et al*. (2006)
Bacteria	*Lawsonia intracellularis*	Rabbit feces	Protein A–coated paramagnetic beads	Anti-LsaA antibody	Infection diagnosis and epidemiological investigations	Watarai, Suwa and Iiguni (2004)
Bacteria	*Escherichia coli*	Ground beef	Dynabeads™ anti-*E. coli* 0157	Anti-*E. coli* 0157	Detection and isolation of pathogenic bacteria	Ochoa and Harrington (2005)

MPVA: magnetic polyvinyl alcohol; PECAM-1: platelet cell adhesion molecule-1; LsaA: *Lawsonia* surface antigen A.

effects at nontarget sites. The susceptibility to *in vivo* degradation further reduces the efficiency of gene transfer.

Microparticles, especially MPs, as carriers of DNA can overcome many of these challenges and may help in delivering sustained, therapeutic concentrations of DNA. Frequent dosing regimens and protection of DNA from serum components is possible with the use of biodegradable, biocompatible polymers that are inert, safe, and do not compromise the bioactivity of the DNA. The use of MPs for gene transfection has been termed *magnetofection* by Plank *et al*. (2003a) and comprises the application of a magnetic field in order to drive the magnetic vector toward the target cells or retain it in the target tissue. Preparation of magnetic vectors can be accomplished by linking nucleic acids or nucleic acid vectors to magnetic nanoparticles (Figure 4) using physical (e.g., polyelectrolyte mediated), chemical (e.g., covalently linked), and biological (e.g., biotin–streptavidin, antigen–antibody bound) means (Plank *et al*., 2003b).

Moving to MPs significantly improves the transfection rates not only through magnetically forced contact (Mah *et al*., 2002; Scherer *et al*., 2002) (Figure 4), but also by increasing the plasmid concentration (Hughes, Galea-Lauri, Farzaneh and Darling, 2001). Gersting *et al*. (2004) compared the efficiency of magnetofection with that of standard transfection methods and found that the level of transgene expression resulting from magnetofection was 400-fold higher when compared with dendrimer- or poly(ethyleneimine) (PEI)-mediated transfection (polyfection) and 2500-fold higher when compared with lipofectamine-mediated transfection (lipofection) (Hirao *et al*., 2003). *PolyMAG100* (Chemicell) is one of the commercially available MP preparations for high-efficiency nucleic acid delivery in research. It consists of 100-nm-sized magnetic nanoparticles that are mixed with the nucleic acid to be transfected in a one-step procedure. Magnetic transfection with this reagent is rapid and efficient, uses low vector doses and thus less expensive transfection reagents, has higher transfection rates (percentage of cells transfected), and results in increased levels of transgene expression even with short incubation times. Figure 5 shows a typical example of magnetic transfection efficiency in endothelial cells.

Magnetic gene transfection is being studied with great fervor and holds great promise for gene delivery. One advantage over other methods is that an MP does not need

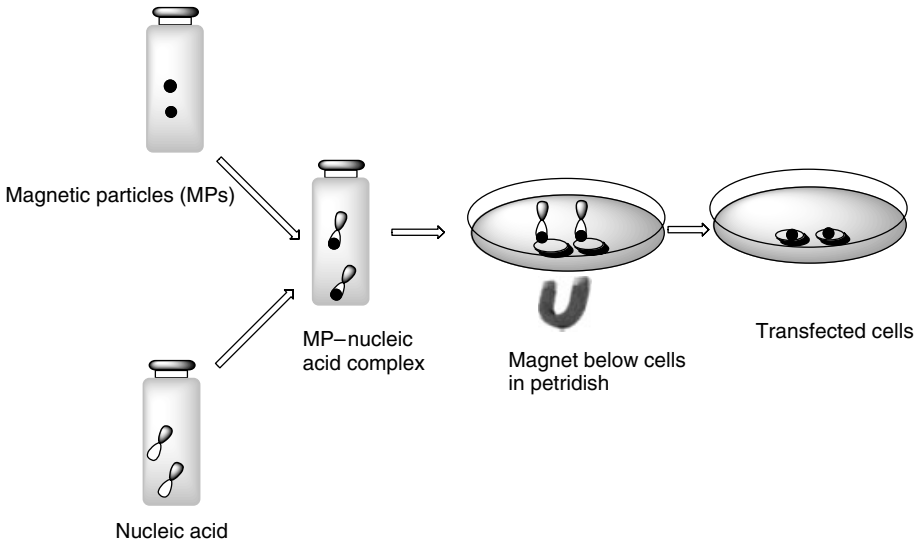

Figure 4. Magnetic transfection uses a magnetic force to guide the gene vectors associated with MPs in close contact with the target cells. Very high vector doses can thus be reached in the cells within a few minutes.

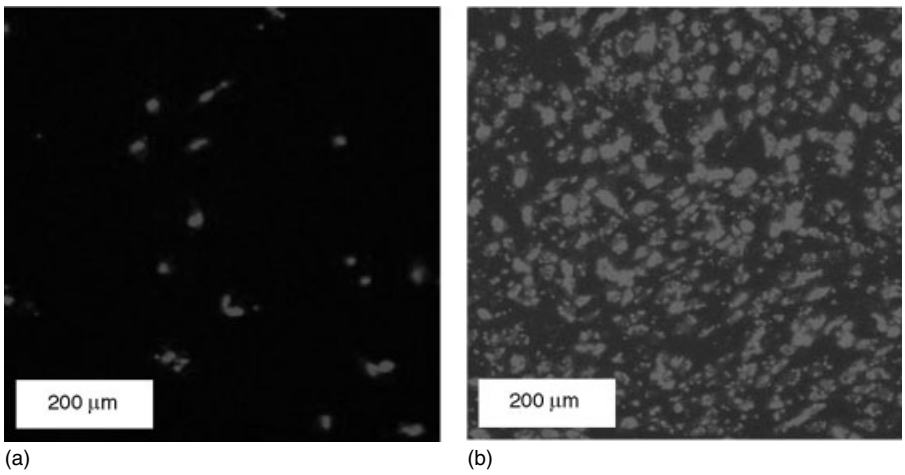

Figure 5. Primary human umbilical vein endothelial cells positioned on the MagnetoFACTOR plate were incubated for 15 min with a Cy3 fluorescence-labeled antisense-oligonucleotide complexed with (a) the transfection reagent Effectene^{TM} (Qiagen) or (b) Effectene^{TM} plus the magnetofection reagent CombiMAG (Chemicell), followed by further cultivation in cell culture medium for 24 h. (Data kindly provided by F. Krötz, Ludwig-Maximilians University, Munich.)

receptors or membrane-bound proteins to enter the cells, which makes it possible to also transfect cells that are not normally susceptible to it (Scherer *et al*., 2002). Some recent examples of magnetic gene transfection are given in Table 3.

3 THERAPEUTIC APPLICATIONS OF MAGNETIC CARRIERS

3.1 Introduction

The application of MPs as a medical means to cure diseases dates back to ancient times when pulverized magnetite was utilized to treat different external as well as internal illnesses (Häfeli, 2006a). It was, however, not until the middle of the last century that this idea enjoyed a renaissance with the proposal to treat cancer using local hyperthermia via the heating of MPs exposed to alternating magnetic fields (Gilchrist *et al*., 1957). Whereas this therapeutic modality is described in more detail in Section 4, the initial sections deal primarily with MPs as carriers of drugs.

The delivery of drugs to specific preidentified targets within the body, maximizing the drug concentration in the target and minimizing toxic effects in nontarget tissue, is known as *targeted drug delivery*. Two known mechanisms of drug delivery with carrier systems include passive and

Table 3. Examples of gene transfection using magnetic particles (MPs).

Transfection vector	Delivery system	Particle size (nm)	References
HVJ-E plasmid	Protamine or heparin-coated maghemite nanoparticles (Nanotek, C.I. Kasei)	29	Morishita *et al*. (2005)
p55pCMV-IVS-luc^{+} (luciferase reporter gene)	Magnetic beads (CombiMag)	100–200	Krötz *et al*. (2003)
GFP-C2 plasmid	Superparamagnetic iron oxide dextran nanoparticles	59	Cao *et al*. (2004)
PCMVluc plasmid DNA (luciferase reporter gene)	Cationic polymer-coated iron oxide nanoparticles (transMAG^{PEI})	200	Gersting *et al*. (2004)
pGL3 plasmid DNA	Magnetic cationic liposomes	40	Hirao *et al*. (2003)

GFP-C2: green fluorescent protein C2

Table 4. General advantages and disadvantages of the magnetic targeting approach.

Advantages	Disadvantages
• Increased and very high drug concentrations are possible in the target region, organ, and suborgan, as compared to other systemic passive or active targeting approaches • Very low drug concentrations are seen in other body parts • Side effects and toxicity are much reduced or missing • Total amount of drug use can be decreased substantially • Local capillary diffusion of drugs is maximized • Extravasation of MPs into interstitial/extravascular space is possible and has been reported in several investigations • Magnetic targeting supports the EPR effect • MPs can be targeted away from the RES	• Treatment depth (e.g., deep body targeting) is limited owing to rapid magnetic field fall-off • Production of defined, directed magnetic fields and field gradients can be a challenge • Magnet-induced agglomeration of MPs can lead to clogging (embolizations) of small blood vessels

EPR: enhanced permeation and retention.

active targeting. In passive targeting, the final biodistribution of the carriers is determined by the physical properties of the particles. For example, the ability of some colloids to be taken up by the reticuloendothelial system (RES), especially in the liver and the spleen, has made them the vectors of choice for passive drug targeting to these organs. In active targeting, the final biodistribution is determined by the way the receptors on specific cells and organs recognize the carriers. In order to facilitate binding to target cells, the carriers are engineered to contain target-specific ligands, such as antibodies, peptide sequences, sugar moieties, charge, and other specific molecular entities.

In addition to passive and active targeting, a third targeting option is magnetic drug delivery. Magnetic drug delivery is a physical method of delivering nano- or microsized MPs, possibly loaded with a drug, to a target organ or region. Like the other two methods, magnetic drug delivery has both advantages and disadvantages. Table 4 lists them in a comprehensive form. Combinations of all three methods are also possible and are under investigation.

3.2 Mechanism of magnetic drug delivery

Magnetic drug delivery uses external magnets to produce or to orient a magnetic moment in MPs, to guide drug-loaded

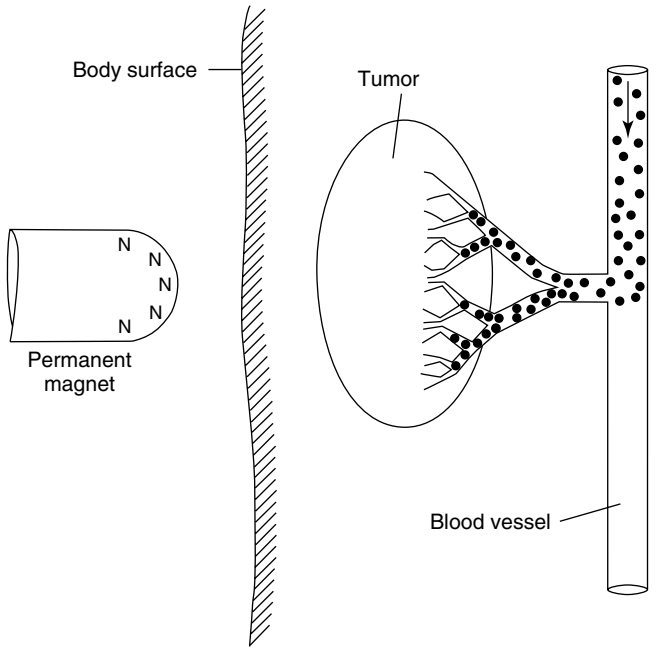

Figure 6. Principle of magnetic drug targeting. The magnetic carriers are administered into the vascular system of a patient and then 'pulled' toward the target organ, in this case a tumor. Blood flow within the capillary bed of the tumor is too weak to overcome the magnetic forces and magnetic particles get trapped within the target organ.

MPs to a target organ, and to hold them there for a controlled treatment period (Figure 6). Treatment can then be accomplished in a number of ways. These include slow release of a chemotherapeutic drug from the MPs, local irradiation from MPs containing radioactive β emitters, and locally induced hyperthermia from MPs in an alternating magnetic field.

In magnetic drug targeting, particle size is the most important parameter with respect to biodistribution, toxicity, magnetic responsiveness, and even drug release kinetics. On the one hand, smaller particles can reach a larger volume of the patient because they can enter smaller blood vessels. Particles with a diameter of less than 50 nm (see Figure 7a and b), especially with the help of magnetic forces, can even pass the fenestrations of capillary walls and, in this way, reach most of the cells in the human body. On the other hand, smaller particles experience a dramatically reduced magnetic force because the magnetic moment in a magnetic field gradient decreases with decreasing particle diameter (see equation (6)). As a result, the magnetic forces induced in superparamagnetic particles (smaller than about 50 nm) are not likely to overcome the Stokes drag and the collisions with red blood cells in the bloodstream (Grief and Richardson, 2005). These theoretical calculations have not been supported in practice. In particular, experimental studies have provided evidence that superparamagnetic particles in the bloodstream can be concentrated or prevented from clearance by magnetic forces. This seeming contradiction might be explained by an agglomeration tendency that MPs experience in a magnetic field with magnetic moments much larger than the ones of isolated units (see equation (6)). This phenomenon is illustrated by the clusters in Figure 7(c), which may disintegrate as soon as the field is switched off and can then pass through the narrow blood vessels of the vascular system.

The earliest experiments utilizing magnetic forces on MPs were carried out with particle sizes well above the superparamagnetic range. One of the earliest studies concerned a magnetic selection procedure of Kupffer cells (Rous and Beard, 1934). In this investigation, particles of milled γ-Fe_2O_3 (diameter $\leqslant 1\,\mu m$) were taken up by the Kupffer cells and could then be manipulated with a pair of horseshoe magnets.

The most common method of producing a magnetic field and field gradient capable of attracting MPs is through the use of permanent magnets or electromagnets. The strongest permanent magnets available today are rare-earth magnets made from NdFeB, a material that has only been known since 1983 (Kirchmayr, 1996). Small-sized NdFeB button magnets of the best grade with sizes of 1.0 cm diameter and 0.5 cm thickness are able to stop MPs up to 2.5 cm from their surface, although this is always dependent on the MPs as well. It has been reported that, using a larger, 2.5-cm-wide and 7.5-cm-thick NdFeB magnet, magnetic iron particles coated with carbon could be stopped within defined liver regions up to 14 cm away (Johnson *et al*., 2002). The strongest electromagnets are superconducting magnets that can be bought in easy-to-use electrically cooled configurations and produce 12 or more teslas from a barrel-sized, laboratory-compatible instrument (JASTEC: Japan Superconductor Technology) or 2.2 T from a tonguelike desktop system (Takeda *et al*., 2007) (Figure 8). A superconducting system from Stereotaxis Inc, St. Louis, MO, USA was approved by the U.S. FDA in 2003 and is now available to direct catheters with a small magnetic tip to otherwise difficult or even impossible-to-reach areas in the brain or heart. It is easy to imagine how useful such systems would be for drug delivery, (micro)surgical procedures, electrical interventions, or ablation catheter procedures. More recently, Stereotaxis developed a permanent magnet system termed *Niobe*^{TM} for the same applications (Ernst *et al*., 2004). Two outer permanent magnets align a third small magnet integrated in the tip of a mapping and ablation catheter along its magnetic field lines. By changing the orientation of the outer magnets, the orientation of the magnetic field lines also change, thereby allowing navigation of the ablation catheter. In combination with an automated advancer system, this novel technique is the first to allow for complete remote catheter ablation.

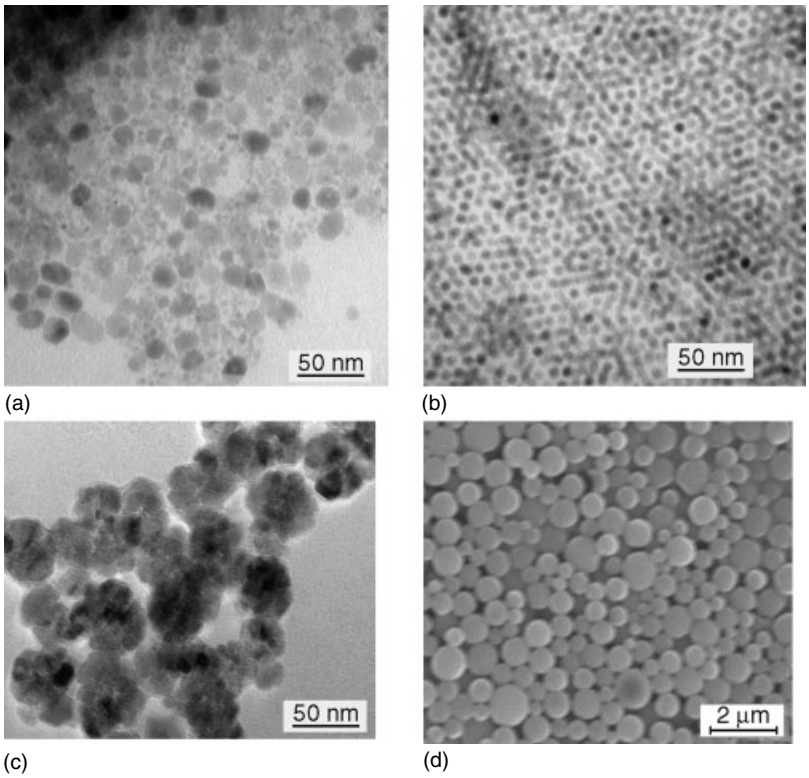

Figure 7. Transmission and scanning electron microscopy pictures of primary and composite magnetic particles. (a) Hydrophilic magnetite nanoparticles prepared by the Elmore method (Elmore, 1938). (b) Monosized oleic acid–coated lipophilic magnetite nanoparticles prepared by the iron pentacarbonyl decomposition method (Hyeon *et al*., 2001). (c) Clusters of iron oxide particles prepared by a wet chemical precipitation procedure and subsequent coating done with carboxymethyldextran. (Courtesy C. Oestreich, Institute of Ceramic Materials, Freiberg University of Mining and Technology.) (d) Magnetic biodegradable composite poly(lactide-*co*-glycolide) microspheres incorporating the magnetite particles shown in (a) (Zhao, Gagnon and Häfeli, 2007).

Two other methods can produce strong, local, and directed magnetic fields that can be used to accumulate MPs in a target organ. The first method consists in placing small magnets internally as unipolar probes next to the target organ, such as in a diseased intracerebral artery (Alksne, Fingerhut and Rand, 1966). The second method is to implant a ferromagnetic object, such as a seed, stent, wire, or needle, in the target area and then to place the patient in a strong external magnetic field (Iacob, Rotariu, Strachan and Häfeli, 2004). Magnetized magnetic meshes were able to accumulate large amounts of 2-µm or 370-nm particles, even at $5\,\mathrm{cm\,s^{-1}}$ flow rates, while nonmagnetized control wires attracted no particles at all (Yellen *et al*., 2005). Interestingly, the magnetic fields do not need to exceed 0.1 T according to the authors of this study. One disadvantage of both procedures, however, is their invasiveness, since a ferromagnetic element or magnet must first be placed inside the patient.

Although many magnetic drug delivery investigations were reported (see the following text), not much quantitative information is known about the targeting efficiency of the MPs. The reason for this is that most people are interested in the success of an attempted therapy and therefore generally are more interested in the biodistribution of the delivered drug than the carrier (MP) distribution. One of the few reported targeting efficiency studies used the old technique of radiolabeled MPs in combination with γ camera or single photon emission computed tomography (SPECT) imaging. A preliminary *in vivo* investigation tested the binding stability and magnetic targeting ability of ^{90}Y-labeled iron–carbon particles of sizes 1–5 µm (Yu *et al*., 2002). Eleven mCi of ^{90}Y-MP was administered intra-arterially into the hepatic artery of a swine. Blood samples taken following the administration showed that less than 3% of the total injected activity had escaped into the blood supply 30 min after the administration. A γ-camera image taken 24 h after the injection using the Bremsstrahlung emission associated with ^{90}Y qualitatively showed a single source of emission in the region of the liver where the ^{90}Y-MP had been targeted with a strong permanent magnet. Even 72 h after the injection, more than 85% of the injected activity was still present at the target location (unpublished data). In addition to these radioactive measurements, and histological

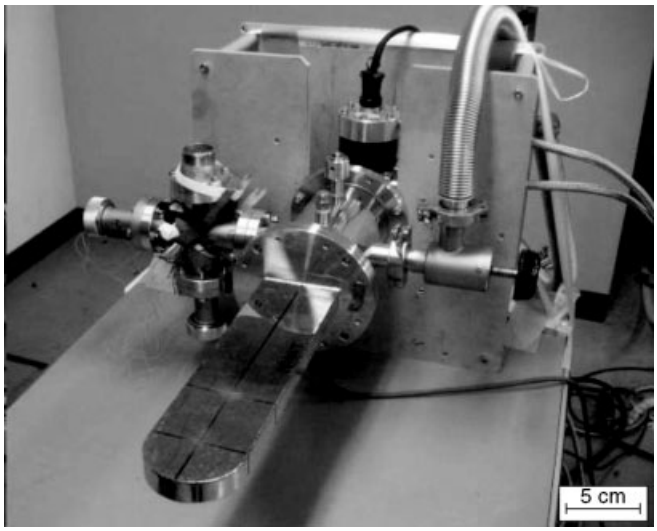

Figure 8. Tonguelike magnet system producing fields of 2.2 T.

methods and magnetic resonance imaging (MRI) for the detection of the MPs, which are at best semiquantitative, some efforts have been made in recent years to develop new and improved tools for quantitative *in vivo* measurements. These methods include magnetorelaxometric measurements (Eberbeck, Wiekhorst, Steinhoff and Trahms, 2006) and X-ray or neutron-spectroscopy measurements (Brunke *et al*., 2006). Both techniques are very promising, but have, to this point, been applied only to feasibility studies and not to complete magnetic targeting studies.

More studies are still needed to give information about the distribution of MPs *in vivo*. It would be especially useful if it was possible to simulate and predict magnetic targeting efficiency, once the MPs, magnet, and blood flow parameters are known. What is clear, however, is that there will always be some loss of the injected MPs into the blood circulation as compared to local application of a drug where there is none. The distribution of the drug-carrying MPs throughout the target organ, however, may be much better. Also, it has been shown that intra-arterial application of MPs is able to deliver much more of the drug to the target tissue than intravenous injection. Intra-arterial injection prevents the MPs from being filtered immediately by fixed macrophages in the liver and lungs.

3.3 Magnetic drug delivery systems (microspheres, nanospheres, liposomes)

The most commonly used magnetic drug delivery systems include magnetic microspheres (see Figure 7d), nanospheres, and liposomes filled with drugs or containing drugs bound to their surface. The MPs contained in these drug delivery systems are often grouped according to size. At the lower end, we have the ferrofluids, which are colloidal iron oxide solutions. Encapsulated MPs in the range of 10–500 nm are usually called *magnetic nanospheres* and any MPs of just below 1–100 µm are magnetic microspheres. Magnetic liposomes, which are phospholipid vesicles incorporating a magnetic compound, are also included when speaking about magnetic carriers. The materials for the preparation of MPs include both nonbiodegradable materials, such as ethyl cellulose and the synthetic polymers polymethylmethacrylates (PMMAs) and polystyrene, and biodegradable materials, such as albumin, phospholipids, starch, poly(lactic acid), dextran, polyalkylcyanoacrylates, and polyethylene imines (Schütt *et al*., 1997).

The amount and nature of the magnetic component incorporated into the MPs is an important material consideration. Today, materials with higher magnetic susceptibility and magnetization compared to the aforementioned iron oxides (Gupta and Gupta, 2005) are being investigated and developed to increase the magnetic response of MPs to an applied magnetic field further. Riffle at Virginia Tech in the United States and Bönnemann at the Max Planck Institute in Germany, for example, are independently and with different methods spearheading the development of oxidation-proof nanocobalt particles (Bönnemann *et al*., 2003; Riffle *et al.,* 2003). Similarly, passivated nanoiron is being developed by Materials Modifications Inc. in the United States (Williams and Kotha, 2003). The alloy Fe_3Co has also recently been prepared by Hütten at the University of Bielefeld in Germany in the form of highly uniform nanoparticles, with excellent size control between 1 and 11 nm (Hütten *et al*., 2005).

Smaller nanosized MPs containing up to a 100% of the magnetic material can be made with methods such as the decomposition of iron pentacarbonyl precursors. Typically, however, the MPs must be protected from agglomeration, oxidation, and further reactions, and coating materials such as detergents and longer-chain fatty acids are thus introduced or are already present during the synthesis.

Importantly, magnetic drug delivery systems follow the same rules as other pharmaceutical drug delivery devices. For example, magnetically delivering a chemotherapeutic drug to a tumor alone does not eradicate it. The drug must first be released from the particles in order to be efficacious. Furthermore, the particles have to follow the same strict rules regarding sterility, nonimmunogenicity, nontoxicity, and biocompatibility as any other invasive drug delivery systems.

MPs consisting of iron, nickel, or cobalt can be cytotoxic owing to the production of positively charged metal ions. Magnetite, maghemite, and superparamagnetic iron oxide nanoparticles coated and stabilized with hydrophilic polymers, however, have been found to be quite thermodynamically stable under physiological conditions and

not to exert obvious toxic effects. Pharmacokinetic studies of small magnetite nanoparticles destined for MRI (Weissleder *et al*., 1989) have shown that the magnetite nanoparticles are taken up by the cells of the RES and are transported intracellularly to lysosomes, where they slowly oxidize at low pH and are then recycled by the body (Lawaczeck *et al*., 1997). Within 20–40 days, up to 60% of the iron is recovered in red blood cells, as determined using radiolabeled ^{59}Fe. On the basis of these studies, magnetic nanoparticles have been approved as MRI contrast agents.

Recent discussions have centered on toxic effects of (magnetic) nanoparticles in humans after inhalation. Rodent models have shown that the potential problematic effects of such particles include the induction of asthma, inflammation, and even cancer (Nel, Xia, Madler and Li, 2006). Some of these effects might be due the fact that particles smaller than 100 nm are not exhaled, but are almost completely retained in the alveoli (Kreyling, Semmler and Möller, 2006). For this reason, acute effects can rapidly turn into chronic effects. Although many effects seen in rodents do not develop in humans, it is still prudent to carefully monitor all health effects from nanoparticles.

3.4 Magnetic drug delivery systems for chemotherapy

Many tumors, especially those of pancreas, liver, lung, stomach, brain, and head and neck, are untreatable because of inaccessibility, inoperability, lymph node infiltration, and the unacceptably high risk of toxicity to nearby organs. Magnetic drug delivery is able to concentrate the drugs in a tumor once it has been outlined by imaging methods such as MRI and computerized, single photon emission, and positron emission tomography. For magnetic drug delivery, the tumor must be accessible through the arterial system and have a good blood supply. The magnetic delivery method promises longer survival, fewer side effects, and shorter and less toxic treatments.

The era of drug-filled microspheres started with the use of albumin MPs filled with the anticancer drug doxorubicin (adriamycin) (Widder, Senyei and Ranney, 1979). As is typical for many other MPs, maximum magnetite contents of up to 50 wt% were reported. The era of albumin particles was followed by that of MPs made from many different matrix materials incorporating or adsorbing just about any chemotherapeutic drugs imaginable. The drugs tested *in vitro* or *in vivo* included mitomycin C (Kato *et al*., 1980, 1981), camptothecin, ara-C, tumor necrosis factor (TNF-α), paclitaxel, mitoxanthrone, 5-fluorouracil (5-FU), and dactinomycin, just to name a few (Häfeli, 2006b).

The application of drug-filled MPs by intravenous injection is not ideal, because it results in substantial dilution of MPs throughout the body and in the successive MP uptake by the RES, particularly in the spleen, liver, and lungs. As a result, typically only a threefold increase in MP concentration is reached in the target location with the attached magnet compared to the contralateral side of the body with no magnet as was shown, for example, with dactinomycin-filled magnetic nanoparticles (Ibrahim, Couvreur, Roland and Speiser, 1983). Approximately twofold enhancement between the effect of activated and non-activated electromagnets was seen when another group targeted gliomas in rats (Pulfer and Gallo, 1998; Pulfer, Ciccotto and Gallo, 1999). Even the intravenous injection of MPs very close to the tumor only marginally increases MP uptake, as shown in one of the first well-controlled patient trials with 14 patients using the drug 4′-epidoxorubicin adsorbed onto MPs with an anhydroglucose coating (Lübbe *et al*., 1996; Lübbe, Alexiou and Bergemann, 2001). Most of the drug was released over 30 min after injection, and the system was shown to be nontoxic. However, it was also not very effective, probably owing to the small particle size (about 100 nm) and the not so strong magnets used.

A better way to inject drug-filled MPs and achieve more effective magnetic targeting is intra-arterial injection proximal to the tumor. The first animal trials using this injection technique involved the delivery of MPs to a distinct area of a rat's tail (Widder, Morris, Howard and Senyei, 1981; Widder *et al*., 1983). It resulted in the delivery of 200 times more drug to the target area compared to what could be achieved through intravenous application of the same amount of free drug (Senyei, Reich, Gonczy and Widder, 1981). The company FeRx further improved on this method by employing MPs made of carbon-coated pure iron with a diameter of 1 to 5 µm. Their MPs are the most magnetic particles ever used *in vivo*. The drug doxorubicin was adsorbed to the carbon coating and then slowly released at the tumor site, as seen in a clinical phase I trial performed between 2001 and 2004 in patients with primary liver cancer (hepatocellular carcinoma or HCC) (Goodwin, 2000; Johnson *et al*., 2002). X-ray and magnetic resonance images such as those in Figure 9 confirmed excellent particle retention in the liver tumors upon employing an 8-cm-long and 2.5-cm-diameter NdFeB magnet.

Only one other clinical trial has been described in the literature. This trial used ferrocarbon particles of about 100 nm diameter that within minutes adsorbed about 2 wt% of the anticancer drug carminomycine (Kuznetsov *et al*., 1997). The authors report that more than a hundred patients have received this treatment in different Russian hospitals since 1990. Unfortunately, the clinical results were not reported in

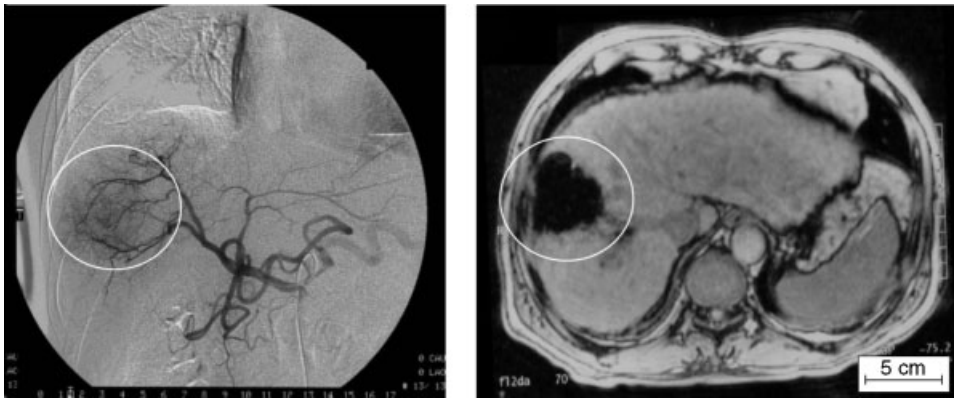

Figure 9. Postdosing angiogram (a) and MRI (b) after magnetic targeting with doxorubicin-loaded MTC by FeRx Inc.

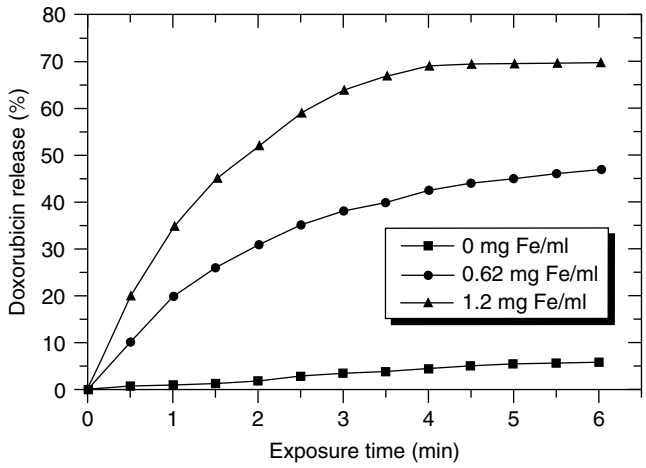

Figure 10. Dependence of doxorubicin release from magnetoliposomes with various concentrations of ferrocolloid. The results are mean values from four independent measurements. (Reprinted with permission M. Babincova *et al*., copyright 2002, Elsevier.)

a very detailed manner and the definitive treatment outcome is still unclear.

To date magnetic liposomes sized like nanoparticles have yet to be used clinically. There are, however, ongoing animal experiments using magnetoliposomes that incorporate paclitaxel (Zhang *et al*., 2005). Although the incorporation of large amounts of magnetite into liposomes is more difficult than into nanoparticles, up to 25 wt% of magnetite has been recently enclosed into dipalmitoylphosphatidylcholine liposomes that also contained crystal violet as a model drug (Koneracka *et al*., 2005). Another group made similar magnetoliposomes, without any drugs, to be used for hyperthermia treatment (Gonzales and Krishnan, 2005).

Most drug release from MPs occurs passively, by desorption from and diffusion out of the MP matrix. The main driving forces are pH, osmolarity (of the blood), and concentration differences between the MPs and the blood/tissue. One group investigated the active release of chemotherapeutic drugs upon local heating using an alternating current (AC) magnetic field with a frequency of $\sim$1 MHz (Babincova *et al*., 2002). Their doxorubicin magnetoliposomes made with 8-nm magnetic oxide particles released the drug upon irradiation. Depending on the ferrocolloid concentration in the magnetoliposomes and the length of the exposure to the alternating magnetic field, significant amounts of doxorubicin were released (see Figure 10). The release of drug seemed to be owing to local heating of the liposomal membrane, which has a phase transition temperature of 42 $^{\circ}$C. Similar results have been reported *in vivo* (Viroonchatapan *et al*., 1998). In particular, upon placement in an alternating electromagnetic field, the tumor temperature could be kept at 42 $^{\circ}$C despite blood flow and the entrapped 5-FU was almost completely released within the next hour.

Overall, as already described in an excellent review (Gupta and Hung, 1994), different chemotherapeutic drugs have already been combined with MPs made from different matrices, and many new ones will likely become available in the future. Magnetic targeting of solid animal tumors has been shown to enhance the tumor drug concentration two to several hundred times. It is hoped that the use of more magnetic and more uniform MPs will further extend the indication of such particles to lung, pancreas, and breast cancer and move them into clinical trials.

3.5 Magnetic drug delivery systems for radiotherapy

The biggest challenge in the use of radioactive isotopes for the killing of cancer cells is the delivery of a sufficiently high radiation dose without harming the surrounding tissue. MPs that incorporate radioisotopes either in the matrix or

bound to the surface can be used to address this challenge (Häfeli, 2001a). The advantage of this method over the external beam therapy typically used in radiation oncology departments is that the local dose can be very high, resulting in improved tumor cell eradication, and that it can be given in one application rather than in the standard six weeks of daily radiotherapy. Different radioisotopes can be used to treat different treatment ranges (Häfeli, 2001b). The β emitter ^{90}Y, for example, will irradiate up to a range of 12 mm in tissue while ^{131}I will irradiate only up to 2.4 mm. Unlike chemotherapeutic drugs, the radioactivity is not released. Instead, the radioactive MPs are delivered to and held at the target site and from there irradiate the area within the specific treatment range of the isotope. Once the MPs are no longer radioactive, they ideally biodegrade, as is the case with poly(lactic acid) or gelatin microspheres.

Initial experiments in mice have shown that intraperitoneally injected radioactive poly(lactic acid) based MPs could be concentrated near a subcutaneous tumor in the belly area above which a small magnet had been attached (Häfeli *et al*., 1997). The dose-dependent irradiation from the β emitter ^{90}Y-containing MPs resulted in the complete disappearance of more than half of the tumors. To improve the magnetic targeting efficiency, magnetic targeted carriers (MTCs; from FeRx), which are more magnetically responsive iron–carbon particles, have been recently radiolabeled with isotopes such as ^{188}Re (Häfeli, Pauer, Failing and Tapolsky, 2001), ^{111}In (Häfeli, 2004), ^{90}Y, and ^{125}I (Yu *et al*., 2002), but have yet to be tested.

Enhancement of tumor cell kill without harming the patient can also be achieved by combining drug delivery with internally given radioactive isotopes or external radiation. Gelatin MPs with metronidazole, an efficient sensitizer of hypoxic mammalian cells to the effects of radiation, have been prepared and shown to release the drug in a defined way (Leucuta, 1986). Such a slow drug release over a few hours sensitizes even normally radioresistant cancer cells, lowers the overall radiation dose necessary for successful treatment, and prevents side effects.

Internal radiotherapy may soon be feasible not only with β and γ emitters, but also with short-range auger emitters given that tat peptides have recently been shown to penetrate cell membranes and shuttle MPs inside cells (Lewin *et al*., 2000). For this purpose, MPs must be able to penetrate the cell surface efficiently. Tat peptide, a positively charged peptide, has been shown to induce the internalization of therapeutic agents such as radioactively complexed ^{99m}Tc and ^{188}Re (Polyakov *et al*., 2000) and superparamagnetic iron oxides known as *tat-CLIO* (tat-cross-linked iron oxides) (Wunderbaldinger, Josephson and Weissleder, 2002). Weissleder's group, who developed the tat-CLIO, was able to accumulate the tat-CLIO intracellularly in a highly specific manner (Wunderbaldinger, Josephson and Weissleder, 2002).

Overall, the advantages of local radiation treatment using magnetically delivered MPs are similar to those of magnetically delivered chemotherapy. In addition, there is no resistance formation, the doses can be planned in advance using treatment software, the treatment range and therefore also the range of expected toxicity is well known, and the targeting success can be imaged and possibly altered with commonly used nuclear medicine techniques.

3.6 Other magnetic drug targeting applications

Magnetic drug delivery can be used to deliver not only chemotherapeutic, radioactive, peptide, and hyperthermia drugs, but also antiinfective, blood-clot-dissolving, anti-inflammatory, antiarthritic, photodynamic therapy, and paralysis-inducing drugs. The magnetic delivery of genes, another successful example, has already been reviewed in Section 2 of this chapter.

One of the most successful examples in this group of drug targeting applications is the preparation of magnetite coated with the blood-clot-dissolving drug urokinase (Inada *et al*., 1987) or streptokinase (Torchilin *et al*., 1988), which was used to dissolve surgically induced thrombi in the carotid arteries of a dog (Torchilin *et al*., 1988). The control side received no special treatment while the experimental side had a magnet attached above it. One hour after the procedure, streptokinase bound to the surface of MPs was injected into the animal at a dose 10 times lower than the normal, non-MP-bound streptokinase dose. The side without the magnet completely occluded within 4 h, while the side with the magnet returned to initial blood flow after about 30 min and appeared completely open at histological examination (Figure 11).

The magnetic drug delivery potential is enormous, especially for highly potent – and thus also potentially very toxic – drugs. Many organs and systems in the body can be targeted. For most applications, it is obvious that systemic effects can be minimized or completely eliminated while the sought-after effect is enhanced. A good example is the magnetic delivery of the curare-like drug diadonium to the limbs of cats (Kharkevich, Alyautdin and Filippov, 1989), during which their limbs became paralyzed with only slight respiratory depression.

3.7 Magnetic particles that exert therapeutic effects by embolization

Under the influence of a magnetic field, MPs align in chains and eventually agglomerate. Depending on particle size and shape, this can lead to embolization (clogging) of the blood

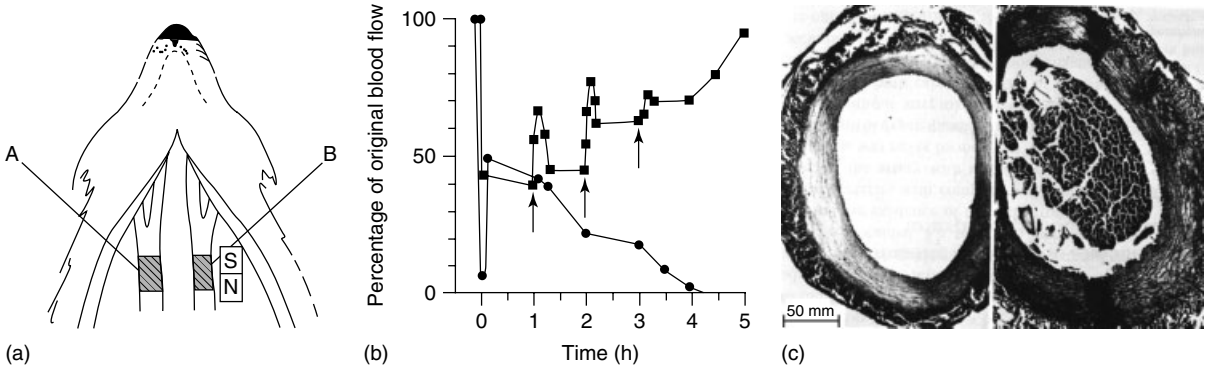

Figure 11. Magnetically driven thrombolysis with streptokinase-coated magnetite particles is possible by placing a magnet close to the area of the vascular flap in the carotid artery (a). Blood flow resumed in the targeted artery within 4 h, while the nontargeted carotid artery was completely clogged (b and c) (Torchilin *et al*., 1988).

vessels and especially of the small capillaries 7–10 µm in diameter. This accumulation of particles alone can be used to starve the target tissue of oxygen, producing hypoxia and inducing necrosis. The first embolization applications in the 1960s and 1970s included the occlusion of cerebral and renal aneurysms (Alksne, Fingerhut and Rand, 1966; Hilal, Michelsen, Driller and Leonard, 1974; Roth, 1969) and were followed by the occlusion of the feeding vessels of carcinomas. Rand *et al*. described the technique of injecting a mixture of liquid silicone and microspheres of carbonyl iron into the intraparenchymal vascular bed followed by intravascular vulcanization without heat transfer from the outside (Mosso and Rand, 1973). The ferrosilicone was retained in the required position by a strong magnetic field generated by a superconducting coil. Another successful example of cancer embolization therapy is the magnetic accumulation of a so-called 10–30-µm-diameter iron sponge in viscous solution in rabbit tumors (Sako *et al*., 1982).

To maximize efficacy, embolization therapy is generally used in combination with a second treatment approach such as radiotherapy, chemotherapy, or hyperthermia. This was shown in the 1970s when Rand *et al*. continued their above-described investigations (Snyder and Rand, 1975) with needle-shaped γ-Fe_2O_3 particles and introduced additional radiofrequency (RF) heating to more than 55 °C on the renal surface of rabbits (Rand, Snyder, Elliott and Snow, 1976; Rand, Snow, Elliott and Snyder, 1981; Rand, Snow and Brown, 1982). In this way, total coagulation necrosis of a renal cancer model was achieved, possibly more as a result of the hyperthermic treatment than because of the occlusion. The treated animals survived the procedures and the exposure to both magnetic fields and ferromagnetic compounds without evidence of ill effects. The combination of embolization and hyperthermia and its medical use is still being pursued (Mitsumori *et al*., 1994, 1996; Moroz, Jones and Gray, 2002).

3.8 Summary

Owing to space constraints, this section about the therapeutic applications of magnetic carriers could only cover a limited sampling of the literature. The interested reader is directed to a much more complete and in-depth review of the field (Häfeli, 2006b). Magnetic drug delivery covers a wide area of applications, with a lot of research currently being performed worldwide. None of the applications, with the exception of several magnetic hyperthermia trials (Gneveckow *et al*., 2005), have reached the clinical trial stage yet. Preclinical animal research, however, is being performed in the areas of magnetic gene delivery, tumor targeting, rheumatoid arthritis treatment, and blood detoxification. This ongoing work, in combination with enormous advances in the field of magnetic nanoparticle synthesis and analytical characterization methods, is expected to lead to new and successful clinical uses of magnetic carriers.

4 MAGNETIC PARTICLE HYPERTHERMIA

4.1 Principles of magnetic particle hyperthermia

The application of heat as a traditional healing method has been known for a long time. Soon after the discovery that the metabolism of tumor cells is more susceptible to high temperatures than that of normal cells, views on how hyperthermia could be used for tumor therapy emerged. Besides whole body hyperthermia where the systemic temperature has to be carefully controlled to, for example, 41.8 °C (Robins *et al*., 1997), there is a spectrum of ways of local intracorporal heat generation using focused microwave radiation, capacitive or inductive coupling of RF fields, implanted electrodes, focused ultrasound, or lasers. For the clinical state of the

art of hyperthermia in oncology, see the review given by Falk and Issels (2001). As an alternative therapy, magnetic particle hyperthermia (MPH) is a method where MPs are deposited in tumor tissue with subsequent heating by means of an external alternating magnetic field. For biomedical applications, the vast number of known magnetic materials is strongly restricted by the demand of biocompatibility (e.g., nontoxicity, sufficient chemical stability in bioenvironment, appropriate circulation time in blood, and finally, harmless biodegradability). Although attempts to use metallic iron particles, spinel ferrites, as well as special magnetic alloys for MPH have been made, the majority of investigations is focused on the magnetic iron oxides Fe_3O_4 (magnetite) and γ-Fe_2O_3 (maghemite). These materials are well tolerated by the human body. At present, a variety of approved types of magnetic iron oxide particles for specific contrast enhancement in nuclear MRI are available on the market (cf. Section 5). However, these relatively small, superparamagnetic particles are not well suited for MPH owing to insufficient heating power. Besides localized heat generation, the application of magnetic nanoparticles offers the possibility of a self-limitation of the temperature enhancement by using a magnetic material with suitable Curie temperature (e. g., Rand, Snow, Elliott, Haskins, 1985).

Since there is no strict borderline between tolerable and mortal temperatures, both on the systemic as well as the cellular level, there is a range of temperature elevation considered to be therapeutically useful. With increasing temperature, different mechanisms of cell damaging occur and accordingly two therapy modalities were conceived: Treatments at temperatures of 42–45 °C for up to few hours – commonly denoted as *hyperthermia* – need to be combined with other assisting toxic agents (mostly irradiation or chemotherapy) for reliable damage of tumor cells. In contrast, thermoablation aims at the thermal killing of all tumor cells by applying temperatures in excess of at least 50 °C in the tumor region for exposure times of at least a few minutes. Though these short treatment times and reliable tumor damage seem advantageous, there is the risk of critical systemic side effects such as a shock syndrome due to sudden release of large amounts of necrotic tumor material and major inflammatory response (Moroz, Jones and Gray, 2002).

In addition to the therapeutically useful tumor heating effect of MPs, the alternating magnetic field can also cause an unwanted nonselective heating of healthy tissue due to the generation of eddy currents. According to the induction law, the latter is proportional to the square of $(H{\cdot}f{\cdot}D)$, where H is field amplitude, f is the frequency, and D is the induced current loop diameter. The induction heating of iron oxide nanoparticles is practically negligible, but with the specific electrical conductivity of tissue ($0.6\,\Omega^{-1}\,m^{-1}$) the critical current density for irreversible cell damaging (in the order of $20\,mA\,cm^{-2}$, e.g., Siegenthaler, 1994) may be reached in macroscopic loops of the patient's body. Experimentally, Brezovich (1988) found for a loop diameter of about 30 cm that a *test person had a sensation of warmth, but was able to withstand the treatment for more than one hour without major discomfort* if the product $H{\cdot}f$ was below $4.85 \times 10^8\,A\,m^{-1}\,s^{-1}$. Depending on the diameter of the exposed body region and the seriousness of the illness, this critical product may be exceeded. For instance, for the first commercially developed equipment for treatment of human patients, a frequency of 100 kHz and a field amplitude up to $18\,kA\,m^{-1}$ was reported (Gneveckow *et al*., 2004).

4.2 Loss processes in magnetic particle systems

The generation of heat by magnetic substances in an external alternating magnetic field may be caused by several physical loss processes. The main mechanism of heat production with magnetic nanoparticles is associated with hysteresis occurring during reversal of the magnetization. With decreasing particle size, the energy barriers for magnetization reversal decrease and hysteresis is increasingly influenced by thermal fluctuations. In addition to hysteresis, in fluid suspensions of MPs viscous losses may arise owing to particle rotations induced by the external alternating magnetic field. Particles can be immobilized by adhesion, for example, to cell membranes and tissue surfaces, or by uptake by fibroblasts. Free rotations are thus suppressed, while the still possible oscillations lead to complex loss contributions. In comparison to magnetic losses, eddy current induced heating of small MPs is negligibly small. The often used term *inductive heating* in biomedical literature for MP heating is thus misleading.

4.2.1 Hysteresis losses

Hysteresis losses are represented in a well-known manner by the area of hysteresis loops (e.g., Bertotti, 1998). Below a critical particle size, domain walls do not exist and the simplest process of magnetization reversal is the uniform mode (Stoner and Wohlfarth, 1948). In this case, for an ensemble of randomly oriented, noninteracting, ellipsoidal, uniaxial single-domain particles, hysteresis loss energy density is given by twice the anisotropy energy density K. It may be enhanced by a factor of 4 if particle axes are aligned with the external field. Besides the simple model of uniform magnetization reversal, there are different theoretical models dealing with more complicated magnetization distributions (e.g., curling, buckling, fanning; see, e.g., Aharoni, 1996; Hubert and Schäfer, 1998), which are described in terms of the micromagnetic theory (Kronmüller and Fähnle, 2003). For cubic magnetite crystals, Butler and Banerjee (1975)

derived from theoretical estimations an upper limit of about 80 nm for the single-domain size range, which increases considerably with tetragonal particle elongation. The same order of magnitude is obtained from micromagnetic calculations (Fabian *et al*., 1996) considering more sophisticated magnetization patterns like the so-called flower and vortex states. For further recent theoretical and experimental results from literature, see **Magnetization Configurations and Reversal in Small Magnetic Elements, Volume 2**. Experimentally, for magnetite crystals in the mean diameter range above about 50 nm, the coercivity and remanence was found to decrease with increasing particle size d according to an empirically well established $d^{-0.6}$ power law (Heider, Dunlop and Sugiura, 1987), which implies a decrease of hysteresis losses in the multidomain size range. A strong decrease in coercivity with increasing particle size in the range 30–100 nm measured for maghemite was interpreted by Eagle and Mallinson (1967) as an indication for a nonuniform reversal mode. Since, on the other hand, magnetite particles with size below about 25 nm become superparamagnetic (see the following text), a maximum of hysteresis losses may be expected for single-domain iron oxide particles with a mean diameter of close to 30 nm.

However, for utilization of the full hysteresis loop for heat generation, alternating field amplitudes well above the coercivity field are needed, which imposes strong technical demands on the magnetic field generator. For instance, with a 15 kW 400 kHz AC generator in a coil for treatment of breast cancer (Hilger, Hergt and Kaiser, 2005) using field amplitudes of not more than 10 kA m^{-1}, one is restricted to minor loops. The large coercivities of acicular maghemite particles (typically 50 kA m^{-1}) used for magnetic recording are rarely of value for medical heating problems. In general, for single-domain particles with nearly rectangular hysteresis loop, one may expect only minor values of hysteresis losses for field amplitudes below the effective anisotropy field. By comparing different types of MPs with respect to their suitability for hyperthermia (Hergt *et al*., 1998), it was shown that hysteresis losses of different types of magnetite particles may differ by orders of magnitude in the range 1–10 kA m^{-1} of field amplitudes owing to differences of particle size, shape, and microstructure. As an illustration, Figure 12 shows the dependence of hysteresis loss on field amplitude for different classes of magnetic iron oxide particles (e.g., a typical sample m6.3 prepared by chemical precipitation, a sample BASF1 of acicular particles for recording applications, and magnetosomes synthesized by bacteria) in comparison with the theoretical curve for a Stoner–Wohlfarth (SW) system. Though the mean particle diameters of about 30 nm – as determined by transmission electron microscopy – for all samples are in the single-domain range, there are considerable deviations between the experimental results of different particle types

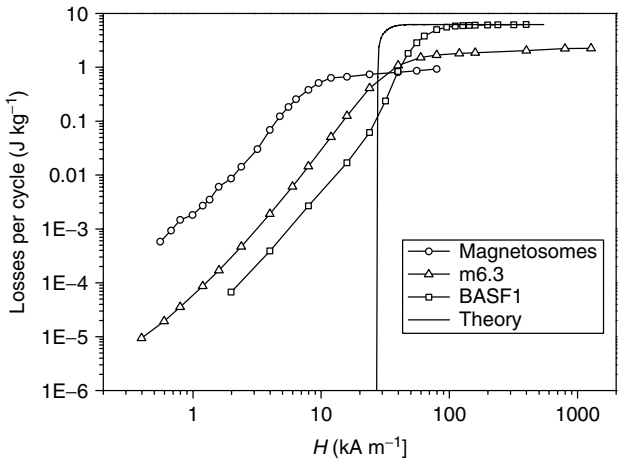

Figure 12. Dependence of hysteresis losses per cycle on field amplitude for different types of magnetic nanoparticles (a chemically precipitated sample m6.3 (Dutz *et al*., 2007), bacterial magnetosomes (Hergt *et al*., 2005), and a sample of commercial magnetic recording particles BASF1) in comparison with the theoretical curve for randomly oriented Stoner–Wohlfarth (SW) particles. The SW coercivity is adjusted to that of BASF1. (Reprinted with permission Hergt R. Hiergeist *et al*., copyright 2005, Elsevier.)

and SW theory. In particular, experimental results for low field amplitudes generally show a third-order power law for the amplitude dependence of hysteresis losses, which is known as the so-called *Rayleigh law* for multidomain objects if the motion of domain walls is hindered by pinning centers (e.g., Kronmüller and Fähnle, 2003). Many magnetite and maghemite powders in a broad size range of about 10 nm up to 100 nm were investigated (Dutz *et al*., 2007) but in no case the high specific losses at low amplitudes of bacterial iron oxide magnetosomes shown in Figure 12 were met.

4.2.2 Thermal relaxation effects

With decreasing particle volume V, the energy barriers impeding the reversal of the magnetic moments decrease and the probability of spontaneous jumps of the magnetization due to thermal activation processes increases. As a consequence, loss energy per cycle derived from hysteresis loops becomes smaller than calorimetrically measured loss data if the characteristic time of measurement τ_m is larger than the relaxation time of the particle system. For the simple case of two stable states separated by a barrier that is proportional to the anisotropy energy KV, the so-called Neél relaxation time of the system is determined by the ratio of KV to the thermal energy kT (Néel, 1949):

$$\tau_N = \tau_o \exp[KV/(kT)] \quad (\tau_o \sim 10^{-9}\text{s}) \tag{7}$$

A critical particle volume V_c may be defined by $\tau_N(V_c) = \tau_m$. For a measuring frequency of 300 kHz and a magnetic anisotropy energy density of 10^4 J m^{-3} (for magnetite

particles of ellipsoidal shape with an aspect ratio of 1.4), the critical diameter is about 20 nm. Below the critical size, the relaxation effects cause remanence, coercivity as well as hysteresis losses to vanish. This transition to the so-called superparamagnetism (for details see **Superparamagnetic Particles, Volume 4**) occurs in a narrow size range. The frequency dependence of the relaxation of the particle system may be well investigated by measuring spectra of the complex susceptibility, the imaginary part $\chi''(f)$ of which is related to the loss power density P according to (e.g., Landau and Lifshitz, 1960)

$$P(f, H) = \mu_o \pi \chi''(f) H^2 f \tag{8}$$

where $\chi''(f)$ may commonly be described by the well-known expression (see e.g., Delaunay, Neveu, Noyel and Monin, 1995)

$$\chi''(f) = \chi_o \phi/(1+\phi^2), \quad \phi = f\tau_N,$$
$$\chi_o = \mu_o M_S^2 V/(kT) (M_S : \text{saturation magnetization}) \tag{9}$$

According to these equations, at low frequencies ($\phi \ll 1$), that is, in the superparamagnetic regime, losses increase with the square of frequency while for $\phi \gg 1$ losses approach a frequency-independent saturation value $P = \mu_o \pi H^2 (\chi_o/\tau)$. At the transition between these two regimes, the spectrum of the imaginary part of the susceptibility has a peak that is related via equation (7) to the anisotropy energy KV. The very strong size dependence of the relaxation time according to this equation leads to a very sharp maximum of the loss power density in dependence on particle size (Hergt *et al*., 1998; Hergt, Hiergeist, Hilger and Kaiser, 2002). Accordingly, a remarkable output of heating power occurs only for particle systems with narrow size (and anisotropy) distribution. The effect of size distribution on loss power density was elucidated theoretically by Rosensweig (2002).

In addition to Neél relaxation, which is related to the reversal of magnetic moments inside the particles, a second relaxation path is possible in liquid suspensions: the so-called Brownian relaxation is due to particle reorientation, which becomes essential if the magnetic moment direction is strongly coupled to the particle itself, for example, by a large value of the magnetic anisotropy, combined with easy particle rotation due to a low viscosity η of the suspension liquid. For spherical particles with the hydrodynamic radius r_h (which due to, e.g., particle coating may be essentially larger than the radius of the MP core), the relaxation time is given by

$$\tau_B = 4\pi\eta r_h^3/(kT) \tag{10}$$

which was first derived by Debye (1929) for rotational polarization of molecules. The loss power density for Brown relaxation is given by introducing equation (10) instead of equation (7) into equations (9) and (8). In the general case, if both Néel and Brown relaxation are present, an effective relaxation time may be used according to

$$\frac{1}{\tau_{\text{eff}}} = \frac{1}{\tau_N} + \frac{1}{\tau_B} \tag{11}$$

A general treatment of the relaxation in ferrofluids based on a Fokker–Planck equation was given by Shliomis and Stepanov (1994).

The role of Brown relaxation may be estimated from the measured susceptibility spectra shown in Figure 13 (Hergt *et al*., 2004a). By comparing the experimental data points measured for the fluid suspension with the data of the same particles immobilized in gel, the effect of Brown relaxation becomes clear. The low frequency peak of χ'' for the liquid suspension represents Brown losses. It has vanished after immobilization of the particles in gel. Consequently, a considerable reduction of specific heating power may be expected when particles circulating in blood adhere to tumor cells or enter a cell by (typically) endocytosis. However, the results of Figure 13 show that this detrimental effect may be avoided by choosing a suitable frequency of the external magnetic field well above the Brown peak. The experimental data points may be satisfyingly approximated (full and dashed line) by combining equations (7–11) with the experimental size distribution determined by electron microscopy (for details see Hergt *et al*., 2004a). The loss power density calculated by equation (8) is well confirmed by calorimetric measurements, which give a specific loss power (SLP) of 600 W per gram maghemite in a field of 400 kHz and 11 kA m^{-1}. There, the loss power density given in (W cm^{-3}) is related to the measured SLP (W g^{-1}) by the mass density $\rho = 4.8$ g cm^{-3} of maghemite. In medical literature, the SLP is often denoted as *specific absorption rate* (SAR).

4.2.3 *Viscous losses*

Losses related to viscous friction of rotating MPs in a liquid suspension are not restricted to the above case of superparamagnetic particles. In general, a rotating magnetic field H exerts a torque moment $T = \mu_o M_R H V$ onto a particle, which may be regarded as a permanent magnet (M_R means its remanent magnetization) rotating in a liquid of viscosity η. In the steady state, the viscous drag in the liquid $12\pi\eta V f$ is counteracted by the magnetic torque T and the loss energy per cycle is simply given by $2\pi T$. In steady state, the minimum field amplitude H needed to sustain stationary rotation is related to the frequency according to the balance

$$12\pi\eta f = \mu_o M_R H \tag{12}$$

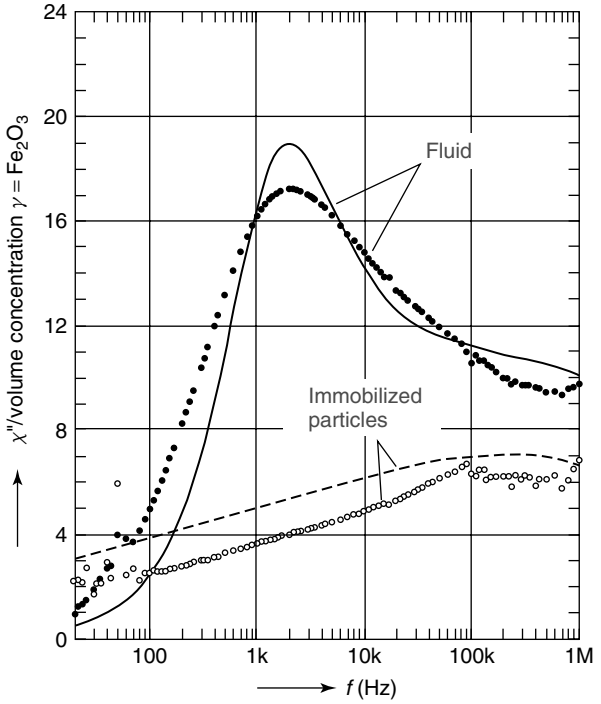

Figure 13. Imaginary part of the specific susceptibility as a function of frequency. Experimental results of an aqueous maghemite ferrofluid and of the same particles immobilized in gel are plotted (dots) in comparison with calculated spectra (full and dashed line). (Reprinted with permission Hergt R. Hiergeist *et al*., copyright 2004, Elsevier.)

For example, for an aqueous suspension (viscosity $\eta = 10^{-3}$ Pa·s) of magnetite ($M_R \approx 2.3 \times 10^5$ A m^{-1}), the minimum necessary field is 10 kA m^{-1} at a frequency of 70 kHz. For the latter AC-field parameters, the SLP given by $24\pi^2\eta f^2/\rho$ is about 240 W g^{-1}.

The effect of viscous losses was clearly demonstrated in experiments with relatively large (some 100 nm) crushed magnetite particles suspended in aqueous sol containing commercial gelatin, which is stiff below about 30 °C and a liquid at temperatures higher than 35 °C (Hiergeist *et al*., 1999). On heating above the melting point, the SLP increases by nearly an order of magnitude up to 200 W g^{-1} at a field amplitude of 6.5 kA m^{-1} and a frequency of 410 kHz.

4.3 Physical limitations of magnetic particle hyperthermia

The amount of nanoparticles necessary to increase the tissue temperature by MPH depends strongly on the SLP of the applied nanoparticles. In particular, for systemic delivery of nanoparticles (in contrast to local intratumorally injection), for instance, by means of antibody targeting (e.g., Suzuki, Shinkai, Kamihira and Kobayashi, 1995), the expected target concentration is very low (smaller than 1 mg of magnetite per cm^3 of tumor tissue) and, consequently, SLP must be rather high. For a quantitative estimation of the demand of SLP, one has to consider that the intratumoral temperature elevation is a result of the balance of two competing processes: Heat generation within magnetic nanoparticles is counteracted by heat depletion into surrounding tissue due to blood perfusion and heat conduction. In general, this needs the consideration of the so-called bioheat equation (e.g., Nyborg, 1988). However, if there are no large vessels in the immediate neighborhood of the tumor, the problem reduces to the solution of the heat conductivity equation (Andrä *et al*., 1999). As a result, in nearly steady state, for an approximately spherical tumor of radius r one gets a correlation between the size of the particle containing volume (i.e., the tumor size), the particle concentration c within it, the temperature elevation ΔT, and the SLP:

$$\Delta T = \frac{SLP \cdot c \cdot r^2}{(3\lambda)} \tag{13}$$

where λ is the thermal conductivity of body tissue, which is similar to that of water. As an important result, the demand of SLP increases with decreasing tumor size according to an inverse power law r^{-2}. Considering, for instance, thermoablation ($\Delta T = 15$ K) using a typical ferrofluid ($SLP < 100$ W g^{-1} of iron oxide) in tissue concentrations of about 10 mg cm^{-3} (provided by intratumoral injection), it follows from equation (13) that the diameter of the heated tissue region must not be smaller than 1 cm even if the tumor should be considerably smaller. In the case of antibody targeting only a low concentration of magnetic material may be achieved in the tumor region and a reasonable temperature elevation may be expected only for relatively large tumors (for details see Hergt, Hiergeist, Hilger and Kaiser, 2002; Hergt and Andrä, 2006). A volume reduction would demand a considerable increase of SLP according to equation (13). In particular, a significant temperature increase for isolated tumor cells that take up MPs cannot be expected. As stated by Rabin (2002), thermal effects on the cellular level are negligible as far as there is no macroscopic heating of cells within the tissue. Insofar, there is no reason to differentiate extracellular macroscopic heating and 'intracellular hyperthermia', which was claimed to be a particularly effective way for damaging tumor cells by some authors (e.g., Bacri *et al*., 1997; Jordan *et al*., 1999).

It should be pointed out that the scenario discussed is 'best case'. In practice, tumor shape deviates considerably from being spherical, and a homogeneous filling of tumor tissue by MPs will rarely be achievable. Consequently, the demand of heating power may be considerably larger than

expected from the above given estimations. In addition, for an optimum choice of particles with sufficient SLP, one has to take into account the limitation for the product $H{\cdot}f$ discussed in the preceding text (Section 4.1). The favorable combination of AC-field amplitude and frequency depends strongly on the type of particles provided for the therapy. For particles with mean size in the superparamagnetic regime, the frequency dependence of losses is mainly determined by the imaginary part of the susceptibility given in equation (9). On the contrary, for ferromagnetic particles, the frequency dependence of hysteresis losses is linear. The dependence of magnetic losses on field amplitude obeys a square law for superparamagnetic particles as given in equation (8) compared to a third-order power law for larger ferromagnetic particles in the Rayleigh regime. It is reasonable that for particles with hysteresis losses within the validity range of the Rayleigh regime one should favor the field amplitude against frequency in the limiting product $H{\cdot}f{\cdot}\mathrm{D}$.

It follows from the discussion of loss mechanisms given earlier – and is confirmed empirically – that the SLP of different types of magnetic nanoparticles may differ by orders of magnitude. The most important parameter is the mean particle size in combination with a narrow size distribution. For superparamagnetic particles, there is a steep decline in SLP with decreasing particle size (Hergt *et al*., 2004b). Insofar, the occasionally used very small particles below about 10 nm mean diameter are not the optimum choice for effective tumor heating. A maximum of SLP is expected for single-domain particles in the diameter range between the multidomain and the superparamagnetic regime, while, however, the coercivity should be not too high. As a confirmation, a very large value of SLP of nearly $1000\,\mathrm{W\,g^{-1}}$ at an AC-field amplitude of $10\,\mathrm{kA\,m^{-1}}$ and a frequency of 410 kHz was found by Hergt *et al*. (2005) for bacterial magnetosomes having a mean diameter of the magnetite crystals of about 35 nm (cf. Figure 12).

In addition to mean particle diameter, the particle size distribution has a strong effect on the value of the SLP as discussed in Section 4.2. As an experimental confirmation, by magnetic fractionation a high-SLP fraction with a mean core diameter of 18 nm that delivered $400\,\mathrm{W\,g^{-1}}$ (at 410 kHz and $11\,\mathrm{kA\,m^{-1}}$) could be gained from a commercial ferrofluid (Hergt *et al*., 2004b). A similar value of SLP of $600\,\mathrm{W\,g^{-1}}$ was found for magnetite particles with mean diameter of 15 nm, which owing to a special preparation procedure show a rather narrow normal size distribution instead of a commonly observed log-normal distribution (Hergt *et al*., 2004a).

In general, the mean particle concentration and especially inhomogeneities within the particles may affect the magnetic properties. The remanence of ferromagnetic particle ensembles decreases with increasing packing density owing to dipole–dipole interactions. As a consequence, the hysteresis losses decrease as well. The situation is more complicated in the case of superparamagnetic particles. Agglomerated clusters (see, e.g., Figure 7c) tend to behave like weak ferromagnetic bodies. The mean concentration in fluids, however, is usually low and the mean distance between particles too large to cause measurable modifications of magnetic properties.

Another important factor determining magnetic losses is the effective magnetic anisotropy. Considering the relatively small crystal anisotropy of the ferrimagnetic iron oxides in the order of some kilojoules per cubic meter (e.g., McCurrie, 1994), even relatively small deviations from isometric shapes lead to remarkable shape anisotropy and a wide spread of relaxation times. Moreover, magnetic anisotropy may be considerably influenced by the particle coating (Berkowitz *et al*., 1975), which is necessary for stabilization of the suspension as well as for coupling of functional groups. Finally, the coating may have a direct influence on the SLP if there is a contribution of Brown relaxation losses.

Considering all factors that may influence SLP, it is difficult to estimate a theoretical limit for the SLP of magnetic nanoparticles but it seems very questionable whether the above cited value of $1000\,\mathrm{W\,g^{-1}}$ may be exceeded by more than an order of magnitude. If this could be achieved, treatment of tumors whose diameter is a few millimeters using MPH would need a particle concentration of only $1\,\mathrm{mg\,cm^{-3}}$ in tissue. However, it is open at present whether such a concentration may be really attained by targeting with antibody-functionalized MPs.

To summarize, a good knowledge of structural and magnetic properties of magnetic nanoparticles is a prerequisite for designing particle systems with large SLP for hyperthermia or thermoablation. The manifold methods available for magnetic nanoparticle preparation has been recently reviewed (Tartaj *et al*., 2003).

4.4 Biomedical results of magnetic particle hyperthermia

4.4.1 Results with animals and cell cultures

Gilchrist *et al*. (1957) performed the first basic animal experiments with MPH, taking into account not only physical aspects of particle magnetism but also how the process could be technically implemented. Work performed since then in cell cultures and animals such as mice, rats, rabbits, dogs, and pigs are summarized in a review (Moroz, Jones and Gray, 2002). The conclusion of this experimental work is that temperature elevations sufficient for tumor degradation may be realized in animal experiments under tolerable systemic particle concentrations. Successful tumor cell killing was proved by histological evaluation of treated tissue. Although

many specific questions of MPH could be cleared in those experiments, the posttreatment survival rates – if at all determined – were rather scattered and predictions of successful human therapy will still need to be shown. The best survival rates of 87.5% in rats with no tumor regrowth within three months were reported by Yanase *et al*. (1998a). These authors also reported on observations of an antitumor immunity induction by MPH using magnetite cationic liposomes (Yanase *et al*., 1998b). Successful tumor control using magnetoliposomes coated with antibody fragments was reported (Le *et al*., 2001). For more detailed information, see the review given by Hergt and Andrä (2006).

Research on MPH was also supplemented by a lot of *in vitro* experiments using cell cultures. The main purpose of these experiments was the testing of the biocompatibility of coated magnetic iron oxides and investigation of interactions of magnetic nanoparticles with different cell species in aqueous suspension. Nanoparticle coatings used for MPH are mainly dextran, carboxydextran, citrate, polyethylene glycol, or starch. Toxicity of various coatings was studied, for example, by Häfeli and Pauer (1999). Several authors (cf. Moroz, Jones and Gray, 2002) have shown the differences of the cellular uptake of magnetic nanoparticles for different cell types as well as particle coatings by *in vitro* experiments. A very specific cellular uptake was achieved by coupling tumor-specific monoclonal antibodies on a polyethylene glycol coating of magnetite particles (Suzuki, Shinkai, Kamihira and Kobayashi, 1995). After incubation with BM314 cells, 90-pg magnetite per tumor cell was detected, which was four times that of the unlabeled control. However, much more specific antibody labeling is necessary to achieve MP enrichment in tumor tissue to meet the requirements of MPH. Chan, Kirpotin and Bunn (1993) have compared survival fractions of human lung adenocarcinoma cells following heating using water bath and MPH. They concluded that cancer cell damage was purely due to thermal effects. Being in accordance with theoretical considerations of Rabin (2002), this result contradicts the repeated claim of biomedical literature (e.g., Jordan *et al*., 1999) that 'intracellular hyperthermia' is a particularly effective way of tumor cell damaging.

To summarize, animal and cell culture experiments clarified some essential preconditions for human therapy.

4.4.2 Application to human patients

Although Gilchrist *et al*. (1957) were very optimistic about application of their new method in humans – and since then promising reports have repeatedly appeared in public media – almost half a century passed before first trials with humans were announced (Gneveckow *et al*., 2005). Provided suitable magnetic nanoparticles are available, the most critical problem to be solved is the reliable particle delivery to tumors, which may be achieved mainly in two different ways: first, injection of the particle suspension directly into the tumor or, secondly, a remote application in the blood vessel system followed by targeted delivery to the tumor. The latter may be performed, in principle, by labeling of MPs with tumor-specific antibodies or by particle guidance by means of inhomogeneous magnetic fields. At present, only direct injection is under practical consideration. The key problem of direct injection is the realization of an adequate particle distribution in the tumor tissue. Since the temperature elevation caused by the external alternating magnetic field is mainly confined to tissue regions containing MPs in sufficient concentration, the tissue distribution of the applied particle suspension should fit the tumor shape in the ideal case. However, there are serious practical difficulties in achieving this situation. Matching an infiltrative growing tumor, such as a glioblastoma, with a magnetic nanoparticle suspension seems difficult. On the basis of high-resolution imaging of the tumor shape, the physician has to realize a sufficiently homogeneous coverage of the tumor by the particle suspension avoiding excessive involvement of the healthy tissue. Even for a globular, well-bounded tumor, homogeneous injection is difficult owing to the tissue inhomogeneity, which causes the injected suspension to spread irregularly out of the tumor into the normal tissue, which is softer and differently textured compared to the relatively dense tumor tissue. To avoid these difficulties, a very slow infiltration and/or repeated multisite injections have been recommended (Jordan *et al*., 1997), although the latter bears the danger of needle track implantation or local tumor spread, as pointed out by Moroz, Jones and Gray (2002). It is therefore indispensable to check the particle distribution after injection by suitable diagnostic means, including sonography, radiography, or MRI. With knowledge of the spatial distribution of MPs and the particle concentration in tissue as well as the SLP of the applied particle type, one may estimate the temperature increase using the physical principles discussed earlier (Section 4.3, equation (13)). By measuring the local temperature increase using temperature sensors (e.g., optical fiber sensors) introduced into the tumor tissue, it is possible to control heating by adjustment of field amplitude and duration of the field exposure. A technically advanced hyperthermia and thermoablation system for clinical application was recently reported (Gneveckow *et al*., 2004) and clinical trials on the feasibility and tolerability of MPH are ongoing (Gneveckow *et al*., 2005).

For improving the site specificity of MPH, the labeling of MPs with target-specific ligands (e.g., antibodies) was suggested. Although often mentioned in the literature, only preliminary results of this appealing method have been published. They are restricted to *in vitro* experiments with cell cultures (Suzuki, Shinkai, Kamihira and Kobayashi,

1995) or *in vivo* experiments with animals using intratumoral injection (Shinkai *et al*., 1999; Le *et al*., 2001). The targeting efficiency, that is, the concentration enhancement on the tumor site in comparison to the systemic particle level and the content in organs of the reticuloendothelial system (RES), was not thoroughly investigated for remote (e.g., intravenous) particle application. The expected concentrations are so low that achieving a useful heating effect would need a considerable enhancement of the specific heating power of magnetic nanoparticles as discussed earlier.

The enrichment of magnetic nanoparticles in a target region of the body by application of external magnetic fields is in principle possible as shown by several authors. The method, however, suffers from the limitation that the center of attraction for the particles cannot be positioned within the body with extracorporeal magnets. After theoretically modeling magnetically targeted drug delivery, Grief and Richardson (2005) concluded that this method 'is appropriate only for targets close to the surface of the body'. Further, since magnetic attraction is proportional to the magnetic moment of the particles, superparamagnetic particles develop insufficient forces for magnetic targeting. On the other hand, for larger single-domain particles, there is the tendency of agglomeration with the hazard of unintended embolization. However, it is also possible to take advantage of embolization and use it for arterial embolization hyperthermia (for a review see Moroz, Jones and Gray 2002).

To summarize, MPH promises highly selective cancer therapy provided some practical problems of controlled particle delivery are solved.

5 MAGNETIC NANOPARTICLES FOR DIAGNOSTIC IMAGING

5.1 Contrast enhancement in magnetic resonance imaging

5.1.1 Introduction

One of the most valuable and widely used imaging methods in medical diagnostics is MRI. Though the diagnostic potential of conventional MRI is immense and a variety of different contrast modes are well established, further improvements of the method have been pursued in the last years by the application of magnetic nanoparticles for contrast enhancement based on functional site specificity. Since there are several introductory books and excellent review papers on MRI (e.g., Oppelt, 1998), only a short summary of the principles of the method is provided, so that the role of magnetic nanoparticles for enhancing the diagnostic value of MRI can be understood.

In MRI, the nuclear magnetic moment of protons is used as a sensitive probe of the chemical neighborhood of protons in different tissues and organs of the human body. Nuclear moments are aligned by means of an external magnetic bias field (commonly 0.2–3 T) and precession of the spins is excited by transverse RF pulses at the proton resonance frequency of about 43 MHz T^{-1} (NMR: nuclear magnetic resonance). After applying the pulse sequence, the induced magnetization decays and the longitudinal (T_1) and transverse (T_2) relaxation times of the precessing nuclear magnetic moments show tissue-specific differences that are used to generate image contrast. Imaging is performed by controlling external field gradients so that the resonance condition is fulfilled only in a restricted local region, and then scanning the resonant volume over the body part to be imaged. Magnetic response signals are detected by pick-up coils. The 'read-out' of the decaying magnetization is performed at defined delay after the end of excitation pulses. In this way, the tissue-specific differences of the relaxation times T_1 and/or T_2 may be used for construction of the so-called T_1- or T_2-weighted images showing optimal contrast of special tissue features. In practice, for optimization of tissue contrast, a variety of different pulse sequences (e.g., the widely applied 'spin echo' methods) may be used. For details, the specialized literature should be consulted (e.g., Mansson and Bjornerud, 2001).

5.1.2 Nuclear magnetic relaxation

In general, relaxation of the excited nuclear spins to equilibrium is stimulated by fluctuations of the local magnetic field due to random thermal agitation of the surrounding medium. The longitudinal relaxation is governed mainly by spin–lattice interactions, while transversal relaxation is related to spin–spin interactions, which are sensitive to local inhomogeneities of the magnetic field. In addition to random fluctuations of the local magnetic field, 'dephasing' of the excited spin system is caused by temporally constant inhomogeneities of the magnetic bias field. This latter dephasing contribution may be corrected by the so-called echo techniques.

The tissue-specific differences of relaxation times T_1 and T_2 bearing the main contrast information may be additionally influenced by paramagnetic or superparamagnetic contrast media supplied to the patient's blood vessels, to single organs, or parts thereof. Target-specific contrast enhancement may either rely on natural physiological enrichment processes or may be mediated by special ligand tags (e.g., tumor-specific antibodies) coupled to the contrast agents. Consequently, those substances may be used as markers in physiological processes and owing to their site specificity one may detect pathological deviations or malfunctions of organs.

In general, the change of relaxation times is proportional to the concentration of contrast agents in the sample volume and, accordingly, for characterizing the ability of those agents for imaging enhancement one uses the so-called 'relaxivity', which is the change in the inverse of T_1 or T_2 per unit concentration measured in ($s^{-1}\,mol^{-1}$). Commonly, both T_1 and T_2 are reduced by usual contrast agents and for good image contrast the pulse sequence used for imaging has to be chosen adequately (see, e.g., Bulte and Brooks, 1997). Of course, contrast agents approved for clinical use must show sufficient biocompatibility and the temporal biodistribution (e.g., circulation time in blood, elimination from organs) is essential to obtain useful contrast.

5.1.3 Paramagnetic contrast agents

One established group of contrast media are paramagnetic metal-ion chelates (e.g., Gd-DTPA, a chelating agent containing diethylenetriaminepentaacetic acid). The chelation of the strong paramagnetic Gd^{3+} ion is necessary to avoid toxicity effects of free ions, though in this way the 'contact area' to the bulk water protons – and correspondingly the relaxivity – is considerably reduced. In theoretical models for explaining the effect of MRI contrast agents on proton spin relaxation, one differentiates inner- and outer-sphere relaxation, which determines the 'transmission' of the paramagnetic fluctuations toward the bulk neighborhood of the contrast molecule. The inner sphere is the first coordination sphere of the metal ion, the chelation of which commonly leaves room for only one water molecule. This water molecule is in rapid exchange with the bulk water molecules via the outer sphere, which is the next shell of water molecules surrounding the chelate. The coupling of the proton spin relaxation with the paramagnetic relaxation is described by the Solomon–Bloembergen–Morgan theory. For details, see the book edited by Merbach and Toth (2001) on the chemistry of contrast agents for medical MRI. The theory relates the observed relaxation rate enhancement to microscopic time constants characterizing diffusion of proton spins, electron spin relaxation, and rotational correlation of proton and electron spin.

Present experimental investigations aim at the development of improved Gd chelates with enhanced relaxivity and site preference for targeting of special epitope binding sites (e.g., tumor antigens). The size of Gd-based water-soluble macromolecules may be adjusted for optimum contrast depending on vascular distribution dynamics and the targeting area. For instance, Winter *et al*. (2005) investigated lipid-encapsulated perfluorocarbon nanoparticle contrast agents functionalized with different new Gd chelates for the sensitive and specific detection and localization of fibrin and molecular signatures of angiogenesis. The special molecular design of the relatively large paramagnetic constructs (about 200 nm in diameter) ensures, with a paramagnetic load of about 50 000 gadolinium ions, very high relaxivity per particle in the order of $10^6\,s^{-1}\,m\,mol^{-1}$. In order to guarantee sufficient accumulation at the target area, site-specific contrast agents should circulate longer than the common blood-pool MR agents. Accordingly, adequate chemical stability of the Gd complexes in physiological environment ought to be provided for minimizing toxic side effects.

5.1.4 Magnetic nanoparticles as contrast agents

Local magnetic fields much larger than those due to paramagnetic ions are caused by superparamagnetic particles of the magnetic iron oxides (maghemite and magnetite). The most important parameter in determining the destiny of such particles after introduction into the vascular system (e.g., elimination by phagocytosis or extravasation into interstitial compartment) is the mean size of the particles. Small objects below about 10 nm diameter may leak from blood vessels and distribute in the extracellular fluid (therefore occasionally termed *ECF agents*). Agents that are normally prevented from extravasating to the healthy brain by the blood–brain barrier are suitable, for instance, to trace various neuropathological deviations. A prolonged intravascular circulation time of the so-called blood-pool agents with a diameter range of 10–50 nm ensures great utility in MR angiography. Enhanced uptake of particles in cancerous tissue related to the tumor angiogenesis (e.g., Folkman, 1985) may lead to an initial contrast enhancement after contrast agent application, providing an improved sensitivity for carcinoma detection. Further examples are enrichments at thrombi or the detection of arteriosclerotic plaques. Since particle elimination by phagocytosing cells is most effective in a medium size range of 50–150 nm, the group of contrast agents in this size range and with a circulation time in the order of hours addresses diagnostic needs for organs of the RES (e.g., liver, spleen, bone marrow, lymphatic system). In contrast, site-specific MRI contrast agents should have a long circulation time, which is a prerequisite for sufficient accumulation on a specific target site. A special group is the contrast agents for diagnostics of the gastrointestinal tract: mainly relatively large particles of 0.3–3 µm, which must be protected by suitable coatings against rapid excretion. For an overview on biomedical indications of contrast agent application including many recent references, see, for instance, La Conte, Nitin and Bao (2005).

The useful particle diameters discussed earlier comprise the magnetic oxide core plus an organic coating (e.g., dextran), which is necessary for stabilizing the aqueous particle suspensions against particle aggregation. The coating is

the boundary to the physiological environment and accordingly it is important for possible interactions with proteins (e.g., immunoglobulins of the blood plasma). For instance, hydrophilic coatings like dextran help prevent particle elimination by macrophages. The coating may be functionalized by bioactive molecular groups such as tumor-specific antibodies for receptor-specific targeting.

Important particle parameters for the relaxivity are core magnetization, mean size of the magnetic core, and size distribution. While in the case of paramagnetic contrast agents inner-sphere contributions are particularly important for the relaxivity, magnetic nanoparticles create considerable local fluctuating field gradients and interact with proton nuclear spins by dipolar interaction in the outer-sphere diffusion range. The classical outer-sphere relaxation theory was improved by different authors (for a review, see, e.g., Bulte and Brooks, 1997; Muller *et al*., 2001) taking into account the dynamics of the core magnetization. For superparamagnetic particles with a core diameter in the order of 10 nm, the dependence of relaxivity on the magnetic field was introduced by the Langevin function. In general, the existing different theoretical models rely on various microscopic parameters (mainly elementary time constants), which are rarely accessible by experimental means. Consequently, the uncertainties allow for some fitting freedom. Theoretical predictions are often checked experimentally by measuring the so-called NMRD (nuclear magnetic resonance dispersion) profiles, which is the dependence of proton relaxation rate on the magnetic field. Fitting the observed field dependence of T_2 relaxivities at high fields is only successful if a 'susceptibility term' corresponding to a linear nonsaturating component in the particle magnetization is taken into account. This term may be explained by a 'paramagnetic' surface of the nanoparticles. On the other hand, in the low field range (roughly below 0.1 T), the observed dispersion of the longitudinal relaxivity may be only explained by taking into account the anisotropy energy of the particles, which determines the Néel relaxation of the particle moment (see, e.g., Muller *et al*., 2001). The T_2 shortening by strongly magnetized spheres was treated by Gillis, Moiny and Brooks (2002) using computer simulation, taking into account partial refocusing by echo pulse sequences. For small particle sizes (up to about 30 nm), relaxivity increases with the square of the diameter in agreement with the outer-sphere theory. For larger particles above 30 nm, the relaxivity remains constant in the static dephasing regime while the relaxivity decreases for different types of echo sequences with increasing core size (cf. Figure 10.6 in the review by Muller *et al*., 2001).

While experimental investigations are usually carried out on well-defined dilute aqueous suspensions, modifications are expected for particles in dense tissue, where particles could get stuck or adhere to cell surfaces, for example, in a tumor. The effect of clustering of magnetic nanoparticles in water suspensions was investigated by Roch, Gossuin, Muller and Gillis (2005). Recently, relaxivities of several paramagnetic and superparamagnetic substances in blood as well as in water were compared by Coroiu and Cristea (2005). Data on commercially available superparamagnetic iron oxide–based contrast media are compiled in a review paper of Taupitz, Schmitz and Hamm (2003). There, an overview on several medical applications of superparamagnetic contrast media is given. The contrast change due to magnetic nanoparticles may be positive or negative for 'T_1 weighting' depending on particle concentration and the choice of the pulse sequences used for imaging, while for 'T_2-weighting' negative contrast generally arises (e.g., Bulte and Brooks, 1997). At high local particle concentrations, artifacts may arise, which mask all finer image details. This problem is relevant for assessment of the particle enrichment on a target site for MPH since at present relatively high therapeutic particle concentrations are needed.

More complicated types of nanoparticles are under development for tumor diagnostics and therapy. For instance, Kopelman *et al*. (2005) describe photodynamic nanoparticles consisting of a polyacrylamide core combined with photosensitizer and MP MRI contrast agent. One promising goal in MPH is the combination of diagnostics and therapy by using the same magnetic nanoparticles for contrast enhancement and hyperthermia. In addition, the integration of controlling the increase of tumor temperature under hyperthermia as demonstrated by Carter *et al*. (1998) and on-line checking of tumor damage by MRI would be important steps toward establishment of magnetic particle hyperthermia as a reliable tumor therapy.

5.2 Magnetic particle imaging (MPI)

When Lauterbur published his seminal paper (Lauterbur, 1973), he did not specifically restrict it to magnetic resonance but more generally described 'image formation by induced local interactions'. A recent approach in applying this idea is magnetic particle imaging (MPI), which was proposed by Gleich (2003) and further described by Gleich and Weizenecker (2005) and Trabesinger (2005). The principle of the method is based on highlighting a small region within a larger surrounding volume by marking with MPs and taking advantage of their specific magnetization curve. The large difference between the strongly nonlinear magnetization dependence of MPs as a function of the magnetic field and the magnetization of tissue, which is proportional to the field, can be utilized for medical applications. The particle magnetization as a function of the magnetic field

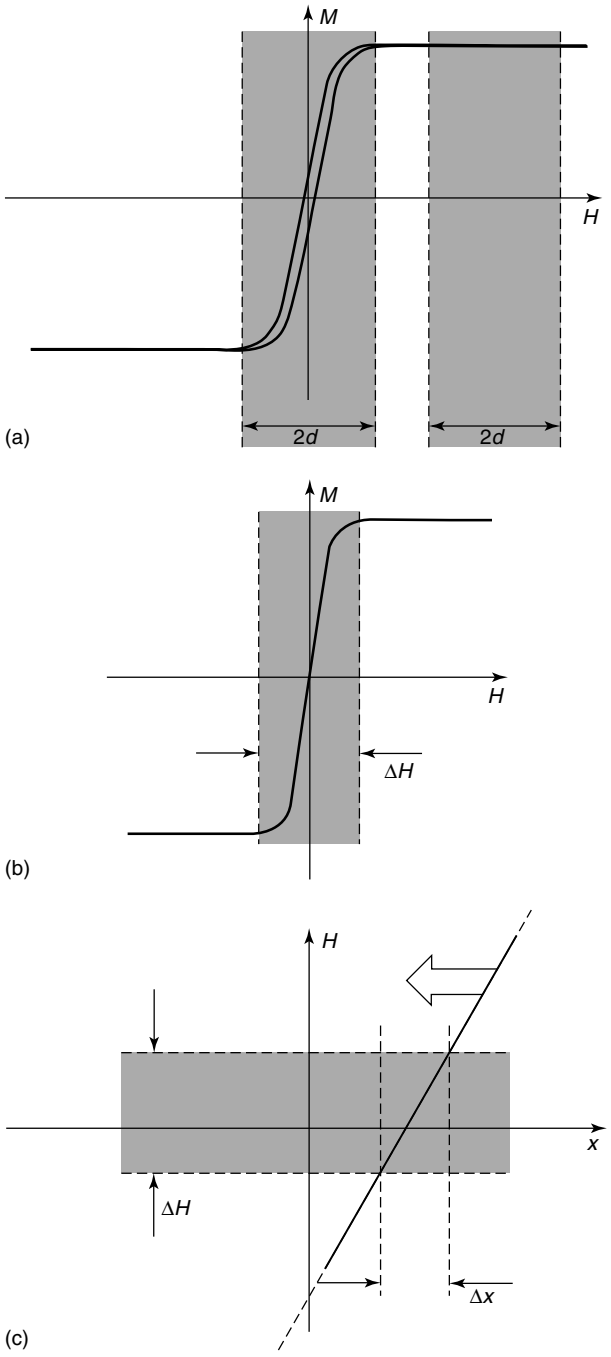

Figure 14. Two variants of magnetic particle imaging (MPI): (a) An alternating modulation field of the amplitude d (gray region) is superimposed on a selection field, which is realized by a field gradient slowly moving across the investigated volume; only if the selection field is nearly zero, the exposed particles respond with harmonics of the modulation frequency. (b) A strong magnetic field with high gradient $\mathrm{d}H/\mathrm{d}x$ is quickly moved across the examined volume; all those particles that experience the field range ΔH of their steep change of magnetization (gray region) respond with a single remagnetization pulse; the spatial resolution Δx (c) is determined by the magnitude of the field gradient $\mathrm{d}H/\mathrm{d}x$ and the field range ΔH of steeply changing particle magnetization.

may coarsely be subdivided into three different sections: for high strengths of positive and negative fields, there are two regions where the magnetization is almost constant (saturation) while in a restricted field region near zero the magnetization changes steeply with the field (Figure 14). This latter small field range (selection field) is moved by either one of two scanning procedures across the examined volume. In the first variant of MPI, an AC magnetic field with small amplitude (modulation field) is superimposed on the slowly moving selection field and causes only those particles that are exposed to the selection field to respond with harmonics of the modulation frequency, which can be selectively measured. The second variant of MPI uses a strong field with high gradient that is moved with high speed across the examined volume, thereby switching the magnetization of all particles in the small region where the actual field is about zero. In both variants, the actual position of the selection field must be known and, at the same time, the responding stray field of the particles has to be detected by suitable means, for example, by pick-up coils carefully compensated with respect to the externally applied fields.

The general operability of MPI was demonstrated by Gleich and Weizenecker (2005) with an array of small holes of 0.5 mm diameter filled with an undiluted, commercially available MRI contrast agent (Resovist®, Schering Ag, Berlin, Germany) containing magnetic oxide particles with a magnetic core well below 100 nm. The holes could be clearly resolved.

For medical applications of MPI, the regions of interest have to be marked selectively, for example, by methods of drug targeting, including the labeling of magnetic carriers and the guidance of the labeled particles to the corresponding sites. Even with the moderate resolving power demonstrated in the initial experiments mentioned earlier, the novel concept may provide the possibility to develop relatively cheap scanners that can be adapted to particular applications. An interesting feature of MPI is its use of harmless radio waves that can pass through the body without significant attenuation.

6 CONCLUSIONS AND PERSPECTIVES

Microparticles can easily pass through the narrow capillary blood vessels of humans. Nanoparticles that are still smaller with a diameter of below 50 nm can even squeeze through the fenestrations of blood vessels and, in this way, can reach most of the cells in the human body. Nanoparticles are therefore predestined to act as carriers for drugs and other agents. Making micro- or nanoparticles magnetic gives them even more favorable properties including the following:

- Their magnetic stray field enhances the contrast in MRI and can also act as source for other contrast mechanisms such as MPI.
- Their magnetic moment generates forces and torques after the application of external magnetic fields. In this way, retention and guidance of MPs can be realized.
- Their magnetic core exhibits losses in alternating or rotating magnetic fields, which leads to temperature increase in MPs. Thus they can act as localized heat sources and produce direct effects such as hyperthermia and thermoablation or indirect effects such as an enhanced rate of chemical reactions.

Together with the fact that magnetic fields in the low frequency region penetrate human tissue without significant attenuation, these particular properties make MPs unique tools for diagnosis and therapy. Despite numerous applications in technology, medicine, and biology, there is still immense research going on in this field, as judged by the large increase in relevant articles over time. Current investigations comprise the synthesis of large amounts of MPs with narrow size distributions and high magnetic susceptibilities, the optimization of magnetic targeting and the magnets to use, and the increasing the particles' heat production for magnetic hyperthermia. Magnetosomes grown in magnetotactic bacteria hold the record in specific heat production for magnetic hyperthermia, and several research groups are trying to learn from these microorganisms and apply natural processes to laboratory techniques.

REFERENCES

Aharoni, A. (1996). *Introduction to the Theory of Ferromagnetism*, Clarendon Press: Oxford.

Alksne, J.F., Fingerhut, A.G. and Rand, R.W. (1966). Magnetically controlled focal intravascular thrombosis in dogs. *Journal of Neurosurgery*, **25**, 516–525.

Andrä, W., d'Ambly, C.G., Hergt, R., *et al*. (1999). Temperature distribution as function of time around a small spherical heat source of local magnetic hyperthermia. *Journal of Magnetism and Magnetic Materials*, **194**, 197–203.

Andrä, W. and Schwabe, E. (1955). Eine einfache Methode, magnetische Elementarbezirke mit trockenem Pulver sichtbar zu machen. *Annalen der Physik*, **17**, 55–56.

Apel, M., Heinlein, U.A.O., Miltenyi, S., *et al*. (2006). Magnetic cell separation for research and clinical applications. In *Magnetism in Medicine*, *Second Edition*, Andrä, W. and Nowak, H. (Eds.), Wiley-VCH: Berlin, pp. 571–595.

Babincova, M., Cicmanec, P., Altanerova, V., *et al*. (2002). AC-magnetic field controlled drug release from magnetoliposomes: design of a method for site-specific chemotherapy. *Bioelectrochemistry*, **55**, 17–19.

Bacri, J.C., da Silva, M.F., Perzynski, R., *et al*. (1997) Use of magnetic nanoparticles for thermolysis of cells in a ferrofluid. In *Scientific and Clinical Applications of Magnetic Carriers*, Häfeli, U., Schütt, W., Teller, J. and Zborowski, M. (Eds.), Plenum Press: New York, London, pp. 597–606.

Berkowitz, A.E., Lahut, J.A., Jacobs, I.S., *et al*. (1975). Spin pinning at ferrite-organic interfaces. *Physical Review Letters*, **34**, 594.

Bertotti, G. (1998). *Hysteresis in Magnetism*, Academic Press: London.

Bönnemann, H., Brijoux, W., Brinkmann, R., *et al*. (2003). A size-selective synthesis of air stable colloidal magnetic cobalt nanoparticles. *Inorganica Chimica Acta*, **350**, 617–624.

Bosnes, M., Deggerdal, A., Rian, A., *et al*. (1997). Magnetic separation in molecular biology. In *Scientific and Clinical Applications of Magnetic Carriers*, Häfeli, U., Schütt, W., Teller, J. and Zborowski, M. (Eds.), Plenum Press: New York, pp. 269–285.

Brezovich, I.A., (1988). Low frequency hyperthermia: capacitive and ferromagnetic thermoseed methods. In *Medical Physics Monograph*, Palivan, P.R. and Hetzel, F.W. (Eds.), American Institute of Physics: New York, pp. 82–111, Vol. 16.

Brunke, O., Odenbach, S., Jurgons, R., *et al*. (2006). Determination of the magnetic particle distribution in tumour tissue by means of x-ray tomography. *Journal of Physics: Condensed Matter*, **18**, S2903–S2918.

Bulte, J.W.M. and Brooks, R.A. (1997). Magnetic nanoparticles as contrast agents for MR imaging – an overview. In *Scientific and Clinical Applications of Magnetic Carriers*, Häfeli, U., Schütt, W., Teller, J. and Zborowski, M. (Eds.), Plenum Press: New York, London, pp. 527–543.

Butler, R.F. and Banerjee, S.K. (1975). Theoretical single-domain grain size range in magnetite and titanomagnetite. *Journal of Geophysical Research*, **80**, 4049–4058.

Campbell, J.D., Piechaczek, C., Winkels, G., *et al*. (2005). Isolation and generation of clinical-grade dendritic cells using the CliniMACS system. *Methods in Molecular Medicine*, **109**, 55–70.

Cao, Z.G., Zhou, S.W., Sun, K., *et al*. (2004). Preparation and feasibility of superparamagnetic dextran iron oxide nanoparticles as gene carrier. *Chinese Journal of Cancer*, **23**, 1105–1109.

Carter, D.L., MacFall, J.R., Clegg, S.T., *et al*. (1998). Magnetic resonance thermometry during hyperthermia for human high-grade sarcoma. *International Journal of Radiation Oncology Biology Physics*, **40**, 815–822.

Chan, D.C.F., Kirpotin, D.B. and Bunn, P.A. (1993). Synthesis and evaluation of colloidal magnetic iron oxides for the site specific rf-induced hyperthermia of cancer. *Journal of Magnetism and Magnetic Materials*, **122**, 374–378.

Coroiu, I. and Cristea, V. (2005). Proton NMR relaxivity of blood samples in the presence of iron, gadolinium and dysprosium compounds. *Journal of Magnetism and Magnetic Materials*, **293**, 520–525.

Debye, P. (1929). *Polar Molecules*, Dover Publications: New York.

Delaunay, L., Neveu, S., Noyel, G. and Monin, J. (1995). A new spectrometric method using magneto-optical effect to study magnetic liquids. *Journal of Magnetism and Magnetic Materials*, **149**, L239–L249.

Dumetre, A. and Darde, M.L. (2005). Immunomagnetic separation of Toxoplasma gondii oocysts using a monoclonal antibody directed against the oocyst wall. *Journal of Microbiological Methods*, **61**, 209–217.

Dutz, S., Hergt, R., Mürbe, J., *et al*. (2007). Hysteresis losses of magnetic nanoparticle powders in the single domain size range. *Journal of Magnetism and Magnetic Materials*, **308**, 305–312.

Eagle, D.F. and Mallinson, J.C. (1967). On the coercivity of γ-Fe_2O_3 particles. *Journal of Applied Physics*, **38**, 995–997.

Eberbeck, D., Wiekhorst, F., Steinhoff, U. and Trahms, L. (2006). Aggregation behaviour of magnetic nanoparticle suspensions investigated by magnetorelaxometry. *Journal of Physics: Condensed Matter*, **18**, S2829–S2846.

Elmore, W.C. (1938). Ferromagnetic colloid for studying magnetic structure. *Physical Review*, **54**, 309–310.

Ernst, S., Ouyang, F., Linder, C., *et al*. (2004). Modulation of the slow pathway in the presence of a persistent left superior caval vein using the novel magnetic navigation system Niobe. *Europace*, **6**, 10–14.

Fabian, K., Kirchner, A., Williams, W., *et al*. (1996). Three-dimensional micromagnetic calculations for magnetite using FFT. *Geophysical Journal International*, **124**, 89–104.

Falk, M.H. and Issels, R.D. (2001). Hyperthermia in oncology. *International Journal of Hyperthermia*, **17**, 1–18.

Folkman, J. (1985). Tumor angiogenesis. *Advances in Cancer Research*, **43**, 175–203.

Gersting, S.W., Schillinger, U., Lausier, J., *et al*. (2004). Gene delivery to respiratory epithelial cells by magnetofection. *The Journal of Gene Medicine*, **6**, 913–922.

Gilchrist, R.K., Medal, R., Shorey, W.D., *et al*. (1957). Selective inductive heating of lymph nodes. *Annals of Surgery*, **146**, 596–606.

Gillis, P., Moiny, F. and Brooks, R.A. (2002). On T2-Shortening by strongly magnetized spheres: A partial refocusing model. *Magnetic Resonance in Medicine*, **47**, 257–263.

Gleich, B. (2003). *Verfahren zur Ermittlung der räumlichen Verteilung magnetischer Partikel*, German patent application DE 101 51 778 A1.

Gleich, B. and Weizenecker, J. (2005). Tomographic imaging using the nonlinear response of magnetic particles. *Nature*, **435**, 1214–1217.

Gneveckow, U., Jordan, A., Scholz, R., *et al*. (2004). Description and characterization of the novel hyperthermia-and thermoablation-system MFH® 300F for clinical magnetic fluid hyperthermia. *Medical Physics*, **31**, 1444–1451.

Gneveckow, U., Jordan, A., Scholz, R., *et al*. (2005). Magnetic force nanotherapy: with nanoparticles against cancer. Experiences from three clinical trials. *Biomedizinische Technik*, **50**, 92–93.

Gonzales, M. and Krishnan, K.M. (2005). Synthesis of magnetoliposomes with monodisperse iron oxide nanocrystal cores for hyperthermia. *Journal of Magnetism and Magnetic Materials*, **293**, 265–270.

Goodwin, S. (2000). Magnetic targeted carriers offer site-specific drug delivery. *Oncology News International*, **9**, 22.

Grief, A.D. and Richardson, G. (2005). Mathematical modelling of magnetically targeted drug delivery. *Journal of Magnetism and Magnetic Materials*, **293**, 455–463.

Gupta, A.K. and Gupta, M. (2005). Synthesis and surface engineering of iron oxide nanoparticles for biomedical applications. *Biomaterials*, **26**, 3995–4021.

Gupta, P.K. and Hung, C.T. (1994). Magnetically controlled targeted chemotherapy. In *Microspheres and Regional Cancer Therapy*, Willmott, N. and Daly, J. (Eds.), CRC Press: Boca Raton, pp. 71–116.

Häfeli, U. (1998). The history of magnetism in medicine. In *Magnetism in Medicine*, Andrä, W. and Nowak, H. (Eds.), Wiley-VCH: Berlin, pp. 15–34.

Häfeli, U.O. (2001a). Chapter 18: radiolabeled magnetic microcapsules for magnetically targeted radionuclide therapy. In *Microspheres, Microcapsules and Liposomes: Radiolabeled and Magnetic Particulates in Medicine and Biology*, Arshady, R. (Ed.), Citus Books: London, pp. 559–584.

Häfeli, U.O. (2001b). Radioactive microspheres for medical applications. In *Physics and Chemistry Basis of Biotechnology*, Bulte, J. and de Kuyper, M. (Eds.), Kluwer Academic Publishers: Dordrecht, Holland, pp. 213–248.

Häfeli, U.O. (2004). Magnetically modulated therapeutic systems. *International Journal of Pharmaceutics*, **277**, 19–24.

Häfeli, U.O. (2006a). The history of magnetism in medicine. In *Magnetism in Medicine: A Handbook*, Andrä, W. and Nowak, H. (Eds.), Wiley-VCH: Berlin, pp. 3–25.

Häfeli, U.O. (2006b). Magnetic nano-and microparticles for targeted drug delivery. In *Smart Particles in Nanomedicine – the MML Series*, Arshady, R. and Kono, K. (Eds.), Kentus Books: London, pp. 77–126, Vol. 8.

Häfeli, U.O. and Pauer, G.J. (1999). In vitro and in vivo toxicity of magnetic microspheres. *Journal of Magnetism and Magnetic Materials*, **194**, 76–82.

Häfeli, U., Pauer, G., Failing, S. and Tapolsky, G. (2001). Radiolabeling of magnetic particles with rhenium-188 for cancer therapy. *Journal of Magnetism and Magnetic Materials*, **225**, 73–78.

Häfeli, U.O., Pauer, G.J., Roberts, W.K., *et al*. (1997). Magnetically targeted microspheres for intracavitary and intraspinal Y-90 radiotherapy. In *Scientific and Clinical Applications of Magnetic Carriers*, Häfeli, U., Schütt, W., Teller, J. and Zborowski, M. (Eds.), Plenum Publishing: New York, pp. 501–516.

Hatch, G.P. and Stelter, R.E. (2001). Magnetic design considerations for devices and particles used for biological high-gradient magnetic separation (HGMS) systems. *Journal of Magnetism and Magnetic Materials*, **225**, 262–276.

Heider, F., Dunlop, D.J. and Sugiura, N. (1987). Magnetic properties of hydrothermally recrystallized magnetite crystals. *Science*, **236**, 1287–1290.

Hergt, R. and Andrä, W. (2006) Magnetic hyperthermia and thermoablation. In *Magnetism in Medicine*, *Second Edition*, Andrä, W. and Nowak, H. (Eds.), Wiley-VCH: Berlin, pp. 550–570.

Hergt, R., Andrä, W., d'Ambly, C.G., *et al*. (1998). Physical limits of hyperthermia using magnetite fine particles. *IEEE Transactions on Magnetics*, **34**, 3745–3754.

Hergt, R., Hiergeist, R., Hilger, I. and Kaiser, W.A. (2002). Magnetic nanoparticles for thermoablation. *Recent Research Development in Materials Science*, **3**, 723–742.

Hergt, R., Hiergeist, R., Hilger, I., *et al*. (2004a). Maghemite nanoparticles with very high AC-losses for application in RF-magnetic hyperthermia. *Journal of Magnetism and Magnetic Materials*, **270**, 345–357.

Hergt, R., Hiergeist, R., Zeisberger, M., *et al*. (2004b). Enhancement of AC-losses of magnetic nanoparticles for heating applications. *Journal of Magnetism and Magnetic Materials*, **280**, 358–368.

Hergt, R., Hiergeist, R., Zeisberger, M., *et al*. (2005). Magnetic properties of bacterial magnetosomes as potential diagnostic and therapeutic tools. *Journal of Magnetism and Magnetic Materials*, **293**, 80–86.

Hiergeist, R., Andrä, W., Buske, N., *et al*. (1999). Application of magnetite ferrofluids for hyperthermia. *Journal of Magnetism and Magnetic Materials*, **201**, 420–422.

Hilal, S.K., Michelsen, W.J., Driller, J. and Leonard, E. (1974). Magnetically guided devices for vascular exploration and treatment. *Radiology*, **113**, 529–540.

Hilger, I., Hergt, R. and Kaiser, W.A. (2005). Use of magnetic nanoparticle heating in the treatment of breast cancer. *IEE Proceedings Nanobiotechnology*, **152**, 33–39.

Hirao, K., Sugita, T., Kubo, T., *et al*. (2003). Targeted gene delivery to human osteosarcoma cells with magnetic cationic liposomes under a magnetic field. *International Journal of Oncology*, **22**, 1065–1071.

Holschuh, K. and Schwammle, A. (2005). Preparative purification of antibodies with protein A-an alternative to conventional chromatography. *Journal of Magnetism and Magnetic Materials*, **293**, 345–348.

Hubert, A. and Schäfer, R. (1998). *Magnetic Domains*, Springer: Berlin, Heidelberg, New York, Barcelona, Budapest, Hong Kong, London, Milan, Paris, Singapore, Tokyo.

Hughes, C., Galea-Lauri, J., Farzaneh, F. and Darling, D. (2001). Streptavidin paramagnetic particles provide a choice of three affinity-based capture and magnetic concentration strategies for retroviral vectors. *Molecular Therapy*, **3**, 623–630.

Hütten, A., Sudfeld, D., Ennen, I., *et al*. (2005). Ferromagnetic FeCo nanoparticles for biotechnology. *Journal of Magnetism and Magnetic Materials*, **293**, 93–101.

Hyeon, T., Lee, S.S.L., Park, J., *et al*. (2001). Synthesis of highly crystalline and monodisperse maghemite nanocrystallites without a size-selection process. *Journal of the American Chemical Society*, **123**, 12798–12801.

Iacob, G., Rotariu, O., Strachan, N.J.C. and Häfeli, U.O. (2004). Magnetizable needles and wires-modeling an efficient way to target magnetic microspheres in vivo. *Biorheology*, **41**, 599–612.

Ibrahim, A., Couvreur, P., Roland, M. and Speiser, P. (1983). New magnetic drug carrier. *The Journal of Pharmacy and Pharmacology*, **35**, 59–61.

Inada, Y., Ohwada, K., Yoshimoto, T., *et al*. (1987). Fibrinolysis by urokinase endowed with magnetic property. *Biochemical and Biophysical Research Communications*, **148**, 392–396.

Johnson, J., Kent, T., Koda, J., *et al*. (2002). The MTC technology: a platform technology for the site-specific delivery of pharmaceutical agents. *European Cells and Materials*, **3**, 12–15.

Jordan, A., Scholz, R., Wust, P., *et al*. (1997). Effects of magnetic fluid hyperthermia on C3H mammary carcinoma in vivo. *International Journal of Hyperthermia*, **13**, 587–605.

Jordan, A., Scholz, R., Wust, P., *et al*. (1999). Endocytosis of dextran and silan-coated magnetite nanoparticles and the effect of intracellular hyperthermia on human mammary carcinoma cells in vitro. *Journal of Magnetism and Magnetic Materials*, **194**, 185–196.

Kato, T., Nemoto, R., Mori, H., *et al*. (1980). An approach to magnetically controlled cancer chemotherapy. I. Preparation and properties of ferromagnetic mitomycin C microcapsules (author's transl). *Nippon Gan Chiryo Gakkai shi*, **15**, 876–880.

Kato, T., Nemoto, R., Mori, H., *et al*. (1981). An approach to magnetically controlled cancer chemotherapy. V. Preparation, properties and pharmacokinetics of microcapsules encased with magnetic particles and mitomycin C (author's transl). *Nippon Gan Chiryo Gakkai Shi*, **16**, 1351–1357.

Kharkevich, D.A., Alyautdin, R.N. and Filippov, V.I. (1989). Employment of magnet-susceptible microparticles for the targeting of drugs. *The Journal of Pharmacy and Pharmacology*, **41**, 286–288.

Kinoshita, T., Seino, S., Mizukoshi, Y., *et al*. (2005). Magnetic separation of amino acids by gold/iron-oxide composite nanoparticles synthesized by gamma-ray irradiation. *Journal of Magnetism and Magnetic Materials*, **293**, 106–110.

Kirchmayr, H.R. (1996). Permanent magnets and hard magnetic materials. *Journal of Physics D: Applied Physics*, **29**, 2763–2778.

Kirschvink, J.L. and Gould, J.L. (1981). Biogenic magnetite as a basis for magnetic field detection in animals. *Biosystems*, **13**, 181–201.

Kobayashi, A. and Kirschvink, J.L. (1995). Magnetoreception and electromagnetic field effects: sensory perception of the geomagnetic field in animals and humans. In *Electromagnetic Fields: Biological Interactions and Mechanisms*, *Vol. 250 ACS Advances in Chemistry*, Blank, M. (Ed.), American Chemical Society, pp. 367–394.

Koneracka, M., Kopcansky, P., Sosa, P., *et al*. (2005). Interliposomal transfer of crystal violet dye from DPPC liposomes to magnetoliposomes. *Journal of Magnetism and Magnetic Materials*, **293**, 271–276.

Kopelman, R., Koo, Y-E.L., Philbert, M., *et al*. (2005). Multifunctional platforms for in vivo MRI enhancement and photodynamic therapy of a rat brain cancer. *Journal of Magnetism and Magnetic Materials*, **293**, 404–410.

Korecka, L., Jezova, J., Bilkova, B., *et al*. (2005). Magnetic enzyme reactors for isolation and study of heterogeneous glycoproteins. *Journal of Magnetism and Magnetic Materials*, **293**, 349–357.

Kreyling, W., Semmler, M. and Möller, W. (2006). Health implications of nanoparticles. *Journal of Nanoparticle Research*, **8**, 543–562, DOI 10.1007/s11051-005-9068-z.

Kronick, P.L., Campbell, G.L. and Joseph, K. (1978). Magnetic microspheres prepared by redox polymerisation used in a cell separation based on gangliosides. *Science*, **200**, 1074–1076.

Kronmüller, H. and Fähnle, M. (2003). *Micromagnetism and the Microstructure of Ferromagnetic Solids*, University Press Cambridge.

Krötz, F., Sohn, H.Y., Gloe, T., *et al*. (2003). Magnetofection potentiates gene delivery to cultured endothelial cells. *Journal of Vascular Research*, **40**, 425–434.

Kurland, H-D., Grabow, J., Staupendahl, G., *et al*. (2007). Magnetic iron oxide nanopowders produced by CO_2 laser evaporation. *Journal of Magnetism and Magnetic Materials*, **311**, 73–77.

Kuznetsov, A.A., Harutyunyan, A.R., Dobrinsky, E.K., *et al*. (1997). Ferro-carbon particles: preparation and clinical applications. In *Scientific and Clinical Applications of Magnetic Carriers*, Häfeli, U., Schütt, W., Teller, J. and Zborowski, M. (Eds.), Plenum Publishing: New York, pp. 379–389.

La Conte, L., Nitin, N. and Bao, G. (2005). Magnetic nanoparticle probes. *Nanotoday*, **19**, 32–38.

Landau, L.D. and Lifshitz, E.M. (1960). *Electrodynamics of Continuous Media*, Pergamon Press: London.

Lauterbur, P.C. (1973). Image formation by induced local interactions: examples employing nuclear magnetic resonance. *Nature*, **232**, 190–191.

Lawaczeck, R., Bauer, H., Frenzel, T., *et al*. (1997). Magnetic iron oxide particles coated with carboxydextran for parenteral administration and liver contrasting. Pre-clinical profile of SH U555A. *Acta Radiologica*, **38**, 584–597.

Le, B., Shinkai, M., Kitade, T., *et al*. (2001). Preparation of tumour specific magnetoliposomes and their application for hyperthermia. *Journal of Chemical Engineering of Japan*, **34**, 66–72.

Leucuta, S.E. (1986). Magnetic microspheres and microcapsules as carriers for intravascular administration of metronidazole. *Drug Development and Industrial Pharmacy*, **12**, 2281–2288.

Lewin, M., Carlesso, N., Tung, C.H., *et al*. (2000). Tat peptide-derivatized magnetic nanoparticles allow in vivo tracking and recovery of progenitor cells. *Nature Biotechnology*, **18**, 410–414.

Lowenstam, H.A. (1962). Magnetite in denticle capping in recent chitons (Polyplacophora). *Geological Society of America Bulletin*, **73**, 435–438.

Lübbe, A.S., Alexiou, C. and Bergemann, C. (2001). Clinical applications of magnetic drug targeting. *The Journal of Surgical Research*, **95**, 200–206.

Lübbe, A.S., Bergemann, C., Riess, H., *et al*. (1996). Clinical experiences with magnetic drug targeting: a phase I study with 4'-epidoxorubicin in 14 patients with advanced solid tumors. *Cancer Research*, **56**, 4686–4693.

Lutz, P., Heitmann, A., Herzog, P., *et al*. (2005). Magnetic bead technology in RNA, DNA extraction form plasma minipools. *Transfusion*, **45**, 1106–1110.

Mah, C., Fraites, T.J. Jr., Zolotukhin, I., *et al*. (2002). Improved method of recombinant AAV2 delivery for systemic targeted gene therapy. *Molecular Therapy*, **6**, 106–112.

Mansson, S. and Bjornerud, A. (2001). Physical principles of medical imaging by nuclear magnetic resonance. In *The Chemistry of Contrast Agents in Medical Magnetic Resonance Imaging*, Merbach, A.E. and Toth, E. (Eds.), John Wiley & Sons, pp. 1–43.

McCurrie, R.A. (1994). *Ferromagnetic Materials*, Academic Press: London.

Meldrum, F.C., Heywood, B.R. and Mann, S. (1992). Magnetoferritin: in vitro synthesis of a novel magnetic protein. *Science*, **257**, 522–523.

Merbach, A.E. and Toth, E. (2001). *The Chemistry of Contrast Agents in Medical Magnetic Resonance Imaging*, John Wiley & Sons: Chichester.

Mertz, C., Kaminski, M., Xie, Y., *et al*. (2005). In vitro studies of functionalized magnetic nanospheres for selective removal of a stimulant biotoxin. *Journal of Magnetism and Magnetic Materials*, **293**, 572–577.

Miebach, S., Grau, S., Hummel, V., *et al*. (2006). Isolation and culture of microvascular endothelial cells from gliomas of different WHO grades. *Journal of Neuro-Oncology*, **76**, 39–48.

Miltenyi, S., Muller, W., Weichel, W. and Radbruch, A. (1990). High gradient magnetic cell separation with MACS. *Cytometry*, **11**, 231–238.

Mitsumori, M., Hiraoka, M., Shibata, T., *et al*. (1994). Development of intra-arterial hyperthermia using a dextran-magnetite complex. *International Journal of Hyperthermia*, **10**, 785–793.

Mitsumori, M., Hiraoka, M., Shibata, T., *et al*. (1996). Targeted hyperthermia using dextran magnetite complex: a new treatment modality for liver tumors. *Hepato-Gastroenterology*, **43**, 1431–1437.

Morishita, N., Nakagami, H., Morishita, R., *et al*. (2005). Magnetic nanoparticles with surface modification enhanced gene delivery of HVJ-E vector. *Biochemical and Biophysical Research Communications*, **334**, 1121–1126.

Moroz, P., Jones, S.K. and Gray, B.N. (2002). Magnetically mediated hyperthermia: current status and future directions. *International Journal of Hyperthermia*, **18**, 267–284.

Mosso, J.A. and Rand, R.W. (1973). Ferromagnetic silicone vascular occlusion: a technique for selective infarction of tumors and organs. *Annals of Surgery*, **178**, 663–668.

Müller, R., Hergt, R., Zeisberger, M. and Gawalek, W. (2005). Preparation of magnetic nanoparticles with large specific loss for heating applications. *Journal of Magnetism and Magnetic Materials*, **289**, 13–16.

Muller, R.N., Roch, A., Colet, J-M., *et al*. (2001). Particulate magnetic contrast agents. In *The Chemistry of Contrast Agents in Medical Magnetic Resonance Imaging*, Merbach, A.E. and Toth, E. (Eds.), John Wiley & Sons: Chichester, pp. 417–434.

Néel, L. (1949). Influence des fluctuations thermiques a l'aimantation des grains ferromagnétiques très fins. *Comptes Rendus de l' Academie des Sciences*, **228**, 664–668.

Nel, A., Xia, T., Madler, L. and Li, N. (2006). Toxic potential of materials at the nanolevel. *Science*, **311**, 622–627.

Nyborg, W.L. (1988). Solutions of the bio-heat transfer equation. *Physics in Medicine and Biology*, **33**, 785–792.

Ochoa, M.L. and Harrington, P.B. (2005). Immunomagnetic isolation of enterohemorrhagic Escherichia coli O157:H7 from ground beef and identification by matrix-assisted laser desorption/ionization time-of-flight mass spectrometry and database searches. *Analytical Chemistry*, **77**, 5258–5267.

Oppelt, A. (1998). Physical principles and technology. In *Magnetism in Medicine*, Andrä, W. and Nowak, H. (Eds.), Wiley-VCH: Berlin, pp. 305–347.

Plank, C., Scherer, F., Schillinger, U., *et al*. (2003a). Magnetofection: enhancing and targeting gene delivery with superparamagnetic nanoparticles and magnetic fields. *Journal of Liposome Research*, **13**, 29–32.

Plank, C., Schillinger, U., Scherer, F., *et al*. (2003b). The magnetofection method: using magnetic force to enhance gene delivery. *Biological Chemistry*, **384**, 737–747.

Polyakov, V.R., Sharma, V., Dahlheimer, J., *et al*. (2000). Novel tat-peptide chelates for direct transduction of Tc-99m and rhenium into human cells for imaging and radiotherapy. *Bioconjugate Chemistry*, **11**, 762–771.

Pouliquen, D. (2001). *Magnetic Microparticles, Historical Introduction*, *First Edition*, Citus Books: London, Vol. 3.

Pulfer, S.K., Ciccotto, S.L. and Gallo, J.M. (1999). Distribution of small magnetic particles in brain tumor-bearing rats. *Journal of Neuro-Oncology*, **41**, 99–105.

Pulfer, S.K. and Gallo, J.M. (1998). Enhanced brain tumor selectivity of cationic magnetic polysaccharide microspheres. *Journal of Drug Targeting*, **6**, 215–227.

Rabin, Y. (2002). Is intracellular hyperthermia superior to extracelluar hyperthermia in the thermal sense. *International Journal of Hyperthermia*, **18**, 194–199.

Rand, R.W., Snow, H.D. and Brown, W.J. (1982). Thermomagnetic surgery for cancer. *The Journal of Surgical Research*, **33**, 177–183.

Rand, R.W., Snow, H.D., Elliott, D.G. and Haskins, G.M. (1985). *Induction Heating Method for Use in Causing Necrosis of Neoplasm*, US Patent 4,545,368.

Rand, R.W., Snow, H.D., Elliott, D.G. and Snyder, M. (1981). Thermomagnetic surgery for cancer. *Applied Biochemistry and Biotechnology*, **6**, 265–272.

Rand, R.W., Snyder, M., Elliott, D. and Snow, H. (1976). Selective radiofrequency heating of ferrosilicone occluded tissue: a preliminary report. *Bulletin of the Los Angeles Neurological Societies*, **41**, 154–159.

Riffle, J.S., Baranauskas, V.V., Vadala, M., *et al*. (2003). Oxidatively stable cobalt nanoparticles, *DARPA Biomagnetics Meeting*, San Diego, p. 27.

Risoen, P.A., Struksnes, K., Myrset, A.H. and Gabrielsen, O.S. (1995). One-step magnetic purification of recombinant DNA-binding proteins using magnetizable phosphocellulose. *Protein Expression and Purification*, **6**, 272–277.

Robins, H.I., Rushin, D., Kutz, M., *et al*. (1997). Phase I clinical trial of melphalan and 41.8 C whole-body hyperthermia in cancer patients. *Journal of Clinical Oncology*, **15**, 158–164.

Roch, A., Gossuin, Y., Muller, R.N. and Gillis, P. (2005). Superparamagnetic colloid suspensions: water magnetic relaxation and clustering. *Journal of Magnetism and Magnetic Materials*, **293**, 532–539.

Rosensweig, R.E. (2002). Heating magnetic fluid with alternating magnetic field. *Journal of Magnetism and Magnetic Materials*, **252**, 370–374.

Rotariu, O., Ogden, I.D., Macrae, M., *et al*. (2005). An immunomagnetic separator for concentration of pathogenic microorganisms from large volume samples. *Journal of Magnetism and Magnetic Materials*, **293**, 589–596.

Roth, D.A. (1969). Occlusion of intracranial aneurysms by ferromagnetic thrombi. *Journal of Applied Physics*, **40**, 1044–1045.

Rous, P. and Beard, J.W. (1934). Selection with the magnet and cultivation of reticulo-endothelial cells (Kupffer cells). *The Journal of Experimental Medicine*, **59**, 577–591.

Safarik, I., Ptackova, L. and Safarikova, M. (2001). Large-scale separation of magnetic bioaffinity adsorbents. *Biotechnology Letters*, **23**, 1953–1956.

Safarik, I. and Safarikova, M. (1999). Use of magnetic techniques for the isolation of cells. *Journal of Chromatography B: Biomedical Sciences and Applications*, **722**, 33–53.

Safarik, I. and Safarikova, M. (2004). Magnetic techniques for the isolation and purification of proteins and peptides. *Biomagnetic Research and Technology*, **2**, 7–7.

Safarikova, M., Kibrikova, I., Ptackova, L., *et al*. (2005). Magnetic solid phase extraction of non-ionic surfactants from water. *Journal of Magnetism and Magnetic Materials*, **293**, 377–381.

Sako, M., Yokogawa, S., Sakomoto, K., *et al*. (1982). Transcatheter microembolization with ferropolysaccharide: a new approach to ferromagnetic embolization of tumors: preliminary report. *Investigative Radiology*, **17**, 573–582.

Scheef, E., Wang, S., Sorenson, C.M. and Sheibani, N. (2005). Isolation and characterization of murine retinal astrocytes. *Molecular Vision*, **11**, 613–624.

Scheffel, A., Gruska, M., Faivre, D., *et al*. (2006). An acidic protein aligns magnetosomes along a filamentous structure in magnetotactic bacteria. *Nature*, **440**, 110–114.

Scherer, F., Anton, M., Schillinger, U., *et al*. (2002). Magnetofection: enhancing and targeting gene delivery by magnetic force in vitro and in vivo. *Gene Therapy*, **9**, 102–109.

Schüler, D. and Frankel, R.B. (1999). Bacterial magnetosomes: microbiology, biomineralization and biotechnological applications. *Applied Microbiology and Biotechnology*, **52**, 464–473.

Schütt, W., Grüttner, C., Häfeli, U., *et al*. (1997). Applications of magnetic targeting in diagnosis and therapy – possibilities and limitations. A mini-review. *Hybridoma*, **16**, 109–117.

Senyei, A.E., Reich, S.D., Gonczy, C. and Widder, K.J. (1981). In vivo kinetics of magnetically targeted low-dose doxorubicin. *Journal of Pharmaceutical Sciences*, **70**, 39–41.

Shinkai, M., Yanase, M., Suzuki, M., *et al*. (1999). Intracellular hyperthermia for cancer using magnetite cationic liposomes. *Journal of Magnetism and Magnetic Materials*, **194**, 176–184.

Shliomis, M.I. and Stepanov, V.I. (1994). Theory of dynamic susceptibility of magnetic fluids. In *Relaxation Phenomena in Condensed Matter*, Coffey, W. (Ed.), John Wiley & Sons: Cichester.

Siegenthaler, U. (1994). *Klinische Pathophysiologie*, Thieme: Stuttgart.

Snyder, M. and Rand, R.W. (1975). Utilization of barium-impregnated ferromagnetic silicone in vascular occlusion. *Bulletin of the Los Angeles Neurological Societies*, **40**, 145–152.

Somia, N. and Verma, I.M. (2000). Gene therapy: trials and tribulations. *Nature Reviews Genetics*, **1**, 91–99.

Stoner, E.C. and Wohlfarth, E.P. (1948). A mechanism of magnetic hysteresis in heterogeneous alloys. *Philosophical Transactions of the Royal Society*, **A240**, 599–642.

Sun, S. and Zeng, H. (2002). Size controlled synthesis of magnetic nanoparticles. *Journal of the American Chemical Society*, **124**, 8204–8205.

Suzuki, M., Shinkai, M., Kamihira, M. and Kobayashi, T. (1995). Preparation and characteristics of magnetite labelled antibody with the use of polyethylene glycol derivatives. *Biotechnology and Applied Biochemistry*, **21**, 1179–1186.

Takeda, S., Mishima, F., Fujimoto, S., *et al*. (2007). Development of magnetically targeted drug delivery system using superconducting magnet. *Journal of Magnetism and Magnetic Materials*, **311**, 367–371.

Tartaj, P., del Puerto-Morales, M., Veitemillas-Verdaguer, S., *et al*. (2003). The preparation of magnetic nanoparticles for applications in biomedicine. *Journal of Physics D: Applied Physics*, **36**, R182–R197.

Taupitz, M., Schmitz, S. and Hamm, B. (2003). Superparamagnetische Eisenoxidpartikel: Aktueller Stand und zukünftige Entwicklungen. *Fortschritte auf dem Gebiete der Rontgenstrahlen*, **175**, 752–765.

Teotia, S. and Gupta, M.N. (2001). Purification of alpha-amylases using magnetic alginate beads. *Applied Biochemistry and Biotechnology*, **90**, 211–220.

Thomas, T.E., Richards, A.J., Roath, O.S., *et al*. (1993). Positive selection of human blood cells using improved high gradient magnetic separation filters. *Journal of Hematotherapy*, **2**, 297–303.

Torchilin, V.P., Papisov, M.I., Orekhova, N.M., *et al*. (1988). Magnetically driven thrombolytic preparation containing immobilized streptokinase-targeted transport and action. *Haemostasis*, **18**, 113–116.

Trabesinger, A. (2005). Particular magnetic insights. *Nature*, **435**, 1173–1174.

Ugelstad, J., Berge, A., Ellingsen, T., *et al*. (1992). Preparation and application of new monosized polymer particles. *Progress in Polymer Science*, **17**, 87–161.

Ugelstad, J. and Mork, P.C. (1980). Swelling of oligomer-polymer particles. New methods for preparation of emulsions and polymer dispersions. *Advances in Colloid and Interface Science*, **13**, 101–140.

Viroonchatapan, E., Sato, H., Ueno, M., *et al*. (1998). Microdialysis assessment of 5-fluorouracil release from thermosensitive magnetoliposomes induced by an electromagnetic field in tumor-bearing mice. *Journal of Drug Targeting*, **5**, 379–390.

Watarai, H., Suwa, M. and Iiguni, Y. (2004). Magnetophoresis and electromagnetophoresis of microparticles in liquids. *Analytical and Bioanalytical Chemistry*, **378**, 1693–1699.

Weissleder, R., Stark, D.D., Engelstad, B.L., *et al*. (1989). Superparamagnetic Iron Oxide: Pharmacokinetics and toxicity. *American Journal of Roentgenology*, **152**, 167–173.

Widder, K.J., Morris, R.M., Howard, D.P. and Senyei, A.E. (1981). Tumor remission in Yoshida sarcoma-bearing rats by selective targeting of magnetic albumin microspheres containing doxorubicin. *Proceedings of the National Academy of Sciences of the United States of America*, **78**, 579–581.

Widder, K.J., Morris, R.M., Poore, G.A., *et al*. (1983). Selective targeting of magnetic albumin microspheres containing low-dose doxorubicin: total remission in Yoshida sarcoma-bearing rats. *European Journal of Cancer and Clinical Oncology*, **19**, 135–139.

Widder, K.J., Senyei, A.E. and Ranney, D.F. (1979). Magnetically responsive microspheres and other carriers for the biophysical targeting of antitumor agents. *Advances in Pharmacology and Chemotherapy*, **16**, 213–271.

Williams, C.M. and Kotha, S. (2003). Exploration of novel technique employing cell injected magnetic nanoparticles to control hemorrhaging resulting from battlefield wounds, *DARPA Biomagnetics Meeting*, San Diego, p. 13.

Winter, P., Athey, P., Kiefer, G., *et al*. (2005). Improved paramagnetic chelate for molecular imaging with MRI. *Journal of Magnetism and Magnetic Materials*, **293**, 540–545.

Wunderbaldinger, P., Josephson, L. and Weissleder, R. (2002). Tat peptide directs enhanced clearance and hepatic permeability of magnetic nanoparticles. *Bioconjugate Chemistry*, **13**, 264–268.

Yanase, M., Shinkai, M., Honda, H., *et al*. (1998a). Intracellular hyperthermia for cancer using magnetite cationic liposomes: an in vivo study. *Japanese Journal of Cancer Research*, **89**, 463–469.

Yanase, M., Shinkai, M., Honda, H., *et al*. (1998b). Antitumour immunity induction by intracellular hyperthermia using magnetite cationic liposomes. *Japanese Journal of Cancer Research*, **89**, 775–782.

Yellen, B.B., Forbes, Z.G., Halverson, D.S., *et al*. (2005). Targeted drug delivery to magnetic implants for therapeutic applications. *Journal of Magnetism and Magnetic Materials*, **293**, 647–654.

Yu, J.F., Häfeli, U.O., Dong, Y., *et al*. (2002). Radiolabeling of magnetic targeted carriers with several therapeutic and imaging radioisotopes. *European Cells and Materials*, **3**(Suppl. 2), 16–18.

Zborowski, M. (1997). Physics of magnetic cell sorting. In *Scientific and Clinical Applications of Magnetic Carriers*, Häfeli, U., Schütt, W., Teller, J. and Zborowski, M. (Eds.), Plenum Publishing: New York, pp. 205–231.

Zhang, J.Q., Zhang, Z.R., Yang, H., *et al*. (2005). Lyophilized paclitaxel magnetoliposomes as a potential drug delivery system for breast carcinoma via parenteral administration: in vitro and in vivo studies. *Pharmaceutical Research*, **22**, 573–583.

Zhao, H., Gagnon, J. and Häfeli, U.O. (2007). Process and formulation variables in the preparation of injectable and biodegradable magnetic microspheres. *Biomagnetic Research and Technology 5.2*.

Magnetic Tunnel Junctions

Stuart Parkin, Hyunsoo Yang, See-Hun Yang and Masamitsu Hayashi
IBM Almaden Research Center, San José, CA, USA

1 INTRODUCTION

More than 70 years ago it was realized that in simple ferromagnetic metals such as Fe, Co, and Ni, current is carried by spin-polarized electrons because of a significant spin-dependent scattering of the majority ('up') and minority ('down') spin-polarized electrons (Mott and Jones, 1936). Many of the magnetotransport properties of these elements and their alloys can be understood within a 'two-current' model in which the electrical current is comprised of independent up- and down-spin currents. It took more than half a century, however, before it was appreciated that these currents can be manipulated in inhomogeneous magnetic systems comprising magnetic and nonmagnetic regions so as to modify the flow of current in these systems and thereby their resistance. Examples include magnetic multilayers composed of alternating thin magnetic and nonmagnetic layers such as Fe/Cr, Co/Ru, and Co/Cu (Baibich *et al*., 1988; Parkin, More and Roche, 1990; Parkin, Bhadra and Roche, 1991) and granular magnetic alloys composed of immiscible magnetic and nonmagnetic metals such as Co and Cu (Berkowitz *et al*., 1992; Chien, 1995). These systems exhibit very large changes in resistance at room temperature in response to magnetic fields as the magnetization directions of neighboring magnetic layers or regions are changed. This phenomenon is often referred to as *giant magnetoresistance* (GMR) (Parkin, 1994, 1995; Fert and Bruno, 1994; Gijs and Bauer, 1997; Mathon, 1991; Levy, 1994; Parkin *et al*., 2003; Barthélémy *et al*., 2002; Parkin, Li and Smith, 1991).

The largest GMR effects are found in Co/Cu multilayers (Parkin, 1993) with changes in resistance exceeding 100% at room temperature. However, these large effects are found in multilayers in which the individual Co and Cu layers are ultrathin – just two to three atomic layers thick – because GMR arises largely from spin-dependent scattering, not within the interior of the magnetic layers ('bulk' scattering, as Mott had considered; Mott and Jones, 1936) but rather from the interfaces between the individual layers ('interface' scattering; Parkin, 1993). The relative importance of interface scattering as compared to bulk scattering was a topic of considerable debate in the early days of GMR but now it is generally agreed that the contribution of spin-dependent scattering from a magnetic interface layer is perhaps 100 times that from an interior magnetic layer. This is very

Handbook of Magnetism and Advanced Magnetic Materials. Edited by Helmut Kronmüller and Stuart Parkin. Volume 5: *Spintronics and Magnetoelectronics*. ISBN: 978-0-470-02217-7.

important technologically because of the need to minimize and control the influence of long-range magnetic dipolar fields emanating from the magnetic component.

GMR has found one extremely important application in the form of a highly sensitive magnetic recording read head for magnetic hard disk drives (see Parkin *et al*., 2003). The GMR effect in magnetic multilayers is not suitable for sensors but can be engineered to create useful devices through several concepts of 'spin engineering' (Parkin *et al*., 2003). In particular, one important concept is fixing the direction of the magnetic moment of individual magnetic layers in a thin-film device by the phenomenon of exchange bias (Meiklejohn and Bean, 1956; Nogués and Schuller, 1999): exchange bias is a magnetic exchange interaction at the interface between a ferromagnet and an antiferromagnet, which can lead to a unidirectional exchange anisotropy in the ferromagnet. This interaction can be so large that the magnetic hysteresis loop of a ferromagnetic film can be shifted from zero field by an 'exchange bias' field which can exceed 1 T or more in magnitude. A second important concept is the use of oscillatory interlayer exchange coupling of 3d transition-metal (TM) ferromagnetic layers through intermediate nonmagnetic layers of the 3d, 4d, and 5d TMs and the noble metals, Cu, Ag, and Au (Parkin, More and Roche, 1990; Parkin, 1991). All these nonmagnetic metals exhibit a long-range indirect interlayer exchange coupling, which oscillates between ferro- and antiferromagetic coupling. By using specific thicknesses of these nonmagnetic metals, which give rise to antiferromagnetic coupling, artificial antiferromagnetic (AAF) thin-film structures that have zero or small net magnetic moment, and consequently, significantly reduced magnetic dipolar fields can be created. These concepts are illustrated in Figure 1. Figure 1(d) shows the basic structure of the most commonly used GMR read head device today. The device, a 'spin valve', contains a reference magnetic electrode formed from an exchange biased AAF separated by a thin Cu layer (second layer from the top), ∼20 Å thick, from the sensing layer which is typically formed from a soft ferromagnetic alloy with the insertion of a very thin interface layer for enhanced interface scattering. The AAF layer universally contains an ultrathin ruthenium layer just 5–10 Å thick to provide the antiferromagnetic coupling layer. These devices act, in some ways, like a valve, where the flow of current through them is modified by applying a magnetic field.

In the past two decades since the discovery of GMR and oscillatory interlayer coupling in TM systems, the magnitude of the GMR signal exhibited by spin-valve structures has changed very little. The resistance of such structures is typically about 10–15% higher when the sensing and reference magnetic moments are antiparallel (AP) as compared to that when they are parallel (P) to one another. Partly for this reason, interest has been renewed in the past decade in devices based not on spin-dependent diffusive scattering but rather on spin-dependent tunneling through an ultrathin dielectric layer forming a tunnel barrier. These structures are the focus of this review.

2 FUNDAMENTALS OF MAGNETIC TUNNEL JUNCTIONS (MTJs)

The essential element of a magnetic tunnel junction (MTJ) is a sandwich of two thin ferro- or ferrimagnetic layers separated by a thin insulating spacer layer which forms a tunnel barrier. When a bias voltage is applied across the barrier, finite current flows through the junction because of quantum-mechanical tunneling. This means that a distinctive property of an MTJ, compared to spin valves, but common to any tunneling device, is the exponential dependence of the tunneling current on the thickness of the tunnel barrier (Simmons, 1963). From a device perspective, this is very interesting, since the resistance of an MTJ can be varied over many orders of magnitude simply by varying the thickness of the dielectric spacer layer. This allows tuning of the device resistance depending on the application. On the other hand small variations in this layer thickness, perhaps due to subtle variations in a deposition process, can lead to large changes in the device resistance. Moreover, for many device applications, it is the signal-to-noise ratio in the frequency range of interest that determines the sensitivity of the MTJ device (Nowak, Weissman and Parkin, 1999). The main sources of noise in an MTJ are Johnson noise, which scales with the square root power of the resistance of the device, and shot noise, which increases with the square root power of the current through the device. Thus, for many high-frequency applications, which require that the resistance of the MTJ must be very low (on the order of ∼20 Ω), the tunnel barrier must be very thin – just a few atomic layers thick. This is a considerable challenge.

In MTJs, the magnitude of the tunneling current depends on the relative orientation of the magnetization direction of the two ferromagnetic metal layers. The tunneling magnetoresistance (TMR) is defined as:

$$TMR = \frac{I_{\max} - I_{\min}}{I_{\min}} \tag{1}$$

where $I_{\max}$ and $I_{\min}$ are the maximum and minimum currents, respectively, that flow through the barrier. For MTJs with conventional ferromagnetic metals (Ni, Fe, Co), the current flow is maximized (minimized) when the magnetization directions of the two ferromagnetic layers are parallel (antiparallel) to each other.

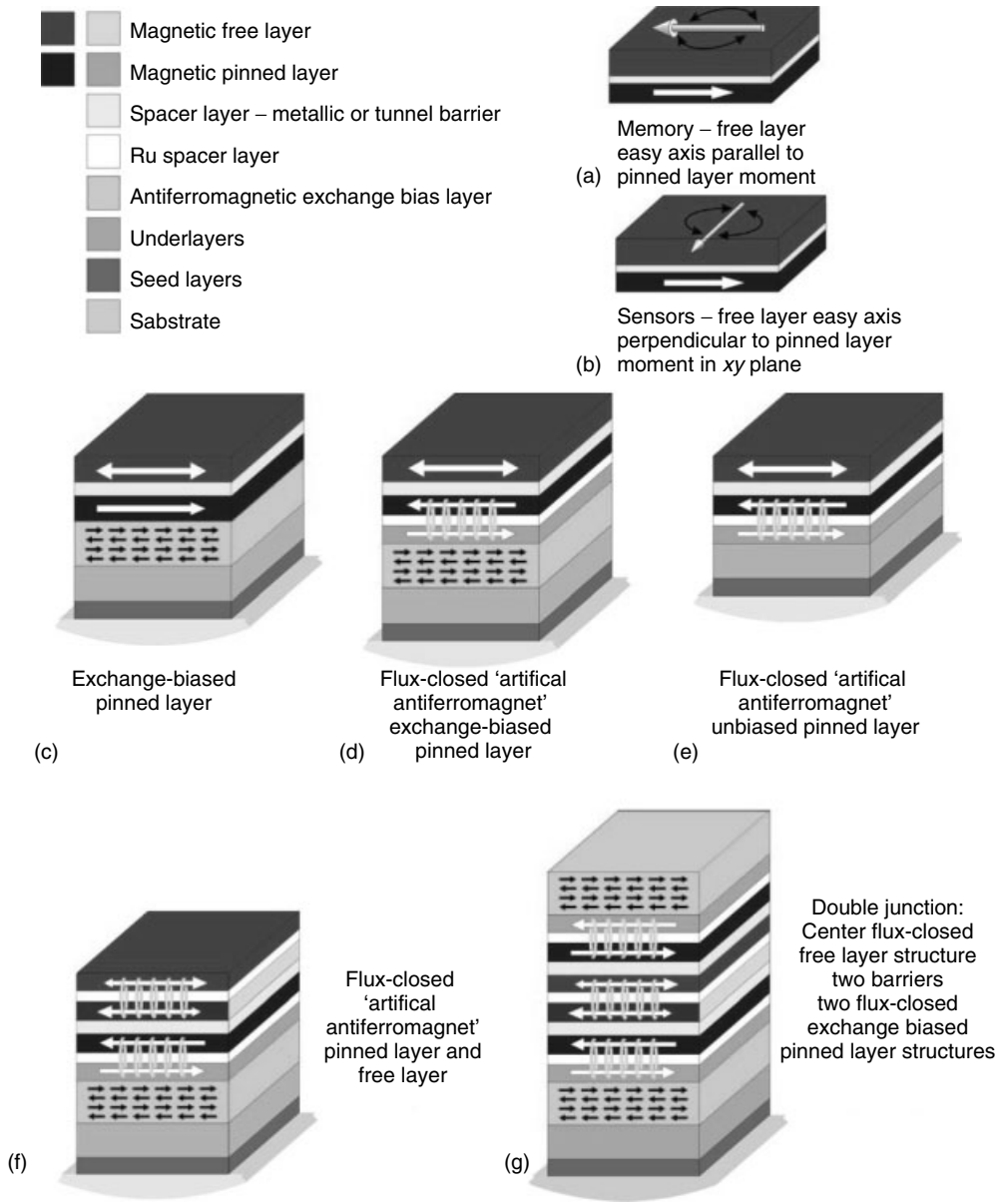

Figure 1. Spin-engineered magnetic devices. (a,b) The easy axis of the 'free' ferromagnetic layer in a magnetoresistive device is oriented based on the purpose for which it is engineered. Field sensor devices such as read heads rely on a free layer with an easy axis at right angles to the moment of the 'pinned' layer. Impinging magnetic fields will rotate the moment away from this middle position and the sensor resistance changes. On the other hand, MR devices designed for use in memory applications will have a free layer easy axis parallel to that of the pinned layer. (c) A very basic GMR/TMR stack consisting of a pinned ferromagnetic layer magnetically locked by exchange bias to the interfacial field of an antiferromagnetic layer, and a simple ferromagnetic free layer. The 'spin valve' is such a stack using a conducting spacer layer between the ferromagnetic layers. (d) In this case the pinned layer is in fact an element consisting of a pair of ferromagnetic layers antiferromagnetically coupled through a ruthenium (Ru) spacer layer; the lower layer in this artificial antiferromagnet is pinned via exchange bias as in (c). This flux closure increases the pinned layer magnetic stability and reduces coupling to the free layer. (e) Pinned element consists of an AF-coupled pair of ferromagnetic layers acting as a single 'hard' layer. There is no exchange bias layer to discourage rotation of the pinned element. (f) Both the pinned and free elements consist of AF-coupled pairs. (g) A double-tunnel junction. All ferromagnetic elements consist of AF-coupled pairs. There are two pinned ferromagnets, both exchange biased by antiferromagnetic layers. Spin filtering occurs both as current tunnels from the first pinned layer to the free element and again as it tunnels from the free element to the second pinned element. (Reprinted with Permission from S.S.P. Parkin *et al*. Copyright 1999, American Institute of Physics.)

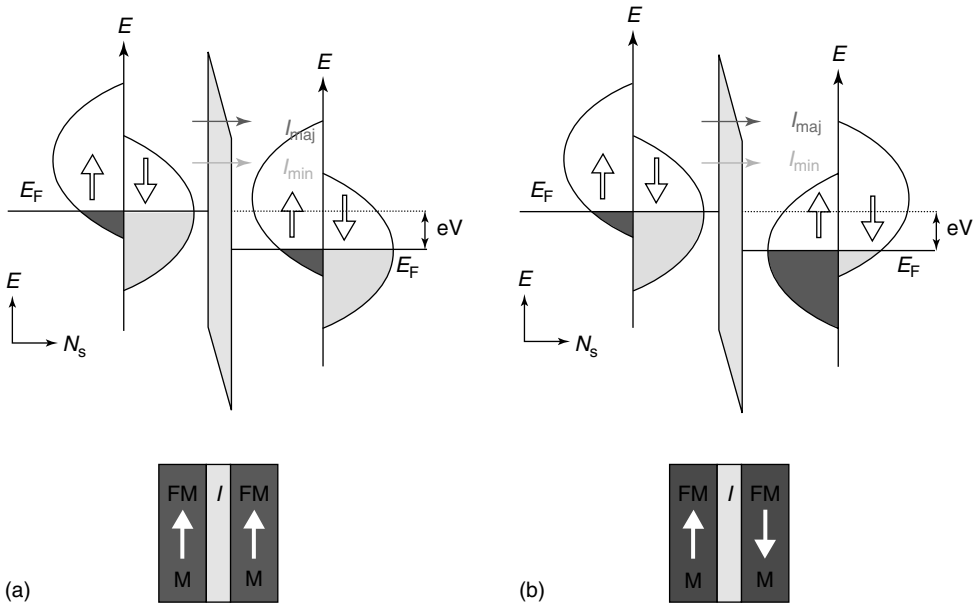

Figure 2. Schematic illustration of the tunneling process. The densities of states for the left and right electrode are shown for (a) parallel and (b) antiparallel configuration. The horizontal arrows represent the electron spin direction. The bottom panel shows the corresponding magnetization configuration of the MTJ.

The origin of tunnel magnetoresistance was first described by Julliere (1975) using a simple transport model. This model makes two important assumptions. First, the electrons do not change their spin direction during the tunneling process. Second, the tunneling current is carried by two independent conductance channels whose carriers are the electrons with spin up and down. The total current is then the sum of the current of the two independent channels within the two-current model (McGuire and Potter, 1975; Mott, 1936, 1964; Fert and Campbell, 1968) which, as mentioned in the preceding text, can account for the GMR (Baibich *et al*., 1988; Valet and Fert, 1993) effect and which has also proved valid to describe anisotropic magnetoresistance (Smit, 1951; Campbell, Fert and Jaoul, 1970; Banhart, Ebert and Vernes, 1997). In the two-current model, the conduction electrons are generally assumed to originate from the free electron–like s bands. The localized d or f states act as scattering centers. By contrast, in MTJs we take the localized d- or f-state electrons as the carriers responsible for the tunneling currents.

Figure 2 shows a simplified density of states (DOS) of an MTJ when the magnetization directions of the two ferromagnetic metals are (a) parallel and (b) antiparallel to each other. The DOS of each electron spin in the ferromagnetic electrode is shifted against the other because of the exchange splitting caused by the internal magnetic field (Mott, 1964; O'Handley, 1999). In Figure 2, the DOS of the ferromagnetic metals are weak ferromagnets, that is, the number of electrons at the Fermi energy is larger for the majority states as compared to the minority states. A bias voltage is applied across the barrier to generate tunneling current; here the voltage is applied such that the electrons tunnel through the barrier from the left to the right electrode. The tunneling current is predominantly carried by the electrons whose states are near the Fermi energy (Duke, 1969; Wolf, 1989). In order to conserve the spin during the tunneling process, the electron that travels from one spin state on the left electrode must be accepted by the same unfilled spin state on the right electrode. Consequently, the number of electrons that can tunnel through the barrier is limited by the number of filled states on the left electrode and the number of the unfilled states on the right electrode.

The tunneling current that flows through the junction for the parallel (I_P) and antiparallel (I_{AP}) states can be expressed as:

$$I_P \propto N_\uparrow^L N_\uparrow^R + N_\downarrow^L N_\downarrow^R$$
$$I_{AP} \propto N_\uparrow^L N_\downarrow^R + N_\downarrow^L N_\uparrow^R \tag{2}$$

where $N_{\uparrow\downarrow}^{L,R}$ are the density of majority ($\uparrow$) and minority ($\downarrow$) spin states at the Fermi energy for the two ferromagnetic electrodes (L and R). Equation (2) shows that the current for the AP state is suppressed compared to that of the P state. This difference in the current is the origin of the TMR effect.

From equations (1) and (2), the TMR ratio is written as

$$TMR = \frac{I_P - I_{AP}}{I_{AP}} = \frac{2P_L P_R}{1 - P_L P_R} \tag{3}$$

Here, $P_i \equiv \frac{N_\uparrow^i - N_\downarrow^i}{N_\uparrow^i + N_\downarrow^i}$, i = L, R is the spin polarization of the left (L) or right (R) ferromagnetic electrodes. As evident from equation (3), the TMR ratio is proportional to the spin polarization P_i of the ferromagnetic electrodes. Methods to experimentally determine the magnitude and sign of the spin polarization are discussed later.

A more accurate theoretical description of the TMR effect was given by Slonczewski (1989). His model included the effect of the insulator on the TMR effect, where the tunneling current was assumed to depend on the barrier height and width of the insulator. The ferromagnetic electrodes were treated within the free electron approximation with two separate bands for each spin direction (Stearns, 1977). Since the insulator possesses finite barrier height and width, the electron wave function from the ferromagnetic electrodes can penetrate inside the insulator. Consequently, an additional factor of the spin polarization arises from the interface between the insulator and the ferromagnetic electrode. The effective spin polarization becomes

$$P_{\mathrm{EFF}} = P_i A (-1 < A < 1) \tag{4}$$

where A is a constant that depends on the barrier height and width of the insulator as well as the DOS of the ferromagnetic electrode. Julliere's model ($P_{\mathrm{EFF}} = P_i$) is recovered when the barrier height or the width becomes infinite, that is, for a perfect insulator. Interestingly, Slonczewski's model predicts that the effective spin polarization can be negative at low barrier height ($A < 0$). This indicates that the spin polarization in MTJs is not an intrinsic property of the ferromagnetic metals, but depends both on the electrode and the barrier characteristics.

Although Slonczewski's model does not take into account other complications such as the multiband structure of the ferromagnetic electrodes and the complex band structure of the insulator, or the electron–electron interactions, spin-wave emission and absorption, and inelastic tunneling processes, nevertheless, it provides a reasonable basis for an appreciation of spin-dependent tunneling in MTJs. In order to include band structure effects, one needs to perform first-principle electronic structure calculations, such as the density function theory. However, even using such an elaborate method, it is difficult to predict the TMR ratio precisely in a quantitative way, since it is known that the tunneling current also depends on defects and impurities inside the barrier as well as on the roughness of the interface layer, which are difficult to include even in numerical calculations.

The first successful MTJ was prepared by Julliere (1975). The MTJ consisted of Fe/Ge/Co, where the semiconducting Ge acted as an insulating barrier. A conductance change as high as ∼14% was observed at 4.2 K. After Julliere's initial discovery, other barriers, such as nickel oxide (NiO) (Maekawa and Gafvert, 1982), gadolinium oxide (GdO_x) (Nowak and Rauluszkiewicz, 1992), and aluminum oxide (AlO_x) (Suezawa, Takahashi and Gondo, 1992; Miyazaki, Yaoi and Ishio, 1991), were explored over a period of nearly 20 years, with the observation of modest TMR effects of up to several percent at room temperature. In 1995, two groups reported TMR ratios of about 10% at room temperature, using an amorphous aluminum oxide barrier and Fe–Co electrodes (Moodera *et al.*, 1995; Miyazaki and Tezuka, 1995). These results sparked much interest in MTJs, largely due to their promising applications in recording read heads for hard disk drives and in novel magnetic random access memories (MRAMs), as discussed later in this chapter.

Most work in this period of time used amorphous aluminum oxide tunnel barriers, which had been extensively studied for Josephson junction superconducting devices. A method of forming the tunnel barrier in which a few monolayers of aluminum metal were first deposited and then were subsequently oxidized, either thermally using molecular oxygen or reactively using atomic oxygen, had been successful in creating high-quality tunnel barriers with very low leakage currents (Rowell, Gurvitch and Geerk, 1981; Mallison, Miller and Kleinsasser, 1995). In MTJs, it is not only the formation of a tunnel barrier without pinholes that is important for the observation of large TMR signals, but also the preparation of high-quality interfaces between the barrier and the electrodes which preserve the magnetic integrity of the surface layers of the ferromagnetic electrodes. Thus, the magnitude of the TMR ratio highly depends on the detailed preparation method of forming the tunnel junction. The observed increase in the TMR ratio over the past decades owes much to the improvements in these methods.

Magnetron sputtering methods are typically used for deposition, including the ferromagnetic electrodes as well as the insulator layer. To form the junction, it is ideal to grow the MTJ *in situ* since the interface between the insulator and the ferromagnetic metals needs to be extremely clean to maintain the polarization of the tunneling electrons. For exploring new materials and refining MTJ device structures it is very useful to use a *in situ* shadow masking technique to pattern first, the bottom ferromagnetic electrode, second, the tunnel barrier and third, the top ferromagnetic counterelectrode. Thus MTJs, which, unlike spin-valve structures, require patterned top and bottom electrodes to pass current through the device for testing purposes, can be prepared quickly and efficiently without using conventional lithography methods, which would otherwise be needed. Figure 3 shows a schematic illustration of a magnetron sputtering system with an *in situ* computer-controlled system for placing a sequence of shadow masks onto any 1 of 20 substrates. A shadow mask, here formed from a thin metal sheet (black layer), is

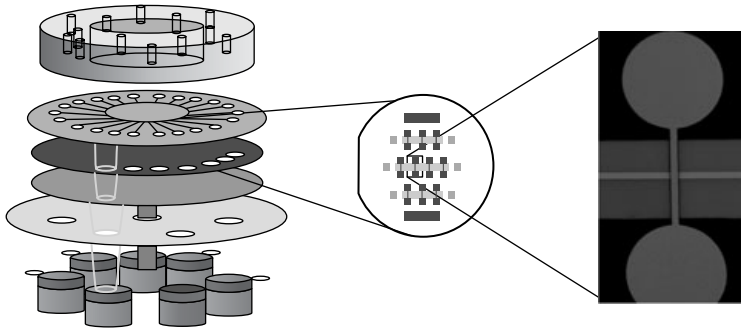

Figure 3. Schematic illustration of magnetron sputtering with a shadow mask (black plate) technique introduced. The middle panel shows the deposited MTJs. Scanning electron microscopy image of the junction is shown in the right panel.

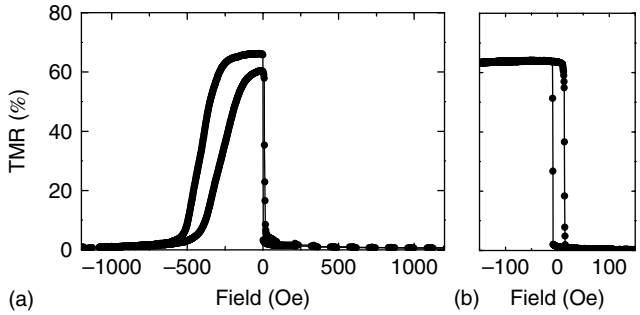

Figure 4. TMR ratio plotted against the applied magnetic field for an MTJ consisting of 50 TaN | 50 Ta | 150 IrMn | 35 $Co_{70}Fe_{30}$ | 22 Al | 10 $Co_{70}Fe_{30}$ | 65 $Co_{59.5}Fe_{25.5}Zr_{15}$ | 50 TaN | 50 Ta | (units in Å). The Al layer is plasma oxidized for 240 s to form an AlO_x barrier. (a) Major loop and (b) minor loop.

inserted between the target (bottom layer) and the substrate (second layer from the top) to define the deposited structure. Typically, three different shadow masks are used to form, respectively, the bottom electrode, the insulator, and the top electrode, although many more masks can be used for the definition of more complex structures or for the use of isolation pads. Using shadow masking techniques the junction size is limited by the apertures within metal masks, which are typically on the order of 25–100 μm, and, in sputtering systems by the sputter gas pressure and the distance from the source to the substrate. It is interesting to recall that shadow masking techniques were used in the 1960s for the manufacture of microelectronic devices including transistors with dimensions as small as ∼10 μm (Brody and Page, 1968; Brody, 1996). Shadow masks, often termed *stencil masks*, can be formed from silicon nitride membranes with dimensions as small as 10 nm and have been used to successfully define metal nanowires on this length scale (Deshmukh *et al*., 1999). Clogging of the apertures prevents the deposition of significant amounts of material.

In AlO_x-based MTJs, the AlO_x layers are usually formed either by depositing an aluminum layer followed by a subsequent oxidation, or by depositing Al in an oxygen atmosphere. The oxidation of the ultrathin Al layer, typically 6–15-Å thick, needs to be optimized to achieve a high TMR ratio. Excess oxidation of the Al layer leads to oxidation of the bottom ferromagnetic metal, which significantly influences the spin polarization of the interface states that contribute to tunneling. Deficient oxidation creates local electrically conducting paths (pinholes) in the insulator and degrades the quality of the barrier. Such pinholes are believed to provide conductive channels that are not spin polarized. A number of oxidation methods have been used to optimize the oxidation of the ultrathin Al layer. Plasma oxidation of the Al layer has been commonly used, since the optimum oxidation time to obtain high TMR ratio is usually faster compared to thermal oxidation. It has been found that annealing the MTJ typically increases the TMR ratio by improving the quality of the interfaces between the insulator and the ferromagnetic metal.

In a few years after 1995 the TMR of MTJs increased rapidly with values of up to ∼60% for MTJs with CoFe electrodes and up to ∼70% for MTJs with amorphous ferromagnetic electrodes formed by incorporating small amounts (10–25 at.%) of glass forming elements such as B, Zr, or Hf in the CoFe alloy. Interestingly, the magnitude of the TMR signal was found to be rather insensitive to the ferromagnetic electrode material (Parkin *et al*., 1999). Figure 4 shows a plot of TMR versus applied magnetic field for an MTJ with an AlO_x barrier and ferromagnetic electrodes formed from CoFe (lower electrode) and an amorphous ferromagnetic alloy (upper electrode) which shows a TMR of about 70% at room temperature. This is the maximum value of TMR which has yet been reported at room temperature for MTJs using an AlO_x barrier (Parkin unpublished; Wang *et al*., 2004; Sakuraba *et al*., 2005).

MTJs with other barrier materials, such as titanium oxide (TiO_2) (Bibes *et al*., 2003), aluminum nitride (AlN) (Sharma *et al*., 2000; Yoon *et al*., 2004), tantalum oxide (TaO_x) (Sharma, Wang and Nickel, 1999), strontium titanium oxide

(STO) (de Teresa *et al*., 1999a,b), and magnesium oxide (MgO) (Bowen *et al*., 2001; Faure-Vincent *et al*., 2003) have also been studied. TiO_2 barrier has found its way into application as a magnetic recording read head (Mao *et al*., 2006) owing to its ultralow resistance–area product. TaO_x and STO have been reported to show an inverse or negative TMR ratio, which will be briefly discussed in the following section.

The basic origin of TMR lies in the degree of spin polarization P of the tunneling current in the MTJ device. For many years this was considered to be related to the fundamental electronic structure of the ferromagnetic electrodes and, in particular, to the degree of spin polarization of the DOS at the Fermi energy of the electrodes. Similar to the two-current model of transport in ferromagnetic metals, the tunneling current in an MTJ device may be considered to be composed of independent majority and minority spin-polarized currents. Assuming that these currents are proportional to the corresponding spin-polarized DOS in the emitting and receiving magnetic electrodes, the TMR can be defined as $TMR = P_1P_2/(1-P_1P_2)$ where $P_{1,2}$ are the spin polarizations of the DOS of the two magnetic electrodes (Julliere, 1975; Meservey and Tedrow, 1994). In this simple model the TMR is determined solely by the electronic structure of the magnetic electrodes and is insensitive to the tunnel barrier properties. It has become clear recently that this model is much too simple and that the properties of the tunnel barrier and its interface with the magnetic electrodes are extremely important in determining the degree of spin polarization of the tunnel current and, consequently, the TMR, as discussed in the following sections.

3 INFLUENCE OF CHEMICAL BONDING ON SPIN-POLARIZED TUNNELING

It is well known in metal–insulator–metal (MIM) tunneling structures that the tunneling characteristics are strongly influenced by the electronic structure of the metal interface layers (Wolf, 1989). Similarly, in MTJs the interface electronic structure and the nature of the bonding between the ferromagnet (F) and the insulator are clearly very important. Indeed, it was long postulated that the positive sign (majority spin electrons) of the polarization of the tunneling current from Co and Ni ferromagnetic electrodes reflects the predominant tunneling of the more delocalized conduction band electrons with sp character rather than the more localized electrons with d character, even though the DOS near the Fermi energy of the latter is considerably higher (Stearns, 1977). Slight variations in the nature of the bonding between Fe and Co and oxygen in alumina tunnel barriers have been calculated to affect both the magnitude and sign of the polarization of the tunneling current (Tsymbal, Oleinik and Pettifor, 2000; Oleinik, Tsymbal and Pettifor, 2000). Unfortunately, the role of oxygen bonding is difficult to probe experimentally because of the ease of formation of TM oxides many of which are nonferromagnetic or antiferromagnetic.

An interesting system in which to explore the role of oxygen bonding on spin-dependent tunneling is TM alloys formed from Fe, Ni, and Co diluted with nonmagnetic elements, in conjunction with tunnel barriers which do and do not contain oxygen. Figure 5(a,b) compiles results on alloys of Co–Pt and Co–V with tunnel barriers formed from Al_2O_3 and AlN (Kaiser *et al*., 2005). The figure includes measurements of the spin polarization of the tunneling current measured by superconducting tunneling spectroscopy (STS) in ferromagnet-insulator-superconductor (FIS) junctions formed by replacing one of the ferromagnetic electrodes in an MTJ with a superconducting (S) layer of Al. Analysis of the voltage dependence of the conductance of such structures at temperatures well below the superconducting transition temperature of Al ($\sim$2 K) allows the direct determination of the tunnel current polarization (Meservey and Tedrow, 1994). The figure shows that for Al_2O_3 barriers the tunneling spin polarization (TSP) decreases rapidly when Co is diluted with V but hardly changes at all when Co is diluted with up to 50% Pt. When the Al_2O_3 barrier is replaced with AlN then the results are quite different. For the case of V the TSP now decreases more slowly as the Co is diluted with V but for the case of Pt the TSP decreases more quickly with increasing Pt concentration.

These results can be rationalized on the basis of the different strength of the chemical bonds formed between the metal electrodes and O or N in the barrier as illustrated schematically by the cartoon in Figure 5(c). Assuming that the tunneling process is highly localized in nature and that the tunneling current may vary significantly between neighboring atomic sites in the metal interface layer, the net tunneling current comprises currents tunneling from individual Co and Pt or V atoms. If we conjecture that these currents are directly related to the strength of the local chemical bonds formed at the interface with the tunnel barrier, then since Pt forms a much weaker bond with oxygen than Co does, we conclude that the tunneling current from Co–Pt alloys for alumina tunnel barriers will be dominated by tunneling from the Co atoms. If we further assume that the current from the Co component is spin polarized and that from Pt (or V) is not then we can model the dependence of the spin polarization of the tunneling current on the Co–Pt and Co–V concentrations, as shown in Figure 5(a,b). For Co–Pt/Al_2O_3 the experimental measurements can be fit with such a model if the probability of tunneling from Co is about 3.5 times higher than that from Pt. Perhaps coincidentally, this is nearly

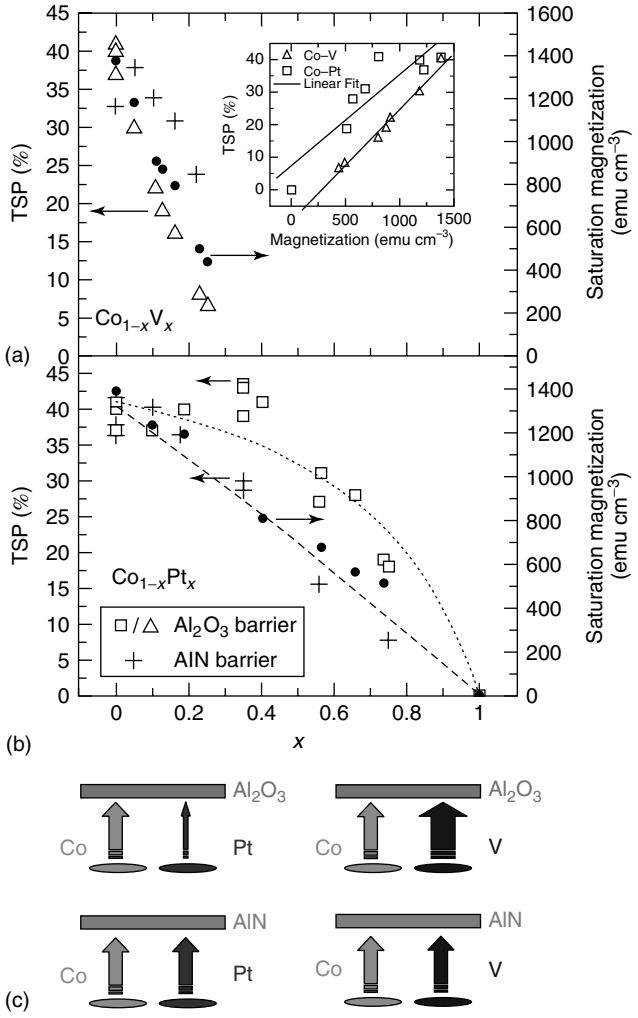

Figure 5. (a)Tunneling spin polarization at 0.25 K and magnetization at 5 K for (a) $Co_{1-x}V_x$ and (b) $Co_{1-x}Pt_x$ alloys as a function of the V and Pt atomic functions. The results show a tunneling probability from Pt sites that is ∼3.8 times lower than from Co sites for the case of Al_2O_3 barriers (dotted line) and ∼1.1 times lower for the case of AlN barriers (dashed line) (Kaiser *et al*., 2005). (c) Schematic representation of the relative magnitude of the tunneling currents from the constituent elements in Co–Pt and Co–V alloys for tunneling for Al_2O_3 and AlN tunnel barriers.

the same ratio as that of the strength of the Co–O to Pt–O bonds (as inferred from heat of enthalpies).

By contrast with Pt, V forms a much stronger bond with O than does Co so the same model would predict a fast decrease of TSP as the Co is diluted with V since the (non-spin-polarized) tunneling current from V would increase rapidly (faster than in proportion to the V concentration). This is as observed in Figure 5(a,b).

As mentioned above when $Al_2O_3$is substituted by AlN the dependence of TSP on Pt and V concentrations is quite different but the results are consistent with a model in which the local tunneling probability is related to the local chemical bonding. The bonding of Co, Pt, and V with nitrogen is quite weak so the TSP is then diluted approximately in proportion to the Pt and V concentrations, as is found experimentally (see Figure 5). These results suggest that the magnitude of the TSP and, consequently, the TMR can be strongly modified by 'chemically engineering' the bonding at the interfaces between the ferromagnetic electrodes and the tunnel barrier.

4 INFLUENCE OF WAVE-FUNCTION SYMMETRY ON SPIN-POLARIZED TUNNELING

The influence of the chemical bonds formed at the ferromagnet/insulator interface on the magnitude of the tunneling current can be described in terms of a tunneling matrix element. The tunneling current is proportional to the DOS multiplied by the corresponding tunneling matrix element. Similarly, the tunneling matrix elements will also be strongly influenced by the symmetry of the wave functions of the conduction band states in the ferromagnet. The electronic wave functions decay into the tunnel barrier evanescently with a decay length that depends on the symmetry of the wave functions. Thus states with a more delocalized character will decay less quickly into the tunnel barrier and so have a corresponding larger tunneling matrix element. This means that if the majority and minority spin-polarized conduction band states in the ferromagnet have significantly different symmetries then these states will decay at different rates across the tunnel barrier leading to an increased (or decreased) spin polarization of the tunneling current. Thus the tunnel barrier can act as a spin filter. This scenario was predicted for MTJs formed from single crystalline Fe/MgO/Fe sandwiches oriented in the (100) direction (Butler *et al*., 2001; Mathon and Umerski, 2001), where the Fe is bcc and the MgO simple cubic and the two lattices are rotated with respect to each other by 45° to allow for a nearly perfect epitaxial relationship.

Theoretical calculations of the electronic DOS at zero temperature in the Fe/MgO/Fe(100) system by Butler *et al*. (2001) are shown in Figures 6 and 7. Figure 6 shows the dependence of the transmission of electrons through a tunnel barrier composed of eight MgO (100) layers as a function of their in-plane momentum $k_{\|} = k_x + k_y$ parallel to the Fe/MgO/Fe interface. Results are shown for the majority and minority electron channels, for P orientation of the Fe layer magnetizations (a and b, respectively), and for electron transmission for AP orientation of the Fe moments (c). The most obvious feature is that the transmission probability is much higher in the majority than in the minority channel by about 3 orders of magnitude. This clearly shows that the

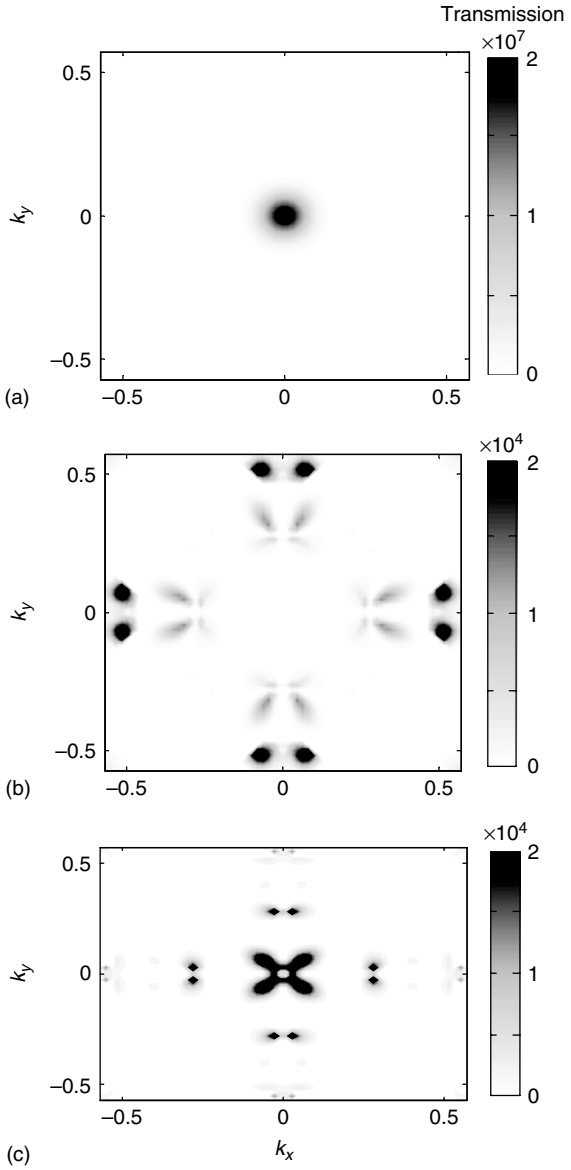

Figure 6. Majority (a), minority (b), and antiparallel (c) conductance versus the crystal momentum in the film plane for a (100) Fe/8 ML MgO/Fe structure (Butler *et al*., 2001). (American Physical Society.)

MgO barrier strongly spin filters the majority spin-polarized electrons even when just a few atomic layers thick. The origin of this spin-filtering effect is revealed by comparing the transmission probability of electrons in the various majority and minority bands at the Fermi energy. Figure 7 shows the calculated DOS for electrons incident from the left electrode for the individual majority and minority spin-polarized conduction bands. There is one majority spin-polarized band with Δ_1 symmetry, that is, with s angular momentum character that decays very slowly across the MgO barrier compared to the other majority spin-polarized

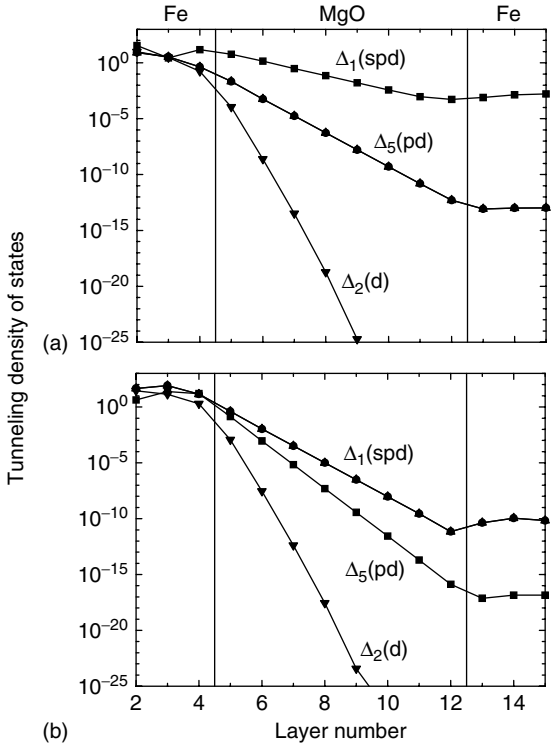

Figure 7. Tunneling density of states (TDOS) of the (a) majority and (b) minority channels at $k_\parallel = 0$ from Fe(100)/8 ML MgO/Fe(100) (Butler *et al*., 2001). (American Physical Society.)

bands and all the minority bands, which have predominant p and d wave-function symmetry. One can interpret this simplistically as the higher tunneling probability for the electrons in the more extended s-wave character states compared to the less extended p and d character states.

A second important feature shown in Figure 6 is the very different $k_\parallel$ dependence of the electron transmission probability in the majority and minority bands. In the majority band the electron transmission is very high close to the center of the Brillouin zone at $k_\parallel = 0$. This corresponds to that expected for free electrons incident on a thick tunnel barrier for which the electron transmission is decreased rapidly away from the forward direction because of an effective increase in the barrier thickness through which the electrons propagate. Note that the half-angle of the cone of the forward transmitted electrons increases as the barrier thickness is decreased. By contrast the $k_\parallel$ dependence of the transmission in the minority channel is quite unlike the simple free electron case and the transmission near the forward direction is very weak. Again this reflects the different wave-function symmetries in these channels.

In summary, for coherent tunneling of electrons through a single crystalline MgO(100) tunnel barrier, in which the electron momentum parallel to the interface is conserved,

very high TMR is expected, owing to the preferential transmission of majority spin-polarized electrons in the Δ_1 band. Fe Δ_1 states, which are highly spin polarized at the Fermi energy, couple with MgO Δ_1 evanescent states at $k_\parallel = 0$. The coupling between these states is very sensitive to details of the Fe–MgO interface. When the surface Fe layer is oxidized this coupling is calculated to be significantly weakened leading to a weakened spin-filtering effect (Zhang, Butler and Bandyopadhyay, 2003), namely, a tunneling matrix element effect.

Following the theoretical predictions of very high TMR values in (100) Fe/MgO/Fe a number of groups attempted to prepare single crystalline epitaxial thin-film Fe/MgO/Fe sandwiches and, although highly perfect structures were prepared, only modest TMR values were obtained for several years (Klaua *et al*., 2001; Bowen *et al*., 2001; Faure-Vincent *et al*., 2003; Mitani, Moriyama and Takanashi, 2003). In 2001 Parkin *et al*. used magnetron sputter deposition techniques to successfully prepare highly (100) textured, exchange biased MTJs with MgO(100)-oriented tunnel barriers which exhibited very high TMR values exceeding 180% (Parkin *et al*., 2004; Butler and Gupta, 2004). Nearly identical MTJ structures with amorphous alumina barriers exhibited much lower TMR values of ∼70%. These results are consistent with the theoretical predictions of Butler *et al*. (2001). With slight modifications of the structure reported in Parkin *et al*. (2004) even higher TMR values of more than 350% at room temperature and nearly 600% at helium temperatures are obtained, as discussed in Parkin (2006). These structures are useful technologically both because they are formed at room temperature using simple sputter deposition techniques and also because they are prepared on amorphous substrates – here an amorphous SiO_2 layer formed on Si(100). Other groups have obtained similar results in highly textured MTJs prepared on silicon oxide in closely related structures (Djayaprawira *et al*., 2005) with reported values of more than 450% TMR at room temperature (Ikeda *et al*., 2006).

A cross-section transmission electron micrograph of a typical MTJ is shown in Figure 8. Underlayers of TaN/Ta are deposited first on the SiO_2 substrate; they form a template on which grows a highly (100)-textured fcc antiferromagnetic exchange bias layer of $Ir_{76}Mn_{24}$. Subsequently, a reference ferromagnetic electrode of $Co_{70}Fe_{30}$is deposited, which is bcc and grows (100) oriented. The MgO barrier is formed by first depositing a thin layer of Mg, ∼4–6 Å thick, followed by the reactive sputter deposition of Mg in an ArO_2 plasma (∼2% oxygen) to form MgO. The Mg underlayer is used to prevent oxidation of the underlying ferromagnetic electrode but this layer is converted to MgO by the reactive oxygen introduced into the sputter chamber during the deposition of the MgO layer. Finally, a counterferromagnetic

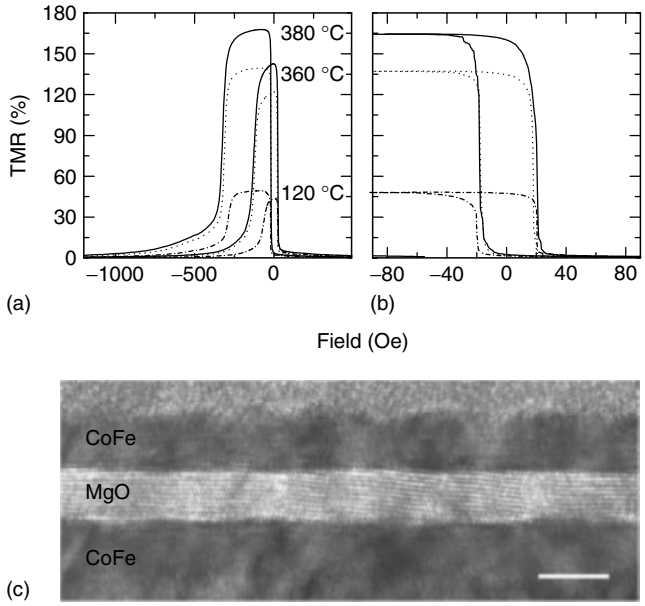

Figure 8. (a) Plots of TMR versus field for MTJs with structures of 100 TaN/250 IrMn/8 $Co_{84}Fe_{16}$/30 $Co_{70}Fe_{30}$/29 MgO/150 $Co_{84}Fe_{16}$/100 Mg. The corresponding final anneal temperature T_A, after which the data is measured at room temperature, is shown in the figure. (a) and (b) The major and minor loop, respectively. (c) High-resolution transmission electron micrograph along the (Sun *et al*., 1998) zone axes showing atomically resolved lattice planes with (100) planes perpendicular to the growth direction. (Reprinted with Permission from S.S.P. Parkin *et al*. Copyright 2004, Nature Publishing Group.)

electrode is formed from a nominally amorphous alloy of $[Co_{70}Fe_{30}]_{80}B_{20}$. The TMR of this structure, as deposited, is modest (∼60–80% at room temperature) but on annealing at temperatures of up to 450 °C the TMR is significantly increased to values of more than 350% at room temperature (see Figure 8) (Parkin *et al*., 2004).

Giant TMR values have also been reported by Yuasa *et al*. (2004) in single crystal Fe/MgO/Fe(100) MTJs prepared by molecular-beam epitaxy on MgO(100) single crystalline substrates. Figure 9 shows the dependence of the TMR ratio measured at 20 and 293 K on the thickness of the MgO barrier. As predicted by theoretical calculations (Butler *et al*., 2001; Mathon and Umerski, 2001), the TMR ratio increases as the MgO thickness is increased. This is attributed to the suppression of the un-spin-polarized states in the Fe band contributing to the tunnel current at large MgO thicknesses. Surprisingly, the TMR ratio oscillates with the MgO thickness, with an oscillation period of 0.3 nm. This oscillation was interpreted as a consequence of coherent tunneling across the barrier, although the detailed mechanism is still under investigation.

Faure-Vincent *et al*. (2002) and Katayama *et al*. (2006) have studied the interlayer exchange coupling between the

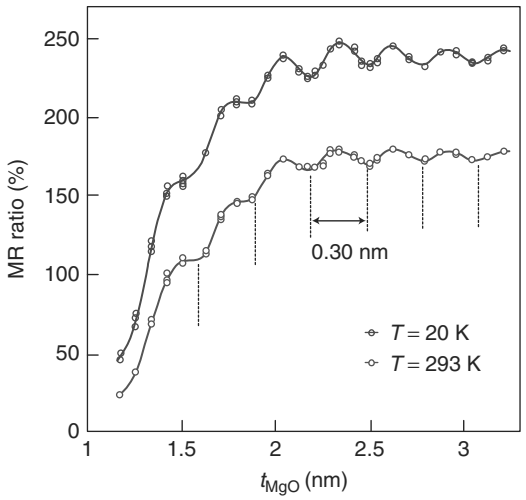

Figure 9. Tunnel magnetoresistance of Fe(001)/MgO(001)/Fe(001) junctions. MR ratio at $T = 293$ and 20 K (measured at a bias voltage of 10 mV) versus t_{MgO} is plotted. (Reprinted with Permission from S. Yuasa *et al*. Copyright 2004, Nature Publishing Group.)

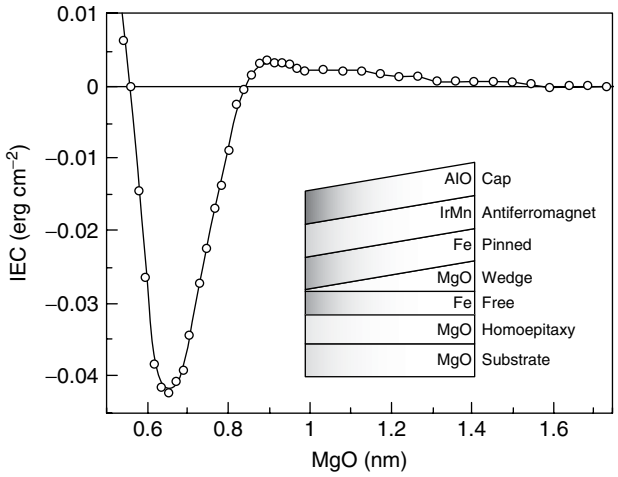

Figure 10. Interlayer exchange coupling versus MgO thickness measured for Fe(001)/MgO(001)/Fe(001) junctions. The thickness of the Fe free layer is 15 nm. Inset shows the cross section of the sample (Katayama *et al*., 2006). (American Physical Society.)

two ferromagnetic layers across an MgO barrier. When the spacer layer between the two ferromagnetic layers is a nonmagnetic metal, it is known that the exchange coupling oscillates with the thickness of the spacer layer between ferromagnetic and antiferromagnetic coupling (Parkin, More and Roche, 1990; Parkin, 1991). This coupling is mediated by the conduction electrons in the spacer layer, which is reminiscent of RKKY coupling (Bruno and Chappert, 1991; Bruno, 1995). When an insulating spacer layer is used, it is predicted that the exchange coupling is ferromagnetic and that it decays exponentially with the spacer thickness. Figure 10 shows the measured interlayer exchange coupling in MTJs consisting of a single crystal Fe/MgO/Fe. Interestingly, the exchange coupling is antiferromagnetic when the MgO thickness is in the range of 0.5–0.8 nm. From first-principle calculations, it was concluded that the coupling was mediated by oxygen vacancy states located within the MgO barrier (Zhuravlev, Tsymbal and Vedyayev, 2005).

5 RELATIONSHIP OF TUNNELING MAGNETORESISTANCE TO TUNNELING SPIN POLARIZATION

The fundamental origin of TMR is the spin polarization of the tunneling current. Therefore, the measurement of the magnitude and sign of the TSP is very important for further understanding of TMR (Julliere, 1975). The spin polarization can be probed by a variety of techniques such as photoemission (Feder, 1985; Dedkov, Rüdiger and Güntherodt, 2002), point-contact Andreev reflection (Soulen *et al*., 1998) and STS (Meservey and Tedrow, 1994). Photoemission experiments determine the unweighted DOS at the Fermi energy and, therefore, for the 3d TM ferromagnets, are sensitive mainly to the contribution of the d electrons, whereas most of the tunneling current is due to electrons from the more extended sp bands (Gadzuk, 1969). Andreev reflection measures the magnitude (but not the sign) of the polarization of electrons at a diffusive interface between the ferromagnetic metal and a superconductor, whereas MTJs involve electrons tunneling across a thin dielectric layer. The STS technique uses a superconducting electrode (S) in the presence of a large magnetic field to detect both the magnitude and the sign of the spin polarization of current tunneling from a ferromagnetic electrode (F) at the Fermi energy across an insulating layer (I) in FIS junctions. Thus, STS is the technique most closely related to spin-dependent tunneling in MTJs.

Figure 11 illustrates the superconducting DOS in a magnetic field as well as the conductance of a FIS junction. Note that the Zeeman splitting of the quasiparticle states due to the applied magnetic field parallel to the surface of the superconducting counterelectrode displaces the spin-up and spin-down DOS peaks of the superconductor by $2\mu_B H$. Thus the conductance curve in the presence of a magnetic field has four peaks with the peak height being asymmetric with respect to zero bias. Note that the inner two peaks are due to predominantly one spin component of the tunneling electrons from the ferromagnetic electrode, either spin up or spin down. The degree of the asymmetry between these two peaks is a measure of the TSP from the ferromagnet.

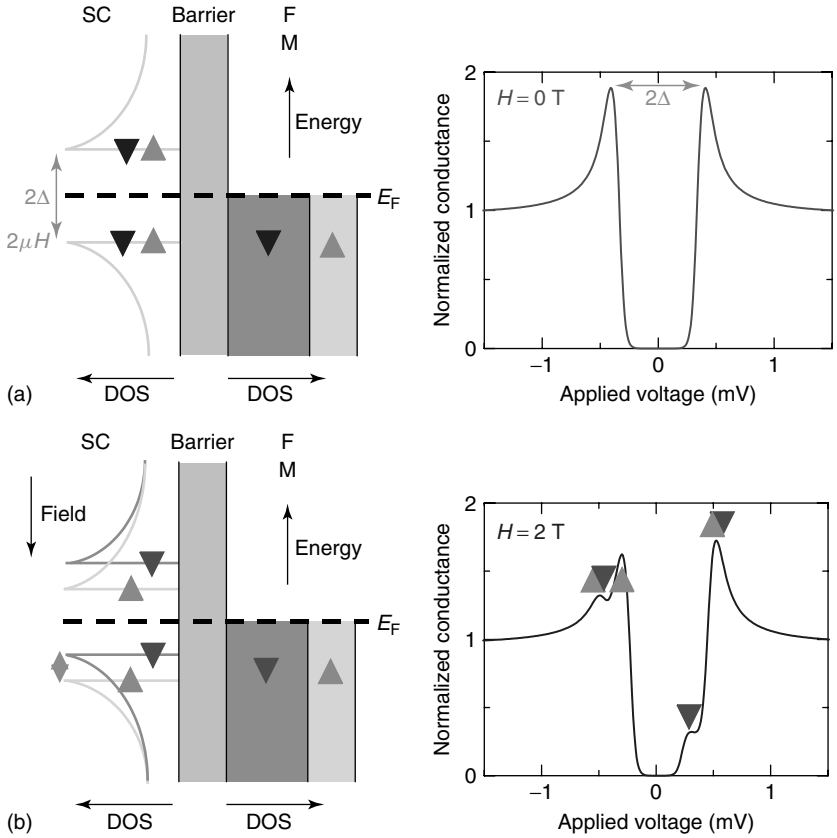

Figure 11. Superconductor–insulator–ferromagnet tunneling at zero magnetic field (a) and at 2 T (b). The figures on the left illustrate the DOS of a BCS superconductor and a ferromagnetic metal. The figures on the right show the theoretical normalized conductance from such a junction.

The STS technique was first developed by Meservey and Tedrow using aluminum superconducting electrodes (Meservey and Tedrow, 1994) and has been applied to many ferromagnetic and ferrimagnetic metals including the 3d TMs and many of their alloys (Kaiser *et al*., 2005), the rare-earth (RE) metals (Meservey and Tedrow, 1994) and RE–TM alloys (Kaiser, Panchula and Parkin, 2005). Al has been widely used ever since this early work because Al has a low spin-orbit scattering, a high superconducting critical field (∼4 T), and readily forms an insulating barrier (Al_2O_3). However, the measurements must be made at low temperatures (<0.4 K) since the superconducting critical temperature of Al is typically below ∼2.5 K. It is possible to use other superconducting electrodes. Using NbN superconducting electrodes STS measurements can be made at higher temperatures (∼1.2 K) without the need for a ^{3}He cryostat (Yang *et al*., 2006).

For many years, the determination of TSP was based simply on using four values of the conductance at the four nominal peak positions (Meservey and Tedrow, 1994; Tedrow and Meservey, 1973). This method tends to overestimate the polarization, thereby requiring a more accurate method of analysis (Worledge and Geballe, 2000). Later, spin-orbit scattering and orbital depairing in the superconductor were taken into account by using the DOS derived by Maki (1964).

Meservey and Tedrow determined the TSP of Co, Fe, and Ni as well as alloys of these elements (Meservey and Tedrow, 1994; Paraskevopoulos, Meservey and Tedrow, 1977). Results are shown in Figure 12 together with TSP data from Monsma and Parkin (2000) and the magnetic moments per atom from the Slater–Pauling curves (Cullity, 1972). Monsma and Parkin's values of TSP are slightly higher than those of Meservey and Tedrow's; this can be attributed to improved sample preparation. Ni and Ni-rich alloys appear to have low TSP values as compared to Fe- and Co-rich alloys, but this is likely due to problems in creating a high-quality interface with aluminum oxide tunnel barriers. Indeed, recent experiments have found TSP values for Ni that are much higher and similar to those of Co and Fe (Nadgorny *et al*., 2000; Kim and Moodera, 2004).

The TSP is measured to be positive for Co, Fe, and Ni as well as for all their alloys. This is not consistent with the spin-polarized DOS in the bulk band structure of Co and Ni at the Fermi energy in which the density of filled states is higher for minority spin-polarized electrons. Moreover, an

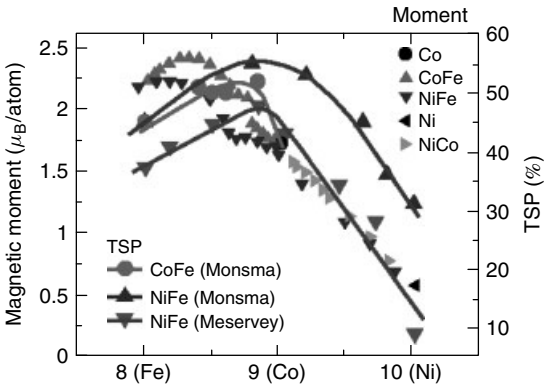

Figure 12. Tunneling spin polarization and magnetic moment per atom for different Co–Fe and Ni–Fe alloys. TSP data from Meservey and Monsma are shown for comparison with the Slater–Pauling curves (Monsma and Parkin, 2000; Cullity, 1972). (American Physical Society.)

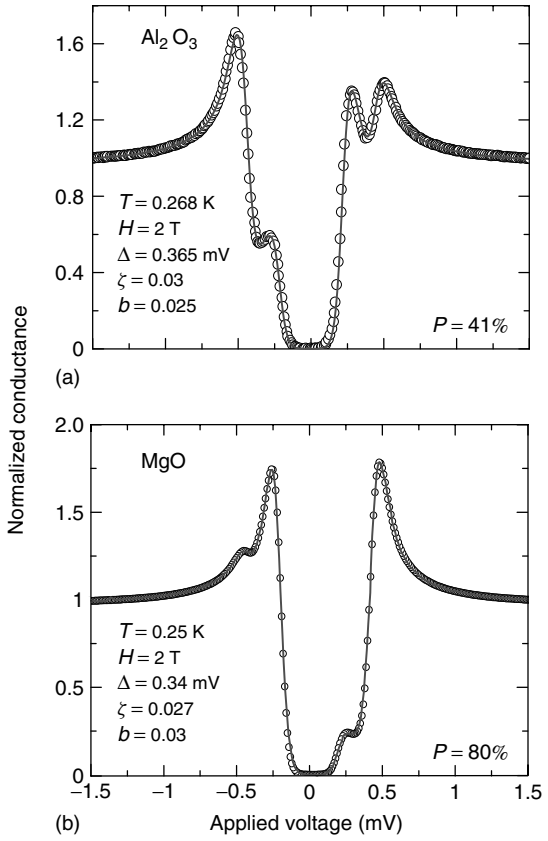

Figure 13. Conductance versus bias voltage curves (symbols) and fits (solid lines) from the structure of (a) AlSi/AlO_x/Co and (b) $Co_{70}Fe_{30}$/MgO/AlSi. The measurements were taken at ∼0.25 K in a field of 2 T applied in the plane of the films. The values for the TSP were extracted by fitting the data curves with the following fitting parameters indicated in the figure: superconducting gap Δ, depairing parameter ζ, and spin-orbit parameter b.

approximately linear relationship between magnetic moment per atom and spin polarization was found by Paraskevopoulos *et al*. who measured the spin polarization of ferromagnetic alloys comprising Ni diluted with the paramagnetic elements Cr, Cu, Mn, and Ti (Paraskevopoulos, Meservey and Tedrow, 1977). Since magnetization and spin polarization have very different physical origins, such a simple proportionality would be surprising. Indeed, for Ni alloys, this relationship appears to be derived from the decreasing tendency of oxidation of Ni as impurities are added to the metal. Indeed, with improved deposition techniques, and vacuum deposition systems with much lower base pressures, the TSP of Ni, Fe, Co, and their alloys has steadily increased over the years since the early measurements in the 1970s. Moreover, as discussed in Section 3 the dependence of the TSP on the magnetic moment of Co and Fe alloys is very sensitive to the diluent (Kaiser *et al*., 2005).

Using conventional amorphous alumina tunnel barriers TSP values of up to ∼55% (Monsma and Parkin, 2000) are found for conventional 3d ferromagnets, such as CoFe, but using highly textured crystalline MgO tunnel barriers TSP values of more than 85% (Parkin *et al*., 2004) can be achieved for otherwise the same ferromagnet, as illustrated in Figure 13. Such TSP values rival those previously observed only with half-metallic ferromagnets (Parker *et al*., 2002).

The magnitude and the sign of the TMR are strongly influenced by the electrode and tunnel barrier materials as well as the barrier/ferromagnet interface structure and chemistry. A particularly interesting example is that of the work by de Teresa *et al*. (1999b) who studied the magnetotransport properties of MTJs with one ferromagnetic electrode formed from a single crystalline thin film of the perovskite, $La_{1-x}Sr_xMnO_3$, which is nominally a majority spin-polarized half-metal, an epitaxial tunnel barrier formed from $SrTiO_3$, and a counterelectrode formed from a conventional 3d TM, cobalt. As shown in Figure 14, this MTJ device exhibits a negative TMR at zero bias, that is, the resistance is lowest when the $La_{1-x}Sr_xMnO_3$ and the Co moments are antiparallel to each other. Since the manganite is known to have only majority spin-polarized electrons at the Fermi energy (Park *et al*., 1998), de Teresa *et al*. concluded, therefore, that the polarization of the empty Co states into which the electrons tunnel across the $SrTiO_3$ barrier in the AP configuration must be predominantly *minority* spin polarized. This is exactly the opposite sign of polarization for electrons tunneling to and from Co through amorphous alumina tunnel barriers. de Teresa *et al*. argue that the $SrTiO_3$ barrier preferably favors tunneling of electrons with d character rather than the s character as in alumina because of the d character provided by the Ti. This interpretation is subject to some debate. For example, Oleinik, Tsymbal, and Pettifor (2002) suggest that

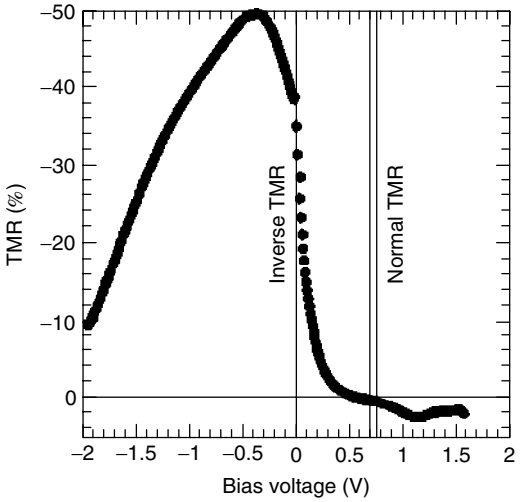

Figure 14. Bias dependence of the TMR ratio in Co/STO/LSMO tunnel junction. (Reprinted with permission de Teresa *et al*. copyright 1999, AAAs.)

the inversion of the TMR sign could be due to the formation of moments on the Ti atoms in the $SrTiO_3$ barrier which they calculate are exchange coupled antiparallel to the Co moments in the electrode. Another possibility is that defects in the tunnel barrier can give rise, through resonant tunneling, to an inversion of the TMR, as calculated by Tsymbal *et al*. (2003). Indeed, Sharma, Wang, and Nickel (1999) using composite tunnel barriers formed from bilayers of Ta_2O_5/Al_2O_3, and $Ni_{80}Fe_{20}$ electrodes, report a voltage dependence of TMR similar to that of de Teresa *et al*. They find negative TMR values, albeit small values of just a few percent, for electrons tunneling into the $NiFe/Ta_2O_5$ interface, which they find is strongly dependent on the oxidation time used to form the barrier, perhaps indicating the role of defects.

Another interesting system with regard to the relationship between TMR and TSP is tunnel junctions formed with RE–TM alloys, in particular, ferrimagnetic alloys formed from Co and Fe, and the RE metal Gd. In these alloys, which are amorphous, the TM moments are aligned antiparallel to that of Gd. These alloys show both negative and positive TSP, depending on their composition, and, the temperature, as shown in Figure 15 (Kaiser, Panchula and Parkin, 2005). This behavior that can be understood from the stronger temperature dependence of the magnetization of the RE subnetwork compared to that of the TM subnetwork, and the larger RE moment compared to the TM moment at low temperatures. Thus, there is a compensation temperature where the RE and TM subnetwork magnetizations exactly balance and the alloy has a zero net magnetization. Correspondingly, there is a compensation composition of the alloy at a given temperature where the net moment goes through zero as the RE/TM ratio is varied. As the temperature or composition

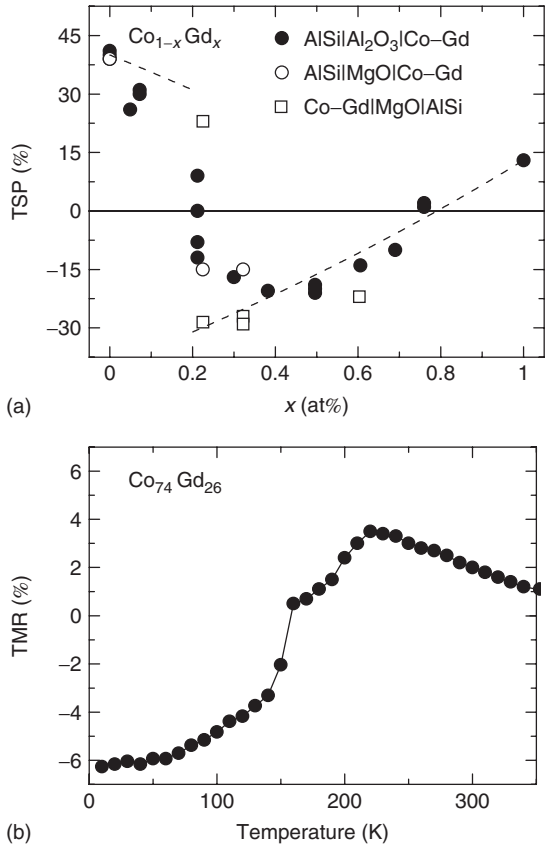

Figure 15. (a) TSP for Co–Gd alloys with various compositions. The line is a fit to the data. (b) TMR versus temperature for an MTJ with a $Co_{70}Fe_{30}$ electrode and a 50-Å thick $Co_{74}Gd_{26}$ counterelectrode (Kaiser, Panchula and Parkin, 2005). (American Physical Society.)

is varied through the corresponding compensation point, the sign of the TSP changes but the magnitude of the TSP is observed to be substantial at the compensation point when the net moment of the alloy goes to zero. This illustrates that a magnetic material can, in principle, have zero magnetization but a finite spin polarization, clearly proving that the two quantities are not related to one another in any simple way.

By inserting a thin CoFe layer at the interface between a CoFeGd alloy and a MgO tunnel barrier, large negative TMR values of $\sim -50\%$ can be achieved at room temperature (Kaiser and Parkin, 2006). The high negative spin polarization, as well as the tunable coercivity, amorphous structure, and low uniaxial anisotropy of RE–TM alloys make them promising candidates for use in MTJ-based devices, such as flux-closed double-tunnel junctions for MRAM memory cells (Kaiser and Parkin, 2006).

The Julliere relationship shown in equation (3) indicates that the magnitude of the TMR ratio diverges when the spin polarization of the ferromagnetic electrode approaches 100%. This is one of the reasons why half-metallic ferromagnets

have been of considerable interest in recent years. There are several classes of half-metals, as discussed in **Half-metals, Volume 4**, which can be both minority spin polarized, as, for example, magnetite (Fe_3O_4) (Walz, 2002; Ziese, 2002), and majority spin polarized, as, for example, $La_{1-x}Sr_xMnO_3$, mentioned in the preceding text. MTJs with $La_{1-x}Sr_xMnO_3$ electrodes and $SrTiO_3$ (and $CaTiO_3$) barriers have been demonstrated to show very high TMR values, exceeding ∼1000% (Sun *et al*., 1998; Bowen *et al*., 2003), but only at low temperatures. Though the Curie temperature of $La_{1-x}Sr_xMnO_3$ is close to or just above room temperature (depending on the oxygen concentration and the Sr dopant concentration), the TSP has a much stronger dependence than the magnetization, and typically falls to zero at about half the Curie temperature, for reasons which are not fully understood.

Recently, several groups have reported substantial TMR ratios in MTJs formed with Heusler alloy electrodes (Park *et al*., 1998; Webster, 1969; Kubler, Williams and Sommers, 1983; Galanakis, Dederichs and Papanikolaou, 2002). Heusler alloys are a large class of ternary intermetallic compounds with the chemical formula X_2YZ, which have been predicted to be half-metallic. Sakuraba *et al*. (2005) have fabricated Co_2MnSi/AlO_x/CoFe MTJs, which display a TMR ratio of 70% at room temperature, which is comparable to the highest TMR ratios reported in MTJs with TM electrodes and AlO_x tunnel barriers. They have successfully grown highly oriented Co_2MnSi layers on single crystal MgO substrates. Theoretical calculations predict that Co_2MnSi with the $L2_1$ crystal structure can achieve nearly 100% spin polarization, but chemical disorder or the formation of other crystal structures, such as B2 and A2, can significantly affect the spin polarization (Galanakis, Dederichs and Papanikolaou, 2002; Picozzi, Continenza and Freeman, 2004). Therefore, in addition to providing a clean interface between the ferromagnetic electrode and the insulator, the highly textured $L2_1$-ordered Co_2MnSi was essential to finding a high TMR ratio.

A number of other reports on MTJs using various Heusler alloys have been reported including alloys such as Co_2MnAl (Sakuraba *et al*., 2006a), Co_2FeSi (Gercsi *et al*., 2006), $Co_2FeAl_{0.5}Si_{0.5}$ (Tezuka *et al*., 2006a,b), and $Co_2Cr_{0.6}Fe_{0.4}Al$ (Marukame *et al*., 2007). It is interesting to note that the TMR ratio is very sensitive to the temperature in many MTJs with Heusler alloy electrodes. It is interesting that this is similar to the case of MTJs with manganite electrodes. For example, Sakuraba *et al*. (2006a) find that an MTJ formed with a Co_2MnAl electrode and a MgO barrier displays a TMR ratio of 570% at 4 K, but that this is more than eight times higher than its room-temperature value (see Figure 16). The large TMR ratio at low temperature indicates that Co_2MnAl is nearly half-metallic. In addition, bias-voltage-dependent conductance measurements revealed that the energy gap (Δ) between the Fermi level and the bottom of the minority spin conduction band is only ∼10 meV (Sakuraba *et al*., 2006b), which is more than two times smaller than the thermal fluctuation energy at room temperature (26 meV). The drop of the TMR ratio at the temperature is thus associated with thermal mixing of the spin state of the

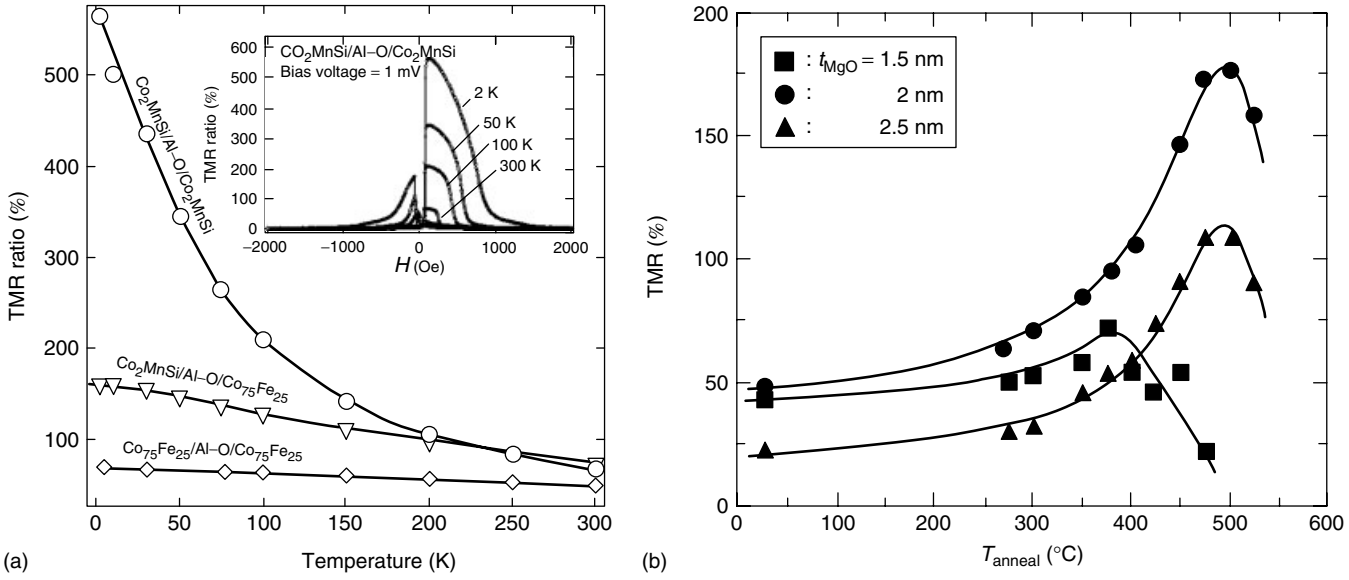

Figure 16. (a) Temperature dependence of the TMR ratio for $Co_2MnSi/Al-O/Co_2MnSi$ MTJ. TMR curves at the corresponding temperature are shown in the inset. All measurements were conducted under an applied bias voltage of +1 mV (Sakuraba *et al*., 2006a). (b) Annealing temperature dependence of TMR measured at RT for an MTJ consisting of 30-nm $Co_2FeAl_{0.5}Si_{0.5}/t_{MgO}$ MgO/5-nm $Co_2FeAl_{0.5}Si_{0.5}$/3-nm $Co_{75}Fe$/15-nm $Ir_{22}Mn_{78}$/Ta (Tezuka *et al*., 2006b). (American Physical Society.)

electrons, which thereby obscures the half-metallic nature of the Heusler alloy. Increasing the energy gap Δ by varying the composition of the Heusler alloy leads to half-metallic behavior at higher temperatures. Indeed, TMR values exceeding $\sim$100% at room temperature have recently been reported by several groups (Tezuka *et al*., 2006b; Marukame *et al*., 2007). The highest TMR values to date at room temperature have been reported in MTJs with $L2_1$-$Co_2FeAl_{0.5}Si_{0.5}$ full Heusler alloys for both electrodes and a MgO tunnel barrier (Tezuka *et al*., 2006b).

6 TEMPERATURE AND BIAS VOLTAGE DEPENDENCE OF TMR

In many MTJs the magnitude of the TMR decreases strongly with increasing temperature. There are several possible mechanisms that can be responsible for such an effect including thermally excited magnons in the ferromagnetic electrodes, thermal excitation of magnetic impurities or defects in the tunnel barrier or at the electrode/barrier interfaces, and thermal variations of the electronic structure at elevated temperatures. These effects give rise to a decrease in the interfacial magnetization and, thereby, the spin polarization (MacDonald, Jungwirth and Kasner, 1998; Shang *et al*., 1998; Moodera, Nowak and van de Veerdonk, 1998; Bratkovsky, 1998). A strong temperature dependence of the TMR is often related to a poor quality of the interface between the ferromagnetic electrode and the tunnel barrier. Since the most commonly used tunnel barriers are oxides, small amounts of excess oxygen, for example, oxygen physisorbed on the surface of the oxide barrier before deposition of the ferromagnetic electrode, can result in oxidation of ferromagnetic metal electrodes. Since oxides of Ni and Co are antiferromagnetic, and several oxides of Fe are antiferromagnetic, any oxidation of the electrode is likely to lead to a decrease in the spin polarization of the tunneling current. This is likely to be strongly temperature dependent because of the comparatively low Neel temperatures of the antiferromagnetic oxides. 'Loose' spins can readily depolarize the tunneling current.

It is interesting to note that the temperature dependence of the tunneling current is usually much weaker in the P as compared to the AP alignment of the magnetic electrodes as shown in Figure 17. In the case of MgO tunnel barriers, the temperature dependence of the junction resistance for P alignment of the ferromagnetic electrodes is almost negligible compared to that of Al_2O_3 barriers. In both barriers, most of the increase in the TMR at lower temperatures is due to the increase in the resistance of the AP state.

Most MTJs show a substantial decrease of TMR as the bias voltage is increased. Zhang *et al*. (1997) proposed that this was due to inelastic scattering by magnon excitations at the ferromagnet/insulator interface. When hot electrons tunnel from one electrode across the insulating barrier into the opposing ferromagnet/insulator interface, they may lose their energy by emitting a magnon, which may result in flipping of the electron's spin. More magnons are created with increasing bias voltage, resulting in reduced TMR values. The energy dependence of the spin polarization of the DOS in the ferromagnetic electrodes due to details of their band structure, especially the magnitude of the exchange splitting and the energy width of the exchange split bands, will also reduce the TMR at high bias (Moodera, Nowak and van de Veerdonk, 1998).

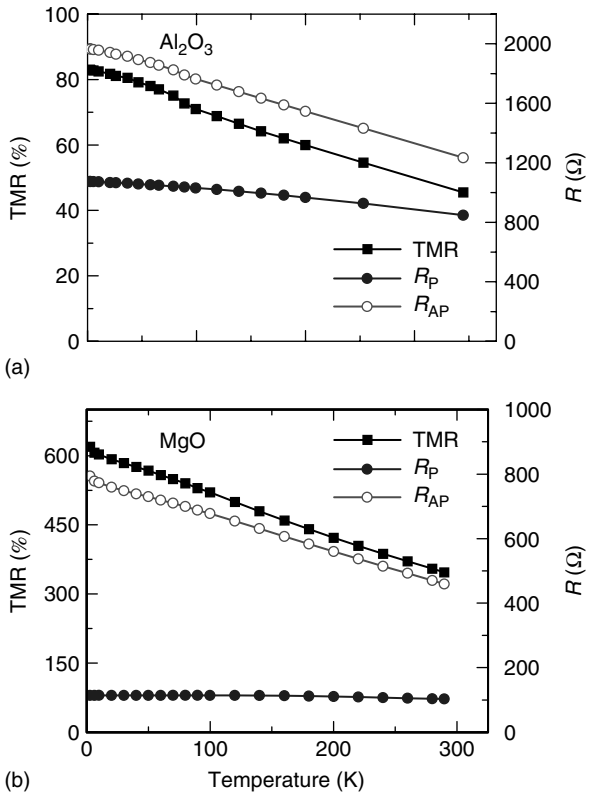

Figure 17. (a) Temperature dependence of TMR, parallel (R_P) and antiparallel (R_{AP}) resistance of (a) Ta/IrMn/CoFe/26 AlO_x/CoFe and (b) Ta/IrMn/CoFe/MgO(100)/CoFe.

Ding *et al*. (2003) reported the absence of a zero-bias anomaly and an almost constant TMR with bias voltage for spin-polarized electron tunneling between a Co(0001) surface and an amorphous magnetic tip across a vacuum barrier using a scanning tunneling microscopy technique. The zero-bias anomaly, very often observed in planar tunnel junctions with insulator barriers, was therefore attributed to defect scattering from localized states in the barrier, rather than to magnon creation or spin excitations at the interfaces (Zhang and White, 1998; Tsymbal, Mryasov and LeClair, 2003). Planar

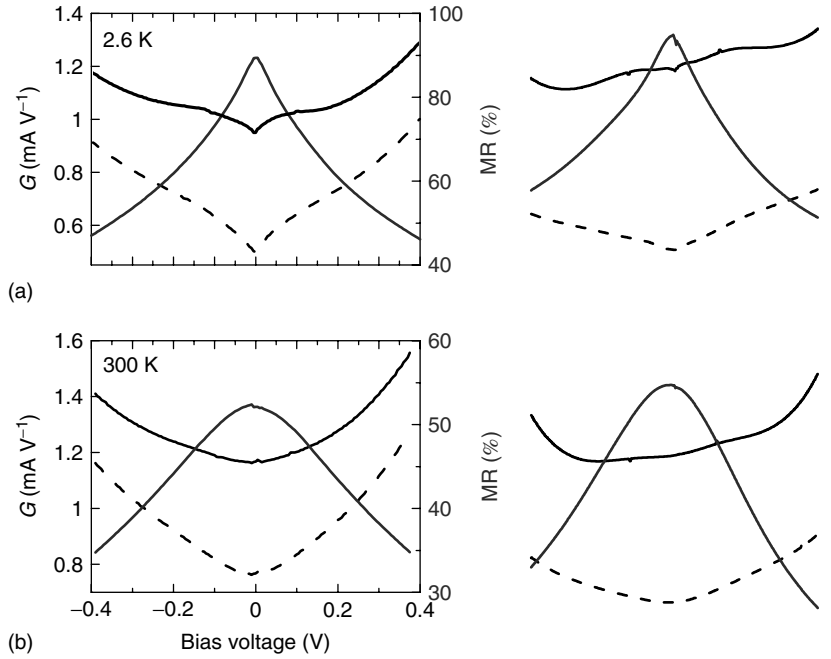

Figure 18. Conductance and TMR curves for MTJs with AlO_x barrier measured at (a) 2.6 K and (b) room temperature.

tunnel junctions often contain significant defects within the barrier and at its interfaces which can lead to significant decreases in the effective tunneling barrier height (Rippard, Perrella and Buhrman, 2001).

The bias voltage dependence of TMR should be symmetric with regard to positive and negative voltages when the magnetic electrodes are identical, and the barrier is symmetric in shape. Figure 18 shows typical bias voltage dependences of TMR and conductance for Al_2O_3 (left panels) and MgO (right panels) barriers at 2.6 K and room temperature. The Al_2O_3 barrier shows a symmetric bias dependence while the MgO does not, which may be due to the different growth methods (Al_2O_3: plasma oxidation, MgO: reactive sputtering). At low temperatures, both barriers display zero-bias anomalies in the P configuration but MgO does not show as prominent a zero-bias anomaly as Al_2O_3 in the AP configuration. Also the prominent broad valleys in conductance at $\sim$0.27 V are shown for P configuration in MgO barrier; these may be ascribed to the coherent tunneling of certain symmetries as mentioned in the preceding text.

The TMR of MTJs decreases with increased voltage and temperature. This is thought to be due to inelastic tunneling from phonons and magnons at the interface between the ferromagnetic electrode and the insulator, and impurities both at these interfaces and within the interior of the tunnel barrier, which may result in flipping of the electron spin and so a decrease in the spin polarization of the tunneling electrons. The predominant elastic tunneling, where incident electrons from one electrode tunnel through the barrier without loss of energy to the opposite electrode, gives rise to a significant background of the conductance versus voltage curve. It is thus important to clarify the relationship between the tunnel conductance and the interface structure of an MTJ. Inelastic electron tunneling spectroscopy (IETS), is the measurement of $\mathrm{d}^2I/\mathrm{d}V^2$ versus V and was first developed by Jaklevic and Lambe (1966). This is a very sensitive spectroscopic technique, which has been used to study the electronic structure of chemical compounds and complexes incorporated within insulating barriers, as well as the detailed electronic nature of interfaces within MIM tunnel junctions. The observation of both the vibrational as well as electronic spectra (defects, impurities, magnons, and phonons) has been carried out. Higher-order derivatives of the conductance versus voltage curves often reveal peaks at energies corresponding to those of the inelastic tunneling channels, where incident electrons lose energy inside the tunnel barrier or at the barrier/electrode interfaces.

A typical measurement is shown in Figure 19 for both Al_2O_3 and MgO barriers. The IETS signal from the AP configuration compared to the P configuration is large and more sensitive to the spin-dependent scattering, indicating that the spin-flip inelastic excitations are dominant for the AP configuration. In case of Al_2O_3, typical phonon spectra of the Al (33 mV) and the Al–O longitudinal optical (LO) modes (20 and 120 mV) were observed as shown in Figure 19(a). For MgO barriers in Figure 19(b), typical phonon spectra for the MgO optical (O) phonon at 27 mV (Klein *et al.*, 1973) and the MgO LO surface mode at 83 mV (Plesiewicz

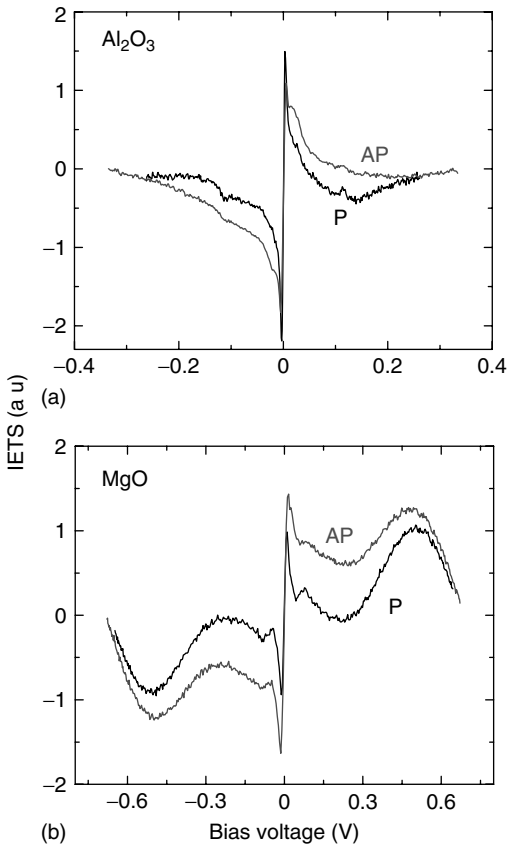

Figure 19. (a) Inelastic tunneling spectroscopy (IETS) of (a) CoFe/AlO_x/CoFe and (b) CoFe/(100)MgO/CoFe measured at 2.8 K.

and Adler, 1986) were observed. Huge peaks around zero bias from both orientations result from magnon excitations, which are reported to be absent with nonmagnetic electrodes (Moodera, Nowak and van de Veerdonk, 1998; van de Veerdonk, Moodera and de Jonge, 1999; Han *et al*., 2001). The broad peaks appearing around 500–600 mV have never been observed in the MTJs with Al–O tunnel barriers. The high-energy peaks reveal the information on the wave-function-dependent conductance channels in MgO that are related to the opening of the additional conduction channels when the applied bias is higher than the band edge of that spin Δ_x band (Ando *et al*., 2005).

7 SPIN-DEPENDENT TUNNELING IN OTHER SYSTEMS

When a tunnel barrier is itself a ferromagnetic insulator the tunnel barrier height will be different for spin-up and spin-down electrons. This means that the tunneling current will be spin filtered since the probability of tunneling is extremely sensitive to the barrier height. This is a very efficient method for polarizing current even when the metal electrodes are nonmagnetic and is of interest for spin injection into semiconductors without the need for ferromagnetic metal electrodes. However, it has so far been difficult to create MTJs with useful properties because of the difficulty of independently setting the magnetic moment direction of the insulating barrier and that of one of the metallic electrodes, which is required to observe a TMR effect. One recent example is that of Leclair *et al*. (2002) who reported a TMR ratio of more than 100% at 7 K in an MTJ with a barrier formed from EuS with one nonmagnetic electrode formed from Al and one ferromagnetic electrode formed from Gd. However, the magnetic switching characteristics of this device were quite poor. Moreover, since EuS has a very low Curie temperature, well below room temperature, this material is not useful for applications at room temperature and above.

Finally, we briefly discuss spin-dependent tunneling in granular systems. Owing to the quantized nature of electron charge, a tunneling current is associated with a series of events in which individual electrons tunnel across a barrier. Consequently, Coulomb interaction of electrons can significantly influence the tunneling process. Consider a double barrier tunnel junction, where the electron has to first tunnel through the first barrier and land on a middle electrode before tunneling through the second barrier. Suppose that the middle electrode is temporarily occupied by the preceding electrons that tunneled through the first barrier. In order for the next electron to tunnel through the first barrier, it has to overcome the charging energy associated with the Coulomb interaction with the other electrons placed in the middle electrode. This effect is called *Coulomb blockade*, in which the Coulomb interaction 'blocks' the electron from tunneling through a barrier. The magnitude of this charging energy is inversely proportional to the size of the middle electrode. Consequently, it is possible to trap a single electron in the middle 'island' (electrode) by reducing the island size such that the charging energy exceeds the thermal fluctuation energy. Double-tunnel junction devices capable of trapping a single electron in the middle island are typically called *single electron transistors*, since the middle island can act as a gate, which controls the tunneling current between the two barriers. Intensive efforts have been made to create useful single electron transistors, in particular, by using semiconductor quantum dots.

The Coulomb blockade effect has been observed in tunnel junctions using ferromagnetic granular nanoparticles as the middle islands (Mitani *et al*., 1998; Zare-Kolsaraki, Hackenbroich and Micklitz, 2002). Granular nanoparticles can be formed, for example, by cosputtering aluminum and gold in an oxygen atmosphere (Barsadeh *et al*., 1994), which results in segregated gold particles embedded in the

aluminum oxide matrix since gold is inert to oxygen. Typical diameter of the nanoparticles is in the range of a few nanometers with a relatively large distribution. A number of groups have reported observation of the Coulomb blockade effect via nanoparticles embedded in an insulating matrix.

Coulomb blockade is a pure charge effect of the electrons. Recently, the role of the spin degree of freedom on single electron tunneling has attracted great interest. In particular, much theoretical work has been carried out on the prediction of the TMR ratio for the case of single electron tunneling (Barnas and Fert, 1998; Takahashi and Maekawa, 1998). Experimentally, Yakushiji *et al*. have reported oscillations of the TMR ratio with the bias voltage across the barrier in MTJs with Co nanoparticles embedded in an AlO_x layer (Yakushiji *et al*., 2005). Interestingly, the TMR ratio was observed to oscillate between −10 and 15% when the voltage was increased from 0 to ∼0.2 V. This oscillation was attributed to an oscillation of the position of the Fermi level lying between either the majority or the minority spin states which are discretized due to the geometrical confinement of the nanoparticle.

Spin accumulation occurs frequently in magnetic/nonmagnetic hybrid systems. For example, when electron flows from a nonmagnetic layer to a ferromagnetic layer, electrons whose spin direction are opposite to the magnetization direction of the ferromagnetic layer will be reflected from the layer. Consequently, electrons with a certain spin direction will pile up at the interface of the magnetic/nonmagnetic layer. This effect can occur, for example, in current perpendicular to the plane (CPP) GMR devices.

8 CONCLUSION

Spin-dependent tunneling junctions have a long history dating back to more than 30 years but it is only in the past decade that MTJs with significant values of TMR at room temperature have been fabricated. A detailed understanding of the relationship of the TMR and the corresponding spin polarization of the tunneling current to the ferromagnetic and tunnel barrier materials forming the MTJ is developing. It is clear that it is not simply the electronic structure of the ferromagnetic electrode that determines the magnitude of the spin-dependent tunneling. Rather the spin polarization of the tunneling current can be strongly modified by tunneling matrix elements that themselves depend on chemical bonding at the ferromagnet/tunnel barrier interface and also on the symmetry of the conduction band wave functions. This means that magnetic metals which are only weakly magnetic can give rise, by suitable wave function or chemical bond engineering, to highly spin-polarized currents. Conversely, strongly magnetic metals may give only very weakly spin-polarized tunnel currents. An important conclusion is that the TSP is not related in any simple way to the magnetization of the magnetic electrodes. For example, RE–TM ferrimagnetic electrodes with no net magnetic moment can give rise to highly spin-polarized tunneling current (Miyazaki and Tezuka, 1995).

MTJs have a promising future both as highly sensitive field sensors and as magnetic memory storage elements (Parkin *et al*., 2003). By contrast with metallic spin-valve sensors whose magnetoresistance is limited to 10–20% at room temperature there is no theoretical limit to the TMR of MTJs. Whilst the very high TMR of >350% at room temperature observed with crystalline MgO tunnel barriers is very attractive for sensing and memory applications it seems likely that new materials with even higher magnetoresistance values will be found in the future which could have even wider technological applications.

REFERENCES

Ando, Y., *et al*. (2005). *Applied Physics Letters*, **87**, 142502.

Baibich, M.N., *et al*. (1988). *Physical Review Letters*, **61**, 2472.

Banhart, J., Ebert, H. and Vernes, A. (1997). *Physical Review B*, **56**, 10165.

Barnas, J. and Fert, A. (1998). *Europhysics Letters*, **44**, 85.

Barsadeh, E., *et al*. (1994). *Physical Review B*, **50**, 8961.

Barthélémy, A., *et al*. (2002). *Journal of Magnetism and Magnetic Materials*, **242**, 68.

Berkowitz, A.E., *et al*. (1992). *Physical Review Letters*, **68**, 3745.

Bibes, M., *et al*. (2003). *Applied Physics Letters*, **82**, 3269.

Bowen, M., *et al*. (2001). *Applied Physics Letters*, **79**, 1655.

Bowen, M., *et al*. (2003). *Applied Physics Letters*, **82**, 233.

Bratkovsky, A.M. (1998). *Journal of Applied Physics*, **72**, 2334.

Brody, T.P. (1996). *Journal of the Society for Information Display*, **4**, 117.

Brody, P. and Page, D. (1968). *Electronics*, **41**, 100.

Bruno, P. (1995). *Physical Review B*, **52**, 411.

Bruno, P. and Chappert, C. (1991). *Physical Review Letters*, **67**, 1602.

Butler, W.H., *et al*. (2001). *Physical Review Bhysical Review B*, **63**, 054416.

Butler, W.H. and Gupta, A. (2004). *Nature Materials*, **3**, 845.

Campbell, I.A., Fert, A. and Jaoul, O. (1970). *Journal of Physics C: Solid State Physics*, **3**, S95.

Chien, C.L. (1995). In *Annual Review of Materials Science*, Wessels, B.W. (Ed.), Annual Reviews Inc.: Palo Alto, p. 129.

Cullity, B.D. (1972). *Introduction to Magnetic Materials*, Addison Wesley, Reading, MA.

Dedkov, Y.S., Rüdiger, U. and Güntherodt, G. (2002). *Physical Review B*, **65**, 064417.

Deshmukh, M.M., *et al*. (1999). *Applied Physics Letters*, **75**, 1631.

Ding, H.F., *et al*. (2003). *Physical Review Letters*, **90**, 116603.

Djayaprawira, D.D., *et al*. (2005). *Applied Physics Letters*, **86**, 092502.

Duke, C.B. (1969). *Tunneling in Solids*, Academic: New York.

Faure-Vincent, J., *et al*. (2002). *Physical Review Letters*, **89**, 107206.

Faure-Vincent, J., *et al*. (2003). *Applied Physics Letters*, **82**, 4507.

Feder, R. (1985).

Fert, A. and Bruno, P. (1994). In *Ultrathin Magnetic Structures*, Heinrich, B. and Bland, J.A.C. (Eds.), Springer-Verlag: Berlin, p. 82.

Fert, A. and Campbell, I.A. (1968). *Physical Review Letters*, **21**, 1190.

Gadzuk, J.W. (1969). *Physical Review*, **182**, 416.

Galanakis, I., Dederichs, P.H. and Papanikolaou, N. (2002). *Physical Review B*, **66**, 174429.

Gercsi, Z., *et al*. (2006). *Applied Physics Letters*, **89**, 082512.

Gijs, M.A.M. and Bauer, G.E.W. (1997). *Advances in Physics*, **46**, 285.

Han, X-F., *et al*. (2001). *Applied Physics Letters*, **78**, 2533.

Ikeda, S., Hayakawa, J., Min Lee, Y., *et al*. (2006). Dependence of tunnel magnetoresistance on ferromagnetic electrode materials in MgO-barrier magnetic tunnel junctions. http://arxiv.org/abs/cond-mat/060855.

Jaklevic, R.C. and Lambe, J. (1966). *Physical Review Letters*, **17**, 1139.

Julliere, M. (1975). *Physics Letters A*, **54**, 225.

Kaiser, C., *et al*. (2005). *Physical Review Letters*, **94**, 247203.

Kaiser, C., Panchula, A.F. and Parkin, S.S.P. (2005). *Physical Review Letters*, **95**, 047202.

Kaiser, C. and Parkin, S.S.P. (2006). *Applied Physics Letters*, **88**, 112511.

Katayama, T., *et al*. (2006). *Applied Physics Letters*, **89**, 112503.

Kim, T.H. and Moodera, J.S. (2004). *Physical Review B*, **69**, 020403(R).

Klaua, M., *et al*. (2001). *Physical Review B*, **64**, 134411.

Klein, J., *et al*. (1973). *Physical Review B*, **7**, 2336.

Kubler, J., Williams, A.R. and Sommers, C.B. (1983). *Physical Review B*, **28**, 1745.

LeClair, P. *et al*. (2002). *Applied Physics Letters*, **80**, 625.

Levy, P.M. (1994). In *Solid State Physics*, Ehrenreich, H. and Turnbull, D. (Eds.), Academic Press: New York, p. 367.

MacDonald, A.H., Jungwirth, T. and Kasner, M. (1998). *Physical Review Letters*, **81**, 705.

Maekawa, S. and Gafvert, U. (1982). *IEEE Transactions on Magnetics*, **18**, 707.

Maki, K. (1964). *Progress of Theoretical Physics*, **32**, 29.

Mallison, W.H., Miller, R.E. and Kleinsasser, A.W. (1995). *IEEE Transactions on Applied Superconductivity*, **5**, 2330.

Mao, S.N., *et al*. (2006). *IEEE Transactions on Magnetics*, **42**, 97.

Marukame, T., *et al*. (2007). *Applied Physics Letters*, **90**, 012508.

Mathon, J. (1991). *Contemporary Physics*, **32**, 143.

Mathon, J. and Umerski, A. (2001). *Physical Review B*, **63**, 220403.

McGuire, T.R. and Potter, R.I. (1975). *IEEE Transactions on Magnetics*, **11**, 1018.

Meiklejohn, W.H. and Bean, C.P. (1956). *Physical Review*, **102**, 1413.

Meservey, R. and Tedrow, P.M. (1994). *Physics Reports*, **238**, 173.

Mitani, S., *et al*. (1998). *Physical Review Letters*, **81**, 2799.

Mitani, S., Moriyama, T. and Takanashi, K. (2003). *Journal of Applied Physics*, **93**, 8041.

Miyazaki, T. and Tezuka, N. (1995). *Journal of Magnetism and Magnetic Materials*, **139**, L231.

Miyazaki, T., Yaoi, T. and Ishio, S. (1991). *Journal of Magnetism and Magnetic Materials*, **98**, L7.

Moodera, J.S., *et al*. (1995). *Physical Review Letters*, **74**, 3273.

Moodera, J.S., Nowak, J. and van de Veerdonk, R.J.M. (1998). *Physical Review Letters*, **80**, 2941.

Monsma, D.J. and Parkin, S.S.P. (2000). *Applied Physics Letters*, **77**, 720.

Mott, N.F. (1936). *Proceedings of the Royal Society of London*, **A153**, 699.

Mott, N.F. (1964). *Advances in Physics*, **13**, 325.

Mott, N.F. and Jones, H. (1936). *Theory of the Properties of Metals and Alloys*, Oxford University Press.

Nadgorny, B., *et al*. (2000). *Physical Review B*, **61**, R3788.

Nogués, J. and Schuller, I.K. (1999). *Journal of Magnetism and Magnetic Materials*, **192**, 203.

Nowak, J. and Rauluszkiewicz, J. (1992). *Journal of Magnetism and Magnetic Materials*, **109**, 79.

Nowak, E.R., Weissman, M.B. and Parkin, S.S.P. (1999). *Applied Physics Letters*, **74**, 600.

O'Handley, R.C. (1999). *Modern Magnetic Materials: Principles and Applications*, John Wiley & Sons.

Oleinik, I.I., Tsymbal, E.Y. and Pettifor, D.G. (2000). *Physical Review B*, **62**, 3952.

Oleinik, I.I., Tsymbal, E.Y. and Pettifor, D.G. (2002). *Physical Review B*, **65**, 020401(R).

Paraskevopoulos, D., Meservey, R. and Tedrow, P.M. (1977). *Physical Review B*, **16**, 4907.

Park, J.H., *et al*. (1998). *Nature*, **392**, 794.

Parkin, *et al*. unpublished.

Parkin, S.S.P. (1991). *Physical Review Letters*, **67**, 3598.

Parkin, S.S.P. (1993). *Physical Review Letters*, **71**, 1641.

Parkin, S.S.P. (1994). In *Ultrathin Magnetic Structures*, Heinrich, B. and Bland, J.A.C. (Eds.), Spinger-Verlag, Berlin, p. 148.

Parkin, S.S.P. (1995). In *Annual Review of Materials Science*, Wessels, B.W. (Ed.), Annual Reviews Inc.: Palo Alto, p. 357.

Parkin, S.S.P. (2006). *Materials Research Society Bulletin*, **31**, 389.

Parkin, S.S.P., *et al*. (1999). *Journal of Applied Physics*, **85**, 5828.

Parker, J.S., *et al*. (2002). *Physical Review Letters*, **88**, 196601.

Parkin, S.S.P., *et al*. (2003). *Proceedings of the IEEE*, **91**, 661.

Parkin, S.S.P., *et al*. (2004). *Nature Materials*, **3**, 862.

Parkin, S.S.P., Bhadra, R. and Roche, K.P. (1991). *Physical Review Letters*, **66**, 2152.

Parkin, S.S.P., Li, Z.G. and Smith, D.J. (1991). *Applied Physics Letters*, **58**, 2710.

Parkin, S.S.P., More, N. and Roche, K.P. (1990). *Physical Review Letters*, **64**, 2304.

Picozzi, S., Continenza, A. and Freeman, A.J. (2004). *Physical Review B*, **69**, 094423.

Plesiewicz, W. and Adler, J.G. (1986). *Physical Review B*, **34**, 4583.

Rippard, W.H., Perrella, A.C. and Buhrman, R.A. (2001). *Applied Physics Letters*, **78**, 1601.

Rowell, J.M., Gurvitch, M. and Geerk, J. (1981). *Physical Review B*, **24**, 2278.

Sakuraba, Y., *et al*. (2005). *Japanese Journal of Applied Physics*, **44**, L1100.

Sakuraba, Y., *et al*. (2006a). *Applied Physics Letters*, **88**, 192508.

Sakuraba, Y., *et al*. (2006b). *Applied Physics Letters*, **89**, 052508.

Simmons, J.G. (1963). *Journal of Applied Physics*, **34**, 1793.

Shang, C.H., *et al*. (1998). *Physical Review B*, **58**, R2917.

Sharma, M., *et al*. (2000). *Applied Physics Letters*, **77**, 2219.

Sharma, M., Wang, S.X. and Nickel, J.H. (1999). *Physical Review Letters*, **82**, 616.

Slonczewski, J.C. (1989). *Physical Review B*, **39**, 6995.

Smit, J. (1951). *Physica*, **17**, 612.

Soulen, R.J. Jr., Byers, J.M., Osofsky, M.S., *et al*. (1998). Measuring the spin polarization of a metal with a superconducting point contact. *Science*, **282**, 85.

Stearns, M.B. (1977). *Journal of Magnetism and Magnetic Materials*, **5**, 167.

Suezawa, Y., Takahashi, F. and Gondo, Y. (1992). *Japanese Journal of Applied Physics*, **31**, L1415.

Sun, J.Z., *et al*. (1998). *Applied Physics Letters*, **73**, 1008.

Takahashi, S. and Maekawa, S. (1998). *Physical Review Letters*, **80**, 1758.

Tedrow, P.M. and Meservey, R. (1973). *Physical Review B*, **7**, 318.

de Teresa, J.M., *et al*. (1999a). *Physical Review Letters*, **82**, 4288.

de Teresa, J.M., *et al*. (1999b). *Science*, **286**, 507.

Tezuka, N., *et al*. (2006a). *Applied Physics Letters*, **89**, 112514.

Tezuka, N., *et al*. (2006b). *Applied Physics Letters*, **89**, 252508.

Tsymbal, E.Y., *et al*. (2003). *Physical Review Letters*, **90**, 186602.

Tsymbal, E.Y., Mryasov, O.N. and LeClair, P.R. (2003). *Journal of Physics: Condensed Matter*, **15**, R109.

Tsymbal, E.Y., Oleinik, I.I. and Pettifor, D.G. (2000). *Journal of Applied Physics*, **87**, 5230.

Valet, T. and Fert, A. (1993). *Physical Review B*, **48**, 7099.

van de Veerdonk, R.J.M., Moodera, J.S. and de Jonge, W.J.M. (1999). *Journal of Magnetism and Magnetic Materials*, **198–199**, 152.

Walz, F. (2002). *Journal of Physics: Condensed Matter*, **14**, R285.

Wang, D.X., *et al*. (2004). *IEEE Transactions on Magnetics*, **40**, 2269.

Webster, P.J. (1969). *Contemporary Physics*, **10**, 559.

Wolf, E.L. (1989). *Principles of Electron Tunneling Spectroscopy*, Oxford University Press: New York.

Worledge, D.C. and Geballe, T.H. (2000). *Physical Review B*, **62**, 447.

Yakushiji, K., *et al*. (2005). *Nature Materials*, **4**, 57.

Yang, H., *et al*. (2006). *Applied Physics Letters*, **88**, 182501.

Yoon, T.S., *et al*. (2004). *Applied Physics Letters*, **85**, 82.

Yuasa, S., *et al*. (2004). *Nature Materials*, **3**, 868.

Zare-Kolsaraki, H., Hackenbroich, B. and Micklitz, H. (2002). *Europhysics Letters*, **57**, 866.

Zhang, S., *et al*. (1997). *Physical Review Letters*, **79**, 3744.

Zhang, X-G., Butler, W.H. and Bandyopadhyay, A. (2003). *Physical Review B*, **68**, 092402.

Zhang, J. and White, R.M. (1998). *Journal of Applied Physics*, **83**, 6512.

Zhuravlev, M.Y., Tsymbal, E.Y. and Vedyayev, A.V. (2005). *Physical Review Letters*, **94**, 026806.

Ziese, M. (2002). *Reports on Progress in Physics*, **65**, 143.

FURTHER READING

LeClair, P., *et al*. (2000). *Physical Review Letters*, **86**, 1066.

LeClair, P., *et al*. (2001). *Physical Review B*, **64**, 100406.

Moodera, J.S., *et al*. (1999). *Physical Review Letters*, **83**, 3029.

Nagahama, T., *et al*. (2001). *Applied Physics Letters*, **79**, 4381.

Yuasa, S., Nagahama, T. and Suzuki, Y. (2002). *Science*, **297**, 234.

Spin Angular Momentum Transfer in Magnetoresistive Nanojunctions

Jonathan Z. Sun
IBM T.J. Watson Research Center, Yorktown Heights, NY, USA

1 INTRODUCTION

Spin-angular momentum transfer (or spin transfer for short) concerns the influence of a spin-polarized current on its host magnetic conductor. This phenomenon originates from the exchange of angular momentum between a spin-polarized current and the magnetization – a concept that has been developing over the years (Berger, 1978, 1984, 1988, 1992, 1996; Hung and Berger, 1986; Bazaliy, Jones and Zhang, 1998), which resulted in the theoretical prediction of the spin-current-induced magnetic excitation and reversal (Slonczewski, 1989, 1996), and its quantitative experimental verification (Katine *et al*., 2000; Albert, Katine, Buhrman and Ralph, 2000).

A sketch for the basic concept of spin-transfer effect is shown in Figure 1. The lower left corner of the figure presents a two-ferromagnet layered spin-valve structure. A current passes through the left ferromagnet (F1) and becomes spin polarized. When it passes through the second, thinner ferromagnet on the right (F2), the spin polarization of the current may have to change direction, depending on the relative alignment of the magnetization between F1 and F2. This is illustrated at the upper left of the figure. Here N denotes a nonmagnetic conductor, or in the case of a magnetic tunnel junction (MTJ), the N between F1 and F2 could also be a tunnel barrier.

In essence, it is the repolarization process that causes F2 to experience an effective torque. This spin-current-induced torque, or spin torque for short, appears along the same direction as the damping torque experienced by the precessing F2. The spin torque can either be in the same direction as the damping or in the opposite direction, depending on the direction of current flow and the relative spin orientation between F1 and F2. When the spin torque is in the direction opposite to the damping of F2, the magnetization would amplify any deviation from its equilibrium state. When the spin torque is sufficiently strong, this amplification process can cause F2 to precess with an ever-increasing cone angle going past $\pi/2$, eventually settling into the opposite direction, causing a complete magnetic reversal. The situation for reversed current direction is a bit more complex, but the net spin torque on F2 remains proportional to the current, and the reversal process remains essentially the same.

Handbook of Magnetism and Advanced Magnetic Materials. Edited by Helmut Kronmüller and Stuart Parkin. Volume 5: *Spintronics and Magnetoelectronics*. ISBN: 978-0-470-02217-7.

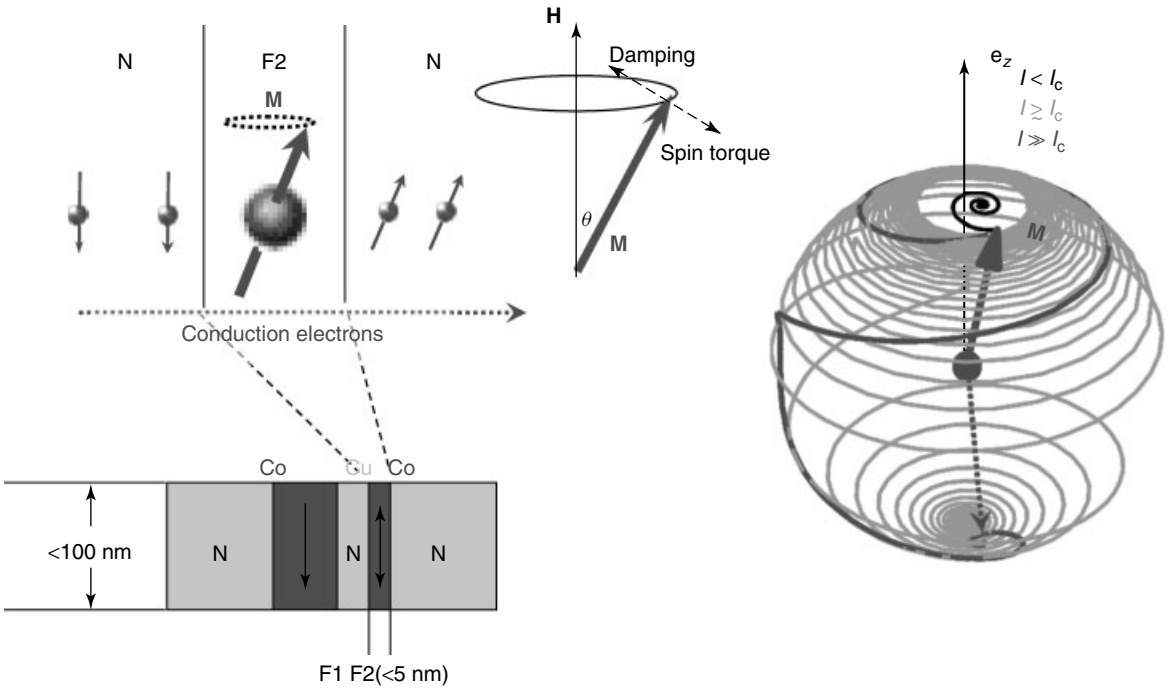

Figure 1. An illustration of the spin-torque-related dynamics for a macrospin. A uniaxial anisotropy is assumed along the $\mathbf{e}_z$ axis, as is an applied magnetic field **H**.

The presence of a spin torque affects the magnetotransport problem at many levels. The spin torque is, first of all, microscopic and quantum mechanical in nature. The collective effect of a spin-polarized current brings a torque on the ferromagnetic conductor carrying the current. The response of the ferromagnet to this torque would in turn affect the current transport, making it in general a complex coupled system. Fortunately, in most cases, the timescales are quite different between the magnetodynamics of the ferromagnet (which tends to be around the ferromagnetic resonance frequency or of the order of tens to hundreds of picoseconds) and that of the spin-polarized electronic transport process, which involves spin-flip lifetimes of the order of several picoseconds or less (Levy, 2002). This allows for an effective separation of the two processes, and a meaningful definition of a spin torque when used in the context of a description of the magnetodynamics of the ferromagnet, with the torque strength characterizable by phenomenological parameters such as the spin polarization of the current and the instantaneous angle between the two ferromagnets (F1 and F2 in Figure 1). These phenomenological parameters can in principle be derived from first-principle transport theories. The same set of parameters can also be used as input for the description of the (slower) magnetodynamics of the ferromagnet electrodes. For detailed analysis of the relationship between the spin torque and the microscopic transport properties of given materials systems, readers are referred to more advanced discussions presented in Bazaliy, Jones and Zhang (1998); Slonczewski (1996, 1999, 2002), Stiles and Zangwill (2002a,b), Bauer, Tserkovnyak, Huertas-Hernando and Brataas (2003), Stiles, Xiao and Zangwill (2004), Waintal, Myers, Brouwer and Ralph (2000), and Polianski and Brouwer (2004).

Here we focus on the macroscopic consequences of spin torque. We present a brief description of the magnetodynamics of a macrospin as it experiences the action of a spin torque. We then survey a series of experiments on the effect of spin torque, including the observation of an instability threshold current for spin-torque-induced magnetic precession and reversal, and a spin-torque-driven amplification of thermal fluctuation.

2 ZERO-TEMPERATURE MACROSPIN DYNAMICS

A macrospin model treats a nanomagnet with the assumption that its internal magnetic degrees of freedom are frozen. The only relevant parameters are the total magnetic moment **m** and the magnetic anisotropy energy $U(\theta, \varphi)$, where θ and φ are the polar-coordinate angles of **m**. The physical shape of the nanomagnet is relevant only in that its related shape demagnetization energy contributes to the total anisotropy energy function $U(\theta, \varphi)$.

2.1 Macrospin dynamics and the presence of a spin-torque term

The macrospin dynamics without the presence of a spin torque is well described by the classical Landau–Lifshitz–Gilbert (LLG) equation (Lifshitz and Pitaevskii, 1981)

$$\left(\frac{1}{\gamma}\right)\frac{\mathrm{d}\mathbf{m}}{\mathrm{d}t} = \mathbf{m}\times\mathbf{H} - \left(\frac{\alpha}{\gamma m^2}\right)\mathbf{m}\times\frac{\mathrm{d}\mathbf{m}}{\mathrm{d}t} \qquad (1)$$

Here $\mathbf{m}$ is the magnetic moment of the macrospin, $\gamma = g\mu_\mathrm{B}/\hbar \approx 2\mu_\mathrm{B}/\hbar$ is the gyromagnetic ratio, and α is the LLG damping coefficient. The first term in equation (1) describes the magnetic-field-induced torque on a magnetic moment $\mathbf{m}$. The second term describes damping.

When a spin-polarized current passes through a ferromagnetic electrode that is $\mathbf{m}$, $\mathbf{m}$ will attempt to repolarize the current in the direction of its magnetization, $\mathbf{n}_m$. In the process, some of the angular momentum from the electron spins will be absorbed by $\mathbf{m}$. This exerts a net torque on $\mathbf{m}$.

For a nanomagnet $\mathbf{m}$ within which magnetization is uniform, the transverse component of spin torque is (Slonczewski, 1996)

$$\Gamma = -g\left(\mathbf{n}_m, \mathbf{n}_\mathrm{s}\right)\left[\frac{\hbar}{(2e)}\right]\left(\frac{\eta I}{m^2}\right)\left(\mathbf{n}_\mathrm{s}\times\mathbf{m}\right)\times\mathbf{m} \qquad (2)$$

where $\mathbf{n}_m$ is the unit vector direction of $\mathbf{m}$, $\mathbf{n}_\mathrm{s}$ is the direction of spin polarization of the incoming current, and $\eta = \left(I_\uparrow - I_\downarrow\right)/\left(I_\uparrow + I_\downarrow\right)$ is the spin-polarization factor, where $I_\uparrow$ and $I_\downarrow$ are the majority and minority spin-polarized currents with their polarization axis $\mathbf{n}_\mathrm{s}$ defined by the polarizing magnet (F1 in Figure 1). $g\left(\mathbf{n}_m, \mathbf{n}_\mathrm{s}\right)$ is a numerical prefactor that describes the angular dependence of the efficiency of spin-angular momentum transfer, originating from the dependence of net spin polarization of the current on the relative orientation of the two ferromagnets. Because the net spin polarization depends on the exact arrangements of the electrodes, so does $g\left(\mathbf{n}_m, \mathbf{n}_\mathrm{s}\right)$ (Slonczewski, 1996; Stiles and Zangwill, 2002a; Waintal, Myers, Brouwer and Ralph, 2000). For all-metal spin valves, the detailed angular dependence of $g\left(\mathbf{n}_m, \mathbf{n}_\mathrm{s}\right)$ is model dependent, and is microscopically never an angle-independent quantity. Its macroscopic form as seen in real materials systems relates to the angular dependence of magnetoresistance (MR), and is to be established experimentally.

The case of a constant $g\left(\mathbf{n}_m, \mathbf{n}_\mathrm{s}\right) \equiv 1$ describes a spin current whose polarization is independent of the relative angle, and the macrospin simply redirects the spin-current polarization direction, and in the process completely absorbs its transverse angular momentum. For simplicity of discussion, on a semiquantitative level, we assume a constant $g\left(\mathbf{n}_m, \mathbf{n}_\mathrm{s}\right)$, and use equation (2) as the basic interaction that enters the magnetodynamics equation for the motion of the macrospin. The LLG equation (Lifshitz and Pitaevskii, 1981) with the spin-torque term therefore is

$$\left(\frac{1}{\gamma}\right)\frac{\mathrm{d}\mathbf{m}}{\mathrm{d}t} = \mathbf{m}\times\left[\mathbf{H} - (\alpha/m)\,\mathbf{m}\times\left(\mathbf{H} + \frac{\eta\hbar I}{2em\alpha}\mathbf{n}_\mathrm{s}\right)\right] \qquad (3)$$

Equation (3) can also be viewed as a local constitutive equation for magnetodynamics studies including the nanomagnet's internal degrees of magnetic freedom. Together with an exchange-stiffness term, the vector field equation then describes the dynamics of the nanomagnet in continuous medium limit, a special case of which is when the nanomagnet is a thin film with thickness much smaller than the lateral dimensions and the exchange length. In this case, the in-plane degrees of magnetic freedom can be taken into account by replacing $\mathbf{H} \to \mathbf{H} + (D/2\mu_\mathrm{B})\,\nabla^2\mathbf{n}_m$, where $\nabla^2 = \partial_x^2 + \partial_y^2$ with x, y being the in-plane position coordinates, D the exchange-stiffness constant, and $\mathbf{n}_m = \mathbf{M}/M$ the local direction of magnetization $\mathbf{M}$ at point (x, y).

2.2 Threshold current for magnetic amplification

For simple geometries and under a macrospin approximation, equation (3) can be linearized and solved for its stability boundary. For a thin, free-layer nanomagnet in a collinear geometry, with its uniaxial anisotropy field's easy axis aligned to that of the field applied in the film plane, and the easy-plane anisotropy sharing its easy plane with the film plane, this gives a stability threshold current I_c of (Slonczewski, 1996; Sun, 1999, 2000a)

$$I_\mathrm{c} = \left(\frac{2e}{\hbar}\right)\left(\frac{\alpha}{\eta}\right)m\left(H + H_k + 2\pi M_\mathrm{s}\right) \qquad (4)$$

Here α is the LLG damping coefficient, $m = (abt)\,M_\mathrm{s}$ is the total magnetic moment of the free layer, with a, b as its lateral dimensions and t its thickness. M_s is the saturation magnetization of the free layer (F2). H_k is the uniaxial anisotropy field.

Equation (4) gives a current threshold, above which the *linearized* LLG equation becomes unstable over time, and a net gain of precession cone angle results. While comparing with experimental results, however, effects of large cone-angle precession often need to be carefully taken into account, since the development of an initial cone-angle increase as dictated by a linear stability threshold may not necessarily lead to complete magnetic reversal (Sun, 2000a). Although in many simple geometries, such as systems with uniaxial-only anisotropy or thin-film nanomagnets with a strong easy-plane anisotropy due to demagnetization and a

moderate in-plane uniaxial anisotropy, oftentimes the linear stability threshold does lead to the reversal of the magnetic moment.

There are several other factors that determine the experimentally observable switching current, making the simple stability threshold expression equation (4) insufficient. Chief among these factors is finite temperature. Other uncertainties include the relatively poor knowledge of the actual LLG damping coefficient for a particular device structure, and that of the exact spin-polarization value η. Detailed calculations for specific spin-transport models would give rise to additional angular dependences of spin torque as a function of the relative orientation between F1 and F2. The damping coefficient α may also become angle dependent, especially for large-angle dynamics.

A simple way of comparing equation (3) with experiment is to examine the intercept-to-slope ratio of the experimentally observed threshold boundary $I_c(H)$, defined as $R_{IS} = I_c(0)/(\mathrm{d}I_c/\mathrm{d}H)$. For equation (4), $R_{IS} = H_k + 2\pi M_s$. Early experimental data, mostly measured quasistatically over the timescale of less than a few milliseconds, appears to consistently underestimate the value of R_{IS}, by almost an order of magnitude (Sun *et al.*, 2003; Sun, Kuan, Katine and Koch, 2004). This is because equation (4) represents the zero-temperature stability threshold. With finite temperature, additional thermal agitation is present, making the apparent threshold current lower and also causing it to give a differently shaped $I_c(H)$, resulting in smaller R_{IS} (Sun, Kuan, Katine and Koch, 2004), as will be discussed later.

2.3 Size consideration: why is spin torque most visible only in nanomagnets?

There are two known mechanisms that can cause interaction between a magnetic moment and a transport current: current-induced magnetic field (the Oersted field) and spin-polarized current-induced spin torque. A current-induced magnetic field for a wire of radius r would give a relation between the maximum field (usually around the surface of the wire) and the current passing through the wire I. From Maxwell's equations, the relation is $I = (c/2)\,rH$ (in Gaussian units, c is the speed of light). A spin valve of similar lateral size ($2r$) would have a spin-torque threshold current of the order (following equation (4)) of $I_c \approx (H + H_k + 2\pi M_s)\left(4r^2 t\right) M_s\,(\alpha/\eta)\,(2e/\hbar)$. The spin-torque threshold is proportional to r^2, and the Oersted field–related current is (for a given threshold field, such as the anisotropy field H_k) proportional to r. Thus, at large dimensions, the threshold from the Oersted field is the lower threshold. The crossover point is roughly (for high-moment thin films like cobalt with $H \sim H_k \ll 2\pi M_s$)

$$r_c \sim \left(\frac{c\hbar}{4e}\right)\left(\frac{\eta}{\alpha}\right)\left(\frac{1}{M_s t}\right)\left(\frac{H_k}{2\pi M_s}\right) \tag{5}$$

which gives for 30-Å-thick cobalt, an $r_c \sim 0.04\,\mu\mathrm{m}$, assuming a spin-polarization factor of $\eta \approx 0.1$, a damping coefficient $\alpha \approx 0.01$, and $H_k \sim 100\,\mathrm{Oe}$. Thus, a practical crossover dimension for a pillar-structured, cobalt-based spin valve is of the order of $2r_c \sim 0.1\,\mu\mathrm{m}$, below which the spin-torque effect is more significant. For larger spin polarization or for free-layer materials with different moment and anisotropy, the crossover dimensions may be larger. For example, spin-transfer-induced magnetic switching has been observed in MTJs with sizes around $0.1 \times 0.2\,\mu\mathrm{m}^2$ (Pakala *et al.*, 2005; Kubota *et al.*, 2005a).

3 EARLY EXPERIMENTAL EVIDENCE OF SPIN-CURRENT-INDUCED MAGNETIC EXCITATION

Spin-torque-induced magnetic excitation has been experimentally observed in many different systems. Earlier experiments (Berger, 1978, 1984, 1988), for example, illustrate the effect of a carrier electron's spin-angular momentum on abrupt magnetic domain walls. Slonczewski (1996) predicted the presence of a spin torque from spin-polarized current in a metallic magnetic multilayer geometry. Experiments show current-induced magnetic excitation in point-contact junction on giant-magnetoresistance (GMR) multilayers (Tsoi *et al.*, 1998, 2000; Myers *et al.*, 1999), and magnetic switching in highly spin-polarized manganite junctions (Sun, 1999). These experiments reveal the sometimes dramatic effect of the spin torque, leading to the quantitative, experimental observation of the spin-transfer-induced magnetic reversal (Sun, 1999), and the eventual unambiguous experimental demonstration (Katine *et al.*, 2000) of the reversal and magnetic excitation effects in lithographically defined nanomagnet spin-valve junctions.

Tsoi *et al.* (1998) showed that magnetic excitation can be the result of bringing a point-contact tip made of silver in contact with a multilayered Cu|Co|Cu|Co . . . thin film. The current density under the point contact is high enough to exceed the spin-torque excitation threshold. As a consequence, an excitation and reversal of magnetic moment results – most likely only for the first cobalt layer. This manifests itself as a step in the point-contact junction's current–voltage (IV) characteristics. The threshold voltage (or current, since the junction is basically a linear resistor with only small nonlinear deviations) varies linearly with

the magnetic field, which is applied perpendicular to the film surface and is large enough to overcome the easy-plane demagnetization field of cobalt (which is about $4\pi M_s \approx 17.6\,\text{kOe}$). This linear dependence of threshold current on applied field is consistent with equation (4), although in this geometry the threshold refers to the generation of spin waves irradiating away from the point contact, as analyzed by Slonczewski (1999). The spin-wave radiation through exchange-stiffness coupling contributes to a finite intercept of the threshold current versus magnetic-field line, which was also subsequently confirmed by experiments (Rippard, Pufall and Silva, 2003).

Another possible interpretation of this data is the presence of a voltage threshold for spin-wave (magnon) emission at a certain energy, with the voltage threshold determined by the Zeeman splitting, $V_c \approx (g\mu_B/e)\,H$. Why these two apparently different interpretations may have some intrinsic relationship remains an intriguing subject (Sun *et al*., 2005).

Another form of the point contact onto magnetic layers was done by Myers *et al*. (1999). In this experiment, a special substrate with a SiN membrane was used, with a nanometer-size hole lithographically fabricated into the SiN membrane. The magnetic multilayers were then deposited on one side of the wafer, and the metal point contact (copper in this case) was deposited *in situ* on the other side, forming a metallic constriction contact through the SiN hole, and thus a point-contact junction. There, they not only observed signatures of magnetic excitation, but also observed current-induced, hysteretic magnetic reversal.

Earlier, current-induced magnetic reversal was observed in manganites-based all-oxide trilayer magnetic junctions. The junction is $1 \times 2\,\mu\text{m}^2$ in size, although the actual current path is likely to be much smaller, perhaps of the order of several hundred angstroms. Later, more systematic measurements of junctions with similar behavior were carried out, as the junction switching behavior was found to be consistent with a spin-transfer-induced magnetic reversal process (Sun, 1999, 2000b). The phenomena in these manganite-based junctions occur only in a small fraction of junctions prepared. The phenomenon is likely to have originated from interface-inhomogeneity-related current paths, and the switching occurs only for those junctions where the interface inhomogeneity is at the right place with the right size. These particular junctions, while rare, did switch with a well-defined threshold current (Sun, 1999), whose value showed a systematic dependence on applied magnetic field, in ways consistent with a simple spin-angular momentum transfer model (Slonczewski, 1996; Sun, 1999).

Other experiments during this period explored the interplay between spin-polarized current and the magnetic-field-driven reversal in nanomagnet electrodes. An example was the work by Wegrowe *et al*. (1999), where an electroplated Ni wire, 80 nm in diameter and about 500 nm in length was used. The experiment demonstrated a shift in the threshold magnetic field for a resistance-field hysteresis loop when a $10^7\,\text{A cm}^{-2}$ pulsed current was present. The change of threshold field was about 100 Oe at 0.15 mA of current pulse, larger than any induced magnetic field the current could generate. The authors argue that the spin-polarized current affects the magnetic reversal threshold field.

The quantitative proof of a spin-transfer-induced magnetic reversal was shown in all-metal current-perpendicular (CPP) spin-valve nanomagnets in 1999 by Katine *et al*. (2000) and Albert, Katine, Buhrman and Ralph (2000). Their experiments used electron-beam lithography to define a CPP spin-valve nanopillar, about 100 nm across in lateral dimension. An example of one such junction device is given in Figure 2.

A clear signature of magnetic reversal was seen, driven by current with a threshold current density around $\text{mid}-10^7\,\text{A cm}^{-2}$. The threshold current demonstrated the characteristic linear dependence on applied magnetic field with a slope consistent with spin-transfer model prediction (Katine *et al*., 2000; Albert, Katine, Buhrman and Ralph, 2000).

4 MAGNETOTRANSPORT OF A SPIN-VALVE-BASED SPIN-TRANSFER JUNCTION

4.1 Quasistatic magnetoresistance properties

For a spin-valve-based magnetic junction, its MR response to the combined effect of an applied magnetic field H and a bias current I shows distinctively different response regions that can be readily identified in the (I, H) parameter space.

Such MR measurement is usually taken in a quasistatic setup (with measurement response time at 1 ms or slower). A dc-bias current is applied to the junction. Often the junction resistance is measured by an ac lock-in method by superimposing a small ac current on top of the dc bias. This method is particularly useful when the junction MR is only a small percentage of the resistance. In a typical quasistatic measurement in our lab, the bias current is stepped at a rate around $0.1-1\,\text{mA min}^{-1}$, while the magnetic-field sweep rate (if swept) is of the order of $100-1000\,\text{Oe min}^{-1}$.

Generally speaking, the resistance response is hysteretic against both applied-field sweep and bias-current sweep. The values of the switching threshold current I^+ and I^-, corresponding to the resistance high-to-low and low-to-high switching thresholds, are functions of the applied magnetic field and the current history.

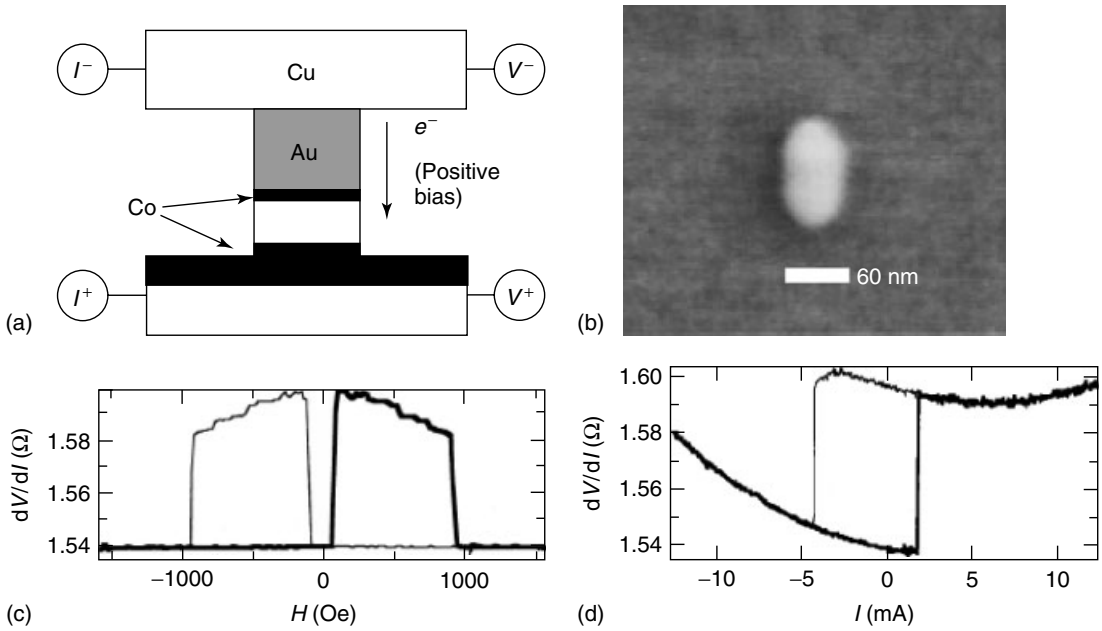

Figure 2. Current-induced reversal of magnetization in a current-perpendicular spin valve. The first definitive proof of current-induced magnetic switching was shown by Katine *et al*. (2000) in 1999 using a structure similar to the one shown in (a). The lateral size of the junction range from the earlier 120 nm or so in diameter (Katine *et al*., 2000) to the later geometry of $70 \times 120\,\mathrm{nm}^2$ (Albert, Katine, Buhrman and Ralph, 2000), as shown in the scanning electron micrograph (SEM) in (b). The resistance versus magnetic field sweep is shown in (c), and the resistance versus bias-current sweep is shown in (d). Resistance corresponds to $\mathrm{d}V/\mathrm{d}I$ measured using a lock-in detection method with an ac-bias current superimposed on the dc-bias current. (Reused with permission from F.J. Albert, J.A. Katine, R.A. Buhrman and D.C. Ralph, *Applied Physics Letters*, **77**, 3809 (2000). Copyright 2000, American Institute of Physics.)

Figure 3 describes the basic experimental observations of the hysteretic current and field dependence of the junction resistance. This phase diagram is a simplified version from Kiselev *et al*. (2003). Note that this phase diagram is obtained with quasistatic measurements, and hence it is not a simple stability boundary but a thermal-activation-determined transition-rate boundary. In principle, the exact position of the lines as well as their shape depend on the system temperature and the measurement speed, as discussed later.

There are generally three types of behaviors observed from these experimental switching boundary phase diagrams. The first corresponds to the region that shows hysteretic switching between parallel and antiparallel states, those represented by the area P/AP in Figure 3(a). The second region shows a large amount of telegraph noise, often involving two-level fluctuations, signaling thermally activated transitions between two metastable states (Myers *et al*., 2002; Urazhdin, Birge, Pratt and Bass, 2003). These two states could be two orbits of persistent precession, or they could be between two stable points, or they could be between one stable point and one orbit of persistent precession. A third type of behavior is usually observed in the high-field, high current density region, where continuous magnetic precession at microwave frequency is present. This can be accompanied by a reversible step in a junction's IV curve. It appears in $\mathrm{d}V/\mathrm{d}I$ measurement as a peak, whose amplitude and width depend on the step's shape as well as measurement conditions.

A direct correspondence between these quasistatically measured $R(H)$ phase diagrams and microwave emission characteristics was established experimentally (Kiselev *et al*., 2003). Most features observed experimentally can be found in monodomain LLG models (Sun, 2000a; Li and Zhang, 2003; Bazaliy and Jones, 2004; Grollier *et al*., 2003; Valet, 2004, private communications; Özyilmaz *et al*., 2003), as direct comparisons were made in a magnetic field perpendicular to the junction film surface geometry (Kiselev *et al*., 2004). There are, however, some features observed in the relatively high bias region that were not accounted for by the simple monodomain LLG model (Kiselev *et al*., 2003). More recent experiment has further probed the nature of these dynamic excitations beyond the monodomain limit (Kiselev *et al*., 2004). Modeling of these behaviors, in general, requires numerical treatment of the LLG equation. Comparison of such numerical simulation (e.g., see Lee *et al*. (2004)) and experiment (Kiselev *et al*., 2003) gives satisfactory agreement to the leading order.

In general, the regions outside the hysteretic P/AP part involve steady-state or chaotic dynamic motion, often in large amplitudes. As such, the exact behavior is

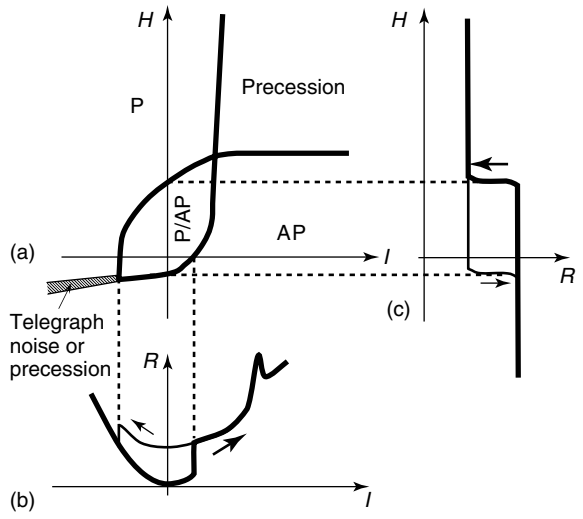

Figure 3. A sketch of the phase diagram of a spin-transfer device. (a) The phase diagram in (I, H) space. P designates 'parallel' state and AP, antiparallel. P/AP is the hysteresis region. The curvatures of the phase boundaries shown here are a result of finite temperature effect that is discussed later. (b) A horizontal cut of the phase space, showing a current-induced resistance switch. (c) A vertical cut of the phase space, showing a magnetic-field-induced resistance switch. The difference between the precessional states on the upper right region of (a) and the telegraph noise/precession states on the lower left region of (a) is not fundamental. The nanomagnet may exhibit either a persistent precessional state or a telegraph noise state, depending on the relative strength between the spin torque, the effective anisotropy field experienced by the nanomagnet, which includes the effect of applied field, as well as the effect of temperature in relation to these magnetic energy scales.

sensitive to factors beyond simple macrospin models. Factors such as the exact shape of the nanomagnet, the uniformity (or lack of uniformity) of the spin current passing through, and the magnetic boundary conditions imposed on the nanomagnet all contribute to determining the nature of the dynamics. The internal magnetic degrees of freedoms are also involved, giving rise to various modes of spin-wave excitations, further complicating the behavior.

At very high current densities (above $10^8\,\mathrm{A\,cm^{-2}}$, e.g., for typical Co|Cu structures with 30 Å or so Co), spin transfer can even amplify the magnetic inhomogeneities in a single-layer, thin- film nanomagnet, be it initially structural and static in nature or thermal and dynamic. The process involves spin diffusion current in the lateral direction parallel to the film surface, which couples magnetization of the film surfaces from different locations and amplifies the angular deviation from equilibrium. This has been theoretically described (Polianski and Brouwer, 2004; Stiles, Xiao and Zangwill, 2004) and experimentally observed (Özyilmaz *et al*., 2004).

4.2 Time-dependent magnetoresistance during magnetic reversal

The response of a nanomagnet to spin torque is dynamic. This can be investigated by time-resolved transport measurements. Time-dependent measurement also directly answers the question of spin-torque switching time and its dependence on the conditions of the driving current, which is important for applications.

Spin-transfer-induced magnetic reversal follows a different type of dynamics than magnetic-field-driven reversal. For spin-valve-based spin-transfer devices, direct measurement of the switching speed of spin-transfer junctions is nontrivial because of the small signal level involved. For CPP spin valves, even at lateral sizes of 100 nm or below, the junction resistance still is less than 10 Ω or so, and the MR change is even smaller – usually only about 3∼5% of the total junction resistance. This results in an MR-related voltage signal typically below 0.1 mV. Dynamic calculations (Sun, 2000a) give the generic timescale of the precession to be around $(2\pi M_s)\,\gamma \sim 50$–$100$ ps for cobalt, and places the precessional-reversal time in the order of 1∼10 ns.

Most switching dynamics measurements were performed at ambient temperature. One earlier experiment probed the switching speed as a function of driving current amplitude (Koch, Katine and Sun, 2004). Owing to the small MR signal level on top of the large primary signal from the current step, an elaborate signal averaging sequence was devised to extract the time-dependent evolution of the junction voltage related to magnetic reversal. With proper averaging, the output voltage difference can be normalized to reflect the ensemble-averaged reversal probability, which is presented in Figure 4(a). The corresponding switching speed as a function of the drive current amplitude is shown in Figure 4(b) on a linear scale, and on a log-linear scale in Figure 4(c).

Two points are noted for the data shown in Figure 4(b–c). First, at the high-speed limit, the dependence of τ^{-1} on bias current I is linear. Second, in the subthreshold, large-τ regime, this linearity gives way to a curved onset which turns out to be exponentially dependent on the bias current as shown in Figure 4(c). The linear τ^{-1} versus I dependence stems from spin-transfer angular momentum conservation, and the curved onset relates to thermal activation. Both can be adequately described by the spin-transfer dynamics with thermal noise. In addition, the quasistatically measured I_c on the same sample under the same environment is more than a factor of 2 less than the threshold current observed in Figure 4(b). The difference is due to the different timescales of the two measurements.

This experiment only reveals the envelope of the switching junction's voltage response in time. The detailed oscillation in the voltage related to magnetic precession is sensitive

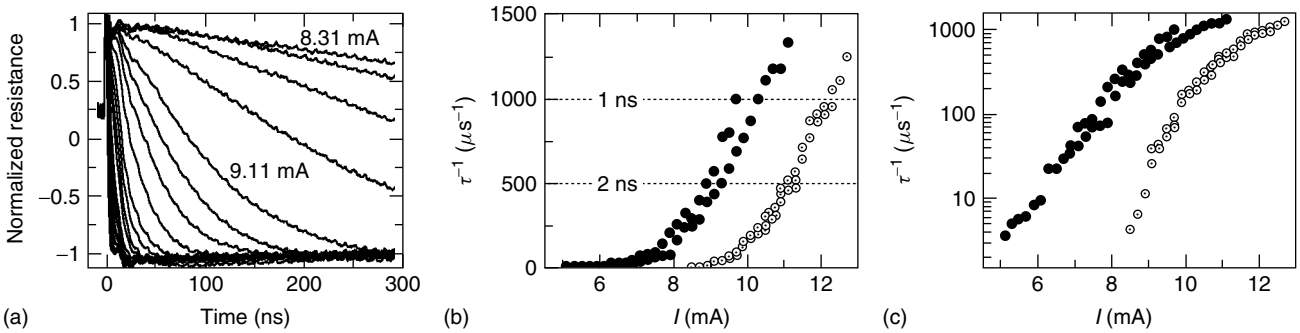

Figure 4. (a) Time-dependent switching probability. (b) Switching speed τ^{-1} extracted from (a). Horizontal dashed lines with labels indicate the switching speed corresponding to a reversal time of 1 and 2 ns, respectively; (c) Switching speed plotted on log-linear scale. Open and closed circle symbols represent the switching threshold on the positive and the negative current step of the junction. (Reproduced from J. Sun *et al*., 2004, with permission from the International Society for Optical Engineering (SPIE). © 2004.)

to the initial condition which is thermally randomized and smeared out. A more recent experiment by Krivorotov *et al*. reveals not only the envelope of the switching junction's dynamic voltage output but also the actual oscillation that reflects the dynamic precession accompanying the reversal (Krivorotov *et al*., 2005). This was done by using a junction with a noncollinear magnetic moment arrangement between the fixed and the free layers. At sufficiently large angles (around 45°), it introduces a distinctive initial condition for the precession dynamics upon the presence of a step-function driving current, thus preserving the phase information of the oscillations upon multitrace average. This way, they directly observed the effect of spin current on the damping characteristics of the nanomagnet by relating the oscillation envelope to the spin-current amplitude.

5 FINITE TEMPERATURE MACROSPIN DYNAMICS

A simple macrospin finite temperature dynamic model for spin-transfer-induced switching was first described in Sun, Kuan, Katine and Koch (2004) and Koch, Katine and Sun (2004), which capture the essentials with an analysis of a collinear geometry between the macrospin's direction and that of the spin-polarized current. A more careful analysis of the model on the basis of the Fokker–Plank equation formalism can be found in Li and Zhang (2004a) and Apalkov and Visscher (2005a).

5.1 Review of the zero-temperature model

Define a macrospin with its magnetic moment $\mathbf{m}$ having a direction described by a unit direction vector $\mathbf{n}_m = \mathbf{n}_m(\theta, \varphi) = \sin\theta\sin\varphi\mathbf{e}_x + \sin\theta\cos\varphi\mathbf{e}_y + \cos\theta\mathbf{e}_z$, where θ and φ are direction angles in a polar-coordinate system. The moment $\mathbf{m}$ is situated in a combined energy potential of $U = U(\theta, \varphi)$ that includes all energy conserving torques experienced by $\mathbf{m}$. The normalized gradient of U, expressed in terms of $\mathbf{H}_{\text{eff}} = (1/m)\,\nabla U(\theta, \varphi)$ includes terms of the applied magnetic field $\mathbf{H}$, a uniaxial anisotropy whose strength can be characterized by a uniaxial anisotropy field H_k, and an easy-plane anisotropy field that could be used to describe a macrospin in thin-film geometry, experiencing the demagnetization effect from the flat thin-film geometry. Here the operator $\nabla = \mathbf{e}_\theta\,(\partial/\partial\theta) + \mathbf{e}_\varphi\,(1/\sin\theta)\,(\partial/\partial\varphi)$, with unit vectors $\mathbf{e}_\theta$ and $\mathbf{e}_\varphi$ denoting the direction of rotation for θ and φ, respectively. Note that except for the applied field $\mathbf{H}$, $\mathbf{H}_{\text{eff}}$ here is in general not a simple magnetic-field vector but a function of the angular position of $\mathbf{m}$.

The precession dynamics of the macrospin $\mathbf{m}$ under the potential well U in the classical limit can be described by the phenomenological LLG equation

$$\left(\frac{1}{\gamma}\right)\frac{\mathrm{d}\mathbf{m}}{\mathrm{d}t} = \mathbf{m}\times\left[\mathbf{H}_{\text{eff}} - \left(\frac{\alpha}{m}\right)\mathbf{m}\times\mathbf{H}_{\text{eff}}\right] \tag{6}$$

As was shown for equation (3), adding the spin-torque term of equation (2) gives

$$\left(\frac{1}{\gamma}\right)\frac{\mathrm{d}\mathbf{m}}{\mathrm{d}t} = \mathbf{m}\times\left[\mathbf{H}_{\text{eff}} - \left(\frac{\alpha}{m}\right)\mathbf{m}\times(\mathbf{H}_{\text{eff}} + \mathbf{H}_{\text{s}})\right] \tag{7}$$

where $\mathbf{H}_{\text{s}} = I\eta\,(\hbar/2e)\,(1/m\alpha)\,\mathbf{n}_{\text{s}}$ is the spin-angular momentum transfer term. For simplicity $g = 1$ is assumed while using equation (2).

Examine the simple case when only an applied magnetic field $\mathbf{H}$ is present in $\mathbf{H}_{\text{eff}}$, and $\mathbf{H}$ and $\mathbf{H}_{\text{s}}$ are collinear. In this simple limit

$$\left(\frac{1}{\gamma}\right)\frac{\mathrm{d}\mathbf{m}}{\mathrm{d}t} = \mathbf{m}\times\left[\mathbf{H} - \left(\frac{\widetilde{\alpha}}{m}\right)\mathbf{m}\times\mathbf{H}\right] \tag{8}$$

with $\widetilde{\alpha} = \alpha + \hbar\eta I/(2emH) = \alpha(1 + I/I_c)$, where $I_c = (2e/\hbar)(\alpha/\eta)(abtM_s)H_a$, a special case of the threshold current as defined in equation (4). This reveals the role of spin-polarized current I: it modifies the effective damping coefficient of the nanomagnet. When the effective damping α becomes negative, the nanomagnet will amplify disturbances away from its equilibrium position, resulting in a magnetic instability, leading to a magnetic reversal.

For more general situations, since $\mathbf{H}_{\text{eff}}$ contains the angular position (θ, φ) of $\mathbf{m}$, a full stability analysis of equation (7) is required. This, in the small cone-angle limit $(\theta \ll \pi)$, can be done analytically with a linearized equation (7), as was done in Sun (2000a) When averaged over a timescale longer than the natural precession period $\Omega_K = \gamma H_k$, it gives an effective damping coefficient of $\widetilde{\alpha} = \alpha + \hbar\eta I/[2em(H + H_k + 2\pi M_s)]$ that describes the average cone-angle evolution $\langle\theta(t)\rangle$. Here, the uniaxial anisotropy field H_k and the orthogonal easy-plane anisotropy term are included. A thin-film demagnetization-related easy-plane anisotropy energy is assumed, therefore $M_s = m/v$, where $v = abt$ is the volume of the nanomagnet. The resulting instability threshold when $\widetilde{\alpha} = 0$ is just equation (4) $|I_c| = (1/\eta)(2e/\hbar)m\alpha(H + H_k + 2\pi M_s)$. This threshold current $I_c(H)$ depends linearly on the applied field H. It should have an intercept-to-slope ratio of $H_k + 2\pi M_s$. Experimental results (Sun *et al*., 2003), however, suggest that the actual slope-to-intercept ratio falls well below, and finite temperature effect plays an important role.

The effect of finite temperature on the macrospin system's response to a spin-transfer excitation is twofold. First, it affects the average precession motion of the macrospin by adding thermal agitation, resulting in finite probabilities for thermal activation over the magnetic energy barrier. Secondly, it adds a thermally distributed initial condition to the macrospin.

5.2 Finite temperature LLG equation

Following the approach of Brown (1963) and Grinstein and Koch (2003), a Langevin random field $\mathbf{H}_L$ can be added to the effective magnetic-field term $\mathbf{H}_{\text{eff}}$. $\mathbf{H}_L$ relates to the system temperature T as $H_{L,i} = \sqrt{2\alpha k_B T/\gamma m}\, I_{\text{ran},i}(t)$, $(i = x, y, z)$; where $I_{\text{ran}}(t)$ is a Gaussian random function with the first two moments of $\langle I_{\text{ran}}(t)\rangle = 0$ and $\langle I^2_{\text{ran}}(t)\rangle = 1$. Each of the x, y, z components has its own uncorrelated $I_{\text{ran}}(t)$. Without the spin-transfer effect, the finite temperature LLG equation with a Langevin random field reads

$$\left(\frac{1}{\gamma}\right)\frac{\mathrm{d}\mathbf{m}}{\mathrm{d}t} = \mathbf{m} \times \left[\mathbf{H}_{\text{eff}} + \mathbf{H}_L - \left(\frac{\alpha}{m}\right)\mathbf{m} \times \mathbf{H}_{\text{eff}}\right] \quad (9)$$

which describes the dynamics of a macrospin $\mathbf{m}$ sitting in a potential well $U(\theta, \varphi)$, with a thermally activated motion and a finite lifetime of staying inside the potential well, namely, a thermal lifetime τ approximately following the Boltzmann statistics of

$$\tau = \tau_0 \exp\left(\frac{\Delta U}{k_B T}\right) \quad (10)$$

where ΔU is the potential barrier height as seen from the local minimum in which $\mathbf{m}$ fluctuates, and $\tau_0 \sim 1/\gamma H_k$ is the reciprocal attempt frequency. Equation (9) should work well when $\Delta U/k_B T \gg 1$. The thermal-activation lifetime equation (10) is determined once a system is defined by equation (9) and an energy landscape $U(\theta, \varphi)$, represented in equation (9) by $\mathbf{H}_{\text{eff}}(\theta, \varphi) = (1/m)\nabla U(\theta, \varphi)$.

5.3 Finite temperature LLG equation with spin torque: amplified thermal activation

Spin-transfer excitation adds an additional torque. Similar to equation (7), after including the spin-transfer torque and assuming the spin-polarized current carries no entropy flow into the macrospin, equation (9) reads

$$\left(\frac{1}{\gamma}\right)\frac{\mathrm{d}\mathbf{m}}{\mathrm{d}t} = \mathbf{m} \times \left[\mathbf{H}_{\text{eff}} + \mathbf{H}_L - \left(\frac{\alpha}{m}\right)\mathbf{m} \times (\mathbf{H}_{\text{eff}} + \mathbf{H}_s)\right] \quad (11)$$

with $\mathbf{H}_s$ representing the spin-transfer torque related contribution, as defined in equation (7).

It is instructive to look at a special case when $\mathbf{H}_s$ and $\mathbf{H}$ are both collinear to the easy axis of the uniaxial anisotropy term $\mathbf{H}_k$ inside $\mathbf{H}_{\text{eff}}$, and the easy-plane anisotropy is zero. In this case and for small cone angle $\theta \ll 1$, the effect of $\mathbf{H}_s$ is simply to modify $\mathbf{H}_{\text{eff}} \to \widetilde{\mathbf{H}}_{\text{eff}} = (H_k + H + H_s)\mathbf{n}_s = (H_k + H)\left(1 + \frac{H_s}{H_k + H}\right)\mathbf{n}_s = \left(1 + \frac{H_s}{H_k + H}\right)\mathbf{H}_{\text{eff}}$. Thus, one can rewrite equation (11) in the form of equation (9)

$$\left(\frac{1}{\gamma}\right)\frac{\mathrm{d}\mathbf{m}}{\mathrm{d}t} = \mathbf{m} \times \left[\mathbf{H}_{\text{eff}} + \mathbf{H}_L - \left(\frac{\widetilde{\alpha}}{m}\right)\mathbf{m} \times \mathbf{H}_{\text{eff}}\right] \quad (12)$$

where $\widetilde{\alpha} = \left[1 + H_s/(H_k + H)\right]\alpha = (1 + I/I_c)\alpha$, with $I_c = (2e/\hbar)(\alpha/\eta)(abtM_s)(H + H_k)$, another special case of equation (4).

Equation (12) is a mathematically equivalent description of a macrospin system as equation (9) with the same amplitude of $\mathbf{H}_L$. This then suggests that $H_{L,i} = \sqrt{2\alpha k_B T/\gamma m}\, I_{\text{ran},i}(t)$ remains valid for this hypothetical macrospin's LLG equation (12). However, in equation (12), the damping coefficient α is replaced by $\widetilde{\alpha}$. To maintain $H_{L,i}$, it means the macrospin would see a fictitious temperature $\widetilde{T}$, such that $\widetilde{\alpha}\widetilde{T} = \alpha T$.

Since equation (12) is equivalent to a macrospin situated at temperature $\widetilde{T}$ with damping $\widetilde{\alpha}$, one may further deduce that the thermal-activation lifetime of the system can also be expressed in the form of equation (10), with its temperature rescaled to $\widetilde{T}$, that is,

$$\tau = \tau_0 \exp\left(\frac{\Delta U}{k_{\mathrm{B}}\widetilde{T}}\right) = \tau_0 \exp\left[\frac{\Delta U}{k_{\mathrm{B}}T}\left(\frac{\widetilde{\alpha}}{\alpha}\right)\right]$$
$$= \tau_0 \exp\left[\frac{\Delta U}{k_{\mathrm{B}}T}\left(1 - \frac{I}{I_{\mathrm{c}}}\right)\right] \tag{13}$$

This conclusion of a linearly current-dependent apparent temperature can be directly compared with experiment done in subthreshold driving current ($|I| < I_{\mathrm{c}}$).

More rigorous theoretical treatments that give equation (13) can be found in Li and Zhang (2004a) and Visscher and Apalkov (2005). The energy distribution of a macrospin under spin-current excitation is calculated by Apalkov and Visscher (2005b).

Equation (13) is the basic function that determines the shape of the quasistatically measured magnetic switching phase boundary as illustrated in Figure 3. The increase in switching rate as $H \to H_k$ and/or as $I \to I_{\mathrm{c}}$ gives rise to the increased slope, making the experimentally observed intercept-to-slope ratio well below what is expected from zero temperature $I_{\mathrm{c}}(H)$ (Sun *et al.*, 2003; Sun, Kuan, Katine and Koch, 2004), as illustrated in Figure 5. The overall shape of this quasistatic switching boundary is consistent with what is observed experimentally (Kiselev *et al.*, 2003), which is illustrated in Fig.3. The boundary here corresponds to observing a switching event during a period of τ. The expression can be readily derived from equation (13) to be

$$I(H) = I_{\mathrm{c}}(H)\left[1 - \frac{1}{(1 - H/H_k)^2}\left(\frac{k_{\mathrm{B}}T}{\Delta U}\right)\ln\left(\frac{\tau}{\tau_0}\right)\right] \tag{14}$$

In addition to measuring the averaged switching speed versus switching current as shown in Figure 4, a direct measurement of the apparent threshold current can also be done using a pulsed current bias. These experiments (Pakala *et al.*, 2005; Yagami, Tulapurkar, Fukushima and Suzuki, 2004, 2005) verify the description of equation (14) and also provide a quick estimate of the zero-temperature threshold current without requiring full dynamic measurements down to the nanosecond level.

5.4 Thermally distributed initial condition

In the simple collinear geometry, the initial condition of the macrospin system under spin-transfer excitation is most important when the spin-transfer excitation is large – such as when it is near or exceeding the zero-temperature threshold current I_{c}. In this case, when the spin-transfer current is applied suddenly at time t_0, it will result in a fairly quick magnetic reversal. The switching time required at zero temperature is estimated to be (Sun, 2000a)

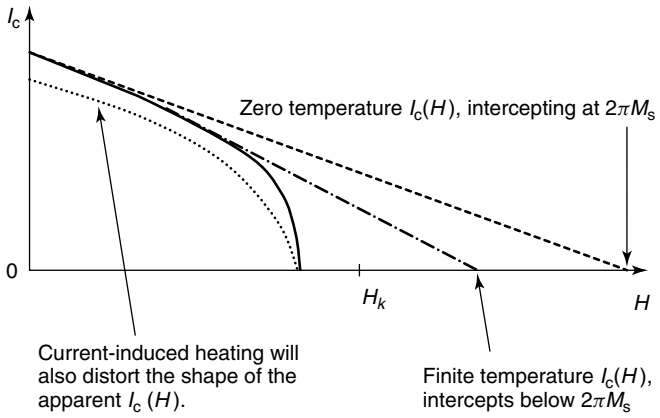

Figure 5. The effect of finite temperature and quasistatic measurement. The quasistatic measurement over a laboratory timescale τ allows an appreciable amount of probability for the nanomagnet to thermally switch out of its lowest potential well, completing a magnetic reversal. The closer to H_k and/or I_{c}, the more pronounced this thermal activation becomes, causing the observed switching boundary to curve below that of the zero temperature $I_{\mathrm{c}}(H)$, and giving an artificially low intercept on the field axis. The Joule heating of the device is often more significant for MTJs than for spin valves. In such cases, the apparent switching boundary may become further distorted, as illustrated here by the thick dotted line.

$$\tau^{-1} = \frac{\alpha\gamma}{m\ln(\pi/2\theta_0)}(H + H_k + 2\pi M_{\mathrm{s}})\left[(I/I_{\mathrm{c}}) - 1\right]$$
$$= \frac{\eta(\mu_{\mathrm{B}}/e)}{m\ln(\pi/2\theta_0)}(I - I_{\mathrm{c}}), \quad (I > I_{\mathrm{c}}) \tag{15}$$

with θ_0 being the initial deviation of $\mathbf{m}$ from its easy-axis direction. The last step in equation (15) reveals angular momentum conservation. A finite temperature brings a thermally distributed θ_0. Thus the precise switching speed will vary from measurement to measurement. At the same time, the thermal agitation during the course of reversal will add some uncertainty to the exact speed and trajectory of the reversal. This disturbance is likely to be small compared to the large cone-angle motion involved in these reversal events as long as $\Delta U/k_{\mathrm{B}}T \gg 1$.

To see the consequence of a thermally distributed initial θ_0, examine a special case with $U(\theta,\varphi) = \Delta U\left(\sin^2\theta + h_p\sin^2\theta\cos^2\varphi - 2h\cos\theta\right)$, where $\Delta U = mH_k/2$ is the uniaxial anisotropy energy constant, $h_{\mathrm{p}} = 4\pi M_{\mathrm{s}}/H_k$ is the easy-plane anisotropy field in dimensionless unit, and $h = H/H_k$ is the applied field, assuming a collinear

geometry between $\mathbf{H}$ and $\mathbf{H}_k$. Assume further a small thermal fluctuation amplitude when $\Delta U/k_{\mathrm{B}}T \gg 1$. In such limit, the main effect of finite temperature on delay τ is through the initial angular position of θ, which in the limit of $\Delta U/k_{\mathrm{B}}T \gg h_{\mathrm{p}} \gg 1$ gives a switching speed based on the ensemble-averaged switching time as (Sun, Kuan, Katine and Koch, 2004)

$$\langle\tau\rangle^{-1} \approx \frac{\eta\mu_{\mathrm{B}}}{me}\left[\frac{\ln\left(4\pi^2 h_{\mathrm{p}}\right)}{\pi\ln\left(\Delta U/k_{\mathrm{B}}T\right)}\sqrt{\frac{1+h}{h_{\mathrm{p}}}}\right](I - I_{\mathrm{c}}) \quad (16)$$

In this particular limit, the ensemble-averaged switching speed has a current-dependence slope that is directly dictated by the thermal-activation-induced initial angle. This is true only if there are no transient disturbance fields during the application of the current pulse. Such transient fields would create a sudden rotation of the effective easy-axis direction, and in effect create a nonzero and nonthermal initial angle θ_0, dictating the speed of the spin-transfer switch.

Summarizing the temperature-dependence results discussed so far, we conclude

$$\langle\tau\rangle^{-1} \approx \begin{cases} \tau_0^{-1}\exp\left[-\frac{\Delta U}{k_{\mathrm{B}}T}(1-h)^2\left(1-\dfrac{I}{I_{\mathrm{c}}}\right)\right], \\ \qquad \text{when} \quad (I \ll I_{\mathrm{c}}) \\ \left(\dfrac{\eta\mu_{\mathrm{B}}}{me}\right)\left[\dfrac{\ln\left(4\pi^2 h_{\mathrm{p}}\right)}{\pi\ln\left(\Delta U/k_{\mathrm{B}}T\right)}\sqrt{\dfrac{1+h}{h_{\mathrm{p}}}}\right](I - I_{\mathrm{c}}), \\ \qquad \text{when} \quad (I \gg I_{\mathrm{c}}) \end{cases} \quad (17)$$

Equation (17) describes the experimental observation presented in Figure 4: a linear dependence of switching speed and drive current amplitude above a switching threshold current I_{c}, and a log-linear dependence below the threshold.

The dependence of thermal-activation dwell time as a function of bias current on the spin valve was also directly probed by a set of careful experiments by Krivorotov *et al.* (2004), which confirmed the linear current-dependence factor in the exponential.

In the dynamic switch region ($I > I_{\mathrm{c}}$), the slope of switching speed versus drive current reflects angular momentum conservation. The product $(I - I_{\mathrm{c}})\langle\tau\rangle$ is also an important figure of merit for the possible application of this two-terminal switch as a memory element.

Recently two other experiments have revealed a similar set of relationships between the pulse-width and pulse-height dependences for a spin-current-driven magnetic switch (Tulapurkar *et al.*, 2005; Kaka *et al.*, 2005). A generally similar behavior is reported, although these experiments measure the magnetic switching probability in the long-time limit, including switching events that may occur after the removal of the pulsed driving current. Therefore, the statistics for the switching probability of the nanomagnet should be somewhat different from equation (17).

6 SPIN-TRANSFER SWITCHING IN MAGNETIC TUNNEL JUNCTIONS

Another class of magnetoresistive two-terminal devices is the so-called magnetic tunnel junction. Publications on MTJ research date back to the 1970s (Julliere *et al.*, 1975; Suezawa and Gondo, 1987; Maekawa and Gäfvert, 1982). Theoretical work published as early as 1989 described the MTJ's MR and also predicted a spin-current-induced magnetic excitation (Slonczewski, 1989). In the 1990s, on the experimental front, sizable room-temperature MR was observed in a relatively simple ferromagnet–oxide–ferromagnet stack structure (Moodera, Kinder, Wong and Meservey, 1995; Miyazaki and Tezuka, 1995). Since then, AlO_x-barrier-based MTJs have been successfully optimized for both low RA recording head and higher impedance devices for magnetic random access memory (MRAM) applications. More recently, explorations of MgO as a crystalline tunnel barrier material led further to dramatic improvements in MTJ's performance, both in terms of the magnitude of MR (Parkin *et al.*, 2004; Yuasa *et al.*, 2004; Djayaprawira *et al.*, 2005) and in terms of a successful reduction of the junction-specific resistance–area product (the RA).

For an MTJ to show spin-transfer-induced switching effect, it has to meet some fairly stringent requirements. For most experimental situations, the junction is required to support a tunnel current of the order of $10^7\,\mathrm{A\,cm^{-2}}$ across the tunnel barrier. This can be done only with junctions having high tunnel conductance as well as reasonable tunnel barrier breakdown voltage. At the same time, the junction has to be lithographically patterned down to around 200 nm in size to avoid having excess amount of total current, as discussed earlier. It turns out that these requirements are similar to those of recording-head applications of MTJ, where such properties are desirable for handling signal-to-noise ratio concerns and for compatibility with existing read-out electronics. To a large extent, it is the technology development surrounding the recording-head application that brought us to the age of spin-transfer switching in MTJs.

Spin-transfer-induced magnetic switching in MTJs was first unambiguously observed by Huai *et al.* (2004). Independently, Fuchs *et al.* (2004) also published their work on spin-transfer switching of MTJs. These experiments used AlO_x-based tunnel barriers. The junctions used in Huai *et al.* (2004) had MRs ranging 1–20%, for RAs in the range of $0.5–10\,\Omega\mu\mathrm{m}^2$. The junction stack was of the type

‖ substrate SiO_2 |PtMn|CoFe|Ru|CoFe| Al_2O_3 |CoFe|NiFe‖. The junctions were patterned using deep UV photolithography with resist trimming, followed by Ar ion-mill etch, to about $0.1 \times 0.2\,\mu m^2$ in size. Junctions in Fuchs *et al.* (2004) were patterned, using electron-beam lithography and ion milling, down to a size of $40 \times 130\,nm^2$. For Fuchs *et al.* (2004), because their free layer is predominantly permalloy ($Ni_{81}Fe_{19}$), the junctions were superparamagnetic at ambient temperature. They varied junction temperature to investigate the effect of spin-transfer torque on magnetic switching as the free layer moves across its superparamagnetic transition.

Recently a new tunnel barrier, MgO, was being explored as a superior barrier for MTJs, because it provides much larger tunnel magnetoresistance (TMR) than that achieved with AlO_x-based MTJs. Crystalline MgO was predicted to allow for extremely high TMR values if interfaced with (001)-textured Fe surfaces (Butler *et al.*, 2001; Mathon and Umerski, 2001). This is related to the directional electronic states that are highly spin polarized in the direction perpendicular to the interface of a (001)Fe|(100)MgO|(001)Fe stack. Such large TMR effects have now been experimentally observed (Yuasa *et al.*, 2004; Parkin *et al.*, 2004) as materials and device refinements are underway to further improve the junction characteristics (Ikeda *et al.*, 2005).

An example of spin-transfer-induced magnetic switching in an MgO-based MTJ is shown in Figure 6. The free layer for the junction shown here is composed of 2 nm of CoFeB (Assefa *et al.*, 2006). A current-induced switching is seen between these two branches both at positive and at negative currents. Here positive current designates the direction where electrons tunnel from the free layer into the fixed layer. It is clear the magnetic-field-induced switch and the current-induced switch in this case resulted in exactly the same change in low-bias junction resistance. One may therefore conclude that the current-induced magnetic switching is a complete magnetic reversal, resulting in the same final magnetic state as the one achieved by magnetic-field-induced reversal. The junction shown here is nominally $50 \times 100\,nm^2$ in size. The junction dynamic resistance R_J was measured with a lock-in detection of an ac sine-wave signal, 10 μA in rms amplitude at 331 Hz, superimposed on the dc-bias current. When measuring $R_J(H)$, the field sweep speed was about $2\,Oe\,s^{-1}$. When measuring $R_J(I)$, the bias current varies with a speed of around $0.01\,mA\,s^{-1}$. The switching boundaries thus measured are determined by assisted thermal activation, as described by the first equation in equation (17).

Spin-transfer-induced magnetic switching in MTJs is in many aspects very similar to that in all-metal spin valves. A relationship similar to that in equation (4) exists, which describes the instability current threshold (Slonczewski,

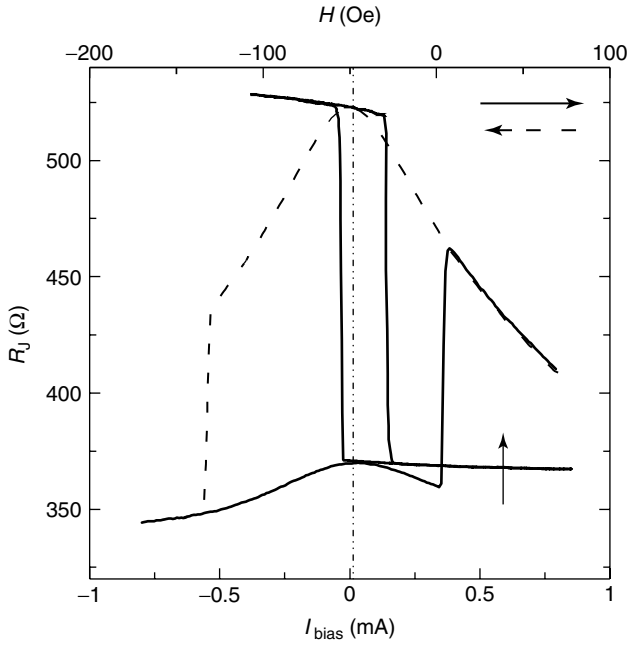

Figure 6. An example of an MTJ undergoing spin-transfer-induced magnetic switching. The solid and dash-dot lines represent the two branches of the MTJ's dynamic resistance $R_J = dV/dI$, measured as a function of a dc-bias current. To illustrate the relationship between the current-induced switching and magnetic switching, a low-bias magnetoresistance versus magnetic-field curve is shown as the faint solid line for comparison. The vertical dashed line here represents the bias magnetic field at which the current sweep for junction dynamic resistance is taken. (Data is related to work in Assefa *et al.* (2006).) The junction shown here is $0.05 \times 0.10\,\mu m^2$ in size. (Reproduced from J.Z. Sun *et al.*, 2006, *Journal of Res. And Dev*, with permission from IBM. © 2006.)

2005). In a stack containing an MTJ, the spin polarization of the tunnel current is usually determined by the spin-dependent tunnel matrices. Since a tunnel barrier usually has much higher RA than the corresponding spin-valve resistance, it tends to determine the transport current and the amount of spin polarization, while the resistances from the rest of the stack structure and that from the leads do not affect the spin-polarization current through the free layer as much as they did in an all-metal spin valve. However this difference is only quantitative. With very low RA tunnel junctions, the spin-dependent conductances from the rest of the pillar do come into play, in ways similar to that of an all-metal spin valve.

Another important issue is the bias dependence of the tunnel current's spin polarization, and its relationship with the bias dependence of the junction TMR. The bias-dependent TMR is relevant to spin transfer because both phenomena relate to the spin-dependent tunnel matrices. The spin current relating to the spin transfer of an MTJ is determined by the initial states of the tunneling electrons involved

(Slonczewski, 2005). This relates to the efficiency of conversion between the total charge current and the spin current responsible for spin torque on the free layer. The TMR of an MTJ, on the other hand, depends on both the initial and the final state densities of the tunnel electrons. It is commonly observed experimentally that an MTJ's TMR decreases upon increasing the bias (Lu *et al*., 1998; Sun *et al*., 1998; Zhang, Levy, Marley and Parkin, 1997).

Experimentally, it was shown early on that at bias currents sufficient to induce spin-transfer switching, the TMR value is significantly diminished from its low-bias value. This, however, does not appear to significantly diminish the ability of the MTJ to produce spin-transfer switching (Fuchs *et al*., 2004). More recently, the same group reported (Fuchs *et al*., 2005a) the observation of a rather constant spin-polarization factor of the tunnel current over the bias range enclosing spin-transfer switching, unlike the TMR value of the same MTJ which shows significant bias dependence over the same bias range. These seem to suggest that empirically, the spin-transfer-related spin-polarization efficiency of an MTJ is much less bias dependent than its TMR and is not significantly diminished at high bias.

It has also been experimentally shown that a correlation exists between the value of the low-bias TMR and the threshold current for a spin-transfer switching (Diao *et al*., 2005).

As in their spin-valve cousins, MTJ-based spin-transfer switching was also most often observed in quasistatic measurements. This is not surprising as quasistatic switching threshold currents are usually lower than dynamic thresholds, and MTJ devices have less tolerance for high current density bias than spin valves. Experimentally, it has been observed that a thermally activated switching process nearly identical to those described in the previous section (Koch, Katine and Sun, 2004; Sun, Kuan, Katine and Koch, 2004; Yagami, Tulapurkar, Fukushima and Suzuki, 2004) is at play. This can be quantitatively verified by careful measurements of the statistically averaged switching threshold current as a function of the current pulse width used to switch the junction (Pakala *et al*., 2005; Kubota *et al*., 2005b; Hosomi *et al*., 2005).

To access deterministic switching requires larger current density than necessary for thermal-activation-assisted switching. MTJs tend to have lower breakdown current density than spin valves. Therefore, spin-transfer switching experiments on MTJs were first done in the thermal-activation-assisted region. Further improvement in MTJ materials will make it easier access the precessional switching process. These would require improvements of the tunnel barrier strength for providing larger breakdown current densities. More importantly, this will require magnetic anisotropy engineering for the magnetic free layer so as to eliminate the dominating effect of shape-induced easy-plane anisotropy in threshold current (Sun, 2000a). The same requirements will be necessary for successful demonstration and application of MTJ in producing persistent magnetic precessions necessary for the generation of microwave emissions.

In the meantime, a convenient way of estimating the equivalent zero-temperature switching current threshold is to use an extrapolated value of the threshold current as a function of the switching time in the thermal-activation regime (Pakala *et al*., 2005; Diao *et al*., 2005) This is equivalent to using the deviation from log-linear behavior in Figure 4(c) as a way of estimating I_{c0}. The accuracy of this estimate, however, will depend on the details of the switching layer's magnetic properties, especially its uniaxial anisotropy barrier height compared to $k_B T$. In simplistic single-domain models, it is the value of $\Delta U / k_B T$.

Another important factor to be considered for MTJ-based (and to a lesser degree, for spin-valve-based) spin-transfer switching is Joule heating induced by the current. Estimates for the amount of current-induced Joule heating in a typical metallic spin valve run from less than 20 K (Krivorotov *et al*., 2004) to about 50 K (Deac *et al*., 2005). A tunnel junction on the other hand, because of its larger RA value, dissipates more power, resulting in more heating (Fuchs *et al*., 2005b). This effect could introduce an additional term in the current dependence of equation (13) through a current-dependent temperature T. It modifies the appearance of the phase boundaries and equation (14). The net effect of this heating is to tilt the apparent switching boundary $I(H)$ for large I, as illustrated in Figure 5, as also seen in experiments (Krivorotov *et al*., 2004; Fuchs *et al*., 2005a,b).

7 POSSIBLE APPLICATIONS

Spin-transfer-induced magnetic excitation and magnetic reversal is a relatively new phenomenon that dominates magnetic behavior for junction devices only in high current density transport and below about 0.1 μm in lateral size. As the critical dimensions of the modern day electronic devices shrink below this length scale, the spin-transfer mechanism becomes important in several aspects. It may be used for localized write addressing of a magnetic random memory element or it could be used for on-chip generation of tunable microwave radiation. The mechanism also affects the operation of a magnetic hard-disk's read heads.

A two-terminal spin valve or MTJ that can be current switched between two stable resistance states constitutes a memory element. To integrate such a memory element into existing CMOS circuit technologies, some basic device

requirements must be met. Chief among them are three items: the device impedance, the voltage swing between the two stable states, and the threshold current required to switch the device. Switching speed and its relationship and trade-off with switching current are also important.

To be integrable, the current density required for device switching must be comparable to what a typical CMOS circuit of comparable density can supply. If this were supplied by a MOSFET transistor, it usually is of the order of $0.5-1\,\mathrm{mA}\,\mu\mathrm{m}^{-1}$ channel width for the transistors. This determines the upper limit of the switching current. Diode selection could in principle allow for higher current density, although there are additional concerns over impedance (mis)match and uniformity of device characteristics over large numbers of junctions and diodes.

The other constraint on the junction switching current is that it has to be sufficient to switch a nanomagnet that has the thermal stability to retain its remanent state at room temperature. For this, one needs a magnetic anisotropy energy $U_k = (1/2)mH_k$ of the order $40-60\,k_\mathrm{B}T$. It turns out that the high-speed switching threshold current I_c in equations (17) and (4) can be directly related to this uniaxial anisotropy energy in the form (Sun, 1999, 2000a), $I_\mathrm{c} \approx (2e/\hbar)\,(\alpha/\eta)\,U_k$. This, depending on the damping α and spin-polarization factor η, places $I_\mathrm{c} \approx 10-100\,\mu\mathrm{A}$ for $U_k \sim 60\,k_\mathrm{B}T$.

Present-day spin-transfer switching junction devices typically involve a quasistatic switching current of the order of $0.1-1\,\mathrm{mA}$ for a device cross- sectional size of around $50-100\,\mathrm{nm}$. This places the quasistatic switching threshold current density in the order $10^6\,\mathrm{A\,cm}^{-2}$. To be useful for CMOS integration, at least another order-of-magnitude reduction is necessary. The high-speed switching threshold, as shown earlier, can be significantly higher (by perhaps a factor of 2–5 depending on device structure details).

Existing low-impedance ($1-10\,\Omega\,\mu\mathrm{m}^{-2}$) MTJs can support a transport current of the order $10^7\,\mathrm{A\,cm}^{-2}$ before barrier-related breakdown. Such current density is sufficient to demonstrate spin-transfer effect. In 2005, SONY Corporation presented the first successful implementation of a CMOS-integrated MTJ switch using spin-transfer as the switching mechanism (Hosomi *et al*., 2005). In this device, switchings of up to 10^{12} cycles were demonstrated at a write-pulse width of around 20 ns, although write-success probability still needs improvement.

A large part of the threshold current of a present-day spin-transfer device comes from the easy-plane demagnetization field because of the thin film geometry. This type of anisotropy does not contribute to thermal stability, yet since the spin-transfer excitation involves significant out-of-film-plane precession, this easy-plane anisotropy significantly increases the spin-transfer switching current. One possibility of reducing the switching current of the spin-transfer devices, therefore, is to reduce or eliminate this easy-plane anisotropy from the system (Sun, 2000a). This can be seen by generalizing equation (4) to include an additional uniaxial anisotropy term in the form of

$$I_\mathrm{c} = \left(\frac{2e}{\hbar}\right)\left(\frac{\alpha}{\eta}\right) m\left(H + H_k + \mid 2\pi M_\mathrm{s} - H_\mathrm{p} \mid\right) \qquad (18)$$

where $\mid 2\pi M_\mathrm{s} - H_\mathrm{p} \mid$ is the combined anisotropy field corresponding to an anisotropy energy expression of equation (1) in Sun (2000a), with the perpendicular anisotropy energy prefactor $K_\mathrm{p} = (1/2)\,m\left(4\pi M_\mathrm{s} - H_\mathrm{p}\right)$. When $K_\mathrm{p} > 0$, an easy-plane anisotropy results. For $K_\mathrm{p} < 0$, this anisotropy term becomes uniaxial with its axis perpendicular to the film surface (and therefore perpendicular to the usually shape-defined in-plane uniaxial anisotropy noted here as H_k). A sizable, perpendicular anisotropy component H_p can be achieved by the careful engineering of the free-layer's interface magnetism, or by controlling its stress field (for materials with large magnetostriction coefficient), or a combination of both. These propositions are theoretically feasible but are likely to raise significant material and fabrication challenges before they can be successfully implemented in a manufacturable fashion.

The threshold current as expressed in relations such as equations (4) and (18) provides only an order-of-magnitude estimate for the switching current necessary for memory circuit operation. To achieve sufficiently fast and deterministic switching, the drive current has to be above the threshold, sometimes by a significant amount. The switching speed versus switching time trade-off is well captured by the curves presented in Figure 4. This trade-off is described by the linear current-dependence in second equation in equation (17). For the $50 \times 100 \times 3\,\mathrm{nm}^3$ cobalt nanomagnet presented in Figure 4, the figure of merit for $(I - I_\mathrm{c})\,\langle\tau\rangle$ is about 8 pC.

For finite temperature operation as a memory element, the collinear switching is unlikely to be the best geometry, as the initial condition of the switch will depend sensitively on thermal distribution. A noncollinear arrangement between the 'free'-layer nanomagnet's orientation and that of the spin-polarized current may be desirable. At the same time, it may be helpful to add, through layout design, a current-induced magnetic field as a transient 'tipping' field to create a nonequilibrium initial state when switching the nanomagnet.

In addition to possible applications as a bistable resistor for memory circuits, spin-transfer devices have also been explored for potential use as compact, on-chip microwave oscillators (Rippard *et al*., 2004). Experiment has demonstrated tunable microwave output from spin-transfer-based magnetic junction structures whose frequencies range from

1 to 20 GHz and whose full-width-half-maximum power linewidth is at least 1000 times below its center frequency. Phase locking between magnetic precession–induced microwave oscillation and additional input tune has also been demonstrated (Rippard *et al*., 2005). Future work in this area is likely to be aimed at reducing the current density required for microwave generation, at increasing the device impedance, and more importantly its output signal amplitude, as well as at the reduction of required external bias magnetic field.

Spin transfer also affects the performance of magnetic read heads in modern hard drives (Covington, Rebei, Parker and Seigler, 2004; Covington *et al*., 2005; Zhu *et al*., 2004). There it can act as a negative influence, at times amplifying thermal and other magnetic noises of the read head, causing stability problems and raising concerns over the signal-to-noise ratio and dynamic characteristics.

Spin-transfer-related magnetic excitation has also been observed to move magnetic domain walls in narrow ferromagnetic wires (Yamaguchi *et al*., 2004; Kläui *et al*., 2005; Saitoh, Miyajima, Yamaoka and Tatara, 2004; Yamanouchi, Chiba, Matsukura and Ohno, 2004; Vernier *et al*., 2004; Grollier *et al*., 2003). In fact, the interaction between spin-polarized current and a ferromagnetic domain wall has been one of the first areas where a spin-angular momentum transfer process was considered (Berger, 1978, 1984). Recent experiments demonstrated unambiguous presence of a spin-torque term in the cause of domain wall motion under applied current. This mechanism (Li and Zhang, 2004b; Tatara and Kohno, 2004; Thiaville, Nakatani, Miltat and Suzuki, 2005; Waintal and Viret, 2004; Zhang and Li, 2004), if harnessed with sufficiently low current density, could have significant implications for memory devices as well.

In short, for applications in integrated circuits, the spin-transfer device has to have lower threshold current density – by at least another order of magnitude than what is demonstrated in all-metal spin valves, and it has to have much larger voltage output than the demonstrated values of several hundred microvolts in spin valves. The recently demonstrated spin-current switchable MTJ devices may prove effective as spin switches that are impedance-matched to CMOS transistors. The switching current density, even in MTJs, remains too high. Various strategies are being proposed for the improvement of spin-transfer devices.

One proposal for reducing the current required to switch a nanomagnet was presented by Berger (2003). For a free nanomagnet sandwiched in between two oppositely fixed magnetic polarizer layers, Berger predicted a sizable enhancement of the spin-transfer effect and an approximately sixfold net reduction of the threshold current.

Several recent experiments (Jiang *et al*., 2004) seem to confirm the existence of this enhancement, although quantitative comparison with model results is yet to be made.

Some recent work has further explored this three-magnetic-layer structure in combination with an MTJ, in which one side of the ferromagnetic (FM) free layer in the middle is interfaced with the FM fixed layer through a tunnel barrier (Fuchs *et al*., 2005b). In this case, the magnetic alignment between the fixed and the free layer on the spin-valve side is seen to affect the spin-transfer threshold current for the free-layer reversal, either to reduce the threshold when the two fixed layers are antiparallel or to increase the threshold when they are parallel. Furthermore, the authors have used this extra degree of freedom in the structure to investigate the effect of junction stack heating, using the apparent magnetic switching field of the free layer as a measure for the free-layer temperature through the thermal-activation model.

8 CONCLUDING REMARKS

In this chapter, we have described how spin-transfer-induced magnetic excitation has been demonstrated both in all-metal spin-valve magnetic nanojunctions and in MTJs. The spin-torque effect can generate persistent magnetic precession as well as complete reversal of a nanomagnet moment's orientation, depending on the details of the bias current and field environment. The main effect of spin torque is to oppose or assist the effective magnetic damping of the nanomagnet, absorbing part of the spin current depending on the relative direction of the nanomagnet moment with respect to the spin-polarization direction and the current flow direction of the spin current. The spin-torque-related effects become most visible when the magnetic junction is small – approximately below 200 nm in lateral dimensions and a film thickness of less than 5 nm in the case of cobalt, for example, macrospin dynamics capture the main experimental features well. It is a good starting point to the quantitative understanding of these new magnetodynamics. For more quantitative and detailed understanding, finite wavelength magnetic excitation has to be carefully taken into account. This in most cases can only be done numerically. Finite temperature problems of micromagnetics with the presence of a spin torque remains a challenge.

Spin torque has important implications for solid-state device applications. For MRAM, it can be used to locally write address a nanomagnet bit by passing an electrical (or spin) current through the particular nanomagnet. This write operation will not disturb the neighboring nanomagnet bit, as it is easier to localize the write current path than is if the write operation were done through current-induced magnetic field. It may also be possible to use spin-transfer junction in its

persistent precession mode, acting as an extremely compact tunable microwave generator. Spin transfer and spin torque also affect the performance of the read heads in magnetic disk drives. In this case, the challenge is to avoid the amplification of thermal (and other) noises present in the read head by the spin-transfer excitation.

The current density required for spin-torque effect to result in magnetic reversal and persistent precession is still a bit too high for ready integration with CMOS technology. The threshold current density is, for the moment, limited mostly by the thin-film shape-determined easy-plane anisotropy $4\pi M_s$. Reduction or elimination of this energy could reduce the threshold current, although the materials and processing challenges associated with this proposition is significant.

The signal voltage output from spin-valve-based spin-transfer junctions is too low. These are all-metal-based junctions with very low impedances which made their integration with CMOS difficult. MTJs, with their much wider range of impedances, seem to have a much better future as spin-transfer switching (or oscillation) devices for circuit integration. This will become feasible once the spin-transfer excitation current density is reduced to a level compatible with MTJs with the desired impedance.

There are relatively stringent requirements on the switching current for reversing a nanomagnet if the nanomagnet is to avoid entering its superparamagnetic state. For room-temperature data retention of the nanomagnet state, the corresponding switching threshold current has been estimated to be of the order of 10–100 μA depending on the choice of material parameters.

ACKNOWLEDGMENTS

I wish to thank D. W. Abraham, R. A. Buhrman, W. Y. Chen, J. DeBrosse, G. D. Fuchs, W. J. Gallagher, Xin Jiang, J. A. Katine, A. D. Kent, R. H. Koch, T. S. Kuan, D. J. Monsma, B. Özylimaz, S. S. P. Parkin, D. C. Ralph, C. T. Rettner, W. H. Rippard, M. J. Rooks, J. C. Slonczewski, M. D. Stiles, B. D. Terris, M. Tsoi, P. L. Trouilloud, and D. C. Worledge for stimulating discussions.

REFERENCES

Albert, F.J., Katine, J.A., Buhrman, R.A. and Ralph, D.C. (2000). Spin-polarized current switching of a co thin film nanomagnet. *Applied Physics Letters*, **77**, 3809.

Apalkov, D.M. and Visscher, P.B. (2005a). Spin-torque switching: Fokker-planck rate calculation. *Physical Review B*, **72**, 180405.

Apalkov, D.M. and Visscher, P.B. (2005b). Slonczewski spin-torque as negative damping: Fokker-plank computation of energy distribution. *Journal of Magnetism and Magnetic Materials*, **286**, 370.

Assefa, S., Sun, J.Z., Ruiz, N., *et al*. (2006). *Proceedings of Intermag* in San Diego: California USA, May 8–12, 2006.

Bauer, G.E.W., Tserkovnyak, Y., Huertas-Hernando, D. and Brataas, A. (2003). Universal angular magnetoresistance and spin torque in ferromagnetic/normal metal hybrids. *Physical Review B*, **67**, 094421.

Bazaliy, Ya.B. and Jones, B.A. (2004). Current-induced magnetization switching in small domains of different anisotropies. *Physical Review B*, **69**, 094421.

Bazaliy, Ya.B., Jones, B.A. and Zhang, S-C. (1998). Modification of the laudau0lifshitz equation in the presence of a spin-polarized current in colossal- and giant-magnetoresistive materials. *Physical Review B*, **57**, R3213.

Berger, L. (1978). Low-field magnetoresistance and domain drag in ferromagnets. *Journal of Applied Physics*, **49**, 2156.

Berger, L. (1984). Exchange interaction between ferromagnetic domain wall and electric current in very thin metallic films. *Journal of Applied Physics*, **55**, 1954.

Berger, L. (1988). Exchange interaction between electric current and magnetic domain wall containing Bloch lines. *Journal of Applied Physics*, **63**, 1663.

Berger, L. (1992). Motion of a magnetic domain wall traversed by fast-rising current pulses. *Journal of Applied Physics*, **71**, 2721.

Berger, L. (1996). Emission of spin waves by a magnetic multilayer traversed by a current. *Physical Review B*, **54**, 9353.

Berger, L. (2003). Novel multilayer configuration for experiments of spin precession induced by a dc current. *Journal of Applied Physics*, **93**, 7693.

Brown, W.F. (1963). Thermal fluctuations of a single-domain particle. *Physical Review*, **130**, 1677.

Butler, W.H., Zhang, X-G., Schulthess, T.C., *et al*. (2001). Spin-dependent tunneling conductance of Fe/MgO/Fe sandwiches. *Physical Review B*, **63**, 054416.

Covington, M., AlHajDarwish, M., Ding, Y., *et al*. (2005). Spin transfer effects in current perpendicular to the plane spin valves. *Journal of Magnetism and Magnetic Materials*, **287**, 325.

Covington, M., Rebei, A., Parker, G.J. and Seigler, M.A. (2004). Spin momentum transfer in current perpendicular to the plane spin valves. *Applied Physics Letters*, **84**, 3103.

Deac, A., Lee, K.J., Liu, Y., *et al*. (2005). Current-induced magnetization switching in exchange-biased spin valves for current-perpendicular-to-plane giant magnetoresistance heads. *Physical Review B*, **73**, 064414.

Diao, Z., Apalkov, D., Pakala, M., *et al*. (2005). Spin transfer switching and spin polarization in magnetic tunnel junctions with mgo and alox barriers. *Applied Physics Letters*, **87**, 232502.

Djayaprawira, D.D., Tsunekawa, K., Nagai, M., *et al*. (2005). 230% room- temperature magnetoresistance in CoFeB/MgO/CoFeB magnetic tunnel junctions. *Applied Physics Letters*, **86**, 092502.

Fuchs, G.D., Emley, N.C., Krivorotov, I.N., *et al*. (2004). Spin-transfer effects in nanoscale magnetic tunnel junctions. *Applied Physics Letters*, **85**, 1205.

Fuchs, G.D., Katine, J.A., Kiselev, S.I., *et al*. (2005).Spin torque, tunnel-current spin polarization and magnetoresistance in mgo mag- netic tunnel junctions. *Physical Review Letters*, **96**, 186603.

Fuchs, G.D., Krivorotov, I.N., Braganca, P.M., *et al*. (2005). Adjustable spin torque in magnetic tunnel junctions with two fixed layers. *Applied Physics Letters*, **86**, 152509.

Grinstein, G. and Koch, R.H. (2003). Coarse graining in micromagnetics. *Physical Review Letters*, **90**, 207201.

Grollier, J., Boulenc, P., Cros, V., *et al*. (2003). Switching a spin valve back and forth by current-induced domain wall motion. *Applied Physics Letters*, **83**, 509.

Grollier, J., Cros, V., Jaffrés, H., *et al*. (2003). Field dependence of magnetization reversal by spin transfer. *Physical Review B*, **67**, 174402.

Hosomi, M., Yamagishi, H., Yamamoto, T., *et al*. (2005). IEEE International electron devices meeting (IEDM IEEE 0-7803-9269-8/05), *A Novel Nonvolatile Memory with Spin Torque Transfer Magnetization Switching: Spin-RAM*.

Huai, Y., Albert, F., Nguyen, P., *et al*. (2004). Observa- tion of spin-transfer switching in deep submicron-sized and low-resistance magnetic tunnel junctions. *Applied Physics Letters*, **84**, 3118.

Hung, C-Y. and Berger, L. (1986). Exchange forces between domain wall and electric current in permalloy films of variable thickness. *Journal of Applied Physics*, **63**, 4276.

Ikeda, S., Hayakawa, J., Lee, Y.M., *et al*. (2005). Dependence of tunnel magnetoresistance in mgo based magnetic tunnel junctions on ar pressure during mgo sputtering. *Japanese Journal of Applied Physics*, **44**, L1442.

Jiang, Y., Abe, S., Ochiai, T., *et al*. (2004). Effective reduction of critical current for current-induced magnetization switching by a ru layer insertion in an exchange-biased spin valve. *Physical Review Letters*, **92**, 167204.

Julliere, M., (1975). Tunneling between ferromagnetic films. *Physics Letters*, **54A**, 225.

Kaka, S., Pufall, M.R., Rippard, W.H., *et al*. (2005). Spin transfer switching of spin valve nanopillars using nanosecond pulsed currents. *Journal of Magnetism and Magnetic Materials*, **286**, 375.

Katine, J.A., Albert, F.J., Buhrman, R.A., *et al*. (2000). Current-driven magentization reversal and spin-wave excitation in co/cu/co pillars. *Physical Review Letters*, **84**, 3149.

Kiselev, S.I., Sankey, J.C., Krivorotov, L.N., *et al*. (2003). Microwave oscillations of a nanomagnet driven by a spin-polarized current. *Nature*, **425**, 380.

Kiselev, S.I., Sankey, J.C., Krivorotov, I.N., *et al*. (2004). Current-induced nanomagnet dynamics for magnetic fields perpendicular to the sample plane. *Physical Review Letters*, **93**, 036601.

Kläui, M., Vaz, C.A.F., Bland, J.A.C., *et al*. (2005). Controlled and reproducible domain wall displacement by current pulses injected into ferromagnetic ring structures. *Physical Review Letters*, **94**, 106601.

Koch, R.H., Katine, J.A. and Sun, J.Z. (2004). Time-resolved reversal of spin-transfer switching in a nanomagnet. *Physical Review Letters*, **92**, 088302.

Krivorotov, I.N., Emley, N.C., Garcia, A.G.F., *et al*. (2004). Temperature dependence of spin-transfer-induced switching of nanomagnets. *Physical Review Letters*, **93**, 166603.

Krivorotov, I.N., Emley, N.C., Sankey, J.C., *et al*. (2005). Time-domain measurements of nanomagnet dynamics driven by spin-transfer torques. *Science*, **307**, 228.

Kubota, H., Fukushima, A., Ootani, Y., *et al*. (2005a). Magnetization switching by spin-polarized current in low-resistance magnetic tunnel junction with mgo (001) barrier. *IEEE Transactions on Magnetics*, **41**, 2633.

Kubota, H., Fukushima, A., Ootani, Y., *et al*. (2005b). Evaluation of spin-transfer switching in CoFeB/MgO/CoFeB magnetic tunnel junctions. *Japanese Journal of Applied Physics*, **44**, L1237.

Lee, K-J., Deac, A., Redon, O., *et al*. (2004). Excitations of incoherent spin-waves due to spin-transfer toruque. *Nature Materials*, **3**, 877.

Levy, P.M. (2002). The role of spin accumulation in current-induced switching of magnetic layers, or the first 10^{-12} s in a magnetic multilayer after the current is switched on. *Journal of Physics D: Applied Physics*, **35**, 2448.

Li, Z. and Zhang, S. (2003). Magnetization dynamics with a spin-transfer torque. *Physical Review B*, **68**, 024404.

Li, Z. and Zhang, S. (2004a). Thermally assisted magnetization reversal in the presence of a spin- transfer torque. *Physical Review B*, **69**, 134416.

Li, Z. and Zhang, S. (2004b). Domain wall dynamics and spin wave excitations with spin-transfer torques. *Physical Review Letters*, **92**, 207203.

Lifshitz, E.M. and Pitaevskii, L.P. (1981). Chapter 7, magnetism. *Statistical Physics Part 2*, A. Wheaton & Co. Ltd.: Exeter, p. 285, Vol. 2.

Lu, Yu., Li, X.W., Xiao, G., *et al*. (1998). Bias voltage and temperature dependence of magnetotunneling effect. *Journal of Applied Physics*, **83**, 6515.

Mathon, J. and Umerski, A. (2001). Theory of tunneling magnetoresistance of an epitaxial Fe/MgO/Fe(001) junction. *Physical Review B*, **63**, 220403.

Maekawa, S. and Gäfvert, U. (1982). *IEEE Transactions on Magnetics*, **MAG-18**, 707.

Myers, E.B., Albert, F.J., Sankey, J.C., *et al*. (2002). Thermally activated magnetic reversal induced by a spin-polarized current. *Physical Review Letters*, **89**, 196801.

Miyazaki, T. and Tezuka, N. (1995). Giant magnetic tunneling effect in Fe/Al2O3/Fe junction. *Journal of Magnetism and Magnetic Materials*, **139**, L231.

Moodera, J.S., Kinder, L.R., Wong, T.M. and Meservey, R. (1995). Large magnetoresistance at room temperature in ferromagnetic thin film tunnel junctions. *Physical Review Letters*, **74**, 3273.

Myers, E.B., Ralph, D.C., Katine, J.A., *et al*. (1999). Current-induced switching of domains in magnetic multilayer devices. *Science*, **285**, 867.

Özyilmaz, B., Kent, A.D., Monsma, D., *et al*. (2003). Current-induced magnetization reversal in high magnetic fields in co/cu/co nanopillars. *Physical Review Letters*, **91**, 067203.

Özyilmaz, B., Kent, A.D., Sun, J.Z., *et al*. (2004). Current-induced excitations in single cobalt ferromagnetic layer nanopillars. *Physical Review Letters*, **93**, 176604.

Pakala, M., Huai, Y., Valet, T., *et al*. (2005). Critical current distribution in spin-transfer-switched magnetic tunnel junctions. *Journal of Applied Physics*, **98**, 056107.

Parkin, S.S.P., Kaiser, C., Panchula, A., *et al*. (2004). Giant tunnelling magnetoresistance at room temperature with mgo(100) tunnel barriers. *Nature Materials*, **3**, 862.

Polianski, M.L. and Brouwer, P.W. (2004). Current-induced transverse spin-wave instability in a thin nanomagnet. *Physical Review Letters*, **92**, 026602.

Rippard, W.H., Pufall, M.R., Kaka, S., *et al*. (2004). Direct-current induced dynamics in co90fe10/ni80fe20 point contacts. *Physical Review Letters*, **92**, 027201.

Rippard, W.H., Pufall, M.R., Kaka, S., *et al*. (2005). Injection locking and phase control of spin transfer nano-oscillators. *Physical Review Letters*, **95**, 067203.

Rippard, W.H., Pufall, M.R. and Silva, T.J. (2003). Quantitative studies of spin-momentum-transfer-induced excitation in co/cu multilayer fllms using point-contact spectroscopy. *Applied Physics Letters*, **82**, 1260.

Saitoh, E., Miyajima, H., Yamaoka, T. and Tatara, G. (2004). Current-induced res- onance and mass determination of a single magnetic domain wall. *Nature*, **42**, 203.

Slonczewski, J.C. (1989). Conductance and exchange coupling of two ferromagnets separated by a tunneling barrier.. *Physical Review B*, **39**, 6995.

Slonczewski, J.C. (1996). Current-driven excitation of magnetic multilayers. *Journal of Magnetism and Magnetic Materials*, **159**, L1.

Slonczewski, J.C. (1999). Excitation of spin waves by an electric current. *Journal of Magnetism and Magnetic Materials*, **195**, L261.

Slonczewski, J.C. (2002). Currents and torques in metallic magnetic multilayers. *Journal of Magnetism and Magnetic Materials*, **247**, 324.

Slonczewski, J.C. (2005). Currents, torques and polarization factors in magnetic tunnel junctions. *Physical Review B*, **71**, 024411.

Stiles, M.D., Xiao, J. and Zangwill, A. (2004). Phenomenological theory of current-induced magnetization precession. *Physical Review B*, **69**, 054408.

Stiles, M.D. and Zangwill, A. (2002a). Noncollinear spin transfer in co/cu/co multilayers. *Journal of Applied Physics*, **91**, 6812.

Stiles, M.D. and Zangwill, A. (2002b). Anatomy of spin-transfer torque. *Physical Review B*, **66**, 014407.

Suezawa, Y. and Gondo, Y. (1987). In *Proceedings of the International Symposium on Physics of Magnetic Materials*, Takahashi, M. Maekawa, S., Gondo, Y. and Nose, H. (Eds.), World Scientific: Singapore, p. 303.

Sun, J.Z. (1999). Current-driven magnetic switching in manganite trilayer junctions. *Journal of Magnetism and Magnetic Materials*, **202**, 157.

Sun, J.Z. (2000a). Spin-current interaction with a monodomain magnetic body, a model study. *Physical Review B*, **62**, 570.

Sun, J.Z. (2000b). Spin-dependent transport in trilayer junctions of doped manganites. *Physica C*, **350**, 3201.

Sun, J.Z., Abraham, D.W., Roche, K., *et al*. (1998). Temperature- and bias-dependence of magnetoresistance in doped manganite thin film trilayer junctions. *Applied Physics Letters*, **73**, 1008.

Sun, J.Z., Kuan, T.S., Katine, J.A. and Koch, R.H. (2004). Spin angular momentum transfer in a current-perpendicular spin-valve nanomagnet. *Proceedings of the SPIE*, **5359**, 445.

Sun, J.Z., Monsma, D.J., Kuan, T.S., *et al*. (2003). Spin-torque transfer in batch-fabricated spin-valve magnetic nano- junctions. *Journal of Applied Physics*, **93**, 6859.

Sun, J.Z., Özyilmaz, B., Chen, W., *et al*. (2005). Spin-transfer-induced magnetic excitation: the role of spin-pumping induced damping. *Journal of Applied Physics*, **97**, 10C714.

Tatara, G. and Kohno, H. (2004). Theory of current-driven domain wall motion: spin transfer versus momentum transfer. *Physical Review Letters*, **92**, 086601.

Thiaville, A., Nakatani, Y., Miltat, J. and Suzuki, Y. (2005). Micromagnetic understanding of current-driven domain wall motion in patterned nanowires. *Europhysics Letters*, **69**, 990.

Tsoi, M., Jansen, A.G.M., Bass, J., *et al*. (1998). Excitation of a magnetic multilayer by an electric current. *Physical Review Letters*, **80**, 4281.

Tsoi, M., Jansen, A.G.M., Bass, J., *et al*. (2000). Generation and detection of phase-coherent current-driven magnons in magnetic multilayers. *Nature*, **406**, 46.

Tulapurkar, A.A., Devolder, T., Yagami, K., *et al*. (2005). Subnanosecond magnetization reversal in magnetic nanopillars by spin angular momentum transfer. *Applied Physics Letters*, **85**, 5358.

Urazhdin, S., Birge, N.O., Pratt, W.P. Jr. and Bass, J. (2003). Current-driven magnetic exitations in permalloy-based multilayer nanopillars. *Physical Review Letters*, **91**, 146803.

Valet, T. (2004), private communications.

Vernier, N., Allwood, D.A., Atkinson, D., *et al*. (2004). Domain wall propagation in magnetic nanowires by spin-polarized current injection. *Europhysics Letters*, **65**, 526.

Visscher, P.B. and Apalkov, D.M. (2005). Fokker-planck calculation of spin-torque resistance hyseteresis and switching currents. *Journal of Applied Physics*, **97**, 10C704.

Waintal, X., Myers, E.B., Brouwer, P.W. and Ralph, D.C. (2000). Role of spin-dependent interface scattering in generating current-induced torques in magnetic multilayers. *Physical Review B*, **62**, 12317.

Waintal, X. and Viret, M. (2004). Current-induced distortion of a magnetic domain wall. *Europhysics Letters*, **65**, 427.

Wegrowe, J-E., Kelly, D., Jaccard, Y., *et al*. (1999). Current-induced magnetization reversal in magnetic nanowires. *Europhysics Letters*, **45**, 626.

Yagami, K., Tulapurkar, A.A., Fukushima, A. and Suzuki, Y. (2004). Low-current spin-transfer switching and its thermal durability in a low-saturation-magnetization nanomaget. *Applied Physics Letters*, **85**, 5634.

Yagami, K., Tulapurkar, A.A., Fukushima, A. and Suzuki, Y. (2005). Estimation of thermal durability and intrinsic critical currents of magnetization switching for spin-transfer based magnetic random access memory. *Journal of Applied Physics*, **97**, 10C707.

Yamaguchi, A., Ono, T., Nasu, S., *et al*. (2004). Real-space observation of current-driven domain wall motion in submicron magnetic wires. *Physical Review Letters*, **92**, 077205.

Yamanouchi, M., Chiba, D., Matsukura, F. and Ohno, H. (2004). Current-induced domain-wall switch- ing in a ferromagnetic semiconductor structure. *Nature*, **428**, 539.

Yuasa, S., Nagahama, T., Fukushima, A., *et al*. (2004). Giant room-temperature magnetoresistance in single-crystal Fe/MgO/Fe magnetic tunnel junctions. *Nature Materials*, **3**, 868.

Zhang, S., Levy, P.M., Marley, A.C. and Parkin, S.S.P. (1997). Quenching of magnetoresistance by hot electrons in magnetic tunnel junctions. *Physical Review Letters*, **79**, 3744.

Zhang, S. and Li, Z. (2004). Roles of nonequilibrium conduction electrons on the magnetization dynamics of ferromagnets. *Physical Review Letters*, **93**, 127204.

Zhu, J-G., Kim, N., Zhou, Y., *et al*. (2004). Current induced noise in cpp spin valves. *Journal of Applied Physics*, **40**, 2323.

Spin-transfer in High Magnetic Fields and Single Magnetic Layer Nanopillars

Andrew D. Kent
New York University, New York, NY, USA

1 INTRODUCTION

Spin transfer is a newly discovered interaction between itinerant electrons and the background magnetization of a ferromagnet, first predicted by Slonczewski (1996) and Berger (1996). This interaction is remarkable in many respects, some of which have been discussed in previous chapters in this volume. From a fundamental perspective, it acts contrary to conventions in condensed matter physics. The large number of conduction electrons in a metal ($n \simeq 10^{22}$ electrons/cm^3) typically determines the characteristics of electrons or quasiparticles at the Fermi surface, which in turn determine the material's thermodynamic and transport characteristics. The ratio of the number of electrons at the Fermi surface to those in the Fermi sea at 4 K is $kT/E_F = 10^{-4}$ for a metal. A ferromagnetic (FM) metal has different numbers of up- and down-spin electrons in the Fermi sea. The up-spin electrons are those whose magnetic moment align with the magnetization and are known as *majority electrons*. The excitations for spin-up and spin-down quasiparticles are distinct, as are their conductivities, which is the basis for the phenomena of giant magnetoresistance (GMR). However, through the spin-transfer interaction, electrons at the Fermi surface change the characteristics of the Fermi sea, leading to excitations of the background magnetization and even magnetization reversal. So there is a role reversal: a small number of electrons at the Fermi surface influence the entire background charge configuration.

The phenomena of spin transfer is distinct from that associated with the flow of charge currents and the magnetic fields that result from such flows; the Oersted fields (Figure 1). Spin transfer is predicted and is found to lead to fundamentally new types of magnetic excitations. For instance, a dc spin current has been shown to lead to steady-state precession of the magnetization at gigahertz frequencies (Kiselev *et al.*, 2003; Rippard *et al.*, 2004). A steady-state charge current cannot produce a steady-state precession –illustrating, perhaps most clearly, that new physics is needed to understand the influence of a spin current on the background magnetization. Of particular interest, spin transfer is leading to new insights into the injection, diffusion, and coherence of electron spins in materials. In addition, many questions about the microscopic theory of the interactions remain open to further study, both from the theoretical and experimental view points (Zhang, Levy and Fert, 2002; Shapiro, Levy and Zhang, 2003; Levy and Zhang, 2004; Brataas, Bauer and Kelly, 2006; Stiles and Miltat, 2006).

Spin-current-induced magnetic excitations in single magnetic layer and bilayer nanopillars are discussed in this chapter. In contrast with earlier chapters, which focus on

Handbook of Magnetism and Advanced Magnetic Materials. Edited by Helmut Kronmüller and Stuart Parkin. Volume 5: *Spintronics and Magnetoelectronics*. ISBN: 978-0-470-02217-7.

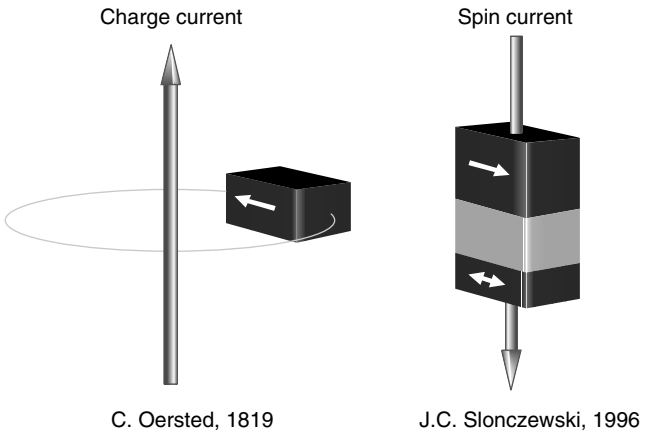

Figure 1. Oersted discovered in 1819 that a charge current produces a magnetic field which acts on a magnet. The interaction predicted by Slonczewski (1996) is distinct and is associated with the flow of spin current directly through a ferromagnetic layer. In the illustration, this is a thick 'fixed' magnetic layer and a thin 'free' layer, a prototype spin-transfer structure.

low-field switching and precession, we emphasize phenomena that occur at high current and magnetic field.

We begin with an outline of the Slonczewski model. We then present high-field experiments that reveal hysteresis in current and magnetic field sweeps in magnetic bilayers. These experiments suggest that even in very large magnetic fields a spin current may induce a complete reversal of the thin magnetic layer to align antiparallel (AP) to the applied field – that is, to a state of maximum magnetic energy. This is consistent with the Slonczewski model within a single domain or macrospin picture. We then review experiments on single magnetic layer structures that require physics beyond the macrospin model. These experiments illustrate that spin transfer can create nonuniform spin-wave excitations. The most elementary samples that exhibit spin-transfer effects thus consist of just a single thin magnetic layer, not two magnetic layers. Nonuniform spin-wave excitations are also seen in traditional bilayer structures, which experiment reveals to have a rich phase diagram of current-induced excitations. We conclude with a summary and perspectives on spin transfer.

2 SPIN-TRANSFER INTERACTION

In Slonczewski's model, spin-angular momentum is transferred to the background magnetization when the spin current enters the ferromagnet – within the first few atomic layers Stiles and Zangwill (2002). The transverse component of spin current is filtered by the FM layer and, by conservation of angular momentum, there is a back reaction on the magnetization. Absorption of the transverse component of spin-angular momentum by the background magnetization is the fundamental origin of the spin-transfer torque.

In magnetic nanopillars that consist of a thick and thin magnetic layer separated by a nonmagnetic (NM) layer, the thick (fixed) layer polarizes the current and dynamics is usually induced in the thin (free) layer. The magnetization of the free layer can be described by the Landau–Lifshitz–Gilbert (LLG) equation with an additional term. In a macrospin model, which assumes that the two layers are uniformly magnetized:

$$\frac{\mathrm{d}\hat{m}}{\mathrm{d}t} = -\gamma \hat{m} \times \vec{H}_{\mathrm{eff}} + \alpha \hat{m} \times \frac{\mathrm{d}\hat{m}}{\mathrm{d}t} + \gamma a_{\mathrm{J}} \hat{m} \times (\hat{m} \times \hat{m}_P) \quad (1)$$

$\hat{m}$ and $\hat{m}_P$ are unit vectors in the direction of magnetization of the free and fixed magnetic layers, respectively. The first term on the right leads to precession of the magnetization about the effective field, $\vec{H}_{\mathrm{eff}}$, γ is the gyromagnetic ratio. The second term on the right is the damping term, where α is the Gilbert damping constant. The last term is due to spin transfer. The vector cross product, $\hat{m} \times (\hat{m} \times \hat{m}_P)$, is in the direction of spin angular momentum transverse to the free layer magnetization and in the plane containing $\hat{m}$ and $\hat{m}_P$. To see this explicitly, note that:

$$\hat{m} \times (\hat{m} \times \hat{m}_P) = (\hat{m} \cdot \hat{m}_P)\hat{m} - \hat{m}_P \quad (2)$$

The prefactor of the spin-transfer term, a_{J}, depends on the current, the spin polarization of the current, P, and the angle between the free and pinned magnetic layers Θ, $a_{\mathrm{J}} = \frac{\hbar I}{eMV} g(P, \Theta)$ (Slonczewski, 1996). Here I is the charge current and g is a function of the polarization P that increases with Θ. V is the volume of the magnetic element. An increase in a_{J} with an increase in the angle has been found in a number of different approaches to modeling the spin-transfer effect (Bauer, Tserkovnyak, Huertas-Hernando and Brataas, 2003; Stiles and Zangwill, 2002; Waintal, Myers, Brouwer and Ralph, 2000; Shapiro, Levy and Zhang, 2003). Spin-current-induced torques of the form $b_{\mathrm{J}} \hat{m} \cdot \hat{m}_P$ are also possible, where b_{J} is proportional to the current (Zhang, Levy and Fert, 2002). This has the form of torque due to a magnetic field in a direction $\hat{m}_P$, with a magnitude proportional to the current. This term and the spin-torque term define a basis in the plane orthogonal to $\hat{m}$ and, therefore, an arbitrary torque on the magnetization can always be decomposed into these two terms. There is experimental evidence for this interaction, which is found to be somewhat smaller in magnitude than the spin-torque term (Zimmler *et al.*, 2004). However, this term does not, by itself, lead to magnetization dynamics distinct from that of Oersted fields,

so we emphasize magnetization dynamics associated with the spin torque in this chapter.

The effective magnetic field, $\vec{H}_{\rm eff}$, in equation (1) is the vector sum of the applied field, $\vec{H}$, and the anisotropy fields. Studies are typically conducted on thin elements with an asymmetric shape, approximating a rectangle or ellipse. In this case, the effective field is given by

$$\vec{H}_{\rm eff} = \vec{H} + H_{\rm a}(\hat{m}\cdot\hat{x})\hat{x} - 4\pi M_{\rm s}(\hat{m}\cdot\hat{z})\hat{z} \qquad (3)$$

Here $H_{\rm a}$ is an anisotropy field that accounts for the asymmetric shape of the element ($H_{\rm a} = 2K/M_{\rm s}$, where K is in the uniaxial anisotropy constant) and $4\pi M_{\rm s}$ characterizes the easy-plane anisotropy. $H_{\rm a}$ ($\sim$0.1 T) is typically much smaller than $4\pi M_{\rm s}$ ($\sim$1 T).

In equilibrium, the magnetization is aligned with the effective magnetic field. The spin-transfer torque competes with damping and, at a threshold current, leads to excitation of the magnetization. This is illustrated in Figure 2. Deviation of the free layer magnetization direction from the effective field leads to precession of the magnetization about the field at an angular frequency $\omega = \gamma H_{\rm eff}$. The damping torque acts to bring the magnetization back into alignment with the effective field. If the pinned layer magnetization is also parallel (P) to the effective field, then the spin-transfer torque and damping are collinear. In this case, the spin-transfer torque can enhance or oppose the damping torque depending on the sign of the current. In the latter case, excitation of the magnetization occurs, which may drive the free layer magnetization into a precessional state (PS) or new static configuration.

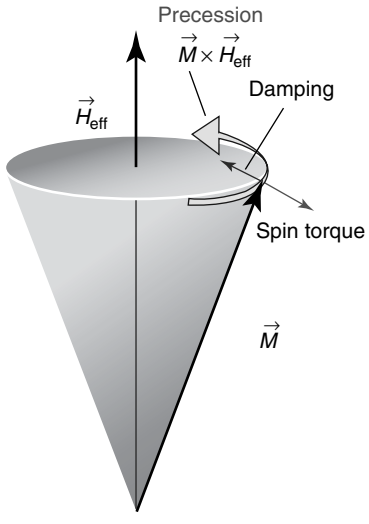

Figure 2. Schematic of magnetization dynamics with a spin-transfer torque. In large fields, when the pinned layer magnetization, effective field, and applied field are parallel, the spin-transfer torque is collinear with the damping. Instabilities occur when the spin torque opposes and exceeds the damping torque.

3 HIGH-FIELD STUDIES OF BILAYERS

Studies in large magnetic fields applied perpendicular to the layers provide insight into the physics of spin transfer. For fields greater than the layer demagnetization field ($4\pi M_{\rm s}$), the Zeeman energy ($E = -M_{\rm s}H$) becomes the dominant term in the magnetic energy and, in equilibrium, the magnetization is aligned with the applied field. In this limit (i.e., assuming that $H \gg H_{\rm a}$), there is axial symmetry about the field direction, and the precession is circular, with the precession frequency increasing linearly with the applied field.

Initial point-contact experiments on magnetic multilayers were conducted in high perpendicular fields (Tsoi *et al*., 1998, 2000; Myers *et al*., 1999) (Figure 3a). A peak structure in the differential resistance ($\mathrm{d}V/\mathrm{d}I$) versus current graph was observed and interpreted as the onset of current-induced excitation of long wavelength ($k \simeq 0$) spin waves (Tsoi *et al*., 1998, 2000; Slonczewski, 1999) (Figure 3a). Subsequent experiments have focused on nanopillar structures (Figure 3b), in which the magnetic bilayers, such as Co/Cu/Co layered films, are patterned down to the 100-nm lateral scale (Katine *et al*., 2000; Grollier *et al*., 2001, 2003; Albert, Katine, Buhrman and Ralph, 2000; Albert *et al*., 2002; Sun *et al*., 2002, 2003). Spin-transfer torque studies on pillar devices (PDs) are usually conducted with small magnetic fields applied in the layer plane. In the low-field regime, a hysteretic jump in the differential resistance was observed (Figure 3b). These experiments provide clear evidence for current-induced magnetization switching (Katine *et al*., 2000; Grollier *et al*., 2001, 2003; Albert, Katine, Buhrman and Ralph, 2000; Albert *et al*., 2002; Sun *et al*., 2002, 2003; Urazhdin, Birge, Pratt and Bass, 2003). Hence, the effect of the spin-polarized current on the magnetization seemed to be quite distinct in the low- and high-field regimes; at low fields, switching is observed, whereas high-field data is interpreted in terms of spin-wave excitations. Current-induced hysteretic magnetization reversal was only observed at low *in-plane* fields in nanopillar devices.

3.1 Experiments on nanopillar junctions

Nanopillar junctions were used to study current-induced magnetization dynamics in large fields and currents in Özyilmaz *et al*. (2003). The layer structure was |3-nm Co| 10-nm Cu|12-nm Co|300-nm Cu| 10-nm Pt| and the typical lateral size of the sample was $90 \times 140\,\mathrm{nm}^2$. The thin Co layer has a lower coercivity and is the 'free' layer in the device. The thick Co layer is the 'fixed' layer in the device and acts to set up a spin-polarized current in the intervening Cu layer. The inset in Figure 4 shows a sketch of the PD. Details of fabrication and transport properties at low in-plane

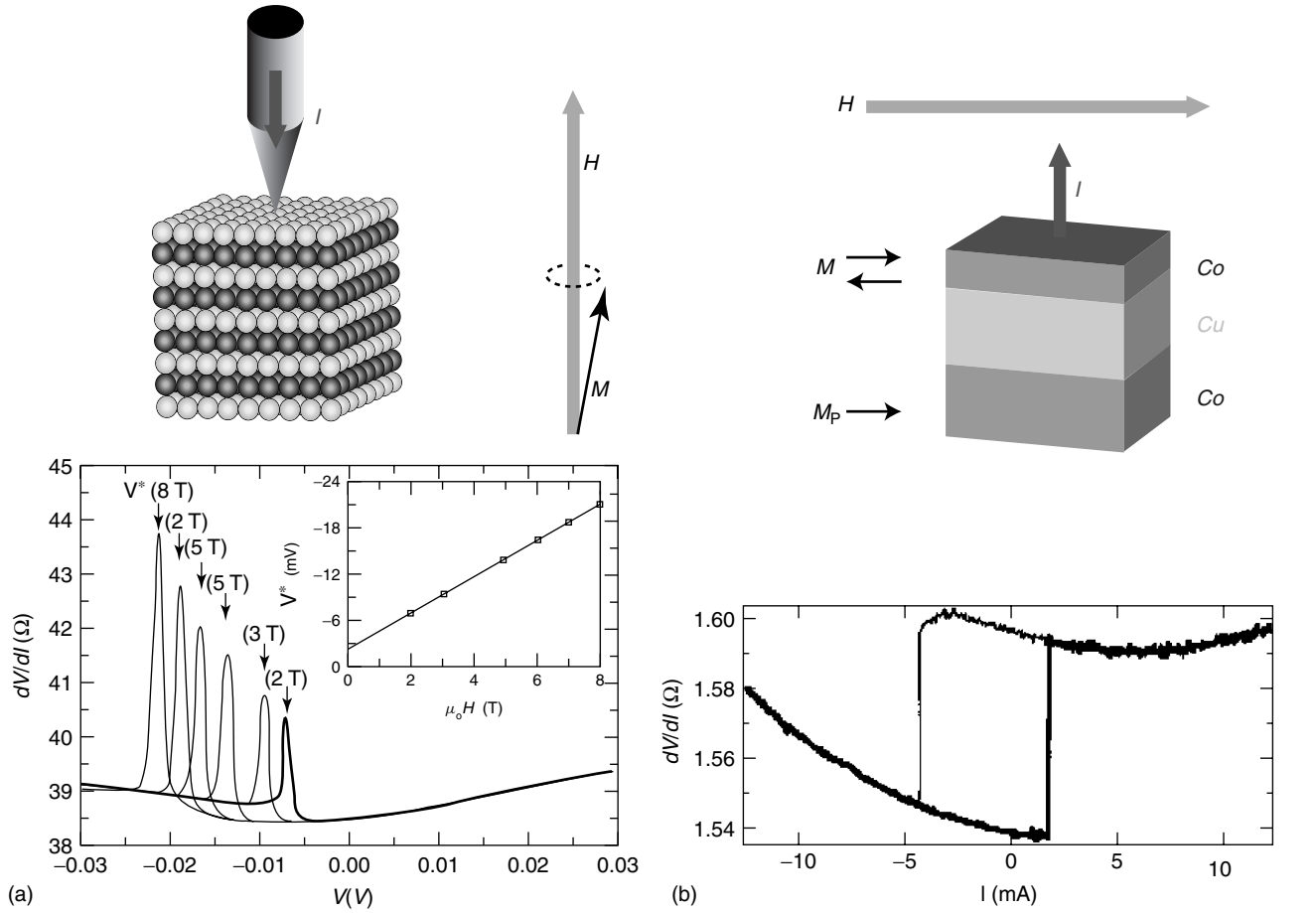

Figure 3. Spin-transfer experiments. (a) Initial studies were conduced using mechanical point contacts to magnetic multilayers. In high fields perpendicular to the plane, peaks in differential resistance were observed and interpreted as the onset spin-wave excitations. (b) Experiments on magnetic bilayer thin-film elements patterned into nanopillars showed the first evidence for current-induced magnetization reversal in small in-plane applied magnetic fields. (Reprinted with permission of Tsoi *et al*. copyright 1998, American Physical Society.)

fields can be found elsewhere (Sun *et al*., 2003). Transport measurements were conducted in a four-point measurement configuration at 4.2 K to minimize the effect of thermal fluctuations on the magnetization dynamics. Positive current bias is defined such that electrons flow from the thin to the thick layer.

A typical magnetoresistance (MR) measurement with in-plane magnetic fields is shown in Figure 4(a). The device exhibits a clean transition between a low-resistance and high-resistance state corresponding to P and AP alignment of the magnetization of the two Co layers. The MR of this sample is 5.4% at 4.2 K. Owing to magnetostatic interactions between the layers, the high-resistance state is reached before the sign of H is reversed, which is typical of pillars in which both magnetic layers are patterned.

Figure 4(b) shows dV/dI versus I with the applied field perpendicular to the film. Here the applied field ($H = 2.2$ T) is larger than the demagnetization field of the Co thin layer ($4\pi M_s \approx 1.5$ T). The sweep to negative currents is shown as the dashed line in the figure. An abrupt change in resistance occurs only for one current direction. In addition, the onset of this change in resistance is sharp and takes place at a critical current, I_c ($j_c \approx 2.3 \times 10^8 \mathrm{A\,cm^{-2}}$). The signature is a peak in the differential resistance. In simultaneous dc measurement (shown in an inset of Figure 4b), this feature corresponds to a steplike increase of the dc voltage. The parabolic increase in the background resistance for both directions of the current is due to increased electron scattering at high current densities.

In earlier reports, the peak structure in the differential resistance of point contacts was attributed to the excitation of a uniform precession of the free layer (Tsoi *et al*., 1998, 2000; Slonczewski, 1999). However, this picture does not explain the data on nanopillars for several reasons. First, the resistance change is large. This can be seen by either looking at the change of slope in the dc voltage at the critical current I_c or by comparing the differential resistance for I greater

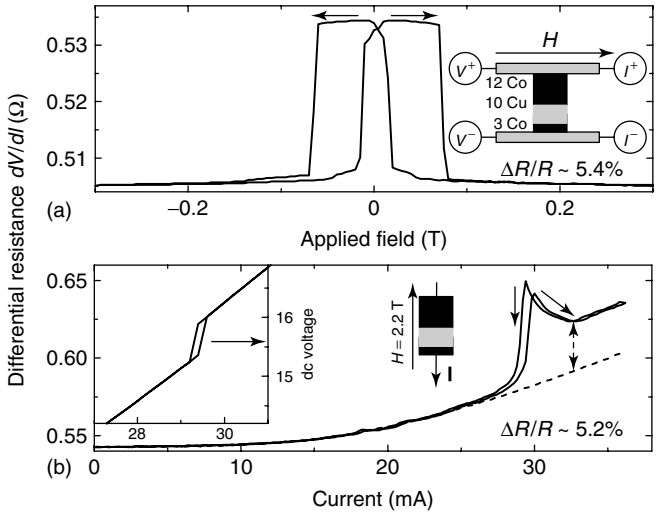

Figure 4. (a) $\mathrm{d}V/\mathrm{d}I$ versus H for in-plane fields and small bias currents. The inset show the sequence of the layers (in nm) and the four-point measurement geometry. The lateral dimensions of the sample are $90 \times 140\,\mathrm{nm}^2$. (b) $\mathrm{d}V/\mathrm{d}I$ versus I of the same device in an applied perpendicular field of $H = 2.2\,\mathrm{T}$. Differential resistance $\mathrm{d}V/\mathrm{d}I$ was measured by means of a phase-sensitive lock-in technique with a 100-μA modulation current at $f = 800\,\mathrm{Hz}$ added to a dc bias current. The dc voltage was recorded simultaneously. At a critical current, a peak structure occurs in the differential resistance. The dotted line shows $\mathrm{d}V/\mathrm{d}I$ at negative currents, for which the peak structure is absent. The inset shows the simultaneous dc voltage measurement. (Reprinted with permission of Özyilmaz *et al*. copyright 2003, American Physical Society.)

than I_c with the differential resistance at the same current value but with opposite polarity at which the abrupt change in resistance is absent. Either comparison shows a change in resistance of about 5%, similar to the GMR value of the same device (Figure 4a). Therefore, an explanation in terms of a small deviation of the free layer magnetization from its P alignment with respect to the static layer is not sufficient to explain the observed resistance change. With the measurement of a resistance change comparable to the GMR effect, it seems plausible to assume that even at high fields the spin-transfer effect can produce a full reversal of the magnetization. Second, the change in device resistance is hysteretic, occurring at higher current density for increasing current (Figure 4b). The excitation of small amplitude spin waves would decay rapidly on the timescale of such measurements and thus appear reversible in such $I-V$ measurements. Further, as we show in the following text, this interpretation is consistent with micromagnetic modeling.

The critical current for excitations has a nonmonotonic dependence on the applied perpendicular field. This is shown in Figure 5. At low fields, the critical current decreases with increasing applied fields (Figure 5a). While at fields greater than 1.5 T, the critical current increases with applied field (Figure 5b). In addition, at high fields, the current sweeps are hysteretic, particularly above 2 T. The magnetic field dependence of the critical current is summarized in Figure 6(a), in which the differential resistance is plotted in grayscale. Here the current is swept up from 20 to 36 mA, while the magnetic field is held constant for each current sweep. For subsequent current sweeps, the field is raised from 0.34 to 2.7 T in steps of 5 mT. In this grayscale plot, a critical current I_c separates the 'applied field-current bias' plane into two regions. Below the critical current, the device remains in its low-resistance state, in a P or nearly P magnetization state. Above the critical current, the magnetization of the device is in a higher resistance state, in which the relative orientation of the magnetization of the two layers deviates strongly from a P configuration.

The critical current for decreasing current is shown as the dashed line in this figure. As noted in the preceding text, for fields greater than 1.4 T, the critical current increases with applied magnetic field. In this region, the current hysteresis, ΔI_c, also generally increases with increasing field. (There is a deviation from this behavior between 2.0 and 2.4 T, in which ΔI_c actually decreases. We suspect this to be due to the onset of nonuniform excitations.) While below 1.2 T, the critical current decreases linearly with applied magnetic field. In this field region ($1.1\,\mathrm{T} \rightarrow 0.35\,\mathrm{T}$), the hysteresis is near the limit of our experimental resolution. The resistance jumps for both regions are similar in magnitude, that is, close to the GMR value.

The general features of the data can be understood on the basis of the LLG equations with the spin-torque term, equation (1). In the large-field regime ($H > 4\pi M_s$), we neglect the in-plane magnetic anisotropy and take $\vec{H}_{\mathrm{eff}} = H - 4\pi M_s(\hat{m}\cdot\hat{z})\hat{z}$. In this case, there is axial symmetry and the equations of motion can be greatly simplified. Initially, both layers are parallel to the applied field and the z component of the free layer magnetization satisfies (neglecting terms of order α^2):

$$\frac{\mathrm{d}m_z}{\gamma\,\mathrm{d}t} = (1 - m_z^2)[\alpha(H - 4\pi M_s m_z) - a_J] \qquad (4)$$

It is clear that an initial state $m_z = 1$ aligned with the applied field in the z direction will become unstable when $a_J > \alpha(H - 4\pi M_s)$. The threshold current, $a = \alpha(H - 4\pi M_s)$ increases with increasing applied field, as observed in experiment. More generally, this relation illustrates that the critical current for the onset of magnetic excitations is proportional to the ferromagnetic resonance (FMR) frequency, $\omega = \gamma(H - 4\pi M_s)$. This follows because the spin-transfer torque competes with the damping torque, which is proportional to the precession frequency. The critical current is also predicted to be zero when $H = 4\pi M_s$.

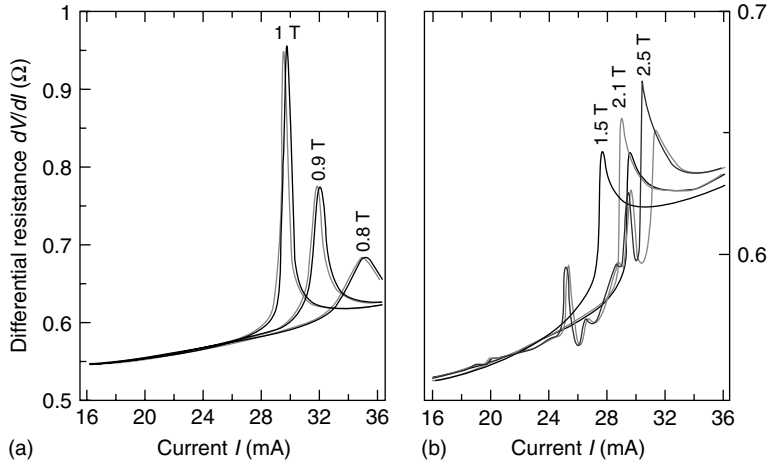

Figure 5. dV/dI versus I at several applied perpendicular fields, acquired both for increasing and decreasing current sweeps. (a) Low-field regime: here the critical current decreases with increasing field. (b) High-field regime: the critical current increases with the magnetic field and clear hysteresis is observed sweeping up and down in current.

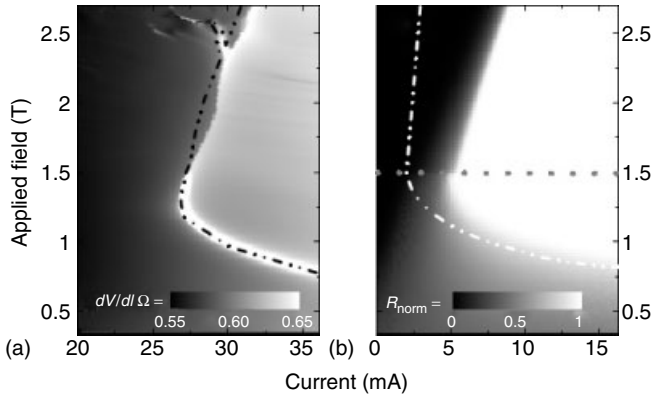

Figure 6. (a) Magnetic field dependence of dV/dI versus I. The grayscale represents the differential resistance of the junction. Light color corresponds to high resistance and dark to low resistance. The dashed line shows the position of the jump in resistance for downsweep of the bias current. (b) Micromagnetic simulations of the experiment as described in the text. (Reprinted with permission of Özyilmaz *et al*. copyright 2003, American Physical Society.)

A solution with magnetization antiparallel to the effective field ($m_z = -1$) occurs for $a_J > \alpha(H + 4\pi M_s)$ and corresponds to a static magnetization ($(d\hat{m}/dt) = 0$). In this case, the spin torque leads to a state of maximum magnetic energy of the free layer. Similar high-energy states have also been observed in numerical studies for the field in-plane geometry (Sun, 2000; Li and Zhang, 2003). As a_J increases with Θ, the transition between a precessing state with $|m_z| < 1$ and $m_z = -1$ occurs rapidly with increasing current and is hysteretic. For example, hysteresis occurs when $a_J > \alpha(H + 4\pi M_s)$ for $\hat{m}\cdot\hat{m}_P = -1$, while at the same current $a_J < \alpha(H - 4\pi M_s)$ when $\hat{m}\cdot\hat{m}_P = 1$. In addition, for increasing applied field, the transition occurs at a higher current and the width of the hysteresis increases.

It is important to note that the hysteresis here is a characteristic of the spin-transfer interaction. Hysteresis in ferromagnets is typically associated with magnetic anisotropy or dipolar interactions that result in local minima in the energy (Hubert and Schäfer, 1998). In large applied fields, however, there is only one minimum in the energy, when the magnetization and field are aligned. Here the hysteresis is due to the angular dependence of the spin-torque interaction. The spin torque per unit angle for small deviations of the layer magnetizations from collinear is largest in the AP state and therefore starting in an AP state and reducing the current results in a lower critical current than starting in a P state and increasing the current.

Figure 6(b) shows the result of integration of the equation (1) under the conditions approximating the experiment ($P = 0.4$ for Co and $\alpha = 0.007$ (Schreiber *et al*., 1995)). The device resistance is plotted in grayscale versus I and H and is computed from the angle between the fixed and free layers using the analytic expression: $R_{norm} = (R(\theta) - R(0))/(R(\pi) - R(0)) = (1 - \cos^2(\theta/2))/(1 + \cos^2(\theta/2))$ (Wang, Zhang and Levy, 1996; Bauer, Tserkovnyak, Huertas-Hernando and Brataas, 2003; Shapiro, Levy and Zhang, 2003). For $H < 4\pi M_s$ (below the horizontal dashed line in the figure) the pinned layer magnetization tilts into the plane and thus the pinned layer and effective field are no longer collinear. In this case, there are PSs of the magnetization, with the projection of $\hat{m}$ on $\hat{m}_P$ decreasing with increasing current. The average resistance is plotted below this line. The dashed–dotted line shows the transition to a low-resistance state for decreasing currents, that is, starting with the layers initially antiparallel.

Qualitatively, there is a good correspondence between the data and the model. The model captures the general features in the data, including the high-field region of increasing critical current with increasing applied field and the low-field region ($H < 1.4\,\mathrm{T}$) in which the critical current increases with decreasing field. It is now straightforward to understand why the critical current is a nonmonotonic function of field. This follows because the critical current is proportional to the FMR frequency which itself is a nonmonotonic function of applied field. The FMR frequency for magnetization in the film plane is given by the Kittel equation, $\omega = \gamma\sqrt{H_\mathrm{a}(H_\mathrm{a} + 4\pi M_\mathrm{s})}$ (Kittel, 1996). When a field is applied perpendicular to the plane, the FMR frequency decreases until the applied field is sufficient to orient the magnetization in the field direction, when $H = 4\pi M_\mathrm{s}$. Further increase of the field leads to an increasing resonance frequency and a linear dispersion of the critical current with applied magnetic field –the critical current follows the same trend.

There are also clear discrepancies between the data and the model. In particular, the model predicts significantly lower critical currents (factor of ∼5) and greater hysteresis than observed in the experiment. The latter is perhaps not surprising as we have assumed single domain dynamics in the model and likely the relaxation to the low-energy magnetic state occurs via nonuniform magnetic states of the free layer. In more recent experimental studies, the critical current is found to be within a factor of ∼2 of the model, likely reflecting the improvements in sample quality, both layer structure and lithography (Chen *et al*., 2006a,b).

MR measurements at fixed current bias also show hysteresis at high fields. Figure 7 shows MR measurements at fixed and large current bias. There are five field regions bounded by H_1, H_2, H_3, and H_4, which depend on current bias. For fields, $H_1 < H < H_2$, the field is sufficient to lead to P alignment of the layer magnetizations. In the next region ($H_2 < H < H_3$), PSs driven by the spin current become possible and a gradual and *reversible* transition from P to AP alignment takes place. In the interval $H_3 < H < H_4$. The layers are in an AP state. At the boundary H_4, a reversible but sharp transition from AP back to P configuration takes place. The width of the hysteresis depends on the current bias and the polarity of the applied field. In general, it increases with increasing current bias.

This behavior is distinct from that of point contacts (Tsoi *et al*., 1998, 2000). It is also different from the characteristics found when large in-plane fields are applied to PDs (Katine *et al*., 2000; Grollier *et al*., 2003). In the latter case, a large plateau in the MR with intermediate resistance R_int value ($R_\mathrm{P} < R_\mathrm{int} < R_\mathrm{AP}$) was observed. The resistance plateau was attributed to a precessing spin-wave state in between P and AP alignment. From Figure 7, it is clear that in the field perpendicular geometry there is not a large plateau in the MR. In comparison to point-contact

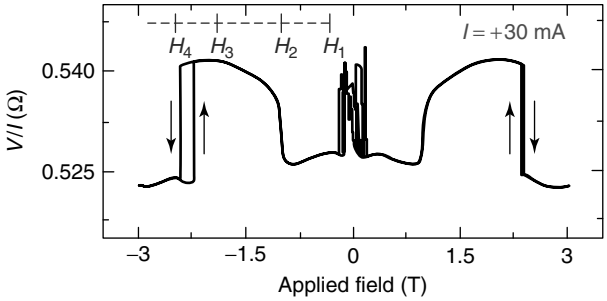

Figure 7. Magnetoresistance measurement at large positive applied bias current. For fields greater than $|H_1|$, there is a low-resistance state with parallel alignment of the layer magnetizations. In the field range $|H_3| > |H| > |H_2|$, current-induced torques lead toward antiparallel alignment through PS states. For $|H| > |H|$, the layers are forced back to a parallel alignment. The transition to parallel alignment is abrupt and hysteretic, whereas the gradual transition starting at H_2 is reversible. (Reprinted with permission of Özyilmaz *et al*. copyright 2003, American Physical Society.)

experiments (Tsoi *et al*., 1998, 2000), high bias currents in PDs appear to lead to a complete magnetization reversal even at high magnetic fields. In addition, there is a recent report that an energy-threshold mechanism explains spin-transfer-induced magnetic excitations in nanopillars in the field perpendicular geometry, based on temperature dependent studies of the critical current (Tsoi *et al*., 2004). However, a reduction in the critical current with increasing temperature is naturally explained within the standard model of spin-transfer model as a result of thermal fluctuations of the magnetization (see Li and Zhang, 2004). Finally, these results and analysis suggest that the main peak in $\mathrm{d}V/\mathrm{d}I$ in large perpendicular magnetic fields marks the end, not the onset of magnetization dynamics. Recent high-frequency studies in the field perpendicular geometry are consistent with this interpretation (Kiselev *et al*., 2004).

3.2 Phase diagram for magnetic excitations in the field perpendicular geometry

The phase diagram for magnetic excitations in the field perpendicular geometry is intricate even within the macrospin approximation. This can be seen with a simple form for the angular dependence of the spin torque proposed in Li and Zhang (2004),

$$\tau_\mathrm{ST} = \frac{a_\mathrm{J}}{1 + \eta\hat{m}\cdot\hat{m}_\mathrm{P}}\hat{m} \times (\hat{m} \times \hat{m}_\mathrm{P}), \tag{5}$$

with the single parameter η characterizing the angular dependence of the torque and with $a_\mathrm{J} = (\hbar I P/2eM_\mathrm{s}V)$ (i.e., with the angular dependence removed from this factor). Note that angular variations of the torque in equation (5) closely

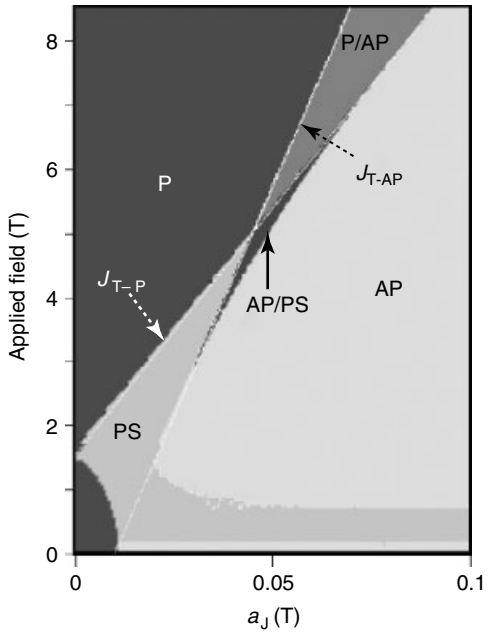

Figure 8. Phase diagram of a nanopillar in the field perpendicular geometry for $\eta = 0.3$, $\alpha = 0.01$, and $4\pi M_s = 1.5\,\mathrm{T}$, with a small (0.1 T) in-plane uniaxial anisotropy. The labels refer to parallel (P), antiparallel (AP), and precessional states (PS). The threshold current density for instability of the P state, J_{T-P}, and the AP state, J_{T-AP}, are indicated.

match those given by Slonczewski (1996). (For example, $\eta = 0.45$ here corresponds to a polarization, $P = 0.2$, in Slonczewski (1996)). This form of the torque was also chosen because it permits a greater degree of analytical analysis of spin-torque-induced magnetization dynamics.

A phase diagram computed using this form of the spin torque and the effective field given in equation (3) is shown in Figure 8. For fields greater than $4\pi M_s$, the P state becomes unstable at a threshold current given by

$$J_{T-P} = \frac{2e\alpha}{\hbar P}(1+\eta)M_s t(H - 4\pi M_s) \tag{6}$$

leading to a PS. Here t is the free layer thickness. Further increase in the current results in the free layer switching to an AP state. On decreasing the current, the AP becomes unstable and switches back to a PS or P state when

$$J_{T-AP} = \frac{2e\alpha}{\hbar P}(1-\eta)M_s t(H + 4\pi M_s) \tag{7}$$

As mentioned in the preceding text, hysteresis is associated with the angular dependence of the spin-transfer torque; the fact that the torque is larger in the AP state ($\eta > 0$).

J_{T-P} and J_{T-AP} are equal and cross when $H_c = 4\pi M_s/\eta$. However, hysteresis appears at a smaller field, corresponding to the lowest field at which the AP/PS region appears in the phase diagram. Within this model, η can be determined from experiment, from the lowest field at which hysteresis occurs. For example, on the basis of the data shown in Figure 6, η must be greater than 0.3. This implies that, for a constant current, the derivative of the torque with respect to the angle between the layers for small deviations from collinear alignment is approximately a factor of 2 larger for the AP state than the P state. This is close to that found in measurements by Smith *et al*. of the angular dependence of the spin torque in GMR read heads (Smith, Katine, Childress and Carey, 2005).

Recent experiments give a critical current threshold in semiquantitative agreement with equations (6) and (7). The main discrepancy is in the intercept of the threshold boundary, as is the case for the data presented in Figure 6. This discrepancy may reflect the fact that the macrospin model greatly underestimates the principal mode frequency in the field perpendicular geometry because of finite size effects (McMichael and Stiles, 2005; Kakazei *et al*., 2004). As the critical current is proportional to the mode frequency, this changes the intercept of the threshold current versus field, resulting in a greater threshold current at a given field. However, this does not change the slope of the threshold current versus field, which is set by the gyromagnetic ratio, γ. It would clearly be of interest to conduct full micromagnetic simulations to better understand the experimentally determined phase diagrams and the breakdown of the macrospin approximation in the high-field limit. Simulations of this sort have already been conducted for small in-plane magnetic fields (Lee *et al*., 2004; Montigny and Miltat, 2005). High-frequency experiments, like those reported in Kiselev *et al*. (2003) and Rippard *et al*. (2004), would also shed light on magnetization dynamics in the high-field limit.

4 SINGLE MAGNETIC LAYER EXCITATIONS

4.1 Background

It is of interest to study the most elementary sample or device that exhibits current-induced excitations. The concept proposed by Slonczewski requires two magnetic layers, one which serves to polarize the current and the second which responds to the polarized current (Slonczewski, 1996). This bilayer structure is also considered necessary for a more practical reason. The magnetic state of the layers is inferred from resistance measurements. The layer that polarizes the current also serves as a reference layer, and changes in magnetization are detected through the GMR effect. Therefore, a sample with only a single magnetic layer would seem to preclude

both the excitation as well as the detection of magnetic excitations. Nonetheless, experiments have demonstrated current-induced excitations in electrical transport studies, sometimes with characteristics quite similar to those seen in traditional bilayer structures. Further, recent theory suggests that the same spin-transfer interaction responsible for reversal and excitations in bilayers leads to magnetic instabilities in structures that contain only a single magnetic layer.

The spin-transfer interaction requires a component of spin-angular momentum transverse to the direction of the background magnetization of the ferromagnet. Slonczewski and Berger considered a one-dimensional model in a macrospin approximation. In this case, two magnetic layers are needed for the spin-transfer interaction –the interaction is present when the magnetizations of the layers are noncollinear. However, going beyond the macrospin and one-dimensional transport model, it is found that only one magnetic layer is needed to have a nonzero spin-torque interaction. In this case, fluctuations in the magnetization direction transverse to the current direction are allowed. This coupled with spin diffusion parallel to the layer interfaces leads to a transverse component of spin at the FM interface and magnetic excitations. This is the basis for single-layer excitations.

Polianski and Brouwer (2004) first proposed a model for single-layer magnetic excitations. They emphasized that the spin-filtering characteristic of ferromagnets is the fundamental cause of the spin-transfer torque. Spin filtering occurs whenever a current crosses a NM/FM interface. For example, in a pillar that consists of a NM/FM/NM structure in a current perpendicular to the plane (CPP) geometry, spin currents flow at the interfaces and there is spin accumulation at both FM/NM interfaces, on either side of the FM (Figure 9). Fluctuations in the magnetization direction of the FM combined with spin diffusion parallel to the NM/FM interface lead to a transverse component of spin at the interface and a spin-transfer torque (Figure 10). At each interface, these torques act to align the magnetization along the direction of the spin accumulation. In a structure that has mirror symmetry about the center of the magnetic layer, the resulting torques are of equal magnitude but are opposite in direction and cancel each other. However, if the mirror symmetry is broken, the torques acting on each NM/FM interface have different magnitudes. In this case, Polianski and Brouwer (2004) and Stiles, Xiao and Zangwill (2004) predict that an unpolarized current can induce spin-wave instabilities and generate spin-wave excitations with wave vectors in the film plane. Instabilities occur when the current bias is such that the direction of the larger spin accumulation is antiparallel to the direction of the magnetization of the FM. This leads to a specific prediction for the dependence of the excitations on current polarity. Polianski and Brouwer (2004) studied the case of a thin FM where the magnetization does not

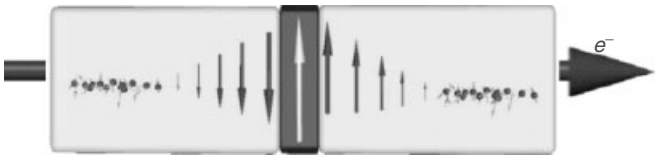

Figure 9. Electron current flow through a single ferromagnetic layer leads to spin accumulation on either side of the ferromagnet, that is, a magnetization is induced in the contacts to the layer.

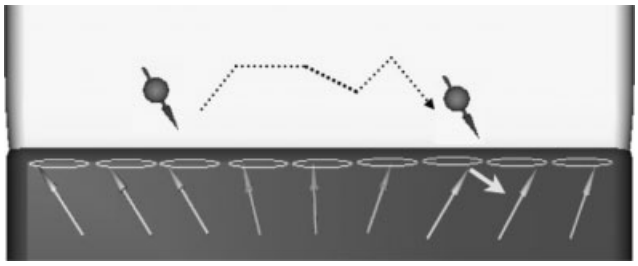

Figure 10. Mechanism of spin-wave generation proposed in Polianski and Brouwer (2004). Spin diffusion of down-spin reflected electrons are shown as dashed lines. This results in a spin torque that enhances the spin-wave amplitude. The torque on the background magnetization is shown as a white arrow. (Reprinted with permission Polanski *et al*., copyright 2004, American Physical Society.)

have any spatial variation along the current flow direction. Here, the break in symmetry requires asymmetric contacts. Stiles, Xiao and Zangwill (2004) relaxed this requirement and allowed the magnetization to vary along the current flow direction, which also breaks the mirror symmetry. In either case, in ideal asymmetric junctions, current-induced excitations are predicted to occur for only one current polarity and are expected to be absent in perfectly symmetric structures. Both groups made predictions on how single-layer instabilities depend on parameters such as the current bias polarity, the FM layer thickness, the degree of asymmetry of the single-layer junction, and the applied field.

4.2 Experiments

In order to study spin transfer, high current densities must be injected into the ferromagnet. This has been achieved in three different geometries: (i) lithographically patterned point-contact junctions, (ii) mechanical point contacts, and (iii) nanopillar junctions. The first technique was pioneered at Cornell University and has been used in many types of studies. In fact, in initial spin-transfer experiments in bilayer films subject to high current densities, samples with only one magnetic layer were also studied (Myers *et al*., 1999). Here, high current densities were achieved by means of lithographically patterned point contacts (Figure 11a). Mechanical point contacts were used in studies of magnetic

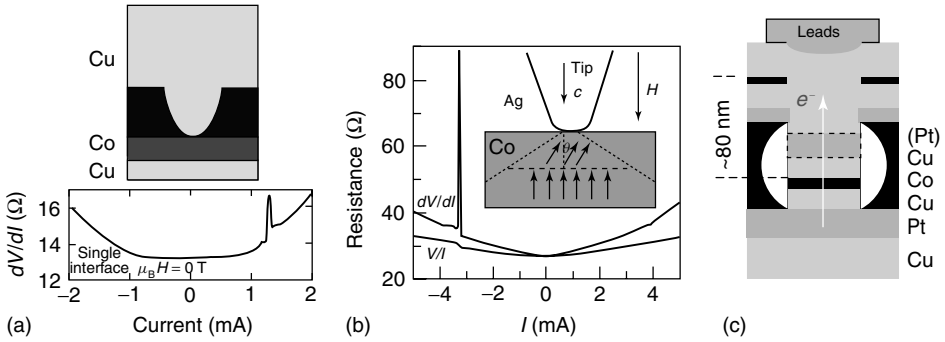

Figure 11. Single-layer experiments. (a) Observation of current-induced excitations in lithographically produced point-contact junctions. (Reprinted with permission E.B. Myers *et al*., copyright 1999, AAAS.) (b) First systematic point-contact experiments on a single ferromagnetic layer. (Reprinted with permission Ji *et al*., copyright 2003, American Physical Society.) Inset of (b) illustrates a model for the magnetization dynamics with a highly nonuniform current density. Note that the current polarity convention is opposite in (a) and (b). (c) Schematic of a single Co-layer pillar junction fabricated via the nanostencil mask process. (Reprinted with permission Özyilmaz *et al*., copyright 2004, American Physical society.) Electron flow indicates the definition of positive current bias. Symmetric junctions are fabricated by addition of a Pt layer (dashed box).

multilayers (Tsoi *et al*., 1998) and employed by Ji, Chien and Stiles (2003) to study single FM layers (Figure 11b). The first studies of single FM layer nanopillar junctions, illustrated in Figure 11(c), were done by Özyilmaz, Kent, Rooks and Sun (2005) and are discussed in detail in the following text.

These distinct sample geometries place different boundary conditions on the current and magnetization. In point-contact methods, the current density is very high at the contact and thus also highly nonuniform. This nonuniformity creates a situation in which a single magnetic layer may act as its own reference and polarizing layer. The region removed from the contact and experiencing a lower current density serves this function. The experiments of Ji, Chien and Stiles (2003) are performed on relatively thick FM layers (300 nm of Co) that allow for spatial variations of the magnetization along the current direction, or longitudinal excitation of the magnet. The excitation envisioned in this experiment is illustrated schematically in Figure 11(b). The authors propose that magnetic excitations localized near the contact result in a nonuniform magnetization in the film. They suggest that the added resistance of the contact is associated with a longitudinal excitation of the magnetization–essentially, a domain wall forms near the contact. This mechanism is similar to that operative in bilayers. The phenomena observed are in fact quite similar to those discussed in previous sections. Increases in resistance and peaks in differential resistance are observed that disperse to higher current as the magnetic field increases.

Nanopillar junctions have several key advantages in the study of spin-transfer excitation of single magnetic layers. First, the current density is uniform across the nanomagnet interface and thus there is no *a priori* spin-polarizing reference magnetic layer to generate a transverse component of spin or lead to resistance changes; these effects must come from the same magnetic layer through which the current passes. Second, there is the possibility of creating excitations that are transverse to the current flow direction. In particular, very thin magnetic layers can be realized in which the creation of longitudinal excitations would be energetically very costly. Excitations can also be studied as a function of layer thickness. This geometry is thus well suited to explore the basic physics of spin transfer in single magnetic layers. We thus focus on such experiments in this article.

4.2.1 Single-layer nanopillar devices

Experiments on PDs were conducted by Özyilmaz, Kent, Rooks and Sun (2005). Junctions ∼50 nm in diameter were fabricated by means of a nanostencil mask process (Sun *et al*., 2002), which has been used earlier for spin-transfer torque studies in Co/Cu/Co bilayer spin valves (Sun *et al*., 2003; Özyilmaz *et al*., 2003). To study the thickness dependence of single-layer excitations, a nanostencil mask process was combined with an *in situ* wedge growth mechanism. With this approach, PDs were fabricated with a single Co layer of continuously varied thickness across a single wafer. As shown in Figure 11(c), structures fabricated by means of an undercut template are intrinsically asymmetric due to the requirement of an inert bottom electrode surface, usually Pt, on top of which the pillar structure is grown. Here, asymmetry refers to the spin-accumulation pattern generated within the PD with respect to the Co-layer position. The strong asymmetry due to the choice of Pt as bottom electrode is removed by inserting a second Pt layer. Therefore, the study of spin transfer in symmetric single-layer structures requires the 'capping' of the pillar with a Pt layer, as indicated in Figure 11(c).

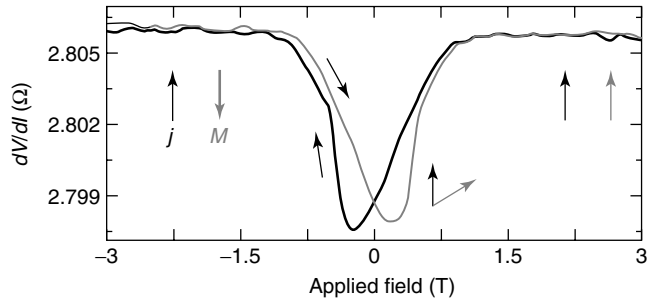

Figure 12. Typical $\mathrm{d}V/\mathrm{d}I$ versus H data at zero dc bias and 4.2 K. The junction size is $50 \times 50\,\mathrm{nm}^2$ and $t \approx 17\,\mathrm{nm}$. An increase in junction resistance ($\sim$0.1%) is observed when j and M are collinear. (Reprinted with permission Özyilmaz *et al*. copyright 2004, American Physical society.)

Junctions with an FM layer thickness varying from 2 to 17 nm and lateral dimensions from $30 \times 60\,\mathrm{nm}^2$ up to $70 \times 140\,\mathrm{nm}^2$ have been studied as a function of bias current and applied field. The range of Co-layer thicknesses covers both, the case where the thickness t is smaller than the exchange length l_{ex} of Co and the case where the thickness is comparable to the latter ($t \geq l_{\mathrm{ex}}$). All junctions in this thickness range exhibit single-layer excitations. To confirm that the excitations are caused by asymmetric contacts, the experiments were repeated with symmetric PDs with a stack sequence of |PtRh 15 nm|Cu 10 nm|Co 10 nm|Cu 10 nm|Pt 15 nm|.

A typical MR measurement of a single-layer junction at zero dc bias is shown in Figure 12. The resistance R has its minimum when the magnetization M lies in the thin-film plane, that is, when M is orthogonal to $\hat{j}$. It gradually increases with applied field which tilts the magnetization vector out of the thin-film plane. Once the applied field exceeds $4\pi M_{\mathrm{s}}$, M is parallel to $\hat{j}$ and the resistance saturates at its maximum. From this, it is clear that the MR is sensitive enough to register (*field-induced*) changes of relative orientation of $\hat{j}$ and M. MR can also be used to detect *current-induced* changes of the magnetization, as we show in the following text.

A typical $I(V)$ curve for an asymmetric single-layer PD is shown in Figure 13. Here $\mathrm{d}V/\mathrm{d}I$ versus I is plotted for fields $H = 1.5, 2, 2.5$, and 3.1 T for a $30 \times 60\,\mathrm{nm}^2$ junction with $t \approx 8\,\mathrm{nm}$. At fields above the demagnetization field ($H > 1.5\,\mathrm{T}$), we observe anomalies in the form of small dips at negative current polarity only. Note that in the field perpendicular geometry the onset of these excitations always leads to a (small) decrease in resistance, which is opposite to what has been observed in both point-contact experiments (Myers *et al*., 1999; Ji, Chien and Stiles, 2003) and bilayer PDs. We discuss this further in the following text.

To distinguish these excitations from the parabolic background resistance, we plot $\mathrm{d}^2V/\mathrm{d}I^2$, which is sensitive to abrupt features in $\mathrm{d}V/\mathrm{d}I$. Plotted in grayscale as a function

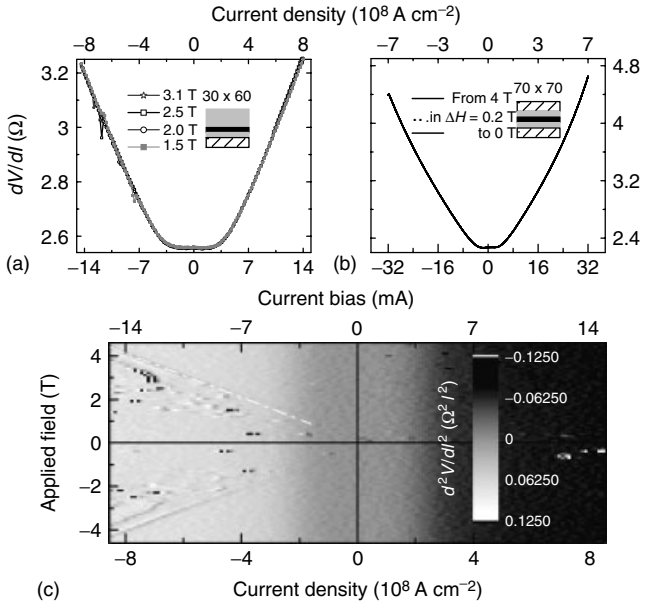

Figure 13. $\mathrm{d}V/\mathrm{d}I$ versus I at constant fields. (a) Asymmetric junction ($30 \times 60\,\mathrm{nm}^2$, $t \approx 8\,\mathrm{nm}$) with Pt as bottom electrode. For $H > 4\pi M_{\mathrm{s}}$ dips are observed at negative bias only. (b) Symmetric junction ($70 \times 70\,\mathrm{nm}^2$, $t \approx 10\,\mathrm{nm}$) with Pt on either side of the Co layer ($t \approx 10\,\mathrm{nm}$). $I(V)$ curves at different field values overlap fully. (c) Phase diagram for current-induced excitations in single-layer junctions; same junction as in Figure 13(a). $\mathrm{d}^2V/\mathrm{d}I^2$ is plotted in grayscale. The white dashed–dotted line indicates the boundary for excitations. (Reprinted with permission Özyilmaz *et al*. copyright 2004, American Physical society.)

of the applied field and the current bias, it represents a phase diagram for single-layer excitations. An example of such a plot is shown in Figure 13(c). Here, the current is swept from -15 to $+15$ mA, while the magnetic field is held constant for each current sweep. For subsequent sweeps, the field is stepped from -4.6 to $+4.6$ T in 100 mT steps. The 'current bias–applied field' plane segregates into two regions separated by a straight line, which we associate with the critical current I_{c} for single-layer excitations. For fields with $H > 4\pi M_{\mathrm{s}}$, excitations only occur for negative current polarities. At negative current bias, excitations are absent below the critical current, whereas above the critical current many modes are excited. I_{c} shows a linear dependence on the applied field and can be extrapolated approximately to the origin. Dividing I_{c} by the *nominal* junction area A, we estimate the field dependence of the critical current density $j_{\mathrm{c}} = bH$ with $b \approx 1.9 \times 10^8\,\mathrm{A\,cm^{-2}\,T^{-1}}$. We obtain a more accurate estimate for j_{c} by multiplying I_{c} with the junction resistance $R \approx 2.55\,\Omega$, which is equivalent to dividing by an *effective* junction area: $j_{\mathrm{c}} \propto I_{\mathrm{c}}R = \beta H$ with $\beta \approx 8.8 \times 10^{-3}$ ($\mathrm{A\Omega\,T^{-1}}$).

A better way to distinguish the small features of current-induced excitations from the varying background resistance

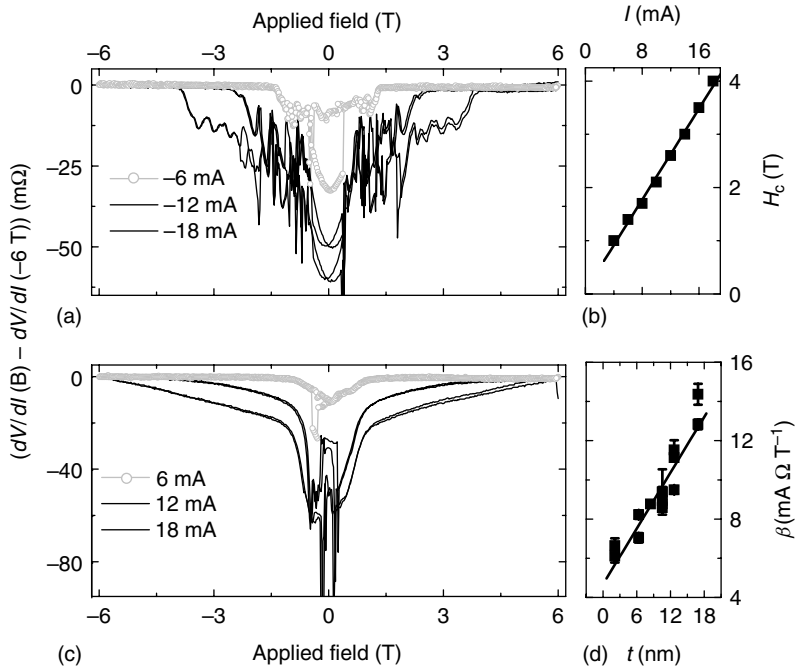

Figure 14. (a) dV/dI versus H at negative current bias. The zero dc bias field sweep of this junction is shown in Figure 13. (b) Current bias dependence of the critical fields above which excitations are not observed. (c) dV/dI versus H for positive current bias; excitations are absent. (d) Thickness dependence of the 'critical currents'. Here, the slope β of I_cR is plotted as a function of Co-layer thickness t. (Reprinted with permission Özyilmaz *et al*. copyright 2004, American Physical society.)

is to fix the latter. This can be done by keeping the current constant and sweeping the applied field instead. Here, an example of such a measurement is given in Figure 14(a) and (c). Field sweeps at fixed negative current bias are shown in Figure 14(a), whereas Figure 14(c) shows the MR at fixed positive currents. The strongest evidence for current-induced excitations in single-layer junctions comes from the comparison of these two figures. As shown in Figure 14(c), excitations at fields $H > 4\pi M_s$ are absent in the field traces. However, high current densities at positive bias gradually increase the applied field at which the differential resistance saturates. This effect cannot be attributed solely to the presence of additional (Oersted) fields related to the charge current and is not yet fully understood.

There is a dramatic change in the field traces if one applies a negative current bias to the junction. For each fixed current value, there is now a critical field H_c, above which the resistance remains constant. However, below H_c, the observation of peaks and dips indicates the presence of many (current-induced) excitations. H_c is a linear function of the bias current and shifts to higher values as one increases the current. As can be seen in Figure 14(b), the linear fit of the critical fields can once more be extrapolated to the origin. Hence, in both field sweeps at fixed currents and current sweeps at fixed fields one obtains a linear dependence of the critical parameter on the running variable, that is, $j_c = bH$ and $H_c = cj$. For a particular Co-layer thickness, the slopes b and c are equivalent, that is, $b \cong c^{-1}$. From Figure 14(b) and the nominal junction area A, we estimate the current density dependence of $H_c = cj$ with $c \approx 5.2 \times 10^{-9}\,\mathrm{T\,A^{-1}\,cm^{-2}}$. Using the junction resistance $R \approx 2.80\,\Omega$ as an approximation for the effective junction area, we obtain $H_c \propto \zeta(IR)$ with $\zeta \approx 73.8\,\mathrm{T/(A\Omega)}$. Note that for $H < 4\pi M_s$ there are large changes in the hysteresis for both current polarities. This effect cannot be explained by the interaction of the Oersted fields with magnetic domain configurations at fields $H < 4\pi M_s$. In fact, recent experiments show current-induced switching in a single layer, reflecting the domain structure in low fields even in these deep submicron magnetic elements (Özyilmaz and Kent, 2006). Related studies also indicate MR when switching between domain configurations of permalloy single magnetic layers (Urazhdin, Chien, Guslienko and Novozhilova, 2006).

The thickness dependence of these excitations has also been studied and the results are summarized in Figure 14(d). For all thicknesses, the observed boundary in the 'current bias/applied field plane' can be extrapolated close to the origin. Here we only plot the slope β of the field dependence of I_cR ($\propto j_c$) as a function of Co-layer thickness t. We observe an *increase* in β with increasing t, $\Delta\beta/\Delta t \approx 0.48 \pm 0.05\,\mathrm{m\Omega\,T^{-1}\,nm^{-1}}$. The critical currents increase by approximately a factor of 2 as one increases the Co-layer

thickness t from 2 to 17 nm. Over the same thickness range, the junction resistance R increases only by ≈25% (not shown).

To clarify the origin of these excitations, we have repeated these experiments in symmetric single-layer PDs. An example of current sweeps at fixed fields in these structures is shown in Figure 13(b). Here, the current is swept from +32 to −32 mA in a $70 \times 70\,\mathrm{nm}^2$ junction. In magnetic fields up to 4 T, features such as dips or peaks are absent in the current-voltage characteristics. Also, field sweeps at fixed current do not exhibit any of the strong polarity dependence observed in asymmetric PDs. To summarize, in symmetric junctions, current-induced excitations are absent up to $j \leq 7 \times 10^8\,\mathrm{A\,cm^{-2}}$.

The plots in Figures 13(c) and 14 make it appear that beyond a threshold current the excitations occur randomly as a function of I and H. However, this reflects the data sampling in Figure 13(c), which is too coarse to capture the pattern of excitations. Data taken at smaller field intervals reveal a regular pattern of excitations beyond the threshold (Figure 15). The data were obtained with a $30 \times 60\,\mathrm{nm}^2$ junction with $t \simeq 10$ nm. Here, we plot the second derivative of the signal in grayscale. The plot reveals distinct branches of current-induced excitations for currents $|I| > |I_c(H)|$. These new features only occur over a limited field range, δH. Within each narrow field region, excitations shift to higher currents with decreasing applied fields. This behavior is opposite to the applied field dependence of the onset of the single-layer excitations. This pattern likely reflects the discrete spin-wave spectrum in such elements. Recently, the theory presented in Polianski and Brouwer (2004) has been extended beyond the critical current for spin-wave instabilities (Adam, Polianski and Brouwer, 2006) – and this approach seems promising toward explaining single-layer characteristics and the data in Figure 15.

Generally, experimental results and theoretical predictions are in good agreement. Both models give the correct current polarity, magnitude, and thickness dependence of j_c in asymmetric structures. For the current polarity, strong spin-flip scattering at the Pt/Cu interface effectively forces the spin accumulation at the Pt/Cu interface to zero. This leads to a smaller spin accumulation at the Cu/Co interface facing the Pt bottom electrode. Excitations are therefore expected at negative current when the large spin accumulation is in a direction opposite to that of the magnetization, as observed. The theory also predicts a decrease in resistance upon magnetization excitation, as observed. This is counterintuitive because one might expect that the creation of spin-wave excitations leads to additional energy dissipation and therefore resistance. However, when the layer is excited and its magnetization is nonuniform, additional conduction channels are opened. Qualitatively, this is because electron spins reflected from the layer interface can diffuse back to the layer and be transmitted through a region with a different magnetization orientation. Alternatively stated, the nonuniformly magnetized layer leads to a smaller spin accumulation than a uniform magnetization and thus a lower resistance.

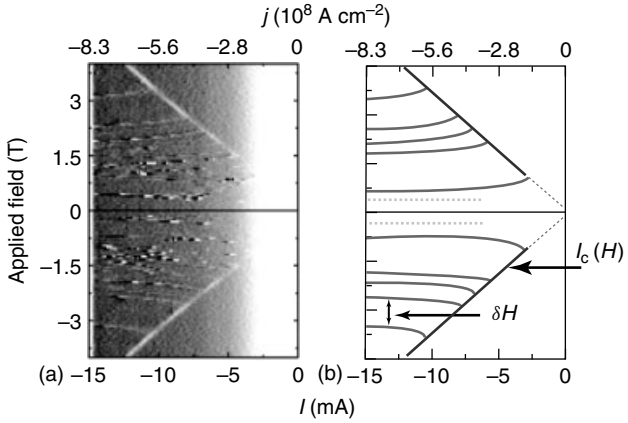

Figure 15. Phase diagram of current-induced excitations in a $30 \times 60\,\mathrm{nm}^2$ junction at negative current. Smaller field steps reveal the applied field dependence of additional features. (a) Grayscale plot of the second derivative as a function of applied field and current bias. (b) The excitation boundaries are retraced to render the pattern clear. For $|I| > |I_c(H)|$ additional features are observed. Each additional feature takes place in a narrow field range, δH. The features shift to higher currents with decreasing applied field value.

In terms of the current magnitude for the excitations, Polianski and Brouwer (2004) studied the case where **M** does not have any spatial variation along the direction parallel to the current $\hat{\mathbf{j}}$. Stiles, Xiao and Zangwill (2004) extended this model by allowing **M** to vary along $\hat{\mathbf{j}}$. For this case, excitations are expected to occur independent of current polarity even in *symmetric* PDs. However, the predicted critical currents are much larger ($j_c > 10^{10}\ \mathrm{A\,cm^{-2}}$) than for the asymmetric case. For example, for an asymmetric junction with $t \approx 17$ nm, the necessary *positive* current densities ($j_c > 2.5 \times 10^9\,\mathrm{A\,cm^{-2}}$) far exceed the value which can be sustained by existing PDs. The linear dependence of j_c on H can be explained by both models. However, the (near) zero intercept of j_c is somewhat peculiar, as the expectation is that the relevant field is the internal field in the layer or $H - 4\pi M_s$. With this reasoning, the critical current intercept should be for $H = 4\pi M_s$. There are two possible explanations for the near zero field intercept. The first is associated with the shape and finite size of the pillar junction. The principle spin-wave modes in such a disk are nonuniform and have a frequency greater than that of an extended thin film, $\omega = \gamma(H - 4\pi M_s)$. This can be seen in micromagnetic calculations of the dependence of the mode frequency on magnetic field (McMichael and Stiles, 2005). For a disk geometry, the frequency of the

modes can also be found analytically (Kakazei *et al*., 2004). A second possible explanation is that the critical current observed may not correspond to small amplitude excitations of the magnetization. As in the case of bilayers discussed in Section 3, large amplitude excitations occur at higher current densities, resulting in a smaller intercept.

The increase in the critical current j_c with increasing Co-layer thickness t is in agreement with theoretical predictions. An *increase* in j_c with increasing t is expected because of an increase in the (bulk) damping (Polianski and Brouwer, 2004; Stiles, Xiao and Zangwill, 2004). According to Stiles, Xiao and Zangwill (2004), in thicker films ($t \gtrapprox l_{ex}$), the variation of $\mathbf{M}$ along $\hat{\mathbf{j}}$ introduces an additional source of asymmetry. This should activate a competing effect, which by itself would *decrease* j_c with increasing t. However, to determine which effect would dominate, details of layer structure and junction geometry need to be considered. For the device geometry considered and for Co-layer thicknesses up to $t \sim 17\,\text{nm}$ ($t > l_{ex}$), the dominant source of the current-induced excitations appears to be the asymmetry of the leads.

In sum, these studies have established that magnetic excitations occur in single-layer asymmetric junctions and are absent in symmetric junctions at similar current densities. The current density for excitations in asymmetric junctions increases with Co-layer thickness. While these experiments demonstrate current-induced excitations in single layers, there are outstanding issues regarding the nature of the excitations. For instance, it is important to know whether they correspond to dynamical excitations. In this regard, it is of interest to study the high-frequency response associated with these excitations. Such studies would also shed light on the nature of the nonuniform modes that are excited. It would also be of interest to examine nanopillar structures with thicker Co layers to examine the onset of longitudinal excitations.

4.3 Bipolar excitations in bilayer nanopillars

The physics of single-layer or nonuniform spin-wave excitations is also relevant to the more widely studied bilayer structures. Bilayer nanopillars generally have asymmetries in the spin-accumulation pattern either due to asymmetric contacts or due to differences between the two magnetic layers in the device. Thus, asymmetries in the spin accumulation across the layers can induce nonuniform magnetic excitations. Therefore, in such structures, nonuniform and uniform current-induced excitation may compete, resulting in a rich phase diagram of magnetic excitations as well as distinct bilayer resistance states. This has been observed in experiments (Özyilmaz, Kent, Rooks and Sun, 2005) and explained in a recent theory (Brataas, Tserkovnyak and Bauer, 2006).

The consequences of single-layer excitations in asymmetric bilayer nanopillars, which consist of a thick ('fixed') and a thin ('free') magnetic layer, are outlined here. It is important to recall that current-induced excitations have been observed for only one polarity of the current at high field (see Section 3), nominally because of the asymmetry in the layer structure. This observation is considered to be clear evidence for physics associated with a spin-transfer torque –as opposed to the effects of charge-current-induced magnetic fields. In addition, the lowest resistance state was always considered to be the static state of P alignment of the layer magnetizations.

Single-layer excitations modify this picture. For sufficiently large current densities, anomalies in $\mathrm{d}V/\mathrm{d}I$ at high fields occur *independent* of current polarity, which decrease the junction resistance. The bipolarity of the excitations and the *decrease* in resistance cannot be understood in terms of spin-transfer-torque-induced single domain dynamics. These results show that high current densities can induce excitations of the magnetization independent of current polarity and relative alignment of the magnetizations of the two magnetic layers. Further, the results illustrate that at high currents the nanopillar resistance can be lower than that of a state of P magnetic alignment. Finally, modifying the contact geometry, by making the contacts more symmetric, is shown to suppress such excitations, consistent with theory (Chen *et al*., 2006a).

4.3.1 Experiments

The layer structure studied is illustrated schematically in Figure 16. The samples studied have lateral dimensions $\sim 50 \times 50\,\text{nm}^2$ and consist of a Pt 15 nm|Cu 10 nm|Co 3 nm|Cu 10 nm|Co 12 nm|Cu 300 nm multilayer.

Figure 17(a) shows typical measurements of $\mathrm{d}V/\mathrm{d}I$ versus I in large applied fields ($B \gg B_{\text{demag}} \sim 1\,\text{T}$). Current-induced excitations (peaks in $\mathrm{d}V/\mathrm{d}I$) appear to occur at positive current bias. However, a more careful look at the current sweeps reveals the presence of excitations even at negative currents (Figure 17b). Here, we observe anomalies in $\mathrm{d}V/\mathrm{d}I$ in the form of *dips*. These dips correspond to decreases in the differential resistance of about 0.5%. These excitations shift to higher currents with increasing field. They may be distinguished from the parabolic background resistance by plotting the second derivative in grayscale as a function of current bias and applied field. From this plot (Figure 17d), it is clear that the excitations depend approximately linearly on the applied field for both polarities of current.

Peaks in $\mathrm{d}V/\mathrm{d}I$ at positive currents are known to be related to magnetization excitations. In Section 3, we have discussed how their position indicates the critical current, I_c, necessary to switch the free layer magnetization into the

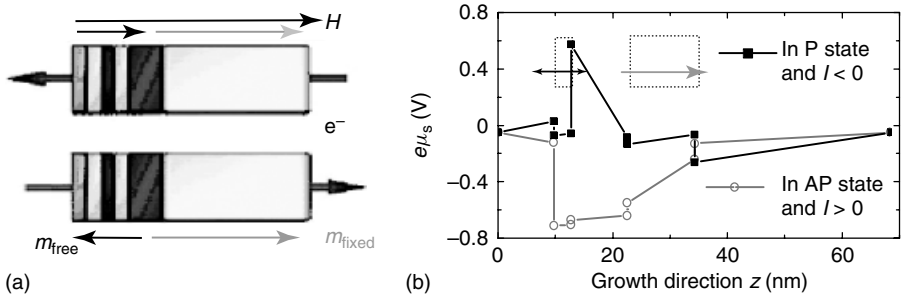

Figure 16. (a) Structure of a nanopillar device. The layer structure from left to right is Pt/Cu/Co/Cu/Co/Cu. The field, electron flow, and magnetization directions are indicated. (b) Calculated spin-accumulation pattern in the P state for negative currents and in the AP state for positive currents, based on a two-channel model, including interface resistances. (Reprinted with permission Özyilmaz *et al*. copyright 2005, American Physical Society.)

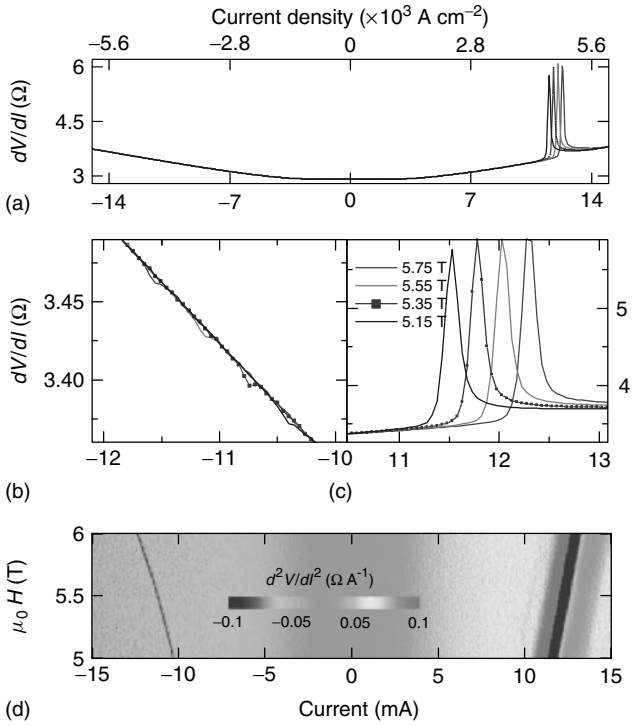

Figure 17. (a–c) Differential resistance versus current with large applied perpendicular fields. (b) Dips in $\mathrm{d}V/\mathrm{d}I$ are observed at negative current bias under conditions for which instabilities are not expected in a single domain model. (c) The peak in $\mathrm{d}V/\mathrm{d}I$ at positive current and the change in differential resistance after the peak is due to switching into an AP state. (d) A plot showing $\mathrm{d}^2V/\mathrm{d}I^2$ versus current and applied field. The dispersion of the dip in $\mathrm{d}V/\mathrm{d}I$ at negative current with increasing field is clearly visible. (Reprinted with permission Özyilmaz *et al*. copyright 2005, American Physical Society.)

high-resistance AP state. However, excitations at negative currents are unexpected. In the P configuration, negative currents are expected to suppress any deviation of the free layer from P alignment with the fixed layer. In particular, in large applied fields, the layer magnetizations should therefore remain in the P state. In addition, we observe dips instead of peaks in $\mathrm{d}V/\mathrm{d}I$, indicating that excitations at negative currents decrease the junction resistance. However, within a single domain model, GMR should lead to an increase in the junction resistance whenever the layer magnetizations deviate from the P alignment.

At positive currents in a single domain model in which the thick-layer magnetization remains fixed, there are no further excitations once the AP state is achieved, that is, once $I > I_c$, after the main peak in $\mathrm{d}V/\mathrm{d}I$ (see Figure 8). However, there is structure in $\mathrm{d}V/\mathrm{d}I$ beyond the main peak, again in the form of dips in $\mathrm{d}V/\mathrm{d}I$. The results are shown in Figure 18. Here, we plot the differential resistance as a function of current for selected applied fields, $0.7\,\mathrm{T} < B < 4.7\,\mathrm{T}$. We observe both peaks *and* dips in $\mathrm{d}V/\mathrm{d}I$. However, at fields $B > 1\,\mathrm{T}$, dips occur only for $I > I_c(H)$. Also, most current sweep traces show multiple dips in $\mathrm{d}V/\mathrm{d}I$. The field dependence of these excitations is best seen when the second derivative $\mathrm{d}^2V/\mathrm{d}I^2$ is plotted in grayscale as a function of current bias and applied field (Figure 18a). Such a plot reveals two boundaries, which can be best distinguished at fields with $B > 1.5\,\mathrm{T}$. The first boundary (B) represents the currents $I_c(H)$ at which the free layer switches into the AP state. Note that in many samples we also observe additional peaks in $\mathrm{d}V/\mathrm{d}I$ for $I < I_c(H)$ (region A). These peaks coincide with small upward jumps of the junction resistance (not shown), which we associate with transitions between PSs (Kiselev *et al*., 2004).

At higher currents, the plot reveals a second boundary (C). The latter marks the critical currents $I_+(H)$ above which we observe dips in $\mathrm{d}V/\mathrm{d}I$. The current bias and field dependence of these additional excitations is nontrivial, but the observed features are both stable and reproducible. A good demonstration of the latter is their applied field dependence. The latter is best described by first considering cuts parallel to the current axis of the plots (Figure 18, dashed–dotted line) and then cuts parallel to the field axis (dotted line). In the first case, the applied field is constant.

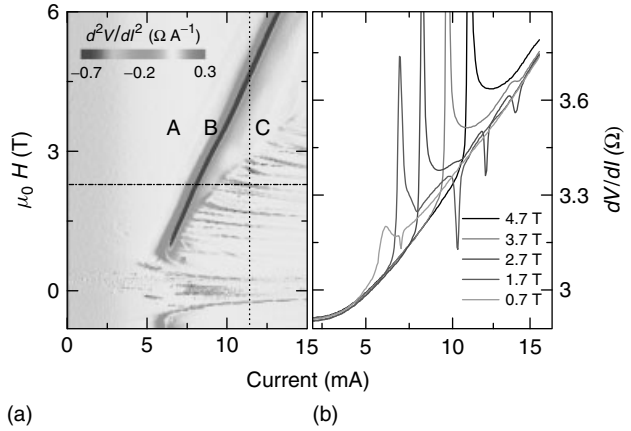

Figure 18. (a) Plot showing $\mathrm{d}^2V/\mathrm{d}I^2$ versus current and applied field. Dips in differential resistance after the main peak in $\mathrm{d}V/\mathrm{d}I$ (labeled B) are visible and correspond to boundary C. *A* labels the region where peaks in $\mathrm{d}V/\mathrm{d}I$ with $\Delta R/R$ much smaller than the GMR value are observed. (Reprinted with permission Özyilmaz *et al*. copyright 2005, American Physical Society.) (b) $\mathrm{d}V/\mathrm{d}I$ versus current at large positive current.

Now, as we increase the current, we cross several branches corresponding to distinct excitations. At each of these crossings, we observe dips in $\mathrm{d}V/\mathrm{d}I$. From cuts parallel to the field axis (constant current bias), we see that each excitation exists only in a very narrow field range, that is, they have a weak dependence on magnetic field. Note that these excitations have a very similar structure to those observed in single magnetic layers (Figure 15). Also, here the excitations shift to lower currents as we increase the applied field. In addition, different branches of excitations are separated by narrow stripes of high-resistance regions. We suspect that these gaps reflect the quantization of transverse spin-wave modes in these small elements. As in the case of excitation of single magnetic layers, current-induced excitation can also be characterized by performing field sweeps at fixed current bias. Such measurements were reported in Özyilmaz, Kent, Rooks and Sun (2005).

We now discuss an interpretation of these results in terms of spin-wave instabilities that are expected in the presence of strong asymmetries in the longitudinal spin accumulation (Polianski and Brouwer, 2004; Stiles, Xiao and Zangwill, 2004). The necessary condition for such instabilities is that the current bias has to be such that the sum of the longitudinal spin accumulation on either side of the FM layer, that is, the net spin accumulation, is in the direction opposite to that of the magnetization (Polianski and Brouwer, 2004; Stiles, Xiao and Zangwill, 2004).

We have modeled the spin-accumulation pattern in our bilayer junctions using the two-current model, with the spin-dependent bulk and interface resistances of Yang *et al*. (1995) in the limit in which the spin-diffusion length is much larger than the layer thicknesses ($\lambda_{\mathrm{sf}} \to \infty$). Figure 16 shows that in the P state at negative current bias the spin accumulation about the thick layer is asymmetric; the net spin accumulation is in the direction opposite to that of the magnetization. According to the condition governing spin-wave instabilities in single layers (Polianski and Brouwer, 2004; Stiles, Xiao and Zangwill, 2004), this accumulation pattern can excite nonuniform spin-waves in the thick layer.

To explain the new region of excitations at currents beyond $I_+(H)$, that is, excitations at positive current bias in the AP state, we also consider the spin accumulation in this case (Figure 16, AP state graph). From this we see that the switching of the free layer has an important effect on the spin accumulation pattern at the fixed layer. The sign of the net spin accumulation changes as the system is switched by the current from the P state into the AP state. Therefore, excitations of the fixed layer now require a *positive* current bias. This is in agreement with the experimental observation. From this we conclude that dips in $\mathrm{d}V/\mathrm{d}I$ at *both* positive and negative currents are caused by excitation of the thick magnetic layer. While at positive currents these excitations could be associated with uniform excitations of the fixed layer, the pattern of the excitations matches well the nonuniform excitations found in single layers (Özyilmaz *et al*., 2004). Similar features at high positive currents have been observed in permalloy nanopillars. Narrow peaks are seen in the voltage spectrum at gigahertz frequencies at these 'dips' in differential resistance, which are consistent with the excitation of the thicker layer in the nanopillar (Kiselev *et al*., 2005). A longitudinal spin accumulation in the direction opposite to that of the magnetization on both sides of this layer seems to be the most likely cause for these excitations.

A detailed theory that explains the experiments presented in the preceding text is in Brataas, Tserkovnyak and Bauer (2006). A schematic phase diagram this theory provides is shown in Figure 19. Here, layer 1 is the thin ferromagnet and layer 2 is the thick ferromagnet. At zero current, the layers are aligned in the large magnetic field. Applying a positive current first produces a macrospin instability of layer 1,

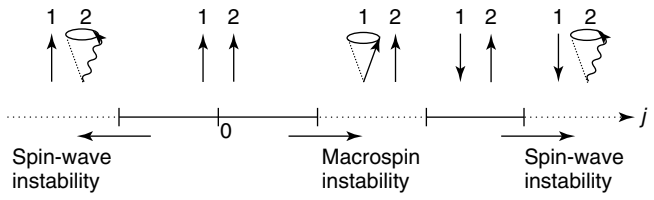

Figure 19. Phase diagram for thin (1) and thick (2) ferromagnet, starting in a parallel configuration, as a function of current. (Reprinted with permission Brataas *et al*. copyright 2006, American Physical Society.)

leading to a reversal of magnetization in the layer. A further increase in the current leads to a spin-wave instability in FM2. For negative currents, a spin-wave instability of the thick layer (FM2) is predicted. The slope of the phase boundaries with respect to applied field ($\mathrm{d}J_c/\mathrm{d}H$) are in semiquantitative agreement with the experiments (Brataas, Tserkovnyak and Bauer, 2006). Further, in the model asymmetries in the spin diffusion to the left and right of the ferromagnets are the main origin of the short wavelength spin-wave excitations of the magnetization. Subsequently, we have prepared nanopillar samples with identical top and bottom leads with respect to spin diffusion, by inserting a thin Pt layer in the right Cu leads shown in Figure 16 (Chen *et al*., 2006a). In these structures, bipolar excitations are suppressed and no excitations are observed beyond the main peak in $\mathrm{d}V/\mathrm{d}I$, confirming theoretical predictions. This result is also of importance in applications of spin transfer since a macrospin response is usually desirable.

5 SUMMARY AND OUTLOOK

The discovery of spin transfer in 1996 has led to rapid advances in the understanding of the influence of spin currents on magnetization dynamics. Spin currents have been shown to lead to nonequilibrium magnetization dynamics, including magnetization reversal, precession, and the excitation of nonuniform spin-wave modes. The resulting phenomena are clearly quite distinct from the action of charge currents or Oersted fields on ferromagnets.

This has been highlighted in this article by emphasizing experimental results on nanopillars in the high-field and high-current limit. In particular, spin currents in magnetic bilayer nanopillars have been shown to lead to magnetic hysteresis in high fields. Micromagnetic modeling shows that sufficient spin current results in a state of maximum magnetic energy, with the field and magnetization antiparallel. This modeling also shows that hysteresis may result from the angular dependence of the spin-torque interaction – distinct from the usual origin of hysteresis in magnets, namely, magnetic anisotropy and the dipole interaction.

Spin transfer also results in intriguing new phenomena in nanopillars with only a single magnetic layer. Here, current-induced excitations lead to a decrease in resistance. These excitations have been shown to be associated with an asymmetry of the contact configuration to the magnetic layer, as predicted by theory. A spin current may therefore excite nonuniform modes of a nanomagnet. The exact nature of the excitations is a topic of active investigation. Explaining such nonuniform magnetic excitations requires physics beyond the macrospin and one-dimensional transport models. It requires coupling micromagnetic and three-dimensional spin-transport calculations, a challenging but important problem. Finally, we have shown evidence for nonuniform excitations in the traditional bilayer nanopillar structures. Results illustrate that the resistance of a nanopillar may be lower than that with the layer magnetizations aligned; the P state. A lower resistance state is realized at high currents, with the onset of nonuniform spin-wave excitations. The contacts to the pillar again play an important role in these excitations.

While new phenomena have been discovered and explored, there are still fundamental questions as to the nature of the spin-transfer interaction. The form of the interaction and its dependence on layer composition and structure is only beginning to be understood quantitatively. The magnetization dynamics excited by the spin-transfer interaction is also poorly understood. For example, the spatial structure of the modes excited and the relaxation and switching pathways are unknown. Improved modeling, nanomagnet, and material structures as well as more detailed transport and magnetic characterization should lead to a better understanding of the physics of spin transfer.

ACKNOWLEDGMENTS

I would like to particularly acknowledge Barbaros Özyilmaz, whose thesis research formed the basis for this article. There were also very important contributions from Jonathan Sun and Wenyu Chen. I would also like to thank P. M. Levy, M. Stiles, and A. Brataas for many insights and useful discussions of this work. This research was supported by grants from NSF-DMR-0405620, DMR-0706322 and by ONR N0014-02-1-0995.

REFERENCES

Adam, S., Polianski, M.L. and Brouwer, P.W. (2006). Current-induced transverse spin-wave instability in thin ferromagnets: Beyond linear stability analysis. *Physical Review B: Condensed Matter and Materials Physics*, **73**(2), 024425.

Albert, F.J., Emley, N.C., Myers, E.B., *et al*. (2002). Quantitative study of magnetization reversal by spin-polarized current in magnetic multilayer nanopillars. *Physical Review Letters*, **89**(22), 226802.

Albert, F.J., Katine, J.A., Buhrman, R.A. and Ralph, D.C. (2000). Spin-polarized current switching of a Co thin film nanomagnet. *Applied Physics Letters*, **77**(23), 3809–3811.

Bauer, G.E.W., Tserkovnyak, Y., Huertas-Hernando, D. and Brataas, A. (2003). Universal angular magnetoresistance and spin torque in ferromagnetic/normal metal hybrids. *Physical Review B: Condensed Matter and Materials Physics*, **67**(9), 094421.

Berger, L. (1996). Emission of spin waves by a magnetic multilayer traversed by a current. *Physical Review B: Condensed Matter and Materials Physics*, **54**(13), 9353–9358.

Brataas, A., Bauer, G.E.W. and Kelly, P.J. (2006). Non-collinear magnetoelectronics. *Physics Reports*, **427**(4), 157–255.

Brataas, A., Tserkovnyak, Y. and Bauer, G.E.W. (2006). Current-induced macrospin versus spin-wave excitations in spin valves. *Physical Review B: Condensed Matter and Materials Physics*, **73**(1), 014408.

Chen, W., Kent, A.D., Rooks, M.J., *et al*. (2006a). Spin-transfer-induced excitations in bilayer magnetic nanopillars at high fields: The effects of contact layers. *Journal of Applied Physics*, **99**(8), 08G511.

Chen, W., Rooks, M.J., Ruiz, N., *et al*. (2006b). Spin-transfer in bilayer magnetic nanopillars at high fields as a function of free layer thickness. *Physical Review B: Condensed Matter and Materials Physics*, **74**(8), 144408.

Grollier, J., Cros, V., Hamzic, A., *et al*. (2001). Spin-polarized current induced switching in Co/Cu/Co pillars. *Applied Physics Letters*, **78**(23), 3663–3665.

Grollier, J., Cros, V., Jaffres, H., *et al*. (2003). Field dependence of magnetization reversal by spin transfer. *Physical Review B: Condensed Matter and Materials Physics*, **67**(17), 174402.

Hubert, A. and Schäfer, R. (1998). *Magnetic Domains*, *First Edition*, Springer.

Ji, Y., Chien, C.L. and Stiles, M.D. (2003). Current-induced spin-wave excitations in a single ferromagnetic layer. *Physical Review Letters*, **90**(10), 106601.

Kakazei, G.N., Wigen, P.E., Guslienko, K.Y., *et al*. (2004). Spin-wave spectra of perpendicularly magnetized circular submicron dot arrays. *Applied Physics Letters*, **85**(3), 443–445.

Katine, J.A., Albert, F.J., Buhrman, R.A., *et al*. (2000). Current-driven magnetization reversal and spin-wave excitations in Co/Cu/Co pillars. *Physical Review Letters*, **84**(14), 3149–3152.

Kiselev, S.I., Sankey, J.C., Krivorotov, I.N., *et al*. (2003). Microwave oscillations of a nanomagnet driven by a spin-polarized current. *Nature*, **425**, 380.

Kiselev, S.I., Sankey, J.C., Krivorotov, I.N., *et al*. (2004). Current-induced nanomagnet dynamics for magnetic fields perpendicular to the sample plane. *Physical Review Letters*, **93**(3), 036601.

Kiselev, S.I., Sankey, J.C., Krivorotov, I.N., *et al*. (2005). Spin-transfer excitations of permalloy nanopillars for large applied currents. *Physical Review B: Condensed Matter and Materials Physics*, **72**(6), 064430.

Kittel, C. (1996). *Introduction to Solid State Physics*, *Seventh Edition*, Wiley.

Lee, K.J., Deac, A., Redon, O., *et al*. (2004). Excitations of incoherent spin-waves due to spin-transfer torque. *Nature Materials*, **3**(12), 877–881.

Levy, P.M. and Zhang, J. (2004). Current-induced spin flip scattering at interfaces in noncollinear magnetic multilayers. *Physical Review B: Condensed Matter and Materials Physics*, **70**(13), 132406.

Li, Z. and Zhang, S. (2003). Magnetization dynamics with a spin-transfer torque. *Physical Review B: Condensed Matter and Materials Physics*, **68**(2), 024404.

Li, Z. and Zhang, S. (2004). Thermally assisted magnetization reversal in the presence of a spin-transfer torque. *Physical Review B: Condensed Matter and Materials Physics*, **72**(13), 212411.

McMichael, R.D. and Stiles, M.D. (2005). Magnetic normal modes of nanoelements. *Journal of Applied Physics*, **97**(10), 10J901.

Montigny, B. and Miltat, J. (2005). Micromagnetic simulations of current-induced microwave excitations. *Journal of Applied Physics*, **97**(10), 10C708.

Myers, E.B., Ralph, D.C., Katine, J.A., *et al*. (1999). Current-induced switching of domains in magnetic multilayer devices. *Science*, **285**(5429), 867–870.

Özyilmaz, B. and Kent, A.D. (2006). Current-induced switching in single ferromagenetic layer nanopillar junctions. *Applied Physics Letters*, **88**(16), 162506.

Özyilmaz, B., Kent, A.D., Monsma, D., *et al*. (2003). Current-induced magnetization reversal in high magnetic fields in Co/Cu/Co nanopillars. *Physical Review Letters*, **91**(6), 067203.

Özyilmaz, B., Kent, A.D., Rooks, M.J. and Sun, J.Z. (2005). Bipolar high-field excitations in Co/Cu/Co nanopillars. *Physical Review B: Condensed Matter and Materials Physics*, **71**(14), 140403.

Özyilmaz, B., Kent, A.D., Sun, J.Z., *et al*. (2004). Current-induced excitations in single cobalt ferromagnetic layer nanopillars. *Physical Review Letters*, **93**(17), 176604.

Polianski, M.L. and Brouwer, P.W. (2004). Current-induced transverse spin-wave instability in a thin nanomagnet. *Physical Review Letters*, **92**(2), 026602.

Rippard, W.H., Pufall, M.R., Kaka, S., *et al*. (2004). Direct-current induced dynamics in Co_{90} $Fe_1$10/Ni[sub 80]fe[sub 20] point contacts. *Physical Review Letters*, **92**(2), 027201.

Schreiber, F., Pflaum, J., Frait, Z., *et al*. (1995). Gilbert damping and g-factor in fexco1-x alloy films. *Solid State Communications*, **93**(12), 965–968.

Shpiro, A., Levy, P.M. and Zhang, S. (2003). Self-consistent treatment of nonequilibrium spin torques in magnetic multilayers. *Physical Review B: Condensed Matter and Materials Physics*, **67**(10), 104430.

Slonczewski, J. (1996). Current-driven excitation of magnetic multilayers. *Journal of Magnetism and Magnetic Materials*, **159**, L1.

Slonczewski, J.C. (1999). Excitation of spin waves by an electric current. *Journal of Magnetism and Magnetic Materials*, **195**(2), 261–268.

Smith, N., Katine, J.A., Childress, J.R. and Carey, M.J. (2005). Angular dependence of spin torque critical currents for cpp- gmr read heads. *IEEE Transactions on Magnetics*, **41**(10), 2935–2940.

Stiles, M. and Miltat, J. (2006). *Spin Dynamics in Confined Magnetic Structures III*, Springer: Berlin.

Stiles, M.D., Xiao, J. and Zangwill, A. (2004). Phenomenological theory of current-induced magnetization precession. *Physical Review B: Condensed Matter and Materials Physics*, **69**(5), 054408.

Stiles, M.D. and Zangwill, A. (2002). Anatomy of spin-transfer torque. *Physical Review B: Condensed Matter and Materials Physics*, **66**(1), 014407.

Sun, J.Z. (2000). Spin-current interaction with a monodomain magnetic body: A model study. *Physical Review B: Condensed Matter and Materials Physics*, **62**(1), 570–578.

Sun, J.Z., Monsma, D.J., Abraham, D.W., *et al*. (2002). Batch-fabricated spin-injection magnetic switches. *Applied Physics Letters*, **81**(12), 2202–2204.

Sun, J.Z., Monsma, D.J., Kuan, T.S., *et al*. (2003). Spin-torque transfer in batch-fabricated spin-valve magnetic nanojunctions (invited). *Journal of Applied Physics*, **93**(10), 6859–6863.

Tsoi, M., Jansen, A.G.M., Bass, J., *et al*. (1998). Excitation of a magnetic multilayer by an electric current. *Physical Review Letters*, **80**(19), 4281–4284.

Tsoi, M., Jansen, A.G.M., Bass, J., *et al*. (2000). Generation and detection of phase-coherent current-driven magnons in magnetic multilayers. *Nature*, **406**(6791), 46–48.

Tsoi, M., Sun, J.Z., Rooks, M.J., *et al*. (2004). Current-driven excitations in magnetic multilayer nanopillars from 4.2 k to 300 k. *Physical Review B: Condensed Matter and Materials Physics*, **69**(10), 100406.

Urazhdin, S., Birge, N.O., Pratt, J.W.P. and Bass, J. (2003). Current-driven magnetic excitations in permalloy-based multilayer nanopillars. *Physical Review Letters*, **91**(14), 146803.

Urazhdin, S., Chien, C.L., Guslienko, K.Y. and Novozhilova, L. (2006). Effects of current on the magnetic states of permalloy nanodiscs. *Physical Review B: Condensed Matter and Materials Physics*, **73**(5), 054416.

Waintal, X., Myers, E.B., Brouwer, P.W. and Ralph, D.C. (2000). Role of spin-dependent interface scattering in generating current-induced torques in magnetic multilayers. *Physical Review B: Condensed Matter and Materials Physics*, **62**(18), 12317–12327.

Wang, K., Zhang, S. and Levy, P.M. (1996). Angular dependence of giant magnetoresistance in a superlattice. *Physical Review B: Condensed Matter and Materials Physics*, **54**(17), 11965–11968.

Yang, Q., Holody, P., Loloee, R., *et al*. (1995). Prediction and measurement of perpendicular giant magnetoresistances of co/cu/$ni_{84}fe_{16}$/cu multilayers. *Physical Review B: Condensed Matter and Materials Physics*, **51**(5), 3226–3229.

Zhang, S., Levy, P.M. and Fert, A. (2002). Mechanisms of spin-polarized current-driven magnetization switching. *Physical Review Letters*, **88**(23), 236601.

Zimmler, M.A., Özyilmaz, B., Chen, W., *et al*. (2004). Current-induced effective magnetic fields in co/cu/co nanopillars. *Physical Review B: Condensed Matter and Materials Physics*, **70**(18), 184438.

Microwave Excitations in Spin Momentum Transfer Devices

Frederick B. Mancoff[1] and Shehzaad Kaka[2,3]

[1] *Technology Solutions Organization, Freescale Semiconductor Inc., Chandler, AZ, USA*
[2] *National Institute of Standards and Technology, Boulder, CO, USA*
[3] *Seagate Technology, Pittsburgh, PA, USA*

1 INTRODUCTION: SPIN-TRANSFER EFFECTS IN NANOMAGNETS

Present applications of thin-film giant magnetoresistance (GMR) spin valves (Dieny, 1994) and magnetic tunnel junctions (Moodera, Nassar and Mathon, 1999) include read-back heads for magnetic information storage in hard drives (Wang and Taratorin, 1999), storage bits in magnetoresistive random access memory (MRAM) (Åkerman *et al*., 2004; Debrosse *et al*., 2004), and magnetic sensors for biological, robotic, and automotive systems (Daughton, 2003; Freitas *et al*., 2004). For such devices, the relative alignment of the individual magnetic moments, and thus also the magnetoresistive signal, is manipulated by a magnetic field. Spin transfer, first predicted by Slonczewski (1996) and Berger (1996), offers a new way to control the magnetic alignment in nanostructured devices using applied electric current instead of magnetic field. When a current flows through a trilayer of two ferromagnets separated by a nonmagnetic spacer, the electrons acquire a spin polarization after passing through the first, or fixed, ferromagnet. As the spin-polarized electrons are incident on the second, or free, ferromagnet, the transfer of spin angular momentum produces a torque on the free magnetization. Magnetic excitations observed as a result of the spin transfer include both a hysteretic reversal (Myers *et al*., 1999; Wegrowe *et al*., 1999; Katine *et al*., 2000; Grollier *et al*., 2001; Mancoff and Russek, 2002; Sun *et al*., 2002; Mancoff *et al*., 2003) or sustained high-frequency precession (Tsoi *et al*., 2000; Kiselev *et al*., 2003; Rippard *et al*., 2004a; Covington *et al*., 2004; Kiselev *et al*., 2004; Rippard *et al*., 2004b) of the magnetization.

The dynamics of the free layer's magnetic moment under a spin-polarized applied current I_{dc} can be described using the Landau–Lifshitz–Gilbert equation with the inclusion of the spin-transfer torque (Slonczewski, 1996):

$$\frac{\mathrm{d}\vec{m}}{\mathrm{d}t} = -\mu_0\gamma\vec{m}\times\vec{H}_{\mathrm{eff}} - \mu_0\gamma\alpha\vec{m}\times(\vec{m}\times\vec{H}_{\mathrm{eff}}) + \frac{\varepsilon I_{\mathrm{dc}}\hbar\gamma}{2eMAt}\vec{m}\times(\vec{m}\times\vec{p}) \quad (1)$$

where $\vec{m}$ and $\vec{p}$ are the free and fixed layer magnetization directions, γ is the gyromagnetic ratio, $\vec{H}_{\mathrm{eff}}$ is the effective

Handbook of Magnetism and Advanced Magnetic Materials. Edited by Helmut Kronmüller and Stuart Parkin. Volume 5: *Spintronics and Magnetoelectronics*. ISBN: 978-0-470-02217-7.

magnetic field including the applied and demagnetizing fields, α is the damping parameter, μ_0 is the permeability of free space, ε is the spin-transfer efficiency, $\hbar$ is Planck's constant, e is the electron charge, M is the free layer saturation magnetization, A is the particle area, and t is the layer thickness. The first term on the right describes the usual precession of $\vec{m}$ about $\vec{H}_{\text{eff}}$. The second term on the right gives the magnetic damping, which tends to drive $\vec{m}$ toward $\vec{H}_{\text{eff}}$. The spin-transfer torque is given by the final term on the right, which is proportional to I_{dc}. For the correct sign of I_{dc}, the spin-transfer torque opposes the magnetic damping term and possibly cancels it out completely. In this case, spin transfer will produce either a hysteretic switch or a steady-state coherent oscillation of $\vec{m}$ depending on the relative strength of I_{dc} and the applied magnetic fields and anisotropies (Slonczewski, 1996, 1999). In this single-domain model, the spin-transfer dynamics depend on the current density I_{dc}/A and would be identical for devices with different diameters when driven with the same current density. The single-domain model, however, ignores effects due to current-generated oersted fields, nonuniform magnetization, and associated exchange energies.

Spin transfer generally becomes significant for nanosized ferromagnets, in which the reduced device dimension d allows the large critical current densities of $10^{10}-10^{11}\,\text{A m}^{-2}$ required for large spin-transfer effects. The spin-transfer torque is proportional to the current density and so varies as d^{-2}. The oersted magnetic field from the current flow also acts on the magnetic moment and varies as d^{-1}. Thus, spin transfer dominates at small d (Slonczewski, 1996). Experimental observations of spin-transfer effects have been reported for $d < 30-200\,\text{nm}$ and include systems such as patterned magnetic nanopillars (Katine *et al*., 2000; Grollier *et al*., 2001; Mancoff and Russek, 2002; Sun *et al*., 2002; Kiselev *et al*., 2003; Mancoff *et al*., 2003; Kiselev *et al*., 2004; Covington *et al*., 2004), mechanical point contacts (Tsoi *et al*., 2000; Rippard, Pufall and Silva, 2003; Ji, Chien and Stiles, 2003; Pufall, Rippard and Silva, 2003), lithographic point contacts (Myers *et al*., 1999; Rippard *et al*., 2004a,b), magnetic tunnel junctions (Huai *et al*., 2004; Fuchs *et al*., 2004), and magnetic nanowires (Wegrowe *et al*., 1999). The possibility for electrical control of magnetization through an applied current, as well as the increasing importance of spin transfer at reduced device sizes, makes spin transfer relevant for nanoscale device applications. Spin-transfer-induced hysteretic magnetic switching could allow a low-power, high-density MRAM written by applied current, rather than applied magnetic field. Also, the microwave output power from the spin-transfer high-frequency magnetic precession state can form the basis for a frequency-tunable, current-controlled nanoscale oscillator. Potential spin-transfer applications are discussed later.

In this article, we discuss spin-transfer-induced high-frequency precession, focusing on experiments at both Freescale Semiconductor and the National Institute of Standards and Technology (NIST) on GMR point contacts. We describe two issues of importance both for fundamental understanding as well as for potential applications: the dependence of spin-transfer precession properties on the area of a single point contact, as well as the observation of phase locking between separate spin-transfer oscillators. First, with regard to the area dependence, we discuss measurements at Freescale of spin-transfer resonance in contacts with diameter d ranging from less than 50 nm to almost 300 nm (Mancoff, Rizzo, Engel and Tehrani, 2006). The resonance frequency f increased nearly linearly with I_{dc}, but the decreasing dependence of the slope $\text{d}f/\text{d}I_{\text{dc}}$ on d deviated from a simple d^{-2} form given by the current density. Instead, the data was fit by an empirical model in which the large-angle precession region extends beyond the contact diameter by a ring of width $\delta \approx 50\,\text{nm}$. Also, the increase of the spin-transfer precession critical current I_{c} with contact area could be fit equivalently well by the model including the ring δ or by previous theory (Slonczewski, 1999).

Next, with regard to phase locking between spin-transfer oscillators, we examined devices with two separate point contacts to a single GMR spin valve film. The Freescale group measured the dependence of spin-transfer phase locking on the intercontact spacing (Mancoff, Rizzo, Engel and Tehrani, 2005). For two 80-nm diameter contacts electrically connected in parallel to a single top electrode, we observed an onset of phase locking between the two resonances for center-to-center spacings less than around 200 nm. The NIST group investigated devices with two contacts spaced by 500 nm and with separate electrical connections (Kaka *et al*., 2005). The current bias of one contact was varied to tune its resonance frequency toward that of the second contact with constant current bias. Over a range in current bias, the precession of both contacts phase locked. For both the Freescale and NIST data, the phase-locked resonance possessed an increased output power and a decreased linewidth due to coherence between the oscillators.

2 EXPERIMENTAL DETAILS

Figure 1(a) shows a typical cross section of a metallic point contact through a thick insulator to a GMR spin valve. The GMR film was patterned with lateral dimensions greater than 8 μm, so any edge defects were far from the point contact. The GMR film was insulated either by a cross-linked PMMA electron-beam (e-beam) lithography resist or SiO_2. The use of SiO_2 has some advantages, including more compatibility with industrial fabrication of spintronics

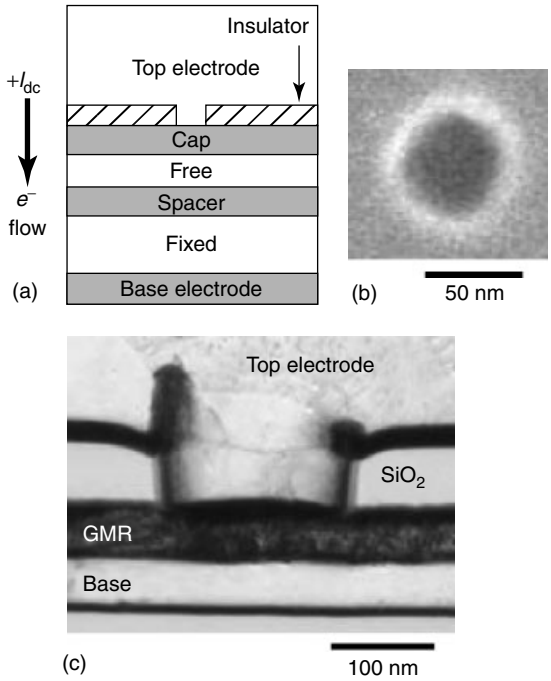

Figure 1. (a) Cross section of a via through an insulator to a GMR film. (b) Plan-view SEM image of a nominal 60-nm diameter contact. (c) Cross-section TEM image of a point contact to a GMR film. (Reproduced from F.B. Mancoff *et al*., 2006, with permission from the American Institute of Physics. © 2006.)

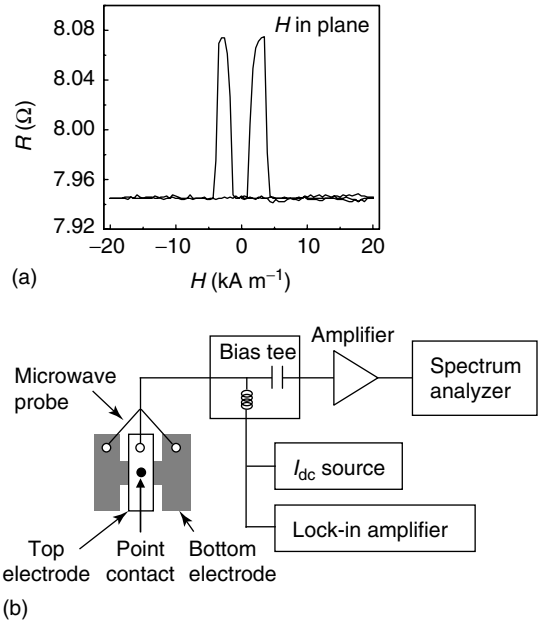

Figure 2. (a) Resistance R versus applied magnetic field H for a nominally 50-nm diameter point contact to a CPP GMR spin valve film. (b) Diagram of high-frequency measurement setup.

devices such as MRAM, allowing optical lithography to pattern the contact via, and avoiding the time-consuming high-dose e-beam exposure needed to cross-link the PMMA. The nominal lithographic contact diameter ranged from less than 50 nm up to 300 nm. Figure 1(b) is a plan-view scanning electron microscope (SEM) image of a nominally 60-nm contact written by e-beam lithography and etched through SiO_2. Figure 1(c) is a cross-section transmission electron microscope (TEM) image of a nominally 160-nm optical lithography contact, also using a SiO_2 insulator.

The GMR film typically consisted of a nonmagnetic base electrode, a relatively thick ferromagnetic fixed layer, a nonmagnetic Cu spacer layer, a relatively thin ferromagnetic free layer, and a nonmagnetic cap. Figure 2(a) shows a measurement at low current bias of the current-perpendicular-to-plane (CPP) GMR in a nominally 50-nm diameter contact. The fixed layer was 20-nm $Co_{81}Fe_{19}$, the Cu spacer was 6 nm thick, and the free layer was 4.5-nm $Ni_{80}Fe_{20}$. The CPP GMR switching was determined by the $Ni_{80}Fe_{20}$ and $Co_{81}Fe_{19}$ coercivities.

The high-frequency electrical measurement setup (top-down view in Figure 2b) was similar to that used for other high bandwidth measurements of magnetic devices (Russek and Kaka, 2000; Stutzke, Burkett and Russek, 2003; Kaka and Russek, 2002). The GMR film was patterned into part of the bottom electrode. I_{dc} flowed from a current source into a bias tee and then into the device via a high-frequency microwave probe. A lock-in amplifier measured the device resistance at low frequencies (<kHz). I_{dc} excited spin-transfer precession of the free layer and an associated oscillation of the device resistance through the GMR. The microwave voltage output is the product of I_{dc} and the oscillating resistance. The high-frequency signal passed through the bias tee into a microwave amplifier and then a spectrum analyzer. The amplifier gain was divided out of all data presented. Measurements were at room temperature with $+I_{dc}$ defined as electron flow from the free to the fixed magnetic layer. The chip and probe were mounted on a rotatable stage for which a magnetic field applied to the device could be varied between in plane and out of plane.

3 CONTACT AREA DEPENDENCE OF SPIN-TRANSFER RESONANCE

In this section, we describe measurements at Freescale of spin-transfer resonance in devices with a single GMR point contact, as in Figure 1, focusing on the dependence of the spin-transfer precession as a function of the contact size (Mancoff, Rizzo, Engel and Tehrani, 2006). In recent measurements of high-frequency (5–40 GHz) spin-transfer magnetization precession, the dependence on the lateral device area has not been examined (Kiselev *et al*., 2003,

Rippard *et al*., 2004a; Covington *et al*., 2004; Kiselev *et al*., 2004; Rippard *et al*., 2004b). However, understanding the area dependence is important in determining the details of the spin-transfer-induced dynamics, particularly the precession's spatial extent and lateral coherence, the importance of the oersted field, and the type of magnetic spin-wave excitations generated. The area dependence is also critical for understanding the scaling of spin-transfer devices in applications such as low-power, high-density MRAM or nanoscale current-driven, tunable microwave oscillators.

The measured device contact resistance versus the nominal designed contact diameter d_{nominal} (squares) from 50 to 300 nm is plotted in Figure 3(b). The data are averages for 35 contacts total of varied size. The dashed line is a fit of a Sharvin–Maxwell calculation for the point contact resistance (Wexler, 1966), for which we let the contact area differ from the nominal area by an amount equal to a ring of constant width. This area difference was determined by the fit as a decrease from the nominal diameter by a ring of width ≈8 nm, likely due to a slight loss in pattern fidelity in forming the contact.

For the experiments, the spin valve typically contained a 20-nm $Co_{81}Fe_{19}$ fixed layer, a 6-nm Cu spacer, and a 4.5-nm $Ni_{80}Fe_{20}$ free layer. Figure 3(a) shows the frequency spectrum amplitude measured for a nominally 300-nm diameter contact at I_{dc} from 50 to 75 mA in an applied magnetic field of approximately 1 T normal to the thin-film plane. At this magnetic field, the $Ni_{80}Fe_{20}$ free magnetization was saturated out of plane while the $Co_{81}Fe_{19}$ fixed magnetization pointed ≈30° out of plane, according to Stoner–Wohlfarth calculations. The spin-transfer precession manifested itself as a sharp peak in the frequency spectrum above a critical current at $+I_{\text{dc}}$. The signal resulted from the GMR as the $Ni_{80}Fe_{20}$ free layer magnetization moved while the $Co_{81}Fe_{19}$ magnetization was fixed with respect to spin transfer due to its larger thickness and magnetization compared to the $Ni_{80}Fe_{20}$. The peak precession frequency increased monotonically with I_{dc} (Figure 3(a)). This increasing trend is also demonstrated in Figure 4 as a map of the voltage amplitude which is a function of both the frequency spectrum and I_{dc}. The peak precession frequency increased with I_{dc} at an average rate of around 120 MHz mA^{-1} for this device, demonstrating an electrically controlled resonance frequency that may be of use in a practical oscillator device. The peak precession frequency displays occasional discontinuous jumps at certain values of I_{dc}, such as at around 57 mA and a larger jump at around 73 mA as seen in Figure 4. The origin of these discontinuities is unknown (Rippard *et al*., 2004a,b; Kiselev *et al*., 2004) but may be associated with spin-transfer excitation of the nominally fixed magnetic layer or a change in the mode structure within the free layer.

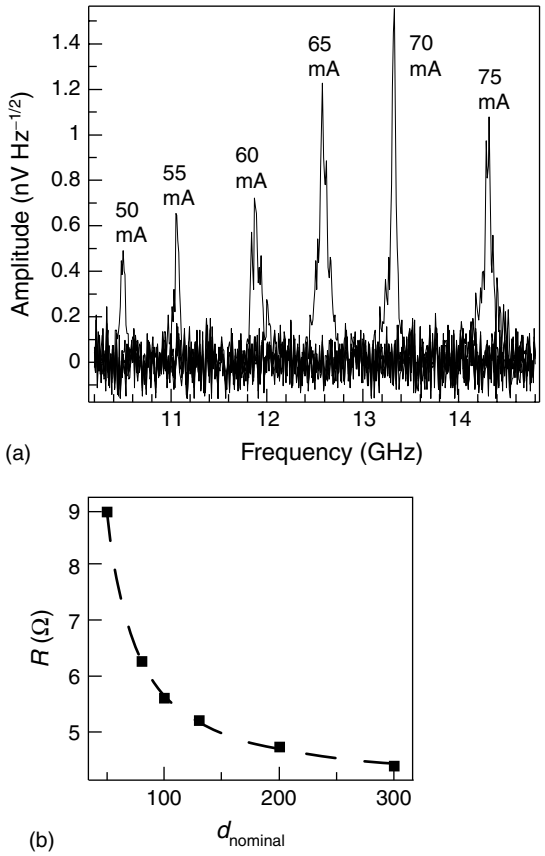

Figure 3. (a) Voltage amplitude versus frequency for a GMR contact of nominal diameter 300 nm. (b) Contact resistance versus nominal diameter d_{nominal} (squares). The dashed line is a Sharvin–Maxwell fit. Error bars in (b) are smaller than the data points. (Reproduced from F.B. Mancoff *et al*., 2006, with permission from the American Institute of Physics. © 2006.)

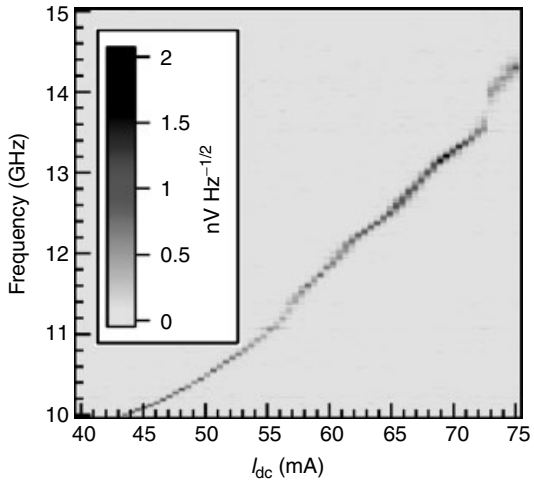

Figure 4. Map of voltage spectrum amplitude versus frequency and current bias I_{dc} for the GMR contact of nominal diameter 300 nm from Figure 3(a).

In this geometry, with the magnetic field applied perpendicular to the film plane, the fixed layer does not have a large Zeeman energy to fix the direction of the layer in the azimuthal direction, and motion of the fixed layer can occur.

Figures 3(a) and 4 demonstrate spin-transfer precession in the largest area devices to date. Such clear spin-transfer precession in larger devices is somewhat surprising since, as described previously, spin transfer competes with the self-generated magnetic field from the current flow and is typically dominant only at small contact diameters (Slonczewski, 1996). Nevertheless, we observed robust spin-transfer resonance in devices as large as almost 300 nm diameter. Although the data in Figures 3(a) and 4 were from a contact formed using e-beam lithography, we also observed similar spin-transfer resonance in contacts patterned with optical lithography (Figure 1c). Optical lithography offers simplified fabrication for applications by avoiding e-beam lithography, which was used for almost all spin-transfer studies so far (See Huai *et al*., 2004 for an exception).

As a function of the physical diameter d_{SM} determined from the Sharvin–Maxwell fit in Figure 3(b), the measured frequency full-width at half-maximum (*FWHM*) was as small as <10 MHz (Figure 5a) and the quality factor *f/FWHM* was as large as >1700 (Figure 5b), both roughly constant with d_{SM} from 35 nm to almost 300 nm. Each data point in Figure 5(a) and (b) is the minimum *FWHM* and maximum *f/FWHM* measured for a given contact over the range of I_{dc} and magnetic fields examined. The solid lines are the average of the data points for a given diameter. The maximum integrated resonance power ranged from around 200 pW at the smaller sizes to 1–5 pW in the largest devices.

The spin-transfer peak precession frequency f versus I_{dc} measured for nominal contact diameters from 50 to 300 nm is shown in Figure 6(a), with the labels giving d_{SM} for each contact. For all sizes, the measured f (crosses) increased approximately linearly with I_{dc} (dotted lines are linear fits). This linear dependence agrees with Landau–Lifshitz–Gilbert calculations using a spin-transfer torque term for a single-domain particle (Slonczewski, 1996; Lee, Redon and Dieny, 2005), and also for the spatially nonuniform case including nonlinearities from both exchange and dipole coupling (Hoefer *et al*., 2005). The physical picture is as follows: normally, the damping torque aligns the $Ni_{80}Fe_{20}$ free moment with the effective magnetic field and produces a non-precessing, zero torque steady state. The spin-transfer torque opposes the magnetic damping torque so the free moment can have a nonzero angle with the field in equilibrium and undergo steady-state precession. Increased I_{dc} and spin-transfer torque drive the $Ni_{80}Fe_{20}$ free layer to larger steady-state precession angles with the 1 T applied magnetic field. Then, the demagnetizing field of the $Ni_{80}Fe_{20}$ is reduced

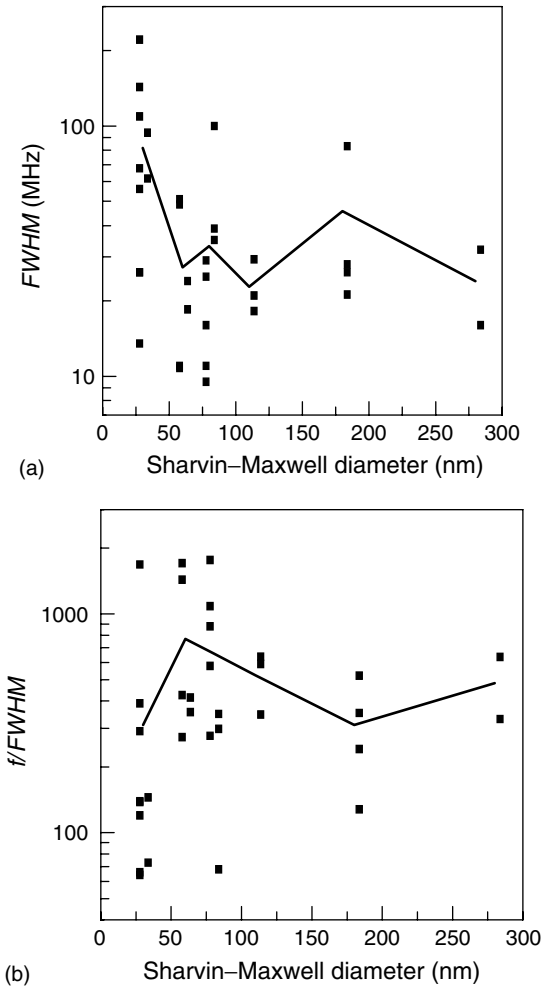

Figure 5. (a) Minimum spin-transfer resonance full-width at half-maximum *FWHM* of the voltage spectrum and (b) maximum resonance quality factor *f/FWHM* versus physical contact diameter d_{SM} from the Sharvin–Maxwell fit in Figure 3(b). Solid lines show the average data points.

and no longer nearly cancels the applied field, so that the net internal field, the magnetic torque, and therefore also the precession frequency f increase.

The slope df/dI_{dc} (squares) versus the contact diameter d_{SM} from the fit to the Sharvin–Maxwell calculation is shown in Figure 6(b). The data are averages of 17 contacts total of varied size. The error bars are the standard error in df/dI_{dc}. The dashed line is a fit of $df/dI_{dc} \propto 1/d^2_{SM}$, which assumes f to be proportional to the current per area defined by the contact diameter d_{SM}. As shown, this fit was quite poor (reduced $\chi^2 \gg 1$). Compared to the dashed fit, the observed slope df/dI_{dc} increases much more slowly with decreasing d_{SM}, which implies that the contacts require more current (or torque) to increase f than expected from the physical contact diameter. This difference is largest for the smallest contacts.

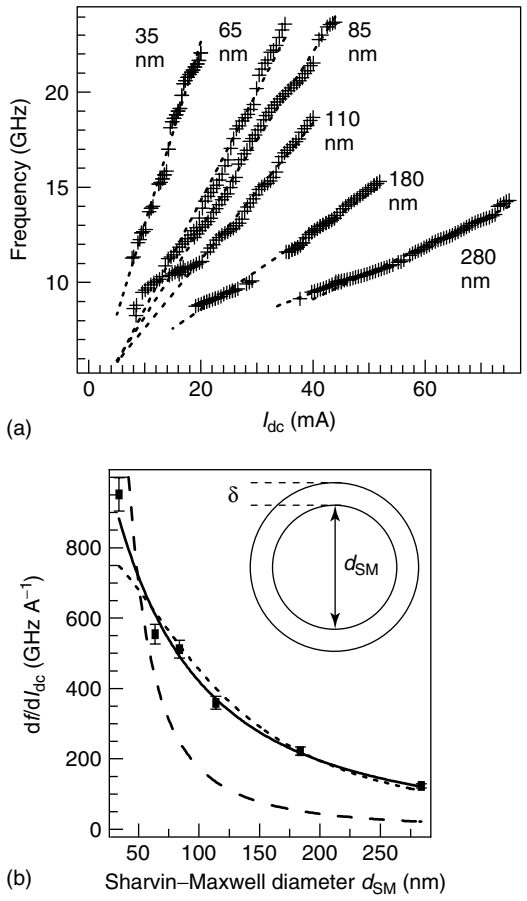

Figure 6. (a) Peak frequency f versus current I_{dc} for varied contact size (labels give the physical diameters d_{SM} from the Sharvin–Maxwell fit in Figure 3b). (b) Slope df/dI_{dc} versus d_{SM}. The solid line fit to $df/dI_{dc} \propto 1/(d_{SM}/2+\delta)^2$ determines $\delta \approx 50$ nm. A similar fit with $\delta = 0$ (dashed line) does not match the data. The dotted fit to $df/dI_{dc} \propto 1/(\pi(d_{SM}/2)^2 + C)$ with a constant area C does not fit the data as well as the solid line. (inset) Top-down view of a GMR contact, showing d_{SM} and δ. (Reproduced from F.B. Mancoff *et al.*, 2006, with permission from the American Institute of Physics. © 2006.)

As a starting model, we hypothesized that the contacts have a larger area of precessing spins than given by $A_{SM} = \pi(d_{SM}/2)^2$, since the strong magnetic exchange coupling must create a finite transition between the coherently precessing spins under the contact and the approximately static spins far outside it. In addition, energy losses due to dipolar radiation and spin-wave generation will increase the effective contact area. Spin-wave radiation losses were previously included in the theory of the critical current I_c for spin-transfer precession in point contacts (Slonczewski, 1999), but as a constant term independent of area.

As a first approximation, we assumed that the strongly precessing region extends into the continuous $Ni_{80}Fe_{20}$ film by a ring of constant width δ around the physical diameter d_{SM} (see a schematic, overhead view of the contact in the inset to Figure 6b). The modified fit of $df/dI_{dc} \propto 1/(d_{SM}/2+\delta)^2$ to the data (solid line in Figure 6b) was good (reduced $\chi^2 \approx 1.8$). The fit determined $\delta \approx 50$ nm, which results from magnetic excitation in the surrounding $Ni_{80}Fe_{20}$ film. This δ value for the excitation length is several times greater than the magnetic exchange length, which is ≈6 nm for the $Ni_{80}Fe_{20}$ film (Hoefer *et al.*, 2005). For interactions between two contacts in close proximity, each with $d_{SM} \approx 65$ nm, for example, this δ value implies that for a center-to-center spacing of $d_{SM} + 2\delta \approx 170$ nm, the precessing regions will interact. This estimate is consistent with our observation (see next section) of phase locking of the spin-transfer resonances for two $d_{SM} \approx 65$ nm contacts at center-to-center spacings <200 nm in the Freescale devices (Mancoff, Rizzo, Engel and Tehrani, 2005).

We also fit the form $df/dI_{dc} \propto 1/(\pi(d_{SM}/2)^2 + C)$ to the data in Figure 6(b) (dotted line), where C is a constant area of magnetic excitation in addition to $\pi(d_{SM}/2)^2$. We were motivated to use this form by a theoretical expression for I_c versus area (see Slonczewski, 1999 and equation (2) in the following text) in which I_c is proportional to the sum of the contact area and a constant term independent of area due to spin-wave radiation to the surrounding film. The fit determined a minimum spin precession area of $C \approx \pi(110\,\text{nm}/2)^2$, but did not match the data nearly as well (reduced $\chi^2 \approx 8.3$) as the solid line fit using the δ-ring model. In addition, as another comparison for the data in Figure 6(b), a decreasing trend for df/dI_{dc} versus contact size has also been recently calculated in the case of a spatially nonuniform precession for the contact (Hoefer *et al.*, 2005).

We used finite element simulations to estimate the increase in precessing area due to current spreading from the current injection site. The injected current density's lateral extent was approximately 3 nm (6 nm) outside the physical contact area in a horizontal plane at the top (bottom) of the 6-nm-thick Cu spacer layer. We thus conclude that current spreading is a relatively minor contribution to the increased magnetically active area given by the ring width $\delta \approx 50$ nm.

We also measured the spin-transfer critical current I_c versus area $A_{SM} = \pi(d_{SM}/2)^2$ for an out-of-plane applied magnetic field of 1 T (Figure 7a). I_c is the lowest current for which the spin-transfer peak in frequency was observed. The data are averages of a total of 17 contacts of varied size, and the error bars show the standard error in I_c. A theoretical form for I_c versus contact area A derived using the spin-transfer torque is (Slonczewski, 1999):

$$I_c = \frac{etM}{\hbar\varepsilon}\left[\frac{23D}{2\hbar\gamma} + 2A\alpha\left(B_{app} - \mu_0 M\right)\right] \qquad (2)$$

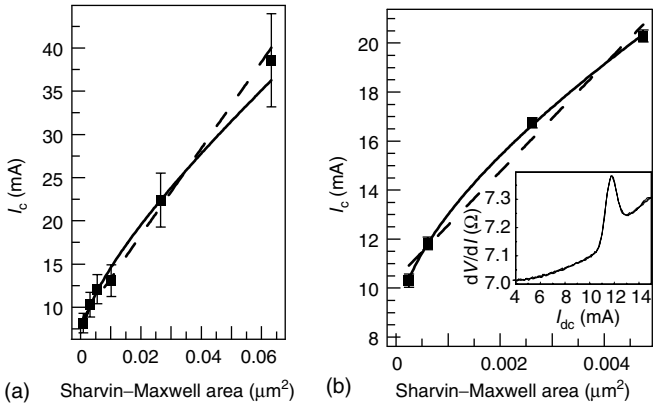

Figure 7. (a) Spin-transfer resonance critical current I_c versus area from the physical contact diameter d_{SM} from the Sharvin–Maxwell fit in Figure 3(b). A 1 T magnetic field was applied out of plane. (b) I_c versus area, with an in-plane field of 40 mT and with I_c measured from peaks in quasistatic dV/dI versus I_{dc} (inset), which correspond to the onset of spin-transfer-induced low frequency noise. The data in the inset is from a nominally 50-nm diameter contact. Dashed lines are fits to equation (2) for (a) or equation (3) for (b), and the solid curves are fits to modified forms including a ring δ in the area calculation. (Reproduced from F.B. Mancoff *et al*., 2006, with permission from the American Institute of Physics. © 2006.)

where e is the electron charge, t is the free layer thickness, M is the magnetization, $\hbar$ is Planck's constant, ε is the spin-transfer efficiency, D is the exchange parameter, γ is the gyromagnetic ratio, α is the damping parameter, B_{app} is the applied magnetic field, and μ_0 is the permeability of free space. The first term on the right in equation (2) represents damping of the spin-transfer torque due to spin-wave radiation losses to the surrounding magnetic film, while the second term in equation (2) results from the conventional magnetic damping. For small contact areas, the spin-wave radiation term dominates the dissipation of the spin-transfer excitation, while the conventional damping term becomes more significant for larger contacts.

The fit of equation (2) is shown in Figure 7(a) (dashed line). Using $t = 4.5\,\text{nm}$, $M \approx 640\,\text{kA m}^{-1}$ from vibrating sample magnetometry, and $D = 3.5\,\text{meV-nm}^2$ (Pufall, Rippard and Silva, 2003) for the $Ni_{80}Fe_{20}$ free layer, we find $\varepsilon \approx 0.18$ and $\alpha \approx 0.07$. This ε is in fair agreement with results by a different technique where $\varepsilon \approx 0.29$–0.56 for $Co_{90}Fe_{10}$/Cu multilayers or $\varepsilon \approx 0.17$–0.38 for $Ni_{80}Fe_{20}$/Cu multilayers (Pufall, Rippard and Silva, 2003). ε is reduced in our devices since the fixed layer magnetization is $\approx 30^\circ$ out of plane instead of 90° as assumed for equation (2). The in-plane magnetization and corresponding spin polarization do not contribute to precession, so ε is reduced, in this case by a factor of $\approx$2, compared to when the fixed layer magnetization is 90° out of plane. The α value is somewhat large compared to that measured for continuous $Ni_{80}Fe_{20}$ films ($\alpha \approx 0.01$) but closer to that measured for large-angle precession in patterned nanostructures ($\alpha \approx 0.03$) (Kaka *et al*., 2003).

We also fit the data to a modified form of equation (2) with $I_c \propto (A_{SM} + \Delta A)$, where ΔA is the extra area of the ring of width δ and the proportionality constant contains the same prefactors as the area term in equation (2). This modified form incorporates the spin-wave radiation loss term using the additional excitation ring δ, instead of the constant term independent of area (first term on the right in equation (2)). The fit to this equation (solid curve in Figure 7a) determined $\delta \approx 90\,\text{nm}$ (comparable to $\delta \approx 50\,\text{nm}$ from Figure 6) as well as $\alpha/\varepsilon \sim 0.16$, which gave $\alpha \approx 0.03$ assuming $\varepsilon \approx 0.18$ as found previously. The quality of the two fits in Figure 7(a) was roughly equal given the data uncertainty, though the fit incorporating the ring δ gave a more reasonable α.

In Figure 7(b), we again plot I_c versus A_{SM}, but now for an in-plane applied magnetic field of 40 mT. The data are averages of more than 80 devices of varied size. Error bars showing the standard error in I_c are smaller than the data points. The I_c values in Figure 7(b) were from quasistatic measurements of the differential resistance dV/dI versus I_{dc}, as shown in the inset to Figure 7(b) for a nominally 50-nm diameter contact. The observed peak in dV/dI at $I_{dc} \approx 11\,\text{mA}$ marks the onset of spin-transfer-induced magnetic excitations. Corresponding frequency spectrum measurements showed these dV/dI peaks were actually due to low frequency ($< \approx 2\,\text{GHz}$) noise rather than a coherent high-frequency resonance as in Figure 7(a). This low frequency noise presumably results from switching between multiple metastable magnetic configurations (Pufall *et al*., 2004). Whereas this noise is not due to coherent precession as in Slonczewski (1999), its onset is still due to the spin-transfer torque exceeding a critical value. Therefore, we fit these spin-transfer features using equation (2), but modified for the in-plane magnetic field (Rippard, Pufall and Silva, 2003):

$$I_c = \frac{etM}{\hbar\varepsilon}\left[\frac{23D}{2\hbar\gamma} + 2A\alpha\left(B_{app} + \frac{\mu_0 M}{2}\right)\right] \qquad (3)$$

The fit of equation (3) (dashed line in Figure 7b) gave $\varepsilon \approx 0.14$ and $\alpha \approx 0.08$, in reasonable agreement with the field out-of-plane measurements. Figure 7(b) also shows a fit (solid curve) using the alternate form of equation (3) $I_c \propto (A_{SM} + \Delta A)$, which determined $\delta \approx 70\,\text{nm}$ and $\alpha/\varepsilon \sim 0.15$, or $\alpha \approx 0.02$ assuming $\varepsilon \approx 0.14$. This second form for I_c fits the data in Figure 7(b) much better (reduced $\chi^2 \approx 0.2$ as compared to $\approx$9.5 for equation (3) itself) and gives a more reasonable α. In general, an understanding of the area dependence of spin-transfer resonance is important both for

testing spin-transfer theory and for future applications of spin transfer to magnetic oscillators or nonvolatile memory.

4 PHASE LOCKING BETWEEN SPIN-TRANSFER OSCILLATORS

4.1 Introduction to phase locking

This section reviews data from two independent groups that studied a system of two interacting nanocontact oscillators. The results support a single conclusion: the localized magnetic oscillations of two nanocontact oscillators in submicrometer proximity can phase lock (synchronize) to a single microwave frequency. These investigations, conducted at Freescale Semiconductor (Mancoff, Rizzo, Engel and Tehrani, 2005) and at NIST in Boulder, Colorado (Kaka *et al*., 2005), are motivated by the technological possibilities of increased microwave power output from a large array of phase-locked spin-transfer oscillators. For the present geometry of point contacts to an extended magnetic film, possible coupling mechanisms between contacts include oscillating dipolar magnetic fields, spin-wave radiation, or exchange coupling. A related experiment at NIST demonstrated injection locking of a single spin-transfer oscillator to a microwave current applied from an external source (Rippard *et al*., 2005). In addition, phase locking in arrays of multiple spin-transfer oscillators was recently investigated both by analytical calculations (Slavin and Tiberkevich, 2005) and numerical simulations (Grollier, Cros and Fert, 2005).

Phase locking via mutual interactions occurs in a variety of settings beyond magnetic materials. Examples of solid-state devices include arrays of phase-locked, oscillating Josephson junctions (Wengler, Guan and Track, 1995; Benz and Burroughs, 1991) and Metal-semiconductor transistors (MESFETS) (Popovic, Weikle, Kim and Rutledge, 1991) as well as coupled semiconductor oscillator designs for achieving high-frequency purity (Rohde, Poddar and Bock, 2005). Historically, the first scientific observation of phase locking dates back to 1665 when Christian Huygens noticed synchronized motion of two pendulum clocks caused by mechanical vibrations transmitted through a wall (Bennet, Schatz, Rockwood and Wiesenfeld, 2002). Synchronized behavior also occurs in biological systems, including the light flashing of certain colonies of fireflies in Malaysia (Strogatz, 2003) and the dependence of the periodicity of light emission from individual flies on the received stimulus of neighboring light flashes (Buck and Buck, 1968). Another example is human heart muscle, composed of thousands of pacemaker cells that fire in synchrony to produce a single heartbeat despite slight differences between neighbor cells. However, under certain conditions, synchrony is lost, disrupting the heartbeat and leading to a life threatening medical condition (Strogatz, 2003).

4.2 Measurement of phase locking as a function of contact separation

In this section, we focus on measurements at Freescale on the dependence of phase locking between spin-transfer resonances in two neighboring GMR point contacts as a function of the physical separation between the contacts (Mancoff, Rizzo, Engel and Tehrani, 2005). The two contacts are to the same section of the GMR film and are connected electrically in parallel to each other with a single top electrode (schematic cross section in Figure 8a). The sputter-deposited film consisted of a 5-nm Pd/25-nm Cu base electrode, a 20-nm $Co_{81}Fe_{19}$ fixed magnetic layer, a 6-nm Cu spacer, a 4.5-nm $Ni_{80}Fe_{20}$ free magnetic layer, and a 2-nm Cu/3.5-nm Pd cap. Figure 8(b) shows a cross-section SEM image of the contacts. The center-to-center spacing was 120 nm, and the nominal diameters were 80 nm. As described in the previous section, an actual diameter $d_{SM} \approx 65$ nm was determined

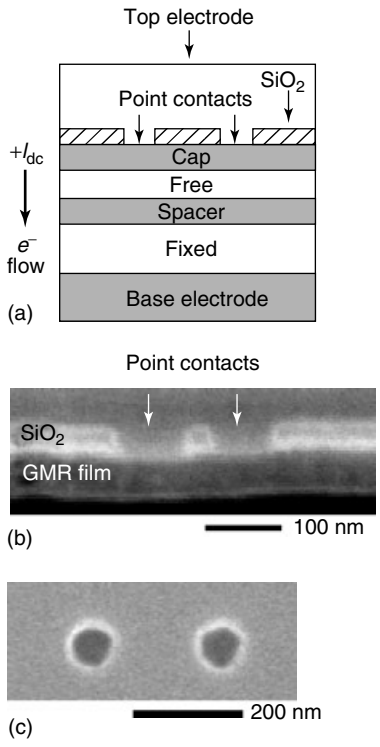

Figure 8. (a) Cross section of two point contacts. (b) Cross-section SEM image of two 80-nm diameter contacts with a 120 nm center-to-center spacing. (c) Plan-view SEM image of two 80-nm contacts with a 240 nm spacing. (Reproduced from Mancoff *et al*., 2005, with permission from Nature Publishing Group. © 2005.)

from a Sharvin–Maxwell calculation. Figure 8(c) is a plan-view SEM image of a similar sample with 240 nm spacing.

For high-frequency measurements on double point contacts in this section, a total dc current I_{dc} was applied to the contact pair. Figure 9 shows the measured frequency spectrum voltage amplitude versus I_{dc} for three devices with center-to-center spacings of 800 nm (Figure 9a), 150 nm (Figure 9b), and 120 nm (Figure 9c). All the data in this section was taken in a magnetic field of between 0.8 and 1.2 T applied perpendicular to the plane of the film. The spin-transfer precession, or resonance, appeared as a frequency spectrum peak at a given I_{dc}. The peak frequencies for all spacings increased approximately linearly with increased I_{dc}, over a frequency range of <10 to >24 GHz, in agreement with similar measurements on single GMR point contacts (Rippard *et al*., 2004a; Mancoff, Rizzo, Engel and Tehrani, 2006). The number and behavior of the observed spin-transfer peaks depended on the two contacts' relative spacing. For the widely spaced device (Figure 9a) with 800 nm spacing, we observed two separate peaks for nearly all I_{dc}. The two peaks had comparable resonance frequencies that increased at similar average rates versus I_{dc}. Each peak displayed frequency jumps at multiple I_{dc} values, similar to discontinuities observed for single point contacts (Rippard *et al*., 2004a; Mancoff, Rizzo, Engel and Tehrani, 2006). The two sets of jumps were uncorrelated, so the pair of contacts at 800 nm spacing was undergoing independent, uncoupled spin-transfer oscillations.

In contrast, the closely spaced contact pair (Figure 9c) at 120 nm spacing displayed only a single peak in frequency for all I_{dc}. The change from two independent peaks at 800 nm spacing to a single peak at 120 nm spacing indicates interactions between the point contacts at closer spacing coupled the spin-transfer oscillations. The coupling strength is sufficient to bring together in frequency the resonances from the two different contacts that would otherwise be separated by several hundred megahertz for uncoupled devices, as in Figure 9(a). For the device with a somewhat greater spacing of 150 nm (Figure 9b), we detected two separate peaks for most I_{dc}. However, here the two peaks progressed nearly parallel in frequency versus I_{dc}, compared to the two independent sets of frequency jumps for the 800 nm

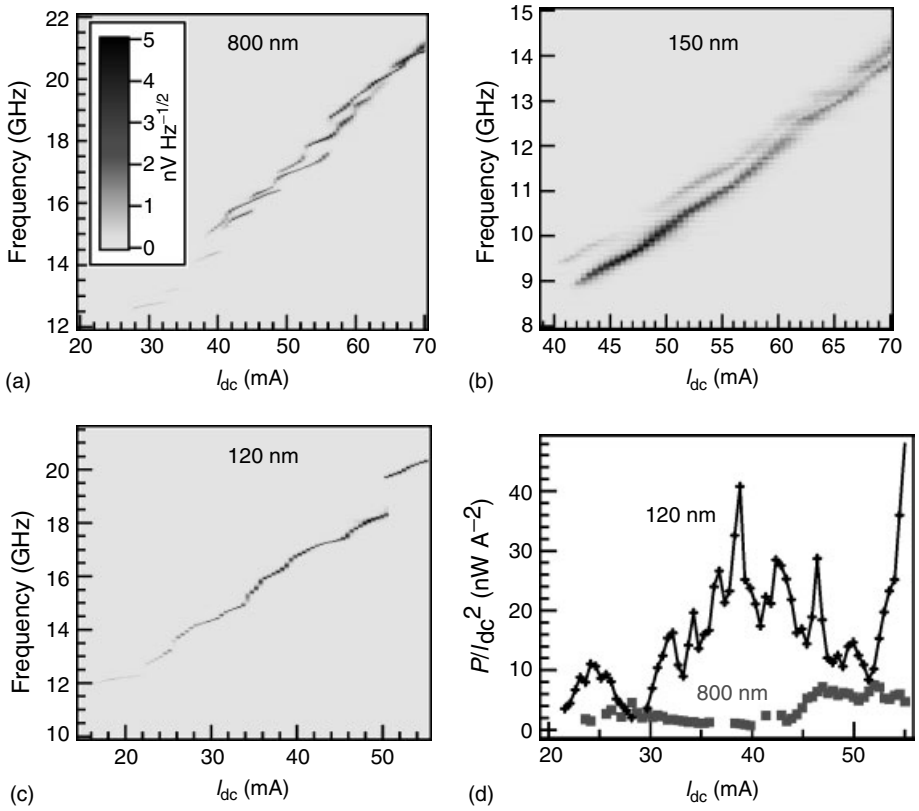

Figure 9. Maps of spectrum amplitude versus frequency and applied current bias I_{dc} for devices with varied center-to-center intercontact spacing of (a) 800 nm, (b) 150 nm, and (c) 120 nm. (d) Integrated power P normalized by I_{dc}^2 versus I_{dc} for double point contact devices with 120 nm (crosses) and 800 nm (squares) spacings. Corresponding frequency spectra show either one or two spin-transfer peaks, respectively. The curve for the 800-nm spaced sample includes the sum of the power in its two peaks. (Reproduced from Mancoff *et al*., 2005, with permission from Nature Publishing Group. © 2005.)

spacing device (Figure 9a). Thus, the 150 nm spacing data in Figure 9(b) behaved with a coupling strength intermediate between the two independent peaks at 800 nm spacing and the single peak at 120 nm spacing.

We observed a significant difference in power output between devices with a relatively close spacing and a single resonance peak compared to devices with larger spacing and two independent peaks. Figure 9(d) shows that the typical integrated power normalized by $I_{dc}{}^2$ for the single peak in a device with 120 nm spacing (crosses) was clearly greater than the combined power for the two peaks in a device with 800 nm spacing (squares). Among seven devices (with spacings of 120–200 nm) showing a single peak similar to Figure 9(c), the average output power was $11 \pm 2\,\mathrm{nW\,A^{-2}}$ (where specified uncertainty is the standard error) in 1 T applied magnetic field. In contrast, for all seven devices (with spacings of 400 and 800 nm) showing two independent peaks similar to Figure 9(a) the average output power was $5 \pm 0.5\,\mathrm{nW\,A^{-2}}$ for the two peaks combined in a 1 T field. A similar factor of ≈2 difference in power was also observed in 1.2 T, with $8 \pm 1\,\mathrm{nW\,A^{-2}}$ for devices with small spacing and one peak and $4 \pm 0.5\,\mathrm{nW\,A^{-2}}$ for devices with large spacing and two peaks.

The factor of ≈2 difference in output power indicates the closely spaced double point contacts were phase locked. We modeled the two contacts as resistors R_1 and R_2 in parallel with each other and in series with a single current source I_{dc}. The two resistances oscillate in time with a phase difference ϕ and equal amplitude ΔR and frequency ω about an average value R_0: $R_1(t) = R_0 + (\Delta R/2)\cos\omega t$ and $R_2(t) = R_0 + (\Delta R/2)\cos(\omega t + \phi)$. The ac voltage V_{ac} generated by the device is then $V_{ac}(\phi) = I_{dc}\,((R_1R_2/(R_1 + R_2)) - (R_0/2))$, and the power measured across the 50 Ω load of the spectrum analyzer is $P(\phi) = \frac{1}{2} \cdot (V_{ac}^2(\phi)/50\,\Omega)$. For simplicity, we assumed the 50 Ω load impedance is much greater than the contact resistances, as is in the experiment. The power for two in-phase oscillators is found by evaluating $P(\phi = 0)$. The power for two uncoupled contacts oscillating independently with random ϕ, as expected in Figure 9(a), is given by averaging over ϕ from 0 to 2π: $P_{\mathrm{random}\,\phi} = \int_0^{2\pi} \frac{P(\phi)\mathrm{d}\phi}{2\pi}$. Evaluating these expressions, we find: $P(\phi = 0) = 2P_{\mathrm{random}\,\phi}$, so that the modeled total power for two uncoupled contacts is half the power for two in-phase oscillators. Thus, we conclude that the two point contact oscillators with close intercontact spacing (Figure 9c) are phase locked with $\phi = 0$, whereas those with wide spacing (Figure 9a) are uncoupled.

We measured spin transfer in over 30 devices with various spacings and repeatedly observed the trend in Figure 9(a–c). The statistical distributions for these measurements are shown in Figure 10 where we plot histograms for the three types of spin-transfer frequency-domain behavior (two peaks, intermediate, and one peak) versus intercontact spacing. The solid lines are guides to the eye. The 'two peaks' histogram (solid diamonds) is maximum for the largest spacings of 400 nm and greater and drops to 0 at small spacings. These data correspond to devices with two spin-transfer peaks observed at each I_{dc} and with each peak showing its own independent frequency jumps, indicating that the point contact pair was uncoupled. The 'one peak' histogram (open squares) is maximum at the smallest spacings of 120–150 nm and decreases to 0 above 200 nm. These data correspond to devices with a single resonance peak observed at each I_{dc}, indicating strong coupling and associated phase locking between the oscillators. Finally, the 'intermediate' histogram (solid triangles) shows a third category of spin-transfer data with a maximum around 200 nm spacing. These data correspond to devices which showed a transition from one peak to two within an I_{dc} sweep, or a single peak over most I_{dc} values with an occasional weaker second peak, or two peaks moving nearly parallel in frequency with I_{dc} as in Figure 9(b). This intermediate category represents devices in a transition range between those with strong coupling with phase locking and those with very weak or no coupling between the two independent oscillators.

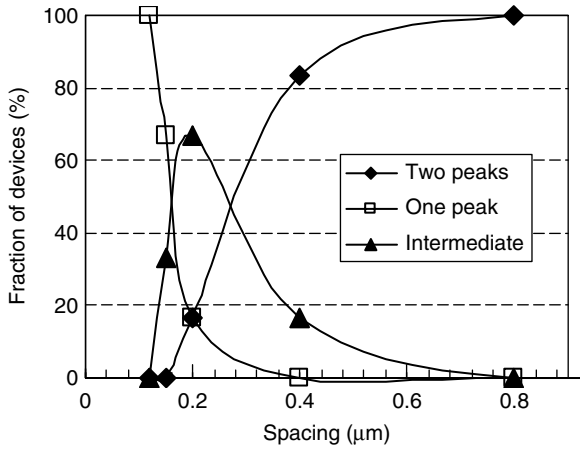

Figure 10. Histogram of spin-transfer behavior for devices with two contacts and varied center-to-center spacing. Squares show the devices for which a single spin-transfer peak was observed, as in Figure 9(c). Diamonds show the devices for which two peaks were observed, as in Figure 9(a). Triangles show the devices with intermediate spin-transfer characteristics. Solid lines are guides to the eye. (Reproduced from Mancoff *et al.*, 2005, with permission from Nature Publishing Group. © 2005.)

Figure 10 indicates consistent likelihood of phase locking in the Freescale double point contact devices at center-to-center spacings <200 nm. As described in the previous section, the region of large-angle precession for each point contact exceeds the physical contact area in the extended $Ni_{80}Fe_{20}$ free layer magnetic film. For a single contact

of nominally 80 nm diameter (with a Sharvin–Maxwell diameter $d_{SM} \approx 65$ nm, as described in the previous section), we estimated an effective magnetic excitation diameter of approximately 170 nm (Mancoff, Rizzo, Engel and Tehrani, 2006). This value suggests the possibility that an overlap in the regions of strong dynamic excitation existing for center-to-center spacings of 200 nm (Figure 10) leads to a spontaneously phase-locked state above the critical current of the oscillators. We see in the next section that phase locking can occur for a larger contact separation (500 nm) with the requirement that each oscillator's resonance frequency be independently tuned to closely coincide.

Figure 11 gives another example of spin-transfer oscillations in a double point contact device with 150 nm intercontact spacing and an intermediate coupling strength. For the frequency spectra map versus I_{dc} in Figure 11(a), we observed the onset of one spin-transfer peak for $I_{dc} > \approx 28$ mA followed by a second peak of comparable amplitude for $I_{dc} > \approx 35$ mA. The two separate peaks then coexisted for I_{dc} up to $\approx$47 mA followed by a transition to a single peak above this current, likely indicating that the contacts have phase locked. Figure 11(b) shows the corresponding integrated output power normalized by ${I_{dc}}^2$. The closed triangles are for the single peak at high I_{dc}, whereas the open squares and closed diamonds are the individual powers in the two peaks at lower I_{dc}, with the open squares (closed diamonds) showing the data for the lower (higher) frequency peak of these two. We observed an average power $\approx 5\,\mathrm{nW\,A^{-2}}$ in each of the two peaks with a total $\approx 10\,\mathrm{nW\,A^{-2}}$ just below the transition at $I_{dc} \approx 47$ mA, as compared to $\approx 20\,\mathrm{nW\,A^{-2}}$ in the single peak at higher current. This factor of 2 power increase is consistent with phase locking with $\phi = 0$, as discussed in the preceding text. Thus, Figure 11 illustrates an electrically tunable transition of the double point contact device into phase locking. For this device, the linewidth *FWHM* decreases across the transition, from $\approx$200 MHz for each of the two peaks at low I_{dc} narrowing to $\approx$80 MHz for the single peak at high I_{dc}.

A decreased linewidth upon phase locking is expected if thermal fluctuations contribute significantly. Then for the phase-locked pair, thermal energy fluctuations act on a device with greater coherent magnetic volume, so the effective fluctuation field and *FWHM* will decrease, as in Figure 11 (Russek *et al.*, 2005). On average, we observed a slight ($\approx$10–30%) decrease in the *FWHM* for the closely spaced devices with one peak compared to $\approx$200 MHz *FWHM* for widely spaced devices with two peaks.

In this section, the Freescale devices with two nanosized spin-transfer oscillators in parallel phase locked when the intercontact spacing was <200 nm. We observed only one resonance for closely spaced contacts and found the average power was approximately twice the total for two separate resonances at large spacings, indicating phase locking for the closely spaced contacts.

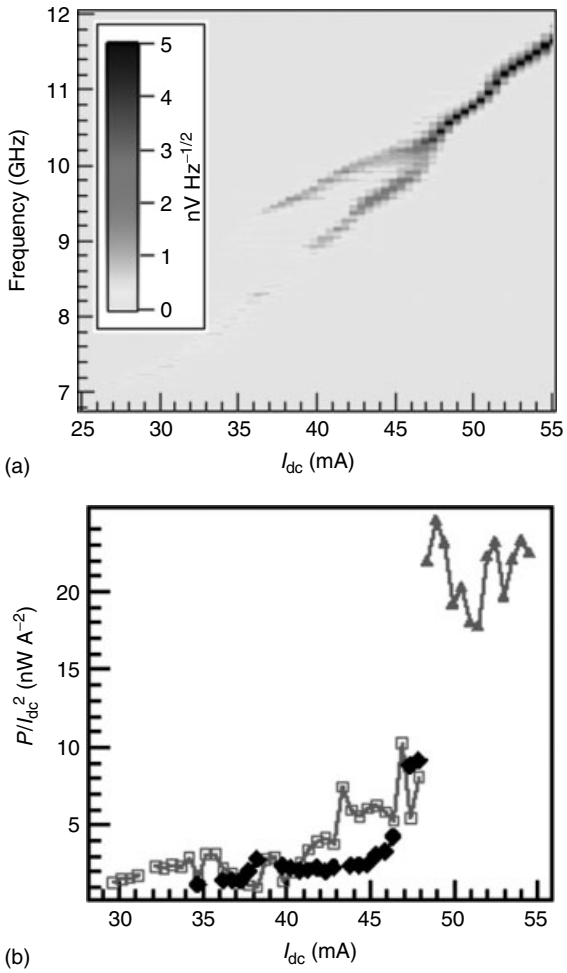

Figure 11. (a) Map of spectrum amplitude versus frequency and applied current bias I_{dc} for two contacts with 150 nm intercontact spacing. (b) Integrated power P normalized by I_{dc}^2 versus I_{dc} for the frequency spectra in (a). The data for I_{dc} below the transition at $\sim$47 mA is given by the open squares and closed diamonds for the lower and higher frequency peaks respectively. Closed triangles show the data for the single peak observed at larger I_{dc}. (Reproduced from Mancoff *et al.*, 2005, with permission from Nature Publishing Group. © 2005.)

4.3 Measurement of phase locking with independent frequency control of each oscillator

In this section, we discuss measurements at NIST on the two-nanocontact system utilizing a slightly different device structure and measurement method (Kaka *et al.*, 2005). Sputter-deposited spin valve films were patterned into 10 μm × 20 μm rectangular mesas with the following

layer structure: 5-nm Ta/50-nm Cu/20-nm $Co_{90}Fe_{10}$/5-nm Cu/5-nm $Ni_{80}Fe_{20}$/1.5-nm Cu/2.5-nm Au. The $Co_{90}Fe_{10}$ layer is the fixed layer of the spin valve because its moment and thickness are larger than the $Ni_{80}Fe_{20}$ layer. E-beam lithography was used to pattern two 40-nm diameter metallic contacts (nanocontacts) to the top of the mesa through a PMMA insulator. The contacts were separated by 500 nm and wires were fabricated connecting each nanocontact to a separate set of probe pads. Ground contacts are made to the sides of the mesa. This device structure (Figure 12a) allows independent current control of each contact. Each nanocontact is connected to its own current source through the inductive port of a bias tee (Figure 12b). The capacitive port of each bias tee transmits the high-frequency output of each device, when active. Both of these high-frequency channels are input to the isolated ports of a microwave power combiner that has a bandwidth of 2–18 GHz. The output of the power combiner is amplified and then measured by a spectrum analyzer. When both nanocontacts are active, and their respective frequencies are within the bandwidth of the power combiner, then the high-frequency signals from both contacts can be displayed simultaneously. All the data in this section were taken with an external magnetic field of 0.74 T oriented at 75° from the film plane. This particular applied magnetic field vector is known to produce relatively high output power from a nanocontact oscillator (Rippard *et al*., 2004b).

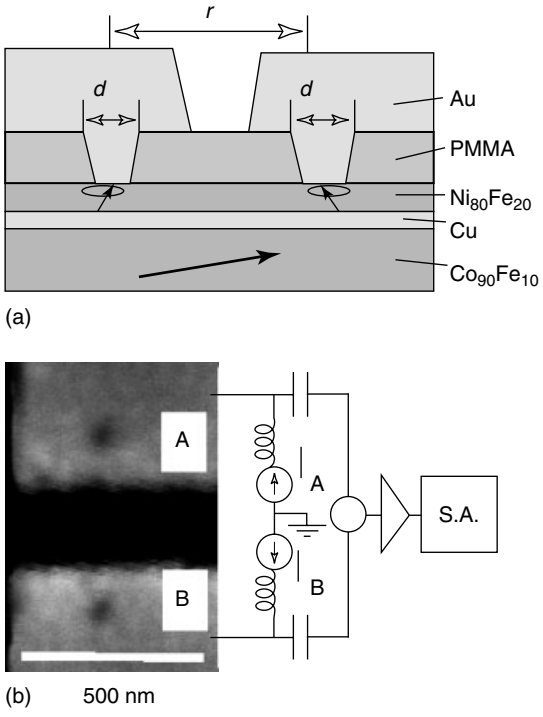

Figure 12. (a) Cross section of two nanocontacts (with diameter $d = 40$ nm) made to a spin valve stack. The contacts were separated by $r = 500$ nm. Arrows show assumed magnetization directions and motion. (b) Micrograph of a two-nanocontact device. At right is a measurement schematic including a bias tee connected to each contact, a microwave power combiner (circle), an amplifier, and the spectrum analyzer (designated by S.A.). (Reproduced from Kaka *et al*., 2005, with permission from Nature Publishing Group. © 2005.)

When only one oscillator was active (no current through the other contact), we detected the noninteracting (free-running) behavior of that particular oscillator. Figure 13(a) shows the free-running peak frequencies for each oscillator as a function of applied current. The two oscillators are designated as A and B. Figure 13(b) shows the output power (area under the spectral peak) in the free-running state for A and B. The frequencies exhibited by both oscillators were close to previous measurements in nanocontact oscillators at this particular field and angle (Rippard *et al*., 2004b). However, small differences existed in the frequency and power output of each oscillator. This difference, possibly due to slight variations in the geometry of the fabricated contacts, enabled unique identification of each oscillator.

When currents were applied to both contacts making both oscillators simultaneously active, interactions between the oscillators altered their frequencies from their free-running values. First, there was a static oersted magnetic field generated by the current through the neighboring contact. An estimate of the in-plane field at a neighboring contact can be given by the simple formula of field from an infinite current: $B = \mu_0 I (2\pi r)^{-1}$. For a 12 mA current and a 500 nm separation, the estimated field is only 4.8 mT, whereas the in-plane component of the applied field in our measurement was 191.5 mT. The result of this additional small oersted field was an approximately linear shift in the oscillator frequency as a function of current through the *other* contact as seen in Figure 14. This effect persisted for negative current through

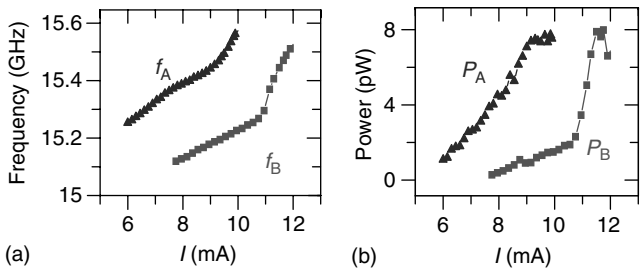

Figure 13. Free-running oscillator behavior. (a) Frequency of oscillator A alone versus current through A (triangles). Frequency of oscillator B alone versus current through B (squares). (b) Power from oscillator A alone versus current through A (triangles). Power from oscillator B alone versus current through B (squares). (Reproduced from Kaka *et al*., 2005, with permission from Nature Publishing Group. © 2005.)

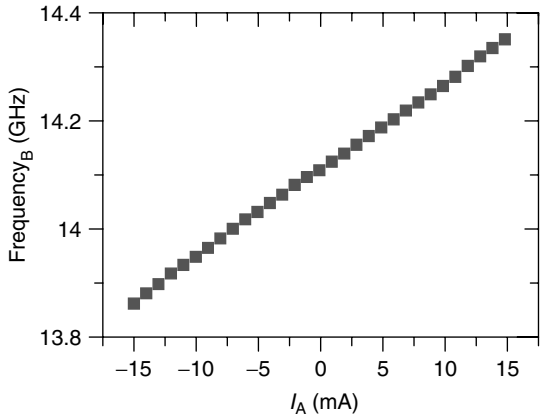

Figure 14. Effect of oersted field from neighboring contact on oscillator frequency. Frequency of oscillator B versus current through contact A.

the other contact (the other oscillator is inactive), and the slope of the frequency shift with current changed sign if the sign of the applied field was switched.

Second, and more remarkably, a mutual nonlinear interaction between the two oscillators led to phase coherence of both oscillators at a single frequency over a range in applied current. This behavior was experimentally examined through the following protocol: current through A (I_A) was fixed at 8 mA, current through B (I_B) was ramped, and at each point during the ramp, the spectrum of the combined signals from A and B was detected. Figure 15(a) shows the evolution of the spectrum as I_B is ramped for a particular device. Color on the contour plot represents spectral intensity. Initially, only the signal from A was present. As I_B was ramped, a signal from B emerged above its critical current, and the frequency increased with the same slope as its free-running case. In addition, the frequency of A decreased slightly because of the ampere field from current through B. Figure 15(b) shows the spectrum consisting of both peaks at $I_B = 8.65$ mA. Near $I_B = 9.2$ mA, both oscillators suddenly united to produce a single frequency. This locked state remained until about $I_B = 11$ mA. Above 11 mA, the system unlocked, and two separate signals reemerged. The spectrum of the locked state in Figure 15(c) ($I_B = 9.5$ mA) was a peak that was both narrower and much stronger than either peak in Figure 15(b).

The high-frequency signal from each individual oscillator as it evolved through locking was accessed by disconnecting the other oscillator's high-frequency channel from the power combiner. The results are shown in Figure 16. Both oscillators emitted at the same frequencies for $I_B > 9.2$ mA, albeit with very different power output. Figure 16(b) shows that power from A was roughly constant at 4.2 pW (the

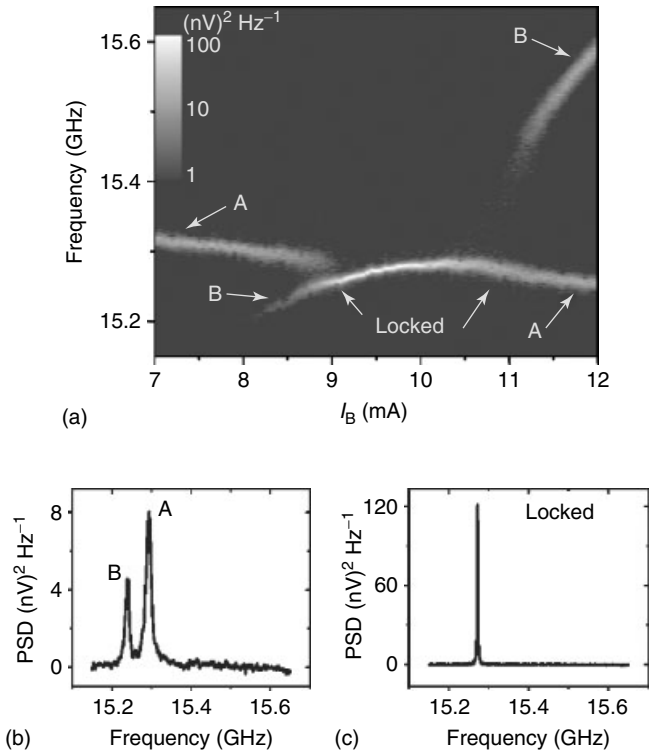

Figure 15. (a) Contour plot showing the evolution of spectra from both oscillators as current through A was fixed at 8 mA and current through B was ramped from 7 to 12 mA. Spectral intensity is on a logarithmic scale. Locking occurred in the region where only one frequency was present. (b) Spectrum taken before locking occurred showing peaks for A and B. Current through B is 8.65 mA. (c) Spectrum of locked state. Only one peak was visible. Current through B was 9.5 mA. (Reproduced from Kaka *et al*., 2005, with permission from Nature Publishing Group. © 2005.)

free-running power at $I_A = 8$ mA) until B activated. Interaction with B caused the power from A to vary, and during locking, power from A increased. As seen in Figure 16(d), the power from oscillator B increased with current much like in its free-running condition. The spectral linewidths, measured as the *FWHM* of the signal peaks, abruptly decreased during locking. This is shown in Figure 17 for both oscillators. During locking, the linewidth was about 2 MHz. In comparison, the free-running oscillator linewidths were greater than 4 MHz. Apparently the feedback mechanism that sustained a phase-locked state also ensured greater frequency stability of the oscillators.

The phase coherence of the two oscillators during locking was demonstrated by including a phase shifting coaxial element in the high-frequency channel of A leading to the power combiner. I_A was again fixed at 8 mA, and I_B was fixed at 9.55 mA to lock both oscillators. The phase shifter was fully adjusted producing about a 300° change in phase length between the two high-frequency channels.

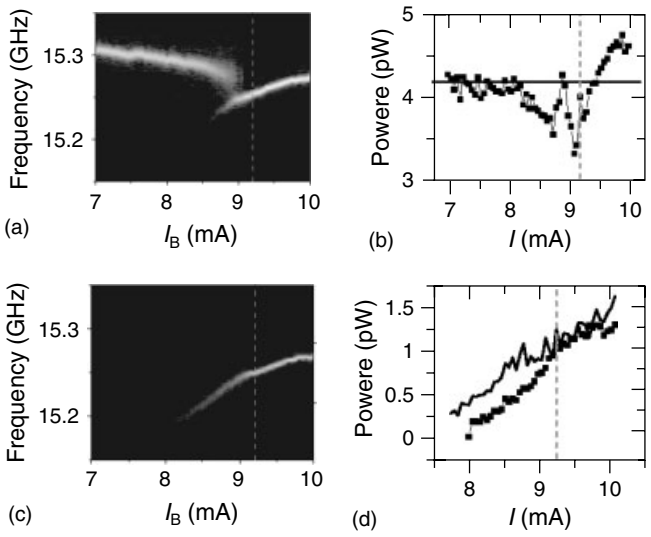

Figure 16. Behavior of individual oscillators. Start of the locking range indicated by vertical dashed line in each panel. (a) Evolution of spectra from A only as current was ramped through B. A was still fixed with current of 8 mA. (b) The power from A only (squares) varied as A interacted with B. The free-running power from A when current through A was 8 mA (line) is also shown. (c) Evolution of spectra from B only as current was ramped through B. (d) Power from B only (squares) increased with current. The free-running power from B versus current through B (line) is also shown. (Reproduced from Kaka *et al*., 2005, with permission from Nature Publishing Group. © 2005.)

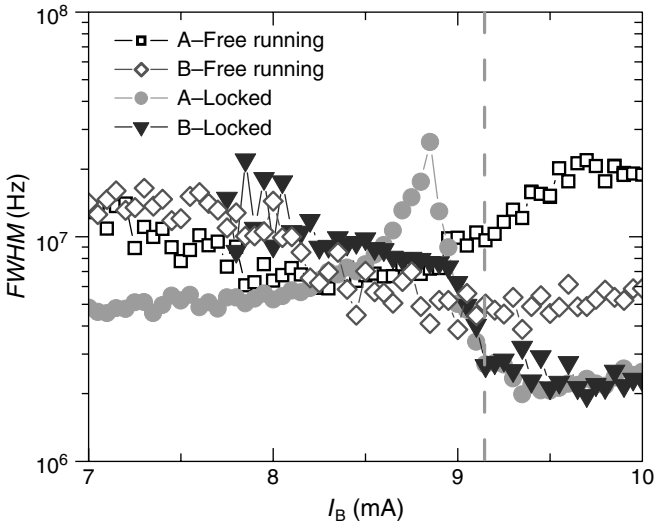

Figure 17. Free-running linewidths with current for A (open squares) and B (open diamonds) are shown. Linewidths for the interacting oscillators A (solid circles) and B (solid triangles) showed an abrupt drop at locking. Onset of locking is designated by the vertical dashed line. (Reproduced from Kaka *et al*., 2005, with permission from Nature Publishing Group. © 2005.)

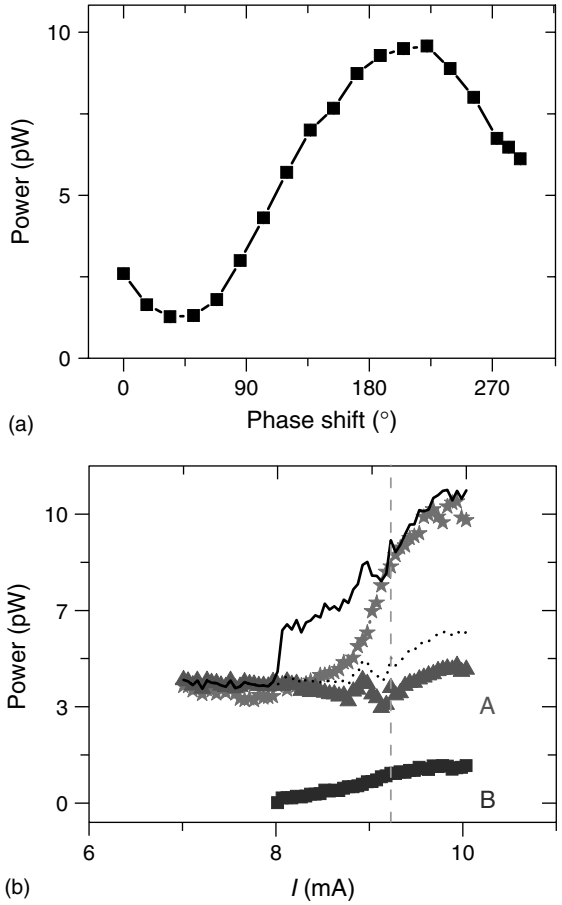

Figure 18. (a) Combined power output versus phase shift where the current through A was 8 mA and the current through B was 9.55 mA. An interference pattern between signals from A and B resulted. (b) Power outputs versus current through B. Power from A only (triangles), power from B only (squares), and combined power (stars). Sum of power from A and B (dotted line) and coherent sum of power from A and B (solid line) are also shown. The vertical dashed line indicates the start of the locking range. (Reproduced from Kaka *et al*., 2005, with permission from Nature Publishing Group. © 2005.)

The resulting combined power as the phase was shifted is shown in Figure 18(a). The sinusoidal variation in time-averaged power as the phase was shifted is an interference pattern that can only occur because of a time-independent phase relationship between the signals from A and B. Although the data shows that A and B were phase coherent during locking, we have not determined the absolute phase difference (if any) between the oscillations of A and B. However, this phase difference could be determined using this measurement method if the phase length of each high-frequency channel is known.

With the phase shifter set to maximize the combined output with $I_A = 8\,\text{mA}$ and $I_B = 9.55\,\text{mA}$, the power measured was $P_{MAX} = 9.90\,\text{pW}$. Here, the phase shifter adjusted the

phase length such that the signals from A and B were in phase at the power combiner. At those same currents, the individual oscillator powers were 4.37 and 1.19 pW from A and B respectively. A and B were phase coherent ac voltage sources, thus the combined output power was the coherent sum given by $P_c = (V_A + V_B)^2(50\,\Omega)^{-1} = P_A + P_B + 2(P_A P_B)^{1/2}$ where V_i and P_i are the individual oscillator voltage and power output respectively. The coherent sum should be 10.15 pW, which is close to P_{MAX}. Conversely, if A and B were coincidentally at the same frequency but not phase coherent, the time-averaged combined power would be given by $P = ({V_A}^2 + {V_B}^2)(50\,\Omega)^{-1} = P_A + P_B = 5.56$ pW. Figure 18(b) shows the measured combined power as well as the individual output powers. A dotted line is added to represent $P_A + P_B$, which is substantially less than the combined power during locking. Outside the locking range, the measured combined power (power from both peaks) was less than the calculated coherent sum of power, yet during locking the calculated coherent sum and the actual measured combined power matched well. Maximized power output by coherent addition is an important and perhaps useful property of phase-locked nano-oscillators that can lead to significantly increased output levels for applications.

5 DEVICE APPLICATIONS OF SPIN-TRANSFER OSCILLATORS

Synchronized nanocontact oscillators can potentially both compete with existing microwave oscillators and drive new applications. A single oscillator produces a wide range of microwave frequencies depending on current and applied field. The high-frequency output typically has narrow linewidth, that is, a high-frequency stability, as characterized by a quality factor *f/FWHM*, where f is the oscillator frequency and *FWHM* is the full-width at half-maximum of the spectral peak. Quality factors from 10^2 to 10^4 have been demonstrated (Rippard *et al*., 2004b). Furthermore, the oscillations are generated from a small footprint device. As mentioned previously, the region of large-angle magnetic precession is of the same order as the contact area (diameter ≈100 nm). The full device dimensions are determined by the magnetic mesa size, which is several micrometers on a side. In contrast, commercially available tunable oscillators depend on resonators, such as quartz crystals, yttrium-iron-garnet (YIG) spheres, and LC networks, which have footprints ≈1 mm on a side (Burns, 2003; Rohde, Poddar and Bock, 2005). Finally, the nanocontact oscillator is fabricated using standard sputtered magnetic thin films. This technology is compatible with both MRAM (Åkerman *et al*., 2004) and mainstream complementary metal oxide semiconductor (CMOS) fabrication, permitting cost effective manufacturing.

Synchronized nanocontact oscillators allow for increased high-frequency power output. At present, the output from a single nanocontact oscillator has been measured as high as few nanowatts. By coherently combining the power from N phase-locked oscillators electrically connected in a series array, for example, the output power to a load should increase as N^2 in the case where the load resistance is much greater than the array resistance. In addition to the increased power, phase-locked spin-transfer oscillators also appear to provide enhanced frequency stability.

Certain challenges exist to take advantage of spin-transfer nanocontact oscillators in applications. Nanocontact oscillators require a large magnetic field directed out of plane to produce the highest output powers (Rippard *et al*., 2004b). This field could be introduced by compact permanent magnets by an appropriate exchange bias. Another concern is the efficiency of converting the dc input power to high-frequency output power. For example, 10 mA is typically sufficient to produce oscillations in a 20 Ω GMR device leading to an input power P_{dc} of 2 mW. The output power P_{ac} is in the picowatt to the nanowatt range, yielding efficiencies P_{ac}/P_{dc} from 10^{-8} to 10^{-6}. Replacing the GMR signal ≈1% with a tunneling magnetoresistance (TMR) signal of 100–200% for MgO-based tunnel junctions could dramatically increase the efficiency. For either GMR or TMR devices, the substantial dc current to excite spin-transfer oscillations can create difficulties from electromigration, heating, or tunnel barrier breakdown. Materials engineering, which has been successful for developing disk drive read heads and MRAM bits, may lead to an optimized device structure containing a proper internal magnetic field bias and requiring less current. Finally, a microwave design needs to be developed that allows for dc current biasing and high-frequency power combining of an array of phase-locked nanocontact oscillators.

Spin-transfer oscillator properties allow for exciting application possibilities. Compared to typical voltage controlled oscillators, spin-transfer oscillators can offer wide frequency tunability, small device size, and fast modulation capability (Pufall *et al*., 2005). One application is as reference oscillators for portable electronics and communications. The footprint of a nanocontact oscillator array is 10 μm on a side. The conventional timing reference in cellular phones, for example, is a crystal oscillator with a footprint of a few millimeters. The much smaller magnetic oscillator array would allow the direct integration of the timing source within a single transceiver communications chip. The small footprint, high frequency, and frequency agility of the nanocontact oscillators may lead to application as a local oscillator within a heterodyne detector. This could provide RF spectrum analysis within a single chip. Finally, magnetic nanocontact oscillators may find application within a wireless communication

system that operates between the separate components within a computer, enabling the fast electronic data transfer that is increasingly important as computer systems move toward multiprocessor parallel computing schemes.

6 SUMMARY

When biased with a dc current, lithographic point contacts to GMR films can produce a microwave signal due to spin-transfer resonance. The frequency is tunable from at least 5–40 GHz as a function of current and magnetic field, and the linewidths can be as narrow as <5 MHz with resonance quality factors exceeding 10 000. We examined the area dependence of spin-transfer precession and also observed phase locking between neighboring excitations. First, as a function of nominal contact diameter from 50 to 300 nm, devices at Freescale showed a decreasing slope of precession frequency versus current and an increasing critical current. This data was fit using a model in which the magnetically precessing region extends beyond the contact edge by a ring of width ≈50 nm. Other effects, such as the oersted field, the spin-wave radiation pattern, and other magnetic nonuniformities with a more detailed spatial dependence than can be accounted for with this model, may also affect the size dependence.

With regard to phase locking, experiments at Freescale detected phase locking between two nominally 80-nm diameter spin-transfer oscillators, electrically connected in parallel to a single top electrode, when the intercontact spacing was $< \approx$200 nm. On average, the total power in the single resonance peak for these closely spaced devices was approximately twice the combined power in the two separate peaks observed for devices with two widely spaced contacts. The experiments at NIST examined devices with independent electrical control of two nanocontact oscillators spaced by 500 nm and found that the two resonances phase locked when the current bias through one contact was varied so as to shift its frequency close to that of the second contact. The difference in the spacing length scale for phase locking is not fully understood and may be due to the different bias geometries, for which the independent electrical biasing in the NIST experiment may permit more precise frequency matching and longer-range phase locking. Further experiments may also identify the coupling mechanism that causes phase locking, such as spin-wave radiation or oscillating magnetic fields emitted by each contact. The increased output power and decreased resonance linewidth for phase-locked contacts promise to enable control of even larger arrays of spin-transfer oscillators and make possible new applications for these devices in microwave electronics.

ACKNOWLEDGMENTS

We acknowledge N. Rizzo, B. Engel, and S. Tehrani, with whom the work at Freescale was performed, and M. Pufall, W. Rippard, T. Silva, S. Russek, and J. Katine, with whom the work at NIST was performed. We thank B. Butcher for help with device fabrication at Freescale, P. Kabos and A. Kos for assistance with microwave apparatus, and A. Slavin, M. Stiles, T. Gerrits, and R. Goldfarb for discussions. This work was supported in part by the DARPA SPINS program through Motorola. Portions reprinted with permission from Mancoff *et al*. (2006). Copyright 2006. American Institute of Physics.

REFERENCES

Åkerman, J., DeHerrera, M., Durlam, M., *et al*. (2004). Magnetic tunnel junction based magnetoresistive random access memory. In *Magnetoelectronics*, Johnson, M. (Ed.), Elsevier Academic Press: Amsterdam, pp. 231–272.

Bennet, M., Schatz, M.F., Rockwood, H. and Wiesenfeld, K. (2002). Huygen's clocks. *Proceedings of the Royal Society of London A*, **458**, 563–579.

Benz, S.P. and Burroughs, C.J. (1991). Coherent emission from two dimensional Josephson junction arrays. *Applied Physics Letters*, **58**, 2162–2164.

Berger, L. (1996). Emission of spin waves by a magnetic multilayer traversed by a current. *Physical Review B*, **54**, 9353–9358.

Buck, J. and Buck, E. (1968). Mechanism of rhythmic synchronous flashing of fireflies. *Science*, **159**, 1319–1327.

Burns, R. (2003). Why Oscillators are the best frequency sources for wireless designs. *RF Design*, 38-42. Also available on the World Wide Web, http://rfdesign.com/images/archive/308RF_Burns 38.pdf.

Covington, M., AlHajDarwish, M., Ding, Y., *et al*. (2004). Current-induced magnetization dynamics in current perpendicular to the plane spin valves. *Physical Review B*, **69**, 184406-1–184406-8.

Daughton, J. (2003). Spin-dependent sensors. *Proceedings of the IEEE*, **91**, 681–686.

Debrosse, J., Dietmar, G., Bette, A., *et al*. (2004). A high-speed 128-kb MRAM core for future universal memory applications. *IEEE Journal of Solid-State Circuits*, **39**, 678–683.

Dieny, B. (1994). Giant magnetoresistance in spin-valve multilayers. *Journal of Magnetism and Magnetic Materials*, **136**, 335–339.

Freitas, P.P., Ferreira, H.A., Graham, D.L., *et al*. (2004). Magnetoresistive DNA chips. In *Magnetoelectronics*, Johnson, M. (Ed.), Elsevier Academic Press: Amsterdam, pp. 331–373.

Fuchs, G.D., Emley, N.C., Krivorotov, I.N., *et al*. (2004). Spin-transfer effects in nanoscale magnetic tunnel junctions. *Applied Physics Letters*, **85**, 1205–1207.

Grollier, J., Cros, V. and Fert, A. (2005). Synchronization of spin-transfer oscillators driven by stimulated microwave currents. *Physical Review B*, **73**, 060409-1–060409-4.

Grollier, J., Cros, V., Hamzic, A., *et al*. (2001). Spin-polarized current induced switching in Co/Cu/Co pillars. *Applied Physics Letters*, **78**, 3663–3665.

Hoefer, M., Ablowitz, M., Ilan, B., *et al*. (2005). Theory of magnetodynamics induced by spin torque in perpendicularly magnetized thin films. *Physical Review Letters*, **95**, 267206-1–267206-4.

Huai, Y., Albert, F., Nguyen, P., *et al*. (2004). Observation of spin-transfer switching in deep submicron-sized and low-resistance magnetic tunnel junctions. *Applied Physics Letters*, **84**, 3118–3120.

Ji, Y., Chien, C. and Stiles, M. (2003). Current-induced spin-wave excitations in a single ferromagnetic layer. *Physical Review Letters*, **90**, 106601-1–106601-4.

Kaka, S., Nibarger, J.P., Russek, S.E., *et al*. (2003). High-frequency measurements of spin-valve films and devices. *Journal of Applied Physics*, **93**, 7539–7544.

Kaka, S., Pufall, M.R., Rippard, W.H., *et al*. (2005). Mutual phase-locking of microwave spin torque nano-oscillators. *Nature*, **437**, 389–392.

Kaka, S. and Russek, S.E. (2002). Precessional switching of submicrometer spin valves. *Applied Physics Letters*, **80**, 2958–2960.

Katine, J.A., Albert, F.J., Buhrman, R.A., *et al*. (2000). Current-driven magnetization reversal and spin-wave excitation in Co/Cu/Co pillars. *Physical Review Letters*, **84**, 3149–3152.

Kiselev, S.I., Sankey, J.C., Krivorotov, I.N., *et al*. (2003). Microwave oscillations of a nanomagnet driven by a spin-polarized current. *Nature*, **425**, 380–383.

Kiselev, S.I., Sankey, J.C., Krivorotov, I.N., *et al*. (2004). Current-induced nanomagnet dynamics for magnetic fields perpendicular to the sample plane. *Physical Review Letters*, **93**, 036601-1–036601-4.

Lee, K.J., Redon, O. and Dieny, B. (2005). Analytical investigation of spin-transfer dynamics using a perpendicular-to-plane polarizer. *Applied Physics Letters*, **86**, 022505-1–022505-3.

Mancoff, F.B., Dave, R.W., Rizzo, N.D., *et al*. (2003). Angular dependence of spin-transfer switching in a magnetic nanostructure. *Applied Physics Letters*, **83**, 1596–1598.

Mancoff, F.B., Rizzo, N.D., Engel, B.N. and Tehrani, S. (2005). Phase-locking in double-point-contact spin-transfer devices. *Nature*, **437**, 393–395.

Mancoff, F.B., Rizzo, N.D., Engel, B.N. and Tehrani, S. (2006). Area dependence of spin-transfer resonance in giant magnetoresistance contacts up to 300 nm diameter. *Applied Physics Letters*, **88**, 112507-1–112507-3.

Mancoff, F.B. and Russek, S.E. (2002). Spin-current-induced magnetotransport in Co-Cu-Co nanostructures. *IEEE Transactions on Magnetics*, **38**, 2853–2855.

Moodera, J.S., Nassar, J. and Mathon, G. (1999). Spin-tunneling in ferromagnetic junctions. *Annual Review Of Materials Science*, **29**, 381–432.

Myers, E.B., Ralph, D.C., Katine, J.A., *et al*. (1999). Current-induced switching of domains in magnetic multilayer devices. *Science*, **285**, 867–890.

Popovic, Z.B., Weikle, R.M., II, Kim, M. and Rutledge, D.B. (1991). A 100-MESFET planar grid oscillator. *IEEE Transactions on. Microwave Theory and Techniques*, **39**, 193–200.

Pufall, M.R., Rippard, W.H., Kaka, S., *et al*. (2004). Large-angle gigahertz-rate random telegraph switching induced by spin momentum transfer. *Physical Review B*, **69**, 214409-1–214409-5.

Pufall, M.R., Rippard, W.H., Kaka, S., *et al*. (2005). Frequency modulation of spin transfer oscillators. *Applied Physics Letters*, **86**, 082506-1–082506-3.

Pufall, M.R., Rippard, W.H. and Silva, T.J. (2003). Materials dependence of the spin-momentum transfer efficiency and critical current in ferromagnetic metal/Cu multilayers. *Applied Physics Letters*, **83**, 323–325.

Rippard, W.H., Pufall, M.R., Kaka, S., *et al*. (2004a). Direct-current induced dynamics in $Co_{90}Fe_{10}/Ni_{80}Fe_{20}$ point contacts. *Physical Review Letters*, **92**, 027201-1–027201-4.

Rippard, W.H., Pufall, M.R., Kaka, S., *et al*, (2004b). Current-driven microwave dynamics in magnetic point contacts as a function of applied field angle. *Physical Review B*, **70**, 100406-1–100406-4.

Rippard, W.H., Pufall, M.R., Kaka, S., *et al*. (2005). Injection locking and phase control of spin transfer nano-oscillators. *Physical Review Letters*, **95**, 067203-1–067203-4.

Rippard, W.H., Pufall, M.R. and Silva, T.J. (2003). Quantitative studies of spin-momentum-transfer-induced excitations in Co/Cu multilayer films using point-contact spectroscopy. *Applied Physics Letters*, **82**, 1260–1262.

Rohde, U.L., Poddar, A.K. and Bock, G. (2005). *The Design of Modern Microwave Oscillators for Wireless Applications*, Wiley-Interscience: New Jersey.

Russek, S.E. and Kaka, S. (2000). Time and frequency domain measurements of ferromagnetic resonance in small spin-valve. *IEEE Transactions on Magnetics*, **36**, 2560–2562.

Russek, S.E., Kaka, S., Rippard, W.H., *et al*. (2005). Finite-temperature modeling of nanoscale spin-transfer oscillators. *Physical Review B* **71**, 104425-1–104425-6.

Slavin, A.N. and Tiberkevich, V.S. (2005). Nonlinear self-phase-locking effect in an array of current-driven magnetic nanocontacts. *Physical Review B*, **72**, 092407-1–092407-4.

Slonczewski, J. (1996). Current-driven excitation of magnetic multilayers. *Journal of Magnetism and Magnetic Materials*, **159**, L1–L7.

Slonczewski, J. (1999). Excitation of spin waves by an electric current. *Journal of Magnetism and Magnetic Materials*, **195**, L261–L268.

Strogatz, S. (2003). *Sync: The Emerging Science of Spontaneous Order*, Hyperion: New York.

Stutzke, N., Burkett, S.L. and Russek, S.E. (2003). Temperature and field dependence of high-frequency magnetic noise in spin valve devices. *Applied Physics Letters*, **82**, 91–93.

Sun, J.Z., Monsma, D.J., Abraham, D.W., *et al*. (2002). Batch-fabricated spin-injection magnetic switches. *Applied Physics Letters*, **81**, 2202–2204.

Tsoi, M., Jansen, A.G.M., Bass, J., *et al*. (2000). Generation and detection of phase-coherent current-driven magnons in magnetic multilayers. *Nature*, **406**, 46–48.

Wang, S.X. and Taratorin, A.M. (1999). *Magnetic Information Storage Technology*, Academic Press: San Diego.

Wegrowe, J-E., Kelly, D., Jaccard, Y., *et al*. (1999). Current-induced magnetization reversal in magnetic nanowires. *Europhysics Letters*, **45**, 626–632.

Wengler, M.J., Guan, B. and Track, E.K. (1995). 190-GHz radiation from a quasioptical Josephson junction array. *IEEE Transactions on Microwave Theory and Techniques*, **43**, 984–988.

Wexler, G. (1966). The size effect and the non-local Boltzmann transport equation in orifice and disk geometry. *London*, **89**, 927–941.

Theory of Spin-polarized Current and Spin-transfer Torque in Magnetic Multilayers

John Slonczewski[1]

IBM Research Division, Yorktown Heights, NY, USA

[1] *IBM RSM Emeritus*

1 INTRODUCTION

In 1996, Luc Berger predicted that electric current flowing across a normal metal spacer between two magnets could excite forward-propagating spin waves (Berger, 1996). In the same year, a ballistic model predicted that a steady current may create a spin-transfer torque that would excite magnetic precession in one of two so separated single-domain magnets having lithographed dimensions of order 100 nm (Slonczewski, 1996). If the sign of uniaxial anisotropy is negative, this precession may remain steady, making conceivable a radio frequency oscillator. If the anisotropy is positive, a spiral precession followed by magnetic reversal may occur, in which case writing for magnetic memory is conceivable. Subsequent experiments supported these predictions and led to the vast array of new spin-transfer phenomena under investigation today (Stiles and Miltat, 2005).

However, the first copious experimental evidence for any current-driven magnetic excitation was that of Tsoi *et al*. (1998), who passed currents through mechanical point contacts into unpatterned (not single-domain) multilayers. In the absence of lithography, spin waves radiate energy transversally away from the contact region, greatly increasing the current required for excitation (Slonczewski, 1999). The year 1999 saw the beginning of monodomain excitation in magnets having lithographic dimensions $\leq$150 nm. In one case a magnetic oxide particle was excited, (Sun, 1999) and in another, one layer of a lithographed all-metallic multilayer (Myers *et al*., 1999).

Equivalent circuits of spin-polarized current play a large role in the theory of giant magnetoresistance and spin-transfer torque (Brataas, Nazarov and Bauer, 2000; Brataas, Bauer and Kelly, 2006). Sections 2–4 present a *majority-spin transparency* model for diffusive noncollinear magnetoresistance and current-driven torque (Slonczewski, 2002). It takes explicit account of the band structures of the elements Co, Ni, and Cu used in many experiments. The question of torque is reduced to that of solving an effective circuit whose branches consist of the four spin-channel currents flowing through the two ferromagnets in a device pillar. The key formulas for cross-spacer connection of spin-channel voltages and currents enable algebraic solution of effective circuit equations.

Handbook of Magnetism and Advanced Magnetic Materials. Edited by Helmut Kronmüller and Stuart Parkin. Volume 5: *Spintronics and Magnetoelectronics*. ISBN: 978-0-470-02217-7.

Their application predicts the currents and torques, requiring only prior analytic solution of the linear coupled diffusion equations (Valet and Fert, 1993) governing the current-voltage relations of the separate halves of the device pillar (see also **Theory of Spin-transfer Torque, Volume 2**).

Section 5 illustrates theoretical results for currents and torques for the simple case of a symmetric pillar with purely resistive spin channels lacking spin relaxation. Section 6 presents the barest essentials of the magnetic dynamics resulting from spin-transfer torque. It assumes uniaxial anisotropy and illustrates both the switching and steady precession of a monodomain produced by a steady electric current.

More recently, spin-transfer switching was also observed in magnetic tunnel junctions (MTJs). Two laboratories, at Grandis, Inc. (Huai *et al*., 2003) and Cornell U., (Fuchs *et al*., 2004) reported it independently, thus making possible higher signal voltages in spin-transfer memory elements. Sections 8 and 9 treat noncollinear magnetoresistance and spin-transfer torque for the case of MTJs, employing Bardeen tunneling theory, introduced in Section 7.

For a given voltage V, one has the two-parameter formula $J = VG_0(1 + g\cos\theta)$ for the electric current density versus the angle θ between the moments. Section 8 presents the theory for left and right-torque densities $(\hbar/2e)VG_0\tau_{L,R}\sin\theta$ with respective dimensionless coefficients $\tau_L$and τ_R. Assuming elasticity of the tunneling and validity of the polarization factors P_L, P_R for the two electrode-and-barrier compositional combinations, one predicts the mutual relation $g = \tau_L\tau_R$, with $\tau_L = P_R$ and $\tau_R = P_L$.

The concept of polarization factor is less convenient at the high voltages and small barrier thicknesses needed in devices, for then inelastic tunneling becomes more important. Responding to the recent advent of very highly magnetoresistive MTJs with MgO barriers, Section 9 describes an appropriate phenomenological model which concludes with predicted observational signatures of conductance and torque caused by special conditions at the ferromagnet-insulator interfaces.

2 TWO-CHANNEL SPIN-POLARIZED TRANSPORT

2.1 Suppression of transverse polarization

The internal exchange field giving rise to the spontaneous magnetization of a ferromagnet such as Fe, Co, or Ni is so strong that, in equilibrium, it creates a relative shift eV_{ex} between spin-up and spin-down energy bands amounting to about 2 eV for Fe and Co, and 1 eV for Ni. Suppose that an additional out-of-equilibrium electron should initially occupy a state in which the spin lies orthogonal to the spontaneous magnetization. It then precesses at this terrific frequency $eV_{ex}/\hbar$ which is orders of magnitude greater than the frequencies (in gigahertz) encountered in the magnetic dynamics of nanoscale device elements described by classical Landau–Lifshitz equations. Consequently, the transverse polarization and its current are very strongly suppressed within the thickness ($\geq$3 atomic layers) and time scales (>100 ps) of usual interest in magnetic memory.

More precisely, it is not exchange alone, but a *combination of three effects* which creates such a strong exchange splitting of those band regions near the Fermi surface which are important in electron transport. To begin, a free atom of Fe, Co, or Ni has the electron configuration $3d^n4s^2$ outside of the argon core. The values of n are 6 for Fe, 7 for Co, and 8 for Ni. When the atoms bond to form a pure metal, the strong spin-diagonal (nonexchange) crystalline electric field causes two effects. The first effect is that the electrostatic field of neighboring point-charge nuclei disrupts the atomic orbitals and 'quenches' the atomic-orbital angular momentum, thus suppressing to a degree spin relaxation via spin-orbit coupling. Secondly, it permits electron waves at the Fermi level to propagate with relative freedom through the lattice. Quantum-mechanically, both of these effects cause the atomic s ($l = 0$) wave functions to mix strongly with p ($l = 1$) and d ($l = 2$) wave functions. Indeed, the sheer number of p (3) and d (5) states is so great compared to the one s state per atom, that none of the band states at the Fermi surface have predominantly s character. (The one-electron V_{sd} matrix element in first-principle band structure computations is of order 1–2 eV.) Thirdly, it follows that this mixing generally subjects the Fermi-energy electrons to the mean-field atomically *internal* d–d exchange interaction. This exchange is extremely large, amounting to a level splitting of order $J_{dd} \approx$ 1–2 eV. Generally, very few of the wave functions approach the character of 4s or free-electron waves for which the exchange splitting would be smaller ($\approx$0.1 eV). This fact accounts for the strong suppression of transverse spin momentum mentioned in the preceding text.

This suppression makes credible the *spin-channel model* of electron transport (Valet and Fert, 1993). Consider, for example, the layered submicron metallic pillar joining two nonmagnetic semi-infinite conductors N_L and N_R shown in Figure 1. It is rotated 90° so that the deposition plane is oriented vertically. The pillar includes left (F_L) and right (F_R) magnets separated by a very thin nonmagnetic metallic spacer N. The cross section in the plane parallel to the substrate is an ellipse with dimensions typically 100 × 60 nm.

Of interest is electron transport through this pillar between the voltages $V = V_1$ deep within a relatively bulky electric lead on the left and another voltage $V = 0$ deep within a similarly bulky lead on the right. In metals a convenient

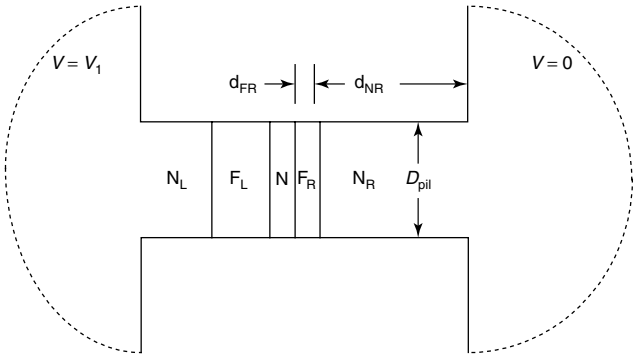

Figure 1. Magnetic multilayer pillar laid sideways. N: normal metal; F: ferromagnet; L: left; R: right.

measure of spin relaxation is the characteristic so-called spin 'diffusion' (relaxation, really) length (λ_N or λ_F) measuring the *spatial* decay of polarization $\langle\sigma_z\rangle$ proportional to the function $\exp(-x/\lambda_N)$ or $\exp(-x/\lambda_F)$ (Valet and Fert, 1993).

The dimensions of experimental pillars often approach the condition that they are too small for relaxation to be of consequence. The thickness of each sublayer component must be less than the corresponding diffusion length. Sufficient such conditions for the pillar of Figure 1 are

$$d_{NL}, d_{NR} \ll \lambda_N; \quad d_{FL}, d_{FR} \ll \lambda_F \tag{1}$$

If satisfied, they make valid the effective resistive circuit of Figure 2 featuring four channel resistors $R_{L\pm}$, $R_{R\pm}$. Our representation of spin relaxation in the external leads by means of the shorts shown in Figure 2 requires an opposite sort of condition, namely that dimensions of the leads are greater than $\lambda_{N,R}$. If one of these conditions is violated, the problem requires solution of a two-component diffusion equation (Valet and Fert, 1993).

2.2 Half-pillar resistors

We embrace the limits (1) and the spin-channel shorts shown in Figure 2. This will focus attention on the problem created by noncollinear spin-quantization axes. For the moment, we put aside the central 'junction box' appearing in the figure. One may decompose each of the four *half-pillar* unit-area channel resistors $R_{L\pm}$ and $R_{R\pm}$ into terms in series arising from two-channel bulk resistivity $\rho_\pm$, from two-channel unit-area interfacial resistance $r_\pm$, and from an end-effect term occurring at the pillar-lead connection. Thus, half-pillar unit-area resistances between either lead and the spacer (see Figure 1), with the subscripts R and L here elided, are

$$R_\pm = \rho_\pm d_F + 2r_\pm + \rho_N\left(2d_N + \frac{\pi D_{pil}}{2}\right) \tag{2}$$

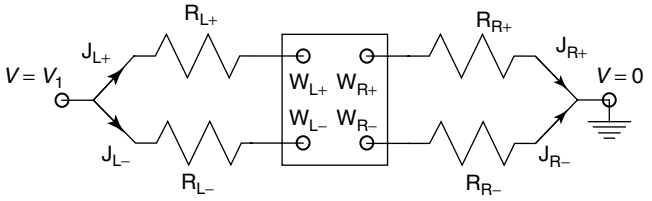

Figure 2. Effective two-channel circuit for the pillar of Figure 1 containing an N/F/N multilayer. Properties of the central 'junction box' are key to electron transport when $\mathbf{M}_L$ and $\mathbf{M}_R$ are not collinear.

where d_F and d_N are layer thicknesses and D_{pil} is the pillar diameter. (Section 3.2 justifies our neglect of bulk resistivity *within* the central spacer.) The final term $\pi\rho_N D_{pil}/2$ is due to the lead-to-pillar contact, approximated by half of a *constriction* resistance ρ_N/D_{pil} derived long ago by J. C. Maxwell. (The conducting constriction in Maxwell's case joins two semi-infinite conductors of homogeneous resistivity.)

A group at Michigan State University (Bass and Pratt, 2001) systematically measured collinear magnetoresistance of magnetron-sputtered periodic N/F/N/F/N . . . multilayers, numbering as many as 40 periods, at 4.2 K. This study established values of the specific resistance parameters appearing in equation (2). These values, together with independent values of ρ_N and spin diffusion distances λ_F and λ_N occurring in conditions (1) appear in the table below.

The low-temperature resistivity of Cu and Ag varies with sputtering conditions but is typically about three times its 300 K value given in the table. Sometimes the magnet F_L is part of the substrate; then, in the limiting cases $\lambda_{FL} \ll D_{pil}$ and $\lambda_{FL} \gg D_{pil}$, this equation for L is replaced by the

Table 1. Transport parameters for multilayers composed of sputtered Co, Cu, and Ag.

Parameter (K)	Units	Co/Cu	Co/Ag
$\rho_N(300)$	nΩm	17	16
$\lambda_F(4.2)$	nm	50	50
$\lambda_N(4.2,\ 300)$	nm	1500, 350	
From collinear GMR experiments (Bass and Pratt, 2001) at 4.2 K			
ρ_+	nΩm	81	111
ρ_-	nΩm	220	320
r_+	10^{-15} Ωm^2	0.24	0.17
r_-	10^{-15} Ωm^2	1.8	2.1
G, equation (21)	10^{15} Ω^{-1}m^{-2}	1.32	1.04

estimate

$$R_{L\pm} = r_{\pm} + \rho_{\pm} \cdot \min(\Lambda_{sf}, \pi D_{pil}/4) \tag{3}$$

where D_{pil} is the diameter of the pillar. (See **Spin-transfer in High Magnetic Fields and Single Magnetic Layer Nanopillars, Volume 5** for effects of more general conditions of spin relaxation.)

3 EFFECTIVE CIRCUIT FOR A NONCOLLINEAR ALL-METALLIC PILLAR

We now address the crucial properties of the spacer N represented by the junction box in Figure 2.

3.1 Spin polarization in a rotated reference frame

The term *spin-accumulation*, or spin-polarization density, in a *normal* metal refers to the expectation value $\langle \sigma_z \rangle$ of σ_z for the electrons occupying a unit volume. Of course, its value depends on the orientation of the quantization axis ζ. How it transforms in a spacer under coordinate-axis rotation is crucial to electron transport in noncollinear magnetic multilayers.

Consider a total of $2n_0$ electrons occupying only given numbers $n_0 + n_{\pm}$ of *pure* eigenstates $|\pm\rangle$ of $\sigma_z = \pm 1$, respectively, in the unprimed spin-quantization frame. By definition, the spin accumulation in a normal metal n is

$$\Delta n \equiv \langle \sigma_z \rangle = n_+ - n_- \tag{4}$$

with $n_+ = n_-$ to preserve neutrality of charge density which occurs in the absence of significant electrostatic capacitance. Consider the primed frame, whose z' axis lies in the xy-plane at an angle θ from the z axis. The same electrons have the new spin accumulation

$$\Delta n' \equiv \langle \sigma_{z'} \rangle = n'_+ - n'_- \tag{5}$$

where $n_0 + n'_{\pm}$ is the expectation value of $\sigma_{z'}$. Applying the square-law of probability, n'_+ is obtained from the first column of the spin rotation matrix (Sakurai, 1985)

$$\langle \sigma | \sigma' \rangle = \begin{pmatrix} \cos(\theta/2) & \sin(\theta/2) \\ -\sin(\theta/2) & \cos(\theta/2) \end{pmatrix} \tag{6}$$

The result is

$$n'_+ = n_+ \cos^2 \frac{\theta}{2} + n_- \sin^2 \frac{\theta}{2} \tag{7}$$

From the second column of equation (6), one finds

$$n'_- = n_+ \sin^2 \frac{\theta}{2} + n_- \cos^2 \frac{\theta}{2} \tag{8}$$

After substitution of equations (7), (8), and (4), equation (5) reduces to

$$\Delta n' = \Delta n \cos\theta \tag{9}$$

Application of this equation requires caution because it involves no interaction, no physical change in the condition of the system during the transformation. The spins states remain pure eigenstates $|\pm\rangle$ of σ_z in the unprimed frame throughout.

3.2 Spin-dependent electron distribution within the spacer

Our treatment of noncollinear spin-dependent transport here neglects all scattering within the spacer. It is equivalent to special cases of the computational drift-diffusion approach of M. Stiles and coworkers (Stiles and Miltat, 2005). It is also a special case of independent circuit theory by Wainthal, Myers, Brouer and Ralph (2000). It differs from a formulation leading to a general circuit theory (See Brataas, Nazarov and Bauer, 2000 and Section 6.2 of Brataas, Bauer and Kelly, 2006) by taking into account explicitly the momentum dependence of spin state within a spacer free of scatterers. Our theory is appropriate to many experiments in which the copper spacer thickness is much smaller than the mean free path Λ due to phonon scattering of about 40 nm at 300 K. At much lower temperatures, where the parameter values in Table 1 were determined, defect scattering dominates Λ which may be three times greater still. Nonetheless, in the appropriate limit, the general theory (Brataas, Bauer and Kelly, 2006) reduces to our connection formulas given in the subsequent text (Bauer, G.E.W. private communication).

Figure 3 indicates a left ferromagnet F_L, having spontaneous magnetization $\mathbf{M}_L = -M_L\mathbf{l}$, separated from a right ferromagnet F_R, having spontaneous magnetization $\mathbf{M}_R = -M_R\mathbf{r}$, by a nonmagnetic metal N. Here, $\mathbf{l}$ and $\mathbf{r}$ are unit vectors forming the general mutual angle $\theta = \cos^{-1}(\mathbf{l} \cdot \mathbf{r})$. We assume the presence of steady state spin-dependent currents within each ferromagnet The proximity of two different ferromagnetic polarization axes $\mathbf{l}$ and $\mathbf{r}$ implies the absence of any single axis of spin polarization appropriate to electrons within N. To deal with this situation, we describe in the subsequent text the statistically steady electron state within N that is consistent with the channel currents and potentials of the ferromagnets.

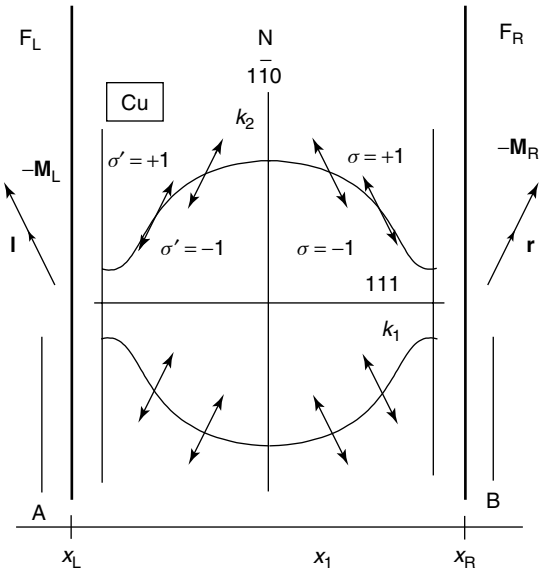

Figure 3. Notations for a metallic trilayer including ferromagnetic layers F_L with magnetization vector $\mathbf{M}_L$ at left and F_R with magnetization $\mathbf{M}_R$ at right, separated by a nonmagnetic spacer N. Shown schematically is a $11\bar{2}$-section of the Fermi surface for a Cu spacer with 111-axis normal to the layer plane. Arrows on the surface depict spin-polarization axes described in the text. The right (left) half of the Fermi surface is polarized parallel to the moment axis of the left (right) magnet.

We distinguish alternative **l**- and **r**- quantization axes for Pauli spin with operators σ_l and σ_r satisfying eigenstate equations $\sigma_l|\mathrm{L},\sigma\rangle = \sigma|\mathrm{L},\sigma\rangle$ ($\sigma = \pm 1$, sometimes abbreviated as $\sigma = \pm$) and $\sigma_r|\mathrm{R},\sigma'\rangle = \sigma'|\mathrm{R},\sigma'\rangle$ ($\sigma' = \pm 1$, or $\pm$). The spin states satisfy

$$\langle i,\sigma|i,\sigma''\rangle = \delta_{\sigma,\sigma''} \quad (i = \mathrm{L},\mathrm{R}) \tag{10}$$

and the plane spin rotation transformation

$$\langle \mathrm{L},\sigma|\mathrm{R},\sigma'\rangle = \begin{pmatrix} \cos(\theta/2) & -\sin(\theta/2) \\ \sin(\theta/2) & \cos(\theta/2) \end{pmatrix} \tag{11}$$

in equation (6).

Total absences of exchange coupling and scattering within N are assumed. Whatever atomic-scale subregion within the spacer, adjoining F_L or F_R, contains significant decaying exchange, or any interface-related scattering centers which may be present, is considered to belong to that magnetic region ($x_1 < x_L$ or $x_1 > x_R$) rather than to N.

Note, however, that any electron within N ($x_L < x_1 < x_R$) moving *rightward*, thus satisfying $v_1(\mathbf{k}) > 0$ and represented by decoration with the symbol $\rightarrow$, last *either* passed through (transmitted), *or* backscattered from, the *left* (F_L/N) interface. If transmitted, its final polarization is clearly $|\mathrm{L},+\rangle$ or $|\mathrm{L},-\rangle$ according to the two-channel model of spin-polarized current flowing in F_L. If backscattered, the electron spin has *the single polarization* $|\mathrm{L},-\rangle$ under an assumed condition of *perfect majority-spin transmission* (PMST; see in the subsequent text.) through the interface. Therefore, a rightward-moving electron [$\rightarrow$,with $v_1(\mathbf{k}) > 0$] has pure spin polarization $|\mathrm{L},+\rangle$ or $|\mathrm{L},-\rangle$, with no mixing that would describe a spin tilt away from this quantization axis. Similarly, a leftward-moving electron [$\leftarrow$,with $v_1(\mathbf{k}) < 0$] has only pure spin polarization $|\mathrm{R},+\rangle$ or $|\mathrm{R},-\rangle$. This scheme for the case of a 111-textured multilayer is illustrated in the $11\bar{2}$-section of the copper Fermi surface sketched within Figure 3.

The PMST condition is supported very well by the very small experimental values of interfacial resistance r_+ for Co/Cu and Co/Ag interfaces seen in Table 1 of Section 2.2. (They are one order of magnitude smaller than the respective r_-. They are consistent with a mean reflection coefficient of $\approx$5%.) If this were 0% then reflected electrons could have only the minority-spin orientation and the polarization scheme in Figure 3 would be exact. Therefore, for pillars composed of Co and Cu or Ag this electron distribution is well justified.

Why do the majority-spin electrons reflect so weakly? The answer lies in the following peculiarity of ferromagnetic electron structure: In experimental sputtered films, the metals Co, Ni, and Cu all have face-centered cubic (fcc) structure. As atomic number A increases in the sequence Co($A = 27$), Ni(28), Cu(29), the majority-spin electrons have the constant configuration $3d^5s^1$. Then in this range of A, each additional electron enters the minority band (Kübler, 2000). Consequently, the majority-spin energy bands differ very little. As indicated in the schematic cross section shown in Figure 3, the majority-spin Fermi surface for Co (and Ni) differs from a free-electron sphere mainly by the presence of small 'necks' which lie along 111-axes and join the surface to the Brillouin-zone boundary. The diameter of the neck increases a little in passing to Cu, but the remainder of the Fermi surface hardly changes. A majority-spin electron incident onto such an interface feels little change in potential. For this reason, majority-spin electrons reflect weakly at Co/Cu and Ni/Cu interfaces. Results of first-principle numerical computations (Xia *et al*., 2002) support this qualitative conclusion.

3.3 Connecting channels across a spacer without scatterers

Spin-channel currents through a magnet are driven by a *chemical potential* in addition to the ordinary electrostatic potential. To explain this fact, consider $T = 0\,\mathrm{K}$. Begin at thermal equilibrium with fully occupied states in the spacer having energy $\varepsilon \leq \varepsilon_{F0}$, with ε_{F0} the Fermi level. Then

apply the electrostatic voltage V to the spacer. Clearly, the new Fermi level for each σ is $\varepsilon_F \to \varepsilon_{F0} - eV$ and the particle potential $-eV$ provides impetus to drive electrons away from (or attract them to) the spacer. Suppose that some nonequilibrium process now adds the number n_σ of electrons per unit volume to the channel $\sigma = \pm$ within the spacer. Because of the exclusion principle, the Fermi level must rise in first-order approximation by the amount n_σ/n_F, where $2n_F$ is the electron density per unit energy and volume at $\varepsilon = \varepsilon_{F0}$, in order to make room for the added electrons. Clearly, now the Fermi level is spin-dependent and given by $\varepsilon_{F,\sigma} = \varepsilon_{F0} - eV + (n_\sigma/n_F)$. Surely, the 'chemical' voltage $-n_\sigma/en_F$ is able to drive a channel current just as well as the equivalent amount of electric voltage V. It follows that transport in spin channels requires augmenting the electric voltage to form the total *electrochemical* voltage defined by

$$W_\sigma = V - \frac{n_\sigma}{en_F} \tag{12}$$

One must hasten to add that in the absence of appreciable electrostatic capacitance, which we assume, charge neutrality is preserved. Thus, one has the condition $n_+ = -n_-$. It is easy to see that this expression for W_σ is correct at $T > 0\,\mathrm{K}$ as long as kT is small compared to the width of the energy band.

So now we know that electric current density J_σ in our simplified (see Section 2.2) half-pillar spin channel $\sigma(= \pm)$ must be written $J_\sigma = W_\sigma/R_\sigma$, where R_σ is the unit-area resistance. According to the laws of electric circuits, the ordinary *electric* voltage $V = (W_+ + W_-)/2$ and true *electric* current $J = J_+ + J_-$ must be continuous everywhere, and in particular across the central normal-metal spacer N in Figure 1. But we need four continuity relations altogether, so we must find two more in order to solve the complete circuit in Figure 2. We attach the subscripts L and R to specify values for every quantity *evaluated within the spacer*, using the left and right spin-coordinate axes, respectively. Thus, left and right so-called *spin-accumulation* or polarization densities are

$$\Delta n_L \equiv n_{L,+} - n_{L,-} \text{ and } \Delta n_R \equiv n_{R,+} - n_{R,-} \tag{13}$$

Accordingly, we have

$$\Delta W_L \equiv W_{L,+} - W_{L,-} = -\left(\frac{\Delta n_L}{en_F}\right) \text{ and}$$
$$\Delta W_R = -\left(\frac{\Delta n_R}{en_F}\right) \tag{14}$$

Finding two relations connecting ΔW_R and ΔJ_R to ΔW_L and ΔJ_L will suffice, together with continuity of V and J, to provide the four relations needed to solve the circuit of Figure 2.

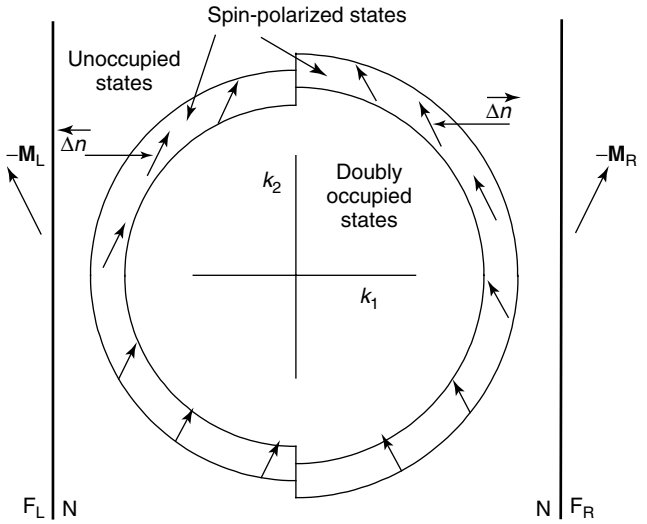

Figure 4. Scheme of **k**-dependent spin accumulation within the normal spacer N. It illustrates the parameterization of the nonequilibrium spin polarization of the Bloch states in a metallic spacer having a spherical Fermi surface.

To proceed further, we need to parameterize the spin-polarization scheme shown in Figure 4. For simplicity, the Fermi surface is spherical. This figure indicates that the spin polarization of electrons within N is concentrated within two hemispherical shells located on the Fermi surface and marked with scalar *partial spin accumulations* $\overleftarrow{\Delta n}$ and $\overrightarrow{\Delta n}$. The thicknesses of these shells are infinitesimal for linear transport. The left-(right-) arrow above the symbol $\overleftarrow{\Delta n}$ ($\overrightarrow{\Delta n}$) means that the electrons are moving leftward(rightward), $v_1 < (>)0$. In accordance with our discussion of the PMST condition connected with Figure 3, the polarization axis for $\overleftarrow{\Delta n}(\overrightarrow{\Delta n})$ is $-\mathbf{M}_R(-\mathbf{M}_L)$. The electron states outside of these shells are either doubly occupied or empty and therefore unpolarized in both cases.

To evaluate Δn_L, note that the shell marked $\overrightarrow{\Delta n}$ is already polarized along axis $-\mathbf{M}_L$ so it contributes to the total as it stands. But the one marked $\overleftarrow{\Delta n}$ is polarized along the other axis $-\mathbf{M}_R$ so its contribution must be projected upon the axis $-\mathbf{M}_L$. Therefore, one has from equation (9)

$$\Delta n_L = \overrightarrow{\Delta n} + \overleftarrow{\Delta n}\cos\theta \tag{15}$$

One then has from equation (14), and similarly using $\Delta n_R = \overleftarrow{\Delta n} + \overrightarrow{\Delta n}\cos\theta$

$$\Delta W_L = -\frac{(\overrightarrow{\Delta n} + \overleftarrow{\Delta n}\cos\theta)}{en_F},$$
$$\Delta W_R = -\frac{(\overleftarrow{\Delta n} + \overrightarrow{\Delta n}\cos\theta)}{en_F} \tag{16}$$

Evaluation of the current difference $\Delta J_{\mathrm{L}} \equiv J_{\mathrm{L}+} - J_{\mathrm{L}-}$ is similar, except that to obtain current, one must weight the terms $\overleftarrow{\Delta n}(\overrightarrow{\Delta n})$ in equation (15) with $\mp e\overline{v}$, where $\overline{v}$ is the mean of $v_1(\mathbf{k})$ over the right hemisphere of the Fermi surface. (Similarly for ΔJ_{R}.) Thus the current differences are

$$\Delta J_{\mathrm{L}} = e\overline{v}(\overleftarrow{\Delta n}\cos\theta - \overrightarrow{\Delta n}), \quad \Delta J_{\mathrm{R}} = e\overline{v}(\overleftarrow{\Delta n} - \overrightarrow{\Delta n}\cos\theta) \tag{17}$$

From the four equations (16) and (17), one may eliminate the two variables $\overleftarrow{\Delta n}$, $\overrightarrow{\Delta n}$ to find the two desired connection equations:

$$\Delta J_{\mathrm{R}} = \left[\Delta J_{\mathrm{L}}(1+\cos^2\theta) - G\Delta W_{\mathrm{L}}\sin^2\theta\right]/2\cos\theta \tag{18}$$

$$\Delta W_{\mathrm{R}} = \left[-G^{-1}\Delta J_{\mathrm{L}}\sin^2\theta + \Delta W_{\mathrm{L}}(1+\cos^2\theta)\right]/2\cos\theta \tag{19}$$

where the single spacer-material parameter required is

$$G = \frac{e^2 n_{\mathrm{F}}\overline{v}}{2} \tag{20}$$

These equations are verifiable by substitution of equations (16) and (17).

Since the mean of v_1^2 equals $v_{\mathrm{F}}^2/3$ where v_{F} is the Fermi velocity of an assumed spherical Fermi surface of the spacer composition, the rms relation $\overline{v} \approx v_{\mathrm{F}}/3^{1/2}$ may be used to estimate $\overline{v}$. For a parabolic band this formula then becomes

$$G = \frac{e^2 k_{\mathrm{F}}^2}{3^{1/2}\pi h} \tag{21}$$

which is $2/3^{1/2}$ times the Sharvin ballistic conductance G_{Sh} (2 spins) per unit area of a constriction whose diameter is smaller in order of magnitude than the mean free path. (Note, however, that the Sharvin ballistic resistance *phenomenon,* which occurs when the aperture *diameter* is smaller than Λ, plays no role in the present theory because all our potentials and currents are independent of x_1 within the spacer region N.) Equation (21) gives $G = 1.32 \times 10^{15}\ \Omega^{-1}\mathrm{m}^{-2}$ for a free-electron gas having the electron density of Cu.

The crucial role of equation (15) in this derivation must be understood. Validity of the two-channel model in a half-pillar does not require the spins within the adjoining spacer to occupy pure eigenstates of σ_ζ where ζ is parallel to $\mathbf{M}$ of the ferromagnet. One *does* need a correct electron distribution within the spacer as parameterized by our model for the partial spin accumulations $\overleftarrow{\Delta n}$ and $\overrightarrow{\Delta n}$ indicated in Figure 4. From these, one needs to evaluate only the *expectation* values of the properly evaluated *expectation* values of the accumulations to evaluate $\Delta W_{\mathrm{L,R}}$ and $\Delta J_{\mathrm{L,R}}$. The fact that not all spins are parallel to the same axis $\mathbf{l}$ or $\mathbf{r}$ does not matter.

The connection formulas (18) and (19) may reasonably be applied to Co, Ni, and alloys that lie on the negative-slope side of the Neel–Slater–Pauling curve (Kübler, 2000) in which the majority-spin 3d-band is fully occupied. For then the majority-spin electrons at the Fermi level belong to the sp-band and therefore approach the condition of 100% transparency assumed in the derivation in the preceding text. In particular, these formulas should not be applied when an electrode is composed of Fe. Nor do they apply to the case $\Lambda \ll$ (spacer thickness) treated elsewhere (Barnaś *et al.*, 2005).

4 CURRENT-DRIVEN PSEUDOTORQUE

Our object is to calculate the electric resistance and current-driven torque for a pillar with noncollinear moments. The important thing is to solve the circuit equations for the noncollinear condition considered in Section 3. As illustrated in Section 5, the connection formulas (18) and (19) are key to this solution. With this solution in hand, the resistance will be simply

$$R(\theta) = \frac{V}{(J_{\mathrm{L},+} + J_{\mathrm{L},-})} \text{ or } = \frac{V}{(J_{\mathrm{R},+} + J_{\mathrm{R},-})} \tag{22}$$

But the current-driven torque needs the detailed discussion given in the present section.

4.1 Torque mechanism

We explain first how the exchange-reaction torque created by scattering of preferentially polarized electrons incident from a normal metal onto a ferromagnet concentrates on the magnetization located within a distance equal to $d_{\mathrm{impact}} \approx 4$ atomic layers of the interface.

Figure 5 depicts schematically the local spin vector of the stationary-state wave function for an electron incident rightward onto an N/F interface located at position $\xi \equiv x_1 = 0$. (The spin-coordinate axes η, ζ in Figure 5 have no special relation to the position coordinates x_2, x_3 of the

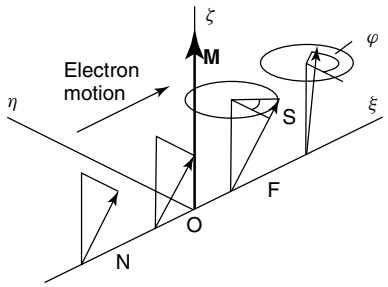

Figure 5. Illustration of spin precession for an electron passing from a nonmagnetic metal ($\xi < 0$) into a ferromagnetic metal ($\xi > 0$).

pillar illustrated in Figure 1.) Within the region N, the local expectation of vector spin operator $\mathbf{s} = \hbar\sigma/2$ for the incident wave is a general constant. Dynamical reaction to the spin momentum scattered by the magnet causes a torque on **M**. Under the PMST assumption in Section 3.2 only minority spin $\sigma = -$ can scatter backwards into N. (This reflected wave is not indicated in Figure 5.) But this *reflected* momentum is collinear with **M**, therefore its reaction does not contribute torque.

The local expectation of **s** for the wave component *transmitting* into the ferromagnet ($\xi > 0$) has an azimuthal angle with respect to the moment **M** of F given by

$$\varphi(\xi) = \varphi(0) + (k_{\xi+} - k_{\xi-})\xi, (\xi > 0) \tag{23}$$

where $k_{\xi\pm}$ are the normal components of electron wave vectors at $\varepsilon = \varepsilon_F$ for $\sigma = +$ and $\sigma = -$. (For graphical simplicity, Figure 5 shows $\mathbf{M}\|\zeta$, but actually **M** may have any direction.) For a given energy, the two values of $k_{\xi\pm}(k_\eta, k_\zeta)$ depend on the conserved transverse momentum components $\hbar(k_\eta, k_\zeta)$ and differ because of internal exchange.

In diffusive metallic transport, the wave vectors of all incident electrons having a given **s** lie very near all parts of the Fermi surface. Therefore the quantity $k_{\xi+} - k_{\xi-}$ varies over a great range. It follows that the averages of $s_\xi \propto \cos\varphi$ and $s_\eta \propto \sin\varphi$ at a given plane ξ approach 0 within an impact depth $\xi = d_{\text{impact}}$ of a few atomic layers (Xia *et al.*, 2002; Stiles and Zangwill, 2002). If the scale of micromagnetic homogeneity treated in the continuum representation with the Landau–Lifshitz equations is greater than this impact depth, as for the monodomain treated in Section 6, the reaction of this precession communicates to the magnet the net of the **s** components transverse to **M** of all of the electrons passing through the I/F interface into the magnet F. It follows also that the reactive momentum impulse given to F acts essentially at the interface and lies within the **M–s** plane determined by the incident electrons.

Crucial is the principle of conservation of spin momentum which follows from absence of spin operators in the *N*-electron Hamiltonian for a solid:

$$\mathcal{H} = \sum_i \frac{\mathbf{p}_i^2}{2m} + \sum_{i<j} \frac{e^2}{|\mathbf{r}_i - \mathbf{r}_j|} - \sum_{i,l} \frac{e^2 Z_l}{|\mathbf{r}_i - \mathbf{R}_l|} \tag{24}$$

The first of three terms above is kinetic energy with $\mathbf{p}_i$ the electron momentum operator, the second is coulomb interaction between electrons at positions $\mathbf{r}_{i,j}$, and the third is the coulomb interaction between electron i and atomic nucleus l carrying charge Z_l at fixed position $\mathbf{R}_l$. (Internal exchange coupling responsible for the formation of spontaneous magnetization of a ferromagnet arises from the antisymmetry principle even though spin operators are absent from $\mathcal{H}$.)

Note that we neglect the small spin-orbit effect. Spin-orbit coupling, in combination with defect scattering, determines the spin relaxation lengths λ_N and λ_F tabulated in Table 1. Its neglect is valid in the following derivation of torque from currents because λ_N, λ_F, and Λ are much greater than d_{impact} (see Section 4.1).

4.2 A general torque relation

Spin-momentum conservation causes the corresponding effective vectorial surface-torque densities $\mathbf{T}_L$ and $\mathbf{T}_R$ (with $\mathbf{l}\cdot\mathbf{T}_L = 0$ and $\mathbf{r}\cdot\mathbf{T}_R = 0$) to satisfy the vector equation

$$\mathbf{T}_L + \mathbf{T}_R = K_R\mathbf{r} - K_L\mathbf{l} \tag{25}$$

Here

$$K_n \equiv \hbar(J_{n,-} - J_{n,+})/2e \tag{26}$$

is the rightward flowing *spin-momentum* current (or spin current for brevity) density within magnet n(=L or R), $-e$ is the electron charge and $J_{n\pm}$ is the *electric* current density flowing in the majority- or minority-spin channel of the respective magnet in the two-channel model of perpendicular magnetoresistance. By convention, both charge and momentum *current* directions are reckoned positive along the $+x_1$ direction in Figure 3. (These densities are assumed independent of x_2 and x_3.) Accordingly, the right-hand side of equation (25) represents the net rate of spin momentum flowing into the region enclosed by two geometric planes A and B (see Figure 3) located inside the magnets at the distance d_{impact} from the F/N interfaces; the left side gives the consequent sum of macroscopic torques concentrated on the magnets at these interfaces. The great strength of the internal exchange stiffness within a pillar device insures that this torque is conveyed to their entire thickness as a whole.

As explained in the preceding text, the coplanar orientation of $\mathbf{T}_L(t)$ and $\mathbf{T}_R(t)$ with the moments $\mathbf{M}_L$ and $\mathbf{M}_R$ displayed in Figure 6 are general. Their scalar magnitudes are obtained by forming the scalar products of equation (25) alternatively with $\mathbf{M}_L$ and $\mathbf{M}_R$:

$$T_L = \frac{(K_L\cos\theta - K_R)}{\sin\theta} \tag{27}$$

$$T_R = \frac{(K_R\cos\theta - K_L)}{\sin\theta} \tag{28}$$

where the sign convention for the scalars is indicated in the Figure 6.

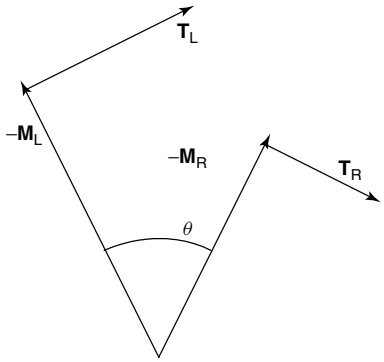

Figure 6. The torque vectors $\mathbf{T}_L$ and $\mathbf{T}_R$ lie within the plane containing the instantaneous magnetization vectors.

Equations (26)–(28) are key to current-driven torque for, given the spin-channel currents obtained by solving the effective circuit, these equations predict the corresponding torques to be included in the Landau–Lifshitz equations used later to treat domain dynamics and switching. Thus both questions of conductance (see equation (22)) and torque are reduced to solution of the effective circuit equations introduced Section 3 (see also **Theory of Spin-transfer Torque, Volume 2**).

5 MAGNETORESISTANCE AND CURRENT-DRIVEN TORQUE OF A SYMMETRIC PILLAR

5.1 The magnetoresistance

The two relations (18) and (19) provide the connection across spacers needed to complete the effective circuit Kirchoff equations for angular dependence of perpendicular magnetoresistance. A method of solution for broad classes of pillars, with significant complication due to spin relaxation, are published (Manchon and Slonczewski, 2006). To take a simple example, the magnetoelectronics of a trilayer $F_L/N/F_R$ is described by the circuit diagram of Figure 7 in the special

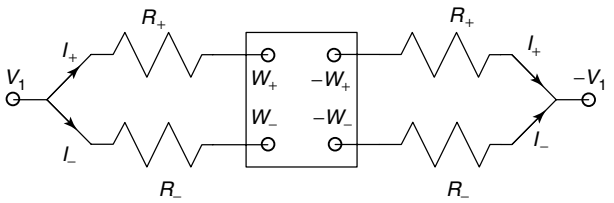

Figure 7. Effective circuit for the trilayer when magnets F_L and F_R are equal. $R_\pm$ are the channel resistances of each magnet and lead combination. Equations (18) and (19) connect the currents and voltages across the spacer and equation (32) gives the total resistance.

case that F_L and F_R have identical properties and thicknesses and spin relaxation within the magnets can be neglected. The channel resistances $R_\pm$ should include both the bulk and interfacial contributions given in equation (2).

To take advantage of the resulting odd voltage symmetry and even current symmetry, electric voltage V_1 is applied to the left contact and $-V_1$ to the right. Then symmetry permits omission of the subscripts L and R and dictates the disposition of current densities, $J_\pm \equiv J_{L\pm} = J_{R\pm}$, voltages $W_\pm \equiv W_{L\pm} = -W_{R\pm}$, shown in Figure 7, as well as the relations $\Delta J \equiv J_+ - J_-$, $\Delta J_R = \Delta J_L$ and $\Delta W_R = -\Delta W_L$. ($J_\pm$ is shown as $I_\pm$ in Figure 7.) The total unit-area resistance is

$$R = \frac{2V_1}{(J_+ + J_-)} \tag{29}$$

Our neglect of spacer resistance means $V_L = V_R = 0$, implying $W_+ = -W_-$ according to equation (12).

Each relation (18) and (19) now reduces to the single independent equation

$$(J_+ - J_-)(1 - \cos\theta)^2 = G(W_+ - W_-)\sin^2\theta \tag{30}$$

Kirchoff's laws give the two relations

$$W_\pm = V_1 - R_\pm J_\pm \tag{31}$$

Simple elimination between equations (29–31) gives the result

$$R(\theta) = \frac{(R_+ + R_-)\sin^2(\theta/2) + 2GR_+R_-\cos^2(\theta/2)}{2\sin^2(\theta/2) + G(R_+ + R_-)\cos^2(\theta/2)} \tag{32}$$

Experimental data is usefully reduced to the dimensionless variable

$$r = \frac{R(\theta) - R(0)}{R(\pi) - R(0)} \tag{33}$$

Interpretation of experiments sometimes centers on deviation of the r data from linearity with respect to the variable $\cos^2(\theta/2)$ as measured by the parameter χ in the formula

$$r = \frac{1 - \cos^2(\theta/2)}{1 + \chi\cos^2(\theta/2)} \tag{34}$$

Figure 8 illustrates this relation. In these terms, the formulas (32) and (33) combine to give

$$\chi = \frac{1}{2}G(R_+ + R_-) - 1 \quad (> -1) \tag{35}$$

Experimental values of χ thus far are positive, including those for trilayers FeCo/Cu/FeCo and NiFe/Cu/NiFe having

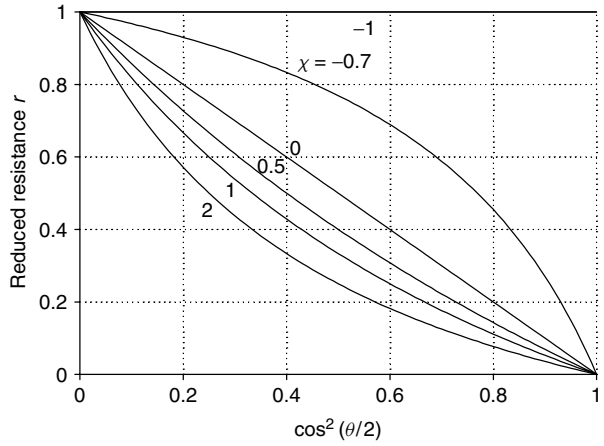

Figure 8. Angular dependence of reduced magnetoresistance on angle θ between magnetic moments defined by equation (33), according to equations (34) and (35).

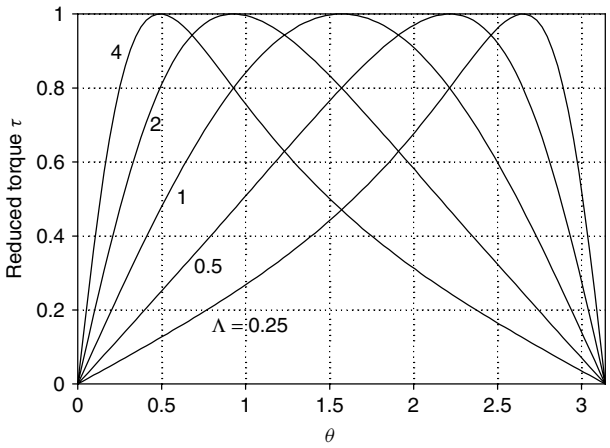

Figure 9. Dependence of reduced torque on angle θ for a trilayer with identical ferromagnetic sublayers. The parameter Λ is given by equation (37).

equal magnets. Application of the present theory to these experiments would require G to be about half of our expected $1.4 \times 10^{15}\ \Omega^{-1}\,\mathrm{m}^{-2}$ (Bass, J. private communication). However, the present theory takes no account of the antiferromagnetic and superconducting connecting layers used in the experiments. In addition, since the magnets are composed of alloys that include Fe, we do not know how well they satisfy the condition of negligible majority-spin interfacial reflection assumed by the theory (see Section 3.2) (see also **Enhanced Magnetoresistance, Volume 1**).

5.2 Torques on a symmetric trilayer

Specializing now to our illustrative case of two identical magnets in the preceding text (see Figure 7), application of the relations (30) and (31) reduces equation (28) to the new torque relation for either magnet:

$$T = \frac{\hbar J P_\mathrm{r} \Lambda \tau(\theta)}{4e} \tag{36}$$

with

$$P_\mathrm{r} = \frac{(R_- - R_+)}{(R_+ + R_-)},\ \ \Lambda = \left[\frac{G(R_+ + R_-)}{2}\right]^{1/2} \tag{37}$$

and

$$\tau(\theta) = \frac{\sin\theta}{\Lambda \cos^2(\theta/2) + \Lambda^{-1}\sin^2(\theta/2)} \tag{38}$$

The latter reduced torque relation is plotted in Figure 9. Section 6 treats the effect of such a current-driven torque on the dynamic behavior of a monodomain using the Landau–Lifshitz equation.

6 DYNAMICS OF MAGNETIZATION DRIVEN BY CURRENT

Other chapters treat this subject in depth (see also **Magnetization Dynamics Including Thermal Fluctuations: Basic Phenomenology, Fast Remagnetization Processes and Transitions Over High-energy Barriers, Volume 2**, **Nonlinear Magnetization Dynamics in Nanomagnets, Volume 2**, **Microwave Generation in Magnetic Multilayers and Nanostructures, Volume 2**, **Spin Angular Momentum Transfer in Magnetoresistive Nanojunctions, Volume 5**, and **Microwave Excitations in Spin Momentum Transfer Devices, Volume 5**).

Our treatment here is minimal: For simplicity, consider a uniformly magnetized monodomain having uniaxial effective anisotropy field $H_\mathrm{u} = 2K_\mathrm{u}/M_\mathrm{s}$ where $K_\mathrm{u}\sin^2\theta$ is the total energy per unit volume, including material and shape terms. The free motion of the monodomain is a circular precession about the easy axis with constant θ and circular frequency $\omega = \gamma H_\mathrm{u}\cos\theta$.

In the presence of small damping (measured by the Gilbert coefficient α) and exchange (spin-transfer) torques, the time-dependence of the cone angle satisfies

$$\mathrm{d}\theta/\mathrm{d}t = \dot\theta_\mathrm{damp} + \dot\theta_\mathrm{exch} \quad \text{with} \tag{39}$$

$$\dot\theta_\mathrm{damp} = -\frac{1}{2}\gamma\alpha H_\mathrm{u}\sin 2\theta \quad \text{and} \tag{40}$$

$$\dot\theta_\mathrm{exch} = \frac{\gamma\hbar J g(\theta)}{eM_\mathrm{s}d_\mathrm{F}}\sin\theta \tag{41}$$

The latter three functions are plotted in Figure 10 for three values of dimensionless current I. (Units for all physical quantities are arbitrary.) The function $g(\theta)$ employed is

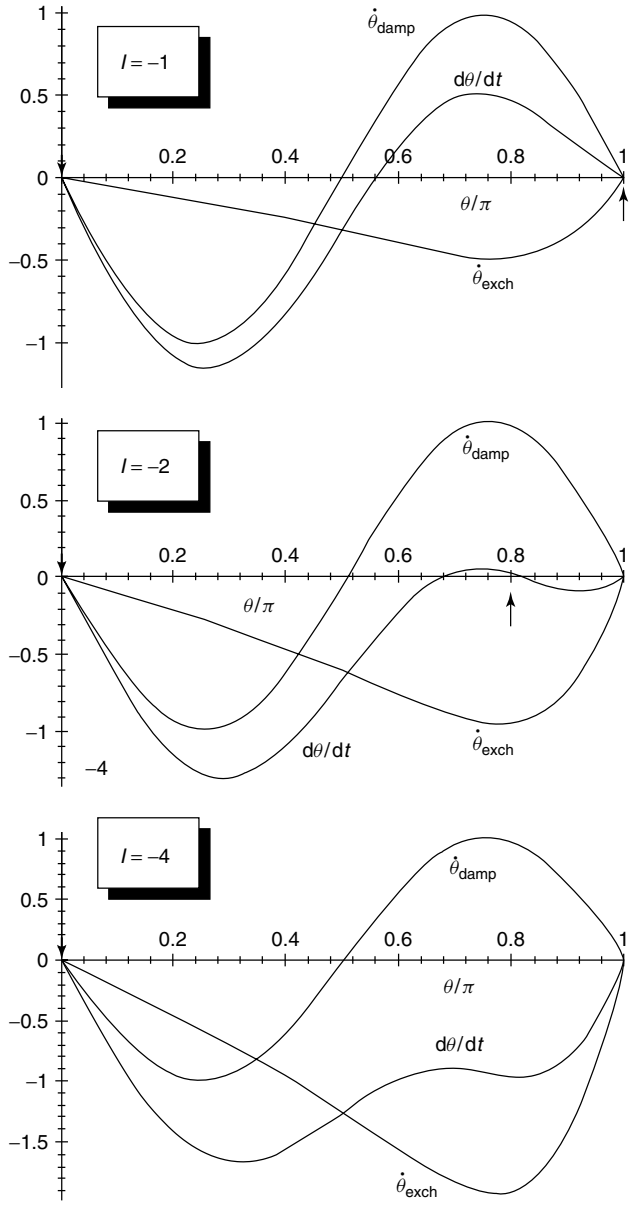

Figure 10. Instantaneous angular velocity versus angle θ of the precession cone for a uniaxial monodomain pillar magnet subject to viscous damping and three values of dimensionless current I, according to equation (39). Points of stable dynamic equilibrium are indicated by $\uparrow$ or $\downarrow$.

from an earlier theory (Slonczewski, 1996) and corresponds approximately to the symmetric pillar case $\Lambda = 0.4$ in Figure 9. Obvious conditions for the stability of any cone angle are $\mathrm{d}\theta/\mathrm{d}t = 0$ (equilibrium) and $\mathrm{d}[\mathrm{d}\theta/\mathrm{d}t]/\mathrm{d}\theta < 0$ (stability).

For $I = -1$, the remanent states $\theta = 0, \pi$ satisfy both conditions, but the intermediate equilibrium point $\theta = 0.56\pi$ is not stable. Therefore the current value $I = -1$ does not excite either of the two remanent states. In the time domain, consider a small initial fluctuation (e.g., thermal) $\theta = 0.95\pi$ from one remanent state. Then, integration of equation (39) shows that the current $I = -1$ permits the moment to relax exponentially to the nearby remanent state as illustrated by the top curve in Figure 11.

For $I = -2$, only two, ($\theta = 0,\ 0.79\pi$) of the four equilibrium states are stable. Therefore this value of current drives the moment out of the neighborhood of $\theta = \pi$ toward the first stable equilibrium $\theta = 0.79\pi$. (See Figure 11.) After it relaxes to this point, the moment continues to precess steadily at circular frequency $\omega = \gamma H_{\mathrm{u}} \cos 0.79\pi$ as long as the constant current $I = -2$ is maintained. If the current is subsequently turned off, then the moment falls to the nearer remanent state, $\theta = \pi$ in this case. This example illustrates the fact that the criterion $\mathrm{d}[\mathrm{d}\theta/\mathrm{d}t]/\mathrm{d}\theta = 0$ for instability threshold does not necessarily imply a full moment reversal.

For $I = -4$, only one state has a stable equilibrium, so that a complete reverse switch from $\theta = \pi^-$ to $\theta = 0$ occurs. (See Figure 11) Note that the current speeds up the relaxation to the final state.

Clearly, positive I of sufficient magnitude will switch in the forward direction from $\theta = 0^+$ to $\theta = \pi$. In this case ($I > 0$) it happens that a steady precessing state does not exist and the threshold current for instability of $\theta = 0$ does also cause a full switch. Thus for $H_{\mathrm{u}} > 0$, the possibility of a steady precessing state depends on the value of P and the sign of I. However, for $H_{\mathrm{u}} < 0$ there exists a range including both signs of I supporting a steady precession.

(For details of dynamic micromagnetic theory, see **Nonlinear Magnetization Dynamics in Nanomagnets, Volume 2**. For pillar dynamics, see **Spin Angular Momentum Transfer in Magnetoresistive Nanojunctions,**

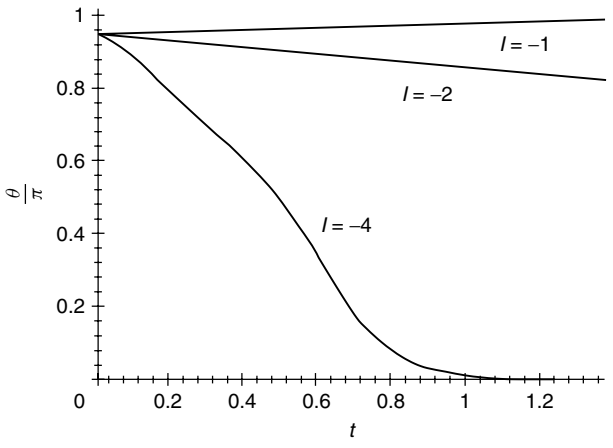

Figure 11. Dependence of precession-cone angle θ on time computed from equation (39) in arbitrary units. The initial state is $\theta = 0.95\pi$. The dimensionless current $I = -1$ causes no switch, $I = -2$ causes a partial switch to the precessing state $\theta = 0.79\pi$ and $I = -4$ causes a full switch to $\theta = 0$.

Volume 5 and **Spin-transfer in High Magnetic Fields and Single Magnetic Layer Nanopillars, Volume 5**. For point-contact excitation, see **Microwave Generation in Magnetic Multilayers and Nanostructures, Volume 2**. For devices, see **Microwave Excitations in Spin Momentum Transfer Devices, Volume 5**.)

7 QUANTUM TUNNELING THEORY

Beginning with this section, we replace the metallic spacer in the magnetic multilayer with a tunneling barrier. A powerful way to treat tunneling is with the method of Bardeen, which uses Fermi's Golden Rule of time-dependent perturbation theory to describe the flow of electrons from one electrode to the other (Duke, 1969). It is best derived using the interaction picture for perturbation theory (Sakurai, 1985).

7.1 Interaction picture

Let ψ satisfy the Schroedinger wave equation

$$i\hbar\dot{\psi} = H\psi \tag{42}$$

for the one-particle Hamiltonian

$$H = -\frac{\left(\frac{\hbar \mathrm{d}}{\mathrm{d}x}\right)^2}{2m} + V(x) \tag{43}$$

in one dimension. Let $\phi_n(x)$ $(n = 0, 1, 2, \ldots)$ be a complete orthonormal set of basis functions. A general wave function may be expanded thus:

$$\psi = \sum_n C_n(t)\phi_n(x) \tag{44}$$

The matrix equivalent of the Schröedinger equation is found as usual to be

$$i\hbar\dot{C}_n = \Sigma_{n'} H_{n,n'} C_{n'} \tag{45}$$

with $\bullet \equiv \mathrm{d}/\mathrm{d}t$ and the matrix form of the Hamiltonian

$$H_{n,n'} = \langle \phi_n | H | \phi_{n'} \rangle \tag{46}$$

Now let H' be a small general perturbation:

$$H = H_0 + H' \tag{47}$$

Also, let $\lambda(x) \equiv \phi_0$ be a single initially occupied unperturbed state having vanishing energy: $H_0\lambda = 0$. Assume also $H'_{0,0} \equiv 0$. Each of the initially unoccupied remaining unperturbed states ϕ_n satisfy

$$(H_0 - \hbar\omega_n)\phi_n = 0 \ (n = 1, 2, \ldots) \tag{48}$$

with energy $\hbar\omega_n$. Use the interaction picture (Sakurai, 1985)

$$C_n = a_n(t)e^{-i\omega_n t} \tag{49}$$

with initial values $a_0(0) = 1$ and $a_n(0) = 0$ for $n = 1, 2, \ldots$ For $n \neq 0$, consider $H'_{n,n'}$, a_n, and ω_n to be first-order quantities. Upon substitution of equation (49), equation (45) reduces in first-order approximation to

$$\dot{a}_0 = 0, \quad \dot{a}_n = -iH'_{n,0}e^{i\omega_n t} \ \ (n = 1, 2 \ldots) \tag{50}$$

These are the linearized perturbation equations in the interaction picture. Our next goal is a special expression for $H'_{n,0}$ for the case of tunneling.

7.2 Tunneling rate

To describe tunneling from left to right, specialize to the case of V approaching the constant barrier height B within much of the barrier (see Figure 12). Let our $\lambda(x) \equiv \phi_0$ be one initial state having energy $E = 0$ which is localized within the *left* electrode by the potential $B + V_{\mathrm{L}}(x)$ where B is constant with $V_{\mathrm{L}} \leq 0$ for all x, and $V_{\mathrm{L}} = 0$ for $x > a$. Let the remaining ϕ_n be localized on the right of the barrier by the potential $B + V_{\mathrm{R}}(x)$ where $V_{\mathrm{R}} \leq 0$ for all x, and $V_{\mathrm{R}} = 0$ for $x < b$. The total potential of the system is $V = B + V_{\mathrm{L}}(x) + V_{\mathrm{R}}(x)$. The basic approximation of Bardeen is to neglect the nonorthogonality of λ to ϕ_n $(n = 1, 2, \ldots)$ due to the small wave function overlap within the barrier (Duke, 1969). (See Figure 12)

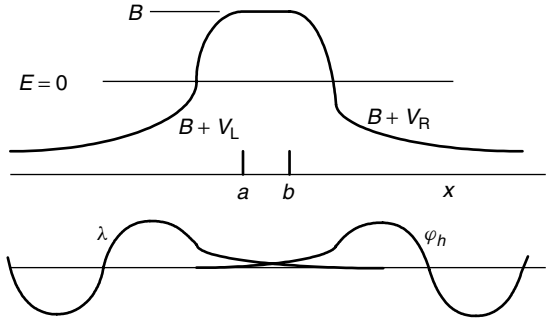

Figure 12. Potentials $V = B + V_{\mathrm{L}}$ and $V = B + V_{\mathrm{R}}$, plotted above, which define left $\lambda(x)$ and right $\phi_n(x)$ $n = 1, 2, 3, \ldots$ electrode basis functions, plotted schematically in the subsequent text, for Bardeen tunnel theory.

Equation (44) in the interaction picture for tunneling becomes

$$\psi = \lambda + \sum\nolimits_n a_n(t)\phi_n e^{-i\omega_n t} \tag{51}$$

The probability P_n for occupation of the state ϕ_n and its rate of increase $\dot{P}_n$ are

$$P_n = a_n^*\, a_n, \qquad \dot{P}_n = (\dot{a}_n^*\, a_n) + \text{c.c.} \tag{52}$$

Let's calculate this rate from perturbation theory. Substitute equation (50) into equation (52) and find

$$\dot{P}_n = i\hbar H'_{0,n} a_n e^{-i\omega_n t} + \text{c.c.} \tag{53}$$

Note that we may assume that our basis states λ and ϕ_n are real, because we are free to use either the real or imaginary part of any complex unperturbed solution. Therefore, the matrix $H'_{n,n'}$ is real and symmetric. Since the expectation of velocity $(-i\hbar \mathrm{d}/\mathrm{d}x)/m$ for a real wave function vanishes identically, the Bardeen method cannot describe flow of current through the electrodes − only between them.

Now calculate the one-particle current j from the general expression (Bohm, 1951)

$$j(c) = \frac{i\hbar}{2}(\psi_x^*\,\psi - \psi^*\,\psi_x)_{x=c} = \frac{i\hbar}{2}\left(\psi_x^*\,\psi\right)_{x=c} + \text{c.c.} \tag{54}$$

at the point $x = c$, where $\psi_x \equiv \partial\psi/\partial x$. We let $x = c$ be a point within the barrier and substitute equation (51) into equation (54) to find

$$j = \left[\frac{i\hbar}{2}\left(\lambda_x\varphi_n - \lambda\varphi_{n,x}\right)_{x=c} a_n(t_1)e^{-i\omega_n t}\right] + \text{c.c.} \tag{55}$$

Now compare this with equation (53), identifying $j = \sum_n \dot{P}_n$. They are equal for all initial conditions only if we identify

$$H'_{0,n} = \frac{1}{2}\left(\lambda_x\varphi_n - \lambda\varphi_{n,x}\right)_{x=c} \tag{56}$$

for all n. In this equation, c must satisfy $a \le c \le b$ in Figure 12. We conclude that equation (56) is the general formula for Bardeen's transfer Hamiltonian.

Fermi's Golden Rule for the total transition rate gives:

$$\frac{\mathrm{d}P}{\mathrm{d}t} = \frac{2\pi}{\hbar} H'^2_{n,0}\rho(E) \tag{57}$$

where $\rho \equiv \hbar(\mathrm{d}\omega_n/\mathrm{d}n)$ is the density of states assumed to be very closely spaced (Sakurai, 1985). This equation with the matrix element (56) substituted comprises the essential tool for calculating the current through an insulating barrier.

8 CURRENTS AND TORQUES IN MAGNETIC TUNNEL JUNCTIONS

8.1 Currents

For adaptation (Slonczewski, 2005) of the Bardeen method to the MTJ illustrated schematically in Figure 13(a), a stationary basis state $|p, \sigma\rangle$ within the left ferromagnetic electrode $\mathrm{F_L}$ is assigned the orbital index p and majority/minority spin $\sigma = \pm$ quantized along axis **l**. It satisfies $(H + eV - \epsilon_{p,\sigma})|p, \sigma\rangle = 0$, and decays exponentially within the barrier, considered semi-infinite in width when defining the basis states, as in Section 7.2. From this point forward, $-V$ is the external voltage applied to $\mathrm{F_L}$. Here, $H = (\mathbf{p}^2/2m) + \Sigma_\sigma|\sigma\rangle U_\sigma(x, y, z)\langle\sigma|$, where the potential U_σ depends on spin $\sigma(= \pm)$ within the ferromagnets but not within the barrier. Within $\mathrm{F_R}$, a similar state satisfies $(H - \epsilon_{q,\sigma'})|q, \sigma'\rangle = 0$ with quantization axis **r**. Because the barrier is assumed to dominate all other resistances of this circuit, the spin channels are shown in Figure 13(b) as shorted in each magnet and external-contact region by spin-lattice relaxation due to spin-orbit coupling. One may disregard *spin accumulation* and the related distinction between electric and

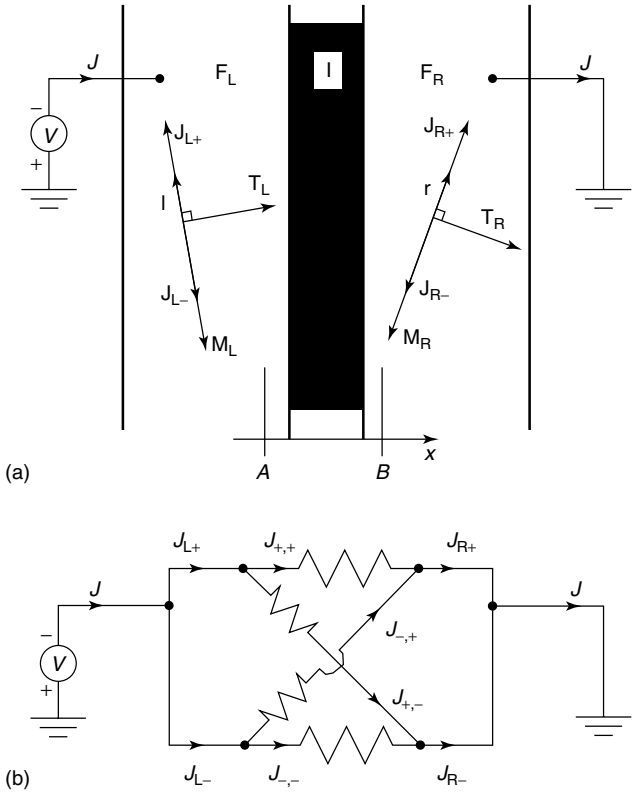

Figure 13. (a) Scheme of magnetic tunnel junction and key to notations. (b) Equivalent circuit for spin-channel currents and further key to notations.

electrochemical potentials which were important previously in connection with metallic spacers. U_σ includes all elastic terms arising from atomic disorder due to alloying, defects, interfacial atomic interdiffusion, and so on. The state indices p, q simply enumerate the exact eigenstates $|p,\sigma\rangle$, $|q,\sigma'\rangle$ of H in the Bardeen basis. Each such state incorporates effects of all multiple elastic scatterings without limit.

Employing the spinor transformation connecting quantization axes **l** and **r**, the transfer matrix element takes the form

$$\langle p,\sigma|H-\varepsilon|q,\sigma'\rangle = \begin{bmatrix} \gamma_{p,+;q,+}\cos\frac{\theta}{2} & \gamma_{p,+;q,-}\sin\frac{\theta}{2} \\ -\gamma_{p,-;q,+}\sin\frac{\theta}{2} & \gamma_{p,-;q,-}\cos\frac{\theta}{2} \end{bmatrix} \quad (\sigma,\sigma'=\pm) \tag{58}$$

Here the purely orbital factor $\gamma_{p,\sigma;q,\sigma'}$ is evaluated by extending our tunnel matrix expression (56) to three dimensions. Then, inclusion of spin indices gives the expression

$$\gamma_{p,\sigma;q,\sigma'}(x) = \frac{-\hbar^2}{2m}\int \mathrm{d}y\mathrm{d}z(\psi_{p,\sigma}\partial_x\varphi_{q,\sigma'} - \varphi_{q,\sigma'}\partial_x\psi_{p,\sigma})_{x=c} \tag{59}$$

Here the integral is over unit area with coordinate $x = c$ lying inside the barrier. The energies $\epsilon_{p,\sigma}$ and $\epsilon_{q,\sigma'}$ may differ only infinitesimally from a fixed value ε. The Hamiltonian H, the left ($\psi_{p,\sigma}$) and right ($\varphi_{q,\sigma'}$) orbital wave functions, and these matrix elements (59) are real.

Only the neglect of cross-barrier overlaps $\langle p,\sigma|q,\sigma'\rangle$ allows use of the Fermi golden rule (57) of perturbation theory which is strictly valid only for an orthonormal basis. Substitution of the perturbation (58) into this rule is followed by summation over the initial states in the energy band of width eV. Thus, for infinitesimal V, the partial electric current density flowing between channel σ in $\mathrm{F_L}$ and channel σ' in $\mathrm{F_R}$ becomes

$$J_{\sigma,\sigma'} = \frac{-2\pi e^2 V}{\hbar}\sum\nolimits'_{p,q}\langle p,\sigma|H-\varepsilon_\mathrm{F}|q,\sigma'\rangle^2 \tag{60}$$

at $T = 0$ K. The $'$ in $\sum'_{p,q}$ imposes the conditions $\varepsilon_\mathrm{F} < (\varepsilon_{p,\sigma}, \varepsilon_{q,\sigma'}) < \varepsilon_\mathrm{F} + eV$.

8.2 Genesis of polarization factors

Although MTJ relations depending on polarization factors are often used to interpret experiments, their validity is theoretically justified only under a severe restriction: The barrier is so thick that only a narrow selection of basis functions on each side penetrates it. To explain, consider the Schroedinger equation in two dimensions within the region of a flat barrier of height B:

$$\left[\frac{-\hbar^2}{2m}\left(\partial_x^2+\partial_y^2\right)+B-E_\mathrm{F}\right]\psi = 0 \tag{61}$$

A solution is

$$\psi \propto e^{-\kappa_x x}\cos(k_y y+\beta) \tag{62}$$

and the eigenvalue equation may be written

$$\kappa_x^2 = k_y^2+\kappa, \quad \kappa = \left[2m(B-E_\mathrm{F})/\hbar^2\right]^{1/2} \tag{63}$$

This equation says that the greater the y-momentum, the steeper the decay of ψ. Therefore the tunnel current concentrates near the single state with $k_y = 0$. The barrier collimates the current. Under this extreme condition, drop the indices p and q. On both sides of the barrier, the wave functions $\psi_\sigma \propto e^{-\kappa x}$ and $\varphi_{\sigma'} \propto e^{\kappa x}$ are independent of y. The matrix element (59) reduces to

$$\gamma_{\sigma,\sigma'} = \frac{-\hbar^2}{m}\kappa\int \mathrm{d}y\psi_\sigma\varphi_{\sigma'} \tag{64}$$

In the notation of Figure 13(b), the total tunnel electric current density flowing from R to L is

$$J = \Sigma_{\sigma,\sigma'}J_{\sigma,\sigma'} \tag{65}$$

with

$$J_{\sigma,\sigma'} = c_1 e^{-2\kappa w}\begin{pmatrix} \psi_+^2\varphi_+^2\cos^2(\theta/2) & \psi_+^2\varphi_-^2\sin^2(\theta/2) \\ \psi_-^2\varphi_+^2\sin^2(\theta/2) & \psi_-^2\varphi_-^2\cos^2(\theta/2) \end{pmatrix} \tag{66}$$

for any x within the barrier. Here w is the barrier thickness and the constant c_1 results from integrating $\int \mathrm{d}k_y$. For a rectangular barrier, the relative error of the Bardeen approximation is of the order $\exp(-kw)$ (Duke, 1969).

Substitute the identities

$$2\cos^2(\theta/2) = 1+\cos\theta \quad \text{and} \quad 2\sin^2(\theta/2) = 1-\cos\theta \tag{67}$$

to find

$$J = \frac{c_1}{2}e^{-2\kappa w}\left[(\psi_+^2+\psi_-^2)(\varphi_+^2+\varphi_-^2)+(\psi_+^2-\psi_-^2)\times(\varphi_+^2-\varphi_-^2)\cos\theta\right] \tag{68}$$

This may be written

$$J(\theta) = J_0(1+\iota\cos\theta), \quad \iota = P_\mathrm{L}P_\mathrm{R} \tag{69}$$

where J_0 is constant and the right and left *tunnel-polarization* factors are

$$P_{\rm L} = \frac{\psi_+^2 - \psi_-^2}{\psi_+^2 + \psi_-^2}\ , \quad P_{\rm R} = \frac{\varphi_+^2 - \varphi_-^2}{\varphi_+^2 + \varphi_-^2} \tag{70}$$

Note that the polarization factor relevant to tunneling is evaluated at any $x = c$ within the barrier. A realistic evaluation of J_0 generally requires *ab initio* numerical computation. Experimental data for the resistance $R(\theta)$ are often summarized by the magnetoresistance ratio

$$\mathrm{MR} \equiv \frac{R(\pi) - R(0)}{R(0)} = \frac{J(0) - J(\pi)}{J(\pi)} \tag{71}$$

Whenever polarization factors are legitimate, this formula reduces to that of Julliere's model (Julliere, 1975)

$$\mathrm{MR} = \frac{2P_{\rm L}P_{\rm R}}{1 - P_{\rm L}P_{\rm R}} \tag{72}$$

according to equation (69). (For more MTJ theory, see **Theory of Spin-dependent Tunneling, Volume 1** and **Spin-dependent Tunneling: Role of Evanescent and Resonant States, Volume 5**.)

8.3 Torques

Now apply the torque relations (27) and (28). (Some caution is demanded by the fact that the electron collimating effect of tunneling may cause $d_{\rm impact}$ in MTJs to be greater than that present with metallic spacers.) Substitute the relations

$$J_{{\rm L},\sigma} = J_{\sigma,+} + J_{\sigma,-}, \quad J_{{\rm R},\sigma'} = J_{+,\sigma'} + J_{-,\sigma'}, \quad (\sigma, \sigma' = \pm) \tag{73}$$

implied by the circuit diagram in Figure 13. The torque on the right magnet becomes

$$T_{\rm R} = -\left(\frac{\hbar\tau_{\rm R}J_0}{2e}\right)\sin\theta \tag{74}$$

or, in coordinate-free form

$$\mathbf{T}_{\rm R} = \left(\frac{\hbar\tau_{\rm R}J_0}{2e}\right)\mathbf{r}\times(\mathbf{l}\times\mathbf{r}) \tag{75}$$

with the torque coefficient

$$\tau_{\rm R} = P_{\rm L} \tag{76}$$

Similarly, the torque on the left magnet is

$$T_{\rm L} = -\left(\frac{\hbar\tau_{\rm L}J_0}{2e}\right)\sin\theta, \quad \tau_{\rm L} = P_{\rm R} \tag{77}$$

or, in coordinate-free form

$$\mathbf{T}_{\rm L} = \frac{\hbar\tau_{\rm L}}{2e}J_0\mathbf{l}\times(\mathbf{r}\times\mathbf{l}) \tag{78}$$

The equations (69), (76), and (78) show the very close relation between current-driven torques and magnetoconduction at the same voltage, summarized by the relation $\iota = \tau_{\rm L}\tau_{\rm R}$ connecting observables in the limit of large barrier thickness.

9 JUNCTIONS USING MGO BARRIERS

At this time (2007), rapid improvements of magnetoresistance ratio (MR) and voltage-driven torque effects in MTJs using MgO barriers are taking place. Initially, first-principle computations by Mathon and Umerski (2001) and by Butler, Zhang, Schulthess and MacLaren (2001) predicted enormous values of magnetoresistance ratio MR for epitaxial junctions of composition (001)Fe/MgO/Fe. The large MR is due to a selection rule prohibiting the transition of the minority band Δ_5 wave function at transverse momentum $k_\parallel = 0$ to the most-slowly decaying Δ_1 wave function within the MgO barrier. Subsequently (Zhang and Butler, 2004) further predicted even greater ratios in such junctions with Co or ordered FeCo substituted for Fe.

Indeed, many experiments using compositions of the class $\mathrm{Fe}_x\mathrm{Co}_y\mathrm{B}_z$/(001)MgO/$\mathrm{Fe}_x\mathrm{Co}_y\mathrm{B}_z$ reported MR as great as 270% at $T = 300$ K, but smaller than predicted (see **Magnetic Tunnel Junctions, Volume 5**). The measured MR depends greatly on extrinsic conditions including annealing, dislocations, added elements inserted at interfaces, and sputtering conditions. It appears likely that details of microstructure at interfaces mix Δ_5 and Δ_1 states, thus permitting greater minority-spin current which decreases MR from its first-principle value. Switching experiments confirm spin-transfer phenomena in MTJs (Huai *et al*., 2003; Fuchs *et al*., 2004).

Here, we predict observable signatures of voltage-driven torque whose measurement could discriminate between various effects of the microstructural conditions mentioned in the preceding text (Slonczewski and Sun, 2007). As yet no experimental tests exist. Possibly applicable methods of directly measuring the current-driven torque have appeared recently in two reports: (Tulapurkar *et al*., 2005) use an external field to orient the two magnetic moments at an angle of 30°. The torque created by an AC current flowing through the junction causes the free moment to oscillate. A voltmeter detects the DC magnetoresistive voltage proportional, by virtue of nonlinearity, to the square of the oscillation amplitude. Sankey *et al*. (2006) similarly use current-driven torque to drive ferromagnetic resonance in the free magnet. These techniques

show promise for the experimental investigation of the torque signatures predicted in the subsequent text.

Sections 7 and 8 assume the tunneling is elastic. Here we take advantage of the more general nature of relations derived there. Our present model, includes inelastic as well as elastic mechanisms of spin-polarized tunneling (Slonczewski and Sun, 2007). It is inspired in part by awareness of conductance data for $Fe_xCo_yB_z/MgO/Fe_xCo_yB_z$ of the sort shown in Figure 14. We find in the subsequent text that the antiparallel conduction G_{AP} resembling the nonanalytic function $a + b|V|$ for $|V| > 80\,\text{mV}$ (which we call *pseudolinear*), apparent in the lower curve of Figure 14, does not arise from elastic tunneling. But *inelastic* tunneling theory can explain pseudolinear voltage dependence observed for various non-MTJ tunneling junction compositions (Kirtley and Scalapino, 1990). Inclusion of inelastic tunneling is a key feature of our model for MgO-based tunneling junctions. (For MTJ experiments, see **Magnetic Tunnel Junctions, Volume 5**.)

9.1 Magnetoconductance and torkance

We employ notation compatible with the above-mentioned experimental techniques for measuring differential current- or voltage-driven torque (Tulapurkar *et al*., 2005; Sankey *et al*., 2006). In particular, we use the coefficients $G_{\sigma,\sigma'}$ of cross-channel *conductance amplitude,* defined in the subsequent text, for electric current flowing through any of the four spin channel combinations $\sigma, \sigma'(= \pm)$ (see Figure 13).

The *physical* electric conductance density flowing between spin channel σ' (R) and σ (L) of the barrier (see equation (66)) are

$$\mathrm{d}J_{\sigma,\sigma'}/\mathrm{d}V = G_{\sigma,\sigma'}(V)\langle\sigma|\sigma'\rangle^2, \quad (G_{\sigma,\sigma'}) \leq 0 \tag{79}$$

with the spin-coordinate transformation matrix elements $\langle\pm|\pm\rangle = \cos(\theta/2)$ and $\langle\pm|\mp\rangle = \pm\sin(\theta/2)$. The first-principle calculations for MTJs with (100)MgO barriers (Mathon and Umerski, 2001; Zhang and Butler, 2004), express, for $V = 0$, the conductance density for parallel and antiparallel moments with the formulas (in a different notation)

$$G_P = G_{++} + G_{--}, \quad G_{AP} = G_{+-} + G_{-+} \tag{80}$$

These equations follow easily for any V from the condition of spin conservation. When tunneling is inelastic, $G_{\sigma,\sigma'}$ necessarily varies with voltage V, as explained in the subsequent text.

Now we eschew use of polarization factors (70) because their validity in inelastic tunneling is not established. In place of equation (75), we introduce the following expression for what we may call *torkance*:

$$\frac{\mathrm{d}\mathbf{T}_R}{\mathrm{d}V} = \frac{\hbar}{4e}(G_{++} - G_{--} + G_{+-} - G_{-+})\mathbf{r} \times (\mathbf{l} \times \mathbf{r}) \tag{81}$$

Here the factor $-\hbar/2e$ converts the electric current carried by a particle flux to the equivalent current of spin angular momentum.

Equation (81) follows from equations (28) and (79). To verify equation (81) more transparently for the special case $\mathbf{l} \perp \mathbf{r}$, define the vector spin moment per unit area of one metallic nanomagnet:

$$\mathbf{S} = (\hbar/2)(n_+ - n_-)\mathbf{s} \qquad (n_+ > n_-) \tag{82}$$

where $\mathbf{s}$ is a unit vector, $n_\pm$ are total electron numbers for spin-polarized subbands $\sigma = \pm$. The spin-current density flowing rightward through the magnet is

$$\mathbf{K} = (K_+ - K_-)s \equiv (\hbar/2)(\Sigma_i v_{i,+} - \Sigma_i v_{i,-})\mathbf{s} \tag{83}$$

where $v_{i,\sigma}$ is the velocity of an occupied state. Consider the volume Ω lying between the planes marked A and B in Figure 13. The mean spin components transverse to local $\mathbf{M}$ vanish at all points outside Ω. Neglect all terms in the Hamiltonian $\mathcal{H}$ except kinetic and coulomb energies as given in equation (24). Since $\mathcal{H}$ contains no spin operators, the total vectorial spin $\mathbf{S}_{tot}$ contained in Ω changes only by inward flow of vectorial spin currents. Then its time derivative satisfies the equations

$$\dot{\mathbf{S}}_{tot} = \dot{\mathbf{S}}_L + \dot{\mathbf{S}}_R = \mathbf{K}_L - \mathbf{K}_R \tag{84}$$

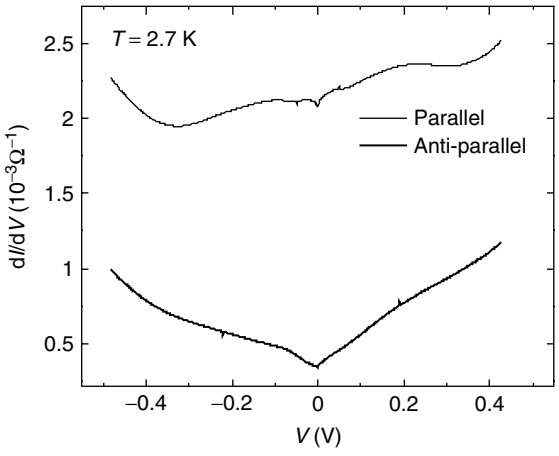

Figure 14. Measured conductance versus voltage for an MTJ having a very large MR. The parallel conductance G_P lies above, the antiparallel G_{AP} below. The composition is Co70Fe30/(8 Å)Mg-(26 Å)MgO/Co70Fe30. Junction dimensions are $240 \times 80\,\mu\text{m}^2$. (Unpublished data, by courtesy of S. S. P. Parkin.)

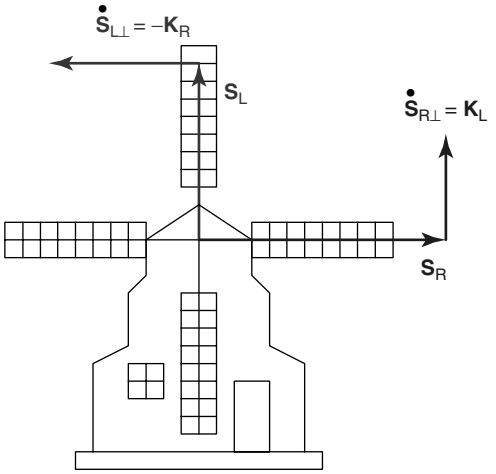

Figure 15. (Colored on line) Illustrating relations between pseudo-torque and spin-current vectors when moments are perpendicular. Assumed is the usual case in which each spin-current vector $\mathbf{K}_{\mathrm{L}}$ and $\mathbf{K}_{\mathrm{R}}$ have the same sign relative to $\mathbf{S}_{\mathrm{L}}$ and $\mathbf{S}_{\mathrm{R}}$, respectively.

The Bardeen method predicts only pseudotorque vector components lying within the $\mathbf{l}$–$\mathbf{r}$ plane. Now consider the special case $\mathbf{l} \perp \mathbf{r}$. Since $\dot{\mathbf{S}}_{\mathrm{L}} \bullet \mathbf{l} = \dot{\mathbf{S}}_{\mathrm{R}} \bullet \mathbf{r} = 0$, we have the cross-relations $\dot{\mathbf{S}}_{\mathrm{L}\perp} = -\mathbf{K}_{\mathrm{R}}$ and $\dot{\mathbf{S}}_{\mathrm{R}\perp} = \mathbf{K}_{\mathrm{L}}$. See Figure 15. According to equation (79), the $\perp$ condition implies that, from equation (83), $K_{\mathrm{L}\pm}$ has 1/2 the strength it would have for the given $G_{\sigma,\sigma'}$ if the spin axes were optimally aligned:

$$\mathrm{d}K_{\mathrm{L}\sigma}/\mathrm{d}V = \left(\frac{1}{2}\right)\left(\frac{-\hbar}{2e}\right)\left(G_{\pm,+} + G_{\pm,-}\right) \tag{85}$$

The result of combining this with the first of equations (83) and substituting into $\dot{\mathbf{S}}_{\mathrm{R}\perp} = \mathbf{K}_{\mathrm{L}}$ agrees with equation (81).

9.2 Elastic tunneling

Consider a special phenomenological model of F/MgO/F having symmetric chemical composition exemplified by the MTJ whose conductances are plotted in Figure 14. Compose each channel current density of elastic and inelastic terms: $J_{\sigma,\sigma'} = J^{\mathrm{el}}_{\sigma,\sigma'} + J^{\mathrm{inel}}_{\sigma,\sigma'}$. Define a tunnel-rate coefficient $U_{\sigma,\sigma'}$ proportional to the mean-square matrix element for elastic tunneling between the orbital states of spin channels $\sigma(=\pm)$ and $\sigma'(=\pm)$. It is averaged over the index p of real Bardeen orbital basis states $|p,\sigma\rangle$ on the left and over q of $|q,\sigma'\rangle$ on the right, with the factor depending on θ omitted. Including all other factors in the conventional tunneling expression for current except the state densities $\rho_\sigma, \rho_{\sigma'}$, it may be approximated by the form

$$U_{\sigma,\sigma'} = Ce^{-2\kappa d}\overline{\langle p,\sigma|H|q,\sigma'\rangle^2} \tag{86}$$

where κ is the decay coefficient for a real pseudo-Bloch function with $k_\parallel = 0$ and symmetry type Δ_1 having its energy within the forbidden band of MgO (Mathon and Umerski, 2001; Zhang and Butler, 2004). The predicted local density in the $\sigma = -$, Δ_5-propagation channel at $\geq$3 atomic layers of MgO from the initial F/I interface amounts to $\lessapprox 10^{-2}$ times that of the $\sigma = +$, Δ_1-channel. (See Figure 7 of Butler, Zhang, Schulthess and MacLaren, 2001.) This prediction makes reasonable our neglect of tunneling via the Δ_5 channel in experimental MTJs. We assume that disorder or dislocations within the electrodes or interface regions enables the $\sigma = -$, Δ_5-state of an electrode to couple to the Δ_1-channel of MgO to an extent governed by details of the atomic-scale structure.

For finite V, we may integrate the transition rate of the golden rule (57) with respect to V. Then, in view of the relation (60), the current density due to elastic tunneling at $T = 0\,\mathrm{K}$ reduces to the phenomenological form

$$J^{\mathrm{el}}_{\sigma,\sigma'}(V,\theta) = U_{\sigma,\sigma'}\langle\sigma,\sigma'\rangle^2\int_0^V \mathrm{d}v\rho_\sigma(v-V)\rho_{\sigma'}(v) \tag{87}$$

upon adjustment of C. Here, for convenience, we have replaced the energy ε argument in the state density ρ_σ, measured from the Fermi level $\varepsilon_{\mathrm{F}} = 0$, with voltage using $\varepsilon = eV$. We assume that, whatever lack of symmetry is present in this system, it will not be in the composition, therefore not in the state density ρ_σ. Rather it will lie in the coefficient $U_{\sigma,\sigma'}$, reflecting asymmetry of the concentration of defects or dopants in the interfacial microstructure; thus we omit the subscripts L and R from ρ_σ.

In many cases, as in Figure 14, the relative dependence of G_{P} on V is much weaker than that of G_{AP}. Thus, we take G_{P} constant and assume, to first order in v,

$$\rho_+ = \text{ const.}, \quad \rho_- = \rho_{-,0} + \rho_{-,1}v \tag{88}$$

Then in view of equation (79), equation (87) reduces in first order to

$$\begin{aligned} G^{\mathrm{el}}_{++} &= U_{++}\rho_+^2, \quad G^{\mathrm{el}}_{+-} = U_{+-}\rho_+(\rho_{-,0} + \rho_{-,1}V) \\ G^{\mathrm{el}}_{-+} &= U_{-+}\rho_+(\rho_{-,0} - \rho_{-,1}V), \quad G^{\mathrm{el}}_{--} = U_{--}\rho^2_{-,0} \end{aligned} \tag{89}$$

Notice here that U_{+-} is distinct from U_{-+} because breaking of the selection rule forbidding coupling of a $k_\parallel = 0$ minority state in a magnetic electrode to Δ_1 in MgO is allowed only by disorder in the electrode or interface, or presence of a foreign interfacial layer. Thus U_{+-} and U_{-+} depend on microstructural conditions which may differ on the two sides of the barrier. In an MTJ having large MR, such as the one in Figure 14, G^{el}_{--} is anyway small, so no correction is attempted.

Substitution of equation (89) into (80), gives the linear form $G_{\mathrm{AP}} = a + bV$ and not the *broken* linear form $a + b|V|$ which would reasonably represent the data appearing in Figure 14. To obtain a better representation of the data, we consider the possibility of inelastic tunneling in the subsequent text.

9.3 Inelastic tunneling

The following argument sketches the crux of a general theory (Kirtley and Scalapino, 1990) for the V-dependence of inelastic tunneling current density J^{inel} at $T = 0$ K: For $V > 0$, write

$$J^{\mathrm{inel}} = \int_0^V \mathrm{d}v \rho_{\mathrm{L}}(v - V) \int_0^v F^{\mathrm{inel}}(v - v')\mathrm{d}v' \rho_{\mathrm{R}}(v') \quad (90)$$

where the excitation, proportional to the spectral weight $F^{\mathrm{inel}}(v - v')$ (> 0) of excitation by some subsystem compensates for the difference $e(v - v')$ between initial and final energies in the electrodes. Then, assuming F^{inel}, ρ_{L}, ρ_{L} are constants, the result, written for both signs of V, is the broken linear function $G^{\mathrm{inel}} = \mathrm{d}J^{\mathrm{inel}}/\mathrm{d}V = F^{\mathrm{inel}}\rho_{\mathrm{L}}\rho_{\mathrm{R}}|V|$ we seek. In the present case, the nature of this subsystem (maybe magnons, electron traps at oxygen vacancies, or correlated coulomb excitation of electrons (Slonczewski and Sun, 2007)) is not known.

In the case of a perfectly ordered, epitaxial crystalline MTJ having a composition in the class (Fe,Co,FeCo)/MgO/(Fe,Co,FeCo), a quantum-theoretical selection rule forbids mixing of the minority-spin Bloch waves at $k_{\parallel} = 0$, having little-group symmetry Δ_5, with the MgO gap wave function having the lowest decay coefficient κ (Mathon and Umerski, 2001; Zhang and Butler, 2004). An enormous magnetoconductance ratio is predicted from the consequently small values of G_{+-} and G_{-+} appearing in equation (80). We assume that some inelastic mechanism provides channels additional to those of the defect-induced elastic coefficients U_{+-} and U_{-+} for breaking this selection rule. From the previous paragraph follow the formulas $G^{\mathrm{inel}}_{+-} = D_{\mathrm{R}}|V|$ and $G^{\mathrm{inel}}_{-+} = D_{\mathrm{L}}|V|$, where the adjustable coefficients satisfy $D_{\mathrm{L}} > D_{\mathrm{R}}$ or $D_{\mathrm{L}} < D_{\mathrm{R}}$ depending on which interface the inelastic mechanism favors. Since the ++ connection does not involve the selection rule, and the $--$ involves it twice, we take $G^{\mathrm{inel}}_{++} = G^{\mathrm{inel}}_{--} = 0$.

Substitution of equation (89) into (80), with $G^{\mathrm{inel}}_{\sigma\sigma'}$ included, gives

$$G_{\mathrm{AP}} = (U_{+-} + U_{-+})\rho_+\rho_{-,0} + (D_{\mathrm{L}} + D_{\mathrm{R}})|V| + (U_{+-} - U_{-+})\rho_+\rho_{-,1}V \quad (91)$$

By eliminating G_{++} between equations (80) and (81), and including $G^{\mathrm{inel}}_{\sigma\sigma'}$, one gets:

$$\mathrm{d}T_{\mathrm{R}}/\mathrm{d}V = (\hbar/4e)[G_{\mathrm{P}} + (U_{+-} - U_{-+})\rho_+\rho_{-,0} + (D_{\mathrm{L}} - D_{\mathrm{R}})|V| + (U_{+-} + U_{-+})\rho_+\rho_{-,1}V]\sin\theta \quad (92)$$

where we have neglected G_{--} altogether.

9.4 Observable signatures from magnetoconductance and torkance

With the aid of our equations (91) and (92), combined observation of G_{AP} and $\mathrm{d}T_{\mathrm{R}}/\mathrm{d}V$ may serve to reflect interfacial microstructures of a compositionally symmetric MTJ having a large magnetoconductive ratio $G_{\mathrm{P}}/G_{\mathrm{AP}}$. To illustrate this, we assume G_{P} is constant and plot schematically G_{AP} and $\mathrm{d}T_{\mathrm{R}}/\mathrm{d}V$ in Figure 16 for 5 special cases A–E reflecting terms in these equations:

1. *Symmetric reference case*, (A) with $U_{+-} - U_{-+} = \rho_{-,1} = D_{\mathrm{L}} - D_{\mathrm{R}} = 0$: Here G_{AP} has the pseudolinear dependence on $|V|$ due to inelastic scattering exemplified by the data in Figure 14. The torkance $\mathrm{d}T_{\mathrm{R}}/\mathrm{d}V = (\hbar/4e)G_{\mathrm{P}}\sin\theta$ is constant. A predicted independence of torkance on V for magnon-induced tunneling is one example of this broad phenomenological prediction (Levy and Fert, 2006).
   The remaining cases in the subsequent text illustrate possible changes from case A leaving the sums $U_{+-} + U_{-+}$ and $D_{\mathrm{L}} + D_{\mathrm{R}}$ unchanged:
2. *Asymmetry of elastic tunneling*, (B): Let $U_{+-} > U_{-+}$, which reflects the difference in degrees of disorder or dislocation density at the two F/I interfaces. G_{AP} does not change. But now the torkance makes a constant shift amounting to $(U_{+-} - U_{-+})\rho_+\rho_{-,0}\sin\theta$, according to equation (92).
3. *Dependence of state density on energy*, (C): Let $\rho_{-,1} > 0$. This does not change G_{AP} but gives the torkance a true linear dependence.

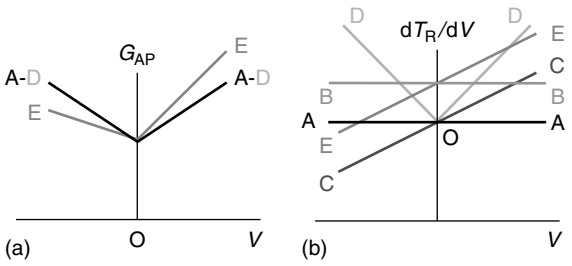

Figure 16. (Color on-line) Scheme of predicted antiparallel conductance G_{AP} (a) and torkance $\mathrm{d}T_{\mathrm{R}}/\mathrm{d}V$ (b). The separate cases A–E are described in the text.

4. *Asymmetry of distribution of inelastic tunneling centers*, (D): Let $D_L > D_R$. This causes no change in G_{AP}, but gives pseudolinear dependence to torkance. Depending on the sign of $D_L - D_R$, the torkance rises with $|V|$ as shown, or falls.
5. *Combine tunnel matrix asymmetry with dependence of ρ_- on energy*, (E): Let both $U_{+-} > U_{-+}$ *and* $\rho_{-,1} > 0$. This gives G_{AP} a true linear bias. The torkance acquires a superposition of the effects in cases B and C, namely a shift and a tilt.

It is significant how much more information about spin-dependent tunnel transport observation torkance is capable than the conductance. For example, any one of the cases A, B, C, or D could account for the data in Figure 14. They are indistinguishable in Figure 16(a), but in (b) we see significant differences in the torkance signature, potentially enabling experimental discrimination between microstructural mechanisms.

Case E is particularly interesting because the dislocation densities at the two interfaces of epitaxial (001)Fe/MgO/Fe are known to differ markedly. This difference may cause the inequality $U_{+-} \neq U_{-+}$. Indeed, a plot of G_{AP} in sample B reported by (Tiusan *et al*., 2006) reveals tilted-V behavior resembling that shown in case E of Figure 16(a). If the present model is correct, then the torkance in a pillar of the same composition should show, as a minimum, the shift and true linear tilt seen in panel (b), case E.

10 A FINAL COMMENT

Worth summarizing are the complementary natures predicted in the preceding text for currents and spin-transfer torques through metallic versus MgO-tunneling spacers: (i) When the spacer is metallic, current density J is the natural independent variable; but in the case of a barrier, the voltage V is better. (ii) At constant intermoment angle θ, the relations for $V(J)$ and torque $\mathbf{T}(J)$ predicted when the spacer is metallic are linear for a significant range of J; but the $J(V)$, $\mathbf{T}(J)$, and $\mathbf{T}(V)$ relations predicted in MTJs for general θ may be significantly nonlinear. (One linear exception is $G_P(V)$ and others are $\mathbf{T}(V)$ in the special cases A and B illustrated in Figure 16.) (iii) With a metallic spacer, the $V(\theta)$ and $\mathbf{T}(\theta)$ relations are typically not unique under any condition; but with a tunneling barrier *at given* V, they *are* simple: $J \propto \cos\theta$ and $\mathbf{T} \propto \sin\theta$.

REFERENCES

Barnaś, J., Fert, A., Gmitra, M., *et al*. (2005). From giant magnetoresistance to current-induced switching by spin transfer. *Physical Review B*, **72**, 024426–4.

Bass, J. and Pratt,W.P. Jr. (2001). Current-perpendicular (CPP) magnetoresistance in magnetic metallic multilayers. *Journal of Magnetism and Magnetic Materials*, **200**, 274.

Berger, L. (1996). Emission of spin waves by a magnetic multilayer traversed by a current. *Physical Review B*, **54**, 9353–9361.

Bohm, D. (1951). *Quantum Theory*, Prentice-Hall: New York. Sec. 17.7.

Brataas, A., Bauer, G.E.W. and Kelly, P.J. (2006). Non-collinear magnetoelectronics. *Physics Reports*, **427**, 157–255.

Brataas, A., Nazarov, Y.V. and Bauer, G.E.W. (2000). Finite-element theory of transport in ferromagnet-normal metal systems. *Physical Review Letters*, **84**, 2481–2484.

Butler, W.H., Zhang, X-G., Schulthess, T.C. and MacLaren, J.M. (2001). Spin-dependent tunneling conductance of Fe—MgO—Fe sandwiches. *Physical Review B*, **63**, 54416–54427.

Duke, C.B. (1969). *Tunneling in Solids*, Academic Press: New York.

Fuchs, G.D., Emley, N.C., Krivorotov, I.N., *et al*. (2004). Spin-transfer effects in nanoscale magnetic tunnel junctions. *Applied Physics Letters*, **85**, 1205–1213.

Huai, Y., Albert, F., Nguyen, P., *et al*. (2003). Observation of spin-transfer switching in deep submicron-sized and low-resistance magnetic tunnel junctions. *Applied Physics Letters*, **84**, 3118–3120.

Julliere, M. (1975). Tunneling between ferromceqnetic films. *Physics Letters*, **54A**,225–227.

Kirtley, J.R. and Scalapino, D.J. (1990). Inelastic-tunneling model for the linear conductance background in the high-Tc superconductors. *Physical Review Letters*, **65**, 798–800, and references therein.

Kübler, J. (2000). *Theory of Itinerant Electron Magnetism*, Clarendon Press: Oxford, p. 234.

Levy, P.M. and Fert, A. (2006). Spin transfer in magnetic tunnel junctions with hot electrons. *Physical Review Letters*, **97**, 97205–97208.

Manchon, A. and Slonczewski, J.C. (2006). Generalization of a circuit theory for current perpendicular to plane magnetoresistance and current-driven torque. *Physical Review B*, **73**, 184419–184425.

Mathon, J. and Umerski, A. (2001). Theory of tunneling magnetoresistance of an epitaxial Fe/MgO/Fe(001) junction. *Physical Review B*, **63**, 220403–220405.

Myers, E.B., Ralph, D.C., Katine, J.A., *et al*. (1999). Current-induced switching of domains in magnetic multilayer devices. *Science*, **285**, 867–870.

Sakurai, J.J. (1985). *Modern Quantum Mechanics*, Bemjamin/Cummings: Menlo Park, Secs. 5.5 and 5.6.

Sankey, J.C., Braganca, P.M., Garcia, A.G.F., *et al*. (2006). Spin-transfer-driven ferromagnetic resonance of individual nanomagnets. *Physical Review Letters*, **96**, 227601–227604.

Slonczewski, J.C. (1996). Current-driven excitation of magnetic multilayers. *Journal of Magnetism and Magnetic Materials*, **159**, L1–L7.

Slonczewski, J.C. (1999). Excitation of spin waves by an electric current. *Journal of Magnetism and Magnetic Materials*, **195**, L261–L268.

Slonczewski, J.C. (2002). Currents and torques in metallic magnetic multilayers. *Journal of Magnetism and Magnetic Materials*, **247**, 324–338.

Slonczewski, J.C. (2005). Currents, torques, and polarization factors in magnetic tunnel junctions. *Physical Review B*, **71**, 24411–24420.

Slonczewski, J.C. and Sun, J.Z. (2007). Theory of voltage-driven current and torque in magnetic tunnel junctions. *Journal of Magnetism and Magnetic Materials*, **310**, 169–175.

Stiles, M.D. and Miltat, J. (2005). *Spin-Transfer Torque and Dynamics in Spin Dynamics in Confined Magnetic Structures III*, Hillebrands, B. and Thiaville, A. (Eds.), Springer: Berlin.

Stiles, M.D. and Zangwill, A. (2002). Anatomy of spin-transfer torque. *Physical Review B*, **66**, 14407–14420.

Sun, J.Z. (1999). Current-driven magnetic switching in manganite trilayer junctions. *Journal of Magnetism and Magnetic Materials*, **202**, 157–162.

Tiusan, C., Sicot, M., Faure-Vincent, J., *et al*. (2006). Static and dynamic aspects of spin tunnelling in crystalline magnetic tunnel junctions. *Journal of Physics: Condensed Matter*, **18**, 941–956.

Tsoi, M., Jansen, A.G.M., Bass, J., *et al*. (1998). Excitation of a magnetic multilayer by an electric current. *Physical Review Letters*, **80**, 4281–4284.

Tulapurkar, A.A., Suzuki, Y., Fukushima, A., *et al*. (2005). Spin-torque diode effect in magnetic tunnel junctions. *Nature*, **438**, 339–342.

Valet, T. and Fert, A. (1993). Theory of the perpendicular magnetoresistance in magnetic multilayers. *Physical Review B*, **48**, 7099–7113.

Wainthal, X., Myers, E.B., Brouer, P.W. and Ralph, D.C. (2000). Role of spin-dependent interface scattering in generating current-induced torques in magnetic multilayers. *Physical Review B*, **62**, 12317–12327.

Xia, K., Kelly, P.J., Bauer, G.E.W., *et al*. (2002). Spin torques in ferromagnetic/normal-metal structures. *Physical Review B*, **65**, 220401–220404.

Zhang, X-G. and Butler, W.H. (2004). Large magnetoresistance in bcc Co/MgO/Co and FeCo/MgO/FeCo tunnel junctions. *Physical Review B*, **70**, 172407–172410.

High-temperature Superconductivity – Magnetic Mechanisms

Michael R. Norman
Argonne National Laboratory, Argonne, IL, USA

1 A BRIEF HISTORY – PART 1

The histories of superconductivity and magnetism have been much intertwined. The discovery of the Meissner effect in 1933, where magnetic flux is expelled from a superconductor as it is cooled below its transition temperature T_c, demonstrated that superconductors were more than just perfect conductors, leading to the famous proposal by London of the existence of a macroscopic condensate that accounts for the supercurrent. This was quite startling given the fermionic nature of the charge carriers in a metal, whose statistics do not prefer condensate formation as in the case of bosons. This idea was codified by Ginzburg and Landau in 1950, who introduced an order parameter field describing the condensate of electrons. The resulting Ginzburg–Landau Hamiltonian has been exploited in many areas of physics, including those dealing with the origin of the universe. One of the early successes of the Ginzburg–Landau theory was the prediction of type II superconductivity by Abrikosov in 1957, in which magnetic flux penetrates in the form of quantized vortices above a lower critical field H_{c1}. Recently, such vortices have been observed in cold atom condensates as well.

It was the development of a microscopic theory by Bardeen, Cooper, and Schrieffer (BCS) in 1957 and the subsequent proof by Gor'kov in 1959 of the equivalence of this theory to the Ginzburg–Landau formalism which began the modern era of superconductivity (Schrieffer, 1964). The crucial finding of Cooper in 1956 was that in the presence of a Fermi sea, arbitrarily weak attraction could lead to pair formation. Such pairs behave as bosons, thus explaining how a condensate could exist. The attraction that forms the pairs is a consequence of the positive ions and the fact that the ions and electrons have different timescales. Figure 1 illustrates how this works. Positive ions are attracted to negative electrons. This polarizes the ions toward the electron. When the electron leaves, a second electron sees this positive cloud and is attracted to this location, leading to pair formation. As the interaction is local in space, one forms s-wave pairs that are spin singlets by fermion antisymmetry. The pairs form despite the presence of the Coulomb repulsion of the individual electrons as they are at the same place, but at different times. Once the electrons become energetic enough relative to the ion vibrations (phonons), the attraction goes away, and the Coulomb repulsion wins out. This 'retardation' effect is responsible for limiting the superconducting transition temperature of electron–phonon systems to values significantly smaller than room temperature.

Handbook of Magnetism and Advanced Magnetic Materials. Edited by Helmut Kronmüller and Stuart Parkin. Volume 5: *Spintronics and Magnetoelectronics*. ISBN: 978-0-470-02217-7.

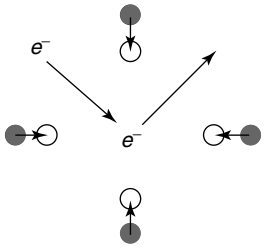

Figure 1. The electron–phonon interaction leads to an induced attraction between electrons. Arrows joining circles show displaced ions; the timescale of these ions for relaxation back to their original positions is slow compared to the electron dynamics.

The development of the BCS theory also led to the understanding of why proximity to magnetism is usually detrimental to superconductivity. In 1960, Abrikosov and Gor'kov showed, using the powerful Matsubara technique for finite temperature quantum field theory, that magnetic impurities are pair breaking (Abrikosov and Gor'kov, 1961). This result is easy to appreciate, since spin flip scattering will destroy singlet pairs. This argument was generalized to the dynamic case by Berk and Schrieffer, who showed, by summing a ladder series representing repeated scattering between the two electrons of the pair, that ferromagnetic spin fluctuations were detrimental to spin singlet superconductivity (Berk and Schrieffer, 1966) (Figure 2).

However, Fay and Layzer (1968) turned this argument around. The same formalism can be used to show that ferromagnetic spin fluctuations will promote spin triplet pairing, which is p wave due to fermion antisymmetry. This relies on the fact that the bare contact interaction is zero in the triplet channel (due to the Pauli exclusion principle), but the induced interaction (again, from the ladder sum of repeated

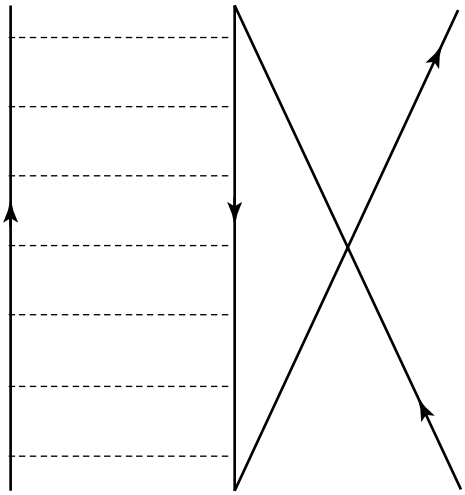

Figure 2. Particle–particle interaction from spin fluctuations. Note the particle–hole ladder sum buried inside this diagram.

scattering of two electrons via spin fluctuations shown in Figure 2) is attractive. Physically, this 'attraction' is due to the fact that an up spin electron prefers to have other up spin electrons nearby. The node in the pair wave function for the p-wave case acts to prevent the two electrons from coming too close together, thus minimizing the detrimental effects due to the direct Coulomb repulsion. They suggested that this mechanism could apply to nearly ferromagnetic metals such as Pd and also to the charge-neutral case of ^{3}He.

In 1972, Osheroff, Richardson, and Lee indeed discovered p-wave superfluidity in ^{3}He. It was soon realized that there were two superfluid phases, an anisotropic A phase and an isotropic B phase. This was difficult to understand, since the free energy of the isotropic phase should be the lowest according to Ginzburg–Landau theory. But in the following year, Anderson and Brinkman (1973) showed how the anisotropic A phase could be stabilized. The development of an energy gap removes some of those spin fluctuations that lead to pairing in a spin fluctuation model, thus leading to a decrease in the pairing kernel. This gapping effect is less pronounced in the anisotropic A phase than in the isotropic B phase, explaining how the A phase can be stabilized. This would seem to have been the 'smoking gun' for spin fluctuations, but in subsequent years, it was realized that there are many contributions to the pairing kernel besides spin fluctuations, such as density fluctuations, transverse current fluctuations, and so on. In fact, alternates to spin fluctuation theory have been proposed in the case of ^{3}He, including the 'nearly localized' approach of Vollhardt and the polarization potential model of Bedell and Pines (Vollhardt and Wolfle, 1990).

At this point, an important issue should be realized. Unlike the electron–phonon case where electrons and ions can be approximately treated as separate systems, the spin fluctuations themselves are composed of electrons. This makes the whole notion of 'pairing glue' suspect in this case. One consequence of this is that spin fluctuations do not appear to obey Migdal's theorem. How this theorem works for the classic phonon case is as follows. The ratio of the electron mass to the ion mass is very small, thus leading to a controlled perturbation expansion. For most cases, it is sufficient to stop at lowest order when evaluating the electron and phonon self-energies. The exception is the pairing instability, which requires summing a ladder series of repeated scattering. This neglect of vertex corrections, though, is not generally valid in the case of spin fluctuations, as shown by Hertz, Levin, and Beal-Monod (1976).

In 1979, Frank Steglich's group discovered superconductivity in the heavy electron alloy $CeCu_2Si_2$. This came in the face of existing wisdom that proximity to magnetism was deadly for superconductivity in metals (^{3}He obviously differs in that its pairs are composed of charge-neutral atoms). Soon,

several of these materials were discovered, and one of them, UPt_3, was known to exhibit strong spin fluctuation behavior. As expected, various spin fluctuation theories based on ^{3}He were proposed to explain the superconductivity seen in these materials. But subsequent neutron scattering revealed that these metals were nearly antiferromagnetic, rather than nearly ferromagnetic. In 1986, several theories were formulated for heavy fermions on the basis of neutron-scattering data (Miyake, Schmitt-Rink and Varma, 1986; Scalapino, Loh and Hirsch, 1986). The prediction was the formation of a singlet pair, this time due to the fact that in the presence of antiferromagnetic correlations an up spin electron prefers to be surrounded by down spin electrons. To avoid the strong on-site Coulomb repulsion, the pair state has d-wave symmetry. For a simple cubic lattice, the pairs take the form $(x^2-y^2) \pm i(3z^2-r^2)$. In real space, this pair wave function corresponds to six lobes that point from a given atomic site to its near neighbors.

In hexagonal symmetry, this two-dimensional group representation instead becomes isomorphic to $L = 2$, $M = \pm 1$ spherical harmonic. This E_{1g} model is a leading candidate to describe various experimental data in UPt_3, including the observation of the three different superconducting phases seen in the H, T phase diagram (Joynt and Taillefer, 2002). But problems with this model have led to a variety of other proposals, including the A, B model of Garg (two nearly degenerate single dimensional group representations), the p-wave model of Machida, and the f-wave model of Norman and Sauls. This last model (E_{2u}) provides a particularly good description of the H, T phase diagram, thermal conductivity, and transverse ultrasound data (Sauls, 1994). Triplet models (p, f) for UPt_3 are particularly attractive, since there has been no observed change in the Knight shift (i.e., the static spin susceptibility) when going below T_c, as opposed to other heavy fermion superconductors such as UPd_2Al_3 and $CeCu_2Si_2$ (Tou, Ishida and Kitaoka, 2005). The point to be made, though, is that despite many claims in the literature, the actual pairing symmetry of any heavy electron superconductor is unknown at present.

2 A BRIEF HISTORY – PART 2

In early 1986, high-temperature superconductivity was discovered by Bednorz and Mueller in the doped perovskite $La_{2-x}Ba_xCuO_4$ (LBCO) (Bednorz and Müller, 1986). It was not until November of that year, though, before the results were verified and thus led to wide-scale recognition. By January of 1987, superconductivity above the temperature at which air liquefies was found in the related compound $YBa_2Cu_3O_7$ (YBCO) by Chu and collaborators. The same month, a theory for these materials was proposed by Anderson (1987). He recognized that the undoped compound La_2CuO_4 would likely be a Mott insulator. He speculated that the Néel (antiferromagnetic) order of the insulator would be melted by quantum fluctuations (due to the low spin $S = 1/2$ of the d^9 Cu ion and the two-dimensional nature of the CuO_2 planes). Although Néel order was discovered subsequently, it indeed disappears when only a few percent of holes are doped into the material. Anderson denoted this melted Néel state as a *resonating valence bond* (*RVB*) state, which represents a liquid of spin singlet pairs. When the system is doped, the presence of charge carriers causes this spin pairing state to condense into a superconducting state. Originally, it was thought that the resulting pair symmetry would be s-wave-like, but subsequent work in 1988 predicted d-wave symmetry instead (Kotliar and Liu, 1988; Zhang, Gros, Rice and Shiba, 1988).

It was not long after Anderson's theory was announced in 1987 that more traditional spin fluctuation–based approaches were brought to bear on this matter. Bickers, Scalapino, and Scalettar observed that the 3D pairing state discussed earlier in the context of heavy fermion materials would reduce to $dx^2 - y^2$ in two dimensions (Bickers, Scalapino and Scalettar, 1987). Scalapino (1995) subsequently gave an intuitive picture of how such a pair state arises. In momentum space, the zero frequency limit of the real part of the effective potential coming from the Coulomb interaction is repulsive for all wave vectors, with a maximum at a wave vector (π, π) which would be the ordering wave vector for the undoped antiferromagnet (Figure 3). But Fourier transformed into real space, the effective potential has Friedel oscillations. Although obviously repulsive at short distances, the potential is attractive for near neighbor separations (Figure 3). In momentum space, this is reflected in the gap equation, where the sign change of the d-wave tight binding gap function $\Delta(\mathbf{k}) = \cos(k_x a) - \cos(k_y a)$ upon translation by (π, π) compensates for the repulsive sign of the potential V: $\Delta(\mathbf{k}) = \Sigma_{\mathbf{k}'} V_{\mathbf{k}\mathbf{k}'} \Delta(\mathbf{k}')$ where the pairing kernel $V_{\mathbf{k}\mathbf{k}'} = U + J(\cos(q_x a) + \cos(q_y a))$ with $\mathbf{q} = \mathbf{k} - \mathbf{k}'$, U positive and J negative.

Despite this initial success, there were no indications from experiment at that time supporting the existence of a d-wave pairing state. In fact, because the cuprates are somewhat dirty systems replete with impurities, the feeling was that the order parameter would have to be s-wave-like to avoid pair breaking. To understand this, we note that the d-wave order parameter changes sign under a reflection operation $xy \rightarrow yx$. Any impurity scattering that mixes these two states destroys the d-wave phasing relation.

In the early 1990s, though, experimental evidence began to emerge supporting a d-wave picture. The temperature dependence of the nuclear magnetic resonance (NMR) spin relaxation rate, the Knight shift, and the in-plane penetration depth

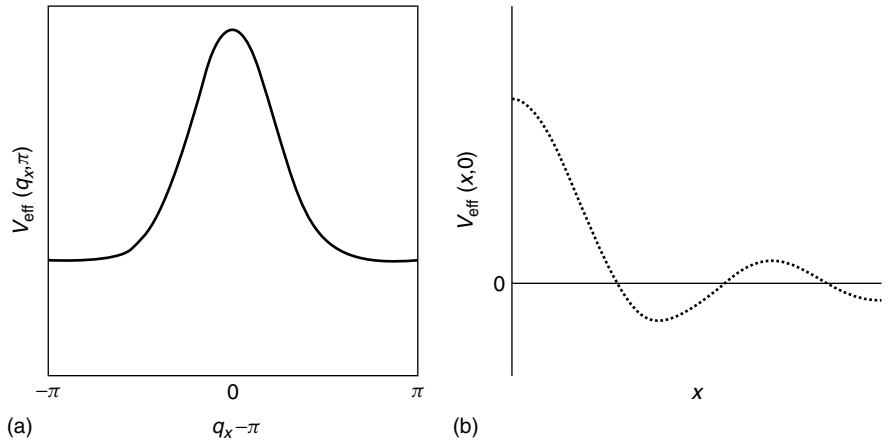

Figure 3. Effective interaction for spin fluctuation–mediated pairing (antiferromagnetic case). (a) Momentum space (a repulsive potential peaked at $\mathbf{q} = (\pi, \pi)$) and (b) real space (repulsive potential on site, attractive potential for a near neighbor separation).

did not follow the exponential behavior predicted for s-wave pairing, but rather the power law behavior predicted for a d-wave state due to the presence of a node (zero) in the order parameter. This node was subsequently imaged directly by angle-resolved photoemission. Then phase-sensitive Josephson tunneling saw the predicted sign change of the d-wave order parameter upon 90° rotation. Since then, a large body of experimental evidence has accumulated, including the dependence of T_c on impurities, that overwhelmingly confirms the d-wave nature of the pairs. At the same time, there has been great progress in the theory of spin fluctuations as applied to cuprates, as well as in solving the underlying microscopic theories based on the Hubbard model. In addition, there have been recent advances made in the RVB theories as well.

3 ELECTRONIC STRUCTURE OF THE CUPRATES

In the undoped cuprates, the copper ions are in a d^9 configuration. This corresponds to a single hole in the x^2-y^2 orbital (not to be confused with the d-wave pair state discussed earlier). Of all transition-metal oxides, the cuprates are unusual in that the copper d orbital and the oxygen p orbital have energies that are nearly degenerate (Pickett, 1989). As a consequence, the dominant energy scale in the problem is the large ($\sim$6 eV) bonding–antibonding splitting between the copper $dx^2 - y^2$ orbital and the oxygen p_x and p_y orbitals (Figure 4). This leaves the highest energy band (the antibonding one) as half filled. Adding Coulomb repulsion, this band splits into two, a lower Hubbard band and an upper Hubbard band. The resulting Mott insulating gap is of the order of 2 eV. Keeping all three bands, this is known as the *three-band Hubbard model*, but keeping

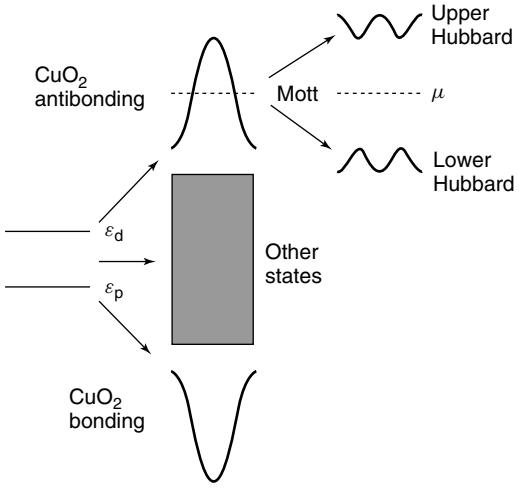

Figure 4. Electronic structure of the layered cuprates. The copper d and oxygen p levels hybridize, resulting in a partially filled antibonding band. A Mott gap due to Coulomb correlations splits this band, leading to the formation of an upper Hubbard band and a lower Hubbard band, with the chemical potential, μ, inside this gap for zero doping.

just the antibonding band it is known as the *single-band Hubbard model*. Almost all treatments assume the latter, though Varma has argued that important physics is thrown out upon such a reduction (as will be discussed later). In the limit of large Coulomb repulsion, U, one can then project onto the subspace which does not allow double occupation of the Cu site, leading to the $t - J$ model, where J, the superexchange interaction, is proportional to t^2/U and t is the effective hopping integral between Cu sites. J prefers antiferromagnetic orientation of the copper spins (one spin per site in the undoped case). This can be seen by the fact that the Pauli exclusion principle does not allow virtual double occupation unless the two spins are antialigned.

There are no exact solutions of either the single band Hubbard model or the simpler $t-J$ model in two dimensions. Approximate treatments have been done using quantum Monte Carlo, density matrix renormalization group, dynamical mean-field theory (and its various cluster extensions), and exact diagonalization of small clusters. Although there is no solid proof at this time, results are encouraging enough that there is a strong probability that a true d-wave pairing instability exists in these models. It is beyond the scope of this article to review these techniques. Instead, we give an overview of the spin fluctuation approach and its RVB counterpart, discuss these theories in relation to experimental data, and then end with a discussion of alternate mechanisms for cuprate superconductivity.

4 SPIN FLUCTUATION THEORIES

The literature on this subject is vast, so this brief review can only give the highlights. The basic idea is that in spin fluctuation theories, the pair potential V is found to be proportional to $I^2\mathrm{Im}\chi(\mathbf{q},\omega)$ where I is the effective spin interaction between electrons and $\mathrm{Im}\chi(\mathbf{q},\omega)$ is the imaginary part of the dynamic spin susceptibility, with the proportionality prefactor of order unity ($-3/2$ for spin singlet pairs and $+1/2$ for spin triplet pairs). 'I' itself is dependent on the underlying theory. For instance, in the Hubbard model, this would be the Hubbard interaction U, but if one used an effective low-energy theory, then it would be J, the superexchange interaction. At this level, the theory is equivalent to random phase approximation (RPA) where $\chi(\mathbf{q},\omega)=\chi_0(\mathbf{q},\omega)/(1-I\chi_0(\mathbf{q},\omega))$ with $\chi_0(\mathbf{q},\omega)$ the polarization bubble calculated using bare Greens functions.

There are several ways to consider going beyond RPA. One is simply to add fluctuation corrections to $\chi(\mathbf{q},\omega)$. To understand this approach (Lonzarich and Taillefer, 1985), we note that in a Ginzburg–Landau expansion for magnetism, the free energy would be of the form aM^2+bM^4 where M is the magnetization (staggered magnetization in the antiferromagnetic case). With fluctuations included, we note that upon factorization of M^4 one obtains a term of the form $6\langle M^2\rangle M^2$ where $\langle M^2\rangle$ is the expectation value of M^2 averaged over all statistical ensembles. This $6bM^2\langle M^2\rangle$ term then renormalizes the aM^2 term, leading to an $a_{\mathrm{eff}}=a+6b\langle M^2\rangle$, noting that a is simply the inverse (RPA) susceptibility (in statistical field theory, this is often denoted as the *Hartree approximation*). This approach has been enormously successful in describing transition-metal magnets, for instance, predicting the lack of magnetic long-range order in lower dimensions, and understanding why most magnets have transition temperatures strongly suppressed relative to mean-field (Stoner) theory. In turn, these fluctuations enter into the pair kernel, and this approach has been extensively studied by Moriya and coworkers in the context of a spin fluctuation–mediated picture for cuprate superconductivity (Moriya and Ueda, 2000, 2003).

Another way to go beyond RPA is to use dressed Greens functions rather than bare ones when constructing the polarization bubble. This is the basis behind the fluctuation exchange (FLEX) approximation (Bickers, Scalapino and White, 1989), where the self-energy used to dress the single-particle Greens functions is chosen to satisfy a certain self-consistency relation involving the free energy, the self-energy, and the Greens function (the conserving approximation of Gordon Baym). Subsequently, this method has been applied by many authors, to address not only the single-particle spectral function and the dynamic spin susceptibility but also the pairing interaction.

One issue with such approximations is that it is usually dangerous to dress the Greens functions without including vertex corrections in the spin susceptibility. In the 'two-particle self-consistent' approach of Vilk and Tremblay (1997), a similar procedure to FLEX is done, but now the interaction U (they assumed a Hubbard model) is replaced by U_{sp}, with U_{sp} a screened interaction (again chosen to satisfy certain self-consistent relations), which enters the susceptibility, $\chi(\mathbf{q},\omega)=\chi_0(\mathbf{q},\omega)/(1-U_{\mathrm{sp}}\chi_0(\mathbf{q},\omega))$, where as in FLEX χ_0 is calculated using dressed Greens functions. In essence, U_{sp} represents a constant vertex correction. More sophisticated approximations would allow U_{sp} to depend on momentum and frequency. Note that in such approaches, the U^2 prefactor of the pairing kernel is now replaced by UU_{sp}. A recent review of this and related approaches based on dynamical mean-field theory (and its cluster extensions) has been offered by Tremblay, Kyung, and Senechal (2006).

One can, of course, attempt to go beyond these approximations by performing a systematic diagrammatic expansion including vertex corrections, for instance, the work of Doug Scalapino and coworkers (Bulut, 2002). These authors have used quantum Monte Carlo simulations as a fundamental check of their work (as has the Tremblay group). The limitation is that such quantum Monte Carlo simulations cannot be carried out at low temperatures because of the so-called fermion sign problem (the many-body wave function having both positive and negative regions in the fermionic case leads to the problem of negative probabilities in the context of the simulations).

And, there have been some attempts to combine all of these ideas into a single approach. A good example is the extensive work of Chubukov and collaborators on a quantum field theoretical approach to the spin fluctuation problem, dealing with matters concerning the strong influence of quantum and thermal fluctuations, with the resulting non-Fermi liquid behavior. Space prohibits an adequate summary of this work,

and the reader is referred to a review article done by this group (Abanov, Chubukov and Schamlian, 2003).

Finally, one can go via the phenomenological route and replace $\chi(\mathbf{q}, \omega)$ in the pairing kernel by the experimental dynamic spin susceptibility. This approach has been exploited by a number of authors, in particular David Pines and coworkers (Monthoux and Pines, 1994), where they modeled $\chi(\mathbf{q}, \omega)$ based on the NMR data of Slichter's group. Subsequent work has exploited the growing amount of data for $\chi(\mathbf{q}, \omega)$ obtained by inelastic neutron scattering (INS).

So, what is the upshot of these approaches? For doping ranges relevant for experiment, they predict d$x^2 - y^2$ pairing. The physics is essentially equivalent to that discussed earlier in this article, and in the context of the cuprates, this was first discussed by Bickers, Scalapino and Scalettar (1987) as mentioned before. But what does this all mean when addressing experimental data?

5 SPIN FLUCTUATION THEORIES – CONFRONTING EXPERIMENT

First, we deal with the 'if' story; that is, does d-wave pairing really emerge from the underlying Hamiltonians (single-band Hubbard, $t - J$) that underlie these spin fluctuation approaches? Interestingly, the jury is still out on this question. The most detailed diagrammatic studies of Scalapino and coworkers (Bulut, 2002) have not definitely answered this question (the issue being whether vertex corrections do or do not suppress the pairing instability). Quantum Monte Carlo simulations have yielded conflicting results, some indicating an enhancement of pairing, others not, though the most recent studies indicate an enhancement (Sorella *et al*., 2002). The issue, of course, is the inability to access very low temperatures because of the fermion sign problem.

Of course, virtually all such approaches do yield d-wave pairing (within a given approximation), but the predicted values of T_c vary quite a bit. This even occurs in phenomenological models, where there was an interesting debate between two groups (Pines and Levin) concerning whether such models did or did not generate high T_c. Besides the obvious differences of the two phenomenologies (choice of U_{eff}, etc.), the main issue concerned how far in energy the dynamic susceptibility extended (Schuttler and Norman, 1996). Most INS studies are confined to less than 100 meV, but we now know that significant weight must be present beyond this energy scale to obtain a high T_c. Fortunately, recent INS measurements on underdoped LBCO and YBCO indicate spectral weight up to and beyond 200 meV (for the undoped material, spin fluctuations extend up to 400 meV). On the other hand, the susceptibility decreases with doping, and it is certainly not clear whether there is enough magnetic spectral weight in overdoped materials to be consistent with the relatively high T_c seen.

Of course, arguing about values of T_c might seem analogous to asking how many angels can dance on the head of a pin. After all, in BCS theory, T_c depends exponentially on its coupling constant. Of more relevance is what such theories tell us about experimental data.

Let us start with the one most debated, which is the nature of the phase diagram in cuprates. There are (of course) a number of versions of this, but Figure 5 gives a representative one. Besides the well-known magnetic (Néel) insulator at low doping and the superconducting phase at intermediate doping, several other phases have been proposed. Likely, at low temperatures, the Néel state continues as a disordered (spin glass) state, though the range of doping and the ubiquity of this phase are still debated. At high dopings, there is increasing evidence that the normal state is a Fermi liquid, with scattering rates roughly quadratic in temperature and energy, and thus with well-defined single-particle (quasiparticle) states. Near optimal doping above T_c, one sees a 'strange metal' phase characterized by 'marginal Fermi liquid'–like behavior (Varma *et al*., 1989). By this, we mean a scattering rate that is linear in temperature and energy. But of most interest is the pseudogap phase in the underdoped regime, first inferred from NMR measurements, and later studied extensively by INS, infrared conductivity, tunneling, specific heat, and perhaps most spectacularly by angle-resolved photoemission (ARPES). These studies

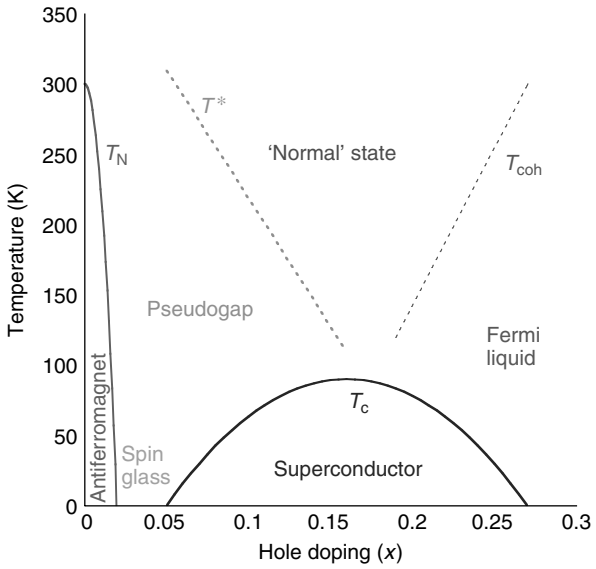

Figure 5. Phase diagram of the cuprates versus x, the number of doped holes per copper ion. Solid lines represent true thermodynamic phase transitions; dotted lines indicate crossover behavior.

indicate that an anisotropic gap emerges in the electronic excitations well above T_c. The question is about the nature of this gap.

One thought is that the pseudogap is a precursor to the superconducting gap (Randeria, Trivedi, Moreo and Scalettar, 1992). After all, in almost all magnets, the exchange splitting exists far above the ordering temperature, this temperature being strongly reduced by fluctuations as discussed in the preceding text. Stated equivalently, the exchange gap is not proportional to $\langle M \rangle^2$ but rather to $\langle M^2 \rangle$. Superconductors, though, usually do not demonstrate these effects. But cuprates are characterized by small carrier densities, short coherence lengths, and reduced (quasi-2D) dimensionality. All of these conspire to make fluctuation effects more profound. Some spin fluctuation models do advocate that the pseudogap is a pairing gap. But most assume that it is actually the magnetic exchange gap itself.

To understand this, note that because of the Mermin–Wagner theorem, long-range magnetic order at finite T would not occur in two dimensions. This is why the transition temperature of the undoped material is strongly suppressed relative to the value of J (which is of the order of 1500 K); that is, T_N is determined by residual three-dimensional coupling between the CuO_2 planes. But this 'three-dimensional' T_N is rapidly destroyed by doping. What is left then is a pseudogap state characterized by short-range antiferromagnetic fluctuations. As these are known to disappear with overdoping, this provides a natural explanation of the strong doping dependence of the T^* (pseudogap) crossover line. In some sense, the pseudogap phase is the 'renormalized classical' regime that exists above what is presumably a $T = 0$ magnetic phase transition. The effect is pronounced because of the quasi-two dimensionality (Vilk and Tremblay have demonstrated that this pseudogap is a property of two dimensions and would be very weak in the three-dimensional case (Vilk and Tremblay, 1997)).

These approaches have emphasized the potential 'quantum critical' nature of the phase diagram shown in Figure 5 (Laughlin, Lonzarich, Monthoux and Pines, 2001). The idea is that at a critical doping, antiferromagnetic fluctuations would disappear (T^* would go to zero). This purported 'quantum critical point' is buried under the superconducting dome. Is this coincidental? The spin fluctuation proponents say it is not, and note the similarity of the cuprate phase diagram to that determined in a number of heavy fermion magnets. In those cases, the systems are three dimensional, and thus the T^* line actually corresponds to the phase line for long-range ordering. And in several cases, a superconducting dome appears in the vicinity of where this phase line goes to zero temperature. This was first elucidated by Gil Lonzarich's group for $CeIn_3$ and $CePd_2Si_2$ under pressure (Mathur *et al.*, 1998), but this has now been seen for several other materials as well, including the first known heavy fermion superconductor, $CeCu_2Si_2$. This quantum critical point scenario, though, is not unique to magnetic models.

Despite first appearances, this 'nearly antiferromagnetic' picture of the pseudogap phase is quite different from the RVB one presented in the next section. In the RVB approach, the fluctuations are singlet in character, but in the spin fluctuation approach, they are antiferromagnetic in nature. Note that a singlet is $S = 0$, but an antiferromagnet corresponds to a mixture of $S = 0$ and $S = 1$, $S_z = 0$. They are obviously not the same object. This controversy is best highlighted by two recent papers, one by Barzykin and Pines (Barzykin and Pines, 2006) and the other, the RVB review article by Lee, Nagaosa, and Wen (2006). In both cases, spin susceptibility data are compared to results of the 2D Heisenberg antiferromagnet. In the former case, there is a match (Figure 6) and in the latter case there is a large discrepancy. Part of this disagreement is due to the assumed 'offset' of the susceptibility: the former assumes a temperature-independent but doping-dependent Fermi liquid component and the latter, that the only offset is due to the van Vleck contribution. But the major disagreement concerns the magnitude of J: the latter use the value of 130 meV appropriate for the insulator, but the former assume that T^* is actually J itself, and, thus, strongly doping dependent. To justify this, these authors ironically quote the RVB result that the effective exchange J_{eff} should be $J - tx$ (where t is the hopping and x is the doping).

The nature of the dynamic spin susceptibility itself is more controversial. In Figure 7, the famous 'hourglass' plot of the energy–momentum relation of the spin fluctuations is presented (Tranquada *et al.*, 2004). This was first elucidated for underdoped YBCO in its superconducting state (Arai

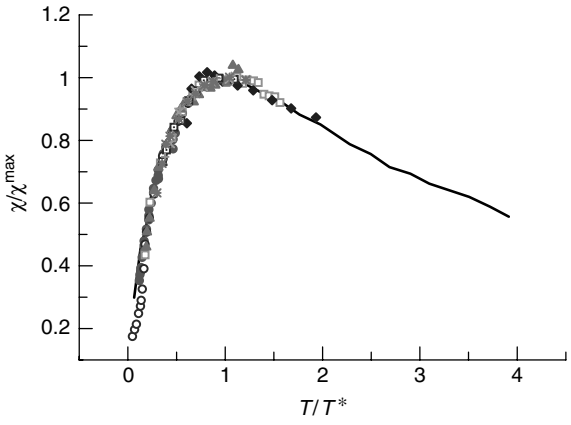

Figure 6. Comparison of the 2D Heisenberg model to experimental susceptibility data in YBCO. (Reproduced from V. Barzykin *et al.*, 2006, with permission from the American Physical Society. © 2006.) The data are scaled assuming that the effective exchange at a given doping is equal to the pseudogap onset temperature T^*.

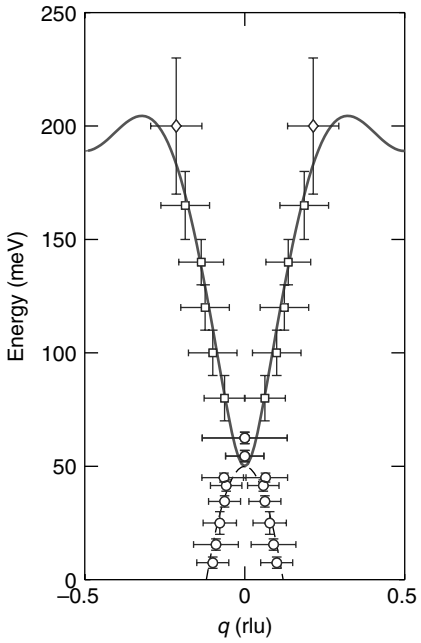

Figure 7. Hourglass-like dispersion of the spin excitations in the stripe-ordered phase of LBCO, measured with respect to $\mathbf{q} = (\pi, \pi)$, as revealed by inelastic neutron scattering. (Reproduced from J.M. Tranquada *et al*., 2004, with permission from Nature Publishing Group. © 2004.) A similar dispersion is seen in the superconducting state of underdoped YBCO (Hayden *et al*., 2004).

et al., 1999). It is characterized by strong intensity at the neck of the hourglass which occurs at a commensurate wave vector of $\mathbf{q} = (\pi, \pi)$ known as the *resonance*, with two incommensurate 'bowls' above and below. Although not apparent in Figure 7, it is now known that the hourglass has a 45° twist in momentum space, with the incommensurability below resonance oriented along the CuO bond directions and that above resonance oriented along the diagonals (Hayden *et al*., 2004).

This unusual pattern has been reproduced by various RPA-type calculations. To understand this result, note that in the superconducting state, the polarization bubble becomes $G_{\mathrm{k}}G_{\mathrm{k+q}} + F_{\mathrm{k}}F_{\mathrm{k+q}}$ where G_{k} is the normal Greens function and F_{k} the anomalous (Gor'kov) Greens function. The latter is proportional to the gap, Δ_{k}. For s-wave superconductors, the presence of a gap causes a 2Δ gap in $\mathrm{Im}\chi_0$. But because the gap is constant in the s-wave case, these two terms (*GG* and *FF*) destructively interfere in such a way that no pole develops in the RPA expression $\chi = \chi_0/(1 - I\chi_0)$. On the other hand, for the d-wave case, the two terms reinforce near $\mathbf{q} = (\pi, \pi)$ since the gap product $\Delta_{\mathrm{k}}\Delta_{\mathrm{k+q}}$ is negative (Fong *et al*., 1995). As a consequence $\mathrm{Im}\chi_0$ has a step jump at the 2Δ threshold. By Kramers–Kronig, this translates into a log divergence in the real part at $\omega = 2\Delta$, and thus a pole in χ is guaranteed at some $\omega < 2\Delta$. The dispersion of $\mathrm{Im}\chi$ away from (π, π) can either be upward (magnonlike) or downward (reverse magnonlike), depending on the Fermi surface geometry. In the latter case, one reproduces the downward part of the hourglass in Figure 7. The upper part of the hourglass is a consequence of the fact that the RPA response is typically incommensurate for frequencies above that of the (π, π) resonance, and some calculations also reproduce the 45° twist effect mentioned above (Eremin *et al*., 2005).

There is, though, an alternate explanation for the data based on 'stripes' (Tranquada *et al*., 2004). The idea is illustrated in Figure 8 (Tranquada *et al*., 1995). All of the above theories assume homogeneous behavior. But what if instead the system prefers to be inhomogeneous. To understand this, note that each doped hole in a CuO_2 plane breaks the four magnetic bonds that connect a given copper ion to its four neighbors. This is energetically costly, and one way to minimize this effect is having the holes clump together. But the long-range part of the Coulomb interaction will not prefer this clumping of charge. As a compromise, it was proposed some years ago that the system would instead organize into a lamellar phase where 'stripes' composed of the doped holes would be separated by undoped (antiferromagnetic) regions (Zaanen and Gunnarsson, 1989). This idea naturally explains why the separation of the incommensurate wave vector from (π, π) (width of the bottom of the 'hourglass' in Figure 7) scales with the doping (the well-known Yamada plot (Fujita *et al*., 2002) shown in Figure 9). In this picture, the incommensurability is due to the 'skip' of the antiferromagnetic structure across the stripe (that is, the antiferromagnetic

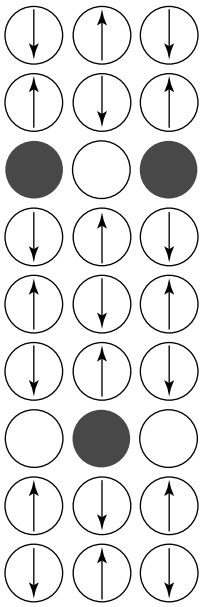

Figure 8. Stripe picture for $x = 1/8$ doping–circles are copper sites, arrows represent spins, and dark circles are doped holes.

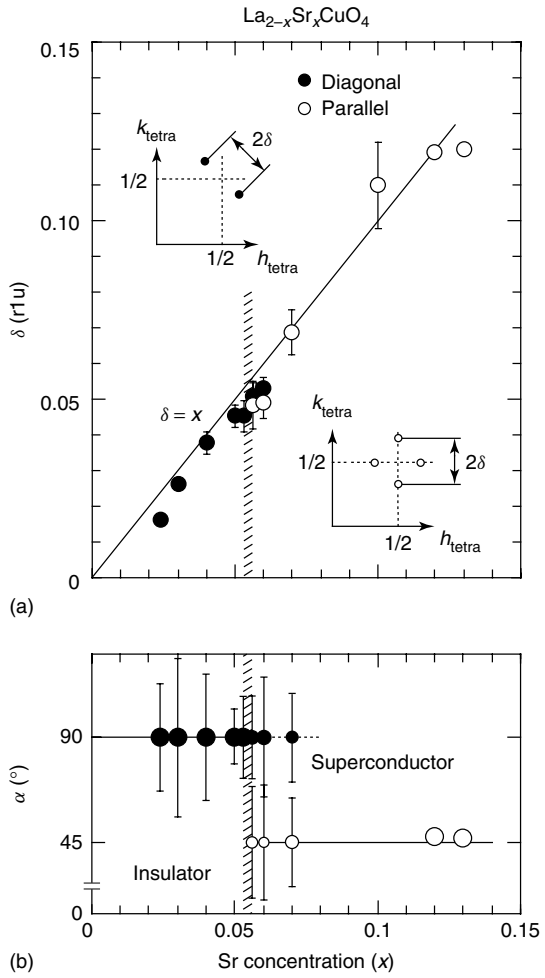

Figure 9. (a) Neutron-scattering peaks versus doping for $La_{2-x}Sr_xCuO_4$ (LSCO). (b) The spot pattern rotates by 45° at the spin glass/superconducting boundary. δ is the incommensurability and α, the angle of the spots in momentum space relative to the (π, π) wave vector. (Reproduced from M. Fujita *et al*., 2002, with permission from the American Physical Society. © 2002.)

domains themselves are commensurate), as opposed to RPA, where the incommensurability is due to the 2D Fermi surface geometry (which under certain assumptions (Si, Zha, Levin and Lu, 1993) can also reproduce the Yamada plot). And, detailed simulations by several groups have also reproduced the hourglass itself (Uhrig, Schmidt and Gruninger, 2004). The upper part of the hourglass is just the gapped magnonlike dispersion one would obtain for an undoped two-leg ladder (which is used to model the antiferromagnetic domains). The lower part of the hourglass is due to spin-wave-like excitations associated with the stripe periodicity (in the simulations, they are due to the much weaker exchange that couples one spin ladder across a stripe to the next spin ladder). The 'twist' of the hourglass also naturally emerges from these simulations.

The important point to emphasize is how different these two explanations of the 'hourglass' are. In the RPA case, the assumption is a homogeneous 2D material. The spin excitations are derived from underlying fermionic and pair excitations (from G_k and F_k). The d-wave symmetry of the gap and the shape of the 2D Fermi surface are crucial for the obtained results. In the stripes case, though, the simulations are essentially undoped spin ladders connected by weak exchange. There are no underlying fermionic degrees of freedom. The physics is crucially dependent on the inhomogeneity of the stripes and their quasi-1D character (the spin gap associated with the upper part of the hourglass is the ladder analog of the Haldane gap associated with a linear chain of spins). In support of the 'stripes' picture, Tranquada's group has seen the hourglass as well for LBCO at $x = 1/8$ (Tranquada *et al*., 2004) which is not superconducting because of the formation of static stripes (Tranquada *et al*., 1995). On the other hand, it is quite possible that the RPA-like theories would work in this case as well if the pseudogap had d-wave symmetry. A recent ARPES study has indicated that the $T = 0$ pseudogap state indeed has the same nodal structure as the d-wave superconducting state (Kanigel *et al*., 2006), and new ARPES results indicate a similar story as well for LBCO at $x = 1/8$ (Valla *et al*., 2006).

The next experimental controversy concerns unusual features seen in the single-particle spectral function measured by ARPES and the resulting density of states measured by tunneling spectroscopy. Both find a very unusual spectral lineshape in the superconducting state (Figure 10), with a sharp peak at the gap energy followed at higher energies by a spectral dip and at even higher energies by a broad hump (peak-dip hump). It was speculated early on that this might be some strong coupling feature as seen previously in tunneling spectra for conventional superconductors. The idea is that the spectral dip represents a singularity in the electron self-energy. This results in a two-branch spectrum, the low-energy branch (associated with the sharp peak) represents a renormalized quasiparticle-like dispersion, and a higher-energy branch (the 'hump'), a dispersion which at high energies traces out the bare one (Norman *et al*., 1997). The theory for this had been worked out in by Engelsberg and Schrieffer (1963) in the context of the electron–phonon interaction. The singular energy would then be the sum of the gap energy Δ and the boson energy Ω (in their case, a phonon), and thus a subtraction of the gap and dip energies would yield Ω (the physics of this can be seen from the Feynman diagram in Figure 11). Norman *et al*. noticed that for a slightly overdoped Bi2212 sample the peak-dip-hump structure was only visible below T_c; above T_c one simply saw a single broad peak (Figure 10). On this basis, they felt that the effect was unlikely to be due to a phonon (which would of course still be present above T_c) and more likely

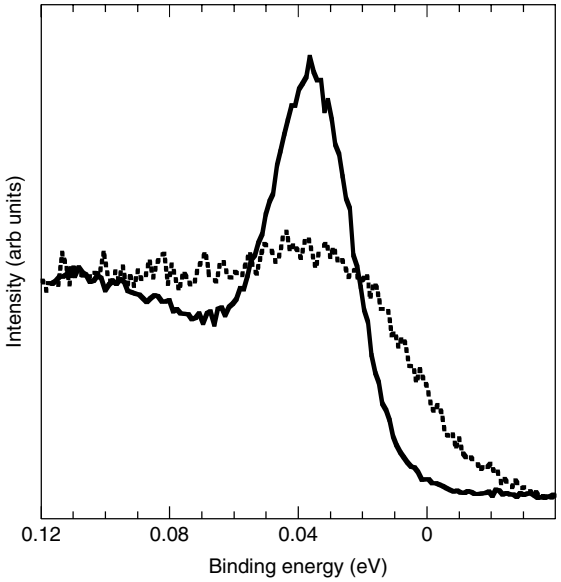

Figure 10. ARPES spectra at $k = (\pi, 0)$ for an overdoped ($T_c = 87$ K) Bi2212 sample in the normal state (dotted line) and superconducting state (solid line). (Reproduced from M.R Norman *et al*., 1997, with permission from the American Physical Society. © 1997.)

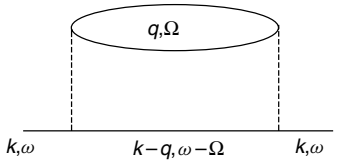

Figure 11. Lowest-order Feynman diagram for electron–electron scattering. For the spin resonance case, the bubble labeled by (**q**, Ω) is replaced by the dynamic spin susceptibility. For the phonon case, it is replaced by the phonon propagator.

due to some kind of electronic collective excitation. Noting that (i) the peak-dip-hump effect was strongest at the $(\pi, 0)$ point of the Brillouin zone that are connected to one another by (π, π) wave vectors and (ii) the energy of the boson was inferred to be 40 meV, the same as seen for the (π, π) spin resonance in optimal doped YBCO (the neck of the hourglass in Figure 7), Norman *et al*. speculated that the boson instead was the spin resonance and in a later paper by this group, they gave evidence that the doping dependence of the boson energy was consistent with INS, which finds that the resonance energy falls with underdoping (Campuzano *et al*., 1999). This was very unusual since the gap energy increases strongly as the doping is reduced. Subsequently, Zasadzinski *et al*. (2001) traced the mode energy in great detail with tunneling, exploiting its higher-energy resolution (Figure 12). They found that the boson energy scales as $5T_c$, just as the resonance does in neutron data. Moreover, with overdoping, the boson energy approaches

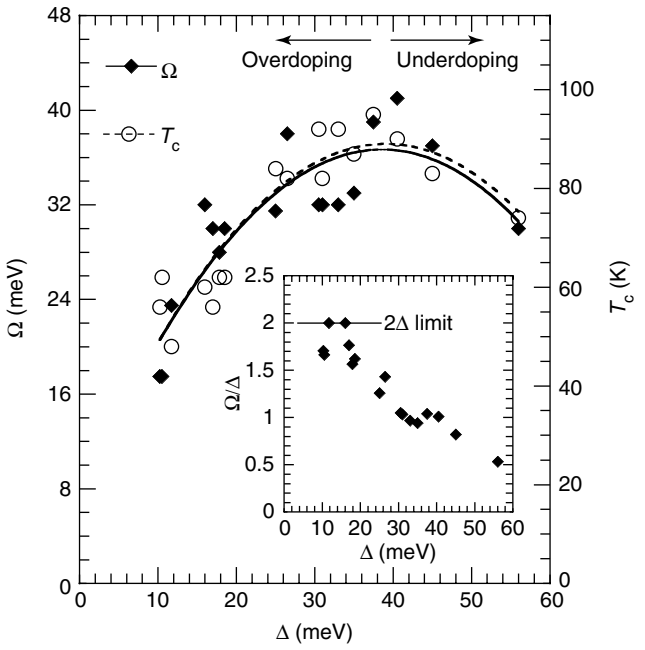

Figure 12. Resonance energy versus doping inferred from tunneling data, showing scaling with T_c. The inset demonstrates that this energy saturates to 2Δ in the overdoped limit. (Reproduced from J.F. Zasadzinski *et al*., 2001, with permission from the American Physical Society. © 2001.)

but never exceeds 2Δ, as would be expected for a collective mode inside of a 2Δ gap (as occurs in the RPA calculations discussed above).

With the development of improved (Scienta) detector technology, the momentum and frequency dependence of this effect in ARPES has been mapped out in much greater detail. The peak-dip-hump spectra in constant momentum slices energy distribution curves (EDCs) are reflected in a two-branch dispersion which is translated to a single 'S'-shaped dispersion when traced used constant energy slices momentum distribution curves (MDCs). As with the peak-dip hump, this 'S'-shaped anomaly disappears when going above T_c (Sato *et al*., 2003). All of these effects become less pronounced as one moves in the zone from the $(\pi, 0)$ point toward the d-wave node (Kaminski *et al*., 2001). Along the nodal direction, the MDC dispersion forms a kink behavior (Bogdanov *et al*., 2000) instead of an 'S', and the resulting EDC at the node itself has a 'break' (Kaminski *et al*., 2000) rather than a clear spectral 'dip'. But the spectral behavior seems to continuously evolve as a function of momentum, indicating that all the strong coupling effects have a similar origin (Kaminski *et al*., 2001).

This picture, though, has been challenged by a number of groups. Kee, Kivelson, and Aeppli (2002) have questioned whether there is enough spectral weight in the resonance (typically a few percent of the total spin fluctuation spectral

weight) to account for the strong effects seen in ARPES and tunneling. This reduces to an argument concerning the size of the interaction I in the boson spectral function $3/2I^2\chi(\mathbf{q}, \omega)$ (Abanov *et al*., 2002). More seriously, Lanzara *et al*. (2001) have seen the nodal kink in a variety of different cuprates for different dopings at essentially the same energy. They also see a weaker kinklike effect above T_c. Because of this, they speculated that the boson was instead a phonon. Extra evidence for phonons was given in later experiments that found an oxygen isotope effect (Gweon *et al*., 2004) (yet to be reproduced by other groups), and the idea was extended by Cuk *et al*. (2004) to deal with other regions of the zone (they propose a breathing mode to explain the nodal 'kink' and a buckling mode to explain the antinodal 'S'). Cuk *et al*. advocate that the rapid appearance of the 'S' below T_c is due to the gapping of the internal fermion line in the Feynman diagram in Figure 11. Further support for this picture has been given in a recent scanning tunneling microscopy (STM) study, where an analysis of the peak-dip-hump structure indicated (i) a doping-independent boson energy and (ii) a significant oxygen isotope effect (Lee *et al*., 2006). An advantage of this study is that it was a local probe, and thus the local gap energy (which changes significantly with location in most STM studies of Bi2212) could be subtracted off to determine the local boson energy. A disadvantage of this analysis was that the boson energy was not associated with the dip energy scale as in other studies, but rather with a maximum in the derivative $(\mathrm{d}^2I/\mathrm{d}V^2)$ spectrum (which corresponds to an energy intermediate between the dip and hump energies). The physical significance of this alternate energy scale is not apparent, since there is no feature in the raw $\mathrm{d}I/\mathrm{d}V$ data at this energy.

One mysterious fact concerns the doping independence of the nodal kink energy mentioned above. From the Feynman diagram in Figure 11, this energy should be $\Delta + \Omega$ (where Δ is the gap value at the antinode), but Δ is known to be a strong function of doping. This requires Ω to have an opposite doping dependence to compensate. There is no evidence that this occurs for phonons, but this would occur in the spin case for underdoped materials (with Ω and Δ having opposite doping dependences (Eschrig, 2006)). A way out is to assume forward (small $\mathbf{q}$) scattering (Kulic and Dolgov, 2005) in Figure 11 instead (so that at the node Δ reduces to zero), but this is not consistent with the $\mathbf{q}$ dependence of the above-mentioned phonons (or the spin fluctuations for that matter).

Of course, one could argue that all of these results are suspect in that they implicitly assume Figure 11, which is a lowest-order result (and thus inherently assumes a Migdal approximation). It was already mentioned that such an approximation can be suspect for spin fluctuations. Moreover, some authors have advocated that the hump is a polaron effect, with the hump maximum representing multiple phonon shake offs (Shen *et al*., 2004). In the spin case, the ultimate strong coupling picture is that advocated by Anderson and coworkers based on the RVB picture (Anderson *et al*., 2004).

6 RVB THEORY

This concept was proposed early on by Anderson (1987). Anderson assumed that quantum fluctuations (due to the low spin $S = 1/2$ of the Cu d^9 ion and the quasi-two dimensionality of the crystal structure) would melt the Néel order typically associated with Mott insulators. He proposed that the resulting state would be a liquid of spin singlets. As a given singlet involves coupling two of the copper ions, and each copper ion is surrounded by four other copper ions, then each bond can be either part of a singlet or not (Figure 13). Therefore, each bond can 'resonate' between being part of a singlet or not, hence the notation 'resonating valence bond' (after the work of Pauling, where in benzene, say, one can think of each carbon–carbon link as resonating between a single electron and a double electron bond). Now, imagine doping a hole into such a configuration. Since each copper ion in the undoped case participates in a singlet, then one singlet is broken. This leaves a free chargeless spin (denoted as a *spinon*) and a spinless charged hole (denoted as a *holon*). This implies the presence of spin-charge separation. The jury is still out on this particular question. In one dimension, spin-charge separation with its resulting non-Fermi liquid characteristics do occur (and is one of the major motivations for those pursuing models based on stripes). But to date, there is no exact answer to this question in two dimensions.

Regardless, Anderson's idea had a profound influence on the field. It emphasized that the cuprates should be thought of as doped Mott insulators, that a 'single-band'

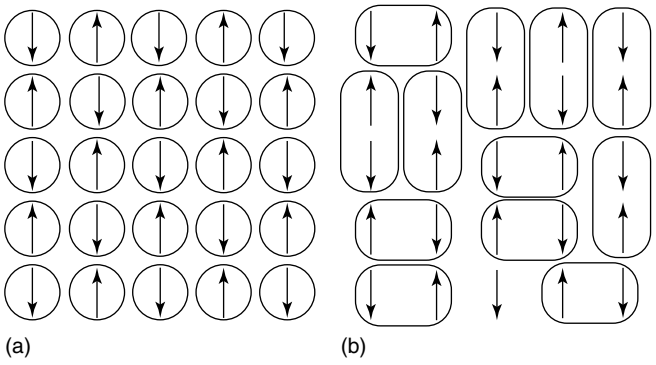

Figure 13. Néel lattice (a) versus RVB (b). The RVB state is a liquid of spin singlets. Circles are copper sites, arrows represent spins, and ovals are spin singlets.

approximation should be adequate, and that non-Fermi liquid effects would be pronounced. It also suggested a novel mechanism for superconductivity. Once the doped holes became phase coherent (at temperatures below the phase coherence temperature, which is roughly proportional to the doping), then spin-charge recombination would occur. The resulting charged singlets would be superconducting because of bose condensation of the holons. Although the original prediction for this superconducting state was s wave, it was realized by several groups within a year that the actual lowest free-energy state would be d wave (Kotliar and Liu, 1988; Zhang, Gros, Rice and Shiba, 1988).

One interesting prediction of this theory is that the pairing (spin) gap would be maximal at zero doping and then decay approximately linearly with doping (the $J_{\text{eff}} = J - tx$ relation mentioned before). On the other hand, the superconducting order parameter would initially be linear in doping, reach a maximum, and then follow the pairing gap for overdoped materials, forming the famous superconducting dome (Figure 14). The resulting phase diagram (also shown in Figure 14) reveals four different states, a superconducting state, a strange metal phase, a Fermi liquid, and a spin gap phase (Nagaosa and Lee, 1992). The RVB spin gap was probably the first prediction for the subsequently observed pseudogap phase. In RVB theory, the pseudogap phase corresponds to a spin singlet state (with its resulting spin gap) but no phase coherence in the charge degrees of freedom. One of the interesting ideas to emerge from this was an explanation for transport in this phase, which reveals a metallic behavior for in-plane conduction, but an insulating behavior for conduction between the planes. In the RVB picture, the metallic behavior is due to the fact that the holons can freely propagate. But to tunnel between the planes, the holons and spinons must recombine to form physical electrons, and this costs the spin gap energy, thus one obtains insulating like behavior for the c-axis conduction (Lee, Nagaosa, Wen, 2006). This 'gap' has now been directly seen in c-axis infrared conductivity data (Homes *et al*., 1993).

At the mean-field level, the RVB physics is relatively well understood. Going beyond mean-field theory has been a challenge. One way is to note that when considering a $t - J$ model, the RVB ground state corresponds to a projected BCS wave function (the projection designed to remove all d^{10} copper sites, which would be at infinite energy in the infinite U limit). One can perform variational Monte Carlo simulations with such a wave function. At zero doping, this state is energetically competitive with the true (Néel) ground state (there is no sign problem in the undoped case, so extensive Monte Carlo simulations have been performed). Though no proof exists for finite doping, we know that the Néel state is rapidly destroyed with doping, and it is anticipated that the RVB state, if anything, will be more

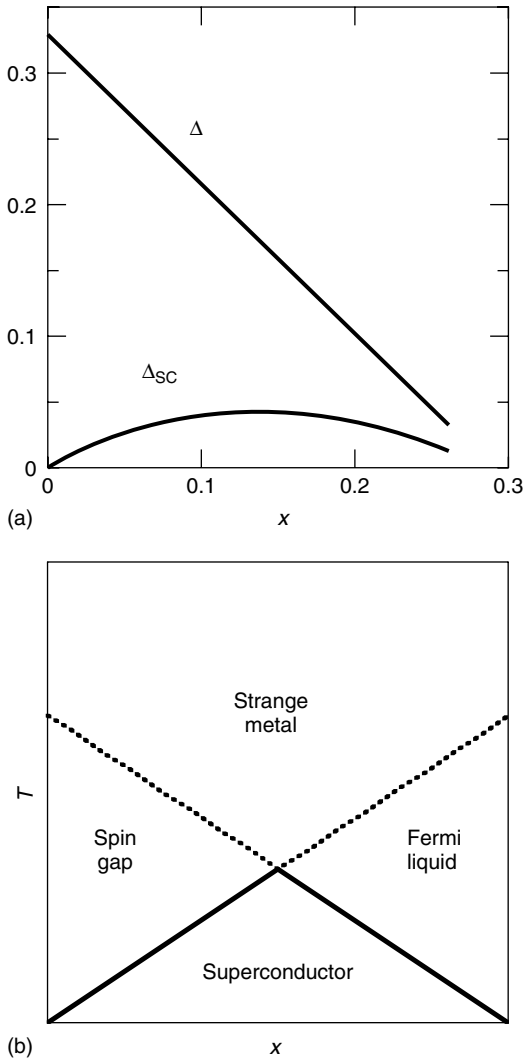

Figure 14. Spin gap, Δ, and superconducting order parameter, Δ_{SC}, as a function of doping from RVB theory (a). RVB phase diagram (b).

competitive once the magnetism disappears. Recent advances in Monte Carlo technology has allowed other quantities besides the group state energy to be calculated. Paramekanti, Randeria, and Trivedi have exploited this to calculate a variety of properties at zero temperature, in particular, the doping dependence of the spin gap, the superfluid weight, the quasiparticle residue, the Drude weight, and the nodal Fermi velocity (Paramekanti, Randeria and Trivedi, 2001). The results are in favorable agreement with experiment. Extending these studies to finite temperature and excited state properties remains a challenge for the future. As an aside, one can also perform a partial projection. This is the basis of the gossamer superconductivity theory of Laughlin (2006), that predicts a ghostly form of superconductivity for small dopings.

The other approach (Lee, Nagaosa, Wen, 2006) has been to exploit the same quantum field theoretic treatments used for heavy fermion materials (the slave boson approach for the Kondo lattice). The spinons and holons are not physical objects, and there is an arbitrary phase relation between the two. This introduces a U(1) gauge degree of freedom in the problem (that cancels for the physical electron). Associated with this is a vector gauge field that acts to satisfy the constraint that the spinon and holon currents balance (the scalar component of the field satisfying the no double occupation constraint). In this formalism, the mean-field state is the saddle point of the resulting Lagrangian. Fluctuations are represented by the quadratic terms associated with the gauge fields. This theory has had some successes (some of the calculated properties qualitatively follow the doping trends found later by the variational Monte Carlo simulations). In particular, it gave the first understanding of how the Fermi surface could be large for hole doped materials (scaling like $1 - x$), whereas the quasiparticle, Drude, and superfluid spectral weights scale as x (Kotliar, 1995). In essence, the Fermi surface remains large as the doping is reduced, but its spectral weight continuously disappears, so it ends up vanishing, much in the way of the Cheshire cat in Alice in Wonderland. This picture is more or less consistent with photoemission and optics data.

There were problems with the U(1) theory, though. Such a theory predicted that the linear T term in the superconducting penetration depth (due to thermally excited carriers near the d-wave node) scales as x^2, which has not been observed. This led Patrick Lee and collaborators to look at an SU(2) generalization (Lee, Nagaosa, Wen, 2006). In the undoped case, the presence of a down spin on a copper site is equivalent to the absence of an up spin (because in the undoped case, every copper site has exactly one spin). As Affleck *et al*. point out (Affleck, Zou, Hsu and Anderson, 1988), this implies that the U(1) symmetry previously mentioned expands to an SU(2) symmetry in the undoped case. Connected to this is the fact that in the undoped case, the d-wave spin pairing state is quantum mechanically equivalent to the so-called π flux phase where currents flow around a copper plaquette (Figure 15), these two states being connected by a rotation in particle–hole space. Obviously, this SU(2) symmetry is reduced to U(1) upon the introduction of holes, but the fluctuations implied by this enlarged symmetry group are certainly relevant. In this SU(2) picture, the above-mentioned problem is 'fixed' (the linear T term in the penetration depth become roughly doping independent (Wen and Lee, 1998)), and in such a formalism, the pseudogap phase can be thought of as a state that fluctuates between a 'superconducting' direction and a 'flux phase' direction. In other words, the pseudogap phase is a fluctuating mother phase, from which various long-range ordered phases emerge

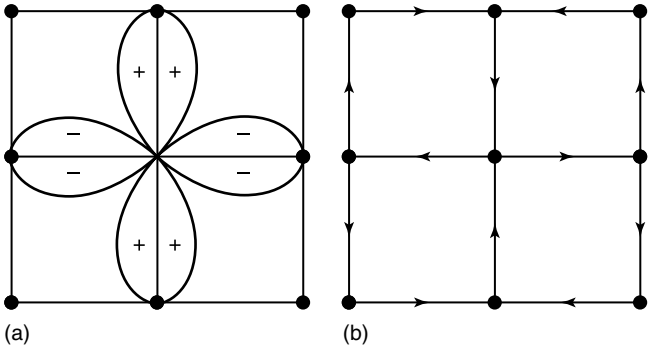

Figure 15. Two RVB states that are equivalent at zero doping: d-wave spin pairing state (a) and π flux state (b). Dots are copper ions and arrows are bond currents.

at lower temperatures (magnetic and spin glass states at low doping, superconductivity at intermediate doping). Note that the flux phase state is an orbital current phase, and is related to the d-density wave state that has been advocated by others as a phenomenological approach to the pseudogap phase (Chakravarty, Laughlin, Morr and Nayak, 2001).

This formalism also gives some idea into the existence of a Nernst effect above T_c (Xu *et al*., 2000). In normal metals, the Nernst effect (a transverse voltage generated by a thermal gradient) is small due to approximate particle–hole symmetry. But in superconductors, it can be very large in the presence of unpinned vortices (whose flow due to the thermal gradient generates a transverse voltage). Surprisingly, in cuprates, this Nernst effect extends significantly far above T_c, implying the existence of vortices well above T_c. But we know the superconducting gap is large, so how can such vortices be energetically favorable? In the SU(2) picture, this occurs since the vortex core is the pseudogap phase itself (rather than some gapless normal state) (Lee, Nagaosa, Wen, 2006). This pseudogap, in fact, has been seen in the vortex core of superconducting samples by STM measurements (Renner *et al*., 1998).

One issue with these types of theories is that they predict certain topological excitations associated with the gauge fields that have yet to be seen by experiment. Until they are, there will always be doubts about such approaches, since they are difficult to employ and the gauge fluctuation expansion is not well controlled, a common bane of strong coupling theories.

On more general grounds, one can ask how different these strong coupling approaches are from the more 'weak coupling' approaches discussed earlier. A famous debate has arisen on this subject, with Laughlin claiming that RVB and spin fluctuations represent two different limits of the same underlying theory (Laughlin, 1998), whereas Anderson has strongly differed (Anderson, 1997). As we pointed out earlier, there is one significant difference between these two

types of approaches. The spin fluctuation based approaches assume antiferromagnetic fluctuations, whereas in RVB, the fluctuations are singlet in character. It is somewhat surprising that this fundamental distinction has yet to be definitely cleared up by experiment.

7 ALTERNATE MECHANISMS

Space prohibits a detailed summary of the countless theories that have been proposed in the context of cuprate superconductors. But in this section, those of some note will be mentioned, especially in connection to what was discussed in the preceding text. This section (and article) is then ended with a brief discussion of the 'phonon' question.

The SO(5) approach of Zhang and collaborators (Demler, Hanke and Zhang, 2004) is similar in spirit to the SU(2) approach just mentioned. Instead of fluctuating between a flux phase and a superconducting phase, one fluctuates between the two known ground states (antiferromagnetism and superconductivity). The minimal group which contains these two order parameters is SO(5) (the 'five' being the real and imaginary values of the superconducting order parameter, and the three spatial components of the Néel vector). SO(5) has 10 generators, 4 of them being the charge operator and the 3 spin components, the other 6 are so-called π operators that connect the superconducting and Néel sectors of the theory. These operators, acting on the superconducting ground state, create the previously mentioned (π, π) resonance – that is, this resonance can be thought of as an excited triplet pair state with center of mass momentum (π, π). In the SO(5) case, though, this resonance is a property of the particle–particle channel, and only appears in neutron scattering because of particle–hole mixing in the superconducting state. This theory thus naturally explains why the resonance is only seen below T_c, and why its doping and temperature dependences scale with the superconducting order parameter (a property which does not obviously follow from the RPA calculations previously discussed). It also predicts that the vortex core is antiferromagnetic (Arovas, Berlinsky, Kallin and Zhang, 1997) and that charge modulation effects seen in tunneling for underdoped samples are from a checkerboard pair density wave state (Chen *et al*., 2002) (as opposed to stripes). There are some issues connected with this theory, though. The (π, π) resonance in this theory is an antibound state, as opposed to RPA where it is a bound state. Available data are much more consistent with the latter, as the resonance energy is less than 2Δ (that is, it lies below the particle–hole continuum rather than above (Tchernyshyov, Norman and Chubukov, 2001)). Moreover, although the theory incorporates the fact that the undoped material is an antiferromagnet, it does not take into account the fact that it is a Mott insulator (where the charge excitations are strongly gapped). To correct this obvious deficiency, a modified theory known as *projected SO(5)* has been developed, and the reader is referred to the literature for a discussion of this technique and how it addresses spectroscopy data like photoemission in the low doping regime (Zacher, Hanke, Arrigoni and Zhang, 2000). Space also prohibits a discussion of other 'preformed' pairs scenarios, such as the QED_3 theory of Franz and Tesanovic that advocates that the pseudogap phase is a phase disordered superconductor characterized by a proliferation of vortexlike excitations (Franz and Tesanovic, 2001).

The π flux phase mentioned in the context of RVB theories is an orbital current phase with an associated wave vector of (π, π). Such a phase is characterized by point nodes, that have been recently inferred as the $T = 0$ ground state of the pseudogap phase by thermal conductivity (Sutherland *et al*., 2005) and more recently photoemission data (the latter directly imaging the nodes (Kanigel *et al*., 2006)). On the other hand, there is no evidence from photoemission that the pseudogap (at least the low-energy one associated with the leading edge of the ARPES spectrum) has a finite $\mathbf{q}$ vector associated with it. In fact, current ARPES data are consistent with the pseudogap being tied to both the Fermi surface and to the Fermi energy, as would be expected for a $\mathbf{q} = 0$ state (a superconductor is a $\mathbf{q} = 0$ state, since the center of mass momentum of the pair is zero). But the π flux phase state is not the only orbital current phase that has been proposed. Varma has argued that when one reduces from the three-band model (copper $d x^2 - y^2$ orbital and oxygen p_x and p_y orbitals) to the commonly employed single-band model (the antibonding mixture of the copper and oxygen states), one has thrown out the baby with the bathwater so to speak (Varma, 2006). He believes a complete theory must keep all of these degrees of freedom. Although a discussion of this important topic would take us far outside the bounds of this review, it should be noted that optics data have revealed changes in spectrum when passing through T_c which extend up to several electronvolts (Rübhausen *et al*., 2001). If these degrees of freedom are important for superconductivity, then indeed neglecting higher-energy degrees of freedom could be dangerous. In Varma's theory, a unique orbital current phase emerges because of a nontrivial (Berry) phase involving the three different orbitals. This shows up in the antibonding band at the Fermi energy as an orbital current which flows in the subplaquette formed by a copper ion and its surrounding oxygen neighbors (Figure 16). Since the structure is based on the unit cell itself, it is a $\mathbf{q} = 0$ state. Originally, the theory had a current pattern such that would generate magnetic reflections for diagonal aligned Bragg vectors (Figure 16b). These were searched for by neutron scattering and not found. A related circular dichroism experiment was performed in photoemission by Kaminski *et al*. (2002) and found a

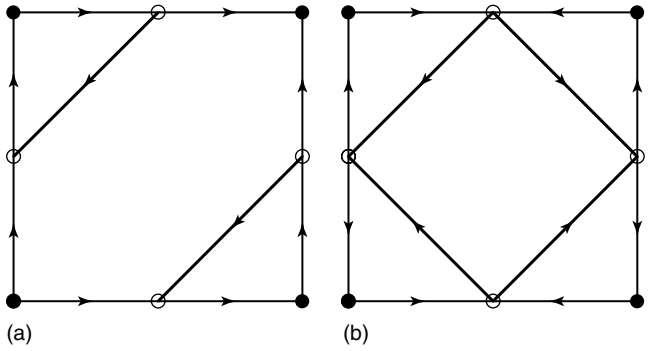

Figure 16. Two orbital current patterns proposed by Varma. Solid dots are copper ions, open dots are oxygen ions, and arrows are bond currents. The pattern in (a) has been used to interpret recent polarized ARPES and neutron results in the pseudogap phase.

dichroism shift along the $(\pi, 0)$–(π, π) direction (not yet reproduced by other groups, though). To account for this, Varma rotated his current pattern by 45° (Figure 16a). The resulting magnetic reflections would then be along the bond directions, and these were recently seen by neutron scattering (Fauque *et al*., 2006) (but again, not reproduced by other groups). Varma's theory also predicts nodes in the pseudogap phase, as has been recently inferred from experiment (as mentioned in the preceding text). Recently, a dichroism signal has been found by X rays that matches the ARPES one (Kubota, Ono, Oohara and Eisaki, 2006), but the claim was that the signal was structural, not magnetic, in origin.

Another inhomogeneous pattern, as mentioned before, is stripes. These patterns have been seen in several transition-metal oxides, and in the low temperature tetragonal (LTT) structural phase of doped lanthanum cuprate near $x = 1/8$ (Tranquada *et al*., 1995). As mentioned before, stripes give a natural explanation of the Yamada plot, have been proposed (in their dynamic version) as an explanation for the unusual hourglass-shaped spin dispersion seen in neutron scattering, and can account for various Fourier charge peaks seen in STM data (Kivelson *et al*., 2003). From a theoretical perspective, the advantage is that the quasi-1D nature of the stripes naturally yields spin-charge separation and its resulting non-Fermi liquid properties (which are more difficult to generate in homogeneous 2D models). The holes pick up their pairing gap by virtually hopping from the stripes to the undoped antiferromagnetic domains (Emery, Kivelson and Zachar, 1997) (even leg spin ladders having a spin gap). The much lower value of T_c as compared to the gap is determined by Josephson coupling of the stripes. The stripes picture has been important in focusing the physics community on the fundamental question of real space–based approaches as compared to the traditional momentum space–based approaches used in the past to address superconductivity. It emphasizes the role of inhomogeneity, which has been spectacularly seen in STM experiments (Pan *et al*., 2001). It provides a unique (quasi-1D) approach to the cuprate problem. But this approach has also raised a number of questions. A recent X-ray analysis of the $x = 1/8$ stripe phase in LBCO has found a smooth sine wave for the charge modulations, as opposed to the square wave picture of Figure 8 (Abbamonte *et al*., 2005). Charge modulation effects seen in STM are weak in intensity and, moreover, tend to trace out a checkerboard pattern (Hanaguri *et al*., 2004) as opposed to a stripe one (a checkerboard has been advocated for the spin pattern in doped LSCO as well in a recent neutron-scattering study (Christensen *et al*., 2004)). Even the large inhomogeneity effects seen by STM have been challenged by others (the group of Oystein Fischer typically does not observe them). Alternate explanations have also been given with reference to the STM Fourier peaks (McElroy *et al*., 2003) (for instance, similar ARPES autocorrelation studies are consistent with a joint density of states explanation for the Fourier peaks (Chatterjee *et al*., 2006)). But an interesting aspect of the stripes scenario is the possible coupling of lattice and charge/spin degrees of freedom. It is well known that certain phonons show anomalies that are thought to be connected with static stripes or their dynamic variants (Reznik *et al*., 2006).

Having mentioned the lattice, it is time to end this review with a discussion of the 'phonon' question. As mentioned earlier, it has been advocated that the peak-dip-hump lineshape seen in tunneling and ARPES is a strong polaron effect. Polarons are certainly prominent in other transition-metal oxides, such as manganites, and in fact were an integral part of the guiding principle that led Bednorz and Mueller to their original discovery. Whether they are present at optimal doping is an entirely different matter (the normal state actually being quite a good metal with well-developed screening as characterized by the 1-eV plasmon). And, as mentioned before, it has been advocated by several photoemission and STM groups that the strong coupling anomalies seen in those spectra are caused by phonons rather than magnetic excitations.

Of course, the one known thing in superconductivity is that phonons can definitely cause pairing. All finite frequency phonons contribute positively to the s-wave pairing channel (Bergmann and Rainer, 1973). Obviously, only some of them do for the d-wave channel. An advantage of the d-wave channel is the strong reduction in the direct Coulomb repulsion (due to the nodes in the pair wave function), but then again, we do not know of any s-wave electron–phonon superconductors which occur at 150 K, much less in the d-wave channel with its reduced coupling constant. So, it is a rather far stretch to believe that phonons can account for cuprate superconductivity. This does not mean

that they cannot be responsible for certain anomalies in experimental spectra, and even those authors advocating such are careful not to claim that phonons are solely responsible for superconductivity. But what is somewhat disturbing is the trend to fit the entire spectrum assuming phonons (or polarons) and ignore the underlying strong electron–electron interactions that presumably give rise to the various states (Mott insulator, d-wave superconductor) to begin with. It is difficult, of course, to properly treat all degrees of freedom (charge, spin, lattice), particularly for doped systems, and then one is faced with the 'everything but the kitchen sink' scenario for describing the material. In ^{3}He, it is a known fact that many degrees of freedom enter the various interactions, including the pairing one. But there, a spin fluctuation–based approach captures the fundamental essence of the problem. It is quite likely that such a spin fluctuation approach (or a strong coupling analog like RVB) will also capture the essence of the cuprate problem. But only time will tell.

ACKNOWLEDGMENTS

The author would like to thank many people for discussions that led to his thoughts as laid down in this review. A far-from-exhaustive list would include Phil Anderson, J C Campuzano, Andrey Chubukov, Seamus Davis, Matthias Eschrig, Steve Kivelson, Alessandra Lanzara, Bob Laughlin, David Pines, Mohit Randeria, Doug Scalapino, Z-X Shen, and Chandra Varma. The author acknowledges support from the US Department of Energy, Office of Science, under Contract No. W-31-109-ENG-38.

REFERENCES

Abanov, Ar., Chubukov, A.V., Eschrig, M., *et al*. (2002). Neutron resonance in the cuprates and its effect on fermionic excitations. *Physical Review Letters*, **89**, 177002.

Abanov, Ar., Chubukov, A.V. and Schamlian, J. (2003). Quantum critical theory of the spin fermion model and its application to cuprates: normal state analysis. *Advances in Physics*, **52**, 119–218.

Abbamonte, P., Rusydi, A., Smadici, S., *et al*. (2005). Spatially modulated 'mottness' in $La_{2-x}Ba_xCuO_4$. *Nature Physics*, **1**, 155–158.

Abrikosov, A.A. and Gor'kov, L.P. (1961). Contribution to the theory of superconducting alloys with paramagnetic impurities. *Soviet Physics JETP*, **12**, 1243–1253.

Affleck, I., Zou, Z., Hsu, T. and Anderson, P.W. (1988). SU(2) gauge symmetry of the large-U limit of the Hubbard model. *Physical Review B*, **38**, 745–747.

Anderson, P.W. (1987). The resonating valence bond state in La_2CuO_4 and superconductivity. *Science*, **235**, 1196–1198.

Anderson, P.W. (1997). A re-examination of concepts in magnetic metals: the 'nearly antiferromagnetic Fermi liquid'. *Advances in Physics*, **46**, 3–11.

Anderson, P.W. and Brinkman, W.F. (1973). Anisotropic superfluidity in ^{3}He: a possible interpretation of its stability as a spin-fluctuation effect. *Physical Review Letters*, **30**, 1108–1111.

Anderson, P.W., Lee, P.A., Randeria, M., *et al*. (2004). The physics behind high temperature superconducting cuprates: the plain vanilla version of RVB. *Journal of Physics: Condensed Matter*, **16**, R755–R769.

Arai, M., Nishijima, T., Endoh, Y., *et al*. (1999). Incommensurate spin dynamics of underdoped superconductor $YBa_2Cu_3O_{6.7}$. *Physical Review Letters*, **83**, 608–611.

Arovas, D.P., Berlinsky, A.J., Kallin, C. and Zhang, S-C. (1997). Superconducting vortex with an antiferromagnetic core. *Physical Review Letters*, **79**, 2871–2874.

Barzykin, V. and Pines, D. (2006). Phenomenological model of protected behavior in the pseudogap state of underdoped cuprate superconductors. *Physical Review Letters*, **96**, 247002.

Bednorz, J.G. and Müller, K.A. (1986). Possible high T_c superconductivity in the Ba-La-Cu-O system. *Zeitschrift fur Physik B*, **64**, 189–193.

Bergmann, G. and Rainer, D. (1973). The sensitivity of the transition temperature to changes in $\alpha^2F(\omega)$. *Zeitschrift fur Physik*, **263**, 59–68.

Berk, N.F. and Schrieffer, J.R. (1966). Effect of ferromagnetic spin correlations on superconductivity. *Physical Review Letters*, **17**, 433–435.

Bickers, N.E., Scalapino, D.J. and Scalettar, R.T. (1987). CDW and SDW mediated pairing interactions. *International Journal of Modern Physics B*, **1**, 687–695.

Bickers, N.E., Scalapino, D.J. and White, S.R. (1989). Conserving approximation for strongly correlated electron systems: Bethe-Salpeter equation and dynamics for the two dimensional Hubbard model. *Physical Review Letters*, **62**, 961–964.

Bogdanov, P.V., Lanzara, A., Kellar, S.A., *et al*. (2000). Evidence for an energy scale for quasiparticle dispersion in $Bi_2Sr_2CaCu_2O_8$. *Physical Review Letters*, **85**, 2581–2584.

Bulut, N. (2002). $dx^2 - y^2$ superconductivity and the Hubbard model. *Advances in Physics*, **51**, 1587–1667.

Campuzano, J.C., Ding, H., Norman, H.R., *et al*. (1999). Electronic spectra and their relation to the (π, π) collective mode in high T_c superconductors. *Physical Review Letters*, **83**, 3709–3712.

Chakravarty, S., Laughlin, R.B., Morr, D.K. and Nayak, C. (2001). Hidden order in the cuprates. *Physical Review B*, **63**, 094503.

Chatterjee, U., Shi, M., Kaminski, A., *et al*. (2006). Non-dispersive Fermi arcs and absence of charge ordering in the pseudogap phase of $Bi_2Sr_2CaCu_2O_{8+\delta}$. *Physical Review Letters*, **96**, 107006.

Chen, H-D., Hu, J-P., Capponi, S., *et al*. (2002). Antiferromagnetism and hole pair checkerboard in the vortex state of high T_c superconductors. *Physical Review Letters*, **89**, 137004.

Christensen, N.B., McMorrow, D.F., Ronnow, H.M., *et al*. (2004). Dispersive excitations in the high-temperature superconductor $La_{2-x}Sr_xCuO_4$. *Physical Review Letters*, **93**, 147002.

Cuk, T., Baumberger, F., Lu, D.H., *et al*. (2004). Coupling of the B_{1g} phonon to the antinodal electronic states of $Bi_2Sr_2Ca_{0.92}Y_{0.08}Cu_2O_8$. *Physical Review Letters*, **93**, 117003.

Demler, E., Hanke, W. and Zhang, S-C. (2004). SO(5) theory of antiferromagnetism and superconductivity. *Review of Modern Physics*, **76**, 909–974.

Emery, V.J., Kivelson, S.A. and Zachar, O. (1997). Spin-gap proximity effect mechanism of high-temperature superconductivity. *Physical Review B*, **56**, 6120–6128.

Engelsberg, S. and Schrieffer, J.R. (1963). Coupled electron-phonon system. *Physical Review*, **131**, 993–1008.

Eremin, I., Morr, D.K., Chubukov, A.V., *et al*. (2005). Novel neutron resonance mode in d_{x2-y2}-wave superconductors. *Physical Review Letters*, **94**, 147001.

Eschrig, M. (2006). The effect of collective spin 1 excitation on electronic spectra in high T_c superconductors. *Advances in Physics*, **55**, 47–183.

Fauque, B., Sidis, Y., Hinkov, V., *et al*. (2006). Magnetic order in the pseudogap phase of high-T_c superconductors. *Physical Review Letters*, **96**, 197001.

Fay, D. and Layzer, A. (1968). Superfluidity of low density fermion systems. *Physical Review Letters*, **20**, 187–190.

Fong, H.F., Keimer, B., Anderson, P.W., *et al*. (1995). Phonon and magnetic neutron scattering at 41 meV in $YBa_2Cu_3O_7$. *Physical Review Letters*, **75**, 316–319.

Franz, M. and Tesanovic, Z. (2001). Algebraic Fermi liquid from phase fluctuations: topological fermions, vortex baryons and QED_3 theory of cuprate superconductors. *Physical Review Letters*, **87**, 257003.

Fujita, M., Yamada, K., Hiraka, H., *et al*. (2002). Static magnetic correlations near the insulating-superconducting phase boundary in $La_{2-x}Sr_xCuO_4$. *Physical Review B*, **65**, 064505.

Gweon, G.H., Sasagawa, T., Zhou, S.Y., *et al*. (2004). An unusual isotope effect in a high-transition-temperature superconductor. *Nature*, **430**, 187–190.

Hanaguri, T., Lupien, C., Kohsaka, Y., *et al*. (2004). A 'checkerboard' electronic crystal state in lightly hole-doped $Ca_{2-x}Na_xCuO_2Cl_2$. *Nature*, **430**, 1001–1005.

Hayden, S.M., Mook, H.A., Dai, P., *et al*. (2004). The structure of the high-energy spin excitations in a high-transition temperature superconductor. *Nature*, **429**, 531–534.

Hertz, J.A., Levin, K. and Beal-Monod, M.T. (1976). Absence of a Migdal theorem for paramagnons and its implications for superfluid He^3. *Solid State Communications*, **18**, 803–806.

Homes, C.C., Timusk, T., Liang, R., *et al*. (1993). Optical conductivity of c axis oriented $YBa_2Cu_3O_{6.7}$: evidence for a pseudogap. *Physical Review Letters*, **71**, 1645–1649.

Joynt, R. and Taillefer, L. (2002). The superconducting phases of UPt_3. *Review of Modern Physics*, **74**, 235–294.

Kaminski, A., Mesot, J., Fretwell, H., *et al*. (2000). Quasiparticles in the superconducting state of $Bi_2Sr_2CaCu_2O_{8+\delta}$. *Physical Review Letters*, **84**, 1788–1791.

Kaminski, A., Randeria, M., Campuzano, J.C., *et al*. (2001). Renormalization of spectral line shape and dispersion below T_c in $Bi_2Sr_2CaCu_2O_{8+\delta}$. *Physical Review Letters*, **86**, 1070–1073.

Kaminski, A., Rosenkranz, S., Fretwell, H.M., *et al*. (2002). Spontaneous breaking of time reversal symmetry in the pseudogap state of a high-T_c superconductor. *Nature*, **416**, 610–613.

Kanigel, A., Norman, M.R., Randeria, M., *et al*. (2006). Evolution of the pseudogap from Fermi arcs to the nodal liquid. *Nature Physics*, **2**, 447–451.

Kee, H-Y., Kivelson, S.A. and Aeppli, G. (2002). Spin-1 resonance peak cannot account for electronic anomalies in the cuprate superconductors. *Physical Review Letters*, **88**, 257002.

Kivelson, S.A., Bindloss, I.P., Fradkin, E., *et al*. (2003). How to detect fluctuating stripes in the high temperature superconductors. *Review of Modern Physics*, **75**, 1201–1241.

Kotliar, G. (1995). The large N expansion in the strong correlation problem. In *Strongly Interacting Fermions and High T_c Superconductivity*, Doucot, B. and Zinn-Justin, J. (Eds.), Elsevier: Amsterdam, pp. 197–247.

Kotliar, G. and Liu, J. (1988). Superexchange mechanism and d-wave superconductivity. *Physical Review B*, **38**, 5142–5145.

Kubota, M., Ono, K., Oohara, Y. and Eisaki, H. (2006). X-ray optical activity in underdoped Bi-based high T_c superconductor. *Journal of the Physical Society of Japan*, **75**, 053706.

Kulic, M.L. and Dolgov, O.V. (2005). Dominance of the electron-phonon interaction with forward scattering peak in high-T_c superconductors: theoretical explanation of the ARPES kink. *Physical Review B*, **71**, 092505.

Lanzara, A., Bogdanov, P.V., Zhou, X.J., *et al*. (2001). Evidence for ubiquitous strong electron-phonon coupling in high-temperature superconductors. *Nature*, **412**, 510–514.

Laughlin, R.B. (1998). A critique of two metals. *Advances in Physics*, **47**, 943–958.

Laughlin, R.B. (2006). Gossamer superconductivity. *Philosophical Magazine*, **86**, 1166–1171.

Laughlin, R.B., Lonzarich, G.G., Monthoux, P. and Pines, D. (2001). The quantum criticality conundrum. *Advances in Physics*, **50**, 361–365.

Lee, J., Fujita, K., McElroy, K., *et al*. (2006). Interplay of electron-lattice interactions and superconductivity in $Bi_2Sr_2CaCu_2O_{8+\delta}$. *Nature*, **442**, 546–550.

Lee, P.A., Nagaosa, N. and Wen, X-G. (2006). Doping a Mott insulator: physics of high temperature superconductivity. *Review of Modern Physics*, **78**, 17–85.

Lonzarich, G.G. and Taillefer, L. (1985). Effect of spin fluctuations on the magnetic equation of state of ferromagnetic and nearly ferromagnetic metals. *Journal of Physics C*, **18**, 4339–4371.

Mathur, N.D., Grosche, F.M., Julian, S.R., *et al*. (1998). Magnetically mediated superconductivity in heavy fermion compounds. *Nature*, **394**, 39–43.

McElroy, K., Simmonds, R.W., Hoffman, J.E., *et al*. (2003). Relating atomic-scale electronic phenomena to wave-like quasiparticle states in $Bi_2Sr_2CaCu_2O_{8+\delta}$. *Nature*, **422**, 592–596.

Miyake, K., Schmitt-Rink, S. and Varma, C.M. (1986). Spin fluctuation mediated even parity pairing in heavy fermion superconductors. *Physical Review B*, **34**, 6554–6556.

Monthoux, P. and Pines, D. (1994). Spin-fluctuation-induced superconductivity and normal-state properties of $YBa_2Cu_3O_7$. *Physical Review B*, **49**, 4261–4278.

Moriya, T. and Ueda, K. (2000). Spin fluctuations and high temperature superconductivity. *Advances in Physics*, **49**, 555–606.

Moriya, T. and Ueda, K. (2003). Antiferromagnetic spin fluctuation and superconductivity. *Reports on Progress in Physics*, **66**, 1299–1341.

Nagaosa, N. and Lee, P.A. (1992). Ginzburg-Landau theory of the spin-charge-separated system. *Physical Review B*, **45**, 966–970.

Norman, M.R., Ding, H., Campuzano, J.C., *et al*. (1997). Unusual dispersion and lineshape of the superconducting state spectra of $Bi_2Sr_2CaCu_2O_{8+\delta}$. *Physical Review Letters*, **79**, 3506–3509.

Pan, S.H., O'Neal, J.P., Badzey, R.L., *et al*. (2001). Microscopic electronic inhomogeneity in the high T_c superconductor $Bi_2Sr_2CaCu_2O_{8+x}$. *Nature*, **413**, 282–285.

Paramekanti, A., Randeria, M. and Trivedi, T. (2001). Projected wavefunctions and high temperature superconductivity. *Physical Review Letters*, **87**, 217002.

Pickett, W.E. (1989). Electronic structure of the high-temperature oxide superconductors. *Review of Modern Physics*, **61**, 433–512.

Randeria, M., Trivedi, T., Moreo, A. and Scalettar, R.T. (1992). Pairing and spin gap in the normal state of short coherence length superconductors. *Physical Review Letters*, **69**, 2001–2004.

Renner, Ch., Revaz, B., Kadowaki, K., *et al*. (1998). Observation of the low temperature pseudogap in the vortex core of $Bi_2Sr_2CaCu_2O_{8+\delta}$. *Physical Review Letters*, **80**, 3606–3609.

Reznik, D., Pintschovius, L., Ito, M., *et al*. (2006). Electron-phonon coupling reflecting dynamic charge inhomogeneity in copper oxide superconductors. *Nature*, **440**, 1170–1173.

Rübhausen, M., Gozar, A., Klein, M.V., *et al*. (2001). Superconductivity-induced optical changes for energies of 100Δ in the cuprates. *Physical Review B*, **63**, 224514.

Sato, T., Matsui, H., Takahashi, T., *et al*. (2003). Observation of band renormalization effects in hole doped high T_c superconductors. *Physical Review Letters*, **91**, 157003.

Sauls, J.A. (1994). The order parameter for the superconducting phase of UPt_3. *Advances in Physics*, **43**, 113–141.

Scalapino, D.J. (1995). Distinguishing high T_c theories. *Journal of Physics and Chemistry of Solids*, **56**, 1669–1672.

Scalapino, D.J., Loh, E. and Hirsch, J.E. (1986). d-wave pairing near a spin density wave instability. *Physical Review B*, **34**, 8190–8192.

Schrieffer, J.R. (1964). *Theory of Superconductivity*, Benjamin/Cummings: Reading.

Schuttler, H-B. and Norman, M.R. (1996). Contrasting dynamic spin susceptibility models and their relation to high temperature superconductivity. *Physical Review B*, **54**, 13295–13305.

Shen, K.M., Ronning, F., Lu, D.H., *et al*. (2004). Missing quasiparticles and the chemical potential puzzle in the doping evolution of the cuprate superconductors. *Physical Review Letters*, **93**, 267002.

Si, Q., Zha, Y., Levin, K. and Lu, J.P. (1993). Comparison of spin dynamics in $YBa_2Cu_3O_{7-\delta}$ and $La_{2-x}Sr_xCuO_4$: effects of Fermi surface geometry. *Physical Review B*, **47**, 9055–9076.

Sorella, S. Martins, G.B., Becca, F., Gazza, C., *et al*. (2002). Superconductivity in the two-dimensional t-J model. *Physical Review Letters*, **88**, 117002.

Sutherland, M., Li, S.Y., Hawthorn, D.G., *et al*. (2005). Delocalized fermions in underdoped cuprate superconductors. *Physical Review Letters*, **94**, 147004.

Tchernyshyov, O., Norman, M.R. and Chubukov, A.V. (2001). Neutron resonance in high-T_c superconductors is not the π particle. *Physical Review B*, **63**, 144507.

Tou, H., Ishida, K. and Kitaoka, Y. (2005). Quasiparticle spin susceptibility in heavy fermion superconductors: an NMR study compared with specific heat results. *Journal of the Physical Society of Japan*, **74**, 1245–1254.

Tranquada, J.M., Sternlieb, B.J., Axe, J.D., *et al*. (1995). Evidence for stripe correlations of spins and holes in copper oxide superconductors. *Nature*, **375**, 561–563.

Tranquada, J.M., Woo, H., Perring, T.G., *et al*. (2004). Quantum magnetic excitations from stripes in copper oxide superconductors. *Nature*, **429**, 534–538.

Tremblay, A.M.S., Kyung, B. and Senechal, D. (2006). Pseudogap and high temperature superconductivity from weak to strong coupling: towards a quantitative theory. *Low Temperature Physics*, **32**, 424–451.

Uhrig, G.S., Schmidt, K.P. and Gruninger, M. (2004). Unifying magnons and triplons in stripe-ordered cuprate superconductors. *Physical Review Letters*, **93**, 267003.

Valla, T. Federov, A.V., Lee, J., Davis, J.C., *et al*. (2006). Science **314**, 1914–1916.

Varma, C.M. (2006). Theory of the pseudogap state of the cuprates. *Physical Review B*, **73**, 155113.

Varma, C.M., Littlewood, P.B., Schmitt-Rink, S., *et al*. (1989). Phenomenology of the normal state of Cu-O high-temperature superconductors? *Physical Review Letters*, **63**, 1996–1999.

Vilk, Y.M. and Tremblay, A.M.S. (1997). Non perturbative many body approach to the Hubbard model and single particle pseudogap. *Journal of Physics I France*, **7**, 1309–1368.

Vollhardt, D. and Wolfle, P. (1990). *The Superfluid Phases of Helium 3*, Taylor & Francis: London.

Wen, X-G. and Lee, P.A. (1998). Theory of quasi-particles in the underdoped high T_c superconducting state. *Physical Review Letters*, **80**, 2193–2197.

Xu, Z.A., Ong, N.P., Wang, Y., *et al*. (2000). Vortex-like excitations and the onset of superconducting phase fluctuation in underdoped $La_{2-x}Sr_xCuO_4$. *Nature*, **406**, 486–488.

Zaanen, J. and Gunnarsson, O. (1989). Charged magnetic domain lines and the magnetism of high T_c oxides. *Physical Review B*, **40**, 7391–7394.

Zacher, M.G., Hanke, W., Arrigoni, E. and Zhang, S-C. (2000). Interrelation of superconducting and antiferromagnetic gaps in high T_c compounds: a test case for the SO(5) theory. *Physical Review Letters*, **85**, 824–827.

Zasadzinski, J.F., Ozyuzer, L., Miyakawa, N., *et al*. (2001). Correlation of tunneling spectra in $Bi_2Sr_2CaCu_2O_{8+\delta}$ with the resonance spin excitation. *Physical Review Letters*, **87**, 067005.

Zhang, F.C., Gros, C., Rice, T.M. and Shiba, H. (1988). A renormalized Hamiltonian approach to a resonant valence bond wavefunction. *Superconductor Science and Technology*, **1**, 36–46.

Magnetic Polarons

Stephan von Molnár[1] and Patricia A. Stampe[2]

[1] *Florida State University, Tallahassee, FL, USA*
[2] *Florida A & M University, Tallahassee, FL, USA*

1 INTRODUCTION

The concept of magnetic polarons is by now ubiquitous in any discussion concerning the physical properties of both concentrated and diluted magnetic semiconductors [1]. It is the goal of this brief overview to provide a historical perspective of the conceptual development of magnetic polarons based, in large part, on selected experimental findings. Our theme is to highlight the importance of the magnetic state of semiconductors in any discussion of their physical properties. The chapter describes the most important magnetic semiconductors, the europium and other rare-earth chalcogenides, having the NaCl- or thorium phosphide–type cubic structures, the mixed valence perovskites (see also **Ferromagnetic Manganite Films, Volume 5**), and the magnetically dilute II–VI and III–V semiconductors (see also **Ferromagnetic Semiconductors, Volume 5** and **Diluted Ferromagnetic Semiconductors – Theoretical Aspects, Volume 5**). The development of the concept of the magnetic polaron will be outlined and experimental evidence for the existence of this many-body state will be presented. This description borrows much from the well-studied dielectric polaron, in which the local environment around a charge defect is modified due to the effective dielectric susceptibility function. In a magnetic polaron the magnetic susceptibility plays a similar role. The discussion will end with a description of applications of these ideas to magnetically dilute oxides, where, however, experimental evidence is far more controversial.

Handbook of Magnetism and Advanced Magnetic Materials. Edited by Helmut Kronmüller and Stuart Parkin. Volume 5: *Spintronics and Magnetoelectronics*. ISBN: 978-0-470-02217-7.

2 MIXED VALENCE PEROVSKITES (see also Ferromagnetic Manganite Films, Volume 5)

The most important early work on (diluted) magnetic semiconductors was the discovery by Jonker and van Santen (1950) (Jonker, 1956) that the $(La_{1-x}Ca_x)MnO_3$ manganite perovskites are ferromagnetic and conducting. Volger (1954) showed that $La_{0.8}Sr_{0.2}MnO_3$ displayed very large negative magnetoresistance which peaked near the Curie temperature, depending on the dopant concentration of manganese. As is now known, these effects have been reborn within the past 13 years (von Helmolt *et al*., 1993; Jin, McCormack, Tiefel and Ramesh, 1994) as 'colossal magnetoresistance' and have been the subject of massive research activities to this day. A

review by Coey, Viret and von Molnár (1999) gives a detailed account of work done up to the year 1999. The materials are very complicated, however, and spin and charge ordering, the Jahn–Teller distortion, as well as magnetic polaron formation may all contribute energetically over various portions of the phase diagram in describing the transport and spectroscopic properties of these materials. Direct evidence for the formation of small magnetic clusters in $LaMnO_3$ came from small angle neutron scattering (SANS) experiments and the concomitant anomalous volume lattice distortions observed by De Teresa *et al*. (1997).

To explain the origin of conductivity-induced ferromagnetism in $LaMnO_3$, Zener and others (Zener, 1951; Anderson and Hasegawa, 1955) proposed a spin-dependent electron transfer between 3d levels of the magnetic transition element ions. de Gennes, considering both antiferromagnetic superexchange and the Zener double exchange term (Zener, 1951), was able to describe in detail the magnetic phase diagram of the mixed valence manganites (de Gennes, 1960). He was also the first to point out that the presence of localized carriers results in a large deformation of the magnetic environment provided by the Mn spins. This realization and the suggestion of motion of the magnetic disturbance in the presence of a magnetic or electric field provided an initial guide for subsequent experimental observations (von Molnár and Methfessel, 1967). de Gennes' work foreshadowed the concept of the magnetic impurity state which was first investigated in detail by Kasuya and Yanase (1968), and independently by Nagaev (1974), for the case of the NaCl-type Eu chalcogenides. Before discussing Kasuya's model of the magnetic impurity state or bound magnetic polaron in detail, we summarize in the following paragraphs the physical properties of the rare-earth chalcogenides that led to the theoretical model.

3 RARE-EARTH CHALCOGENIDES

3.1 NaCl-type Eu chalcogenides (O, S, Se, Te)

The discovery in 1961 of the first ferromagnetic insulator, europium oxide (Matthias, Bozorth and Van Vleck, 1961), focused almost all research effort in the following years on the development and understanding of this general class of concentrated magnetic semiconductors, and interests in the perovskites abated. The europium chalcogenides are a particularly simple crystal structure, NaCl, and therefore are far more amenable to both experimental and theoretical analysis. It might be mentioned, parenthetically, that the observation of ferromagnetism in an insulating material was in itself a major theoretical challenge since conduction electrons, which normally provide the magnetic glue among magnetic ions, are in this case absent. Furthermore, the seven electrons having an $^8S_{7/2}$ ground state are very tightly bound to the atom core with a radial extent maximum at $\leq$0.1 nm (1 Å) (Friedman, Choppin and Feuerbacher, 1964). Kasuya (1970a) was the first to provide a theoretical basis for ferromagnetism that involved the virtual excitation of 4f electrons of the europium ion to a more extended d state which could overlap the wave function of the nearest-neighbor 4f electrons. The idea that (empty) 3d and 2s conduction band states could be partially filled by doping with trivalent rare earths (initially to produce impurity states and at more concentrated levels to lead to degenerate magnetic semiconductors), and thus increase the ferromagnetic transition temperatures was an almost natural consequence of the early findings (Matthias, Bozorth and Van Vleck, 1961). Experimental evidence was provided by the work of Holtzberg, Methfessel, Suits, and McGuire (1964). The figure of their data (Figure 1) gives dramatic proof of the interdependence of magnetism and carrier concentration or more broadly of magnetism and all other carrier-dependent physical properties in these concentrated systems.

3.1.1 Evidence for polaron formation

To the best of these authors' knowledge, the first reference to magnetic polaron formation was given by Heikes and Chen (1964) in a discussion concerning transport in sintered La-doped EuS that displayed a strong temperature-dependent peak in the resistivity near ferromagnetic order. Since this is an obscure reference, it is generally not recognized as part of the

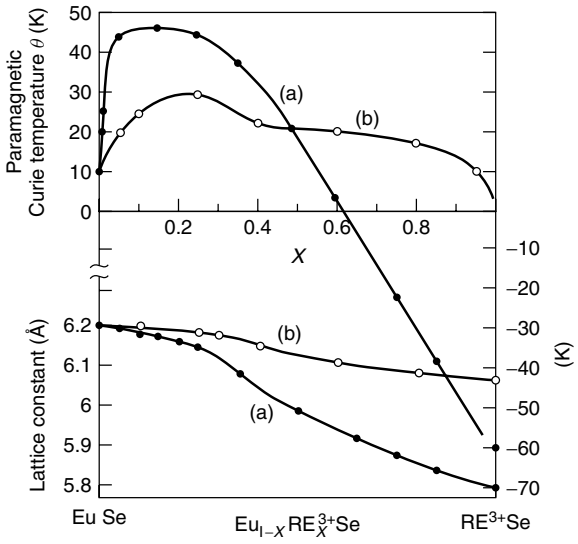

Figure 1. Variation of the paramagnetic Curie temperature and the lattice constant of EuSe with rare-earth substitution: (a) $Eu_{1-x}Gd_xSe$ and (b) $Eu_{1-x}La_xSe$. (Reproduced from Holtzberg *et al*., 1964, with permission from the American Physical Society. © 1964.)

history of the development of these ideas. Heikes suggested a model of impurity band conductivity in which the radius of the overlapping impurity wave function critically depended on magnetic order (magnetic polaron formation). The high resistivity near T_C results from a thermally activated hopping mechanism between occupied and unoccupied impurity sites. This suggestion is analogous to dielectric polaron formation and transport, discussed by, for example, Snyder *et al*. (1996), for mixed valence perovskites.

Figure 2 is a characteristic example of the effects observed and summarizes findings for a single crystal of EuS containing nominally 5% La. The observed experimental increase in resistivity above the paramagnetic Curie temperature θ_ρ ($\sim$35 K), which decreases with decreasing temperature as magnetic order increases, and the dramatic negative magnetoresistance clearly demonstrate that the transport properties depend on the magnetic state of the sample. These findings confirm the first detailed magnetotransport study in single crystal EuGdSe (von Molnár and Methfessel, 1967) and, combined with Hall and thermoelectric power measurements that point toward a mobility effect in EuGdSe, led to

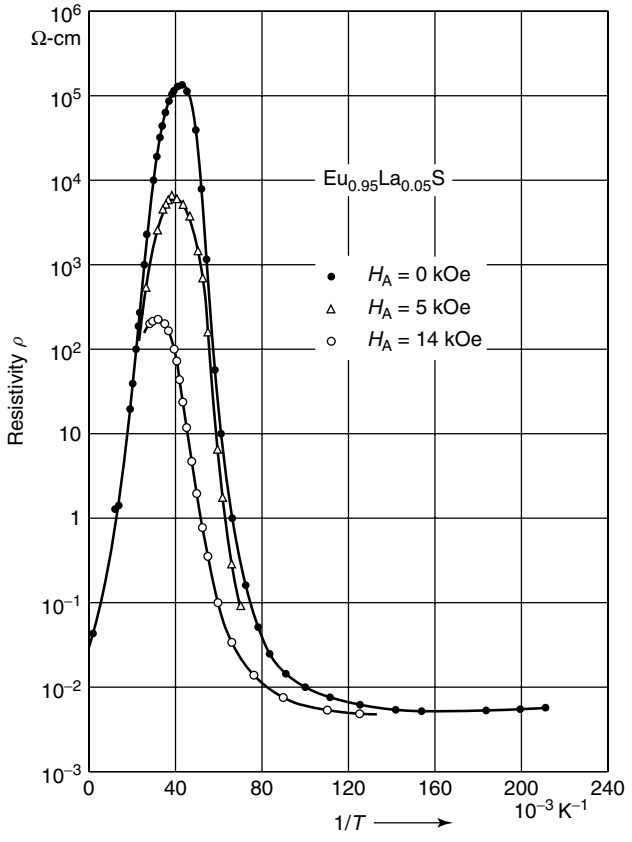

Figure 2. The peak in the resistivity of $Eu_{0.95}La_{0.05}S$ measured in various applied fields. (Reproduced from Methfessel *et al*., 1968, with permission from Springer-Verlag GmbH. © 1968.)

the conclusion that magnetic polarons are formed in these systems near and above T_C, only to be destroyed as ferromagnetic order develops. We quote verbatim from that paper:

'The possibility of reducing the kinetic energy by hopping to neighbors with parallel spin increases the effective ferromagnetic exchange interaction between neighboring $4f$ ions by an "indirect" type of double exchange mechanism resulting from the intra-atomic $4f-5d$ exchange. Therefore, we find here again the trapped electron surrounded by a polaron-like spin cluster. With decreasing temperature we expect the size of the polarons to increase and the accidental overlap of neighboring polarons to become more and more abundant. The proposed spin clusters, it should be pointed out, are not stationary in the lattice, but fluctuate by their interaction with phonons and spin waves. For temperatures below T_C, we visualize the electrons to move along chains of ferromagnetically aligned spin groups, which are interrupted by unordered spins. The decrease in the number of unordered spins with temperature is a function of the reduced (i.e., normalized) magnetization, and results in the observed resistivity decrease below T_C.'

It is to be noted that this description applies to many of the physical effects that will be discussed presently. In particular, the suggestion of magnetic phase separation plays an important role in theories of the metal insulator phase transition in the perovskite manganites (Gor'kov and Kresin, 1998, 2004), and was first mapped out experimentally in a detailed neutron diffraction study by Wollan (1955). It has also been seen in tunneling microscopy (Fath *et al*., 1999), noise spectroscopy (Raquet *et al*., 2000; Merithew *et al*., 2000), and in many other techniques (von Molnár and Coey, 1998). An analysis of critical scattering near the ferromagnetic transition temperature in the Eu compounds by von Molnár and Kasuya (1968) gave further credence to the magnetic polaron model. Critical scattering, first discussed by de Gennes and Friedel (1958) and later elaborated by Fisher and Langer (1968), was unable to explain the magnitude and width in temperature of the observed effect. Since the scattering amplitude depends on the correlation of spin fluctuations with respect to the Fermi wavelength of electrons in metals or degenerate semiconductors, larger objects, the magnetic polarons, were invoked as an explanation.

Other than the transport properties already mentioned, experimental evidence for magnetic polarons in concentrated magnetic semiconductors came from optical studies, reported first by Busch, Streit and Wachter (1970), in which they studied the emission and excitation spectrum of the photoluminescence of insulating EuTe, an antiferromagnet. These authors found that an observed increase in the luminescence intensity with decreasing temperature could be accounted for by the formation of magnetic polarons. The physical idea was that the polaron would shrink the wave function, and thereby

increase the probability of recombination. These authors also discovered that applying a large magnetic field reversed this process. The intensity became much smaller, presumably because the magnetic polaron was no longer bound, thereby reducing the probability of recombination.

3.2 Thorium phosphide–type rare-earth chalcogenides

von Molnár and colleagues (von Molnár, Holtzber, McGuire and Popma 1972; von Molnár and Holtzberg, 1973; von Molnár, Briggs, Flouquet and Remenyi, 1983; Washburn *et al*., 1984) studied the transport properties of $Gd_{3-x}v_xS_4$. Here v means vacancies that can be considered as donor dopants. The end member Gd_2S_3 is an antiferromagnetic insulator, whereas Gd_3S_4 is a ferromagnetic metal. Principal results are shown in Figure 3, where the logarithm of the resistivity at various fields and temperatures is presented. The main result is that while resistivity rises without bound with decreasing temperature at zero and low magnetic fields, a field of approximately 3.2 T transforms the material into a metal with a resistivity that is independent of temperatures below 10 K. The study by Penney,

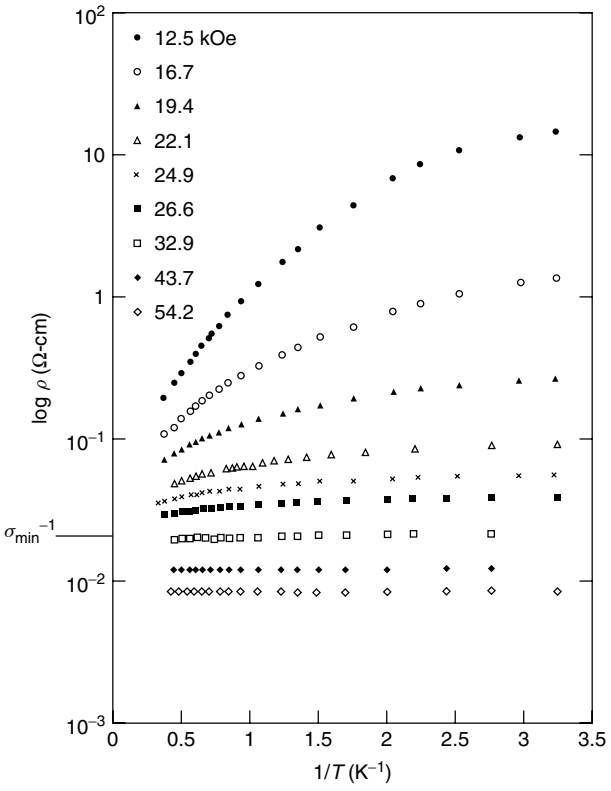

Figure 3. Temperature dependence of the magnetoresistance of $Gd_{3-x}v_xS_4$. (Reproduced from von Molnar *et al*., 1983, with permission from the American Physical Society. © 1983.)

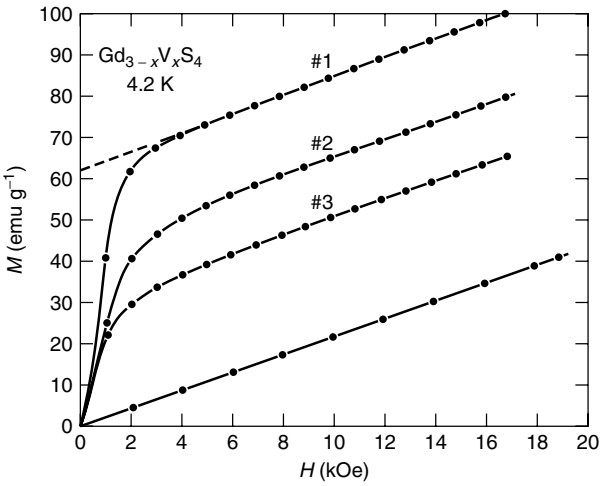

Figure 4. Field dependence of magnetization for $Gd_{3-x}v_xS_4$ for samples of varying carrier concentration. (Reproduced from Penney *et al*., 1974, with permission from the American Institute of Physics. © 1974.)

Holtzberg, Tao and von Molnár (1974) of the magnetic properties of these compounds provided the first magnetic proof that magnetic polarons in this otherwise antiferromagnetic material do exist. These results, given in Figure 4, show the magnetization of several samples with various carrier concentrations as a function of the applied magnetic field at 4.2 K. The significance of these data is that the pure material without any carriers (lowest curve) shows a magnetization rising linearly from zero with the field, as would be expected for a canting antiferromagnet, whereas with increasing electron concentration the extrapolated slope of magnetization versus field to zero field has a positive intercept on the magnetization axis. This remnant ferromagnetic component represents the polaron.

Finally, we again emphasize that the material undergoes a magnetic field–driven insulator-to-metal transition (Washburn *et al*., 1984), demonstrating, once again, that the electron, bound principally by magnetic interactions, can become a free carrier if the magnetic state of the lattice becomes similar to that of the polaron. A detailed study by Shapira, Foner, Reed and Oliveira (1972) in defect doped EuTe (also an antiferromagnet insulator) had arrived at this conclusion independently.

4 THE POLARON MODEL

In this section, we describe the polaron model originally envisioned to account for experimental observations in Eu chalcogenides, but also applicable with minor modifications to any magnetic system in which the magnetic species with moment $\vec{S}$ may be thought of as localized and interacting with the spin, $\vec{s}$, of an electron. Magnetic semiconductors

are interesting because this exchange coupling gives rise to an extraordinarily large Zeeman splitting expressed in the mean-field approximation as

$$E = g^* \mu_B \vec{s} \cdot H + 2J\vec{s} \cdot \left\langle \vec{S} \right\rangle \tag{1}$$

where g^* is the spectroscopic splitting factors for the carriers, μ_B is the Bohr magneton, and H is the applied magnetic field. $\langle S \rangle$ is the average value of the local moments over the region occupied by the band electrons. The second term of equation (1) can produce enormous splitting, amounting to fractions of an electron volt in Eu compounds below the magnetic ordering temperature and as large as 10 meV T^{-1} in (paramagnetic) diluted magnetic semiconductors. However, when the electronic states are not extended, the exchange J can lead to an additional localization beyond the normal Coulomb binding and correlations observed in nonmagnetic semiconductors. In an antiferromagnet (a paramagnet is much the same), this can lead to the formation of 'ferromagnetic' clusters – the magnetic polarons (Kasuya and Yanase, 1968; Dietl and Spalek, 1982; Heiman, Wolff and Warnock, 1983).

As has already been mentioned, Zener (1951) and de Gennes (1960) introduced spin-dependent electron transfer and spin polarons, respectively, to account for conductivity-induced ferromagnetism in $LaMnO_3$. Here we present Kasuya's arguments for the stability of the spin polaron (Kasuya, 1970a; Coey, Viret and von Molnár, 1999). It is assumed that a single electron or hole is introduced into an otherwise antiferromagnetic or paramagnetic lattice. In the absence of defects or impurities, the differential free energy ΔF_f, of a spherical polarized cluster in this background may be expressed as

$$\Delta F_f = \frac{E_0}{\gamma^2} - \frac{J}{2\gamma^3} \tag{2}$$

where $E_0 = (\pi^2 h^2 / 2ma^2)$, $\gamma = R/a$ and a is defined by the equation $4\pi a^3 = 1/N_{Eu}$. Here, we are specifically addressing the case for Eu chalcogenides, in which a magnetic Eu spin sits at every lattice site, and N_{Eu} is the number of Eu^{2+} ions per unit volume. Minimizing this free energy with respect to the radius, R, results in a nonphysical solution with $R \to 0$ or ∞. A more realistic model introduces the additional energy term found in equation (3) due to the Coulomb attraction of an electron to an oppositely charged center:

$$\Delta F = \Delta F_f - \frac{e^2}{\varepsilon R} \tag{3}$$

Of course, this is the situation most often encountered in bulk semiconductors, since the (concentrated) magnetic semiconductors are insulators, unless doped, and the dopant acts as an attractive center, just as it would in any ordinary semiconductor. Under these conditions, minimization with respect to R yields a stable configuration, and Kasuya referred to this as the bound magnetic polaron or magnetic impurity state. Although the second term in equation (3) describes a simple Coulomb attraction, a screened Coulomb or other inverse R dependence should also lead to a solution at finite R. More complex descriptions may be appropriate when the Coulomb attractive term is weak or absent, such as the recent developments in (Cd,Mn)Te (Jaroszynski *et al*., 2006). Below the Neél temperature of an antiferromagnet, the polarons will not move easily in the presence of an electric field, since they have to drag their polarization cloud along, which leads to a large effective mass (diffusive motion) (Kasuya, 1970b; Wolfram and Callaway, 1962) or localization. It also becomes clear how an applied magnetic field can produce an insulator–metal transition. The magnetic contribution to the localization comes about from the difference between the antiferromagnetic or paramagnetic order of the host and the ferromagnetic order of the polaron. In a magnetic field, as the sublattice develops an ever increasing net magnetization, this energy difference decreases and ultimately the carrier becomes unbound. If there are defects present, this polaron, which might be describable as a heavy but band-like particle moving diffusively (Kasuya, 1970b; Wolfram and Callaway, 1962), will typically be bound to defects such as the Coulomb potential described earlier. Transport under these conditions occurs via 'hopping', which may also be magnetic field dependent. The previous description is in the limit of small carrier concentration in a concentrated magnetic lattice. These ideas, however, may be applied also to situations where carrier concentration is large, but the magnetic lattice is diluted. As will be seen (Ohno *et al*., 1996), a large polaron results. The type of transport will still be stipulated by the proximity of the Fermi energy with respect to the mobility edge, a concept that also embraces the physical picture of percolating clusters more magnetically ordered and more conducting than the sublattice background.

5 II–VI DILUTED MAGNETIC SEMICONDUCTOR (see also Ferromagnetic Semiconductors, Volume 5)

The prototypical example of this class of semiconductors is CdTe doped with Mn (Mn^{2+} is a $^6S_{5/2}$ ion), which substitutes for Cd sites in this zinc blende structure. In this case, however, additional doping of, for example, In is necessary to provide carriers to this otherwise insulating system. Several magnetotransport studies have been interpreted in terms of magnetic polaron formation (Sawicki *et al*., 1986; Wojtowicz *et al*., 1986). A number of transport and concomitant magnetic studies made use of the fact that In:$Cd_{1-x}Mn_xTe$

is a persistent photoconductor in which, for suitably low temperatures, the carrier concentration may be varied continuously by temporary illumination, that is, the material may be photodoped (Terry *et al*., 1992b). Over the concentration range between 4×10^{16} and $2 \times 10^{17}\,\mathrm{cm}^{-3}$, in a regime where low-temperature transport occurs by hopping, the conductivity changes from a $1/T^{1/2}$ law, characteristic of variable range hopping with Coulomb interactions to simple activation, $1/T$, as temperature is decreased. This 'hard gap' of inaccessible states was interpreted as the difference between unrelaxed magnetically disordered empty states and the magnetically relaxed state, which occurs after the electron has hopped and formed a bound magnetic polaron. Applying a large magnetic field eliminates the energy difference between magnetically disordered and ordered states and the $T^{1/2}$ law is recovered (Terry, Penney and von Molnár, 1992a). The most direct evidence, however, comes from a number of ingenious optical studies (Dietl and Spalek, 1982; Heiman, Wolff and Warnock, 1983; Harris and Nurmikko, 1983; Awschalom *et al*., 1985; Awschalom, Warnock and von Molnár, 1987). Dietl and Spalek (1982) and Heiman, Wolff and Warnock (1983) independently developed theories introducing magnetic polarons to explain spin-flip Raman data, with finite spin-flip energies even at zero applied magnetic field. They concluded that the effective field is provided by the fluctuating magnetic polaron. More recent Raman studies of the Eu chalcogenides and their interpretation utilizing polaron concepts have been reported by Cooper *et al*. (Rho *et al*., 2002a,b; Snow *et al*., 2001).

Some of the most exciting developments in the study of magnetic polarons have, however, employed time-resolved techniques. Polaron formation has been studied by observations of the time evolution of the polaron-binding energy, on picosecond timescales, in transmission and luminescence (Harris and Nurmikko, 1983; Awschalom *et al*., 1985). A remarkable innovative experiment by Awschalom, Warnock and von Molnár (1987) succeeded in direct observations of spin dynamics responsible for polarons through time-resolved magnetic measurements. This elegant magnetic spectroscopy employs a planar DC SQUID as a detector to measure the statically and dynamically induced magnetization as a function of impinging radiant energy. Finally, this spectroscopy was employed to study polaron formation even in confined geometries (Awschalom *et al*., 1991). These results are shown in Figure 5. Samples were constructed of multiple quantum wells of (zinc-blende type) $Cd_{1-x}Mn_xSe$ confined by ZnTe barriers. These magnetic heterostructures are type II, that is, optically excited electrons are confined to the $Cd_{1-x}Mn_xSe$ layer and holes to the ZnTe layer. The magnetization induced by electrons optically excited from the valence to the conduction bands of the heterostructure are then monitored as a function of excitation energy, both statically and dynamically. Here we focus on the static results. For an excitation energy of the impinging circularly polarized light in the vicinity of the quantum well ground state, a magnetic peak is observed for energies somewhat lower than the $n = 1$ quantum level. This is due to magnetic polaron formation. For energies lower than the polaron energy, the absorption is minimal.

Magnetization rises, however, with the onset of absorption into the impurity level at which polarons form. The subsequent decrease for higher energies is due to spin scattering, which results in a relaxation of polaron orientation and a much smaller net magnetization in a direction perpendicular to the pickup loop of the SQUID. It is to be noted that the polaron peak exists despite the fact that the bulk polaron radius is estimated to be approximately 9 nm, whereas the thinnest quantum well is only 1.8 nm wide. Clearly, the polaron can no longer be thought of as being spherical, but must by necessity, take on a pancake-like shape. The observed time-dependent polaron magnetization also deserves comment. It grows and decays at relatively long timescales, on the order of 400 ps, characteristic of spin lattice relaxation times. This means that this process leaves a magnetic imprint that lasts far longer than the lifetime of the photoexcited electron (femtosecond) which caused it in the first place.

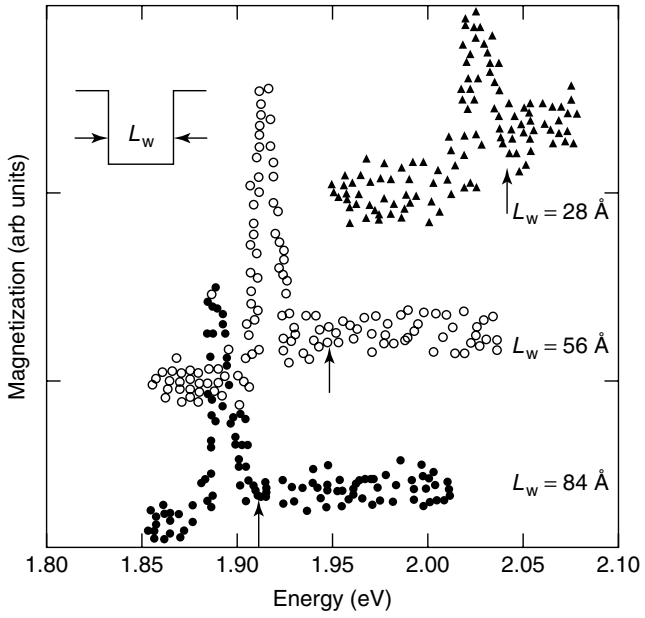

Figure 5. Magnetic excitation spectra measured at 1.5 K for three quantum well structures with widths L_w as indicated. (Reproduced from Awschalom *et al*., 1991, with permission from the American Physical Society. © 1991.)

6 III–V DILUTED MAGNETIC SEMICONDUCTORS (see also Ferromagnetic Semiconductors, Volume 5 and Diluted Ferromagnetic Semiconductors – Theoretical Aspects, Volume 5)

Following seminal work by Story, Galazka, Frankel and Wolff (1986), who discovered ferromagnetism in PbSnMnTe diluted magnetic semiconductors, III–V diluted magnetic semiconductors were first produced in InAs and GaAs (Munekata *et al*., 1989). Although transition-metal (TM) ions have by now been introduced into many additional members of the III–V semiconductor family, in this discussion, we confine ourselves to InMnAs and GaMnAs, since these materials have been studied in the greatest detail and evidence for magnetic polaron formation exists.

The first evidence comes from an analysis of magnetotransport and magnetization in thin films of p-doped InMnAs close to the insulator–metal transition by Ohno *et al*. (1992). These authors observed an anomalous Hall effect which dominates Hall measurements for temperatures between ∼0.4 K and close to room temperature. Partially ferromagnetic order is observed below ∼7.5 K (Figure 6). The coexistence of remanent magnetization and unsaturated spins, as well as large negative magnetoresistance at low temperatures, was interpreted as being due to the formation of large magnetic polarons with average magnetic correlation lengths exceeding 10 nm. The measured hole concentration of $\sim 2 \times 10^{19}$ cm^{-3} implies that many electrons contribute to the magnetic cluster. A theoretical description of these large magnetic polarons in diluted systems was first advanced by Isaacs and Wolff (1987).

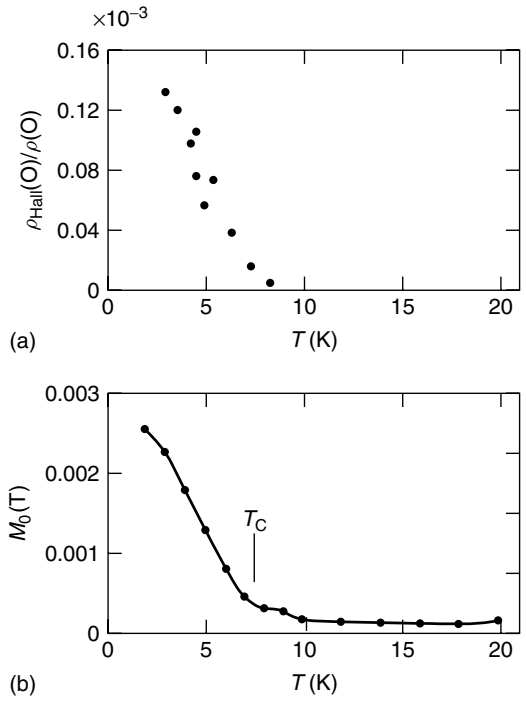

Figure 6. (a) Temperature dependence of the remanent part of Hall resistivity divided by the zero field resistivity of InMnAs. (b) Temperature dependence of the remanent magnetization of the film. (Reproduced from Ohno *et al*., 1992, with permission from the American Physical Society. © 1992.)

Other evidence comes from magnetic circular dichroism studies in GaMnAs by Beschoten *et al*. (1999). These authors show that the evolution of ferromagnetism in p-type GaMnAs can be separated into two distinct spectral contributions as a function of applied field depending on the excitation energy. A high-energy ferromagnetic and lower-energy antiferromagnetic signal is observed. The low-energy signal is attributable to antiferromagnetic exchange between holes and Mn^{2+} ions, which leads to a polaron cloud that forms below T_C.

The renaissance in studies of diluted systems following the discovery that GaMnAs can reach ferromagnetic transition temperatures in excess of 110 K (Ohno *et al*., 1996; Ohno, 1998, 1999; Furdyna *et al*., 2002; Ku *et al*., 2003; Maksimov *et al*., 2004) has also resulted in theoretical reexamination of magnetic polaron formation and transition to the ferromagnetic (conducting) state. In particular, a magnetic polaron model has been developed for purely insulating or highly resistive III–V materials, which often exhibit Mott variable range hopping at low temperatures, consistent with carriers localized in polarons (Wolff, Bhatt and Durst, 1996; Bhatt, Berciu, Kennett and Wan, 2002; Kaminski and Das Sarma, 2002; Durst, Bhatt and Wolff, 2002; Das Sarma, Hwang and Kaminski, 2003). The magnetic polaron percolation description assumes that the carrier density n_c is much lower than the impurity dopant density n_i. The carriers are localized in hydrogenic orbitals forming polarons. The polaron radius, r_H, depends on the dielectric constant, ε, and the effective mass m^* viz.

$$r_H = \varepsilon \left(\frac{m}{m^*}\right) a_0 \tag{4}$$

where a_0 is the Bohr radius, 5.3×10^{-11}m. The dopant impurities are assumed to be substitutional at the cation site. Magnetic exchange between the magnetic moment of the dopant impurities and the moment of the localized carrier results in ferromagnetic alignment of the impurity moments and a large effective moment that naturally depends on the impurity density in the cation site. The radius, r_P, over which the impurity moments are bound to those of the carrier, varies inversely with temperature, as (Bhatt, Berciu, Kennett and Wan, 2002; Das Sarma, Hwang and Kaminski, 2003;

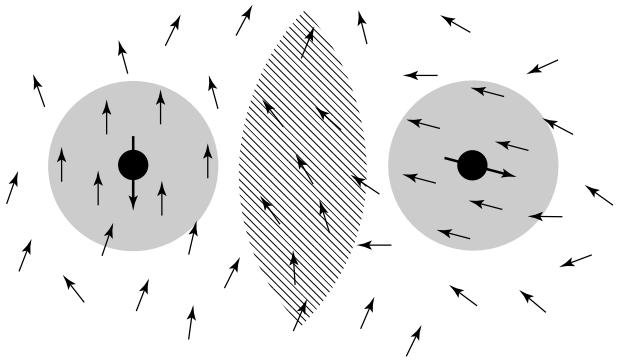

Figure 7. A schematic diagram showing the interaction between two bound magnetic polarons (gray circles). The large arrows represent impurity spins while the small arrows represent carrier spins. The lens-shaped shaded region indicates the region that is important for the interaction of the two polarons. (Reproduced from Kaminski *et al*., 2002, with permission from the American Physical Society. © 2002.)

Kaminski and Das Sarma, 2002)

$$r_{\mathrm{P}} = \frac{r_{\mathrm{H}}}{2} \ln\left(\frac{sSJ}{T}\right) \tag{5}$$

where J is the effective exchange constant. If the polarons are spaced sufficiently far apart, the magnetic exchange between polarons will be small, and the material will be paramagnetic. As the temperature decreases, the polaron radius increases, allowing overlap. Ferromagnetic exchange between neighboring magnetic polarons (Figure 7), the mechanism for which was detailed by Wolff, Bhatt and Durst (1996), results in bulk ferromagnetic ordering of the material.

Assuming the polarons to act as rigid spheres, percolation will be achieved when

$$r_{\mathrm{P}} \left(n_{\mathrm{c}}\right)^{1/3} = 0.86 \tag{6}$$

From this, an expression for the Curie temperature below which percolation (and magnetic ordering) is achieved can be obtained.

$$T_{\mathrm{C}} \approx sSJ \left(r_{\mathrm{H}}^3 n_{\mathrm{c}}\right)^{1/3} n_{\mathrm{i}}^{1/2} n_{\mathrm{c}}^{-1/2} \exp\left(\frac{-0.86}{\left(r_{\mathrm{H}}^3 n_{\mathrm{c}}\right)^{1/3}}\right) \tag{7}$$

No attempt has been made to compare the theoretical T_{C} with experimental values owing to the experimental difficulty in obtaining accurate values for n_{c} in highly insulating specimens as well as uncertainties in actual dopant concentration. In addition, as pointed out by Gor'kov and Kresin (1998), the assumption of a rigid sphere model should be modified owing to site correlation.

The magnetic moment as a function of temperature below T_{C} can be calculated on the basis of the number of impurity atoms contained within the percolating cluster, and yields concave $M(T)$ curves similar to those obtained in low carrier concentration samples of InMnAs (Ohno *et al*., 1992) and $Ge_{1-x}Mn_x$ (Park *et al*., 2002; Li *et al*., 2005). This model also explains the lower-than-anticipated magnetic moment observed in these III–V materials, since at a given temperature not all impurity atoms are within the percolating cluster and do not contribute to the observed ferromagnetic moment. The bound magnetic polaron picture has also been used, with some expansion, to explain some of the properties of the dilute magnetic oxides discussed in the following section.

7 DILUTE MAGNETIC OXIDES

Triggered by the prediction, in 2000 (Dietl *et al*., 2000), of room-temperature ferromagnetism in p-type ZnO doped with 5% Mn, considerable research has been focused on the development of dilute magnetic semiconductors based on wide-band gap oxides such as ZnO, TiO_2, and SnO_2 doped with small amounts of TMs. A large body of work already exists and has been reviewed elsewhere (Pearton *et al*., 2003a, 2004; Janisch, Gopal and Spaldin, 2005). Several overall trends have been revealed as follows:

1. *Lack of reproducibility*: Samples of nominally the same material prepared by different research groups often appear to have very different properties, ranging from paramagnetic to ferromagnetic.
2. *Anomalously large moments*: Some materials doped with small amounts of TM have been reported to have measured moments per dopant atom larger than that expected for the spin-only moment of the dopant atom (Fitzgerald *et al*., 2005; Ogale *et al*., 2003; Hong *et al*., 2005a; Hong, Sakai, Prellier and Hassini, 2005b). However, it should be noted that these large moments per impurity atom occur for TM concentrations of typically 1% or lower. This leads to very small sample moments on the order of 10^{-5}–10^{-4} emu, which are difficult to measure accurately. Also, small uncertainties in dopant concentration can lead to large uncertainties in the calculated moment per impurity atom.
3. *Decrease in moment with dopant concentration*: A general trend of reduced moment per dopant atom is observed as a function of increased TM dopant concentration (Ogale *et al*., 2003; Fitzgerald *et al*., 2005; Janisch, Gopal and Spaldin, 2005).
4. *High-transition temperatures*: Observed Curie temperatures are above room temperature. These transition temperatures are very high for such low magnetic dopant concentrations.

5. *Magnetism/carrier concentration*: Ferromagnetism has been reported in both conducting and insulating specimens. To our knowledge, there has been no convincing conclusive evidence of the relationship between magnetism and carrier concentration, which would be expected if the magnetic exchange is carrier mediated. In some cases, it has been observed that the addition of a donor codopant, such as lithium in ZnO (Lee, Jeong, Hwang and Cho, 2003), increases the magnetic properties of the material. In contradiction though, recent results show that H doping results in significant ferromagnetism but little change in carrier concentration (Lee *et al*., 2006).
6. *Substrate dependence*: A number of groups have shown that the magnetic properties of the thin films are strongly dependent on the substrate on which the material is grown. In general, the lowest quality film crystallinity gives the most magnetic films (Hong *et al*., 2005a; Hong, Sakai, Prellier and Ruyter, 2005c; Kaspar *et al*., 2005).
7. *Moment in d^0 systems*: There have also been reports of magnetism in ZnO films doped with Sc and in HfO_2, both materials with no intrinsic magnetism (Coey, Venkatesan and Fitzgerald, 2005a; Coey *et al*., 2005c).
8. *Anisotropy*: Several researchers have noticed a strong dependence of the saturation magnetization on the direction of the applied field (Coey *et al*., 2005b).

These features have led to a debate over whether the magnetism in these materials is truly intrinsic or extrinsic. In particular, the lack of reproducibility and giant moments has led to suggestions of the formation of secondary phases or contamination during sample preparation. For example, it has been shown that the ferromagnetic moment in bulk Mn:ZnO prepared by sintering (Sharma *et al*., 2003) can be explained by the formation of such ferromagnetic secondary phases (Kundaliya *et al*., 2004). Recently, Colis *et al*. have been able to detect secondary phases in Mn-doped ZnO via the presence of additional signatures in Raman spectroscopy data (Colis *et al*., 2005), even though X-ray data on the same sample showed a single phase material. The authors conclude that the observed ferromagnetism results solely from these secondary effects. There also exists the possibility of clusters of the ferromagnetic dopant occurring as seen in TiO_2:Co (Kim *et al*., 2002; Kennedy *et al*., 2004). It is clear therefore that detailed microstructural characterization must be done before analysis of the origin of ferromagnetism can be made. Although such measurements have been done for much of the data presented in the literature, secondary phases that could cause ferromagnetic signals at room temperature can be very small in size, and are close to the current measurement limitations. This makes it difficult to preclude definitely extrinsic sources of magnetism in these doped oxides.

In most experimental setups, starting materials and finished samples are handled numerous times by metal implements such as stainless-steel tweezers, which can transfer small amounts of ferromagnetic material to a specimen (Abraham, Frank and Guha, 2005). In addition, the growth environment (furnace, vacuum chamber) can contain amounts of magnetic impurities, which, unless great care is taken, can be transferred to the sample. Varying amounts of contamination could easily be a cause for the lack of reproducibility between research groups worldwide, and may explain the spread in reported results.

Despite these reservations, there has been a growing consensus that a number of these features can be explained using models based on magnetic polarons. Although the polaron percolation model described earlier appears to explain the doped III–V materials, it is not clear whether it can be applied equally well to the dilutely doped magnetic oxide materials described earlier. Owing to the large Curie temperatures observed in the oxides, there are few measurements of $M(T)$ and even of T_C with which to compare. Also, the magnetic oxides often exhibit moments higher than expected, rather than the lower moments predicted by the above model.

Defects are expected to play a key role in both the magnetic and transport properties of the doped magnetic oxides. In these materials, it is generally considered that the TM dopant cations substitute for the cation in the crystal structure. We let the symbol x, with values from 0 to 1, represent the degree of substitution in the cation site, that is, $Zn_{1-x}M_xO$ and $Ti_{1-x}M_xO_2$, where M is the TM dopant. It should be noted that while in ZnO the TM cation substitutes for a cation with a valency of 2 (Zn^{2+}), in TiO_2 and SnO_2, the TM cation substitutes for a cation with a valency of 4. Most TMs form ions with valencies of either 2 or 3. This means that when substitutional in either TiO_2 or SnO_2, oxygen vacancies will form in order to ensure charge neutrality of the crystal. Also, ZnO and SnO_2 show a tendency toward the formation of cation intersitials, further increasing the nonstoichiometry. In general, then, the chemical formula for these oxides should include the possibility of oxygen nonstoichiometry, that is, $Ti_xM_{1-x}O_{2-\delta}$. In this case δ is a representation of the defect concentration in the material.

Recently, Coey has expanded the polaron percolation model to incorporate conduction through the formation of a conducting impurity band at sufficiently high defect concentration in the oxides (Coey, Venkatesan and Fitzgerald, 2005a; Coey, 2005). It is assumed that the n-type carriers are localized at donor defect sites, and thus the polaron distribution is directly dependent on defect concentration and distribution. In the high dielectric oxides under consideration here, the polaron radius r_H can be on the order of several nanometers, since it is directly proportional to the dielectric constant of the material. This large polaron radius can

encompass hundreds of cation sites and thus a number of dopant sites.

At low defect concentrations the carriers are trapped and the material is insulating. As the defect concentration (and carrier concentration) increases, the wave functions of the weakly bound localized carriers overlap. This forms an impurity band, and the material becomes metallic. Generalized phase diagrams for such a system have been proposed (Janisch, Gopal and Spaldin, 2005; Coey, Venkatesan and Fitzgerald, 2005a). Figure 8, from Coey, Venkatesan and Fitzgerald (2005a), shows an oxide system in which the magnetic state changes as a function of both TM dopant concentration and defect concentration. The shaded regions in the figure denote regions in which the carrier concentration is low, and the system is insulating. Clearly, as observed in experimental systems, ferromagnetism is predicted in both conducting and insulating films. In this model, the degree of magnetic coupling is strongly dependent on the defect (polaron) density, and thus the growth conditions. This argument could be used to explain the wide variation in moments reported by different groups for materials produced by different methods or in different conditions. This could also explain why poorer-quality, defect-rich films have been observed to exhibit stronger moments than high-quality films (Kaspar *et al*., 2005; Hong *et al*., 2005a).

When the dopant concentration, x, increases sufficiently to form pairs of dopant ions on neighboring sites, superexchange interactions will occur. The superexchange interaction is expected, in general, to be antiferromagnetic, so these pairs will yield a net reduction in the observed moment. Once the dopant concentration exceeds the percolation threshold, x_p, nearest-neighbor pairs will form throughout the material and it will become antiferromagnetic. The experimentally observed trend toward reduced moment with increased dopant agrees with the prediction of the formation of antiferromagnetically coupled pairs of magnetic dopant ions at high dopant concentrations.

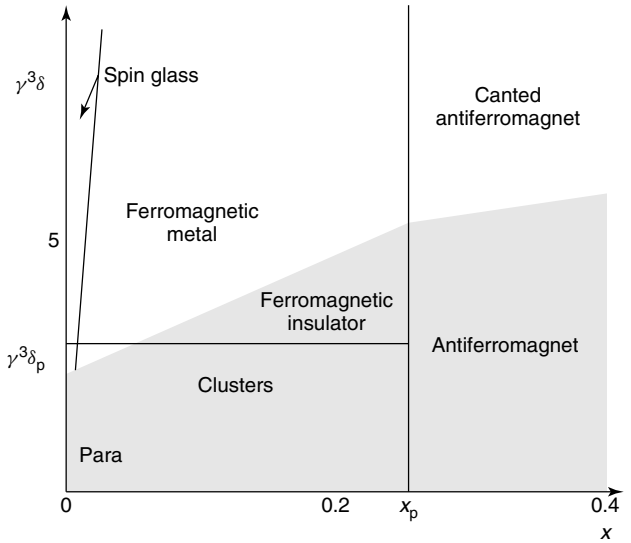

Figure 8. Proposed phase diagram for TM-doped oxides. The shaded region indicates insulating material. (Reproduced from Coey *et al*., 2005, with permission from Nature Publishing Group. © 2005.)

The Curie temperatures calculated for this model using typical material parameters are much lower than those actually observed, suggesting the need for extension of the model. Potentially, reasonable values for T_C could be obtained by hybridization of the donor impurity band orbitals with empty 3d bands from the magnetic impurities. Such hybridization would be most likely to occur near the beginning and the end of the 3d series of TM dopants where empty 3d bands cross the Fermi level. In support of this, experiments on a series of ZnO samples doped with small amounts of TM elements have shown that the magnetization of the resultant material varies across the TM series with peaks near the beginning and end of the series where hybridization is most likely to occur (Coey *et al*., 2005c).

Further supporting evidence is needed to confirm the impurity band model. In particular, it would be necessary to be able to quantify the defect concentration in a specimen in order to allow it to be compared with films grown by others or within the same group. Then the samples could be arranged by defect and dopant concentration to determine whether the phase diagram is reproduced. Another potential method for confirming the proposed phase diagram would be to vary the defect concentration within a specimen with a given dopant concentration to allow the effect of defect concentration on the magnetic and electrical properties to be reproducibly measured.

Finally we mention briefly the work on nitride materials. Magnetic doping of nitrides has paralleled the research on oxides, although to a large extent the research has concentrated primarily on Mn as the magnetic dopant. It is possible that magnetism in these materials may be described using similar models. Reviews of work on nitrides can be found in Pearton *et al*. (2003a,b). There have been two recent experimental reports of giant magnetic moments ($400-4000\,\mu_B$) in insulating material (Dhar *et al*., 2005a,b), GaN:Gd epilayers, and a theoretical description for conducting samples (Dalpian and Wei, 2005). Verification of these observations and the existing band structure calculations are necessary to provide impetus to further consider polarization effects in this system.

7.1 New developments

In this context, we note that a very recent analysis of magnetotransport effects in (Cd,Mn)Te quantum wells indicates that

a magnetic field induced increase in magnetic cluster size leads to large negative magnetoresistive effects (Jaroszynski *et al*., 2006) near but on the metallic side of the metal insulator transition. The change in carrier concentration in one and the same sample is achieved by gating of the device. The authors note the resemblance of these effects to mixed valence perovskites. Although the negative magnetoresistance is absent at higher temperatures, our view is that the effects in both systems are in the spirit of magnetic polarons described earlier in this text (von Molnár and Methfessel, 1967) and theoretically by Gor'kov and Kresin (1998, 2004). The authors point out, correctly, that in the present 2D modulation-doped system, the coulomb binding term is weak and thus the stability of the polarization cloud is not describable in the spirit of a strongly bound magnetic polaron. In fact, an observed concentration-independent conductivity requires that the polarization cloud maintain a constant radius regardless of carrier concentration. This is in striking contrast to, for example, Penney, Holtzberg, Tao and von Molnár (1974) and requires a modified model for the stability of the ferromagnetic conducting local polarization, that is, the magnetic polaron. Some of the physics associated with the formation of these magnetic polarons may have their origin in newly published data in the cobaltites. While $La_{1-x}Sr_xCoO_3$ can be described by classic magnetic polarons in the dilute limit (Giblin *et al*., 2005), in the more concentrated regions, the physical properties are more like those of conducting clusters in a dielectric matrix (Wu *et al*., 2005). This is similar to the mode of formation suggested by the results mentioned earlier on modulation-doped II–VI diluted heterostructures (Jaroszynski *et al*., 2006). Wu *et al*. prove conclusively, utilizing SANS, that $La_{1-x}Sr_xCoO_3$ phase separates into ferromagnetic metallic clusters having limited size distribution embedded in an insulating nonferromagnetic matrix. This, the authors argue persuasively, is a result of spontaneous magnetoelectronic, not chemical, phase separation. There is, furthermore, no direct spectroscopic evidence of the latter (Wu *et al*., 2005). Other indirect experimental evidence, such as a hopping transport signature with $\ln \rho \sim T^{-1/2}$ (Kennedy *et al*., 2004) as well as an intergranular giant magnetoresistance, however, are characteristic of chemically multiphase materials as well. It is apparent that these novel experimental results will require further theoretical understanding of magnetic polarons.

8 CONCLUSION

In summary, we have shown, utilizing specific experimental evidence drawn principally from transport, optics, and scattering experiments that magnetic polaron descriptions can explain many of the observed properties of magnetic semiconductor systems, both dilute and concentrated. They also show promise of being able to describe the properties of systems of recent interest such as the dilute magnetic oxides. Extensions of these concepts to the cobaltites and modulation-doped II–VI diluted two dimensional electron systems (2DES) will require improved understanding of polaron stability.

NOTES

[1] This chapter represents an expansion on and an update of a review published earlier. von Molnár, S., Terry, I. and Penney, T. (1995) in *Polarons and Bipolarons in High-T_C Superconductors and Related Materials* (Eds, Salje, E. K. H., Alexandrov, A. S. and Liang, W. Y.) Press Syndicate of the University of Cambridge, Cambridge, pp. 437.

ACKNOWLEDGMENTS

The authors first and foremost thank Mrs Linda Lynes who spent many hours assuring accuracy of references and the general format of the manuscript. They are also grateful to Drs C. Leighton, V. Dobrosavljevic, and R.J. Kennedy for several enlightening discussions which we hope improved this brief review.

REFERENCES

Abraham, D.W., Frank, M.M. and Guha, S. (2005). Absence of magnetism in hafnium oxide films. *Applied Physics Letters*, **87**, 252502-1–252502-3.

Anderson, P.W. and Hasegawa, H. (1955). Considerations on double exchange. *Physical Review*, **100**, 675–681.

Awschalom, D.D., Freeman, M.R., Samarth, N., *et al*. (1991). Observation of polaron dynamics in magnetic quantum-wells. *Physical Review Letters*, **66**, 1212–1215.

Awschalom, D.D., Halbout, J.M., von Molnár, S., *et al*. (1985). Dynamic spin organization in dilute magnetic systems. *Physical Review Letters*, **55**, 1128–1131.

Awschalom, D.D., Warnock, J. and von Molnár, S. (1987). Low-temperature magnetic spectroscopy of a dilute magnetic semiconductor. *Physical Review Letters*, **58**, 812–815.

Beschoten, B., Crowell, P.A., Malajovich, I., *et al*. (1999). Magnetic circular dichroism studies of carrier-induced ferromagnetism in $(Ga_{1-x}Mn_x)As$. *Physical Review Letters*, **83**, 3073–3076.

Bhatt, R.N., Berciu, M., Kennett, M.P. and Wan, X. (2002). Diluted magnetic semiconductors in the low carrier density regime. *Journal of Superconductivity*, **15**, 71–83.

Busch, G., Streit, P. and Wachter, P. (1970). Effect of magnetic ordering on photoluminescence of EuS and EuTe. *Solid State Communications*, **8**, 17–59.

Coey, J.M.D. (2005). High-temperature ferromagnetism in dilute magnetic oxides. *Journal of Applied Physics*, **97**, 10D313-1-3.

Coey, J.M.D., Venkatesan, M. and Fitzgerald, C.B. (2005a). Donor impurity band exchange in dilute ferromagnetic oxides. *Nature Materials*, **4**, 173–179.

Coey, J.M.D., Venkatesan, M., Fitzgerald, C.B., *et al*. (2005b). Anisotropy of the magnetization of a dilute magnetic oxide. *Journal of Magnetism and Magnetic Materials*, **290**, 1405–1407.

Coey, J.M.D., Venkatesan, M., Stamenov, P., *et al*. (2005c). Magnetism in hafnium dioxide. *Physical Review B*, **72**, 244–250.

Coey, J.M.D., Viret, M. and von Molnár, S. (1999). Mixed-valence manganites. *Advances in Physics*, **48**, 167–293.

Colis, S., Alaria, J., Turek, P., *et al*. (2005). No ferromagnetism in Mn doped ZnO semiconductors. *Chemical Physics Letters*, **415**, 337–341.

Dalpian, G.M. and Wei, S.H. (2005). Electron-induced stabilization of ferromagnetism in $Ga_{1-x}Gd_xN$. *Physical Review B*, **72**, 115201-1–115201-5.

Das Sarma, S., Hwang, E.H. and Kaminski, A. (2003). Temperature-dependent magnetization in diluted magnetic semiconductors. *Physical Review B*, **67**, 155–201.

de Gennes, P.G. (1960). Effects of double exchange in magnetic crystals. *Physical Review*, **118**, 141–154.

de Gennes, P.G. and Friedel, J. (1958). Anomalies de resistivite dans certains metaux magnetiques. *Journal of Physics and Chemistry of Solids*, **4**, 71–77.

De Teresa, J.M., Ibarra, M.R., Algarabel, P.A., *et al*. (1997). Evidence for magnetic polarons in the magnetoresistive perovskites. *Nature*, **386**, 256–259.

Dhar, S., Brandt, O., Ramsteiner, M., *et al*. (2005a). Colossal magnetic moment of Gd in GaN. *Physical Review Letters*, **94**, 37–205.

Dhar, S., Perez, L., Brandt, O., *et al*. (2005b). Gd-doped GaN: A very dilute ferromagnetic semiconductor with a Curie temperature above 300 K. *Physical Review B*, **72**, 203–245.

Dietl, T., Ohno, H., Matsukura, F., *et al*. (2000). Zener model description of ferromagnetism in zinc-blende magnetic semiconductors. *Science*, **287**, 1019–1022.

Dietl, T. and Spalek, J. (1982). Effect of fluctuations of magnetization on the bound magnetic polaron – comparison with experiment. *Physical Review Letters*, **48**, 355–358.

Durst, A.C., Bhatt, R.N. and Wolff, P.A. (2002). Bound magnetic polaron interactions in insulating doped diluted magnetic semiconductors. *Physical Review B*, **65**, 235–205.

Fath, M., Freisem, S., Menovsky, A.A., *et al*. (1999). Spatially inhomogeneous metal-insulator transition in doped manganites. *Science*, **285**, 1540–1542.

Fisher, M.E. and Langer, J.S. (1968). Resistive anomalies at magnetic critical points. *Physical Review Letters*, **20**, 665–668.

Fitzgerald, C.B., Venkatesan, M., Lunney, J.G., *et al*. (2005). Cobalt-doped ZnO – a room temperature dilute magnetic semiconductor. *Applied Surface Science*, **247**, 493–496.

Friedman Jr., H.G., Choppin, G.R. and Feuerbacher, D.G. (1964). The shapes of the f orbitals. *Journal of Chemical Education*, **41**, 354.

Furdyna, J.K., Liu, X., Sasaki, Y., *et al*. (2002). Ferromagnetic III-Mn-V semiconductor multilayers: manipulation of magnetic properties by proximity effects and interface design. *Journal of Applied Physics*, **91**, 7490–7495.

Giblin, S.R., Terry, I., Clark, S.J., *et al*. (2005). Observation of magnetic excitions in $LaCoO_3$. *Europhysics Letters*, **70**, 677–683.

Gor'kov, L.P. and Kresin, V.Z. (1998). Manganites at low temperatures and light doping: band approach and percolation. *JETP Letters*, **67**, 934.

Gor'kov, L.P. and Kresin, V.Z. (2004). Mixed-valence manganites: fundamentals and main properties. *Physics Reports: Review Section of Physics Letters*, **400**, 149–208.

Harris, J.H. and Nurmikko, A.V. (1983). Formation of the bound magnetic polaron in (Cd,Mn)Se. *Physical Review Letters*, **51**, 1472–1475.

Heikes, R.R. and Chen, C.W. (1964). Evdence for impurity bands in La-Doped EuS. *Physics*, **1**, 159.

Heiman, D., Wolff, P.A. and Warnock, J. (1983). Spin-flip Raman-scattering, bound magnetic polaron, and fluctuations in (Cd,Mn)Se. *Physical Review B*, **27**, 4848–4860.

Holtzberg, F., Methfessel, S., Suits, J.C. and McGuire, T.R. (1964). Effect of electron concentration on magnetic exchange interactions in rare earth chalcogenides. *Physical Review Letters*, **13**, 18–21.

Hong, N.H., Sakai, J., Huong, N.T., *et al*. (2005a). Role of defects in tuning ferromagnetism in diluted magnetic oxide thin films. *Physical Review B*, **72**, 45–336.

Hong, N.H., Sakai, J., Prellier, W. and Hassini, A. (2005b). Transparent Cr-doped SnO2 thin films: ferromagnetism beyond room temperature with a giant magnetic moment. *Journal of Physics: Condensed Matter*, **17**, 1697–1702.

Hong, N.H., Sakai, J., Prellier, W. and Ruyter, A. (2005c). Room temperature ferromagnetism in laser ablated transition-metal-doped TiO2 thin films on various types of substrates. *Journal of Physics D: Applied Physics*, **38**, 816–821.

Isaacs, E.D. and Wolff, P.A. (1987). Spin-Texture in Acceptor-Bound Magnetic Polarons, in *Diluted Magnetic (Semimagnetic) Semiconductors*, Aggarwal, R.L., Furdyna, J.K. and von Molnár, S. (Eds.), Materials Research Society: Pittsburgh, pp. 91–95, Vol. 89.

Janisch, R., Gopal, P. and Spaldin, N.A. (2005). Transition metal-doped TiO2 and ZnO - present status of the field. *Journal of Physics: Condensed Matter*, **17**, R657–R689.

Jaroszynski, J., Andrearczyk, T., Karczwski, G.,*et al*. (2006). An intermediate phase at the metal-insulator boundary in a magnetically doped two-dimensional electron system. to be published.

Jin, S., McCormack, M., Tiefel, T.H. and Ramesh, R. (1994). Colossal magnetoresistance in La-Ca-Mn-O ferromagnetic thin-films (invited). *Journal of Applied Physics*, **76**, 6929–6933.

Jonker, G.H. (1956). Magnetic compounds with perovskite structure .4. conducting and non-conducting compounds. *Physica*, **22**, 707–722.

Jonker, G. and van Santen, J. (1950). Ferromagnetic compounds of manganese with perovskite structure. *Physica*, **16**, 337.

Kaminski, A. and Das Sarma, S. (2002). Polaron percolation in diluted magnetic semiconductors. *Physical Review Letters*, **88**, 247–202.

Kaspar, T.C., Heald, S.M., Wang, C.M., *et al*. (2005). Negligible magnetism in excellent structural quality $Cr_xTi_{1-x}O_2$ anatase: Contrast with high-T_C ferromagnetism in structurally defective $Cr_xTi_{1-x}O_2$. *Physical Review Letters*, **95**, 217–203.

Kasuya, T. (1970a). Exchange mechanisms in europium chalcogenides. *IBM Journal of Research and Development*, **14**, 214.

Kasuya, T. (1970b). Mobility of the antiferromagnetic large polaron. *Solid State Communications*, **8**, 16–35.

Kasuya, T. and Yanase, A. (1968). Anomalous transport phenomena in Eu-Chalcogenide alloys. *Reviews of Modern Physics*, **40**, 684.

Kennedy, R.J., Stampe, P.A., Hu, E.H., *et al*. (2004). Hopping transport in TiO_2: Co: A signature of multiphase behavior. *Applied Physics Letters*, **84**, 2832–2834.

Kim, D.H., Yang, J.S., Lee, K.W., *et al*. (2002). Formation of Co nanoclusters in epitaxial $Ti_{0.96}Co_{0.04}O_2$ thin films and their ferromagnetism. *Applied Physics Letters*, **81**, 2421–2423.

Ku, K.C., Potashnik, S.J., Wang, R.F., *et al*. (2003). Highly enhanced Curie temperature in low-temperature annealed Ga,Mn As epilayers. *Applied Physics Letters*, **82**, 2302–2304.

Kundaliya, D.C., Ogale, S.B., Lofland, S.E., *et al*. (2004). On the origin of high-temperature ferromagnetism in the low-temperature-processed Mn-Zn-O system. *Nature Materials*, **3**, 709–714.

Lee, H.J., Jeong, S.Y., Hwang, J.Y. and Cho, C.R. (2003). Ferromagnetism in Li co-doped ZnO:Cr. *Europhysics Letters*, **64**, 797–802.

Lee, H.J., Park, C.H., Jeong, S.Y., *et al*. (2006). Hydrogen-induced ferromagnetism in ZnCoO. *Applied Physics Letters*, **88**, 62–504.

Li, A.P., Wendelken, J.F., Shen, J., *et al*. (2005). Magnetism in Mn_xGe_{1-x} semiconductors mediated by impurity band carriers. *Physical Review B*, **72**, 195–205.

Maksimov, O., Sheu, B.L., Xiang, G., *et al*. (2004). Enhancement of Curie temperature in $Ga_{1-x}Mn_xAs$ epilayers grown on cross-hatched $In_yGa_{1-y}As$ buffer layers.*Journal of Crystal Growth*, **269**, 298–303.

Matthias, B.T., Bozorth, R.M. and Van Vleck, J.H. (1961). Ferromagnetic interaction in Euo. *Physical Review Letters*, **7**, 160–161.

Merithew, R.D., Weissman, M.B., Hess, F.M., *et al*. (2000).Mesoscopic thermodynamics of an inhomogeneous colossal-magnetoresistive phase. *Physical Review Letters*, **84**, 3442–3445.

Methfessel, S. and Mattis, D.C. (1968). *Handbuch der Physik*, Springer Verlag: Berlin.

Munekata, H., Ohno, H., von Molnár, S., *et al*. (1989). Diluted magnetic III-V semiconductors. *Physical Review Letters*, **63**, 1849–1852.

Nagaev, E.L. and Grigin, A.P. (1974). Spin polaron theory for magnetic semiconductors with narrow bands. *Physical Status Solidi B*, **65**, 11.

Ogale, S.B., Choudhary, R.J., Buban, J.P., *et al*. (2003). High temperature ferromagnetism with a giant magnetic moment in transparent Co-doped SnO_2-delta. *Physical Review Letters*, **91**, 77–205.

Ohno, H. (1998). Making nonmagnetic semiconductors ferromagnetic. *Science*, **281**, 951–956.

Ohno, H. (1999). Properties of ferromagnetic III-V semiconductors. *Journal of Magnetism and Magnetic Materials*, **200**, 110–129.

Ohno, H., Munekata, H., Penney, T., *et al*. (1992). Magnetotransport properties of p-Type (In,Mn)As diluted magnetic III-V semiconductors. *Physical Review Letters*, **68**, 2664–2667.

Ohno, H., Shen, A., Matsukura, F., *et al*. (1996). (Ga,Mn)As: A new diluted magnetic semiconductor based on GaAs. *Applied Physics Letters*, **69**, 363–365.

Park, Y.D., Hanbicki, A.T., Erwin, S.C., *et al*. (2002). A group-IV ferromagnetic semiconductor: Mn_xGe_{1-x}. *Science*, **295**, 651–654.

Pearton, S.J., Abernathy, C.R., Overberg, M.E., *et al*. (2003a). Wide band gap ferromagnetic semiconductors and oxides. *Journal of Applied Physics*, **93**, 1–13.

Pearton, S.J., Heo, W.H., Ivill, M., *et al*. (2004). Dilute magnetic semiconducting oxides. *Semiconductor Science and Technology*, **19**, R59–R74.

Pearton, S.J., Park, Y.D., Abernathy, C.R., *et al*. (2003b). GaN and other materials for semiconductor spintronics. *Journal of Electronic Materials*, **32**, 288–293.

Penney, T., Holtzber. F., Tao, L.J. and von Molnár, S. (1974). Localized Ferromagnetic Polarons in Antiferromagnetic Gd3-xvxS4 in *Magnetism and Magnetic Materials-1973*, Graham, C.D. and Rhyne, J.J. (Eds.), AIP (American Institute of Physics) Conference Proceedings, New York, p. 908–912, Vol. 18.

Raquet, B., Anane, A., Wirth, S., *et al*. (2000). Noise probe of the dynamic phase separation in $La_{2/3}Ca_{1/3}MnO_3$. *Physical Review Letters*, **84**, 4485–4488.

Rho, H., Snow, C.S., Cooper, S.L., *et al*. (2002a). Evolution of magnetic polarons and spin-carrier interactions through the metal-insulator transition in $Eu_{1-x}Gd_xO$. *Physical Review Letters*, **88**, 127–401.

Rho, H., Snow, C.S., Cooper, S.L., *et al*. (2002b). The evolution of magnetic polarons in $Eu_{1-x}Gd_xO$: A light scattering study. *Physica B: Condensed Matter*, **312**, 775–776.

Sawicki, M., Dietl, T., Kossut, J., *et al*. (1986). Influence of S-D exchange interaction on the conductivity of $Cd_{1-x}Mn_xSe$-in in the weakly localized regime. *Physical Review Letters*, **56**, 508–511.

Shapira, Y., Foner, S., Reed, T.B. and Oliveira, N.F. (1972). Eute II. resistivity and hall-effect. *Physical Review B*, **5**, 26–47.

Sharma, P., Gupta, A., Rao, K.V., *et al*. (2003). Ferromagnetism above room temperature in bulk and transparent thin films of Mn-doped ZnO. *Nature Materials*, **2**, 673–677.

Snow, C.S., Cooper, S.L., Young, D.P., *et al*. (2001). Magnetic polarons and the metal-semiconductor transitions in (Eu,La)B6 and EuO: Raman scattering studies. *Physical Review B*, **64**, 174412-1–174412-12.

Snyder, G.J., Hiskes, R., DiCarolis, S., *et al*. (1996). Intrinsic electrical transport and magnetic properties of $La_{0.67}Ca_{0.33}MnO_3$ and $La_{0.67}Sr_{0.33}MnO_3$ MOCVD thin films and bulk material. *Physical Review B*, **53**, 14434–14444.

Story, T., Galazka, R.R., Frankel, R.B. and Wolff, P.A. (1986). Carrier-concentration induced ferromagnetism in PbSnMnTe. *Physical Review Letters*, **56**, 777–779.

Terry, I., Penney, T. and von Molnár, S. (1992a). Low-temperature transport-properties of $Cd_{0.91}Mn_{0.09}Te$:In and evidence for a magnetic hard gap in the density of states. *Physical Review Letters*, **69**, 1800–1803.

Terry, I., Penney, T., Vonmolnar, S., *et al*. (1992b). Band tails and the insulator-metal transition in the persistent photoconductor Cd1-xMnxTe:In. *Solid State Communications*, **84**, 235–240.

Volger, J. (1954). Further experimental investigations on some ferromagnetic oxidic compounds of manganese with perovskite structure. *Physica*, **20**, 49.

von Helmolt, R., Wecker, J., Holzapfel, B., *et al*. (1993). Giant negative magnetoresistance in perovskitelike $La_{2/3}Ba_{1/3}MnO_x$ ferromagnetic-films. *Physical Review Letters*, **71**, 2331–2333.

von Molnár, S., Briggs, A., Flouquet, J. and Remenyi, G. (1983). Electron localization in a magnetic semiconductor – $Gd_{3-x}v_xS_4$. *Physical Review Letters*, **51**, 706–709.

von Molnár, S. and Coey, J.M.D. (1998). Heterogeneity in mixed-valence manganites. *Current Opinion in Solid State and Materials Science*, **3**, 171–174.

von Molnár, S. and Holtzberg, F. (1973). The Effect of Coulombic and Magnetic Disorder on Transport in Magnetic Semiconductors in *Magnetism and Magnetic Materials – 1972* Graham, C.D. and Rhyne, J.J. (Eds.), AIP (American Institute of Physics) Conference Proceedings, New York, p. 1259–1273, Vol. 10.

von Molnár, S., Holtzberg, F., McGuire, T.R. and Popma, T.J.A. (1972). Transport in the Ferromagnetic Semiconductor $Gd_{3-x}v_xS_4$ in *Magnetism and Magnetic Materials-1971*, Graham, C.D. and Rhyne, J.J. AIP ((American Institute of Physics) Conference Proceedings, New York, p. 869, Vol. 5.

von Molnár, S. and Kasuya, T. (1968). Evidence of band conduction and critical scattering in dilute Eu-Chalcogenide alloys. *Physical Review Letters*, **21**, 17–57.

von Molnár, S. and Methfessel, S. (1967). Giant negative magnetoresistance in ferromagnetic $Eu_{1-x}Gd_xSe$. *Journal of Applied Physics*, **38**, 959.

von Molnár, S., Terry, I. and Penney, T. (1995). Magnetic Polarons in Concentrated and Diluted Magnetic Semiconductors in *Polarons and Bipolarons in High-T_C Superconductors and Related Materials*, Salje, E.K.H., Alexandrov, A.S. and Liang, W.Y. (Eds.), Press Syndicate of the University of Cambridge: Cambridge, pp. 437–452.

Washburn, S., Webb, R.A., von Molnár, S., *et al*. (1984). Absence of minimum metallic conductivity in $Gd_{3-x}v_xS_4$ at very low-temperature and evidence for a coulomb gap. *Physical Review B*, **30**, 6224–6226.

Wojtowicz, T., Dietl, T., Sawicki, M., *et al*. (1986). Metal-insulator-transition in semimagnetic semiconductors. *Physical Review Letters*, **56**, 2419–2422.

Wolff, P.A., Bhatt, R.N. and Durst, A.C. (1996). Polaron-polaron interactions in diluted magnetic semiconductors. *Journal of Applied Physics*, **79**, 5196–5198.

Wolfram, T. and Callaway, J. (1962). Exchange narrowing of D bands in ferromagnets. *Physical Review*, **127**, 1605–1611.

Wollan, E.O. (1955). Neutron diffraction study of the magnetic properties of the series of perovskite-type compounds [(1-x)La,xCa]MnO_3. *Physical Review*, **100**, 545–563.

Wu, J., Lynn, J.W., Glinka, C.J., *et al*. (2005). Intergranular giant magnetoresistance in a spontaneously phase separated perovskite oxide. *Physical Review Letters*, **94**, 037201-1-4.

Zener, C. (1951). Ferromagnetic compounds of manganese. *Physical Review*, **82**, 403.

The Kondo Effect in Mesoscopic Quantum Dots

Michael Grobis[1], Ileana G. Rau[1], Ronald M. Potok[1,2] and David Goldhaber-Gordon[1]

[1] *Stanford University, Stanford, CA, USA*
[2] *Harvard University, Cambridge, MA, USA*

1 INTRODUCTION

At low temperatures, a small concentration of magnetic impurities – atoms or ions with a nonzero magnetic moment – can dramatically affect the behavior of conduction electrons in an otherwise pure metal. This phenomenon, known as the *Kondo effect* (Kondo, 1964), has been a leitmotif of solid-state physics since the 1960s. Nearly a decade ago, the Kondo effect was discovered in a new system (Goldhaber-Gordon *et al*., 1998a), in which the local magnetic moment belongs not to an atom but to a lithographically defined droplet of electrons known as a *quantum dot* or *artificial atom* (Kastner, 1993). When the droplet contains an odd number of electrons, it has a net spin and hence may be thought of as a magnetic artificial atom. Nearby metal or semiconducting electrical leads play the role of the host metal.

Handbook of Magnetism and Advanced Magnetic Materials. Edited by Helmut Kronmüller and Stuart Parkin. Volume 5: *Spintronics and Magnetoelectronics*. ISBN: 978-0-470-02217-7.

The artificial atom system offers several important advantages for the study of the Kondo effect:

1. A single site is measured, rather than a statistical average over many sites.
2. The microscopic states of the system are better defined and easier to tailor than in bulk systems.
3. Most of the important parameters can be precisely measured and tuned *in situ*.
4. The local site can be studied out of equilibrium and in regimes that are inaccessible in other contexts.

In this chapter of the handbook, we review how researchers around the world have applied these advantages to create a renaissance in the study of the Kondo effect. Though this approach was initially inspired by theory (Glazman and Raikh, 1988; Ng and Lee, 1988) and continues to be strongly informed by it, we organize our review around experimental developments in mesoscopic systems.

1.1 Background of the Kondo effect: dilute magnetic alloys

At relatively high temperatures, the resistivity of a metal is dominated by electron–phonon scattering. As the temperature is lowered well below the Debye temperature, the scattering rate, and hence the phonon contribution to resistivity, decreases as T^5. At sufficiently low temperatures, phonon-induced scattering becomes insignificant and resistivity saturates at a finite value determined by scattering from defects in the crystal lattice. In the 1930s, researchers noticed that this simple picture did not always hold. Measurements of Au cooled below 10 K sometimes showed a resistivity

rise rather than saturation as the temperature was lowered further (de Haas, de Boer and van den Berg, 1934). The effect remained an enigma until the 1960s when experimental evidence correlated the low-temperature resistivity rise with the presence of dilute magnetic impurities in the metal (Sarachik, Corenzwit and Longinotti, 1964). Inspired by the strong evidence that individual magnetic impurities were responsible for the resistivity rise, Kondo considered a model involving an antiferromagnetic interaction between the local moment and the sea of conduction electrons (Kondo, 1964). Using perturbation theory, Kondo found that the antiferromagnetic interaction leads to a logarithmic rise in electron-impurity scattering with decreasing temperature.

Though Kondo's work was a crucial breakthrough, calculations using this theoretical framework inherently produced unphysical logarithmic divergences. Finding a solution to this conundrum became known as the *Kondo Problem*. The problem was finally solved by Wilson (1975), who developed a new renormalization group (RG) technique for the purpose. Wilson's RG calculations showed that at temperatures below a characteristic Kondo temperature T_K, a magnetic impurity would form a singlet with the surrounding sea of conduction electrons. Despite this success in determining the ground state (and thermodynamic properties) of a magnetic impurity in a metal, nearly two decades would pass before the development of numerical renormalization group (NRG) techniques that could accurately calculate transport properties such as resistivity over a broad range of temperatures (Costi, Hewson and Zlatic, 1994).

1.2 Tunneling: Kondo in a new geometry

Since the Kondo effect is a property of magnetic impurities in a host metal, it should also be observable in transport through magnetic impurities sandwiched between two metal leads (Appelbaum, 1966). This was borne out in both large tunnel junctions with many impurities (Wyatt, 1964) and more recently in a nanometer-scale junction containing a single impurity (Gregory, 1992; Ralph and Buhrman, 1994). In this geometry, the Kondo effect enhances conductance rather than resistivity at low temperature and low bias voltage (Appelbaum, 1966).

The advent of high-mobility GaAs heterostructures in the 1980s ushered in the modern era of mesoscopic semiconductor physics: the study of electronic phenomena at intermediate spatial scales, between atomic and macroscopic. Through concurrent advancement in lithographic technology, the first artificial atoms were created in patterned GaAs heterostructures in the late 1980s (Reed *et al*., 1988; van Wees *et al*., 1989; Meirav, Kastner and Wind, 1990). Around the same time, two theoretical teams pointed out that this type of system can behave like a magnetic impurity and hence should exhibit the Kondo effect (Glazman and Raikh, 1988; Ng and Lee, 1988). Indeed, ten years later the Kondo effect was observed in lithographically defined quantum dots (Goldhaber-Gordon *et al*., 1998a; Cronenwett, Oosterkamp and Kouwenhoven, 1998; Simmel *et al*., 1999). Due to the unprecedented degree of flexibility and control available in artificial atom systems, a wave of experimental work followed, exploring a variety of Kondo regimes untouched by previous efforts.

Several other new and interesting Kondo systems have emerged in recent years, as well. The Kondo effect has also been observed in scanning tunneling microscopy (STM) measurements of individual surface adatoms (Madhavan *et al*., 1998; Li, Schneider, Berndt and Delley, 1998) and metal complexes (Zhao *et al*., 2005), allowing, for example, the study of the spatial characteristics of Kondo interactions (Madhavan *et al*., 1998; Manoharan, Lutz and Eigler, 2000). Electrons localized on a single molecule or a single carbon nanotube can exhibit Kondo effects stemming from local degeneracies not easily achieved in a GaAs artificial atom (Park *et al*., 2002; Liang *et al*., 2002), and can be coupled to reservoirs with exotic properties (superconducting, ferromagnetic). Though a wide range of Kondo systems have played important roles in developing our understanding of the Kondo effect, this review will focus mainly on the diverse set of experiments performed using mesoscopic quantum dot systems.

2 EXPERIMENTAL SIGNATURES OF THE SPIN-1/2 KONDO EFFECT

In this section, we review the characteristic signatures of the Kondo effect in the context of a spin-1/2 quantum dot coupled to two reservoirs. Consideration of more complex scenarios is left to later sections.

2.1 Quantum dots

Our discussion of experimental results draws primarily on work performed on three types of quantum dots, each offering a different set of advantages: lateral and vertical semiconductor dots, and carbon nanotube quantum dots (Figure 1). Lateral quantum dots are formed by depleting a subsurface two-dimensional electron gas (2DEG) using lithographically defined metallic gates, as shown in Figure 1(a). The 2DEG resides at the interface of a semiconductor heterostructure (e.g., GaAs/AlGaAs), located tens to hundreds of nanometers below the surface. The quantum dot consists of a pool of confined electrons, tunnel coupled to extended sections of the

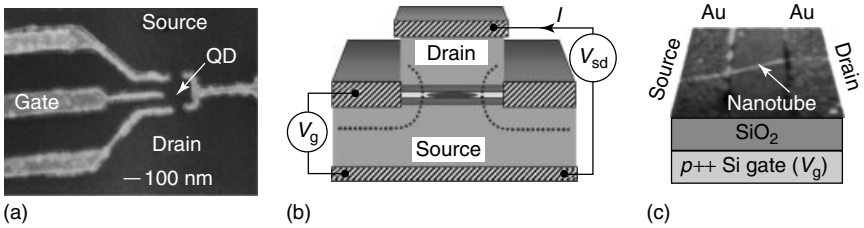

Figure 1. The Kondo effect has been seen in a variety of quantum dot geometries such as (a) lateral quantum dots (scanning electron microscopy (SEM) image). (b) Vertical quantum dots (schematic). (Reproduced from S. Sasaki *et al*., 2000, with permission from Nature Publishing Group. © 2000.) (c) Carbon nanotubes (SEM and schematic). (Reproduced from Jesper *et al*., 2000, with permission from Nature Publishing Group. © 2000.)

2DEG, which serve as leads. Several nearby gate electrodes electrostatically control the quantum dot electron occupancy, as well as the dot–lead couplings. In principle, the number of electrons can be reduced to zero; however, in many lateral quantum dot geometries, the conductance through the quantum dot's contacts is 'pinched off' by the increasingly negative gate voltage before the dot is entirely emptied.

The vertical quantum dot geometry, shown in Figure 1(b), allows the formation of a small, well-coupled, few-electron quantum dot whose conductance remains measurable all the way down to the expulsion of the last electron. This allows accurate determination of the electron occupancy, as discussed later in this section. Another important difference between lateral and vertical quantum dots is the number of tunneling modes, or channels, that couple the dot to the leads [1]. Typically, the dot–lead contacts in lateral dots are single-mode quantum point contacts (QPCs), while the wide lead–dot contact area in vertical dots contains several partially transmitting modes.

A carbon nanotube quantum dot is created using a single carbon nanotube deposited on a conducting substrate covered by a thin insulator (e.g., SiO_2/n^{++}-Si). Lithographically defined metal leads contact the nanotube, and the conducting substrate is biased to modify the electron occupancy of the nanotube (Figure 1c). While the nanotube–lead couplings cannot be finely controlled, this geometry allows for the creation of a wide variety of leads, such as superconducting and magnetic, which are difficult, if not impossible, to achieve in semiconductor heterostructures. For a further discussion of quantum dots, including the Kondo effect, we encourage readers to examine several recent reviews (Kouwenhoven *et al*., 1997; Kouwenhoven, Austing and Tarucha, 2001; Yoffe, 2001; Pustilnik and Glazman, 2004; Giuliano, Naddeo and Tagliacozzo, 2004).

2.2 Theoretical background

Here, we present only a brief theoretical description of the Kondo effect. The reader may consult several references for a more complete theoretical description (Gruner and Zawadowski, 1974; Wilson, 1975; Nozières and Blandin, 1980; Andrei, Furuya and Lowenstein, 1983; Hewson, 1993; Costi, Hewson and Zlatic, 1994; Pustilnik and Glazman, 2004 (See also **The Kondo Effect, Volume 1**).

2.2.1 Kondo Hamiltonian

The Kondo effect arises when a degenerate local state is coupled to a reservoir of mobile electrons. The system is well described by the Anderson Hamiltonian

$$H = \sum_{k,\sigma} \varepsilon_k c^\dagger_{k\sigma} c_{k\sigma} + \sum_{\sigma} \varepsilon_0 d^\dagger_\sigma d_\sigma + U d^\dagger_\uparrow d_\uparrow d^\dagger_\downarrow d_\downarrow + \sum_{k,\sigma} \left(v_k d^\dagger_\sigma c_{k\sigma} + v^*_k \, c^\dagger_{k\sigma} d_\sigma \right) \quad (1)$$

which was originally proposed to describe a magnetic impurity atom in a metal (Anderson, 1961). The first term represents the kinetic energy of electrons in the reservoir, labeled by their momentum (k) and spin (σ). The second term is the quantized energy of localized electrons in a single spin-degenerate state near E_F – all other quantum dot levels are assumed to be either completely full (well below E_F) or completely empty (well above E_F), and hence can be safely ignored. The third term accounts for interactions among localized electrons: a second electron added to the local site costs more than the first electron, by an amount denoted as the *charging energy* U. This is crucial, since it allows for the possibility that the doubly degenerate site can be occupied by just a single electron. In this case, the site acts as a magnetic impurity and can exhibit the Kondo effect. The final term describes spin-conserving tunneling on and off the local site, with strength v_k. A schematic of the Anderson model is shown in Figure 2. A spin-degenerate quantum dot is probably the most exact experimental realization of the Anderson model.

With a few simple assumptions, which are generally well justified for a quantum dot with odd occupancy,

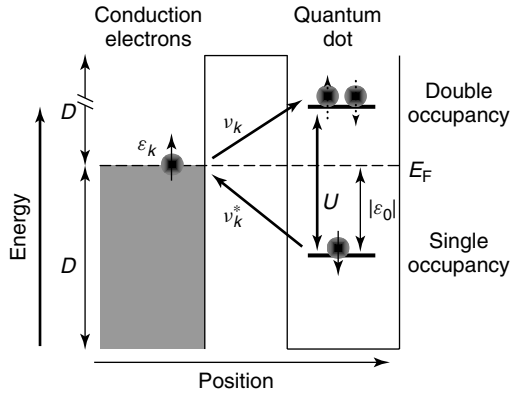

Figure 2. Schematic diagram of the Anderson model as applied to a singly occupied spin-degenerate quantum dot state coupled to an electron reservoir. The parameters are discussed in the text.

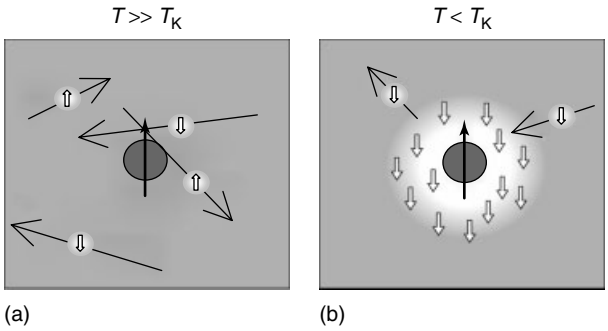

Figure 3. A magnetic impurity in a sea of conduction electrons. (a) Above the Kondo temperature (T_K), the conduction electrons are only weakly scattered by the magnetic impurity. (b) Below T_K, the conduction electrons screen the local spin to form a spin singlet. The formation of the Kondo screening cloud enhances the effective scattering cross section of the magnetic impurity.

the interaction between the conduction electrons and the quantum dot (final term in equation (1)) can be approximated as an antiferromagnetic coupling,

$$H_{\text{int}} = J s_{\text{cond}} \cdot S_{\text{QD}} \tag{2}$$

Equation 2 is known as the s–d or the *Kondo Hamiltonian* (Kondo, 1964; Schrieffer and Wolff, 1966; Kasuya, 1956; Yosida, 1957), as alluded to previously. S_{QD} is the net spin of the quantum dot, while s_{cond} is the sum of spin operators for the conduction electrons (cf. Pustilnik and Glazman, 2004). The strength of the antiferromagnetic coupling depends on the microscopic parameters of the Anderson model, according to

$$J \sim |v|^2 \left(\frac{1}{-\varepsilon_0} + \frac{1}{\varepsilon_0 + U} \right) \tag{3}$$

Here, ε_0 is measured relative to E_F and the interaction strength is taken to be a constant ($v_k = v$) over a finite bandwidth (D) and zero otherwise, as indicated in Figure 2.

2.2.2 *Kondo ground state*

The ground state of the Kondo Hamiltonian is not twofold degenerate, but is instead a spin singlet in which the spin of a localized electron is matched with the spin of delocalized electrons to yield a net spin of zero. This 'Kondo screening cloud' is shown schematically in Figure 3. Due to phase space constraints, the Kondo interaction predominantly affects electrons near the Fermi surface. This mixing of conduction and local electron states leads to the characteristic signature of the formation of the Kondo singlet: the appearance of a narrow resonance at the Fermi energy with width proportional to the strength of the Kondo interaction [2].

Owing to its nonconventional nature, the Kondo singlet's 'binding energy' is not simply proportional to J. Typically expressed as a Kondo temperature (T_K), the binding energy can be calculated perturbatively using equation (2) to give

$$T_K \sim D\sqrt{\rho J}\exp(-1/2\rho J) \tag{4}$$

where ρ is the density of states in the reservoir at energy E_F (Hewson, 1993). The formation of the Kondo singlet is a continuous phase transition, and T_K should be interpreted as the cross-over energy scale for this transition. It is important to realize that T_K is not a well-defined energy scale: equally valid definitions can differ by a constant multiplicative factor. In this review, we use a definition suggested by Costi, Hewson, and Zlatic (1994) and introduced for quantum dots by Goldhaber-Gordon *et al*. (1998b): T_K is the temperature at which the Kondo conductance has risen to half its extrapolated zero-temperature value (see Section 2.3.3).

The expression for T_K can be rewritten in terms of quantities that are more easily controlled and measured in quantum dot experiments (Haldane, 1978):

$$T_K \sim \sqrt{\Gamma U}\exp(\pi\varepsilon_0(\varepsilon_0 + U)/\Gamma U) \tag{5}$$

Here, Γ is the rate for electron on and off the dot. The spin-1/2 Kondo effect occurs only when the local site is singly occupied ($\varepsilon_0 < 0$ and $\varepsilon_0 + U > 0$), so the exponent in equation (5) is negative, as expected from equation (4). These equations break down near the charge degeneracy points ($\varepsilon_0 = 0$ and $\varepsilon_0 + U = 0$), where charge fluctuations produce mixed valence rather than Kondo behavior (Costi, Hewson and Zlatic, 1994). Coupling additional leads to the quantum dot modifies Γ, but does not affect the overall Kondo behavior. The leads behave as a single collective reservoir, as long as Kondo processes can freely exchange

electrons between each pair of reservoirs (Glazman and Raikh, 1988).

T_K is maximized when the quantum dot state is energetically close to E_F ($\varepsilon_0 \sim 0$) and strongly coupled to the leads (large Γ). Finite charging energy (U) and level spacing (Δ) put a limit on T_K in quantum dots, since electrons are no longer localized on the dot for $\Gamma > \min(U, \Delta)$. U and Δ increase with decreasing device size, yielding a maximal T_K in the range of 0.1–1 K for typical semiconductor quantum dots and up to 10 K in carbon nanotube–based devices. For comparison, T_K in excess of 500 K has been observed for atomic impurities in bulk systems (Gruner and Zawadowski, 1974).

The formal spatial scale of the Kondo cloud is given by

$$\xi_K \sim \hbar v_F / k_B T_K \tag{6}$$

where v_F is the Fermi velocity (Sorensen and Affleck, 1996). $\xi_K \sim 1\,\mu m$ for typical semiconductor quantum dots in the Kondo regime, which gives an estimate of the spatial extent of Kondo correlations. The spatial properties of the Kondo cloud have proved difficult to measure for several reasons. The Kondo screening cloud mainly involves spin rearrangement. However, local spin density is dynamic, since the spin on the local site is rapidly changing, and the exponential decay is modulated further by polynomial decay factors (Barzykin and Affleck, 1996). In addition, charge rearrangement due to Kondo singlet formation is minimal and occurs only at length scales on the order of λ_F. Local probes, such as STM, generally measure the total density of states, which is modified on similar short spatial scales (Madhavan *et al*., 1998; Újsághy, Kroha, Szunyogh and Zawadowski, 2000). This is understood to stem from oscillations and polynomial decay that modulate the slow exponential decay of spin polarization in the electron gas at distances greater than λ_F from the local moment (Barzykin and Affleck, 1996).

2.3 Kondo transport in quantum dots

The formation of the Kondo screening cloud enhances the scattering of conduction electrons by the local magnetic site. Hence, the resistivity of a bulk metal with a small concentration of magnetic impurities rises as temperature is decreased below the characteristic Kondo temperature for that impurity/metal system. In a geometry where transport is dominated by tunneling through a magnetic site, the enhanced scattering has the opposite effect: *conductance* rises for $T < T_K$, as a new mechanism for transport becomes available (Appelbaum, 1966; Ng and Lee, 1988; Costi, Hewson and Zlatic, 1994). In transport through semiconductor quantum dots, the Kondo effect emerges whenever the dot contains an unpaired spin, as is the case when an odd number of electrons occupy the dot. As the occupancy of a dot is tuned by a nearby gate, the low-temperature conductance alternates between high (odd occupancy) and low (even occupancy), as seen in Figure 4(a). The high conductance for odd occupancy disappears as the coupling to the leads (Γ) is reduced (Figure 4b): T_K becomes lower than the base temperature of the measurement apparatus (cf. equation (5)). In this 'Coulomb blockade' (CB) regime, conduction occurs only near the charge degeneracy points.

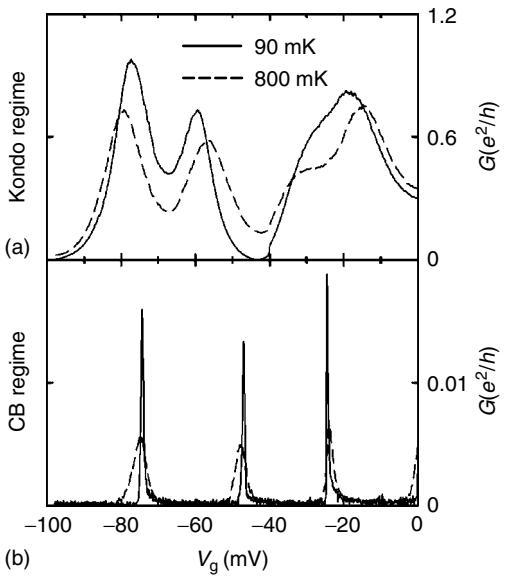

Figure 4. Linear conductance through the lateral quantum dot shown in Figure 1(a), as a function of gate voltage. From left to right, the quantum dot electron occupancy increases by four and three in (a) and (b) respectively. (a) Kondo regime: For strong lead–dot coupling, the Kondo effect enhances conductance for odd occupancy at 90 mK. At higher temperatures (800 mK), the Kondo effect is partially suppressed and transport proceeds through temperature-broadened single-particle levels. (b) Coulomb blockade (CB) regime: For weak dot–lead coupling ($\Gamma \ll U, \Delta$), the Kondo temperature is lower than the base temperature of the experiment (90 mK) and transport occurs only at the charge degeneracy points. Note: the peaks in (b) have been shifted by +120 mV and do not correspond to the same electronic states as in (a). (Reproduced from D. Goldhaber-Gordon *et al*., 1998, with permission from the American Physical Society. © 1998.)

The Kondo-mediated transport through a quantum dot may be distinguished from other mechanisms for conductance enhancement by the following distinctive features:

1. Even–odd alternation of conductance as a function of dot occupancy (the Kondo effect occurs only for odd occupancy).
2. Enhanced conductance at low temperature, with a characteristic temperature dependence.
3. Enhanced conductance at zero bias relative to finite bias.

4. Suppression of conductance by magnetic field, which splits the local spin degeneracy.
5. Recovery of enhanced conductance at finite magnetic field by application of a bias voltage equal to the Zeeman splitting.

The above list is useful for demonstrating the occurrence of a Kondo effect, but is not an exhaustive or quantitative description of spin-1/2 Kondo. Note that some of the listed features can only be observed in systems where the local site occupancy can be tuned (i.e., 1) or where a finite bias can be applied across the local site(s) (i.e., 3 and 5).

2.3.1 *Even–odd effect*

The low-temperature Kondo conductance enhancement is expected to occur whenever a local state is degenerate and partially filled. In the absence of additional degeneracies, this occurs whenever the number of electrons on the dot is odd. Though early Kondo dot measurements exhibited conductance enhancements in alternating CB valleys, the researchers could not directly demonstrate that the enhancement occurred for odd rather than even occupancies, since the initial occupancy of the dot was unknown (Goldhaber-Gordon *et al*., 1998a). Indeed, in later sections, we discuss a variety of Kondo effects that do not require a spin-1/2 dot state and hence do not follow the even–odd rule. More recent quantum dot devices use either of two methods to conclusively determine the total electron occupancy. In one method, the electron number is determined by counting CB peaks as the quantum dot is emptied by an increasingly negative gate voltage. This technique works best in vertical quantum dots (Tarucha *et al*., 1996) (Figure 1b), as well as certain lateral dots (Ciorga *et al*., 2000), which remain conducting as the occupancy is reduced and counted down to zero. A second technique uses a QPC fabricated close to the quantum dot, to serve as a detector of the dot's occupancy (Sprinzak *et al*., 2002). Each electron added to the quantum dot electrostatically alters the conductance of the QPC. This method works even if transport through the quantum dot is so slow as to be immeasurable with conventional methods (fewer than around 1000 electrons per second). These methods confirm that in small GaAs quantum dots spin-1/2 Kondo and even–odd conductance alternation are the rule rather than the exception.

2.3.2 *Dependence on external parameters*

Kondo conductance through a quantum dot has a characteristic and calculable dependence on external parameters such as temperature, magnetic field, and voltage across the dot (Pustilnik and Glazman, 2004). We can consider two regimes: low energy and high energy, distinguished by whether the perturbations $k_B T$, eV, and $g\mu_B B$ are small or large compared to $k_B T_K$. At low energy, a Kondo impurity acts as an elastic scatterer, and nearby conduction electrons behave as in a conventional Fermi liquid, albeit with slightly modified numerical parameters (Nozières, 1974). Hence, for $k_B T$, eV, and $g\mu_B B \ll k_B T_K$ the Kondo spectral function and the associated transport through a spin-1/2 Kondo dot display quadratic dependence on external parameters, reflecting the E^2 scattering rate of quasiparticles in a Fermi liquid,

$$G(X) \sim G_0(1 - C(X/k_B T_K))^2$$
$$X = k_B T, eV, g\mu_B B \ll k_B T_K \quad (7)$$

$G_0 = G(X = 0)$, and the constant C is slightly different for the three perturbations.

In the opposite extreme, $k_B T$, eV, or $g\mu_B B \gg k_B T_K$, Kondo transport is well described by a perturbative treatment of the excitation and shows a logarithmic dependence on energy,

$$G(X) \sim 1/ln^2(X/k_B T_K)$$
$$X = k_B T, eV, g\mu_B B \gg k_B T_K \quad (8)$$

The two regimes evolve smoothly and monotonically into one another with no sharp features appearing at T_K. No analytic expression linking the two regimes has been derived, though an empirical expression for $G(T)$ that matches NRG calculations (Costi, Hewson and Zlatic, 1994) over the entire temperature range has been widely adopted by experimentalists (Goldhaber-Gordon *et al*., 1998b). We note that even though the three perturbations have similar effects on conductance, the mechanism is slightly different in each case, as discussed in the next two sections. The evolution of shot noise is predicted to follow forms similar to equations (7) and (8) (Meir and Golub, 2002), but with an effective fractional charge of $5/3e$, reflecting the presence of both elastic and inelastic scattering even at low temperatures (Sela, Oreg, von Oppen and Koch, 2006).

2.3.3 *Temperature dependence*

The conductance behavior predicted by equations (7) and (8) can be seen in temperature-dependent conductance measurements of a Kondo dot, as shown in Figure 5. As temperature is raised, the conductance in the odd valleys decreases because of suppression of the Kondo effect. In contrast, conductance in the even valleys increases because of thermal broadening of the bare quantum dot levels (Pustilnik and Glazman, 2004). The scaled temperature-dependent conductance for several gate voltage values in the Kondo valley is shown in Figure 5(b). The Kondo conductance shows

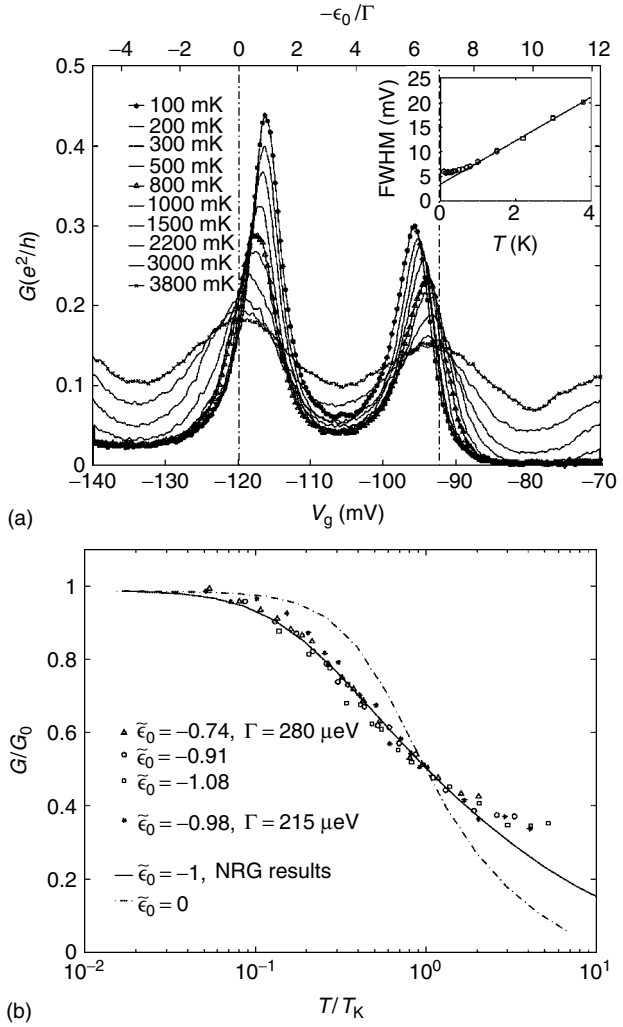

Figure 5. (a) Temperature dependence of the conductance in the Kondo valley. The vertical dashed lines indicate the location of the charge degeneracy points (i.e., $\varepsilon_0 = 0$ or $\varepsilon_0 + U = 0$), as deduced from data for $T \gg T_K$. Inset: The extrapolated linear temperature dependence of the Coulomb blockade peak width at $T = 0$ gives $\Gamma = 295 \pm 20\,\mu$eV. The slope of the line determines the conversion factor between the applied gate voltage (V_g) and ε_0. (b) Normalized conductance (G/G_0) as a function of normalized temperature (T/T_K) for several points along the Kondo valley. Here $\sim\varepsilon = \varepsilon_0/\Gamma$. G_0 and T_K were extracted by fitting the temperature dependence to equation (9). The data shown here are from the lateral quantum dot device shown in Figure 1(a). (Reproduced from D. Goldhaber-Gordon *et al.*, 1998, with permission from the American Physical Society. © 1998.)

the characteristic T^2 saturation at low temperatures, crossing over to a logarithmic temperature dependence as T approaches T_K. The empirically derived formula alluded to above,

$$G(T) = G_0(T_K'^2/(T^2 + T_K'^2))^s \qquad (9)$$

provides a remarkably good fit over the whole temperature range (Goldhaber-Gordon *et al.*, 1998b). The constant s determines the slope of the conductance falloff. Using a value $s = 0.22$ matches the slope found in NRG calculations for spin-1/2 Kondo systems (Costi, Hewson and Zlatic, 1994). Here, $T_K' = T_K/(2^{1/s} - 1)^{1/2}$, which is equivalent to defining T_K such that $G(T_K) = G_0/2$, as noted earlier. The extracted values of T_K and G_0 across the Kondo valley are shown in Figure 6. As predicted by equation (5), T_K is maximal when the quantum level resides close to E_F.

At temperatures above T_K, non-Kondo conductance channels can develop (Pustilnik and Glazman, 2004), and this

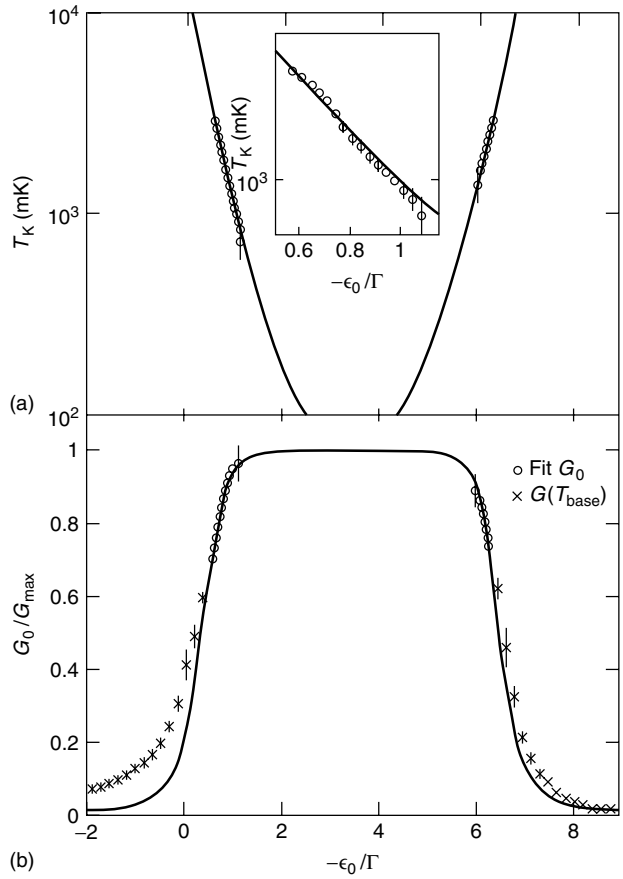

Figure 6. (a) Values of T_K across the Kondo valley shown in Figure 5, extracted by fitting the temperature-dependent conductance to the Kondo form (equation (9)). The behavior is well described by equation (5) (solid line). Inset: Expanded view of the left side of the figure, showing the quality of the fit. (b) Values of G_0 across the Kondo valley extracted from the temperature fits in part (a) (open circles) or from base temperature conductance (crosses). The solid line shows $G_0(\varepsilon_0)$ predicted by Wingreen and Meir (1994). $G_{max} = 0.49e^2/h$ and $0.37e^2/h$ for the left and right peak, respectively. (Reproduced from D. Goldhaber-Gordon *et al.*, 1998, with permission from the American Physical Society. © 1998.)

leads to deviations from equation (9). Occasionally a better fit to $G(T)$ can be achieved by adding a temperature-independent offset to the Kondo form (equation (9)). Though convenient, using such an offset in analyzing Kondo behavior is not yet well-established as physically valid.

2.3.4 *Dependence on bias and magnetic field*

The E^2 dependence of the Kondo spectral function can be probed by applying a bias across the dot (Goldhaber-Gordon *et al*., 1998a; Cronenwett, Oosterkamp and Kouwenhoven, 1998). The spectrum shows a narrow zero-bias anomaly, referred to as the *Kondo resonance*, that is present across the whole odd-occupancy Coulomb valley (Figure 7). For small biases, the Kondo conductance peak falls off with V^2. The Kondo peak broadens with increasing temperature, and the extrapolated zero-temperature half width at half maximum is approximately $2T_K$ (Costi, 2000). Exact interpretation of the Kondo peak shape is complicated by nonequilibrium processes (Wingreen and Meir, 1994; Schiller and Hershfield, 1995), which are discussed further in Section 3.2.

An applied magnetic field lifts the degeneracy between the two spin states on the quantum dot. The asymmetry between the two spin states acts to suppress Kondo correlations in much the same way as the asymmetry created by an applied bias. Progressively higher magnetic fields split the Kondo spectral function, which can be probed by the measurement of differential conductance as a function of bias (Goldhaber-Gordon *et al*., 1998a; Cronenwett, Oosterkamp and Kouwenhoven, 1998). These measurements are discussed in Section 3.2.

2.3.5 *Universal scaling*

The similarity of the effects of temperature, bias, and magnetic field on the Kondo effect is neatly encompassed by a series of theoretically predicted universal scaling relations. In the context of Kondo transport, the behavior of different Kondo systems can be collapsed onto a single curve once each curve is scaled appropriately using only the Kondo temperature and the zero-temperature conductance, T_K and G_0, respectively (Ralph, Ludwig, von Delft and Buhrman, 1994; Schiller and Hershfield, 1995). The relation between temperature and bias can be expressed as

$$\frac{(G(V=0,T)-G(V,T))/G_0}{CT^{\alpha}} = F(eV/k_BT) \qquad (10)$$

Here, $F(eV/k_BT)$ is a universal function that depends on the type of Kondo effect, but not on the exact details of the Kondo system at hand. The scaling constants G_0 and C are defined by the low-temperature expansion for $G(T)$ (equation (7)). The exponent $\alpha = 2$ for a spin-1/2 quantum dot, but can take on different values in more exotic Kondo systems (Ralph, Ludwig, von Delft and Buhrman, 1994). Though the scaling properties of Kondo systems are frequently used in analyzing Kondo measurements (Figure 5b), few experimental measurements of universal Kondo scaling functions or the expected deviation from universality (Majumdar, Schiller and Hershfield, 1998) have been reported to date (Ralph, Ludwig, von Delft and Buhrman, 1994).

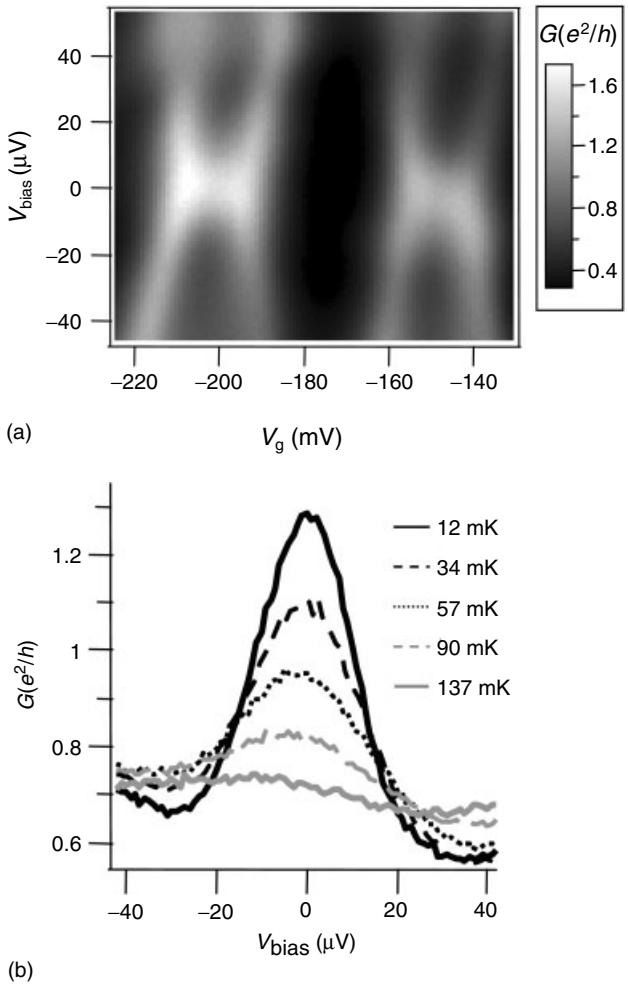

Figure 7. (a) Low-temperature ($T = 12$ mK) differential conductance (dI/dV) through a lateral quantum dot, as a function of gate voltage and applied bias in the Kondo regime. In the absence of the Kondo effect, dI/dV is nonzero only when a quantum dot energy level is aligned with the Fermi energy of one of the leads (cf. Kouwenhoven, Austing and Tarucha, 2001). The resulting 'Coulomb diamonds' are modified by the Kondo effect: a Kondo resonance appears at zero bias across the whole Coulomb valley for odd occupancy. The Kondo effect also alters finite bias conduction through the quantum dot levels. (b) Temperature dependence of the Kondo resonance in the middle of the Kondo valley ($V_g = -203.5$ mV).

2.4 Transmission phase shift and unitary limit

The zero-temperature Kondo conductance through a two-lead quantum dot can also be derived via the Landauer formalism and Friedel sum rule, giving

$$G_0 = \frac{2e^2}{h}\left[\frac{2\Gamma_1\Gamma_2}{\Gamma_1^2+\Gamma_2^2}\right]^2 \frac{1}{2}\sum_\sigma \sin^2(\delta_\sigma) \qquad (11)$$

where Γ_i is the rate of tunneling between the local site and the ith lead and δ_σ is the transmission phase shift of the σ spin channel (see Pustilnik and Glazman, 2004). For tunneling through a quantum dot in the CB regime, the transmission phase shift is changed by π each time one CB peak is tuned through the Fermi energy. Surprisingly, owing to the equivalence of the two spin states brought about by the Kondo effect, the transmission phase shift evolves instead by $\pi/2$ in the Kondo regime at $T = 0$ (Figure 8d) (Gerland, von Delft, Costi and Oreg, 2000). As the temperature is raised to $T \sim T_K$, the phase shift evolves to the more conventional π phase shift, as seen in Figure 8(b).

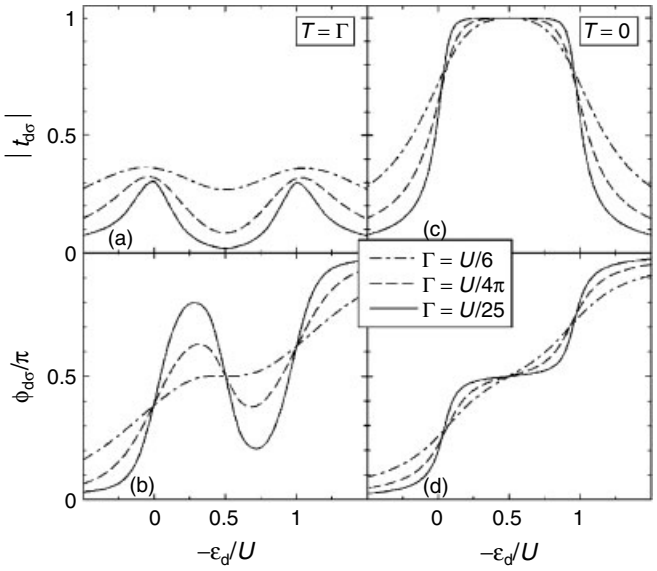

Figure 8. Theoretical temperature and coupling dependence of the transmission amplitude ($|_{d\sigma}|$) and phase ($\Phi_{d\sigma}$) for transport through a quantum dot, as a function of the normalized energy of the quantum dot level (ε_0/U). Each pane plots results for three values of dot–lead coupling (Γ). The transmission amplitude is normalized to $2e^2/h$. (a and b) The two panels on the left show calculations for $T = \Gamma > T_K$. In this regime, transport occurs mainly through thermally broadened quantum dot levels. (c and d) The two panels on the right show calculations for $T = 0$. The Kondo effect is in the unitary limit, giving a $2e^2/h$ conductance throughout the Kondo valley. In this regime, the phase shift is $\pi/2$ in the Kondo valley. (Reproduced from Ulrich Gerland *et al.*, 2000, with permission from the American Physical Society. © 2000.)

While the Kondo phase shift cannot be determined in bulk measurements, several mesoscopic measurements can determine it directly (Ji *et al.*, 2000; Sato *et al.*, 2005). One of the most successful approaches to measuring transmission phase shifts involves using an Aharonov–Bohm (AB) interferometer geometry like the one shown in Figure 9(a) (Yacoby, Heiblum, Mahalu and Shtrikman, 1995). Electrons can either tunnel through the quantum dot or travel ballistically through a reference arm. The relative phase of these two paths depends on the magnetic flux through the loop and the transmission phase shift acquired in tunneling through the quantum dot. The transmission phase shift is deduced by examining how the interference pattern changes as a function of the energy ε_0 of a localized state on the quantum dot. The Kondo phase shifts extracted from these experiments are somewhat larger than the theoretically predicted value, as seen in Figure 9(c) (Ji *et al.*, 2000; Ji, Heiblum and Shtrikman, 2002). Transmission phase shifts can be measured using other two-path interference geometries, such as a quantum wire side-coupled to a quantum dot (Sato *et al.*, 2005). In these devices, the measured phase shift is closer to the theoretically predicted value of $\pi/2$. More recent experiments (Avinun-Kalish *et al.*, 2005; Neder *et al.*, 2006) and theoretical work (Aharony, Entin-Wohlman and Imry, 2003; Aharony and Entin-Wohlman, 2005; Jerez, Vitushinsky and Lavagna, 2005) have elucidated some of the intricacies of phase shifts measured in mesoscopic electron interferometers.

An additional consequence of the equivalence of the two spin transport channels is that the zero-temperature conductance through a Kondo dot is $2e^2/h$ for symmetric reservoir–dot coupling (equation (11)). In contrast, the maximum conductance on a conventional Coulomb charging peak is only e^2/h in the absence of Kondo correlations, since only one spin state can be transmitted at a time. The configuration of equal reservoir coupling and $T = B = V = 0$ is commonly referred to as *Kondo in the unitary limit*. This limit can be achieved experimentally as long as k_BT, eV, $g\mu_BB \ll k_BT_K$ and the coupling asymmetry is small compared to Γ, as observed by van der Wiel *et al.* (2000).

3 KONDO EFFECT IN MODIFIED ENVIRONMENTS

In the previous section, we briefly discussed how the Kondo state is suppressed by external perturbations such as temperature and magnetic field. In this section, we provide a more general description of how the spin-1/2 Kondo state evolves in response to modified environments.

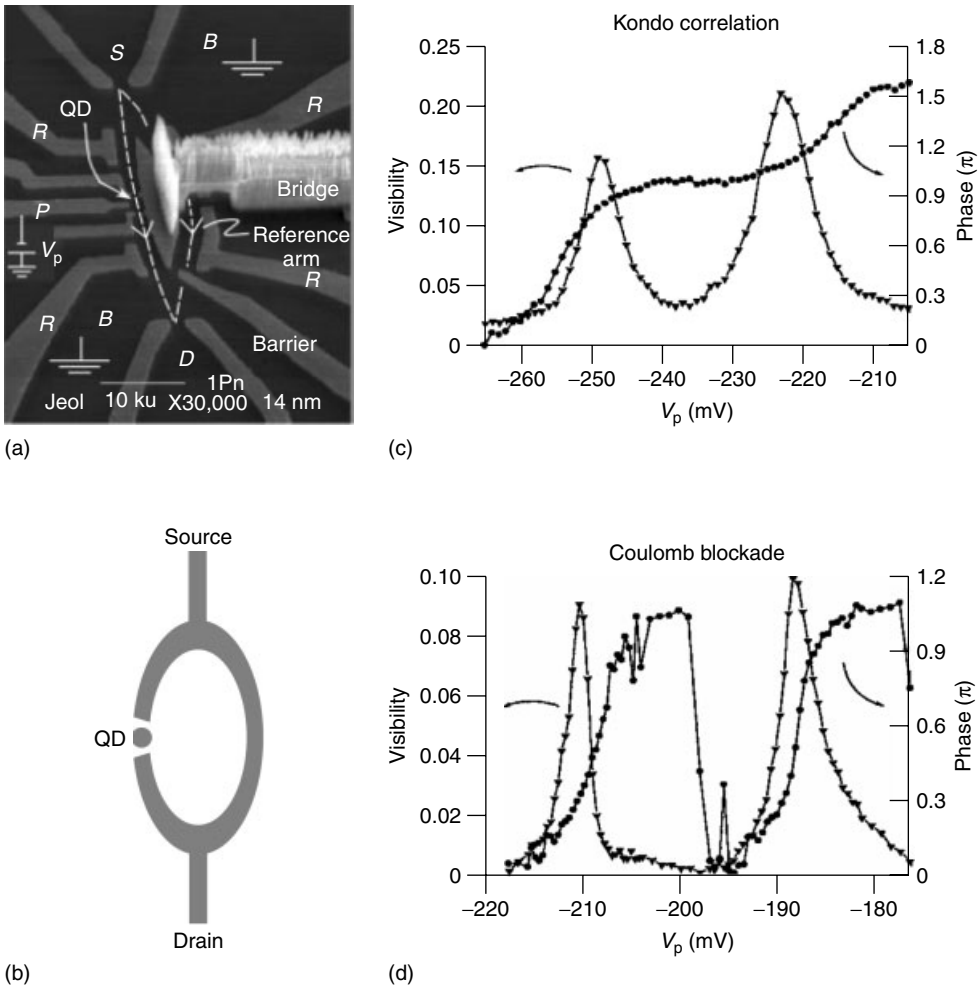

Figure 9. (a) SEM image of a mesoscopic Aharonov–Bohm interferometer with (Reproduced from Y. Ji *et al*., 2000, with permission from Science AAAS. © 2000) (b) a rough schematic of the device. (c) Evolution of the transmission phase and interference visibility as a function of the quantum dot energy level in the Kondo regime. The phase shift plateaus at π in the middle of the Kondo valley before rising to 1.5π when the quantum level is doubly occupied. (Reproduced from Y. Ji *et al*., 2000, with permission from Science AAAS. © 2000.) (d) In the Coulomb blockade regime ($T_K < T_{base}$), the phase shift increases and then falls by π each time the quantum dot occupancy is increased by one electron. (Reproduced from Y. Ji *et al*., 2000, with permission from Science AAAS. © 2000.)

In addition to temperature, magnetic field, and bias, nonideal conduction reservoirs and other external couplings can affect the Kondo behavior. The effects of perturbations on the Kondo state can be categorized as follows: (i) the Kondo state is suppressed because of the decoherence of the Kondo singlet (e.g., suppression of Kondo by thermal fluctuations), (ii) a non-Kondo ground state becomes the lowest-energy ground state (e.g., formation of spin-polarized ground state in high magnetic field), or (iii) a new Kondo state is created. The Kondo energy scale ($k_B T_K$) is a useful scale for determining how a perturbation will affect the Kondo state. Weak perturbations ($E < k_B T_K$) typically only partially suppress the Kondo state, while stronger perturbations ($E > k_B T_K$) are needed to significantly alter or destroy the Kondo singlet.

3.1 Decoherence of the Kondo state

We first discuss how various processes can lead to decoherence of the Kondo singlet. The Kondo singlet state is created by spin-flip cotunneling processes between conduction electrons and the local state. Non-Kondo processes, such as emission or absorption of a phonon or photon, disturb the necessary superposition of electronic states in the Kondo singlet. At zero temperature and bias, the phase space available for these non-Kondo processes is nearly eliminated and delocalized electrons within length ξ_K (equation (7)) form a Kondo singlet with the local spin. At finite temperature, thermal fluctuations drive non-Kondo transitions, progressively destroying these correlations. These non-Kondo transitions are facilitated by smearing of the sharp Fermi

distribution of the leads with temperature, which increases the available phase space for the transitions. Similarly, a small bias ($eV < k_B T_K$) applied across the dot also opens up phase space for non-Kondo transitions, leading to a suppression of the Kondo state. Larger biases have a more profound affect on the Kondo state, as discussed later in this section.

Coupling the quantum dot to other noise sources can have similar decohering effects. Avinun-Kalish *et al*. (2004) experimentally investigated the suppression of the Kondo state due to a capacitively coupled QPC. Conceptually, the QPC can be treated either as a source of shot noise or as a quantum dot charge measurement device, as discussed in Section 2.3.1. The authors observed stronger-than-expected suppression of Kondo transport, which they attributed to the long residence time of an electron in the Kondo cloud that extends well into the leads (Avinun-Kalish *et al*., 2004). The Kondo state can also be decohered by irradiating the sample with microwave radiation (Kaminski, Nazarov and Glazman, 1999; Elzerman *et al*., 2000). Here the random population and decay of excited states by photons takes over the role of thermal fluctuations in destroying the Kondo state.

3.2 Nonequilibrium Kondo effect

An applied bias across the quantum dot can have several interesting consequences on the Kondo state. For a quantum dot coupled equally to two leads at the same potential, the Kondo screening cloud spans both leads. An applied bias between the leads exposes the quantum dot to different Fermi levels, which opens up inelastic (decohering) channels for electron scattering between different leads. Kondo exchange with each individual lead, however, is not affected. For biases above $k_B T_K$, the Kondo spectral function splits into two resonances centered on the Fermi energies of each reservoir, as shown in Figure 10(a) (Wingreen and Meir, 1994; Schiller and Hershfield, 1995). The two Kondo resonances slowly fade with increasing bias because of decoherence associated with the exchange of electrons between the leads, but they remain visible for biases far exceeding $k_B T_K$. Two-terminal quantum dot measurements cannot accurately map out the nonequilibrium spectral function, but instead measure a convolution of two evolving spectral functions. The splitting can be observed experimentally through the addition of a weakly coupled third lead (Lebanon and Schiller, 2001; Leturcq *et al*., 2005), as shown in Figure 10(b). An alternative approach to probing the out-of-equilibrium Kondo spectral function has been investigated using a split Fermi distribution in a quantum wire side-coupled to a quantum dot (de Franceschi *et al*., 2002).

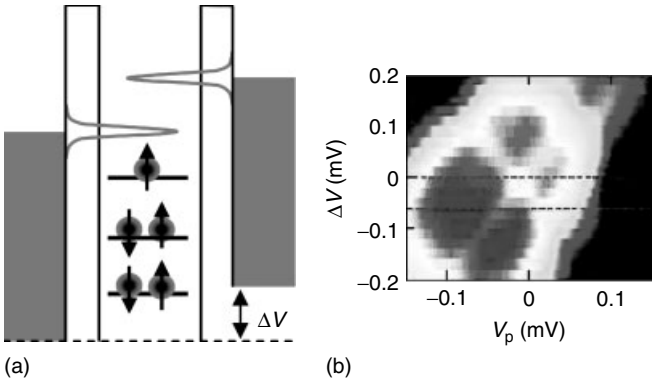

Figure 10. (a) A schematic of the splitting of the Kondo spectral function with an applied bias. The relative amplitude of the Kondo resonance in each lead depends on the respective dot–lead coupling. In the extreme case, where one lead is well coupled and the other is weakly coupled (typical of STM experiments), the weakly coupled lead can be treated as a spectroscopic probe (Lebanon and Schiller, 2001; Nagaoka, Jamneala, Grobis and Crommie, 2002). (b) The splitting of the Kondo resonance with applied bias can be probed by weakly coupling an additional lead. The plot shows the current through the weakly coupled lead as a function of the voltage difference (ΔV) between the two strongly coupled leads. A Kondo conductance enhancement is observed when the Fermi energy of the weakly coupled lead is aligned with the Fermi energy of either one of the strongly coupled leads, leading to the cross pattern seen in the figure. (Reproduced from R. Leturcq *et al*., 2005, with permission from the American Physical Society. © 2005.)

3.2.1 Recovery of the Kondo state

An applied bias can also provide the necessary energy to form a Kondo singlet when the Kondo ground state is not otherwise the favored configuration. The first example of this phenomenon is the recovery of the Kondo effect at finite bias in an applied magnetic field. A magnetic field breaks the spin degeneracy of the quantum dot ground state favoring a spin-polarized ground state over the Kondo singlet. As a result, spin-flip transitions incur an energy cost, leading to a characteristic suppression of Kondo conductance, as described in Section 2.3.2. The spin-flip energy cost can be compensated by applying a bias across the quantum dot. Here, the Kondo state reemerges when the applied bias is equal to the spin-flip energy ($eV \sim g\mu_B B$) (Goldhaber-Gordon *et al*., 1998a; Cronenwett, Oosterkamp and Kouwenhoven, 1998; Kogan *et al*., 2004a). Experimentally, this produces two Kondo peaks, separated by twice the spin-flip energy (Figure 11). Surprisingly, the measured splitting of the Kondo resonance exceeds the expected Zeeman splitting, an effect which is not fully understood (Kogan *et al*., 2004a; Costi, 2000; Moore and Wen, 2000).

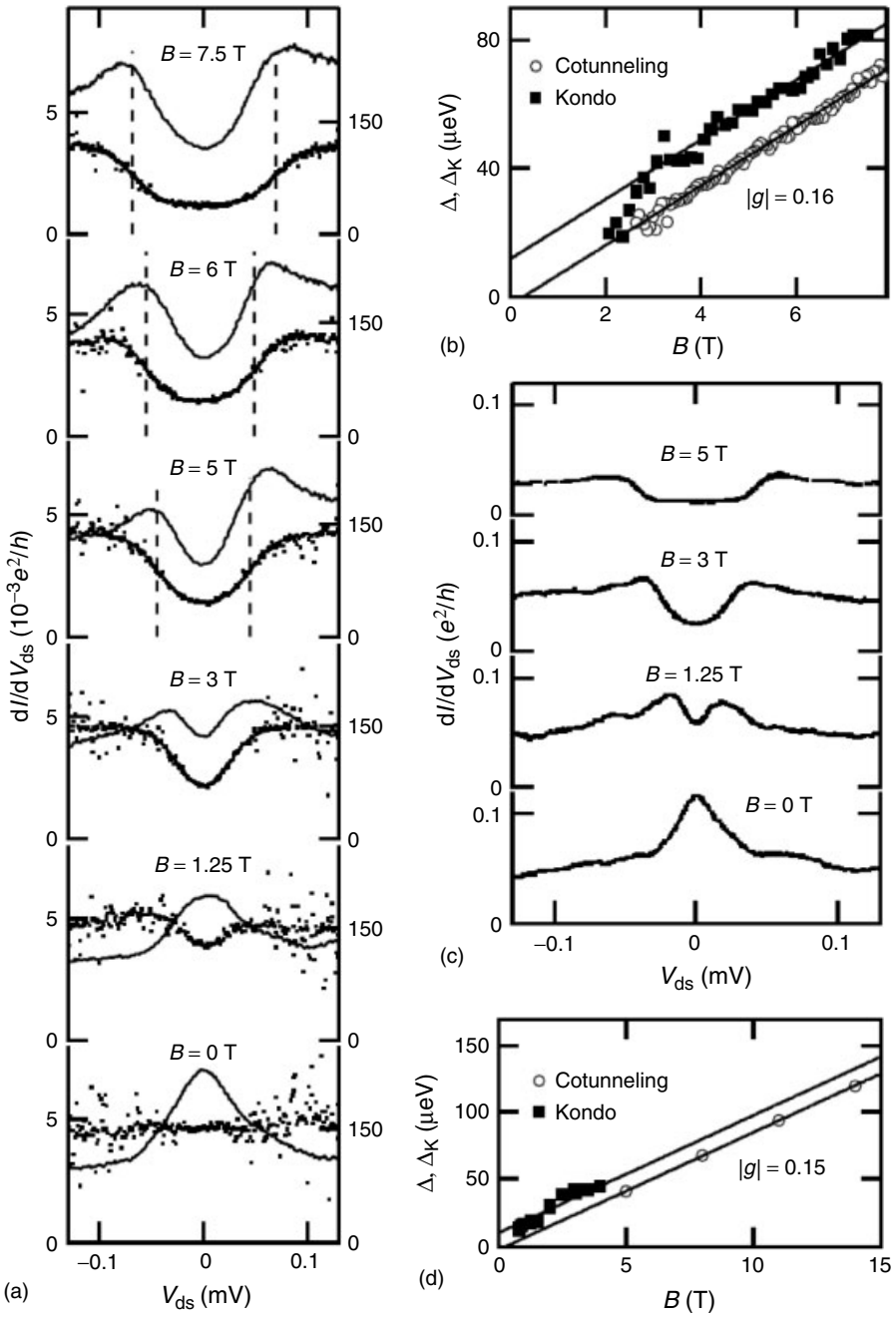

Figure 11. Evolution of the Kondo resonance and the inelastic spin-flip cotunneling gap with applied magnetic field for two different quantum dot devices. Device 1: (a) The solid line (dots) shows the evolution of the Kondo peak (cotunneling gap) with applied field. (b) The Kondo peak splitting ($2\Delta_K$, solid squares) is larger than the spin-flip cotunneling gap (2Δ, open circles), indicating that $\Delta_K > g\mu_B B$. Device 2: (c) The split Kondo peak seamlessly evolves into an inelastic spin-flip cotunneling signal as the magnetic field is increased. (d) The transition to inelastic cotunneling is marked by a decrease in the measured gap, indicating again that $\Delta_K > g\mu_B B$. (Reproduced from A Kogan *et al*., 2004, with permission from the American Physical Society. © 2004.)

High-frequency microwave radiation ($hf > k_B T_K$) can break up the Kondo singlet and destroy the Kondo effect, as described previously. On the other hand, microwave radiation can also drive Tien–Gordon photon-assisted tunneling processes (Kouwenhoven *et al*., 1994). By tuning the applied bias to the photon energy ($eV \sim hf$), a unique Kondo state can exist in which coherent spin-flip tunneling events coincide with simultaneous absorption or emission of photons. Kogan and coworkers found that such a state can be achieved experimentally if the monochromatic microwave radiation

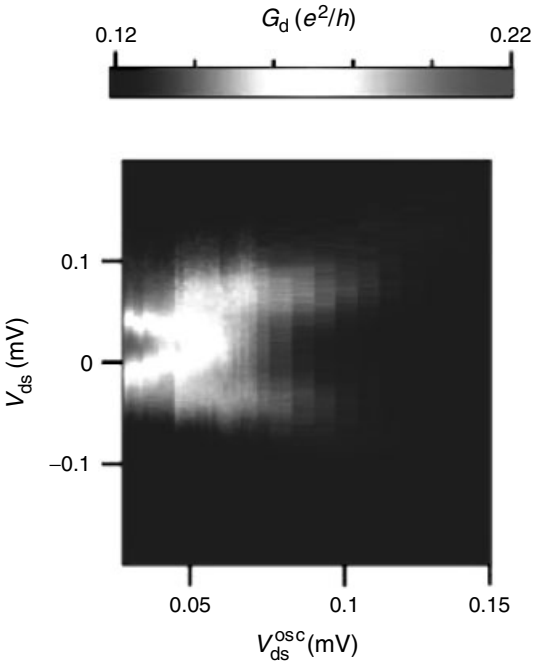

Figure 12. Splitting of the Kondo peak as a function of microwave irradiation amplitude. (Reproduced from A. Kogan *et al*., 2004, with permission from Science AAAS. © 2004.)

intensity is tuned so that $eV_{osc} \sim hf$ (Kogan, Amasha and Kastner, 2004b). These conditions ensure that the photon field is strong enough to modify Kondo processes, but not strong enough to decohere them altogether. The experimental signature of this state is a splitting of the Kondo peak into two peaks separated by twice the photon frequency, as seen in Figure 12.

3.2.2 Crossover to cotunneling

In the examples of nonequilibrium Kondo effects presented here, a finite bias is essential for the creation of the Kondo state even though it also introduces decoherence processes. Inevitably, the Kondo state will decohere completely when exposed to strong enough perturbations ($E \gg k_B T_K$). Incoherent, or inelastic, cotunneling processes can still enhance conductance in this regime, though to a much lesser extent than the analogous coherent processes that compose the Kondo effect (de Franceschi *et al*., 2001). The transition from coherent Kondo tunneling to incoherent cotunneling has been investigated by several groups (Sasaki *et al*., 2000; Kogan *et al*., 2004a). Figure 11(c) and (d) shows the seamless transition from Kondo to incoherent cotunneling as a function of an applied magnetic field (Kogan *et al*., 2004a; Heinrich, *et al*., 2004).

3.3 Kondo in Landau levels

Though an applied magnetic field generally suppresses the Kondo state, several novel Kondo states can form at intermediate fields. The electronic states of a 2DEG in magnetic fields are Landau levels (LLs), which for our purposes are circular orbits at quantized multiples of the cyclotron energy. Quantum dot states can acquire an LL character once the electron cyclotron radius is comparable to the spatial dimensions of the dot. The quantum dot LL states behave in much the same way as regular quantum dot states and can exhibit Kondo behavior (Schmid, Weis, Eberl and von Klitzing, 2000; Sprinzak *et al*., 2002; Stopa *et al*., 2003; Keller *et al*., 2001). Typically, the lowest spin-degenerate LL is most strongly coupled to the leads, and Kondo processes occur when this level contains an unpaired spin (Stopa *et al*., 2003; Keller *et al*., 2001). The occupancy of the LL can be tuned by changing the total number of electrons with an applied gate voltage or by redistributing the existing electrons among the LLs using an applied magnetic field. As a result, the Kondo conductance shows a 'checkerboard' pattern as a function of gate voltage and magnetic field, as shown in Figure 13 (Schmid, Weis, Eberl and von Klitzing, 2000; Sprinzak *et al*., 2002; Stopa *et al*., 2003; Keller *et al*., 2001). At higher magnetic fields, the Zeeman splitting spin polarizes the leads, and the Kondo conductance vanishes. In high magnetic fields, electrons can form closed orbits around a depleted region of a 2DEG. The resulting 'antidot' can act as a magnetic impurity and exhibit the Kondo effect (Kataoka, Ford, Simmons and Ritchie, 2002).

3.4 Modified conduction reservoir

In order for Kondo correlations to persist, the quantum dot must be able to freely exchange electrons with the leads. Metallic leads facilitate electron exchange by providing a large smooth density of states near the Fermi level. However, distinctive Kondo states can exist even if the leads have additional electronic structure.

3.4.1 Finite level spacing (Kondo box)

A natural question to ask is what happens to Kondo processes when the mean level spacing of the leads (Δ) becomes comparable to the Kondo temperature (T_K) (Thimm, Kroha and von Delft, 1999; Simon and Affleck, 2002). Thimm, Kroha, and von Delft (1999) explored this question theoretically in the context of a single-electron transistor and found three unique signatures: (i) the Kondo resonance splits up into a series of subpeaks, (ii) the conductance depends on the even/odd occupancy of the combined lead–quantum dot

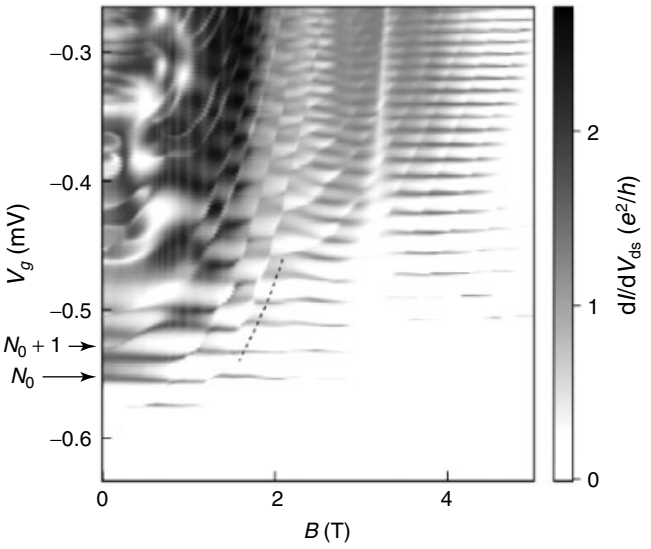

Figure 13. In a high magnetic field applied perpendicular to the quantum dot, the states of a quantum dot organize into Landau levels. If the dot is strongly coupled to its leads, the Kondo effect occurs whenever the occupancy of the outer Landau level (LL) is odd. As a result, the differential conductance shows a checkerboard pattern as the LL occupancy can be tuned by both a gate voltage and the magnetic field. (Reproduced from J. Weis *et al*., 2000, with permission from the American Physical Society. © 2000.)

system, and (iii) quantum dot transport exhibits Fano-like line shapes with anomalous temperature dependence. A 'Kondo box' exhibiting these features has yet to be quantitatively studied experimentally despite several interesting approaches (Odom, Huang, Cheung and Lieber, 2000; Manoharan, Lutz and Eigler, 2000; Booth *et al*., 2005).

3.4.2 Magnetic leads

Ferromagnetic leads create spin imbalances, which affect the dynamics of Kondo spin-flip exchange. The behavior of these systems depends on the relative magnetic orientation of the two leads connected to the quantum dot (Sergueev *et al*., 2002; Martinek *et al*., 2003; Choi, Sánchez and López, 2004). If both leads have the same magnetic orientation, the reservoir spin imbalance acts similar to a magnetic field. Here, the Kondo spectral function is suppressed and split, whenever the quantum dot is not electron–hole symmetric ($\varepsilon_0 \neq -U/2$) (Choi, Sánchez and López, 2004). The Kondo effect for antiparallel magnetic lead alignment is equivalent to the nonmagnetic case, though with a different nonequilibrium behavior. Experimental realizations of ferromagnetic coupled leads in mesoscopic systems have been hampered by the difficulty in reliably creating magnetic semiconductor structures. Some of the predicted magnetic behavior has been seen, however, in single molecular transistors (Pasupathy *et al*., 2004).

3.4.3 Superconducting and Luttinger-liquid leads

More exotic systems have also been considered, such as coupling a quantum dot to superconducting (Fazio and Raimondi, 1998; Sun, Guo and Lin, 2001) or Luttinger-liquid leads (Kane and Fisher, 1992; Lee and Toner, 1992; Furusaki and Nagaosa, 1994). In both cases, the leads have no density of single-electron states at the Fermi level, where the Kondo screening cloud would normally form. Therefore, the Kondo ground state competes with the native ground state of the leads. For superconducting leads, the Kondo effect will develop if the Kondo energy scale, $k_B T_K$, exceeds the superconducting single-electron excitation energy gap, Δ, as seen experimentally in carbon nanotube quantum dots (Buitelaar, Nussbaumer and Schönenberger, 2002). Kondo behavior in Luttinger liquids depends sensitively on the Luttinger parameter of the leads (Komnik and Gogolin, 2003), but has not been examined in mesoscopic experiments.

4 EXOTIC KONDO SYSTEMS

The Kondo effect, as described by the Anderson model (equation (1)), arises when a localized degenerate state is coupled to a reservoir of conduction electrons. Though our discussion has focused on spin-1/2 degeneracy, the Kondo effect can also arise from a twofold degeneracy with other physical origins (Figure 14), or from a higher local degeneracy. In this section, we review recent mesoscopic systems that demonstrate such scenarios.

4.1 Nonspin Kondo systems

4.1.1 Twofold electrostatic degeneracy

One of the most striking examples of a non-spin-1/2 Kondo system is the spinless Kondo effect observed in a capacitively coupled double quantum dot system (Wilhelm, Schmid, Weis and von Klitzing, 2002). The experimental configuration (shown in Figure 15a) consists of two parallel quantum dots, each coupled to its own independent set of leads. The two dot–lead systems cannot exchange electrons with each other, but can communicate via electrostatic coupling between the two quantum dots. A charge degeneracy can be created by tuning the two quantum dots so that the quantum state corresponding to having an extra electron on

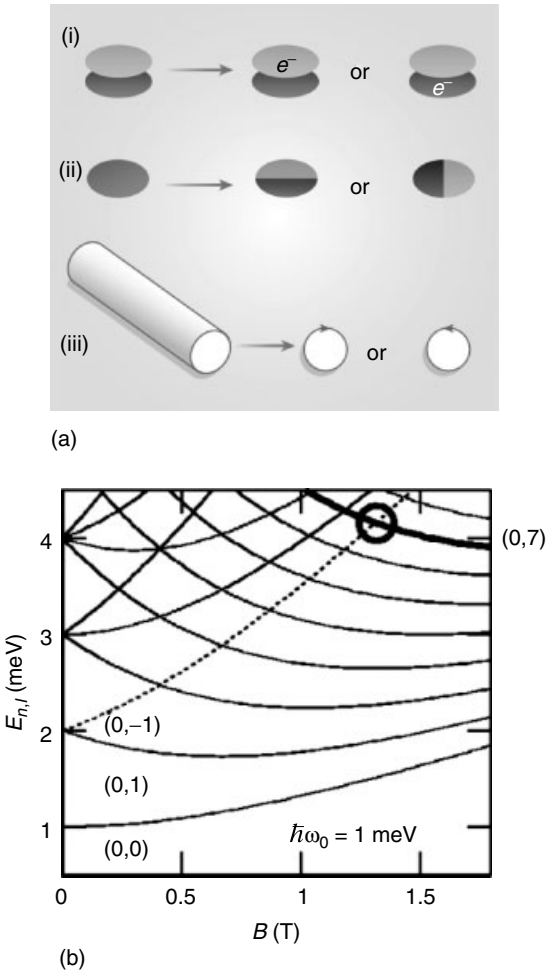

Figure 14. (a) The spin-1/2 Kondo effect stems from the twofold spin degeneracy of a quantum dot level. Degeneracies with origins other than spin can also lead to a completely equivalent Kondo effect. Such degeneracies can arise from the following: (i) two spatially separated sites of which only one can be occupied due to Coulomb repulsion, (ii) a spatial symmetry that leads to two degenerate orbitals, and (iii) the lattice symmetry of a carbon nanotube which gives rise to a twofold orbital degeneracy. (Reproduced from Ronald M. Potok *et al*., 2005, with permission from Nature Publishing Group. © 2005.) (b) Orbitals with different energies can be made degenerate by tuning their energies with an applied magnetic field. Shown here is the evolution of circular quantum dot states with magnetic field. Degeneracies occur at level crossings, such as the one indicated by the circle. (Reproduced from S. Sasaki *et al*., 2004, with permission from the American Physical Society. © 2004.)

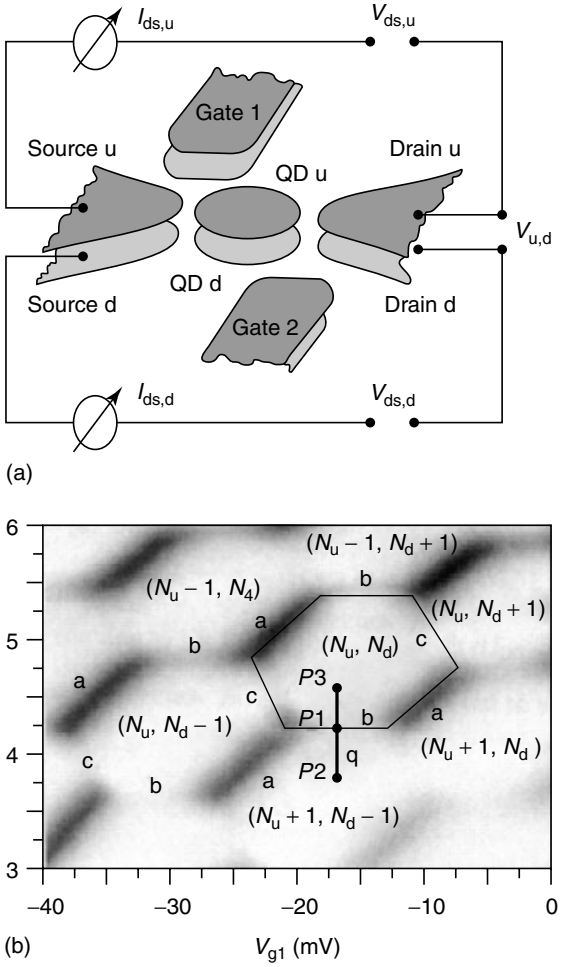

Figure 15. (a) Schematic of a capacitively coupled double quantum dot system used to observe the spinless Kondo effect (scenario (i) in Figure 14(a)). (b) Current through the upper quantum dot as a function of V_{G1} and $V_{u,d}$ shows a honeycomb pattern because of electrostatic interaction with the lower quantum dot ($V_{DS,u} = 80\,\mu$V; 'white' = no current). The spinless Kondo effect leads to the faint conductance observed along the line marked 'b'. (Reproduced from U. Wilhelm *et al*., 2002, with permission from Elsevier. © 2002.)

dot 1 ($N_1 + 1$, N_2) is degenerate with the state corresponding to an extra electron on dot 2 (N_1, $N_2 + 1$). This charge degeneracy takes over the role normally played by spin degeneracy, mapping this system onto the Anderson impurity model (Pohjola *et al*., 2000; Wilhelm, Schmid, Weis and von Klitzing, 2001).

Transport through one of the dots as a function of the occupancy of both dots reveals a honeycomb pattern (Figure 15b), similar to that seen in transport through double quantum dot systems (van der Wiel *et al*., 2003). The faint conductance feature on side b of the hexagon in Figure 15(b) (at the charge degeneracy point described earlier) is the feature of interest in this experiment. While single-electron transport is forbidden because of CB, two-electron processes give rise to nonzero conductance. Here an electron jumps off one dot, while another electron simultaneously jumps onto the other. These processes drive the Kondo effect, screening the electrostatic (as opposed to magnetic) degeneracy and giving rise to a nonzero conductance.

4.1.2 Twofold orbital degeneracy

A more common nonspin degeneracy in quantum dot systems is orbital degeneracy, which typically arises from spatial symmetries. The orbital Kondo effect has been observed in a circular quantum dot (Sasaki *et al*., 2004). Carbon nanotubes have an intrinsic orbital degeneracy due to their structure, and several groups have reported Kondo effects stemming from this degeneracy (Nygård, Cobden and Lindelof, 2000; Jarillo-Herrero *et al*., 2005a,b). Nondegenerate orbital states can be brought into degeneracy by applying a magnetic field, as shown in Figure 14(b), leading to analogous Kondo effects (Sasaki *et al*., 2004). Spin degeneracy may also combine with orbital degeneracy, leading to exotic Kondo physics as described in the following subsections.

4.2 Multiple-degeneracy Kondo systems

Quantum dots with a multiple degenerate grounds state can exhibit a variety of interesting Kondo effects. The Kondo behavior of these systems depends on the allowed transitions between the N degenerate states. If transitions can occur equally between any pair of degenerate states, the system has $SU(N)$ symmetry and is described by the Coqblin–Schrieffer model (Coqblin and Schrieffer, 1969). The Kondo temperature is predicted theoretically to be larger in these systems than in equivalent spin-1/2 Kondo systems and depends exponentially on N:

$$T_K \sim D e^{-1/N\rho(E_F)J} \tag{12}$$

where J, $\rho(E_F)$, and D are the exchange coupling, density of states, and interacting electron bandwidth, respectively. Like the spin-1/2 Kondo ground state, the $SU(N)$ Kondo ground state is no longer degenerate. In contrast, for an impurity with a high spin degeneracy ($S > 1/2$), a single conduction channel will only couple states with $\Delta S_z = 1$. In these systems, the Kondo effect will underscreen the magnetic moment, leaving behind a ground state of lower degeneracy, associated with a net spin reduced by 1/2 from its native value (Mattis, 1967). Other systems, such as the singlet–triplet degeneracy discussed later, can have a more complicated coupling structure (Eto, 2005).

4.2.1 Spin and orbital degeneracy: SU(4) Kondo effect

When the electronic state of a system contains both orbital and spin degeneracy, the same delocalized lead electrons that magnetically screen the unpaired spin may also electrostatically screen the orbital degeneracy. The two degrees of freedom can produce an $SU(4)$ Kondo effect, which has been observed in vertical GaAs dots (Sasaki *et al*., 2004) and carbon nanotubes (Jarillo-Herrero *et al*., 2005b). In the vertical quantum dot system, T_K is not large enough for the spin-1/2 Kondo effect to be observed in the absence of orbital degeneracy (odd valleys in Figure 16a). Kondo conductance enhancement is observed, however, when the dot is tuned to an orbital crossing point using an applied magnetic field. Here an $SU(4)$ fourfold degeneracy is present,

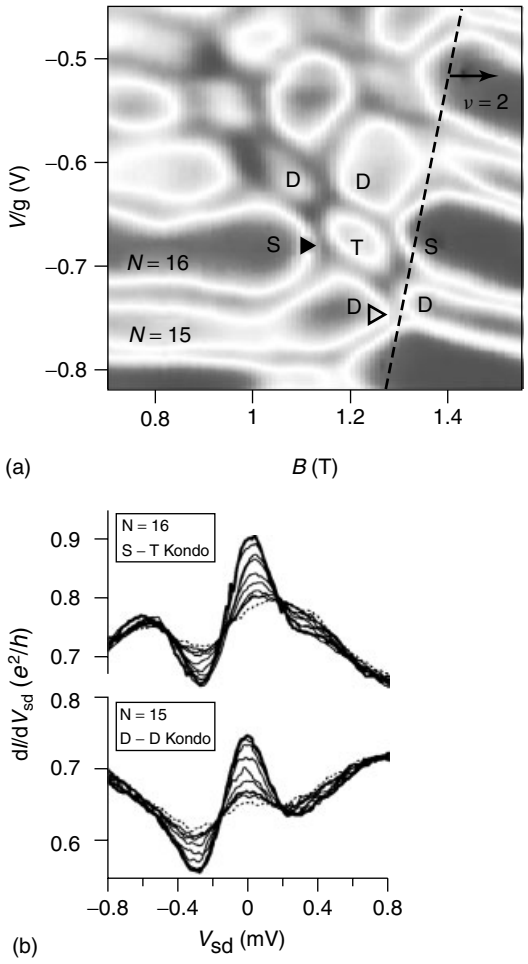

Figure 16. (a) Zero-bias conductance measured in a vertical quantum dot as a function of gate voltage and magnetic field. Orbital states are brought into and out of degeneracy by the magnetic field, which leads to two types of Kondo effects. For odd occupancy, a doublet–doublet (D–D) Kondo effect arises at orbital crossings where a fourfold degeneracy is present. A singlet–triplet (S–T) Kondo effect occurs at level crossings for even occupancy. To the right of the dotted line, all electrons occupy the lowest Landau level. (b) The temperature dependence of the Kondo resonance for the S–T and D–D Kondo effects from 60 mK (thick solid line) to 1.5 K (dashed line). Both systems show a similar Kondo temperature. (Reproduced from S. Sasaki *et al*., 2004, with permission from the American Physical Society. © 2004.)

which enhances the Kondo temperature (Eto, 2005). This 'doublet–doublet' Kondo state produces a zero-bias Kondo peak, as seen in Figure 16(b).

Carbon nanotubes have an intrinsic orbital degeneracy in addition to a spin degeneracy, which can lead to $SU(4)$ Kondo physics (Jarillo-Herrero *et al.*, 2005b). Owing to electron–hole symmetry, the $SU(4)$ Kondo effect is observed when the two orbitals are occupied by either one or three electrons (Figure 17a). The fourfold degeneracy responsible for the Kondo ground state is demonstrated by the splitting of the Kondo resonance into four peaks with magnetic field (Figure 17b). The magnetic field suppresses the $SU(4)$ Kondo effect by first lifting the orbital degeneracy. The resulting spin-1/2 Kondo effect survives until the Zeeman splitting becomes comparable to the Kondo temperature. A pure orbital $SU(2)$ Kondo effect is attained at orbital level crossings, which one can attain by applying a magnetic field (dashed lines in Figure 17a). In these experiments, the Kondo temperature for the $SU(4)$ Kondo effect is larger than the Kondo temperature for the $SU(2)$ Kondo effect, as predicted by equation (12). It is not yet clear why the electrons in the (metal) leads have the requisite fourfold symmetry to fully screen the local state on the nanotube.

4.2.2 *Triplet and singlet–triplet Kondo effect*

The ground state of a quantum dot with an even number of electrons is usually a spin singlet at zero magnetic field, where each occupied orbital contains a pair of electrons. The triplet state will have lower energy, however, if the exchange energy gained for parallel spin filling exceeds the level separation between adjacent orbitals (Tarucha *et al.*, 2000). A quantum dot with $S = 1$ no longer has the same spin symmetry as the spin-1/2 reservoir electrons. As discussed earlier, Kondo correlations will partially screen the $S = 1$ quantum dot, leaving behind a residual spin-1/2, as long as only a single reservoir mode is coupled to the quantum dot. Perhaps owing to a low T_K predicted for these systems (Wan, Phillips and Li, 1995; Izumida, Sakai and Shimizu, 1998), a pure spin-1 Kondo effect has not been unambiguously observed in mesoscopic systems.

Alternatively, the singlet and triplet state can be brought into degeneracy using an applied magnetic field. At low magnetic fields, the Zeeman splitting of the triplet is negligible and the singlet–triplet degeneracy point is fourfold degenerate, though not $SU(4)$ symmetric (Eto and Nazarov, 2000; Pustilnik and Glazman, 2000). The singlet–triplet Kondo temperature is expected to be higher than for spin-1/2 Kondo systems and comparable to that found in $SU(4)$ Kondo systems (Eto, 2005). A singlet–triplet Kondo effect has been observed in transport measurements through vertical quantum dots (Sasaki *et al.*, 2000, 2004) (shown in Figure 16), lateral quantum dots (Schmid, Weis, Eberl and von Klitzing, 2000; van der Wiel *et al.*, 2002; Kogan *et al.*, 2003), and carbon nanotubes (Nygård, Cobden and Lindelof, 2000; Jarillo-Herrero *et al.*, 2005a,b) (Figure 17a). Even if the singlet and triplet states are not energetically degenerate, a finite bias can compensate for the energy difference and lead to a nonequilibrium singlet–triplet Kondo effect, as seen recently in a carbon nanotube quantum dot (Paaske *et al.*, 2006).

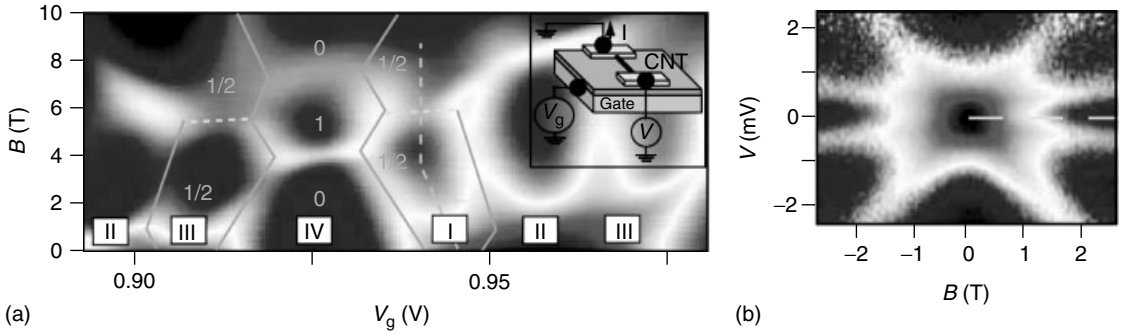

Figure 17. (a) Conductance through a carbon nanotube quantum dot (shown schematically in the inset) as a function of magnetic field (B) and gate voltage (V_G). The solid lines highlight the evolution of the Coulomb blockade peaks with B. The Roman numerals indicate the number of electrons occupying the partially occupied four-electron shell at $B = 0$, while the Arabic numbers represent the spin of the ground state. At $B = 0$, an $SU(4)$ Kondo effect occurs for single (I) and triple occupancy (III), while a singlet–triplet Kondo effect is observed for double occupancy (II). A purely orbital Kondo effect is observed at magnetic-field-induced level crossings, as indicated by the horizontal dotted lines. (b) A magnetic field will split the four degenerate states (two spin × two orbital) that generate the $SU(4)$ Kondo effect. Since the orbital magnetic moment is approximately three times larger than the spin magnetic moment in a carbon nanotube, the orbital states are split at a different rate than the spin states, and four peaks are observed at finite B field. (Reproduced from Jarillo-Herrero *et al.*, 2005, with permission from Nature Publishing Group. © 2005.)

4.2.3 Two-stage Kondo effect

A system on the border of a singlet–triplet transition can exhibit a remarkable two-stage Kondo effect. If coupled to two reservoir modes, the transport properties of an $S = 1$ quantum dot are theoretically predicted to have a nonmonotonic dependence on temperature and bias (Pustilnik and Glazman, 2001). The two modes create two different Kondo screening channels with different associated Kondo temperatures, T_{K1} and T_{K2}. At unitary coupling, the two modes interfere and reduce Kondo conductance when T is below both T_{K1} and T_{K2}. A second screening channel can form in systems containing only one tunneling mode if the dot–lead couplings are asymmetric (Pustilnik and Glazman, 2001). A quantum dot just on the singlet side of the singlet–triplet transition is also predicted to undergo a similar two-stage Kondo effect, even if only a single tunneling mode is coupled to the dot (Hofstetter and Schoeller, 2002). Such two-stage Kondo effects have been observed in lateral quantum dots (van der Wiel *et al*., 2002; Granger *et al*., 2005). In experiments by van der Wiel, a magnetic field tunes the quantum dot near a singlet–triplet degeneracy point. Conductance measurements show a dip in the zero-bias anomaly at low temperatures (Figure 18). From the available data, it is not possible to unambiguously distinguish whether a singlet or triplet ground state is responsible for the observed effect.

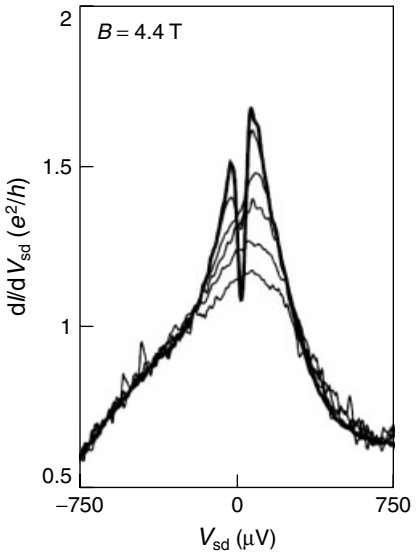

Figure 18. The two-stage Kondo effect is characterized by enhanced conductance at intermediate energies and suppressed conductance at low energies, as demonstrated by the dip in the zero-bias Kondo resonance. Shown here is the temperature dependence of the Kondo peak from 15 mK (solid line) to 800 mK. (Reproduced from W.G. van der Wiel *et al*., 2002, with permission from the American Physical Society. © 2002.)

5 RECENT DEVELOPMENTS AND FUTURE DIRECTIONS

As we have seen, the designability and *in situ* control of parameters in semiconductor quantum dots have enabled highly quantitative tests of Kondo physics and observation of Kondo effects in new regimes and scenarios. This new approach has brought fresh insight and excitement to what was legitimately considered one of the best-understood phenomena in solid-state physics. The continuing flow of theoretical predictions and experimental investigations – around 100 papers per year in mesoscopic physics alone – attests that Kondo physics remains a rich and vibrant field. We conclude our review with a few remarks about the future of mesoscopic Kondo experiments, as suggested by recent trends.

5.1 Spatial and temporal Kondo physics

Mesoscopic experiments have illuminated the effect on Kondo transport of external parameters (e.g., temperature, magnetic field) and dot–lead coupling. In short, spin-1/2 Kondo phenomenology is broadly well understood. However, several important issues remain on the cutting edge: How do a pair of magnetic impurities interact (Jeong, Chang and Melloch, 2001; Craig *et al*., 2004; Simon, Lopez and Oreg, 2005; Vavilov and Glazman, 2005)? What are the dynamics and spatial extent of the Kondo screening cloud (Sorensen and Affleck, 1996; Nordlander *et al*., 1999) and how do these depend on the dimensionality of the screening reservoirs (Simon and Affleck, 2002)? How can we understand and control the processes that lead to decoherence of the Kondo state, especially out of equilibrium (Avinun-Kalish *et al*., 2004; Kogan *et al*., 2004a; Leturcq *et al*., 2005)?

5.2 Novel Kondo systems

As discussed in Sections 3 and 4, design of a quantum dot's states has enabled studies of a broad family of Kondo effects with different local degeneracies. However, several proposed exotic Kondo systems have not yet been addressed by extensive experiments. Controlling the electronic properties of the conduction reservoir, as discussed in Section 3.4, has proved difficult in mesoscopic systems. Manipulating the coupling of quantum dots to superconducting, magnetic, or one-dimensional leads will be exciting and is likely to advance fastest in hybrid molecular-metal systems, in which the material of the metal leads can be selected to yield desired electronic structure (Buitelaar, Nussbaumer

and Schönenberger, 2002; Pasupathy *et al*., 2004). Tantalizing theoretical predictions abound for multichannel Kondo systems, such as the two-channel Kondo effect (Cox and Zawadowski, 1998; Matveev, 1995; Oreg and Goldhaber-Gordon, 2003; Pustilnik, Borda, Glazman and von Delft, 2004), which occurs when two reservoirs independently attempt to screen a spin-degenerate state. The resulting frustrated system is predicted to exhibit both local non-Fermi liquid behavior and a model quantum phase transition, as recently observed by some of the present authors in a novel double-dot geometry (Potok *et al*., 2007). This offers hope that the tools of mesoscopic physics can bear on complex correlated electrons systems normally realized only in bulk systems. Finally, several experimental observations indicate that the celebrated 0.7 structure seen in QPC transport might have Kondo origins (Cronenwett *et al*., 2002; Rejec and Meir, 2006). This effect is yet to be fully understood and should continue to attract both experimental and theoretical attention.

NOTES

[1] Though the terms *tunneling channels* and *tunneling modes* are often used interchangeably, we will avoid using the former to avoid confusion with the concept of independent Kondo screening channels, which lead to the multichannel Kondo effect (Section 5.2).

[2] In the mixed-valence regime, the Kondo resonance is expected to move away from E_F and no longer be symmetric about its maximum (Costi, Hewson and Zlatic, 1994; Wahl *et al*., 2004).

REFERENCES

Aharony, A. and Entin-Wohlman, O. (2005). Measuring the Kondo effect in the Aharonov-Bohm interferometer. *Physical Review B*, **72**, 073311.

Aharony, A., Entin-Wohlman, O. and Imry, Y. (2003). Measuring the transmission phase of a quantum dot in a closed interferometer. *Physical Review Letters*, **90**, 156802.

Anderson, P.W. (1961). Localized magnetic states in metals. *Physical Review*, **124**, 41.

Andrei, N., Furuya, K. and Lowenstein, J.H. (1983). Solution of the Kondo problem. *Reviews of Modern Physics*, **55**, 331–402.

Appelbaum, J. (1966). S-D exchange model of zero-bias tunneling anomalies. *Physical Review Letters*, **17**, 91.

Avinun-Kalish, M., Heiblum, M., Silva, A., *et al*. (2004). Controlled dephasing of a quantum dot in the Kondo regime. *Physical Review Letters*, **92**, 156801.

Avinun-Kalish, M., Heiblum, M., Zarchin, O., *et al*. (2005). Crossover from 'mesoscopic' to 'universal' phase for electron transmission in quantum dots. *Nature*, **436**, 529–533.

Barzykin, V. and Affleck, I. (1996). The Kondo screening cloud: What can we learn from perturbation theory? *Physical Review Letters*, **76**, 4959–4962.

Booth, C.H., Walter, M.D., Daniel, M., *et al*. (2005). Self-contained Kondo effect in single molecules. *Physical Review Letters*, **95**, 267202.

Buitelaar, M.R., Nussbaumer, T. and Schönenberger, C. (2002). Quantum dot in the Kondo regime coupled to superconductors. *Physical Review Letters*, **89**, 256801.

Choi, M.S., Sánchez, D. and López, R. (2004). Kondo effect in a quantum dot coupled to ferromagnetic leads: a numerical renormalization group analysis. *Physical Review Letters*, **92**, 056601.

Ciorga, M., Sachrajda, A.S., Hawrylak, P., *et al*. (2000). Addition spectrum of a lateral dot from Coulomb and spin-blockade spectroscopy. *Physical Review B*, **61**, R16315–R16318.

Coqblin, B. and Schrieffer, J.R. (1969). Exchange interaction in alloys with cerium impurities. *Physical Review*, **185**, 847.

Costi, T.A. (2000). Kondo Effect in a Magnetic Field and the Magnetoresistivity of Kondo Alloys. *Physical Review Letters*, **85**, 1504.

Costi, T.A., Hewson, A.C. and Zlatic, V. (1994). Transport-coefficients of the Anderson model via the numerical renormalization-group. *Journal of Physics: Condensed Matter*, **6**, 2519–2558.

Cox, D.L. and Zawadowski, A. (1998). Exotic Kondo effects in metals: magnetic ions in a crystalline electric field and tunnelling centres. *Advances in Physics*, **47**, 599–942.

Craig, N.J., Taylor, J.M., Lester, E.A., *et al*. (2004). Tunable nonlocal spin control in a coupled-quantum dot system. *Science*, **304**, 565–567.

Cronenwett, S.M., Lynch, H.J., Goldhaber-Gordon, D., *et al*. (2002). Low-temperature fate of the 0.7 structure in a point contact: a Kondo-like correlated state in an open system. *Physical Review Letters*, **88**, 226805.

Cronenwett, S.M., Oosterkamp, T.H. and Kouwenhoven, L.P. (1998). A tunable Kondo effect in quantum dots. *Science*, **281**, 540–544.

Elzerman, J.M., de Franceschi, S., Goldhaber-Gordon, D., *et al*. (2000). Suppression of the Kondo effect in a quantum dot by microwave radiation. *Journal of Low Temperature Physics*, **118**, 375–389.

Eto, M. (2005). Enhancement of Kondo effect in multilevel quantum dots. *Journal of the Physical Society of Japan*, **74**, 95–102.

Eto, M. and Nazarov, Y.V. (2000). Enhancement of Kondo effect in quantum dots with an even number of electrons. *Physical Review Letters*, **85**, 1306–1309.

Fazio, R. and Raimondi, R. (1998). Resonant Andreev tunneling in strongly interacting quantum dots. *Physical Review Letters*, **80**, 2913–2916.

de Franceschi, S., Hanson, R., van der Wiel, W.G., *et al*. (2002). Out-of-equilibrium Kondo effect in a mesoscopic device. *Physical Review Letters*, **89**, 156801.

de Franceschi, S., Sasaki, S., Elzerman, J.M., *et al*. (2001). Electron cotunneling in a semiconductor quantum dot. *Physical Review Letters*, **86**, 878–881.

Furusaki, A. and Nagaosa, N. (1994). Kondo effect in a tomonaga-luttinger liquid. *Physical Review Letters*, **72**, 892–895.

Gerland, U., von Delft, J., Costi, T.A. and Oreg, Y. (2000). Transmission phase shift of a quantum dot with Kondo correlations. *Physical Review Letters*, **84**, 3710–3713.

Giuliano, D., Naddeo, A. and Tagliacozzo, A. (2004). Linear Kondo conductance in a quantum dot. *Journal of Physics: Condensed Matter*, **16**, S1453–S1483.

Glazman, L.I. and Raikh, M.E. (1988). Resonant Kondo transparency of a barrier with quasilocal impurity states. *JETP Letters*, **47**, 452–455.

Goldhaber-Gordon, D., Göres, J., Kastner, M.A., *et al*. (1998a). From the Kondo regime to the mixed-valence regime in a single-electron transistor. *Physical Review Letters*, **81**, 5225–5228.

Goldhaber-Gordon, D., Shtrikman, H., Mahalu, D., *et al*. (1998b). Kondo effect in a single-electron transistor. *Nature*, **391**, 156–159.

Granger, G., Kastner, M.A., Radu, I., *et al*. (2005). Two-stage Kondo effect in a four-electron artificial atom. *Physical Review B*, **72**, 165309.

Gregory, S. (1992). Experimental-observation of scattering of tunneling electrons by a single magnetic-moment. *Physical Review Letters*, **68**, 2070–2073.

Gruner, G. and Zawadowski, A. (1974). Magnetic-impurities in non-magnetic metals. *Reports on Progress in Physics*, **37**, 1497–1583.

de Haas, W.J., de Boer, J. and van den Berg, G.J. (1934). The electrical resistance of gold, copper, and lead at low temperatures.*Physica*, **1**, 1115.

Haldane, F.D.M. (1978). Scaling theory of asymmetric Anderson model. *Physical Review Letters*, **40**, 416–419.

Heinrich, A.J., Gupta, J.A., Lutz, C.P. and Eigler, D.M. (2004). Single-Atom Spin-Flip Spectroscopy. *Science* **306**, 466.

Hewson, A.C. (1993). *The Kondo Problem to Heavy Fermions*, Cambridge University Press: Cambridge.

Hofstetter, W. and Schoeller, H. (2002). Quantum phase transition in a multilevel dot. *Physical Review Letters*, **88**, 016803.

Izumida, W., Sakai, O. and Shimizu, Y. (1998). Kondo effect in single quantum dot systems – study with numerical renormalization group method. *Journal of the Physical Society of Japan*, **67**, 2444–2454.

Jarillo-Herrero, P., Kong, J., van der Zant, H.S.J., *et al*. (2005a). Electronic transport spectroscopy of carbon nanotubes in a magnetic field. *Physical Review Letters*, **94**, 156802.

Jarillo-Herrero, P., Kong, J., van der Zant, H.S.J., *et al*. (2005b). Orbital Kondo effect in carbon nanotubes. *Nature*, **434**, 484–488.

Jeong, H., Chang, A.M. and Melloch, M.R. (2001). The Kondo effect in an artificial quantum dot molecule. *Science*, **293**, 2221–2223.

Jerez, A., Vitushinsky, P. and Lavagna, M. (2005). Theoretical analysis of the transmission phase shift of a quantum dot in the presence of Kondo correlations. *Physical Review Letters*, **95**, 127203.

Ji, Y., Heiblum, M. and Shtrikman, H. (2002). Transmission phase of a quantum dot with Kondo correlation near the unitary limit. *Physical Review Letters*, **88**, 076601.

Ji, Y., Heiblum, M., Sprinzak, D., *et al*. (2000). Phase evolution in a Kondo-correlated system. *Science*, **290**, 779–783.

Kaminski, A., Nazarov, Y.V. and Glazman, L.I. (1999). Suppression of the Kondo effect in a quantum dot by external irradiation. *Physical Review Letters*, **83**, 384–387.

Kane, C.L. and Fisher, M.P.A. (1992). Transmission through barriers and resonant tunneling in an interacting one-dimensional electron-gas. *Physical Review B*, **46**, 15233–15262.

Kastner, M.A. (1993). Artificial Atoms. *Physics Today*, **46**, 24–31.

Kasuya, T. (1956). A theory of metallic ferromagnetism and antiferromagnetism on Zener's model. *Progress of Theoretical Physics*, **16**, 45–57.

Kataoka, M., Ford, C.J.B., Simmons, M.Y. and Ritchie, D.A. (2002). Kondo effect in a quantum antidot. *Physical Review Letters*, **89**, 226803.

Keller, M., Wilhelm, U., Schmid, J., *et al*. (2001). Quantum dot in high magnetic fields: correlated tunneling of electrons probes the spin configuration at the edge of the dot. *Physical Review B*, **64**, 033302.

Kogan, A., Amasha, S., Goldhaber-Gordon, D., *et al*. (2004a). Measurements of Kondo and spin splitting in single-electron transistors. *Physical Review Letters*, **93**, 166602.

Kogan, A., Amasha, S. and Kastner, M.A. (2004b). Photon-induced Kondo satellites in a single-electron transistor. *Science*, **304**, 1293–1295.

Kogan, A., Granger, G., Kastner, M.A., *et al*. (2003). Singlet-triplet transition in a single-electron transistor at zero magnetic field. *Physical Review B*, **67**, 113309.

Komnik, A. and Gogolin, A.O. (2003). Resonant tunneling between luttinger liquids: a solvable case. *Physical Review Letters*, **90**, 246403.

Kondo, J. (1964). Resistance minimum in dilute magnetic alloys. *Progress of Theoretical Physics*, **32**, 37.

Kouwenhoven, L.P., Austing, D.G. and Tarucha, S. (2001). Few-electron quantum dots. *Reports on Progress in Physics*, **64**, 701–736.

Kouwenhoven, L.P., Jauhar, S., McCormick, K., *et al*. (1994). Photon-assisted tunneling through a quantum-dot. *Physical Review B*, **50**, 2019–2022.

Kouwenhoven, L.P., Marcus, C.M., McEuen, P.L., *et al*. (1997) Electron transport in quantum dots. In *Mesoscopic Electron Transport*, Sohn, L.L., Kouwenhoven, L.P. and Schon, G. (Eds.), Kluwer.

Lebanon, E. and Schiller, A. (2001). Measuring the out-of-equilibrium splitting of the Kondo resonance. *Physical Review B*, **65**, 035308.

Lee, D.H. and Toner, J. (1992). Kondo effect in a luttinger liquid. *Physical Review Letters*, **69**, 3378–3381.

Leturcq, R., Schmid, L., Ensslin, K., *et al*. (2005). Probing the Kondo density of states in a three-terminal quantum ring. *Physical Review Letters*, **95**, 126603.

Li, J.T., Schneider, W.D., Berndt, R. and Delley, B. (1998). Kondo scattering observed at a single magnetic impurity. *Physical Review Letters*, **80**, 2893–2896.

Liang, W.J., Shores, M.P., Bockrath, M., *et al*. (2002). Kondo resonance in a single-molecule transistor. *Nature*, **417**, 725–729.

Madhavan, V., Chen, W., Jamneala, T., *et al*. (1998). Tunneling into a single magnetic atom: spectroscopic evidence of the Kondo resonance. *Science*, **280**, 567–569.

Majumdar, K., Schiller, A. and Hershfield, S. (1998). Nonequilibrium Kondo impurity: perturbation about an exactly solvable point. *Physical Review B*, **57**, 2991–2999.

Manoharan, H.C., Lutz, C.P. and Eigler, D.M. (2000). Quantum mirages formed by coherent projection of electronic structure. *Nature*, **403**, 512–515.

Martinek, J., Utsumi, Y., Imamura, H., *et al*. (2003). Kondo effect in quantum dots coupled to ferromagnetic leads. *Physical Review Letters*, **91**, 127203.

Mattis, D.C. (1967). Symmetry of ground state in a dilute magnetic metal alloy. *Physical Review Letters*, **19**, 1478.

Matveev, K.A. (1995). Coulomb-blockade at almost perfect transmission. *Physical Review B*, **51**, 1743–1751.

Meir, Y. and Golub, A. (2002). Shot noise through a quantum dot in the Kondo regime. *Physical Review Letters*, **88**, 116802.

Meirav, U., Kastner, M.A. and Wind, S.J. (1990). Single-electron charging and periodic conductance resonance in GaAs Nanostructures. *Physical Review Letters*, **65**, 771–774.

Moore, J.E. and Wen, X.-G. (2000). Anomalous Magnetic Splitting of the Kondo Resonance. *Physical Review Letters*, **85**, 1722.

Nagaoka, K., Jamneala, T., Grobis, M. and Crommie, M.F. (2002). Temperature dependence of a single Kondo impurity. *Physical Review Letters*, **88**, 077205.

Neder, I., Heiblum, M., Levinson, Y., *et al*. (2006). Unexpected behavior in a two-path electron interferometer. *Physical Review Letters*, **96**, 016804.

Ng, T.K. and Lee, P.A. (1988). On-site Coulomb repulsion and resonant tunneling. *Physical Review Letters*, **61**, 1768–1771.

Nordlander, P., Pustilnik, M., Meir, Y., *et al*. (1999). How long does it take for the Kondo effect to develop? *Physical Review Letters*, **83**, 808–811.

Nozières, P. (1974). Fermi-liquid description of Kondo problem at low temperatures. *Journal of Low Temperature Physics*, **17**, 31–42.

Nozières, P. and Blandin, A. (1980). Kondo effect in real metals. *Journal de Physique*, **41**, 193–211.

Nygård, J., Cobden, D.H. and Lindelof, P.E. (2000). Kondo physics in carbon nanotubes. *Nature*, **408**, 342–346.

Odom, T.W., Huang, J.L., Cheung, C.L. and Lieber, C.M. (2000). Magnetic clusters on single-walled carbon nanotubes: the Kondo effect in a one-dimensional host. *Science*, **290**, 1549–1552.

Oreg, Y. and Goldhaber-Gordon, D. (2003). Two-channel Kondo effect in a modified single electron transistor. *Physical Review Letters*, **90**, 136602.

Paaske, J., Rosch, A., Wolfle, P., *et al*. (2006). Non-equilibrium singlet-triplet Kondo effect in carbon nanotubes. *Nature Physics*, **2**, 460–464.

Park, J., Pasupathy, A.N., Goldsmith, J.I., *et al*. (2002). Coulomb blockade and the Kondo effect in single-atom transistors. *Nature*, **417**, 722–725.

Pasupathy, A.N., Bialczak, R.C., Martinek, J., *et al*. (2004). The Kondo effect in the presence of ferromagnetism. *Science*, **306**, 86–89.

Pohjola, T., Boese, D., Schoeller, H., *et al*. (2000). Resonant tunneling through quantum dots. *Physica B*, **284**, 1762–1763.

Potok, R.M., Rau, I.G., Shtrikman, H., *et al*. (2007). Observation of two-channel Kondo effect, *Nature*, **446**, 167–171.

Pustilnik, M., Borda, L., Glazman, L.I. and von Delft, J. (2004). Quantum phase transition in a two-channel-Kondo quantum dot device. *Physical Review B*, **69**, 115316.

Pustilnik, M. and Glazman, L.I. (2000). Conduction through a quantum dot near a singlet-triplet transition. *Physical Review Letters*, **85**, 2993–2996.

Pustilnik, M. and Glazman, L.I. (2001). Kondo effect in real quantum dots. *Physical Review Letters*, **87**, 216601.

Pustilnik, M. and Glazman, L.I. (2004). Kondo effect in quantum dots. *Journal of Physics: Condensed Matter*, **16**, R513–R537.

Ralph, D.C. and Buhrman, R.A. (1994). Kondo-assisted and resonant-tunneling via a single charge trap – a realization of the Anderson model out of equilibrium. *Physical Review Letters*, **72**, 3401–3404.

Ralph, D.C., Ludwig, A.W.W., von Delft, J. and Buhrman, R.A. (1994). 2-channel Kondo scaling in conductance signals from 2-level tunneling systems. *Physical Review Letters*, **72**, 1064–1067.

Reed, M.A., Randall, J.N., Aggarwal, R.J., *et al*. (1988). Observation of discrete electronic states in a zero-dimensional semiconductor nanostructure. *Physical Review Letters*, **60**, 535–537.

Rejec, T. and Meir, Y. (2006). Magnetic impurity formation in quantum point contacts. *Nature*, **442**, 900.

Sarachik, M.P., Corenzwit, E. and Longinotti, L.D. (1964). Resistivity of Mo-Nb + Mo-Re alloys containing 1% Fe. *Physical Review*, **135**, A1041.

Sasaki, S., Amaha, S., Asakawa, N., *et al*. (2004). Enhanced Kondo effect via tuned orbital degeneracy in a spin 1/2 artificial atom. *Physical Review Letters*, **93**, 017205.

Sasaki, S., de Franceschi, S., Elzerman, J.M., *et al*. (2000). Kondo effect in an integer-spin quantum dot. *Nature*, **405**, 764–767.

Sato, M., Aikawa, H., Kobayashi, K., *et al*. (2005). Observation of the Fano-Kondo antiresonance in a quantum wire with a side-coupled quantum dot. *Physical Review Letters*, **95**, 066801.

Schiller, A. and Hershfield, S. (1995). Exactly solvable nonequilibrium Kondo problem. *Physical Review B*, **51**, 12896–12899.

Schmid, J., Weis, J., Eberl, K. and von Klitzing, K. (2000). Absence of odd-even parity behavior for Kondo resonances in quantum dots. *Physical Review Letters*, **84**, 5824–5827.

Schrieffer, J.R. and Wolff, P.A. (1966). Relation between Anderson and Kondo Hamiltonians. *Physical Review*, **149**, 491.

Sela, E., Oreg, Y., von Oppen, F. and Koch, J. (2006). Fractional shot noise in the Kondo regime. *Physical Review Letters*, **97**, 086601.

Sergueev, N., Sun, Q.F., Guo, H., *et al*. (2002). Spin-polarized transport through a quantum dot: Anderson model with on-site Coulomb repulsion. *Physical Review B*, **65**, 165303.

Simmel, F., Blick, R.H., Kotthaus, J.P., *et al*. (1999). Anomalous Kondo effect in a quantum dot at nonzero bias. *Physical Review Letters*, **83**, 804–807.

Simon, P. and Affleck, I. (2002). Finite-size effects in conductance measurements on quantum dots. *Physical Review Letters*, **89**, 206602.

Simon, P., Lopez, R. and Oreg, Y. (2005). Ruderman-Kittel-Kasuya-Yosida and magnetic-field interactions in coupled Kondo quantum dots. *Physical Review Letters*, **94**, 086602.

Sorensen, E.S. and Affleck, I. (1996). Scaling theory of the Kondo screening cloud. *Physical Review B*, **53**, 9153–9167.

Sprinzak, D., Ji, Y., Heiblum, M., *et al*. (2002). Charge distribution in a Kondo-correlated quantum dot. *Physical Review Letters*, **88**, 176805.

Stopa, M., van der Wiel, W.G., Franceschi, S.D., *et al*. (2003). Magnetically induced chessboard pattern in the conductance of a Kondo quantum dot. *Physical Review Letters*, **91**, 046601.

Sun, Q.F., Guo, H. and Lin, T.H. (2001). Excess Kondo resonance in a quantum dot device with normal and superconducting leads: the physics of Andreev-normal co-tunneling. *Physical Review Letters*, **87**, 176601.

Tarucha, S., Austing, D.G., Honda, T., *et al*. (1996). Shell filling and spin effects in a few electron quantum dot. *Physical Review Letters*, **77**, 3613–3616.

Tarucha, S., Austing, D.G., Tokura, Y., *et al*. (2000). Direct Coulomb and exchange interaction in artificial atoms. *Physical Review Letters*, **84**, 2485–2488.

Thimm, W.B., Kroha, J. and von Delft, J. (1999). Kondo box: a magnetic impurity in an ultrasmall metallic grain. *Physical Review Letters*, **82**, 2143–2146.

Újsághy, O., Kroha, J., Szunyogh, L. and Zawadowski, A. (2000). Theory of the Fano resonance in the STM tunneling density of states due to a single Kondo impurity. *Physical Review Letters*, **85**, 2557–2560.

Vavilov, M.G. and Glazman, L.I. (2005). Transport spectroscopy of Kondo quantum dots coupled by RKKY interaction. *Physical Review Letters*, **94**, 086805.

Wahl, P., Diekhoner, L., Schneider, M.A., *et al*. (2004). Kondo temperature of magnetic impurities at surfaces. *Physical Review Letters*, **93**, 176603.

Wan, Y., Phillips, P. and Li, Q.M. (1995). Suppression of the Kondo effect in quantum dots by even-odd asymmetry. *Physical Review B*, **51**, 14782–14785.

van Wees, B.J., Kouwenhoven, L.P., Harmans, C.J.P.M., *et al*. (1989). Observation of zero-dimensional states in a one-dimensional electron interferometer. *Physical Review Letters*, **62**, 2523–2526.

van der Wiel, W.G., de Franceschi, S., Fujisawa, T., *et al*. (2000). The Kondo effect in the unitary limit. *Science*, **289**, 2105–2108.

van der Wiel, W.G., de Franceschi, S., Elzerman, J.M., *et al*. (2002). Two-stage Kondo effect in a quantum dot at a high magnetic field. *Physical Review Letters*, **88**, 126803.

van der Wiel, W.G., de Franceschi, S., Elzerman, J.M., *et al*. (2003). Electron transport through double quantum dots. *Reviews of Modern Physics*, **75**, 1–22.

Wilhelm, U., Schmid, J., Weis, J. and von Klitzing, K. (2001). Two electrostatically coupled quantum dots as a realization of the Anderson impurity model. *Physica E: Low-Dimensional Systems and Nanostructures*, **9**, 625–630.

Wilhelm, U., Schmid, J., Weis, J. and von Klitzing, K. (2002). Experimental evidence for spinless Kondo effect in two electrostatically coupled quantum dot systems. *Physica E: Low-Dimensional Systems and Nanostructures*, **14**, 385–390.

Wilson, K.G. (1975). Renormalization group – critical phenomena and Kondo problem. *Reviews of Modern Physics*, **47**, 773–840.

Wingreen, N.S. and Meir, Y. (1994). Anderson model out of equilibrium – noncrossing-approximation approach to transport through a quantum-dot. *Physical Review B*, **49**, 11040–11052.

Wyatt, A.F.G. (1964). Anomalous densities of states in normal tantalum and niobium. *Physical Review Letters*, **13**, 401.

Yacoby, A., Heiblum, M., Mahalu, D. and Shtrikman, H. (1995). Coherence and phase-sensitive measurements in a quantum-dot. *Physical Review Letters*, **74**, 4047–4050.

Yoffe, A.D. (2001). Semiconductor quantum dots and related systems: electronic, optical, luminescence and related properties of low dimensional systems. *Advances in Physics*, **50**, 1–208.

Yosida, K. (1957). Anomalous electrical resistivity and magnetoresistance due to an S-D interaction in Cu-Mn alloys. *Physical Review*, **107**, 396–403.

Zhao, A.D., Li, Q.X., Chen, L., *et al*. (2005). Controlling the Kondo effect of an adsorbed magnetic ion through its chemical bonding. *Science*, **309**, 1542–1544.

Ferromagnetic Manganite Films

Vasily Moshnyaga and Konrad Samwer
Universität Göttingen, Göttingen, Germany

1 INTRODUCTION

As a starting point in the history of perovskite manganites one should note 1950 as the year in which Jonker and van Santen (1950) published the first paper on mixed valent manganites with perovskite structure and composition $La_{1-x}Ae_xMnO_3$ (Ae = Ca, Sr, Ba). They demonstrated for the first time the existence of positive or ferromagnetic (FM) exchange interaction between Mn^{3+} and Mn^{4+} ions in an oxide compound and found optimal compositions $x = 25–40\%$ to obtain maximum values of Curie temperatures, T_C, and magnetization close to saturation.

However, it has taken a long time up to the last decade of the twentieth century, when the discovery of the high-T_C superconductivity in perovskite cuprates (Bednorz and Müller, 1986) and related huge progress in oxide thin-film technologies have renewed a great interest in other oxide systems, including perovskite manganites. In 1993, the so-called colossal magnetoresistance (CMR) was discovered in thin manganite films (von Helmolt *et al*., 1993; Chahara, Ohno, Kasai and Kozono, 1993). The effect, quantified as difference between the resistance in zero (ambient) field, $R(0)$, and the resistance in applied field, $R(B)$, normalized to $R(B)$, that is, $CMR = 100\% \times \{[R(0) - R(B)]/R(B)\}$, can be extremely large: $CMR = 10^5–10^8\%$ (McCormack *et al*., 1994). This means that electrical resistance of a magnetic material can drop by few orders of magnitude by applying an external magnetic field $B \sim 5\,T$. The discovery of the CMR effect has initiated a boom both in fundamental and technological research in the nineties.

During the past few years, perovskite manganites examine the second renaissance, which is naturally connected with great progress in nanoscience and nanotechnology. It was observed experimentally (Uehara, Mori, Chen and Cheong, 1999) and also argued theoretically (Moreo, Yunoki and Dagotto, 1999) that the electronic properties of manganites may be spatially inhomogeneous. Metallic and insulating electronic phases can coexist within the same sample of a definite chemical composition over different length scales: from micrometer down to few nanometers. The mesoscopic, nanometer-scale, electronic inhomogeneities might be interesting for the future nanotechnology – self-organized nanostructures with different functionality may be created within a chemically homogeneous medium (Mathur and Littlewood, 2003). Closely connected to the preceding issue are nanostructured manganite films and manganite-based nanocomposites. Reduced dimensions of manganites as well as novel architecture and second-phase counterpartners in composites offer additional opportunity to control the magnetotransport. Therefore, thin manganite films and corresponding thin-film technologies become important also for fundamental research because they allow creation of some specific conditions, like negative pressure (Moshnyaga *et al*., 2003), which cannot be

Handbook of Magnetism and Advanced Magnetic Materials. Edited by Helmut Kronmüller and Stuart Parkin. Volume 5: *Spintronics and Magnetoelectronics*. ISBN: 978-0-470-02217-7.

realized in bulk samples and single crystals. In summary, immense and continuous research interest in the perovskite manganites is directly related to their complexity: they possess a number of crystallographic, electronic, and magnetic phases. These phases are not 'static', they can interact with each other as well as can be strongly influenced by external factors (temperature, pressure, magnetic field, electromagnetic radiation), yielding very interesting and potentially useful effects.

The chapter is organized in the following way. In Section 2, crystalline structure, the phase diagram, and phase transitions in perovskite manganites are discussed. Moreover, experimental evidences and theoretical ideas on the inhomogeneous electronic ground state in manganites are briefly overviewed. Special attention is paid to the lattice strain and disorder effects, which are important to understand the electronic properties of manganites. Section 3 is devoted to thin-film deposition techniques, mostly used for the preparation of multinary oxide films. Physical vapor deposition (PVD) techniques and chemical routes are compared. Moreover, the peculiarities of the structure and microstructure of manganese thin films as well as thin-film composites are reviewed. Section 4 is focused on the different magnetoresistance (MR) effects in individual manganese thin films, multilayers, and nanocomposites. CMR effect at the metal–insulator (MI) transition is discussed in relation to electronic phase separation (EPS) and percolation models. Artificially grown thin-film phase-separated systems containing second insulating phase is also discussed. Low-field MR effects in multilayers (tunneling magnetoresistance, TMR) as well as in individual epitaxial manganite films (domain–wall and anisotropic MR) may have potential for spintronics due to full spin polarization of charge carriers on the Fermi level in manganites.

2 FUNDAMENTAL ASPECTS

Since the discovery of CMR effect, the manganites are still in the focus of both fundamental and applied research. During this intense study, a few comprehensive reviews (Tokura, 2000; Coey, Viret and Molnar, 1999; Dagotto, Hotta and Moreo, 2001; Dagotto, 2003) have been published, where practically all aspects of crystalline and electronic structure as well as their relations to electronic properties and phase transitions were discussed in detail. Here, we limit ourselves to summarizing remarks on the preceding topics with a special focus on the lattice strain and cation disorder effects, which, in our opinion, are of great importance for understanding magnetotransport phenomena and different MR effects in thin manganite films.

2.1 Crystalline structure and lattice strain effects

As was revealed earlier (Jonker and van Santen, 1950), the most interesting manganites, which later were shown to possess CMR effect (von Helmolt *et al*., 1993; Chahara, Ohno, Kasai and Kozono, 1993), crystallize in ABO_3 perovskite–type structure as shown in Figure 1. The manganites can be described by the general chemical formula $Re_{1-x}Ae_xMnO_3$, where Re = La, Nd, Pr are rare-earth trivalent elements, and Ae = Ca, Sr, Ba are divalent alkali earth elements. Large three-(La) and divalent (Ca) cations, shown by green color, are located in the so-called *A-site* positions, which are 12-coordinated. The small Mn ions fill the B sites, coordinated by six oxygen atoms. The structure can be also viewed as a cubic close-packed array, formed by oxygen anions and A cations, in which Mn cations occupy octahedral interstitial sites.

A very important feature of the perovskite structure is the ability to accommodate lattice distortions by means of lowering the symmetry from the cubic one down to rhombohedral, orthorhombic, tetragonal, and monoclinic. Accommodation of lattice strain seems to be a driving force for the formation of different perovskite structural modifications with contrasting electronic behavior. There are two possible reasons for lattice distortions in the perovskite manganites. *First* is the Jahn–Teller (JT) effect (Jahn and Teller, 1937), which assumes the change of local symmetry at the Mn^{3+} ion of the isolated Mn^{3+} O_6 octahedron from cubic to tetragonal with elongation along z axis and compression in the (a, b) plane when a high spin state ($S = 2$) is realized. JT effect lifts orbital degeneracy and stabilizes electronic occupation of the lowest e_g orbital. The *second* source of lattice distortions is the size mismatch between the Re and Ae cations, occupying A-site positions. Perovskite

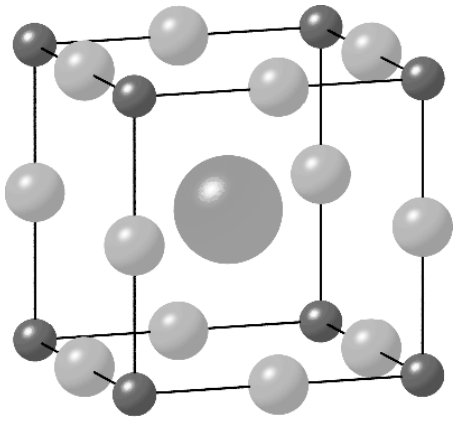

Figure 1. Fragment of perovskite structure: large Re, Ae (La, Ca) cations are shown by green color, small Mn cations (red) any oxygen anions (blue).

structure tries to expel the resulting internal or chemical pressure by corresponding cooperative rotations and tilting of MnO_6 octahedra, which form a 3D network according to orthorhombic or rhombohedral structures as shown in Figure 1.

Various perovskite structures are described by the tolerance factor, t:

$$t = (r_A + r_O)/\sqrt{2}(r_B + r_O) \tag{1}$$

where r_A and r_B are ionic radii of A and B cations, respectively, and r_O is the ionic radius of oxygen. Tolerance factor is a geometrical parameter, which quantifies the ionic size mismatch when A cation is too small to fit into the space between MnO_6 octahedra. In the cubic structure with perfect matching of (A–O) and (B–O) planes $t = 1$, which implies $r_A = r_O = 0.140\,\text{nm}$ and $r_B = (\sqrt{2} - 1)r_O = 0.058\,\text{nm}$ (Coey, Viret and Molnar, 1999). For the parent compound $LaMnO_3$ (LMO) with well-defined radius of A-site cation $r_{La} = 0.136\,\text{nm}$ and $r_{Mn^{3+}} = 0.0645\,\text{nm}$ (Shannon and Prewitt, 1976), one can get $t \approx 0.954$. This value is significantly smaller than $t = 1$ and is in accordance with observed O′-type orthorhombic structure (Urushibara *et al*., 1995). Prototypic optimally doped CMR compounds, such as $La_{0.7}$(Ca or Sr or Ba)$_{0.3}MnO_3$, which are of most interest in the present review, possess $t \approx 0.969$, $t \approx 0.979$, and $t \approx 0.997$, respectively. Thus, only the $La_{0.7}Ba_{0.3}MnO_3$ (LBMO) compound with the largest average radius of A-site cation, $\langle r_A \rangle = 0.1435\,\text{nm}$ shows the structure close to cubic. LSMO ($\langle r_A \rangle = 0.1384\,\text{nm}$) and LCMO ($\langle r_A \rangle = 0.1354\,\text{nm}$) manganites possess rhombohedral, *R-3c* (Urushibara *et al*., 1995), and orthorhombic, P_{nma} (Radaelli *et al*., 1995), structures, respectively.

A very important structural characteristic is the (Mn–O–Mn) bond angle, the value of which is close to 180° for the cubic as well as for rhombohedral structures. However, the bond angle for the orthorhombic structure becomes significantly smaller than 180° (Mitchel *et al*., 1996) and decreases continuously with decreasing tolerance factor in the region $0.89 < t < 0.96$ (Radaelli *et al*., 1997). The bond angle distortions provide a mechanism for the so-called *bandwidth control* (Hwang *et al*., 1995). It was shown that isovalent substitutions in the A-site positions, affecting both $\langle r_A \rangle$ and t values to a large extent, control the Curie temperature, T_C, and MI transition temperature, T_{MI}, in a broad range from 50 K for $t = 0.89$ up to 370 K ($t = 0.98$). Another possibility provided by the perovskite structures is the so-called *filling control*. As was shown already (Jonker and van Santen, 1950), the perovskite structure is extremely robust against chemical substitutions on the A-site positions, allowing to obtain a complete row of solid solutions like $La_{1-x}Ca_xMnO_3$ for $0 < x < 1$. Therefore, the doping by charge carriers (holes) through divalent substitutions in the A-site positions becomes available.

2.2 Phase transitions and phase diagram

Perovskite manganites, depending on their composition and structural modifications, show a rich variety of electronic phases such as metallic and insulating; ferromagnetic and antiferromagnetic; charge and orbitally ordered states. These phases interact with each other and can be strongly influenced by different external fields (temperature, magnetic field, pressure, etc.), resulting in a peculiar electronic transport and magnetic behavior.

Traditionally viewed, a parent stoichiometric compound LMO with $t = 0.954$ and orthorhombic P_{nma} structure is well known as *A-type antiferromagnet* with a Neel temperature $T_N = 140\,\text{K}$ (Wollan and Kohler 1955). The spins of Mn ions are ordered ferromagnetically within the (a, b) plane along the a axis. The sublattice moment, $3.87\,\mu_B$, is close to the spin-only contribution of the Mn ions. However, adjacent planes are ordered antiferromagnetically, yielding zero or very weak total moment. Moreover, LMO shows insulating behavior because of the localized electrons on the lowest occupied e_g orbitals of the Mn^{3+} ions due to the JT distortions of the MnO_6 octahedron. The insulating gap $E_{JT} \sim 0.25\,\text{eV}$ (Dessau and Shen, 2000) is provided by JT splitting of previously orbitally degenerated e_g states. JT distortions in LMO are coherent, that is, long and short (Mn–O) bonds alternate in a 'checkerboard' pattern leading to the so-called "cooperative JT distortion" or "orbital ordering" (OO). The OO state is characterized by ordering of the lowest occupied $3z^2 - r^2$ in a real space as shown in Figure 2 (Ishihara, Inoue and Maekawa, 1997). As was first argued by Goodenough (1955), the reason for OO is minimization of elastic strain originated due to different lengths of Mn–O bonds. The OO state becomes energetically favorable for $T_{ST} \leq 873\,\text{K}$, at which a transition from the high-temperature rhombohedral phase to the low-temperature orthorhombic phase occurs (Wold and Arnott, 1959). Note that OO phase transition takes place at much higher temperature than antiferromagnetic Neel temperature, $T_N = 140\,\text{K}$.

As we have mentioned in the preceding text, the filling control occurs by means of hole doping when a part of La cations are substituted with Ca, Sr, or Ba, forming a compound like $La_{1-x}Ca_xMnO_3$. This is equivalent to the creation of xMn^{4+} ions with $3d^3$ configuration and one hole on their e_g orbital, which can take part in charge transfer. The Mn^{4+} ion is not a JT ion in contrast to that of Mn^{3+} and can be viewed as a perturbation of the long-range OO state in LMO matrix. By increasing the doping level 'x', the OO state

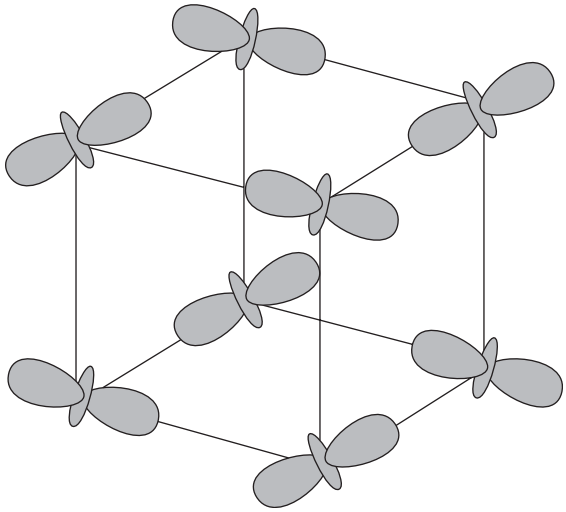

Figure 2. Ordering of $3z^2$-r^2 orbitals in $LaMnO_3$. (Reproduced from S. Ishihara *et al*., 1997, with permission from the American Physical Society. © 1997.)

will be progressively diluted and e_g holes become mobile (itinerant) dominating the charge transport by means of hopping between different Mn sites. Itinerancy of e_g electrons (holes), or strictly speaking, one-electron bandwidth, W, is provided by covalent mixing of e_g orbitals of Mn and those of 2p of oxygen (Goodenough, 1955). Another part of 3d electrons occupying the orbital triplet t_{2g} states stabilized by crystal-field splitting is localized, forming the local spin ($S = 3/2$) and being responsible for magnetic properties. Thus, the covalent character of Mn–O bonds as well as strong on-site Hund coupling between conducting e_g electrons with spin $S = 1/2$ and those of $t_{2g}(S = 3/2)$ both lead to the long-range FM ordering between Mn^{3+} and Mn^{4+} ions via the so-called *double exchange* (*DE*) interaction (Zener, 1951; Anderson and Hasegawa, 1955; de Gennes, 1960). In the framework of tight-binding approximation, the following expression for the spin-dependent hopping resonance integral d_{ij} was obtained (Anderson and Hasegawa, 1955):

$$d_{ij} \approx \varepsilon_\sigma \lambda_\sigma^2 \cos\theta \cos(\varphi/2) \tag{2}$$

where ε_σ is a one-electron energy, λ_σ is the covalent-mixing parameter between e_g orbitals of Mn ions and σ-bonding oxygen p orbitals, $(180^\circ - \theta)$ is the O–Mn–O bond angle, and φ is the angle between the spins of adjacent Mn^{3+} and Mn^{4+} ions. In this formalism, the hopping probability, or in other words bandwidth W, can be increased (the carriers become more itinerant) (i) by decreasing angle θ down to 0, that is, increasing the tolerance factor t up to 1; (ii) by applying external hydrostatic pressure, which increases covalent-mixing parameter λ_σ, that is, reduces Mn–O bond length; and (iii) by means of long-range magnetic ordering for $T < T_C$, which aligns adjacent Mn spins parallel to each other and thus reduces angle φ down to 0. The phase diagram for prototypic $La_{1-x}Ca_xMnO_3$ (Schiffer, Ramirez, Bao and Cheong, 1995), shown in Figure 3, demonstrates complex behavior of different electronic and magnetic phases as a function of doping level, x. Low-doped LMO, being an antiferromagnetic insulator (AFI), transforms into a canted antiferromagnet (CA) for $0 < x < 0.07$, and then to a ferromagnetic insulator (FI) for $0.1 < x < 0.15$. Insulator-to-metal transition occurs at $x = 0.175$ and further for $0.2 < x < 0.45$ ferromagnetic metallic (FMM) phase becomes stable below Curie temperatures, $T_C \approx 170$–250 K. The optimal doping level is found to be around $x = 0.33$, thus yielding maximal $T_C \approx 250$–270 K. With further increasing of Ca doping $0.45 < x < 0.87$ a *charge ordered insulating* (COI) phase appears for $100 < T < 250$ K, which transforms into an AFI at low temperatures. The COI phase first observed by Chen and Cheong for LCMO with $x = 0.5$ (Chen and Cheong, 1996) represents itself the ordering of Mn^{3+} and Mn^{4+} ions in real space in the form of Mn^{3+}/Mn^{4+} stripes with corresponding OO. Therefore, in spite of increased charge density ($x \sim 0.5$), charges are localized within these stripes owing to cooperative JT effect, which is manifested by superstructural ordering of Mn^{3+} O_6 and Mn^{4+} O_6 octahedra as reflected by electron diffraction. The end member of the family, $CaMnO_3$, shows AFI phase of G-type, in which the spin of each Mn^{4+} ion is ordered antiparallel to its six nearest neighbors owing to the antiferromagnetic superexchange Mn–O–Mn interaction (Goodenough, 1955).

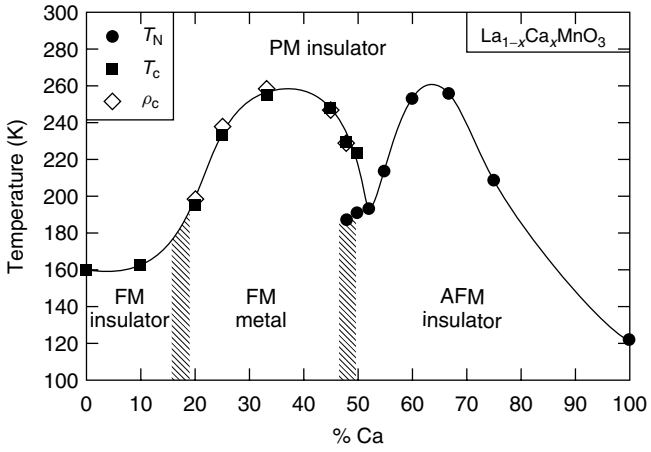

Figure 3. Phase diagram for $La_{1-x}Ca_xMnO_3$. FM: ferromagnetic metal; FI: ferromagnetic insulator; CAF: canted antiferromagnetic; AF: antiferromagnetic insulator; CO: charge ordered insulator. (Reproduced from P. Schiffer *et al*., 1995, with permission from the American Physical Society. © 1995.)

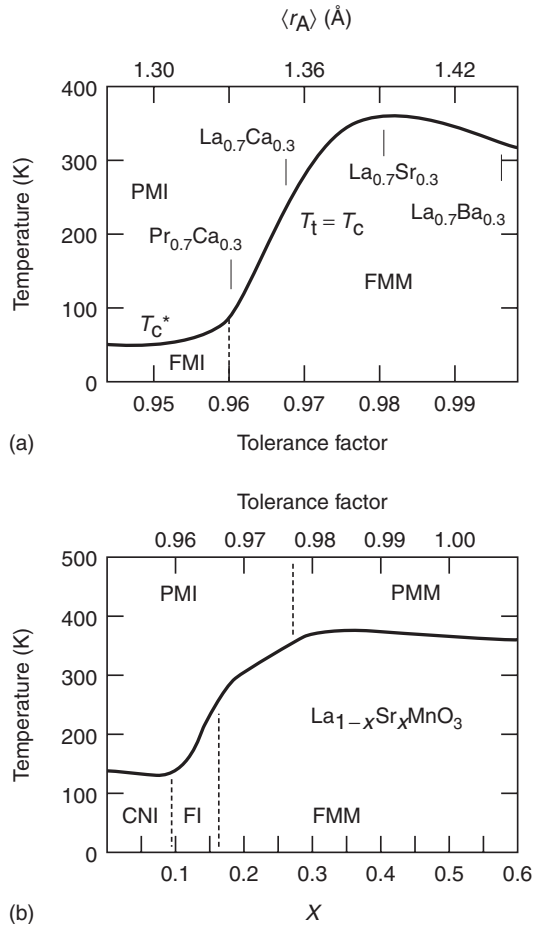

Figure 4. Phase diagram for isovalent substituted manganites $Ln_{0.7}Ae_{0.3}MnO_3$ (Ln = La, Pr; and A = Ca, Sr, Ba) (a) and for $La_{1-x}Sr_xMnO_3$. (Reproduced from W. Archibald *et al*., 1996, with permission from the American Physical Society. © 1996.)

Another phase diagram with data from Hwang *et al*. (1995) and Urushibara *et al*. (1995) is shown in Figure 4 in the form adopted from Archibald, Zhou and Goodenough (1996). It illustrates the influence of lattice effects or internal chemical pressure, quantified by the tolerance factor, t, and average A-site cation radius, $\langle r_A \rangle$. Modification of internal lattice strain can be achieved either by isovalent substitutions on the A site for $Ln_{0.7}Ae_{0.3}MnO_3$ system (see Figure 4a), while keeping doping level constant, or by changing doping level as well, as exemplified for canonic DE system $La_{1-x}Sr_xMnO_3$ (Figure 4b). Maximal Curie temperature, $T_C = 360$ K, and the strongest DE were reported for $La_{0.7}Sr_{0.3}MnO_3$ with $t = 0.98$. Remarkably, LBMO with the largest value $\langle r_A \rangle = 0.1435$ nm and practically cubic structure ($t = 0.998$) has a lower $T_C = 320$ K in disagreement with the DE model. A similar $T_C - \langle r_A \rangle$ phase diagram was reported in Hwang, Palstra, Cheong and Battlog (1995), where the lattice strain was additionally increased by hydrostatic pressure for the same manganites as in Figure 4(b). T_C increases with hydrostatic pressure in accordance with DE predictions. Remarkably, the strongest changes of T_C occurs for $0.96 < t < 0.98$, that is, for the LCMO system, in which the DE contribution is weakened compared to that in LSMO. A competing electron-lattice (EL) interaction (Millis, Littlewood and Shraiman, 1995) due to the JT effect becomes dominant in manganites with small values of $\langle r_A \rangle$, that is, for $t < 0.96$, which show distorted perovskite structure. For example, $Pr_{0.7}Ca_{0.3}MnO_3$ (PCMO) with $t = 0.95$ is no more ferromagnetic, instead a *COI* state becomes stable for $T < T_{CO} \sim 240$ K and transforms into an AFI state at lower temperatures. Thus, the tolerance factor may be viewed as a structural parameter, which reflects a relative strength of the DE and EL interactions (Hwang *et al*., 1995). Perovskite manganites are classified with respect to their bandwidth, W, as *large bandwidth* materials, which are definitely LSMO and LBMO with $t \sim 1$ and DE < EL; *middle bandwidth* (LCMO) $t = 0.97$ and DE ∼ EL; and *small bandwidth* (PCMO) $t = 0.95$ and EL > DE.

2.3 Cation disorder

As we have seen in the previous paragraph, both *bandwidth* and *filling* control are carried out by chemical substitutions on the A sites in the perovskite lattice with corresponding changes of the average ionic radius of the A-site cation, $\langle r_A \rangle$, and the tolerance factor, t. This inevitably leads, in most cases, to the A-site *cation disorde*r because of the different ionic radius of A-site cations.

Rodriguez-Martinez and Attfield (1996) have quantified the disorder in terms of the variance of ionic radii $\sigma^2 = \sum y_i r_i^2 - \langle r_A \rangle^2$ about the mean $\langle r_a \rangle$ (y_i is the fractional occupancy, $\sum y_i = 1$). They performed a systematic study of bulk compounds $R_{0.7}M_{0.3}MnO_3$ (R = La-Sm; and M = Ca, Sr, and Ba) with the same $\langle r_a \rangle = 0.123$ nm but different values of disorder, $\sigma^2 = 0.001 - 0.024$. Surprisingly, they found that Curie temperature, T_C, decreases linearly with increasing σ^2, as shown in Figure 5, from 363 down to 60 K. The samples with very large disorder, $\sigma^2 > 0.015$ Å^2, seem to be not more microscopically homogeneous due to possible segregation of A-site cations, although they look single phased in X-ray powder diffraction. These samples show electronically inhomogeneous behavior, indicated by two maxima on the R(T) curves, and by disparity between T_C and T_{MI} for $\sigma^2 = 0.024$ Å^2. A mixture of antiferromagnetic and ferromagnetic regions for $T > T_C$ was also suggested for 'disordered' samples, based on the observed deviation of the inverse magnetization from the classical Curie–Weiss behavior.

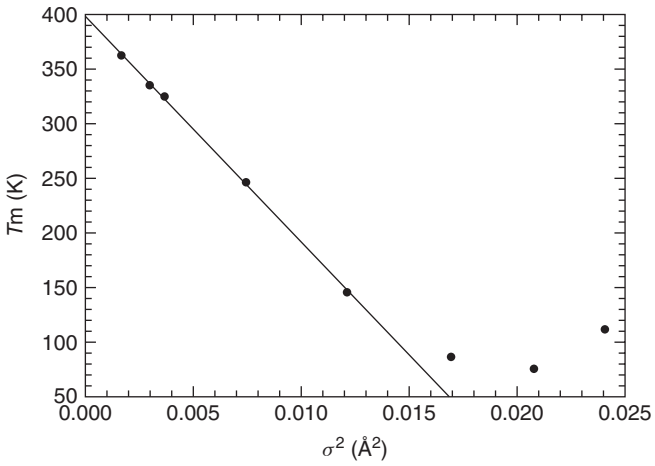

Figure 5. Decrease of the Curie temperature by increasing of the disorder. (Reproduced from L.M. Rodriguez-Martinez *et al*., 1996, with permission from the American Physical Society. © 1996.)

The disorder-induced reduction of T_C was assigned to the size mismatch–induced strain fields with corresponding JT distortions of the MnO_6 octahedra, resulting from oxygen displacements, and shown to obey the following form:

$$T_m = T_m(0) - pQ^2 \tag{3}$$

Here, $T_m(0)$ is the transition temperature for an ideal cubic ($t = 1$) manganite with $r_A{}^0 \approx 1.4$ nm and without cation disorder, $\sigma^2 = 0$. The strain term is proportional to anion displacements $Q = \sigma$ (p is force constant), which are random due to A-site disorder, or can be ordered due to changing of average A-site radius: $Q_0 = r_A{}^0 - \langle r_A \rangle$. The important conclusion was that for relatively small average ionic radii $\langle r_A \rangle < 0.122$ nm the A-site disorder is small and a true variation of T_C with tolerance factor, as shown in Figure 4, can be observed. For large $\langle r_A \rangle >$ 0.123 nm (Ba doping) the A-site disorder dominates, yielding to almost no dependence of T_C on $\langle r_A \rangle$ (see Figure 4). Thus, the A-site disorder seems to be responsible for the lowering of the Curie temperature for LBMO ($T_C = 320$ K), which despite the optimal large $\langle r_a \rangle$ reveals a very large disorder, $\sigma^2 = 0.0131$ Å^2. In comparison, the LSMO with small disorder, $\sigma^2 = 0.0018$ Å^2, shows $T_C = 370$ K. Another important result of Rodriguez-Martinez and Attfield (1996) is that so-called *ideal cubic manganite* without disorder, $\sigma^2 = 0$, would show the highest $T_{MI} \approx 530$ K. The calculations based on the DE model alone give $T_{MI} = 2500$–5000 K (Millis, Littlewood and Shraiman, 1995), whereas those considering the JT distortions of MnO_6 octahedra result in a more realistic value ~500 K (Millis, Littlewood and Shraiman, 1995; Roder, Zang and Bishop, 1996), similar to the estimated T_{MI} without disorder.

The A-site disorder seems to play a key role in the CMR effect. Well-known small bandwidth $Pr_{1-x}Ca_xMnO_3$ (PCMO) has a very small size variance, $\sigma^2 < 10^{-4}$ Å^2, because of close matching of the ionic radii of Pr^{3+} and Ca^{2+}. Remarkably, $Pr_{0.75}Ca_{0.20}Sr_{0.05}MnO_3$ (additional Sr doping is necessary to obtain an insulator-to-metal transition) also with small disorder $\sigma^2 = 1.3 \times 10^{-3}$ Å^2 demonstrates extremely large value of CMR = 10^8% for $T = 85$ K (Raveau, Maignan and Caignaert, 1995). In contrast, other small bandwidth manganites with similar $\langle r_a \rangle$ and T_{MI}, for example, $La_{0.6}Ca_{0.3}Y_{0.1}MnO_3$, but with larger disorder, $\sigma^2 = 2.5 \times 10^{-3}$ Å^2 show only CMR = 4×10^3% at $T = 120$ K (Maignan, Simon, Caignaert and Raveau, 1996).

Recently, the A-site ordered configuration was reported for the so-called *half-doped* manganites, $Ln_1Ba_1Mn_2O_6$ (Arima *et al*., 2002; Akahoshi *et al*., 2003). Owing to specific composition (ratio La/Ba = 1), they form a layered structure, in which both size and charge mismatch can result in A-site ordering. The microstructure of the ordered half-doped manganites, visualized by high-resolution transmission electron microscopy (TEM) and shown in Figure 6, contain the LnO and BaO layers alternately stacked along the c axis with intervening MnO_2 sheets, which thus suffer from no random Coulomb potential. Such an ordering for Ln = Y with small $\langle r_A \rangle = 1.18$ Å was found to stabilize long-range charge/orbital ordered (COO) insulating phase at high temperatures up to $T_{CO} = 500$ K. In contrast, in the disordered LnBMO a random distribution of the Ln and Ba cations between the A positions generates a random Coulomb potential and/or local strain in the MnO_2 sheets. This leads to the collapse of long-range COO insulating phase due to Mn^{3+}/Mn^{4+} frustrations, yielding a spin-glass (SG) state at low temperatures. Remarkably, as shown for disordered $Eu_{0.5}Ba_{0.5}MnO_3$ (Mattheu *et al*., 2004), such an SG state can be responsible for a pronounced CMR effect. Thus, the size mismatch as well as different charge of the constituting A-site cations may strongly influence the phases and the magnetotransport properties in manganites, depending on whether A-site disordered or ordered structure is realized.

2.4 Electronic inhomogeneity of manganites

As we have seen in the previous sections, the spin, charge, and lattice degrees of freedoms compete with one another leading to complex phase diagram of perovskite manganites. However, the complexity of manganites can be even higher – a lot of experimental results (Urushibara *et al*., 1995; Hennion *et al*., 1998; Allodi, De Renzi and Guidi,

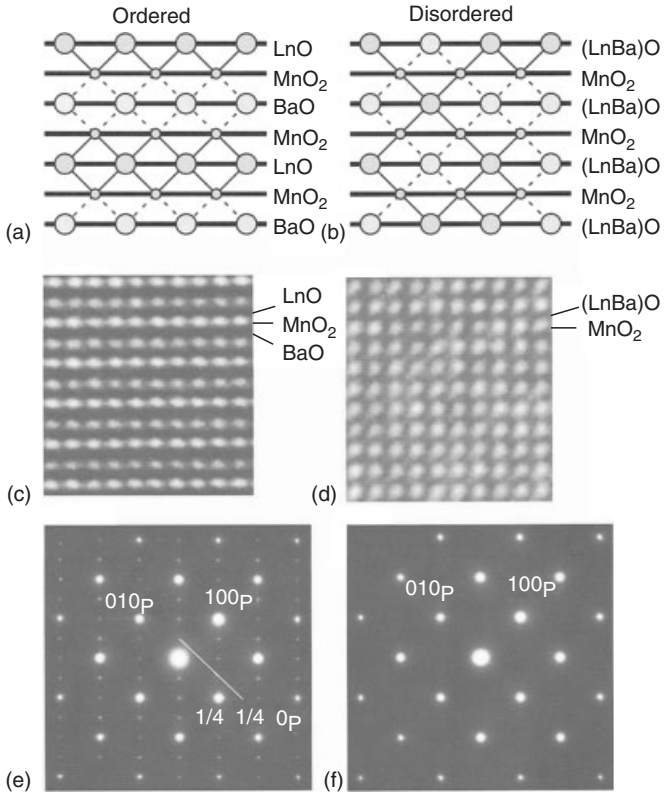

Figure 6. Schematic structure of ordered (a, c, e) and disordered (b, d, f) half-doped manganites $Ln_{0.5}Ba_{0.5}MnO_3$. (Reproduced from D. Akahoshi *et al*., 2003, with permission from the American Physical Society. © 2003.)

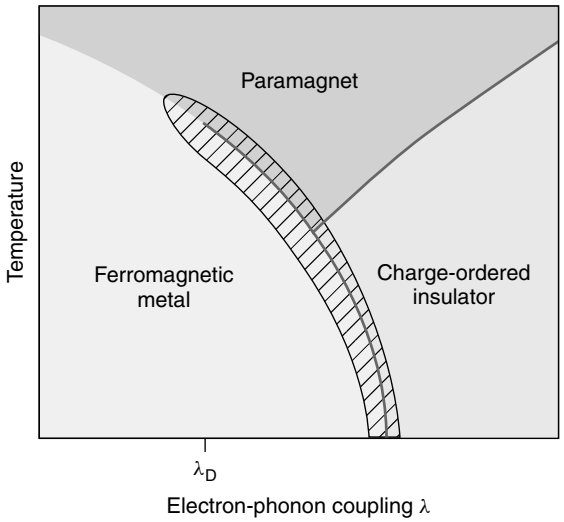

Figure 7. Generic phase diagram as a function of electron-phonon coupling. (Reproduced from N. Mathur *et al*., 2003, with permission from the American Institute of Physics. © 2003.)

1998; de Teresa *et al*., 1997; Linn *et al*., 1996; Fernandez-Baca *et al*., 1998; Mori, Chen and Cheong, 1998) as well as theoretical computational models (Moreo, Yunoki and Dagotto, 1999; Dagotto, Hotta and Moreo, 2001; Moreo *et al*., 2000; Burgy *et al*., 2001; Ahn, Lookman and Bishop, 2004) evidence the coexistence of mixed electronic phases or *electronic inhomogeneity*. In the literature one can also find a term *electronic phase separation* (*EPS*). Actually, a pronounced tendency to EPS has been usually observed for the intermediate (LCMO) and small bandwidth (PCMO) manganites in which FM–DE interaction is weakened in comparison with competing COO. Moreover, for these manganites, the phase transition from para- to ferromagnetic phase was found to be of the first order. In contrast, canonical DE compounds like LSMO and LBMO with second-order phase transition for $T_C = 320–360\,K$ and no signatures for COO (no static JT effect) show no EPS to the best of our knowledge. Thus, it was supposed that electronic inhomogeneity is intimately related to the first-order phase transition whatever the phase coordinate such as temperature, doping level, magnetic field, or hydrostatic pressure is considered. The parameter controlling the EPS tendency seems to be electron-phonon coupling, λ, as summarized in generic phase diagram in Figure 7 (from Mathur and Littlewood, 2003). For $\lambda < \lambda_0$, the lattice effects are small and FM–PM transition is continuous or of the second order; one finds no reasons for mixed phases. There is a critical value λ_0, exceeding of which the transition becomes discontinuous (first order) with discontinuous jump in order parameter and latent heat. Thus, mixed electronic phases were assumed to appear in the vicinity of FM/paramagnetic (PM) or FM/COI phase boundaries as illustrated by the hatched area in Figure 7. Equilibrium coexistence of thermodynamically stable phases at the first-order phase transition is well known to occur owing to disorder or imposed conservation law (Mathur and Littlewood, 2001). The peculiarity of manganites is the quite large scale, compared to the lattice parameter, of the phase coexistence, which can vary from tens to hundreds of nanometers, as well as its sensitivity to quite small external forces.

One of the first direct experimental observations of remarkable electronically inhomogeneous state was the TEM study in LCMO with $x \approx 0.5$ (Mori, Chen and Cheong, 1998), that is, at the border between the FMM/AF-COI phases (see Figure 3). Note that such coexistence contradicts the DE model because charge localization (precursor state to charge ordering) assumes exclusively an AF insulating but not an FMM state. The latter one requires delocalization (hopping) of charge carriers. However, these phases were indeed observed as a mixture between incommensurate charge ordered (CO) and ferromagnetic metallic (FM) charge disordered clusters with a size of 20–30 nm. CO domains consist of paired and unpaired JT distorted Mn^{3+} stripes.

A phase separation (PS) on a much larger submicrometer scale was observed by Uehara, Mori, Chen and Cheong (1999) for $La_{0.625-y}Pr_yCa_{0.325}MnO_3$ system ($y = 0.25–0.4$), in which a CO state is stable for $T < T_{CO} = 210\,K$. The CO AF- and charge-disordered FM domains with characteristic sizes of about 0.3–0.5 μm were revealed by electron microscopy at $T = 17\,K$ in the macroscopically FM state.

A useful local probe technique, scanning tunneling spectroscopy (STS), combined with scanning tunneling microscopy (STM), allows one to study tunneling conductivity, σ, at the surfaces of thin films and single crystals for ultrahigh vacuum conditions. In such experiments, the change of local σ can be observed as a function of temperature as well as magnetic field. We will consider STS/STM observations for thin films in detail in Section 4.

Another group of experiments provide indirect evidences for PS in manganites related to macroscopic effects observed close and far away from phase boundaries in Figure 3. For example, a small angle neutron scattering (SANS) (Hennion *et al*., 1998) and magnetic resonance experiments (Allodi, De Renzi and Guidi, 1998) reported on the FM/AF coexistence in $La_{1-x}Ca_xMnO_3$ bulk samples for $x = 0.05$, 0.08, that is, far away from the MI phase boundary, $x = 0.175$. de Teresa *et al*. (1997) have found short-range FM correlations in LCMO with optimal doping, $x = 0.33$, in the form of small magnetic clusters or *magnetic polarons* with diameter ∼1.2 nm, which exist in the macroscopically PM state for $T > T_C$. Moreover, FM–PM transition according to SANS (Linn *et al*., 1996; Fernandez-Baca *et al*., 1998) has an unconventional character, that is, in contrast to conventional ferromagnet the spin-wave excitations decrease as the temperature approaches T_C from below but a new contribution due to quasielastic spin diffusion grows and then dominates at the transition region. Thus, a two-phase model, FMM with well-defined spectrum of spin waves and PM insulating (spin diffusion), was proposed (Linn *et al*., 1996), in which the fractions of two phases depend on the temperature.

After first experimental observations, some new theoretical computational models appeared, which account for the competition between FM and atomic force microscopy (AFM) phases in the presence of electronic density fluctuations, chemical disorder, and very recently, lattice strain. Within EPS scenario (Moreo, Yunoki and Dagotto, 1999), it was assumed that the observed inhomogeneities are due to different hole densities in competing FM and AFM phases (Figure 2). However, mesoscopic scale coexistence (Uehara, Mori, Chen and Cheong, 1999; Mori, Chen and Cheong, 1998) of electrically charged domains is energetically unfavorable due to a drastic increase of the Coulomb energy. Another model, disorder-induced PS, was also proposed by the Dagotto's group (Dagotto, Hotta and Moreo, 2001; Moreo *et al*., 2000; Burgy *et al*., 2001) to avoid the problems related to Coulomb energy. The model focuses on the first-order transition, for example, FMM/AFI insulator at $x \sim 0.5$, in the presence of A-site cation disorder discussed in the preceding text. Such a transition without disorder is characterized by a discontinuous jump of the order parameter and latent heat over the phase boundary. The stable ground state is then essentially metallic or insulating depending on the location on the phase diagram. Moreo *et al*. (2000) have shown by means of Monte Carlo simulations within 'one'- and 'two'-orbital models that cation disorder, resulting in random distribution of hopping probabilities and exchange interactions, generates mixed phases with coexisting FM and AF domains in the vicinity of the phase transition, which now becomes continuous or percolative. Qualitatively, a phase-separated state can be stable due to two competing opposite tendencies. Firstly, the increase of the interface energy in coexisting FM and AF domains makes PS energetically unfavorable, thus tending to increase the domain size. Secondly, the disorder tends to minimize the size of domains down to the lattice spacing, at which the system can be either the FM or AF according to disorder, fluctuating over the FM/AF phase boundary. As a result, an equilibrium size of PS domains is stabilized. Note that the hole density, for instance, $x \sim 0.5$, is constant and no limitations from the Coulomb energy on the size of competing clusters arise. Thus, even micrometer cluster sizes become possible. Another interesting feature is that the larger the disorder, the smaller the competing AF and FM domains. This seems to be important for understanding the CMR results on Pr-based compounds with small disorder, which assume that very large CMR is compatible with a large size of AF and FM domains.

A recent model (Ahn, Lookman and Bishop, 2004) assumes that strain, instead of electron density or disorder, is a driving force of the PS. The basic assumptions of the new model are (i) without strain (undistorted state) the system is metallic and under strain (distorted state) it is insulating and (ii) there exist coupled short- and long-wavelength lattice distortions of the JT type, which modify elastic energy of the system yielding local (undistorted) and global (distorted) energy minima. Such a 'structural template' governs the formation and topology of the coexisting mixed phases.

3 THIN MANGANITE FILMS

Usually, the preparation of thin films and study of their structure and physical properties are believed to be the topics of applied research. This is mainly because films due to their planar geometry can be easily integrated into different electronic devices. However, as for manganites and likely for other complex oxides, the thin-film aspects become

interesting not only with respect to potential applications, which sometimes even look quite illusive now, but rather for fundamental research. First, because of extreme chemical and structural complexity, even single crystals are not perfect – owing to macroscopic structural defects like twinning and mosaic blocks (Eremenko *et al*., 2001) and corresponding mechanical stress, their electrical and magnetic properties can be far from ideal. Stress-free epitaxial thin films look very attractive because at least along the growth direction due to reduced size their structure is quite perfect. Even more interestingly, thin films with their reduced dimensionality down to nanometer scale provide new boundary conditions and new effects, which cannot be obtained in single crystals. The new branches of fundamental research, nanoscience and nanotechnology, are definitely based on thin-film aspects. Thus, oxide thin-film growth techniques as well as understanding of the processes of film growth become very important.

3.1 Preparation techniques

It is widely accepted that all known oxide thin-film techniques can be subdivided into two large classes: (i) PVD and (ii) chemical deposition techniques. PVD can be realized as a co-evaporation process, that is, when different metals condense on a substrate under ultrahigh vacuum (usually within *molecular-beam epitaxy* technique) with subsequent or simultaneous oxidation. Another possibility is material transfer from the preliminary synthesized target to the substrate realized by means of laser ablation, *pulsed-laser deposition* (*PLD*) or by *magnetron sputtering* techniques. In the following text, we will discuss PLD, because this is a technique that is mostly used for the preparation of complex oxide thin films.

Chemical deposition techniques imply that the desired oxide compound grows as a result of a chemical reaction between the *precursor* compounds (metal-halogenides or metal-organics), that is, chemicals with required metal atoms, bound to a ligand group, containing oxygen, carbon, and hydrogen, usually. The precursors can react being in vapor phase or in a solid phase. The former is the so-called *chemical vapor deposition* (*CVD*), one of which modifications *metalorganic chemical vapor deposition technique* (MOCVD) is a basic industrial technique for the preparation of $A^{III}B^{V}$ semiconductors. The techniques with precursors reacting in solid phase are called *chemical decomposition* routes; they are compatible with spin and deep coating techniques as well as with spray pyrolysis technique. In Section 3.1.2, a chemical deposition route, for example, *metalorganic aerosol deposition* (MAD), combining the principles of MOCVD and technical arrangement of spray pyrolysis, will be discussed in detail.

3.1.1 Pulsed-laser deposition

In Figure 8, a schematic diagram of a typical PLD set up is shown (Krebs *et al*., 2003). Short (few nanoseconds) pulses of high-energy laser radiation (usually KrF laser with wavelength $\lambda = 248$ nm) are focused on the surface of a target, yielding to rapid heating or superheating of all constituting elements up to their evaporation temperature. The removal of the material from the target occurs by means of an explosion mechanism with the resulting plume containing the ions, atomic aggregates as well as liquid droplets. In contrast to thermal evaporation, which yields a vapor composition in accordance with equilibrium vapor pressures of the target elements, the laser-induced expulsion produces a plume of material with stoichiometry similar to the target. This is a decisive advantage of PLD in obtaining complex oxides, containing elements with significantly different evaporation temperatures. Despite the quite clear operation setup, preparation of films by PLD seems to be very complex phenomenon, including different stages such as interaction of laser beam with the target, dynamics of ablated materials, deposition of ablated materials on the substrate, and finally nucleation and growth of a thin film. These processes as well as recently developed modifications of PLD were discussed in detail in the literature (Venkatesan, 1994; Willmott, 2004). Here we note only that stimulated by the discovery of high-T_C superconductivity, PLD technique has been succeeded with Y–Ba–Cu–O films in Dijkkamp *et al*. (1987). The main further developments include the 'off-axis' variant (Holzapfel *et al*., 1992), which has essentially solved the problem of droplets, and later the 'molecular-beam' PLD (DeLeon *et al*., 1998) with realization of controllable layer-by-layer (LL) growth. Thus, PLD has become a basic technique for the preparation of multicomponent oxide films as well as oxide multilayers and superlattices

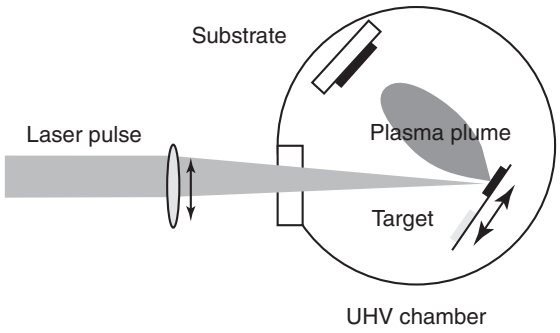

Figure 8. Schematic diagram of a typical PLD setup. (Reproduced from H.-U. Krebs *et al*., 2003, with permission from Springer-Verlag GmbH. © 2003.)

of different functionality. As was already emphasized, first manganite films, showing pronounced CMR effect (von Helmolt *et al*., 1993; Chahara, Ohno, Kasai and Kozono, 1993; McCormack, *et al*., 1994), were also obtained by PLD.

With respect to the growth of high temperature superconductivity (HTSC) as well as of manganite oxide thin films, the oxygen deficiency still remains a problem for PLD or for other PVD techniques using vacuum. As was shown in many papers, the film structure and magnetotransport properties of manganite films are very sensitive to oxygen deficiency, which may result due to insufficient oxygen partial pressure (usually 1 mbar) during deposition. Preparation of oxide films at higher oxygen partial pressures within a vacuum technique seems to be quite sophisticated. In this sense, *chemical deposition* routes compatible with up to 1 bar oxygen pressure look more appropriate.

3.1.2 Metalorganic aerosol deposition (MAD)

Thin manganite films can be grown by means of unconventional MAD technique (Moshnyaga *et al*., 1999). MAD is a chemical route, originally developed for the preparation of HTSC $YBa_2Cu_3O_{7-x}$ films (Khoroshun *et al*., 1990) and also used for other oxide films of different functionality (Ivashchenco *et al*., 1995; Kuliuk *et al*., 1995; Moshnyaga *et al*., 1997). Similar to other chemical deposition techniques (CVD, MOCVD) to obtain an oxide film within MAD, one should be able to carry out the following pyrolysis reaction:

$$\mathrm{Me(C_3H_5O_2)}_x + \mathrm{O_2} \xrightarrow{T\,^\circ\mathrm{C}} \mathrm{MeO}_{x/2} + y\mathrm{CO_2}\uparrow + z\mathrm{H_2O}\uparrow \tag{4}$$

Here, $\mathrm{Me(C_3H_5O_2)}_x$ is an organometallic precursor, Me(acetylacetonate) (Me = La, Ca, or Mn), which decomposes under heating or electron beam or UV radiation with the formation of a metal oxide compound in an oxygen containing media. Two types of chemical reactions are important for applications: (i) *homogeneous* pyrolysis, which occurs in a gas phase, is used for the preparation of oxide nanoparticles (Konrad *et al*., 1999) and (ii) *heterogeneous* pyrolysis, which takes place at the interface between gas and a solid, is suitable for growth of thin films. CVD and MOCVD techniques require volatile precursors, large quantities of which can be congruently vaporized at relatively low temperatures (20–100 °C). Sol–gel and spray pyrolysis both use the nonvolatile precursors, which react being in solid state. The MAD technique uses *β-diketonates* of metal chelates as precursors, which have low decomposition temperature $\sim$ 250–300 °C and usually low volatility or even are thought to be nonvolatile (precursors for rare-earth elements). Very fine droplets (aerosols) of a few micrometer sizes allow one to perform the so-called *flash* or fast evaporation (Wahl, Stadel, Gorbenko and Kaul, 2000), which is advantageous for precursors with low volatility. The decomposition/vaporization of aerosols occurs on the heated substrate, thus preventing gas-phase reaction and possible contamination of the growing film with nanoparticles.

The scheme of the MAD is shown in Figure 9. The mixture of organometallic precursors, typically acetylacetonates of the corresponding metals, has been dissolved in an organic solvent. The precursor solution in the form of aerosols with diameter of about 10–20 μm, obtained by a pneumatic nozzle, was transferred onto heated substrate by a carrier gas (compressed air or oxygen). Aerosol flow rate was controlled in the range $v = 0.05$–$10\,\mathrm{mL\,min^{-1}}$ by measuring diffusion light scattering on the droplets. The substrate temperature can be controlled in the region $T_S = 400$–$1000\,^\circ\mathrm{C}$ by detecting the radiation emitted from the substrate heater, using a photodiode optically coupled to the heater by a fiber-optic waveguide. Deposition rate can be varied in the range $v = 5$–$300\,\mathrm{nm\,min^{-1}}$ by changing the concentration of the precursor solution and aerosol flow rate. MAD, compared with other techniques, possesses several advantages: (i) precise control of the film composition, (ii) no vacuum and gas transport lines, (iii) high deposition rates, and (iv) high oxygen partial pressure up to 10^5 Pa.

3.2 Thin-film effects

3.2.1 Growth mechanisms

There are two well-known basic growth modes of thin films: (i) LL growth, also named by Frank and van der Merwe (1949), which takes place when the atoms of growing film

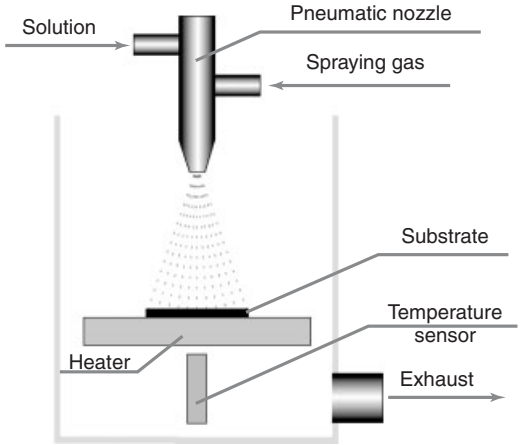

Figure 9. The scheme of the MAD process. (Reproduced from V. Moshnyaga *et al*., 2005, with permission from Springer-Verlag GmbH. © 2005.)

bound preferentially to the substrate surface as to each other promoted by fast diffusion as well; and (ii) 3D island nucleation (Volmer and Weber, 1926), which takes place when the adatoms bound more to each other than to the substrate, favored by slow diffusion. Quantitatively, these two cases can be described within the Young's equation (Lüth, 2001):

$$\gamma_{SV} = \gamma_{SF} + \gamma_{FV} \cos\theta \tag{5}$$

Here γ_{sv}, γ_{sf}, and γ_{fv} are interface energies between substrate (s) and vacuum (v), substrate/film (f) and film/vacuum, respectively. θ is the contact angle between the nucleus and the substrate (see Figure 10). LL growth take place if $\theta = 0$ or undefined, which requires $\gamma_{SV} \geq \gamma_{SF} + \gamma_{FV}$, whereas 3D growth occurs when $0 < \cos\theta < 1$ and thus $\gamma_{SV} \leq \gamma_{SF} + \gamma_{FV}$. Energetically, this means that in the case of LL growth the energy gain (γ_{sv}) due to coating of a substrate by a film exceeds the energy cost ($\gamma_{sf} + \gamma_{fv}$) related with the formation of new interfaces; the film 'wets' the substrate completely. In contrast, for 3D growth the growing film tries to minimize the interface energy, γ_{sf}, and its own surface energy, γ_{fv}, thus 'balling up' on the substrate. Actually, due to condensation of a film from a supersaturated vapor phase, there is an additional energy gain proportional to the Gibbs's free enthalpy per unit volume $G_V = k_B T \ln(p_0/p)$ ($k_B T$ is thermal energy, p and p_0 are partial pressures in the supersaturated vapor phase and equilibrium pressure for the film material for given substrate temperature T) (Willmott, 2004). The supersaturation degree, $S = p_0/p$, is an important parameter, which describes how far away from equilibrium the process of film growth is. S values can be significantly different for various deposition techniques. For example, the PLD technique can be viewed as essentially nonequilibrium – the plasma nature of ablated material plume leads to extreme high supersaturation, $S \sim 10^9$, yielding very high fractional density of stable nucleating sites $N_S = 0.6$ (Willmott, 2004). The rate of nucleation (growth rate) is proportional to N_S as well as to the rate of impingement, therefore the high supersaturation in turn results in films composed of large amount of small crystallites similar to rapid thermal deposition at low temperatures. The PLD technique operates close to this regime (Krebs, Bremert, Störmer and Luo, 1995). For comparison within molecular-beam epitaxy, the growth of films can be close to thermal equilibrium ($S \sim 10^4$ and $N_S \sim 5 \times 10^{-4}$), resulting in perfect large crystal domains (Tersoff, Johnson and Orr, 1997). Thus, growth conditions close to equilibrium, that is, low supersaturation and impingement rate as well as high diffusion rate would inhibit nucleation tendency, that is, 3D growth and would promote LL growth with atomically smooth and large terraces. As for complex oxides like manganites with perovskite crystalline structure, the preparation of LL films is intimately coupled to heteroepitaxial growth on the appropriate single crystalline oxide substrates.

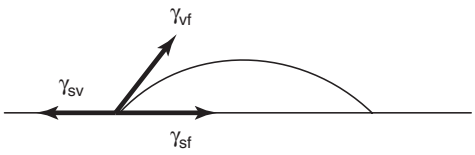

Figure 10. Nucleation site of a film on the substrate.

3.2.2 Epitaxial growth, misfit stress

Preparation of atomically smooth manganite films with perfect crystalline structure is a challenging task not only for the better understanding of intrinsic magnetotransport phenomena but also for the so-called *interface engineering* (Yamada *et al.*, 2004). The latter was recently shown to be extremely important both for low-field TMR in LSMO/$SrTiO_3$ (STO)/LSMO structures (Kwon *et al.*, 1997) as well as for architecting and growth of novel synthetic magnetic (Ogawa *et al.*, 2003) and ferroelectric (FE) materials (Haeni *et al.*, 2004). In many earlier reports, epitaxial manganite thin films can be successively grown using deposition techniques as discussed in Section 3.1 on single crystalline standard substrates like STO, $LaAlO_3$ (LAO) and $NdGaO_3$ (NGO), which have similar perovskite structure. Less used were the substrates of cubic MgO or ZrO_2:Y (YSZ).

In Figure 11, we present an example of heteroepitaxy of LSMO film on STO substrate, obtained by PLD technique (Izumi *et al.*, 1998) within LL-growth mode, controlled by reflection of high-energy electron diffraction (RHEED). Oscillations of specular spot in RHEED patterns as a function of deposition time with a period corresponding to one unit cell clearly demonstrate LL growth. The surface of the film studied by AFM was extremely smooth and flat – one can evidently see flat terraces of about 100 nm width and steps of 0.4 nm height. The alignment and spacing between steps were found to be the same as those of the STO substrate. By means of coaxial impact collision ion scattering technique (CAICISS) (Kawasaki *et al.*, 1994), it was observed that the top atomic layer is MnO_2. Thus LSMO film is considered to be an alternative stack of (La,Sr)O and MnO_2 atomic layers along the [001] direction. The in- and out-of-plane lattice parameters of the LSMO/STO film were found to be significantly different, $a = 0.391$ nm and $c = 0.383$ nm, indicating that film structure changes from the rhombohedral (see Section 1) with pseudocubic lattice constant $a = 0.387$ nm (see Section 1) to a tetragonal, $a \approx b > c$. The reason is *epitaxy misfit stress*, $\varepsilon = (a_{STO} - a_{LSMO})/a_{STO} \sim 0.9\%$, which being relatively small prevents the formation of misfit dislocations at the interface and results in coherently strained

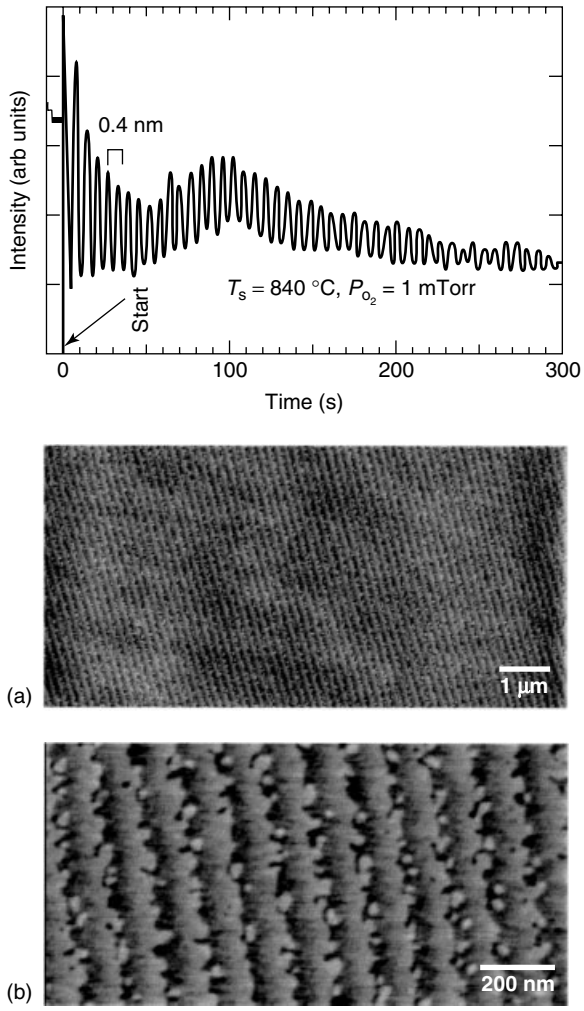

Figure 11. Layer-by-layer grown $La_{0.6}Sr_{0.4}MnO_3$ film. (Reproduced from Izumi *et al.*, 1998, with permission from the American Institute of Physics. © 1998.)

atomic planes. The strain has biaxial nature, that is, the film is tensile strained in (a, b) plane, that is, $a_{\text{film}} > a_{\text{bulk}}$ and compressively strained along the [001] direction, $a_{\text{film}} < a_{\text{bulk}}$, yielding tetragonal large lattice distortion in the film. Surprisingly, the strain persists up to the thickness of about 100 nm and leads to the significant change of the bulk film properties: (i) Curie temperature $T_C = 310$ K instead of 370 K seen in the bulk and (ii) the resistance of the films was about 1 order of magnitude larger than that for single crystal.

Substrate-induced lattice strain effects in thin manganite films were studied in a number of papers (Gommert, Cerva, Wecker and Samwer, 1999; Wang *et al.*, 2000; Bibes *et al.*, 2001; Wiedenhorst *et al.*, 1999; Lebedev *et al.*, 1998; Rao *et al.*, 1998, 1999) by means of changing the substrate nature and film thickness. Usually, the substrates of STO ($a = 0.3905$ nm), resulting in tensile in-plane stress, and LAO ($a = 0.3793$ nm), yielding a compressive in-plane stress, were used. The dependence of lattice strain in epitaxial $La_{0.8}Ca_{0.2}MnO_3$ films as a function of their thickness is shown in Figure 12 both, for films grown on STO and LAO substrates (Rao *et al.*, 1998, 1999). A clear difference between STO and LAO can be seen, namely, the LCMO/STO films are coherently strained up to the thickness of about 100 nm. In contrast, the LCMO/LAO films do not overtake the in-plane lattice constant of the substrate, that is, they are not coherently strained even down to 2–5 nm. This was ascribed to a very large lattice misfit between LCMO and LAO, $\varepsilon = 2.7\%$, which cannot be elastically accommodated, thus resulting in interface dislocations and stress relaxation. Moreover, as was also shown (Rao *et al.*, 1998, 1999; Biswas *et al.*, 2000), stress relaxation under large lattice misfit yields 3D- rather than LL-growth mode.

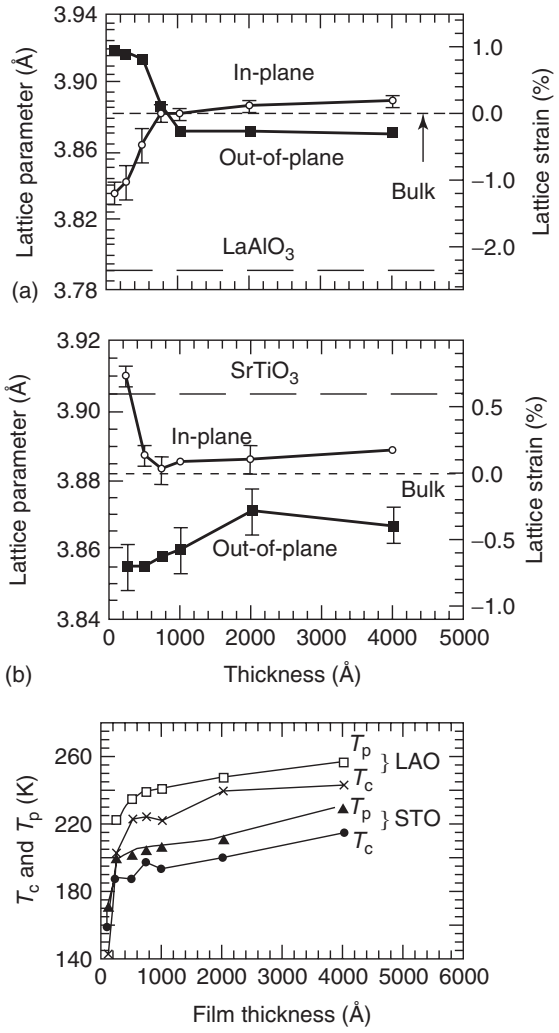

Figure 12. Stress effect induced by substrate-film lattice misfit. (Reproduced from Rao *et al.*, 1999, with permission from the American Institute of Physics. © 1999.)

As is shown in Figure 12(b), the MI transition at T_p as well as Curie temperature, T_C, are extremely sensitive to the lattice strain and decrease about 80–100 K. Millis, Darling and Migliori (1998) quantified the lattice strain effect on T_C due to both bulk strain, ε_b, and JT stress, ε_{JT}, which acts as tetragonal distortion. The obtained dependence of T_C on the lattice strain is described by equation (3):

$$T_C(\varepsilon) = T_C(0)(1 - \alpha\varepsilon_b - 1/2\Delta\varepsilon^{*2}) \quad (6)$$

Here $\alpha = 1/T_C(dT_C/d\varepsilon_b)$ and $\Delta = 1/T_C(d^2T_C/d\varepsilon^{*2})$ are the strain coefficients for bulk and JT strain respectively. The second, symmetry conserving, term in equation (4) describes the change of kinetic energy as a function of strain, which can be either positive due to compressive strain or negative (tensile) leading to increasing or decreasing of T_C, respectively. The bulk strain can be naturally assigned to the change of Mn–O distances as a result of applying pressure. The third, symmetry braking, term relates to the electron localization due to splitting of e_g states of Mn ions caused by static JT effect (see Section 1); the Mn–O–Mn bond angle is corresponding structural parameter, which changes due to JT strain (Radaelli *et al.*, 1997). Being in qualitative agreement with experimental results, the model lacks in detailed description because the strain effects were found to be accompanied with increasing disorder (Aarts, Freisem, Hendrikx and Zandbergen, 1998). This is because the change of film volume due to epitaxy (contraction or expansion) can be stabilized also by the formation of defects like oxygen deficiency (Sun *et al.*, 2000) or partial cation substitution (Rao *et al.*, 1997). Summarizing, the stress-induced effects usually lead to degradation of magnetic and electric properties of manganite films. Hence, preparation of strain-free manganite films on appropriate substrates becomes extremely important problem.

Single crystalline perovskite NGO with (110) orientation possesses lattice constant $a = 0.386$ nm, which is very close to lattice parameter of manganite films, $a = 0.387$ nm; the lattice misfit is only about 0.2%. Recently, (Mitra *et al.*, 2005) have demonstrated LL growth of strain-free LCMO films on NGO substrates by PLD technique. The morphology of the films studied by STM shows large terraces of about 360 nm width and mean square roughness, $RMS = 0.03$ nm. High MI transition temperature $T_P \approx T_C = 268$ K accompanied by very sharp transition were observed. Earlier (Gommert, Cerva, Wecker and Samwer, 1999), a potential of cubic MgO substrates ($a = 0.421$ nm) for the preparation of high quality manganite films by PLD was shown. In this case the lattice misfit is extremely large, $\epsilon = 8\%$, and misfit dislocations, indeed, were present in a 2 nm thick interface region with enhanced disorder but then after the film was almost defect free showing magnetization close to the bulk LCMO. Using MAD technique, we have demonstrated a possibility to grow LL LCMO films on MgO substrate (Moshnyaga, 2005). Typical surface morphology image, obtained by STM, is shown in Figure 13. The film is very smooth, $RMS = 0.1$ nm, and contains large terraces of 100–200 nm, divided by one unite cell steps of ∼0.4 nm height. Interestingly, the LCMO/MgO interface looks quite different from that in Gommert, Cerva, Wecker and Samwer (1999) – it is sharp and smooth with only two to three distorted atomic layers of LCMO. Remarkably, misfit dislocations are present, but located almost exactly on the film-substrate interface, causing an effective mechanism of misfit stress accommodation already in the first atomic layers of growing LCMO film.

3.2.3 Grain boundaries and interfaces

In early studies of manganites, it was already shown that despite intrinsic magnetotransport, related to MI transition

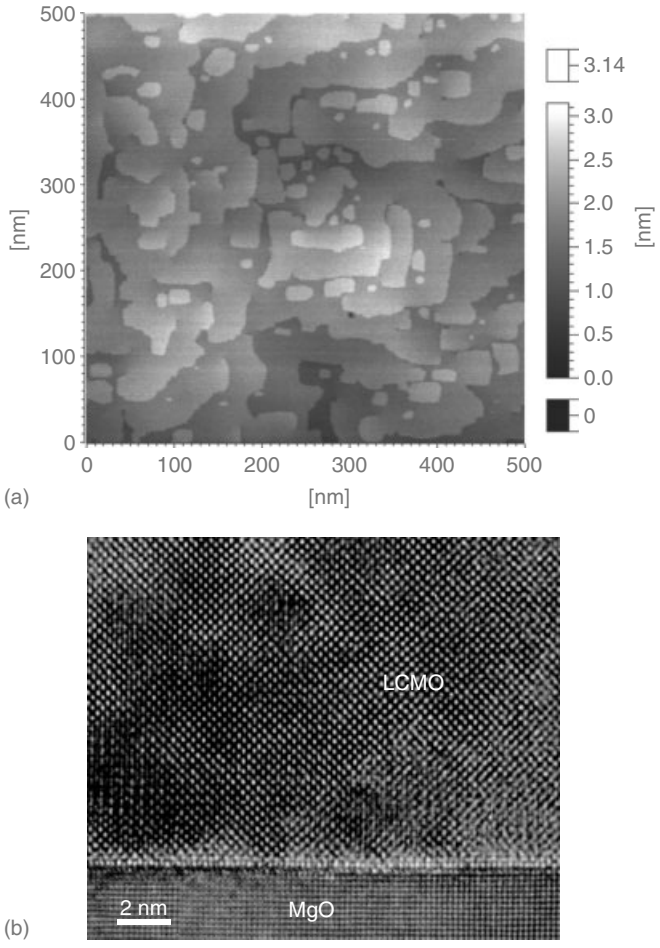

Figure 13. (a) Surface morphology and (b) HREM image (Courtesy of O. Lebedev, EMAT RUCA, University of Antwerp.) of the film interface of a layer-by-layer LCMO/MgO(100) film grown by MAD technique.

and CMR, extrinsic effects like TMR (Hwang, Cheong, Ong and Battlog, 1996) due to static disorder on the interfaces like Grain boundaries (GB) look interesting for low-field applications. Another important feature is that manganites can be viewed as half-metallic compounds (Park *et al*., 1998) with almost fully spin polarized charge carriers on the Fermi level for $T < T_C$. This causes the importance of manganites for *spin electronics*, which along with charge of electron takes into account also the spin degree of freedom, thus dealing with spin-dependent electron transport. In the following text, we discuss the structure and properties of artificially made interfaces.

GB in bulk materials are of limited interest because it is very difficult to control them. To obtain controllable GB in thin films, the bicrystal substrates, usually of STO, were used (Gupta *et al*., 1996; Steenbeck *et al*., 1998; Phillip *et al*., 2000). Such substrates are composed of two misoriented crystalline blocks, thus forming one well-defined wide angle GB. The misorientation angle can be varied usually in the range 8–36°. A manganite film then grows epitaxially on these crystalline blocks, resulting in a well-defined one GB in the film as schematically shown in Figure 14(a). The local structure of grain boundary (Gross *et al*., 2000), visualized by high-resolution electron microscopy (HREM), is shown in Figure 14(b). The GB interface in the film looks as a straight line and is composed of about few nanometer-wide structurally distorted region likely due to accumulation of misfit dislocations and/or nonstoichiometry defects. Moreover, charge carrier concentration in the GB region can be also reduced due to band bending effects similar to that known for high-T_C superconductors (Chisholm and Penneycook, 1991). Hammerl *et al*. (2000) have demonstrated that the GB in Y–Ba–Cu–O films can be additionally doped with Ca to compensate the depletion of charge carrier concentration and thus to increase critical current density.

Another way to design TMR elements is to create interfaces containing manganite/insulator/manganite layers. The in-plane heterostructures with insulating STO layer grown by PLD technique were used for magnetic tunnel junctions (Lu *et al*., 1996; Sun *et al*., 1996; Luo and Samwer, 2001; Pailloux *et al*., 2002; Bowen *et al*., 2003). An example of such trilayer heterostructure is reproduced in Figure 15; it demonstrates sharp and coherent LSMO/STO/LSMO interfaces. No indications on the appearance of misfit dislocations were observed. Köster *et al*. (2002) have shown a possibility to obtain vertical LSMO/MgO/LSMO interfaces by means of self-assembled simultaneous growth of nanocomposite (nanocolumnar) in $(LSMO)_{1-x}$:$(MgO)_x$ on sapphire substrates by MAD technique. The films exhibit pronounced TMR at low temperatures due to MgO insulating layer working as a vertical tunneling barrier. In Figure 15 (b) one can see two types of 45°-misoriented

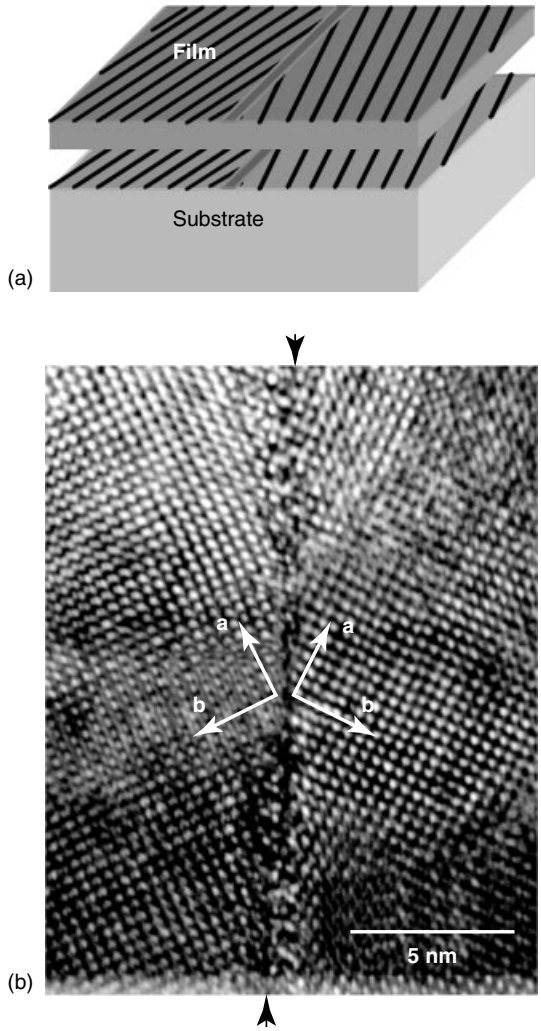

Figure 14. (a) Schematic view of a film epitaxially grown on bicrystal substrate. (b). HREM image of grain boundary region. (Reproduced from Gross *et al*., 2000, with permission from Elsevier. © 2000.)

interfaces: (a) undoped LSMO/LSMO interfaces which show no TMR and are similar to epitaxial films and (b) 'doped' of 'filled' LSMO/MgO/LSMO interfaces, composed of crystalline LSMO domains, separated by MgO layer. The latter interfaces build a network of vertical tunneling barriers. Very recently (Esseling *et al*., 2005), the vertical LSMO/MgO/LSMO interfaces were characterized with respect to (1/f)-noise, which is a well-known limiting factor for device applications. The noise level characterized by a dimensionless parameter, $\langle a_V \rangle \sim 10^{-27}\,m^3$, was found to be comparable with the noise from epitaxial films: strained film on STO has $\langle a_V \rangle \sim 10^{-24}\,m^3$ and unstrained grown on NGO substrate possess $\langle a_V \rangle \sim 10^{-30}\,m^3$ (Reutler *et al*., 2000). These data confirm high quality of LSMO/MgO/LSMO

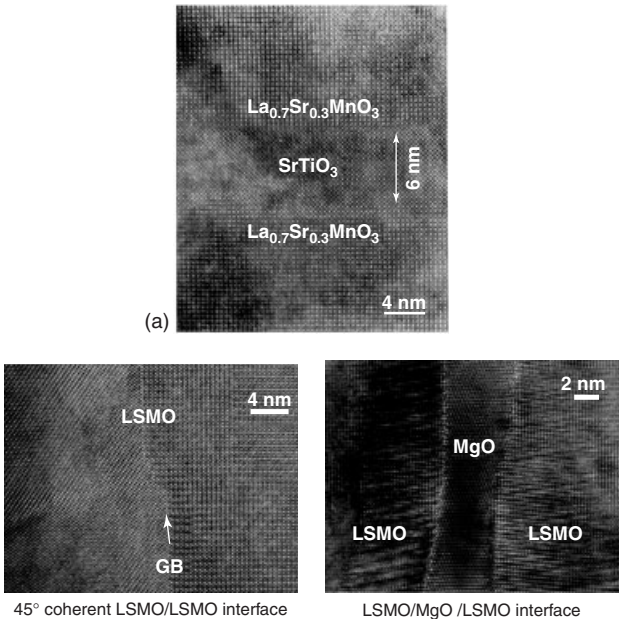

Figure 15. (a) HREM image of the tunnel magnetic junction interface. (Reproduced from Y. Lu *et al*., 1996, with permission from the American Physical Society. © 1996.) (b). Vertical interfaces in LSMO/MgO/LSMO nanocomposite films. (Reproduced from S.A. Köster *et al*., 2002, with permission from the American Institute of Physics. © 2002.)

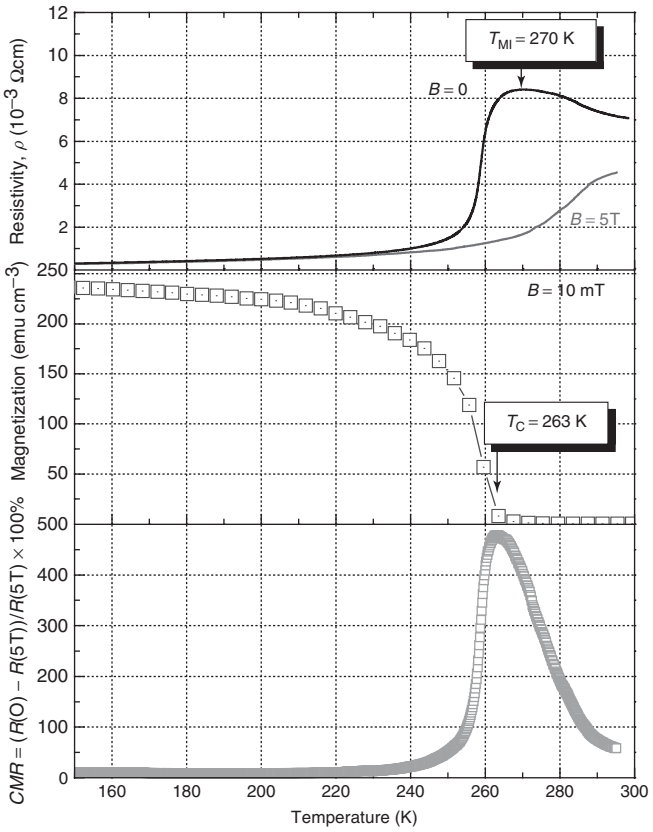

Figure 16. Temperature dependences of resistance (a), magnetization (b) and CMR (c) for an epitaxial LCMO film.

interfaces, prepared by self-assembled growth within MAD technique.

4 MAGNETORESISTANCE EFFECTS IN MANGANITE FILMS

4.1 Metal–insulator transition and colossal magnetoresistance

4.1.1 General comments

As was mentioned in Section 2 continuous and broad interest to the perovskite manganites is basically caused by the fact that they show MI transition and CMR effect. To illustrate the interrelations between different phase transitions, in Figure 16 we present temperature dependence of the resistance (a), magnetization (b), and CMR (c) for an epitaxial LCMO/MgO film, grown by MAD technique. One can see that for $T > T_{\mathrm{MI}}{\sim}270\,\mathrm{K}$, the film shows insulating-like behavior in the sense that $\mathrm{d}\rho/\mathrm{d}T < 0$, which changes to a metallic-like dependence with $\mathrm{d}\rho/\mathrm{d}T > 0$ for $T < T_{\mathrm{MI}}$. Very close to the preceding transition is the Curie temperature, $T_{\mathrm{C}} = 263\,\mathrm{K}$, defined as the temperature of the minimum of the function $(1/M)(\mathrm{d}M/\mathrm{d}T)$, where M is the film magnetization (Rajeswari *et al*., 1998). Apparently, CMR is very large only in a narrow region in the vicinity of T_{C}, or in other words, large CMR is coupled to the highest level of magnetic disorder (Ashckroft and Mermin, 1981), which is very sensitive to applied magnetic field as well as other factors like temperature, hydrostatic pressure, or even electromagnetic radiation. For completely ferromagnetically ordered material, for $T < T_{\mathrm{C}}$ as well as for noncorrelating (disordered) PM spins ($T \gg T_{\mathrm{C}}$) CMR is negligibly small.

Basically, the CMR phenomenology is in accordance with DE model (Zener, 1951; Anderson and Hasegawa, 1955; de Gennes, 1960). See Section 2 for the large bandwidth manganites like LSMO, showing highest $T_{\mathrm{C}} \sim 370\,\mathrm{K}$, second-order para-ferromagnetic phase transition (Mira *et al*., 1999) and metallic-like behavior also in PM phase. For middle bandwidth manganites like LCMO with moderate $T_{\mathrm{C}} \sim 260\,\mathrm{K}$ and first-order MI phase transition as was first suggested by Millis, Darling and Migliori (1998), the larger resistance as well as an insulating-like behavior in PM phase cannot be explained within the DE model. An additional EL interaction due to JT effect should be taken into account.

The charge localization (see Section 2.1) occurs by means of static or dynamic JT distortions of MnO_6 octahedra resulting in the formation of lattice *polarons* for $T > T_C$, that is, localized carriers tightly bound to the local lattice deformation (Billinge *et al*., 1996; Kim *et al*., 1996; Jaime *et al*., 1997). Such a carrier with corresponding local distortion can move through the lattice by means of a temperature activated hopping mechanism (Mott, 1990) with insulating-like temperature dependence of the resistivity, $\rho \sim \exp(T_0/T)^{1/4}$ (Viret, Ranno and Coey, 1997). Moreover, PM state shows the *correlated lattice distortions* observed by small angle neutron (SANS) and X-ray scattering techniques (Dai *et al*., 2000; Adams *et al*., 2000; Kiryukhin *et al*., 2003). The correlation length was found to be of several lattice constants, varying in the range 1.2–2.8 nm for LCMO with different doping level (Dai *et al*., 2000). Remarkably the scattering intensity, proportional to the concentration of these nanoscaled correlated regions, increases approaching T_C and can be suppressed by applied magnetic field (Koo *et al*., 2001), thus mimicking temperature dependence of the resistivity and CMR effect. Furthermore (Kiryukhin *et al*., 2003), it was shown that correlated polarons are compatible with orthorhombic structure but not with the rhombohedral one. Figure 17 illustrates the temperature behavior of the nanoscaled structural correlations in the $La_{0.75}(Ca_{0.45}Sr_{0.55})_{0.25}MnO_3$ system, for which (P_{nma}/R-3c) structural phase transition occurs for $T_0 = 370$ K. One can see that polaron correlations are suppressed both for $T < T_C$ due to the increase of DE in FM phase and for $T > T_0$ in PM state within the rhombohedral structure. The latter, being a more symmetric pseudocubic structure with three equivalent crystallographic axes, seems to be incompatible with the existence of long-range strain fields in nanoscaled regions with static JT effect.

Summarizing, one can view correlated polarons in the form of nanoscaled structural correlations as a precursor state for the long-range COO state, which builds up when DE contribution is progressively suppressed by means of bandwidth or filling controls. By enhancing delocalizing tendencies due to DE in an optimally doped materials for $T < T_C$, the correlated polaron regions will 'melt' at the expense of metallic regions, characterized by conventional spin-wave excitations rather than by diffusive inelastic contribution from correlated polarons, both detected by SANS (Linn *et al*., 1996; Fernandez-Baca *et al*., 1998). Metallic phase can be also treated as charge and orbitally disordered. Thus, competing DE and electron–lattice interactions may result in an electronically inhomogeneous ground state with coexisting domains of FMM and AFI phases. On the basis of effective medium approach, Jaime *et al*. (1999) proposed a two-phase model with magnetic field and temperature dependent concentration of metallic regions, embedded in a polaronic background, having an activated electrical conductivity.

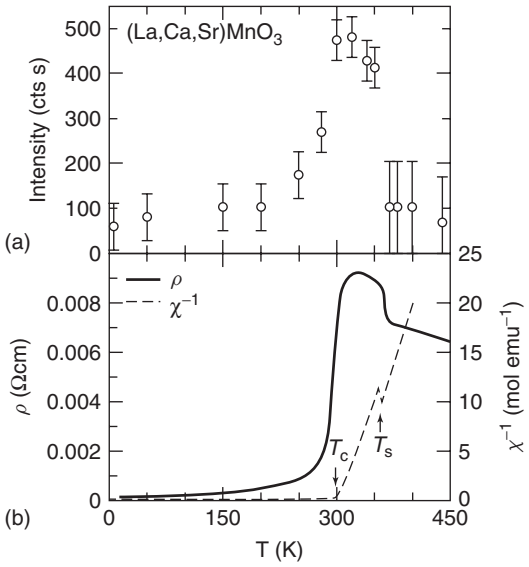

Figure 17. (a) Temperature dependence of the intensity of the peak due to the structural correlations in $La_{0.75}(Ca_{045}Sr_{0.55})_{0.25}MnO_3$; (b) Temperature dependence of the electrical resistivity (solid) line and inverse magnetic susceptibility (dashed line). (Reproduced from Kiryukhin *et al*., 2003, with permission from the American Physical Society. © 2003.)

4.1.2 Phase separation studied by local probe techniques

To study the phase coexistence in manganites, the local probe techniques like STM coupled to STS were used (Fäth *et al*., 1999; Becker *et al*., 2002; Renner *et al*., 2002; Chen *et al*., 2003; Moshnyaga *et al*., 2006). These techniques allow one not only to visualize the surface morphology of a manganite thin film or single crystalline sample under ultrahigh vacuum (UHV) conditions but also by measuring the $I-V$ characteristics, to obtain the information on the local surface electronic structure with very high spatial resolution. Owing to modern developments of the STM, such measurements can be performed additionally by varying temperature and magnetic field. Fäth *et al*. (1999) have done the first STS study on the single crystals of $La_{1-x}Ca_xMnO_3$ ($x = 0.25$ and 0.3) as well as on epitaxial LCMO film grown on STO substrate. STS on the LCMO film was measured both for $T < T_C$ and $T > T_C$; unfortunately the temperatures were not specified. For all temperatures the ($I-V$) curves were found to be essentially nonlinear in the range of voltages $V = 0$–4 V. Even for small voltages, one can hardly see linear behavior. However, there was observed a correlation between measurements of four-probe bulk resistivity and tunneling resistivity. Namely, for $T < T_C$, that is, in macroscopically FM and metallic state, the film shows relatively high values of differential

tunneling conductivity $\mathrm{d}I/\mathrm{d}V_{V=0} \sim 1$ ns, which were thus assigned to be 'metallic' (M). In contrast, a low conductivity, $\mathrm{d}I/\mathrm{d}V_{\mathrm{V}=0} \sim 10^{-2}$–$10^{-3}$ ns, measured for $T > T_{\mathrm{C}}$ in the macroscopically PM and insulating state were assigned to be 'insulating' (I). In Figure 18 the distribution of the tunneling conductance $\sigma = \mathrm{d}I/\mathrm{d}V$ taken at 3 V on LCMO/STO film from Fäth *et al*. (1999) is shown for temperature close but lower than T_{C}. One can see that σ is inhomogeneously distributed over the measured area ($500 \times 500\,\mathrm{nm}^2$), containing more conducting regions, colored on the 'red' to 'black' color scale, and less conducting regions ('yellow' to 'white'), both having a cloudlike shape. Characteristic sizes of these electronic structures vary within several tens of nanometers. By applying magnetic field, the average conductivity increases at least for fields close to 9 T (one can see that the conductivity map becomes darker). This behavior is in qualitative agreement with the bulk CMR effect and DE model (Zener, 1951; Anderson and Hasegawa, 1955; de Gennes, 1960), assuming the decrease of electrical resistance in magnetic field due to suppression of magnetic disorder and increase of one-electronic bandwidth (see equation (2). However, locally, σ still remains inhomogeneous in contradiction with DE even at 9 T. A remarkable feature, which was not discussed by Fäth *et al*. (1999), is that magnetic field does not necessary lead to the increase of local σ. Indeed, in some regions (follow, for instance, the 'red' central part at $B = 0$ in Figure 18), one can evidently see that σ decreases (the color changes from red to yellow) with increasing field. Very similar behavior

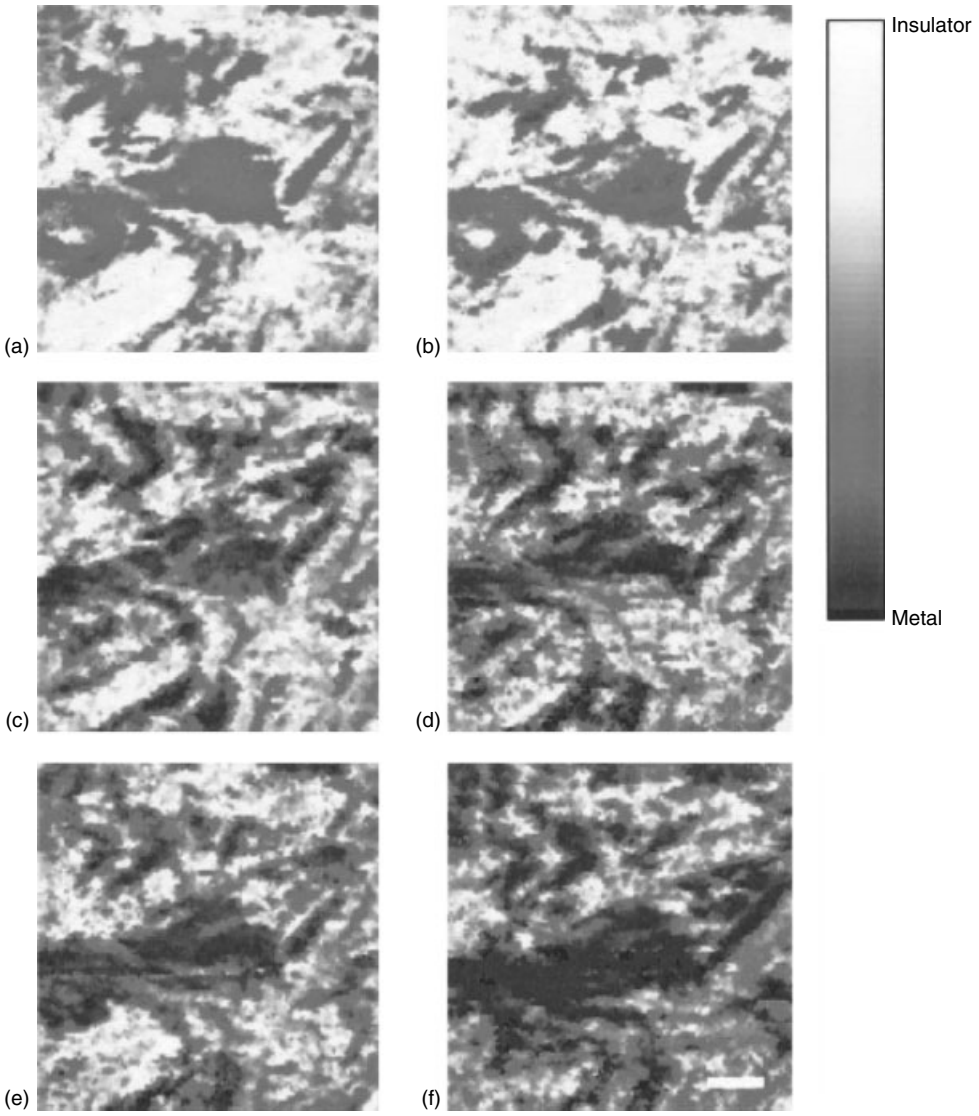

Figure 18. Conductivity maps at 3 V bias for LCMO thin film for magnetic fields of 0, 0.3, 1, 3, 5, and 9 T (a–e). The color represents the slope of the local (I–V) curve at a bias of 3V. (Reproduced from M. Fäth *et al*., 1999, with permission from Science AAAS. © 1999.)

was also seen by Chen *et al*. (2003). Moreover, they have observed that after the field was scanned from 0–5 T and back to 0, the tunneling conductivity map was looking significantly different from the initial STS map, taken before the application of magnetic field. This clearly indicates that field-induced changes in tunneling conductivity are irreversible. Thus, nonmonotonous local $\sigma(H)$ behavior, if considered on a scale 50–100 nm, which is comparable to the size of cloud-like features in Figure 18, may be in disagreement with bulk CMR-like behavior, assuming decrease of the resistance in applied field, and DE model as well. One can rather say that external magnetic field induces rearrangement of metallic and insulating regions. This, likely, indicates that M and I phases are not free – they are coupled together leading to a peculiar magnetic field behavior.

Becker *et al*. (2002) have studied local tunneling conductivity, taken however at $V = 0$, for different temperatures for LSMO and LCMO films. STS images, qualitatively similar to those from Fäth *et al*. (1999) and Chen *et al*. (2003), with coexisting M and I regions were obtained. Moreover, the evaluated concentration of metallic phase was found to be temperature dependent similar to temperature dependence of the bulk material. This confirms similarity between the bulk and surface measurements and rules out a possible 'surface' nature of the observed PS in thin films and single crystals. Renner *et al*. (2002) have obtained STS with atomic resolution on $Bi_{0.24}Ca_{0.76}MnO_3$ single crystal, which behaves as CO insulator for $T < T_{CO}{\sim}240$ K and orders antiferromagnetically at low temperatures. Remarkably, they also observed a coexistence of metallic and insulating domains, which occurs at room temperature, that is, higher than T_{CO}. Owing to success in atomic resolution, a structural characterization of both metallic and insulating phases have been done. The M-phase was found to be cubic with O–Mn–O angle close to 180°, whereas the I phase was orthorhombic showing a 'zig-zag' type structural distortion of Mn–O bonds. Very sharp M/I phase boundary was observed. Thus, as could be expected from structural consideration discussed in Section 1, the manifestation of metallicity is directly related to a more symmetric cubic (or rhombohedral R-3c) structure, while the insulating behavior is caused by lattice distortions within less symmetric orthorhombic P_{nma} structure due to JT effect.

These results make a quantitative basis to discuss other local STS studies, which could be more or less related to extrinsic PS in thin films. Biswas *et al*. (2000) have seen inhomogeneous electronic behavior caused by incomplete strain relaxation in LCMO/LAO films grown according to 3D growth mode. They found an insulating-like tunneling conductivity near the edges of crystalline grains, whereas the central part of the grain was metallic. Bibes *et al*. (2001) observed nanoscale PS on LCMO/STO interfaces and interpreted it within a stress-induced PS due to coherently strained LCMO on the interface. These data seem to be important for the experiments on TMR (see Section 4.2) because stress-induced PS, accompanied by weakening of DE interaction, can decrease spin polarization of a manganite layer at the interface. Mitra *et al*. (2005) have demonstrated that stress-free LL LCMO/NGO films do not show nanoscale or mesoscopic PS; they possess rather homogeneous distribution of tunneling conductivity $\sigma = dI/dV_{0.1V} = 1.07–1.13\,\text{nA V}^{-1}$ over the measured area ($1 \times 1\,\mu\text{m}^2$) for $T < T_C$. The temperature dependence of tunneling conductivity shows a pronounced minimum by $T \sim T_C$, reflecting a bulk MI transition. No real insulating behavior with $\sigma = 0$ for $T > T_C$ was observed in agreement with results of Fäth *et al*. (1999). Very recently, Moshnyaga *et al*., (2006) have prepared LCMO/MgO films, showing unusual rhombohedral R-3c crystalline structure and unique ordering of A-site cations (La and Ca). Note that the relatively small ionic radius of Ca leads to the formation of orthorhombic P_{nma} structure (Radaelli *et al*., 1995, 1997) in LCMO manganites for the whole range of Ca doping ($0 < x < 1$). The A-site ordered film shows a unique superstructure with superlattice constant $a_s = 4a_{per} \approx 1.55$ nm due to ordered 3D arrangement of La and Ca cations. Such ordering suppresses (compensates) La/Ca size mismatch lattice stress within one supercell, resulting in a stress-free state of LCMO film. Remarkably, no PS on the scale down to 1 nm for $T < T_C$ was detected by STM/STS technique. In sharp contrast, an orthorhombic LCMO/MgO film does show PS for $T < T_C$, similar to the results of Fäth *et al*. (1999); Becker *et al*. (2002); Chen *et al*. (2003) with the size of insulating clusters 10–50 nm. No correlation with morphology (microstructure) was observed, indicating intrinsic nature of PS.

Thus, we believe that realization of tendencies to PS should be closely related to the crystallographic structure. As was shown in Section 1, the structure close to cubic ($t \sim 1$) favors DE interaction resulting in FMM behavior. Typical example is a canonic DE material LSMO, which being optimally doped shows high-$T_C{\sim}360$ K, accompanied by second-order phase transition; to the best of our knowledge no PS was observed in such LSMO up to now. By lowering the crystal symmetry down the orthorhombic, the competing EL interaction increases, leading to PS in the presence of cation disorder, imposed on the first-order phase transition (LCMO).

4.1.3 Percolative MI transition and CMR effect

The electronic inhomogeneity revealed by STM/STS technique in thin manganite films (Fäth *et al*., 1999; Becker *et al*., 2002; Chen *et al*., 2003; Moshnyaga *et al*., 2006) seems to be incompatible with polaronic scenario. This is because the

PS length scale, which varies in the range 10–100 nm, is much larger than the size of homogeneously distributed small polarons (Billinge *et al*., 1996; Kim *et al*., 1996; Jaime *et al*., 1997) and even larger than characteristic length of correlated polarons (Dai *et al*., 2000; Adams *et al*., 2000; Kiryukhin *et al*., 2003), which does not exceed 1–3 nm. The observed PS state rather assumes the existence of spatial fluctuations of stress and/or Coulomb potential due to quenched disorder (Moreo, Yunoki and Dagotto, 1999; Moreo *et al*., 2000; Dagotto, Hotta and Moreo, 2001; Burgy *et al*., 2001), discussed in Sections 2.3 and 2.4. Moreo *et al*. (2000) have obtained theoretically within one- and two-orbital models that the size of competing FM and AF clusters close to first-order phase transition in the presence of quenched disorder can be much larger than the lattice spacing. The cluster size varies in the range of few tens to few hundreds of lattice spacing; that is, within 10–400 nm. Moreover, the cluster size depends on the strength of disorder, σ^2, that is, the larger the disorder, the smaller the cluster size. The disorder-induced PS explains the observed inhomogeneities by STM/STS (Fäth *et al*., 1999; Becker *et al*., 2002; Chen *et al*., 2003; Moshnyaga *et al*., 2006) as well as those seen by TEM (Uehara, Mori, Chen and Cheong, 1999).

The important theoretical prediction was the *percolative* character of PS scenario as a function of magnetic field or temperature, intuitively concluded already in earlier experiments (Uehara, Mori, Chen and Cheong, 1999). Moreo *et al*. (2000) have shown that under applied magnetic field, the previously disconnected FM clusters grow in size and start to connect each other. Thus, a *percolation*, that is, formation of an infinite metallic cluster (Shklovsky and Efros, 1979), accompanied with formation of a current path emerges. The MI transition in the PS scenario occurs as a percolation transition within the two-phase model, simulated by the resistor network (Mayr *et al*., 2001). By decreasing temperature, starting from PM state, the concentration of metallic phase increases from zero up to a value called *percolation threshold*, p_0, which consists of 40 and 50% for 2D and 3D percolation models, respectively (Shklovsky and Efros, 1979). For $p > p_0$ a metallic filament builds up, forming the current path through the whole sample. Very large values of CMR $\sim 10^5\%$ (McCormack *et al*., 1994) can be quantitatively explained within the resistor network model, which shows that the resistance close to percolation threshold is very sensitive to small changes in concentration of metallic phase p, resulting in extreme large, up to several orders of magnitude, changes of the resistance (Mayr *et al*., 2001).

We proposed an approach (Moshnyaga *et al*., 2003; Lebedev *et al*., 2002) to create artificial phase-separated system, based on epitaxial nanocomposite manganite (LCMO) thin films, containing a second insulating phase (MgO), which chemically and crystallograhically fits the primary manganite phase. Such composites can be viewed also as an artificially created 'phase-separated' system, consisting of 3D manganite nanoclusters, imbedded in an appropriate insulating oxide matrix. Thus, chemical PS will lead to an artificial EPS of the MI type, parameters, and the scale of which can be controlled by processing conditions. Magnetotransport properties can then be compared with those recently observed in 'naturally existing' electronic phase-separated samples (Uehara, Mori, Chen and Cheong, 1999). The microstructure of $(LCMO)_{1-x}$:$(MgO)_x$ nanocomposite films grown on MgO substrate by MAD technique is shown in Figure 19. In the cross-sectional image (Figure 19a), one can see that both LCMO and MgO phases grow epitaxially on the MgO substrate. The mean diameter of the LCMO domains varies as $D = 40–50$ nm. Sharp interfaces are also seen in an HREM plane view image in Figure 19(b). Remarkably, we did not observe misfit dislocations at these LCMO/MgO interfaces similar to the case of individual LCMO films grown on

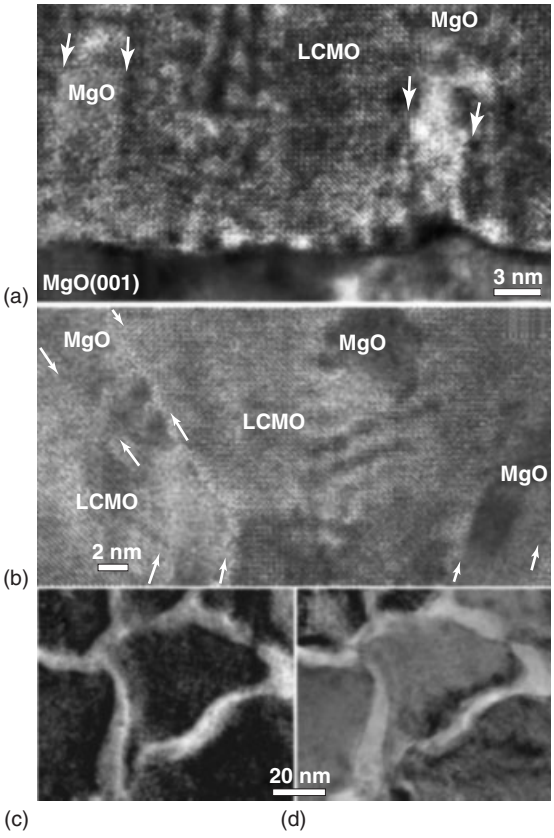

Figure 19. Cross section (a) and plane view (b) HREM images of epitaxial nanocomposite (LCMO):(MgO) films. Mg (bright) map obtained by EELS (c) and plane view TEM image (d) of the same region showing clear chemical phase separation between LCMO and MgO. (Reproduced from V. Moshnyaga *et al*., 2003, with permission from Nature Publishing Group. © 2003.)

MgO substrate by MAD technique (see Section 3.3). Energy filtered TEM in a plane view, shown in Figure 19(c), demonstrates no chemical intermixture between LCMO and Mg (bright regions), which is in good agreement with the sharp contrast between these phases in the HREM image (Figure 19d). Thus, we conclude that composite films contain chemically well-separated nanocrystalline LCMO and MgO domains, which are epitaxially oriented with respect to each other as well as to the substrate. By varying the concentration of MgO, x, one can control magnetotransport behavior as we as the structure of the LCMO phase. The percolation threshold in conductivity was found for $x_c = 0.33$. This means that for $x > x_c$ resistivity at room temperature drastically increases as shown in Figure 20 and no MI transition at zero (ambient) magnetic field was observed for temperatures down to 4.2 K. Remarkably, in such artificial PS system, the CMR effect is manifested as a field-induced MI transition (see Figure 20) and exactly at the percolation threshold CMR reaches very large values of more than $10^5\%$ for B = 5 T. This is in very good agreement with computational models (Mayr *et al*., 2001) and probably explains the nature of very large CMR in earlier experiments (McCormack *et al*., 1994) as really caused by the PS scenario. Another interesting result of this study (Moshnyaga *et al*., 2003) was the observation of strong elastic coupling between the LCMO and MgO nanophases. This coupling provides an additional opportunity to control the behavior of LCMO by means of volume tensile stress or 'negative' pressure, actuated by MgO second phase. As a result, the structure of LCMO changes from a usual orthorhombic (P_{nma}) to the rhombohedral (R-3c), which is shown on the phase diagram in Figure 20(b). The structural phase transition (see Figure 20b) occurs also at the percolation threshold, when an infinite MgO cluster emerges, connecting all LCMO domains and yielding homogeneous and very large volume stress. According to Lebedev *et al*. (2002), this structural phase transition to a more symmetric rhombohedral phase provides a stress accommodation mechanism, which is necessary to release very large bulk tensile stress induced by the MgO second phase.

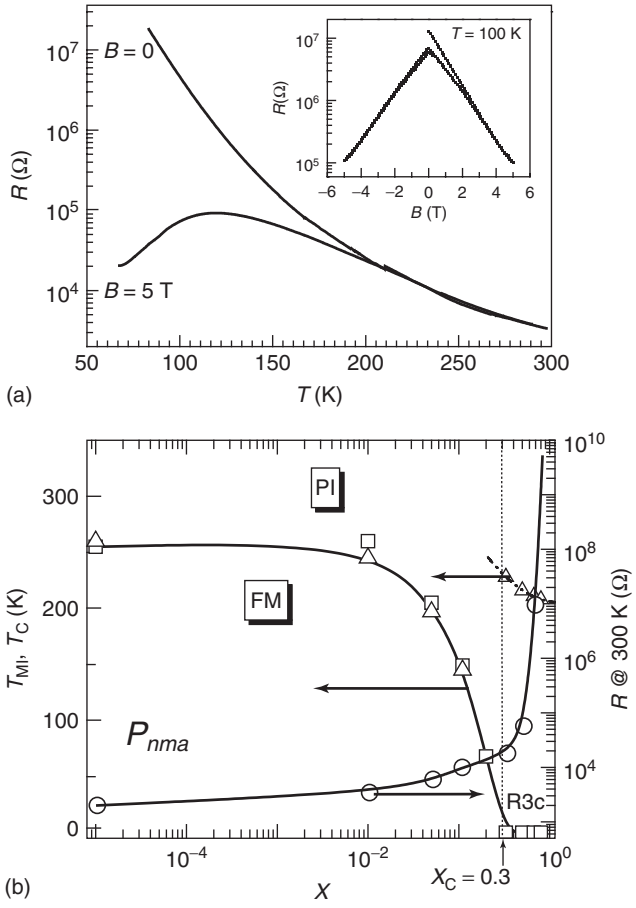

Figure 20. CMR effect as magnetic field-induced metal-insulator transition at the percolation threshold for $x = 0.33$ (a) and phase diagram of LCMO:MgO system (b), showing tight coupling between structural, magnetic, and electronic properties. (Reproduced from V. Moshnyaga *et al*., 2003, with permission from Nature Publishing Group. © 2003.)

4.2 Low-field magnetoresistance

As is commonly believed, the CMR effect being limited within narrow temperature region close to T_C and strong magnetic fields of several Tesla has no potential for applications. The device applications like magnetic sensors or magnetic random access memory (MRAM) require both low-field sensitivity and broad operation temperature region. The low-field sensitivity is provided with the TMR effect on the interfaces between manganite and insulating phase (usually STO). The structure of such interfaces realized in planar geometry or as GB was discussed in Section 3.2. Another possibility for low-field MR provides intrinsic magnetic disorder, that is, magnetic domain structure naturally existing in a FM material. For low-field applications one can try to use the interaction between the transport current, $\vec{J}$, and fluctuations of magnetization vector $\overrightarrow{M}$ in a structurally homogeneous ferromagnet because of two different MR effects: (i) direct scattering of charge carriers on domain walls, called *domain-wall magnetoresistance* (*DWMR*) and (ii) spin-orbit interaction induced difference in scattering amplitude when the current flows parallel and perpendicular to the magnetization direction, called *anisotropic magnetoresistance* (*AMR*). In the following text we discuss these low-field MR effects with respect to manganite films, but concentrate first on the TMR effect.

4.2.1 Tunneling magnetoresistance (TMR)

The main idea of TMR is based on spin-dependent scattering of charge carriers (Moodera, Kinder, Wong and Meservey, 1995), which are assumed to be spin polarized, that is, the electrons possess a definite projection of spin, on the interfaces (see Figure 21). Because of broken translational symmetry of the manganite films on the interfaces, there are two magnetically decoupled manganite layers (electrodes), having in between an insulating tunneling transparent barrier layer with the thickness typically about 1–2 nm. When a dc bias is applied electrons can tunnel through the barrier. The resistance of such magnetic tunnel junction depends on the relative orientation of magnetization in FM electrodes for $T < T_C$, which can be controlled by applied magnetic field. The TMR ratio is

$$TMR = (R_{AP} - R_P)/R_{AP} \tag{7}$$

With R_{AP} and R_P are resistances of magnetic tunnel junction for antiparallel and parallel orientation of magnetization

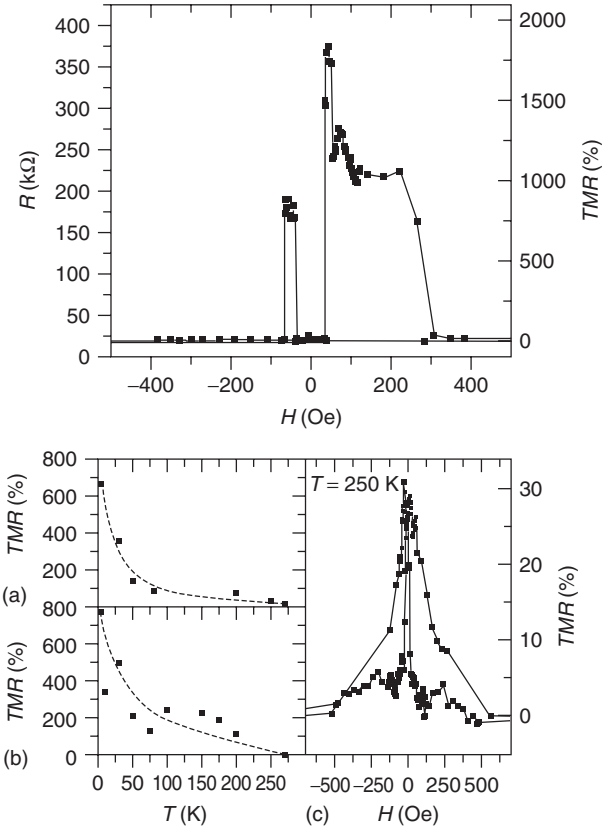

Figure 21. Field dependence of the resistance of a magnetic tunnel junction from (upper panel) and temperature dependences of the TMR effect (lower panel). (Reproduced from M. Bowen *et al.*, 2003, with permission from the American Institute of Physics. © 2003.)

of electrodes, respectively (Bowen *et al.*, 2003). $R_P < R_{AP}$ because, under assumption that spin of charge carrier does not changes by tunneling process, the parallel configuration account for minimum energy while to realize the antiparallel configuration an additional energy to reorient spin of an electron is required. Julliere (1975) has formulated that TMR ratio of a magnetic tunnel junction depends on the spin polarization of electrons on the Fermi level in both electrodes, P_1 and P_2, as the following:

$$TMR = 2P_1P_2/(P_1 - P_2) \tag{8}$$

The advantage of manganites for TMR is that the spin polarization, as measured by spin resolved photoemission spectroscopy, can be very high reaching almost 100% (Park *et al.*, 1998). One calls manganites *half-metallic* with practically fully spin polarized electrons on the Fermi level. In comparison, spin polarization of transition element FM metals like Fe, Ni, or Co does not exceed 50% (Monsma and Parkin, 2000), yielding usually maximum TMR $\sim$ 60%. According to Julliere's model, manganites should show very high TMR, which even can diverge when $P_1 = P_2 = 1$. On the other hand, by constructing a magnetic tunnel junction, one electrode of which has known P value, one can estimate the spin polarization for another electrode. Indeed, manganite base tunnel junctions (Bowen *et al.*, 2003), prepared as trilayer structure LSMO/STO/LSMO, reveal extremely high TMR = 1800% as shown in Figure 21. One can see that resistance change can exceed 1 order of magnitude for very low magnetic fields, comparable to coercive field $H_C \sim 100$ Oe. The estimated spin polarization degree in LSMO was 95% in good agreement with spectroscopy measurements (Park *et al.*, 1998). However, such high TMR value was observed only for low temperatures. In Figure 21(b) one can see that TMR decreases strongly with increasing temperature and even for $T \sim$250 K, that is, much lower than bulk $T_C = 360$ K for LSMO TMR vanishes. Similar temperature dependences were obtained on TMR structures prepared by different techniques with tunneling barriers grown between planar interfaces, vertical interfaces as well as a GB (Hwang, Cheong, Ong and Battlog, 1996; Steenbeck *et al.*, 1998; Gupta *et al.*, 1996; Phillip *et al.*, 2000; Lu *et al.*, 1996; Sun *et al.*, 1996; Pailloux *et al.*, 2002; Luo and Samwer, 2001; Köster *et al.*, 2002), thus indicating a common temperature behavior of TMR in manganite-based magnetic tunnel junctions. The degradation of T_C and, hence, of spin polarization in the manganite layer close to the interface caused, likely, by stress effect or interface doping was suggested. Commonly used barrier material, STO, with small lattice mismatch, $\varepsilon \approx 0.9\%$ indeed induces coherent strain in LSMO layer up to about 100 nm distance from the barrier, leading to decrease of T_C for LSMO from the bulk value 360 down

to 310 K in the strained film (Izumi *et al*., 1998). However, such reduction of T_C does not explain the suppression of TMR for temperatures much lower than room temperature. Moreover, the LCMO/NGO/LCMO tunnel junctions (Moon-Ho, Mathur, Evetts and Blamire, 2000) with perfectly matched NGO barrier also show drastic reduction of TMR for temperatures around 150–200 K, that is, far away from bulk T_C of LCMO as discussed in the following text.

An interesting way to increase the interface magnetization of LSMO and thus to increase spin polarization at room temperature was proposed by Yamada *et al*. (2004). They suggested that degradation of the interface magnetization occurs because of the doping effect, that is, of increased Sr concentration on the interface resulted from the SrO termination layer of $SrTiO_3$ barrier. By means of interface LL engineering, they introduced a two-unit-cell-thick LMO between the LSMO/STO interface. As a result, the interface magnetization, probed by second-harmonic-generation (SHG) technique, was significantly increased at room temperature. Without LMO layer no magnetic SHG was observed already for $T \sim 250$ K. Another source of interface degradation (Bibes *et al*., 2001), is related to a nanoscale PS on the LCMO/STO interfaces induced by coherent strain effect. As a result, the FM coupling within the metallic regions is depressed. This accounts for the reduction of the Curie temperature and conductivity in the manganite layer close to the interface. Although the precise cause for the reduction of interface magnetism (stress, disorder, doping, PS, etc.) is difficult to determine in any concrete case, from structural considerations it seems probably that the problem is closely related to the interface symmetry of d orbitals of Mn, resulting in the change of Mn–O bond length and/or O–Mn–O angle, which both are crucial for magnetism in manganites. In this sense very important becomes the problem of termination layer, that is, whether (La,Sr)O or MnO_2 layer terminates a manganite film at the interface. Pailloux *et al*. (2002) have shown that (La,Sr)O termination does not disturb average valence of Mn close to interface and allows one to keep TMR still measurable close to the bulk T_C in Co/STO/LSMO tunnel junctions. Interesting interface properties were shown by Giesen *et al*. (2004), who observed that all-manganite multilayers like $(LSMO/LCMO)_n$, prepared by PLD technique, do not show PS induced reduction of magnetic and electric properties of LCMO layer down to the thickness of 6 nm. This was interpreted within the preservation of Mn–O–Mn chains at the interfaces. In this context, an insulating manganite barrier layer for TMR structures looks very interesting (Kleine, Luo and Samwer, 2006). One can suppose that LMO with the same perovksite structure and practically the same lattice parameter as electrodes (LSMO) would not suppress interface magnetism in LSMO.

4.2.2 Domain-wall and anisotropic magnetoresistance (DWMR and AMR)

The information on the DWMR in manganite films (Mathur *et al*., 1999; Wolfman *et al*., 2001; Ziese, 2002) is limited and contradictory. This is caused by the fact that both DWMR and AMR effects lead to very small relative changes in the resistance, $\Delta R/R \leq 0.1$–1 %, which can be hardly separated between DWMR and AMR effect and/or can be even hindered by other extrinsic (TMR) or intrinsic (CMR) effects (Ziese, 2002). Moreover, the observation of DWMR requires a definite geometry of magnetic domain structure, which is usually achieved by the preparation of nanocontacts and nanoconstrictions. Micromagnetic simulations of the domain structure accounting additionally for stress-induced changes in magnetic anisotropy in thin manganite films (O'Donnell, Rzchowski, Eckstein and Bozovic, 1998) are also extremely important. To obtain reliable experimental data, well-defined samples made from epitaxial thin films of high crystalline quality, usually grown by LL mode, are required. Mathur *et al*. (1999) have seen a step like of about 1% jumps in the resistance at T = 77 K of a LCMO thin-film array, containing constricted areas of micrometer size, which were assumed to pin the domain walls close to constrictions. The estimated value of domain wall × area resistance, DWRA = $8 \times 10^{-14} \Omega m^2$, was about 4 orders of magnitude smaller than that for a grain boundary, but much larger than DWRA in FM cobalt. The DWMR = 16% at room temperature was obtained for a LSMO film with a nanoconstricted area, produced by electron beam lithography (Wolfman *et al*., 2001). In Figure 22, the vertical nanoconstriction geometry with $h = 90$ nm-wide gaps lying in the film plane is shown. The resistance of a such nanobridge as a function of magnetic field shows very sharp 1.8 kΩ large jumps for $H \sim 0.75$–1.5 kOe with a hysteresis in switching, thus evidencing magnetic origin of the resistance change. The very large resistance × area product DWRA = $10^{-11} \Omega m^2$ implies that the width of domain wall is strongly reduced due to nanoconstriction.

The AMR effect, which is governed by the magnetization state of a structurally homogeneous FM material, seems to be more appropriate for low-field applications (Ciureanu and Middelhoek, 1992) – at least no special geometric limitations like nanoconstrictions are required. Spontaneous AMR, originating from spin-orbit interaction (Smit, 1951; McGuire and Potter, 1975; Malozemoff, 1985), results in the anisotropy of the resistivity, $\Delta\rho = \rho_{||} - \rho_{\perp}$, with respect to the magnetization direction. Here $\rho_{||}$ and $\rho_{\perp}$ is the resistivity parallel and perpendicular to the magnetization direction, respectively, of a single-domain ferromagnet. Depending on whether the voltage is probed parallel (V_X) or perpendicular (V_Y) to the current density, the electric field related to the AMR is given

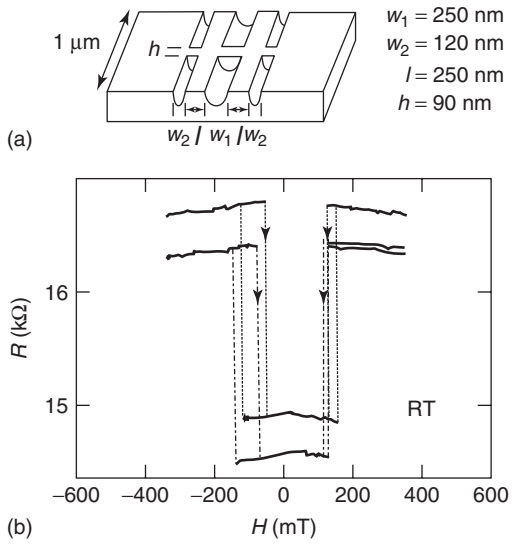

Figure 22. (a) Scheme of a nanoconstriction device and (b) field dependence of the resistance at room temperature. (Reproduced from J. Wolfman *et al*., 2001, with permission from the American Institute of Physics. © 2001.)

by Li *et al*. (1999):

$$E_x = j\rho_\perp + j(\Delta\rho)\cos^2\alpha \quad \text{(Longitudinal geometry)} \quad (9)$$

$$E_y = (j/2)(\Delta\rho)\sin(2\alpha) \quad \text{(Transverse geometry)} \quad (10)$$

Here, j is the transport current density in x direction, and α is the angle between current and the magnetization. AMR is quantified by a ratio $\gamma = \Delta\rho/\rho_0$ (ρ_0 is bulk resistively of the material at zero filed), which is only about 1% for most FM materials as well as for magnates (Mathur *et al*., 1999; Malozemoff, 1985; Li *et al*., 1999). Therefore, AMR, usually hardly seen in longitudinal geometry ($\Delta\rho \ll \rho_\perp\rho_0$), can be detected in the transverse geometry (equation (10) using a properly microstructured epitaxial films.

We have studied in detail the AMR effect in transverse geometry (also known as *planar Hall effect*) for epitaxial $La_{0.7}(Ca_{0.5}Sr_{0.5})MnO_3$ (LSCMO, $T_C = 310–320$ K) thin films grown by MAD technique (Moshnyaga, Damaschke, Tidecks and Samwer, 2003) and built a prototype low-field manganite sensor operating at room temperature. The film was patterned photo-lithographically as shown in Figure 23. The length of the current line was $L = 6$ mm and the width $W = 0.3$ mm. The transverse voltage was detected with the V_Y contacts placed in the perpendicular direction. The magnetic field was aligned parallel to the film surface. The angle dependence of the transverse voltage, $V_Y(\alpha)$, measured at room temperature and magnetic field $H = 0.5$ kOe (see Figure 23) obeys equation (9) for the AMR effect, corrected

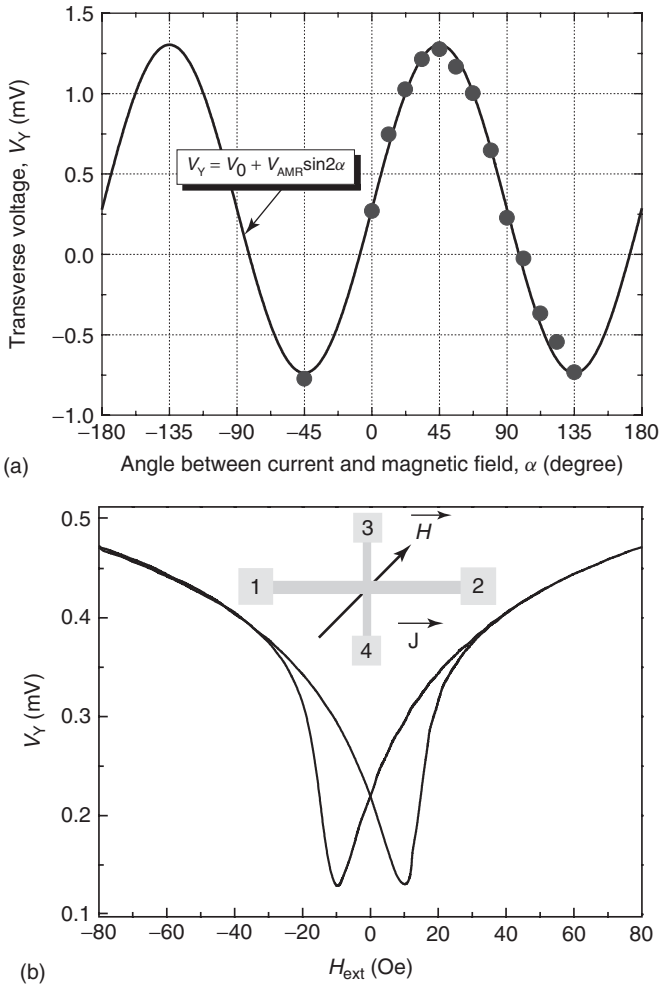

Figure 23. Angle (a) and magnetic field (b) dependences of transverse voltage of a $La_{0.7}(Ca, Sr)_{0.3}MnO_3$ thin film. The sample geometry is shown in the inset of (b): the current flows between contacts (1,2) and the voltage, V_Y, is measured between the opposite contacts (3,4). Magnetic field is aligned parallel to the film plane at angle α to the current line. (Reproduced from V. Moshnyaga *et al*., 2003a, with permission from the American Institute of Physics. © 2003.)

by small isotropic offset voltage, V_0, due to longitudinal misfit of the transverse contacts:

$$V_Y(\alpha, H) = V_0(H) + V_{AMR}(H) \times \sin(2\alpha) \quad (11)$$

here: $V_0 = 0.27$ mV and $V_{AMR} = 1$ mV for $H = 0.5$ kOe. As one can see in Figure 23(b) the magnetic field dependence of the AMR voltage in the LSCMO films is extremely sharp for very low fields $H = 0–20$ Oe, yielding a maximum room-temperature field sensitivity of $S \approx 20\%$/Oe. Another important quantity is the magnetovoltage ratio, $MV = 100\%[V_{AMR}(H)/V_0]$, which describes the relative change of the transverse voltage in an applied magnetic field.

For $\alpha = 45^\circ$ and $H = 500\,\text{Oe}$ with $V_{\text{AMR}} = 1\,\text{mV}$ and $V_0 = 0.25\,\text{mV}$ (see Figure 18) we get MV = 400%. Even for very low fields, $H < 40\,\text{Oe}$, it is $MV\,(40\,\text{Oe}) = 220\%$. The mentioned parameters for manganite films considerably exceed $S = 6\%/\text{Oe}$ and $MV = 130\ \%$ at $H = 35\,\text{Oe}$, observed for the transverse AMR structures based on Co/Ni multilayers at room temperature (Prados *et al*., 1995). Very recently, by improving the measurement conditions of LSCMO-based prototype thin-film sensor, we obtained the output sensitivity as large as $S = 400\,\mu\text{V}\,\text{Oe}^{-1}$ for very low-field $H \sim 1\,\text{Oe}$. With the actual noise level, $V_{\text{N}} \sim 0.1\,\mu\text{V}$, the dc magnetic field sensitivity was $H_{\text{N}} = V_{\text{N}}/S \approx 2 \times 10^{-4}$ Oe at room temperature. All this makes manganite-based MR sensors very attractive for a low-field sensing, which was already demonstrated by us at the International Hannover fair, 1–24 April 2004.

5 SUMMARY AND OUTLOOK

We hope that in spite of limited space, the main features of the physics of manganite thin films were discussed. The most important and most intriguing aspect of the manganites is definitely their *complexity*, related to a rich variety of experimentally observed physical effects like MI transition, CMR, charge, and OO. These phenomena, mediated by different electronic and structural phase transitions, can be strongly influenced by external stimuli (field, temperature, pressure, electromagnetic radiation), resulting in potentially useful effects.

Furthermore, the complexity of manganite also includes the coexistence of different electronic and structural phases (*PS*) as well as the interaction between them. The nature of phase competition or in other words the mechanisms of interaction between different phases within PS scenario seems to be most difficult and thus unexplored problem both for experimental and theoretical physics. Taking into account the major role of lattice strain and disorder effects on the structure and electronic properties of manganites, discussed in Section 1, one can suppose that the phases, FMM and AFI, counteracting in the PS scenario, may be *coupled elastically*. From earlier fundamental studies it is known these phases differ by their crystalline structure (AFI phase is orthorhombic and FMM phase is cubic or rhombohedral) and thus by degree of lattice strain. This point seems to be in good agreement with local STM/STS. Moreover, the observed nonmonotonous magnetic field dependence of the local tunneling conductivity map as well as the irreversibility and 'magnetic history' effects in the PS in thin films of LCMO strongly support the coupling between phases. Note that the irreversibility close to the orthorhombic-rhombohedral structural phase transition in bulk $La_{1-x}SrMnO_3$ (x = 0.17) was clearly seen not only by changing temperature but also as a function of magnetic field, known as *structural phase transition induced by magnetic field* (Asamitsu *et al*., 1995). More generally temperature and magnetic field behavior of the PS in thin films as well as its characteristic scale (10–100 nm) agrees well with the disorder (stress)-induced PS scenario close to the first-order phase transition. Very important becomes the issue of controlling cation disorder, which will allow one to study CMR and electronic manifestations of small and correlated polarons on a very fine scale (1–3 nm) in a so-called *clean limit*. We believe the first step along this line is done by means of preparation of A-site ordered LCMO films.

Along the fundamental importance, the controlling of stress and disorder on the nanoscale seems to be interesting also for future applications. We would like to draw the attention of the reader to the following, may be unexpected, aspect of the PS model: the interaction between metallic and insulating phases occurs at the *interfaces and by means of changing of the interface properties*. This implies also that PS dynamic as a function of field or temperature should be strongly dependent on the interface quality. One can find a very clear analogy with the magnetic tunnel junctions, the performance (spin polarization) of which as we have seen in Section 2.2 depends crucially on the interface quality. Thus, to control PS with a possibility to make a step in nanoscale physics and technology down to at least 10 nm as well as to control the TMR device performance means to be able to control the interfaces. The term *interface engineering* is already known. With respect to the PS problem such interface nanoengineering can be done by creating 'static' interfaces in the preliminary homogeneous electronic template chemically by doping during self-assembled growth of nanophases, like in LCMO:MgO nanocomposites. In this sense, the search of new phase counterparts and further technological development are necessary. Even more interesting seems to be 'dynamic' interfaces created by electromagnetic radiation. It is known that electromagnetic radiation (X ray or visible light) can significantly change the ground state of a manganite resulting even in insulator–metal transition (see for example, Kiryukhin *et al*., 1997; Mishina *et al*., 2004); this topic is out of the frame of this review). However, locally the effect of electromagnetic radiation on the PS was not studied to the best of our knowledge.

Recently, *multiferroic behavior* has become a very hot topic. Such materials combining FM and FE properties are extremely interesting both for fundamental and applied science (Spaldin and Fiebig, 2005). Such materials would, in principle, allow one to get new functions due to magneto-electric effect, that is, magnetization can be controlled by electric field and, vice versa, electrical polarization can be changed by magnetic field. Because of a limited amount of

intrinsic multiferroic materials (note that FM-FE coexistence in the same chemically homogeneous material seems to be mutually exclusive – FE needs empty but FM requires partially filled transition-metal orbitals (for details see Spaldin and Fiebig, 2005)), there is a great demand of composite multiferroic materials, among which thin-film composite will play a major role owing to the possibility of obtaining very large interface area and thus of optimizing elastic coupling between FM and FE constituents with corresponding optimization of magnetoelectric effect. In this case, the problem of controlling thin-film interfaces becomes extremely important. Recently, Zheng *et al*. (2004) have prepared multiferroic $BaTiO_3$–$CoFe_2O_4$ film nanostructures, in which elastically coupled nanocolumnar phases are also coupled magnetoelectrically, that is, magnetization of $CoFe_2O_4$ changes at the FE Curie temperature. It seems reasonable to substitute $CoFe_2O_4$ in such a composite with a manganite (LCMO) phase; the latter should be much more sensitive to mechanic deformation actuated anyway by the FE $BaTiO_3$ component. However, to realize chemical PS (not multilayer geometry) between two phases (LCMO and $BaTiO_3$) having the same perovskite structure looks quite a challenging task for thin-film technology.

REFERENCES

Aarts, J., Freisem, S., Hendrikx, R. and Zandbergen, H.W. (1998). Disorder effects in epitaxial thin films of (La,Ca)MnO_3. *Applied Physics Letters*, **72**, 2975–2977.

Adams, C.P., Lynn, J.W., Mukovskii, Y.M., *et al*. (2000). Charge ordering and polaron formation in the magnetoresistive oxide $La_{0.7}Ca_{0.3}MnO_3$. *Physical Review Letters*, **85**, 3954–3957.

Ahn, K., Lookman, T. and Bishop, A.R. (2004). Strain-induced metal–insulator phase coexistence in perovskite manganites. *Nature*, **428**, 401.

Akahoshi, D., Uchida, M., Tomioka, Y., *et al*. (2003). Random potential effect near the bicritical region in perovskite manganites as revealed by comparison with the ordered perovskite analogs. *Physical Review Letters*, **90**, 177203.

Allodi, G., De Renzi, R. and Guidi, G. (1998). ^{139}La NMR in lanthanum manganites: indication of the presence of magnetic polarons from spectra and nuclear relaxations. *Physical Review B*, **57**, 1024–1034.

Anderson, P.W. and Hasegawa, H. (1955). Considerations on double exchange. *Physical Review*, **100**, 675–681.

Archibald, W., Zhou, J-S. and Goodenough, J.B. (1996). First-order transition at T_C in the orthomanganites. *Physical Review B*, **53**, 14445–14449.

Arima, T., Akahoshi, D., Oikawa, K., *et al*. (2002). Change in charge and orbital alignment upon antiferromagnetic transition in the *A*-site-ordered perovskite manganese oxide $RBaMn_2O_6$ (R = Tb and Sm). *Physical Review B*, **66**, 140408(R).

Asamitsu, A., Moritomo, Y., Tomioka*, Y., *et al*. (1995). A structural phase transition induced by an external magnetic field. *Nature*, **373**, 407–409.

Ashckroft, N.W. and Mermin, N.D. (1981). *Solid State Physics*, Holt Saunders Japan, Ltd,: Tokyo.

Becker, T., Streng, C., Luo, Y., *et al*. (2002). Intrinsic inhomogeneities in manganite thin films investigated with scanning tunneling spectroscopy. *Physical Review Letters*, **89**, 237203.

Bednorz, J.G. and Müller, K.A. (1986). Possible highT_c superconductivity in the Ba–La–Cu–O system. *Zeitschrift fur Physik B*, **64**, 189–193.

Bibes, M., Balcells, Ll., Valencia, S., *et al*. (2001). Nanoscale multiphase separation at $La_{2/3}Ca_{1/3}MnO_3/SrTiO_3$ interfaces. *Physical Review Letters*, **87**, 067210.

Billinge, S.J.L., Di Francesco, R.G., Kwei, G.H., *et al*. (1996). Direct observation of lattice polaron formation in the local structure of $La_{1-x}Ca_xMnO_3$. *Physical Review Letters*, **77**, 715–718.

Biswas, A., Rajeswari, M., Srivastava, R.C., *et al*. (2000). Two-phase behavior in strained thin films of hole-doped manganites. *Physical Review B*, **61**, 9665–9668.

Bowen, M., Bibes, M., Barthelemy, A., *et al*. (2003). Nearly total spin polarization in $La_{2/3}Sr_{1/3}MnO_3$ from tunneling experiments. *Applied Physics Letters*, **82**, 233–235.

Burgy, J., Mayr, M., Martin-Mayor, V., *et al*. (2001). Colossal effects in transition metal oxides caused by intrinsic inhomogeneities. *Physical Review Letters*, **87**, 277202.

Chahara, K., Ohno, T., Kasai, M. and Kozono, Y. (1993). Magnetoresistance in magnetic manganese oxide with intrinsic antiferromagnetic spin structure. *Applied Physics Letters*, **63**, 1990–1992.

Chen, C.H. and Cheong, S-W. (1996). Commensurate to incommensurate charge ordering and its real-space images in $La_{0.5}Ca_{0.5}MnO_3$. *Physical Review Letters*, **76**, 4042–4045.

Chen, S.F., Lin, P.I., Juang, J.Y., *et al*. (2003). Metallic percolation in $La_{0.67}Ca_{0.33}MnO_3$ thin films. *Applied Physics Letters*, **82**, 1242–1244.

Chisholm, M.F. and Penneycook, S.J. (1991). Structural origin of reduced critical currents at $YBa_2Cu_3O_{7-\delta}$ grain boundaries. *Nature*, **351**, 47–49.

Ciureanu, P. and Middelhoek, S. (1992). *Thin Film Resistive Sensors*, Institute of Physics Publishing: New York.

Coey, J.M.D., Viret, M. and Molnar, S. (1999). Mixed-valence manganites. *Advances in Physics*, **48**, 167–293.

Dagotto, E. (2003). *Nanoscale Phase Separation and Colossal Magnetoresistance*, Springer-Verlag: Berlin- Heidelberg.

Dagotto, E., Hotta, T. and Moreo, A. (2001). Colossal magnetoresistant materials: the key role of phase separation. *Physics Reports*, **344**, 1–153.

Dai, P., Fernandez-Baca, J.A., Wakabayashi, N., *et al*. (2000). Short-range polaron correlations in the ferromagnetic $La_{1-x}Ca_xMnO_3$. *Physical Review Letters*, **85**, 2553–2556.

DeLeon, R.L., Joshi, M.P., Rexer, E.F., *et al*. (1998). Progress in thin film formation by laser assisted molecular beam deposition (LAMBD). *Applied Surface Science*, **127–129**, 321–329.

Dessau, D.S. and Shen, Z-H. (2000). Direct electronic structure measurements of the colossal magnetoresistive oxides. In *Colossal Magnetoresistive Oxides*, Tokura, Y. (Ed.), Gordon & Breach Science Publishers: Amsterdam, pp. 149–185.

Dijkkamp, D., Venkatesan, T., Wu, X.D., *et al*. (1987). Preparation of Y-Ba-Cu oxide superconductor thin films using pulsed laser evaporation from high T_C bulk material. *Applied Physics Letters*, **51**, 619–621.

Eremenko, V., Gnatchenko, S., Makedonska, N., *et al*. (2001). X-ray study of $Nd_{0.5}Sr_{0.5}MnO_3$ manganite structure above and below the ferromagnetic metal–antiferromagnetic insulator spontaneous phase transition. *Low Temperature Physics*, **27**, 930–934.

Esseling, M., Moshnyaga, V., Samwer, K., *et al*. (2005). Low-frequency 1/f-noise in $(La_{0.7}Sr_{0.3}MnO_3)_{0.95}$:$(MgO)_{0.05}$ nanocomposite films. *Applied Physics Letters*, **87**, 082509.

Fäth, M., Freisem, S., Menovsky, A.A., *et al*. (1999). Spatially inhomogeneous metal-insulator transition in doped manganites. *Science*, **285**, 1540–1542.

Fernandez-Baca, J.A., Dai, P., Hwang, H.Y., *et al*. (1998). Evolution of the low-frequency spin dynamics in ferromagnetic manganites. *Physical Review Letters*, **80**, 4012–4015.

Frank, F.C. and van der Merwe, J.H. (1949). One-dimensional dislocations: static theory; misfitting monolayers and oriented growth. *Proceedings of the Royal Society Series A*, **198**, 205–225.

de Gennes, P-G. (1960). Effects of double exchange in magnetic crystals. *Physical Review*, **118**, 141–154.

Giesen, F., Damaschke, B., Moshnyaga, V., *et al*. (2004). Suppression of interface-induced electronic phase separation in all-manganite multilayers by preservation of the Mn-O chain network. *Physical Review B*, **69**, 014421.

Gommert, E., Cerva, H., Wecker, J. and Samwer, K. (1999). Influence of misfit stress on the magnetoresistive properties of $La_{0.7}Ca_{0.3}MnO_{3-\delta}$ thin films. *Journal of Applied Physics*, **85**, 5417–5419.

Goodenough, J.B. (1955). Theory of the role of covalence in the perovskite-type manganites [La, M(II)]MnO_3. *Physical Review*, **100**, 564–573.

Gross, R., Alff, L., Büchner, B., *et al*. (2000). Physics of grain boundaries in the colossal magnetoresistance manganites. *Journal of Magnetism and Magnetic Materials*, **211**, 150–159.

Gupta, A., Gong, G.Q., Xiao, G., *et al*. (1996). Grain-boundary effects on the magnetoresistance properties of perovskite manganite films. *Physical Review B*, **54**, R15629–R15632.

Haeni, J.H., Irvin, P., Chang, W., *et al*. (2004). Room-temperature ferroelectricity in strained $SrTiO_3$. *Nature*, **430**, 758–761.

Hammerl, G., Schmehl, A., Schulz, R.R., *et al*. (2000). Enhanced supercurrent density in polycrystalline $YBa_2Cu_3O_{7-\delta}$ at 77 K from calcium doping of grain boundaries. *Nature*, **407**, 162–164.

von Helmolt, R., Wecker, J., Holzapfel, B., *et al*. (1993). Giant negative magnetoresistance in perovskitelike $La_{2/3}Ba_{1/3}MnO_x$ ferromagnetic films. *Physical Review Letters*, **71**, 2331–2333.

Hennion, M., Moussa, F., Biotteau, G., *et al*. (1998). Liquidlike spatial distribution of magnetic droplets revealed by neutron scattering in $La_{1-x}Ca_xMnO_3$. *Physical Review Letters*, **81**, 1957–1960.

Holzapfel, B., Roas, B., Schultz, L., *et al*. (1992). Off-axis laser deposition of $YBa_2Cu_3O_{7-\delta}$ thin films. *Applied Physics Letters*, **61**, 3178–3180.

Hwang, H.Y., Cheong, S.W., Ong, N.P. and Battlog, B. (1996). Spin-polarized intergrain tunneling in $La_{2/3}Sr_{1/3}MnO_3$. *Physical Review Letters*, **77**, 2041–2044.

Hwang, H.Y., Palstra, T.T.M., Cheong, S-W. and Battlog, B. (1995). Pressure effects on the magnetoresistance in doped manganese perovskites. *Physical Review B*, **52**, 15046–15049.

Hwang, H.Y., Cheong, S-W., Radaelli, P.G., *et al*. (1995). Lattice effects on the magnetoresistance in doped $LaMnO_3$. *Physical Review Letters*, **75**, 914–917.

Ishihara, S., Inoue, J. and Maekawa, S. (1997). Effective Hamiltonian in manganites: mStudy of the orbital and spin structures. *Physical Review B*, **55**, 8280–8286.

Ivashchenco, A.I., Karyaev, E.V., Khoroshun, I.V., *et al*. (1995). Relations between structural and electronic properties of SnO_2 polycrystalline thin films prepared by the aerosol MOCVD technique. *Thin Solid Films*, **263**, 122–126.

Izumi, M., Konishi, Y., Nishihara, T., *et al*. (1998). Atomically defined epitaxy and physical properties of strained $La_{0.6}Sr_{0.4}MnO_3$ films. *Applied Physics Letters*, **73**, 2497–2499.

Jahn, H.A. and Teller, E. (1937). Stability of polyatomic molecules in degenerate electronic states. I. Orbital degeneracy. *Proceedings of the Royal Society Series A*, **161**, 220–235.

Jaime, M., Hardner, H.T., Salamon, M.B., *et al*. (1997). Hall-effect sign anomaly and small-polaron conduction in $(La_{1-x}Gd_x)_{0.67}Ca_{0.33}MnO_3$. *Physical Review Letters*, **78**, 951–954.

Jaime, M., Lin, P., Chun, S.H., *et al*. (1999). Coexistence of localized and itinerant carriers near T_C in calcium-doped manganites. *Physical Review B*, **60**, 1028–1032.

Jonker, G. and van Santen, J. (1950). Ferromagnetic compounds of manganese with perovskite structure. *Physica*, **16**, 337–349.

Julliere, M. (1975). Tunneling between ferromagnetic films. *Physics Letters A*, **54**, 225–226.

Kawasaki, M., Takahashi, K., Maeda, T., *et al*. (1994). Atomic control of the $SrTiO_3$ crystal surface. *Science*, **266**, 1540–1542.

Khoroshun, I.V., Karyaev, E.V., Moshnyaga, V.T., *et al*. (1990). Characterization of epitaxial Y-Ba-Cu-O oxide thin films grown by aerosol MOCVD technique. *Superconductor Science and Technology*, **3**, 493–496.

Kim, K.H., Gu, J.Y., Choi, H.S., *et al*. (1996). Frequency shifts of the internal phonon modes in $La_{0.7}Ca_{0.3}MnO_3$. *Physical Review Letters*, **77**, 1877–1880.

Kiryukhin, V., Casa, D., Hill, J.P., *et al*. (1997). An X-ray-induced insulator-metal transition in a magnetoresistive manganite. *Nature (London)*, **386**, 813–815.

Kiryukhin, V., Koo, T.Y., Ishibashi, H., *et al*. (2003). Average lattice symmetry and nanoscale structural correlations in magnetoresistive manganites. *Physical Review B*, **67**, 064421.

Kleine, A., Luo, Y. and Samwer, K. (2006). Electronic phase separation in $LaMnO_{3+\delta}$: usable as tunneling barriers. *Europhysics Letters*. **76**, 135–141.

Konrad, A., Fries, T., Gahn, A., *et al*. (1999). Chemical vapor synthesis and luminescence properties of nanocrystalline cubic Y_2O_3: Eu. *Journal of Applied Physics*, **86**, 3129–3133.

Koo, T.Y., Kiryukhin, V., Sharma, P.A., *et al*. (2001). Magnetic-field-induced collapse of charge-ordered nanoclusters and the colossal magnetoresistance effect in $Nd_{0.7}Sr_{0.3}MnO_3$. *Physical Review B*, **64**, 220405(R).

Köster, S.A., Moshnyaga, V., Samwer, K., *et al*. (2002). Doping of interfaces in $(La_{0.7}Sr_{0.3}MnO_3)_{1-x}$:$(MgO)_x$ composite films. *Applied Physics Letters*, **81**, 1648–1650.

Krebs, H-U., Bremert, O., Störmer, M. and Luo, Y. (1995). Comparison of the structure of laser deposited and sputtered metallic alloys. *Applied Surface Science*, **86**, 90–94.

Krebs, H-U., Weisheit, M., Faupel, J., *et al*. (2003). Pulsed laser deposition (PLD) – a versatile thin film technique. *Advances in Solid State Physics*, **43**, 505–518.

Kuliuk, L., Kravetsky, I., Micu, A., *et al*. (1995). Non-linear optical properties of ZnO thin films prepared by aerosol MOCVD technique. *Proceedings of SPIE*, **2801**, 135–140.

Kwon, C., Robson, M.C., Kim, K-C., *et al*. (1997). Stress-induced effects in epitaxial $(La_{0.7}Sr_{0.3})MnO_3$ films. *Journal of Magnetism and Magnetic Materials*, **172**, 229–236.

Lebedev, O.I., van Tendeloo, G., Amelinckx, S., *et al*. (1998). Structure and microstructure of $La_{1-x}Ca_xMnO_{3-\delta}$ thin films prepared by pulsed laser deposition. *Physical Review B*, **58**, 8065–8074.

Lebedev, O.I., Verbeeck, J., van Tendeloo, G., *et al*. (2002). Structural phase transitions and stress accommodation in $(La_{0.67}Ca_{0.33}MnO_3)_{1-x}$:$(MgO)_x$ composite films. *Physical Review B*, **66**, 104421.

Li, G., Lu, Z., Chai, C., *et al*. (1999). Pseudo-Hall effect in spin-valve multilayers. *Applied Physics Letters*, **74**, 747–749.

Linn, J.W., Erwin, R.W., Borchers, J.A., *et al*. (1996). Unconventional ferromagnetic transition in $La_{1-x}Ca_xMnO_3$. *Physical Review Letters*, **76**, 4046–4049.

Lu, Y., Li, X.W., Gong, G.Q., *et al*. (1996). Large magnetotunneling effect at low magnetic fields in micrometer-scale epitaxial $La_{0.67}Sr_{0.33}MnO_3$ tunnel junctions. *Physical Review B*, **54**, R8357–R8360.

Luo, Y. and Samwer, K. (2001). Structural and magnetotunneling investigations on $La_{0.7}Ca_{0.3}MnO_3/Al_2O_3$ multilayers. *Journal of Applied Physics*, **89**, 6760–6762.

Lüth, H. (2001). *Solid Surfaces, Interfaces and Thin Films*, *Fourth Edition*, Springer.

Maignan, A., Simon, Ch., Caignaert, V. and Raveau, B. (1996). Colossal magnetoresistance properties of the manganese perovskites $La_{0.7-x}Y_xCa_{0.3}MnO_{3\delta}$. *Journal of Applied Physics*, **79**, 7891–7895.

Malozemoff, A.P. (1985). Anisotropic magnetoresistance of amorphous and concentrated polycrystalline iron alloys. *Physical Review B*, **32**, 6080–6083.

Mathur, N.D. and Littlewood, P.B. (2001). The self-organised phases of manganites. *Solid State Communications*, **119**, 271–280.

Mathur, N. and Littlewood, P.B. (2003). Mesoscopic texture in manganites. *Physics Today*, **56**, 25–30.

Mathur, N.D., Littlewood, P.B., Todd, N.K., *et al*. (1999). Resistance of a domain wall in $La_{0.7}Ca_{0.3}MnO_3$. *Journal of Applied Physics*, **86**, 6287–6290.

Mattheu, R., Akahoshi, D., Asamitsu, A., *et al*. (2004). Colossal magnetoresistance without phase separation: disorder-induced spin glass state and nanometer scale orbital-charge correlation in half doped manganites. *Physical Review Letters*, **93**, 227202.

Mayr, M., Moreo, A., Vergés, J.A., *et al*. (2001). Resistivity of mixed-phase manganites. *Physical Review Letters*, **86**, 135–138.

McCormack, M., Jin, S., Tiefel, T.H., *et al*. (1994). Very large magnetoresistance in perovskite-like La-Ca-Mn-O thin films. *Applied Physics Letters*, **64**, 3045–3047.

McGuire, T.R. and Potter, R.I. (1975). Anisotropic magnetoresistance in ferromagnetic 3d alloys. *IEEE Transactions on Magnetics*, **11**, 1018–1024.

Millis, A.J., Darling, T. and Migliori, A. (1998). Quantifying strain dependence in "colossal" magnetoresistance manganites. *Journal of Applied Physics*, **83**, 1588–1591.

Millis, A.J., Littlewood, P.B. and Shraiman, B.I. (1995). Double exchange alone does not explain the resistivity of $La_{1-x}Sr_xMnO_3$. *Physical Review Letters*, **74**, 5144–5147.

Mira, J., Rivas, J., Rivadulla, F., *et al*. (1999). Change from first-to second-order magnetic phase transition in $La_{2/3}(Ca, Sr)_{1/3}MnO_3$ perovskites. *Physical Review B*, **60**, 2998–3001.

Mishina, E., Sherstyuk, N., Sigov, A., *et al*. (2004). Non-linear optical properties of $La_{0.7}Ca_{0.3}MnO_3$ films and dynamics of photoinduced transition. *Transactions of the Magnetics Society of Japan*, **4**, 272–277.

Mitchel, J.F., Argirou, D.N., Potter, C.D., *et al*. (1996). Structural phase diagram of $La_{1-x}Sr_xMnO_{3+\delta}$: relationship to magnetic and transport properties. *Physical Review B*, **54**, 6172–6183.

Mitra, J., Paranjape, M., Raychaudhuri, A.K., *et al*. (2005). Temperature dependence of density of states near the Fermi level in a strain-free epitaxial film of the hole-doped manganite $La_{0.7}Ca_{0.3}MnO_3$. *Physical Review B*, **71**, 094426.

Monsma, D. and Parkin, S. (2000). Spin polarization of tunneling current from ferromagnet/Al_2O_3 interfaces using copper-doped aluminum superconducting films. *Applied Physics Letters*, **77**, 720.

Moodera, J., Kinder, L., Wong, T. and Meservey, R. (1995). Large magnetoresistance at room temperature in ferromagnetic thin film tunnel junctions. *Physical Review Letters*, **74**, 3273–3276.

Moon-Ho, J., Mathur, N.D., Evetts, J.E. and Blamire, M.G. (2000). Coherent magnetic reversal in half-metallic manganite tunnel junctions. *Applied Physics Letters*, **77**, 3803–3805.

Moreo, A., Yunoki, S. and Dagotto, E. (1999). Phase separation scenario for manganese oxides and related materials. *Science*, **283**, 2034–2040.

Moreo, A., Mayr, M., Feiguin, A., *et al*. (2000). Giant cluster coexistence in doped manganites and other compounds. *Physical Review Letters*, **84**, 5568.

Mori, S., Chen, C.H. and Cheong, S-W. (1998). Paired and unpaired charge stripes in the ferromagnetic phase of $La_{0.5}Ca_{0.5}MnO_3$. *Physical Review Letters*, **81**, 3972–3975.

Moshnyaga, V. (2005). Metal-insulator transition and magnetoresistance in manganite films: lattice strain and disorder effects. In *Frontiers in Magnetic Materials*, Narlikar, A.V. (Ed.), Springer-Verlag: Berlin-Heidelberg, pp. 415–458.

Moshnyaga, V., Damaschke, B., Tidecks, R. and Samwer, K. (2003). Low-field transverse magnetovoltage in manganite films. *Journal of Applied Physics*, **93**, 6354–6360.

Moshnyaga, V., Damaschke, B., Shapoval, O., *et al*. (2003). Structural phase transition at the percolation threshold in $(La_{0.7}Ca_{0.3}MnO_3)_{1-x}$:$(MgO)_x$ epitaxial nanocomposite films. *Nature Materials*, **2**, 247–252.

Moshnyaga, V., Khoroshun, I., Petrenko, P., *et al*. (1997). Preparation of $PbTiO_3$ films from heterometallic polynuclear organometallic precursors. *MRS Proceedings*, **495**, 239–242.

Moshnyaga, V., Khoroshun, I., Sidorenko, A., *et al*. (1999). Preparation of rare-earth manganite-oxide thin films by metalorganic aerosol deposition technique. *Applied Physics Letters*, **74**, 2842–2844.

Moshnyaga, V., Sudheendra, L., Lebedev, O.I., *et al*. (2006). *A-site ordering versus electronic inhomogeneity in CMR-manganite films*. *Physical Review Letters*, **97**, 107205.

Mott, N.F. (1990). *Metal-insulator Transitions*, *Second Edition*, Taylor & Francis: London.

O'Donnell, J., Rzchowski, M.S., Eckstein, J.N. and Bozovic, I. (1998). Magnetoelastic coupling and magnetic anisotropy in $La_{0.67}Ca_{0.33}MnO_3$ films. *Applied Physics Letters*, **72**, 1775–1777.

Ogawa, Y., Yamada, H., Ogasawara, T., *et al*. (2003). Nonlinear magneto-optical Kerr rotation of an oxide superlattice with artificially broken symmetry. *Physical Review Letters*, **90**, 217403.

Pailloux, F., Imhoff, D., Sikora, T., *et al*. (2002). Nanoscale analysis of a $SrTiO_3/La_{2/3}Sr_{1/3}MnO_3$ interface. *Physical Review B*, **66**, 014417.

Park, J-H., Vescovo, E., Kim, H-J., *et al*. (1998). Direct evidence for a half-metallic ferromagnet. *Nature*, **392**, 794–796.

Phillip, J.B., Höfener, C., Thienhaus, S., *et al*. (2000). Large two-level magnetoresistance effect in doped manganite grain-boundary junctions. *Physical Review B*, **62**, R9248–R9251.

Prados, C., Garcia, D., Lesmes, F., *et al*. (1995). Extraordinary anisotropic magnetoresistance effect under 35 Oe field at room temperature in Co/Ni multilayers. *Applied Physics Letters*, **67**, 718–720.

Radaelli, P.G., Cox, D.E., Marezio, M., *et al*. (1995). Simultaneous structural, magnetic, and electronic transitions in $La_{1-x}Ca_xMnO_3$ with $x = 0.25$ and 0.50. *Physical Review Letters*, **75**, 4488–4491.

Radaelli, P.G., Iannone, G., Marezio, M., *et al*. (1997). Structural effects on the magnetic and transport properties of perovskite $A_{1-x}A'_x$ MnO_3 ($x = 0.25$, 0.30). *Physical Review B*, **56**, 8265–8276.

Rajeswari, M., Shreekala, R., Goyal, A., *et al*. (1998). Correlation between magnetic homogeneity, oxygen content, and electrical and magnetic properties of perovskite manganite thin films. *Applied Physics Letters*, **73**, 2672–2674.

Rao, R.A., Gan, Q., Eom, C.B., *et al*. (1997). Strain stabilized metal–insulator transition in epitaxial thin films of metallic oxide $CaRuO_3$. *Applied Physics Letters*, **70**, 3035–3037.

Rao, R.A., Lavric, D., Nath, T.K., *et al*. (1998). Three-dimensional strain states and crystallographic domain structures of epitaxial colossal magnetoresistive $La_{0.8}Ca_{0.2}MnO_3$ thin films. *Applied Physics Letters*, **73**, 3294–3296.

Rao, R.A., Lavric, D., Nath, T.K., *et al*. (1999). Effects of film thickness and lattice mismatch on strain states and magnetic properties of $La_{0.8}Ca_{0.2}MnO_3$ thin films. *Journal of Applied Physics*, **85**, 4794–4796.

Raveau, B., Maignan, A. and Caignaert, V. (1995). Spectacular GMR effects in the polycrystalline perovskite $Pr_{0.7}Sr_{0.05}Ca_{0.25}$ MnO_{3-d}. *Journal of Solid State Chemistry*, **117**, 424–426.

Renner, Ch., Aeppli, G., Kim, B-G., *et al*. (2002). Atomic-scale images of charge ordering in a mixed-valence manganite. *Nature*, **416**, 518–521.

Reutler, P., Bensaid, A., Herbstritt, F., *et al*. (2000). Local magnetic order in manganite thin films studied by $1/f$ noise measurements.*Physical Review B*, **62**, 11619–11625.

Roder, H., Zang, J. and Bishop, A.R. (1996). Lattice effects in the colossal-magnetoresistance manganites. *Physical Review Letters*, **76**, 1356–1359.

Rodriguez-Martinez, L.M. and Attfield, J.P. (1996). Cation disorder and size effects in magnetoresistive manganese oxide perovskites. *Physical Review B*, **54**, R15622–R15625.

Schiffer, P., Ramirez, A.P., Bao, W. and Cheong, S-W. (1995). Low temperature magnetoresistance and the magnetic phase diagram of $La_{1-x}Ca_xMnO_3$. *Physical Review Letters*, **75**, 3336–3339.

Shannon, R.D. and Prewitt, C.T. (1976). Revised effective ionic radii and systematic studies of interatomic distances in halides and chalcogenides. *Acta Crystallographica Section A*, **32**, 751–767.

Shklovsky, B.I. and Efros, A.L. (1979). *Electronic Properties of Doped Semiconductors*, Moscow: Nauka.

Smit, J. (1951). *Physica*, **16**, 612–635.

Spaldin, N.A. and Fiebig, M. (2005). The renaissance of magnetoelectric multiferroics. *Science*, **309**, 391–392.

Steenbeck, K., Eick, T., Kirsch, K., *et al*. (1998). Tunneling-like magnetoresistance in bicrystal $La_{0.8}Sr_{0.2}MnO_{3-\delta}$ thin films. *Applied Physics Letters*, **73**, 2506–2508.

Sun, J.Z., Gallagher, W.J., Duncombe, P.R., *et al*. (1996). Observation of large low-field magnetoresistance in trilayer perpendicular transport devices made using doped manganate perovskites.*Applied Physics Letters*, **69**, 3266–3268.

Sun, J.R., Yeung, C.F., Zhao, K., *et al*. (2000). Strain-dependent vacuum annealing effects in $La_{0.67}Ca_{0.33}MnO_{3-\delta}$ films. *Applied Physics Letters*, **76**, 1164–1166.

de Teresa, J.M., Ibarra, M.R., Algarbel, P.A., *et al*. (1997). Evidence for magnetic polarons in the magnetoresistive perovskites. *Nature*, **386**, 256–259.

Tersoff, J., Johnson, M.D. and Orr, B.G. (1997). Adatom densities on GaAs: evidence for near-equilibrium growth. *Physical Review Letters*, **78**, 282–285.

Tokura, Y. (Ed.) (2000). *Colossal Magnetoresistance Oxides*, Gordon & Breach Science Publishers: Amsterdam.

Uehara, M., Mori, S., Chen, C.H. and Cheong, S-W. (1999). Percolative phase separation underlies colossal magnetoresistance in mixed-valent manganites. *Nature*, **399**, 560–563.

Urushibara, A., Moritomo, Y., Arima, T., *et al*. (1995). Insulator-metal transition and giant magnetoresistance in $La_{1-x}Sr_xMnO_3$. *Physical Review B*, **51**, 14103–14109.

Venkatesan, T. (1994). Pulsed laser deposition: future trends. In *Pulsed Laser Deposition of Thin Films*, Chrisey, D.B. and Hubler, G.K. (Eds.), John Wiley & Sons: New York, pp. 313–326.

Viret, M., Ranno, L. and Coey, J.M.D. (1997). Magnetic localization in mixed-valence manganites. *Physical Review B*, **55**, 8067–8070.

Volmer, M. and Weber, J. (1926). *Zeitschrift fur Physikalische Chemie*, **119**, 277–283.

Wahl, G., Stadel, O., Gorbenko, O. and Kaul, A. (2000). High-temperature chemical vapor deposition. An effective tool for the production of coatings. *Pure and Applied Chemistry*, **72**, 2167–2176.

Wang, H.S., Wertz, E., Hu, Y.F., *et al*. (2000). Role of strain in magnetotransport properties of $Pr_{0.67}Sr_{0.33}MnO_3$ thin films. *Journal of Applied Physics*, **87**, 7409–7414.

Wiedenhorst, B., Höfener, C., Lu, Y., *et al*. (1999). Strain effects and microstructure of epitaxial manganite thin films and heterostructures. *Applied Physics Letters*, **74**, 3636–3638.

Willmott, P.R. (2004). Deposition of complex multielemental thin films. *Progress in Surface Science*, **76**, 163–217.

Wold, A. and Arnott, R.J. (1959). Preparation and crystallographic properties of the systems $LaMn_{1-x}Mn_xO_{3+\lambda}$ and $LaMn_{1-x}Ni_xO_{3+\lambda}$ JA-1106. *Journal of Physics and Chemistry of Solids*, **9**, 176–180.

Wollan, E.O. and Kohler, W.C. (1955). Neutron diffraction study of the magnetic properties of the series of perovskite-type compounds $[(1-x)\mathrm{La}, x\mathrm{Ca}]MnO_3$. *Physical Review*, **100**, 545–563.

Wolfman, J., Haghiri-Gosnet, A.M., Raveau, B., *et al*. (2001). Large domain wall magnetoresistance up to room temperature in $La_{0.7}Sr_{0.3}MnO_3$ bridges with nanoconstrictions. *Journal of Applied Physics*, **89**, 6955–6957.

Yamada, H., Ogawa, Y., Ishii, Y., *et al*. (2004). Engineered interface of magnetic oxides. *Science*, **305**, 646–648.

Zener, C. (1951). Interaction between the *d* shells in the transition metals. *Physical Review*, **81**, 440–444.

Zheng, H., Wang, J., Lofland, S.E., *et al*. (2004). Multiferroic $BaTiO_3$-$CoFe_2O_4$ nanostructures. *Science*, **203**, 661–663.

Ziese, M. (2002). Extrinsic magnetotransport phenomena in ferromagnetic oxides. *Reports on Progress in Physics*, **65**, 143–249. and references therein.

Ferromagnetic Semiconductors

Fumihiro Matsukura[1,2] and Hideo Ohno[1,2]

[1] *Tohoku University, Sendai, Japan*
[2] *Japan Science and Technology Agency, Sendai, Japan*

1 INTRODUCTION

Ferromagnetic semiconductors are semiconductors that exhibit ferromagnetism. Owing to spontaneous spin splittings in the band structure caused by exchange interaction, they exhibit a variety of spin-dependent optical and transport properties that are not readily available in other materials. Owing to this additional spin degree of freedom, ferromagnetic semiconductors can combine semiconductor heterostructure physics and ferromagnetism, which may lead us to new usage of semiconductor properties and ferromagnetism that was not realized by other systems (Awschalom, Loss and Samarth, 2002; Žutić, Fabian and Das Sarma, 2004). The study of ferromagnetic semiconductors was initiated by extensive theoretical and experimental studies on rare-earth chalcogenides and chromite spinels since the 1960s (Methfessel and Mattis, 1968; Holtberg *et al*., 1980; Mauger and Godart, 1986). However, difficulties in preparation of materials and their heterostructures made these materials less attractive. Recent progress in ferromagnetic semiconductors was made in a class of semiconductors called *diluted magnetic semiconductors* (DMSs), where a part of host atoms is replaced by magnetic elements. In the early stage of the DMS research, studies were done on paramagnetic II–VI compound semiconductor-based DMSs (Furdyna and Kossut, 1988; Kossut and Dobrowolski, 1993; Dietl, 1994). These paramagnetic II–VI DMSs showed antiferromagnetic superexchange interaction among magnetic ions and exhibited a number of new spin-dependent phenomena including giant Zeeman splitting of band states induced by an external magnetic field H. Giant Zeeman splitting is caused by the exchange interaction among band carriers (sp states) and magnetic spins (d states), which is often called the *sp–d exchange interaction*. This interaction is the source of most of the unique properties of II–VI DMSs and determines properties such as the magnitude of the Faraday effect and allows one to realize a new class of low-dimensional structures, such as spin superlattice (Kossut, 2001; Dobrowolski, Kossut and Story, 2003).

Synthesis (Munekata *et al*., 1989) and subsequent discovery of ferromagnetism in III–V-based DMSs, (In,Mn)As and (Ga,Mn)As, in the 1990s (Ohno *et al*., 1992, 1996) added a new dimension to the magnetic semiconductor research because of possible seamless integration of ferromagnetism with well-established III–V heterostructures and devices. (Ga,Mn)As and (In,Mn)As are now most well-investigated and well-understood ferromagnetic semiconductors and the material and their heterostructures provide an ideal test

Handbook of Magnetism and Advanced Magnetic Materials. Edited by Helmut Kronmüller and Stuart Parkin. Volume 5: *Spintronics and Magnetoelectronics*. ISBN: 978-0-470-02217-7.

bench for demonstrating new concepts in physics and device operation (Ohno, 1999; Matsukura, Ohno and Dietl, 2002; Jungwirth *et al*., 2006). It has been established that the existence of holes brings about the ferromagnetic interaction among Mn spins in (Ga,Mn)As and (In,Mn)As. The p–d Zener model has been shown to describe qualitatively and, in many cases, even quantitatively a number of experimental results on these materials (Dietl, Ohno and Matsukura, 2001; Dietl *et al*., 2000). In this review, we intend to summarize the present state of the experimental results on ferromagnetic semiconductors focusing mainly on the prototypal (Ga,Mn)As and (In,Mn)As and their device structures.

2 PREPARATION AND BASIC CHARACTERIZATION

A number of methods have been employed for the synthesis of DMSs. These include Bridgman and Czochralski methods for bulk materials, and molecular-beam epitaxy (MBE), diffusion, ion implantation, and pulsed-laser deposition methods for thin films. The Bridgman method was adopted to obtain single-crystal bulk II–VI DMSs, in which the solubility of transition metals can be high due to the isoelectronic nature of magnetic ions; for example, highest Mn composition $x \sim 0.8$ for representative II–VI DMS, $Cd_{1-x}Mn_xTe$ (Furdyna and Kossut, 1988). MBE growth has been adopted for nearly all heterostructures and low-dimensional structures based on II–VI materials. It has also been used to prepare (In,Mn)As with $x < 0.18$ (Munekata *et al*., 1989), overcoming the solubility limit of transition metals in III–V, which is of the order of 10^{18}–$10^{19}\,cm^{-3}$, together with the surface segregation and phase separation (DeSimone, Wood and Evans, 1982; Kordoš, Janšák and Benč, 1975). The growth of single-crystal (In,Mn)As was achieved by employing low-temperature molecular-beam epitaxy (LT-MBE), performing epitaxial growth at low growth temperature T_S below 300 °C compared to typical $T_S \sim 500\,^{\circ}C$ for InAs, where, importantly, T_S was still high enough to provide metastable single crystal and low enough to suppress the formation of thermodynamically stable second phases such as MnAs. This initial success of (In,Mn)As was followed by the growth of (Ga,Mn)As (Ohno *et al*., 1996). Most of Mn in III–V DMSs substitute the third-group cation site and provide both localized spins and holes due to their acceptor nature.

2.1 Molecular-beam epitaxy of (Ga,Mn)As

Typical MBE of (Ga,Mn)As is carried out in an ultrahigh vacuum MBE chamber with elemental sources, Ga, Mn, and As, on GaAs(001) substrates with surfaces under As-stabilized conditions. After the removal of surface oxide and the growth of buffer layer for the preparation of a flat starting surface, the growth of (Ga,Mn)As is initiated by simply commencing the Mn flux during the LT-GaAs growth while keeping T_S constant at ∼250 °C. The reflection high-energy electron diffraction (RHEED) pattern is used as a common tool to monitor the growth front. The RHEED pattern for (Ga,Mn)As shows a streaky (1 × 2) pattern, confirming the growth of (Ga,Mn)As with a zinc-blende structure. Maximum x reported so far is 0.15 (Chiba, Takamura, Matsukura and Ohno, 2003). When T_S and/or Mn flux is too high, one can recognize the segregation of the hexagonal MnAs phase from a spotty RHEED pattern (Shen *et al*., 1997a). Further decreasing T_S or employing the migration-enhanced epitaxy (MEE) method, where Ga + Mn and As fluxes are supplied alternately, have been reported to help increase maximum x, but not dramatically (Takamura, Matsukura, Ohno and Ohno, 2001; Sadowski *et al*., 2001). If the growth condition is appropriate, a clear RHEED intensity oscillation is observed at the initial stage of growth (Shen *et al*., 1997a), where the surfactant effect of Mn and excess As may be responsible for the two-dimensional growth at low T_S (Shen, Horikoshi, Ohno and Guo, 1997b; Yasuda and Ohno, 1999; Guo *et al*., 2000). Magnetic and electrical properties of (Ga,Mn)As are strongly affected by the growth condition, such as V/III beam-flux ratio and T_S as well as x (Matsukura *et al*., 1999; Shimizu, Hayashi, Nishinaga and Tanaka, 1999; Ohno, 1998; Myers *et al*., 2006), which is related to the degree of compensation due to the existence of As antisites and Mn interstitials, both known as donors in GaAs.

2.2 Determination of Mn composition and lattice constants

Mn composition in the epitaxial film can be calculated from the beam-equivalent pressure (BEP) measured by an ion gauge inserted in the path of the beam flux and later calibrated to relate BEP to the beam flux and/or from the periods of the RHEED intensity oscillation observed at the initial stage of growth (Ohno *et al*., 1996; Sadowski *et al*., 2000). Other conventional analyses are also applicable, such as Auger microprobe measurement, electron probe-microanalysis (EPMA), and secondary ion mass spectroscopy (SIMS) (Ohno *et al*., 1996; Sadowski *et al*., 2001). Of all others, the most widely used method is the use of lattice constant a determined by X-ray diffraction (XRD) as the measure of x due to its experimental simplicity.

(Ga,Mn)As on a GaAs buffer layer has compressive lattice strain, and the free-standing lattice constant a is calculated with assumptions that the (Ga,Mn)As layer is fully strained, that is, the lateral lattice constant of the epitaxial layer is equal to the GaAs one, and that (Ga,Mn)As has the same elastic constant as GaAs (Ohno *et al*., 1996). The pseudomorphic growth without the indication of strain relaxation has been confirmed by asymmetric XRD at least up to a thickness of 2 µm with $x = 0.057$ (Shen *et al*., 1999). For (Ga,Mn)As, a is known to follow the Vegard's law, $a = a_{\text{LT-GaAs}}(1-x) + a_{\text{ZB-MnAs}}x$, where $a_{\text{LT-GaAs}}$ and $a_{\text{ZB-MnAs}}$ are the lattice constants of low-temperature-grown GaAs (LT-GaAs) ∼0.566 nm and hypothetical zinc-blende MnAs ∼0.598 nm respectively (Ohno *et al*., 1996). However, this way of determining a is known to suffer from uncertainties due to the degree of incorporation of defects like As antisites and Mn interstitials (Shimizu, Hayashi, Nishinaga and Tanaka, 1999; Hayashi, Hashimoto, Katsumoto and Iye, 2001; Schott, Faschinger and Molenkamp, 2001; Schott *et al*., 2003; Sadowski and Domagala, 2004).

Most of Mn in (Ga,Mn)As substitutes Ga; that is why we write this alloy as (Ga,Mn)As. For Mn-doped GaAs,

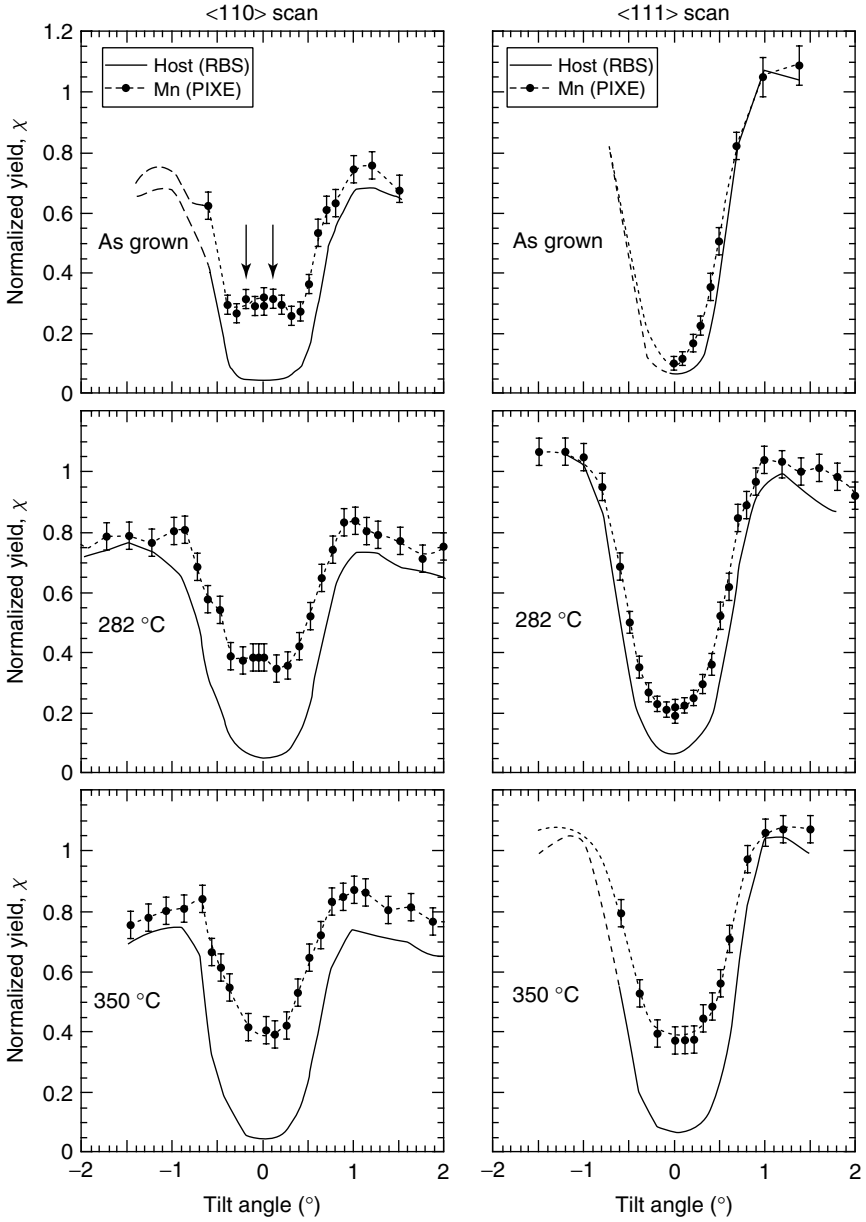

Figure 1. Angular scans of RBS and PIXE about ⟨110⟩ along {110} planar channel and ⟨111⟩ axes for three (Ga,Mn)As samples with $x \sim 0.08$ before and after LT annealing. (Reproduced from Yu *et al*., 2002, with permission from the American Physical Society. © 2002.)

with the doping level less than $10^{19}\,\mathrm{cm}^{-3}$, substitutional Mn was confirmed by an electron paramagnetic resonance (EPR) and cross-sectional scanning tunneling microscopy (XSTM) (Ilegrams, Dingle and Rupp, 1975; Schneider *et al*., 1987; Tsuruoka *et al*., 2002). For (Ga,Mn)As, the extended X-ray absorption fine structure (EXAFS) study showed that most of Mn are in the substitutional position, that is, on the Ga sublattice of the zinc-blende lattice (Shioda, Ando, Hayashi and Tanaka, 1998). The ion-channeling measurements (Rutherford backscattering (RBS) and particle-induced X-ray emission (PIXE)) shown in Figure 1 later revealed that those Mn atoms (∼17% of the introduced Mn atoms in the case of Figure 1) that were not incorporated in the substitional site reside in the interstitial sites (Yu *et al*., 2002a). Post-growth low-temperature annealing (LT annealing) at or below the growth temperature (Hayashi, Hashimoto, Katsumoto and Iye, 2001) was found to decrease the number of Mn interstitials, $\mathrm{Mn_I}$, and simultaneously increases hole concentration p (Potashnik *et al*., 2001; Edmonds *et al*., 2002a,b), indicating that the $\mathrm{Mn_I}$ is unstable and mobile donor. The double-donor nature of $\mathrm{Mn_I}$ is also shown from the *ab initio* calculation (Máca and Mašek, 2003). Further annealing at 350 °C results in MnAs precipitates having NiAs structure, which has T_C of ∼310 K. Theoretical study shows that double-donor $\mathrm{Mn_I}$ does not participate in ferromagnetic order and may form pairs with substitutional Mn, $\mathrm{Mn_{Ga}}$. This results in antiferromagnetic coupling by superexchange interaction and reduces net Mn moment (Blinowski and Kacman, 2003).

2.3 Determination of carrier concentration of (Ga,Mn)As

Since the presence of holes stabilizes ferromagnetism in (Ga,Mn)As, it is important to determine the hole concentration p. In conventional semiconductors, p can readily be determined by magnetotransport measurements, using the Hall effect. For ferromagnetic semiconductors, however, it is not straightforward due to the presence of the anomalous Hall effect, which can play a role even at room temperature, and of the negative magnetoresistance (MR) at low temperatures. Hall resistance R_{Hall} in ferromagnetic semiconductors is expressed as the sum of the ordinary Hall resistance and anomalous Hall resistance,

$$R_{\mathrm{Hall}} = \frac{R_0}{d}\mu_0 H + \frac{R_S}{d}M \qquad (1)$$

where R_0 and R_S are the ordinary and anomalous Hall coefficients respectively, d is the thickness of the ferromagnetic layers, M is the component of the magnetization perpendicular to the sample surface. R_S is usually proportional to $R_{\mathrm{sheet}}^{\gamma}$ (R_{sheet}: sheet resistance) with γ = 1 or 2, depending on the origin of the scattering (Chien and Westgate, 1980) or $\gamma = 2$ due to a scattering-independent topological contribution (Jungwirth, Qian and MacDonald, 2002). The dominance of the anomalous Hall term hinders the straightforward determination of the carrier type and concentration from the ordinary Hall term; the carrier concentration is given as $1/(eR_0)$ (e: elementary charge) and its positive (negative) sign corresponds to p-type (n-type) conduction. Only at low temperatures and under very high H, the anomalous Hall term almost saturates, so that R_0 can be determined from the remaining linear change of R_{Hall} in the H dependence, as shown in Figure 2 (Omiya *et al*., 2000; see also Sadowski *et al*., 2002; Edmonds *et al*., 2002a). Note that, although M saturates at relatively low H, negative MR persists to high H, and generates the H dependence of the anomalous Hall effect through the change in the anomalous Hall coefficient. Thus, this method is applicable only for (Ga,Mn)As with metallic conductivity because of the very large MR and resistance for insulating (Ga,Mn)As.

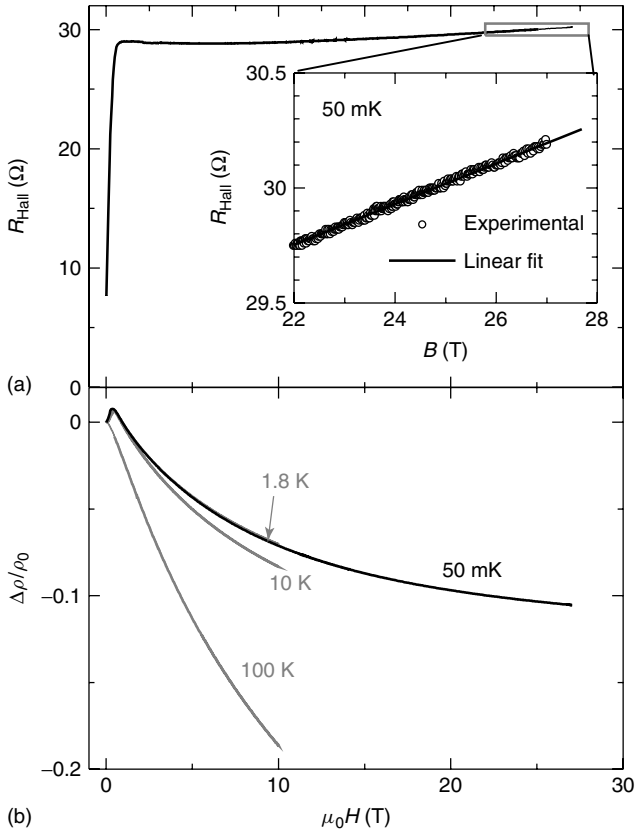

Figure 2. (a) R_{Hall} and (b) R_{sheet} measured at low temperatures. The inset shows that R_{Hall} is the linear function of H in the high-field region. (Reproduced from T. Omiya *et al*., 2000, with permission from Elsevier. © 2000.)

Another powerful method for determining p is the electrochemical capacitance–voltage (ECV) profiling. The reliability of this method was confirmed by comparison of p obtained from ECV and Hall measurements for Be-doped LT-GaAs (Yu *et al*., 2002b; see also Koeder *et al*., 2003; Moriya and Munekata, 2003). The determination of p by other methods, such as thermoelectric power measurements (Osinny *et al*., 2001) and the Raman scattering analysis of the coupled plasmon-LO-phonon modes, is also possible (Limmer *et al*., 2002; Seong *et al*., 2002).

These measurements revealed that p is often less than $10^{21}\,\mathrm{cm}^{-3}$ (smaller than nominal x) for as-grown samples, and increases significantly to $p = x$, consistent with the acceptor nature of Mn, after appropriate annealing as long as x is below 0.07 and the film is thin enough (Wang *et al*., 2004).

3 PROPERTIES OF (Ga,Mn)As

3.1 Magnetic properties

Magnetization M of (Ga,Mn)As is usually measured using a superconducting quantum interference device (SQUID) magnetometer. The diamagnetic response of thick GaAs substrate determined by a separate measurement must be subtracted from the measured magnetization curve in order to obtain the response from the thin epitaxial layer. When H is applied in the direction of magnetic easy axis of (Ga,Mn)As, M shows a sharp and clear hysteresis in its H dependence at low temperatures, which is one of the evidences of the presence of extended ferromagnetic order in the film. T_C can be determined by measuring the temperature dependence of the remanent magnetization, from the Arrott plots, and/or from the Curie–Weiss plot. The value of T_C has a strong correlation with the electrical conductivity, that is, for a given x, the T_C is higher for more metallic samples. The highest T_C reported so far is 173 K for (Ga,Mn)As with $x = 0.09$ after annealing (Wang *et al*., 2005a; Jungwirth *et al*., 2005). The p–d Zener model with mean-filed approximation is capable of explaining the observed magnetic properties, including the magnitude of T_C (Dietl *et al*., 2000; Dietl, Ohno and Matsukura, 2001).

The magnetic domain structure, which is another evidence of the presence of the extended ferromagnetic phase, has been observed in (Ga,Mn)As samples by a scanning Hall microscope and magneto-optical microscopes (Shono *et al*., 2000; Welp *et al*., 2003; Thevenard *et al*., 2006). The computed value of the domain width in (Ga,Mn)As by the p–d Zener model combined with micromagnetic theory (Dietl, König and MacDonald, 2001) is in reasonable agreement with the experimental ones.

3.2 Electrical properties

The spin–orbit interaction and the p–d exchange interaction manifest themselves in sizable magnetotransport phenomena, including the anomalous Hall effect, anisotropic magnetoresistance (AMR), and the planar Hall effect, which provide valuable information on the magnetism of (Ga,Mn)As. Because of the high sensitivity, the determination of magnetization behavior from transport is an important technique for thin films of diluted magnets, where the total of the magnetic moments is small. In addition, the sensitivity of transport measurements does not depend on the lateral size of the device with the fixed lateral aspect ratio.

The temperature and magnetic field dependence of R_{Hall} reflects the temperature and field dependence of magnetization because R_{Hall} is dominated by the anomalous Hall effect term of equation (1) (Matsukura, Ohno, Shen and Sugawara, 1998; Matsukura *et al*., 2004). From the same procedure as that for magnetization measurements, T_C can be determined by the Arrott plots and the Curie–Weiss plot, as shown in Figure 3 (Ohno and Matsukura, 2001). Since the (Ga,Mn)As layers grown directly on GaAs usually have in-plane magnetic easy axis, R_{Hall} measured in perpendicular H probes the magnetization process along the hard axis for the magnetization.

In contrast with R_{Hall} measured in perpendicular H, the planar Hall resistance is the transverse resistance measured by the same probes as R_{Hall} in an in-plane H (Jan, 1957). For (Ga,Mn)As, the signal of the planar Hall resistance is large and can be used to detect the in-plane M reversal (Tang, Kawakami, Awschalom and Roukes, 2003).

It has been found that MR of (Ga,Mn)As depends on the relative orientation of the current direction, the magnetic field direction, and their direction with respect to crystal axes (Hayashi *et al*., 2000). For metallic (Ga,Mn)As, the lowest resistance is observed when H is parallel to the current, as shown in Figure 4 (Baxter *et al*., 2002; Matsukura *et al*., 2004). The direction of H for the highest resistance, however, was predicted theoretically to be different for compressive and lattice strain (Jungwirth *et al*., 2002). This is corroborated by experiments; for the sample with compressive strain, the highest resistance is measured when H is perpendicular to the surface, and for the sample with a tensile strain it is observed when H is in-plane perpendicular to the current (Matsukura *et al*., 2004).

Resistance maximum observed around T_C and the negative MR associated with it are attributed to the critical scattering. The resistance maximum can be interpreted in terms of a spin-dependent scattering by packets of ferromagnetically coupled spins, whose correlation length is comparable to the wavelength of the carriers at the Fermi level. The

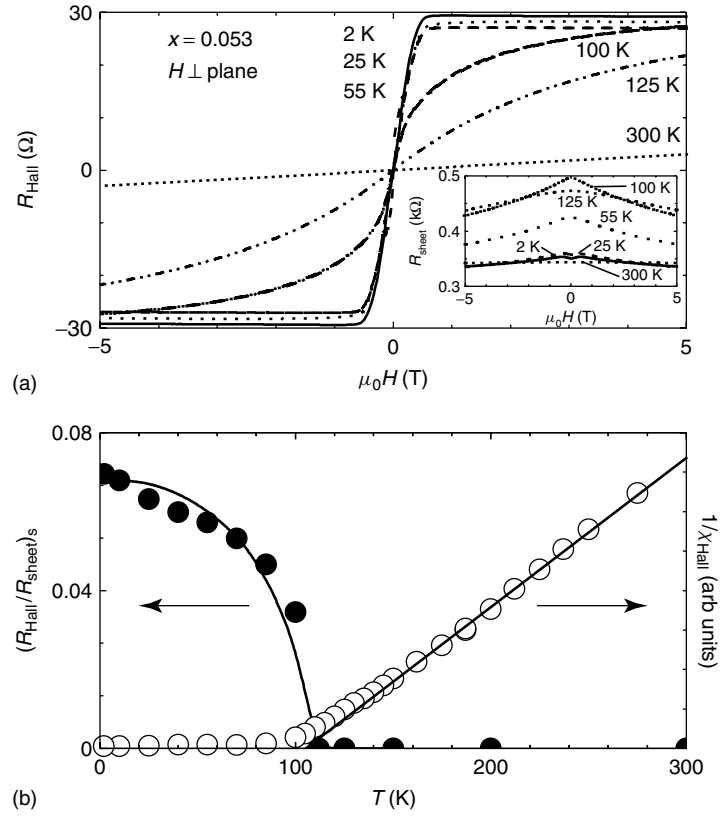

Figure 3. (a) Temperature dependence of R_{Hall} and MR (inset). (b) The temperature dependence of spontaneous magnetization, $(R_{\mathrm{Hall}}/R_{\mathrm{sheet}})_{\mathrm{S}}$ obtained from Arrott plots and the Curie–Weiss plot. (Reproduced from H. Ohno *et al*., 2001, with permission from Elsevier. © 2001.)

negative MR occurs because the H-induced spin alignment reduces the spin-disorder scattering (Matsukura, Ohno, Shen and Sugawara, 1998). From the numerical fitting to the data of the temperature dependence and H dependence of the resistance reproduces the data well and gives the magnitude of p–d exchange interaction as $|N_0\beta| = 1.5 \pm 0.2$ (Omiya *et al*., 2000), which compares favorably with that determined by photoemission experiments, $N_0\beta = -1.2\,\mathrm{eV}$ (Okabayashi *et al*., 1998).

At low temperatures, the negative MR extends to rather high H, where magnetic spins are fully ordered ferromagnetically according to the anomalous Hall effect response. This cannot be accounted for by the suppression of spin-disorder scattering. Here, one should note that the giant splitting of the valence band makes both spin-disorder and spin-orbit scattering ineffective. Under such conditions, negative MR due to weak localization can show up at low temperatures, where phase breaking scattering ceases to operate. The weak localization MR is expressed as

$$\frac{\Delta\rho}{\rho} \sim -\frac{\Delta\sigma}{\sigma} = -\frac{n_v e^2 C_0 \rho (eB/\hbar)^{1/2}}{(2\pi^2\hbar)} \qquad (2)$$

where $C_0 \sim 0.605$, ρ is resistivity, σ is conductivity, $\hbar$ is the reduced Planck constant, and $1/2 \leq n_v \leq 2$, depending on whether one or all four hole subbands (spin-split bands of light and heavy holes) contribute to the charge transport (Kawabata, 1980). The fitting to equation (2) with n_v as a fitting parameter reproduces the data at 2 K quite well for samples under compressive as well as for those under tensile strain (Matsukura *et al*., 2004). Metal–insulator transition (MIT)-associated feature can also be observed for insulating (Ga,Mn)As, which shows an anisotropic hopping conduction with 2 orders of magnitude difference between the resistivity along [110] and [−110] directions below 1 K (Katsumoto *et al*., 1998).

The Baukhausen noise caused by the scattering due to the existence of magnetic domain walls (DWs) has been observed in the resistance measurement (Hayashi *et al*., 2000). Magnetic DW is known to contribute to the electrical resistance. The domain wall resistance (DWR) of a single DW has been measured for (Ga,Mn)As; a negative sign of DWR was reported for (Ga,Mn)As with in-plane easy axis, and a positive was reported for that with perpendicular easy axis (Tang *et al*., 2004; Chiba *et al*., 2006). The former negative DWR may be explained by the destruction

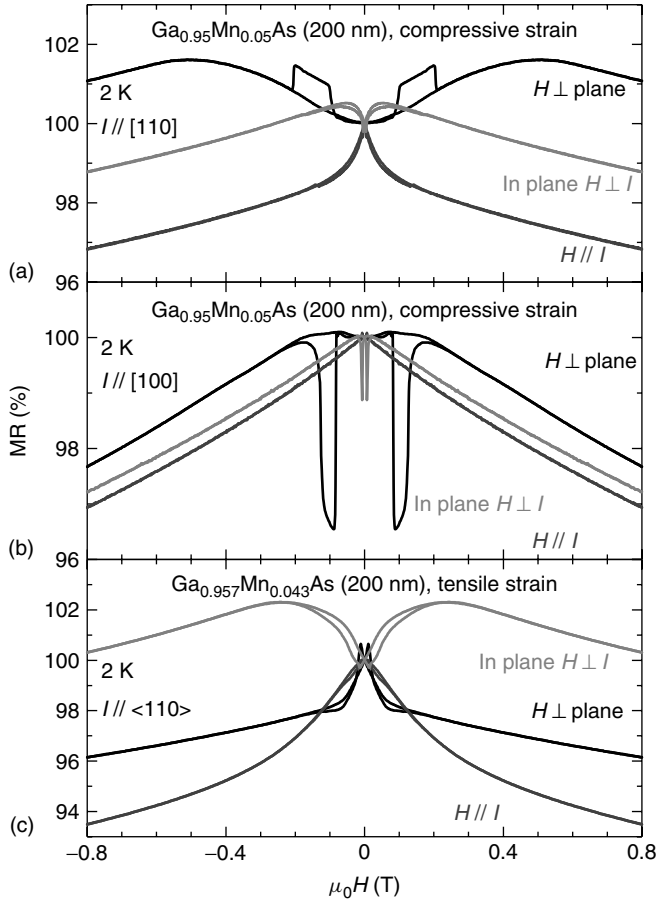

Figure 4. AMR of (Ga,Mn)As with compressive (a and b) and tensile strain (c). The current direction is (a) along [110], (b) [100], and (c) ⟨110⟩. (Reproduced from F. Matsukura *et al*., 2001, with permission from Elsevier. © 2001.)

of quantum coherence of electrons at the DW (Tatara and Fukuyama, 1997) and/or by the AMR contribution. The latter positive DWR can be decomposed into the extrinsic and intrinsic DWR components. Numerical calculation can explain well, as shown in Figure 5, that the extrinsic DWR is dominated by the zigzag current due to the alternating polarity of the anomalous Hall effect at DW (Partin, Karnezos, de Menezes and Berger, 1974), and that the remaining DWR is shown to be of the same order of the resistance due to the mistracking of the carrier spins inside DW (Chiba *et al*., 2006; Levy and Zhang, 1997).

The spin polarization of holes in (Ga,Mn)As has been measured by the Andreev reflection to be as high as ∼80% and similar effective polarization determined from the magnitude of tunneling magnetoresistance (TMR) (290%) at low temperatures (Barden *et al*., 2003; Chiba, Matsukura and Ohno, 2004). These results are consistent with the theoretical calculations of (Ga,Mn)As (Ogawa, Shirai, Suzuki and Kitagawa, 1999; Dietl, Ohno and Matsukura, 2001).

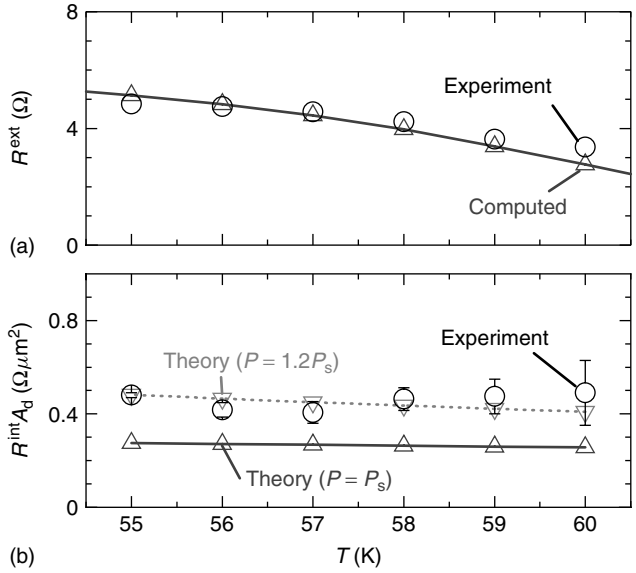

Figure 5. The temperature dependence of experimental and numerical DW resistance per one DW for (a) extrinsic and (b) intrinsic components. (After Chiba *et al*. (2006).)

3.3 Magnetic anisotropy

The direction as well as the magnitude of the magnetocrystalline anisotropy of (Ga,Mn)As can be tuned by the direction and the magnitude of the lattice strain as well as p. A number of methods have been employed to determine the magnetic anisotropy of (Ga,Mn)As, for example, magnetization, ac susceptibility, ferromagnetic resonance (FMR), anomalous Hall effect, planar Hall effect, AMR, TMR, and magneto-optical microscope measurements (Sawicki *et al*., 2004, 2005; Wang *et al*., 2005b; Liu, Sasaki and Furdyna, 2003; Liu, Lim, Dobrowolska and Furdyna, 2005; Shen *et al*., 1997a; Tang, Kawakami, Awschalom and Roukes, 2003; Hamaya *et al*., 2003, 2004; Uemura, Sone, Matsuda and Yamamoto, 2005; Welp *et al*., 2003). The layers under compressive strain, (Ga,Mn)As on GaAs, usually show in-plane magnetic easy axis, while the layers under tensile strain, like (Ga,Mn)As on (In,Ga)As, show magnetic easy axis perpendicular to the plane (Shen *et al*., 1997a). The single ion anisotropy of Mn in GaAs is confirmed to be too small to explain this sizable magnetic anisotropy (Fedorych, Hankiewicz, Wilamowski and Sadowski, 2002). The origin of this strain-dependent magnetic anisotropy is explained in terms of the warped anisotropic valence band due to the spin–orbit interaction and the lattice stain in the framework of the p–d Zener model, which also predicts that the magnetic anisotropy is p dependent (Dietl *et al*., 2000; Dietl, Ohno and Matsukura, 2001; Abolfath, Jungwirth, Brum and MacDonald, 2001). The p-dependent part has later been confirmed experimentally in (Al,Ga,Mn)As, where Al reduces

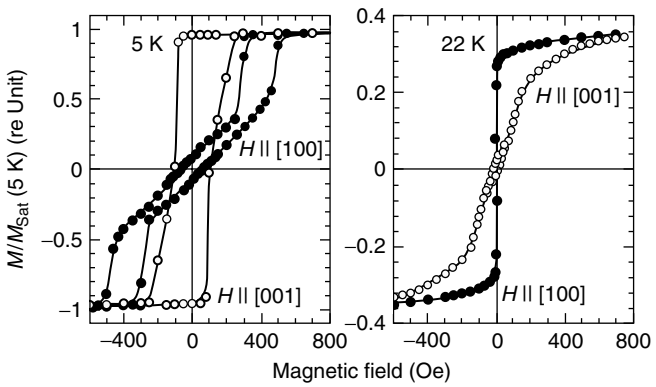

Figure 6. H dependence of magnetization normalized by its saturation value at 5 K for two directions of the film in respect to H (closed symbols and open symbols are for in-plane and perpendicular H respectively) at two temperatures. (After Sawicki *et al.* (2004).)

hole concentration, and in (Ga,Mn)As with a high degree of compensation. There the direction of magnetic easy axis is temperature dependent and changes its direction from in plane to perpendicular as temperature decreases, as shown in Figure 6 (Takamura, Matsukura, Chiba and Ohno, 2002; Sawicki *et al.*, 2003, 2004), in accordance with what is predicted for the low p case by the p–d Zener model. Furthermore, (Ga,Mn)As shows fourfold in-plane easy axis along ⟨100⟩ and uniaxial easy axis along [110] or [−110] (Hayashi *et al.*, 2000; Sawicki *et al.*, 2005). The in-plane uniaxial anisotropy cannot be explained by the p–d Zener model, without assuming the presence of shear strain, which has not yet been confirmed experimentally, and its exact origin remains unclear. It has been suggested that it may be related to the anisotropic (1×2) surface reconstruction during MBE growth, the lack of top–bottom symmetry in epilayers, or the existence of a trigonal distortion (Welp *et al.*, 2003; Sawicki *et al.*, 2004, 2005).

The magnetic overlayers on (Ga,Mn)As can induce the additional anisotropy to (Ga,Mn)As. The pinning of the M direction or exchange biasing of (Ga,Mn)As is shown to be possible with overlayers of spin glass (Zn,Mn)Se and antiferromagnetic MnO (Liu, Sasaki and Furdyna, 2001; Fid *et al.*, 2004).

3.4 Low-temperature annealing

Low-temperature annealing (Hayashi, Hashimoto, Katsumoto and Iye, 2001) is now a standard process to improve the quality of (Ga,Mn)As. An appropriate LT-annealing process increases the electrical conductivity due to the increase in p and at the same time increases T_C. LT annealing allows us to measure the correlation between the electrical conductivity and T_C using a set of samples cleaved from the same wafer, where a monotonic positive dependence of T_C on the conductivity was observed. This is one of the evidences of the hole-induced ferromagnetism (Edmonds *et al.*, 2002b). Initially, the effect was suspected to be due to As antisites, which act as a double donor in GaAs. A series of studies established that the annealing effect is coming from reducing the number of Mn_I. As shown by the EXAFS and the channeling measurements (Shioda, Ando, Hayashi and Tanaka, 1998; Yu *et al.*, 2002a), Mn occupies two distinct positions, Ga and interstitial sites, in zinc-blende host GaAs lattice. Mn_{Ga} acts as a single acceptor, while Mn_I as a double donor. When Mn can be considered the only dopant, p can be expressed by the concentrations of Mn_{Ga} and Mn_I, as $p = [Mn_{Ga}] - 2[Mn_I]$. This relationship was confirmed experimentally by a combination of channeling and ECV measurements, as shown in Figure 7 (Wojtowicz *et al.*, 2004). In addition, Mn_{Ga} and Mn_I can form antiferromagnetic pairs, in which the Mn moments are cancelled. Thus, if all Mn_I form a pair with Mn_{Ga}, the effective Mn composition contributing to ferromagnetic order is the difference in the compositions of Mn_{Ga} and Mn_I, $x_{eff} = ([Mn_{Ga}] - [Mn_I])/N_0$, where N_0 is the density of the cation sites. If one assumes this relation, the magnetization data have been shown to yield $\sim 5\,\mu_B$ per Mn atom, consistent with the expected value for Mn^{2+}, in a wide range of x from 0.02 to 0.09, as shown in Figure 8 (Wang *et al.*,

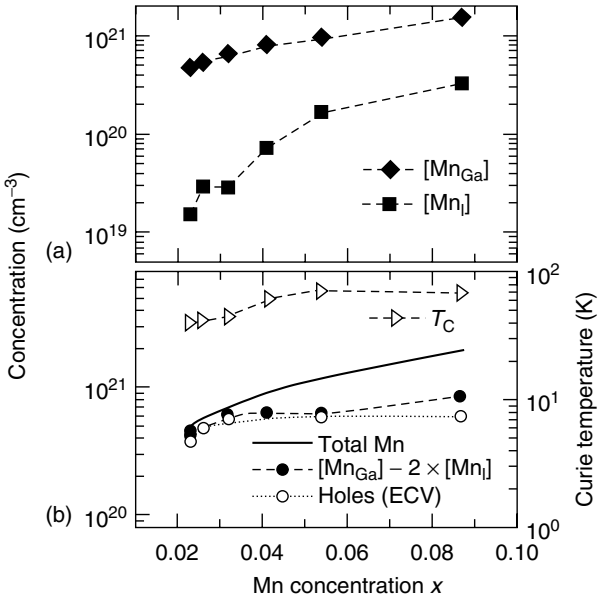

Figure 7. (a) The concentration of Mn_{Ga} and Mn_I versus x. (b) The x dependence of concentration of uncompensated Mn_{Ga}, $[Mn_{Ga}]-2[Mn_I]$ and p measured by ECV. T_C and concentration of total Mn concentration, $Mn_{Ga} + Mn_I$, are also plotted. (Reproduced from T. Wojtowicz *et al.*, 2004, with permission from Elsevier. © 2004.)

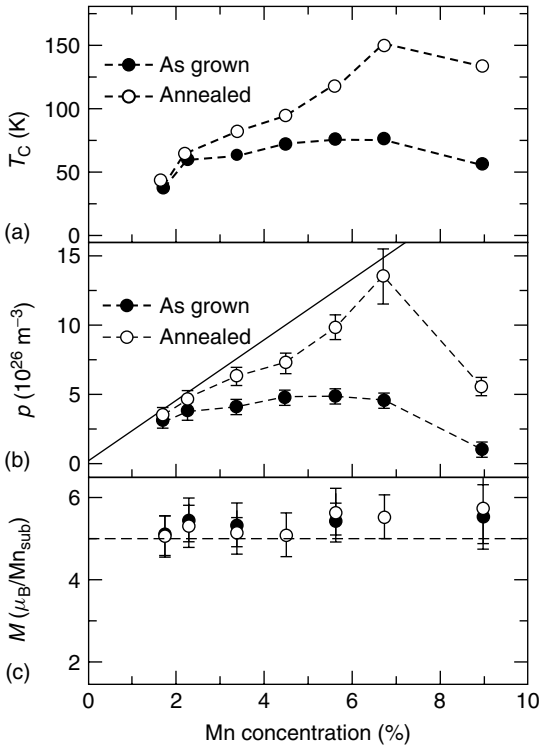

Figure 8. (a) T_C (b) p dependence on x for as-grown and annealed samples. The linear solid line in (c) presents the p expected without compensation. (c) Estimated magnetic moment per uncoupled Mn_{Ga} with the assumption of the antiferromagnetic coupling of Mn_{Ga} and Mn_I. (Reproduced from K.Y. Wang *et al*., 2004, with permission from the American Institute of Physics. © 2004.)

2004). The good agreement for both as-grown and annealed samples seen in Figure 8 also indicates that the increase in T_C after LT annealing is a combined result of increased p and x_{eff} due to the reduction of $[Mn_I]$.

The self-compensation of Mn is enhanced at higher x, and results in almost the same p for as-grown (Ga,Mn)As with x greater than 0.02, but overcompensation has never been observed. Thus, the self-compensation is believed to be related to the Fermi level pinning effect (Walukiewicz, 1988). This suggests that once the Fermi level reaches a certain position in the valence band, it becomes energetically favorable to form Mn_I as a counterdopant (Yu *et al*., 2003).

The effect of the LT annealing is strongly structure dependent. The increase in T_C by LT annealing is greater for thinner (Ga,Mn)As and is observed for the (Ga,Mn)As layers with bare surface, that is, LT-annealing effect is suppressed with a cap GaAs layer with thickness beyond 10 monolayers (Chiba, Takamura, Matsukura and Ohno, 2003; Stone *et al*., 2003). These results indicate that diffusion to and/or from the surface plays a role in the LT-annealing process. The surface Mn Auger signal increases after annealing, indicating that Mn out diffuses and accumulates at the surface during the process (Edmonds *et al*., 2004). This is shown to be modeled by a one-dimensional out-diffusion model (Edmonds *et al*., 2004). It has also been suggested that the diffusion of Mn to the substrate side may be limited electrostatically by the formation of a p–n junction by Mn_I and Mn_{Ga}. According to this scenario, Mn_I becomes electrically inactive at the surface and is trapped as a result of oxidation or some other unknown reasons; thus, the LT annealing is expected to depend on the atmosphere and an additional layer on the surface. More efficient LT-annealing effects are observed for (Ga,Mn)As annealed in O_2 and (Ga,Mn)As with an amorphous As capping layer, where the formation of Mn–O and Mn–As at the surface may work to reduce the number of Mn_I (Malfait *et al*., 2005; Adell *et al*., 2005). Another important effect is that the LT annealing can produce a more homogeneous magnetization depth profile than that of an as-grown sample, which was confirmed by polarized neutron reflectometry measurements (Kirby *et al*., 2004).

Postgrowth hydrogenation of (Ga,Mn)As results in reduction of p and is shown to lead to suppression of ferromagnetism (Gonnenwein *et al*., 2004).

3.5 Magneto-optical properties

Magneto-optical properties have been studied to elucidate the origin of ferromagnetism of (Ga,Mn)As because they can probe the spin-split band structure induced by the sp–d exchange interaction. When the origin of the ferromagnetism is intrinsic, a large magneto-optical response should be observed at the critical points of the host zinc-blende semiconductors. This is indeed the case for (Ga,Mn)As, and a large Faraday rotation and magnetic circular dichroism (MCD) signals have been observed at critical points E_0 and E_1, whose H dependence traces the magnetization curves well (Kuroiwa *et al*., 1998; Ando, Hayashi, Tanaka and Twardowski, 1998; Beshoten *et al*., 1999). The sign of these signals is opposite to that of most of the II–VI DMSs with a negative p–d exchange. This can be explained by a spin-dependent Burnstein–Moss shift caused by hole redistribution that is taken into consideration (Szczytko *et al*., 1999; Dietl, Ohno and Matsukura, 2001).

4 HETEROSTRUCTURES AND DEVICE STRUCTURES

In order to show new spin-dependent phenomena and to explore the possibility of their future device application, a

number of ferromagnetic semiconductor-based heterostructures are now being investigated experimentally as well as theoretically. In this section, we review the results of heterostructures and device structures, which exhibit new phenomena that are not available in existing semiconductor devices.

4.1 Control of magnetism and magnetization reversal by external means

Since the ferromagnetism in (Ga,Mn)As and (In,Mn)As is stabilized by the presence of holes, it is expected that one can switch magnetic phases without changing the temperature by electrical means, which controls the value of p. This has been shown to be possible using a metal–insulator–semiconductor field-effect transistor (MISFET) structure with a thin (In,Mn)As layer ($\leq$5 nm) as a semiconductor channel (Ohno *et al*., 2000). The (In,Mn)As layers are grown on a GaAs substrate with a thick (Al,Ga)Sb buffer layer to relax the large lattice mismatch between (In,Mn)As and GaAs. The devices have a Hall-bar shape, in order to probe the magnetization through the anomalous Hall effect. Since the channel is p-type, the application of positive (negative) gate electric field E_G decreases (increases) p; for the structure under discussion $|E_G| = 1.5\,\mathrm{MV\,cm^{-1}}$ changes several percents of total p. In the vicinity of T_C, the magnetization curves show a more square shape under negative E_G, indicating an enhanced ferromagnetic order, while they show a paramagnetic-like response under positive E_G, as shown in Figure 9. This reversible change of T_C by $E_G = \pm 1.5\,\mathrm{MV\,cm^{-1}}$ determined using the Arrott plots can be as large as 4 K for 4-nm-thick (In,Mn)As (Chiba, Yamanouchi, Matsukura and Ohno, 2003). Control of T_C by electrical means is also a proof that the ferromagnetism in this material is carrier induced.

Another important effect of E_G is the change of the coercive force H_C below T_C; larger (smaller) H_C for negative (positive) E_G. By using this phenomenon, a new scheme of electrical magnetization reversal, electric-field-assisted magnetization reversal, has been demonstrated as follows: After saturation of magnetization at positive H under $E_G = -1.5\,\mathrm{MV\,cm^{-1}}$, one reduces H through zero to a small negative H but still less than the coercive force, H_C. Then, E_G is switched to zero, which reduces $|H_C|$ below $|H|$ and switching takes place (Chiba, Yamanouchi, Matsukura and Ohno, 2003).

Although there has only been limited success on (Ga,Mn)As (Chiba *et al*., 2003), recent progress in low-temperature deposition of high-quality insulators made it possible to observe a similar electrical modulation of T_C and H_C in (Ga,Mn)As (Chiba, Matsukura and Ohno, 2006a).

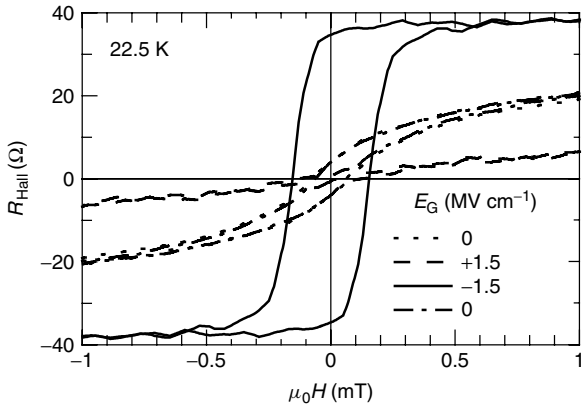

Figure 9. R_{Hall} versus $\mu_0 H$ under three different E_G. R_{Hall} is measured at $E_G = 0$ before and after the application of E_G. (Reproduced from Ohno *et al*., 2000, with permission from Nature Publishing Group. © 2000.)

The change in magnetic properties and H_C in (In,Mn)As has also been demonstrated by light irradiation, where the photogenerated carriers play a role (Koshihara *et al*., 1997; Oiwa, Słupinski and Munekata, 2001; Kanamura *et al*., 2002; Liu *et al*., 2004). Owing to the existence of persistent photoconductivity, the phenomena are occasionally not isothermal: in which case one needs to warm up the sample to return to the original state. The magnetization enhancement of (Ga,Mn)As by circularly polarized light illumination has also been observed for (Ga,Mn)As and Mn δ-doped GaAs (Oiwa *et al*., 2002; Nazmul, Kobayashi, Sugahara and Tanaka, 2004).

4.2 Tunneling magnetoresistance and current-induced magnetization switching

Magnetic tunnel junctions (MTJs) based on (Ga,Mn)As, such as (Ga,Mn)As/AlAs/(Ga,Mn)As and (Ga,Mn)As/GaAs/(Ga,Mn)As, show TMR (Hayashi, Shimada, Shimizu and Tanaka, 1999; Chiba *et al*., 2000), where parallel and antiparallel configurations of the magnetization of the two (Ga,Mn)As layers result in low- and high-resistance (R_P and R_{AP}) states, just as metal MTJs. Note that GaAs acts as a barrier layer for holes in (Ga,Mn)As (Ohno, Arata, Matsukura and Ohno, 2002). The highest TMR ratios [$= (R_{AP} - R_P)/R_P$] so far are 75 and 290% for AlAs and GaAs intermediate barrier layer, as shown in Figure 10, respectively. The latter corresponds to effective carrier spin polarization $P = 77\%$, according to the Julliere's formula, TMR ratio $= 2P^2/(1-P^2)$ (Tanaka and Higo, 2001; Chiba, Matsukura and Ohno, 2004).

In submicron (Ga,Mn)As MTJs, current-induced magnetization switching (CIMS) has been observed (Chiba *et al*., 2004; Elsen *et al*., 2006). On the R_P state, the current pulse, injected from the thicker to thinner (Ga,Mn)As, induces

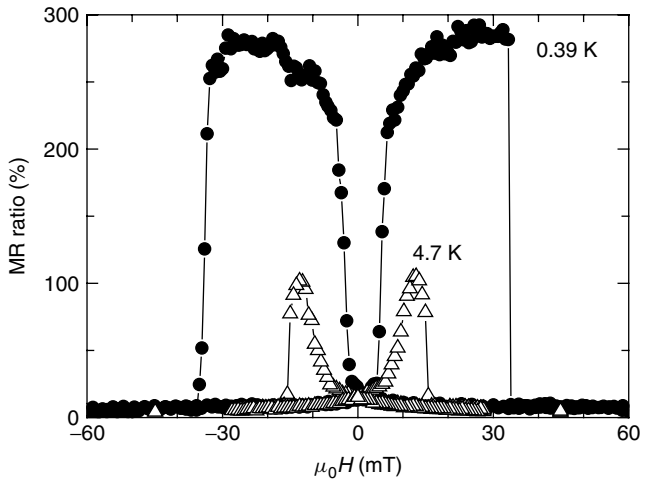

Figure 10. Tunneling magnetoresistance of (Ga,Mn)As/GaAs/(Ga,Mn)As under H // [100] measured at low temperatures. (Reproduced from D. Chiba *et al*., 2004a, with permission from Elsevier. © 2004a.)

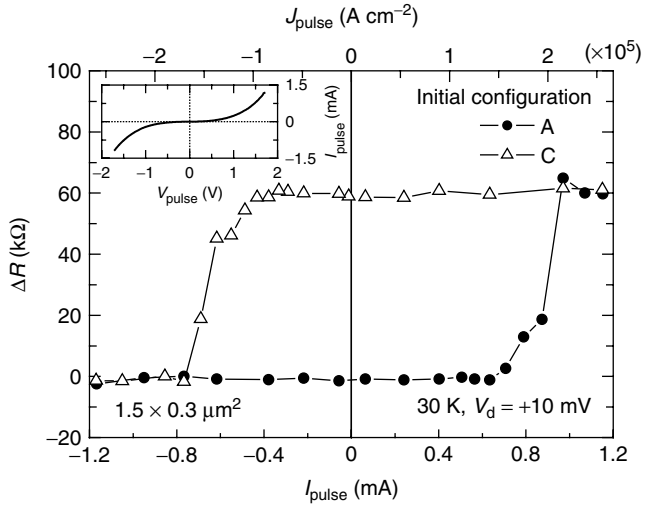

Figure 11. The magnitude of the current pulse dependence ΔR, which is the difference of the resistance after current pulse injection and R_P of $1.5 \times 0.3\,\mu m^2$ device at 30 K. Closed circles show ΔR for initial configuration A (parallel M) and open triangles for initial configuration C (antiparallel M). The inset shows current–voltage characteristic of the device. (After Chiba *et al*. (2004).)

the magnetization reversal in the thinner (Ga,Mn)As, and results in the R_{AP} state. The opposite sign of current induces the magnetization reversal again in the thinner (Ga,Mn)As layer and results in the R_P state, as shown in Figure 11. The critical current density J_C for switching is of the order of $10^4 \sim 10^5\,A\,cm^{-2}$. The CIMS in (Ga,Mn)As-based MTJ can be explained qualitatively by the Slonczewski's spin-transfer torque model (Slonczewski, 1996), although the model predicts an order of magnitude greater J_C than the observed one. The large bias dependence of TMR ratio and its possible role in the CIMS process is not understood at the moment, along with the nature of the possible incoherent switching process, such as the formation of domain structure (Chiba *et al*., 2004; Chiba, Matsukura and Ohno, 2006b; Chiba, Kita, Matsukura and Ohno, 2006; Elsen *et al*., 2006; Moriya, Hamaya, Oiwa and Munekata, 2004).

A very large tunnel anisotropic magnetoresistance (TAMR) up to 150 000% has been reported in (Ga,Mn)As-based MTJs in vertical and lateral device structures (Rüster *et al*., 2003, 2005; Giddings *et al*., 2005). Although it needs further work to firmly establish the origin of TAMR (Saito, Yuasa and Ando, 2005), it has been attributed to anisotropic valence band structure induced by the spin–orbit interaction and lattice strain in combination with the MIT.

4.3 Current-induced domain wall motion

By the application of a current pulse across the DW, it has been found that the position of DW can electrically be manipulated in the absence of a magnetic field (Yamanouchi, Chiba, Matsukura and Ohno, 2004). The electrical channel made from (Ga,Mn)As used in the experiment has magnetic easy axis perpendicular to the surface by inserting the (In,Ga)As or (In,Al)As buffer layer. This easy axis direction is not only useful in monitoring the DW position through the anomalous Hall effect and by the magneto-optical Kerr effect (MOKE) microscope but also essential in observing the effect, as discussed in the following text. The DW switching was observed for the channel with three regions with different thickness, where the thinnest region was set to the center of the channel. Note that this stepped structure allows patterning H_C due to slight nonuniformity in the film and each step acts as a confinement potential for DW. The DW position was initialized to one of the stepped boundaries of the thinnest region by H. After setting $H = 0$, a current pulse of $10^5\,A\,cm^{-2}$ for 100 ms at 80 K (T_C of this film is 90 K) was applied. Both the anomalous Hall signals and MOKE images indicated that the DW moved to the other step boundary, in the direction opposite to the current direction. The application of a subsequent current pulse in the opposite direction switched back the DW to its initial position. The DW was confined by the two stepped boundaries, as expected from the increase in the DW energy in the adjacent layers.

The temperature dependence as well as the current density (j) dependence of the DW velocity have been measured systematically using a 5-μm-wide (Ga,Mn)As channel with a single step (Yamanouchi *et al*., 2006). The DW initially at the step was moved by the current pulse, and the DW swept area was monitored by MOKE to obtain the effective DW speed, v_{eff}, from the effective DW displacement, the

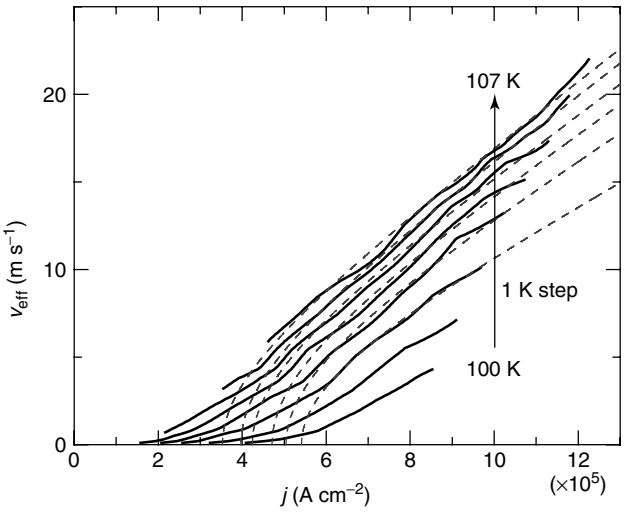

Figure 12. DW velocity as a function of current density at various device temperatures. The thin broken lines show fitted theoretical dependence of velocity on current density. (After Yamanouchi *et al.* (2006).)

value of the area being divided by the width, for a given pulse width; the displacement was linearly dependent on the pulse width. The change in the device temperature by the Joule heating was calibrated by measuring the device resistance during the pulse application and compared with the temperature dependence of the device resistance. The j dependence of $v_{\rm eff}$ at a fixed temperature showed that there are at least two regimes separated by a critical current density $j_{\rm C}$, which is of a few hundreds of thousands of amperes per centimeter square, as shown in Figure 12. Beyond $j_{\rm C}$, $v_{\rm eff}$ increased linearly with j, while below $j_{\rm C}$ the DW velocity was slow and its functional form much more involved. The linear dependence of $v_{\rm eff}$ above $j_{\rm C}$ and the value of $j_{\rm C}$ were found to be explained quantitatively well, including the direction of the movement by the spin-transfer mechanism with an intrinsic DW pinning (Tatara and Kohno, 2004). The j dependence of $v_{\rm eff}$ below $j_{\rm C}$ obeys an empirical scaling law, suggesting the existence of current-induced DW creep (Lemerle *et al.*, 1998).

We note that in metallic structures this intrinsic $j_{\rm C}$ is too high and is beyond one's reach, and thus the velocity versus current density curves are the first of this kind determined in ferromagnetic materials. Even with (Ga,Mn)As, the in-plane anisotropy is expected to result in an order of magnitude higher $j_{\rm C}$ due to magnetocrystalline anisotropy.

4.4 Spin injection into nonmagnetic semiconductors

Owing to spontaneous magnetization, spontaneous spin polarization of carriers exists in ferromagnetic semiconductors below $T_{\rm C}$. Thus, these materials can be used as a spin-polarized carrier emitter into the nonmagnetic structures under the absence of magnetic field. Spin injection from (Ga,Mn)As to nonmagnetic GaAs has been demonstrated by devices combining a GaAs-based nonmagnetic light-emitting diode (LED) structure as spin-polarized carrier detectors (Ohno *et al.*, 1999). In the electroluminescence (EL) measurements, partial spin polarization of injected carriers from (Ga,Mn)As through GaAs to (In,Ga)As quantum well, where they recombine with unpolarized electrons from backside n-type GaAs, was detected in the form of circular polarization of the EL signals. Injection of spin-polarized electrons has also been demonstrated successfully using an Esaki tunnel diode structure as a spin emitter, where spin-polarized holes in the valence band of (Ga,Mn)As are injected into the conduction band of an adjacent n-GaAs by interband tunneling (Kohda *et al.*, 2001; Jonston-Halperin *et al.*, 2002; Van Dorpe *et al.*, 2004). By the use of a three-terminal device structure to control bias voltages of Esaki diode and LED independently, as shown in Figure 13, the efficiency of the spin injection to LED has been measured as a function of the bias voltage. EL polarization up to 32.4% was obtained, suggesting that the injected electrons have high spin polarization of over 85% (Kohda *et al.*, 2006).

5 TOWARD HIGH CURIE TEMPERATURE FERROMAGNETIC SEMICONDUCTORS

5.1 Other ferromagnetic semiconductors

Following theoretical predictions (Dietl *et al.*, 2000; Dietl, Ohno and Matsukura, 2001; Sato and Katayama-Yoshida, 2000), a worldwide effort for synthesizing ferromagnetic semiconductors with high $T_{\rm C}$ is now underway. Ferromagnetic semiconductors based on wide-gap semiconductors such as GaN and ZnO have extensively been investigated (Pearton *et al.*, 2003), as the chemical trend pointed out by the theoretical studies indicates that this is the right direction to be followed. There are many encouraging reports on the observation of room-temperature ferromagnetism in wide-gap materials doped with transition metals or rare earths. Some of them have shown to be able to see a correlation between magnetization and MCD signals at semiconductor critical points and/or the anomalous Hall effect (Saito, Zayets, Yamagata and Ando, 2003; Toyosaki *et al.*, 2004). In order to firmly establish whether the observed ferromagnetic order is intrinsic and is what one is looking for, it is now becoming increasingly clear that one needs to do a series of measurements to carefully rule out the possibilities

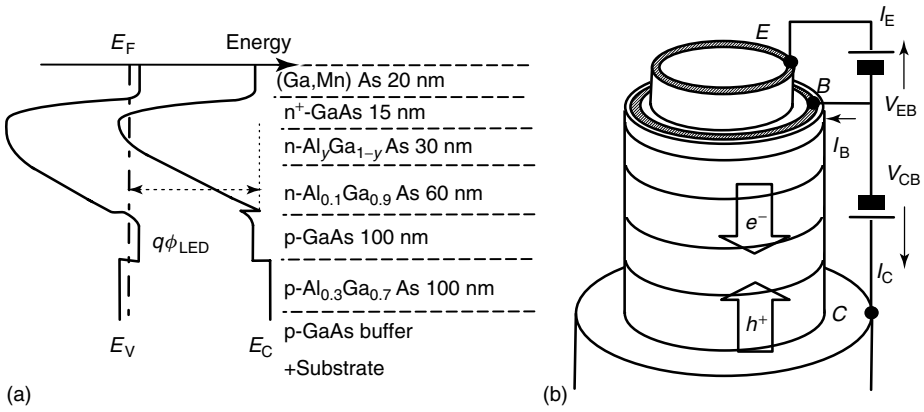

Figure 13. (a) The schematic band diagram and (b) the three-terminal device of Esaki diode on LED. (Reproduced from M. Kohda *et al*., 2006, with permission from the American Institute of Physics. © 2006.)

of having magnetic precipitates (Dietl, this volume). These precipitates can be of the same crystal structure stabilized by the host lattice, meaning that there is no bulk counterpart. They may have an elongated structure (Singh *et al*., 2005) with a high blocking temperature, thereby exhibiting hysteresis and anisotropy. They can even be antiferromagnetic clusters with uncompensated spins.

In an effort to integrate room-temperature ferromagnetic materials to nonmagnetic semiconductor monolithically, metal materials that have the same crystal structure as that of the host semiconductor have also been investigated. So far, single-crystal zinc-blende CrAs and CrSb were grown by MBE and were confirmed to show ferromagnetism over 400 K (Akinaga, Manago and Shirai, 2000; Zhao *et al*., 2001). Theoretical calculation predicts that these materials have half-metallic band structure (Shirai, 2003).

5.2 Perspective and remarks

According to the p–d Zener model, higher values of x_{eff} and p are keys to increase T_C of (Ga,Mn)As, and more material science is needed in this direction, where challenges are the solubility limit and self-compensation. In order to overcome these obstacles, there are several proposals, such as codoping of donors to reduce the number of Mn_I, the optimization of annealing condition, and the use of high-index substrate to increase Mn incorporation efficiency (Yu *et al*., 2003; Wang *et al*., 2005c). The artificial structure to increase local Mn composition and hole concentration simultaneously is another promising direction to be followed; T_C of 250 K was observed in a Mn δ-doped structure with modulation doping to increase hole concentration (Nazmul *et al*., 2005).

Synthesis of ferromagnetic semiconductors based on wide-band gap semiconductors, which are expected to have greater p–d exchange, is another method that was adopted to increase T_C. Although there are a number of encouraging reports, recent theoretical work has pointed out the presence of attractive chemical interactions between magnetic ions and the possibility of having spinodal decomposition (Sato, Katayama-Yoshida and Dederichs, 2005; Fukushima, Sato, Katayama-Yoshida and Dederichs, 2006). It has also been argued that high x is necessary due to the lack of long-range exchange interaction among magnetic spins in these materials (Bergvist *et al*., 2004; Sato, Scheika, Dederichs and Katayama-Yoshida, 2004).

If one is searching for carrier-induced ferromagnetism, then the dependence of magnetic properties on carrier type and its concentration is one of the critical indicators of intrinsic ferromagnetism. The existing theories imply that T_C depends on x, for example, $T_C \propto x$ by the p–d Zener model and $T_C \propto x^{1/2}$ by the double-exchange model (Dietl *et al*., 2000; Dietl, Ohno and Matsukura, 2001; Sato, Dederics and Katayama-Yoshida, 2003), and thus the dependence of magnetic properties on x conveys important information. The existence of the correlation among magnetization, magneto-optical, and magnetotransport properties is one of the necessary conditions of intrinsic ferromagnetism, although large magneto-optical and magnetotransport phenomena for the material with small spin–orbit interaction are not expected. The measurement of carrier spin polarization includes typical properties for ferromagnetic semiconductors reflecting spin-split subband states induced by sp–d exchange interaction (Barden *et al*., 2003; Chiba, Matsukura and Ohno, 2004). The controllability of magnetism by external means is important to confirm the intrinsic ferromagnetism and to demonstrate the possibility in applications (Ohno *et al*., 2000).

Finally, we point out that even if the ferromagnetism-like response has turned out to be originating from precipitates, having ferromagnetic-like inclusion seamlessly integrated into a host semiconductor can be useful depending on what we want to do with semiconductor-magnetism integration.

6 SUMMARY

Ferromagnetic semiconductors are providing an excellent test bench for exploring spin-dependent phenomena in semiconducting materials and to demonstrate new phenomena, ranging from electric-field manipulation of ferromagnetism through CIMS and current-induced DW motion to spin injection in an integrated semiconductor structure for possible spintronic applications, where both charge and spins play critical roles. Directions as well as precautions to be taken for pursuing high transition temperature ferromagnetic semiconductors are also discussed.

ACKNOWLEDGMENTS

The authors thank T. Dietl, D. Chiba, and M. Yamanouchi for their collaboration and discussions. A part of the study done at Tohoku University was supported by the IT Program of RR2002 from MEXT.

REFERENCES

Abolfath, M., Jungwirth, T., Brum, J. and MacDonald, A.H. (2001). Theory of magnetic anisotropy in $III_{1-x}Mn_xV$ ferromagnets. *Physical Review B*, **63**, 054418-1–054418-14.

Adell, M., Ilver, L., Kanski, J., *et al*. (2005). Postgrowth annealing of (Ga,Mn)As under As capping: an alternative way to increase T_C. *Applied Physics Letters*, **86**, 112501-1–112501-3.

Akinaga, H., Manago, T. and Shirai, M. (2000). Material design of half-metallic zinc-blende CrAs and the synthesis by molecular-beam epitaxy. *Japanese Journal of Applied Physics*, **39**, L1118–L1120.

Ando, K., Hayashi, T., Tanaka, M. and Twardowski, A. (1998). Magneto-optic effect of the ferromagnetic diluted magnetic semiconductor $Ga_{1-x}Mn_xAs$. *Journal of Applied Physics*, **83**, 6548–6550.

Awschalom, D.D., Loss, D. and Samarth, N. (2002). *Semiconductor Spintronics and Quantum Computation*, Springer-Verlag: Berlin.

Barden, J.G., Parker, J.S., Xiong, P., *et al*. (2003). Direct measurement of the spin polarization of the magnetic semiconductor (Ga,Mn)As. *Physical Review Letters* **91**, 056602-1–056602-4.

Baxter, D.V., Ruzmetov, D., Schreschiligt, J., *et al*. (2002). Anisotropic magnetoresistance in $Ga_{1-x}Mn_xAs$. *Physical Review B*, **65**, 212407-1–212407-4.

Bergvist, L., Eriksson, O., Kudrnocský, D.V., *et al*. (2004). Magnetic percolation in diluted magnetic semiconductors. *Physical Review Letters*, **93**, 137202-1–137202-4.

Beshoten, B., Crowell, P.A., Malajovich, I., *et al*. (1999). Magnetic circular dichroism studies of carrier-induced ferromagnetism in $(Ga_{1-x}Mn_x)As$. *Physical Review Letters*, **83**, 3073–3076.

Blinowski, J. and Kacman, P. (2003). Spin interactions of interstitial Mn ions in ferromagnetic GaMnAs. *Physical Review B*, **67**, 121204(R)-1–121204(R)-4.

Chiba, D., Akiba, N., Matsukura, F., *et al*. (2000). Magnetoresistance effect and interlayer coupling of (Ga,Mn)As trilayer structure. *Applied Physics Letters*, **77**, 1873–1875.

Chiba, D., Kita, T., Matsukura, F. and Ohno, H. (2006). Pulse-width and magnetic-field dependences of current-induced magnetization switching in a (Ga,Mn)As magnetic tunnel junction. *Journal of Applied Physics*, **99**, 08G514-1–08G514-3.

Chiba, D., Matsukura, F. and Ohno, H. (2004). Tunneling magnetoresistance in (Ga,Mn)As-based heterostructures with a GaAs barrier. *Physica E*, **21**, 966–969.

Chiba, D., Matsukura, F. and Ohno, H. (2006a). Electric-field control of ferromagnetism in (Ga,Mn)As. *Applied Physics Letters*, **89**, 162505-1–162505-4.

Chiba, D., Matsukura, F. and Ohno, H. (2006b). Electrical magnetization reversal in ferromagnetic III-V semiconductors. *Journal of Physics D: Applied Physics*, **39**, R1–R11.

Chiba, D., Sato, Y., Kita, T., *et al*. (2004). Current-driven magnetization reversal in a ferromagnetic (Ga,Mn)As/GaAs/(Ga,Mn)As tunnel junction. *Physical Review Letters*, **93**, 216602-1–216602-4.

Chiba, D., Takamura, K., Matsukura, F. and Ohno, H. (2003). Effect of low-temperature annealing on (Ga,Mn)As trilayer structures. *Applied Physics Letters*, **82**, 3020–3022.

Chiba, D., Yamanouchi, M., Matsukura, F., *et al*. (2003). Electric field effect on the magnetic properties of III-V ferromagnetic semiconductor (In,Mn)As and ((Al),Ga,Mn)As. *Journal of Superconductivity: Incorporating Novel Magnetism*, **16**, 179–182.

Chiba, D., Yamanouchi, M., Matsukura, F., *et al*. (2006). Domain-wall resistance in ferromagnetic (Ga,Mn)As. *Physical Review Letters*, **96**, 096602-1–096602-4.

Chiba, D., Yamanouchi, M., Matsukura, F. and Ohno, H. (2003). Electrical manipulation of magnetization reversal in a ferromagnetic semiconductor. *Science*, **301**, 943–945.

Chien, C.L. and Westgate, C.R. (1980). *The Hall Effect and its Application*, Plenum Press: New York.

DeSimone, D., Wood, C.E.C. and Evans, C.A. Jr. (1982). Manganese incorporation behavior in molecular beam epitaxial gallium arsenide. *Journal of Applied Physics*, **53**, 4938–4942.

Dietl, T. (1994). (Diluted) magnetic semiconductors. In *Handbook on Semiconductors, Completely Revised and Enlarged Edition*, Mahajan, S. (Ed.), North-Holland: Amsterdam, 1251–1342, Vol. 3B.

Dietl, T., König, J. and MacDonald, A.H. (2001). Magnetic domains in III-V magnetic semiconductors. *Physical Review B*, **64**, 241201(R)-1–241201(R)-4.

Dietl, T., Ohno, H., Matsukura, F., *et al*. (2000). Zener model description of ferromagnetism in zinc-blende magnetic semiconductors. *Science*, **287**, 1019–1022.

Dietl, T., Ohno, H. and Matsukura, F. (2001). Hole-mediated ferromagnetism in tetrahedrally coordinated semiconductors. *Physical Review B*, **63**, 195205-1–195205-21.

Dobrowolski, W., Kossut, J. and Story, T. (2003). II–VI and IV–VI diluted magnetic semiconductors – new bulk materials

and low-dimensional quantum structures. In *Handbook of Magnetic Materials*, Bushchow, K.H.J. (Ed.), North-Holland: Amsterdam, pp. 289–377, Vol. 15.

Edmonds, K.W., Boguslawski, P., Wang, K.Y., *et al*. (2004). Mn interstitial diffusion in (Ga,Mn)As. *Physical Review Letters*, **92**, 037201-1–037201-4.

Edmonds, K.W., Wang, K.Y., Campion, R.P., *et al*. (2002a). Hall effect and hole densities of $Ga_{1-x}Mn_xAs$. *Applied Physics Letters*, **81**, 3010–3012.

Edmonds, K.W., Wang, K.W., Campion, R.P., *et al*. (2002b). High-Curie-temperature of $Ga_{1-x}Mn_xAs$ obtained by resistance-monitored annealing. *Applied Physics Letters*, **81**, 4991–4993.

Elsen, M., Boulle, O., George, J.M., *et al*. (2006). Spin transfer experiments on (Ga,Mn)As/(In,Ga)As/(Ga,Mn)As tunnel junctions. *Physical Review B*, **73**, 035303-1–035303-4.

Fedorych, O.M., Hankiewicz, E.M., Wilamowski, Z. and Sadowski, J. (2002). Single ion anisotropy of Mn-doped GaAs measured by electron paramagnetic resonance. *Physical Review B*, **66**, 045201-1–045201-16.

Fid, K.F., Stone, M.B., Ku, K.C., *et al*. (2004). Exchange biasing of the ferromagnetic semiconductor $Ga_{1-x}Mn_xAs$. *Applied Physics Letters*, **85**, 1556–1558.

Fukushima, T., Sato, K., Katayama-Yoshida, H. and Dederichs, P.H. (2006). Spinodal decompositions under layer by layer growth condition and high Curie-temperature quasi-one dimensional nano-structure in diluted magnetic semiconductors. *Japanese Journal of Applied Physics*, **45**, L416–L418.

Furdyna, J.K. and Kossut, J. (1988). *Semiconductors and Semimetals, Diluted Magnetic Semiconductors*, Academic Press: London, Vol. 25.

Giddings, A.D., Khalid, M.N., Jungwirth, T., *et al*. (2005). Large tunneling anisotropic magnetoresistance in (Ga,Mn)As nanoconstrictions. *Physical Review Letters*, **94**, 127202-1–127202-4.

Gonnenwein, S.T.B., Wassner, T.A., Huebl, H., *et al*. (2004). Hydrogen control of ferromagnetism in a dilute magnetic semiconductor. *Physical Review Letters*, **91**, 227202-1–227202-4.

Guo, S.P., Shen, A., Yasuda, H., *et al*. (2000). Surfactant effect of Mn on the formation of self-organized InAs nanostructures. *Journal of Crystal Growth*, **208**, 799–803.

Hamaya, K., Moriya, R., Oiwa, A., *et al*. (2004). Contribution of shape anisotropy to the magnetic configuration of (Ga,Mn)As. *Japanese Journal of Applied Physics*, **43**, L306–L308.

Hamaya, K., Taniyama, T., Kitamoto, Y., *et al*. (2003). Magneto-transport study of temperature dependent magnetic anisotropy in a (Ga,Mn)As epilayer. *Journal of Applied Physics*, **94**, 7657–7661.

Hayashi, T., Hashimoto, Y., Katsumoto, S. and Iye, Y. (2001). Effect of low-temperature annealing on transport and magnetism of diluted magnetic semiconductor (Ga,Mn)As. *Applied Physics Letters*, **78**, 1691–1693.

Hayashi, T., Katsumoto, S., Hashimoto, Y., *et al*. (2000). Anisotropy and Barkhausen jumps in diluted magnetic semiconductor (Ga,Mn)As. *Physica B*, **284–288**, 1175–1176.

Hayashi, T., Shimada, H., Shimizu, M. and Tanaka, M. (1999). Tunneling spectroscopy and tunneling magnetoresistance in (Ga,Mn)As ultrathin heterostrucures. *Journal of Crystal Growth*, **201/202**, 689–692.

Holtberg, F., von Molnár, S. and Coey, J.M. (1980). Rare earth magnetic semiconductors. In *Handbook on Semiconductors*, Ketler, S.P. (Ed.), North-Holland: Amsterdam, pp. 803–856, Vol. 3.

Ilegrams, M., Dingle, R. and Rupp L.W. Jr. (1975). Optical and electrical properties of Mn-doped GaAs grown by molecular-beam epitaxy. *Journal of Applied Physics*, **46**, 3059–3065.

Jan, J.P. (1957). Galvanomagnetic and thermomagnetic effects in metals. In *Solid State Physics*, Seitz, F. and Turnbull, D. (Eds.), Academic Press: New York, pp. 1–96, Vol. 5.

Jonston-Halperin, L.D., Kawakami, R.K., Young, D.K., *et al*. (2002). Spin-polarized Zener tunneling in (Ga,Mn)As. *Physical Review B*, **65**, 041306-1–041306-4.

Jungwirth, T., Abolfath, M., Sinova, J., *et al*. (2002). Boltzmann theory of engineered anisotropic magnetoresistance in (Ga,Mn)As. *Applied Physics Letters*, **81**, 4029–4031.

Jungwirth, T., Qian, N. and MacDonald, A.H. (2002). Anomalous hall effect in ferromagnetic semiconductors. *Physical Review Letters*, **88**, 207208-1–207208-4.

Jungwirth, T., Sinova, S., Mašek, J., *et al*. (2006). Theory of ferromagnetic (III,Mn)V semiconductors. *Reviews of Modern Physics*, **78**, 809–863.

Jungwirth, J., Wang, K.Y., Mašek, J., *et al*. (2005). Prospects for high temperature ferromagnetism in (Ga,Mn)As semiconductors. *Physical Review B*, **72**, 165204-1–165204-13.

Kanamura, M., Zhou, Y.K., Okunuma, S., *et al*. (2002). Growth of InMnAsSb/InSb heterostructures with mid-infrared-light induced ferromagnetic properties. *Japanese Journal of Applied Physics*, **41**, 1019–1021.

Katsumoto, S., Oiwa, A., Iye, Y., *et al*. (1998). Strongly anisotropic hopping conduction in (Ga,Mn)As/GaAs. *Physica Status Solidi (B)*, **205**, 115–118.

Kawabata, A. (1980). Theory of negative magnetoresistance in three-dimensional systems. *Solid State Communications*, **34**, 431–432.

Kirby, B.J., Borchers, J.A., Rhyne, J.J., *et al*. (2004). Annealing-dependent magnetic depth profile in $Ga_{1-x}Mn_xAs$. *Physical Review B*, **69**, 081307(R)-1–081307(R)-4.

Koeder, A., Frank, S., Schoch, W., *et al*. (2003). Curie temperature and carrier concentration gradients in epitaxy-grown $Ga_{1-x}Mn_xAs$ layers. *Applied Physics Letters*, **82**, 3278–3280.

Kohda, M., Kita, T., Ohno, Y., *et al*. (2006). Bias voltage dependence of the electron spin injection studied in a three-terminal device based on a (Ga,Mn)As/n^+ -GaAs Esaki diode. *Applied Physics Letters*, **89**, 012103-1–012103-3.

Kohda, M., Ohno, Y., Takamura, K., *et al*. (2001). A spin Esaki diode. *Japanese Journal of Applied Physics*, **40**, L1274–L1276.

Kordoš, P., Janšák, L. and Benč, V. (1975). Preparation and properties of Mn-doped epitaxial gallium arsenide. *Solid-State Electronics*, **18**, 223–226.

Koshihara, S., Oiwa, A., Hirasawa, M., *et al*. (1997). Ferromagnetic order induced by photogenerated carriers in magnetic III–V semiconductor heterostructures of (In,Mn)As/GaSb. *Physical Review Letters*, **78**, 4617–4620.

Kossut, J. (2001). Low-dimensional structures of diluted magnetic (semimagnetic) semiconductors – a subjective review. *Acta Physica Polonica A, Supplement*, **100**, 111–138.

Kossut, J. and Dobrowolski, W. (1993). Diluted magnetic semiconductors. In *Handbook of Magnetic Materials*, Bushchow, K.H.J. (Ed.) North-Holland: Amsterdam, pp. 231–305, Vol. 7.

Kuroiwa, T., Yasuda, T., Matsukura, F., *et al*. (1998). Faraday rotation of ferromagnetic (Ga,Mn)As. *Electronics Letters*, **34**, 190–192.

Lemerle, S., Ferre, J., Chappert, C., *et al*. (1998). Domain wall creep in an ising ultrathin magnet film. *Physical Review Letters*, **80**, 849–852.

Levy, P.M. and Zhang, S. (1997). Resistivity due to domain wall scattering. *Physical Review Letters*, **79**, 5110–5113.

Limmer, W., Glunk, M., Schoch, W., *et al*. (2002). Micro-Raman scattering study of $Ga_{1-x}Mn_xAs$. *Physica E*, **13**, 589–592.

Liu, X., Lim, W.L., Dobrowolska, M. and Furdyna, J.K. (2005). Ferromagnetic resonance study of the free-hole contribution to magnetization and magnetic anisotropy in modulation-dopes $Ga_{1-x}Mn_xAs/Ga_{1-y}Al_yAs$:Be. *Physical Review B*, **71**, 035307-1–035307-7.

Liu, X., Lim, W.L., Titova, L.V., *et al*. (2004). External control of the direction of the magnetization in ferromagnetic InMnAs/GaSb heterostructures. *Physica E*, **20**, 370–373.

Liu, X., Sasaki, Y. and Furdyna, J.K. (2001). Enhancement of magnetic coercivity and ferromagnetic transition temperature by proximity effects in the GaMnAs-ZnMnSe multilayer system. *Applied Physics Letters*, **79**, 2414–2416.

Liu, X., Sasaki, Y. and Furdyna, J.K. (2003). Ferromagnetic resonance in $Ga_{1-x}Mn_xAs$: effects of magnetic anisotropy. *Physical Review B*, **67**, 205204-1–205204-9.

Máca, F. and Mašek, J. (2003). Electronic states in $Ga_{1-x}Mn_xAs$: substitutional versus interstitial position of Mn. *Physical Review B*, **66**, 235209-1–235209-6.

Malfait, M., Vanacken, J., Moschchalkov, V.V., *et al*. (2005). Enhanced annealing effect in an oxygen atmosphere on $Ga_{1-x}Mn_xAs$. *Applied Physics Letters*, **86**, 132501-1–132501-3.

Matsukura, F., Ohno, H. and Dietl, T. (2002). III-V ferromagnetic semiconductors. In *Handbook of Magnetic Materials*, Bushchow, K.H.J. (Ed.), North-Holland: Amsterdam, pp. 1–87, Vol. 14.

Matsukura, F., Ohno, H., Shen, A. and Sugawara, Y. (1998). Transport properties and origin of ferromagnetism in (Ga,Mn)As. *Physical Review B*, **57**, R2037–R2040.

Matsukura, F., Sawicki, M., Dietl, T., *et al*. (2004). Magnetotransport properties of metallic (Ga,Mn)As films with compressive and tensile strain. *Physica E*, **21**, 1032–1036.

Matsukura, F., Shen, A., Sugawara, Y., *et al*. (1999). *Properties of (Ga,Mn)As and their Dependence of Molecular Beam Growth Conditions*, Institute of Physics: Conference Series No. 162, pp. 547–552.

Mauger, A. and Godart, C. (1986). The magnetic, optical, and transport properties of representatives of a class of magnetic semiconductors: the europium chalcogenides. *Physics Reports*, **141**, 51–176.

Methfessel, S. and Mattis, D.C. (1968). Magnetic semiconductors. In *Encyclopedia of Physics, Volume XVIII/1, Magnetism*, Wijn H.P.J. (Ed.), Springer-Verlag: Berlin, pp. 389–562.

Moriya, R., Hamaya, K., Oiwa, A. and Munekata, H. (2004). Current-induced magnetization reversal in a (Ga,Mn)As-based magnetic tunnel junction. *Japanese Journal of Applied Physics*, **43**, L825–L827.

Moriya, R. and Munekata, H. (2003). Relation among concentrations of incorporated Mn atoms, ionized Mn acceptors, and holes in *p*-(Ga,Mn)As epilayers. *Journal of Applied Physics*, **93**, 4603–4609.

Munekata, H., Ohno, H., von Molnar, S., *et al*. (1989). Diluted magnetic III-V semiconductors. *Physical Review Letters*, **63**, 1849–1852.

Myers, R.C., Sheu, B.L., Jackson, A.W., *et al*. (2006). Antisite effect on hole-mediated ferromagnetism in (Ga,Mn)As. *Physical Review B* **74**, 155203-1–155203-9.

Nazmul, A.M., Amemiya, T., Shuto, Y., *et al*. (2005). High temperature ferromagnetism in GaAs-based heterostructures with Mn δ doping. *Physical Review Letters*, **95**, 017201-1–017201-4.

Nazmul, A.M., Kobayashi, S., Sugahara, S. and Tanaka, M. (2004). Electrical and optical control of ferromagnetism in III-V semiconductor heterostructures at high temperature ($\sim$100 K). *Japanese Journal of Applied Physics*, **43**, L233–L236.

Ogawa, T., Shirai, M., Suzuki, N. and Kitagawa, I. (1999). First-principle calculations of electronic structures of diluted magnetic semiconductors (Ga,Mn)As. *Journal of Magnetism and Magnetic Materials*, **196–197**, 428–429.

Ohno, H. (1998). Making nonmagnetic semiconductors ferromagnetic. *Science*, **281**, 951–956.

Ohno, H. (1999). Properties of ferromagnetic III-V semiconductors. *Journal of Magnetism and Magnetic Materials*, **200**, 110–129.

Ohno, Y., Arata, I., Matsukura, F. and Ohno, H. (2002). Valence band barrier at (Ga,Mn)As/GaAs interfaces. *Physica E*, **13**, 521–524.

Ohno, H., Chiba, D., Matsukura, F., *et al*. (2000). Electric-field control of ferromagnetism. *Nature*, **408**, 944–946.

Ohno, H. and Matsukura, F. (2001). A ferromagnetic III-V semiconductor: (Ga,Mn)As. *Solid State Communications*, **117**, 179–186.

Ohno, H., Munekata, H., Penny, T., *et al*. (1992). Magnetotransport properties of p-type (In,Mn)As diluted magnetic III-V semiconductors. *Physical Review Letters*, **68**, 2664–2667.

Ohno, H., Shen, A., Matsukura, F., *et al*. (1996). (Ga,Mn)As: a new diluted magnetic semiconductor based on GaAs. *Applied Physics Letters*, **69**, 363–365.

Ohno, Y., Young, D.K., Beschoten, B., *et al*. (1999). Electrical spin injection in a ferromagnetic semiconductor heterostructure. *Nature*, **402**, 790–792.

Oiwa, A., Mitsumori, Y., Moriya, R., *et al*. (2002). Effect of optical spin injection on ferromagnetically coupled Mn spins in the III-V magnetic alloy semiconductor (Ga,Mn)As. *Physical Review Letters*, **88**, 137202-1–137202-4.

Oiwa, A., Słupinski, T. and Munekata, H. (2001). Control of magnetization reversal process by light illumination in ferromagnetic semiconductor heterostructure p-(In,Mn)As/GaSb. *Applied Physics Letters*, **78**, 518–520.

Okabayashi, J., Kimura, A., Rader, O., *et al*. (1998). Core-level photoemission study of $Ga_{1-x}Mn_xAs$. *Physical Review B*, **58**, R4211–R4214.

Omiya, T., Matsukura, F., Dietl, T., *et al*. (2000). Magnetotransport properties of (Ga,Mn)As investigated at low temperature and high magnetic field. *Physica E*, **7**, 976–980.

Osinny, V., Jędrzejczak, A., Arciszewska, M., *et al*. (2001). Fermi level position in GaMnAs – a thermoelectric study. *Acta Physica Polonica A*, **100**, 327–334.

Partin, D.L., Karnezos, M., de Menezes, L.C. and Berger, L. (1974). Nonuniform current distribution in the neighborhood of a ferromagnetic domain wall in cobalt at 4.2 K. *Journal of Applied Physics*, **45**, 1852–1859.

Pearton, S.J., Abernathy, C.R., Overberg, M.E., *et al*. (2003). Wide band gap ferromagnetic semiconductors and oxides. *Journal of Applied Physics*, **93**, 1–13.

Potashnik, S.J., Ku, K.C., Chun, S.H., *et al*. (2001). Effects of annealing time on defect-controlled ferromagnetism in $Ga_{1-x}Mn_xAs$. *Applied Physics Letters*, **79**, 1495–1497.

Rüster, C., Borzenko, T., Gould, C., *et al*. (2003). Very large magnetoresistance in lateral ferromagnetic (Ga,Mn)As wires with nanoconstrictions. *Physical Review Letters*, **91**, 216602-1–216602-4.

Rüster, C., Gould, C., Jungwirth, J., *et al*. (2005). Very large tunneling anisotropic magnetoresistance of a (Ga,Mn)As/GaAs/(Ga,Mn)As stack. *Physical Review Letters*, **94**, 027203-1–027203-4.

Sadowski, J. and Domagala, J.Z. (2004). Influence of defects on the lattice constant of GaMnAs. *Physical Review B*, **69**, 075206-1–075206-5.

Sadowski, J., Domagała, J.Z., Bąk-Misiuk, J., *et al*. (2000). Structural and magnetic properties of molecular beam epitaxy grown GaMnAs layers. *Journal of Vacuum and Science Technology B*, **18**, 1697–1700.

Sadowski, J., Mathieu, R., Svedlindh, P., *et al*. (2001). Structural and magnetic properties of GaMnAs layers with high Mn-content grown by migration-enhance epitaxy on GaAs (100) substrates. *Applied Physics Letters*, **78**, 3271–3273.

Sadowski, J., Mathieu, R., Svedlindh, P., *et al*. (2002). Ferromagnetic GaMnAs/GaAs superlattice – MBE growth and magnetic properties. *Thin Solid Films*, **412**, 122–128.

Saito, H., Yuasa, S. and Ando, K. (2005). Origin of the tunnel anisotropic magnetoresistance in $Ga_{1-x}Mn_xAs$/ZnSe/$Ga_{1-x}Mn_xAs$ magnetic tunnel junctions of II-VI/III-V heterostructures. *Physical Review Letters*, **95**, 086604-1–086604-4.

Saito, H., Zayets, V., Yamagata, S. and Ando, K. (2003). Room-temperature ferromagnetism in a III-V diluted magnetic semiconductor $Zn_{1-x}Cr_xTe$. *Physical Review Letters*, **90**, 207202-1–207202-4.

Sato, K., Dederics, P.H. and Katayama-Yoshida, H. (2003). Curie temperature of III-V diluted magnetic semiconductors calculated from first principles. *Europhysics Letters*, **61**, 403–408.

Sato, K. and Katayama-Yoshida, H. (2000). Material design for transparent ferromagnets with ZnO-based magnetic semiconductors. *Japanese Journal of Applied Physics*, **39**, L555–L558.

Sato, K., Katayama-Yoshida, H. and Dederichs, P.H. (2005). High Curie temperature and nano-scale spinodal decomposition phase in diluted magnetic semiconductors. *Japanese Journal of Applied Physics*, **44**, L948–L951.

Sato, K., Scheika, W., Dederichs, P.H. and Katayama-Yoshida, H. (2004). Low-temperature ferromagnetism in (Ga,Mn)N: Ab initio calculations. *Physical Review B*, **70**, 201202(R)-1–201202(R)-4.

Sawicki, M., Matsukura, F., Dietl, T., *et al*. (2003). Temperature peculiarities of magnetic anisotropy in (Ga,Mn)As: the role of the hole concentration. *Journal of Superconductivity: Incorporating Novel Magnetism*, **16**, 7–10.

Sawicki, M., Matsukura, F., Idziaszek, A., *et al*. (2004). Temperature dependent magnetic anisotropy in (Ga,Mn)As layers. *Physical Review B*, **70**, 245325-1–245325-6.

Sawicki, M., Wang, K.Y., Edmonds, K.W., *et al*. (2005). In-plane uniaxial anisotropy rotations in (Ga,Mn)As thin films. *Physical Review B*, **71**, 121302(R)-1–121302(R)-4.

Schneider, J., Kaufmann, U., Wilkening, W., *et al*. (1987). Electronic structure of the neutral manganese acceptor in gallium arsenide. *Physical Review Letters*, **59**, 240–243.

Schott, G.M., Faschinger, W. and Molenkamp, L.W. (2001). Lattice constant variation and complex formation in zincblende gallium arsenide. *Applied Physics Letters*, **79**, 1807–1809.

Schott, G.M., Schmidt, G., Karczewski, G., *et al*. (2003). Influence of growth conditions on the lattice constant and composition of (Ga,Mn)As. *Applied Physics Letters*, **82**, 4678–4680.

Seong, M.J., Chun, S.H., Cheong, H.M., *et al*. (2002). Spectroscopic determination of hole density in the ferromagnetic semiconductor $Ga_{1-x}Mn_xAs$. *Physical Review B*, **66**, 033202-1–033202-4.

Shen, A., Horikoshi, Y., Ohno, H. and Guo, S.P. (1997b). Reflection high-energy electron diffraction oscillation during growth of GaAs at low temperatures under As over pressure. *Applied Physics Letters*, **71**, 1540–1542.

Shen, A., Matsukura, F., Guo, S.P., *et al*. (1999). Low-temperature molecular beam epitaxial growth of GaAs and (Ga,Mn)As. *Journal of Crystal Growth*, **201/202**, 679–683.

Shen, A., Ohno, H., Matsukura, F., *et al*. (1997a). Epitaxy of (Ga,Mn)As, a new diluted magnetic semiconductor based on GaAs. *Journal of Crystal Growth*, **175/176**, 1069–1074.

Shimizu, H., Hayashi, H., Nishinaga, Y. and Tanaka, M. (1999). Magnetic and transport properties of III-V based magnetic semiconductor (Ga,Mn)As: growth condition dependence. *Applied Physics Letters*, **74**, 398–400.

Shioda, R., Ando, K., Hayashi, T. and Tanaka, M. (1998). Local structure of III-V diluted magnetic semiconductors $Ga_{1-x}Mn_xAs$ studied using extended x-ray-absorption fine structure. *Physical Review B*, **58**, 1100–1102.

Shirai, M. (2003). Possible half-metallic ferromagnetism in zinc blende CrSb and CrAs. *Journal of Applied Physics*, **93**, 6844–6846.

Shono, T., Hasegawa, T., Fukumura, T., *et al*. (2000). Observation of magnetic domain structure in a ferromagnetic semiconductor (Ga,Mn)As with a scanning Hall probe microscope. *Applied Physics Letters*, **77**, 1363–1365.

Singh, R.K., Wu, S.Y., Liu, H.X., *et al*. (2005). The role of Cr substitution on the ferromagnetic properties of $Ga_{1-x}Cr_xN$. *Applied Physics Letters*, **86**, 012504-1–012504-3.

Slonczewski, J.C. (1996). Current-driven excitation of magnetic multilayers. *Journal of Magnetism and Magnetic Materials*, **159**, L1–L7.

Stone, M.B., Ku, K.C., Potashnik, S.J., *et al*. (2003). Capping-induced suppression of annealing effect on $Ga_{1-x}Mn_xAs$. *Applied Physics Letters*, **83**, 4568–4570.

Szczytko, J., Mac, W., Twardowski, A., *et al*. (1999). Antiferromagnetic p-d exchange in ferromagnetic $Ga_{1-x}Mn_xAs$. *Physical Review B*, **59**, 12935–12939.

Takamura, K., Matsukura, F., Chiba, D. and Ohno, H. (2002). Magnetic properties of (Al,Ga,Mn)As. *Applied Physics Letters*, **81**, 2590–2592.

Takamura, K., Matsukura, F., Ohno, Y. and Ohno, H. (2001). Growth and properties of (Ga,Mn)As films with high Mn concentration. *Journal of Applied Physics*, **89**, 7024–7025.

Tanaka, M. and Higo, Y. (2001). Large tunneling magnetoresistance in GaMnAs/AlAs/GaMnAs ferromagnetic semiconductor tunnel junctions. *Physical Review Letters*, **87**, 026602-1–026602-4.

Tang, H.X., Kawakami, R.K., Awschalom, D.D. and Roukes, M.L. (2003). Giant planar Hall effect in epitaxial (Ga,Mn)As devices. *Physical Review Letters*, **90**, 107201-1–107201-4.

Tang, H.X., Masmanidis, S., Kaeakami, R.K., *et al*. (2004). Negative intrinsic resistivity of and individual domain wall in epitaxial (Ga,Mn)As microdevices. *Nature*, **431**, 52–56.

Tatara, G. and Fukuyama, H. (1997). Resistivity due to a domain wall in ferromagnetic metal. *Physical Review Letters*, **78**, 3773–3776.

Tatara, G. and Kohno, H. (2004). Theory of current-driven domain wall motion: spin transfer versus momentum transfer. *Physical Review Letters*, **92**, 086601-1–086601-4.

Thevenard, L., Largeau, L., Mauguin, O., *et al*. (2006). Magnetic properties and domain structure of (Ga,Mn)As film with perpendicular anisotropy. *Physical Review B*, **73**, 195331-1–195331-7.

Toyosaki, H., Fukumura, T., Yamada, Y., *et al*. (2004). Anomalous Hall effect governed by electron doping in a room-temperature transparent ferromagnetic semiconductor. *Nature Materials*, **3**, 221–224.

Tsuruoka, T., Tanimoto, R., Tachikawa, N., *et al*. (2002). Microscopic identification of dopant atoms in Mn-doped GaAs layers. *Solid State Communications*, **121**, 79–82.

Uemura, T., Sone, T., Matsuda, K. and Yamamoto, M. (2005). Magnetic anisotropy study for GaMnAs-based magnetic tunnel junction. *Japanese Journal of Applied Physics*, **44**, L1352–L1354.

Van Dorpe, P., Liu, Z., Van Roy, W., *et al*. (2004). Very high spin polarization in GaAs by injection from a (Ga,Mn)As Zener diode. *Applied Physics Letters*, **84**, 3945–3947.

Walukiewicz, W. (1988). Mechanism of Fermi-level stabilization in semiconductors. *Physical Review B*, **37**, 4760–4763.

Wang, K.Y., Campion, R.P., Edmonds, K.W., *et al*. (2005a). Magnetism in (Ga,Mn)As thin films with T_C up to 173 K. In *AIP Conference Proceedings Volume 772, Physics of Semiconductors: 27th International Conference on the Physics of Semiconductors–ICPS-27*, Menéndez, J. and Van der Walle, C.G. (Eds.), American Institute of Physics: Melville, pp. 333–334.

Wang, K.Y., Edmonds, K.W., Campion, R.P., *et al*. (2004). Influence of the Mn interstitial on the magnetic and transport properties of (Ga,Mn)As. *Journal of Applied Physics*, **95**, 6512–6514.

Wang, K.Y., Edmonds, K.W., Zhao, L.X., *et al*. (2005c). (Ga,Mn)As grown on (311) GaAs substrates: Modified Mn incorporation and magnetic anisotropies. *Physical Review B*, **72**, 115207-1–115207-6.

Wang, K.Y., Sawicki, S., Edmonds, K.W., *et al*. (2005b). Spin reorientation transition in single-domain (Ga,Mn)As. *Physical Review Letters*, **95**, 217204-1–217204-4.

Welp, U., Vlasko-Vlasov, V.K., Liu, X., *et al*. (2003). Magnetic domain structure and magnetic anisotropy in $Ga_{1-x}Mn_xAs$. *Physical Review Letters*, **90**, 167206-1–167206-4.

Wojtowicz, T., Furdyna, J.K., Liu, X., *et al*. (2004). Electronic effects determining the formation of ferromagnetic $III_{1-x}Mn_xV$ alloys during epitaxial growth. *Physica E*, **25**, 171–180.

Yamanouchi, M., Chiba, D., Matsukura, F., *et al*. (2006). Velocity of domain-wall motion induced by electrical current in the ferromagnetic semiconductor (Ga,Mn)As. *Physical Review Letters*, **96**, 096601-1–096601-4.

Yamanouchi, M., Chiba, D., Matsukura, F. and Ohno, H. (2004). Current-induced domain-wall switching in a ferromagnetic semiconductor structure. *Nature*, **428**, 539–542.

Yasuda, H. and Ohno, H. (1999). Monte Carlo simulation of reentrant reflection high-energy electron diffraction intensity oscillation observed during low-temperature GaAs growth. *Applied Physics Letters*, **74**, 3275–3277.

Yu, K.M., Walukiewicz, W., Wojtowicz, T., *et al*. (2002a). Effect of the location of Mn sites in ferromagnetic $Ga_{1-x}Mn_xAs$ on its Curie temperature. *Physical Review B*, **65**, 201303(R)-1–201303(R)-4.

Yu, K.M., Walukiewicz, W., Wojotowicz, T., *et al*. (2002b). Determination of free hole concentration in ferromagnetic $Ga_{1-x}Mn_xAs$ using electrochemical capacitance-voltage profiling. *Applied Physics Letters*, **81**, 844–846.

Yu, K.M., Walukiewick, T., Wojtowicz, T., *et al*. (2003). Curie temperature limit in ferromagnetic $Ga_{1-x}Mn_xAs$. *Physical Review B*, **68**, 041308(R)-1–041308(R)-4.

Zhao, J.H., Matsukura, F., Takamura, K., *et al*. (2001). Room-temperature ferromagnetism in zincblende CrSb grown by molecular-beam epitaxy. *Applied Physics Letters*, **79**, 2776–2778.

Žutić, I., Fabian, J. and Das Sarma, S. (2004). Spintronics: fundamentals and applications. *Reviews of Modern Physics*, **76**, 323–410.

Diluted Ferromagnetic Semiconductors – Theoretical Aspects

Tomasz Dietl
Institute of Physics and Warsaw University, Warszawa, Poland

1 INTRODUCTION

The family of diluted magnetic semiconductors (DMS) encompasses standard semiconductors, in which a sizable portion of atoms is substituted by such elements, which produce localized magnetic moments in the semiconductor matrix. Usually, magnetic moments originate from 3d or 4f open shells of transition metals (TMs) or rare earths (REs) (lanthanides), respectively, so that typical examples of DMS are $Cd_{1-x}Co_xSe$, $Ga_{1-x}Mn_xAs$, $Pb_{1-x}Eu_xTe$ and, in a sense, Si:Er. A strong spin-dependent coupling between the band and localized states accounts for outstanding properties of DMS. This coupling gives rise to spin-disorder scattering, giant spin splittings of the electronic states, formation of magnetic polarons, and strong indirect exchange interactions between the magnetic moments, the latter leading to collective spin glass, antiferromagnetic, or ferromagnetic spin ordering. Owing to the possibility of controlling and probing magnetic properties by the electronic subsystem or vice versa, DMS have been successfully employed to address a number of important questions concerning the nature of various spin effects in various environments and at various length and timescales. At the same time, DMS exhibit a strong sensitivity to the magnetic field and temperature as well as constitute important media for generation of spin currents and for manipulation of localized or itinerant spins by, for example, strain, light, electrostatic, or ferromagnetic gates. These properties, complementary to both nonmagnetic semiconductors and magnetic metals, open doors for application of DMS as functional materials in spintronic devices.

Extensive studies of DMS started in 1970s, particularly in the group of Robert R. Gałązka in Warsaw, when appropriately purified Mn was employed to grow bulk II–VI Mn-based alloys by various modifications of the Bridgman method (Gałązka, 1978). Comparing to magnetic semiconductors, such as Eu chalcogenides (e.g., EuS) and Cr spinels (e.g., $CdCr_2Se_4$) investigated earlier (Nagaev, 1983), DMS exhibited smaller defect concentrations and were easier to dope by shallow impurities. Accordingly, it was possible to examine their properties by powerful magneto-optical and magnetotransport techniques (Dietl, 1994; Gałązka, 1978, 1981; Furdyna and Kossut, 1988; Awschalom and Samarth, 2002). Since, in contrast to magnetic semiconductors, neither narrow magnetic bands nor long-range magnetic ordering affected low-energy excitations, DMS were named semimagnetic semiconductors. More recently, research on DMS have been extended toward materials containing magnetic elements other than Mn as well as to III–VI, IV–VI (Bauer, Pascher and Zawadzki, 1992), and III–V (Matsukura,

Handbook of Magnetism and Advanced Magnetic Materials. Edited by Helmut Kronmüller and Stuart Parkin. Volume 5: *Spintronics and Magnetoelectronics*. ISBN: 978-0-470-02217-7.

Ohno and Dietl, 2002) compounds as well as group IV elemental semiconductors and various oxides (Prellier, Fouchet and Mercey, 2003). In consequence, a variety of novel phenomena had been discovered, including effects associated with narrow bands and magnetic phase transformations, making the borderline between properties of DMS and magnetic semiconductors more and more elusive.

A rapid progress of DMS research in 1990s stemmed, to a large extent, from the development of methods of crystal growth far from thermal equilibrium, primarily by molecular-beam epitaxy (MBE) but also by laser ablation. These methods have made it possible to obtain DMS with the content of the magnetic constituent beyond thermal equilibrium solubility limits (Ohno, 1998). Similarly, the doping during MBE process allows one to increase substantially the electrical activity of shallow impurities (Haury *et al*., 1997; Ferrand *et al*., 2001). In the case of III–V DMS (Matsukura, Ohno and Dietl, 2002), in which divalent magnetic atoms supply both spins and holes, the use of the low-temperature MBE provides thin films of, for example, $Ga_{1-x}Mn_xAs$ with x up to 0.08 and the hole concentration approaching $10^{21}\,cm^{-3}$, in which ferromagnetic ordering is observed up to 170 K (Wang *et al*., 2005). Remarkably, MBE and processes of nanostructure fabrication, make it possible to add magnetism to the physics of semiconductor quantum structures. Particularly important are DMS, in which ferromagnetic ordering was discovered, as discussed here and in the chapter **Ferromagnetic Semiconductors, Volume 5**.

Owing to novel functionalities (Ohno *et al*., 2000) and theoretical expectations (Dietl *et al*., 2000), an enormous activity has been directed to developing diluted ferromagnetic semiconductors sustaining ferromagnetic order up to high temperatures (Dietl, 2005; Liu, Yun and Morkoç, 2005) as well as to describing their properties theoretically (Jungwirth *et al*., 2006a). In fact, a ferromagnetic response, often persisting up to above room temperature, has been detected in a number of semiconductor and oxide thin layers doped with minute amount of magnetic ions (Dietl, 2005; Liu, Yun and Morkoç, 2005). As known, a highly sensitive SQUID magnetometer is necessary to detect the corresponding small signals, which are often inferior to those coming from typical remanent fields, sample holders, substrates, or residual magnetic nanoparticles originating from nominally nonmagnetic source materials or processing procedures. In rather rare cases, the ferromagnetic signal of DMS layers could univocally be assigned to precipitates of a known ferromagnetic or ferrimagnetic material. In few other cases, its magnitude has been greater than that evaluated from the nominal concentration of magnetic ions. More often, however, the ferromagnetic response of the layer coexists with paramagnetic characteristics, indicating that only a fraction of magnetic spins remains correlated at high temperatures.

A particularly important question that arises in this context is whether at the length scale appropriately greater than the mean distance between magnetic ions a spatially uniform ferromagnetic spin order is a real ground state of ferromagnetic DMS. Actually, the existence and the role of spatially nonuniform ferromagnetic spin order was an important theme in research on both magnetic semiconductors (Nagaev, 1983) and colossal magnetoresistance oxides (Dagotto, Hotta and Moreo, 2001). Nanoscale phase separation effects that were invoked to explained pertinent properties of those materials may *a priori* be even more relevant in ferromagnetic DMS, in which carrier correlation and electrostatic disorder associated with ionized impurities coexist with alloy disorder in the magnetic sublattice. We recall in this context that uncoupled nanoscale ferromagnetic regions of the volume V give rise to macroscopic ferromagnetic signatures, such as spontaneous magnetization and magnetic hysteresis, below the blocking temperature (e.g., Shinde *et al*., 2004), $T_B = KV/[k_B \ln(t_{lab}/\tau)]$, where K is the density of the magnetic anisotropy energy, and $\ln(t_{lab}/\tau) \approx 25$ for a typical ratio of a relevant spin-flip relaxation time τ to the time of hysteresis measurements, t_{lab}.

In the remaining part of this review, we focus on semiconductors which under doping with TM or RE become ferromagnetic but *remain* in the initial crystal structure or, in the other words, do not undergo any *crystallographic* phase separation. Therefore, the ferromagnetism of DMS considered here does not result simply from the precipitation of any known ferromagnetic or ferrimagnetic material. In particular, in the next section, we describe the present theoretical understanding of DMS showing *uniform* ferromagnetic order, such as (Ga,Mn)As or heavily doped p-(Zn,Mn)Te, in which interactions between randomly distributed magnetic ions are mediated by delocalized holes in the valence band. We then turn to DMS, in which a competition between long-range ferromagnetic and short-range antiferromagnetic interactions and/or the proximity to the localization boundary lead to the *electronic* nanoscale phase separation into areas of differing spin orders. Finally, we discuss, in some detail, systems exhibiting the *chemical* nanoscale phase separation into regions with a small and a large concentration of magnetic atoms, respectively.

2 SPATIALLY UNIFORM FERROMAGNETIC DMS

2.1 Overview

Since for decades, III–V semiconductor compounds have been applied as photonic and microwave devices, the discovery of ferromagnetism first in (In,Mn)As (Ohno *et al*.,

1992) and then in (Ga,Mn)As (Ohno *et al*., 1996) came as a landmark achievement. In these materials, substitutional divalent Mn ions provide localized spins and function as acceptor centers that provide holes which mediate the ferromagnetic coupling between the parent randomly distributed Mn spins (Dietl, Haury and Merle d'Aubigné, 1997; Matsukura, Ohno, Shen and Sugawara, 1998; Jungwirth, Atkinson, Lee and MacDonald, 1999). In another technologically important group of semiconductors, in II–VI compounds, the densities of spins and carriers can be controlled independently, similar to the case of IV–VI materials, in which hole-mediated ferromagnetism was discovered already in the 1980s (Story, Gałązka, Frankel and Wolff, 1986). Stimulated by the theoretical predictions (Dietl, Haury and Merle d'Aubigné, 1997), search for carrier-induced ferromagnetism in II–IV materials containing Mn was undertaken. Experimental studies conducted with the use of magneto-optical and magnetic methods led to the discovery of ferromagnetism in 2D (Haury *et al*., 1997) and 3D (Ferrand *et al*., 2001) II–VI Mn-based DMS doped by nitrogen acceptors.

Since magnetic properties are controlled by band holes, an appealing possibility is to influence the magnetic ordering isothermally, by light or by the electric field, which affect the carrier concentration in semiconductor quantum structures. Such tuning capabilities of the materials systems in question were put into the evidence in (In,Mn)As/(Al,Ga)Sb (Koshihara *et al*., 1997; Ohno *et al*., 2000) and modulation-doped p-(Cd,Mn)Te/(Cd,Mg,Zn)Te (Haury *et al*., 1997; Boukari *et al*., 2002) heterostructures. Actually, these findings can be quantitatively interpreted by considering the effect of the electric field or illumination on the hole density under stationary conditions and, therefore, on the Curie temperature in the relevant magnetic layers. Interestingly, according to experimental findings and theoretical modeling, photocarriers generated in II–VI systems by above barrier illumination destroy ferromagnetic order in the magnetic quantum well residing in an undoped (intrinsic) region of a p–i–p structure (Haury *et al*., 1997; Boukari *et al*., 2002) but they enhance the magnitude of spontaneous magnetization in the case of a p–i–n diode (Boukari *et al*., 2002). Furthermore, the current-induced magnetization reversal was demonstrated in submicron pillars of (Ga,Mn)As/GaAs/(Ga,Mn)As (Chiba *et al*., 2004; Elsen *et al*., 2006). Spin-polarized current was also shown to displace magnetic domain walls in (Ga,Mn)As with the easy axis perpendicular to the film plane (Yamanouchi, Chiba, Matsukura and Ohno, 2004, 2006).

Guided by the growing amount of experimental results, including informative magnetic resonance (Szczytko *et al*., 1999; Fedorych, Hankiewicz, Wilamowski and Sadowski, 2002) and photoemission (Mizokawa *et al*., 2002; Rader *et al*., 2004; Hwang *et al*., 2005) studies, a theoretical model of the hole-controlled ferromagnetism in III–V, II–VI, and group IV semiconductors containing Mn was proposed (Dietl *et al*., 2000, 2001). These materials exhibit characteristics specific to both charge transfer insulators and strongly correlated disordered metals. Moreover, complexities specific to strongly correlated systems coexist in DMS with features exhibited by heavily doped semiconductors and semiconductor alloys, such as Anderson–Mott localization (Dietl, 1994), defect generation by self-compensation mechanisms (Dietl, Ohno and Matsukura, 2001; Mašek and Máca, 2001; Yu *et al*., 2002), and the breakdown of the virtual-crystal approximation (Benoit à la Guillaume, Scalbert and Dietl, 1992). Nevertheless, the theory built on p–d Zener's model of carrier-mediated ferromagnetism and on either Kohn-Luttinger's kp (Dietl *et al*., 2000; Dietl, Ohno and Matsukura, 2001; Abolfath, Jungwirth, Brum and MacDonald, 2001) or multiorbital tight-binding (Vurgaftman and Meyer, 2001; Sankowski and Kacman, 2005; Timm and MacDonald, 2005) descriptions of the valence band in tetrahedrally coordinated semiconductors has qualitatively, and often quantitatively, described thermodynamic, micromagnetic, transport, and optical properties of DMS with delocalized holes (Dietl, 2004; Jungwirth *et al*., 2006a; Sankowski, Kacman, Majewski and Dietl, 2006a), challenging competing theories. It is often argued that owing to these studies (Ga,Mn)As has become one of the best-understood ferromagnets. Accordingly, this material is now serving as a testing ground for various *ab initio* computational approaches to strongly correlated and disordered systems.

2.2 Magnetic impurities in semiconductors

A good starting point for the description of DMS is the Vonsovskii model, according to which the electron states can be divided into two categories: (i) localized magnetic d or f shells and (ii) extended band states built up of s, p, and sometimes d atomic orbitals. The former give rise to the presence of local magnetic moments and intracenter optical transitions. The latter form bands, much alike as in the case of nonmagnetic semiconductor alloys. Indeed, the lattice constant of DMS obeys the Vegard low, and the energy gap E_g between the valence and the conduction band depends on x in a manner qualitatively similar to nonmagnetic counterparts. According to the Anderson model, the character of magnetic impurities in solids results from a competition between (i) hybridization of local and extended states, which tends to delocalized magnetic electrons and (ii) the on-site Coulomb interactions among the localized electrons, which stabilizes the magnetic moment in agreement with Hund's rule.

Figure 1 shows positions of local states derived from 3d shells of TM impurities with respect to the band energies

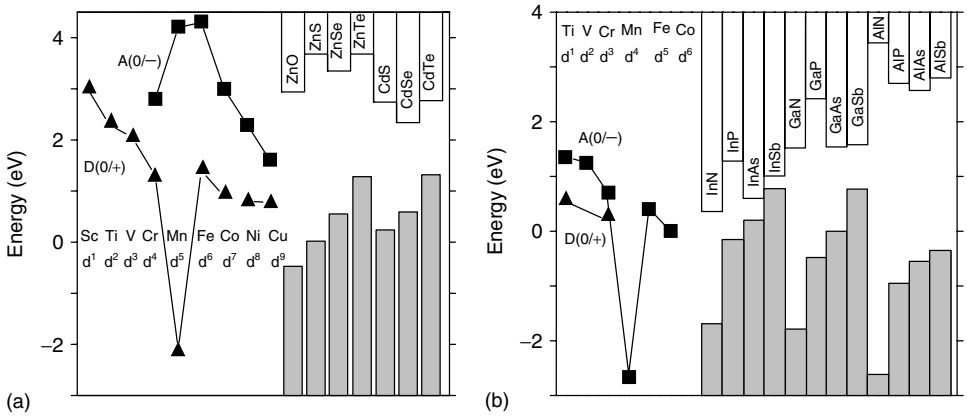

Figure 1. Approximate positions of transition-metal levels relative to the conduction and valence band edges of II–VI (a) and III–V (b) compounds. By triangles the d^N/d^{N-1} donor and by squares the d^N/d^{N+1} acceptor states are denoted. (Adapted from Langer, Delerue, Lannoo and Heinrich, 1988 and Zunger, 1986.)

of the host II–VI and III–V compounds. In Figure 1, the levels labeled 'donors' denote the ionization energy of the magnetic electrons ($TM^{2+} \rightarrow TM^{3+}$or $d^n \rightarrow d^{n-1}$), whereas the 'acceptors' correspond to their affinity energy ($TM^{2+} \rightarrow TM^{1+}$or $d^n \rightarrow d^{n+1}$). The difference between the two is the on-d-shell Coulomb (Hubbard) repulsion energy U in the semiconductor matrix. In addition, the potential introduced by either neutral or charged TM can bind a band carrier in a Zhang-Rice-type singlet or hydrogenic-like state, respectively. Such bound states are often experimentally important, particularly in III–V compounds, as they correspond to lower energies than the competing d-like states, such as presented in Figure 1.

In the case of Mn, in which the d shell is half-filled, the d-like donor state lies deep in the valence band, whereas the acceptor level resides high in the conduction band, so that $U \approx 7\,\text{eV}$ according to photoemission and inverse photoemission studies. Thus, Mn-based DMS can be classified as charge transfer insulators, $E_g < U$. The Mn ion remains in the 2+ charge state, which means that it does not supply any carriers in II–VI materials. However, it acts as a hydrogenic-like acceptor in the case of III–V antimonides and arsenides, while the corresponding Mn-related state is deep, presumably due to a stronger p–d hybridization, in the case of phosphides and nitrides. According to Hund's rule, the total spin $S = 5/2$ and the total orbital momentum $L = 0$ for the d^5 shell in the ground state. The lowest excited state d^{*5} corresponds to $S = 3/2$ and its optical excitation energy is about 2 eV. Thus, if there is no interaction between the spins, their magnetization is described by the paramagnetic Brillouin function. In the case of other TMs, the impurity-induced levels may appear in the gap, and then compensate shallow impurities, or even act as resonant dopant, for example, Sc in CdSe, Fe in HgSe or Cu in HgTe. Transport studies of such systems have demonstrated that intersite Coulomb interactions between charged ions lead to the Efros-Shklovskii gap in the density of the impurity states, which makes resonant scattering to be inefficient in semiconductors (Wilamowski, Świątek, Dietl and Kossut, 1990). Furthermore, spin-orbit interaction and Jahn–Teller effect control positions and splittings of the levels in the case of ions with $L \neq 0$. If the resulting ground state is a magnetically inactive singlet there is no permanent magnetic moment associated with the ion, the case of Fe^{2+}, whose magnetization is of the Van Vleck type at low temperatures.

2.3 Exchange interaction between band and localized spins

The important aspect of DMS is a strong spin-dependent coupling of the effective mass carriers to the localized d electrons, first discovered in (Cd,Mn)Te (Komarov *et al.*, 1977; Gaj, Gałązka and Nawrocki, 1978) and (Hg,Mn)Te (Bastard *et al.*, 1978; Jaczyński, Kossut and Gałązka, 1978). Neglecting nonscalar corrections that can appear for ions with $L \neq 0$, this interaction assumes the Kondo form,

$$H_K = -I(\vec{r} - \vec{R}^{(i)})\vec{s}\vec{S}^{(i)} \tag{1}$$

where $I(\vec{r} - \vec{R}^{(i)})$ is a short-range exchange energy operator between the carrier spin $\vec{s}$ and the TM spin localized at $\vec{R}^{(i)}$. When incorporated to the kp scheme, the effect of H_K is described by matrix elements $\langle u_i|I|u_i\rangle$, where u_i are the Kohn-Luttinger amplitudes of the corresponding band extreme. In the case of carriers at the Γ point of the Brillouin zone in zinc-blende DMS , the two relevant matrix elements $\alpha = \langle u_c|I|u_c\rangle$ and $\beta = \langle u_v|I|u_v\rangle$ involve s-type and p-types wave functions, respectively. There are two

mechanisms contributing to the Kondo coupling (Dietl, 1981; Bhattacharjee, Fishman and Coqblin, 1983; Kacman, 2001): (i) the exchange part of the Coulomb interaction between the effective mass and localized electrons; (ii) the spin-dependent hybridization between the band and local states. Since there is no hybridization between Γ_6 and d-derived (e_g and t_{2g}) states in zinc-blende structure, the s–d coupling is determined by the direct exchange. The experimentally determined values are of the order of $\alpha N_o \approx 0.25\,\mathrm{eV}$, where N_o is the cation concentration, somewhat reduced comparing to the value deduced from the energy difference between $S1/2$ states of the free singly ionized Mn atom $3d^5 4s^1$, $\alpha N_o = 0.39\,\mathrm{eV}$. In contrast, there is a strong hybridization between Γ_8 and t_{2g} states, which affects their relative position, and leads to a large magnitude of $|\beta N_o| \approx 1\,\mathrm{eV}$. If the relevant effective mass state is above the t_{2g} level (the case of, e.g., Mn-based DMS, $\beta < 0$ but otherwise β can be positive (the case of, e.g., $Zn_{1-x}Cr_xSe$ (Mac *et al.*, 1993)).

2.4 p–d Zener model

It is convenient to apply the Zener model of carrier-controlled ferromagnetism by introducing the functional of free-energy density, $\mathcal{F}[\vec{M}(\vec{r})]$. The choice of the local magnetization $\vec{M}(\vec{r})$ as an order parameter means that the spins are treated as classical vectors, and that spatial disorder inherent to magnetic alloys is neglected. In the case of magnetic semiconductors $\mathcal{F}[\vec{M}(\vec{r})]$ consists of two terms, $\mathcal{F}[\vec{M}(\vec{r})] = \mathcal{F}_S[\vec{M}(\vec{r})] + \mathcal{F}_c[\vec{M}(\vec{r})]$, which describe, for a given magnetization profile $\vec{M}(\vec{r})$, the free energy densities of the Mn spins in the absence of any carriers and of the carriers in the presence of the Mn spins, respectively. A visible asymmetry in the treatment of the carries and of the spins corresponds to an adiabatic approximation: the dynamics of the spins in the absence of the carriers is assumed to be much slower than that of the carriers. Furthermore, in the spirit of the virtual-crystal and molecular-field approximations, the classical continuous field $\vec{M}(\vec{r})$ controls the effect of the spins upon the carriers. Now, the thermodynamics of the system is described by the partition function Z, which can be obtained by a functional integration of the Boltzmann factor $\exp(-\int \mathrm{d}\vec{r}\mathcal{F}[\vec{M}(\vec{r})]/k_B T)$ over all magnetization profiles $\vec{M}(\vec{r})$, an approach developed for bound magnetic polarons (Dietl and Spałek, 1983; Dietl, 1983), and directly applicable for spin physics in quantum dots as well. In the mean-field approximation (MFA), which should be valid for spatially extended systems and long-range spin–spin interactions, a term corresponding to the minimum of $\mathcal{F}[\vec{M}(\vec{r})]$ is assumed to determine Z with a sufficient accuracy.

If energetics is dominated by spatially uniform magnetization $\vec{M}$, the spin part of the free energy density in the magnetic field $\vec{H}$ can be written in the form (Świerkowski and Dietl, 1988)

$$\mathcal{F}_S[\vec{M}] = \int_0^{\vec{M}} \mathrm{d}\vec{M}_o \vec{h}(\vec{M}_o) - \vec{M}\vec{H} \tag{2}$$

Here, $\vec{h}(\vec{M}_o)$ denotes the inverse function to $\vec{M}_o(\vec{h})$, where $\vec{M}_o$ is the available experimentally macroscopic magnetization of the spins in the absence of carriers in the field h and temperature T. In DMS, it is usually possible to parameterize $M_o(h)$ by the Brillouin function $B_S(T, H)$ that takes the presence of intrinsic short-range antiferromagnetic interactions into account. Near T_C and for $H = 0$, M is sufficiently small to take $M_o(T, h) = \chi(T)h$, where $\chi(T)$ is the magnetic susceptibility of localized spins in the absence of carriers. Under these conditions,

$$\mathcal{F}_S[M] = \frac{M^2}{2\chi(T)} \tag{3}$$

which shows that the increase of $\mathcal{F}_S$ with M slows down with lowering temperature, where $\chi(T)$ grows. Turning to $\mathcal{F}_c[M]$ we note that owing to the giant Zeeman splitting of the bands proportional to M, the energy of the carriers, and thus $\mathcal{F}_c[M]$, decreases with $|M|$, $\mathcal{F}_c[M] - \mathcal{F}_c[0] \sim -M^2$. Accordingly, a minimum of $\mathcal{F}[M]$ at nonzero M may develop in $H = 0$ at sufficiently low temperatures signalizing the appearance of a ferromagnetic order.

The present authors and coworkers (Dietl *et al.*, 2000) found that the minimal Hamiltonian necessary to describe properly effects of the complex structure of the valence band in tetrahedrally coordinated semiconductors upon $\mathcal{F}_c[M]$ is the Luttinger $6 \times 6\,kp$ model supplemented by the p–d exchange contribution taken in the virtual-crystal and molecular-field approximations,

$$H_{pd} = \frac{\beta \vec{s}\vec{M}}{g\mu_B} \tag{4}$$

This term leads to spin splittings of the valence subbands, whose magnitudes – owing to the spin-orbit coupling – depend on the hole wave vectors $\vec{k}$ in a complex way even for spatially uniform magnetization $\vec{M}$. It would be technically difficult to incorporate such effects to the Ruderman-Kittel-Kasuya-Yosida (RKKY) model, as the spin-orbit coupling leads to nonscalar terms in the spin–spin Hamiltonian. At the same time, the indirect exchange associated with the virtual spin excitations between the valence subbands, the Bloembergen-Rowland mechanism, is automatically included. The model allows for strain, confinement, and was developed for both zinc-blende and wurzite materials (Dietl, Ohno and Matsukura, 2001). Furthermore, the direct influence of the magnetic field on the hole spectrum

was taken into account. Carrier–carrier spin correlation was described by introducing a Fermi-liquid-like parameter A_F (Dietl, Haury and Merle d'Aubigné, 1997; Haury *et al*., 1997; Jungwirth, Atkinson, Lee and MacDonald, 1999), which enlarges the Pauli susceptibility of the hole liquid. No disorder effects were taken into account on the ground that their influence on thermodynamic properties is relatively weak except for strongly localized regime. Having the hole energies, the free energy density $\mathcal{F}_c[\vec{M}]$ was evaluated according to the procedure suitable for Fermi liquids of arbitrary degeneracy. By minimizing $\mathcal{F}[\vec{M}] = \mathcal{F}_S[\vec{M}] + \mathcal{F}_c[\vec{M}]$ with respect to $\vec{M}$ at given T, H, and hole concentration p, Mn spin magnetization $M(T, H)$ was obtained as a solution of the mean-field equation,

$$\vec{M}(T, H) = x_{\text{eff}} N_o g \mu_B S B_S \left[\frac{g\mu_B \left(-\frac{\partial \mathcal{F}_c[\vec{M}]}{\partial \vec{M}} + \vec{H} \right)}{k_B (T + T_{AF})} \right] \quad (5)$$

where the carrier energy and entropy as well as peculiarities of the valence band structure, such as the presence of various hole subbands, anisotropy, and spin-orbit coupling, are hidden in $F_c[\vec{M}]$. Near the Curie temperature T_C and at $H = 0$, where M is small, we expect $\mathcal{F}_c[M] - \mathcal{F}_c[0] \sim -M^2$. It is convenient to parameterize this dependence by a generalized carrier spin susceptibility, which is related to the magnetic susceptibility of the carrier liquid according to $\chi_c = A_F (g^* \mu_B)^2 \tilde{\chi}_c$. In terms of $\tilde{\chi}_c$,

$$\mathcal{F}_c[M] = \mathcal{F}_c[0] - \frac{A_F \tilde{\chi}_c \beta^2 M^2}{2(g\mu_B)^2} \quad (6)$$

By expanding $B_S(M)$ for small M one arrives to the mean-field formula for $T_C = T_F - T_{AF}$, where T_F is given by

$$T_F = \frac{x_{\text{eff}} N_o S(S+1) A_F \tilde{\chi}_c(T_C) \beta^2}{3k_B} \quad (7)$$

For a strongly degenerate carrier liquid $|\epsilon_F|/k_B T \gg 1$, as well as neglecting the spin-orbit interaction $\tilde{\chi}_c = \rho/4$, where ρ is the total density of states for intraband charge excitations, which in the 3D case is given by $\rho = m^*_{DOS} k_F / \pi^2 \hbar^2$. In this case and for $A_F = 1$, T_F assumes the well-known form, derived already in 1940s in the context of carrier-mediated nuclear ferromagnetism (Fröhlich and Nabarro, 1940). In general, however, $\tilde{\chi}_c$ has to be determined numerically by computing $\mathcal{F}_c[M]$ for a given band structure and degeneracy of the carrier liquid. The model can readily be generalized to various dimensions as well as to the case, when $\vec{M}$ is not spatially uniform in the ground state, a case of spin-density waves expected in the case of 1D systems.

The same formalism, in addition to T_C and Mn magnetization $M(T, H)$, as discussed in the preceding text, provides also quantitative information on spin polarization and magnetization of the hole liquid (Dietl, Ohno and Matsukura, 2001). Furthermore, it can be exploited to describe chemical trends as well as micromagnetic, transport, and optical properties of ferromagnetic DMS (Jungwirth *et al*., 2006a). In particular, a detail theoretical analysis of anisotropy energies and anisotropy fields in films of (Ga,Mn)As was carried out for a number of experimentally important cases within the p–d Zener model (Dietl, Ohno and Matsukura, 2001; Abolfath, Jungwirth, Brum and MacDonald, 2001). The cubic anisotropy as well as uniaxial anisotropy under biaxial epitaxial strain were examined as a function of the hole concentration p. Both shape and magnetocrystalline anisotropies were taken into account. The perpendicular and in-plane orientation of the easy axis is expected for the compressive and tensile strain, respectively, provided that the hole concentration is sufficiently small. However, according to theory, a reorientation of the easy axis direction is expected at higher hole concentrations. Furthermore, in a certain concentration range the character of magnetic anisotropy is found to depend on the magnitude of spontaneous magnetization, that is on the temperature. The computed phase diagram for the reorientation transition compared to the experimental results for a (Ga,Mn)As film is shown in Figure 2. In view that theory is developed with no adjustable parameters the agreement between experimental and computed concentrations and temperature corresponding to the reorientation transition is very good. Furthermore, the computed magnitudes of the anisotropy field H_u (Dietl, Ohno and Matsukura, 2001) are consistent with the available findings for both compressive and tensile strain.

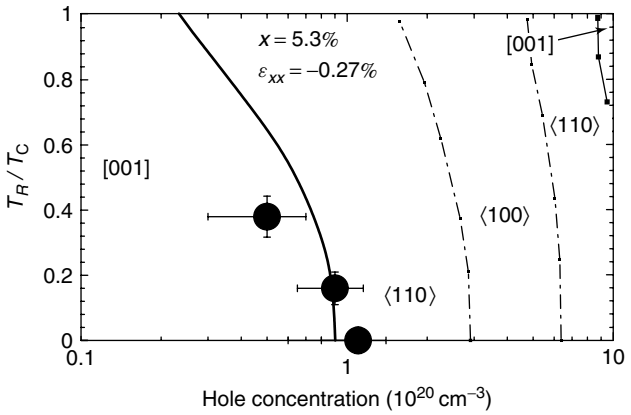

Figure 2. Experimental (full points) and computed values (thick lines) of the ratio of the reorientation to Curie temperature for the transition from perpendicular to in-plane magnetic anisotropy. Dashed lines mark expected temperatures for the reorientation of the easy axis between ⟨100⟩ and ⟨110⟩ in-plane directions. (Reproduced from Sawicki *et al*., 2005, with permission from the American Physical Society. © 2005.)

It should be emphasized that the preceding description of ferromagnetic DMS is strictly valid only in the weak coupling limit (Dietl *et al*., 2000). On going from antimonides to nitrides or from tellurides to oxides, the p–d hybridization increases. In the strong-coupling limit, the short-range part of the TM potential may render the virtual-crystal approximation and molecular-field approximation invalid (Benoit à la Guillaume, Scalbert and Dietl, 1992; Matsukura and Ohno, 2002), leading to properties somewhat reminiscent of those specific to alloys which cannot be described by the virtual crystal approximation, like Ga(As,N) (Wu, Shan and Walukiewicz, 2002). Here, dynamic mean-field approximation (DMFA) may capture relevant physics (Chattopadhyay, Das Sarma and Millis, 2001). In particular, in the strong-coupling limit, the short-range potential of the TM ion admixes to the itinerant carrier wave function a local component. This, together with quantum effects of Anderson–Mott localization, may generate modifications in optical and transport characteristics, such as an apparent increase in the carrier effective mass (Burch *et al*., 2006).

The issue how various corrections to the mean-field p–d Zener model (Dietl *et al*., 2000) affect theoretical values of T_C was recently examined in some detail for (Ga,Mn)As (Brey and Gómez-Santos, 2003; Timm and MacDonald, 2005; Jungwirth *et al*., 2005; Popescu *et al*., 2006) with the conclusions that the overall picture remains quantitatively valid. Figure 3 shows one of the recent theoretical modelings of T_C in comparison to experimental findings for (Ga,Mn)As (Jungwirth *et al*., 2005). These results confirm, in particular, that T_C values above 300 K could be achieved in $Ga_{0.9}Mn_{0.1}As$ if such a large magnitude of the substitutional Mn concentration could be accompanied by a corresponding increase of the hole density (Dietl *et al*., 2000).

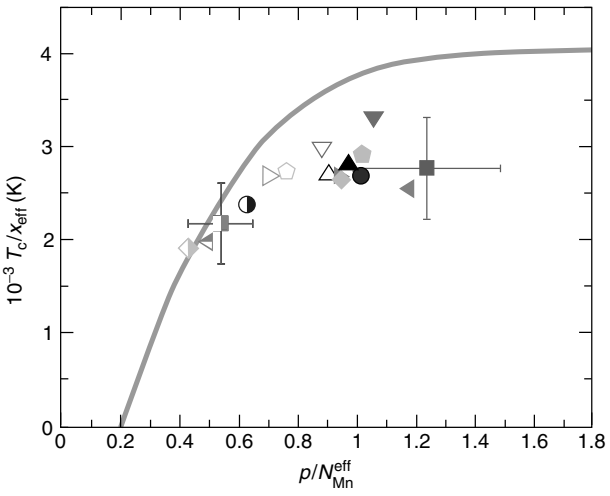

Figure 3. Experimental Curie temperatures versus hole density p relative to effective concentration of Mn moments, $N_{Mn} = 4x_{eff}/a_o^3$, where x_{eff} is the content of Mn in the substitutional positions and a_o is the lattice constant. Gray line is theoretical computed within the tight-binding and coherent potential approximations. (Reproduced from Jungwirth *et al*., 2005, with permission from the American Physical Society. © 2005.)

2.5 Theory of modulated structures of diluted ferromagnetic semiconductors

The discovery of carrier-induced ferromagnetism in zinc-blende III–V and II–VI compounds has made it possible to consider physical phenomena and device concepts for previously unavailable combinations of quantum structures and magnetism in semiconductors. Indeed, it has already been demonstrated that various modulated structures of (Ga,Mn)As show functionalities relevant for spintronic devices including spin injection of holes (Ohno *et al*., 1999; Young *et al*., 2002) and electrons (Kohda *et al*., 2001, 2006; Johnston-Halperin *et al*., 2002), interlayer coupling (Chiba *et al*., 2000; Sadowski *et al*., 2002), exchange bias (Eid *et al*., 2005), giant magnetoresistance (GMR) (Chiba *et al*., 2000), tunneling magnetoresistance (TMR) (Tanaka and Higo, 2001; Mattana *et al*., 2003; Chiba, Matsukura and Ohno, 2004), tunneling anisotropic magnetoresistance (TAMR) (Ruster *et al*., 2005; Giddings *et al*., 2005), and domain-wall resistance (Tang *et al*., 2004; Chiba *et al*., 2006).

Because of paramount importance of interfaces as well of Rashba and Dresselhaus terms, spin properties of modulated semiconductor structures cannot be meaningfully modeled employing a standard kp theory. Accordingly, an empirical multiorbital tight-binding theory of multilayer structures has been developed (Oszwałdowski, Majewski and Dietl, 2006; Sankowski and Kacman, 2005; Sankowski, Kacman, Majewski and Dietl, 2006a,b). The employed procedure describes properly the carrier dispersion in the entire Brillouin zone and takes into account the presence of magnetic ions in the virtual-crystal and molecular-field approximations. Furthermore, since the phase coherence and spin diffusion lengths are comparable in these devices and, moreover, they are typically longer than the length of the active region, the formulation of spin transport model in terms of the Boltzmann distribution function f for particular spin orientations is not appropriate. Recently, theory that combines a Landauer-Büttiker formalism with tight-binding approximation has been developed (van Dorpe *et al*., 2005; Sankowski, Kacman, Majewski and Dietl, 2006a,b). In contrast to the standard kp method (Petukhov, Chantis and Demchenko, 2002; Brey, Fernández-Rossier and Tejedor, 2004), this theory, in which $sp^3d^5s^*$ orbitals are taken into account, describes properly the interfaces and inversion symmetry breaking as well as the band dispersion in the entire Brillouin zone, so that the essential for the spin-dependent tunneling Rashba and

Dresselhaus terms as well as the tunneling via $\vec{k}$ points away from the zone center are taken into account.

The approach in question, developed with no adjustable parameters, provided information on sign of the interlayer coupling (Sankowski and Kacman, 2005), explained experimentally observed large magnitudes of both electron current spin polarization up to 70% in the (Ga,Mn)As/n-GaAs Zener diode (van Dorpe *et al*., 2005) and TMR of the order of 300% in a (Ga,Mn)As/GaAs/(Ga,Mn)As trilayer structure (Sankowski, Kacman, Majewski and Dietl, 2006b), as shown in Figure 4. Furthermore, theory reproduced a fast decrease of these figures with the device bias as well as it indicated that the magnitude of TAMR should not exceed 10% under usual strain conditions and for hole densities corresponding to the metal side of the metal-to-insulator transition (MIT) (Sankowski, Kacman, Majewski and Dietl, 2006a). A similar model was employed to examine an intrinsic domain-wall resistance in (Ga,Mn)As (Oszwałdowski, Majewski and Dietl, 2006).

3 NONUNIFORM FERROMAGNETIC DMS – ELECTRONIC NANOSCALE PHASE SEPARATIONS

3.1 Effects of competing magnetic interactions

A number of effects has been identified, which may lead to deviations from a simple ferromagnetic spin order in carrier-controlled diluted ferromagnetic semiconductors even if the spatial distribution of magnetic ions is uniform. In particular, spin-density waves appear to be in the ground state in the case of 1D systems (Dietl, Cibert, Ferrand and Merle d'Aubigné, 1999). Another proposal involves canted ferromagnetism stemming from a nonscalar form of spin–spin interactions, brought about by spin-orbit coupling (Zaránd and Jankó, 2002), though a large value of saturation magnetization in (Ga,Mn)As indicates that the effect is not large (Jungwirth *et al*., 2006b). Finally, a competition between long-range ferromagnetic interactions and intrinsic short-range antiferromagnetic interactions (Kępa *et al*., 2003) may affect the character of magnetic order (Kechrakos, Papanikolaou, Trohidou and Dietl, 2005). It appears that the effect is more relevant in II–VI DMS than in III–V DMS where Mn centers are ionized, so that the enhanced hole density at closely lying Mn pairs may compensate antiferromagnetic interactions (Dietl, Ohno and Matsukura, 2001).

The above-mentioned competition between the long-range RKKY merely ferromagnetic interaction and short-range merely antiferromagnetic superexchange was shown to affect in a nontrivial way magnetic properties of modulation-doped p-type (Cd,Mn)Te quantum wells (Kechrakos, Papanikolaou, Trohidou and Dietl, 2005). In this system, the temperature T_C at which spontaneous spin splitting of electronic levels appears as well as its temperature dependence (Haury *et al*., 1997; Kossacki *et al*., 2000, 2002; Boukari *et al*., 2002) follow predictions of a simple mean-field Zener-like model of ferromagnetism (Dietl, Haury and Merle d'Aubigné, 1997). A reasonable accuracy of the MFA in this low-dimensional system was linked to the long-range

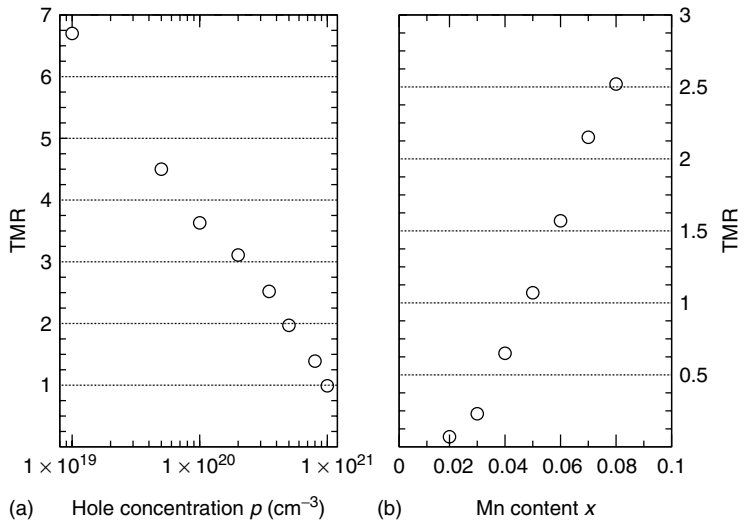

Figure 4. Difference in resistance for antiparallel and parallel magnetization orientations normalized by resistance for parallel orientation for tunneling structures p-$Ga_{1-x}Mn_xAs$/GaAs/p-$Ga_{1-x}Mn_xAs$ as a function of: (a) hole concentration p (for $x = 0.08$); (b) Mn content x (for $p = 3.5 \times 10^{20}\,\mathrm{cm}^{-3}$) in the limit of small bias voltage. (Reproduced from Sankowski, P. *et al*., 2006, with permission from Elsevier. © 2006.)

character of the ferromagnetic interactions as well as to the combined effects of spin-orbit interaction and confinement that lead to the Ising-type universality class (Haury *et al*., 1997). At the same time, however, wide hysteresis loops and the associated spontaneous macroscopic magnetization in zero magnetic field, which are expected within this model (Lee, Jungwirth and MacDonald, 2002), have not been observed. Instead, according to polarization-resolved photoluminescence measurements, the global spin polarization of the carrier liquid increases slowly with the external magnetic field along the easy axis, reaching saturation at a field by a factor of 20 greater than what could be accounted for by demagnetization effects (Kossacki *et al*., 2000, 2002).

In order to explain this behavior, Monte Carlo simulations were employed (Kechrakos, Papanikolaou, Trohidou and Dietl, 2005), in which the Schrödinger equation was solved at each Monte Carlo sweep. Such a model is capable to assess the influence of magnetization fluctuations, short-range antiferromagnetic interactions, disorder, magnetic polaron formation, and spin-Peierls instability on the carrier-mediated ferromagnetism in two-dimensional electronic systems. It has been found that the determined critical temperatures and hystereses are affected in a nontrivial way by the presence of short-range antiferromagnetic interactions, as shown in Figure 5. In particular, the antiferromagnetic interactions decrease T_C less than expected within the MFA. However, the presence of competing interactions reduces strongly the remanence and the coercive field. It appears that in order to satisfy both ferromagnetic and antiferromagnetic spin couplings in an optimum way, the system breaks into nanoscale ferromagnetic domains, so that the global magnetization averages to zero. At the same time, the magnitude of the external magnetic field that can align these domains is set by the strength of the antiferromagnetic interactions, not by demagnetization or magnetic anisotropy energies.

3.2 Effects of Anderson–Mott localization

Similar to other doped semiconductors, p-type DMS undergo MIT, when an average distance between the carriers becomes 2.5 times greater than the Bohr radius. The insulator regime can be reached not only by reducing the acceptor density but also by increasing the concentration of compensation donors or by depleting the film of holes either by electrostatic gates or by charge transfer to surface states or to neighbor undoped layers. In has been found that, in contrast to charge transport characteristics, the Curie temperature, like other thermodynamic properties, does not show up any critical behavior on crossing the MIT (Matsukura, Ohno, Shen and Sugawara, 1998; Ferrand *et al*., 2001).

Two competing models have been put forward in order to explain the existence of ferromagnetic order on the insulator side of the MIT. According to the magnetic polaron scenario (Durst, Bhatt and Wolff, 2002; Kaminski and Das Sarma, 2002) the holes stay localized by the individual parent acceptors, so that their localization length corresponds to the Bohr radius, usually diminished – particularly in the strong-coupling regime – by the hole interaction with the short-range part of the TM potential. In such a case, the ferromagnetic transition can be viewed as the percolation threshold of bound magnetic polarons.

Another scenario was put forward by the present author and coworkers (Dietl, Haury and Merle d'Aubigné, 1997; Dietl *et al*., 2000; Ferrand *et al*., 2001). Within this model, the hole localization length, which diverges at the MIT,

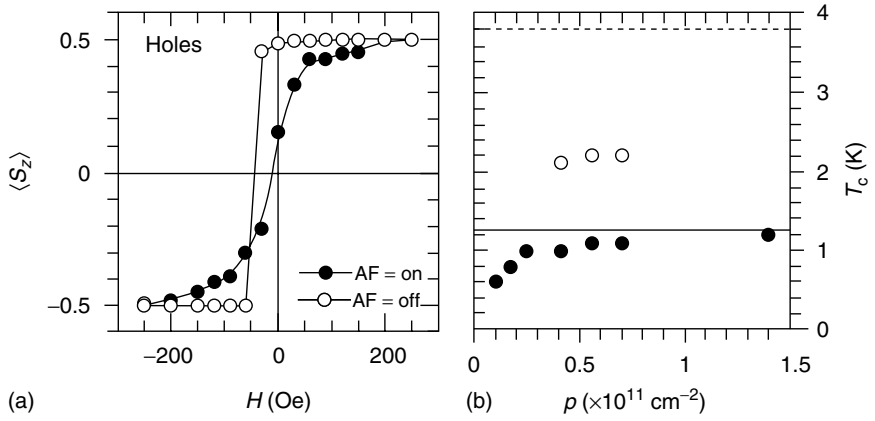

Figure 5. (a) Upper branch of the magnetization hysteresis loop of hole spins in a $Cd_{0.96}Mn_{0.04}Te$ quantum well at $T = 0.7T_C$, where T_C is the Curie temperature, as determined by Monte Carlo simulations neglecting (open symbols) an taking into account (full symbols) the presence of antiferromagnetic interactions. The sheet hole density is $p = 0.41 \times 10^{11}\,cm^{-2}$. (b) The simulated dependence of T_C on p. Horizontal lines are the mean-field results neglecting (dashed line) and taking into account (solid line) antiferromagnetic interactions. (Reproduced from Kechrakos *et al*., 2005, with permission from the American Physical Society. © 2005.)

remains much greater than an average distance between the acceptors for the experimentally important range of the hole densities. Accordingly, the holes can be regarded as delocalized at the length scale relevant for the coupling between magnetic ions. Hence, the spin–spin exchange interactions are effectively mediated by the itinerant carriers, so that the p–d Zener or RKKY model can be applied also on the insulator side of the MIT. At the same time, however, large mesoscopic fluctuations in the local value of the density of states are expected near the MIT. As a result, nanoscale phase separation into paramagnetic and ferromagnetic regions takes place below and in the vicinity of the apparent Curie temperature. The paramagnetic phase persists down to the lowest temperatures in the locations that are *not* visited by the holes or characterized by a low value of the blocking temperature T_B defined in Introduction. The ferromagnetic order develops in the regions, where the carrier liquid sets long-range ferromagnetic correlation between the randomly distributed TM spins. According to this model, the portion of the material encompassing the ferromagnetic bubbles, and thus the magnitude of the saturated ferromagnetic moment, grows with the net acceptor concentration, extending over the whole sample on the metallic side of the MIT.

It is still a formidable task, even in nonmagnetic semiconductors, to describe quantitatively effects of both disorder and carrier–carrier correlation near the Anderson–Mott transition. However, there is a growing amount of experimental results indicating that the model outlined in the previous paragraph is qualitatively correct. In particular, for samples on the insulator side of MIT, the field dependence of magnetization shows the presence of superimposed ferromagnetic and paramagnetic contributions in both (Ga,Mn)As (Oiwa *et al*., 1997) and p-(Zn,Mn)Te (Ferrand *et al*., 2001). Interestingly, the paramagnetic component is less visible in the anomalous Hall effect data, presumably because it probes merely the regions visited by the carriers (Ferrand *et al*., 2001). At the same time, colossal negative magnetoresistance is observed, leading to the field-induced insulator-to-metal transition in samples with the appropriate acceptor densities (Ferrand *et al*., 2001; Katsumoto *et al*., 1998). The enhanced conductance in the magnetic field can be linked to the ordering of ferromagnetic bubbles and to the alignment of the spins in the paramagnetic regions. Remarkably, the corresponding effects have recently been found in modulation-doped quantum well of (Cd,Mn)Te, where no localization of carriers by individual ionized impurities and, thus, no formation of bound magnetic polarons is expected (Jaroszyński *et al*., 2005). The question whether the holes bound by individual acceptors or rather the holes residing in weakly localized states mediate ferromagnetism in DMS on the insulating side of the MIT was also addressed by inelastic neutron scattering in (Zn,Mn)Te:P (Kępa *et al*., 2003). In that work, the difference in the nearest-neighbor Mn pairs exchange energy J_1 in the presence and in the absence of the holes was determined. The hole-induced contribution to J_1 was found to be by a factor of 4 smaller than that calculated under the assumption that the holes reside on individual acceptors. By contrast, if the hole states are assumed to be metallic-like at length scale of the nearest-neighbor distance, the calculated value is smaller than the experimental one by a factor of 1.5, a discrepancy well within combine uncertainties in the input parameters to theory and experimental determination.

4 NONUNIFORM FERROMAGNETIC DMS – CHEMICAL NANOSCALE PHASE SEPARATIONS

4.1 Spinodal decomposition

It is well known that phase diagrams of a number of alloys exhibit a solubility gap in a certain concentration range. This may lead to spinodal decomposition into regions with a low and a high concentration of particular constituents. If the concentration of one of them is small, it may appear in a form of coherent nanocrystals embedded by the majority component. For instance, such a spinodal decomposition is known to occur in the case of (Ga,In)N (Farhat and Bechstedt, 2002), where In-rich quantum-dot-like regions are embedded by an In-poor matrix. However, according to the pioneering *ab initio* work of van Schilfgaarde and Mryasov (2001) and others (Sato, Katayama-Yoshida and Dederichs, 2005) particularly strong tendency to form nonrandom alloy occurs in the case of DMS: the evaluated gain in energy by bringing two Ga-substitutional Mn atoms together is $E_d = 120\,\text{meV}$ in GaAs and 300 meV in GaN, and reaches 350 meV in the case of Cr pair in GaN (van Schilfgaarde and Mryasov, 2001).

Since spinodal decomposition does not usually involve a precipitation of another crystallographic phase, it is not easy detectable experimentally. Nevertheless, its presence was found by transmission electron microscopy (TEM) (Moreno *et al*., 2002; Yokoyama, Yamaguchi, Ogawa and Tanaka, 2005) in (Ga,Mn)As, where coherent zinc-blende Mn-rich (Mn,Ga)As nanocrystals led to the apparent Curie temperature up to 360 K (Yokoyama, Yamaguchi, Ogawa and Tanaka, 2005). Furthermore, coherent hexagonal and diamond-type Mn-rich nanocrystals were detected by spatially resolved X-ray diffraction in (Ga,Mn)N (Martinez-Criado *et al*., 2005) and by TEM in (Ge,Mn) (Bougeard, Ahlers, Trampert and Abstreiter, 2006), respectively.

In view of typically limit solubility of magnetic atoms in semiconductors, it may, therefore, be expected that such a

spinodal decomposition is a generic property of a number of DMS. Owing to the high concentration of the magnetic constituent, the nanocrystals form in this way order magnetically at a relatively high temperature T_m, usually much greater than room temperature. Obviously, either ferromagnetic or ferrimagnetic nanocrystals possess a nonzero magnetic moment. Interestingly enough, nanocrystals in which antiferromagnetic interactions dominate can also show a nonzero magnetic moment owing to the presence of uncompensated spins at their surface, whose relative magnitude grows with decreasing nanocrystal size (Trohidou, Zianni and Blackman, 2002).

As an example we consider (Zn,Cr)Se (Karczewski *et al*., 2003) and (Zn,Cr)Te (Saito, Zayets, Yamagata and Ando, 2003), which show (Karczewski *et al*., 2003; Kuroda *et al*., 2005) the well-known superparamagnetic behavior (Shinde *et al*., 2004; Goswami *et al*., 2005), indicating that the system is to be viewed rather as an ensemble of noninteracting ferromagnetic particles than a uniform magnetic alloy. In such a case the temperature dependencies of magnetization and magnetic susceptibility are described by four distinguished temperatures: T_m, the blocking temperature T_B that corresponds to a maximum of zero-field cooled magnetization; the apparent Curie temperature $T_C^{(app)}$ of the composite material, and the Curie–Weiss temperature Θ characterizing a weighted magnitude of the exchange interactions between the Cr spins within the nanocrystal. A maximum value of $T_C^{(app)} \approx 320\,\mathrm{K}$ is obtained for (Zn,Cr)Te with x_{Cr} above the percolation limit for 3D, $x \approx 0.2$.

These remarkable observations can readily be interpreted under the assumption that the relevant magnetic nanoparticles are built of a metallic zinc-blende CrTe or Cr-rich (Zn,Cr)Te characterized by $T_m \approx 320\,\mathrm{K}$ and by the lattice constant imposed by a paramagnetic semiconductor host, either ZnTe or (Zn,Cr)Te with a rather small Cr concentration. This conjecture is consistent with *ab initio* computations (Zhao and Zunger, 2005) predicting zinc-blende CrTe to be a ferromagnetic half-metal as well as with experimental results for CrTe in a bulk NiAs-type structure for which $T_m \equiv T_C = 340 \pm 10\,\mathrm{K}$ (Ohta, Kanomata, Kaneko and Yoshida, 1993). Within this scenario, for small ferromagnetic nanocrystals we expect $T_B < T_C^{(app)} < T_C$, T_B being proportional to a mean nanoparticle volume V, $T_B \approx KV/(25k_B)$, where K is the density of the magnetic anisotropy energy. Similarly, $T_C^{(app)}$ provides information on the upper bound of the V distribution. Furthermore, we note that broken magnetic bonds at the nanocrystal surface reduce the Curie–Weiss temperature Θ from its anticipated value for large V, $\Theta_{max} \geq T_C$.

It is, therefore, legitimate to suppose that coherent nanocrystals with a large concentration of magnetic constituent account for high apparent Curie temperatures detected in a number of DMS. This model explains, in particular, a long staying puzzle about the origin of ferromagnetic response in DMS, in which an average concentration of magnetic ions is below the percolation limit for the nearest neighbor coupling and, at the same time, the free-carrier density is too low to mediate an efficient long-range exchange interaction. Remarkably, the presence of magnetically active nanocrystals leads to an enhanced magneto-optical (Yokoyama, Yamaguchi, Ogawa and Tanaka, 2005) and magnetotransport (Shinde *et al*., 2004; Ye *et al*., 2003) properties. This opens doors for various applications of such hybrid systems provided that methods for controlling nanocrystal characteristics and distribution would be elaborated. So far, the most rewarding method of self-organized growth of coherent nanocrystals or quantum dots has exploited strain fields generated by lattice mismatch at interfaces of heterostructures (Stangl, Holý and Bauer, 2004). Remarkably, it becomes possible to fabricate highly ordered three-dimensional dot crystals under suitable spatial strain anisotropy (Stangl, Holý and Bauer, 2004). A further progress in this direction is particularly timely as it could result in the development of high-density 3D memories and spatial light modulators for advanced display technologies. A new method of self-organized growth has recently been proposed by the present author (Dietl, 2006). In this approach, long-range Coulomb forces serve to control the aggregation of alloy constituents.

4.2 Controlling spinodal decomposition by interion coulomb interactions

It is well known that in most DMS the levels derived from the open d or f shells of magnetic ions reside in the band gap of the host semiconductor (Dietl, 2002). This property of magnetic ions has actually been exploited for a long time to fabricate semi-insulating materials, in which carriers introduced by residual impurities or defects are trapped by the band-gap levels of magnetic impurities. The essential ingredient of the proposal in question (Dietl, 2006) is the observation that such a trapping alters the charge state of the magnetic ions and, hence, affect their mutual Coulomb interactions. Accordingly, codoping of DMS with shallow acceptors or donors modifies E_d and thus provides a mean for the control of ion aggregation. Indeed, the energy of the Coulomb interaction between two elementary charges residing on the nearest-neighbor cation sites in the GaAs lattice is 280 meV. This value indicates that the Coulomb interaction can preclude the aggregation, as the gain of energy associated with the bringing two Mn atoms in (Ga,Mn)As is $E_d = 120\,\mathrm{meV}$.

It is evident that the model in question should apply to a broad class of DMS as well to semiconductors and insulators, in which a constituent, dopant, or defect can exist

in different charge states under various growth conditions. As important examples we consider (Ga,Mn)N and (Zn,Cr)Te, in which remarkable changes in ferromagnetic characteristics on codoping with shallow impurities have recently been reported (Reed *et al*., 2005; Ozaki *et al*., 2005). In particular, a strong dependence of saturation magnetization M_s at 300 K on codoping with Si donors and Mg acceptors has been found (Reed *et al*., 2005) for (Ga,Mn)N with an average Mn concentration $x_{Mn} \approx 0.2\%$. Both double exchange and superexchange are inefficient at this low Mn concentration and for the midgap Mn level in question. At the same time, the model of nanocrystal self-organized growth in question explains readily why M_s goes through a maximum when Mn impurities are in the neutral Mn^{3+} state, and vanishes if codoping by the shallow impurities makes all Mn atoms to be electrically charged.

It has also been found that $T_C^{(app)}$ depends dramatically on the concentration of shallow N acceptors in (Zn,Cr)Te. Actually, $T_C^{(app)}$ decreases monotonically when the concentration x_N of nitrogen increases, and vanishes when x_{Cr} and x_N become comparable. This supports the model as in ZnTe the Cr state (Godlewski and Kamińska, 1980) resides about 1 eV above the nitrogen level (Baron, Saminadayar and Magnea, 1998). Accordingly, for $x_N \approx x_{Cr}$ all Cr atoms become ionized and the Coulomb repulsion precludes the nanocrystal formation. At the same time, the findings are not consistent with the originally proposed double exchange mechanism (Ozaki *et al*., 2005), as undoped ZnTe is only weakly p type, so that T_C should be small for either $x_N \approx 0$ and $x_N \approx x_{Cr}$, and pick at $x_N \approx x_{Cr}/2$, not at $x_N \approx 0$.

Finally, we mention the case of Mn doped GaAs, InAs, GaSb, and InSb. In those materials, owing to a relatively shallow character of Mn acceptors and a large Bohr radius, the holes reside in the valence band. Thus, the Mn atoms are negatively charged, which – according to our model – reduces their clustering, and makes it possible to deposit, by low-temperature epitaxy, a uniform alloy with a composition beyond the solubility limit. Codoping with shallow donors, by reducing the free-carrier screening, will enhance repulsions among Mn, and allow one to fabricate homogenous layers with even greater x_{Mn}. On the other hand, codoping by shallow acceptors, along with the donor formation by a self-compensation mechanism (Yu *et al*., 2002), will enforce the screening and, hence, lead to nanocrystal aggregation.

5 SUMMARY

The findings discussed here demonstrate that a number of pertinent properties of spatially uniformed carrier-controlled diluted ferromagnetic semiconductors and their heterostructures can be understood qualitatively, if not quantitatively, by the present theory. The accumulated data point clearly to the importance of spin-orbit interactions in the physics of hole-mediated ferromagnetism in semiconductors. These interactions control the magnitude of the Curie temperature, the saturation value of the magnetization, the anomalous Hall effect as well as the character and magnitude of magnetic and transport anisotropies. A growing amount of evidences shows that under various conditions the spatial distribution of carriers and/or magnetic ions is by no means uniform. The nanoscale phase separation can be driven either by randomness in the carrier and spin subsystems or by limited solubility of TMs in the host semiconductor, which leads to spinodal decomposition into regions with a small and a large concentration of the magnetic constituent. Interestingly, by manipulating the charge state of magnetic ions, it becomes possible to control the spinodal decomposition. This constitutes an appealing avenue toward self-organized coherent epitaxy of magnetic nanocrystals over a wide range of their dimensions. It is expected that further works will indicate how to tailor nanocrystal size dispersion and spatial distribution. In this context, engineering of local strains by exploiting various combinations of dopants and hosts may turn out to be of relevance. The self-organized growth mode in question (Dietl, 2006) is rather universal – it applies to dopants exhibiting a solubility gap, and different charge states that are stable under the growth conditions. The existence of this nano-assembling mechanism, as exemplified here by the case of (Zn,Cr)Te and (Ga,Mn)N codoped with shallow impurities, explains outstanding properties of a broad class of composite DMS, and offer prospects for exploiting their novel functionalities. In particular, the nanocrystals, rather than the host, are shown to account for ferromagnetic signatures in magnetic and magneto-optical characteristics of these systems. These findings imply also that today's *ab initio* methods of computational materials science, assigning the high-temperature ferromagnetism of, for example, (Zn,Cr)Te (Bergqvist *et al*., 2004; Fukushima, Sato, Katayama-Yoshida and Dederichs, 2004) to the uniform diluted alloy, overestimate substantially long-range ferromagnetic correlation, presumably because effects of Mott–Hubbard and Anderson–Mott localization of paramount importance in the case of the narrow d band are implicitly disregarded in the codes developed so far. It thus appears that delocalized or weakly localized valence band holes are necessary to transmit magnetic information between the diluted spins (Dietl *et al*., 2000; Jungwirth *et al*., 2006a). In addition to (Ga,Mn)As, (Zn,Mn)Te:N, and related systems, recent indications of ferromagnetism in p-(Ga,Mn)N (Edmonds *et al*., 2005; Sarigiannidou *et al*., 2006) and p-(Ga,Mn)P (Scarpulla *et al*., 2005) appear to support this conclusion. However, in those and other experimentally relevant cases, nonuniformity associated with hole localization is seen to affect strongly ferromagnetic properties. It is still

to be found out experimentally whether nitrides, oxides or diamond containing 5% of randomly distributed magnetic impurities and more than 3×10^{20} valence band holes/cm^3 show ferromagnetic ordering above the room temperature.

ACKNOWLEDGMENTS

This work was supported in part by ERATO Semiconductors Spintronics Project of Japan Science and Technology Agency, by NANOSPIN E. C. project (FP6-2002-IST-015728), by Humboldt Foundation, and carried out in collaboration with M. Sawicki, K. Osuch, H. Przybylińska, M. Kiecana, A. Lipińska, and P. Kossacki in Warsaw, as well as with groups of H. Ohno in Sendai, S. Kuroda in Tsukuba, K. Trohidou in Athens, J. Cibert and D. Ferrand in Grenoble, J. Jaroszyński and D. Popović in Tallahassee, L. Molenkamp in Würzburg, B. Gallagher in Nottingham, and A. Bonanni in Linz.

REFERENCES

Abolfath, M., Jungwirth, T., Brum, J. and MacDonald, A. (2001). Theory of magnetic anisotropy in $III_{1-x}Mn_xV$ ferromagnets. *Physical Review B*, **63**, 054418.

Awschalom, D. and Samarth, N. (2002). Optical manipulation, transport and storage of spin coherence in semiconductors, In *Semiconductor Spintronics and Quantum Computation*, Awschalom, D., Loss, D. and Samarth, N. (Eds.) Springer: Berlin, pp. 147–194.

Baron, T., Saminadayar, K. and Magnea, N. (1998). Nitrogen doping of Tebased II-VI compounds during growth by molecular beam epitaxy. *Journal of Applied Physics*, **83**, 1354.

Bastard, G., Rigaux, C., Guldner, Y., *et al*. (1978). Effect of exchange on interband magneto-absorption in zero gap $Hg_{1-x}Mn_xTe$ mixed crystals. *Journal de Physique (Paris)*, **39**, 87.

Bauer, G., Pascher, W. and Zawadzki, W. (1992). Magneto-optical properties of semimagnetic lead chalcogenides. *Semiconductor Science and Technology*, **7**, 703.

Benoit à la Guillaume, C., Scalbert, D. and Dietl, T. (1992). Wigner-Seitz approach to spin splitting in diluted magnetic semiconductors. *Physical Review B*, **46**, 9853(R).

Bergqvist, L., Eriksson, O., Kudrnovský, J., *et al*. (2004). Magnetic percolation in diluted magnetic semiconductors. *Physical Review Letters*, **93**, 137202.

Bhattacharjee, A.K., Fishman, G. and Coqblin, B. (1983). Virtual bound state model for the exchange interaction in semimagnetic semiconductors such as $Cd_{1-x}Mn_xTe$. *Physica B & C*, **117–118**, 449.

Bougeard, S., D. Ahlers, A. Trampert, and G. Abstreiter, 2006, Clustering in a precipitate free GeMn magnetic semiconductor. *Physical Review Letters*, **97**, 237202.

Boukari, H., Kossacki, P., Bertolini, M., *et al*. (2002). Light and electric field control of ferromagnetism in magnetic quantum structures. *Physical Review Letters*, **88**, 207204.

Brey, L., Fernández-Rossier, J. and Tejedor, C. (2004). Spin depolarization in the transport of holes across GaMnAs/GaAlAs/p-GaAs. *Physical Review B*, **70**, 235334.

Brey, L. and Gómez-Santos, G. (2003). Magnetic properties of GaMnAs from an effective Heisenberg Hamiltonian. *Physical Review B*, **68**, 115206.

Burch, K.S., Shrekenhamer, D.B., Singley, E.J., *et al*. (2006). Impurity band conduction in a high temperature ferromagnetic semiconductor. *Physical Review Letters*, **97**, 087208.

Chattopadhyay, A., Das Sarma, S. and Millis, A.J. (2001). A dynamical mean field theory for the magnetic transition temperature of ferromagnetic semiconductors. *Physical Review Letters*, **87**, 227202.

Chiba, D., Akiba, N., Matsukura, F., *et al*. (2000). Magnetoresistance effect and interlayer coupling of (Ga, Mn)As trilayer structures. *Applied Physics Letters*, **77**, 1873.

Chiba, D., Matsukura, F. and Ohno, H. (2004). Tunneling magnetoresistance in (Ga,Mn)As-based heterostructures with a GaAs barrier. *Physica E*, **21**, 966.

Chiba, D., Sato, Y., Kita, T., *et al*. (2004). Currentdriven magnetization reversal in a ferromagnetic semiconductor (Ga,Mn)As/GaAs/(Ga,Mn)As tunnel junction. *Physical Review Letters*, **93**, 216602.

Chiba, D., Yamanouchi, M., Matsukura, F., *et al*. (2006). Domain wall resistance in ferromagnetic (Ga,Mn)As. *Physical Review Letters*, **96**, 096602.

Dagotto, E., Hotta, T. and Moreo, A. (2001). Colossal magnetoresistant materials: the key role of phase separation. *Physics Reports*, **344**, 1.

Dietl, T. (1981). Semimagnetic semiconductors in high magnetic fields. In *Physics in High Magnetic Fields*, Chikazumi, S. and Miura, N. (Eds.), Springer: Berlin, p. 344.

Dietl, T. (1983). Optical properties of bound magnetic polarons in n-$Cd_{1-x}Mnx$Se. *Journal of Magnetism and Magnetic Materials*, **38**, 34.

Dietl, T. (1994). Diluted magnetic semiconductors. In *Handbook of Semiconductors*, Mahajan, S. (Ed.), North Holland: Amsterdam, p. 1251, Vol. 3B.

Dietl, T. (2002). Ferromagnetic semiconductors. *Semiconductor Science and Technology*, **17**, 377.

Dietl, T. (2004). Magnetic anisotropy and domain structure in carriercontrolled ferromagnetic semiconductors. *Journal of Physics: Condensed Matter*, **16**, 5471.

Dietl, T. (2005). Spintronics and ferromagnetism in wide-band-gap semiconductors. In *Proceedings 27th International Conference on the Physics of Semiconductors, Flagstaff, USA, 2004*, van de Walle, C.G. and Menèndez, J. (Eds.), AIP: Melville, p. 56.

Dietl, T. (2006). Self-organized growth controlled by charged states of magnetic impurities. *Nature Materials*, **5**, 673.

Dietl, T., Cibert, J., Ferrand, D. and Merle d'Aubigné, Y. (1999). Carriermediated ferromagnetic interactions in structures of magnetic semiconductors. *Materials Science and Engineering*, **63**, 103.

Dietl, T., Haury, A. and Merle d'Aubigné, Y. (1997). Free carrier-induced ferromagnetism in structures of diluted magnetic semiconductors. *Physical Review B*, **55**, R3347.

Dietl, T., Matsukura, F. and Ohno, H. (2002). Ferromagnetism of magnetic semiconductors: Zhang-Rice limit. *Physical Review B*, **66**, 033203.

Dietl, T., Ohno, H. and Matsukura, F. (2001). Hole-mediated ferromagnetism in tetrahedrally coordinated semiconductors. *Physical Review B*, **63**, 195205.

Dietl, T., Ohno, H., Matsukura, F., *et al*. (2000). Zener model description of ferromagnetism in zinc-blende magnetic semiconductors. *Science*, **287**, 1019.

Dietl, T. and Spałek, J. (1983). Effect of thermodynamic fluctuations of magnetization on the bound magnetic polaron in dilute magnetic semiconductors. *Physical Review B*, **28**, 1548.

van Dorpe, P., van Roy, W., de Boeck, J., *et al*. (2005). Voltage controlled spin injection in a (Ga,Mn)As/(al,ga)as zener diode. *Physical Review B*, **72**, 205322.

Durst, A.C., Bhatt, R.N. and Wolff, P.A. (2002). Bound magnetic polaron interactions in insulating doped diluted magnetic semiconductors. *Physical Review B*, **65**, 235205.

Edmonds, K.W., Novikov, S.V., Sawicki, M., *et al*. (2005). Transport and magnetism in p-type cubic (Ga,Mn)N. *Applied Physics Letters*, **86**, 152114.

Eid, K.F., Stone, M.B., Maksimov, O., *et al*. (2005). Exchange biasing of the ferromagnetic semiconductor (Ga,Mn)As by MnO. *Journal of Applied Physics*, **97**, 10D304.

Elsen, M., Boulle, O., George, J-M., *et al*. (2006). Spin transfer experiments on (Ga,Mn)As/(In,Ga)As/(Ga,Mn)As tunnel junctions. *Physical Review B*, **73**, 035303.

Farhat, M. and Bechstedt, F. (2002). First-principles calculations of gap bowing in $In_xGa_{1-x}N$ and $In_xAl_{1x}N$ alloys: Relation to structural and thermodynamic properties. *Physical Review B*, **65**, 075213.

Fedorych, O.M., Hankiewicz, E.M., Wilamowski, Z. and Sadowski, J. (2002). Single ion anisotropy of Mn-doped GaAs measured by electron paramagnetic resonance. *Physical Review B*, **66**, 045201.

Ferrand, D., Cibert, J., Wasiela, A., *et al*. (2001). Carrier-induced ferromagnetism in p-$Zn_{1-x}Mn_xTe$. *Physical Review B*, **63**, 085201.

Fröhlich, F. and Nabarro, F. (1940). Orientation of nuclear spins in metals. *Proceedings of the Royal Society of London Series A*, **175**, 382.

Fukushima, T., Sato, K., Katayama-Yoshida, H. and Dederichs, P.H. (2004). Theoretical prediction of Curie temperature in (Zn,Cr)S, (Zn,Cr)Se and (Zn,Cr)Te by first principles calculations. *Japanese Journal of Applied Physics*, **43**, L1416.

Furdyna, J. and Kossut, J. (1988). *Diluted Magnetic Semiconductors*, *Volume 25 of Semiconductor and Semimetals*, Academic Press: New York.

Gaj, J.A., Gałązka, R.R. and Nawrocki, M. (1978). Giant exciton Faraday rotation in $Cd_{1-x}Mn_xTe$ mixed crystals. *Solid State Communications*, **25**, 193.

Gałązka, R. (1978). Semimagnetic semiconductors. In *Proceedings 14th International Conference on Physics of Semiconductors, Edinburgh 1978*, Wilson, B. (Ed.), IoP: Bristol, p. 133.

Giddings, A., Khalid, M., Jungwirth, T., *et al*. (2005). Large tunneling anisotropic magnetoresistance in (Ga,Mn)As nanoconstrictions. *Physical Review Letters*, **94**, 127202.

Godlewski, M. and Kamińska, M. (1980). The chromium impurity photogeneration transitions in ZnS, ZnSe and ZnTe. *Journal of Physics: Condensed Matter*, **13**, 6537.

Goswami, R., Kioseoglou, G., Hanbicki, A.T., *et al*. (2005). Growth of ferromagnetic nanoparticles in Ge:Fe thin films. *Applied Physics Letters*, **86**, 032509.

Haury, A., Wasiela, A., Arnoult, A., *et al*. (1997). Observation of a ferromagnetic transition induced by two-dimensional hole gas in modulation-doped CdMnTe quantum wells. *Physical Review Letters*, **79**, 511.

Hwang, J.I., Ishida, Y., Kobayashi, M., *et al*. (2005). High-energy spectroscopic study of the III-V nitride-based diluted magnetic semiconductor $Ga_{1-x}Mn_xN$. *Physical Review*, **B 72**, 085216.

Jaczyński, M., Kossut, J. and Gałązka, R.R. (1978). Influence of exchange interaction on quantum transport phenomena in $Hg_{1-x}Mn_xTe$. *Physical Status Solidi A*, **88**, 73.

Jaroszyński, J., Andrearczyk, T., Karczewski, G., *et al*. (2005). Nanoscale clusterization at the metal-insulator boundary in diluted magnetic 2D quantum wells unpublished, available at http://arXivorg/abs/cond-mat/0509189.

Johnston-Halperin, E., Lofgreen, D., Kawakami, R., *et al*. (2002). Spin-polarized Zener tunneling in (Ga,Mn)As. *Physical Review B*, **65**, 041306(R).

Jungwirth, T., Atkinson, W., Lee, B. and MacDonald, A.H. (1999). Interlayer coupling in ferromagnetic semiconductor superlattices. *Physical Review B*, **59**, 9818.

Jungwirth, T., Sinova, J., Mašek, J., *et al*. (2006a). Theory of ferromagnetic (III,Mn)V semiconductors. *Reviews of Modern Physics*, **78**, 809.

Jungwirth, T., Wang, K.Y., Mašek, J., *et al*. (2006b). Low tempearature magnetization of (Ga,Mn)As. *Physical Review B*, **73**, 165205.

Jungwirth, T., Wang, K., Mašek, J., *et al*. (2005). Prospects of high temperature ferromagnetism in (Ga,Mn)As semiconductors. *Physical Review B*, **72**, 165204.

Kacman, P. (2001). Spin interactions in diluted magnetic semiconductors and magnetic semiconductor structures. *Semiconductor Science and Technology*, **16**, R25–R39.

Kaminski, A. and Das Sarma, S. (2002). Polaron percolation in diluted magnetic semiconductors. *Physical Review Letters*, **88**, 247202.

Karczewski, G., Sawicki, M., Ivanov, V., *et al*. (2003). Ferromagnetism in (Zn,Cr)Se layers grown by molecular beam epitaxy. *Journal of Superconductivity/Novel Magnetism*, **16**, 55.

Katsumoto, S., Oiwa, A., Iye, Y., *et al*. (1998). Strongly Anisotropic Hopping Conduction in (Ga, Mn)As/GaAs. *Physical Status Solidi A*, **205**, 115.

Kechrakos, D., Papanikolaou, N., Trohidou, K.N. and Dietl, T. (2005). Monte Carlo simulations of ferromagnetism in p-$Cd_{1-x}Mn_xTe$ quantum wells. *Physical Review Letters*, **94**, 127201.

Kępa, H., Khoi, L.V., Brown, C.M., *et al*. (2003). Probing hole-induced ferromagnetic exchange in magnetic semiconductors. *Physical Review Letters*, **91**, 087205.

Kohda, M., Kita, T., Ohno, Y., *et al*. (2006). Spectroscopic analysis of ballistic spin injection in a three-terminal device based on a p-(Ga,Mn)As/n$^+$-GaAs Esaki diode. *Applied Physics Letters*, **89**, 012103.

Kohda, M., Ohno, Y., Takamura, K., *et al*. (2001). A spin Esaki diode. *Japanese Journal of Applied Physics*, **40**, L1274.

Komarov, A., Ryabchenko, S., Terletskii, O., *et al*. (1977). Magneto-optical investigations and double magneto-optic resonance of the exciton band in CdTe:Mn^{2+}. *Soviet Physics JETP*, **46**, 318.

Koshihara, S., Oiwa, A., Hirasawa, M., *et al*. (1997). Ferromagnetic order induced by photogenerated carriers in magnetic III-V semiconductor heterostructures of (In,Mn)As/GaSb. *Physical Review Letters*, **78**, 4617.

Kossacki, P., Ferrand, D., Arnoult, A., *et al*. (2000). Ordered magnetic phase in $Cd_{1-x}Mn_xTe/Cd_{1-y-z}Mg_yZn_zTe$:N heterostructures: magnetooptical studies. *Physica E*, **6**, 709.

Kossacki, P., Kudelski, A., Gaj, J., *et al*. (2002). Light controlled and probed ferromagnetism of (Cd,Mn)Te quantum wells. *Physica E*, **12**, 344.

Kuroda, S., Ozaki, N., Nishizawa, N., *et al*. (2005). Growth and magnetic properties of novel ferromagnetic semiconductor (Zn,Cr)Te. *Science and Technology of Advanced Materials*, **6**, 558.

Langer, J., Delerue, C., Lannoo, M. and Heinrich, H. (1988). Transition-metal impurities in semiconductors and heterojunction band lineups. *Physical Review B*, **38**, 7723.

Lee, B., Jungwirth, T. and MacDonald, A.H. (2002). Field effect magnetization reversal in ferromagnetic semiconductor quantum wells. *Physical Review B*, **65**, 193311.

Liu, C., Yun, F. and Morkoç, H. (2005). Ferromagnetism of ZnO and GaN: A review. *Journal of Materials Science: Materials in Electronics*, **16**, 555.

Mac, W., Khoi, N.T., Twardowski, A., *et al*. (1993). Ferromagnetic p-d exchange in $Zn_{1-x}Cr_xSe$ diluted magnetic semiconductor. *Physical Review Letters*, **71**, 2327.

Martinez-Criado, G., Somogyi, A., Ramos, S., *et al*. (2005). . clusters in GaN: Hexagonal or cubic symmetry?. *Applied Physics Letters*, **86**, 131927.

Matsukura, F., Ohno, H. and Dietl, T. (2002). III-V ferromagnetic semiconductors, *Handbook of Magnetic Materials*, Vol. 14, p. 1–87.

Matsukura, F., Ohno, H., Shen, A. and Sugawara, Y. (1998). Transport properties and origin of ferromagnetism in (Ga,Mn)As. *Physical Review B*, **57**, R2037.

Mattana, R., George, J-M., Jaffrès, H., *et al*. (2003). Electrical detection of spin accumulation in a p-type GaAs quantum well. *Physical Review Letters*, **90**, 166601.

Mašek, J. and Máca, F. (2001). Self-compensating incorporation of Mn in $Ga_{1-x}Mn_xAs$. *Acta Physica Polonica A*, **100**, 319.

Mizokawa, T., Nambu, T., Fujimori, A., *et al*. (2002). Electronic structure of the oxide-diluted magnetic semiconductor $Zn_{1-x}Mn_xO$. *Physical Review B*, **B 66**, 085209.

Moreno, M., Trampert, A., Jenichen, B., *et al*. (2002). Correlation of structure and magnetism in GaAs with embedded Mn(Ga)As magnetic nanoclusters. *Journal of Applied Physics*, **92**, 4672.

Nagaev, R. (1983). *Physics of Magnetic Semiconductors*, Mir: Moscow.

Nagaev, E.L. (1993). *Physics of Magnetic Semiconductors*, Mir: Moscow.

Ohno, H. (1998). Making nonmagnetic semiconductors magnetic. *Science*, **281**, 951.

Ohno, H., Chiba, D., Matsukura, F., *et al*. (2000). Electric-field control of ferromagnetism. *Nature*, **408**, 944.

Ohno, H., Munekata, H., Penney, T., *et al*. (1992). Magnetotransport properties of p-type (In,Mn)As diluted magnetic III-V semiconductors. *Physical Review Letters*, **68**, 2664.

Ohno, H., Shen, A., Matsukura, F., *et al*. (1996). (Ga,Mn)As: A new diluted magnetic semiconductor based on GaAs. *Applied Physics Letters*, **69**, 363.

Ohno, Y., Young, D.K., Beschoten, B., *et al*. (1999). Electrical spin injection in a ferromagnetic semiconductor heterostructure. *Nature*, **402**, 790.

Ohta, S., Kanomata, T., Kaneko, T. and Yoshida, H.Y. (1993). Pressure effect on the Curie temperature and thermal expansion of CrTe. *Journal of Physics: Condensed Matter*, **5**, 2759.

Oiwa, A., Katsumoto, S., Endo, A., *et al*. (1997). Nonmetal-metal-nonmetal transition and large negative magnetoresistance in (Ga, Mn)As/GaAs. *Solid State Communications*, **103**, 209.

Oszwałdowski, R., Majewski, J.A. and Dietl, T. (2006). Influence of band structure effects on domain-wall resistance in diluted ferromagnetic semiconductors. *Physical Review B*, **74**, 153310.

Ozaki, N., Okabayashi, I., Kumekawa, T., *et al*. (2005). Suppression of ferromagnetism due to hole doping in $Zn_{1-x}Cr_xTe$ grown by molecular-beam epitaxy. *Applied Physics Letters*, **87**, 192116.1.

Petukhov, A.G., Chantis, A.N. and Demchenko, D.O. (2002). Resonant enhancement of tunneling magnetoresistance in double-barrier magnetic heterostructures. *Physical Review Letters*, **89**, 107205.

Popescu, F., Yildirim, Y., Alvarez, G., *et al*. (2006). Critical temperatures of a two-band model for diluted magnetic semiconductors. *Physical Review B*, **73**, 075206.

Prellier, W., Fouchet, A. and Mercey, B. (2003). Oxide-diluted magnetic semiconductors: a review of the experimental status. *Journal of Physics: Condensed Matter*, **15**, R1583.

Rader, O., Pampuch, C., Shikin, A.M., *et al*. (2004). Resonant photoemission of $Ga_{1-x}Mn_xAs$ at the Mn L edge. *Physical Review B*, **69**, 075202.

Reed, M.J., Arkun, F.E., Berkman, E.A., *et al*. (2005). Effect of doping on the magnetic properties of GaMnN: Fermi level engineering. *Applied Physics Letters*, **86**, 102504.

Ruster, C., Gould, C., Jungwirth, T., *et al*. (2005). Tunneling anisotropic magnetoresistance: Creating a spin-valve-like signal using a single ferromagnetic semiconductor layer. *Journal of Applied Physics*, **97**, 10C506.

Sadowski, J., Mathieu, R., Svedlindh, P., *et al*. (2002). Ferromagnetic GaMnAs/GaAs superlattices – MBE growth and magnetic properties. *Thin Solid Films*, **412**, 122.

Saito, H., Zayets, V., Yamagata, S. and Ando, K. (2003). Room-temperature ferromagnetism in a II-VI diluted magnetic semiconductor $Zn_{1-x}Cr_xTe$. *Physical Review Letters*, **90**, 207202.

Sankowski, P. and Kacman, P. (2005). Interlayer exchange coupling in (Ga,Mn)As-based superlattices. *Physical Review B*, **71**, 201303(R).

Sankowski, P., Kacman, P., Majewski, J. and Dietl, T. (2006a). Spin-dependent tunnelling in modulated structures of (Ga,Mn)As. *Physica E*, **32**, 375.

Sankowski, P., Kacman, P., Majewski, J. and Dietl, T. (2006b). Tight-binding model of spin-polarized tunnelling in (Ga,Mn)As-based structures. *Physica E*, **32**, 375.

Sarigiannidou, F., Wilhelm, E., Monroy, E., *et al*. (2006). Intrinsic ferromagnetism in wurtzite (Ga,Mn)N semiconductor. *Physical Review B*, **74**, 041306(R).

Sato, K., Katayama-Yoshida, H. and Dederichs, P.H. (2005). High Curie temperature and nano-scale spinodal decomposition phase in dilute magnetic semiconductors. *Japanese Journal of Applied Physics*, **44**, L948.

Sawicki, M., Wang, K-Y., Edmonds, K.W., *et al*. (2005). In-plane uniaxial anisotropy rotations in (Ga,Mn)As thin films. *Physical Review*, **B 71**, 121302.

Scarpulla, M.A., Cardozo, B.L., Farshchi, R., *et al*. (2005). Ferromagnetism in $Ga_{1-x}Mn_xP$: Evidence for inter-Mn exchange mediated by localized holes within a detached impurity band. *Physical Review Letters*, **95**, 207204.

van Schilfgaarde, M. and Mryasov, O.N. (2001). Anomalous exchange interactions in III-V dilute magnetic semiconductors. *Physical Review B*, **63**, 233205.

Shinde, S.R., Ogale, S.B., Higgins, J.S., *et al*. (2004). Co-occurrence of superparamagnetism and anomalous hall effect in highly reduced cobalt-doped rutile TiO_2-films. *Physical Review Letters*, **92**, 166601.

Stangl, J., Holý, V. and Bauer, G. (2004). Structural properties of self-organized semiconductor nanostructures. *Reviews of Modern Physics*, **76**, 725.

Story, T., Gałązka, R.R., Frankel, R.B. and Wolff, P.A. (1986). Carrier-concentration-induced ferromagnetism in PbSnMnTe. *Physical Review Letters*, **56**, 777.

Świerkowski, L. and Dietl, T. (1988). Stability of self-trapped magnetic polarons. *Acta Physica Polonica A*, **73**, 431.

Szczytko, J., Twardowski, A., Swiatek, K., *et al*. (1999). Mn impurity in $Ga_{1-x}Mn_xAs$ epilayers. *Physical Review*, **B 60**, 8304.

Tanaka, M. and Higo, Y. (2001). Large tunneling magnetoresistance in GaMnAs/AlAs/GaMnAs ferromagnetic semiconductor tunnel junctions. *Physical Review Letters*, **87**, 026602.

Tang, H., Masmanidis, S., Kawakami, R., *et al*. (2004). Negative intrinsic resistivity of an individual domain wall in epitaxial (Ga,Mn)As microdevices. *Nature*, **431**, 52.

Timm, C. and MacDonald, A. (2005). Influence of non-local exchange on RKKY interactions in III-V diluted magnetic semiconductors. *Physical Review B*, **71**, 155206.

Trohidou, K.N., Zianni, X. and Blackman, J.A. (2002). Magnetic behavior of antiferromagnetic and composite ferro-antiferromagnetic nanoparticles. *Physical Status Solidi A*, **189**, 305.

Vurgaftman, I. and Meyer, J. (2001). Nonmetal-metal-nonmetal transition and large negative magnetoresistance in (Ga, Mn)As/GaAs. *Physical Review B*, **64**, 245207.

Wang, K., Edmonds, K., Campion, R., *et al*. (2005). Magnetism and transport in ferromagnetic semiconductor (Ga,Mn)As films with tc up to 175 K In *Proceedings 27th International Conference on the Physics of Semiconductors*, Flagstaff, USA, 2004, Van de Walle, C. G. Mendez, J. (Ed.), AIP: Melville, p. 333.

Wilamowski, Z., Świątek, K., Dietl, T. and Kossut, J. (1990). Resonant states in semiconductors: A quantitative study of HgSe:Fe. *Solid State Communications*, **74**, 833.

Wu, J., Shan, W. and Walukiewicz, W. (2002). Band anticrossing in highly mismatched III–V semiconductor alloys. *Semiconductor Science and Technology*, **17**, 860.

Yamanouchi, M., Chiba, D., Matsukura, F., *et al*. (2006). Velocity of domain-wall motion induced by electrical current in a ferromagnetic semiconductor (Ga,Mn)As. *Physical Review Letters*, **96**, 096601.

Yamanouchi, M., Chiba, D., Matsukura, F. and Ohno, H. (2004). Current-induced domain-wall switching in a ferromagnetic semiconductor structure. *Nature*, **428**, 539.

Ye, S., Klar, P.J., Hartmann, T., *et al*. (2003). Anisotropy of the magnetotransport in (Ga,Mn)As/MnAs paramagnetic-ferromagnetic hybrid structures. *Applied Physics Letters*, **83**, 3927.

Yokoyama, M., Yamaguchi, H., Ogawa, T. and Tanaka, M. (2005). Zinc-blende-type MnAs nanoclusters embedded in GaAs. *Journal of Applied Physics*, **97**, 10D317.

Young, K., Gupta, J.A., Johnston-Halperin, E., *et al*. (2002). Optical, electrical and magnetic manipulation of spins in semiconductors. *Semiconductor Science and Technology*, **17**, 275.

Yu, K.M., Walukiewicz, W., Wojtowicz, T., *et al*. (2002). Effect of the location of Mn sites in ferromagnetic $Ga_{1-x}Mn_xAs$ on its Curie temperature. *Physical Review B*, **65**, 201303.

Zaránd, G. and Jankó, B. (2002). $Ga_{1-x}Mn_xAs$: a frustrated ferromagnet. *Physical Review Letters*, **89**, 047201.

Zhao, Y-J. and Zunger, A. (2005). Zinc-blende half-metallic ferromagnets are rarely stabilized by coherent epitaxy. *Physical Review B*, **71**, 132403.

Zunger, A. (1986). Electronic structure of 3d transition-atom impurities in semiconductors. In *Solid State Physics*, Seitz, F. and Turnbull, D. (Eds.), Academic Press: New York, pp. 275–464, Vol. 39.

Spin Engineering in Quantum Well Structures

Roberto C. Myers and Arthur C. Gossard
University of California, Santa Barbara, CA, USA

1 INTRODUCTION

The band engineering afforded in heterostructures (Kroemer, 2001) can be tailored at monolayer length scales by using layer-by-layer growth techniques, such as molecular-beam epitaxy (MBE) (Gossard, 1986). Depositing a thin ($\sim$10–100 Å) narrow band-gap material within a wider band-gap material confines band electrons in one dimension at length scales at which this confinement quantizes the wave functions, energy levels, and band structure. These quantum wells (QWs) are essential components in countless optoelectronic devices, such as QW laser diodes, avalanche photodiodes, quantum cascade lasers, and high electron mobility transistors to name a few. In addition to modern device application, QWs have been at the forefront of condensed matter research, providing systems in which band structure, density of states, carrier density, and confinement energy are adjustable.

Recently, the possibility of utilizing the spin of electrons for additional or fundamentally new device functionality, spintronics, has sparked a broad research effort in semiconductors. QWs offer a unique means for controlling the interactions between free carrier spins and localized magnetic-ion or nuclear spins and have the advantage of a high level of technological versatility via advanced growth techniques like MBE. Additionally, QWs have advantageous optical properties for probing and polarizing spin. In spin-LEDs, for example, the degree of circular polarization of electroluminescence from QWs is used as a probe of spin-polarized current through these devices, which is made possible by the unique spin-sensitive optical selection rules.

We review recent developments in semiconductor spintronics, in which electric and magnetic fields are used to polarize, orient, and couple quantum-confined spins. Heterostructure band engineering is used to modify the spin-dependent terms in the Hamiltonian of carriers confined to QWs. This is accomplished in nonmagnetic semiconductors by exploiting the dependence of the spin-orbit interaction on the effective band gap, which is modified by chemical composition and quantum confinement. Vertically biased QWs provide electronic control of the spatial position of carrier wave functions in QWs. Such carrier shifting modifies the spin-dependent terms in the Hamiltonian owing to g-factor gradients or local exchange interactions in magnetically doped QWs. High-frequency modulation of these interactions can be used *in lieu* of an external transverse magnetic field to resonantly manipulate electron and nuclear spins. These techniques are applied in magnetic structures, where the strong exchange interaction between local moments and band electrons massively enhances the energy of the spin interactions compared with nonmagnetic wells. The intrinsic

Handbook of Magnetism and Advanced Magnetic Materials. Edited by Helmut Kronmüller and Stuart Parkin. Volume 5: *Spintronics and Magnetoelectronics*. ISBN: 978-0-470-02217-7.

coupling of magnetic and carrier spins can be tailored in QWs to engineer exchange effects through modulation doping or kinetic confinement effects. Increasing the hole carrier density in magnetic wells results in the creation or enhancement of ferromagnetism, while confinement energy modifies the exchange interactions due to band mixing.

2 *g*-FACTORS IN QUANTUM WELLS

2.1 Electron *g*-factor

Band structure strongly alters the spin-orbit interaction in semiconductors QWs. The change in band structure between QW and barrier materials leads to a change in the effective g-factors. Figure 1(a) plots g-factors as a function of band gap for a number of semiconductors and their alloys (Madelung, 2004; Kosaka *et al*., 2001), the traditional map of band gap versus lattice constant is plotted in Figure 1(b), and the g-factor versus lattice constant is in Figure 1(c). The spin splitting between spin-up and spin-down electrons ($\Delta E_{\uparrow\downarrow}$) per unit of magnetic field is also plotted in Figure 1(a), $\Delta E_{\uparrow\downarrow} = g\mu_B B$, showing the range of conduction-band spin splittings possible in these systems, where μ_B is the Bohr magneton and B is the applied magnetic field. The sign change of $\Delta E_{\uparrow\downarrow}$ corresponds to a change in orientation of the electron spin ground state with magnetic field, with electron spins pointing opposite the field when $g > 0$ ($\Delta E_{\uparrow\downarrow} > 0$) and spins pointing parallel with the field for $g < 0$ ($\Delta E_{\uparrow\downarrow} < 0$). The origin of the sign and magnitude change of the effective g-factor for electrons in bulk crystals is the spin-orbit interaction and interband mixing (Roth, Lax and Zwerdling, 1959). Following from a perturbative treatment in k·p theory, the following expression describes the effective g-factor (Hermann and Weisbuch, 1977),

$$g = g_0 - \frac{2}{3}\left(\frac{2p_{sp}^2}{m_0}\right)\frac{\Delta}{(E_g[E_g + \Delta])} \qquad (1)$$

where $g_0 \sim 2.002$ is the g-factor for free electrons, p_{sp} is proportional to the conduction and valence band mixing, and Δ is the spin-orbit splitting of the valence band (spin-split-off band). Equation 1 explains, for example, why wider band-gap materials, such as GaN and ZnO exhibit g-factors close to the free electron value ($\sim$2) and why narrow band-gap semiconductors exhibit negative g-factors, such as GaAs (~ -0.44) and InAs (~ -15). Further, the unusually large and negative value of the conduction-band electron g-factors in InSb (~ -51) and InAs are due to the large Δ in these materials. Alloying semiconductors provides one route for engineering g-factors. In GaAs, by alloying with Al the conduction-band g-factor can be increased from -0.44 in pure GaAs to $+0.6$ in $Al_{0.4}Ga_{0.6}As$ (Chadi, Clark and Burnham, 1976; Weisbuch and Hermann, 1977). It was also shown that alloying GaAs

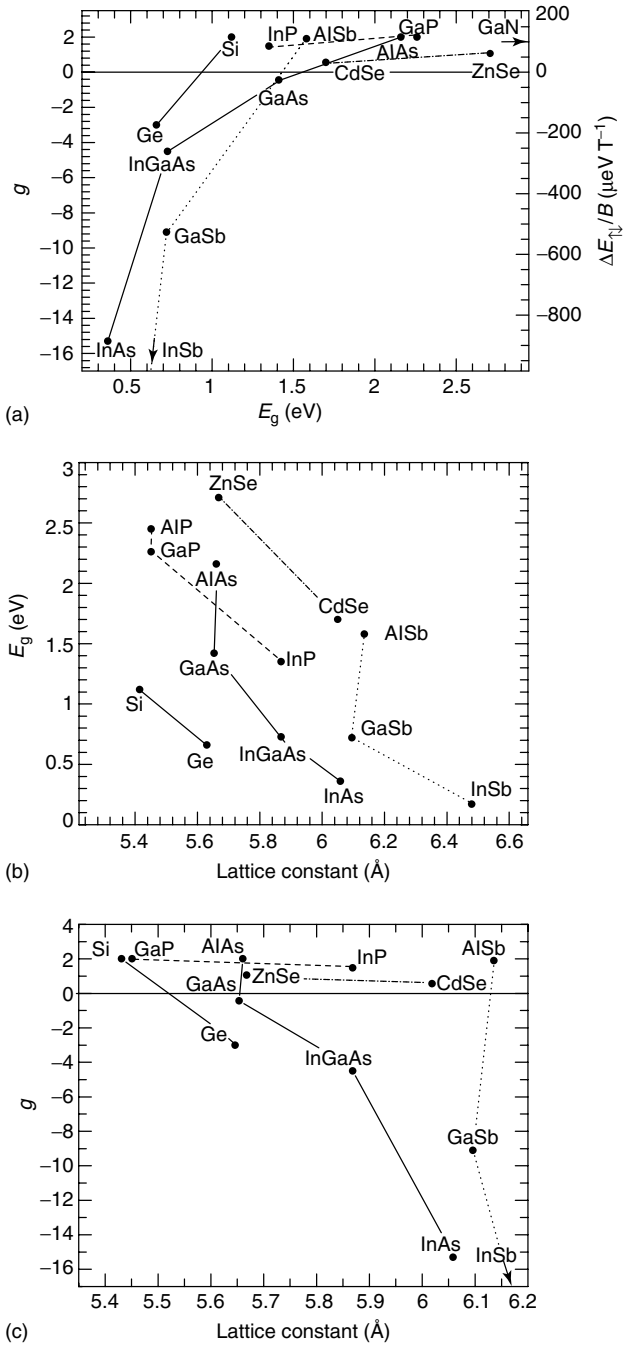

Figure 1. (a) Summary of electron g-factors versus band gap in several semiconductors. Lines connect alloy systems. The corresponding spin splitting in the conduction band is plotted in the right vertical axis per unit of magnetic field. (b) Band gap versus lattice constant for several semiconductors. (c) Electron g-factor versus lattice constant. (Data from Madelung, 2004; Kosaka *et al*., 2001 and references therein.)

with In decreases the g-factor from -0.44 to -0.8 in $In_{0.1}Ga_{0.9}As$ (Weisbuch and Hermann, 1977) and reaches -4.07 in $In_{0.53}Ga_{0.47}As$ lattice matched to InP (Kowalski, Linke and Omling, 1996). An additional modification of g-factors exists in QWs, where spatial confinement of carriers along the growth direction increases the effective band gap (Ivchenko and Kiselev, 1992). The simple substitution of $E_g \rightarrow E_g^*$ in equation (1) provides a rough estimate for the effective g-factor in QWs.

Optical measurements of electron g-factors in a number of QW systems experimentally demonstrate the effect of confinement on carrier spin splittings. Snelling *et al.* used measurements of polarization-resolved photoluminescence (PL) in the Voigt geometry–the Hanle effect–to extract effective electron g-factors and spin lifetimes in GaAs–$Al_xGa_{1-x}As$ QWs (Snelling *et al.*, 1991). These measurements demonstrated that for Al concentrations of 30%, QW width modifies the g-factor from negative values in wide wells to positive values in narrow wells and an effective $g = 0$ for widths near 5.5 nm. These time-averaged measurements were later confirmed by optical measurement of electron spin dynamics in the time domain of similar structures using the technique of time-resolved Kerr or Faraday rotation (Malinowski and Harley, 2000; Poggio *et al.*, 2004; Myers *et al.*, 2005b). Note that such measurements only provide information about the magnitude of the g-factor and not its sign. Figure 2 plots the effective electron g-factor and $\Delta E_{\uparrow\downarrow}$ from (Snelling *et al.*, 1991; Malinowski and Harley, 2000; Poggio *et al.*, 2004; Myers *et al.*, 2005b) showing the wide range in sign and magnitude available in GaAs–AlGaAs and InGaAs–GaAs QWs.

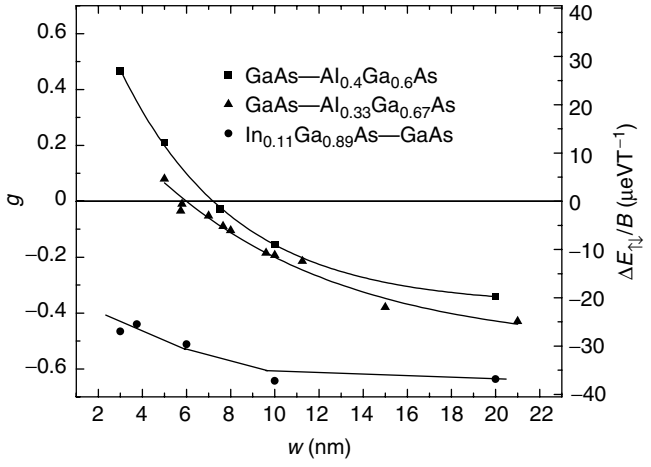

Figure 2. Effective in-plane electron g-factors in some III–V quantum wells plotted as a function of well width (w). (Data reproduced from Snelling *et al.*, 1991; Malinowski and Harley, 2000; Poggio *et al.*, 2004; Myers *et al.*, 2005b.)

2.2 Hole *g*-factor

The energy landscape for electron spins in the valence band is more complex than for the conduction band due to the strong spin-orbit interaction and band mixing of the heavy, light, and spin-split-off bands. In QWs, the degeneracy of the heavy and light hole bands is lifted due to symmetry breaking from confinement and/or strain, whereby the heavy hole band becomes the ground state for holes. The label of these valence bands becomes somewhat of a misnomer in QWs since the heavy hole band in bulk becomes lighter in QWs (larger d^2E/dk^2) and the light hole band becomes heavier (smaller d^2E/dk^2). Away from $k = 0$, the bands therefore cross and result in strong mixing. This results in an anisotropy of the angular momentum that pins the heavy hole spin (3/2) parallel to the growth axis and light hole spin (1/2) perpendicular to the growth axis (Martin *et al.*, 1990).

Polarization-resolved PL was used to measure the Zeeman splittings in GaAs–AlGaAs and InGaAs–GaAs QWs (Snelling, Blackwood, McDonagh and Harley, 1992; Traynor, Harley and Warburton, 1995). From these excitonic spin splittings, the g-factor for heavy holes and heavy hole excitons were extracted. In such experiments, the g-factor of the exciton is defined as the sum of the hole and electron g-factors, which implicitly assumes that exciton binding and electron–hole exchange coupling does not significantly modify the g-factor. In the GaAs–AlGaAs system, heavy hole g-factors undergo a similar sign change as does the electron g-factor near 5.5 nm well width. In the GaAs–AlGaAs system, however, the complexity of the valence band results in nonlinear Zeeman splittings at high magnetic fields making precise determination of the hole g-factors difficult. Usually, the short spin lifetimes ($\sim$110 fs in GaAs) (Hilton and Tang, 2002) of hole spins in bulk semiconductors renders it inaccessible in the time domain, resulting from the fourfold degeneracy of the valence band at $k \sim 0$. However, the degeneracy lifting of the heavy and light hole bands in QWs, discussed in the preceding text, increases the hole-spin lifetime (Uenoyama and Sham, 1990). Measurements of polarization-resolved PL at zero field have shown hole-spin lifetimes of up to 1 ns in 7.5 nm GaAs–$Al_{0.33}Ga_{0.67}As$ QWs (Roussignol *et al.*, 1992). In n-doped QWs of GaAs–AlGaAs, time-resolved/polarization-resolved PL was used to measure the spin precession of optically injected heavy holes in a transverse field, allowing for the observation of heavy hole-spin precession with lifetimes up to 700 ps (Marie *et al.*, 1999). Surprisingly, hole-spin procession has not been observed in almost identical samples using the technique of time-resolved Kerr rotation, where only electron spin precession has been observed (Malinowski and Harley, 2000; Poggio *et al.*, 2004; Myers *et al.*, 2005b). The difference in Fermi level is a possible explanation since the sensitivity of these techniques

changes depending on the density of states. PL is sensitive only to nonequilibrium spin polarization that is optically injected, whereas Kerr and Faraday rotation are sensitive to any spin polarization. It should also be considered that sample-to-sample variation could alter the relaxation processes, especially in samples where both electron and hole g-factors change in sign and magnitude with small changes in well width.

2.3 *g*-factor anisotropy in quantum wells

Quantum confinement alters the g-factor ($g_\parallel$) parallel and perpendicular to the growth axis ($g_\perp$) leading to anisotropic spin splittings (Ivchenko and Kiselev, 1992). This results from the anisotropy inherent to the valence band, where the heavy and light hole bands are split in QWs. Such a splitting affects the anisotropy of both holes and electrons. Heavy hole spins are pinned along the growth axis, while light holes align perpendicular to it, and consequently the g-factors have large anisotropy. The anisotropy of the hole g-factors in QWs has been measured in GaAs–AlGaAs QWs. The g-factors parallel to the growth axis for heavy holes vary from about -2 to $+1$ with QW width as measured from the Zeeman splitting in the Faraday geometry (Snelling, Blackwood, McDonagh and Harley, 1992). The in-plane heavy hole g-factor is more than 10 times smaller, $\sim$0.03 as measured from hole-spin precession in a transverse field (Marie *et al*., 1999) (Voigt geometry), reflecting the strong pinning of heavy hole spins along the growth axis.

The effective band gap has an anisotropy depending on whether the band gap from the light hole or heavy hole is considered. Following from equation (1), the electron g-factor is therefore anisotropic in QWs depending on the splitting between the heavy and light hole bands. Optically detected magnetic resonance (ODMR) was used to measure the anisotropy of the electron g-factor in single–sided modulation p-doped InGaAs–InP QWs (Kowalski *et al*., 1994). In the bulk limit of $In_{0.53}Ga_{0.47}As$, the g-factor was measured to be isotropic with $g \sim 4$. In QWs, the anisotropy increases as the well width narrows, which is plotted in Figure 3. In the narrowest wells measured the ratio, $g_\parallel/g_\perp = 4$. Strain was also modified by changing the concentration of Ga while maintaining the same QW width. Both $g_\parallel$ and $g_\perp$ were modified by the change in strain; however, the ratio of the two remained roughly constant, suggesting that the g-factor anisotropy was strain independent. Similar measurements of g-factor anisotropy by angle-dependent time-resolved Kerr rotation in strained InGaAs–GaAs wells and in unstrained GaAs–AlGaAs wells confirm the strong g-factor anisotropies owing to quantum confinement and weaker dependence on strain (Malinowski and Harley, 2000; Sih *et al*., 2004; Salis, Awschalom, Ohno and Ohno, 2001).

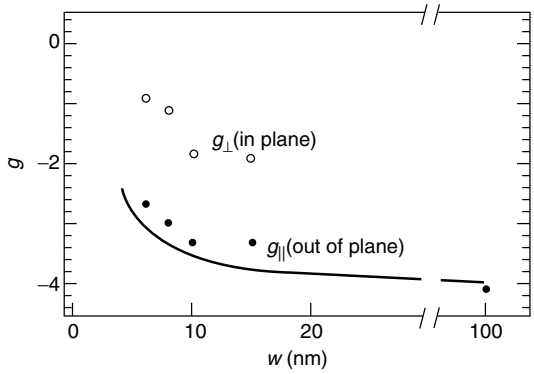

Figure 3. Anisotropic electron g-factor in $In_{0.53}Ga_{0.47}As$–InP quantum wells measured at a temperature of 1.6 K. The g-factor parallel to the growth axis, $g_\parallel$ (solid circles), and perpendicular to the growth axis, $g_\perp$ (open circles), are plotted as a function of well width (w). (Reproduced from Kowalski *et al*., 1994.)

Electron spin precession in a transverse magnetic field is altered by g-factor anisotropy. Since the g-factor is a tensor, the Larmor frequency (Ω_L) gains vector dependence. It is necessary to define the spin precession vector, $\mathbf{\Omega}_\mathrm{L} = \hat{g}\mu_\mathrm{B}\mathbf{B}/\hbar$, which defines the frequency and axis about which electron spins precess. The g-factor anisotropy is responsible for an enhancement of dynamic nuclear spin polarization (DNP) (Salis, Awschalom, Ohno and Ohno, 2001). In a later section, we discuss how these anisotropies can be controlled with a vertical bias leading to a new form of electron spin resonance (ESR) based on manipulation of $\mathbf{\Omega}_L$ through the g-tensor.

3 EXCHANGE INTERACTIONS IN MAGNETIC QUANTUM WELLS

In addition to the spin-orbit interaction, magnetically doped QWs contain the exchange interaction between carriers and localized magnetic-ion spin. In dilute magnetic semiconductor (DMS) theory, the exchange interaction appears as a δ-function-like operator centered on the magnetic-ion impurities in the crystal, which usually consist of transition-metal (TM) ions occupying cation sites. This approximation is successful at modeling a wide range of magnetic semiconductor systems, most notably the $II_{1-x}TM_xVI$ systems (Dietl, 1994). Here, the exchange-induced spin splitting between spin-up and spin-down electrons is given as

$$\Delta E_{\mathrm{s-d}} = -xN_0\alpha\langle S_\mathrm{z}\rangle, \quad \Delta E_{\mathrm{p-d}} = xN_0\beta\langle S_\mathrm{z}\rangle \qquad (2)$$

where x is the concentration of TM impurities, N_0 is the cation density, $\langle S_\mathrm{z}\rangle$ is the projection of the 3d electron spins of the TM ions along the applied field B_z, and $\alpha(\beta)$ is

the s–d (p–d) exchange parameter for conduction (valence) band electrons. The 3d electron spins of the TM ion usually maintain a stable configuration in semiconductors with constant g-factor, for example, Mn^{2+} in II–VI maintains $g \sim 2$ and spin $-5/2$. Thus $\langle S_z \rangle$ is known through the magnetic moment of the TM, and for high enough x, the magnetic moment is measurable by magnetometry. By this token, the magnetic field dependence of the exchange terms, $\Delta E_{s,p-d}$, simply tracks the magnetic moment of the TM, such that in paramagnetic semiconductors the carrier spin splitting will follow a Brillouin function and exhibit a hysteresis loop in a ferromagnetic semiconductor.

An important distinction in the definition of x is made between the case for bulk or QW DMS. In QWs, the spatial confinement for carrier wave functions along the growth axis leads to a modification for the effective exchange splitting. This can be understood from equation (2) as a modification of the effective TM concentration experienced by carriers confined to the QWs, such that the effective x is equal to the overlap integral of the carrier probability density $|\psi_{s,p}|^2$ with the TM concentration profile along the growth axis (z).

The exchange interactions tend to have energy scales with orders of magnitude larger than the spin-orbit or hyperfine interactions, and in the case of ferromagnetic semiconductors, they have a strong hysteretic low-field response. Thus, in principle, magnetic semiconductors are more ideal candidates for a practical semiconductor spintronics. In practice, magnetic doping of semiconductors contains many unique challenges owing to the increased complexity of the physical interactions and to the unintentional formation of crystallographic defects.

3.1 II–VI magnetic wells

In II–VI DMS, magnetic impurities are electrically inert, and the solubility of these impurities is relatively high; for example, 10% Mn in ZnCdSe is easily attainable while maintaining high optical quality. These systems enjoy a long and successful history in the literature including the engineering of spin interactions via quantum confinement in II–VI DMS QWs (Awschalom and Samarth, 1999). Giant Faraday rotations, the high solubility of magnetic impurities, and the large energy scale of the resulting exchange splittings enabled these structures to be ideal test systems for confinement and exchange interactions.

Since TM doping usually increases the band gap in II–VI materials, magnetic QWs can be constructed by simply doping the barrier (Gunshor, Kolodziejski, Nurmikko and Otsuka, 1988). In this case, exchange overlap between carriers in the well and magnetic impurities in the barrier occurs through the penetration of the wave function into the barrier, leading to relatively small x values as compared to bulk DMS alloys. Alternatively, magnetic ions can be doped directly in the well. This can be accomplished, for example, by digital doping submonolayers of MnSe layers into ZnSe–ZnCdSe square QWs (Crooker *et al*., 1995). By changing the thickness and position of the digital MnSe layers within a QW, the effective x values are significantly increased, leading to giant Faraday rotations as large as $\sim 10^7$ deg cm^{-1} T^{-1}. Finally, uniform magnetic doping in both QWs and barriers is possible in CdMnTe–CdMnMgTe, where the exchange constants in both the QW and Mg containing barriers are identical (Mackh *et al*., 1994). The uniform magnetic doping profiles in these structures allow for reliable measurements of the effects of quantum confinement on the exchange parameters (Mackh, Ossau, Waag and Landwehr, 1996; Merkulov *et al*., 1999) discussed in later sections.

3.2 III–V magnetic wells

Although most work in magnetic QWs, to date, has been limited to II–VI paramagnetic DMS systems, III–V magnetic semiconductors offer the prospect of ferromagnetic interactions. Most notably, $Ga_{1-x}Mn_xAs$ ($0.01 < x < 0.08$) grown by MBE exhibits ferromagnetism in the bulk phase (Ohno *et al*., 1996; Ohno, 2002) with Curie temperatures as high as $\sim$150 K reported after postgrowth annealing (Ku *et al*., 2003; MacDonald, Schiffer and Samarth, 2005). Unlike for the case of II–VI, Mn doping in GaAs is electronically active, such that a Mn ion occupying a Ga site acts as an acceptor providing a free hole that takes part in long-range ferromagnetic interaction between Mn-ion spins (Jungwirth *et al*., 2006). Unfortunately, the solubility of Mn in GaAs is small at high substrate temperature ($\sim$580 °C) such that GaMnAs is usually grown at $\sim$250 °C in order to attain high enough Mn densities for ferromagnetism ($\sim$5%). At these temperatures and Mn-doping levels, growth defects such as As antisite (As_{Ga}) and interstitial Mn (Mn_I) are incorporated at high concentrations. Subsequently, electronic and optical performance is severely reduced in comparison to high-temperature grown GaAs. Despite this constraint, several recent experiments in quantum-confined GaMnAs structures have been successful, all involving unique layer structures and growth conditions.

4 VERTICALLY BIASED QUANTUM WELLS

QWs may have tilted bands owing to internal electric fields from electronic doping, surface depletion, electric-dipole polarization, and band-gap gradients. Applying a vertical

bias to QWs provides a convenient means for controlling the carrier density and band bending within these structures. Thus, wave function position and shape can be controlled with vertical bias. In this section, we describe how vertically biased QW structures can be used to manipulate the spin of electrons and local moments. The g-factor gradient and band profiles are tailored by heterostructure design. Applying a vertical bias shifts the electron wave function into regions of varying g-factor allowing control over the sign and magnitude of the electron spin splitting using an electric field. Spatial control of the electron wave function is also used to selectively polarize and depolarize local nuclear spins via the hyperfine coupling. Finally, by applying a high-frequency vertical bias, electron and nuclear spin can be resonantly modulated and depolarized.

The g-factor will shift with band bending owing to wave function penetration into the barriers. This g-factor gradient in semiconductor QWs provides a means for controlling the effective g-factors by changing the position of carrier wave functions confined to these structures. This effect was observed in a two-dimensional electron gas (2DEG) of GaAs–AlGaAs in which the ESR frequency was measured as a function of gate bias (Jiang and Yablonovitch, 2001). A shift in the ESR frequency corresponding to a change in effective electron g-factor of $\sim$0.003 (change in $\Delta E_{\uparrow\downarrow} \sim 0.17\mu\text{eV T}^{-1}$) was observed due to gate bias. In the square well and 2DEGs, the application of an electric field along the growth axis (gate bias) results in a triangular distortion of the QW, in which case, wave function distortion and energy shifting owing to the quantum-confined Stark effect are the main results. Although the wave function minimum is displaced, penetration into the energetically forbidden barriers remains a small effect.

4.1 Parabolic quantum wells

A convenient band structure for spatial wave function control exists in parabolic QWs, in which the first-order effect of linear band bending (constant electric field) is to shift the parabola's minimum (Salis *et al*., 1997). Since the potential maintains the same curvature under a linear distortion, the electronic wave functions remain undistorted and shift their center position to the new potential minimum (Figure 4a). The wave function position and effective g-factor of holes will also be changed by the vertical bias, but electrically tunable hole-spin dynamics have not yet been observed by the optical techniques discussed here.

4.1.1 Heterostructure design

GaAs–AlGaAs-type parabolic QWs can be grown using MBE digital-alloying techniques. The Al concentration is digitally graded to achieve the desired harmonic oscillator potential along the growth axis (Gossard, 1986; Miller, Gossard, Kleinman and Munteanu, 1984). This is accomplished by shuttering the Al beam to grow a digital alloy (bilayer) in which the thickness of AlGaAs and GaAs are varied to attain the desired average Al concentration throughout the QW region. Each bilayer period is typically $\sim$20 Å, in order for enough GaAs to be grown in each bilayer to maintain purity and smoothness throughout the structure. Concentration grading is possible by analog alloying (Kopf *et al*., 1992), in which the flux of each effusion cell is adjusted by changing its temperature, but has the disadvantage that the effusion cell must be stabilized at each temperature setting during which time the growth is paused for several minutes. Such pauses are undesirable during QW growths since the probability of impurity incorporation increases with wait time. Digital alloys are controlled through shutter timing and, therefore, require no growth interrupts to grade composition.

As seen in Figure 4(b), energy-resolved PL measurements confirm the harmonic shape of the potential since the rich excitonic spectrum shows a large family of equally spaced energy levels. The analytically soluble nature of the harmonic potential allows for the determination of conduction and valence band offsets from these spectra.

To attain significant displacements of the electron wave function in these structures, large electric fields need to be applied across the front- and backgates. This requires the application of DC voltages at which typical backgated structures breakdown (Linfield, Jones, Ritchie and Thompson, 1993). The development of low-temperature (LT) grown GaAs conduction barriers by Maranowski *et al*. allows for the application of untypically large electric fields to GaAs-based heterostructures (Maranowski, Ibbetson, Campman and Gossard, 1995). LT GaAs resistive layers are grown between the active layer and the conducting backgate, usually n + GaAs. At a substrate temperature of 250 °C and in an As overpressure, the excess As incorporates into GaAs at concentrations of $\sim$1–2% ($\sim 10^{20}\,\text{cm}^{-3}$). After annealing such layers at high temperature, metallic As precipitates form creating a highly resistive metal/semiconductor/metal composite (Warren *et al*., 1990), massively reducing leakage currents. Further modification of these layers can be performed to reduce photocurrent leakage. Simply increasing the Al content of the LT layer shifts the absorption edge to higher energy removing the photocurrent while maintaining the highly resistive character of LT GaAs (Poggio *et al*., 2003).

4.1.2 Optical detection of electron spin precession

Electron spin dynamics can be observed in the Voigt geometry, where a static magnetic field is perpendicular to the

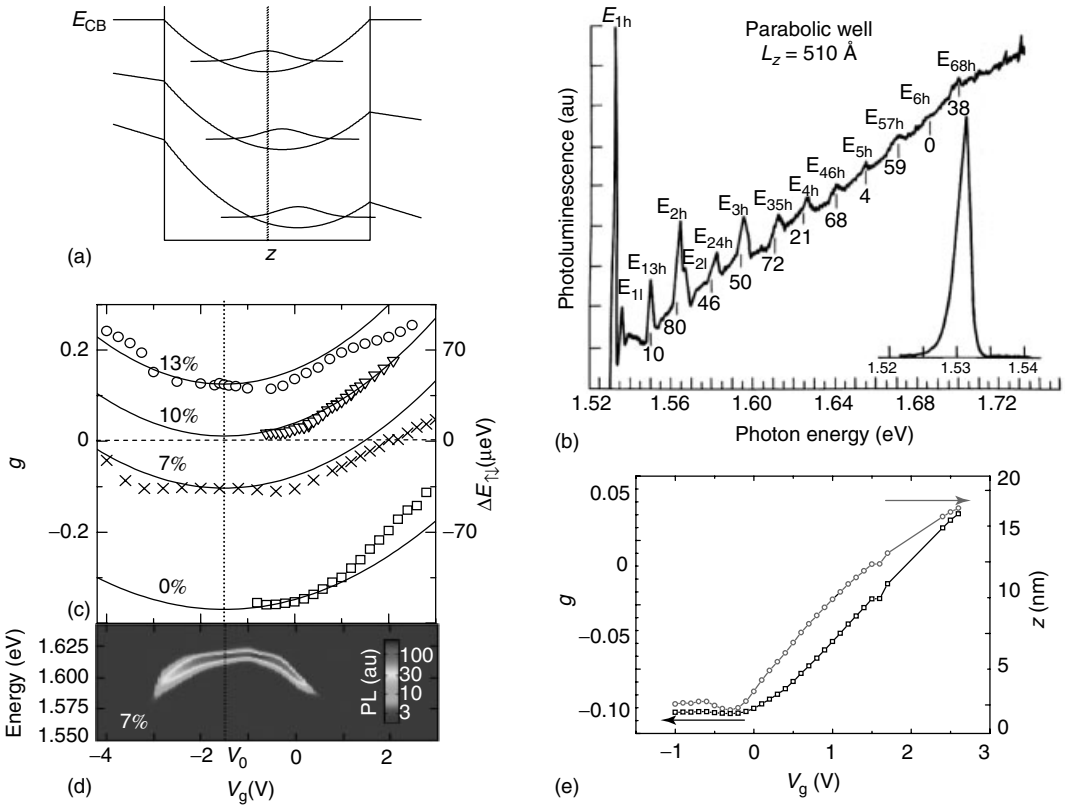

Figure 4. Parabolic quantum wells of GaAs–AlGaAs. (a) Schematic conduction band-edge diagram in a parabolically graded quantum well. The ground state electron wave function displaces along the growth axis (z) with vertical bias. (b) Photoluminescence as a function of excitation energy (PLE) in a 51-nm parabolic quantum well graded from 30% Al in the barriers to 0% in the center of the well. (Reprinted with permission Miller *et al*., copyright 1984, American Physical Society.) (c) g-factor tuning in vertically biased GaAs–$Al_{0.4}Ga_{0.6}As$ parabolic quantum wells from optical measurements of electron spin dynamics via time-resolved Kerr rotation at a temperature of 5 K in a 6 T magnetic field. The wells are 100 nm wide and the percent value represents the concentration of Al in the center of the well. The corresponding spin splitting in the conduction band is plotted in the right vertical axis. (Reprinted with permission G. Salis *et al*., copyright 2001, Nature Publishing Group.) (d) Photoluminesence spectrum showing the quantum-confined Stark effect in a parabolic quantum well at 5 K. (Reprinted with permission G. Salis *et al*., copyright 2001, Nature Publishing Group.) (e) The g-factor versus vertical bias for parabolic quantum well with the corresponding wave function position (z). (Reproduced from Poggio *et al*., 2003.)

optical axis. In this geometry, a circularly polarized excitation pulse excites spin-polarized electrons and holes in the sample that are perpendicular to the magnetic field and thereby induce quantum beating of the spins. The spin dynamics can be optically measured in semiconductor QWs by time-averaged techniques, such as Hanle (Chadi, Clark and Burnham, 1976), or directly in the time domain by using the technique of time-resolved Kerr (or Faraday) rotation (Crooker *et al*., 1996). In the latter technique, the Kerr (or Faraday) rotation of a probe pulse is mapped out in time by controlling the time delay between excitation and probe pulses using a mechanical delay line. The electron spin precession frequency (Ω_L) measures the total spin splitting in the conduction band (along the magnetic field) since $\Delta E_{\uparrow\downarrow} = \hbar\Omega_L = g_z\mu_B B_z$. Hole-spin precession has not been observed in GaAs–AlGaAs using this technique, as discussed previously. In wide parabolic QWs, the weak confinement may not be adequate to increase the hole-spin lifetimes above their usual small values (<1 ps), while electron spin precession is typically observable well into the nanosecond regime.

4.1.3 g-Factor control

Parabolic QWs of GaAs–AlGaAs with LT GaAs (or LT AlGaAs) backgates were used to demonstrate electric-field control of the electron g-factor (Salis *et al*., 2001, 2003). By measuring the electron spin dynamics optically using time-resolved Kerr rotation, the effective electron g-factor was extracted for various bias voltages. Figure 4(c) plots the effective electron g-factor as a function of gate bias in a number of these structures along with the $\Delta E_{\uparrow\downarrow}$. In particular, for samples with 7% Al at the center of the well, g-factor tuning through zero is possible. The g-factor remains constant over a large bias range between 0 and +2 V owing

to exciton binding as evidenced by the loss of PL at biases outside this range, Figure 4(d). PL of these structures displays the quantum-confined Stark effect appearing as a red shift in PL with gate bias, a typical spectroscopic feature of gated QWs (Miller *et al*., 1984). Once the exciton binding between electrons and holes is overcome, PL disappears, electron wave function shifting occurs with less impedance, and the g-factor response to gate bias increases.

The effective electron g-factor in parabolic QWs changes as a function of position along the growth axis because of its dependence on Al concentration (Weisbuch and Hermann, 1977). It can be calculated quantitatively as a weighted average between the electron probability density ($|\psi_s(z)|^2$) and the g-factor at any given position along the QW axis,

$$g^*(z) = \int g(z)|\psi_s(z)|^2 \mathrm{d}z + \Delta g_c \tag{3}$$

where $g^*(z)$ is the effective electron g-factor, $g(z)$ is the g-factor of electrons at each position in the QW due to the local Al concentration, and Δg_c is a phenomenological constant that accounts for confinement effects not included in this simple model. On the basis of the measured values of g^* as a function of gate bias, shown in Figure 4(c), the center position of the wave function (z) can be calculated using equation (3). Figure 4(e) plots the results of this calculation for a 100-nm-wide parabolic QW with 7% Al at the center. The wave function can be displaced ~20 nm at 5 nm V^{-1}.

Recent models of these structures using five-level k·p theory show close agreement with the experiment indicating that the simple picture of g-factor tuning, described above, captures the essential physics (Pfeffer and Zawadzki, 2005).

4.1.4 Shaping nuclear spin profiles

The spatial wave function control in parabolic QWs has also been used to shape nuclear spin profiles (Poggio *et al*., 2003). This experiment exploits the contact hyperfine interaction between electron and nuclear spins to selectively polarize and depolarize nuclear spin profiles at specific positions within a QW (Tifrea and Flatte, 2003). Optically injected spin-polarized electrons in the conduction band of a semiconductor polarize nuclear spins through DNP (Lampel, 1968). This effect only occurs, however, if a longitudinal component of electron spin polarization exists (Salis, Awschalom, Ohno and Ohno, 2001). This is easily accomplished in the Faraday geometry, where the field is parallel to the optical axis, and therefore injects spins parallel to the field. In the Voigt geometry, which is necessary to observe spin precession, spins are, in principle, injected perpendicular to the field and DNP should not be observed since the transverse spin polarization averages to zero. In large magnetic field, the average longitudinal electron spin polarization will not be zero and DNP may occur through the equilibration of electron spins along the field, which were originally polarized transverse to the field (Kikkawa and Awschalom, 2000). Additionally, a direct longitudinal component of spin injection can be created by simply tilting the sample since the excitation beam refracts slightly along the field. In QWs, the g-factor anisotropy leads to a spin precession axis ($\mathbf{\Omega}_L$), which is not parallel with the optical axis (Kalevich and Korenev, 1992). This provides a component of spin injected along the quantization axis and enhances DNP (Salis, Awschalom, Ohno and Ohno, 2001).

If electrons overlap with nuclear spin, the contact hyperfine interaction will modify their spin Hamiltonians, such that the spin splitting is $\Delta E_{\uparrow\downarrow} = \hbar\Omega_L = g_z\mu_B B_z + A_H\langle I_z\rangle$, where A_H is the hyperfine constant and $\langle I_z\rangle$ is the component of nuclear spin along the magnetic field. In analogy to the exchange interaction described in equation (2), the hyperfine constant is weighted by the overlap between electrons and nuclear spin. Thus, control over the electron probability density, as shown in Figure 4(e), will modify the effective strength of the hyperfine term. Nuclear spin profiles were created at arbitrary positions within parabolic QWs by fixing the gate bias, and therefore the electron wave function position, and waiting for 20 min for DNP to saturate. Time-resolved Kerr rotation was used to measure $\Delta E_{\uparrow\downarrow}$ as a function of gate bias once the nuclei were polarized. Subtracting the signal in the unpolarized case allows the extraction of the hyperfine term plotted in Figure 5(a), where the vertical lines plot the center position of the electron wave function during the polarization process (Poggio *et al*., 2003). These nuclear spin profiles can be resonantly depolarized by applying RF to the vertical gates at isotope specific frequencies.

Electrical control over nuclear spin polarization in QWs was recently accomplished in square QWs using a qualitatively different biasing effect than wave function shifting (Sanada *et al*., 2005). In these structures, vertical bias tunes the electron density, which strongly alters the efficiency of the DNP process. Hysteresis in the DNP process has also been reported in similar square QW structures (Sanada *et al*., 2003). Finally, the use of both an RF coil and optical detection of nuclear spin polarization (Poggio and Awschalom, 2005) was used to demonstrate coherent control of nuclear spin in QWs implementing traditional NMR pulse sequences to induce Rabi oscillations (Sanada *et al*., 2006).

4.1.5 Electron spin resonance by g-tensor modulation

So far, we have limited the discussion of electric-field effects to the case of DC bias. It is also possible to apply AC biases to parabolic QWs at frequencies close to the spin

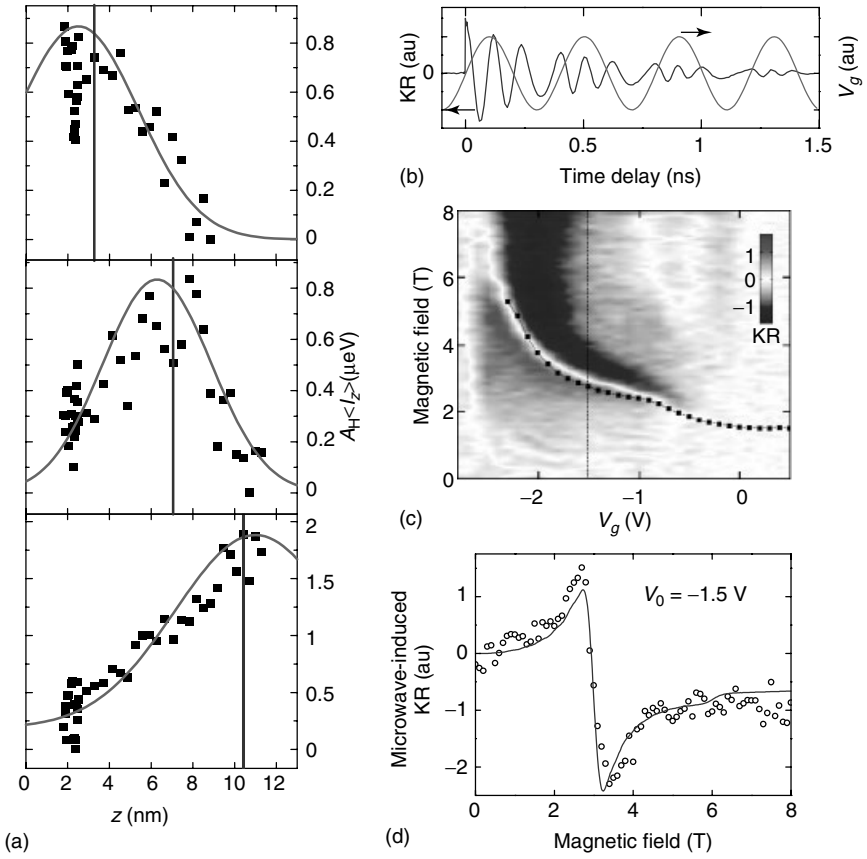

Figure 5. Nuclear and electron spin manipulation in parabolic quantum wells of GaAs–AlGaAs. (a) Spatial profiling of nuclear spin polarization in parabolic QWs of GaAs–AlGaAs at a temperature of 6 K and magnetic field of ∼4 T. The contact hyperfine energy ($A_H\langle I_z\rangle$) due to nuclear spin polarization is plotted along the growth axis (z) with Gaussian fits shown as solid lines. Vertical lines mark the center of the electron wave function when dynamic nuclear polarization was performed. (Part (a) Reproduced from Poggio *et al*., 2003, with permission from the American Physical Society © 2003.) (b) Frequency-modulated electron spin precession due to microwave modulation of the electron g-factor at a temperature of 5 K and magnetic field of 6 T. The microwave signal (2.356 GHz) applied across the front- and backgates is plotted as a sinusoid. (c) The change in electron spin polarization (Kerr rotation) due to the microwave signal (2.66 GHz) as a function of both magnetic field and DC vertical bias. Black squares plot the expected position of g-TMR resonance calculated from the measured anisotropy of the g-factor. (d) Linecut of data in (c) at fixed DC bias showing the resonance structure. (Parts (b), (c), and (d) Reprinted by permission from Kato *et al*., copyright 2003, AAAS.)

precession frequency and resonantly control electron spins (Kato *et al*., 2003). This spin resonance technique, called *g-tensor modulation resonance* (g-TMR), does not require a transverse magnetic field, but makes use of the inherent g-factor anisotropy of QWs. As described in a previous section, the g-factor in a QW is anisotropic because of lateral confinement. Since $g_\perp$ and $g_\parallel$ have different gate bias dependences, electron spins precess about different axes depending on the vertical bias. In gated parabolic QWs, the g-factor anisotropy is modulated by applying AC bias between the front- and backgates, effectively modulating the spin precession vector. Microwave frequency is applied across the front- and backgates of a parabolic QW, while measuring the electron spin precession using time-resolved Kerr rotation. The repetition rate of the laser (∼76 MHz) is used as a reference clock for a frequency tunable microwave amplifier. Thus, nearly gigahertz frequency voltages are applied to the QWs in phase with the laser. Additionally, the laser is operated in a phase-locked loop to maintain a stable repetition rate. Figure 5(b) plots the Kerr rotation as a function of time showing electron spin precession in the presence of ∼2 GHz gate bias. Since the effective g-factor is modulating at ∼2 GHz, electron spin precession is frequency modulated.

When the modulation frequency is brought into resonance with the spin splitting along the quantization axis (g-TMR), electron spins can be tipped either toward or away from the magnetic field. The requirements to observe g-TMR are that the g-tensor must be modulated at the spin-splitting frequency and that the g-factor must be anisotropic. Both criteria are satisfied in these parabolic QW structures. Lock-in amplification was used to measure the microwave-induced

Kerr rotation as a function of magnetic field and an additional DC vertical bias (Figure 5c). The measurements show a clear resonance line that shifts with magnetic field and vertical bias. The position of the resonance matches calculated values (black squares) based on angle-dependent measurements of the g-factor anisotropy. Line cuts at fixed bias voltage (Figure 5d) reveal the shape of the resonance lines and match numerical simulations (solid line).

4.2 Coupled quantum wells

In parabolic QW structures, the electron wave function shifts in a continuous manner. It is also possible to achieve discrete changes in electron position in coupled QWs. These structures consist of adjacent QWs connected by barriers that are thin enough for wave function tunneling to occur (Dingle, Gossard and Wiegmann, 1975). Vertically biased coupled QWs have been used for transition from the spatially direct exciton state, where the exciton resides in one well, to the spatially indirect exciton state, where the exciton is split between adjacent wells (Chen, Koteles, Elman and Armiento, 1987). The resulting change in spatial overlap between the electron and hole drastically alters the transition rates and can be used to modulate absorption (Islam *et al.*, 1987). If the widths of the coupled wells are different, then shifting the electron wave function between wells changes the electron g-factor owing to its strong width dependence (Figure 2).

The electron g-factor was measured in coupled QWs of GaAs–AlGaAs as a function of vertical bias for samples with different tunnel barriers widths (Poggio *et al.*, 2004). Figure 6 plots the g-factors in these structures measured by time-resolved Kerr rotation together with the schematic band-edge diagrams. For uncoupled QWs with a large 20-nm tunnel barrier (Figure 6a), two g-factors are visible over the full bias range corresponding to the different g-factors in the two wells. Tunneling between the wells does not occur within the carrier recombination time. A sharp g-factor transition with vertical bias occurs for a sample with a 6-nm tunnel barrier (Figure 6b), where electron tunneling is incoherent. Finally, strong coupling of the wells is observed in narrow 2-nm tunnel barriers (Figure 6c), where the g-factor is smoothly varied between its value in the two wells.

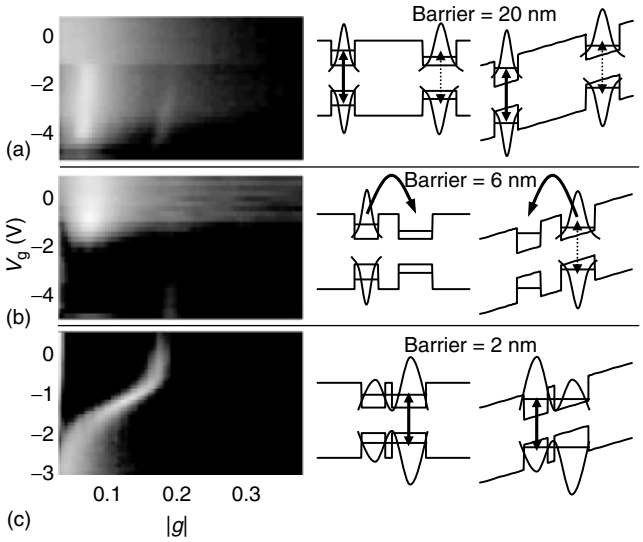

Figure 6. Tuning the electron g-factor in coupled quantum wells of GaAs–$Al_{0.3}Ga_{0.7}As$. The two wells are 7 and 10 nm wide. Color intensity plots the Fourier transform of electron spin precession as a function of vertical bias and g-factor at a temperature of 5 K in a 6 T magnetic field. Schematic band-edge diagrams show the effect of vertical bias for coupled wells with different tunnel barrier widths. Vertical arrows indicate the strong (solid line) and weak (dashed line) photoluminescence transitions and curved arrows show the interwell tunneling. (a) Two distinct g-factors in uncoupled wells with 20-nm-wide tunnel barrier. (b) Sharp g-factor switching for incoherently coupled wells with 6-nm tunnel barriers. (c) Smooth g-factor tuning in coherently coupled wells with 2-nm tunnel barriers. (Reprinted with permission M. Poggio *et al.*, copyright 2004, American Physical Society.)

5 ENHANCEMENT OF MAGNETIC INTERACTIONS IN QUANTUM WELLS

Magnetic doping alters the magnetic field response of $\Delta E_{\uparrow\downarrow}$ from its typical linear field dependence in nonmagnetic structures, to a Brillouin function in paramagnetic structures, and finally showing hysteretic behavior in ferromagnetic structures. Electronic and magnetic doping can be independently engineered in QWs with exchange interactions that are orders of magnitude larger than the spin-orbit induced spin splittings. Confinement also increases the density of carriers near the magnetic impurities, which can have a dramatic effect on the carrier-mediated ferromagnetism. Quantum confinement alters the strength of the exchange interactions extrinsically by increasing the effective TM density experienced by carriers in the wells and intrinsically through more complex kinetic energy effects.

5.1 Vertically biased magnetic wells

The vertical biasing techniques used in nonmagnetic QWs can also be employed in magnetically doped structures to electrically tune the interaction between carrier spin and magnetic-ion spin. The electronic characteristics of magnetic impurities in semiconductors may complicate this task since their associated charges will screen the electric field, damping the effect of bias. This is not a problem in II–VI systems where TM impurities are neutral, but occurs in III–V, for

example, GaMnAs, where the Mn ions act as acceptors. The ionized impurities will screen the electric-field and can act as nonradiative recombination centers. These constraints can be balanced by moving the magnetic layers into the QW barriers or reducing the doping level.

5.1.1 II,Mn-VI parabolic wells

In previous sections, we described the use of digital magnetic doping to achieve large effective magnetic doping densities in II–VI magnetic QWs. This doping technique allows the local placement of magnetic impurities within optically active QWs. Also, we discussed the use of vertically biased parabolic QWs to control the wave function position. Both schemes have been incorporated into parabolic QWs containing local magnetic impurities in which the exchange overlap between carriers in the wells and magnetic impurities can be controlled with vertical bias (Myers *et al*., 2005a). Samples of ZnSe–$Zn_{0.85}Cd_{0.15}Se$ parabolic QWs were grown by MBE. Submonolayers of MnSe were deposited in the center 5 nm of the structures. Electron spin precession at the absorption edge of the QWs was measured using time-resolved Kerr rotation to extract the effective electron g-factor. The inset of Figure 7(a) plots the electron g-factor as a function of vertical bias for a nonmagnetic control sample showing a g-factor shift due to the spatial translation of the electron wave function under vertical bias into regions of varying Cd concentration. For magnetically doped sample, the effective g-factor was increased by an order of magnitude and can be tuned over 400% (Figure 7a, open circles). As the conduction-band exchange term increases, the electron spin lifetime decreases since the spin-flip scattering decoherence mechanism is proportional to the exchange splitting (Crooker *et al*., 1995). At low bias, the exchange overlap is maximized and the spin lifetime is small, whereas at large negative bias when the exchange overlap is minimized the electron spin lifetime increases.

Equally large shifts in the effective g-factor were observed as a function of the optical excitation and probe energy (E_p). As E_p was increased at zero bias, the electron g-factor decreased from 18 to 6 (Figure 7b). This dramatic change was explained as being due to the large difference in exchange overlap, which is due to sublevel filling effects. The wave function ground state has a maximum at the QW center, a position at which the excited state has a node. Estimates of the sublevel spacing and subsequent exchange overlap are consistent with this picture.

In addition to electron spin precession, Mn-ion spin precession is observed in these samples which originates from a spin-flip interaction between optically injected hole spin and Mn-ion spin (Crooker *et al*., 1996). Thus, the amplitude of the Mn-ion spin precessions should be proportional to the exchange overlap between holes and Mn ions, which is significantly altered under vertical bias. At negative bias, the Mn-ion spin precession amplitude was observed to decrease by an order of magnitude and can be explained by the decrease in hole-Mn exchange overlap under negative bias. We have discussed only the effect of exchange interactions on the amplitude of the Mn spin precession. Although Mn-ion spin precession has been observed, the back-action of electron spins on Mn-ion spin splitting has not been observed; the Mn precession frequency always remains constant. Such a shift in the Mn effective g-factor is expected and has been observed, for example, in paramagnetic resonance measurements of n-CdMnTe quantum wells (Teran *et al*., 2003).

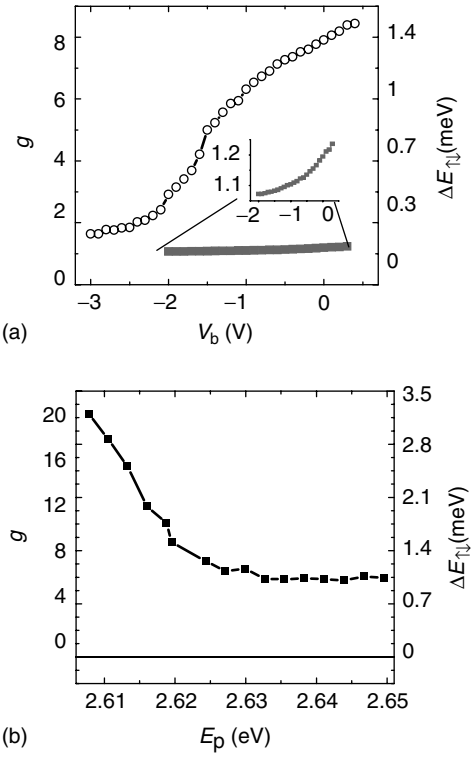

Figure 7. Electrical control of exchange overlap in ZnCdSe–CdSe parabolic quantum wells doped with MnSe. (a) The effective electron g-factor as a function of vertical bias (open circles). The g-factor versus bias in nonmagnetic control samples (closed squares) is enlarged in the inset. (b) Effective electron g-factor as a function of excitation and probe energy (E_p). Corresponding spin-splitting energies are plotted on the right vertical axes. Measurements performed at a temperature of 5 K in a 3 T magnetic field. (Reprinted with permission R.C. Myers *et al*., copyright 2005, American Physical Society.)

5.1.2 III–V wells with a ferromagnetic barrier

In the previous structure, Mn ions are paramagnetic and large magnetic fields (∼10 T) must be applied to fully saturate their moments. Ferromagnetic layers provide lower

saturation field and a hysteretic response. The coupling of ferromagnetic spins to carrier spins in a QW results in strong spin splittings and polarizations at low field. This strategy is advantageous over bulk systems, since QW structures contain an inherent localization of the interactions that can be controlled via heterostructure design. As discussed in previous sections, however, defect control remains a barrier to combine both robust ferromagnetism and high-quality QWs in which spin-sensitive optical or electronic measurements are possible. In the GaMnAs, the level of Mn doping required for ferromagnetism leads to a degenerate hole gas and the incorporation of interstitial Mn defects and As antisites, which limit the optical performance of this material. An alternative approach incorporates submonolayer ferromagnetic layers of MnAs embedded within a GaAs matrix, so-called digital ferromagnetic heterostructures (Kawakami *et al*., 2000). These structures have the advantage that ferromagnetism in the MnAs layers can be independent of the electronic doping in the surrounding GaAs matrix (Johnston-Halperin *et al*., 2003).

Such layers have been incorporated into the top AlGaAs barriers of GaAs QWs, where optical quality in the QW is maintained by combining both the growth of QWs at high temperature with the growth of the magnetic barrier at LT. Design constraints of such hybrid structures dictate that magnetic layers must be grown after the QW layers since high-temperature annealing of the magnetic layers would lead to the formation of Mn-containing second phase defects. Additionally, the ferromagnetic layer must be spaced sufficiently far from the QW to maintain an optical response in the wells, but close enough for coupling effects to be observed.

Polarization-resolved PL in these structures revealed that initially unpolarized photoexcited holes in a GaAs QW become spin polarized opposite to the magnetization of the ferromagnetic barrier (Myers, Gossard and Awschalom, 2004). The optical selection rules in QWs dictate that the spin-polarized holes or electrons will emit circularly polarized photons, thus PL polarization is an indicator of spin polarization. Figure 8(a) shows the circular polarization of the PL emission in the QW, tracking the magnetization of the ferromagnetic layers. A negative vertical bias increases this polarization indicating that its origin is spin-polarized heavy holes coupled through wave function overlap with spins in the ferromagnetic layer. As shown in Figure 8(b) and (c), vertical bias changes the polarization from positive to negative while maintaining the same field response as the ferromagnetic layer. These structures provide a means for electrically controlling spin polarization at low magnetic fields in a QW through wave function overlap.

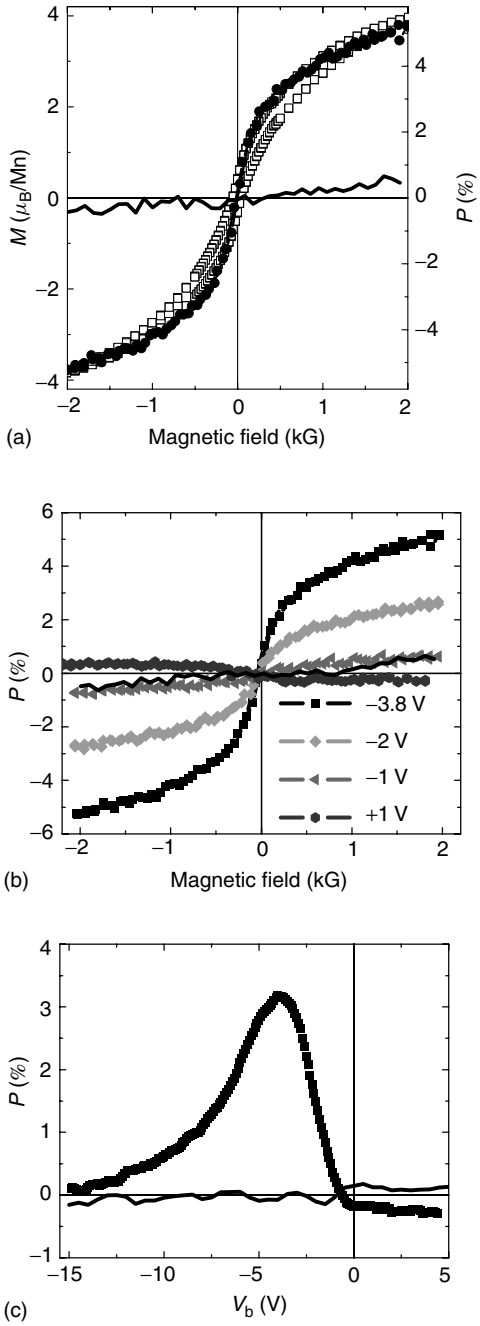

Figure 8. Tunable spin polarization in GaAs–AlGaAs square wells with a ferromagnetic barrier at 5 K. (a) Spin polarization and magnetization as a function of magnetic field (B). Magnetization (M) measured by SQUID magnetometry is plotted in the left vertical axis (open squares). Photoluminescence polarization (P) is plotted in the right vertical axis (closed circles). The P measured in a nonmagnetic control sample is plotted as a solid line. (b) Field dependence of P at various vertical biases for a sample with a ferromagnetic barrier (symbols), and control sample (solid line) in a +1 kGs magnetic field. (c) Vertical bias dependence of P for the sample shown in (b) (solid squares) and for the control sample (solid line). (Reprinted with permission R.C. Myers *et al*., copyright 2004, American Physical Society.)

5.2 Ferromagnetism in modulation doped wells

The inherent coupling of TM spins in II–VI semiconductors is antiferromagnetic (Dietl, 1994). However, upon hole doping, the strong p–d exchange coupling between valence band and magnetic-ion spins enables a long-range ferromagnetic coupling. Here, the itinerant hole spins couple to more than one localized magnetic-ion spin and results in ferromagnetism in both II–VI and III–V systems (Dietl *et al*., 2000). In QW structures, modulation doping may be used to locally increase the hole density over the TM spins and create or enhance the ferromagnetic state.

5.2.1 Ferromagnetic II,Mn-VI wells

As previously discussed, TM doping in II–VI semiconductors is isoelectronic providing no free holes. The direct coupling between magnetic spins is antiferromagnetic, which is observable at high doping levels where these nearest-neighbor interactions dominate. Magnetic spins display paramagnetism when sufficiently diluted. A long-range and hole-mediated ferromagnetic interaction occurs when holes are present. Ferromagnetism has been created in $Cd_{0.976}Mn_{0.024}Te$ QWs by modulation doping holes using specially designed $Cd_{0.66}Mg_{0.27}Zn_{0.07}Te$:N barriers (Haury *et al*., 1997). Figure 9(a) plots the polarization-resolved PL spectra of these QWs at very low magnetic field. A giant Zeeman splitting is observed because of the exchange splitting in the conduction and valence bands (equation (2)). The strong low-field dependence of the spin splitting is indicative of the ferromagnetic state. Quantitative analysis of the field-dependent exchange splitting was used to extract the magnetic susceptibility (χ) as a function of temperature (Figure 9b). The temperature intercept of the inverse susceptibility is the mean-field ordering temperature, essentially the Curie temperature, which is 1.8 K for these structures. In samples without modulation hole doping (open squares in Figure 9b) ferromagnetism is not observed and can be destroyed in the hole-doped samples by illumination (open circles).

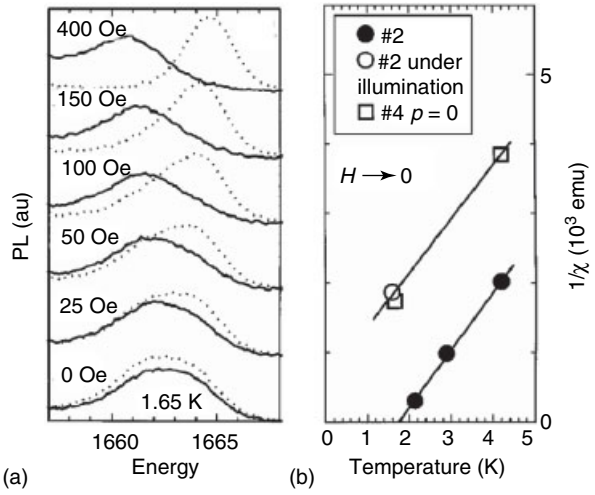

Figure 9. Ferromagnetism in $Cd_{0.976}Mn_{0.024}Te$ quantum wells by modulation hole doping. (a) Polarization-resolved photoluminescence (PL) at 1.65 K. The $\sigma+$ (solid line) and $\sigma-$(dotted line) spectra are plotted at several fields, showing a giant Zeeman splitting at low field indicative of ferromagnetism. (b) Inverse magnetic susceptibility ($1/\chi$) as a function of temperature. Data points were calculated from fits to the field-dependent Zeeman splitting measured by polarization-resolved PL. Data are shown for the modulation hole-doped sample displaying ferromagnetic order (solid circles), for the same sample under white light illumination which destroys the ferromagnetic ordering (open circles), and for a sample without modulation hole doping (open squares). (Reprinted with permission Haury *et al*., copyright 1997, American Physical Society.)

5.2.2 Enhanced Curie temperature in III,Mn-V 2DHGs

The creation of ferromagnetism in II,Mn-VI QWs by modulation hole doping is an impressive demonstration of the controllable coupling between magnetic-ion and free carrier spin in semiconductors. The low ferromagnetic transition temperature, however, makes these structures technologically impractical. Ferromagnetism in GaMnAs is a robust phenomenon, as previously discussed, since Mn acts as an acceptor GaAs providing free holes that mediate the ferromagnetism. Additionally, postgrowth annealing of GaMnAs has been shown to increase the Curie temperature (Ku *et al*., 2003) by diffusing interstitial Mn to the surface that would otherwise compensate holes (Edmonds *et al*., 2004). Thus, GaMnAs is an ideal system for investigating the effects of modulation doping on ferromagnetism.

This strategy has been used in GaAs–AlGaAs two-dimensional hole gases (2DHG) where modulation hole doping in the AlGaAs barrier controls the hole density in the 2DHG which contains a magnetic layer (Nazmul, Sugahara and Tanaka, 2002). Submonolayers of MnAs were incorporated into the 2DHG region using a two-step growth process resulting in the valence band-edge profile shown in Figure 10(a) (Nazmul, Sugahara and Tanaka, 2003a). As discussed previously, such structures contain a design constraint that the substrate temperature cannot be increased after the magnetic layer is grown. Thus the Be-doped AlGaAs barrier and a thin layer of GaAs were grown first at high temperature, while submonolayers of MnAs were deposited within the GaAs 2DHG region at LT. The magnetization of the layers are probed indirectly using the anomalous Hall effect, which is particularly strong in

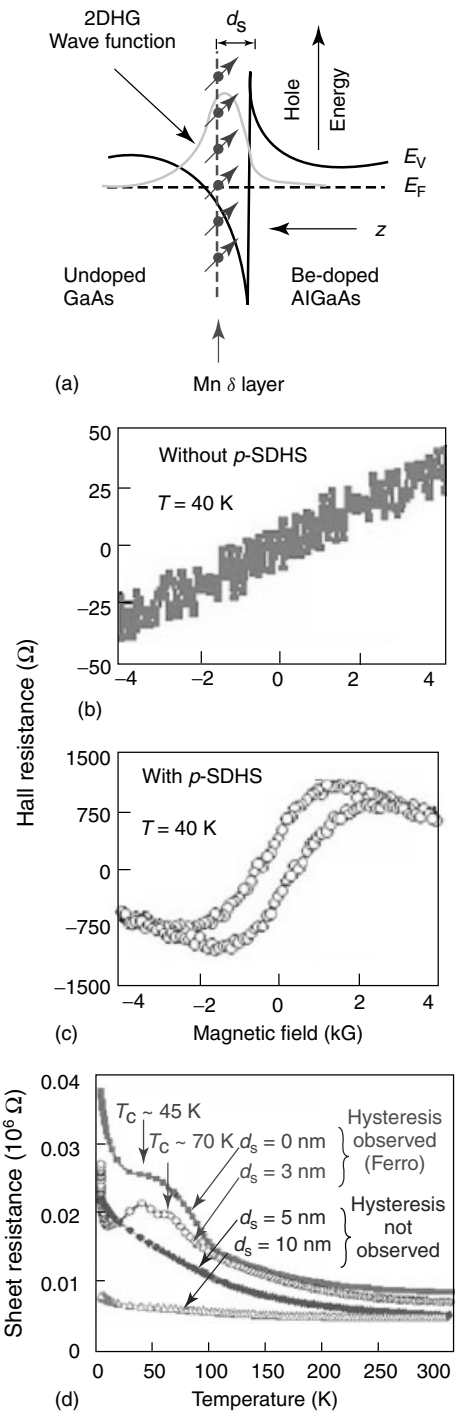

Figure 10. Enhanced ferromagnetism in modulation hole-doped GaAs–AlGaAs two-dimensional hole gases (2DHGs) with MnAs. (a) Valence band edge (E_V) along the growth axis (z) showing the hole wave function, Fermi level (E_F), and position of the Mn ions. (b) Hysteretic field sweeps of the Hall resistance for a sample containing a MnAs layer without hole doping, and (c) for a sample containing hole doping. (d) Resistance as a function of temperature for hole-doped samples with various MnAs positions (d_s) relative to the AlGaAs barrier. (Reprinted with permission Nazmul *et al*., copyright 2003, American Physical Society.)

the GaMnAs system (Ohno, 2002). The Hall resistance in a magnetic layer contains an additional term that tracks the magnetization. Figure 10(b) plots the Hall resistance as a function of field in a sample without modulation hole doping. A hysteresis appears in samples containing modulation doping (Figure 10c) indicating that the MnAs layers are ferromagnetic. Features in the sheet resistance appear near the Curie temperature of the MnAs layer (Figure 10d).

Optimization of the magnetism in these layers has been performed by adjusting the position of the MnAs layers for maximum overlap with the 2DHG. However, postgrowth annealing of the samples leads to the largest increase in Curie temperature (up to 172 K) (Nazmul, Sugahara and Tanaka, 2003b). More recently, the Curie temperature has been further increased in these structures by inverting the 2DHG, such that the p-doped AlGaAs layer is grown after the magnetic layer at LT. After postgrowth annealing, a hysteresis in the Hall resistance was observed up to 250 K, the highest Curie temperature in the GaMnAs system reported to date (Nazmul *et al*., 2005).

The magnetic anisotropy of these layers remains an open question. Hall measurements are performed with the magnetic field applied out of plane. Thus, the appearance of a hysteresis indicates the magnetic easy axis to be out of plane of the film. In submonolayer MnAs layers, the easy axis is typically in plane and shows no hysteresis along the out of plane hard axis (Kawakami *et al*., 2000).

5.3 Kinetic exchange effects in quantum wells

As discussed in a previous section, the conduction-band spin splitting includes both the regular Zeeman splitting plus the exchange interaction,

$$\Delta E_{\uparrow\downarrow} = g\mu_B B + \Delta E_{s-d}, \qquad \Delta E_{s-d} = -xN_0\alpha\langle S_z\rangle \quad (4)$$

The s–d exchange parameter (α) is typically small (0.2 eV) and positive resulting from direct exchange interaction between s-like conduction-band electrons. This contrast with the p–d exchange parameter (β), which is large ($\sim$1 eV) and negative in magnetic semiconductors due to hybridization between p-like valence electrons and the d orbitals localized on the TMs (Dietl, 1994), a mechanism known as *kinetic exchange* (Dietl, 1981; Bhattacharjee, Fishman and Coqblin, 1983). The hybridization occurs due to the virtual transition of electrons from the valence band into d states. The relative strength of these interactions varies with the confinement energy since electrons with larger k values increase their probability of occupying the d states.

5.3.1 II,Mn-VI wells

Quantum confinement has been observed to alter the exchange splittings in II,Mn-VI QWs. Polarization-resolved PL measurements in CdMnTe–CdMnMgTe wells showed a reduction in the exciton exchange splitting of ∼15% compared with bulk (Mackh, Ossau, Waag and Landwehr, 1996). This effect was modeled taking into account the confinement dependence of the p–d exchange parameter, but a full quantitative agreement was lacking (Bhattacharjee, 1998).

Measurements of the conduction-band exchange splitting in these QWs indicated that in addition to a kinetic modification of the p–d exchange term, the s–d exchange term is reduced by quantum confinement by up to 25% of its bulk value (Merkulov *et al*., 1999). Figure 11 plots the normalized s–d exchange parameter in CdMnTe–CdMnMgTe QWs as a function of confinement energy, E_e. The exchange splitting was measured by spin-flip Raman scattering as a function of magnetic field and representative scans are plotted in the inset of Figure 11. The data were modeled (line in Figure 11) by modifying the theory in (Bhattacharjee, 1998) to include the effect of band mixing and virtual transitions, that is, kinetic exchange, of conduction-band electrons into d states. The s–d exchange parameter decreases with confinement mostly because the conduction electrons get larger k values and mix with the valence band. The contribution of the valence band exchange parameter is negative since these p-like states hybridize readily with the magnetic d states, that is, p–d is large and negative.

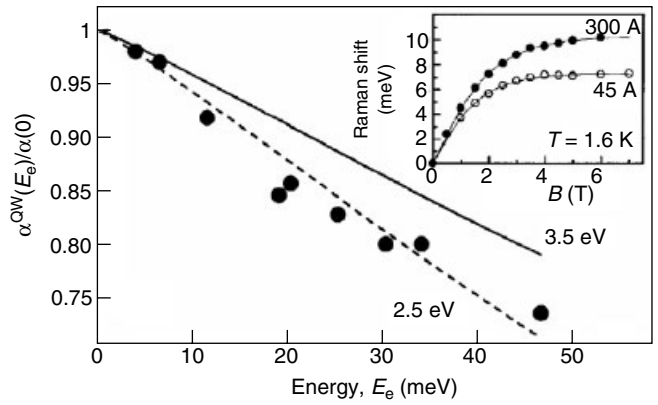

Figure 11. The conduction-band exchange parameter (α) as a function of the confinement energy in a $Cd_{0.98}Mn_{0.02}Te$–$Cd_{0.876}Mn_{0.014}Mg_{0.11}Te$ quantum well. Inset: Magnetic field dependences of the spin-flip Raman shifts in two quantum wells of different width. Fits to these data were used to extract α plotted as solid circles in the main figure. Solid and dashed lines plot calculations based on a kinetic exchange model. (Reprinted with permission Merkulov *et al*., copyright 1999, American Physical Society.)

5.3.2 III,Mn-V wells

The exchange parameters in III,Mn-V semiconductors, in particular GaMnAs, are usually not accessible using traditional band-edge optical techniques because of the high defect densities inherent to these materials. Such measurements have recently become possible in GaMnAs–AlGaAs QWs grown by MBE with low doping levels ($10^{17}-10^{19}\,cm^{-3}$) at intermediate substrate temperatures (Myers *et al*., 2005b). Electronic and structural measurements indicate that most of the Mn resides on substitutional Ga sites (Poggio *et al*., 2005). Time-resolved Kerr rotation measurements were used to measure the total conduction-band spin splitting for a range of Mn-doping concentrations and QW widths. Using equation 4, the effective exchange constant ($xN_0\alpha$) was extracted based on measurements of the g-factor in identical nonmagnetic samples (Figure 2). Figure 12(a) plots the effective exchange constant as a

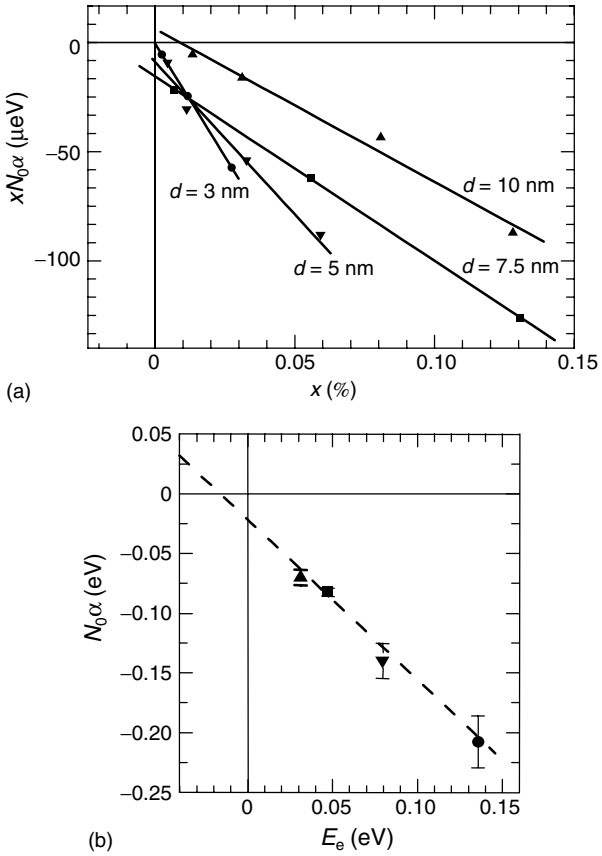

Figure 12. The conduction-band exchange constant in $Ga_{1-x}Mn_xAs$–AlGaAs quantum wells. (a) The conduction-band exchange splitting ($xN_0\alpha$) as a function of x. Linear fits connect data from wells of the same width. (b) The exchange parameter ($N_0\alpha$) as a function of electron confinement energy with a linear fit (dashed line). Data points correspond to linear fits in (a). (Reprinted with permission R.C. Myers *et al*., copyright 2005, American Physical Society.)

function of Mn density demonstrating that the exchange parameter increases linearly with Mn-doping density, while the slope varies with QW width. This indicates that the II,Mn-VI exchange model (equation (4)) is valid in the GaMnAs system, and that quantum confinement appears to alter the exchange parameter as in II,Mn-VI QWs. Figure 12(b) plots the exchange constant as a function of confinement energy for electrons in GaMnAs QWs. Surprisingly, the exchange parameter is negative in all the QWs in contrast to II–VI magnetic semiconductors. However, the confinement leads to a negative contribution to the exchange parameter, the same as observed in (Merkulov *et al*., 1999). Measurements in quantum wells with lower barriers confirms this trend (Stern *et al*., 2007). Recent theoretical investigations predict the confinement-induced negative s–d exchange coupling in GaMnAs QWs (Dalpian and Wei, 2006).

6 SUMMARY

In semiconductor QWs, a control over the interactions between a variety of spin systems are possible, which are unfeasible in the bulk. The atomic layer precision of MBE allows for a precise engineering of g-factor sign and magnitude by quantum confinement and band engineering. In vertically biased wells, the controllable band bending spatially shifts carrier wave functions, thereby modulating their spin splitting through g-factor gradients and through local interactions with nuclear spin. Continuous shifting of the wave function is possible in parabolic QWs, while tunneling between coupled square wells provides more discrete changes in the wave function position. Adding a high-frequency component to the vertical bias allows for resonant control of spin, such as g-TMR and nuclear spin resonant depolarization.

The measurement of these effects relies on the ability to resolve electron spin precession, through ultrafast optical spectroscopy, which in turn places requirements on the transverse electron spin lifetime. Despite much theoretical and experimental work, engineering electron spin lifetimes in QWs remains mostly an empirical endeavor of trial and error. This arises due to competing variables that may enhance or limit spin lifetime, such as electronic doping (either modulation or direct doping), Fermi level, and carrier temperature. This may offer some explanation for the discrepancy between time-resolved Kerr (or Faraday) rotation measurements and time-resolved PL in which hole-spin precession has and has not been observed in nominally identical structures, respectively. Since hole wave functions shift with vertical bias, g-factor tuning of hole spin must also occur. Engineering structures for improved hole-spin lifetimes by carrier doping, strain, or confinement, may allow these hole-spin effects to become observable.

Spin splittings in nonmagnetic structures tend to be of the order of $10\,\mu\mathrm{eV\,T^{-1}}$ and this energetic fragility usually requires low sample temperatures and high magnetic fields to observe the effects. Magnetically doped semiconductors offer orders of magnitude larger and more robust spin splittings that in principle can scale to technologically practical temperatures and magnetic fields. In vertically biased magnetic QW structures, analogous to those used in nonmagnetic wells, such an enhancement of the spin interactions has been observed. In these structures, the exchange overlap between carrier and magnetic-ion spins is electrically controlled, which changes the spin polarization and spin dynamics of carriers in the wells. In principle, the manipulation of Mn-ion spins through electron or hole-spin polarization should be possible; so far only the reverse has been observed. These techniques contrast with indirect spintronic devices such as spin-LED structures, where magnetic layers are remote from the optically active region and measurements of direct spin couplings are not possible.

Engineering the carrier density and quantum confinement in QWs provides, also, a means to alter or enhance the intrinsic interactions between free carriers and magnetic ions. Modulation doping holes in magnetic wells enhances the ferromagnetic ordering temperature above what is achievable in bulk systems. Changing confinement by QW width and depth strongly alters the conduction-band exchange parameter. This is observed in both II–VI and III–V magnetic wells where the kinetic exchange mechanism adds a negative contribution to conduction-band exchange splitting. The use of QW design to engineer spin interactions in magnetic materials could be applied to many materials systems, for example, GaN–AlGaN, in which the effect of magnetic doping in bulk materials has proven difficult to determine. The exchange interactions responsible for ferromagnetic interactions can be probed at low magnetic doping levels since exchange splitting effects are observable at these densities, for example, $10^{19}\,\mathrm{cm^{-3}}$ in GaMnAs QWs. At low doping levels, materials constraints, such as magnetic impurity solubility and associated defect formation can be avoided, which frequently render the origin of ferromagnetism, in some systems, ambiguous and controversial.

ACKNOWLEDGMENTS

The authors thank M. Poggio and Y. K. Kato for helpful discussion and comments.

REFERENCES

Awschalom, D.D. and Samarth, N. (1999). Spin dynamics and quantum transport in magnetic semiconductor quantum structures. *Journal of Magnetism and Magnetic Materials*, **200**, 130–147.

Bhattacharjee, A.K. (1998). Confinement-induced reduction of the effective exchange parameters in semimagnetic semiconductor nanostructures. *Physical Review B*, **58**, 15660–15665.

Bhattacharjee, A.K., Fishman, G. and Coqblin, B. (1983). Virtual bound state model for the exchange interaction in semimagnetic semiconductors such as $Cd_{1-x}Mn_xTe$. *Physica B+C*, **117–118**, 449–451.

Chadi, D.J., Clark, A.H. and Burnham, R.D. (1976). Γ_1 conduction electron g factor and matrix elements in GaAs and $Al_xGa_{1-x}As$ alloys. *Physical Review B*, **13**, 4466–4469.

Chen, Y.J., Koteles, E.S., Elman, B.S. and Armiento, C.A. (1987). Effect of electric fields on excitons in a coupled double-quantum-well structure. *Physical Review B (Rapid Communications)*, **36**, 4562–4565.

Crooker, S.A., Tulchinsky, D.A, Levy, J., *et al*. (1995). Enhanced spin interactions in digital magnetic heterostuctures. *Physical Review Letters*, **75**, 505–508.

Crooker, S.A., Baumberg, J.J., Flack, F., *et al*. (1996). Terahertz spin precession and coherent transfer of angular momenta in magnetic quantum wells. *Physical Review Letters*, **77**, 2814–2817.

Dalpian, G.M. and Wei, S. (2006). Electron-mediated ferromagnetism and negative $s-d$ exchange splitting in semiconductors. *Physical Review B*, **73**, 245204-1–245204-4.

Dietl, T. (1981). In *Proceedings of the Oji International Seminar, Physics in High Magnetic Fields*, Chikazumi, C. and Miura, M. (Eds.), Springer-Verlag: Berlin, p. 344, Vol. 24.

Dietl, T. (1994). Diluted magnetic semiconductors. In *Handbook on Semiconductors*, Moss, T.S. (Ed.), North Holland: Amsterdam, p. 1251, Vol. 3B.

Dietl, T., Ohno, H., Matsukura, F., *et al*. (2000). Zener model description of ferromagnetism in zinc-blende magnetic semiconductors. *Science*, **287**, 1019–1022.

Dingle, R., Gossard, A.C. and Wiegmann, W. (1975). Direct observation of superlattice formation in a semiconductor heterostructure. *Physical Review Letters*, **34**, 1327–1330.

Edmonds, K.W., Boguslawski, P., Wang, K.Y., *et al*. (2004). Mn interstitial diffusion in (Ga,Mn)As. *Physical Review Letters*, **92**, 037201-1–037201-4.

Gossard, A.C. (1986). Growth of microstructures by molecular beam epitaxy. *IEEE Journal of Quantum Electronics*, **22**, 1649–1655.

Gunshor, R.L., Kolodziejski, L.A., Nurmikko, A.V. and Otsuka, N. (1988). Semimagnetic and magnetic semiconductor superlattices. *Annual Review of Materials Science*, **18**, 325–350.

Haury, A., Wasiela, A., Arnoult, A., *et al*. (1997). Observation of a ferromagnetic transition induced by two-dimensional hole gas in modulation-doped CdMnTe quantum wells. *Physical Review Letters*, **79**, 511–514.

Hermann, C. and Weisbuch, C. (1977). $\mathbf{k}\cdot\mathbf{p}$ perturbation-theory in III-V compounds and alloys: a re-examination. *Physical Review B*, **15**, 823–833.

Hilton, D.J. and Tang, C.L. (2002). Optical orientation and femtosecond relaxation of spin-polarized holes in GaAs. *Physical Review Letters*, **89**, 146601-1–14660-14.

Islam, M.N., Hillman, R.L., Miller, D.A.B., *et al*. (1987). Electroabsorption in GaAs/AlGaAs coupled quantum well waveguides. *Applied Physics Letters*, **50**, 1098–1100.

Ivchenko, E.L. and Kiselev, A.A. (1992). Electron g-factor of quantum-wells and superlattices. *Soviet Physics Semiconductors*, **26**, 827–831.

Jiang, H.W. and Yablonovitch, E. (2001). Gate-controlled electron spin resonance in $GaAs/Al_xGa_{1-x}As$ heterostructures. *Physical Review B (Rapid Communications)*, **64**, 041307-1–041307-4.

Johnston-Halperin, E., Schuller, J.A., Gallinat, C.S., *et al*. (2003). Independent electronic and magnetic doping in (Ga,Mn)As based digital ferromagnetic heterostructures. *Physical Review B*, **68**, 165328-1–165328-9.

Jungwirth, T., Sinova, J., Masek, J., *et al*. (2006). Theory of ferromagnetic (III,Mn)V semiconductors. *Reviews of Modern Physics*, **78**, 809–864.

Kalevich, V.K. and Korenev, V.L. (1992). Anisotropy of the electron g-factor in GaAs/AlGaAs quantum-wells. *JETP Letters*, **56**, 253–259.

Kato, Y., Myers, R.C., Driscoll, D.C., *et al*. (2003). Gigahertz electron spin manipulation using voltage controlled g-tensor modulation. *Science*, **299**, 1201–1204.

Kawakami, R.K., Johnston-Halperin, E., Chen, L.F., *et al*. (2000). (Ga,Mn)As as a digital ferromagnetic heterostructure. *Applied Physics Letters*, **77**, 2379–2381.

Kikkawa, J.M. and Awschalom, D.D. (2000). All-optical magnetic resonance in semiconductors. *Science*, **287**, 473–476.

Kopf, R.F., Herman, M.H., Schnoes, M.L., *et al*. (1992). Band offset determination in analog graded parabolic and triangular quantum wells of GaAs/AlGaAs and GaInAs/AlInAs. *Journal of Applied Physics*, **71**, 5004–5011.

Kosaka, H., Kiselev, A.A., Baron, F.A., *et al*. (2001). Electron g factor engineering in III-V semiconductors for quantum communications. *Electronics Letters*, **37**, 464–465.

Kowalski, B., Linke, H. and Omling, P. (1996). Spin-resonance determination of the electron effective g value of $In_{0.53}Ga_{0.47}As$. *Physical Review B*, **54**, 8551–8555.

Kowalski, B., Omling, P., Meyer, B.K., *et al*. (1994). Conduction-band spin splitting of type-I $Ga_xIn_{1-x}As/InP$ quantum wells. *Physical Review B (Rapid Communications)*, **49**, 14786–14789.

Kroemer, H. (2001). Nobel lecture: quasielectric fields and band offsets: teaching electrons new tricks. *Reviews of Modern Physics*, **73**, 783–793.

Ku, K.C., Potashnik, S.J., Wang, R.F., *et al*. (2003). Highly enhanced Curie temperature in low-temperature annealed [Ga, Mn]As epilayers. *Applied Physics Letters*, **82**, 2302–2304.

Lampel, G. (1968). Nuclear dynamic polarization by optical electronic saturation and optical pumping in semiconductors. *Physical Review Letters*, **20**, 491–493.

Linfield, E.H., Jones, G.A.C., Ritchie, D.A. and Thompson, J.H. (1993). The fabrication of a back-gated high electron mobility transistor-a novel approach using MBE regrowth on an in situ ion

beam patterned epilayer. *Semiconductor Science and Technology*, **8**, 415–422.

MacDonald, A.H., Schiffer, P. and Samarth, N. (2005). Ferromagnetic semiconductors: moving beyond (Ga,Mn)As. *Nature Materials*, **4**, 195–202.

Mackh, G., Hilpert, M., Yakovlev, D.R., *et al*. (1994). Exciton magnetic polarons in the semimagnetic alloys $Cd_{1-x-y}Mn_xMg_yTe$. *Physical Review B*, **50**, 14069–14076.

Mackh, G., Ossau, W., Waag, A. and Landwehr, G. (1996). Effect of the reduction of dimensionality on the exchange parameters in semimagnetic semiconductors. *Physical Review B*, **54**, R5227–R5230.

Madelung, O. (2004). *Semiconductors: Data Handbook*, *Third Edition*, Springer-Verlag: Berlin.

Malinowski, A. and Harley, R.T. (2000). Anisotropy of the electron g factor in lattice-matched and strained-layer III-V quantum wells. *Physical Review B*, **62**, 2051–2056.

Maranowski, K.D., Ibbetson, J.P., Campman, K.L. and Gossard, A.C. (1995). Interface between low-temperature grown GaAs and undoped GaAs as a conduction barrier for back gates. *Applied Physics Letters*, **66**, 3459–3461.

Marie, X., Amand, T., Le Jeune, P., *et al*. (1999). Hole spin quantum beats in quantum-well structures. *Physical Review B*, **60**, 5811–5817.

Martin, R.W., Nicholas, R.J., Rees, G.J., *et al*. (1990). Two-dimensional spin confinement in strained-layer quantum wells. *Physical Review B (Rapid Communications)*, **42**, 9237–9240.

Merkulov, I.A., Yakovlev, D.R., Keller, A., *et al*. (1999). Kinetic exchange between the conduction band electrons and magnetic ions in quantum-confined structures. *Physical Review Letters*, **83**, 1431–1434.

Miller, D.A.B., Chemla, D.S., Damen, T.C., *et al*. (1984). Band-edge electroabsorption in quantum well structures: the quantum-confined Stark effect. *Physical Review Letters*, **53**, 2173–2176.

Miller, R.C., Gossard, A.C., Kleinman, D.A. and Munteanu, O. (1984). Parabolic quantum wells with the GaAs-$Al_xGa_{1-x}As$ system. *Physical Review B*, **29**, 3740–3743.

Myers, R.C., Gossard, A.C. and Awschalom, D.D. (2004). Tunable spin polarization in III-V quantum wells with a ferromagnetic barrier. *Physical Review B (Rapid Communications)*, **69**, 161305-1–161305-4.

Myers, R.C., Ku, K.C., Li, X., *et al*. (2005a). Optoelectronic control of spin dynamics at near-terahertz frequencies in magnetically doped quantum wells. *Physical Review B (Rapid Communications)*, **72**, 041302-1–041302-4.

Myers, R.C., Poggio, M., Stern, N.P., *et al*. (2005b). Antiferromagnetic $s-d$ exchange coupling in GaMnAs. *Physical Review Letters*, **95**, 017204-1–017204-4.

Nazmul, A.M., Amemiya, T., Shuto, Y., *et al*. (2005). High temperature ferromagnetism in GaAs-based heterostructures with Mn delta doping. *Physical Review Letters*, **95**, 017201-1–017201-4.

Nazmul, A.M., Sugahara, S. and Tanaka, M. (2002). Transport properties of Mn δ-doped GaAs and the effect of selective doping. *Applied Physics Letters*, **80**, 3120–3122.

Nazmul, A.M., Sugahara, S. and Tanaka, M. (2003a). MBE growth, structural, and transport properties of Mn δ-doped GaAs layers. *Journal of Crystal Growth*, **251**, 303–310.

Nazmul, A.M., Sugahara, S. and Tanaka, M. (2003b). Ferromagnetism and high Curie temperature in semiconductor heterostructures with Mn δ-doped GaAs and p-type selective doping. *Physical Review B (Rapid Communications)*, **67**, 241308-1–241308-4.

Ohno, H. (2002). Ferromagnetic III-V semiconductors and their heterostructures. In *Semiconductor Spintronics and Quantum Computation*, Awschalom, D.D., Loss, D. and Samarth, N. (Eds.), Springer-Verlag: Berlin, pp. 1–30.

Ohno, H., Shen, A., Matsukura, F., *et al*. (1996). (Ga,Mn)As: a new ferromagnetic semiconductor based on GaAs. *Applied Physics Letters*, **69**, 363–365.

Pfeffer, P. and Zawadzki, W. (2005). Theory of spin splitting in $Ga_{1-x}Al_xAs$ parabolic quantum wells controlled by an electric field. *Physical Review B*, **72**, 035325-1–035325-6.

Poggio, M. and Awschalom, D.D. (2005). High-field optically detected nuclear magnetic resonance in GaAs. *Applied Physics Letters*, **86**, 182103-1–182103-3.

Poggio, M., Myers, R.C., Stern, N.P., *et al*. (2005). Structural, electrical, and magneto-optical characterization of paramagnetic GaMnAs quantum wells. *Physical Review B*, **72**, 235313-1–235313-15.

Poggio, M., Steeves, G.M., Myers, R.C., *et al*. (2003). Local manipulation of nuclear spin in a semiconductor quantum well. *Physical Review Letters*, **91**, 207602-1–207602-4.

Poggio, M., Steeves, G.M., Myers, R.C., *et al*. (2004). Spin transfer and coherence in coupled quantum wells. *Physical Review B (Rapid Communications)*, **70**, 121305-1–121305-4.

Roth, L.M., Lax, B. and Zwerdling, S. (1959). Theory of optical magneto-absorption effects in semiconductors. *Physical Review*, **114**, 90–103.

Roussignol, Ph., Rolland, P., Ferreira, R., *et al*. (1992). Hole polarization and slow hole-spin relaxation in an n-doped quantum-well structure. *Physical Review B (Rapid Communications)*, **46**, 7292–7295.

Salis, G., Graf, B., Ensslin, K., *et al*. (1997). Wave function spectroscopy in quantum wells with tunable electron density. *Physical Review Letters*, **79**, 5106–5109.

Salis, G., Kato, Y., Ensslin, K., *et al*. (2001). Electrical control of spin coherence in semiconductor nanostructures. *Nature*, **414**, 619–622.

Salis, G., Awschalom, D.D., Ohno, Y. and Ohno, H. (2001). Origin of enhanced dynamic nuclear polarization and all-optical nuclear magnetic resonance in GaAs quantum wells. *Physical Review B*, **64**, 195304-1–195304-10.

Salis, G., Kato, Y., Ensslin, K., *et al*. (2003). Electrical control of spin precession in semiconductor quantum wells. *Physica E: Low-Dimensional Systems and Nanostructures*, **16**, 99–103.

Sanada, H., Kondo, Y., Matsuzaka, S., *et al*. (2006). Optical pump-probe measurements of local nuclear spin coherence in semiconductor quantum wells. *Physical Review Letters*, **96**, 067602-1–067602-4.

Sanada, H., Matsuzaka, S., Morita, K., *et al*. (2003). Hysteretic dynamic nuclear polarization in GaAs/$Al_xGa_{(1-x)}As$ (110) quantum wells. *Physical Review B (Rapid Communications)*, **68**, 241303-1–241303-4.

Sanada, H., Matsuzaka, S., Morita, K., *et al*. (2005). Gate control of dynamic nuclear polarization in GaAs quantum wells. *Physical Review Letters*, **94**, 097601-1–097601-4.

Sih, V., Lau, W.H., Myers, R.C., *et al*. (2004). Control of electron-spin coherence using Landau level quantization in a two-dimensional electron gas. *Physical Review B (Rapid Communications)*, **70**, 161313-1–161313-4.

Snelling, M.J., Blackwood, E., McDonagh, C.J. and Harley, R.T. (1992). Exciton, heavy-hole, and electron *g* factors in type-I GaAs/$Al_xGa_{1-x}As$ quantum wells. *Physical Review B (Rapid Communications)*, **45**, 3922–3925.

Snelling, M.J., Flinn, G.P., Plaut, A.S., *et al*. (1991). Magnetic *g* factor of electrons in GaAs/$Al_xGa_{1-x}As$ quantum wells. *Physical Review B*, **44**, 11345–11352.

Stern, N.P., Myers, R.C., Poggio, M., *et al*. (2007). Confinement engineering of s-d exchange interactions in GaMnAs/AlGaAs quantum wells. *Physical Review B*, **75**, 045329.

Teran, F.J., Potemski, M., Maude, D.K., *et al*. (2003). Collective character of spin excitations in a system of Mn^{2+}spins coupled to a two-dimensional electron gas. *Physical Review Letters*, **91**, 077201-1–077201-4.

Tifrea, I. and Flatte, M.E. (2003). Electric field tunability of nuclear and electronic spin dynamics due to the hyperfine interaction in semiconductor nanostructures. *Physical Review Letters*, **90**, 237601-1–237601-4.

Traynor, N.J., Harley, R.T. and Warburton, R.J. (1995). Zeeman splitting and *g* factor of heavy-hole excitons in $In_xGa_{1-x}As$/GaAs quantum wells. *Physical Review B (Rapid Communications)*, **51**, 7361–7364.

Uenoyama, T. and Sham, L.J. (1990). Carrier relaxation and luminescence polarization in quantum wells. *Physical Review B*, **42**, 7114–7123.

Warren, A.C., Woodall, J.M., Freeouf, J.L., *et al*. (1990). Arsenic precipitates and the semi-insulating properties of GaAs buffer layers grown by low-temperature molecular beam epitaxy. *Applied Physics Letters*, **57**, 1331–1333.

Weisbuch, C. and Hermann, C. (1977). Optical detection of conduction-electron spin resonance in GaAs, $Ga_{1-x}In_xAs$, and $Ga_{1-x}Al_xAs$. *Physical Review B*, **15**, 816–822.

Hot Electron Spintronics

Xin Jiang[1], Sebastiaan van Dijken[2], and Stuart Parkin[1]

[1] *IBM Almaden Research Center, San José, CA, USA*
[2] *Trinity College, Dublin 2, Ireland*

1 INTRODUCTION

Spin-dependent electron transport in ferromagnetic metals has been extensively investigated, especially in view of its importance for the functionality of spintronic devices. When electron transport occurs at energies much larger than thermal energies of the order of kT ($kT \sim 26\,\text{meV}$ at 300 K), it is often referred to as '*hot' electron transport*. When hot electrons are transmitted through ferromagnetic metals, they interact with the electrons and atoms in the metal and can be scattered. It is well known that the hot electron mean free paths are spin dependent in ferromagnetic metals. The minority electrons usually have a smaller mean free path than the majority electrons, that is, they are more heavily scattered than the majority electrons. This spin-dependent scattering provides a means of studying the interaction between the hot electron spins and the more localized spins constituting the ferromagnet and also forms the basis for building hot electron spintronic devices.

Various techniques have been developed to study hot electron transport in ferromagnetic metals. These techniques usually require a source of hot electrons with a well-defined energy, a medium in which the electrons travel, and an analyzer for the transmitted electrons. Commonly used electron sources include a semiconductor photocathode, a scanning tunneling microscope (STM) tip, a metal/semiconductor Schottky barrier, and a metal/insulator tunnel barrier. The transmission medium normally contains one or more ferromagnetic-metal layers, separated by nonmagnetic metal or dielectric layers. The electron analyzer may detect both the electron spin's polarization and intensity, such as a Mott detector, or may simply be an energy analyzer, such as a metal/semiconductor Schottky barrier.

Spin-resolved electron transmission is one of the most important techniques for studying hot electron transport in ferromagnetic thin films. Moreover, highly spin-polarized hot electron currents can be obtained after transmission due to the highly efficient spin-filtering effect. Understanding of the spin-filtering effect is key to a variety of applications, including, for example, ballistic electron emission microscopy (BEEM), and the spin-valve transistor and magnetic tunnel transistor devices. The high spin polarization, resulting from spin-filtering, also makes it an attractive approach for hot electron spin injection into semiconductors, which is an important ingredient for the development of useful semiconductor-based spintronic devices.

Handbook of Magnetism and Advanced Magnetic Materials. Edited by Helmut Kronmüller and Stuart Parkin. Volume 5: *Spintronics and Magnetoelectronics*. ISBN: 978-0-470-02217-7.

2 SPIN-RESOLVED ELECTRON TRANSMISSION

When a hot electron beam impinges on a ferromagnetic surface or interface, the electrons can be reflected, absorbed, or transmitted. Siegmann, Pierce, Celotta (1981) studied electron absorption of a $Ni_{40}Fe_{40}B_{20}$ film for electron energies between 2 and 500 eV. They found that the absorption depends on the orientation of the incident electron spins with respect to the magnetization of the ferromagnetic film. They attributed this dependence to the influence of exchange interactions on elastic spin-dependent electron scattering. They further proposed that the measurement of the absorption current could be utilized for detecting electron spin polarization and probing surface magnetization.

It was later pointed out by Schönhense and Siegmann (1993) that spin-resolved electron transmission through ferromagnetic metals provides a more efficient way of detecting the spin dependence of hot electron transport due to the large asymmetry in the majority and minority electron mean free paths. In typical transmission experiments the ferromagnetic film can only be a few nanometers thick because the transmission efficiency is quite small, $\sim 10^{-3}$ or less, so that the transmitted beam currents lie in the picoampere to nanoampere range, or even less. The first measurement of spin-dependent electron inelastic mean free paths was conducted by Pappas *et al*. (1991) using spin-resolved photoemission. In these experiments, ultrathin Fe overlayers were grown on Cu(100). When photons from the light source impinge on the sample, hot electrons are emitted from the Cu substrate through the Fe overlayer (Figure 1). In order to track the transport of the hot electrons generated in the Cu substrate, energy-resolved spectra were taken so that these electrons could be identified from their element-specific binding energy. The intensity and spin polarization of the hot electrons after transmission through the Fe overlayer was analyzed by a Mott detector. Pappas *et al*. found that the mean free path of the majority electrons is larger than that of the minority electrons in the energy range of $\sim$10–40 eV, and that the mean free paths increase with decreasing electron energy. The rate of increase is larger for the majority electrons than for the minority electrons. Similar experiments were carried out by Getzlaff, Bansmann, and Schönhense (1993) and Vescovo *et al*. (1995) for hcp Co and bcc Fe overlayers on W(110), and fcc Co overlayers on Cu(111), respectively. A spin asymmetry in electron inelastic mean free paths was also observed in these structures.

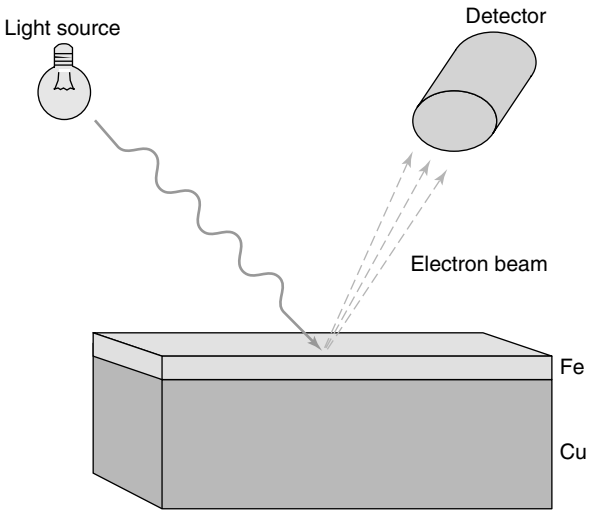

Figure 1. Spin- and energy-resolved photoemission measurements of hot electron transmission through a thin Fe overlayer grown on a Cu substrate.

In the experiments discussed above, the photogenerated electrons are initially unpolarized. They acquire spin polarization while traversing the ferromagnetic overlayer. In a different experiment, Gröbli *et al*. (1995) grew a thin Fe overlayer on a GaAs substrate with a Ag buffer layer between the Fe and GaAs. The Ag layer was used to prevent interdiffusion and reaction between the Fe film and GaAs. Using circularly polarized light (Meier and Zakharchenya, 1984), spin-polarized electrons were created in GaAs and subsequently extracted through the Ag and Fe overlayers. Gröbli *et al*. analyzed the intensity and polarization of the photocurrents as a function of the photon energy and initial electron spin polarization. They found that the transmission was about 1.7 times larger when the electron spin direction was oriented parallel to the Fe magnetization compared to the case when it was antiparallel.

One complication in the overlayer experiments is that the incident light also creates hot electrons inside the overlayer, thereby giving rise to a large background signal. To overcome this problem, self-supporting thin-film structures have been used to study spin-dependent hot electron transmission (Figure 2). The preparation of such structures usually involves deposition of an intermediate layer onto a substrate. Afterwards, the film stack of interest is deposited onto the intermediate layer. Finally, the intermediate layer is removed by dissolving it in a suitable solution, such as water, to obtain freestanding thin films. A GaAs photocathode is often used as the electron source, in which circularly polarized light is used to generate spin-polarized electrons with a polarization vector $\vec{P}$ (Meier and Zakharchenya, 1984). By using self-supporting films, the creation and transmission of hot electrons are no longer intertwined. Consequently, the background signal can be reduced. Lassailly *et al*. (1994) and Drouhin *et al*. (1996) measured hot electron transmission through Au/Co/Au film stacks with the electron spin polarization parallel or antiparallel with the Co magnetization $\vec{M}$. For inelastically scattered electrons, the transmission probability was found to be four

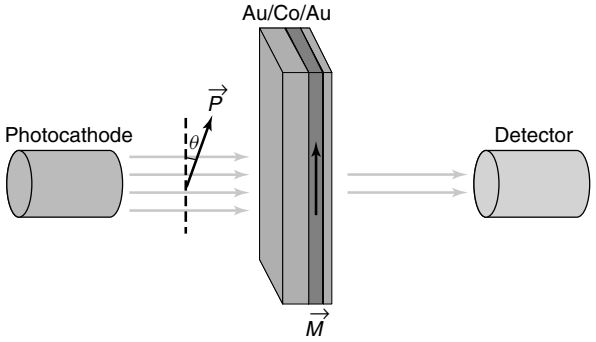

Figure 2. Spin-resolved hot electron transmission measurements through a freestanding ferromagnetic thin-film structure. θ is the angle between the spin polarization of the incident electron beam and the magnetization of the ferromagnet.

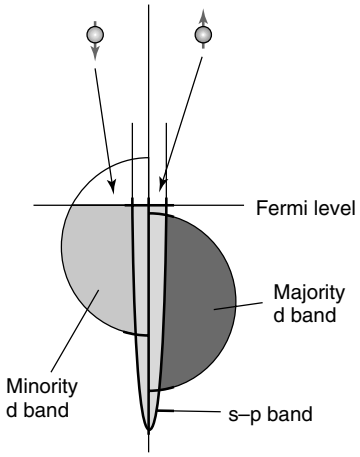

Figure 3. Illustration of spin-dependent electron scattering in 3d transition metals. The horizontal and vertical axes represent the density of states and electron energy, respectively. The filled region represents occupied states. Only the minority electrons (spin-down) can be effectively scattered into the empty minority d band.

times higher for the majority electrons than for the minority electrons. For elastically scattered electrons, the asymmetry in transmission was much smaller, which might be related to the sample preparation (Drouhin *et al*., 1996). Oberli *et al*. (1998) also carried out spin-dependent transmission experiments using a Au/Co/Au film stack. They observed a large transmission asymmetry for elastic electron scattering of up to $\sim$80%.

When the spin polarization vector of the incident electron beam is perpendicular to the magnetization of the ferromagnetic thin film ($\theta = 90^\circ$ in Figure 2), the spin state of the hot electrons can be regarded as a superposition of two components, one parallel and one antiparallel to the film magnetization, with equal amplitude. After the electrons are transmitted through the ferromagnet, the amplitudes of the two components are no longer the same due to spin-dependent absorption. As a result, the spin vector is rotated toward the magnetization direction. Meanwhile, a phase difference between the two components develops and the spin vector precesses around the magnetization. Weber, Riesen, and Siegmann (2001) measured the precession angles of hot electron spins after passing through Fe, Co, and Ni thin films. At an electron energy of 7 eV, they obtained a precession rate of 33, 19, and $7^\circ\,\mathrm{nm}^{-1}$ for Fe, Co, and Ni, respectively. Owing to the conservation of total angular momentum, there must be a corresponding precession of the magnetization of the ferromagnet around the spin vector of the injected hot electrons. It therefore follows that the injection of hot electron spins can be utilized for precessional magnetization reversal (Siegmann *et al*., 1995; Back *et al*., 1998, 1999). Assuming realistic parameters, Weber *et al*. estimated that the switching time using the precession method could be as short as a few picoseconds, which is much faster than conventional magnetic field driven magnetization reversal.

The spin dependence of hot electron scattering in ferromagnetic metals is often considered to be a consequence of electron–electron scattering. In ferromagnetic 3d transition metals the electron d band is split into the majority and minority bands. A portion of the minority electron band is empty, while the majority electron band is almost fully occupied. As a result, minority electron scattering into the empty d band is very effective, giving rise to a shorter mean free path. In contrast, the majority electrons can only be scattered into the less abundant s–p band and thus have a larger mean free path. This simple picture is illustrated in Figure 3. It was found that the inelastic scattering length of hot electrons in transition metals can be described by a simple formula (Schönhense and Siegmann, 1993; Siegmann, 1992), as follows,

$$\frac{1}{\lambda} = \sigma = \sigma_0 + \sigma_d\,(5 - n) \tag{1}$$

where λ and σ are the spin-averaged electron mean free path and scattering cross section, respectively. σ_d accounts for scattering into the empty d bands while σ_0 accounts for other scattering processes. n is the number of occupied d orbitals available to one spin state and since the total number of d orbitals there is 5, $5 - n$ is the number of holes in the d band for one spin state. To account for the different mean free paths of the majority and minority electrons in ferromagnets, Schönhense and Siegmann (1993) extended equation (1) to a spin-dependent format,

$$\frac{1}{\lambda_\pm} = \sigma_\pm = \sigma_0 + \sigma_d\,[5 - (n \pm \Delta n)] \tag{2}$$

where '+' and '−' indicate the corresponding quantities for the majority- and minority-spin electrons, respectively.

$2\Delta n$ is the Bohr magneton number of the ferromagnet. Schönhense and Siegmann obtained good agreement with existing experimental data using equation (2) with a single fitting parameter σ_0/σ_d. They described the spin-dependent hot electron transmission in ferromagnetic transition metals as a spin-filtering effect since the majority electrons are preferentially transmitted while the minority electrons are mostly eliminated after passing through the ferromagnet.

The concept of spin-filtering was successfully used to explain the lack of negative spin polarization observed in photoemission experiments for Co. In strong ferromagnets, such as Co and Ni, the minority d band has a much larger density of states at the Fermi level than the majority d band. Therefore, a negative spin polarization is expected in the photoemission experiments close to the threshold photon energy. This was indeed observed in the case of Ni. For thick Co films, however, the observed polarization is positive at photothreshold (Gröbli *et al*., 1995). This puzzle was understood in light of the spin-filtering effect inside the Co film. Although the light initially excites more minority electrons than majority electrons, they are eliminated from the photocurrent due to their short mean free path. As a result, the majority electrons dominate in the photoemission and a positive spin polarization is observed. If a thin Co film is used with thickness on the order of the minority electron mean free path, a negative spin polarization at photothreshold should be observed since the spin-filtering effect is small for very thin films. Gröbli, Oberli, and Meier (1995) evaporated ultrathin fcc Co overlayers onto Cu(001) and measured the spin polarization of the photocurrent as a function of the Co film thickness. At photo threshold, they obtained a negative spin polarization for film thicknesses up to ∼27 Å. These results provided clear evidence for the spin-filtering effect in ferromagnetic films.

For ultrathin films, the electron mean free path is no longer a well-defined quantity since the motion of the electrons cannot be divided into a succession of single steps. In this sense, spin-dependent electron lifetimes may be a more appropriate quantity to study hot electron transport in ferromagnetic thin films (Aeschlimann *et al*., 1997; Knorren *et al*., 2000). The first direct measurement of spin-dependent electron lifetimes was conducted by Aeschlimann *et al*. (1997) using two-photon photoemission (2PPE) (Figure 4). In the 2PPE experiment, a first laser pulse excites electrons from their ground state into an intermediate state below the vacuum level. After a certain time delay, a second laser pulse excites these electrons above the vacuum level, giving rise to photoemission. The lifetime of the electrons in the intermediate energy state can be extracted by analyzing the intensity and spin polarization of the emitted electrons as a function of the delay time. The energy dependence of the lifetime can be obtained by varying the energy of the laser pulse. Aeschlimann *et al*. measured spin lifetimes in fcc Co films deposited on a Cu(001) single crystal. They found that the electron lifetimes were on the order of a few femtoseconds to 20 fs in the energy range of 0.6–1.1 eV above the Fermi level. The electron lifetime decreased with energy, which was attributed to the increased phase space into which the electrons could be scattered at high energy (Quinn, 1962). The ratio between the majority and minority electron lifetimes was found to be ∼2 at 1 eV and decreased to ∼1.2 at 0.6 eV, which was attributed to the band structure of Co. The density of states of the Co minority electron band has a maximum at ∼1 eV above the Fermi level. When the hot electron energy is less than 1 eV, the number of empty states available for scattering decreases in the minority electron band. On the other hand, the density of states in the majority electron band is more or less constant in this energy range. Therefore, a larger increase in the lifetime of minority electrons than of majority electrons may be expected as the energy is decreased from 1.0 to 0.6 eV.

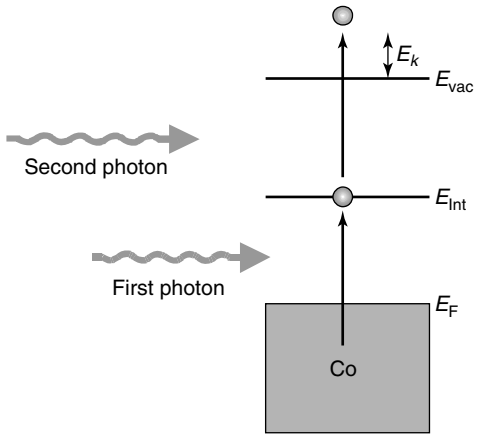

Figure 4. Illustration of the two-photon-photoemission process. E_{Int} and E_{Vac} indicate the energy level of the intermediate state and the vacuum level, respectively. E_k is the kinetic energy of the emitted electrons.

Spin-resolved electron transmission is a powerful technique for investigating spin-dependent hot electron transport in ferromagnetic thin-film structures. Important parameters, such as electron mean free paths and lifetimes, can be extracted from these experiments. These studies provide a solid foundation for developing spintronic devices based on hot electron transport.

3 BALLISTIC ELECTRON EMISSION MICROSCOPY

BEEM was first implemented by Kaiser and Bell (1988). In BEEM, an STM tip is positioned above a metal/semiconductor

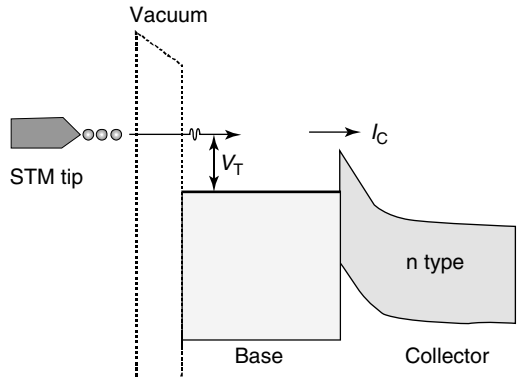

Figure 5. Ballistic electron emission microscopy.

Schottky barrier, where the semiconductor is doped n type (see Figure 5). When a tip bias voltage (V_T) is applied, hot electrons are generated by tunneling from the STM tip into the metal base through the vacuum barrier. If these electrons retain an energy larger than the height of the Schottky barrier (Φ_S) at the metal/semiconductor interface, they can be transmitted into the semiconductor conduction band. The magnitude of the collector current (I_C) is very sensitive to the details of the band structure at the metal/semiconductor interface. Therefore BEEM has been extensively used to probe the electronic structure of buried interfaces (Kaiser and Bell, 1988; Bell and Kaiser, 1988; Schowalter and Lee, 1991; Ludeke and Bauer, 1993; Garcia-Vidal, de Andres and Flores, 1996; Smith and Kogan, 1996; Bell, 1996; Guthrie *et al.*, 1996; Smith, Lee and Narayanamurti, 1998; Weilmeier, Rippard and Buhrman, 1999; Smith *et al.*, 2000). In these studies, the base layer is usually comprised of noble metals, such as Au, which have very large electron mean free paths (Weilmeier, Rippard and Buhrman, 1999).

The hot electrons injected into the metal base have a very high kinetic energy of $\sim E_F + eV_T$. Once they are transmitted into the semiconductor conduction band, their kinetic energy is reduced to $eV_T - \Phi_S$. As a result, the electrons lose a large fraction of their normal momentum component. On the other hand, the transverse momentum component is often assumed to be conserved. This leads to a critical angle of collection (θ_C), and only electrons propagating within this angle may be collected in the semiconductor. θ_C can be calculated using the following formula,

$$\theta_C = \arcsin\sqrt{\frac{m_t}{m}\frac{eV_T - \Phi_S}{E_F + eV_T}} \tag{3}$$

where m_t is the transverse electron effective mass in the semiconductor conduction band and m is the electron mass in the metal base. Assuming typical values of $\frac{m_t}{m} \sim 0.1$, $eV_T -$

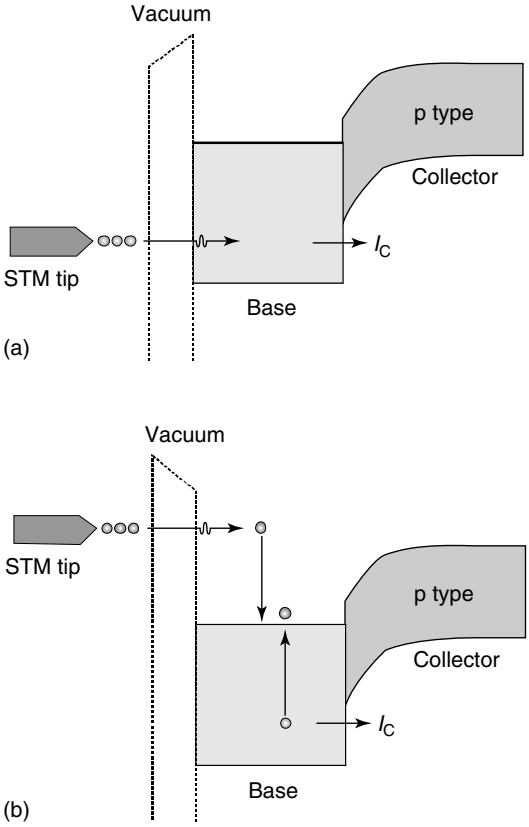

Figure 6. Ballistic hole emission microscopy operating in the normal (a) and reverse (b) modes.

$\Phi_S \sim 0.5\,\text{eV}$, $E_F + eV_T \sim 5\,\text{eV}$, the critical angle is estimated to be less than 6^o. Therefore, the lateral resolution of BEEM can be as high as $\sim$1 nm if the base layer thickness is on the order of 10 nm. The ability to probe subsurface interfaces with such a high resolution is probably the most attractive property of BEEM. Another advantage of BEEM is that the energy of the hot electrons can easily be changed by varying the tip bias voltage, thus allowing for investigations of the energy dependence of hot electron transport over a wide range of energy.

The ballistic transport of hot holes can be studied in a similar manner if the semiconductor collector is doped p type rather than n type (Bell *et al.*, 1990; Hecht *et al.*, 1990). This technique is called *ballistic hole emission microscopy* (BHEM). Figure 6 shows two operation modes of BHEM. When the STM tip is positively biased with respect to the metal base, hot holes are directly injected into the valence band of the collector (Figure 6a). This is the normal operation mode of BHEM. If the STM tip is negatively biased, on the other hand, BHEM operates in the reverse mode (Figure 6b). In this case, hot electrons are first injected into the base, where they are inelastically scattered and lose energy. The energy is transferred to secondary electrons, exciting them to

higher energy states and creating hot holes inside the base layer. Some of these holes then traverse ballistically through the base layer and form the collector current. BHEM has been used to study the transport properties of hot holes, complementary to the study of hot electrons, as well as to probe the electron–hole scattering process in materials.

In order to study the spin dependence of hot electron transport using BEEM, Rippard and Buhrman replaced the noble metal base with single Co films or Co/Cu/Co trilayers (Rippard and Buhrman, 1999, 2000). This variation of BEEM is called *ballistic electron magnetic microscopy* (BEMM). When the hot electrons traverse the Co/Cu/Co base layers, the scattering rate depends on the alignment of magnetization of the two Co layers since the electron mean free paths are spin dependent. As a result, the collector current is maximized when the moments of the two Co layers are parallel and minimized when the moments are antiparallel. By varying the thickness of the Co layers, Rippard and Buhrman extracted spin-dependent electron attenuation lengths of ∼21 and ∼6 Å for the majority and minority electrons in the energy range of 1–2 eV above the Fermi level.

Similar to BEMM, a modification of BHEM allows for the study of the spin dependence of ballistic hole transport in ferromagnetic base layers. This variation is, not surprisingly, referred to as *ballistic hole magnetic microscopy* (BHMM). Banerjee *et al*. (2005) used BHMM to study hot hole transport in Co single layer films and NiFe/Au/Co trilayers grown on a p-type Si collector. For the single layer Co films, they found that the hot hole attenuation length increases from 6 to 10 Å in the energy range from 0.8 to 2 eV at 150 K. For the NiFe/Au/Co base, the transmission of hot holes is clearly spin dependent. The collector current is about 2.3 times larger when the Co and NiFe moments are aligned parallel compared to antiparallel. This corresponds to a large transmission ratio of ∼4.4 for majority and minority holes. Banerjee *et al*. tentatively attributed this spin asymmetry to the difference in group velocities for the majority and minority holes. Further investigation is necessary to determine the origin of the observed spin dependence. BHMM can also operate in the reverse mode. Haq *et al*. (2005) used reverse BHMM to measure hot hole transport in a NiFe/Au/Co spin-valve base. They observed a large collector current change of ∼2.8 times when the alignment of the Co and NiFe moments is switched from antiparallel to parallel.

Another interesting application of BEEM is to study hot electron transport through insulating tunnel barriers, such as Al_2O_3. Tunnel barriers are a key ingredient for spintronic devices such as magnetic tunnel junctions (MTJs) (Julliere, 1975; Miyazaki and Tezuka, 1995; Moodera *et al*., 1995). Understanding the properties of tunnel barriers is therefore crucial for the development of MTJ-based technologies (Parkin *et al*., 1999, 2003). Rippard, Perrella, and Buhrman (2001) fabricated Au/Cu/Co/Al_2O_3/Co/Cu tunnel structures on Si(111), where the Al_2O_3 layer was formed by oxidation of an ultrathin Al film deposited by evaporation or sputtering. They found that evaporated Al formed a uniform tunnel barrier at a much thinner thicknesses (∼6 Å) than sputtered Al. For even thinner films, a significant variation in BEEM current was observed, indicating a nonuniform or discontinuous barrier. The barrier height, on the other hand, was determined to be ∼1.2 eV, independent of the deposition method, barrier thickness, and oxidation conditions. Kurnosikov *et al*. (2002) studied hot electron transport in Ta/Co/Al_2O_3/Ru tunnel junctions without any auxiliary Schottky barriers. A lock-in technique was used in order to extract the small BEEM current from the large background current of the tunnel junction itself. For very thick barriers (∼40 Å), they obtained a barrier height of ∼1.7 eV.

It is worth mentioning that BEEM can be used to probe the luminescence properties of buried structures if a quantum well light-emitting structure is incorporated into the semiconductor collector. This is called *ballistic electron emission luminescence* (BEEL) (Appelbaum *et al*., 2004).

4 SPIN-VALVE TRANSISTOR AND MAGNETIC TUNNEL TRANSISTOR

The use of an STM tip in BEEM as the electron source places a limitation on possible device applications. Monsma *et al*. (1995) introduced a three-terminal solid-state hot electron device–the spin-valve transistor (Figure 7). Similar to BEEM, the spin-valve transistor has a metal base and a semiconductor collector. But instead of an STM tip, a semiconductor emitter is used to create hot electrons by thermionic emission from the emitter Schottky barrier. These electrons subsequently travel across the base layers and are collected by the collector Schottky barrier. To operate the spin-valve transistor, the emitter Schottky barrier height must be

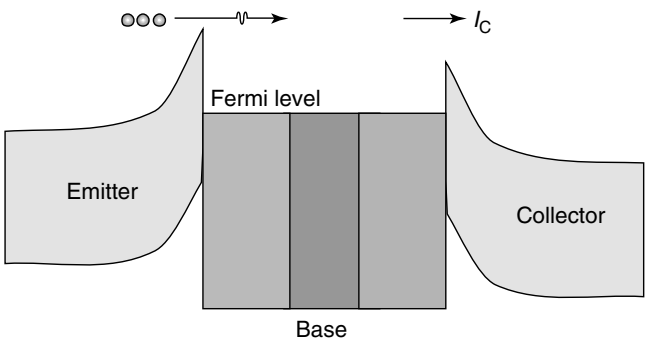

Figure 7. Schematic band diagram of a spin-valve transistor.

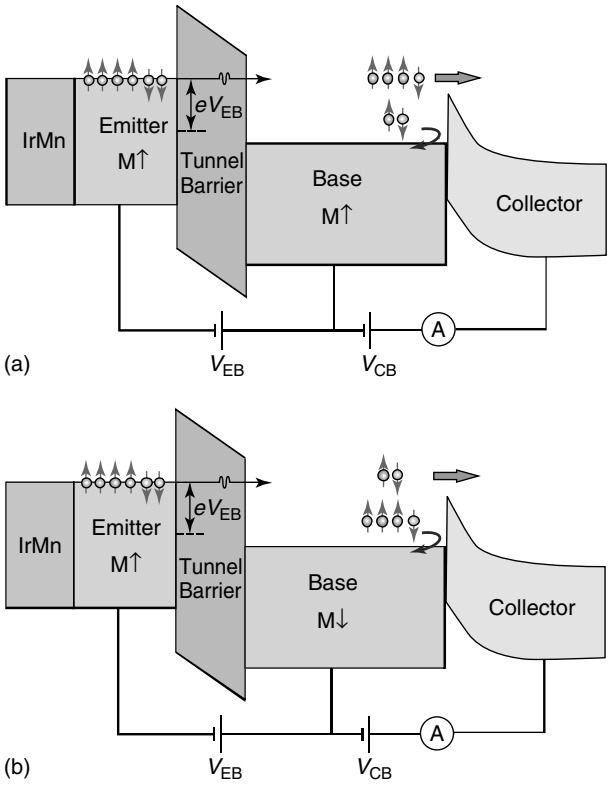

Figure 8. Schematic band diagrams of a magnetic tunnel transistor for a parallel (a) and antiparallel (b) alignment of the emitter and base magnetic moments.

larger than the collector Schottky barrier height. This can be achieved by inserting different metal seed layers at the emitter/base and base/collector interfaces. The base comprises a ferromagnetic-metal/normal-metal/ferromagnetic-metal spin-valve. Thus the magnitude of the collector current can be varied by changing the alignment of the magnetic moments within the spin-valve base. The first room-temperature operation of a spin-valve transistor was realized by Monsma, Vlutters, and Lodder (1998). Spin-dependent hot electron transport in the spin-valve transistor was extensively explored and a very large magnetic field sensitivity was demonstrated at room temperature (Monsma, Vlutters, and Lodder, 1998; Monsma *et al*., (1995); Anil Kumar *et al*., 2000, 2001; Jansen *et al*., 2000, 2001a,b; Vlutters *et al*., 2001, 2002; van 't Erve *et al*., 2002). A detailed review of the spin-valve transistor was given by Jansen (2003).

In the spin-valve transistor, the hot electron energy is determined by the emitter Schottky barrier height. Thus it is not possible to vary the electron energy continuously in one single device. In addition, the difference between the emitter and collector Schottky barrier heights is typically small. Therefore, the collection efficiency of the spin-valve transistor is limited. In order to overcome these problems, a hot electron device called a *magnetic tunnel transistor* was developed (Mizushima *et al*., 1997, 1998; Sato and Mizushima, 2001; van Dijken, Jiang and Parkin, 2002a). One form of the magnetic tunnel transistor consists of a ferromagnetic-metal emitter, a ferromagnetic-metal base, and a semiconductor collector (Figure 8). The emitter and the base are separated by a thin insulating tunnel barrier. A Schottky barrier is formed between the base and the collector with a barrier height Φ_S. Hot electrons are injected from the emitter into the base when an emitter/base bias voltage (V_{EB}) is applied across the tunnel barrier, forming the emitter current (I_E). These electrons traverse the ferromagnetic base layer and are scattered as they do so. The transmitted electrons are subsequently collected in the semiconductor collector but only if their energy remains greater than the Schottky barrier height. Since minority electrons have a short mean free path, they are easily scattered in the base layer. As a result, they lose energy and only a few of them will be collected. In contrast, majority electrons are more likely to maintain their energy due to their large mean free paths. Therefore, more majority electrons will overcome the Schottky barrier and will subsequently be collected. The collector current is very sensitive to the relative alignment of the magnetic moments of the emitter and the base. In the parallel alignment, most of the electrons injected into the base are majority electrons and are scattered less in the base, giving rise to a large collector current (Figure 8a). In the antiparallel alignment, most of the injected electrons are minority electrons and are more heavily scattered, leading to a small collector current (Figure 8b). The switching between the parallel and antiparallel alignment of the magnetic moments can be realized by growing an antiferromagnetic IrMn layer on top of the emitter layer. This IrMn layer is exchange coupled to the emitter and pins the emitter magnetization along a fixed direction. In this case, by applying an appropriate magnetic field, the magnetic moment of the base can be aligned to be either parallel or antiparallel to that of the emitter. The relative change in the collector current when the alignment is switched from antiparallel to parallel can be quantified by the magnetocurrent (MC) parameter, defined as,

$$MC = \frac{I_{C,P} - I_{C,AP}}{I_{C,AP}} \tag{4}$$

where $I_{C,P}$ and $I_{C,AP}$ are the collector current for parallel (P) and antiparallel (AP) alignment of the emitter and base magnetic moments, respectively.

Figure 9(a) shows the collector current as a function of magnetic field at 77 K for a magnetic tunnel transistor with the following structure, GaAs(100)/30-Å $Co_{84}Fe_{16}$/25-Å Al_2O_3/50-Å $Co_{84}Fe_{16}$/300-Å $Ir_{22}Mn_{78}$/50-Å Ta. As the

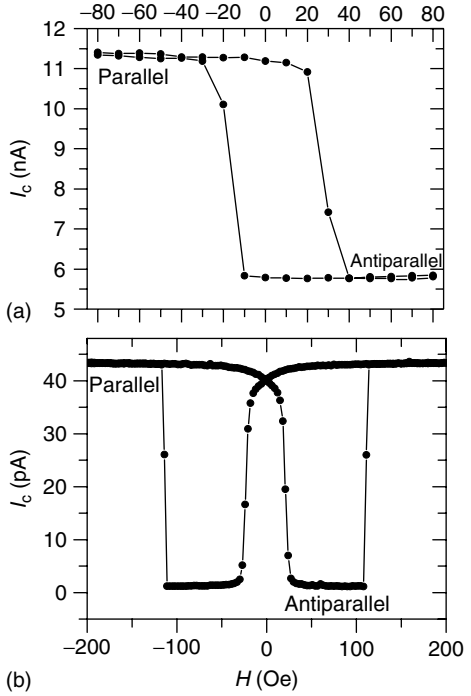

Figure 9. Collector current as a function of the magnetic field for a magnetic tunnel transistor with a single base layer (a) and a spin-valve base (b) at 77 K. The bias voltage is $V_{EB} = 1.0$ V for (a) and 0.8 V for (b).

magnetic field is swept between ± 80 Oe, the base magnetic moment switches at $\sim \pm 20$ Oe, while the emitter magnetic moment remains fixed in the applied field range. At $V_{EB} = 1.0$ V, $I_{C,P}$ ($\sim$11.5 nA) is almost twice as large as $I_{C,AP}$, giving rise to an MC value of 97%.

The moderate MC value in Figure 9(a) is a consequence of the modest tunneling spin polarization of the CoFe/Al_2O_3 emitter, which is typically $\sim$45% (Monsma and Parkin, 2000). Even if spin-filtering in the base is perfect, the maximum MC is of the order of 100%. To enhance the MC effect, a different type of magnetic tunnel transistor was developed using a nonmagnetic metal emitter and a ferromagnetic spin-valve base. In such a device, the initially unpolarized electrons are spin-filtered by the two ferromagnetic layers in the spin-valve base. Much larger MC values can be obtained as spin-filtering can create spin polarization of more than 90% (van Dijken, Jiang and Parkin, 2003a,b). As shown in Figure 9(b), an MC value exceeding 3400% is demonstrated in a magnetic tunnel transistor with the following structure, GaAs(100)/50-Å $Co_{70}Fe_{30}$/40-Å Cu/50-Å $Ni_{81}Fe_{19}$/25-Å Al_2O_3/300-Å Cu. Note that the collector currents shown in Figure 9 are quite small. This is because most of the hot electrons are lost due to scattering in the base and at the base/collector interface. Increasing the hot electron energy can give rise to larger collector currents, up to several microamperes. By optimizing film growth and improving interface properties, the magnitude of the collector current may be further improved (van Dijken, Jiang and Parkin, 2005).

In a simple model ignoring spin-flip processes, the collector current of a magnetic tunnel transistor is carried independently by majority- and minority-spin electrons. The attenuation of hot electron current in each spin channel is described by the corresponding bulk attenuation length and the interface collection efficiency. The collector current for parallel and antiparallel alignments of the emitter and base magnetic moments can be described by the following formula,

$$I_{C,P(AP)} = I_E \frac{1 + P_E}{2} e^{-t/\lambda_{\uparrow(\downarrow)}} \alpha_{C\uparrow(\downarrow)} + I_E \frac{1 - P_E}{2} e^{-t/\lambda_{\downarrow(\uparrow)}} \alpha_{C\downarrow(\uparrow)} \quad (5)$$

where I_E is the tunnel current, P_E is the spin polarization of the electrons injected from the emitter into the base, t is the base layer thickness, $\lambda_{\uparrow(\downarrow)}$ is the attenuation length for the majority (minority) electrons within the ferromagnetic base layer, and $\alpha_{C\uparrow(\downarrow)}$ is the electron collection efficiency at the base/collector interface.

van Dijken, Jiang, and Parkin (2002b) fabricated a series of magnetic tunnel transistors with different CoFe base layer thicknesses and measured the thickness dependence of the collector current for parallel and antiparallel alignments at various emitter/base bias voltages V_{EB} (i.e., hot electron energy). By fitting the data to equation (5), they obtained hot electron attenuation lengths in the energy range of 1–1.9 eV. As shown in Figure 10, the attenuation length of majority electrons is about 5–6 times larger than that of the minority electrons. Moreover, the attenuation length of majority electrons decreases with electron energy, whereas the attenuation length of minority electrons hardly shows any energy dependence. The difference in scattering cross sections for the majority and minority electrons $\Delta\sigma = \sigma_\downarrow - \sigma_\uparrow = 1/\lambda_\uparrow - 1/\lambda_\downarrow$ can be calculated using the attenuation lengths. This result is plotted in the inset of Figure 10 together with some data obtained by Oberli *et al.* for Co thin films at electron energies of $\sim$5–16 eV (Oberli *et al.*, 1998).

The decrease of the attenuation length of majority electrons at elevated energies is due mainly to an enhanced electron–electron scattering rate, which is the most important scattering mechanism for majority electrons (Quinn, 1962; Zarate, Apell and Echenique, 1999; Drouhin, 2001). On the other hand, the minority electrons are subject to more efficient scattering because of the abundant availability of empty minority d band states near the Fermi level and additional scattering mechanisms such as spontaneous spin-wave scattering (Vlutters *et al.*, 2002). As a result, the

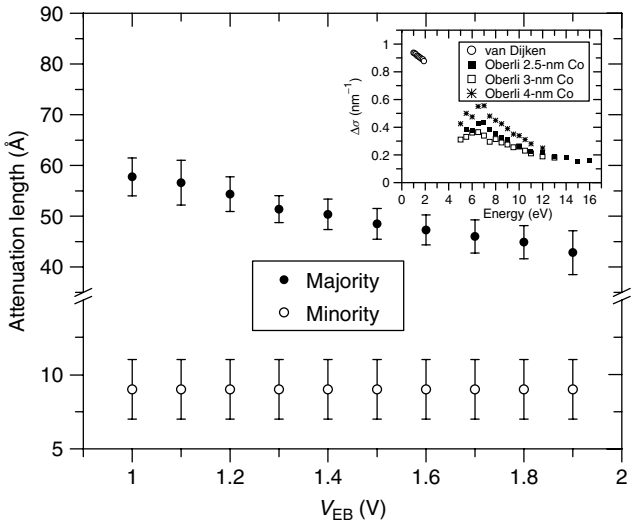

Figure 10. Majority and minority electron attenuation lengths in CoFe thin films as a function of the electron energy (van Dijken, Jiang and Parkin, 2002b). The inset shows the difference in scattering cross sections for majority and minority electrons at electron energy of ∼1–16 eV (Oberli *et al*., 1998; van Dijken, Jiang and Parkin, 2002b).

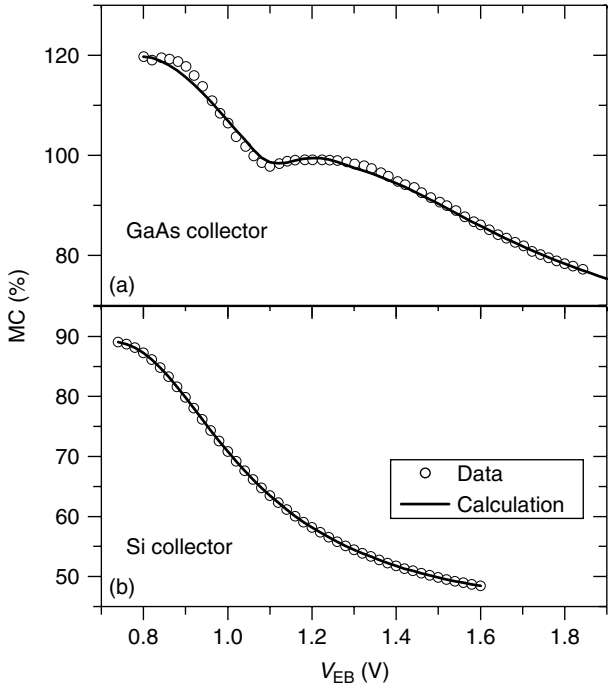

Figure 11. Bias dependence of the MC in magnetic tunnel transistors with a GaAs (a) and Si (b) collector (van Dijken, Jiang and Parkin, 2003c; Jiang *et al*., 2004). The symbols and lines indicate experimental data and model calculation results, respectively.

minority electron attenuation length is much smaller. The large spin asymmetry in the attenuation lengths implies that the hot electron current in the magnetic tunnel transistor, after spin-filtering in the base region, can be highly spin-polarized (van Dijken, Jiang and Parkin, 2002b). Using the attenuation lengths plotted in Figure 10, the spin polarization of the hot electron current at the base/collector interface is more than 95% when the CoFe base layer thickness exceeds ∼35 Å.

The collector current in a magnetic tunnel transistor is determined not only by the electron transmission in the ferromagnetic base layer, but also by the conduction band structure of the semiconductor collector. For example, the bias dependence of the MC is very different for magnetic tunnel transistors with GaAs and Si collectors. This is illustrated in Figure 11, where the MC is measured as a function of V_{EB} for two magnetic tunnel transistors with GaAs and Si collectors (van Dijken, Jiang and Parkin, 2003c; Jiang *et al*., 2004). In the case of a GaAs collector, a pronounced nonmonotonic bias dependence of the MC is observed (Figure 11a). When the bias voltage V_{EB} exceeds the Schottky barrier height (∼0.78 V), a large MC is obtained. The MC decreases with V_{EB} up to ∼1.1 V, then increases slightly, and finally decreases gradually. In contrast, for the magnetic tunnel transistor with a Si collector, the MC decreases continuously as a function of the bias voltage (Figure 11b).

In the magnetic tunnel transistor, the spin-polarized hot electrons that are injected from the emitter into the base initially have very narrow energy distribution because the tunneling process is highly sensitive to the height of the tunnel barrier. Specifically, the electrons are injected with energies close to the emitter Fermi level. As these electrons traverse the base region, they experience inelastic scattering and lose energy. As a consequence, the energy distribution of the hot electrons broadens. Since the scattering rate is normally higher for the minority electrons than for the majority electrons, the minority electrons are more likely to lose energy and thus have a broader energy distribution. Additional electron scattering occurs at the base/collector interface, after which a fraction of the incident electrons are collected by the semiconductor. This interface scattering likely broadens the angular distribution of the hot electrons.

The GaAs conduction band has an energy minimum at the center of the Brillouin zone (Γ valley). At an energy of ∼0.29 eV above the top of the Schottky barrier, there are eight local minima along the ⟨111⟩ axis (L valleys). At even higher energy, ∼0.48 eV above the Schottky barrier height, there are six local minima along the ⟨001⟩ axis (X valleys) (Blakemore, 1982). When the bias voltage exceeds the Schottky barrier height by a small margin, a hot electron current is collected through the central Γ valley. Because of their narrow energy distribution, a relatively large portion of the majority electrons is able to surmount the Schottky barrier and hence contributes to the collector current. On the

other hand, only a small portion of the minority electrons has enough energy to be collected. This large spin asymmetry results in a large MC. At elevated emitter/base bias voltages, increasingly more of the scattered minority electrons are able to surmount the Schottky barrier. The increase of the minority electron current gives rise to a smaller MC. If all the collector conduction bands open up at the same energy level, a monotonic decrease of the MC with bias is expected, as observed in the magnetic tunnel transistor with a Si collector. However, for GaAs, the L and the X valleys open up at higher energies than the Γ valley. When these valleys just become available for hot electron injection, they favor the collection of the majority electrons and thus tend to increase the MC. This leads to the observed nonmonotonic bias dependence of the MC when the collector is GaAs. An implication in this argument is that the hot electrons at the base/collector interface have a broad angular distribution, thus allowing them to access the L valleys in GaAs with large transverse momentum components. This can be justified by strong electron scattering at the base/collector interface (Smith, Lee and Narayanamurti, 1998; van Dijken, Jiang and Parkin, 2002b, 2003; Jiang *et al*., 2004). The calculated results based on this model are shown as lines in Figure 11. An excellent agreement is obtained between the experiments and calculations.

5 HOT ELECTRON SPIN INJECTION

The development of modern-day electronics has followed Moore's law for several decades, in which the channel length of a silicon MOSFET is halved about every 18–24 months, allowing for a doubling of the number of transistors (Moore, 1965). However, as the transistor size continues to shrink towards fundamental physical limits, there is an increasing interest in exploring alternate technologies to both silicon and purely charged based devices. Spintronics is a particularly promising technology, where the spin states of carriers are utilized as an additional degree of freedom for improved information processing and data storage (Zutic, Fabian and Sarma, 2004). The electron's spin has already played an important role in magnetoelectronic devices, such as the spin valve and the magnetic tunnel junction. The discovery of the giant magnetoresistance and the tunneling magnetoresistance effects has had a profound impact on the magnetic recording industry (Julliere, 1975; Miyazaki and Tezuka, 1995; Moodera *et al*., 1995; Parkin *et al*., 1999, 2003; Baibich *et al*., 1988; Binasch *et al*., 1989; Parkin, More and Roche, 1990; Parkin, Bhadra and Roche, 1991). In semiconductor electronics, however, the role of spins is rather passive. It is interesting to note that semiconductors have many desirable properties as far as spins are concerned. In particular, the electron

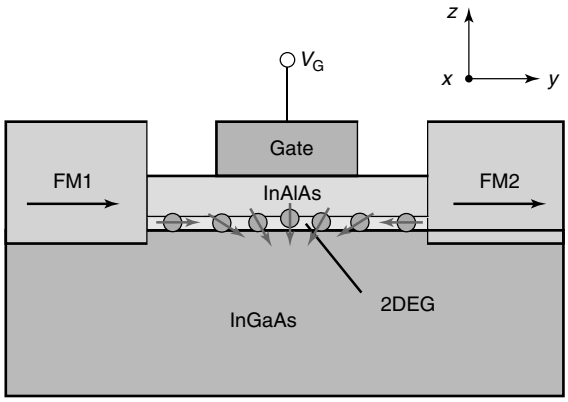

Figure 12. Schematic drawing of the Datta–Das transistor. FM1 and FM2 are two ferromagnetic contacts to the 2DEG.

spin relaxation time in semiconductors can be several orders of magnitude longer than the electron momentum and energy relaxation times (Kikkawa and Awschalom, 1998). Using an electric field, electrons in GaAs can be dragged over a distance of 100 μm without losing their spin coherence (Kikkawa and Awschalom, 1999). In addition to the long spin lifetimes and large spin diffusion lengths, semiconductors offer the flexibility of electrically controlled variable carrier doping densities and profiles and spin relaxation rates, which could be useful for building interesting spintronic devices. For example, Ohno *et al*. (2000) showed that it is possible to control the ferromagnetism of InMnAs thin films by modulating the hole concentration. Sandhu *et al*. (2001) and Karimov *et al*. (2003) demonstrated that the electron spin relaxation rates in GaAs heterostructures can be varied by applying a gate voltage. Murakami *et al*. predicted that a dissipationless spin current flows in GaAs in the presence of an electric field (Murakami, Nagaosa and Zhang, 2003). These studies suggest that spin-based semiconductor electronics has the potential to develop an entirely new generation of devices with high speed, high density, low power consumption, and nonvolatility (Wolf *et al*., 2001).

One of the first semiconductor spintronic devices was proposed by Datta and Das (1990) (Figure 12) and is often referred to as the Datta–Das 'transistor'. This device is comprised of two ferromagnetic contacts placed on top of a semiconductor two-dimensional electron gas (2DEG) formed at an InAlAs/InGaAs interface. The two ferromagnetic contacts serve as the injector and detector of spin-polarized electrons, respectively. The 2DEG forms a channel for electron transport between the contacts. Owing to the Rashba effect (Rashba, 1960; Bychkov and Rashba, 1984), the mobile electrons in the 2DEG sense an effective magnetic field and precess around this field. The strength of the magnetic field can be controlled by applying a gate voltage across the 2DEG (Nitta *et al*., 1997). Therefore, it is possible to modulate the

electron spin precession inside the 2DEG and, consequently, the magnitude of the current. Although simple in concept, the Datta–Das transistor contains all the essential components of a semiconductor spintronic device, the creation, transport, manipulation, and detection of spin-polarized electrons, by electrical means. The first step, the creation of spin-polarized electrons inside semiconductors, can be realized by electrical spin injection. It is a prerequisite for semiconductor spintronics.

It has long been known that spin-polarized electrons can be generated in direct band gap semiconductors by optical pumping with circularly polarized light (Meier and Zakharchenya, 1984). For device applications, however, electrical means of spin injection is more desirable. The first attempts at electrical spin injection were carried out using Ohmic contacts formed by ferromagnetic metals (Monzon and Roukes, 1999; Gardelis *et al*., 1999; Filip *et al*., 2000). Since the electrons in the ferromagnetic metals are spin-polarized, it was expected that the electrons injected into the semiconductors would maintain their spin orientation and thus give rise to successful spin injection. Despite significant effort, however, unambiguous spin injection was not demonstrated. Later on, it was realized that the conductivity mismatch between the metal and the semiconductor might present a fundamental obstacle to spin injection (Schmidt *et al*., 2000). The conductivity mismatch can be understood in a simple picture, as shown in Figure 13. In the spin injection experiment, the resistance of the device can be divided into a spin-independent part $R_0^{\uparrow} = R_0^{\downarrow}$ and a spin-dependent part $R_S^{\uparrow} \neq R_S^{\downarrow}$, where the up (down) arrow represents the majority (minority) electron channel. The semiconductor resistance is normally spin independent, whilst the ferromagnet/semiconductor contact resistance is spin dependent. When an Ohmic contact is used, $R_S^{\uparrow,\downarrow}$ is much smaller than $R_0^{\uparrow,\downarrow}$. Therefore, the electron transport is dominated by the spin-independent semiconductor resistance. As a result, the electron current is not polarized. In order to achieve efficient spin injection, the spin-dependent conductivity needs to be smaller than its spin-independent counterpart. Note that Figure 13 is a rather simplistic picture of the conductivity mismatch problem. A more detailed treatment of this subject was given by Schmidt *et al*. (2000).

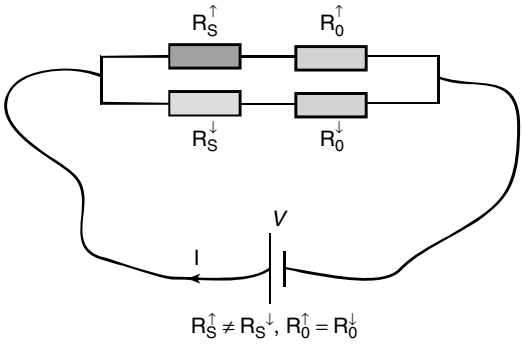

Figure 13. A simplistic picture to illustrate the conductivity mismatch problem in spin injection experiments.

The first evidence of electrical spin injection was reported by Hammar *et al*. (1999). They used NiFe contacts to inject electrons into an InAs 2DEG, with a thick AlGaSb insulating barrier inserted between the NiFe and the 2DEG. Owing to the Rashba effect, the spin degeneracy of the electron density of states in the 2DEG is lifted. As a result, electron transport in the 2DEG channel is spin dependent. When the magnetization of the NiFe contacts is varied by a magnetic field, the resistance of the device is expected to change (Johnson, 1998). Indeed, Hammar *et al*. observed a resistance change of $\sim$0.9%. This observation, although a small effect, was an encouraging step towards spin injection. Hu *et al*. (2001) also reported spin injection from NiFe into an InAs 2DEG, with a smaller resistance change of $\sim$0.2%.

Much larger spin injection effects were obtained using diluted magnetic semiconductors whose conductivity matches that of normal semiconductors. The use of magnetic semiconductors was proposed by Oestreich *et al*. (1999). Using time-resolved photoluminescence, they showed that the magnetic semiconductor $Cd_{0.98}Mn_{0.02}Te$ could serve as a very good spin aligner in a magnetic field of 2.5 T. Moreover, the spin-polarized electrons generated in the $Cd_{0.98}Mn_{0.02}Te$ layer could be efficiently transported into an adjacent CdTe layer. Shortly afterwards, Fiederling *et al*. (1999), Ohno *et al*. (1999), and Jonker *et al*. (2000) demonstrated electrical spin injection using BeMnZnSe, GaMnAs, and ZnMnSe spin injectors, respectively. In these experiments, a quantum well light emitting diode (LED) was used as an optical detector to measure the spin polarization of the injected electrons (Figure 14). The injected electrons recombine with

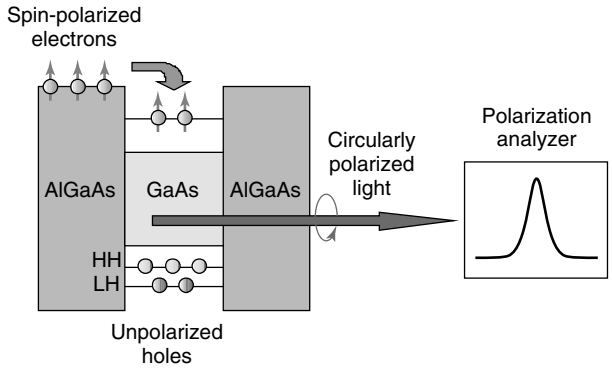

Figure 14. Schematic drawing of a quantum well LED detector used for measuring the spin polarization of injected electrons. HH and LH represent the heavy and light holes in the quantum well, respectively.

holes inside the quantum well and emit light. The degree of circular polarization of the emitted light is correlated to the spin polarization of the electrons prior to recombination through optical selection rules (Meier and Zakharchenya, 1984). Therefore, the spin polarization can be inferred from the luminescence polarization. Very large spin polarizations of more than 80% were reported for magnetic semiconductor injectors (Jonker *et al*., 2001). Such a high spin polarization is very desirable for spintronic applications. However, magnetic semiconductors have limitations. These materials, to date, only possess the desired magnetic properties at temperatures well below room temperature and/or in a large magnetic field, thereby limiting their usefulness.

Ferromagnetic 3d transition metals have Curie temperatures much higher than room temperature, making them attractive for spin injection into semiconductors. However, care must be taken to overcome the conductivity mismatch between the metal and the semiconductor. Rashba pointed out that the mismatch problem can be resolved if the ferromagnetic metal forms a tunnel contact with the semiconductor since the tunneling process is spin dependent and tunnel contacts can have a high impedance (Rashba, 2000). This predication was confirmed by Zhu *et al*. (2001). Using a Fe/GaAs Schottky tunnel contact, they observed a spin polarization of ∼2% in GaAs/InGaAs quantum wells. Following the same route, higher spin polarizations were reported by the Jonker group at the Naval Research Laboratory (Hanbicki *et al*., 2002, 2003) and the Crowell and Palmstrøm groups at the University of Minnesota (Adelmann *et al*., 2005), reaching ∼30% at low temperatures. Crooker *et al*. used a magneto-optical Kerr technique to directly image electrical spin injection and accumulation in a lateral GaAs device with Fe Schottky contacts (Crooker *et al*., 2005). Electrical detection of spin injection and accumulation was recently demonstrated by Lou *et al*. (2006, 2007) who show that the nonequilibrium spin population in the semiconductor gives rise to a measurable voltage signal. Moreover, they show that the suppression of the voltage signal by a small transverse magnetic field is consistent with spin precession and dephasing induced by the magnetic field.

Besides Schottky tunnel contacts, oxide tunnel barriers were also utilized for spin injection. Manago and Akinaga utilized ferromagnetic metals in conjunction with Al_2O_3 tunnel barriers as the spin injector and observed a signal of ∼1% at room temperature (Manago and Akinaga, 2002). van 't Erve *et al*. (2004) fabricated Fe/Al_2O_3 tunnel injectors and measured a spin polarization of 40% at 5 K. Motsnyi *et al*. (2002, 2003) and Van Dorpe *et al*. (2003) used the oblique Hanle effect (Meier and Zakharchenya, 1984) to investigate spin injection from a ferromagnetic-metal/Al_2O_3-tunnel-barrier injector into a GaAs LED. They applied a magnetic field at an angle to the ferromagnetic-metal film plane and measured the circular polarization of the light emitted from the LED. Motsnyi *et al*. (2003) obtained a light polarization of ∼4% at 80 K and ∼1% at room temperature. By model fitting, they concluded that the actual spin injection efficiency is about 21 and 16%, respectively.

When a Schottky or Al_2O_3 tunnel contact is used for spin injection, the maximum spin polarization that can be achieved may be limited by the tunneling spin polarization of the ferromagnetic metal. For instance, for 3d ferromagnetic metals and their alloys, the tunneling spin polarization is normally no more than 50% when an Al_2O_3 tunnel barrier is used (Monsma and Parkin, 2000). To overcome this limit, two approaches can be adopted for spin injection of highly spin-polarized electrons. One is to take advantage of the spin-filtering effect of hot electrons in ferromagnetic metals to obtain high spin polarization. The other is to develop new materials which give rise to high tunneling spin polarization. These two approaches will be discussed below.

In the previous section, it has been shown that the spin polarization of the hot electron current in a magnetic tunnel transistor can be as high as 95% at the base/collector interface due to efficient spin-filtering in the base. Moreover, the presence of a tunnel barrier in the magnetic tunnel transistor solves the conductivity mismatch problem. Because of these properties the magnetic tunnel transistor holds promise as a highly efficient spin injector. To detect the injected electron spin polarization, a quantum well LED structure is incorporated into the collector of the magnetic tunnel transistor. In this scheme, the injected electrons recombine with unpolarized holes from the substrate in the quantum well and emit light. By analyzing the circular polarization of the light, the spin polarization of the electrons can be determined using the optical selection rules (Meier and Zakharchenya, 1984). As shown in Figure 15, there are two types of holes in the quantum well, the heavy holes (HHs) and the light holes (LHs). They both can recombine with the electrons and emit photons with opposite helicity. In general, careful analysis of these data must be made in order to properly extract the electron's spin polarization from the luminescence spectra. However, in the quantum well, the energy degeneracy of the heavy and light hole states is lifted due to confinement and/or strain effects. If the energy splitting between the two hole states (ΔE) is larger than the spectral resolution, it is possible to measure the circular polarization of the HH emission only. In this case, the luminescence polarization is simply equal to the electron spin polarization. Note that the selection rules in Figure 15 are only valid in the Faraday geometry, that is, with the spin

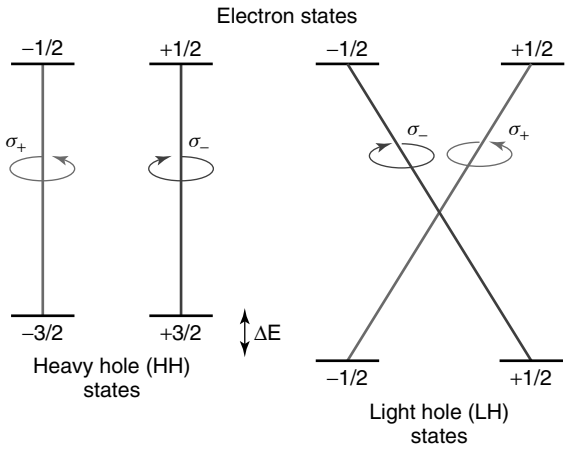

Figure 15. Optical selection rules for electron–hole recombination in the Faraday geometry.

and light propagation directions both perpendicular to the quantum well plane. Experimentally, this requires the use of a large magnetic field to rotate the electron spin moment out of the film plane.

In the spin injection experiment, the quantum well detector is buried inside the semiconductor heterostructure. The injected electrons are first transported into the quantum well region, where they spend a certain amount of time (described by the recombination time) before recombining with the holes and emitting light. The measured electroluminescence (EL) polarization does not take into account any spin relaxation effects prior to recombination and, therefore, sets a lower bound on the spin polarization of the injected electrons. To properly interpret the experimental data, it is necessary to take into account various spin relaxation processes in the semiconductor. Three spin relaxation mechanisms are known to be particularly important, the Elliott–Yafet (EY), D'yakonov–Perel' (DP), and Bir–Aronov–Pikus (BAP) mechanisms. The EY process derives from the mixing of electron wave functions of opposite spin states due to spin-orbit coupling (Elliott, 1954; Yafet, 1963). As a result, electron momentum scattering leads to spin relaxation, with a rate proportional to the momentum scattering rate. The DP process is present in semiconductors without inversion symmetry (D'yakonov and Perel', 1971; D'yakonov and Kachorovskii, 1986). The mobile electrons see an effective magnetic field whose magnitude and orientation depend on the electron momentum. Spin precession around this magnetic field gives rise to spin relaxation. Momentum scattering randomizes the direction of the effective magnetic field and reduces the average precession effect. The DP spin relaxation rate is therefore inversely proportional to the momentum scattering rate, which is opposite to the EY process. The BAP process is due to electron–hole exchange and annihilation interactions (Bir, Aronov and Pikus, 1976). The relative importance of the three processes depends on the details of the sample structure and the experimental conditions, such as the semiconductor doping profile, experiment temperature, and so on.

Jiang *et al*. (2003) conducted spin injection experiments at 1.4 K using a magnetic tunnel transistor as the spin injector. The emitter of the magnetic tunnel transistor was made up of 50-Å CoFe. The base consisted of 35-Å NiFe and 15-Å CoFe with the NiFe layer adjacent to the collector. The tunnel barrier was Al_2O_3 with a thickness of ∼22 Å. Three GaAs/$In_{0.2}Ga_{0.8}$As quantum wells were incorporated in the collector as the optical detector. Figure 16 shows the EL spectra at a hot electron energy of ∼2 eV, where the thin and thick lines represent the left ($\sigma+$) and right ($\sigma-$) hand circular polarization components, respectively. Note that the width of the luminescence peaks is only ∼25 Å, which is limited by the spectrometer resolution for the given signal level. According to absorption studies, the separation in wavelengths between the HH and LH emissions is ∼400 Å in these GaAs/$In_{0.2}Ga_{0.8}$As quantum wells. Therefore, the narrow luminescence linewidth enables the unambiguous detection of recombination between electrons and HHs. As mentioned before, in this case the circular polarization of the EL is equal to the spin polarization of the electrons just before recombination.

The EL in Figure 16 clearly depends on the magnetic field. At zero field, the intensities of the $\sigma+$ (I^+) and $\sigma-$ (I^-) components are equal. At high fields, there is a significant difference between I^+ and I^-. Here, the intensities are calculated by integrating the areas under the peaks. The EL polarization is defined as,

$$P_{\mathrm{EL}} = \frac{I^+ - I^-}{I^+ + I^-} \tag{6}$$

P_{EL} is ∼13% at 2.5 T and ∼ − 13% at −2.5 T. The sign of P_{EL} indicates injection of majority electron spins into the quantum wells. This result is consistent with the sign of the collector current polarization observed in electrical transport measurements in magnetic tunnel transistors. Excitons in $In_{0.2}Ga_{0.8}$As have a large g factor, leading to a large Zeeman splitting energy in the quantum wells, which is shown by the shift of the EL peak center positions for $\sigma+$ and $\sigma-$ components at high fields.

The relatively small collector current of the magnetic tunnel transistor requires the device to operate at high electron energy in order to obtain enough signal in the spin injection experiments. Electron spin relaxation, however, is very efficient at high energy (Meier and Zakharchenya, 1984; Krishnamurthy, van Schilfgaarde and Newman, 2003), leading to a moderate EL polarization of the order of ∼10%. To

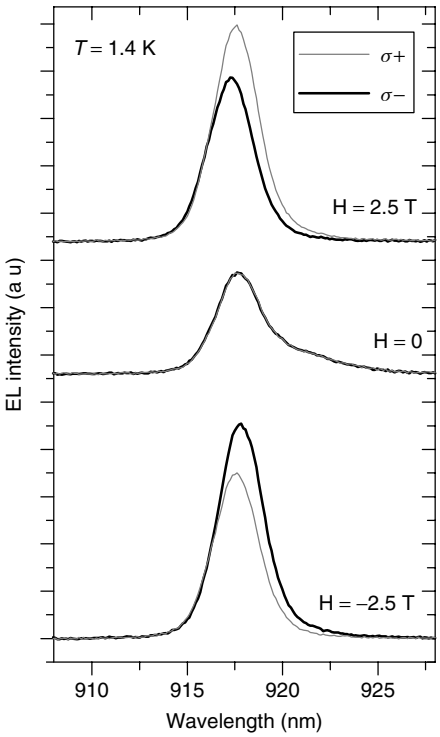

Figure 16. Electroluminescence spectra measured in magnetic fields of 0 and ±2.5 T at 1.4 K for a magnetic tunnel transistor spin injector. The thin and thick lines represent the $\sigma+$ and $\sigma-$ circular polarization components, respectively. (Jiang *et al*., 2003.)

increase the electron current at lower energy while maintaining a high spin polarization, crystalline CoFe/MgO tunnel injectors have been used. The tunneling spin polarization of a CoFe/MgO(100) structure was predicted to be very high using first principle calculation (Butler *et al*., 2001; Mathon and Umerski, 2001; Zhang and Butler, 2004). Experimentally, tunneling spin polarization as high as 85% was reported by Parkin *et al*. (2004). Therefore, a CoFe/MgO tunnel injector is capable of injecting highly spin-polarized electrons into semiconductors.

Successful spin injection using a CoFe/MgO tunnel injector was demonstrated for the first time by Jiang *et al*. (2005). In their experiment, the injector consists of 50-Å $Co_{70}Fe_{30}$ and 30-Å MgO capped with 100-Å Ta, and the detector contains a GaAs/AlGaAs quantum well light-emitting diode. A large electroluminescence polarization of ∼47% was observed at room temperature in a magnetic field of 5 T, as shown in Figure 17. A nonmonotonic temperature dependence of the EL polarization was observed, which was related to the temperature dependence of spin relaxation rate and electron recombination time in the quantum well detector. In spin injection experiments, the measured luminescence polarization P in a steady state is given by (Meier and

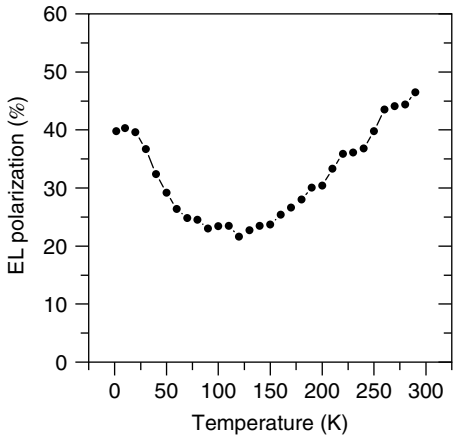

Figure 17. Temperature dependence of the electroluminescence polarization at 5 T for a CoFe/MgO tunnel spin injector (Jiang *et al*., 2005).

Zakharchenya, 1984),

$$P = \frac{\tau_S}{\tau_S + \tau_R} P_0 \tag{7}$$

where P_0 is the initial spin polarization of the electrons injected into the quantum well, τ_S and τ_R are the spin and electron lifetimes, respectively. Both τ_S and τ_R vary with temperature and contribute to the temperature dependence of the luminescence polarization (Meier and Zakharchenya, 1984; Krishnamurthy, van Schilfgaarde and Newman, 2003; Ohno *et al*., 1999; Malinowski *et al*., 2000; Lau, Olesberg and Flatté, 2001; Puller *et al*., 2003; Feldmann *et al*., 1987; Gurioli *et al*., 1991; Tignon *et al*., 1998; Fernández-Alonso *et al*., 2003). Salis *et al*. (2005) measured τ_S and τ_R in GaAs/AlGaAs quantum well detectors using a spin-resolved Kerr technique. They found that the observed dip in the luminescence polarization was largely due to a maximum electron lifetime at intermediate temperatures. On the basis of these measurements, Salis *et al*. suggested that the initial spin polarization of the injected electrons was ∼70%, independent of temperature.

The observation of efficient spin injection at room temperature using a CoFe/MgO tunnel injector is consistent with the high Curie temperature of CoFe and the weak temperature dependence of spin-dependent tunneling. The actual spin injection efficiency is higher than that inferred from the polarization of the quantum well EL because of spin relaxation in the quantum well detector. The MgO-based spin injector can readily be fabricated by sputter deposition. In addition, the MgO barrier prevents intermixing of the ferromagnetic metal and the semiconductor, leading to improved thermal stability (Wang *et al*., 2005). These desirable features make MgO-based tunnel spin injectors attractive for future semiconductor spintronic applications.

6 CONCLUSION

A great deal of progress has been made in the field of hot electron spintronic physics over the decade. These materials and devices are particularly interesting for the study of the physics of the spin-dependent scattering properties of electrons with energies just above the Fermi energy, an energy range which is difficult to access by other techniques. Moreover, spin-based hot electron devices have promise for semiconductor-based spintronic devices, particularly for the purpose of the injection of highly spin-polarized current into semiconductors.

ACKNOWLEDGMENTS

We thank Roger Wang, Robert Shelby, Roger Macfarlane, Gian Salis, Seth Bank, Glenn Solomon, and James Harris for useful discussions.

REFERENCES

Adelmann, C., Lou, X., Strand, J., *et al*. (2005). Spin injection and relaxation in ferromagnet-semiconductor heterostructures. *Physical Review B*, **71**, R121301.

Aeschlimann, M., Bauer, M., Pawlik, S., *et al*. (1997). Ultrafast spin-dependent electron dynamics in fcc co. *Physical Review Letters*, **79**, 5158.

Anil Kumar, P.S., Jansen, R., van 't Erve, O.M.J., *et al*. (2000). Low-field magnetocurrent above 200% in a spin-valve transistor at room temperature. *Journal of Magnetism and Magnetic Materials*, **214**, L1.

Anil Kumar, P.S., Jansen, R., van 't Erve, O.M.J., *et al*. (2001). 300% magnetocurrent in a room temperature operating spin-valve transistor. *Physica C*, **350**, 166–170.

Appelbaum, I., Russell, K.J., Kozhevnikov, M., *et al*. (2004). Room-temperature ballistic electron emission luminescence spectroscopy with a scanning tunneling microscope. *Applied Physics Letters*, **84**, 547.

Back, C.H., Allenspach, R., Weber, W., *et al*. (1999). Minimum field strength in precessional magnetization reversal. *Science*, **285**, 864.

Back, C.H., Weller, D., Heidmann, J., *et al*. (1998). Magnetization reversal in ultrashort magnetic field pulses. *Physical Review Letters*, **81**, 3251.

Baibich, M.N., Broto, J.M., Fert, A., *et al*. (1988). Giant magnetoresistance of (001)Fe/(001)Cr magnetic superlattices. *Physical Review Letters*, **61**, 2472.

Banerjee, T., Haq, E., Siekman, M.H., *et al*. (2005). Spin filtering of hot holes in a metallic ferromagnet. *Physical Review Letters*, **94**, 027204.

Bell, L.D. (1996). Evidence of momentum conservation at a nonepitaxial metal/semiconductor interface using ballistic electron emission microscopy. *Physical Review Letters*, **77**, 3893.

Bell, L.D., Hecht, M.H., Kaiser, W.J., *et al*. (1990). Direct spectroscopy of electron and hole scattering. *Physical Review Letters*, **64**, 2679.

Bell, L.D. and Kaiser, W.J. (1988). Observation of interface band structure by ballistic-electron-emission microscopy. *Physical Review Letters*, **61**, 2368.

Binasch, G., Grünberg, P., Saurenbach, F., *et al*. (1989). Enhanced magnetoresistance in layered magnetic structures with antiferromagnetic interlayer exchange. *Physical Review B*, **39**, 4828.

Bir, G.L., Aronov, A.G. and Pikus, G.E. (1976). Spin relaxation of electrons due to scattering by holes. *Soviet Physics JETP*, **42**, 705.

Blakemore, J.S. (1982). Semiconducting and other major properties of gallium arsenide. *Journal of Applied Physics*, **53**, R123.

Butler, W.H., Zhang, X-G., Schulthess, T.C., *et al*. (2001). Spin-dependent tunneling conductance of Fe|MgO|Fe sandwiches. *Physical Review B*, **63**, 054416.

Bychkov, Y.A. and Rashba, E.I. (1984). Properties of a 2D electron gas with lifted spectral degeneracy. *JETP Letters*, **39**, 78.

Crooker, S.A., Furis, M., Lou, X., *et al*. (2005). Imaging spin transport in lateral ferromagnet/semiconductor structures. *Science*, **309**, 2191.

Datta, S. and Das, B. (1990). Electronic analog of the electro-optic modulator. *Applied Physics Letters*, **56**, 665.

Drouhin, H-J. (2001). Spin-dependent scattering in transistion metals. *Journal of Applied Physics*, **89**, 6805.

Drouhin, H-J., van der Sluijs, A.J., Lassailly, Y., *et al*. (1996). Spin-dependent transmission of free electrons through ultrthin cobalt layers (invited). *Journal of Applied Physics*, **79**, 4734.

D'yakonov, M.I. and Kachorovskii, VY. (1986). Spin relaxation of two-dimensional eelctrons in noncentrosymmetric semiconductors. *Soviet Physics Semiconductors*, **20**, 110.

D'yakonov, M.I. and Perel', VI. (1971). Spin orientation of electrons associated with the interband absorption of light in semiconductors. *Soviet Physics JETP*, **33**, 1053.

Elliott, R.J. (1954). Theory of the effect of spin-orbit coupling on magnetic resonance in some semiconductors. *Physical Reviews*, **96**, 266.

Feldmann, J., Peter, G., E.O., Göbel, *et al*. (1987). Linewidth dependence of radiative exciton lifetimes in quantum wells. *Physical Review Letters*, **59**, 2337.

Fernández-Alonso, F., Righini, M., Franco, A., *et al*. (2003). Time-resolved differential reflectivity as a probe of on-resonance exciton dynamics in quantum wells. *Physical Review B*, **67**, 165328.

Fiederling, R., Keim, M., Reuscher, G., *et al*. (1999). Injection and detection of a spin-polarized current in a light-emitting diode. *Nature*, **402**, 787.

Filip, A.T., Hoving, B.H., Jedema, F.J., *et al*. (2000). Experimental search for the electrical spin injection in a semiconductor. *Physical Review B*, **62**, 9996.

Garcia-Vidal, F.J., de Andres P.L. and Flores, F. (1996). Elastic scattering and the lateral resolution of ballistic electron emission

microscopy: focusing effects on the Au/Si interface. *Physical Review Letters*, **76**, 807.

Gardelis, S., Smith, C.G., Barnes, C.H.W., *et al*. (1999). Spin-valve effects in a semiconductor field-effect transistor: A spintronic device. *Physical Review B*, **60**, 7764.

Getzlaff, M., Bansmann, J., and Schönhense, G. (1993). Spin-polarization effects for electrons passing through thin iron and cobalt films. *Solid State Communications*, **87**, 467.

Gröbli, J.C., Guarisco, D., Frank, S., *et al*. (1995). Spin-dependent transmission of polarized electrons through a ferromagnetic iron film. *Physical Review B*, **51**, 2945.

Gröbli, J.C., Kündig, A., Meier, F., *et al*. (1995). Positive spin polarization of the photoelectrons emitted near photothreshold from cesiated Co (0001). *Physica B*, **204**, 359.

Gröbli, J.C., Oberli, D. and Meier, F. (1995). Crucial tests of spin filtering. *Physical Review B*, **52**, R13095.

Gurioli, M., Vinattieri, A., Colocci, M., *et al*. (1991). Temperature dependence of the radiative and nonradiative recombination time in GaAs/$Al_xGa_{1-x}As$ quantum-well structures. *Physical Review B*, **44**, 3115.

Guthrie, D.K., Harrell, L.E., Henderson, G.N., *et al*. (1996). Ballistic-electron-emission spectroscopy of Au/Si and Au/GaAs interfaces: Low-temperature measurements and ballistic models. *Physical Review B*, **54**, 16972.

Hammar, P.R., Bennett, B.R., Yang, M.J., *et al*. (1999). Observation of spin injection at a ferromagnet-semiconductor interface. *Physical Review Letters*, **83**, 203.

Hanbicki, A.T., Jonker, B.T., Itskos, G., *et al*. (2002). Efficient electrical spin injection from a magnetic metal/tunnel barrier contact into a semiconductor. *Applied Physics Letters*, **80**, 1240.

Hanbicki, A.T., van 't Erve, O.M.J., Magno, R., *et al*. (2003). Analysis of the transport process providing spin injection through an Fe/AlGaAs Schottky barrier. *Applied Physics Letters*, **82**, 4092.

Haq, E., Banerjee, T., Siekman, M.H., *et al*. (2005). Ballistic hole magnetic microscopy. *Applied Physics Letters*, **86**, 082502.

Hecht, M.H., Bell, L.D., Kaiser, W.J., *et al*. (1990). Ballistic-hole spectroscopy of interfaces. *Physical Review B*, **42**, 7663.

Hu, C.-M., Nitta, J., Jensen, A., *et al*. (2001). Spin-polarized transport in a two-dimensional electron gas with interdigital-ferromagnetic contacts. *Physical Review B*, **63**, 125333.

Jansen, R. (2003). The spin-valve transistor: a review and outlook. *Journal of Physics D: Applied Physics*, **36**, R289.

Jansen, R., Anil Kumar, P.S., van't Erve, O.M.J., *et al*. (2000). Thermal spin-wave scattering in hot-electron magnetotransport across a spin valve. *Physical Review Letters*, **85**, 3277.

Jansen, R., Kim, S.D., Vlutters, R., *et al*. (2001a). Anisotropic spin-orbit scattering of hot-electron spins injected into ferromagnetic thin-films. *Physical Review Letters*, **87**, 166601.

Jansen, R., van 't Erve, O.M.J., Kim, S.D., *et al*. (2001b). The spin-valve transistor: Fabrication, characterization, and physics (invited). *Journal of Applied Physics*, **89**, 7431.

Jiang, X., van Dijken, S., Wang, R., *et al*. (2004). Bias voltage dependence of magnetocurrent in magnetic tunnel transistors. *Physical Review B*, **69**, 014413.

Jiang, X., Wang, R., Shelby, R.M., *et al*. (2005). Highly spin-polarized room-temperature tunnel injector for semiconductor spintronics using MgO(100). *Physical Review Letters*, **94**, 056601.

Jiang, X., Wang, R., van Dijken, S., *et al*. (2003). Optical detection of hot-electron spin injection into GaAs from a magnetic tunnel transistor. *Physical Review Letters*, **90**, 256603.

Johnson, M. (1998). Theory of spin-dependent transport in ferromagnet-semiconductor heterostructures. *Physical Review B*, **58**, 9635.

Jonker, B.T., Hanbicki, A.T., Park, Y.D., *et al*. (2001). Quantifying electrical spin injection: Component-resolved electroluminescence from spin-polarized light-emitting diodes. *Applied Physics Letters*, **79**, 3098.

Jonker, B.T., Park, Y.D., Bennett, B.R., *et al*. (2000). Robust electrical spin injection into a semiconductor heterostructure. *Physical Review B*, **62**, 8180.

Julliere, M. (1975). Tunneling between ferromagnetic films. *Physics Letters*, **54A**, 225.

Kaiser, W.J. and Bell, L.D. (1988). Direct investigation of subsurface interface electronic structure by ballistic-electron-emission microscopy. *Physical Review Letters*, **60**, 1406.

Karimov, O.Z., John, G.H., Harley, R.T., *et al*. (2003). High temperature gate control of quantum well spin memory. *Physical Review Letters*, **91**, 246601.

Kikkawa, J.M., Awschalom, D.D. (1998). Resonant spin amplification in n-type GaAs. *Physical Review Letters*, **80**, 4313.

Kikkawa, J.M., Awschalom, D.D. (1999). Lateral drag of spin coherence in gallium arsenide. *Nature (London)*, **397**, 139.

Knorren, R., Bennemann, K.H., Burgermeister, R., *et al*. (2000). Dynamics of excited electrons in copper and ferromagnetic transition metals: Theory and experiment. *Physical Review B*, **61**, 9427.

Krishnamurthy, S., van Schilfgaarde, M. and Newman, N. (2003). Spin lifetimes of electrons injected into GaAs and GaN. *Applied Physics Letters*, **83**, 1761.

Kurnosikov, O., de Jong, J.E.A., Swagten, H.J.M., *et al*. (2002). Direct observation of local hot electron transport through Al_2O_3 tunnel junctions. *Applied Physics Letters*, **80**, 1076.

Lassailly, Y., Drouhin, H-J., van der Sluijs, A.J., *et al*. (1994). Spin-dependent transmission of low-energy electrons through ultrathin magnetic layers. *Physical Review B*, **50**, 13054.

Lau, W.H., Olesberg, J.T. and Flatté, M.E. (2001). Electron-spin decoherence in bulk and quantum-well zinc-blende semiconductors. *Physical Review B*, **64**, 161301R.

Lou, X., Adelmann, C., Crooker, S.A., *et al*. (2007). Electrical detection of spin transport in lateral ferromagnet-semiconductor devices. *Nature Physics*. **3**, 197.

Lou, X., Adelmann, C., Furis, M., *et al*. (2006). Electrical detection of spin accumulation at a ferromagnet-semiconductor interface. *Physical Review Letters*, **96**, 176603.

Ludeke, R. and Bauer, A. (1993). Hot electron scattering processes in metal films and at metal-semiconductor interfaces. *Physical Review Letters*, **71**, 1760.

Malinowski, A., Britton, R.S., Grevatt, T., *et al*. (2000). Spin relaxation in GaAs/$Al_xGa_{1-x}As$ quantum wells. *Physical Review B*, **62**, 13034.

Manago, T. and Akinaga, H. (2002). Spin-polarized light emitting diode using metal/insulator/semiconductor structures. *Applied Physics Letters*, **81**, 694.

Mathon, J. and Umerski, A. (2001). Theory of tunneling magnetoresistance of an epitaxial Fe/MgO/Fe(001) junction. *Physical Review B*, **63**, 220403.

Meier, F. and Zakharchenya, B.P. (1984). *Optical Orientation*, North Holland: Amsterdam.

Miyazaki, T. and Tezuka, N. (1995). Giant magnetic tunneling effect in Fe/Al2O3/Fe junction. *Journal of Magnetism and Magnetic Materials*, **139**, L231.

Mizushima, K., Kinno, T., Yamauchi, T., *et al*. (1997). Energy-dependent hot electron transport across a spin-valve. *IEEE Transactions on Magnetics*, **33**, 3500.

Mizushima, K., Kinno, T., Tanaka, K., *et al*. (1998). Strong increase of the effective polarization of the tunnel current in Fe/AlOx/Al junctions with decreasing Fe layer thickness. *Physical Review B*, **58**, 4660.

Monsma, D.J., Lodder, J.C., Popma, Th.J.A., *et al*. (1995). Perpendicular hot electron spin-valve effect in a new magnetic field sensor: the spin-valve transistor. *Physical Review Letters*, **74**, 5260.

Monsma, D.J. and Parkin, S.S.P. (2000). Spin polarization of tunneling current from ferromagnet/Al_2O_3 interfaces using copper-doped aluminum superconducting films. *Applied Physics Letters*, **77**, 720.

Monsma, D.J., Vlutters, R. and Lodder, J.C. (1998). Room temperature-operating spin-valve transistors formed by vacuum bonding. *Science*, **281**, 407.

Monzon, F.G. and Roukes, M.L. (1999). Spin injection and the local Hall effect in InAs quantum wells. *Journal of Magnetism and Magnetic Materials*, **198–199**, 632.

Moodera, J.S., Kinder, L.R., Wong, T.M., *et al*. (1995). Large magnetoresistance at room temperature in ferromagnetic thin film tunnel junctions. *Physical Review Letters*, **74**, 3273.

Moore, G.E. (1965). Cramming more components onto integrated circuits. *Electronics*, **38**, 114.

Motsnyi, V.F., Boeck, J.D., Das, J., *et al*. (2002). Electrical spin injection in a ferromagnetic/tunnel barrier/semiconductor heterostructure. *Applied Physics Letters*, **81**, 265.

Motsnyi, V.F., Dorpe, P.V., Roy, W.V., *et al*. (2003). Optical investigation of electrical spin injection into semiconductors. *Physical Review B*, **68**, 245319.

Murakami, S., Nagaosa, N. and Zhang, S-C. (2003). Dissipationless quantum spin current at room temperature. *Science*, **301**, 1348.

Nitta, J., Akazaki, T., Takayanagi, H., *et al*. (1997). Gate control of spin-orbit interaction in an inverted In0.53Ga0.47As/In0.52Al0 .48As heterostructure. *Physical Review Letters*, **78**, 1335.

Oberli, D., Burgermeister, R., Riesen, S., *et al*. (1998). Scattering cross section and spin motion of low energy electrons passing through a ferromagnet. *Physical Review Letters*, **81**, 4228.

Oestreich, M., Hübner, J., Hägele, D., *et al*. (1999). Spin injection into semiconductors. *Applied Physics Letters*, **74**, 1251.

Ohno, H., Chiba, D., Matsukura, F., *et al*. (2000). Electric-field control of ferromagnetism. *Nature*, **408**, 944.

Ohno,Y., Terauchi, R., Adachi, T., *et al*. (1999). Spin relaxation in GaAs(110) quantum wells. *Physical Review Letters*, **83**, 4196.

Ohno, Y., Young, D.K., Beschoten, B., *et al*. (1999). Electrical spin injection in a ferromagnetic semiconductor heterostructure. *Nature*, **402**, 790.

Pappas, D.P., Kämper, K.P., Miller, B.P., *et al*. (1991). Spin-dependent electron attenuation by transmission through thin ferromagnetic films. *Physical Review Letters*, **66**, 504.

Parkin, S.S.P., Bhadra, R. and Roche, K.P. (1991). Oscillatory magnetic exchange coupling through thin copper layer. *Physical Review Letters*, **66**, 2152.

Parkin, S., Jiang, X., Kaiser, C., *et al*. (2003). Magnetically engineered spintronic sensors and memory. *Proceedings of IEEE*, **91**, 661.

Parkin, S.S.P., Kaiser, C., Panchula, A.F., *et al*. (2004). Giant tunneling magnetoresistance at room temperature with MgO (100) tunnel barriers. *Nature Materials*, **3**, 862.

Parkin, S.S.P., More, N. and Roche, K.P. (1990). Oscillations in exchange coupling and magnetoresistance in metallic superlattice structures: Co/Ru, Co/Cr, and Fe/Cr. *Physical Review Letters*, **64**, 2304.

Parkin, S.S.P., Roche, K.P., Samant, M.G., *et al*. (1999). Exchange-biased magnetic tunnel junctions and application to nonvolatile magnetic random access memory. *Journal of Applied Physics*, **85**, 5828.

Puller, V.I., Mourokh, L.G., N.J.M., Horing, *et al*. (2003). Electron spin relaxation in a semiconductor quantum well. *Physical Review B*, **67**, 155309.

Quinn, J.J. (1962). Range of excited electrons in metals. *Physical Reviews*, **126**, 1453.

Rashba, E.I. (1960). Properties of semiconductors with an extremum loop I0 cyclotron and combinational resonance in a magnetic field perpendicular to the plane of the loop. *Soviet Physics Solid State*, **2**, 1109.

Rashba, E.I. (2000). Theory of electrical spin injection: Tunnel contacts as a solution of the conductivity mismatch problem. *Physical Review B*, **62**, R16267.

Rippard, W.H. and Buhrman, R.A. (1999). Ballistic electron magnetic microscopy: Imaging magnetic domains with nanometer resolution. *Applied Physics Letters*, **75**, 1001.

Rippard, W.H. and Buhrman, R.A. (2000). Spin-dependent hot electron transport in Co/Cu thin films. *Physical Review Letters*, **84**, 971.

Rippard, W.H., Perrella, A.C. and Buhrman, R.A. (2001). Ballistic electron microscopy study of ultrathin oxidized aluminum barriers for magnetic tunnel junctions. *Applied Physics Letters*, **78**, 1601.

Salis, G., Wang, R., Jiang, X., *et al*. (2005). Temperature independence of the spin-injection efficiency of a MgO-based tunnel spin injector. *Applied Physics Letters*, **87**, 262503.

Sandhu, J.S., Heberle, A.P., Baumberg, J.J., *et al*. (2001). Gateable suppression of spin relaxation in semiconductors. *Physical Review Letters*, **86**, 2150.

Sato, R. and Mizushima, K. (2001). Spin-valve transistor with an Fe/Au/Fe(001) base. *Applied Physics Letters*, **79**, 1157.

Schmidt, G., Ferrand, D., Molenkamp, L.W., *et al*. (2000). Fundamental obstacle for electrical spin injection from a ferromagnetic metal into a diffusive semiconductor. *Physical Review B*, **62**, R4790.

Schönhense, G. and Siegmann, H.C. (1993). Transmission of electrons through ferromagnetic material and applications to detection of electron spin polarization. *Annalen der Physik*, **2**, 465.

Schowalter, L.J. and Lee, E.Y. (1991). Role of elastic scattering in ballistic-electron-emission microscopy of Au/Si(001) and Au/Si(111) interfaces. *Physical Review B*, **43**, 9308.

Siegmann, H.C. (1992). Surface and 2D magnetism. *Journal of Physics: Condensed Matter*, **4**, 8395 and references therein.

Siegmann, H.C., Garwin, E.L., Prescott, C.Y., *et al*. (1995). Magnetism with picosecond field pulses. *Journal of Magnetism and Magnetic Materials*, **151**, L8.

Siegmann, H.C., Pierce, D.T., and Celotta, R.J. (1981). Spin-dependent absorption of electrons in a ferromagnetic metal. *Physical Review Letters*, **46**, 452.

Smith, D.L. and Kogan, Sh.M. (1996). Theory of ballistic-electron-emission microscopy of buried semiconductor heterostructures. *Physical Review B*, **54**, 10354.

Smith, D.L., Kozhevnikov, M., Lee, E.Y., *et al*. (2000). Scattering theory of ballistic-electron-emission microscopy at nonepitaxial interfaces. *Physical Review B*, **61**, 13914.

Smith, D.L., Lee, E.Y. and Narayanamurti, V. (1998). Ballistic electron emission microscopy for nonepitaxial metal/semiconductor interfaces. *Physical Review Letters*, **80**, 2433.

Tignon, J., Heller, O., Roussignol, Ph., *et al*. (1998). Excitonic recombination dynamics in shallow quantum wells. *Physical Review B*, **58**, 7076.

van Dijken, S., Jiang, X. and Parkin, S.S.P. (2002a). Room temperature operation of a high output current magnetic tunnel transistor. *Applied Physics Letters*, **80**, 3364.

van Dijken, S., Jiang, X. and Parkin, S.S.P. (2002b). Spin-dependent hot electron transport in $Ni_{81}Fe_{19}$ and $Co_{84}Fe_{16}$ films on GaAs(001). *Physical Review B*, **66**, 094417.

van Dijken, S., Jiang, X. and Parkin, S.S.P. (2003a). Comparison of magnetocurrent and transfer ratio in magnetic tunnel transistors with spin-valve bases containing Cu and Au spacer layers. *Applied Physics Letters*, **82**, 775.

van Dijken, S., Jiang, X. and Parkin, S.S.P. (2003b). Giant magnetocurrent exceeding 3400% in magnetic tunnel transistors with spin-valve base layers. *Applied Physics Letters*, **83**, 951.

van Dijken, S., Jiang, X. and Parkin, S.S.P. (2003c). Non-monotonic bias voltage dependence of the magnetocurrent in GaAs-based magnetic tunnel transistors. *Physical Review Letters*, **90**, 197203.

van Dijken, S., Jiang, X. and Parkin, S.S.P. (2005). The influence of nonmagnetic seed layers on the magnetotransport properties of magnetic tunnel transistors with a silicon collector. *Journal of Applied Physics*, **97**, 043712.

Van Dorpe, P., Motsnyi, V.F., Nijboer, M., *et al*. (2003). Highly efficient room temperature spin injection in a metal-insulator-semiconductor light emitting diode. *Japanese Journal of Applied Physics*, **42**, L502.

van 't Erve, O.M.J., Kioseoglou, G., Hanbicki, A.T., *et al*. (2004). Comparison of Fe/Schottky and Fe/Al2O3 tunnel barrier contacts for electrical spin injection into GaAs. *Applied Physics Letters*, **84**, 4334.

van 't Erve, O.M.J., Vlutters, R., Anil Kumar, P.S., *et al*. (2002). Transfer ratio of the spin-valve transistor. *Applied Physics Letters*, **80**, 3787.

Vescovo, E., Carbone, C., Alkemper, U., *et al*. (1995). Spin-dependent electron scattering in ferromagnetic Co layers on Cu(111). *Physical Review B*, **52**, 13497.

Vlutters, R., van 't Erve, O.M.J., Jansen, R., *et al*. (2001). Modeling of spin-dependent hot-electron transport in the spin-valve transistor. *Physical Review B*, **65**, 024416.

Vlutters, R., van 't Erve, S.D., Kim, O.M.J., *et al*. (2002). Interface, volume, and thermal attenuation of hot-electron spins in Ni80Fe20 and Co. *Physical Review Letters*, **88**, 027202.

Wang, R., Jiang, X., Shelby, R.M., *et al*. (2005). Increase in spin injection efficiency of a CoFe/MgO(100) tunnel spin injector with thermal annealing. *Applied Physics Letters*, **86**, 052901.

Weber, W., Riesen, S. and Siegmann, H.C. (2001). Magnetization precession by hot spin injection. *Science*, **291**, 1015.

Weilmeier, M.K., Rippard W.H. and Buhrman, R.A. (1999). Ballistic electron transport through Au(111)/Si(111) and Au(111)/Si(100) interfaces. *Physical Review B*, **59**, R2521.

Wolf, S.A., Awschalom, D.D., Buhrman, R.A., *et al*. (2001). Spintronics: A spin-based electronics vision for the future. *Science*, **294**, 1488.

Yafet, Y. (1963). In *Solid State Physics*, Seitz, F. and Turnball, D. (Eds.), Academic: New York, p. 1, Vol. 14.

Zarate, E., Apell, P. and Echenique, P.M. (1999). Calculation of low-energy-electron lifetimes. *Physical Review B*, **60**, 2326.

Zhang, X.-G. and Butler, W.H. (2004). Large magnetoresistance in bcc Co/MgO/Co and FeCo/MgO/FeCo tunneling junctions. *Physical Review B*, **70**, 172407.

Zhu, H.J., Ramsteiner, M., Kostial, H., *et al*. (2001). Room-temperature spin injection from Fe into GaAs. *Physical Review Letters*, **87**, 016601.

Zutic, I., Fabian, J. and Sarma, S.D. (2004). Spintronics: fundamentals and applications. *Reviews of Modern Physics*, **76**, 323.

Spin-dependent Transport of Carriers in Semiconductors

Roland Winkler

Northern Illinois University, DeKalb, IL, USA and Argonne National Laboratory, Argonne, IL, USA

1 INTRODUCTION

Broadly speaking, spin-dependent transport phenomena in semiconductors can be divided into two categories. On the one hand, we have those effects such as spin drift, spin diffusion, and spin precession that refer to the transport of spin-polarized carriers. These effects are of central importance for spintronics device concepts where the generation of spin-polarized distributions of carriers are spatially separated from those elements that manipulate and detect the spins. On the other hand, we also have spin-dependent phenomena such as the spin Coulomb blockade or weak localization and spin-split Shubnikov–de Haas oscillations visible in magneto-transport of two-dimensional (2D) electron systems. The latter effects provide important insights into the nature of the spin-dependent interactions, such as exchange and spin-orbit coupling, that can be exploited for the manipulation of spin systems. In this review, we will focus mostly on the former class of phenomena. Also, we will focus mostly on homogenous systems and touch only briefly on the properties of structured devices that are discussed in **Semiconductor Spintronic Devices, Volume 5**.

We begin with a discussion of optical orientation of electron spins in semiconductors (Section 2). Then we review nonequilibrium spin flow including spin drift and diffusion (Section 3.1), and spin precession (Section 3.2). Coulomb effects in spin transport are discussed in Section 3.3. Finally, we review in Section 4 spin photocurrents and the reverse effect, the electrical generation of a spin polarization.

Handbook of Magnetism and Advanced Magnetic Materials. Edited by Helmut Kronmüller and Stuart Parkin. Volume 5: *Spintronics and Magnetoelectronics*. © 2007 John Wiley & Sons, Ltd. ISBN: 978-0-470-02217-7.

2 OPTICAL ORIENTATION OF ELECTRON SPINS

Various schemes have been developed to generate spin-polarized carrier distributions in nonmagnetic semiconductors. Broadly speaking, these fall into three categories. First, optical excitation allows creation of spin-polarized electrons inside the semiconductor. Second, magnetic layers can be used to inject spin-polarized carriers into the semiconductors. These magnetic layers can be semimagnetic semiconductors (see also **Diluted Ferromagnetic Semiconductors – Theoretical Aspects, Volume 5**), ferromagnetic semiconductors (see also **Ferromagnetic Semiconductors, Volume 5**) or ferromagnetic metal electrodes attached to the semiconductor (Jonker, 2003). Finally, dynamic phenomena based on electric fields and charge currents can give rise to

spin polarization inside the semiconductor or spin accumulation at the edges of the sample (see Section 4.2 and **Theory of Spin Hall Effects in Semiconductors, Volume 5**).

Here, we will focus on the *optical orientation* of electrons that has proven to be a powerful technique since some of the earliest studies of spin-related phenomena in semiconductors were performed (Lampel, 1968; Meier and Zakharchenya, 1984). In direct semiconductors like GaAs, the electron states in the conduction band have spin $S = 1/2$, whereas the hole states in the valence band have an effective spin $S = 3/2$. The hole states with spin z component $S_z = \pm 3/2$ are denoted heavy-hole (HH) states, whereas the light-hole (LH) states have $S_z = \pm 1/2$. Left (right) circularly polarized photons carry a z component of angular momentum of -1 $(+1)$ so that conservation of angular momentum results in the selection rules for optical transitions depicted in Figure 1. A more detailed analysis shows that the probabilities for transitions from the HH states to the conduction band are three times larger than the probability for optical transitions from the LH states. In bulk semiconductors, the maximum attainable degree of spin polarization is thus $P = 50\%$, where P is defined as

$$P = \frac{N_+ - N_-}{N_+ + N_+} \tag{1}$$

and N_+ (N_-) is the number of electrons with spin up (down), respectively. In 2D systems, the degeneracy of the HH and LH states is lifted as sketched in Figure 1. For resonant excitation at the HH energy we thus expect a rise of the maximum attainable degree of polarization up to $P = 100\%$.

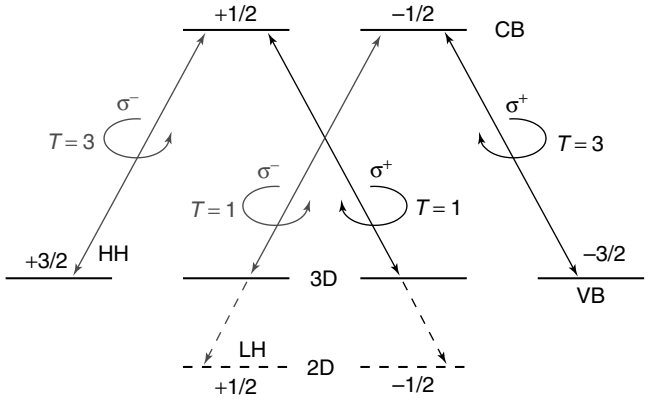

Figure 1. Selection rules and relative transition rates T for optical transitions between valence band (VB) states having an effective spin $S = 3/2$ and conduction band (CB) states with $S = 1/2$ (Dyakonov and Perel, 1984)). In bulk semiconductors, the HH states ($S_z = \pm 3/2$) are degenerate with the LH states ($S_z = \pm 1/2$) whereas in quasi-2D systems the LH states (dashed bold lines) are lower in energy than the HH states.

A particular advantage of the optical orientation scheme lies in the fact that it holds both for absorption and emission, so that it can be used for creating and for detecting spin-polarized carrier distributions. However, the holes lose their spin orientation significantly faster than the electrons, and the oriented electrons can recombine with *any* hole. Therefore, Figure 1 implies that the polarization of the recombination photoluminescence (PL) in bulk semiconductors does not exceed ∼25%. (This does not apply to 2D systems where the recombination PL is due to a transition from the lowest electron to the lowest HH state.)

Even in a single-particle picture for the optical excitation, the 3 : 1 ratio of HH and LH transitions is obtained only if HH–LH coupling of the hole states at nonzero wave vectors $\mathbf{k}$ is neglected. Owing to this HH–LH coupling, the hole states with $k > 0$ are not spin eigenstates. Furthermore, a realistic picture must take into account that optical absorption gives rise to the formation of excitons, that is, Coulomb correlated electron-hole pairs. Thus even for excitations close to the absorption edge we get substantial HH–LH coupling because the exciton states consist of electron and hole states with k of the order of $1/a_B^*$, where a_B^* is the effective Bohr radius. The Coulomb coupling between different electron and hole states yields a second contribution to the mixing of single-particle states with different values of S_z. Finally, we must keep in mind that for higher excitation energies we get a superposition of exciton continua that are predominantly HH- or LH-like. These different excitons contribute oppositely to the spin orientation of electrons. We note that these arguments are valid for the optical excitation of bulk semiconductors and quasi-2D systems (Pfalz *et al*., 2005).

Optical orientation in bulk systems was reviewed by Dyakonov and Perel (1984). Early works on 2D systems were published by Weisbuch *et al*. (1981) and Masselink *et al*. (1984) who reported on polarization-resolved transmission and PL experiments on GaAs/AlGaAs quantum wells (QWs) under cw excitation. In later works, the electron-spin polarization in quasi-2D systems was studied using time-resolved PL excitation spectroscopy. For excitation energies even slightly above the HH resonance, several authors (Freeman, Awschalom and Hong, 1990; Dareys *et al*., 1993; Muñoz, Pérez, Viña and Ploog, 1995) observed a polarization that was significantly smaller than one. These measurements were carried out on fairly narrow GaAs/AlGaAs QWs. A first well-width dependent study of optical orientation was performed experimentally by Roussignol *et al*. (1992). For energies near the HH resonance, they found initial spin polarizations in the range of 60–80%.

Twardowski and Hermann (1987) as well as Uenoyama and Sham (1990) studied the polarization of QW PL theoretically, taking into account HH–LH coupling in

the valence band. However, these authors neglected the Coulomb interaction between electron and hole states. On the other hand, Maialle, de Andrada e Silva and Sham (1993) investigated the spin dynamics of excitons taking into account the exchange coupling between electrons and holes, but disregarded the HH–LH coupling in the valence band. Recently, a detailed experimental and theoretical study of optical orientation in 2D systems was performed by Pfalz *et al*. (2005) confirming that the polarization of the measured PL reflects the spin polarization of the excited electrons (equation (1)) over a wide range of excitation energies. As an example, Figure 2 shows the measured and calculated degree of spin polarization P as a function of excitation energy of a 198-Å-wide GaAs/AlAs QW.

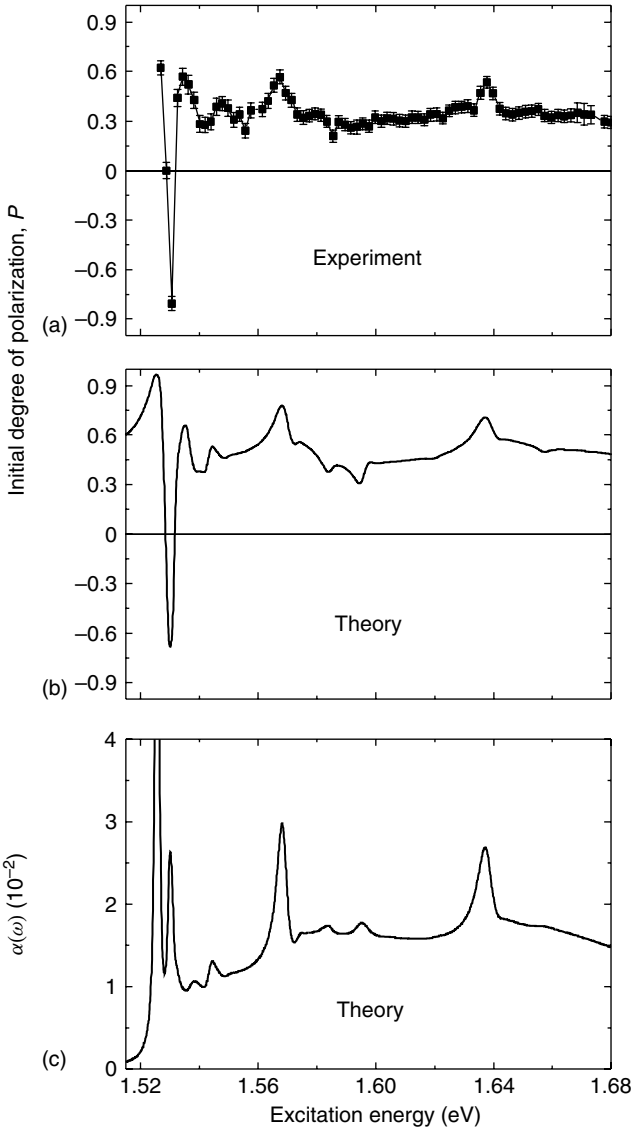

Figure 2. (a) Measured and (b) calculated degree of spin polarization P and (c) calculated absorption coefficient $\alpha(\omega)$ as a function of excitation energy of a 198-Å-wide GaAs/AlAs QW. The lowest peak in the absorption spectrum is an HH exciton that gives rise to a large positive spin orientation. The next peak slightly above the first peak is due to the LH exciton, and it results in a strongly negative spin orientation. The peaks at higher energies are Fano resonances, which give mixed contributions to the spin polarization. (Adapted from Pfalz *et al*., 2005.)

3 NONEQUILIBRIUM SPIN FLOW IN SEMICONDUCTORS

3.1 Spin drift and diffusion

Similar to electric charge distributions in semiconductors, a nonequilibrium spin distribution can spread out diffusively or it can drift in the presence of an electric field. However, these phenomena behave qualitatively different in p- and n-type semiconductors (D'yakonov and Perel', 1971a). In p-type semiconductors, only the spins of the nonequilibrium electrons become oriented. Their number is proportional to the intensity of the light, but the degree of orientation does not depend on the intensity (Figure 1). As drift and diffusion of the spin orientation must preserve charge neutrality, the kinetics of the spin orientation follows the kinetics of the charge distribution. Charge diffusion in doped semiconductors is characterized by the diffusion coefficient of the minority carriers (Smith, 1978). Therefore, electron-spin diffusion in p-type semiconductors is essentially characterized by the charge diffusion coefficient for electrons[1].

In n-type semiconductors, the situation is qualitatively different due to the fact that the optically excited electrons augment the equilibrium electrons (D'yakonov and Perel', 1971a). Therefore, significant optical orientation of electron spins is possible at moderate degrees of excitation when the excess photoelectron density is still much less than the equilibrium electron density. The mechanism underlying this effect is the following. Absorption of circularly polarized light creates electrons with mainly a single spin orientation. The spin relaxation time τ_s of these electrons is typically much greater than the excess carrier lifetime. Holes, on the other hand, have a short spin relaxation time so that the spin orientation of the optically created holes is quickly lost. Therefore, *any* electron can recombine with these holes with a recombination rate that is usually independent of the sign of the spin. Thus, optical excitation is a source for spin-polarized electrons whereas recombination represents a drain for electrons with the 'wrong' spin orientation. Under stationary excitation, the oriented electrons are the equilibrium ones.

In a bulk sample, the light is usually absorbed in a narrow layer near the surface of the crystal. In this case, the excess

carriers penetrate a distance of the order of the diffusion length $L = \sqrt{D_p \tau}$, where D_p is the hole diffusion coefficient in the n-type sample (which is usually small), and τ is the lifetime of the nonequilibrium carriers. On the other hand, the orientation penetrates a depth of the order of the spin-diffusion length $L_s = \sqrt{D_s \tau_s}$, where D_s is the spin-diffusion coefficient of the electrons (which is usually large; it is approximately equal to the electron diffusion coefficient D_e). Under typical experimental conditions we thus have $L_s \gg L$ in an n-type sample (D'yakonov and Perel', 1971a). Beyond a layer of thickness $\sim L$, recombination cannot change the degree of polarization P that falls off like $P(z) = P(0)\exp(-z/L_s)$, that is, a spin orientation of the order of $P(0)$ penetrates into a layer of depth $\sim L_s$, where there are no excess carriers. (A small number of photoexcited carriers can be present within this layer because of reabsorption (Dzhioev, Zakharchenya, Korenev and Stepanova, 1997).)

In general, the motion of the spin density $\mathbf{S}$ is characterized by a drift-diffusion equation (D'yakonov and Perel', 1976; Garbuzov, Merkulov, Novikov and Fleisher, 1976; Dyakonov and Perel, 1984)

$$\frac{\partial \mathbf{S}}{\partial t} = D_s \nabla^2 \mathbf{S} + \frac{e\mathcal{E} \cdot \nabla \mathbf{S}}{k_B T} + \mathbf{\Omega} \times \mathbf{S} - \frac{\mathbf{S}}{\tau_s} - \frac{\mathbf{S} - \mathbf{S}_0}{\tau} \quad (2)$$

similar to the drift and diffusion of charge. Here $\mathcal{E}$ is a built-in or external electric field; T is the temperature; and Ω is the spin precession frequency, which can be due to an external magnetic field $\mathbf{B}$, that is, $\mathbf{\Omega} = g^* \mu_B \mathbf{B}/\hbar$, or due to spin-orbit coupling at $B = 0$ (see Section 3.2). The last two terms reflect two reasons for the spin orientation to vanish, spin relaxation and recombination, where $\mathbf{S}_0$ is the average spin orientation at the moment of photocreation. Recently, the drift-diffusion equation (2) was reconsidered by Flatté and Byers (2000) and Yu and Flatté (2002).

Spin drift and diffusion have been studied experimentally by several groups. Dzhioev, Zakharchenya, Korenev and Stepanova (1997) estimated that the spin diffusion length in their n-type GaAs sample was $L_s = 10\,\mu\text{m}$. Hägele *et al.* (1998) found that the spin orientation in intrinsic GaAs was almost completely preserved over a distance of $4\,\mu\text{m}$. Kikkawa and Awschalom (1999) performed a detailed study of spin transport in intrinsic and n-type GaAs samples in which gates allowed one to stir the drift of the spin-polarized electrons. Using nonlocal Faraday rotation, they found that the drift distance of the spin-oriented electrons was linear in the electric field, and it could exceed a distance of $100\,\mu\text{m}$ for electric fields of $16\,\text{V cm}^{-1}$. Fiederling *et al.* (1999) used semimagnetic $\text{Be}_x\text{Mn}_y\text{Zn}_{1-x-y}\text{Se}$ to inject spin-polarized electrons into a 0.1-μm-thick layer of n-type AlGaAs followed by a 15-nm-wide GaAs, where the spin-polarized electrons recombined with holes that were injected from the other side of the QW (a spin light-emitting diode). Similar experiments were also performed by Jonker *et al.* (2000) and Ohno *et al.* (1999) who used semimagnetic ZnMnSe and ferromagnetic GaMnAs, respectively, to create spin-polarized electrons that were injected into a nonmagnetic layer followed by a light-emitting diode[2].

It has been found that interfaces between different semiconductors do not affect spin transport. This was first noticed by Garbuzov, Merkulov, Novikov and Fleisher (1976), who studied spin orientation for a sample that contained a GaAs QW embedded in thick graded layers of p-type $\text{Al}_x\text{Ga}_{1-x}\text{As}$. Malajovich *et al.* (2000) found that even the interface between ZnSe and GaAs, a II–VI and a III–V semiconductor, did not suppress spin transport.

Lateral spin diffusion was studied by Cameron, Riblet and Miller (1996). When two laser beams with crossed polarizations interfere, the light intensity on the sample is uniform, but the polarization alternates between left polarized, linear, and right polarized. Therefore, a spin grating is generated in the sample where the optical orientation of the electrons alternates across the excitation region. By analyzing the orientation decay as a function of time, these authors could determine the spin-diffusion coefficient D_s and the spin relaxation time τ_s. The spin-diffusion length $L_s = \sqrt{D_s \tau_s}$ appeared to be approximately $8\,\mu\text{m}$ (Kavokin, 2002). Stotz, Hey, Santos and Ploog (2005) achieved a controlled lateral spin transport using two interfering traveling beams of coherent acoustic phonons. These beams resulted in dynamic quantum-dot like confining potentials that could take along the spin-polarized electrons.

3.2 Spin precession

The magnetic-field-dependent term $\mathbf{\Omega} \times \mathbf{S}$ in equation (2) describes the precessional motion of the oriented spins in an external field $\mathbf{B}$ or an effective field due to spin-orbit coupling. For a transverse external field $\mathbf{B}$, this term gives rise to the Hanle effect, a depolarization of luminescence induced by the field $\mathbf{B}$ (Dyakonov and Perel, 1984). In a homogenous system (i.e., $\nabla \mathbf{S} = 0$ in equation (2)), we get the expression for the Hanle curve

$$S_z(B) = \frac{S_z(0)}{1 + (\Omega T_s)^2}, \quad \text{where} \quad S_z(0) = \frac{S_0}{1 + \tau/\tau_s} \quad (3)$$

Here we have assumed that the z direction is the direction of the exciting radiation with $\mathbf{S}_0 \perp \mathbf{B}$, and T_s is the 'spin lifetime' defined by $T_s^{-1} = \tau^{-1} + \tau_s^{-1}$. From the Hanle curve as a function of field B, one can thus extract the lifetime τ and the spin relaxation time τ_s of the carriers (provided the effective Landé factor g^* is known). However,

a particular situation arises in n-type semiconductors where recombination is not possible past the surface layer of thickness $\sim L$. The depolarization induced by the magnetic field thus changes the gradient of the degree of polarization within the layer where electrons are oriented. Therefore, the spin-diffusion rate becomes magnetic-field-dependent, which results in a distinct change of the functional form of the Hanle curve as a function of magnetic field (D'yakonov and Perel', 1976).

In the presence of both time-inversion symmetry and space-inversion symmetry, all electron states in a solid with a given wave vector $\mathbf{k}$ are twofold degenerate. When the potential through which the carriers move is inversion-asymmetric, however, the spin degeneracy is removed even in the absence of an external magnetic field B. We then obtain two branches of the energy dispersion, $E_+(\mathbf{k})$ and $E_-(\mathbf{k})$. This spin splitting can be the consequence of a bulk inversion asymmetry (BIA) of the underlying crystal (e.g., a zinc blende structure; Dresselhaus, 1955), and of a structure inversion asymmetry (SIA) of the confinement potential (Ohkawa and Uemura, 1974; Bychkov and Rashba, 1984). Strain gives rise to a third contribution to $B = 0$ spin splitting (Seiler, Bajaj and Stephens, 1977; Howlett and Zukotynski, 1977). A fourth contribution can be the low microscopic symmetry of the atoms at an interface (Rössler and Kainz, 2002). $B = 0$ spin splitting has been reviewed, for example, by Pikus, Marushchak and Titkov (1988) and Winkler (2003). In the present context, it is important that the spin splitting can be ascribed to an effective Zeeman term $H = (\hbar/2)\boldsymbol{\sigma} \cdot \boldsymbol{\Omega}(\mathbf{k})$ with an effective magnetic field $\boldsymbol{\Omega}(\mathbf{k})$. In leading order of $\mathbf{k}$, the effective field in a 2D electron system on a (001) surface reads

$$\boldsymbol{\Omega}(\mathbf{k}_\parallel) = \frac{2\gamma}{\hbar} \begin{pmatrix} k_x \left(k_y^2 - \langle k_z^2 \rangle\right) \\ k_y \left(\langle k_z^2 \rangle - k_x^2\right) \\ 0 \end{pmatrix} + \frac{2\alpha}{\hbar} \begin{pmatrix} k_y \\ -k_x \\ 0- \end{pmatrix} \qquad (4)$$

The first term characterizes the BIA spin splitting of the electron states. It is called the *Dresselhaus* or k^3 term (Dresselhaus, 1955; Braun and Rössler, 1985). It exists already in bulk zinc blende semiconductors due to the broken inversion symmetry. In quasi-2D systems only the in-plane wave vector $\mathbf{k}_\parallel = (k_x, k_y, 0)$ is a continuous variable. In first-order perturbation theory, the wave vector components k_z and powers thereof are replaced by expectation values with respect to the subband wave functions. The field $\boldsymbol{\Omega}(\mathbf{k}_\parallel)$ due to BIA is depicted in Figure 3(a). We note that in 2D systems, the Dresselhaus term depends on the crystallographic orientation of the substrate. For 2D systems on an $[mmn]$ surface with integers m and n, the Dresselhaus term was given by Braun and Rössler (1985).

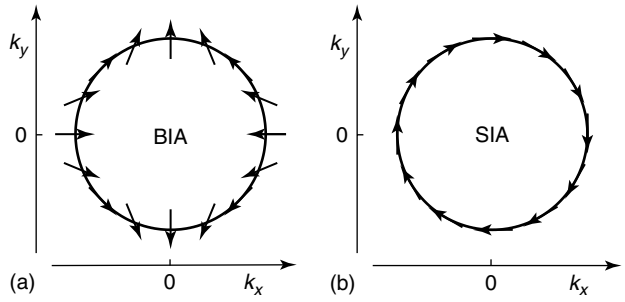

Figure 3. Effective magnetic field $\boldsymbol{\Omega}(\mathbf{k}_\parallel)$ along a contour of constant energy (a) due to the Dresselhaus term in a system with BIA and (b) due to the Rashba term in a system with SIA.

The momentum scattering of electrons off other electrons, impurities, phonons, etc., results in a random-walk type precession of the electron spins in the field $\boldsymbol{\Omega}(\mathbf{k})$, which gives rise to the so-called Dyakonov–Perel spin relaxation (D'yakonov and Perel', 1972; Pikus and Titkov, 1984). A *controlled* precession of electrons in the Dresselhaus field $\boldsymbol{\Omega}(\mathbf{k})$ was first demonstrated by Riechert *et al*. (1984), who investigated the polarization of photoemission following optical orientation. After deposition of Cs and O on the (110) surface of their strongly p-doped GaAs sample, a surface inversion layer was formed where the bands were strongly bent downward. Electrons moving through this layer gain a large kinetic energy. Yet if the layer is very narrow, they move ballistically with $\mathbf{k}$ normal to the surface so that the direction of $\boldsymbol{\Omega}$ is the same for all escaping electrons. The photoelectron orientation is thus rotated away from the initial direction defined by the pumping light beam, as observed by Riechert *et al*[3].

In asymmetric QWs, SIA gives rise to the second term in equation (4), which is frequently called the *Rashba* term (Rashba, 1960; Bychkov and Rashba, 1984). The coefficients γ and α depend on the underlying semiconductor bulk material; but α depends also on the asymmetry of the QW in the growth direction (Winkler, 2003). It can be tuned by means of front and back gates (Nitta, Akazaki, Takayanagi and Enoki, 1997). This is exploited in the famous spin-field-effect transistor proposed by Datta and Das (1990), see **Semiconductor Spintronic Devices, Volume 5**. The field $\boldsymbol{\Omega}(\mathbf{k}_\parallel)$ due to SIA is depicted in Figure 3(b).

A third contribution to $\boldsymbol{\Omega}(\mathbf{k})$ at $B = 0$ is obtained by means of strain. In lowest order of $\mathbf{k}$ and of the components ε_{ij} of the strain tensor we get (Pikus and Titkov, 1984)

$$\boldsymbol{\Omega}(\mathbf{k}) = \frac{C_3}{\hbar} \begin{pmatrix} \varepsilon_{xy}k_y - \varepsilon_{xz}k_z \\ \varepsilon_{yz}k_z - \varepsilon_{yx}k_x \\ \varepsilon_{zx}k_x - \varepsilon_{zy}k_y \end{pmatrix} + \frac{C_3'}{\hbar} \begin{pmatrix} k_x(\varepsilon_{yy} - \varepsilon_{zz}) \\ k_y(\varepsilon_{zz} - \varepsilon_{xx}) \\ k_z(\varepsilon_{xx} - \varepsilon_{yy}) \end{pmatrix} \qquad (5)$$

The first term depends on the off-diagonal components of the strain tensor, that is, these components describe a shear strain. They are nonzero, for example, when uniaxial stress is applied in the crystallographic directions [111] or [110] of a bulk crystal (Trebin, Rössler and Ranvaud, 1979). The prefactor C_3' of the second term in equation (5) is nonzero only because of coupling to remote bands outside the usual 8×8 Kane Hamiltonian. Therefore, this term is rather small, so usually it can be neglected (Pikus and Titkov, 1984; D'yakonov, Marushchak, Perel' and Titkov, 1986).

For bulk InSb, the effect of strain on spin splitting has been studied by measuring Shubnikov–de Haas oscillation (Seiler, Bajaj and Stephens, 1977) and cyclotron resonance (Ranvaud, Trebin, Rössler and Pollak, 1979). D'yakonov, Marushchak, Perel' and Titkov (1986) analyzed the Hanle effect in the presence of strain in order to obtain $C_3 = 20\,\text{eVÅ}$ for GaSb, $C_3 = 5\,\text{eVÅ}$ for GaAs, and $C_3 = 3\,\text{eVÅ}$ for InP. The decrease of these values from GaSb to InP correlates with the decrease in the spin-orbit interaction gap in these crystals from 0.82 to 0.11 eV.

The effect of strain on spin transport in *n*-type (001) GaAs was first studied by Kato, Myers, Gossard and Awschalom (2004a) using time and spatially resolved Faraday rotation spectroscopy. However, they did not quantify or tune the strain in their samples. The implications of equation (5) have been confirmed in detail in experiments by Crooker and Smith (2005). Similar experiments have been published also by Beck, Metzner, Malzer and Döhler, 2005. Crooker and Smith used a small vise to apply tunable uniaxial strain along the [110] or $[1\bar{1}0]$ direction of their *n*-GaAs sample, while a circularly polarized 1.58-eV laser focused to a 4-μm spot was used to create locally a spin orientation along [001]. In spatially resolved measurements using Kerr rotation they studied the electron-spin precession while the electrons drifted and diffused away from the position of the laser spot, where the spin orientation was created (see Figure 4).

Crooker and Smith found that the spin precession of electrons drifting and diffusing in the strain field (5) is more robust than the precession of electrons moving in an external magnetic field. The reason is that in a transverse magnetic field the ensemble spin orientation dephases quickly when the precession period falls below the spin-diffusion length (the Hanle effect discussed in the preceding text). The strain-induced field (5), on the other hand, is linear in the wave vector $\mathbf{k}$ so that slowly moving electrons experience a smaller field $\boldsymbol{\Omega}(\mathbf{k})$ than the faster electrons. But the distance the electrons must travel for a complete precession period is the same for slow and fast electrons so that the electrons remain in phase (Figures 4c and d). This argument also implies that the precession period should be independent of the magnitude of the external electric field used to push the electrons, as

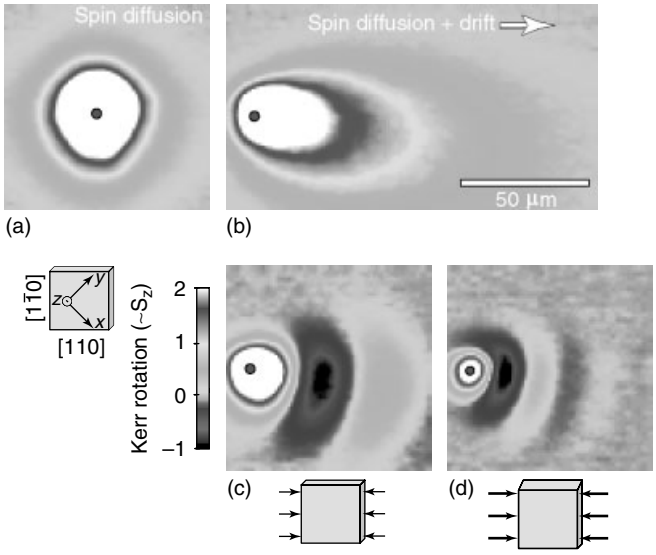

Figure 4. Images of the electron-spin flow in a 1-μm-thick *n*-GaAs epilayer ($n = 1 \times 10^{16}\,\text{cm}^{-3}$) at 4 K, acquired via Kerr-rotation microscopy. (a) Shows the spin polarization due to spin diffusion alone. In (b)–(d), a lateral electric field $E = 10\,\text{V cm}^{-1}$ was applied. Finally, E was complemented by (c) weak and (d) large uniaxial stress along [110]. The white bar in (b) gives the length scale for all four panels. (Adapted from Crooker and Smith, 2005.)

confirmed by the experiments of Crooker and Smith and Beck, Metzner, Malzer and Döhler.

The strain-induced field (5) has a pronounced dependence on the wave vector $\mathbf{k}$. If a uniaxial strain is applied along the direction [110], we have $\Omega = 0$ for $\mathbf{k}$ along [001]. This is analogous to the fact that we have no Dresselhaus spin splitting in symmetric QWs on a (110) surface for $\mathbf{k}_\parallel$ along [001] (Winkler, 2003). Within the (001) plane the $\mathbf{k}$ dependence of $\boldsymbol{\Omega}$ is the same as for the Rashba term, see Figure 3(b). If, in addition to the strain-induced field (5) an external magnetic field $\mathbf{B}$ is applied, the electrons with $\boldsymbol{\Omega}(\mathbf{k})$ approximately parallel to $\mathbf{B}$ precess faster than the electrons with $\boldsymbol{\Omega}(\mathbf{k})$ approximately antiparallel to $\mathbf{B}$. This was confirmed by the experiments of Crooker and Smith. To show this they used the fact that the radial diffusion in a pure strain-induced field (5) *or* an external magnetic field $\mathbf{B}$ is independent of the direction of $\mathbf{k}$, which reflects the fact that the magnitude of $\boldsymbol{\Omega}$ does not depend on the direction of the $\mathbf{k}$ vector of the electrons. The superposition of both fields, on the other hand, results in an anisotropic total field $\boldsymbol{\Omega}$ the magnitude of which depends on the direction of $\mathbf{k}$. This is similar to the fact that, to lowest (i.e., linear) order in $\mathbf{k}_\parallel$, the magnitude of both the Dresselhaus and Rashba spin splitting in 2D systems are independent of the direction of $\mathbf{k}_\parallel$ (see Figure 3), yet the superposition of both terms gives rise to anisotropic spin splitting even in linear order of $\mathbf{k}_\parallel$ (de Andrada e Silva, 1992).

The interplay of diffusion, drift in electric fields, and precession in external magnetic fields was studied theoretically by Qi and Zhang (2003) using a semiclassical Boltzmann equation for the 2×2 spin density matrix in order to cope with the different length scales of this problem, such as the diffusion length L, the spin-diffusion length L_s, and the spin precession length. Spin diffusion equations for systems with Rashba spin-orbit interaction in an electric field were studied by Bleibaum (2006). Drift and diffusion were also studied theoretically by Hruška *et al*. (2006) for an experimental setup similar to the one used by Crooker and Smith (2005) as described in the preceding text.

3.3 Coulomb effects

So far, we have completely neglected the Coulomb interaction between the electrons. Although this interaction does not couple to the spin degree of freedom of the electrons, it has a great influence on spin-dependent transport. This has long been known in the context of spin diffusion in spin-polarized liquid ^{3}He. Leggett and Rice (1968) and Leggett (1970) have shown that the spin polarization gives rise to a molecular field, and any given spin will then see (and precess around) a total field that is the sum of the molecular field and the external field. This molecular field cannot affect the precession of the total spin density $\mathbf{S}$, since it is automatically parallel to it. However, it produces a torque on the spin current, which is present in the equation of continuity for the latter. Leggett showed that, as a result, the equation for $\mathbf{S}$ in the hydrodynamic limit no longer has a simple form similar to equation (2) but he derived a significantly more complicated hydrodynamic-type spin-diffusion equation. More recently, Takahashi, Shizume and Masuhara (1999) have applied these ideas to the spin diffusion and drift in 2D electron systems. They solved the quantum kinetic equation derived from the equation of motion for the nonequilibrium real-time Green's functions in order to show that the spin rotation term known for ^{3}He is indeed also present in degenerate 2D electron systems at low temperatures.

In a sequence of papers, D'Amico and Vignale (2000, 2001, 2002, 2003) performed a detailed theoretical analysis of how the Coulomb interaction affects spin-polarized transport and diffusion in electron systems (see also Flensberg, Jensen and Mortensen (2001)). D'Amico and Vignale showed that the Coulomb interaction gives rise to a spin Coulomb drag between the electrons moving with spin up and the electrons moving with spin down, similar to the Coulomb drag that has been observed for electrons in two spatially separated layers (Gramila *et al*., 1991; Rojo, 1999). The spin Coulomb drag reflects the fact that while, in the absence of impurities, the total momentum $\mathbf{P} = \sum_i \mathbf{p}_i$ of the electrons is preserved, the 'up' and 'down' components of the total momentum, $\mathbf{P}_\uparrow = \sum_i \mathbf{p}_i(1 + \sigma_{zi})/2$ and $\mathbf{P}_\downarrow = \sum_i \mathbf{p}_i(1 - \sigma_{zi})/2$, are not separately preserved, even in the absence of impurities. Here $\mathbf{p}_i$ is the momentum of the ith electron, and σ_{zi} is the Pauli matrix for the z component of the ith electron spin. Coulomb scattering can transfer momentum between spin-up and spin-down electrons, thereby effectively introducing a 'friction' for the relative motion of the two spin components, which tends to equalize the net momenta of the spin components (see Figure 5).

In a more rigorous formulation, Ohm's law can be written in the form

$$\begin{pmatrix} \mathcal{E}_\uparrow \\ \mathcal{E}_\downarrow \end{pmatrix} = \begin{pmatrix} \rho_{\uparrow\uparrow} & \rho_{\uparrow\downarrow} \\ \rho_{\downarrow\uparrow} & \rho_{\downarrow\downarrow} \end{pmatrix} \begin{pmatrix} \mathbf{j}_\uparrow \\ \mathbf{j}_\downarrow \end{pmatrix} \tag{6}$$

Here, the effective electric fields $\mathcal{E}_\sigma$ are the sums of a spin-independent external electric field plus the gradient of the local chemical potential, which can be spin-dependent, and $\mathbf{j}_\sigma$ is the electric current carried by the electrons with spin σ. The spin Coulomb drag gives rise to a spin transresistivity $\rho_{\uparrow\downarrow}$ in equation (6), which is the ratio of the gradient of the spin-down electrochemical potential to the spin-up current density when the spin-down current is zero. D'Amico and Vignale (2000) evaluated $\rho_{\uparrow\downarrow}$ in a generalized random-phase approximation.

D'Amico and Vignale (2001) showed that the Coulomb interaction usually gives rise to a significant reduction of the spin-diffusion coefficient D_s in equation (2) as compared to its value D_{ni} in a noninteracting system. They obtained

$$D_s = \frac{\mu k_{\mathrm{B}} T}{e} \frac{\mathcal{S}}{\mathcal{S}_c} \frac{1}{1 - \rho_{\uparrow\downarrow}/\rho_{\mathrm{D}}} \tag{7}$$

where $\mu k_{\mathrm{B}} T/e$ is the diffusion constant of a noninteracting system in the high-temperature limit (Einstein's relation), $\mathcal{S}$ is the spin stiffness (i.e., the inverse of the spin

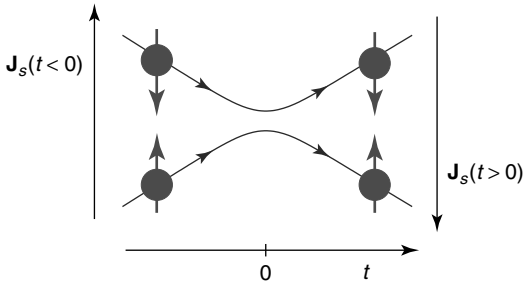

Figure 5. At $t < 0$ both electrons contribute equally to an upward spin current $\mathbf{J}_s = (e/m)(\mathbf{P}_\uparrow - \mathbf{P}_\downarrow)$. At $t = 0$, the directions of the orbital motions of the electrons are inverted due to Coulomb scattering. The direction of the spin current $\mathbf{J}_s$ at $t > 0$ is thus reversed.

susceptibility), $\mathcal{S}_c = k_B T n/(4n_\uparrow n_\downarrow)$ is the Curie spin stiffness of an ideal classical gas, and $\rho_D = m^*/(ne^2\tau_D)$ is the Drude resistivity. Figure 6 shows the ratio D_s/D_{ni} as a function of density n, assuming a dielectric constant $\varepsilon = 12$ appropriate for GaAs and mobility $\mu = 3 \times 10^3\,\mathrm{cm^2\,V^{-1}\,s^{-1}}$. Different line styles correspond to different temperatures as indicated. The curves labeled SD correspond to the case in which interactions in D_s are taken into account only through the spin Coulomb drag (i.e., the third factor in equation (7)).

Figure 6 shows that the interaction correction is quite significant and reduces the value of D_s. For large densities or $T \lesssim T_F$, where T_F is the Fermi temperature for density n, the dominant effect in the full calculation stems from the softening of the spin stiffness. On the other hand, the spin drag contribution dominates at small densities (the nondegenerate limit $T \gg T_F$). Note that $T_F = 1.6$, 20, and 300 K correspond to $n = 7.4 \times 10^{15}$, 3.2×10^{17}, and $1.9 \times 10^{19}\,\mathrm{cm^{-3}}$, respectively.

The spin Coulomb drag in a 2D electron gas was studied theoretically by D'Amico and Vignale (2003) and Flensberg, Jensen and Mortensen (2001), giving results quantitatively similar to three-dimensional (3D) electron systems. It was also observed experimentally by Weber *et al*. (2005). These authors used spin gratings as discussed at the end of Section 3.1 to measure the spin-diffusion coefficient D_s in a 2D electron gas in a GaAs/AlGaAs QW (circles in Figure 7). Its value as a function of temperature is significantly smaller than the charge diffusion coefficient D_c obtained from transport measurements for samples from the same wafer (solid lines in Figure 7). Yet good agreement is achieved between the measured D_s and calculations taking into account the spin Coulomb drag effect (i.e., the last factor in equation (7)), see the dashed line in Figure 7.

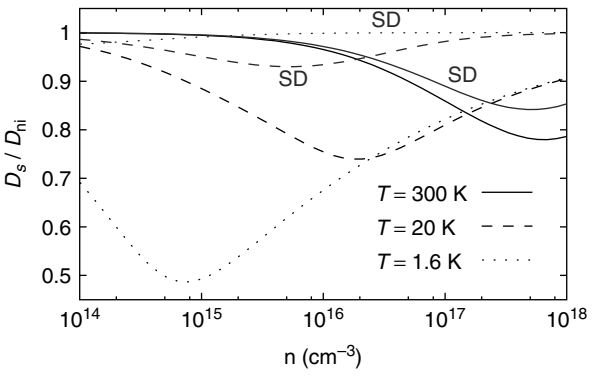

Figure 6. Ratio D_s/D_{ni} between the spin-diffusion coefficient D_s of an interacting electron system and the spin-diffusion coefficient D_{ni} of the corresponding noninteracting system, plotted as a function of density n, and assuming a dielectric constant $\varepsilon = 12$ appropriate for GaAs and mobility $\mu = 3 \times 10^3\,\mathrm{cm^2\,V^{-1}\,s^{-1}}$. The curves labeled SD correspond to the case in which interactions in D_s are taken into account only through the spin Coulomb drag (i.e., the third factor in equation (7)). (Reprinted figure with permissions from D'Amico *et al*., *Phys. Rev. B*, Vol 65, 085109, 2002. Copyright 2002 by the American Physical Society.)

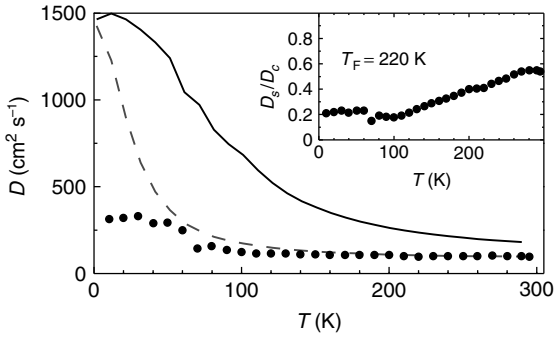

Figure 7. Measured (circles) and calculated (dashed line) spin-diffusion coefficient D_s and charge diffusion coefficient D_c (solid line) in a 2D electron gas in a GaAs/AlGaAs QW. The electron concentration is $n = 4.3 \times 10^{11}\,\mathrm{cm^{-2}}$, which corresponds to a Fermi temperature $T_F = 220\,\mathrm{K}$. The inset shows the ratio between the measured D_s and D_c. (Reproduced from Weber *et al*., 2005, with permission from Nature Publishing Group. © 2005.)

4 SPIN POLARIZATION AND CHARGE CURRENTS

4.1 Spin photocurrents

The optical creation of spin-oriented electrons can give rise to charge currents, the so-called spin photocurrents, which are characterized by the fact that these currents reverse their direction when the radiation helicity is changed from left-handed to right-handed and vice versa. Spin photocurrents are described by an axial tensor (or pseudotensor) of second rank. Such tensors play an important role in the context of gyrotropy, so that systems permitting nonzero axial second-rank tensors are often denoted gyrotropic systems. We note that gyrotropy is found neither in inversion-symmetric systems nor in systems with a zinc blende structure. The 18 gyrotropic crystal classes are listed, for example, by Agranovich and Ginzburg (1984)[4]. Semiconductors with a zinc blende (or diamond) structure become gyrotropic when the symmetry is reduced by means of, for example, quantum confinement or uniaxial strain. We note that gyrotropy is also a required and sufficient condition for the existence of k-linear spin splitting of the energy spectrum of spin-1/2 electron systems.

Two mechanisms contribute to spin photocurrents in gyrotropic media, the circular photogalvanic effect (CPGE) and the spin-galvanic effect (SGE) (Ganichev and Prettl, 2003). The CPGE was independently predicted by Ivchenko

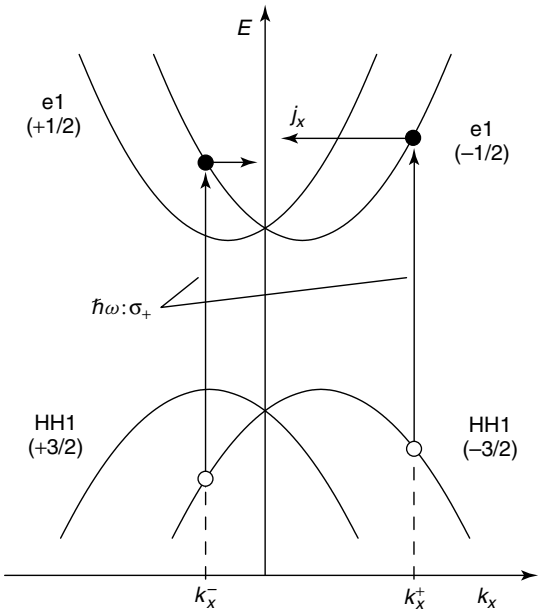

Figure 8. Microscopic picture of the circular photogalvanic effect (after Ganichev *et al*. (2001)). σ_+ excitation with photon energy $\hbar\omega$ induces optical transitions between the valence subband hh1 and the conduction subband e1 (vertical arrows). The concurrence of energy conservation, spin splitting of the electron and hole states, and optical selection rules results in an unbalanced occupation of the positive (k_x^+) and negative (k_x^-) states yielding a spin-polarized photocurrent. (Reprinted from *Journal of Magnetism and Magnetic Materials*, vol 300, Ganichev *et al*., p127, 2006 with permission from Elsevier.)

and Pikus (1978) and Belinicher (1978). Subsequently, this effect was observed in bulk Te by Asnin *et al*. (1978). The mechanism is illustrated in Figure 8. Excitation with σ_+-polarized light induces direct optical transitions between the valence subband hh1 and the conduction subband e1 (vertical arrows in Figure 8). For a given photon energy $\hbar\omega$, the optical selection rules and spin splitting result in an unbalanced occupation of the positive (k_x^+) and negative (k_x^-) states such that the 'center of mass' of these transitions is shifted from $k_x = 0$ to some average value $\langle k_x \rangle \neq 0$. This wave vector $\langle k_x \rangle$ translates into an average electron velocity $v = \hbar\langle k_x \rangle / m^*$ of the optically oriented electrons, which corresponds to a spin-polarized charge current, that is, the current is carried by electrons with one spin orientation. For interband transitions in 2D systems, as depicted in Figure 8, a detailed theory for the CPGE has been formulated by Golub (2003). Spin photocurrents can also be generated in a similar way by means of intersubband and intrasubband transitions (Ganichev *et al*., 2001; Ganichev and Prettl, 2003). Sherman, Najmaie and Sipe (2005) and Tarasenko and Ivchenko (2005) have shown that pure spin photocurrents not accompanied by charge transfer or spin orientation can be generated by means of absorption of unpolarized light in low-dimensional semiconductor systems.

Up to now, we have discussed spin photocurrents obtained by means of one-photon absorption. These currents can also be generated by means of two-photon excitation (Bhat and Sipe, 2000). In this case, the spin polarization of the resulting charge currents has been confirmed directly by measuring the phase-dependent spatial shift of the circularly polarized PL (Hübner *et al*., 2003). Pure spin photocurrents not accompanied by charge transfer have been generated through quantum interference of one- and two-photon absorption by Stevens *et al*. (2003).

Besides the CPGE, the SGE is a second mechanism that contributes to spin photocurrents (Ivchenko, Lyanda-Geller and Pikus, 1989; Ganichev *et al*., 2002). The SGE is caused by asymmetric spin-flip relaxation of spin-polarized electrons. The mechanism is illustrated in Figure 9. An unbalanced population of spin-up and spin-down subbands is generated, for example, by optical orientation. The current flow is caused by **k**-dependent spin-flip relaxation processes. Spins oriented in the up direction are scattered along k_x from the more occupied, for example, spin-up branch, to the less filled spin-down branch. Four quantitatively different spin-flip scattering events exist and are sketched in Figure 9 as bent arrows. The spin-flip scattering rate depends on the values of the wave vectors of the initial and the final states. Therefore, the spin-flip transitions marked by solid arrows in Figure 9 have the same rates. They preserve the distribution of carriers in the branches and, thus, do not yield a current. However, the two scattering processes shown by dashed arrows are inequivalent and generate an asymmetric carrier distribution around the branch minima. This asymmetric population results in a current flow along the x-direction. Within this model of elastic scattering the current is not spin polarized, since the same number of spin-up and spin-down

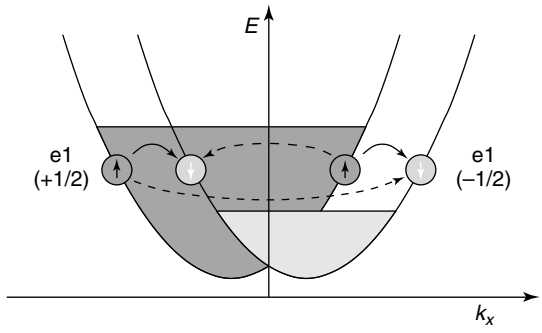

Figure 9. One-dimensional microscopic picture of the spin-galvanic effect (after Ganichev *et al*. (2001)). If one spin subband is preferentially occupied, for example, by optical excitation, asymmetric spin-flip scattering results in a current in the x direction.

electrons move in the same direction with the same velocity (Ganichev *et al*., 2002).

Assuming a linear relation between the components S_β of the electrons' averaged spin density and the components j_α of the resulting spin photocurrent, we get for the SGE

$$j_\alpha = \sum_\beta \mathcal{T}_{\alpha\beta} S_\beta \qquad \alpha, \beta = x, y, z \tag{8}$$

where $\mathcal{T}_{\alpha\beta}$ is an axial tensor of second rank[5]. This equation shows clearly that, unlike the case of the CPGE, optical excitation is not required for the SGE. The CPGE, however, is always accompanied by the SGE. Formally, this is due to the fact that both effects are characterized by axial tensors of second rank. Even in a completely optical experiment, CPGE and SGE can be distinguished by their different behaviors when the light source is switched off. Then the circular photogalvanic current decays with the momentum relaxation time whereas the spin-galvanic current decays with the spin relaxation time. If spin relaxation is absent, the spin-galvanic current vanishes (Ganichev and Prettl, 2003).

In recent years, detailed experimental and theoretical investigations of the CPGE and SGE in different systems have been performed by Ganichev *et al*. This work and related work have been reviewed by Ganichev and Prettl (2003, 2006).

4.2 Electrical generation of a spin polarization

In general, two possibilities exist for orienting electron spins with electric currents in a semiconductor. The first one is the spin Hall effect. For semiconductor systems, this idea was first discussed by D'yakonov and Perel' (1971b). It yields a spin accumulation at the *edges* of the sample in the direction perpendicular to the current. A detailed discussion of the spin Hall effect can be found in **Theory of Spin Hall Effects in Semiconductors, Volume 5**. In gyrotropic media, a second mechanism exists that yields a spin polarization in the *bulk* of the sample (Aronov and Lyanda-Geller, 1989; Edelstein, 1990). We note that equation (8), relating the given spin orientation $\mathbf{S}$ with the resulting current $\mathbf{j}$, can obviously be inverted, that is, an electric current $\mathbf{j}$ can give rise to a spin density $\mathbf{S}$ (Ivchenko and Pikus, 1978). As discussed in detail by Aronov, Lyanda-Geller and Pikus (1991), the different mechanisms contributing to the spin polarization of electrons induced by a current $\mathbf{j}$ can be classified analogously to the different spin relaxation mechanisms for $\mathbf{j} = 0$: for $\mathbf{j} = 0$, these mechanisms drive the system toward its equilibrium configuration characterized by equal occupations of the spin states. For $\mathbf{j} \neq 0$, on the other hand, the nonequilibrium configuration is characterized by an unequal filling of the spin states. Apart from a prefactor Q of order one, the details of which depend on the scattering mechanisms present in the electron system, the spin polarization is given by the ratio between the spin splitting $\hbar\Omega(\mathbf{k}_\mathcal{E})$ (assumed to be linear in $\mathbf{k}$) and the average energy $\overline{E}$ of the involved electrons (Aronov, Lyanda-Geller and Pikus, 1991)

$$\mathbf{S} = Qn \frac{\hbar\mathbf{\Omega}(\mathbf{k}_\mathcal{E})}{\overline{E}} \tag{9}$$

Here $\mathbf{k}_\mathcal{E} = e\mathcal{E}\tau_p/\hbar$ is the shift of the Fermi sphere caused by the electric field $\mathcal{E}$, and τ_p is the momentum relaxation time. In degenerate systems, we have $\overline{E} = \hbar^2 k_\mathrm{F}^2/(2m^*)$. In nondegenerate systems we have $\overline{E} = (d/2)k_\mathrm{B}T$, where d is the dimension. Finally, $n = k_\mathrm{F}^d/(d\pi)$ is the number density. The prefactor Q for different scattering mechanisms in $d = 2$ and $d = 3$ dimensions is given in Table I of Aronov, Lyanda-Geller and Pikus (1991).

The electric-field-induced spin orientation inside a semiconductor was also studied theoretically by Magarill, Chaplik and Éntin (2001) in 2D and Culcer, Yao, MacDonald and Niu (2005) in 2D and 3D. The effect was first observed experimentally in bulk Te by Vorob'ev *et al*. (1979). More recently, it was used by Hammar, Bennett, Yang and Johnson (1999, 2000) to analyze the spin injection from a ferromagnetic film into a 2D electron system, see also Monzon, Tang and Roukes (2000) van Wees (2000) and Silsbee (2001). Moreover, the effect was measured in strained bulk InGaAs by Kato, Myers, Gossard and Awschalom (2004b) and in 2D GaAs systems by Silov *et al*. (2004) and Ganichev *et al*. (2004, 2006). As an example, we want to discuss the experiment of Ganichev *et al*. They used a p-type GaAs multi-QW grown on an intentionally miscut (001) surface (tilted by 5° toward the [110] direction). The symmetry of this system is thus fully characterized by one mirror plane $(1\bar{1}0)$ (i.e., point group C_s), and electric spin orientation is expected only for a current in the ('active') direction $[1\bar{1}0]$ of the 2D plane, but not for the perpendicular ('passive') direction. In a transmission measurement using linearly polarized light, it is then possible to identify the current-induced spin orientation via a rotation of the polarization vector of the transmitted light (dichroic absorption and Faraday rotation) in a crossed polarizer setup, see the inset of Figure 10. For the 'active' direction $[1\bar{1}0]$, Ganichev *et al*. observed a significantly larger signal in the photodetector than for the 'passive' direction (Figure 10). The nonzero signal for the 'passive' direction was ascribed to imperfections of the infrared polarizers and carrier heating by the current, as confirmed by control experiments.

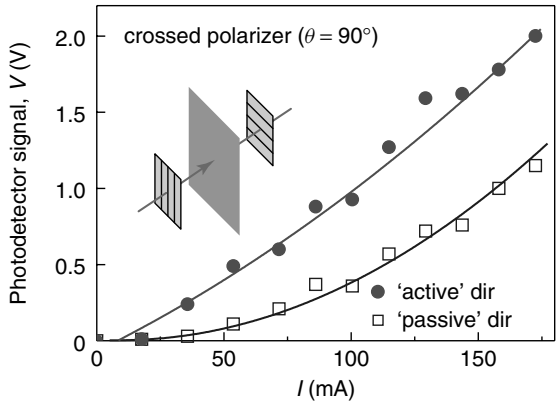

Figure 10. Transmission of a GaAs multi-QW as a function of current I in a crossedpolarizer setup (sketched in the inset). The sample was grown on a miscut (001) surface so that spin orientation is expected for the 'active' direction $[1\bar{1}0]$ but not for the perpendicular 'passive' direction. (Reproduced from Ganichev *et al*., 2006, with permission from Elsevier. © 2006.)

Finally, we note that Kalevich and Korenev (1990) predicted and observed a current-induced spin precession in the field $\mathbf{\Omega}(\mathbf{k}_{\mathcal{E}})$.

5 OUTLOOK

We focused here on the fundamental physics underlying the spin-dependent transport of carriers in semiconductors. These phenomena have many important and fascinating applications in the field of spintronics that are discussed elsewhere in this volume. Particularly important are various laterally structured systems such as the Datta-Das spin transistor (Datta and Das, 1990) and hybrid devices combining nonmagnetic semiconductors with semimagnetic and ferromagnetic materials.

ACKNOWLEDGMENTS

The author appreciates stimulating discussions with M. Beck, D. Culcer, S. D. Ganichev, and L. E. Golub. Also, he is grateful to S. A. Crooker for Figure 4. The research at Argonne National Laboratory was supported by the U.S. Department of Energy, Office of Science, Office of Basic Energy Sciences, under Contract No. DE-AC02-06CH11357.

NOTES

[1] When a semiconductor has a large absorption coefficient near the band edge, an emitted photon is usually reabsorbed before it can escape the crystal (Dumke, 1957). The detailed analysis of spin diffusion in p-type semiconductors performed by Garbuzov, Merkulov, Novikov and Fleisher (1976) and Gioev, Zakharchenya, Kavokin and Pak (1994) showed that allowance for diffusion and reabsorption was essential for the proper interpretation of their experimental data. Even in n-type GaAs it was found that reabsorption can be important for spin diffusion (Dzhioev, Zakharchenya, Korenev and Stepanova, 1997). Please note that the first authors of the latter two publications are, in fact, the same.

[2] The broad field of spin injection into semiconductors was recently reviewed, for example, by Jonker (2003).

[3] The Rashba spin splitting discussed below was not taken into account by Riechert, Alvarado, Titkov and Safarov (1984) for the interpretation of their experiment. However, this does not change the qualitative picture.

[4] As certain aspects of gyrotropy require a symmetric material tensor, the discussion of gyrotropy is often restricted to those 15 crystal classes that permit a symmetric axial tensor of second rank (Nye, 1957; Landau and Lifshitz, 1984), thus excluding the crystal classes C_{3v}, C_{4v}, and C_{6v} (the latter includes wurtzite materials). Spin photocurrents and the electric generation of spin discussed below do not require that the corresponding material tensors are symmetric. Therefore, these effects can be observed for all 18 crystal classes that permit an axial tensor of second rank. A general discussion of the symmetry of material tensors was given, for example, by Bir and Pikus (1974).

[5] For many crystal classes permitting nonzero axial tensors of second rank it is nonetheless required by symmetry that certain components of these tensors must vanish, see, for example, the discussion of the experiment of Ganichev *et al*. (2004, 2006) in Section 4.2 below.

REFERENCES

Agranovich, V.M. and Ginzburg, V.L. (1984). *Crystal Optics with Spatial Dispersion, and Excitons*, Second Edition, Springer: Berlin.

Aronov, A.G. and Lyanda-Geller, Y.B. (1989). Nuclear electric resonance and orientation of carrier spins by an electric field. *JETP Letters*, **50**, 431–434.

Aronov, A.G., Lyanda-Geller, Y.B. and Pikus, G.E. (1991). Spin polarization of electrons by an electric current. *Soviet Physics JETP*, **73**, 537–541.

Asnin, V.M., Bakun, A.A., Danishevskiĭ, A.M., *et al*. (1978). Observation of a photo-emf that depends on the sign of the circular polarization of the light. *JETP Letters*, **28**, 74–77.

Beck, M., Metzner, C., Malzer, S. and Döhler, G.H. (2005). *Spin Lifetimes and Strain-controlled Spin Precession of Drifting*

Electrons in Zinc Blende Type Semiconductors, http://arxiv.org/abs/cond-mat/0504668.

Belinicher, V. (1978). Space-oscillating photocurrent in crystals without symmetry center. *Physics Letters*, **66A**, 213–214.

Bhat, R.D.R. and Sipe, J.E. (2000). Optically injected spin currents in semiconductors. *Physical Review Letters*, **85**, 5432–5435.

Bir, G.L. and Pikus, G.E. (1974). *Symmetry and Strain-Induced Effects in Semiconductors*, Wiley: New York.

Bleibaum, O. (2006). Spin diffusion equations for systems with Rashba spin-orbit interaction in an electric field. *Physical Review B*, **73**, 035322.

Braun, M. and Rössler, U. (1985). Magneto-optic transitions and non-parabolicity parameters in the conduction band of semiconductors. *Journal of Physics C: Solid State Physics*, **18**, 3365–3377.

Bychkov, Y.A. and Rashba, E.I. (1984). Oscillatory effects and the magnetic susceptibility of carriers in inversion layers. *Journal of Physics C: Solid State Physics*, **17**, 6039–6045.

Cameron, A.R., Riblet, P. and Miller, A. (1996). Spin gratings and the measurement of electron drift mobility in multiple quantum well semiconductors. *Physical Review Letters*, **76**, 4793–4796.

Crooker, S.A. and Smith, D.L. (2005). Imaging spin flows in semiconductors subject to electric, magnetic, and strain fields. *Physical Review Letters*, **94**, 236601.

Culcer, D., Yao, Y., MacDonald, A.H. and Niu, Q. (2005). Electrical generation of spin in crystals with reduced symmetry. *Physical Review B*, **72**, 045215.

D'Amico, I. and Vignale, G. (2000). Theory of spin Coulomb drag in spin-polarized transport. *Physical Review B*, **62**, 4853–4857.

D'Amico, I. and Vignale, G. (2001). Spin diffusion in doped semiconductors: the role of Coulomb interactions. *Europhysics Letters*, **55**, 566–572.

D'Amico, I. and Vignale, G. (2002). Coulomb interaction effects in spin-polarized transport. *Physical Review B*, **65**, 085109.

D'Amico, I. and Vignale, G. (2003). Spin Coulomb drag in the two-dimensional electron liquid. *Physical Review B*, **68**, 045307.

Dareys, B., Marie, X., Amand, T., *et al*. (1993). Spin dynamics of exciton states in GaAs/AlGaAs multiple quantum wells. *Superlattices and Microstructures*, **13**, 353–358.

Datta, S. and Das, B. (1990). Electronic analog of the electro-optic modulator. *Applied Physics Letters*, **56**, 665–667.

de Andrada e Silva, E.A. (1992). Conduction-subband anisotropic spin splitting in III-V semiconductor heterojunctions. *Physical Review B*, **46**, 1921–1924.

Dresselhaus, G. (1955). Spin-orbit coupling effects in zinc blende structures. *Physical Review*, **100**, 580–586.

Dumke, W.P. (1957). Spontaneous radiative recombination in semiconductors. *Physical Review*, **105**, 139–144.

D'yakonov, M.I., Marushchak, V.A., Perel', V.I. and Titkov, A.N. (1986). The effect of strain on the spin relaxation of conduction electrons in III-V semiconductors. *Soviet Physics JETP*, **63**, 655–661.

D'yakonov, M.I. and Perel', V.I. (1971a). Feasibility of optical orientation of equilibrium electrons in semiconductors. *JETP Letters*, **13**, 144–146.

D'yakonov, M.I. and Perel', V.I. (1971b). Possibility of orienting electron spins with current. *JETP Letters*, **13**, 467–469.

D'yakonov, M.I. and Perel', V.I. (1972). Spin relaxation of conduction electrons in noncentrosymmetric semiconductors. *Soviet Physics Solid State*, **13**, 3023–3026.

D'yakonov, M.I. and Perel', V.I. (1976). Theory of the Hanle effect in optical orientation of electrons in *n*-type semiconductors. *Soviet Physics Semiconductors*, **10**, 350–353.

Dyakonov, M.I. and Perel, V.I. (1984). Theory of optical spin orientation of electrons and nuclei in semiconductors. In *Optical Orientation*, Meier, F. and Zakharchenya, B.P. (Eds.), Elsevier: Amsterdam, pp. 11–71.

Dzhioev, R.I., Zakharchenya, B.P., Korenev, V.L. and Stepanova, M.N. (1997). Spin diffusion of optically oriented electrons and photon entrainment in *n*-gallium arsenide. *Physics of the Solid State*, **39**, 1765–1768.

Edelstein, V.M. (1990). Spin polarization of conduction electrons induced by electron current in two-dimensional asymmetric electron systems. *Solid State Communications*, **73**, 233–235.

Fiederling, R., Keim, M., Reuscher, G., *et al*. (1999). Injection and detection of a spin-polarized current in a light-emitting diode. *Nature*, **402**, 787–790.

Flatté, M.E. and Byers, J.M. (2000). Spin diffusion in semiconductors. *Physical Review Letters*, **84**, 4220–4223.

Flensberg, K., Jensen, T.S. and Mortensen, N.A. (2001). Diffusion equation and spin drag in spin-polarized transport. *Physical Review B*, **64**, 245308.

Freeman, M.R., Awschalom, D.D. and Hong, J.M. (1990). Picosecond photoluminescence excitation spectroscopy of GaAs/AlGaAs quantum wells. *Applied Physics Letters*, **57**, 704–706.

Ganichev, S.D., Danilov, S.N., Schneider, P., *et al*. (2004). Can an Electric Current Orient Spins in Quantum Wells? http://arxiv.org/abs/cond-mat/0403641.

Ganichev, S.D., Danilov, S.N., Schneider, P., *et al*. (2006). Electric current-induced spin orientation in quantum well structures. *Journal of Magnetism and Magnetic Materials*, **300**, 127–131.

Ganichev, S.D., Ivchenko, E.L., Bel'kov, V.V., *et al*. (2002). Spin-galvanic effect. *Nature*, **417**, 153–156.

Ganichev, S.D., Ivchenko, E.L., Danilov, S.N., *et al*. (2001). Conversion of spin into directed electric current in quantum wells. *Physical Review Letters*, **86**, 4358–4361.

Ganichev, S.D. and Prettl, W. (2003). Spin photocurrents in quantum wells. *Journal of Physics: Condensed Matter*, **15**, R935–R983.

Ganichev, S. and Prettl, W. (2006). *Intense Terahertz Excitation of Semiconductors*, Oxford University Press: Oxford.

Garbuzov, D.Z., Merkulov, I.A., Novikov, V.A. and Fleisher, V.G. (1976). Diffusion of 'spin-labelled' electrons in a double heterostructure. *Soviet Physics Semiconductors*, **10**, 552–555.

Gioev, R.I., Zakharchenya, B.P., Kavokin, K.V. and Pak, P.E. (1994). Study of diffusional and radiative electron transport in *p*-GaAs by the optical orientation method. *Physics of the Solid State*, **36**, 1501–1506.

Golub, L.E. (2003). Spin-splitting-induced photogalvanic effect in quantum wells. *Physical Review B*, **67**, 235320.

Gramila, T.J., Eisenstein, J.P., MacDonald, A.H., *et al*. (1991). Mutual friction between parallel two-dimensional electron systems. *Physical Review Letters*, **66**, 1216–1219.

Hägele, D., Oestreich, M., Rühle, W.W., *et al*. (1998). Spin transport in GaAs. *Applied Physics Letters*, **73**, 1580–1582.

Hammar, P.R., Bennett, B.R., Yang, M.J. and Johnson, M. (1999). Observation of spin injection at a ferromagnet-semiconductor interface. *Physical Review Letters*, **83**, 203–206.

Hammar, P.R., Bennett, B.R., Yang, M.J. and Johnson, M. (2000). A reply to the comment by F. G. Monzon, H. X. Tang, and M. L. Roukes, and also to the comment by B. J. van Wees. *Physical Review Letters*, **84**, 5024–5025.

Howlett, W. and Zukotynski, S. (1977). Effect of deformation on the conduction band of III-V semiconductors. *Physical Review B*, **16**, 3688–3693.

Hruška, M., Kos, Š., Crooker, S.A., *et al*. (2006). Effects of strain, electric, and magnetic fields on lateral electron-spin transport in semiconductor epilayers. *Physical Review B*, **73**, 075306.

Hübner, J., Rühle, W.W., Klude, M., *et al*. (2003). Direct observation of optically injected spin-polarized currents in semiconductors. *Physical Review Letters*, **90**, 216601.

Ivchenko, E.L., Lyanda-Geller, Y.B. and Pikus, G.E. (1989). Photocurrent in structures with quantum wells with an optical orientation of free carriers. *JETP Letters*, **50**, 175–177.

Ivchenko, E.L. and Pikus, G.E. (1978). New photogalvanic effect in gyrotropic crystals. *JETP Letters*, **27**, 604–608.

Jonker, B.T. (2003). Progress toward electrical injection of spin-polarized electrons into semiconductors. *Proceedings of IEEE*, **91**, 727–740.

Jonker, B.T., Park, Y.D., Bennett, B.R., *et al*. (2000). Robust electrical spin injection into a semiconductor heterostructure. *Physical Review B*, **62**, 8180–8183.

Kalevich, V.K. and Korenev, V.L. (1990). Effect of electric field on the optical orientation of 2D electrons. *JETP Letters*, **52**, 230–235.

Kato, Y., Myers, R.C., Gossard, A.C. and Awschalom, D.D. (2004a). Coherent spin manipulation without magnetic fields in strained semiconductors. *Nature*, **427**, 50–53.

Kato, Y.K., Myers, R.C., Gossard, A.C. and Awschalom, D.D. (2004b). Current-induced spin polarization in strained semiconductors. *Physical Review Letters*, **93**, 176601.

Kavokin, K.V. (2002). Optical manifestations of electron spin transport and relaxation in semiconductors. *Physical Status Solidi A*, **190**, 221–227.

Kikkawa, J.M. and Awschalom, D.D. (1999). Lateral drag of spin coherence in gallium arsenide. *Nature*, **397**, 139–141.

Lampel, G. (1968). Nuclear dynamic polarization by optical electronic saturation and optical pumping in semiconductors. *Physical Review Letters*, **20**, 491–493.

Landau, L.D. and Lifshitz, E.M. (1984). *Electrodynamics of Continuous Media*, Second Edition, Pergamon: Oxford.

Leggett, A.J. (1970). Spin diffusion and spin echoes in liquid ^{3}He at low temperature. *Journal of Physics C: Solid State Physics*, **3**, 448–459.

Leggett, A.J. and Rice, M.J. (1968). Spin echoes in liquid He^3 and mixtures: a predicted new effect. *Physical Review Letters*, **20**, 586–589.

Magarill, L.I., Chaplik, A.V. and Éntin, M.V. (2001). Spin response of 2D electrons to a lateral electric field. *Semiconductors*, **35**, 1081–1087.

Maialle, M.Z., de Andrada e Silva, E.A. and Sham, L.J. (1993). Exciton spin dynamics in quantum wells. *Physical Review B*, **47**, 15776–15788.

Malajovich, I., Kikkawa, J.M., Awschalom, D.D., *et al*. (2000). Coherent transfer of spin through a semiconductor heterointerface. *Physical Review Letters*, **84**, 1015–1018.

Masselink, W.T., Sun, Y.L., Fischer, R., *et al*. (1984). Enhanced luminescence from AlGaAs/GaAs single quantum well structures through improved interfaces. *Journal of Vacuum Science and Technology B*, **2**, 117–122.

Meier, F. and Zakharchenya, B.P. (Eds.) (1984). *Optical Orientation*, Elsevier: Amsterdam.

Monzon, F.G., Tang, H.X. and Roukes, M.L. (2000). Magnetoelectronic phenomena at a ferromagnet-semiconductor interface. *Physical Review Letters*, **84**, 5022.

Muñoz, L., Pérez, E., Viña, L. and Ploog, K. (1995). Spin relaxation in intrinsic GaAs quantum wells: Influence of excitonic localization. *Physical Review B*, **51**, 4247–4257.

Nitta, J., Akazaki, T., Takayanagi, H. and Enoki, T. (1997). Gate control of spin-orbit interaction in an inverted $In_{0.53}Ga_{0.47}$ As/$In_{0.52}$ $Al_{0.48}$As heterostructure. *Physical Review Letters*, **78**, 1335–1338.

Nye, J.F. (1957). *Physical Properties of Crystals*, Oxford University Press: Oxford.

Ohkawa, F.J. and Uemura, Y. (1974). Quantized surface states of narrow-gap semiconductors. *Journal of the Physical Society of Japan*, **37**, 1325–1333.

Ohno, Y., Young, D.K., Beschoten, B., *et al*. (1999). Electrical spin injection in a ferromagnetic semiconductor heterostructure. *Nature*, **427**, 790–792.

Pfalz, S., Winkler, R., Nowitzki, T., *et al*. (2005). Optical orientation of electron spins in GaAs quantum wells. *Physical Review B*, **71**, 165305.

Pikus, G.E., Marushchak, V.A. and Titkov, A.N. (1988). Spin splitting of energy bands and spin relaxation of carriers in cubic III-V crystals (review). *Soviet Physics Semiconductors*, **22**, 115–124.

Pikus, G.E. and Titkov, A.N. (1984). Spin relaxation under optical orientation in semiconductors. In *Optical Orientation*, Meier, F. and Zakharchenya, B.P. (Eds.), Elsevier: Amsterdam, pp. 73–131.

Qi, Y. and Zhang, S. (2003). Spin diffusion at finite electric and magnetic fields. *Physical Review B*, **67**, 052407.

Ranvaud, R., Trebin, H-R., Rössler, U. and Pollak, F.H. (1979). Quantum resonances in the valence bands of zinc-blende semiconductors. II. Results for *p*-InSb under uniaxial stress. *Physical Review B*, **20**, 701–715.

Rashba, E.I. (1960). Properties of semiconductors with an extremum loop: I. Cyclotron and combinational resonance in a magnetic

field perpendicular to the plane of the loop. *Soviet Physics Solid State*, **2**, 1109–1122.

Riechert, H., Alvarado, S.F., Titkov, A.N. and Safarov, V.I. (1984). Precession of the spin polarization of photoexcited conduction electrons in the band-bending region of GaAs(001). *Physical Review Letters*, **52**, 2297–2300.

Rojo, A.G. (1999). Electron-drag effects in coupled electron systems. *Journal of Physics: Condensed Matter*, **11**, R31–R52.

Rössler, U. and Kainz, J. (2002). Microscopic interface asymmetry and spin-splitting of electron subbands in semiconductor quantum structures. *Solid State Communications*, **121**, 313–316.

Roussignol, P., Rolland, P., Ferreira, R., *et al*. (1992). Time-resolved spin-polarization spectroscopy in GaAs/AlGaAs quantum wells. *Surface Science*, **267**, 360–364.

Seiler, D.G., Bajaj, B.D. and Stephens, A.E. (1977). Inversion-asymmetry splitting of the conduction band in InSb. *Physical Review B*, **16**, 2822–2833.

Sherman, E.Y., Najmaie, A. and Sipe, J.E. (2005). Spin current injection by intersubband transitions in quantum wells. *Applied Physics Letters*, **86**, 122103.

Silov, A.Y., Blajnov, P.A., Wolter, J.H., *et al*. (2004). Current-induced spin polarization at a single heterojunction. *Applied Physics Letters*, **85**, 5929–5931.

Silsbee, R.H. (2001). Theory of the detection of current-induced spin polarization in a two-dimensional electron gas. *Physical Review B*, **63**, 155305.

Smith, R.A. (1978). *Semiconductors*, Second Edition, Cambridge University Press: Cambridge.

Stevens, M.J., Smirl, A.L., Bhat, R.D.R., *et al*. (2003). Quantum interference control of ballistic pure spin currents in semiconductors. *Physical Review Letters*, **90**, 136603.

Stotz, J.A.H., Hey, R., Santos, P.V. and Ploog, K.H. (2005). Coherent spin transport through dynamic quantum dots. *Nature Materials*, **4**, 585–588.

Takahashi, Y., Shizume, K. and Masuhara, N. (1999). Spin diffusion in a two-dimensional electron gas. *Physical Review B*, **60**, 4856–4865.

Tarasenko, S.A. and Ivchenko, E.L. (2005). Pure spin photocurrents in low-dimensional structures. *JETP Letters*, **81**, 231–235.

Trebin, H-R., Rössler, U. and Ranvaud, R. (1979). Quantum resonances in the valence bands of zinc-blende semiconductors. I. Theoretical aspects. *Physical Review B*, **20**, 686–700.

Twardowski, A. and Hermann, C. (1987). Variational calculation of polarization of quantum-well photoluminescence. *Physical Review B*, **35**, 8144–8153.

Uenoyama, T. and Sham, L.J. (1990). Carrier relaxation and luminescence polarization in quantum wells. *Physical Review B*, **42**, 7114–7123.

van Wees, B.J. (2000). Comment on "Observation of spin injection at a ferromagnet-semiconductor interface". *Physical Review Letters*, **84**, 5023.

Vorob'ev, L.E., Ivchenko, E.L., Pikus, G.E., *et al*. (1979). Optical activity in tellurium induced by a current. *JETP Letters*, **29**, 441–445.

Weber, C.P., Gedik, N., Moore, J.E., *et al*. (2005). Observation of spin Coulomb drag in a two-dimensional electron gas. *Nature*, **437**, 1330–1333.

Weisbuch, C., Miller, R.C., Dingle, R., *et al*. (1981). Intrinsic radiative recombination from quantum states in GaAs-AlGaAs multi-quantum well structures. *Solid State Communications*, **37**, 219–222.

Winkler, R. (2003). *Spin-orbit Coupling Effects in Two-dimensional Electron and Hole Systems*, Springer: Berlin.

Yu, Z.G. and Flatté, M.E. (2002). Electric-field dependent spin diffusion and spin injection into semiconductors. *Physical Review B*, **66**, 201202.

Semiconductor Spintronic Devices

Michael E. Flatté
University of Iowa, Iowa City, IA, USA

1 INTRODUCTION

Semiconductors, more than any other class of material, are very sensitive to external electrical perturbations, and as a result the properties of a semiconducting material can often be dramatically changed with gate contacts. This ability to drive a material far from equilibrium using external controls permits the amplification and switching behavior of transistors, as well as a variety of other nonlinear properties. For transistors based on charge motion, such as field-effect transistors, the typical modification of equilibrium achieved with the gate contact is the back-and-forth change of the material's conductance between the insulating and the metallic regime. For spin-based devices, it will be the controllable and reversible change of a spin-dependent or magnetic property.

Handbook of Magnetism and Advanced Magnetic Materials. Edited by Helmut Kronmüller and Stuart Parkin. Volume 5: *Spintronics and Magnetoelectronics*. ISBN: 978-0-470-02217-7.

The first demonstration that the fundamental magnetic properties of a ferromagnetic semiconductor could be manipulated with an external contact was the demonstration of a voltage dependence of the Curie temperature in the ferromagnetic semiconductor InMnAs (Ohno *et al*., 2000). Since then an electric field has been shown to modify the coercive field of InMnAs (Chiba, Yamanouchi, Matsukura and Ohno, 2003) and as a result permit magnetization reversal. These demonstrations rely on the unusual nature of ferromagnetism in these materials. In order to modify the magnetic properties of these materials with an electric field, a sufficient number of carriers must be removable from the material with a modest-sized voltage, and the ferromagnetic state must depend on the density of these carriers. The requirement of carriers that mediate the magnetism suggests magnetic insulators would be poor candidates for gate control of magnetism. Magnetic metals are also poor candidates, for the density of carriers in a typical metal is orders of magnitude higher than in ferromagnetic semiconductors, and therefore it is not possible to remove enough carriers with a modest voltage to significantly modify the magnetic properties of a metal. Thus electrically switchable magnets, and the potential applications of such materials (e.g., electrically switchable magneto-optical elements or voltage-tunable sources of spin-polarized current) are likely restricted to devices made from ferromagnetic semiconductors.

The spin-dependent properties of carriers moving through nonmagnetic semiconductors can also be modified by the application of electric fields. Even though there is no equilibrium magnetization in these materials, the orbital properties of a specific electronic state are entangled with the spin properties of that state through the spin-orbit interaction. Semiconductors with inversion-symmetric crystal structures (such as silicon, germanium, and diamond) have doubly degenerate electronic states for all crystal momenta, but owing to the

spin-orbit interaction, the wave functions cannot be factored into a spin component multiplying an orbital component. This entanglement of spin and orbit leads to transport-dependent spin dynamics, including relaxation of spin-polarized distributions of carriers toward an equilibrium unpolarized state. For semiconductors with inversion-asymmetric crystal structures (such as gallium arsenide, zinc selenide, and other materials with zincblende or wurtzite crystal structures), the effect of the spin-orbit interaction is even more pronounced, leading to momentum-dependent spin splittings of the electronic states throughout the zone. An applied external electric field provides an additional inversion-asymmetric contribution to the overall crystal potential, and thus introduces a nonzero spin splitting into the electronic states of an inversion-symmetric material or modifies the spin splittings of an inversion-asymmetric material.

A seminal proposal (Datta and Das, 1990) described this mechanism for electric-field manipulation of the spin orientation of electrons moving through a high-mobility semiconductor channel. Since then many other manipulation proposals and device configurations have been discussed in the literature. These include both the use of electric fields to change the electronic structure of a region of the device (modifying the spin splittings of moving electrons) and the use of electric fields to change the average velocity of carriers which thus experience different average electronic structures (Koga, Nitta, Takayanagi and Datta, 2002). Some recent transistor suggestions have focused on simply modifying the spin relaxation time of carriers within a nonmagnetic semiconductor as a way of achieving gain (Hall *et al*., 2003b). Electric-field manipulation of the spin relaxation time has been demonstrated in GaAs/AlGaAs and InAs/AlSb quantum wells. On the basis of these observations and theoretical estimates of the fundamental limits of transistor performance (both for charge-based and spin-based devices) it has been suggested that spin-based transistor devices have superior fundamental performance limits than charge-based devices (Hall and Flatté, 2006).

The final category of devices to be considered here are those in which the electric fields, rather than controlling the properties of a single layer (magnetic or nonmagnetic), are used to control the relative potentials of two elements of the device. This type of control is commonly used in charge-based electronics, such as changing the relative potential of the p and n regions of a diode. These adjustments are then used to change the carrier transport through the device as a whole. When the elements of the structure are magnetic, then the magnetic properties of the current can be adjusted in addition to the total current, or the device functionality itself can be manipulated. One example of this type of device is a ferromagnetic semiconductor with 100% or nearly 100% spin-polarized carriers. A domain wall in such a material behaves similar to a p−n diode, but can be removed if desired to replace a nonlinear circuit element with a linear one (Flatté and Vignale, 2001).

2 GATE-CONTROLLED MAGNETS AND SEMICONDUCTOR SPINTRONIC DEVICES

2.1 Gate control of the properties of carrier-mediated ferromagnetic semiconductors

The fundamental physical properties of carrier-mediated ferromagnetic semiconductors differ significantly from those of magnetic insulators or magnetic metals and provide clues to the potential applications of such materials when they become available at and above room temperature. Magnetic semiconductors of this type, such as InMnAs (Munekata *et al*., 1989) and GaMnAs (Ohno *et al*., 1996) are grown by adding both magnetic ions and carriers to an initially nonmagnetic, insulating semiconductor. If only magnetic ions are added to a nonmagnetic semiconductor, such as in the case of Mn substituted for the group-II atom in a II−VI semiconductor such as ZnSe, then these ions are very weakly coupled and do not establish ferromagnetic order. This situation is shown in Figure 1. Although these materials are not ferromagnetic, their magnetic response can be very unusual. When the magnetic ion Mn replaces the group-III atom in a III−V semiconductor, such as InAs or GaAs, then the different valence of Mn provides an additional hole for each substitutional Mn. At low concentrations, each hole is bound to a substitutional Mn in an acceptor state with a radius of ∼1 nm, as shown in Figure 1. Shown in Figure 2 is a scanning tunnelling microscope (STM) measurement of the acceptor state associated with Mn when substituted in GaAs. The state itself is highly anisotropic due to the breaking of spherical symmetry by the cubic lattice of GaAs.

Although the hole would bind to the Mn location simply because of the attractive Coulomb potential from the effective negative charge of the Mn site, the acceptor level is much more strongly bound than would be expected for a shallow level. This additional binding originates from p−d hybridization, the coupling of the p-like valence states of GaAs with the core electronic d-like states of the Mn ion. As this coupling is highly spin-selective, the bound acceptor state is nearly 100% spin polarized, with the hole spin direction oriented antiparallel to the $S = 5/2$ core spin of the Mn ion. At the valence band edge the holes are members of a $J_h = 3/2$ multiplet, and thus the ground state of the combined core-spin-valence-hole Mn complex is $J = 1$.

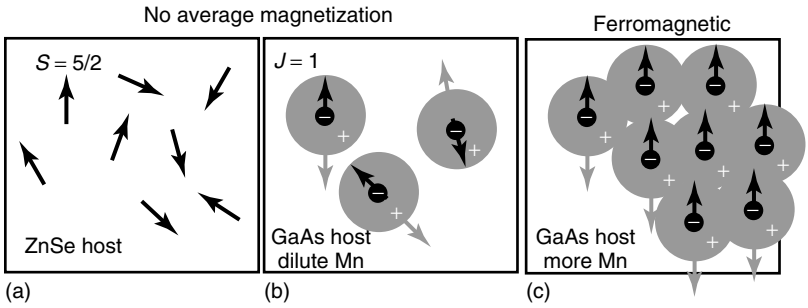

Figure 1. (a) When magnetic ions are placed in a nonmagnetic semiconductor without additional carriers the spins are very weakly coupled and not ferromagnetic. (b) Magnetic ions with bound holes placed in a nonmagnetic semiconductor are weakly coupled when at very dilute concentrations. (c) When the density of magnetic ions with bound holes is high enough, the carriers overlap, coupling the magnetic ions and producing ferromagnetism.

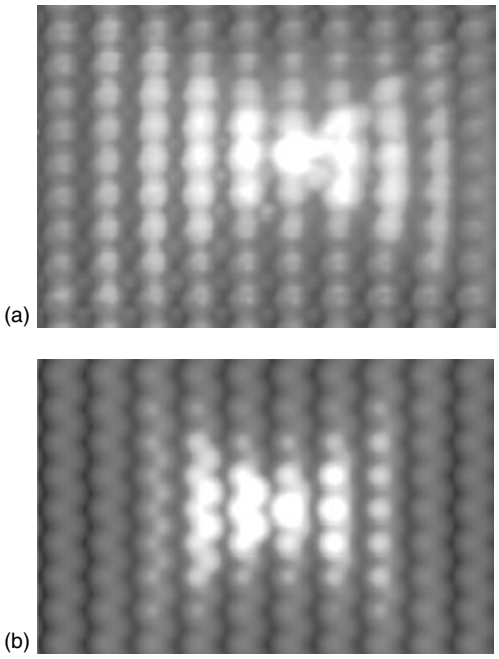

Figure 2. (a) STM image of neutral Mn. Big and small round features correspond to As and Ga related surface states, respectively. Mn is located in the fifth subsurface atomic layer; (b) simulated image of the Mn situated in the fifth subsurface atomic layer. (Reprinted with permission Yakunin *et al*., copyright 2004, American Physical Society.)

These properties of the ground state have been confirmed by electron-spin-resonance measurements on individual substitutional Mn ions (Schneider, Kaufmann, Wilkening and Baeumler, 1987).

When a sufficient density of Mn has been added these acceptor states overlap. If the spin orientations of the holes on two neighboring Mn are parallel then each hole can delocalize into a molecular state around both Mn. If, however, the spin orientations are antiparallel then the two acceptor states cannot hybridize with each other and each hole must remain localized around its own Mn. As the holes are more delocalized for parallel Mn alignment, and thus have lower energy, the ferromagnetic configuration is energetically favored. The energy splittings between these molecular states are observable with scanning tunneling spectroscopy and confirm the ferromagnetic alignment between neighboring Mn (Kitchen *et al*., 2006). As the acceptor state itself, seen in Figure 2, is spatially anisotropic, it is not surprising that the Mn–Mn coupling mediated by the bound holes is also spatially anisotropic. The consequence of this carrier-mediated coupling is a ferromagnetic state when the Mn doping density is sufficiently high (as shown in Figure 1).

Impressive quantitative calculations of the properties of ferromagnetic GaMnAs and other Mn-doped III–V ferromagnetic semiconductors have been achieved using a highly simplified picture of the electronic structure in Figure 1. In the 'mean-field' approach (Dietl, Ohno and Matsukura, 2001; Abolfath, Jungwirth, Brum and MacDonald, 2001; MacDonald, Schiffer and Samarth, 2005), the effective spin-dependent potential of the individual Mn ions is smeared out to a uniform spin-dependent potential throughout the solid. The hole density is also smeared out to a uniform value and the polarization of the Mn ions and the holes is determined self-consistently given the hole–Mn–ion interaction energy. This mean-field approach has successfully described the conductivity of GaMnAs, the magnetic anisotropy and magnetoelastic constants (Masmanidis *et al*., 2005), the dependence of the Curie temperature on doping and strain, and some of the chemical trends of other magnetic semiconducting materials. Limitations include predictions of room-temperature ferromagnetism in the semiconductors GaMnN and ZnMnO – predictions that have yet to be convincingly demonstrated.

Figure 1 also suggests how reducing the density of holes can reduce the Curie temperature of such a magnetic semiconductor. As the coupling between neighboring Mn core spins is mediated by the carriers, if there are fewer carriers the coupling will be weaker. The density of Mn required

to achieve the ferromagnetic state is only around 1% (with the largest Curie temperatures achieved for doping densities >5%). This means that only one hole for every 10–100 unit cells must be removed to fully deplete the material of carriers (and the Curie temperature can be observably modified even if only a small fraction of the carriers present have been removed). This behavior is possible because the host material for the magnetic ions is a nonmagnetic semiconductor. If the host material were a nonmagnetic insulator rather than a semiconductor any carriers would be strongly bound to the magnetic atoms inserted into the lattice. Thus the overlap with nearby spins would be of far shorter range, and ferromagnetism would not be achievable via carrier mediation until magnetic atoms were placed on a much larger fraction of lattice sites than required for these ferromagnetic semiconductors. If the host were a nonmagnetic metal then the density of carriers present at the start (typically of order one per unit cell) would be much larger than the density in these magnetic semiconductors, precluding the possibility of gating the magnetism. Carrier-mediated ferromagnetism itself would be less effective, for the sign of the spin–spin interaction mediated by a dense sea of carriers would oscillate rapidly in space (Ruderman–Kittel–Kasuya–Yosida coupling) owing to the Fermi surface structure. As a result, the behavior of a dilute alloy of magnetic atoms in a nonmagnetic host would be characterized by varying magnitudes and signs of spin–spin coupling, which tends to produce a spin glass rather than a ferromagnet.

2.2 Switchable Faraday isolators

Potential applications of gateable ferromagnets include switchable magneto-optical elements and voltage-tunable sources of highly spin-polarized current. One popular example of a magneto-optical element is the Faraday isolator, shown schematically in Figure 3. This device, commonly used to prevent feedback into laser cavities, provides one-way transmission of light. A one-way mirror violates time-reversal invariance, so a magnetic element is required to implement the device. In a magnetic material, the index of refraction differs for left and right circularly polarized light, an effect called *magnetic circular dichroism*. In the configuration of Figure 3, light that is linearly polarized passes through a Faraday rotator. A linearly polarized light beam can be decomposed into a coherent sum of a left and right circularly polarized beam. The index difference for these two components in the Faraday rotator generates a phase difference between the two that results in a rotation of the linear polarization direction for the beam as it passes through the material. In the schematic, the magnetization and length of the material is chosen so the beam rotates 45° counterclockwise. That beam can then pass through another linear polarizer mounted at the other end of the device and oriented at 45° to the initial polarizer. If light enters from the far end, however, it is filtered by the linear polarizer to a 45° polarization and is rotated an additional 45° while passing in the other direction through the Faraday rotator. As the sense of rotation is the same for light traveling in either direction through the Faraday rotator, when light enters from the far side it is rotated into a 90° oriented beam that cannot pass through the original linear polarizer. For communication wavelengths the material commonly used is yttrium iron garnet (YIG), which provides a large Faraday rotation and low optical loss. Use of a switchable ferromagnet would permit the one-directional transmission to be turned on or off, or the direction of the allowed transmission to be changed dynamically. Such magnetically switchable mirrors may find applications in high-speed switching and in high-speed displays.

2.3 Voltage-tunable sources of spin-polarized current

As the spin polarization of a carrier-mediated ferromagnetic semiconductor depends sensitively on the carrier density, applying a voltage to deplete the carriers will also modify the carrier spin polarization. This produces a voltage-tunable source of spin-polarized carriers. The spin polarization of this current, however, can be amplified by placing this ferromagnetic semiconductor in a transistor-like structure called a *magnetic bipolar transistor* (Flatté, Yu, Johnston-Halperin and Awschalom, 2003).

Shown in Figure 4 is a schematic of an $n-p_{\uparrow}-n$ transistor structure, consisting of an emitter and collector that are nonmagnetic n-doped semiconductors and a base that is a p-doped ferromagnetic semiconductor. In this structure, three general types of spin-selective processes can potentially cause minority electrons injected from the nonmagnetic n-doped emitter into the p-doped base to become spin polarized before passing into the collector. The first is a dramatic spin-filtering effect on carriers passing from the emitter to the $p_{\uparrow}$ base, the second is spin-selective conduction electron-spin flipping within the $p_{\uparrow}$ region, and the third is spin-selective recombination within the $p_{\uparrow}$ region. The result is a large current of highly spin-polarized electrons into the nonmagnetic collector of the device. This spin-polarized current can be controlled by any scheme that controls the orientation or magnitude of the base magnetization.

The spin-filtering effect originates from the spin splitting of the minority (conduction electron) band edges in the $p_{\uparrow}$ base (shown in Figure 4). Estimates of the spin splitting of the valence band in a p-doped magnetic semiconductor, such as GaMnAs, range from 20–100 meV. The conduction band

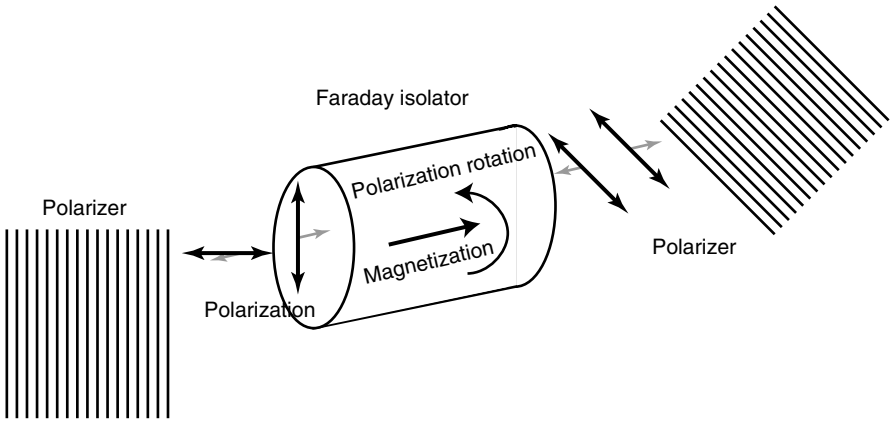

Figure 3. Schematic of a Faraday isolator. The breaking of time-reversal invariance for light propagation through the Faraday rotator leads, in combination with polarizers, to one-way transmission of light. Magnetic semiconductors may permit switchable Faraday isolators.

is split as well (Myers *et al*., 2005) through hybridization with the valence band and the d-levels, although by a smaller energy (S_c). The influence of the conduction band spin splitting on this proposed device is quite dramatic even for small splittings, for the equilibrium spin polarization of minority carriers in the base,

$$\frac{n_{\mathrm{B}\downarrow 0} - n_{\mathrm{B}\uparrow 0}}{n_{\mathrm{B}\downarrow 0} + n_{\mathrm{B}\uparrow 0}} = \tanh(S_c/2k_{\mathrm{B}}T) \tag{1}$$

where $n_{\mathrm{B}s0}$ is the equilibrium density of spin s conduction electrons in the base. When the device is biased the Shockley approximations fix the minority carrier quasichemical potential on the emitter side of the base equal to the chemical potential in the emitter (Figure 4). In an ordinary transistor this gives rise to the exponential dependence of the base's minority carrier density on the emitter–base voltage, V_{EB}. For a magnetic base, the enhanced minority carrier densities $n_{\mathrm{B}s}$ injected from the emitter will likewise increase exponentially, and retain the spin polarization of equation (1),

$$\frac{n_{\mathrm{B}\downarrow}}{n_{\mathrm{B}\uparrow}} = \frac{n_{\mathrm{B}\downarrow 0}}{n_{\mathrm{B}\uparrow 0}} \tag{2}$$

If the band alignment is as shown in Figure 4 then $n_{\mathrm{B}\downarrow} > n_{\mathrm{B}\uparrow}$, however, the other case is straightforward. The degree of spin polarization is considerably more dramatic than that expected for tunneling through a spin-split barrier (Moodera, Hao, Gibson and Meservey, 1988; Hao, Moodera and Meservey, 1990) and occurs in any base region thick enough to eliminate tunneling from emitter to collector.

A related structure, the spin-valve transistor (Monsma, Lodder, Popma and Dieny, 1995; Jansen, 2003; van Dijken, Jiang and Parkin, 2003), places a metallic spin valve (Ziese and Thornton, 2001) in the base region of a silicon transistor. Large variations in the collector current were found in such a device; however, in the spin-valve transistor the collector current is very small compared to the emitter and base currents. The magnetic bipolar transistor, however, potentially has a collector current that greatly exceeds the base current, yielding a gain much larger than one.

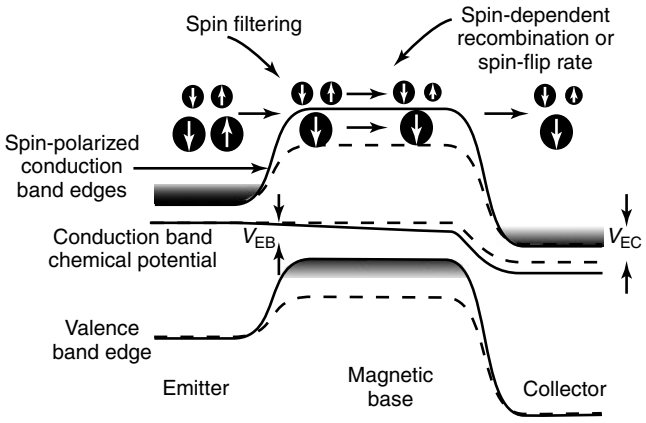

Figure 4. $\mathrm{n}-\mathrm{p}_{\uparrow}-\mathrm{n}$ transistor. Thermally excited unpolarized electrons in the emitter are filtered at the emitter–base interface and can be further polarized through spin relaxation or carrier recombination in the base. The spin-split conduction and valence band edges are shown in the magnetic base, as well as the conduction band quasichemical potential. Dashed (solid) lines are for spin-down (spin-up). Occupied states (electron or hole) are indicated with shading. (Reprinted with permission M.E. Flatte *et al*., copyright 2003, American Institute of Physics.)

The unusual device functionalities suggested by electrically tunable ferromagnetic semiconductors have yet to become practical for commercial devices. Limitations include the Curie temperatures of carrier-mediated ferromagnets (which remain far below room temperature at this time) and the material quality of the known ferromagnetic semiconductors. Increases in the highest Curie temperatures achieved for true carrier-mediated ferromagnets over the past

several years suggest that room-temperature carrier-mediated ferromagnets may be possible. Even if those are demonstrated, however, there are additional characteristics that must be improved before such materials could be used in the devices described in the preceding text. For Faraday isolators the optical loss must be small compared to the rotation angle, and current ferromagnetic semiconductor tend to have very poor optical properties, characterized by high optical losses at all wavelengths. The electric fields required to modify the magnetic properties of gate-tunable devices should be as small as possible; now the voltages required to deplete enough carriers to change the Curie temperature by as little as a single degree are much larger than practical for high-speed integrated devices.

3 CONTROL OF SPIN RELAXATION IN NONMAGNETIC SEMICONDUCTORS

Semiconductor spintronic devices may not require magnetic materials. It has already been established experimentally that the flow of current through nonmagnetic semiconductors can produce spin-polarized distributions, either uniformly in space (Kato, Myers, Gossard and Awschalom, 2004a; Silov *et al*., 2004) or by spatially separating a moving, initially unpolarized distribution into two oppositely polarized distributions (Kato, Myers, Gossard and Awschalom, 2004c; Wunderlich, Kaestner, Sinova and Jungwirth, 2005; Sih *et al*., 2005). Both effects, current-induced spin polarization and the spin-Hall effect, have recently been demonstrated at room temperature (Stern *et al*., 2006). The spin-orbit interaction, which couples the motion of the electrons to the spin dynamics, plays an important role in these phenomena (D'yakonov and Perel', 1971; Levitov, Nazarov and Éliashberg, 1985; Edelstein, 1990; Hirsch, 1999; Murakami, Nagaosa and Zhang, 2003; Sinova *et al*., 2004). See also **Theory of Spin Hall Effects in Semiconductors, Volume 5** in this volume will address these topics in more detail.

Once an initial nonequilibrium spin polarization has been generated, then additional methods can be used to manipulate the population's spin orientation. One method is interfering one population with another (Kato, Myers, Gossard and Awschalom, 2005). As the spin coherence lengths in semiconductors are exceptionally long (Kikkawa and Awschalom, 1999; Sogawa *et al*., 2001) and can exceed 100 μm in some materials, manipulations that rely on spin population interference can work over much longer length scales than possible for devices relying on orbital coherence. Distributions can also be moved into regions with different spin lifetimes to either store or destroy spin coherence (Malajovich, Berry, Samarth and Awschalom, 2001).

In addition to these effects, the simple act of transporting the spin population through a nonmagnetic semiconductor with spin-orbit interaction can cause the spin orientation to precess, even without applied magnetic fields. When electrons move through a crystal, the electric fields associated with the crystal potential are relativistically transformed into effective magnetic fields acting in the rest frame of the electrons. These effective magnetic fields depend on the direction of electron motion through the crystal, and thus will cause the spin orientation to precess in a path-dependent way (Kato, Myers, Gossard and Awschalom, 2004b; Crooker and Smith, 2005; Crooker *et al*., 2005).

3.1 Electric-field control of internal effective magnetic fields

As the internal effective magnetic fields arise from a relativistic transformation of the crystal's electric fields into the rest frame of a moving electron, those magnetic fields can be controlled in any way that changes the crystal's electric fields in the laboratory frame. A simple way to do this is to apply a uniform electric field. The tunable effective magnetic field experienced by moving electrons that arises from this electric field provides additional strategies to manipulate a spin population. In the seminal work of Datta and Das (1990), the spin orientation of carriers moving ballistically from source to drain in a transistor geometry is controlled by such an effective magnetic field induced with a uniform electric field applied to the crystal. This 'Rashba' field **B** (Rashba, 1960; Bychkov and Rashba, 1984) has the form

$$\mathbf{B} = \alpha\ \mathbf{E} \times \mathbf{k} \tag{3}$$

where **E** is an effective electric field, **k** is the carrier's crystal momentum, and α depends on the strength of the spin-orbit interaction in the material. Even in the absence of a true applied electric field, the presence of inversion-symmetry breaking in a structure ('structural inversion asymmetry') can produce an effective electric field and a resulting Rashba field. For an electric field generated by a gate and pointing parallel to z, the Rashba field will point in the xy plane perpendicular to **k**. When carriers move ballistically along x from source to drain in a transistor geometry, for example in a quantum wire, all the carriers have the same **k**, and the Rashba field (parallel to y) is the same for all carriers. In more general situations in which carriers are distributed through momentum space, the spins of the individual carriers will precess relative to each other (in a phenomenon called *dephasing*), and the total spin polarization moving from source to drain will decay.

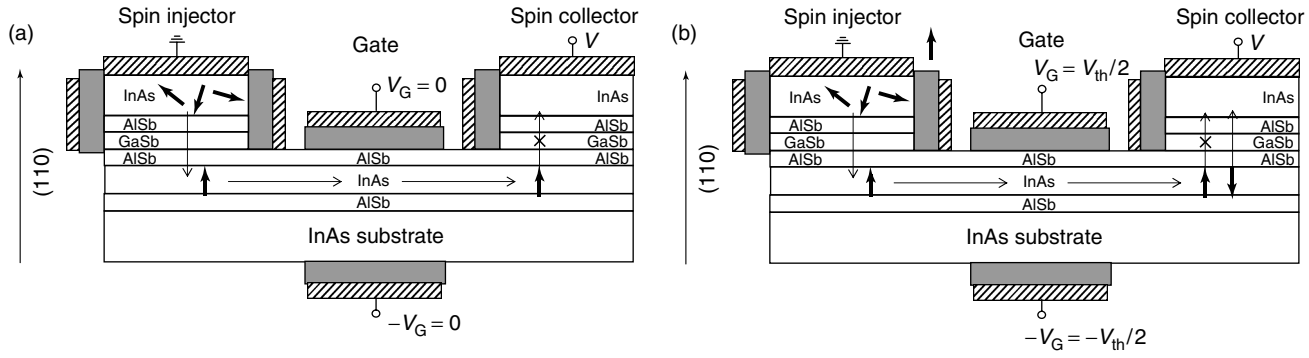

Figure 5. Schematic of the spin transistor of (Hall *et al*., 2003b) in (a) the 'off' and (b) the 'on' state. The spin injector (source) and collector (drain) are configured to select opposite spin polarizations. If the spin lifetimes are very long (gate voltage off) in the channel then no current will flow from source to drain. If the spin lifetimes are short (gate voltage on), then current can flow easily from source to drain. (Reprinted with permission K. Hall *et al*., copyright 2003, American Institute of Physics.)

If carriers move through a material by diffusion, rather than by ballistic transport, the varying momenta of the carriers leads to dephasing of the carriers relative to each other and an overall loss of spin polarization. Through the choice of a clever geometry, balancing the gate electric field with the internal electric fields from a crystal structure (Schliemann, Egues and Loss, 2003), partially coherent spin manipulation is possible even for diffusing carriers. In current structures near room temperature, however, the propagating carriers lose their spin polarization in less than 1 ns (Lau and Flatté, 2005). Thus an alternate approach for diffusive carriers is desirable.

A simpler design relies on the controllable decay of spin polarization rather than its reorientation. In zinc-blende semiconductors, the spin lifetime originates from differing effective magnetic fields for different carriers (D'yakonov and Perel', 1972; Dresselhaus, 1955). Zinc-blende quantum wells grown in the (110) direction are special, for the spin lifetime for spins oriented parallel to the (110) direction is very long (D'yakonov and Kachorovskii, 1986; Winkler, 2004; Ohno *et al*., 1999a; Hall *et al*., 2003a). If an electric field is applied in the (110) direction, however, a Rashba field is generated perpendicular to (110), causing the spin lifetimes to shorten (Lau and Flatté, 2002) by several orders of magnitude. Reductions of a factor of 10 in the spin lifetime in a GaAs/AlGaAs quantum well (Karimov *et al*., 2003) and of a factor of 4 in the spin lifetime in an InAs/AlSb quantum well (Hall *et al*., 2005) have been observed experimentally.

3.2 Spin transistor action in a nonmagnetic semiconductor

This controllable spin lifetime forms the basis for transistor action in the device (Hall *et al*., 2003b) shown in Figure 5. Once polarized spins (to be specific, spin-up) have been injected into a channel, either from a magnetic material (Fiederling *et al*., 1999; Ohno *et al*., 1999b; Hanbicki *et al*., 2002; Adelmann *et al*., 2005) or using a nonmagnetic spin filter (Andrada e Silva and La Rocca, 1999; Voskoboynikov, Lin, Lee and Tretyak, 2000; Koga, Nitta, Takayanagi and Datta, 2002; Hall *et al*., 2003b), their motion through the device can be controlled according to whether they remain spin polarized or not (Hall *et al*., 2003b). If they remain spin polarized and the drain contact spin filter only accepts spin-down carriers, then current does not flow from source to drain. This is the situation (Figure 5a) when no electric field is applied using the gate contact. When an electric field is applied (Figure 5b) then the spin polarization decays rapidly in the channel. In this situation, current flows easily from source to drain. Hence, in this design, there is no moveable barrier between source and drain. The spin-dependent barriers in this device permit carriers of one spin orientation to pass while preventing those of the other spin polarization. The spin-dependent barriers are not raised or lowered. The switching is performed instead by changing the spin orientation in the channel.

Transistor action in a CMOS field effect transistor (FET), by contrast, requires raising and lowering a barrier whose height is set by the gate voltage. When the barrier is high the source–drain current cannot flow, whereas when it is low the source–drain current flows easily. For low standby power (LSTP) CMOS (Semiconductor Industry Association, 2003) the switchable range of the height of the barrier, V_{th}, must be at least 400 mV, corresponding to $16k_BT$, or a thermally excited current over the barrier in the 'off' state of 10^{-7} the 'on' current. Here k_B is Boltzmann's constant and T is the temperature. The gate capacitance of the CMOS FET, C_g, is proportional to the area of the region of the channel that

is blocked with this barrier. The power-delay product (twice the switching energy) is $C_g V_{th}^2$ and the switching time is proportional to C_g. If the gate capacitance is too low then the barrier becomes thin enough that carriers can tunnel through it and the leakage current rises above that expected from V_{th}, but if the capacitance is too high the switching time is long and the switching energy high.

Although the difference in 'on' and 'off' gate voltages for low standby power (LSTP) CMOS cannot be reduced below 400 mV for a 10^7 on–off current ratio at room temperature ($\sim$280 mV for a 10^5 on–off current ratio), the difference in 'on' and 'off' gate voltages for the spin transistor described in the preceding text can be much less. The source–drain current is proportional to the spin relaxation rate, so for a 10 ps spin lifetime in the 'on' state and a 10^5 on–off ratio the spin lifetime must be 1 µs in the off state (100 µs for a 10^7 on–off ratio). Spin lifetimes in excess of 150 ns have been observed experimentally in bulk GaAs (Kikkawa and Awschalom, 1998), so here the 1 µs value will be used. It only requires an average 1 meV spin splitting (associated with a random effective magnetic field direction) to cause a spin to relax within 1 ps. This spin splitting is not generated directly by the gate voltage, but is induced by the applied electric field and the spin-orbit interaction of the material as described by equation (3). For the 20 nm thick InAs quantum well of Hall *et al.*, 2003b the required electric field to reduce the spin lifetime to 10 ps at room temperature is 50 kV cm^{-1}. Thus, the threshold voltage will be 100 mV, a factor of 4 less. It can be reduced even further if a material with a larger spin-orbit interaction than InAs (such as InSb or an InAs/GaSb superlattice) is used instead.

The other quantity entering the dynamic power dissipation (power-delay product) is the gate capacitance, from

$$C_g = \epsilon_0 \epsilon_s \frac{A}{d} \tag{4}$$

where ϵ_0 is the dielectric permittivity of vacuum, ϵ_s the relative dielectric constant of the semiconductor, A the area of the gate, and d the thickness of the region the electric field is applied to. In CMOS the thickness of the oxide layer determines d, whereas for the spin transistor the quantum well thickness determines d. For a spin transistor based on InAs/AlSb with a gate of the same area as a CMOS gate the gate capacitance is a factor of 5 smaller (as the 20 nm thick quantum well is much thicker than the CMOS gate oxide). The threshold voltage and the gate capacitance indicates that the dynamic power dissipation would be a factor of 500 times smaller for the spin transistor than LSTP CMOS in 2018 (Hall and Flatté, 2006).

The other important form of power dissipation is the static power dissipation. In CMOS, the dominant source of static power dissipation is the source–drain leakage current. The target value for 2018 LSTP CMOS is 100 pA/µm^{-1}. In the spin transistor, the dominant source is the spin relaxation in the 'off' state. For the gate length target in 2018 LSTP CMOS of 10 nm, a quantum well doping of 2×10^{12} cm^{-2} and a 1 µs spin relaxation time, the leakage current for the spin transistor will be 16 pA/µm^{-1}, a factor of 6 smaller than for LSTP CMOS in 2018.

The switching speed is also an important metric and depends on the source–drain current in the 'on' state, the threshold voltage, and the gate capacitance. For a 10 ps 'on' spin relaxation time and the parameters above, the switching time will be 3 ps, 10 times longer than the target for 2018 LSTP CMOS. Increasing the carrier doping level in the quantum well reduces the switching time, although it also increases the static leakage current. The switching time can be reduced without increasing the leakage current if the spin transistor quantum well uses a material with a larger spin-orbit interaction, such as InSb or InAs/GaSb superlattices.

Direct comparisons are possible between spin transistor design performance and CMOS performance. These comparisons suggest that the static power dissipation and the dynamic power dissipation would be smaller for the spin transistor (Hall and Flatté, 2006). This improved performance originates from the lower threshold voltage and the lower gate capacitance of the spin transistor design. The switching speed of the design of Hall *et al.*, 2003b is slower than CMOS. It can be made faster if the InAs quantum well is replaced with a material that has a larger spin-orbit interaction.

Progress toward implementing a scalable side-gate structure that would permit spin injection from a nonmagnetic material has been achieved; a prototype of the side-gated structure has been demonstrated using fabrication techniques that are scalable to deep submicron scales, although the spin-switching properties have yet to be confirmed in that prototype (Moon *et al.*, 2004). Use of the (110) growth direction as described here reduces the effect of spin-orbit interaction on the spin lifetime in the 'off' state, for the spin lifetime for (110)-oriented spins should be very long. The rapid spin relaxation in the 'on' state is still retained for the (110) growth direction. Narrow-gap semiconductor materials are the subject of intense investigation for high-speed low-power integrated circuit applications, although the considerations that will determine whether they are competitive with other material systems (especially silicon CMOS) differ for spin-based devices relative to charge-based devices.

The spin transistor described here works through electric-field control of the decay of spin polarization, and hence could be considered an incoherent semiconductor spintronic device. Spin transistors also permit the manipulation of their output currents through reorienting the source and drain

magnetic layers (Hall *et al*., 2003b; Sugahara and Tanaka, 2004) in a fashion similar to spin valves (Ziese and Thornton, 2001). Other logical elements may be possible which depend on electrical control of the coherent propagation properties of spin in semiconductors, including the spatial period of spin precession originating from the Rashba field described in the preceding text. Such devices may be able to perform more complicated operations than a transistor or may provide an efficient method of implementing analog logic. The behavior of such devices, and comparisons with competing charge-based devices, is not as thoroughly explored as those of 'spin transistors' and offers fertile ground for future theoretical device physics research.

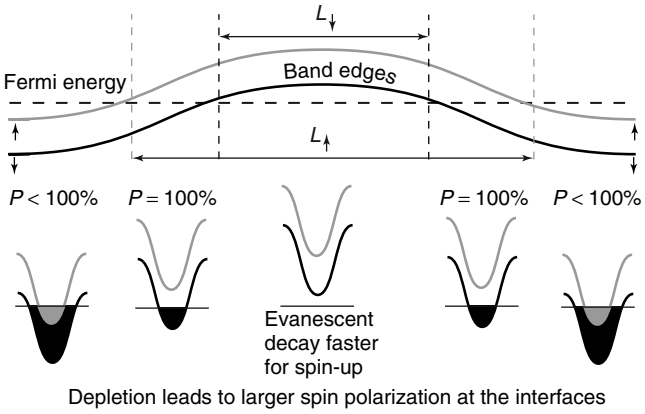

Figure 6. Schematic of the spin-split band edges of a carrier-mediated ferromagnetic semiconductor as the carrier density is varied from metallic to insulating and back to metallic. If the variation occurs over a length scale small compared to the range of the exchange interaction then the bands remain spin split even without carriers. Thus depleted ferromagnetic semiconductors can be natural half-metals.

4 NONLINEAR TRANSPORT IN MAGNETICALLY INHOMOGENEOUS STRUCTURES

The low carrier density of carrier-mediated ferromagnetic semiconductors, which permits electric-field control of magnetism, also suggests that unusual transport phenomena might occur near interfaces and edges. If the carrier density is very high, such as in magnetic metals, or the range of spin–spin interaction is short, such as in magnetic insulators, then bulk behavior is usually recovered within one atomic layer of the interface. Frequently the final atomic layer of a magnet is a 'magnetically dead' region, with much lower or negligible spin polarization, or very high levels of spin-flip scattering. In a tunnel-junction geometry, this magnetically dead region can dominate the transport, greatly reducing the apparent spin polarization of the magnetic material.

4.1 Depletion and spin polarization near the edge of a magnetic semiconductor

Ordinarily if there are no carriers in the carrier-mediated ferromagnet then the spin polarization of the region vanishes and the material ceases to be magnetic. However, the lower carrier density and the long-range spin–spin interaction in magnetic semiconductors (see Figure 1) suggest that the region of modified magnetic properties should extend a distance of order the radius of the acceptor state away from the interface. Over this region of $\sim 1-2$ nm there is a strong exchange interaction even though there are few or no carriers. The situation is shown schematically in Figure 6 for an electron-doped carrier-mediated ferromagnetic semiconductor, although the situation for a hole-doped material is very similar. If the length scale of the variation in carrier density is small compared to the range of the exchange interaction (this $\sim 1-2$ nm), then the spin splitting of the band edge should roughly remain constant through the region of carrier density change.

As shown in Figure 6, upon moving from a region with higher carrier density to one of lower carrier density it is possible that the remaining carriers would become much more highly spin polarized than they would be either in the bulk of the magnetic semiconductor or in a bulk material with the same carrier density as the depleted region near the edge. Thus, a 100% spin polarized or nearly 100% spin-polarized material might be achievable near the edge of an ordinary magnetic semiconductor whose carriers are polarized significantly less than 100%. If the carrier depletion is continued until all carriers have been depleted (of both spin polarizations), then the remaining spin splitting in the electronic structure can still affect the transport by modifying the evanescent decay of the wave functions differently for spin-up and spin-down carriers. As shown in Figure 6, the width of the effective depleted region of the electron gas for carriers oriented spin-up, $L_\uparrow$, is much wider than that for carriers oriented spin-down, $L_\downarrow$. The evanescent decay of spin-up wave functions should also be much more rapid than that of spin-down wave functions. As a result, the resistance of this interface region to the tunneling of spin-up carriers should be much larger than the tunneling resistance for spin-down carriers. A treatment of the interface behavior when the depletion length is shorter than the exchange interaction predicts tunneling magnetoresistances much larger than would be expected from the bulk spin polarization of the magnetic semiconductor. This effect was seen in GaMnAs nanoconstrictions (Rüster *et al*., 2003), for which 2000% magnetoresistances were observed even

though GaMnAs in bulk has a spin polarization closer to 85% (Braden *et al*., 2003).

4.2 Unipolar spin diodes and transistors

Although the very large magnetoresistance described in the preceding text is considerably greater than that seen in metallic systems, it remains a linear resistive property. Most of the interesting properties of semiconductor charge-based devices are nonlinear transport properties, which suggests examining the nonlinear transport properties associated with inhomogeneous magnetic materials for unusual behavior. One interesting situation, that will now be analyzed, is that of the transport properties of a domain wall between 100% spin-polarized ferromagnetic semiconductors.

The current–voltage characteristics of this domain wall can be simply understood through an analogy between unipolar ferromagnetic semiconductors and nonmagnetic bipolar materials. This analogy is best visualized in the relationship between transport through the 180° domain wall between 100% spin-polarized semiconductors, which will be referred to as a 'spin diode', and transport through the traditional p–n diode. Shown in Figure 7(a) are the band edges of the conduction and valence band for a traditional p–n diode in equilibrium. The quasi Fermi levels are shown as dashed lines. To assist in exploring the analogy with the spin diode, Figure 7(b) shows the energies of the elementary carriers in those bands: conduction electrons and valence holes. This unfamiliar diagram is obtained merely by noting that the energy of a hole in the valence band is the negative of the energy of the valence electron (relative to the chemical potential). Figure 7(b) more clearly illuminates the similarities with the band edges for the spin diode, which are shown in Figure 7(c). Just as for the p–n diode, in the unipolar spin diode the majority carriers on one side are the minority carriers on the other side.

A major difference, however, is that the two types of carriers in the p–n diode have opposite charge, whereas in the spin diode they have the same charge. One implication of this is that in the p–n diode the interface between the layers is a *charge* depletion layer, whereas in the spin diode the interface is a *spin* depletion layer. Another major difference resulting from the charges of the carriers is the way the carrier energies shift under bias.

In the p–n diode under forward bias, the barriers for both valence hole and conduction electron transport across the junction are reduced. As shown in Figure 7(d) and 7(e) this leads to an increase in the conduction electron current to the left-hand side and the valence hole current to the right-hand side. Because the carriers have opposite charge, both increases result in an increased charge current to the right-hand side. For the spin diode (Figure 7(f)), only the barrier for spin-up electrons moving to the left-hand side is reduced – the barrier for spin-down electrons moving to the right-hand side is increased. The charge current is thus directed to the right-hand side and the spin current to the left-hand side. Under reverse bias, the barriers for carrier transport are both increased in the p–n diode Figure 7(g) and 7(h), yielding rectification of the charge current. For the spin diode Figure 7(i), again one barrier is reduced and the other increased. Thus the charge current is not rectified but the spin current is. With analogous assumptions to the Shockley assumptions for an ideal diode, the charge current density J_q and the spin current density J_s depend on the voltage V according to:

$$J_q = 2qJ_o\sinh(qV/k_BT) \tag{5}$$

$$J_s = 2\hbar J_o\sinh^2(qV/2k_BT) \tag{6}$$

where $J_o = Dn_m/L_m$, q is the electron charge, $\hbar$ is the Planck's constant, D is the diffusion constant, n_m is the minority carrier density, and L_m is the minority spin diffusion length. The resulting spin polarization of the current is

$$P = (2qJ_s/\hbar J_q) = \tanh(qV/2k_BT) \tag{7}$$

Thus the spin polarization approaches unity as V gets large, and approaches 0 for small V. The relative directions of the charge and spin currents are shown on Figure 7 for the cases of forward and reverse bias.

For ease of use as components in integrated circuits, a magnetoelectronic device should allow for magnetic manipulation of the charge current gain – to achieve this, back-to-back spin diodes are required (shown in Figure 8). Analyzing this structure in a similar way to a bipolar nonmagnetic transistor, the collector current density is

$$\begin{aligned} I_C = &-\frac{qJ_o}{\sinh(W/L)} \\ &\times [(e^{-qV_{EB}/k_BT} - 1) - (e^{-qV_{CB}/k_BT} - 1)\cosh(W/L)] \\ &- qJ_o[e^{qV_{CB}/k_BT} - 1] \end{aligned} \tag{8}$$

and the emitter current is

$$\begin{aligned} I_E = &-\frac{qJ_o}{\sinh(W/L)} \\ &\times [(e^{-qV_{EB}/k_BT} - 1)\cosh(W/L) - (e^{-qV_{CB}/k_BT} - 1)] \\ &+ qJ_o[e^{qV_{EB}/k_BT} - 1] \end{aligned} \tag{9}$$

The base width is W, the voltage between emitter and base is $V_{BE} < 0$, and the voltage between collector and

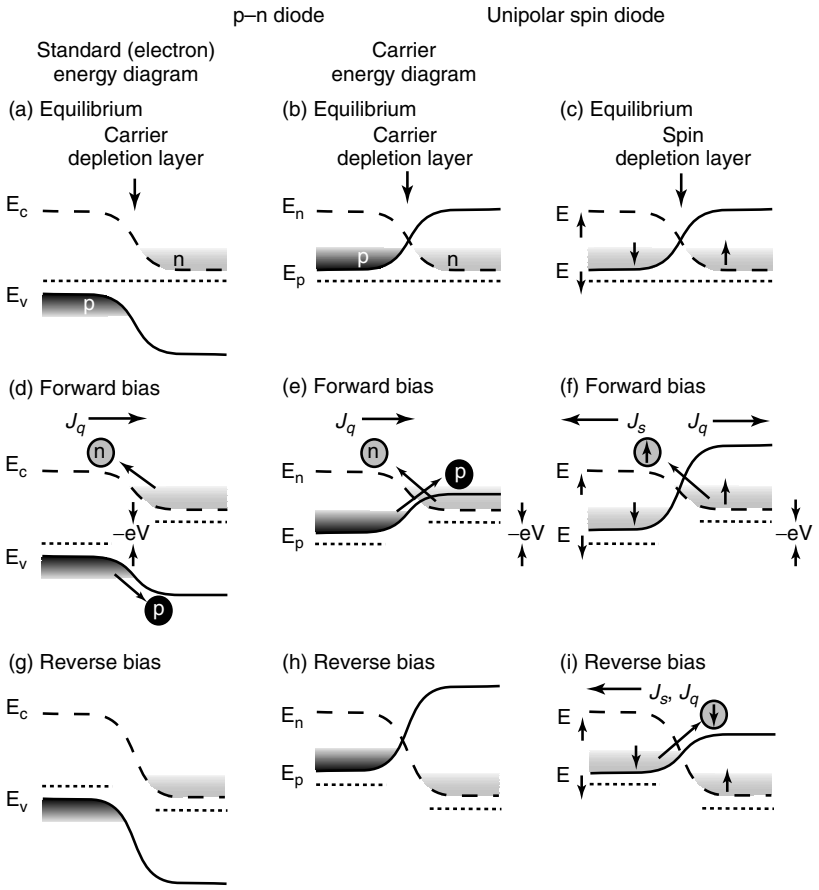

Figure 7. Standard and carrier energy diagrams for a traditional p–n diode versus unipolar spin diode under equilibrium conditions (a)–(c), forward bias (d–f), and reverse bias (g–i). (Reprinted with permission from M.E. Flatte & G. Vignale, copyright 2001, American Institute of Physics.)

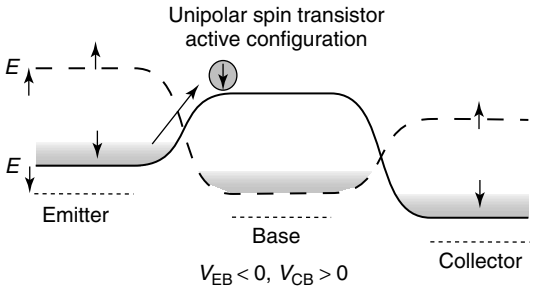

Figure 8. Carrier energy diagram for the unipolar spin transistor in the normal active configuration. (Reprinted with permission from M.E. Flatte & G. Vignale, copyright 2001, American Institute of Physics.)

base is $V_{CB} > 0$. The base current is $I_B = I_E - I_C$. When W/L is small, $I_B \ll I_C$, which is the desired situation for transistor operation (current gain $I_C/I_B \gg 1$). Leakage from the base to the collector (a process in this device similar to leakage from the base to the emitter in an ordinary bipolar transistor) can be suppressed (Flatté and Vignale, 2005) by making the collector spin splitting larger than that of the base or emitter (a similar approach to making a heterostructure bipolar transistor).

Thus it should be possible to program a logical circuit which behaves like a bipolar logical circuit using a uniformly doped unipolar magnetic material. The p-like regions correspond to regions with the magnetization pointing one way and the n-like regions correspond to region with the magnetization pointing in the opposite direction. Such logical circuits can include memory circuits, thus indicating that nonvolatile memory can be constructed as well.

Spin-flip of carriers moving through the domain wall acts like a recombination current in a bipolar device, and so should be reduced if at all possible. This can be done by making the domain wall thinner. Calculations of ballistic spin-preserving transport through domain walls, both with (Vignale and Flatté, 2002) and without (Deutsch, Vignale and Flatté, 2004) a bias applied to the spin diode, indicate that the transport can be predominately spin-preserving under reasonable conditions for transistor operation.

5 SUMMARY

The semiconductor spintronic devices described here function because of either the unique properties of carrier-mediated ferromagnetic semiconductors or the possibility of controlling the internal effective magnetic fields in nonmagnetic semiconductors. Many of the same characteristics that make semiconductors tremendously useful for ordinary charge transport, such as the ability to modify the electronic structure and carrier concentration with relatively weak electric fields, the intrinsic nonlinearities of transport in semiconductor systems, and the large length scales over which semiconductors return to equilibrium (compared with both metals and insulators), are essential to the subtle spin-dependent phenomena described here.

The single improvement in material properties that would be most helpful in the commercialization of these devices is the demonstration of a true carrier-mediated ferromagnetic semiconductor at a temperature exceeding room temperature. Ideally the carrier density in such a semiconductor would be relatively low, permitting modification of the Curie temperature with a small electric field. For the magneto-optical elements described here, such as Faraday isolators, such room temperature carrier-mediated ferromagnetic semiconductors would also need to generate large Faraday rotation angles with relatively small optical losses. For nonmagnetic spin transistors, the demonstration of extremely efficient spin injection (the injection of distributions that are nearly 100% spin polarized) is the next significant technological step. For unipolar and bipolar spin diodes and transistors, the key roadblock is to reduce the carrier density of the ferromagnetic semiconductors to the point where a voltage can be sustained across the depletion layer.

REFERENCES

Abolfath, M., Jungwirth, T., Brum, J. and MacDonald, A.H. (2001). Theory of magnetic anisotropy in $III_{1-x}Mn_xV$ ferromagnets. *Physical Review B*, **63**, 054418.

Adelmann, C., Lou, X., Strand, J., *et al*. (2005). Spin injection and relaxation in ferromagnet-semiconductor heterostructures. *Physical Review B*, **71**, 121301(R).

Andrada e Silva, E.A. and La Rocca, G.C. (1999). Electron-spin polarization by resonant tunneling. *Physical Review B* **59**, R15583–R15585.

Braden, J.G., Parker, J.S., Xiong, P., *et al*. (2003). Direct measurement of the spin polarization of the magnetic semiconductor (Ga,Mn)As. *Physical Review Letters*, **91**, 056602.

Bychkov, Y.A. and Rashba, E.I. (1984). Oscillatory effects and the magnetic susceptibility of carriers in inversion layers. *Journal of Physics C*, **17**, 6039–6045.

Chiba, D., Yamanouchi, M., Matsukura, F. and Ohno, H. (2003). Electrical manipulation of magnetization reversal in a ferromagnetic semiconductor. *Science*, **301**, 943–945.

Crooker, S.A., Furis, M., Lou, X., *et al*. (2005). Imaging spin transport in lateral ferromagnet/semiconductor structures. *Science*, **309**, 2191–2195.

Crooker, S.A. and Smith, D.L. (2005). Imaging spin flows in semiconductors subject to electric, magnetic, and strain fields. *Physical Review Letters*, **94**, 236601.

Datta, S. and Das, B. (1990). Electronic analog of the electro-optic modulator. *Applied Physics Letters*, **56**, 665–667.

Deutsch, M., Vignale, G. and Flatté, M.E. (2004). Effect of electrical bias on spin transport across a magnetic domain wall. *Journal of Applied Physics*, **96**, 7424–7427.

Dietl, T., Ohno, H. and Matsukura, F. (2001). Hole-mediated ferromagnetism in tetrahedrally coordinated semiconductors. *Physical Review B*, **63**, 195205.

van Dijken, S., Jiang, X. and Parkin, S.S.P. (2003). Giant magnetocurrent exceeding 3400% in magnetic tunnel transistors with spin-valve base layers. *Applied Physics Letters*, **83**, 951–953.

Dresselhaus, G. (1955). Spin-orbit coupling effects in zinc blende structures. *Physical Review*, **100**, 580–586.

D'yakonov, M.I. and Kachorovskii, V.Y. (1986). Spin relaxation of two-dimensional electrons in noncentrosymmetric semiconductors. *Soviet Physics Semiconductors*, **20**, 110–112.

D'yakonov, M.I. and Perel', V.I. (1971). Current-induced spin orientation of electrons in semiconductors. *Physics Letters A*, **35**, 459–460.

D'yakonov, M.I. and Perel', V.I. (1972). Spin relaxation of conduction electrons in noncentrosymmetric semiconductors. *Soviet Physics Solid State*, **13**, 3023–3026.

Edelstein, V.M. (1990). Spin polarization of conduction electrons induced by electric current in two-dimensional asymmetric electron systems. *Solid State Communications*, **73**, 233–235.

Fiederling, R., Keim, M., Reuscher, G., *et al*. (1999). Injection and detection of a spin-polarized current in a light-emitting diode. *Nature*, **402**, 787–790.

Flatté, M.E. and Vignale, G. (2001). Unipolar spin diodes and transistors. *Applied Physics Letters*, **78**, 1273–1275.

Flatté, M.E. and Vignale, G. (2005). Heterostructure unipolar spin transistors. *Journal of Applied Physics*, **97**, 104508.

Flatté, M.E., Yu, Z.G., Johnston-Halperin, E. and Awschalom, D.D. (2003). Theory of semiconductor magnetic bipolar transistors. *Applied Physics Letters*, **82**, 4740–4742.

Hall, K. and Flatté, M.E. (2006). Performance of a spin-based insulated gate field effect transistor. *Applied Physics Letters*, **88**, 162503.

Hall, K., Gündoğdu, K., Altunkaya, E., *et al*. (2003a). Spin relaxation in (110) and (001) InAs/GaSb superlattices. *Physical Review B*, **68**, 115311.

Hall, K., Lau, W.H., Gündoğdu, K., *et al*. (2003b). Nonmagnetic semiconductor spin transistor. *Applied Physics Letters*, **83**, 2937–2939.

Hall, K., Gündoğdu, K., Hicks, J.L., *et al*. (2005). Room-temperature electric-field controlled spin dynamics in (110) InAs quantum wells. *Applied Physics Letters*, **86**, 202114.

Hanbicki, A.T., Jonker, B.T., Itskos, G., *et al*. (2002). Efficient electrical spin injection from a magnetic metal/tunnel barrier contact into a semiconductor. *Applied Physics Letters*, **80**, 1240–1242.

Hao, X., Moodera, J.S. and Meservey, R. (1990). Spin-filter effect of ferromagnetic europium sulfide tunnel barriers. *Physical Review B*, **42**, 8235–8243.

Hirsch, J. E. (1999). Spin Hall effect. *Physical Review Letters*, **83**, 1834–1837.

Jansen, R. (2003). The spin-valve transistor: a review and outlook. *Journal of Physics D*, **36**, R289–R308.

Karimov, O.Z., John, G.H., Harley, R.T., *et al*. (2003). High temperature gate control of quantum well spin memory. *Physical Review Letters*, **91**, 246601.

Kato, Y., Myers, R.C., Gossard, A.C. and Awschalom, D.D. (2004a). Current-induced spin polarization in strained semiconductors. *Physical Review Letters*, **93**, 176601.

Kato, Y.K., Myers, R.C., Gossard, A.C. and Awschalom, D.D. (2004b). Coherent spin manipulation without magnetic fields in strained semiconductors. *Nature*, **427**, 50–53.

Kato, Y.K., Myers, R.C., Gossard, A.C. and Awschalom, D.D. (2004c). Observation of the spin Hall effect in semiconductors. *Science*, **306**, 1910–1913.

Kato, Y., Myers, R.C., Gossard, A.C. and Awschalom, D.D. (2005). Electron spin interferometry using a semiconductor ring structure. *Applied Physics Letters*, **86**, 162107.

Kikkawa, J.M. and Awschalom, D.D. (1998). Resonant spin amplification in *n*-type GaAs. *Physical Review Letters*, **80**, 4313–4316.

Kikkawa, J.M. and Awschalom, D.D. (1999). Lateral drag of spin coherence in gallium arsenide. *Nature*, **397**, 139–141.

Kitchen, D., Richardella, A., Tang, J-M., *et al*. (2006). Atom-by-atom substitution of Mn in GaAs and visualization of their hole-mediated interactions. *Nature*, **442**, 436–439.

Koga, T., Nitta, J., Takayanagi, H. and Datta, S. (2002). Spin-filter device based on the Rashba effect using a nonmagnetic resonant tunneling diode. *Physical Review Letters*, **88**, 126601.

Lau, W.H. and Flatté, M.E. (2002). Tunability of electron spin coherence in III-V quantum wells. *Journal of Applied Physics*, **91**, 8682–8684.

Lau, W.H. and Flatté, M.E. (2005). Electric field dependence of spin coherence in (001) GaAs/$Al_xGa_{1-x}As$ quantum wells. *Physical Review B*, **72**, 161311(R).

Levitov, L.S., Nazarov, Y.V. and Éliashberg, G.M. (1985). Magnetoelectric effects in conductors with mirror isomer symmetry. *Soviet Physics JETP*, **61**, 133–135.

MacDonald, A.H., Schiffer, P. and Samarth, N. (2005). Ferromagnetic semiconductors: moving beyond (Ga,Mn)As. *Nature Materials*, **4**, 195–202.

Malajovich, I., Berry, J.J., Samarth, N. and Awschalom, D.D. (2001). Persistent sourcing of coherent spins for multifunctional semiconductor spintronics. *Nature*, **411**, 770–772.

Masmanidis, S.C., Tang, H.X., Myers, E.B., *et al*. (2005). Nanomechanical measurement of magnetostriction and magnetic anisotropy in (Ga,Mn)As. *Physical Review Letters*, **95**, 187206.

Monsma, D.J., Lodder, J.C., Popma, T.J.A. and Dieny, B. (1995). Perpendicular hot electron spin-valve effect in a new magnetic field sensor: the spin-valve transistor. *Physical Review Letters*, **74**(26), 5260–5263.

Moodera, J.S., Hao, X., Gibson, G.A. and Meservey, R. (1988). Electron-spin polarization in tunnel junctions in zero applied field with ferromagnetic EuS barriers. *Physical Review Letters*, **61**, 637–640.

Moon, J.S., Chow, D.H., Schulman, J.N., *et al*. (2004). Experimental demonstration of split side-gated resonant interband tunneling devices. *Applied Physics Letters*, **85**, 678–680.

Munekata, H., Ohno, H., von Molnár, S., *et al*. (1989). Diluted magnetic III-V semiconductors. *Physical Review Letters*, **63**, 1849–1852.

Murakami, S., Nagaosa, N. and Zhang, S-C. (2003). Dissipationless quantum spin current at room temperature. *Science*, **301**, 1348–1351.

Myers, R.C., Poggio, M., Stern, N.P., *et al*. (2005). Antiferromagnetic $s-d$ exchange coupling in GaMnAs. *Physical Review Letters*, **95**, 017204; 229902(E).

Ohno, H., Chiba, D., Matsukura, F., *et al*. (2000). Electric-field control of ferromagnetism. *Nature*, **408**, 944–946.

Ohno, H., Shen, A., Matsukura, F., *et al*. (1996). (Ga,Mn)As: A new diluted magnetic semiconductor based on GaAs. *Applied Physics Letters*, **69**, 363–365.

Ohno, Y., Terauchi, R., Adachi, T., *et al*. (1999a). Spin relaxation in GaAs(110) quantum wells. *Physical Review Letters*, **83**, 4196–4199.

Ohno, Y., Young, D.K., Beschoten, B., *et al*. (1999b). Electrical spin injection in a ferromagnetic semiconductor heterostructure. *Nature (London)*, **402**, 790–792.

Rashba, E.I. (1960). Properties of semiconductors with an extremum loop I. Cyclotron and combinational resonance in a magnetic field perpendicular to the plane of the loop. *Soviet Physics Solid State*, **2**, 1109–1122.

Rüster, C., Borzenko, T., Gould, C., *et al*. (2003). Very large magnetoresistance in lateral ferromagnetic (Ga,Mn)As wires with nanoconstrictions. *Physical Review Letters*, **91**, 216602.

Schliemann, J., Egues, J.C. and Loss, D. (2003). Nonballistic spin-field-effect transistor. *Physical Review Letters*, **90**, 146801.

Schneider, J., Kaufmann, U., Wilkening, W. and Baeumler, M. (1987). Electronic structure of the neutral manganese acceptor in gallium arsenide. *Physical Review Letters*, **59**, 240–243.

Semiconductor Industry Association (2003). *International Technology Roadmap for Semiconductors*, Semiconductor Industry Association: San Jose, http://public.itrs.net.

Sih, V., Myers, R.C., Kato, Y.K., *et al*. (2005). Spatial imaging of the spin Hall effect and current-induced polarization in two-dimensional electron gases. *Nature Physics*, **1**, 31–35.

Silov, A.Y., Blajnov, P.A., Wolter, J.H., *et al*. (2004). Current-induced spin polarization at a single heterojunction. *Applied Physics Letters*, **85**, 5929–5931.

Sinova, J., Culcer, D., Niu, Q., *et al*. (2004). Universal intrinsic spin hall effect. *Physical Review Letters*, **92**, 126603.

Sogawa, T., Santos, P.V., Zhang, S.K., *et al*. (2001). Transport and lifetime enhancement of photoexcited spins in GaAs by surface acoustic waves. *Physical Review Letters*, **87**, 276601.

Stern, N.P., Ghosh, S., Xiang, G., *et al*. (2006). Current-induced polarization and the spin hall effect at room temperature. *Physical Review Letters*, **97**, 126603.

Sugahara, S. and Tanaka, M. (2004). A spin metal-oxide-semiconductor field-effect transistor using half-metallic-ferromagnet contacts for the source and drain. *Applied Physics Letters*, **84**, 2307–2309.

Vignale, G. and Flatté, M.E. (2002). Nonlinear spin-polarized transport through a ferromagnetic domain wall. *Physical Review Letters*, **89**, 098302.

Voskoboynikov, A., Lin, S.S., Lee, C.P. and Tretyak, O. (2000). Spin-polarized electronic current in resonant tunneling heterostructures. *Journal of Applied Physics*, **87**, 387–391.

Winkler, R. (2004). Spin orientation and spin precession in inversion-asymmetric quasi-two-dimensional electron systems. *Physical Review B*, **69**, 045317.

Wunderlich, J., Kaestner, B., Sinova, J. and Jungwirth, T. (2005). Experimental observation of the spin-hall effect in a two-dimensional spin-orbit coupled semiconductor system. *Physical Review Letters*, **94**, 047204.

Yakunin, A.M., Silov, A.Y., Koenraad, P.M., *et al*. (2004). Spatial structure of an individual Mn acceptor in GaAs. *Physical Review Letters*, **92**, 216806.

Ziese, M. and Thornton, M.J. (Eds.) (2001). *Spin Electronics*, *Lecture Notes in Physics*, Springer-Verlag: Heidelberg, Vol. 569.

Theory of Spin Hall Effects in Semiconductors

Hans-Andreas Engel, Emmanuel I. Rashba and Bertrand I. Halperin
Harvard University, Cambridge, MA, USA

1 INTRODUCTION

In the simplest version of a spin Hall effect, an electrical current passes through a sample with spin-orbit interaction, and induces a spin polarization near the lateral edges, with opposite polarization at opposing edges (D'yakonov and Perel', 1971). This effect does not require an external magnetic field or magnetic order in the equilibrium state before the current is applied. If conductors are connected to the lateral edges, spin currents can be injected into them. Electrical current in a sample can also produce a bulk spin polarization, far from the edges, which is not generally classified *per se* as a spin Hall effect, though it is intimately related and is an important ingredient of spin Hall calculations.

Spin Hall effects have received a great deal of theoretical attention recently, in part because the subject includes ingredients of spintronics, electrical generation, transport, and control of nonequilibrium spin populations, and also because analysis has shown that the problem has remarkable subtlety. Theoretical efforts were also fueled by recent experimental observations of these effects.

In the following we consider semiconductors, where the various mechanisms of spin-orbit coupling are well known and can be roughly classified into two categories. First, the extrinsic mechanism is only present in the vicinity of impurities and leads to spin-dependent scattering, including Mott skew scattering. Second, the intrinsic spin-orbit coupling remains finite away from impurities and can be understood as a (often spatially homogeneous) spin-orbit field inherent in the band structure. Furthermore, the spin-orbit couplings are strongly symmetry dependent and are therefore different for electron and for hole carriers, and are different for two- and three-dimensional systems. Thus, the microscopic processes involved in generating a spin Hall effect can depend critically on such system properties. Initially, there was hope that spin-transport theory can be formulated in terms of universal spin currents that would simplify our understanding; however, it turned out that there is no such universality. As there is no unique description of the spin Hall effect, we should rather refer to it as a set of spin Hall effects.

There is already a vast amount of theoretical literature available on spin Hall effects and on the related spin currents. It is beyond the scope of this chapter to provide a historical overview or to give an explanation of all the theoretical techniques used. We rather provide an overview of the various mechanisms, explain them using intuitive and qualitative physical pictures, and give a summary of some key theoretical descriptions and results.

In contrast, the number of experiments on spin Hall effects is small and an overview is straightforward. In the experiment by Kato, Myers, Gossard and Awschalom (2004b),

Handbook of Magnetism and Advanced Magnetic Materials. Edited by Helmut Kronmüller and Stuart Parkin. Volume 5: *Spintronics and Magnetoelectronics*. ISBN: 978-0-470-02217-7.

electrical currents in three-dimensional n-GaAs layers (2 μm thick) induced a spin Hall effect, which was optically detected via Kerr microscopy. Measurements in strained samples showed little dependence of the effect on the crystal orientation and it was concluded that the extrinsic mechanism proposed by D'yakonov and Perel' (1971) was causing the spin Hall effect (Kato, Myers, Gossard and Awschalom, 2004b). Indeed, the experimental data can be described with reasonable accuracy by the extrinsic mechanism in a model based on scattering by screened Coulomb impurities (Engel, Halperin and Rashba, 2005), as well as one based on short-range scatterers (Tse and Das Sarma, 2006a) (see Section 4.3). Similar experiments in ZnSe (Stern *et al*., 2006) were also in agreement with theory, and a spin Hall effect was observed at room temperature. In another experiment, Wunderlich, Kaestner, Sinova and Jungwirth (2005) observed a spin Hall effect in two-dimensional layers of p-GaAs by detecting the polarization of recombination radiation at the edges of the sample. They ascribed this effect to the intrinsic mechanism, which is consistent with the magnitude of the observation (Schliemann and Loss, 2005; Nomura *et al*., 2005). Furthermore, in measurements on a two-dimensional electron system in an AlGaAs quantum well, a spin Hall effect was also observed and ascribed to the extrinsic mechanism (Sih *et al*., 2005). Finally, Valenzuela and Tinkham (2006) observed a reciprocal spin Hall effect in Al, where a spin current induced a transverse voltage via the extrinsic mechanism (Hirsch, 1999).

In addition to theoretical works in the traditional sense, there is also a large amount of numerical simulations on concrete realizations of disordered systems, for example, on a finite lattice. It has generally been difficult to make direct comparisons between numerical simulations and theoretical predictions, in part because theoretical works usually assume that the spin-orbit splittings are much less than the Fermi energy, whereas simulations tend to employ larger spin-orbit splittings in order to obtain numerically significant results. See, for example, (Ando and Tamura, 1992; Sheng, Sheng and Ting, 2005; Nikolić, Zârbo and Souma, 2005; Li, Hu and Shen, 2005).

In Section 2 below, we review the mechanisms for spin-orbit coupling in the semiconductors of interest, and we discuss forms of the effective Hamiltonians that describe the carriers in various situations. In Section 3, we see how the various effective Hamiltonians can influence spin transport and accumulation. We discuss spin precession, produced by the intrinsic spin-orbit coupling, as well as skew scattering and the so-called side-jump effect, resulting from the extrinsic spin-orbit coupling. We introduce Boltzmann-type kinetic equations which can describe spin transport and accumulation in various situations, and we discuss the simpler spin and charge diffusion equations which can be typically used in situations where the spin-relaxation rate is much slower than momentum relaxation.

In Section 4, we discuss explicitly the spin polarization and spin transport arising from an electrical current in a semiconductor with spin-orbit coupling. We introduce the notion of a spin current and the spin Hall conductivity, and we discuss results that have been obtained for these quantities in various situations. We also discuss a relation between the spin Hall conductivity and the so-called anomalous Hall effect that can result from spin-orbit coupling in a ferromagnet or in semiconductor with a spin polarization induced by an external magnetic field.

Spin currents are not directly observed in experiments, however. If spin-relaxation rates are slow, one may expect that spin currents with a nonzero divergence can lead to observable local spin polarizations, in which relaxation of excess spin balances the accumulation of spin that is transported into a region by the spin current. Furthermore, boundary effects may be important and nontrivial; in the presence of an electric current, spin polarization may be generated directly at a sample boundary. These issues are discussed in Section 4.5. We also briefly discuss mesoscopic systems, where all parts of the sample are close to a boundary.

A different type of spin Hall effect, associated with edge states, has been predicted to occur in certain systems that are insulating in the bulk, where the topology of the band structure has been altered due to spin-orbit coupling. In Section 5, we discuss this concept, along with the possibility that such effects may occur and be observable in a number of materials.

2 SPIN-ORBIT COUPLING IN SEMICONDUCTORS

For a nonrelativistic electron in vacuum, the Dirac equation can be reduced to the Pauli equation, describing a two-component spinor and containing the Zeeman term. The Pauli equation also contains relativistic corrections – including the spin-orbit coupling

$$H_{\mathrm{SO,\,vac}} = \lambda_{\mathrm{vac}}\, \boldsymbol{\sigma} \cdot (\mathbf{k} \times \nabla \tilde{V}) \tag{1}$$

Here, we used $\lambda_{\mathrm{vac}} = -\hbar^2/4m_0^2c^2 \approx -3.7 \times 10^{-6}$ Å^2, vacuum electron mass m_0, velocity of light c, and $\mathbf{k} = \mathbf{p}/\hbar$. In a semiconductor, we split the total potential $\tilde{V} = V_{\mathrm{cr}} + V$ into the periodic crystal potential V_{cr} and an aperiodic part V, which contains the potential due to impurities, confinement, boundaries, and external electrical field. One then tries to eliminate the crystal potential as much as possible and to

describe the charge carriers in terms of the band structure. The simplest systems of this sort can be exemplified by electrons in cubic direct-gap semiconductors. Then, the minimum of the energy spectrum is usually near the center of the Brillouin zone, and the twofold Kramers degeneracy is the only degeneracy of the spectrum at $k = 0$. It follows from symmetry arguments that for slow electrons in such crystals, and for slow carriers (electrons and holes) in high symmetry two-dimensional systems, the effective single-particle Hamiltonian is

$$H_{\text{eff}} = \epsilon_k + V + H_{\text{int}} + H_{\text{ext}} \tag{2}$$

$$H_{\text{int}} = -\frac{1}{2}\,\mathbf{b}(\mathbf{k}) \cdot \boldsymbol{\sigma} \tag{3}$$

$$H_{\text{ext}} = \lambda\, \boldsymbol{\sigma} \cdot (\mathbf{k} \times \nabla V) \tag{4}$$

where $\mathbf{k}$ is the crystal wave vector relative to the zone center, and we assumed that V is only slowly varying on the scale of the lattice constant. Here, $\boldsymbol{\sigma}$ is the vector of Pauli matrices for the pseudo spin-$\frac{1}{2}$ of the Kramer's doublet at $k = 0$; it is customarily called a *spin-$\frac{1}{2}$ system*. $\mathbf{b}(\mathbf{k})$ is the intrinsic spin-orbit field, with $\mathbf{b}(\mathbf{k}) = -\mathbf{b}(-\mathbf{k})$ due to time reversal symmetry. Thus, for a three-dimensional system, $\mathbf{b}$ can only be present if the inversion symmetry of the host crystal is broken. In the case of a two-dimensional system, it is conventional to talk about its two-dimensional band structure, and to include the confinement potential in ϵ_k and $\mathbf{b}(\mathbf{k})$ (instead of including it explicitly in V); in this case $\mathbf{b}$ can also result from an asymmetry in the confinement.

In contrast, H_{ext} does not require broken inversion symmetry of the pure crystal or of the structure. It is important to note that λ in equation (4) can be many orders of magnitude larger than the vacuum value λ_{vac}; this is due to the large spin-orbit interaction when the Bloch electrons move close to the nuclei, with velocities that are close to relativistic. Both H_{int} and H_{ext} may be important for the spin Hall effect, as we will discuss in this chapter. We present specific forms of these effective Hamiltonians in Sections 2.3 and 2.4.

2.1 Band structure of materials with spin-orbit interaction

We now consider the electron wave functions near the forbidden gap of a semiconductor. These wave functions are often described by the Kohn–Luttinger $\mathbf{k} \cdot \mathbf{p}$ method, where one expands the Hamiltonian in terms of band-edge Bloch functions. Here, we present a brief overview of this method; more detailed explanations can be found, for example, in Blount's (1962) review article or in the books by Bir and Pikus (1974) and by Winkler (2003).

For a given $\mathbf{k}$, the solutions of the Schrödinger equation are Bloch functions $e^{i\mathbf{k}\cdot\mathbf{r}} u_{\nu',\mathbf{k}}(\mathbf{r})$. Here, ν' is the band index and includes the spin degree of freedom. The lattice-periodic part $u_{\nu',\mathbf{k}}(\mathbf{r})$ of these Bloch functions can be expanded in the functions $u_{\nu,\,\mathbf{k}=0}(\mathbf{r}) = \langle \mathbf{r} | u_{\nu,0} \rangle$, which provide a complete basis when all bands ν are taken. For semiconductors with a direct gap at the center of the Brillouin zone, which we discuss here, one may consider states in close vicinity of $\mathbf{k} = 0$, truncate this expansion, and only take the closest bands into account. Therefore, it is sufficient to know the matrix elements of the full Hamiltonian H in the truncated basis $|\phi_\nu\rangle = e^{i\mathbf{k}\cdot\mathbf{r}} |u_{\nu,0}\rangle$, that is, one considers $H_{\nu\nu'}(\mathbf{k}) = \langle \phi_\nu | H | \phi_{\nu'} \rangle$. More concretely, one evaluates

$$H_{\nu\nu'}(\mathbf{k}) = E_\nu \delta_{\nu\nu'} + \frac{\hbar^2 k^2}{2m_0}\delta_{\nu\nu'} + \frac{\hbar}{m_0}\mathbf{k} \cdot \langle u_{\nu,0} | \boldsymbol{\pi} | u_{\nu',0} \rangle \tag{5}$$

where E_ν is the energy offset of the band at $\mathbf{k} = 0$, that is, $[p^2/2m_0 + V_{\text{cr}} + (\lambda_{\text{vac}}/\hbar)\,\boldsymbol{\sigma} \cdot (\mathbf{p} \times \nabla V_{\text{cr}})] |u_{\nu,0}\rangle = E_\nu |u_{\nu,0}\rangle$. Further, $\boldsymbol{\pi} = \mathbf{p} + (\lambda_{\text{vac}}/\hbar)\,(\nabla V_{\text{cr}} \times \boldsymbol{\sigma})$, and one usually approximates $\boldsymbol{\pi} \approx \mathbf{p}$; then the last term of equation (5) is proportional to the matrix element of $\mathbf{k} \cdot \mathbf{p}$, giving this method its name. Finally, this finite-dimensional Hamiltonian $H(\mathbf{k})$ now describes the band structure in terms of a few parameters – band offsets and momentum matrix elements of $\mathbf{k} = 0$ Bloch functions – and is well suited for analyzing charge carriers.

Alternatively, one can use a second method and construct a Hamiltonian by allowing all contributions (up to some order in k) that are invariant under the symmetry operations of the system – the coupling constants are material-dependent parameters. For example, when considering the top of the valence band in Figure 1 and in the absence of inversion asymmetry, magnetic field, and strain, the most general form up to quadratic terms in k (i.e., in the effective mass approximation), is the 4×4 Luttinger Hamiltonian,

$$H_{\text{L}} = \frac{\hbar^2}{m_0}\left[\left(\gamma_1 + \frac{5}{2}\gamma_2\right)\frac{k^2}{2} - \gamma_3 (\mathbf{k} \cdot \mathbf{J})^2 + (\gamma_3 - \gamma_2)\sum_{\text{i}} k_{\text{i}}^2 J_{\text{i}}^2\right] \tag{6}$$

which is consistent with the cubic symmetry. Here, $\mathbf{J} = (J_x, J_y, J_z)$ and J_{i} are the angular momentum matrices for spin $\frac{3}{2}$, and γ_{i} are the material-dependent Luttinger parameters. H_{L} describes p-doped Si and Ge; for GaAs, due to broken inversion symmetry, terms linear in k arise as well.

By contrast, using the first method ($\mathbf{k} \cdot \mathbf{p}$ method) instead, the Hamiltonian $H_{\nu\nu'}(\mathbf{k})$ (equation (5)) is evaluated directly for the eight bands ν (including spin) shown in Figure 1, and one arrives at the simplest version of the 8×8 Kane model. It only includes three parameters, namely, the energy gap E_0,

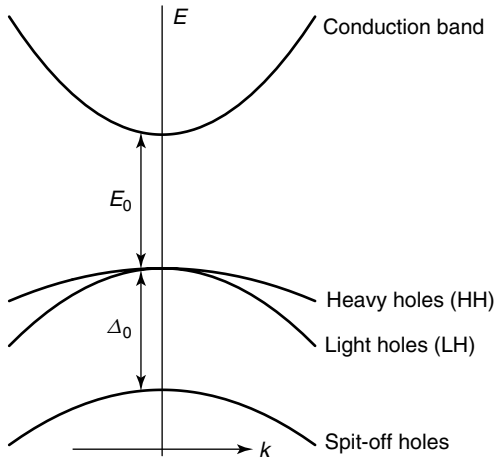

Figure 1. Schematic band structure of a cubic direct gap semiconductor. When spin-orbit interaction is disregarded, one finds an s-like conduction band and a p-like threefold degenerate valence band. The spin-orbit interaction due to crystal potential V_{cr} (entering as $\tilde{V}$ in equation (1)) partially lifts this degeneracy and leads to a substantial splitting between the valence bands with total angular momentum $J = 3/2$ (heavy and light holes) and those with $J = 1/2$ (split-off holes).

the energy of the split-off holes Δ_0, and the matrix element P of the momentum (multiplied by $\hbar/m_0$) between s- and p-type states. P is nearly universal for III–V compounds, while the other parameters depend on the material. This eight-dimensional description is accurate for narrow band materials; for wider gaps it still provides understanding at a qualitative level.

Furthermore, one can then derive an effective, lower-dimensional Hamiltonian by block diagonalizing $H_{\nu\nu'}$; this is an efficient way to calculate the band structure in the vicinity of $\mathbf{k} = 0$. One can do this either exactly or by using time-independent degenerate perturbation theory (see Section 2.2). Considering a particular block, this allows estimating the magnitude of the symmetry-allowed terms. Terms that were not present before block diagonalization are called contributions from remote bands. For example, using the 8×8 Kane model, one can calculate the parameters γ_{i} that enter the 4×4 Luttinger Hamiltonian (equation (6)) for the top of the valence band; because the model is isotropic, one gets $\gamma_2 = \gamma_3$. To estimate corrections due to the cubic symmetry, one needs to take more bands into account.

In addition to the crystal field, we also wish to consider electric fields that are applied externally or that result from charged impurities. Assuming that the corresponding potential $V(\mathbf{r})$ varies slowly on the scale of a lattice constant, we can apply the envelope function approximation (EFA), that is, we replace the plain waves $\mathrm{e}^{i\mathbf{k}\cdot\mathbf{r}}$ by slowly varying envelope functions $\psi_\nu(\mathbf{r})$. Evaluating matrix elements of V in the basis $\langle \mathbf{r}|\psi, \nu\rangle = \psi_\nu(\mathbf{r})u_{\nu,\,\mathbf{k}=0}(\mathbf{r})$, the main contribution is diagonal with respect to the band index ν. However, because $\mathbf{k}$ and $V(\mathbf{r})$ do not commute, off-diagonal elements (in ν) can arise in the Hamiltonian when expanding in $\mathbf{k}$, see, for example, equation (4). Magnetic fields can be included in a similar way, using the Perierls substitution $\hbar\mathbf{k} = -i\hbar\nabla - (e/c)\mathbf{A}$. Here, we use $e < 0$ for electrons and $e > 0$ for holes. Then, the components of $\mathbf{k}$ no longer commute, $\mathbf{k} \times \mathbf{k} = i(e/\hbar c)\mathbf{B}$; this leads to Zeeman coupling, which is described by an effective g factor.

2.2 Effective Hamiltonian

The $\mathbf{k}\cdot\mathbf{p}$ method leads to high-dimensional Hamiltonians (equation (5)), for example, an 8×8 matrix for the Kane model, thus further simplifications are desirable. For this, one can use time-independent degenerate perturbation theory and describe a subset of states (say, the lowest conduction-band states) with an effective Hamiltonian. Löwdin partitioning is a straightforward and convenient method to implement such a perturbative expansion (Winkler, 2003); it is also known as Foldy-Wouthuysen transformation in the context of the Dirac equation and as Schrieffer-Wolf transformation in the context of the Anderson model. The idea is to find a unitary transformation e^{-S} (i.e., S is anti-Hermitian) such that the transformed Hamiltonian $\mathrm{e}^{-S}H\mathrm{e}^{S}$ is block diagonal, that is, contains no off-diagonal elements between the states we are interested in and any other states. This procedure assumes that the states of interest (e.g., the conduction band) are separated from the other states (all other bands) by an energy much larger than the Fermi energy. Then, because these off-diagonal elements are small, one can eliminate the off-diagonal blocks of $\mathrm{e}^{-S}H\mathrm{e}^{S}$ order by order (or even exactly). In our example, the transformed Hamiltonian consists of one 2×2 and one 6×6 block. The smaller block describes the conduction-band electrons – we can understand the two dimensions as (pseudo-) spin $\frac{1}{2}$. At the level of wave functions, the periodic part of the electron wave function at a given $\mathbf{k} \neq 0$ is mainly described by the conduction band Bloch function at $k = 0$, but also contains a small admixture from the valence band Bloch functions.

2.3 Intrinsic spin-orbit coupling

One generally distinguishes between intrinsic and extrinsic mechanisms of spin-orbit coupling; however, this classification is not unique across the literature. In this section, we classify it according to the individual terms of the effective Hamiltonians. Namely, we refer to the spin-orbit contributions to the Hamiltonian that depend on impurity potentials as *extrinsic*. The other spin-orbit contributions arise even in the

absence of impurities and we call them *intrinsic* – we also call effects resulting from these contributions intrinsic, even if we have to allow for a small concentration of impurities to make the theory of dc transport properties consistent [1].

For a (pseudo-) spin-$\frac{1}{2}$ system, the spin-orbit part of the intrinsic one-particle Hamiltonian has the general form $H_{\rm int}$ (equation (3)). In the following, we discuss the origin and the functional form of such spin-orbit fields. We focus on such spin-$\frac{1}{2}$ descriptions, because they are relevant for low-dimensional systems and are the basis of most theoretical works.

We first consider a n-doped bulk (3D) semiconductor and the effective Hamiltonian of conduction-band electrons. III–V and II–VI semiconductors lack inversion symmetry and are available in two modifications: in cubic zinc blende or in hexagonal wurtzite structure. In zinc blende modification, the bulk inversion asymmetry (BIA) leads to the Dresselhaus term

$$H_{\rm D,\,3d} = \mathcal{B}\, k_x (k_y^2 - k_z^2)\sigma_x + \text{c.p.} \tag{7}$$

where $k_{\rm i}$ are along the principal crystal axes. Here, c.p. stands for cyclic permutation of all indices, and the symmetrized product of the components $k_{\rm i}$ must be used if a magnetic field is applied. The Dresselhaus term originates from bands further away than the basic eight bands, and one finds the coupling constant in terms of the band parameters; when using the extended 14×14 Kane model its numerical value is $\mathcal{B} \approx 27\ \text{eV\AA}^3$, for both GaAs and InAs (Winkler, 2003). However, tight-binding calculations and interpretation of weak-localization experiments indicate lower values, at least for GaAs (Knap *et al.*, 1996; Krich and Halperin, 2007).

When the electrons are confined to two dimensions, the expectation value of the Dresselhaus term along the confinement direction (that we always assume to be along [001]) should be taken, $\langle H_{\rm D,\,3d}\rangle$. While $\langle k_z\rangle = 0$, we see that the terms in $\langle k_z^2\rangle \approx (\pi/d)^2$ are large for small confinement width d, thus the main BIA contribution becomes

$$H_\beta = \beta(k_x\sigma_x - k_y\sigma_y) \tag{8}$$

with $\beta \approx -\mathcal{B}(\pi/d)^2$. In addition to the k-linear term in equation (8), there is also a k^3 term,

$$H_{\rm D,\,2d} = \mathcal{B}\, k_x k_y (k_y\sigma_x - k_x\sigma_y) \tag{9}$$

which is small compared to H_β in the strong confinement (low carrier density) limit $\pi/d \gg k_{\rm F}$, where $k_{\rm F}$ is the Fermi wave vector. Additionally, a spin-orbit coupling term arises if the confinement potential $V(z)$ along the z direction is not symmetric, that is, if there is a structure inversion asymmetry (SIA). Equation (4) provides an explicit connection between such a potential and spin-orbit coupling. Taking the expectation value $\langle H_{\rm ext}\rangle$ along the z direction and noting that the only contribution of the confinement field is $\propto \langle \nabla_z V\rangle$, one finds the Rashba Hamiltonian,

$$H_\alpha = \alpha(k_y\sigma_x - k_x\sigma_y) \tag{10}$$

corresponding to $\mathbf{b}(\mathbf{k}) = 2\alpha\,\hat{\mathbf{z}}\times\mathbf{k}$. More generally, for spinors with $J_z = \pm 1/2$, H_α is the only k-linear invariant of the group $C_{\infty v}$ that takes into account the confinement potential $V(z)$ but disregards the discrete symmetry of the crystal. The magnitude of the coupling constant α depends on the confining potential and it can be modified by applying an additional field via external gates. It also defines the spin-precession wave vector $k_\alpha = \alpha m/\hbar^2$. Finally, such a term H_α is also present for three-dimensional electrons in systems of hexagonal wurtzite structure (or in cubic systems with strain, see Section 2.5).

Next, we consider a p-doped three-dimensional semiconductor, that is, the $J = 3/2$ valence band, described by the four-dimensional Luttinger Hamiltonian. Remote bands lead to a BIA contribution to the Hamiltonian, which is given by equation (7) after replacing $\sigma_{\rm i}$ by the angular momentum matrices $J_{\rm i}$ for spin $\frac{3}{2}$ and using a different coupling constant. If the system is reduced to two dimensions, size quantization lifts the fourfold degeneracy at $\mathbf{k} = 0$ and creates heavy-hole (HH) bands with $J_z = \pm 3/2$ and light-hole (LH) bands with $J_z = \pm 1/2$ (for confinement along the [001] axis). Usually the HH bands are higher in energy, thus for small doping it is sufficient to consider only them. For spinors with $J_z = \pm 3/2$, the only invariant of the group $C_{\infty v}$ (again, we do not discuss invariants of discrete symmetries here) respecting time reversal symmetry is

$$H_{\alpha,\rm h} = i\alpha_{\rm h}\left(k_-^3\sigma_+ - k_+^3\sigma_-\right) \tag{11}$$

where $a_\pm \equiv a_x \pm i a_y$ for any a. As distinct from H_α (equation (10)), the Rashba Hamiltonian for HHs is cubic in k, as it was discussed in (Winkler, 2000; Schliemann and Loss, 2005).

2.4 Extrinsic spin-orbit coupling

Electric fields due to impurities lead to extrinsic contributions to the spin-orbit coupling. Externally applied electrical fields lead to analogous contributions. To derive the dominant extrinsic term, it is sufficient to restrict ourselves to the simplest 8×8 Kane Hamiltonian; higher bands will give rise to small corrections. Using third-order perturbation theory and for conduction-band electrons, we find $H_{\rm ext}$ as given in equation (4), with (Nozières and Lewiner, 1973;

Winkler, 2003)

$$\lambda \approx \frac{P^2}{3}\left[\frac{1}{E_0^2} - \frac{1}{(E_0+\Delta_0)^2}\right] \tag{12}$$

and where V is the potential due to impurities and an externally applied field. It is noteworthy that equation (4) has the same analytical form as the vacuum spin-orbit coupling (equation (1)); this is because both the Dirac equation and the simplest Kane Hamiltonian have spherical symmetry and because both the Pauli equation and equation (4) are obtained in a low-energy expansion. However, for $\Delta_0 > 0$ the coupling constant λ has the *opposite sign* as in vacuum.

One finds $\lambda \approx 5.3\,\text{Å}^2$ for GaAs and $\lambda \approx 120\,\text{Å}^2$ for InAs, that is, spin-orbit coupling in n-GaAs is by 6 orders of magnitude stronger than in vacuum, and even larger for InAs due to its smaller gap. This enhancement of spin-orbit coupling is critical for developing large extrinsic spin currents. Furthermore, for a two-dimensional system, when considering V as averaged along the $\hat{\mathbf{z}}$ direction, both ∇V and $\mathbf{k}$ are in plane, thus we have $H_{\text{ext, e}} = \lambda\,\sigma_z(\mathbf{k}\times\nabla V)_z$.

For a 3D hole system, we consider the $J = 3/2$ valence band. Then, the dominant extrinsic spin-orbit term in third-order perturbation theory describing the valence band states is

$$H_{\text{ext, v}} = \lambda_{\text{v}}\,\mathbf{J}\cdot(\mathbf{k}\times\nabla V) \tag{13}$$

with $\lambda_{\text{v}} = -P^2/3E_0^2$, that is, for GaAs $\lambda_{\text{v}} \approx -15\,\text{Å}^2$ (Winkler, 2003) and has to be added to the Luttinger Hamiltonian H_{L} (equation (6)). When considering a two-dimensional hole system with HH–LH splitting, we can restrict equation (13) to the HH states, where $J_z = \pm 3/2$. Expressing this two-dimensional subspace in terms of a pseudo spin $\frac{1}{2}$ leads to

$$H_{\text{ext, v}} = -\frac{P^2}{2E_0^2}\,(\mathbf{k}\times\nabla V)_z\sigma_z \tag{14}$$

Thus, the extrinsic spin-orbit interaction for two-dimensional HH states has the same form as for two-dimensional electrons.

Finally, we point out that extrinsic spin-orbit coupling arises because the long-range Coulomb potential of the impurities does not commute with the intrinsic Hamiltonian of the hosting crystal. The extrinsic Hamiltonian H_{ext} (equations (4) and (13)) is obtained in the framework of the EFA, which disregards short-range contributions to the spin-orbit coupling arising from the chemical properties of dopants. This is why the coupling λ depends only on the parameters of the perfect crystal lattice.

2.5 Strain

Nonhydrostatic strain reduces the symmetry of the system and in this way leads to additional spin-orbit terms in the Hamiltonian. In third-order perturbation theory of the Kane Hamiltonian, the effective conduction-band Hamiltonian due to strain is dominated by

$$H_{\varepsilon,\,\text{e}} = \frac{-2C_2\Delta_0 P}{3E_0(E_0+\Delta_0)}\,\boldsymbol{\sigma}\cdot(\mathbf{k}\times\boldsymbol{\varepsilon}_{\text{s}}) \equiv \frac{1}{2}C_3\,\boldsymbol{\sigma}\cdot(\mathbf{k}\times\boldsymbol{\varepsilon}_{\text{s}}) \tag{15}$$

where $\boldsymbol{\varepsilon}_{\text{s}} = (\varepsilon_{yz},\ \varepsilon_{xz},\ \varepsilon_{xy})$ describes the shear strain. Here, C_2 is the interband deformation-potential constant that arises in noncentrosymmetric semiconductors (Winkler, 2003; Trebin, Rössler and Ranvaud, 1979). Note that Pikus and Titkov (1984) as well as Ivchenko and Pikus (1997) use the opposite sign in the definition of this constant, $C_2^{\text{PT/IP}} = -C_2$. Further, if a shear is applied such that only $\varepsilon_{xy} \neq 0$, equation (15) has the same form as the Rashba Hamiltonian (equation (10)).

For three-dimensional $J = 3/2$ valence band states, the main strain contribution is (Pikus and Titkov, 1984)

$$H_{\varepsilon,\,\text{v}} = \frac{2C_2P}{3E_0}\,\mathbf{J}\cdot(\mathbf{k}\times\boldsymbol{\varepsilon}_{\text{s}}) \tag{16}$$

Note that when the system is confined to two dimensions, equation (16) implies a k-linear spin-orbit contribution for HH states due to strain, $(C_2P/E_0)\ (\mathbf{k}\times\boldsymbol{\varepsilon}_{\text{s}})_z\,\sigma_z$. This linear term arises due to the low symmetry of the strained material, in contrast to the Rashba term (cf. equation (11)), which is dominated by terms cubic in k and where the k-linear terms are numerically small (Winkler, 2003).

2.6 Anomalous velocity and coordinate

As a consequence of the spin-orbit interaction, velocity and coordinate operators are modified and become spin dependent – this will be important when considering currents. When an effective Hamiltonian is derived in perturbation theory, as explained in Section 2.2, a unitary transformation e^{-S} is applied. Thus, the coordinate operator $\mathbf{r} = i(\partial/\partial\mathbf{k})$ is also transformed, $\mathbf{r}\mapsto\tilde{\mathbf{r}} = \text{e}^{-S}\mathbf{r}\text{e}^{S} = \mathbf{r} + \delta\mathbf{r}$ and we call $\delta\mathbf{r}$ the anomalous coordinate. In particular, because S couples to spin, $\delta\mathbf{r}$ is spin dependent. This correction $\delta\mathbf{r}$ is known as the *Yafet term* (Yafet, 1963); also, it can be expressed in terms of a Berry connection, $\langle u_{v',\mathbf{k}}\,|i\nabla_{\mathbf{k}}|\,u_{v,\mathbf{k}}\rangle$ (Kohmoto, 1985; Sundaram and Niu, 1999; Nagaosa, 2006). In perturbation theory, one finds

$$\delta\mathbf{r}_{\text{SO, e}} = \lambda(\boldsymbol{\sigma}\times\mathbf{k}) \tag{17}$$

$$\delta\mathbf{r}_{\text{SO, v}} = \lambda_{\text{v}}(\mathbf{J}\times\mathbf{k}) \tag{18}$$

for conduction-band electrons and for $J = 3/2$ HH states, respectively. Note that coordinate operators no longer commute, $\mathbf{r} \times \mathbf{r} = i\lambda\boldsymbol{\sigma}$ and $\mathbf{r} \times \mathbf{r} = i\lambda_{\mathrm{v}}\mathbf{J}$, respectively. Finally, $\delta\mathbf{r}_{\mathrm{SO}}$ leads to an extra term in the equations of motion that can be understood as anomalous velocity (Blount's, 1962).

Formally, we can derive the anomalous velocity similar to the coordinate, namely, $\mathbf{v} \mapsto \mathrm{e}^{-S}\mathbf{v}\mathrm{e}^{S} = \mathbf{v}_0 + \delta\mathbf{v}$, where $\delta\mathbf{v}$ is the anomalous velocity and, for a parabolic band, $\mathbf{v}_0 = \hbar\mathbf{k}/m^*$. Alternatively, one can obtain the velocity operator from the Heisenberg equation, $\mathbf{v} = (i/\hbar)\left[H, \tilde{\mathbf{r}}\right]$. For $H = H_0 + H_{\mathrm{SO}}$, where H_{SO} contains the (small) spin-orbit coupling, we get $\mathbf{v} = \mathbf{v}_0 + (i/\hbar)\,[H_{\mathrm{SO}}, \mathbf{r}] + (i/\hbar)\,[H_0, \delta\mathbf{r}_{\mathrm{SO}}]$. Thus, H_{SO} leads to an anomalous velocity because it does not commute with the unperturbed coordinate $\mathbf{r}$, and, additionally, the contribution from the anomalous coordinate $\delta\mathbf{r}_{\mathrm{SO}}$ should also be taken into account, as it can be significant.

When the impurity potential V is included, the above argument remains the same, but now H_{SO} contains the extrinsic contribution as well. Note that for extrinsic spin-orbit $H_{\mathrm{SO}} = H_{\mathrm{ext,\,e}}$ (equation (4)) the commutator $\left[H_{\mathrm{ext,\,e}}, \mathbf{r}\right]$ and the anomalous coordinate $\delta\mathbf{r}_{\mathrm{SO}}$ give equal contributions to $\delta\mathbf{v}$ (Nozières and Lewiner, 1973).

3 MECHANISMS OF SPIN TRANSPORT

We now address how the microscopic mechanism of spin-orbit interaction, given by effective Hamiltonians, influences spin transport and accumulation. In the following, we assume a noninteracting system in the absence of a magnetic field. Because we ignore electron–electron interaction, we do not consider the spin-drag effect here (Hankiewicz and Vignale, 2006), which can lead to a suppression of spin transport at high temperatures, and suppression of spin relaxation (Glazov and Ivchenko, 2002). We also restrict ourselves to Boltzmann transport and do not discuss the hopping regime (Entin-Wohlman *et al*., 2005).

3.1 Intrinsic: spin precession

In a system with weak intrinsic spin-orbit coupling H_{int} (equation (3)), consider a carrier with spin aligned along the spin-orbit field $\mathbf{b}(\mathbf{k})$. When an electrical field $\mathbf{E} = E\hat{\mathbf{x}}$ is applied, the particle is accelerated: $\dot{\mathbf{k}} = e\mathbf{E}/\hbar$ in lowest order in spin-orbit interaction; and its spin-orbit field changes: $\dot{\mathbf{b}} = (\partial\mathbf{b}/\partial k_x)\,eE/\hbar$. For a small acceleration, the spin follows adiabatically the direction of $\mathbf{b}(\mathbf{k})$. Additionally, there will be a nonadiabatic correction that can be derived as follows. Suppose that the direction of $\mathbf{b}$ rotates in the xy plane (as it is the case for Rashba interaction H_α). Because the rotation frequency ω is the component of $\dot{\mathbf{b}}/b$ perpendicular to $\mathbf{b}$, it is $\omega = (\mathbf{b} \times \dot{\mathbf{b}})_z/b^2$. In the corotating frame, there is a field b along the x axis and a field $\hbar\omega$ along the z axis. As we are interested in the next-to-adiabatic correction, we assume that ω changes slowly and that the spin remains aligned along the total field in the rotating frame, thus it has a component $s_z \approx (\hbar/2)\,\hbar\omega/b$. Therefore, the first nonadiabatic correction to the spin is $\delta\mathbf{s}(\mathbf{k}) = \hbar^2(\mathbf{b} \times \dot{\mathbf{b}})_z/2b^3$. In particular, the electrical field drives this spin precession (via $\dot{\mathbf{b}}$), leading to such out-of-plane component $\delta\mathbf{s}(\mathbf{k})$, which could be important in spin transport (Sinova *et al*., 2004), see Section 4.3. However, when considering dc properties, one must be careful and also allow for impurities that decelerate the carriers to reach a steady state. In particular, if $\mathbf{b}(\mathbf{k})$ is linear in $\mathbf{k}$, it turns out that the deceleration at impurities cancels this spin precession, see Section 4.3.

3.2 Extrinsic: skew scattering

When a carrier scatters at an impurity potential V, because of the extrinsic spin-orbit interaction (equations (4) and (14)) the scattering cross section depends on the spin state (Smit, 1958), see Figure 2. This effect is known as *Mott skew scattering* (Mott and Massey, 1965) and was originally considered for high-energy electrons that are elastically scattered by an atom and that are described by the vacuum Hamiltonian, equation (1). Skew scattering does not appear in the first-order Born approximation, thus is at least of the order V^3. For band electrons, skew scattering was originally considered as the origin of the anomalous Hall

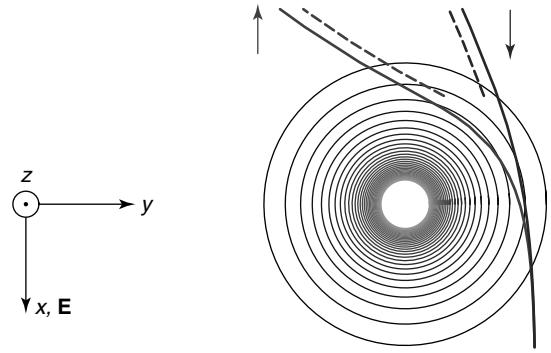

Figure 2. Spin-dependent scattering of electrons at an attractive impurity. We show the classical trajectories (solid lines), for a screened Coulomb potential and for strongly exaggerated extrinsic spin-orbit coupling (using equation (4) with $\lambda > 0$) and with spin quantization axis perpendicular to the plane. The skew-scattering current results from different scattering angles for spin-↑ and spin-↓ electrons and leads to a positive spin Hall conductivity, $\sigma_{\mathrm{SS}}^{\mathrm{SH}} = -j_{\mathrm{SS},y}^{z}/E_x > 0$. The dashed lines show the horizontal displacement due to the side-jump effect, contributing to the spin current with opposite sign.

effect, see Section 4.4. As applied to spin Hall effect, the relevance of this extrinsic mechanism was recognized early on (D'yakonov and Perel', 1971; Hirsch, 1999; Zhang, 2000).

3.3 Extrinsic: side-jump mechanism

The side-jump mechanism (Berger, 1970) describes the lateral displacement of the wave function during the scattering event. (Such a displacement does not modify the skew scattering cross section introduced in Section 3.2, because it does not change the scattering angle measured at large distances.) The side-jump contribution is obtained when the anomalous velocity $\delta\mathbf{v}$ (see Section 2.6) is integrated over the duration of the scattering process. As indicated in Section 2.6, the anomalous coordinate for electrons (equation (17)) leads to an anomalous-velocity contribution $\lambda(\boldsymbol{\sigma} \times \dot{\mathbf{k}})$; and there is an equal term due to $(i/\hbar)[H_{\mathrm{ext,\,e}},\ \mathbf{r}]$. For impurity scattering with momentum transfer $\delta\mathbf{k}$, this results in a total lateral displacement $2\lambda(\boldsymbol{\sigma} \times \delta\mathbf{k})$ (and analogously for holes, using equation (18)). When the effect of the anomalous velocity owing to an applied electrical field is considered, the side-jump contribution to spin transport becomes a subtle issue; for a detailed analysis and intuitive description see (Nozières and Lewiner, 1973). Because the side-jump mechanism is not contained in the Boltzmann approach, in such a framework it needs to be evaluated separately. The side-jump contribution can be found using the Kubo formula and diagrammatic approaches; see (Lewiner, Betbeder and Nozières, 1973; Crépieux and Bruno, 2001; Tse and Das Sarma, 2006a).

3.4 Kinetic equation

We consider the Hamiltonian H_{eff} (equation (2)) containing both intrinsic (H_{int}) and extrinsic (H_{ext}) spin-orbit contributions, and with V that describes the electrical field $\mathbf{E}$ and the impurity potential V_{i}. For a homogeneous system of noninteracting particles, one can derive the kinetic equation (Khaetskii, 2006; Shytov, Mishchenko, Engel and Halperin, 2006)

$$\frac{\partial \hat{f}}{\partial t} + \frac{1}{\hbar}\,\boldsymbol{\sigma}\cdot(\mathbf{b}\times\mathbf{f}) + e\mathbf{E}\cdot\frac{1}{\hbar}\frac{\partial \hat{f}_0}{\partial \mathbf{k}} = \left(\frac{\partial \hat{f}}{\partial t}\right)_{\mathrm{coll}} \tag{19}$$

that is, a spin-dependent Boltzmann equation, where the distribution function is written as a 2×2 spin matrix $\hat{f} = \hat{f}_0(\mathbf{k}) + \frac{1}{2}n(\mathbf{k})\,\mathbb{1} + \mathbf{f}(\mathbf{k})\cdot\boldsymbol{\sigma}$, with equilibrium distribution function $\hat{f}_0$. Here, n is the excess particle density and $\mathbf{f}$ describes the spin-polarization density. Formally, the Boltzmann equation is obtained by an expansion in $1/k_{\mathrm{F}}\ell$, where ℓ is the mean free path, that is, it is applicable for dilute impurities. Traditionally, the Boltzman equation describes the distribution function $n(\mathbf{k})$, which is the *probability* density of a state $\mathbf{k}$ to be occupied – in contrast, here it describes $\hat{f}(\mathbf{k})$, which corresponds to the 2×2 *density matrix* for a spin-$\frac{1}{2}$ particle.

All terms on the lhs of equation (19) arise in the absence of impurities. The first term is the derivative of $\hat{f}$ with respect to its explicit time dependence. The second term describes the spin precession; it is obtained from the Heisenberg equation, $\mathbf{f}\cdot\dot{\boldsymbol{\sigma}} = \mathbf{f}\cdot(i/\hbar)\left[-\frac{1}{2}\mathbf{b}\,(\mathbf{k})\cdot\boldsymbol{\sigma},\ \boldsymbol{\sigma}\right]$. The third term is the driving term due to the electrical field, given in lowest order of $\mathbf{E}$. Finally, for inhomogeneous particle and spin distributions, the term $\mathbf{v}\cdot\nabla\hat{f}$ has to be added to the lhs.

The rhs of the Boltzmann equation (equation (19)) is the collision term, symbolically given by

$$\left(\frac{\partial \hat{f}(\mathbf{k})}{\partial t}\right)_{\mathrm{coll}} = n_{\mathrm{i}} v \sum_{\mathbf{k}';\ \epsilon'=\epsilon} \frac{\mathrm{d}\overleftrightarrow{\sigma}}{\mathrm{d}\Omega}\left[\hat{f}(\mathbf{k}') - \hat{f}(\mathbf{k})\right] \tag{20}$$

Here, n_{i} is the impurity density and we only consider elastic scattering $\mathbf{k}\to\mathbf{k}'$ and $\mathbf{k}'\to\mathbf{k}$. The scattering cross-section tensor $\mathrm{d}\overleftrightarrow{\sigma}/\mathrm{d}\Omega$ and the summation over final states $\mathbf{k}'$ are spin dependent because (i) the extrinsic interaction H_{ext} leads to skew scattering, (ii) the intrinsic spin-orbit Hamiltonian H_{int} induces a spin-dependent density of states (DOS), and (iii) H_{int} causes spin-dependent momentum transfer – in general, the spin dependence of scattering is rather complex. The description of scattering is simplified for weak spin orbit coupling, as the collision term can be expanded in spin-orbit coupling, and we can discuss the individual corrections separately. Note that the Boltzmann equation does not include the side-jump effect (cf. Section 3.3), which is of higher order in $1/k_{\mathrm{F}}\ell$.

When considering only spin-orbit coupling due to H_{ext}, the collision term including skew scattering for a central symmetric impurity potential is (Engel, Halperin and Rashba, 2005)

$$\left(\frac{\partial \hat{f}(\mathbf{k})}{\partial t}\right)_{\mathrm{coll}} = n_{\mathrm{i}} v_\epsilon \int \mathrm{d}\Omega(\mathbf{k}')\left\{I(\vartheta)\left[\hat{f}(\mathbf{k}') - \hat{f}(\mathbf{k})\right] + \frac{1}{2}I(\vartheta)S(\vartheta)\,\boldsymbol{\sigma}\cdot\mathbf{m}[n(\mathbf{k}) + n(\mathbf{k}')]\right\} \tag{21}$$

where $\mathbf{m} = \mathbf{k}'\times\mathbf{k}/\left|\mathbf{k}'\times\mathbf{k}\right|$ is the unit vector normal to the scattering plane and $\vartheta = \vartheta_{\mathbf{k}\mathbf{k}'}$ is the angle between $\mathbf{k}'$ and $\mathbf{k}$. The coefficient $I(\vartheta)$ is the spin-independent part of the scattering cross section, while $S(\vartheta)$ is the so-called Sherman function (Mott and Massey, 1965; Motz, Olsen and Koch, 1964; Huang, Voskoboynikov and Lee, 2003), describing the polarization of outgoing particles (which is

normal to the scattering plane) scattered into direction $\mathbf{k}$ from an unpolarized incoming beam of momentum $\mathbf{k}'$. Note that $I\,S$, as mentioned earlier in Section 3.2, vanishes in first-order Born approximation; the lowest term is $\propto V^3$. Also, S is proportional to spin-orbit coupling, this is why in the second term in equation (21), only the spin-independent part of $\hat{f}$, $\frac{1}{2}n$, is retained.

So far, we considered the distribution function $\hat{f}(\mathbf{k})$ as density in $\mathbf{k}$ space. In the presence of intrinsic spin-orbit interaction, the energy spectrum contains two branches: for a given $\mathbf{k}$, there are two energies, split by the intrinsic field $\mathbf{b}(\mathbf{k})$. Thus, for elastic scattering, energy is conserved but $|\mathbf{k}|$ is not. It is now more convenient to choose a distribution as function of energy ϵ and direction φ in $\mathbf{k}$ space. Namely, the distributions $\Phi_{\mathrm{c}}(\varphi,\,\epsilon)$ and $\mathbf{\Phi}(\varphi,\,\epsilon)$ are derived from the distributions $n(\mathbf{k})$ and $\mathbf{f}(\mathbf{k})$, and can again be written as matrix $\hat{\Phi}(\varphi,\,\epsilon)$. Note that $\hat{\Phi}$ contains the spin-dependent DOS. We now consider a two-dimensional system, $\mathbf{k} = (k\cos\varphi,\ k\sin\varphi)$, and assume that the spectrum ϵ_k in the absence of spin-orbit interaction is isotropic (cf. equation (2)), and we define k_ϵ such that $\epsilon_{k_\epsilon} = \epsilon$ and define $v_\epsilon = \epsilon'_{k_\epsilon}/\hbar$. For $\mathbf{E} = E\hat{\mathbf{x}}$ and for $b \ll E_{\mathrm{F}}$, the kinetic equation becomes (Shytov, Mishchenko, Engel and Halperin, 2006)

$$\frac{\partial\hat{\Phi}}{\partial t} + \boldsymbol{\sigma}\cdot\left[\frac{\mathbf{b}\times\mathbf{\Phi}}{\hbar} - \frac{\Phi_{\mathrm{c}}}{4\hbar^2 v_\epsilon}\,\mathbf{b}\times\frac{\partial\mathbf{b}}{\partial k}\right] + \frac{eE}{(2\pi)^2}\,\frac{\partial f_0}{\partial\epsilon}\left[\frac{k_x}{\hbar} + \frac{1}{2\hbar^2 v_\epsilon}\,\frac{\partial}{\partial\varphi}\,(\mathbf{b}\cdot\boldsymbol{\sigma}\,\sin\varphi)\right] = \left(\frac{\partial\hat{\Phi}}{\partial t}\right)_{\mathrm{coll}} \tag{22}$$

where f_0 is the Fermi distribution function and $\mathbf{b}$ is evaluated for $|\mathbf{k}| = k_\epsilon$.

Now, considering only H_{int}, the collision integral can be found in a Golden Rule approximation (Shytov, Mishchenko, Engel and Halperin, 2006),

$$\left(\frac{\partial\hat{\Phi}(\varphi,\,\epsilon)}{\partial t}\right)_{\mathrm{coll}} = \int_0^{2\pi}\mathrm{d}\varphi'\,K(\vartheta)\left[\hat{\Phi}(\varphi') - \hat{\Phi}(\varphi)\right] + \int_0^{2\pi}\mathrm{d}\varphi'\,\boldsymbol{\sigma}\cdot\left[\mathbf{M}(\varphi,\varphi')\Phi_{\mathrm{c}}(\varphi') - \mathbf{M}(\varphi',\varphi)\Phi_{\mathrm{c}}(\varphi)\right] \tag{23}$$

Here, the first term describes the spin-independent scattering, with $K(\vartheta) = K(\varphi'-\varphi) = W(q)k_\epsilon/2\pi\hbar^2 v_\epsilon$ and $q = 2k_\epsilon\sin(|\vartheta|/2)$. The factor $W(q) = \left\langle\,|V_{\mathrm{i}}(\mathbf{q})|^2\,\right\rangle$ does not depend on the direction of the momentum transfer $\mathbf{q}$ because the problem is isotropic (while, of course, the individual scattering event is anisotropic, that is, depends on the scattering angle ϑ). This spin-independent term coincides with first term of equation (21), with $K(\vartheta) = n_{\mathrm{i}}v_\epsilon I(\vartheta)$, and should only be included once. The second term in equation (23) is given in first order in the intrinsic spin-orbit interaction $\mathbf{b}$ and contains the kernel (Shytov, Mishchenko, Engel and Halperin, 2006)

$$\mathbf{M}(\varphi,\varphi') = \frac{v_\epsilon}{4k_\epsilon}\,K(\vartheta)\,\frac{\partial}{\partial\epsilon}\left[\frac{k_\epsilon\mathbf{b}(\varphi)}{v_\epsilon}\right] + \frac{\mathbf{b}(\varphi)+\mathbf{b}(\varphi')}{4\hbar k_\epsilon v_\epsilon}\,\frac{\partial K(\vartheta)}{\partial\vartheta}\,\tan\frac{\vartheta}{2} \tag{24}$$

where the first term results from the spin-dependent DOS of the outgoing wave. The second term in $\mathbf{M}$ arises, because for a given energy ϵ, $|\mathbf{k}|$ depends on the spin state. Thus the incoming and outgoing states can have different momenta, leading to spin-dependent corrections to q.

For a very smooth scattering potential such that typically $q < b/v_{\mathrm{F}}$, the spin motion is adiabatic and should be treated differently (Govorov, Kalameitsev and Dulka, 2004; Khaetskii, 2006).

3.5 Diffusion equation

A spin-diffusion equation can be derived, starting from the Boltzmann equation, for a dirty system when the spin-relaxation time τ_{s} is much longer than the momentum relaxation time τ, that is, $\tau_{\mathrm{s}} \gg \tau$. It describes the carrier density $N(\mathbf{r})$ and spin-polarization density $\mathbf{s}(\mathbf{r})$; say, s_z is the excess density of particles polarized along $\hat{\mathbf{z}}$. For conduction-band electrons, the (pseudo-) spin density is $\mathbf{S} = (\hbar/2)\mathbf{s}$. The diffusion equation is simpler to solve than the kinetic equation (19), as the dependence on $\mathbf{k}$ is integrated out. Also, it is usually sufficient to know $\mathbf{s}$, because it is an experimentally accessible quantity, while $\hat{f}(\mathbf{k})$ is not directly accessible, cf. Sections 4.2 and 4.5 below. For a two-dimensional system with Rashba spin-orbit interaction H_α (equation (10)), the diffusion equation is (Burkov, Núñez and MacDonald, 2004; Mishchenko, Shytov and Halperin, 2004)

$$\dot{N} = D\nabla^2(N + \rho_0 V_{\mathrm{E}}) + \Gamma_{\mathrm{sc}}(\nabla\times\mathbf{s})_z \tag{25}$$

$$\dot{s}_i = D\nabla^2 s_i - \tau_i^{-1}s_i + \Gamma_{\mathrm{ss}}[(\hat{\mathbf{z}}\times\nabla)\times\mathbf{s}]_i + \Gamma_{\mathrm{sc}}\,(\hat{\mathbf{z}}\times\nabla)_i(N + \rho_0 V_{\mathrm{E}}) \tag{26}$$

with diffusion constant $D = \frac{1}{2}v_{\mathrm{F}}^2\tau$, anisotropic Dyakonov–Perel (1972) spin-relaxation rates $\tau_x^{-1} = \tau_y^{-1} = \tau_\perp^{-1} = 2\tau(\alpha k_{\mathrm{F}}/\hbar)^2$ and $\tau_z^{-1} = 2\tau_\perp^{-1}$, spin-charge coupling $\Gamma_{\mathrm{sc}} = -2\alpha(\alpha k_{\mathrm{F}}\tau)^2/\hbar^3$, spin–spin coupling

$\Gamma_{\rm ss} = 4\alpha E_{\rm F}\tau/\hbar^2$, density of states $\rho_0 = m/\pi\hbar^2$, and potential energy $V_{\rm E}$ of a carrier in the electrical field. The charge current is

$$\mathbf{J}^{\rm c} = -D\nabla(N + \rho_0 V_{\rm E}) + \Gamma_{\rm sc}\,\hat{\mathbf{z}} \times \mathbf{s} \tag{27}$$

Further, Mal'shukov, Wang, Chu and Chao (2005) derived diffusion equations for two-dimensional electrons with the Dresselhaus Hamiltonian $H_{\rm D,\,2d}$ (equation (9)).

The boundary conditions of the diffusion equation for a system with spin-orbit interaction are not trivial and one expects that they depend on the microscopic properties of the boundaries. A number of papers have been written about the boundary conditions corresponding to various physical circumstances, and have partly clarified this issue (Govorov, Kalameitsev and Dulka, 2004; Mal'shukov, Wang, Chu and Chao, 2005; Adagideli and Bauer, 2005; Galitski, Burkov and Das Sarma, 2006; Bleibaum, 2006; Tserkovnyak, Halperin, Kovalev and Brataas, 2006). Depending on the particular boundary condition, there may or may not be an s_z spin accumulation near the boundary of a 2D system, see Section 4.5. Somewhat related to this question, Shekhter, Khodas and Finkel'stein (2005) considered the boundary between a diffusive and ballistic system and allowed for spin-dependent scattering at the boundary, resulting from a spatially dependent Rashba Hamiltonian H_α.

4 ELECTRICALLY INDUCED SPIN POLARIZATION AND SPIN TRANSPORT

4.1 Spin current and spin Hall conductivity

In this section, we define the spin current in a homogeneous system with density n as

$$j_k^i \equiv \frac{1}{2}\, n\langle \sigma_{\rm i} v_k + v_k \sigma_{\rm i}\rangle \tag{28}$$

where $\langle\cdot\rangle$ is the expectation value of single-particle operators and with $\langle 1\rangle = 1$. Thus, the spin current is defined as the difference of the particle current densities (measured in numbers of particles) for carriers with opposite spins. This is in accordance with many studies (Murakami, Nagaosa and Zhang, 2003; Sinova *et al*., 2004; Sinova, Murakami, Shen and Choi, 2006), where a definition as in equation (28) was chosen, up to numerical prefactors. In many definitions, an additional prefactor of $\frac{1}{2}$ is used, which results from $\hbar/2$ angular momentum per electron spin and setting $\hbar = 1$. With the same argument, for the HH band, sometimes a prefactor $3/2$ is used; but sometimes only a factor $\frac{1}{2}$ is used to have the same definition of $\mathbf{j}^\mu$ for electrons and holes. Furthermore, the rhs of equation (28) is sometimes multiplied by the charge e to obtain the same units for charge and for spin currents. In particular, this means that the sign of the definition of $\mathbf{j}^\mu$ may change if $e < 0$ for electrons is taken.

Next, we define the spin Hall conductivity

$$\sigma^{\rm SH} \equiv -\frac{j_y^z}{E_x} \tag{29}$$

where j_y^z is the spin current density resulting from a small applied electrical field E_x. The negative sign in equation (29) results from writing a formal similar definition for $\sigma^{\rm SH}$ as for the charge conductivity σ_{xy}; however, sometimes a definition with an opposite sign for $\sigma^{\rm SH}$ is used.

These various prefactors are only some technicality – the main question is whether defining j_k^i as in equation (28) makes sense. To describe spin transport it sounds attractive to find a scheme similar to the charge transport theory. Because of charge conservation, charge densities $\rho^{\rm c}$ and charge currents $\mathbf{j}^{\rm c}$ satisfy the continuity equation $\dot{\rho}^{\rm c} + \mathrm{div}\,\mathbf{j}^{\rm c} = 0$. For spin transport, we can consider the spin density $S_{\rm i}$ instead of $\rho^{\rm c}$. Mott's (1936) two-channel model of electron transport in ferromagnetic metals is based on independent and conserved currents of up- and down-spin electrons, and $\mathbf{S}$ and j_k^i obey a continuity equation. Definition (28) is the natural generalization of Mott's model; however, spin-orbit coupling violates spin conservation, and the continuity equation for spin densities and currents does not hold. In this chapter, we still use equation (28) as definition of the spin current, as it is widely used, but we remain aware of its limitations. Despite the fact that it cannot be directly related to spin accumulation, it is a useful model quantity to compare the effect of different spin-orbit coupling mechanisms. While the continuity equation does not hold, one can, for a concrete Hamiltonian, evaluate source terms arising on the rhs (Burkov, Núñez and MacDonald, 2004; Erlingsson, Schliemann and Loss, 2005), which is often termed as torque (Culcer *et al*., 2004).

Other definitions of spin currents have also been proposed. Zhang and Yang (2005) analyzed the current of the total angular momentum $L_z + S_z$ and argued that it vanishes for the Rashba Hamiltonian H_α in the absence of impurities (owing to the rotational invariance of H_α) and that thus the impurity scattering would determine angular momentum currents. Shi, Zhang, Xiao and Niu (2006) discussed spin currents, introducing a definition that is not proportional to our j_k^i, but is given as time-derivative of the 'spin displacement' $S_{\rm i}(\mathbf{r})\, r_k$. A somewhat related definition was used by Bryksin and Kleinert (2006), who found that such spin currents diverge when the frequency $\omega \to 0$.

4.2 Spin polarization

In experiments, the spin polarization can be detected optically (Meier and Zakharchenya, 1984). Electrically induced polarizations were inferred from measurements of the Kerr rotation, where the polarization of a linearly polarized beam of light rotates when the beam is reflected at a spin-polarized sample (Kato, Myers, Gossard and Awschalom, 2004b; Sih *et al*., 2005). Alternatively, the circular polarization of the recombination light at a p–n junction can be used to determine the initial polarization of the carriers (Wunderlich, Kaestner, Sinova and Jungwirth, 2005). Finally, the inverse effect, the photo-galvanic effect, can be observed, where a spin polarization is produced by polarized light and the induced electrical current is detected (Ganichev and Prettl, 2003).

In the bulk of a two- or three-dimensional sample, spin polarizations arise because an electrical field shifts the Fermi sea; $\langle \mathbf{k} \rangle = e\mathbf{E}\tau/\hbar$ for small E and with transport lifetime τ. This implies that owing to intrinsic terms, there is on average a finite spin-orbit field, $\langle \mathbf{b}(\mathbf{k}) \rangle$. This leads to a bulk spin polarization, which, in simple cases, is aligned along $\langle \mathbf{b} \rangle$ (Ivchenko and Pikus, 1978; Vas'ko and Prima, 1979; Levitov, Nazarov and Eliashberg, 1985; Edelstein, 1990; Aronov, Lyanda-Geller and Pikus, 1991). Such a polarization was observed experimentally in two-dimensional GaAs hole systems: Silov *et al*. (2004) used a (001) surface and detected the polarization of the photoluminescense from the side of the cleaved sample, while Ganichev *et al*. (2006) used samples of low crystallographic symmetry and detected the polarization along the growth direction. Furthermore, in the presence of anisotropic scattering (see Section 3.4), a magnetic field $\mathbf{B}$ can lead to polarization perpendicular to both $\langle \mathbf{b} \rangle$ and $\mathbf{B}$ (Engel, Rashba and Halperin, 2007) – such a perpendicular polarization was already observed by Kato, Myers, Gossard and Awschalom (2004a).

4.3 Spin currents in bulk

The bulk spin current j_k^i was analyzed for many different spin-orbit Hamiltonians. For a two-dimensional electron system, the intrinsic effect of the Rashba coupling H_α lead to some debate. Because j_k^i is invariant under time reversal, it is allowed to be finite in equilibrium. Indeed, such equilibrium spin currents are predicted theoretically; however, they are of order α^3 and usually small (Rashba, 2003).

Now we discuss bulk spin currents driven by an external electrical field for systems with either intrinsic or extrinsic spin-orbit interaction. We do not discuss the more complicated case when both terms are present.

When an electrical field is applied and the electrons are accelerated, the precession described in Section 3.1 was considered. Because the initial spin density for a given direction of $\mathbf{k}$ is proportional to α, but the nonadiabatic correction is proportional to $1/\alpha$, the spin-orbit coupling constant cancels. Initially, it was believed that a small concentration of impurities has no effect and a 'universal' spin Hall conductivity $\sigma^{\mathrm{SH}} = e/4\pi\hbar$ was predicted (Sinova *et al*., 2004). However, it turns out that when the impurities are properly taken into account, the vertex correction cancels the bubble term, see Figure 3. Thus, the dc conductivity σ^{SH} vanishes (Inoue, Bauer and Molenkamp, 2004; Raimondi and Schwab, 2005),

$$\sigma^{\mathrm{SH}} = 0 \tag{30}$$

which was confirmed in numerical calculations (Sheng, Sheng, Weng and Haldane, 2005). Only when the ac conductivity $\sigma^{\mathrm{SH}}(\omega)$ is considered, in the regime $1/\tau \ll \omega \ll b/\hbar$ the universal value is recovered (Mishchenko, Shytov and Halperin, 2004).

That there are no bulk spin Hall currents can be understood by the following argument given by Dimitrova (2005). Using the Heisenberg equation and for parabolic bands, one finds the identity $\mathrm{d}\sigma_y/\mathrm{d}t = -(m\alpha/\hbar^2)(\sigma_z v_y + v_y \sigma_z)$ for single-particle operators (Burkov, Núñez and MacDonald, 2004; Erlingsson, Schliemann and Loss, 2005). For a homogeneous system, one then takes the expectation value of this identity and finds that $j_y^z \propto \mathrm{d}S_z/\mathrm{d}t$. When we consider dc properties, we must assume that the system is in a stationary state (i.e., we need impurity scattering). Then, the spin polarization S_z is constant and thus $j_y^z = 0$. These arguments, as well as spin current cancellation in a magnetic field in the absence of scatterers (Rashba, 2004) show that the cancellation is an intrinsic property of the free electron Hamiltonian H_α and is not related to any specific property of the scatterers.

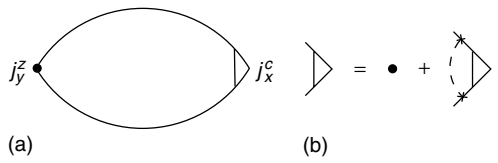

Figure 3. Diagram for spin Hall conductivity. The Kubo formula for σ^{SH} is proportional to $\mathrm{Tr}\,\langle\langle j_y^z G_{\mathrm{R}} j_x^c G_{\mathrm{A}} \rangle\rangle$, with charge current operator j_x^c and retarded and advanced Green's functions $G_{\mathrm{R/A}}$, and where $\langle\langle \cdot \rangle\rangle$ includes averaging over impurity configuration. In lowest order in $1/k_{\mathrm{F}}\ell$, we can neglect crossed impurity lines and σ^{SH} is given by the diagram shown in (a). Here, the full lines symbolize the renormalized Green's functions including self-energy. In (b), the vertex renormalization due to impurity scatterings (connected by dashed line) is defined recursively. When only the first term of (b) is taken, we get the bubble contribution to σ^{SH}; when all terms are summed, this leads to the additional (ladder) vertex correction.

Furthermore, Chalaev and Loss (2005) find that the weak localization contribution to j_y^z vanishes, and show more generally that j_y^z vanishes even if both H_α and H_β are present. Grimaldi, Cappelluti and Marsiglio (2006) find vanishing j_y^z for arbitrary values of $\alpha k_F/E_F$.

This cancellation is special to k-linear spin-orbit interaction (for nonparabolic bands, there can be a small finite contribution, proportional to α^2 (Krotkov and Das Sarma, 2006)). For example, for two-dimensional hole systems, the coupling $H_{\alpha,\mathrm{h}}$ is cubic in k (equation (11)). Then, if isotropic scattering is assumed, the vertex correction vanishes, and a 'universal' value $\sigma^{\mathrm{SH}} = 3e/4\pi\hbar$ is found in the clean limit $b\tau \gg \hbar$ (Murakami, 2004; Schliemann and Loss, 2005). Quite generally, for a 2D system where the spin-orbit field $\mathbf{b}(\mathbf{k})$ winds $N \neq 1$ times around a circle in the xy plane when $\mathbf{k}$ moves once around the Fermi circle (i.e., $N = 3$ for $H_{\alpha,\mathrm{h}}$), a universal value

$$\sigma^{\mathrm{SH}} = \frac{eN}{4\pi\hbar} \tag{31}$$

is found in the clean limit and for isotropic scattering (Shytov, Mishchenko, Engel and Halperin, 2006; Khaetskii, 2006).

Also for the k^3-Dresselhaus couplings, $H_{\mathrm{D,\,3d}}$ and $H_{\mathrm{D,\,2d}}$ (equations (8) and (9)), the vertex corrections vanish for isotropic scattering. This leads to a finite spin Hall conductivity for two-dimensional systems when $H_{\mathrm{D,\,2d}}$ is included (Mal'shukov and Chao, 2005). Similarly, σ^{SH} is finite for $H_{\mathrm{D,\,3d}}$ (Bernevig and Zhang, 2004).

The results cited above are only valid for isotropic scattering, except equation (30), which holds more generally. Recently, more general descriptions using kinetic equation (cf. Section 3.4) allowed to include arbitrary angular dependence of impurity scattering (Shytov, Mishchenko, Engel and Halperin, 2006; Khaetskii, 2006). It turns out that σ^{SH} significantly depends on the shape of the scattering potential and does not reduce to a simple form, in general. For example, in the clean limit $b\tau \gg \hbar$ and in the regime of small angle scattering (but still for a typical momentum transfer $q > b/v_F$, i.e., not too small angles), one finds

$$\sigma^{\mathrm{SH}} = -\frac{eN}{2\pi\hbar}\left(\frac{N^2-1}{N^2+1}\right)(\tilde{N} - \zeta - 2) \tag{32}$$

where ζ describes the nonparobalicity of the band, $v_\epsilon \propto k_\epsilon^{1+\zeta}$, and for $|\mathbf{b}| \propto k^{\tilde{N}}$ (Shytov, Mishchenko, Engel and Halperin, 2006). For example, taking $\zeta = 0$ and $H_{\alpha,\mathrm{h}}$, with $N = \tilde{N} = 3$, we see that the sign of σ^{SH} in equation (32) is *opposite* to the case of isotropic scattering (equation (31)). Similarly, Liu and Lei (2005) found in a numerical study of system with spin-orbit coupling $H_{\alpha,\mathrm{h}}$ that σ^{SH} strongly depends on the type of the scattering potential. Therefore, the spin Hall conductivity is not a universal quantity, as its numerical prefactor and its sign depend on sample parameters. On the other hand, for clean systems with $N \neq 1$, the order of magnitude is consistently $\left|\sigma^{\mathrm{SH}}\right| \sim e/4\pi\hbar$.

The above results are valid for weak spin-orbit coupling, $k_\alpha \ll k_F$. Conversely, there are also materials with strong spin-orbit coupling, as it was recently found in Bi/Ag (111) and Pb/Ag (111) surface alloys (Ast *et al.*, 2007). This motivated Grimaldi, Cappelluti and Marsiglio (2006) to generalize the theory, however, relying on an extensive numerical procedure.

The extrinsic contribution $H_{\mathrm{ext,\,e}}$ for electrons also leads to spin currents (D'yakonov and Perel', 1971; Hirsch, 1999). These currents are often evaluated only for isotropic impurity scattering (Zhang, 2000; Shchelushkin and Brataas, 2005). Assuming absence of intrinsic spin-orbit interaction, for arbitrary angular dependence of scattering, the extrinsic spin Hall conductivity equals (Engel, Halperin and Rashba, 2005)

$$\sigma^{\mathrm{SH}} = -\frac{\gamma}{2e}\sigma_{xx} + 2n\lambda\frac{e}{\hbar} \tag{33}$$

where the first term is due to skew scattering (see Section 3.2). The second term is due to the side-jump mechanism (Section 3.3); as this mechanism goes beyond transport equation, this term has to be evaluated separately. Here, σ_{xx} is the electrical conductivity and we defined the transport skewness

$$\gamma = \frac{\int \mathrm{d}\Omega\, I(\vartheta) S(\vartheta) \sin\vartheta}{\int \mathrm{d}\Omega\, I(\vartheta)(1-\cos\vartheta)} \tag{34}$$

that depends on the structure of the scattering center and on the Fermi energy, and I, S are defined below in equation (21). For screened Coulomb scatterers, equation (33) can be evaluated without any free parameters (Engel, Halperin and Rashba, 2005) and the resulting absolute value of spin current is in quantitative agreement (within error bars) with the observation by Kato, Myers, Gossard and Awschalom (2004b) in GaAs and seems comparable with the data by Stern *et al.* (2006) in ZnSe – implying that the observed spin currents are due to the extrinsic effect. Note that in equation (33) the skew scattering and the side-jump contributions have opposite signs. The skew-scattering term dominates in standard transport theory where one expands in $\hbar/E\tau$ where E is a typical electron energy; however, for dirty samples both terms can be of comparable magnitude. Stern *et al.* (2006) found that the measured σ^{SH} in ZnSe has the sign of the skew-scattering contribution and that the same is likely to be the case for the σ^{SH} observed by Kato, Myers, Gossard and Awschalom (2004b). Finally, assuming short-range scatterers, Tse and Das Sarma (2006a) found the

same order of magnitude for extrinsic spin currents. However; later they concluded that intrinsic spin-orbit coupling can cancel skew-scattering and reduce side-jump contributions to σ^{SH} (Tse and Das Sarma, 2006b).

Remarkably, despite the fact that the side-jump term in equation (33) was derived by including electron dynamics during the scattering event, it does not contain any factors related to the scattering probability – it only depends on the coupling constant λ, which is an intrinsic property of the material and is directly related to a Berry connection through the spin-orbit contribution to the operator of electron coordinate, cf. Section 2.6. Thus, while in this review and commonly in the literature the side-jump contribution is considered as extrinsic, it is clear that the distinction between intrinsic and extrinsic is somewhat arbitrary for this contribution.

4.4 Anomalous Hall effect and its relation to spin Hall effect

In the anomalous Hall effect (AHE), equilibrium polarization of a ferromagnet combined with spin-orbit interaction leads to electrical Hall currents transverse to an applied field. The theory of AHE has a long history and reveals many problems typical of spin transport in media with spin-orbit coupling, including the competing mechanisms of spin-orbit scattering by impurities and the role of intrinsic spin precession; for reviews see (Nozières and Lewiner, 1973; Crépieux and Bruno, 2001; Nagaosa, 2006). For noninteracting electrons and negligible spin relaxation, AHE and SHE are closely related; this is true for extrinsic spin-orbit interaction because λ is small and spin relaxation is of order λ^2 (Elliott, 1954; Yafet, 1963). In the SHE, we can decompose the spin currents $\mathbf{j}^{\mu}$ as a difference in particle currents of two spin species with polarizations $\pm\hat{\boldsymbol{\varepsilon}}_{\mu}$. Regarding these species separately, each carries the anomalous Hall current $\mathbf{J}^{\uparrow,\downarrow}_{\mathrm{AH}}$ of a system with spins fully aligned along the $\pm\hat{\boldsymbol{\varepsilon}}_{\mu}$ direction and with density $n_{\mathrm{AH}} = \frac{1}{2}n$, because we consider the SHE in nonmagnetic media, where electrons are unpolarized in equilibrium. We can express the spin Hall current as (Engel, Halperin and Rashba, 2005)

$$\mathbf{j}^{\mu}_{\mathrm{SH}} = \mathrm{e}^{-1}\left(\mathbf{J}^{\uparrow}_{\mathrm{AH}} - \mathbf{J}^{\downarrow}_{\mathrm{AH}}\right) \tag{35}$$

This relation allows to make use of the extensive literature on the AHE to gain further insights into mechanisms of the SHE, at least on its extrinsic part.

4.5 Spin accumulation and transport at boundaries

For only extrinsic spin-orbit coupling, because the spin relaxation is negligible for small λ, the spin is almost a conserved quantity and thus spin density and spin current satisfy a continuity equation with a small relaxation term. In this case, bulk spin currents will produce a spin polarization at the edge of the sample, that is, spin currents and spin accumulation are directly related (D'yakonov and Perel', 1971; Hirsch, 1999; Zhang, 2000). The polarization at a $y = 0$ edge is $S_z = (\hbar/2)\, s_z = (\hbar/2)\sqrt{\tau_{\mathrm{s}}/D_{\mathrm{s}}}\, j^z_y$, with spin-relaxation time τ_{s} and spin-diffusion coefficient D_{s} (which is identical to the electron diffusion coefficient D in the absence of electron–electron interaction).

For intrinsic spin-orbit interaction, it is not clear whether any general relation exists between spin accumulation and bulk spin currents, but spin accumulation can be studied directly. We discuss here the situation of a semi-infinite two-dimensional electron system, with Rashba coupling, located in the upper half-plane ($y > 0$). We assume a uniform applied electric field parallel to the x axis, and we consider the diffusive limit, where the spin diffusion length is large compared to the mean free path, so equations (25) and (26) apply far from the boundary. The spin density near the edge will depend on the boundary conditions for the diffusion equations at $y = 0$, and these will depend, in turn, on the boundary conditions of the microscopic Hamiltonian, as discussed in the various articles cited in the last paragraph of Section 3.5.

In the case of an ideal reflecting boundary, the spin density $\mathbf{s}(y)$ is found to be constant, and the same as in the bulk, right up to the edge (Bleibaum, 2006). Thus, one finds $s_z = 0$, while s_y has a value proportional to the charge current and to the Rashba coupling constant α. By contrast, if there is strong spin-orbit scattering at the boundary, all components of $\mathbf{s}$ should vanish there. In this case, the coupled diffusion equations predict that for $y > 0$, there will be *nonzero* values of both s_z and s_y, with oscillating behavior, in a region near the edge whose width is of the order of spin-precession length $k_{\alpha}^{-1} = \hbar^2/m\alpha$, which is about the Dyakonov–Perel spin-diffusion length $\sqrt{D_s \tau_s}$ (Rashba, 2006).

What happens if the boundary at $y = 0$ is partially or completely transmitting and there is a second conductor in the region $y < 0$ which has no spin orbit coupling? As noted by Adagideli and Bauer (2005), one should expect, in general, to find nonzero oscillatory values of both s_z and s_y in the Rashba conductor near the boundary, and injection of spin into the non-spin-orbit material. However, it was found by Tserkovnyak, Halperin, Kovalev and Brataas (2006) that this actually will not happen in the simplest case that one might consider: a boundary between a pair of two-dimensional systems with identical properties except for different values of α. There will quite generally be a discontinuity in the spin densities at a lateral boundary between systems with different Rashba coupling. If the electron mobility is a constant across the boundary, the discontinuity turns out to be equal to the

difference between the bulk spin densities of the systems. Then, on each side of the boundary one finds $s_z = 0$, while s_y is the same as the respective bulk value. There will thus be no spin injection if the second two-dimensional electron system has $\alpha = 0$.

Mal'shukov, Wang, Chu and Chao (2005) have argued that there should be spin accumulation near a reflecting edge, in the diffusive case, when the cubic Dresselhaus coupling $H_{\mathrm{D,2d}}$ is important. In the opposite limit of ballistic transport and near a sharp specular edge, Usaj and Balseiro (2005) have found spin magnetization due to H_α that oscillates rapidly with a period of k_{F}^{-1} and shows beating on a length scale of k_α^{-1}.

There are also numerical approaches analyzing the edge spin accumulation. Nomura *et al*. (2005) simulated a two-dimensional hole system, using the coupling $H_{\alpha,\mathrm{h}}$ (equation (11)). They found a spin accumulation that was consistent with the experiments by Wunderlich, Kaestner, Sinova and Jungwirth (2005).

4.6 Mesoscopic systems and spin interferometers

So far we have not considered interference effects – for example, in Section 3.4, we used an expansion in lowest order $1/k_{\mathrm{F}}\ell$ which does not include interference between electron propagation paths that follow different trajectories. To include such coherent effects in systems with impurities, one needs to consider the next order in $1/k_{\mathrm{F}}\ell$: the weak localization corrections. Alternatively, one can consider clean systems that are ballistic on length scales of the device. Spin interference effects in mesoscopic systems open up a new set of technical possibilities, for example, in rings or ringlike arrays with spin-orbit interaction, one can use Berry phase and Aharonov–Casher phase effects to study a variety of phenomena. In the presence of an applied magnetic field, spin-orbit effects can modify the Aharonov–Bohm or Altshuler–Aronov–Spivak oscillations in the electrical conductance. For theoretical discussions, see (Aronov and Lyanda-Geller, 1993; Bulgakov *et al*., 1999; Engel and Loss, 2000; Frustaglia, Hentschel and Richter, 2001; Koga, Nitta and van Veenhuizen, 2004; Aeberhard, Wakabayashi and Sigrist, 2005). For experimental results, see (Morpurgo *et al*., 1998; Yau, Poortere and Shayegan, 2002; Yang, Yang and Lyanda-Geller, 2004; Koga, Sekine and Nitta, 2006; Koenig *et al*., 2006; Bagraev *et al*., 2006).

For practical applications, it is not only important to generate nonequilibrium spin polarization in media with spin-orbit coupling, but also inject spin currents produced by such populations into 'normal' conductors, that is, conductors with negligible spin-orbit coupling. In normal conductors, spin is conserved and spin currents are well defined. Spin injection can be achieved using spin-orbit coupling, even in devices without magnetic fields and without ferromagnetic components. Proposals for such devices, in the mesoscopic regime, have been made by (Kiselev and Kim, 2003; Shekhter, Khodas and Finkel'stein, 2005; Souma and Nikolić, 2005; Eto, Hayashi and Kurotani, 2005; Silvestrov and Mishchenko, 2006).

Generally, spin interference devices make use of the intrinsic and extrinsic spin-orbit couplings presented in Section 2 and the spin-transport mechanisms discussed in Section 3 are important. However, we do not present more concrete descriptions of interference effects or details of microscopic structures; this could be done by solving the Schrödinger equation analytically, by simulating it numerically, or by using weak localization calculations. On the other hand, we can assess the length scales on which spin precession effects are expected: both diffusion equation (Section 3.5) and its solution near boundaries (Section 4.5) indicate spin-precession length $\ell_\alpha = 1/k_\alpha$ as a characteristic length for spin distributions. Furthermore, for clean systems, responses to an inhomogeneous field diverge at the wave vector $q = 2k_\alpha$ of the field (Rashba, 2005). This 'breakdown' suggests the length ℓ_α as an optimal size for achieving large spin polarizations. For a more generic Hamiltonian H_{int}, this scale can be estimated as $\ell_{\mathrm{eff}} \sim \hbar^2 k_{\mathrm{F}}/m\,|\mathbf{b}|$, establishing a 'mesoscopic' scale at which one can expect largest static spin responses to electric fields. Because ℓ_{eff} is also of the order of the Dyakonov–Perel spin-diffusion length, this estimate seems applicable both to the ballistic and diffusive regimes.

5 SPIN HALL EFFECT DUE TO EDGE STATES IN INSULATORS

In the previous parts of Section 4, we discussed spin currents j_y^z driven by electric field E_x, their relevance to spin transport and spin accumulation, and also the techniques for calculating conductivities σ^{SH} (equation (29)). Even when these nondiagonal components of the tensor j_j^i were not directly influenced by dissipation, they were calculated for ordinary metallic conductors whose longitudinal electric conductivity σ_{xx} was controlled by electron scattering, hence, electron transport in the bulk was dissipative. More recently, Murakami, Nagaosa and Zhang (2004) proposed that some centrosymmetric 3D systems possess properties of 'spin insulators'. These are media with gapped electron spectra and zero bulk electrical conductivities σ_{xx} but finite and dissipationless spin conductivities σ^{SH}.

The basic idea is as follows. A set of electron bands that in absence of SO coupling belongs to orbital momentum $\mathbf{L}$, in presence of SO coupling is described by the total angular

momentum $\mathbf{J} = \mathbf{L} + \mathbf{S}$. When some of the bands belonging to the $\mathbf{J}$ multiplet are filled, while different bands of the same multiplet are empty and are separated from the filled bands by a gap, all filled bands contribute to spin current. Uniaxially strained zero-gap semiconductors α-Sn and HgTe, and narrow-gap semiconductors of PbTe type were proposed as model systems. Spin conductivity σ^{SH} is large in these materials: it is about $e/\hbar a$ in 3D, a being the lattice constant. In 2D, σ^{SH} is quantized when the Fermi level is inside the gap (Qi, Wu and Zhang, 2006; Onoda and Nagaosa, 2005). However, for reasons similar to those discussed in Section 4.1, the relation of this σ^{SH} to spin transport is not obvious and was already questioned (Kane and Mele, 2005a; 2005b).

A different concept of spin transport in an insulating phase has been developed by Kane and Mele as applied to graphene (Kane and Mele, 2005a; 2005b). It is based on the Haldane model of quantum Hall effect (QHE) with spinless fermions under the conditions of zero total magnetic flux across the unit cell (Haldane, 1988). It has been emphasized (Onoda and Nagaosa, 2005; Kane and Mele, 2005a) that this model differs fundamentally from the model by Murakami, Nagaosa and Zhang (2004), in particular, in the properties of edge channels. Their crucial role for the QHE has been clarified by Halperin (1982), and they play a similar role in the physics of spin Hall effect in graphene. In what follows, we consider properties of graphene in more detail. The graphene model is not only of conceptual interest but is also attractive because of the very recent experimental achievements in measuring electron transport in graphene (Novoselov *et al.*, 2004; Zhang, Tan, Stormer and Kim, 2005).

Graphene is a monoatomic layer of graphite. Its honeycomb 2D lattice is shown in Figure 4. The elementary cell includes two atoms shown as A and B. The phase diagram of

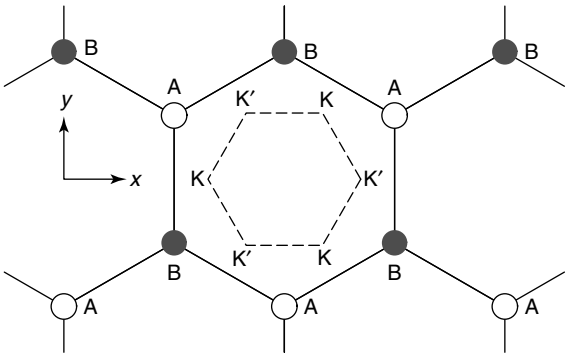

Figure 4. Schematics of honeycomb lattice of graphene. The hexagon in the center is an elementary cell containing two carbon atoms that belong to two sublattices. Atoms of these sublattices are marked as A and B and are shown by empty and filled circles, respectively. Brillouin zone is shown by a dashed line. K and K′ indicate nonequivalent corners of the zone where the gap opens.

graphene can be understood from the tight-binding Hamiltonian (Kane and Mele, 2005b)

$$H = t\sum_{\langle ij\rangle} c_i^+ c_j + \frac{2i}{\sqrt{3}}\lambda_{\mathrm{SO}}\sum_{\langle\langle ij\rangle\rangle} \nu_{ij} c_i^+ \sigma_z c_j + i\lambda_{\mathrm{R}}\sum_{\langle ij\rangle} c_i^+ (\boldsymbol{\sigma}\times\hat{\mathbf{d}}_{ij})_z c_j + \lambda_{\mathrm{v}}\sum_i \xi_i c_i^+ c_i \quad (36)$$

where c_{i} are annihilation operators at lattice cites i, spin indices in them being suppressed. The first term is the nearest neighbor hopping term between two sublattices. For the following, of the critical importance is the second term with $\nu_{ij} = (2/\sqrt{3})(\hat{\mathbf{d}}_1 \times \hat{\mathbf{d}}_2)_z = \pm 1$ that describes second neighbor hopping. Here $\hat{\mathbf{d}}_1$ and $\hat{\mathbf{d}}_2$ are unit vectors along two bonds that an electron traverses when going from the site j to the site i. The cross product of $\hat{\mathbf{d}}_1$ and $\hat{\mathbf{d}}_2$ produces a screw that in the Haldane model of spinless fermions couples them to inhomogeneous magnetic flux, while in the present model it couples the orbital motion of an electron to Pauli matrix σ_z. Hence, λ_{SO} is a coupling constant of a mirror symmetric, $z \to -z$, spin-orbit interaction. The third term is a nearest neighbor Rashba term, $\hat{\mathbf{d}}_{ij}$ being a unit vector in the direction connecting i and j nodes. It explicitly violates $z \to -z$ symmetry and originates from the coupling to the substrate or from an external electric field. The fourth term is a staggered sublattice potential with ξ_{i} taking values $\xi_{\mathrm{i}} = \pm 1$ for A and B lattice sites. It vanishes for graphene but would be present for a similar boron nitride (BN) film. Including this term is a clue for explaining the difference between the 'quantum spin Hall' (QSH) phase and a usual insulator (Kane and Mele, 2005a; 2005b).

The remarkable spin properties of graphene are seen from the one-dimensional projection of its energy spectrum, Figure 5, found by solving the Hamiltonian of equation (36) in the geometry of a strip with finite extent in the y direction (defined in Figure 4), that is, having 'zigzag' edges aligned along the x direction. The spectrum comprises four energy bands, of which the two lower bands are occupied; each bulk band is twofold spin degenerate. Narrow gaps at K and K′ open because of $\lambda_{\mathrm{SO}}, \lambda_{\mathrm{v}} \neq 0$ – for $\lambda_{\mathrm{SO}}, \lambda_{\mathrm{v}} = 0$, electrons possess a k-linear spectrum of Dirac fermions, $\varepsilon(k) = \hbar c^* k$. In addition to bulk states, there are edge states connecting K and K′ bulk continua. Their topology in the panels (a) and (b) is rather different.

In the panel (a) drawn for a small λ_{v}, edge states traverse the gap. For each edge of the strip, there are two such states. They are Kramers conjugate and propagate in opposite directions. This behavior reflects unusual cross-symmetry of bulk states that manifests itself in the opposite signs of the gap function at K and K′ points. The small-λ_{v} phase has been dubbed as QSH phase by Kane and Mele (2005a). It is the

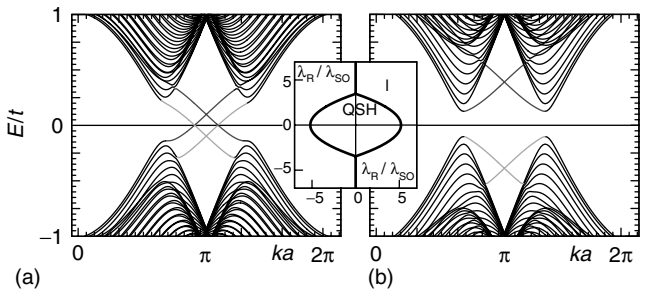

Figure 5. Energy bands of a one-dimensional strip of graphene with 'zigzag' edges, that is, the strip has finite extent along the y direction shown in Figure 4. Narrow gaps in the bulk spectrum are achieved at the K- and K′ vertices of the Brillouin zone. Branches of the spectrum originating from the edges of bulk continua show energies of edge states. Edge states at a given edge of the strip cross at $ka = \pi$, a being the lattice spacing. (a) QSH phase for $\lambda_v = 0.1t$; edge states at a given edge of the strip cross at $ka = \pi$, a being the lattice spacing. (b) A normal insulating phase for $\lambda_v = 0.4t$. In both cases, $\lambda_{SO} = 0.06t$ and $\lambda_R = 0.05t$. The inset shows the phase diagram in the λ_v–λ_R plane for $0 < \lambda_{SO} \ll t$. (Reproduced from C.L. Kane *et al*., 2005, with permission from the American Physical Society. © 2005.)

distinctive property of this phase that at any energy inside the gap there is one pair of edge modes (more generally, an odd number of such pairs).

When $\lambda_R = 0$, σ_z is conserved, and the pattern of dissipationless spin transport become especially simple. Each of independent subsystems of $\sigma_z = \uparrow$ and $\sigma_z = \downarrow$ electrons is equivalent to Haldane spinless fermions (Haldane, 1988). One pair of such 'spin filtered' states propagates along each edge. The states with opposite σ_z polarizations propagate in opposite directions. Because they form a Kramers doublet, potential backscattering is forbidden and transport is dissipationless. This model predicts two-terminal electric conductivity $G = 2e^2/h$. Propagation of charge current through edge states results in antisymmetric spin accumulation at these edges. In four-terminal geometry, spin currents flow between adjacent contacts, and related spin conductances are quantized; when normalized on a number of transported spins, $G^s = \pm e/2\pi\hbar$. For $\lambda_R \neq 0$, however, σ_z is not conserved. Nevertheless, spin currents persist (if λ_R is small, see the following text) but they are no longer exactly quantized. An early argument that the spin Hall conductance can be quantized was given by Froehlich, Studer and Thiran (1995) when considering incompressible 2D systems.

Panel (b) of Figure 5, drawn for a larger staggered potential λ_v, shows properties of a normal narrow-gap insulator. The gap function has the same sign at K and K′, as a result, one pair of edge states runs between two conduction-band valleys and the second pair between two valence band valleys. For some boundary conditions at the strip edges, edge states can penetrate the gap. However, there is always an even number of Kramers conjugate pairs of edge states at any given energy inside the gap, hence, backscattering is no longer forbidden. Therefore, it is the topology of edge states that defines the difference between the QSH and insulating phases in a simple and concise form.

The QSH phase is formed due to the bulk spin-orbit coupling λ_{SO}. Increasing asymmetric λ_R or staggered λ_v potentials destroy it when they become large enough. A phase diagram of the competing phases, QSH phase, and a normal insulator, is shown in the inset to Figure 5. The QSH phase exists inside an ovaloid in the λ_v/λ_{SO}–λ_R/λ_{SO} plane. Outside it, graphene shows properties of a normal narrow-gap insulator.

Another factor suppressing the gap and spin conductivity is electron scattering in the bulk. Its effect has been investigated numerically by Sheng, Sheng, Ting and Haldane (2005) for a four-probe spin Hall setup using the Landauer–Büttiker formula (Landauer, 1988; Büttiker, 1988); their spin conductivity σ^{SH} describes real spin transport. Disorder was modeled as $\sum_i \epsilon_i c_i^+ c_i$ with ϵ_i randomly distributed in the interval $[-W/2, W/2]$. They found that σ^{SH} remains within a few percent of its quantized value when $W < t$ and the Fermi level stays inside the gap; and σ^{SH} drops fast with increasing W for $W \gtrsim 1.5t$. Under the same conditions, σ^{SH} remains stable for $\lambda_R \lesssim 0.2t$. These results allow to establish the parameter range inside which edge spin channels remain robust and carry dissipationless and nearly quantized spin currents. Inside this range, there exist close analogy between QSH and QHE systems.

Currently, there is no direct experimental indication of the spin gap in graphene. A crude theoretical estimate of it by Kane and Mele (2005a) results in the gap $2\Delta_{SO} \sim 2.4\,\mathrm{K}$ which is in a reasonable agreement with different data (Brandt, Chudinov and Ponomarev, 1988). However, more recent calculations indicate that the actual value of Δ_{SO} is considerably smaller. Meantime, estimates of $\hbar/\tau$ based on transport data result in $\hbar/\tau \gtrsim 25\,\mathrm{K}$ for typical mobilities of $\mu \approx 10\,000\,\mathrm{cm^2\,V^{-1}\,s^{-1}}$, τ being the momentum relaxation time. Comparison of these data can easily explain suppression of spin-polarized transport through edge channels by disorder in the samples that are currently available. An independent mechanism of suppression is the λ_R constant that develops when electron concentration is controlled by a gate, and the ratio λ_R/λ_{SO} is unknown. Unfortunately, all estimates are crude because electron transport in graphene is still not understood. Novoselov *et al*. (2005) recently reported the minimum metallic conductivity $4e^2/h$ when the Fermi level passes through the conic point of the spectrum; it is nearly independent of the mobility μ. A nonuniversal and even larger conductivity of about $6e^2/h$ was reported by (Zhang, Tan, Stormer and Kim, 2005). The closest theoretical value $2e^2/h$ comes from the spin channel model (Kane and Mele,

2005a), followed by $4e^2/\pi h$ and $2e^2/\pi h$ found from different models of the bulk transport of Dirac fermions (Ziegler, 1998; Shon and Ando, 1998). Because there exists a region of parameter values where spin transport through edge channels is robust, honeycomb lattices lithographically produced from semiconductors with strong spin-orbit coupling may also be of interest (Zheng and Ando, 2002).

Abanin, Lee and Levitov (2006) argued that in the QHE regime, the exchange-enhanced gap for chiral edge modes, originating from Zeeman splitting, may be as large as 100 K. Another system where edge spin channels may play a role was proposed by Bernevig and Zhang (2006); it includes parabolic confinement in conjunction with inhomogeneous shear deformation. More recently, Fu and Kane (2006) proposed $Bi_{1-x}Sb_x$ semiconductor alloys and α-Sn and HgTe under uniaxial strain as materials that satisfy the necessary symmetry requirements for the QSH phase and that are expected to have a large Δ_{SO}. Independently, Bernevig, Hughesm, and Zhang (2006) showed that HgTe/CdTe quantum wells are also good candidates for the QSH phase.

NOTES

[1] This is reminiscent of the definition of an 'intrinsic semiconductor', which is so pure that (at a sufficiently high temperature) the impurity contribution to the carrier density is negligible. The conductivity of such a sample is known as *intrinsic* conductivity (again, a finite transport lifetime τ is required to make the conductivity well defined). At lower temperatures, the carrier density mainly results from the impurities and now one refers to *extrinsic* properties.

ACKNOWLEDGMENTS

We acknowledge discussions with A.A. Burkov, D. Loss, A.H. MacDonald, C.M. Marcus, E.G. Mishchenko, A.V. Shytov, and R. Winkler. This work was supported by NSF Grants No. DMR-05-41988 and No. PHY-01-17795, and the Harvard Center for Nanoscale Systems.

REFERENCES

Abanin, D.A., Lee, P.A. and Levitov, L.S. (2006). Spin filtered edge states and quantum Hall effect in graphene. *Physical Review Letters*, **96**, 176803.

Adagideli, I. and Bauer, G.E.W. (2005). Intrinsic spin Hall edges. *Physical Review Letters*, **95**, 256602.

Aeberhard, U., Wakabayashi, K. and Sigrist, M. (2005). Effect of spin-orbit coupling on zero-conductance resonances in asymmetrically coupled one-dimensional rings. *Physical Review B*, **72**, 075328.

Ando, T. and Tamura, H. (1992). Conductance fluctuations in quantum wires with spin-orbit and boundary-roughness scattering. *Physical Review B*, **46**, 2332.

Aronov, A.G. and Lyanda-Geller, Y.B. (1993). Spin-orbit Berry phase in conducting rings. *Physical Review Letters*, **70**, 343.

Aronov, A.G., Lyanda-Geller, Y.B. and Pikus, G.E. (1991). Spin polarization of electrons by an electric current. *Soviet Physics JETP*, **73**, 537.

Ast, C.R., Henk, J., Ernst, A., *et al*. (2007). Giant Spin Splitting through Surface Alloying. *Physical Review Letters*, **98**, 186807.

Bagraev, N.T., Galkin, N.G., Gehlhoff, W., *et al*. (2006). Spin interference in silicon one-dimensional rings. *Physica B*, **378**, 894.

Berger, L. (1970). Side-jump mechanism for the Hall effect of ferromagnets. *Physical Review B*, **2**, 4559.

Bernevig, B.A. and Zhang, S-C. (2004). Intrinsic Spin-Hall Effect in *n*-Doped Bulk GaAs. http://arxiv.org/cond-mat/0412550.

Bernevig, B.A. and Zhang, S-C. (2006). Quantum spin Hall effect. *Physical Review Letters*, **96**, 106802.

Bernevig, B.A., Hughes, T.L., and Zhang, S-C. (2006). Quantum Spin Hall Effect and Topological Phase Transition in HgTe Quantum Wells. http://arxiv.org/cond-mat/0611399.

Bir, G.L. and Pikus, G.E. (1974). *Symmetry and Strain-Induced Effects in Semiconductors*, Wiley: New York.

Bleibaum, O. (2006). Boundary Conditions for Spin Diffusion Equations with Rashba Spin-Orbit Interaction. *Physical Review B*, **74**, 113309.

Blount's, E. (1962). Formalisms of band theory. In *Solid State Physics*, Seitz, F. and Turnbull, D. (Eds.), Academic Press: New York, p. 305, Vol. 13.

Brandt, N.B., Chudinov, S.M. and Ponomarev, Y.G. (1988). *Semimetals 1. Graphite and its Compounds*, North Holland: Amsterdam.

Bryksin, V.V. and Kleinert, P. (2006). Theory of electric-field-induced spin accumulation and spin current in the two-dimensional Rashba model. *Physical Review B*, **73**, 165313.

Bulgakov, E.N., Pichugin, K.N., Sadreev, A.F., *et al*. (1999). Hall-like effect induced by spin-orbit interaction. *Physical Review Letters*, **83**, 376.

Burkov, A.A., Núñez, A.S. and MacDonald, A.H. (2004). Theory of spin-charge-coupled transport in a two-dimensional electron gas with Rashba spin-orbit interactions. *Physical Review B*, **70**, 155308.

Büttiker, M. (1988). Symmetry of electrical conduction. *IBM Journal of Research and Development*, **32**, 317.

Chalaev, O. and Loss, D. (2005). Spin-Hall conductivity due to Rashba spin-orbit interaction in disordered systems. *Physical Review B*, **71**, 245318.

Crépieux, A. and Bruno, P. (2001). Theory of the anomalous Hall effect from the Kubo formula and the Dirac equation. *Physical Review B*, **64**, 014416.

Culcer, D., Sinova, J., Sinitsyn, N.A., *et al*. (2004). Semiclassical spin transport in spin-orbit-coupled bands. *Physical Review Letters*, **93**, 046602.

Dimitrova, O.V. (2005). Spin-Hall conductivity in a two-dimensional Rashba electron gas. *Physical Review B*, **71**, 245327.

D'yakonov, M.I. and Perel', V.I. (1971). Possibility of orienting electron spins with current. *JETP Letters*, **13**, 467.

D'yakonov, M.I. and Perel', V.I. (1972). Spin relaxation of conduction electrons in noncentrosymmetric semiconductors. *Soviet Physics Solid State*, **13**, 3023.

Edelstein, V.M. (1990). Spin polarization of conduction electrons induced by electric current in two-dimensional asymmetric electron systems. *Solid State Communications*, **73**, 233.

Elliott, R.J. (1954). Theory of the effect of spin-orbit coupling on magnetic resonance in some semiconductors. *Physical Review*, **96**, 266.

Engel, H-A., Halperin, B.I. and Rashba, E.I. (2005). Theory of spin Hall conductivity in n-doped GaAs. *Physical Review Letters*, **95**, 166605.

Engel, H-A. and Loss, D. (2000). Conductance fluctuations in diffusive rings: Berry phase effects and criteria for adiabaticity. *Physical Review B*, **62**, 10238.

Engel, H-A., Rashba, E.I. and Halperin, B.I. (2007). Out-Of-Plane Spin Polarization From In-Plane Electric and Magnetic Fields. *Physical Review Letters*, **98**, 036602.

Entin-Wohlman, O., Aharony, A., Galperin, Y.M., *et al*. (2005). Orbital ac spin-Hall effect in the hopping regime. *Physical Review Letters*, **95**, 086603. (references therein).

Erlingsson, S.I., Schliemann, J. and Loss, D. (2005). Spin susceptibilities, spin densities, and their connection to spin currents. *Physical Review B*, **71**, 035319.

Eto, M., Hayashi, T. and Kurotani, Y. (2005). Spin polarization at semiconductor point contacts in absence of magnetic field. *Journal of the Physical Society of Japan*, **74**, 1934.

Froehlich, J., Studer, U. and Thiran, E. (1995). Quantum Theory of Large Systems of Non-Relativistic Matter. http://arxiv.org/cond-mat/9508062.

Frustaglia, D., Hentschel, M. and Richter, K. (2001). Quantum transport in nonuniform magnetic fields: aharonov-bohm ring as a spin switch. *Physical Review Letters*, **87**, 256602.

Fu, L. and Kane, C.L. (2006). Topological Insulators with Inversion Symmetry. http://arxiv.org/cond-mat/0611341.

Galitski, V.M., Burkov, A.A. and Das Sarma, S. (2006). Boundary conditions for spin diffusion in disordered systems. *Physical Review B*, **74**, 115331.

Ganichev, S.D. and Prettl, W. (2003). Spin photocurrents in quantum wells. *Journal of Physics: Condensed Matter*, **15**, R935.

Ganichev, S., Danilov, S., Schneider, P., *et al*. (2006). Electric current-induced spin orientation in quantum well structures. *Journal of Magnetism and Magnetic Materials*, **300**, 127.

Glazov, M.M. and Ivchenko, E.L. (2002). Precession spin relaxation mechanism caused by frequent electron-electron collisions. *JETP Letters*, **75**, 403.

Govorov, A.O., Kalameitsev, A.V. and Dulka, J.P. (2004). Spin-dependent transport of electrons in the presence of a smooth lateral potential and spin-orbit interaction. *Physical Review B*, **70**, 245310.

Grimaldi, C., Cappelluti, E. and Marsiglio, F. (2006). Off-Fermi surface cancellation effects in spin-Hall conductivity of a two-dimensional Rashba electron gas. *Physical Review B*, **73**, 081303.

Haldane, F.D.M. (1988). Model for a quantum Hall effect without Landau levels: condensed-matter realization of the "parity anomaly". *Physical Review Letters*, **61**, 2015.

Halperin, B.I. (1982). Quantized Hall conductance, current-carrying edge states, and the existence of extended states in a two-dimensional disordered potential. *Physical Review B*, **25**, 2185.

Hankiewicz, E.M. and Vignale, G. (2006). Spin Coulomb drag corrections to the extrinsic spin-Hall effect of a two-dimensional electron gas. *Physical Review B*, **73**, 115339.

Hirsch, J.E. (1999). Spin Hall effect. *Physical Review Letters*, **83**, 1834.

Huang, H.C., Voskoboynikov, O. and Lee, C.P. (2003). Spin-orbit interaction and electron elastic scattering from impurities in quantum wells. *Physical Review B*, **67**, 195337.

Inoue, J.I., Bauer, G.E.W. and Molenkamp, L.W. (2004). Suppression of the persistent spin Hall current by defect scattering. *Physical Review B*, **70**, 041303.

Ivchenko, E.L. and Pikus, G. (1978). New photogalvanic effect in gyrotropic crystals. *JETP Letters*, **27**, 604.

Ivchenko, E. and Pikus, G. (1997). *Superlattices and Other Heterostructures*, Springer: Berlin.

Kane, C.L. and Mele, E.J. (2005a). Quantum spin Hall effect in graphene. *Physical Review Letters*, **95**, 226801.

Kane, C.L. and Mele, E.J. (2005b). Z_2 topological order and the quantum spin Hall effect. *Physical Review Letters*, **95**, 146802.

Kato, Y.K., Myers, R.C., Gossard, A.C. and Awschalom, D.D. (2004a). Current-induced spin polarization in strained semiconductors. *Physical Review Letters*, **93**, 176601.

Kato, Y.K., Myers, R.C., Gossard, A.C. and Awschalom, D.D. (2004b). Observation of the spin Hall effect in semiconductors. *Science*, **306**, 1910.

Khaetskii, A. (2006). Intrinsic spin current for an arbitrary Hamiltonian and scattering potential. *Physical Review B*, **73**, 115323.

Kiselev, A.A. and Kim, K.W. (2003). T-shaped spin filter with a ring resonator. *Journal of Applied Physics*, **94**, 4001.

Knap, W., Skierbiszewski, C. and Zduniak, A., *et al*. (1996). Weak antilocalization and spin precession in quantum wells. *Physical Review B*, **53**, 3912.

Koenig, M., Tschetschetkin, A., Hankiewicz, E., *et al*. (2006). Direct observation of the Aharonov-Casher phase. *Physical Review Letters*, **96**, 076804.

Koga, T., Nitta, J. and van Veenhuizen, M. (2004). Ballistic spin interferometer using the Rashba effect. *Physical Review B*, **70**, 161302.

Koga, T., Sekine, Y. and Nitta, J. (2006). Experimental realization of a ballistic spin interferometer based on the Rashba effect using a nanolithographically defined square loop array. *Physical Review B*, **74**, 041302.

Kohmoto, M. (1985). Topological invariant and the quantization of the Hall conductance. *Annals of Physics*, **160**, 343.

Krich, J.J. and Halperin, B.I. (2007). Cubic Dresselhaus Spin-Orbit Coupling in 2D Electron Quantum Dots. http://arxiv.org/cond-mat/0702667.

Krotkov, P. and Das Sarma, S. (2006). Intrinsic spin Hall conductivity in a generalized Rashba model. *Physical Review B*, **73**, 195307.

Landauer, R. (1988). Spatial variation of currents and fields due to localized scatterers in metallic conduction. *IBM Journal of Research and Development*, **32**, 306.

Levitov, L.S., Nazarov, Y.N. and Eliashberg, G.M. (1985). Magnetoelectric effects in conductors with mirror isomer symmetry. *Soviet Physics JETP*, **61**, 133.

Lewiner, C., Betbeder, O. and Nozières, P. (1973). Field theoretical approach to anomalous Hall-effect in semiconductors. *Journal of Physics and Chemistry of Solids*, **34**, 765.

Li, J., Hu, L. and Shen, S-Q. (2005). Spin-resolved Hall effect driven by spin-orbit coupling. *Physical Review B*, **71**, 241305.

Liu, S.Y. and Lei, X.L. (2005). Disorder effects on the spin-Hall current in a diffusive Rashba two-dimensional heavy-hole system. *Physical Review B*, **72**, 155314.

Mal'shukov, A.G. and Chao, K.A. (2005). Spin Hall conductivity of a disordered two-dimensional electron gas with Dresselhaus spin-orbit interaction. *Physical Review B*, **71**, 121308.

Mal'shukov, A.G., Wang, L.Y., Chu, C.S. and Chao, K.A. (2005). Spin Hall effect on edge magnetization and electric conductance of a 2D semiconductor strip. *Physical Review Letters*, **95**, 146601.

Meier, F. and Zakharchenya, B.P. (Eds.) (1984). *Optical Orientation*, North Holland.

Mishchenko, E.G., Shytov, A.V. and Halperin, B.I. (2004). Spin current and polarization in impure two-dimensional electron systems with spin-orbit coupling. *Physical Review Letters*, **93**, 226602.

Morpurgo, A.F., Heida, J.P., Klapwijk, T.M., *et al*. (1998). Ensemble-average spectrum of Aharonov-Bohm conductance oscillations: evidence for spin-orbit-induced Berry's phase. *Physical Review Letters*, **80**, 1050.

Mott, N.F. (1936). The electrical conductivity of transition metals. *Proceedings of the Royal Society of London Series A*, **153**, 699.

Mott, N.F. and Massey, H.S.W. (1965). *The Theory of Atomic Collisions*, Oxford University Press: London.

Motz, J.W., Olsen, H. and Koch, H.W. (1964). Electron scattering without atomic or nuclear excitation. *Reviews of Modern Physics*, **36**, 881. Sec. VI and Eqs. (1A-107) and (1A-403).

Murakami, S. (2004). Absence of vertex correction for the spin Hall effect in p-type semiconductors. *Physical Review B*, **69**, 241202.

Murakami, S., Nagaosa, N. and Zhang, S-C. (2003). Dissipationless quantum spin current at room temperature. *Science*, **301**, 1348.

Murakami, S., Nagaosa, N. and Zhang, S-C. (2004). Spin-Hall insulator. *Physical Review Letters*, **93**, 156804.

Nagaosa, N. (2006). Anomalous Hall effect - a new perspective. *Journal of the Physical Society of Japan*, **75**, 042001.

Nikolić, B.K., Zârbo, L.P. and Souma, S. (2005). Mesoscopic spin Hall effect in multiprobe ballistic spin-orbit-coupled semiconductor bridges. *Physical Review B*, **72**, 075361.

Nomura, K., Wunderlich, J., Sinova, J., *et al*. (2005). Edge spin accumulation in semiconductor two-dimensional hole gases. *Physical Review B*, **72**, 245330.

Novoselov, K.S., Geim, A.K., Morozov, S.V., *et al*. (2004). Electric field effect in atomically thin carbon films. *Science*, **306**, 666.

Novoselov, K.S., Geim, A.K., Morozov, S.V., *et al*. (2005). Two-dimensional gas of massless Dirac fermions in graphene. *Nature*, **438**, 197.

Nozières, P. and Lewiner, C. (1973). A simple theory of the anomalous Hall effect in semiconductors. *Journal of Physiology (Paris)*, **34**(10), 901.

Onoda, M. and Nagaosa, N. (2005). Spin current and accumulation generated by the spin Hall insulator. *Physical Review Letters*, **95**, 106601.

Pikus, G.E. and Titkov, A.N. (1984). Spin relaxation under optical orientation in semiconductors. In *Optical Orientation*, Meier, F. and Zakharchenya, B.P. (Eds.), North Holland, p. 73, Chapter 3.

Qi, X-L., Wu, Y-S. and Zhang, S-C. (2006). Topological quantization of the spin Hall effect. *Physical Review B*, **74**, 085308.

Raimondi, R. and Schwab, P. (2005). Spin-Hall effect in a disordered two-dimensional electron system. *Physical Review B*, **71**, 033311.

Rashba, E.I. (2003). Spin currents in thermodynamic equilibrium: the challenge of discerning transport currents. *Physical Review B*, **68**, 241315.

Rashba, E.I. (2004). Sum rules for spin Hall conductivity cancellation. *Physical Review B*, **70**, 201309.

Rashba, E.I. (2005). Spin dynamics and spin transport. *Journal of Superconductivity*, **18**, 137.

Rashba, E.I. (2006). Spin-orbit coupling and spin transport. *Physica E*, **34**, 31.

Schliemann, J. and Loss, D. (2005). Spin-Hall transport of heavy holes in III-V semiconductor quantum wells. *Physical Review B*, **71**, 085308.

Shchelushkin, R.V. and Brataas, A. (2005). Spin Hall effects in diffusive normal metals. *Physical Review B*, **71**, 045123.

Shekhter, A., Khodas, M. and Finkel'stein, A.M. (2005). Diffuse emission in the presence of an inhomogeneous spin-orbit interaction for the purpose of spin filtration. *Physical Review B*, **71**, 125114.

Sheng, L., Sheng, D.N. and Ting, C.S. (2005). Spin-Hall effect in two-dimensional electron systems with Rashba spin-orbit coupling and disorder. *Physical Review Letters*, **94**, 016602.

Sheng, L., Sheng, D.N., Ting, C.S. and Haldane, F.D.M. (2005). Nondissipative spin Hall effect via quantized edge transport. *Physical Review Letters*, **95**, 136602.

Sheng, D.N., Sheng, L., Weng, Z.Y. and Haldane, F.D.M. (2005). Spin Hall effect and spin transfer in a disordered Rashba model. *Physical Review B*, **72**, 153307.

Shi, J., Zhang, P., Xiao, D. and Niu, Q. (2006). On a proper definition of spin current. *Physical Review Letters*, **96**, 076604.

Shon, N.H. and Ando, T. (1998). Quantum transport in two-dimensional graphite system. *Journal of the Physical Society of Japan*, **67**, 2421.

Shytov, A.V., Mishchenko, E.G., Engel, H-A. and Halperin, B.I. (2006). Small-angle impurity scattering and the spin Hall

conductivity in two-dimensional semiconductor systems. *Physical Review B*, **73**, 075316.

Sih, V., Myers, R.C., Kato, Y.K., *et al*. (2005). Spatial imaging of the spin Hall effect and current-induced polarization in two-dimensional electron gases. *Nature Physics*, **1**, 31.

Silov, A.Y., Blajnov, P.A., Wolter, J.H., *et al*. (2004). Current-induced spin polarization at a single heterojunction. *Applied Physics Letters*, **85**, 5929.

Silvestrov, P.G. and Mishchenko, E.G. (2006). Polarized Electric Current in Semiclassical Transport with Spin-Orbit Interaction. *Physical Review B*, **74**, 165301.

Sinova, J., Murakami, S., Shen, S-Q. and Choi, M-S. (2006). Spin-Hall effect: back to the beginning on a higher level. *Solid State Communications*, **138**, 214.

Sinova, J., Culcer, D., Niu, Q., *et al*. (2004). Universal intrinsic spin Hall effect. *Physical Review Letters*, **92**, 126603.

Smit, J. (1958). The spontaneous Hall effect in ferromagnetics–II. *Physica*, **24**, 39.

Souma, S. and Nikolić, B.K. (2005). Spin Hall current driven by quantum interferences in mesoscopic rashba rings. *Physical Review Letters*, **94**, 106602.

Sundaram, G. and Niu, Q. (1999). Wave-packet dynamics in slowly perturbed crystals: Gradient corrections and Berry-phase effects. *Physical Review B*, **59**, 14915.

Stern, N.P., Ghosh, S., Xiang, G., *et al*. (2006). Current-Induced Polarization and the Spin Hall Effect at Room Temperature. *Physical Review Letters*, **97**, 126603.

Trebin, H.R., Rössler, U. and Ranvaud, R. (1979). Quantum resonances in the valence bands of zinc-blende semiconductors. I. Theoretical aspects. *Physical Review B*, **20**, 686.

Tse, W-K. and Das Sarma, S. (2006a). Spin Hall effect in doped semiconductor structures. *Physical Review Letters*, **96**, 056601.

Tse, W-K. and Das Sarma, S. (2006b). Intrinsic spin Hall effect in the presence of extrinsic spin-orbit scattering. *Physical Review B*, **74**, 245309.

Tserkovnyak, Y., Halperin, B.I., Kovalev, A.A. and Brataas, A. (2006). Boundary Spin Hall Effect in a Rashba Semiconductor. http://arxiv.org/cond-mat/0610190.

Usaj, G. and Balseiro, C.A. (2005). Spin accumulation and equilibrium currents at the edge of 2DEGs with spin-orbit coupling. *Europhysics Letters*, **72**, 631.

Valenzuela, S.O. and Tinkham, M. (2006). Direct electronic measurement of the spin Hall effect. *Nature*, **442**, 176.

Vas'ko, F.T. and Prima, N.A. (1979). Spin splitting of spectrum of two-dimensional electrons. *Soviet Physics Solid State*, **21**, 994.

Winkler, R. (2000). Rashba spin splitting in two-dimensional electron and hole systems. *Physical Review B*, **62**, 4245.

Winkler, R. (2003). *Spin-Orbit Coupling Effects in Two-Dimensional Electron and Hole System*, Springer: Berlin.

Wunderlich, J., Kaestner, B., Sinova, J. and Jungwirth, T. (2005). Experimental observation of the spin-Hall effect in a two-dimensional spin-orbit coupled semiconductor system. *Physical Review Letters*, **94**, 047204.

Yafet, Y. (1963). *g*-factors and spin-lattice relaxation of conduction electrons. In *Solid State Physics*, Seitz, F. and Turnbull, D. (Eds.), Academic Press: New York, p. 1, Vol. 14.

Yang, M.J., Yang, C.H. and Lyanda-Geller, Y.B. (2004). Quantum beating in ring conductance: observation of spin chiral states and Berry's phase. *Europhysics Letters*, **66**, 826.

Yau, J-B., Poortere, E.P.D. and Shayegan, M. (2002). Aharonov-Bohm oscillations with spin: evidence for Berry's phase. *Physical Review Letters*, **88**, 146801.

Zhang, S. (2000). Spin Hall effect in the presence of spin diffusion. *Physical Review Letters*, **85**, 393.

Zhang, Y., Tan, Y-W., Stormer, H.L. and Kim, P. (2005). Experimental observation of the quantum Hall effect and Berry's phase in graphene. *Nature*, **438**, 201.

Zhang, S. and Yang, Z. (2005). Intrinsic spin and orbital angular momentum Hall effect. *Physical Review Letters*, **94**, 066602.

Zheng, Y. and Ando, T. (2002). Hall conductivity of a two-dimensional graphite system. *Physical Review B*, **65**, 245420.

Ziegler, K. (1998). Delocalization of 2D dirac fermions: the role of a broken supersymmetry. *Physical Review Letters*, **80**, 3113.

Manipulation of Spins and Coherence in Semiconductors

Nathaniel P. Stern, Jesse Berezovsky, Sayantani Ghosh and David D. Awschalom

University of California, Santa Barbara, CA, USA

1 INTRODUCTION

The physics of spins in semiconductors was first seriously explored in pioneering theoretical and experimental work in the 1960s (Meier and Zakharechenya, 1984). Since then, advances in materials science and semiconductor processing technology have opened up vast new territories of conceptual space, rich in fascinating spin-related phenomena. This chapter highlights recent measurements involving spin coherence in semiconductor structures.

There is currently significant interest in the potential applications of spins in semiconductors (referred to as *spintronics* (Wolf *et al*., 2001)). Existing semiconductor devices rely solely on the charge of the electron and the orbital part of the electron wave function. However, it is becoming evident that the electron spin, previously ignored, can also be manipulated and detected in a number of ways in semiconductor systems. Novel interactions between spins and light have been explored, allowing for all-optical control of spin coherence (Gupta, Knobel, Samarth and Awschalom, 2001; Hübner *et al*., 2003; Gurudev Dutt *et al*., 2006); structures can be engineered for spin manipulation through the introduction of magnetic dopants; and significantly, all-electrical methods for spin generation, manipulation, and detection have been developed that do not require magnetic fields or magnetic materials (Kato, Myers, Gossard and Awschalom, 2004a,b,c; 2003, Hanbicki, van 't Erve and Magno, 2003; Lou *et al*., 2006). To date, no commercially viable device has been demonstrated in the field of semiconductor spintronics, but as we gain understanding of the underlying physical phenomena, it seems increasingly evident that God would not have created such an extraordinary garden if man were not meant to enjoy its bounty.

Handbook of Magnetism and Advanced Magnetic Materials. Edited by Helmut Kronmüller and Stuart Parkin. Volume 5: *Spintronics and Magnetoelectronics*. ISBN: 978-0-470-02217-7.

2 COHERENT SPIN ENSEMBLES AND OPTICAL MEASUREMENT

A significant barrier to the practical use of spins in semiconductors is the ephemeral nature of the spin state – unlike charge, spin is not a conserved quantity. The average time for the loss of spin information is described by two quantities, the longitudinal spin lifetime, T_1 (also known as the *spin-flip time*), and the transverse spin lifetime T_2 (also known as

the *coherence time*). In general, T_1 refers to the time for the relative amplitudes of the spin eigenstates (e.g., spin-up and spin-down) to become scrambled and T_2 refers to the time for the relative phase of the eigenstates to be lost. In the case where many spins are measured simultaneously, inhomogeneities in the spin dynamics over the ensemble result in a reduced effective transverse spin lifetime, referred to as T_2^* .

There are several mechanisms that contribute to the decay and decoherence of spins in semiconductors. Through spin–orbit (SO) coupling in a noncentrosymmetric crystal (e.g., zinc blende, wurtzite), an electron's momentum acts as a magnetic field seen by the electron spin (Yu and Cardona, 1996). In the D'yakonov–Perel mechanism (D'yakonov and Perel, 1971a), as the electron momentum is repeatedly scattered, the electron spin state is randomized as it precesses about this fluctuating effective field. Furthermore, the SO interaction mixes the spin and momentum eigenstates, directly linking momentum scattering with spin scattering. This path to spin decoherence is known as the *Elliot–Yafet mechanism* (Elliot, 1954). These two spin-orbit mediated mechanisms show opposite dependence on the momentum scattering rate. In the Elliot–Yafet mechanism, more momentum scattering leads to more spin scattering. In contrast, as momentum scattering increases, the fluctuating effective field of the D'yakonov–Perel mechanism tends to 'cancel out', in an effect akin to motional narrowing seen in nuclear magnetic resonance (NMR) (Abragam, 1961).

Electron spins can also be flipped through interactions with other spin systems, such as through the electron–hole exchange interaction (Bir–Aronov–Pikus mechanism (Bir, Aronov and Pikus, 1976)), or through the hyperfine interaction with nuclear spins (Lampel, 1968). These mechanisms become significant when the electron wave function has significant overlap with the holes or with nuclei, respectively.

Despite the inevitability of spin decoherence, relatively long spin lifetimes have been measured in some semiconductor systems. In bulk n-type GaAs, T_2^* has been found to exceed 100 ns at low temperature (Kikkawa and Awschalom, 1998). The spin lifetime in GaAs is found to depend strongly on the donor concentration, with a maximum occurring near the metal–insulator transition owing to the changing strength of the different spin relaxation mechanisms (Dzhioev *et al*., 2002). Some II–VI semiconductors, such as ZnSe, show robust spin coherence up to room temperature (Kikkawa, Smorchkova, Samarth and Awschalom, 1997). Such materials have relatively large band gaps and small SO coupling, and therefore less spin decoherence owing to the D'yakonov–Perel or Elliot–Yafet mechanisms. Furthermore, by confining electrons within a quantum dot (QD), momentum scattering is suppressed, leading to longer spin lifetimes. T_1 times up to 0.85 ms have been measured in GaAs QDs at 300 mK in a magnetic field of 8 T (Elzerman *et al*., 2004) and 20 ms in InAs QDs at 1 K in a 4 T field (Kroutvar *et al*., 2004). A time-averaged *transverse* electron spin lifetime, T_2^*, of 16 ns has been observed in single GaAs QD (Bracker *et al*., 2005). In variants of the spin-echo technique used in NMR (Abragam, 1961), the T_2 time of InAs QDs has been measured to be ∼3 µs at 6 K (Greilich *et al*., 2006), and the singlet–triplet coherence time in a double QD structure has been found to be greater than 1 µs at 135 mK (Petta *et al*., 2005).

The selection rules governing optical transitions from the valence band to the conduction band of noncentrosymmetric crystals provide a useful means for initializing and detecting spin polarization in these materials (Meier and Zakharechenya, 1984) (see Figure 1). The conduction band minimum (the Γ-point) is twofold degenerate, corresponding to the two spin states ($S = 1/2$, $S_z = \pm 1/2$). The six states at the valence band maximum are split into the fourfold degenerate heavy holes ($J = 3/2$, $J_z = \pm 3/2$) and light holes ($J = 3/2$, $J_z = \pm 1/2$), and the doubly degenerate split-off holes ($J = 1/2$, $J_z = \pm 1/2$). The split-off band is typically sufficiently far from the heavy and light holes that split-off hole transitions can be ignored for excitation near the band edge.

A circularly polarized photon carries angular momentum of 1 $\hbar$, and thus can only drive transitions with $\Delta L_z = \pm 1$. For example, absorption of a photon with $l = 1$ can drive the transition from a heavy-hole state with $J_z = -3/2$ to an electron state with $S_z = -1/2$, or the transition from a light-hole state with $J_z = -1/2$ to an electron state with $S_z = 1/2$. Calculating the dipole transition matrix elements for these

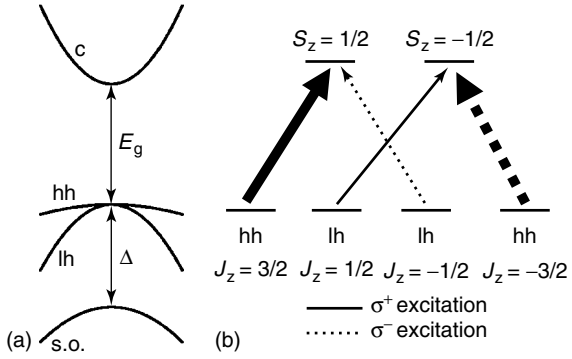

Figure 1. (a) Schematic of the band structure of a zinc-blende semiconductor, showing the conduction band (c), heavy-hole band (hh), light-hole band (lh), and split-off hole band (s.o.). Also indicated are the energy gap, E_g, and the spin-orbit splitting Δ. (b) Diagram of the four band-edge transitions and selection rules for circularly polarized light. The width of the lines indicates the strength of the transition.

two transitions, one finds that the heavy-hole transition is more likely than the light-hole transition by a factor of 3. In this way, circularly polarized optical excitation near the band edge results in the pumping of a net electron spin polarization in the conduction band.

The situation is improved further in strained crystals or with quantum confinement, which can lift the degeneracy between the heavy and light holes. In this case, transitions from only one hole band can be driven resulting in nearly 100% spin polarization.

These spin-dependent selection rules not only allow for the initialization of spin-polarized electrons and holes, but also the measurement of spin polarization. In the opposite process of optical spin pumping, when spin-polarized electrons and holes recombine radiatively, the resulting luminescence is circularly polarized. By measuring this polarization, the spin polarization at the time of the recombination can be inferred.

In a Hanle measurement (Figure 2a), spins are optically initialized using circularly polarized light perpendicular to an applied magnetic field. As the injected spins precess about this field, the steady-state spin polarization is reduced. The resulting curve of polarization versus magnetic field typically shows a Lorentzian lineshape, with width proportional to the transverse spin lifetime. The Hanle technique was used extensively in early measurements of spins in semiconductors (Meier and Zakharechenya, 1984), and have been used more recently in experiments to measure a single electron spin in a GaAs QD (Bracker *et al*., 2005) and in measurements of spins injected from a ferromagnetic metal into a semiconductor light-emitting diode (Strand *et al*., 2003).

A more direct measurement of spin polarization can be obtained through the Faraday effect (Faraday, 1846). Here, a net spin polarization in a material results in a different index of refraction for left and right circularly polarized light. Thus when linearly polarized light is transmitted through the material, the two circularly polarized components acquire a relative phase shift, yielding a rotation of the polarization of the transmitted light. The angle through which the polarization is rotated is proportional to the spin polarization along the axis of the light propagation. The same effect occurs upon reflection off the sample, in this case known as *Kerr rotation* (*KR*).

Faraday rotation (or KR) can be used to probe the steady-state spin polarization, similar to the Hanle measurement discussed in the preceding text (Figure 2b). By using Faraday rotation instead of a traditional Hanle measurement, one gains the ability to measure spins that do not undergo radiative recombination. Additionally, Faraday rotation provides spectroscopic information about the energy levels occupied by the spins through the energy-dependence of the Faraday effect (Meier and Awschalom, 2005). This measurement technique proves especially useful for spins that are not

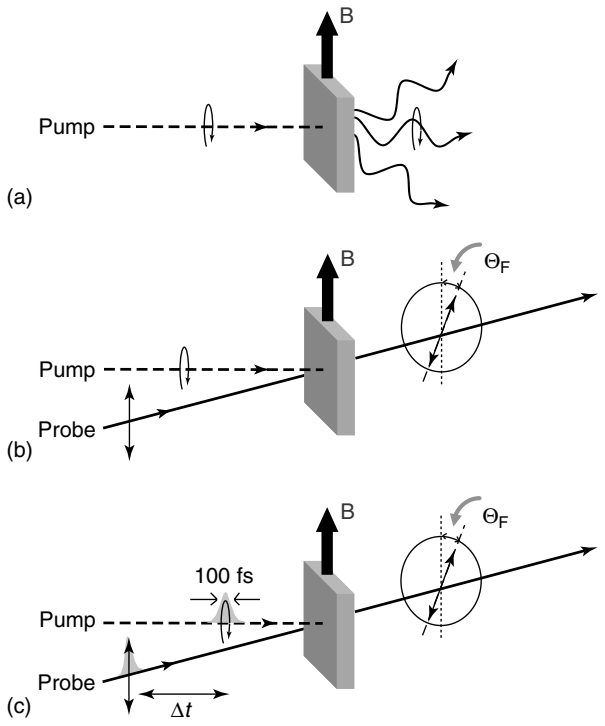

Figure 2. (a) Schematic of a Hanle measurement. Spins are injected with circularly polarized excitation, and the degree of circular polarization of the photoluminescence is measured. (b) Schematic of a DC Faraday rotation measurement. Spin polarization is measured through the rotation of a linearly polarized probe beam. (c) Schematic of a time-resolved Faraday rotation measurement. A circularly polarized pump pulse excites spins, which are probed a time Δt later through the rotation of a linearly polarized probe pulse.

optically injected. DC Faraday or KR measurements have recently been used for studying electrical spin injection and accumulation in ferromagnetic metal/nonmagnetic semiconductor heterostructures (Stephens *et al*., 2004; Crooker *et al*., 2005). Also, measurements of intrinsically generated spin polarizations through the spin Hall effect (Kato, Myers, Gossard and Awschalom, 2004c) or current-induced spin polarization (Kato, Myers, Gossard and Awschalom, 2004b) are also possible using this method.

The Faraday and Kerr effects can be used in conjunction with ultrafast optical techniques for time-resolved measurements of spin coherence in semiconductors (Awschalom *et al*., 1985; Baumberg *et al*., 1994; Östreich, Schönhammer and Sham, 1995; Crooker *et al*., 1997), (Figure 2c). In such measurements, a mode-locked Ti:Sapphire laser provides a train of pump and probe pulses with subpicosecond duration, which are both focused to a spot on the sample. The pump pulse is circularly polarized, and serves to optically inject spin-polarized electrons into the conduction band. The arrival of the probe pulse is delayed from the pump by changing

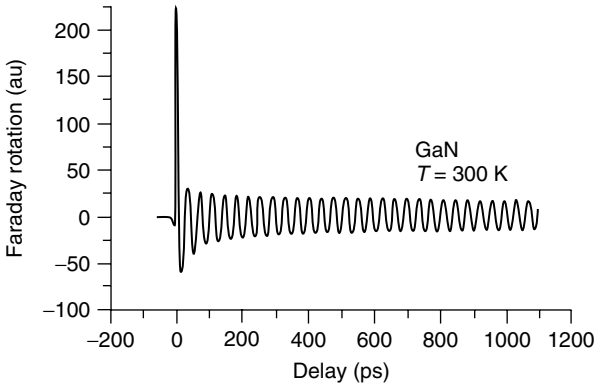

Figure 3. Coherent spin precession in GaN measured by time-resolved Faraday rotation. (Adapted from Beschoten *et al.*, 2001.)

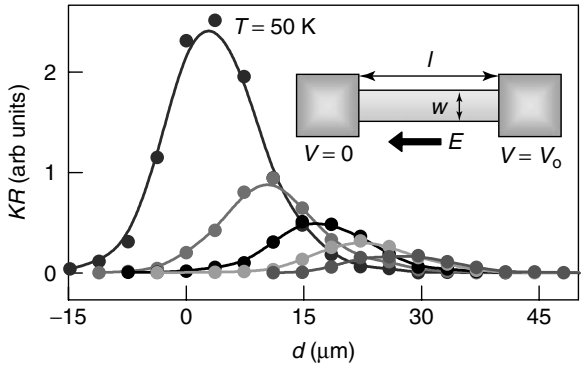

Figure 4. Schematic of the device geometry for spin drag measurements $l = 300\,\mu\text{m}$, $w = 100\,\mu\text{m}$. Spatial profiles of the optically injected spin packet, in n-type bulk ZnSe, extracted from Fourier transforms of θ_K at $E = 60\,\text{mV}\,\mu\text{m}^{-1}$ for $\Delta t = 13.1\,\text{ns}$, $\Delta t = 26.2\,\text{ns}$, $\Delta t = 39.3\,\text{ns}$, $\Delta t = 52.4\,\text{ns}$, and $\Delta t = 65.5\,\text{ns}$, in the order of decreasing amplitude. (Reprinted with permission Stern *et al.*, copyright 2006, American Physical Society.)

the optical path length of the probe. The probe is linearly polarized, and the resulting Faraday (or Kerr) rotation of the probe serves as an instantaneous measurement of the spin polarization at the moment of incidence on the sample. If the spins are initialized into a coherent superposition of spin eigenstates, the projection of the resulting dynamics along the probe direction can be observed as a function of time. For example, Figure 3 shows the coherent quantum beating between electron spin levels Zeeman-split by a transverse magnetic field in GaN at room temperature. By fitting such a curve, the transverse spin lifetime and the electron g-factor can be extracted.

3 ELECTRICAL GENERATION AND MANIPULATION OF SPIN POLARIZATION

In the previous section, we have demonstrated the ability to create and detect electron spin coherence using optical means. Here, we address the issue of using electric fields to create, manipulate, and transport spin-polarized electrons in semiconducting materials. A significant challenge in the transport of spin-polarized carriers over useful length scales and through heterointerfaces is the ability to do so without destroying the spin coherence. Spatially resolved KR allows the study of mesoscopic lateral spin transport in devices with an externally applied, in-plane electric field. In this pump-probe technique, two beams are normally incident on the sample and focused to a 15-μm spot. The KR of the probe maps the electron spin polarization as the relative separation d of the pump and probe is varied in the direction of the electric field. Figure 4 follows the optically injected spin packet as it is dragged along the channel by an electric field of $60\,\text{mV}\,\mu\text{m}^{-1}$ in the n-type ZnSe channel ($n = 5 \times 10^{16}\,\text{cm}^{-3}$). Extracting the drift velocity from the center of the spin packets allows an estimate of the spin mobility of $\mu_s = 89 \pm 14\,\text{cm}^2\,\text{V}^{-1}\text{s}^{-1}$. This is 20 times less than that measured in GaAs, where time and spatially resolved measurements show that spin lifetimes can exceed hundreds of nanoseconds, and spin packets can be transported over a hundred microns (Kikkawa and Awschalom, 1999). These lateral spin drag experiments in both II–VI and III–V semiconductors demonstrate that spin polarization can be transported over micron-scale distances in semiconductors with the application of an electric field.

The interaction between a spin magnetic moment and a magnetic field **B** gives rise to the Zeeman energy splitting and the precession of a spin about a transverse magnetic field mentioned in Section 2:

$$H_Z = \mu_B \vec{B} \cdot \overleftrightarrow{g} \cdot \vec{\sigma} \tag{1}$$

where μ_B is the Bohr magneton, $\vec{\sigma}$ is the spin operator, and $\overleftrightarrow{g}$ is the Landé g-tensor. Semiconductors allow a great amount of control of this interaction through the material-dependent g-factor (See also **Spin Engineering in Quantum Well Structures, Volume 5**). For example, spin precession can be modulated at GHz frequencies using an electric field to control the g-factor of electrons in parabolically graded heterostrcutures (Kato, Myers, Gossard and Awschalom, 2003). Conventional spin manipulation through the g-factor is limited, however, in that it still requires the application of an external magnetic field. But, the capability of manipulating electron spins in nonmagnetic semiconductors in the absence of such an external magnetic field has practical implications for spin-based quantum information processing (Loss and DiVincenzo, 1998) and spin-based electronics (Awschalom, Loss and Samarth, 2002;

Wolf *et al*., 2001). Single qubit operations require a local Hamiltonian, which is tunable within coherence times that generally do not exceed a few nanoseconds. The scaling down of devices for on-chip integration requires precise control of magnetic fields at micron-scale dimensions or even smaller. External magnetic fields are limited on both accounts – it is both difficult to create large fields in a short timescale, as well as to spatially localize a field without complicated architectures.

The SO interaction provides a unique pathway for spin manipulation through electric fields without magnetic fields or magnetic materials (Aronov, Lander-Geller and Pikus, 1991). The SO Hamiltonian, given by

$$H_{\mathrm{SO}} = \frac{\hbar}{4m_0^2c^2}[\vec{\nabla}V(\vec{r}) \times \vec{p}] \cdot \vec{\sigma} \tag{2}$$

is a consequence of relativity arising from the transformation of an electric field into a magnetic field in the frame of a moving electron. According to the form of equation 2, the electric field and orbital momentum create an effective magnetic field that acts on the spin operator in the same way as the magnetic field in equation 1. This electric field need not be a real field, but a 'quasi electric field', arising from asymmetries in the crystal field, the band gap, or strain-induced spin splitting. In this part of the chapter, we describe experiments investigating the existence of strain-induced internal magnetic field in *n*-GaAs and *n*-ZnSe and show electrical generation of spin polarization in these semiconductors through SO coupling, performed at low temperatures in GaAs (Kato, Myers, Gossard and Awschalom, 2004b) and at higher temperatures persisting to 300 K, in ZnSe (Stern *et al*., 2006).

The GaAs samples are grown by molecular-beam epitaxy (MBE) and consist of a 2-μm *n*-GaAs layer ($n = 3 \times 10^{16}\,\mathrm{cm}^{-3}$) acting as a spin probe layer at the surface and a 2-μm film of $Al_{0.4}Ga_{0.6}As$ underneath serving as a stressor/etch layer. The semi-insulating GaAs (001) substrate is removed by chemical etching in order to form a rectangular membrane with dimensions ∼100 by ∼300 μm. The processed membrane has curvature, possibly due to the larger lattice constant or the oxidation of the $Al_{0.4}Ga_{0.6}As$ layer, thereby straining the *n*-GaAs film. Ohmic contacts are evaporated on the surface in order to apply an in-plane electric field **E** along the $[1\bar{1}0]$ crystallographic direction. The in-plane strain, estimated using optical interference fringes at room temperature, is $\sim 10^{-5}$.

Electron spin dynamics is probed using the same time-resolved KR technique mentioned earlier for studying spin transport. Figure 5(a)–(d) shows the spatiotemporal evolution of a coherent electron spin packet with zero external field, under various applied E. The spin packet

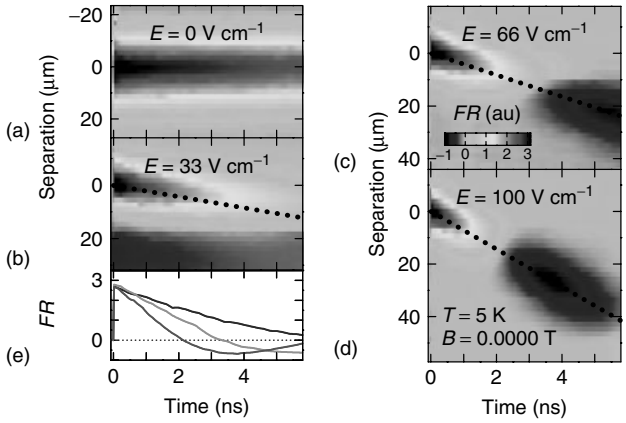

Figure 5. Spatiotemporal evolution of the photoexcited spin packet at zero magnetic field. (a)–(d) FR as a function of pump-probe separation and time delay for $E = 0, 33, 67, 100\,\mathrm{V\,cm}^{-1}$, respectively. The dotted lines are determined by the drift velocity of the spin packet. (e) Linecuts along the dotted lines in (b)–(d). (Reprinted by permission from *Nature* Kato *et al*., copyright 2004 Nature Publishing Group.)

drifts in the electric field, as expected, but it also coherently precesses in time about an internal magnetic field B_{int} generated by SO coupling for momentum $k \neq 0$. The precession angle is in excess of 3π over 60 μm in 13 ns and is proportional to the electric field. To accurately characterize B_{int}, KR is measured as a function of an *external* magnetic field B_{ext}. As in the case of time-resolved KR, the spin polarization signal oscillates and decays in time according to $\theta_0 \exp(-\Delta t/T_2^*)\cos(g\mu_{\mathrm{B}}B\Delta t/\hbar)$, where Δt is the pump-probe time delay (in these measurements, fixed at 13.1 ns), θ_0 is the initial amplitude at $\Delta t = 0$, T_2^* is the transverse spin coherence time, g is the electron g-factor, and B is the magnitude of the transverse magnetic field experienced by the electron spins. In the absence of an applied electric field (Figure 6, top trace), the average $k = 0$ and therefore $B_{\mathrm{int}} = 0$ and the oscillations are centered at $B = B_{\mathrm{ext}} = 0$. With an applied E perpendicular to B_{ext} (center trace), both the external and internal magnetic fields are along y and add directly so that $B = B_{\mathrm{ext}} + B_{\mathrm{int}}$ and the oscillatory signal is centered at $-B_{\mathrm{int}}$. For E parallel to B_{ext}, B_{int} is perpendicular to B_{ext} (Kato, Myers, Gossard and Awschalom, 2004a; Sih *et al*., 2006a) resulting in a total field magnitude of $B = \sqrt{B_{\mathrm{ext}}^2 + B_{\mathrm{int}}^2}$ which is always greater than zero for a nonzero B_{int}, causing suppression of the center peak (bottom trace).

In both cases in the preceding text, with nonzero electric field the amplitude of the signal decreases with increasing voltage, which is further investigated by spatially separating the pump and the probe by a distance d along the direction of E (Figure 7). Owing to the laser profile of the pump beam, the optically injected spins have a Gaussian spatial

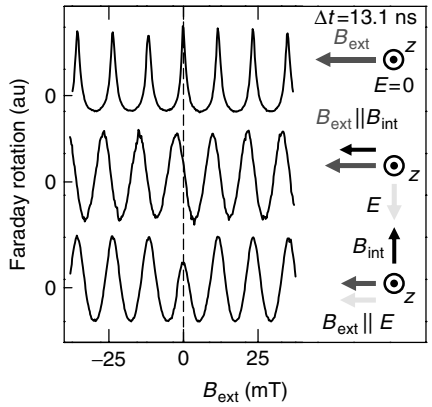

Figure 6. Characterization of the internal magnetic field showing the dependence of FR on the external magnetic field in three different geometries, with $E = 0$, $E||B_{\rm ext}$, and $E \perp B_{\rm ext}$. The curves are offset and scaled for clarity. (Reprinted by permission from *Nature* Kato *et al*., copyright 2004 Nature Publishing Group.)

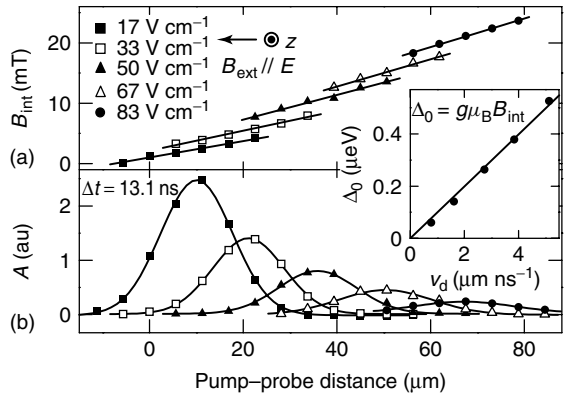

Figure 7. $B_{\rm int}$ (a) and A (b) as a function of the pump-probe separation d in the $E||B_{\rm ext}$ geometry for $E = 17$ (solid squares), 33 (open squares), 50 (solid triangles), 67 (open triangles), and 83 (solid circles) V cm^{-1}. Symbols are data and the lines are fits. The inset shows the spin splitting Δ_0 as a function of $v_{\rm d}$. (Reprinted by permission from *Nature* Kato *et al*., copyright 2004 Nature Publishing Group.)

profile which is centered at $d = 0$ when $E = 0$. An applied voltage ($E \neq 0$) imparts a nonzero average momentum k to the injected spin packet, causing it to drift with an average velocity $v_{\rm d}$. Spins at the leading edge of the packet experience a larger $B_{\rm int}$ than the trailing edge. This variation is due to the spread in the drift velocities of the spin packet arising from spin diffusion. The reported value of $B_{\rm int}$ for each E are obtained from a linear fit at the center of the spin packet, and is observed to be more than 20 mT. The spin splitting arising from this $B_{\rm int}$, $\Delta_0 = g\mu_{\rm B}B_{\rm int}$, is plotted as a function of $v_{\rm d}$. Figure 7 (inset) shows a phenomenological linear relation $\Delta_0 = \beta v_{\rm d}$. In the data presented, $\beta = 99$ neV ns μm^{-1}, while in an unstrained sample (without substrate removal) β is almost an order of magnitude smaller, decisively linking the internal magnetic field to the strain-induced spin splitting in the semiconductor.

The electrical manipulation of spin states discussed so far still requires the creation of coherent spins by optical injection. Encoding of spin information without optical or magnetic techniques offers a significant step toward an all-electrical protocol for spintronic devices. Early theoretical work points out the possibility of using a current flow to obtain magnetization in materials lacking inversion symmetry (Levitov, Nazarov and Eliashberg, 1985) (such as the zinc-blende semiconductors n-GaAs and n-ZnSe). Prior experiments for detection of current-induced spin polarization (CISP) in other systems (Hammar, Bennet, Yang and Johnson, 1999; Vorob'ev *et al*., 1979) had added complications.

The same materials and techniques described above can be used to investigate CISP. Figure 8(a) shows the measurement geometry for studying CISP in an n-$In_{0.07}Ga_{0.93}As$ channel with a built-in strain field. An alternating electric field with amplitude $E = V_{\rm pp}/(2l)$ is established along the InGaAs channel of width w and length l. The current-induced KR is lock-in detected and is measured as a function of magnetic field $B_{\rm ext}$ applied parallel to the alternating E (Figure 8b). The curves in Figure 8(b) can be explained by assuming a constant orientation rate γ for spins polarized along the y axis. In a similar process to the Hanle measurement (Figure 2a), the z component of spin per unit volume $\rho_{\rm z}$ can be written as

$$\rho_{\rm z} = \int_0^\infty {\rm d}t\gamma \exp(-t/T_2^*)\sin(\omega_{\rm L}t) = \rho_{el}\frac{\omega_{\rm L}T_2^*}{(\omega_{\rm L}T_2^*)^2 + 1} \quad (3)$$

where γ is the number of spins oriented along the y axis per unit time per unit volume, T_2^* is the transverse spin coherence time, $\omega_{\rm L} = g\mu_{\rm B}B/\hbar$ is the electron Larmor frequency, and $\rho_{\rm el} = \gamma T_2^*$ is the steady-state spin density due to electrical excitation. The upper limit for the integration is taken as infinity because the modulation period is much longer than T_2^* . This odd Lorentzian shape is indicative of spins generated in plane and perpendicular to E. Temperature dependence of this effect shows $\rho_{\rm el}(\sim 10\,\mu{\rm m}^{-3})$ not varying significantly up to $T = 60$ K. At higher T, $\rho_{\rm el}$ becomes smaller due to the decline of T_2^* , and is below the noise level for $T > 150$ K. Similar measurements in 1.5 μm-thick n-ZnSe samples yield a $\rho_{\rm el} \sim 12\,\mu{\rm m}^{-3}$ at $T = 20$ K, with CISP signal persisting up to room temperature.

Although qualitatively understood as arising from SO coupling, the microscopic origin of CISP is not well understood. Strain-enhanced inversion asymmetry terms in the Hamiltonian manifest as $B_{\rm int}$ and could generate the

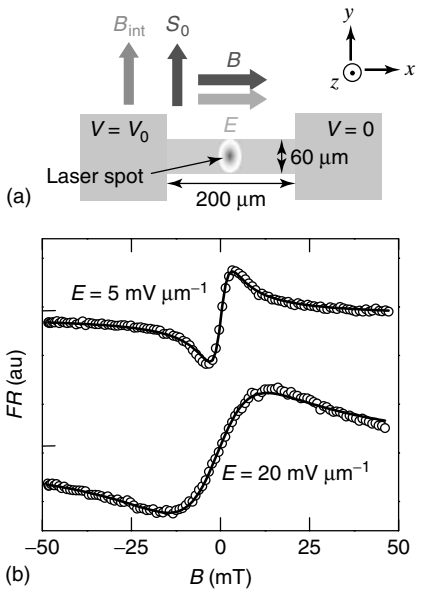

Figure 8. (a) Schematic of the device and geometry in measuring current-induced spin polarization. Squares are the metal contacts at the ends of the channel. (b) Voltage-induced FR as a function of B_{ext} for $E = 5$ and $20\,\text{mV}\,\mu\text{m}^{-1}$ with $\mathbf{E}||[1\bar{1}0]$. Open circles are data and the solid lines are the fits to equation (3). (Data originally presented in Kato, Myers, Gossard and Awschalom, 2004b.)

spin polarization. In general, the internal magnetic field strength shows a close correlation to the amount of strain in *n*-GaAs structures, but the CISP shows little correlation to the strength of B_{int}. In the experiment with *n*-ZnSe epilayers, the CISP is comparable in magnitude to that observed in GaAs, which is most surprising, since no B_{int} is measured in these thick *n*-ZnSe samples.

4 EXPERIMENTAL OBSERVATION OF THE SPIN HALL EFFECT

Electrically induced spin polarization can also be generated when current flows in a semiconductor with SO coupling, where carriers can be deflected in spin-dependent directions through the spin Hall effect. The spin Hall effect refers to the generation of a spin current transverse to a charge current in the absence of an applied magnetic field. A pure spin current can be interpreted as an equal number of spin-up and spin-down electrons moving in opposite directions, resulting in a flow of a spin angular momentum with no net charge current. The source of the transverse spin current can be either extrinsic or intrinsic spin-orbit mechanisms, analogous to the origin of the anomalous Hall effect. The extrinsic spin Hall effect was first predicted due to spin-dependent scattering off impurities in a semiconductor crystal (D'yakonov and Perel, 1971b). SO coupling mixes spin and momentum eigenstates leading to skew and side-jump scattering mechanisms which drive the transverse spin current (Engel, Halperin and Rashba, 2005). More recently, an intrinsic spin Hall effect was predicted as arising from the momentum-dependent internal magnetic field B_{int} which arises from SO coupling (Murakami, Nagaosa and Zhang, 2003; Sinova *et al*., 2004). These Dresselhaus and Bychkov–Rashba fields arise from bulk inversion asymmetry or structural inversion asymmetry, respectively, and generate spin splitting in the electron bands for momentum $k \neq 0$ in semiconductors without an inversion center. These effective internal magnetic fields are inherent in the band structure of the crystal and do not depend on the presence of impurities.

4.1 Observation of the spin Hall effect in bulk Gallium arsenide

The first optical detection of the spin Hall effect (Kato, Myers, Gossard and Awschalom, 2004c) was performed on a series of 2 μm-thick GaAs epilayers with a Si doping density $n = 3 \times 10^{16}\,\text{cm}^{-3}$ grown by MBE on a (001) semi-insulating GaAs substrate. The epilayers were patterned by photolithography and etched into a semiconducting channel with a metallic contact on each end. The structures are cooled to $T = 30\,\text{K}$ in a helium flow cryostat. When current is sent through the semiconducting channel, a transverse spin current develops due to the spin Hall effect. This pure spin current cannot be measured directly, but it does result in a spin accumulation on the edges of the channel, which can be detected optically.

Figure 9(a) shows an unstrained GaAs sample with a channel of width $w = 77\,\mu\text{m}$ and length $l = 300\,\mu\text{m}$ patterned parallel to the [110] crystallographic direction. The sample is measured with a scanning Kerr microscope (Stephens *et al*., 2003) which provides ∼1 μm spatial resolution to detect the KR of a linearly polarized 825-nm-wavelength probe beam. Figure 9(b) shows KR as a function of external applied magnetic field B_{ext}. The curves are analogous to the Hanle effect (Meier and Zakharechenya, 1984) previously discussed in terms of both luminescence polarization and DC Kerr measurements. Spin polarization is generated out of the plane of the channel by the spin Hall effect, which precesses about the transverse magnetic field B_{ext} as it decoheres. The KR of the spatially resolved probe measures the time-averaged polarization projected along the beam direction (z axis), which is well-fit by a Lorentzian function given by

$$\theta_{\text{K}} = \frac{\theta_0}{(\omega_{\text{L}}\tau)^2 + 1} \tag{4}$$

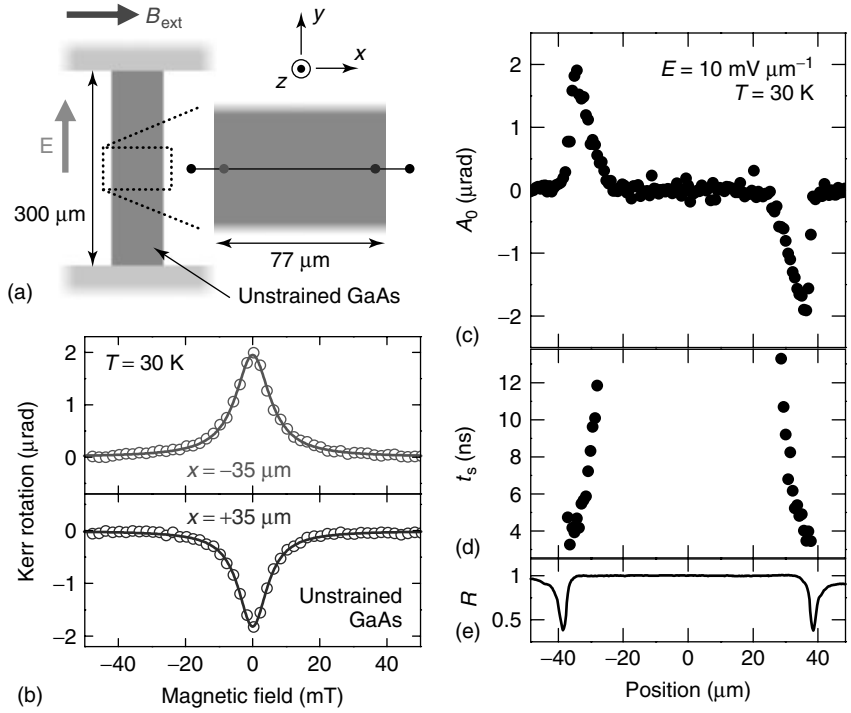

Figure 9. The spin Hall effect in unstrained GaAs. Data are taken at $T = 30\,\mathrm{K}$ and a linear background has been subtracted from each B_{ext} scan. (a) Schematic of the unstrained GaAs sample and the experimental geometry. (b) Typical measurement of KR as a function of B_{ext} for $x = -35\,\mu\mathrm{m}$ (top) and $x = +35\,\mu\mathrm{m}$ (bottom) for $E = 10\,\mathrm{mV}\,\mu\mathrm{m}^{-1}$. Solid lines are fits as explained in text. (c)–(d) Spatial dependence of peak KR A_0 and spin lifetime across the channel, respectively, obtained along the linecut in (a). (e) Reflectivity R as a function of x. R is normalized to the value on the GaAs channel. The two dips indicate the position of the edges and the width of the dips gives an approximate spatial resolution. (Reprinted with permission Kato *et al.*, copyright 2004, AAAS.)

where θ_0 is the amplitude of KR and $\omega_{\mathrm{L}} = g\,\mu_{\mathrm{B}} B/\hbar$. ($g = -0.44$ for this sample as measured using time-resolved KR). This Lorentzian form is analogous to equation 3, except the spin polarization is generated out of plane along the probe beam direction rather than in the plane. θ_0 is of equal magnitude and opposite sign for the two edges of the sample (Figure 9c), as expected for the spin Hall effect (Hirsch, 1999; Zhang, 2000). The density of accumulated spin polarization (which is proportional to θ_0) is a maximum at the edges of the channel and decreases with distance from the edge. The accumulation can be quantitatively analyzed using solutions to a drift-diffusion model for the spin current (Zhang, 2000), giving a spin diffusion length of $L_{\mathrm{s}} \sim 3 - 4\,\mu\mathrm{m}$.

A two-dimensional spatially resolved image of the entire channel shows the electrically induced spin accumulation of opposite sign on either edge of the sample (Figure 10). The polarization is uniform over the length of the channel but decreases near the contacts as would be expected from the unpolarized electrons injected at the contacts.

The origin of the spin Hall effect in the GaAs epilayers is likely extrinsic spin-dependent scattering. The k-dependent spin splitting in unstrained GaAs is weak, and similar observations in strained InGaAs show no marked crystallographic direction dependence that would link the spin accumulation to the band structure. Measurements in strained InGaAs channels show similar spin accumulation with an additional B_{int}, but the presence of this intrinsic SO field does not qualitatively change the effect.

4.1.1 The intrinsic spin Hall effect in a two-dimensional hole gas

The spin Hall effect was also observed in a two-dimensional hole gas (Wunderlich, Kaestner, Sinova and Jungwirth, 2005). In this experiment, a novel p−n junction light-emitting diode microdevice in coplanar geometry was fabricated using optical and electron beam lithography in modulation-doped AlGaAs/GaAs heterostructures grown by MBE (see Figure 1 in Wunderlich, Kaestner, Sinova and Jungwirth, 2005). The sample was cooled to a temperature of 4.2 K, and an in-plane electric field is applied along the p channel of the microdevice (see Figure 3 in Wunderlich, Kaestner, Sinova and Jungwirth, 2005) generating a nonzero out-of-plane hole spin polarization. The polarization of the emitted light depends on the direction of the hole spins,

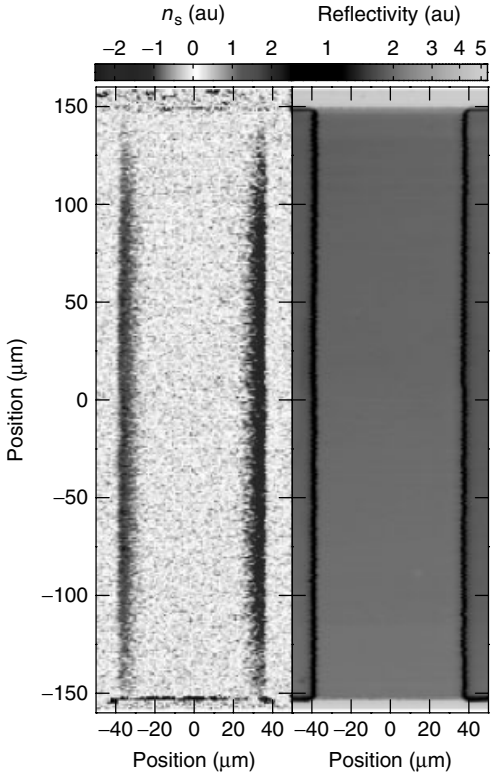

Figure 10. Two-dimensional images of spin density n_s (left) and reflectivity R (right) for an unstrained GaAs channel measured at $T = 30\,\mathrm{K}$ and $E = 10\,\mathrm{mV\,\mu m^{-1}}$. The region on the left (right) corresponds to the spin polarization in the $z(-z)$ direction. (Reprinted with permission Kato *et al*., copyright 2004, AAAS.)

allowing optical detection of the spin polarization at the edges of the p channel. The polarization of this light changes sign for the opposite edges of the channel. In addition, the polarization of the emitted light also changes sign when the direction of the applied electric field is reversed, consistent with the predicted spin Hall effect. In contrast to the measurement of extrinsic spin Hall effect through KR, microscopic quantum transport calculations suggest that the observed spin Hall effect is intrinsic owing to the strong SO coupling of the two-dimensional hole gas (Wunderlich, Kaestner, Sinova and Jungwirth, 2005).

4.1.2 The spin Hall effect in a two-dimensional electron gas

The spin Hall effect can also be measured in two-dimensional electron systems, first done in modulation-doped single quantum wells are grown by MBE on (110) semi-insulating GaAs substrates (Sih *et al*., 2005). Similar devices and measurement techniques are used as those used in the original KR measurement of the spin Hall effect. Figure 11(c) shows a one-dimensional spatial profile of the spin accumulation

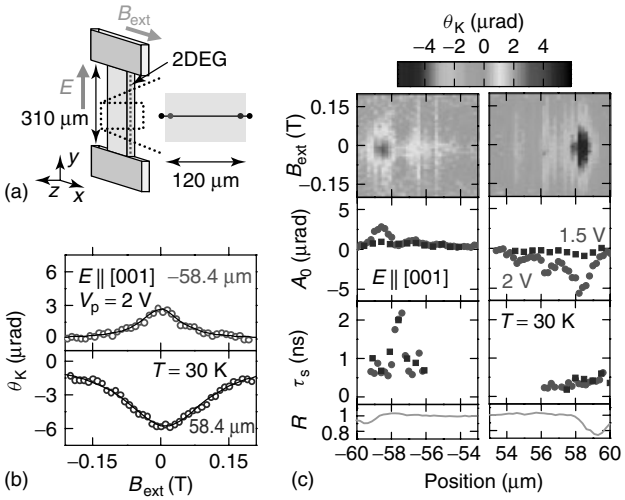

Figure 11. Spin Hall effect in a two-dimensional electron gas (a) Device schematic and measurement geometry. (b) Kerr rotation (hollow symbols) and fits (lines) as a function of applied in-plane magnetic field B_{ext} for $x = -58.4\,\mu\mathrm{m}$ (top) and $x = +58.4\,\mu\mathrm{m}$ (bottom). The channel has width $w = 120\,\mu\mathrm{m}$, length $l = 310\,\mu\mathrm{m}$, and mesa height $0.1\,\mu\mathrm{m}$. A linear background is subtracted for clarity. (c) B_{ext} scans as a function of position near the edges of the channel of a device for $V_p = 2\,\mathrm{V}$. Amplitude A_0, spin coherence time τ_s, and reflectivity R are plotted for $V_p = 1.5\,\mathrm{V}$ (squares) and $2\,\mathrm{V}$ (circles). (See the original figure in color in Sih *et al*., 2005.) (Reprinted with permission V. Sih *et al*., copyright 2005, Nature Publishing Group.)

near the edges of the channel. Two spin Hall peaks at each edge of the channel are visible, one at $x = \pm 58.6\,\mu\mathrm{m}$ and one of smaller amplitude at $x = \pm 56.4\,\mu\mathrm{m}$. This structure could be due to an additional contribution from spin-polarized carriers undergoing spin precession about the in-plane Bychkov–Rashba field as they diffuse from the edges toward the center of the channel.

Optical measurements in (110)-oriented quantum wells also allow study of the two spin-orbit mechanisms responsible for internal magnetic fields by allowing one to isolate the contributions of the Dresselhaus and Bychkov–Rashba effects. In two-dimensional systems, the Dresselhaus field is oriented along the growth direction in (110) quantum wells, whereas this field is in plane in (001) quantum wells. Since the Dresselhaus and Bychkov–Rashba fields are mutually perpendicular, one can observe a dependence of the CISP on the direction of the current flow in the semiconductor and the interplay of the Dresselhaus and Bychkov–Rashba fields (Sih *et al*., 2005).

4.1.3 Evidence of pure spin current generated by the spin Hall effect

Despite the strong evidence for the observation of the spin Hall effect, the source of the spin accumulation is not

clear. Theory of the spin Hall effect would suggest that a transverse spin current is created in the bulk of the semiconductor channel, but since spin is not a conserved quantity in a material with SO interactions, the very concept of a spin current is not well defined (Sih *et al.*, 2005). This difficulty causes uncertainty about the existence of a real pure spin current causing spin accumulation in the experiments. Indeed, models of spin accumulation are sensitive to the boundary conditions imposed at the edges (Tse, Fabian, Zutic and Das Sarma, 2005). Edge effects such as carrier depletion can cause local effective magnetic fields, which could potentially give rise to spin accumulation without the production of a bulk spin current.

Devices can be engineered to distance the boundary of the current in the channel from the edges of the sample, thereby separating spin accumulation from the physical edge of the sample (Sih *et al.*, 2006b). Using the same GaAs material described previously, 60-μm-wide channels are fabricated along the $[1\bar{1}0]$ crystallographic direction with smaller 40-μm-wide channels extending from the main channel transverse to the current flow, shown schematically in Figure 12(a).

The spin polarization amplitude for a 60-μm-wide channel and for 10-, 20-, and 40-μm-wide side arms are displayed in Figure 12(b). The spin polarization amplitude near the left edge at $x = -30\,\mu\text{m}$ is unaltered in the presence of the side arms. In contrast, the spin polarization amplitude near the right edge $x = 30\,\mu\text{m}$ is modified by the addition of the side arms. The spin polarization amplitude is not always largest near the edge of the channel, indicating that the spin accumulation is not a local effect caused by the sample's physical boundary. The amplitude of the spin polarization is smaller for longer side arms at any position x, consistent with spins drifting from the main channel toward the end of the side arms. The measurements can be successfully modeled by a spin drift-diffusion model (Crooker *et al.*, 2005; Lou *et al.*, 2006) of a spin current being generated throughout the bulk of the channel and drifting into the side arms, where there is no generation of spin polarization since there is negligible electron current (Figure 12). These measurements demonstrate that the spin polarization from the spin Hall effect is not restricted to the sample edges. The spin current generated in the bulk of the channel can drive spin transport over length scales significantly longer than the spin diffusion length $L_s = 9\,\mu\text{m}$ in the sample.

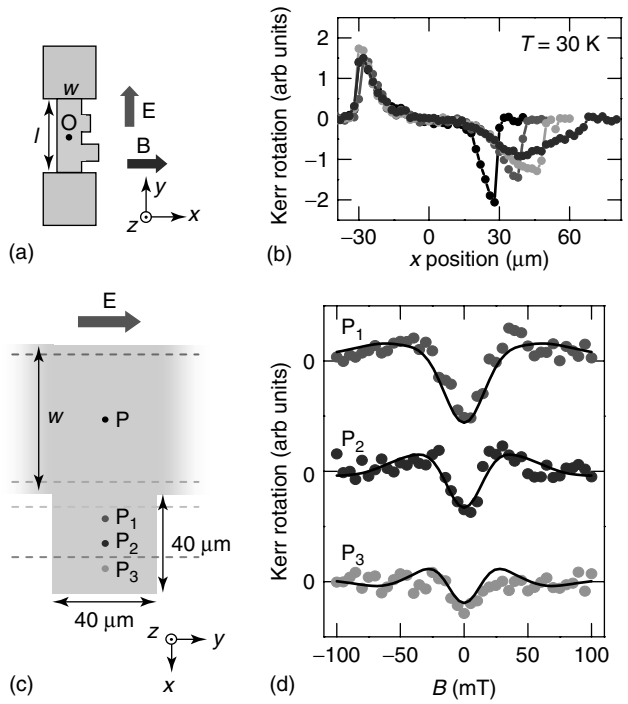

Figure 12. (a) Measurement schematic and experimental geometry. The center of the channel is taken to be the origin O. (b) Spin polarization amplitude as a function of position measured for the channel and with 10 μm, 20 μm, and 40 μm side arms. Data are taken at $T = 30\,\text{K}$ and $V = 6\,\text{V}$. (c) Measurement schematic showing where the spatial scans are made. P indicates the position $(x, y) = (0\,\mu\text{m}, -50\,\mu\text{m})$. (d) Kerr rotation as a function of magnetic field for three different x positions at $y = -50\,\mu\text{m}$ on the 40 μm side arm. Measurements are shown for $x = 40\,\mu\text{m}$ (P_1, top), $x = 50\,\mu\text{m}$ (P_2, middle) and $x = 60\,\mu\text{m}$ (P_3, bottom). Solid lines are calculated from a model that accounts for spin drift. (Reprinted with permission Sih *et al.*, copyright 2006, American Physical Society.)

4.2 Electrical measurement of the spin Hall effect

Optical measurements enable measurement of the spin Hall effect through the direct connection between light polarization and carrier spin through the selection rules in zinc-blende semiconductors. Since the spin Hall effect is an example of all-electrical generation of spin, it is desirable to be able to detect spin accumulation entirely on-chip without the need for external laser systems. Further, electrical detection may enable a more direct measurement of the spin Hall conductivity of a material. Various proposals have been made to measure the spin Hall effect electrically in metals and semiconductors (Hankeiwicz, Molenkamp, Jungwirth and Sinova, 2004; Shchelushkin and Brataas, 2005).

Direct electronic detection of the spin Hall effect was first demonstrated in a diffusive metallic conductor (aluminum) (Valenzuela and Tikham, 2006). In this measurement, the device, which consists of an aluminum strip with side arms and a ferromagnetic electrode, was fabricated using electron beam lithography and a shadow mask evaporation technique (see Figure 1 in Valenzuela and Tikham, 2006). The measurements are performed at 4.2 K. Spin-polarized electrons are injected from the ferromagnetic electrode into

the Al strip by applying a voltage between the electrode and one end of the Al strip. The spin-polarized charge current flowing in the Al strip creates a spin current flowing in the opposite direction due to diffusion of spin-polarized carriers. SO interactions separate the spin-up and spin-down electrons generating a transverse spin current that leads to spin accumulation at the edges of the Al strip. Unequal numbers of spin-up and spin-down electrons in the Al strip leads to a charge imbalance across the strip producing a spin Hall voltage proportional to the spin polarization. This process is based on the same principles as the anomalous Hall effect, but occurs in a nonmagnetic material. The measured spin conductivity is consistent with the result of the theoretical calculations using semiclassical Boltzmann approximation (Zhang, 2000). The measured spin Hall voltage in this experiment is of the order of 10 nV, and the corresponding spin Hall conductivity (σ_{SH}) is approximately $10^{-3}\Omega^{-1}\,m^{-1}$ which is 10^{-4} times smaller than the charge conductivity (σ_C) in Al.

4.3 The spin Hall effect at room temperature in Zinc selenide

Optical measurements of the spin Hall effect and other forms of all-electrical spin generation were typically performed in the III–V semiconductor GaAs, which has long spin coherence times as well as strong SO coupling effects. Despite the typically weaker SO coupling in II–VI semiconductors (Winkler, 2003), both CISP and the spin Hall effect have been observed through KR in 1.5-μm-thick *n*-type Cl-doped ZnSe epilayers with $n = 9 \times 10^{18}\,cm^{-3}$ (Stern *et al*., 2006). Observation of the spin Hall effect is highly dependent on *n*-doping, as no spin Hall signature is measured in samples with lower *n*.

In this experiment, careful attention was paid to measure the sign of the spin accumulation, with the results shown in Figure 13(a). The spin Hall conductivity is measured to be of the same order of magnitude and the same sign to what has been predicted by theory for GaAs with a dominant extrinsic spin Hall effect (Engel, Halperin and Rashba, 2005; Tse and Das Sarma, 2006). ZnSe exhibits long spin coherence times even up to room temperature (Malajovich *et al*., 2000), and both the CISP and the spin Hall effect persist up to room temperature as well (Figure 13d and e) with little decrease in the spin diffusion length and only an order of magnitude decrease in spin polarization and spin Hall conductivity. The spin Hall conductivity is proportional to the charge conductivity, suggesting extrinsic spin-orbit mechanisms. This result is the first evidence of all-electrical generation and separation of spin polarization

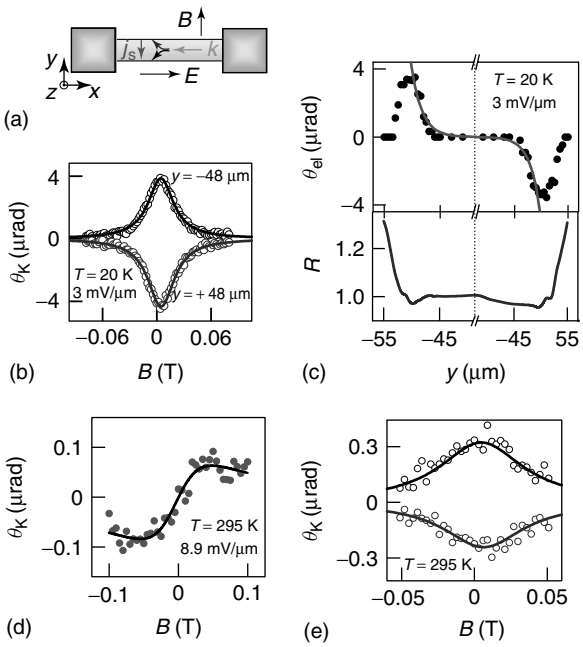

Figure 13. (a) Schematic showing the measurement geometry for the spin Hall effect, with $B_{ext}||x$. For $E > 0$, $j_x^s < 0$. (b) θ_K (open circles) and fits (lines) at $y = 0\,\mu m$ as a function of B_{ext} for $x = -48\,\mu m$ (top) and $x = +48\,\mu m$ (bottom) at $T = 20\,K$. (c) Spatial dependence of the fit parameters θ_{el} and τ_s, as well as the reflectivity R of the beam (normalized to 1 at $x = 0$). (d) KR (circles) and fit (line) of CISP at room temperature. Adjacent-point averaging was done to improve signal-to-noise. (e) KR (circles) and fits (lines) of spin Hall polarization at $x = -48\,\mu m$ (top) and $x = +48\,\mu m$ (bottom) for $T = 295\,K$. (Reprinted with permission Stern *et al*., copyright 2006, American Physical Society.)

at room temperature, hinting at the possibility of utilizing these phenomena in functional spintronics devices.

5 SPIN COHERENCE IN MAGNETIC SEMICONDUCTORS

In previous sections, we discussed the possibilities for generating and manipulating coherent ensembles of spins in semiconductors using optical and electrical techniques. Spins also interact with local moments in a semiconductor, such as magnetic impurities. The interactions between coherent spins and magnetic moments in a semiconductor offer a pathway for realizing hybrid materials which can take advantage of the long-lived spins of localized impurities and the ability to optically and electrically manipulate coherence in semiconductors.

Magnetic coupling between two spins in most semiconductors is dominated by the electrostatic exchange interaction. In semiconductors doped with only small amounts of magnetic atoms, even the exchange interactions are too

short-ranged for magnetic ordering to occur. But, the itinerant band carriers are strongly affected by exchange with the doped magnetic atoms in the lattice due to their spatial overlap with the random local magnetic moments. Even in dilute magnetic systems, exchange interactions are not negligible, causing a giant Zeeman spin splitting in a magnetic field where the energy difference between spin-up and spin-down states of electrons can be increased by orders of magnitude.

Carrier–ion spin interactions in dilute magnetic semiconductors include both direct and kinetic exchange processes (Kacman, 2001). The interaction between the s-symmetry conduction band or p-symmetry valence band and the localized d states of magnetic impurities are known and the s–d and p–d exchange interactions, respectively. In this section, we will discuss a series of phenomena that arise in magnetic semiconductors due to the sp–d exchange interactions between spin-polarized carriers and a dilute system of magnetic moments doped into the host semiconductor.

5.1 Manipulating carrier exchange interactions in semiconductors

Early experiments on spins in magnetic semiconductors were typically performed in II–VI semiconductors where high solubility of magnetic dopants is achieved because of the compatible valence between typical transition-metal dopants and the group II cations. Conduction and valence band spins can be accessed through optical techniques such as photoluminescence and absorption, where spin energy splittings can be readily extracted. Treating sp–d exchange as a mean-field, dilute paramagnetic impurities induce an additional effective magnetic field on the carriers. Time-resolved measurements of coherent spin precession in paramagnetic semiconductors reveal an enhanced spin-flip scattering due to the magnetic impurities and an enhanced spin-splitting energy. The Larmor precession ν_{L} in a transverse magnetic field (e.g., along the x axis) is proportional to the total conduction band spin-splitting energy between spin-up and spin-down electrons ($\Delta E = E_{\uparrow} - E_{\downarrow}$) and can be expressed in terms of the Zeeman splitting (ΔE_{g}), and the s–d exchange splitting (ΔE_{sd}):

$$h\nu_{\mathrm{L}} = \Delta E = \Delta E_g + \Delta E_{\mathrm{sd}} = g\mu_{\mathrm{B}} B_x - xN_0\alpha \langle S_x \rangle \quad (5)$$

Here $\langle S_x \rangle$ is the component of Mn^{2+} spin along B, x is the concentration of magnetic ions, and $N_0\alpha$ is the s–d exchange parameter. Measuring the precession frequency of electron spins in a paramagnetic semiconductor allows extraction the s–d exchange energy in the material (Figure 14).

The strength of sp–d exchange interactions depends directly on the overlap of the carrier wave functions and the d orbitals of magnetic atoms. A graded parabolic

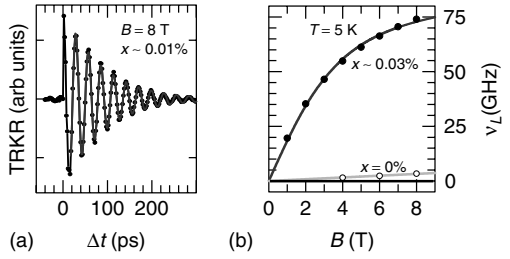

Figure 14. (a) Coherent electron spin precession in a paramagnetic AlGaAs/$Ga_{1-x}Mn_xAs$ quantum well. (b) Enhancement of the Larmor precession frequency in a similar quantum well (solid data) compared with the linear frequency of a nonmagnetic quantum well. The Brillouin function shape from the magnetization of the paramagnetic Mn impurities is evident in the curvature of ν_{L} with magnetic field. (Reprinted with permission Myers *et al*., copyright 2005, American Physical Society.)

quantum well allows for direct tuning of the exchange energy of electrons by electrical gating after the heterostructure growth. In an experiment by Myers *et al*. (2005a), a gated quantum well of $Zn_{1-x}Cd_xSe$ with x parabolically graded from $x = 0$ in the barriers to $x = 0.15$ at the center is grown by MBE. Four submonolayer digital regions of MnSe are deposited in the center of the well. When an electrical bias is applied to a parabolic potential, the center position of the confined electron will shift with minimal distortion in the wave function (Figure 15a). The tails of the electron wave function will overlap with the MnSe layers less than the center, thereby allowing direct electrical tuning of the s–d exchange in the device. Time-resolved Kerr rotation (TRKR) is used to measure the precession frequency of the electrons as a function of the electrical bias (Figure 15b). Whereas spins in a nonmagnetic quantum well show little tuning, the precession frequency of the electrons in the magnetic quantum well have an effective enhancement to their g-factor from the magnetic layers which tunes as the bias is changed. The TRKR measurements also reveal that the Mn spin system is tipped by the p–d exchange away from its equilibrium magnetization in a process that will be discussed in more detail later. The precession frequency of the photoexcited carriers can be further tuned by laser excitation energy. The s–d exchange is effectively reduced using higher laser energy, At higher excitation energies, the carriers are injected in higher exciton sublevels of the quantum well whose wave functions do not overlap as efficiently with the Mn^{2+}-doped layers as the s-symmetry ground state. The resulting effective electron g-factor is reduced closer to the nonmagnetic value (Figure 15c).

The sp–d exchange interactions are sensitive to changes in band symmetry caused by quantum confinement. Figure 16 shows measurements of the s–d exchange energy extracted from TRKR of coherent spin precession in $Ga_{1-x}Mn_xAs$ quantum wells of varying confinement energy (Myers *et al*.,

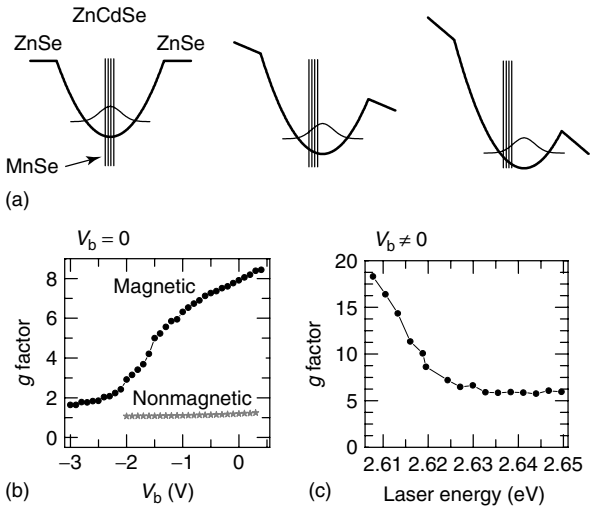

Figure 15. (a) Schematic of a parabolic ZnSe/ZnCdSe quantum well with digital MnSe doping in the center. Under electrical bias ($V_b \neq 0$), the parabolic potential is translated, which translates the electron wave function with minimal distortion and alters the effective overlap of the electron wave function with the magnetic region. (b) Tuning of the electron effective g-factor (proportional to ΔE) with bias V_b showing the increased exchange coupling near zero-bias. (c) Tuning of the effective g-factor with the laser energy showing the decreased s-d interaction for electrons in higher sublevels. (Reprinted with permission Myers *et al*., copyright 2005, American Physical Society.)

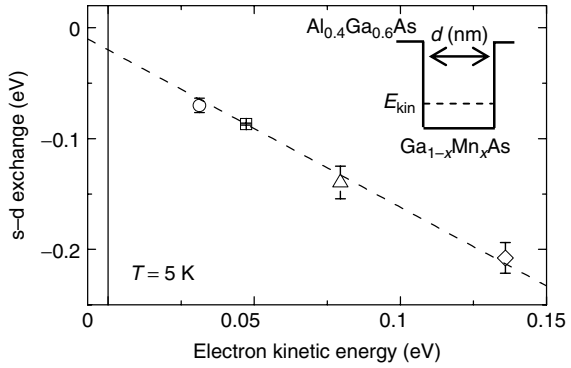

Figure 16. Variation of the s−d exchange in AlGaAs/GaMnAs quantum wells with the kinetic energy of the ground state (inset). The antiferromagnetic s−d exchange was originally presented in Myers *et al*. (2005b). (Reprinted with permission Myers *et al*., copyright 2005, American Physical Society.)

2005b; Poggio *et al*., 2005). The quantum well confinement is controlled varying the quantum well width. The s−d exchange becomes more antiferromagnetic with increasing confinement energy. This trend was first observed in CdMnTe quantum wells (Mackh, Ossau, Waag and Landwehr, 1996) and explained as a confinement-induced band mixing (Merkulov *et al*., 1999). Quantum confinement increases the kinetic energy of electrons in the quantum wells, bringing the electrons away from the zone center in k space. Away from $k = 0$, mixing of the conduction and valence bands alters the symmetry of electron states. Since p−d exchange is antiferromagnetic (negative), the partial p symmetry of the conduction band for $k \neq 0$ causes the s−d exchange to become more antiferromagnetic. This phenomenon is general to both II−VI and III−V paramagnetic quantum wells, providing a broad method of engineering electron exchange interactions in heterostructure devices.

5.2 Coherent spins and local magnetic moments

In addition to the effects of magnetic interactions on carrier spins discussed in the preceding text, spin polarization in the bands also influences the magnetic atoms in the semiconductor, in some cases inducing magnetic order. One of the earliest indications of the importance of carrier spin to the magnetic ordering of a magnetic semiconductor was the bound magnetic polaron, invoked to explain a decrease of resistivity with increasing magnetic field in Eu-chalcogenides (von Molnar and Methfessel, 1967; Kasuya and Yanase, 1968). A bound magnetic polaron forms when carriers are captured near magnetic donors or acceptors. Exchange interactions between the trapped spins and the paramagnetic impurities align nearby magnetic spins, causing an indirect, band-mediated ferromagnetism between the magnetic impurities. The resulting 'ball' of polarized atoms around the trapped carrier is the magnetic polaron. This dynamic magnetic ordering into polarons has been found to be a universal phenomenon in magnetic semiconductors (Kasuya and Yanase, 1968).

The dynamics of polaronic spin ordering can be observed optically with TRKR, as was first done in CdMnTe (Awschalom *et al*., 1985). In this experiment, a strong laser pump pulse injects spin-polarized acceptor bound excitons into the material. A subsequent probe pulse does not measure the bound excitons, but rather detects a low-temperature magnetization signal which increases rapidly over ∼200 ps before decaying away. Exchange interactions between the photoexcited electron and the Mn ions surrounding the exciton polarize the spins of the magnetic impurities forming the polaron. Larger magnetic fields increase the strength of the resulting Mn polarization detected. The magnetization disappears above $T = 10$ K, but at low temperatures the time-resolved technique captures this dynamical magnetization of the semiconductor in real time.

Angular momentum from photo-injected spin-polarized carriers can be coherently transferred to the magnetic system. TRKR measurements from magnetic ZnSe/(Zn, Cd, Mn)Se quantum wells reveal THz-frequency electron spin precession at the enhanced g-factor due to s−d exchange

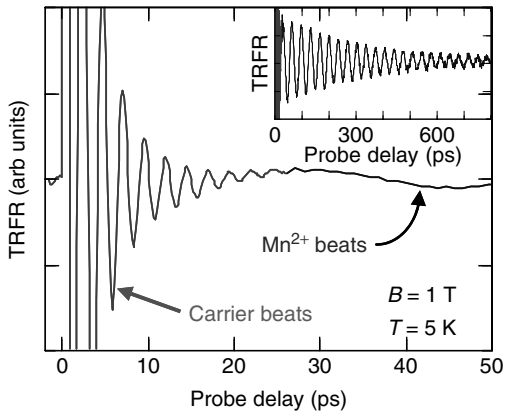

Figure 17. TRFR from a ZnSe/(Zn, Cd, Mn)Se quantum well showing the s−d exchange-enhanced THz spin precession of the electrons transitioning into the slower GHz spin precession of the Mn^{2+} moments. The inset shows the Mn spin beats persisting for ∼1 ns, much longer than the photoexcited carrier beats. (Reprinted with permission Crooker *et al*., copyright 1996, American Physical Society.)

(Figure 17). Further, the decoherence time of the electrons is only ∼20 ps due to the enhanced spin-flip relaxation from the magnetic impurities (Crooker *et al*., 1996).

The measurements from these quantum wells also reveal an oscillating component, which persists for nanoseconds longer than the spin polarization of the optically injected electrons (Figure 17). The frequency of this long-lived precession corresponds to $g = 2$, and is unchanged with temperature or sample parameters. The photoexcited carriers impart a transverse magnetization to the ensemble of Mn spins, which then precess at microwave frequencies about the applied magnetic field independently of the electron spins. This transfer of angular momentum from the optically injected spin-polarized carriers occurs through the p−d exchange coupling. The hole magnetization provides an effective exchange field which tips the Mn spin polarization away from the equilibrium direction of the external field. The magnetization vector precesses around the magnetic field at $g = 2$ as detected in the TRKR as if it were optically injected by the pump beam. This result demonstrates that spin information can be coherently transferred to the magnetic lattice where it will remain long after the original spin-polarized carriers have recombined.

5.3 Ferromagnetic semiconductors and outlook

When the concentration of magnetic atoms and carriers is high enough in some magnetic semiconductors, the delocalized carriers can mediate a ferromagnetic interaction between the magnetic impurities (Kacman, 2001). This carrier-mediated ferromagnetism was first observed in the III–V dilute magnetic semiconductors InMnAs and GaMnAs (Ohno *et al*., 1992, 1996) grown through low-temperature MBE to increase the solubility of Mn in the III–V lattice. Beyond the rich scientific interest, carrier-mediated ferromagnetism is attractive from a technological standpoint because the magnetic interaction can be electrically tuned through the electrical properties of the semiconductor (Ohno *et al*., 2000). Ferromagnetic semiconductors provide a medium to combine the capabilities of magnetic and semiconductor devices in a single material, driving research in the fields of spintronics and materials science to improve the understanding and engineering of these materials.

Because of the low-temperature MBE necessary to increase the solubility of magnetic dopants to ferromagnetic levels, the defect levels in ferromagnetic semiconductors are high. As such, optically injected spin coherence has not yet been measured in ferromagnetic III–V semiconductors. Coherent spin dynamics have recently been observed in GaMnAs quantum wells (Myers *et al*., 2005b), but the materials are only paramagnetic because of the low Mn^{2+} concentration required to observe coherent dynamics. It would be revolutionary to combine ferromagnetic semiconducting materials with the ability to manipulate coherent spin phenomena. Such a union would not only allow the scientific study of dynamic magnetization by coherent spin-polarized carriers, but also bring powerful new functionality to spintronic devices relevant for both logic and memory applications.

ACKNOWLEDGMENTS

We would like to thank AFOSR, DARPA, DMEA, NSF, and ONR for financial support. We greatly thank W. Lau and J. Stephens for assistance in preparation of this manuscript. N. P. S. acknowledges the Fannie and John Hertz Foundation.

REFERENCES

Abragam, A. (1961). *The Principles of Magnetic Resonance*, Clarendon: Oxford.

Aronov, A.G., Lander-Geller, Y.B. and Pikus, G.E. (1991). Spin polarization of electrons by an electric current. *Soviet Physics Journal of Experimental and Theoretical Physics*, **73**, 537–541.

Awschalom, D.D., Halbout, J-M., von Molnar, S., *et al*. (1985). Dynamic spin organization in dilute magnetic systems. *Physical Review Letters*, **55**, 1128–1131.

Awschalom, D.D., Loss, D. and Samarth, N. (2002). *Semiconductor Spintronics and Quantum Computation*, Springer: Berlin.

Baumberg, J.J., Awschalom, D.D., Samarth, N., *et al*. (1994). Spin beats and dynamical magnetization in quantum structures. *Physical Review Letters*, **72**, 717–720.

Beschoten, B., Johnston-Halperin, E., Young, D.K., *et al*. (2001). Spin coherence and dephasing in GaN. *Physical Review B*, **63**, 121202(R).

Bir, G., Aronov, A. and Pikus, G. (1976). Spin relaxation of electrons due to scattering by holes. *Journal of Experimental and Theoretical Physics*, **42**, 705–712.

Bracker, A.S., Stinaff, E.A., Gammon, D., *et al*. (2005). Optical pumping of the electronic and nuclear spin of single charge-tunable quantum dots. *Physical Review Letters*, **94**, 047402-1–047402-4.

Crooker, S.A., Awschalom, D.D., Baumberg, J.J., *et al*. (1997). Optical spin resonance and transverse spin relaxation in magnetic semiconductor quantum wells. *Physical Review B*, **56**, 7574–7588.

Crooker, S.A., Baumberg, J.J., Flack, F., *et al*. (1996). Terahertz spin precession and coherent transfer of angular momenta in magnetic quantum wells. *Physical Review Letters*, **77**, 2814–2817.

Crooker, S.A., Furis, M., Lou, X., *et al*. (2005). Imaging spin transport in lateral ferromagnet/semiconductor structures. *Science*, **309**, 2191–2195.

Dzhioev, R.I., Kavokin, K.V., Koronev, V.L., *et al*. (2002). Low temperature spin-relaxation in *n*-type GaAs. *Physical Review B*, **66**, 245204-1–245204-7.

D'yakonov, M.I. and Perel, V.I. (1971a). Spin orientation of electrons associated with interband absorption of light in semiconductors. *Journal of Experimental and Theoretical Physics*, **33**, 1053–1059.

D'yakonov, M.I. and Perel, V.I. (1971b). Possibility of orienting electron spins with current. *Journal of Experimental and Theoretical Physics Letters*, **13**, 467–469.

Elliot, R.J. (1954). Theory of the effect of spin-orbit coupling on magnetic resonance in some semiconductors. *Physical Review*, **96**, 266–279.

Elzerman, J.M., Hanson, R., Willems van Beveren, L.H., *et al*. (2004). Single-shot read-out of an individual electron spin in a quantum dot. *Nature*, **430**, 431–435.

Engel, H-A., Halperin, B.I. and Rashba, E.I. (2005). Theory of spin Hall conductivity in *n*-doped GaAs. *Physical Review Letters*, **95**, 166605-1–166605-4.

Faraday, M. (1846). On the magnetization of light and the illumination of magnetic lines of force. *Philosophical Transactions of the Royal Society of London*, **136**, 1–26.

Greilich, A., Yakovlev, D.R., Shabaev, A., *et al*. (2006). Mode locking of electron spin coherences in singly charged quantum dots. *Science*, **313**, 241–345.

Gupta, J.A., Knobel, R., Samarth, N. and Awschalom, D.D. (2001). Ultrafast manipulation of electron spin coherence. *Science*, **292**, 2458–2461.

Gurudev Dutt, M.V., Cheng, J., Wu, Y., *et al*. (2006). Ultrafast optical control of electron spin coherence in charged GaAs quantum dots. *Physical Review B*, **74**, 125306-1–125306-6.

Hammar, P.R., Bennet, B.R., Yang, M.J. and Johnson, M. (1999). Observation of spin injection at a ferromagnet-semiconductor interface. *Physical Review Letters*, **83**, 203–206.

Hanbicki, A.T., van 't Erve, O.M.J., Magno, R., *et al*. (2003). Analysis of the transport process providing spin injection through an Fe/AlGaAs Schottky barrier. *Applied Physics Letters*, **82**, 4092–4094.

Hankeiwicz, E.M., Molenkamp, L.W., Jungwirth, T. and Sinova, J. (2004). Manifestation of the spin Hall effect through charge-transport in the mesoscopic regime. *Physical Review B*, **70**, 241301R-1–241301R-4.

Hirsch, J.E. (1999). Spin Hall effect. *Physical Review Letters*, **83**, 1834–1837.

Hübner, J., Rühle, W.W., Klude, M., *et al*. (2003). Direct observation of optically injected spin-polarized currents in semiconductors. *Physical Review Letters*, **90**, 216601-1–216601-4.

Kacman, P. (2001). Spin interactions in diluted magnetic semiconductors and magnetic semiconductor structures. *Semiconductor Science and Technology*, **16**, R25–R39.

Kasuya, T. and Yanase, A. (1968). Anomalous transport phenomena in eu-chalcogenide alloys. *Review of Modern Physics*, **40**, 684–696.

Kato, Y.K., Myers, R.C., Gossard, A.C. and Awschalom, D.D. (2003). Gigahertz electron spin manipulation using voltage-controlled g-tensor modulation. *Science*, **299**, 1201–1204.

Kato, Y.K., Myers, R.C., Gossard, A.C. and Awschalom, D.D. (2004a). Coherent spin manipulation without magnetic fields in strained semiconductors. *Nature*, **427**, 50–53.

Kato, Y.K., Myers, R.C., Gossard, A.C. and Awschalom, D.D. (2004b). Current-induced spin polarization in strained semiconductors. *Physical Review Letters*, **93**, 176601–176604.

Kato, Y.K., Myers, R.C., Gossard, A.C. and Awschalom, D.D. (2004c). Observation of the spin Hall effect in semiconductors. *Science*, **306**, 1910–1913.

Kikkawa, J.M. and Awschalom, D.D. (1998). Resonant spin amplification in n-type GaAs. *Physical Review Letters*, **80**, 4313–4316.

Kikkawa, J.M. and Awschalom, D.D. (1999). Lateral drag of spin coherence in gallium arsenide. *Nature*, **397**, 139–141.

Kikkawa, J.M., Smorchkova, I.P., Samarth, N. and Awschalom, D.D. (1997). Room-temperature spin memory in two-dimensional electron gases. *Science*, **277**, 1284–1287.

Kroutvar, M., Ducommun, Y., Heiss, D., *et al*. (2004). Optically programmable electron spin memory using semiconductor quantum dots. *Nature*, **432**, 81–84.

Lampel, G. (1968). Nuclear dynamic polarization by optical electronic saturation and optical pumping in semiconductors. *Physical Review Letters*, **20**, 491–493.

Levitov, L.S., Nazarov, Y.V. and Eliashberg, G.M. (1985). Magnetoelectric effects in conductors with mirror isomer symmetry. *Soviet Physics Journal of Experimental and Theoretical Physics*, **61**, 133–137.

Loss, D. and DiVincenzo, D.P. (1998). Quantum computation with quantum dots. *Physical Review A*, **57**, 120–126.

Lou, X., Adelmann, C., Furis, M., *et al*. (2006). Electrical detection of spin accumulation at a ferromagnet-semiconductor interface. *Physical Review Letters*, **96**, 176603-1–176603-4.

Mackh, G., Ossau, W., Waag, A. and Landwehr, G. (1996). Effect of the reduction of dimensionality on the exchange parameters in semimagnetic semiconductors. *Physical Review B*, **54**, 5227–5230(R).

Malajovich, I., Kikkawa, J.M., Awschalom, D.D., *et al*. (2000). Resonant amplification of spin transferred across a GaAs/ZnSe interface. *Journal of Applied Physics*, **87**, 5073–5075.

Meier, F. and Awschalom, D.D. (2005). Faraday rotation spectroscopy of quantum-dot quantum wells. *Physical Review B*, **71**, 205315-1–205316-9.

Meier, F. and Zakharechenya, B.P. (1984). *Optical Orientation*, Elsevier: Amsterdam.

Merkulov, I.A., Yakovlev, D.R., Keller, A., *et al*. (1999). Kinetic exchange between the conduction band electrons and magnetic ions in quantum-confined structures. *Physical Review Letters*, **83**, 1431–1434.

von Molnar, S. and Methfessel, S. (1967). Giant negative magnetoresistance in ferromagnetic $Eu_{1-x}Gd_xSe$. *Journal of Applied Physics*, **38**, 959–964.

Murakami, S., Nagaosa, N. and Zhang, S.C. (2003). Dissipationless quantum spin current at room temperature. *Science*, **301**, 1348–1351.

Myers, R.C., Ku, K.C., Li, X., *et al*. (2005a). Optoelectronic control of spin dynamics at near-terahertz frequencies in magnetically doped quantum wells. *Physical Review B*, **72**, 041302-4(R).

Myers, R.C., Poggio, M., Stern, N.P., *et al*. (2005b). Antiferromagnetic s-d exchange coupling in GaMnAs. *Physical Review Letters*, **95**, 017204-4.

Ohno, H., Chiba, D., Matsukura, F., *et al*. (2000). Electric-field control of ferromagnetism. *Nature*, **408**, 944–946.

Ohno, H., Munekata, H., Penney, T., *et al*. (1992). Magnetotransport properties of *p*-type (In,Mn)As diluted magnetic III-V semiconductors. *Physical Review Letters*, **68**, 2664–2667.

Ohno, H., Shen, A., Matsukura, F., *et al*. (1996). (Ga,Mn)As: a new diluted magnetic semiconductor based on GaAs. *Applied Physics Letters*, **69**, 363–365.

Östreich, T., Schönhammer, K. and Sham, L.J. (1995). Theory of spin beatings in the Faraday rotation of semiconductors. *Physical Review Letters*, **75**, 2554–2557.

Petta, J.R., Johnson, A.C., Taylor, J.M., *et al*. (2005). Coherent manipulation of coupled electron spins in semiconductor quantum dots. *Science*, **309**, 2180–2184.

Poggio, M., Myers, R.C., Stern, N.P., *et al*. (2005). Structural, electrical, and magneto-optical characterization of paramagnetic GaMnAs quantum wells. *Physical Review B*, **72**, 235313–235315.

Shchelushkin, R.V. and Brataas, A. (2005). Spin Hall effects in diffusive normal metals. *Physical Review B*, **71**, 045123-1–045123-10.

Sih, V., Knotz, H., Stephens, J., *et al*. (2006a). Mechanical control of spin-orbit splitting in GaAs and $In_{0.04}Ga_{0.96}As$ epilayers. *Physical Review B*, **73**, 241316(R).

Sih, V., Lau, W., Myers, R.C., *et al*. (2006b). Generating spin currents in semiconductors with the spin Hall effect. *Physical Review Letters*, **97**, 096605-1–096605-4.

Sih, V., Myers, R.C., Kato, Y.K., *et al*. (2005). Spatial imaging of the spin Hall effect and current-induced spin polarization in a two-dimensional electron gas. *Nature Physics*, **1**, 31–35.

Sinova, J., Culcer, D., Niu, Q., *et al*. (2004). Universal intrinsic spin Hall effect. *Physical Review Letters*, **92**, 126603-1–126603-4.

Stephens, J., Berezovsky, J., McGuire, J.P., *et al*. (2004). Spin accumulation in forward-biased MnAs/GaAs Schottky diodes. *Physical Review Letters*, **93**, 097602-1–097602-4.

Stephens, J., Kawakami, R.K., Berezovsky, J., *et al*. (2003). Spatial imaging of magnetically patterned nuclear spins in GaAs. *Physical Review, B*, **68**, 041307-1–041307-4.

Stern, N.P., Ghosh, S., Xiang, G., *et al*. (2006). Current-induced polarization and the spin Hall effect at room temperature. *Physical Review Letters*, **97**, 126603-1–126603-4.

Strand, J., Schultz, B.D., Isakovic, A.F., *et al*. (2003). Dynamic nuclear polarization by electrical spin injection in ferromagnetic-semiconductor heterostructures. *Physical Review Letters*, **91**, 036602-1–036602-4.

Tse, W-K. and Das Sarma, S. (2006). Spin Hall effect in doped semiconductor structures. *Physical Review Letters*, **96**, 056601-1–056601-4.

Tse, W-K., Fabian, J., Zutic, I. and Das Sarma, S. (2005). Spin accumulation in the extrinsic spin Hall effect. *Physical Review B*, **72**, 241303-1–241303-4.

Valenzuela, S.O. and Tikham, M. (2006). Direct electronic measurement of the spin Hall effect. *Nature*, **442**, 176–179.

Vorob'ev, L.E., Ivchenko, E.L., Pikus, G.E., *et al*. (1979). Optical activity in tellurium induced by a current. *Journal of Experimental and Theoretical Physics Letters*, **29**, 441.

Winkler, R. (2003). *Spin-Orbit Coupling Effects in Two-Dimensional Electron and Hole Systems*, Springer: New York.

Wolf, S.A., Awschalom, D.D., Buhrman, R.A., *et al*. (2001). Spintronics: a spin-based electronics vision for the future. *Science*, **294**, 1488–1495.

Wunderlich, J., Kaestner, B., Sinova, J. and Jungwirth, T. (2005). Experimental observation of the Spin-Hall effect in a two-dimensional spin-orbit coupled semiconductor system. *Physical Review Letters*, **94**, 047204-1–047204-4.

Yu, P. and Cardona, M. (1996). *Fundamentals of Semiconductors*, Springer: Berlin.

Zhang, S. (2000). Spin Hall Effect in the presence of spin diffusion. *Physical Review Letters*, **85**, 393–396.

FURTHER READING

Aronov, A.G. and Lyanda-Geller, Y.B. (1989). Nuclear electric resonance and orientation of carrier spins by an electric field. *Journal of Experimental and Theoretical Physics Letters*, **50**, 431–434.

Bychkov, Y.A. and Rashba, E.I. (1984). Oscillatory effects and the magnetic susceptibility of carriers in inversion layers. *Journal Physics C. Solid State Physics*, **17**, 6039–6045.

Dresselhaus, G. (1955). Spin-orbit coupling effects in zinc blende structures. *Physical Review*, **100**, 580–586.

Edelstein, V.M. (1990). Spin polarization of conduction electrons induced by electric current in two-dimensional asymmetric electron systems. *Solid State Communications*, **73**, 233–235.

Jain, S.C., Willander, M. and Maes, H. (1996). Stresses and strains in epilayers, stripes and quantum structures of III – V compound semiconductors. *Semiconductor Science and Technology*, **11**, 641–671.

Rashba, E.I. (2004). Spin currents, spin populations, and dielectric function of noncentrosymmetric semiconductors. *Physical Review B*, **70**, 161201.

Shi, J., Zhang, P., Xiao, D. and Niu, Q. (2006). Proper definition of spin current in spin-orbit coupled systems. *Physical Review Letters*, **96**, 076604-1–076604-4.

Silov, A.Y., Blajnov, P.A., Wolter, J.H., *et al*. (2004). Current-induced spin polarization at a single heterojunction. *Applied Physics Letters*, **85**, 5929–5931.

Quantum Computing with Spins in Solids

William A. Coish and Daniel Loss
University of Basel, Basel, Switzerland

1 INTRODUCTION

Recent advances in semiconductor spintronics and, more specifically, spin-based quantum computing in solid-state systems, have encouraged significant research efforts in the last years (Prinz, 1998; Wolf *et al*., 2001; Awschalom, Loss and Samarth, 2002). Much of this research is motivated by pressure on the electronics industry to maintain Moore's-law growth in systems with components that are very quickly approaching the nanoscale, where quantum mechanics becomes important (ITRS, 2005). Additionally, nanoscale devices provide a unique opportunity to study the fundamental physics of quantum phenomena in a controllable environment.

Independent of the particular motivation, if quantum information processing is to progress beyond basic proof-of-principle experiments, it must be based on a viable, scalable qubit (a quantum-mechanical two-level system, which can be placed in an arbitrary superposition of its basis states: $|\psi\rangle = a\,|0\rangle + b\,|1\rangle$). The two states of single electron spins ($|\uparrow\rangle = |0\rangle$ and $|\downarrow\rangle = |1\rangle$), confined to semiconductor quantum dots (the Loss–DiVincenzo proposal), are one such qubit (Loss and DiVincenzo, 1998). These qubits are viable, in the sense that they make use of fabrication techniques and electrical control concepts that have been developed over the last five decades in research laboratories and industry. The secret to scalability in the Loss–DiVincenzo proposal lies in local gating; this proposal would implement gating operations through the exchange interaction, which can be tuned locally with exponential precision, allowing pairs of neighboring qubits to be coupled and decoupled independently. This is to be contrasted with proposals that make use of long-ranged interactions (e.g., dipolar coupling) for which scalability may be called into question. The local, tunable nature of interqubit interactions in the Loss–DiVincenzo proposal is what makes it possible to consider first isolated one-qubit (single quantum dot), then isolated two-qubit (double quantum dot) systems. Once single and double quantum dots are understood, along with environmental coupling mechanisms, a quantum computation can proceed through a series of one- and two-qubit operations, without great concern regarding interactions between three, four, and more qubits.

There are many other proposals for qubits and associated quantum control processes. Some examples include various proposals that use superconducting devices (for reviews, see Makhlin, Schön and Shnirman, 2001; Burkard, 2004),

Handbook of Magnetism and Advanced Magnetic Materials. Edited by Helmut Kronmüller and Stuart Parkin. Volume 5: *Spintronics and Magnetoelectronics*. ISBN: 978-0-470-02217-7.

proposals for 'adiabatic quantum computing', in which quantum computations are performed through adiabatic manipulation of coupling constants in physically realizable Hamiltonians (Farhi, Goldstone, Gutmann and Sipser, 2000; Farhi *et al*., 2001; Wu, Zanardi and Lidar, 2005) (this might be used to perform fast quantum simulations of, for example, superconducting pairing models (Wu, Byrd and Lidar, 2002)), electron-spin qubits encoded in two-spin states (Levy, 2002) or many-spin chains (Meier, Levy and Loss, 2003a,b) (recent work showing that such spin chains can be built-up atom-by-atom on a surface (Hirjibehedin, Lutz and Heinrich, 2006) is a possible first step to implementing such a proposal), cavity-QED schemes (Sleator and Weinfurter, 1995; Domokos, Raimond, Brune and Haroche, 1995), trapped-ion proposals (Cirac and Zoller, 1995), and so on. Each of these proposals has advantages and disadvantages. Here we do not compare the relative merits of all proposals, but instead focus on proposals involving electron spins confined to quantum dots.

Before a quantum computation can begin, the qubits in a working quantum computer must be initialized to some state, for example, $|0\rangle$. These qubits must be sufficiently isolated from the surrounding environment to reduce decoherence, there must be some way to perform fast single- and two-qubit operations in a timescale much less than the qubit decoherence time, and it must be possible to read out the final state of the qubits after any quantum computation (DiVincenzo, 2000). In the following sections, we address these issues and others which are important for the Loss–DiVincenzo proposal. In the process, we survey some recent work on quantum computing with electron spins in quantum dots.

Owing to the rapid development of this field, there have been many recent reviews on quantum-dot quantum computing. Among these numerous reviews, there has been work that focuses on single-electron charge qubits in double dots (Fujisawa, Hayashi and Sasaki, 2006), the implementation of single-electron spin resonance (ESR), and the molecular wave functions of coupled double dots (van der Wiel *et al*., 2006), various proposals for spin-based quantum computing (Cerletti, Coish, Gywat and Loss, 2005), silicon-based proposals for quantum computing (Koiller *et al*., 2005), general quantum computing in the solid state, including both quantum dots and superconducting systems (Burkard, 2004), experiments and experimental proposals for quantum-dot-confined electrons (Engel, Kouwenhoven, Loss and Marcus, 2004), the many coupling schemes and decoherence mechanisms for quantum-dot spin qubits (Hu, 2004), and optical properties of quantum dots (Hohenester, 2004). In this review, we analyze the Loss–DiVincenzo proposal from the viewpoint that this proposal can be decomposed into first single and then double quantum dots, with a special emphasis on double-dot physics.

This review is organized as follows: in Section 2, we give a brief summary of the Loss–DiVincenzo proposal for quantum computing. In Section 3, we discuss the characterization and manipulation of spin and charge states of electrons in single quantum dots. Section 4 contains a description of double quantum dots that emphasizes the single-electron regime, which is relevant for quantum-dot quantum computing. In Section 5 we survey important decoherence mechanisms for electron spins in single and double quantum dots. In Section 6, we briefly review some proposals for the generation and detection of nonlocal entanglement of electron spins in nanostructures, and in Section 7 we conclude with a brief summary of important topics for future study.

2 SPINS IN QUANTUM DOTS: AN OVERVIEW OF THE LOSS–DIVINCENZO PROPOSAL

In the original Loss–DiVincenzo proposal, the qubits are stored in the two spin states of single confined electrons. The considerations discussed in (Loss and DiVincenzo, 1998) are generally applicable to electrons confined to any structure (e.g., atoms, molecules, defects, etc.), although the original proposal focused on applications in gated semiconductor

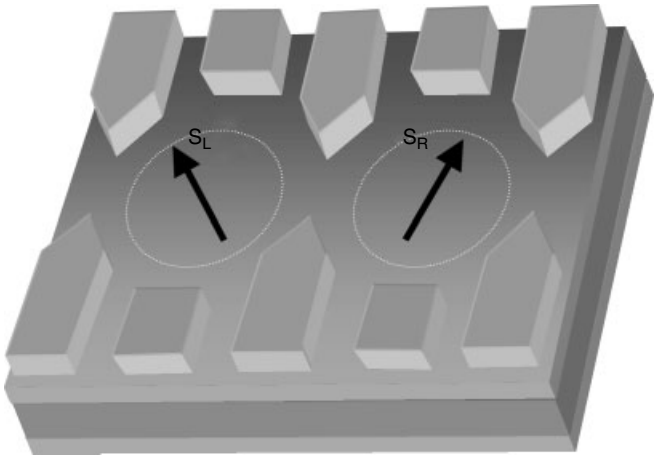

Figure 1. A double quantum dot. Top gates are set to an electrostatic voltage configuration that confines electrons in the two-dimensional electron gas (2DEG) below to the circular regions shown. Applying a negative voltage to the back gate, the dots can be depleted until they each contain only one single electron, each with an associated spin-1/2 operator $\mathbf{S}_{\mathrm{L(R)}}$ for the electron in the left (right) dot. The $|\uparrow\rangle$ and $|\downarrow\rangle$ spin-1/2 states of each electron provide a qubit (two-level quantum system).

quantum dots, as shown in Figure 1. Voltages applied to the top gates of such structures provide a confining potential for electrons in a two-dimensional electron gas (2DEG), below the surface. A negative voltage applied to a back-gate depletes the 2DEG locally, allowing the number of electrons in each dot to be reduced down to one (the single-electron regime). Advances in materials fabrication and gating techniques have now allowed for the realization of single electrons in single vertical (Tarucha *et al*., 1996) and gated lateral (Ciorga *et al*., 2000) dots, as well as double dots (Elzerman *et al*., 2003; Hayashi *et al*., 2003; Petta *et al*., 2004).

Initialization of all qubits in the quantum computer to the Zeeman ground state $|\uparrow\rangle = |0\rangle$ could be achieved by allowing all spins to reach thermal equilibrium at temperature T in the presence of a strong magnetic field B, such that $|g\mu_B B| > k_B T$, with g-factor $g < 0$, Bohr magneton μ_B, and Boltzmann's constant k_B (Loss and DiVincenzo, 1998). For example, assuming $g = -0.44$ (the bulk value for GaAs) and a temperature of $T = 100\,\text{mK}$, initialization with a probability $p > 99\%$ is achieved in a field of $B > 1\,\text{T}$. (For further initialization schemes, see Section 3.2.)

Once the qubits have been initialized to some state, they should remain in that state until a computation can be executed. In the absence of environmental coupling, the spins-1/2 of single electrons are intrinsic two-level systems, which cannot 'leak' into higher excited states. Additionally, since electron spins only couple to charge degrees of freedom indirectly through the spin-orbit (or hyperfine) interactions, they are relatively immune to fluctuations in the surrounding electronic environment.

Single-qubit operations in the Loss–DiVincenzo quantum computer could be carried out by varying the Zeeman splitting on each dot individually (Loss and DiVincenzo, 1998). It may be possible to do this through g-factor modulation (Salis *et al*., 2001), the inclusion of magnetic layers (Myers *et al*., 2005) (see also Figure 2), modification of the local Overhauser field due to hyperfine couplings (Burkard, Loss and DiVincenzo, 1999), or with nearby ferromagnetic dots (Loss and DiVincenzo, 1998). There are a number of alternate methods that could be used to perform single-qubit rotations (see Section 3.2).

Two-qubit operations would be performed within the Loss–DiVincenzo proposal by pulsing the exchange coupling between two neighboring qubit spins 'on' to a nonzero value ($J(t) = J_0 \neq 0$, $t \in \{-\tau_s/2 \ldots \tau_s/2\}$) for a switching time τ_s, then switching it 'off' ($J(t) = 0$, $t \notin \{-\tau_s/2 \ldots \tau_s/2\}$). This switching can be achieved by briefly lowering a center-gate barrier between neighboring electrons, resulting in an appreciable overlap of the electron wave functions (Loss and DiVincenzo, 1998), or alternatively, by pulsing the relative back-gate voltage of neighboring dots (Petta *et al*., 2005a) (see Section 4.3). Under such an operation (and in the absence of Zeeman or weaker spin-orbit or dipolar interactions), the effective two-spin Hamiltonian takes the form of an isotropic Heisenberg exchange term, given by (Loss and DiVincenzo, 1998; Burkard, Loss and DiVincenzo, 1999)

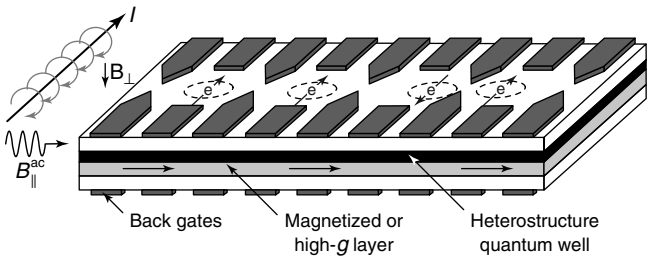

Figure 2. A series of exchange-coupled electron spins. Single-qubit operations could be performed in such a structure using electron-spin resonance (ESR), which would require an ac transverse magnetic field $B_{\parallel}^{ac}$, and a site-selective Zeeman splitting $g(x)\mu_B B_{\perp}$, which might be achieved through g-factor modulation or magnetic layers. Two-qubit operations would be performed by bringing two electrons into contact, introducing a nonzero wave function overlap and corresponding exchange coupling for some time (two electrons on the right). In the idle state, the electrons can be separated, eliminating the overlap and corresponding exchange coupling with exponential accuracy (two electrons on the left).

$$H_{ex}(t) = J(t)\mathbf{S}_L \cdot \mathbf{S}_R \tag{1}$$

where $\mathbf{S}_{L(R)}$ is the spin-1/2 operator for the electron in the left (right) dot, as shown in Figure 1. The Hamiltonian $H_{ex}(t)$ generates the unitary evolution $U(\phi) = \exp[-i\phi \mathbf{S}_L \cdot \mathbf{S}_R]$, where $\phi = \int J(t)dt/\hbar$. If the exchange is switched such that $\phi = \int J(t)dt/\hbar = J_0\tau_s/\hbar = \pi$, $U(\phi)$ exchanges the states of the two neighboring spins, that is, $U(\pi)\left|\mathbf{n}, \mathbf{n}'\right\rangle = \left|\mathbf{n}', \mathbf{n}\right\rangle$, where $\mathbf{n}$ and $\mathbf{n}'$ are two arbitrarily oriented unit vectors and $\left|\mathbf{n}, \mathbf{n}'\right\rangle$ indicates a simultaneous eigenstate of the two operators $\mathbf{S}_L \cdot \mathbf{n}$ and $\mathbf{S}_R \cdot \mathbf{n}'$. $U(\pi)$ implements the so-called SWAP operation. If the exchange is pulsed on for the shorter time $\tau_s/2$, the resulting operation $U(\pi/2) = (U(\pi))^{1/2}$ is known as the *square-root-of-SWAP* ($\sqrt{SWAP}$). The $\sqrt{\text{SWAP}}$ operation in combination with arbitrary single-qubit operations is sufficient for universal quantum computation (Barenco *et al*., 1995; Loss and DiVincenzo, 1998). The $\sqrt{\text{SWAP}}$ operation has now been successfully implemented in experiments involving two electrons confined to two neighboring quantum dots (as in Figure 1) (Petta *et al*., 2005a; Laird *et al*., 2006). Errors during the $\sqrt{\text{SWAP}}$ operation have been investigated due to nonadiabatic transitions to higher orbital states (Schliemann, Loss and MacDonald, 2001; Requist, Schliemann, Abanov and Loss, 2005), spin-orbit interaction (Bonesteel, Stepanenko and DiVincenzo, 2001; Burkard and Loss, 2002; Stepanenko *et al*., 2003), and hyperfine coupling to surrounding nuclear spins (Petta *et al*., 2005a; Coish and Loss, 2005;

Klauser, Coish and Loss, 2006; Taylor *et al*., 2006). The isotropic form of the exchange interaction given in equation (1) is not always valid. In realistic systems, a finite spin-orbit interaction leads to anisotropic terms which may cause additional errors, but could also be used to perform universal quantum computing with two-spin encoded qubits, in the absence of single-spin rotations (Bonesteel, Stepanenko and DiVincenzo, 2001; Lidar and Wu, 2002; Stepanenko and Bonesteel, 2004; Chutia, Friesen and Joynt, 2006) (see also Section 4.4 below for more on two-spin encoded qubits).

In the Loss–DiVincenzo proposal, readout could be performed using spin-to-charge conversion. This could be accomplished with a 'spin filter' (spin-selective tunneling) to leads or a neighboring dot, coupled with single-electron charge detection (see also Section 3.2).

3 SINGLE QUANTUM DOTS

There are many different types of quantum dot that can be manufactured, each with distinct characteristics. Gated lateral quantum dots (as shown in Figures 1 and 2) offer the benefit that their shape and size can be controlled to suit a particular study, and the tunnel coupling between pairs of these dots can be tuned in a straightforward manner: by raising or lowering the barrier between the dots. Gated vertical dots (Tarucha *et al*., 1996) are created by etching surrounding material to form a pillar structure, with vertical confinement provided by a double-barrier heterostructure. Vertical dots allow for the controlled fabrication of quantum dots with large level spacing, although tunability of the coupling in these structures is restricted due to the fabrication process. To resolve this issue, hybrid laterally coupled vertical double-quantum dots have been manufactured, in which the interdot tunnel coupling is controllable (Hatano, Stopa and Tarucha, 2005). Self-assembled quantum dots are yet another type of dot that can be used for quantum information processing. Self-assembled dots form spontaneously during epitaxial growth due to a lattice mismatch between the dot and substrate materials. These dots can be made with very large single-particle level spacing, but typically form at random locations, which makes controlled coupling through a tunnel junction difficult. Such dots can, however, potentially be coupled with optical cavity modes (Imamoğlu *et al*., 1999), and new techniques have now allowed the fabrication of cavities with modes that couple maximally directly at the positions of isolated dots (Badolato *et al*., 2005).

In the rest of this section, we focus on lateral quantum dots, as shown in Figures 1 and 2. After a brief review of charge and spin control in single quantum dots, we will address issues specific to double quantum dots in Section 4.

3.1 Charge control: Coulomb blockade

To ensure a single two-level system is available to be used as a qubit, it is practical to consider single isolated electron spins (with intrinsic spin 1/2) confined to single orbital levels. A natural first step to implementing the Loss–DiVincenzo proposal was therefore to demonstrate control over charging electron-by-electron in a single gated quantum dot. This is typically done by operating a quantum dot in the Coulomb-blockade regime, where the energy for the addition of an electron to the dot is larger than the energy that can be supplied by electrons in leads coupled to the dot. In this case, the charge on the quantum dot is conserved, and no electrons can tunnel onto or off of the dot. For a general review of Coulomb blockade phenomena and the characterization of many-electron states in single quantum dots, see Kouwenhoven, Austing and Tarucha (2001).

3.2 Spin control: initialization, operations, and readout

As mentioned in Section 2, initialization of all electron spins to the 'up' state $|\uparrow\rangle$ could be achieved by allowing all spins to equilibrate in a strong magnetic field. Depending on the particular architecture, this may take a long time or it may be inconvenient to have large magnetic fields in the region of the apparatus. Initialization could also be achieved through spin injection from a ferromagnet, as has been performed in bulk semiconductors (Fiederling *et al*., 1999; Ohno *et al*., 1999), with a spin-polarized current from a spin-filter device (Prinz and Hathaway, 1995; Prinz, 1998; Loss and DiVincenzo, 1998; DiVincenzo, 1999; Recher, Sukhorukov and Loss, 2000), or by optical pumping (Cortez *et al*., 2002; Shabaev, Efros, Gammon and Merkulov, 2003; Gywat *et al*., 2004; Bracker *et al*., 2005), which has now allowed the preparation of spin states with very high fidelity, in one case as high as 99.8% (Atature *et al*., 2006) [1].

Single-qubit operations could be performed in the Loss–DiVincenzo proposal whenever the Zeeman energy of the quantum-dot spins can be tuned locally, as mentioned in Section 2. Alternative single-qubit-rotation schemes may require global magnetic field gradients with pulsed magnetic and electric fields (Wu, Lidar and Friesen, 2004) or static magnetic, but ac electric fields (Tokura, van der Wiel, Obata and Tarucha, 2006), ESR (see Figure 2) or, in the presence of spin-orbit interaction, electric-dipole spin resonance (EDSR) techniques. EDSR has been analyzed in great detail for two-dimensional systems in theory (Rashba and Efros, 2003; Duckheim and Loss, 2006) and experiment (Kato, Myers,

Gossard and Awschalom, 2004), and can also be applied to lower-dimensional systems (quantum wires and quantum dots) (Levitov and Rashba, 2003; Golovach, Borhani and Loss, 2006), with the advantage that single-qubit operations could then be performed using fast all-electrical control. New experiments have now shown that it may be possible in practice to perform single-spin operations on spins in single quantum dots using ESR, as depicted in Figure 2 (Koppens *et al*., 2006).

In an alternative to the above proposals, it has recently been shown that arbitrary single-spin rotations could be performed with high fidelity in a quantum dot with a pulsed electric field, but a time-independent magnetic field gradient (Coish and Loss, 2006). This scheme would avoid 'heating' effects due to ac power dissipation (van der Wiel *et al*., 2006) since this scheme involves no ac electromagnetic fields, and could make use of large permanent magnetic field gradients ($\simeq 1\,\mathrm{T}/\mu\mathrm{m}$) arising from, for example, nanomagnets on the surface of semiconductors (Wróbel *et al*., 2004).

As mentioned in Section 2, quantum-dot spin readout can be performed using a spin filter. Experimentally, spin filters have been reported in the open (Potok, Folk, Marcus and Umansky, 2002) and Coulomb-blockade regimes (Folk, Potok, Marcus and Umansky, 2003), and have even been used to determine the longitudinal spin decay (T_1) time (Hanson *et al*., 2003; 2004) using an n-shot readout scheme, which has been analyzed in detail (Engel *et al*., 2004). A single-shot readout has also been demonstrated (Elzerman *et al*., 2004) and improved upon (Hanson *et al*., 2005). Non-invasive readout schemes using spin-to-charge conversion and quantum-point-contact (QPC) measurements have been used on two-spin encoded qubits (Johnson *et al*., 2005a; Petta *et al*., 2005a; Petta *et al*., 2005b; Johnson *et al*., 2005b) (see also Section 4.4).

To measure the transverse spin coherence time T_2, there have been proposals to perform ESR and detect the resulting resonance in stationary current (Engel and Loss, 2001), changes in the resistivity of a neighboring field-effect transistor (FET) (Martin, Mozyrsky and Jiang, 2003), optically (Gywat *et al*., 2004), or from current noise (Schaefers and Strunz, 2005). ESR in single quantum dots has not been observed until very recently, in part because it is challenging to generate high-frequency magnetic fields with sufficient power for single-spin manipulation without 'heating' electrons on the quantum dot or in the surrounding leads through the associated electric field (van der Wiel *et al*., 2006). Recent experiments overcome this problem (Koppens *et al*., 2006) by employing a double-quantum dot in the spin-blockade regime, where a smaller Zeeman splitting can be resolved, allowing the use of low-power ac magnetic fields (Burkard, 2006) (see also the discussion on spin blockade near the end of Section 5.2 below).

4 DOUBLE QUANTUM DOTS

Single qubits are the fundamental unit of quantum information in quantum computing. However, universal quantum computation still requires both single-qubit and two-qubit operations (Barenco, Deutsch, Ekert and Jozsa, 1995). In the Loss–DiVincenzo proposal, two-qubit gates are performed with exchange-coupled electron spins confined to two neighboring quantum dots (double dots). Double dots are also important for two-electron encoded qubits (Levy, 2002), in which qubits are encoded into a two-dimensional pseudospin-1/2 subspace of a four-dimensional two-electron spin system.

In this section, we discuss characterization and manipulation techniques that are commonly used to extract microscopic parameters of double quantum dots. In Section 4.1, we review the charge stability diagram and illustrate its connection to a commonly used microscopic model Hamiltonian. In Section 4.2, we review work on the coherent coupling of double quantum dots, which is required to generate a large exchange interaction for two-qubit gating. In Section 4.3, we discuss the use of double quantum dots as two-qubit gates, and in Section 4.4 we review some work on using double quantum dots to control single 'encoded' qubits (Levy, 2002), a topic which has now come into vogue (Petta *et al*., 2005a; Taylor *et al*., 2005; Burkard and Imamoglu, 2006; Hanson and Burkard, 2007).

4.1 The double-dot charge stability diagram

Just as transport through a single quantum dot and Coulomb blockade phenomena give information about the orbital level spacing, charging energy, and spin states of single quantum dots, similar studies can be carried out on double quantum dots. Whereas for single dots, transport phenomena are typically understood in terms of one-dimensional plots of conductance versus gate voltage, the primary tool used to understand double quantum dots is the double-dot charge stability diagram. The stability diagram is a two-dimensional plot of current or differential conductance through the double dot or through a neighboring QPC, given as a function of two independent back-gate voltages (one applied locally to each dot). The plot differentiates regions where the double-dot ground state has a charge configuration (N_1, N_2), for various N_1, N_2, where N_1 is the number of charges on the left dot and N_2 is the number of charges on the right. Transport through double quantum dots and the relevant charge stability diagram have been discussed thoroughly in (van der Wiel *et al*., 2003). In the rest of this section, we review some features of the double-dot stability diagram with an emphasis on the connection to a model Hamiltonian that is commonly used in the literature (Klimeck, Chen and Datta, 1994; Pals

and MacKinnon, 1996; Golden and Halperin, 1996; Ziegler, Bruder and Schoeller, 2000).

An isolated double quantum dot is described by the Hamiltonian

$$H_{\mathrm{dd}} = H_{\mathrm{C}} + H_{\mathrm{T}} + H_{\mathrm{S}} \tag{2}$$

where H_{C} gives the single-particle and interparticle charging energies due to Coulomb interaction as well as the orbital energy, H_{T} is the interdot tunneling term due to a finite overlap of dot-localized single-particle wave functions, which ultimately gives rise to exchange, and H_{S} contains explicitly spin-dependent terms, which may include spin-orbit interaction, dipole–dipole interaction, and the contact hyperfine interaction between the confined electron spins and nuclear spins in the surrounding lattice.

There are several approaches that can be taken to writing the various components of the double-dot Hamiltonian H_{dd}, corresponding to several degrees of microscopic detail. In the simplest form, the Hubbard model, details of the electron wave functions are neglected and the Coulomb interaction is modeled by on-site and nearest-neighbor terms. Since this description relies only on very few parameters, it is the most commonly used in the literature on transport phenomena through quantum dots. The shape of the confining potential, quantum-dot localized wave functions, and form of the Coulomb interaction may become important in certain circumstances, in which case it is more appropriate to apply either the Heitler–London method (which neglects doubly occupied dot levels), or the Hund–Mulliken method, which includes the effects of double-occupancy. These methods predict, for instance, a variation of the interdot exchange interaction through zero with increasing out-of-plane magnetic field (Burkard, Loss and DiVincenzo, 1999). Experimentally, it has been confirmed that the exchange coupling can be tuned with an out-of-plane magnetic field in single vertical (Fujisawa *et al*., 2002) and single lateral quantum dots (Zumbühl, Marcus, Hanson and Gossard, 2004), which behave effectively as double-dot structures. Here we ignore these effects and focus on the simplest Hubbard model that reproduces much of the double-dot physics that can be seen in transport phenomena.

We model the Coulomb interaction with simple on-site ($U_{1(2)}$ for the left (right) dot) and nearest-neighbor (U') repulsion. The single-particle charging energy is given in terms of a local dot potential $V_{1(2)}$. The charging Hamiltonian is then

$$H_{\mathrm{C}} = \frac{1}{2}\sum_{l} U_l N_l\,(N_l - 1) + U' N_1 N_2 - |e| \sum_{l} V_l N_l + \sum_{kl} \epsilon_{lk} n_{lk} \tag{3}$$

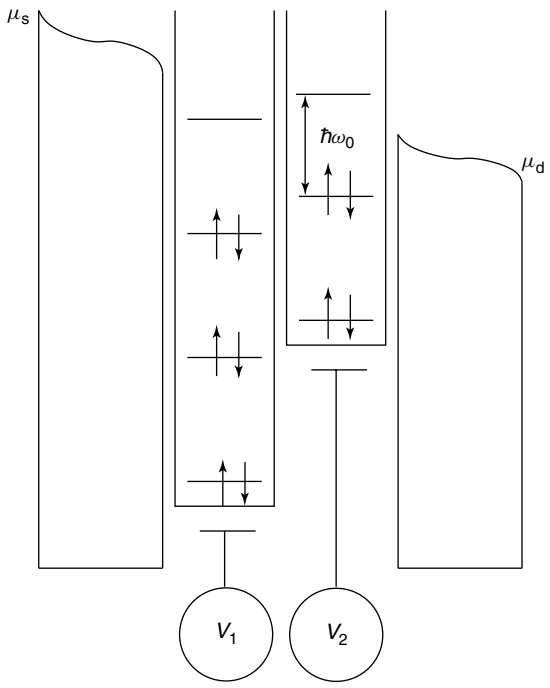

Figure 3. Ground state configuration for a double quantum dot with large orbital and charging energies, and negligible dot-lead and interdot coupling. $\mu_{\mathrm{s(d)}}$ is the source (drain) chemical potential, $V_{1(2)}$ is the left (right) local dot potential, which is related to applied gate potentials by a linear transformation (see equation (5), below), and both dots are assumed to have the same uniform level spacing $\hbar\omega_0$.

where $N_l = \sum_k n_{lk}$ counts the total number of electrons in dot l, with $n_{lk} = \sum_\sigma d^\dagger_{lk\sigma} d_{lk\sigma}$, and here $d_{lk\sigma}$ annihilates an electron on dot l, in orbital k, with spin σ. ϵ_{lk} is the energy of single-particle orbital level k in dot l, which gives rise to the typical orbital level spacing $\epsilon_{lk+1} - \epsilon_{lk} \approx \hbar\omega_0$ (see Figure 3).

Within the capacitive charging model described by the equivalent circuit in the inset of Figure 4(a), the microscopic charging energies are related to capacitances by (Ziegler, Bruder and Schoeller, 2000; van der Wiel *et al*., 2003)

$$U_l = \frac{C_1 C_2}{C_1 C_2 - C_{\mathrm{m}}^2}\frac{e^2}{C_l},\quad U' = \frac{2e^2 C_{\mathrm{m}}}{C_1 C_2 - C_{\mathrm{m}}^2} \tag{4}$$

where $C_1 = C_{\mathrm{s}} + C_{\mathrm{m}} + C_{\mathrm{g1}}$, $C_2 = C_{\mathrm{d}} + C_{\mathrm{m}} + C_{\mathrm{g2}}$, and all capacitances are defined in the inset of Figure 4(a). In experiments, the local quantum-dot potentials $V_{1,2}$ are controlled indirectly in terms of gate voltages $V_{\mathrm{g1,2}}$, which are capacitively coupled to the dots through gate capacitances $C_{\mathrm{g1,2}}$. For fixed quantum-dot charges $(Q_1, Q_2) = -|e|\,(N_1, N_2) =$ const., differences in the dot voltages ΔV_1 and ΔV_2 are related to differences in the gate voltages ΔV_{g1} and ΔV_{g2} through (Ziegler, Bruder and Schoeller, 2000; van der Wiel

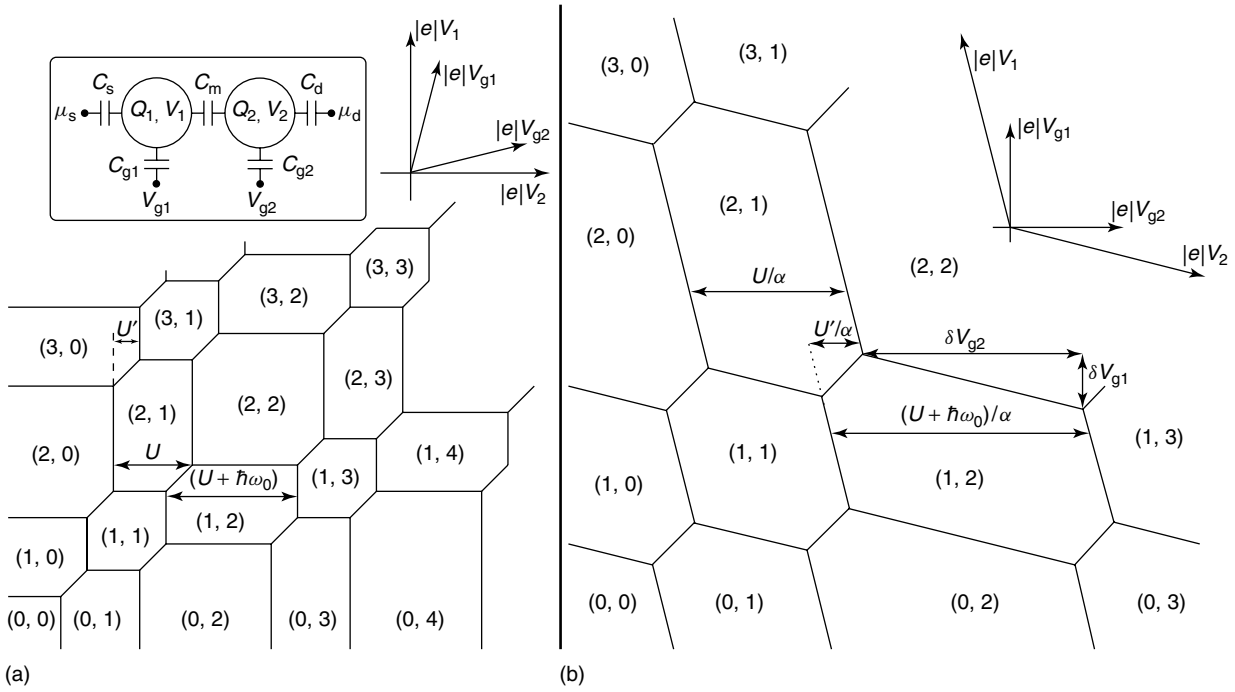

Figure 4. Stability diagram plotted in terms of (a) local dot potentials $V_{1,2}$ and (b) applied gate potentials $V_{g1,2}$, with on-site charging energies $U_l = U$, $l = 1, 2$, nearest-neighbor charging energy U', and dot orbital level spacing $\hbar\omega_0$ satisfying $U{:}\hbar\omega_0{:}U' = 3{:}2{:}1$. In addition, for (b) we have assumed the voltage scaling factors are the same for both dots, and are given by $\alpha_1 = \alpha_2 = \alpha = 1/2$. (a) inset: capacitive charging model for a double quantum dot, indicating the source (drain) chemical potential $\mu_{s(d)}$, the charge on the left (right) dot $Q_{1(2)}$, the capacitances to source (drain) $C_{s(d)}$, the mutual capacitance C_m, and gate capacitances $C_{g1,2}$. (b) Horizontal lines in the $|e|\,V_{1(2)}$ plane become skewed with slope $\delta V_{g1}/\delta V_{g2} = -C_m C_{g2}/C_2 C_{g1}$ when plotted versus $|e|\,V_{g1(2)}$.

et al., 2003)

$$\begin{pmatrix} C_1 & -C_m \\ -C_m & C_2 \end{pmatrix} \begin{pmatrix} \Delta V_1 \\ \Delta V_2 \end{pmatrix} = \begin{pmatrix} C_{g1}\Delta V_{g1} \\ C_{g2}\Delta V_{g2} \end{pmatrix} \tag{5}$$

The double-dot stability diagram can then be given equivalently as a two-dimensional plot with energy axes $|e|\,V_1$, $|e|\,V_2$, or with axes $|e|\,V_{g1}$, $|e|\,V_{g2}$, which are skewed and stretched with respect to the original axes according to the transformation given in equation (5). The end effect is that parallel horizontal (vertical) lines in the $|e|\,V_{1(2)}$ plane separated by a distance $dV_{1(2)}$ transform to skewed parallel lines, separated by $dV_{g1(2)} = dV_{1(2)}/\alpha_{1(2)}$ along the vertical (horizontal) of the new coordinate system, where (see Figure 4).

$$\alpha_l = \frac{C_{gl}}{C_l}, \quad l = 1, 2 \tag{6}$$

Additionally, horizontal lines in the $|e|\,V_{1(2)}$ plane become skewed with a slope $\delta V_{g1}/\delta V_{g2} = -C_m C_{g2}/C_2 C_{g1}$ (see Figure 4b), and vertical lines are skewed with slope $\delta V_{g1}/\delta V_{g2} = -C_1 C_{g2}/C_m C_{g1}$.

The Hamiltonian in equation (3) conserves the number of electrons on each dot: $[H_C, N_l] = 0$, so we label the ground state by the two dot occupation numbers, (N_1, N_2), and indicate where each configuration is the ground state in Figure 4 for equivalent quantum dots that satisfy $\alpha_1 = \alpha_2 = \alpha = 1/2$, $U_1 = U_2 = U$, $\epsilon_{lk+1} - \epsilon_{lk} = \hbar\omega_0$ for all k, l, and $U : \hbar\omega_0 : U' = 3 : 2 : 1$. The charge stability diagram is described by a 'honeycomb' of irregular hexagons with dimensions that are determined by three typical energy scales: (i) The on-site repulsion U, (ii) the nearest-neighbor repulsion U', and (iii) the typical orbital energy $\hbar\omega_0$. Figure 4 assumes a ground state electron filling as shown in Figure 3, with constant orbital energy $\hbar\omega_0$. In this case, the orbital energy appears in the dimensions of only every second honeycomb cell of the stability diagram, along the horizontal or vertical direction, since the spin-degenerate orbital states fill with two electrons at a time according to the Pauli principle. This even–odd behavior may not be visible in dots of high symmetry, where the orbital levels are manifold degenerate (such an orbital degeneracy may make it difficult to generate a well-defined two-level system for electron spins in carbon nanotubes or gated graphene, although there are potential solutions to this problem (Trauzettel, Bulaev, Loss and Burkard, 2007)). Alternatively, the absence of an even–odd effect in low-symmetry single dots has previously been attributed to the absence of spin degeneracy due to

many-body effects (Stewart *et al*., 1997; Fujisawa, Tokura and Hirayama, 2001; van der Wiel *et al*., 2003).

Each vertex of a honeycomb cell corresponds to a triple-point, where three double-dot charge states are simultaneously degenerate. For a double dot connected to source and drain leads at low temperature, and in the absence of relaxation or photo-assisted tunneling processes, it is only at these points where resonant sequential transport can occur, through shuttling processes of the form $(0, 0) \rightarrow (1, 0) \rightarrow (0, 1) \rightarrow (0, 0)$. This picture changes when a strong interdot tunnel coupling H_{T} is considered in addition.

4.2 Molecular states in double dots

Molecule-like states have been observed and studied in detail in two-electron single vertical (Fujisawa *et al*., 2002) and lateral quantum dots (Zumbühl, Marcus, Hanson and Gossard, 2004) (the latter behave as an effective double-dot structure, showing good agreement with theory (Golovach and Loss, 2004)). Evidence of molecular states forming also in double quantum dots due to a strong interdot tunnel coupling has been found in a variety of systems (Schmidt *et al*., 1997; Schedelbeck, Wegscheider, Bichler and Abstreiter, 1997; Blick *et al*., 1998; Brodsky *et al*., 2000; Bayer *et al*., 2001; Ota *et al*., 2005; Hüttel *et al*., 2005; Fasth, Fuhrer, Bjork and Samuelson, 2005; Mason, Biercuk and Marcus, 2004; Biercuk *et al*., 2005; Graeber *et al*., 2006). For example, molecular states have been observed in many-electron gated quantum dots in linear transport (Blick *et al*., 1998) (solid lines of Figure 5b) and transport through excited states (Hüttel *et al*., 2005) (dashed lines in Figure 5b). In addition, molecular states have been observed in vertical-lateral gated double-quantum dots (Hatano, Stopa and Tarucha, 2005), gated dots formed in quantum wires (Fasth, Fuhrer, Bjork and Samuelson, 2005) and gated carbon-nanotube double dots (Mason, Biercuk and Marcus, 2004; Biercuk *et al*., 2005; Graeber *et al*., 2006). A large interdot tunnel coupling is essential for generating a large exchange interaction J (see equation (23) below), and is therefore very important for the implementation of fast two-qubit gates in the Loss–DiVincenzo proposal.

In this section, we analyze changes to the double-dot stability diagram that occur due to the interdot tunneling term H_{T}. We focus on the relevant regime for quantum computing, where only a single orbital state is available for occupation on each quantum dot (the lower-left region of Figure 4a and b). In the subspace of these lowest dot orbital states, H_{T} is given by:

$$H_{\mathrm{T}} = t_{12} \sum_{\sigma} d_{1\sigma}^{\dagger} d_{2\sigma} + \mathrm{H.c.} \tag{7}$$

where t_{12} is the tunneling amplitude between the two dots, and $d_{l\sigma}$, $l = 1, 2$, annihilates an electron in the lowest single-particle orbital state localized on quantum dot l with spin σ.

When the double dot is occupied by only $N = 0, 1$ electrons and is coupled weakly to leads, an explicit expression can be found for the current passing through a sequentially coupled double dot, as shown in Figure 5(a) (Ziegler, Bruder and Schoeller, 2000; Graeber *et al*., 2006). It is straightforward to diagonalize $H_{\mathrm{C}} + H_{\mathrm{T}}$ in the subspace of $N = 1$ electrons on the quantum dot. This gives the (spin-degenerate) eigenenergies and corresponding eigenvectors:

$$E_{\pm}(\Delta, \epsilon) = -\frac{1}{\sqrt{2}} \left(\Delta \pm \sqrt{\epsilon^2 + 2t_{12}^2} \right) \tag{8}$$

$$|E_{\pm}\rangle = \cos\left(\frac{\theta_{\pm}}{2}\right) |1, 0\rangle + \sin\left(\frac{\theta_{\pm}}{2}\right) |0, 1\rangle \tag{9}$$

$$\tan\left(\frac{\theta_{\pm}}{2}\right) = \frac{\epsilon \mp \sqrt{\epsilon^2 + 2t_{12}^2}}{\sqrt{2} t_{12}} \tag{10}$$

Here, $E_{\pm}(\Delta, \epsilon)$ is written in terms of new energy coordinates ϵ, Δ, which are related to the old (voltage) coordinates through a rotation of the axes by 45° (see also Figure 5b):

$$\begin{pmatrix} \Delta \\ \epsilon \end{pmatrix} = \frac{1}{\sqrt{2}} \begin{pmatrix} 1 & 1 \\ -1 & 1 \end{pmatrix} \begin{pmatrix} |e| V_1 \\ |e| V_2 \end{pmatrix} \tag{11}$$

We then define double-dot chemical potentials:

$$\mu_{\pm}(\Delta, \epsilon) = E_{\pm}(\Delta, \epsilon) - E_0 \tag{12}$$

where $E_0 = 0$ is the energy of the $(0, 0)$ charge configuration. In the presence of a strong tunnel coupling, the eigenstates of the double dot are no longer labeled separately by the quantum numbers N_1, N_2. Instead, the sum $N = N_1 + N_2$ is conserved. If we add to H_{dd} the double-dot-lead coupling Hamiltonian $H_{\mathrm{dd-}L} = \sum_{k\sigma} t_{\mathrm{s}} c_{\mathrm{s}k\sigma}^{\dagger} d_{1\sigma} + t_{\mathrm{d}} c_{\mathrm{d}k\sigma}^{\dagger} d_{2\sigma} + \mathrm{H.c.}$, where $c_{\mathrm{s(d)}k\sigma}^{\dagger}$ creates an electron in the source (drain), in orbital k with spin σ, then N can fluctuate between 1 and 0 if the double-dot and lead chemical potentials are equal. We identify double-dot sequential-tunneling processes as those that change the total charge on the double-dot by one: $N \rightarrow N \pm 1$ (Golovach and Loss, 2004). One can evaluate golden-rule rates for all sequential-tunneling processes, taking the dot-lead coupling $H_{\mathrm{dd-L}}$ as a perturbation to obtain the stationary current from a standard Pauli master equation (the Pauli master equation is valid for sufficiently high temperature, $k_{\mathrm{B}}T > \Gamma_{\mathrm{s(d)}}$, so that off-diagonal elements can be ignored in the double-dot density matrix). For weak dot-lead coupling, at low temperature $k_{\mathrm{B}}T < \hbar\omega_0$, and at zero bias ($\mu = \mu_s = \mu_d + \Delta\mu$, with $\Delta\mu \rightarrow 0$), transport occurs only through the $N = 1$ ground state, with chemical

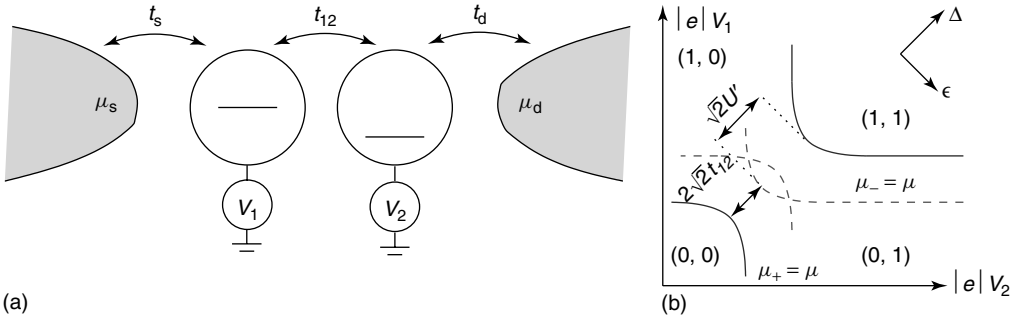

Figure 5. (a) A tunnel-coupled double quantum dot, with tunneling amplitude t_{12}. The source and drain leads, at chemical potentials μ_s and μ_d, are connected to the left and right dots through tunnel barriers with tunneling amplitudes t_s and t_d, respectively. The left and right dots are set to local potentials V_1 and V_2. (b) Modification of the stability diagram in the case of a significant tunnel coupling t_{12}. To generate this figure we have chosen the ratio of tunnel coupling to the mutual (nearest-neighbor) charging energy to be $t_{12}/U' \approx 1/5$. At solid lines, transport occurs via the double-dot ground state $|E_+\rangle$ and at dashed lines additional transport can occur through the first excited state $|E_-\rangle$ (see equations (9) and (10) below).

potential μ_+. The differential conductance near the $N = 0, 1$ boundary is then given by

$$\frac{\mathrm{d}I}{\mathrm{d}(\Delta\mu)} = |e|\,\Gamma\left(\frac{-2f'(\mu_+)}{1+f(\mu_+)}\right)$$

$$\Gamma = \frac{\sin^2(\theta_+)\,\Gamma_s\Gamma_d}{4\left(\cos^2\left(\frac{\theta_+}{2}\right)\Gamma_s + \sin^2\left(\frac{\theta_+}{2}\right)\Gamma_d\right)} \qquad (13)$$

where $f(E) = 1\Big/\left[1+\exp\left(\frac{E-\mu}{k_BT}\right)\right]$ is the Fermi function at chemical potential μ and temperature T, $f'(E) = \mathrm{d}f(E)/\mathrm{d}E$, and $\Gamma_{s(d)} = \frac{2\pi\nu}{\hbar}\left|t_{s(d)}\right|^2$ is the tunneling rate to the source (drain) with a lead density of states per spin ν at the Fermi energy. If spin degeneracy is lifted, the quantity in brackets in equation (13) is replaced by the familiar term $-f'(\mu_+) = 1\Big/\left[4k_BT\cosh^2\left(\frac{\mu_+-\mu}{2k_BT}\right)\right]$ (Beenakker, 1991). The differential conductance (equation (13)) reaches a maximum near the point where the double-dot chemical potential matches the lead chemical potential, $\mu_+(\Delta,\epsilon) = \mu$, which we indicate with a solid line in Figure 5(b). Transport through the excited state can occur where $\mu_-(\Delta,\epsilon) = \mu$, and when the bias $\Delta\mu = \mu_s - \mu_d$ or temperature T are sufficiently large to generate a significant population in the excited state $|E_-\rangle$. Dashed lines indicate where $\mu_-(\Delta,\epsilon) = \mu$ in Figure 5(b).

There are several qualitative changes to the double-dot stability diagram that take place in the presence of strong tunnel coupling. First, the number of electrons on each dot is not conserved individually. Instead, the sum $N = N_1 + N_2$ is conserved, which means that there are no longer lines separating, for example, the (1,0) and (0,1) states in Figure 5(b). Second, sequential-tunneling processes allow current to be transported through the double dot along the length of the 'wings' that define the boundaries between N and $N \pm 1$-electron ground states. This is in contrast to the case where t_{12} is weak, in which resonant sequential transport can only occur at triple points, where the shuttling processes of the type $(0,0) \to (1,0) \to (0,1) \to (0,0)$ are allowed by energy conservation.

4.3 Two-qubit gates in double quantum dots

The $\sqrt{\mathrm{SWAP}}$ operation described in Section 2 requires significant control of the exchange coupling J. The value of J can be controlled by raising/lowering the interdot barrier, thus changing the tunnel coupling t_{12} (Loss and DiVincenzo, 1998), or with an out-of-plane magnetic field or weak in-plane electric field (Burkard, Loss and DiVincenzo, 1999). More recently, experiments have controlled J by varying the back-gate voltages on two neighboring quantum dots through a large parameter regime, independently (Petta *et al*., 2005a). Here we discuss this last method to control J, which has been analyzed in several recent papers (Petta *et al*., 2005b; Coish and Loss, 2005; Taylor *et al*., 2006; Stopa and Marcus, 2006).

We consider a double quantum dot in the region of the charge stability diagram indicated in the lower inset of Figure 6. Specifically, we consider the regime of gate voltages where the double dot contains $N = 2$ electrons near the degeneracy point of the $(1,1)$ and $(0,2)$ charge states, and aim to diagonalize the Hamiltonian $H_C + H_T$ in the basis of three spin triplets and two relevant singlets:

$$|S(0,2)\rangle = d^\dagger_{2\downarrow}d^\dagger_{2\uparrow}\,|\mathrm{vac.}\rangle \qquad (14)$$

$$|S(1,1)\rangle = \frac{1}{\sqrt{2}}\left(d^\dagger_{2\downarrow}d^\dagger_{1\uparrow} - d^\dagger_{2\uparrow}d^\dagger_{1\downarrow}\right)|\mathrm{vac.}\rangle \qquad (15)$$

$$|T_0\rangle = \frac{1}{\sqrt{2}}\left(d^\dagger_{2\downarrow}d^\dagger_{1\uparrow} + d^\dagger_{2\uparrow}d^\dagger_{1\downarrow}\right)|\mathrm{vac.}\rangle \qquad (16)$$

$$|T_+\rangle = d^\dagger_{2\uparrow} d^\dagger_{1\uparrow} |\text{vac.}\rangle \tag{17}$$

$$|T_-\rangle = d^\dagger_{2\downarrow} d^\dagger_{1\downarrow} |\text{vac.}\rangle \tag{18}$$

In the absence of additional spin-dependent terms, the triplets are degenerate, with energy $E_{\text{Triplet}} = E_{(1,1)} = -\sqrt{2}\Delta'$, whereas the two singlet states have energies and associated eigenvectors

$$E^{\pm}_{\text{Singlet}} = E_{\text{Triplet}} - \frac{1}{\sqrt{2}}\left(\epsilon' \pm \sqrt{(\epsilon')^2 + 4t_{12}^2}\right) \tag{19}$$

$$\left|E^{\pm}_{\text{Singlet}}\right\rangle = \cos\left(\frac{\theta^S_{\pm}}{2}\right)|S(1,1)\rangle + \sin\left(\frac{\theta^S_{\pm}}{2}\right)|S(0,2)\rangle \tag{20}$$

$$\tan\left(\frac{\theta^S_{\pm}}{2}\right) = \frac{\epsilon' \mp \sqrt{(\epsilon')^2 + 4t_{12}^2}}{2t_{12}} \tag{21}$$

Here, Δ' and ϵ' are related to the previous coordinates (Δ, ϵ) through a simple translation of the origin:

$$\begin{pmatrix}\Delta' \\ \epsilon'\end{pmatrix} = \begin{pmatrix}\Delta \\ \epsilon\end{pmatrix} + \frac{1}{\sqrt{2}}\begin{pmatrix}-U' \\ U' - U\end{pmatrix} \tag{22}$$

This gives rise to the Heisenberg exchange for large negative ϵ' (from equation (19)):

$$J(\epsilon') = E_{\text{Triplet}} - E^{+}_{\text{Singlet}} \approx \frac{\sqrt{2}t_{12}^2}{|\epsilon'|}, \quad \epsilon' < 0, \quad |\epsilon'| \gg 2t_{12} \tag{23}$$

By pulsing $\epsilon' = \epsilon'(t)$, the exchange $J(\epsilon'(t))$ can be pulsed on and off again in order to implement the $\sqrt{\text{SWAP}}$ operation, as described in Section 2 (see the inset of Figure 6). This operation has now been achieved experimentally with a gating time on the order of 180 ps (Petta *et al*., 2005a), in good agreement with the predictions in (Burkard, Loss and DiVincenzo, 1999) for an achievable switching time.

4.4 Initialization of two-spin encoded qubits

Fluctuations in a nuclear spin environment can lead to rapid decoherence of single-electron spin states due to the contact hyperfine interaction (see Section 5). The effects of these fluctuations can be reduced, in part, by considering a qubit encoded in two-electron singlet $|0\rangle = |S(1,1)\rangle$ and triplet states $|1\rangle = |T_0\rangle$, as defined in equations (15) and (16). A qubit encoded in this two-dimensional subspace would be immune to global magnetic field fluctuations, and is then only susceptible to fluctuations in the difference of the magnetic field on the two dots. With this encoding scheme, the qubit energy splitting would be provided through the exchange coupling (equation (23)), and single-qubit rotations

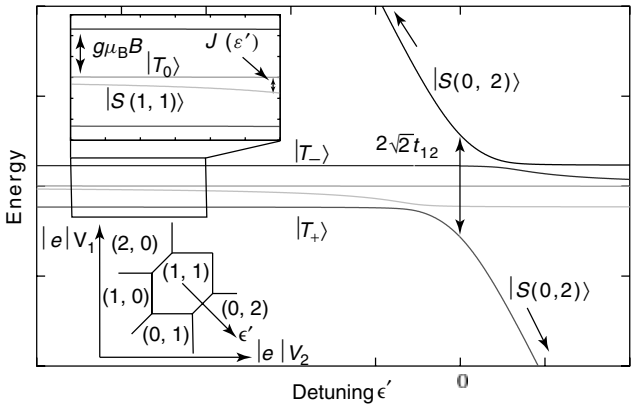

Figure 6. Energy level spectrum for two electrons in the two lowest orbital states of a double quantum dot. The triplet states $|T_\pm\rangle$ are split off from $|T_0\rangle$ and $|S(1,1)\rangle$ by the Zeeman splitting $g\mu_B B$ (see the upper inset). The exchange coupling J (which gives the splitting between $|T_0\rangle$ and $|S(1,1)\rangle$) can be changed by varying the detuning ϵ' (pictured in the lower inset).

could be performed using an inhomogeneous magnetic field (Levy, 2002). Two-qubit operations in this scheme could be performed, for example, using capacitive coupling due to the relative charge distributions of the triplet and singlet states in neighboring double dots (Taylor *et al*., 2005), although the difference in these charge distributions can lead to additional dephasing due to fluctuations in the electrical environment (Coish and Loss, 2005) (see also Section 5, below). An alternative scheme to couple such encoded qubits over long distances with optical cavity modes has also been proposed (Burkard and Imamoglu, 2006). One additional advantage of the two-spin encoded qubit scheme is that adiabatic tuning of the gate voltages can be used to initialize and read out information stored in the singlet–triplet basis (Johnson *et al*., 2005a; Petta *et al*., 2005a). We discuss this initialization scheme in the rest of this section.

We consider the singlet ground state $\left|E^{+}_{\text{Singlet}}\right\rangle$, given by equations (20) and (21). For large positive detuning, $|\epsilon'| \gg t_{12}, \epsilon' > 0$, the mixing angle in equation (21) is $\theta^S_+ \approx \pi$ and the singlet ground state is approximately given by $|S(0,2)\rangle$. For large negative detuning $|\epsilon'| \gg t_{12}, \epsilon' < 0$, we find $\theta^S_+ \approx 0$ and the lowest-energy singlet is instead given by $|S(1,1)\rangle$ (see Figure 6). If the two-electron system is allowed to relax to its ground state $|S(0,2)\rangle$ at large positive detuning ϵ' and the detuning is then varied adiabatically slowly to large negative values, the encoded qubit can be initialized to the state $|0\rangle = |S(1,1)\rangle$ (see Figure 6 and insets). It is a straightforward exercise to estimate the error in such an operation for a two-dimensional Hamiltonian.

For a linear ramp of ϵ' over an infinite interval (i.e., $\epsilon' = (\Delta\epsilon/\tau_{\text{sw}})\,t$, $t = -\infty \ldots \infty$ with characteristic switching time τ_{sw} to sweep over an interval $\Delta\epsilon$), the result of Zener,

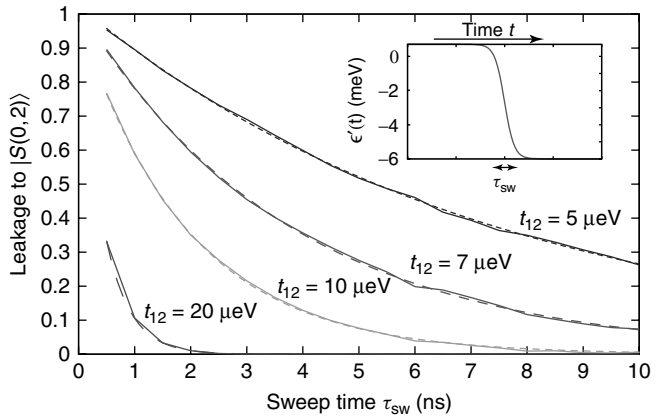

Figure 7. Leakage (the occupation probability of the state $|S(0,2)\rangle$ at the end of the sweep) due to nonadiabatic transitions after sweeping from $\epsilon' = 0.7\,\text{meV}$ to $\epsilon' = -6\,\text{meV}$. Leakage is given as a function of the characteristic sweep time τ_{sw}, where $\epsilon'(t) = \epsilon_0 - \frac{\Delta\epsilon}{2}\tanh(2t/\tau_{\text{sw}})$, with $\epsilon_0 = -2.65\,\text{meV}$ and $\Delta\epsilon = 6.7\,\text{meV}$. We show results for $t_{12} = 5, 7, 10, 20\,\mu\text{eV}$. Solid lines show the results of numerical integration of the Schrödinger equation and dashed lines give exponential fits, which decay with the time constants τ_{fit}, given in Table 1.

for the nonadiabatic Landau–Zener transition probability is (Zener, 1932)

$$P = \exp\left(-\frac{\tau_{\text{sw}}}{\tau_{LZ}}\right), \quad \tau_{LZ} = \frac{\hbar\sqrt{2}\Delta\epsilon}{4\pi t_{12}^2} \tag{24}$$

Here, the Landau–Zener tunneling probability is controlled in terms of two timescales: the switching time τ_{sw} for a typical range of $\Delta\epsilon$ and the Landau–Zener time constant τ_{LZ}, which has a strong dependence ($\propto 1/t_{12}^2$) on the interdot tunnel coupling. For a realistic voltage pulse, ϵ' is swept over a finite interval, and the pulse shape, in general, will not be linear for the entire sweep. Performing an analysis similar to that used for single-spin gates (Schliemann, Loss and MacDonald, 2001; Requist, Schliemann, Abanov and Loss, 2005) for this case, one can perform a numerical integration of the time-dependent Schrödinger equation in the subspace formed by the two singlets for an arbitrary pulse shape. We have done this for a pulse of the form $\epsilon'(t) = \epsilon_0 - \frac{\Delta\epsilon}{2}\tanh(2t/\tau_{\text{sw}})$, $t = -5\tau_{\text{sw}} \ldots 5\tau_{\text{sw}}$ [2], where we find an approximately exponential dependence of P on the switching time τ_{sw} (see Figure 7). Fitting to this exponential dependence, we find a time constant τ_{fit} analogous to the Landau–Zener time τ_{LZ}. The time constants τ_{LZ} (from equation (24)) and τ_{fit} from the numerical data in Figure 7 are compared in Table 1 for various values of the interdot tunnel coupling t_{12}. The results of Figure 7 and Table 1 suggest that (for this set of parameters) adiabatic switching for initialization or readout on a timescale of $\tau_{\text{sw}} \lesssim 1\,\text{ns}$ can only be performed without significant error if the tunnel coupling t_{12} is made larger than $t_{12} > 20\,\mu\text{eV}$. It is important to note that this analysis ignores additional effects due to magnetic-field inhomogeneities, spin-orbit coupling, or the hyperfine interaction, all of which can lead to additional singlet–triplet anticrossings (see Section 5.2, below) and hence, to additional initialization or readout errors.

Table 1. Landau–Zener time constant τ_{LZ} for a linear ramp of ϵ' and the time constant τ_{fit} for fits to numerically evaluated data at various values of the tunnel coupling t_{12}.

t_{12} (μeV)	τ_{LZ} (ns)	τ_{fit} (ns)
5	20	7.4
7	10	3.8
10	4.9	1.9
20	1.2	0.43

5 DECOHERENCE

Decoherence is the process by which information stored in a quantum bit is lost. There are two timescales used to describe decoherence processes for a spin that decays exponentially in the presence of an applied magnetic field. T_1 is the longitudinal spin decay time, or spin-flip time, which describes the timescale for random spin flips: $|\uparrow\rangle \rightarrow |\downarrow\rangle$. T_2, the transverse spin decay time, describes the decay of a superposition state $a|\uparrow\rangle + b|\downarrow\rangle$. Both of these timescales are important for quantum computing, since both effects lead to qubit errors.

An experiment performed on an ensemble of systems with different environments can lead to additional decoherence, beyond that described by the 'intrinsic' T_2 time (Slichter, 1980). For such an experiment, the ensemble-averaged transverse spin decay time is therefore often denoted T_2^* to distinguish it from the single-spin decay time. Other symbols such as τ_c (the correlation time) and T_{M} (the magnetization envelope decay time) are often used to distinguish decay that is nonexponential.

For a quantum-dot-confined electron-spin state to decay, it is necessary for the spin to couple in some way to fluctuations in the environment. There are two important sources of this coupling for electron spins in quantum dots. First, the spin-orbit interaction couples electron spin states to their orbital states, and therefore makes spins indirectly sensitive to fluctuations in the electric environment. Second, the Fermi contact hyperfine interaction between electrons and surrounding nuclear spins in the host material can lead to rapid decay if fluctuations in the nuclear spin environment

are not properly controlled. In the rest of this section we discuss recent progress in understanding decoherence due to these two coupling mechanisms.

5.1 Spin-orbit interaction

For a 2DEG formed in GaAs, the spin-orbit interaction is given in terms of two terms:

$$H_{\mathrm{SO}} = \alpha\left(p_x\sigma_y - p_y\sigma_x\right) + \beta\left(p_y\sigma_y - p_x\sigma_x\right) + O\left(|\mathbf{p}|^3\right) \tag{25}$$

where $\sigma_{x,y}$ are Pauli matrices and $\mathbf{p} = (p_x, p_y)$ is the momentum operator in the plane of the 2DEG. The first term, proportional to α, is the Rashba (or structure-inversion-asymmetry) spin-orbit coupling term. The Rashba term is due to asymmetry in the confining potential and can therefore be tuned to some degree with applied gates. The second term, proportional to β, is the Dresselhaus (bulk-inversion-asymmetry) term, and is due to the fact that GaAs, which has a zinc-blende lattice, has no center of inversion symmetry. Corrections to this spin-orbit Hamiltonian of order $|\mathbf{p}|^3$ are smaller than the linear-momentum terms in quantum dots by the ratio of z-confinement length to the quantum-dot Bohr radius, and are negligible in the two-dimensional limit (Cerletti, Coish, Gywat and Loss, 2005).

H_{SO} obeys time-reversal symmetry (i.e., H_{SO} is invariant under the operation $\mathbf{p} \to -\mathbf{p}, \boldsymbol{\sigma} \to -\boldsymbol{\sigma}$). Thus, in the absence of a magnetic field, the ground state of a single electron confined to a quantum dot is twofold degenerate due to Kramer's theorem, and H_{SO} alone cannot cause decoherence. The character of the ground-state doublet does change, however, due to the presence of H_{SO}, mixing orbital and spin states. Thus, any fluctuations that couple to the orbital degree of freedom can cause decoherence in combination with spin-orbit coupling. These fluctuations can come from lattice phonons, surrounding gates, electron-hole pair excitations, and so on (Golovach, Khaetskii and Loss, 2004). The longitudinal spin relaxation rate $1/T_1$ due to spin-orbit coupling and lattice phonons has been calculated, and shows a strong suppression for confined electrons (with large level spacing $\hbar\omega_0$) in weak magnetic fields B: $1/T_1 \propto B^5/(\hbar\omega_0)^4$ (Khaetskii and Nazarov, 2000; 2001). This calculation has been extended to a larger range of magnetic fields, showing that the B-field dependence of $1/T_1$ saturates and is then suppressed when the wavelength of the phonons with energy $g\mu_{\mathrm{B}}B$ is comparable to the dot size (Golovach, Khaetskii and Loss, 2004). Further, this calculation has also been extended to include the transverse spin decay time due to spin-orbit interaction alone, showing that dephasing is limited by relaxation, or $T_2 = 2T_1$ to leading order in the spin-orbit coupling, independent of the particular source of fluctuations (Golovach, Khaetskii and Loss, 2004). Additionally, $1/T_1$ has been shown to have a strong dependence on the magnetic field direction, relative to the crystal axes (Fal'ko, Altshuler and Tsyplyatyev, 2005), shows a strong enhancement near avoided level crossings, which may allow independent measurements of the Rashba and Dresselhaus coupling constants (Bulaev and Loss, 2005a), and plays a role in phonon-assisted cotunneling current through quantum dots (Lehmann and Loss, 2006). The relaxation rate of quantum-dot-confined hole spins due to spin-orbit coupling and phonons has also been investigated. In some cases, recent work has shown that the hole spin relaxation time may even exceed the relaxation time of electron spins (Bulaev and Loss, 2005b). In addition to lattice phonons, electric-field fluctuations can result from the noise in a QPC readout device, which results in spin decoherence when considered in combination with spin-orbit coupling. This mechanism shows a strong dependence of the decoherence rate $\left(\sim 1/r^6\right)$ on the dot-QPC separation r (Borhani, Golovach and Loss, 2005), and can therefore be controlled with careful positioning of the readout device.

Measurements of relaxation times for single-electron spins have been performed in gated lateral quantum dots (Hanson *et al*., 2003; Elzerman *et al*., 2004), giving a T_1 time in good agreement with the theory of Golovach, Khaetskii and Loss (2004) and in self-assembled quantum dots (Kroutvar *et al*., 2004), which confirmed the expected magnetic field dependence: $1/T_1 \propto B^5$ (Khaetskii and Nazarov, 2001). Additionally, singlet–triplet decay has been measured in single vertical (Fujisawa *et al*., 2002), and lateral (Hanson *et al*., 2005) dots, as well as lateral double dots (Petta *et al*., 2005b; Johnson *et al*., 2005a).

There is a general consensus that spin relaxation for quantum-dot-confined electrons proceeds through the spin-orbit interaction and phonon emission at high magnetic fields. However, in weak magnetic fields, and for the transverse spin decay time T_2, there are stronger effects in GaAs. These effects are due to the contact hyperfine interaction between confined electron spins and nuclear spins in the surrounding lattice.

5.2 Hyperfine interaction

For a collection of electrons in the presence of nuclear spins, the Fermi contact hyperfine interaction reads

$$H_{\mathrm{hf}} = Av\sum_k \mathbf{I}_k \cdot \mathbf{S}(\mathbf{r}_k),\ \mathbf{S}(\mathbf{r}_k) = \frac{1}{2}\sum_{\sigma,\sigma'=\uparrow,\downarrow} \psi^\dagger_\sigma(\mathbf{r}_k)\boldsymbol{\sigma}_{\sigma\sigma'}\psi_{\sigma'}(\mathbf{r}_k) \tag{26}$$

where A is the hyperfine coupling strength, v is the volume of a crystal unit cell containing one nuclear spin, $\mathbf{I}_k$ is the spin operator for the nuclear spin at site k, $\mathbf{S}(\mathbf{r}_k)$ is the electron spin density at the nuclear site, given

in terms of field operators $\psi_\sigma(\mathbf{r}) = \sum_n \Psi_n(\mathbf{r}) c_{n\sigma}$. Here, $c_{n\sigma}$ annihilates an electron with orbital envelope function $\Psi_n(\mathbf{r})$ and spin σ. The $\Psi_n(\mathbf{r})$ form a complete orthonormal set, from which it follows that $\left\{\psi_\sigma(\mathbf{r}), \psi^\dagger_{\sigma'}(\mathbf{r}')\right\} = \delta(\mathbf{r} - \mathbf{r}')\delta_{\sigma,\sigma'}$, $\left\{\psi_\sigma(\mathbf{r}), \psi_{\sigma'}(\mathbf{r}')\right\} = 0$, and we have denoted matrix elements by $\boldsymbol{\sigma}_{\sigma\sigma'} = \langle\sigma|\boldsymbol{\sigma}|\sigma'\rangle$, where $\boldsymbol{\sigma} = (\sigma_x, \sigma_y, \sigma_z)$ is the vector of Pauli matrices. The significance of the general form given in equation (26) is that there can be interplay of orbital and spin degrees of freedom due to the contact hyperfine interaction. When the orbital level spacing is not too large, this interplay can be the limiting cause of electron-spin relaxation (Erlingsson, Nazarov and Fal'ko, 2001; Erlingsson and Nazarov, 2002) in weak magnetic fields, where the spin-orbit interaction is less effective, and leads to enhanced nuclear spin relaxation in the vicinity of sequential-tunneling peaks for a quantum dot connected to leads, where $\mathbf{S}(\mathbf{r})$ fluctuates significantly (Lyanda-Geller, Aleiner and Altshuler, 2002; Hüttel *et al.*, 2004).

The orbital level spacing in lateral quantum dots is usually much larger than the typical energy scale of $H_{\rm hf}$. In this case, it is possible to solve for the ground state orbital envelope wave function $\Psi_0(\mathbf{r})$ in the absence of the hyperfine interaction, and write an effective hyperfine Hamiltonian for a single electron projected onto the quantum-dot orbital ground state:

$$H_{\rm hf,0} \approx \mathbf{h}_0 \cdot \mathbf{S}_0, \;\; \mathbf{h}_0 = Av \sum |\Psi_0(\mathbf{r}_k)|^2 \mathbf{I}_k \qquad (27)$$

where here $\mathbf{S}_0$ is the spin-1/2 operator for a single electron in the quantum-dot orbital ground state. The primary material used to make lateral quantum dots is GaAs. All natural isotopes of Ga and As carry nuclear spin $I = 3/2$. Each isotope has a distinct hyperfine coupling constant, but the average coupling constant, weighted by the relative abundance of each isotope in GaAs gives $A \approx 90\,\mu$eV (Paget, Lampel, Sapoval and Safarov, 1977).

Dynamics under $H_{\rm hf,0}$ have now been studied extensively under many various approximations and in many parameter regimes. Here we give a brief account of some part of this study. For an extensive overview, see reviews in (Schliemann, Khaetskii and Loss, 2003; Cerletti, Coish, Gywat and Loss, 2005). The first analysis of the influence of equation (27) on quantum-dot electron-spin dynamics showed that the long-time longitudinal spin-flip probability, $P_{\uparrow\downarrow} \approx 1/p^2 N$ (Burkard, Loss and DiVincenzo, 1999) was suppressed in the limit of large nuclear spin polarization p and number of nuclear spins in the dot, N. It may be possible to reach high polarizations in a 2DEG by allowing the system to equilibrate at low temperature, below which the nuclei are predicted to undergo a ferromagnetic phase transition (Simon and Loss, 2007). An exact solution for the case of a fully polarized nuclear spin system ($p = 1$) has shown that both the longitudinal and transverse components of the electron spin decay by a fraction $\sim 1/N$ according to a long-time power law $\sim 1/t^{3/2}$ on a timescale of $\tau \sim \hbar N/A$ (Khaetskii, Loss and Glazman, 2002) ($\hbar N/A \sim 1\,\mu$s for a GaAs dot containing $N \simeq 10^5$ nuclei). This exact solution for $p = 1$, which shows a nonexponential decay, demonstrates that the electron spin decay is manifestly non-Markovian since the timescale for motion in the nuclear spin bath is much longer than the decay timescale of the electron spin. For unpolarized systems, the ensemble-averaged mean-field dynamics show a transverse spin decay on a timescale $\tau \sim \hbar\sqrt{N}/A \sim 5\,$ns (Khaetskii, Loss and Glazman, 2002; Merkulov, Efros and Rosen, 2002). The exact solution has been extended to the case of nonzero polarization $p \neq 1$ using a generalized master equation, valid in the limit of large magnetic field or polarization $p \gg 1/\sqrt{N}$ (Coish and Loss, 2004). This work has shown that, while the longitudinal spin decay is bounded by $\sim 1/p^2 N$, due to the quantum nature of the nuclear field, the transverse components of spin will decay to zero in a time $t_c \approx 5\,\text{ns}/\sqrt{1-p^2}$ (without necessarily ensemble averaging and without making a mean-field ansatz), unless an electron spin-echo sequence is performed or the nuclei are prepared in an eigenstate of the operator h_0^z through measurement (Coish and Loss, 2004). There are several recent suggestions for methods that could be used to measure the operator h_0^z (Giedke *et al.*, 2006; Klauser, Coish and Loss, 2006; Stepanenko, Burkard, Giedke and Imamoglu, 2006) in order to extend the electron-spin decay times. Once the nuclear spin system is forced into an eigenstate of h_0^z, the lowest-order corrections for large magnetic field still show incomplete decay for the transverse spin (Coish and Loss, 2004), suggesting that dynamics induced by the nuclear dipolar interaction may limit spin coherence in this regime (de Sousa and Das Sarma, 2003), although higher-order corrections have been reported to lead to complete decay (Deng and Hu, 2006), even when the nuclear spin system is static. There have been several efforts to understand the hyperfine decoherence problem numerically (Schliemann, Khaetskii and Loss, 2002; Shenvi, de Sousa and Whaley, 2005b), and other studies have investigated electron spin-echo envelope decoherence under the hyperfine interaction alone (Coish and Loss, 2004; Shenvi, de Sousa and Whaley, 2005b; Shenvi, de Sousa and Whaley, 2005a) or the combined influence of hyperfine and nuclear dipolar interactions (de Sousa and Das Sarma, 2003; de Sousa, Shenvi and Whaley, 2005; Witzel, de Sousa and Das Sarma, 2005; Yao, Liu and Sham, 2006, 2007). Other approaches to understanding the hyperfine decoherence problem include semiclassical theories that replace the quantum nuclear field by a classical dynamical vector (Erlingsson and Nazarov, 2004; Yuzbashyan, Altshuler, Kuznetsov and Enolskii, 2005) or a classical distribution

function (Al-Hassanieh, Dobrovitski, Dagotto and Harmon, 2006).

Experiments on electron-spin decoherence in single quantum dots (Bracker *et al*., 2005; Dutt *et al*., 2005) and double-quantum dots (Petta *et al*., 2005a; Koppens *et al*., 2005) have now confirmed that the ensemble-averaged electron-spin dephasing time is indeed given by $\tau \sim \hbar\sqrt{N}/A \sim 5\text{–}10\,\text{ns}$.

For two electron spins confined to a double quantum dot, the hyperfine Hamiltonian (equation (26)) can be cast in the form (Coish and Loss, 2005)

$$H_{\text{hf,dd}} = \epsilon_z \sum_l S_l^z + \sum_l \mathbf{h}_l \cdot \mathbf{S}_l$$
$$= \epsilon_z S_l^z + \mathbf{S}\cdot\mathbf{h} + \delta\mathbf{S}\cdot\delta\mathbf{h} \tag{28}$$

$$\mathbf{S}_l = \frac{1}{2} \sum_{\sigma,\sigma'=\uparrow,\downarrow} d_{l\sigma}^{\dagger} \boldsymbol{\sigma}_{\sigma\sigma'} d_{l\sigma'} \tag{29}$$

where $\epsilon_z = g\mu_B B$ is the Zeeman splitting, $d_{1(2)\sigma}$ annihilates an electron in the single-particle orbital state with envelope wave function $\Psi_{1(2)}(\mathbf{r})$ and spin σ, we define $\mathbf{h} = (\mathbf{h}_1 + \mathbf{h}_2)/2$, $\delta\mathbf{h} = (\mathbf{h}_1 + \mathbf{h}_2)/2$, where the quantum nuclear field operators are $\mathbf{h}_{1(2)} = Av \sum_k \left|\Psi_{1(2)}(\mathbf{r}_k)\right|^2 \mathbf{I}_k$, the sum of electron spins is $\mathbf{S} = \mathbf{S}_1 + \mathbf{S}_2$ and the difference is $\delta\mathbf{S} = \mathbf{S_1} - \mathbf{S_2}$. While the sum $\mathbf{S}$ conserves the total squared electron spin, and can only couple states of different z-projection (e.g., $|T_0\rangle$ to $|T_\pm\rangle$), the difference $\delta\mathbf{S}$ does not preserve the total spin, and therefore couples singlet to triplet (e.g., $|S(1,1)\rangle$ to $|T_0\rangle$ and $|T_\pm\rangle$). The difference term $\propto \delta\mathbf{S}$ will therefore lead to anticrossings in the energy level spectrum, where $|S(1,1)\rangle$ and $|T_\pm\rangle$ or $|T_0\rangle$ cross. Adding equation (29) to the previous double-dot Hamiltonian, $H_{\text{dd}} = H_{\text{C}} + H_{\text{T}} + H_{\text{hf,dd}}$, and making a mean-field ansatz for the nuclear field operators, that is, replacing operators by their expectation values: $\mathbf{h} \to \langle\mathbf{h}\rangle$ [3], leads to the energy level spectrum shown in Figure 6. In the limit of large Zeeman splitting ϵ_z and large negative detuning ϵ', an effective two-level Hamiltonian can be derived in the subspace of lowest-energy singlet and $S^z = 0$ triplet ($|S\rangle$, $|T_0\rangle$) (Coish and Loss, 2005):

$$H_{\text{dd,eff}} = \frac{J}{2}\mathbf{S}\cdot\mathbf{S} + \delta h^z \delta S^z + O\left(\frac{1}{\epsilon_z}\right) \tag{30}$$

An exact solution can be found for pseudospin dynamics in the two-dimensional subspace of $|S\rangle$ and $|T_0\rangle$ under the action of $H_{\text{dd,eff}}$. This solution shows that a singlet–triplet correlator undergoes an interesting power-law decay in a characteristic timescale that can be extended by increasing J (Coish and Loss, 2005), and has been verified in experiment (Laird *et al*., 2006). As is true for the transverse components of a single-electron spin, the singlet–triplet correlator shows a rapid decay if the nuclear spin environment is not in an eigenstate of the relevant nuclear field operator (in this case, δh^z). The decay time can be significantly extended by narrowing the distribution in δh^z eigenstates through measurement (Klauser, Coish and Loss, 2006) or by performing a spin-echo sequence (Petta *et al*., 2005a). Remaining sources of dephasing include the corrections to $H_{\text{dd,eff}}$ (of order $1/\epsilon_z$, which cannot be removed easily) and fluctuations in the electrostatic environment, although the effect of these fluctuations can be removed to leading order at zero-derivative points for the exchange interaction (Coish and Loss, 2005), where:

$$\frac{\mathrm{d}J(\epsilon)}{\mathrm{d}\epsilon} = 0 \tag{31}$$

Recent calculations suggest that these zero-derivative points should be achievable with appropriate control of the confinement potential or magnetic field (Hu and Das Sarma, 2006; Stopa and Marcus, 2006).

Since the hyperfine interaction does not preserve the total spin quantum number of electrons, this interaction plays a very important role in studies on spin-dependent transport. In particular, spin blockade (Weinmann, Häusler and Kramer, 1995; Weinmann, 2003) occurs in double quantum dots (Ono, Austing, Tokura and Tarucha, 2002) when tunneling is allowed between spin singlet $|S(1,1)\rangle \to |S(0,2)\rangle$, but not between spin triplets $|T(1,1)\rangle \nrightarrow |T(0,2)\rangle$, because of a large energy cost due to orbital level spacing and the Pauli principle. This blockade allows for the extraction of features at energy scales much less than temperature, making it an ideal parameter regime in which to perform spectroscopy on double dots (Pioro-Ladrière *et al*., 2003) and spin-resonance experiments, which previously suffered from 'heating' effects in single dots (van der Wiel *et al*., 2003; Koppens *et al*., 2006). The hyperfine interaction mixes the $|S(1,1)\rangle$ and $|T(1,1)\rangle$ states, allowing transport, and effectively removing spin blockade when these states are nearly degenerate. This behavior leads to a number of intriguing effects, including stable undriven oscillations in transport current (Ono and Tarucha, 2004; Erlingsson, Jouravlev and Nazarov, 2005), and a striking magnetic field dependence of leakage current, which allows the extraction of information about the nuclear spin system (Koppens *et al*., 2005; Jouravlev and Nazarov, 2006). Even–odd effects in the spin blockade of few-electron quantum dots have further revealed the shell-filling illustrated in Figure 3 (Johnson *et al*., 2005b).

The influence of spin-dependent terms, causing decoherence or unwanted evolution, is a central issue in quantum-dot spin quantum computing. The requirements for fault-tolerant quantum information processing are very stringent. This raises the bar for required understanding of these environmental influences to a very high level, and guarantees that

Table 2. Experimentally determined energy relaxation and decoherence times in single and double quantum dots. (Reproduced by permission of W.A. Coish *et al*., copyright 2006 Wiley VCH.)

	Decay type	Measured decay time (s)
(i)	Energy relaxation time T_1 between Zeeman-split sublevels	$T_1 > 50\,\mu$s (Hanson *et al*., 2003) (lateral GaAs dot), $T_1 = 0.85$ ms at $B = 8$ T (Elzerman *et al*., 2004) (lateral GaAs dot), $T_1 = 20$ ms at $B = 4$ T (Kroutvar *et al*., 2004) (self-assembled Ga(In)As dot), $T_1 = 170$ ms at $B = 1.75$ T (Amasha *et al*., 2006) (lateral GaAs dot).
(ii)	Single-spin coherence time τ_c due to the hyperfine interaction	$\tau_c = 1 - 10$ns (Bracker *et al*., 2005; Braun, *et al*., 2005; Dutt *et al*., 2005).
(iii)	Singlet–triplet energy relaxation time $T_{1,\mathrm{ST}}$	$T_{1,\mathrm{ST}} \simeq 10 - 500\,\mu$s (Fujisawa *et al*., 2002; Sasaki, Fujisawa, Hayashi and Hirayama, 2005) (vertical dot), $T_{1,\mathrm{ST}} \simeq 0.2 - 2.5$ ms (Hanson *et al*., 2005) (lateral dot), $T_{1,\mathrm{ST}} \simeq 1\,\mu\mathrm{s} - 10$ ms (Petta *et al*., 2005b; Johnson *et al*., 2005a) (lateral double dot).
(iv)	Singlet–triplet coherence time due to hyperfine $\tau_{\mathrm{c,ST}}$	$\tau_{\mathrm{c,ST}} \simeq 10$ ns (Petta *et al*., 2005a) (free-induction decay time), $\tau_{\mathrm{c,ST,echo}} \simeq 1.2\,\mu$s (Petta *et al*., 2005a) (spin-echo envelope decay time).
(v)	Orbital inelastic relaxation time $T_{1,\mathrm{orb}}$ for a single-electron charge state in a double quantum dot	$T_{1,\mathrm{orb}} \simeq 16$ ns (Petta *et al*., 2004).
(vi)	Orbital dephasing time τ_ϕ for a single-electron charge state in a double quantum dot	$\tau_\phi \simeq 1$ ns (Hayashi *et al*., 2003), $\tau_\phi \simeq 400$ ps (Petta *et al*., 2004), (see also the comprehensive review in Fujisawa, Hayashi and Sasaki, 2006).

quantum-dot spin decoherence will remain a challenge for some time to come.

5.3 Experimentally measured decay times

To complete this section on decoherence, here we include a table with some of the most relevant measurements of decoherence and energy relaxation times found in single and double quantum dots (see Table 2).

6 ENTANGLEMENT GENERATION, DISTILLATION, AND DETECTION

In addition to the usual requirements for control and coherence, to demonstrate the true quantum nature of qubits, there have been many suggestions to create and measure nonlocal multiparticle entanglement of electron spins in nanostructures (DiVincenzo and Loss, 1999; Burkard, Loss and Sukhorukov, 2000; Loss and Sukhorukov, 2000; Choi, Bruder and Loss, 2000; Egues, Burkard and Loss, 2002; Burkard and Loss, 2003; Samuelsson, Sukhorukov and Büttiker, 2004; Recher, Sukhorukov and Loss, 2001; Lesovik, Martin and Blatter, 2001; Mélin, 2001; Costa and Bose, 2001; Oliver, Yamaguchi and Yamamoto, 2002; Bose and Home, 2002; Recher and Loss, 2002, 2003; Bena, Vishveshwara, Balents and Fisher, 2002; Saraga and Loss, 2003; Bouchiat *et al*., 2003; Beenakker and Schoenenberger, 2003; Saraga, Altshuler, Loss and Westervelt, 2004; Egues *et al*., 2005). These proposals include suggestions to extract a spin singlet from a superconductor through two quantum dots (Recher, Sukhorukov and Loss, 2001) or nanotubes (Recher and Loss, 2002; Bena, Vishveshwara, Balents and Fisher, 2002), or to create entanglement near a magnetic impurity (Costa and Bose, 2001), through a single quantum dot (Oliver, Yamaguchi and Yamamoto, 2002), from biexcitons in double quantum dots (Gywat, Burkard and Loss, 2002), or through a triple dot (Saraga and Loss, 2003). It may also be possible to distill entanglement (Bennett *et al*., 1997) from an unentangled Fermi gas through Coulomb scattering in a 2DEG (Saraga, Altshuler, Loss and Westervelt, 2004).

As well as providing a proof of quantum-mechanical behavior, entanglement can be used as a resource for measurement-based quantum computing. Some measurement-based schemes rely on the creation of highly entangled cluster states (Raussendorf and Briegel, 2001), which could be generated in quantum-dot arrays using the Heisenberg exchange interaction (Borhani and Loss, 2005). Other measurement-based schemes generate entanglement through partial Bell-state (parity) measurements (Beenakker, DiVincenzo, Emary and Kindermann, 2004), which could also be implemented for spins in quantum dots using spin-to-charge conversion (Engel and Loss, 2005; Coish, Golovach, Egues and Loss, 2006). Independent of the method used, the generation or purification and subsequent detection of entangled electron spins would present a significant milestone on the road to a working quantum-dot quantum computer.

7 CONCLUSIONS AND OUTLOOK

We have presented some of the theoretical and experimental challenges to quantum-dot quantum computing with electron spins. The last few years have seen an extremely rapid rate of progress in experiments which show that many of the required elements of a spin-based quantum-dot quantum computer can be realized in principle. The most significant advances include the reduction of the number of electrons confined to gated quantum dots down to a single electron (Ciorga *et al*., 2000), the demonstration (Hanson *et al*., 2003) and improvement (Hanson *et al*., 2005) of electron-spin readout in gated lateral dots, which has led to the measurement of a spin T_1 time (Elzerman *et al*., 2004), the demonstration of the $\sqrt{\text{SWAP}}$ operation, allowing for the extraction of an ensemble-averaged T_2^* time, and spin-echo methods to extend the decay time within a two-spin encoded subspace (Petta *et al*., 2005a), and most recently the demonstration of single-spin rotations under resonant conditions (Koppens *et al*., 2006, 2007).

To demonstrate viability of the Loss–DiVincenzo proposal, more experiments are needed. Although the Loss–DiVincenzo proposal is scalable in principle, it remains to be seen if there are significant practical obstacles to scaling-up the number of electrons involved well beyond two.

NOTES

[1] Optical initialization is likely more practical for the proposal of (Imamoğlu *et al*., 1999), in which the qubit spins can be widely separated and addressed individually or coupled with optical excitation, rather than the Loss–DiVincenzo proposal, where quantum dots are close, in order to maximizing wave function overlap for exchange-mediated qubit coupling.

[2] Note that this type of pulse will generally lead to a smaller value of P for a given set of parameters since here, $\mathrm{d}\epsilon'/\mathrm{d}t \leq \Delta\epsilon/\tau_{\mathrm{sw}}$, whereas for the linear pulse $\mathrm{d}\epsilon'/\mathrm{d}t = \Delta\epsilon/\tau_{\mathrm{sw}}$ for the entire sweep.

[3] In general, great care should be taken in making such a replacement. See the discussion, for example, in (Coish and Loss, 2005) or (Coish, Yuzbashyan, Altshuler and Loss, 2006).

ACKNOWLEDGMENTS

We acknowledge financial support from the Swiss NSF, the NCCR Nanoscience, EU NoE MAGMANet, DARPA, ARO, ONR, and JST ICORP.

REFERENCES

Al-Hassanieh, K.A., Dobrovitski, V.V., Dagotto, E. and Harmon, B.N. (2006). Numerical modeling of the central spin problem using the spin-coherent-state p-representation. *Physical Review Letters*, **97**, 037204.

Amasha, S., MacLean, K., Zumbühl, D., *et al*. (2006). Measurements of the spin relaxation rate at low magnetic fields in a quantum dot, http://arXiv.org/cond-mat/0607110.

Atature, M., Dreiser, J., Badolato, A., *et al*. (2006). Quantum-dot spin-state preparation with near-unity fidelity. *Science*, **312**, 551–553.

Awschalom, D.D., Loss, D. and Samarth, N. (2002). *Semiconductor Spintronics and Quantum Computing*, Springer-Verlag: Berlin.

Badolato, A., Hennessy, K., Atature, M., *et al*. (2005). Deterministic coupling of single quantum dots to single nanocavity modes. *Science*, **308**, 1158–1161.

Barenco, A., Bennett, C.H., Cleve, R., *et al*. (1995). Elementary gates for quantum computation. *Physical Review A*, **52**, 3457–3467.

Barenco, A., Deutsch, D., Ekert, A. and Jozsa, R. (1995). Conditional quantum dynamics and logic gates. *Physical Review Letters*, **74**, 4083–4086.

Bayer, M., Hawrylak, P., Hinzer, K., *et al*. (2001). Coupling and entangling of quantum states in quantum dot molecules. *Science*, **291**, 451–453.

Beenakker, C.W.J. (1991). Theory of coulomb-blockade oscillations in the conductance of a quantum dot. *Physical Review B*, **44**, 1646–1656.

Beenakker, C.W., DiVincenzo, D.P., Emary, C. and Kindermann, M. (2004). Charge detection enables free-electron quantum computation. *Physical Review Letters*, **93**, 020501.

Beenakker, C.W.J. and Schoenenberger, C. (2003). Quantum shot noise. *Physics Today*, **56**, 37.

Bena, C., Vishveshwara, S., Balents, L. and Fisher, M.P. (2002). Quantum entanglement in carbon nanotubes. *Physical Review Letters*, **89**, 037901.

Bennett, C.H., Brassard, G., Popescu, S., *et al*. (1997). Purification of noisy entanglement and faithful teleportation via noisy channels. *Physical Review Letters*, **78**, 2031.

Biercuk, M., Garaj, S., Mason, N., *et al*. (2005). Gate-defined quantum dots on carbon nanotubes. *Nano Letters*, **5**, 1267–1271.

Blick, R.H., Pfannkuche, D., Haug, R.J., *et al*. (1998). Formation of a coherent mode in a double quantum dot. *Physical Review Letters*, **80**, 4032–4035.

Bonesteel, N.E., Stepanenko, D. and DiVincenzo, D.P. (2001). Anisotropic spin exchange in pulsed quantum gates. *Physical Review Letters*, **87**, 207901.

Borhani, M., Golovach, V.N. and Loss, D. (2005). Spin decay in a quantum dot coupled to a quantum point contact. *Physical Review B*, **73**, 155311.

Borhani, M. and Loss, D. (2005). Cluster states from Heisenberg interactions. *Physical Review A*, **71**, 034308.

Bose, S. and Home, D. (2002). Generic entanglement generation, quantum statistics, and complementarity. *Physical Review Letters*, **88**, 050401.

Bouchiat, V., Chtchelkatchev, N., Feinberg, D., *et al*. (2003). Single-walled carbon nanotube superconductor entangler: noise correlations and Einstein Podolsky Rosen states. *Nanotechnology*, **14**, 77–85.

Bracker, A.S., Stinaff, E.A., Gammon, D., *et al*. (2005). Optical pumping of the electronic and nuclear spin of single charge-tunable quantum dots. *Physical Review Letters*, **94**, 047402.

Braun, P-F., Marie, X., Lombez, L., *et al*. (2005). Direct observation of the electron spin relaxation induced by nuclei in quantum dots. *Physical Review Letters*, **94**, 116601.

Brodsky, M., Zhitenev, N.B., Ashoori, R.C., *et al*. (2000). Localization in artificial disorder: two coupled quantum dots. *Physical Review Letters*, **85**, 2356–2359.

Bulaev, D.V. and Loss, D. (2005a). Spin relaxation and anticrossing in quantum dots: Rashba versus Dresselhaus spin-orbit coupling. *Physical Review B*, **71**, 205324.

Bulaev, D.V. and Loss, D. (2005b). Spin relaxation and decoherence of holes in quantum dots. *Physical Review Letters*, **95**, 076805.

Burkard, G. (2004). Theory of solid state quantum information processing, http://arXiv.org/cond-mat/0409626.

Burkard, G. (2006). Quantum physics: a spin solo. *Nature*, **442**, 749–750.

Burkard, G. and Imamoglu, A. (2006). Ultra-long distance interaction between spin qubits. *Physical Review B*, **74**, 041307(R).

Burkard, G. and Loss, D. (2002). Cancellation of spin-orbit effects in quantum gates based on the exchange coupling in quantum dots. *Physical Review Letters*, **88**, 047903.

Burkard, G. and Loss, D. (2003). Lower bound for electron spin entanglement from beam splitter current correlations. *Physical Review Letters*, **91**, 087903.

Burkard, G., Loss, D. and DiVincenzo, D.P. (1999). Coupled quantum dots as quantum gates. *Physical Review B*, **59**, 2070–2078.

Burkard, G., Loss, D. and Sukhorukov, E.V. (2000). Noise of entangled electrons: Bunching and antibunching. *Physical Review B*, **61**, 16303.

Cerletti, V., Coish, W.A., Gywat, O. and Loss, D. (2005). Recipes for spin-based quantum computing. *Nanotechnology*, **16**, R27.

Choi, M-S., Bruder, C. and Loss, D. (2000). Spin-dependent Josephson current through double quantum dots and measurement of entangled electron states. *Physical Review B*, **62**, 13569–13572.

Chutia, S., Friesen, M. and Joynt, R. (2006). Detection and measurement of the dzyaloshinskii-moriya interaction in double quantum dot systems. *Physical Review B*, **73**, 241304.

Ciorga, M., Sachrajda, A.S., Hawrylak, P., *et al*. (2000). Addition spectrum of a lateral dot from Coulomb and spin-blockade spectroscopy. *Physical Review B*, **61**, 16315.

Cirac, J.I. and Zoller, P. (1995). Quantum computations with cold trapped ions. *Physical Review Letters*, **74**, 4091–4094.

Coish, W.A., Golovach, V.N., Egues, J.C. and Loss, D. (2006). Measurement, control, and decay of quantum-dot spins. *Physica Status Solidi B*, **243**, 3658.

Coish, W.A. and Loss, D. (2004). Hyperfine interaction in a quantum dot: non-markovian electron spin dynamics. *Physical Review B*, **70**, 195340.

Coish, W.A. and Loss, D. (2005). Singlet-triplet decoherence due to nuclear spins in a double quantum dot. *Physical Review B*, **72**, 125337.

Coish, W.A. and Loss, D. (2006). Exchange-controlled single-spin rotations in quantum dots, http://arXiv.org/cond-mat/0610443.

Coish, W.A., Yuzbashyan, E.A., Altshuler, B.L. and Loss, D. (2006). Quantum vs. classical hyperfine-induced dynamics in quantum dots, http://arXiv.org/cond-mat/0610633.

Cortez, S., Krebs, O., Laurent, S., *et al*. (2002). Optically driven spin memory in *n*-doped inas-gaas quantum dots. *Physical Review Letters*, **89**, 207401.

Costa, A.T. and Bose, S. (2001). Impurity scattering induced entanglement of ballistic electrons. *Physical Review Letters*, **87**, 277901.

Deng, C. and Hu, X. (2006). Analytical solution of electron spin decoherence through hyperfine interaction in a quantum dot. *Physical Review B*, **73**, 241303.

DiVincenzo, D.P. (1999). Quantum computing and single-qubit measurements using the spin-filter effect. *Journal of Applied Physics*, **85**, 4785–4787.

DiVincenzo, D.P. (2000). The physical implementation of quantum computation. *Fortschritte Der Physik*, **48**, 771.

DiVincenzo, D.P. and Loss, D. (1999). Quantum computers and quantum coherence. *Journal of Magnetism and Magnetic Materials*, **200**, 202–218.

Domokos, P., Raimond, J.M., Brune, M. and Haroche, S. (1995). Simple cavity-QED two-bit universal quantum logic gate: the principle and expected performances. *Physical Review A*, **52**, 3554–3559.

Duckheim, M. and Loss, D. (2006). Electric-dipole-induced spin resonance in disordered semiconductors. *Nature Physics*, **2**, 195–199.

Dutt, M.V., Cheng, J., Li, B., *et al*. (2005). Stimulated and spontaneous optical generation of electron spin coherence in charged GaAs quantum dots. *Physical Review Letters*, **94**, 227403.

Egues, J.C., Burkard, G. and Loss, D. (2002). Rashba spin-orbit interaction and shot noise for spin-polarized and entangled electrons. *Physical Review Letters*, **89**, 176401.

Egues, J.C., Burkard, G., Saraga, D.S., *et al*. (2005). Shot noise and spin-orbit coherent control of entangled and spin-polarized electrons. *Physical Review B*, **72**, 235326.

Elzerman, J.M., Hanson, R., Greidanus, J.S., *et al*. (2003). Few-electron quantum dot circuit with integrated charge read out. *Physical Review B*, **67**, 161308.

Elzerman, J.M., Hanson, R., Willems van Beveren, L.H., *et al*. (2004). Single-shot read-out of an individual electron spin in a quantum dot. *Nature*, **430**, 431–435.

Engel, H-A., Golovach, V.N., Loss, D., *et al*. (2004). Measurement efficiency and n-shot read out of spin qubits. *Physical Review Letters*, **93**, 106804.

Engel, H-A., Kouwenhoven, L.P., Loss, D. and Marcus, C.M. (2004). Controlling spin qubits in quantum dots. *Quantum Information Processing*, **3**, 115–132.

Engel, H-A. and Loss, D. (2001). Detection of single spin decoherence in a quantum dot via charge currents. *Physical Review Letters*, **86**, 4648.

Engel, H-A. and Loss, D. (2005). Fermionic bell-state analyzer for spin qubits. *Science*, **309**, 586–588.

Erlingsson, S.I., Jouravlev, O.N. and Nazarov, Y.V. (2005). Coherent oscillations of current due to nuclear spins. *Physical Review B*, **72**, 033301.

Erlingsson, S.I. and Nazarov, Y.V. (2002). Hyperfine-mediated transitions between a Zeeman split doublet in GaAs quantum dots: the role of the internal field. *Physical Review B*, **66**, 155327.

Erlingsson, S.I. and Nazarov, Y.V. (2004). Evolution of localized electron spin in a nuclear spin environment. *Physical Review B*, **70**, 205327.

Erlingsson, S.I., Nazarov, Y.V. and Fal'ko, V.I. (2001). Nucleus-mediated spin-flip transitions in GaAs quantum dots. *Physical Review B*, **64**, 195306.

Fal'ko, V.I., Altshuler, B.L. and Tsyplyatyev, O. (2005). Anisotropy of spin splitting and spin relaxation in lateral quantum dots. *Physical Review Letters*, **95**, 076603.

Farhi, E., Goldstone, J., Gutmann, S., *et al*. (2001). A quantum adiabatic evolution algorithm applied to random instances of an NP-complete problem. *Science*, **292**, 472.

Farhi, E., Goldstone, J., Gutmann, S. and Sipser, M. (2000). Quantum computation by adiabatic evolution, http://arXiv.org/quant-ph/0001106.

Fasth, C., Fuhrer, A., Bjork, M. and Samuelson, L. (2005). Tunable double quantum dots in inas nanowires defined by local gate electrodes. *Nano Letters*, **5**, 1487–1490.

Fiederling, R., Keim, M., Reuscher, G., *et al*. (1999). Injection and detection of a spin-polarized current in a light-emitting diode. *Nature*, **402**, 787–790.

Folk, J.A., Potok, R.M., Marcus, C.M. and Umansky, V. (2003). A gate-controlled bidirectional spin filter using quantum coherence. *Science*, **299**, 679–682.

Fujisawa, T., Austing, D.G., Tokura, Y., *et al*. (2002). Allowed and forbidden transitions in artificial hydrogen and helium atoms. *Nature*, **419**, 278.

Fujisawa, T., Hayashi, T. and Sasaki, S. (2006). Time-dependent single-electron transport through quantum dots. *Reports on Progress in Physics*, **69**, 759–796.

Fujisawa, T., Tokura, Y. and Hirayama, Y. (2001). Transient current spectroscopy of a quantum dot in the Coulomb blockade regime. *Physical Review B*, **63**, 081304.

Giedke, G., Taylor, J.M., D'Alessandro, D., *et al*. (2006). Quantum measurement of the nuclear spin polarization in quantum dots. *Physical Review A*, **74**, 032316.

Golden, J.M. and Halperin, B.I. (1996). Relation between barrier conductance and coulomb blockade peak splitting for tunnel-coupled quantum dots. *Physical Review B*, **53**, 3893–3900.

Golovach, V.N., Borhani, M. and Loss, D. (2006). Electric dipole induced spin resonance in quantum dots. *Physical Review B*, **74**, 165319.

Golovach, V.N., Khaetskii, A. and Loss, D. (2004). Phonon-induced decay of the electron spin in quantum dots. *Physical Review Letters*, **93**, 016601.

Golovach, V.N. and Loss, D. (2004). Transport through a double quantum dot in the sequential- and co- tunneling regimes. *Physical Review B*, **69**, 245327.

Graeber, M.R., Coish, W.A., Hoffmann, C., *et al*. (2006). Molecular states in carbon nanotube double quantum dots. *Physical Review B*, **74**, 075427.

Gywat, O., Burkard, G. and Loss, D. (2002). Biexcitons in coupled quantum dots as a source of entangled photons. *Physical Review B*, **65**, 205329.

Gywat, O., Engel, H-A., Loss, D., *et al*. (2004). Optical detection of single-electron spin decoherence in a quantum dot. *Physical Review B*, **69**, 205303.

Hanson, R., van Beveren, L.H.W., Vink, I.T., *et al*. (2005). Single-shot readout of electron spin states in a quantum dot using spin-dependent tunnel rates. *Physical Review Letters*, **94**, 196802.

Hanson, R. and Burkard, G. (2007). Universal set of quantum gates for double-dot spin qubits with fixed inter-dot coupling. *Physical Review Letters*, **98**, 050502.

Hanson, R., Vandersypen, L.M., van Beveren, L.H., *et al*. (2004). Semiconductor few-electron quantum dot operated as a bipolar spin filter. *Physical Review B*, **70**, 241304.

Hanson, R., Witkamp, B., Vandersypen, L.M., *et al*. (2003). Zeeman energy and spin relaxation in a one-electron quantum dot. *Physical Review Letters*, **91**, 196802.

Hatano, T., Stopa, M. and Tarucha, S. (2005). Single-electron delocalization in hybrid vertical-lateral double quantum dots. *Science*, **309**, 268–271.

Hayashi, T., Fujisawa, T., Cheong, H.D., *et al*. (2003). Coherent manipulation of electronic states in a double quantum dot. *Physical Review Letters*, **91**, 226804.

Hirjibehedin, C.F., Lutz, C.P. and Heinrich, A.J. (2006). Spin coupling in engineered atomic structures. *Science*, **312**, 1021–1024.

Hohenester, U. (2004). Optical properties of semiconductor nanostructures: decoherence versus quantum control, http://arXiv.org/cond-mat/0406346.

Hu, X. (2004). Spin-based quantum dot quantum computing, http://arXiv.org/cond-mat/0411012.

Hu, X. and Das Sarma, S. (2006). Charge-fluctuation-induced dephasing of exchange-coupled spin qubits. *Physical Review Letters*, **96**, 100501.

Hüttel, A.K., Ludwig, S., Lorenz, H., *et al*. (2005). Direct control of the tunnel splitting in a one-electron double quantum dot. *Physical Review B*, **72**, 081310.

Hüttel, A.K., Weber, J., Holleitner, A.W., *et al*. (2004). Nuclear spin relaxation probed by a single quantum dot. *Physical Review B*, **69**, 073302.

Imamoğlu, A., Awschalom, D.D., Burkard, G., *et al*. (1999). Quantum information processing using quantum dot spins and cavity QED. *Physical Review Letters*, **83**, 4204–4207.

ITRS (2005). International technology roadmap for semiconductors, http://public.itrs.net/.

Johnson, A.C., Petta, J.R., Marcus, C.M., *et al*. (2005b). Singlet-triplet spin blockade and charge sensing in a few-electron double quantum dot. *Physical Review B*, **72**, 165308.

Johnson, A.C., Petta, J.R., Taylor, J.M., *et al*. (2005a). Relaxation of single electron spins by nuclei in a double quantum dot. *Nature*, **435**, 925.

Jouravlev, O.N. and Nazarov, Y.V. (2006). Electron transport in a double quantum dot governed by a nuclear magnetic field. *Physical Review Letters*, **96**, 176804.

Kato, Y., Myers, R.C., Gossard, A.C. and Awschalom, D.D. (2004). Coherent spin manipulation without magnetic fields in strained semiconductors. *Nature*, **427**, 50–53.

Khaetskii, A.V., Loss, D. and Glazman, L. (2002). Electron spin decoherence in quantum dots due to interaction with nuclei. *Physical Review Letters*, **88**, 186802.

Khaetskii, A.V. and Nazarov, Y.V. (2000). Spin relaxation in semiconductor quantum dots. *Physical Review B*, **61**, 12639–12642.

Khaetskii, A.V. and Nazarov, Y.V. (2001). Spin-flip transitions between Zeeman sublevels in semiconductor quantum dots. *Physical Review B*, **64**, 125316.

Klauser, D., Coish, W.A. and Loss, D. (2006). Nuclear spin state narrowing via gate–controlled rabi oscillations in a double quantum dot. *Physical Review B*, **73**, 205302.

Klimeck, G., Chen, G. and Datta, S. (1994). Conductance spectroscopy in coupled quantum dots. *Physical Review B*, **50**, 2316–2324.

Koiller, B., Hu, X., Capaz, R.B., *et al*. (2005). Silicon-based spin and charge quantum computation. *Anais Da Academia Brasileira De Ciencias*, **77**, 201, http://arXiv.org/cond-mat/0505169.

Koppens, F.H.L., Buizert, C., Tielrooij, K.J, *et al*. (2006). Driven coherent oscillations of a single electron spin in a quantum dot. *Nature*, **442**, 766–771.

Koppens, F.H.L., Folk, J.A., Elzerman, J.M., *et al*. (2005). Control and detection of singlet-triplet mixing in a random nuclear field. *Science*, **309**, 1346–1350.

Koppens, F.H.L., Klauser, D., Coish, W.A, *et al*. (2007). Universal phase shift and non-exponential decay of driven single-spin oscillations, http://arXiv.org/cond-mat/0703640.

Kouwenhoven, L.P., Austing, D.G. and Tarucha, S. (2001). Few-electron quantum dots. *Reports on Progress in Physics*, **64**, 701–736.

Kroutvar, M., Ducommun, Y., Heiss, D., *et al*. (2004). Optically programmable electron spin memory using semiconductor quantum dots. *Nature*, **432**, 81.

Laird, E.A., Petta, J.R., Johnson, A.C., *et al*. (2006). Effect of exchange interaction on spin dephasing in a double quantum dot. *Physical Review Letters*, **97**, 056801.

Lehmann, J. and Loss, D. (2006). Cotunneling current through quantum dots with phonon-assisted spin-flip processes. *Physical Review B*, **73**, 045328.

Lesovik, G.B., Martin, T. and Blatter, G. (2001). Electronic entanglement in the vicinity of a superconductor. *European Physical Journal B*, **24**, 287–290.

Levitov, L.S. and Rashba, E.I. (2003). Dynamical spin-electric coupling in a quantum dot. *Physical Review B*, **67**, 115324.

Levy, J. (2002). Universal quantum computation with spin-1/2 pairs and Heisenberg exchange. *Physical Review Letters*, **89**, 147902.

Lidar, D.A. and Wu, L-A. (2002). Reducing constraints on quantum computer design by encoded selective recoupling. *Physical Review Letters*, **88**, 017905.

Loss, D. and DiVincenzo, D.P. (1998). Quantum computation with quantum dots. *Physical Review A*, **57**, 120.

Loss, D. and Sukhorukov, E.V. (2000). Probing entanglement and nonlocality of electrons in a double-dot via transport and noise. *Physical Review Letters*, **84**, 1035–1038.

Lyanda-Geller, Y.B., Aleiner, I.L. and Altshuler, B.L. (2002). Coulomb "blockade" of nuclear spin relaxation in quantum dots. *Physical Review Letters*, **89**, 107602.

Makhlin, Y., Schön, G. and Shnirman, A. (2001). Quantum-state engineering with Josephson-junction devices. *Reviews of Modern Physics*, **73**, 357–400.

Martin, I., Mozyrsky, D. and Jiang, H.W. (2003). A scheme for electrical detection of single-electron spin resonance. *Physical Review Letters*, **90**, 018301.

Mason, N., Biercuk, M.J. and Marcus, C.M. (2004). Local gate control of a carbon nanotube double quantum dot. *Science*, **303**, 655–658.

Meier, F., Levy, J. and Loss, D. (2003a). Quantum computing with antiferromagnetic spin clusters. *Physical Review B*, **68**, 134417.

Meier, F., Levy, J. and Loss, D. (2003b). Quantum computing with spin cluster qubits. *Physical Review Letters*, **90**, 047901.

Mélin, R. (2001). Electronic EPR-like experiments with superconductors, http://arXiv.org/cond-mat/0105073.

Merkulov, I.A., Efros, A.L. and Rosen, M. (2002). Electron spin relaxation by nuclei in semiconductor quantum dots. *Physical Review B*, **65**, 205309.

Myers, R.C., Ku, K.C., Li, X., *et al*. (2005). Optoelectronic control of spin dynamics at near-terahertz frequencies in magnetically doped quantum wells. *Physical Review B*, **72**, 041302(R).

Ohno, Y., Young, D.K., Beschoten, B., *et al*. (1999). Electrical spin injection in a ferromagnetic semiconductor heterostructure. *Nature*, **402**, 790–792.

Oliver, W.D., Yamaguchi, F. and Yamamoto, Y. (2002). Electron entanglement via a quantum dot. *Physical Review Letters*, **88**, 037901.

Ono, K., Austing, D.G., Tokura, Y. and Tarucha, S. (2002). Current rectification by Pauli exclusion in a weakly coupled double quantum dot system. *Science*, **297**, 1313–1317.

Ono, K. and Tarucha, S. (2004). Nuclear-spin-induced oscillatory current in spin-blockaded quantum dots. *Physical Review Letters*, **92**, 256803.

Ota, T., Rontani, M., Tarucha, S., *et al*. (2005). Few-electron molecular states and their transitions in a single InAs quantum dot molecule. *Physical Review Letters*, **95**, 236801.

Paget, D., Lampel, G., Sapoval, B. and Safarov, V.I. (1977). Low field electron-nuclear spin coupling in gallium arsenide under optical pumping conditions. *Physical Review B*, **15**, 5780–5796.

Pals, P. and MacKinnon, A. (1996). Coherent tunnelling through two quantum dots with Coulomb interaction. *Journal of Physics: Condensed Matter*, **8**, 5401–5414.

Petta, J.R., Johnson, A.C., Marcus, C.M., *et al*. (2004). Manipulation of a single charge in a double quantum dot. *Physical Review Letters*, **93**, 186802.

Petta, J.R., Johnson, A.C., Taylor, J.M., *et al*. (2005a). Coherent manipulation of coupled electron spins in semiconductor quantum dots. *Science*, **309**, 2180–2184.

Petta, J.R., Johnson, A.C., Yacoby, A., *et al*. (2005b). Pulsed-gate measurements of the singlet-triplet relaxation time in a two-electron double quantum dot. *Physical Review B*, **72**, 161301.

Pioro-Ladrière, M., Ciorga, M., Lapointe, J., *et al*. (2003). Spin-blockade spectroscopy of a two-level artificial molecule. *Physical Review Letters*, **91**, 026803.

Potok, R.M., Folk, J.A., Marcus, C.M. and Umansky, V. (2002). Detecting spin-polarized currents in ballistic nanostructures. *Physical Review Letters*, **89**, 266602.

Prinz, G.A. (1998). Magnetoelectronics. *Science*, **282**, 1660–1663.

Prinz, G. and Hathaway, K. (1995). Magnetoelectronics - special issue. *Physics Today*, **48**, 24–25.

Rashba, E.I. and Efros, A.L. (2003). Orbital mechanisms of electron-spin manipulation by an electric field. *Physical Review Letters*, **91**, 126405.

Raussendorf, R. and Briegel, H. (2001). A one-way quantum computer. *Physical Review Letters*, **86**, 5188–5191.

Recher, P. and Loss, D. (2002). Superconductor coupled to two Luttinger liquids as an entangler for electron spins. *Physical Review B*, **65**, 165327.

Recher, P. and Loss, D. (2003). Dynamical coulomb blockade and spin-entangled electrons. *Physical Review Letters*, **91**, 267003.

Recher, P., Sukhorukov, E.V. and Loss, D. (2000). Quantum dot as spin filter and spin memory. *Physical Review Letters*, **85**, 1962–1965.

Recher, P., Sukhorukov, E.V. and Loss, D. (2001). Andreev tunneling, Coulomb blockade, and resonant transport of nonlocal spin-entangled electrons. *Physical Review B*, **63**, 165314.

Requist, R., Schliemann, J., Abanov, A.G. and Loss, D. (2005). Double occupancy errors in quantum computing operations: Corrections to adiabaticity. *Physical Review B*, **71**, 115315.

Salis, G., Kato, Y., Ensslin, K., *et al*. (2001). Electrical control of spin coherence in semiconductor nanostructures. *Nature*, **414**, 619–622.

Samuelsson, P., Sukhorukov, E.V. and Büttiker, M. (2004). Electrical current noise of a beamsplitter as a test of spin entanglement. *Physical Review B*, **70**, 115330.

Saraga, D.S., Altshuler, B.L., Loss, D. and Westervelt, R.M. (2004). Coulomb scattering in a 2D interacting electron gas and production of EPR pairs. *Physical Review Letters*, **92**, 246803.

Saraga, D.S. and Loss, D. (2003). Spin-entangled currents created by a triple quantum dot. *Physical Review Letters*, **90**, 166803.

Sasaki, S., Fujisawa, T., Hayashi, T. and Hirayama, Y. (2005). Electrical pump-and-probe study of spin singlet-triplet relaxation in a quantum dot. *Physical Review Letters*, **95**, 056803.

Schaefers, H. and Strunz, W.T. (2005). Electron spin tomography through counting statistics: a quantum trajectory approach. *Physical Review B*, **71**, 075321.

Schedelbeck, G., Wegscheider, W., Bichler, M. and Abstreiter, G. (1997). Coupled quantum dots fabricated by cleaved edge overgrowth: from artificial atoms to molecules. *Science*, **278**, 1793.

Schliemann, J., Khaetskii, A.V. and Loss, D. (2002). Spin decay and quantum parallelism. *Physical Review B*, **66**, 245303.

Schliemann, J., Khaetskii, A. and Loss, D. (2003). Electron spin dynamics in quantum dots and related nanostructures due to hyperfine interaction with nuclei. *Journal of Physics: Condensed Matter*, **15**, R1809–R1833.

Schliemann, J., Loss, D. and MacDonald, A.H. (2001). Double-occupancy errors, adiabaticity, and entanglement of spin qubits in quantum dots. *Physical Review B*, **63**, 085311.

Schmidt, T., Haug, R.J., Klitzing, K.V., *et al*. (1997). Spectroscopy of the single-particle states of a quantum-dot molecule. *Physical Review Letters*, **78**, 1544–1547.

Shabaev, A., Efros, A., Gammon, D. and Merkulov, I.A. (2003). Optical readout and initialization of an electron spin in a single quantum dot. *Physical Review B*, **68**, 201305(R).

Shenvi, N., de Sousa, R. and Whaley, K.B. (2005a). Nonperturbative bounds on electron spin coherence times induced by hyperfine interactions. *Physical Review B*, **71**, 144419.

Shenvi, N., de Sousa, R. and Whaley, K.B. (2005b). Universal scaling of hyperfine-induced electron spin echo decay. *Physical Review B*, **71**, 224411.

Simon, P. and Loss, D. (2007). Nuclear spin ferromagnetic phase transition in an interacting 2D electron gas. *Physical Review Letters*, **98**, 156401.

Sleator, T. and Weinfurter, H. (1995). Realizable universal quantum logic gates. *Physical Review Letters*, **74**, 4087–4090.

Slichter, C.P. (1980). *Principles of Magnetic Resonance*, Springer-Verlag: Berlin.

de Sousa, R. and Das Sarma, S. (2003). Electron spin coherence in semiconductors: considerations for a spin-based solid-state quantum computer architecture. *Physical Review B*, **67**, 033301.

de Sousa, R., Shenvi, N. and Whaley, K.B. (2005). Qubit coherence control in a nuclear spin bath. *Physical Review B*, **72**, 045330.

Stepanenko, D. and Bonesteel, N.E. (2004). Universal quantum computation through control of spin-orbit coupling. *Physical Review Letters*, **93**, 140501.

Stepanenko, D., Bonesteel, N.E., DiVincenzo, D.P., *et al*. (2003). Spin-orbit coupling and time-reversal symmetry in quantum gates. *Physical Review B*, **68**, 115306.

Stepanenko, D., Burkard, G., Giedke, G. and Imamoglu, A. (2006). Enhancement of electron spin coherence by optical preparation of nuclear spins. *Physical Review Letters*, **96**, 136401.

Stewart, D.R., Sprinzak, D., Marcus, C.M., *et al*. (1997). Correlations between ground and excited state spectra of a quantum dot. *Science*, **278**, 1784–1788.

Stopa, M. and Marcus, C.M. (2006). Magnetic field control of exchange and noise immunity in double quantum dots, http://arxiv.org/cond-mat/0604008.

Tarucha, S., Austing, D.G., Honda, T., *et al*. (1996). Shell filling and spin effects in a few electron quantum dot. *Physical Review Letters*, **77**, 3613.

Taylor, J.M., Engel, H.A., Dur, W., *et al*. (2005). Fault-tolerant architecture for quantum computation using electrically controlled semiconductor spins. *Nature Physics*, **1**, 177–183.

Taylor, J.M., Petta, J.R., Johnson, A.C., *et al*. (2006). Relaxation, dephasing, and quantum control of electron spins in double quantum dots, http://arXiv.org/cond-mat/0602470.

Tokura, Y., van der Wiel, W.G., Obata, T. and Tarucha, S. (2006). Coherent single electron spin control in a slanting Zeeman field. *Physical Review Letters*, **96**, 047202.

Trauzettel, B., Bulaev, D.V., Loss, D. and Burkard, G. (2007). Spin qubits in graphene quantum dots. *Nature Physics*, **3**, 192–196.

Weinmann, D. (2003). Spin blockades in the transport through quantum dots. *LNP Vol. 630: Anderson Localization and Its Ramifications: Disorder, Phase Coherence and Electron Correlations*, **630**, 289–301.

Weinmann, D., Häusler, W. and Kramer, B. (1995). Spin blockades in linear and nonlinear transport through quantum dots. *Physical Review Letters*, **74**, 984–987.

van der Wiel, W.G., de Franceschi, S., Elzerman, J.M., *et al*. (2003). Electron transport through double quantum dots. *Reviews of Modern Physics*, **75**, 1–22.

van der Wiel, W.G., Stopa, M., Kodera, T., *et al*. (2006). Semiconductor quantum dots for electron spin qubits. *New Journal of Physics*, **8**, 28.

Witzel, W.M., de Sousa, R. and Das Sarma, S. (2005). Quantum theory of spectral-diffusion-induced electron spin decoherence. *Physical Review B*, **72**, 161306.

Wolf, S.A., Awschalom, D.D., Buhrman, R.A., *et al*. (2001). Spintronics: a spin-based electronics vision for the future. *Science*, **294**, 1488–1495.

Wróbel, J., Dietl, T., Łusakowski, A., *et al*. (2004). Spin filtering in a hybrid ferromagnetic-semiconductor microstructure. *Physical Review Letters*, **93**, 246601.

Wu, L., Byrd, M. and Lidar, D. (2002). Polynomial-time simulation of pairing models on a quantum computer. *Physical Review Letters*, **89**, 57904.

Wu, L-A., Lidar, D.A. and Friesen, M. (2004). One-spin quantum logic gates from exchange interactions and a global magnetic field. *Physical Review Letters*, **93**, 030501.

Wu, L., Zanardi, P. and Lidar, D. (2005). Holonomic quantum computation in decoherence-free subspaces. *Physical Review Letters*, **95**, 130501.

Yao, W., Liu, R-B. and Sham, L.J. (2006). Theory of electron spin decoherence by interacting nuclear spins in a quantum dot. *Physical Review B*, **74**, 195301.

Yao, W., Liu, R-B. and Sham, L.J. (2007). Restoring coherence lost to a mesoscopic bath. *Physical Review Letters*, **98**, 077602.

Yuzbashyan, E.A., Altshuler, B.L., Kuznetsov, V.B. and Enolskii, V.Z. (2005). Solution for the dynamics of the bcs and central spin problems. *Journal of Physics A: Mathematical and General*, **38**, 7831.

Zener, C. (1932). Non-adiabatic crossing of energy levels. *Proceedings of the Royal Society of London*, **137**, 696.

Ziegler, R., Bruder, C. and Schoeller, H. (2000). Transport through double quantum dots. *Physical Review B*, **62**, 1961–1970.

Zumbühl, D.M., Marcus, C.M., Hanson, M.P. and Gossard, A.C. (2004). Cotunneling spectroscopy in few-electron quantum dots. *Physical Review Letters*, **93**, 256801.

The Magnetic Resonance Force Microscope

P. Chris Hammel and Denis V. Pelekhov
Ohio State University, Columbus, OH, USA

1 INTRODUCTION

The emerging technique of magnetic resonance force microscopy (MRFM) (Sidles, 1991) was conceived by Sidles (1992) as a tool that could provide the revolutionary capability for three-dimensional imaging of single-copy biomolecules. This challenging goal has been augmented by a growing interest in applying it to imaging, especially subsurface imaging, of a broad range of materials and devices including those that are the subject of this handbook.

New materials and devices with unprecedented capabilities and levels of performance are being created by tailoring the structure and composition of multicomponent materials at the nanometer scale. Some of the most important examples are systems incorporating and exploiting electronic spin in its many manifestations including ferromagnetism. A central component of a successful materials development program is the availability of characterization tools. Progress in the development of spin electronics materials and devices will depend on tools capable of providing detailed microscopic information about the electronic, magnetic, and structural properties of these materials systems. In addition to studying the constituents of these systems the ability to image and characterize buried interfaces in multicomponent systems is a particularly important requirement.

The MRFM is a novel scanned-probe instrument which combines the three-dimensional imaging capabilities of magnetic resonance imaging (MRI) with the high sensitivity and resolution of atomic force microscopy. It will enable nondestructive, chemical-specific, high-resolution microscopic studies and imaging of *subsurface* properties of a broad range of materials. Dramatic improvements in the capabilities of the MRFM in the last decade have confirmed the validity of the approach in nuclear magnetic resonance (NMR) (Rugar *et al*., 1994), electron spin resonance (ESR) (Rugar, Yannoni and Sidles, 1992; Hammel, Zhang, Moore and Roukes, 1995; Bruland *et al*., 1998) and ferromagnetic resonance (FMR) experiments (Zhang, Hammel and Wigen, 1996; Wago, Botkin, Yannoni and Rugar, 1998; Zhang *et al*., 1998; Hammel, Zhang and Midzor, 1998). In the quest for improved sensitivity a recent milestone – the detection of a single electronic spin using by MRFM – has been demonstrated by the IBM group (Rugar, Budakian, Mamin and Chui, 2004). Several good reviews are available (Sidles *et al*., 1995; Yannoni, Züger, Rugar and Sidles, 1996; Pelekhov *et al*., 2002; Wigen, Roukes and Hammel, 2006).

Because spatial resolution in MRI is limited by the requirement that adequate signal (compared to detection noise) be obtained from the resolved volume, this breakthrough heralds new horizons in magnetic resonance imaging. This is a unique accomplishment amongst single spin detectors in that MRFM couples directly to the electron's magnetic

Handbook of Magnetism and Advanced Magnetic Materials. Edited by Helmut Kronmüller and Stuart Parkin. Volume 5: *Spintronics and Magnetoelectronics*. ISBN: 978-0-470-02217-7.

dipole moment. Other high sensitivity approaches exploit mechanisms that couple the spin of the electron to its spatial degrees of freedom, hence allowing the spin to be detected through its coupling to the electronic charge. The much larger interaction force afforded by coupling to the charge carries the limitations associated with the particular environment required to obtain the needed interaction between the electron spin and orbital degrees of freedom. MRFM is a general technique applicable wherever conventional magnetic resonance would apply, this generality of applicability is a central strength of the MRFM.

The development of MRFM instruments capable of fulfilling these goals will be built on techniques that improve sensitivity and overcome the challenges inevitable in applying them under various the experimental conditions these applications entail. In this chapter, we focus on these two aspects of MRFM: Sections 2–4 discuss the fundamentals of the technique and the various components of a microscope, and in Section 5 several applications to problems will be discussed.

2 UNDERLYING TECHNOLOGIES

2.1 Magnetic resonance

2.1.1 Fundamentals

Electrons and many atomic nuclei possess a magnetic moment μ. This moment is related their spin angular momentum J by the gyromagnetic ratio γ which is unique for each moment

$$\boldsymbol{\mu} = \gamma \mathbf{J} \tag{1}$$

The electronic moment $\mu_e = 9.28 \times 10^{-24}\,\mathrm{J\,T^{-1}} \approx \mu_\mathrm{B}$ is approximately 10^3 times larger than nuclear moments. Because spin moments possess both magnetic moment and angular momentum, the torque exerted by an external magnetic field H results in precession of the moment about the field:

$$\frac{\mathrm{d}\boldsymbol{\mu}}{\mathrm{d}t} = \boldsymbol{\mu} \times \gamma \mathbf{H} \tag{2}$$

The precession frequency (the Larmor frequency) is $\omega_\mathrm{L} = \gamma H$.

A magnetic moment in a magnetic field H exhibits a resonant response to a transverse magnetic field H_1 oscillating at frequency ω_L. This effect emerges in a simple quantum mechanical as well as classical picture. The Hamiltonian for a magnetic moment in a magnetic field H applied along the $\hat{z}$ direction, is

$$\mathcal{H} = -\boldsymbol{\mu} \cdot \mathbf{H} \tag{3}$$

hence,

$$E_m = -\gamma \hbar H m \tag{4}$$

where $m = J, J-1, \ldots, -J+1, -J$ is the projection of the spin angular momentum $\mathbf{J}$ along the field axis $\mathbf{H}$. Therefore the energy of the transition between states having initial and final spin projections m_i and m_f is

$$\Delta E = -\gamma \hbar H \Delta m \tag{5}$$

where $\Delta m = m_f - m_i$. The transition is stimulated by a transverse oscillating field $H_1 = H_1 \hat{x} \cos(\omega t)$. The matrix element for this perturbation is

$$\left\langle m_f \left| -\gamma \hbar H_1 J_x \right| m_i \right\rangle \tag{6}$$

Writing $J_x = (1/2)(J_+ + J_-)$ we see it is nonzero only for $\Delta m = \pm 1$. Thus the energy of the allowed resonant transitions is

$$|\Delta E| = \gamma \hbar H = \hbar \omega_\mathrm{L} \tag{7}$$

and therefore energy is absorbed at the resonant excitation frequency $\omega_\mathrm{L} = \gamma H$.

2.1.2 Spin susceptibility

The spin polarization of an ensemble of N particles of spin J in thermal equilibrium at temperature T with a magnetic field of magnitude H_0 is governed by Boltzmann statistics (Abragam, 1961). The populations of energy levels of the spin system are proportional to $\exp(-E_m/k_\mathrm{B}T)$. The net equilibrium magnetization M of the ensemble is

$$M = N\gamma\hbar \frac{\sum_{m=-J}^{J} m \exp(-E_m/k_\mathrm{B}T)}{\sum_{m=-J}^{J} \exp(-E_m/k_\mathrm{B}T)} \tag{8}$$

Exploiting the high-temperature approximation (usually an excellent approximation) $E_m/k_\mathrm{B}T \ll 1$ we obtain the following expression for M and the spin susceptibility $\chi_0 = M/H_0$:

$$M = \frac{N\gamma^2\hbar^2 J(J+1)}{3k_\mathrm{B}T} H_0 = \chi_0 H_0 \tag{9}$$

2.1.3 Spin relaxation

A spin system that is removed from this thermal equilibrium state will regain it through interactions with its environment, a thermal reservoir, typically the crystal lattice hosting the spin, at temperature T. This process requires transitions between spin states, and these

require fluctuating magnetic fields analogous to the field H_1 described in Section 2.1.1 above. These fields must fluctuate at ω_L and have a component oriented perpendicular to the direction of the polarizing magnetic field H_0. The time evolution of ensemble magnetization M is given by

$$\frac{dM_z}{dt} = -\frac{M_z - M_0}{T_1} \tag{10}$$

where T_1 is the longitudinal spin relaxation time that is determined by the intensity of fluctuations of the transverse local field at the frequency $\omega_L = \gamma H_0$. It describes the process of realigning the spin with the direction of polarizing magnetic field. It can be expressed (Abragam, 1961) in terms of the transverse fluctuating fields $H_\pm$ capable of driving $\Delta m = \pm 1$ transitions between $|m\rangle$ states:

$$\frac{1}{T_1} = \gamma^2 \int_{-\infty}^{\infty} \langle H_\pm(0) H_\pm(\tau)\rangle e^{i\gamma H_0 \tau} d\tau \tag{11}$$

The integral is the spectral density $J_\pm$ of the field fluctuations, given by the Fourier transform of the time autocorrelation function of the field fluctuations, and it describes the intensity of these fluctuations at frequency ω:

$$J_\pm(\omega) = \int_{-\infty}^{\infty} \langle H_\pm(0) H_\pm(\tau)\rangle e^{i\omega\tau} d\tau \tag{12}$$

Hence we see that the rate at which spins relax is proportional to this spectral density evaluated at the Larmor frequency, that is, those fluctuating fields capable of causing $\Delta m = \pm 1$ transitions.

A monochromatic transverse field H_1 can coherently rotate M_z into the $\hat{x}-\hat{y}$ plane thus generating a transverse magnetization M_x and M_y; this magnetization will subsequently decay for two reasons. Inhomogeneous relaxation results if different spins experience different magnetizing fields due to spatial inhomogeneity. Different spins will precess at different frequencies causing loss of coherence and eventually loss of the transverse magnetization. A Lorentzian distribution of fields with a half-width ΔH will decohere the transverse magnetization on a timescale:

$$T_2^* = (\gamma \Delta H)^{-1} \tag{13}$$

Interactions between nuclear spins also cause decoherence of the transverse magnetization; these are described by transverse spin relaxation time T_2: (Abragam, 1961)

$$\frac{dM_x}{dt} = -\frac{M_x}{T_2}, \frac{dM_y}{dt} = -\frac{M_y}{T_2} \tag{14}$$

2.1.4 Rotating frame of reference

It is helpful in understanding the dynamics of spins simultaneously experiencing static and oscillating transverse fields to apply a simple transformation (Slichter, 1989) into a frame of reference that rotates about the axis defined by the applied field $\mathbf{H}_0$ (typically $\hat{z}$). The linearly polarized transverse oscillating rf field $H_x = 2H_1 \cos(\omega_{rf} t)$ that is applied in magnetic resonance can be written as a superposition of two oppositely circularly polarized fields of amplitude H_1 rotating with frequencies $\pm\omega_{rf}$ (Abragam, 1961). In practice, only one of the circularly polarized components need be considered since the counter-rotating component is far off resonance ($2\omega_{rf}$) and has little effect on the spin system. In a frame rotating at ω_{rf} the first oscillating field is static, so the magnetic field seen by a spin (see Figure 1) is given by:

$$\mathbf{H}_{eff} = \left(H_z^{tot} - \frac{\omega_{rf}}{\gamma}\right)\hat{z} + H_1\hat{x} \tag{15}$$

Here $H_z^{tot} = H_0 + H_z^{tip}$ to explicitly allow for the fact that in MRFM the field of the micromagnetic tip H_{tip} adds to the field experienced by the sample. In the rotating frame, the resonance condition leads to a particularly simple situation:

$$\frac{\Delta\omega}{\gamma} = H_z^{tot} - \frac{\omega_{rf}}{\gamma} = 0 \Rightarrow \mathbf{H}_{eff} = H_1\hat{x} \tag{16}$$

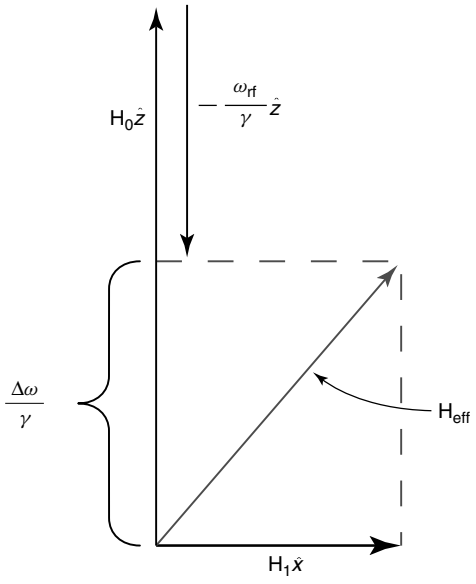

Figure 1. Diagram of magnetic fields in a frame of reference rotating about $\hat{\mathbf{z}}$ with angular frequency ω_{rf}. The resulting effective field $\mathbf{H}_{eff}$ is the vector sum of the applied magnetic field $\mathbf{H}_0$, the transverse field $\mathbf{H}_1$ and the field $-(\omega_{rf}/\gamma)\hat{z}$ that accounts for the transformation to the rotating frame of reference.

Hence the magnetization precesses about $H_1\hat{x}$ at a frequency γH_1, the Rabi frequency. The $\hat{x}$ component of H^{tip} is static and much less than H_0, so it can be neglected.

2.1.5 The Bloch equations

The equations of motion (equation (2)) for the magnetization **M** can be written in the rotating frame of reference including longitudinal and transverse spin relaxation as

$$\frac{\mathrm{d}\mathbf{M}}{\mathrm{d}t} = \gamma\,(\mathbf{M} \times \mathbf{H}_{\text{eff}}) - \frac{M_x\hat{x} + M_y\hat{y}}{T_2} - \frac{M_z - M_0}{T_1}\hat{z} \quad (17)$$

The steady-state solutions of these, the well-known Bloch equations (Bloch, 1946; Abragam, 1961), are

$$M_x = \frac{\Delta\omega\gamma H_1 T_2^2}{1 + (T_2\Delta\omega)^2 + \gamma^2 H_1^2 T_1 T_2} M_0 \quad (18)$$

$$M_y = \frac{\gamma H_1 T_2}{1 + (T_2\Delta\omega)^2 + \gamma^2 H_1^2 T_1 T_2} M_0 \quad (19)$$

$$M_z = \frac{1 + (\Delta\omega T_2)^2}{1 + (T_2\Delta\omega)^2 + \gamma^2 H_1^2 T_1 T_2} M_0 \quad (20)$$

where $\Delta\omega = \omega_{\text{rf}} - \omega_{\text{L}}$. The frequency dependence of $M_z(\omega)$, related to the magnetic resonance lineshape, is a (negative-going) Lorentzian whose minimum occurs at $\Delta\omega = 0$. The linewidth, or full width at half intensity, $\delta\omega$ is

$$\delta\omega = 2\frac{\sqrt{1 + \gamma^2 H_1^2 T_1 T_2}}{T_2} \quad (21)$$

2.2 Magnetic resonance imaging

Magnetic resonance imaging (MRI) is a large and rich field that employs an applied magnetic field gradient to map the spatial location of a particular volume onto either the frequency or the applied homogeneous field of a detected magnetic resonance signal. The relationship between the frequency ω_{L} of a spin and the magnetic field H it experiences is

$$\omega_{\text{L}} = \gamma H \quad (22)$$

A magnetic field gradient applied along the $\hat{z}$ direction $\mathrm{d}H/\mathrm{d}z$ creates a spatial distribution of spin resonant frequencies:

$$\omega_{\text{L}}(z) = \gamma\left(H_0 + \frac{\mathrm{d}H_z}{\mathrm{d}z}z\right) \quad (23)$$

Conventional MRI (Callaghan, 1991) employs pulsed magnetic resonance techniques that produce a time-domain spin echo signal. This signal will decay rapidly as a consequence of the broad range of fields present, that is, it will exhibit a short T_2^* (see equation (13)). The Fourier transform of this time-domain decay will produce spectrum in which the signal intensity at a particular frequency corresponds to the number spins at the z-coordinate prescribed by the field gradient.

Alternatively, one can employ monochromatic rf radiation of frequency ω_{rf}, then only those spins lying on a surface of constant field (perpendicular to the field gradient) at z_{res} will contribute to the signal:

$$z_{\text{res}} = \frac{\left(\frac{\omega_{\text{rf}}}{\gamma} - H_0\right)}{\frac{\mathrm{d}H_z}{\mathrm{d}z}} \quad (24)$$

The thickness δz of the resonance volume is determined by the *homogeneous* linewidth of the sample $(\gamma T_2)^{-1}$

$$\delta z = \frac{(\gamma T_2)^{-1}}{\frac{\mathrm{d}H_z}{\mathrm{d}z}} \quad (25)$$

This width determines the spatial resolution of MRI.

The resolution of MRI is limited by detection sensitivity and the requirement that the resolved volume be large enough to provide acceptable signal-to-noise ratio. Pulsed MRI protocols employ pulsed spatial field gradients applied along three orthogonal directions combined with rf pulses to assign a unique value of spin precession frequency and phase to spins within a resolved region having volume $(\delta z)^3$. We see from equation (25) that spatial resolution can be improved by increasing the field gradient strengths. This improvement comes at the price of diminished signal which is proportional to the number of spins $N_{\text{spins}} = n(\delta z)^3$ in the volume element (n is the spin density). Conventional spectrometers can detect the signal from 10^9 electron spins ($\sim 10^{15}$ nuclear spins) in bandwidths of order 1 Hz. The finest spatial resolution reported in inductively detected nuclear micro-MRI is at the level of $(\sim 3\,\mu\text{m})^3$ (Ciobanu, Seeber and Pennington, 2002).

2.3 Scanned-probe microscopy

Scanned-probe microscopy (SPM) refers to a large family of experimental techniques based on detection of a local interaction between a sample and a microscale probe that can be precisely positioned over the sample. Raster scanning of the microprobe over the sample surface provides a spatial map of the detected interaction.

2.3.1 Scanning tunneling microscopy

The first scanned-probe microscope was the scanning tunneling microscope (STM) invented by Gerd Binnig and Heini Rohrer in 1982. In this instrument an atomically sharp

conducting needle is brought close to conducting surface, close enough for electrons tunnel through the vacuum gap (typically $\sim$1 Å) between the tip and the surface in the presence of a potential difference. The extremely short range of the tunneling interaction allows mapping of the local density of electronic states with atomic scale resolution. Mapping of surface topography, local state spectroscopy, and atomic manipulation have all been accomplished with the STM. The STM is, however, limited to conducting surfaces.

2.3.2 Atomic force microscopy

The atomic force microscope (AFM) uses as a probe a flexible micromechanical cantilever with a sharp tip. The interaction between this probe and the surface is detected by measuring the resulting displacement of the cantilever. The typical magnitude of the forces involved is 10^{-9}–10^{-12} N. The displacement of the cantilever is measured using optical displacement detection. The AFM can operate on insulating as well as conducting surfaces, and also provides information about the surface of the sample. AFM can be used for mapping surface topography, stiffness, local friction, and for surface manipulation. It is usually operated in one of two modes: contact mode and noncontact mode. In contact mode the cantilever is in hard contact with the surface and the displacement of the cantilever under the influence of the force of Pauli repulsion is measured. In noncontact mode, an oscillating cantilever hovers above the sample surface and the local gradient of the long-range dipolar (Van der Waals) force is measured by detecting the consequent shift of the natural frequency of the cantilever ω_c. The spatial resolution of AFM is defined, depending on the mode of operation, by parameters such as the radius of the cantilever tip (typically $\sim$10 nm) and the probe–sample separation. Under proper conditions atomic resolution is achievable (Giessibl, 2003).

2.3.3 Magnetic force microscope

The magnetic force microscope (MFM) is a form of AFM that detects the dipolar magnetostatic interaction between the magnetic tip and magnetic dipoles in a ferromagnetic sample. The tip is scanned at a controlled distance above the sample without direct contact. The typical probe–sample interaction has similar magnitude: 10^{-9}–10^{-12} N.

3 THE MRFM INSTRUMENT

MRFM is similar to MFM; the essential difference is the addition of an applied rf field to enable the sample magnetization to be manipulated by magnetic resonance techniques. Because the goal is high spatial resolution imaging, the signal detected is, in general, from a small number of paramagnetic spins, hence the forces are much smaller than in the case of other force microscopies.

A micromechanical cantilever with a micromagnetic probe tip is brought close to the sample surface. The force F exerted on the magnetic tip by magnetic moments in the sample is

$$\mathbf{F} = -(\mathbf{m} \cdot \nabla)\mathbf{B} \tag{26}$$

where $\mathbf{m}$ is the magnetic moment of the sample and $\nabla\mathbf{B}$ is the gradient of the magnetic field of the micromagnetic tip. This force will deflect the compliant cantilever; sensitive displacement detection allows this force to be measured. Using magnetic resonance techniques, the sample magnetization is manipulated at or near the resonant frequency ω_c of the cantilever. The amplitude of the cantilever response is multiplied by Q thus reducing the demands on the displacement detection. Forces as small as 10^{-18} N have been detected (Hoen *et al*., 1994). MRFM can be applied for detection of any kind of magnetic resonance: ESR, NMR, and FMR. Force detection of magnetic resonance detection is far more sensitive than conventional inductive detection, and recently Rugar and coworkers demonstrated MRFM detection of a single electron spin (Rugar, Budakian, Mamin and Chui, 2004). By comparison, the sensitivity of a commercially available inductively detected ESR spectrometer is $\sim 10^9$ spins.

3.1 Micromechanical resonator

The heart of the MRFM is the resonant micromechanical force sensor. The most commonly used structure is a micromechanical beam of length L, width W and thickness T typically clamped at one end, that is, configured as a cantilever, though doubly clamped is also feasible. Other structures such as torsional oscillators (Barrett *et al*., 1998) have also been used for MRFM force detection however, cantilevers are by far more popular and we will focus on them here. MRFM cantilevers with characteristic dimensions $L \approx 300$–$500\,\mu$m, $W \approx 20\,\mu$m and $T \approx 0.5\,\mu$m (see Figure 2) can be fabricated by standard surface micromachining techniques (Madou, 2002). Most commonly MRFM cantilevers are made from Si and Si_3N_4.

3.1.1 The cantilever as a simple harmonic oscillator

The motion of a micromechanical beam resonator is described by the Euler- Bernoulli equation

$$\frac{\partial^2}{\partial x^2}\left[EI(x)\frac{\partial^2}{\partial x^2}z(x,t)\right] + \rho A(x)\frac{\partial^2}{\partial t^2}z(x,t) = F(x,t) \tag{27}$$

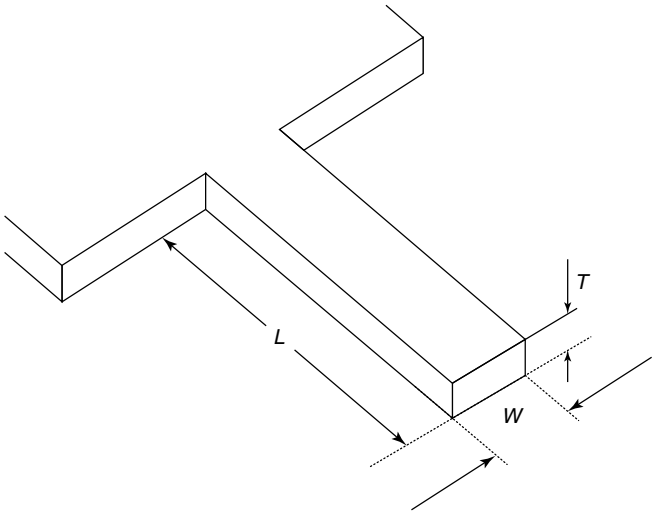

Figure 2. Schematic diagram of simple rectangular micromechanical cantilever.

where $z(x,t)$ is the transverse displacement of the beam, x is the coordinate along the beam, t is time, E is Young's modulus, ρ is the mass density, $I(x)$ is the moment of inertia about the centroid of the beam, $A(x)$ is the cross-sectional area of the beam and $F(x,t)$ is the external applied force. It can be shown that small vibrations at a coordinate x on the beam can be described by a point mass-on-spring model with effective parameters obtained from equation (27) using appropriate boundary conditions. The resulting equation of motion, with dissipation terms included, is that of a simple harmonic oscillator (SHO):

$$m\frac{\partial^2}{\partial t^2}z(t) + \frac{m\omega_c}{Q}\frac{\partial}{\partial t}z(t) + kz(t) = F(t) \tag{28}$$

where the effective parameters are the resonant frequency of the cantilever ω_c, the effective mass m of the resonator, the quality factor Q and the spring constant k of the resonator.

3.1.2 Resonator parameters

The effective parameters in equation (28) for the fundamental vibration mode are obtained from equation (27)

$$\omega_0 = a_1\sqrt{\frac{ET^2}{\rho L^4}} \tag{29}$$

$$k = a_2\frac{ET^3W}{L^3} \tag{30}$$

$$m = a_3\rho LTW \tag{31}$$

The numerical prefactors depend on x and the boundary conditions used to solve equation (27). If x corresponds to the free end of a simple rectangular cantilever (shown in Figure 2), the prefactors are $a_1 \approx 1.0$, $a_2 \approx 0.25$ and $a_3 \approx 0.25$.

3.1.3 Resonator response to oscillatory excitation

MRFM force detection exploits the response of a cantilever to an oscillatory force

$$F(t) = F_0 e^{\iota\omega t} \tag{32}$$

In the low damping approximation ($Q \gg 1$) the cantilever displacement is

$$z(\omega,t) = A_0 e^{\iota(\omega t+\theta_0)} + e^{-\frac{\omega_c}{2Q}t}\left(C_1 e^{-\iota\omega_c t} + C_2 e^{\iota\omega_c t}\right) \tag{33}$$

where

$$A_0(\omega) = \frac{F_0/m}{\sqrt{(\omega_c^2-\omega^2)^2 + (\omega_c\omega/Q)^2}} \tag{34}$$

$$\theta_0(\omega) = \arctan\left[\frac{\omega_c\omega}{Q(\omega^2-\omega_c^2)}\right] \tag{35}$$

where C_1 and C_2 are complex coefficients determined by initial conditions.

The first term of equation (33) gives the steady-state response of the cantilever. While the response of the cantilever to a static force F_0 is $A_0(0) = F_0/k$ the response to an oscillatory force of the same magnitude at $\omega = \omega_c$ is $A_0(\omega_c) = QF_0/k$, that is the oscillation amplitude is multiplied by the quality factor Q of the cantilever, typically 10^4–10^5, compared to the off-resonant response. This has the important consequence of reducing the *displacement readout* sensitivity (see Section 3.2) needed to ensure that it doesn't limit overall sensitivity.

The second term in equation (33) represents the transient response of the cantilever which decays on the oscillator response timescale

$$\tau = \frac{2Q}{\omega_c} \tag{36}$$

This reflects the fact that changing the amplitude involves changing the oscillator energy by means of the rather small signal force. When an oscillatory force is applied to an otherwise undriven resonator its oscillation amplitude will grow until a steady state is reached in which the work done by the external force (on resonance the force is in phase with the velocity, so it performs work) is balanced by the energy dissipated per cycle ($\propto Q^{-1}$). The response time τ reflects the time required to increase the energy of the resonator to this equilibrium. This time can be long for the high Q cantilevers used in MRFM: typically $Q \sim 5\times10^4$ and $\omega_0 = 2\pi\times10^4$ Hz, so $\tau \approx 1.6$ s. This slow response

can be substantially improved by the application of negative force feedback without significantly degrading the cantilever force sensitivity (Mertz, Marti and Mlynek, 1993; Bruland, Garbini, Dougherty and Sidles, 1996) if necessary.

3.2 Displacement detection

3.2.1 Optical interferometry

Optical displacement detection based on fiber-optic interferometry (Albrecht, Grütter, Rugar and Smith, 1992) is currently nearly universal in MRFM experiments. Laser light launched into one port of a directional fiber coupler (see Figure 3) propagates to the end of the fiber positioned a distance δ from the backside of the cantilever. The gap between the end of the fiber and the reflective cantilever surface forms an interferometric cavity. Cantilever motion changes this gap altering the interference between the reference beam internally reflected off the end of the fiber and the signal beam reflected off the cantilever and back into the fiber. The dependence of the light power on δ is

$$P_p \propto P_{s0} + P_{r0} + 2\sqrt{P_{s0}P_{r0}}\cos\left(\frac{4\pi}{\lambda}\delta\right) \tag{37}$$

where λ is the wavelength of the laser light and P_{s0} and P_{r0} are the powers of the signal and reference beams respectively. To maximize the displacement sensitivity $\mathrm{d}P_p/\mathrm{d}\delta$, the interferometric cavity should be tuned such that

$$\delta = \frac{\lambda}{4}\left(\frac{1}{2} \pm n\right), \quad n = 1, 2, 3 \ldots \tag{38}$$

The amplitude of the reference and the signal beams depends on the power of the laser light P_{laser} and on the reflectivity R_s of the cantilever and R_r of the end of the fiber, so the displacement sensitivity is

$$\left|\frac{\mathrm{d}P_p}{\mathrm{d}\delta}\right| = \frac{8\pi}{\lambda}P_{\mathrm{laser}}(1 - R_r)R_sR_r \tag{39}$$

The sensitivity can be optimized by tuning the reflectivity of the interferometric surfaces with a metallic coating. A displacement noise floor of $10^{-13}\,\mathrm{m\,Hz^{-1/2}}$ can be straightforwardly achieved.

3.2.2 Alternative displacement detection methods

While optical fiber interferometric displacement detection is quite popular, there are other approaches that offer advantages, for instance, in applications to photosensitive samples or where straightforward electrical readout is desired, perhaps at the expense of displacement sensitivity.

Piezoresistive

Piezoresistive displacement detection is based on measuring the change in resistance of the cantilever material resulting from stress induced by cantilever displacement. This approach has been implemented (Arlett *et al.*, 2006) with good sensitivity in Si cantilevers supported by two thin legs with a thin piezoresistive (p^+ Si) top layer. The p^+ layer forms a continuous current path through the legs, and bending will induce a stress σ leading to a change ΔR in the resistance of this path. This can in turn be related to displacement Δz of the end of the cantilever:

$$D \equiv \frac{\Delta R}{R}\frac{1}{\Delta z} = \frac{\Pi_{\mathrm{eff}}\sigma}{\Delta z} = \Pi_{\mathrm{eff}}\frac{3}{2}E\frac{h}{L^2}\left(1 - \frac{\lambda}{2L}\right) \tag{40}$$

where Π_{eff} is the effective piezoresistive coefficient of the material, E is Young's modulus, L is the length of the cantilever, h is its thickness and λ is the length of the piezoresistive region.

The minimum detectable displacement δz_{min} of the cantilever, limited by the Johnson noise in the resistor and $1/f$ noise (Yu *et al.*, 2001), is

$$\delta z_{\mathrm{min}} = \frac{4}{DV}\left[\frac{\alpha V^2}{N}\ln\frac{f_1}{f_2} + 4k_{\mathrm{B}}TR(f_1 - f_2)\right]^{1/2} \tag{41}$$

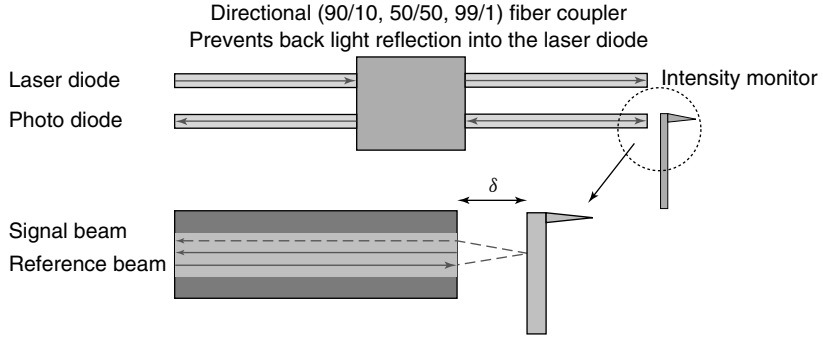

Figure 3. Schematic diagram of the optical fiber interferometer. δ is the distance between the end of the fiber and the cantilever.

where V is the bias voltage, α the $1/f$ noise parameter, N the number of carriers and f_1 and f_2 the upper and the lower limits of the measurement bandwidth. The typical displacement noise floor reported with piezoresistive cantilevers is of the order of $10^{-11}\,\mathrm{m\,Hz^{-1/2}}$ at room temperature. Experimental force sensitivities of $235\,\mathrm{aN\,Hz^{-1/2}}$ and $17\,\mathrm{aN\,Hz^{-1/2}}$ have been obtained at room temperature and 4.2 K, respectively (Arlett *et al*., 2006); optimal performance was obtained at an excitation current that balanced the opposing influences of readout noise and self heating.

Though this detection scheme has yet to be used in MRFM experiments, an integrated piezoresistive displacement detector offers the advantage that there is no need for precision alignment of the cantilever with the detector. This step can be time consuming and its elimination could simplify MRFM experiments and hasten the dissemination of MRFM techniques to a broad research community.

Capacitive displacement detection using a microwave tank circuit

The capacitance between two electrodes varies with separation, so the displacement of a cantilever can be detected by measuring the capacitance C_p between the micromechanical resonator and a sensing electrode. Assuming small cantilever displacements, the corresponding change of the capacitance δC_p is

$$|\delta C_p| = C_p \frac{\delta d}{d} = \epsilon\epsilon_0 \frac{A}{d}\frac{\delta d}{d} \tag{42}$$

where A is the area of capacitor plates, d the distance between the plates and δd is the displacement of the resonator.

When added in parallel to the capacitance of a microwave tank circuit, C_p will lead to a measurable shift in its resonance frequency ω_{res}. The analysis of the noise performance of a tank circuit is identical to that of an SHO. The minimum detectable displacement (Pelekhov *et al*., 2005) depends on temperature T and the quality factor Q of the tank circuit. Capacitive displacement detection promises extremely high displacement detection sensitivity. For typical cantilever parameters we can expect a displacement noise floor of $10^{-13}\,\mathrm{m\,Hz^{-1/2}}$ at room temperature. Because the signal depends on the area of the electrode on the cantilever, this approach does not scale well as cantilevers become smaller.

This method has been used for MRFM signal detection (Pelekhov *et al*., 2005) but self heating of the tank circuit by the drive was evident at low temperatures. The tradeoff between displacement sensitivity and self heating can be helped by lithographic integration of the detection circuit with the cantilever.

Capacitive displacement detection using a single electron transistor

Another approach to capacitive displacement detection (LaHaye, Buu, Camarota and Schwab, 2004) exploits the excellent charge sensitivity of the radio frequency single electron transistor (rf SET) (Devoret and Schoelkopf, 2000). The SET is a superconducting island coupled to drain and source contacts through two tunnel junctions. The conductivity and hence the impedance of the SET arises from the tunneling of individual electrons through the tunnel contacts, and is very sensitive to the alignment of the chemical potential of the drain and source contacts. Slight changes of the island potential are evident in the SET conductance. A microwave tank circuit is used to match a room temperature detector to the impedance of the SET. On resonance, the impedance of the tank circuit is small and therefore the reflectance of the circuit is determined by the differential resistance R_d of the SET. This enables continuous, sensitive readout of the SET impedance.

When the cantilever is voltage biased and capacitively coupled to the SET, its displacement will modify R_d and hence the reflected rf power. At the low temperatures (below 300 mK) where the SET is typically operated its displacement noise is dominated by the tunnel current shot noise and the back action noise of the SET on the cantilever (LaHaye, Buu, Camarota and Schwab, 2004; Zhang and Blencowe, 2001). Theoretical estimates predict a displacement noise floor as low as $10^{-16}\,\mathrm{m\,Hz^{-1/2}}$; in the lab $3.8 \times 10^{-15}\,\mathrm{m\,Hz^{-1/2}}$ has been demonstrated using a 20 MHz beam resonator (LaHaye, Buu, Camarota and Schwab, 2004). Although it requires ultralow temperatures and has only been applied to doubly clamped beams to date, SET displacement detection is currently the most sensitive available.

3.3 Radio frequency magnetic fields

A fundamental requirement for MRFM is the transverse rf magnetic field used to manipulate the sample magnetization. The quality of the resulting force signal depends sensitively on the strength of the transverse oscillatory magnetic field H_1 that manipulates the magnetization. Standard rf field generation techniques are difficult to apply for MRFM because its scanning probe microscope arrangement makes placement of the sample and the MRFM probe inside of an rf coil (NMR) or a microwave cavity (ESR, FMR) virtually impossible. Instead, the sample must be placed as close as possible to the microstrip resonator or a microcoil used to generate the field which must be impedance matched to the 50 Ω source impedance of the rf/microwave signal generator. The nature of the impedance matching network depends on the frequency.

In the rf regime (∼100 MHz) a standard NMR tank circuit using lumped capacitive elements works well (see, e.g., Fukushima and Roeder, 1981). The microwave field needed for ESR or FMR experiments is somewhat more involved since lumped capacitive elements become impractical at these frequencies (3–10 GHz). Design strategies based on distributed microwave structures constructed from microstriplines (50 Ω planar transmission geometry with a signal line separated from a planar ground plane by a dielectric sheet) are useful. Resonant structures are desirable to increase the field; these can be based on either resonant microstriplines or microcoils.

3.3.1 Microstrip resonator

A microstrip resonator (Wallace and Silsbee, 1991) is a section of a microstrip line whose length is half the wavelength λ of the electromagnetic wave at the desired frequency $\omega_{\rm rf}$. The rf power is delivered by a transmission line that is capacitively or inductively coupled to the conducting island. The planar nature of microstrip resonators is convenient for use in scanned-probe experiments as the sample can be placed directly on the resonator (Zhang *et al.*, 1998).

3.3.2 Microcoil

A conventional coil provides a somewhat larger H_1 since the field is a sum of contributions from several windings of the coil. The need to generate rf field in GHz regime limits the inductance of the coil and therefore its size and the number of windings. The coil can be matched to the rf source by a distributed impedance matching network (Wallace and Silsbee, 1991; Zhang *et al.*, 1998; Mamin, Budakian and Rugar, 2003). Typically, ∼250 μm diameter coils with 2–2.5 windings are used. The sample is placed outside the coil on its main axis within one coil radius of the coil to achieve reasonable H_1 intensity so alignment is more demanding than for a microstrip resonator. A normal metal coil implementation delivers 1–3 G (up to ∼9 GHz) with about 10 mW of rf power delivered to the circuit.

Superconducting circuits provide strong H_1 at low power input (Mamin, Budakian and Rugar, 2003). Using this approach, a 7 G microwave field has been demonstrated ∼100 μm from a 220 μm diameter coil with 2.5 windings using only 400 μW of applied power (Mamin, Budakian and Rugar, 2003). Low applied power is important in a cryogenic environment where the heat load must be minimized. There is, however, a significant limitation imposed by superconducting resonators: the applied static field must be well below the superconducting critical field of Nb which limits the applied field to ≈2000 G. This is sufficient for ESR experiments but limiting for NMR detection.

3.4 Micromagnetic probe tips

One of the most powerful means of increasing the tip-sample interaction (equation (45)) and hence MRFM sensitivity is to increase the magnetic field gradient of the probe tip. The component of the field gradient that generates the needed force perpendicular to the plane of the cantilever will depend on the orientation of the cantilever relative to the sample surface and on the polarization of magnetic moments in the sample. For a typical geometry (as in Figure 6) we seek to maximize $\mathrm{d}B_z/\mathrm{d}z$. In a $\sim 10^5\,\mathrm{T\,m^{-1}}$ field gradient, a single electron spin generates a force of 10^{-18} N; much higher gradients will be needed for single nuclear spin sensitivity. This will require close approach to a micromagnetic probe tip.

Although not necessarily the optimal shape, we can consider a spherical ferromagnetic micromagnet to illustrate the challenge. A sphere of radius a uniformly magnetized along $\hat{z}$ with saturation magnetization M_s will have total moment $m_0 = (4/3)\pi a^3 M_s$ (see Figure 6). The field gradient a distance z from the center of the sphere is given by

$$\frac{\mathrm{d}B_z}{\mathrm{d}z} = -6\frac{\mu_0}{4\pi}\frac{m_0}{z^4} \tag{43}$$

Here $z = a + d$, where d is the gap between the sample an the magnetic sphere. For a given operating distance d, the maximum field gradient of a spherical probe magnet is achieved for a radius $a = 3d$. Given state-of-art force detection sensitivity (Rugar, Budakian, Mamin and Chui, 2004) gradients of 10^7–$10^8\,\mathrm{T\,m^{-1}}$ will be needed for single nuclear spin detection. To obtain this from an ($\mu_0 M_s = 2.2$ T) nanosphere will require $d = 46$ nm and $a = 138$ nm ($10^7\,\mathrm{T\,m^{-1}}$) or $d = 4.6$ nm and $a = 14$ nm ($10^8\,\mathrm{T\,m^{-1}}$).

The selection of the magnetic tip goes beyond the size of magnetic particle. Depending on the goals of the experiment, which might not necessarily be a single nuclear spin detection, magnetic coercivity, material stability, ease of fabrication, and the response of the magnetic tip to applied magnetic and rf fields should be considered.

3.4.1 Tip materials

Magnetic materials available for MRFM tip fabrication can be divided into magnetically 'soft' and 'hard' magnetic materials according to their coercivity.

Typically transition metals such as Co, Fe, and Ni have low coercivity, but high saturation magnetization. Fabrication is straightforward and compatible with typical microlithographic processes. This makes soft magnets attractive fabricating magnetic tips.

Hard magnetic materials such as the rare-earth alloys $SmCo_5$, Sm_2Co_{17} and $Nd_2Fe_{14}B$ exhibit coercive fields as

high as 2–3 T. Magnetic tips fabricated out of hard magnetic materials have the advantage that they can be used in MRFM experiments where an externally applied field B_{ext} antiparallel to the orientation of the tip magnetization is desired; there are applications for which this is valuable (see Section 5).

High coercivity offers another advantage. When mounted on an oscillating cantilever in an applied magnetic field, soft magnets are dissipative (Stipe *et al*., 2001a) due to magnetic 'friction' occurring as the particle's moment rotates while trying to follow the direction of the external magnetic field. This dissipation reduces the quality factor Q of the cantilever thus reducing MRFM sensitivity.

We will see in Section 5.2.1 that a long spin lifetime is crucial for ultrasensitive MRFM detection as the noise bandwidth is set by the inverse of this lifetime. Magnetic field fluctuations arising from thermal fluctuations of the tip moment will contribute to spin relaxation in the sample (see Section 2.1.3). Magnetic materials with large magnetic anisotropy K (typically larger in hard magnetic materials) reduce this effect.

3.4.2 Tip fabrication

High coercivity tips are important for high sensitivity MRFM to minimize relaxation due to tip moment fluctuations. Micromagnetic rare-earth tips are fabricated by a two step process: first small particles of the tip material are glued to the cantilever in the presence of an applied magnetic field to orient the tip moment in the desired direction. The tip is then shaped using focused ion beam milling (FIB). This technique can generate tips with gradients exceeding $10^5\,\text{T}\,\text{m}^{-1}$ ($1\,\text{G}\,\text{nm}^{-1}$). An example is shown in Figure 4.

3.4.3 Tip characterization

Characterizing the magnetic moment and the field gradient of the micromagnetic probe tip is essential and challenging due to the very small magnitude the probe magnetic moment and the need to accurately map the spatial variation of the tip field on the scale of tens or hundreds of nanometers.

Vibrating cantilever magnetometry (Zhang and Hammel, 1999; Chabot and Moreland, 2003; Stipe *et al*., 2001b) is a convenient method uniquely capable of measuring the magnetic moment of a small ferromagnetic particle mounted on a micromechanical cantilever. This approach is sensitive to moments as small as $10^4\mu_{\text{B}}$ (Stipe *et al*., 2001b) and so is suitable for the study of nanoscale magnetic tips. The motion of a magnetic particle at the end of a cantilever entails rotation its magnetic moment with respect to the externally applied magnetic field; this leads to a restoring torque that depends on the position of the cantilever and so changes the effective cantilever spring constant. The cantilever is driven at constant amplitude its natural frequency ω_c by means of positive feedback, and the change of its frequency is measured as a function of external magnetic field. The resulting frequency shift $\Delta\omega$ (Stipe *et al*., 2001b) is

$$\Delta\omega = \omega_c \frac{m H H_k}{2kL_e^2(H + H_{\text{K}})} \tag{44}$$

where m is the magnetic moment of the particle, L_e is the effective length of the cantilever, H_k is the anisotropy field of the tip and H is the applied magnetic field. Typical cantilever magnetometry data is shown in Figure 5. The magnetic moment of the magnetic tip can be extracted from the slope of the field dependence. Parameters such as coercivity can also be extracted. Reversals of the magnetization in response to field reversal in a soft magnet are clearly evident as slope changes.

4 FORCE DETECTION OF MAGNETIC RESONANCE

At the heart of MRFM is sensitive detection of the force $\mathbf{F}$ between a magnetic tip generating a field gradient $\nabla\mathbf{B}$ and the magnetization $\mathbf{m}$ in a localized region of the sample

$$\mathbf{F} = -(\mathbf{m}\cdot\nabla)\mathbf{B} \tag{45}$$

The characteristic force scale for MRFM is 1 atto-newton ($1\ \text{aN} = 10^{-18}\,\text{N}$) set by the interaction between a single electronic moment interacting through a field gradient of $10^5\,\text{T}\,\text{m}^{-1}$ ($1\,\text{G}\,\text{nm}^{-1}$). Detecting the force exerted by a single nuclear spin will require higher field gradients and improved force sensitivity. Detecting such forces is challenging; for comparison, forces measured in conventional SPM are usually not lower than $10^{-12}\,\text{N}$.

The transduction of a force signal into a voltage involves two stages of signal detection: first the mechanical resonator converts the oscillatory force to displacement, then this displacement is detected by a position sensitive readout. Sensitive force detection then requires the following

- System noise should be minimized
  - System noise should be dominated by thermal fluctuations of the cantilever.
  - Noise spectral density and bandwidth should be minimized.
- The signal force must be comparable to or larger than the system noise (referred to the input):

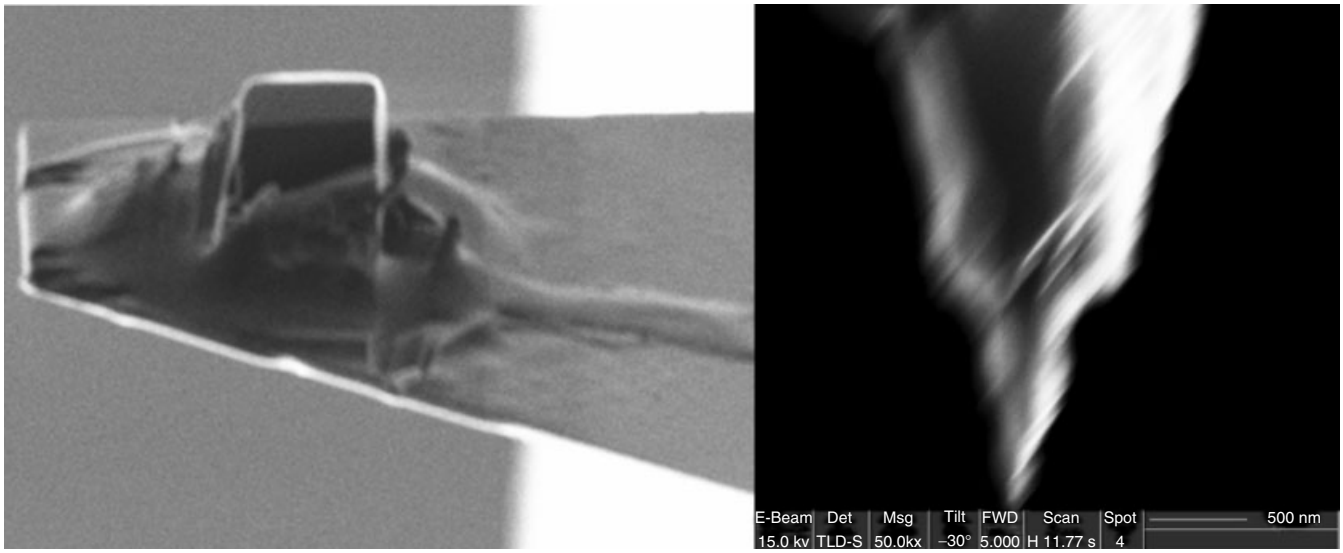

Figure 4. FIB fabricated rare-earth micromagnets (provided by P. Banerjee and R. Steward).

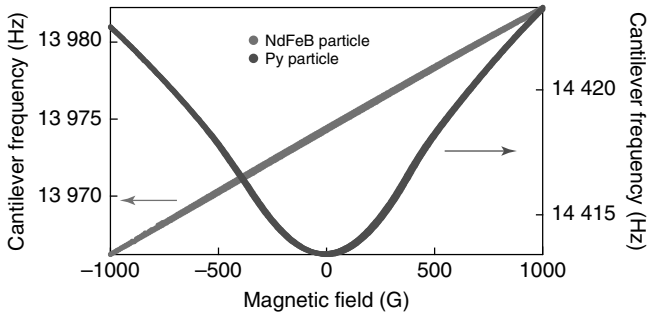

Figure 5. Cantilever magnetometry data for 'hard' NdFeB and 'soft' permalloy probe magnets. The magnetic moment of the particle can be extracted from the slope of the cantilever frequency dependence on the applied magnetic field. It can be seen that, unlike the soft-probe magnet, the hard-probe magnet preserves the direction of its magnetization as the direction of the applied field is reversed. (Provided by P. Banerjee.)

  - The field gradient should be as large as possible.
  - The force signal can be imprinted with an optimal time signature to aid detection and reject nonthermal noise.
- The noise added in reading out the resulting cantilever displacement must be negligible compared to the thermal noise of the cantilever.

This entails engineering the interaction in such a way that the resulting cantilever displacement exceeds both the cantilever displacement noise in the measurement bandwidth and the noise floor of the displacement detection scheme. The readout requirement essentially requires driving the cantilever at its resonant frequency to enhance the oscillation amplitude for a given drive.

4.1 Sensitive oscillatory force detection

The response of a cantilever to an externally applied force is well described by the model of a linear harmonic oscillator. The displacement δz of the end of a cantilever under the influence of a static force F is

$$\delta z_{\text{stat}} = \frac{F}{k} \tag{46}$$

where k is the mechanical spring constant of the cantilever. Thus, a 1 aN force acting on a soft ($k = 10^{-3}\,\text{N}\,\text{m}^{-1}$) cantilever will produce a static displacement $\delta z_{\text{stat}} = 10^{-15}$ m, well below the noise floor of available displacement detection schemes. By driving on resonance, the amplitude of the steady-state oscillations are increased by the quality factor Q:

$$\delta z_{\text{osc}} = Q\frac{F}{k} = Q\delta z_{\text{stat}} \tag{47}$$

Typically Q is $10^4 - 10^5$, resulting in an amplification of the cantilever response sufficient to render displacement readout noise negligible.

4.1.1 Fundamentals of force detection

Force sensitivity for resonant force detectors

The sensitivity of force detection using a micromechanical resonator is ultimately limited by the thermal motion δz_{th} of the resonator. By the equipartition theorem, the average thermal energy per degree of freedom of an SHO is (Albrecht,

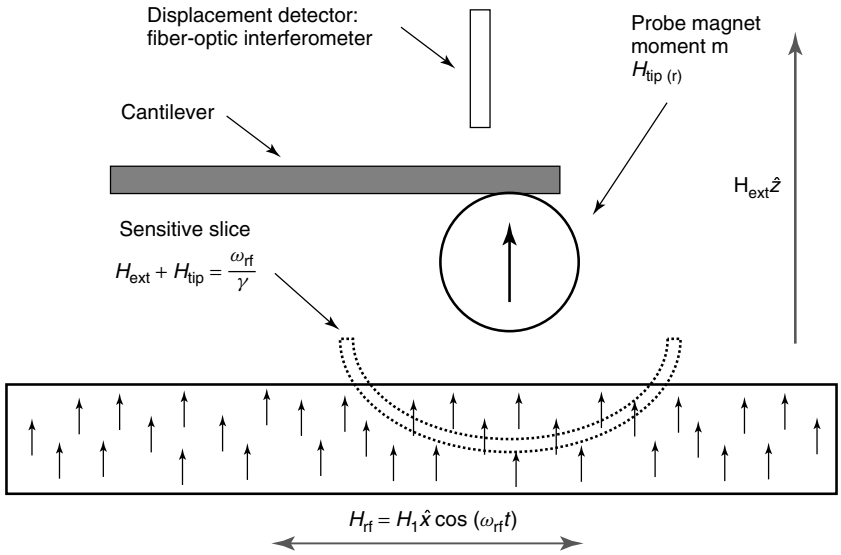

Figure 6. Schematic diagram of an MRFM experiment with probe magnet mounted on the cantilever. The cantilever is parallel to the sample surface. The sensitive slice is shown schematically.

Grutter, Horne and Rugar, 1991)

$$\frac{k\langle\delta z_{\rm th}^2\rangle}{2} = \frac{k_{\rm B}T}{2} \tag{48}$$

Equivalently we can consider the cantilever to be driven by a white noise force $F_{\rm th}$ given by (Stowe *et al.*, 1997)

$$F_{\rm th} = \sqrt{\frac{4kk_{\rm B}T\,\Delta\nu}{Q\omega_c}} \tag{49}$$

where $\Delta\nu$ is the measurement bandwidth. This expression provides a guide to the steps that can be taken to reduce $F_{\rm th}$ such as increasing Q and working at low temperature. In order to be detectable the force arising from the magnetic resonance signal should be greater than $F_{\rm th}$.

Frequency shift detection

It is often convenient, as discussed in the subsequent text, to detect the magnetic resonance signal by measuring the small induced shift in the cantilever resonance frequency ω_c. This approach requires that the cantilever be driven at its resonance frequency; we call the oscillation amplitude $z_{\rm osc}$. The fundamental limit of the sensitivity of frequency detection also arises from the thermal excitation of cantilever. The resulting thermal frequency noise $\delta\omega_{\rm th}$ is given by Albrecht, Grutter, Horne and Rugar (1991)

$$\delta\omega_{\rm th} = \sqrt{\frac{\omega_c k_{\rm B}T\,\Delta\nu}{kQ\langle z_{\rm osc}^2\rangle}} \tag{50}$$

Displacement detection sensitivity

It is important that displacement readout add negligibly to the total detection noise. A resonant oscillatory force of 10^{-18} N acting on a soft ($k = 10^{-3}\,{\rm N\,m^{-1}}$), high Q cantilever will produce cantilever oscillations $\delta z_{\rm osc} \sim 10^{-10} - 10^{-11}$ m. Hence we require displacement readout sensitivity better than $10^{-12}\,{\rm m\,Hz^{-1/2}}$. Thus, displacement sensitivity can be well managed by working at the cantilever resonance frequency.

4.1.2 Amplitude detection

Amplitude detection is the most straightforward approach to MRFM signal detection: a signal force oscillating at ω_c is applied to the cantilever, and the amplitude of the steady-state oscillations, proportional to the applied force, is measured. This approach is the most straightforward to implement and will deliver reliable results in the case of a strong magnetic resonance signal. However, amplitude detection has several disadvantages that complicate its application for high sensitivity measurements. One is the long response time τ (see equation (36) and associated discussion) required for the high Q micromechanical resonator to increase its energy and achieve its steady-state oscillation amplitude. This determines the waiting time between two consecutive signal measurements and thus the rate at which data can be acquired. For a high Q cantilever this time can be as long as 1–10 s, making acquisition of large amounts of data unacceptably time consuming. This problem can be mitigated by using negative feedback (Bruland *et al.*, 1998; Bruland, Garbini, Dougherty and Sidles, 1998) to nondissipatively increase signal bandwidth without increasing $F_{\rm th}$.

Another problem encountered in amplitude detection is the sensitivity of the cantilever frequency to conditions such as the applied field and temperature. This leads to a mismatch between the signal frequency and ω_c thus introducing a spurious variation in the oscillation amplitude that can obscure the desired signal. This is more severe the higher the Q. The solution is to update the frequency ω_{mod} at which the signal force is modulated to match real-time cantilever frequency measurements. This leads naturally to signal detection based on frequency shift detection (Albrecht, Grutter, Horne and Rugar, 1991), a powerful alternative to amplitude detection.

4.1.3 Frequency detection

The magnetic resonance force signal can be transduced into a shift in the cantilever resonance frequency by arranging that the signal force be applied *in phase* with the cantilever position (note that the displacement of a harmonic oscillator driven at its resonance frequency lags the driving force by 90°). Using the equation of motion for an SHO

$$m\frac{\partial^2}{\partial t^2}z + \frac{m\omega_c}{Q}\frac{\partial}{\partial t}z + kz = k_1 z \tag{51}$$

where m is the effective mass of the cantilever and the term on the right side is the signal force $F = k_1 z$, manifestly synchronized with cantilever position z. This requires that the cantilever be separately driven (by means of e.g., a piezoelectric actuator) at its resonance frequency at constant amplitude z_{osc} by means of a positive feedback circuit in which the cantilever is the frequency determining element. The frequency shift is given by

$$\frac{\delta\omega}{\omega_c} = \frac{F}{2kz_{\mathrm{osc}}} \tag{52}$$

The magnitude of F is given by the change in signal force over a half cycle of cantilever oscillation; the frequency shift is

4.2 Spin manipulation protocols

There are several methods that can be used to manipulate spin magnetization at the resonance frequency of the micromechanical force sensor. The choice of a preferred spin manipulation protocol will depend on spin system properties such as relaxation time T_1.

4.2.1 Cyclic suppression

The Bloch equation (25) show that M_z is suppressed by the application of a strong resonant ($\omega_{\mathrm{rf}} = \omega_{\mathrm{L}}$) field H_1. Either shifting the frequency off resonance or reducing the amplitude allows M_z to recover (on a timescale T_1). In order to achieve the goal of modulating M_z at ω_c the magnetization must substantially recover during one period of cantilever oscillation. Hence $1/T_1$ must be larger than ω_{mod}.

Cyclic suppression is straightforward to apply and effective (Zhang, Roukes and Hammel, 1996). Its primary disadvantage arises from the potential for spurious feedthrough forces due to the modulation of the rf field at ω_c. This undesired excitation can easily swamp the magnetic resonance signal which is occurring at the same modulation frequency.

4.2.2 Anharmonic modulation

A solution to this problem (Bruland, Krzystek, Garbini and Sidles, 1995) lies in simultaneous anharmonic modulation of two experimental parameters such as rf field strength and applied magnetic field H_0:

$$H_0(t) = H_0 + H_0^{\mathrm{mod}}\cos(\omega_z t) \tag{53}$$

$$H_1(t) = H_1^0 + H_1^{\mathrm{mod}}\cos(\omega_1 t) \tag{54}$$

with modulation frequencies satisfying $|\omega_z - \omega_1| = \omega_c$. The intrinsic nonlinearity of magnetic resonance leads to a term in the spin magnetization oscillating at ω_c, whereas spurious excitations occur at frequencies far from ω_c and therefore have negligible influence.

4.2.3 Adiabatic inversion

For systems with long spin relaxation times $1/T_1 \ll \omega_{\mathrm{mod}}$ a method based on coherent, periodic rotation of the spin orientation is preferable. This approach is based on the fact that orientation of the magnetization will follow that of $\mathbf{H}_{\mathrm{eff}}$ if $\mathbf{H}_{\mathrm{eff}}$ is rotated sufficiently slowly, that is if the rotation is adiabatic. This amounts to requiring that the magnetization precess many times about $\mathbf{H}_{\mathrm{eff}}$ in the time required to significantly rotate $\mathbf{H}_{\mathrm{eff}}$ itself. $\mathbf{H}_{\mathrm{eff}}$ can be periodically rotated by modulating either the magnitude of external magnetic field H_0 or by frequency modulation (FM) of H_1 (see Figure 1). Initially a spin ensemble is prepared with a thermal equilibrium magnetization $\mathbf{M}_z$ parallel to $\mathbf{H}_0$ and with $\Delta\omega$ sufficiently large that $\mathbf{H}_{\mathrm{eff}}$ is essentially parallel to $\mathbf{H}_0$. The magnetization is inverted by rotating of $\mathbf{H}_{\mathrm{eff}}$ through 180°, that is, $\Delta\omega$ is swept from a large positive value through zero (resonance) to a large negative value. Adiabaticity is determined by the rate of rotation of $\mathbf{H}_{\mathrm{eff}}$ compared to the magnitude of γH_{eff}; which passes through a minimum on resonance where its magnitude is γH_1. The values of $H_1 \sim 1\text{–}10\,\mathrm{G}$ achievable in MRFM set a limit on

the allowed modulation rate $\omega_{\rm mod}$. For inversion by FM the adiabatic condition requires

$$\omega_{\rm mod} \ll \frac{\gamma^2 H_1^2}{\Delta\omega} \tag{55}$$

4.2.4 MRFM excitation by adiabatic reversals

Examination of equation (15) in Section 2.1.4 reveals two ways to modulate the $\hat{z}$-component of $\mathbf{H}_{\rm eff}$: modulation of $\omega_{\rm rf}$ or modulation of $H^{\rm tot}$. We first consider FM to cyclically reverse $\mathbf{H}_{\rm eff}$:

$$\omega_{\rm rf} = \Omega_{\rm FM}\cos(\omega_{\rm mod} t) \tag{56}$$

In order to generate a frequency shift signal the cantilever is driven into oscillation at its natural resonance frequency ω_c with oscillation amplitude $z_{\rm osc}$, and we set $\omega_{\rm mod} = \omega_c$ and phase lock the reversals to the cantilever position (see Section 4.1.3).

Starting with the magnetization parallel to $\mathbf{H}_0$, $\omega_{\rm rf}$ is set to be far below $\omega_{\rm L}$ for the spins of interest (remember that due to the tip field gradient $\omega_{\rm L}$ varies with position). At the moment the cantilever is at an extremum of its oscillation we begin FM centered on $\omega_{\rm L}$ thus generating adiabatic reversals of the magnetization that will shift the cantilever resonant frequency ω_c. This frequency shift is continuously monitored as it decays with time (Figure 7).

The spins will follow $\mathbf{H}_{\rm eff}$ only if it is rotated sufficiently slowly that the adiabatic condition is satisfied, that is, only if spins precess about $\mathbf{H}_{\rm eff}$ much faster than its orientation rotates. The most demanding moment is at resonance when $|H_{\rm eff}|$ is minimum and equal to H_1; typically $\sim$1–10 G in the microwave regime. Hence, the magnitude of H_1 sets the limit on the modulation rate $\omega_{\rm mod}$ achievable with this method. If $\mathbf{H}_{\rm eff}$ is inverted by rf FM the adiabatic condition is

$$\omega_{\rm mod} \ll \frac{\gamma^2 H_1^2}{\Omega_{\rm FM}} \tag{57}$$

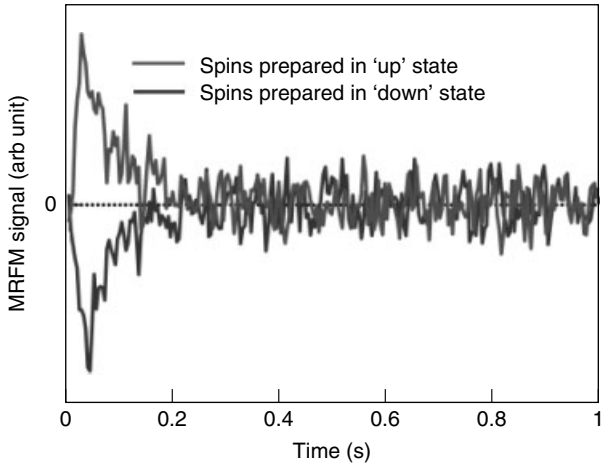

Figure 7. ESR signal at $T = 4$ K from E'-centers in silica detected using OSCAR. The sign of the signal is reversed by preparing the spin system in an inverted state. (Provided by P. Banerjee.)

The lifetime τ_m of the signal generated by cyclic adiabatic inversion cannot exceed the spin relaxation time in the rotating frame $T_{1\rho}$. In practice it is also limited by unavoidable violations of adiabatic condition due to insufficient applied rf field strength H_1.

The sign of the frequency shift can be reversed selecting an opposite sign of the signal force relative to the cantilever position, that is, by reversing the cantilever extremum at which FM is commenced. This allows the sign of the signal to be reversed with minimal change to the spurious background providing a means to subtract off this background.

4.2.5 Oscillating cantilever-driven adiabatic reversals

The technique dubbed oscillating cantilever-driven adiabatic reversals (OSCAR) (Stipe *et al.*, 2001c) was pioneered explicitly for situations where few spins are detected and hence very large gradients are used. OSCAR relies on field modulation in equation (15) to rotate $\mathbf{H}_{\rm eff}$, but uses a clever trick: rather than modulate H_0 advantage is taken of the large field gradient generated by the tip. As the cantilever oscillates this large gradient means that $H_{\rm tip}$ experienced by the spins of interest will be modulated:

$$\delta H_z^{\rm tot} = \delta H_z^{\rm tip} = z_{\rm osc}\frac{{\rm d}H^{\rm tip}}{{\rm d}z} \tag{58}$$

OSCAR naturally inverts the effective field $H_{\rm eff}$ and hence the magnetization with a phase appropriate for frequency shift detection: because the modulation of the field is due to cantilever motion the oscillations are perfectly synchronous with the position of the cantilever (see Figure 1). Consequently, as long as the adiabatic condition (equation (57)) is satisfied the force on the cantilever will be explicitly phase-locked to the position of the cantilever and so the force will shift the resonance frequency of the cantilever.

The OSCAR protocol also begins with the magnetization polarized along $\mathbf{H}_0$. The rf field with its frequency $\omega_{\rm rf}$ well below $\gamma H_{\rm tot}$ is turned on when the cantilever is at an extremum so the effective field $\mathbf{H}_{\rm eff}$ is nearly aligned with $\mathbf{H}_0$. The tip motion will modulate the field causing adiabatic reversals that shift ω_c.

The sign of the frequency shift depends on the phase of the cantilever oscillations relative to the magnetization reversals again providing a means to subtract off spurious backgrounds. This relative phase can be changed, for example, by

preparing spins in a state aligned in the direction opposite to $\mathbf{H}_0$ by means, for example, of an rf π pulse such as is shown in Figure 7. This enables detection of the spin polarization state using MRFM.

We return to the requirement OSCAR places on the field gradient. Successful adiabatic reversal requires $\Delta H_{\mathrm{tot}} \gg H_1$, and since $\Delta H_{\mathrm{tot}} = z_{\mathrm{osc}} \mathrm{d}H^{\mathrm{tip}}/\mathrm{d}z$ we need

$$\frac{\mathrm{d}H^{\mathrm{tip}}}{\mathrm{d}z} \gg \frac{H_1}{z_{\mathrm{osc}}} \tag{59}$$

It is unproductive to make z_{osc} much larger than 100 nm because this reduces the frequency shift (see equation (52)), so for $H_1 \sim 1$–10 G, gradients of order of 0.1–$1\,\mathrm{G\,nm^{-1}}$ are needed.

4.3 Probe–sample interactions

The MRFM probe–sample interaction is given by equation (45). Though this expression is convenient it fails to convey many salient features of the general case. Let us consider a probe magnet creating a spatially nonuniform magnetic field $\mathbf{H}^{\mathrm{tip}}(\mathbf{r})$, where $\mathbf{r}$ is the spatial coordinate, interacting with a time dependent spin magnetization of the sample $\mathbf{m}(\mathbf{r}, t) = \mathbf{m}_0(\mathbf{r}) + \delta\mathbf{m}(\mathbf{r}, t)$ with the time dependent component originating from rf manipulation of spins in the sample. In this case, the time dependent component of the total force between the MRFM probe and the sample will be

$$\mathbf{F}(t) = \int_V (\delta\mathbf{m}(\mathbf{r}, t) \cdot \nabla)\, \mathbf{B}^{\mathrm{tip}}(\mathbf{r})\, \mathrm{d}\mathbf{r} \tag{60}$$

where the integration done over the entire sample volume. The static component of the interaction with $\mathbf{m}_0(\mathbf{r})$ will not be detected by the resonant detection scheme employed in MRFM. To understand MRFM probe–sample interaction, we must analyze the spatial and time dependence of $\delta\mathbf{m}(\mathbf{r}, t)$ and the spatial variation of the gradient of the magnetic field $\mathbf{H}(\mathbf{r})$ of the micromagnetic tip.

4.3.1 Sensitive slice evolution

The spatial variation of $\delta\mathbf{m}(\mathbf{r}, t)$ will depend on the method used for spin manipulation. As an illustrative example we consider the case of cyclic suppression (Section 4.2.1) by means of a 100% amplitude modulation of the intensity of the rf field. The frequency of the rf radiation is ω_{rf}. For simplicity, we assume that the sample is placed in the external magnetic field $\mathbf{H}_0 \parallel \hat{z}$ such that $|\mathbf{H}_0| \gg |\mathbf{H}^{\mathrm{tip}}(\mathbf{r})|$. The thermal spin polarization in this case is $\mathbf{m}_0 = m_0\hat{z}$. The probe magnet is a small magnetic sphere magnetized in the $\hat{z}$ direction. The (spatially dependent) response of the magnetization to the applied rf field is given by equation (25); we find

$$\delta m_z(\mathbf{r}) = \frac{m_0\gamma^2 H_1^2 T_1 T_2}{1 + [T_2(\gamma\left|\mathbf{H}_0 + \mathbf{H}^{\mathrm{tip}}(\mathbf{r})\right| - \omega_{\mathrm{rf}})]^2 + \gamma^2 H_1^2 T_1 T_2} \tag{61}$$

This equation shows that the applied rf radiation will have the greatest effect on the spins in the spatial volume known as the *sensitive slice* where the following condition is satisfied:

$$\left|\gamma\left|\mathbf{H}_0 + \mathbf{H}^{\mathrm{tip}}(\mathbf{r})\right| - \omega_{\mathrm{rf}})\right| \leq \frac{\delta\omega}{2} \tag{62}$$

Here $\delta\omega = T_2^{-1}$ is the linewidth of the magnetic resonance signal (see equation (25)). The shape of the sensitive slice, a bowl centered on the probe magnet, is defined by both $\mathbf{H}_0$ and $\mathbf{H}^{\mathrm{tip}}(\mathbf{r})$; this shape is shown in Figure 8 for various values of H_0. The radius of the bowl increases with increasing $|\mathbf{H}_0|$ until it transforms into a doughnut-like shape when $|\mathbf{H}_0| > \omega_{\mathrm{rf}}/\gamma$.

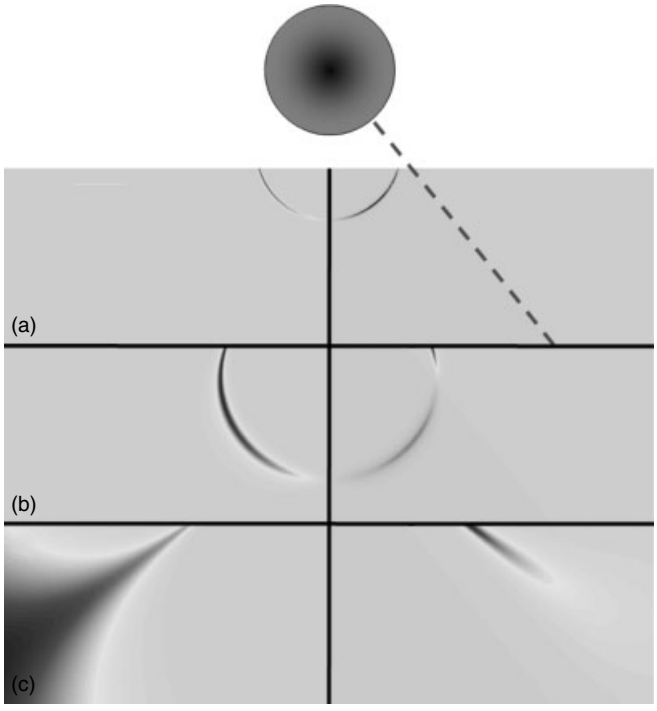

Figure 8. Evolution of the sensitive slice (left panel) and the force slice (right panel) with applied field H_0 increasing from (a) to (c), with (c) corresponding to $H_0 = \omega_{\mathrm{rf}}/\gamma$. The probe magnet of diameter a (shown as the black circle above the sample) and the magnet-sample separation are presented to scale, with the sample width being $5\,a$. The dashed line marks the line of the zero gradient $\mathrm{d}H_z/\mathrm{d}z$. (A color version of this figure is presented in Suter, Pelekhov, Roukes and Hammel, 2002.) (Reprinted with permission A Suter *et al*., copyright 2002, Elsevier.)

4.3.2 Evolution of the force

The magnetization couples to the cantilever through the $\hat{z}$ component of the force $-(\mathbf{m}\cdot\nabla)\mathbf{B}(\mathbf{r})$, hence for the geometry shown in Figure 6 the component of primary interest is $\mathrm{d}H_z/\mathrm{d}z$. The dipolar nature of the probe field means the sign $\mathrm{d}H_z/\mathrm{d}z$ reverses for magnetization off to the side of the tip (see Figure 8), therefore different parts of the sample contribute forces of different sign and, under certain conditions, can cancel one another. Figure 8 shows the evolution of the 'force slice' which is essentially the 'sensitive slice' convolved with the position dependence of the tip gradient. Spins located along the lines of zero gradient do not contribute to the interaction.

4.3.3 Leading edge signal

The spectrum, that is, the evolution of the signal force with field H_0, can be simulated by integrating the force over the entire sample for a series of applied fields. It is typical that the signal changes sign as the shape of the sensitive slice evolves with H_0 (Suter, Pelekhov, Roukes and Hammel, 2002). An important feature of the spectrum is its 'leading edge', that is, the minimum field H_0 at which the signal appears; this occurs as the sensitive slice just enters the surface of the sample. The field offset of this feature from $\omega_{\mathrm{rf}}/\gamma$ measures the strength of the field due to the probe magnet for a particular tip-sample separation.

Measuring the tip field as a function of separation is useful for mapping the spatial variation of tip field with nanometer scale resolution. From this the gradient of the tip field can be accurately obtained. Precise characterization of MRFM probe magnets is essential for correct interpretation of MRFM data.

5 APPLICATIONS

MRFM is a powerful and inventive approach to imaging and characterization of a broad variety of materials. As in the case of conventional magnetic resonance, MRFM is based on direct coupling of the detector to the dipole moment of the target spin. As we have seen in the preceding text because this interaction is quite weak this entails great care in the detection of the signal and has implications for quality and bandwidth of the signal detected. On the other hand, this allows the approach to be applicable to the detection of any spin or spin ensemble that can be brought into the proximity of the micromagnetic probe tip. This excellent breadth of applicability and flexibility distinguishes it from the array of powerful spin sensitive detection techniques currently in use and development.

The true power of MRFM will be determined by the impact of its application to problems studying and developing electronic, magnetic, and structural materials as well as to the biomedical community with extensive need for structural and functional characterization and visualization of biological materials. The rapid pace at which MRFM has improved capabilities such as sensitivity, signal bandwidth, and the rapidly expanding range of materials to which it has been successfully applied suggest a robust technique with the broad flexibility necessary to adapt to the diversity of experimental conditions that will be encountered in performing compelling studies of currently interesting materials.

MRFM offers the excellent sensitivity required to achieve very high spatial resolution. Just as important, this excellent sensitivity comes with a noninvasive probe that will benefit fields from nano-electronics to biomolecular imaging. As electronic elements become smaller, they become sensitive to even individual impurities and dopants; hence three-dimensional atomic scale characterization becomes crucial. Perhaps most notably, the field of spin-based quantum computation will require single spin detection technology both for quantum state readout and for device characterization; single spin MRFM promises to aid in this challenging undertaking.

5.1 Ferromagnetic resonance

There are two motivations for performing FMR experiments using the MRFM. First is the tremendous promise of microscopic FMR experiments for elucidating the nature of scientifically and technologically important magnetic materials such as layered magnetic systems exploiting spin dependent electron transport phenomena. It is important to understand how the performance of such devices is influenced by microscopic spatial variations in properties like interface quality, exchange coupling, and magnetic anisotropy. Conventional FMR has proved to be a powerful technique in evaluating the average values of these properties within the sample.

With the addition of the microscopic imaging capability of MRFM, FMR/MRFM could become one of the primary characterization techniques for such devices (see Wigen, Roukes and Hammel, 2006) for a review of FMR microscopy. Furthermore, unlike conventional inductive detection force detection of magnetic resonance is uniquely sensitive to M_z, the longitudinal component of the magnetization. In the subsequent text, we outline some experiments that exploit these strengths and demonstrate the potential MRFM holds for studies of ferromagnetic materials and devices.

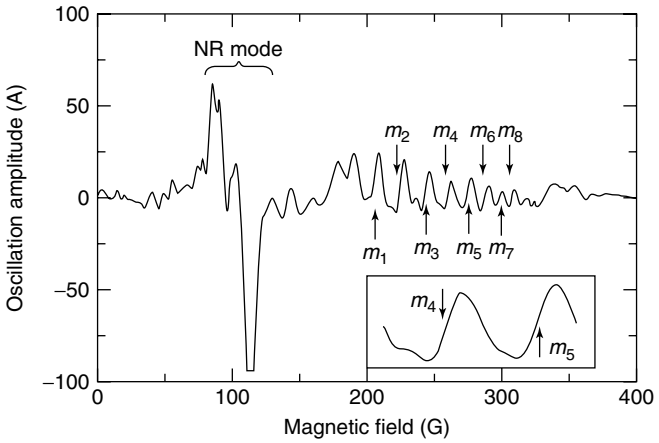

Figure 9. An experimental FMR/MRFM spectrum (cantilever oscillation amplitude as a function of applied field in Gauss) of a single crystal YIG film (Reprinted with permission Z Zhang *et al*., copyright 1996, American Institute of Physics.) which shows the nonresonance (NR) mode and a family of magnetostatic modes (labeled m_1, m_2, ...). The locations of the magnetostatic modes are indicated by arrows in the inset. The resonance was excited by a 2 G, 825 MHz magnetic field; the rf field was 100% amplitude modulated at 41.27 kHz. The bias field was ramped at $1.5\,\mathrm{G\,s^{-1}}$ and modulated at a frequency of 36.01 kHz and with a modulation amplitude of 4 G.

5.1.1 MRFM detection of FMR

The first MRFM detection of FMR (see Figure 9) was demonstrated on a film sample of yttrium iron garnet (YIG) by Zhang, Hammel and Wigen (1996). The sample was an approximately rectangular parallelepiped $20 \times 40 \times 3\,\mu\mathrm{m}^3$ YIG chip that was mounted on the cantilever; the gradient magnet was stationary. The signal was sufficiently large that the experiments were performed in ambient air to reduce Q and the cantilever's oscillatory response. The signal was generated by anharmonic modulation (Bruland, Krzystek, Garbini and Sidles, 1995). The applied magnetic field ranged from 150 to 400 Oe, so the sample was not entirely saturated. As a consequence strong spurious coupling was observed at lower fields where the field was just sufficient to saturate the center of the sample, so modulation of the field significantly altered M_z.

At higher fields, a family of resonance modes, the magnetostatic modes first calculated by Damon and Eshbach (DE) (1961) were observed. The application of DE theory was complicated by the small size and irregular shape of the sample and by the fact that the sample is not fully saturated at resonance. Nonetheless, the results agreed qualitatively with estimates based on DE theory in a rectangularly-shaped, saturated YIG medium. The tip field strength was insufficient to enable local imaging, so the resonance modes observed arose from the resonance behavior of the entire sample.

Wago, Botkin, Yannoni and Rugar (1998) performed FMR on a similar sample, but with gradients as large as $10\,\mathrm{G\,\mu m^{-1}}$ and found similar behavior, namely, that the detected modes were collective modes of the entire sample defined by sample dimensions. Images consistent with this conclusion were observed.

5.1.2 Damping in ferromagnets

Klein and coworkers have performed experiments in which they used MRFM to perform FMR experiments on a 160 μm diameter YIG disk (Klein, Charbois, Naletov and Fermon, 2003; de Loubens, Naletov and Klein, 2005). They exploited both the fact that force detection is sensitive to the longitudinal component of the magnetization rather than the transverse component as in inductive detection and the high sensitivity of MRFM to allow measurements not possible by conventional means. Their measurements were performed on the entire YIG disk with the tip far removed. This work has provided quantitative results that provided unique insights into fundamental dynamic behaviors in ferromagnets.

MRFM detection of FMR differs from conventional approaches in that M_z is directly measured in contrast to measurement of the absorption of microwave power as in conventional FMR detection. They compared power absorbed (proportional to the square of the transverse magnetization M_t^2) to M_z to identify various contributions to the observed FMR linewidth. The enhanced sensitivity provided MRFM detection also allowed detection of the longitudinal moment across a broad range of microwave frequencies even far from the resonance frequency of the microwave resonator.

Their MRFM measurement of the FMR linewidth as a function of frequency from 5 to almost 14 GHz revealed a linear response, that a frequency dependent component and a frequency independent component. The frequency dependent component that is associated with Gilbert damping because of the proportionality to $\partial M/\partial t$, while frequency independent component can have various origins including inhomogeneous broadening and impurity scattering of magnons. The frequency dependence revealed a peak in the linewidth at the resonant frequency of the microwave resonator that was attributed to loading of the resonator by the sample so as to reduce the intensity of H_1 near the Larmor frequency.

While providing insight the homogeneous and inhomogeneous contributions to the linewidth cannot be distinguished on the basis of the frequency dependence alone. It is known that by measuring the dependence of the FMR signal amplitude on the frequency at which the microwave excitation frequency is modulated the relaxation times associated with relaxation via magnetostatic and exchange modes can be

extracted. MRFM detection of the longitudinal magnetization as a function of modulation frequency was used for this measurement in addition to traditional FMR techniques to measure the dependence of the transverse magnetization on the same quantity. For MRFM detection the signal must be generated at ω_c (see Section 4); in order to allow modulation at a broad range of frequencies, Klein *et al*. employed anharmonic modulation (Bruland, Krzystek, Garbini and Sidles, 1995) involving simultaneous frequency and amplitude modulation (at ω_a) of the microwave excitation such that $\left|\omega_f \pm \omega_a\right| = \omega_c$.

The group took advantage of MRFM's unique ability to directly measure M_z They observed a rapid suppression of M_z as saturation of the resonance is approached. This provides new insight into the spin dynamics occurring at saturation. Spin relaxation arises from the generation of spin waves (Suhl and Phys, 1957; Fletcher, LeCraw and Spencer, 1960), but the transverse magnetization is largely insensitive to short wavelength spin wave modes because their transverse component averages to zero, so only measures the number of fundamental mode spin waves. However each spin wave mode reduces the longitudinal magnetization by $\gamma\hbar$ so the longitudinal magnetization measures the total number of spin waves of all wavelengths. As shown in Figure 10, at saturation $1/T_1$ decreases rapidly as the generation of fundamental mode spin waves saturates. Instead there is a rapid increase in the generation of short length spin waves that cannot be detected in conventional transverse linewidth measurements.

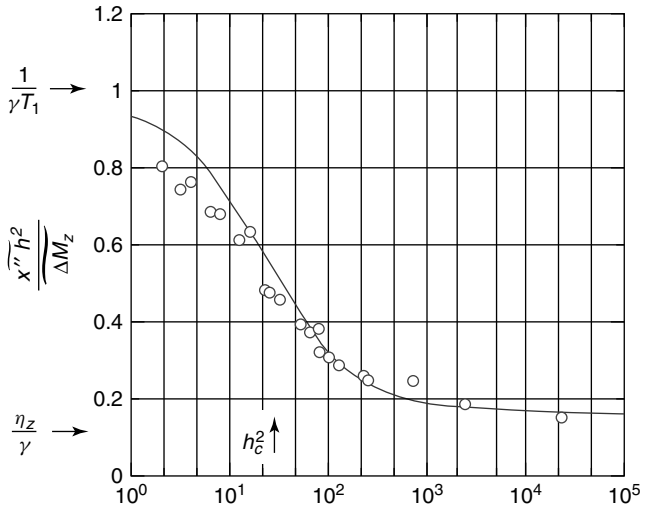

Figure 10. A plot of the ratio of the transverse component of the magnetization relative to the longitudinal component versus microwave power. (Reprinted with permission de Loubens *et al*., copyright 2005, American Physical Society.) This ratio is equal to $1/\gamma T_1$. By comparing conventional and MRFM detected linewidth data, the authors showed the rapid decrease of $1/T_1$ at saturation.

5.1.3 FMR imaging

Mewes *et al*. have demonstrated the ability of MRFM to observe spin dynamics of ferromagnets in micron-scale ferromagnetic structures (Mewes *et al*., 2006). The experiments were performed on an array of permalloy disks 50 nm thick and 1.5 μm in diameter. Experiments were performed both with the tip far from the dots and very close. When distant the tip field was very small and magnetostatic modes in good agreement with theoretical expressions (Kalinikos, 1980) were observed. The MRFM tip used was characterized by means of ESR experiments on DPPH (1,1-Diphenyl-2-picrylhydrazyl) to determine the dependence of the tip field on tip-sample separation.

The sample experiences tip fields in excess of 400 Oe when the tip approaches closely. The external magnetic field was tuned to the spectral feature associated with the fundamental magnetostatic mode and the tip was scanned over the sample (Figure 11). The resolution of the image is much better than that achievable using the same tip (tip width ~1 μm) for MFM of the dots. In fact the spatial resolution is roughly consistent with the ratio of the linewidth of the mode selected for imaging (~40 Oe) and the field gradient (~300 G μm^{-1}); the same ratio that sets spatial resolution in MRI of paramagnetic materials. Thus MRFM allows studies of static and dynamic spin properties in patterned magnets with resolution not set by the tip dimensions as in MFM. However the detailed mechanism of imaging is not understood and the question of spatial resolution achievable in extended ferromagnets remains an area of active study (Mewes *et al*., 2006; Midzor *et al*., 2000; Urban *et al*., 2006).

5.2 Electron spin resonance

Mechanical detection of magnetic resonance was first demonstrated using ESR (Rugar, Yannoni and Sidles, 1992) using an organic molecule DPPH with an unpaired spin that has a rapid (and temperature independent) spin relaxation rate ($T_1 \approx T_2 \approx 60$ ns) and a high spin density (2×10^{21} cm^{-3}). Because $\omega_c \ll 1/T_1$ cyclic suppression must be used to modulate M_z (see Section 4.2.1).

The push to improve detection sensitivity has relied on samples with very long spin relaxation times ($\gg \omega_c^{-1}$) to enable long data collection times and therefore reduced noise bandwidths. In this case, modulation of M_z is accomplished by means of cyclic adiabatic inversion (Section 4.2.3).

That effort produced the milestone of MRFM detection of a single electron spin by (Rugar, Budakian, Mamin and Chui, 2004). This is a signal achievement that dramatically alters the horizons for high-resolution imaging and experimentation on nanoscale systems. It confirms the extraordinary sensitivity of MRFM and underlines the breadth and flexibility of

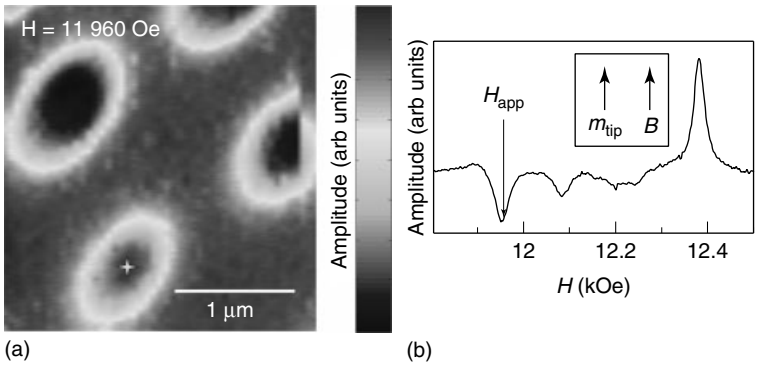

Figure 11. Images obtained at a tip-sample separation of 150 nm and a microwave frequency of $f_{mw} = 7.7\,\text{GHz}$ 60% amplitude modulated at the cantilever frequency are shown. (b) shows the MRFM spectrum obtained with the tip located over the center of the permalloy dot (indicated by the star). (a) shows the cantilever response obtained in lateral scans over an area $2.5 \times 2.5\,\mu\text{m}^2$ at a field $H = 11\,960\,\text{Oe}$. The external magnetic field was aligned parallel to the moment of the tip.

the method. The experiment was done on a silica sample containing a low density ($\sim 10^{14}\,\text{cm}^{-3}$) of electronic spins known as E′ centers that are created by γ-irradiation of the silica. The low spin density ensured that an isolated spin could be found for detection by the MRFM micromagnetic tip.

5.2.1 Single electron spin detection

The ultrahigh sensitivity regime involves several extreme parameter values that lead to new phenomena:

- Very high sensitivity enables detection of ensembles sufficiently small that the thermal fluctuations of the net spin polarization dominate over the thermal equilibrium polarization.
- The large tip field gradients necessary for high sensitivity lead to large temporal variations of the magnetic field as a consequence of cantilever motion; these can be beneficial or detrimental.

Statistical spin polarization

For sufficiently small ensembles thermal fluctuations of the net spin polarization can be an important effect: the net spin polarization is proportional to

$$\Delta N = N_\uparrow - N_\downarrow = \sqrt{N} \tag{63}$$

This 'statistical polarization' becomes comparable to the thermal equilibrium Boltzmann polarization at $T = 4\,\text{K}$ and $H = 1\,\text{kOe}$ for samples containing of order 10^4 spins. One can then achieve larger signals and can collect data continuously avoiding the need to wait for the spin polarization to recover to thermal equilibrium by means of spin-lattice relaxation before the next measurement.

On the other hand the average polarization and hence average signal is zero, and so the spin magnetic resonance response is manifested only in the variance of the force signal (Budakian, Mamin, Chui and Rugar, 2005). Instead of a definite frequency shift the cantilever undergoes random frequency fluctuations (see Figure 12) of magnitude

$$\delta f_c = \pm f_c \frac{2\mu_B \sqrt{N} \nabla H_z}{\pi k z_{osc}} \tag{64}$$

With field gradient $\nabla H_z \approx 2\,\text{G nm}^{-1}$ and a very small cantilever spring constant $k \approx 0.1\,\text{mN m}^{-1}$ the frequency shift per electronic spin is $\sim$3–5 mHz assuming $z_{osc} = 16\,\text{nm}$.

Interrupted OSCAR

This challenge led to the development of a variant of the OSCAR (Rugar, Budakian, Mamin and Chui, 2003) technique (Section 4.2.5) in which the motion of the micromagnetic tip mounted on the driven cantilever cyclically reverses the orientation of H_{eff} and hence the spin orientation. Dubbed iOSCAR (Mamin, Budakian, Chui and Rugar, 2003) it employs an interruption of the rf field for half a cantilever period that allows the cantilever to move from one extremum to another without rotating H_{eff}. The spin force remains proportional to the cantilever position, but the phase of the oscillatory force exerted on the cantilever relative to its position is reversed thus changing the sign of the resulting frequency shift (see Figure 13). This modulates the OSCAR signal and imprints the signal with a time signature that allows it to be identified at nonzero offset frequency from $f_c = \omega_c/2\pi$.

If the rf power is interrupted at a frequency $f_{int} = 86\,\text{Hz}$ the cantilever frequency is modulated at $f_{sig} = f_{int}/2 = 43\,\text{Hz}$. The frequency shift associated with the magnetic

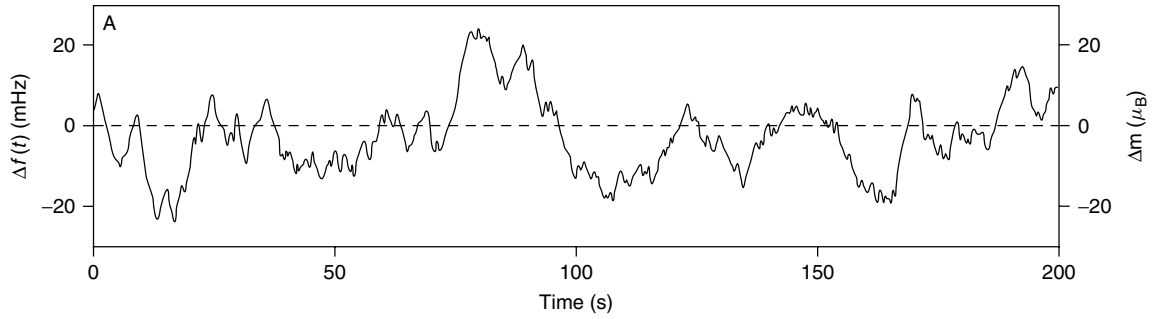

Figure 12. Trace showing a time record of the statistical fluctuations. (Reprinted with permission Budakian *et al*., copyright 2005, AAAS.) The frequency shift recorded in a 83-mHz bandwidth is converted to equivalent number of spins (right-hand axis) by dividing Δf by the average frequency shift per spin ($\overline{|\delta f|} = 0.8$ mHz/spin).

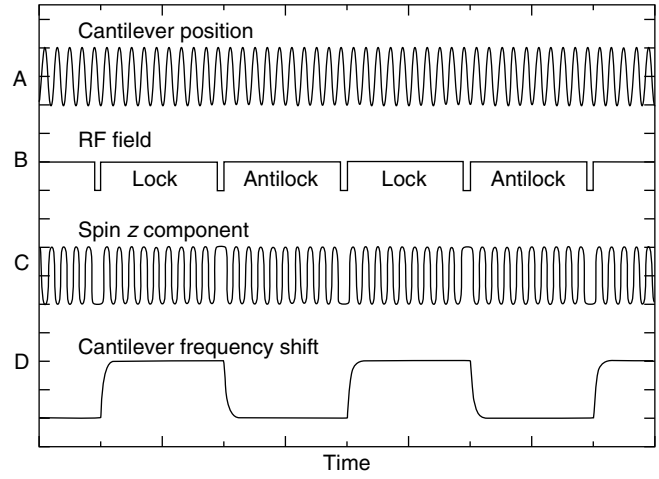

Figure 13. Timing diagram for the interrupted OSCAR protocol. (Reprinted with permission Mami *et al*., copyright 2003, American Physical Society.) The cantilever is oscillated continuously at its resonance frequency, and the microwave field (curve B) is normally on, but is periodically interrupted for one-half cantilever cycle. The z component of the magnetization (C) oscillates in response to the cantilever motion due to adiabatic rapid passage when the microwaves are on, but is left static when they are off. The oscillating magnetization reverses phase with respect to the cantilever for each microwave interruption, giving a cantilever frequency shift (D) that oscillates at one-half the microwave interrupt frequency (F).

resonance alone will manifest itself at this frequency with an intensity

$$\Delta f(t) = \frac{4}{\pi}|\delta f_c|A(t) \tag{65}$$

where $A(t)$ represents the random statistical fluctuations (Rugar, Budakian, Mamin and Chui, 2004).

Signal averaging presents an unusual challenge in this case since the average signal is zero: $\langle A(t)\rangle = 0$, hence $\langle \Delta f(t)\rangle = 0$, and $\langle [A(t)]^2\rangle = 1$. Hence to obtain a signal the square of the frequency shift $[\Delta f(t)]^2$, that is, the signal energy (Rugar, Budakian, Mamin and Chui, 2004) was detected. The phase sensitive lock-in detection can be adjusted such that the signal force appears only in the in-phase variance of the measured signal can be written as $\sigma_I^2 = \sigma_{\text{spin}}^2 + \sigma_{\text{noise}}^2$, where σ_{spin}^2 and σ_{noise}^2 are uncorrelated variances of the spin signal and the noise respectively; the quadrature variance σ_Q^2 will then contain only noise, that is, $\sigma_Q^2 = \sigma_{\text{noise}}^2$. The spin signal is $\sigma_{\text{spin}}^2 = \sigma_I^2 - \sigma_Q^2$ and the signal-to-noise ratio $\text{SNR} = \sigma_{\text{spin}}^2/\sigma_I^2$.

Using this technique the signal from a single electron spin was detected. The low spin density of the sample provides for a 200–500 nm spacing between the spins, whereas while the detected spin sufficiently dilute that the probe can interact only with one spin at a time (see Figure 14). The force variance was $|\delta f_c| = 4.2$ mHz in very good agreement with the expected value. The consistency spatial shift of the signal with change of microwave frequency and the expected value of the force signal variance verified that the signal originates indeed from a magnetic resonance signal.

5.2.2 *Spin relaxation by thermal motion of high gradient tip*

The lifetime of a spin signal during a cyclic inversion measurement is a crucial parameter as short lifetimes spread the signal in frequency space requiring wider bandwidth and hence increased noise. Sensitive experiments require close approach of the magnetic tip to the spin to be detected, but early ESR MRFM experiments showed substantial reduction of the rotating frame electron spin relaxation time τ_m as the tip approached the spin. Rugar *et al*. found that τ_m was reduced from 275 ms to 68 ms as the tip-spin spacing was reduced from 1500 nm to 800 nm (Stipe *et al*., 2001c).

The excess relaxation was found to arise from the magnetic field fluctuations that result when thermal vibrations displace the high gradient tip (Mozyrsky, Martin, Pelekhov and Hammel, 2003). As discussed in Section 2.1.3 the component of

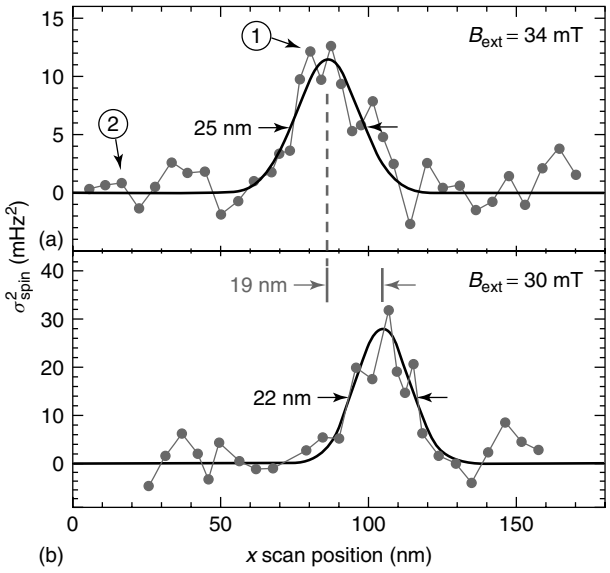

Figure 14. A graph (Reprinted with permission D Rugar *et al*., copyright 2004, Nature Publishing Group.) showing the spin signal as the probe magnet is scanned laterally in the **x** direction across a single electron in a SiO_2 for two values of external field: (a), B_{ext} = 34 mT, and (b), B_{ext} = 30 mT. The smooth curves are Gaussian fits to guide the eye. The 19 nm shift in peak position reflects the movement of the resonant slice induced by the 4 mT change in external field. The difference in absolute peak height is primarily due to different lock-in amplifier detection bandwidths: 0.18 Hz and 0.59 Hz for (a) and (b), respectively.

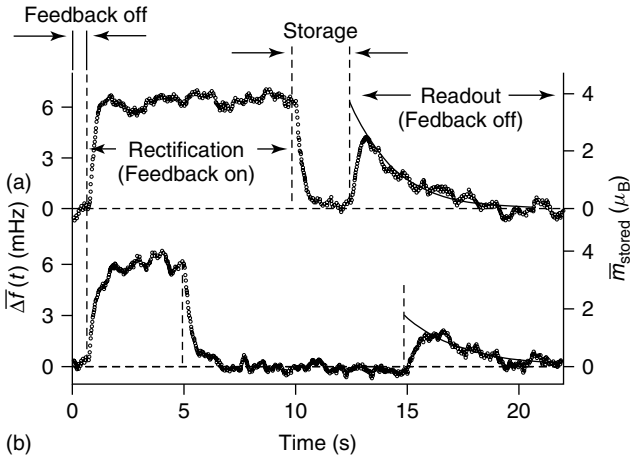

Figure 15. Control of the spin magnetization of few spin ensembles using MRFM (Reprinted with permission Budakian *et al*., copyright 2005, AAAS.) is shown. (a) An average polarization of about 3.7 μ_B was created in an ensemble of $N \approx 70$ spins through active feedback, stored in the laboratory frame for 2.5 seconds, and subsequently read out. (b) Data taken under the same conditions as (a) except that the storage time has been extended to 10 s.

these transverse magnetic field fluctuations at the Larmor frequency ω_L will induce spin relaxation. During the adiabatic inversion the magnetization precesses at frequency $\omega_L(t) = \gamma H_{eff}(t)$; the minimum frequency will be $\omega_L = \gamma H_1$, corresponding to a precession frequency of $\omega_L/2\pi \approx 3$–10 MHz. Though the fundamental cantilever mode is at $\omega_c/2\pi$, typically in the range 1–10 kHz, higher cantilever harmonics can significantly contribute to spin relaxation. It was shown (Mozyrsky, Martin, Pelekhov and Hammel, 2003; Berman, Gorshkov, Rugar and Tsifrinovich, 2003) that the electron spin relaxation rate due to the higher order cantilever modes is

$$\frac{1}{\tau_m} \approx \frac{3.4\mu_B \nabla \mathbf{H}_{probe}}{\hbar} \left(\frac{k_B T}{k\sqrt{z_0^2 - z_1^2}} \right) \left(\frac{\omega_c}{\gamma H_1} \right)^{3/2} \qquad (66)$$

where z_0 is the amplitude of thermal cantilever motion, z_1 is the tip-sample separation, k is the cantilever spring constant and T is temperature. As the probe is brought close to the sample the strength of the probe field gradient $\nabla \mathbf{H}_{probe}$ and hence the induced relaxation rate increases. It is noteworthy that increasing H_1 also reduces excess relaxation.

This problem was conclusively addressed in the single spin experiment (Rugar, Budakian, Mamin and Chui, 2004) where a cantilever designed with an extra mass at its tip to suppress high order vibrational modes effectively eliminated the excess relaxation (Chui *et al*., 2003). H_1 intensity was increased to 7 G through use of a superconducting microwave circuit (Mamin, Budakian and Rugar, 2003). As a result the rotating frame electron spin relaxation τ_m of a single electron was estimated to be 760 ms in the tip field gradient of 2.0 G nm^{-1} ≈250 nm away from the detected spin.

5.2.3 Creating order in spin ensembles

Complementary to high-resolution imaging is the ability MRFM provides to controllably manipulate spin magnetization using spatially localized magnetic resonance. This kind of close control has been nicely demonstrated in experiments that have built on the high sensitivity ESR detection (Budakian, Mamin, Chui and Rugar, 2005).

The first experiment involved hyperpolarizing an electron spin ensemble by capturing an especially large statistical fluctuation (Budakian, Mamin, Chui and Rugar, 2005). In this experiment, the cantilever signal frequency shift $\Delta f(t)$ was continuously monitored, and when the frequency shift exceeded a certain threshold value the rf field was turned off (see Figure 15). Without an rf field cantilever electron spins remain oriented along $\hat{\mathbf{z}}$ and are unaffected by cantilever oscillation so their polarization is effectively preserve for times of order T_1 (measured to be ≈30 s). Spin polarization exceeding anything achievable by thermal polarization could be generated and used in other experiments.

The second experiment building on this idea controlled the spin dynamics of the through real-time feedback. Whenever the frequency shift fell below a certain value a π-inversion was applied. This prevented the system from evolving beyond the predefined polarization. By this means the spin system was locked into a relatively well defined polarization state.

5.3 Nuclear magnetic resonance

NMR is a powerful tool for material studies. Nuclear spins are prevalent in most materials and chemical specificity is achieved since each nuclear spin has a unique gyromagnetic ratio. This has made high sensitivity MRFM detection of NMR a key goal. Excellent progress has been made since the first detection of NMR by means of MRFM in 1993 (Rugar *et al*., 1994).

5.3.1 Detection and manipulation of statistical polarization

State-of-the-art sensitivity has been demonstrated in an experiment (Mamin, Budakian, Chui and Rugar, 2005) that detected the statistical spin polarization of nuclear spins. Nuclear moments are $\sim 10^3$ times smaller than electronic moments, so this approach requires very high sensitivity. The ability to achieve substantial polarization without waiting T_1 is even more advantageous than for electron spin detection because nuclear T_1s can exceed hours at low temperatures.

Three nuclear spin systems were used in this study: ^{19}F nuclei in CaF_2, and ^{1}H spins in the polymer polymethylmethacrylate (PMMA) and collagen. The CaF_2 experiment demonstrated spin sensitivity of $\approx$2000 nuclear spins with a 2.5 h averaging time.

Techniques based on short rf pulses inserted into the interrupted OSCAR protocol described in Section 5.2.1 were developed for spin nutation and transverse spin relaxation measurements using statistically polarized spin ensembles. During the nutation experiment, an rf pulse of length t_p was inserted during the cantilever cycle when the nuclear spins are precisely on resonance causing them to precess about the $\mathbf{H}_{\text{eff}}$ which lies in the $\hat{x}$ plane in the rotating frame of reference. As the pulse length, and therefore the angle of spin rotation, is changed the signal oscillates with period $T = 2\pi/\gamma H_1$ as shown in Figure 16.

The inhomogeneous transverse spin relaxation time measurement is similar but is based on sequence of two $\pi/2$ pulses separated by a time τ inserted into the iOSCAR sequence. The first pulse rotates spins into the $\hat{x}$-$\hat{y}$ plane where the spin polarization decays due to transverse spin relaxation in a time $T_2^* = 4\,\mu$s. For τ significantly longer than T_2^*, the final polarization vanishes so the signal will be half of the value observed for short τ.

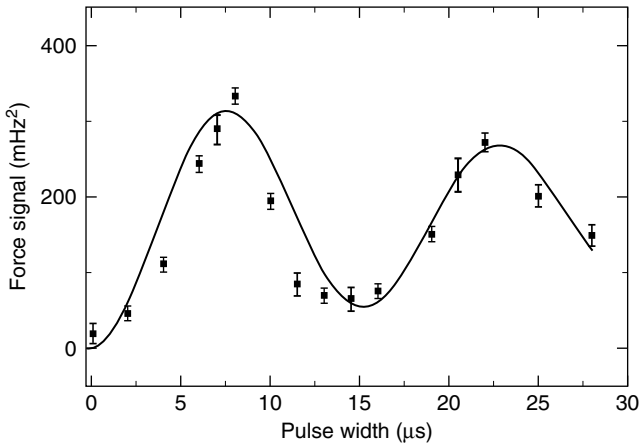

Figure 16. Nutation of the statistical polarization in CaF_2. (Reprinted with permission H J Mamin *et al*., copyright 2005, American Physical Society.) The signal is shown as a function of the pulse width t_p. The spin oscillation period about the effective field indicates an rf field strength $H_1 = 17$ Oe.

This demonstration of standard pulse techniques in combination with ultrasensitive NMR detection reinforces the expectation that MRFM detected NMR will be a powerful tool for microscopic studies of materials.

5.3.2 NMR double resonance in force microscopy

We have seen that MRFM allows NMR detection with the sensitivity much higher than that of the conventional NMR (2000 spins in the IBM experiment, (Mamin, Budakian, Chui and Rugar, 2005) compared to at least 10^{12}–10^{13}). To fully exploit this strength the conventional pulsed NMR techniques must be brought to bear. Important steps in this direction have been demonstrated by (Lin *et al*., 2006). Here we briefly describe their application of solid-state double resonance techniques in an MRFM experiment performed on ^{19}F and ^{31}P nuclei in a KPF_6 crystal.

A useful and commonly used solid-state NMR double resonance technique is Hartmann–Hahn cross polarization (CP) in which polarization transfer from a more easily polarized spin species (e.g., due to a higher gyromagnetic ratio) to a less polarized species provides increased detection sensitivity for the latter. The technique employs irradiation at two rf frequencies (ω_{L}^I and ω_{L}^{II}) with H_1 intensities chosen such that $\gamma^{\text{I}} H_1^{\text{I}} = \gamma^{\text{II}} H_1^{\text{II}}$.

The applicability of these techniques to MRFM detection in the presence of the gradient from a 0.5-mm iron wire has been explored in samples containing $\sim 10^{15}$ spins. Figure 17 shows the growth of the ^{31}P spin polarization as a function of the time τ_{cp} the cross polarization rf field is applied. The

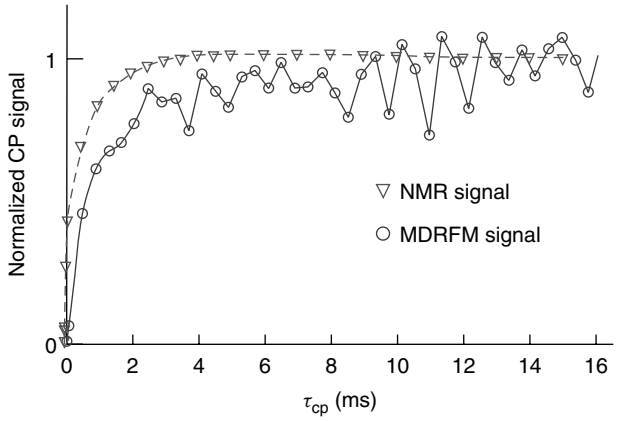

Figure 17. The buildup of the ^{31}P spin polarization as a function of τ_{cp} of the CP pulse sequence was measured using cyclic adiabatic inversion (○). Data acquired in a conventional NMR experiment on the same spin system (▽). (Reprinted with permission Q Lin *et al*., copyright 2006, American Physical Society.)

MRFM data are in good agreement with data acquired in a conventional NMR experiment.

Spin decoupling

Another application of double resonance is to narrow resonance lines in to enhance the resolution of solid-state NMR spectroscopy. A common broadening mechanism in solids results from the interaction between the target spin and neighboring dissimilar spins (heteronuclear coupling). This interaction can be reduced by irradiating at the Larmor frequency of the offending species to average the interaction to zero. During decoupling the target signal is detected at its Larmor frequency.

The Meier group has also demonstrated (Lin *et al*., 2006) narrowing of the ^{31}P line through continuous wave (CW) decoupling applied at the ^{19}F Larmor frequency. The ^{31}P linewidth was measured using a Hahn echo technique in which the echo amplitude is measured using cyclic adiabatic inversion to generate the MRFM signal (Degen *et al*., 2005). The Hahn echo alone will also reduce heteronuclear line broadening but CW decoupling is superior. The linewidth after the echo was 1.4 kHz, this was reduced to 900 Hz by decoupling.

The ability to use pulsed techniques to improve spectral resolution in MRFM is an important advance: when combined with high sensitivity MRFM detection it points toward the potential for local NMR spectroscopy with unprecedented spatial resolution.

5.3.3 1D NMR MRFM imaging of GaAs

The demonstration of NMR/MRFM imaging of Ga in GaAs by D. Smith and colleagues (Thurber, Harrell and Smith, 2003) indicates the promise MRFM holds for studies of microelectronic devices composed of important electronic semiconductors. For multicomponent devices the unique ability of MRFM to observe buried structures is a key strength.

Thurber and Smith *et al*. have obtained 1D NMR/MRFM images of a GaAs sample mounted on the cantilever. Even at $T = 5$ K in a 4 T applied magnetic field the nuclear spin polarization is small, so they optically pumped the electron spin polarization with circularly polarized light to enhance the nuclear polarization. Distinct NMR signals from three nuclear isotopes: (^{71}Ga, ^{69}Ga, and ^{75}As), were detected using cyclic adiabatic inversion. In addition, they obtained high resolution, 1D ^{71}Ga MRFM images from the GaAs sample whose nuclear spin polarization was controllably modified prior to imaging. The optically pumped nuclear magnetization was artificially suppressed by prolonged cyclic adiabatic inversion in two spatial regions separated by a volume of unperturbed magnetization. The MRFM signal was subsequently recorded as the sensitive slice was swept through the sample during the imaging cycle; this revealed the two regions of diminished magnetization at different values of the applied field as shown in Figure 18. The regions can still be resolved as their separation is reduced to 500 nm. The authors estimate their limiting 1D spatial resolution in the experiment to be 170 nm with detection sensitivity of $\sim 4 \times 10^{11}$ ^{71}Ga Hz$^{-1/2}$.

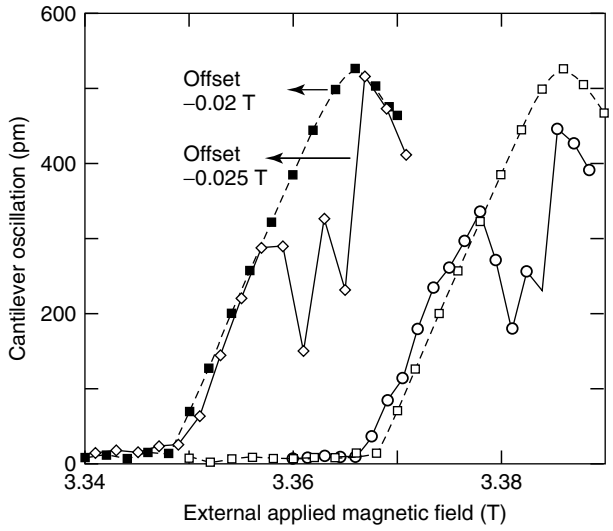

Figure 18. Demonstration of spatially resolved NMR in optically pumped ^{71}Ga. (Reprinted with permission K R Thurber *et al*., copyright 2003, Elsevier.) The spin polarization was suppressed in two closely spaced slices and then imaged for two slice separations: 670 nm (◇) and 500 nm (○). For comparison, spectra obtained from optically pumped sample with no slice saturation are shown (□ and ■). (The difference in offset between the unmodified (■, offset −0.02 T) and the 670 nm (◇, offset −0.025 T) data is believed to be caused by a slight change <1 μm in the separation between the sample and magnet for these data runs done on different days.

6 CONCLUSIONS

We have discussed the methods and techniques of MFRM, an emerging fully three-dimensional high-resolution scanned-probe technique. While focusing on detailed discussions of the experimental approaches used, we have also pointed out several successful applications. The rapid improvement in the capabilities of the technique culminating notably in the detection of individual electronic spins demonstrate that it is a robust and flexible technique. The range of successful applications serve to confirm this and indicate its broad potential.

ACKNOWLEDGMENTS

We thank P. Banerjee and R. Steward for allowing us to use unpublished figures. We also gratefully acknowledge the Department of Energy Office of Basic Energy Sciences, the Army Research Office and the National Science Foundation for their support of the authors' work reported in this article.

REFERENCES

Abragam, A. (1961). *The Principles of Nuclear Magnetism*, Clarendon: Oxford.

Albrecht, T.R., Grutter, P., Horne, D. and Rugar, D. (1991). Frequency Modulation detection using High-Q cantilevers for enhanced force microscopy sensitivity. *Journal of Applied Physics*, **69**, 668.

Albrecht, T.R., Grütter, P., Rugar, D. and Smith, D.P.E. (1992). Low temperature force microscope with all-fiber interferometer. *Ultramicroscopy*, **42–44**, 1638–1646.

Arlett, J.L., Maloney, J.R., Gudlewski, B., *et al*. (2006). Self-sensing micro- and nanocantilevers with attonewton-scale force resolution. *Nano Letters*, **6**(5), 1000–1006.

Barrett, T.A., Miers, C.R., Sommer, H.A., *et al*. (1998). Design and construction of a sensitive nuclear magnetic resonance force microscope. *Journal of Applied Physics*, **83**, 6235.

Berman, G.P., Gorshkov, V.N., Rugar, D. and Tsifrinovich, V.I. (2003). Spin relaxation caused by thermal excitations of high-frequency modes of cantilever vibrations. *Physical Review B*, **68**, 94402.

Bloch, F. (1946). Nuclear induction. *Physical Review*, **70**, 460.

Bruland, K.J., Dougherty, W.M., Garbini, J.L., *et al*. (1998). Force-detected magnetic resonance in a field gradient of 250,000 Tesla per meter. *Applied Physics Letters*, **73**, 3159.

Bruland, K.J., Garbini, J.L., Dougherty, W.M. and Sidles, J.A. (1996). Optimal control of force microscope cantilevers. II. Magnetic coupling implementation. *Journal of Applied Physics*, **80**, 1959.

Bruland, K.J., Garbini, J.L., Dougherty, W.M. and Sidles, J.A. (1998). Optimal control of ultrasoft cantilevers for force microscopy. *Journal of Applied Physics*, **83**, 3972.

Bruland, K.J., Krzystek, J., Garbini, J.L. and Sidles, J.A. (1995). Anharmonic modulation for noise reduction in magnetic resonance force microscopy. *Review of Scientific Instruments*, **66**, 2853.

Budakian, R., Mamin, H.J., Chui, B.W. and Rugar, D. (2005). Creating order from random fluctuations in small spin ensembles. *Science*, **307**, 408.

Callaghan, P.T. (1991). *Principles of Nuclear Magnetic Resonance Microscopy*, Clarendon Press: Oxford.

Chabot, M.D. and Moreland, J. (2003). Micrometer-scale magnetometry of thin Ni80Fe20 films using ultrasensitive microcantilevers. *Journal of Applied Physics*, **93**, 7897.

Chui, B.W., Hishinuma, Y., Budakian, R., *et al*. (2003). *TRANSDUCERS '03. 12th International Conference on Solid-State Sensors, Actuators and Microsystems*, Digest of Technical Papers, IEEE: Piscataway, pp. 1120–1123, Vol. 2.

Ciobanu, L., Seeber, D.A. and Pennington, C.H. (2002). 3D MR microscopy with resolution. 3.7 μm by 3.3 μm. *Journal of Magnetic Resonance*, **158**, 178.

Damon, R. and Eshbach, J. (1961). Magnetostatic modes of a ferromagnet slab. *Journal of Physics and Chemistry of Solids*, **19**, 308.

Degen, C.L., Lin, Q., Hunkeler, A., *et al*. (2005). Microscale localized spectroscopy with a magnetic resonance force microscope. *Physical Review Letters*, **94**, 207601.

Devoret, M.H. and Schoelkopf, R.J. (2000). Amplifying quantum signals with the single-electron transistor. *Nature*, **406**, 1039.

Fletcher, R.C., LeCraw, R.C. and Spencer, E.G. (1960). Electron spin relaxation in ferromagnetic insulators. *Physical Review*, **117**, 955.

Fukushima, E. and Roeder, S.B.W. (1981). *Experimental Pulse NMR a Nuts and Bolts Approach*, Addison-Wesley: Reading.

Giessibl, F.J. (2003). Advances in atomic force microscopy. *Reviews of Modern Physics*, **75**, 949.

Hammel, P.C., Zhang, Z., Midzor, M. (1998). In *Frontiers in Magnetism of Reduced Dimension Systems*, Wigen, P.E. (Ed.), Kluwer Academic Publishers: Dordrecht.

Hammel, P.C., Zhang, Z., Moore, G.J. and Roukes, M.L. (1995). Subsurface imaging with the magnetic-resonance force microscope. *Journal of Low Temperature Physics*, **101**, 59.

Hoen, S.T., Züger, O., Yannoni, C.S., *et al*. (1994). *Solid-State Sensor and Acutator Workshop*, Hilton Head South Carolina, 13–16 June, Vol. 75, p. 6211.

Kalinikos, B.A. (1980). Excitation of propagating spin waves in ferromagnetic films. *IEEE Proceedings*, **127**, (pt.H), 4.

Klein, O., Charbois, V., Naletov, V.V. and Fermon, C. (2003). Measurement of the ferromagnetic relaxation in a micron-size sample. *Physical Review B: Condensed Matter and Materials Physics*, **67**, 220407.

LaHaye, M.D., Buu, O., Camarota, B. and Schwab, K. (2004). Approaching the quantum limit of a nanomechanical resonator. *Science*, **304**, 74.

Lin, Q., Degen, C.L., Tomaselli, M., *et al*. (2006). Magnetic double resonance in force microscopy. *Physical Review Letters*, **96**, 137604.

de Loubens, G., Naletov, V.V. and Klein, O. (2005). Reduction of the spin-wave damping induced by nonlinear effects. *Physical Review B: Condensed Matter and Materials Physics*, **71**, 180411.

Madou, M.J. (2002). *Fundamentals of Microfabrication: the Science of Miniaturization*, *Second Edition*, CRC Press: Boca Raton.

Mamin, H.J., Budakian, R., Chui, B.W. and Rugar, D. (2003). Detection and manipulation of statistical polarization in small spin ensembles. *Physical Review Letters*, **91**, 207604.

Mamin, H.J., Budakian, R., Chui, B.W. and Rugar, D. (2005). Magnetic resonance force microscopy of nuclear spins: Detection and manipulation of statistical polarization. *Physical Review B: Condensed Matter and Materials Physics*, **72**, 024413.

Mamin, H.J., Budakian, R. and Rugar, D. (2003). Superconducting microwave resonator for millikelvin magnetic resonance force microscopy. *Review of Scientific Instruments*, **74**, 2749.

Mertz, J., Marti, O. and Mlynek, J. (1993). Regulation of a microcantilever response by active control. *Applied Physics Letters*, **62**, 2344.

Mewes, T., Kim, J., Pelekhov, D.V., *et al*. (2006). Ferromagnetic resonance force microscopy studies of arrays on micron size permalloy dots. *Physical Review B*, **74**, 144424.

Midzor, M.M., Wigen, P.E., Pelekhov, D.V., *et al*. (2000). Imaging mechanisms of force detected FMR microscopy. *Journal of Applied Physics*, **87**, 6493.

Mozyrsky, D., Martin, I., Pelekhov, D. and Hammel, P.C. (2003). Theory of spin relaxation in magnetic resonance force microscopy. *Applied Physics Letters*, **82**, 1278.

Pelekhov, D.V., Martin, I., Suter, A., *et al*. (2002). Magnetic resonance force microscopy and the solid state quantum computer. *Proceedings of the SPIE - The International Society for Optical Engineering*, **4656**, 1.

Pelekhov, D.V., Selcu, C., Banerjee, P., *et al*. (2005). Light-free magnetic resonance force microscopy for studies of electron spin polarized systems. *Journal of Magnetism and Magnetic Materials*, **286**, 324.

Rugar, D., Budakian, R., Mamin, H.J. and Chui, B.W. (2003). Manipulation and detection of electron spins by magnetic resonance force microscopy authors. *AIP Conference Proceedings*, **696**, 45.

Rugar, D., Budakian, R., Mamin, H.J. and Chui, B.W. (2004). Single spin detection by magnetic resonance force microscopy. *Nature*, **430**, 329.

Rugar, D., Yannoni, C.S. and Sidles, J.A. (1992). Mechanical detection of magnetic resonance. *Nature*, **360**, 563.

Rugar, D., Züger, O., Hoen, S.T., *et al*. (1994). Force detection of nuclear magnetic resonance. *Science*, **264**, 1560.

Sidles, J.A. (1991). Noninductive detection of single-proton magnetic resonance. *Applied Physics Letters*, **58**, 2854.

Sidles, J.A. (1992). Folded stern-gerlach experiment as a means for detecting nuclear magnetic resonance in individual nuclei. *Physical Review Letters*, **68**, 1124.

Sidles, J.A., Garbini, J.L., Bruland, K.J., *et al*. (1995). Magnetic resonance force microscopy. *Reviews of Modern Physics*, **67**, 249.

Slichter, C.P. (1989). *Principles of Magnetic Resonance*, Springer-Verlag: New York.

Stipe, B.C., Mamin, H.J., Stowe, T.D., *et al*. (2001a). Noncontact friction and force fluctuations between closely spaced bodies. *Physical Review Letters*, **87**(9), 096801.

Stipe, B.C., Mamin, H.J., Stowe, T.D., *et al*. (2001b). Noncontact friction and force fluctuations between closely spaced bodies. *Physical Review Letters*, **86**, 2874.

Stipe, B.C., Mamin, H.J., Yannoni, C.S., *et al*. (2001c). Electron spin relaxation near a micron-size ferromagnet *Physical Review Letters*, **87**(27), 277602.

Stowe, T., Yasumura, K., Kenny, T., *et al*. (1997). Attonewton force detection using ultrathin silicon cantilevers. *Applied Physics Letters*, **71**, 288.

Suhl, H. and Phys, J. (1957). The theory of ferromagnetic resonance at high signal powers. *Chemistry of Solids*, **1**, 209.

Suter, A., Pelekhov, D.V., Roukes, M.L. and Hammel, P.C. (2002). Probe-sample coupling in the magnetic resonance force microscope. *Journal of Magnetic Resonance*, **154**, 210.

Thurber, K.R., Harrell, L.E. and Smith, D.D. (2003). 170 nm nuclear magnetic resonance imaging using magnetic resonance force microscopy. *Journal of Magnetic Resonance*, **162**, 336–340.

Urban, R., Putilin, A., Wigen, P., *et al*. (2006). Perturbation of magnetostatic modes observed by ferromagnetic resonance force microscopy. *Physical Review B*, **73**, 212410.

Wago, K., Botkin, D., Yannoni, C.S. and Rugar, D. (1998). Paramagnetic and ferromagnetic resonance imaging with a tip-on-cantilever magnetic resonance force microscope. Microstrip resonators for electron-spin resonance. *Applied Physics Letters*, **72**, 2757.

Wallace, W.J. and Silsbee, R.H. (1991). *Review of Scientific Instruments*, **62**, 1754.

Wigen, P.E., Roukes, M.L. and Hammel, P.C. (2006). In *Spin Dynamics in Confined Magnetic Structures III*, *Vol. 101/2006 of Topics in Applied Physics*, Hillebrands, B. and Thiaville, A. (Eds.), Springer-Verlag: Berlin, Heidelberg, pp. 105–136, Chapter 3.

Yannoni, C.S., Züger, O., Rugar, D. and Sidles, J.A. 1996). In *Encyclopedia of Nuclear Magnetic Resonance*, Grant, D.M. and Harris, R.K. (Eds.), Wiley: Chichester, pp. 2093–2100.

Yu, X-M., Jiang, X-L., Thaysen, J., *et al*. (2001). Noise and sensitivity in polysilicon piezoresistive cantilevers. *Chinese Physics*, **10**, 918.

Zhang, Y. and Blencowe, M.P. (2001). Intrinsic noise of a micromechanical displacement detector based on the radio-frequency single-electron transistor. *Journal of Applied Physics*, **91**, 4249.

Zhang, Z. and Hammel, P.C. (1999). *Solid State Nuclear Magnetic Resonance*, **11**, 65.

Zhang, Z., Hammel, P.C., Midzor, M., *et al*. (1998). Ferromagnetic resonance force microscopy on microscopic cobalt single layer films. *Applied Physics Letters*, **73**, 2036.

Zhang, Z., Hammel, P.C. and Wigen, P.E. (1996). Sensitivity and spatial resolution for electron-spin-resonance detection by magnetic resonance force microscopy. *Applied Physics Letters*, **68**, 2005.

Zhang, Z., Roukes, M.L. and Hammel, P.C. (1996). *Journal of Applied Physics*, **80**, 6931.

Tunneling Magnetoresistance in Semiconductors

Shinobu Ohya[1,2] and Masaaki Tanaka[1,2]

[1] *University of Tokyo, Tokyo, Japan*
[2] *Japan Science and Technology Agency, Saitama, Japan*

1 INTRODUCTION

Over the past few years, tunneling magnetoresistance (TMR) and related phenomena have been extensively studied in magnetic tunnel junctions (MTJs) composed of ferromagnetic semiconductors (FMSs), such as (In,Mn)As (Munekata *et al*., 1989; Ohno, Munekata, Molnar and Chang, 1991; Ohno *et al*., 1992) and (Ga,Mn)As (Ohno *et al*., 1996; Hayashi *et al*., 1997a; Van Esch *et al*., 1997). These FMS-based MTJs are fully epitaxial and single crystalline, and have atomically flat interfaces; thus reductions of leak current and roughness scattering are expected, leading to large TMR. Moreover, novel functions induced by quantum-size effects are expected in FMS-based quantum heterostructures.

Among these semiconductor-based MTJ structures, (Ga,Mn)As-based MTJs have been extensively studied, because (Ga,Mn)As is a ferromagnetic (FM) p-type semiconductor with a zinc blende–type crystal structure having almost the same lattice constant as GaAs and AlAs. Therefore, (Ga,Mn)As/(GaAs or AlAs) III–V-based heterostructures can be epitaxially grown with abrupt interfaces and with atomically controlled layer thicknesses (Hayashi *et al*., 1997b; Ohno, 1999; Ohno *et al*., 1999; Tanaka *et al*., 2000a,b). Several advantages are expected in MTJs of GaMnAs-based III–V heterostructures: (i) One can form high-quality single crystalline MTJs made of all-semiconductor heterostructures, which can be easily integrated with other III–V-based structures and devices. (ii) In principle, many parameters such as the barrier height, barrier thickness, and the Fermi energy of FM electrodes are controllable. (iii) Introduction of quantum heterostructures, such as double-barrier resonant tunneling diodes, is probably easier than any other material system. In Section 2, we mainly focus on the GaMnAs-based single-barrier MTJs. The basic characteristics of TMR and the theoretical understanding in these single-barrier structures are presented. In the last part of Section 2, recent progress of TMR studies in semiconductor-based single-barrier MTJs including other materials is reviewed.

Combining the quantum-size effect and TMR is one of the very important issues for adding novel functionalities to semiconductor-based spin-electronic devices. Recently, theoretical calculations and experiments of GaMnAs-based double-barrier MTJs have been carried out. The theoretical calculations predict that TMR is largely enhanced by the quantum-size effect. In Section 3, these theoretical predictions and experiments on GaMnAs-based double-barrier MTJs are reviewed.

In Section 4, recently observed novel phenomena, materials, and structures related to TMR in semiconductors are described. The first of them is the tunneling anisotropic magnetoresistance (TAMR), which was observed in GaMnAs-based heterostructures (Gould *et al*., 2004; Rüster *et al*., 2005). TAMR seems very similar to TMR, but the

Handbook of Magnetism and Advanced Magnetic Materials. Edited by Helmut Kronmüller and Stuart Parkin. Volume 5: *Spintronics and Magnetoelectronics*. ISBN: 978-0-470-02217-7.

characteristics differ considerably. Although the mechanism of TAMR has not been fully understood, experimental results and present understandings of TAMR are briefly mentioned in this section. Second, the recent observation of TMR in MnAs/AlAs/GaAs:MnAs MTJ structures, where the bottom electrode is composed of FM MnAs nanoclusters embedded in GaAs (we refer to as GaAs:MnAs), is presented (Hai, Yokoyama, Ohya and Tanaka, 2006). In this structure, TMR is induced by spin-polarized carriers moving through the MnAs nanoclusters. Because the T_C value of MnAs is above room temperature, it is expected that TMR devices operating at room temperature could be realized. Also, it was clarified that the bias voltage V_{half} at which the TMR ratio is reduced by half is surprisingly as high as 1200 mV, which is much higher than V_{half}($\sim$40 mV) of FMS-based MTJs. Here, the basic characteristics of GaAs:MnAs-based MTJs are introduced. Finally, application of TMR to three terminal devices is described. In the recently proposed spin transistors of metal-oxide-semiconductor (MOS) gate structure (spin MOSFET; Sugahara and Tanaka, 2004, 2005), spin injection from the FM source into the semiconductor channel via spin-polarized tunneling is essential for device operation. The device structure, operation principle, and applications of the spin MOSFET are reviewed.

2 TMR IN SINGLE-BARRIER MAGNETIC TUNNEL JUNCTIONS

2.1 Early studies of TMR in GaMnAs-based MTJs

The first observation of TMR in a GaMnAs-based heterostructure was reported by Hayashi, Shimada, Shimizu, and Tanaka (1999). TMR was observed in a fully epitaxial MTJ structure of $Ga_{0.961}Mn_{0.039}As$ (200 nm)/AlAs (3 nm)/$Ga_{0.961}Mn_{0.039}As$ (200 nm) grown by low-temperature molecular-beam epitaxy (LT-MBE). Figure 1 shows the TMR curve observed in GaMnAs/AlAs/GaMnAs MTJ with a magnetic field applied in plane along the [110] direction at 4.2 K. Because the lattice constant of GaMnAs is slightly larger than that of GaAs, the GaMnAs film grown on GaAs receives a compressive strain, having an in-plane magnetic anisotropy, so as to minimize the magnetostatic energy. Thus, hysteretic MR curves can be obtained when a magnetic field is applied along the in-plane direction of the GaMnAs film. In this study, the TMR ratio of around 5% was obtained at 4.2 K. Here, we define the TMR ratio as $(R_{AP} - R_0)/R_0$, where R_{AP} and R_0 are resistances in antiparallel magnetization and in parallel magnetization at zero magnetic field, respectively. (When the TMR ratio

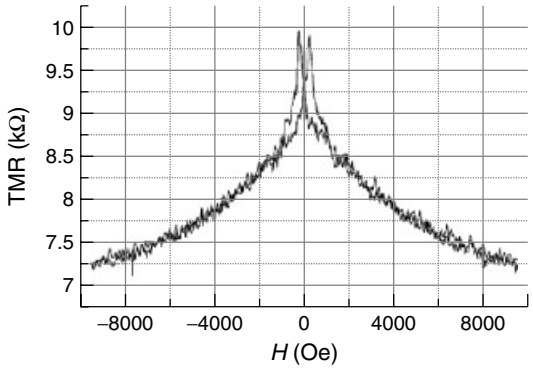

Figure 1. Magnetic-field dependence of tunneling resistance measured at 4.2 K on $Ga_{0.961}Mn_{0.039}As$ (200 nm)/AlAs (3 nm)/$Ga_{0.961}Mn_{0.039}As$ (200 nm). (Reproduced from Hayashi *et al*., 1999, with permission from Elsevier. © 1999.)

is defined as $(R_{max} - R_{min})/R_{min}$, where R_{max} and R_{min} are the maximum and minimum resistances respectively, in Figure 1, it is 36% at 4.2 K). After this experiment, in 2000, Chiba *et al*. observed TMR in a $Ga_{0.95}Mn_{0.05}As$/AlAs (3 nm)/$Ga_{0.97}Mn_{0.03}As$ MTJ (Chiba *et al*., 2000). They grew this structure on an InGaAs buffer layer whose lattice constant is larger than GaMnAs. In this case, the GaMnAs films receive a tensile strain, leading to an out-of-plane magnetic anisotropy. They applied magnetic field perpendicular to the film plane, and observed the TMR ratio of around 5.5% at 20 K.

2.2 Basic characteristics of TMR in GaMnAs-based MTJs

In 2001, a large TMR ratio (>70%, maximum 75%) was observed by Tanaka and Higo in GaMnAs/AlAs/GaMnAs MTJs at 8 K (Tanaka and Higo, 2001, 2002). This large increase of TMR was achieved by the improved quality of the GaMnAs layers and the tunnel barrier, and by optimization of the device structures. In the GaMnAs MTJ structures, it is known that there are many defects such as the As antisites (Grandidier *et al*., 2000) and the Mn interstitials (Yu *et al*., 2002), whose concentration strongly depends on the MBE growth conditions. Thus, controlling these defects is important for fabricating the GaMnAs MTJ structures. In this study, systematic investigations, such as AlAs barrier-thickness dependence, temperature dependence, and magnetic-field-direction dependence of TMR, were carried out. Here, these basic characteristics of TMR in GaMnAs-based single-barrier MTJs are reviewed.

Figure 2 illustrates the sample structure and preparation process, using LT-MBE and patterning by photolithography. After a 100-nm-thick Be-doped GaAs buffer layer was grown at 580 °C on a p^+-GaAs(001) substrate, a $Ga_{1-x}Mn_xAs$

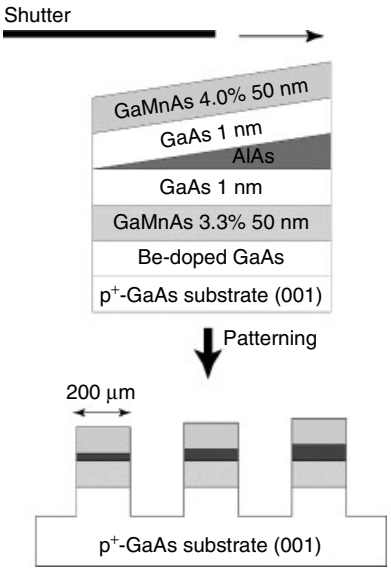

Figure 2. Preparation of a wedge-type ferromagnetic semiconductor trilayer heterostructure by LT-MBE and mesa-etched round-shaped MTJs, 200 μm in diameter. (Reproduced from Tanaka *et al*., 2001, with permission from the American Physical Society. © 2001.)

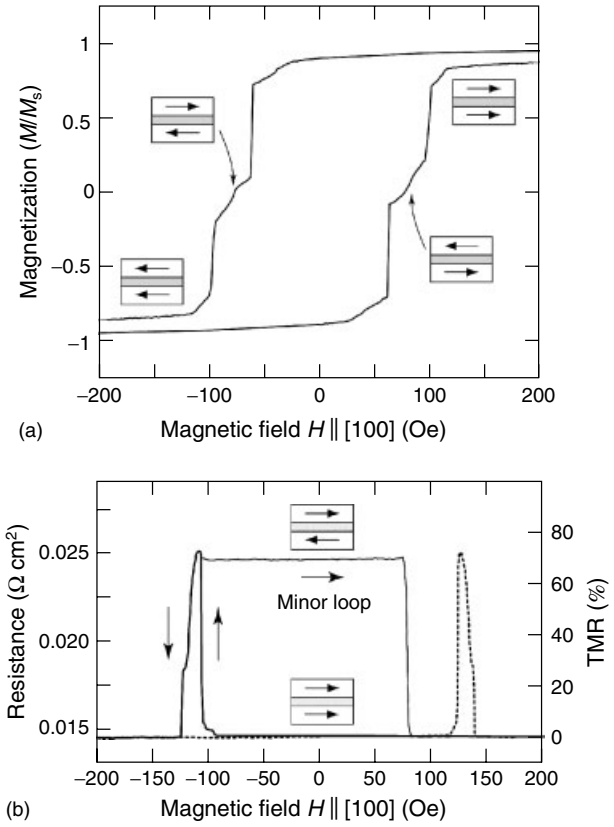

Figure 3. (a) Magnetization of a $Ga_{1-x}Mn_xAs$ ($x = 4.0\%, 50\,nm$)/AlAs (3 nm)/$Ga_{1-x}Mn_xAs$ ($x = 3.3\%, 50\,nm$) trilayer measured by SQUID at 8 K. The specimen size was $3 \times 3\,mm^2$. The vertical axis shows the normalized magnetization M/M_s, where M_s is the saturation magnetization. (b) TMR curves at 8 K of a $Ga_{1-x}Mn_xAs$ ($x = 4.0\%, 50\,nm$)/AlAs (1.6 nm)/$Ga_{1-x}Mn_xAs$ ($x = 3.3\%, 50\,nm$) tunnel junction. The tunnel junctions were mesa-etched diodes 200 μm in diameter. Bold solid and dashed curves are major loops, with the magnetic-field sweep direction from positive to negative and negative to positive, respectively. A minor loop is shown by a thin solid curve. In both (a) and (b), the magnetic field was applied along the [100] axis in the plane. (Reproduced from Tanaka *et al*., 2001, with permission from the American Physical Society. © 2001.)

($x = 4.0\%, 50\,nm$)/AlAs (d_{AlAs})/$Ga_{1-x}Mn_xAs$ ($x = 3.3\%$, 50 nm) trilayer was grown at 250°C. By using a shutter moving linearly in front of the substrate, the barrier thickness d_{AlAs} was changed from 1.3 to 2.8 nm within a wafer of $20 \times 20\,mm^2$. The slope of the wedge was estimated by the growth rate of AlAs, which was obtained by reflection high-energy electron diffraction (RHEED) oscillations and the moving speed of the shutter. Preparation of wedge-type samples is important in order to characterize the dependence of the TMR of MTJs on the barrier thickness, because the electronic and magnetic properties of the GaMnAs layers are very sensitive to the growth conditions (Shimizu, Hayashi, Nishinaga and Tanaka, 1999). In addition, undoped 1-nm-thick GaAs spacers were inserted between GaMnAs and AlAs to make the interfaces smooth and to avoid Mn diffusion into the barrier, which may cause spin-flip scattering. In order to measure the tunneling transport, the sample was patterned by photolithography and mesa etching, into arrays of round-shaped mesa junctions, 200 μm in diameter with various barrier thicknesses ranging from 1.3 nm to 2.8 nm.

2.2.1 *Experimental results of TMR in the GaMnAs/AlAs/GaMnAs MTJs*

The magnetization of the $Ga_{1-x}Mn_xAs$ ($x = 4.0\%, 50\,nm$)/AlAs (3 nm)/$Ga_{1-x}Mn_xAs$ ($x = 3.3\%, 50\,nm$) trilayer measured by superconducting quantum interference device (SQUID) at 8 K is shown in Figure 3(a). In the SQUID measurements, the trilayer sample was cleaved into a square shape with an area of $3 \times 3\,mm^2$. The magnetic field was applied along the [100] axis in the plane. Pairs of arrows in the figure indicate the magnetization directions of the top and bottom GaMnAs layers at different fields. Owing to the different coercivity of the two GaMnAs layers, a double-step magnetization curve with coercive fields of about 60 and 100 Oe was observed. The easy magnetization axis of the FM GaMnAs layers lies in the film plane.

Figure 3(b) shows tunnel resistance versus magnetic field, that is, TMR curves measured at 8 K on a junction with $d_{AlAs} = 1.6\,nm$ when the magnetic field was applied along the [100] axis in the plane. The measurements were done at

a constant bias of 1 mV, and so there is no hot carrier effect. Bold solid and dashed curves (major loops) in Figure 3(b) were obtained by sweeping the field from positive to negative and negative to positive, respectively. As shown by the bold solid curve, when the magnetic field H was swept from the positive saturation field down to negative, the tunnel resistance $R(H)$ increased from 0.014 to 0.025 $\Omega\,\mathrm{cm}^2$ (corresponding TMR was 72%) at $H = -110$ Oe, where the magnetization of one GaMnAs layer reversed and the magnetization configuration changed from parallel to antiparallel. Sweeping the field further to the negative direction, $R(H)$ and TMR decreased to their initial values ($R(H) = 0.014\,\Omega\,\mathrm{cm}^2$) at $H = -125$ Oe, where the magnetization of the other GaMnAs layer reversed and the magnetization configuration became parallel again. The difference of the coercive fields between the M–H curve in Figure 3(a) and the TMR curve in Figure 3(b) is caused by the difference in the shape and size of the measured specimens. Note that the TMR value is over 70%, much higher than the TMR previously reported. A thin solid curve in Figure 3(b) shows a minor loop, indicating that the antiparallel magnetization configuration is stable, as well as the parallel magnetization configuration. The switching fields of the major and minor loops are different. This is a general feature of the coercivity in GaMnAs films and it depends on the maximum magnetic field applied just before the switching. This is probably related to the domain wall pinning, whose unpinning energy depends on the maximum magnetic field applied just before the switching of magnetization. In this case, the minor loop is measured with the maximum magnetic field of -120 Oe, while the major loops are measured with the maximum magnetic fields of ± 1 T. Therefore, the switching field of the minor loop is smaller than that of the major loop.

Figure 4(a) shows the tunnel resistance R for the tunnel junctions measured at 8 K as a function of the barrier thickness d_{AlAs}. The resistance exponentially increased over a wide range from 10^{-3} to $10\,\Omega\,\mathrm{cm}^2$ as d_{AlAs} increased, which means that high-quality tunnel junctions were formed with a constant barrier height. In the WKB approximation, the slope of ln R–d_{AlAs} characteristics is given by $2[2m^* V_{\mathrm{b}}]^{1/2}/\hbar$, thereby estimating the product $m^* V_{\mathrm{b}}$ to be $0.32 m_0$ kg·eV, where m_0 is the free-electron mass, m^* is the effective mass of holes, and V_{b} is the barrier height. The valence band offset between GaMnAs and AlAs is unknown but it is considered to be close to that ($\sim$0.55 eV) of GaAs and AlAs, and the Fermi energy of holes in GaMnAs is 0.1 to 0.2 eV, thus the barrier height V_{b} is $\sim$0.45 eV. Therefore, the effective mass m^* of holes that are responsible for tunneling is roughly estimated to be $\sim 0.7 m_0$.

Figure 4(b) shows barrier-thickness dependence of TMR at 8 K when the magnetic field was applied in plane along the [100] and [1$\bar{1}$0] axes. The maximum TMR was 75%

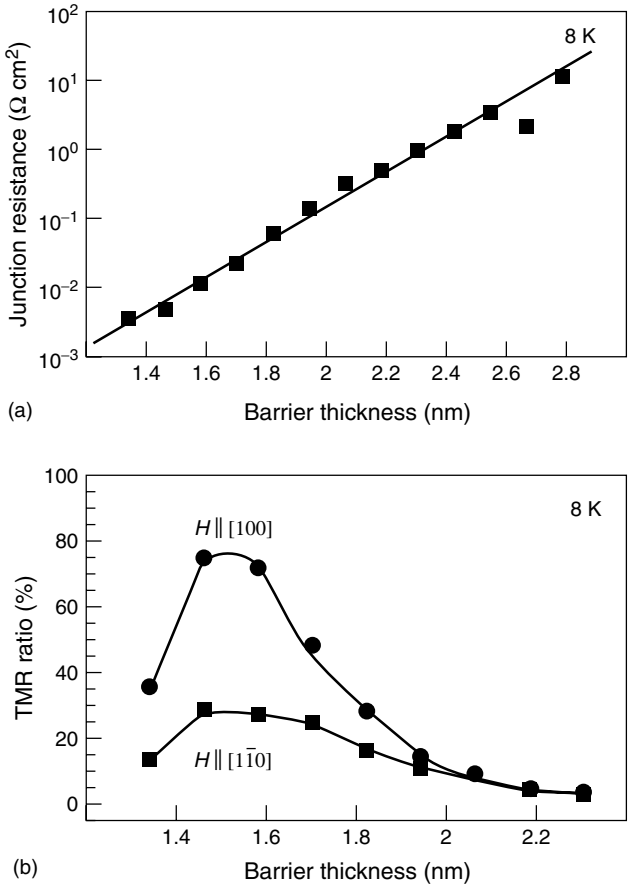

Figure 4. Barrier-thickness dependence of (a) the tunnel resistance and (b) the TMR in $Ga_{1-x}Mn_xAs$ ($x = 4.0\%$, 50 nm)/AlAs (d_{AlAs})/$Ga_{1-x}Mn_xAs$ ($x = 3.3\%$, 50 nm) tunnel junctions measured at 8 K. In (b), the TMR values were measured with the magnetic field applied along the [100] and [1$\bar{1}$0] axes. (Reproduced from Tanaka *et al.*, 2001, with permission from the American Physical Society. © 2001.)

at $d_{\mathrm{AlAs}} = 1.46$ nm when the field was applied along the [100] axis. In both field directions, with increasing d_{AlAs} (>1.5 nm), the TMR was found to rapidly decrease. At all the values of d_{AlAs}, the TMR was higher when the field was applied along the [100] axis than along the [1$\bar{1}$0] axis. The difference of the TMR between the two directions of the field is due to the cubic magnetocrystalline anisotropy induced by the zinc blende–type GaMnAs crystal structure, where the easy magnetization axis of GaMnAs is ⟨100⟩, the details of which is reported in the literature (Higo, Shimizu and Tanaka, 2001). Although the reason for the drop in the TMR for the junction with $d_{\mathrm{AlAs}} < 1.4$ nm is not clear at present, this drop could be caused by the decrease of the effective barrier height because of the interface roughness or the image potential. Another possible reason is the FM interlayer exchange coupling between GaMnAs layers separated by a very thin AlAs layer.

When TMR was measured on many round-shaped mesa tunnel junctions, a variety of different characteristics were observed, as shown in Figure 5(a)–(d). Here, the magnetic field was applied in plane along the [100] axis. Because the present tunnel junctions are totally monocrystalline and GaMnAs is considered to have the magnetocrystalline anisotropy with the easy magnetization axis of ⟨100⟩, the magnetization direction of the top and bottom GaMnAs layers favors to be along one of the four easy axes ([100], [010], [$\bar{1}$00], [0$\bar{1}$0]) in the film plane. These TMR behaviors are attributed to the different magnetization configurations, as illustrated in the lower panel of Figure 5. Here, solid and gray arrows are the magnetization directions of the two GaMnAs layers, and time evolutions of magnetization configuration are depicted when the applied magnetic field is changed from positive (+200 Oe) to negative (−200 Oe). These TMR behaviors are well explained by the analysis of magnetization rotation based on the single domain theory. The multivalue characteristics of TMR owing to the magnetocrystalline anisotropy could lead to interesting applications such as multivalue recording and novel logic circuitry.

Temperature dependence of the TMR for these various junctions with different d_{AlAs} are measured and the normalized conductance difference data $\Delta G = \Delta G(T)/\Delta G$ (8 K) are plotted in Figure 6, where T is temperature, $\Delta G(T) = G_{\mathrm{P}}(T) - G_{\mathrm{AP}}(T)$, $G_{\mathrm{P}}(T)$ and $G_{\mathrm{AP}}(T)$ are the

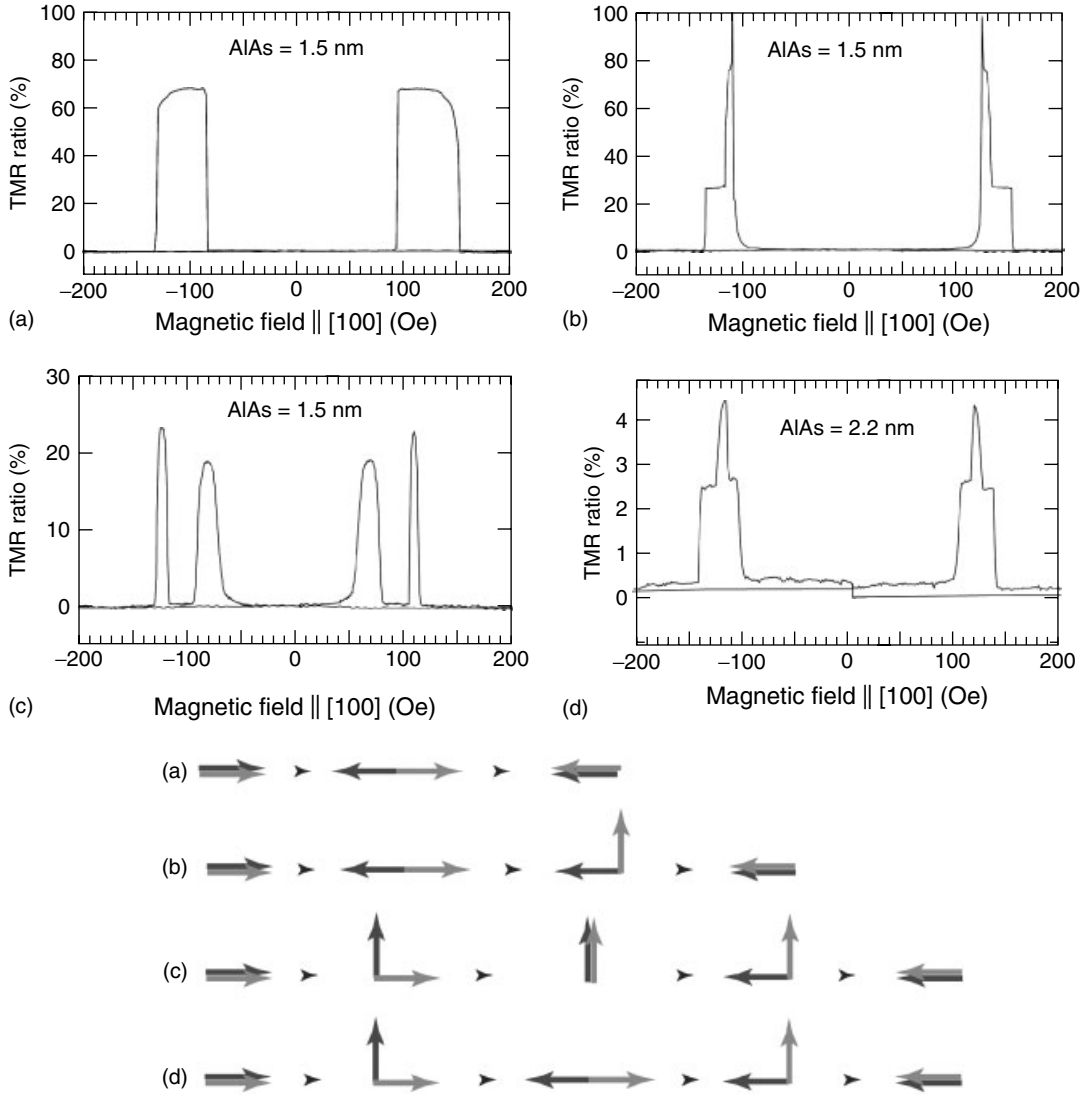

Figure 5. A variety of TMR characteristics of round-shaped mesa tunnel junctions at 8 K. The magnetic field was applied in plane along the [100] axis. In the lower panel, time evolutions of magnetization configuration are depicted when the applied magnetic field is changed from positive (+200 Oe) to negative (−200 Oe). Solid and gray arrows are the magnetization directions of the two GaMnAs layers. (Reproduced from Tanaka *et al*., 2002, with permission from Elsevier. © 2002.)

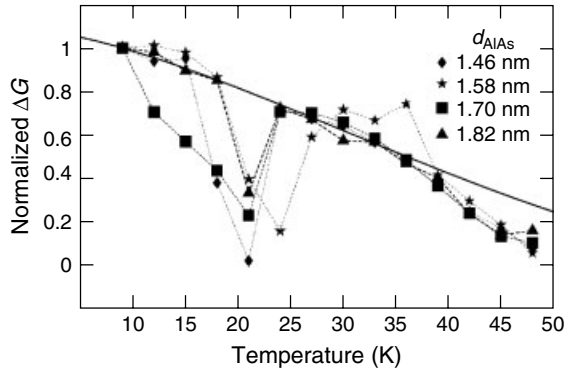

Figure 6. Temperature dependence of the normalized conductance difference ΔG (equivalently TMR) for various junctions with different $d_{\mathrm{AlAs}} = 1.46, 1.58, 1.70, 1.82$ nm. The solid line is the fit to the theory based on thermal spin-wave excitations (Tanaka and Higo, 2001, 2002). (Reproduced from M. Tanaka *et al*., 2002, with permission from Elsevier. © 2002.)

junction conductances at T K for parallel and antiparallel magnetization, respectively. ΔG (equivalently, TMR) basically decreased with increasing temperature and vanished at ∼50 K, which is the Curie temperature of one of the GaMnAs layers. ΔG dropped once at ∼20 K, because the coercivity of the top and bottom GaMnAs layers is so close (almost same) that the window for antiparallel magnetization is too small, which was confirmed by temperature-dependent magnetization measurements, thus ΔG was difficult to be observed at around 20 K. A solid line in Figure 6 is the fit to the theory $\Delta G(T) = \Delta G_0(1 - \alpha T^{3/2})^2$, where ΔG_0 is a constant and α is fitted to $1.5 \times 10^{-3}\,\mathrm{K}^{-3/2}$, based on thermal spin-wave excitations (Shang, Nowak, Jansen and Moodera, 1998). The theory can explain the present data, as it did for conventional $Co/Al_2O_3/Co(NiFe)$ MTJs. This means that the dominant contribution to the tunnel conductance is direct elastic tunneling with the tunneling carrier spin polarization P decreasing as $1 - \alpha T^{3/2}$. Both the excellent scaling of the junction resistance with the AlAs barrier thickness (Figure 4a) mentioned earlier and this temperature dependence of ΔG give strong evidence for TMR junctions.

2.2.2 *Tight binding calculations of TMR*

In the conventional Jullière's model (Jullière, 1975), the TMR depends only on the spin-dependent density of states (DOSs) in the two FM electrodes and does not depend on the barrier thickness d, and hence the Jullière model cannot explain these experimental results. Because the present GaMnAs/AlAs/GaMnAs heterostructures are epitaxially grown single crystals, the wave vector $\boldsymbol{k}_\parallel$ of carriers parallel to the interface should be conserved in tunneling. Calculations using the tight binding theory including $\boldsymbol{k}_\parallel$ conservation by Mathon (1997) is consistent with the experimental results of barrier-thickness dependence of TMR mentioned earlier.

The experimental results can be qualitatively explained as follows: Figure 7 shows the Fermi surfaces for up and down spins in two FM electrodes, calculated by the single orbital, tight binding model, when the magnetization configuration is (a) parallel and (b) antiparallel. Also, the dispersion of the decaying factor κ_z in the barrier layer was calculated and shown in the middle of the figure. The wave vector $k_z(E_F, \boldsymbol{k}_\parallel)$ normal to the interface in the FM electrodes is determined from $E_F = E_0 + 2t\cos(k_z a) + w(\boldsymbol{k}_\parallel)$, and the decaying factor $\kappa_z(E_F, \boldsymbol{k}_\parallel)$ in the barrier layer is determined from $E_F = E_0 + 2t\cosh(\kappa_z a) + w(\boldsymbol{k}_\parallel)$, where $w(\boldsymbol{k}_\parallel) = 2t[\cos(k_x a) + \cos(k_y a)]$, $\boldsymbol{k}_\parallel = (k_x, k_y)$ is the wave vector parallel to the film plane, E_F is the Fermi energy, E_0 is the on-site energy in each layer, t is the nearest-neighbor hopping parameter, and a is the lattice constant (Mathon, 1997). The spin polarization in the FM electrodes was regarded as the difference of E_0 between the majority and minority carriers. When the magnetizations of the two FM electrodes are parallel as shown in Figure 7(a), the majority (minority) spin is the up (down) spin in both electrodes, so that the carriers can tunnel through all the channels $(\boldsymbol{k}_\parallel, \sigma)$. When the magnetizations of the two FM electrodes are antiparallel as shown in Figure 7(b), the down spin is the majority spin in the right electrode, thus the carriers with $k_\parallel = |\boldsymbol{k}_\parallel| > k_{\mathrm{cutoff}}$ cannot tunnel, where k_{cutoff} is the cutoff wave vector which is the largest $k_\parallel$ in the minority spin band. This difference of tunneling between parallel and antiparallel configurations indicates that the TMR is mainly caused by carriers with large $k_\parallel (> k_{\mathrm{cutoff}})$. However, these carriers with larger $k_\parallel$ exponentially decay more rapidly during tunneling in the barrier because of larger κ_z, as shown in the middle of Figure 7. Because of this in-plane dispersion of $\kappa_z(\boldsymbol{k}_\parallel)$, when the barrier thickness d is large, the tunneling conductance is dominated by the carriers with smaller $k_\parallel$, which do not contribute much to the TMR. Therefore, the TMR decreases as d increases.

In order to compare with the experimental TMR obtained in the GaMnAs/AlAs/GaMnAs tunnel junctions, the dependence of TMR on d_{AlAs} was calculated using the spin-orbit nearest-neighbor sp^3s^* model (Vogl, Hjalmarson and Dow, 1983; Chadi, 1977). The tight binding parameters reported by Schulman and Chang were used to obtain the realistic band structures of GaAs and AlAs (Schulman and Chang, 1985). The effect of Mn ions in GaMnAs was simplified by introducing an additional term ΔJ_x into the intralayer coupling matrices in the sp^3s^* Hamiltonian. Here J_x is a 10×10 matrix derived from the x component of the total angular momentum $\boldsymbol{J}$ in the planar-orbital basis. J_x was used because the magnetization was along the [100] axis. This additional

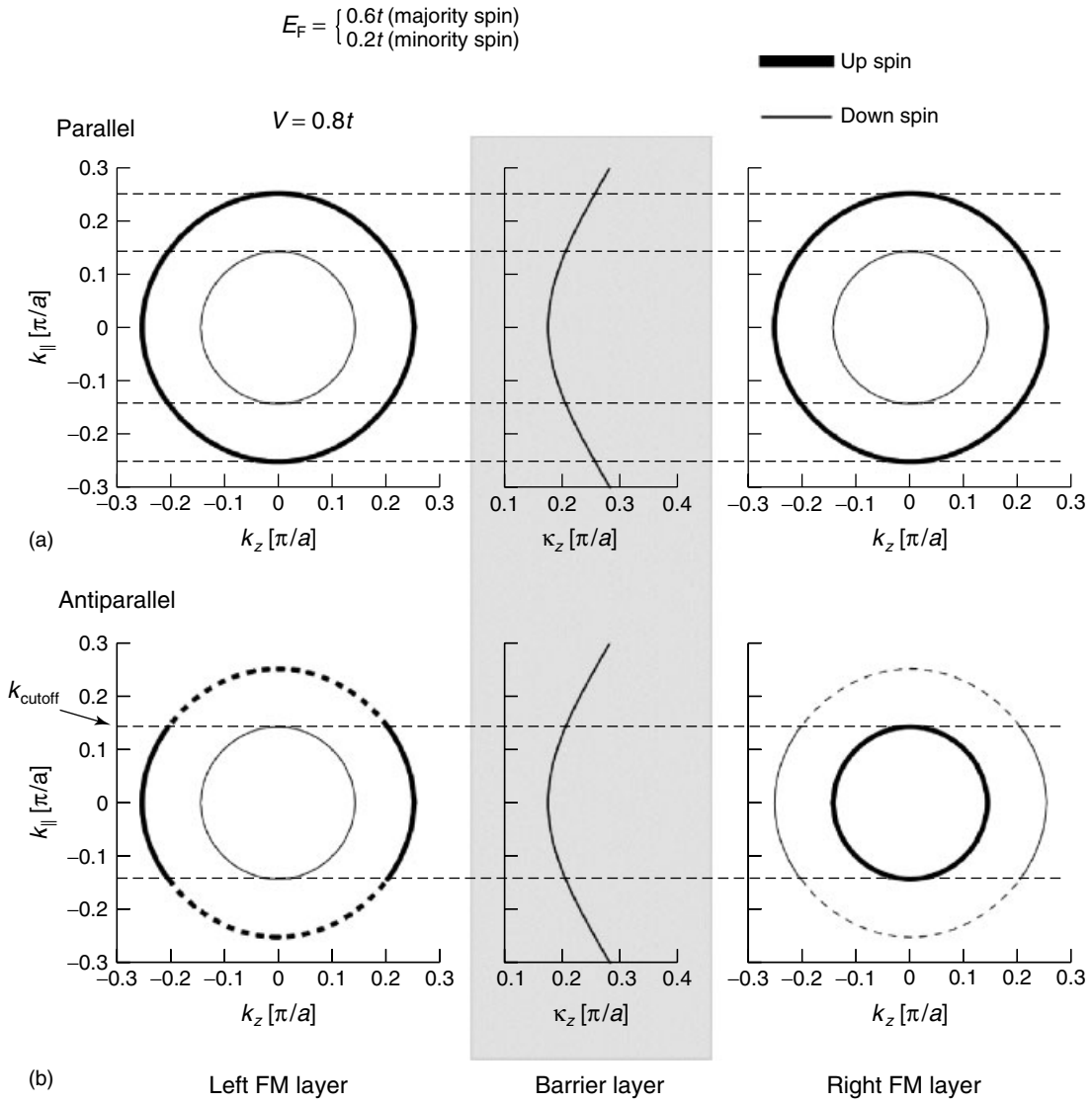

Figure 7. Fermi surfaces of the simple cubic lattice calculated by the single orbital tight binding model for up and down spins with the spontaneous spin splitting in (a) parallel and (b) antiparallel magnetization configurations. Dependence of the decaying factor κ_z in the barrier on $\mathbf{k}_\parallel$ is also shown in the middle of the Figure. (Reproduced from Tanaka *et al.*, 2001, with permission from the American Physical Society. © 2001.)

term causes the changes of the on-site energies proportional to J_x. The scalar proportional coefficient Δ corresponds to the spin-splitting energy between the two holes $|3/2, 1/2>$ and $|3/2, -1/2>$ at the Γ point.

In order to calculate TMR, tunneling probability T was first calculated, as shown in Figure 8, and plotted in the $\boldsymbol{k}_\parallel$ plane ($-0.3\pi/a < k_x < 0.3\pi/a$, $-0.3\pi/a < k_y < 0.3\pi/a$), both for parallel and antiparallel magnetization. The $\boldsymbol{k}_\parallel$ dependence of T is complex because of the complexity of the valence band structure of GaMnAs and AlAs. The band parameters used here are shown in the inset of Figure 9. Despite the complexity, the essential point is as follows. When the AlAs barrier thickness is as thin as 1 monolayer (ML), T has some nonzero values even at large $k_\parallel$ for parallel magnetization, whereas T is zero at large $k_\parallel$ for antiparallel magnetization. This difference in T between parallel and antiparallel magnetization leads to large TMR. In contrast, when the AlAs barrier thickness is greater (5 MLs), T is significantly suppressed at large $k_\parallel$ for parallel magnetization due to large κ_z, as described above, thus the difference in T between parallel and antiparallel magnetization is smaller, resulting in smaller TMR.

Figure 9 shows the calculated (solid curve) and measured (solid circles) barrier-thickness dependences of the TMR in the present GaMnAs/AlAs/GaMnAs tunnel junctions. We assumed that E_F, V, and Δ were 0.2, 0.67, and 0.08 eV,

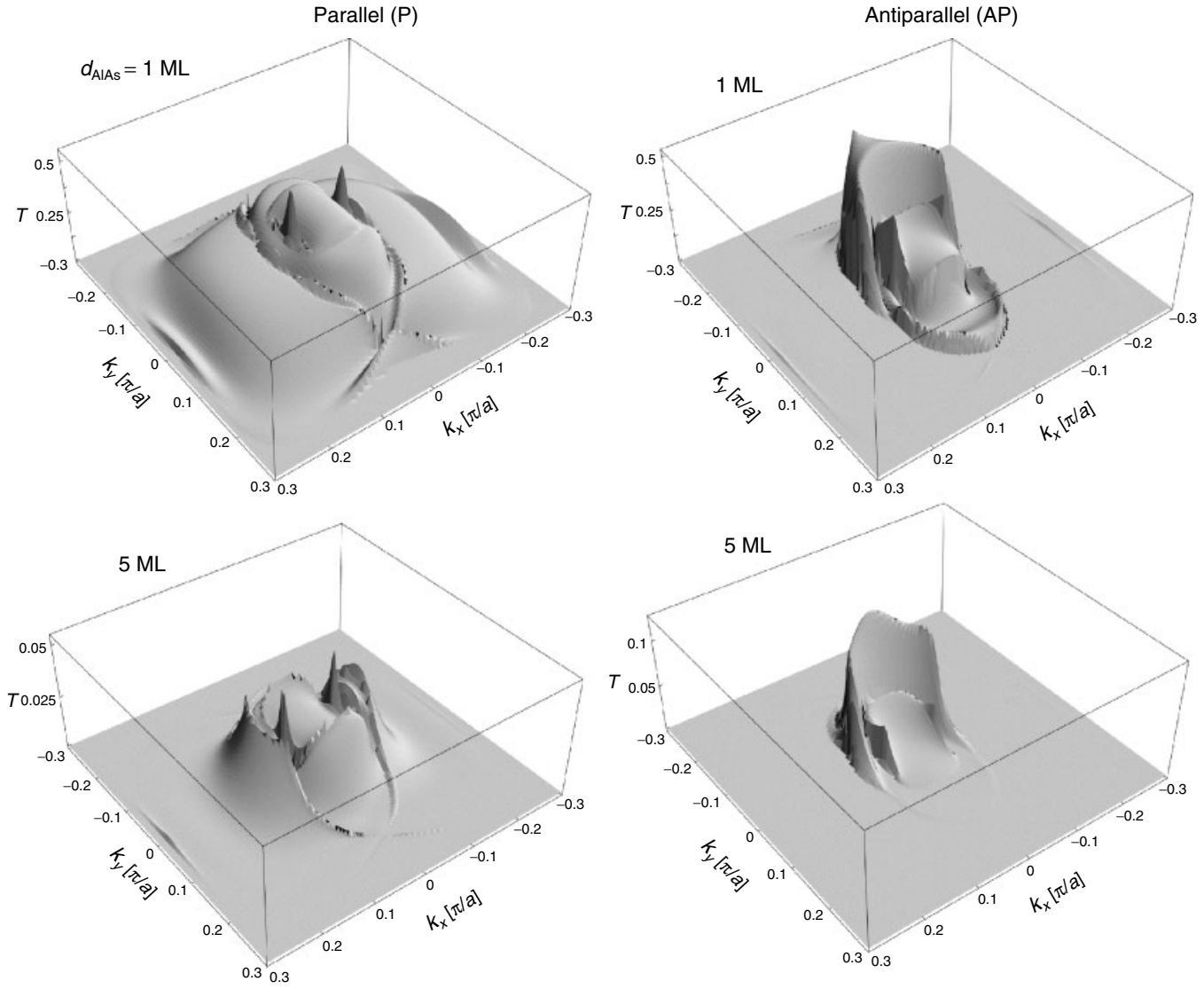

Figure 8. Tunneling probability T in GaMnAs/AlAs (d_{AlAs})/GaMnAs tunnel junctions plotted in the $\boldsymbol{k}_{\parallel}$ plane ($-0.3\pi/a \leq k_x \leq 0.3\pi/a$, $-0.3\pi/a \leq k_y \leq 0.3\pi/a$), both for parallel and antiparallel magnetization configurations, when the AlAs barrier thickness $d_{AlAs} = 1$ ML and 5 ML. (Reproduced from M. Tanaka *et al*., 2002, with permission from Elsevier. © 2002.)

respectively. The Fermi energy E_F and the valence band offset V were measured from the top of the valence band in the calculated GaMnAs band structure, as shown in the inset of Figure 9. $V = 0.67$ eV gives the valence band offset of 0.55 eV when $\Delta = 0$, that is, the case for normal GaAs/AlAs interfaces, which is a reasonable value. Compared with the experimental results, the calculated TMR decreases rapidly in the thinner barrier region. The barrier thickness was evaluated from RHEED oscillations and the moving speed of the shutter, as mentioned before. Because completely accurate alignment of the moving shutter with the substrate in the MBE chamber is difficult, the absolute values of the estimated barrier thickness may not be reliable (though the relative values are reliable), hence the calculated dependence was horizontally shifted towards right by 0.7 nm (only 2.5 ML) to fit to the experimental results, as shown by a dashed curve in Figure 9. The fitting is fairly good, but not perfect partly because the band structure of GaMnAs is not fully known yet, the model is simple compared with the more complex band structure, and/or partly because there could be spin scattering at the interfaces or in the tunnel barrier which is not taken into account. However, the present spin-orbit nearest-neighbor sp^3s^* model is found to explain the most essential part of the experimental barrier-thickness dependence of the TMR. Note that there are three essential points in this model. (i) The cutoff wave vector

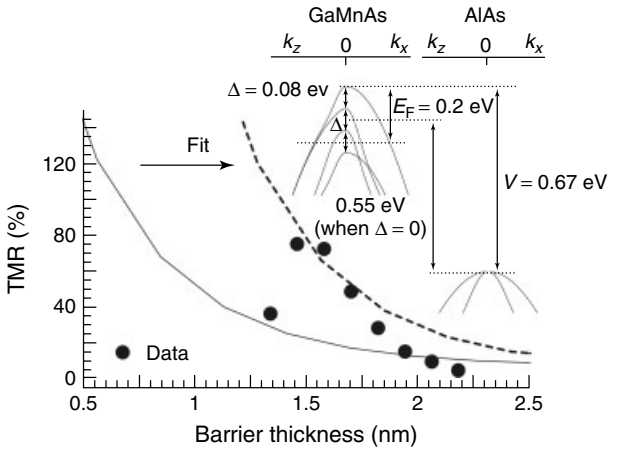

Figure 9. Solid curve represents the calculated dependence of TMR on the barrier thickness d_{AlAs} when the Fermi energy $E_{\mathrm{F}} = 0.2\,\mathrm{eV}$, the band offset $V = 0.67\,\mathrm{eV}$ (both measured from the top of the valence band of GaMnAs), and the spin splitting $\Delta = 0.08\,\mathrm{eV}$ between the two light holes $|3/2, 1/2\rangle$ and $|3/2, -1/2\rangle$ at the Γ point. Inset shows the band dispersion and the relationship of these parameters. The solid curve is horizontally shifted to the dashed curve by 0.7 nm (only 2.5 ML) to fit to the experimental results (solid circles, the magnetic field was along the [100] axis), because the absolute barrier thicknesses of the junctions are nominal. (Reproduced from Tanaka *et al*., 2001, with permission from the American Physical Society. © 2001.)

k_{cutoff} in the plane exists in the antiparallel configuration. (ii) The decaying factor κ_z in the barrier increases with increasing $k_{\parallel}$. (iii) $\boldsymbol{k}_{\parallel}$ is conserved in tunneling. Although these points may not be valid in the conventional MTJs with polycrystalline metallic electrodes, they are valid in the present $Ga_{1-x}Mn_xAs/AlAs/Ga_{1-x}Mn_xAs$ tunnel junctions, which are epitaxially grown single crystals.

2.3 More recent works on single-barrier MTJ

Recently, many materials have been used in the studies of semiconductor-based single-barrier MTJs, and furthermore the TMR ratio is increasing. Chiba *et al*. used GaAs as a tunneling barrier of the GaMnAs-based MTJ (Chiba, Matsukura and Ohno, 2004). They fabricated a $Ga_{0.926}Mn_{0.074}As$ (20 nm)/GaAs (6 nm)/$Ga_{0.956}Mn_{0.044}As$ (20 nm) MTJ, and observed high TMR ratios of 90% at 15 K, 105% at 4.7 K, and 290% at a very low temperature of 0.39 K with a magnetic field applied in plane along [100]. They also realized current-driven magnetization reversal in the GaMnAs (80 nm)/GaAs (6 nm)/GaMnAs (15 nm) MTJs (Chiba *et al*., 2004). The critical current densities, which are necessary to change parallel magnetization to antiparallel magnetization and *vice versa*, were $j_{\mathrm{AP}} = 1.92 \times 10^5\,\mathrm{A\,cm^{-2}}$ and $j_{\mathrm{P}} = 1.4 \times 10^5\,\mathrm{A\,cm^{-2}}$ at 30 K, respectively. These values are two orders of magnitude smaller than those observed in metal systems, resulting from the smaller magnetization of GaMnAs. For the current-driven magnetization reversal, a lower energy barrier is more appropriate. Elsen *et al*. fabricated a GaMnAs-based MTJ with a 6-nm-thick $In_{0.25}Ga_{0.75}As$ barrier, and realized current-driven magnetization reversal with smaller current densities of $j_{\mathrm{AP}} = 1.23 \times 10^5\,\mathrm{A\,cm^{-2}}$ and $j_{\mathrm{P}} = 1.37 \times 10^5\,\mathrm{A\,cm^{-2}}$ at 3 K ($j_{\mathrm{AP}} = 9.39 \times 10^4\,\mathrm{A\,cm^{-2}}$ and $j_{\mathrm{P}} = 9.86 \times 10^4\,\mathrm{Acm^{-2}}$ at 30 K) (Elsen *et al*., 2006). In the structure, also, a high TMR ratio of 155% was observed at 3 K.

Chun *et al*. used a FM metal of MnAs as a top electrode in order to investigate the spin injection from a metal to a semiconductor (Chun *et al*., 2002). They fabricated MnAs(45 nm)/GaAs(1 nm)/AlAs(d = 1, 2, 5, 10 nm)/GaAs (1 nm)/$Ga_{0.97}Mn_{0.03}As$(120 nm) MTJ structures, and obtained a TMR ratio of around 30% at 4.2 K when d is 5 nm.

Saito *et al*. used wide-gap (2.8 eV) II–VI semiconductor ZnSe as a barrier of the GaMnAs MTJ structure (Saito, Yuasa and Ando, 2005). The lattice constant of ZnSe (0.5669 nm) is very close to that of GaAs (0.5654 nm), and its optimum growth condition is comparable to that of GaMnAs (∼250 °C). These structural properties make it possible to grow epitaxial ZnSe/GaMnAs heterostructures. They fabricated a $Ga_{0.928}Mn_{0.072}As$ (50 nm)/ZnSe (1 nm)/$Ga_{0.928}Mn_{0.072}As$ (50 nm) MTJ structure, observing a TMR ratio of around 100% at 2 K. This result is expected to open a new possibility of realizing II–VI/III–V spin devices.

As mentioned earlier, large TMR ratios were obtained in GaMnAs-based MTJs, therefore GaMnAs is an excellent model material for realizing spin-electronic devices. For device application, however, there is a problem of low Curie temperature (T_{C}) of GaMnAs. When the FM transition of GaMnAs was first observed, T_{C} was only around 60 K (Ohno *et al*., 1996; Hayashi *et al*., 1997a). After that, the T_{C} value of GaMnAs was increased year after year and has reached 173 K in GaMnAs alloy films (Wang *et al*., 2005) and 250 K in the Mn δ-doped GaAs heterostructures (Nazmul *et al*., 2005). However, it is still lower than room temperature. On the other hand, the fabrication of new FMSs with T_{C} higher than room temperature has also been reported. $TiCoO_2$ is one of the recently developed FSs whose T_{C} is above 400 K (Matsumoto *et al*., 2001a,b). Toyosaki *et al*. used $TiCoO_2$ as a bottom electrode of MTJ (Toyosaki *et al*., 2005). They fabricated a $Fe_{0.1}Co_{0.9}/AlO_x/TiCoO_2$ MTJ, and observed a TMR ratio of ∼11% at 15 K. TMR was observed up to 180 K, but it disappeared above 180 K, which is much lower than T_{C} of $TiCoO_2$ (∼400 K). They pointed out that this was the result of inelastic tunneling in the amorphous barrier layer or the junction interface. If an epitaxial tunnel barrier can be grown on the $TiCoO_2$ bottom layer with high-quality interfaces, it is expected that the operating temperature of TMR can be improved.

3 DOUBLE-BARRIER MTJs

3.1 Theoretical predictions of the TMR behavior in GaMnAs-based resonant tunneling diodes

Combining spin-dependent tunneling and quantum-size effect is one of the very important issues for future semiconductor-based spintronic devices. By combining these effects, a large TMR enhancement and novel functions are expected to be realized, hence, theoretical calculations on the TMR behavior in GaMnAs-based resonant tunneling diodes (RTDs) have been carried out.

Hayashi *et al*. calculated the transmission probability of an RTD structure composed of GaMnAs/AlAs (28 Å)/GaMnAs (80 Å)/AlAs (28 Å)/GaMnAs, using a transfer matrix formalism (Hayashi, Tanaka and Asamitsu, 2000). They assumed a valence band profile along the direction perpendicular to the material interfaces shown in Figure 10(a). In this model, the magnetization directions of both GaMnAs electrodes are parallel to one another, and only the magnetization direction of the GaMnAs FM quantum well (angle θ, as shown in Figure 10(a) is changeable relative to the magnetization directions of the electrodes, because the coercive force of thin GaMnAs films is larger than that of thick GaMnAs films. Figure 10(b) and (c) show the calculated results of the energy dependence of the transmission probability ($TT^*(E_z)$) from one majority spin band to the other majority spin band. Figure 10(b) and (c) correspond to heavy holes ($m_{hh} = 0.45m_0$) and light holes ($m_{lh} = 0.08m_0$), respectively. The peak energies shift in both cases, depending on the magnetization direction of the FM quantum well. This result indicates that a FM quantum well works as a very sharp spin filter as well as an energy filter, leading to the enhancement and unique bias dependence of TMR.

Petukhov *et al*. calculated the TMR behavior in GaMnAs/AlAs/GaAs/AlAs/GaMnAs RTD structures comprising a nonmagnetic quantum well between two insulating AlAs barriers (Petukhov, Chantis and Demchenko, 2002). In the calculation, they used a multiband transfer matrix method with a Luttinger–Kohn and an exchange mean-field Hamiltonian (Dietl, Ohno and Matsukura, 2001). They predicted that a large TMR enhancement occurs even with such a nonmagnetic GaAs quantum well. This mechanism is depicted in Figure 11, and is explained as follows: (a) and (b) show the majority and minority spin bands in parallel magnetization, respectively; (c) and (d) show those in antiparallel magnetization, respectively. In this model, the resonant level E_R is assumed to exist between the bottoms of valence up-spin and down-spin bands. In parallel magnetization, the up-spin carriers can go through the RTD structure. In antiparallel magnetization, however, no carrier can go through, thus the

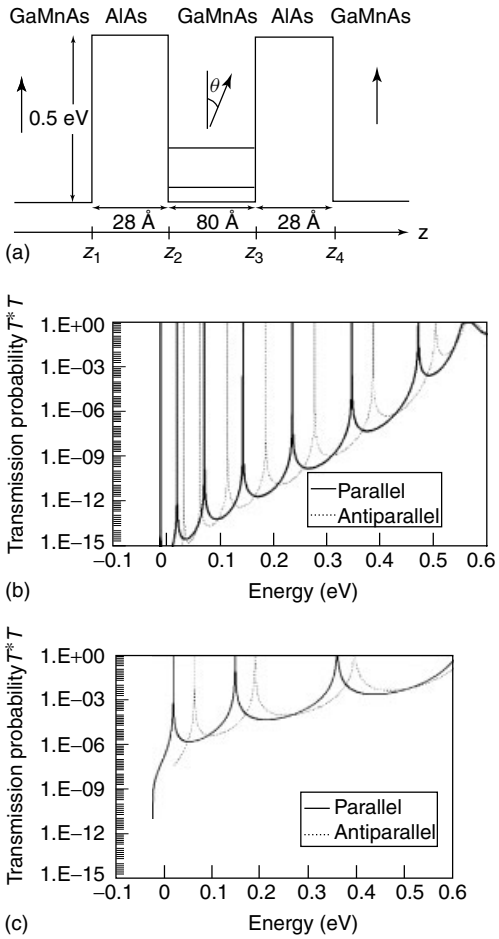

Figure 10. (a) Valence band profile of the GaMnAs-based double-barrier heterostructure. (b) Transmission probability for heavy holes ($m_{hh} = 0.45m_0$ for GaMnAs and $0.75m_0$ for AlAs, respectively). (c) Transmission probability for light holes ($m_{lh} = 0.08m_0$ for GaMnAs and $0.143m_0$ for AlAs, respectively). (Reproduced from Hayashi *et al*., 2000, with permission from the American Physical Society. © 2000.)

TMR ratio becomes very large. Figure 12 shows the calculated TMR ratio as a function of the thickness of the GaAs quantum well when the AlAs thickness w is 1, 1.5, and 2 nm. The inset is the schematic valence band diagram of these RTD structures. At a specific quantum well width, the TMR ratio is enhanced to 800% when the AlAs thickness is 2 nm.

3.2 Experimental studies on TMR in GaMnAs-based double-barrier MTJ structures

In order to observe the quantum-size effect in the GaMnAs-based RTD, Hayashi *et al*. fabricated a $Ga_{0.955}Mn_{0.045}As$/AlAs (2.8 nm)/$Ga_{0.965}Mn_{0.035}As$(8 nm)/AlAs (2.8 nm)/$Ga_{0.955}Mn_{0.045}As$ RTD structure on a p^+-GaAs(001) substrate, and

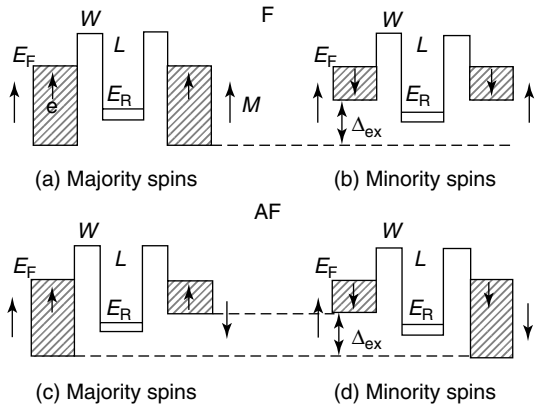

Figure 11. Band alignments of GaMnAs/AlAs/GaAs/AlAs/GaMnAs assumed by Petukhov *et al*. (a) and (b) The majority (up spin) and minority spin (down spin) bands in parallel magnetization, respectively; and (c) and (d) are those in antiparallel magnetization. Here, W, L, E_R, and Δ_{ex} are the AlAs thickness, the GaAs quantum well width, the resonant level, and the exchange energy, respectively. (Reproduced from Petukhov *et al*., 2002, with permission from the American Physical Society. © 2002.)

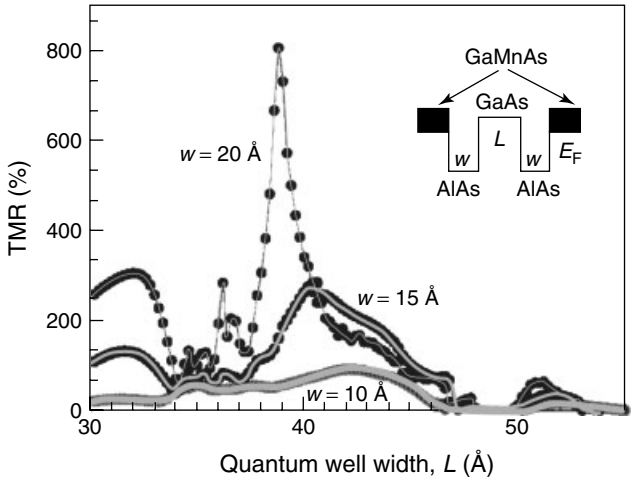

Figure 12. Calculated TMR ratios by Petukhov *et al*. as a function of the GaAs quantum well width when the AlAs thickness (w) is 1, 1.5, and 2 nm. The inset is the schematic valence band diagram of these RTD structures. (Reproduced from Petukhov *et al*., 2002, with permission from the American Physical Society. © 2002.)

investigated TMR (Hayashi, Tanaka and Asamitsu, 2000). In this RTD structure, TMR ratio of around 7% was observed at 4.2 K; when it is defined as $(R_{AP} - R_0)/R_0$, where R_{AP} and R_0 are resistances in antiparallel magnetization and in parallel magnetization at zero magnetic field, respectively. (When the TMR ratio is defined as $(R_{max} - R_{min})/R_{min}$, where R_{max} and R_{min} are the maximum and minimum resistance in the TMR loop, it is about 170% at 4.2 K). This value is higher than the TMR value observed in the GaMnAs-based single-barrier MTJ at that time (∼5%). Although the shape of the derivative $dI/dV - V$ of this RTD sample looked wavy, negative differential resistance was not clearly observed in the $I-V$ curve. It has not been clarified whether this TMR enhancement is induced by the quantum-size effect.

Mattana *et al*. fabricated a GaMnAs/AlAs (1.5 nm)/GaAs (5 nm)/AlAs (1.5 nm)/GaMnAs double-barrier MTJ structure, investigating the TMR behavior (Mattana *et al*., 2003). Figure 13(a) shows the TMR curve and (b) shows the bias dependence of TMR obtained in this double-barrier MTJ structure at 4 K. The inset of (b) shows the $I-V$ curve. Neither TMR enhancement nor negative differential resistance was observed. They explained that this is attributable to

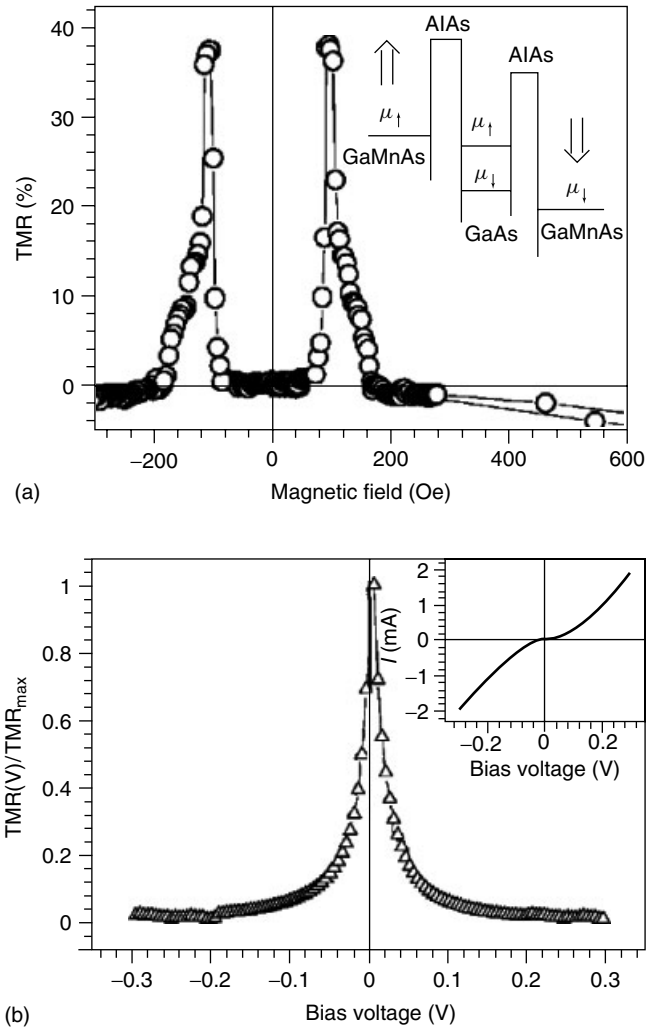

Figure 13. (a) TMR curve for a 20-μm-diameter double-barrier junction. Inset: Schematic picture of the spin splitting of the electrochemical potentials $\mu_\uparrow$, and $\mu_\downarrow$ in the nonmagnetic central layer of a GaMnAs/AlAs/GaAs/AlAs/GaMnAs structure in the antiparallel state. (b) Bias dependence of TMR obtained in the double-barrier MTJ structure at 4 K. The inset of (b) shows its I-V curve. (Reproduced from Mattana *et al*., 2003, with permission from the American Physical Society. © 2003.)

the sequential tunneling without spin relaxation in the GaAs middle layer, where the spin relaxation time is longer than the mean time τ_n spent by holes in the GaAs middle layer between tunneling in and tunneling out. Considering the tunnel resistance as a function of the barrier thickness observed by Tanaka and Higo (2001) (shown in Figure 4), τ_n is estimated to be a few 100 ps at a typical energy of some tens of millielectron volts in a few nanometer-thick quantum well. This is much longer than the time of the phase breakdown, which generally does not exceed a few picoseconds at 4 K. They concluded that this condition does not fulfill that of the coherent resonant tunneling and that sequential tunneling is dominant in their double-barrier MTJ structure.

Ohya *et al*. suggested that one of the possible reasons for the difficulty in the observation of TMR associated with the resonant tunneling effect in GaMnAs/AlAs/GaAs/AlAs/GaMnAs RTDs is its band profile. Because the valence band bottom energy of GaAs is higher than the Fermi level of GaMnAs by 87–140 meV ($\equiv v$) in terms of hole energy (Ohno, Arata, Matsukura and Ohno, 2002), the energy of the valence band bottom of the GaAs quantum well is higher than the Fermi level of GaMnAs. Therefore, a high bias voltage of at least about 200 mV ($\approx 2v/e$) has to be applied in order to observe the resonant levels formed above the valence band bottom of the GaAs quantum well. However, as shown in Figure 13(b), and reported by Mattana *et al*. (2003), when a bias voltage higher than 200 mV is applied to the GaMnAs-based double-barrier structure, the TMR ratio becomes very small or almost zero because of the strong bias dependence of TMR. Therefore, it is difficult to observe TMR and the resonant tunneling effect at the same time in this structure.

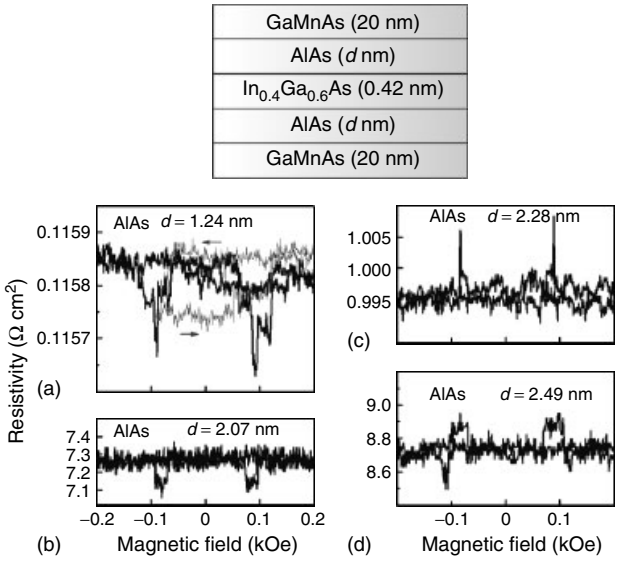

Figure 14. TMR curves of the $Ga_{0.94}Mn_{0.06}As$/AlAs (d nm)/$In_{0.4}Ga_{0.6}As$ (0.42 nm)/AlAs (d nm)/$Ga_{0.94}Mn_{0.06}As$ RTD junctions with d of (a) 1.24, (b) 2.07, (c) 2.28, and (d) 2.49 nm. The measurements were done at 7 K with a bias voltage of 10 mV and a magnetic field applied in plane along the [100] axis. In (a), bold and thin curves indicate a major loop and a minor loop, respectively (Ohya, Hai and Tanaka, 2005). (Reproduced from Ohya *et al*., 2005, with permission from the American Institute of Physics. © 2005.)

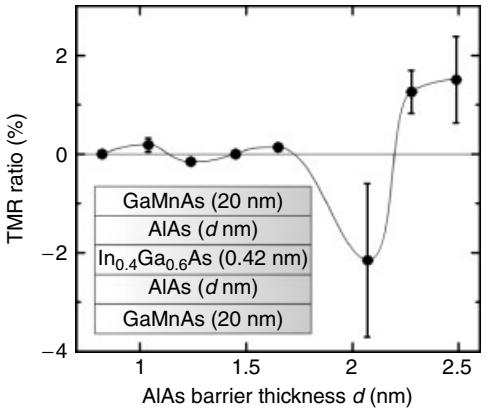

Figure 15. TMR ratio versus AlAs barrier thickness d of the $Ga_{0.94}Mn_{0.06}As$/AlAs (d nm)/$In_{0.4}Ga_{0.6}As$ (0.42 nm)/AlAs (d nm)/$Ga_{0.94}Mn_{0.06}As$ RTD. The measurements were carried out at 7 K with a bias voltage of 10 mV and a magnetic field applied in plane along the [100] axis. (Reproduced from Ohya *et al*., 2005, with permission from the American Institute of Physics. © 2005.)

For these reasons, Ohya *et al*. used an $In_{0.4}Ga_{0.6}As$ quantum well instead of GaAs. The energy of the heavy-hole band of $In_{0.4}Ga_{0.6}As$ is estimated to be about 200 meV lower than the Fermi level of GaMnAs (Van de Walle, 1989). Owing to the strong strain in the $In_{0.4}Ga_{0.6}As$ quantum well, it is difficult to grow a thick InGaAs layer, hence a very thin InGaAs quantum well of 4.2 Å was used. $Ga_{0.94}Mn_{0.06}As$/AlAs (d nm)/$In_{0.4}Ga_{0.6}As$ (0.42 nm)/AlAs (d nm)/$Ga_{0.94}Mn_{0.06}As$ RTD junctions were grown with the AlAs thickness d varied from 0.8 to 2.7 nm by controlling the in-plane position of the mobile shutter in front of the sample surface equipped with the MBE growth chamber. Figure 14(a), (b), (c), and (d) show the TMR curves of this sample with d of 1.24, 2.07, 2.28, and 2.49 nm at 7 K, respectively. In (a) and (b), usual positive TMR was obtained, while in (c) and (d) inverse TMR was observed. Figure 15 shows the TMR ratio as a function of d. With increasing d, the TMR ratio oscillated between positive and negative values with a period of around 0.8 nm.

It is difficult to explain this peculiar TMR behavior by the multiple magnetic domain formation, the impurity level in the barrier (Tsymbal, Sokolov, Sabirianov and Doudin, 2003), or the interference of two states with complex wave vectors in the barrier (Yuasa *et al*., 2004; Bultler, Zhang, Schulthess and MacLaren, 2001). The most possible mechanism for explaining this TMR behavior is the resonant

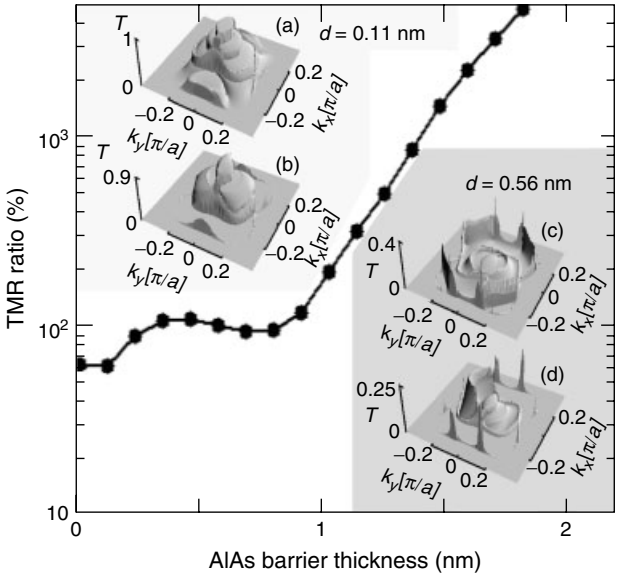

Figure 16. Calculated TMR ratio of GaMnAs/AlAs (d nm)/$In_{0.4}Ga_{0.6}As$ (0.42 nm)/AlAs (d nm)/GaMnAs RTD structures as a function of d, where exchange energy Δ and E_F are assumed to be 80 meV and 270 meV, respectively. The insets (a) and (b) show the tunneling probabilities as functions of $\mathbf{k}_\parallel$ with $d = 0.11$ nm in parallel magnetization and in antiparallel magnetization, respectively; and (c) and (d) show those with $d = 0.56$ nm in parallel magnetization and in antiparallel magnetization, respectively. (Reproduced from Ohya *et al*., 2005, with permission from the American Institute of Physics. © 2005.)

tunneling effect. To evaluate the influence of the resonant tunneling effect, the TMR ratios were calculated for the GaMnAs/AlAs/$In_{0.4}Ga_{0.6}As$/AlAs/GaMnAs RTDs using the transfer matrix method with 4×4 Luttinger–Kohn $k \cdot p$ Hamiltonian and the p–d exchange Hamiltonian (Dietl, Ohno and Matsukura, 2001). Figure 16 shows the calculated TMR ratio of GaMnAs/AlAs (d nm)/$In_{0.4}Ga_{0.6}As$ (0.42 nm)/AlAs (d nm)/GaMnAs RTD structures as a function of d when E_F is 270 meV. Inset figures are tunneling probabilities as functions of $\mathbf{k}_\parallel$ with $d = 0.11$ nm in (a) parallel and (b) antiparallel magnetization, and with $d = 0.56$ nm in (c) parallel and (d) antiparallel magnetization, respectively. The calculated TMR ratio oscillated with a period of around 0.8–1.5 nm. When d is less than 0.7 nm, the contribution of the resonant tunneling effect is small. For example, in (a) and (b), the shape of the tunneling probabilities are almost the same as those obtained in GaMnAs/AlAs/GaMnAs single-barrier heterostructures, where resonant peaks are hardly seen. Therefore, the TMR ratio decreases with increasing d like the case of GaMnAs/AlAs/GaMnAs single-barrier heterostructures, as can be seen when d is $0.4 - 0.7$ nm in Figure 16. When d becomes 0.5 nm, the resonant tunneling effect begins to occur. For example, as shown in (c) in parallel magnetization, octagon-shaped sharp resonant peaks are formed at $|\mathbf{k}_\parallel|$ around $0.2 - 0.3\pi/a$. On the other hand, as shown in (d) in antiparallel magnetization, resonant peaks are hardly formed because the $\mathbf{k}_\parallel$ region contributing to the tunneling is smaller than the octagon at which the resonant peaks are formed in parallel magnetization. As d increases above 0.7 nm, the resonant tunneling effect becomes stronger, thus the TMR ratio increases. In this way, TMR oscillation occurs. Such a TMR oscillation was obtained when E_F was higher than 210 meV, and a similar resonant tunneling effect was also obtained.

In this calculation, the oscillatory behavior was obtained, but the inverse TMR was not reproduced. This is possibly because diffusive scattering induces inverse TMR. This mechanism of inverse TMR induced by diffusive scattering was proposed by Itoh, Inoue, Umerski, and Mathon (2003), and their calculations reproduced the experimental results well in the NiFe/Al_2O_3/Cu/Co MTJ (Yuasa, Nagahama and Suzuki, 2002). In GaMnAs-based heterostructures, it is known that there are point defects, such as Mn interstitials (Yu *et al*., 2002) and As anti-site defects (Grandidier *et al*., 2000), thus this scenario may occur. However, further theoretical investigations are needed to verify it.

At present, in FMS-based quantum heterostructures, clear observation of the negative differential resistance in I–V characteristics or TMR enhancement induced by the quantum-size effect has not been accomplished. The reason has not been clarified yet. In future, more considerations on how to realize the quantum-size effect should be done, and TMR enhancement and realization of novel functions by quantum-size effect are to be expected. Very recently, TMR enhancement associated with resonant tunneling. (Ohya, Hai, Mizuno and Tanaka, 2007).

4 NOVEL PHENOMENA AND STRUCTURES RELATED TO TMR IN SEMICONDUCTORS

4.1 Tunneling anisotropic magnetoresistance (TAMR)

Recently, a novel phenomenon called TAMR was observed in GaMnAs-based heterostructures. TAMR is very similar to TMR, but the characteristics of TAMR are significantly different from those of TMR. While TMR is a phenomenon caused by the difference of the tunnel resistance between parallel and antiparallel magnetization, TAMR is a phenomenon where the tunnel resistance differs depending on the magnetization direction in GaMnAs. In contrast to TMR, which is observed in the MTJ structures composed of two FM layers, TAMR can be observed even in a 'single' FM GaMnAs layer. TAMR was observed in Au/AlO_x/GaMnAs structures

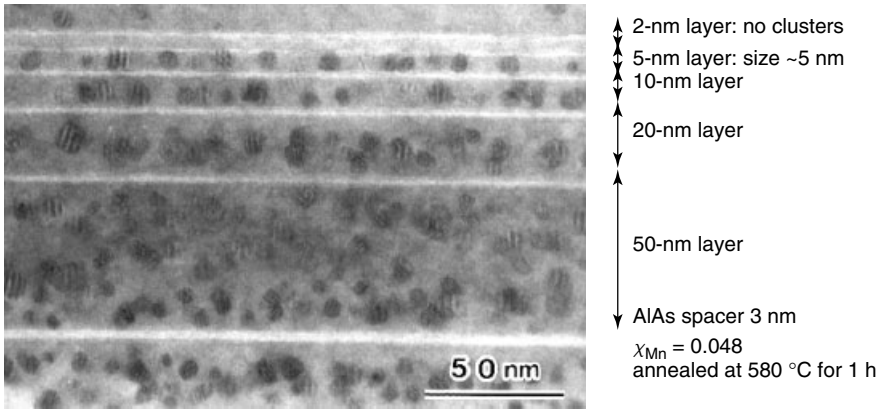

Figure 17. Cross-sectional transmission-electron microscopy (TEM) image of MnAs nanoclusters with different GaAs:MnAs thicknesses of 50, 20, 10, 5, and 2 nm. These layers are sandwiched by 3-nm-thick AlAs spacer layers. The Mn concentration is fixed at 4.8% in all the GaMnAs layers (as-grown), which turned into GaAs:MnAs layers by phase separation during annealing at 580 °C. (Reproduced from Shimizu and Tanaka, 2001, with permission from the American Institute of Physics. © 2001.)

containing only one FM GaMnAs layer (Gould *et al*., 2004). They observed spin-valve-like MR curves which are very similar to those of TMR. However, the switching field, at which the resistance state changes from low to high or high to low, and the sign of the (TA)MR ratio (∼3% at 4.2 K) change depending on the magnetic-field angle and temperature. From the measurement results of magnetic-field angle dependence of TAMR, it was clarified that the tunnel resistance becomes high when the magnetization lies along the [100] or the [$\bar{1}$00] crystallographic direction of GaMnAs, and becomes low when it is along [010] or [0$\bar{1}$0]. These results suggest that TAMR is induced by the anisotropic DOSs of GaMnAs. They calculated the anisotropic DOS of GaMnAs using the $k \cdot p$ envelope function description, and indicated that TAMR is reproduced when assuming a small in-plane uniaxial strain of around 0.1%. Because GaMnAs has a large spin-orbit interaction, such a small strain can induce the anisotropic DOS, leading to a TAMR of several percent.

Large TAMR, up to 150 000%, was observed in a GaMnAs/GaAs (2 nm)/GaMnAs MTJ structure with a bias voltage of 1 mV at 1.7 K (Rüster *et al*., 2005). As in the case of TAMR observed in the single GaMnAs layer mentioned earlier, the sign of TAMR observed in this MTJ structure also changes when the direction of the magnetic field is rotated. It was found that TAMR has a very strong bias dependence and temperature dependence. For these mechanisms, they proposed several factors, such as the zero-bias anomaly (Lee, Tejedor and Fernández-Rossier, 2004) in tunneling from a dirty metal which appears because of the opening of an Efros–Shklovskii gap (Efros and Shklovskii, 1975) at E_F when crossing the metal–insulator transition, disorder and impurity-mediated tunneling, and so on. At present, however, the mechanism of TAMR has not been completely understood yet, thus further studies are needed.

4.2 TMR in MTJ structures with MnAs nanoclusters embedded in GaAs

Recently, it was reported that FM MnAs nanoclusters embedded in GaAs, that is GaAs:MnAs, can be used as the magnetic electrode of semiconductor-based MTJs (Hai, Yokoyama, Ohya and Tanaka, 2006). GaAs:MnAs is a granular material formed by annealing GaMnAs at 500 ∼ 700 °C. It has good compatibility with III–V heterostructures (Tanaka, Shimizu and Miyamura, 2001). Also, because of the high T_C of MnAs around 313 ∼ 318 K, GaAs:MnAs-based structures are expected to be used for semiconductor-based spin-electronic devices operating at room temperature. Figure 17 shows the transmission-electron microscopy (TEM) image of the GaAs:MnAs layers sandwiched by thin AlAs layers (Shimizu and Tanaka, 2001). The black dot regions correspond to the hexagonal MnAs nanoclusters. A high-quality heterostructure without any dislocations was obtained. One important feature of the GaAs:MnAs-based heterostructures is the controllability of the size of the MnAs clusters. When the distance between the AlAs layers decreases, the size of

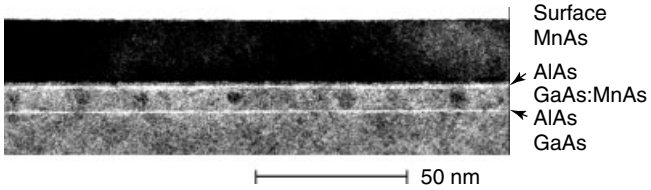

Figure 18. Cross-sectional TEM image of the MnAs (type-A, 20 nm)/GaAs (1 nm)/AlAs (2.2 nm)/GaAs:MnAs (5 nm)/AlAs (1.5 nm)/p-GaAs(001) heterostructure (from top to bottom), in which uniform (5 nm in diameter) MnAs nanoparticles are found between the two AlAs layers. (Reproduced from Hai, P. *et al*., 2006, with permission from Elsevier. © 2006.)

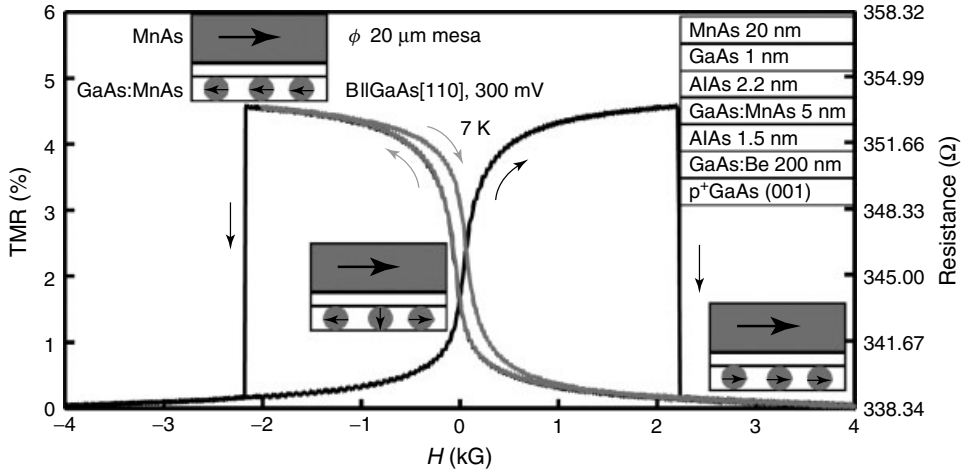

Figure 19. TMR at 7 K with a bias voltage of 300 mV of an MTJ, whose structure is MnAs (20 nm)/GaAs (1 nm)/AlAs (2.2 nm)/GaAs:MnAs (5 nm)/AlAs (1.5 nm)/p-GaAs(001). The diameter of the MTJ was 20 μm. The solid and gray curves are major and minor loops, respectively. The magnetic field was applied in the film plane and parallel to the GaAs [110] azimuth. (Reproduced from Hai, P. *et al*., 2006, with permission from Elsevier. © 2006.)

the MnAs clusters becomes uniform, because it is limited by the distance between the two AlAs layers. By using this technique, the magnetic characteristics of MnAs nanoclusters can be controlled.

Hai *et al*. fabricated MnAs (type-A, 20 nm)/GaAs(1 nm)/Al As(2.2 nm)/GaAs:MnAs(5 nm)/AlAs (1.5 nm)/p-GaAs(001) heterostructures and mesa-shaped MTJs with 20-μm diameter. Figure 18 shows cross-sectional TEM image of this MTJ structure, in which uniform (5 nm in diameter) MnAs nanoparticles are embedded between the two ultrathin AlAs layers. Figure 19 shows the TMR loops of this MTJ at 7 K with a bias voltage of 300 mV. The magnetic field was applied along the easy magnetization axis of type-A MnAs thin film, which is parallel to the in-plane GaAs [110] azimuth. Clear TMR with major and minor loops was observed. The jump of the major loop at ±2.2 kG corresponds to the abrupt magnetization reversal of the top MnAs electrode. The hysteresis of the minor loop indicates that the thermal magnetization fluctuation of the MnAs nanoclusters is quenched. The appearance of TMR shows that MnAs nanoclusters with 5-nm diameter can work as spin injectors. Figure 20 shows the bias voltage dependence of the TMR ratio. The bias polarity is defined by the voltage of the top electrode with respect to the substrate. Up to +300 mV, the TMR increases monotonously and reaches a maximum value of 4.5% at +300 mV. Over +300 mV, the TMR decreases slowly but the bias voltage V_{half} at which the TMR is reduced by half is surprisingly as high as +1200 mV. This value of V_{half} is much higher than that (∼40 mV) of FMS-based MTJs. The peak of TMR at 300 mV reflects a local maximum of spin polarization at an energy level above the Fermi level of MnAs, which is predicted by theoretical calculations (Ravindran *et al*., 1999; Pangulur *et al*., 2003). A similar picture is also observed at the negative biases. The appearance of

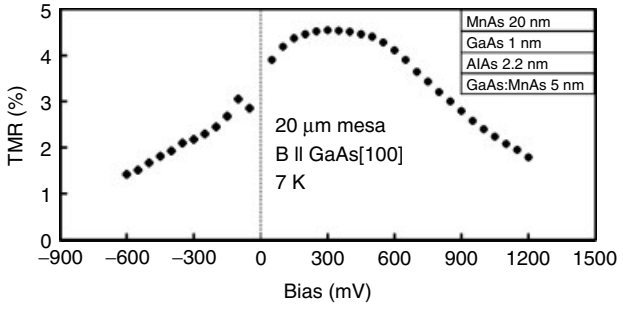

Figure 20. Bias voltage dependence of TMR of the same MTJ of Figure 19 at 7 K. The magnetic field is applied in the film plane and parallel to the GaAs [110] azimuth. The V_{half} is as high as 1200 mV. (Reproduced from Hai, P. *et al*., 2006, with permission from Elsevier. © 2006.)

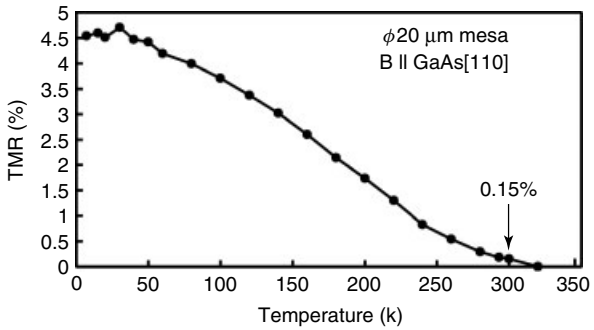

Figure 21. Temperature dependence of TMR of the same MTJ of Figure 19. TMR was observed up to room temperature. (Reproduced from Hai, P. *et al*., 2006, with permission from Elsevier. © 2006.)

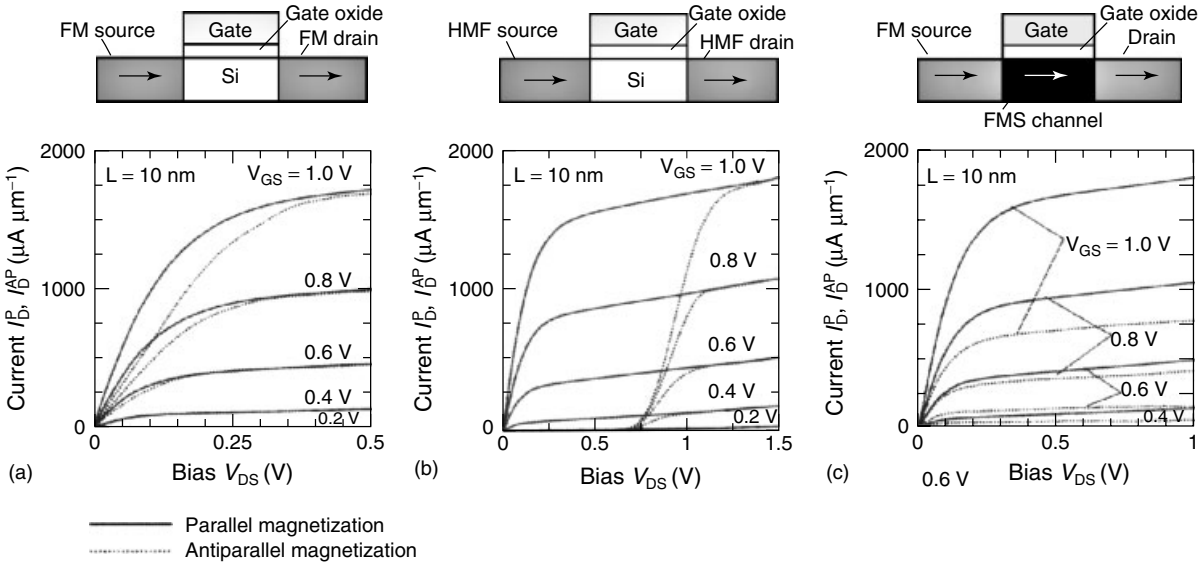

Figure 22. Schematic device structures and output characteristics of the spin MOSFETs. The devices have (a) ferromagnetic-metal (FM) source and drain and Si channel; (b) half-metallic ferromagnet (HMF) source and drain, and Si channel; (c) FM source and drain, and ferromagnetic semiconductor (FMS) channel. Each device has a MOS gate. The drain current I_{D^-} drain-source voltage V_{DS} characteristics in parallel and antiparallel magnetization are plotted by solid and broken curves, respectively, with various gate-source biases V_{GS}. (Reproduced from Sugahara and Tanaka, 2004; Matsuno *et al*., 2004, with permission from the American Institute of Physics. © 2004.)

TMR at negative biases shows that MnAs nanoclusters can also work as spin detectors. Figure 21 shows the temperature dependence of TMR. TMR was observed up to room temperature and remains at 300 K. Theoretically, the TMR value increases by increasing the size of the MnAs clusters. Higher TMR ratio is expected to be obtained in the future.

4.3 TMR in spin transistor structures

A recently proposed metal-oxide-semiconductor field-effect-transistor (MOSFET) type of spin transistor, referred to as spin MOSFET, is expected to give new functionalities in semiconductor integrated electronics (Sugahara and Tanaka, 2004; Matsuno, Sugahara and Tanaka, 2004). The spin MOSFET has a simple device structure consisting of an ordinary MOS structure and FM (or half-metallic) contacts for the source/drain, resulting in good compatibility with well-established Si technology. Figure 22 shows the structures of the spin MOSFET. In this device, spin-polarized carriers are injected from the source through the Schottky tunnel barrier at the FM source/channel contact into the semiconductor channel, are transported in the channel keeping the spin polarization, and reach the drain. It can be regarded as a three terminal device with magnetoresistance (or TMR) and transistor functions (Sugahara, 2005; Sugahara and Tanaka, 2006).

The most important feature of the spin MOSFET is magnetization-dependent output characteristics: The current-drive capability of the spin MOSFET can be controlled by the relative magnetization configuration of the two FM components in the device (for example the source and the drain in Figure 22a and b), that is, the output current (or current-drive capability) is large (small) in parallel (antiparallel) magnetization, as shown in the lower panel of Figure 22. Furthermore, it is predicted from theoretical calculations that the spin MOSFET exhibits excellent transistor performance, such as high transconductance and low power-delay product that are important requirements for integrated circuit applications. These features make the spin MOSFET a functional building-block device for nonvolatile memory and reconfigurable logic (Sugahara, 2005; Tanaka, 2005; Sugahara and Tanaka, 2006).

Here we show how the TMR effect is used in the spin transistors, taking the structure of Figure 22(c) as an example, where the device has a MOS structure with an FMS channel, and a FM source and drain, as shown in Figure 23 (Sugahara and Tanaka, 2005). The interfaces between the FM source/drain and the FMS channel are Schottky junctions. (It is not necessary that both the source and the drain are FM/FMS Schottky junctions.) A nonmagnetic metal/FMS Schottky junction can be used for one of the source and drain contacts. Possible candidates for the channel materials are FMSs using Si, Ge, and SiGe as host material. Recently, it has been well recognized that SiGe and Ge, as well as Si and strained Si, are important as channel materials for advanced MOSFETs with high performance. $Si_{1-x}Mn_x$ and $Ge_{1-x}Mn_x$ are theoretically predicted to be FMSs (Araki, Sato and Katayama-Yoshida, 2002; Araki, Shirai, Sato and

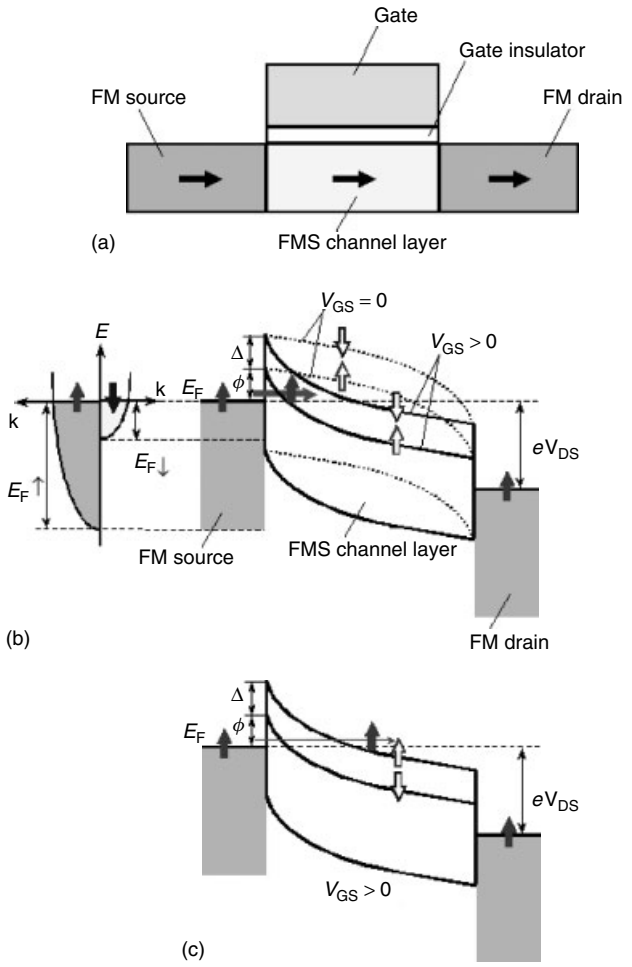

Figure 23. Schematic (a) device structure and (b), (c) band diagrams of an *n*-channel accumulation-type spin MOSFET with the channel of a nondegenerate ferromagnetic semiconductor (FMS); (b) and (c) show parallel and antiparallel magnetization configurations, respectively. (Reproduced from Sugahara *et al*., 2005, with permission from IEEE. © 2005.)

Katayama-Yoshida, 2003; Stroppa, Picozzi, Continenza and Freeman, 2003), and experimental investigations have been performed by several groups. The successful epitaxial growth of FM $Ge_{1-x}Mn_x$ films and their field-effect control of ferromagnetism were demonstrated (Park *et al*., 2002; D'Orazio *et al*., 2003). High Curie temperatures close to room temperature were also reported for $Ge_{1-x}Mn_x$ and $Ge_{1-x-y}Mn_xCo_y$ (Cho *et al*., 2002; Tsui *et al*., 2003). Recently reported n-type iron silicide–based FMSs, $Fe_xCo_{1-x}Si$ and $Fe_xMn_{1-x}Si$ (Manyala *et al*., 2004), may also be candidates for the channel material. Possible materials for the source/drain are FMs with a large spin polarization, such as iron-based alloys and half-metallic ferromagnets (HMFs). CoFe and CoFeB are commonly used in MTJs as the FM electrodes, which exhibit a large TMR, indicating a large spin polarization (Han *et al*., 2000; Wang *et al*., 2004; Maehara, Djayaprawira, Nagai and Watanabe, 2006). Fe_3Si is also an attractive candidate (Nakane, Tanaka and Sagahara, 2006), since Fe_3Si is a Heusler alloy and thus half-metallicity or an extremely large spin polarization is expected. Recently, a high-spin injection efficiency from Fe_3Si into a semiconductor was reported using an Fe_3Si/GaAs Schottky junction (Ramsteiner *et al*., 2004).

In the following, an *n*-channel accumulation-type spin MOSFET with the channel of a nondegenerate FMS is presented to explain its operating principle. Hereafter, it is assumed that the FMS channel is a free layer and the FM source/drain is a pinned layer, and that the magnetization direction of the FM drain is always the same as that of the FM source. Figure 23(b) schematically shows the band diagram of the spin MOSFET under a common source bias condition with and without a gate–source bias V_{GS}, where the relative magnetization configuration of the FMS channel and FM source/drain is parallel. Assuming that the nonmagnetic metal/FMS Schottky junction model given by Lebedeva and Kuivalainen (Lebedeva and Kuivalainen, 2003) can be extended to the FM/FMS Schottky junction, a spin-dependent Schottky barrier (SB) appears due to the energy splitting Δ of the up- and down-spin bands at the conduction band edge of the FMS channel, that is, a lower SB height ϕ for up-spin electrons and a higher SB height $\phi + \Delta$ for down-spin electrons, as shown in Figure 23(b). When a drain–source bias $V_{DS}(>0)$ is applied with $V_{GS} = 0$, neither up-spin nor down-spin electrons are injected from the source to the channel because of the reverse-biased SB of the source (as shown by the upper two dotted curves in Figure 23b). By applying $V_{GS}(>0)$, the SB width is reduced (as shown by the upper two solid curves in Figure 23b), and thus up- and down-spin electrons in the FM source can tunnel through the thinned SB into the channel. When the magnetization configuration of the FMS channel and FM source is parallel, the SB height is low for the majority spin (up spin) electrons in the FM source. Thus, a large output (drain) current can flow. When the magnetization configuration becomes antiparallel because of flipping the magnetization of the FMS channel, the SB height for the majority spin electrons in the FM source is higher, as shown in Figure 23(c). Thus, current by majority spin electrons is drastically reduced, since the tunnel current decreases exponentially as the barrier height increases. Although the SB height is lower for the minority spin (down spin) electrons in the FM source, tunneling current through the SB is small due to the small carrier density of the minority spin electrons. Therefore, the output current depends on the relative magnetization of the FMS channel and FM source/drain, as shown in Figure 22(c). A large magnetocurrent ratio can be obtained and it is insensitive to the drain–source bias conditions, owing to the spin filter effect of the FMS/FM Schottky junction.

Furthermore, excellent transistor performance such as high transconductance and small subthreshold swing is predicted. This device can be applied to a new nonvolatile memory architecture using a single spin MOSFET cell, in which the programming current can be drastically reduced using the electrical manipulation of magnetization reversal of the FMS channel (Sugahara and Tanaka, 2005).

REFERENCES

Araki, K., Sato, K. and Katayama-Yoshida, H. (2002). A study of transition metal doped group-IV magnetic semiconductors by first-principles computations. Presented at *The 63rd Autumn Meeting*, The Japan Society of Applied Physics: Niigata, 26p-ZA-3.

Araki, K., Shirai, M., Sato, K. and Katayama-Yoshida, H. (2003). Materials design of IV-based ferromagnetic semiconductors by inhomogeneous doping. Presented at *The 50th Spring Meeting*, The Japan Society of Applied Physics: Yokohama, 29a-ZH-2.

Bultler, W.H., Zhang, X.G., Schulthess, T.C. and MacLaren, J.M. (2001). Spin-dependent tunneling conductance of Fe| MgO| Fe sandwiches. *Physical Review B*, **63**, 054416.

Chadi, D.J. (1977). Spin-orbit splitting in crystalline and compositionally disordered semiconductors. *Physical Review B*, **16**, 790–796.

Chiba, D., Akiba, N., Matsukura, F., *et al*. (2000). Magnetoresistance effect and interlayer coupling of (Ga, Mn)As trilayer structures. *Applied Physics Letters*, **77**, 1873–1875.

Chiba, D., Matsukura, F. and Ohno, H. (2004). Tunneling magnetoresistance in (Ga,Mn)As-based heterostructures with a GaAs barrier. *Physica E*, **21**, 966–969.

Chiba, D., Sato, Y., Kita, T., *et al*. (2004). Current-driven magnetization reversal in a ferromagnetic semiconductor (Ga,Mn)As/GaAs/(Ga,Mn)As tunnel junction. *Physical Review Letters*, **93**, 216602.

Cho, S., Choi, S., Hong, S.C., *et al*. (2002). Ferromagnetism in Mn-doped Ge. *Physical Review B*, **66**, 033303.

Chun, S.H., Potashnik, S.J., Ku, K.C., *et al*. (2002). Spin-polarized tunneling in hybrid metal-semiconductor magnetic tunnel junctions. *Physical Review B*, **66**, 100408.

Dietl, T., Ohno, H. and Matsukura, F. (2001). Hole-mediated ferromagnetism in tetrahedrally coordinated semiconductors. *Physical Review B*, **63**, 195205.

D'Orazio, F., Lucari, F., Santucci, S., *et al*. (2003). Magneto-optical properties of epitaxial Mn_xGe_{1-x} films. *Journal of Magnetism and Magnetic Materials*, **262**, 158.

Efros, A.L. and Shklovskii, B.I. (1975). Coulomb gap and low temperature conductivity of disordered systems. *Journal of Physics C*, **8**, L49–L51.

Elsen, M., Boulle, O., George, J-M., *et al*. (2006). Spin transfer experiments on (Ga,Mn)As/(In,Ga)As/(Ga,Mn)As tunnel junctions. *Physical Review B*, **73**, 035303.

Gould, C., Rüster, C., Jungwirth, T., *et al*. (2004). Tunneling anisotropic magnetoresistance: a spin-valve-like tunnel magnetoresistance using a single magnetic layer. *Physical Review Letters*, **93**, 117203.

Grandidier, B., Nys, J.P., Delerue, C., *et al*. (2000). Atomic-scale study of GaMnAs/GaAs layers. *Applied Physics Letters*, **77**, 4001–4003.

Hai, P.N., Yokoyama, M., Ohya, S. and Tanaka, M. (2006). Spin polarized tunneling in III-V based heterostructures with a ferromagnetic MnAs thin film and GaAs:MnAs nanoclusters. *Physica E*, **32**, 416–418.

Han, X., Oogane, M., Kubota, H., *et al*. (2000). Fabrication of high-magnetoresistance tunnel junctions using $Co_{75}Fe_{25}$ ferromagnetic electrodes. *Applied Physics Letters*, **77**, 283–285.

Hayashi, T., Shimada, H., Shimizu, H. and Tanaka, M. (1999). Tunneling spectroscopy and tunneling magnetoresistance in (GaMn)As ultrathin heterostructures. *Journal of Crystal Growth*, **201/202**, 689–692.

Hayashi, T., Tanaka, M. and Asamitsu, A. (2000). Tunneling magnetoresistance of a GaMnAs-based double barrier ferromagnetic tunnel junction. *Journal of Applied Physics*, **87**, 4673–4675.

Hayashi, T., Tanaka, M., Nishinaga, T., *et al*. (1997a). (GaMn)As: GaAs-based IIIV diluted magnetic semiconductors grown by molecular beam epitaxy. *Journal of Crystal Growth*, **175/176**, 1063–1068.

Hayashi, T., Tanaka, M., Seto, K., *et al*. (1997b). III–V based magnetic(GaMnAs)/nonmagnetic(AlAs) semiconductor superlattices. *Applied Physics Letters*, **71**, 1825–1827.

Higo, Y., Shimizu, H. and Tanaka, M. (2001). Anisotropic tunneling magnetoresistance in GaMnAs/AlAs/GaMnAs ferromagnetic semiconductor tunnel junctions. *Journal of Applied Physics*, **89**, 6745–6747.

Itoh, H., Inoue, J., Umerski, A. and Mathon, J. (2003). Quantum oscillation of magnetoresistance in tunneling junctions with a nonmagnetic spacer. *Physical Review B*, **68**, 174421.

Jullière, M. (1975). Tunneling between ferromagnetic films. *Physics Letters A*, **54**, 225–226.

Lebedeva, N. and Kuivalainen, P. (2003). Modeling of ferromagnetic semiconductor devices for spintronics. *Journal of Applied Physics.*, **93**, 9845–9864.

Lee, M., Tejedor, J.G. and Fernández-Rossier, J. (2004). Tunnel magnetoresistance in GaMnAs: going beyond Jullière formula. *Applied Physics Letters*, **85**, 1996–1998.

Maehara, H., Djayaprawira, D.D., Nagai, M. and Watanabe, N. (2006). Huge magnetoresistance and low junction resistance in magnetic tunnel junctions with crystalline MgO barrier. *IEEE Transactions on Magnetics*, **42**, 103–107.

Manyala, N., Sidis, Y., Ditusa, J.F., *et al*. (2004). Large anomalous Hall effect in a silicon-based magnetic semiconductor. *Nature Materials*, **3**, 255–262.

Mathon, J. (1997). Tight-binding theory of tunneling giant magnetoresistance. *Physical Review B*, **56**, 11810–11819.

Matsumoto, Y., Murakami, M., Shono, T., *et al*. (2001a). Room-temperature ferromagnetism in transparent transition metal-doped titanium dioxide. *Science*, **291**, 854–856.

Matsumoto, Y., Murakami, M., Shono, T., *et al*. (2001b). Ferromagnetism in Co-doped TiO2 rutile thin films grown by laser molecular beam epitaxy. *Japanese Journal of Applied Physics*, **40**, L1204–L1206.

Matsuno, T., Sugahara, S. and Tanaka, M. (2004). Novel reconfigurable logic gates using spin metal-oxide-semiconductor field-effect transistors. *Japanese Journal of Applied Physics*, **43**, 6032–6037.

Mattana, R., George, J-M., Jaffrès, H., *et al*. (2003). Electrical detection of spin accumulation in a p-type GaAs quantum well. *Physical Review Letters*, **90**, 166601.

Munekata, H., Ohno, H., Molnar, Svon., *et al*. (1989). Diluted magnetic III-V semiconductors. *Physical Review Letters*, **63**, 1849–1852.

Nakane, R., Tanaka, M. and Sugahara, S. (2006). Preparation and characterization of ferromagnetic DO_3-phase Fe_3Si thin films on silicon-on-insulator substrates for Si-based spin-electronic device applications. *Applied Physics Letters*, **89**, 192503.

Nazmul, A.M., Amemiya, T., Shuto, Y., *et al*. (2005). High temperature ferromagnetism in GaAs-based heterostructures with Mn δ doping. *Physical Review Letters*, **95**, 017201.

Ohno, H. (1999). Properties of ferromagnetic III–V semiconductors. *Journal of Magnetism and Magnetic Materials*, **200**, 110–129.

Ohno, Y., Arata, I., Matsukura, F. and Ohno, H. (2002). Valence band barrier at (Ga,Mn)As/GaAs interfaces. *Physica E*, **13**, 521–524.

Ohno, H., Munekata, H., Molnar, S. von and Chang, L.L. (1991). New III-V diluted magnetic semiconductors. *Journal of Applied Physics*, **69**, 6103–6108.

Ohno, H., Munekata, H., Penney, T., *et al*. (1992). Magnetotransport properties of *p*-type (In,Mn)As diluted magnetic III-V semiconductors. *Physical Review Letters*, **68**, 2664–2667.

Ohno, H., Shen, A., Matsukura, F., *et al*. (1996). (Ga,Mn)As: a new diluted magnetic semiconductor based on GaAs. *Applied Physics Letters*, **69**, 363–365.

Ohno, Y., Young, D.K., Benschoten, B., *et al*. (1999). Electrical spin injection in a ferromagnetic semiconductor heterostructure. *Nature*, **402**, 790–792.

Ohya, S., Hai, P.N. and Tanaka, M. (2005). Tunneling magnetoresistance in GaMnAs/AlAs/InGaAs/AlAs/GaMnAs double-barrier magnetic tunnel junctions. *Applied Physics Letters*, **87**, 012105.

Ohya, S., Hai, P.N., Mizuno, Y. and Tanaka, M. (2007). Quantum size effect and tunneling magnetoresistance in ferromagnetic-semiconductor quantum heterostructrues. *Physical Review B*, in press.

Pangulur, R.P., Tsoi, G., Nadgorny, B., *et al*. (2003). Point contact spin spectroscopy of ferromagnetic MnAs epitaxial films. *Physical Review B*, **68**, 201307.

Park, Y.D., Hanbicki, A.T., Erwin, S.C., *et al*. (2002). A group-IV ferromagnetic semiconductor: Mn_xGe_{1-x}. *Science*, **295**, 651–654.

Petukhov, A.G., Chantis, A.N. and Demchenko, D.O. (2002). Resonant enhancement of tunneling magnetoresistance in double-barrier magnetic heterostructures. *Physical Review Letters*, **89**, 107205.

Ramsteiner, M., Kawaharazuka, A., Herfort, J., *et al*. (2004). Spin injection from Fe_3Si into GaAs. *Applied Physics Letters*, **85**, 3492–3494.

Ravindran, P., Delin, A., James, P., *et al*. (1999). Magnetic, optical, and magneto-optical properties of MnX (X = As, Sb, or Bi) from full-potential calculations. *Physical Review B*, **59**, 15680.

Rüster, C., Gould, C., Jungwirth, T., *et al*. (2005). Very large tunneling anisotropic magnetoresistance of a (Ga,Mn)As/GaAs/(Ga,Mn)As stack. *Physical Review Letters*, **94**, 027203.

Saito, H., Yuasa, S. and Ando, K. (2005). Origin of the tunnel anisotropic magnetoresistance in $Ga_{1-x}Mn_xAs$/ZnSe/$Ga_{1-x}Mn_xAs$ magnetic tunnel junctions of II-VI/III-V heterostructures. *Physical Review Letters*, **95**, 086604.

Schulman, J.N. and Chang, Y.C. (1985). Band mixing in semiconductor superlattices. *Physical Review B*, **31**, 2056–2068.

Shang, C.H., Nowak, J., Jansen, R. and Moodera, J.S. (1998). Temperature dependence of magnetoresistance and surface magnetization in ferromagnetic tunnel junctions. *Physical Review B*, **58**, R2917–R2920.

Shimizu, H., Hayashi, T., Nishinaga, T. and Tanaka, M. (1999). Magnetic and transport properties of III–V based magnetic semiconductor (GaMn)As: growth condition dependence. *Applied Physics Letters*, **74**, 398–400.

Shimizu, H. and Tanaka, M. (2001). Magneto-optical properties of semiconductor-based superlattices having GaAs with MnAs nanoclusters. *Journal of Applied Physics*, **89**, 7281–7283.

Stroppa, A., Picozzi, S., Continenza, A. and Freeman, A.J. (2003). Electronic structure and ferromagnetism of Mn-doped group-IV semiconductors. *Physical Review B*, **68**, 155203.

Sugahara, S. (2005). Spin metal-oxide-semiconductor field-effect transistors (spin MOSFETs) for integrated spintronics. *IEE Proceeding: Circuits Devices and Systems*, **152**(4), 355–365.

Sugahara, S. and Tanaka, M. (2004). A spin metal-oxide-semiconductor field-effect transistor using half-metallic-ferromagnet contacts for the source and drain. *Applied Physics Letters*, **84**, 2307–2309.

Sugahara, S. and Tanaka, M. (2005). A spin metal-oxide-semiconductor field-effect transistor (spin MOSFET) using a ferromagnetic semiconductor for the channel. *Journal of Applied Physics*, **97**, 10D503.

Sugahara, S. and Tanaka, M. (2006). Spin metal-oxide-semiconductor field-effect transistors (spin MOSFETs) and their integrated circuit applications. *ACM Transactions on Storage*, **2**, 197–219.

Tanaka, M. (2000a). Epitaxial growth and properties of III–V magnetic semiconductor (GaMn)As and its heterostructures. *Journal of Vacuum Science and Technology*, **B16**, 2267–2274.

Tanaka, M. (2000b). Ferromagnetic semiconductor heterostructures based on (GaMn)As. *Journal of Vacuum Science and Technology*, **A18**, 1247–1253.

Tanaka, M. (2005). Spintronics: recent progress and tomorrow's challenges. *Journal of Crystal Growth*, **278**, 25–37.

Tanaka, M. and Higo, Y. (2001). Large tunneling magnetoresistance in GaMnAs/AlAs/GaMnAs ferromagnetic semiconductor tunnel junctions. *Physical Review Letters*, **87**, 026602.

Tanaka, M. and Higo, Y. (2002). Tunneling magnetoresistance in GaMnAs/AlAs/GaMnAs ferromagnetic semiconductor heterostructures. *Physica E*, **13**, 495–503.

Tanaka, M., Shimizu, H. and Miyamura, M. (2001). Enhancement of magneto-optical effect in a GaAs: MnAs hybrid nanostructure sandwiched by GaAs/AlAs distributed Bragg reflectors: epitaxial semiconductor-based magneto-photonic crystal. *Journal of Crystal Growth*, **227**, 839–846.

Toyosaki, H., Fukumura, T., Ueno, K., *et al*. (2005). A ferromagnetic oxide semiconductor as spin injection electrode in magnetic tunnel junction. *Japanese Journal of Applied Physics*, **44**, L896–L898.

Tsui, F., He, L., Ma, L., *et al*. (2003). Novel germanium-based magnetic semiconductors. *Physical Review Letters*, **91**, 177203.

Tsymbal, E.Y., Sokolov, A., Sabirianov, I.F. and Doudin, B. (2003). Resonant inversion of tunneling magnetoresistance. *Physical Review Letters*, **90**, 186602.

Van de Walle, Chris G. (1989). Band lineups and deformation potentials in the model-solid theory. *Physical Review B*, **39**, 1871–1883.

Van Esch, A., Van Bockstal, L., De Boeck, J., *et al*. (1997). Interplay between the magnetic and transport properties in the III-V diluted magnetic semiconductor $Ga_{1-x}Mn_xAs$. *Physical Review B*, **56**, 13103–13112.

Vogl, P., Hjalmarson, H.P. and Dow, J.D. (1983). A semi-empirical tight-binding theory of the electronic structure of semiconductors. *Journal of Physics and Chemistry of Solids*, **44**, 365–378.

Wang, K.Y., Campion, R.P., Edmonds, K.W., *et al*. (2005). Magnetism in (Ga,Mn)As thin films with T_C up to 173 K. *AIP Conference Proceedings*, **772**, 333–334.

Wang, D., Nordman, C., Daughton, J., *et al*. (2004). Magnetostriction effect of amorphous CoFeB thin films and application in spin-dependent tunnel junctions. *Journal of Applied Physics*, **97**, 10C906.

Yu, K.M., Walukiewicz, W., Wojtowicz, T., *et al*. (2002). Effect of the location of Mn sites in ferromagnetic $Ga_{1-x}Mn_xAs$ on its Curie temperature. *Physical Review B*, **65**, 201303.

Yuasa, S., Nagahama, T., Fukushima, A., *et al*. (2004). Giant room-temperature magnetoresistance in single-crystal Fe/MgO/Fe magnetic tunnel junctions. *Nature Material*, **3**, 868–871.

Yuasa, S., Nagahama, T. and Suzuki, Y. (2002). Spin-polarized resonant tunneling in magnetic tunnel junctions. *Science*, **297**, 234–237.

Spin-dependent Tunneling: Role of Evanescent and Resonant States

Evgeny Y. Tsymbal
University of Nebraska, Lincoln, NE, USA

1 INTRODUCTION

The phenomenon of spin-dependent tunneling (SDT) is an imbalance in the electric current carried by up- and down-spin electrons tunneling from a ferromagnetic metal through an insulating barrier. The field of SDT was founded by the pioneering experiments of Tedrow and Meservey (1971, 1973). They used ferromagnet/insulator/superconductor (FM/I/S) tunnel junctions and measured the spin polarization (SP) of the tunneling current originating from various ferromagnetic metals across an amorphous alumina barrier (Meservey and Tedrow, 1994).

The phenomenon of tunneling magnetoresistance (TMR), first observed in experiments by Jullière (1975), is the manifestation of SDT in magnetic tunnel junctions (MTJs). An MTJ consists of two ferromagnetic metal electrodes separated by a thin insulating barrier layer. The most important property of an MTJ is that the tunneling current across the barrier depends on the relative orientation of the magnetizations of the two ferromagnetic electrodes, which can be changed by an applied magnetic field. This phenomenon is called *tunneling magnetoresistance* (*TMR*). The discovery of a large reproducible TMR at room temperature in MTJs based on amorphous Al_2O_3 by Moodera, Kinder, Wong, and Meservey (1995) has attracted considerable interest due to the potential application of MTJs in spin-electronic devices such as magnetic sensors and magnetic random access memories (MRAMs). This interest was further boosted by a recent discovery of large TMR values in crystalline Fe/MgO/Fe and similar MTJs by Parkin *et al.* (2004) and Yuasa *et al.* (2004), and triggered tremendous activity in the experimental and theoretical investigations of the electronic, magnetic, and transport properties of MTJs (for reviews on MTJs see Levy and Zhang (1999), Moodera and Mathon (1999), Tsymbal, Mryasov and LeClair (2003), Zhang and Butler (2003), Heiliger, Zahn and Mertig (2006) and Parkin (2006)).

Theoretical understanding of SDT has an interesting history. Tedrow and Meservey analyzed their experiments in terms of SDT currents carried from a ferromagnet through an amorphous alumina barrier into the up- and down-spin states of a superconductor (Tedrow and Meservey, 1971, 1973). They measured a SP of the tunneling conductance which is defined by

$$P = \frac{G^{\uparrow} - G^{\downarrow}}{G^{\uparrow} + G^{\downarrow}} \tag{1}$$

Handbook of Magnetism and Advanced Magnetic Materials. Edited by Helmut Kronmüller and Stuart Parkin. Volume 5: *Spintronics and Magnetoelectronics*. ISBN: 978-0-470-02217-7.

where $G^{\uparrow}$ and $G^{\downarrow}$ are the up- and down-spin conductance of the tunnel junction. The results of these early experiments on SDT were interpreted in terms of spin-dependent density of states (DOS) of the ferromagnetic electrodes at the Fermi energy, $\rho_{\mathrm{F}}^{\uparrow}$ and $\rho_{\mathrm{F}}^{\downarrow}$. Assuming that the spin-dependent conductance is proportional to $\rho_{\mathrm{F}}^{\uparrow}$ for majority-spin electrons and is proportional to $\rho_{\mathrm{F}}^{\downarrow}$ for minority-spin electrons, the measured values of the SP of the tunneling conductance, P, should be equal to the SP of the DOS at the Fermi energy of the ferromagnet,

$$P_{\mathrm{FM}} = \frac{\rho_{\mathrm{F}}^{\uparrow} - \rho_{\mathrm{F}}^{\downarrow}}{\rho_{\mathrm{F}}^{\uparrow} + \rho_{\mathrm{F}}^{\downarrow}} \tag{2}$$

This result demonstrates, however, inconsistency between the measured and predicted values of the SP. Experimentally it was found that the SP of the tunneling conductance from all the 3d ferromagnetic metals and their alloys is positive, which implies that the majority-spin electrons tunnel more efficiently than the minority-spin electrons (Meservey and Tedrow, 1994). This is in the contradiction with the bulk band structure, at least, for the two ferromagnetic metals, Co and Ni, which have the dominant contribution of the minority spins at the Fermi energy causing the respective SP of the DOS to be negative. This fact was later explained by Stearns (1977), who assumed that the most dispersive bands provide essentially all the tunneling current. On the basis of this argument and using a realistic band structure of Fe and Ni, Stearns was able to explain experimental values (measured at that time) of the SP for these ferromagnets. Despite the success of Stearns' idea, this model did not provide a clear understanding of the origin of the dominance of the 'itinerant' electrons in transport properties.

The relationship between SDT and TMR was explained by Jullière within a simple model assuming that the SP of the tunneling current is determined solely by the SP of the electronic DOS of the ferromagnetic electrodes at the Fermi energy (Jullière, 1975). Although Jullière's model served as a useful basis for interpreting a number of experiments on TMR, this model is too simple to describe all the available experimental data. In particular, experimental results show that the tunneling SP strongly depends on the structural quality of MTJs. Improvements in the quality of the alumina barrier and the metal/alumina interfaces resulted in the enhancement of the measured values of the SP (Monsma and Parkin, 2000). Experiments also show that the SP depends on the choice of the tunneling barrier. De Teresa *et al*. (1999a,b) found that Co exhibits a negative value of the SP when tunneling occurs through a $SrTiO_3$ barrier. This is opposite to the tunneling SP across an Al_2O_3 barrier, for which all 3d ferromagnets show positive SPs. Also, experiments by LeClair *et al*. demonstrated the decisive role of the electronic structure of the interfaces in SDT (LeClair *et al*., 2000, 2001a,b). It is evident, therefore, that the tunneling SP is *not* an intrinsic property of the ferromagnet alone but depends on the structural and electronic properties of the entire junction including the insulator and the ferromagnet/insulator interfaces.

More recent theoretical studies provided a new insight into the phenomenon of SDT. It was stated that the expected spin dependence of the tunneling current can be deduced from the symmetry of the Bloch states in the bulk ferromagnetic electrodes and the complex band structure of the insulator (MacLaren, Zhang, Butler and Wang, 1999; Mavropoulos, Papanikolaou and Dederichs, 2000). By identifying those bands in the electrodes that are coupled efficiently to the evanescent states decaying most slowly in the barrier, one can make conclusions about the SP of the conductance. It was emphasized that for a broad class of insulating materials the states that belong to the identity representation should have minimum decay rates. This representation is comparable to the s character suggesting that s bands should be able to couple most efficiently across the interface and decay most slowly in the barrier. For Fe, Co, and Ni ferromagnets the majority-spin states at the Fermi energy have more s character than the minority-spin states, which tend to have mainly d character. Thus, the majority conductance is expected to be greater than the minority conductance resulting in a slower decay with barrier thickness for the former. These symmetry arguments satisfactorily explain large values of TMR predicted for epitaxial Fe/MgO/Fe junctions (Butler, Zhang, Schulthess and MacLaren, 2001; Mathon and Umerski, 2001). These conclusions are also expected to be valid for MTJs with an Al_2O_3 barrier which is consistent with the experimental observations (Meservey and Tedrow, 1994). They are also in agreement with the earlier hypothesis by Stearns (1977).

Despite the undoubted importance, the symmetry arguments have their limitations. First, they assume that the barrier is sufficiently thick so that only a small focused region of the surface Brillouin zone contributes to the tunneling current. For realistic MTJs with barrier thickness of about 1 nm this assumption is usually unjustified. Moreover, for amorphous barriers like alumina where the transverse wave vector is not conserved in the process of tunneling, the entire surface Brillouin zone might contribute almost equally to the conductance. Second, despite the presence of certain selection rules for tunneling, there is no general rule preventing the Bloch states composed mostly of the d orbitals from tunneling through the barrier states that have no d character. For example, it was demonstrated experimentally that the tunneling current from a ferromagnetic Ni tip (Alvarado and Renaud, 1992) and from a hcp Co(0001) surface (Okuno, Kishi and Tanaka, 2002) through vacuum is negatively spin

polarized. The negative SP is due to the dominant contribution of the d electrons in tunneling, despite the fact that there are no d states in vacuum. Therefore, symmetry considerations alone applied to bulk materials are not always sufficient to predict the SP. It is critical to take into account the electronic structure of the ferromagnet/barrier interfaces which, as was shown experimentally, control the SP (LeClair *et al*., 2000, 2001a,b).

An important mechanism by which the interfaces affect the SP of the conductance is the bonding between the ferromagnetic electrodes and the insulator (Tsymbal and Pettifor, 1997). The interface bonding determines the effectiveness of transmission across the interface, which can be different for electrons of different orbital character (and/or symmetry) carrying an unequal SP. Also the interface bonding is responsible for the appearance of interface states which, as was predicted theoretically (Wunnicke *et al*., 2002), affect the conductance dramatically. Experimentally, the effect of bonding at the ferromagnet/insulator interface was proposed to explain the inversion of the SP of electrons tunneling from Co across a $SrTiO_3$ barrier (De Teresa *et al*., 1999a,b). The bonding mechanism was also put forward to elucidate positive and negative values of TMR depending on the applied voltage in MTJs with Ta_2O_5 and Ta_2O_5/Al_2O_3 barriers (Sharma, Wang and Nickel, 1999). Interface states in MgO-based tunnel junctions were indirectly observed in transport measurements (Tiusan *et al*., 2004, 2006). Theoretically, strong sensitivity of the magnitude of TMR to the sp–d mixing at the ferromagnet/alumina interface was predicted in the presence of imperfectly oxidized Al or O ions (Itoh and Inoue, 2001). It was found that oxygen deposited on the Fe(001) surface reverses the SP of the DOS in vacuum due to the strong exchange splitting of the antibonding oxygen states (Tsymbal, Oleinik and Pettifor, 2000). It was predicted that an atomic layer of iron oxide at the interface between Fe and MgO layers greatly reduces TMR in Fe/MgO/Fe junctions because of the bonding between Fe and O atoms (Zhang, Butler and Bandyopadhyay, 2003). The significant effect of the interface atomic structure on current–voltage characteristics was predicted for Fe/MgO/Fe junctions (Heiliger, Zahn, Yavorsky and Mertig, 2006).

The main objective of this article is to discuss two important factors that control the SP in MTJs: the complex band structure of the insulating barrier which determines selection rules for tunneling of spin-polarized bands from ferromagnets and the bonding at the ferromagnet/barrier interface resulting in the appearance of resonant interface states that significantly affect the SP of the conductance. We consider several theoretical models illustrating the significance of these two mechanisms in different kinds of MTJs. We start our discussion from Jullière's model and a simple description of SDT within a free-electron model.

2 JULLIÈRE'S MODEL

Jullière's model for TMR is based on two assumptions. First, it assumes that spin of electrons is conserved in the tunneling process. It follows, then, that tunneling of up- and down-spin electrons are two independent processes, so that the conductance occurs in the two independent spin channels. Such a two-current model has also been used to interpret the closely related phenomenon of giant magnetoresistance (see, Tsymbal and Pettifor, 2001 for a review). According to this assumption, electrons originating from one spin state of the 'left' ferromagnetic electrode are accepted by unfilled states of the same spin of the 'right' electrode. If the two ferromagnetic films are magnetized parallel, the minority spins tunnel to the minority states and the majority spins tunnel to the majority states. If, however, the two films are magnetized antiparallel, the identity of the majority- and minority-spin electrons is reversed so that the majority spins of the left electrode tunnel to the minority states in the right electrode and vice versa. Second, Jullière's model assumes that the conductance for a particular spin orientation is proportional to the product of the DOS of the two ferromagnetic electrodes. According to these assumptions, the conductance for the parallel and antiparallel alignment, G_P and G_{AP} respectively, can be written as follows:

$$\begin{aligned} G_P &\propto \rho_L^{\uparrow}\rho_R^{\uparrow} + \rho_L^{\downarrow}\rho_R^{\downarrow} \\ G_{AP} &\propto \rho_L^{\uparrow}\rho_R^{\downarrow} + \rho_L^{\downarrow}\rho_R^{\downarrow} \end{aligned} \tag{3}$$

where $\rho_n^{\uparrow}$ and $\rho_n^{\downarrow}$ are the DOS of the left and right ferromagnetic electrodes (designated by index n = L, R) for the majority- and minority-spin electrons. It follows from equation (3) that the parallel- and antiparallel-magnetized MTJs have different conductances, which implies a nonzero TMR. If we define a TMR ratio as the conductance difference between parallel and antiparallel magnetizations, normalized by the antiparallel conductance, we arrive then at Jullière's formula

$$TMR \equiv \frac{G_P - G_{AP}}{G_{AP}} = \frac{2P_L P_R}{1 - P_L P_R} \tag{4}$$

which expresses the TMR in terms of the SPs of the two ferromagnetic electrodes

$$P_n = \frac{\rho_n^{\uparrow} - \rho_n^{\downarrow}}{\rho_n^{\uparrow} + \rho_n^{\downarrow}} \tag{5}$$

where n = L, R.

This approach allows linking the known values of the SP obtained from the Tedrow–Meservey experiments to the values of TMR. It is important to note, however, that the

correlation between the SP and TMR using equation (4) disregards the nature of the DOS entering equation (3). As long as the conductance per spin can be represented as a product of two quantities characterizing the left and right electrodes (and may be left and right interfaces), we arrive at equation (4) for TMR and equation (5) for the SP. Therefore, $\rho_{\rm n}^{\uparrow}$ and $\rho_{\rm n}^{\downarrow}$ can be interpreted as an *effective* tunneling DOS of the ferromagnetic electrodes which make the applicability of Jullière's formula more general.

It appears that the most recent SP values with Al_2O_3 barriers obtained via the SDT technique agree well with the maximum TMR values reported with Al_2O_3 barriers within Jullière's model (see Tsymbal, Mryasov and LeClair, 2003 for details). The possible reason for this agreement is discussed in the next section. However, we caution that Jullière's model is only a phenomenological guide to estimate the magnitude of the TMR effect when SPs of the tunneling current across the *same* barriers are known.

3 A FREE-ELECTRON MODEL

A little more insight into TMR can be obtained using a simple free-electron model for tunneling through a rectangular potential barrier. Within this model the exchange splitting of the free-electron bands is included by using different potentials for the up- and down-spin electrons, $V_{\rm n}^{\sigma}$, where index ${\rm n}={\rm L}$, R denotes the left or right ferromagnetic electrode and σ is the spin index, $\sigma=\uparrow,\downarrow$. A solution for the free-electron model can be obtained taking into account the fact that the transverse wave vector $\mathbf{k}_{\parallel}$ is conserved in the tunneling process. Assuming that the barrier thickness d is not too small, the transmission coefficient per spin is given by

$$T^{\sigma}(\mathbf{k}_{\parallel}) = 16\kappa^2 \frac{k_{\rm L}^{\sigma}}{\kappa^2 + k_{\rm L}^{\sigma 2}} \frac{k_{\rm R}^{\sigma}}{\kappa^2 + k_{\rm R}^{\sigma 2}} e^{-2\kappa d} \tag{6}$$

Equation (6) assumes that transmission occurs between two bulk states in the ferromagnetic electrodes that are characterized by the wave vector normal to the interfaces $k_{\rm n}^{\sigma} = \sqrt{(2m/\hbar^2)(E_{\rm F} - V_{\rm n}^{\sigma}) - k_{\parallel}^2}$. $\kappa = \sqrt{(2m/\hbar^2)(U - E_{\rm F}) + k_{\parallel}^2}$ is the decay constant in the barrier, and U is the potential barrier height. As follows from equation (6), for a given value of $\mathbf{k}_{\parallel}$ the transmission coefficient can be decoupled into the product of two interface transmission functions $T_{\rm L}^{\sigma}(\mathbf{k}_{\parallel})$ and $T_{\rm R}^{\sigma}(\mathbf{k}_{\parallel})$ characterizing the left and right electrodes interfaces respectively and the exponential decay factor (see Zhang and Butler, 2003 and Belashchenko *et al.*, 2004 for discussion of the validity of this approximation in a more general case)

$$T^{\sigma}(\mathbf{k}_{\parallel}) = T_{\rm L}^{\sigma}(\mathbf{k}_{\parallel}) e^{-2\kappa d} T_{\rm R}^{\sigma}(\mathbf{k}_{\parallel}) \tag{7}$$

where

$$T_{\rm n}^{\sigma}(\mathbf{k}_{\parallel}) = \frac{4\kappa k_{\rm n}^{\sigma}}{\kappa^2 + k_{\rm n}^{\sigma 2}} \tag{8}$$

The physical meaning of $T_{\rm n}^{\sigma}(\mathbf{k}_{\parallel})$ is the transmission probability from the left (right) electrode to the barrier across the interface. For a given value of $\mathbf{k}_{\parallel}$ the interface transmission function determines the transport SP of the ferromagnet/interface.

The total spin-resolved conductance G^{σ} is determined by the sum of equation (6) over transverse wave vectors $\mathbf{k}_{\parallel}$

$$G^{\sigma} = \frac{e^2}{h} \sum_{\mathbf{k}_{\parallel}} T^{\sigma}(\mathbf{k}_{\parallel}) \tag{9}$$

This implies that, in general, the total conductance is not factorized, which makes Jullière's formula (4) inapplicable. However, for a sufficiently thick barrier only electronic states that lie in the vicinity $\mathbf{k}_{\parallel}=0$ primarily contribute the conductance because of the dependence of the decay constant κ on $k_{\parallel}$. In this case the total conductance is proportional to the product of $T_{\rm L}^{\sigma}(\mathbf{k}_{\parallel}=0)$ and $T_{\rm R}^{\sigma}(\mathbf{k}_{\parallel}=0)$, and Jullière's formula becomes valid if the effective SP of the two ferromagnetic electrodes are defined by

$$P_{\rm n} = \frac{T_{\rm n}^{\uparrow}(\mathbf{k}_{\parallel}=0) - T_{\rm n}^{\downarrow}(\mathbf{k}_{\parallel}=0)}{T_{\rm n}^{\uparrow}(\mathbf{k}_{\parallel}=0) + T_{\rm n}^{\downarrow}(\mathbf{k}_{\parallel}=0)} \tag{10}$$

where ${\rm n}={\rm L}$, R. Equation (10) is identical to Slonczewski's result (Slonczewski, 1989):

$$P_{\rm n} = \frac{k_{\rm n}^{\uparrow} - k_{\rm n}^{\downarrow}}{k_{\rm n}^{\uparrow} + k_{\rm n}^{\downarrow}} \frac{\kappa^2 - k_{\rm n}^{\uparrow} k_{\rm n}^{\downarrow}}{\kappa^2 + k_{\rm n}^{\uparrow} k_{\rm n}^{\downarrow}} \tag{11}$$

Note that here $k_{\rm n}^{\uparrow,\downarrow} = \sqrt{(2m/\hbar^2)(E_{\rm F} - V_{\rm n}^{\uparrow,\downarrow})}$ are the spin-dependent Fermi wave vectors, and $E_{\rm F}$ is the Fermi energy. As follows from equation (11), the SP of the tunneling current is not uniquely defined by the wave vector of the ferromagnet and contains a factor that depends on the barrier height. For a high potential barrier ($\kappa \gg k_{\rm n}^{\uparrow}, k_{\rm n}^{\downarrow}$) this expression reduces to

$$P_{\rm n} = \frac{k_{\rm n}^{\uparrow} - k_{\rm n}^{\downarrow}}{k_{\rm n}^{\uparrow} + k_{\rm n}^{\downarrow}} \tag{12}$$

which might be considered as the original definition of the SP within Jullière's formula in terms of bulk DOS of the ferromagnet at the Fermi energy. Indeed, within a free-electron model the bulk DOS is proportional to the Fermi wave vector which makes equations (12) and (5) identical.

In real experiments, however, the barriers may not be sufficiently thick to provide the only contribution to the conductance from electrons tunneling normal to the interfaces. In this case the SP depends on the barrier thickness and height due to the redistribution of tunneling electrons in the $\mathbf{k}_{||}$ space which makes Jullière's formula inapplicable (MacLaren, Zhang and Butler, 1997). This fact makes it surprising that Jullière's formula provides a reasonable agreement between measured values of the tunneling SP and the TMR values measured for alumina barriers.

The likely reason for this consistently is the fact that alumina barrier is amorphous. In this case, it is natural to expect that the transmission through the insulator is nonzero between states in the electrodes characterized by different values of $\mathbf{k}_{||}$. In the limit of strong disorder, scattering in the insulator becomes random and hence the transmission between $\mathbf{k}_{||}$ states occurs with equal probability. In this case the total conductance is proportional to a product of the average transmission functions characterizing the left and right interfaces

$$G^{\sigma} \propto \left\langle T_{\mathrm{L}}^{\sigma} \right\rangle \left\langle T_{\mathrm{R}}^{\sigma} \right\rangle \tag{13}$$

where $\left\langle T_{\mathrm{n}}^{\sigma} \right\rangle = \sum_{\mathbf{k}_{\|}} T_{\mathrm{n}}^{\sigma}(\mathbf{k}_{\|})$ and n = L, R. Thus the effective tunneling DOS entering the expression for polarization (5) in Jullière's formula is determined by the average interface transmission functions so that

$$P_{\mathrm{n}} = \frac{\left\langle T_{\mathrm{n}}^{\uparrow} \right\rangle - \left\langle T_{\mathrm{n}}^{\downarrow} \right\rangle}{\left\langle T_{\mathrm{n}}^{\uparrow} \right\rangle + \left\langle T_{\mathrm{n}}^{\downarrow} \right\rangle} \tag{14}$$

This explains the agreement between the SPs measured in Tedrow–Meservey experiments with values of TMR obtained using Jullière's formula (see Belashchenko *et al.*, 2004 for further discussion).

Although free-electron models capture some important features of SDT, they cannot be used for the quantitative description of TMR. In particular, free-electron models ignore the multiband electronic structure of the ferromagnetic electrodes and the ferromagnet/insulator interfaces. Also the free-electron models do not take into account the complex band structure of the insulator that, as we will see in the next section is decisive for selecting bands which tunnel most efficiently across the barrier.

4 COMPLEX BAND STRUCTURE AND SYMMETRY

A powerful method to make qualitative predictions about SDT in epitaxial tunnel junction taking into account a multiband electronic structure was proposed by Mavropoulos, Papanikolaou, and Dederichs (2000). Using a notion of the complex band structure they emphasized the importance of symmetry of the evanescent gap states in the tunneling barrier for SDT. Below we describe the basic idea of this method.

Electronic transport in tunnel junctions is largely determined by the electronic properties of the insulator within the band gap. These properties are described by a complex band structure and evanescent electronic states. Although such states can exist only at a surface or interface, their general properties can be derived from the bulk band structure of the material by letting the wave vector to be complex. Perfect epitaxial tunnel junctions have two-dimensional periodicity and therefore the wave vector, $\mathbf{k}_{||}$, parallel to the interface is conserved. For each (real) value of $\mathbf{k}_{||}$ one can then describe the evanescent states in terms of dispersion relations $E(k_{\mathrm{z}})$, where $k_{\mathrm{z}} = q + i\kappa$ is the complex wave vector perpendicular to the interface. The imaginary part κ is the decay rate, so that the corresponding wave functions fall off exponentially as $e^{-\kappa z}$. Obviously, those evanescent states that have reasonably small decay rate play the decisive role in electron tunneling. In fact, in the limit of large barrier thickness the state with the smallest decay rate, $\kappa_{\min}$, controls the tunneling current.

Similar to real bands, complex bands can be described in terms of irreducible representations of the symmetry group. Symmetry of the evanescent states determines which Bloch states of the metal electrodes can couple to the evanescent states and thus contribute to the conductance. Symmetry of the evanescent state with the smallest decay rate determines bands of the electrode that can most efficiently tunnel through the insulator. For ferromagnetic electrodes, at the Fermi energy the majority-spin bands may have symmetry different from that of the minority-spin bands, resulting in a different coupling to the evanescent states. These considerations allow conclusions about the SP of the conductance and the TMR in MTJs to be made.

4.1 Fe/MgO/Fe tunnel junctions

Let us consider epitaxial Fe/MgO/Fe(001) tunnel junctions as an example of the application of this method. We will see that symmetry arguments predict very large values of TMR in these junctions consistent with first-principles (Butler, Zhang, Schulthess and MacLaren, 2001) and tight-binding (Mathon and Umerski, 2001) calculations.

MgO, like many other insulators, has a direct band gap at the Γ point and for not too thin MgO barriers the dominant contribution to the conductance comes from electrons near the $\overline{\Gamma}$ point ($\mathbf{k}_{||} = 0$). Decay constants of the two relevant

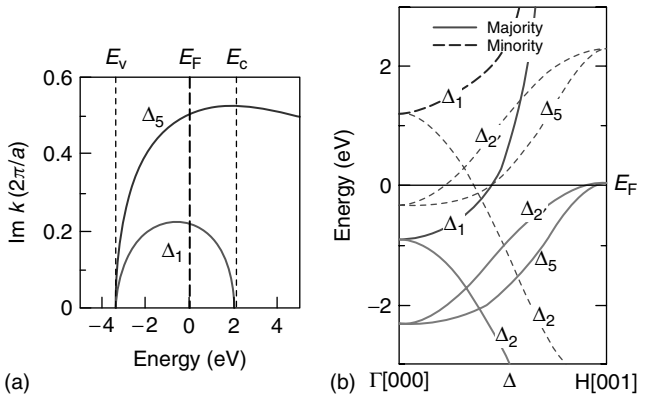

Figure 1. (a) Complex band structure of MgO at the $\overline{\Gamma}$ point. Two evanescent states which have lowest decay rates are shown. The position of the Fermi level, E_F, in a Fe/MgO/Fe MTJ and the top of the valence band, E_v, and the bottom of the conduction band, E_c, are displayed by dashed lines. (b) Spin- resolved band structure of Fe along the [001] direction. Bands are labeled by their symmetry representation. Thick lines mark the Δ_1 bands which match the symmetry of the evanescent state in MgO which has the lowest decay rate. (Courtesy of J.P. Velev.)

evanescent states with $\mathbf{k}_{||} = 0$ are shown in Figure 1(a) as a function of energy. We see that the state that has a minimum decay constant $\kappa_{\min}$ belongs to a Δ_1 symmetry (the identity representation). If any electron originating from the Fe electrode is to tunnel via this state, it must belong to a state in Fe that also belongs to Δ_1 symmetry, so that it can couple to the evanescent state. In the Fe electrode, the k-space direction Δ corresponding to the (001) surface is $\Gamma - H$. Looking at the band structure of Fe in this direction (Figure 1b), we see that the relevant band of symmetry Δ_1 at the Fermi energy appears *only* within the majority-spin channel. This band couples to the Δ_1 evanescent state in MgO and passes to the other side of the barrier. Electrons of other symmetries are cut off by a thick enough MgO barrier. For example, electrons of Δ_5 symmetry which appear at the Fermi energy of Fe both within the majority- and minority-spin channels (Figure 1b) are coupled to the evanescent state of Δ_5 symmetry which has larger decay constant (Figure 1a) and therefore decay faster in the barrier. This makes the SP of the conductance across Fe/MgO interface to be positive and close to 100% for sufficiently thick barriers. Therefore, when coupled to MgO barrier, Fe(001) behaves like a half-metal because it has the Δ_1 band contributing to the conductance only in the one spin channel.

When the electron has reached the interface of the second electrode, it will or will not be allowed to continue, depending on the relative magnetization orientation of the two electrodes. For the parallel orientation, it will couple efficiently to the majority Δ_1 state and continue. For the antiparallel orientation, however, majority-spin electrons tunnel to minority-spin bands which have no Δ_1 symmetry states at the Fermi energy. This implies that there is no conductance for the parallel configuration and hence infinitely large TMR. These arguments are exact for the state of $\kappa_{\min}$, at $\mathbf{k}_{||} = 0$, but for reasons of continuity they will almost hold for $\mathbf{k}_{||}$ near the $\overline{\Gamma}$ point. The presence of the spin-dependent electron reflection from MgO thin films grown on Fe(001) has recently been demonstrated experimentally using spin-polarized low-energy electron microscopy (Wu, Schmid and Qiu, 2006).

In addition to bcc Fe, other crystalline ferromagnetic metals such as bcc Co and bcc FeCo alloys have the Δ_1 symmetry band at the Fermi energy only within the majority-spin channel. Using the symmetry arguments discussed above, we can conclude that large values of TMR are expected for MTJs with these electrodes and MgO barriers if they are stacked in the (001) direction. This is confirmed by first-principles calculations (Zhang and Butler, 2004) and has recently been observed experimentally (Yuasa *et al.*, 2006). The considerations based on symmetry explain large values of TMR which are observed experimentally in crystalline MgO-based tunnel junctions (Faure-Vincent *et al.*, 2003; Parkin *et al.*, 2004; Yuasa *et al.*, 2004; Djayaprawira *et al.*, 2005; Hayakawa *et al.*, 2006).

In a broad class of insulating materials the states that belong to the identity representation have minimum decay rates. For semiconductors (insulators) with a direct band gap (such as GaAs, ZnSe, or semiconductors with a higher atomic number or/and ionicity) these states are centered on the Γ point. One would therefore expect a large TMR in epitaxial MTJs with these barriers and bcc Fe (Co, FeCo) if they stacked along the (001) direction. For example, a large TMR has been predicted for Fe/ZnSe/Fe(100) MTJs (MacLaren, Zhang, Butler and Wang, 1999). Unfortunately, experimentally epitaxial Fe/ZnSe/FeCo MTJs show much less impressive behavior compared to MgO-based MTJs demonstrating a sizable magnetoresistance of 16% only at low temperatures (Gustavsson, George, Etgens and Eddrief, 2001). This is a consequence of a semiconducting nature of the ZnSe barrier which makes the mechanism of conductance to be different from that considered theoretically. Owing to a smaller band gap the presence of impurity/defect states close to the Fermi energy makes the ballistic approach inadequate for the description of SDT in these junctions at such barrier thicknesses where according to the symmetry arguments the TMR should be large.

We note that the presence of disorder in the barrier layer may also produce notable effects on electronic transport in MgO-based tunnel junctions. Localized states in MgO have been observed using scanning tunneling spectroscopy measurements (Klaua *et al.*, 2001; Mather, Read and Buhrman, 2006). These states are attributed to O vacancies or other structural defects, arising because of nonideal

growth conditions. It is known that the mechanism of electron transport in such imperfect MTJs is very different compared to ideal junctions (Tsymbal and Pettifor, 1998), which may affect significantly the transport SP (Vedyayev, Bagrets, Bagrets and Dieny, 2001) and even lead to the reversal of TMR (Tsymbal, Sokolov, Sabirianov and Doudin, 2003). Recent first-principles calculations predict that O vacancies in MgO produce nonresonant scattering of tunneling electrons causing a reduction of TMR (Velev, Belashchenko, Jaswal and Tsymbal, 2007). For thicker barriers, tunneling mediated by O vacancies may explain the observed slope of the logarithm of resistance as a function of MgO thickness independent of the magnetization orientation (Yuasa *et al*., 2004). This behavior is inconsistent with direct tunneling, because in perfect Fe/MgO/Fe MTJs the decay lengths of the evanescent states controlling the conductance for parallel and antiparallel magnetizations are different (Butler, Zhang, Schulthess and MacLaren, 2001).

4.2 Co/$SrTiO_3$/Co tunnel junctions

A completely different behavior is predicted for perovskite barrier electrodes, such as $SrTiO_3$, in which the symmetry of the complex band structure of $SrTiO_3$ enables efficient tunneling of the minority d electrons from bcc Co, causing the SP of the conductance across the $SrTiO_3$interface to be negative (Velev *et al*., 2005). Using the structural model of an epitaxial Co/$SrTiO_3$/Co(001) MTJ (Oleinik, Tsymbal and Pettifor, 2002) a very large TMR was predicted for this junctions.

The fact that the tunneling current is dominated by minority-spin electrons can be explained by taking into account the band structure of bcc Co and decay rates of the Co states in $SrTiO_3$. The majority-spin 3d band in bcc Co is filled, so that the DOS at the Fermi level has a large negative SP (Bagayoko, Ziegler and Callaway, 1983). Actually, the band structure of bcc Co along the Δ direction is very similar to that of bcc Fe shown in Figure 1(b) with the Fermi energy shifted up by about 1 eV. Owing to the symmetry of the evanescent states with lowest decay rates in $SrTiO_3$ the 3d states could efficiently tunnel through the barrier. Indeed, as is seen from the complex band structure of $SrTiO_3$ shown in Figure 2(a) at the $\overline{\Gamma}$ point ($\mathbf{k}_{||} = 0$), the Δ_5 and Δ_1 states have comparable decay rates in the gap of $SrTiO_3$. Therefore, both the majority-spin Δ_1 band and the minority-spin Δ_5 band of bcc Co can tunnel efficiently through the $SrTiO_3$ barrier.

While the $\overline{\Gamma}$ point analysis is instructive, it is not sufficient in this case because the conductance is not dominated by this point. This fact can be understood from Figure 2(b), showing the three lowest decay rates of the evanescent states at the Fermi energy. It is seen that a very large area of the Brillouin zone, forming a cross pattern along the $\overline{\Gamma}$–M directions, exhibits two lowest decay rates that are very close to those at the $\overline{\Gamma}$ point. Clearly, at large barrier thickness the states lying in this 'cross' area should dominate the conductance. This feature is in sharp contrast to sp-bonded insulators like MgO and Al_2O_3 where the decay rate has a deep parabolic minimum in the vicinity of the $\overline{\Gamma}$ point. This difference is due to the conduction band of $SrTiO_3$, which is formed by fairly localized 3d states of Ti instead of free-electron-like states of a metal atom in simple oxides. Therefore, the minority-spin d states which have much larger DOS at the Fermi energy than the majority-spin states dominate the conductance providing a negative SP of the tunneling current in Co/$SrTiO_3$/Co MTJs. This finding is in agreement with the experimental observations of (De Teresa *et al*., 1999a,b), who found that the transport SP of the Co/$SrTiO_3$ interface is negative, opposite to that of the Co/Al_2O_3 interface.

5 INTERFACE RESONANT STATES AND INTERFACE BONDING

The presence of surface electronic states on a surface of a metal is well known. If these states are coupled to bulk Bloch states, they are called *surface resonant states* or *surface resonances*. For example, the presence of minority-spin resonant states on the Fe(001) surface is well established experimentally, for example, by STM measurements (Stroscio *et al*., 1995).

Interface resonances may appear in MTJs and influence their transport properties (Wunnicke *et al*., 2002). The minority-spin interface resonances are present at the Fe(001)/MgO interface, as was found from first-principle calculations (Butler, Zhang, Schulthess and MacLaren, 2001) and was indirectly observed in tunneling experiments (Tiusan *et al*., 2004, 2006). Within a two-dimensional Brillouin zone these resonant states represent a surface band sharply peaked near the Fermi energy. Calculations show that the interface Fe(001)/MgO band is very flat making it extremely sensitive to electron energy (Belashchenko, Velev and Tsymbal, 2005). This can be seen from Figure 3, which shows the density of electronic states resolved with respect to the transverse wave vector $\mathbf{k}_{||}$ for different energies. It is evident that a significant change in the location of these bands within the first Brillouin zone occurs when energy is shifted by a tiny amount of 0.02 eV.

The formation of interface resonant states is largely controlled by the atomic structure and bonding at the interface. This can already be seen within a simple tight-binding model (Tsymbal and Belashchenko, 2005) which shows that the interplay between the interface on-site atomic

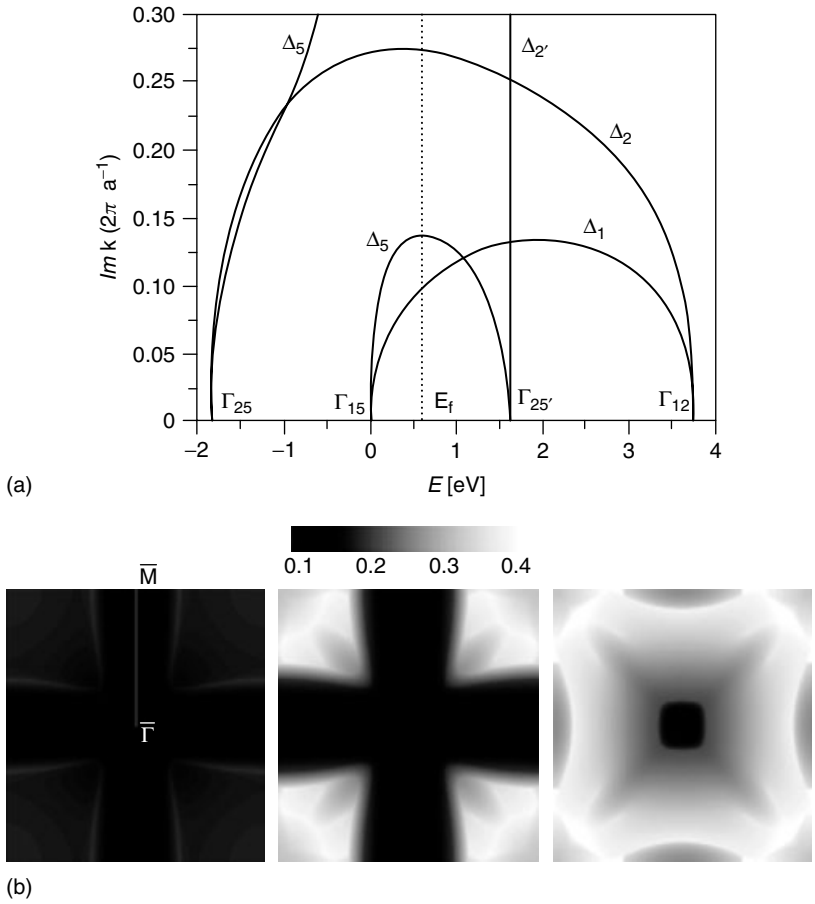

Figure 2. (a) Complex band structure of $SrTiO_3$ at the $\overline{\Gamma}$ point showing evanescent states which have lowest decay rates. The position of the Fermi level E_F in a Co/$SrTiO_3$/Co MTJ is indicated by a dashed line. (b) Three lowest decay rates (in units of $2\pi/a$) of the evanescent states in $SrTiO_3$ as a function of $\mathbf{k}_{||}$ at the Fermi energy. (Reproduced from J. Velev *et al*., 2005, with permission from the American Physical Society. © 2005.)

energies and the strength of interface bonding may result in the appearance of an interface resonance. The width of this resonance is controlled by its coupling to bulk states that is determined by the interface bonding and the interface potential.

Theoretically, interface resonant states can produce a very large tunneling current if they match identical resonances at the opposite interface (Wunnicke *et al*., 2002; Tusche *et al*., 2005). In practice, however, this situation is unlikely because the interface resonances are always mismatched by structural disorder, inelastic scattering and a small applied bias voltage (Velev, Belashchenko and Tsymbal, 2006). This is the consequence of the fact that the intrinsic damping of resonant states is very small as a result of their weak coupling to bulk states. Inelastic scattering and structural disorder broaden the resonant states thereby strongly reducing the conductance through this channel. A small applied bias voltage produces a similar effect due to a mismatch of resonances at the opposite interfaces. The detrimental effect of disorder is seen from calculations using realistic structure models (Xu *et al*., 2006; Mathon and Umerski, 2006).

The situation described above does not, however, diminish the role of interface resonant states and interface bonding in transport properties of MTJs. Actually, as was mentioned in the introduction, in many cases the interface atomic and electronic structure play a decisive role in spin transport. Below we consider three examples where interface bonding and interface resonant states control the SP of the tunneling current in MTJs.

5.1 Interface resonant states in Fe/MgO/Fe tunnel junctions

First, we consider epitaxial Fe/MgO/Fe(001) MTJs. As explained in Section 4.1 on the basis of symmetry arguments, these junctions should possess very large values of TMR for sufficiently thick MgO barriers. This is due to the

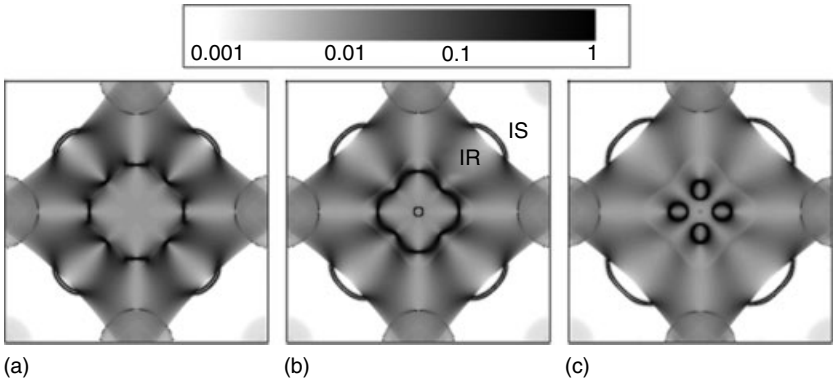

Figure 3. $\mathbf{k}_{||}$-resolved minority-spin density of states (in arb units) for Fe(001)/MgO interface calculated for three different energies near the Fermi energy (E_F): (a) $E = E_F - 0.02\,eV$, (b) $E = E_F$, (c) $E = E_F + 0.02\,eV$. Interface resonant states are denoted by IR. (Reproduced from K.D. Belashchenko *et al.*, 2005, with permission from the American Physical Society. © 2005.)

contribution from the Δ_1 band which is present at the $\overline{\Gamma}$ point only in the majority-spin channel of Fe at the Fermi energy. At small barrier thickness, however, the conductance is not dominated by the $\overline{\Gamma}$ point, and symmetry arguments are no longer valid. Calculations of Belashchenko, Velev and Tsymbal (2005) show that the contribution from the interface resonant states becomes appreciable at MgO thickness below six monolayers (MLs) which results in the decrease of TMR. This is consistent with the experimental results which show that TMR in Fe/MgO/Fe(001) MTJs drops down precipitously for barrier thickness below 1.5 nm (Yuasa *et al.*, 2004). The interface resonant states may also affect the bias-voltage dependence of TMR (Zhang *et al.*, 2004).

Figure 4(a–c) shows the spin-resolved conductance for the MTJ with four MLs of MgO for the parallel and antiparallel magnetization. The large contribution to the conductance near the $\overline{\Gamma}$ point (Figure 4a) is due to the matching of the majority Δ_1 band in Fe and the respective evanescent state in the MgO. The conductance for the minority-spin channel (Figure 4b) and the conductance for the antiparallel magnetization (Figure 4c) are strongly enhanced for certain $\mathbf{k}_{||}$ points in the Brillouin zone. The comparison to Figure 3(b) indicates that this is due to the contribution from a resonant interface band. The enhancement of the conductance is most pronounced for small barrier thickness, because the interface band lies away from the $\overline{\Gamma}$ point, and therefore the resonant contribution to the transmission decays faster with barrier thickness compared to the nonresonant contribution. The enhanced contribution of these interface resonances leads to the decrease of TMR at low barrier thickness. Indeed, on grounds explained above (Velev, Belashchenko and Tsymbal, 2006), the contribution from the minority-spin channel for the parallel magnetization should be disregarded. On the other hand, the interface resonances *do* contribute to the conductance in the antiparallel configuration, where they tunnel into majority-spin states of the other electrode. The latter have no fine structure in the Brillouin zone, and hence the conductance is weakly sensitive to a potential mismatch at the two interfaces that might occur in real junctions.

The contribution from the interface resonance can be suppressed and consequently, the TMR can be enhanced if a thin epitaxial Ag layer is deposited at the two Fe/MgO interfaces. It is known that an epitaxial Ag overlayer on Fe(001) surface notably modifies the electronic structure of the surface states (Vescovo *et al.*, 1995). If the minority-spin interface DOS is reduced by Ag, the antiparallel conductance will be suppressed. On the other hand, the majority-spin conductance should not be strongly affected due to almost perfect transmission through the Fe/Ag(001) interface (Stiles, 1996). This is indeed what is predicted by the theory (Belashchenko, Velev and Tsymbal, 2005).

Figure 4(d–f) shows the $\mathbf{k}_{||}$- and spin-resolved conductance of Fe/MgO/Fe junctions with Ag interlayers. Not unexpectedly, for parallel magnetization the conductance is weakly affected by the Ag interlayers, whereas for antiparallel magnetization the conductance changes dramatically. The most pronounced difference is the disappearance of the contribution from interface resonances that dominated the conductance of the Fe/MgO/Fe junction with no Ag interlayers (compare Figure 4c and f). This strong change occurs owing to the Fe–Ag hybridization which makes the interface resonant band more dispersive and removes the Fermi level crossing responsible for the highly conductive resonant states. The significant reduction of the conductance in the antiparallel configuration leads to a dramatic enhancement of the TMR. Thus, Ag interlayers practically eliminate the contribution from the interface resonances and enhance TMR for thin barriers.

The noble metal interlayer may also enhance the TMR because of quantum-well states formed within the interlayer

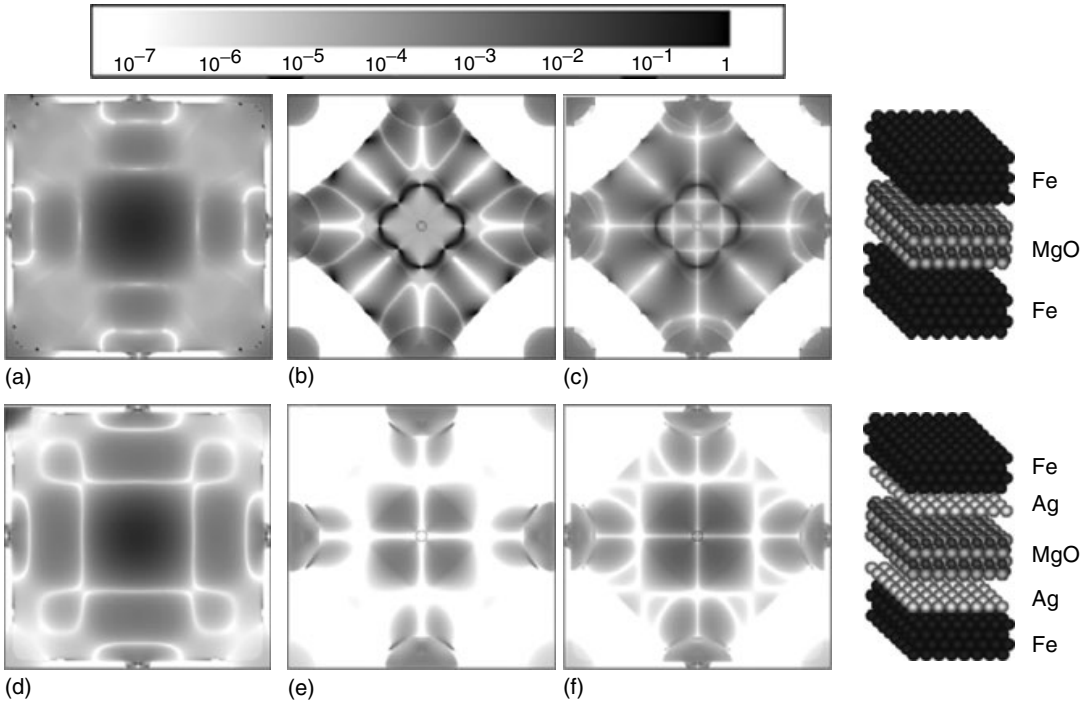

Figure 4. Conductance (in units of e^2/h) as a function of $\mathbf{k}_{||}$ for Fe/MgO/Fe (a, b, and c) and Fe/Ag/MgO/Ag/Fe (d, e, and f) tunnel junctions with four monolayers of MgO for majority spins (a), (d), minority spins (b), (e), each spin channel in the antiparallel configuration (c), (f). (Reproduced from K.D. Belashchenko *et al*., 2005, with permission from the American Physical Society. © 2005.)

(Mathon and Umerski, 2005). With increasing the interlayer thickness, a theory predicts an oscillatory dependence of TMR (Vedyayev *et al*., 1997; Mathon and Umerski, 1999) with a possibility of strong enhancement of the conductance and TMR at resonant conditions (Lu, Zhang and Pantelides, 2005) and tuning of quantum-well states by impurities (Kalitsov *et al*., 2004). Yuasa, Nagahama, and Suzuki (2002) found experimentally quantum-well oscillations in $Co/Cu/Al_2O_3/Ni_{80}Fe_{20}$ tunnel junctions with the bottom epitaxial Co/Cu(001) electrodes. Recently, quantum oscillations of the tunneling conductance in fully epitaxial double barrier Fe(001)/MgO/Fe/MgO/Fe MTJs were observed experimentally (Nozaki, Tezuka and Inomata, 2006) and calculated from first principles (Wang, Lu, Zhang and Han, 2006).

5.2 Tunneling from clean and oxidized Co surfaces through vacuum

Another interesting example that demonstrates the importance of interface states is tunneling from clean and oxidized Co surfaces through vacuum studied by Belashchenko *et al*. (2004). It shows the crucial role of bonding between Co and O atoms on the surface for SDT. This work investigates the SP of the tunneling current from a Co(111) electrode to a nonmagnetic Al(111) which serves as a detector of the tunneling SP in the spirit of the Tedrow–Meservey experiments.

Figure 5(a) and (b) show the $\mathbf{k}_{||}$-resolved conductance for the majority- and minority-spin electrons within the first surface Brillouin zone for a clean Co(111) surface. The Co Fermi surface viewed along the [111] direction has holes close to the $\overline{\Gamma}$ point with no bulk states in both spin channels, which results in zero conductance in this area. The majority-spin conductance (Figure 5a) varies rather smoothly and is appreciable over a relatively large area of the Brillouin zone. On the other hand, the minority-spin conductance (Figure 5b) has a narrow crown-shaped 'hot ring' around the edge of the Fermi surface hole. The analysis of layer and $\mathbf{k}_{||}$-resolved DOS shows that it is not associated with surface states, but rather with an enhancement of bulk $\mathbf{k}_{||}$-resolved DOS near the Fermi surface edge. As is seen from Figure 5(a) and (b), the Fermi surface hole is smaller for majority spins. Therefore, the conductance should become fully majority-spin polarized in the limit of very thick barriers. This occurs, however, only at barrier thickness $d \sim 10\,\text{nm}$, while for typical values of $d \sim 2\,\text{nm}$ the SP is about -60% and depends weakly on d.

An oxidized Co surface is modeled by placing an O monolayer on top of the Co(111) electrode such that O atoms lie in the threefold hollow-site positions above the subsurface Co layer (Figure 5f). The oxygen monolayer

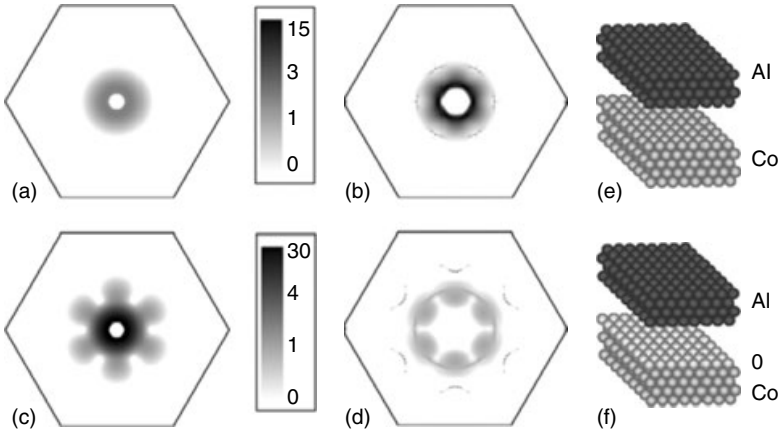

Figure 5. $\mathbf{k}_{||}$-resolved conductance (in units of e^2/h) from clean and oxidized (111) Co surfaces through vacuum into Al: (a) clean surface, majority spin; (b) clean surface, minority spin; (c) oxidized surface, majority spin; (d) oxidized surface, minority spin. Vacuum layer thickness is 2 nm for clean and 1.7 nm for oxidized Co surface. Units are $10^{-11}e^2/h$ for (a), (b) and $10^{-14}e^2/h$ for (c), (d). Geometry for clean and oxidized Co surfaces are shown in (e) and (f), respectively. (Reproduced from K.D. Belashchenko *et al*., 2004, with permission from the American Physical Society. © 2004.)

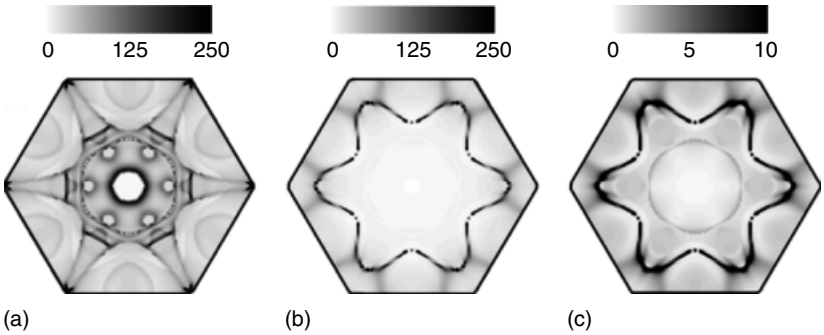

Figure 6. $\mathbf{k}_{||}$-resolved minority-spin local DOS (arb units) at the Fermi energy for the oxidized Co(111) surface: (a) bulk Co; (b) subsurface Co monolayer; (c) surface O monolayer. (Reproduced from K.D. Belashchenko *et al*., 2004, with permission from the American Physical Society. © 2004.)

dramatically changes the electronic structure reducing the magnetic moment of the underlying Co to 0.17 μ_B. Interestingly, the presence of the almost magnetically dead monolayer of Co at the interface does not kill the SP of the conductance; it rather changes sign of the SP from negative to positive. This fact is evident from Figure 5(c) and (d) which indicates that the overall reduction in the conductance due to oxidation is accompanied by the dominant suppression of the minority-spin transmission.

The origin of this behavior can be understood from Figure 6 which displays the $\mathbf{k}_{||}$- and layer-resolved minority-spin DOS at the Fermi energy. For bulk Co the Fermi surface edges are strongly emphasized in the DOS (Figure 6a). One of them representing a ring around the $\overline{\Gamma}$ point dominates the minority-spin conductance for the clean Co surface (compare to Figure 5b). The oxidation results in the strong covalent bonding between Co and O atoms at the surface producing an antibonding band which is clearly seen in the $\mathbf{k}_{||}$-resolved DOS for Co and O surface monolayers (Figure 6b and c). This resonant band appears only in the minority-spin channel and removes the spectral weight from the center of the Brillouin zone. As a result, the bulk minority-spin states responsible for most tunneling transmission from the clean surface encounter a band gap in the surface Co and O layers which is equivalent to adding an additional tunneling barrier. Thus, the tunneling conductance for the MTJ with the oxidized Co surface is fully dominated by the majority-spin channel, resulting in the SP of about +100%.

Experimentally, the reversal of the SP associated with surface oxidation may be detected using spin-polarized STM measurements (Bode, 2003). Since the ferromagnetic tip is sensitive to the SP of the total local DOS above the surface, the TMR in the system surface/vacuum/tip should change sign when Co surface is oxidized. In other words, for the clean Co(111) surface the tunneling current should be higher when the magnetizations of the tip and the surface are aligned

parallel, but for the oxidized surface it should be higher for the antiparallel alignment.

5.3 Role of interface Co–O bonding in $Co/Al_2O_3/Co$ tunnel junctions

Interface bonding plays a decisive role in SDT in $Co/Al_2O_3/Co$ MTJs as is shown by Belashchenko, Tsymbal, Oleinik and van Schilfgaarde (2005). Assuming crystalline epitaxy at the interface between fcc Co(111) electrodes and an Al_2O_3 barrier this work considers two fully-relaxed atomic configurations of the O-terminated interface that differ only by the presence or absence of an adsorbed oxygen atom at the interface (Figure 7). Model 1 (Figure 7a and b) represents the O-terminated $Co/Al_2O_3/Co$ structure with three oxygen atoms per unit cell (Oleinik, Tsymbal and Pettifor, 2000). These oxygen atoms participate in bonding with the two adjacent Al atoms, making the bonds of the latter fully saturated. Model 2 (Figure 7c and d) adds an additional O atom in the threefold hollow site. This O atom and the neighboring Co atoms are labeled 'II' in Figure 7(c) and (d), whereas the other O and surface Co atoms are labeled 'I'. Structural sites occupied by O(I) and O(II) atoms are very dissimilar. O(II) atoms lie much closer to the Co surface compared to O(I) atoms and, hence, are more strongly coupled to Co than O(I) atoms.

This distinction is evident in the local DOS for the interfacial atoms shown in Figure 8. Similar to the Co(111) surface with an adsorbed oxygen monolayer, Co(II) and O(II) atoms in model 2 form bonding and antibonding orbitals which are clearly seen in the local DOS plots. The bonding states lie below the bottom of the Co 3d band, while the antibonding states are slightly above the Fermi level. While the magnetic moment of Co(II) atoms is notably reduced ($1.30\,\mu_B$), this effect is much smaller compared to the oxidized Co surface, because in model 2 there is only one 'adsorbed' O(II) atom per three Co(II) atoms. The local DOS for Co(I) atoms remains quite similar to bulk Co, while the local DOS for O(I) atoms shows a small but notable 'echo' of the Co(II)–O(II) antibonding states.

The spin asymmetry of the conductance for these tunnel junctions can be analyzed by calculating the spin-resolved conductance per unit cell area for the parallel orientation of electrodes. Model 1 shows that the majority-spin conductance $G_{\uparrow\uparrow} = 0.0042e^2/h$ is smaller than the minority-spin conductance $G_{\downarrow\downarrow} = 0.023e^2/h$. This implies that the SP $P = \left(G_{\uparrow\uparrow} - G_{\downarrow\downarrow}\right) / \left(G_{\uparrow\uparrow} + G_{\downarrow\downarrow}\right)$ is negative and equals -70%. Note that, although this quantity is not directly measurable, it correlates with the measurable SP. This situation changes dramatically when an additional O atom is placed at the interface. The model 2 exhibits a reversal of the SP from negative to positive. The total conductances per cell area are $G_{\uparrow\uparrow} = 0.087e^2/h$ and $G_{\downarrow\downarrow} = 0.045e^2/h$, and the $P = +32\%$.

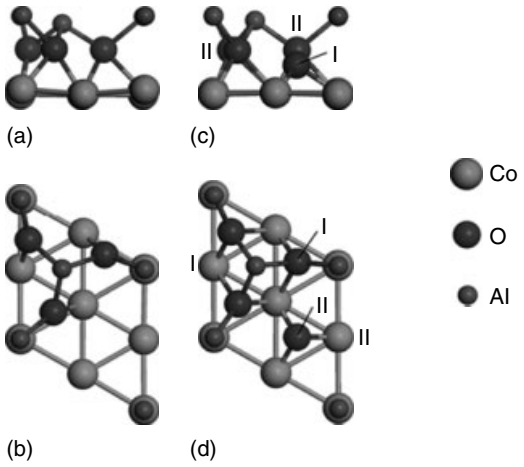

Figure 7. Interface structure of the $Co/Al_2O_3/Co$ MTJ for model 1 (a, b) and model 2 (c, d). (a) and (c) 'Front' views from a direction normal to the threefold axis. (b) and (d) 'Top' views along the threefold axis. There are two types of Co and O atoms at the interface for model 2: three O(I) atoms, one O(II) atom, one Co(I) atom, and three Co(II) atoms per unit cell. (Reproduced from K.D. Belashchenko *et al*., 2005, with permission from the American Physical Society. © 2005.)

Thus, we see that the strong interface bonding with O atoms is responsible for the positive SP of the tunneling current in $Co/Al_2O_3/Co$ tunnel junctions. This bonding produces antibonding Co–O states that are present at the Fermi level in the majority-spin channel. These interface states moderately mix with the bulk states, forming interface resonances, which strongly assist tunneling. On the other hand, the minority-spin antibonding Co–O states lie above the Fermi energy because of exchange splitting and do not affect the conductance.

These results suggest that the common argument of the dominant s-electron contribution to tunneling, which is often used to explain the positive SP of the alumina-based tunnel junctions is not justified. The strong interfacial bonding between Co and O atoms at the interface may be the major factor resulting in the positive SP as is observed in experiment.

6 CONCLUSIONS

It was believed for a long time that the tunneling SP in MTJs is solely determined by the electronic and magnetic properties of ferromagnetic electrodes (such as the total DOS or the DOS of itinerant bands the at the Fermi energy). This idea was, in particular, based on the agreement between measured values of the SP of the tunneling

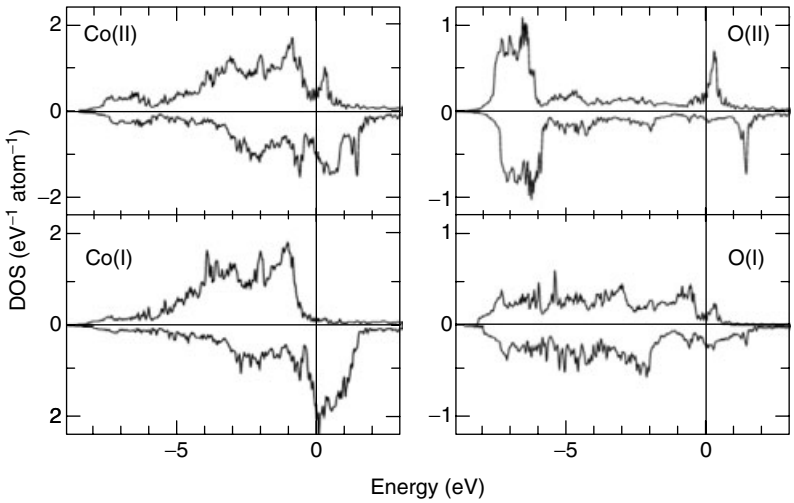

Figure 8. Local DOS per atom for interfacial atoms in model 2. In each panel, top half shows the majority-spin DOS, and bottom half, the minority-spin DOS per atom. The vertical line denotes the position of the Fermi level. (Reproduced from K.D. Belashchenko *et al*., 2005, with permission from the American Physical Society. © 2005.)

current across Al_2O_3 barriers using the Tedrow–Meservey technique and the maximum TMR values reported for Al_2O_3 barriers within Jullière's model. However, later it became clear that not only the electronic structure of ferromagnets but also the electronic structure of the ferromagnet/insulator interface and the evanescent states in the insulator control the tunneling SP. It is now commonly accepted that the SP entering the Jullière's formula is due to the ferromagnet/barrier complex rather than the ferromagnet alone. Theoretically, this concept can be explained in terms of the interface transmission function (Belashchenko *et al*., 2004), which explains the essence of the effective tunneling DOS used in the Jullière's formula.

We have considered a few examples that illustrate the role of evanescent states in the insulating barrier and bonding at the ferromagnet/barrier interface in controlling the SP of the tunneling current in epitaxial tunnel junctions (MTJs). Symmetry of the evanescent states selects spin-polarized bands in the ferromagnetic electrodes that are able to efficiently tunnel through the barrier. In particular, the matching of the majority-spin Δ_1 band in ferromagnetic Fe(001) to the Δ_1 complex band in MgO which has the lowest decay rate at the Fermi energy and the absence of the minority-spin Δ_1 band at the Fermi energy in bulk Fe are responsible for large values of TMR observed in crystalline Fe/MgO/Fe and similar junctions.

The complex band structure of $SrTiO_3$ explains a large negative tunneling SP in bcc $Co/SrTiO_3/Co(001)$ MTJs. This is the consequence of the localized 3d states of Ti, which contribute to the band structure of $SrTiO_3$ and allow efficient tunneling of minority d electrons of Co that have a large weight at the Fermi energy. This behavior is a drastic departure from the mechanism of tunneling in MTJs based on sp-bonded insulators such as Al_2O_3 and explains the experimental observation of the negative SP of electrons tunneling from Co through $SrTiO_3$ (De Teresa *et al*., 1999a,b).

The interface bonding may result in the appearance of interfaces resonant states which dramatically affect the SP of the tunneling current. These states are responsible for a decrease of TMR in Fe/MgO/Fe(001) MTJs for small barrier thickness. A monolayer of Ag epitaxially deposited at the interface between Fe and MgO suppresses tunneling through the interface band and may thus be used to enhance the TMR in these junctions.

The SP of the tunneling current from Co(111) through vacuum is predicted to be negative but can be reversed by deposition of a monolayer of oxygen on the Co(111) surface which makes the SP close to +100%. This effect occurs owing to the formation of surface bands that mix well with bulk majority-spin states but create an additional tunneling barrier for minority-spin states. This phenomenon could be observed using STM measurements.

The strong interface bonding between Co and O atoms at the interface in $Co/Al_2O_3/Co$ MTJs explains positive values of the SP observed experimentally. These results show that the common argument suggesting that s electrons dominate tunneling, which is often used to explain positive SPs observed experimentally in Al_2O_3-based tunnel junctions is quantitatively incorrect. In reality, the SP in these junctions is controlled by the interfacial structure and bonding. The strong interface bonding between a ferromagnetic atom and O is likely responsible for the positive SP in these junctions.

The sensitivity of the tunneling SP and TMR to the interface atomic and electronic structure expands the possibilities for engineering optimal MTJ properties for device applications.

ACKNOWLEDGMENTS

The author is grateful to Kirill Belashchenko, Sitaram Jaswal, Ivan Oleynik, Mark van Schilfgaarde, Derek Stewart, and Julian Velev for their contribution to the research work, results of which have been discussed in this article. This work was supported by NSF (DMR-0203359 and MRSEC DMR-0213808) and the Nebraska Research Initiative.

REFERENCES

Alvarado, S.F. and Renaud, P. (1992). Observation of spin-polarized-electron tunneling from a ferromagnet into GaAs. *Physical Review Letters*, **68**, 1387.

Bagayoko, D., Ziegler, A. and Callaway, J. (1983). Band structure of bcc cobalt. *Physical Review B*, **27**, 7046–7049.

Belashchenko, K.D., Tsymbal, E.Y., Oleinik, I.I. and van Schilfgaarde, M. (2005). Positive spin polarization in $Co/Al_2O_3/Co$ tunnel junctions driven by oxygen adsorption. *Physical Review B*, **71**, 224422.

Belashchenko, K.D., Tsymbal, E.Y., van Schilfgaarde, M., *et al*. (2004). Effect of interface bonding on spin-dependent tunneling from the oxidized Co surface. *Physical Review B*, **69**, 174408.

Belashchenko, K.D., Velev, J. and Tsymbal, E.Y. (2005). Effect of interface states on spin-dependent tunneling in Fe/MgO/Fe tunnel junctions. *Physical Review B*, **72**, R140404.

Bode, M. (2003). Spin-polarized scanning tunnelling microscopy. *Report on Progress in Physics*, **66**, 523–582.

Butler, W.H., Zhang, X-G., Schulthess, T.C. and MacLaren, J.M. (2001). Spin-dependent tunneling conductance of Fe|MgO|Fe sandwiches. *Physical Review B*, **63**, 054416.

De Teresa, J.M., Barthélémy, A., Fert, A., *et al*. (1999a). Inverse tunnel magnetoresistance in $Co/SrTiO_3/La_{0.7}Sr_{0.3}MnO_3$: new ideas on spin-polarized tunneling. *Physical Review Letters*, **82**, 4288–4291.

De Teresa, J.M., Barthélémy, A., Fert, A., *et al*. (1999b). Role of metal-oxide interface in determining the spin polarization of magnetic tunnel. *Science*, **286**, 507–509.

Djayaprawira, D., Tsunekawa, K., Nagai, M., *et al*. (2005). 230% room-temperature magnetoresistance in CoFeB/MgO/CoFeB magnetic tunnel junctions. *Applied Physics Letters*, **86**, 092502.

Faure-Vincent, J., Tiusan, C., Jouguelet, E., *et al*. (2003). High tunnel magnetoresistance in epitaxial Fe/MgO/Fe tunnel junctions. *Applied Physics Letters*, **82**, 4507–4509.

Gustavsson, F., George, J.M., Etgens, V.H. and Eddrief, M. (2001). Structural and transport properties of epitaxial Fe/ZnSe/FeCo magnetic tunnel junctions. *Physical Review B*, **64**, 184422.

Hayakawa, J., Ikeda, S., Lee, Y.M., *et al*. (2006). Effect of high annealing temperature on giant tunnel magnetoresistance ratio of CoFeB/MgO/CoFeB magnetic tunnel junctions. *Applied Physics Letters*, **89**, 232510.

Heiliger, C., Zahn, P. and Mertig, I. (2006). Microscopic origin of magnetoresistance. *Materials Today*, **9**, 46–54.

Heiliger, C., Zahn, P., Yavorsky, B.Y. and Mertig, I. (2006). Interface structure and bias dependence of Fe/MgO/Fe tunnel junctions: *ab initio* calculations. *Physical Review B*, **73**, 214441.

Itoh, H. and Inoue, J. (2001). Interfacial electronic states and magnetoresistance in tunnel junctions. *Surface Science*, **493**, 748–756.

Jullière, M. (1975). Tunneling between ferromagnetic films. *Physics Letters A*, **54**, 225–226.

Kalitsov, A., Coho, A., Kioussis, N., *et al*. (2004). Impurity-induced tuning of quantum-well states in spin-dependent resonant tunneling. *Physical Review Letters*, **93**, 046603.

Klaua, M., Ullmann, D., Barthel, J., *et al*. (2001). Growth, structure, electronic, and magnetic properties of MgO/Fe(001) bilayers and Fe/MgO/Fe(001) trilayers. *Physical Review B*, **64**, 134411.

LeClair, P., Hoex, B., Wieldraaijer, H., *et al*. (2001). Sign reversal of spin polarization in $Co/Ru/Al_2O_3/Co$ magnetic tunnel junctions. *Physical Review B*, **64**, 100406.

LeClair, P., Kohlhepp, J.T., Swagten, H.J.M. and de Jonge, W.J.M. (2001). Interfacial density of states in magnetic tunnel junctions. *Physical Review Letters*, **86**, 1066–1069.

LeClair, P., Swagten, H.J.M., Kohlhepp, J.T., *et al*. (2000). Apparent spin polarization decay in Cu-dusted $Co/Al_2O_3/Co$ tunnel junctions. *Physical Review Letters*, **84**, 2933–2296.

Levy, P.M. and Zhang, S.F. (1999). Spin dependent tunneling. *Current Opinion in Solid State and Materials Science*, **4**, 223–229.

Lu, Z.Y., Zhang, X-G. and Pantelides, S.T. (2005). Spin-dependent resonant tunneling through quantum-well states in magnetic metallic thin films. *Physical Review Letters*, **94**, 207210.

MacLaren, J.M., Zhang, X-G. and Butler, W.H. (1997). Validity of the Julliere model of spin-dependent tunneling. *Physical Review B*, **56**, 11827–11832.

MacLaren, J.M., Zhang, X-G., Butler, W.H. and Wang, X.D. (1999). Layer KKR approach to Bloch-wave transmission and reflection: application to spin-dependent tunneling. *Physical Review B*, **59**, 5470–5478.

Mather, P.G., Read, J.C. and Buhrman, R.A. (2006). Disorder, defects, and band gaps in ultrathin (001) MgO tunnel barrier layers. *Physical Review B*, **73**, 205412.

Mathon, J. and Umerski, A. (1999). Theory of tunneling magnetoresistance in a junction with a nonmagnetic metallic interlayer. *Physical Review B*, **60**, 1117.

Mathon, J. and Umerski, A. (2001). Theory of tunneling magnetoresistance of an epitaxial Fe/MgO/Fe(001) junction. *Physical Review B*, **63**, R220403.

Mathon, J. and Umerski, A. (2005). Theory of resonant tunneling in an epitaxial Fe/Au/MgO/Au/Fe(001) junction. *Physical Review B*, **71**, 220402.

Mathon, J. and Umerski, A. (2006). Theory of tunneling magnetoresistance in a disordered Fe/MgO/Fe(001) junction. *Physical Review B*, **74**, 140404.

Mavropoulos, Ph., Papanikolaou, N. and Dederichs, P.H. (2000). Complex band structure and tunneling through ferromagnet/insulator/ferromagnet junctions. *Physical Review Letters*, **85**, 1088–1091.

Meservey, R. and Tedrow, P.M. (1994). Spin-polarized electron-tunneling. *Physics Reports*, **238**, 173–243.

Monsma, D.J. and Parkin, S.S.P. (2000). Temporal evolution of spin-polarization in ferromagnetic tunnel junctions. *Applied Physics Letters*, **77**, 883–885.

Moodera, J.S., Kinder, L.R., Wong, T.M. and Meservey, R. (1995). Large magnetoresistance at room-temperature in ferromagnetic thin-film tunnel-junctions. *Physical Review Letters*, **74**, 3273–3276.

Moodera, J.S. and Mathon, G. (1999). Spin polarized tunneling in ferromagnetic junctions. *Journal of Magnetism and Magnetic Materials*, **200**, 248–273.

Nozaki, T., Tezuka, N. and Inomata, K. (2006). Quantum oscillation of the tunneling conductance in fully epitaxial double barrier magnetic tunnel junctions. *Physical Review Letters*, **96**, 027208.

Okuno, S.N., Kishi, T. and Tanaka, K. (2002). Spin-polarized tunneling spectroscopy of Co(0001) surface states. *Physical Review Letters*, **88**, 066803.

Oleinik, I.I., Tsymbal, E.Y. and Pettifor, D.G. (2000). Structural and electronic properties of cobalt/alumina tunnel junctions from first principles. *Physical Review B*, **62**, 3952–3959.

Oleinik, I.I., Tsymbal, E.Y. and Pettifor, D.G. (2002). Atomic and electronic structure of Co/$SrTiO_3$/Co tunnel junctions. *Physical Review B*, **65**, R020401.

Parkin, S.S.P. (2006). Spin-polarized current in spin valves and magnetic tunnel junctions. *Materials Research Society Bulletin*, **31**, 389–394.

Parkin, S.S.P., Kaiser, C., Panchula, A., *et al*. (2004). Giant tunneling magnetoresistance at room temperature with MgO (100) tunnel barriers. *Nature Materials*, **3**, 862–867.

Sharma, M., Wang, S.X. and Nickel, J.H. (1999). Inversion of spin polarization and tunneling magnetoresistance in spin-dependent tunneling junctions. *Physical Review Letters*, **82**, 616–619.

Slonczewski, J.C. (1989). Conductance and exchange coupling of two ferromagnets separated by a tunneling barrier. *Physical Review B*, **39**, 6995.

Stearns, M.B. (1977). Simple explanation of tunneling spin-polarization of Fe, Co, Ni and its alloys. *Journal of Magnetism and Magnetic Materials*, **5**, 167–171.

Stiles, M.D. (1996). Spin-dependent interface transmission and reflection in magnetic multilayers. *Journal of Applied Physics*, **79**, 5805–5810.

Stroscio, J.A., Pierce, D.T., Davies, A., *et al*. (1995). Tunneling spectroscopy of bcc (001) surface states. *Physical Review Letters*, **75**, 2960–2963.

Tedrow, P.M. and Meservey, R. (1971). Spin-dependent tunneling into ferromagnetic nickel. *Physical Review Letters*, **26**, 192–195.

Tedrow, P.M. and Meservey, R. (1973). Spin polarization of electrons tunneling from films of Fe, Co, Ni, and Gd. *Physical Review B*, **7**, 318–326.

Tiusan, C., Faure-Vincent, J., Bellouard, C., *et al*. (2004). Interfacial resonance state probed by spin-polarized tunneling in epitaxial Fe/MgO/Fe tunnel junctions. *Physical Review Letters*, **93**, 106602.

Tiusan, C., Sicot, M., Faure-Vincent, J., *et al*. (2006). Static and dynamic aspects of spin tunnelling in crystalline magnetic tunnel junctions. *Journal of Physics: Condensed Matter*, **18**, 941–956.

Tsymbal, E.Y. and Belashchenko, K.D. (2005). Role of interface bonding in spin-dependent tunneling. *Journal of Applied Physics*, **97**, 10C910.

Tsymbal, E.Y., Mryasov, O.N. and LeClair, P.R. (2003). Spin-dependent tunneling in magnetic tunnel junctions. *Journal of Physics: Condensed Matter*, **15**, R109–R142.

Tsymbal, E.Y., Oleinik, I.I. and Pettifor, D.G. (2000). Oxygen-induced positive spin polarization from Fe in the vacuum barrier. *Journal of Applied Physics*, **87**, 5230–5232.

Tsymbal, E.Y. and Pettifor, D.G. (1997). Modelling of spin-polarized electron tunnelling from 3*d*-ferromagnets. *Journal of Physics: Condensed Matter*, **9**, L411–L417.

Tsymbal, E.Y. and Pettifor, D.G. (1998). Spin-polarized electron tunneling across a disordered insulator. *Physical Review B*, **58**, 432–437.

Tsymbal, E.Y. and Pettifor, D.G. (2001). Perspectives of giant magnetoresistance. In *Solid State Physics*, Ehrenreich, H. and Spaepen, F. (Eds.), Academic Press, pp. 113–237, Vol. 56.

Tsymbal, E.Y., Sokolov, A., Sabirianov, I.F. and Doudin, B. (2003). Resonant inversion of tunneling magnetoresistance. *Physical Review Letters*, **90**, 186602.

Tusche, C., Meyerheim, H.L., Jedrecy, N., *et al*. (2005). Oxygen-induced symmetrization and structural coherency in Fe/MgO/Fe(001) magnetic tunnel junctions. *Physical Review Letters*, **95**, 176101.

Vedyayev, A., Bagrets, D., Bagrets, A. and Dieny, B. (2001). Resonant spin-dependent tunneling in spin-valve junctions in the presence of paramagnetic impurities. *Physical Review B*, **63**, 064429.

Vedyayev, A., Ryzhanova, N., Lacroix, C., *et al*. (1997). Resonance in tunneling through magnetic wave tunnel junctions. *Europhysics Letters*, **39**, 219.

Velev, J.P., Belashchenko, K.D., Jaswal, S.S. and Tsymbal, E.Y. (2007). Effect of O vacancies on spin-dependent tunneling in Fe/MgO/Fe magnetic tunnel junctions. *Applied Physics Letters*, **90**, 072502.

Velev, J.P., Belashchenko, K.D., Stewart, D.A., *et al*. (2005). Negative spin polarization and large tunneling magnetoresistance in epitaxial Co/$SrTiO_3$/Co magnetic tunnel junctions. *Physical Review Letters*, **95**, 216601.

Velev, J.P., Belashchenko, K.D. and Tsymbal, E.Y. (2006). Destructive effect of disorder and bias voltage on interface resonance transmission in symmetric tunnel junctions. *Physical Review Letters*, **96**, 119601.

Vescovo, E., Rader, O., Redinger, J., *et al*. (1995). 2-dimensional spin-polarized states of Ag on Fe(100). *Physical Review B*, **51**, 12418–12424.

Wang, Y., Lu, Z-Y., Zhang, X-G. and Han, X.F. (2006). First-principles theory of quantum well resonance in double barrier

magnetic tunnel junctions. *Physical Review Letters*, **97**, 087210.

Wu, Y.Z., Schmid, A.K. and Qiu, Z.Q. (2006). Spin-dependent quantum interference from epitaxial MgO thin films on Fe(001). *Physical Review Letters*, **97**, 217205.

Wunnicke, O., Papanikolaou, N., Zeller, R., *et al*. (2002). Effects of resonant interface states on tunneling magnetoresistance. *Physical Review B*, **65**, 064425.

Xu, P.X., Karpan, V.M., Xia, K., *et al*. (2006). Influence of roughness and disorder on tunneling magnetoresistance. *Physical Review B*, **73**, 180402.

Yuasa, S., Fukushima, A., Kubota, H., *et al*. (2006). Giant tunneling magnetoresistance up to 410% at room temperature in fully epitaxial Co/MgO/Co magnetic tunnel junctions with bcc Co(001) electrodes. *Applied Physics Letters*, **89**, 042505.

Yuasa, S., Nagahama, T., Fukushima, A., *et al*. (2004). Giant room-temperature magnetoresistance in single-crystal Fe/MgO/Fe magnetic tunnel junctions. *Nature Materials*, **3**, 868–871.

Yuasa, S., Nagahama, T. and Suzuki, Y. (2002). Spin-polarized resonant tunneling in magnetic tunnel junctions. *Science*, **297**, 234.

Zhang, X-G. and Butler, W.H. (2003). Band structure, evanescent states, and transport in spin tunnel junctions. *Journal of Physics: Condensed Matter*, **15**, R1603–R1639.

Zhang, X-G. and Butler, W.H. (2004). Large magnetoresistance in bcc Co/MgO/Co and FeCo/MgO/FeCo tunnel junctions. *Physical Review B*, **70**, 172407.

Zhang, X-G., Butler, W.H. and Bandyopadhyay, A. (2003). Effects of the iron-oxide layer in Fe-FeO-MgO-Fe tunneling junctions. *Physical Review B*, **68**, 092402.

Zhang, C., Zhang, X-G., Krstic, P.S., *et al*. (2004). Electronic structure and spin-dependent tunneling conductance under a finite bias. *Physical Review B*, **69**, 134406.

Geometry-driven Magnetoresistance

Stuart A. Solin[1] and L. Ramdas Ram-Mohan[2]

[1] *Washington University in St. Louis, St. Louis, MO, USA*
[2] *Worcester Polytechnic Institute, Worcester, MA, USA*

1 INTRODUCTION

The continuing technological demand for high sensitivity, fast, and inexpensive magnetic macro and nanosensors for use in a number of applications including ultrahigh-density magnetic recording (Childress and Fontaua, 2005), medical instrumentation (Rinck, 1993), consumer electronics (Fraden, 1993), machine tool positioning (Kuze and Shibasaki, 1997), and for rotation and speed sensing in vehicles (Heremans, 1997), has, during the past two decades, stimulated an extensive worldwide research effort to improve the properties of magnetic sensors in general and magnetic nanosensors in particular. The natural focus of this research has been on materials and material structures that exhibit significant magnetoresistance (MR) at room temperature.

Two classes of fundamental physical phenomena that give rise to MR have received the overwhelming bulk of this research attention. One which is based on spintronic effects associated with the perturbation to the interfacial spin-dependent scattering cross section (Dieny, 1994) by the applied magnetic field, usually in layered structures composed of ferromagnetic metals, nonmagnetic metals and/or nonmagnetic insulators, gives rise to the well-known giant magnetoresistance (GMR) (Egelhoff, 1995) and tunneling magnetoresistance (TMR) (Mitra *et al*., 2001) effects that have been addressed elsewhere in this volume. The other which is based on the change in resistance associated with a bulk magnetic phase transition is responsible for the colossal magnetoresistance (CMR) (Rao and Raveau, 1998) effect. While GMR has had huge technological impact in the form of read-head sensors in modern computer hard disk drives (Daughton and Chen, 1993) and TMR represents the next generation read-head device (Song *et al*., 2000), CMR has and is unlikely to have a concomitant effect because it requires relatively low temperatures and high magnetic fields to exhibit acceptable sensing properties (Rao and Raveau, 1998).

The high sensitivity of magnetic devices exhibiting GMR, TMR, and CMR is based on the physical or intrinsic contributions to the MR (Popovic, 1991). Such physical contributions involve the dependence of carrier mobility, energy-band structure, spin−spin interactions and carrier concentration on the applied magnetic field. However, the magnetotransport property of any physical object also depends on a geometric contribution (Popovic, 1991). These geometric contributions depend on the shape of the device, the location of the contacts, and the location, shape, and relative conductivity of any macroscopic or nanoscopic inhomogeneities that might be present in the device structure. For most of the familiar MR devices such as those based on GMR, TMR or CMR, it is the physical contribution that dominates the

Handbook of Magnetism and Advanced Magnetic Materials. Edited by Helmut Kronmüller and Stuart Parkin. Volume 5: *Spintronics and Magnetoelectronics*. ISBN: 978-0-470-02217-7.

transport properties. Nevertheless, it has been recently shown that by judicious design of simple structures, the geometric contribution can be made to play an important, indeed even dominant role (Lee, Wingreen, Solin and Wolff, 1994; Lee, Solin and Hines, 1993; Thio and Solin, 1998; Thio *et al*., 1998a,b; Solin, Thio, Hines and Heremans, 2000). An example of the former is the phenomenon of ballistic magnetoresistance (BMR) while an example of the latter is extraordinary magnetoresistance (EMR). It is these two unconventional phenomena that we address in this chapter. To facilitate an in-depth discussion of EMR and BMR it is useful to illustrate the impact of geometry on magnetotransport with a succinct example.

To establish the magnetotransport properties of a material it is usual to perform a measurement of the Hall effect (Seeger, 1985; Popovic, 1991) by fabricating a Hall bar structure from (what is assumed to be) homogeneous material as indicated in Figure 1(a). Here, a bias current is applied along the x axis, the Hall voltage is measured along the y axis and the magnetic field is applied along the z axis (e.g., into the plane of the figure). One can also employ the Hall bar to measure the MR along the x axis. Now assume that the material being measured has one dominant carrier, say electrons whose mobility is typically much larger than that of holes (Zawadzki, 1974), and assume that these carriers have a δ-function velocity distribution, for example, they all move with the same velocity, the drift velocity. On application of a magnetic field, there will be a transient period during which the electrons are deflected, by the Lorentz force, to one side of the Hall bar. Eventually, a steady state excess of electrons will accumulate on one side of the Hall bar to form a negative space charge. This space charge generates a Hall field as indicated in Figure 1(a), and the force on the carriers from the Hall field just counter balances the Lorentz force. Thus, after the short transient during which the space charge is developed, there is no net force in the y direction and the current flows unperturbed along the x axis. Then, no current flows in the y direction and the x current is independent of the magnetic field. In this case, the MR $\Delta\rho(H)/\rho_0 \equiv [\rho(H) - \rho_0]/\rho_0 \equiv 0$, where H is the applied field, $\rho(H)$ is the field-dependent resistivity, and $\rho_0 = \rho(H = 0)$.

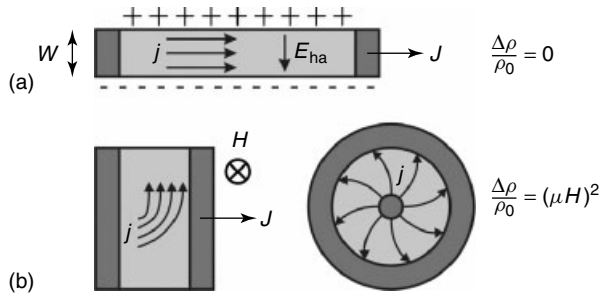

Figure 1. (a) A schematic representation of a Hall bar with the semiconductor region in dark gray and the metallic contacts in light gray. The current density, magnetic field are represented by J, H, and E_{ha}, respectively. For the conduction model discussed in the text, the magnetoresistance of this structure measured along the long axis is identically zero. (b) A schematic representation of a Corbino disk structure. For the conduction model discussed in the text, the magnetoresistance of this structure is $(\mu H)^2$ where μ is the carrier mobility.

Now consider the measurement configuration shown in Figure 1(b). Here the same material employed in Figure 1(a) is arranged in a so-called Corbino disk (Kleinman and Schawlow, 1960) with a cylindrical inner electrode and a concentric outer electrode between which is embedded the material to be measured. Current flows from the inner to the outer electrode or vice versa and the magnetic field is applied normal to the plane of the disk. Since the outer electrode is an equipotential, no asymmetric space charge can build up on its surface. Therefore, no Hall field develops to quench the effect of the Lorentz force on the carriers, which now follow a curved path to the outer electrode. The larger the applied field, the longer is this path and the higher is the field-dependent resistance of the disk. In this case, the MR is given by $\Delta\rho/\rho_0 = \mu^2 H^2$ where μ is the dominant carrier mobility (Popovic, 1991). The MR of the Corbino disk structure can be quite large, depending on the magnitudes of μ and H.

Obviously, the only difference between the measurements depicted in Figures 1(a) and (b) is in the geometry of the contact configurations since the intrinsic material properties are the same for both measurements. Moreover, for a homogeneous material with a two-contact configuration, it can be shown using the Onsager relations (Streater, 1999) that the maximum MR is obtained with a Corbino disk or its topological equivalent (Thio *et al*., 1998), for example, an electrode within an electrode but not constrained to cylindrical symmetry. Now that we have illustrated the general impact of geometry on magnetotransport, we will address specific examples in the following discussions of EMR and BMR.

2 EXTRAORDINARY MAGNETORESISTANCE

2.1 Background

During the course of their attempted study of a one-dimensional Mott transition in GaAs/$Ga_{1-x}Al_xAs$ superlattices, Solin and coworkers observed a room-temperature MR that was quadratic in the magnetic field, similar to that of a Corbino disk but much larger, and characterized the effect as GMR despite the fact that the system was

composed of nonmagnetic materials (Solin and Lee, 1995). Indeed, the effect was also larger than the GMR that is normally associated with ferromagnetic/metallic multilayers. Realizing that if the material in the Corbino structure was inhomogeneous and/or contained more than two contacts, then the 'Corbino maximum' MR could be exceeded, they quantitatively accounted for their observations by attributing the GMR to Corbino-like regions associated with interface fluctuations in the superlattice structure but with three or more isolated contacts on the outer edge of the disk.

Reasoning that for a given H, maximal MR is achieved with a material of maximum μ because, for semiconductors, μ is inversely proportional to carrier effective mass, m*, and m* is proportional to the energy gap, Solin, Thio and Hines (2000) concluded that narrow-gap materials were attractive candidates for nonmagnetic MR devices (Solin *et al*., 1999). They therefore launched a series of studies (Thio and Solin, 1998; Thio *et al*., 1998a,b) of $Hg_{1-x}Cd_xTe$ a material with an x-dependant gap that could be tuned through zero (Dornhaus and Nimtz, 1976). This nonmagnetic material also exhibited GMR (Thio and Solin, 1998; Thio *et al*., 1998a,b) which was associated with the presence of phase separated Hg precipitates that acted as metallic inhomogeneities but in a symmetric four-contact van der Pauw disc configuration (Wolfe, Stillman and Rossi, 1972) such as that shown in the inset of Figure 2. Clearly, it was much more desirable to control the shape and properties of the metallic inhomogeneity by lithographic patterning than to rely on nature. Accordingly, Solin *et al*. focused on InSb, a high-mobility narrow-gap semiconductor, which when patterned into vdP disks with concentric metallic inhomogeneities yielded such a large room-temperature MR (Solin, Thio, Hines and Heremans, 2000) that it was dubbed EMR (Solin *et al*., 2002a).

2.2 EMR in internally shunted circular macroscopic structures – experimental results

The proof of principal demonstration of EMR was accomplished with symmetric four-probe macroscopic vdP disc structures such as the one depicted in Figure 2 inset. Structures of this type are referred to as metal–semiconductor hybrids (MSH). The centered vdP disks which had an outer radius of 1 mm were prepared from metal organic vapor phase epitaxy (MOVPE) grown epilayers of Te-doped n-type InSb (Solin, Thio, Hines and Heremans, 2000). A buffer layer of 200 nm undoped InSb was grown on a 4 in semi-insulating GaAs substrate (resistivity $>1 \times 10^{17}\,\Omega\,\mathrm{cm}$). A 1.3 µm active layer of InSb (concentration $n = 2.11 \times 10^{16}\,\mathrm{cm}^{-3}$and mobility $\mu = 40\,200\,\mathrm{cm}^2\,\mathrm{Vs}^{-1}$) was deposited on the buffer layer and capped by a 50-nm InSb contacting

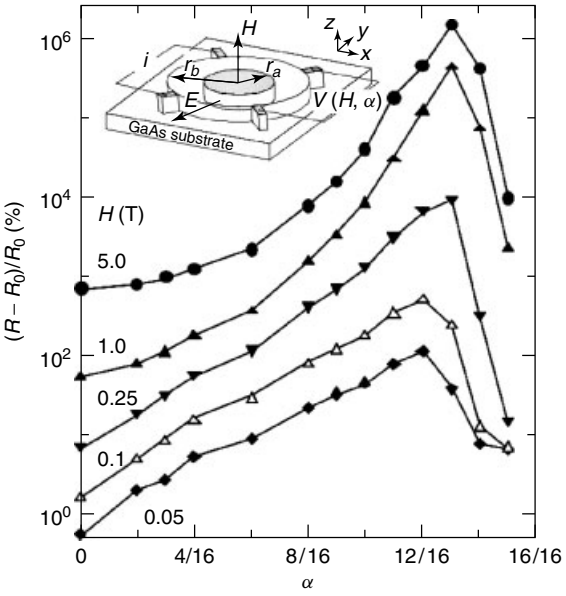

Figure 2. The field dependence of the magnetoresistance, $(R - R_0)/R_0$, of a Te-doped InSb van der Pauw disk of radius r_b in which is embedded a concentric right circular cylinder of Au of radius r_a. The filling factor is $a = r_a/r_b$. Inset: a schematic diagram of the hybrid disk structure. (Reprinted with permission Solin *et al*., copyright 2000, AAAS.)

layer ($n \sim 1.5 \times 10^{17}\,\mathrm{cm}^{-3}$). This epitaxial sequence was passivated by a 200 nm layer of Si_3N_4. The wafers were photolithographically patterned into chips bearing mesas for the vdP disks. The internal circular shunt embedded in the disk, together with the mesa contact pads were simultaneously metallized with a Ti/Pt/Au stack, with Au the dominant component. Additional details of the sample preparation and measurement are given elsewhere (Solin and Zhou, 2001).

Solin *et al*. also showed that in general,

$$EMR\,(\Delta H, H_{\mathrm{bias}}) = \frac{R^{\mathrm{eff}}\,(\Delta H + H_{\mathrm{bias}}) - R^{\mathrm{eff}}\,(H_{\mathrm{bias}})}{R^{\mathrm{eff}}\,(H_{\mathrm{bias}})} \quad (1)$$

where ΔH is the applied (signal) field normal to the plane of the device, $R^{\mathrm{eff}}(H)$ is the effective field-dependent resistance measured in a four-probe configuration, H_{bias} is the bias field and ΔH is the applied or signal field (not the field gradient; Solin, 2005). For small signals

$$EMR\,(\Delta H \to 0, H_{\mathrm{bias}}) = \left[\frac{1}{R^{\mathrm{eff}}\,(H_{\mathrm{bias}})}\right] \times \left[\frac{\mathrm{d}R^{\mathrm{eff}}(H)}{\mathrm{d}H}\right]_{H_{\mathrm{bias}}} \Delta H \quad (2)$$

where $\left[\mathrm{d}R^{\mathrm{eff}}\,(H)\,/\mathrm{d}H\right]_{H_{\mathrm{bias}}}$ is the current sensitivity. In the zero bias large signal but still low field limit, $\mu\Delta H \ll 1$, the EMR can be defined relative to either the zero-field resistance

or to the minimum resistance, the latter definition yielding the larger value which is comparable to the usual definition of MR adopted by the GMR community (Levy, 1994). Thus,

$$EMR(\Delta H) = \frac{R^{\text{eff}}(\Delta H) - R_j^{\text{eff}}}{R_j^{\text{eff}}} = G_j^{\text{S}}(\Delta H)\,[\mu \Delta H]^2 + G_j^{\text{AS}}(\Delta H)\,[\mu \Delta H] \quad j = 0, \min \tag{3}$$

Here $G_j^{\text{S}}(\Delta H)$ and $G_j^{\text{AS}}(\Delta H)$ are, respectively, symmetric and antisymmetric geometric factors which depend on the shape, location, and physical properties of the conducting inhomogeneity and contacts. (For the symmetric structure shown in the inset of Figure 2, $G_{\text{AS}}(\Delta H) = 0$.) Clearly, narrow-gap high-mobility semiconductors such as InSb and InAs are choice materials for EMR devices (Madelung, 1991).

The room-temperature magnetotransport properties of the macroscopic vdP structure shown in the inset of Figure 2 are shown in the main panel of Figure 2 as a function of the radius ratio $\alpha = r_a/r_b$, where r_a is the variable radius of a cylindrical embedded Au inhomogeneity and r_b is the fixed radius of the bulk thin film Te-doped InSb matrix. As can be seen from Figure 2, the room-temperature EMR is of order 10^6% at an applied field of 5 T. More importantly, the EMR exceeds 100% at the low field of 0.05 T. Values as high as 600% at 0.05 T have been achieved with galvanomagnetically equivalent externally shunted rectangular vdP plate structures (Zhou, Solin and Hines, 2000).

The EMR phenomenon can be readily understood using a simple though nonintuitive classical physics analysis based on diffusive transport (Seeger, 1985). The magnetoconductivity tensor for the semiconductor in the axial configuration shown in the inset of Figure 2 is

$$\sigma\,(H) = \begin{bmatrix} \dfrac{\sigma}{1+\beta^2} & \dfrac{-\sigma\beta}{1+\beta^2} & 0 \\ \dfrac{+\sigma\beta}{1+\beta^2} & \dfrac{\sigma}{1+\beta^2} & 0 \\ 0 & 0 & \sigma \end{bmatrix} \tag{4}$$

with σ being the dc conductivity and $\beta = \mu H$. If the electric field on the vertical surface of the inhomogeneity is $\vec{E} = E_x\hat{x} + E_y\hat{y}$, the current density is $\vec{J} = \underline{\sigma\,(H)}\vec{E}$. The electric field is everywhere normal to the equipotential surface of a highly conducting inhomogeneity. At $H = 0$, $\underline{\sigma\,(H)}$ is diagonal so $\vec{J} = \sigma\vec{E}$ and the current flows into the inhomogeneity which acts as a short circuit. At high $H(\beta > 1)$, the off-diagonal components of $\underline{\sigma\,(H)}$ dominate so $\vec{J} = (\sigma/\beta)\left[E_y\hat{x} - E_x\hat{y}\right]$ and $\vec{J} \perp \vec{E}$. Equivalently, the Hall angle (Popovic, 1991) between the electric field and the current density approaches 90°, and the current becomes tangent to, that is, deflected around, the inhomogeneity. Thus, the inhomogeneity acts as an *open circuit*. The transition of the inhomogeneity from short circuit at low H to open circuit at high H results in a geometric enhancement of the MR of the semiconductor even if its resistivity (conductivity) is field-independent (i.e., the physical MR is zero).

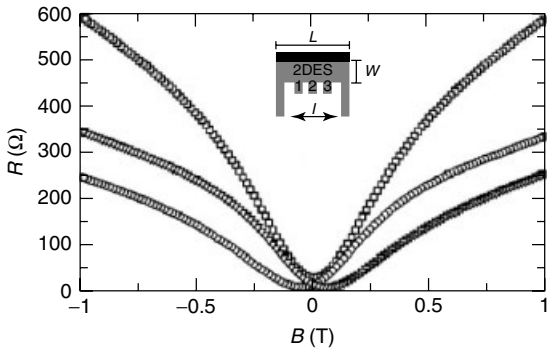

Figure 3. Resistance of an EMR van der Pauw plate device with W 520 mm at 4.2 K before illumination to increase carrier density by the persistent photo effect. (□) represents the data set of the symmetric configuration $R_{1,3}$. −(▽) and (○) symbolize the asymmetric ones, $R_{2,3}$ and $R_{1,2}$, respectively. Inset: a schematic diagram of the EMR device with the semiconductor in gray and the metal in black. (Reprinted with permission Moeller *et al*., copyright 2002, American Institute of Physics.)

Following the demonstration of EMR in macroscopic InSb–Au MSHs, Grundler and coworkers demonstrated low temperature (4.2 K) EMR in microscopic MSHs with dimensions of order 100 µm constructed from an InAs/InGaAs two-dimensional electron gas (2DEG) contacted by Au electrodes and a Au shunt (Moeller *et al*., 2002). This choice of materials provided an extremely low specific contact resistance of $10^{-8}\,\Omega\,\text{cm}^2$ which is important for technological applications. The results of Grundler and coworkers are shown in Figure 3 which depicts the field dependence of the resistance of their devices which were rectangular analogues of off-centered vdP disks (see further discussion in the subsequent text). They achieved an EMR as high as 115 000% at a field of 1 T (Moeller *et al*., 2002). In addition, they showed that the transport properties of low temperature EMR devices based on a 2DEG could be tailored for applications by manipulating the carrier mobility, density, and the geometry of the device. Moreover, they confirmed that EMR was due to current reallocation as outlined in the model proposed by Solin, Thio, Hines and Heremans (2000).

2.3 EMR in circular macroscopic structures – theoretical analysis

The centered vdP structure shown in the inset of Figure 2 was selected, in part, because its high symmetry allows one to readily obtain an analytic solution for the electric field

and current distribution by solving the Laplacian boundary value problem (Zhou, Solin and Hines, 2000). Indeed, this same construct and the analytic solution was first employed by Wolfe, Stillman and Rossi (1972) to explain the unusually large mobility exhibited by inhomogeneous GaAs. A similar approach was used by Solin *et al*. to analytically calculate the magnetotransport properties of the centered vdP disks with a series of discrete but increasing geometric factors with $0 \leq \alpha \leq 15/16$ (Zhou, Hines and Solin, 2001).

In Figure 4(a) is shown the room-temperature field dependence of the resistance of a series of InSb–Au vdP disks of the type and measuring configuration shown in the inset of Figure 2. This is the raw data from which the curves shown in Figure 2 were deduced. The corresponding plots shown in Figure 4(b) were obtained from the above-described solution to the Laplacian boundary value problem *with no adjustable parameters* (Zhou, Hines and Solin, 2001; Wolfe, Stillman and Rossi, 1972). As can be seen by comparing Figures 4(a) and (b), the calculated curves are in quantitative agreement with the measurements with one notable exception. The curve for $\alpha = 0$, for example, for the response of an un-shunted semiconductor shows a small MR effect as evidenced by the concave curvature near $\mathrm{H} = 0$ whereas the calculated curve for $\alpha = 0$ is flat. The origin of this discrepancy is the fact that the small MR for $\alpha = 0$ is due to the physical contribution which has not been including in the analytic calculation. This also highlights the clear dominance of the geometric contribution at higher values of α.

An alternate and more versatile approach to the calculation of the magnetotransport properties of EMR structures is the finite element method (FEM) (Ram-Mohan, 2002). The coauthors and their colleagues have shown that FEM is the ideal approach to modeling EMR since it can account for the spatially varying properties of arbitrarily shaped hybrid structures (Moussa *et al*., 2001). This method can also accommodate every type of boundary condition at interfaces and at boundaries/edges. In this case, the governing relation is the constitutive relation between the current and the field: $j_i = \sigma_{ij}(H)E_j$. With $E_i = -\partial_i \phi$, the current continuity condition takes the form $\partial_i \left(\sigma_{ij}\partial_j \phi(x, y)\right) = 0$. This partial differential equation has been solved using the FEM (Moussa *et al*., 2001) together with an approach based on the principle of least action (Zienkiewicz and Taylor, 1994; Hughes, 1987). In the EMR case, the action integral is given by

$$A = \frac{1}{2}\iint \mathrm{d}x\,\mathrm{d}y\,(\partial_i \phi(x, y))\sigma_{ij}(\partial_j \phi(x, y)) + \int_{\Delta_1} \mathrm{d}l\left[\phi(x, y)\right]|_{\Delta_1} j_{\mathrm{in}} - \int_{\Delta_2} \mathrm{d}l\left[\phi(x, y)\right]|_{\Delta_2} j_{\mathrm{out}} \quad (5)$$

where the current boundary conditions at the leads are easily incorporated into the calculations. The action is defined with an integral over time of the Lagrangian. Here the system is represented in the steady state. Consequently, the integral over time is suppressed for convenience. The double integral in equation (5) is just the electrostatic energy in the system. The presence of the field-dependent conductivity tensor poses no issue. In the FEM, the physical region is subdivided into triangles and action is evaluated in each triangle by representing the potential in terms of interpolation polynomials multiplied by unknown coefficients. On integrating the spatial dependence, the action is expressed as a binomial in the nodal coefficients with

$$A = \frac{1}{2}\phi_\alpha M_{\alpha\beta}\phi_\beta + \int_{\Delta_1} \mathrm{d}l\left[\phi(x, y)\right]|_{\Delta_1} j_{\mathrm{in}} - \int_{\Delta_2} \mathrm{d}l\left[\phi(x, y)\right]|_{\Delta_2} j_{\mathrm{out}} \quad (6)$$

The variational principle then leads to a matrix equation representing the discretized differential equation. This is solved for the unknown nodal values of the potential function. With no adjustable parameters, using the standard inputs for the conductivity of Au and InSb in the FEM calculations, excellent agreement is obtained between the experimental magnetotransport (or EMR) and its theoretically predicted values, as shown in Figure 4(c). The field-dependent current flow patterns for the centered vdP disk can also be determined from the FEM as indicated in Figures 5(a) and (b) (Moussa *et al*., 2001). Notice from Figure 5(a) that for zero field, current flows into the shunt along paths that are normal to the metal–semiconductor interface, whereas at high field current is mostly ejected from the shunt along paths that are approximately tangent to the interface.

2.4 Externally shunted rectangular EMR macroscopic structures based on conformal mapping

The centered vdP structure shown in the inset of Figure 2 is not compatible with the scaling of EMR devices to the nanoscale regime for applications such as read-head sensors because of the difficulty of fabricating and filling nanoscopic holes. However, one can use the concept of bilinear conformal mapping (Churchill, 1960) to generate structures that will exhibit EMR and at the same time will be compatible with nanoscale fabrication.

It is known (Popovic, 1991; Solin, 2004; Zhou, Hines and Solin, 2001) that any homogeneous device with a circular boundary of unit radius in the two-dimensional complex t plane with orthogonal axes r and is where $t = r + is$ can be

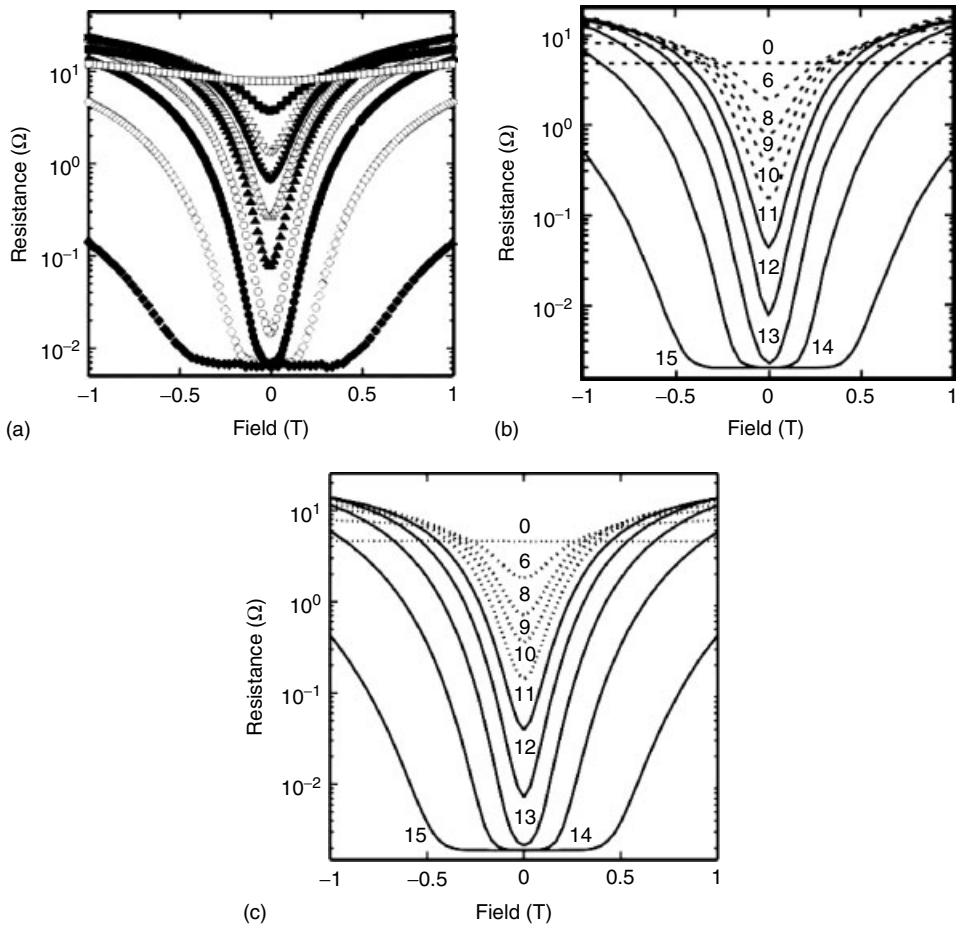

Figure 4. (a) The measured room-temperature field-dependent resistance up to 1 T of a composite van der Pauw disk of Te:InSb and Au for a number of values of $\alpha = r_a/r_b$. This is the data that was used to compute the EMR shown in Figure 2. The data traces in the region of zero field correspond (top to bottom) to increasing α in the following steps: $16\alpha = 0, 6, 8, 9, 10, 11, 12, 13, 14, 15$. (b) Field-dependent resistance calculated analytically using Laplace's equation with no adjustable parameters. (c) Field-dependent resistance calculated using the finite element method with no adjustable parameters. (Reprinted with permission Solin *et al*., copyright 2000, AAAS and Moussa *et al*., copyright 2001, American Physical Society.)

mapped into the complex upper half Cartesian z plane with orthogonal axes x and iy where $z = x + iy$ (see Figure 6a) by using the bilinear transformation (Popovic, 1991).

$$z(t) = -i\,\frac{t\ +\ i}{t\ -\ i} \tag{7}$$

The preceding mapping equation transforms the four symmetrically spaced electrical contacts on the perimeter of the disk in the t plane (shown in Figure 6a in the configuration for a MR measurement) to the corresponding contacts on the line $y = 0$ in the z plane. Although the mapped contacts are symmetric about the line $x = 0$ they are not of equal size as they are when viewed in the t plane. If one embeds an off-centered hole of radius r_1 into the homogeneous disk of Figure 6(a) as shown in Figure 6(b), that hole maps to a line that truncates the upper half plane at height $y_1 = 1/(r_1 + 1)$. In other words, the vacuum inside the hole of radius r_1 in the disk in the t plane maps to the vacuum above the line y_1 in the z plane. Consider now the circle of radius r_2 which creates an evacuated notch in the disk in the t plane as shown in Figure 6(c). That circle maps to a line which truncates the z plane at the position $x = x_2 = 1/r_2$ as is also shown in Figure 6(c). A symmetrically displaced circle of equal radius on the left of the vertical bisector of the disk in the t plane truncates the z plane with a line at position $-x_2 = -(1/r_2)$ as shown in Figure 6(d). By a selection of circular cuts in the t plane, the truncated disk can be exactly mapped to a rectangular structure of appropriate dimension in the z plane.

Of the structures depicted in Figures 6(a–d), that shown in Figure 6(b) is the simplest one which contains a fully enclosed inhomogeneity, for example, a circular hole displaced from the center of the disk. Zhou, Hines and Solin (2001) showed that if one embeds this hole with a highly

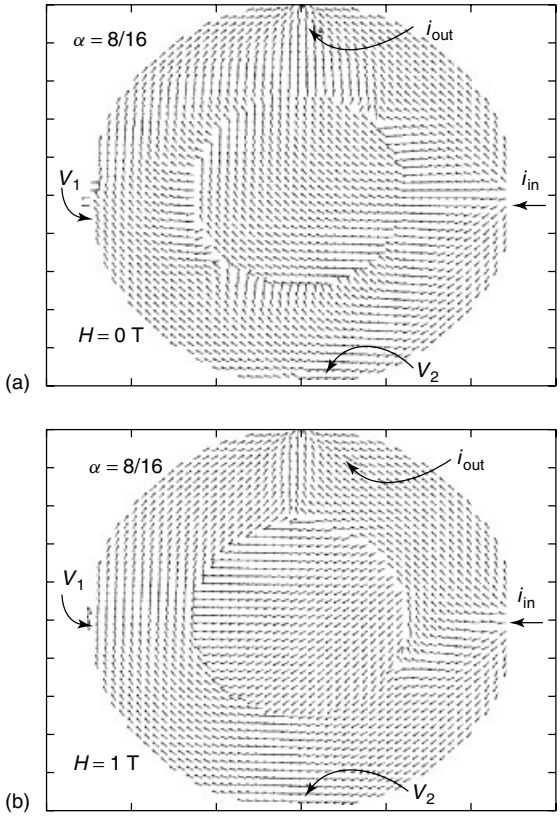

Figure 5. The current flow in the van der Pauw geometry for a circular InSb wafer with a concentric metallic inhomogeneity and $\alpha' = 8/16$, (a) at $H = 0$ and (b) at $H = 1\,\mathrm{T}$. The lengths of the arrows are not to scale. (Reprinted with permission Moussa *et al*., copyright 2001, American Physical Society.)

conducting metal, then the resultant structure which they called an off-center vdP disk is similar to the centered vdP disk which yielded the large EMR values cited in the preceding text. However, the corresponding rectangular mapped structure in the z plane would be of infinite extent in the $+x$ and $-x$ directions and would contain an external shunt of infinite height in the $+y$ direction. To avoid these complications, Solin *et al*. defined a structure which contains not only the r_2 cuts of Figure 6(d) but also an additional circle of radius r_3 in the t plane as shown in Figure 6(e). The latter maps to the line $y = y_3$ in the z plane. The modified off-centered vdP disk now contains a metallic inhomogeneity embedded into the space between the circles of radii r_1, r_2, and r_3 while the space between the circle of radius r_1 and the disk perimeter contains a narrow-gap semiconductor. Thus, the t-plane disk with an *internal* embedded shunt maps to a rectangle in the z plane with a corresponding *external* metallic shunt, which was called a *van der Pauw plate* (Zhou, Hines and Solin, 2001). Moreover, for the exact mapping depicted in Figure 6(e), the galvanomagnetic behavior of the two structures will be identical (Popovic, 1991).

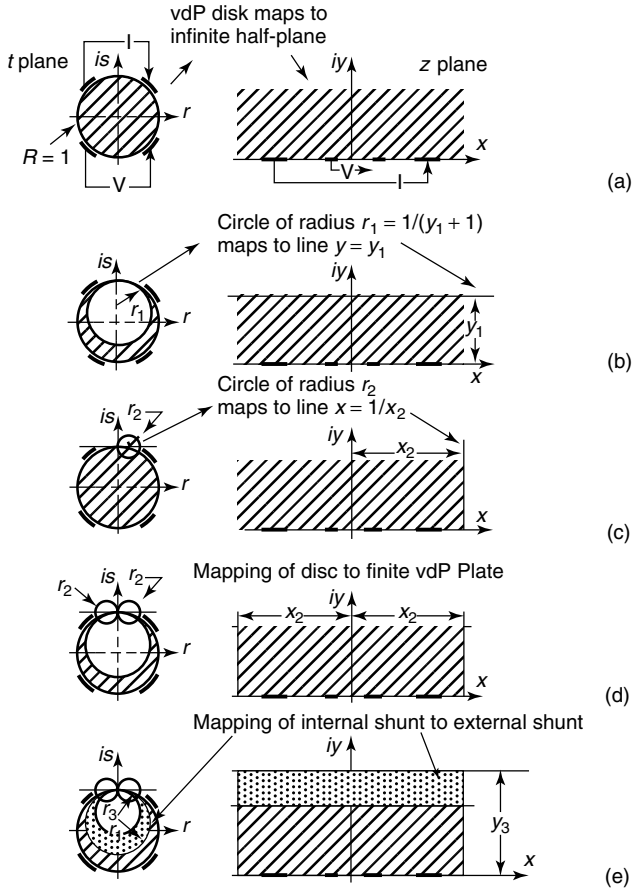

Figure 6. Schematic diagram of bilinear mapping of (a) a van der Pauw disk in the t plane mapped to the upper half space of the z plane. Also shown is the contact configuration for measuring magnetoresistance. (b) an off-center hole in the t plane mapped to a line in the z plane, (c) a circular perimeter cut in the t plane mapped to a line in the z plane, (d) repeat of (c) with a symmetric perimeter cut, (e) an internal shunt in the t plane mapped to an external shunt in the z plane. (Reprinted with permission T. Zhou *et al*., copyright 2001, American Institute of Physics.)

Although the mapping technique described in the preceding text, has been known, (Popovic, 1991) the adaptation of this technique to the design of rectangular structures with external shunts (Zhou, Hines and Solin, 2001) had not been previously considered. Furthermore, for mapped plates with $x_2 > 4$, the cuts represented by the circles of radius r_2 in the left panel of Figure 6(e) are small/negligible. Therefore, the externally shunted plate structure shown on the right panel of Figure 6(e) is, to a good approximation, electrically equivalent to the vdP disk shown in the left panel of Figure 6(e) without the r_2 cuts. Moreover, an expression for the filling factor of the rectangular EMR structure, though more complex than that of the concentric circular structure has been derived as a function of the geometric properties of the structure (Zhou, Hines and Solin, 2001).

In order to confirm that the mapping procedure described in the preceding text is viable it was tested using symmetric and asymmetric four-probe macroscopic vdP plate EMR structures of the type shown in the insets to Figures 7(a) and (b) (Solin, 2005). The results of these tests are shown in the main panels of Figure 7. The material constituents of the vdP plate structures depicted in the insets of Figure 7 were the same as those used for the internally shunted circular hybrid structures depicted in the inset Figure 2. Two features are noteworthy in the data of Figure 7(a) the room-temperature EMR is very large reaching values in excess of 100% at a field of 0.05 T. In Figure 7(b) the EMR is asymmetric with respect to the applied field when the leads are placed asymmetrically on the rectangular narrow-gap semiconductor plate. The latter feature constitutes a condition of self-biasing which is important for a number of applications in which the sign of the applied magnetic field must be determined.

The magnetotransport properties of the externally shunted vdP plate clearly depend strongly on the placement of the current and voltage leads, for example, on lead geometry.

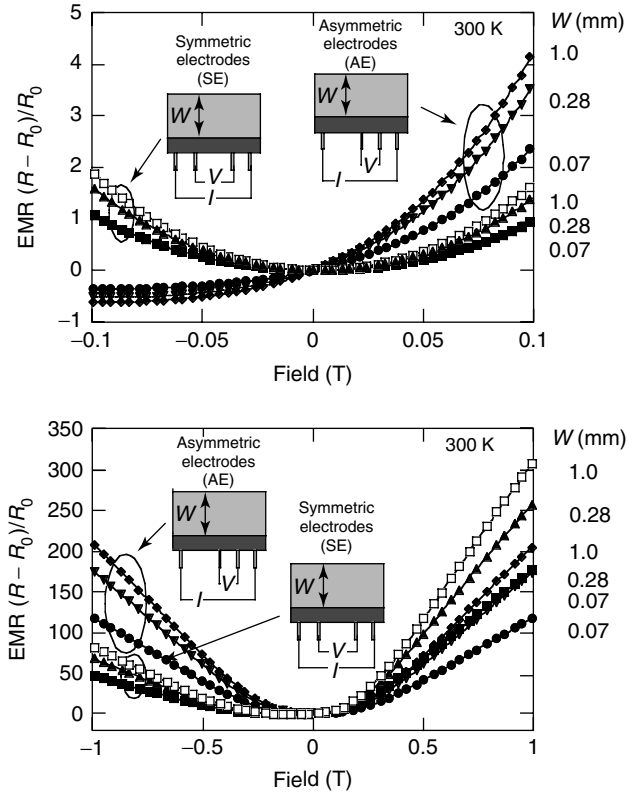

Figure 7. The low field (a) and high field (b) room-temperature EMR of van der Pauw plates with symmetric and asymmetric electrode configurations as a function of the width, W, of the external shunt. The dark (light) rectangle represents Te:InSb (Au). (Adapted from Figure 2 of Solin, 2004.)

These properties also depend strongly on the shape and relative dimensions of the semiconductor and metal components of the hybrid structure itself as can be seen from the dependence of the EMR in Figure 7 on the width, W, of the shunt for a semiconductor region of fixed width. Note that in the range of filling factors addressed in Figure 7 which is below the optimum filling factor of 13/16, as depicted in Figure 3, the EMR systematically increases with increasing filling factor. In addition, an added feature of the data of Figure 7 is the enhancement of the EMR in the structure with asymmetric leads relative to the structure with symmetric lead placement.

Moussa, Ram-Mohan, Rowe and Solin (2003) have used the FEM to calculate the EMR of four-probe vdP plates as a function of the position of a magnetic spot along the long axis of the semiconductor. They showed that the EMR response was strongly dependent on the wiring configuration of the four leads of the vdP plate and on the spot position along the long axis of the plate. For instance, as can be seen from Figure 8, the IVVI configuration gives an asymmetric response for the position dependent MR while the VIVI configuration yields a larger but inverted quasisymmetric response. Holz, Kronenwerth and Grundler (2005a) also employed the FEM to extend the theoretical studies of Moussa, Ram-Mohan, Rowe and Solin (2003). They showed that for an inhomogeneous field of a spot, the field-dependent resistance exhibits a symmetry reversal (*vis-à-vis* symmetric and antisymmetric) relative to that of a homogeneous field and that the active device area depended not only on the voltage probe positions but also on the locations of the current probes.

Holz, Kronenwerth and Grundler (2005a) also developed a clever method for assessing and illustrating the effect of an inhomogeneous field. They defined the MR of a dot as $MR_{\mathrm{dot}} = [R\,(B_{\mathrm{dot}} = +50\,\mathrm{mT}) - R\,(B_{\mathrm{dot}} = -50\,\mathrm{mT})]\,/\,R\,(0)$ and displayed MR_{dot} for different lateral positions as a grey-scale pattern as shown in Figure 9. Holtz *et al.* have also studied the response of vdP plate EMR structures with the FEM to determine the optimal EMR as a function of the geometry, for example, length (L) to width (W) ratio and material parameters (Holz, Kronenwerth and Grundler, 2003). They confirmed the correlation of the asymmetric (symmetric) response with and IVVI (IVIV) lead configuration and found that EMR is optimal for devices with $L/W = 0.025$. Most importantly, they showed (i) that EMR vdP plates are inversely scalable, for example, their performance improves with *decreasing* size, (ii) that the EMR can be further enhanced/optimized by selective placement of the voltage and current leads (Holz, Kronenwerth and Grundler, 2005b), and (iii) that for the IVIV configuration, the Hall effect and EMR cooperate to enhance sensitivity (Holz, Kronenwerth and Grundler, 2005b).

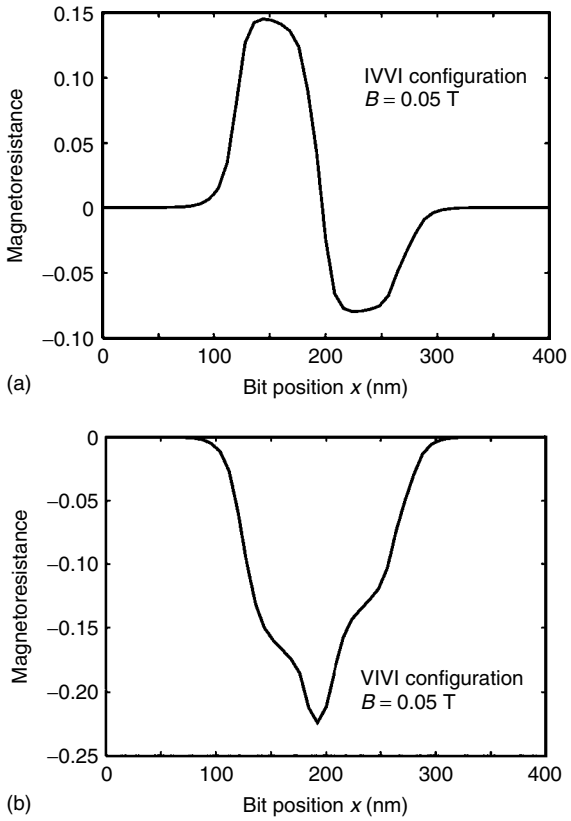

Figure 8. (a) The calculated magnetoresistance of a symmetric van der Pauw plate structure (see insets of Figure 7) as a function of the position of an $80 \times 50\,\mathrm{nm}^2$ magnetic bit with a magnetic field of 0.05 T. The external leads are 20 nm thick, with the leads centered at ± 150 nm and ± 30 nm. The leads are wired in the IVVI configuration. (b) The same as (a) but with the leads wired in the IVIV configuration. (Reprinted with permission Moussa *et al.*, copyright 2003, American Institute of Physics.)

2.5 Nanoscopic EMR devices

Several applications of state-of-the-art magnetic sensors including imaging, medical devices, and read heads for ultrahigh-density magnetic recording require structures with three-dimensional spatial resolution at the nanoscale. In the case of EMR sensors, one requires an ultrathin (<100 nm) film, which can be patterned into device structures with lateral dimensions of order 50 nm. Unfortunately, the mobility of InSb on GaAs (100) drops drastically with thickness for thicknesses below 1000 nm as a result of carrier scattering from dislocations induced by the 14% lattice mismatch (Zhang *et al.*, 2004). To overcome this problem, Solin and coworkers designed a nanoscopic four-lead vdP plate EMR device (Solin *et al.*, 2002a,b) based on an InSb/AlInSb quantum-well heterostructure (Chung *et al.*, 1999) which exhibits relatively high mobility for carriers in the very thin well.

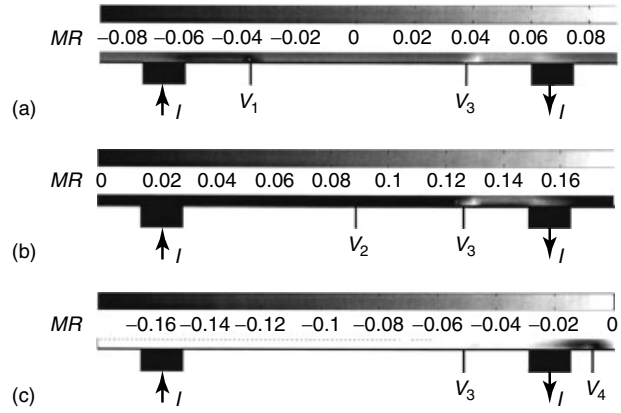

Figure 9. Magnetoresistance, $MR_{\mathrm{dot}} = [R(B_{\mathrm{dot}} = +50\,\mathrm{mT}) - R(B_{\mathrm{dot}} = -50\,\mathrm{mT})]/R(0)$, of the hybrid structure for different voltage probe configurations: (a) $V_1 - V_3$, (b) $V_2 - V_3$, and (c) $V_3 - V_4$ as a function of the dot's position in the semiconductor. For clarity, the metal is not shown here. In each figure, black represents the lowest and white the highest possible value. Note that the dynamic range in each sub figure is the same. (Reprinted with permission M. Holz *et al.*, copyright 2005, American Institute of Physics.)

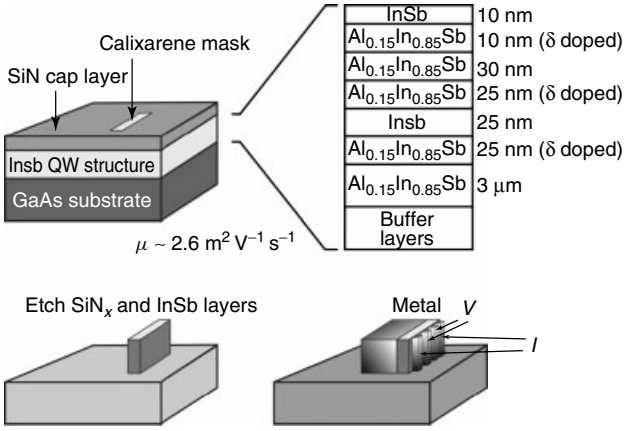

Figure 10. A schematic representation of the process used to fabricate nanoscopic EMR structures.

In Figure 10 is shown schematically the nano-EMR quantum well layer stacking arrangement together with the (simplified) fabrication steps that are required. To achieve lateral feature sizes below 100 nm, a multistep state-of-the-art electron beam (e-beam) lithography process was utilized (Solin *et al.*, 2002a). First, a 30-nm-thick insulating film of Si_3N_4 was deposited on the thin-film-quantum-well wafer as a cap layer and macroscopic Au strips for wire bonding were deposited. Then a 30-nm-thick film of calixarene, a new high-resolution negative resist (Yasin, Hasko and Carecenac, 2001) was spin-coated on. The desired lithographic pattern was delineated in the calixarene by e-beam lithography. This calixarene pattern and the macroscopic Au strips

serve as a mask for reactive ion etching (RIE) (Roosmalen, Baggermann and Brader, 1995) of the Si_3N_4 layer using standard methods (Sugawara, 1998). This etching process produces a raised mesa of the thin film on its supporting substrate. For InSb films, the appropriate etchant is a CH_4+H_2 mixture. The residual Si_3N_4 and Au strips serve as an RIE mask. Au leads and Au bridging contacts were then deposited using a Ge stencil mask and shadow evaporation technique. To minimize leakage current through the floor of the mesa, as evidenced by finite EMR observed in shuntless devices, an insulating Al_2O_3 barrier was first prepared by depositing and subsequently oxidizing a layer of Al close to the mesa sidewall. In addition, extremely high alignment accuracy of about ± 10 nm was required to effect sidewall contacting of the Au strips to mesa at the location of the quantum well.

The above-described e-beam lithographic methods, were used to fabricate the nano-EMR structure shown in Figure 11. The active volume of this structure has dimensions of order the width of the mesa at the height of the quantum well (30 nm) $\times$ the spacing of the voltage probes (40 nm) $\times$ the thickness of the quantum well (25 nm). The field dependence of the room-temperature MR of that device is shown in the main panel and upper-right inset of Figure 12. As can be seen, the EMR reaches values as high as 5% at zero bias and a signal field of 0.05 T. This was claimed to be the highest room-temperature MR level obtained to date for a patterned magnetic sensor with this spatial resolution (Solin*et al*., 2002b). Moreover, with a modest bias field of 0.2 T corresponding to the zero-field offset (Solin *et al*., 1996) in Figure 12, the measured EMR is 35% at a signal field of 0.05 T. (The offset is associated with the asymmetric placement of the voltage leads.) Also, note that the device can be biased into a field region where the EMR response is linear with field, a feature that can simplify signal amplification. Equally significant is the fact that the current sensitivity, at

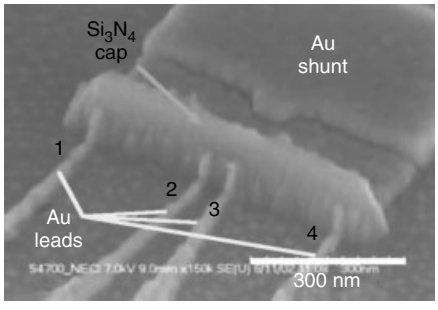

Figure 11. An electron micrograph of a hybrid nanoscopic van der Pauw EMR plate structure fabricated from an InSb/$In_{1-x}Al_xSb$ quantum-well heterostructure. The current leads, voltage leads, and external shunt are labeled as indicated. The four contacts shown in the micrograph extend along the mesa floor and up the side of the mesa to the upper 25 nm $Al_{0.15}In_{0.85}Sb$ barrier. (Adapted from Figure 3 of Solin, 2005.)

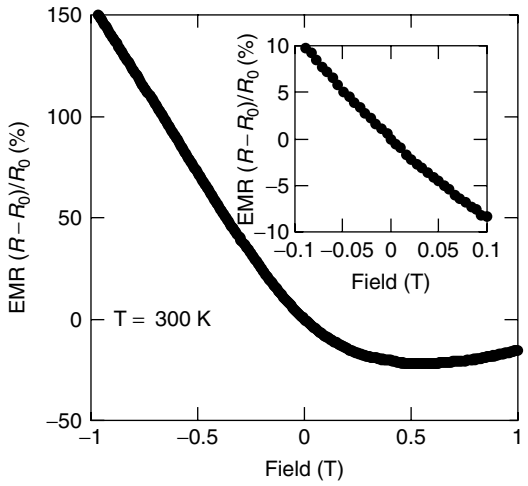

Figure 12. The field dependence of the magnetoresistance of the mesoscopic van der Pauw plate structure shown in Figure 11. The bias current density is 5×10^3 A cm^{-2}.

a magnetic field bias of 0.2 T has a large measured value of 585 Ω T^{-1} at room temperature. It is this figure that enters directly into the calculation of the signal-to-noise ratio (SNR) as will be discussed in the subsequent text.

The room-temperature mean free path of the carriers in an InSb quantum well is $\ell = \hbar\sqrt{2\pi\tilde{n}}(\mu/e) = 200$ nm (Jablonski *et al*., 1984). Thus one would expect the transport in a nanostructure to be ballistic in which case it can be shown that the expected EMR would be at least a factor of 5 lower than what is observed in Figure 12. However, Solin *et al*. have suggested that the transport is in fact still diffusive as a result of the randomization of the carrier velocities due to scattering off of the rough mesa sidewalls (Solin *et al*., 2002a,c) (see Figure 11). The scattering process is enhanced because the roughness wavelength is of the order of the Fermi wavelength of the carriers $\lambda_F = \sqrt{2\pi/\tilde{n}} =$ 48 nm (Jablonski *et al*., 1984). Given the assumption of diffusive transport, the EMR of the nanoscopic device though noteworthy, is still about a factor of 20 lower than that obtained with a macroscopic plate of the same geometry fabricated from thin film Te-doped InSb with a room-temperature mobility of 4.5×10^4 cm^2 Vs^{-1} (Zhou, Hines and Solin, 2001). Part of this difference is due to the mobility difference thus yielding a reduction in EMR of a factor of $(4.5 \times 10^4/2.3 \times 10^4)^2 = 3.8$. The additional order of magnitude reduction derives from current leakage through the mesa floor (quantum well lower barrier) which carries a much higher proportion of the current than does the quantum well itself.

The performance of a magnetic sensor is, of course, measured by the SNR at the operating conditions under which it will be employed. For nano-EMR devices of the

type shown in Figure 11, only two noise sources are relevant, $1/f$ noise and thermal or Johnson noise. In this case, if the effective resistance is quadratic with field, for example, $R^{\text{eff}} = R_0^{\text{eff}}\left[1 + G\mu^2(H - H_0)^2\right]$ where H_0 is the zero-field offset, the voltage SNR can be written in the following form (Weissman, 1988; Solin 2007):

$$SNR(f) = \frac{I_{\text{in}}\left|\left(\frac{\mathrm{d}R^{\text{eff}}}{\mathrm{d}H}\right)_{H_{\text{bias}}}\right|\Delta H}{\left[\left(\frac{V}{L}\right)^2\gamma\mu e R_{\text{out}}\frac{\Delta f}{f} + 4kTR_{\text{out}}\Delta f\right]^{\frac{1}{2}}} = \frac{\left|El[(2G_S\mu^2 H_{\text{Bias}} \pm G_{\text{AS}}\mu)\Delta H]\right|}{\left[\frac{E^2\gamma l}{nwt}\frac{\Delta f}{f} + \frac{4kTl\Delta f}{nwte\mu}\right]^{\frac{1}{2}}} \quad (8)$$

where I_{in} is the input current, V is input voltage, $L(l)$ is the spacing of the current (voltage) leads, γ is the dimensionless Hooge parameter (van der Ziel, 1988), e is the electron charge, f is the operating frequency, Δf is the detection bandwidth, k is Boltzmann's constant, T is temperature in Kelvin, R_{out} is the two terminal resistance between the voltage probes including the contact resistance at the interface between the voltage probes and the device, $E = V/L$ is the bias electric field, l is the voltage probe spacing, n is the carrier (electron) density, wt is the cross-sectional area for bias current flow and the other variables in equation (8) have been previously defined. The first term in each of the denominator brackets is the 1/f noise while the second term is the thermal noise. By equating these two terms we can deduce the crossover frequency $f_c = E^2(\gamma e\mu/4kT)$. For $f \gg f_c$ thermal noise dominates and the SNR is frequency independent, while for $f \ll f_c$ 1/f noise dominates and the SNR is independent of the bias field.

It is useful to estimate the crossover frequency for a nanoscopic EMR sensor of the type shown in Figure 11. The relevant parameters are $\gamma \sim 10^{-8}$, $\mu \sim 2.3 \times 10^4\,\text{cm}^2\,\text{V}^{-1}\,\text{s}^{-1}$, $E \sim 4 \times 10^2\,\text{V cm}^{-1}$ in which case $f_c \sim 400\,\text{Hz}$ at 300 K. Clearly, it is desirable to operate the EMR nanosensor at sufficiently high frequency to be in the thermal noise limited region. Note that l, w, and t are set by the required three-dimensional resolution, and ΔH is set by the available signal so these parameters are deemed uncontrollable.

In the thermal noise regime, the SNR increases as $n\mu^{5/2}$. Therefore, it is advantageous to maximize this product. Since for $n(T) > n_c(T)$ mobility decreases with increasing n (Seeger, 1985), where $n_c(T)$ is a critical concentration, EMR nano sensors operate optimally at or near $n_c(T) = n_c(300\,\text{K})5 \times 10^{17}\,\text{cm}^{-3}$ for InSb (Madelung, 1991). For an EMR nanosensor with this carrier concentration and dimensions shown in Figure 11, the calculated noise equivalent field (NEF) (Deeter, Day, Beahn and Manheimer, 1993) that is obtained from equation (8) by setting $SNR(f) = 1$ and solving for the resultant value of $\Delta H/\sqrt{\Delta f}$ is NEF = $4.1\mu\,\text{T Hz}^{-1/2}$ for a bias current of 2.2×10^{-6} A, a current sensitivity of $585\,\Omega\,\text{T}^{-1}$. For comparison, nano-Hall sensors with active area $50 \times 50\,\text{nm}^2$ made from bismuth have a reported NEF of $100\,\mu\text{T(Hz)}^{-1/2}$ (Sandu, Kurosawa, Dede and Oral 2004), while micron-size Hall devices based on GaAs/AlGaAs quantum wells have been demonstrated in scanning probe systems that show NEF of $4\,\mu\text{T(Hz)}^{-1/2}$, but only at low temperature (<77 K) (Bending, 1999). Also TMR and GMR sensors with flux concentrators show NEF as low as $0.1\,\text{nT(Hz)}^{-1/2}$ at room temperature but this corresponds to spatial resolutions of the order of microns (Stutzke, Russek, Papas and Tondra, 2006).

3 BALLISTIC MAGNETORESISTANCE

3.1 Transport through a point contact

In the BMR phenomenon (Garcia, Munoz and Zhao, 1999), we again see a manifestation of the *geometric* enhancement of the MR. The resistance in a point contact between two ferromagnetic wires, as shown in Figure 13, is governed by quantum-mechanical effects associated with the ballistic transport of electrons from one wire to the other through a channel of nanometer dimensions. The wires can be considered to be reservoirs of electrons with a difference in their chemical potentials due to a bias, so that a current can flow from one side of the device to the other. The actual resistance depends on the size of the diameter at the contact, which is typically over several atomic 'channels' all the way down to a single atomic point contact. Each channel acts as a waveguide for the electron, and the transmission coefficient for the waveguide defines the strength of the contribution for each mode in the waveguide; the transmission coefficient depends strongly on the geometry of the waveguide.

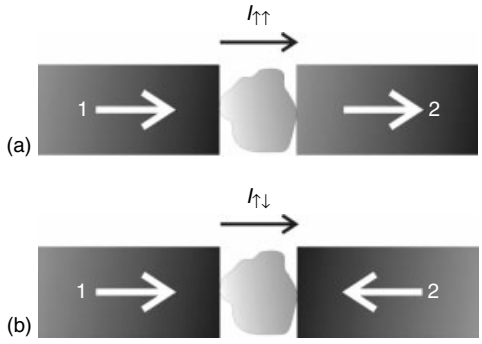

Figure 13. A schematic of a cluster of Ni or Co atoms deposited between two ferromagnetic wires for which the magnetization in the two wires is (a) parallel, or (b) antiparallel.

For normal metallic point contacts with N noninteracting independent channels and with unit transmission, the quantization of the conductance G is described by Landauer (1957, 1970, 1988), and Buttiker, Imry, Landauer and Pinhas (1985) to be

$$G = 2e^2 \frac{N}{h} = \frac{N}{(25.8\,\mathrm{k}\Omega)} \tag{9}$$

Because this result is central to our understanding of BMR we provide, in Appendix A, a detailed derivation of it. The factor of 2 in the conductance formula accounts for the fact that in such metallic contacts electrons of both spin polarization are transported across the contact. For ferromagnetic leads with a point contact between them, the transport of electrons across from one wire to the other is, in general, a spin-dependent process. We are then concerned with *spin*-ballistic transport through the junction. In the case of BMR, the two reservoirs are ferromagnetic and have particular spin polarizations which are either parallel or antiparallel to each other. The unit of conductance is defined by $G_{0\uparrow\uparrow} = e^2/h$, without the factor of 2 of the usual theory that accounts for both electron spins (Ono, Ooka and Miyajima, 1999). In Figure 13, which show a schematic of a BMR contact structure, the magnetization of the two ferromagnetic wires is parallel in configuration (a), and antiparallel in configuration (b). The nanoscale point contact between the wires is represented by a cluster of atoms between the tips of the wires. The switching of the magnetization in the wire labeled 2 on the right can be controlled by an external magnetic field applied to this wire. The conductance of the nanochannel changes with the application of the external magnetic field leading to the BMR which is defined as

$$[\mathrm{BMR}] = \frac{\Delta G}{G} = \frac{G_{\uparrow\uparrow} - G_{\uparrow\downarrow}}{G_{\uparrow\downarrow}} \tag{10a}$$

or equivalently as

$$[\mathrm{BMR}] = \frac{\Delta R}{R} = \frac{R_{\uparrow\downarrow} - R_{\uparrow\uparrow}}{R_{\uparrow\uparrow}} \tag{10b}$$

In 1999, the initial observations (Garcia, Munoz and Zhao, 1999, 2000; Landauer, 1957; Ono, Ooka and Miyajima, 1999; Zhao, Munoz, Tatara and Garcia, 2001) at room temperature were of a BMR of 280% with 3d transition metals (Fe, Co, Ni) using atomic size contacts. These were followed by a BMR of 700% in electrodeposited Ni–Ni nanocontacts of 30 nm (Garcia *et al*., 2001). More recently, Chopra and Hua (2002) have observed a room-temperature BMR of 3150% using electrodeposition of the nanocontact.

The reader should beaware that the experimental evidence for BMR is still in a state of flux because of the difficulties and pitfall with the experiments (Eglekoff *et al*., 2005).

3.2 Theoretical aspects of domain wall scattering

Theoretical considerations suggest that the BMR effect is generated by spin scattering at domain walls (DWs). The presence of a DW in the nanochannel for the antiparallel configuration, then leads to enhanced scattering that depends on the geometry of the contact and the structural (and spatial) details of the DW. The width of the wall depends on the area of contact and the size of the junction. The enhanced scattering in the antiparallel configuration corresponds to the relation

$$G_{\uparrow\uparrow} > G_{\uparrow\downarrow} \tag{11}$$

The early work of Cabrera and Falicov (1974) on the scattering mechanism for an electron scattering off a DW in a bulk material provides a framework to consider the effect of scattering. Their work was based on a classical Boltzmann equation model, and was in the limit that the thickness of the DW, d_w, is much less than the mean free path. It showed that the resistivity is large only when the spin splitting is comparable to the Fermi energy and $k_\mathrm{F} d_\mathrm{w} \leq 1$, where k_F is the Fermi wave vector. A limitation of their work is that it considers only one-dimensional motion for the electrons. Tatara and Fukuyama (1997) treated the three-dimensional motion of the electrons and considered the effect of a DW on the resistivity in a mesoscopic wire of width L_T with the DW thickness $d_\mathrm{w} \geq L_T \gg k_\mathrm{F}^{-1}$. However, again, in this case, the electron spin can accommodate itself adiabatically from one side of the DW to the other. Thus, the reflection of the electron at the wall is negligible, resulting in a very small MR.

In both cases, the overall MR effect is small as compared with nanoscale point contacts. In thick DWs, the MR is reduced because the spin can rotate and align with the local magnetization adiabatically as the electron travels through the wall. Conversely, for very thin DWs ($\sim$1 nm) the spin is almost completely conserved as the electron crosses the wall. However, this is no longer true if the contact size is of nanometer scale and we have quantized conductance. The thickness of the DW may then be very thin, of the order of the contact size, and yet the BMR should be very large even at room temperature (RT) because, in this case, the adiabatic accommodation of the spin polarization as the electron traverses the DW does not hold. This has indeed been indicated in the calculation in the limit of a vanishing DW width by van Hoof *et al*. (1999). Through the use of realistic band structure calculations they were able to show that the DW MR is enhanced by orders of

magnitude over the results from earlier theories. Tatara, Zhao, Munoz and Garcia (1999) calculated the resistivity based on the exchange interaction between the local spin S of the ferromagnetic ions and the electron spin. Using a Hamiltonian of the form

$$H = \sum_{k\sigma} \varepsilon_k c^+_{k\sigma} c_{k\sigma} - J \int \mathrm{d}x\, S(x)(c^+ \sigma\, c) \tag{12}$$

with $\varepsilon_k = \frac{\hbar^2 k^2}{2m} - \varepsilon_\mathrm{F}$ and a local spin S having the spatial dependence of a DW ($S_z = S_0$ tanh (x/d_w)), they showed that the resistance due to the DW is given by

$$R_\mathrm{w} = \frac{h}{e^2}\frac{1}{N}\frac{\pi^2}{4}\frac{\zeta^2}{1-\zeta^2}F(\zeta, d_\mathrm{w}) \tag{13}$$

with N being the number of channels in the cross-sectional area of the contact, while $\zeta = (k_{\mathrm{F}\uparrow} - k_{\mathrm{F}\downarrow})/(k_{\mathrm{F}\uparrow} + k_{\mathrm{F}\downarrow})$, and $k_\mathrm{F} = (k_{\mathrm{F}\uparrow} + k_{\mathrm{F}\downarrow})/2$. The parameter ζ is the spin polarization at the Fermi level ε_F and it also corresponds to the ratio of the density of states at ε_F, so that $\zeta = (D_\uparrow - D_\downarrow)/(D_\uparrow + D_\downarrow)$. The function $F(\zeta, d_\mathrm{w})$ is

$$F(\zeta, d_\mathrm{w}) = \frac{1}{2}\left[\frac{1}{\cosh^2 \pi\, k_\mathrm{F} d_\mathrm{w}} + \frac{1}{\cosh^2 \pi\, k_\mathrm{F}\zeta\, d_\mathrm{w}}\right] \tag{14}$$

and is shown in Figure 14. In the absence of a DW the conductance is given in terms of the number, N, of channels through the contact as $G_{\uparrow\uparrow} = Ne^2/h$. The DW resistance R_w and $G^{-1}_{\uparrow\uparrow}$ arise from different mechanisms and the total resistance is $R = G^{-1}_{\uparrow\uparrow} + R_\mathrm{w}$. We can then identify the BMR as arising from the presence or absence of R_w in $G = R^{-1}$

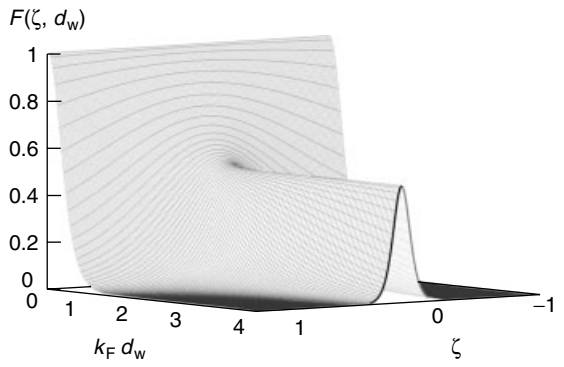

Figure 14. The function $F(\zeta, d_\mathrm{w})$ is plotted as a function of the spin polarization parameter ζ and the effective domain wall thickness expressed as $k_\mathrm{F} d_\mathrm{w}$. As $d_\mathrm{w} \to 0$, we have $F(\zeta, d_\mathrm{w}) \to 1$. For large values of $k_\mathrm{F} d_\mathrm{w}$, the function $F(\zeta, d_\mathrm{w})$ shows a peak at $\zeta \to 0$ with a maximum of 0.5.

and we have

$$\frac{\Delta G}{G} = \frac{G_{\uparrow\uparrow} - G_{\uparrow\downarrow}}{G_{\uparrow\downarrow}} = \frac{\pi^2}{4}\frac{\zeta^2}{1-\zeta^2}F(\zeta, d_\mathrm{w}) \tag{15}$$

For further details of the derivation, the reader is referred to the article by Tatara, Zhao, Munoz and Garcia (1999). The function $F(\zeta, d_\mathrm{w}) \to 1$ as the DW d_w goes to zero (see Figure 14). This prediction of the theory is in agreement with the model of Julliere (1975), who investigated the tunneling across an interface between two ferromagnetic films, when the spin is conserved across the interface. In other words, the BMR is given by the degree of polarization only. Also, $F(\zeta, d_\mathrm{w}) \to 0$ as the DW thickness increases, so that $k_\mathrm{F} d_\mathrm{w} \geq 1$, and the electron spin accommodates the spin variation in the DW. When the material has only one spin-polarized band we have $\zeta \to 1$, and the magnetoconductance (MC) goes to infinity, according to equation (15). This corresponds to total reflection at the interface.

In explicitly obtaining $F(\zeta, d_\mathrm{w})$, for the ferromagnetic materials, it is necessary to know the density of states at the Fermi level from band structure calculations (Moruzzi, Janak and Williams, 1978), since both s and d bands contribute to the density of states at the Fermi level. The ratio of the total density of states for the two bands to that of the s band at the Fermi level, $\beta = D_{\mathrm{d+s}}/D_\mathrm{s}$, is large since it is the d-band density of states that dominates in these materials. Assuming that the band structure in the thin ferromagnetic wires on either side of the nanocontact is close to that of the bulk material we can‘ theoretically estimate for Ni that $\beta \approx D_\uparrow/D_\downarrow = 13$, and that $\zeta = 0.87$. Garcia *et al.* (2001) estimated that this provides a maximum MR of 400% which agrees remarkably well with experiments (Garcia, Munoz and Zhao, 1999). For Co, the values of the parameters are $\beta \approx 11$ and $\zeta = 0.83$. The number of channels N participating in the ballistic transport can be estimated using Sharvin's formula (Sharvin, 1965a,b) in which the β parameter, representing the large density of states at the Fermi level, and the geometric parameter a, the radius of the contact, play a role. We have

$$N = \beta\frac{(k_\mathrm{F} a)^2}{4} \tag{16}$$

Now, d_w, is also related to the number of channels through the fact that in nanocontacts the restricted channels alter the geometry of the DW so that with the assumption $d_\mathrm{w} \approx a$, equation (16) leads to the relation

$$k_\mathrm{F} d_\mathrm{w} = k_\mathrm{F} a = \left(\frac{4N}{\beta}\right)^{1/2} \tag{17}$$

Analytical calculations showing that $d_\mathrm{w} \approx a$ have been performed by Bruno (1999).

Thus, the MC, equation (15) is large, even for small N, when $\zeta \approx 1$ and decreases rapidly as the number of channels increases beyond $N \geq \beta/4$.

The ballistic transport through a connecting narrow nanochannel between two ferromagnetic regions has been modeled by Tagirov, Vodopyanov and Efetov (2001, 2002) and Tagirov, Vodopyanov and Garipov (2003) by considering actual circular and rectangular geometries for the contact. The effect of a DW and its width, in comparison with the spin mean free path, on the BMR can then be studied, and the models reproduce the experimental results of Garcia, Munoz and Zhao (1999) fairly well. The location of the DW in the ballistic channel, between the two ferromagnetic regions, is included in their discussion. A tight-binding model for the theory of tunneling magnetoresistance has been developed by Mathon (1997), who shows that the tunneling MR approaches rapidly the same saturation value when either the interelectrode hopping decreases or the height of the insulating barrier increases. When the insulating barrier is high (i.e., the band gap is large), the tunneling MR depends only weakly on the thickness of the insulating layer. However, when the band gap is small compared to the conduction bandwidth, the tunneling MR decreases rapidly with increasing thickness of the insulator. Mathon's numerical results for a Co(001) junction, based on a fully realistic band structure of the Co electrodes, show a very similar behavior. As the tight-binding hopping matrix between the Co electrodes is gradually turned off, the tunneling MR ratio drops initially very rapidly from its value of 280% in the metallic regime to about 40% but then stabilizes in the range 40–65%. This is in a very good agreement with the observed value of 40%. It is thus noteworthy that he obtains very reasonable values for MR, using the tight-binding model, that agree with experiment. The tunneling MR in this model calculation is the BMR.

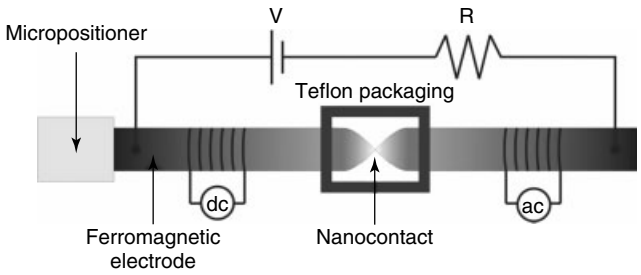

Figure 15. A schematic of the experimental setup employed by Garcia *et al*. is shown. (Reprinted with permission Chung *et al*., copyright 2003, American Institute of Physics.)

3.3 Experimental results on BMR

We now turn to the experimental results reported by Garcia, Munoz and Zhao (2000) and Garcia *et al*. (2001). A typical experimental schematic (Chung *et al*., 2003) is shown in Figure 15. The nanocontacts are formed by mechanically putting into contact the polished ends of two Ni wires of 2 mm diameter. The Teflon packaging mechanically holds and aligns the structure in place. By systematically moving the position of one of the wires, the contact area can be adjusted. The two ferromagnetic wires have wires wrapped around them to provide control in the direction of magnetization. At the tip of the nickel rods a field of up to 150 Oe is generated at 0.2 A. Alternating the current in one of the wire wrappings, leads to an alternating field on one of the ferromagnetic wire. This permits a clean measurement of the BMR. To determine the BMR, a 100 mV bias voltage was applied across the junction. Other materials could be deposited at the tip to investigate the BMR in nanochannels made with these materials. To summarize the experimental outcomes, the results (Garcia, 2003) of several measurements of the MC plotted against the conductance, or equivalently the number of channels N, is shown in Figure 16. Data from Co, Ni, and Fe nanochannels are presented in the same figure simultaneously. Reproducible results have been reported for the BMR (Chung *et al*., 2003). The measurements of BMR ranging from over 300% for narrow (atomic) channels of size ∼0.5 nm with $N = 1$, to 20% with N ∼ 20 channels with 2 nm^2 area of contact are shown. The full and dashed curves in Figure 16

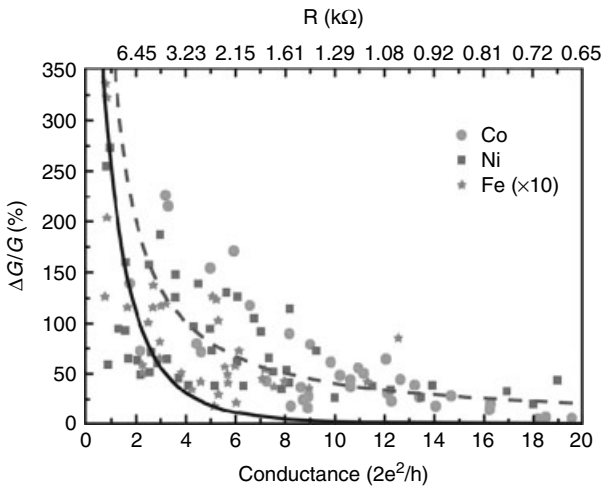

Figure 16. Magnetoconductance as a function of the contact conductance (bottom x axis) and the contact resistance (top x axis) for Ni, Co, and Fe contacts. Solid and dashed curves are the theory approximations in the limits of a small and large number of conducting channels, respectively. (Adapted from Figure 1 of Garcia, 2003.)

correspond to values of $\beta \approx 11$ and $\beta \approx 40$, respectively. It is seen that all the data lie between these two curves. While the lower value of the ratio of the density of states, β, is given by theoretical estimates of the band structure of the bulk material, this does not necessarily apply to the nanostructure.

3.4 Scaling and universality in BMR experiments

On putting together all the data on MC (or equivalently MR, as seen from equations (10a and b) for nanocontacts between Ni–Ni, Co–Co, Fe–Fe, CrO_2–CrO_2, and CrO_2–Ni heterojunctions, it was noticed by Chung *et al.* (2002) that the largest MR was observed at a conductance of $0.05\,G_0$ where $G_0 = 2e^2/h$. This is shown in Figure 17(a). This is different from the maximum for MR of ∼210% observed in Ni–Ni nanojunctions at a conductance of G_0. The behavior of CrO_2–Ni nanojunction is similar to that of CrO_2–CrO_2 in that the peak MC occurs at very low conductance although the maximum MR is lower, as seen in Figure 17(b). Chung *et al.* then combined the data for all nanocontacts by plotting the MC that is scaled by the maximum value of the MC in each of the heterojunctions. The quantity $(\Delta G/G_{\uparrow\downarrow})/(\Delta G/G_{\uparrow\downarrow})_{\max}$ was plotted against the conductance G_0. All the experimental data essentially fit *around* the solid curve and *within* the cross-hatched area between the solid and dashed curves of Figure 18. The solid and dashed curves are obtained from Tatara, Zhao, Munoz and Garcia (1999) for small N and for large N, the number of conducting channels, or equivalently when the DW

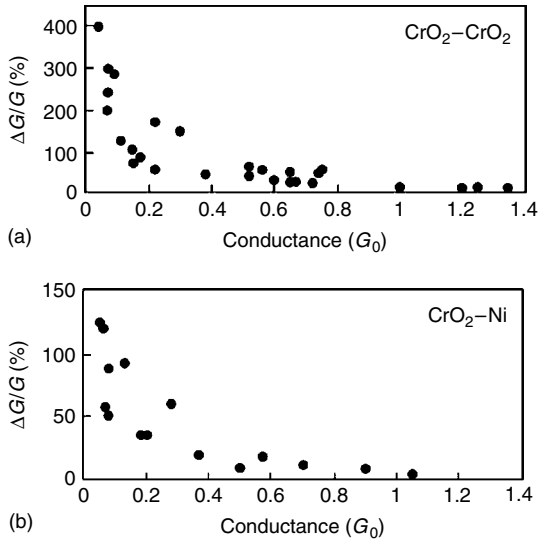

Figure 17. The experimental data for magnetoconductance versus contact conductance for (a) CrO_2-CrO_2, and (b) CrO_2-Ni nanocontacts. (Reprinted with permission Chung *et al.*, copyright 2003, American Institute of Physics.)

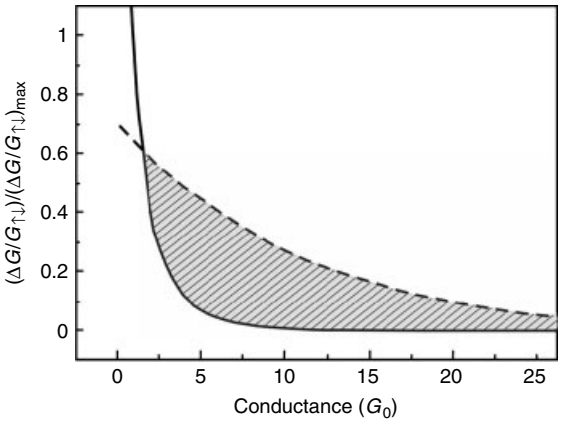

Figure 18. The universality of scaled BMR discovered by Garcia *et al.* is shown. The normalized magnetoconductance scaled by the ratio of the maximum BMR for the material. All experimental data essentially fit *around* the solid curve and *within* the cross-hatched area between the solid and dashed curves. The curves are obtained from Tatara *et al.* for small and large number of conducting channels. (Reprinted with permission Chung *et al.*, copyright 2003, American Institute of Physics and Chung *et al.*, copyright 2002, American Physical Society.)

magnetization profile varies smoothly or is constant in the DW, respectively. In the case of the CrO_2–Ni heterojunction, the scaling was performed using the conductance value of CrO_2. Figure 18 is a summary of the data for Ni, Co, Fe, the half-metallic CrO_2, Ni–CrO_2, and for the Verwey insulator Fe_3O_4 (Versluijs, Bari and Coey, 2001).

A universal picture for BMR for such a wide variety of materials occurs when the scaling of the data proposed by Chung *et al.* (2002) is performed. The normalized MC in nanocontacts has a universal behavior versus the scaled conductance, and is independent of the electron transport mechanism. The only consideration is spin conservation in the ballistic transport through the DW at the nanocontact. We follow the arguments of Chung *et al.* (2002) in presenting their analysis of the BMR. The behavior of the normalized MC is defined by the spin scattering function $F(\zeta, d_w)$ that incorporates the influence of the dependence on d_w and density of states at the Fermi level. When the Landauer conductance, $G = G_0 \sum_i T_i$, where T_i are the transmission coefficients, is reexpressed using Sharvin's version (Sharvin, 1965a,b), we have

$$G = G_0 \left(\frac{d_w}{\lambda_F}\right)^2 \gamma \tag{18}$$

where the number of channels $N = (d_w/\lambda_F)^2$, λ_F is the electron wavelength at the Fermi level, and γ is the transmission coefficient per channel. We can analyze the data after scaling using equation (18). Here the various factors take into account the different material resistivities since the DW scattering occurs in the nanochannel and the channel

transmission coefficient depends on the transport process and hence the resistivity. Therefore if $\gamma \ll 1$, then the conductance can be much smaller than G_0 even if the number of channels is larger than 1. The half-metallic oxide samples manifest this behavior whereas normal metals do not, and this explains the difference in scale on the graphs in Figures 16 and 17.

The theoretical work of Tagirov, Vodopyanov and Efetov (2001, 2002) and Tagirov, Vodopyanov and Garipov (2003) shows that large MR can occur in nanocontacts even in the diffusive regime. According to their quasiclassical theory of spin transport through magnetic nanocontact, large MR can be obtained if strong spin scattering at the DW is achieved for antiparallel alignment of magnetization in the magnetic nanocontact. Figure 19 provides a schematic representation of the DW within a nanocontact. To realize such large spin scattering, the electron spin orientation should be preserved during transit through nanocontacts. If DW width d_w is shorter than the mean distance between spin-flip scattering $d_{spn} = v_F T_{spin}$, where v_F is the Fermi velocity and T_{spin} is the spin-relaxation time, the spin can be preserved and large MR can be obtained even in the diffusive transport regime. Furthermore, they have predicted that the nanocontact of highly spin-polarized metals such as LSMO and CrO_2 would show very large MR of 1000% or higher. The mean free path ℓ of CrO_2 is about 1.4 nm or less at room temperature, as shown theoretically by Lewis, Allen and Sasaki (1997). The value is very small compared to that of normal metals, which is in the range of a few tens of nanometers. Also, Park *et al*. do obtain short spin diffusion lengths $\sim 3 \pm 1$ nmin another system, VIZ., NiCr (Park *et al*., 1999). Therefore, diffusive transport seems to be dominant at CrO_2 nanocontacts when $\ell < d_w$. On the other hand, the spin orientation can be preserved even after many scattering events. Therefore, when the DW width, assumed to be of the order of the square root of the nanocontact cross section, is smaller than the spin-relaxation length, the electron spin relaxation cannot be accommodated by the abrupt magnetization gradient and thus strong spin scattering, that is, high MR, can be achieved. The reader interested in further details of the scaling and universality in BMR and the nuances for each material is referred to Chung *et al*. (2002, 2003).

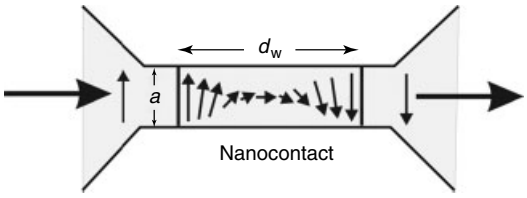

Figure 19. The nanocontact between two ferromagnetic wires is shown schematically. The domain wall in the nanocontact has a lateral thickness of d_w and a width corresponding to that of the nanochannel, a. The current through the nanochannel is shown by the horizontal arrows. The magnetization vector rotates across the domain between the initial and final magnetization directions in the two wires.

4 CONCLUDING REMARKS

In summary, geometry plays an important role in determining the magnetotransport properties of EMR and BMR structures on both the macroscale (EMR) and on the nanoscale (EMR and BMR). EMR derives from the orbital motion of carriers in nonmagnetic materials while BMR results from the interactions of spins with domains in magnetic materials. EMR has been observed in both InSb and InAs narrow-gap semiconductors with a variety of structures and at a range of temperatures down to that of liquid helium. The narrow-gap semiconductors are choice materials for EMR devices because of their concomitantly high carrier mobility. Following the discovery of EMR it has been realized that it is but one example of a broad class of geometry-driven interfacial 'EXX' effects in MSHs where proof of principal has been demonstrated for XX = piezoconductance (PC) (Rowe, Hines and Solin, 2003), optoconductance (OC) (Wieland *et al*., 2006) and electroconductance (EC) (Wang, Wieland and Solin, 2007).

The initial controversy about BMR, and the uncertainties about the governing mechanisms (e.g., as to whether it is due to magnetostriction), have now been resolved (Sullivan *et al*., 2005) by more careful experiments from several research groups. It is evident that the phenomenon of BMR is dependent heavily on the geometry of the nanocontact. A large value of BMR depends on the two key parameters, a large value for the ratio of the density of states at the Fermi level associated with the electron distributions with the two electron spin polarizations, and on a small value for the ratio of the DW thickness d_w to the mean free path ℓ for spin reversal. In ballistic nanocontacts, the length ℓ is essentially the length of the nanochannel. With the anticipated technological applications, research on BMR in novel materials, the dependence on quantum effects, and its geometric enhancement will continue to be a fascinating aspect of research on the physical behavior of materials at the nanoscale.

Both EMR and BMR portend significant potential for impact on magnetic sensor technology, particularly in the area of ultrahigh-density magnetic recording. Nevertheless, neither of these new phenomena have, to date, had any 'kinetic' impact on technology as is usually the case for discoveries that represent a new paradigm competing with an established conventional technology, for example, GMR

and TMR. Accordingly, it will be very interesting to monitor the development of EMR and BMR over the next few years to see if their promise as novel magnetic sensors is actually fulfilled.

ACKNOWLEDGMENTS

Our work on the EMR and FEM described in this review has benefited from the stimulating interactions and major contributions of our collaborators and students. Included among the former group are D.R. Hines, T. Thio, J. Bennett, the late R.A. Stradling, J. Heremans, J.S. Tsai, Y. Pashkin, M.B. Santos, A.C.H. Rowe, M. Lee, N. Wingreen, P.A. Wolff, S. Schwed, T. Zhou, S.J. Chung, and N. Goel. In the latter group, we include A. Girgis, J. Moussa, K. Weiland, Y. Shao and Y. Wang. Naturally, the responsibility for any errors or omissions in the content of this article rests solely with the authors. We gratefully acknowledge the support of the US National Science Foundation (NSF) under grant ECS-0329347. SAS also acknowledges support of the US National Institute of Health (NIH) under grant 1U54CA11934201 and of the UK Engineering and Physical Sciences Research Council (EPSRC) under grant EP/C511816/1 (L.F. Cohen, PI).

REFERENCES

Baranger, H.U. and Stone, A.D. (1989). Electrical linear-response theory in an arbitrary magnetic-field - a new fermi-surface formation. *Physical Review B*, **40**, 8169.

Beenakker, C.W.J. and van Houten, H. (1991). Quantum transport in semiconductor nanostructures. In *Solid State Physics*, Ehrenreich, H. and Turnbull, D. (Eds.), Academic Press: New York, Vol. 44.

Bending, S.J. (1999). Local magnetic probes of superconductors. *Advances in Physics*, **48**, 449–535.

Bruno, P. (1999). Geometrically constrained magnetic wall. *Physical Review Letters*, **83**, 2425.

Buttiker, M., Imry, Y., Landauer, R. and Pinhas, S. (1985). Generalized manychannel conductance formula with application to small rings. *Physical Review B*, **31**, 6207.

Cabrera, G.G. and Falicov, L.M. (1974). Theory of residual resistivity of Bloch walls. *Physical Status Solidi B*, **61**, 539.

Childress, J.R. and Fontaua, R.E. (2005). Magnetic recording read head sensor technology. *Comptes Rend us Phisique*, **6**, 997–1012.

Chopra, H.D. and Hua, S.Z. (2002). Magnetoresistance of half-metallic oxide nanocontacts. *Physical Review B*, **66**, R020403.

Chung, S.J., Goldammer, K.J., Lindstrom, S.C., *et al*. (1999). A study of factors limiting electron mobility in InSb quantum wells. *Journal of Vacuum Science and Technology B*, **17**, 1151.

Chung, S.H., Munoz, M. and Garcia, N. (2003). Universal scaling of magnetoconductance in magnetic nanocontacts. *Journal of Applied Physics*, **93**, 7939.

Chung, S.H., Munoz, M., Garcia, N., *et al*. (2002). Universal scaling of ballistic magnetoresistance in magnetic nanocontacts. *Physical Review Letters*, **89**, 287201–287203.

Churchill, R.V. (1960). *Complex Variables and Applications*, McGraw-Hill: New York.

Daughton, J. and Chen, Y. (1993). GMR materials for low field applications. *IEEE Transactions on Magnetics*, **29**, 2705.

Deeter, M.N., Day, G.W., Beahn, T.J. and Manheimer, M. (1993). Magneto-opticmagnetic field sensor with 1.4 pT/*(Hz) minimum detectable field at 1 kHz. *Electronics Letters*, **29**, 933.

Dieny, B., (1994). Giant magnetoresistance in spin valve multilayers. *Journal of Magnetism and Magnetic Materials*, **136**, 335–359.

Dornhaus, R. and Nimtz, G. (1976). *Springer Tracts in Modern Physics*, Springer-Verlag: New York, Vol. 78 references therein.

Eglekoff, W.F., Ettedgui, G.H., Kadmon, Y., *et al*. (2005) Artifacts that mimic ballistic Magnetoresistance. *Journal of Magnetism and Magnetic Materials*, **287**, 496–500.

Egelhoff, W.F., Jr., Ha, T., Misra, R.D.K., *et al*. (1995). Magnetoresistance values exceeding 21% in symmetric spin valves. *Journal of Applied Physics*, **78**, 273.

Fraden, J. (1993). *AIP Handbook of Modern Sensors: Physics Designs and Applications*, American Institute of Physics: New York, pp. 243–262.

Garcia, N. (2003). Magnetoresistance and magnetostriction in magnetic contacts. *Europhysics News*, **34**(6), 1–10.

Garcia, N., Munoz, M., Qian, G.G., *et al*. (2001). An effective gate for spintronics. *Applied Physics Letters*, **79**, 4550.

Garcia, N., Munoz, M. and Zhao, Y-W. (1999). Magnetoresistance in excess of 200% in Ballistic Ni Nanocontacts at Room Temperature and 100 Oe. *Physical Review Letters*, **82**, 2923.

Garcia, N., Munoz, M. and Zhao, Y-W. (2000). Ballistic magnetoresistance in transition-metal nanocontacts: The case of iron. *Applied Physics Letters*, **76**, 2586.

Heremans, J.P. (1997). Magnetic Field Sensors for Magnetic Position Sensing in Automotive Applications. *Materials Research Society Symposia Proceedings*, **475**, 63.

van Hoof, J.B.A.N., Schep, K.M., Brataas, A., *et al*. (1999). Electronic transport through magnetic domain walls'. *Physical Review B*, **59**, 138.

Holz, M., Kronenwerth, O. and Grundler, D. (2003). Optimization of semiconductor–metal hybrid structures for application in magnetic-field sensors and read heads. *Applied Physics Letters*, **83**, 3344.

Holz, M., Kronenwerth, O. and Grundler, D. (2005a). Semiconductor-metal hybrid structures as local magnetic-field probes: magnetoresistance and spatial sensitivity profile. *Applied Physics Letters*, **87**, 172501.

Holz, M., Kronenwerth, O. and Grundler, D. (2005b). Enhanced sensitivity due to current redistribution in the Hall effect of semiconductor-metal hybrid structures. *Applied Physics Letters*, **86**, 172513.

van Houten, H., Beenakker, C.W.J. and van Wees, B.J. (1992). *Semiconductors and Semimetals*, Reed, M. (Ed.), Academic Press: New York, Vol. 35.

Hughes, T.J.R. (1987). *The Finite Element Method*, Prentice-Hall: Englewood Cliffs.

Imry, Y. (1986). Physics of mesoscopic systems. In *Directions in Condensed Matter Physics*, Grinstein, G. and Mazenko, G. (Eds.), World Scientific: Singapore.

Jablonski, A., Mrozek, P., Gergely, G., *et al*. (1984). The inelastic mean free path of electrons in some semiconductor compounds and metals. *Surface and Interface Analysis*, **6**, 291.

Julliere, M. (1975). Tunneling between ferromagnetic films. *Physics Letters*, **54A**, 225.

Kleinman, D.A. and Schawlow, A.L. (1960). Corbino Disk. *Journal of Applied Physics*, **31**, 2176.

Kuze, N. and Shibasaki, I. (1997). MBE research and production of hall sensors, MBE review. *III-V's Review*, **10**, 28.

Landauer, R. (1957). Spatial variation of currrents and fields due to localized scatterers in metallic conduction. *IBM Journal of Research and Development*, **1**, 223.

Landauer, R. (1970). Electrical resistance of disordered one-dimensional lattices. *Philosophical Magazine*, **21**, 863.

Landauer, R. (1988). Generalizd many-channel conductance formula with application to small rings. *IBM Journal of Research and Development*, **32**, 306.

Lee, M., Solin, S.A. and Hines, D.R. (1993). Electron-localization mechanisms in GaAs/$Ga_{0.7}Al_{0.3}$As superlattices. *Physical Review*, **B48**(11), 921.

Lee, M., Wingreen, N.S., Solin, S.A. and Wolff, P.A. (1994). Giant growth axis longitudinal magnetoresistance from In-plane conduction in semiconductor superlattices. *Solid State Communications*, **89**, 687.

Levy, P.M. (1994). Giant Magnetoresistance in Magnetic Layered and Granular Materials. *Solid State Physics*, **47**, 367.

Lewis, S.P., Allen, P.B. and Sasaki, T. (1997). Band structure and transport properties of CrO_2. *Physical Review*, **55**, 10253.

Madelung, O. (Ed.) (1991). *Semiconductors: Group IV Elements and III –V Compounds*, Springer-Verlag: New York.

Mathon, J. (1997). Tight-binding theory of tunneling giant magnetoresistance. *Physical Review B*, **56**, 11810.

Mclennan, M.J., Lee, Y. and Datta, S. (1991). Voltage drop in mesoscopic systems: a numerical study using a quantum kinetic equation. *Physical Review B*, **43**, 13846.

Mitra, C., Raychaudhuri, P., Kobernik, G., *et al*. (2001). p-n diode with hole-. and electron-doped lanthanum manganites. *Applied Physics Letters*, **79**, 2408.

Moeller, C.H., Kronenwerth, O., Grundler, D., *et al*. (2002). Extraordinary magnetoresistance effect in a microstructured metal-semiconductor hybrid structure. *Applied Physics Letters*, **80**, 3988.

Moruzzi, V.L., Janak, J.F. and Williams, A.R. (1978). *Calculated Electronic Properties of Metals*, Pergamon Press: New York.

Moussa, J., Ram-Mohan, L.R., Sullivan, J., *et al*. (2001). Finite element modeling of extraordinary magnetoresistance in thin film semiconductors with metallic inclusions. *Physical Review B*, **64**, 184410.

Moussa, J., Ram-Mohan, L.R., Rowe, A.C.H. and Solin, S.A. (2003). Response of an extraordinary magnetoresistance read head to a magnetic bit. *Journal of Applied Physics*, **94**, 1110.

Ono, T., Ooka, Y. and Miyajima, H. (1999). 2e2/h to e2/h switching of quantum conductance associated with a change in nano-scale ferromagnetic domain structure. *Applied Physics Letters*, **75**, 1622.

Park, W., Loloee, R., Caballero, J.A., *et al*. (1999). Test of unified picture of spin-dependent transport in perpendicular (CPP) giant magnetoresistance and bulk alloys. *Journal of Applied Physics*, **85**, 4542–4544.

Popovic, R.S. (1991). *Hall Effect Devices*, Adam Hilger: Bristol.

Rao, C.N.R. and Raveau, B. (Eds.) (1998). *Colossal Magnetoresistance, Charge Ordering and Related Properties of Manganese Oxides*, World Scientific: Singapore.

Ram-Mohan, L.R. (2002). *Finite Element and Boundary Element Applications to Quantum Mechanics*, Oxford University Press: Oxford.

Rinck, P.A. (1993). *Magnetic Resonance in Medicine*, Third Edition, Blackwell Scientific Publishing.

Roosmalen, A.J., Baggermann, G. and Brader, S.J.H. (1995). Dry Etching for VLSI, update in *Applied Physics and Electrical Technology*, Plenum Press: New York.

Rowe, A.C.H., Hines, D.R. and Solin, S.A. (2003). Enhanced room-temperature piezoconductance of metal–semiconductor hybrid structures. *Applied Physics Letters*, **83**, 1160.

Sandu, A., Kurosawa, K., Dede, M. and Oral, A. (2004). 50 nm Hall Sensors for room temperature scanning Hall probe microcopy. *Japanese of Journal of Applied Physics*, **43**, 777–778.

Seeger, K. (1985). *Semiconductor Physics*, Third Edition, Springer-Verlag: Berlin.

Sharvin, Yu.V. (1965a). A possible method for measuring Fermi surfaces. *Zhurnal Eksperimentalnoi I Teoreticheskoi Fiziki*, **48**, 984.

Sharvin, Yu.V. (1965b). A possible method for studying fermi surfaces. *Soviet Physics Jetp*, **21**, 655–656.

Solin, S.A. (2007). Design and properties of a scanning EMR probe microscope in Proc. of the Indo-US workshop on nanoscale materials. Sahu, S.N. and Rao, B.K. (eds.) Puri, 2004, in press.

Solin, S.A. (2004). *Proceedings of the International Conference on Condensed Matter Theory*, Louis, St. and Clark, J.W. (Ed.) (in press).

Solin, S.A. (2005). In *Clusters and Nano-Assemblies: Physical and Biological Systems*, Jena, P., Khanna, S.N. and Rao, B.K. (Eds.), World Scientific: New Jersey, p. 247.

Solin, S.A., Hines, D.R., Rowe, A.C.H., *et al*. (2002a). Nonmagnetic semiconductors as read-head sensors for ultra-high-density magnetic recording. *Applied Physics Letters*, **80**, 4012.

Solin, S.A., Hines, D.R., Rowe, A.C.H., *et al*. (2002). In *Physics of Semiconductors 2002, Proceedings of the 26th International Conference on the Physics of Semiconductors*, *Conference Series No. 171*, Long A.R. and Davies, J.H. (Eds.), Institute of Physics: Edinburgh, paper N1-2.

Solin, S.A., Hines, D.R., Tsai, J.S., *et al*. (2002b). Room temperature extraordinary magneto resistance of non-magnetic narrow-gap semiconductor/metal composites: application to read-head sensors for ultra high density magnetic recording. *IEEE Transactions on Magnetics*, **38**, 89.

Solin, S.A. and Lee, M. (1995). Temperature dependence and angular dependence of the giant longitudinal magnetoresistance in

GaAs-AlGaAs superlattices. *Materials Science and Engineering*, **B31**, 147.

Solin, S.A., Thio, T., Bennett, J.W., *et al*. (1996). Self-biasing nonmagnetic giant magnetoresistance sensor. *Applied Physics Letters*, **69**, 4105.

Solin, S.A., Thio, T. and Hines, D.R. (2000). Controlled GMR enhancement from conducting inhomogeneities in non-magnetic semiconductors. *Physica*, **B279**, 37.

Solin, S.A., Thio, T., Hines, D.R. and Heremans, J.J. (2000). Enhanced geometric magnetoresistance at room-temperature in inhomogeneous narrow-gap semiconductors. *Science*, **289**, 1530.

Solin, S.A., Thio, T., Hines, D.R., *et al*. (1999). Large enhancement of the giant magnetoresistance in inhomogeneous semiconductors: dependence on magnetic field direction. *Journal of Applied Physics*, **85**, 5789.

Solin, S.A. and Zhou, T. (2001). *Proceedings of the International Conference on Solid State Devices and Materials*. Tokyo, Japan p. 570.

Song, D., Nowak, J., Larson, R., *et al*. (2000). Spin tunneling heads above 20 Gb/in/sup 2/. *IEEE Transactions on Magnetics*, **36**, 2545.

Streater, R.F. (1999). Onsager symmetry in statistical dynamics. *Open Systems and Information Dynamics*, **6**, 87.

Stutzke, N.A., Russek, S.E. Papas, D.P. and Tondra, M. (2006). Low-frequency noise measurements on commercial magnetoresistive magnetic field sensors. *Journal of Applied Physics*, **97**, 10Q107–10Q109.

Sugawara, M. (1998). *Plasma Etching: Fundamentals and Applications*, Oxford: New York.

Sullivan, M.R., Boehm, D.A., Ateya, D.A., *et al*. (2005). Ballistic magntoresistance in nickel single-atom conductors without magnetostriction. *Physical Review B*, **71**, 024412.

Tagirov, L.R., Vodopyanov, B.P. and Efetov, K.B. (2001). Ballistic versus diffusive magnetoresistance of a magnetic point contact. *Physical Review B*, **63**, 104428.

Tagirov, L.R., Vodopyanov, B.P. and Efetov, K.B. (2002). Multivalued dependence of the magnetoresistance on the quantized conductance in nanosize magnetic contacts. *Physical Review B*, **65**, 214419.

Tagirov, L.R., Vodopyanov, B.P. and Garipov, B.M. (2003). Magnetoresistance of a semiconducting magnetic wire with a domain wall. *Journal of Magnetism and Magnetic Materials*, **258–259**, 61.

Tatara, G. and Fukuyama, H. (1997). Resistivity due to a domain wall in ferromagnetic metal. *Physical Review Letters*, **78**, 3773.

Tatara, G., Zhao, Y-W., Munoz, M. and Garcia, N. (1999). Domain wall scattering explains 300% ballistic magnetoconductance of nanocontacts. *Physical Review Letters*, **83**, 2030.

Thio, T. and Solin, S.A. (1998). Giant magnetoresistance enhancement in inhomogeneous semiconductors. *Applied Physics Letters*, **72**, 3497.

Thio, T., Solin, S.A., Bennett, J.W., *et al*. (1998a). Giant magnetoresistance in $Hg_{1-x}Cd_xTe$ and applications for high density magnetic recording. *Journal of Crystal Growth*, **184–185**, 1293.

Thio, T., Solin, S.A., Bennett, J.W., *et al*. (1998b). Giant magnetoresistance in zero-bandgap $Hg_{1-x}Cd_xTe$. *Physical Review*, **B57**(12), 12,239–12,244.

Versluijs, J.J., Bari, M.A. and Coey, J.M.D. (2001). Magnetoresistance of half-metallic oxide nanocontacts. *Physical Review Letters*, **87**, 026601.

Wang, Y., Wieland, K.A. and Solin, S.A. (2007). Electroconductance in In-GaAs metal-semiconductor hybrid structures. *Journal of Applied Physics*, in press.

van Wees, B.J., Kouwenhoven, L.P., Willems, E.M.M., *et al*. (1991). Quantum ballistic and adiabatic electron transport studied with quantum point contacts. *Physical Review B*, **43**, 12431–12453.

van Wees, B.J., van Houten, H., Beenakker, C.W.J., *et al*. (1988). Quantised conductance of point contacts in a two-dimensional electron gas. *Physical Review Letters*, **60**, 848.

Weissman, M.B. (1988). 1/f noise and other slow, nonexponential kinetics in condensed matter. *Reviews of Modern Physics*, **60**, 537.

Wieland, K.A., Wang, Yun., Ram-Mohan, L.R., *et al*. (2006). Extraordinary optoconductance in metal-semiconductor hybrid structures. *Applied Physics Letters*, **88**, 052105.

Wharam, D.A., Thronton, T.J., Newbury, R., *et al*. (1988). One-Dimensional transport and the quantization of the ballistic resistance. *Journal of Physics C: Solid State Physics*, **21**, L209.

Wolfe, C.M., Stillman, G.E. and Rossi, J.A. (1972). High apparent mobility in inhomogeneous semiconductors. *Journal of the Electrochemical Society: Solid-State Science and Technology*, **119**, 250–255.

Yasin, S., Hasko, D.G. and Carecenac, F. (2001). Nanolithography using ultrasonically assisted development of calixarene negative electron beam resist. *Journal of Vacuum Science and Technology B: Microelectronics and Nanometer Structures*, **19**, 311.

Zawadzki, W. (1974). Electron transport phenomena in small-gap semiconductors. *Advances in Physics*, **23**, 435.

Zhang, T., Clowes, S.K., Debnath, M., *et al*. (2004). High-mobility thin InSb films grown by molecular beam epitaxy. *Applied Physics Letters*, **84**, 4463–4465.

Zhao, Y-W., Munoz, M., Tatara, G. and Garcia, N. (2001). Extraordinary magnetoresistance in externally shunted Van Der Pauw plates. *Journal of Magnetism and Magnetic Materials*, **223**, 169.

Zhou, T., Hines, D.R. and Solin, S.A. (2001). Extraordinary magnetoresistance in externally shunted Van Der Pauw Plates. *Applied Physics Letters*, **78**, 667.

Zhou, T., Solin, S.A. and Hines, D.R. (2000). Extraordinary magnetoresistance of a semiconductor-metal composite van der Pauw Disk. *Journal of Magnetism and Magnetic Materials*, **226**, 1976.

van der Ziel, A. (1988). Semiclassical derivation of Handel's expression for the hooge parameter. *Journal of Applied Physics*, **63**, 2456.

Zienkiewicz, O.C. and Taylor, R.L. (1994). *The Finite Element Method*, Fourth Edition, McGraw-Hill: New York.

APPENDIX

A LANDAUER FORMULA FOR QUANTIZED CONDUCTANCE

In this Appendix, it is useful to provide a brief derivation of the Landauer formula (Landauer, 1957; Buttiker, Imry, Landauer, and Pinhas 1985) for quantized conductance in ballistic electron transport through very narrow structures since it provides a frame of reference for the discussion on BMR. Electrons in the devices of dimensions ≈50 nm or less, so-called mesoscopic devices, start behaving more like waves than particles. With the mean free path becoming comparable to the dimensions of the electronic device, an electron is transmitted through the device ballistically with no scattering. The electron waves will display phase coherence, however, and undergo quantum interference effects as defined by the *geometry* of the mesoscopic device. These features of electron transport change the usual macroscopic nature of resistance, leading to a quantization of resistance. We give a qualitative derivation of the Landauer relation defining the quantized conductance in terms of the transmission coefficient of electron waves through the device. The electron waves are guided through the device in a manner similar to optical waveguides.

It is useful to visualize the structure used in the original experiments. A two-dimensional electron gas (2DEG) created at the interface between a thin layer of GaAs and n-doped AlGaAs was used. By placing contacts for gates on the surface of the GaAs layer, as in Figure 20, it is possible to measure the electrical resistance, R, of the 2DEG in its flow through the split-gate channel. When the channel is constricted by the application of a gate voltage, the resistance of the device is essentially the resistance of the channel. In the absence of any scattering one might anticipate that the carriers will go through ballistically with no resistance at all; however, this is not so, and the resistance of the device remains finite.

One of the results of Landauer's theory (Landauer, 1957; Buttiker, Imry, Landauer, and Pinhas 1985) of conductance in mesoscopic devices is that the device may be thought of as two-contact reservoirs of carriers maintained at constant electro-chemical potentials μ_1 and μ_2 with the 'quantum device' in between, as shown in Figure 20. The current I through the device is proportional to $\mu_1 - \mu_2$, and its conductance $G = 1/R$ is given by

$$G = \frac{2e^2}{\hbar} \sum_{\mu\nu} T_{\mu\nu} \tag{A1}$$

The device is treated as a waveguide with input and output modes labeled by μ and ν with the transmission coefficients $T_{\mu\nu}$ at the Fermi energy being labeled accordingly.

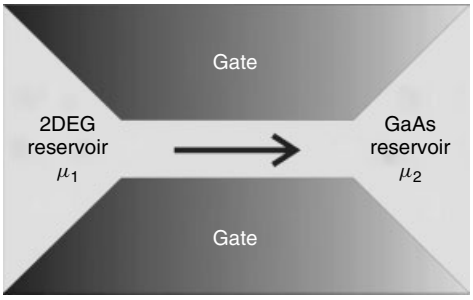

Figure 20. A narrow channel created by a split-gate structure in a 2DEG under bias. The electrons flow from the reservoir with Fermi level μ_1 to the reservoir with Fermi level μ_2 through the narrow channel. The arrow indicates the direction of the electron flow under bias.

Experiments performed independently by Wharam *et al*. (1988) and by van Wees *et al*. (1988, 1991) confirmed this remarkable quantization of resistance. Here we follow the arguments given by Wharam *et al*. (1988) and by Sharvin (1965a,b) to derive this result. The waveguide of Figure 17, which is an idealization of an actual experimental structure, has transverse modes, labeled by an index μ, having energy

$$E_y^{(\mu)} = \frac{\hbar^2 k_\mu^2}{2m^*} = \frac{\hbar^2}{2m^*} \frac{\pi^2 \mu^2}{L^2} \tag{A2}$$

Here L is the transverse width of the waveguide and m^* is the electron's effective mass in the medium. The current in a given subband μ associated with the energy of motion along the lateral direction of the waveguide is given by

$$I_\mu = n_\mu e \, \delta v_\mu \tag{A3}$$

where n_μ is *half* of the number of carriers per unit length in the subband, since only half the electrons have wave vectors in the $+x$ direction. In the preceding equation, e is the electron charge and δv_μ is the increase in velocity. The number of carriers n_μ contributing to the current, including a spin degeneracy factor of 2, is

$$n_\mu = \frac{2}{2\pi} \int_0^{k_{\max}} \mathrm{d}k = \frac{2m^* \, v_\mathrm{F}}{2\pi\hbar} \tag{A4}$$

The change in kinetic energy is given in terms of the applied voltage as

$$eV = \mu_1 - \mu_2 = \frac{1}{2} m^* \, (v_\mathrm{F} + \delta v_{\mu\mathrm{F}})^2 - \frac{1}{2} m^* \, v_\mathrm{F}^2 \tag{A5}$$

so that for $\delta v_{\mu\mathrm{F}} \ll v_F$ we have

$$\delta v_{\mu\mathrm{F}} = \frac{eV}{m^* \, v_{\mu\mathrm{F}}} \tag{A6}$$

Now the current in the channel is given by

$$I = \frac{2e^2}{2\pi\hbar}V \tag{A7}$$

and the conductance corresponding to carriers in one subband is

$$G_0 = \frac{2e^2}{h} \tag{A8}$$

This conductance is dependent only on fundamental physical constants and is the same for any transmission mode. The resistance standard defined by this relation has the value: $R = 1/G_0 = 25,812.8056 \pm 0.0012\,\Omega$. For transmission in more than one transverse mode of the waveguide, we can estimate the total conductance assuming that the transport of carriers in the various modes is independent of each other. In this case, the double sum over incoming and outgoing modes reduces to just one and we have

$$G = \frac{2e^2}{h}N \tag{A9}$$

for N channels.

The preceding derivation leads to a resistance quantization essentially because there is a cancellation of the velocity dependence of the number density and the change in the velocity, in the expression for the current in one dimension. The resistance of the system may be thought of as arising from the contacts between the waveguide and the reservoirs at the two ends.

For more elaborate treatments for the calculation of the quantized resistance the reader is referred to the original articles of Landauer (1957), and Buttiker, Imry, Landauer, and Pinhas (1985) and the review articles by Beenakker and van Houten (1991) and van Houten, Beenakker and van Wees (1992) and by Imry (1986) A treatment using quantum kinetic equations is given by Mclennan, Lee and Datta (1991). A derivation using the usual Kubo formalism for linear response theory is also available (Baranger and Stone, 1989).

Similar considerations apply for the BMR in point contacts, except that the spin polarization of the electrons has to be taken into account. The transport through the point contact from one ferromagnetic lead into another depends on the spin polarizations of the initial and the final leads. The factor of 2 arising from spin in equation (A9) is then dropped and the conductances in the parallel and antiparallel spin polarizations in the leads are denoted by $G_{\uparrow\uparrow}$ and $G_{\uparrow\downarrow}$, respectively. These are used in the definition of the BMR in the earlier sections.